EURODYN 2020

XI International Conference on Structural Dynamics

PROCEEDINGS

Volume I

M. Papadrakakis, M. Fragiadakis, C. Papadimitriou (Eds.)

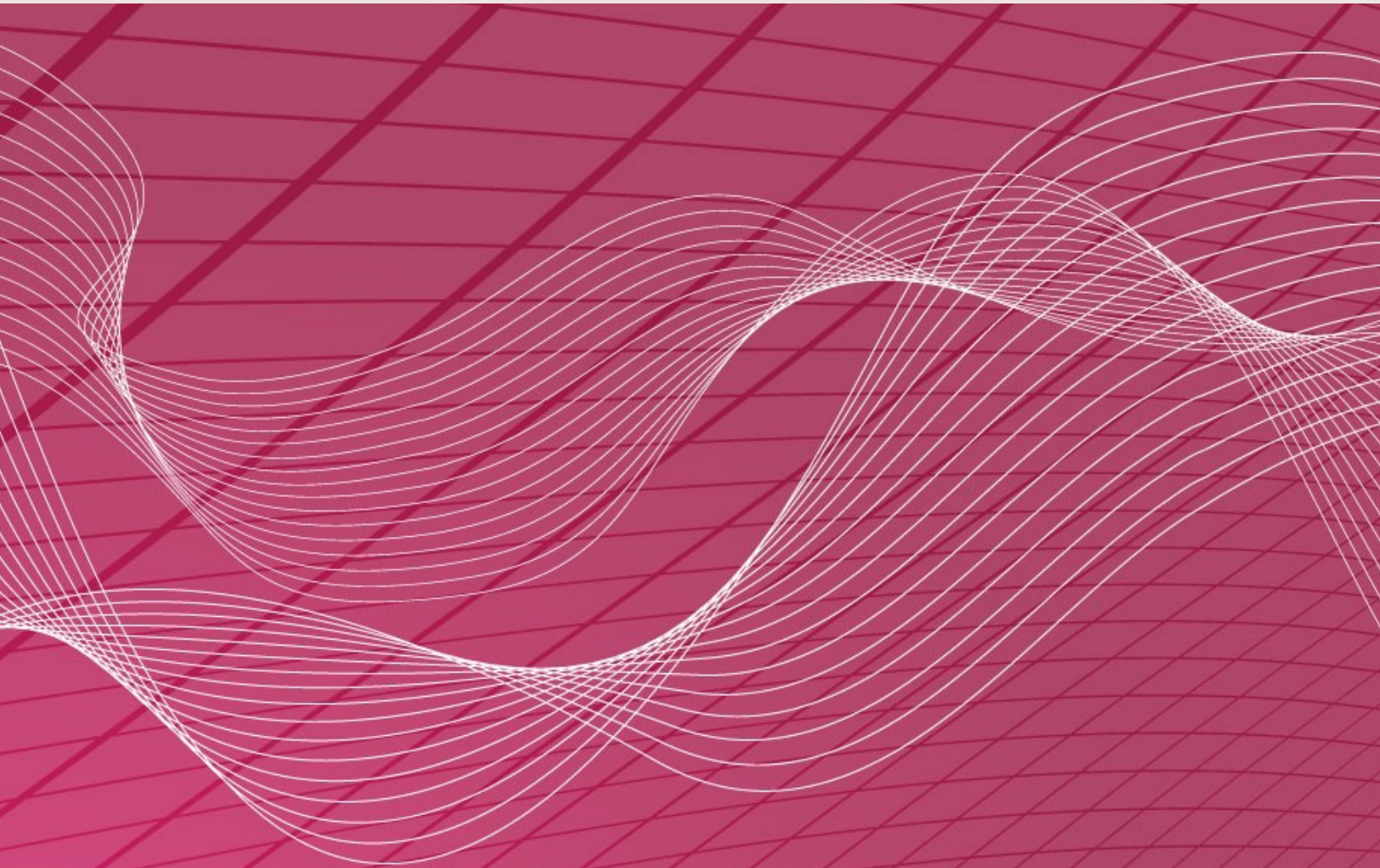

EASD
European Association
for Structural Dynamics

EURODYN 2020

Proceedings of the XI International Conference on Structural Dynamics

Streamed from Athens, Greece

23-26 November 2020

Edited by:

M. Papadrakakis

National Technical University of Athens, Greece

M. Fragiadakis

National Technical University of Athens, Greece

C. Papadimitriou

University of Thessaly, Greece

A publication of:

Institute of Structural Analysis and Antiseismic Research

School of Civil Engineering

National Technical University of Athens (NTUA)

Greece

EURODYN 2020

XI International Conference on Structural Dynamics

M. Papadrakakis, M. Fragiadakis, C. Papadimitriou (Eds.)

First Edition, September 2020

ISBN (set): **978-618-85072-2-7**
ISBN (vol I): **978-618-85072-0-3**

PREFACE

This volume contains the full-length papers accepted for presentation at the XI International Conference on Structural Dynamics EURODYN 2020, streamed online from Athens, Greece on November 23-26, 2020.

EURODYN Conference Series is organized under the auspices of the European Association of Structural Dynamics (EASD). EASD was founded in 1990 as a joint European initiative of experts in Structural Dynamics, with the purpose of sponsoring and overseeing the organization of the EURODYN conferences, scheduled to take place with a three-year interval. The first EURODYN Conference was held in Bochum in 1990, organized by the founding president of EASD Prof. Wilfried Krätzig. Following Bochum, the conferences were held in Trondheim (1993), Florence (1996), Prague (1999), Munich (2002), Paris, (2005), Southampton (2008), Leuven (2011), Porto (2014), Rome in 2017 and this year in Athens, the city where the EURODYN 2020 conference would have taken place in June 2020.

In view of the first signs of the COVID-19 pandemic at the beginning of this year, we were forced to postpone the conference dates at the end of November 2020. This was expected to give the opportunity to the participants to attend the conference either physically or remotely. Unfortunately, and contrary to what we had all anticipated, the COVID-19 was still around at the end of June 2020, and hence we were left with no other choice but to abandon the idea of a physical conference and organize a fully online event. This transition was very painful and created many administration complications. Nevertheless, EASD and the organizing committee have seen this sanitary crisis as an opportunity to organize a different type of event and to propose a new approach for scientific collaboration and communication that respects both the legacy of the conference series and the health of the members of the European Community of Structural Dynamics.

EURODYN conferences have been established as the top scientific events in the area of theoretical, numerical and experimental Structural Dynamics worldwide and are highly-anticipated every three years by the international community of Structural Dynamics. For the 2020 edition of EURODYN series, more than 1000 abstracts were submitted, of which 830 were selected for presentation and among them 400 full-length papers were accepted for publication in the EASD Open Access Procedia, indexed by Scopus Database.

The editors of this volume would like to thank all authors for their contributions. Special thanks go to the 88 colleagues who were involved in the organization of 38 Minisymposia and to the reviewers who contributed to the scientific quality of this e-book with their work.

We would particularly like to thank the Members of the EASD Executive Board, and especially Álvaro Cunha, the President of EASD, Guido De Roeck, the Honorary Chairman of EURODYN 2020 and Fabrizio Vestroni the Chair of the EURODYN 2017, for their valuable advice, suggestions and interest, during the three-year preparation period of EURODYN 2020. Their contributions were significant to the successful outcome of this undertaking.

Manolis Papadrakakis
National Technical University of Athens, Greece

Michalis Fragiadakis
National Technical University of Athens, Greece

Costas Papadimitriou
University of Thessaly, Greece

ACKNOWLEDGEMENTS

The conference organizers acknowledge the support towards the organization of the "XI International Conference on Structural Dynamics", to the following organizations: European Association for Structural Dynamics (EASD), Greek Association for Computational Mechanics (GRACM), Hellenic Society for Earthquake Engineering (HSEE), School of Civil Engineering, National University of Athens (NTUA).

Plenary, Semi-Plenary Speakers and Minisymposia Organizers

We would also like to thank the Plenary and Semi-Plenary Speakers and the Minisymposia Organizers for their help in the setting up of a high standard Scientific Programme.

Plenary Speakers: Geert Degrande, Tracy Kijewski-Correa, Yi Qing Ni

Semi-Plenary Speakers: Eleni Chatzi, Joel P. Conte, Geert Lombaert, Andrei Metrikine, Sotirios Natsiavas, Filippo Ubertini

MS Organizers: I. Antoniadis, M. Arnst, K. Bakalis, B. Balachandran, C.C. Baniotopoulos, M. Barbato, J. Beck, M. Beer, G. Bonnet, C. Borri, C. Boutin, L. Bruno, E. Caetano, F. Casciati, C.A. Castiglioni, E. Chatzi, A. Cicirello, F. Clementi, D. Clouteau, J. Conte, M. Corradi, A. Cunha, G. De Roeck, G. Degrande, V. Denoël, D. Duhamel, J. Edelmann, D. Forcellini, A. Formisano, F. Foti, M. Fragiadakis, V. C. Fragkoulis, V. Fragkoulis, C. Gentile, R. Ghanem, D. Giagopoulos, A. Giaralis, P.B. Gonçalves, R. Höffer, A. Kanyilmaz, I. A. Kougioumtzoglou, S. Lenci, G. Lombaert, F. Magalhães, C. Maniatakis, E. Marino, T. Mazilu, C. E. N. Mazzilli, V. Melissianos, A. Metrikine, A.V. Metrikine, G. Milani, I.P. Mitseas, B. Moaveni, C. Moutinho, H. Mouzakis, H. P. Mouzakis, G. Müller, J. Naprstek, S. Natsiavas, P. Omenzetter, C. Papadimitriou, M. Papadrakakis, I. Papaioannou, A. Pavic, F. Pellicano, F. Perotti, M. Ploechl, I. Psycharis, G. Rega, J. Rodellar, E. Sapountzakis, J-F. Semblat, V. Sepe, C. Soize, S. Sorokin, C. Spyrakos, A. Taflanidis, F. Tubino, D. Vamvatsikos, K.N. van Dalen, P. Van den Broeck, K. Van Nimmen, M. Vasta, P-M. Vasta, I. Vayas, D. Wagg, K. Worden, W.M. Zhai

SUMMARY

VOLUME I

Minisymposia

VOLUME II

Minisymposia

CONTENTS

VOLUME I

Minisymposia

MS 1: ADVANCES IN COMPUTATIONAL STRUCTURAL DYNAMICS

MS 4: DYNAMICS OF COMPOSITE MATERIALS

MS 8: STRUCTURAL HEALTH MONITORING

MS 9: STRUCTURAL CONTROL

MS 10: ADVANCES ON INERTER-BASED STRUCTURAL VIBRATION CONTROL

MS 11: BRIDGE DYNAMICS

MS 12: FOOTBRIDGE VIBRATIONS

MS 13: HUMAN INDUCED VIBRATIONS IN FLOORS, STAIRCASES AND STADIA

MS 14: WIND INDUCED VIBRATIONS OF SLENDER STRUCTURES AND FATIGUE

MS 16: VIBRATION-BASED ASSESSMENT AND SHM OF CULTURAL HERITAGE STRUCTURES

MS 17: VIBRATIONS DUE TO CONSTRUCTION AND INDUSTRIAL ACTIVITIES

VOLUME II

Minisymposia

MS 18: VIBRO-ACOUSTICS

MS 19: BLAST AND IMPACT LOADS

MS 20: MOVING LOADS

MS 21: TRAFFIC INDUCED VIBRATIONS

MS 22: DYNAMIC SOIL-STRUCTURE INTERACTION AND WAVE PROPAGATION

MS 23: ASSESSMENT OF INDUSTRIAL STRUCTURES AND INFRASTRUCTURE UNDER NATURAL HAZARDS

MS 24: SEISMIC PROTECTION OF STEEL STRUCTURES BY MEANS OF DISSIPATIVE SYSTEMS AND COMPONENTS

MS 25: EXPERIMENTAL EARTHQUAKE ENGINEERING

MS 26: UQ AND PROBABILISTIC LEARNING IN COMPUTATIONAL DYNAMICS

MS 27: STOCHASTIC DYNAMICS AND RELIABILITY ANALYSIS OF STRUCTURAL AND MECHANICAL SYSTEMS UNDER ENVIRONMENTAL EXCITATION

MS 28: UNCERTAINTIES ON MATERIALS AND ENVIRONMENTAL LOADS

MS 29: BAYESIAN UPDATING, FILTERING AND INVERSION FOR DYNAMIC SYSTEMS

MS 30: RECENT ADVANCES IN PERFORMANCE-BASED ENGINEERING AND DESIGN OF STRUCTURES AND CIVIL INFRASTRUCTURE SYSTEMS SUBJECTED TO SINGLE OR MULTIPLE HAZARDS

MS 31: EUROPEAN ETN "DYNAMIC VIRTUALISATION: MODELLING PERFORMANCE OF ENGINEERING STRUCTURES" (DYVIRT)

MS 34: VIBRATION ABSORPTION

MS 35: NEW TRENDS IN THE COMPUTATIONAL AND EXPERIMENTAL STRUCTURAL DYNAMICS FOR THE PRESERVATION OF HISTORICAL MASONRY STRUCTURES IN SEISMIC AREAS

MS 38: GENERAL SESSION ON STRUCTURAL DYNAMICS, STABILITY AND VIBRATIONS

EURODYN 2020
XI International Conference on Structural Dynamics
M. Papadrakakis, M. Fragiadakis, C. Papadimitriou (eds.)
Athens, Greece, 23-26 November 2020

A MODE MATCHING TECHNIQUE FOR THE SEISMIC RESPONSE OF LIQUID STORAGE TANKS INCLUDING SOIL-STRUCTURE INTERACTION

Apostolos Tsouvalas[1], Timo Molenkamp[1], Khairina Canny[2], David Kroon[1], Marco Versluis[2], Yaxi Peng[1], and Andrei V. Metrikine[1]

[1] Delft University of Technology
Faculty of Civil Engineering and Geosciences
Stevinweg 1, 2628 CN Delft, The Netherlands
e-mail: {a.tsouvalas,t.molenkamp,d.p.kroon,y.peng,a.metrikine}@tudelft.nl

[2] Witteveen+Bos Raadgevende ingenieurs B.V.
Leeuwenbrug 8, 7411 TJ Deventer, The Netherlands
e-mail:{khairina.canny,marco.versluis}@witteveenbos.com

Keywords: liquid storage tank, seismic response, soil-structure interaction, fluid-structure interaction, shells

Abstract. *The paper establishes a computationally inexpensive method to deal with the dynamic response of liquid storage tanks subjected to seismic excitation including dynamic soil-structure interaction. The tank is modelled as a thin shell, the stored liquid is described as an inviscid and incompressible fluid and the soil medium is modelled as an elastic continuum. The dynamic response of the tank-liquid-soil system is derived in the frequency domain using dynamic substructuring and mode matching. The tank vibrations are first expressed in terms of the in-vacuo shell modes while the liquid motion is described as a superposition of linear potentials. The soil reaction to the plate of the tank is derived on the basis of a boundary integral formulation with the excitation field being the seismic free-field ground motion. Due to its high computational efficiency, the proposed method is suitable when a large number of simulations is required as is the case in seismic risk analysis. It overcomes the limitations of most mechanical analogues used nowadays, while at the same time maintains an accuracy comparable to that of finite element models within a fraction of the computation time of the latter.*

1 INTRODUCTION

The dynamic response of liquid storage tanks subjected to ground excitation has been a subject of continuous research over the past decades [1]. Despite the many modelling techniques available, most models can be classified into two broad categories: Finite Element (FE) models [2] and simplified mechanical analogues with a few degrees of freedom [3, 4].

In a simplified model, the various components of the tank-liquid system are described by point masses, springs and dashpots at certain locations [5]. Such models are useful for engineering purposes since they can prognosticate the base shear force and the overturning moment [6], however, they have certain limitations. First, they provide estimations of the design stresses at the base of the tank alone. Second, when they need to consider shells of non-uniform thickness or dynamic soil-structure interaction, they become needlessly complex, and even though procedures are described in the design codes to incorporate some of these effects [7], these procedures are approximate and cannot always guarantee accurate solutions. On the contrary, when a detailed dynamic analyis is required, FE modelling is often considered. Detailed FE models can overcome most of the limitations of the simpler models described earlier, however, they are computationally expensive and require experienced end users. In addition, the modelling of the unbounded soil domain and the proper inclusion of the seismic excitation remain always a challenge.

To overcome the disadvantages of the aforementioned modelling methods, this paper introduces an alternative method of numerical analysis of the tank-liquid-soil system. By doing so, one can overcome the main disadvantage of the FE models while, at the same time, computational accuracy stays uncompromised. The linear dynamic response of the tank-liquid-soil system is derived in the frequency domain using a mode-matching, dynamic substructuring technique. The substructuring technique, together with the Rayleigh-Ritz method, have been previously employed in [8, 9] for the solution of tank-liquid dynamic problems albeit in the absence of dynamic soil-structure interaction (SSI). In contrast to these earlier works, in this paper the eigenvalue problems are first formulated to obtain the modes of vibration of the tank and the liquid satisfying a set of predefined boundary conditions in an exact manner. Once the vibration modes of the tank and the liquid are determined to within a set of unknown complex-valued coefficients, the latter are obtained by ensuring the kinematic compatibility at the tank-liquid interface and by satisfying the equations of motion of the shell structure subjected to seismic motion. In addition to that, the dynamic reaction of the soil at the bottom side of the plate is considered through a boundary integral formulation in line with Lin et al. [10], thus coupling the tank-liquid system to the soil modelled as a three-dimensional continuum.

The main novelty of the paper lies in the establishment of a computationally inexpensive method to obtain the solution of the fully coupled tank-liquid-soil system subjected to seismic excitation. The computational efficiency stems from the adoption of the dynamic substructuring technique and the fact that for each substructure a standard eigenvalue problem is first solved before the forced response is treated. As will be shown, for low frequency seismic excitations, a few modes usually suffice to reach satisfactory convergence which adds to the computational speed. Furthermore, the solution technique proposed is very efficient and does not require the treatment of the whole coupled problem anew every time one of the substructures alters, i.e. varying liquid volume in the tank or soil composition. Given that, the authors believe that the proposed method is especially useful when a large number of simulations are required as, for example, is the case in seismic risk analyses and probabilistic assessments; cases in which the engineer is usually restricted to the use of simplistic models not capable of capturing all possible

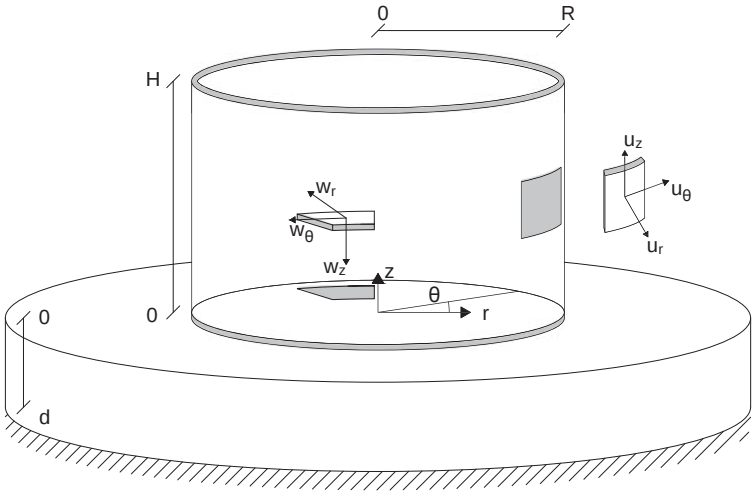

Figure 1: Definition of the displacement components and of the local coordinate system of the tank-liquid-soil system.

failure mechanisms.

In chapter 2, the model is described including the governing equations. The solution method for each subsystem is covered in detail in chapter 3, while chapter 4 establishes the algebraic system of equations that yields the solution to the coupled tank-liquid-soil problem subjected to a seismic excitation. In chapter 5, a convergence analysis is performed and model predictions are compared with FE simulations. Finally, chapter 6, summarises the main results of the paper.

2 MODEL DESCRIPTION

A typical liquid storage tank is shown in Fig.1. The shell structure consists of a circular plate and a cylindrical wall with the parameters E, ν, h and ρ corresponding to the Young's modulus, the Poisson's ratio, the thickness, and the density of the various parts of the shell, respectively. A cylindrical global coordinate system is adopted (r, θ, z) in which r is the radial coordinate, θ is the circumferential coordinate and z is the vertical coordinate. The tank is filled with liquid up to a height of $H_l \leq H$ with H being the height of the wall of the tank. The liquid is assumed inviscid and incompressible with a density ρ_l. The soil column of depth d that supports the tank is modelled as a linear elastic continuum with material parameters ρ_s, λ, μ corresponding to the density and the two Lamè constants of the elastic continuum, respectively. The seismic excitation is included through the free-field ground motion.

The governing equations describing the tank dynamic response read:

$$\boldsymbol{L}_p \boldsymbol{w}_p(r,\theta,t) + \rho_p h_p \ddot{\boldsymbol{w}}_p(r,\theta,t) = \boldsymbol{\sigma}_s(r,\theta,t) + \boldsymbol{p}_p(r,\theta,t) \tag{1}$$

$$\boldsymbol{L}_w \boldsymbol{u}_w(\theta,z,t) + \rho_w h_w \ddot{\boldsymbol{u}}_w(\theta,z,t) = \boldsymbol{p}_w(\theta,z,t) \tag{2}$$

in which $\boldsymbol{w}_p = [w_r, w_\theta, w_z]^{\mathrm{T}}$ is the displacement vector of the mid-surface of the plate, $\boldsymbol{L}_p$ is the stiffness operator of the plate [11], $\boldsymbol{\sigma}_s = [\tau_{rz}, \tau_{r\theta}, \sigma_z]^{\mathrm{T}}$ represents the boundary stress vector induced by the interaction with the soil (including the seismic excitation), and $\boldsymbol{p}_p = [0, 0, p_{liq}]^{\mathrm{T}}$ accounts for the pressure of the stored liquid. Next to that, $\boldsymbol{u}_w = [u_r, u_\theta, u_z]^{\mathrm{T}}$ denote

the displacement of the mid-surface of the wall along the radial, circumferential and vertical directions, respectively. The operator $\boldsymbol{L}_w$ accounts for the stiffness of the cylindrical shell [12] and the force vector $\boldsymbol{p}_w = [p_{liq}, 0, 0]^{\mathrm{T}}$ includes the pressure exerted by the motion of the stored liquid normal to the shell surface. In Eqs.(1–2), the overdot represents a derivative with respect to the time variable.

Supplementary to the equations of motion, a set of boundary and interface conditions need to be formulated to complete the statement of the problem shown in Fig.1:

$$\boldsymbol{u}_w|_{z=0} - \boldsymbol{u}_p|_{r=R} = \boldsymbol{0}\,,\; \phi_{w,z}|_{z=0} - \phi_{p,r}|_{r=R} = 0\,,\; \boldsymbol{f}_w|_{z=0} - \boldsymbol{f}_p|_{r=R} = \boldsymbol{0}\,,\; \boldsymbol{f}_w|_{z=H} = \boldsymbol{0} \tag{3}$$

In Eqs.(3), $\phi_{w,z} = -\partial u_r/\partial z$ and $\phi_{p,r} = -\partial w_z/\partial r$ and $\boldsymbol{f}_w = [M_{zz}, N_{zz}, V_{zr}, T_{z\theta}]^{\mathrm{T}}$ is the generalised force vector of the wall segment which includes the moment M_{zz}, the membrane force N_{zz} and the shear forces V_{zr} and $T_{z\theta}$ [12]. Similarly, $\boldsymbol{f}_p = [M_{rr}, V_r, N_{rr}, N_{r\theta}]^{\mathrm{T}}$ corresponds to the generalised force vector of the plate at the connection with the wall.

Considering a liquid that is inviscid and incompressible, and limiting the scope to linear vibrations, the governing equation for the liquid reads:

$$\nabla^2\phi(r,\theta,z,t) = 0 \tag{4}$$

in which $\phi(r,\theta,z,t)$ denotes the velocity potential. The interface and boundary conditions for the liquid region read:

$$\left.\frac{\partial\phi(r,\theta,z,t)}{\partial r}\right|_{r=R} = \dot{u}_r(\theta,z,t)\,,\; \left.\frac{\partial\phi(r,\theta,z,t)}{\partial z}\right|_{z=0} = \dot{w}_z(r,\theta,t) \tag{5}$$

$$\left.\left(\frac{1}{g}\ddot{\phi}(r,\theta,z,t) - \frac{\partial\phi(r,\theta,z,t)}{\partial z}\right)\right|_{z=H_l} = 0 \tag{6}$$

A single soil layer is considered and the local coordinate system is employed with the z-coordinate pointing downwards, such that the soil surface is at $z = 0$ and the bedrock at $z = d$. The equations of motion read [13]:

$$(\lambda+\mu)\nabla\nabla\boldsymbol{u}_s(r,\theta,z,t) + \mu\nabla\times\nabla\times\boldsymbol{u}_s(r,\theta,z,t) = \rho_s\ddot{\boldsymbol{u}}_s(r,\theta,z,t) \tag{7}$$

in which $\boldsymbol{u}_s = [u_{s,r}, u_{s,\theta}, u_{s,z}]^{\mathrm{T}}$. The boundary conditions and interface conditions of the soil domain at $z = 0$ and $z = d$ read:

$$\begin{array}{rcll} \boldsymbol{u}_s(r,\theta,d,t) & = & \boldsymbol{0} & \\ \boldsymbol{u}_s(r,\theta,0,t) & = & \boldsymbol{u_p}(r,\theta,t) & r \le R \\ \boldsymbol{\sigma}_s^s(r,\theta,0,t) & = & \left\{ \begin{array}{ll} \boldsymbol{0} & r > R \\ -\boldsymbol{K}_s(r,\theta,t) * \left(\boldsymbol{u}_s^f(r,\theta,0,t) - \boldsymbol{u}_p(r,\theta,t)\right) & r \le R \end{array} \right. & \end{array} \tag{8}$$

in which $\boldsymbol{\sigma}_s^s$ is the surface traction acting on the plate along the r-, θ- and z-coordinate at $z = 0$ and the asterisk denotes a convolution operation. The term $\boldsymbol{K}_s(r,\theta,t)$ denotes the dynamic stiffness of the soil column evaluated at the surface of the ground as explained in section 3.3 and $\boldsymbol{u}_s^f(r,\theta,0,t)$ is the free-field ground motion which defines here the excitation mechanism. Equations (1–8) govern the dynamics of the tank-soil-liquid system in the time domain.

3 SOLUTION APPROACH PER SUBSTRUCTURE

The governing equations (1–8) are first transformed to the frequency domain by introducing the Fourier transform pair with respect to time as follows:

$$\tilde{G}(\omega) = \int_{-\infty}^{\infty} g(t) \mathrm{e}^{-\mathrm{i}\omega t} \, \mathrm{d}t \;\text{ and }\; g(t) = \frac{1}{2\pi} \int_{-\infty}^{\infty} \tilde{G}(\omega) \mathrm{e}^{\mathrm{i}\omega t} \mathrm{d}\omega, \tag{9}$$

in which $g(t)$ is understood here as the examined quantity. Complex-valued variables in the frequency domain are indicated with a tilde over the variable.

The resulting set of coupled partial differential equations need to be solved for each excitation frequency. The solution approach is based on the following steps: (i) Solution to the eigenvalue problem of the tank *in-vacuo* (section 3.1); (ii) Eigensolutions of the liquid domain (section 3.2); (iii) Derivation of the dynamic stiffness matrix of the soil at the interface with the tank in the frequency domain (section 3.3); (iv) Solution to the coupled tank-liquid-soil system by making use of the steps (i–iii) as described further in section 4.

3.1 Eigenvalue problem of the tank *in-vacuo*

The equations of motion, boundary and interface conditions for the plate and wall of the tank, neglecting the presence of the water and the soil, are transformed into the frequency domain by means of Eq.(9). The solution is found via separation of variables [14]. A set of algebraic equations is found for the *in-vacuo* shell modes after substituting the assumed solutions for the plate and the wall into the boundary and interface conditions.

$$\boldsymbol{G}_n \cdot \boldsymbol{a} = 0 \tag{10}$$

$\boldsymbol{G}_n$ denotes the coefficient matrix and $\boldsymbol{a}$ is a vector composed of the unknown constants. For a non-trivial solution, the determinant of the coefficient matrix $\boldsymbol{G}_n$ is set equal to zero, i.e. $\det(\boldsymbol{G}_n) = 0$. This results at a transcendental equation which yields an infinite set of eigenvalues ω_{nm} with $m = 0, 1, 2, 3, ...$ for each circumferential order n. A numerical algorithm is developed with the frequency ω (for every circumferential order n) defined as the running variable which is then iterated numerically to find the zeroes of the determinant. Once the values of ω_{nm} are obtained, the tank motion can be expressed as a summation of modes in the frequency domain:

$$\tilde{\boldsymbol{w}}_p(r, \theta, \omega) = \sum_{n=0}^{\infty} \sum_{m=0}^{\infty} \tilde{X}_{nm} \boldsymbol{D}_n^t(\theta) \boldsymbol{W}_{nm}(r) \tag{11}$$

$$\tilde{\boldsymbol{u}}_w(\theta, z, \omega) = \sum_{n=0}^{\infty} \sum_{m=0}^{\infty} \tilde{X}_{nm} \boldsymbol{D}_n^t(\theta) \boldsymbol{U}_{nm}(z) \tag{12}$$

$\boldsymbol{D}_n^t(\theta) = \textit{diag}\ [\cos(n\theta), \sin(n\theta), \cos(n\theta)]$ contains the circumferential dependency of the tank modes and $\boldsymbol{W}_{nm} = [W_{z,nm}, W_{\theta,nm}, W_{r,nm}]^{\mathrm{T}}$ and $\boldsymbol{U}_{nm} = [U_{z,nm}, U_{\theta,nm}, U_{r,nm}]^{\mathrm{T}}$ are the eigenvectors of the plate and the wall, respectively. The indices n, m define the circumferential and axial mode numbers, respectively. The unknown complex-valued amplitudes $\tilde{X}_{nm}$ can be obtained by satisfying the forced vibration problem. The eigenvectors satisfy the following orthogonality condition:

$$\rho_p h_p \iint_S \boldsymbol{D}_q^t \boldsymbol{U}_{ql}^{\mathrm{T}} \boldsymbol{D}_n^t \boldsymbol{U}_{nm} \mathrm{d}S + \rho_w h_w \iint_{S_0} \boldsymbol{D}_q^t \boldsymbol{W}_{ql}^{\mathrm{T}} \boldsymbol{D}_n^t \boldsymbol{W}_{nm} \mathrm{d}S_0 = a_n \Gamma_{nm} \delta_{qn} \delta_{lm} \,, \tag{13}$$

in which δ_{np} and δ_{ml} are the *Kronecker* deltas and S, S_0 denote the surface of integration for the wall and the plate of the tank, respectively. The scalar quantity a_n denotes an integration constant related to the circumference, i.e. $\int_0^{2\pi} D_q^t D_n^t d\theta = a_n \delta_{qn}$; a_n equals π for $n = 0$ and 2π otherwise.

3.2 Eigensolutions of the liquid domain

The liquid potential function is separated into three scalar functions, each one satisfying a subset of the imposed boundary and interface conditions. This allows an analytical treatment of the problem [15]. The total liquid potential is decomposed into three velocity potentials, namely: (i) $\phi^{(1)}(r, \theta, z, t)$ which satisfies the homogeneous boundary conditions at $z = 0$ and $z = H_l$ as well as the imposed kinematic constraint at the interface with the wall; (ii) $\phi^{(2)}(r, \theta, z, t)$ which satisfies the homogeneous boundary conditions at $r = R$ and $z = H_l$, and the imposed kinematic constraint at the interface with the plate; and (iii) $\phi^{(3)}(r, \theta, z, t)$ which does not alter the conditions satisfied already at $z = 0$ and $r = R$ but allows exact satisfaction of the boundary condition at $z = H_l$.

The superposition of the three scalar functions provides the total solution which can be expressed as follows [8]:

$$\tilde{\phi}(r, \theta, z) = \sum_{n=0}^{\infty} \sum_{a=1}^{\infty} \tilde{\phi}_{na}^{(1)} + \tilde{\phi}_{00}^{(2)} + \sum_{n=0}^{\infty} \sum_{b=1}^{\infty} \tilde{\phi}_{nb}^{(2)} + \tilde{\phi}_{00}^{(3)} + \sum_{n=0}^{\infty} \sum_{c=1}^{\infty} \tilde{\phi}_{nc}^{(3)}, \tag{14}$$

in which the following definitions hold:

$$\tilde{\phi}_{na}^{(1)}(r, \theta, z) = \tilde{P}_{na} \phi_{z,na}^{(1)}(z) \phi_{r,na}^{(1)}(r) \cos(n\theta) \tag{15}$$

$$\tilde{\phi}_{00}^{(2)}(r, \theta, z) = \tilde{Q}_{00}(z - H_l) \tag{16}$$

$$\tilde{\phi}_{nb}^{(2)}(r, \theta, z) = \tilde{Q}_{nb} \phi_{z,nb}^{(2)}(z) \phi_{r,nb}^{(2)}(r) \cos(n\theta) \tag{17}$$

$$\tilde{\phi}_{00}^{(3)}(r, \theta, z) = \tilde{S}_{00} \tag{18}$$

$$\tilde{\phi}_{nc}^{(3)}(r, \theta, z) = \tilde{S}_{nc} \phi_{z,nc}^{(3)}(z) \phi_{r,nc}^{(3)}(r) \cos(n\theta) \tag{19}$$

The modal amplitudes $\tilde{P}_{na}$, $\tilde{Q}_{nb}$, and $\tilde{S}_{nc}$ are the unknown complex constants for the liquid domain which will be determined together with the modal amplitudes of the structure by satisfying the forced equations of motion and the kinematic conditions at the tank-liquid interfaces described previously. The index n denotes the circumferential mode number of each potential. The indices a, b and c denote the axial mode numbers. The terms ε_{nb} and ε_{nc} are the roots obtained by setting $J_n'(\varepsilon) = 0$.

3.3 Dynamic stiffness of the soil

To obtain the dynamic stiffness of the soil, the equations are first transformed into the frequency-Hankel domain by means of a Fourier-Hankel transform. In this transformed domain, the dynamic stiffness matrix of a single soil layer reads [13]:

$$\begin{bmatrix} \bar{\boldsymbol{p}}(k, 0) \\ \bar{\boldsymbol{p}}(k, d) \end{bmatrix} = \begin{bmatrix} \bar{\boldsymbol{S}}_{11} & \bar{\boldsymbol{S}}_{12} \\ \bar{\boldsymbol{S}}_{21} & \bar{\boldsymbol{S}}_{22} \end{bmatrix} \begin{bmatrix} \bar{\boldsymbol{u}}(k, 0) \\ \bar{\boldsymbol{u}}(k, d) \end{bmatrix}, \tag{20}$$

in which $\bar{\boldsymbol{p}}(k, 0; d)$, $\bar{\boldsymbol{u}}(k, 0; d)$ correspond to the boundary stress and displacement vectors, respectively, and the bar denotes functions in the frequency-wavenumber domain. The matrix $\bar{\boldsymbol{S}}$

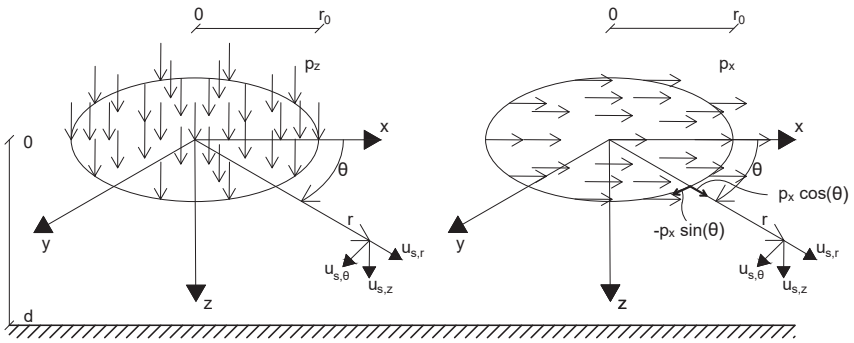

Figure 2: Vertical and horizontal loads distributed evenly over a circular subdisk.

is the dynamic stiffness matrix in the wavenumber-frequency domain. The only terms of interest in $\bar{\boldsymbol{S}}$ are $\bar{\boldsymbol{S}}_{11}$, since the stiffness is needed only at the ground surface. For the sake of brevity of the notations hereafter, we adopt $\bar{\boldsymbol{u}}(k) = \bar{\boldsymbol{u}}(k,0)$, $\bar{\boldsymbol{p}}(k) = \bar{\boldsymbol{p}}(k,0)$ and $\bar{\boldsymbol{p}}(k) = \bar{\boldsymbol{S}}_{11}\bar{\boldsymbol{u}}(k)$. The inverse of the dynamic stiffness matrix of the ground surface, i.e. the flexibility matrix, is of the form:

$$\bar{\boldsymbol{S}}_{11}^{-1} = \bar{\boldsymbol{F}} = \begin{bmatrix} \bar{F}_{11} & 0 & \bar{F}_{13} \\ 0 & \bar{F}_{22} & 0 \\ \bar{F}_{31} & 0 & \bar{F}_{33} \end{bmatrix} \tag{21}$$

Having established a relation between the stresses and displacements at the surface of the ground, one can derive the dynamic stiffness in a straightforward manner. The plate of the tank is assumed to contact the ground surface through circular areas referred to as subdiscs. The loads over a circular subdisk are expanded in Fourier series in the circumferential direction, where $n = 0$ relates to an axisymmetric load and $n = 1$ to an antisymmetric load. The complex amplitudes of the load are related by the following Fourier-Hankel transform pair [13]:

$$\begin{aligned} \bar{\boldsymbol{p}}_n(k) &= a_n \int_{r=0}^{\infty} r\boldsymbol{C}_n(kr) \int_{\theta=0}^{2\pi} \boldsymbol{D}_n(\theta)\tilde{\boldsymbol{p}}(r,\theta)\mathrm{d}\theta\mathrm{d}r \\ \tilde{\boldsymbol{p}}(r,\theta) &= \sum_{n=0}^{\infty} \boldsymbol{D}_n(\theta) \int_{k=0}^{\infty} k\boldsymbol{C}_n(kr)\bar{\boldsymbol{p}}_n(k)\mathrm{d}k \end{aligned} \tag{22}$$

In Eq.(22), a_n is a normalization factor that is equal to $1/2\pi$ or $1/\pi$ for $n = 0$ and $n \neq 0$ respectively. $\boldsymbol{D}_n$ is a diagonal matrix with trigonometric functions, describing the circumferential dependency and $\boldsymbol{C}_n$ contains Bessel functions. Three load cases are considered. A vertical load case and two horizontal load cases; one symmetric and one anti-symmetric with respect to $\theta = 0$. The derivation of the latter two cases is identical but for the trigonometric functions in $\boldsymbol{D}_n$.

The radius of each subdisk equals r_0 and the amplitudes of the vertical and horizontal loads are denoted as p_z and p_x, respectively, as shown in Fig.2. The vertical load, that is assumed uniformly distributed over the subdisc, is transformed into the wavenumber domain by means of Eq.(22):

$$\bar{\boldsymbol{p}}_0(k) = \frac{1}{2\pi} \int_{r=0}^{r_0} r\boldsymbol{C}_0(kr) \int_{\theta=0}^{2\pi} [0,0,p_z]^{\mathrm{T}}\mathrm{d}\theta\mathrm{d}r = -\frac{r_0}{k} J_1(kr_0)[0,0,p_z]^{\mathrm{T}} \tag{23}$$

$\bar{\boldsymbol{p}}_0(k)$ relates to $\bar{\boldsymbol{u}}(k)$ through the flexibility matrix Eq.(21):

$$\bar{\boldsymbol{u}}_0(k) = -\frac{p_z r_0}{k} J_1(kr_0)[\bar{F}_{13},0,\bar{F}_{33}]^{\mathrm{T}} \tag{24}$$

The displacements of the surface at any r and θ are found by:

$$\tilde{\boldsymbol{u}}_s^z(r,\theta) = -r_0 p_z \int_{k=0}^{\infty} J_1(kr_0)\boldsymbol{C}_0(kr)\left[\bar{F}_{13}, 0, \bar{F}_{33}\right]^{\mathrm{T}} \mathrm{dk} \tag{25}$$

Following a similar procedure for the horizontal load one obtains:

$$\tilde{\boldsymbol{u}}_s^x = r_0 p_x \boldsymbol{D}_1(\theta) \int_{k=0}^{\infty} J_1(kr_0)\boldsymbol{C}_1(kr)\left[\bar{F}_{11}, \bar{F}_{22}, \bar{F}_{31}\right]^{\mathrm{T}} \mathrm{dk} \tag{26}$$

Applying the load in y-direction ($\theta = \pi$), via the same steps, an expression can be found similar to Eq.(26).

The integrals in Eqs.(25–26) are evaluated by making use of contour integration. The solution derived holds both within and outside the subdisk. The resulting expressions for $r \leq r_0$ read:

$$\tilde{\boldsymbol{u}}_s^z(r,\theta) = \tilde{p}_z \left(r_0 \pi \mathrm{i} \sum_{k_r} H_1^{(2)}(k_r r_0)\boldsymbol{C}_0(k_r r) \left[\frac{\bar{F}_{13}^n}{\tilde{F}_{p,k}^d}, 0, \frac{\bar{F}_{33}^n}{\bar{F}_{p,k}^d} \right]^{\mathrm{T}} + \left[0, 0, \bar{F}_{33}(0)\right]^{\mathrm{T}} \right), \tag{27}$$

$$\tilde{\boldsymbol{u}}_s^x = -\tilde{p}_x \boldsymbol{D}_1(\theta) \left(r_0 \pi \mathrm{i} \sum_{k_r} H_1^{(2)}(k_r r_0)\boldsymbol{C}_1(k_r r) \left[\frac{\bar{F}_{11}^n}{\bar{F}_{p,k}^d}, \frac{\bar{F}_{22}^n}{\bar{F}_{s,k}^d}, \frac{\bar{F}_{31}^n}{\bar{F}_{p,k}^d} \right]^{\mathrm{T}} - \left[\bar{F}_{11}(0), \bar{F}_{11}(0), 0\right]^{\mathrm{T}} \right) \tag{28}$$

Similarly, the expressions for $r \geq r_0$ read:

$$\tilde{\boldsymbol{u}}_s^z(r,\theta) = r_0 \tilde{p}_z \pi \mathrm{i} \sum_{k_r} J_1(k_r r_0)\boldsymbol{C}_0(k_r r) \left[\frac{\bar{F}_{13}^n}{\bar{F}_{p,k}^d}, 0, \frac{\bar{F}_{33}^n}{\bar{F}_{p,k}^d} \right]^{\mathrm{T}} \tag{29}$$

$$\tilde{\boldsymbol{u}}_s^x = -r_0 \tilde{p}_x \pi \mathrm{i} \boldsymbol{D}_1(\theta) \sum_{k_r} J_1(k_r r_0)\boldsymbol{C}_1(k_r r) \left[\frac{\bar{F}_{11}^n}{\bar{F}_{p,k}^d}, \frac{\bar{F}_{22}^n}{\bar{F}_{s,k}^d}, \frac{\bar{F}_{31}^n}{\bar{F}_{p,k}^d} \right]^{\mathrm{T}} \tag{30}$$

Equations (27–30) define the frequency response functions (FRFs) for a constant distributed force over a circular area with radius r_0. The superscript n here denotes the numerator of the flexibility functions and d the denominator of those; in all cases the derivative of the denominator is taken with respect to k, indicated with subscript k. The FRFs are derived for a single subdisk around the origin. By normalizing the amplitude of the stresses (p_x, p_y, p_z), the dynamic impedance $\tilde{\boldsymbol{R}}_s(r,\theta)$ is obtained which upon inversion yields the dynamic stiffness of the soil $\tilde{\boldsymbol{K}}_s(r,\theta)$.

4 COUPLED TANK-LIQUID-SOIL SYSTEM

The motion of the liquid is described by Eqs.(14–19) and the motion of the tank by Eqs.(11–12). Upon substitution of these expressions into the interface and boundary conditions given by

Eqs.(5–6), and after the use of the orthogonality conditions, one obtains:

$$\Gamma_{na}\tilde{P}_{na} = -\mathrm{i}\omega \sum_{m=0}^{\infty} \tilde{X}_{nm} \int_0^{H_l} \phi^{(1)}_{z,na}(z) U_{r,nm}(z) \mathrm{d}z \tag{31}$$

$$\Gamma_{nb}\tilde{Q}_{nb} = -\mathrm{i}\omega \sum_{m=0}^{\infty} \tilde{X}_{nm} \int_0^{R} \phi^{(2)}_{r,nb}(r) W_{z,nm}(r) r \mathrm{d}r \tag{32}$$

$$\begin{aligned}\Gamma_{nc}\tilde{S}_{nc} = &\sum_{a=1}^{\infty} \tilde{P}_{na} \left.\frac{\partial \phi^{(1)}_{z,na}(z)}{\partial z}\right|_{z=H_l} \int_0^{R} \phi^{(3)}_{r,nc}(r)\phi^{(1)}_{r,na}(r) r \mathrm{d}r \\ &+ \sum_{b=1}^{\infty} \tilde{Q}_{nb} \left.\frac{\partial \phi^{(2)}_{z,nb}(z)}{\partial z}\right|_{z=H_l} \int_0^{R} \phi^{(3)}_{r,nc}(r)\phi^{(2)}_{r,nb}(r) r \mathrm{d}r\end{aligned} \tag{33}$$

The integration constants derived directly from the orthogonality relations are omitted here for the sake of brevity. Next to the satisfaction of the kinematic conditions at the tank-liquid interface, the forced equations of motion of the structure need to be satisfied. Considering Eqs. (11–12) and the fact that for every mode of vibration of the shell $\boldsymbol{L}_w \boldsymbol{u}_{nm} = \omega^2_{nm} \rho_w h_w \boldsymbol{u}_{nm}$ and $\boldsymbol{L}_p \boldsymbol{w}_{nm} = \omega^2_{nm} \rho_p h_p \boldsymbol{w}_{nm}$, the stiffness terms can be replaced by the inertia ones, i.e.:

$$\sum_{n=0}^{\infty}\sum_{m=0}^{\infty} \left(\left(\omega^2_{nm} - \omega^2\right) \rho_p h_p + \tilde{\boldsymbol{K}}_s \right) \tilde{X}_{nm} \boldsymbol{D}^t_n \boldsymbol{W}_{nm} - \tilde{\boldsymbol{p}}_{p,n} \cos(n\theta) = \tilde{\boldsymbol{K}}_s \tilde{\boldsymbol{u}}^f_s \tag{34}$$

$$\sum_{n=0}^{\infty}\sum_{m=0}^{\infty} \left(\omega^2_{nm} - \omega^2\right) \rho_w h_w \tilde{X}_{nm} \boldsymbol{D}^t_n \boldsymbol{U}_{nm} - \tilde{\boldsymbol{p}}_{w,n} \cos(n\theta) = 0 \tag{35}$$

in which the liquid pressures are $\tilde{\boldsymbol{p}}_{n,p} = [0, 0, \tilde{p}_{n,l}|_{z=0}]^{\mathrm{T}}$ and $\tilde{\boldsymbol{p}}_{n,w} = [\tilde{p}_{n,l}|_{r=R}, 0, 0]^{\mathrm{T}}$. $\boldsymbol{W}_{nm}$ and $\boldsymbol{U}_{nm}$ are the eigenvectors of the plate and wall respectively with respect to circumferential mode number n and axial mode number m. By substituting Eqs.(15–19) into $\tilde{\boldsymbol{p}}_{n,p}$ and $\tilde{\boldsymbol{p}}_{n,w}$ one can expand the liquid pressures in terms of the summation of the potential functions. By summing up the components of Eqs.(34–35), one can make use of Eq.(13) to eliminate part of the modal summations. By considering the above, the final set of infinite equations that needs to be solved for every n-mode number reads:

$$\begin{aligned}\sum_{m=0}^{\infty} \left(\omega^2_{nm} - \omega^2\right) \Gamma_{nm} - \int_0^{R} \boldsymbol{W}^{\mathrm{T}}_{nm} \tilde{\boldsymbol{p}}_{p,n} \mathrm{d}r - \int_0^{H} \boldsymbol{W}^{\mathrm{T}}_{nm} \tilde{\boldsymbol{p}}_{w,n} \mathrm{d}z \\ = \frac{1}{a_n} \iint_{S_0} \boldsymbol{D}^t_n \boldsymbol{W}^{\mathrm{T}}_{nm} \tilde{\boldsymbol{K}}_s \left(\tilde{\boldsymbol{u}}^f_s - \tilde{X}_{nm} \boldsymbol{D}^t_n \boldsymbol{W}_{nm} \right) \mathrm{d}S_0\end{aligned} \tag{36}$$

This approach is valid as shown in [16] for a pile foundation embedded into the soil. The final matrix equation can be represented in a condensed form as follows:

$$\boldsymbol{Q}_n \cdot \boldsymbol{c}_n = \boldsymbol{F}_n \tag{37}$$

$\boldsymbol{Q}_n$ is the modal coefficient matrix of dimensions $(a+b+c+m) \times (a+b+c+m)$ which is fully-populated, complex-valued, and gathers the multipliers of the amplitude coefficients resulting from equations (31–33) and (36). Vector $\boldsymbol{c}_n$ contains the liquid unknowns P_{na}, Q_{nb}, S_{nc} and modal amplitude coefficients of the structure X_{nm} and is of size $(a + b + c + m)$. Vector $\boldsymbol{F}_n$ represents the modal projection of the dynamic loading. By following a straightforward matrix operation, i.e. $\boldsymbol{c}_n = \boldsymbol{Q}^{-1}_n \boldsymbol{F}_n$, one can obtain both the liquid and the structure unknown constants once a proper truncation scheme of the infinite system is established.

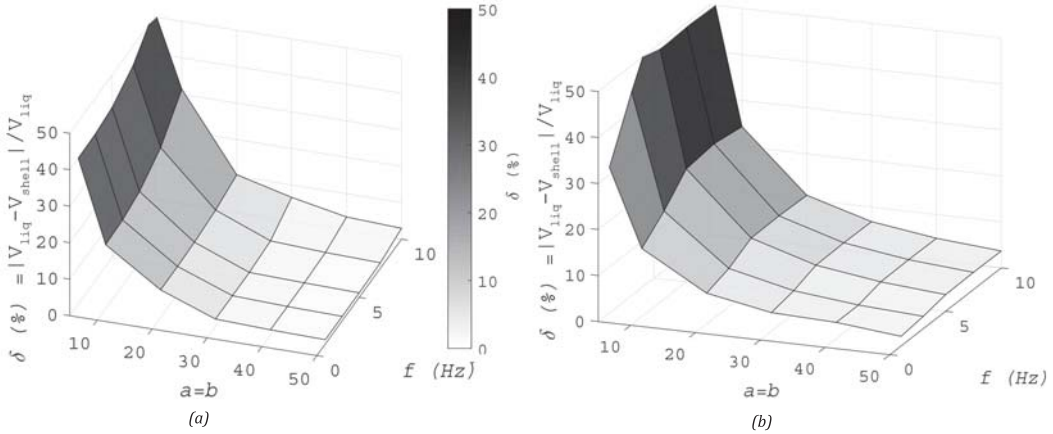

Figure 3: Convergence of the solution for increasing number of axial mode numbers of the liquid domain ($a = b = c$) for: (a) $n = 0$; and (b) $n = 1$.

5 MODEL VALIDATION

The tank-liquid system is validated with a FE model using a Kelvin-Voigt foundation with frequency independent springs and dashpots to represent the SSI effects. The soil domain is validated separately by comparing the results of a harmonically excited rigid massless plate [17, 18].

5.1 Convergence criteria and eigenvalues of the liquid-tank system

The base case considered for validation is a tank with $H/R = 0.71$ and $H = 22$m. The tank is composed of steel material ($\nu = 0.30$ and $\rho = 7850$ kg m^{-3}) with a plate thickness of $h_w = 19$mm and $h_w/h_p = 1.267$. The plate rests on elastic foundation with $k_v = 40$MNm^{-2} and $k_v/k_h = 16$. The stored liquid has a density of 1000kgm^{-3} and a fill level ratio $H_l/H = 1.0$. The adopted computational method involves the truncation of the infinite set of algebraic equations to obtain the unknown modal coefficients. It has been found that the results are most sensitive to the truncation limits of the liquid modes and rather insensitive to the number of structural modes considered as long as a reasonable criterion is adopted for the latter. The number of structural modes to be considered can be estimated by examining the energy spectrum of the dynamic excitation and choosing a truncation limit for the structural modes such that the eigenfrequency of the upper limit in the summation is twice as high as the highest frequency of interest-based on the energy spectrum [19]. Figure 3 depicts the average error at the shell-liquid interface for varying number of liquid modes and for a range of frequencies for two cases of circumferential mode numbers, i.e. $n = 0$ and $n = 1$. As can be seen, when the number of axial modes increases for a given circumferential order, the error decreases monotonically. For the case study considered here, about 30 modes suffice to reduce the error to below 5% for $n = 0$ and about 40 modes to stay within the same limit for $n = 1$.

The proposed model is validated against results obtained by FEM simulations in Comsol Multiphysics® COMSOL Multiphysics® [20]. The validation is performed for several key parameters; here results are shown for a varying liquid volume. As can be seen in Table 1, the differences in the computed eigenvalues between the present model and the FEM are less than 10% in all cases and in most cases below 5%. In Fig. 4, a few mode shapes obtained with the two models are shown. As can be seen, the modes are very similar which proves the validity of the developed model.

$\mathbf{n=1}$	**Present model**		**FEM [20]**		$\lvert\delta f\rvert$ **[%]**	
H_l/H	$f_{1,1}(Hz)$	$f_{1,2}(Hz)$	$f_{1,1}$	$f_{1,2}(Hz)$	$\delta f_{1,1}$	$\delta f_{1,2}$
0%	6.29	12.06	6.42	12.14	2.00	0.63
50%	2.65	6.35	2.39	6.07	9.97	4.55
100%	1.31	3.99	1.24	3.70	5.52	5.80

Table 1: Eigenvalues (in Hertz) obtained by using a FE model in COMSOL Multiphysics® [20] and the present model for the $n = 1$ family of modes and for varying fill height of the liquid.

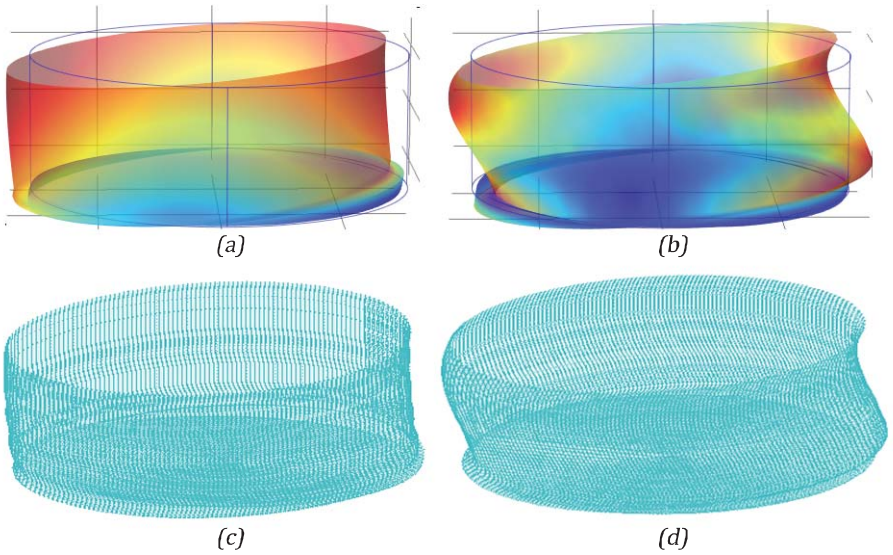

Figure 4: Comparison of the modal shapes of the tank-liquid system obtained by using the FE model in COMSOL Multiphysics® [20] and the present model for a filled tank:(a) FE mode $(1, 1)$; (b) FE mode $(1, 2)$ (c) present model mode $(1, 1)$; (d) present model mode $(1, 2)$.

5.2 Dynamic soil stiffness

The derivation of the dynamic stiffness is benchmarked against results presented in the literature for the case of a rigid plate. To facilitate a direct comparison with literature, a normalized frequency is introduced as $a_0 = \omega R/2\pi c_s$. The dynamic stiffness and damping coefficients in the horizontal direction are defined as:

$$\tilde{K}_{xx} = K^0_{xx}\left(k_{xx} + \mathrm{i}\frac{\omega R}{c_s}c_{xx}\right)(1 + 2\mathrm{i}\beta) \tag{38}$$

in which K^0_{xx} is the static stiffness and k_{xx}, c_{xx} denote the dynamic stiffness and damping coefficients, respectively, and c_s denotes the shear wave speed in the soil.

For the validation case the following values are chosen: $d/R = 2; 4$, $\nu = 1/3$, damping ratio $\beta = 5\%$. The comparison is based on a discretisation of the plate surface in 15 rings yielding in total 709 subdisks. Figure 5 shows that the dynamic stiffness k_{xx} and damping coefficients c_{xx} are in very good agreement with literature [17, 18]. Moreover, the solution for the static case converges relatively fast as shown in Fig.6. It is expected that this is an extreme case since peak stresses are located at the edge of the plate. The subdisks have only one node; thus, the more elements included, the better the stress representation at the edge. When travelling waves with short wavelengths compared to the plate radius are excited, a higher number of elements might be required, albeit in the field of earthquake engineering this is not expected.

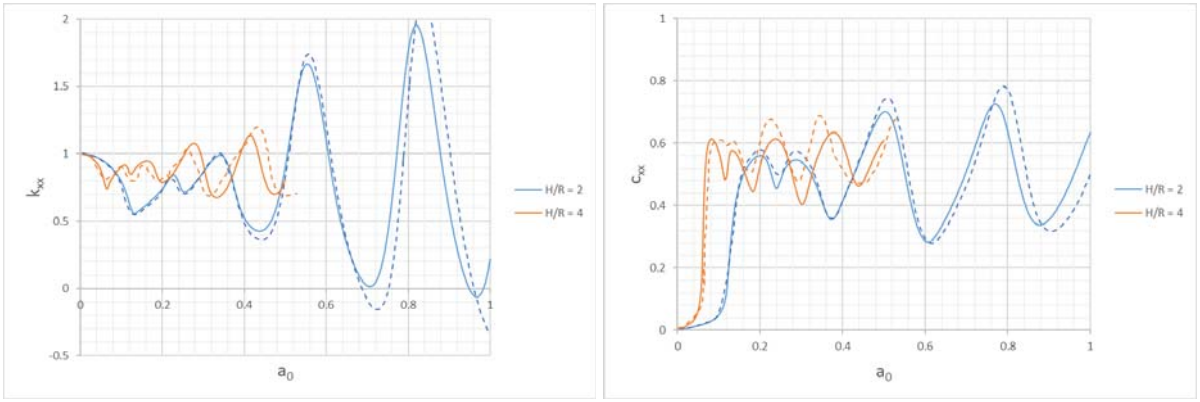

(a) Horizontal stiffness coefficient (b) Horizontal damping coefficient

Figure 5: Comparison of model results (solid lines) and references (dashed lines) [17, 18].

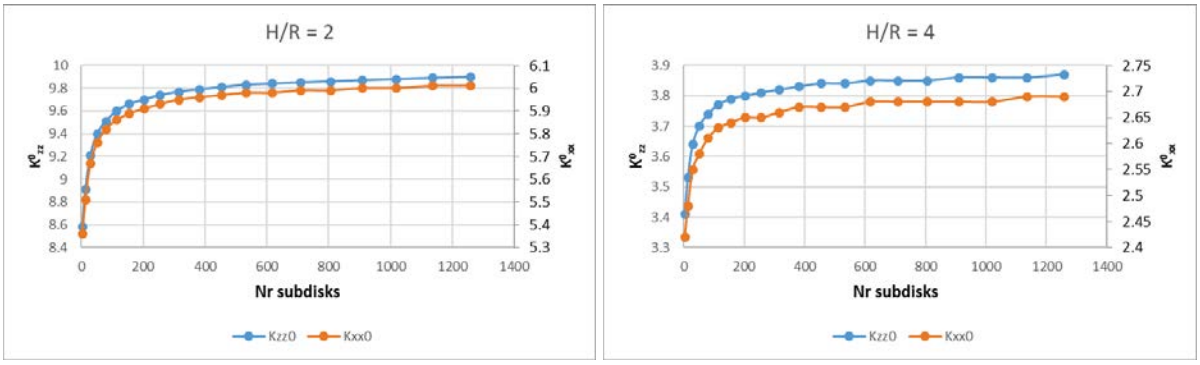

Figure 6: Convergence of the static stiffness for d/R = 2 and d/R = 4.

6 CONCLUSIONS

A computationally inexpensive method is developed for the prediction of the dynamic response of a liquid storage tank subjected to seismic excitation. The model consists of three main subsystems, namely: the shell structure representing the tank, the stored liquid and the soil domain. Emphasis is placed on the theoretical development of the model and the description of an elegant method of solution to the final system of coupled differential equations. The strength of the method is that it can cope with a full dynamic analysis of a coupled tank-liquid-soil system and it can easily be expanded in cases of non-uniform shell thickness and multi-layered soils. Next to that, due to the fact that substructuring forms the basis of the solution technique, the model is suitable for a large number of computations in which some parts of the total system are altered whereas others remain unchanged. The authors believe that the proposed model can be especially useful when a large number of simulations is required as, for example, is the case in seismic risk analyses.

REFERENCES

[1] F. G. Rammerstorfer, K. Scharf, and F. D. Fisher. Storage Tanks Under Earthquake Loading. *Applied Mechanics Reviews*, 43:261–282, 2008.

[2] L. Zhou, Y. Fan, B. Gao, and X. Wang. Seismic response analysis of LNG storage tank

under the vertical earthquake excitation. *Applied Mechanics and Materials*, pages 1743–1746, 2013.

[3] G. W. Housner. The dynamic behavior of water tanks. *Bulletin of the Seismological Society of America*, 53(2):381–387, 1963.

[4] P. K. Malhotra, T. Wenk, and M. Wieland. Simple procedure for seismic analysis of liquid-storage tanks. *Structural Engineering International*, 10(3):197–201, 2000.

[5] G. C. Drosos, A. A. Dimas, and D. L. Karabalis. Discrete Models for Seismic Analysis of Liquid Storage Tanks of Arbitrary Shape and Fill Height. *Journal of Pressure Vessel Technology*, 130(4), 09 2008. ISSN 0094-9930. 041801.

[6] I. P. Christovasilis and A. S. Whittaker. Seismic analysis of conventional and isolated LNG tanks using mechanical analogs. *Earthquake Spectra*, 24:599–616, 2008.

[7] European Commitee for Standardization. EN 1998-4:2006 - Eurocode 8: Design of structures for earthquake resistance - Part 4: Silos, tanks and pipelines. *Eurocode 8: Desing of structures for earthquake resistance*, 4(2006):84, 2006.

[8] M. Amabili. Ritz method and substructuring in the study of vibration with strong fluid-structure interaction. *Journal of Fluids and Structures*, 11:507–523, 1997.

[9] M. Amabili, M. P. Paidoussis, and A. A. Lakis. Vibrations of partially filled cylindrical tanks with ring-stiffeners and flexible bottom. *Journal of Sound and Vibration*, 213:259–299, 1998.

[10] Gao Lin, Zejun Han, and Jianbo Li. An efficient approach for dynamic impedance of surface footing on layered half-space. *Soil Dynamics and Earthquake Engineering*, 49: 39–51, 2013. ISSN 02677261.

[11] A.W. Leissa. *Vibration of Plates*. NASA SP. Scientific and Technical Information Division, National Aeronautics and Space Administration, 1969.

[12] W. Soedel. *Vibrations of Shells and Plates*. McGraw-Hill professional engineering: Mechanical engineering. M. Dekker, 1981. ISBN 9780824711931.

[13] J. P. Wolf. *Dynamic soil-structure interaction*. Prentice-Hall, Englewood Cliffs, 1985. ISBN 0-13-221565-9.

[14] A. Tsouvalas and A. V. Metrikine. Seismic response of the outer shell of a liquefied natural gas storage tank using a semi-analytical dynamic substructuring technique. *International Journal of Earthquake and Impact Engineering*, 1(1-2):98–130, 2016.

[15] J. Habenberger. Fluid damping of cylindrical liquid storage tanks. *SpringerPlus*, 4(1):515, 2015. ISSN 2193-1801.

[16] A. Tsouvalas and A.V. Metrikine. A three-dimensional vibroacoustic model for the prediction of underwater noise from offshore pile driving. *Journal of Sound and Vibration*, 333(8):2283 – 2311, 2014. ISSN 0022-460X.

[17] J. L. Tassoulas. *Elements for the numerical analysis of wave motion in layered media*. Ph.d. thesis, Massachusetts Institute of Technology, 1981.

[18] A. Pais and E. Kausel. Approximate formulas for dynamic stiffnesses of rigid foundations. *Soil Dynamics and Earthquake Engineering*, 7(4):213 – 227, 1988. ISSN 0267-7261.

[19] A. Tsouvalas, K. N. van Dalen, and A. V. Metirikne. The significance of the evanescent spectrum in structure-waveguide interaction problems. *The Journal of the Acoustical Society of America*, 138(4):2574–2588, 2015.

[20] COMSOL Multiphysics®. *www.comsol.com*. Stockholm, Sweden, 2015.

EURODYN 2020
XI International Conference on Structural Dynamics
M. Papadrakakis, M. Fragiadakis, C. Papadimitriou (eds.)
Athens, Greece, 23-26 November 2020

APPLICATION OF THE WAVE FINITE ELEMENT METHOD TO MULTI-SPAN BRIDGES

G. Paratore[2], T. Hoang[1], G. Foret[1], M.P. Limongelli[3], and D. Duhamel[1]

[1]Ecole des Ponts ParisTech
Champs sur Marne, France
e-mail: {denis.duhamel,tien.hoang,gilles.foret}@enpc.fr

[2]Politecnico di Torino
Torino, Italy
e-mail: gabriele.paratore@studenti.polito.it

[3]Politecnico di Milano
Milano, Italy
e-mail: mariagiuseppina.limongelli@polimi.it

Keywords: Wave Finite Element, support, bridge, dynamics.

Abstract. *The Wave Finite Element (WFE) method is based on wave propagation in periodic structures. Starting from a Finite Element (FE) analysis of a single period (sub-structure) we are able to derive the dynamic behaviour relative to the entire structure. Thanks to a reduction in the degrees of freedom (dofs) of the system and by decomposing the response of the structure on a wave basis, the calculation time is considerably reduced compared to the classic FEM. Numerous structures have been solved with this method but it can not deal easily on the boundary conditions. In this study, we develop a technique of WFE to deal with more general cases of structures constrained in a arbitrary manner as a multiple supported bridge. By using the WFE method, the vectors of dofs and loads will be decomposed on the wave basis in function of loads and reaction forces of the supports. Then, by substituting the boundary condition in this wave decomposition, we obtain a relation between the reaction forces and the loads which permits to calculate the structure response. The numerical applications show that the WFE and FEM agree well and the new method permits to reduce significantly the calculation time.*

1 INTRODUCTION

The Wave Finite Element (WFE) is a powerful numerical method that allows to drastically reduce the number of degrees of freedom of a structural model providing a great advantage in terms of computational time. This method has been developed for periodic structures where the geometry repeats itself in a certain direction, and is based on wave propagation. The objective is to compute the wave modes which constitute a base that, similarly to the eigen modes often used in the dynamic analysis, can be used to decompose the structural response in terms of forces and displacements at the considered degrees of freedom. The wave modes are characteristics of the elementary periodic element therefore they can be computed by solving an eigenvalues problem consistently formulated for this element. According to the approach proposed by Duhamel et al. [1, 2, 3] the periodic element can be modelled using the conventional finite element method to retrieve its mass, stiffness and damping matrices. In this approach, these matrices are then used to obtain the dynamic stiffness of the cell in the frequency domain and the theory of periodic structure is used to build the dynamic stiffness matrix of the whole structure. Once the wave base has been determined for the period of the structure and the dynamic problem formulated in terms of this base, the solution of the dynamic equation can be carried out by imposing the boundary conditions. This approach has been followed in Hoang et al. [4] that proposed the wave approach, based on the computation of the dynamic response as the sum of different wave contributions generated by the forces acting on the structure. In previous studies [4, 5], the WFE has been applied considering constrains applied only at the ends of the structure or included inside the periodic element, as for the case of railway tracks. The objective of this paper is to extend the application of the WFE to the study of the dynamic response of multi-supported periodic structures, including the possibility to account for different types of boundary conditions. The extension proposed in this paper allows to analyse structures, such as bridges, whose supports may be of different types and are not necessarily equally spaced. The paper is structured in four sections. The second is dedicated to the introduction of the WFE starting from the type of structures considered in the study and the approaches of resolution. The third section contains the original part of this paper dealing with the analytical formulation of the WFE of a periodic structure with multiple intermediate supports. Finally, in the fourth section the numerical results will be presented with reference to a number of case studies.

2 WAVE FINITE ELEMENT

2.1 Discrete formulation

A periodic system consists of a number of identical elements, in terms of geometric shape, physical properties, boundary conditions, and connections with other substructures, coupled together to form the whole system, see Figure (1). Using the FE method, the generic element is modelled and two types of nodes can be defined: *internal nodes* and *boundary nodes*. The boundary nodes are in turn divided into *left nodes* and *right nodes* with d *degrees of freedom* (dofs) for each side. The kinematic behaviour of the system is described by the column vector of nodal displacements $\mathbf{q}$ which number of components is equal to the total number of dofs of the substructure. On the other hand, the respective nodal forces are described by the column vector $\mathbf{F}$. Their relation is given by the discrete equation of motion:

$$(\mathbf{K} + i\omega\mathbf{C} - \omega^2\mathbf{M})\mathbf{q}(\omega) = \mathbf{D}(\omega)\mathbf{q}(\omega) = \mathbf{F}(\omega) \tag{1}$$

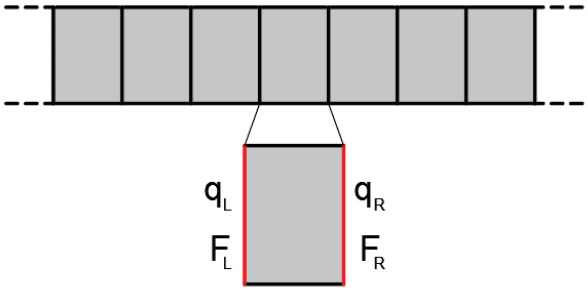

Figure 1: General substructure.

where $\mathbf{D}$ is the *dynamic stiffness matrix* (DSM), and $\mathbf{M}$, $\mathbf{C}$ and $\mathbf{K}$ are respectively the Mass, Dumping and Stiffness Matrix. The dynamic equation can be rewritten in the expanded form in order to separate the degrees of freedom into left (L), inner (I) and right (R) ones.

$$\begin{bmatrix} \mathbf{D}_{LL} & \mathbf{D}_{LI} & \mathbf{D}_{LR} \\ \mathbf{D}_{IL} & \mathbf{D}_{II} & \mathbf{D}_{IR} \\ \mathbf{D}_{RL} & \mathbf{D}_{RI} & \mathbf{D}_{RR} \end{bmatrix} \begin{bmatrix} \mathbf{q}_L \\ \mathbf{q}_I \\ \mathbf{q}_R \end{bmatrix} = \begin{bmatrix} \mathbf{F}_L \\ \mathbf{F}_I \\ \mathbf{F}_R \end{bmatrix} \tag{2}$$

Writing the inner degrees of freedom $\mathbf{q}_I$ in function of the boundary dofs $\mathbf{q}_R$ and $\mathbf{q}_L$, we can reduce the inner nodes in order to obtain a condensed form of the dynamic stiffness matrix.

$$\begin{bmatrix} \bar{\mathbf{D}}_{LI}\mathbf{F}_I \\ \bar{\mathbf{D}}_{RI}\mathbf{F}_I \end{bmatrix} + \begin{bmatrix} \bar{\mathbf{D}}_{LL} & \bar{\mathbf{D}}_{LR} \\ \bar{\mathbf{D}}_{RL} & \bar{\mathbf{D}}_{RR} \end{bmatrix} \begin{bmatrix} \mathbf{q}_L \\ \mathbf{q}_R \end{bmatrix} = \begin{bmatrix} \mathbf{F}_L \\ \mathbf{F}_R \end{bmatrix} \tag{3}$$

Where,

$$\bar{\mathbf{D}}_{LL} = \mathbf{D}_{LL} - \mathbf{D}_{LI}\mathbf{D}_{II}^{-1}\mathbf{D}_{IL},\ \bar{\mathbf{D}}_{LR} = \mathbf{D}_{LR} - \mathbf{D}_{LI}\mathbf{D}_{II}^{-1}\mathbf{D}_{IR},\ \bar{\mathbf{D}}_{RL} = \mathbf{D}_{RL} - \mathbf{D}_{RI}\mathbf{D}_{II}^{-1}\mathbf{D}_{IL}$$
$$\bar{\mathbf{D}}_{RR} = \mathbf{D}_{RR} - \mathbf{D}_{RI}\mathbf{D}_{II}^{-1}\mathbf{D}_{IR},\ \bar{\mathbf{D}}_{LI} = \mathbf{D}_{LI}\mathbf{D}_{II}^{-1},\ \bar{\mathbf{D}}_{RI} = \mathbf{D}_{RI}\mathbf{D}_{II}^{-1}$$

Considering two consecutive substructures (n) and $(n+1)$, two fundamental conditions must be always satisfied: continuity of the displacement along the junction $\mathbf{q}_R^{(n)} = \mathbf{q}_L^{(n+1)}$, equilibrium of the forces acting in the junction: $\mathbf{F}_R^{(n)} + \mathbf{F}_L^{(n+1)} = \mathbf{F}_B^{(n)}$. These equations can be manipulated in order to write the terms regarding substructure $(n+1)$ in function of those regarding the preceding substructure (n).

$$\begin{bmatrix} \mathbf{q}_L^{(n+1)} \\ -\mathbf{F}_L^{(n+1)} \end{bmatrix} = \mathbf{S} \begin{bmatrix} \mathbf{q}_L^{(n)} \\ -\mathbf{F}_L^{(n)} \end{bmatrix} + \begin{bmatrix} \bar{\mathbf{D}}_{qI}\mathbf{F}_I^{(n)} \\ \bar{\mathbf{D}}_{fI}\mathbf{F}_I^{(n)} - \mathbf{F}_B^{(n)} \end{bmatrix} \tag{4}$$

Where, $\mathbf{S}$ is the *transfer matrix* given by:

$$\mathbf{S} = \begin{bmatrix} -\bar{\mathbf{D}}_{LR}^{-1}\bar{\mathbf{D}}_{LL} & -\bar{\mathbf{D}}_{LR}^{-1} \\ \bar{\mathbf{D}}_{LR} - \bar{\mathbf{D}}_{RR}\bar{\mathbf{D}}_{LR}^{-1}\bar{\mathbf{D}}_{LL} & -\bar{\mathbf{D}}_{RR}\bar{\mathbf{D}}_{LR}^{-1} \end{bmatrix} \tag{5}$$

with $\bar{\mathbf{D}}_{qI} = -\bar{\mathbf{D}}_{LR}^{-1}\bar{\mathbf{D}}_{LI}$ and $\bar{\mathbf{D}}_{fI} = \bar{\mathbf{D}}_{RI} - \bar{\mathbf{D}}_{RR}\bar{\mathbf{D}}_{LR}^{-1}\bar{\mathbf{D}}_{LI}$.
The nodal displacements $\mathbf{q}^{(n)}$ and the nodal forces $\mathbf{F}^{(n)}$, together describe the state of the substructure. For this reason we define the *state vector* $\mathbf{u}^{(n)}$ of the substructure (n) and $\mathbf{b}^{(n)}$ the vector of external loads acting on the substructure (n) as:

$$\mathbf{u}^{(n)} = \begin{bmatrix} \mathbf{q}_L^{(n)} \\ -\mathbf{F}_L^{(n)} \end{bmatrix}, \quad \mathbf{b}^{(n)} = \begin{bmatrix} \bar{\mathbf{D}}_{qI}\mathbf{F}_I^{(n)} \\ \bar{\mathbf{D}}_{fI}\mathbf{F}_I^{(n)} - \mathbf{F}_B^{(n)} \end{bmatrix} \tag{6}$$

Equation (4) can be written in a more synthetic form:

$$\mathbf{u}^{(n+1)} = \mathbf{S}\mathbf{u}^{(n)} + \mathbf{b}^{(n)} \tag{7}$$

This last equation represents the relation between the generic substructure (n) and its next substructure $(n+1)$ by means of the transfer matrix $\mathbf{S}$. This leads to:

$$\mathbf{u}^{(n)} = \mathbf{S}^{n-1}\mathbf{u}^{(1)} + \sum_{k=1}^{n-1} \mathbf{S}^{n-k-1}\mathbf{b}^{(k)} \tag{8}$$

Equation (8) represents the relation between the state vector of the first substructure and the state vector of the substructure (n). One also has

$$\mathbf{u}^{(N+1)} = \mathbf{S}^{N-n+1}\mathbf{u}^{(n)} + \sum_{k=n}^{N} \mathbf{S}^{N-k}\mathbf{b}^{(k)} \tag{9}$$

2.2 Wave formulation

The wave modes are the eigenvectors solution of

$$\mathbf{S}\begin{bmatrix}\mathbf{q}_L \\ -\mathbf{F}_L\end{bmatrix} = \lambda \begin{bmatrix}\mathbf{q}_L \\ -\mathbf{F}_L\end{bmatrix} \tag{10}$$

Hence, each eigenvalue of the matrix $\mathbf{S}$ provides a propagation constant λ_i while the eigenvector Φ_i represents the wave shapes, namely the way in which the substructure deforms. For each eigenvalue λ_i of eigenvector Φ_i, there is an eigenvalue $1/\lambda_i$ associated to an eigenvector denoted Φ_i^*.

The matrix $\mathbf{S}$ is symplectic meaning that ${}^t\mathbf{S}\mathbf{J}\mathbf{S} = \mathbf{J}$ with $\mathbf{J} = \begin{bmatrix}\mathbf{O} & \mathbf{I} \\ -\mathbf{I} & \mathbf{O}\end{bmatrix}$. The orthogonality properties are such that ${}^t\mathbf{\Phi}^*\mathbf{J}\mathbf{\Phi} = \mathbf{I}$, ${}^t\mathbf{\Phi}^*\mathbf{J}\mathbf{\Phi}^* = {}^t\mathbf{\Phi}\mathbf{J}\mathbf{\Phi} = \mathbf{O}$ with $\mathbf{\Phi} = [\Phi_1, ..., \Phi_d]$.

We can decompose the state vector $\mathbf{u}^{(n)}$ and the load vector $\mathbf{b}^{(n)}$ in the wave base as a combination of positive and negative waves:

$$\begin{aligned} \mathbf{u}^{(n)} &= \mathbf{\Phi}\mathbf{Q}^{(n)} - \mathbf{\Phi}^*\mathbf{Q}^{*(n)} \\ \mathbf{b}^{(n)} &= \mathbf{\Phi}\mathbf{Q}_B^{(n)} - \mathbf{\Phi}^*\mathbf{Q}_B^{*(n)} \end{aligned} \tag{11}$$

Where $\mathbf{Q}^{(n)}$ and $\mathbf{Q}^{*(n)}$ represent the vectors of *wave amplitude* of the positive-going and negative-going waves. The terms $\mathbf{Q}_B^{(n)}$ and $\mathbf{Q}_B^{*(n)}$ are the vectors of wave amplitude generated by the external loads $\mathbf{F}_I^{(n)}$ and $\mathbf{F}_B^{(n)}$. The wave amplitudes of the external loads can be derived from equation (11), by multiplying both sides by $\mathbf{\Phi}^{*T}\mathbf{J}$ as follow:

$$\begin{aligned} \mathbf{\Phi}^{*T}\mathbf{J}\mathbf{b}^{(n)} &= \mathbf{\Phi}^{*T}\mathbf{J}\mathbf{\Phi}\mathbf{Q}_B^{(n)} - \mathbf{\Phi}^{*T}\mathbf{J}\mathbf{\Phi}^*\mathbf{Q}_B^{*(n)} \\ &= \mathbf{Q}_B^{(n)} \\ &= (\mathbf{\Phi}_q^{*T}\bar{\mathbf{D}}_{fI} - \mathbf{\Phi}_F^{*T}\bar{\mathbf{D}}_{qI})\mathbf{F}_I^{(n)} - \mathbf{\Phi}_q^{*T}\mathbf{F}_B^{(n)} \end{aligned} \tag{12}$$

The same thing can be done to compute the value of $\mathbf{Q}_B^{*(k)}$. Multiplying both sides by $\mathbf{\Phi}^T\mathbf{J}$:

$$\begin{aligned} \mathbf{\Phi}^{T}\mathbf{J}\mathbf{b}^{(n)} &= \mathbf{\Phi}^{T}\mathbf{J}\mathbf{\Phi}\mathbf{Q}_B^{(n)} - \mathbf{\Phi}^{T}\mathbf{J}\mathbf{\Phi}^*\mathbf{Q}_B^{*(n)} \\ &= \mathbf{Q}_B^{*(n)} \\ &= (\mathbf{\Phi}_q^{T}\bar{\mathbf{D}}_{fI} - \mathbf{\Phi}_F^{T}\bar{\mathbf{D}}_{qI})\mathbf{F}_I^{(n)} - \mathbf{\Phi}_q^{T}\mathbf{F}_B^{(n)} \end{aligned} \tag{13}$$

3 WFE FOR STRUCTURES WITH SEVERAL SUPPORTS

3.1 Derivation of the intermediate reactions

In this section, a technique of WFE will be developed to deal with more general cases of structures constrained in a arbitrary manner as a multiple supported bridge. By convention, the constrain can be placed only in the junction between two substructures. If we consider the reactions as external forces acting on the structure, from the equilibrium of external forces and internal forces we have:

$$\mathbf{F}_R^{(k)} + \mathbf{F}_L^{(k+1)} = \mathbf{F}_{ext}^{(k)} + \mathbf{R}^{(k)} \tag{14}$$

Hence this time $\mathbf{F}_B$ is given by:

$$\mathbf{F}_B^{(k)} = \mathbf{F}_{ext}^{(k)} + \mathbf{R}^{(k)} \tag{15}$$

The wave amplitudes can be expressed in function of the external loads $\mathbf{F}_{ext}^{(k)}$ and reactions $\mathbf{R}^{(k)}$ as follows from (12) and (13):

$$\mathbf{Q}_B^{(k)} = (\mathbf{\Phi}_q^{*T}\bar{\mathbf{D}}_{fI} - \mathbf{\Phi}_F^{*T}\bar{\mathbf{D}}_{qI})\mathbf{F}_I^{(k)} - \mathbf{\Phi}_q^{*T}(\mathbf{F}_{ext}^{(k)} + \mathbf{R}^{(k)}) \tag{16}$$

$$\mathbf{Q}_B^{*(k)} = (\mathbf{\Phi}_q^{T}\bar{\mathbf{D}}_{fI} - \mathbf{\Phi}_F^{T}\bar{\mathbf{D}}_{qI})\mathbf{F}_I^{(k)} - \mathbf{\Phi}_q^{T}(\mathbf{F}_{ext}^{(k)} + \mathbf{R}^{(k)}) \tag{17}$$

The sum (8) can be written as

$$\mathbf{\Phi}\mathbf{Q}^{(n)} - \mathbf{\Phi}^*\mathbf{Q}^{*(n)} = \mathbf{S}^{n-1}\left(\mathbf{\Phi}\mathbf{Q}^{(1)} - \mathbf{\Phi}^*\mathbf{Q}^{*(1)}\right) + \sum_{k=1}^{n-1}\mathbf{S}^{n-k-1}\left(\mathbf{\Phi}\mathbf{Q}_B^{(k)} - \mathbf{\Phi}^*\mathbf{Q}_B^{*(k)}\right) \tag{18}$$

Multiplying by $\mathbf{\Phi}^{*T}\mathbf{J}$, using $\boldsymbol{\mu} = [\lambda_1, ..., \lambda_d]$, this gives

$$\mathbf{Q}^{(n)} = \boldsymbol{\mu}^{n-1}\mathbf{Q}^{(1)} + \sum_{k=1}^{n-1}\boldsymbol{\mu}^{n-k-1}\mathbf{Q}_B^{(k)} \tag{19}$$

In the same way, from (9), one has

$$\mathbf{Q}^{*(N+1)} = \boldsymbol{\mu}^{*N-n+1}\mathbf{Q}^{*(n)} + \sum_{k=n}^{N}\boldsymbol{\mu}^{*N-k}\mathbf{Q}_B^{*(k)} \tag{20}$$

with $\boldsymbol{\mu}^* = \boldsymbol{\mu}^{-1}$. We get

$$\mathbf{Q}^{*(n)} = \boldsymbol{\mu}^{N+1-n}\mathbf{Q}^{*(N+1)} - \sum_{k=n}^{N}\boldsymbol{\mu}^{k+1-n}\mathbf{Q}_B^{*(k)} \tag{21}$$

If we call $\mathbf{R}^{(n_s)}$ the vector of reaction corresponding to the constrain s placed in n_s, the state vector is given as follow using (11):

$$\begin{aligned}\mathbf{u}^{(n)} = \mathbf{\Phi}\boldsymbol{\mu}^{n-1}\mathbf{Q}^{(1)} - \mathbf{\Phi}^*\boldsymbol{\mu}^{N+1-n}\mathbf{Q}^{*(N+1)} + \mathbf{T}^{(n)} + \\ - \mathbf{\Phi}\sum_{n_s<n}\boldsymbol{\mu}^{n-1-n_s}\mathbf{\Phi}_q^{*T}\mathbf{R}^{(n_s)} + \mathbf{\Phi}^*\sum_{n_s\geq n}\boldsymbol{\mu}^{n_s+1-n}\mathbf{\Phi}_q^{T}\mathbf{R}^{(n_s)}\end{aligned} \tag{22}$$

$\mathbf{T}^{(n)}$ gathers all the known terms obtained from $\mathbf{F}_{ext}^{(k)}$ and $\mathbf{F}_I^{(k)}$.

3.2 Boundary conditions

The application of the conditions can be written in a synthetic way at support s as:

$$\mathbf{L}_s \mathbf{u}^{(n_s)} = \mathbf{B}_s \tag{23}$$

The matrix $\mathbf{L}_s$ is a *logical matrix* or $(0, 1)$ *matrix*. It can assume different forms depending on the type of constrain and his position along the structure. For a one-dimensional beam and a fixed support, $\mathbf{L}_s$ is given by:

$$\mathbf{L}_s = \begin{bmatrix} 1 & 0 & 0 & 0 & 0 & 0 \\ 0 & 1 & 0 & 0 & 0 & 0 \\ 0 & 0 & 1 & 0 & 0 & 0 \end{bmatrix}$$

The index matrix $\mathbf{L}_s$ for two-dimensional and three-dimensional structures is not so easy to find. The strategy used is to construct the matrix $\mathbf{L}_s$ by means of sub-matrices that subsequently can be assembled. For multiple node junctions, the column state vector is composed by the d nodal displacements followed by the d nodal forces. The Matrix $\mathbf{L}_s$, that multiplies the state vector (see equation (23)) can be seen as the composition of two square sub-matrices $\mathbf{L}_q$ and $\mathbf{L}_F$ that apply to displacements and forces respectively:

$$\mathbf{L}_s \mathbf{u}^{(n_s)} = \left[\begin{array}{c|c} \mathbf{L}_q & \mathbf{L}_F \end{array} \right] \begin{bmatrix} \{\mathbf{q}\} \\ \\ \{\mathbf{F}\} \\ \\ \end{bmatrix} \tag{24}$$

The matrices $\mathbf{L}_q$ and $\mathbf{L}_F$, in turn, consist of sub-matrices, corresponding to each node, named $\mathbf{L}_{q,sub}$ and $\mathbf{L}_{F,sub}$. These sub-matrices are square, identical for every node and depend on the kind of support. Their dimensions correspond to the number of dof for each node.

$$\mathbf{L}_q = \begin{bmatrix} \mathbf{L}_{q,sub} & & \\ & \ddots & \\ & & \mathbf{L}_{q,sub} \end{bmatrix}, \quad \mathbf{L}_F = \begin{bmatrix} \mathbf{L}_{F,sub} & & \\ & \ddots & \\ & & \mathbf{L}_{F,sub} \end{bmatrix} \tag{25}$$

The sub-matrices $\mathbf{L}_{q,sub}$ and $\mathbf{L}_{F,sub}$ have to be constructed for every type of structure (beam, shell, plates, etc.) from whom the number of dof per node depends. The boundary conditions are denoted by the column vector $\mathbf{B}_s$, where the subscript refers to the respective constrain s. Each component represents the admitted displacement of each dof. The vector $\mathbf{B}_s$ depend on the type of constrain:

- rigid constrains: $\mathbf{B}_s = [\mathbf{0}]$
- elastic constrain: $\mathbf{B}_s \neq [\mathbf{0}]$

3.3 Solution of the problem

In order to apply the boundary conditions, equation (22) has to be multiplied for the index matrix $\mathbf{L}_s$ and equalled to the vector $\mathbf{B}_s$. For each support s, the boundary conditions can be written as $\mathbf{B}_s = \mathbf{L}_s \mathbf{u}^{(n_s)}$ so that:

$$\begin{aligned} \mathbf{L}_s \mathbf{\Phi} \boldsymbol{\mu}^{n_s - 1} \mathbf{Q}^{(1)} - \mathbf{L}_s \mathbf{\Phi}^* \boldsymbol{\mu}^{N+1-n_s} \mathbf{Q}^{*(N+1)} + \mathbf{L}_s \mathbf{T}^{(n_s)} + \\ - \mathbf{L}_s \mathbf{\Phi} \sum_{n_i < n_s} \boldsymbol{\mu}^{n_s - 1 - n_i} \mathbf{\Phi}_q^{*T} \mathbf{R}^{(n_i)} + \mathbf{L}_s \mathbf{\Phi}^* \sum_{n_i \geq n_s} \boldsymbol{\mu}^{n_i + 1 - n_s} \mathbf{\Phi}_q^{T} \mathbf{R}^{(n_i)} = \mathbf{B}_s \end{aligned} \tag{26}$$

The next step consists in replacing the vector $\mathbf{R}^{(n_i)}$ with the expression $\mathbf{L}_i^T\tilde{\mathbf{R}}^{(n_i)}$ in order to consider only the non zero components of the reaction. For a notation issue, the following assumption are made:

$$\mathbf{\Phi}_s = \mathbf{L}_s\mathbf{\Phi}; \quad \mathbf{\Phi}_s^* = \mathbf{L}_s\mathbf{\Phi}^\star \tag{27}$$

Finally:

$$\begin{aligned}\mathbf{\Phi}_s\boldsymbol{\mu}^{n_s-1}\mathbf{Q}^{(1)} - \mathbf{\Phi}_s \sum_{n_i<n_s} \boldsymbol{\mu}^{n_s-1-n_i}\mathbf{\Phi}_i^{*T}\tilde{\mathbf{R}}^{(n_i)} \\ + \mathbf{\Phi}_s^* \sum_{n_i\geq n_s} \boldsymbol{\mu}^{n_i+1-n_s}\mathbf{\Phi}_i^T\tilde{\mathbf{R}}^{(n_i)} - \mathbf{\Phi}_s^*\boldsymbol{\mu}^{N+1-n_s}\mathbf{Q}^{*(N+1)} = \mathbf{B}_s - \mathbf{L}_s\mathbf{T}^{(n_s)}\end{aligned} \tag{28}$$

Equation (28) can be written for every constrain s, leading to a system of linear equations in the form:

$$\mathbf{AX} = \mathbf{F} \tag{29}$$

The vector of the unknowns is:

$$\mathbf{X} = \begin{bmatrix} \mathbf{Q}^{(1)} \\ \tilde{\mathbf{R}}^{(n_1)} \\ \vdots \\ \tilde{\mathbf{R}}^{(n_s)} \\ \vdots \\ \tilde{\mathbf{R}}^{(n_S)} \\ \mathbf{Q}^{*(N+1)} \end{bmatrix} \tag{30}$$

Once matrix $\mathbf{A}$ and vector $\mathbf{F}$ are defined, it is possible to solve the problem:

$$\mathbf{X} = \mathbf{A}^{-1}\mathbf{F} \tag{31}$$

Replacing the reactions $\mathbf{R}$ and wave amplitudes $\mathbf{Q}^{(1)}$ and $\mathbf{Q}^{*(N+1)}$ in equation (22), the response of the entire periodic structure is obtained.

4 APPLICATIONS

In order to validate this technique, two applications have been developed. The two structures will present different dimensions and types of constraints placed in an arbitrary manner. For each application the frequency response function (FRF) of the structure will be calculated with respect to a specific point. To confirm the results, every problem will be solved both by the FE method and the WFE method. Furthermore, for both methods the calculation time will be given so that the efficiency can be compared. The general procedure consists in dividing the structure into a certain number of identical substructures. Using the software Abaqus, the substructure is modelled and the stiffness and mass matrix obtained. By importing this data, the problem can be solved by the software Matlab. In fact, from the stiffness and mass matrix it is possible to obtain the dynamic stiffness matrix and the transfer matrix $\mathbf{S}$.

4.1 1D Beam

The structure considered is the multi supported beam represented in Figure (2) with $L = 50m$. The objective of this application is to demonstrate the possibility of considering different types of constrained not necessarily equispaced.

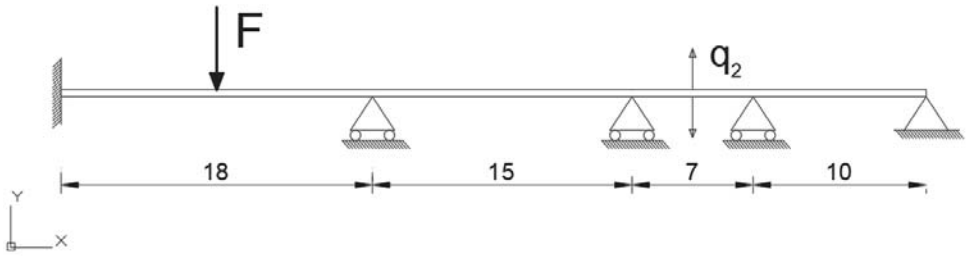

Figure 2: Multi-supported beam

The section of the beam is a IPE 400, see Figure (7) and Table (3). The external force is a vertical point force and acts to the middle of the first span. His value is $F = 5\,kN$. The material considered is steel and the mechanical properties are summarized in Table (1).

Steel	
Density	$d = 7850\,kg/m^3$
Elastic modulus	$E = 210\,GPa$
Poisson modulus	$\nu = 0.3$

Table 1: Mechanical properties of steel.

The beam is composed by 220 substructures of length $l = 0.2m$ with 33 dofs by period and 6603 dofs in the whole structure. The type of element is a 2-node linear beam in a plane. In Figure (3) are reported the results of the analysis. The results match perfectly. The computational time is drastically reduced being $49.31s$ for FEM and $5.57s$ for WFEM.

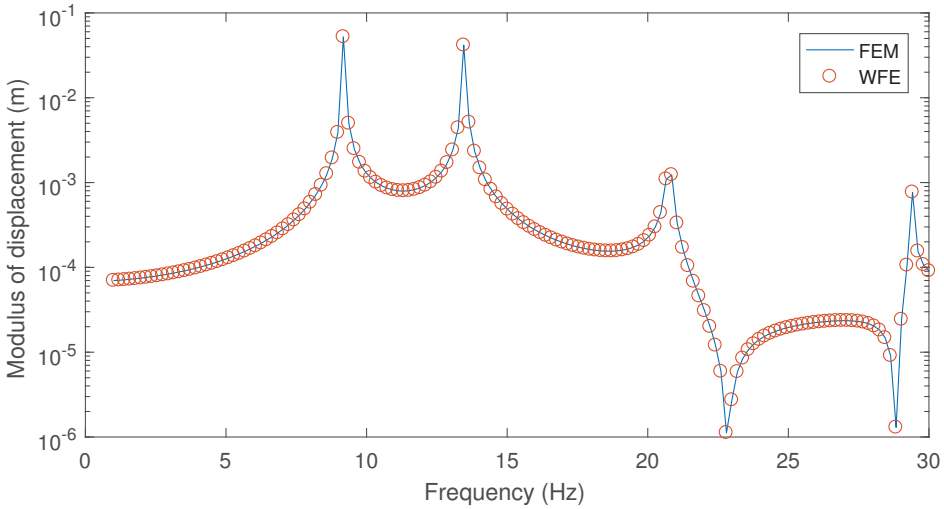

Figure 3: Frequency response function. Logarithm of the modulus of the displacement in function of the frequency.

4.2 Multi-supported bridge

In this section, the dynamic behaviour of a multi-supported bridge is studied. The total length is $L = 120m$. The bridge is fixed to the ends and supported by two equispaced roller supports.

The maximum span is $L_{span} = 40m$. The longitudinal scheme of the bridge is represented in Figure (4). The bridge presents a box-beam deck which dimensions are represented in Figure

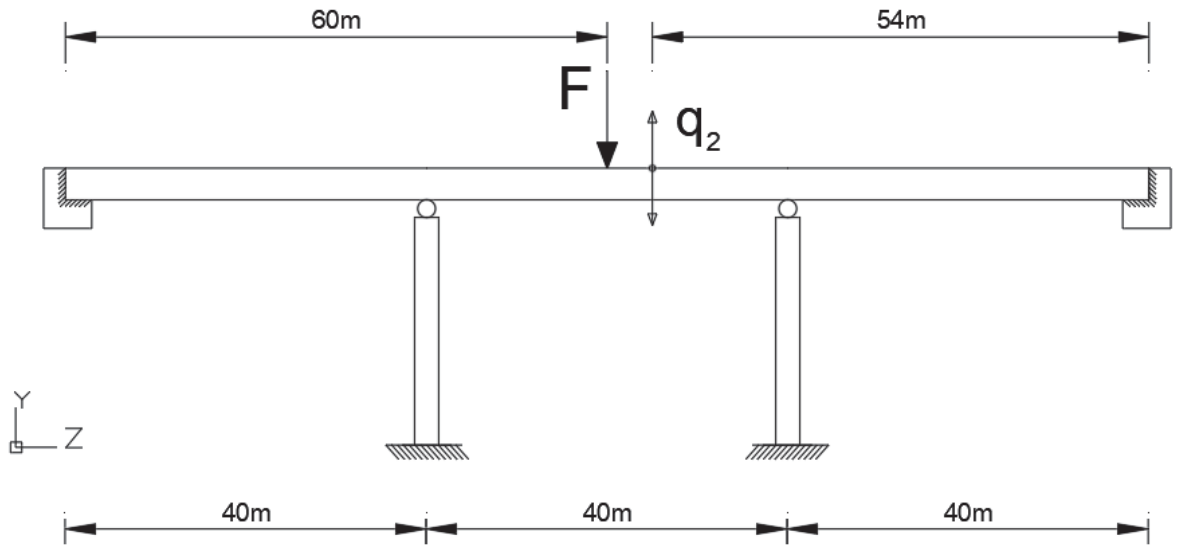

Figure 4: Multi-supported bridge

(5). The external force is a vertical point force and acts to the middle of the structure; its value

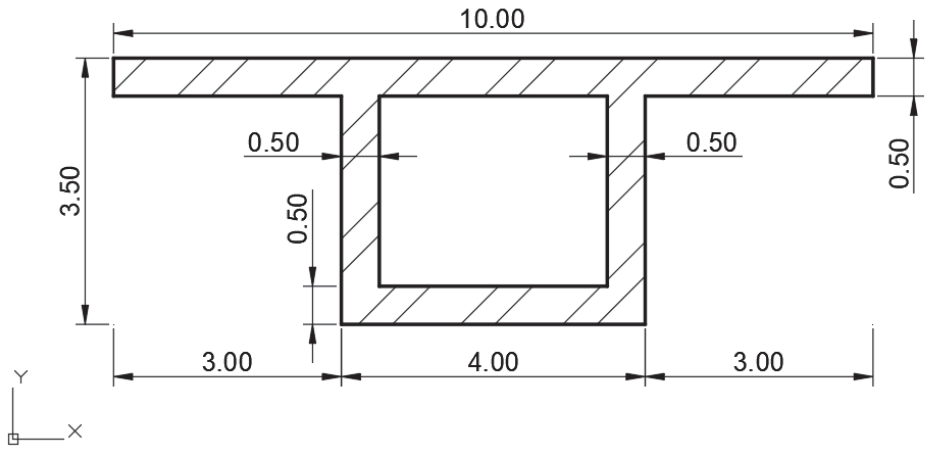

Figure 5: Section of the bridge (m).

is $F = 10\,kN$. The position is at the right upper corner of Figure (5). The response is also computed at the right upper corner. The material considered is concrete and the mechanical property are summarized in Table (2).

The bridge is composed by 480 substructures of length $l = 0.25m$ with 1368 dofs by period and 329004 dofs in the whole structure. The substructure has been modelled by a 8-node linear brick of dimensions $0.25m$. The FRF has been computed every $0.15\,Hz$ in the range of frequencies $0 - 30\,Hz$. The result obtained by applying the WFE method and showed in Figure (6) matches with the one obtained with the FEM. Moreover the computational time is halved being 204 minutes for FEM and 100 minutes for WFEM equivalent to 51% of time reduction.

HP Concrete	
Density	$d = 2500\,kg/m^3$
Elastic modulus	$E = 48\,GPa$
Poisson modulus	$\nu = 0.2$

Table 2: Physical and Mechanical characteristic of concrete.

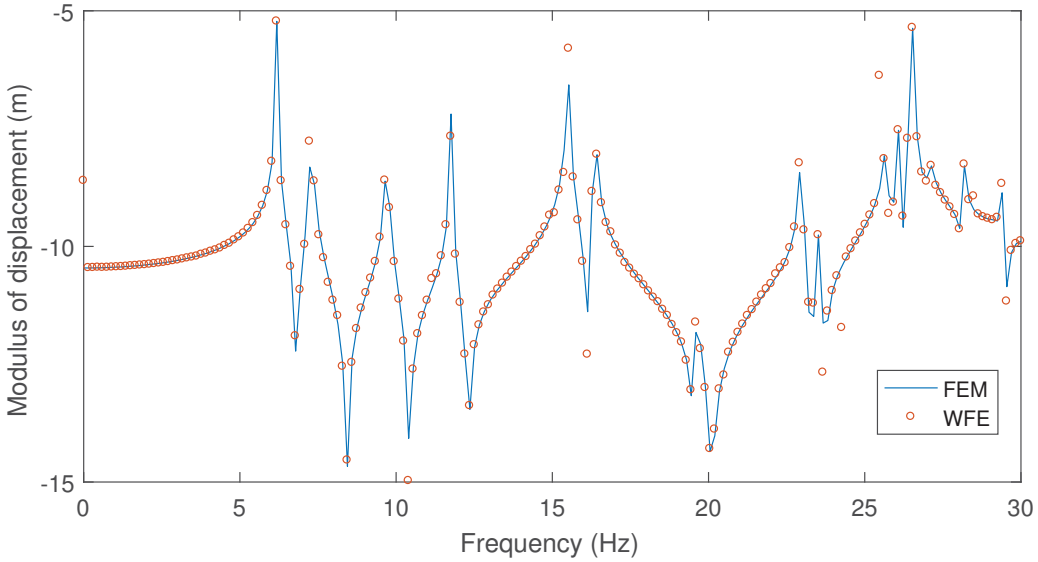

Figure 6: FRF of the bridge. Comparison between the WFEM (o) and the FEM (-)

5 CONCLUSIONS

As already mentioned, the WFE method has proved to be an excellent calculation tool to obtain results in a definitely shorter time compared to FEM. The proposed technique, that can be seen as a way to impose the boundary conditions, is simple but at the same time very effective. It is important to highlight the high efficiency in terms of time reduction and memory used during the computation. Finally, through practical applications, we have validated the method by finding results that coincide with the FEM but with the advantages of obtaining a computational time that in the worst case is halved.

IPE 400	
h	$400\,mm$
b	$180\,mm$
t_w	$8.6\,mm$
t_f	$\nu = 13.5\,mm$

Table 3: Dimensions of IPE 400 section

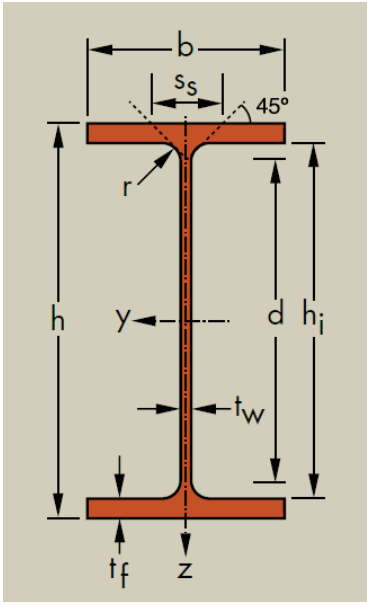

Figure 7: IPE 400

REFERENCES

[1] D. Duhamel, B.R. Mace, M.J. Brennan, Finite element analysis of the vibrations of waveguides and periodic structures, *Journal of sound and vibration*, **294**(1-2), 205-220, 2006

[2] B. Mace, D. Duhamel, M. Brennan, L. Hinke, Finite element prediction of wave motion in structural waveguides, *The Journal of the Acoustical Society of America*, **117**, 2835-43, 2005

[3] J.M. Mencik, D. Duhamel, A wave-based model reduction technique for the description of the dynamic behavior of periodic structures involving arbitrary-shaped substructures and large-sized finite element models, *Finite Elements in Analysis and Design*, **101**, 1-14, 2015

[4] T. Hoang, D. Duhamel, G. Foret, *Wave finite element method for vibration of periodic structures subjected to external loads, 6th European Conference on Computational Mechanics (ECCM 6), June 2018, Glasgow, United Kingdom*

[5] T. Hoang, D. Duhamel, G. Foret, J.L Pochet, F. Sabatier, *Wave finite element method and moving loads for the dynamic analysis of railway tracks, 13th World Congress on Computational Mechanics (WCCM XIII), Jul 2018, New York, United States*

EURODYN 2020
XI International Conference on Structural Dynamics
M. Papadrakakis, M. Fragiadakis, C. Papadimitriou (eds.)
Athens, Greece, 23-26 November 2020

A VARIATIONAL APPROACH TO ASYNCHRONOUS TIME-INTEGRATION OF STRUCTURAL DYNAMICS PROBLEMS IN THE CONTEXT OF FETI AND SPURIOUS OSCILLATIONS ON THE INTERFACES

Andreas S. Seibold[1], **Daniel J. Rixen**[2]

[1]Technichal University of Munich
Boltzmannstraße 15
85748 Garching, Germany
e-mail: andreas.seibold@tum.de

[2] Technichal University of Munich
Boltzmannstraße 15
85748 Garching, Germany
e-mail: rixen@tum.de

Keywords: domain decomposition, time-integration, FETI, asynchronous, multirate, multi-time-step, variational

Abstract. *In this contribution we derive a nonlinear version of the BGC-macro asynchronous time-integration method and investigate the resulting spurious oscillations on the interface, resulting from the coupling on a course time-grid. The main difference to the nonlinear PH-method lies in a different coupling condition, which is only based on the coupling of velocities by Lagrange-Multipliers. We give a brief introduction to our implementation in our in-house developed open-source software AMfe and PyFETI. Afterwards we address the possibility of wave-reflections on the interfaces in certain cases. In the last part of the paper we derive a different asynchronous coupling-method from the variational principle utilizing a generalized midpoint-rule. Due to weak instabilities, when the constraint is formulated on displacment-level, we modify the arising condition such that it is enforced on velocity-level but still represents an energy with the interface-forces. As a prove of concept and for comparability to the BGC-macro method we only use a coarse discretization of the Lagrange-Multiplier-field. Then we show that spurious oscillations couldn't be eliminated in our special test-case, due to that coarse discretization, but incompatibilities in the displacements-filed were smoothed. The amplitude of energy-oscillations is kept similar compared to the BGC-macro method.*

1 INTRODUCTION

When it comes to parallelization of large structural dynamics simulations, domain decomposition methods are widely used in Finite Elements codes. One family of such domain decomposition techniques are the Finite Elements Tearing and Interconnecting (FETI)-methods, originally proposed by Farhat e.a. [2] for linear static structures. Later they've been extended to nonlinear dynamic problems and equipped with efficient preconditioning and recycling-techniques [4, 5, 9]. Things get more troublesome with local highly nonlinear phenomena, as load-balancing becomes an issue and the portion of communication increases. One approach to improve efficiency is a localization approach, where local nonlinear problems are solved [13]. A different idea is the adaptation of the time-step to the physics of each substructure and saving unnecessary computations. Originally the GC-method has been proposed, which allows subcycling on one substructure and enforces compatibility on the small time-steps [6]. Although both this method and its extension to α-integration-schemes, the BGC-micro method [1], share the characteristic that they are derived from a pseudo-energy method, they dissipate energy on the interface. This issue is resolved by non-dissipative methods, that enforce compatibility only at a coarse syncronization time-step, such as the PH- and BGC-macro-methods [14, 1]. However, these methods lead to spurious oscillations on the interface, as shown by Prakash and Hjelmstad [15]. Despite these oscillations it has been shown for a sandwitch-beam with an impact-load, that this asynchronous approach leads to less computations for a nonlinear impact-simulation compared to a completely fine time-discretization and a model, that is decomposed into two subdomains [15]. So the goal of future work is to transfer this computational efficiency to a FETI-solver while avoiding spurious oscillations and conserving energy. A different approach is to derive methods from the variational principle or Hamilton's principle. That approach is well known in structural dynamics from the derivation of differential equations of motion. In the discrete case, this approach can be used to derive time-integration-schemes, that conserve linear and angular momentum and are symplectic and have energy-oscillations bounded, such as the non-dissipative Newmark-β scheme [8]. This technique can also be extended to asynchronous or multirate cases, as it has been done by Leyendecker and Ober-Blöbaum, but instead of spacial decomposition, the separation of dynamics with respect to their speeds is used [12]. In Wenger e.a. higher order variational integrators for synchronous constrained systems have been constructed with a more generalized discretization of the displacements and Lagrange-Multipliers via polynomials in time [16]. In the following chapters we extend the BGC-macro method to nonlinear systems for a Newmark-β scheme and compare it with the nonlinear PH-method in terms of spurious oscillations. For that we start with an introduction to FETI for nonlinear structural dynamics in chapter 2. Subsequently we derive the nonlinear BGC-macro and show the possibility of wave-reflections on a disadvantageous example in chapter 3. In the third part of this article, we give an introduction to the variational principle and derive a variational coupling method for asynchronous time-integration over the generalized midpoint-rule in chapter 4.

2 FETI FOR NONLINEAR STRUCTURAL DYNAMICS

2.1 Nonlinear structural dynamics

We consider a nonlinear structural dynamics problem, which differential equation of motion can be described by d'Alembert's principle as

$$\mathbf{M}\ddot{\vec{q}} + \vec{f}_{int}(\vec{q}) - \vec{f}_{ext}(t) = \vec{0} \tag{1}$$

The system's displacements and their time-derivatives, velocities and accelerations, are represented by $\vec{q}$ and $\dot{\vec{q}}$ and $\ddot{\vec{q}}$ respectively. Moreover $\mathbf{M}$ is the mass-matrix, $\vec{f}_{int}$ the internal forces, resulting from the structure's deformation, which can be nonlinear in $\vec{q}$ and $\vec{f}_{ext}$ are the external forces, which might be time-dependent. The previously mentioned FETI-methods utilize a non-overlapping domain-decomposition approach to subdivide the whole domain of our problem or structure into smaller pieces and solve them on separate computing cores [2]. These socalled subdomains or substructures are coupled by Lagrange-Multipliers on the interfaces only. The equations of motion in (1) are therefore described locally on a substructure s

$$\mathbf{M}^{(s)}\ddot{\vec{q}}^{(s)} + \vec{f}_{int}^{(s)}(\vec{q}^{(s)}) + \mathbf{B}^{(s)^T}\vec{\lambda} - \vec{f}_{ext}^{(s)}(t) = \vec{0} \tag{2}$$

and extended by a global compatibility-condition for the accelerations on the interface Γ_λ

$$\sum_{s=1}^{N_s} \mathbf{B}^{(s)}\ddot{\vec{q}}^{(s)} = \vec{0} \tag{3}$$

where $\mathbf{B}$ is a signed Boolean matrix, that condenses the local degrees of freedom on the interface Γ_λ. It has been shown by Farhat e.a., that coupling on the accelerations doesn't cause a drift of the displacements and leads to more stable computations than in case of displacement-coupling [3, 4]. The solution procedure of both equations (2) and (3) now consists of a time-integration scheme, such as the well known Newmark-β scheme

$$\begin{aligned}
\dot{\vec{q}}_{n+1} &= \dot{\vec{q}}_n + (1-\gamma)\Delta t\ddot{\vec{q}}_n + \gamma\Delta t\ddot{\vec{q}}_{n+1} \\
\vec{q}_{n+1} &= \vec{q}_n + \Delta t\dot{\vec{q}}_n + \left(\frac{1}{2} - \beta\right)\Delta t^2\ddot{\vec{q}}_n + \beta\Delta t^2\ddot{\vec{q}}_{n+1}
\end{aligned}$$

with $\beta \in [0, \frac{1}{4}]$ and $\gamma \in [0, \frac{1}{2}]$ being parameters, that tune accuracy and numerical damping of the integration scheme. Hence we have the solutions of the next time-step $n+1$ related to the previous time-step n only. To solve the nonlinear system for the upcoming time-step $n+1$ we can use a Newton-Raphson scheme and linearize equations (2) and (3), resulting in

$$\begin{aligned}
\mathbf{M}^{(s)}\Delta\ddot{\vec{q}}^{(s)} + \frac{\partial\vec{f}_{int}^{(s)}(\vec{q}_{n+1,i}^{(s)})}{\partial\vec{q}^{(s)}}\frac{\partial\vec{q}^{(s)}}{\partial\ddot{\vec{q}}^{(s)}}\Delta\ddot{\vec{q}}^{(s)} + \mathbf{B}^{(s)^T}\Delta\vec{\lambda} + \\
+\mathbf{M}^{(s)}\ddot{\vec{q}}_{n+1,i}^{(s)} + \vec{f}_{int}^{(s)}(\vec{q}_{n+1,i}^{(s)}) + \mathbf{B}^{(s)^T}\vec{\lambda}_{n+1,i} - \vec{f}_{ext}^{(s)}(t_{n+1}) &= \vec{0} \qquad (4) \\
\sum_{s=1}^{N_s}\mathbf{B}^{(s)}\Delta\ddot{\vec{q}}^{(s)} + \mathbf{B}^{(s)}\ddot{\vec{q}}_{n+1,i}^{(s)} &= \vec{0} \qquad (5)
\end{aligned}$$

with i being the Newton-iteration's index and the Newton-updates

$$\begin{aligned}
\ddot{\vec{q}}_{n+1,i+1}^{(s)} &= \ddot{\vec{q}}_{n+1,i}^{(s)} + \Delta\ddot{\vec{q}}^{(s)} \\
\dot{\vec{q}}_{n+1,i+1}^{(s)} &= \dot{\vec{q}}_{n+1,i}^{(s)} + \gamma\Delta t\Delta\ddot{\vec{q}}^{(s)} \\
\vec{q}_{n+1,i+1}^{(s)} &= \vec{q}_{n+1,i}^{(s)} + \beta\Delta t^2\Delta\ddot{\vec{q}}^{(s)} \\
\vec{\lambda}_{n+1,i+1} &= \vec{\lambda}_{n+1,i} + \Delta\vec{\lambda}.
\end{aligned}$$

2.2 Solving the interface-problem

The solution of the linearized equations in (4) and (5) with the unknowns $\Delta\ddot{\vec{q}}^{(s)}$ and $\Delta\vec{\lambda}$ is usually obtained by an iterative procedure, such as a Conjugate Gradient in case of symmetric systems. The local solutions $\Delta\ddot{\vec{q}}^{(s)}$ depend of the global Lagrange Multipliers $\Delta\vec{\lambda}$ and are determined by

$$\Delta\ddot{\vec{q}}^{(s)}(\Delta\vec{\lambda}) = -\mathbf{J}^{(s)^{-1}}\left(r\vec{e}s^{(s)} + \mathbf{B}^{(s)^T}\Delta\vec{\lambda}\right)$$

with the local Jacobian $\mathbf{J}$ and the associated residual $r\vec{e}s$. By reinserting these local solutions into the compatibility condition (5) we get the global interface-problem

$$\underbrace{\sum_{s=1}^{N_s}\mathbf{B}^{(s)}\mathbf{J}^{(s)^{-1}}\mathbf{B}^{(s)^T}}_{\mathbf{F}}\Delta\vec{\lambda} = \underbrace{\sum_{s=1}^{N_s}\mathbf{B}^{(s)}\mathbf{J}^{(s)^{-1}}r\vec{e}s^{(s)} - \mathbf{B}^{(s)}\ddot{\vec{q}}^{(s)}_{n+1,i}}_{\vec{d}}$$

which is solved iteratively and solves the local problems in each iteration with updated $\Delta\vec{\lambda}$ as external forces. This means in a Conjugate Gradient the operation $\mathbf{F}\Delta\vec{\lambda}$ is performed once every iteration. For implementation purposes we can formulate this operation as

$$\mathbf{F}\Delta\vec{\lambda} = \sum_{s=1}^{N_s}\mathbf{B}^{(s)}\Delta\ddot{\vec{q}}^{(s)}(\Delta\vec{\lambda}) - \vec{d} \tag{6}$$

3 ASYNCHRONOUS TIME-INTEGRATION ON NONLINEAR SYSTEMS

3.1 Derivation of the nonlinear BGC-macro method

In the previous chapter 2.1 the FETI method has been applied to a nonlinear structural dynamics problem, where the same time-step-size has been used on every substructure. This is often referred to as synchronous time-integration. In certain cases different adapted time-step-sizes might come in handy. For example in cases with different dynamics in substructures, like due to different material-stiffnesses or fast nonlinear processes in a substructure, e.g. cracks. Having different time-steps on substurctures is usually referred to as *asynchronous time-integration* [7], multi-timestep [6, 14, 15] or multirate method [12]. In the following we

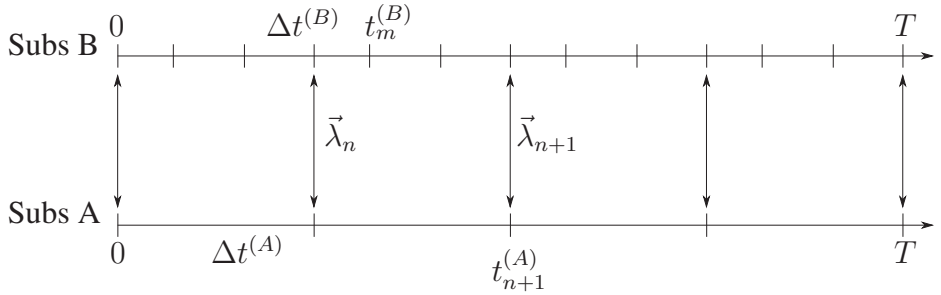

Figure 1: Page layout.

focus on a method, that couples substructures only at a syncronization time-step, as depicted in Figure 1 and proposed by Prakash e.a. [14]. Between these synchronization time-steps the Lagrange-Multipliers are interpolated linearly in time and applied locally on the substructures.

Hence we can extend the nonlinear residuals (2) and (3) by the linear interpolation on the local time-step m of the Lagrange-Multipliers

$$\vec{\lambda}_{m+1} = \vec{\lambda}_n \frac{t_{n+1} - t_{m+1}}{t_{n+1} - t_n} + \vec{\lambda}_{n+1} \frac{t_{m+1} - t_n}{t_{n+1} - t_n}$$

and apply them on the local residual

$$\mathbf{M}^{(s)} \ddot{\vec{q}}^{(s)}_{m+1} + \vec{f}^{(s)}_{int}(\vec{q}^{(s)}_{m+1}) + \mathbf{B}^{(s)^T} \vec{\lambda}_{m+1} - \vec{f}^{(s)}_{ext}(t_{m+1}) = \vec{0}.$$

As in the formulation of the GC-method we formulate the Newmark-β scheme in residual form, based on the velocities

$$\frac{1}{\gamma \Delta t}(\dot{\vec{q}}_{m+1} - \dot{\vec{q}}_m) - \frac{1-\gamma}{\gamma} \ddot{\vec{q}}_m - \ddot{\vec{q}}_{m+1} = \vec{0}$$

$$\vec{q}_m + \Delta t \dot{\vec{q}}_m + \left(\frac{1}{2} - \frac{\beta}{\gamma}\right) \Delta t^2 \ddot{\vec{q}}_m + \frac{\beta \Delta t}{\gamma}(\dot{\vec{q}}_{m+1} - \dot{\vec{q}}_m) - \vec{q}_{m+1} = \vec{0}$$

and write the local solutions and residuals in concatenated form

$$\tilde{\vec{q}}_m = \begin{bmatrix} \ddot{\vec{q}}_m \\ \dot{\vec{q}}_m \\ \vec{q}_m \end{bmatrix} \quad \tilde{\vec{r}}^{(s)} = \begin{bmatrix} \mathbf{M}^{(s)} \ddot{\vec{q}}^{(s)}_{m+1} + \vec{f}^{(s)}_{int}(\vec{q}^{(s)}_{m+1}) + \mathbf{B}^{(s)^T} \vec{\lambda}_{m+1} - \vec{f}^{(s)}_{ext}(t_{m+1}) \\ \frac{1}{\gamma \Delta t}(\dot{\vec{q}}_{m+1} - \dot{\vec{q}}_m) - \frac{1-\gamma}{\gamma} \ddot{\vec{q}}_m - \ddot{\vec{q}}_{m+1} \\ \vec{q}_m + \Delta t \dot{\vec{q}}_m + \left(\frac{1}{2} - \frac{\beta}{\gamma}\right) \Delta t^2 \ddot{\vec{q}}_m + \frac{\beta \Delta t}{\gamma}(\dot{\vec{q}}_{m+1} - \dot{\vec{q}}_m) - \vec{q}_{m+1} \end{bmatrix} = \vec{0} \quad (7)$$

$$\tilde{\vec{r}}^{I} = \sum_{s=1}^{N_s} \mathbf{B}^{(s)} \dot{\vec{q}}^{(s)}_{N_m} = \vec{0} \quad (8)$$

By linearizing residuals (7) and (8) for these local solutions $\tilde{\vec{q}}_j$, $\tilde{\vec{q}}_{j+1}$ and $\vec{\lambda}_{n+1}$, as it has been done in the nonlinear PH-method [15], we can write the full linearized system in matrix form

$$\tilde{\mathbf{M}}^{(s)} = \begin{bmatrix} \mathbf{M}^{(s)} & \mathbf{0} & \mathbf{K}^{(s)} \\ -\gamma \Delta t^{(s)} \mathbf{I} & \mathbf{I} & \mathbf{0} \\ -\beta {\Delta t^{(s)}}^2 \mathbf{I} & \mathbf{0} & \mathbf{I} \end{bmatrix} \qquad \mathbf{N}^{(s)} = \begin{bmatrix} \mathbf{0} & \mathbf{0} & \mathbf{0} \\ -\Delta t^{(s)}(1-\gamma)\mathbf{I} & -\mathbf{I} & \mathbf{0} \\ -\Delta t^{(s)}(1/2-\beta)\mathbf{I} & -\Delta t^{(s)} \mathbf{I} & -\mathbf{I} \end{bmatrix}$$

$$\tilde{\mathbf{B}}^{(s)^T} = \begin{bmatrix} \mathbf{0} \\ \mathbf{B}^{(s)^T} \\ \mathbf{0} \end{bmatrix} \qquad \tilde{\mathbf{C}}^{(s)} = \begin{bmatrix} \mathbf{B}^{(s)^T} \\ \mathbf{0} \\ \mathbf{0} \end{bmatrix}$$

$$\left[\begin{array}{cccc|c|c} \tilde{\mathbf{M}}^{(B)}_1 & & & & & \frac{1}{N_m}\tilde{\mathbf{C}}^{(B)} \\ \mathbf{N}^{(B)} & \tilde{\mathbf{M}}^{(B)}_2 & & & & \frac{2}{N_m}\tilde{\mathbf{C}}^{(B)} \\ & \ddots & \ddots & & & \vdots \\ & & \mathbf{N}^{(B)} & \tilde{\mathbf{M}}^{(B)}_{N_m} & & \frac{N_m}{N_m}\tilde{\mathbf{C}}^{(B)} \\ \hline & & & & \tilde{\mathbf{M}}^{(A)}_{n+1} & \tilde{\mathbf{C}}^{(A)} \\ \hline & & & \tilde{\mathbf{B}}^{(B)} & \tilde{\mathbf{B}}^{(A)} & \mathbf{0} \end{array}\right] \left[\begin{array}{c} \Delta\tilde{\vec{q}}^{(B)}_1 \\ \Delta\tilde{\vec{q}}^{(B)}_2 \\ \vdots \\ \Delta\tilde{\vec{q}}^{(B)}_{N_m} \\ \hline \Delta\tilde{\vec{q}}^{(A)}_{N_m} \\ \hline \Delta\vec{\lambda}_{n+1} \end{array}\right] = \left[\begin{array}{c} -\tilde{\vec{r}}^{(B)}(\tilde{\vec{q}}^{(B)}_0, \tilde{\vec{q}}^{(B)}_1, \vec{\lambda}_1) \\ -\tilde{\vec{r}}^{(B)}(\tilde{\vec{q}}^{(B)}_1, \tilde{\vec{q}}^{(B)}_2, \vec{\lambda}_2) \\ \vdots \\ -\tilde{\vec{r}}^{(B)}(\tilde{\vec{q}}^{(B)}_{N_m-1}, \tilde{\vec{q}}^{(B)}_{N_m}, \vec{\lambda}_{n+1}) \\ \hline -\tilde{\vec{r}}^{(A)}(\tilde{\vec{q}}^{(A)}_n, \tilde{\vec{q}}^{(A)}_{n+1}, \vec{\lambda}_{n+1}) \\ \hline -\tilde{\vec{r}}^{I}(\tilde{\vec{q}}^{(A)}_{n+1}, \tilde{\vec{q}}^{(B)}_{N_m}) \end{array}\right] \quad (9)$$

The main-difference between this method and the nonlinear PH-method lies in the coupling condition [15]. We didn't formulate the coupling-residual based on a force-residual, but a compatibility of end-point-velocities only. In the BGC-macro method this compatibility condition arises from the Pseudo-energy-method and therefore this method can be seen as a nonlinear version of the BGC-macro method [1].

3.2 Numerical experiments on nonlinear asynchronous time-integration

3.2.1 Implementation

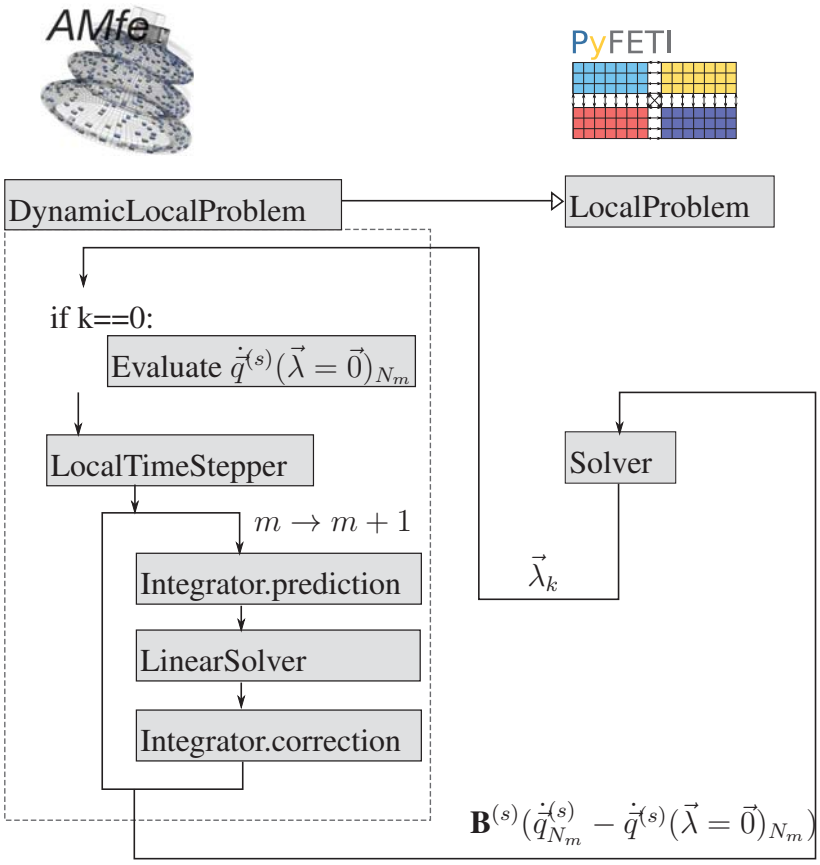

Figure 2: Implementation of the asynchronous time-integration in our FE-framework, which consists of the Python packages AMfe and PyFETI. Here k is the index of each CG-iteration.

For the following experiments we implemented the previous method (9) in a time-stepping manor and integrated it into our FE-framework as depicted in Figure 2. The general framework consists of two open-source Python-packages, the nonlinear FE-library AMfe [17] and the MPI-parallelized FETI-library PyFETI [18]. The softwares' stable master-branches are published on github. As soon as the implementation of the here presented methods is cleaned up and fully integrated in a more flexible and modular manor, they will be published there as well. PyFETI provides the FETI-solver and a local-problem class, which gets the Lagrange-Multipliers as input, does local computations and returns the results to the FETI-solver. This class is customized with local time-stepping routines to implement the method from (9). During the first FETI-iteration the constant $\vec{d}$ from (6) has to be evaluated by performing the local computations with the Lagrange-Multipliers set to a start-value, e.g. $\vec{\lambda} = \vec{0}$.

3.2.2 Spurious oscillations on the interface

As a reference we started with applying our method to the split Duffing-oscillator problem, as used by Prakash e.a.[15], which is shown in Figure 3. The springs' stiffnesses are nonlinear

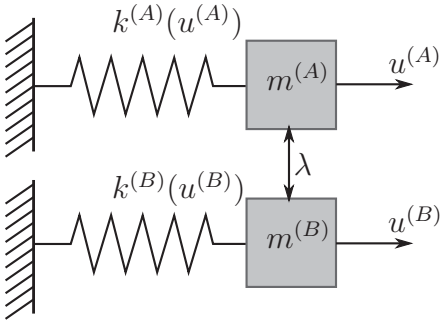

Figure 3: Split Duffing Oscillator.

in the displacements

$$k^{(s)}(q^{(s)}) = k_1 q^{(s)} + k_2 q^{(s)^3}$$

and are set with the parameters from Table 1. In case of rather fine time-discretizations we

	k_1	k_2	m
A	1	1	1
B	10	-5	1

Table 1: Material-parameters for nonlinear Split Duffing Oscillator.

experience a bit more spurious oscillations of the velocities between the synchronization-time-steps, as shown in Figure 4. In the case of a coarser time-discretization in Figure 5 the oscillations increase for both methods, which leads to incompatibilities in the displacements. Hence the force-residuals on the interface of the nonlinear PH-method seem to decrease the amplitude of such spurious oscillations slightly, but require more precomputations, while the method, which is presented here only enforces coupling by Lagrange-Multipliers.

3.2.3 Unphysical reflections on the interface

After the tests on a simple split Duffing-Oscillator, we applied the method to a 2D example beam. The beam's geometry and domain decomposition can be seen in Figure 6. It is loaded with a shock from the right and clamped on the left-hand side. The shock vanishes long before the first syncronization step. The model-parameters can be found in Table 2. With this setup we get a wave in substructure B, which is visualized by the normal-stresses in Figure 7. This wave

l_1	l_2	H	d	f_{max}	t_1	t_2	ΔT	Δt
$40m$	$10m$	$10m$	$2m$	$5.0 \cdot 10^4 N$	$0.00015s$	$0.0003s$	$0.001s$	$0.00001s$

Material-model	Young's-Modulus	Poisson's ratio	Density	thickness
St.Venant-Kirchhoff	$60 \cdot 10^5 N/m^2$	0.34	$2.7 \cdot 10^{-3} kg/m^3$	$0.5m$

Table 2: Model-parameters for 2D beam-example

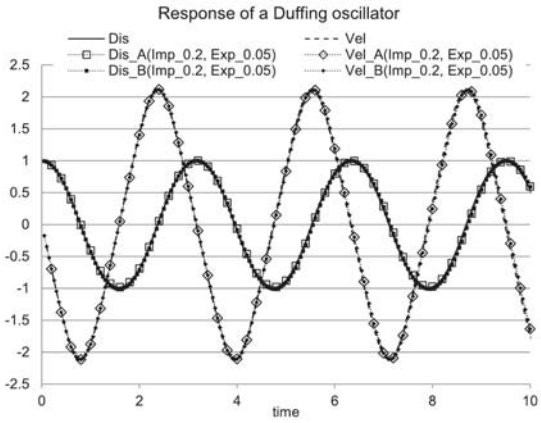

(a) Displacements and velocities of both substructures A, B with nonlinear PH-method [15]

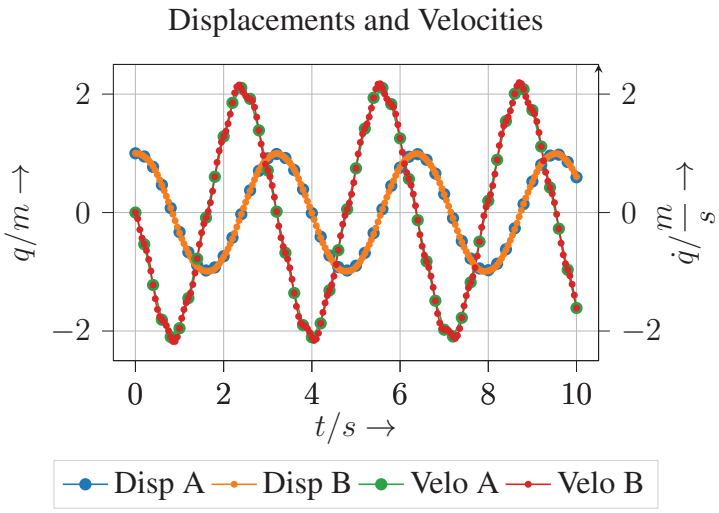

(b) Displacements and velocities of both substructures A, B with nonlinear BGC-macro

Figure 4: Solutions for the split Duffing-oscillator with a rather fine time-discretisation: $\Delta t^{(A)} = 0.2s$ and $\Delta t^{(B)} = 0.05s$

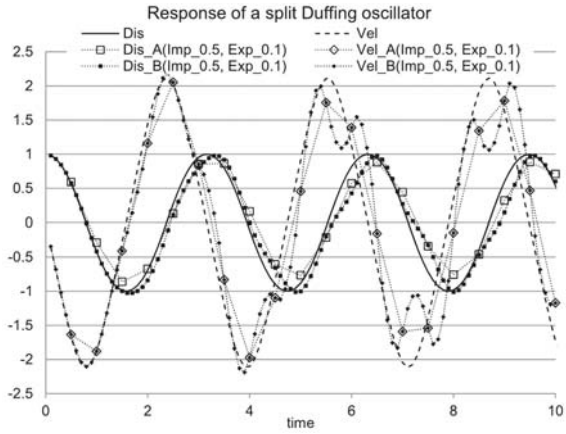

(a) Displacements and velocities of both substructures A, B with nonlinear PH-method [15]

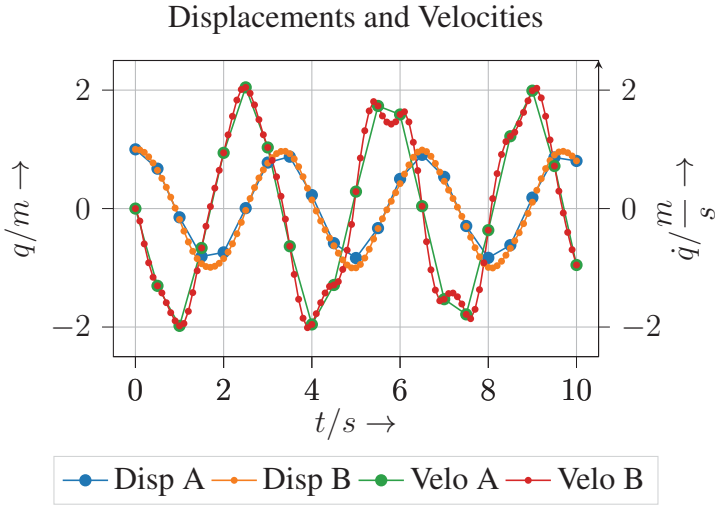

(b) Displacements and velocities of both substructures A, B with nonlinear BGC-macro

Figure 5: Solutions for the split Duffing-oscillator with a rather coarse time-discretisation: $\Delta t^{(A)} = 0.5s$ and $\Delta t^{(B)} = 0.1s$

reaches the interface before the syncronization time-step, high-frequency parts are reflected, as can be seen at the switched sign of the normal stresses in Figure 7, and form a standing wave inside substructure B. During the intermediate time-steps substructure B can be interpreted as a single plate for those high frequencies. The coarse substructure A is not able to follow the fast dynamics of that wave and only captures slower deformations, but overall energy has to be conserved. Hence this fast dynamic stays inside substructure B.

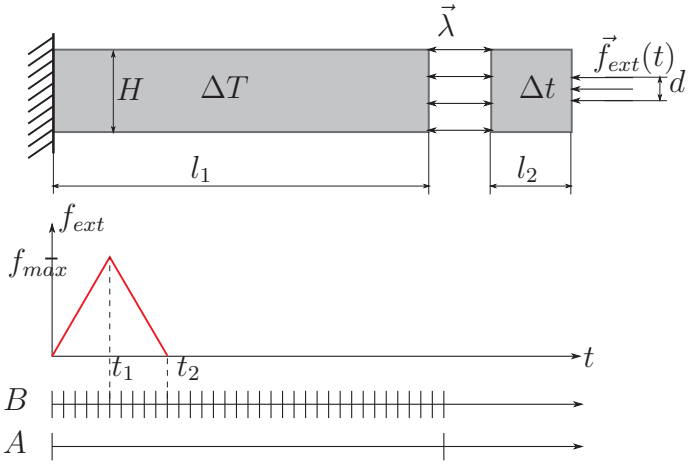

Figure 6: Geometry of the 2D beam and loading with an external shock.

4 A VARIATIONAL APPROACH TO COUPLING CONDITIONS IN TIME

4.1 Construction of a variational asynchronous coupling condition

4.1.1 Introduction to the variational principle in continuous dynamics

In Prakash e.a. it has been stated already, that the spurious oscillations in chapter 3.2.2 pollute the solution [15]. We also showed the appearance of unphysical reflections on the interface in case of inappropriate time-step-sizes and loadings in chapter 3.2.3. These reflections are not just inaccurate, but might also alter the solution by triggering nonlinear cracking events to early or destabilizing the solution with resonances. According to Gravouil e.a. such oscillations don't appear in the micro-step-based methods, such as HATI and BGC-micro, but they suffer from artificial energy-dissipation [7]. An approach, that might be able to resolve these issues is based on the variational principle. For continuous systems this principle, also known as Hamilton's principle, plays a key-role in structural dynamics. Let's consider the Lagrangian

$$\mathcal{L}(\dot{\vec{q}}, \vec{q}) = \mathcal{T}(\dot{\vec{q}}) - \mathcal{V}(\vec{q}) = \frac{1}{2}\dot{\vec{q}}^T \mathbf{M} \dot{\vec{q}} - \mathcal{V}(\vec{q})$$

of a mechanical system, consisting on the kinetic energy $\mathcal{T}$ and potential energy $\mathcal{V}$ of the system. As conservative mechanical systems, meaning systems without loading or dissipation, in nature always move such that energy within the system is kept constant, we can also require, that the Lagrangian integrated over the time-intervall and varied for the displacement $\vec{q}$ stays 0

$$\delta S(\dot{\vec{q}}, \vec{q}) = \delta \int_0^T \mathcal{L}(\dot{\vec{q}}, \vec{q}) dt = \int_0^T \frac{\partial \mathcal{L}}{\partial \vec{q}} \delta \vec{q} + \frac{\partial \mathcal{L}}{\partial \dot{\vec{q}}} \delta \dot{\vec{q}} dt = 0. \tag{10}$$

Here S is called the action integral. With integration by parts we get

$$\delta S(\dot{\vec{q}}, \vec{q}) = \int_0^T \left[\frac{\partial \mathcal{L}}{\partial \vec{q}} - \frac{d}{dt} \frac{\partial \mathcal{L}}{\partial \dot{\vec{q}}} \right] \delta \vec{q} dt + \left[\frac{\partial \mathcal{L}}{\partial \dot{\vec{q}}} \delta \vec{q} \right]_0^T = 0$$

and if we require fixed end-points for $\delta\vec{q}(t=0) = \delta\vec{q}(t=T) = \vec{0}$ now and that the integral has to evaluate 0 for arbitrary variations $\delta\vec{q}$, we get the Euler-Lagrange-equation

$$-\frac{\partial \mathcal{L}}{\partial \vec{q}} + \frac{d}{dt} \frac{\partial \mathcal{L}}{\partial \dot{\vec{q}}} = \frac{d}{dt} \frac{\partial \mathcal{T}}{\partial \dot{\vec{q}}} + \frac{\partial \mathcal{V}}{\partial \vec{q}} = \vec{0}$$

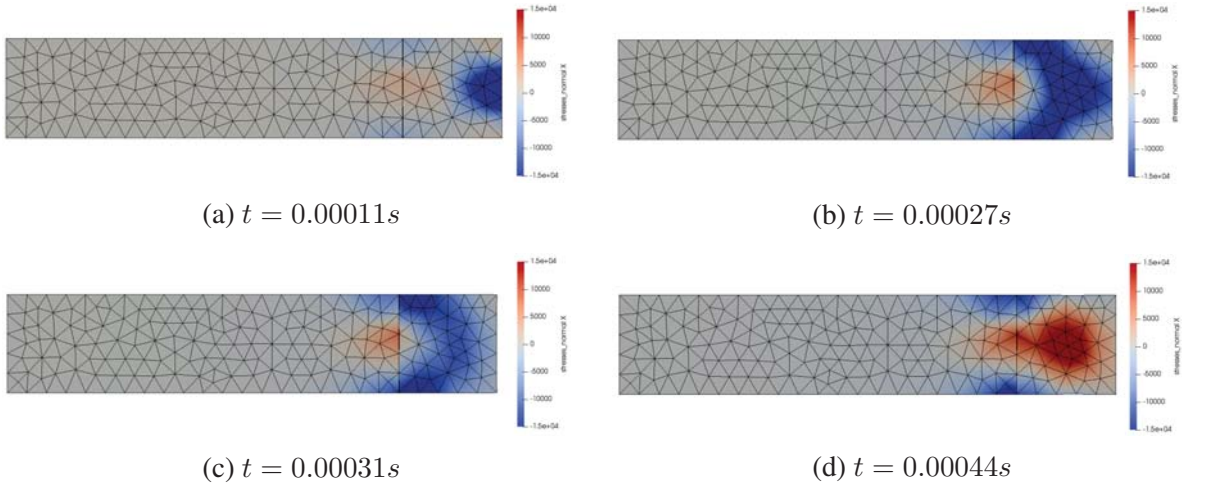

(a) $t = 0.00011s$ (b) $t = 0.00027s$

(c) $t = 0.00031s$ (d) $t = 0.00044s$

Figure 7: Normal stresses in beam-length direction of the 2D-beam at several time-steps. The solution of the coarse substructure have been interpolated linearly onto the fine time-grid for visualization purposes only.

which is our equation of motion from (1) without external loads. Constraints are not taken into account here, but can be included by the interface-energy

$$\mathcal{H}(\vec{q}, \vec{\lambda}) = \vec{g}(\vec{q})^T \vec{\lambda} \tag{11}$$

with the gap-function $\vec{g}(\vec{q})$ [11]. The Lagrangian of such a constrained system is then written as

$$\mathcal{L}(\dot{\vec{q}}, \vec{q}, \vec{\lambda}) = \mathcal{T}(\dot{\vec{q}}) - \mathcal{V}(\vec{q}) - \mathcal{H}(\vec{q}, \vec{\lambda}) \tag{12}$$

4.1.2 Construction of the discrete coupling condition

This approach can be transfered to discrete systems and used for the construction of Variational Time-Integrators, which provide some built-in properties, such as Symplecticity, conservation of linear and angular momentum and bounded oscillations of energy. These properties lead to good long-time behavior of such a Variational Integrator. In fact Kane e.a. showed, that the non-dissipative Newmark-β scheme with $\gamma = \frac{1}{2}$ is variational and can be derived from a Midpoint-rule as integration-scheme [8]. Lew e.a. also developed an asynchronous integrator, based on this principle, but with updating the solutions based on the previous neighboring solution directly and therefore not suitable for a FETI-solver [10]. Leyendecker and Ober-Blöbaum proposed a variational approach for constrained systems and multirate integration, that couples slow and fast dynamics over Lagrange-Multipliers [12]. In the following we use this approach as a basis for the derivation of a new asynchronous coupling technique and domain decomposition. The starting-point of constructing an integrator is the time-discretization of the solutions. Time-dependent shape-functions $\Phi(t)$ and $\Theta(t)$, similar to Wenger [16], lead to a flexible formulation

$$\vec{q}(t) = \sum_{m=0}^{N_m} \Phi(t)_m \vec{q}_m \qquad \dot{\vec{q}}(t) = \sum_{m=0}^{N_m} \frac{d\Phi(t)_m}{dt} \vec{q}_m$$

$$\vec{\lambda}(t) = \sum_{j=0}^{N_j} \Theta(t)_j \vec{\lambda}_j$$

for the approximation of the solutions at any time t. Different indices of displacements and Lagrange-Multipliers indicate the option of different discretizations for both fields and N_m and N_j are the number of time-steps over the full trajectory. These are then inserted into the Lagrangian (12)

$$\mathcal{L}(\vec{q}_0^{(s)}, \dots, \vec{q}_{N_m}^{(s)}, \vec{\lambda}_0, \dots, \vec{\lambda}_{N_j}, t) = \sum_{s=1}^{N_s} \frac{1}{2} \left(\sum_{m=0}^{N_m^{(s)}} \frac{d\Phi(t)_m^{(s)}}{dt} \vec{q}_m^{(s)} \right)^T \mathbf{M}^{(s)} \left(\sum_{m=0}^{N_m^{(s)}} \frac{d\Phi(t)_m^{(s)}}{dt} \vec{q}_m^{(s)} \right) - \\ - \mathcal{V} \left(\sum_{m=0}^{N_m^{(s)}} \Phi(t)_m^{(s)} \vec{q}_m^{(s)} \right)^{(s)} - \mathcal{H} \left(\sum_{m=0}^{N_m^{(s)}} \Phi(t)_m^{(s)} \vec{q}_m^{(s)}, \sum_{j=0}^{N_j} \Theta(t)_j \vec{\lambda}_j)^{(s)} \right) \tag{13}$$

and extended to substructured systems by summing up all local Lagrangians. Due to the free to choose time-discretizations, we still need an appropriate formulation for the gap-function. The gap-function is supposed to measure the gap at any point in time and is written as

$$\vec{g}(\vec{q}_0^{(s)}, \dots, \vec{q}_{N_m}^{(s)}, t) = \sum_{s=1}^{N_s} \mathbf{B}^{(s)} \sum_{m=0}^{N_m^{(s)}} \Phi(t)_m^{(s)} \vec{q}_m^{(s)}$$

where the **B**-matrix is the same as in (3). The next key-point of the integrator's construction is the numerical integration over the time-intervall. The choice of the integration-scheme influences the properties of the constructed integrator. We choose the generalized midpoint-rule here, to have compatibility conditions and time-integration with the non-dissipative Newmark-β derived consistently from the same integration-scheme. One can also choose different integration-schemes for both, compatibility-condition and Lagrangian, as it has been done by Leyendecker e.a. [12]. Moreover the integration requires a segmentation-approach. In our examples here we use the same time-discretization as in chapter 3 to ensure comparability, meaning we have the same time-step-sizes for substructure A and the Lagrange-Multipliers and use a fraction of that time-step-size on the neighboring substructure B. Moreover we use linear time-shape-functions $\Phi(t)$ and $\Theta(t)$ for the solutions

$$\Theta_n(t) = \begin{cases} \frac{t_{n+1}-t}{\Delta T} & t_n \leq t \leq t_{n+1} \\ \frac{t-t_{n-1}}{\Delta T} & t_{n-1} \leq t < t_n \\ 0 & t > t_{n+1} \\ 0 & t < t_{n-1} \end{cases}$$

$$\Phi_n^{(A)}(t) = \begin{cases} \frac{t_{n+1}-t}{\Delta T} & t_n \leq t \leq t_{n+1} \\ \frac{t-t_{n-1}}{\Delta T} & t_{n-1} \leq t < t_n \\ 0 & t > t_{n+1} \\ 0 & t < t_{n-1} \end{cases}$$

$$\Phi_m^{(B)}(t) = \begin{cases} \frac{t_{m+1}-t}{\Delta t} & t_m \leq t \leq t_{m+1} \\ \frac{t-t_{m-1}}{\Delta t} & t_{m-1} \leq t < t_m \\ 0 & t > t_{m+1} \\ 0 & t < t_{m-1} \end{cases}$$

resulting in a discretization as in Figure 8. For the integration of (13) we evaluate the La-

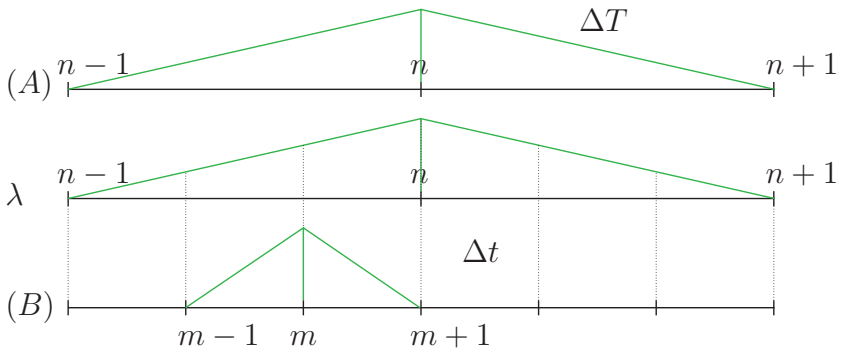

Figure 8: Time-discretization for two substructures A and B and the Lagrange-Multiplier-filed. Additionally the linear shape-function for the Lagrange-Multipliers at time-step n is shown.

grangian at intermediate timesteps

$$t_{m+\alpha/n+\alpha} = (1-\alpha)t_{m/n} + \alpha t_{m+1/n+1}, \qquad \alpha \in [0,1]$$

resulting in

$$\begin{aligned}
&S(\bar{q}_0^{(A)}, \dots, \bar{q}_{N_n}^{(A)}, \bar{q}_0^{(B)}, \dots, \bar{q}_{N_m}^{(B)}, \vec{\lambda}_0, \dots, \vec{\lambda}_{N_n}) = \\
&= \sum_{n=0}^{N_n-1} \Delta T \left[\frac{1}{2} \left(\frac{\bar{q}_{n+1}^{(A)} - \bar{q}_n^{(A)}}{\Delta T} \right)^T \mathbf{M}^{(A)} \left(\frac{\bar{q}_{n+1}^{(A)} - \bar{q}_n^{(A)}}{\Delta T} \right) - \mathcal{V}\left((1-\alpha)\bar{q}_n^{(A)} + \alpha \bar{q}_{n+1}^{(A)} \right) - \right. \\
&\left. - \left((1-\alpha)\bar{q}_n^{(A)} + \alpha \bar{q}_{n+1}^{(A)} \right)^T \mathbf{B}^{(A)^T} \left((1-\alpha)\vec{\lambda}_n + \alpha \vec{\lambda}_{n+1} \right) \right] + \\
&+ \sum_{m=0}^{N_m-1} \Delta t \left[\frac{1}{2} \left(\frac{\bar{q}_{m+1}^{(B)} - \bar{q}_m^{(B)}}{\Delta t} \right)^T \mathbf{M}^{(B)} \left(\frac{\bar{q}_{m+1}^{(B)} - \bar{q}_m^{(B)}}{\Delta t} \right) - \mathcal{V}\left((1-\alpha)\bar{q}_m^{(B)} + \alpha \bar{q}_{m+1}^{(B)} \right) - \right. \\
&\left. - \left((1-\alpha)\bar{q}_m^{(B)} + \alpha \bar{q}_{m+1}^{(B)} \right)^T \mathbf{B}^{(B)^T} \sum_{n=0}^{N_n} \Theta_n(t_{m+\alpha}) \vec{\lambda}_n \right]
\end{aligned}$$

Analogously to the continuous case in (10) the variation of this discrete action integral for its arguments

$$\begin{aligned}
&\delta S(\bar{q}_0^{(A)}, \dots, \bar{q}_{N_n}^{(A)}, \bar{q}_0^{(B)}, \dots, \bar{q}_{N_m}^{(B)}, \vec{\lambda}_0, \dots, \vec{\lambda}_{N_n}) = \\
&= \sum_{n=0}^{N_n} \frac{\partial S}{\partial \bar{q}_n^{(A)}} \delta \bar{q}_n^{(A)} + \sum_{m=0}^{N_m} \frac{\partial S}{\partial \bar{q}_m^{(B)}} \delta \bar{q}_m^{(B)} + \sum_{n=0}^{N_n} \frac{\partial S}{\partial \vec{\lambda}_n} \delta \vec{\lambda}_n = \vec{0}
\end{aligned}$$

must still evaluate as zero. We still require $\delta \bar{q}_0^{(A)} = \delta \bar{q}_{N_n}^{(A)} = 0$, $\delta \bar{q}_0^{(B)} = \delta \bar{q}_{N_m}^{(B)} = 0$, $\delta \vec{\lambda}_0 = \delta \vec{\lambda}_{N_n} = 0$ and that this equation must hold for arbitrary variations $\delta \bar{q}_n^{(A)}$, $\delta \bar{q}_n^{(B)}$, $\delta \vec{\lambda}_n$. This leads

to the equations

$$\Delta T\left[\frac{1}{\Delta T}\mathbf{M}^{(A)}\frac{\vec{q}_n^{(A)}-\vec{q}_{n-1}^{(A)}}{\Delta T}-\alpha\frac{\partial\mathcal{V}\left((1-\alpha)\vec{q}_{n-1}^{(A)}+\alpha\vec{q}_n^{(A)}\right)}{\partial\vec{q}}-\mathbf{B}^{(A)^T}\begin{bmatrix}(1-\alpha)\alpha & \alpha^2\end{bmatrix}\begin{bmatrix}\vec{\lambda}_{n-1}\\ \vec{\lambda}_n\end{bmatrix}\right]+$$
$$+\Delta T\left[-\frac{1}{\Delta T}\mathbf{M}^{(A)}\frac{\vec{q}_{n+1}^{(A)}-\vec{q}_n^{(A)}}{\Delta T}-(1-\alpha)\frac{\partial\mathcal{V}\left((1-\alpha)\vec{q}_n^{(A)}+\alpha\vec{q}_{n+1}^{(A)}\right)}{\partial\vec{q}}-\right.$$
$$\left.-\mathbf{B}^{(A)^T}\begin{bmatrix}(1-\alpha)^2 & (1-\alpha)\alpha\end{bmatrix}\begin{bmatrix}\vec{\lambda}_n\\ \vec{\lambda}_{n+1}\end{bmatrix}\right]=\vec{0}$$
$$\Delta t\left[\frac{1}{\Delta t}\mathbf{M}^{(B)}\frac{\vec{q}_m^{(B)}-\vec{q}_{m-1}^{(B)}}{\Delta t}-\alpha\frac{\partial\mathcal{V}\left((1-\alpha)\vec{q}_{m-1}^{(B)}+\alpha\vec{q}_m^{(B)}\right)}{\partial\vec{q}}-\alpha\mathbf{B}^{(B)^T}\sum_{n=0}^{N_n}\Theta_n(t_{m-1+\alpha})\vec{\lambda}_n\right]+$$
$$+\Delta t\left[-\frac{1}{\Delta t}\mathbf{M}^{(B)}\frac{\vec{q}_{m+1}^{(B)}-\vec{q}_m^{(B)}}{\Delta t}-(1-\alpha)\frac{\partial\mathcal{V}\left((1-\alpha)\vec{q}_m^{(B)}+\alpha\vec{q}_{m+1}^{(B)}\right)}{\partial\vec{q}}-\right.$$
$$\left.-(1-\alpha)\mathbf{B}^{(B)^T}\sum_{n=0}^{N_n}\Theta_n(t_{m+\alpha})\vec{\lambda}_n\right]=\vec{0}$$

for each $\vec{\lambda}_n$:

$$\sum_{m=0}^{N_m-1}\Delta t\mathbf{B}^{(B)}\begin{bmatrix}(1-\alpha)\Theta_n(t_{m+\alpha}) & \alpha\Theta_n(t_{m+\alpha})\end{bmatrix}\begin{bmatrix}\vec{q}_m^{(B)}\\ \vec{q}_{m+1}^{(B)}\end{bmatrix}+$$
$$+\Delta T\left[\mathbf{B}^{(A)}\begin{bmatrix}(1-\alpha)\alpha & \alpha^2\end{bmatrix}\begin{bmatrix}\vec{q}_{n-1}^{(A)}\\ \vec{q}_n^{(A)}\end{bmatrix}\right]+\Delta T\left[\mathbf{B}^{(A)}\begin{bmatrix}(1-\alpha)^2 & \alpha(1-\alpha)\end{bmatrix}\begin{bmatrix}\vec{q}_n^{(A)}\\ \vec{q}_{n+1}^{(A)}\end{bmatrix}\right]=\vec{0}$$

The first two equations result in the Newmark-β scheme for $\alpha=0.5$

$$\begin{aligned}\vec{q}_{m+1} &= (1-\alpha)\Delta t\dot{\vec{q}}_{m+1}+\alpha\Delta t\dot{\vec{q}}_n+\vec{q}_n\\ \ddot{\vec{q}}_{m+1} &= -\tfrac{1-\alpha}{\alpha}\ddot{\vec{q}}_m+\tfrac{1}{\alpha\Delta t}(\dot{\vec{q}}_{m+1}-\dot{\vec{q}}_m)\end{aligned}$$

and the local equilibrium of forces at generalized midpoints

$$\mathbf{M}^{(A)}\ddot{\vec{q}}_{n+\alpha}^{(A)}+\underbrace{\frac{\partial\mathcal{V}}{\partial\vec{q}}\left(\vec{q}_{n+\alpha}^{(A)}\right)}_{\vec{f}_{int}}+\mathbf{B}^{(A)^T}\begin{bmatrix}(1-\alpha) & \alpha\end{bmatrix}\begin{bmatrix}\vec{\lambda}_n\\ \vec{\lambda}_{n+1}\end{bmatrix}=\vec{0}$$
$$\mathbf{M}^{(B)}\ddot{\vec{q}}_{m+\alpha}^{(B)}+\underbrace{\frac{\partial\mathcal{V}}{\partial\vec{q}}\left(\vec{q}_{m+\alpha}^{(B)}\right)}_{\vec{f}_{int}}+\mathbf{B}^{(B)^T}\begin{bmatrix}\Theta_n(t_{m+\alpha}) & \Theta_{n+1}(t_{m+\alpha})\end{bmatrix}\begin{bmatrix}\vec{\lambda}_n\\ \vec{\lambda}_{n+1}\end{bmatrix}=\vec{0}.$$

The third equation is the new coupling condition. In this form it leads to unstable computations after a few time-steps though and if we compare it with previous coupling conditions from BGC-macro (7) and dynamic FETI (3), we notize the unfavorable displacement-coupling here. As this is just a numerics issue related to Lagrange-Multipliers without masses, we replace them by corrected velocities

$$\Delta\vec{q}^{(s)}=(1-\alpha)\Delta t^{(s)}\Delta\dot{\vec{q}}^{(s)}$$

, which result from the integration-scheme

$$\sum_{m=0}^{N_m-1} \Delta t^2(1-\alpha)\mathbf{B}^{(B)} \left[(1-\alpha)\Theta_n(t_{m+\alpha}) \quad \alpha\Theta_n(t_{m+\alpha})\right] \begin{bmatrix} \dot{\vec{q}}_m^{(B)} \\ \dot{\vec{q}}_{m+1}^{(B)} \end{bmatrix} +$$
$$+\Delta T^2(1-\alpha) \left[\mathbf{B}^{(A)} \left[(1-\alpha)\alpha \quad \alpha^2\right] \begin{bmatrix} \dot{\vec{q}}_{n-1}^{(A)} \\ \dot{\vec{q}}_n^{(A)} \end{bmatrix}\right] +$$
$$+\Delta T^2(1-\alpha) \left[\mathbf{B}^{(A)} \left[(1-\alpha)^2 \quad \alpha(1-\alpha)\right] \begin{bmatrix} \dot{\vec{q}}_n^{(A)} \\ \dot{\vec{q}}_{n+1}^{(A)} \end{bmatrix}\right] \qquad = \vec{0}$$

$$\mathbf{M}^{(A)}\ddot{\vec{q}}_{n+\alpha}^{(A)} + \underbrace{\frac{\partial \mathcal{V}}{\partial \vec{q}}\left(\vec{q}_{n+\alpha}^{(A)}\right)}_{\vec{f}_{int}} + \mathbf{B}^{(A)^T}\left[(1-\alpha) \quad \alpha\right]\begin{bmatrix}\vec{\lambda}_n \\ \vec{\lambda}_{n+1}\end{bmatrix} = \vec{0}$$

$$\mathbf{M}^{(B)}\ddot{\vec{q}}_{m+\alpha}^{(B)} + \underbrace{\frac{\partial \mathcal{V}}{\partial \vec{q}}\left(\vec{q}_{m+\alpha}^{(B)}\right)}_{\vec{f}_{int}} + \mathbf{B}^{(B)^T}\sum_{n=0}^{N_n}\Theta_n(t_{m+\alpha})\vec{\lambda}_n = \vec{0}.$$

4.2 Numerical experiments on variational coupling

In this section we apply our new variational asynchronous midpoint (VAMP) coupling condition to the Split Duffing Oscillator, known from chapter 3.2, but for now just with linear stiffnesses and $\alpha = 0.5$, which resembles the well known Newmark-β scheme. As a prove of concept we only solve the interface-problem with a direct solver here. In Figure 9 the displacements and velocities from the VAMP-coupling are compared with the BGC-macro. Both are referenced to the solutions from the synchronous coupling. The positive mainly positive energy in the BGC-macro case doesn't necessarily mean, that overall energy is growing, as the sign depends on the signs of the **B**-matrices. With the weak coupling of the VAMP-method the interface-oscillations of velocities couldn't be reduced, but incompatibilities in the displacement-field are smoothed. Hence a coarse discretization of the Lagrange-Multiplier-field always leads to such oscillations. We'ld like to point out, that the interface-energy in Figure 10 is oscillating, as expected, but bounded and the amplitude is similar for the VAMP-method compared to the strong coupling. The interface-energy is calculated by multiplying the current gap with the current Lagrang-Multiplier according to (11).

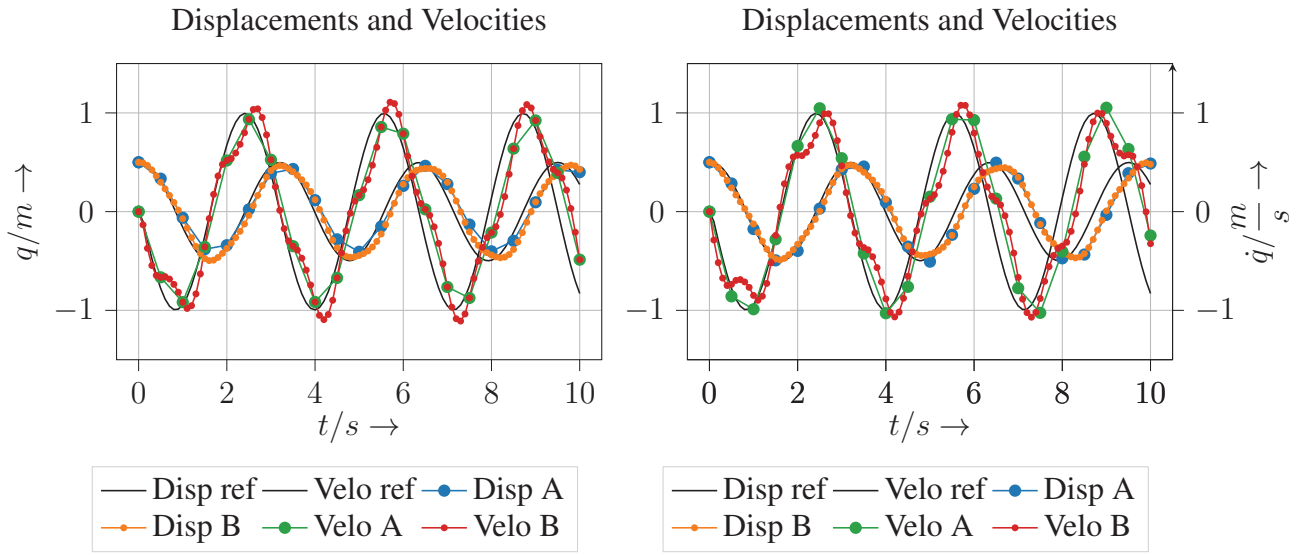

(a) Displacements and velocities of both substructures A, B with linear BGC-macro

(b) Displacements and velocities of both substructures A, B with VMP-coupling

Figure 9: Solutions for the linear split Duffing-oscillator with a rather coarse time-discretisation: $\Delta t^{(A)} = 0.5s$ and $\Delta t^{(B)} = 0.1s$, Stiffnesses: $k^{(A)} = 1.75N/m$, $k^{(B)} = 6.25N/m$. Black curve as reference from the synchronous case with $\Delta t = 0.1s$.

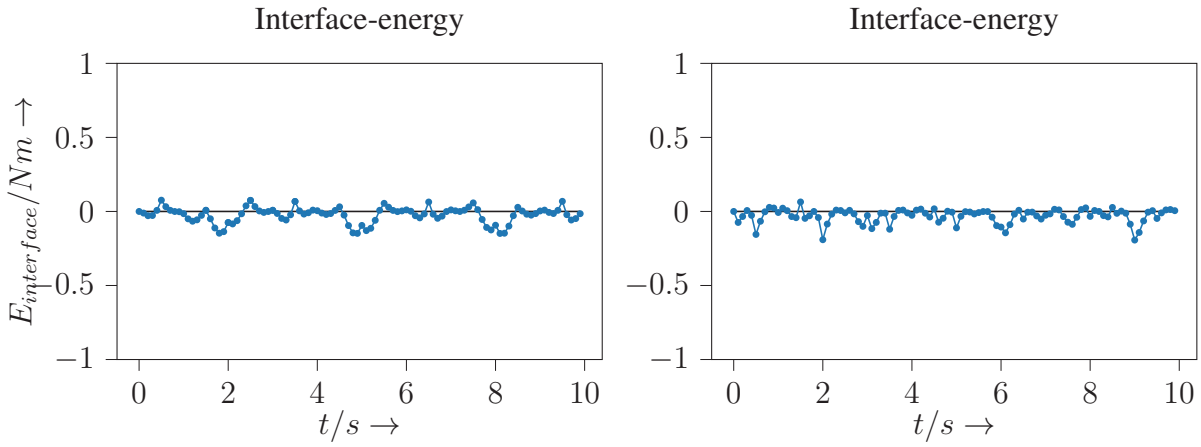

(a) Interface-energy with BGC-macro

(b) Interface-energy with VMP-coupling

Figure 10: Interface-energy for the split Duffing-oscillator with a rather coarse time-discretisation: $\Delta t^{(A)} = 0.5s$ and $\Delta t^{(B)} = 0.1s$. Black curve as reference from the synchronous case with $\Delta t = 0.1s$.

5 CONCLUSIONS

Asynchronous time-integration methods with a strong end-point coupling conserve energy at these synchronization-points, but produce local oscillations between those synchronization steps. Based on the nonlinear PH- and linear BGC-macro-method, we derived a nonlinear version of the BGC-macro for Newmark-β integration schemes. It couples substructures by Lagrange-Multipliers only and doesn't require any presolution-step, but leads to slightly larger amplitudes of the spurious oscillations. Furthermore we show the risk of wave-reflections on the interface in case of adverse time-step-sizes and loadings. In order to find ways of reducing these unphysical effects while keeping the method energy-conserving, we derived a new coupling method from the variational principle. With the variational principle comes a number of inherent properties, such as bounded energy-oscillations and conservation of momentum, while in the BGC-approach the pseudo-energy method was solely used to derive a stable method. Moreover it opens up a large variety of options to create new coupling-methods. In the here presented case of a coarse Lagrange-multiplier discretization this method leads to a weak coupling of the substructures and still produces spurious oscillations in our test-example, while oscillations in the interface-energy are bounded at similar amplitudes as in the strong coupled case of the nonlinear BGC-method. Further research will be done on the velocity-oscillations and whether they can be eliminated by a more fine time-discretization of the Lagrange-Multipliers while keeping the energy bounded. Moreover we have to mention that the variational method couples Lagrange-Multipliers more along the full trajectory, which is disadvantageous in the context of High-Performance-Computing. Different integration-schemes during the construction might reduce these couplings while maintaining the variational properties. The interface-problem of the variational method has been solved with a direct solver as a prove of concept. In future work we will extend this approach to nonlinear problems and solve the interface problem with our FETI-solver, which will enable further performance studies. Moreover further work is needed on the choice of time-shape-functions.

Acknowledgement: *We thank the DFG for the funding of project RI2451/8-1, in which context this work has been done.*

REFERENCES

[1] Brun, M. Gravouil, A. Combescure, A. and Limam, A., Two FETI-based heterogeneous time step coupling methods for Newmark and α-schemes derived from the energy method, *Computer Methods in Applied Mechanics and Engineering*, **283**, 130–176, 2015, doi: 10.1016/j.cma.2014.09.010

[2] Farhat, C. Roux, F.X., A method of finite element tearing and interconnecting and its parallel solution algorithm, *International Journal for Numerical Methods in Engineering*, **32**, 1205–1227, 1991, doi: 10.1002/nme.1620320604

[3] Farhat, C. Crivelli, L. and Géradin, M., On the spectral stability of time integration algorithms for a class of constrained dynamics problems, *AIAA/ASME/ASCE/AHS/ASC Structures, Structural Dynamics, and Materials Conference, 34th and AIAA/ASME Adaptive Structures Forum, La Jolla, CA, Apr. 19-22, 1993, Technical Papers. Pt. 1 (A93-33876 13-39)*, 80–97, 1993

[4] Farhat, C. Crivelli, L. and Roux, F.X., A transient FETI methodology for large-scale parallel implicit computations in structural mechanics, *International Journal for Numerical Methods in Engineering*, **37**, 1945–1975, 1994, doi: 10.1002/nme.1620371111

[5] Rixen, D.J. and Farhat, C., A Simple and Efficient Extension of a Class of Substructure Based Preconditioners to Heterogeneous Structural Mechanics Problems, *International Journal for Numerical Methods in Engineering*, **44**, 489–516, 1999, doi: 10.1002/(SICI)1097-0207(19990210)44:4<489::AID-NME514>3.0.CO;2-Z

[6] Gravouil, A. and Combescure, A., Multi-time-step explicit - Implicit method for non-linear structural dynamics, *International Journal for Numerical Methods in Engineering*, **50**, 199–225, 2001, doi:10.1002/1097-0207(20010110)50:1<199::AID-NME132>3.0.CO;2-A

[7] Gravouil, A. Combescure, A. and Brun, M., Heterogeneous asynchronous time integrators for computational structural dynamics, *International Journal for Numerical Methods in Engineering*, **102**, 202–232, 2015, doi: 10.1002/nme.4818

[8] Kane, C. Marsden, J.E. Ortiz, M. and West, M., Variational integrators and the Newmark algorithm for conservative and dissipative mechanical systems, *International Journal for Numerical Methods in Engineering*, **49**, 1295–1325, 2000, doi: 10.1002/1097-0207(20001210)49:10<1295::AID-NME993>3.0.CO;2-W

[9] Leistner, M.C. Gosselet, P. and Rixen, D.J., Recycling of solution spaces in multipreconditioned FETI methods applied to structural dynamics, *International Journal for Numerical Methods in Engineering*, **116**, 141–160, 2018, doi: 10.1002/nme.5918

[10] Lew, A. Marsden, J.E. Ortiz, M. and West, M., Asynchronous Variational Integrators, *Archive for Rational Mechanics and Analysis*, 2003, doi: 10.1007/s00205-002-0212-y

[11] Leyendecker, S. Marsden, J.E. and Ortiz, M., Variational integrators for constrained dynamical systems, *ZAMM Zeitschrift für Angewandte Mathematik und Mechanik*, **88**, 677–708, 2008, doi: 10.1002/zamm.200700173

[12] Leyendecker, S. and Ober-Blöbaum, S., A Variational Approach to Multirate Integration for Constrained Systems, *Proceedings of the Multibody Dynamics 2011, ECCOMAS Thematic Conference*, Brussels, Belgium, 4-7 July 2011

[13] Pebrel, J. Rey, C. and Gosselet, P., A nonlinear dual domain decomposition method: application to structural problems with damage, *International Journal for Multiscale Computational Engineering*, **6**, 251–262, 2008

[14] Prakash, A. and Hjelmstad, K.D., A FETI-based multi-time-step coupling method for Newmark schemes in structural dynamics, *International Journal for Numerical Methods in Engineering*, **61**, 2183–2204, 2004, doi: 10.1002/nme.1136

[15] Prakash, A. Taciroglu, E. and Hjelmstad, K.D., Computationally efficient multi-time-step method for partitioned time integration of highly nonlinear structural dynamics, *Computers and Structures*, **133**, 51–63, 2014, doi: 10.1016/j.compstruc.2013.11.013

[16] Wenger, T. Ober-Blöbaum, S. and Leyendecker, S., Construction and analysis of higher order variational integrators for dynamical systems with holonomic constraints, *Advances in Computational Mathematics*, **43**, 1163–1195, 2017, doi: 10.1007/s10444-017-9520-5

[17] Applied Mechanics Finite Elements code (AMfe), *https://github.com/AppliedMechanics/AMfe*

[18] Python Finite Elements Tearing and Interconnecting (PyFETI), *https://github.com/jenovencio/PYFETI*

EURODYN 2020
XI International Conference on Structural Dynamics
M. Papadrakakis, M. Fragiadakis, C. Papadimitriou (eds.)
Athens, Greece, 23-26 November 2020

DEVELOPMENT AND VALIDATION OF A MULTIBODY DYNAMICS MODEL FOR THE ASSESSMENT OF THE SEISMIC RETROFIT POTENTIAL OF BRIDGE EXPANSION JOINTS

Michael Tahedl[1], Andreas Taras[2], Fredrik Borchsenius[1], and Daniel Rill[3]

[1]OTH Regensburg
Prüfeninger Str. 58 , 93049 Regensburg, Germany
michael.tahedl@st.oth-regensburg.de, fredrik.borchsenius@oth-regensburg.de

[2] ETH Zürich
Stefano-Franscini-Platz 5, 8093 Zürich, Switzerland
taras@ibk.baug.ethz.ch

[3] Maurer Engineering GmbH
Frankfurter Ring 193, 80807 München, Germany
d.rill@maurer.eu

Keywords: Multibody Dynamics, Bridge Expansion Joints, Earthquake Protection Devices.

Abstract. *Various types of devices are used to protect structures from seismic collapse, such as hydraulic or metallic hysteretic dampers or elastomeric and spherical pendulum bearings as isolators. In this paper however, a component which is already included in almost every medium to long span bridge, will be investigated and optimized to act as an earthquake protection device: the bridge expansion joints. Those structural components are placed between the abutment and the bridge superstructure or between different bridge sections to compensate relative movements, such as heat expansion elongation. Since these devices are often connected to bridge ends, the application of the expansion joints as a seismic protection device is potentially very beneficial. Also, it is expected to be economically advantageous because expansion joints are included by most bridges and under certain circumstances additional and expensive other protection devices can be replaced. The Paper demonstrates an approach of creating a precise and efficient multibody simulation model of expansion joints which will able to computationally determine their impact on seismic events.*

1 INTRODUCTION

The main purpose of the expansion joint in bridges is to cover the gap between the bridge ends and the respective abutment or between several bridge sections which is included to compensate relative movements, such as heat expansion elongation. These gaps need to be covered in order to achieve a continuous roadway for vehicles and pedestrians. In order to bridge this gaps, so called modular expansion joints come into consideration. They partition the gap into several sub-gaps, which for themselves are smaller than the allowed minimum distance. The structural elements, which fulfill this task in most configurations are the so called center beams, which are visible on the surface of the bridge roadway. The underlying support beams, which are significantly more stiff than the center beams, carry the loads induced by crossing vehicles to the gap edges. Because the gaps are not constant, the expansion joint needs to able to partition this movement equidistantly over all sub-gaps. Therefore, several control mechanisms have been developed over time. These mechanisms have in common, that they generate damping forces when the expansion joint is moved due to friction. As a result of this, it shall be investigated more deeply how much those friction forces affects the dynamic behaviour of a bridge under seismic loads.

Several papers like [2], [9] have discussed the dynamic response of bridge expansion joints due to traffic loads, which are capable of evaluating their behaviour in the vertical movement direction. Because it is expected that most of the seismic damping potential of an expansion joint arises from planar movements, those spatial directions need to be considered, too. Others like [10] investigated the pounding response of an expansion joint where the expansion joint is represented as a gap with a simplified, linear spring-damper mechanism. This is acceptable to calculate the effect of pounding towards a flexible bridge model, but is not sufficient when the nonlinear damping force of the expansion joint is of interest. For that case, a spatial multibody dynamics model will be built which is able to reproduce realistic damping forces and is suitable for targeted seismic protection behaviour. This model will be able to investigate the dynamic response of expansion joints which is expected to behave like hydraulic dampers with additional inertial forces. In contrast to that, a static response of the system is not expected, because most response forces are velocity dependent.

2 SWIVEL JOIST EXPANSION JOINTS

2.1 System description

The expansion joint which will be investigated in this paper is the Swivel Joist expansion joint. This type of expansion joint uses a control mechanism that follows the intercept theorem which describes distance relationships of intersecting lines. The task of the swivel joist is fulfilled by the support beam, which can execute rotational movements. Those rotational movement apply a control force to the elastomeric bearings, which are able to slide along the top of the support beam, as well as to the elastomeric springs at the bottom side of the support beam. These elastomeric parts are translationally fixed to the center beams, which are the visible components from the roadway, and can only rotate around the vertical axis. A very basic schematic representation of the control mechanism is displayed in Figure 1.

The elastomeric bearings and springs are preloaded to avoid a lift-off of the center beams. This force generates a significant friction force along the sliding direction of the bearings and springs which is considered as the main reason why the expansion joint is applying damping forces to the moving superstructure.

The outermost center beams of the expansion joint are called the edge beams. These beams

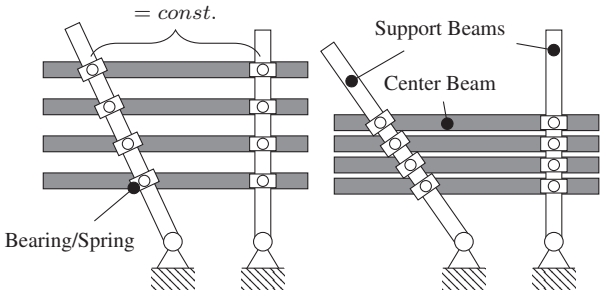

Figure 1: Schematic representation of the kinematic control mechanism of a swivel joist expansion joint

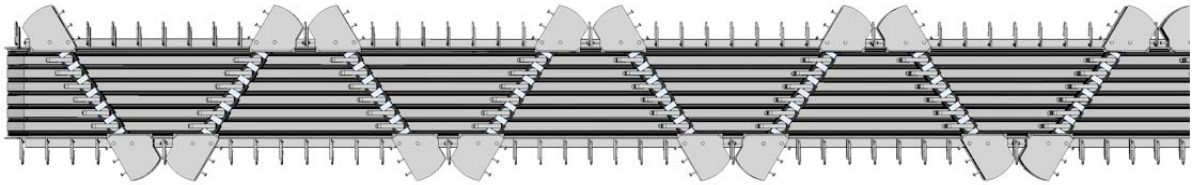

Figure 2: 3D CAD model of a swivel joist expansion joint example in bottom view

are fixed to the corresponding bridge deck and forces the support beams to swivel when one side of the bridge is moving.

3 SIMULATION MODEL

The aim of this work is to build a multibody simulation model of expansion joints which can be used to investigate their seismic retrofit potential. The fact that earthquakes are highly dynamic events which can take up to several minutes, the first requirement to the model is numerical efficiency. Because of high friction forces, it is expected that several force elements like contacts and couplings have to be extremely stiff to conserve a realistic behauviour of the model. On the other hand, such stiff force elements lead to stiff differential equations which need special solvers to gain results in a reasonable computation time.

The second requirement to the model is the possibility for easy adaption to other configurations. Because expansion joints are mostly custom made for a specific bridge, there are many possible configurations to investigate. So it needs to be possible to quickly create new simulation models by only specifying the configuration and the building process of the model itself should be automated.

The third requirement is that the model is easily extendable to other physical simulation environments for future extension possibilities as well as to custom algorithms like special friction models.

All those requirements lead to the conclusion, that it is reasonable to develop a multibody simulation environment which can be extended and automated on demand. The main parts needed to model an expansion joint are presented in the following sections.

3.1 Modeling concept

It is common to reduce the model to the essential components of interest. Parts which have less to no influence on the simulation results are ignored so that only a basic representation of the real system is left. This means for the expansion joint simulation under earthquake loads

that all parts which are affecting the control mechanism must be included. Therefore a model is built with the center beams, the support beams and the included bearings and springs. Figure 3 shows such a reduced simulation model of an example setup.

Figure 3: Reduced model for multibody simulation

The bearings at the top and the springs at the bottom side of the support beam are connected to the overlying center beams and can only rotate about the vertical axis. The contact definition between the bearings and the support beams includes the sidewall, which transmits the control force when the expansion joint is moving, and the top and bottom surface which represent the preloading and the resulting friction force.

Only one edge beam, which applies the external movement, is included because the second edge beam is assumed to be fixed for the first simulations which represent a simple opening and movement cycle. The functionality of this edge beams gets replaced by a kinematic constraint which allows a rotation of the support beams around the vertical axis only. The moving edge beam will be moved by a function of time which is coupled to a 3D force element to measure the force which is necessary to open and close the expansion joint.

3.2 Building simulation model

3.2.1 Rigid body dynamics

The system will be mathematically described by the well known Differential-Algebraic-Equations (DAE) of index 3

$$\begin{aligned} \dot{y} &= Kz \\ M\dot{z} &= F^e + J_g^T \lambda \\ 0 &= g(y) \end{aligned} \tag{1}$$

with the position vector y which containts translational positions and the Euler parameter in this setup and therefore K is the kinematic matrix, the velocity vector z, the mass matrix M, the external forces F^e and the constraint forces $J_g^T \lambda$ which are arising from the kinematic constraint

equations $g(y)$. According to [8], the index of the DAE gets reduced to 1 by two successive time derivations of $g(y)$ which can be solved by any ordinary differential equation solver

$$\dot{y} = Kz \tag{2}$$

$$M\dot{z} = F^e + J_g^T \left(J_g M^{-1} J_g^T\right)^{-1} \left(\dot{J}_g z + J_g M^{-1} F^e\right) \tag{3}$$

The external forces F^e are defined by the included contacts and the jacobian matrix J_g of all constraint equations need to be determined before the system can be solved. This steps are shown in the following sections.

3.2.2 Contacts

Contact mechanics plays an essential role in multibody dynamics and many different approaches have been published. Flores and Lankarani [4] gave a good overview of the relevant contact force models used by many multibody dynamics software. The most basic algorithm with energy dissipation is a linear Kelvin-Voigt contact model which will be implemented to simulate the contact behaviour between the bearings and support beams. It will be used as a point to surface contact where a pre-defined point P_1 represents the contact point and a corresponding surface normal vector n_2 attached to a point P_2 defines a surface. When P_1 penetrates the surface defined by n_2, a force will be applied to both bodies. A contact detection algorithm is implemented to detect whether and how much penetration is established. Therefore the scalar product of the vector between P_2 and P_1 in the local coordinate system of body 2 and the normal vector n_2 calculates the amount of penetration δ. The penetration velocity $\dot{\delta}$ gets calculated in a similar fashion. The linear Kelvin-Voigt contact model then describes the contact normal force as

$$F_n = \begin{cases} k\delta + d\dot{\delta}, & \text{if } \delta > 0 \\ 0, & \text{else} \end{cases} \tag{4}$$

with the contact stiffness k and contact damping d. For stabaility reasons and to make sure that the contact pairs do not stick permanentely, it needs to be guaranteed that

$$k\delta \overset{!}{>} d\dot{\delta} \tag{5}$$

Flores and Lankarani stated in [4] that the linear Kelvin-Voigt contact model may have several weaknesses mainly for high impact velocities. Because relatively slow velocities are considered for the first expansion joint models, this limitations are acceptable. When a more detailed contact behaviour is desired, the contact model described by Hunt and Crossley [6] might be more suitable.

The contact points get applied to the bearing bodies as shown in figure 4. Four contact points are transmitting the control forces from the support beam sidewall. The contact point for the top or bottom surface, depending on which side the bearing is mounted, generates the preloading force through geometrical positioning. These contact points are always closed and slightly overlapping with their contact surface to generate a constant force.

When two bodies get in contact with each other, a friction force tangential to the surface normal n_2 occurs. Many highly detailed models based on the friction model by Dahl [1] which are able to include stick-slip-effects have been developed. This is a common phenomenon which is observed at expansion joints, too. The disadvantage of those models is their complexity and the increasing numerical effort when solving differential equations affected by them. To

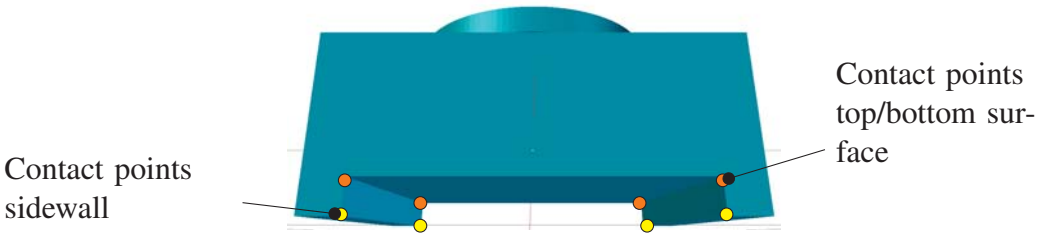

Figure 4: Distribution of the contact points on the bearings

conserve an efficient simulation model of the expansion joint, two basic friction models get implemented instead. The first one represents the statical Coulomb friction model with the tangential velocity dependent friction coefficient $\mu(v_t)$ which is illustrated in figure 5a. To overcome numerical difficulties at $v_t = 0$, μ gets approximated by a linear function when $v_t \in [-v_G, v_G]$ as shown if figure 5b.

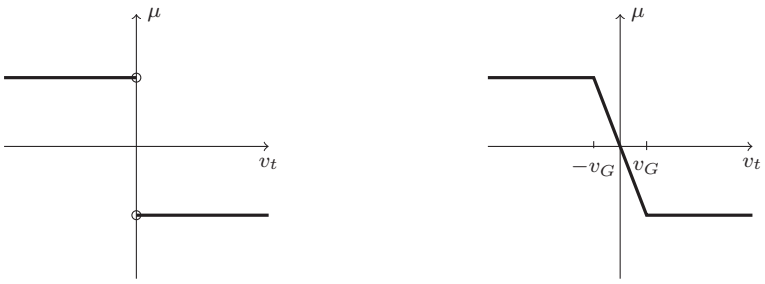

(a) with singularity (b) without singularity

Figure 5: Coulomb friction model

A more enhanced friction model, which includes the Stribeck-effect, is presented by Marques et al. [7]. This effect, illustrated in figure 6a, includes the fact, that the friction coefficient is higher at low velocities than the kinetic friction coefficient is. To simplify the calculation of μ, the continuous function gets approximated by linear sections. It has been observed in the expansion joint simulations that a slightly increasing kinetic friction coefficient is a good approximation of the real friction behaviour, which can be seen in figure 6b. This slightly increasing friction coefficient must be limited to avoid unrealistic high friction at higher velocities. The singularity at zero velocity has to be approximated the same way as in the aforementioned model.

Both friction models are implemented and used for tests within the multibody dynamics environment. Together with the normal forces of the contacts, the friction forces define the external forces F^e from equation 3.

3.2.3 Kinematic constraints

The interaction between the bearings and the center beams could be described either by force elements like so called bushings, which are basically three dimensional springs, or by kinematic constraint equations. Because it is expected that the contacts and those bushings need to be very stiff to ensure a realistic force transmission, the differential equations describing this system will be very stiff, too. To reduce those stiff force elements and the number of degrees of freedom

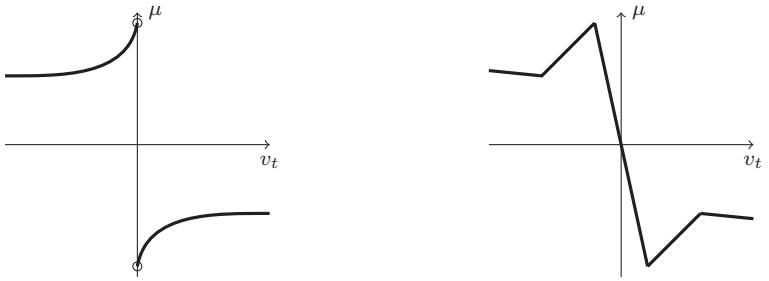

(a) with singularity (b) without singularity

Figure 6: Friction model with Stribeck-effect

of the model at the same time, kinematic constraints come into consideration. The connection between the bearings and the corresponding center beams could be simplified to the effect of a hinge. This constrains two bodies in a way so there is only one rotational degree of freedom left.

To include the effect of this hinge in the dynamic differential equation of the index reduced system 3, the jacobian J_g of the constraint equation $g(y)$ need to be determined. This constraint equation could be built with the basic vector constraints presented by Flores [3] to

$$g(y) = \begin{bmatrix} r_{0P_2,0} - r_{0P_1,0} \\ m_2^T u_2 \\ n_2^T u_2 \end{bmatrix} = 0 \tag{6}$$

where $r_{0P_1,0}$ and $r_{0P_2,0}$ are the vectors from the global coordinate System 0 to the local connection points of the hinge, m_2 and n_2 are the perpendicular vectors to the rotation axis attached to body 1 but transformed to the local coordinate system of body 2 and u_2 is the rotation axis attached to body 2. This equation depicts a hinge constraint because it constrains all translational movement and two rotations by requiring that the perpendicular vectors m_2 and n_2 are always perpendicular to u_2. The first derivative in time of equation 6 delivers the jacobian for each body to

$$\dot{g}(y) = \underbrace{\begin{bmatrix} I_{3\times3} & \tilde{r}_{1P1,0} \\ 0_{1\times3} & -\tilde{m}_2^T u_2 \\ 0_{1\times3} & -\tilde{n}_2^T u_2 \end{bmatrix}}_{J_{g1}} z1 + \underbrace{\begin{bmatrix} -I_{3\times3} & -\tilde{r}_{2P2,0} \\ 0_{1\times3} & A_{12}^T \tilde{m}_2^T u_2 \\ 0_{1\times3} & A_{12}^T \tilde{n}_2^T u_2 \end{bmatrix}}_{J_{g2}} z_2 \tag{7}$$

where $\tilde{r}_{1P1,0}$ and $\tilde{r}_{2P2,0}$ are the skew-symmetric matrices of the vector from the local coordinate system to the connection points transformed to the global coordinate system, z_1 and z_2 are the velocity vectors of the corresponding bodies and A_{12} is the transformation matrix between the local coordinate systems of the bodies. The jacobians of all bodies are collected when building the model providing the global jacobian J_g from equation 3. Another time derivative of the constraint equation delivers the product $\dot{J}_g z$ to

$$\dot{J}_g z = \begin{bmatrix} \dot{A}_{01} \left(\omega_{01,1} \times r_{1P1,1}\right) + \dot{A}_{02} \left(\omega_{02,2} \times r_{2P2,2}\right) \\ \left(\dot{A}_{12} u_2 \times m_2\right) \omega_{02,2} \\ \left(\dot{A}_{12} u_2 \times n_2\right) \omega_{02,2} \end{bmatrix} \tag{8}$$

with the derivatives of the transformation matrices $\dot{A}_{01}$, $\dot{A}_{02}$ and $\dot{A}_{12}$. This product will be collected into a global matrix for all bodies as well.

3.3 Friction coefficient

3.3.1 Test setup

The all determining forces generated by expansion joint are the friction forces generated between the preloaded bearings and the support beam due to the high normal force. In order to build a model which represents this behaviour, it is essential to know the friction coefficient μ. To achieve this, a simple test which should represent a realistic contact and movement scenario is set up as shown in figure 7a.

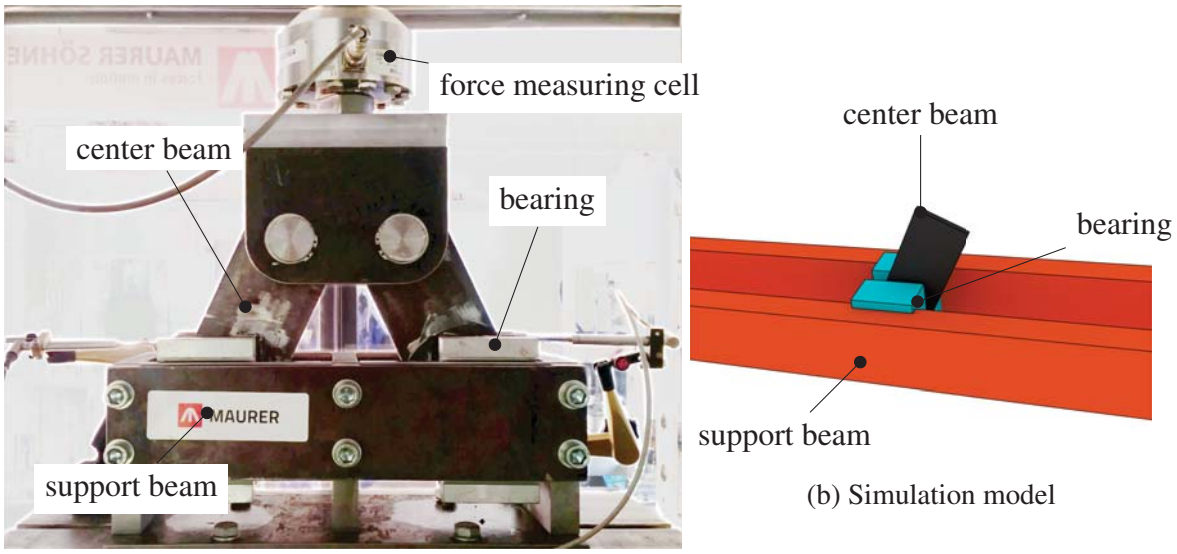

(a) Test

(b) Simulation model

Figure 7: Test setup and simulation model for a realistic friction force determination

With this setup it is intended to reproduce the angled force transmission that is occurring within the expansion joints. The bearings are preloaded with the standard preloading force and the sliding surfaces are identical to the real world contact faces. The force, which is necessary to move the system, is determined by the force measuring cell mounted between a hydraulic cylinder and the representative center beams. The hydraulic cylinder moves up and down with a frequency of $1\,\mathrm{Hz}$.

It has to be considered that friction is not the only physical phenomenon occurring in this setup influencing the time-load curve. Besides friction, there is also a noticeable amount of deformation of the elastomeric rubber bearings due to the high shear forces. This will be approximated by the linear Kelvin-Voigt contact model which allows a limited amount of penetration and represents therefore a deformation of the rubber bearings.

3.3.2 Validation with multibody simulation model

To validate the results from the friction tests, a corresponding multibody simulation model is built as shown in figure 7b. Because the test setup is symmetrical, the simulation model consists of one center beam, two bearings and two fixed support beams only. To generate the preload forces, the contact points of the main sliding surface are defined with a slight penetration of their surfaces and with a contact stiffness of $4 \times 10^7\,\mathrm{kN\,m^{-1}}$. The bearings themselves are connected

to the center beam by kinematic hinges. The results of the test and the simulation results with the basic Coulomb friction model and the Coulomb friction model with the Stribeck effect are compared in figure 8.

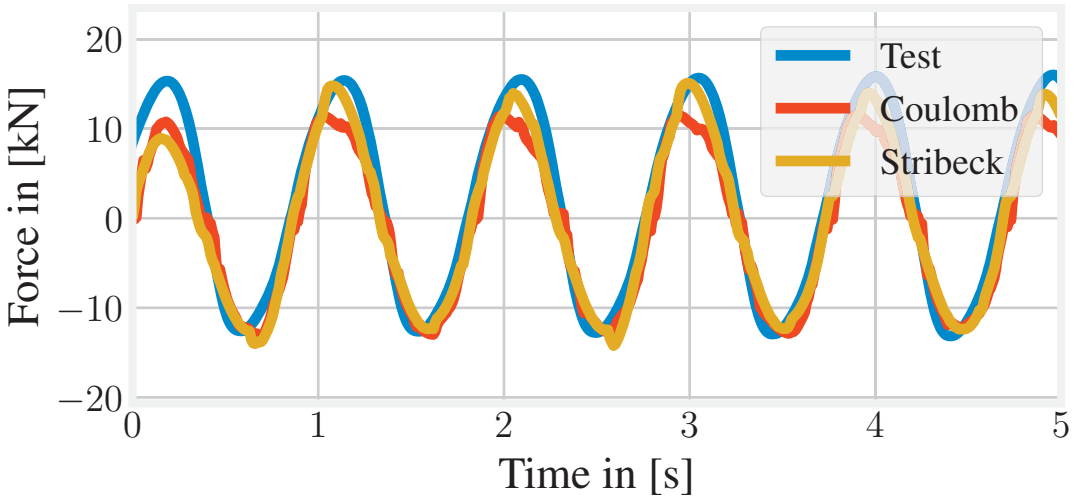

Figure 8: Force from the friction test and the simulations with different friction models

A typical effect within the swivel joist mechanism is the rising force which is needed to open the expansion joint where the angle between the center and support beams become nearly $90°$. This effect is called self-locking and first signs of this could be observed in figure 8 where the pull forces in positive direction are slightly higher than the push forces. This behaviour is represented more precisely by the friction model with the included Stribeck effect with a slightly rising kinematic friction coefficient as shown in figure 6b. This is plausible considering that the relative velocity between the bearing and the support beam increases the more the expansion joint opens and therefore the friction coefficient calculated by this model rises as well. The simulations showed that a static friction coefficient of about $7\,\%$ and a kinematic friction coefficient of $5\,\%$ producing realistic results, hence this values will be used in the follwing sections.

3.4 Numerical aspects

Before a simulation of the actual swivel joist expansion joint model could be done, several numerical aspects need to be considered. The high friction forces require very stiff contact elements to ensure realistic force transmission which leads to stiff initial value problems. Especially for large expansion joints with many bearings and therefore many contacts the simulation for simple opening/closing movements takes weeks with ordinary explicit solvers. Hairer and Wanner [5] suggested implicit methods for such problems. Therefore, the simpliest implicit solver, the backward Euler method

$$q_{k+1} = q_k + hf\left(t_{k+1}, q_{k+1}\right) \tag{9}$$

with the time step size h and

$$q = \begin{bmatrix} y \\ z \end{bmatrix} \tag{10}$$

can be used to solve the initial value problem

$$\dot{q} = f\left(t, q\right) \tag{11}$$

In order to gain the next step at $k+1$, a nonlinear equation system needs to be solved. Hairer and Wanner [5] suggested to solve this with a simplified Newton iteration. The bottleneck of this method is the computation of the jacobian

$$J = \left.\frac{\partial f_i}{\partial q_j}\right|_k \approx \frac{f\left(t, q + \epsilon q_j\right) - f(t, q)}{\epsilon} \tag{12}$$

which is done with a forward difference scheme where i are the functions and j is the number of the degrees of freedom. It has been observed that there are very small changes to the entries of the jacobian from step to step so a recomputation every time step is not necessary which speeds up the simulation tremendously.

A big advantage of the implicit Euler is that it is very efficient because only two function calls are needed per time step. According to [5], this method is also L-stable which means that uninteresting high oscillations of the true solution may be damped by the solver. This often undesired effect called numerical damping allows a reasonable time step size for the expansion joint model without instabilities in the numerical solution.

4 PLANAR OPENING AND CLOSING VALIDATION

To compare the simulation model to a real world example, a simple opening and closing scenario is used. Therefore, a relatively small expansion joint of the type MAURER DS240 is mounted on a test bench and the edge beam is moved by a hydraulic cylinder. This cylinder is equipped with a force measuring cell to determine the force which is needed to move the system. To observe a planar movement, the force is acting in a $45°$ angle, so the expansion joint executes a diagonal movement. The test bench setup is shown in figure 9.

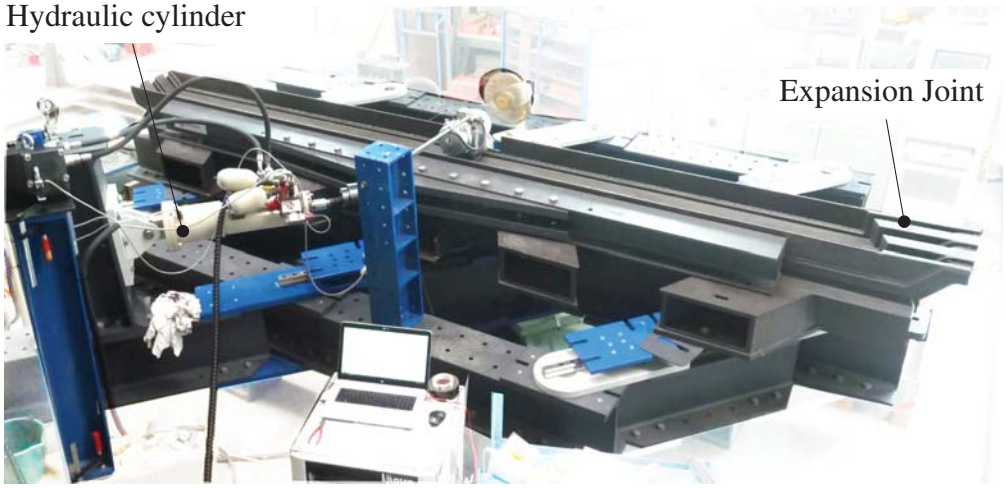

Figure 9: Test bench setup for opening and closing validation

The corresponding simulation model is shown in figure 3. The results from the test and simulations can be seen in figure 10.

Because the friction coefficients are similar, the maximum forces in both simulations are equal. The main difference between those friction models is the curvature of the force needed

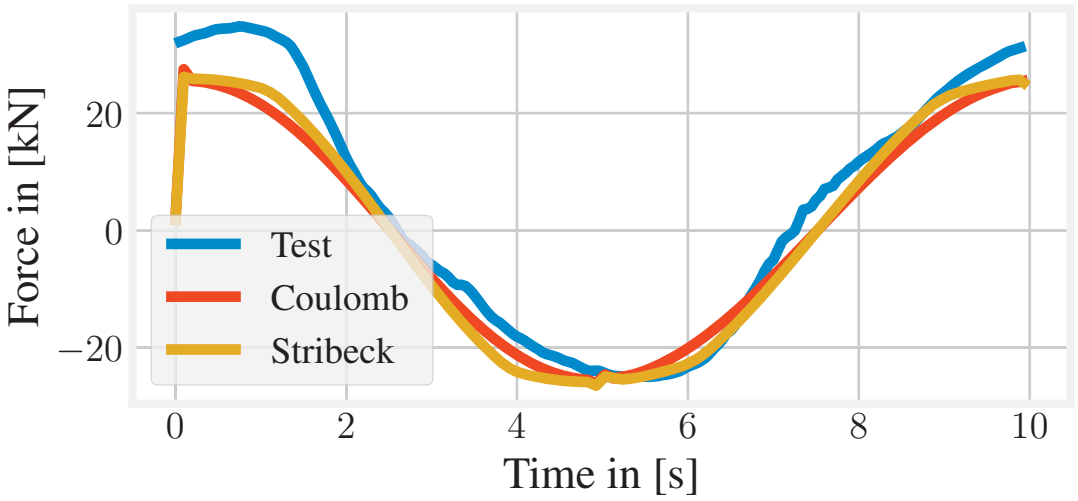

Figure 10: Force from the test and simulations with different friction models

to move the expansion joint, which is considered to be more realistic. Both models are showing a difference in the positive maxima to the measured force. This results from the fact that the test setup is not planar. Instead, the test bench is tilted forward so the hydraulic cylinder has to generate a higher push than pull force. Because of the little movement of only $10\,\mathrm{cm}$, there is not generated any noticeable amount of self-locking.

5 CONCLUSION

This research showed how a multibody dynamic model of an expansion joint for bridges could be created. Different models for the friction forces are presented, tested and compared to real world tests. The simulation model could reproduce realistic forces and movement behaviour. One big challenge is to create an efficient model which can be used in earthquake simulations with a reasonable simulation time. Therefore, stiff force elements are modeled by kinematic constraint equations and the overall stiff differential equations are solved by a simple and efficient Euler backwards method. Further test will include different configurations of the expansion joint and realistic earthquake loads applied to the models.

6 ACKNOWLEDGMENT

I would like to express my very great appreciation the company MAURER SE for the financial support to make this project possible.

REFERENCES

[1] P.R. Dahl. A solid friction model. Technical report, The Aerospace Corporation, California, 1968.

[2] Yong Ding, Wei Zhang, and Francis T.K. Au. Effect of dynamic impact at modular bridge expansion joints on bridge design. *Engineering Structures*, 127:645 – 662, 2016.

[3] P. Flores. *Concepts and Formulations for Spatial Multibody Dynamics*. SpringerBriefs in Applied Sciences and Technology. Springer International Publishing, 2015.

[4] Paulo Flores and Hamid Lankarani. *Contact Force Models for Multibody Dynamics*. 01 2016.

[5] E. Hairer and G. Wanner. *Solving Ordinary Differential Equations II: Stiff and Differential-Algebraic Problems*. Springer Series in Computational Mathematics. Springer Berlin Heidelberg, 2010.

[6] Kenneth Hunt and Erskine Crossley. Coefficient of restitution interpreted as damping in vibroimpact. *Journal of Applied Mechanics*, 1975.

[7] Filipe Marques, Paulo Flores, J.C. Claro, and Hamid Lankarani. Modeling and analysis of friction including rolling effects in multibody dynamics: a review. *Multibody System Dynamics*, 08 2018.

[8] Georg Rill, Thomas Schaeffer, and Fredrik Borchsenius. *Grundlagen und Methodik der Mehrkörpersimulation*. Springer Fachmedien Wiesbaden, 2020.

[9] Michal J.M.M. Steenbergen. Dynamic response of expansion joints to traffic loading. *Engineering Structures*, 26(12):1677 – 1690, 2004.

[10] Tian Wang and Qing Li. Research on pounding response at expansion joint in the linear bridge and the curved bridge under earthquake. *Advanced Materials Research*, 255-260:2303–2307, 05 2011.

EURODYN 2020
XI International Conference on Structural Dynamics
M. Papadrakakis, M. Fragiadakis, C. Papadimitriou (eds.)
Athens, Greece, 23-26 November 2020

A DELAYED FREQUENCY PRECONDITIONER APPROACH FOR SPEEDING-UP FREQUENCY RESPONSE COMPUTATION OF STRUCTURAL COMPONENTS

Guilherme Jenovencio[1], Arul Sivasankar[2], Zeeshan Saeed[3], and Daniel Rixen[1]

[1] Chair of Applied Mechanics
Technical University of Munich
Boltzmannstr. 15, 85785 Garching, Germany
e-mail: {guilherme,rixen}@tum.de

[2] IT4Innovations National Supercomputing Center
Technical University of Ostrava
Studentská 6231, 708 33 Ostrava , Czech Republic
e-mail: sivasankar.arul@gmail.com

[3] Department of Mechanical and Aerospace Engineering
Politecnico di Torino
Corso Duca degli Abruzzi 24, 10129, Turin, Italy
e-mail: zeeshan.saeed@polito.it

Keywords: Reusing preconditioners, Frequence response, Heuristic approach.

Abstract. *In this work, a delayed frequency preconditioner (DFP) is developed and applied in structural problems for speeding-up the frequency response computation. The challenge of computing the frequency response lies in the computation of the linear system that involves the excitation forces and also the dynamic stiffness which is frequency-dependent. For each frequency, the dynamic stiffness must be updated and a new factorization must be performed, which introduces a high computational cost on the solutions of the linear systems. Alternatively, iterative solver such as GMRES can be applied to avoid the cost of factorization, however they require good preconditioners that are traditionally also frequency-dependent. In the new approach, the dynamic stiffness operator is updated with the frequency whereas the preconditioner is kept constant for a range of frequencies serving as a low-cost preconditioner for the iterative solver. This technique saves computation time because a new factorization is avoided for each frequency point. On the other hand, the effectiveness of the delayed preconditioner is destroyed when the frequency of the dynamic operator is too far away from each other. Therefore, we propose a heuristic approach to update the preconditioner when it is underperforming. The algorithm is tested on structural problems and the results show that this approach can drastically reduce the number of iterations for the computation of the frequency response.*

1 INTRODUCTION

Frequency Response (FR) is commonly computed to find the steady-state response of structures under periodic load since they have significantly less computational cost compared to the time integration methods. FR computation is essential in several aspects of design, optimization and analysis [1–6] and in various fields ranging from large aircraft components [7] to micro-electro-mechanical systems [8].

Structural components and assembly models, due to geometrical intricacies and complexity, require very fine three-dimensional discretization. The model order becomes so large that the frequency response computational cost becomes very high. The response is generally desired at more than one frequency, hence, adding extra folds to the computational burden. In such cases, one way of computing the FR is by modal superposition method which helps reduce the problem size depending on the number of mode shapes retained [9]. Another way is to use reduced order models (ROM) that condense static or dynamic information to a smaller number of degrees-of-freedom (DoF) [1]. Even for the ROM, the modal superposition method is preferred over direct solution techniques [10] that require factorization of the dynamic stiffness matrix. Since these methods are approximate, their accuracy highly depends on the selected range of frequency – usually the low frequency range. Specific methods for FR computation avoiding excessive computation burden, that are based on interpolatory model order reduction methods, are reviewed in [11]. In particular, it discusses how several Krylov sequence vectors of dynamics stiffness are computed and used as a reduction basis to find the harmonic response over the frequency range of interest. This approach is called ”Moment Matching” or ”Padé approximation”.

It is well-known that direct solvers are not feasible for very large problems. Iterative solvers, for example, Conjugate Gradient or GMRES method [12], are then employed which use an initial guess of the solution and iterate until the error has been minimized [13]. Preconditioners are used for improving their performance. Preconditioners computed using LU factorization of the matrix are very effective but they are expensive [14]. Computing good preconditioners while reducing the cost of computation is an active area of research since the cost of computing preconditioners influences largely the overall cost of the iterative solver. In [15], a new preconditioner for solving the Helmholtz equation using iterative solver is discussed. Another preconditioner for the same equation is proposed in [16]. Moreover, efficient algorithms and implementation are necessary [17]. Perconditioning also can be done using parallel algorithms [18] when parallel computers are used. Numerous other studies propose new preconditioners for specific problems since there is no ideal preconditioner for every problem [19]. Nevertheless, some examples of popular preconditioners are Incomplete Cholesky, Incomplete LU, Successive over-relaxation (SOR), Symmetric SOR and Multigrid [20] which can be found in most of the computational libraries.

In this paper, a simple method for reusing preconditioners for the FR computation is proposed to reduce the computational cost. The concept of recycling preconditioners has been investigated for other problems. For instance, [21] proposes recycling preconditioners for topology optimization problems and analyses the advantages. Authors in [22, 23] investigate recycling preconditioners for the variational Monte Carlo problem. The simulation involves the solution of a series of Monte-Carlo steps. The preconditioner from one step is updated and mapped to another step. This updated preconditioner is then reused in the next step instead of computing a new preconditioner.

Since frequency response for a structural problem is generally computed for many frequen-

cies, the preconditioner at one frequency is proposed to be reused for some frequencies until its recycling becomes costly for the iterative solver. The so-called Delayed Frequency Preconditioner (DFP) is explained in detail and demonstrated on a beam problem. The method is very simple to implement and saves a lot of preconditioner computations.

The next section presents the system of equations of a typical mechanical system. Section 3 and 4 discuss the iterative solvers and the proposed delayed frequency preconditioner, respectively. In Section 5, results in terms of computation of the DFP are discussed in detail.

2 Equation of Motion of Structural Systems

A simplified structural problem can be represented by the differential equation of motion with mass $\mathbf{M}$, stiffness $\mathbf{K}$ and a viscous damping[1] $\mathbf{C}$ matrix:

$$\mathbf{M}\ddot{\mathbf{u}}(t) + \mathbf{C}\dot{\mathbf{u}}(t) + \mathbf{K}\mathbf{u}(t) = \mathbf{f}(t) \tag{1}$$

where $\mathbf{u}(t)$ is a time varying displacement vector due to action of linear force $\mathbf{f}(t)$. The single dot and double dot over $\mathbf{u}(t)$ denote velocity and acceleration, respectively. Assuming a periodic force $\mathbf{f}(t) = \tilde{\mathbf{f}}e^{i\omega t}$, the equation can be transformed to frequency domain

$$(-\omega^2\mathbf{M} + i\omega\mathbf{C} + \mathbf{K})\tilde{\mathbf{u}}(\omega) = \tilde{\mathbf{f}}(\omega) \tag{2}$$

The expression in parentheses is called dynamic stiffness of the system to be denoted here by

$$\mathbf{Z}(\omega) \triangleq -\omega^2\mathbf{M} + i\omega\mathbf{C} + \mathbf{K} \tag{3}$$

and substituting back in Eq. (2) gives the familiar form of linear system of equations

$$\mathbf{Z}(\omega)\tilde{\mathbf{u}}(\omega) = \tilde{\mathbf{f}}(\omega) \tag{4}$$

Note that Eq. (4) needs to be solved at every frequency $\omega = \omega_j$ in a desired bandwidth $[\omega_1, \omega_N]$ with N spectral points. Keeping in mind that the problem needs to be solved for N excitation frequencies in the frequency range of interest, the above quantities are denoted at j^{th} step for the following discussion as:

$$\tilde{\mathbf{u}}^{(j)} \triangleq \tilde{\mathbf{u}}(\omega_j), \quad \mathbf{Z}^{(j)} \triangleq \mathbf{Z}(\omega_j), \quad \tilde{\mathbf{f}}^{(j)} \triangleq \tilde{\mathbf{f}}(\omega_j) \tag{5}$$

3 Iterative Solution of the Linear System with Preconditioners

The linear system of Eq. (4) needs to be solved at each frequency point within the bandwidth. This can be computed by direct solvers which require factorization of the matrix, for example, LU factorization. It would be eminent immediately that such an operation would be extremely expensive given the size of typical discretized mechanical systems (on the order of 10^6 DoF) and that for all the spectral points. An alternate approach is to use the iterative solvers. Some of the solvers, based on Krylov Subspace, are Conjugate Gradient (CG), BiCG, MINRES, GMRES among many others. The iterative processes require good preconditioners for faster convergence. Some examples of preconditioners are Incomplete Cholesky, Incomplete LU, Successive over-relaxation (SOR), Symmetric SOR and Multigrid [20]. Eq. (4) can be written for the iterative formulation as:

$$\mathbf{Z}^{(j)}(\tilde{\mathbf{u}}_k^{(j)} + \Delta\tilde{\mathbf{u}}) = \tilde{\mathbf{f}}^{(j)} \quad \text{with} \quad \Delta\tilde{\mathbf{u}} \triangleq \tilde{\mathbf{u}}_{k+1}^{(j)} - \tilde{\mathbf{u}}_k^{(j)} \tag{6}$$

[1] The choice of damping model is arbitrary. A linear damping (Rayleigh or proportional) model is used in this work

where $k = 0, 1, , , N_k$ is the iteration index of the iterative solver. Rearranging the terms in Eq. (6)

$$\mathbf{Z}^{(j)} \Delta \tilde{\mathbf{u}} = -\mathbf{Z}^{(j)} \tilde{\mathbf{u}}_k^{(j)} + \tilde{\mathbf{f}}^{(j)} \tag{7}$$

and preconditioning the above equation with $\mathbf{P}^{(j)}$ at ω_j:

$$\begin{aligned} \mathbf{P}^{(j)} \Delta \tilde{\mathbf{u}} &= -\mathbf{Z}^{(j)} \tilde{\mathbf{u}}_k^{(j)} + \tilde{\mathbf{f}}^{(j)} \\ \mathbf{P}^{(j)} (\tilde{\mathbf{u}}_{k+1}^{(j)} - \tilde{\mathbf{u}}_k^{(j)}) &= -\mathbf{Z}^{(j)} \tilde{\mathbf{u}}_k^{(j)} + \tilde{\mathbf{f}}^{(j)} \\ \mathbf{P}^{(j)} \tilde{\mathbf{u}}_{k+1}^{(j)} &= (\mathbf{P}^{(j)} - \mathbf{Z}^{(j)}) \tilde{\mathbf{u}}_k^{(j)} + \tilde{\mathbf{f}}^{(j)} \end{aligned} \tag{8}$$

and muliplying both sides of the last of Eq. (8) with $[\mathbf{P}^{(j)}]^{-1}$ gives the equation used in the iterative solvers.

$$\tilde{\mathbf{u}}_{k+1}^{(j)} = \left(\mathbf{I} - [\mathbf{P}^{(j)}]^{-1} \, \mathbf{Z}^{(j)} \right) \tilde{\mathbf{u}}_k^{(j)} + [\mathbf{P}^{(j)}]^{-1} \, \tilde{\mathbf{f}}^{(j)} \tag{9}$$

Given an iterative solver, Eq. (9) requires that a preconditioner is computed at ω_j for which the solver would take some iterations to converge. Then for all subsequent frequency steps $\omega_{j+1}, \omega_{j+2}, \ldots, \omega_N$, new preconditioners $[\mathbf{P}^{(j+1)}]^{-1}, [\mathbf{P}^{(j+2)}]^{-1}, , \ldots, [\mathbf{P}^{(N)}]^{-1}$ will have to be computed. Since this N times repeated preconditioner computation is a costly operation for frequency response calculation, we aim to reduce it by recycling the preconditioner. This will be presented in the next section.

4 Delayed Frequency Preconditioner (DFP)

Generally, the dynamic stiffness $\mathbf{Z}^{(j)}$ is a different matrix at every ω_j, and therefore, requires a new preconditioner $\mathbf{P}^{(j)}$. The difference lies in the eigenvalues $\mathbf{\Lambda}^{(j)}$ of $\mathbf{Z}^{(j)}$. This is expounded by writing the eigen-decomposition of $\mathbf{Z}$ at two discrete frequency steps.

$$\begin{aligned} \mathbf{Z}^{(j)} &= \mathbf{\Phi} \mathbf{\Lambda}^{(j)} \mathbf{\Phi}^T \\ \mathbf{Z}^{(j+1)} &= \mathbf{\Phi} \mathbf{\Lambda}^{(j+1)} \mathbf{\Phi}^T \end{aligned} \tag{10}$$

where $\mathbf{\Phi}$ are eigenvectors of $\mathbf{Z}$ that remain unchanged at every ω. The eigenvalue matrix $\mathbf{\Lambda}^{(j)}$ and $\mathbf{\Lambda}^{(j+1)}$ have different diagonal elements which can be interpreted as the modal participation factors of the invariant modes $\mathbf{\Phi}$. In the limiting case when $\delta\omega = \omega_{j+1} - \omega_j$ is small, the change in eigenvalues of $\mathbf{Z}^{(j)}$ and $\mathbf{Z}^{(j+1)}$ is small, i.e.

$$\begin{aligned} &\mathbf{\Lambda}^{(j+1)} \approx \mathbf{\Lambda}^{(j)} \quad \text{when} \quad \delta\omega \longrightarrow 0 \\ \implies \; &\mathbf{Z}^{(j+1)} \approx \mathbf{Z}^{(j)} \end{aligned} \tag{11}$$

This property can be exploited to use $\mathbf{P}^{(j)}$ as $\mathbf{P}^{(j+1)} = \mathbf{P}^{(j)}$ at $\omega = \omega_{j+1}$. The preconditioner $[\mathbf{P}^{(j)}]^{-1}$ is thus recycled at $\omega_{j+1}, \omega_{j+2}, \ldots$ in the GMRES or CG iterative solver until a set criterion. If $[\mathbf{P}^{(j)}]^{-1}$ is a good preconditioner for the dynamic matrix $\mathbf{Z}^{(j)}$, it should make the expression $[\mathbf{P}^{(j)}]^{-1}\mathbf{Z}^{(j)}$ in Eq. (9) similar to an identity matrix. Using the same preconditioner in the successive linear system $\mathbf{Z}^{(j+1)}$ (perturbed by small $\delta\omega$ Eq. (3)), $[\mathbf{P}^{(j)}]^{-1}$ is still good enough and so is the resulting Krylov basis (upon which the GMRES or CG solvers are based on). However, the effectiveness of the preconditioner $[\mathbf{P}^{(j)}]^{-1}$ decreases slightly. The solver may take more iterations to converge. By continuing recycling the preconditioner, the solver will take more and more iterations. In order to avoid excessively high iterations, a heuristic

approach can be implemented in the algorithm. For example, as soon as a fixed number of iterations N_k of the iterative solver has been reached, a new preconditioner will be computed and reused for the next linear systems' solutions. However, it should be noted that successive increase in the number of iterations may still be cheaper than computing a new preconditioner at every step. This should be considered when choosing the fixed number of iterations N_k.

Assuming that a preconditioner was computed at frequency ω_j to solve Eq. (9). The same preconditioner was used for some τ number of frequencies. Thus, Eq. (9) can be expressed for the proposed delayed preconditioner in the following form:

$$\tilde{\mathbf{u}}_{k+1}^{(j+\tau)} = \left(\mathbf{I} - [\mathbf{P}^{(j)}]^{-1} \, \mathbf{Z}^{(j+\tau)} \right) \tilde{\mathbf{u}}_{k}^{(j+\tau)} + [\mathbf{P}^{(j)}]^{-1} \, \tilde{\mathbf{f}}^{(j+\tau)} \tag{12}$$

Comparing this equation with Eq. (9), note the change in superscripts of $\tilde{\mathbf{u}}$, $\tilde{\mathbf{f}}$ and $\mathbf{Z}$ while it remains unchanged for the recycled preconditioner $\mathbf{P}^{(j)}$. With the recycled preconditoner, it may not be known a priori the total number of preconditioner computations N_τ in the entire frequency band. However, the recycling is beneficial if $N_\tau < N$ and it scales such that $N_\tau << N$ when N is large in the same bandwidth (higher frequency resolution).

Since the preconditioner computation is delayed by τ in frequency, it is termed as *Delayed Frequency Preconditioner* or DFP. This reduces the computational burden significantly over the whole spectrum. An indicative algorithm of this method is also presented below:

Algorithm 1 Delayed Frequency Preconditioner

$\omega = \omega_{\mathbf{1}}, \omega_{\mathbf{2}} ... \omega_{\mathbf{N}}$ ▷ frequency points
update = $True$ ▷ initialize with preconditioner at ω_1
for $j = 1,\ 2,\ 3\ to\ N$ **do**
    $Z^{(j)} = -\omega_j^2 M + i\omega_j C + K$ ▷ dynamic stiffness matrix
    if (update = $True$) **then**
        $\mathbf{P}$ = compute_preconditioner($Z^{(j)}$) ▷ e.g. iLU preconditioner
    end if
    $\tilde{\mathbf{u}},\ k$ = iterative_solver($\mathbf{Z}^{(j)}, \tilde{\mathbf{f}}^{(j)}, \mathbf{P}$) ▷ Output: solution and number of iterations k
    if ($k \geqslant N_k$) **then**
        update = $True$
    else
        update = $False$
    end if
end for

It should be evident that the DFP is only a recycled preconditioner which can be obtained by any common methods. In this paper, the choice of the preconditioner is restricted to Incomplete and Complete LU. If the system matrix is symmetric and positive definite, the LU can be replaced by Cholesky factorization.

5 Application of the Method

The proposed DFP is tested on a simple beam with a small number of DoF in order to test various parameters. A simple cantilevered steel beam of Fig. 1 is subject to a dynamic load at its free end. It has been discretized into 200 elements. The choice of number of elements arises from the fact that, generally, the reduced order models have a similar model order in many design and optimization studies to conduct parametric studies.

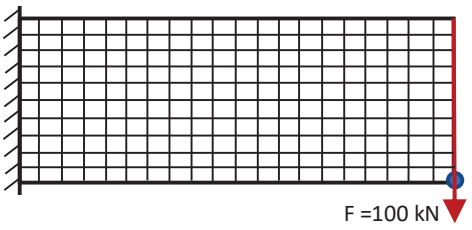

Young's Modulus	$210\ GPa$
Density	$7860\ kg/m^3$
Poisson's ratio	0.3
Beam Size	$8\ m \times 3\ m$
Number of DoF	462
Element Type	Plane-stress
	4-node quadrilateral
Damping Model	$\alpha\mathbf{M} + \beta\mathbf{K}$
α	1×10^{-3}
β	1×10^{-6}

Figure 1: The cantilevered beam with force applied on its unconstrained edge. The beam mechanical properties are also given on the right.

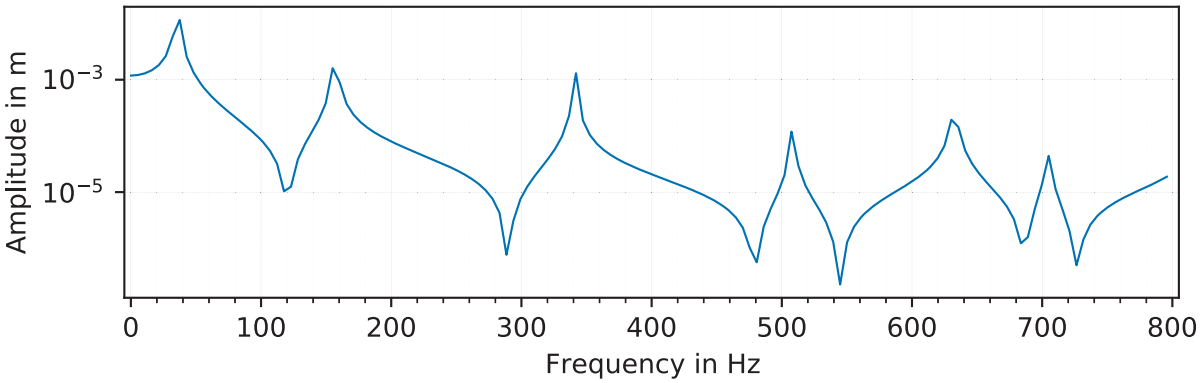

Figure 2: The forced response of the beam at the blue marked DoF in Fig. 1.

A displacement response function of the beam is shown in Fig. 2. The corresponding displacement DoF is shown in Fig. 1 with the blue marker. The frequency band is 0-800 Hz with 150 data points.

The accuracy of an iterative solver is determined by the tolerance limit. In the following analyses, the same tolerance limit is used for frequency response (FR) when a new preconditioner is computed at every frequency and when a delayed preconditioner is used. Therefore, the accuracy of the results from the solver remains the same for both the methods. Due to this reason, the comparison amongst different solvers with preconditioners and the proposed DFP is not deemed necessary. Instead, the results will be discussed only from the perspective of computational performance. The iterative solver chosen for the study is GMRES (in the *scipy* sparse linear algebra library of Python) with two preconditioners i.e. complete and incomplete LU. The two will be used as the DFP.

In Fig. 3, the number of iterations by the GMRES solver is plotted with an incomplete LU preconditioner. It can be seen that it takes mostly 4 or 5 or more iterations for the solver to converge at different frequencies. Since no DFP has been used, a new preconditioner was computed at each step. The small jumps in the number of iterations correspond to the resonance frequencies where the dynamic stiffness is ill-conditioned due to the dominance of the modes.

The DFP algorithm is implemented with the two preconditioners (complete LU and incomplete LU denoted simply by LU and iLU, respectively) in Fig. 4 which has the same axes as Fig. 3. Comparing the two figures, with only iLU preconditioner, the number of iterations is the same at the first frequency. The iterations start to increase gradually (Fig. 4) as the precon-

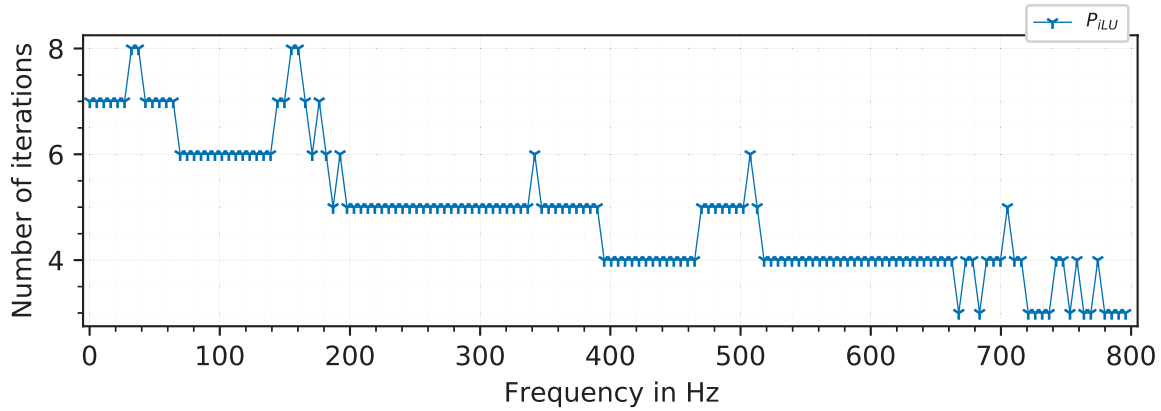

Figure 3: Number of GMRES iterations to convergence when using incomplete LU preconditioners. A new preconditioner is computed at each frequency.

ditioner at the first frequency is being reused until 135 Hz. This is where a new factorization was performed for a new preconditioner indicated by the encircled markers. The criterion for this was set to be 10 iterations $N_k = 10$. As soon as the limit is crossed, a new factorization is performed. The algorithm then continues with the new preconditioner for the next frequencies. Throughout the frequency band, only 17 factorizations were performed with iLU. Again near the resonances, the number of iterations becomes higher and the preconditioner is no longer valid for further frequency points. The complete LU preconditioner is also included in this figure. An LU factorization will be very expensive for a large system, however, in this case, only a few such factorizations are required. This can be afforded and analyzed for the given problem. At the outset of a new factorization, the solver converges in only one iteration since the solution process is direct. But it requires a few iterations as the preconditioner is recycled at the next frequencies. The number of LU factorizations are only 11 compared to 17 for iLU. It should be noted that the computational cost of iLU factorization is cheaper depending on the number of matrix entries that are dropped.

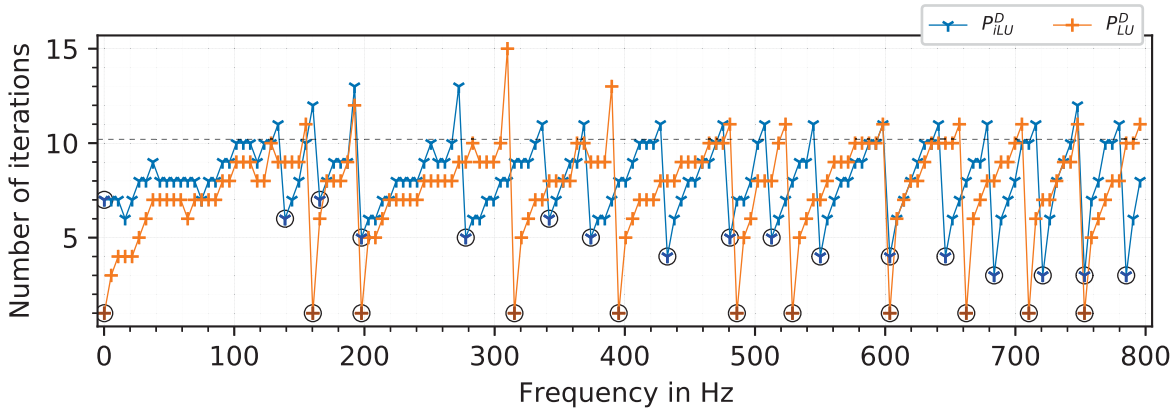

Figure 4: Number of GMRES iterations to convergence when using delayed frequency preconditioners (DFP) algorithm. The delayed preconditioners are incomplete $\mathbf{P}^D_{iLU}$ and complete $\mathbf{P}^D_{LU}$.

The new factorizations with the DFP are correlated with the condition number of the expression $[\mathbf{P}]^{-1}\mathbf{Z}^{(j)}$ which is plotted in Fig. 5 for different $\mathbf{P}$. If $\mathbf{P} = \mathbf{P}_I$ is an identity matrix, the

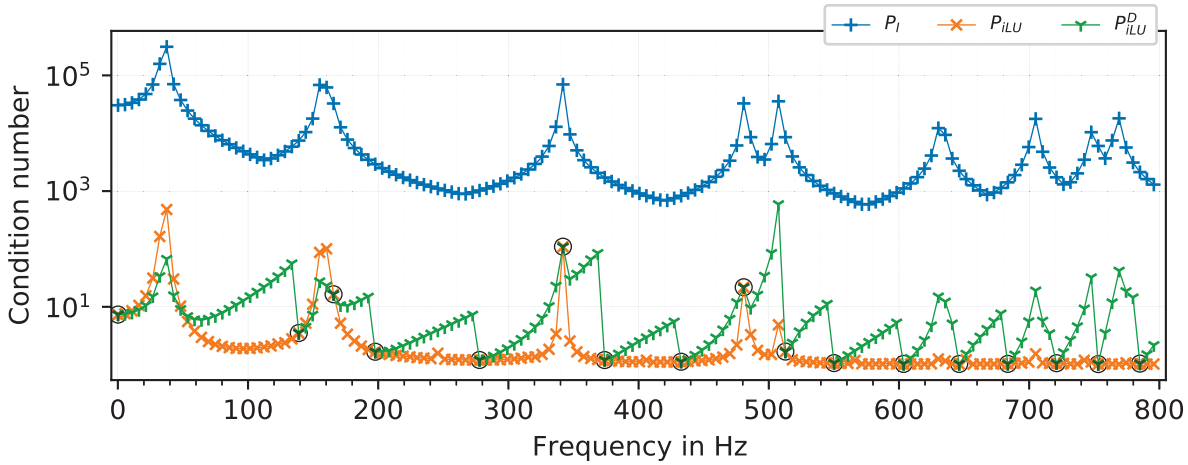

Figure 5: Comparison of condition number with no preconditioner $\mathbf{P}_I$ –an identity matrix, a simple iLU preconditioner $\mathbf{P}_{iLU}$ and the DFP iLU preconditioners $\mathbf{P}^D_{iLU}$.

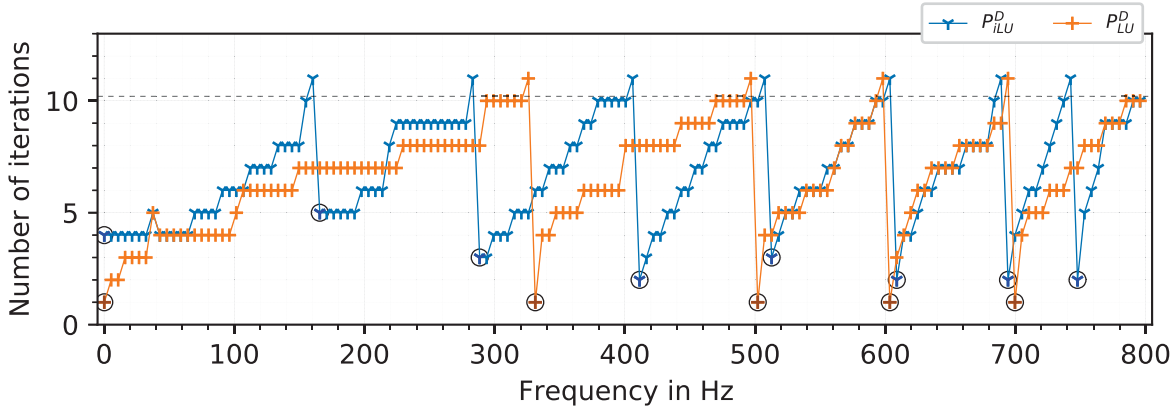

Figure 6: Number of iteration for convergence with BiCGSTAB iterative solver and using delayed preconditioners – incomplete iLU $\mathbf{P}^D_{iLU}$ and complete LU $\mathbf{P}^D_{LU}$.

condition number corresponds exactly to that of the dynamic stiffness $\mathbf{Z}$ which becomes high near the resonances. In its vicinity, the eigenvalues of $\mathbf{Z}^{(j)}$ change rapidly with ω_j. By using the conventional preconditioning technique discussed with iLU preconditioner, the condition number decreases but the behaviour remains the same. It requires more iterations for the solver to converge in the regions where the condition number is high, as was shown in Fig. 3. With the DFP algorithm, the condition number (Fig. 5) behaviour is quite different. It gradually increases and requires more iterations successively (Fig. 3). The change in eigenvalues[2] of $\mathbf{Z}^{(j)}$ renders the reused preconditioner inappropriate. Therefore, a new factorization is performed shown with an encircled marker in Fig. 5.

The method is tested for the same problem with a Bi-Conjugate Gradient Stabilized (BiCG STAB) iterative solver and the same two preconditioners for the DFP method. The number of iterations is shown in Fig. 6. The behaviour is similar to the GMRES solver, however, it

[2]The change in eigenvalues is inferred from the fact that the condition number is the ratio of the largest and smallest singular values of a matrix.

			DFP	
		$\mathbf{P}_{iLU}$	$\mathbf{P}^{D}_{iLU}$	$\mathbf{P}^{D}_{LU}$
	Number of frequencies	150	150	150
GMRES	Number of Iterations	732	1219	1140
	Number of preconditioners	150	17	11
BiCGSTAB	Number of Iterations	423	1024	1005
	Number of preconditioners	150	8	5

Table 1: Performance Comparison of GMRES and BiCGSTAB with and without Delayed Frequency Preconditioner

	Iteration limit N_k	5	10	15	20	25	30	40	50	60
$\mathbf{P}_{iLU}$	Total Iterations	2424	2424	2424	2424	2424	2424	2424	2424	2424
$\mathbf{P}^{D}_{iLU}$	Total Iterations	2424	2419	2430	2580	2749	2981	3249	3375	3661
	Number of preconditioners	150	147	80	15	4	3	2	2	1
	Percentage reduction in computation time	-0.4	1.5	22.5	41.1	41.8	39.2	37.8	33.7	28.5

Table 2: Effect of different iteration limits N_k on the performance of the DFP method. The test was done on the beam problem of Fig. 1with 8122 DoF.

requires a lower number of refactorizations. This is possibly because of the inherent difference of the objective function minimization in the solvers. The comparison of the DFP performance is tabulated in Table 1 for the two solvers. The significant observation is a great reduction in the number of preconditioners from 150 without DFP to 17 and 8 with DFP for GMRES and BiCGSTAB solvers, respectively. It should be noted that BiCGSTAB has also a lesser number of iterations to convergence along with lower refactorizations.

In the following, the computational performance of the method is analyzed. The ratio of the computational cost of computing the LU and iLU preconditioners to the cost of one iteration of the solver increases with an increase in the size of matrices. Since the beam problem considered so far has a small number of DoFs, this ratio is small. Hence, the time saved is not significant. In order to show an appreciable reduction in computation time, a similar problem with 8122 DoFs was used. The time for computing FRF with BiCGSTAB solver using iLU preconditioner with and without the delayed preconditioner was measured for various iteration limits N_k in Table 2 along with the other parameters. When the iteration limit is small, for example, $N_k = 5$, a new preconditioner is computed at all the frequencies. So, the performance of the DFP method is the same as without the DFP. As the iteration limit was increased, the number of preconditioner computations were reduced and there was an improvement in the performance of the method. It can be seen that for $N_k = 25$, the preconditioner was computed only 4 times and there was a 41.8% reduction in the computation time when the DFP algorithm is used. As the iteration limit was further increased, the performance no longer increases. This is due to the fact that the iterative solver then took more total iterations and time to converge, thereby overpowering the time saved by reducing the number of preconditioner computations. As it be seen at $N_k = 60$ that only one preconditioner needed to be computed but it is not quite effective anymore. From the above observations, it can be concluded that the computational time shows an optimum-like behaviour as the iteration limit is changed.

So far, various results were shown for 150 frequency data points in the entire band of frequency. At this point, the scalability for variation in the data points or resolution is discussed.

Table 3 lists the number of preconditioner computations as the number of frequency data points is increased. It is clearly seen that a remarkably smaller number of refactorizations are needed in comparison to the number of data points. In the absence of the DFP, many refactorizations would be needed which is quite expensive. In the limiting case, when the frequency resolution is very coarse, the DFP algorithm will behave as without a delayed preconditioner.

Number of frequencies	10	50	100	150	250	400	1000	2000
Number of $\mathbf{P}$ Computations	4	8	11	11	11	13	14	14

Table 3: Scalability of the DFP: Effect of increasing the number of frequencies in the given range (making $\delta\omega$ smaller) on number of refactorizations for the preconditioners is listed. A complete LU factorization was used and recycled for the data.

6 Conclusions and Future Work

A method for reusing information about preconditioners during frequency response computation was proposed. This method is tested on a beam problem. Two iterative solvers, GMRES and BiCG, were used for this study. The performance of the method was studied for two preconditioners, LU and iLU. The method helps to reduce the number of preconditioner computations significantly, thereby reducing the overall computation cost. The computational performance of the method depends on the iteration limit N_k and shows that an optimum value of N_k may be needed for maximum computational savings. If this limit is low, in the worst-case scenario, factorization has to be done at every other frequency. If the limit is too high, very few preconditioners are computed but it would take more iterations to converge and hence would require more time. Further, it was shown that the method is more effective when the gap between the frequency points becomes smaller.

The method can also be extended to other problems and improvements can be suggested as follows:

- Only linear problems have been considered in this paper. Nonlinearity might arise through material properties or friction contact. This method could be extended to such non-linear problems.
- In this study, only single domain geometries are considered. For very large problems, domain-decomposition method needs to be used. For such cases, the same method can be extended to reuse information from each subdomain.
- The performance of the method can be tested for other linear solvers and preconditioners.

Acknowledgment

This work is a part of the project EXPERTISE that received funding from the European Union's Horizon 2020 research and innovation program under the Marie Sklodowska-Curie grant agreement No 721865.

REFERENCES

[1] D. De Klerk, D. J. Rixen, and S. N. Voormeeren. General framework for dynamic substructuring: History, review, and classification of techniques. *AIAA Journal*, 46(5):1169–1181, may 2008.

[2] Z. D. Ma, N. Kikuchi, and I. Hagiwara. Structural topology and shape optimization for a frequency response problem. *Computational Mechanics*, 13(3):157–174, 1993.

[3] E. Barkanov and J. Gassan. Frequency response analysis of laminated composite beams. *Mechanics of Composite Materials*, 30(5):484–492, 1995.

[4] Loïc Salles, Laurent Blanc, Fabrice Thouverez, A. Gouskov, and Pierrick Jean. Dynamic analysis of a bladed disk with friction and fretting-wear in blade attachments. volume 6, 01 2009.

[5] Z. Saeed, G. Jenovencio, S. Arul, J. Blahoš, A. Sudhakar, L. Pesaresi, J. Yuan, F. El Haddad, H. Hetzler, and L. Salles. A Test-Case on Continuation Methods for Bladed-Disk Vibration with Contact and Friction. In *Conference Proceedings of the Society for Experimental Mechanics Series*, pages 209–212. Springer New York LLC, 2020.

[6] Guilherme Jenovencio and Daniel J Rixen. A dual formulation of cyclic symmetry: Application in free vibration analysis. In *7th International Conference on Computational Methods in Structural Dynamics and Earthquake Engineering (COMPDYN 2019), Crete, Greece*, 2019.

[7] A I Sayma, M Vahdati, S J Lee, and M Imregun. Forced response analysis of a shaft-driven lift fan. *Proceedings of the Institution of Mechanical Engineers, Part C: Journal of Mechanical Engineering Science*, 217(10):1125–1137, 2003.

[8] Alan H Epstein. Millimeter-scale, mems gas turbine engines. In *ASME Turbo Expo 2003, collocated with the 2003 International Joint Power Generation Conference*, pages 669–696. American Society of Mechanical Engineers Digital Collection, 2003.

[9] Weiwei Xiao, Li Li, and Sheng Lei. Accurate modal superposition method for harmonic frequency response sensitivity of non-classically damped systems with lower-higher-modal truncation. *Mechanical Systems and Signal Processing*, 85:204–217, feb 2017.

[10] Z Saeed, C M Firrone, and T M Berruti. Substructuring for contact parameters identification in bladed-disks. *Journal of Physics: Conference Series*, 1264:012037, jul 2019.

[11] U. Hetmaniuk, R. Tezaur, and C. Farhat. Review and assessment of interpolatory model order reduction methods for frequency response structural dynamics and acoustics problems. *International Journal for Numerical Methods in Engineering*, 90(13):1636–1662, 2012.

[12] Youcef Saad and Martin H. Schultz. GMRES: A Generalized Minimal Residual Algorithm for Solving Nonsymmetric Linear Systems. *SIAM Journal on Scientific and Statistical Computing*, 7(3):856–869, jul 1986.

[13] Yousef Saad and Henk A. van der Vorst. Iterative solution of linear systems in the 20th century. *Journal of Computational and Applied Mathematics*, 123(1):1 – 33, 2000. Numerical Analysis 2000. Vol. III: Linear Algebra.

[14] Alan George and Esmond Ng. On the Complexity of Sparse QR and LU Factorization of Finite-Element Matrices. *SIAM Journal on Scientific and Statistical Computing*, 9(5):849–861, sep 1988.

[15] AL Laird and M Giles. Preconditioned iterative solution of the 2D Helmholtz equation. 2002.

[16] Björn Engquist and Lexing Ying. Sweeping Preconditioner for the Helmholtz Equation: Moving Perfectly Matched Layers. *Multiscale Modeling and Simulation*, 9(2):686–710, jul 2010.

[17] John R. Gilbert and Timothy Peierls. Sparse Partial Pivoting in Time Proportional to Arithmetic Operations. 1986.

[18] Youcef Saad. Highly Parallel Preconditioners for General Sparse Matrices. pages 165–199. Springer, New York, NY, 1994.

[19] G. Strang. *Computational Science and Engineering*. Wellesley-Cambridge Press, 2007.

[20] Michele Benzi. Preconditioning techniques for large linear systems: A survey. *Journal of Computational Physics*, 182(2):418–477, nov 2002.

[21] Oded Amir. Revisiting approximate reanalysis in topology optimization: on the advantages of recycled preconditioning in a minimum weight procedure. *Structural and Multidisciplinary Optimization*, 51(1):41–57, may 2015.

[22] Kapil Ahuja, Eric De Sturler, Christopher A Beattie, Jeffrey T Borggaard, David M Ceperley, Serkan Gugercin, and John F Rossi. Recycling Krylov Subspaces and Preconditioners. Technical report, nov 2011.

[23] Arielle Grim-Mcnally. Reusing and Updating Preconditioners for Sequences of Matrices. Technical report, jun 2015.

EURODYN 2020
XI International Conference on Structural Dynamics
M. Papadrakakis, M. Fragiadakis, C. Papadimitriou (eds.)
Athens, Greece, 23-26 November 2020

NONLINEAR FORCE LAW SELECTION AND PARAMETER UPDATE FOR A CANTILEVER BEAM WITH PERIODICALLY REPEATED IMPACTS

Alexandros N. Arailopoulos[1] **and Dimitrios A. Giagopoulos**[1]

[1] Department of Mechanical Engineering, University of Western Macedonia
Bakola & Sialvera, 50100, Kozani, Greece
e-mail: aarailopoulos@uowm.gr, dgiagopoulos@uowm.gr

Keywords: Nonlinear Impact Dynamics, Consecutive Impacts, FE Model Selection, FE Model Updating, Uncertainty quantification, Structural Nonlinearities.

Abstract *Contact-impact events frequently occur between solid contact interfaces in complex dynamic mechanical systems and engineering applications. Impact force models are used to determine the responses of contacting solids. The selection of the impact force model strongly affects the predictions of the dynamic behavior of the contacting bodies, mainly in sequential repeated impacts. In this work, the strong nonlinear dynamic behavior of a cantilever steel beam, repeatedly impacting a steel rigid stop is investigated applying experimental and numerical methodologies. The applicability of a nonlinear constitutive force model selection and model-updating framework at engineering problems where contact-impact phenomena happen in a sequential periodic manner is presented. First, a discrete Finite Element (FE) model of the examined beam was developed. Applying Covariance Matrix Adaptation – Evolution Strategy (CMA-ES) model updating methodology, coupled with robust, accurate and efficient Finite Element Analysis (FEA) software, the linear behavior of the cantilever beam was validated under enforced motion conditions followed by equivalent experimental trials, in order to tune the material and geometrical properties and boundary conditions parameters and develop a high-fidelity linear FE model. Next, the general viscoelastic impact force law based on the Hertz contact theory, augmented with a damping term is integrated in the updated linear FE model. Upon further experimental trials of the impacting cantilever beam under base excitation, a model selection process using Bayesian inference is carried out between nine different expressions of the viscous term at constant nonlinear power exponent, updating the inferred parameters of the most probable force model. A new model selection and updating process including the nonlinear power exponent in the inferred parameters is finally presented in order to tune and study in detail the effect of the contact stiffness, coefficient of restitution, nonlinear power exponent and clearance gap between the contacting bodies in a specific sinusoidal excitation frequency of the impacting cantilever beam, validating the experimental results.*

1 INTRODUCTION

Contact-impact events occur between two colliding bodies that belong to a multibody system or move unconstrained, at an instant of time. During an impact, elastic or plastic deformations locally developed around the contact area, effects related to vibration propagation and abrupt velocity changes and energy dissipation phenomena are detected. These phenomena are augmented and become crucial in engineering applications when involved bodies move intermittently or have clearance joints between them and especially when sequential repeated impacts take place [2-5].

The basic difficulty in order to accurately model and analyze a multibody system with impact-contact phenomena, is the selection of the most appropriate constitutive force model that adequately represents the impact events regarding aspects that include the materials of the contacting bodies and their damping characteristics, their geometry and clearance distance, along with the overall kinematics of the phenomenon involving contact point, impact direction and boundary conditions [7-9]. As the impact model depends on many parameters, coefficient of restitution (COR), c_r, has been introduced as a parameter to determine the energy dissipation during the complete impact event. In all models, the choice of the coefficient of restitution reflects the type of collision. The value of COR is in the range of $0 \le c_r \le 1$, where for a fully elastic contact, the restitution coefficient is equal to the unit, whereas for a fully plastic contact, the restitution coefficient is null. COR is highly depended on the impact speed and direction, material properties and geometry of colliding bodies and duration of contact [10, 11].

In this work, the parameters that contribute to the evaluation of the contact force, including the contact stiffness, contact viscous damping, CORs and clearance, during the strong nonlinear dynamic behavior of a cantilever steel beam, repeatedly impacting a steel rigid stop is investigated applying experimental and numerical methodologies. At first, a high-fidelity finite element (FE) model of the cantilever beam was developed and validated under enforced motion conditions (base excitation) followed by equivalent experimental trials, tuning its material properties and boundary condition parameters. Single objective optimization formulation, without the need of sub-structuring methods, is used for estimating the parameters of the finite element model. The updated FE model is then reduced in order to accommodate a viscoelastic impact force model based on the Hertz contact theory, augmented with a damping term to account for the dissipation of energy during the impact events, as a function of the coefficient of restitutions (COR) between the impacting bodies [12]. The parameters of the applied constitutive impact force model are tuned in order to match the numerical predictions and recorded experimental data. Both unreduced linear FE model and reduced numerical model updating procedures, are achieved implementing response residuals that include time-histories of accelerations [13-18]. A state-of-the-art optimization algorithm, namely, covariance matrix adaptation evolution strategy (CMA-ES) [19-22], is applied in parallel computing, to solve the single-objective optimization problem [23, 24]. The applicability and effectiveness of the methods applied, is explored and issues related to estimating unidentifiable solutions [25-28] arising in FE model updating formulations are also addressed.

The presentation in this work is organized as follows. The theoretical formulation of finite element model updating is briefly presented in section 2. Section 3 presents the viscoelastic dissipative contact force models. Section 4 presents the experimental application. Section 5 presents the updating of the linear FE model. Section 6 presents the experimental set up of the nonlinear model whereas section 7 presents the nonlinear FE model update and results. Conclusions are summarized in section 8.

2 MODEL UPDATING TO MOST PROBABLE PARAMETERS USING CMA-ES

The most probable values (MPVs) of the parameter set $\underline{\theta}$ of the non-linear model are those that maximize the posterior density function (PDF). Numerical acceleration time histories, included in the actual measure of fit, are computed. Thus, Covariance Matrix Adaptation Evolution Strategy (CMA-ES) [1-3], is applied to maximize the natural logarithm of the probability density function, $\ln\left[p(\underline{\theta},\underline{\sigma}\,|\,D,M_i)\right]$. CMA-ES is applied using an already proposed framework in previous works [4-6], to minimize the minus natural logarithm of the probability density function $-\ln\left[p(\underline{\theta},\underline{\sigma}\,|\,D,M_i)\right]$, updating model parameters to the most probable values (MPVs). The algorithm is applied in a parallel computing scheme to compensate for the computation time. Details on the formulation sequence of CMA-ES and the proposed framework can be found in [4].

The objective-function to be minimized that is passed to CMA-ES, is:

$$g\left(\underline{\theta},\underline{\sigma}\right)=-\ln\left[p\left(\underline{\theta},\sigma\,|\,D,M_i\right)\right]=$$

$$=\frac{N_s N_m}{2}\ln\left(2\pi\right)+\frac{N_s N_m}{2}\ln\left(\sigma^2\right)+\frac{1}{2\sigma^2}\sum_{j=1}^{N_s}\frac{\sum_{k=1}^{N_m}\left(\hat{y}_j(k)-y_j\left(k;\underline{\theta}\right)\right)^2}{\sum_{k=1}^{N_m}\left(\hat{y}_j(k)\right)^2}-\ln\pi\left(\underline{\theta},\sigma\,|\,M_i\right) \tag{1}$$

The process terminated when the difference of the best values of two consecutive sets of iterations was less than $\Delta g(\underline{\theta},\underline{\sigma})=10^{-3}$. A version of the CMA-ES algorithm (programmed in C), and the numerical analysis were coupled through a developed C language script, allowing the framework to be compiled and run independently in parallelization. The computer that was used, hosts two (2) Intel® Xeon® Gold Processors 6130 (22M Cache, 3.70 GHz) with 16-cores and 32-threads, resulting in a total number of sixty-four (64) logical (virtual) cores and 128GB of RAM, on Linux Ubuntu 18.04 Operating System.

3 VISCOELASTIC DISSIPATIVE CONTACT FORCE MODELS

Pure elastic contact force constitutive models have the disadvantage of neglecting forces acted upon contacting bodies during compression and restitution phases. Thus, internal damping has been introduced to augment the pure elastic laws and account for energy dissipation during an impact-contact event. A general formulation of the contact force law can be expressed combining elastic and viscous components as [7, 8]:

$$f=K\delta^n+\chi\delta^n\dot{\delta} \tag{2}$$

where K is the generalized contact stiffness depended on the material properties of the colliding bodies and geometry of the local contacting region, δ is the relative indentation between the contacting bodies, n is the nonlinear power exponents, χ represents the hysteresis damping factor and $\dot{\delta}$ is the indentation velocity. **Table 1** presents the most popular expressions of the damping factor χ adopted in the consequent model selection process, where $\dot{\delta}^{(-)}$ represents the initial value of the velocity exactly at the moment of contact-impact occurrence. In all above laws the nonlinear power exponents proposed by all researchers is $n=3/2$ and has been included as such in the implementation of the above expressions during the model selection process.

Table 1. Most popular contact-impact constitutive force models.

Model	Reference of force model	Contact-impact Constitutive force law	Damping factor χ
1	Hertz [9]	$f=K\delta^n$	0

2	Gharib and Hurmuzlu [10]	$f = K\delta^n + \chi\delta^n\dot{\delta}$	$\chi = \frac{1}{c_r}\frac{K}{\dot{\delta}^{(-)}}$
3	Herbert and McWhannel [11]		$\chi = \frac{6(1-c_r)}{(2c_r-1)^2+3}\frac{K}{\dot{\delta}^{(-)}}$
4	Flores et al. [12]		$\chi = \frac{8(1-c_r)}{5c_r}\frac{K}{\dot{\delta}^{(-)}}$
5	Lee and Wang [13]		$\chi = \frac{3(1-c_r)}{4}\frac{K}{\dot{\delta}^{(-)}}$
6	Hunt and Crossley [14]		$\chi = \frac{3(1-c_r)}{2}\frac{K}{\dot{\delta}^{(-)}}$
7	Lankarani and Nikravesh [15]		$\chi = \frac{3(1-c_r^2)}{4}\frac{K}{\dot{\delta}^{(-)}}$
8	Zhiying and Qishao [16]		$\chi = \frac{3(1-c_r^2)e^{2(1-c_r)}}{4}\frac{K}{\dot{\delta}^{(-)}}$
9	Gonthier et al. [17]		$\chi = \frac{1-c_r^2}{c_r}\frac{K}{\dot{\delta}^{(-)}}$

4 EXPERIMENTAL ARRANGEMENT

The experimental set up of the contact-impact cantilever beam is illustrated in **Fig. 1**. A steel beam of total length $745mm$ was tightened on one end, between two compact aluminum blocks for a length of $145mm$ in order to create a fixed support. The bottom aluminum block was mounted on an electromagnetic shaker and a linear variable differential transformer (LVDT) sensor was placed on top of the upper block in order to measure base excitation time histories of displacements, along with accelerometer B recording base excitation time histories of acceleration. Furthermore, three (3) tri-axial accelerometers A1, A2 and A3, were placed at the $2/3s$ of the length of the beam, at the point where contact-impact occurs and at the free end respectively, all in the middle of the width of the beam. Lastly, a load cell was placed below accelerometer A2 at a clearance distance, leaving a gap between the beam and the rigid stop. Load cell was recording imposed impact force during experimental trials.

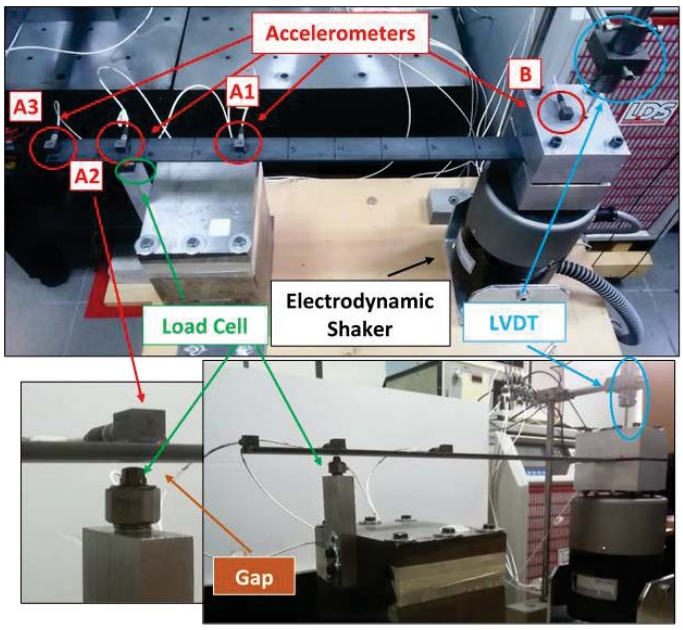

Fig. 1 Experimental arrangement of cantilever beam.

The experimental cantilever beam is a steel beam with Young's modulus $E = 210GPa$, Poisson's ratio $v = 0.3$ and density $\rho = 7850kg/m^3$. Similarly the nominal material properties of the aluminum accelerometers were $E = 69GPa$ for the Young's modulus and $\rho = 2750kg/m^3$. The cantilever steel beam is a simple structural arrangement, which is mounted from one end being free to oscillate under ground motion in the vertical direction. The length of the cantilever is $600mm$, its width is $40mm$ and its thickness is $5mm$.

At first in order to examine the linear response of the cantilever structure, the material and geometrical properties, the boundary condition parameters of the elastic properties of the support, along with the contribution of the accelerometers themselves in the overall response, an experimental arrangement without the rigid stop was introduced. A series of experimental trials were performed under three sinusoidal base motions at 4Hz, 6Hz and 8Hz excitation frequencies and various ranges, recording excitation accelerations at point B and response accelerations at locations A1, A2 and A3.

5 UPDATING OF LINEAR FE MODEL

5.1 Development of linear FE model

Strictly based on the experimental structure, the equivalent finite element model was developed as presented in **Fig. 2** with a schematic diagram of the experimental setup. The accelerometers were also included in the geometry of the structure as its was noticed that their contribution to the overall response of the structure is not negligible. The geometry of the cantilever beam along with the accelerometers themselves is discretized by shell and solid elements respectively, using appropriate pre-processing commercial software [18]. The introduced 2D plane with dimensions $600x40mm$ is modeled with 960 CQUAD shell elements with $5mm$ discretization length and $5mm$ nominal thickness.

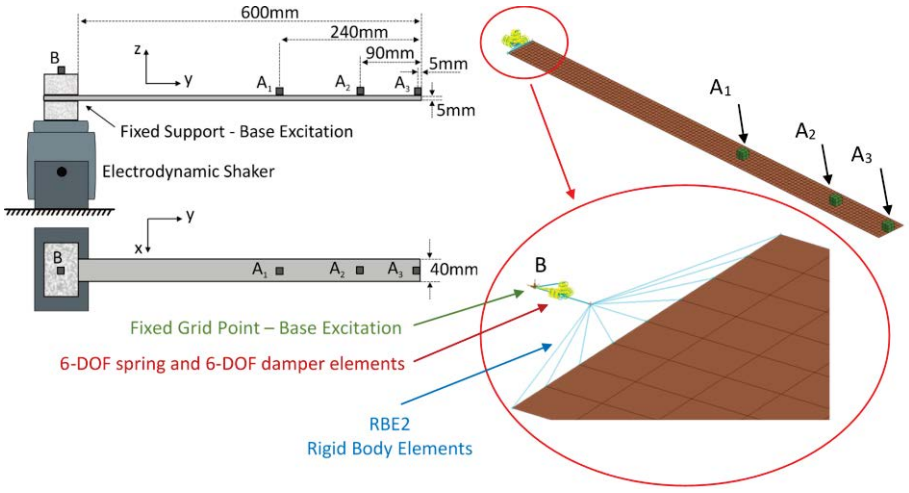

Fig. 2 Schematic diagram of the experimental setup and linear Finite Element model of the cantilever beam.

Because the fixed support (tightening of the beam between two aluminum blocks) is not in fact a rigid connection but has some flexibility, spring and damping elements are used to correctly model this fixed support at all translational and rotational degrees of freedom. In particular, the nodes of the FE model at the end support of the beam are depended and connected through rigid elements (RBE) at one independent node, which corresponds to accelerometer in location B, where the base excitation is applied. At this end of the cantilever beam the support was modeled as elastic with 6-DOF spring and 6-DOF damper elements, whereas the rest of the nodes of the FE model move freely. The total number of DOFs was approximately

3,800. Also, the accelerometers with dimensions $10x10x10mm$ were modeled with 24 CHEXA solid elements with $5mm$ discretization length. The middle node of the bottom surface of accelerometer A1 is located at $240mm$ from the free end, the equivalent node of accelerometer A2 is located at $90mm$ from the free end and the equivalent node of accelerometer A3 is located at $5mm$ from the free end.

5.2 Linear FE model parameterization and updating results

The parameterization of the finite element model of the linear cantilever beam is introduced in order to facilitate the applicability of the updating framework. The parameterized model is consisted of 4 parts, as shown in **Fig. 3**.

Part P1 corresponds to the steel beam and is modeled with shell elements whereas part P2 corresponds to the 3 accelerometers, which are modeled with solid elements. Parts P3 and P4 correspond to 1D elements representing the elasticity of the support using 6 spring and 6 damping elements in all 6 DOFs respectively. The Young's modulus and the material density are used as design variables for the material properties of the beam and accelerometers. The thickness of the shell elements of the beam P1 is also included in the design variables. 6 K_i and 6 C_i where $i=1,\ldots 6$ stiffness and damping parameters are included as design variables for parts P3 and P4. Moreover, damping ratios, using Rayleigh damping in a small and in a large frequency of the linear model were also included in the design values. The total number of design variables resulted in 19 variables.

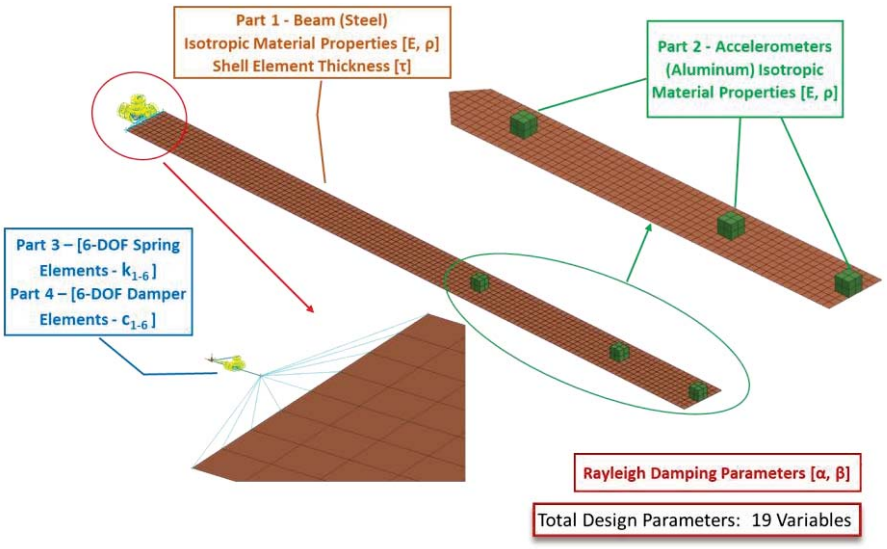

Fig. 3 Linear Finite Element Model Parameterization.

The CMA-ES algorithm is applied to update the developed linear FE model directly comparing raw measured and numerically predicted acceleration responses at all measured locations and directions. **Table 2** presents the design variables, their upper and lower boundaries (LB and UB), as well as the updated results for each parameter.

Table 2: Design variables, CMA-ES design bounds and updated results of material, geometrical and boundary condition parameters.

Part	**Density** ρ $\left[kg/m^3\right]$			**Young's Modulus** E $[GPa]$			**Thickness** τ $[mm]$			**Spring stiffness** K $\cdot 10^5\ kN/m$			**Damper** C $\cdot 10^{-2}\ kNs/m$		
	LB	UB	**Result**	LB	UB	**Result**	LB	UB	**Result**	LB	UB	**Result**	LB	UB	**Result**
P1	7065	8635	**8487.47**	189	231	**226.75**	**4.5**	**5.5**	**5.48**	-	-	-	-	-	-
P2	2475	3025	**2832.50**	62.1	75.9	**65.55**	-	-	-	-	-	-	-	-	-

Part	Density ρ $\left[kg/m^3\right]$			Young's Modulus E $[GPa]$			Thickness τ $[mm]$			Spring stiffness K $\cdot 10^5\ kN/m$			Damper C $\cdot 10^{-2}\ kNs/m$		
	LB	UB	Result	LB	UB	Result	LB	UB	Result	LB	UB	Result	LB	UB	Result
P3	-	-	-	-	-	-	-	-	-	9	15	**12.01**	-	-	-
	-	-	-	-	-	-	-	-	-			**11.58**	-	-	-
	-	-	-	-	-	-	-	-	-			**11.24**	-	-	-
	-	-	-	-	-	-	-	-	-			**9.22**	-	-	-
	-	-	-	-	-	-	-	-	-			**10.57**	-	-	-
	-	-	-	-	-	-	-	-	-			**13.59**	-	-	-
P4	-	-	-	-	-	-	-	-	-	-	-	-	1	9	**4.37**
	-	-	-	-	-	-	-	-	-	-	-	-			**2.61**
	-	-	-	-	-	-	-	-	-	-	-	-			**7.10**
	-	-	-	-	-	-	-	-	-	-	-	-			**5.68**
	-	-	-	-	-	-	-	-	-	-	-	-			**7.06**
	-	-	-	-	-	-	-	-	-	-	-	-			**4.16**

The time-histories of accelerations predicted by the optimal linear FE model (green continuous line) of the cantilever beam are compared, in **Fig. 4**, to the time-histories of accelerations coming directly from the measured data (red continuous line) at A1 and A3 indicative measurement locations at Z local component for three excitation frequencies 4Hz, 6Hz and 8Hz. Although tuning of the FE model was conducted at 6Hz excitation frequency, there is a good correlation of the experimentally obtained and numerically predicted accelerations time histories both at 4Hz and 8Hz excitation frequencies, resulting in a high fidelity linear FE model of the examined structure that could confidently be used in the subsequent nonlinear analysis incorporating the impact force model.

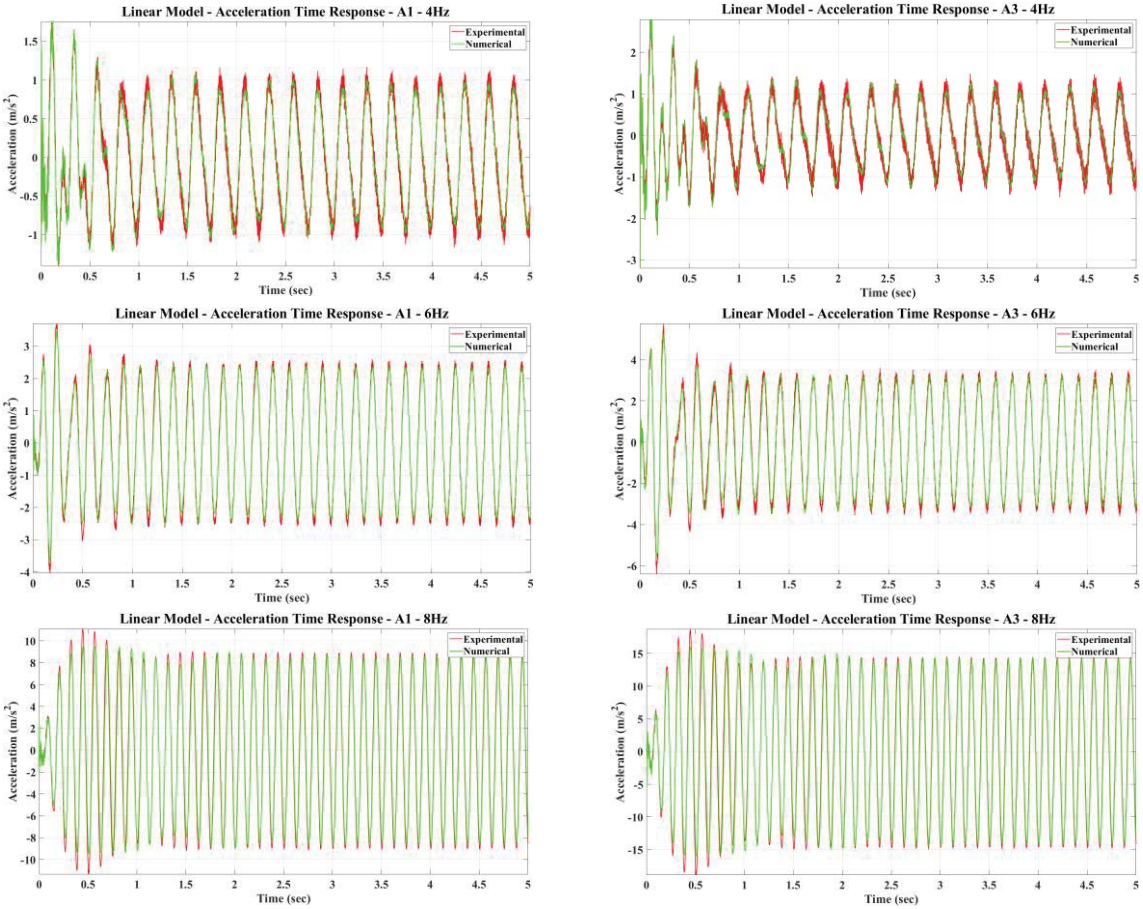

Fig. 4 Time histories of accelerations at A1 and A3 locations from 4Hz, 6Hz and 8Hz excitation frequency.

6 EXPERIMENTAL SET UP OF NONLINEAR MODEL

In this section the nonlinear behavior of the cantilever beam under repeated sequential impacts is closely examined. A schematic illustration of the experimental set up including impact-contact events is presented in **Fig. 5**, which depicts the location and component direction of acceleration measurements along with the location of the load cell that records imposed forces during impacts for comparison purposes.

Excitation and response measurements from ground motion in all direction at 6Hz excitation frequency were recorded in order to measure experimental base excitation at B location and integrate it in the nonlinear FE model at the respective node. The acceleration time histories at locations A1, A2 and A3 at all directions were also recorded in order to be included in the subsequent model selection and model updating processes. Accelerometer A2 is placed on top of the cantilever beam, above the rigid stop where the load cell is located. Thus, measurements recorded from A2 were the most informative since this is the point of contact from which elastic stress waves begin to propagate.

During experimental measurements it was noticed that the dynamic behavior of the beam is fully depended on the dissipation of induced impact energy in the form of transverse and longitudinal elastic stress waves between two consecutive impacts. The impact force and consequently the impact energy are associated to the frequency and range of base excitation. Thus, according to excitation parameters, the elastic stress waves are propagated in the deformable solid medium and do not fade out from one impact event to another, resulting in different impact parameters between impact-contact occurrences.

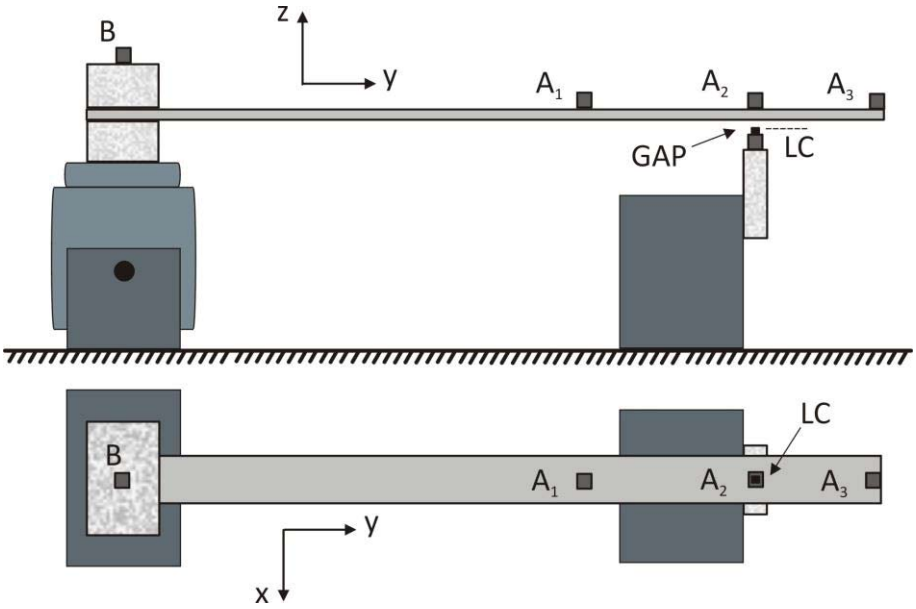

Fig. 5 Schematic illustration of the experimental set up including impact-contact events.

7 NONLINEAR FE MODEL UPDATE

The material and geometrical properties as well as the boundary condition parameters updated using the linear model of the cantilever beam in the previous section, do not depend on the integration of the constitutive force law. Thus, the updated values of modulus of elasticity, density, thickness and spring and damper of the support as presented in **Table 2** were retained constant in the analysis of the nonlinear FE model. The impact parameters are tuned i.e. the generalized contact stiffness K, the coefficient of restitution c_r that affect the imposed force

during each contact-impact event as well as the clearance gap u_g. The nonlinear power exponent was also retained constant at $n_f = 3/2$ as all examined force models proposed.

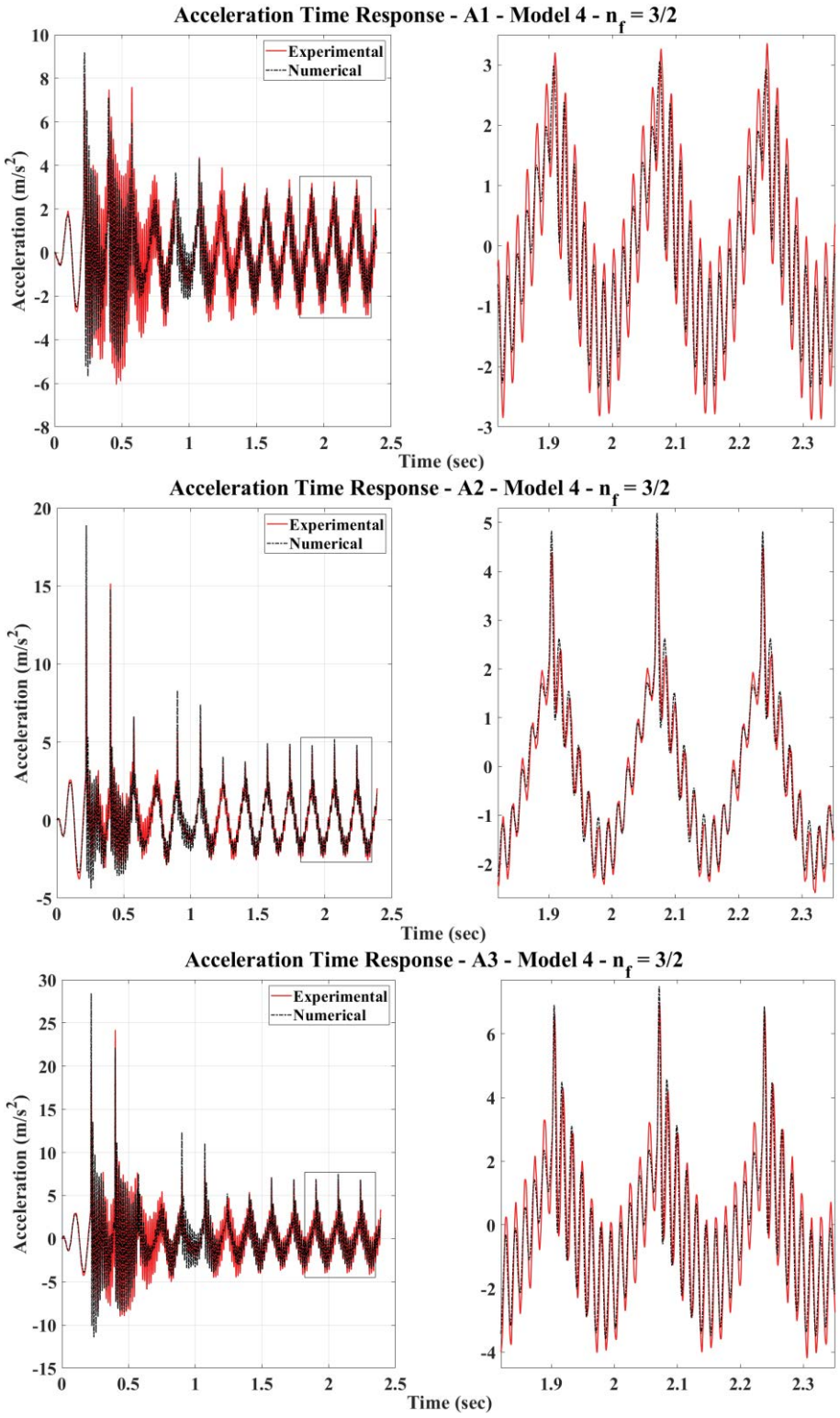

Fig. 6 Time histories of accelerations at A1, A2 and A3 locations, Z component, 6Hz excitation frequency for Model 4 with $n_f = 3/2$.

The prediction error parameters representing modeling and measurements errors at A1, A2, A3 and B sensor locations, were combined in one error parameter σ at a range of variation

$\sigma \in \left[10^{-4},1\right]$. In order to acquire deep insight of the dynamics of the problem, as well as moderate the computational effort, it was chosen to study the $N_c,\{c=1,\ldots,12\}$ first impacts, included in the first $2.5\,\text{sec}$ of the response. This time duration includes impacts both in transient $0 \le t \le 1.5\,\text{sec}$ and steady state response $1.5 < t \le 2.5\,\text{sec}$.

Parameters K^{N_c} and $c_r{}^{N_c}$, the clearance gap u_g and error parameter σ are the updated parameters at a wide enough range based in engineering knowledge and previous experience $\left(\underline{\theta} \in [100,9900]\times[0.1,0.9]\times[1.35,1.45]\times\left[10^{-4},1\right]\right)$. Additionally, as structural damping plays a key role in nonlinear response, Rayleigh damping corresponding to a small and at a large frequency were also included in the inferred parameters with wide range $(\zeta_1,\zeta_2)=[0.1\%,9.9\%]$, in order to fulfill an adequate correlation between the experimental and numerical acceleration time histories.

A comparison of the time histories of acceleration predicted by the optimal nonlinear FE model integrating force Model 4 (Flores et al. [12]) depicted with black dashed-dotted line and the experimental measurements depicted with red continuous line, are presented in **Fig. 6**, at measurement locations A1, A2 and A3 in Z direction and at 6Hz excitation frequency.

Similarly a comparison between the measured imposed impact force at each contact-impact event (red continuous line) and the numerically predicted nonlinear force (black dashed-dotted line) produced by Model 4 (Flores et al. [12]) is presented in **Fig. 7**. Both **Fig. 6** and **Fig. 7** include a zoomed boxed area of the last three impact events from approximately $1.8 \le t \le 2.3\,\text{sec}$ well after the steady state response has been met. It is worth mentioning that all impact parameters of the $N_c = 12$ impact-contact events have been taken into consideration in the nonlinear FE model update scheme, including all transient response and the beginning of the steady state response, increasing difficulty and complexity of the examined engineering problem.

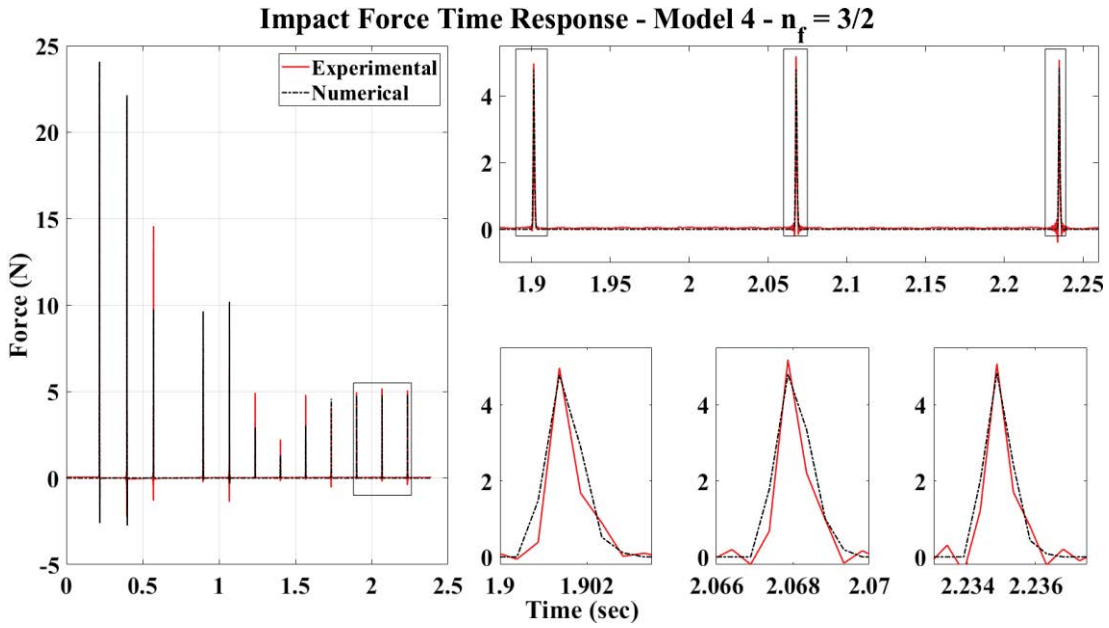

Fig. 7 Experimentally measured and numerically predicted impact force for Model 4 with $n_f = 3/2$.

It is clear that impact force model approaches with great accuracy the peaks of the measured impact force, as clearly presented in the zoomed areas. Thus it could be regarded as a high fidelity impact force model that could be used in further engineering investigation on this specific experimental arrangement and excitation loading.

8 CONCLUSIONS

In conclusion, a nonlinear constitutive force model-updating framework applied at a simple engineering problem (cantilever beam) where contact-impact events occur in a sequential periodic manner is extensively presented. At first, a high-fidelity finite element (FE) model of the experimentally examined cantilever beam was developed and validated in linear response conditions, under enforced motion, followed by equivalent experimental trials, tuning its material and geometrical properties and boundary condition parameters using deterministic single objective function, without the need of sub-structuring. The updated linear FE model is used for the nonlinear response, accommodating a viscoelastic impact force law based on the Hertz contact theory, augmented with a damping term. The impact parameters are updated to the most probable values using CMA-ES and probabilistic objective function. Finally, the updated final model validated with high accuracy the experimental results.

REFERENCES

[1] Hansen, N., *The CMA Evolution Strategy: A Tutorial*. 2011, Research centre Saclay – ˆIle-de-France Universite´ Paris-Saclay, LRI.

[2] Hansen, N., *The CMA Evolution Strategy A Comparing Review.* Towards a New Evolutionary Computation, 2006. **192**(1): p. 75-102.

[3] Hansen, N., S.D. Müller, and P. Koumoutsakos, *Reducing the Time Complexity of the Derandomized Evolution Strategy with Covariance Matrix Adaptation (CMA-ES).* Evolutionary Computation, 2003. **11**(1): p. 1-18.

[4] Giagopoulos, D. and A. Arailopoulos, *Computational framework for model updating of large scale linear and nonlinear finite element models using state of the art evolution strategy.* Computers & Structures, 2017. **192**: p. 210-232.

[5] Giagopoulos, D., A. Arailopoulos, V. Dertimanis, C. Papadimitriou, E. Chatzi, and K. Grompanopoulos, *Structural health monitoring and fatigue damage estimation using vibration measurements and finite element model updating.* Structural Health Monitoring, 2018. **18**(4): p. 1475921718790188.

[6] Arailopoulos, A., D. Giagopoulos, I. Zacharakis, and E. Pipili, *Integrated Reverse Engineering Strategy for Large-Scale Mechanical Systems: Application to a Steam Turbine Rotor.* Frontiers in Built Environment, 2018. **4**(55): p. 1-6.

[7] Alves, J., N. Peixinho, M.T. da Silva, P. Flores, and H.M. Lankarani, *A comparative study of the viscoelastic constitutive models for frictionless contact interfaces in solids.* Mechanism and Machine Theory, 2015. **85**: p. 172-188.

[8] Machado, M., P. Moreira, P. Flores, and H.M. Lankarani, *Compliant contact force models in multibody dynamics: Evolution of the Hertz contact theory.* Mechanism and Machine Theory, 2012. **53**: p. 99-121.

[9] Hertz, H., *Ueber die Berührung fester elastischer Körper*, in *Journal für die reine und angewandte Mathematik (Crelle's Journal)*. 1882. p. 156.

[10] Gharib, M. and Y. Hurmuzlu, *A New Contact Force Model for Low Coefficient of Restitution Impact.* Journal of Applied Mechanics, 2012. **79**(6): p. 064506-064506-5.

[11] Herbert, R.G. and D.C. McWhannell, *Shape and Frequency Composition of Pulses From an Impact Pair.* Journal of Engineering for Industry, 1977. **99**(3): p. 513-518.

[12] Flores, P., M. Machado, M.T. Silva, and J.M. Martins, *On the continuous contact force models for soft materials in multibody dynamics.* Multibody System Dynamics, 2011. **25**(3): p. 357-375.

[13] Lee, T.W. and A.C. Wang, *On The Dynamics of Intermittent-Motion Mechanisms. Part 1: Dynamic Model and Response.* Journal of Mechanisms, Transmissions, and Automation in Design, 1983. **105**(3): p. 534-540.
[14] Hunt, K.H. and F.R.E. Crossley, *Coefficient of Restitution Interpreted as Damping in Vibroimpact.* Journal of Applied Mechanics, 1975. **42**(2): p. 440-445.
[15] Lankarani, H.M. and P.E. Nikravesh, *A Contact Force Model With Hysteresis Damping for Impact Analysis of Multibody Systems.* Journal of Mechanical Design, 1990. **112**(3): p. 369-376.
[16] Zhiying, Q. and L. Qishao, *Analysis of impact process based on restitution coefficient.* J. Dyn. Control, 2006. **4**: p. 294-298.
[17] Gonthier, Y., J. McPhee, C. Lange, and J.-C. Piedbœuf, *A Regularized Contact Model with Asymmetric Damping and Dwell-Time Dependent Friction.* Multibody System Dynamics, 2004. **11**(3): p. 209-233.
[18] BETA CAE Systems, S.A., *ANSA & META-Post*. 2018, BETA CAE Systems, S.A.: Thessaloniki, Greece.

EURODYN 2020
XI International Conference on Structural Dynamics
M. Papadrakakis, M. Fragiadakis, C. Papadimitriou (eds.)
Athens, Greece, 23-26 November 2020

SIMULATION-LEAN TRAINING-SETS FOR HYPER-REDUCTION OF PARAMETRIC GEOMETRIC NON-LINEAR STRUCTURES

Christian H. Meyer[1], **and Daniel J. Rixen**[1]

[1]Technical University of Munich
Chair of Applied Mechanics Boltzmannstr. 15, 85748 Garching
e-mail: christian.meyer, rixen@tum.de

Keywords: Geometric Non-linear Structures, Parametric Systems, Nonlinear Model Reduction, Optimization, Hyperreduction

Abstract. *Parameter studies to design the dynamics of structures that undergo large deformations, such as wind turbine blades or MEMS, can be a tedious task. These studies are usually done with finite element models. The equations of motion provided by the finite element method are nonlinear and high-dimensional. This typically leads to high computation times, especially if the equations must be solved for each parameter variation of the design study.*

Model reduction can reduce the computation time by approximating the high dimensional parametric models. This is done in two steps: First, a Galerkin projection is done that approximates the solution by a linear combination of basis vectors. Second, the evaluation of the nonlinear force term is accelerated by a hyper-reduction. Both steps are challenging if large parameter variations are present because suitable basis vectors as well as the coefficients for the hyper-reduction are dependent on these parameters. An update of the coefficients for the hyper-reduction is very time consuming and can make the benefit of the model reduction useless.

The hyper-reduction method that is used in this contribution is the Energy Conserving Sampling and Weighting method (ECSW). This method requires training sets for computing coefficients for the hyper-reduction. This contribution shows how cost-intensive updates of the reduced order model can be avoided by computing coefficients for the ECSW that are valid for the whole parameter space of interest. We propose to generate training sets for some design parameter samples and compute coefficients that can be used for the whole parameter space. These training sets are computed without the need for expensive time integration of the full order model. Instead, Nonlinear Stochastic Krylov Training Sets (NSKTS) are used that only require static solutions to some applied training forces.

A simple case study of a shape parameterized cantilever beam illustrates the performance of the method. It is shown that computation time can be reduced for large numbers of design changes, but shows worse accuracy compared to local methods.

1 DESIGN STUDIES FOR GEOMETRIC NON-LINEAR STRUCTURES WITH MODEL REDUCTION

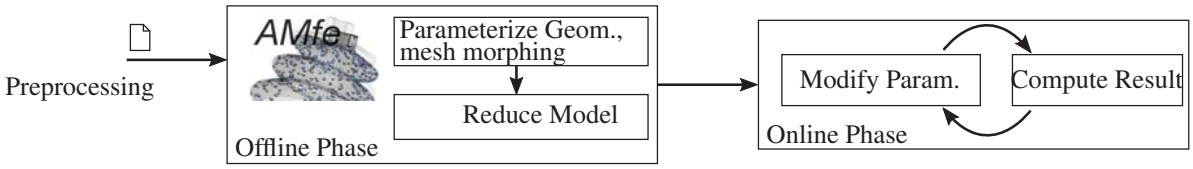

Figure 1: Workflow for faster design studies with model reduction [5]. It consists of two phases: A model is parameterized and reduced in the offline phase. Results and design changes are computed with the reduced order model in the online phase.

Design studies that analyze the dynamics of structures that undergo large deformations can be a tedious task due to high computation times. The reason for this is the nonlinear structure of the equations of motion resulting from the finite element discretization. Computation time can be reduced by applying model reduction. Model reduction reduces the full model to a smaller problem that can be solved in less time. This can be exploited to speed up design studies. A possible workflow is depicted in Figure 1. First, the finite element model is preprocessed and parameterized. Then, model reduction is carried out which results in a reduced order model. This step is called the offline phase. Afterwards, the design study can be performed on the reduced model in the online phase. The online phase consists in the iterative computation of results with the reduced order model and design changes that can be derived from these results. By using the reduced model to iteratively compute results for new designs it is expected that the computation time can be significantly diminished.

The big challenge in this workflow is to provide reduced order models such that the total computation time, that consists of the reduction process (offline costs) and the computation of results (online costs), is smaller than that of direct computations. In general, two different concepts to achieve this goal are distinguished: First, one single reduced order model can be provided, that is valid for the whole parameter space of interest. Second, a new reduced order model is calculated at each design iteration. This contribution proposes an ansatz for the first concept. We will show how a reduction basis can be generated without the need for training simulations and with validity for the whole parameter space. Furthermore, we show how a hyper-reduction with the Energy Conserving Sampling and Weighting method is carried out such that only one reduced order model is needed for the online phase.

The remainder of this contribution is organized as follows: Section 2 gives an overview over how model reduction is performed. This consists of two steps, reduction basis computation and hyper-reduction. Section 3 shows how a reduction basis for the whole parameter space is computed. The hyper-reduction method, namely the Energy Conserving Sampling and Weigthing method, that is summarized in section 2, is extended in section 4 for the parametric case. This section shows how training sets for the hyper-reduction can be computed and how a hyper-reduced order model is created for the whole parameter space. Section 5 demonstrates the performance of the proposed method on a cantilever beam case study. A conclusion is given in the last section.

2 THE TWO STEPS OF MODEL REDUCTION FOR GEOMETRIC NON-LINEAR STRUCTURES

After the finite element discretization, we get the equations of motion

$$\boldsymbol{M}(\boldsymbol{p})\ddot{\boldsymbol{u}}(t) + \boldsymbol{f}(\boldsymbol{p}, \boldsymbol{u}(t), \dot{\boldsymbol{u}}(t)) = \boldsymbol{F}(\boldsymbol{p}, t) \tag{1}$$

where $\boldsymbol{u} \in \mathbb{R}^N$ are the displacements of the finite element nodes, $\boldsymbol{M}$ is the mass matrix, $\boldsymbol{F}$ are the external loads and $\boldsymbol{f}$ is the restoring force that is nonlinear for structures undergoing large deflections. The different quantities also depend on the design parameters $\boldsymbol{p}$ of the system.

The first step to reduce the equations of motion is a Galerkin projection. The displacements $\boldsymbol{u}$ are approximated by a linear combination of n basis vectors $\boldsymbol{v}_i$. This can be written as

$$\boldsymbol{u} = \boldsymbol{V}\boldsymbol{q}, \quad \boldsymbol{V} \in \mathbb{R}^{N \times n} \tag{2}$$

where $\boldsymbol{V}$ is the so called reduction basis and contains column-wise the basis vectors $\boldsymbol{v}_i$. A Galerkin projection on the subspace spanned by these vectors results in

$$\boldsymbol{V}^\mathsf{T}\boldsymbol{M}(\boldsymbol{p})\boldsymbol{V}\ddot{\boldsymbol{q}}(t) + \boldsymbol{V}^\mathsf{T}\boldsymbol{f}(\boldsymbol{p}, \boldsymbol{V}\boldsymbol{q}(t), \boldsymbol{V}\dot{\boldsymbol{q}}(t)) = \boldsymbol{V}^\mathsf{T}\boldsymbol{F}(t)\,. \tag{3}$$

The equations of motion (3) have dimension n and thus must be solved for a reduced number of unknowns compared to equation (1). However, the nonlinear force term still must be evaluated for the full element domain that results in a poor speed-up. Thus, a second step, the hyper-reduction, must be carried out to accelerate the evaluation of the nonlinear force term $\boldsymbol{V}^\mathsf{T}\boldsymbol{f}$.

One method that is able to achieve this acceleration is the Energy Conserving Sampling and Weighting method (ECSW) [1]. It uses the fact that the nonlinear force term

$$\boldsymbol{V}^\mathsf{T}\boldsymbol{f}(\boldsymbol{V}\boldsymbol{q}, \boldsymbol{V}\dot{\boldsymbol{q}}) = \sum_{e \in E} \boldsymbol{V}^\mathsf{T}\boldsymbol{L}_e^\mathsf{T}\boldsymbol{f}_e(\boldsymbol{L}_e\boldsymbol{V}\boldsymbol{q}, \boldsymbol{L}_e\boldsymbol{V}\dot{\boldsymbol{q}}) \tag{4}$$

is an assembly of element forces $\boldsymbol{f}_e$. The matrices $\boldsymbol{L}_e$ map the local degrees of freedom of the element to the global degrees of freedom. The idea of ECSW is to assemble only a subset $\tilde{E} \in E$ of all elements and extrapolate their contribution by introducing weights ξ_e. The hyper-reduced internal storing force

$$\boldsymbol{f}_{hr,ECSW} := \sum_{e \in \tilde{E} \subset E} \xi_e \boldsymbol{V}^\mathsf{T}\boldsymbol{L}_e^\mathsf{T}\boldsymbol{f}_e(\boldsymbol{L}_e\boldsymbol{V}\boldsymbol{q}, \boldsymbol{L}_e\boldsymbol{V}\dot{\boldsymbol{q}}) \tag{5}$$

can be computed faster because much less element forces $\boldsymbol{f}_e$ must be evaluated with the approximation.

The subset $\tilde{E}$ and the weights ξ_e are chosen by forcing

$$\begin{aligned} &|\delta W_{hr}(\boldsymbol{q}_\tau, \boldsymbol{0}) - \delta W(\boldsymbol{q}_\tau, \boldsymbol{0})| \leq \varepsilon_{ECSW} \cdot \delta W(\boldsymbol{q}_\tau, \boldsymbol{0}) \\ \Leftrightarrow\ &|\delta\boldsymbol{q}^\mathsf{T}\boldsymbol{f}_{hr}(\boldsymbol{q}_\tau, \boldsymbol{0}) - \delta\boldsymbol{q}^\mathsf{T}\boldsymbol{V}^\mathsf{T}\boldsymbol{f}(\boldsymbol{V}\boldsymbol{q}_\tau, \boldsymbol{0})| \leq \varepsilon_{ECSW} \cdot \delta\boldsymbol{q}^\mathsf{T}\boldsymbol{V}^\mathsf{T}\boldsymbol{f}(\boldsymbol{V}\boldsymbol{q}_\tau, \boldsymbol{0}) \end{aligned}$$

such that the virtual work δW for a system that is deflected into the direction of training displacements $\boldsymbol{u}_\tau = \boldsymbol{V}\boldsymbol{q}_\tau$ is conserved for any virtual displacement $\delta\boldsymbol{q}$ up to a relative tolerance ε_{ECSW}.

This requirement can be translated to the minimization problem

$$\arg\min_{\xi\in\Phi} \|\boldsymbol{\xi}\|_0 \quad \text{where} \quad \Phi = \{\boldsymbol{\xi} \in \mathbb{R}^{N_e} : \|\boldsymbol{G}\boldsymbol{\xi} - \boldsymbol{b}\| \leq \varepsilon_{ECSW}\|\boldsymbol{b}\| \text{ and } \xi_e \geq 0\} \tag{6}$$

where

$$\boldsymbol{G} = \begin{bmatrix} \boldsymbol{g}_{11} & \cdots & \boldsymbol{g}_{1N_e} \\ \vdots & \ddots & \vdots \\ \boldsymbol{g}_{N_\tau 1} & \cdots & \boldsymbol{g}_{N_\tau N_e} \end{bmatrix} \in \mathbb{R}^{nN_\tau \times N_e} \qquad \text{and} \qquad \boldsymbol{b} = \begin{bmatrix} \boldsymbol{b}_1 \\ \vdots \\ \boldsymbol{b}_{N_\tau} \end{bmatrix} \in \mathbb{R}^{nN_\tau} \tag{7}$$

are built up by the entries

$$\boldsymbol{g}_{le}(\boldsymbol{q}_{\tau_l}) = \boldsymbol{V}^\mathsf{T}\boldsymbol{L}_e^\mathsf{T}\boldsymbol{f}_e(\boldsymbol{L}_e\boldsymbol{V}\boldsymbol{q}_{\tau_l}) \in \mathbb{R}^n \qquad \text{and} \qquad \boldsymbol{b}_l = \boldsymbol{f}_r(\boldsymbol{q}_{\tau_l}) = \sum_{e=1}^{N_e} \boldsymbol{g}_{le}(\boldsymbol{q}_{\tau_l})\,. \tag{8}$$

Here, N_e and N_τ describe the number of elements of the full order model and the number of training sets, respectively. An approximate solution to 6 can be computed by solving a non negative least square problem as described in [1].

3 GLOBAL REDUCTION BASIS

One challenge to reduce geometric nonlinear equations of motion is to compute a proper reduction basis $\boldsymbol{V}$. One option is to use vibration modes of the linearized system and static modal derivatives [2, 3] as basis vectors.

Vibration modes $\boldsymbol{\phi}_i$ are computed by solving the eigenvalue problem

$$(\boldsymbol{K} - \omega_i^2\boldsymbol{M})\boldsymbol{\phi}_i = \boldsymbol{0} \quad \text{with} \quad \boldsymbol{K} = \left.\frac{\partial \boldsymbol{f}(\boldsymbol{u})}{\partial \boldsymbol{u}}\right|_{\boldsymbol{u}=\boldsymbol{0}}\,. \tag{9}$$

The static modal derivatives

$$\Theta_{ij} = -\boldsymbol{K}^{-1} \cdot \nabla_{\boldsymbol{\phi}_j}(\boldsymbol{K}) \cdot \boldsymbol{\phi}_i \tag{10}$$

contain nonlinear information and are important to make the reduction basis able to represent large deflections. A reduction basis is gained by column-wise stacking vibration modes and static modal derivatives into a reduction matrix

$$\boldsymbol{R} = [\ldots, \boldsymbol{\phi}_m, \ldots | \ldots, \Theta_{ij}, \ldots]\,, \qquad m \in M, (i,j) \in T\,. \tag{11}$$

Guidelines for choosing M and T can be found e.g. in [4].

The reduction basis $\boldsymbol{R}$ depends on the mass matrix and the internal restoring force of the system. Thus, it also depends on the design parameters $\boldsymbol{p}$ of the system. If a reduction basis for the whole parameter space is desired, one can process as proposed e.g. in [5]. The parameter space of interest is sampled at some parameter values

$$P_{\text{sample}} = \{\boldsymbol{p}_1,\ \boldsymbol{p}_2, \ldots, \boldsymbol{p}_{N_S}\} \tag{12}$$

and a reduction basis $\boldsymbol{R}_i$ is computed at each sample point $\boldsymbol{p}_i \in P_{\text{sample}}$. Then these bases are concatenated into a matrix

$$\boldsymbol{S} = [\boldsymbol{R}_1\ \boldsymbol{R}_2\ \cdots\ \boldsymbol{R}_{N_S}] \tag{13}$$

which is then deflated to avoid linear dependency and bad conditioning. The deflation can be carried out by computing the singular value decomposition

$$\boldsymbol{S} = \boldsymbol{U}\,\boldsymbol{\Sigma}\,\boldsymbol{W}^{\mathsf{T}} \tag{14}$$

and taking the first n left singular vectors $\boldsymbol{V}_{\text{global}} = [\boldsymbol{u}_1, \boldsymbol{u}_2, \dots \boldsymbol{u}_n]$ whose singular values are greater than a certain tolerance.

4 GLOBAL ECSW WITH NONLINEAR STOCHASTIC KRYLOV TRAINING SETS

To compute the reduced element set $\tilde{E}$ and the corresponding weights ξ (as explained in Section 2), one must have a training set that is typically generated by simulation without hyper-reduction of a reference problem. This incurs significant offline costs. Strategies to obtain training sets without needing to perform a full simulation have been proposed in the past. One of these strategies is called nonlinear stochastic Krylov training sets (NSKTS) which was proposed by Rutzmoser in [6]. This method will be used here and is briefly summarized in the following paragraphs.

First, a force Krylov subspace

$$\boldsymbol{F}_{\text{kry,raw}} = \left[\boldsymbol{V}^{\mathsf{T}}\boldsymbol{b},\ (\bar{\boldsymbol{K}}^{-1}\bar{\boldsymbol{M}})\boldsymbol{V}^{\mathsf{T}}\boldsymbol{b},\ (\bar{\boldsymbol{K}}^{-1}\bar{\boldsymbol{M}})^2\boldsymbol{V}^{\mathsf{T}}\boldsymbol{b},\ \dots,\ (\bar{\boldsymbol{K}}^{-1}\bar{\boldsymbol{M}})^{(q-1)}\boldsymbol{V}^{\mathsf{T}}\boldsymbol{b}\right] \tag{15}$$

is computed where $\boldsymbol{b}$ is the localization vector of the external load $\boldsymbol{F}$ and

$$\bar{\boldsymbol{K}} = \boldsymbol{V}^{\mathsf{T}}\boldsymbol{K}\boldsymbol{V}, \qquad \bar{\boldsymbol{M}} = \boldsymbol{V}^{\mathsf{T}}\boldsymbol{M}\boldsymbol{V}$$

are the reduced stiffness and mass matrices, respectively. The Krylov vectors are orthogonalized such that

$$\boldsymbol{F}_{kry}^{\mathsf{T}}\boldsymbol{K}^{-1}\boldsymbol{F}_{kry} = \boldsymbol{I}\ . \tag{16}$$

Afterwards, β forces are generated by

$$\boldsymbol{f}_{rand,i} = \boldsymbol{F}_{kry} \cdot \boldsymbol{n}_i \tag{17}$$

where $\boldsymbol{n}_i$ is a random vector, such that $\boldsymbol{f}_{rand,i}$ are linear combinations of the vectors from the Krylov subspace (15). Training sets $\boldsymbol{q}_{\tau,i,l}$ are then computed by solving nonlinear static problems

$$\boldsymbol{V}^{\mathsf{T}} \cdot \boldsymbol{f}(\boldsymbol{V}\boldsymbol{q}_{\tau,i,l}) = \frac{l}{k}\boldsymbol{f}_{rand,i} \qquad \text{with } l \in \{1,2,\dots,k\} \text{ and } i \in \{1,2,\dots,\beta\}\ . \tag{18}$$

We use this procedure to compute one set of weights ξ_{global} and elements $\tilde{E}_{\text{global}}$ that is used for all parameter values of interest.

First, we compute NSKTS $\boldsymbol{q}_\tau(\boldsymbol{p}_s)$ for each sample point $\boldsymbol{p}_s \in P_{\text{sample}}$ (c.f. eq. (12)). Then, the quantities

$$\boldsymbol{G}_{\text{global}} = \begin{bmatrix} \tilde{\boldsymbol{g}}_{11} & \cdots & \tilde{\boldsymbol{g}}_{1N_e} \\ \vdots & \ddots & \vdots \\ \tilde{\boldsymbol{g}}_{N_S1} & \cdots & \tilde{\boldsymbol{g}}_{N_SN_e} \end{bmatrix} \in \mathbb{R}^{k\cdot\beta\cdot N_S \times N_e} \qquad \text{and} \qquad \boldsymbol{b}_{\text{global}} = \begin{bmatrix} \tilde{\boldsymbol{b}}_1 \\ \vdots \\ \tilde{\boldsymbol{b}}_{N_S} \end{bmatrix} \in \mathbb{R}^{k\cdot\beta\cdot N_S} \tag{19}$$

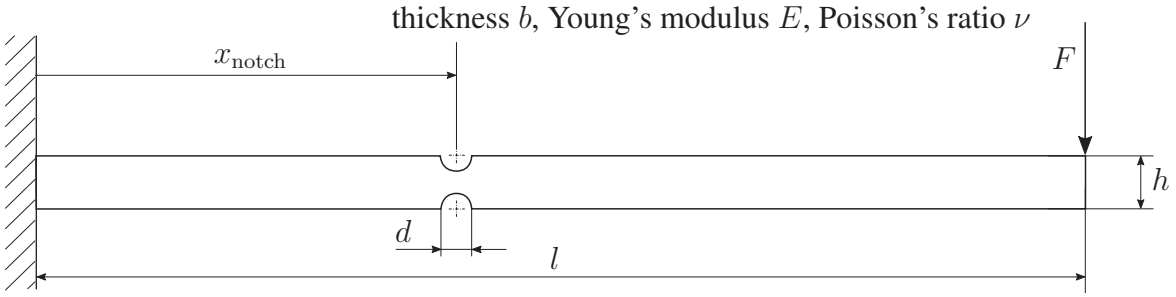

Figure 2: Notched cantilever beam. The design parameter is the position of the notch $\boldsymbol{p} = [x_{\text{notch}}/l]$. Fixed dimensionless parameters: $\frac{F}{El^2} = 3 \cdot 10^{-8} \cdot (\sin(0.0503\,\tau), \nu = 0.49, \frac{h}{l} = 0.05, \frac{d}{l} = 0.03, \frac{b}{l} = 0.1, \tau = \sqrt{\frac{E}{\rho}}\frac{t}{l}$

are built up by the entries

$$\tilde{\boldsymbol{g}}_{se} = \begin{bmatrix} \boldsymbol{V}^{\mathsf{T}}(\boldsymbol{p}_s) \cdot \boldsymbol{L}_e^{\mathsf{T}} \boldsymbol{f}_e(\boldsymbol{p}_s, \boldsymbol{L}_e \boldsymbol{V}(\boldsymbol{p}_s)\, \boldsymbol{q}_{\tau_{1,1}}(\boldsymbol{p}_s)) \\ \vdots \\ \boldsymbol{V}^{\mathsf{T}}(\boldsymbol{p}_s) \cdot \boldsymbol{L}_e^{\mathsf{T}} \boldsymbol{f}_e(\boldsymbol{p}_s, \boldsymbol{L}_e \boldsymbol{V}(\boldsymbol{p}_s)\, \boldsymbol{q}_{\tau_{1,k}}(\boldsymbol{p}_s)) \\ \boldsymbol{V}^{\mathsf{T}}(\boldsymbol{p}_s) \cdot \boldsymbol{L}_e^{\mathsf{T}} \boldsymbol{f}_e(\boldsymbol{p}_s, \boldsymbol{L}_e \boldsymbol{V}(\boldsymbol{p}_s)\, \boldsymbol{q}_{\tau_{2,1}}(\boldsymbol{p}_s)) \\ \vdots \\ \vdots \\ \boldsymbol{V}^{\mathsf{T}}(\boldsymbol{p}_s) \cdot \boldsymbol{L}_e^{\mathsf{T}} \boldsymbol{f}_e(\boldsymbol{p}_s, \boldsymbol{L}_e \boldsymbol{V}(\boldsymbol{p}_s)\, \boldsymbol{q}_{\tau_{\beta,k}}(\boldsymbol{p}_s)) \end{bmatrix} \in \mathbb{R}^{k \cdot \beta \cdot N_S} \tag{20}$$

$$\tilde{\boldsymbol{b}}_s = \sum_{e=1}^{N_e} \tilde{\boldsymbol{g}}_{se} \tag{21}$$

where $N_S = |P_{\text{sample}}|$ is the number of sample points and $\boldsymbol{V}(\boldsymbol{p}_s)$ are local reduction bases that are computed at sampling point $\boldsymbol{p}_s$. The matrix $\boldsymbol{G}_{\text{global}}$ and the vector $\boldsymbol{b}_{\text{global}}$ are used to compute a global set of weights and elements for the ECSW as described by equation (6).

By using the local reduction bases $\boldsymbol{V}(\boldsymbol{p}_s)$ in equation (20), the global hyper-reduction maintains the virtual work, that is produced by a training set $\boldsymbol{q}_\tau(\boldsymbol{p}_s)$, in the directions of its local reduction basis that is computed for the same sample point $\boldsymbol{p}_s$. It is not necessarily maintained in all directions spanned by the global reduction basis $\boldsymbol{V}_{\text{global}}$. Nevertheless, this requirement is fulfilled for all sample points simultaneously.

5 CASE STUDY

The proposed method is demonstrated by means of a case study. Figure 2 shows a drawing of the case study which is a cantilever beam. Its dimensions can be taken from the drawing. The beam is weakened by a notch at position x_{notch}. The case study uses the relative position of this notch $\boldsymbol{p} = x_{\text{notch}}/l$ as design parameter.

The mesh is shape parameterized by modifying the node positions. Thus, the mesh topology is maintained when the parameter is changed. This is illustrated in Figure 3. The mesh consists of $N_e = 1,148$ elements.

The desired parameter range of interest is set to $\boldsymbol{p} \in [0.3, 0.6]$. We have no information about optimal position of sample points a priori. For this reason, we make an attempt by choosing sampling points that are equidistantly distributed in the parameter range of interest. A reduction basis is computed at each of these sample points. The first 5 modes and all their static derivatives are included in this basis. Thus, a reduction basis' dimension is 20 at each sample point. A

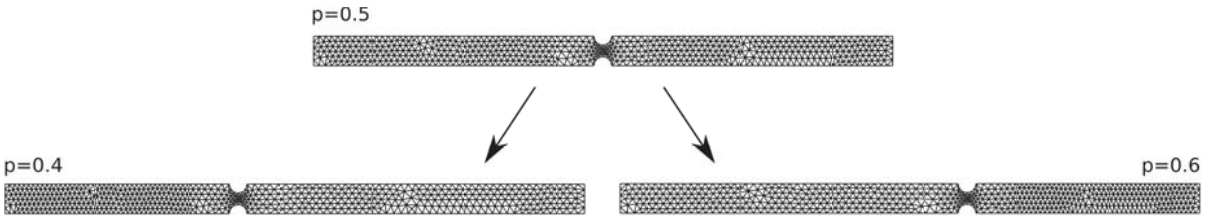

Figure 3: Shape modification by using the mesh morphing technique: The positions of the nodes are changed while the topology is maintained. Top: reference mesh at $\boldsymbol{p} = 0.5$, left: morphed mesh at $\boldsymbol{p} = 0.4$, right: morphed mesh at $\boldsymbol{p} = 0.6$.

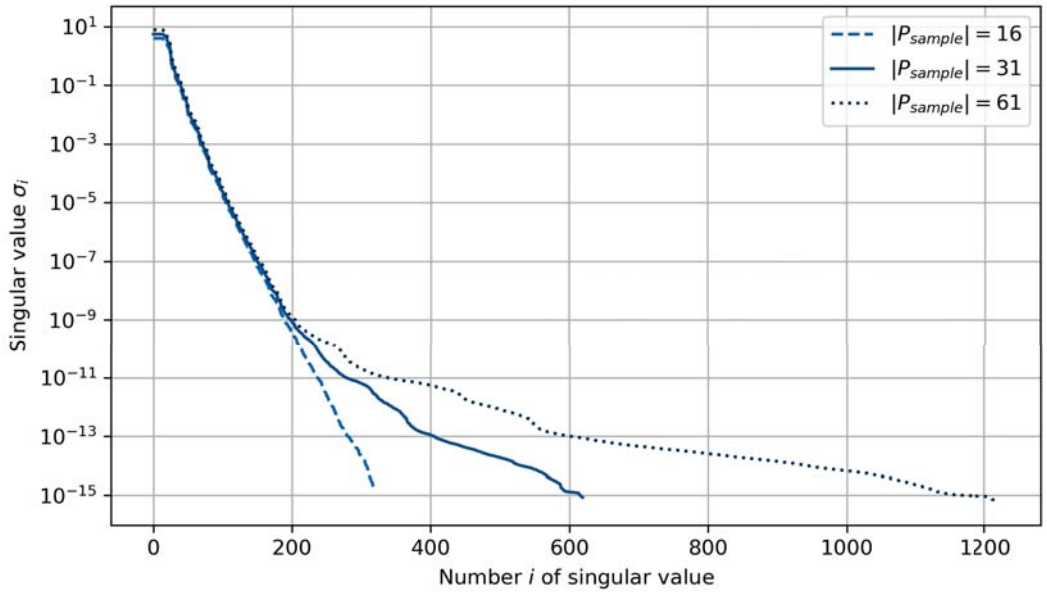

Figure 4: Singular values for deflation of global basis for three different numbers of sampling points.

singular value composition for three different numbers of sampling points is computed according to equation (14) to deflate the global basis. The singular values are shown in figure 4 and give a hint about if the number of sample points has been chosen properly. The singular values show that $|P_{\text{sample}}| = 31$ sample points seem to be a good compromise between the number of sample points and the approximation of the global reduction basis that would be spanned by the full parameter space of interest. For this reason, we present results for

$$P_{\text{sample}} = \{0.30,\ 0.31,\ 0.32,\ \ldots,\ 0.60\} \tag{22}$$

as sample points in the following.

We have $N_s = |P_{\text{sample}}| = 31$ sample points such that the global basis has a dimension of 620 before deflation. A reduction basis $\boldsymbol{V}_{\text{global}}$ is built with the first 300 left singular vectors. Nonlinear stochastic Krylov training sets (NSKTS) are computed for each sample point. The dimension of the Krylov subspace is $q = 4$. $\beta = 6$ linear combinations of Krylov vectors are built for each sample point and $k = 30$ load increments are computed for each linear combination. Figure 5 shows some examples of the computed NSKTS.

This contribution shows results for two parameter values as an example. These values are $\boldsymbol{p} = 0.41$, which is a sample point, and $\boldsymbol{p} = 0.405$, which is between two sample points.

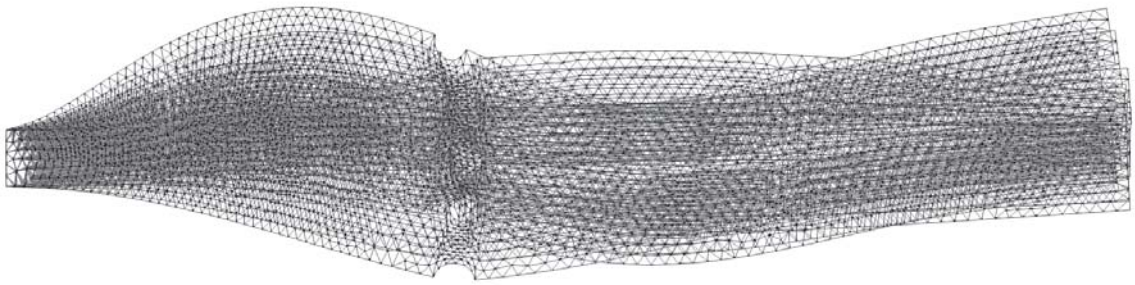

Figure 5: Overlaid examples for NSKTS that are computed for $\boldsymbol{p} = 0.41$

The graph in Figure 6 displays the tip displacement of the beam, simulated with a full order model. Figure 7 displays the absolute error for each time step for different reduced order models. The gray curves are errors for hyper-reduced models that are locally reduced. This means that reduction basis, NSKTS and ECSW-weights are computed directly (locally) for the parameter value of interest. This is the classic approach where a new reduced order model is computed for each parameter of interest. The blue graphs display errors for the global approach described in Section 4. This approach uses a global reduction basis and a global ECSW.

One can see that the error becomes smaller when smaller tolerances ε_{ECSW} are chosen. Furthermore, one can see that the local approach gives smaller errors compared to the global approach if the same tolerance ε_{ECSW} is used.

Table 1 summarizes computation times for different steps of the offline and online phase. One can conclude that much more elements in $\tilde{E}$ are needed for the global approach when the same error is desired. This also leads to higher computation times t_{online} in the online phase. However, as it is a global approach, which means that only one reduced order model must be computed for the whole parameter space of interest, there exists a break-even point where the global approach is beneficial in time compared to the local approach. This is illustrated in Figure 8.

v[a]	p	$\varepsilon_{\mathrm{ECSW}}$	$\lvert\tilde{E}\rvert$[b]	t_{V}[c]	t_{NSKTS}[d]	t_{ECSW}[e]	t_{offline}[f]	t_{online}[g]	t_{full}[h]
g	41.0	1e-05	211	35.9	2.0e+03	293.7	2359.6	300.9	621.1
g	41.0	1e-06	320	35.9	2.0e+03	674.8	2740.6	269.7	621.1
g	41.0	1e-07	471	35.9	2.0e+03	1150.8	3216.6	332.5	621.1
g	40.5	1e-05	211	35.9	2.0e+03	293.7	2359.6	317.0	408.9
g	40.5	1e-06	320	35.9	2.0e+03	674.8	2740.6	356.2	408.9
g	40.5	1e-07	471	35.9	2.0e+03	1150.8	3216.6	378.1	408.9
l	41.0	1e-05	106	0.9	6.0e+01	283.2	343.6	79.9	621.1
l	41.0	1e-06	144	0.9	6.0e+01	274.3	334.7	94.6	621.1
l	41.0	1e-07	187	0.9	6.0e+01	265.5	325.9	92.8	621.1
l	40.5	1e-05	111	0.7	6.0e+01	289.4	349.6	73.8	408.9
l	40.5	1e-06	154	0.7	6.0e+01	288.3	348.6	86.1	408.9
l	40.5	1e-07	197	0.7	6.0e+01	308.2	368.5	95.5	408.9

[a] variant: g=global, l=local
[b] Number of evaluated elements in the ECSW
[c] Time to compute the reduction basis (local or global, respectively)
[d] Time to compute nonlinear stochastic Krylov training sets
[e] Time to compute the element set $\tilde{E}$ and weights ξ
[f] Sum of all offline costs ($t_{\mathrm{V}} + t_{\mathrm{NSKTS}} + t_{\mathrm{ECSW}}$)
[g] Time for one time integration (1,000 timesteps) of the hyper-reduced model
[h] Time for one time integration (1,000 timesteps) of the full order model

Table 1: CPU-times for different computation steps in the case study. All times are measured with the python command `time.process_time()`.

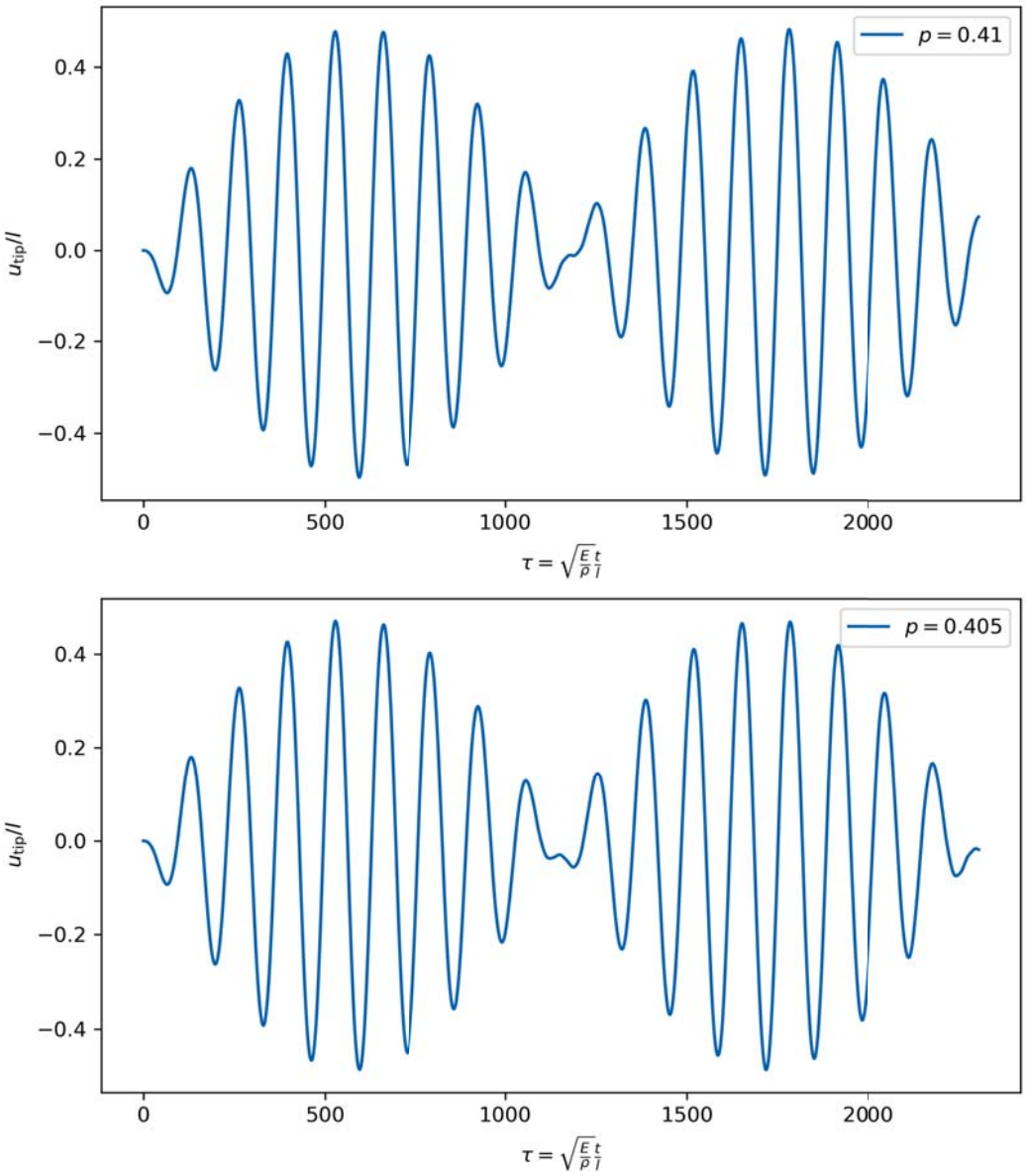

Figure 6: Transient response of the beam's tip displacement. The plots show the results simulated with a full order model.

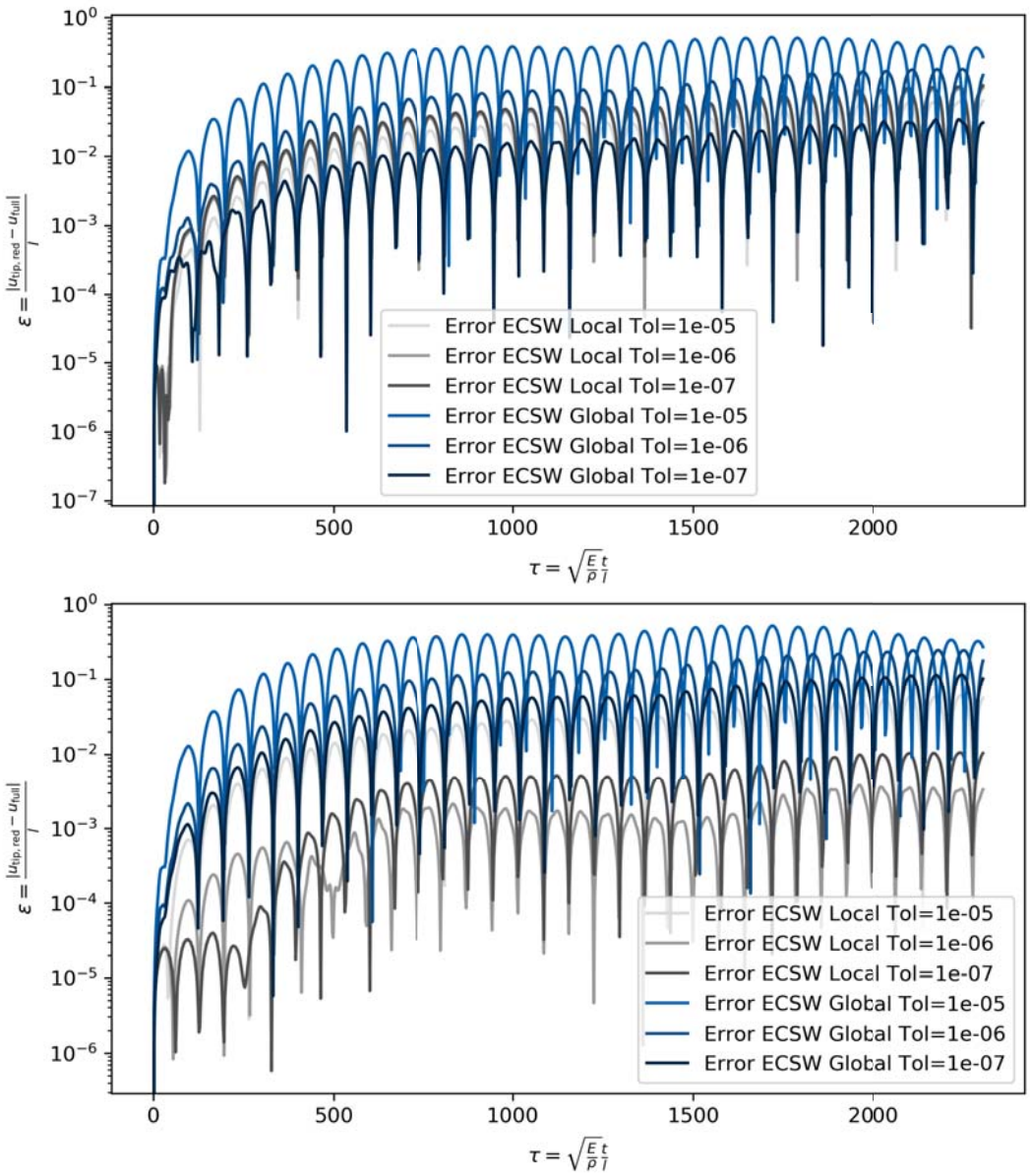

Figure 7: Dimensionless tip displacement error $\varepsilon = \frac{|u_{\mathrm{tip,red}} - u_{\mathrm{full}}|}{l}$ plotted over dimensionless time. Top: errors for simulations at $\boldsymbol{p} = 0.41$, bottom: errors for simulations at $\boldsymbol{p} = 0.405$

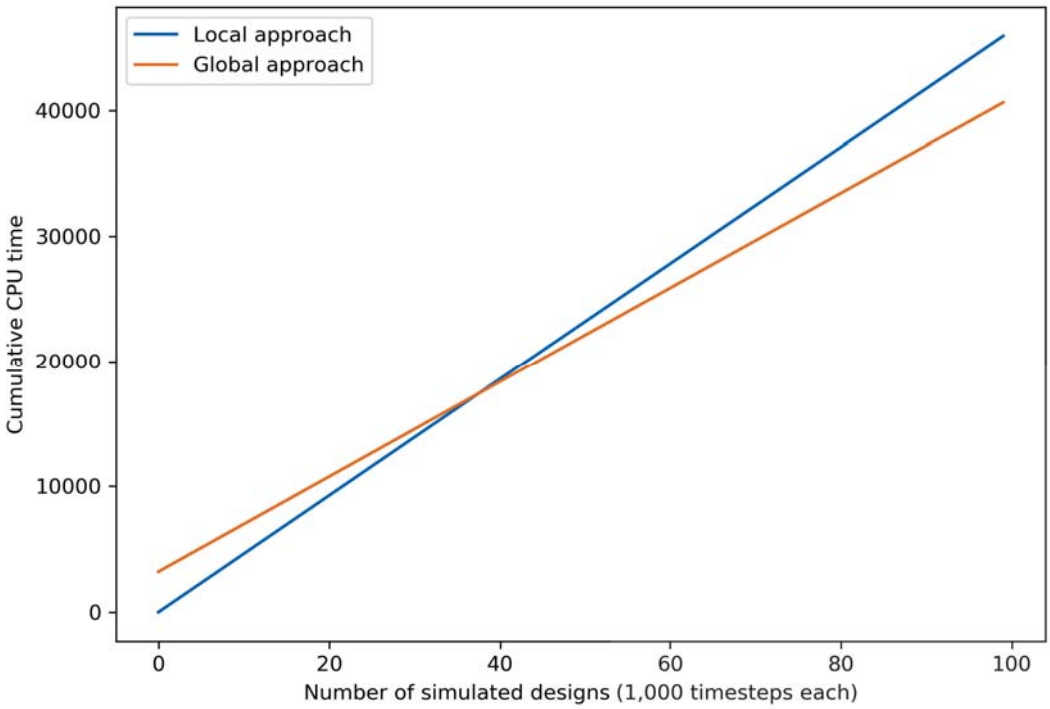

Figure 8: Cumulative Simulation times with local and global model reduction approach. The graphs use t_{offline} and t_{online} data for $\varepsilon_{\text{ECSW}} = 1\text{e} - 7$ of local and global approach, respectively.

6 CONCLUSION

Model reduction can help to reduce computation time when design studies are carried out that investigate the dynamics of geometric nonlinear structures. This contribution proposes a workflow for design studies where only one reduced order model is computed that is used to compute results for all design parameters of interest. This workflow uses nonlinear stochastic Krylov training sets that are computed for some parameter samples. They are used to gain a global set of weights and elements for the Energy Conserving Sampling and Weighting hyper-reduction method. The shape parameterized cantilever beam case study shows that a classic local approach is cheaper and needs less elements in the hyper-reduced element set $\tilde{E}$ and leads to shorter simulation times and smaller approximation errors. In contrast, the global approach only is beneficial if the number of parameter values, that need to be simulated, is very high. Then, the high offline costs for the global reduced order model pay off.

Acknowledgement The presented work is part of the research within the context of the Priority Program 1897 “Calm, Smooth and Smart“, subproject “Model Order Reduction of Parametric Nonlinear Mechanical Systems for Influencing Vibrations”. The authors are grateful to the Deutsche Forschungsgemeinschaft (DFG, eng. German Research Foundation) for the financial support.

REFERENCES

[1] C. Farhat, P. Avery, T. Chapman, J. Cortial, Dimensional reduction of nonlinear finite element dynamic models with finite rotations and energy-based mesh sampling and weighting for computational efficiency, *International Journal for Numerical Methods in Engineering*, **98** (9), 625–662, 2014.

[2] P.M.A. Slaats, J. de Jongh, A.A.H.J. Sauren, Model reduction tools for nonlinear structural dynamics. *Computers and Structures*, **54** (6), 1155–1171, 1995.

[3] J.B. Rutzmoser, Model Order Reduction for Nonlinear Structural Dynamics. *Dissertation*. Technische Universität München, Munich, Germany, 2018.

[4] P. Tiso, Optimal second order reduction basis selection for nonlinear transient analysis, *Conference Proceedings of the Society for Experimental Mechanics Series*, **3**, 27–39, 2011.

[5] C.H. Meyer, D. Rixen, Global proper orthogonal decomposition for parametric model reduction of geometrically nonlinear structures, *PAMM*, **19** (1), e201900436, 2019.

[6] J.B. Rutzmoser, D.J. Rixen, A lean and efficient snapshot generation technique for the Hyper-Reduction of nonlinear structural dynamics, *Computer Methods in Applied Mechanics and Engineering* **325**, 330–349, 2017.

EURODYN 2020
XI International Conference on Structural Dynamics
M. Papadrakakis, M. Fragiadakis, C. Papadimitriou (eds.)
Athens, Greece, 23-26 November 2020

REGULARIZATION METHOD TO INCLUDE MATERIAL SOFTENING IN FIBER BEAM-COLUMN ELEMENTS FOR SEISMIC PERFORMANCE ASSESSMENT OF STEEL FRAMES

Sebastián Pozo[1], Bryam Astudillo[1], Esteban Samaniego[2], and Francisco Flores[1, 3]

[1] Department of Civil Engineering, University of Cuenca, Ecuador
{sebastian.pozo,bryam.astudilloc,francisco.flores}@ucuenca.edu.ec

[2] Department of Hydric Resources and Environmental Science, University of Cuenca, Ecuador
esteban.samaniego@ucuenca.edu.ec

[3] Department of Civil Engineering, University of Azuay, Ecuador
fflores@uazuay.edu.ec

Keywords: Distributed plasticity, mesh-dependence, fiber, seismic performance

Abstract. *Currently, nonlinear analyses are widely used to evaluate the performance of special steel moment frames (Special SMF). Most of the mathematical models used in these analyses used concentrated plasticity approaches whit lumped nonlinearities at the end of beams and columns. Even when these models are highly recommended due to their simplicity and computational efficiency, they present some setbacks related to the axial-flexural interaction and the load protocol calibration dependency. In order to overcome these problems, a distributed plasticity model can be used. However, these models are not intended to capture local geometrical effects such as buckling or necking into the material constitutive law. In addition, these models present localization issues when the constitutive law includes softening, leading to variability in the global response.*

This paper proposes a distributed plasticity beam-column model that overcome these limitations. The constitutive material law proposed herein captures softening due to local buckling under compression stress using a non-symmetric strain-stress curve. The parameters are calibrated through experimental data and validated for different axial loads and loading protocols. Moreover, to solve the softening-localization issue, a method of regularization is proposed. This regularization is verified through static and dynamic analyses of an 8-story Special SMF building. The results show that the proposed model can represent the behavior of W shape sections under different load protocols and axial load demands. In addition, the model can accurately incorporate critical features as maximum flexural capacity, flexure axial interaction, and post-peak softening. The regularization method yielded negligible variations under different plastic lengths of the column for all the analyses. The proposed model is simple to implement, and the results indicate that it can be used to evaluate the seismic performance of Special SMF.

1 INTRODUCTION

Nowadays, the seismic performance of structures is commonly assessing with nonlinear analyses, due to the drastic improvement in computational storage and speed in the last 30 years. As a consequence, several codes such as the ASCE7-16 [1], ASCE-41 [2], and FEMA P-695 [3] require advanced nonlinear analyses to determine the behavior of a structure. However, in order to perform dynamic analyses, where structures are subjected to large deformations, nonlinear models need to capture two significant effects: element deterioration and nonlinear geometric effects. These effects allow the mathematical model to capture large deformations or trigger structural instability [4].

In special steel moment frames (Special SMF), the leading causes of beam-column element deterioration are related to local geometric instabilities. In beams, the deterioration is controlled by local flange buckling [5], while columns are controlled by local flange-web buckling and lateral-torsional buckling [6]. Therefore, a Special SMF model used in seismic performance assessment needs to include these phenomenological effects, as well as the structural geometrical effects (P-delta).

In literature, three main modeling approaches have been used in nonlinear Special SMF models: 1) finite element, 2) concentrated plasticity, and 3) distributed plasticity. The first one is considered the most detailed approach because these models can explicitly capture local instabilities and force interactions in any location within the structure. However, they are not recommended for complex analyses that include many structural members or several nonlinear incursions [7]. In contrast, concentrated plasticity models limit the nonlinear behavior to predefined locations (i.e., at the end of the elements where the inelasticity is expected) using calibrated constitutive curves that represent the element behavior. Even when these models are commonly used due to their simplicity and computational efficiency, they can not capture axial-flexural interaction or plasticity spreading, and they are highly dependent on the calibration load protocol [8].

Distributed plasticity is an approach that is between the other two, and it is a simplification of the finite element method that uses uniaxial materials. A common element of this approach is the fiber beam-column element, which consists of dividing the element into several nonlinear sections where the response is evaluated. This approach requires to define a material constitutive law for the section fibers and an integration method to combine the section responses [9]. Nevertheless, these models obtain the element response as an emergent property entirely related to the constitutive law. Then in order to capture local geometrical instabilities, the constitutive law should include phenomenological effects [7]. Moreover, these models present a critical setback due to strain localization when the constitutive law includes softening, which leads to a spurious mesh-dependence (i.e., non-objective global response) [10].

Even though some authors have proposed constitutive laws that include phenomenological effects, they only utilized a fixed mesh-discretization [8,11]. Therefore, the mesh-sensitivity of these results was not evaluated, consequently a procedure that ensures objective global response is necessary. In this sense, the Smeared-Crack approach is a method that modifies the constitutive law parameters depending on the mesh-discretization to reduce the effects of the localization [12]. This method has been implemented in reinforced concrete fiber models to achieve objective responses [10].

This study proposes a phenomenological calibrated constitutive law and a regularization process applicable to seismic performance assessment of Special SMF. First, the constitutive law is implemented with a non-symmetric curve that represents the section deterioration using compression softening. This curve is calibrated with experimental laboratory tests and validated under different axial load demands and load protocols. Then, the proposed regulariza-

tion method is presented in detail. The regularization process starts with a characterization of the global element response, followed with a sensitivity analysis of mesh-discretization and constitutive parameters to propose a rational set of regularization rules. Finally, the constitutive law and the regularization rules are used on an 8-story Special SMF building under static and dynamic nonlinear analyses to determine its applicability for seismic performance assessment.

2 CONSTITUTIVE LAW

in order to model the element deterioration adequately, the material constitutive law needs to capture not only the steel mechanical properties but also it requires to capture local geometric instabilities. Thus, the constitutive law proposed herein used a non-symmetric behavior with a compression softening branch that represents steel W-Sections local buckling that consequently takes into account the loss of capacity in the section. The open-source software OpenSees [13] was used to implement this behavior. The uniaxial Steel02 and Hysteretic materials were used together (into a Parallel material) to obtain the desired constitutive law. The Steel02 material presents the residual stress (Fig.1(a)) and the Hysteretic material a non-symmetric behavior (Fig.1(b)). The resulting material shows smooth stiffness transition and the compression softening branch until it reaches the residual stress (Fig.1(c-d)).

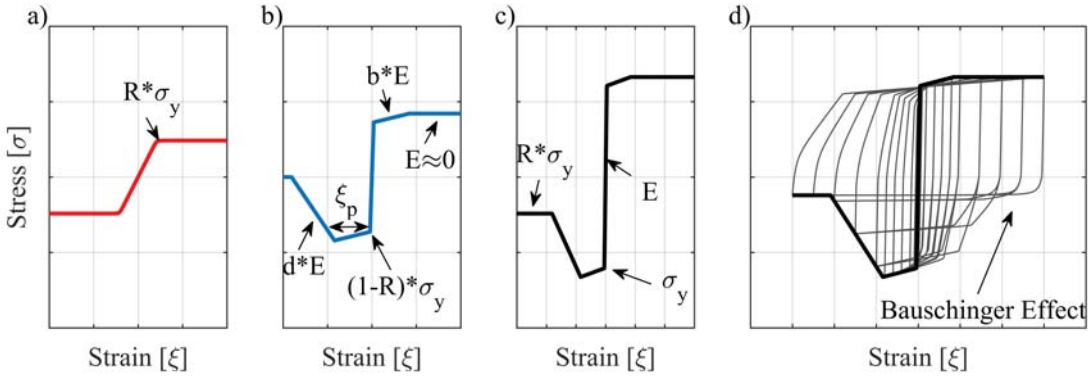

Figure 1: Constitutive law. a) Steel02, b) Hysteretic, c) Proposed material envelope, d) Proposed material cyclic.

The proposed constitutive curve has six characteristic parameters. Two of them are the steel mechanical properties: Young's modulus (E) and yielding stress (σ_y). The additional four calibrated parameters represent the local geometrical instabilities: strain hardening (b), plastic strain (ξ_p), strain softening (d), and residual stress (R).

2.1 Calibration and Validation

The laboratory experiment C4 presented in Elkady and Lignos (2018) [6] was replicated to calibrate the post yielding parameters and to capture the local geometrical effects in W-sections. The calibration test consisted of a cantilever W24x168 column subjected to a lateral collapse consistent load protocol and an axial load demand (P_g) of 0.2 the yielding axial capacity (P_y). The experimental setup is presented in Fig.2(a)), where the column model uses a single fiber-beam column element with the modified Gauss-Radau integration method (Fig.2(b)). In this integration method, the mesh-discretization depends on the plastic length assigned at the element ends, and the plastic length value for the calibration was considered equal to the column depth. The results of Fig.2(c) presents the experimental (Target) and the simulated global responses (Moment-Chord rotation).

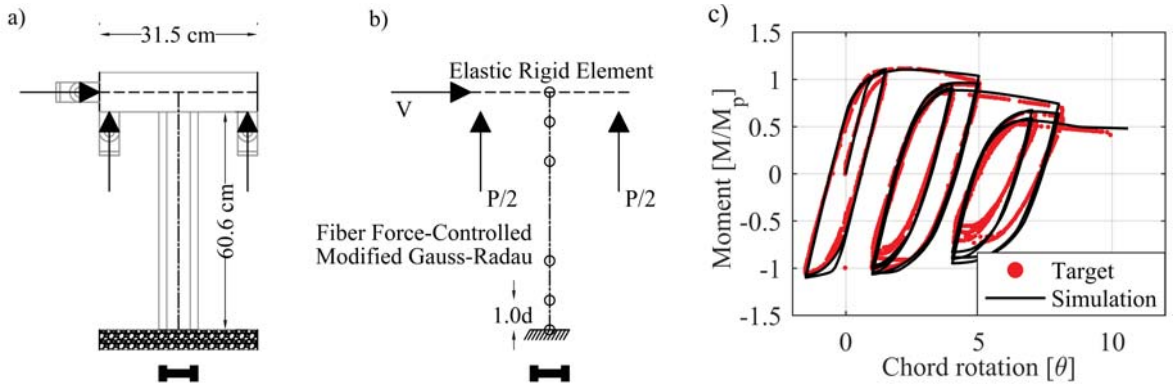

Figure 2: Calibration. a) Experimental setup, b) Numerical model, c) Experimental and simulated responses.

The four parameters related to the local geometrical instabilities were varied until the simulated moment-chord rotation response reached the best visual approximation with the experimental response. The values obtained from the calibration corresponds to 0.005, 0.015, 0.010, and 0.5 for b, ξ_p, d, and R, respectively. With these values, the proposed constitutive law captures the maximum capacity of the column, the smooth transition, the monotonic deterioration, and the cyclic strength and stiffness degradation correctly (Fig.2(c)).

After determining the six parameters, the constitutive law was validated using three additional experimental tests with different axial load demands and load protocols. The experiments correspond to the experiments C2, C3, and C6 obtained from Elkady and Lignos (2018) [6]. These models used the previously calibrated material parameters, and a plastic length equal to the column's depth. The only differences were the load protocol and the axial load demand, as presented in Fig.3(a-c). In addition, Fig.3 shows the comparison between the simulated and the experimental responses.

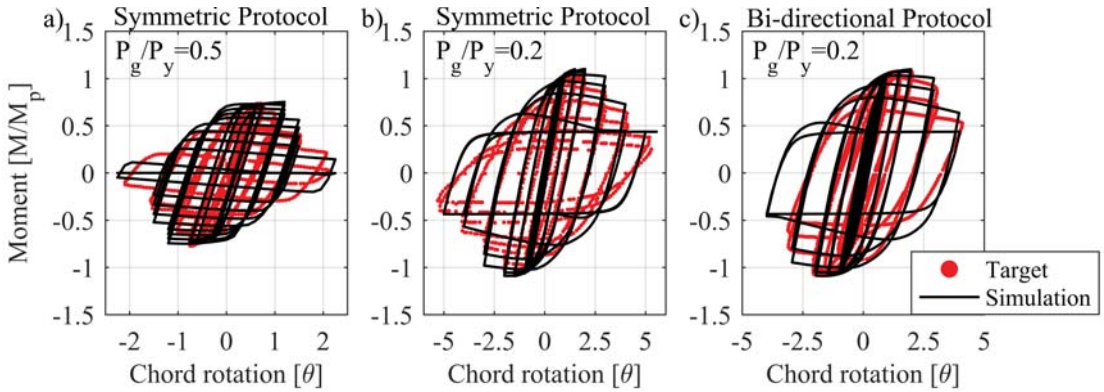

Figure 3: Validation. a) Test C2, b) Test C3, c) Test C6.

The results show that for a high axial load demand (Fig.3(a)), the response is more fragile because it reaches lower rotations than their counterpart with less axial load (Fig.3(b,c)). Fig.3(b-c) show that the simulations capture the stabilization of the moment deterioration when the fragile behavior does not control the response. Additionally, the proposed constitutive curve captures the behavior under the bi-directional symmetric load protocol, capturing the strength deterioration and cyclic degradation adequately (Fig.3(c)).

3 REGULARIZATION METHOD

The selection of an arbitrary plastic length value in the calibration section limits the proposed constitutive law to that unique mesh-discretization. As shown later, mesh-sensitive responses were obtained for different plastic lengths. Therefore, to get an objective response, a regularization method that reduces this spurious mesh-dependence is necessary. The regularization proposed uses the smeared-crack approach, which modifies the constitutive law parameters through regularization rules dependent on the mesh, to obtain an objective global response [12].

Before developing the regularization rules, three steps were necessary to understand the behavior of the global response. First, it was required to idealize the global element response to quantify the variations of the response. Second, addressing the global response differences due to mesh-discretization allowed determining trends in the global response. Finally, a sensitivity analysis of the constitutive law parameters allows determining their influence in the element's response curve. With this information, rational regularization rules can be developed to achieve an objective response.

3.1 Global response behavior.

Contrary to the concentrated plasticity models, the global element response in distributed plasticity models is not previously defined. This response is an emergent behavior that involves the constitutive law, the section geometry, and the element geometry. Therefore, to assess variations in the response curve is necessary to describe its behavior with a certain number of parameters that enable a quantitative comparison. For this purpose, the monotonic global response (moment-chord rotation) was idealized with a multilinear symmetric curve with four regions (Fig.4(a)). The first one represents the elastic element behavior, and it is limited by the yielding point, which is defined when the current stiffness becomes 20% the initial stiffness (K_{init}) (Fig.4(b)). The second region represents the element hardening capacity, and it is limited by the maximum moment and its respective chord rotation. The third region shows the element deterioration behavior, and a residual moment point defines it. Where the residual moment point is computed when the stiffness becomes 50% of the previous step stiffness (K_{curr}) (Fig.4(c)). The last region keeps constant the residual moment capacity.

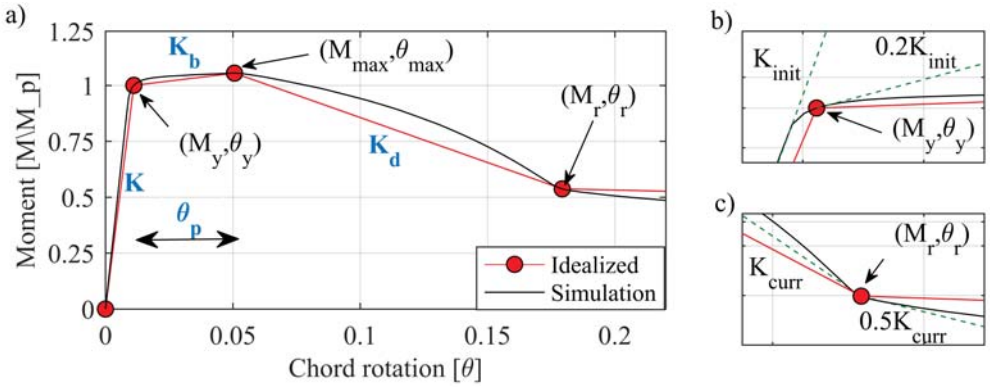

Figure 4: Response idealization. a) Moment chord-rotation, b) Yielding point, c) Residual point, d) Parameters

This idealization allows determining six global parameters presented in Fig.4(a): elastic stiffness (K), yielding moment (M_y), hardening stiffness (K_b), plastic rotation (θ_p), deterioration stiffness (K_d), and residual moment (M_r). These global parameters are coherent with the constitutive law parameters representing similar behavior on a different scale level (constitutive-material, and global-element).

The next step is to determine the mesh-sensitivity of the global response. For this purpose, monotonic static analyses were carried varying only the plastic length (L_p) of the modified Gauss-Radau integration method in the range of 0.3 to 1.8 the plastic length of the calibration (L_{pc}), while keeping the material parameters constant. These analyses illustrate the spurious mesh-dependence of the global moment-chord rotation response (Fig.5(a)). In addition, the analyses allow identifying tendencies in the global parameter values due to the plastic length variations (L_p/L_{pc}). The sub-index c denotes a calibration value or a value obtained using the calibration parameters.

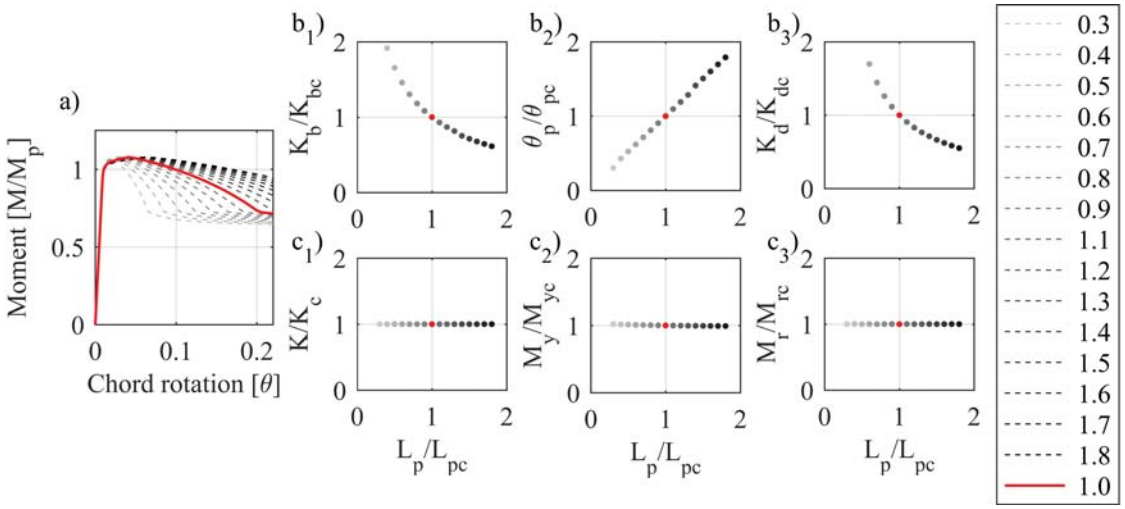

Figure 5: Sensitivity analysis. a) Moment-chord rotation response, b) Main tendencies, c) Null tendencies.

The results show that a variation in the plastic length leads to an inverse variation on hardening stiffness and deterioration stiffness (Fig.5(b_1,b_3)). Meanwhile, the plastic length leads to a direct variation on plastic rotation (Fig.5(b_2)). The other global parameters were not affected (Fig.5(c_1-c_3)), this invariability can be noticed in the moment-chord rotation curves too.

The regularization rules should affect the constitutive law parameters. Therefore, it is required to assess the global response variation due to changes in the constitutive parameters. Three sensitivity analyses were carried varying the constitutive parameters (b, ξ_p, and d) related to the plastic length sensitive global parameter (K_b, θ_p, and K_d). Only one parameter was varied at the time, while the other constitutive law parameters and the plastic length remained equal to the calibrated values. The variation range was kept the same as before from 0.3 to 1.8 the calibrated value. These results lead to determine tendencies in the variations of the global parameters that are critical to defining the regularization rules. Fig.6 shows the moment-chord rotation response of the carried monotonic static analyses varying the constitutive parameters. Also, the normalized tendencies between the constitutive law parameter and the global parameter are presented.

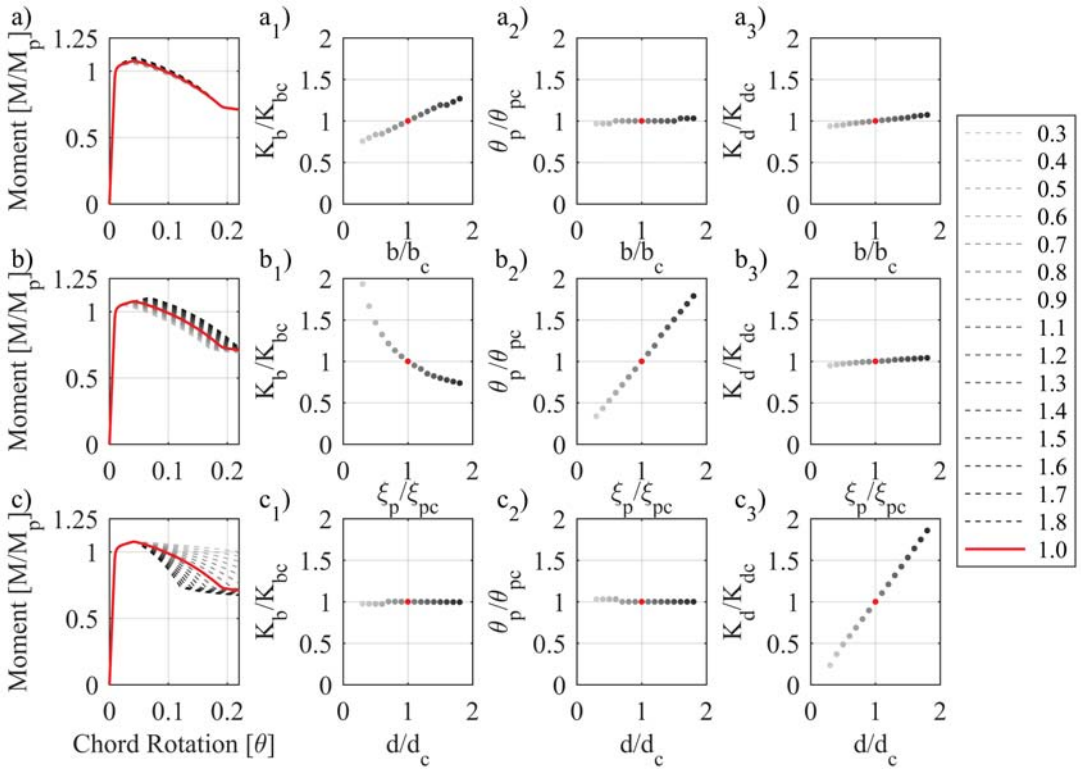

Figure 6: Sensitivity analysis. a) Strain hardening (b), b) Plastic strain (ξ_p), c) Strain deterioration (d).

The three parameters b, ξ_p, and d, show linear tendencies with their respective global parameters K_b, θ_p, and K_d (Fig.6(a_1, b_2, c_3)). Therefore, any variation applied to these parameters affects the global response in the same proportion. A secondary tendency was obtained for the plastic strain, which presents an inverse correlation with the hardening stiffness (Fig.6(b_1)).

3.2 Regularization proposal

The regularization rules should reduce the variations of the global response due to the mesh-discretization and canceling the tendencies showed in (Fig.5(b_1-b_3)). Inverse operations on the global parameter can negate these tendencies. Then, the plastic rotation divided by the plastic length ratio (L_p/L_{pc}), and hardening stiffness and deterioration stiffness multiplied by the same ratio reduces the tendencies. Even more, due to the linear dependence between global parameters and constitutive law parameters (Fig.6(a_1, b_2, c_3)), this operation can be applied to the constitutive law parameters with an equivalent effect on the global response. Consequently, the regularization rules are defined by three equations, one for each sensible constitutive law parameter.

$$b=b_c*(L_p/L_{pc}) \quad (1)$$

$$\xi_p=\xi_{pc}/(L_p/L_{pc}) \quad (2)$$

$$d=d_c*(L_p/L_{pc}) \quad (3)$$

Where L_p, b, ξ_p, and d are the values used in the analysis and L_{pc}, b_c, ξ_{pc}, and d_c are the calibration values, which are the column's depth, 0.005, 0.015, and 0.010, respectively.

With the regularized constitutive law parameters, a new sensitivity analysis varying the plastic length was performed. The element moment-chord rotation response increases its objectivity considerably (Fig.7(a)). In addition, the tendencies presented on the previous sensitivity analysis became negligible for plastic rotation and stiffness deterioration, but hardening

stiffness still presents a slight variation mainly under lower plastic length ratios (Fig.7(a_1)). This difference in stiffness hardening comes from the secondary tendency caused when the plastic strain is modified (Fig.6(b_1)). In order to cancel the variation on stiffness hardening, an alternative regularization rule on the strain hardening was determined:

$$b=b_c*(L_p/L_{pc})^{0.7} \qquad (4)$$

The alternative moment-chord rotation results (Fig.7(b)) show a similar behavior than the obtained with the initial regularization rules. However, the stiffness hardening tendency presents negligible variations to the plastic length (Fig.7(b_1)).

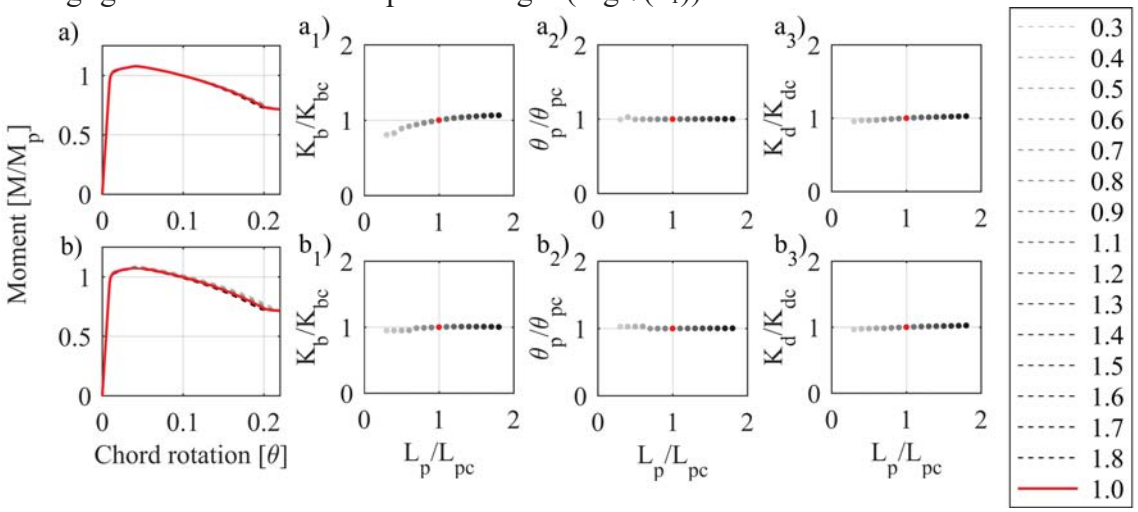

Figure 7: Regularized sensitivity. a) Initial regularization, b) Alternative Regularization.

4 SEISMIC ASSESSMENT

After developing the constitutive law and the regularization rules, these are applied to an eight-story structure with perimetral Special SMF as the lateral system (Fig. 8). The archetype was obtained from the ATC 71 project [14] and was designed for a D_{max} seismic risk category. The building present prequalified reduce beam section (RBS) on beams, and additional web thickness on column-beam connections (Panel Zone). This archetype has been used in several types of Special SMF research, and more detail is presented in [14–16]. The geometrical features of the lateral system are shown in Table 1.

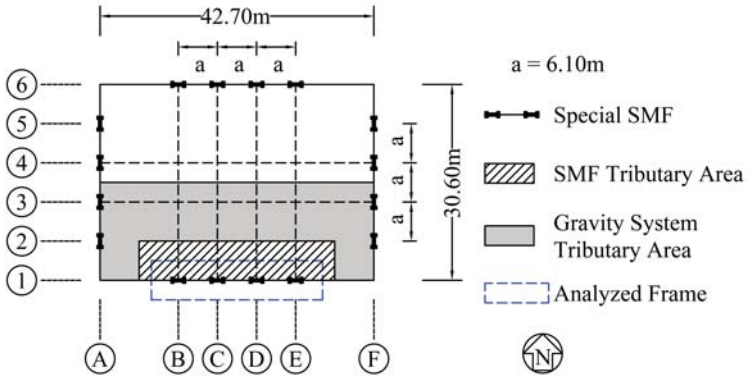

Figure 8. Archetype Plan View

Story	Elevation [m]	Beam Section	Exterior Column Section	Interior Column Section	Doubler Plate Size	
					Exterior [mm]	Interior [mm]
1	4.23	W30X108	W24X131	W24X162	1.59	14.29
2	8.19	W30X116	W24X131	W24X162	1.59	9.53
3	12.16	W30X116	W24X131	W24X162	1.59	17.46
4	16.12	W27X94	W24X131	W24X162	-	9.53
5	20.08	W27X94	W24X131	W24X131	-	14.29
6	24.04	W24X84	W24X131	W24X131	-	11.11
7	28.00	W24X84	W24X94	W24X94	-	14.29
8	31.97	W21X68	W24X94	W24X94	-	7.94

Table 1: Geometrical parameters.

Determine the influence of the regularization method is the main purpose of this research. Therefore, only elements with unknown plastic lengths were modeled with a distributed plasticity approach and the corresponding regularization method. In beams, a fixed plastic length (the RBS connection's length) and the absence of coupled phenomena (i.e., axial-flexural interaction) causes that a concentrated plasticity model can accurately represent the deterioration characteristics of these elements. The constitutive law used in the model was presented by Lignos (2008) [5], and it is known as modified Ibarra-Medina-Krawinkler (mod IMK). This constitutive capture beam's strength deterioration, in addition to strength and stiffness cyclic degradation (Fig.9(c)). More detail of the calibration process and its implementation is presented in [5,16]. The Panel Zones were modeled with the parallelogram methodology proposed in [17]. This approach uses a moment-shear deformation constitutive law that captures the joint nonlinear behavior. (Fig.9(b)), which include an initial stiffness, a secondary stiffness after beam flange yielding, and a hardening slope after columns web yielding.

On the other hand, columns were modeled using a distributed plasticity model with a single force-controlled fiber beam-column element with a modified Gauss-Radau integration method (Fig.9(d)). Three sets of models were developed, varying the plastic length and the regularization method employed. The first set uses the proposed constitutive law without a regularization process, the second set presents the initial regularization rules, and the third set uses the alternative regularization rules. The plastic length was varied from 0.3 to 1.4 the column's depth in the three sets.

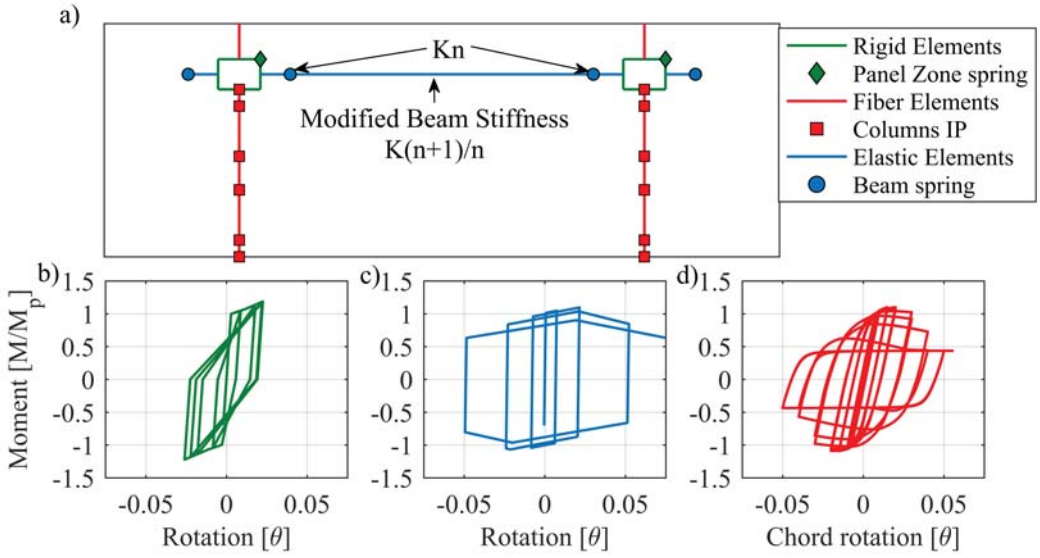

Figure 9: Modeling considerations. a) Frame model, b) Panel zone, c) RBS, d) Column.

The damping assignation considers a Rayleigh damping ratio of 2.5% applied in the first period (T_1) and on $0.2T_1$ according to the recommendations given in [14]. In addition, stiffness damping was not assigned on rotational springs to avoid unexpected damping forces due to stiffness changes after yielding [18]. Therefore, a damping modification was considered for the concentrated plasticity beam elements; the detail of this modification is presented in [19]. Moreover, the P-delta effects were considered with the leaning column approach, which consists of connecting the lateral displacement of the structure with a zero-flexural stiffness column that carries the non-tributary gravity load.

Once defined the model, a seismic performance assessment requires to determine a procedure to verify the behavior of the structure. ASCE 41 [2] establish two nonlinear procedures for seismic evaluations: 1) Nonlinear static procedure, 2) Non-linear time-history procedure. Both approaches are considered using a simplified method that enables determining the model capability of capturing structural instability with a mesh-independent global response.

4.1 Nonlinear static procedure (NSP)

This procedure uses a monotonic static analysis (Pushover) to assess the nonlinear behavior of the structure under an incremental lateral load. The analysis was performed in accordance with FEMA P-695 [3], where the load pattern was proportional to the first modal displacement and the mass distribution. In the nonlinear static procedure, the global acceptance criterion for seismic assessment is related to the maximum drift reached on a target roof displacement. Therefore, the differences showed in the capacity curve are directly related to the differences in the structure's seismic performance using this procedure. The results are presented as the capacity curve with the basal shear/weight ratio (V/W) versus the roof drift (Δ_r/H_r) (Fig.10(a, b, c)). In addition, the structure drift profile is presented at three different events: 1) at the yielding point (0.8%), maximum capacity, and the last step previous basal shear becomes negative.

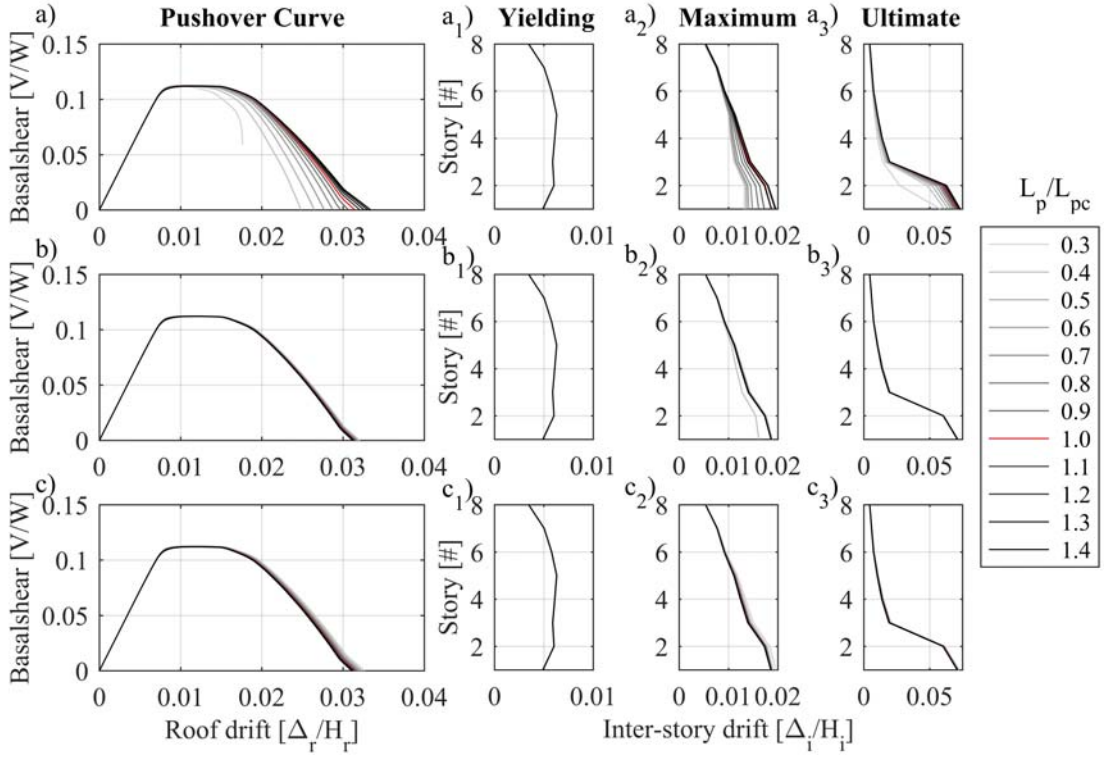

Figure 10: NSP. a) Non-regularized, b) Initial regularization, c) Alternative regularization

It is noticeable that for lower roof drifts demands (less than 0.8%), there is no need for the regularization because the columns do not present softening incursions (Fig.10(a_1, b_1, c_1)). However, on the maximum capacity and the last drift, there is a significant difference in the non-regularized models with variations of 25% and 20%, respectively. Also, it is noticeable that shorter plastic lengths lead to less ductile behavior (Fig.10(a)). In contrast, the regularized results lead to objective responses regardless of the plastic length used in the analysis (Fig.10(b, c)). There is a variation of 5% on the maximum capacity drift profile using the initial regularization rules (Fig.10(b_2)). However, despite that difference, the two regularization rules lead to an objective global response of the structure during the entire analysis.

A more detail summary of the pushover curve is presented in Table 2, where the drift at the maximum basal shear (δ_{Vmax}), the last drift reached by the model (δ_{last}), and the number of Newton-Raphson's iterations until the end of the analysis (NR_{iter}) are presented. This table shows the variations of the non-regularized models not only in the δ_{last}, but also in the δ_{Vmax} which lead to verify the importance of a regularization method even before the secondary (negative) stiffness of the pushover. These differences become negligible whit both regularization methods. These results show that on NSP, it is possible to achieve an objective response despite the weight of the most demanded IP, without increasing the Newton-Raphson iterations.

	Non-regularized			**Initial Regularization**			**Alternative Regularization**		
L_p/L_{pc}	**δ_{Vmax}**	**δ_{last}**	**NR_{iter}**	**δ_{Vmax}**	**δ_{last}**	**NR_{iter}**	**δ_{Vmax}**	**δ_{last}**	**NR_{iter}**
0.3	1.00	1.77	267	1.23	3.21	868	1.27	3.27	871
0.4	1.01	2.49	545	1.23	3.20	858	1.24	3.24	790
0.5	1.02	2.58	615	1.23	3.19	832	1.23	3.22	806
0.6	1.03	2.77	605	1.22	3.18	812	1.23	3.20	737

0.7	1.05	2.85	592	1.22	3.17	843	1.22	3.19	768
0.8	1.11	2.98	475	1.22	3.16	786	1.22	3.17	782
0.9	1.16	3.07	659	1.21	3.16	924	1.22	3.16	739
1.0	1.21	3.15	880	1.21	3.15	880	1.21	3.15	880
1.1	1.24	3.21	760	1.21	3.15	890	1.21	3.14	650
1.2	1.24	3.26	728	1.21	3.14	720	1.21	3.13	849
1.3	1.24	3.31	897	1.21	3.13	653	1.21	3.12	646
1.4	1.20	3.34	753	1.21	3.12	707	1.21	3.11	641
	δ_{Vmax}	δ_{last}	NR_{iter}	δ_{Vmax}	δ_{last}	NR_{iter}	δ_{Vmax}	δ_{last}	NR_{iter}
μ	1.13	2.90	648	1.22	3.16	815	1.22	3.18	764
σ	0.10	0.43	168	0.01	0.03	80	0.02	0.05	81

Table 2: NSP Roof drift and Newton-Raphson's iterations.

4.2 Nonlinear time history procedure (NDP)

This procedure requires to subject the structure to a set of ground motions scaled to the desired seismic intensity, and the median of the maximum responses of the structure is evaluated under specific criteria [2]. In this study, the structure was subjected to one ground motion as a simplified method to verify the constitutive law and the regularization process. The Kocaeli, Turkey ground motion of 1999 was selected and scale under three seismic intensity levels that represent a service level, design level, and maximum considered earthquake (MCE) level. The results of the time-history nonlinear analyses are presented as the 1st inter-story drift response at each intensity level (Fig.11).

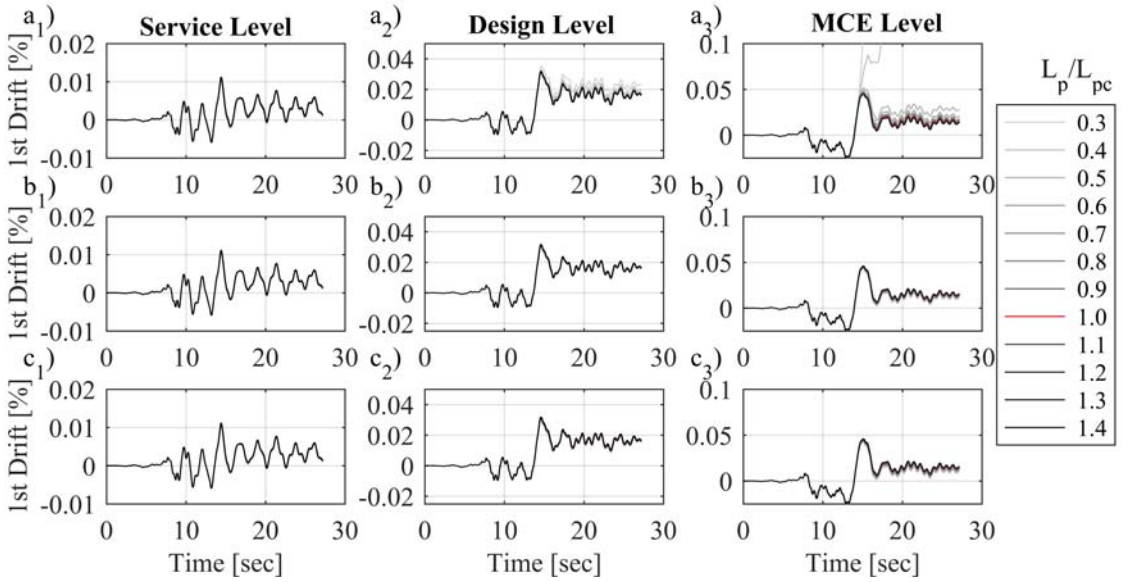

Figure 11: NDP. a) Non-regularized, b) Initial regularization, c) Alternative regularization

The results show that regularization is not necessary for lower intensity levels as the services one (Fig.11(a_1)), and for the design level, the differences are not considerable (Fig.11(a_2)). However, at the MCE level, the non-regularized models show a completely different response, and the localization caused structural instability in two models (Fig.11(a_3)). On the other hand, both regularization rules lead to an objective response (Fig.11(b_1-c_3)). The effect is mainly significative under the highest seismic intensity level, where the differences

are negligible (0.5%, on the maximum drift, and 0.2% on the residual drift). There is no significant difference between the initial and the alternative regularization method.

Similar to the NSP analysis, the maximum inter-story drift (δ_{Max}), the maximum residual inter-story drift (δ_{Res}), and the number of Newton-Raphson iterations until the end of the analysis (NR_{iter}) are presented in Table 3. For instance, the models without regularization and with plastic length lower than the calibration one (L_p/L_{pc}<1.0) present higher deformations than the base case (L_p/L_{pc}=1.0). The opposite behavior is noticeable in models with plastic lengths' higher than the calibration (L_p/L_{pc}>1.0). In contrast, both regularization proposals yield to negligible variations in the δ_{max}, and δ_{Res} with the same computational cost analysis even in a complex nonlinear time-history analysis with high seismic demand.

	Non-regularized			Initial Regularization			Alternative Regularization		
L_p/L_{pc}	**δ_{Max}**	**δ_{Res}**	**NR_{iter}**	**δ_{Max}**	**δ_{Res}**	**NR_{iter}**	**δ_{Max}**	**δ_{Res}**	**NR_{iter}**
0.3	10.04	10.04	3225	4.25	1.06	6015	4.17	0.96	6806
0.4	10.11	10.11	4134	4.31	1.15	6601	4.25	1.07	6656
0.5	5.14	2.72	6421	4.36	1.21	6629	4.31	1.15	5851
0.6	4.84	2.02	6084	4.40	1.26	5911	4.37	1.22	5909
0.7	4.70	1.76	6537	4.43	1.31	6439	4.41	1.28	6111
0.8	4.60	1.58	6430	4.46	1.35	6044	4.45	1.33	5996
0.9	4.55	1.48	6049	4.49	1.38	5916	4.48	1.37	5903
1.0	4.51	1.41	5888	4.51	1.41	5888	4.51	1.41	5888
1.1	4.49	1.36	6614	4.53	1.44	6518	4.54	1.45	6501
1.2	4.47	1.41	5525	4.55	1.47	6137	4.56	1.50	6794
1.3	4.46	1.31	6082	4.56	1.50	6441	4.58	1.45	5984
1.4	4.46	2.92	4278	4.56	1.50	6314	4.59	1.47	6221
L_p/L_{pc}	**δ_{Max}**	**δ_{Res}**	**NR_{iter}**	**δ_{Max}**	**δ_{Res}**	**NR_{iter}**	**δ_{Max}**	**δ_{Res}**	**NR_{iter}**
μ	5.53	3.18	5606	4.45	1.34	6238	4.43	1.30	6219
σ	2.04	3.13	1064	0.10	0.14	271	0.13	0.17	354

Table 3: NDP maximum inter-story drift and Newton-Raphson's iterations for the MCE hazard level.

5 CONCLUSIONS AND RECOMMENDATIONS

This study focuses on assessing regularization rules applied on a phenomenological calibrated steel material that includes softening in the constitutive law. The regularization was tested on a monotonic cantilever test and an eight-story Special SMF building. In addition, the regularization and the constitutive law were assessed under different levels of seismic intensities to determine its applicability for seismic assessment of Special SMF. The main conclusions of this study are:

- The phenomenological calibration captured the behavior of steel W-section adequately under different conditions of load protocol and axial load demands. Also, the phenomenological calibration included the softening branch, which simulated the local geometrical instability of the experimental test.
- The process to define the regularization rules led to identifying essential tendencies of the constitutive law parameters and the mesh-discretization in the global response. Furthermore, this process established an intuitive method to develop regularization rules that reduced the spurious mesh-dependence of the model.

- The seismic assessment of Special SMF using distributed plasticity models showed that regularization was not required in lower levels of seismic intensity because the structure remained substantially elastic. However, in higher demands such as design or MCE, the regularization of the constitutive law became critical to achieving objective responses.
- The regularization rules presented in this study led to objective responses under all the tested analyses. Moreover, there was no significant difference between the two groups of regularization rules, and both of them can be used in seismic performance assessment.
- This regularization process leads to a simple method that controls the mesh-dependence of global results. Furthermore, the procedure does not require additional implementation on OpenSees (i.e., elements, materials, or analyses). Also, since the procedure does not require a fine mesh-discretization, it can be used to reduce the number of elements, or integration points per structural element without compromising the global response.

This study presented limitations regardless of the single archetype used in the seismic assessment section. The effect of the constitutive law and the regularization rules should be tested on a broader range of Special SMF. Also, the performance conditions considered in this structural seismic assessment are related to global performance criteria; a more detailed performance-based analysis is required that includes local conditions such as element rotations.

A significant improvement in considering the distributed plasticity model in columns is that it explicitly captured the axial-flexural interaction. Adding this effect enabled an axial-shortening assessment that was not taking into account in this research. Further research needs to be carried in order to determine if this phenomenon is critical in the seismic performance assessment of Special SMF.

6 BIBLIOGRAPHY

[1] ASCE 7, ed., Minimum design loads and associated criteria for buildings and other structures, American Society of Civil Engineers, Reston, Virginia, 2017.
[2] ASCE 41, Seismic Evaluation and Retrofit of Existing Buildings, (n.d.).
[3] FEMA P695, Quantification of Building Seismic Performance Factors, (2009).
[4] FEMA P-58, Seismic Performance Assessment of Buildings, (2012).
[5] D. Lignos, Sideways Collapse of Deteriorating Structural Systems Under Seismic Excitations, (2008).
[6] A. Elkady, D.G. Lignos, Full-Scale Testing of Deep Wide-Flange Steel Columns under Multiaxis Cyclic Loading: Loading Sequence, Boundary Effects, and Lateral Stability Bracing Force Demands, Journal of Structural Engineering. 144 (2018) 04017189. https://doi.org/10.1061/(ASCE)ST.1943-541X.0001937.
[7] J. Dujc, B. Brank, A. Ibrahimbegovic, Multi-scale computational model for failure analysis of metal frames that includes softening and local buckling, Computer Methods in Applied Mechanics and Engineering. 199 (2010) 1371–1385. https://doi.org/10.1016/j.cma.2009.09.003.
[8] Y. Suzuki, D. Lignos, Fiber-Based Model for Earthquake-Induced Collapse Simulation of Steel Frame Buildings, in: 11 NCEE LA 2018, Earthquake Engineering Research Institute, Los Angeles, California, 2018.
[9] S. Enrico, F. Filip C., T. Fabio F., Fiber Beam-Column Model for nonlinear analysis of R/C frames. Part I. Formulation, EARTHQUAKE ENGINEERING AND STRUCTURAL DYNAMICS. 25 (1996) 711–725.

[10] J. Coleman, E. Spacone, Localization Issues in Force-Based Frame Elements, Journal of Structural Engineering. 127 (2001) 1257–1265. https://doi.org/10.1061/(ASCE)0733-9445(2001)127:11(1257).
[11] M. Farahi, S. Erfani, Efficiency of employing fiber-based finite-length plastic hinges in simulating the cyclic and seismic behavior of steel hollow columns compared with other common modeling approaches, Earthquake Engineering and Engineering Vibration. 18 (2019) 777–794. https://doi.org/10.1007/s11803-019-0536-3.
[12] Y.R. Rashid, Ultimate strength analysis of prestressed concrete pressure vessels, Nuclear Engineering and Design. 7 (1968) 334–344. https://doi.org/10.1016/0029-5493(68)90066-6.
[13] F. McKenna, M.H. Scott, G.L. Fenves, OpenSees: Open system for earthquake engineering simulation., Pacific Earthquake Engineering Center, California, 2006.
[14] NIST, NEHRP, eds., Evaluation of the FEMA P-695 Methodology for Quantification of buildings Seismic Performance Factors, (2010).
[15] F.X. Flores, F.A. Charney, D. Lopez-Garcia, Influence of the gravity framing system on the collapse performance of special steel moment frames, Journal of Constructional Steel Research. 101 (2014) 351–362. https://doi.org/10.1016/j.jcsr.2014.05.020.
[16] F. Zareian, D. Lignos, H. Krawnikler, Evaluation of seismic collapse performance of steel special moment resisting frames using FEMA P695 (ATC-63) methodology, ASCE. (2010) 1275–1284.
[17] A. Gupta, H. Krawinkler, Prediction of seismic demands for SMRFs with ductile connections and elements, SAC Steel Project, 1999.
[18] F.A. Charney, Unintended Consequences of Modeling Damping in Structures, Journal of Structural Engineering. 134 (2008) 581–592. https://doi.org/10.1061/(ASCE)0733-9445(2008)134:4(581).
[19] F. Zareian, R.A. Medina, A practical method for proper modeling of structural damping in inelastic plane structural systems, Computers & Structures. 88 (2010) 45–53. https://doi.org/10.1016/j.compstruc.2009.08.001.

EURODYN 2020
XI International Conference on Structural Dynamics
M. Papadrakakis, M. Fragiadakis, C. Papadimitriou (eds.)
Athens, Greece, 23-26 November 2020

EFFICIENCY OF 1D CNNS IN FINITE ELEMENT MODEL PARAMETER ESTIMATION USING SYNTHETIC DYNAMIC RESPONSES

M. Almutairi[1], **O. Avci** [1], **and N. Nikitas** [1]

[1] University of Leeds
Woodhouse, Leeds LS2 9JT, UK
e-mail: {cnmsek, o.avci, n.nikitas}@leeds.ac.uk

Keywords: Model updating, Parameter estimation, Dynamic response, Damage detection, Convolutional Neural Networks, Deep Learning.

Abstract. *A critical step of building a reliable Finite Element (FE) model is closing the gap between the actual and the simulated structural behaviour by utilizing FE model updating methods. Current updating methods typically require hand-crafted features such as natural frequencies and mode shapes. As a result, limitations in identifying these features are becoming also limitations in the updating process. With the ability to utilize raw data, Deep-Learning (DL) algorithms have the potential to avoid such limitations. This paper aims to validate the efficiency of 1D Convolutional Neural Networks (CNNs) in estimating FE model parameters using synthetic acceleration data. The performance of 1D CNNs was tested on a simple FE beam model. The influence of training pair numbers, and acceleration signal duration on the algorithm performance was evaluated. The results indicate that the 1D CNNs have the ability to estimate FE model parameters with high accuracy. Final results indicate that the standard damage detection and the more novel model parameter estimation, through using 1D CNNs, can be practised synchronously with equally good results.*

1 INTRODUCTION

Finite element (FE) modelling has been in broad use for analysing structural behaviour [1], even though there are uncertainties and assumptions inherent in it (e.g. material properties, boundary conditions) [2]. These uncertainties may compromise the ability of an FE model to simulate the actual static and dynamic behaviour of a structure. To reduce the uncertainties and build a reliable FE model, a reconstruction of it can be considered by calibrating its parameters based on actual structural behaviour data, a process widely known as FE model updating.

FE model updating methods are broadly classified into non-iterative and iterative ones [2, 3]. The former are computationally efficient yet, they tend to produce physically meaningless results. For this reason, they are not widely used in practice [3–5]. On the other hand, iterative methods can overcome this limitation.

Iterative methods estimate a set of FE model parameters by using error minimization techniques; however, there are several concerns associated with their deployment. Namely, some of the methods may converge prematurely to a local optimal solution; such is the case of the Particle Swarm Optimization (PSO). Others rely on a rather complex implementations; such is the case of genetic algorithms [3]. Neural Networks (NNs), being another class of Machine learning (ML) algorithms, provide an alternative solution to avoid such concerns owing to their inherent learning-process step.

NNs can learn any non-linear/complex relationship between the structural response (as embedded for instance within natural frequencies and mode shapes) and a set of FE model parameters [6]. For this reason, several attempts have been made to update FE models using NNs. One of the first attempts was made by Levin and Lieven [7]. In their study, a numerical model of a ten-element cantilever beam was used. They updated the Young's moduli and the density of each element working only with the first five frequencies and mode shapes. They concluded that NNs can withstand the presence of noise even when there is limited data. The limitation of using modal parameters is that the ensuing modal analysis techniques used for extracting them carry assumptions and approximations. On the other hand, the Frequency Response Functions (FRFs) are directly measured in structures. For this reason, Sadr et al. [8] used FRFs to improve NNs' performance in FE model updating. However, training NNs with the large size of FRFs could be time consuming due to the algorithm shallow-learning architecture. To tackle the trade-off between computational cost and algorithm performance, they used Principal Component Analysis (PCA) as a data reduction method. This approach was verified on a numerical (ten-degrees-of-freedom lumped parameter system) and an experimental example (free-free beam). In real-life applications, Sabamehr et al. [9], applied NNs to update FE models of three different bridges. In this study, the change of stiffness of some elements was estimated using NNs and natural frequencies.

A constraint of NNs in FE model updating is that the output data (e.g. FE model parameters) need to be equal or less than the number of input data (e.g. structural responses) [10]. Furthermore, any artefact in the modal parameter identification or the FRFs' reduction would carry over on the final NNs results.

The recent advancements in ML algorithms have led to developing Deep Learning (DL) algorithms, in which the machine can learn by using only raw data [11]. DL algorithms (e.g. Convolutional Neural Networks -CNNs-) have the potential to avoid the drawbacks of traditional NNs.

For instance, modal parameter identification techniques, with their limitations and constraints on the FE model updating process, can be bypassed by utilizing raw acceleration data. As a result, the advantages of the learning process of NNs are maintained and the drawback of utilizing hand-crafted features is overcome.

1D CNNs have already been implemented successfully in vibration-based applications in civil, mechanical and aerospace engineering [12–15]. 1D CNNs can learn from vibration data arranged in the form of a vector, which is convenient for one-point response data, or a matrix, which is convenient for multi-point response data. Abdeljaber et al. [15] used the vector form to identify and locate structural damage at the joints of a laboratory steel grandstand-like frame by using 1D CNNs and acceleration data. The results of this study show that the 1D CNNs have the ability to detect damage at several structural conditions with high accuracy even though these structural conditions were not included in the training data. The limitation of this study is that the number of the structural conditions for training the 1D CNNs should equal the number of the considered joints as well as that the structural condition which represents the undamaged structure needs to exist. To overcome this limitation, Abdeljaber et al. [14] used only two structural conditions, namely, undamaged and severely damaged to assess the overall structural condition of a benchmark structure (four-story, braced steel structure). Different structural conditions, which simulate different level of overall damage, were used to evaluate the algorithm. In their study, a good estimation of the overall structural condition was reported. On the other hand, Zhang et al. [16] used a matrix of acceleration time histories as input data to detect structural damage. The method was validated on three different structures, including an in-service steel girder bridge. In their study, the structural damage was simulated by adding a mass to the structures. Several structural conditions were simulated by changing the position of this mass. The multi-points acceleration responses of each structural condition were used as training and validating data. The latter data was used to evaluate the accuracy of the 1D CNNs performance. The results show a high accuracy (97.2% - 99.5%) in detecting and locating the structural damage.

Inspired by the aforementioned achievements of the 1D CNNs in classification of structural conditions, this paper is aiming to validate the efficiency of 1D CNNs in estimating FE model parameters. A simple numerical cantilever beam model was adopted and different levels of artificial damage were considered for it through the introduction of a non-rigid rotational support. The beam was dynamically loaded for producing synthetic acceleration data. The, multi-point acceleration responses, were formed into an input matrix to estimate the parametrically varying rotational stiffness of the cantilever beam. By this approach, the FE model updating process can be performed simultaneously with detecting and evaluating structural damage.

The paper is organised as follows. The background of 1D CNNs is first reviewed. Then, the proposed method of the FE model updating technique is presented, including reference to previous relevant studies. The performance of the algorithm is then analysed as a function of the number of training data cases, and the acceleration signal duration. Finally, the trained 1D CNNs is tested to validate the proposed methodology.

2 OVERVIEW OF 1D CONVOLUTIONAL NEURAL NETWORKS (1D CNNS)

CNNs used in this study consist of two stages; the feature extractor stage and the fully connected layer stage [17] as illustrated in Figure 1.

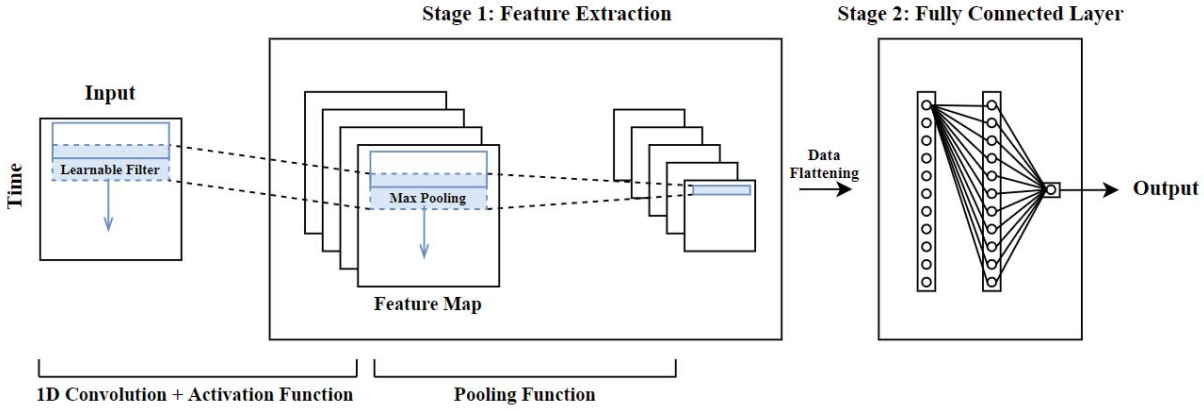

Figure 1: An architecture of 1D CNN includes feature extraction and regression stages.

Extracting features is achieved by stacking and alternating convolutional layers and pooling layers. Figure 1 shows only one convolutional layer and pooling layer for illustration purposes. In the convolutional layer, the input data are convolved by learnable filters and activation functions to generate feature maps. It is worth noting that the activation function is used to introduce nonlinearity to the algorithm, which in turn improves the algorithm learning from complex structural data. There are different types of activation functions such as Rectified Linear Unit (ReLU), sigmoid and linear activation function [18]. As a side effect of generating feature maps, the dimension of data is increasing as shown in Figure 1, where each learnable filter generates a feature map. To reduce the data dimension, pooling layers are used. The pooling layers use a pooling function to operate. The most common pooling function is "max pooling", which convolves over the feature map to select the maximum value of the covered portion. An added benefit of the max pooling function is that it performs a denoising role [19].

In the second stage of CNNs, fully connected layers perform regression based on the extracted features in the first stage. The fully connected layers are the traditional NNs. After the second stage, the prediction error is estimated by a loss function such as the Mean Square Error (MSE). To reduce the error, an optimization function (e.g. Adam as in [20]) is used to update the learnable parameters of the filters in the first stage. In the following section, the FE model updating approach using 1D CNNs is introduced besides related studies which include FE model updating applications using NNs in order to draw similarities for the proposed technique.

3 TRAINING AND VALIDATING THE 1D CNNS

FE model updating by using 1D CNNs, generally, consists of three steps: generating sufficient training data; preparing the training data to train the 1D CNNs; and training and validating the 1D CNNs performance.

Generating training data is a critical step for 1D CNNs' performance. The training data include pair vectors (hereafter called training pairs), where each consists of a vector of FE model parameters (i.e the 1D CNN output), and a vector of their corresponding structural responses (i.e. the 1D CNN input). The training pairs are aimed to cover a wide range of structural conditions. For example, the output vector of Sabamehr et al. [9] includes ± 50% variations of the stiffness of a Pre-Stressed Concrete Box (PSCB) girder bridge. In the case of a voided slab bridge, they assumed variations of ± 20%. In the Lu and Tu [21] study on a numerical model of a lumped-mass stick, which simulates a six-storey building frame, the inter-storey sway stiffness was assumed to range between 100% to 35% to represent undamaged and highly damaged frame members, respectively. After selecting the configuration of the parameter values for each

output vector, the input vectors can be numerically simulated to form the training pairs which would later be prepared for training the 1D CNNs.

Various techniques of preparing training pairs are typically used to improve the algorithm performance, such as data normalisation, data augmentation, padding, shuffling, and the mini-batch technique. Normalising training pairs allows to overcome the drawback of larger values dominating over smaller ones on the algorithm performance [22]. In the Avci et al. [23] study, the acceleration signals of the input vector were normalised in the intuitive range of (-1,1). Because their study was considering damage identification, the output vector was containing only two values, 0 and 1 for the damaged and undamaged cases, respectively. This (0,1) range was used also by Lu and Tu [21] for the output vector in their study of FE model updating using NNs.

Another technique is data augmentation which is often used to increase the number of training pairs when there is limited data [24]. For example, window slicing, which is a data augmentation technique, was introduced for time series in [25]. In this technique, the original time series data is sliced to several segments. Avci et al. [23] applied window slicing in civil engineering application. They sliced the available acceleration signals to several vectors. In this way, each training pair was divided into several training pairs. In the same manner, several acceleration signals, which form a matrix, can be divided into submatrices.

On an adverse note, the introduction of the submatrices leads to compromising the feature extraction process around the border of each submatrix. Namely, the data of the first and the last rows of these submatrices would be scanned only once by the learnable filters. To tackle this issue, the submatrices can be upsized by adding zeros around the borders (padding [26]). In this way, the first and the last rows are covered more than once by the learnable filters.

In addition to the aforementioned techniques, the shuffling of the training pairs is crucial to avoid any bias in the learning process of the algorithm. Finally, updating the learnable parameters after each mini-batch (i.e. portions of the training pairs), instead of one batch (i.e. all the training pairs), can improve the 1D CNN performance and reduce the computational cost. The algorithm requires several passes of all the mini-batches to improve, where each pass is called epoch [11, 27].

For the stage of training and validating the algorithm performance, part of the training pairs (hereafter called validating pairs) are not included in the training process. The validating pairs are utilized to validate the algorithm performance throughout the training process. The validating process is achieved by using a loss function (e.g. MSE). The algorithm can be considered as well-trained when it produces an acceptable error on training pairs as well as validating pairs. Once the algorithm is well-trained, it can be fed the measured structural response of the actual structure to estimate the FE model parameters. These values of the FE model parameters are not necessarily included in the training and validating pairs owing to the regression operation of the 1D CNNs.

Some parameters of 1D CNNs can by adjusted by the user to improve the algorithm performance; such can be the number of the convolutional and pooling layers, the size and number of the learnable filters, the type of activation functions, and the optimization function. The adjusting process of these parameters is called hyperparameter tuning [27]. The manual approach of hyperparameter tuning was adopted by many researchers in mechanical and civil engineering [14, 15, 24, 28]. In this approach, some “rules of thumb” or expert judgment is required. For example, using smaller size learnable filters in multiple convolutional layers would be better than larger size learnable filters in a single convolutional layer. Also, the number of the learnable filters in the first convolutional layers should be more than their number in the last convolutional layers. The ReLU activation function is recommended to be used in the convolutional

layers, while the linear activation function is suitable for regression output layer. Also, the MSE is suggested as a loss function for the regression task of the algorithm [27].

4 NUMERICAL EXAMPLE

A simple numerical example is used in this section for illustrating the implementation of 1D CNNs in FE model updating. The numerical example is a 3D FE model of an I-section cantilever beam which was simulated using shell elements in Abaqus [29]. The cantilever beam is made up of steel with density 7850kg/m^3, Young's modulus 210GPa, and Poisson's ratio 0.3. It has a cross section area cover of 100×100mm, with flange and web thickness of 8mm and 6mm, respectively. The cantilever length is selected as 2.5m so that any shear contributions in the output deflection can be minimised and analytical validation of the FE model can be performed by using standard Euler-Bernoulli beam theory [30], [31].

4.1 Validation of FE model

In this section, the static and dynamic behaviour of the model was validated before pursuing any FE model updating. First, the analytical value of the maximum deflection of the cantilever was calculated. For a static vertical point load of 2kN, applied at the cantilever free end, the corresponding analytical deflection compares with the numerical deflection as shown in Table 1. In a follow-up step, the natural frequencies of the first four modes were calculated analytically and were compared to their numerical counterpart, as shown in Table 2. Results show that both the static and dynamic behaviour of the FE model is in good agreement with the theoretical expectations. It should be noted that although the error in the 2nd bending mode is higher than the error in the other modes, it is not considered significant.

Table 1: Comparison of the numerical and analytical solution of the cantilever tip deflection.

	Numerical solution	Analytical solution	Error %
Vertical displacement	13.55mm	13.44mm	0.8

Table 2: Comparison of the numerical and analytical solution of the cantilever natural frequencies.

Natural frequency (Hz)		Mode type	Error %
Numerical solution	Analytical solution		
11.642	11.663	1st lateral	-0.2
19.265	19.393	1st bending	-0.7
36.441	-	1st torsional	-
72.433	73.096	2nd lateral	-0.9
115.63	121.540	2nd bending	-4.9

After validating the cantilever FE model, different states of the in-plane rotational boundary condition, considered equivalent to damage, were simulated and studied by using different values for the in-plane rotational spring stiffness. It is to be noted that the cantilever mechanism of carrying the main load is having a primarily bending behaviour [32]. The value of the rotational spring (10^{13} N.mm/rad) was selected as the case where the frequency of the 1st bending mode of the rotational spring-supported beam is matching the corresponding frequency of the fixed cantilever beam. For this task, the 1st bending mode is selected since the in-plane rotational spring stiffness is not expected to couple considerably with the lateral modes.

4.2 Generating training pairs and training the 1D CNNs

Specifying the training pairs means specifying both the output and input vectors. The output vectors consist of different values of rotational spring stiffness to simulate different states of the support. To illustrate, a 10% reduction on the initial stiffness value is considered accounting for a nominal 10% damage at the support. The input vectors consist of vertical acceleration responses at four equidistanced locations as shown in Figure 2. For the dynamic excitation of the cantilever beam, a vertical monoharmonic force of 100N amplitude and 10Hz frequency was applied at the free end of the cantilever from zero initial conditions; acceleration response signals were sampled at 200Hz. The four acceleration signals are forming a matrix with four columns, for each rotational spring case.

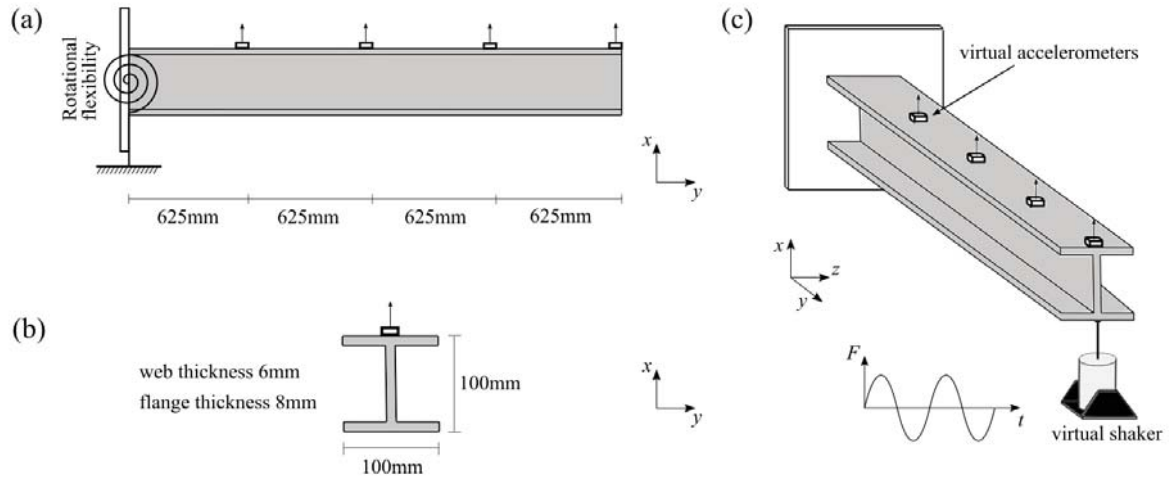

Figure 2: (a) Locations of acceleration response measurements on the spring-supported cantilever beam (not to scale), (b) beam's cross section, and (c) location of monoharmonic force.

Subsequently, the training pairs were prepared to improve the algorithm performance by data normalisation, data augmentation, and padding techniques. First, each input matrix of the training pairs was normalised in a range of (-1,1), while the output vector was normalised in a range of (0,1). Secondly, a data augmentation technique was adopted by dividing the matrices, after each 20 time steps, forming 1000 submatrices. Finally, the padding technique was applied to each submatrix. 10% of the prepared training pairs were used as validating pairs.

Thereafter, the 1D CNN was implemented using the Python library Keras [18]. The 1D CNN was developed in the cloud-based computing service provided by Google called Google Colaboratory (Colab) [33]. This cloud service provides a Graphics Processing Unit (GPU) which accelerates the training phase.

Table 3: Proposed 1D CNNs architecture

No. Layer	Layer type	Filter size	No. filter	Activation function
1	Input layer	-	-	-
2	Convolution	3	32	ReLU
3	Max pooling	2	32	-
4	Convolution	3	64	ReLU
5	Average pooling	2	64	-
6	Fully connected	-	32	ReLU
7	Fully connected	-	1	Linear

The error of the 1D CNNs was estimated by the MSE loss function, after feeding 64 submatrices (i.e. mini-batch size) a time. The MSE was reduced by the Adam optimisation method and the process was repeated for all mini-batches for 80 times (i.e. number of epochs). The algorithm architecture and parameters selected by trial and error are reported in Table 3.

Training the 1D CNN with more data would improve its performance. However, generating more data would increase the computational cost. To find a sufficient data size which yields a good performance of the algorithm, the influence of several data sizes on the algorithm's performance were evaluated. The several data sizes were realised by increasing (1) the number of training pairs, and (2) the acceleration signal duration. It is worth noting that the learnable parameters of the filters have random initial values for improving the algorithm performance. As a consequence, the MSE of a 1D CNN simulation is not a unique value [34]. Inspired by the work of Lee et al. [34], the average MSE of ten simulations was considered for evaluation purposes as shown in Table 4.

Table 4: Example of averaging MSE of ten simulations of a 1D CNN.

No.	MSE
1	0.0015
2	0.00303
3	0.00206
4	0.00358
5	0.00133
6	0.00221
7	0.00372
8	0.00099
9	0.00396
10	0.00123
Average	0.00236

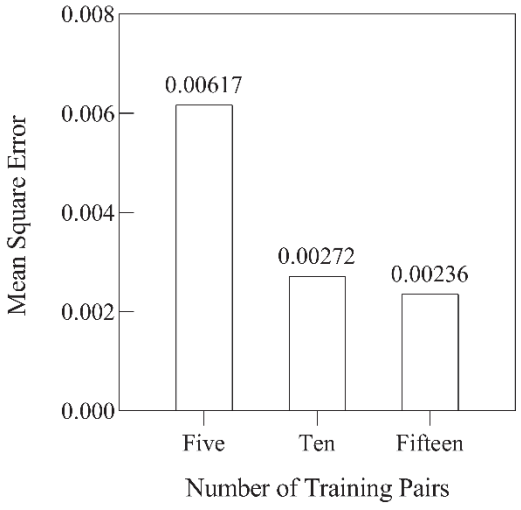

Figure 3: The influence of number of training pairs on the MSE.

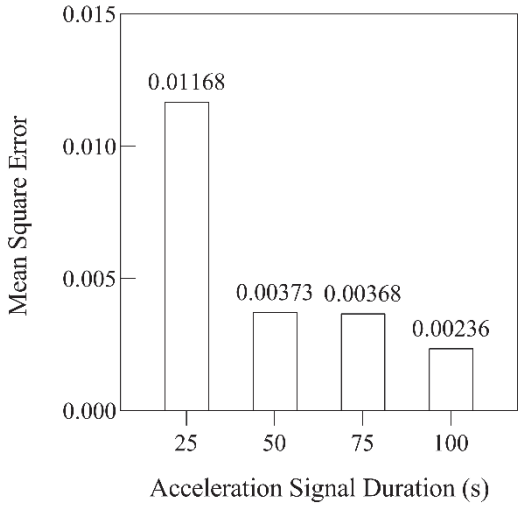

Figure 4: The influence of acceleration signal duration on the MSE.

To evaluate the influence of the number of training pairs, the 1D CNN was trained by (1) five, (2) ten, and (3) fifteen training pairs which were selected randomly within a range of rotational stiffness between 10^{13} and 10^{11} N.mm/rad (i.e. simulating undamaged and 99% damaged support respectively). In the three cases of training pairs, the maximum and minimum spring stiffness values were included. Also, the length of the acceleration response signals were 100s. Figure 3 shows that the averaged MSE in the first case is almost triple its value in the second and third cases. Also, the averaged MSE of the third case differs only marginally from the second case. Therefore, the third case is adopted, as having reached convergence, and used hereafter in this study.

The influence of the acceleration signal duration on the algorithm performance was evaluated by focusing on four different signal durations: 25s, 50s, 75s, and 100s. Figure 4 shows that longer signal duration improves the algorithm performance, as intuitively expected. It can be noticed that the difference of averaged MSE between the 25s and the 50s cases is larger than the difference between the 75s and the 100s cases. Therefore, the adopted acceleration signal duration in this study was selected as 100s.

4.3 Testing the CNN performance

After comparing the averaged MSEs for evaluation purposes, the trained 1D CNNs with the lowest MSE (0.00099) was selected for this section. Throughout the training and validating process, the MSE was calculated after each epoch as shown in Figure 5. The same figure shows good convergence between the MSE of both training and validating pairs, which means that the algorithm is categorized as a "well-trained" one.

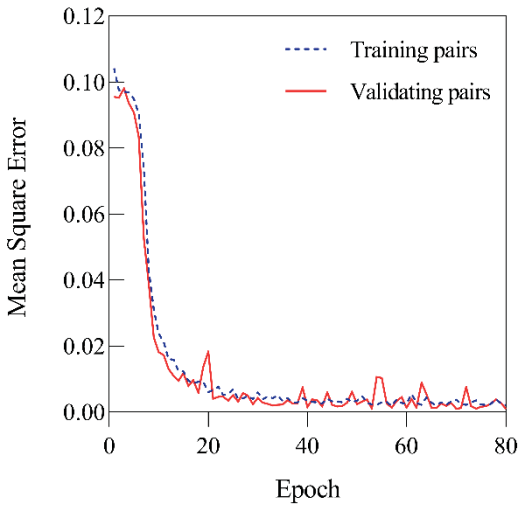

Figure 5: Training performance in term of MSE.

Then, four new cases of rotational spring stiffness (Table 5), which are within the range of stiffnesses that were used in the training pairs, were considered to test the efficiency of the 1D CNNs within an FE model updating approach. These four cases were used to generate four testing pairs. The selection of these testing pairs was done to study the effects of the availability of training pairs around each test pair. To illustrate, the number of training pairs around the first and the fourth testing pairs are more than the second and the third testing pairs.

Table 5: Rotational spring stiffness and corresponding damage for generating testing pairs.

No.	Spring stiffness (N.mm/rad)	Damage %
1	9×10^{12}	10
2	7×10^{12}	30
3	6×10^{12}	40
4	4×10^{12}	60

As mentioned earlier, the input matrix of each pair was divided into 1000 submatrices. In this way, the algorithm is producing 1000 estimations for each testing pair. Table 6 shows an example of some estimations of the algorithm in the case of the first testing pair (i.e. 9×10^{12} N.mm/rad). Subsequently, the estimations were averaged to represent the final selected spring stiffness. The remaining testing pairs were fed to the algorithm one at a time to have 1000 estimations at each time. Table 7 shows the averaged estimations of the four testing pairs compared with the actual spring stiffnesses. It is shown that the errors of the 1D CNN estimations are between -0.4% and 5.1%. From the results, it is clear that the more training pairs around and the testing pair (e.g. the second and the third cases), the higher accuracy can be achieved. The results show that the 1D CNN, in the presence of sufficient data, can not only evaluate the level of damage, but also estimate the value of associated FE model parameters.

Table 6: Example of the 1D CNNs estimations for 9×10^{12} N.mm/rad spring stiffness.

Spring stiffness (N.mm/rad)
9.052×10^{12}
8.25×10^{12}
9.038×10^{12}
..
8.036×10^{12}
9.057×10^{12}

Table 7: The accuracy of the 1D CNNs estimations for four cases of spring stiffness.

Spring stiffness (N.mm/rad)		Error %
Actual	Estimated	
9×10^{12}	8.92×10^{12}	-0.9%
7×10^{12}	7.36×10^{12}	5.1%
6×10^{12}	6.15×10^{12}	2.5%
4×10^{12}	3.98×10^{12}	-0.4%

5 CONCLUSIONS

In this paper, a 1D CNN was implemented for estimating FE model parameters. A numerical example of a 3D cantilever beam was used to validate the efficiency of the algorithm. The 1D CNN was trained to estimate a parametrically varying rotational base spring stiffness, which represented damaged states of the originally rigid support; for input acceleration data from a small number of points was used. The performance of the 1D CNN was evaluated as a function of the number of training pairs, and their actual length/size.

Results show that the benefit of increasing the training data size is significant for the algorithm performance. However, this benefit, generally, is decreasing with progressively increasing data sizes. For the application in hand, the sufficient training data size consists of fifteen training pairs and 100s duration of the acceleration signals.

The well-trained 1D CNNs, having a 0.00099 MSE, was used to estimate different rotational spring stiffness values, = not included within the training pairs. The results prove that the algorithm is capable of estimating the FE model parameter within an error band of -0.4% to 5.1%. The results also indicate that the 1D CNNs can be used in FE model updating with little modification of their more widespread equivalent damage detection version.

REFERENCES

[1] E. Simoen, G. De Roeck, and G. Lombaert, Dealing with uncertainty in model updating for damage assessment: A review, *Mechanical Systems and Signal Processing*, 56, 123–149, 2015.

[2] J. E. Mottershead and M. I. Friswell, Model updating in structural dynamics: a survey, *Journal of sound and vibration*, 167, 2, 347–375, 1993.

[3] T. Marwala, *Finite element model updating using computational intelligence techniques: applications to structural dynamics*. Springer Science & Business Media, 2010.

[4] N. A. Z. Abdullah, M. S. M. Sani, M. M. Rahman, and I. Zaman, A review on model updating in structural dynamics, in *International Conference of Mechanical Engineering Research*, 2015, 100, 1, 12015.

[5] S. Sehgal and H. Kumar, Structural Dynamic Model Updating Techniques: A State of the Art Review, *Archives of Computational Methods in Engineering*, 23, 3, 515–533, 2016.

[6] C. C. Chang, T. Y. P. Chang, and Y. G. Xu, Adaptive neural networks for model updating of structures, *Smart materials and structures*, 9, 1, 59, 2000.

[7] R. I. Levin and N. A. J. Lieven, Dynamic finite element model updating using neural networks, *Journal of Sound and Vibration*, 210, 5, 593–607, 1998.

[8] M. H. Sadr, S. Astaraki, and S. Salehi, Improving the neural network method for finite element model updating using homogenous distribution of design points, *Archive of Applied Mechanics*, 77, 11, 795–807, 2007.

[9] A. Sabamehr, C. Lim, and A. Bagchi, System identification and model updating of highway bridges using ambient vibration tests, *Journal of Civil Structural Health Monitoring*, 8, 5, 755–771, 2018.

[10] J. L. Zapico, A. González-Buelga, M. P. Gonzalez, and R. Alonso, Finite element model updating of a small steel frame using neural networks, *Smart Materials and Structures*, 17, 4, 45016, 2008.

[11] I. Goodfellow, Y. Bengio, A. Courville, and Y. Bengio, *Deep learning*, 1. MIT press Cambridge, 2016.

[12] C. Wu, P. Jiang, C. Ding, F. Feng, and T. Chen, Intelligent fault diagnosis of rotating machinery based on one-dimensional convolutional neural network, *Computers in Industry*, 108, 53–61, Jun. 2019, Accessed: Apr. 14, 2019.

[13] S. Ma, W. Liu, W. Cai, Z. Shang, and G. Liu, Lightweight Deep Residual CNN for Fault Diagnosis of Rotating Machinery Based on Depthwise Separable Convolutions, *IEEE Access*, 7, 57023–57036, 2019.

[14] O. Abdeljaber, O. Avci, M. S. Kiranyaz, B. Boashash, H. Sodano, and D. J. Inman, 1-D CNNs for structural damage detection: Verification on a structural health monitoring benchmark data, *Neurocomputing*, 275, 1308–1317, 2018.

[15] O. Abdeljaber, O. Avci, S. Kiranyaz, M. Gabbouj, and D. J. Inman, Real-time vibration-based structural damage detection using one-dimensional convolutional neural networks, *Journal of Sound and Vibration*, 388, 154–170, 2017.

[16] Y. Zhang, Y. Miyamori, S. Mikami, and T. Saito, Vibration-based structural state identification by a 1-dimensional convolutional neural network, *Computer-Aided Civil and Infrastructure Engineering*, 34, 9, 822–839, 2019.

[17] Y. Zheng, Q. Liu, E. Chen, Y. Ge, and J. L. Zhao, Time series classification using multi-channels deep convolutional neural networks, in *International Conference on Web-Age Information Management*, 2014, 298–310.

[18] F. Chollet, keras. 2015.

[19] M. Jena, S. P. Mishra, and D. Mishra, Empirical Analysis of Activation Functions and Pooling Layers in CNN for Classification of Diabetic Retinopathy, in *2019 International Conference on Applied Machine Learning (ICAML)*, 2019, 34–39.

[20] D. P. Kingma and J. Ba, Adam: A method for stochastic optimization, *arXiv preprint arXiv:1412.6980*, 2014.

[21] Y. Lu and Z. Tu, A two-level neural network approach for dynamic FE model updating including damping, *Journal of Sound and Vibration*, 275, 3–5, 931–952, 2004.

[22] L. Hao and P. L. Lewin, Partial discharge source discrimination using a support vector machine, *IEEE Transactions on Dielectrics and electrical Insulation*, 17, 1, 189–197, 2010.

[23] O. Avci, O. Abdeljaber, S. Kiranyaz, and D. Inman, Structural damage detection in real time: implementation of 1D convolutional neural networks for SHM applications, in *Structural Health Monitoring & Damage Detection, Volume 7*, 2017, 49–54.

[24] J. Jiao, M. Zhao, J. Lin, and J. Zhao, A multivariate encoder information based convolutional neural network for intelligent fault diagnosis of planetary gearboxes, *Knowledge-Based Systems*, 160, 237–250, 2018.

[25] Z. Cui, W. Chen, and Y. Chen, Multi-scale convolutional neural networks for time series classification, *arXiv preprint arXiv:1603.06995*, 2016.

[26] V. Dumoulin and F. Visin, A guide to convolution arithmetic for deep learning, *arXiv preprint arXiv:1603.07285*, 2016.

[27] J. Patterson and A. Gibson, *Deep learning: A practitioner's approach*. " O'Reilly Media, Inc.," 2017.

[28] H. Khodabandehlou, G. Pekcan, and M. S. Fadali, Vibration-based structural condition assessment using convolution neural networks, *Structural Control and Health Monitoring*, 26, 2, e2308, 2019.

[29] Dassault Systèmes Simulia Corp, Abaqus/CAE. Providence, RI, 2017.

[30] T. M. Wang, Natural frequencies of continuous Timoshenko beams, *Journal of Sound Vibration*, 13, 409–414, 1970.

[31] O. W. Blodgett, Design of welded structures, *Cleveland: James F. Lincoln Arc Welding Foundation, 1966*, 1966.

[32] Y.-S. Park, S. Kim, N. Kim, and J.-J. Lee, Finite element model updating considering boundary conditions using neural networks, *Engineering Structures*, 150, 511–519, 2017.

[33] Google, Google Colab. https://colab.research.google.com/ (accessed Mar. 01, 2020).

[34] S. Lee, J. Ha, M. Zokhirova, H. Moon, and J. Lee, Background Information of Deep Learning for Structural Engineering, *Archives of Computational Methods in Engineering*, 25, 1, 121–129, 2018.

EURODYN 2020
XI International Conference on Structural Dynamics
M. Papadrakakis, M. Fragiadakis, C. Papadimitriou (eds.)
Athens, Greece, 23-26 November 2020

INFLUENCE OF SLENDERNESS RATIO IN THE MODAL ANALYSIS BY ANALYTICAL FORMULATION

Jonas P. Falcão[1], Rodolfo A. Carvalho[1], Renan R. Ribeiro[1], Ledymar F. Moreno[2] and José L. V. De Brito[1]

[1]Graduate Program in Structures and Civil Construction, University of Brasilia,
Darcy Ribeiro Campus, Asa Norte, 70910-900, Brasília, DF, Brazil.
email:jonaspfalcao@hotmail.com, carvalho.rodolfo@outlook.com, renan.rocha.ribeiro@gmail.com, jlbrito@unb.br

[2]Graduate Program in Engineering Materials Integrity, University of Brasilia,
Campus of Gama, 72444-240, Gama, DF, Brazil.
e-mail:ingfoncault@gmail.com

Keywords: Natural frequencies, Continuous Euler-Bernoulli model, Slenderness.

Abstract. *This paper presents a dynamic analysis of a single-storey frame composed by one beam and two columns in order to compare the modal analysis results of a full-continuous analytical formulation, based on the Euler-Bernoulli model, to different simplified discrete models. The four models analyzed, through* Maplesoft 2015.1, are: shear *frame model, concentrated mass model, and consistent mass model, which are discrete models, and a full-continuous analytical formulation based on the Euler-Bernoulli model. Historically, simple discrete models, such as the shear building model, have been used rather than continuous analytical formulations due to their simplicity and good accuracy in many practical situations. Nevertheless, geometric characteristics of current structures have changed and, consequently, their dynamic behaviour tends to depart from those ideal for many simplified discrete models. The results obtained illustrated the effect of the element's slenderness and the model type on the first natural frequency obtained with the four different models. The slenderness of 50 represented a benchmark for result analysis, with the concentrated and consistent mass models presenting frequencies similar to the Euler-Bernoulli model when the column slenderness was higher than 50 and the beam slenderness was lesser than 50. Also, the analysis of the first mode shape suggested that this property is not highly influenced by the model type.*

1 INTRODUCTION

Response analysis of structures subjected to dynamic loading, such as earthquakes, winds, waves, rotating machines, and vehicle traffic depends, first of all, on carrying out the modal analysis of the structure [1]. The modal analysis is performed considering only physical and geometric characteristics of the structure, from which it is possible to calculate natural frequencies and mode shapes. Natural frequencies of structure represent physically the number of cycles that each simple harmonic motion of its respective mode shape performs per second [2].

Before carrying out the modal analysis, it is necessary to discretize the structure in a reasonable amount of degrees of freedom for a preliminary assessment. From the results obtained, additional degrees of freedom may be necessary for more detailed investigations on the dynamic behaviour of the structure [3].

The precision and convergence of the results directly depend on how discretized the structure is, that is, they depend on the amount of degrees of freedom that the structural model has. However, there are many structures that can be represented only by its first natural frequencies and mode shape without impairing the accuracy of the results. In this way, the amount of degrees of freedom can be considerably reduced [2].

A full continuous model, including an infinite amount of degrees of freedom, should be used for the best possible accuracy [4]. But sometimes it is not common to use such analysis due to the high complexity equations that arise in this mathematical model [5].

Even when modelling a simple three-bar frame structure, the dynamic analysis turns into a time consuming and error prone algebraic exercise. But due to advances in computational software based on symbolic calculations, such problems can now be easily handled by computers. This turns to be very appropriate, since, in the last instance, the algebraic problem of the dynamic analysis of structures, as continuous systems, is translated in a single transcendental equation, which has only closed form solutions for very simple cases [6]. Usually, a numerical procedure, with the aid of graphical analysis, is then employed to solve this transcendental equation and, finally, the whole dynamic problem, providing the natural frequencies and mode shapes.

A couple of literatures and researches contributed to the development of natural frequencies of some types of structures. Blevins [7] presents tables and formulas for the determination of the natural frequencies and mode shapes, taking into account the effects of bending, shear, torsion and axial forces in beams modelled as continuous systems.

Clough and Penzien [8], Humar [9], and Craig and Kurdila [10] show examples of continuous system analysis of a cantilever beam coupled to a concentrated mass at its free end. Similarly, Clough and Penzien [8] present boundaries conditions, compatibility equations and equilibrium equations of a plane frame continuous model composed by one column and one beam. However, in these literatures, only the algebraic equations obtained from the boundary and equilibrium conditions are presented, without performing any further mathematical development.

Bomtempo [11] and Bomtempo and Pedroso [12] carried out studies regarding the dynamic behaviour of continuous and discrete models of an offshore structure. These models consisted of a cantilever beam coupled to the concentrated mass and mass moment of inertia in order to evaluate the effects of a deck in relation to a monoleg offshore platform.

Vu et al. [13] and Seibel and Copetti [14] developed dynamic analysis under free and forced vibrations of double-beam system. The two beams are connected through spring and damper taking into account different types of loadings and boundary conditions. From Euler-Bernoulli dynamic equation, the natural frequencies were calculated.

Morelato [15], Maiz et al. [16], Migoto [17] and Roncevic et al. [18] performed analytical solutions for natural frequencies and mode shapes of Euler-Bernoulli beams with non classical boundary conditions, for example, translational and rotational spring, inertial and attached mass, and damper.

Koplow et al. [19], Jaworski and Dowell [20], Lu et al. [21] , Giunta and Cicirello [22] and Yu et al. [23] presented closed form solutions for dynamic response for one and multiple stepped beams when there is change of material or cross section shape. The analytical solutions were compared with experimental and finite element numerical results for different boundary conditions.

Tsai [24] used the dynamic stiffness method with the intention to perform a dynamic analysis of a plane frame taking into account the effects of mass distribution in the beam elements. The Wittrick–Williams algorithm was used to identify the natural frequencies.

Failla [25] performed an exact vibration analysis of one and two storey plane frame considering generalised parameters of discrete multi-mass-multi-spring subsystems and elastic rotational joints.

To the best of knowledge of the authors, no work has presented a study about direct comparison between simplified discrete techniques and full continuous formulation based on Euler-Bernoulli theory.

In this sense, this work has the objective to compare the modal analysis results, natural frequencies and mode shapes, obtained from a set of simplified discrete models, such as shear frame, concentrated mass, and consistent mass, to those obtained from a full-continuous analytical model based on Euler Bernoulli theory. A one-storey plane frame is used in the study for the sake of brevity, but the formulations presented here can be easily extended to more complex frame structures. The influence of relevant design parameters, such as beam and columns slenderness, over the fundamental frequency of each analysis model is evaluated and discussed.

In all the results only the fundamental vibration mode was considered, since the shear frame model has only one degree of freedom.

2 MATHEMATICAL FORMULATIONS

In this chapter, mathematical formulations for the case of one-storey building for the four models studied in this work are presented, based on some literatures [6, 8]. The usual simplification of considering only flexure stiffness in the analysis of frame elements is employed. In the formulations, the sub-indexes h and v identify horizontal and vertical elements, respectively. The K, I, M, L, ρ, and ω symbols represent, respectively, the stiffness coefficient, moment of inertia, mass, length of each frame element, mass distributed per unit length and frequency.

2.1 Shear frame model

Figure 1 shows the shear frame model for one-storey building which represents the structure in a single degree of freedom with some unique characteristics.

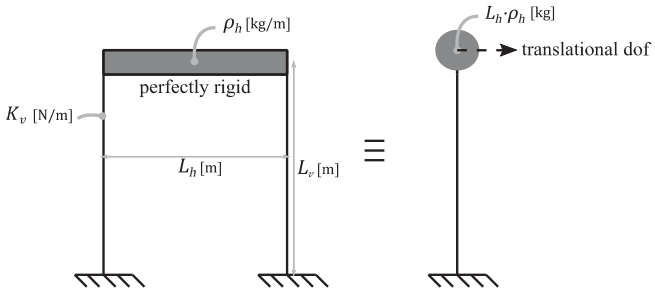

Figure 1: Shear frame model.

The horizontal elements are considered perfectly rigid, contributing only in terms of added mass. Due to its high stiffness, the horizontal element restrains any rotational degrees of freedom in the nodes to which it is connected, allowing only translational movements. The flexibility of the structure is produced just by the vertical elements, whose stiffness coefficients are the well-known flexural stiffness coefficients of bar elements obtained by using the Principle of Virtual Work [26].

The mass of vertical elements is disregarded as insignificant compared to the total mass of structure. This model tends to yield to better results when the horizontal elements have a high flexural stiffness when compared to the vertical elements, such as a slab-beam floor system supported by long columns.

The stiffness and mass matrix degenerate to scalar values, allowing the direct computation of the natural frequency as:

$$\begin{aligned} K &= 2\left(\frac{12EI_v}{L_v^3}\right) \\ M &= \rho_h L_h \\ \omega &= \sqrt{\frac{K}{M}} = \sqrt{\frac{24EI_v}{\rho_h L_h L_v^3}} \end{aligned} \tag{1}$$

2.2 Concentrated mass model

The concentrated, or lumped, mass model extends the shear frame model in two aspects: (i) it considers the flexibility of horizontal element; and (ii) considers the mass of vertical elements. In the case of one-storey frame, two extra degrees of freedom are added to the discrete model which corresponds to the rotation of the nodes.

The masses are still considered concentrated at the nodes of frame, being the mass of vertical and horizontal elements lumped all together in the nodes. The distribution of masses of an element into its nodes is proportional to the relative distance between two consecutive nodes. This model, however, does not include the rotational inertia originated by the lumped masses in the nodes, disregarding its magnitude when compared to the translational inertia.

The concentrated mass model for one-storey frame is illustrated in Figure 2, with all the relevant parameters indicated. Structures with horizontal and vertical elements of similar stiffness tend to be well represented by this model.

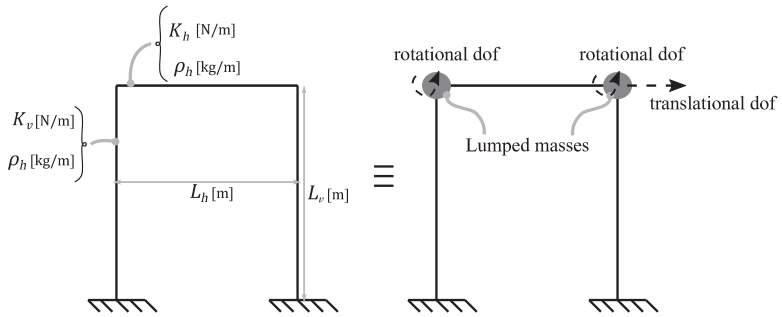

Figure 2: Concentrated mass model.

As shown above, the one-storey frame model is represented by three degrees of freedom: one related to the translational movement in the horizontal direction, and two rotations related to each of the free nodes of the structure. The stiffness and mass matrixes are, therefore, of 3x3 dimension, and are written as:

$$\mathbf{M} = \begin{bmatrix} \rho_v \cdot L_v + \rho_h \cdot L_h & 0 & 0 \\ 0 & 0 & 0 \\ 0 & 0 & 0 \end{bmatrix} \tag{2}$$

$$\mathbf{K} = \begin{bmatrix} \frac{24 \cdot E \cdot I_v}{L_v^3} & \frac{6 \cdot E \cdot I_v}{L_v^2} & \frac{6 \cdot E \cdot I_v}{L_v^2} \\ \frac{6 \cdot E \cdot I_v}{L_v^2} & \frac{4 \cdot E \cdot I_v}{L_v} + \frac{4 \cdot E \cdot I_h}{L_h} & \frac{2 \cdot E \cdot I_h}{L_h} \\ \frac{6 \cdot E \cdot I_v}{L_v^2} & \frac{2 \cdot E \cdot I_h}{L_h} & \frac{4 \cdot E \cdot I_v}{L_v} + \frac{4 \cdot E \cdot I_h}{L_h} \end{bmatrix} \tag{3}$$

The determination of natural frequencies requires the solution of the dynamic equilibrium equation, which ultimately leads, for the case of undamped free vibration, to the following equation:

$$\det\left[-\omega^2 \cdot \mathbf{M} + \mathbf{K}\right] = 0 \tag{4}$$

By solving the previous equation, three roots for the natural frequencies ω, given in rad/s, can be found. They are related to the three vibration modes allowed by the three degrees of freedom present in the discrete model.

2.3 Consistent mass model

The consistent mass model further develops the concentrated mass model by considering the mass as a distributed parameter in the structure, not only as mere lumped masses in the nodes. This can be achieved by using the Principle of Virtual Work. This model is fitted for structures in which the mass is an important factor in the dynamic behaviour and may not be correctly represented by the concentrated mass model. Figure 3 illustrates the consistent mass model, for the case in which each element has a homogeneously distributed mass represented by its mass distributed per unit length ρ.

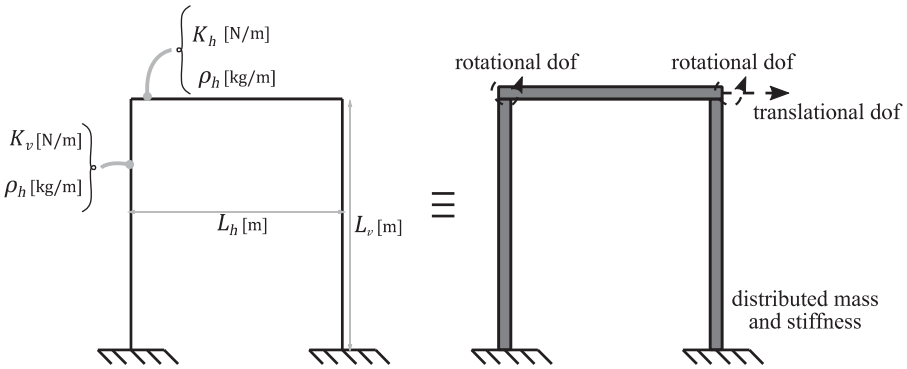

Figure 3: Consistent mass model.

Since the only change in relation to the concentrated mass model is the consideration of distributed mass along the elements, no changes in the stiffness matrix presented on Equation 3 is introduced. By considering mass as distributed along the elements, effects of rotational inertia are added in the model and the mass matrix becomes dense, which becomes:

$$\mathbf{M} = \begin{bmatrix} \frac{26}{35}\rho_v \cdot L_v + \rho_h \cdot L_h & \frac{11}{210}\rho_v \cdot L_v^{\,2} & \frac{11}{210}\rho_v \cdot L_v^{\,2} \\ \frac{11}{210}\rho_v \cdot L_v^{\,2} & \frac{\rho_v \cdot L_v^{\,3}}{105} + \frac{\rho_h \cdot L_h^{\,3}}{105} & -\frac{\rho_h \cdot L_h^{\,3}}{140} \\ \frac{11}{210}\rho_v \cdot L_v^{\,2} & -\frac{\rho_h \cdot L_h^{\,3}}{140} & \frac{\rho_v \cdot L_v^{\,3}}{105} + \frac{\rho_h \cdot L_h^{\,3}}{105} \end{bmatrix} \tag{5}$$

The solution of natural frequencies by this model is of the same type given in Equation 4, and the three roots found correspond to the natural frequencies associated to each mode shape allowed by the degrees of freedom.

The consistent mass model can usually be employed in finite element schemes, and has the following advantages: greater precision and faster convergence with increasing number discretized elements; potential energy and kinetic energy are evaluated in a consistent manner and, because of this, it is possible to determine how the computed values of natural frequencies relate to the exact values [2].

The accuracy of the results obtained through the consistent mass matrix is only slightly better than the results of the concentrated mass matrix, since the inertial forces associated with the rotation of the nodes are not generally significant in many problems of structural engineering. Because of this, the concentrated mass matrix is still widely used [2].On the other hand, Rao [26] questions that it is not obvious which of the two methods presents more accurate results for the response of the structure, since one method can present more satisfactory results than the other depending on the dynamic problem and the discretization of elements.

2.4 Full-continuous Euler-Bernoulli model

A full-continuous model for the dynamic equilibrium of a one-storey frame under free vibration can be constructed by applying the following partial differential equation (PDE) to each element *i*, properly considering the continuity of the frame in the boundary conditions:

$$EI_i \cdot \frac{\partial^4 u_i(x_i,t)}{\partial x_i^{\,4}} + \rho_i \cdot \frac{\partial^2 u_i(x_i,t)}{\partial t^2} = 0 \tag{6}$$

Considering this is a PDE involving two variables, *x* and *t*, a way to solve the problem is using the Separation of Variables for each element *i*, which is given by:

$$u_i(x_i,t) = X_i(x_i)T(t) \tag{7}$$

Substituting Equation 7 into Equation 8, and isolating each variable in a equation side, one arrives at the equation below, which holds only if each side is equal to the same constant denoted by β_i^4:

$$\frac{X_i^{(iv)}}{x_i} = -\frac{\rho_i}{EI_i}\frac{\ddot{T}}{t} = \beta_i^4 \tag{8}$$

This allows to separate the PDE into two ordinary differential equations (ODE) as shown:

$$\begin{cases} X_i^{(iv)}(x_i) - \beta_i^4 X_i(x_i) = 0 \\ \ddot{T}(t) + \dfrac{E_i I_i}{\rho_i}\beta_i^4 T(t) = 0 \end{cases} \tag{9}$$

The solution of these two ODE is given by:

$$\begin{aligned} T(t) &= \bar{A}\cos(\omega t) + \bar{B}\sin(\omega t) \\ X_i(x_i) &= A_i\cos(\beta_i x_i) + B_i\sin(\beta_i x_i) + C_i\cosh(\beta_i x_i) + D_i\sinh(\beta_i x_i) \end{aligned} \tag{10}$$

By inspection of the first equations from both Equation 9 and 10, it can be obtained the relation between the frequency ω and the parameter β_i defined for each element, as given by :

$$\omega = \beta_i^2\sqrt{\frac{EI_i}{\rho_i}} \tag{11}$$

The boundary equations and compatibility equation for each element are indicated in Figure 4, which also presents the local coordinate system for each element and their identification, as considered in the computations performed in this work.

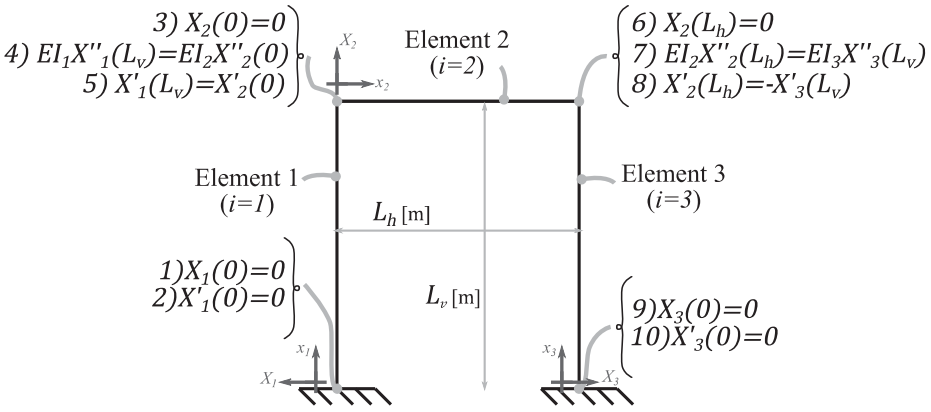

Figure 4: Euler-Bernoulli model boundary conditions.

In the Figure 4, the boundary conditions are presented by the first, second, third, sixth, ninth and tenth equation. The fourth and seventh equation are the compatibility equations for bending moments at nodes and the fifth and eighth equation are the compatibility equations for rotation at nodes.

By applying these boundary conditions to the second equation of Equation 10, considering the appropriate elements, one obtains a set of 10 equations given by:

$$\begin{gathered}
A_1 + C_1 = 0 \\
B_1 + D_1 = 0 \\
A_2 + C_2 = 0 \\
I_v\beta_1^2(-A_1\cos\beta_1 L_v - B_1\sin\beta_1 L_v + C_1\cosh\beta_1 L_v + D_1\sinh\beta_1 L_v) + I_h\beta_2^2(A_2 - C_2) = 0 \\
\beta_1(-A_1\sin\beta_1 L_v + B_1\cos\beta_1 L_v + C_1\sinh\beta_1 L_v + D_1\cosh\beta_1 L_v) - \beta_2(B_2 + D_2) = 0 \\
A_2\cos\beta_2 L_h + B_2\sin\beta_2 L_h + C_2\cosh\beta_2 L_h + D_2\sinh\beta_2 L_h = 0 \\
I_h\beta_2^2(-A_2\cos\beta_2 L_h - B_2\sin\beta_2 L_h + C_2\cosh\beta_2 L_h + D_2\sinh\beta_2 L_h) + I_v\beta_3^2(A_3\cos\beta_3 L_v + B_3\sin\beta_3 L_v - C_3\cosh\beta_3 L_v - D_3\sinh\beta_3 L_v) = 0 \\
\beta_2(-A_2\sin\beta_2 L_h + B_2\cos\beta_2 L_h + C_2\sinh\beta_2 L_h + D_2\cosh\beta_2 L_h) + \beta_3(-A_3\sin\beta_3 L_v + B_3\cos\beta_3 L_v + C_3\sinh\beta_3 L_v + D_3\cosh\beta_3 L_v) = 0 \\
A_3 + C_3 = 0 \\
B_3 + D_3 = 0
\end{gathered} \tag{12}$$

Also, it can be defined two dynamic equilibrium equations, which model the continuity of the frame and the interaction between each connected element, being given by:

$$\begin{aligned}
EI_v X_1^{(iii)}(L_v) &= -\frac{\rho_h}{2}\cdot L_h\cdot\omega^2\cdot X_1(L_v) \\
EI_v X_3^{(iii)}(L_v) &= -\frac{\rho_h}{2}\cdot L_h\cdot\omega^2\cdot X_3(L_v)
\end{aligned} \tag{13}$$

By substituting the second equation of Equation 10, these last two expressions become:

$$\begin{gathered}
EI_v\beta_1^3(A_1\sin\beta_1 L_v - B_1\cos\beta_1 L_v + C_1\sinh\beta_1 L_v + D_1\cosh\beta_1 L_v) + \frac{\rho_h L_h}{2}\omega^2(A_1\cos\beta_1 L_v - B_1\sin\beta_1 L_v + C_1\cos\beta_1 L_v + D_1\cos\beta_1 L_v) = 0 \\
EI_v\beta_3^3(A_3\sin\beta_3 L_v - B_3\cos\beta_3 L_v + C_3\sinh\beta_3 L_v + D_3\cosh\beta_3 L_v) + \frac{\rho_h L_h}{2}\omega^2(A_3\cos\beta_3 L_v - B_3\sin\beta_3 L_v + C_3\cos\beta_3 L_v + D_3\cos\beta_3 L_v) = 0
\end{gathered} \tag{14}$$

Substituting the Equation 11 in the set of equation given by Equations 12 and 14, one ends up with 12 equations involving 13 variables to be determinate: four variables A_i, B_i, C_i and D_i, for each of the three elements, and the ω variable. Since this system of equations is homogeneous, the determinant of the coefficient matrix must be equal to zero in order to the system to have a non-trivial solution.

From this condition, one draws the characteristic polynomial and the transcendental equation, which is solved numerically. The roots found are the values related to the natural frequencies ω of the system. From these values, the parameter β_i can be calculated through Equation 11, for each element and natural frequency. Setting A_1=1, the other 11 constants are calculated and then the mode shape functions for beam and columns are obtained.

3 RESULTS AND DISCUSSIONS

A routine in the software Maplesoft 2015.1 was developed to obtain the fundamental frequencies and mode shapes of a one-storey frame under undamped free vibration modelled by shear frame, concentrated mass, consistent mass, and continuous Euler-Bernoulli models. The influence of the element slenderness on the results of each model was analysed, by varying separately the columns and beam slenderness by changing its length. The slenderness of an element is defined as:

$$\lambda = \frac{L}{\sqrt{\frac{I}{A}}} = \frac{L}{\sqrt{\frac{b\cdot h^3}{12\cdot(b\cdot h)}}} = \frac{L}{h}\cdot\sqrt{12} \tag{15}$$

In which L is the element length, I is the element's cross-section moment of inertia in the axis under flexure, and A is the element's cross-section area. For rectangular cross-sections,

such as those considered in this work, the above properties may be further simplified in terms of the cross-section height, *h*, and base, *b*, defined accordingly to the axis of flexure being considered.

In the analysis presented in this work, the other parameters of the structure are: elastic modulus = 30 [GPa]; mass distributed per unit length of beam = 250 [kg/m]; mass distributed per unit length of columns = 100 [kg/m]; columns with square cross-section of width 0.2 [m]; beam with rectangular cross-section of 0.5 [m] height per 0.2 [m] width. When not subjected to variation to produce different slenderness, the length of the beam and columns are, respectively, 5.0 [m] and 3.0 [m].

Furthermore, since the shear frame model provides a single vibration mode, because it has one degree of freedom, only the first mode will be considered in the modal analysis.

3.1 Fundamental frequency

In Figure 5, it is evaluated the first natural frequency results due to the variation of column slenderness. It can be noticed that the shear frame model best approximated the Euler-Bernoulli model as the column slenderness increased. The concentrated and the consistent mass models present remarkably similar results, with negligible small differences in relation to the Euler-Bernoulli model for slendernesses higher than 50. Overall, the simplified models present a stiffer behaviour, since in all slenderness tested they produced higher natural frequencies.

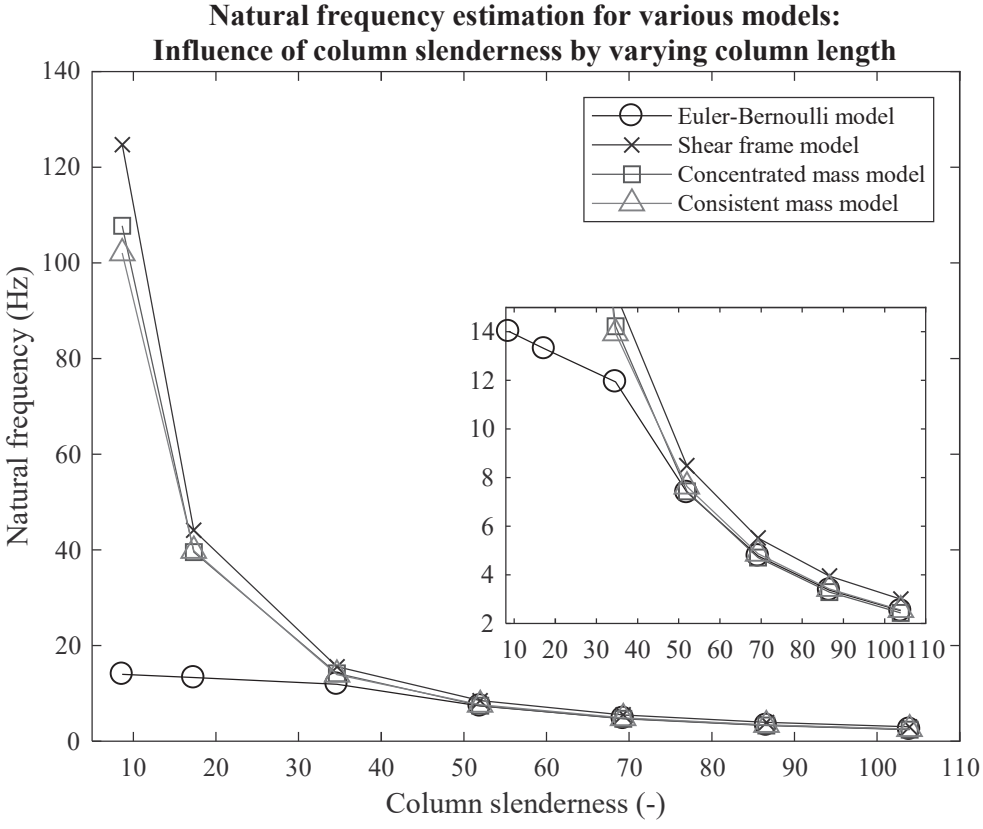

Figure 5: Influence of column slenderness on the first natural frequency, by varying column length

The Euler-Bernoulli model results diverge significantly from the other models for slendernesses lower than 50, indicating that this model still retains most of its flexible behaviour, in comparison to the other models, even when the one-storey frame has very bulk columns. It is

relevant to observe that for bulk elements the Euler-Bernoulli itself may be an inappropriate model since it disregards any flexibility related to the shear stiffness, which results in a much more stiffer model when compared to more realistic models, such as those drawn from Timoshenko Beam theory. For instance, the rule-of-thumb of L/h=10 is usually employed to define a minimum aspect ratio that defines elements slender enough to be modeled with Euler-Bernoulli theory. In the context of the prismatic cross-sections used in this work, this rule-of-thumb corresponds to a slenderness of 34.64. In this way, the observation that for small column slenderness the Euler-Bernoulli model still provided the lowest natural frequencies, i.e. resulted in the most flexible model, while it is clearly already outside the scope of its proper use, is an indicative that the simplified models shall not be used if the columns are considerably bulk.

In Figure 6, it is evaluated the first natural frequency response due to the variation of beam slenderness. Generally speaking, the variation on beam slenderness affects the models' results in a opposite trend when compared to variation of columns' slenderness. In contrast to the previous result, now the shear frame model has better approximation to the Euler-Bernoulli model with the decrease of the element. The concentrated and the consistent mass model continue presenting remarkably similar results, but now better approximated Euler-Bernoulli model when the slenderness was small, with negligible differences for slendernesses lower than 50. Furthermore, from a slenderness equal or higher than 50, the Euler-Bernoulli model diverged significantly from the other models, presenting lower frequency values and thus a more flexible behaviour. Overall, as in the previous analysis, the simplified models still present a stiffer behaviour, since, for all slenderness tested, they continued to produce higher natural frequencies.

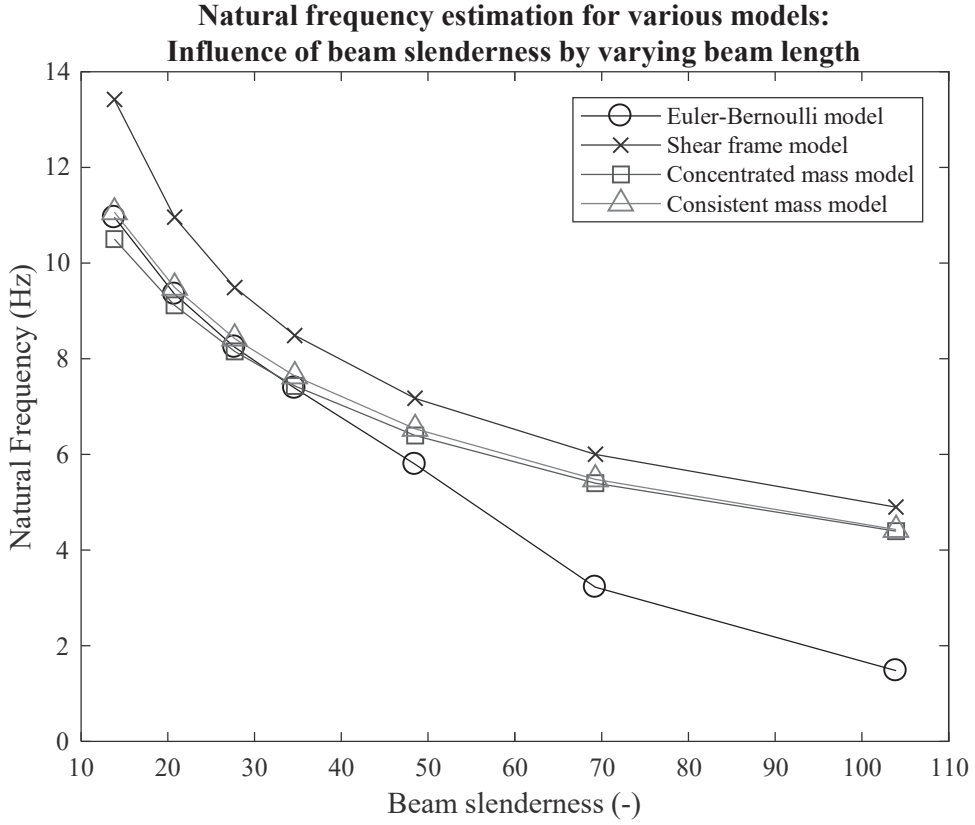

Figure 6: Influence of beam slenderness on the first natural frequency, by varying beam length.

The difference between the effects of beam slenderness and column slenderness on the natural frequencies may reside in the fact that, due to the differences in the adopted cross-section dimensions, to produce the same slenderness the beam length needed to be considerably larger than the column length. This may have led to a problem of poor discretization of elements, which showed in the beam slenderness analysis among the high slendernesses results. The simplified discrete models used in this work modeled each element as a single discrete element, which was probably insufficient to model the long beams produced on the beam slenderness analysis. The Euler model, however, properly retained its flexibility due to its continuous formulation.

For instance, considering the column and beam cross-section dimensions adopted, while a column length equal to 5.77 m leads to a column slenderness equal to 100, a beam length equal to 14.43 m is required to produce this same beam slenderness. Furthermore, while the column slenderness, which was the highest value analysed, was associated to a column length of 6.35 m, a beam slenderness equal to 45 was already associated to a longer beam length, of 6.50 m.

These examples illustrate that the divergence observed in the beam slenderness analysis for higher slenderness are related to the artificial stiffness of simplified discrete models with insufficient discretization. This problem with discrete models is, therefore, related to the discretization capability of the method used, and may be avoided if extended discrete methods, such as finite element or differences methods are employed.

Lastly, from Figures 5 and 6 it can be noticed that there is a slenderness range in both beam and column elements in with the discrete models can produce results close to the continuous model. In contrast, in some extreme cases, the models have no correlation and yield relevant discrepancy in natural frequency results.

3.2 Fundamental mode shape

In order to compare the mode shapes obtained with the different models, it was analysed a standard model with the properties described in the beginning of this section. Again, it is highlighted that only the first mode is considered, since the shear frame model only contains a single degree-of-freedom, which leads to a single mode.

Before discussing the following results, it is important to delve into the process undertook in this work of obtaining the mode shape with the continuous Euler-Bernoulli model by using a symbolic mathematics software such as Maplesoft 2015.1. As previously explained, when assembled the Euler-Bernoulli model leads to a system of trigonometric equations containing 12 equations and 13 variables, whose solution is obtained by invoking the requirement of a non-trivial solution which leads to the determinant of the coefficient's matrix, i.e. the transcendental equation of the system, being equal to zero. The process of computing the determinant of such matrix, even if performed with a symbolic mathematics software, is computed with a numerical method and, therefore, is susceptible to numerical errors and instabilities.

Considering this, Figure 7 presents the results obtained when computing and plotting the coefficient's matrix transcendental equation in terms of the natural frequency ω, which is the 13^{th} variable of the system. From this figure, it is possible to observe that the obtained transcendental equation presents two remarkably close roots, at around 45 rad/s and 48 rad/s. Such closely spaced modes are not expected in frame structures such as the one being considered, and the relatively small local minima between these two roots suggested that one of these modes might be a spurious mode originated by numerical errors.

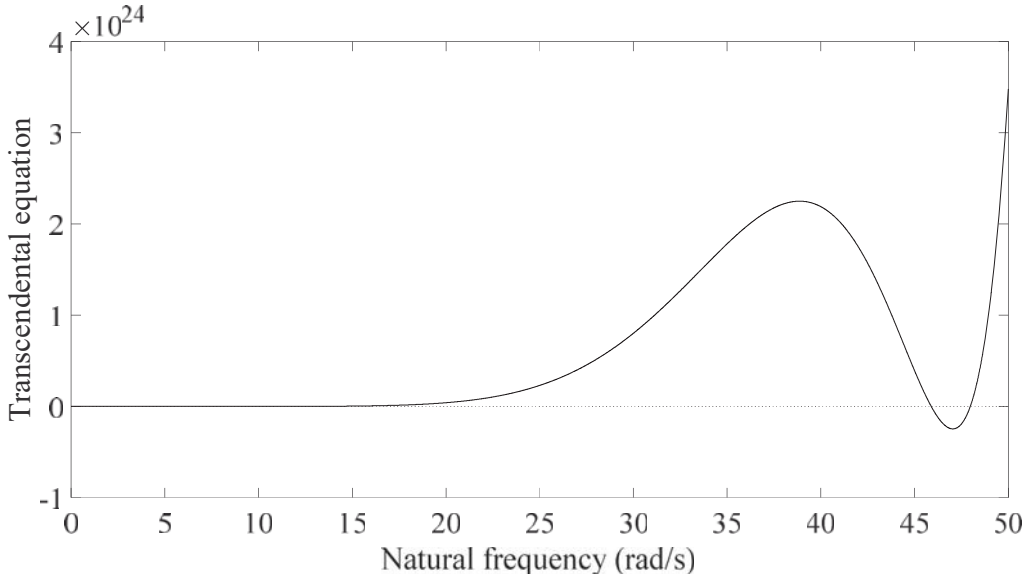

Figure 7: Transcendental equation plot.

In order to assess this possibility, the mode shapes associated to both roots were computed and compared. The results are presented in Figure 8, and the mode shapes were normalized in relation to the displacement at the top of the vertical columns.

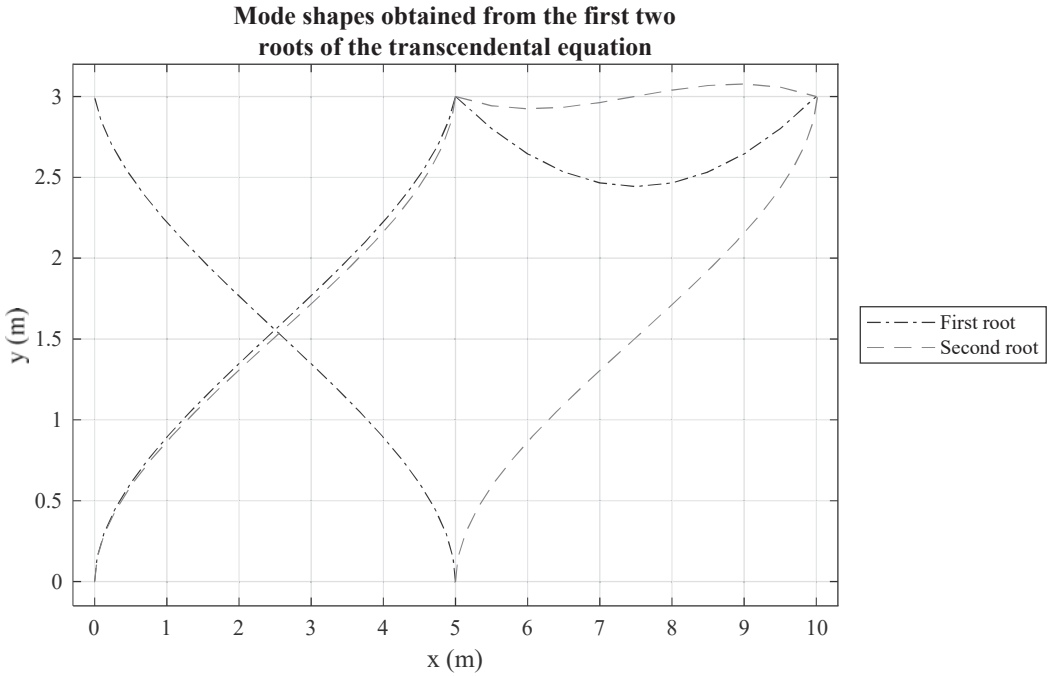

Figure 7: Comparison of the first and second roots of the transcendental equation.

As expected, one of the modes, i.e. the one associated to the first root, presented a non-real mode shape, with the columns displacing in opposite global directions. Such shape is not real, since the horizontal element is not supposed to undergo normal deformations, e.g. extension or reduction, with the structural model being considered. In this way, only modes with the columns displacing in the same global direction are related to real modes.

In this way, the Figure 8 presents the mode shapes obtained with the different models. For the concentrated and consistent models, a third-degree polynomial was assumed to interpolate the displacements between the nodes.

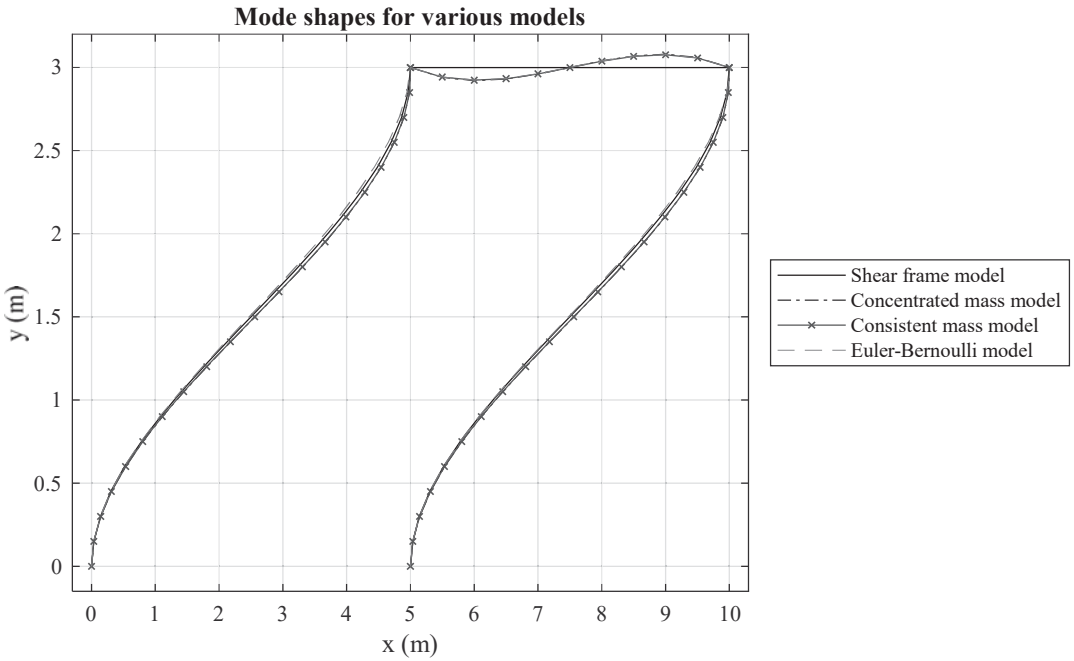

Figure 8: Comparison of mode shapes obtained with the various models.

Apart from the shear frame model, which does not possess flexibility on the horizontal element, all the models present remarkably good coherence between each other. This suggests that the mode shape, at least for the first mode, is not greatly affected by using more complex models, such as the full-continuous Euler-Bernoulli model.

4 CONCLUSIONS

This work presented a comparison of fundamental frequency and mode shape of three simplified models (shear frame, concentrated mass, and consistent mass) in relation to continuous Euler-Bernoulli model for a one-storey framed structure under free vibration. The main conclusions are:

- Both the concentrated and consistent mass models presented remarkably similar results, with accurate results when compared with the continuous model, while shear building model presented the worst results;
- The slenderness of 50 represented a benchmark for evaluating the results from the different models. Concentrated and consistent mass models presented frequencies similar to those obtained from the Euler-Bernoulli model when the column slenderness was higher than 50 and the beam slenderness was lesser than 50;
- The comparison of mode shapes suggested that this property is not highly influenced by the model type.

5 ACKNOWLEGMENTS

The authors of this research are grateful for the financial support of the Brazilian National Council for Scientific and Technological Development (CNPq), Coordination for the Improvement of Higher Education Personnel (CAPES), Program of Alliances for Education and Training, Organization of American States and Coimbra Group of Brazilian Universities (PAEC-OEA/ GCUB).

REFERENCES

[1] S. M. Avila, Hybrid Control for Attenuation of Vibrations in Buildings, Doctoral Thesis, *Pontifical Catholic University - Rio de Janeiro,* 2002. In Portuguese.

[2] A. K. Chopra, Dynamics of Structure: Theory and Applications to Earthquake Engineering, 5th ed, *Pearson Prentice Hall*, 2016.

[3] J. W. Tedesco, W. G. McDougal, C. A. Ross, Structural Dynamics: Theory and Applications, *Pearson Prentice Hall,* 1998.

[4] M. Paz, W. Leigh, Structural Dynamics: Theory and Computation, 5th ed, *Kluwer Academic Publishers*, 2004.

[5] B. K. Donaldson, Introduction to Structural Dynamics, *Cambridge University Press*, 2006.

[6] L. J. Pedroso, Analytics solutions for free vibration in frames and 1st frequency estimates for beams by analytical and numerical methods, Dynamics and Fluid-Structure Research Group, *University of Brasilia*, 2016. In Portuguese.

[7] R. D. Blevins, Formulas for dynamics, acoustics and vibration, Willey-Blackwell, 2015.

[8] R. W. Clough, J. Penzien, Dynamics of structures, 3th ed, *Computers & Structures*, 2003

[9] J. L. Humar, Dynamics of Structures, 3th ed, Taylor & Francis Group, 2012.

[10] R. R. Craig Jr, A. J. Kurdila, Fundamentals of structural dynamics, 2nd ed, *John Wiley & Sons*, 2006.

[11] T. B. S. Bomtempo, A study about influence of deck in the behavior of fixed offshore platforms subjected to dynamic actions, Graduation Tesis, *University of Brasilia*, 2014. In Portuguese.

[12] T. B. S. Bomtempo, L. J. Pedroso, A analytical-numerical study about the influence of deck in dynamic behavior of monoleg offshore platforms in free vibrations, Proceedings of the *XXXVII Iberian Latin-American Congress on Computational Methods in Engineering*, 2014. In Portuguese.

[13] H. V. Vu, A. M. Ordóñez, B. H. Karnopp, Vibration of a double-beam system, *Journal of Sound and Vibration* 229(4), *807-822, 2000.*

[14] A. B. Seibel, R. D. Copetti, Calculus of Frequencies and Mode Shapes of a double-beam system, *Proceeding Series of the Brazilian Society of Applied and Computational Mathematics*, Vol 2, N. 1, 2014. In Portuguese.

[15] T. Morelatto, Calculus of Mode Vibration of Structural Euler-Bernoulli Model with non classical boundary conditions, Graduation Thesis, *Federal University of Rio Grande do Sul,* 2000. In Portuguese.

[16] S. Maiz, D. V. Bambill, C. A. Rossit, P. A. A. Laura, Transverse vibration of Bernoulli-Euler beams carrying point masses and taking into account their rotatory inertia: Exact solution, *Journal of Sound and Vibration* 303, 895-908, 2007.

[17] D. Migotto, Autofunctions and Vibration Frequencies of Euler-Bernoulli Model for Non Classical Beams, Graduation Thesis, *Federal University of Santa Maria,* 2011. In Portuguese.

[18] G. S. Roncevic, B. Roncevic, A. Skoblar, R. Zigulic, Closed form solutions for frequency equation and mode shapes of elastically supported Euler-Bernoulli beams, *Journal of Sound and Vibration* 457, 118-138, 2019.

[19] M. A. Koplow, A. Bhattacharyya, B. P. Mann, Closed form solutions for the dynamic response of Euler-Bernoulli beams with step changes in cross section, *Journal of Sound and Vibration* 295, 214-225, 2006.

[20] J. W. Jaworski, E. H. Dowell, Free vibration of a cantilever beam with multiple steps: Comparison of several theoretical methods with experiment, *Journal of Sound and Vibration* 312, 713-725, 2008.

[21] Z. R. Lu, M. Huang, J. K. Liu, W. H. Chen, W. Y. Liao, Vibration analysis of multiple-stepped beams with the composite element model, *Journal of Sound and Vibration* 322, 1070-1080, 2009.

[22] F. Giunta, A. Cicirello, On the analysis of jointed Euler-Bernoulli beams with step changes in material and cross-section under static and dynamic loads, *Engineering Structures* 179, 66-78, 2019.

[23] H. Yu, Y. Yang, Y. Yuan, Analytical solution for a finite Euler-Bernoulli beam with single discontinuity in section under arbitrary dynamic loads, *Applied Mathematical Modelling* 60, 571-580, 2018.

[24] H. C. Tsai, A distributed-mass approach for dynamic analysis of Bernoulli-Euler plane frames, *Journal of Sound and Vibration* 329, 3744-3758, 2010.

[25] G. Failla, An exact modal analysis approach to vibration analysis of structures with mass-spring subsystems and rotational joints, *Journal of Sound and Vibration* 438, 191-219, 2019.

[26] S. S. Rao, Mechanical Vibrations, 6th ed, *Pearson Prentice Hall*, 2018.

EURODYN 2020
XI International Conference on Structural Dynamics
M. Papadrakakis, M. Fragiadakis, C. Papadimitriou (eds.)
Athens, Greece, 23-26 November 2020

ON SPACE-TIME FORMULATIONS IN STRUCTURAL MECHANICS USING THE PROPER GENERALIZED DECOMPOSITION

Franz Bamer[1], **Nima Shirafkan**[1], **Abdelbacet Oueslati**[2], **Marcus Stoffel**[1], **Géry De Saxcé**[2], **Bernd Markert**[1]

[1] Institute of General Mechanics, RWTH Aachen University, 52062 Aachen, Germany
e-mail: bamer@iam.rwth-aachen.de

[2] Univ. Lille, CNRS, Centrale Lille, FRE 2016 - LaMcube - Laboratoire de mécanique multiphysique et multiéchelle, 59000 Lille, France

Keywords: Newmark integration scheme, proper generalized decomposition, proper orthogonal decomposition, modal analysis, transient excitation

Abstract. *In this contribution, we present the space-time formulations of a nonlinear quasistatic and a linear dissipative dynamic system using the proper generalized decomposition approach. Regarding the quasistatic problem, the equation of equilibrium is transformed into the space-time formulation. Regarding the linear dynamic problem, the set of equations of motion are transformed into one space-time equation, using a space-time formulation of the Newmark integration ansatz. In both cases, the space-time formulation is projected in two coupled space and time equations, which are solved by the fixed point algorithm. The results are compared to the conventional step-by-step algorithm regarding accuracy and efficiency. Solving the problem iteratively in terms of response enrichments, temporal and spatial proper generalized decomposition modes are identified and analyzed during convergence. It is shown that the set of spatial proper generalized decomposition modes of both the quasistatic and the dynamic problem are highly correlated as they can both be replaced by an uncorrelated significantly smaller orthonormal basis representation. In the quasistatic case, it is shown that the response after the first enrichment is purely elastic, while after the second enrichment plastic behavior can be detected. However, plasticity cannot be detected locally by investigation of the proper generalized decomposition modes, but by the uncorrelated orthonormal basis functions using the proper orthogonal decomposition. In the dynamic case, more than only one enrichment is required to evaluate the linear response history as the solution can be decomposed into a set of motion patterns. Nevertheless, the evaluated correlated spatial proper generalized decomposition modes differ significantly from the linear modes of vibration.*

1 Introduction

High-dimensional and finely meshed models are ubiquitous in finite element applications and structural dynamics. They generally demand significant computational efforts, especially, if nonlinearities are involved. However, the latter are inevitable in order to obtain realistic structural response predictions. This, in turn, is essential for reliable decisions about the design of structures and infrastructures and, therefore, has a significant impact on industry and society.

Various computational strategies have been developed in structural dynamics in order to deal with the issue of high-dimensionality.

As a statistical pattern technique the proper orthogonal decomposition can be used to find the dominant motion patterns for the low-order description of nonlinear systems [1]. Here, the transformation into low-order subspaces depends on the set of proper orthogonal modes obtained from structural response pattern [2]. In particular, the applicability of the proper orthogonal decomposition to transient excitations depends mainly on the choice of the observation time period used for the calculations of the proper orthogonal modes [3]. If nonlinearities are not captured in those deformation patterns, they cannot be displayed in the low-order model. However, if the nonlinear response behavior is captured, a surprisingly small number of proper orthogonal modes is sufficient to accurately describe the dynamic response behavior [4, 5].

Another approach is to divide the structure into various substructures. The main goal is to provide low-order representations of the inside areas of the substructures while keeping the number of degrees of freedom of the boundaries unaltered. The Craig-Bampton method [6] and the dual Craig-Bampton method [7] provide powerful techniques in this regard. Although these two strategies are mainly applicable to linear systems, a hierarchical formulation of the Craig-Bampton method has been presented on vibro-impact problems with linear contact formulations [8, 9] and highly nonlinear contact laws [10]. Recently, also a combination of the proper orthogonal decomposition and substructure techniques has been proposed [11].

The proper generalized decomposition (PGD), however, provides a strategy that is neither restricted by the level or type of nonlinearity nor a-priori system identifications are required. This method has firstly been introduced by Ladevéze [12] and has then been applied in many fields such as chemistry [13], thermo-mechanics [14], fluid dynamics [15, 16], geophysics [17] and solid mechanics [18, 19]. Especially, in structural mechanics, first approaches have been proposed to use the proper generalized decomposition ansatz to solve elastoplastic and viscoplastic structures subjected to quasistatic loading [20, 21]. Shirafkan et al. physically interpreted the evolution of spacial and temporal functions, which they refer to as proper generalized decomposition modes, and analyzed these modes during convergence [22]. Furthermore, the Multi-field PGD has been applied to resolve the undamped elastodynamic model and the solution was interpreted by Time Discontinuous Galerkin and Multi-field time-continuous methods [23].

In this contribution, we will develop a new family of efficient and stable algorithms to evaluate the response of linear and nonlinear structures. In particular, we will propose space-time formulations, where we will avoid the step-by-step strategies of conventional time integration schemes and will show that the response is built iteratively in the whole time domain until convergence is achieved. In Section 2, we will develop the strategy in an elastoplastic quasistatic framework. Hereby, the conventional equations of equilibrium will be extended. In Section 3, we will extend this new obtained formulation to dissipative systems in structural dynamics introducing a space-time formulation of the Newmark method. The numerical results of both the quasistatic and dynamic approach will be presented in Section 4. Finally, in Section 5, the conclusion will be given.

2 Formulation of the space-time solution for a quasistatic nonlinear problem

In static equilibrium the terms of inertia are neglected and the external force $\mathbf{F}(t)$ on the system is equal to the resulting internal force $\mathbf{F}_{\text{int}}$:

$$\mathbf{F}(t) - \mathbf{F}_{\text{int}}(\mathbf{u}) = \mathbf{0} \ . \tag{1}$$

Here, $\mathbf{u}$ denotes the unknown structural displacement. The equation is rewritten in the incremental form [24] as

$$\mathbf{K}(\mathbf{u})\Delta\mathbf{u} = \underbrace{\mathbf{F} - \mathbf{F}_{\text{int}}(\mathbf{u})}_{\mathbf{R}(\mathbf{u})} \ , \tag{2}$$

where $\mathbf{R}(\mathbf{u})$ denotes the residual, $\mathbf{K}(\mathbf{u})$ is the tangential stiffness matrix dependent on displacement and $\Delta\mathbf{u}$ is the displacement increment. After discretization of the time domain into in this contribution refered to as temporal nodes t_i $(i = 0, \dots, n_t)$, Equation (2) can be solved incrementally, where static equilibrium is found in a step-by-step manner, as shown in Figure 1a. In each time step an iterative solver, as e.g. the Newton-Raphson algorithm [24], presented in Figure 1b, must be applied.

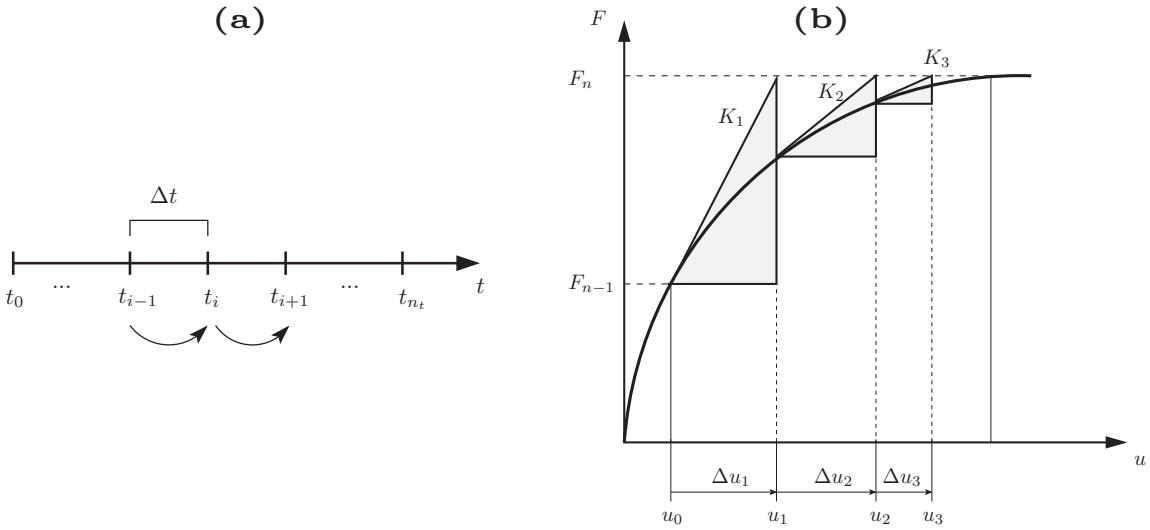

Figure 1: Conventional solution procedure; (a) step-by-step procedure in time; (b) Newton-Raphson iteration within each time step.

In this contribution, we compute the unknowns simultaneously at each temporal node, which will be realized iteratively, as illustrated in Figure 2. Hereby, the quasistatic space-time approach draws on our recently published paper [22].

The solution is then defined by a summation of M functionals, also called enrichments. The solution of a problem f dependent on space and time, can then be written as

$$f(\mathbf{x}, t) \approx \sum_{m=1}^{M} \chi^m(\mathbf{x})\theta^m(t) \ , \tag{3}$$

where $\chi^m(\mathbf{x})$ is the spatial and $\theta^m(t)$ is the temporal function in the m^{th} enrichment. Having defined the space-time solution ansatz, the incremental equation of equilibrium (2) must be

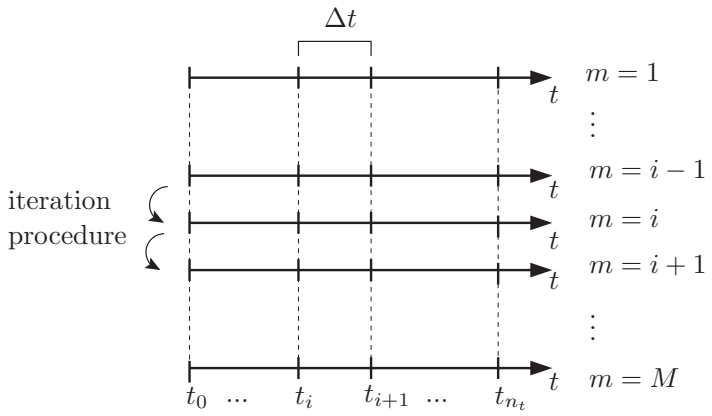

Figure 2: Space-time iteration scheme

reformulated in a space-time framework. According to the spatial discretization of the structure, we define the displacement matrix in each enrichment step in matrix form:

$$\mathbf{u}(\mathbf{x}, t) = [\mathbf{u}(t_0), \ldots, \mathbf{u}(t_{n_t})] \, . \tag{4}$$

Equivalently, the time-dependent internal and external force are expressed as:

$$\begin{aligned} \mathbf{F}_{\text{int}}(\mathbf{u}) &= [\mathbf{F}_{\text{int}}(t_0), \ldots, \mathbf{F}_{\text{int}}(t_{n_t})] \, , \\ \mathbf{F}(t) &= [\mathbf{F}(t_0), \ldots, \mathbf{F}(t_{n_t})] \, . \end{aligned} \tag{5}$$

The residual matrix is then evaluated by $\mathbf{R}(\mathbf{u}, t) = \mathbf{F} - \mathbf{F}_{\text{int}}$. The space-time residual is decomposed into a sum of dyadic products of uncorrelated space and time vectors. Therefore, the singular value decomposition (cf. [4]) is applied:

$$\mathbf{R}(\mathbf{x}, t) = \mathbf{R}_x \mathbf{S} \mathbf{R}_t^T \approx \sum_{j=1}^{n_{tr}} s^j \mathbf{R}_x^j \otimes \mathbf{R}_t^j \tag{6}$$

In this Equation, $\mathbf{R}_x^j$ are the left singular vectors extracted from the $n_x \times n_x$ matrix $\mathbf{R}_\mathbf{x}$, and $\mathbf{R}_t^j$ are the right singular vectors extracted from the $n_t \times n_t$ matrix $\mathbf{R}_\mathbf{t}$. The matrix $\mathbf{S}$ is a $n_x \times n_t$ rectangular diagonal matrix with the singular values s^j in descending order. Each value s^j defines the level of contribution of the j^{th} singular vector pair to the total energy of the space-time residual. Although all singular values must be considered to achieve an exact decomposition, in general, only a small number is necessary for an approximation with sufficiently high accuracy. The truncation number n_{tr} is defined so that the truncated sum contains at least 99.9% of the total sum of the singular values [4].

Furthermore, the space-time formulation of the stiffness matrix is defined by the dyadic product of the spatial and temporal stiffness matrices $\mathbf{K}_x$ and $\mathbf{K}_t$:

$$\mathbf{K} = \mathbf{K}_x \otimes \mathbf{K}_t, \; \mathbf{K}_x \in \mathbb{R}^{n \times n}, \; \mathbf{K}_t \in \mathbb{R}^{n_t \times n_t}. \tag{7}$$

Finally, using the proper generalized decomposition ansatz, the unknown displacement is written as a sum of enrichment functionals:

$$\mathbf{u}(\mathbf{x}, t) = \sum_{m=1}^{M} \Delta \mathbf{u}^m(\mathbf{x}, t) \, . \tag{8}$$

Here, the m^{th} enrichment is decomposed by

$$\Delta\mathbf{u}^m(\mathbf{x},t) = \Delta\mathbf{u}_x^m \otimes \Delta\mathbf{u}_t^m \ . \tag{9}$$

The vectors $\Delta\mathbf{u}_x^m$ and $\Delta\mathbf{u}_t^m$ define the modes of the m^{th} enrichment in the space and time domain.

Having defined the decomposition of the residual (6), the stiffness matrix (7) and the displacements (8), the equation of equilibrium can be reformulated into the space-time equation. For the m^{th} enrichment this yields to:

$$\Big(\mathbf{K}_x \otimes \mathbf{K}_t\Big)\Big(\Delta\mathbf{u}_x^m \otimes \Delta\mathbf{u}_t^m\Big) = \sum_{j=1}^{Tr} s^j \mathbf{R}_x^j \otimes \mathbf{R}_t^j \ . \tag{10}$$

Equation (10) is simplified to:

$$\mathbf{K}_x\Delta\mathbf{u}_x^m \otimes \mathbf{K}_t\Delta\mathbf{u}_t^m = \sum_{j=1}^{Tr} s^j \mathbf{R}_x^j \otimes \mathbf{R}_t^j \ . \tag{11}$$

In this equation, there are two unknowns: $\Delta\mathbf{u}_x^m$ and $\Delta\mathbf{u}_t^m$. However, multiplication by $\big(\Delta\mathbf{u}_t^m\big)^T$ leads to the projection into the space equation

$$\widehat{\mathbf{K}}_t\Delta\mathbf{u}_x^m = \widehat{\mathbf{R}}_x \ , \tag{12}$$

whereby $\widehat{\mathbf{K}}_t$ and $\widehat{\mathbf{R}}_x$ are defined as

$$\begin{aligned} \widehat{\mathbf{K}}_t &= \big(\Delta\mathbf{u}_t^m\big)^T \mathbf{K}_t \Delta\mathbf{u}_t^m \mathbf{K}_x \ , \\ \widehat{\mathbf{R}}_x &= \sum_{j=1}^{Tr} s^j \big(\Delta\mathbf{u}_t^m\big)^T \mathbf{R}_t^j \big(\mathbf{R}_x^j\big)^T \ . \end{aligned} \tag{13}$$

Furthermore, scalar multiplication of Equation (11) by $\big(\Delta\mathbf{u}_x^m\big)^T$ leads to the time equation

$$\widehat{\mathbf{K}}_x\Delta\mathbf{u}_t^m = \widehat{\mathbf{R}}_t, \tag{14}$$

whereby $\widehat{\mathbf{K}}_x$ and $\widehat{\mathbf{R}}_t$ are written as:

$$\begin{aligned} \widehat{\mathbf{K}}_x &= \big(\Delta\mathbf{u}_x^m\big)^T \mathbf{K}_x \Delta\mathbf{u}_x^m \mathbf{K}_t, \\ \widehat{\mathbf{R}}_t &= \sum_{j=1}^{Tr} s^j \big(\Delta\mathbf{u}_x^m\big)^T \mathbf{R}_x^j \big(\mathbf{R}_t^j\big)^T \ . \end{aligned} \tag{15}$$

These two coupled Equations (12) and (14) describe the space-time problem and must be solved simultaneously. Hereby, the fixed point algorithm is applied to iteratively evaluate $\Delta\mathbf{u}_x^m$ and $\Delta\mathbf{u}_t^m$. The spatial unknown $\Delta\mathbf{u}_x^m$ in equation (12) is evaluated while keeping $\Delta\mathbf{u}_t^m$ fixed. Subsequently, the temporal unknown $\Delta\mathbf{u}_t^m$ in equation (14) is evaluated while keeping $\Delta\mathbf{u}_x^m$ fixed. This procedure is repeated until convergence is achieved. The evaluated vectors $\Delta\mathbf{u}_x^m$ and $\Delta\mathbf{u}_t^m$ are inserted into equation (16) in order to obtain the update of the total displacement function after the m^{th} enrichment:

$$\mathbf{u}^m(\mathbf{x},t) = \mathbf{u}^{m-1}(\mathbf{x},t) + \Delta\mathbf{u}_x^m \otimes \Delta\mathbf{u}_t^m \ . \tag{16}$$

In this equation, $\Delta\mathbf{u}_x^m \otimes \Delta\mathbf{u}_t^m$ is the incremental enrichment functional after the current enrichment step and $\mathbf{u}^{m-1}(\mathbf{x},t)$ denotes the total solution of the sum of the preceding $(m-1)$ enrichment functionals. The convergence of the algorithm is examined after each enrichment by means of the Frobenius norm

$$\|\mathbf{Q}\| < \varepsilon_{(conv)} \tag{17}$$

considering

$$\mathbf{Q} = \mathbf{K}_x\Delta\mathbf{u}_x^m \otimes \mathbf{K}_t\Delta\mathbf{u}_t^m - \sum_{j=1}^{Tr} s^j\mathbf{R}_x^j \otimes \mathbf{R}_t^j \ , \tag{18}$$

with $\varepsilon_{(conv)}$ as the chosen convergence interval. Figure 3 shows the proposed space-time solution algorithm.

Enrichments:
for $m = 1 : M$ **do**
  Initialize $\Delta\mathbf{u}_t^0$;

  Fixed point algorithm:
  for $i = 1 : i_{\max}$ **do**
    Solution of space equation: $\Delta\mathbf{u}_x^i = \mathcal{D}^m\left(\Delta\mathbf{u}_t^{i-1}\right)$;
    Solution of time equation: $\Delta\mathbf{u}_t^i = \mathcal{B}^m\left(\Delta\mathbf{u}_x^i\right)$;
    Fixed point convergence check :
      $\|\Delta\mathbf{u}_t^i\|\ \|\Delta\mathbf{u}_x^i\|$ - $\|\Delta\mathbf{u}_t^{i-1}\|\ \|\Delta\mathbf{u}_x^{i-1}\| \leq \varepsilon_{(FP)}$;
  end
  $\Delta\mathbf{u}_x^i \longrightarrow \Delta\mathbf{u}_x^m$;
  $\Delta\mathbf{u}_t^i \longrightarrow \Delta\mathbf{u}_t^m$;

  Update the PGD displacement functional $\mathbf{u}(\mathbf{x},t)$
    $\mathbf{u}^m(\mathbf{x},t) = \mathbf{u}^{m-1}(\mathbf{x},t) + \Delta\mathbf{u}_x^m \otimes \Delta\mathbf{u}_t^m$

  Check convergence:
    $\|\mathbf{K}_x\Delta\mathbf{u}_x^m \otimes \mathbf{K}_t\Delta\mathbf{u}_t^m - \sum_{j=1}^{Tr} S^j\mathbf{R}_x^j \otimes \mathbf{R}_t^j\| < \varepsilon_{(conv)}$
end

Figure 3: Space-time solution algorithm using the proper generalized decomposition ansatz and the fixed point method.

3 Space-time solution of the linear damped dynamic problem

The linear damped set of equations of motion is written as:

$$\mathbf{M}\ddot{\mathbf{u}} + \mathbf{C}\dot{\mathbf{u}} + \mathbf{K}\mathbf{u} = \mathbf{F}(t), \tag{19}$$

where $\mathbf{M}$, $\mathbf{C}$ and $\mathbf{K}$ denote the $n \times n$ mass-, damping- and stiffness matrix. $\mathbf{F}(t)$ denotes the vector of external force. The vectors $\ddot{\mathbf{u}}$, $\dot{\mathbf{u}}$ and $\mathbf{u}$ denote the acceleration, velocity and displacement, respectively. We introduce the Newmark procedure as a representative of implicit

integration methods in structural dynamics. In general, the set of equations of motion is then supposed to be fulfilled at fixed time instants t_i, preferably defined in equidistant time intervals $\Delta t = t_i - t_{i-1}$. Approximation of the solution functions in between those time instants leads to the implicit Newmark equations [26]:

$$\mathbf{u}_i = \mathbf{u}_{i-1} + \big[\Delta t\big]\dot{\mathbf{u}}_{i-1} + \big[(\frac{1}{2} - \beta)\Delta t^2\big]\ddot{\mathbf{u}}_{i-1} + \big[\beta\Delta t^2\big]\ddot{\mathbf{u}}_{i-1} \tag{20}$$

and

$$\dot{\mathbf{u}}_i = \dot{\mathbf{u}}_{i-1} + \big[(1-\gamma)\Delta t\big]\ddot{\mathbf{u}}_{i-1} + \big[\gamma\Delta t\big]\ddot{\mathbf{u}}_{i-1}. \tag{21}$$

The set of equations of motion (19) can be rewritten in the incremental form as:

$$\mathbf{M}\Delta\ddot{\mathbf{u}}_i + \mathbf{C}\Delta\dot{\mathbf{u}}_i + \mathbf{K}\Delta\mathbf{u}_i = \Delta\mathbf{F}_i(t), \tag{22}$$

where $\Delta\ddot{\mathbf{u}}_i$, $\Delta\dot{\mathbf{u}}_i$ and $\Delta\mathbf{u}_i$ are the displacement, velocity and acceleration increments, obtained by:

$$\begin{aligned} \Delta\ddot{\mathbf{u}}_i &= \ddot{\mathbf{u}}_i - \ddot{\mathbf{u}}_{i-1}, \\ \Delta\dot{\mathbf{u}}_i &= \dot{\mathbf{u}}_i - \dot{\mathbf{u}}_{i-1}, \\ \Delta\mathbf{u}_i &= \mathbf{u}_i - \mathbf{u}_{i-1}\ . \end{aligned} \tag{23}$$

The incremental force vector $\Delta\mathbf{F}_i(t)$ is equivalently defined as:

$$\Delta\mathbf{F}_i(t) = \mathbf{F}_i(t) - \mathbf{F}_{i-1}(t)\ . \tag{24}$$

Considering the set of equations of motion (22) and the Newmark formulations (20) and (21), the displacement, velocity and acceleration increments can be obtained step-by-step [24].

Instead of using the conventional approach, we will transform the linear damped dynamic problem into the space-time formulation. To this aim, we, firstly, have to discover a way to convert the incremental displacement vector $\Delta\mathbf{u} = \mathbf{u}_i - \mathbf{u}_{i-1}$ into a space-time matrix. Discretizing the time domain into the temporal nodes t_i $(i = 1, 2, 3, \ldots, n_t)$, we define one displacement matrix as a sequence of displacement vectors in each temporal node:

$$\mathbf{u}(\mathbf{x}, t) = [\mathbf{u}(t_0), \mathbf{u}(t_1), \ldots, \mathbf{u}(t_{n_t})]\ . \tag{25}$$

The incremental space-time displacement matrix is then defined as:

$$\Delta\mathbf{u}(\mathbf{x}, t) = [\mathbf{u}(t_1) - \mathbf{u}(t_0), \mathbf{u}(t_2) - \mathbf{u}(t_1), \ldots, \mathbf{u}(t_{n_t}) - \mathbf{u}(t_{n_{t-1}})]\ . \tag{26}$$

Using this approach, the space-time formulation of initial displacement $\mathbf{u}_0$ must be added by an additional term. The displacement increment is then reformulated as:

$$\mathbf{u}_i - \mathbf{u}_{i-1} \longrightarrow \mathbf{I}_s\mathbf{u}_s \otimes \mathbf{A}_t\mathbf{u}_t - \mathbf{u}_0 \otimes \mathbf{A}_0 \tag{27}$$

The vectors $\mathbf{u}_s$ and $\mathbf{u}_t$ denote the space and time decomposition of the displacement. The matrix $\mathbf{I}_s$ denotes the identity matrix with dimension $n_s \times n_s$, and the matrix $\mathbf{A}_t$ with the dimension $n_t \times n_t$ consists of entries 0, 1 and -1. The vector $\mathbf{A}_0$ consists of one entry equal to one, while the remaining entries are zero. Using this approach, the conventional Newmark equations (20) and (21) are reformulated to the Newmark equations in the space-time framework:

$$\mathbf{I}_s\mathbf{u}_s \otimes \mathbf{A}_1\mathbf{u}_t + \mathbf{I}_s\mathbf{u}_s \otimes \mathbf{A}_2\dot{\mathbf{u}}_t + \mathbf{I}_s\mathbf{u}_s \otimes \mathbf{A}_3\ddot{\mathbf{u}}_t = \mathbf{u}_0 \otimes \mathbf{A}_5 + \dot{\mathbf{u}}_0 \otimes \mathbf{A}_6 + \ddot{\mathbf{u}}_0 \otimes \mathbf{A}_7 \tag{28}$$

$$\mathbf{I}_s\mathbf{u}_s \otimes \mathbf{A}_1\dot{\mathbf{u}}_t + \mathbf{I}_s\mathbf{u}_s \otimes \mathbf{A}_4\ddot{\mathbf{u}}_t = \dot{\mathbf{u}}_0 \otimes \mathbf{A}_5 + \ddot{\mathbf{u}}_0 \otimes \mathbf{A}_8 \tag{29}$$

The matrices $\mathbf{A}_1$, $\mathbf{A}_2$, $\mathbf{A}_3$ and $\mathbf{A}_4$ have the dimension $n_t \times n_t$. The corresponding components are defined according to the respective coefficients of the Newmark equations (20) and (21). Furthermore, $\mathbf{A}_5$, $\mathbf{A}_6$, $\mathbf{A}_7$ and $\mathbf{A}_8$ are vectors. They are necessary to realize the space-time equivalents of the initial displacement $\mathbf{u}_0$, velocity $\dot{\mathbf{u}}_0$ and acceleration $\ddot{\mathbf{u}}_0$ in an equivalent manner to Equation (27). In the next step, the set of equations of motion (19) is transformed into space-time. Thus, we define the stiffness-, damping and mass matrix in the space-time formulation as a dyadic product of the spatial and temporal matrices, c.f. (7):

$$\begin{aligned} \mathbf{M} = \mathbf{M}_s \otimes \mathbf{M}_t,\ \mathbf{M}_s \in \mathbb{R}^{n\times n},\ \mathbf{M}_t \in \mathbb{R}^{n_t\times n_t}. \\ \mathbf{C} = \mathbf{C}_s \otimes \mathbf{C}_t,\ \mathbf{C}_s \in \mathbb{R}^{n\times n},\ \mathbf{C}_t \in \mathbb{R}^{n_t\times n_t}. \end{aligned} \tag{30}$$

Thus, the set of equations of motion can be rewritten in the space-time formulation:

$$(\mathbf{M}_s \otimes \mathbf{M}_t)(\mathbf{u}_s \otimes \ddot{\mathbf{u}}_t) + (\mathbf{C}_s \otimes \mathbf{C}_t)(\mathbf{u}_s \otimes \dot{\mathbf{u}}_t) + (\mathbf{K}_s \otimes \mathbf{K}_t)(\mathbf{u}_s \otimes \mathbf{u}_t) = \mathbf{F} \tag{31}$$

Since the mass, damping and stiffness matrices are considered to be constant during the whole computation process, we apply the simplifications $\mathbf{M}_t = \mathbf{I}_t$, $\mathbf{C}_t = \mathbf{I}_t$ and $\mathbf{K}_t = \mathbf{I}_t$. Consequently, Equation (31) can be simplified to:

$$\mathbf{M}_s\mathbf{u}_s \otimes \mathbf{I}_t\ddot{\mathbf{u}}_t + \mathbf{C}_s\mathbf{u}_s \otimes \mathbf{I}_t\dot{\mathbf{u}}_t + \mathbf{K}_s\mathbf{u}_s \otimes \mathbf{I}_t\mathbf{u}_t = \mathbf{F}. \tag{32}$$

Simplification of the decomposed set of equations of motion (32) and the space-time reformulated Newmark equations (28) and (29) leads to:

$$\begin{aligned} \mathbf{u}\mathbf{A}_1^T + \dot{\mathbf{u}}\mathbf{A}_2^T + \ddot{\mathbf{u}}\mathbf{A}_3^T = \mathbf{u}_0\mathbf{A}_5^T + \dot{\mathbf{u}}_0\mathbf{A}_6^T + \ddot{\mathbf{u}}_0\mathbf{A}_7^T, \\ \dot{\mathbf{u}}\mathbf{A}_1^T + \ddot{\mathbf{u}}\mathbf{A}_4^T = \dot{\mathbf{u}}_0\mathbf{A}_5^T + \ddot{\mathbf{u}}_0\mathbf{A}_8^T, \\ \mathbf{M}_s\ddot{\mathbf{u}} + \mathbf{C}_s\dot{\mathbf{u}} + \mathbf{K}_s\mathbf{u} = \mathbf{F}. \end{aligned} \tag{33}$$

Although the dynamic equation in the space-time has, theoretically, three unknowns, the space-time displacement matrix $\mathbf{u}$, the space-time velocity matrix $\dot{\mathbf{u}}$ and the space-time acceleration matrix $\ddot{\mathbf{u}}$, we take advantage of the fact, that in the linear case, the velocity as well as the acceleration can be written as a function of the displacement. The dynamic linear damped system in the space-time is described by one algebraic space-time equation:

$$\mathbf{K}_s\mathbf{u} - \mathbf{C}_s\mathbf{u}\mathbf{W} + \mathbf{M}_s\mathbf{u}\mathbf{Y} = \mathbf{L}. \tag{34}$$

The matrices $\mathbf{W}$, $\mathbf{Y}$ include the $\mathbf{A}_i$ coefficient matrices written as:

$$\begin{aligned} \mathbf{W} = \mathbf{A}_1^T\big(\mathbf{A}_2^T - \mathbf{A}_1^T(\mathbf{A}_4^T)^{-1}\mathbf{A}_3^T\big)^{-1}, \\ \mathbf{Y} = \mathbf{A}_1^T\big(\mathbf{A}_2^T - \mathbf{A}_1^T(\mathbf{A}_4^T)^{-1}\mathbf{A}_3^T\big)^{-1}\mathbf{A}_1^T\big(\mathbf{A}_4^T\big)^{-1}, \end{aligned} \tag{35}$$

The vector $\mathbf{L}$ contains the external force and the initial conditions, expressed in matrix form:

$$\mathbf{L}(t) = [\mathbf{L}(t_1), \mathbf{L}(t_2), \ldots, \mathbf{L}(t_{n_t})]. \tag{36}$$

In order to decompose the space-time formulation of the vector $\mathbf{L}(t)$ into a sum of dyadic products of uncorrelated space and time vectors, we employ the singular value decomposition [1]:

$$\mathbf{L} = \mathbf{L}_s\mathbf{S}\mathbf{L}_t \approx \sum_{j=1}^{Tr} s^j\mathbf{L}_s^j \otimes \mathbf{L}_t^j. \tag{37}$$

In this equation, $\mathbf{L}_s^j$ are the left singular vectors with dimension n_s and is extracted form the matrix $\mathbf{L}_s$. Analogously, the right singular vector $\mathbf{L}_t^j$ is extracted form the $n_t \times n_t$ matrix $\mathbf{L}_t$. The matrix $\mathbf{S}$ is a $n_s \times n_t$ rectangular diagonal matrix with the singular values s^j in descending order, cf. Equation (6).

Equivalent to the quasistatic approach, the solution is defined as the summation of displacement enrichments:

$$\mathbf{u}(\mathbf{x},t) = \sum_{i=1}^{m-1} \mathbf{u}_s^{(i)} \otimes \mathbf{u}_t^{(i)} + \mathbf{u}_s^{(m)} \otimes \mathbf{u}_t^{(m)}. \tag{38}$$

Having finally defined the decomposition of mass-, damping- and stiffness matrix (32), force matrix (37) and the displacement (38), the main equation of motion (34) is defined in the space-time framework:

$$\begin{aligned} \mathbf{K}_s\big[\sum_{i=1}^{m-1} \mathbf{u}_s^{(i)} \otimes \mathbf{u}_t^{(i)} + \mathbf{u}_s^{(m)} \otimes \mathbf{u}_t^{(m)}\big] - \mathbf{C}_s\big[\sum_{i=1}^{m-1} \mathbf{u}_s^{(i)} \otimes \mathbf{u}_t^{(i)} + \mathbf{u}_s^{(m)} \otimes \mathbf{u}_t^{(m)}\big]\mathbf{W} + \\ \mathbf{M}_s\big[\sum_{i=1}^{m-1} \mathbf{u}_s^{(i)} \otimes \mathbf{u}_t^{(i)} + \mathbf{u}_s^{(m)} \otimes \mathbf{u}_t^{(m)}\big]\mathbf{Y} = \sum_{j=1}^{Tr} s^j \mathbf{L}_s^j \otimes \mathbf{L}_t^j \end{aligned} \tag{39}$$

This equation has the two unknowns $\mathbf{u}_s^m$ and $\mathbf{u}_t^m$. Multiplication by $\left(\Delta \mathbf{u}_t^m\right)^T$ leads to the time equation

$$\mathbf{u}_t^{(m)} = \left(a\mathbf{I}_t - b\mathbf{W}^T + c\mathbf{Y}^T\right)^{-1}\big[\widehat{\mathbf{L}}_t - \mathbf{V}_{s1} + \mathbf{V}_{s2} - \mathbf{V}_{s3}\big]. \tag{40}$$

Analogously, multiplication by $\left(\Delta \mathbf{u}_s^m\right)^T$ leads to the space equation

$$\mathbf{u}_s^{(m)} = \left(e\mathbf{K}_s - f\mathbf{C}_s + g\mathbf{M}_s\right)^{-1}\big[\widehat{\mathbf{L}}_s - \mathbf{V}_{t1} + \mathbf{V}_{t2} - \mathbf{V}_{t3}\big]. \tag{41}$$

Equations (40) and (41) are coupled and solved simultaneously using the fixed point algorithm and describe our space-time problem. The scalars a, b, c, e, f and g are defined as:

$$\begin{aligned} a &= \left(\mathbf{u}_s^{(m)}\right)^T \mathbf{K}_s \mathbf{u}_s^{(m)}, \qquad b = \left(\mathbf{u}_s^{(m)}\right)^T \mathbf{C}_s \mathbf{u}_s^{(m)}, \qquad c = \left(\mathbf{u}_s^{(m)}\right)^T \mathbf{M}_s \mathbf{u}_s^{(m)}, \\ e &= \left(\mathbf{u}_t^{(m)}\right)^T \mathbf{I}_t \mathbf{u}_t^{(m)}, \qquad f = \left(\mathbf{u}_t^{(m)}\right)^T \mathbf{W} \mathbf{u}_t^{(m)}, \qquad g = \left(\mathbf{u}_t^{(m)}\right)^T \mathbf{Y} \mathbf{u}_t^{(m)}. \end{aligned} \tag{42}$$

The external force matrices in the current enrichment m are expressed as:

$$\widehat{\mathbf{L}}_s = \sum_{j=1}^{Tr} s^j \left(\mathbf{L}_t^j\right)^T \mathbf{u}_t^{(m)} \mathbf{L}_s^j, \qquad \widehat{\mathbf{L}}_t = \sum_{j=1}^{Tr} s^j \mathbf{L}_s^j \mathbf{u}_s^{(m)} \mathbf{L}_t^j \tag{43}$$

Furthermore the vectors $\mathbf{V}_{s1}$, $\mathbf{V}_{s2}$, $\mathbf{V}_{s3}$, $\mathbf{V}_{t1}$, $\mathbf{V}_{t2}$ and $\mathbf{V}_{t3}$ are written as:

$$\begin{aligned} \mathbf{V}_{s1} &= \sum_{i=1}^{m-1} \left(\mathbf{u}_s^{(i)}\right)^T \mathbf{K}_s \mathbf{u}_s^{(m)} \mathbf{I}_t \mathbf{u}_t^{(i)}, \qquad \mathbf{V}_{t1} = \sum_{i=1}^{m-1} \left(\mathbf{u}_t^{(i)}\right)^T \mathbf{I}_t^T \mathbf{u}_t^{(m)} \mathbf{K}_s \mathbf{u}_s^{(i)}, \\ \mathbf{V}_{s2} &= \sum_{i=1}^{m-1} \left(\mathbf{u}_s^{(i)}\right)^T \mathbf{C}_s \mathbf{u}_s^{(m)} \mathbf{W}^T \mathbf{u}_t^{(i)}, \qquad \mathbf{V}_{t2} = \sum_{i=1}^{m-1} \left(\mathbf{u}_t^{(i)}\right)^T \mathbf{W} \mathbf{u}_t^{(m)} \mathbf{C}_s \mathbf{u}_s^{(i)}, \\ \mathbf{V}_{s3} &= \sum_{i=1}^{m-1} \left(\mathbf{u}_s^{(i)}\right)^T \mathbf{M}_s \mathbf{u}_s^{(m)} \mathbf{Y}^T \mathbf{u}_t^{(i)}, \qquad \mathbf{V}_{t3} = \sum_{i=1}^{m-1} \left(\mathbf{u}_t^{(i)}\right)^T \mathbf{Y} \mathbf{u}_t^{(m)} \mathbf{M}_s \mathbf{u}_s^{(i)}. \end{aligned} \tag{44}$$

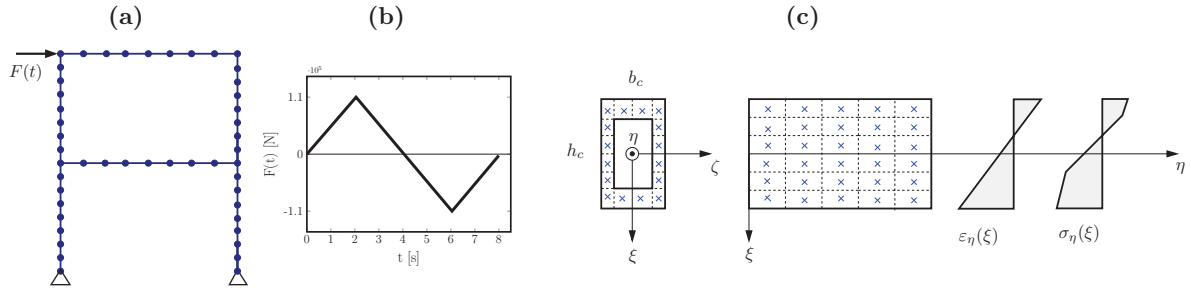

Figure 4: (a) frame structure; (b) sinusoidal quasistatic force history; (c) beam element and nonlinear stress-strain relation

After each enrichment, the evaluated vectors $\mathbf{u}_t^{(m)}$ and $\mathbf{u}_s^{(m)}$ are inserted into Equation (38) to obtain the update of the total displacement function. Equivalent to the quasistatic approach, the convergence of the algorithm is examined after each enrichment by means of the Frobenius norm

$$\|\mathbf{Q}\| < \varepsilon_{conv} \tag{45}$$

with

$$\mathbf{Q} = \mathbf{K}_s\mathbf{u}_s^{(m)} \otimes \mathbf{u}_t^{(m)} - \mathbf{C}_s\mathbf{u}_s^{(m)} \otimes \mathbf{W}^T\mathbf{u}_t^{(m)} + \mathbf{M}_s\mathbf{u}_s^{(m)} \otimes \mathbf{Y}^T\mathbf{u}_t^{(m)} - \sum_{j=1}^{Tr} s^j\mathbf{L}_s^j \otimes \mathbf{L}_t^j \tag{46}$$

and ε_{conv} as the chosen convergence interval.

4 Numerical results

4.1 Numerical results of the elastoplastic problem subjected to quasistatic excitation

As example, we introduce the geometry of a frame structure with two stories and one bay, depicted in Figure 4a (height and width are 8m). The columns and the beam of the structure are discretized by five elements, leading to a total number of 122 degrees of freedom. In Figure 4b, the force history used in this study, is depicted. The force time history is discretized choosing a constant time increment Δt of 0.05 second. An elastoplastic material model with kinematic hardening is implemented, as depicted in Figure 4c. The parameters are chosen as: initial stiffness $E_1 = 240$ GPa, yield stress $\sigma_Y = 220$ MPa, post yielding stiffness $E_2 = 0.1E_1$, Poisson's ratio 0.3. All cross sections of the columns and beam are modeled by quadratic hollow rectangular shapes. The dimensions are 0.3 m $\times$ 0.1 m. The thickness is $t = 10$ mm.

Regarding the conventional step-by-step method, the solution at time t_{i+1} is obtained iteratively based on the foregoing solution at time t_i. However, the proposed space-time procedure solves the problem in the entire time domain. Regarding the classic step-by-step reference method, in total 6237 iterations are performed within 160 time steps, whereas the convergence interval of the residual is set to 1.0 e-3. Regarding the space-time method, only 80 iterations are performed in order to reach the same level of accuracy. The enrichments are composed of a dyadic product of spatial and temporal modes, $\Delta\mathbf{u}_x$ and $\Delta\mathbf{u}_t$, as proposed in Equation (9), which are obtained during each enrichment from Equations (12) and (14). The displacements of the structure are then evaluated by the summation of all already iteratively evaluated enrichments. The results are presented in Figure 5. In particular, Figure 5a shows the evolution of the temporal modes. Figure 5b shows the evolution of the corresponding spatial modes. Additionally, Figure 5c shows the horizontal displacement of the node in the top left corner after each enrichment, and Figure 5d illustrates the corresponding hysteresis of this node.

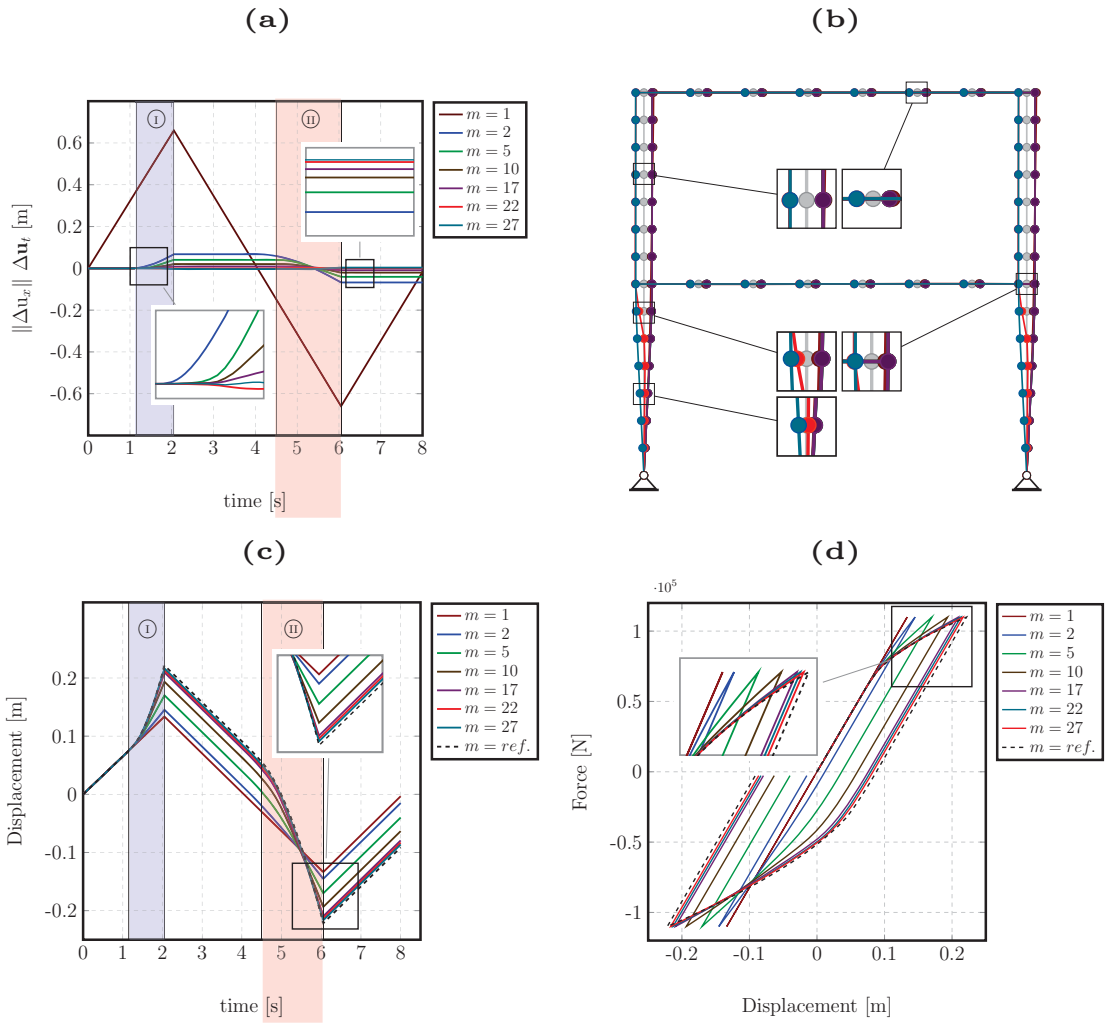

Figure 5: (a) The temporal mode multiplied by the length of the spatial mode $\|\Delta \mathbf{u}_x\| \Delta \mathbf{u}_t$;(b) the spatial mode $\frac{\Delta \mathbf{u}_x}{\|\Delta \mathbf{u}_x\|}$ at different enrichment steps m; (c) displacement response during loading time history; (d) hysteresis behavior after different enrichment steps m, reference solution (ref.). Compare qualitatively with the results in [22].

After the first enrichment step, the linear response is observed. This is seen by the first temporal mode in Figure 5a and the displacement after the first enrichment in Figure 5c. Both of these functions are linearly dependent on the excitation function. This is also verified in Figure 5d, where a linear function of the force-displacement response is observed after the first enrichment. Thus, the displacement in every time step, $\mathbf{u}^{(i)}$, is equal to the solution of the corresponding linear equation $\mathbf{K}^{\text{in}} \mathbf{u}^{(i)} = \mathbf{F}^{(i)}$. From the second enrichment on, the response of the structure evolves into the plastic range. Within the first time period, $0 \leq t \leq 1.15$ s, no plastic deformation is observed and the values of $\Delta \mathbf{u}_t$ are zero for all enrichments except the first one. This can be seen in Figure 5a. Two crucial time periods are defined for this example, in which the plastic strain rate is not equal to zero. This is time period Ⓘ in $1.15 \leq t \leq 2$ s, and time period Ⓘ Ⓘ in $4.5 \leq t \leq 6$ s, as depicted in Figure 5a. Within these time periods, the slopes of the temporal modes $\Delta \mathbf{u}_t^i$ $(i = 2, \ldots, M)$ are not equal to zero, whereas outside those time periods a constant function is observed for all of the temporal modes. With increasing number of enrichments, the amplitude of the temporal modes decreases until convergence. On the one

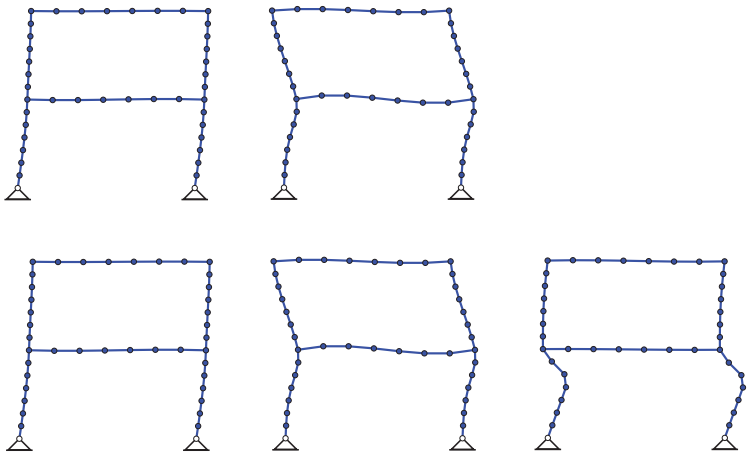

Figure 6: Uncorrelated proper orthogonal decomposition (POD) basis of the spatial modes after five (first row) and after 25 (second row) enrichments.

hand, we observe that $\Delta\mathbf{u}_t^i$ alters if plastic deformation is occurs, as shown in Figure 5a within time period Ⓘ during loading in positive x-direction and within time period Ⓘ. On the other hand, we observe that $\Delta\mathbf{u}_t^i$ remains constant if no additional plastic deformation is induced, as shown in Figure 5a in the time period $2 \leq t \leq 4.5$ s and $6 \leq t \leq 8$ s. These effects can also be observed in Figure 5c, where the solution drifts off the elastic response and converges to the reference solution. Within time periods Ⓘ and Ⓘ, the slope of the converged displacement function varies from the slope of the linear solution $(m = 1)$, whereas, within the remaining time periods, these functions are always parallel to the linear solution. In Figure 5d, it is also shown that the amount of plasticity increases with increasing number of enrichments and the hysteresis becomes broader until convergence to the reference solution.

Having revealed that the first enrichment response is purely linear, we emphasize that the spatial modes of the remaining enrichments, as depicted in Figure 5b, cannot directly be related to a spatial distribution of purely localized plastic deformation. They are rather identified as a set of modes, containing a superposition of global elastic and plastic structural deformation patterns. However, an indication that directly indicates plasticity cannot be seen by this evolution of spatial modes. Considering the horizontal force, as depicted in Figure 4, plastic zones will evolve around both corners of the frame structure. In order to investigate this local effect of the spatial evolution of the inelastic response, an observation matrix after each enrichment is defined that contains a set of correlated spatial modes $\mathbf{Q}^m = [\Delta\mathbf{u}_x^1, \Delta\mathbf{u}_x^2, \ldots, \Delta\mathbf{u}_x^m]$. Using the singular value decomposition (6), this observation matrix represents a set of orthonormal left singular basis vectors $\left[\boldsymbol{\Phi}_1^m, \boldsymbol{\Phi}_2^m, \ldots, \boldsymbol{\Phi}_{n_{tr}}^m\right]$. The singular values provide the amount of energy belonging to each corresponding mode. The number of required basis vectors n_{tr} is then evaluated by ensuring that 99.9% of the total energy of the observation matrix is stored within the set of basis vectors. In Figure 6, this truncated orthonormal basis, evaluated with regard to a varying number of enrichments, is presented. In particular, the first row in this figure shows the orthonormal uncorrelated basis after 5 enrichments, whereas the second row in this figure shows the orthonormal uncorrelated basis after 25 enrichments. The number of required basis vectors that contains almost the whole information of the set of spatial modes increases with increasing number of enrichments. Finally, a maximum number of three basis vectors contains 99.9% of the energy of the observation set obtained using 25 spatial modes. Thus, being able to reduce the number of 25 proper generalized decomposition modes to a number of three uncor-

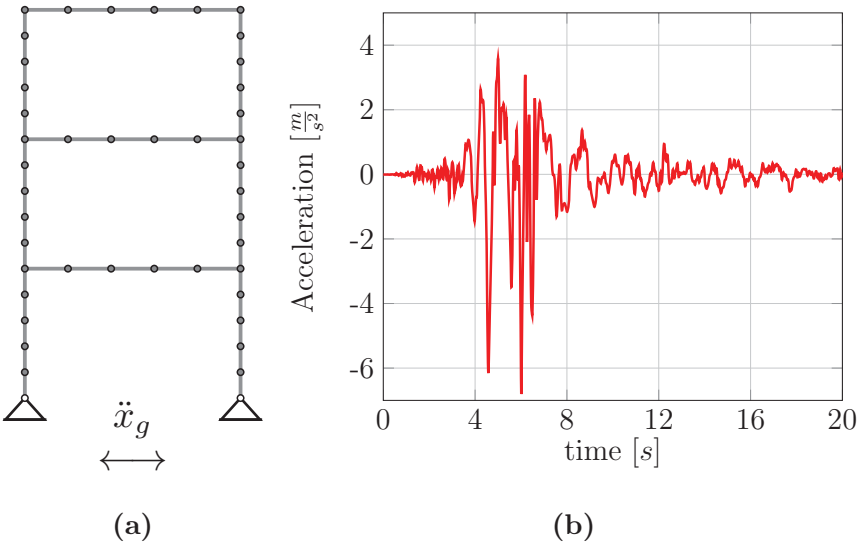

Figure 7: (a) Representative plane frame structure; (b) Horizontal acceleration of Kobe earthquake.

related basis vectors reveals that the spatial modes can be identified as highly correlated. The first uncorrelated basis mode describes the global response behavior of the structure and does not change significantly with increasing number of enrichments. After five enrichments, both basis vectors can only describe rather global response patterns, while local plastic deformations cannot be described. After 25 enrichments, the second and third basis modes clearly show local plastic response behavior around the corners of the frame structures. Consequently, the evolution of localized plastic effects with increasing number of enrichments cannot be interpreted by the set of the spatial modes of the enrichments, as they are highly correlated, but it can be well interpreted by their orthonormal basis representation.

4.2 Numerical results of the dynamic problem including damping subjected to transient excitation

In this section, a linear viscously damped system is solved using the introduced space-time formulation. The results are compared with the conventional Newmark solution. Furthermore, the proper generalized decomposition modes are investigated during convergence. As illustrative example, we investigate the response of two-dimensional frame structure, depicted in Figure 7a subjected to an earthquake record, depicted in Figure 7b. As depicted in this figure, the frame consists of three stories and one bay. Columns as well as beams of the frame structure are discretized by five elements, which leads to 128 degrees of freedom. The chosen time step Δt for the calculation is 10^{-2} s, which is equal to the time resolution of the excitation record. As for the quasistatic example, the whole structure is discretized by a 2 node truss-beam element, applying the Euler-Bernoulli beam theory [25]. The Young's modulus of the material is chosen as $E = 210$ GPa. All cross sections of the columns and beam are modeled by quadratic hollow rectangular shapes. The dimensions are 0.3 m $\times$ 0.1 m. The thickness of the cross sections is chosen as $t = 10$ mm. Rayleigh damping is introduced with a damping parameter of 0.04 for the fourth and 15^{th} mode. Figure 8 presents the horizontal displacement response of the node in the top left corner of the frame after each enrichment. In this figure, we observe convergence to the step-by-step reference solution within the first 18 enrichments. Figure 9 presents the spatial and temporal modes within the first three enrichment steps. In comparison, the first three linear

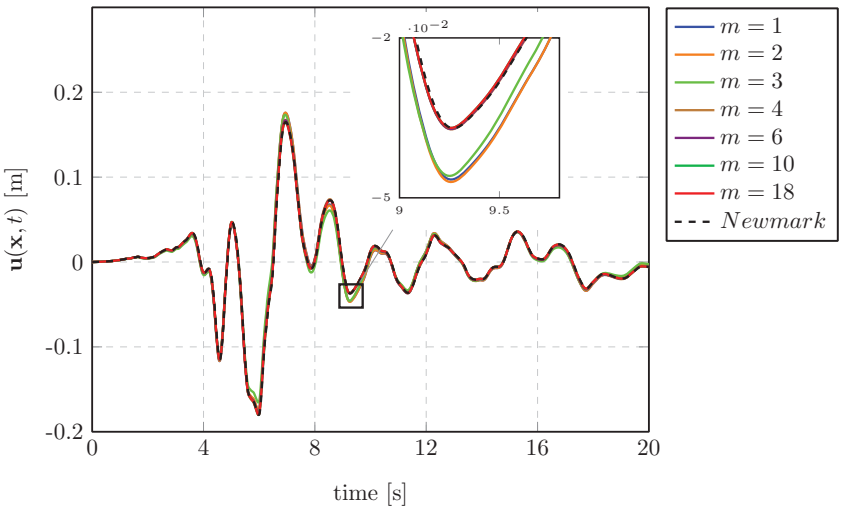

Figure 8: Displacement response during the loading time history after different enrichment.

modes of vibration are presented in red color in this figure. Looking at the patterns of the spatial PGD modes, significant differences can be observed compared to the linear modes of vibration. With increasing number of enrichments, spatial PGD modes are observed to reveal a high correlation with the depicted modes (not shown in this figure). This has also been observed for the quasistatic problem.

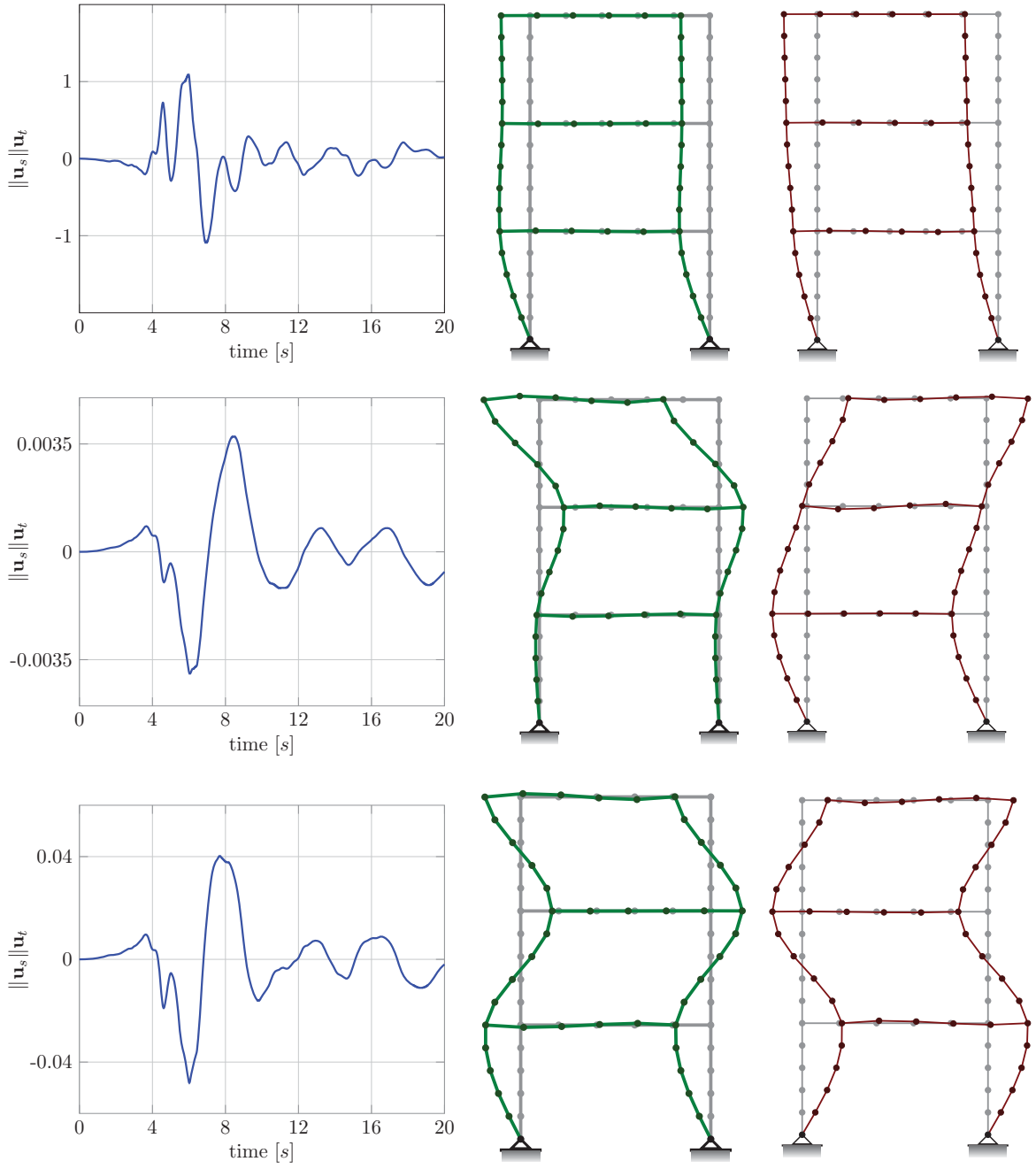

Figure 9: Left column: Expression of the temporal multiplied by the length of spatial mode $\|\mathbf{u}_s\|\mathbf{u}_t$; middle column: the spatial modes $\frac{\mathbf{u}_t}{\|\mathbf{u}_s\|}$ after the first three enrichment steps; right column: the first three modes of vibration.

5 Conclusion

In this paper, a space-time formulation of linear and nonlinear structures has been employed. Firstly, the space-time formulations in the quasistatic elastoplastic framework has been presented. Secondly, a space-time formulation of the Newmark solution for the linear damped equations of motion has been employed. Both formulations have been verified by numerical demonstrations.

Regarding the quasistatic case, the first enrichment represents the solution to the linear equation $\mathbf{K}^{\text{in}}\mathbf{u}^{(i)} = \mathbf{F}^{(i)}$ at all time steps $i = 1 \dots n_t$. However, with the second enrichment the solution starts to evolve into the nonlinear range until convergence is achieved. Regarding the dynamic case, however, a higher number of enrichments is necessary to approximate the linear response function as dynamic motion can be described by a superposition of motion patterns. The spatial proper generalized decomposition modes, however, are significantly different to the linear modes of vibration. Furthermore, the spatial proper generalized decomposition modes reveal a high correlation, so that only a small number of modes differs from each other significantly. This is observed for both, the nonlinear quasistatic and the dynamic problem.

In future studies, we will extend the proposed Newmark space-time method to elastoplastic dynamic problems. Furthermore, it is of great interest whether these types of space-time methods can be applied to vibro-impact problems, such as [27, 28], that can reveal unpredictable dynamical behavior.

REFERENCES

[1] A. Chatterjee, An introduction to the proper orthogonal decomposition, *Curr. Sci.*, **78**, 808–817, 2000.

[2] G. Kerschen, J.C. Golivani, Physical interpretation of the proper orthogonal modes using the singular value decomposition, *Journal of Sound and Vibration*, **249**, 849-865, 2002.

[3] F. Bamer, C. Bucher, Application of the proper orthogonal decomposition for linear and nonlinear structures under transient excitation, *Acta Mechanica*, **223**, 2549–2563, 2012.

[4] F. Bamer, A.K. Amiri, C. Bucher, A new order reduction strategy adapted to nonlinear problems in earthquake engineering,*Earthquake Engng. Strct. Dyn.*, **46**, 537–559, 2017.

[5] F. Bamer, B. Markert, An efficient response identification strategy for nonlinear structures subject to non-stationary generated seismic excitations, *Mechanics based design of structures and machines*, **46**, 313–330, 2017.

[6] D. Craig, M. Bampton, Coupling of Substructures for Dynamics Analyses, *AIAA Journal*, **6** 1313–1319, 1968.

[7] D.J. Rixen, A dual Craig–Bampton method for dynamic substructuring, *Journal of Computational and Applied Mathematics*, **168**, 383–391, 2004.

[8] F. Bamer, J. Shi, B. Markert, Efficient solution of the multiple seismic pounding problem using hierarchical substructure techniques, *Computational Mechanics*, **62**, 761–782, 2018.

[9] J. Shi, F. Bamer, B. Markert, A Structural Pounding Formulation Using Systematic Modal Truncation, *Journal of Shock and Vibration*, **2018**, 1–15, 2018.

[10] J. Shi, F. Bamer, B. Markert, A substructure formulation for the earthquake-induced nonlinear structural pounding problem, *Earthquakes and Structures*, **17**, 101–113, 2019.

[11] L. Zhou, J. W. Simon, S. Reese, Proper orthogonal decomposition for substructures in nonlinear finite element analysis: coupling by means of tied contact, *Archive of Applied Mechanics volume*, **88**, 1975–2001, 2018.

[12] P. Ladevèze, Nonlinear computational structural mechanics, New approaches and non-incremental methods of calculation, *Springer*, ISBN: 0-387-98594-8, 1999.

[13] F. Chinesta, A. Ammar, E. Cueto, On the use of proper generalized decompositions for solving the multidimensional chemical master equation, *Eur. Comput. Mech.*, **19**, 53–64, 2012.

[14] J. V. Aguardo, A. Huerta, F. Chinesta, E. Cueto, Real-time monitoring of thermal processes by reduced-order modeling, *Int. J. Numer. Meth. Engng.*, **102**, 991–1017, 2014.

[15] A. Ammar, B. Mokdad, F. Chinesta, R. Keunings, A new family of solvers for some classes of multidimensional partial differential equations encountered in kinetic theory modeling of complex fluids: Part I, *J. Non-Newtonian Fluid Mech.*, **139**, 153–176, 2006.

[16] A. Ammar, B. Mokdad, F. Chinesta, R. Keunings, A new family of solvers for some classes of multidimensional partial differential equations encountered in kinetic theory modeling of complex fluids: Part II: Transient simulation using space-time separated representations, *J. Non-Newtonian Fluid Mech.*, **144**, 98–121, 2007.

[17] M. Signorini, S. Zlotnik, P. Díez, Proper generalized decomposition solution of the parameterized Helmholtz problem: application to inverse geophysical problems, *Int. J. Numer. Meth. Engng.*, **109**, 1085–1102, 2017.

[18] D. González, E. Cueto, F. Chinesta, Real time direct integration of reduced solid dynamics equations, *Int. J. Numer. Meth. Engng.*, **99**, 633–653, 2014.

[19] F. Chinesta, A. Leygue, F. Bordeu, V. Aguado, E. Cueto, D. Gonzalez, A. Alfaro, A. Ammar, A. Huerta, PGD based computational vademecum for efficient design, optimization and control, *Arch. Comput. Methods. Eng.*, **20**, 31–59, 2013.

[20] J. M. Bergheau, S. Zuchiatti, J. C. Roux, E. Feulvarch, S. Tissot, G. Perrin, The proper Generalized decomposition as a space-time integrator for elastoplastic problems, *C. R. Mecanique*,**344**, 759–768, 2016.

[21] M.A. Nasri, C.Robert, A. Ammar, S.E. Arem, F. Morel, Proper Generalized Decomposition (PGD) for the numerical simulation of polycrystalline aggregates under cyclic loading, *C. R. Mecanique*,**346**, 132–151, 2018.

[22] N. Shirafkan, F. Bamer, M. Stoffel, B. Markert, Quasistatic analysis of elastoplastic structures by the proper generalized deompostion in a space-time approach, *Mechanics research communication*, Online first, 10.1016/j.mechrescom.2020.103500, 2020.

[23] L. Boucinha, A. Gravouil, A. Ammar, Space-time proper generalized decomposition for the resolution of transient elastodynamic models, *Comput. Methods Appl. Mech. Engng.*, **255**, 67–88, 2013.

[24] K.J. Bathe, Dynamics of structures, *Pearson education*, ISBN: 9781621008682, 2012.

[25] G. Falsone, D. Settineri, An Euler–Bernoulli-like finite element method for Timoshenko beams, *Mechanics Research Communications*, **38**, 12–16, 2011.

[26] J. L. Newmark, A Method of Computation for Structural Dynamics, *Journal of the Engineering Mechanics Division*, **85**, 67–94, 1979.

[27] F. Bamer, B. Markert, A nonlinear visco-elastoplastic model for structural pounding, *Earthquake engineering and structural dynamics*, **47**, 2490–2495, 2018.

[28] F. Bamer, A Hertz-pounding formulation with a nonlinear damping and a dry friction element, *Acta Mechanica*, **229**, 4485–4494, 2018.

EURODYN 2020
XI International Conference on Structural Dynamics
M. Papadrakakis, M. Fragiadakis, C. Papadimitriou (eds.)
Athens, Greece, 23-26 November 2020

ISOGEOMETRIC COLLOCATION METHODS FOR THE DYNAMICS OF THREE-DIMENSIONAL GEOMETRICALLY EXACT BEAMS

Enzo Marino[1], Josef Kiendl[2], and Laura De Lorenzis[3]

[1]Department of Civil and Environmental Engineering, University of Florence
Via di S. Marta 3, 50139 Firenze, Italy
e-mail: enzo.marino@unifi.it

[2]Department of Civil Engineering and Environmetal Sciences, Bundeswehr University Munich
Werner-Heisenberg-Weg 39, 85577 Neubiberg, Germany
e-mail: josef.kiendl@unibw.de

[3]Department of Mechanical and Process Engineering
Tannenstrasse 3, 8092 Zürich, Switzerland
e-mail: ldelorenzis@ethz.ch

Keywords: Isogeometric collocation, Nonlinear dynamics, Finite rotations, Timoshenko beams.

Abstract. *In this paper we review some of the most recent computational techniques based on the isogeometric analysis for the solution of the dynamic problem of geometrically exact beams. The kinematics of a spatial Timoshenko beam undergoing finite displacements and rotations involves the Lie group* $\mathrm{SO}(3)$*. Most of the computational complexities originate from the presence of such a non-additive and non-commutative rotation group. By employing the incremental rotation vector to describe the evolution of finite rotations, we discuss how the isogeometric collocation (IGA-C) method can be efficiently used in both explicit and implicit Newmark-based schemes.*

1 INTRODUCTION

For a wide range of engineering problems, accurate and efficient beam formulations able to reproduce large and fast three-dimensional motions are of paramount importance. The isogeometric collocation (IGA-C) method was proposed in [1, 2] with the primary objective of exploiting the higher smoothness of non-uniform rational B-Splines (NURBS) basis functions used in isogeometric analysis (IGA) [3] and the low computational cost of collocation. NURBS basis functions, used both for the geometry representation and the space discretization of the differential problem, significantly simplify the operations of mesh generation and refinement. Moreover, once the initial mesh is generated, refinements do not affect the geometric approximation. IGA has proven to achieve increased accuracy and robustness on a per degree-of-freedom basis compared with standard Finite Element Analysis (FEA) [4, 5, 6].

IGA-C seeks to achieve higher efficiency since, in contrast to Galerkin.based IGA, the need for numerical quadrature is completely removed due to the discretization of the strong form of the governing equations. IGA-C requires only one evaluation point per degree of freedom, regardless of the approximation degree, resulting in a much faster method compared to standard Galerkin-based IGA [7]. IGA-C proved excellent performances in a wide range of applications. Timoshenko beam formulations were successfully proposed in [8, 9, 10, 11, 12, 13]. Bernoulli-Euler beams and Kirchhoff plates were addressed in [14], and Reissner-Mindlin plate and shell problems in [15] and [16], respectively. Kirchhoff-Love plate and shell problems were studied in [17]. In [18, 19, 20] IGA-C was extended to geometrically nonlinear three-dimensional shear-deformable beams. Nonlinear planar Kirchhoff rods were formulated in [21]. In linear dynamics, an explicit IGA-C formulation was introduced in [2] and more recently an explicit higher-order space- and time-accurate method for elastodynamics was proposed in [22]. IGA-C methods for the nonlinear dynamics of geometrically exact beams have been investigated so far only in [23] through an implicit quaternion-based formulation, [24] through an explicit formulation based on the spatial incremental rotation vector, and in [25] through an implicit formulation based on the material incremental rotation vector.

In this work we review and compare the main features of the explicit and implicit formulations we recently proposed in [24] and [25], respectively. In the explicit formulation we adopt one of the best-performing Newmark time integration method for $\mathrm{SO}(3)$ proposed by Krysl & Endres in [26] for the rotational dynamics of rigid bodies. In the implicit formulation we adopt the $\mathrm{SO}(3)$-extended version of the classical Newmark scheme originally proposed in [27].

Both formulations are geometrically consistent, namely the main operations of linearization, variables initialization and kinematic update are made consistently with the geometric structure of the configuration manifold. High efficiency and accuracy are guaranteed by the IGA-C attributes combined with the rotation-vector parameterization for the incremental rotation.

2 THEORETICAL BACKGROUND

2.1 The configuration manifold and its tangent spaces

The motion of any material particle $\boldsymbol{p} \in \mathcal{B}$ of a shear-deformable beam is expressed as follows

$$\boldsymbol{\varphi}(t, \boldsymbol{p}) = \boldsymbol{c}(t, \boldsymbol{q}) + \mathbf{R}(t, \boldsymbol{q})(\boldsymbol{p} - \boldsymbol{q}) \,,$$

where $t \in \boldsymbol{T}$ is the time ($\boldsymbol{T} = [0, T] \subset \mathbb{R}$ being the time domain), $\boldsymbol{q} \in \mathcal{B}$ is the material position of the centroid of the beam cross section containing point $\boldsymbol{p}$. $\mathcal{S} \subset \mathcal{B}$ is the centroid line. (Figure 1).

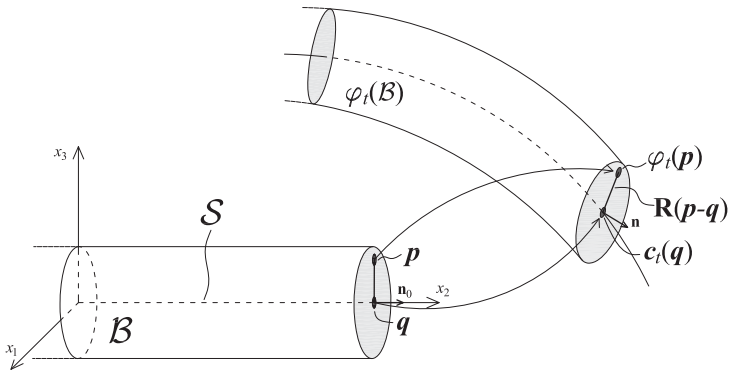

Figure 1: Motion of a three-dimensional shear deformable beam.

The configuration manifold is the set

$$\mathcal{C} = \left\{ (\boldsymbol{c}, \mathbf{R}) \,|\, \boldsymbol{c} : \boldsymbol{T} \times \mathcal{S} \to \mathbb{R}^3 \,, \mathbf{R} : \boldsymbol{T} \times \mathcal{S} \to \mathrm{SO}(3) \right\} \,,$$

where $\boldsymbol{c}(t, \boldsymbol{q})$ is the spatial location of the center of mass of the beam cross section at time t and point $\boldsymbol{q} \in \mathcal{S}$, and $\mathbf{R}(t, \boldsymbol{q})$ is the rigid rotation of the same cross section at the same time. Namely, the (finite) rotation of each beam cross section is described by a time-depending orthogonal operator $\mathbf{R}$ belonging to the non-commutative Lie group $\mathrm{SO}(3)$. On $\mathrm{SO}(3)$ rotation updates, transformations of $\mathrm{SO}(3)$ onto itself, must be consistently performed by a suitable composition of an incremental rotation with the current rotation. Such an operation is non-additive and non-commutative. The latter attribute leads to a substantial difference between spatial and material descriptions of the motion on $\mathrm{SO}(3)$. Indeed, we have that spatial and material tangent spaces to $\mathrm{SO}(3)$ at $\mathbf{R}$ are respectively defined as follows

$$T^s_{\mathbf{R}} \mathrm{SO}(3) = \left\{ \tilde{\boldsymbol{\vartheta}} \mathbf{R} \,|\, \tilde{\boldsymbol{\vartheta}} \in \mathrm{so}(3) \,, \mathbf{R} \in \mathrm{SO}(3) \right\} \,,$$
$$T^m_{\mathbf{R}} \mathrm{SO}(3) = \left\{ \mathbf{R} \widetilde{\boldsymbol{\Theta}} \,|\, \widetilde{\boldsymbol{\Theta}} \in \mathrm{so}(3) \,, \mathbf{R} \in \mathrm{SO}(3) \right\} \,,$$

where $\mathrm{so}(3)$ is the set of 3×3 skew-symmetric matrices [27, 28][1].

Configuration update is made as follows

$$\mathbf{R}_\varepsilon = \exp(\varepsilon \widetilde{\boldsymbol{\vartheta}}) \mathbf{R} = \mathbf{R} \exp(\varepsilon \widetilde{\boldsymbol{\Theta}}); \quad \boldsymbol{c}_\varepsilon = \boldsymbol{c} + \varepsilon \boldsymbol{\eta}$$

where $\widetilde{\boldsymbol{\vartheta}}$ and $\widetilde{\boldsymbol{\Theta}}$ are the spatial and material incremental rotation vectors, respectively; $\boldsymbol{\eta}$ is the incremental displacement, and $\varepsilon \in \mathbb{R}$. (Figure 2).

3 Balance equations in strong form

The displacement-based version of the balance equations is

$$\mu \mathbf{R}^{\mathsf{T}} \boldsymbol{a} = \widetilde{\boldsymbol{K}} \mathbb{C}_N \boldsymbol{\Gamma}_N + \mathbb{C}_N \boldsymbol{\Gamma}_{N,s} + \mathbf{R}^{\mathsf{T}} \bar{\boldsymbol{n}} \tag{1}$$

$$\boldsymbol{J} \boldsymbol{A} + \widetilde{\boldsymbol{W}} \boldsymbol{J} \boldsymbol{W} = \widetilde{\boldsymbol{K}} \mathbb{C}_M \boldsymbol{K}_M + \mathbb{C}_M \boldsymbol{K}_{M,s} + \widetilde{(\mathbf{R}^{\mathsf{T}} \boldsymbol{c}_{,s})} \mathbb{C}_N \boldsymbol{\Gamma}_N + \mathbf{R}^{\mathsf{T}} \bar{\boldsymbol{m}} \tag{2}$$

where μ is the mass per unit length of the beam; $\boldsymbol{a}$ is the spatial acceleration vector of the cross section centroid; $\widetilde{\boldsymbol{K}} = \mathbf{R}^{\mathsf{T}} \mathbf{R}_{,s}$ is the beam curvature in the material form; $\boldsymbol{\Gamma}_N$, $\boldsymbol{K}_M$ are the strain

[1] With the symbol $\sim$ we denote elements of $\mathrm{so}(3)$. Furthermore, for any skew-symmetric matrix $\widetilde{\boldsymbol{a}} \in \mathrm{so}(3)$, $\boldsymbol{a} = \mathrm{axial}(\widetilde{\boldsymbol{a}})$ indicates the axial vector of $\widetilde{\boldsymbol{a}}$ such that $\widetilde{\boldsymbol{a}} \boldsymbol{h} = \boldsymbol{a} \times \boldsymbol{h}$, for any $\boldsymbol{h} \in \mathbb{R}^3$.

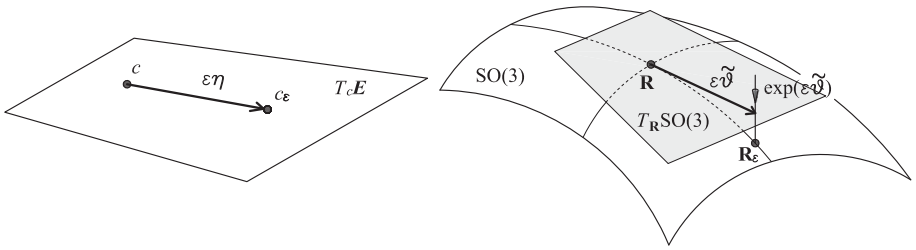

Figure 2: Tangent space to SO(3). Spatial case: $T_{\mathbf{R}}\,\mathrm{SO}(3) = T^s_{\mathbf{R}}\,\mathrm{SO}(3)$.

measure vectors in the material form; $\bar{\boldsymbol{n}}$, $\bar{\boldsymbol{m}}$ are the external forces and moments per unit length in spatial form; $\boldsymbol{J}$ is the material inertia tensor; $\widetilde{\boldsymbol{W}} = \mathbf{R}^{\mathsf{T}}\dot{\mathbf{R}}$ is the material angular velocity tensor and $\boldsymbol{W} = \text{axial}(\widetilde{\boldsymbol{W}})$ its axial vector; $\boldsymbol{A} = \dot{\boldsymbol{W}}$ is the material angular acceleration vector; $\mathbb{C}_N = \text{diag}(GA_1, EA, GA_3)$ and $\mathbb{C}_M = \text{diag}(EJ_1, GJ, EJ_3)$.

The corresponding spatial rotational inertia is given by $\boldsymbol{j}\boldsymbol{\alpha} + \widetilde{\boldsymbol{\omega}}\boldsymbol{j}\boldsymbol{\omega} = \mathbf{R}(\boldsymbol{J}\boldsymbol{A} + \widetilde{\boldsymbol{W}}\boldsymbol{J}\boldsymbol{W})$, where $\boldsymbol{\alpha}$ and $\boldsymbol{\omega}$ are the angular acceleration and velocity in the spatial form.

4 TIME AND SPACE DISCRETIZATIONS

4.1 Explicit (spatial) Newmark scheme

With $\mathcal{I}_u = [0, 1] \subset \mathbb{R}$ as the normalized one-dimensional domain of the basis functions, the spatial approximation of the incremental rotation and displacement is introduced as follows

$$\boldsymbol{\vartheta}(u) \approx \sum_{j=0}^{\mathrm{n}} R_{j,p}(u)\check{\boldsymbol{\vartheta}}_j \quad \text{with} \quad u \in \mathcal{I}_u\,, \tag{3}$$

$$\boldsymbol{\eta}(u) \approx \sum_{j=0}^{\mathrm{n}} R_{j,p}(u)\check{\boldsymbol{\eta}}_j \quad \text{with} \quad u \in \mathcal{I}_u\,, \tag{4}$$

where $\check{()}_j$ indicates the jth control value of the quantity; $R_{j,p}$ indicates the jth NURBS basis function of degree p [29]. Velocities and accelerations are discretized in a similar way through $\check{\boldsymbol{\omega}}_j$, $\check{\boldsymbol{v}}_j$, and $\check{\boldsymbol{\alpha}}_j$, $\check{\boldsymbol{a}}_j$. Note that in the explicit formulation, the latter represent the primary variables of the problem.

At time $t = t^{n-1} = h(n-1)$, h being the time step size and n the time step counter, the control values of the incremental displacement and rotation vectors are expressed as follows

$$\check{\boldsymbol{\eta}}_j^{n-1} = h\check{\boldsymbol{v}}_j^{n-1} + \frac{h^2}{2}\,\check{\boldsymbol{a}}_j^{n-1}; \quad \check{\boldsymbol{\vartheta}}_j^{n-1} = h\check{\boldsymbol{\omega}}_j^{n-1} + \frac{h^2}{2}\,\check{\boldsymbol{\alpha}}_j^{n-1}\,, \tag{5}$$

$$\check{\boldsymbol{v}}_j^{n} = \check{\boldsymbol{v}}_{pj}^{n-1} + \frac{h}{2}\,\check{\boldsymbol{a}}_j^{n}; \quad \check{\boldsymbol{\omega}}_j^{n} = \check{\boldsymbol{\omega}}_{pj}^{n-1} + \frac{h}{2}\,\check{\boldsymbol{\alpha}}_j^{n}\,. \tag{6}$$

By exploiting the above equations, consistent kinematic updates of RHSs of Eqs. (1) and (2) can be done [24] leading to the following time-discretized balance equations

$$\mu\boldsymbol{a}^n = \boldsymbol{\psi}^n; \qquad \boldsymbol{j}^n\boldsymbol{\alpha}^n + \widetilde{\boldsymbol{\omega}}^n\boldsymbol{j}^n\boldsymbol{\omega}^n = \boldsymbol{\chi}^n\,.$$

It is noted that, due to Eq. (6), a nonlinear term in $\boldsymbol{\alpha}^n$ appears in the rotational balance equation. Therefore a linearization is needed leading to the following system of equations

$$\mu\sum_{j=0}^{\mathrm{n}} R_j\check{\boldsymbol{a}}_j^n = \boldsymbol{\psi}_i^n; \quad \frac{\partial\mathbf{r}_i^n(\hat{\boldsymbol{\alpha}}_i^n)}{\partial\boldsymbol{\alpha}_i^n}\sum_{j=0}^{\mathrm{n}} R_j\delta\check{\boldsymbol{\alpha}}_j^n = -\hat{\mathbf{r}}_i^n\,.$$

The complete formulation including the discretizatin of the boundary conditions (not reported here) is available in [24].

4.2 Implicit (material) Newmark scheme

The material form of the Newmark algorithm for $\mathrm{SO}(3)$ [27] is given as follows

$$\mathbf{R}^{n+1} = \mathbf{R}^n \exp(\widetilde{\boldsymbol{\Theta}}^n)\,, \tag{7}$$

$$\boldsymbol{\Theta}^n = h\boldsymbol{W}^n + h^2\left[\left(\frac{1}{2}-\beta\right)\boldsymbol{A}^n + \beta\boldsymbol{A}^{n+1}\right]\,, \tag{8}$$

$$\boldsymbol{W}^{n+1} = \boldsymbol{W}^n + h\left[(1-\gamma)\,\boldsymbol{A}^n + \gamma\boldsymbol{A}^{n+1}\right]\,. \tag{9}$$

The algorithm used to integrate the motion of the beam centroid line is the standard Newmark for nonlinear dynamics, which, for the sake of completeness, is reported in the following

$$\boldsymbol{c}^{n+1} = \boldsymbol{c}^n + \boldsymbol{\eta}^n\,, \tag{10}$$

$$\boldsymbol{\eta}^n = h\boldsymbol{v}^n + h^2\left[\left(\frac{1}{2}-\beta\right)\boldsymbol{a}^n + \beta\boldsymbol{a}^{n+1}\right]\,, \tag{11}$$

$$\boldsymbol{v}^{n+1} = \boldsymbol{v}^n + h\left[(1-\gamma)\,\boldsymbol{v}^n + \gamma\boldsymbol{a}^{n+1}\right]\,. \tag{12}$$

In the implicit formulations the balance equations are written at t^{n+1} as follows

$$-\mu\mathbf{R}^{\mathsf{T}n+1}\boldsymbol{a}^{n+1} + \widetilde{\boldsymbol{K}}^{n+1}\mathbb{C}_N\boldsymbol{\Gamma}_N^{n+1} + \mathbb{C}_N\boldsymbol{\Gamma}_{N,s}^{n+1} + \mathbf{R}^{\mathsf{T}n+1}\bar{\boldsymbol{n}}^{n+1} = \mathbf{0}\,, \tag{13}$$

$$\begin{aligned}&-(\boldsymbol{J}\boldsymbol{A}^{n+1} + \widetilde{\boldsymbol{W}}^{n+1}\boldsymbol{J}\boldsymbol{W}^{n+1}) + \widetilde{\boldsymbol{K}}^{n+1}\mathbb{C}_M\boldsymbol{K}_M^{n+1} + \\ &\mathbb{C}_M\boldsymbol{K}_{M,s}^{n+1} + \mathbf{R}^{\mathsf{T}n+1}\boldsymbol{c}_{,s}^{n+1} \times \mathbb{C}_N\boldsymbol{\Gamma}_N^{n+1} + \mathbf{R}^{\mathsf{T}n+1}\bar{\boldsymbol{m}}^{n+1} = \mathbf{0}\,,\end{aligned} \tag{14}$$

The geometrically consistent linerization of the above equations and the boundary conditions (not reported here) is discussed in detail in [25]. Once linearized equations are obtained, space discretizaion is introduced as follows

$$\delta\boldsymbol{\Theta}^{n+1}(u) = \sum_{j=0}^{\mathrm{n}} R_{j,p}(u)\delta\check{\boldsymbol{\Theta}}_j^{n+1} \quad \text{with} \quad u \in \mathcal{I}_u\,, \tag{15}$$

$$\delta\boldsymbol{\eta}^{n+1}(u) = \sum_{j=0}^{\mathrm{n}} R_{j,p}(u)\delta\check{\boldsymbol{\eta}}_j^{n+1} \quad \text{with} \quad u \in \mathcal{I}_u\,, \tag{16}$$

where incremental rotations and displacements $\delta\check{\boldsymbol{\Theta}}_j^{n+1}$ and $\delta\check{\boldsymbol{\eta}}_j^{n+1}$ represent the primary variable of the implicit formulation. Let $\delta\check{\boldsymbol{\Theta}}_j^{n+1,k}, \delta\check{\boldsymbol{\eta}}_j^{n+1,k}$ be the solution of the linearized system at the iteration kth. Iteration updates are based on the following consistent scheme (we refer to [25] for a comprehensive discussion of the update formulas)

$$\boldsymbol{c}_i^{n+1,k+1} = \sum_{j=0}^{\mathrm{n}} R_j(\check{\boldsymbol{p}}_j^{n+1,k} + \delta\check{\boldsymbol{\eta}}_j^{n+1,k}); \quad \mathbf{R}_i^{n+1,k+1} = \mathbf{R}_i^{n+1,k}\exp(\delta\widetilde{\boldsymbol{\Theta}}_i^{n+1,k})$$

5 NUMERICAL RESULTS

5.1 Cantilever beam

The test, originally proposed in [30], consists of a beam of length $1\,\mathrm{m}$ and with a square cross section with side $0.01\,\mathrm{m}$. The Young's modulus is $E = 210 \times 10^9\,\mathrm{N/m^2}$, the Poisson's ratio is $\nu = 0.2$ and the material density is $\rho = 7800\,\mathrm{kg/m^3}$. With respect to a Cartesian reference system (x_1, x_2, x_3), initially the beam axis is placed along x_2 and the deformation occurs in the (x_2, x_3) plane due to a constant concentrated transversal tip force $\bar{n}_{c_3}$. In Figure 3 the time histories of the beam tip displacements are shown. Two load intensities: $\bar{n}_{c_3} = -10\,\mathrm{N}$ and $\bar{n}_{c_3} = -100\,\mathrm{N}$ are considered. The loads are applied with constant intensity for a duration of $0.5\,\mathrm{s}$ through a step-function without any ramp. For both cases $p = 4$ and $\mathrm{n} = 20$. An excellent agreement is found with [30] (for the small amplitude vibrations case) and between the explicit (see above and [24]) and implicit (see above and [25]) formulations for both small and large amplitude vibrations cases. The implicit formulation appears particularly efficient since it is able to reproduce very fast nonlinear dynamics with impulsive loads (no load ramp functions are applied to any of the two load intensities) with a time step 500 times larger than the explicit formulation. Note that four iterations per time step are required in the Newton-Raphson algorithm with a tolerance on the L_2 norm of the incremental vector of 10^{-10} .

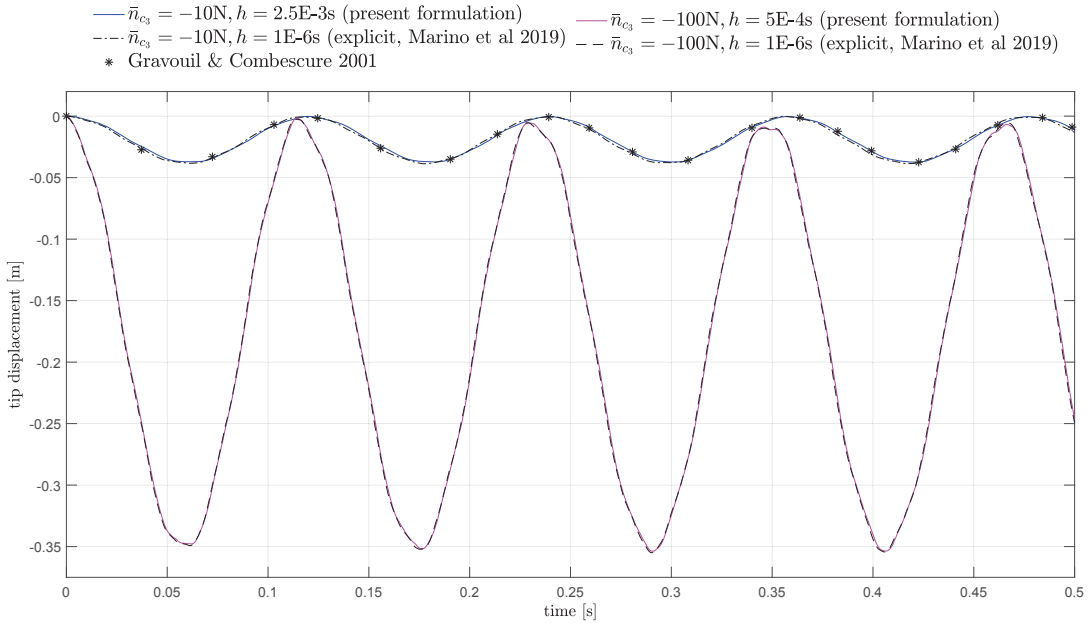

Figure 3: Tip displacement of a cantilever beam subjected to a tip transversal load F_3 with two different intensities. In both cases $p = 4$ and $\mathrm{n} = 20$. Comparisons are made with results obtained in Marino et al 2019 [24] and Gravouil & Combescure 2001 [30].

In Figure 4 four snapshots of the deformed beam are shown. To assess the higher-order space-accuracy of the method when fast and large motions occur, in Figure 5 we show the convergence curves of the L_2 norm of the error for the load case $\bar{n}_{c_3} = -100\,\mathrm{N}$. The error is calculated as $err_{L_2} = ||\boldsymbol{u}^r - \boldsymbol{u}^h||_{L_2}/||\boldsymbol{u}^r||_{L_2}$, where $\boldsymbol{u}^h$ and $\boldsymbol{u}^r$ are the approximate and reference vertical displacements, respectively, evaluated at $t = 1\,\mathrm{ms}$. The reference solution $\boldsymbol{u}^r$ is obtained with $p = 6$, $\mathrm{n} = 80$ and a time step $h = 1 \times 10^{-7}\,\mathrm{s}$.

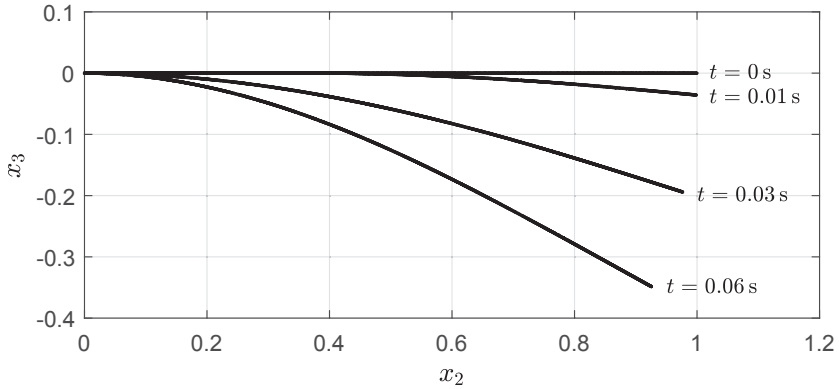

Figure 4: Explicit formulation. Snapshots of a cantilever beam subjected to a tip force $F_3 = -100\,\mathrm{N}$. $p = 4$, $n = 20$, $h = 1 \times 10^{-6}\,\mathrm{s}$. Identical results were obtained with the implicit formulation with $h = 5 \times 10^{-4}$.

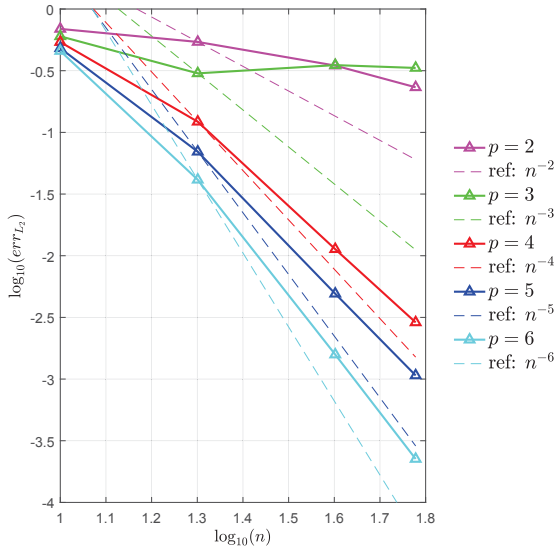

Figure 5: Explicit formulation. L_2 norm of error vs. number of collocation points for a cantilever beam under an in-plane transversal tip force with NURBS basis functions of degrees $p = 2, \ldots, 6$. Dashed lines indicate reference orders of convergence.

5.2 Swinging flexible pendulum

The test consists of an initially straight beam of length $1\,\mathrm{m}$ with a circular cross section of diameter $0.01\,\mathrm{m}$. The Young's modulus is $E = 5 \times 10^6\,\mathrm{N/m^2}$, the Poisson's ratio is $\nu = 0.5$ and the material density is $\rho = 1100\,\mathrm{kg/m^3}$. The beam, initially placed along x_2, is hinged at the end located at $(0, 0, 0)$ and is free at the other end. The motion occurs under the effect of the gravity only.

Figure 6 shows eleven snapshots taken from time 0 to $1\,\mathrm{s}$ with increments of $0.1\,\mathrm{s}$. Results associated with different combinations of basis function degrees, number of collocation points and time step sizes obtained with the implicit formulation are compared. Up to approximately $0.5\,\mathrm{s}$, the results of all cases are almost indistinguishable. After that time, the results with $p = 4$ exhibit some loss of accuracy, while the results with $p = 6$ are always very accurate, also when using a coarser mesh (red line) or when doubling the time step size (green line), indicating that the error due to the space discretization dominates and can be easily (and efficiently) reduced

by order elevation.

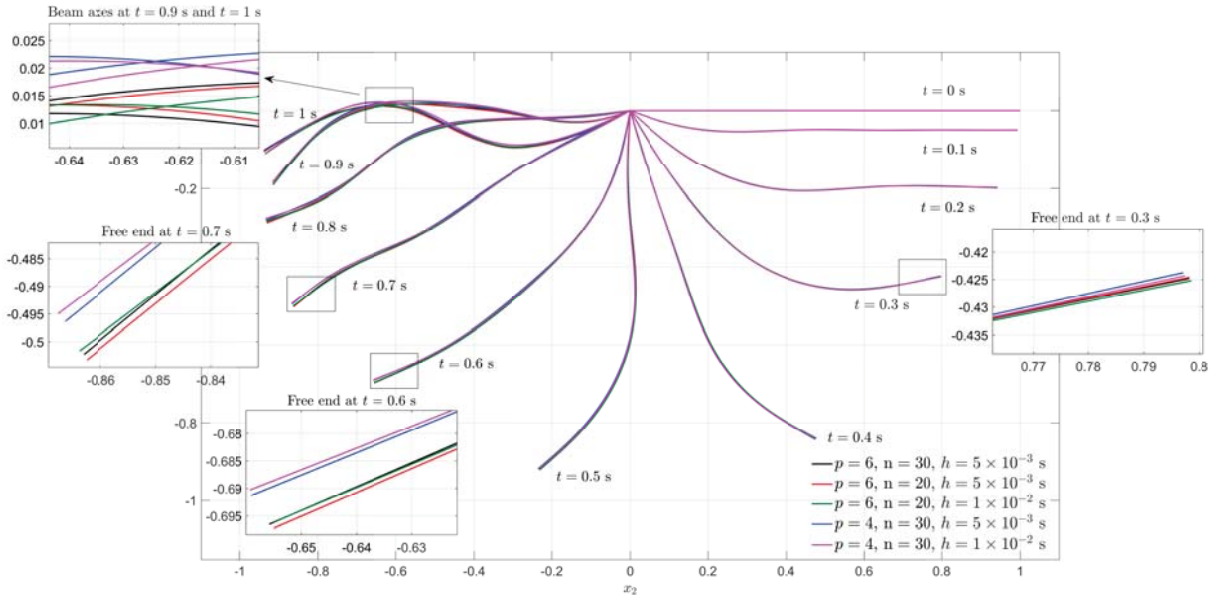

Figure 6: Implicit formulation. Snapshots of a swinging flexible pendulum subjected to gravity only from time 0 to $1\,\mathrm{s}$ with increments of $0.1\,\mathrm{s}$ for different basis function degrees, number of collocation points and time step spans [25].

Figure 7 shows the vertical tip displacement. Comparisons are made with results obtained in [24] (explicit), [25] (implicit), Lang et al 2011 [31] and Weeger et al 2017 [23].

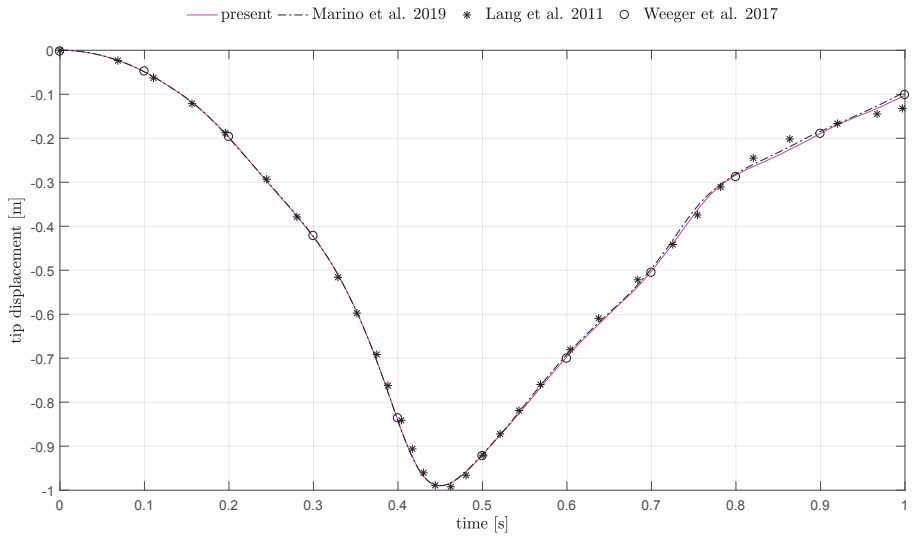

Figure 7: Vertical tip displacement of a swinging flexible pendulum. Comparisons are made with results obtained in Marino et al 2019 [24], Lang et al 2011 [31] and Weeger et al 2017 [23]. Results of the present formulation are obtained with $p = 6$, $\mathrm{n} = 30$, $h = 5 \times 10^{-3}\,\mathrm{s}$ [25].

5.3 Three-dimensional flying beam

The test, proposed originally by Simo & Vu-Quoc in [27], consists of an initially straight free flexible beam with length $L = 10$ placed in the plane (x_2, x_3) subjected at the lower end

to three different time-varying concentrated loads applied simultaneously (Figure 10). Under these loads the beam undergoes a forward translation due to $\bar{n}_{c_2}$, a forward tumbling due to $\bar{m}_{c_1}$ and an out-of-plane deformation due to $\bar{m}_{c_3}$.

The convergence curves of the L_2 norm of the error evaluated at $t = 2\,\mathrm{s}$ vs. the number of collocation points are shown in Figure 8. The error is calculated as above using a reference solution $\boldsymbol{u}^r$ obtained with $p = 8$, $\mathrm{n} = 200$ (approximately 2.3 on the abscissa of Figure 8) and $h = 0.1$. Very good convergence rates are observed up to $p = 5$. They are p for even degrees and $p - 1$ for odd degrees, which is the typical behavior in isogeometric collocation using Greville points [1, 2, 20]. For higher degrees, especially for $p = 8$, as the number of collocation points increases, the temporal error becomes dominant and slightly affects the quality of the convergence rate.

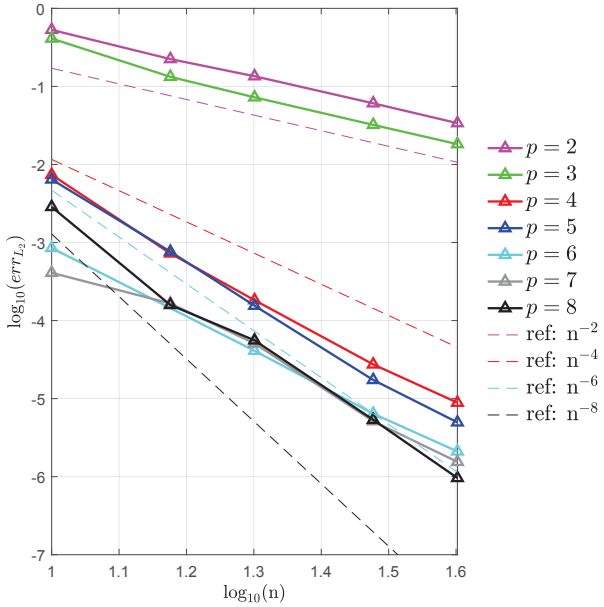

Figure 8: Implicit formulation. L_2 norm of the error evaluated at $t = 2\,\mathrm{s}$ vs. the number of collocation points for the free flying beam for NURBS basis functions of degrees $p = 2, \ldots, 8$. Dashed lines indicate reference orders of convergence. Reference solution computed with $p = 8$, $\mathrm{n} = 200$, $h = 0.1$.

For the implicit formulation, with our choice of β and γ, the standard Newmark time integration scheme is second-order accurate in time [27]. To verify that this attribute is preserved in the implicit IGA-C formulation on $\mathrm{SO}(3)$, we show in Figure 9 the error in L_2 norm associated with time step sizes of 0.05, 0.1, and 0.2. The error is evaluated by comparing the beam configuration at $t = 5$ with a reference solution obtained with $h = 0.01$. In all cases $p = 6$ and $\mathrm{n} = 60$. A perfectly quadratic rate is observed. Figure 10 (right panel) shows some snapshots of the beam centroid line. Results associated with five combinations of p, h, and n are shown. When the largest time step is considered ($h = 0.2$), as expected, the temporal error dominates the spatial one. Reducing the time step size to 0.1, which is more appropriate for this application [27], the accuracy increases significantly. Although unconditional stability is not formally proved in the present nonlinear context, it is noted the high stability of the method even with very large time step sizes. Figure 11 shows snapshots from time 0 to 11.5 with increments of 0.1 in a three-dimensional view.

Very similar results (not reported here) are obtained with the explicit formulations with $h = 1 \times 10^{-5}\,\mathrm{s}$ (see [24]).

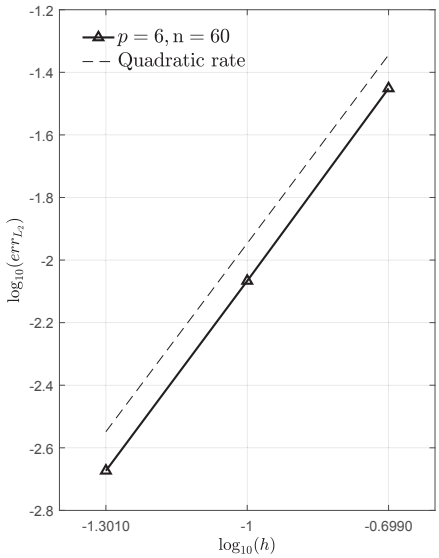

Figure 9: Implicit formulation. L_2 norm of the error vs. time step sizes of 0.05, 0.1, 0.2 for the free flying beam. The error is evaluated by comparing the beam configuration at $t = 5$ with a reference solution obtained with $h = 0.01$. In all cases $p = 6$ and $\mathrm{n} = 60$.

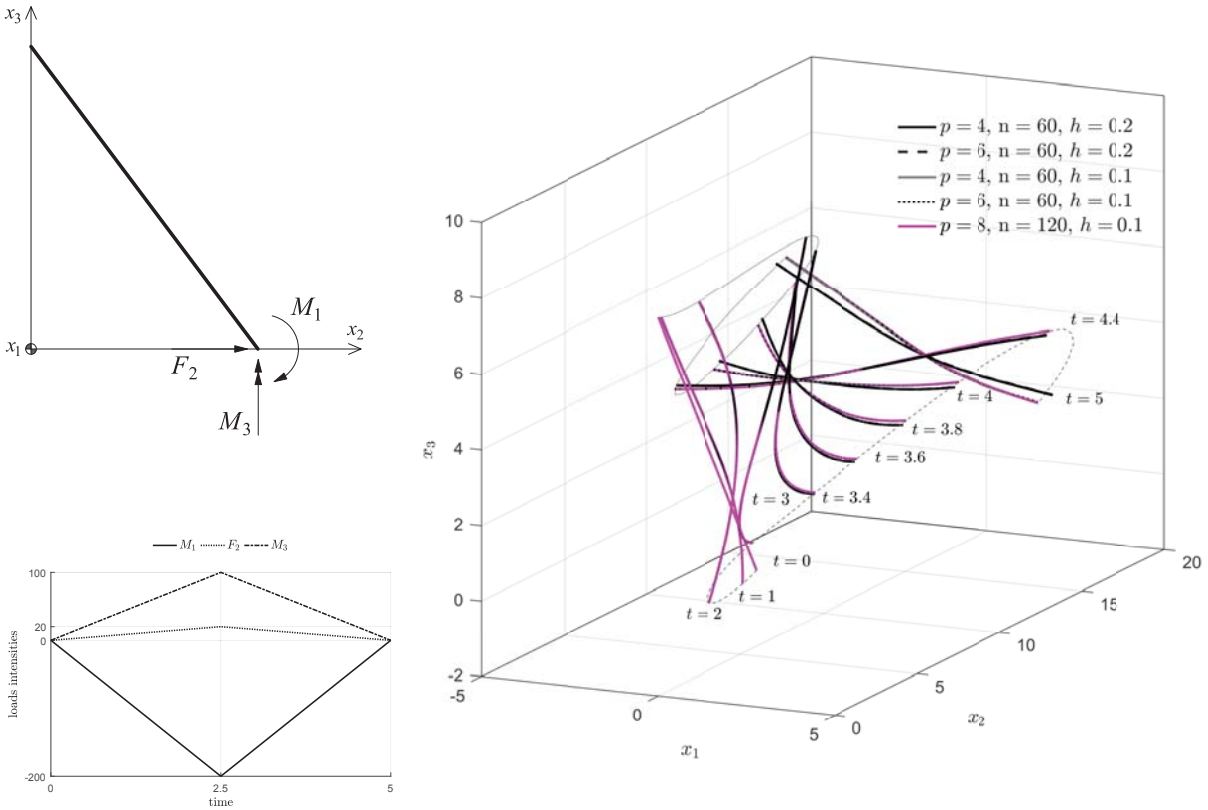

Figure 10: Implicit formulation. Flying flexible beam: initial configuration and loads (left panels). Snapshots in the early tumbling stage for different combinations of polynomial degrees and time step sizes (right panel) [25].

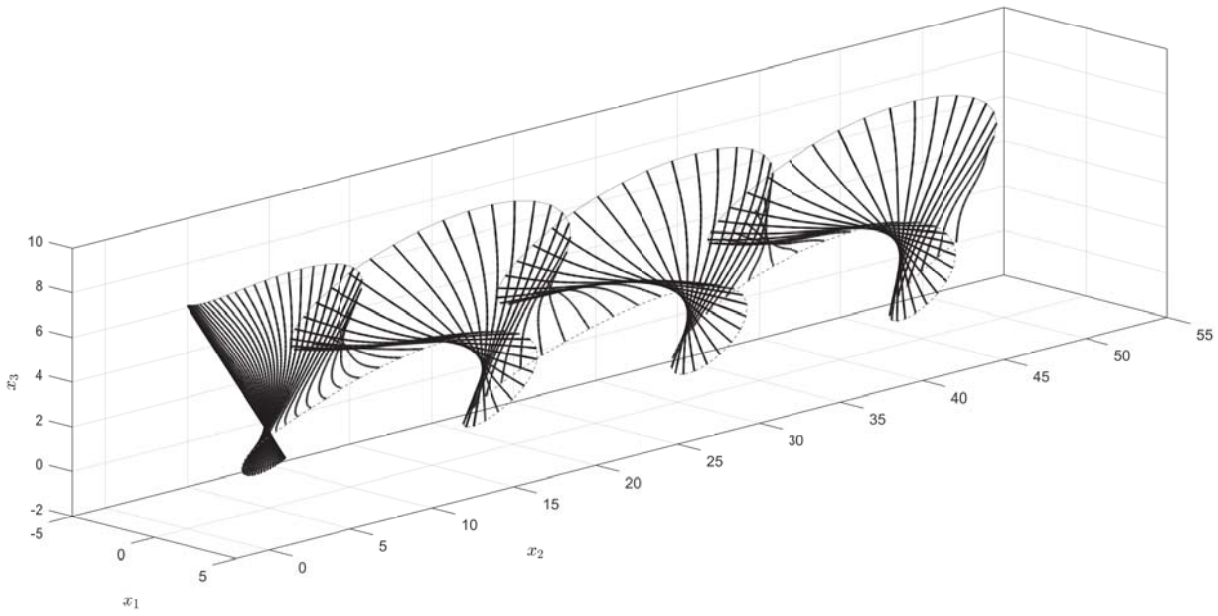

Figure 11: Implicit formulation. Three-dimensional view of the flying flexible beam. Snapshots from time 0 to 11.5 with increments of 0.1 [25].

6 CONCLUSIONS

Both explicit and implicit formulations are geometrically consistent, high-order accurate in space and very efficient. In the explicit formulation, RHSs of the balance equations are obtained by means of consistent update of the kinematic quantities at previous time step. The nonlinear term associated with the angular acceleration has a negligible effect on the overall efficiency of the method since the Newton-Raphson algorithm converges always in one iteration regardless of magnitude and rate of the rotations. The formulation we developed is meant as the basis on which a fully explicit formulation can be developed. With *fully explicit* we mean not only the time integration scheme, but also no equation solving. This can be achieved by developing a suitable mass lumping technique [22] suitable for nonlinear beams.

The implicit method is very stable, even with very large time step sizes, and is able to capture very fast nonlinear dynamics with a remarkable advantage in terms of time step size compared to the explicit version. Order elevation improves the overall accuracy significantly and, in a context where efficiency is one of the major goals, this is a remarkable attribute. Main future developments should be oriented towards energy and momentum preserving IGA-C methods.

REFERENCES

[1] F. Auricchio, L. Beirão Da Veiga, T. J. R. Hughes, A. Reali, G. Sangalli, Isogeometric Collocation Methods, Mathematical Models and Methods in Applied Sciences 20 (11) (2010) 2075–2107.

[2] F. Auricchio, L. Beirão da Veiga, T. J. R. Hughes, A. Reali, G. Sangalli, Isogeometric collocation for elastostatics and explicit dynamics, Computer Methods in Applied Mechanics and Engineering 249-252 (2012) 2–14.

[3] T. Hughes, J. Cottrell, Y. Bazilevs, Isogeometric analysis: CAD, finite elements, NURBS, exact geometry and mesh refinement, Computer Methods in Applied Mechanics and Engineering 194 (39-41) (2005) 4135–4195.

[4] Y. Bazilevs, L. Beirão da Veiga, J. Cottrell, T. J. R. Hughes, G. Sangalli, Isogeometric analysis: approximation, stability and error estimates for h-refined meshes, Mathematical Models and Methods in Applied Sciences 16 (07) (2006) 1031–1090.

[5] T. J. R. Hughes, A. Reali, G. Sangalli, Duality and unified analysis of discrete approximations in structural dynamics and wave propagation: Comparison of p-method finite elements with k-method NURBS, Computer Methods in Applied Mechanics and Engineering 197 (49-50) (2008) 4104–4124.

[6] L. Beirão da Veiga, A. Buffa, J. Rivas, G. Sangalli, Some estimates for h-p-k-refinement in isogeometric analysis., Numerische Mathematik 118 (2011) 271–305.

[7] D. Schillinger, J. Evans, A. Reali, M. Scott, T. J. R. Hughes, Isogeometric collocation: Cost comparison with Galerkin methods and extension to adaptive hierarchical NURBS discretizations, Computer Methods in Applied Mechanics and Engineering 267 (2013) 170–232.

[8] L. Beirão da Veiga, C. Lovadina, a. Reali, Avoiding shear locking for the Timoshenko beam problem via isogeometric collocation methods, Computer Methods in Applied Mechanics and Engineering 241-244 (2012) 38–51.

[9] F. Auricchio, L. Beirão da Veiga, J. Kiendl, C. Lovadina, a. Reali, Locking-free isogeometric collocation methods for spatial Timoshenko rods, Computer Methods in Applied Mechanics and Engineering 263 (2013) 113–126.

[10] J. Kiendl, F. Auricchio, T. Hughes, A. Reali, Single-variable formulations and isogeometric discretizations for shear deformable beams, Computer Methods in Applied Mechanics and Engineering 284 (2015) 988–1004.

[11] J. Kiendl, F. Auricchio, A. Reali, A displacement-free formulation for the Timoshenko beam problem and a corresponding isogeometric collocation approach, Meccanica (2017) 1–11.

[12] G. Balduzzi, S. Morganti, F. Auricchio, Non-prismatic Timoshenko-like beam model: Numerical solution via isogeometric collocation, Computers & Mathematics with Applications 74 (7) (2017) 1531–1541.

[13] E. Marino, S. F. Hosseini, A. Hashemian, A. Reali, Effects of parameterization and knot placement techniques on primal and mixed isogeometric collocation formulations of spatial shear-deformable beams with varying curvature and torsion, Computers & Mathematics with Applications (jun 2020). doi:10.1016/j.camwa.2020.06.006.

[14] A. Reali, H. Gomez, An isogeometric collocation approach for Bernoulli-Euler beams and Kirchhoff plates, Computer Methods in Applied Mechanics and Engineering 284 (2015) 623–636.

[15] J. Kiendl, F. Auricchio, L. Beirão da Veiga, C. Lovadina, A. Reali, Isogeometric collocation methods for the Reissner-Mindlin plate problem, Computer Methods in Applied Mechanics and Engineering 284 (2015) 489–507.

[16] J. Kiendl, E. Marino, L. De Lorenzis, Isogeometric collocation for the Reissner-Mindlin shell problem, Computer Methods in Applied Mechanics and Engineering 325 (2017) 645–665.

[17] F. Maurin, F. Greco, L. Coox, D. Vandepitte, W. Desmet, Isogeometric collocation for Kirchhoff-Love plates and shells, Computer Methods in Applied Mechanics and Engineering 329 (2018) 396–420.

[18] E. Marino, Isogeometric collocation for three-dimensional geometrically exact shear-deformable beams, Computer Methods in Applied Mechanics and Engineering 307 (2016) 383–410.

[19] O. Weeger, S.-K. Yeung, M. L. Dunn, Isogeometric collocation methods for Cosserat rods and rod structures, Computer Methods in Applied Mechanics and Engineering 316 (2017) 100–122.

[20] E. Marino, Locking-free isogeometric collocation formulation for three-dimensional geometrically exact shear-deformable beams with arbitrary initial curvature, Computer Methods in Applied Mechanics and Engineering 324 (2017) 546–572.

[21] F. Maurin, F. Greco, S. Dedoncker, W. Desmet, Isogeometric analysis for nonlinear planar Kirchhoff rods: Weighted residual formulation and collocation of the strong form, Computer Methods in Applied Mechanics and Engineering (2018).

[22] J. A. Evans, R. R. Hiemstra, T. J. R. Hughes, A. Reali, Explicit higher-order accurate isogeometric collocation methods for structural dynamics, Computer Methods in Applied Mechanics and Engineering 338 (2018) 208–240.

[23] O. Weeger, B. Narayanan, M. L. Dunn, Isogeometric collocation for nonlinear dynamic analysis of Cosserat rods with frictional contact, Nonlinear Dynamics (2017) 1–15.

[24] E. Marino, J. Kiendl, L. De Lorenzis, Explicit isogeometric collocation for the dynamics of three-dimensional beams undergoing finite motions, Computer Methods in Applied Mechanics and Engineering 343 (2019) 530–549.

[25] E. Marino, J. Kiendl, L. De Lorenzis, Isogeometric collocation for implicit dynamics of three-dimensional beams undergoing finite motions, Computer Methods in Applied Mechanics and Engineering 356 (2019) 548–570.

[26] P. Krysl, L. Endres, Explicit Newmark/Verlet algorithm for time integration of the rotational dynamics of rigid bodies, International Journal for Numerical Methods in Engineering 62 (15) (2005) 2154–2177.

[27] J. C. Simo, L. Vu-Quoc, On the dynamics in space of rods undergoing large motions — A geometrically exact approach, Computer Methods in Applied Mechanics and Engineering 66 (2) (1988) 125–161.

[28] J. Mäkinen, Rotation manifold SO(3) and its tangential vectors, Computational Mechanics 42 (6) (2008) 907–919.

[29] L. Piegl, W. Tiller, The NURBS Book, Springer-Verlag, New York, NY, 1997.

[30] A. Gravouil, A. Combescure, Multi-time-step explicit-implicit method for non-linear structural dynamics, International Journal for Numerical Methods in Engineering 50 (1) (2001) 199–225.

[31] H. Lang, J. Linn, M. Arnold, Multi-body dynamics simulation of geometrically exact Cosserat rods, Multibody System Dynamics 25 (3) (2011) 285–312.

EURODYN 2020
XI International Conference on Structural Dynamics
M. Papadrakakis, M. Fragiadakis, C. Papadimitriou (eds.)
Athens, Greece, 23-26 November 2020

ANALYTICAL-NUMERICAL MODELING OF FLEXIBLE PYLONS FOR STRUCTURAL HEALTH MONITORING

George D. Manolis[1], George Dadoulis[2], Stylianos I. Pardalopoulos[3] and Kosmas Dragos[4]

[1] Department of Civil Engineering
Aristotle University, Thessaloniki 54124, Greece
e-mail: gdm@civil.auth.gr

[2] Department of Civil Engineering
Aristotle University, Thessaloniki 54124, Greece
georgidi@email.address

[3] Department of Civil Engineering
Aristotle University, Thessaloniki 54124, Greece
sjpard@gmail.com

[4] Chair of Computing in Civil Engineering
Bauhaus University Weimar, 99423 Weimar, Germany
kosmas.dragos@uni-weimar.de

Keywords: Pylons, Antennas, Flexible structures, Structural monitoring, Ambient vibrations, Dynamic loads, Elastic waveguides

Abstract. *The monitoring of flexible structures such towers, antennas and pylons comprising critical infrastructure for power transmission and telecommunications is necessary in order to ensure their continuous operation. This particular field of engineering comes under the umbrella of structural health monitoring, which in recent years has been given high priority in developed countries. There, the built infrastructure is both extensive, encompassing diverse groups of systems such as energy, telecommunication, utility and transportation networks, while at the same time is ageing rapidly. The goal is to set up monitoring schemes with a stand-alone configuration and a wireless transmission of data to central locations for further processing. Thus, it becomes necessary for the sensors employed to have some structural analysis capabilities that can be used in tandem with their data processing functions, all within an artificial intelligence environment. To this end, we develop analytical models for vibrations in elastic waveguides that model flexible structures of variable cross-section and demonstrate their efficiency and accuracy through comparisons with finite element models.*

1 INTRODUCTION

Broadly speaking, infrastructure can be classified as the built environment plus the necessary networks for the supply of energy, water, communications and transportation. Since network operation must remain continuous, Structural Health Monitoring (SHM) is required as a necessary step in setting up maintenance protocols [1]. The data streams generated by monitoring must be evaluated with the aid of Artificial Intelligence (AI) algorithms that will allow authorities to reach rational conclusions regarding the current state of network operation and to assess the need for maintenance, repair, retrofit and rehabilitation [2]. Within this cycle, it is necessary to use numerical models to analyze the current state of the structure as needed [3]. The usual path followed nowadays for modelling either the structure or the structural network under consideration is the Finite Element Method (FEM). This usually requires the setup of meshes for discretizing the continuum that are quite detailed and possibly cannot be accommodated within wireless sensor nodes with limited computational resources and power supply. It then becomes necessary to introduce analytical models with closed-form solutions [4] which can be programmed using computer platforms such as Java [5]. This representation is both accurate and efficient and requires small amounts of computing power. This way, the data streams generated by ambient vibrations and other external loads can be processed and compared with computed response markers [6, 7]. Then, these data streams will be either discarded or transmitted to a central processing unit for further evaluation. The final goal is to produce reliable information through SHM to decide if the structure in question is in need of repairs.

Flexible structures such as antennas and pylons used in power transmission and in telecommunications can be efficiently modelled as elastic waveguides, i.e. base-supported beams of variable cross-section with a continuous mass distribution. In general, these waveguides undergo axial, flexural and torsional vibrations, see Fig. 1. Their motion is governed by partial differential equations in a space variable x (m) and in time t (s). Invariably, a transformation to the frequency domain follows, whereby ordinary differential equations result that are parametric in the frequency ω (rad/s). The change in cross-section along the length results in dispersion phenomena that would otherwise be absent. Furthermore, it might be that the aforementioned three types of vibration patterns are coupled, but this would result in a problem that is probably intractable in terms of a closed-form-solution. Practically speaking, for a circular cylindrical cross-section only flexural vibrations might be influenced by the presence of an axial force, and this would depend on the external loading configuration and frequency content [8]. In here, we will focus on the axial vibration problem as a first step in exploring the suitability of these models to SHM.

2 MECHANICAL MODEL FOR STRUCTURES OF VARIABLE CROSS-SECTION

Figure 1 depicts a free-standing waveguide placed along the X-axis. For transverse $f(x,t)$ and longitudinal $p(x,t)$ loads distributed along the length of the waveguide, plus initial conditions, a bending moment $M(x,t)$, a shear force $Q(x,t)$ and an axial force $N(x,t)$ develop across the cross-section. Also, $u(x,t)$ and $w(x,t)$ are the axial and transverse displacements, respectively, with $\theta=\partial w/\partial x$ being the slope of the neutral axis. The following definitions for the forces and boundary conditions corresponding to a cantilevered waveguide are given below, with initial conditions assumed to be zero:

$$N = EA(x)(\partial u/\partial x), \qquad M = -EI(x)(\partial w^2/\partial x^2), \qquad Q = -EI(x)(\partial w^3/\partial x^3),$$
$$M(a,t) = Q(a,t) = w(b,t) = w'(b,t) = 0, \quad N(a,t) = u(b,t) = 0 \tag{1}$$

In the above, $EA(x)$ and $EI(x)$ are the aggregate axial and flexural stiffness that varies along the antenna length, $a \le L \le b$. Finally, the alternative notation used here involves primes ($'$) and dots ($\cdot$) to respectively denote differentiation with respect to the spatial coordinate x and time t. We will consider the following type of smooth variation for the flexural stiffness, the axial stiffness and the distributed mass of the waveguide as

$$EI(x) = (EI)_{base}(x/b)^3,\ EA(x) = (EA)_{base}(x/b),\ m(x) = (m)_{base}(x/b) \tag{2}$$

Where EI, EA, m are the reference values at the base $x = b$, with the antenna length being $L = b - a$. The type of variation assumed dictates the type of the partial differential equation that will result. When the equations of motion are transformed in the frequency domain, they become Bessel and Euler equations for the axial and flexural vibrations, respectively.

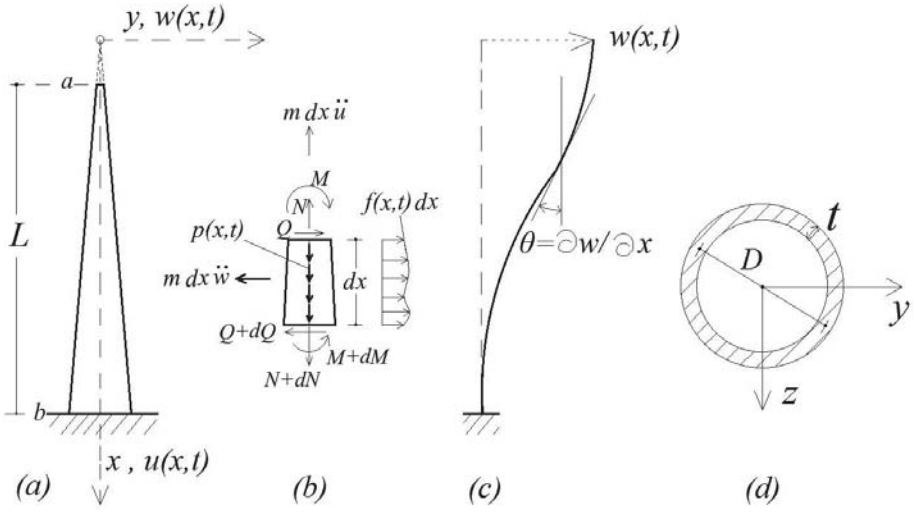

Figure 1: (a) Pylon modelled as base-supported elastic waveguides; (b) longitudinal cross-section of infinitesimal length dx showing the force resultants; (c) deformed pattern; (d) transverse cross-section

3 EQUATIONS OF DYNAMIC EQUILIBRIUM

By considering force and moment equilibrium of the differential segment dx in Fig. 1, we obtain coupled governing equations of dynamic equilibrium for axial and flexural motion as

$$\frac{\partial}{\partial x}\left(EA(x)\,\frac{\partial u(x,t)}{\partial x}\right) - \frac{\partial}{\partial x}\left(Q(x,t)\,\frac{\partial w(x,t)}{\partial x}\right) - m(x)\,\frac{\partial^2 u(x,t)}{\partial t^2} = p(x,t) \tag{3}$$

$$\frac{\partial^2}{\partial x^2}\left(EI(x)\,\frac{\partial^2 w(x,t)}{\partial x^2}\right) - \frac{\partial}{\partial x}\left(N(x,t)\,\frac{\partial w(x,t)}{\partial x}\right) + m(x)\,\frac{\partial^2 w(x,t)}{\partial t^2} = f(x,t) \tag{4}$$

3.1 The time domain

If the coupling terms $\partial/\partial x(Q\cdot\partial w/\partial x)$ in the former and $\partial/\partial x(N\cdot\partial w/\partial x)$ in the latter equation are ignored, then by differentiating the variable stiffness terms we recover the following equations:

$$EA(x)\cdot u'' + (\partial EA(x)/\partial x)\cdot u' - m(x)\cdot \ddot{u} = p(x,t) \quad (5)$$
$$EI(x)\cdot w'''' + 2(\partial EI(x)/\partial x)\cdot w''' + (\partial^2 EI(x)/\partial x^2)\cdot w'' + m(x)\cdot \ddot{w} = f(x,t) \quad (6)$$

Next, by introducing the variable stiffness representations of Eq. (2) and recover the final form for the equations of dynamic equilibrium as follows:

$$(EAx/b)\cdot u'' + (EA/b)\cdot u' - (mx/b)\cdot \ddot{u} = p(x,t) \quad (7)$$

$$(EIx^4/b)\cdot w'''' + 8(EIx^3/b)\cdot w''' + 12(EIx^2/b)\cdot w'' + (mx/b)\cdot \ddot{w} = f(x,t) \quad (8)$$

Remark 1: By examining the uncoupling assertions more carefully, we see that omission of the shear force Q in Eq. (3) implies that $\partial w^3/\partial x^3 = 0$, i.e., we recover a polynomial solution in the spatial coordinate for the transverse displacement in the form of $w(x,t) = g_1(t)x^2 + g_2(t)x + g_3(t)$. A similar state of affairs exists if we neglect the axial force N in Eq. (4), i.e., we get $\partial u/\partial x = 0$ so that $u(x,t) = (a_1 t + a_2)x + (b_1 t + b_2)$. Strictly speaking therefore, Eq. (5) and (6) are no longer mathematically consistent with the original system of Eq. (3) and (4). In essence, what we assume is that axial and flexural vibrations in the waveguide are respectively induced by upwards/downwards travelling pressure (P) and horizontally polarized shear (SH) waves, without conversion from one wave type to another.

3.2 The frequency domain

For harmonic vibrations, we have the displacements as $w(x,t) = W(x)e^{i\omega t}$ and $u(x,t) = U(x)e^{i\omega t}$, where $e^{i\omega t} = \cos(\omega t) + i\sin(\omega t)$, and likewise for the external distributed forces, i.e., $f(x,t) = F(x)e^{i\omega t}$, $p(x,t) = P(x)e^{i\omega t}$. Then,

$$xU'' + U' + a^2 xU(x) = \tilde{P}(x),\ a^2 = (m\omega^2)/EA \quad (9)$$

$$x^4 W(x)'''' + 8x^3 W''' + 12x^2 W'' - \beta^4 xW(x) = \tilde{F}(x),\ \beta^4 = (m\omega^2)/EI \quad (10)$$

Note that both $a(\omega) = \omega/c_p$, $c_p = (E/\rho)^{-1/2}$ (the P-wave speed) and $\beta(\omega)$ are the usual real-valued wavenumbers associated with vibrations of prismatic beams. Also, $\tilde{P}$, $\tilde{F}$ are the scaled spatial variations of the external forces. If the above equations are normalized with respect to the leading derivative terms, we respectively recover a Bessel equation of zero order and an incomplete Euler equation of the fourth order, i.e.,

$$U'' + (1/x)\cdot U' + a^2 \cdot U = \tilde{P} \quad (11)$$
$$W(x)'''' + (8/x)W''' + (12/x^2)W'' - (\beta^4/x^3)W(x) = \tilde{F} \quad (12)$$

Remark 2: We note here that a quadratic variation of the mean radius $D/2$ of a circular cylindrical pylon of constant thickness t yields a complete Euler equation of the fourth order. This will be communicated in future work, since the quadratic variation is a more general representation that can replace the model of Eq. (2). For the above flexural vibration case, although the eigenfrequencies can still be recovered from Eq. (12), the key substitution that will give solutions of the type $W(x) = \sum B_i |x|^{mi}$, $i = 1\ldots4$ will not work.

3.3 Solution for axial vibrations

The homogeneous solutions to the Eq. (11) is

$$U(x) = A_1 J_0(ax) + A_2 Y_0(ax) \tag{13}$$

Where J_0, Y_0 respectively are the Bessel functions of zero order, first and second kind. Next, A_i are constants of integration to be determined from the boundary conditions. For the tapered waveguide with fixity at the base, we have that $U(x = b) = 0$, while for a traction-free condition at the top, we have that $N(x = a) = 0 \rightarrow U'(x = a) = 0$. The second boundary condition requires the first derivative of the displacement solution of Eq. (13). This is accomplished by noting that the spatial derivatives of the Bessel functions are given by the following expressions: $J'_0(ax) = -aJ_1(ax)$, $Y'_0(ax) = -aY_1(ax)$. Now, for the aforementioned homogeneous conditions, constants A_i can only be determined relative to each other. This is done using the displacement derivative evaluated at $x = b$ and setting it equal to zero. Back-substitution into Eq. (13) evaluated at $x = a$ and subsequently also setting it equal to zero yields the following transcendental equation

$$J_0(ab) - \{J_1(aa)/Y_1(aa)\} \cdot Y_0(ab) = 0 \tag{14}$$

An analytical solution for wave number $a_n = \omega_n/c_p$ values which are the roots of the above equation is not possible, and therefore the Newton-Raphson method is used with starting values being the eigenfrequencies ω_n of a reference pylon with constant cross-section. More specifically, if we consider a pylon whose cross-section matches that of the tapered pylon at its base, then $A = 2\pi db$, $m = \rho A$. Closed-form solutions for the displacement vector, the wave numbers, the eigenfrequencies and the eigenfunctions are as follows (Graff, 1975):

$$U(x) = A_1 \sin(ax) + A_2 \cos(ax),\ a_n = (2n - 1)\pi/(2L) \tag{15}$$
$$\omega_n = (2n - 1)\pi c_p/(2L), \quad \varphi_n(x) = \sin(a_n x), \quad n = 1,2,\ldots,\infty$$

Once the eigenfrequencies ω_n of the tapered pylon have been determined, then the corresponding eigenfunctions $\varphi_n(x)$ are the displacements given in Eq. (13), after substitution of the corresponding wave number a_n and with $A_1 = 1$, $A_2 = -J_1(aa)/Y_1(aa)$.

3.4 Modal analysis for axial vibrations

Modal analysis commences with the transformation from the physical displacement coordinates u to the generalized (or modal) coordinates q_i, $i = 1,2,3,\ldots$ by use of the eigenfunctions φ_i as follows:

$$u(x,t) = \sum_{i=1}^{\infty} \left(\varphi_i(x) \cdot q_i(t) \right) \tag{16}$$

Substitution of this expansion into the uncoupled form of the equation of motion, Eq. (4a), pre-multiplication by eigenfunction φ_j and integration over the length of the waveguide gives

$$\sum_{i=1}^{\infty} \left\{ \int_0^L \varphi_j(x) \cdot [EA(x)\varphi'_i(x)]' dx \cdot q_i(t) - \int_0^L \varphi_j(x) \cdot m(x) \cdot \varphi_i(x) dx \cdot \ddot{q}_i(t) \right\} = \sum_{j=1}^{\infty} \int_0^L \varphi_j(x) \cdot p(x,t) dx \tag{17}$$

We note that because of the orthogonality property of the eigenfunctions with respect to the stiffness $EA(x)$ as the weight function, the only non-zero terms remaining are when the two counters coalesce, i.e. $i = j$. This is now followed with integration by parts to shift the spatial derivatives ($'$) outside the brackets to the eigenfunctions $\varphi_i(x)$. Intermediate terms arising in the integration are zero because of the homogeneous spatial boundary conditions. The final result is a system of single degree-of-freedom (SDOF) equations of the form

$$[M]_i \cdot \{\ddot{q}(t)\}_i + [K]_i \cdot \{q(t)\}_i = \{P(t)\}_i \tag{18}$$

where the system matrices involve integration over the waveguide length as

$$[M_i] = \int_0^L m(x) \cdot \varphi^2{}_i(x) dx, \quad [K_i] = \int_0^L EA(x) \{\varphi''{}_i(x)\}^2 dx$$

$$\{P(t)\}_i = \int_0^L \varphi_i(x) \cdot p(x,t) dx$$

As with standard modal analysis, the accuracy achieved in solving for the displacement $u(x,t)$ depends on the number of generalized coordinates $q_i(t)$ retained in the series expansion, which from the previous eigenvalue analysis requires no more than four terms. Finally, the integrals over the length of the waveguide are evaluated by low order Gauss quadrature.

4 NUMERICAL EXAMPLE

We consider a thin-walled steel pylon used, e.g., in supporting electric cable lines for high-speed trains, see Fig. 1. The pylon cross-section has the shape of a ring with mean radius $R=D/2$ and constant thickness t. The length $L = (b - a)$ of the pylon under consideration comprises continuously welded segments for a total length of 12 m, while the base is fixed. Table 1 lists values for the modulus of elasticity E, Poisson's ratio v and the mass density ρ. At any given station $a \le x \le b$, the cross-sectional area is $A = 2\pi Rt$, the principal moment of inertia is $I = \pi R^3 t$ and the mass per unit length is $m = A\rho$. From this information, it is possible to compute both axial $EA(x)$ and flexural $EI(x)$ stiffness, as well as the mass $m(x)$ per length of the pylon. These quantities vary linearly with height for the mass and axial stiffness and cubically for the flexural stiffness, see Eq. (2), with the base of the pylon (btm) considered as the reference point.

E (kPa)	v	ρ (tn/m^3)	a (m)	b (m)
21.0 10^7	0.30	7.85	2.0	14.0

R (m)-outer	t (cm)	A (m^2)-ref	I (m^4)-ref	m (tn/m)-ref
0.20	2.0	0.025	0.0005	0.197

EA (kN)-top	EI (kN·m^2)-top	m (tn/m)-top	EA (kN)-btm	EI (kN·m^2)-btm	m (tn/m)-btm
754,000	15,140	0.028	5,279,000	106,000	0.197

Table 1: Numerical values for the mechanical properties of the steel pylon example.

4.1 Eigenvalue analysis for axial vibrations

As mentioned in sub-section 3.3, we introduce a cantilevered pylon with a constant cross-section whose configuration matches that of the non-homogenous pylon at the base to serve as benchmark for comparison purposes. We now compute its first five eigenfrequencies ω_i and their respective modal masses M_i and stiffnesses K_i, see the left column in Table 2 and also Fig. 3. Similarly, for the tapered pylon, we use the Newton-Raphson method to numerically solve the characteristic polynomial resulting from imposition of the homogeneous boundary conditions to the solution given in Eq. (13). Standard procedure of back-substitution of the recovered eigenfrequencies into the normalized displacement function gives the corresponding eigenfunctions. All these values appear as the right column of Table 2 and in Fig. 3. The computations regarding the tapered pylon were carried out in a Python programming environment [9] requiring negligible running times.

We note that axial vibrations occur at high frequencies, given that the first eigenfrequency of the uniform pylon is 108 Hz and that of the non-uniform one is 146 Hz. Also, the non-uniform pylon consistently has higher values for the eigenfrequencies, because of less mass as compared to the uniform pylon, all other things being equal. Regarding the presence of structural damping in the pylons, it is possible to introduce [10] a complex elasticity modulus in the form $E(1.0+i\eta\omega)$, where the structural damping coefficient η is in the range of 0.1%. This damping is in addition to the dispersion effects for the tapered pylon and results in complex number formalism for the ensuing numerical solution.

Eigenvalue: 1	Eigenvalue: 1
Mi: 1.178 tn	Mi: 0.336655 tn
Ki: 539743.99 kN/m	Ki: 285338.0 kN/m
ωi: 677.04 rad/s	ωi: 920.635 rad/s
fi: 107.75 Hz	fi: 146.524 Hz
Eigenvalue: 2	Eigenvalue: 2
Mi: 1.178 tn	Mi: 0.155565 tn
Ki: 4857695.92 kN/m	Ki: 742137.0 kN/m
ωi: 2031.12 rad/s	ωi: 2184.17 rad/s
fi: 323.26 Hz	fi: 347.621 Hz
Eigenvalue: 3	Eigenvalue: 3
Mi: 1.177 tn	Mi: 0.168852 tn
Ki: 13493599.77 kN/m	Ki: 2.06111e+6 kN/m
ωi: 3385.19 rad/s	ωi: 3493.79 rad/s
fi: 538.77 Hz	fi: 556.054 Hz
Eigenvalue: 4	Eigenvalue: 4
Mi: 1.177 tn	Mi: 0.634078 tn
Ki: 26447455.54 kN/m	Ki: 1.47461e+7 kN/m
ωi: 4739.27 rad/s	ωi: 4822.44 rad/s
fi: 754.28 Hz	fi: 767.516 Hz
Eigenvalue: 5	Eigenvalue: 5
Mi: 1.178 tn	Mi: 1.51583 tn
Ki: 43719263.25 kN/m	Ki: 5.75261e+7 kN/m
ωi: 6093.35 rad/s	ωi: 6160.37 rad/s
fi: 969.79 Hz	fi: 980.453 Hz

Table 2: Steel pylon with constant cross-section (left) and variable cross-section (right): The first five modal masses, modal stiffnesses and eigenvalues

4.2 Comparisons with FEM models

The same cantilevered pylon is now modeled using two types of FEM representations, namely a 'stick' model comprising 2-noded beam elements with 6 degrees-of freedoms (DOF) per node and a 'shell' model comprising 4-noded shell elements with also 6 DOF per node [11]. The convergence study focuses on the axial vibration eigenvalues and examines the necessary number of finite elements along the length and breadth of the pylon to achieve convergence of the results.

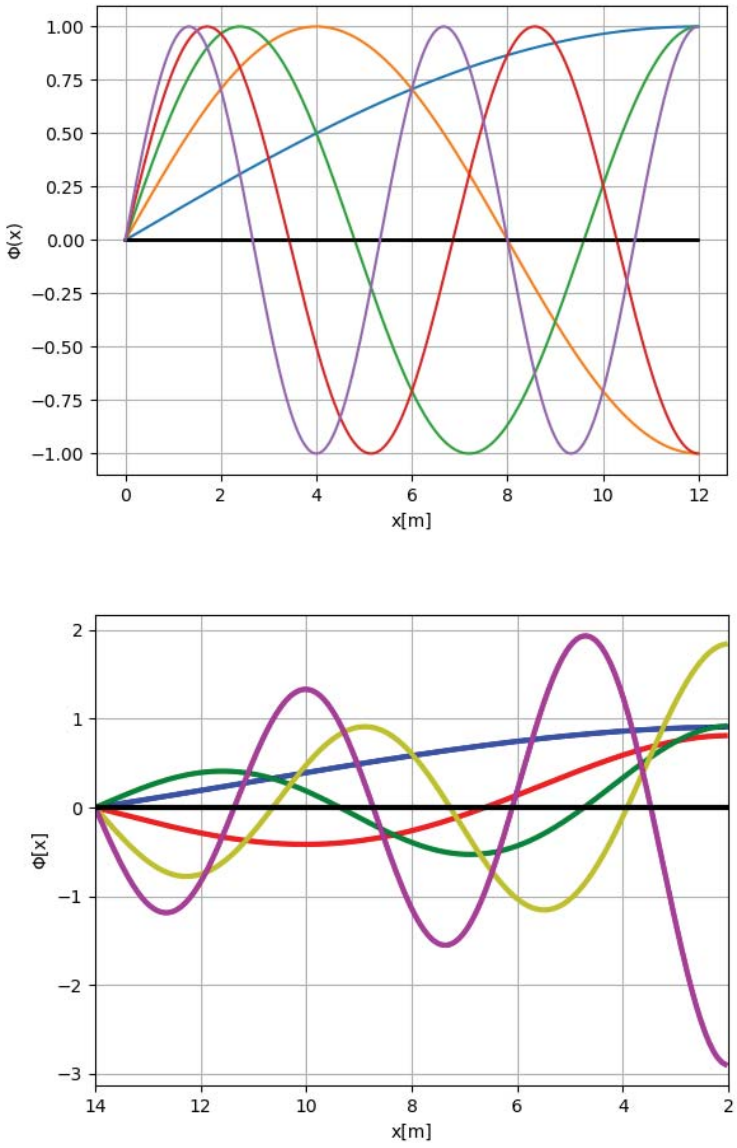

Figure 3: Steel pylon with (top) constant and (bottom) variable cross-section: The first five normalized eigenfunctions $\varphi_i(x)$. Legend: 1 = blue / 2 = red / 3 = green / 4 = yellow / 5 = purple

Starting with the 'stick' model, we begin with 10 uniformly spaced elements for the pylon yielding 60 DOF and reach a maximum of 100 elements resulting in 600 DOF. For the 'shell' model, the smallest acceptable mesh covers the circumference of the cross-section with 3 shell elements spanning 120° sectors each. Therefore, the comparable numbers for the 'shell' model start at 30 elements with 180 DOF and range up to 300 elements with 1800

DOF. Of course, the FEM 'shell' model yields vibration patterns that cannot be captured by the waveguide model, such as 'breathing' modes where the circumference's shape diverges from the original circular one. We see in Fig. 4 that roughly 20 finite elements per length are required in most cases before the eigenfrequencies start to converge, yielding a minimum finite element length of 50 cm. This holds true for both 'stick' and 'shell' models, and we observe that although both FEM models give identical results, they overshoot the analytical waveguide solution by about 2%.

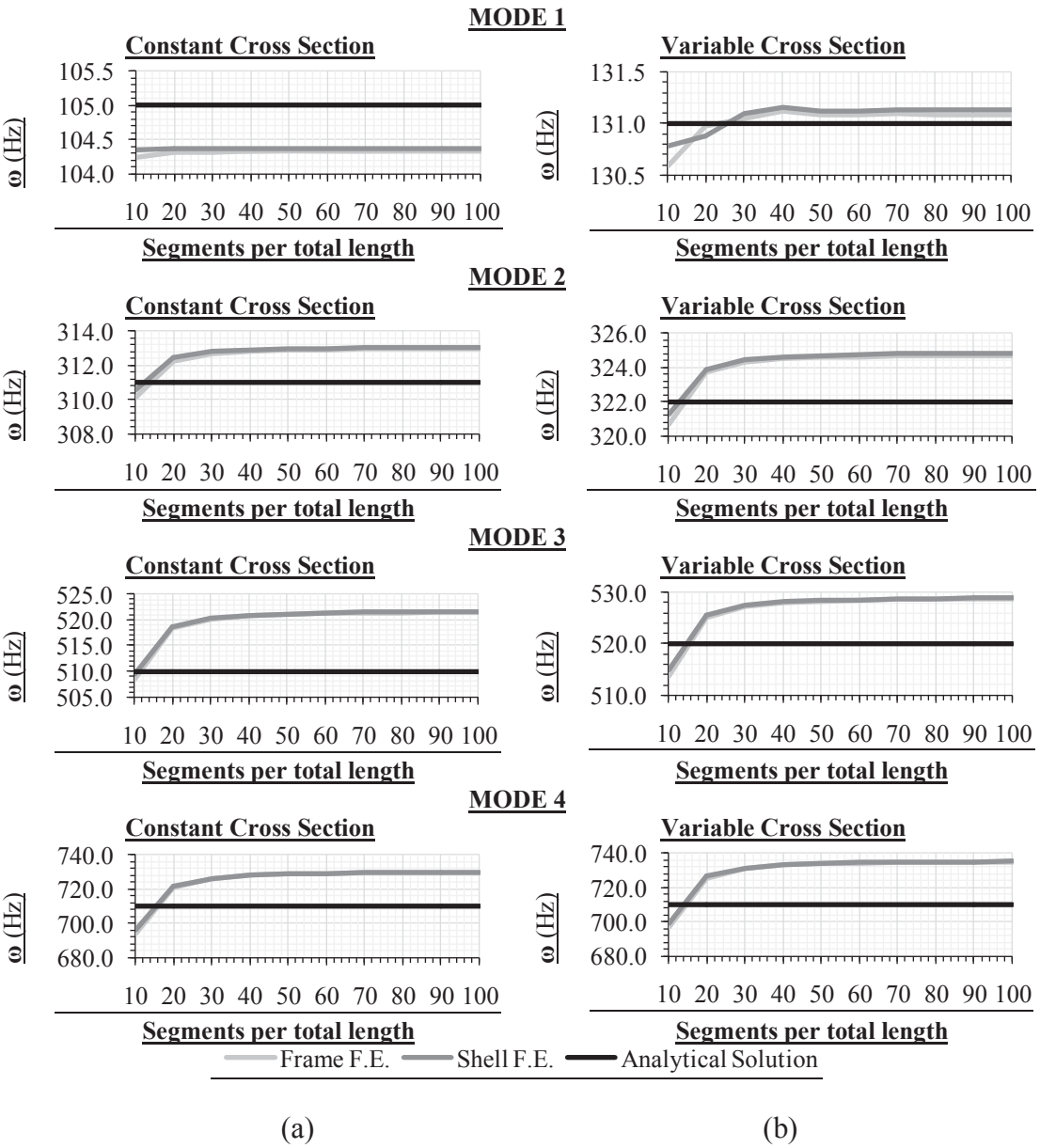

Figure 4: FEM convergence study on the first four axial eigenfrequencies for both (a) constant and (b) variable pylon cross-sections. Note: 3 shell finite elements are used to model the pylon circumference

4.3 Transient axial vibrations

We distinguish two types of quasi-harmonic external loads on pylons supporting electric lines that are generated by the passage of high speed trains: (i) High frequency base accelerations in the vertical direction (axial vibrations) in the range around 50 Hz resulting from the train's wheels running across rails that have minor imperfections; and (ii) low frequency base accelerations in the horizontal direction (flexural vibrations) in the range around 5 Hz as the train moves rapidly forward. Both cases lead to a forcing function in the form $p(x,t) = f(x,t) = -mg\sin(\Omega t)$, where g=9.81 m/s^2 is the acceleration of gravity and Ω (rad/s) is the external frequency of vibration. Focusing on axial vibrations, Fig. 5 is a parametric study summarizing the number of eigenfunctions necessary in the modal analysis to achieve convergence of the transient displacement at the top of the pylon, with the time axis ranging as $0 < t < 0.4$ s. We observe that as the external frequency of vibration increases, so does the number of eigenfunctions necessary for convergence. However, even three eigenfunctions are sufficient, provided the excitation frequency in the axial case does not exceed a value of $f = \Omega/2\pi = 300$ Hz.

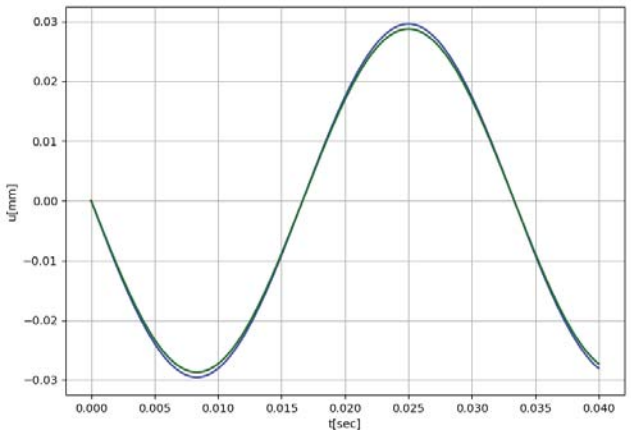

(a)

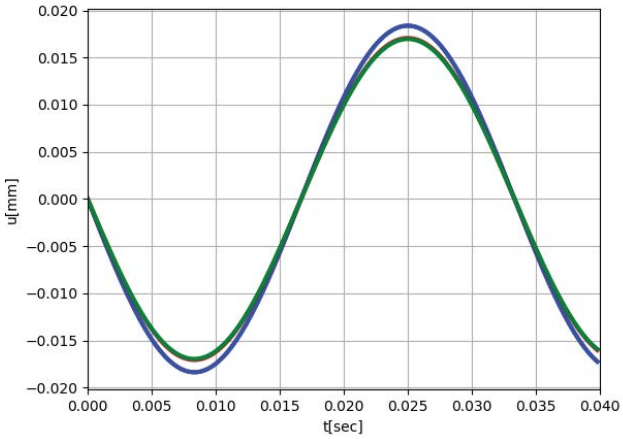

(b)

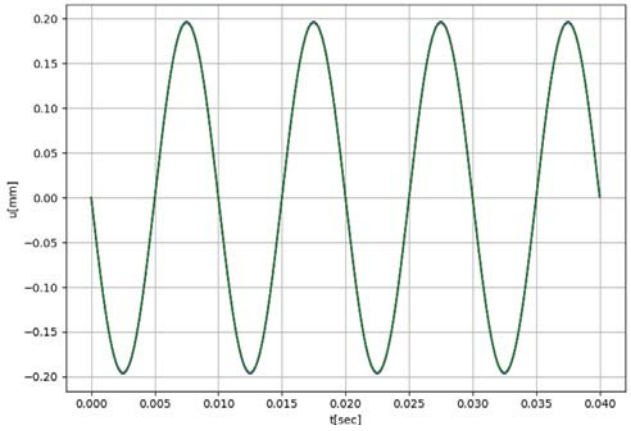

(c)

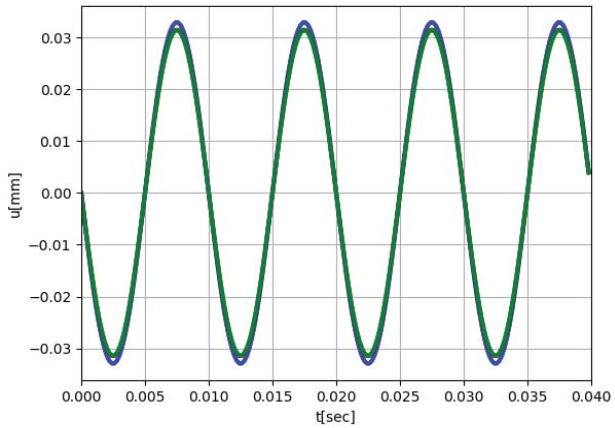

(d)

Figure 5: Modal analysis convergence study for the axial displacement at the top of the steel pylon for a ground acceleration amplitude g = 9.81 m/s^2: (a) Constant and (b) variable pylon cross-sections vibrating at f = 30 Hz and (c) constant and (d) variable pylon cross-sections vibrating at f = 100 Hz .
Legend: 1 (blue), 3 (red), and 5 (green) eigenfunctions are used in the superposition

5 CONCLUSIONS

An analytical model based on elastic waveguides was presented here for determining the dynamic vibrations of flexible structures such as antennas and pylons to environmentally induced loads. The stiffness of these structures may vary with height and both axial and flexural vibrations were considered, with torsional vibrations to be communicated in future work. These solutions are meant to replace large-scale FEM models for reasons of computational economy within the context of real-time data processing in wireless sensor nodes. This is a crucial step in SHM operations, whereby data streams are transmitted by the sensor nodes to a central processing unit only when calculations show that certain tolerance limits are exceed. These limits can be pre-set, but it is necessary to first quantify and then update them over the course of time. To this end, numerical models for monitored structures, which are both accurate and efficient in terms of computing power, must be introduced.

Acknowledgement. The authors acknowledge the German Research Foundation (DFG) program on Initiation of International Collaboration entitled *"Data-driven analysis models for slender structures using explainable artificial intelligence"*, Project No. SM 281/14-1, 2019.

REFERENCES

[1] D.E Adams. *Health Monitoring of Structural Materials and Components: Methods with Applications*. J. Wiley, Chichester, UK, 2007.

[2] B.R. Ellingwood. Risk-informed condition assessment of civil infrastructure: State of practice and research issues. *Structure and Infrastructure Engineering*, 1(1): 7-18, 2007.

[3] A.T. Zimmerman, M. Shiraishi, R.A Swartz and J.P. Lynch. Automated modal parameter estimation by parallel processing within wireless monitoring systems. *ASCE Journal of Infrastructure Systems*, 14(1): 102-113, 2008.

[4] E. Kausel. *Advanced Structural Dynamics*, Cambridge Univ. Press, Cambridge, UK, 2017.

[5] Java (1996). Oracle Corporation, Redwood Shores, CA, USA, 1996. www.java.com

[6] K. Dragos and K. Smarsly. Distributed adaptive diagnosis of sensor faults using structural response data. *Smart Materials and Structures*, 25(10), 105019, 2016.

[7] K. Smarsly and K.H. Law. A migration-based approach towards resource-efficient wireless structural health monitoring. *Advanced Engineering Informatics*, 27(4): 625-635, 2013.

[8] K.F. Graff, K.F. *Wave Motion in Elastic Solids*, Ohio State Univ. Press, Athens, OH, USA, 1975.

[9] Python Software Foundation. Beaverton, OR, USA, 2001. www.python.org

[10] W. Flugge. *Viscoelasticity*. Blaisdell Publishing, Boston, MA, USA, 1967.

[11] SAP 2000 *Integrated Software for Structural Analysis and Design, Version 21*, CSI Inc., Berkeley, CA, USA, 1975. https://www.csiamerica.com/products/sap2000

EURODYN 2020
XI International Conference on Structural Dynamics
M. Papadrakakis, M. Fragiadakis, C. Papadimitriou (eds.)
Athens, Greece, 23–26 November 2020

NONLINEAR DYNAMICS OF A NEGATIVE STIFFNESS OSCILLATOR: EXPERIMENTAL IDENTIFICATION AND MODEL UPDATING

D. Anastasio, A. Fasana, L. Garibaldi, S. Marchesiello

Dipartimento di Ingegneria Meccanica ed Aerospaziale
Politecnico di Torino
Corso Duca degli Abruzzi, 24, 10129, Torino, Italy

Corresponding author: dario.anastasio@polito.it

Keywords: nonlinear dynamics, negative stiffness, double-well Duffing oscillator, experimental identification, model updating.

Abstract. *Systems exhibiting a negative stiffness region are often used as vibration isolators, due to their enhanced damping properties. The device tested in this paper is part of a damping system and it acts like an asymmetric double-well Duffing oscillator, with two stable and one unstable equilibrium positions. The range of motion can either be bounded around one stable position (in-well oscillations) or include all the three positions (cross-well oscillations). Depending on the input amplitude, the oscillator can exhibit linear and nonlinear dynamics, and chaotic motion as well. Due to its asymmetrical design, the two linearized systems associated to small-amplitude oscillations around one stable equilibrium position are different. In this work, the dynamical behavior of the system is first investigated in the case of linear and nonlinear in-well oscillations and then in the case of cross-well oscillations with chaotic motion. To accomplish this task, the device is mounted on a shaking table and it is driven through several excitation levels with both harmonic and random inputs. An experimental bifurcation tracking analysis is also carried out to understand the possible response scenarios. Afterwards, the nonlinear identification is performed using nonlinear subspace algorithms to extract the restoring force of the system. Eventually, the physically-based model of the device is updated to match the identified characteristics via genetic algorithms.*

1 INTRODUCTION

Devices and materials based on a negative stiffness behavior are very often used as vibration isolators due to their amplified damping properties [1,2]. In particular, in the case of engineering structures, examples can be found in automotive suspensions [3,4] or seismic isolation [5,6].

When the negative stiffness effect is coupled to a nonlinear polynomial stiffness contribution, the so-called double-well Duffing oscillator is obtained, whose dynamical properties have been extensively studied in the literature due to the wide kind of motions it can exhibit, ranging from linear to highly nonlinear and chaotic [7]. This oscillator exhibits two stable and one unstable equilibrium positions, and the oscillations can either be bounded around one stable point (in-well or intra-well small oscillations) or include all the three positions (cross-well or infra-well large oscillations). In both cases, periodic oscillations can evolve to steady in-well or cross-well chaotic motions under external excitation [8]. The occurrence of irregular motion, consisting of random-like crossings from oscillations around the two stable equilibrium positions, was first observed experimentally in 1971 [9] and the motion was called "snap-through". A comprehensive literature review about the Duffing equation can be found in [10].

In this work, a negative stiffness oscillator is studied and tested to derive a reliable nonlinear dynamical model. The dynamical properties of the oscillator are first investigated to uncover the possible kind of motions it can exhibit (in-well, cross-well, chaotic). To accomplish this tasks, the device is mounted on a shaking table and it is driven through several excitation levels with harmonic and random inputs. The experimental bifurcation diagram is estimated, together with the attractor surface in the case of chaotic motion.

Afterward, nonlinear system identification is performed to extract the model parameters directly from the measurements. The nonlinear subspace identification (NSI) method [11–14] is adopted to identify the nonlinear restoring force of the system using just one cross-well measurement obtained with random excitation. Eventually, a model updating procedure is implemented with genetic algorithms to refine the physically-based model based on the identified restoring force.

2 NEGATIVE STIFFNESS OSCILLATOR

The device under investigation consists in a U-shaped steel frame connected through rods to a central moving mass. The frame has the purpose to keep the rods under compression during their movement, exerting a compression force $p(\theta)$ depending on the rotation angle θ. A schematic representation of the device is depicted in Figure 1.

It is assumed that the inertia of the moving parts can be concentrated into one central point with mass m, comprising the mass of the central bushing and the equivalent inertia of the rods. The vertical movement of this point is described by the coordinate $y(t)$. The lower surface of the frame is attached to a shaking table, so that displacement $b(t)$ can be imposed to the structure. The free-body-diagram of mass m is depicted in Figure 1.

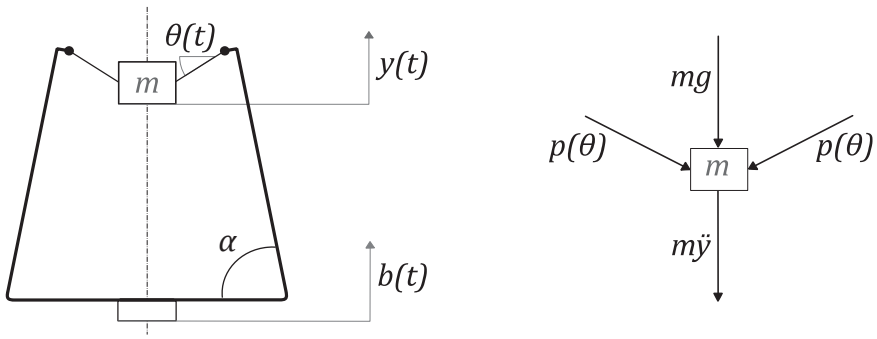

Figure 1: Schematic representation of the negative stiffness oscillator and free-body-diagram of *m*.

With $z(t) = y(t) - b(t)$, the equation of motion of the system in the variable z(t) can be written as

$$m\ddot{z} + k_3 z^3 + k_2 z^2 - k_1 z + k_0 = -m\ddot{b}, \tag{1}$$

where $k_0 = mg$ and the coefficients k_3, k_2, k_1 have to be experimentally estimated. Eq. (1) has the form of a negative-stiffness Duffing equation, and its restoring force K and elastic potential U can be defined as

$$K(z) = k_3 z^3 + k_2 z^2 - k_1 z + k_0, \tag{2}$$

$$U(z) = \frac{1}{4} k_3 z^4 + \frac{1}{3} k_2 z^3 - \frac{1}{2} k_1 z^2 + k_0 z. \tag{3}$$

A qualitative representation of the potential is shown in Figure 2, where its asymmetric double-well characteristic can be observed, together with the three equilibrium positions z^* obtained by setting $K(z^*) = 0$. Two out of three positions represent a stable equilibrium, namely z_-^* and z_+^*, while the central position z_0^* is an unstable point.

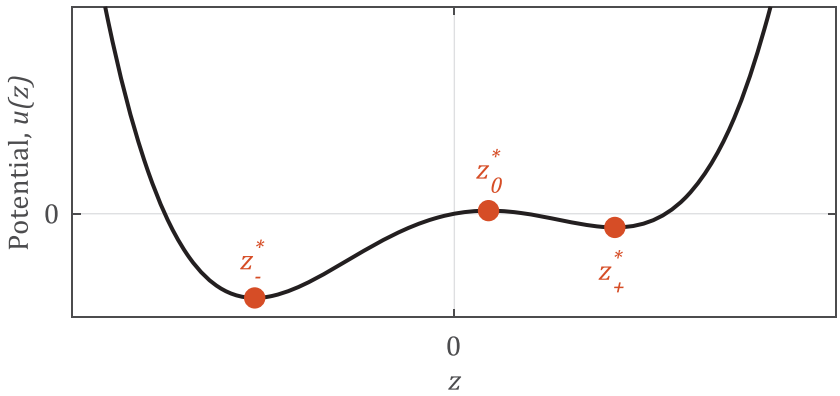

Figure 2: Potential $U(z)$. Orange dots: equilibrium positions.

The oscillations of the moving point are said to be *in-well* when the motion is bounded around one of the two stable equilibrium positions $z_{\pm}^{*}$. The associated linear natural frequency $\omega_{\pm}$ can be computed by

$$\omega_{\pm} = \sqrt{\frac{K'\left(z_{\pm}^{*}\right)}{m}}, \tag{4}$$

$K'\left(z_{\pm}^{*}\right)$ being the derivative of $K(z)$ computed in z_{-}^{*} or z_{+}^{*}.

3 EXPERIMENTAL CHARACTERIZATION

Two photos of the experimental setup corresponding to the two stable equilibrium positions are reported in Figure 3. The moving mass is instrumented with a laser vibrometer to measure its absolute displacement $y(t)$, whose zero position corresponds to the horizontal configuration of the rods ($\theta = 0$). The acceleration of the base $\ddot{b}(t)$ is also recorded through an accelerometer and the displacement $z(t)$ is computed as the difference between the laser measure $y(t)$ and the displacement of the base $b(t)$, obtained by integrating twice its measured acceleration.

The system is driven by harmonic inputs with fixed excitation frequency $\omega = 9 \cdot 2\pi$ rad/s and different amplitudes. The measured signals are sampled at 512 Hz. By applying this set of harmonic excitations, the so-called *bifurcation map* of the system can be built for a specific excitation frequency. The bifurcation map is a snapshot of the kind of steady-state solutions that can be obtained for a given excitation frequency when ranging over the excitation amplitude. Each point in the map represents the amplitude(s) of the steady-state solution for a specific value of the excitation amplitude. Indeed, the system can in principle exhibit super-harmonics of the exciting frequency (meaning frequency contents at $2\omega, 3\omega, 4\omega, \ldots$), sub-harmonics ($1/2\ \omega, 1/3\ \omega, 1/4\ \omega, \ldots$) or chaotic motion.

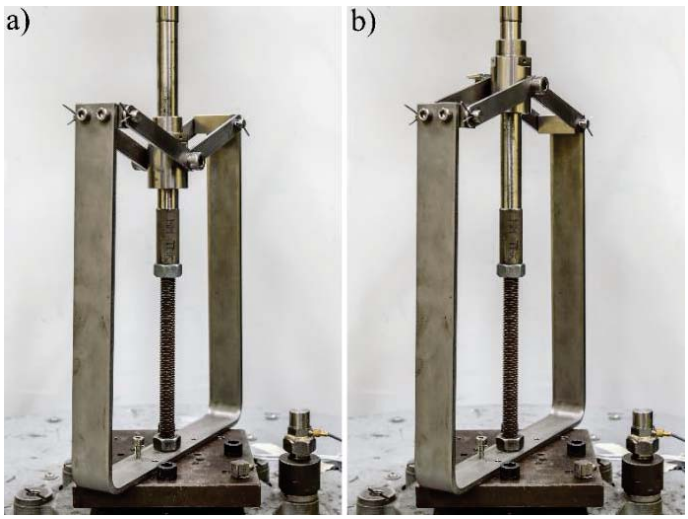

Figure 3: Photos of the experimental setup. a) Negative equilibrium position z_{-}^{*}; b) Positive equilibrium position z_{+}^{*}.

When building the bifurcation map on experimental time series, one should be able to detect the presence of super/sub-harmonics in order to correctly estimate the amplitude(s) of the response. This is done in this work automatically by performing a periodicity analysis of the measured displacement $z(t)$ over a certain number of periods of the input force. The algorithm seeks the number of periods that gives the *best* periodicity of the output signal:

- A *period-1* solution is gathered if the output is periodic with the input. The system in this case might respond with higher harmonics of the excitation frequency ω.
- A *period-2* solution is gathered if the output is periodic with twice the period of the input. The system in this case responds also with the sub-harmonic $1/2\ \omega$.
- A *period-4* solution is gathered if the output is periodic with four times the period of the input. The system in this case responds also with the sub-harmonics $1/2\ \omega, 1/4\ \omega$.
- ...

The experimental bifurcation map is depicted in Figure 4, where the cross-well region is highlighted in grey. Since the map is inferred from experimental measurements, it is not intended to be an exhaustive representation of all the possible bifurcations of the system, as it would be rather difficult to experimentally collect the huge number of points that would be required. Nevertheless, it gives useful information about the range of motions the system exhibits for different input amplitudes. In particular, a cascade of period doublings can be appreciated when the input amplitude is around $12 - 15\ \mathrm{m/s^2}$, especially when starting from the positive equilibrium position ($z_+^* = 0.023$ m).

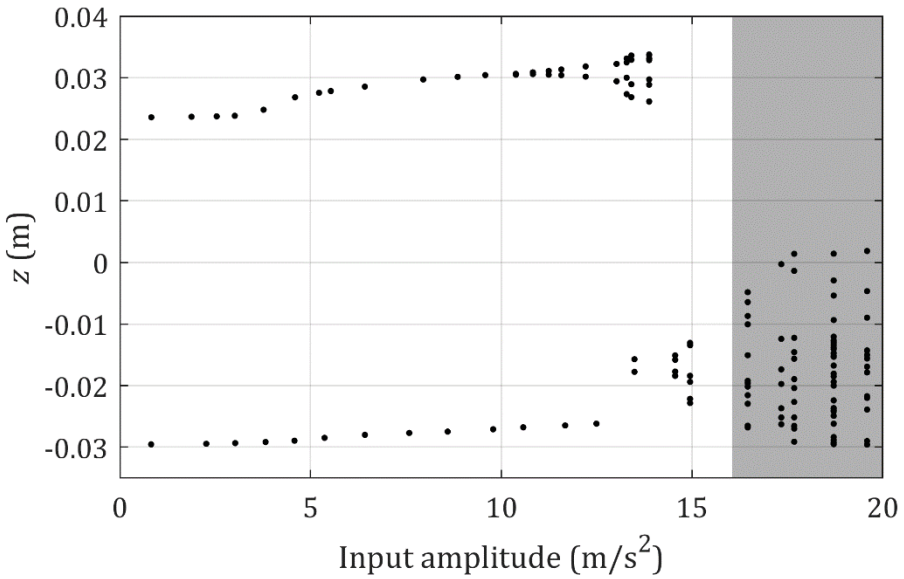

Figure 4: Experimental bifurcation map of the system. The chaotic region is highlighted in grey.

The time series and phase diagrams of some of the points of the bifurcation map are depicted in Figure 5. The selected phase diagrams correspond respectively to a period-1 solution, a period-2 solution, a period-4 solution and to a cross-well motion of the system. The latter in particular can be called *chaotic* in this context, as no periodic solution to a periodic input is retrieved, and this behavior lasts for the entire acquisition time (10 minutes).

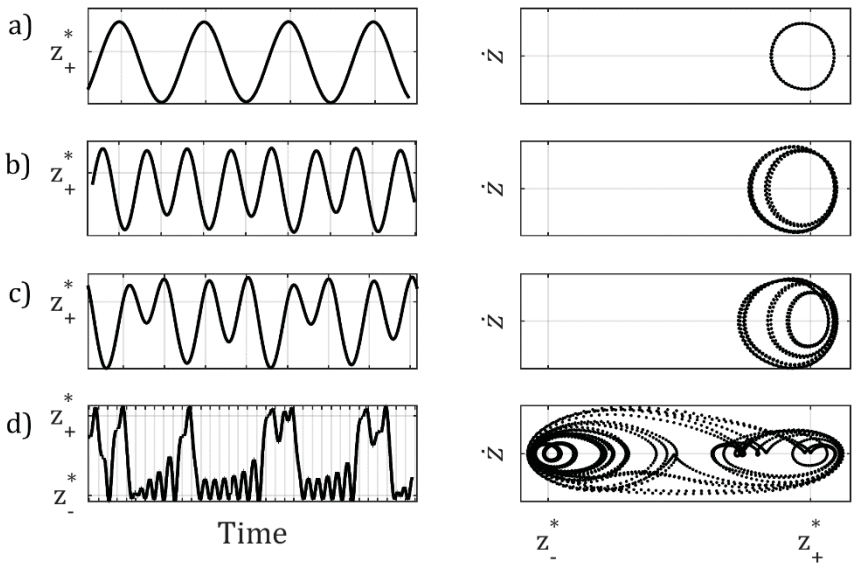

Figure 5: Time series and corresponding phase diagrams of selected measurements. a) Period-1 solution. b) Period-2 solution. c) Period-4 solution. d) Cross-well motion.

It should be recalled that no definition of *chaos* is universally accepted, and this is particularly true when experimental data is considered. The reason is that uncertainties and noise in the data acquisition may interfere with the extreme sensitivity to the initial conditions that characterizes chaotic systems.

The well-known LLE (largest Lyapunov exponent) [15] can be used to check whether the system is behaving chaotically or not: a positive sign means chaotic motion, while a negative sign is representative of a periodic orbit. Several methods exist to compute the LLE from experimental time series, and the one proposed in [16] is adopted here. Results are shown in Figure 6, where a positive sign is retrieved.

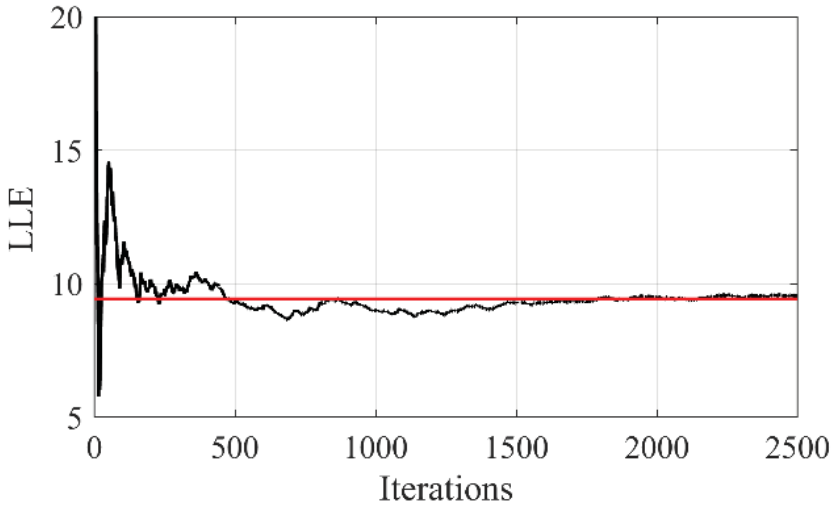

Figure 6: Estimation of the largest Lyapunov exponent. Red line: convergence mean value.

Eventually, the experimental Poincaré sections are computed for different phase synchronizations ϕ of the data with the forcing term [17]. The typical shape of a strange attractor is retrieved [8] and depicted in Figure 7a in a polar plot, while three of its sections are represented in Figure 7b,c,d.

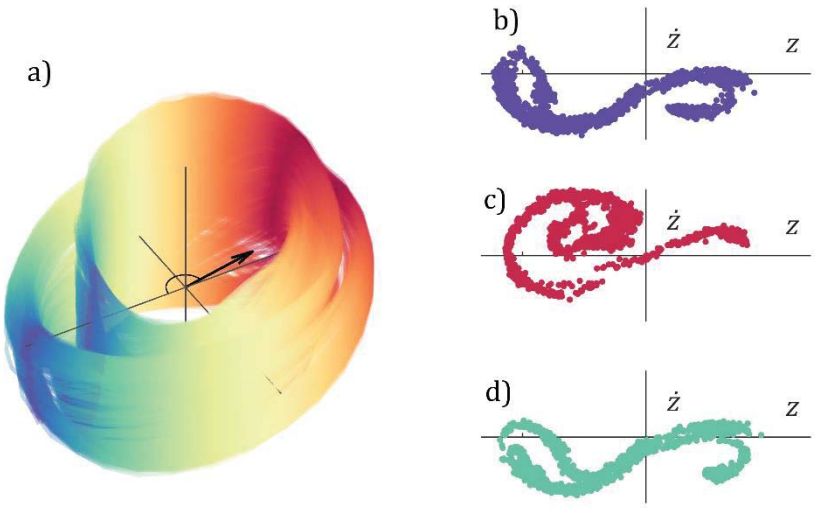

Figure 7: Experimental Poincaré sections. a) Polar representation of the attractor surface; b) Poincaré section, $\phi = 0°$; c) Poincaré section, $\phi = 170°$; d) Poincaré section, $\phi = 320°$.

4 IDENTIFICATION OF THE NONLINEAR RESTORING FORCE AND MODEL UPDATING

The nonlinear subspace identification (NSI) method is adopted in the following to identify the nonlinear state-space model of the system, with the final purpose of estimating its restoring force. NSI relies on the possibility of splitting the nonlinear equation of motion into an underlying-linear (and stable) system (ULS) and a nonlinear feedback. By looking at Eq. (1), this seems not to be possible for the considered system, as the negative linear stiffness creates an unstable ULS. Nevertheless, a workaround can be found by shifting the reference axis and considering the oscillations of the moving point around one *reference position*. This reference position is chosen as one of the two stable equilibrium points $z_{\pm}^{*}$, and it is generally referred to as z^{*}. A new variable $x(t)$ can therefore be defined as

$$x(t) = z(t) - z^{*}, \tag{5}$$

so as to write the equation of motion in the variable x

$$m\ddot{x} + K(x + z^{*}) = -m\ddot{b}, \tag{6}$$

with

$$K(x+z^*) = k_3x^3 + (k_2 + 3k_3z^*)x^2 + \left(3k_3z^{*2} + 2k_2z^* - k_1\right)x \\ = k_3x^3 + \tilde{k}_2x^2 + \tilde{k}_1x. \tag{7}$$

The new coefficients of the restoring force to be identified are therefore k_3, $\tilde{k}_2$ and $\tilde{k}_1$. Also, a nonlinear damping model of the kind $c^{nl}\dot{x}(t)|\dot{x}(t)|$ is sought by the method in addition to a linear viscous damping $c\dot{x}$, to account for the dissipation that comes with the relative motion between the moving point and the vertical steel guide.

Indeed, the ULS depends on the choice of the reference position z^*, therefore:

- When $z^* = z_-^*$ the modal parameters of the underlying-linear small oscillations around the *negative* equilibrium position can be estimated;
- When $z^* = z_+^*$ the modal parameters of the underlying-linear small oscillations around the *positive* equilibrium position can be estimated;

Consequently, two mutually exclusive ULSs can be obtained with NSI. For this reason, a single cross-well measurement under random excitation is fed to the NSI algorithm with two consecutive choices of the reference position: namely $z^* = z_-^*$ and $z^* = z_+^*$. The measurement is sampled at 512 Hz and lasts 300 s, with the last 60 s used for validation purposes.

A model order equal to 2 is chosen for the nonlinear state-space identification, the system being a single-degree-of-freedom system, and the corresponding modal parameters are listed in Table 1.

Reference position	Natural frequency (Hz)	Damping ratio (%)
z_-^*	11.41	11.2
z_+^*	9.19	20.3

Table 1: Modal parameters of the two underlying linear systems identified with NSI.

The validation of the identified model is carried out by simulating the output of the system $x^{SIM}(t)$ with the identified nonlinear state-space model, given the measured input. The simulated and the measured outputs are then compared to estimate the modeling error. Results are reported in Figure 8 in terms of simulated and measured time histories, in time and frequency domains. The statistical parameters of the residual between the measured output $x(t)$ and the simulated one $x^{SIM}(t)$ are listed in Table 2. Generally, the identified state-space model is capable of catching the cross-well motion with a very good accuracy, providing a percentage RMS deviation from the measurement of approximately 8%.

Once the identified model is validated, the coefficients of the nonlinear restoring force can be extracted [11–14], obtaining:

$$K(x+z^*) = k_3x^3 + \tilde{k}_2x^2 + \tilde{k}_1x \\ = 7.35 \cdot 10^5\, x^3 - 6.45 \cdot 10^3\, x^2 + 1.34 \cdot 10^3\, x. \tag{8}$$

The identified restoring force K and the corresponding potential U are depicted in Figure 9a,b. As for the nonlinear damping coefficient c^{nl}, a value of $-5\ \mathrm{Ns^2/m^2}$ is obtained. The total damping force $D(\dot{z}) = c\dot{z} + c^{nl}\dot{z}|\dot{z}|$ is depicted in Figure 9c.

Residual mean (mm)	Residual standard deviation (mm)
0.18	1

Table 2: Statistical parameters of the residual between measured and simulated outputs.

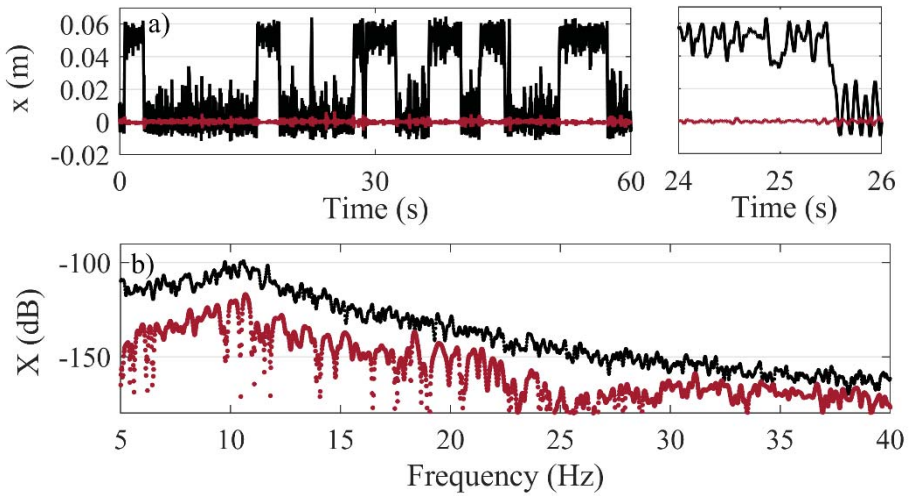

Figure 8: Validation of the nonlinear identification in the time domain (a) and frequency domain (power spectral density, b). Black line: measured output; red line: residual between simulated and measured output.

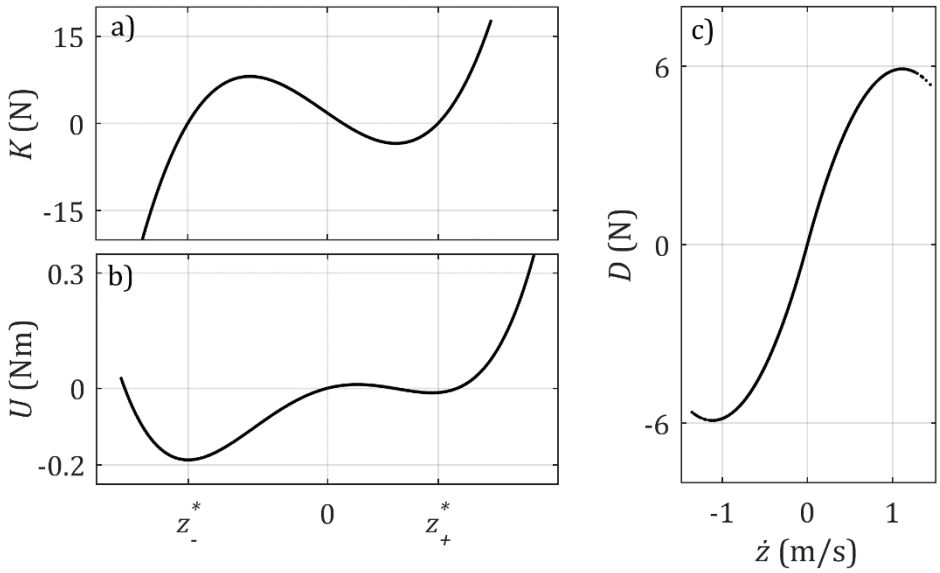

Figure 9: Estimation of the restoring force K (a), the corresponding potential U (b) and the damping force D (c).

4.1 Model updating

Once the parameters of the restoring force have been estimated from the experimental measurements, a comparison with the originally designed values is carried out to validate the model. A model updating procedure is implemented to adjust the physical parameters of the model and minimize the difference between simulated and identified behaviors. A genetic algorithm (GA) [18] is adopted to find the global optimum set of parameters. Genetic algorithms offer the chance to effectively update the model parameters, by exploring the range of feasible values in a smart and fast way. Also, crossover and mutation operators reduce the risk of falling into local minima [18]. The selected fitness function ϵ to be minimized is defined as the sum of two relative error functions ϵ_ω and ϵ_{z^*}. The function ϵ_ω is associated to the residuals on the positive and negative natural frequencies $\omega_\pm$, while ϵ_{z^*} is related to the residuals on the positive and negative equilibrium positions:

$$\epsilon_\omega = \mathrm{RMS}\left\{100\left|\frac{(\omega_-^{MOD} - \omega_-^{EST})}{\omega_-^{EST}}\right|, 100\left|\frac{(\omega_+^{MOD} - \omega_+^{EST})}{\omega_+^{EST}}\right|\right\}$$
$$\epsilon_{z^*} = \mathrm{RMS}\left\{100\left|\frac{(z_-^{*MOD} - z_-^{*EST})}{z_-^{*EST}}\right|, 100\left|\frac{(z_+^{*MOD} - z_+^{*EST})}{z_+^{*EST}}\right|\right\} \tag{9}$$
$$\epsilon = \epsilon_\omega + \epsilon_{z^*}$$

The superscripts *MOD* and *EST* stand respectively for "model" and "estimation". In particular, the estimated natural frequencies $\omega_\pm^{EST}$ are the ones listed in Table 1. The parameters to be optimized are the Young's modulus E of the frame, the frame angle α and the moving mass m. The values of the fitness function across the generations of GA are shown in Figure 10, while the final result is depicted in Figure 11.

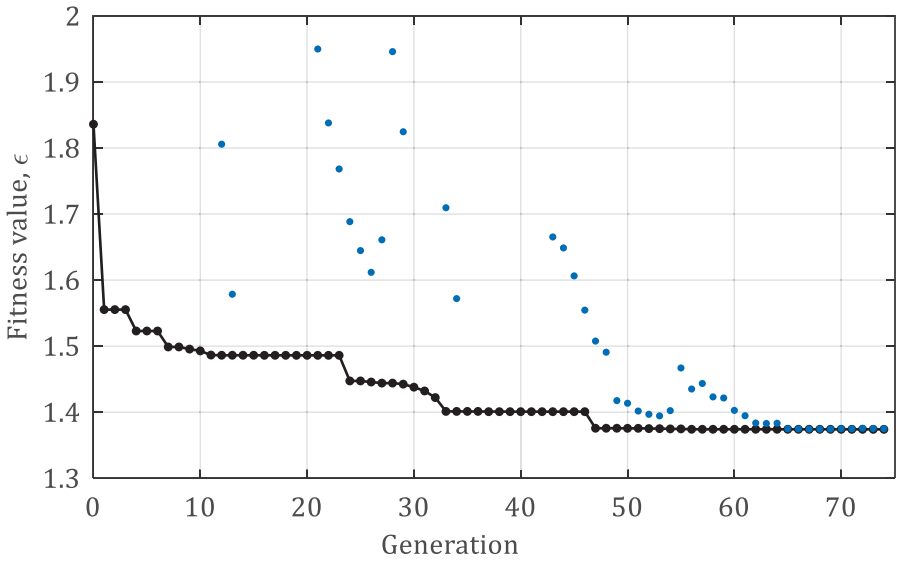

Figure 10: Values of the fitness function across the generations of GA. Black line: best fitness; blue dots: mean fitness values.

The optimization reduces the residual between the experimental characteristics and the model prediction, providing a good match between the final restoring force and potential curves, with a residual ϵ equal to 1.38%.

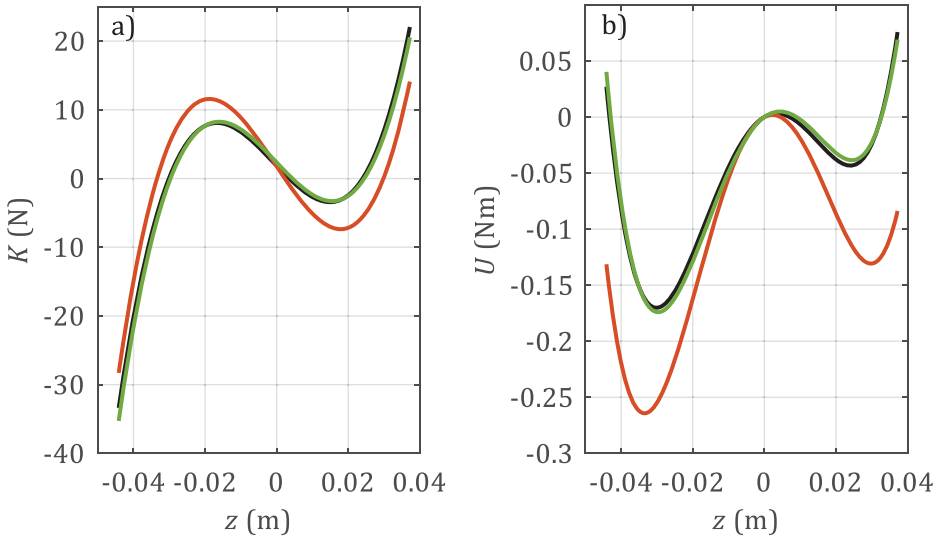

Figure 11: Results of the optimization in terms of restoring force in (a) and potential in (b). Black line: identified curves; orange line: starting values; green line: final values.

5 CONCLUSIONS

A negative stiffness oscillator has been characterized experimentally to exploit its dynamical behavior. A variety of different kind of motions can be obtained because of the bi-stable nature of the device, from in-well to cross-well oscillations, including chaotic motion. These dynamical behaviors have been confirmed by the experimental observations, obtained with harmonic inputs. The bifurcation map of the system has been estimated, together with the attractor surface in the case of chaotic motion. Eventually, the nonlinear restoring force of the system has been identified from the measured time series by applying the nonlinear subspace identification method, and the physically-based model of the device updated via genetic algorithm to match the experimental results.

REFERENCES

[1] R.S. Lakes, Extreme damping in composite materials with a negative stiffness phase, Physical Review Letters. 86 (2001) 2897–2900. https://doi.org/10.1103/PhysRevLett.86.2897.

[2] I. Antoniadis, D. Chronopoulos, V. Spitas, D. Koulocheris, Hyper-damping properties of a stiff and stable linear oscillator with a negative stiffness element, Journal of Sound and Vibration. 346 (2015) 37–52. https://doi.org/10.1016/j.jsv.2015.02.028.

[3] C.M. Lee, V.N. Goverdovskiy, A.I. Temnikov, Design of springs with “negative” stiffness to improve vehicle driver vibration isolation, Journal of Sound and Vibration. 302 (2007) 865–874. https://doi.org/10.1016/j.jsv.2006.12.024.

[4] T.D. Le, K.K. Ahn, A vibration isolation system in low frequency excitation region using negative stiffness structure for vehicle seat, Journal of Sound and Vibration. 330 (2011) 6311–6335. https://doi.org/10.1016/j.jsv.2011.07.039.

[5] H. Iemura, M.H. Pradono, Advances in the development of pseudo-negative-stiffness dampers for seismic response control, Structural Control and Health Monitoring. 16 (2009) 784–799. https://doi.org/10.1002/stc.345.

[6] A.A. Sarlis, D.T.R. Pasala, M.C. Constantinou, A.M. Reinhorn, S. Nagarajaiah, D.P. Taylor, Negative Stiffness Device for Seismic Protection of Structures, Journal of Structural Engineering. 139 (2013) 1124–1133. https://doi.org/10.1061/(ASCE)ST.1943-541X.0000616.

[7] D.W. Jordan, P. Smith, Nonlinear Ordinary Differential Equations: An Introduction for Scientists and Engineers, Fourth, Oxford University Press, New York, 2007.

[8] F.C. Moon, P.J. Holmes, A magnetoelastic strange attractor, Journal of Sound and Vibration. 65 (1979) 275–296. https://doi.org/10.1016/0022-460X(79)90520-0.

[9] W.-Y. Tseng, J. Dugundji, Nonlinear Vibrations of a Buckled Beam Under Harmonic Excitation, Journal of Applied Mechanics. 38 (1971) 467–476. https://doi.org/10.1115/1.3408799.

[10] I. Kovacic, M.J. Brennan, The Duffing Equation, John Wiley & Sons, Ltd, Chichester, UK, 2011. https://doi.org/10.1002/9780470977859.

[11] S. Marchesiello, L. Garibaldi, A time domain approach for identifying nonlinear vibrating structures by subspace methods, Mechanical Systems and Signal Processing. 22 (2008) 81–101. https://doi.org/10.1016/j.ymssp.2007.04.002.

[12] S. Marchesiello, A. Fasana, L. Garibaldi, Modal contributions and effects of spurious poles in nonlinear subspace identification, Mechanical Systems and Signal Processing. 74 (2016) 111–132. https://doi.org/10.1016/j.ymssp.2015.05.008.

[13] D. Anastasio, S. Marchesiello, Free-Decay Nonlinear System Identification via Mass-Change Scheme, Shock and Vibration. 2019 (2019). https://doi.org/10.1155/2019/1759198.

[14] D. Anastasio, S. Marchesiello, G. Kerschen, J.P. Noël, Experimental identification of distributed nonlinearities in the modal domain, Journal of Sound and Vibration. 458 (2019) 426–444. https://doi.org/10.1016/j.jsv.2019.07.005.

[15] S.H. Strogatz, Nonlinear Dynamics and Chaos, CRC Press, 1994. https://www.taylorfrancis.com/books/9780429492563.

[16] A. Wolf, J.B. Swift, H.L. Swinney, J.A. Vastano, Determining Lyapunov exponents from a time series, Physica D: Nonlinear Phenomena. 16 (1985) 285–317. https://doi.org/10.1016/0167-2789(85)90011-9.

[17] F.C. Moon, Experiments on Chaotic Motions of a Forced Nonlinear Oscillator: Strange Attractors, Journal of Applied Mechanics. 47 (1980) 638–644. https://doi.org/10.1115/1.3153746.

[18] K. Deb, Multi-Objective Optimization Using Evolutionary Algorithms, John Wiley & Sons, Inc., 2001.

EURODYN 2020
XI International Conference on Structural Dynamics
M. Papadrakakis, M. Fragiadakis, C. Papadimitriou (eds.)
Athens, Greece, 23–26 November 2020

GEOMETRICALLY NONLINEAR FORCED VIBRATIONS OF MULTIPLE-STEPPED EULER-BERNOULLI BEAMS

I. El Hantati[1], A. Adri[1], H. Fakhreddine[1], S. Rifai[1], R. Benamar[2]

[1] Laboratory of Production Mechanics and Industrial Engineering (LMPGI), Higher School of Technology, Hassan II University of Casablanca,
Km 7, Route El Jadida, B.P. 8012 Oasis, Casablanca, Morocco
e-mail: hantati.issam@gmail.com
e-mail: ahmedadri@gmail.com
e-mail: hatim.fakhreddine@gmail.com
e-mail: said57.rifai@gmail.com
[2] Mohammed V University in Rabat, EMI-Rabat, LERSIM,
Agdal, B.P. 765, Rabat, Morocco
e-mail: rhali.benamar@gmail.com

Keywords: stepped beam, transvers vibration, nonlinear vibration, forced vibration

Abstract. *Stepped beams like structures are extensively used in several mechanical and civil engineering fields, such as for high-rise buildings, robot arms, etc. The objective of the current study is to analyse the geometrically non-linear behaviour of free and forced multi-stepped Euler-Bernouilli beams. The first part consists on determining the multi-stepped beam natural frequencies and associated mode shapes, which constitute the basic functions used afterwards in the non-linear theory. The effect of geometrical non-linearity is based on the Von Karman's assumptions. By deriving the discretized expressions of linear and nonlinear strain and kinetic energies, Hamilton's principle is used to reduce the problem to a non-linear algebraic system solved by means of approximate methods. This leads to the determination of the non-linear modes and their corresponding curvatures, illustrated by application examples showing the effect of geometrical non-linearity on the dynamic behaviour of multi-stepped beams. The effect of the variation of the cross section area and second moment of inertia is also examined. Considering forced vibrations, the single mode approach is used to obtain the non-linear frequency response function in the vicinity of the predominant mode. The effects of the variation in the type of the stepped beam cross section and corresponding parameter ratios are investigated and illustrated by specific application cases.*

1 INTRODUCTION

In many structures encountred in aeronautical, civil or mechanical engineering, stepped beams are used to support loads, transmit motion or to reinforce the entire system. Often in their operation, these types of beams are subjected to vibrations, either free or forced, which require a study in order to be able and predict their dynamic behaviour. Many works have examined the behaviour of this type of beams under various end conditions and under different types of loads.

A review of the literature goes back to N. J. TALEB and E. W. SUPPIGER who applied the Cauchy function method to obtain an approximation of the fundamental frequency and modal configuration of the free transverse vibration of the beams [1]. Balasubramanian and Subramanian studied the performance of a four-degree-of-freedom-per-node element for the vibration analysis of uniform and multi-step beams [2]. S. Naguleswaran gave a brief overview of the work on stepped and multi-stepped beams in [3]. He also examined different cases of vibration of stepped beams in [4,5,6]. In [7,8], MAO used the Adomian Decomposition Method (ADM) to study the free vibration of a stepped beam with two and more uniform sections. Suddoung, Charoensuk and Wattanasakulpong studied the free vibration response of stepped beams made of a functionally graded material (FGM), supported by various types of elastic elements at the ends. In order to obtain the natural frequencies and mode shapes, the solution of the differential equation of motion was performed by the differential transformation method denoted as DTM [9]. R.M. Lin and T.Y. Ng presented in [10] a new method for the calculation of the natural frequencies and mode shapes for the case of free vibration, which is ideally suited for forced vibration applications according to the author.

While most studies on stepped beams have focused on linear vibration analysis, only two works have been found which considered the effect of non-linearity. Sato [11] analysed the non-linear free vibration of stepped beams using the transfer matrix method. Nuttawit Wattanasakulpong and Arisara Chaikittiratana used the Adomian modified decomposition method to study the problems of linear and nonlinear free vibration of stepped beams [12].

None of the works cited above has examined the nonlinear forced response of multi-stepped beams. The purpose of this paper is to present a contribution to the analysis of geometrically nonlinear free and forced vibration of multi-stepped beams assuming Euler-Bernoulli's and Von Karman's hypotheses. The first part consists on determining the stepped beam natural frequencies and associated mode shapes, which are used as basic functions in the non-linear theory. Discretized expressions of the nonlinear and linear strain and kinetic energies are derived, and Hamilton principle is used to reduce the problem to a non-linear algebraic system solved by an approximate method. This leads to determination of the non-linear modes and their corresponding curvatures, which are then illustrated to show the effect of non-linearity on the dynamic behaviour of beams examined. The effect of cross-sectional variation is also examined. Forced vibrations are then examined using the single mode approach to obtain the non-linear frequency response functions are obtained in the neghborhood of the predominant mode. The impact of the variation in the cross section area and second moment of inertia at each step is then illustrated in the forced case.

2 GENERAL FORMULATION

2.1 Linear formulation

The present study concerns three homogeneous Euler-Bernoulli beams shown in Figure 1, characterized by a double change in the rectangulair cross-section. In the first beam (a), the width varies; in the second (b), the height varies, and in the third beam (c), both dimensions vary. For the rest of the study, the beams are suupposed to be fully clamped and are subjected to transverse vibrations.

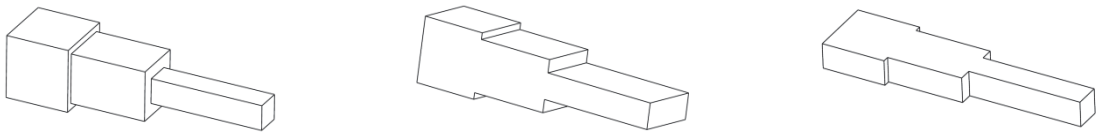

Beam (a) Beam (b) Beam (c)

Figure 1: Three representative cases of the stepped beams examined.

The figure below shows that each of the multi-stepped beams is clamped at both ends and partitioned to three uniform rectangular cross-section subbeams.

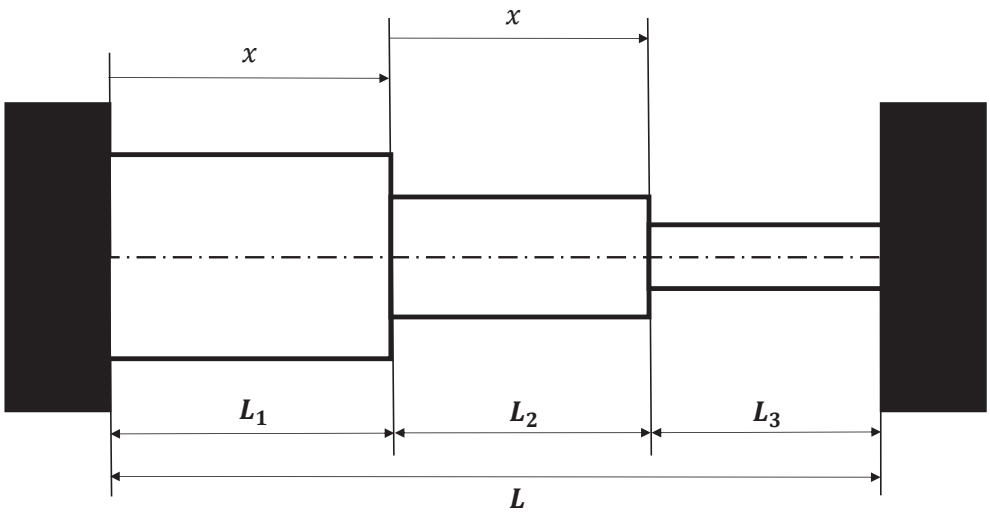

Figure 2: The coordinate system for a stepped beam.

The mechanical and geometrical characteristics of the beams are given in Table1.

	1st subbeam	2nd subbeam	3th subbeam
The length	L_1	L_2	L_3
The young's modulus	E_1	E_2	E_3
The area of cross-section	S_1	S_2	S_3
The second moment of inertia of cross-section	I_1	I_2	I_3
The mass per unit length	ρ_1	ρ_2	ρ_3
The thickness	H_1	H_2	H_3
The eigenvalue parameters	β_1	β_2	β_3
Radius of gyration	$\mathscr{R}_1$	$\mathscr{R}_2$	$\mathscr{R}_3$

Table 1: Characteristics of the three subbeams

The free transverse vibration in each subbeam is governed by the following equation:

$$\frac{d^4 W_i(x)}{dx^4} - \beta_i^4 W_i(x) = 0 \qquad ; x \epsilon [0\ L] \qquad \text{(For i=1,2…, 12)} \tag{1}$$

Where

$$\beta_{ij}^4 = \omega_i^2 \frac{\rho_j S_j}{E_j I_j} \qquad \text{(For j=1 to 3)} \tag{2}$$

Substituting the non-dimensional parameters in eq (2), one obtains the following equation:

$$\frac{d^4 W_i(x^*)}{dx^{*4}} - \beta_i^4 W_i(x^*) = 0 \qquad ; x^* \epsilon [0\ 1] \tag{3}$$

Where

$$x_j^* = \frac{x_j}{L}; R_j^* = \frac{L_j}{L} \quad ; z_j = \frac{\beta_{ij}}{\beta_{i1}}; u_j = \frac{S_j}{S_1}; v_j = \frac{I_j}{I_1} \tag{4}$$

Each step of the beam is defined by the ratio of the cross-section area, the ratio of the second moment of inertia and the eigenvalue parameters (u_j, v_j and z_j). The general solution of eq. (2) may be expressed in each span as:

$$W_i(x^*) = \left\{ \begin{array}{c} W_{ij}(x^*) \rightarrow \{ x_{j-1}^* \le x^* \le x_j^* \} \\ \cdots \\ \cdots \end{array} \right\}$$

$$W_{ij}(x^*) = A_j \cosh\left(\beta_{ij} L\left(x^* - x_{j-1}^*\right)\right) + B_j \sinh\left(\beta_{ij} L\left(x^* - x_{j-1}^*\right)\right) + C_j \cos\left(\beta_{ij} L\left(x^* - x_{j-1}^*\right)\right) + D_j \sin\left(\beta_{ij} L\left(x^* - x_{j-1}^*\right)\right) \tag{5}$$

The satisfaction of the compatibility conditions, at each change of cross-section, as well as the end conditions leads to a homogeneous system.

The end conditions at the left side:

$$W_{i1}(x^*)\Big|_{x^*=0} = 0 \quad ; \frac{dW_{i1}(x^*)}{dx^*}\Big|_{x^*=0} = 0 \tag{6, 7}$$

The end conditions at the right side:

$$W_{i3}(x^*)\Big|_{x^*=0} = 0 \quad ; \frac{dW_{i3}(x^*)}{dx^*}\Big|_{x^*=1} = 0 \tag{8, 9}$$

The compatibility conditions at a change of cross-section are given by:

$$W_{ij}(x^*)\Big|_{x^*=x_j^*} = W_{ij+1}(x^*)\Big|_{x^*=x_j^*} \tag{10}$$

$$\left.\frac{dW_{ij}\left(x^*\right)}{dx^*}\right|_{x^*=x_j^*} = \left.\frac{dW_{ij+1}\left(x^*\right)}{dx^*}\right|_{x^*=x_j^*} \tag{11}$$

$$EI_j \left.\frac{d^2W_{ij}\left(x^*\right)}{dx^{*2}}\right|_{x^*=x_j^*} = EI_{j+1} \left.\frac{d^2W_{ij+1}\left(x^*\right)}{dx^{*2}}\right|_{x^*=x_j^*} \tag{12}$$

$$EI_j \left.\frac{d^2W_{ij}\left(x^*\right)}{dx^{*2}}\right|_{x^*=x_j^*} = EI_{j+1} \left.\frac{d^2W_{ij+1}\left(x^*\right)}{dx^{*2}}\right|_{x^*=x_j^*} \tag{13}$$

The homogeneous system, obtained by satisfying the compatibility and end conditions, is solved by means of the Newton-Raphson algorithm and gives the non-trivial solutions that constitute the natural frequencies beam.

2.2 Nonlinear formulation

2.2.1 Free vibration

The total strain energy V of the beam can be written as:

$$\boldsymbol{V} = \boldsymbol{V_a} + \boldsymbol{V_f} \tag{14}$$

Where $\boldsymbol{V_a}$ is the axial strain energy due to the nonlinear axial forces induced by the large vibration amplitudes and $\boldsymbol{V_f}$ is the strain energy due to bending, expressed as:

$$V_f = \frac{1}{2}\int_0^L E\ I(x)\left(\frac{\delta^2 w}{\delta x^2}\right)^2 dx;\ V_a = \frac{E}{8L}\cdot\left(\int_0^L S(x)\left(\frac{\delta w}{\delta x}\right)^2\right)^2 dx \tag{15, 16}$$

The kinetic energy, denoted by T can be expressed as:

$$T = \frac{1}{2}\rho \int_0^L S(x)\left(\frac{\delta w}{\delta t}\right)^2 dx \tag{17}$$

Assuming harmonic motion and expanding the transverse displacement(w) in the form of a finite series of basic spatial functions, one may write:

$$w(x,t) = a_i W_i(x)\sin(\omega t) \tag{18}$$

Where the a_i are the basic functions contribution coefficients, which vary from [0.1 to 2] with a step of (0.1) . Using the form of w in equation (18), the expressions for total strain and kinetic energy can be written as follows:

$$T = \frac{1}{2}\ \omega^2\, a_i a_i \left(\ \cos(\omega t)\right)^2 M_{ij} \tag{19}$$

$$V = \frac{1}{2}\, a_i a_j\, a_k\, a_l\, (\sin(\omega t))^4 B_{ijkl} + \frac{1}{2}\, a_i a_i \left(\sin(\omega t)\right)^2 K_{ij} \tag{20}$$

In which M_{ij} , K_{ij} and B_{ijkl} are the mass matrix, the rigidity matrix and the nonlinearity tensor. It is well known that the dynamic behaviour of a conservative system can be expressed using Hamilton's principle as:

$$\delta \int_0^{\frac{2\omega}{t}} (V - T)\, dt = 0 \tag{21}$$

After substitution of equations (19 and 20) in equation (21), the mathematical development leads to:

$$2[K]\{A\} + 3\left[B\left(\{A\}\right)\right]\{A\} - 2\omega^2\, [M]\{A\} = 0 \tag{22}$$

Before determining the column vector of the contribution coefficients {A} and the frequency (ω) which are unknowns, equation (22) is put in its dimensionless form by replacing the dimensional parameters with the following parameters.

$$\frac{W_i(x^*)}{W_i^*(x^*)} = \mathscr{R}_{/}; \frac{\omega^2}{\omega^{*2}} = \frac{E I_1}{\rho S_1 L^4}\ ; \frac{M_{ij}}{M_{ij}^*} = \rho S_1 H_1^{\,2} \tag{23, 24, 25}$$

$$K_{ij} = \frac{E I_1 H_1^{\,2}}{L^3} K_{ij}^*; B_{ijkl} = \frac{E I_1 H_1^{\,2}}{L^3} B_{ijkl}^{\,*} \tag{26, 27}$$

The substitution of the above equations equation (22) gives:

$$\left[K^*\right]\{A\} + \frac{3}{2}\left[B^*\left(\{A\}\right)\right]\{A\} - \omega^{*2}\, [M^*]\{A\} = 0 \tag{28}$$

If geometrically nonlinear free vibration is examined, equation (28) is solved by the so-called second formulation, previously developed by M. EL KADIRI AND R. BENAMAR in reference [13].

2.2.2 Forced vibration

To study non-linear forced vibrations, the multi-step beam is supposed to be excited by a concentrated harmonic force, located at the point x0. The concentrated harmonic force can be expressed as in ref [14] by:

$$\mathrm{F}_i^c = F^c \cos(\omega t)\, w_i(x_0) = \mathrm{f}_i^c \cos(\omega t) \tag{29}$$

In order to study of the system dynamic behaviour, Hamilton's principle is applied, with additioN of the term due to the concentrated force, which gives, as in ref[15] :

$$\delta \int_0^{\frac{2\omega}{t}} (V - T + F)\, dt = 0 \tag{30}$$

Substituting equations (19, 20 and 29) in equation (30), leads to the following equation:

$$2[K]\{A\} + 3\left[B\left(\{A\}\right)\right]\{A\} - 2\omega^2\, [M]\{A\} = \left\{F^c\right\} \tag{31}$$

Equation (31) is made dimensionless by putting the dimensionless parameters (23, 24, 25, 26 and 27) in equation (31) to get:

$$\left[K^*\right]\{A\}+\frac{3}{2}\left[B^*\left(\{A\}\right)\right]\{A\}-\omega^{*2}\,[M^*]\{A\}=\left\{F^{c*}\right\} \tag{32}$$

Where f_i^{c*} is the dimensionless force that can be written as:

$$f_i^{c*}=\frac{L^3}{E\,I_1}F^c w_i^*\left(x_0\right) \tag{33}$$

Equation (32) was solved by a method called the single mode approach, presented by M.EL KADIRI AND R. BENAMAR in reference [13]. This approach consists on considering only the predominant mode and neglecting all of the others. In the present case, the predominant mode and the contribution coefficients are denoted by "i" and"a_i", which leads to an equation as follows:

$$1+3\,a_i^{\,2}\frac{B_{iiii}^{\,*}}{K_{ii}^{\,*}}-\frac{f_i^{c*}}{a_i\,K_{ii}^{\,*}}=\left(\frac{\omega_{nl}^*}{\omega_1^*}\right)^2 \tag{34}$$

Where $\omega_1^*=\dfrac{K_{ii}^{\,*}}{M_{ii}^{\,*}}$.

3 NUMERICAL RESULTS AND DISCUSSION

3.1 Free vibration

The cases shown in table (2) and all figures below are for beams with two stepped cross-section changes. The cross-section ratios of the 1st and 2nd step are designated by "u1" and u2 with u1= 0.8 and u2= 0.25. The three beams keep the same ratio u1 and u2. Each of the latter two are expressed differently. The representation of the ratios is as follows:
-Beam 1 is of variable height and width.
-Beam 2 is of a constant width and a variable height.
-Beam 3 is of a constant height and a variable width.

		Mode index			
		1	2	3	4
Beam (c)	Present work	4.598075280254948	7.992296056541504	10.932371269399804	14.162478863118704
	Ref[8]	4.598075164552	7.992295376591	10.932386065194	14.144087111818
	Ref[3]	4.59808	7.99230	10.93237	-
	$Error(\%)=\frac{\text{Ref}[8]-[\text{Present}]}{\text{Ref}[8]}$	2,51633E-06	8,50757E-06	0,000135339	0,130031377
	$Error(\%)=\frac{\text{Ref}[3]-[\text{Present}}{\text{Ref}[3]}$	0,00010265	4,9341E-05	1,1611E-05	-
Beam (b)	Present work	3.374667111927542	5.390268942207863	7.570210029760232	9.212786875568311
	Ref[3]	3.37467	5.39027	7.57021	-
	$Error(\%)=\frac{\text{Ref}[3]-[\text{Present}]}{\text{Ref}[3]}$	8,5581E-05	1,9624E-05	3,9312E-07	-
Beam (a)	Present work	3.741886230810689	6.682789819471814	8.593771164679815	11.602549041679717

Table 2: The first four eigenvalues for clamped–clamped beams with [(u_2=0.8 u_3=0.25) and (R_1=0.25; R_2=0.3; R_3=0.45)]

The first four eigenvalues of beam (a, b and c) in this study are represented in table 2, and a comparison is made between beam (c) and the two beams of ref[8,3] , and between beam (b) and that of ref[3] .

The figure below shows the effect of the variation in the cross-sections on the frequency ratio dependence on the maximum vibration amplitude.

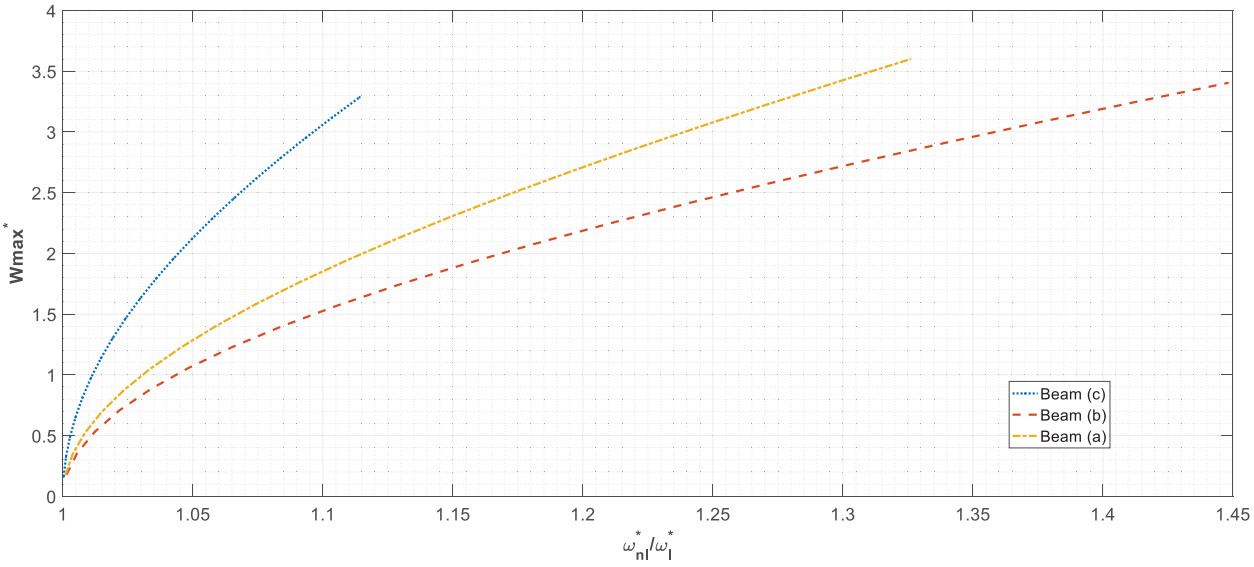

Figure (3) Backbone curves of the three types of beams studied, corresponding to the fundamental nonlinear mode.

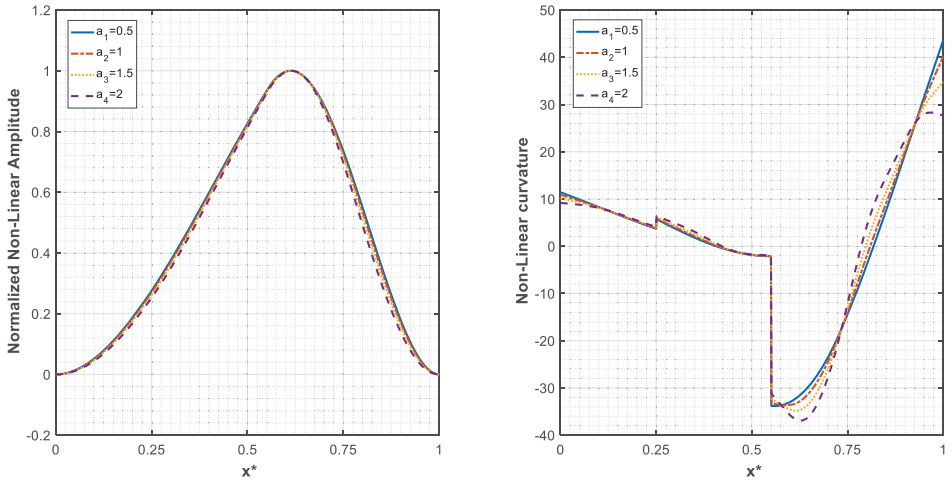

Figure (4): The normalized first non-linear mode and the associated curvature distribution of beam (a) for different values of amplitudes

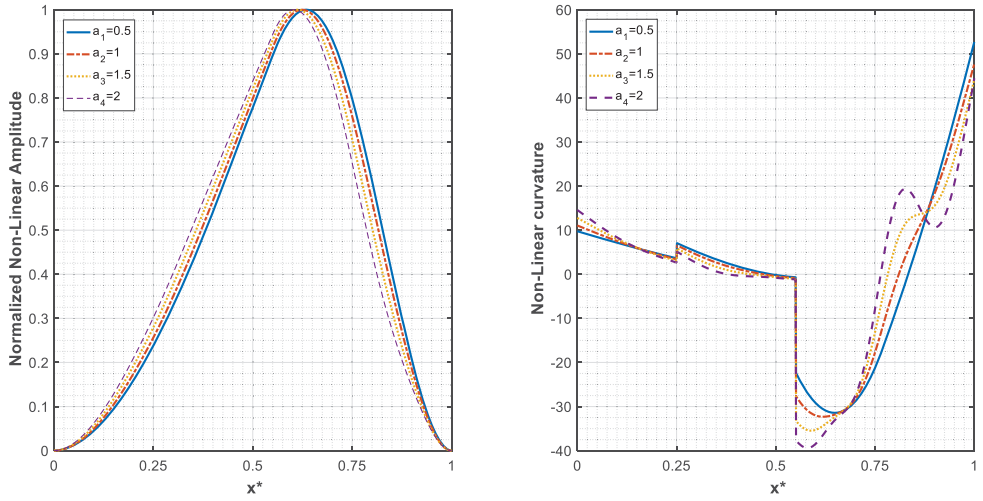

Figure (5): The normalized first non-linear mode and the associated curvature distribution of beam (b) for different values of amplitudes

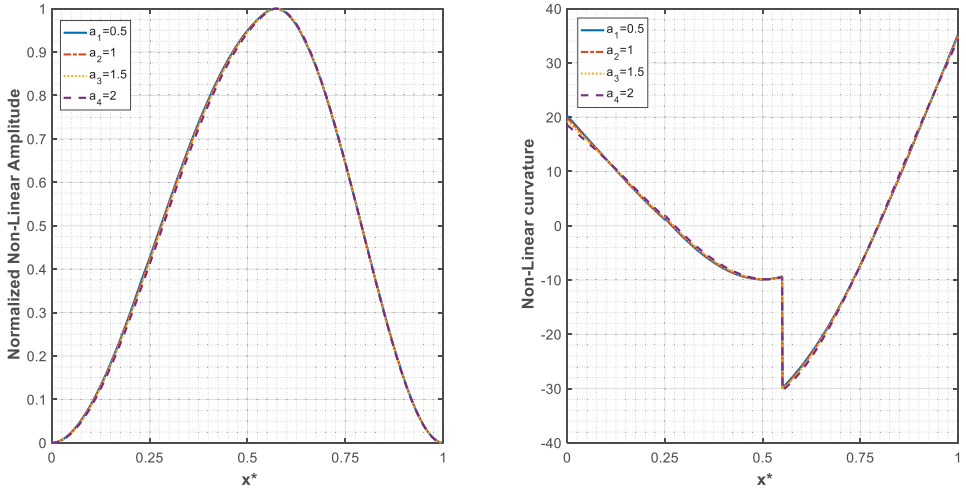

Figure (6): The normalized first non-linear mode and the associated curvature distribution of beam (c) for different values of amplitudes

As shown in the figures above, the non-linearity is highest in beam (b) compared to the other 2 beams. In addition, beam (a) has a higher non-linearity than beam (c). It is also noticed that the geometric non-linearity is not only correlated with the ratio of the cross-section areas, but also with the way it varies.

Moreover, the bending moment results show that for the same beam, the hypothesis of neglecting geometric non-linearity induces an error. For example, the result obtained of the bending moment of the beam (a) at x^*=0.6 with a contribution coefficient a_1= 0.1 is 5.7178629838255, when the contribution coefficient a_1= 2 the result equal to 127.9047642462426, which lead to an error of 13.547% between the linear and non-linear result. The same thing for beam (b) where the bending moment at the same point and with a contribution coefficient a_1= 0.1 equal to 4.9691227579006, when the contribution coefficient a_1= 2 the result equal to 131.27, which lead to an error of 31.88%. Also for beam (b) where the bending moment at the same point and with a contribution coefficient a_1= 0.1 equal to 4.201562264286194, when the contribution coefficient a_1= 2 the result equal to

87.938783062186658, which lead to an error of 3.9075377764628%, hence the interest of the present study.

3.2 Forced vibration

The figures below show the non-linear dynamic behaviour of the forced beam.
The case of the non-linear dynamic behaviour of the forced beam has been studied, using the single-mode approach, in which all modelled beams were excited by a concentrated force, located at the middle of the beam. The study was repeated for three different values of concentrated forces, which were increased according to the following formula [$F^c=10^n$](for n=0,1,2 and 3).

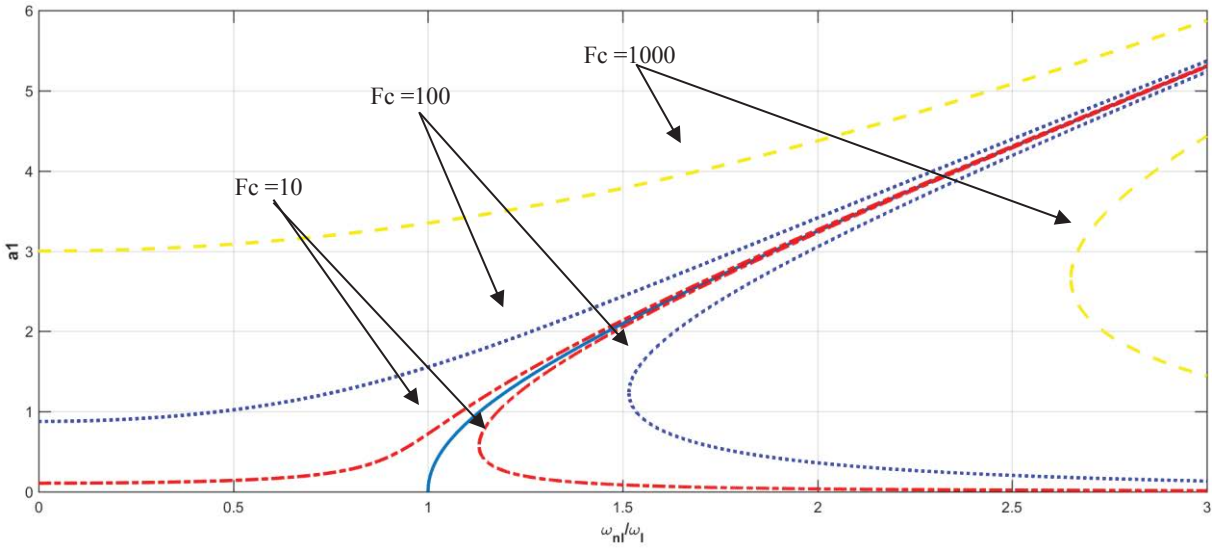

Figure (7) :Nonlinear frequency response functions, based on the single mode approach, for the first beam, subjected to three levels of excitation

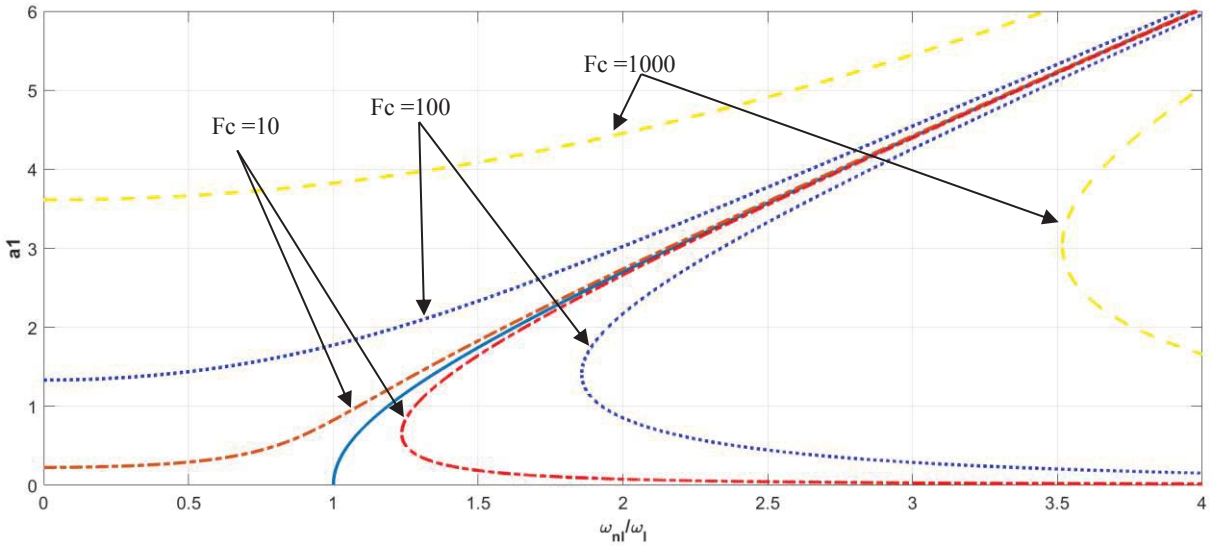

Figure (8): Nonlinear frequency response functions, based on the single mode approach, for the second beam subjected to three levels of excitation

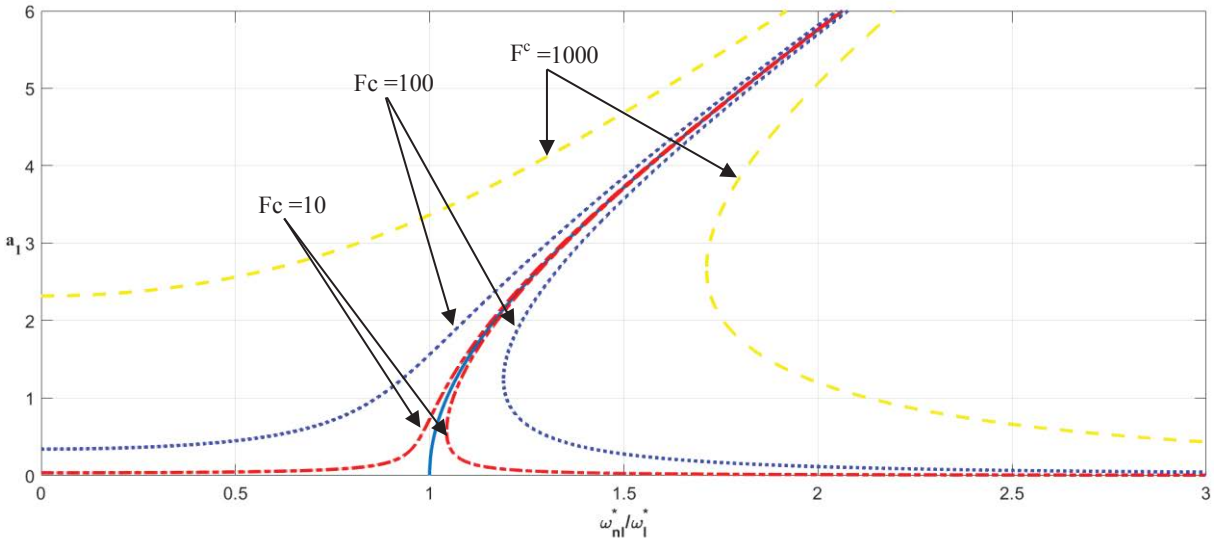

Figure (9): Nonlinear frequency response functions, based on the single mode approach, for the third beam subjected to three levesl of excitation

By assuming the single mode approach, an analysis of the dynamic behaviour of stepped beams was done in the vicinity of the predominant mode. The response curves have been exhibited for the three beams shown in figure (1), which were excited by a concentric harmonic force.

The figures (7, 8 and 9) clearly represent the particular behaviour of non-linear systems, like the jump phenomenon where for the same frequency range, diverse results are possible, also the unproportional progression of the frequency response to the intensity of excitation.

4 CONCLUSION

The analysis of geometrically non-linear, free and forced transverse vibrations of a multi-step beam was examined analytically using Euler-Bernoulli's beams theory and the Von Karman's nonlinearity assumptions. The solution of the linear problem was obtained for three types of beams with different cross-sections, leading to the calculation of frequencies and determination of the mode shapes. The latter were then used as basic functions for the analysis of the non-linear problem. The non-linear algebraic system was subsequently reduced using Hamilton's principle and spectral analysis, and solved using an approximate method called second formulation. This led to examination of the effect of the cross-section variation on the non-linear dynamic behaviour of the beams, illustrated by the backbone curves. The non-linear dynamic behaviour of a beam subjected to a concentric force was also studied using the single-mode approach in the neighbourhood of the predominant mode. The effect of the force level was examined and then illustrated for the three cases.

5 REFERENCES

[1] N.J.Taleb and E.W.Suppiger, Vibration of Stepped Beams, *Journal of the aerospace sciences*, 1961.

[2] TS. Balasubramanian,G. Subramanian, On the performance of a four-degree-of-freedom per node element for stepped beam analysis and higher frequency estimation. *Journal of Sound and Vibration 1985.*

[3] S. Naguleswaran, Vibration of an Euler–Bernoulli beam on elastic end supports and with up to three stepchanges in cross-section, *International Journal of Mechanical Sciences 44* (2002).

[4] S. Naguleswaran, Vibration and stability of an Euler-Bernoulli beam with up to three-step changes in cross-section and in axial force. *International Journal of Mechanical Sciences* 45:1563–79, 2003.

[5] S.Naguleswaran,Vibration of an Euler-Bernoulli stepped beams carrying a nonsymmetrical rigid body at the step. *Journal of Sound and Vibration* 271:1121–32, 2004.

[6] S. Naguleswaran,Vibration and stability of ring-stiffened Euler–Bernoulli tie-bars. *Applied Mathematical Modelling* 30:261–277, (2006)

[7] Q.Mao and S. Pietrzko. Free vibration analysis of stepped beams by using Adomiandecomposition method. *Applied Mathematics and Computation* 217:3429–41, 2010.

[8] Q. Mao, Free vibration analysis of multiple-stepped beams by using Adomian decomposition method. *Mathematical and Computer Modelling* 54:756–64, 2011.

[9] Kittisak Suddoung , Jarruwat Charoensuk and Nuttawit Wattanasakulpong . Vibration response of stepped FGM beams with elastically end constraints using differential transformation method. *Applied Acoustics* 77 (2014)

[10] R.M. Lin, T.Y. Ng. Exact vibration modes of multiple-stepped beams with arbitrary steps and supports using elemental impedance method. *Engineering Structures* 152 24–34, (2017).

[11] H. Sato, Non-linear free vibration of stepped thickness beams. *Journal of Sound and Vibration* 72:415–22, 1980.

[12] Nuttawit Wattanasakulpong and Arisara Chaikittiratanab, Adomian modified decomposition method for large amplitude vibration analysis of stepped beams with elastic boundary conditions, *Mechanics Based Design of Structures and Machines,* 2015.

[13] M. EL Kadiri and R. Benamar, *Journal of Sound and Vibration* 249(2), 263d305, 2002.

[14] R. L. Azrar, R. Benamar and G. White, *Journal of Sound and Vibration* 224 (2), 183-207, 1999.

[15] Hatim Fakhreddine, Ahmed Adri, Saïd Rifai and Rhali Benamar. A Multimode Approach to Geometrically Non-linear Forced Vibrations of Euler–Bernoulli Multispan Beams, *Journal of Vibration Engineering & Technologies,* (2019).

EURODYN 2020
XI International Conference on Structural Dynamics
M. Papadrakakis, M. Fragiadakis, C. Papadimitriou (eds.)
Athens, Greece, 23–26 November 2020

NONSMOOTH MODAL ANALYSIS WITH BOUNDARY ELEMENT METHOD

Tianzheng Lu and Mathias Legrand

Structural Dynamics and Vibration Laboratory, McGill University
817 Sherbrooke St West, Montréal QC H3A 0C3 Canada
e-mail: tianzheng.lu@mail.mcgill.ca
mathias.legrand@mcgill.ca

Keywords: Nonsmooth Modal Analysis, Boundary Element Method, Shooting Method, Harmonic Balance Method, Structural Dynamics

Abstract. *Numerical schemes based on the Boundary Element Method are proposed to perform Nonsmooth Modal Analysis. The latter aims at finding continuous families of periodic orbits of mechanical systems featuring unilateral contact constraints. In this contribution, a simple one-dimensional rod system is targeted. The frequency response, in the form of backbone-curve diagrams, and displacement field are presented. The proposed results compare well with existing studies on this topic.*

1 INTRODUCTION

Within the framework of structural dynamics, linear modal analysis is a daily used tool in industry, aiming at predicting vibratory resonances of periodically forced mechanical systems by searching for continuous families of periodic solutions exhibited by the underlying autonomous (i.e. unforced) system. However, various challenges arise when possibly large-scale *nonlinear* dynamical systems are targeted and for which *nonlinear modal analysis* is needed instead [7]. Nonlinearity has commonly two forms: smooth or nonsmooth function of the state. The nonlinearity is said to be smooth when the governing equation involves a function of the state which is differentiable. Such functions are commonly polynomial. The nonlinearity is said to be nonsmooth otherwise, as for instance, unilateral contact conditions. *Nonsmooth Modal Analysis* (NSM) is a version of modal analysis dedicated to such systems. A few numerical schemes exist to perform NSM, with inherent limitations [11, 12]. In the present work, it is proposed to explore the numerical capabilities of two numerical schemes grounded on the Boundary Element Method (BEM) to perform NSM.

2 SYSTEM OF INTEREST

The system of interest, shown in Figure 1, is a one-dimensional bar of length L with a unilateral contact condition at its right tip. The unknown displacement field is $u(x,t)$, where

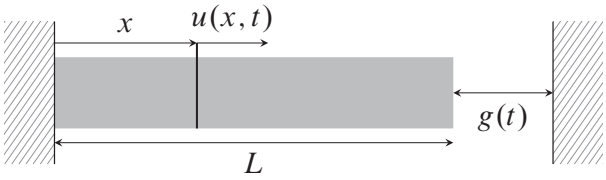

Figure 1: System of interest

x is the space coordinate and t is time. Wave speed c is space-independent and the classical one-dimensional wave equation governs the dynamics, that is

$$u_{,tt} - c^2 u_{,xx} = 0, \quad \forall x \in]0\,;L[. \tag{1}$$

Unilateral contact on the right tip is expressed as a Signorini boundary condition

$$g(t) \geq 0, \quad u_{,x}(L,t) \leq 0, \quad g(L,t)u_{,x}(L,t) = 0. \tag{2}$$

where $g(t) = g_0 - u(L,t)$. Also, since the bar is clamped on the left, $u(0,t) = 0$ applies.

In context of nonlinear modal analysis [7], families of periodic solution forming modal manifolds are computed through a numerical scheme which assumes that no impact law is required as the contact interface but instead, a switch between free-flight and sticking phases occurs.

3 METHODOLOGY

In this paper, two numerical schemes based on the Boundary Element Method are implemented. The BEM forms a family of methods for which the boundary of the domain of interest is the main ingredient of the formulation and full domain discretization is not required when initial condition and body force vanish [6]. It has the notable benefit of reducing the dimension of the formulation. Among the various incarnations of BEM, the Time Domain BEM (TD-BEM)

and Frequency Domain BEM (FD-BEM) are selected to perform nonsmooth modal analysis. The first strategy combines TD-BEM and a simplified shooting method, while the second one combines FD-BEM to Harmonic Balanced Method (HBM).

3.1 Time Domain Boundary Element Method and Shooting Method

TD-BEM is a version of BEM which requires the discretization of both time and space. By pre-multiplying the governing equation (1) with its fundamental solution [4] and performing integration in time and space and then integration by parts, the formulation can be transformed into Boundary Integral Equation (BIE), which here reads [3]

$$\begin{aligned} u(x,t) = &\int_0^t p^*(x,t,\xi,\tau)u(\xi,\tau)\,\mathrm{d}\tau\Big|_{\xi=L} + \int_0^t p^*(x,t,\xi,\tau)u(\xi,\tau)\,\mathrm{d}\tau\Big|_{\xi=0} \\ &- \int_0^t u^*(x,t,\xi,\tau)\,p(\xi,\tau)\,\mathrm{d}\tau\Big|_{\xi=L} - \int_0^t u^*(x,t,\xi,\tau)\,p(\xi,\tau)\,\mathrm{d}\tau\Big|_{\xi=0} \\ &- \frac{1}{c^2}\int_0^L u^*(x,t,\xi,0)v(\xi,0)\,\mathrm{d}\xi + \frac{1}{c^2}\int_0^L \frac{\partial u^*(x,t,\xi,0)}{\partial\tau}\Big|_{\tau=0} u(\xi,0)\,\mathrm{d}\xi \end{aligned} \tag{3}$$

where p represents traction on the boundary ; $u^*(x,t,\xi,\tau)$ and $p^*(x,t,\xi,\tau)$ are the displacement and stress fundamental solutions. Any internal state for $x \in]0\,;L[$ at time t is dependent on the boundary displacement and traction at past times as well as initial states. In order to use TD-BEM, space and time are first discretized. Space integration of the initial states (last two terms in (3)) is performed by discretizing space into n elements and $n+1$ nodes with $\Delta x = L/n$ such that $x_k = k\Delta x$ for $k = 0,\ldots,n$. Time step is set to $\Delta t = \Delta x/c$ to guarantee stability of TD-BEM, such that $t^i = i\,\Delta t$ for $i = 0,\ldots,n$. Equation (3) is discretized by reading it on the boundary, that is $x = 0$ and then $x = L$ for all t^i for all $i = 0,\ldots,n$; it now becomes

$$\mathbf{H}^{ii}\mathbf{u}^i = \mathbf{G}^{ii}\mathbf{p}^i + \sum_{j=0}^{i-1}(\mathbf{G}^{ij}\mathbf{p}^j - \mathbf{H}^{ij}\mathbf{u}^j) + \mathbf{U}^i\mathbf{u}_0 + \mathbf{V}^i\mathbf{v}_0, \quad i = 1,\ldots,n \tag{4}$$

where $\mathbf{u}^i \approx [u(0,t^i), u(L,t^i)]^\top$ and $\mathbf{p}^i \approx [p(0,t^i), p(L,t^i)]^\top$ are displacement and traction vectors on boundary, with size of 2×1. The quantities $\mathbf{H}^{ii}$, $\mathbf{G}^{ii}$, $\mathbf{H}^{ij}$, and $\mathbf{G}^{ij}$ are 2×2 coefficients matrices, evaluated from time-domain integration in (3) of fundamental solutions u^* and p^*. Vectors $\mathbf{u}_0 = [u(x_k,0)_{k=0\ldots,n}]$ and $\mathbf{v}_0 = [v(x_k,0)_{k=0\ldots,n}]$ are the discretized initial displacement and velocity fields, with size $n+1$. The corresponding coefficient matrices of size $2\times(n+1)$ are $\mathbf{U}^i$ and $\mathbf{V}^i$ stemming from space integration of fundamental solutions in (3). For systems without Signorini boundary conditions, Equation (4) can be solved at every time step starting at $i = 1$ where half of the quantities in $\mathbf{u}^i$ and $\mathbf{p}^i$ are unknown, that is $(u(0,t^i), u(L,t^i))$ or $(u(0,t^i), p(L,t^i))$ or $(u(L,t^i), p(0,t^i))$ or $(p(0,t^i), p(L,t^i))$.

In order to account for unilateral contact conditions, TD-BEM is coupled with the floating boundary method [8]. It sees Signorini boundary condition as a switch between non-homogeneous Dirichlet and homogeneous Neumann boundary conditions. This technique does not require an impact law in the BEM format, thus avoiding the chattering or energy dissipation that might exist in other methods [1].

To perform NSM, a shooting method is used. It calculates, here in the discretized framework, the difference between the initial state $\mathbf{q}_0 = (\mathbf{u}_0, \mathbf{v}_0)$ and the corresponding final state $\mathbf{q}(\mathbf{q}_0, T)$ after a yet unknown period T assumed to exist. For a periodic motion, the equality $\mathbf{q}(\mathbf{q}_0, T) = \mathbf{q}_0$

holds. In this work, $\mathbf{v}_0 = \mathbf{0}$ is assumed [11], and the problem to be solved thus reduces to: Find vector $\mathbf{u}_0$ and strictly positive integer m, where $T = m\Delta t$, such that

$$\mathbf{u}_m = \hat{\mathbf{G}}\mathbf{p} - \hat{\mathbf{H}}\mathbf{u} + \hat{\mathbf{U}}^m\mathbf{u}_0 = \mathbf{u}_0 \tag{5}$$

with the notations

$$\hat{\mathbf{G}} = [\hat{\mathbf{G}}^{m1}\ \hat{\mathbf{G}}^{m2}\ \cdots\ \hat{\mathbf{G}}^{mm}],\quad \mathbf{p} = \begin{bmatrix}\mathbf{p}^1\\ \mathbf{p}^2\\ \vdots\\ \mathbf{p}^m\end{bmatrix},\quad \hat{\mathbf{H}} = [\hat{\mathbf{H}}^{m1}\ \hat{\mathbf{H}}^{m2}\ \cdots\ \hat{\mathbf{H}}^{mm}],\quad \mathbf{u} = \begin{bmatrix}\mathbf{u}^1\\ \mathbf{u}^2\\ \vdots\\ \mathbf{u}^m\end{bmatrix}$$

where $\hat{\mathbf{G}}^{mj}$ and $\hat{\mathbf{H}}^{mj}$ are $(n+1)\times 2$ coefficient matrices and $\hat{\mathbf{U}}^m$ is a $(n+1)\times(n+1)$ coefficient matrix. Also, $\mathbf{u}_m = [u(x_k, m\Delta t)_{k=0\ldots,n}]$. Since some $\mathbf{p}^j$ and $\mathbf{u}^j$ in (5) are unknown, Equation (4) is invoked, that is:

$$\mathbf{H}\mathbf{u} = \mathbf{G}\mathbf{p} + \mathbf{U}\mathbf{u}_0 \tag{6}$$

with the notations

$$\mathbf{H} = \begin{bmatrix}\mathbf{H}^{11} & \mathbf{0} & \mathbf{0} & \ldots & \mathbf{0}\\ \mathbf{H}^{21} & \mathbf{H}^{22} & \mathbf{0} & \ldots & \mathbf{0}\\ \mathbf{H}^{31} & \mathbf{H}^{32} & \mathbf{H}^{33} & \ldots & \mathbf{0}\\ \vdots & \vdots & \vdots & \ddots & \vdots\\ \mathbf{H}^{m1} & \mathbf{H}^{m2} & \mathbf{H}^{m3} & \ldots & \mathbf{H}^{mm}\end{bmatrix}, \mathbf{G} = \begin{bmatrix}\mathbf{G}^{11} & \mathbf{0} & \mathbf{0} & \ldots & \mathbf{0}\\ \mathbf{G}^{21} & \mathbf{G}^{22} & \mathbf{0} & \ldots & \mathbf{0}\\ \mathbf{G}^{31} & \mathbf{G}^{32} & \mathbf{G}^{33} & \ldots & \mathbf{0}\\ \vdots & \vdots & \vdots & \ddots & \vdots\\ \mathbf{G}^{m1} & \mathbf{G}^{m2} & \mathbf{G}^{m3} & \ldots & \mathbf{G}^{mm}\end{bmatrix}, \mathbf{U} = \begin{bmatrix}\mathbf{U}^1\\ \mathbf{U}^2\\ \mathbf{U}^3\\ \vdots\\ \mathbf{U}^m\end{bmatrix}.$$

Combining linear systems (5) and (6) yields

$$\begin{bmatrix}\mathbf{H} & -\mathbf{U}\\ \hat{\mathbf{H}} & \mathbf{I}-\hat{\mathbf{U}}\end{bmatrix}\begin{bmatrix}\mathbf{u}\\ \mathbf{u}^0\end{bmatrix} = \begin{bmatrix}\mathbf{G}\\ \hat{\mathbf{G}}\end{bmatrix}\mathbf{p} \tag{7}$$

where $\mathbf{I}$ is a $(n+1)\times(n+1)$ identity matrix. In the floating boundary method, the Signorini condition is considered as a switch between Dirichlet and Neumann conditions. As soon as the contact duration T_c is set, the time step at which the switch happens is known, so does the boundary condition (Dirichlet or Neumann) at each time step at $x = L$. Thus Equation (7) can be solved by reorganizing the known and unknown entries in $\mathbf{u}$ and $\mathbf{p}$, according to the boundary condition at $x = L$ at each time step. Accordingly, by first assuming only one contact switch per period, such a strategy systematically skim through given intervals of values on period T and contact duration T_c (for a chosen Δt). However, physically unacceptable solutions can be found. Accordingly, admissibility is systematically checked to ensure complementary conditions (2) are satisfied. Non-admissible solutions with non-admissible penetration or contact forces are discarded. Such way of Signorini boundary condition enforcement is similar in spirit with a precedent scheme [12], but also shows differences in detail.

3.2 Frequency Domain Boundary Element Method

Frequency Domain Boundary Element Method (FD-BEM) is a frequency-domain form of BEM which targets periodic solutions. Via a Fourier transform in time at frequency ω

$$\tilde{u}(x) = \frac{1}{2\pi}\int_{-\infty}^{\infty} u(x,t)\exp(-i\omega t)\,\mathrm{d}t \tag{8}$$

the wave equation (1) becomes the well-known one-dimensional Helmholtz equation

$$\frac{\mathrm{d}^2\tilde{u}(x)}{\mathrm{d}x^2} + \kappa^2\tilde{u}(x) = 0 \tag{9}$$

where $\kappa = \omega/c$ is the frequency number. Similar to TD-BEM, FD-BEM is based on a weighted residual form of (9), where the weight function is the fundamental solution to the Helmholtz equation [2] with the corresponding BIE

$$2\tilde{u}(x) = \tilde{u}(0)\cos\kappa x + \tilde{u}(L)\cos(\kappa(L-x)) - \frac{1}{\kappa}(\tilde{p}(0)\sin\kappa x - \tilde{p}(L)\sin(\kappa(L-x))) \tag{10}$$

where $\tilde{p}$ is the Fourier Transform of p. Reading (10) on the boundary leads to

$$\begin{bmatrix} \kappa & 0 & -\kappa\cos\kappa L & \sin\kappa L \\ -\kappa\cos\kappa L & \sin\kappa L & \kappa & 0 \end{bmatrix} \begin{bmatrix} \tilde{u}(0) \\ \tilde{p}(0) \\ \tilde{u}(L) \\ \tilde{p}(L) \end{bmatrix} = 0, \quad \kappa \neq 0 \tag{11}$$

Through (11), $\tilde{u}$ at frequency ω can be solved for a combination of Dirichlet and/or Neumann boundary conditions. The time domain solution is then recovered through an inverse Fourier Transform. However, such a formulation is not well adapted when $u(L,t)$ and $p(L,t)$ are both constrained by the complementary condition (2) expressed in time domain. This complementarity condition can be equivalently recast into the equality [9]

$$r(t) \equiv p(L,t) + \max(0, \rho(u(L,t) - g_0) - p(L,t)) = 0, \quad \forall t \tag{12}$$

where $\rho \in \mathbb{R}^+$. In the remainder, the residual $r(t)$ will be made to vanish in an integral sense only. To insert (12) into FD-BEM with the aim of finding periodic solutions, Fourier expansions are considered, that is

$$p(L,t) = \frac{1}{2}a_0 + \sum_{n=1}^{\infty} a_n\cos n\omega_0 t + b_n\sin n\omega_0 t \tag{13}$$

where $\omega_0 = 2\pi/T$ is the base frequency. The corresponding base frequency number is $\kappa_0 = \omega_0/c$. Knowing that $u(0,t) = 0$, it follows from (11) that

$$u(L,t) = \frac{L}{2}a_0 + \sum_{n=1}^{\infty} \frac{\tan n\kappa_0 L}{n\kappa_0}(a_n\cos n\omega_0 t + b_n\sin n\omega_0 t) \tag{14}$$

Since initial velocity is assumed to be zero [11], all sin terms vanishes. Only constant and cos terms remain in equation (13) and equation (14).

The truncated Fourier series of $u(L,t)$ and $p(L,t)$ with m harmonics only is then substituted into (12). The Harmonic Balance Method (HBM) [5] is used to solve for the unknown coefficients $(a_0, a_1, a_2, \ldots, a_m)$. As a special case of Galerkin techniques, HBM reads

$$\int_0^T {}_i(t)r(t)\,\mathrm{d}t = 0, \quad \forall i \tag{15}$$

where the following family of functions is selected: $(1, \cos\omega_0 t, \cos 2\omega_0 t, \ldots, \cos m\omega_0 t)$. With $m+1$ equations, $m+1$ unknown coefficients can be solved for by the (Non-Smooth) Newton method. The function $p(L,t)$ is then reconstructed through (13) and so are other needed functions used to build the Nonsmooth Modes of Vibration. Basic continuation is implemented [7] in order to construct the desired backbone curves, by increasing ω_0 by a small value and solve again, with previous solution as initial guess.

4 RESULTS

In this section, the following is considered: $L = 1$, $c = 1$ and $g_0 = 0.5$. For TD-BEM, the bar is discretized into $n = 50$ elements in space with element length $\Delta x = L/n$ and time step is set accordingly. For FD-BEM, $m = 15$ is used.

The corresponding backbone curves are shown in figure 2. The backbone curve shows the

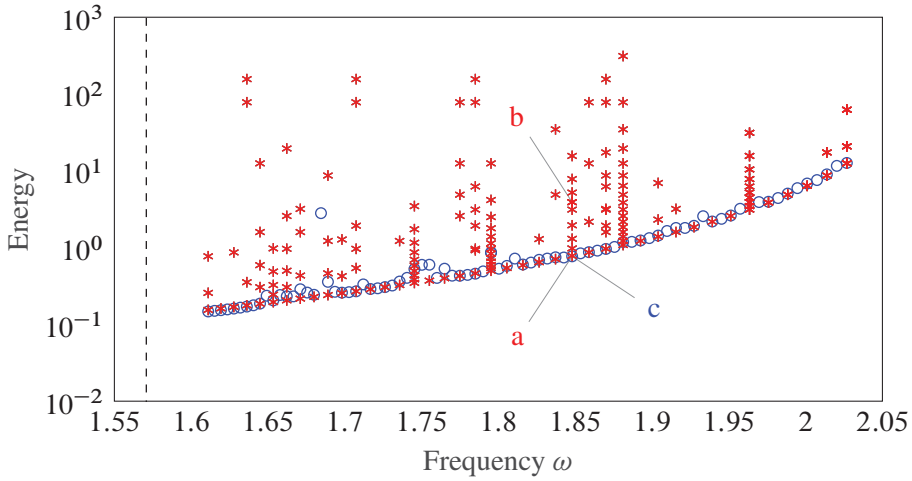

Figure 2: Backbone curve of the first mode. Red stars: TD-BEM/Shooting; blue circles: FD-BEM/HBM. Dashed line: linear mode

frequency-dependence of the total energy, and compares well with existing solutions [11], except for backbone curve near linear mode. Since contact period length decreases as frequency ω decreases [11], short period of contact cannot be evaluated precisely with $m = 15$ harmonics. Due to inaccurate Fourier expansion and residual function, HBM struggles converging to useful periodic solutions. Thus this part of solution is skipped.

It can be observed that TD-BEM captures more than one possible solution for a given frequency of vibration, which shows similar pattern of nonsmooth modes distribution with existing results [10]. Two such solutions feature the same frequency but distinct contact durations, as shown in figure 3 (see points a and b). This is induced by the full internal resonance in the investigated system [12]. Although solution b shows a low-frequency pattern similar to solution a, extra energy is introduced due to higher frequency mode. Comparatively FD-BEM/HBM currently cannot guarantee convergence to internal resonance solutions. More advanced continuation technique might be required to find internal resonance branches.

Displacement solved by FD-BEM/HBM at point c on backbone curve is depicted in Figure 4. Overall, the displacement field is similar to solution at point a in Figure 3. It is worth noting that Signorini conditions in FD-BEM/HBM is enforced in integral sense through (15), unlike in TD-BEM the complementary condition is met pointwise, ie for every time step. Accordingly, residual pointwise penetration occurs as shown in figure 5.

In terms of computational efficiency, FD-BEM/HBM is much superior to TD-BEM/Shooting. With the suggested discretization settings, TD-BEM is about 700 times slower than FD-BEM/HBM to find the whole backbone curve. When n increases, such difference is expected to increase, since the total number of combination between T and T_c to be skimmed increases in $O(n^2)$, while for FD-BEM/HBM the step size of continuation can be arbitrarily controlled.

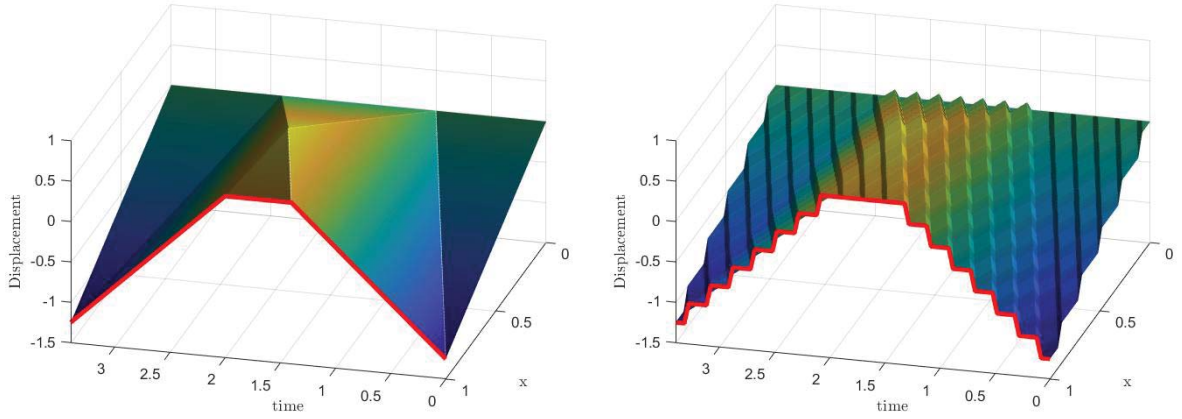

Figure 3: TD-BEM admissible displacement fields $u(x,t)$ at $\omega = 1.848$ with different energy levels. Left: point a in Figure 2, $T_c = 0.6$; Right: point b in Figure 2, $T_c = 0.75$

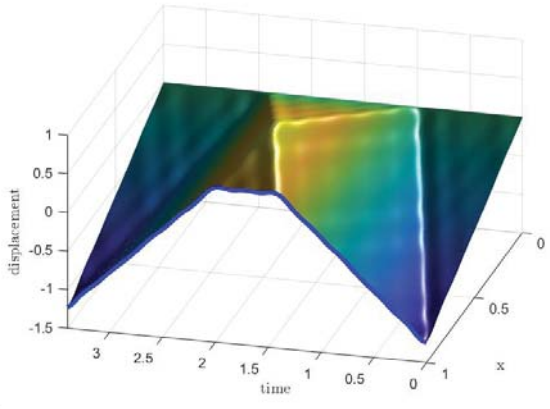

Figure 4: Displacement field found by FD-BEM/HBM at point c in Figure 2

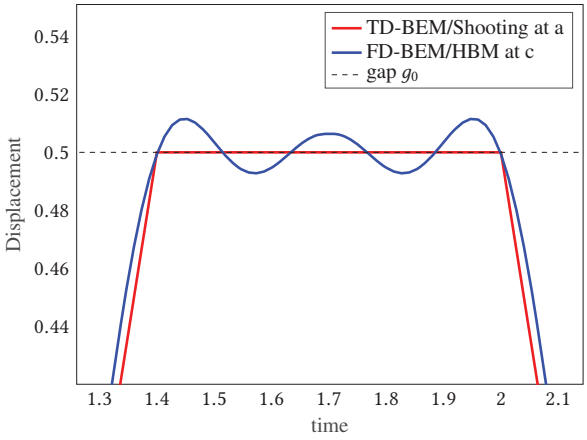

Figure 5: Zoom on displacement $u(L,t)$ found by FD-BEM/HBM at point c in Figure 2

5 CONCLUSIONS

In this paper, two methods have been introduced to perform nonsmooth modal analysis on a simple academic system. Both methods have shown capability to converge to admissible solutions.

The TD-BEM/shooting methodology has shown good capability of capturing highly-detailed step-wise admissible solutions. However, its challenging implementation leads to high computational costs. Although it has shown no numerical energy dissipation in this one-dimensional case, this might be untrue for higher dimensional systems, in which case it would become ineligible for such modal investigations.

Comparatively, FD-BEM/HBM features a much lower computational cost, at the cost of solving Signorini conditions in an integral sense only. This formulation is also energy preserving by construction and could be extended to problems in two or three dimensions. More advanced continuation techniques, such as pseudo-arclength [7], are expected to be coupled into existing FD-BEM/HBM scheme.

References

[1] V. Acary. “Energy conservation and dissipation properties of time-integration methods for nonsmooth elastodynamics with contact”. In: *Journal of Applied Mathematics and Mechanics / Zeitschrift für Angewandte Mathematik und Mechanik* 96.5 (May 2016), pp. 585–603.

[2] H. Antes. “A Short Course on Boundary Element Methods”. Lecture. Technische Universität Braunschweig, Germany, Nov. 2010.

[3] J. A. M. Carrer and V. L. Costa. “Boundary element method formulations for the solution of the scalar wave equation in one-dimensional problems”. In: *Journal of the Brazilian Society of Mechanical Sciences and Engineering* 37.3 (2015), pp. 959–971.

[4] K. F. Graff. *Wave motion in elastic solids*. Courier Corporation, 2012.

[5] J. C. Lindenlaub. “An approach for finding the sinusoidal steady state response of nonlinear systems”. In: *Proc. 7th Ann. Allerton Conf. Circuit and System Theory*. Univ. Illinois. 1969.

[6] W. J. Mansur. “A time-stepping technique to solve wave propagation problems using the boundary element method”. PhD thesis. University of Southampton, 1983.

[7] M. Peeters, R. Viguié, G. Sérandour, G. Kerschen, and J.-C. Golinval. “Nonlinear normal modes, Part II: Toward a practical computation using numerical continuation techniques”. In: *Mechanical Systems and Signal Processing* 23.1 (2009), pp. 195–216.

[8] B. Shorr. *The Wave Finite Element Method*. Foundations of Engineering Mechanics. Springer, 2012.

[9] D. E. Stewart. *Dynamics with Inequalities: impacts and hard constraints*. Vol. 59. SIAM, 2011.

[10] D. Urman and M. Legrand. “Nonlinear modal analysis of the bar in unilateral contact via analytical weak-solutions to the wave equation”. In: *27th Canadian Congress of Applied Mechanics*. Sherbrooke, Canada, May 2019.

[11] J. Venkatesh, A. Thorin, and M. Legrand. “Nonlinear modal analysis of a one-dimensional bar undergoing unilateral contact via the time-domain boundary element method”. In: *ASME 2017 International Design Engineering Technical Conferences*. Cleveland, United States, 2017.

[12] C. Yoong, A. Thorin, and M. Legrand. “Nonsmooth modal analysis of an elastic bar subject to a unilateral contact constraint”. In: *Nonlinear Dynamics* (2018), pp. 1–24.

EURODYN 2020
XI International Conference on Structural Dynamics
M. Papadrakakis, M. Fragiadakis, C. Papadimitriou (eds.)
Athens, Greece, 23–26 November 2020

SUBSONIC STALL FLUTTER ANALYSIS IN 2D BLADE CASCADE USING HYBRID BOUNDARY ELEMENT METHOD

C. Prasad[1] **and L. Pešek**[2]

[1] Institute of Thermomechanics of the CAS, v.v.i.
e-mail: cprasad@it.cas.cz

[2] Institute of Thermomechanics of the CAS, v.v.i.
e-mail: pesek@it.cas.cz

Keywords: Stall flutter, Aeroelasticity, Boundary element method (BEM), Discrete vortex particle method (DVM), Panel method, Blade cascade, Viscous-inviscid coupling.

Abstract. *In this paper study of subsonic stall flutter in the steam turbine blades is carried out. Subsonic stall flutter is one of the dominating and frequently occurring aeroelastic phenomena in large power turbines. The study is carried out by both experimentally and numerically to understand the fundamental physics behind it. Aerodynamics damping (AD) is one of the parameter to analyze the aeroelastic stability of stall flutter in 2D blade cascade. To numerically model the stall flutter in steam turbine a medium fidelity numerical tool is developed. In this research project computationally less expensive potential flow based hybrid boundary element method e.g. panel method, flow model is developed to model the unsteady flow in low pressure turbine blade cascade and to estimate the aeroelastic stability (stall flutter) parameters. A modified version panel method using viscous-inviscid coupling including discrete vortex particle (DVM) free wake model can be used for the separated flow conditions as it is in stall flutter case. These methods are widely adopted for aeroelastic modeling of wind turbines, helicopter rotors, and aircraft aeroelasticity problem . The AD for different Inter blade phase angle (IBPA) is estimated using newly developed hybrid BEM based flow model. The estimated AD will be compared with experimental data and CFD results to evaluate the efficiency and the accuracy of the model.*

1 INTRODUCTION

To meet the exponential growth in electrical power demand world wide the efficiency improvement of the existing power plants and the development of high energy output power plants are being considered in the world. Most of these power plant uses fossil fuel or nuclear material as a heat source to generate electricity with help of power turbines e.g. gas turbine, steam turbines. Therefore, power turbine are key component of whole energy generation system. In the quest to generate more power in the nuclear power plants or coal fired power plants giant steam turbines are being installed fully and efficiently utilize the large volume steam produced in it and this can achieved by increasing the physical dimension of the power turbine, but if one hand increasing the size of power turbine are the solution it poses other type engineering challenges which directly effect the safety and the life cycle of these large power turbines. One of such problem engineer or designer need to address is flow induced vibration. The larger low pressure steam turbine blades are more prone to mechanical vibration due to longer size and less stiffness, which leads to high-cycle fatigue failure and in worse case blade loss and damaging the whole system. The aeroelasticity of low-pressure turbine blade has been the subject of much attention in the past and recent years, [1, 2]

In this paper study of subsonic stall flutter in the steam turbine is carried out. Subsonic stall flutter is one of the dominating and frequently occurring aeroelastic phenomena in large power turbines. Subsonic stall flutter in steam turbine LP stage is very complex physic phenomena and remains a very active topic of research. However, very less work has been done in the subsonic dynamic stall flutter in steam turbine cases in past. The majority of work on subsonic dynamic stall flutter is carried out either on gas turbine or jet engine compressors and fan blades [3, 4]. The problem of dynamic stall flutter in LP turbine blades are getting more important because of ever increasing size of blading to produce more electricity. Therefore, in this research the issue of dynamic stall flutter is studied in details. The study will be carried out by both experimentally, numerically to understand the fundamental physics behind it. Aerodynamics damping (AD) is one of the parameter to study the aeroelastic stability of stall flutter in 2D blade cascade.

Reduced order flow solver: To numerical study the stall flutter in steam turbine there are well developed computational fluid dynamics (CFD) and computational structural dynamics (CSD) based aeroelastic models available for this purpose, however, theses CDF-CSD based models are computationally very expensive. In CFD-CSD based aeroelastic models flow computation is responsible for majority of computational time. Therefore, in this research project computationally less expensive potential flow based hybrid boundary element method (BEM) flow model will be developed to model the unsteady flow in low pressure (LP) turbine blade cascade and to estimate the aeroelastic stability (stall flutter). The panel method (PM) is one of such methods and first proposed by Hess and Smith [5] to model the lifting and non-lifting potential flow around slender bodies. These methods are good compromise of speed and accuracy and can be used for complex geometry until the flow fulfills the criteria of potential flow and free from flow separation. However, for subsonic stall flutter modified PM using viscous-inviscid coupling including discrete vortex particle (DVM) wake model can be used for the separated flow case [6, 7, 8] as it is in stall flutter. These methods are widely adopted for aeroelastic modeling of wind turbines, helicopter rotors, and aircraft aeroelasticity problem [6, 8, 9]. The AD for different Inter blade phase angle (IBPA) is estimated using newly developed hybrid BEM based flow model. The estimated AD will be compared with experimental data and CFD results to evaluate the efficiency and the accuracy of the model. The successful implementation of the proposed aeroelastic model for subsonic stall flutter in 2D cascade will have significant impact

on the computational time reduction and will give researcher and engineering freedom to iterate different blade profile in very short time period at preliminary LP turbine design stage for blade design optimization and to understand the subsonic stall flutter in more details in steam turbine application.

2 Hybrid boundary element method for flow modeling

2.1 Panel method

The panel method is a family of boundary element methods and it is often employed to simulate the aerodynamic flow over lifting and non lifting bodies in attached flow conditions. In the PM flow field is assume to be inviscid and irrotational and it gives the solution of of Laplace's potential flow equation and 2D version can be given by Eq. 1

$$\nabla^2\Phi(x,y) = \frac{\partial^2\Phi}{\partial^2 x} + \frac{\partial^2\Phi}{\partial^2 y} = 0 \tag{1}$$

where $\Phi(x,y)$ is the scalar velocity potential and it is function of position vector $r(x,y)$ .The surface panel method discretization and solution strategy over lifting airfoil is given in the Fig 1. In the PM to construct the flow field and find the solution of the field variables, singularity

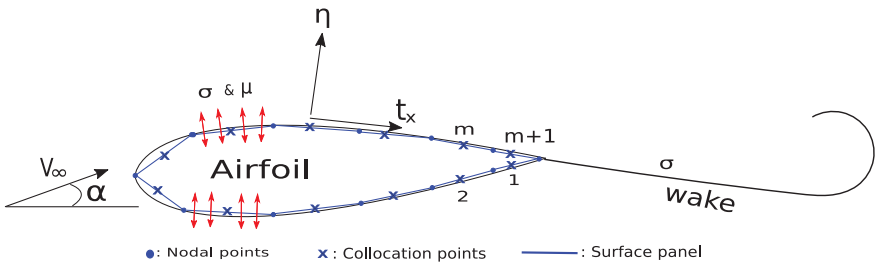

Figure 1: Panel method discretization of airfoil using source and doublet singularities panel

panel elements are placed over the airfoil surface and in the wake. In this work each surface panel elements include a combination of constant strength source (σ) and a doublet (μ) distribution while the wake panels feature only doublet panels because the wake do not carry any aerodynamic load. Notice that in these formulation, the integration is to be carried out along the complete surface of the airfoil. Using the superposition principle, any such distribution of sources and doublet satisfies Laplace's equation, but we will need to find the conditions for (σ) and a doublet (μ) such that the flow tangency boundary condition and the Kutta condition are satisfied. Therefore, boundary conditions (BC) are imposed on control points lying on the centroid of each surface panel as shown in Fig 1.The required BCs are, (1) enforcing the impermeability flow at solid or a fixed normal flow condition ($\nabla\Phi \cdot n = V_n = 0$), (2) Far field: The disturbance created by the singularities on the body and wake must disappear at infinity ($\lim_{|\mathbf{r}|\to\infty} \nabla(\Phi - \Phi_\infty) = 0$). (3) the Kutta condition and Kelvin's theorem, are imposed in order to obtain a complete description of the flow field and the resulting aerodynamic loads. The pressure field (p) is then obtained solving the unsteady Bernoulli equation 6 .

$$\frac{\partial\Phi}{\partial t} + \frac{p}{\rho} + \frac{V^2}{2} = const \tag{2}$$

Furthermore, the surface panels are arranged so as to represent the actual airfoil's geometry. More details about required BC, numerical implementation and determining field variables using unsteady PM can be find in Katz [10]. Apart from many advantages of PM over CFD in terms of speed an accuracy, it suffers from one main disadvantage that is PM can not be employed for separated flow regimes and also it ignores the viscous effect of the fluid. Therefore, in this present paper a modified version of panel method will be used to simulated flow separation including viscous effect close to the body surface in boundary layer (BL) region Fig.2, BL is thin layer of fluid close vicinity of the solid boundary where the fluid viscous effects are dominant. Therefore, in the modified version of the panel method two way viscous-inviscid loose coupling strategy will be adopted to simulate the flow separation and take the account of the viscous effect of the fluid. In this research work BL parameters are estimated with the help of 2D integral boundary layer method.

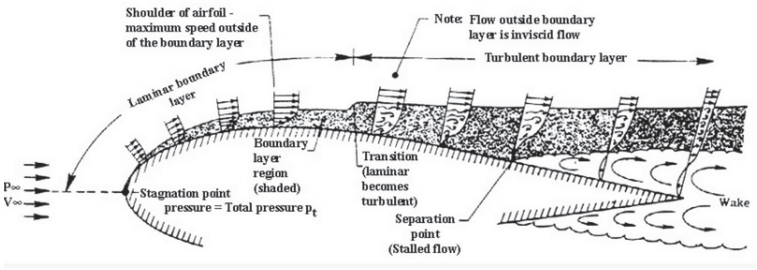

Figure 2: Concept of boundary layer over wing surface [10]

2.2 Integral Boundary layer method :

The integral form of 2D BL equations which relies on the *Von kármán momentum integral equation* can be given by Eq. 3

$$\frac{d\theta}{dx} + \frac{\theta}{U_e}(2+H)\frac{dU_e}{dx} = \frac{1}{2}c_f \tag{3}$$

in which

$$H = \frac{\delta^*}{\theta} \quad and \quad c_f = \frac{2\tau_w}{\rho U_e} \tag{4}$$

Here U_e is the edge velocity, H is the shape factor of the BL velocity profile, θ is momentum thickness of BL, δ^* displacement thickness, τ_w wall shear stress and c_f is the skin friction coefficient of the body surface. The BL equation are solved over airfoil surface along the streamwise direction to determine the separation points. Once the separation points are estimated on the surface a second share layer is shed from the point.

In modified version of PM which is used here, the viscous effect is modeled using integral form of BL equation and the inviscid part with classical PM. A similar modified version of PM with one way viscous-inviscid coupling with double wake technique is adopted by Prasad et al.[9] to simulate the separated flow around wind turbine blades. However, this type of modified PM can successfully simulated steady separated flow cases till the separation occurs only in the suction side of the wing, furthermore, in the Prasad's model static separation points are assumed which means once the separation point is estimated by solving the BL equation it remains unchanged. This is one of the drawback for the model to be employed in dynamic

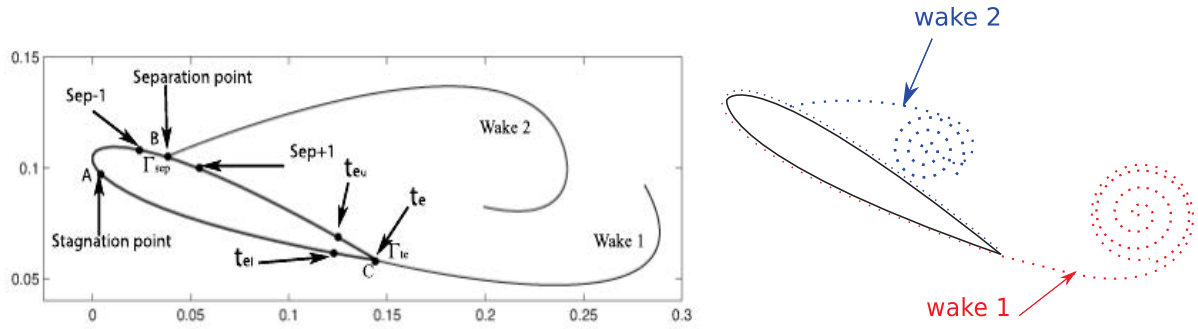

Figure 3: Double wake model using modified PM [9]

stall flow simulation where separation point changes in time, moreover, it is also challenging to model the unsteady wake using continuous doublet vortex sheet due to numerical instability issue. Therefore, a more sophisticated strategy is adopted to model unsteady wake shape in this research with help of discrete vortex particle method (DVM).

2.3 Discrete vortex particle method

Unlike the Prasad et. al. model in the this paper separation points are calculated at each time step not only once for the oscillating airfoil. Moreover, 2D discrete vortex particle method (DVM) will is used to simulate the unsteady wakes using 'vortex blob'. In the DVM the motion and evolution of the vortex blobs are governed by the vorticity transport equation and for the incompressible flow it can be given by Eq. 7

$$\frac{D\omega}{Dt} = (\omega.\nabla)u + \nu\nabla^2\omega \tag{5}$$

where ω is vorticity vector, u velocity vector, ν is kinematic viscosity, and ∇^2 is Laplace's operator respectively. Similar technique to model the unsteady wake is adopted by [7, 8].

2.4 Vortex blob wake conversion

Once the separation point is known a doublet panel is shed from the separation point and second one from the trailing edge.These first panel is nascent wake panel as shown in the Fig. 4. In the next time step these nascent panel converted into vortex blob and a new nascent wake panel is shed again from new separation point. The conversion of doublet wake panel into

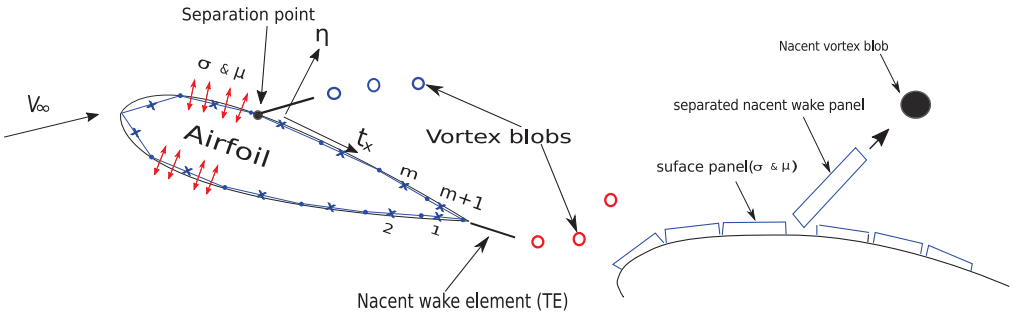

Figure 4: Vortex blob wake conversion model in hybrid PM flow solver

equivalent vortex blob is carried out by similar approach as proposed by [7, 8] to model unsteady wake .The process continue till the edn of the time step or preset convergence criteria of the aerodynamic forces.

3 Flutter analysis Method

The balance between the structure and aerodynamic forces in the system is represented by the aeroelastic Eq. 6

$$[M]\{\ddot{X}\} + [G]\{\dot{X}\} + [K]\{X\} = \{F_{ab}(t)\} \tag{6}$$

where $[M]$, $[G]$, and $[K]$ are the model mass, model damping and model stiffness matrices respectively,$\{X\}$ represents the modal coordinate vector and finally $\{F_{ab}(t)\}$ is the modal unsteady aerodynamic force vector which contains two terms: $F_{disturbance}(t)$ that includes the aerodynamic disturbances upstream and downstream the blade and $F_{damping}(t)$ which represents the aerodynamic damping resulting from the interaction between the blade itself and the flow. For flutter analysis, only the aerodynamic forces due to the vibration of the blade are considered resulting in $F_{disturbance}(t) = 0$ and simplifying the above equation to: Eq. 6

$$[M]\{\ddot{X}\} + [G]\{\dot{X}\} + [K]\{X\} = \{F_{disturbance}(t) + F_{damping}(t)\} \tag{7}$$

The solution of the above equation Eq. 7 allows the determination of the aerodynamic damping and thus the aeroelastic stability of the system.

There are different numerical methods can be used to approximate the aerodynamics characteristics of the system. One of them is “Time Linearized Method” assumes that the unsteady perturbations in the flow are small compared with the mean flow. Then the unsteady flow can be approximated by small harmonic perturbations around a mean value.

In the present research work potential flow based hybrid PM method is used with linearized flow equations assuming the small unsteady perturbation. TWM method with principle of linear superimposition is used to estimate the aerodynamic damping [11, 12] . In the cascade aerodynamic influence of main blade on which the damping is evaluated and the influence other blades on it is superimposed to get the total aerodynamic damping.

Figure 5: Indexing of blades in cascade [13]

Therefore, in TWM the total unsteady response on a blade (here blade “0” in Fig.5) composed of the individual responses from itself and from the other blades lagged by the respective multiple of the IBPA and can be given by Eq. 8

$$\hat{c}^{m,\sigma}_{P,A,twm}(x,y) = \sum_{n=-N/2}^{n=+N/2} \hat{c}^{n,m}_{P,A,ic}(x,y).e^{-i\sigma.n} \tag{8}$$

where $\hat{c}^{m,\sigma}_{P,A,twm}(x,y)$ is the complex pressure coefficient at point (x,y,z) , acting on blade m with the cascade oscillating in traveling wave mode with interblade phase angle σ and

$\hat{c}^{n,m}_{P,A,ic}(x,y)$ is the pressure coefficient of the vibrating blade n , acting on the non-vibrating reference blade m at point (x,y,z) . The coefficients $\hat{c}^{n,m}_{P,A,ic}(x,y)$ are , commonly referred to as local aerodynamic influence coefficients and it is normalized by dynamics pressure "q" and amplitude of oscillation "A". The pressure coefficient is integrated over the surface to get the unsteady force and for the work done for each cycle is obtained by multiplying the total force by respective oscillating displacement. Therefore, aerodynamic damping parameter is given by work done per cycle and normalized by π and amplitude of oscillation "A" and is given in Eq. 9

$$Aerodynamic\ damping(\Xi) = -\frac{c_w}{\pi A^2} \tag{9}$$

where c_w is the aerodynamic work done per cycle. The $positive$ value of Ξ indicates the flow acting in stabilizing manner whereas $negative$ value can cause flutter, therefore, unstable.

3.1 Cascade flutter analysis with unsteady PM

To construct the flow field around oscillating cascade as shown in the Fig.6 using hybrid PM solver each cascade is discretized into small number of panels. Constant strength source and doublet singularity element are distributed over the discretized airfoils, and free wake is modeled using DVM, . In order to evaluate the aerodynamic damping at reference airfoil ("0") the velocity potential (Φ) induced by source and doublet singularity element of the airfoil and the all the other airfoils oscillating in the respective phase lag is superimposed linearly along with the effect of free wakes . This is arranged in matrix form and called aerodynamics influence coefficient matrix (AICM) . With AICM along with zero normal normal flow on the body wall, system of equation $[A]\{x\} = \{y\}$ can be solved to estimate the unknown strength of perturbation potential. More details about the this numerical calculation is given in Katz [10] and the same formulation is adopted here. Once the perturbation potential is known the unsteady pressure coefficient can easily be estimated, hence the aerodynamic force and the work for each time step, the summation of all the time step in one complete cycle gives the total aerodynamic work done in one period.

The experimental test is carried out on 5 blade cascade with NACA0010 series airfoil and flow condition are, constant inlet velocities , 10m to30 m/sec, mean camber line incidence angles ($\alpha_0 = 5°to15°$), pitching amplitudes ($\bar{\alpha} = 2°to5°$), reduced frequencies $k = 0.015\ to\ 0.3$ based on semi chord, and 8 IBPA (φ) = 0, $\pm45°$, $\pm90°$,$\pm135°$, $\pm180°$. This kind of superimposed velocity potential can be obtained for any airfoil in the cascade. The oscillatory motion

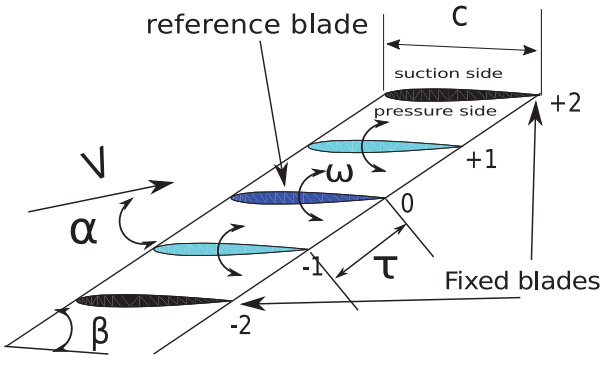

Parameter	Value
Chord (C)	70mm
Flow angle (α)	$+5°to+15°$
Stagger angle (β)	$+15to+25°$
Slant height (τ)	18mm
Oscillating feq.(ω)	10hz to 30hz
Oscillating Amp.($\bar{\alpha}$)	$\pm2mmto\pm$ 5mm

Figure 6: Schematic diagram of and nomenclature of 2D cascade

of the cascade blade can be given in complex form by

$$\alpha(t) = \bar{\alpha} e^{i(\omega t \pm n\varphi)} \tag{10}$$

where n is blade number Fig.5 and the ω is the frequency of oscillation in rad/sec and $\omega = \frac{2.k.U_\infty}{chord}$. Hence the effective angle of attack (α_{eff}) at any time instance is given by Eq. 11

$$\begin{aligned} \alpha_{eff}(t) &= \alpha_0 + \alpha(t) \\ &= \alpha_0 + \bar{\alpha} e^{i(\omega t \pm n\varphi)} = \alpha_0 + \bar{\alpha} sin(\omega t \pm n\varphi) \end{aligned} \tag{11}$$

The blade cascade and geometry and the related parameter values are given in the Fig.6. The wake shape and flow flied around the cascade simulated using hybrid PM is presented in the Fig.7 and Fig.9 for two different time steps. In the Fig.7 the evaluation of the flow field is

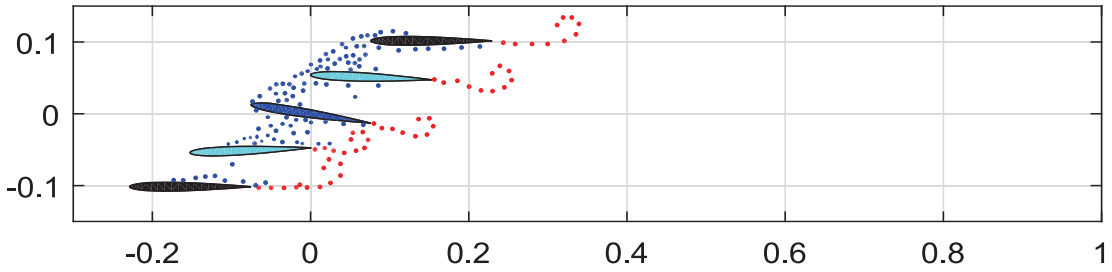

Figure 7: Vortex blob wake shapes at time step T= 15 using hybrid PM at $\alpha_0 = 11°$ and $\bar{\alpha} = 5°$ at reduce frequency $k = 0.115$ and wind speed $Q_\infty = 30.0m/s$

depicted at the first 15 time step the time step size is $\delta t = 0.023$ sec. and oscillating frequency is 15 Hz with amplitude of oscillation is 3 degree and inflow angle 11 degree and k=0.05. The flow start to separate from the suction side of the all airfoils, but the separation position varies in the three oscillating airfoils depending upon the oscillation cycle. In the Fig.9 the wake shapes

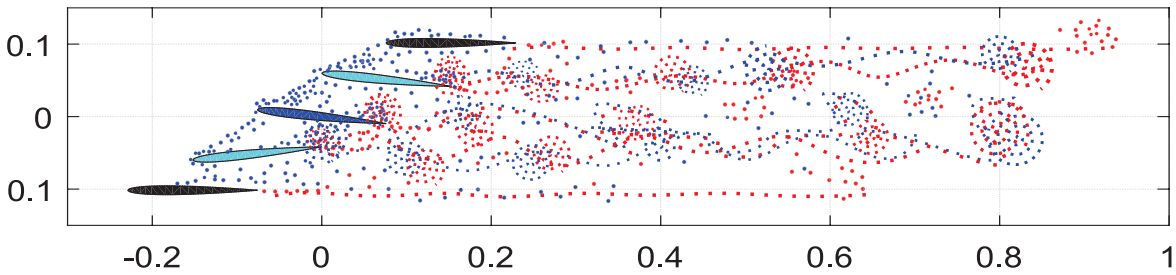

Figure 8: Vortex blob wake shapes at time step T= 150 using hybrid PM at $\alpha_0 = 11°$ and $\bar{\alpha} = 5°$ at reduce frequency $k = 0.115$ and wind speed $Q_\infty = 30.0m/s$

and flow at 150th time step is presented. It can noticed that the leading edge separated shear layer from the lower blade influencing the blade above it strongly, which is complies with the real case. However, there in not significant separation observed in the two fixed airfoils (blade no. -2 and +2 in the Fig.6). Furthermore, in the convergence point of view the proposed hybrid

PM performs very well and starts to converge after 50 time steps for both test cases. Also the fast convergence is due to the fact that PM is based on Laplace's potential flow equation which itself second order linear differential equation, therefore, solution start to converge as soon as starting vortices moves away from the body in unsteady hybrid PM model. For the present tests cases it starts to to happens around 50th time step.

4 Experimental setup for 5 Blade cascade

The physical model of the blade cascade is given in the Fig.9. Five 3D printed blade with NACA0010 profile and 70mm chord length and 100 mm span is attached with base plate. The base plate can be rotate to set the desire angle of attack (α), each blade can also be slide horizontally to set the stagger angle of the cascade. Each of the five blades are attached in the base plate with a mechanism which allows it feed with individual excitation. The experiment is performed in two different configurations. In one configuration the two ends blades (-2 and +2 blade number) in Fig.6 are fixed and the three blades 0, -1 and +1 are excited with the help of shaker, the potion of there shaker are shown in the top right in the Fig.9. All the blades are placed inside rectangular channel with one flow inlet from wind tunnel and the exist as shown in the Fig.9. There gap between channel walls and the blade tip is negligible to ensure the 2D flow field over the cascade and minimize the tip vortex effects. In the second configuration all the blades hang with and free to move in pitching motion, and they are suspended with the help of torsional springs. The experimental test campaign is carried out for wide at different flow speed from 10 m/sec till 50 m/s, different flow angle (from $0°$ till $15°$ and stagger angles (from $10°$ to $25°$). The aerodynamic damping is estimated by multiplying the total force by total pitching displacement in one cycle of oscillation.

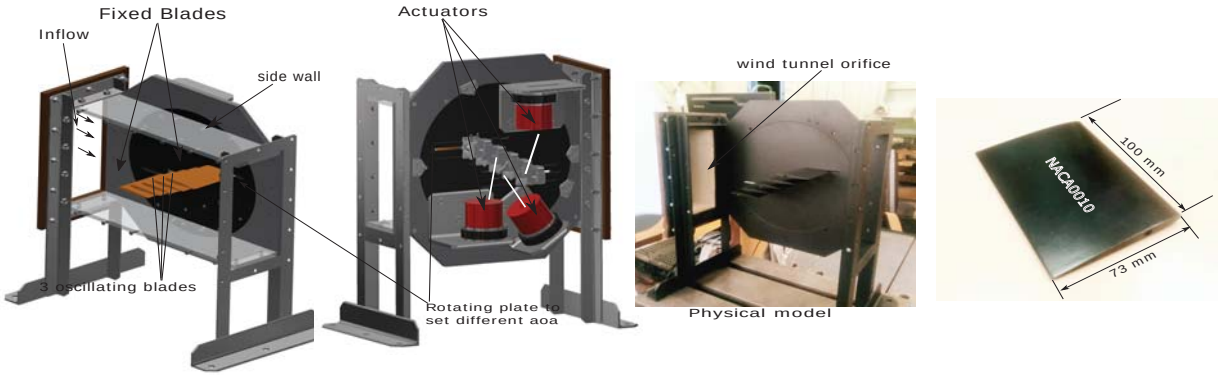

Figure 9: Experimental setup and physical model of the 5 blade cascade

5 Results

At first the the isolated pitching airfoil test is selected for the comparison purpose. The experimental results are obtain from the Galbraith et al. [14]. A cyclic lift coefficient of NACA0015 test results which corresponds the stall flow condition, are compared with simulated results using hybrid PM and presented in the Fig.10. In the Fig.10 results of the present model are in good agreement with the experimental data, although they exhibit a slight overestimation of the lift for high angle of attack (above $15°$). A small deviation in the shape of the C_L loop can be

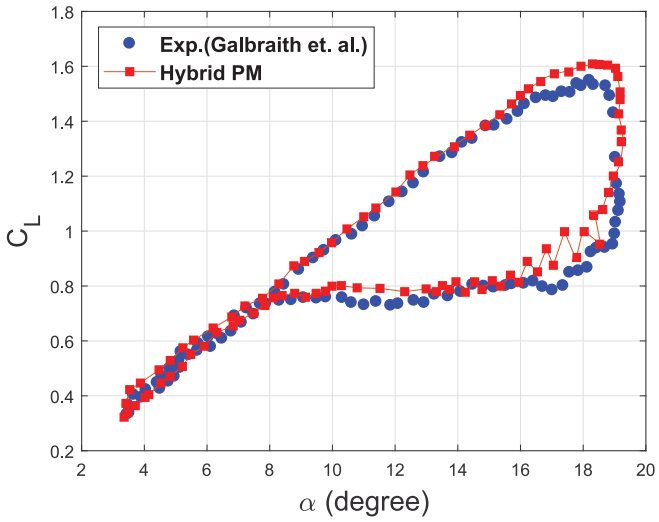

Figure 10: Lift coefficient vs. angle of attack for pitching aerofoil NACA 0015 at Re =1.5×10^{06}, reduce frequency (k) = 0.05

detected in the region close to the maximum pitching angle during the downstroke. This can be caused by strong separated vortex originated due to downstrok motion of the airfoil at the peak maximum angle. Furthermore, the present numerical results exhibit some oscillations when the stall occurs (between 13° to 18°) which is caused by the accumulation of the vortex blob at one point of time which may induce strong velocity potential on the airfoil surface. The problem can be solved by using more sophisticated diffusion method or eliminating the some blobs during the this period. Furthermore, it is worth mentioning that the time computation time taken to achived the converge result for pitching airfoil is approximately 2.5 CPU mins on single core Intel i7, which can be significantly lower then CFD based model, if adopted for the same test case.

The hybrid PM is then employed to estimate the aerodynamic damping for the 5 blade cascade model and the estimated AD vs. IBPA is presented in the Fig.11. the estimated AD curve shows that the present solver managed to predict stable and unstable IBPA region and for the 0 IBPA the cascade is stable for the used flow condition. However, due to lack of experimental result at this moment the accuracy of the results can not be verified. However, a similar linear cascade test case is presented by Prasad et al.[15], but for classical flutter cases. In his study Prasad et al. used CFD model for 11 blade 2D cascade to estimate the AD s-curve, and computational time taken is 13 CPU hrs on 4-core, Intel i7 processor, which is significantly higher compared to present proposed method which takes approximately 12 CPU mins to estimate the AD s-curve as shown in the Fig.11. Hence, the present method can be computationally more efficient than the CFD based model for the stall flutter test condition, if CFD is used, however, the CFD model estimation can be more accurate compared to the hybrid PM, because flow separation effects can be better represented by turbulence models in CFD based numerical models.

6 Conclusion

The paper present the development and implementation of a medium fidelity flow solver based on boundary element panel method to simulate the subsonic stall flutter in the 2D cas-

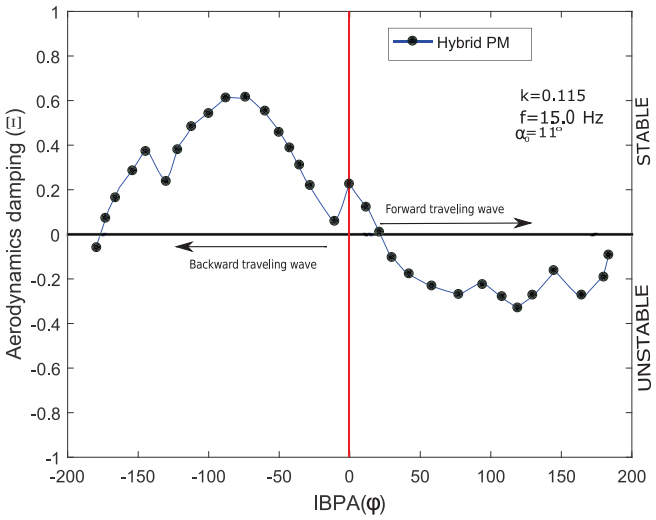

Figure 11: The AD (Ξ) vs IBPA, at $\alpha_0 = 11°$ and $\bar{\alpha} = 5°$ at reduce frequency $k = 0.115$ and wind speed $Q_\infty = 30.0m/s$ using hybrid PM

cades. To model separated flow the classical panel method is modified using viscous-inviscid coupling technique and the free wake is modeled using discrete vortex particles. The hybrid PM is tested for isolated pitching airfoil test case where the estimated cyclic lift coefficient vs angle of attack results shows good agreement with simulated one in Fig.10.Furthermore, the AD for the 5 blade cascade is estimated using the similar method for the subsonic stall flow condition in Fig.11. However, the experimental results were not ready by the time of submission of this paper, therefore, accuracy of the results can not be verified. However, the simulated AD looks reasonable for the similar test case in other literature. Moreover, the present method show significant reduction in the execution compared to CFD based numerical model. Therefore, the proposed method is good compromised of speed and accuracy over CFD based solvers and it has great potential to be used industrial application.The successful implementation of the proposed aeroelastic model for subsonic stall flutter in 2D cascade will have significant impact on the computational time reduction and will give researcher and engineering freedom to iterate different blade profile in very short time period at preliminary LP turbine design stage for blade design optimization and to understand the subsonic stall flutter in more details in steam turbine application.

Future work: In future the experimental results for the 5 blade cascade will be compared with the simulated results for AD and the wake shapes and also unsteady pressure field over the blade surface at different flow conditions.

Acknowledgment: This research is supported by the research project of Technology Agency of the Czech Republic under the NCK framework No. TN1000007, sub-project V1.7.3: "The procedure for calculating the flutter of long blades."

REFERENCES

[1] H. Atassi and T. Akai. Effect of blade loading and thickness on the aerodynamics of oscillating cascades. In *16th Aerospace Sciences Meeting*, page 277. A1AA, 1978.

[2] J Panovsky and R. E Kilelb. A design method to prevent low pressure turbine blade flutter. *Journal of engineering for gas turbines and power*, 122(1):89–98, 2000.

[3] Mehdi Vahdati, Nigel Smith, and Fanzhou Zhao. Influence of Intake on Fan Blade Flutter. *Journal of Turbomachinery*, 137(8), 08 2015.

[4] James D Jeffers and Carl E Meece Jr. F100 fan stall flutter problem review and solution. *Journal of Aircraft*, 12(4):350–357, 1975.

[5] J. L. Hess. Calculation of potential flow about arbitrary three-dimensional lifting bodies. Final Technical Report MDC J5679-01, Naval Air Systems Command, Department of the Navy, 1972.

[6] Vasilis A. Riziotis. and Spyros G. Voutsinas. Dynamic stall modelling on airfoils based on strong viscous-inviscid interaction coupling. *International journal for numerical methods in fluids*, 56:185–208, 2008.

[7] Néstor Ramos García, Antoine Cayron, and Jens Nørkær Sørensen. Unsteady double wake model for the simulation of stalled airfoils. *Journal of Power and Energy Engineering*, 3:20–25, 2015.

[8] Alessandro Zanon, Pietro Giannattasio, and Carlos J Simão Ferreira. A vortex panel model for the simulation of the wake flow past a vertical axis wind turbine in dynamic stall. *Wind Energy*, 16(5):661–680, 2013.

[9] Chandra Shekhar Prasad and Grigorios Dimitriadis. Application of a 3d unsteady surface panel method with flow separation model to horizontal axis wind turbines. *Journal of Wind Engineering and Industrial Aerodynamics*, 166:74 – 89, 2017.

[10] Joseph Katz and Allen Plotkin. *Low-Speed Aerodynamics*. Cambridge University Press, 2nd edition, 2001.

[11] Yoji Hanamura, Hideo Tanaka, and Kazuo Yamaguchi. A simplified method to measure unsteady forces acting on the vibrating blades in cascade. *Bulletin of JSME*, 23(180):880–887, 1980.

[12] Edward F Crawley. Measurements of aerodynamic damping on the mit transonic rotor. Technical report, Cambridge, Mass.: Gas Turbine & Plasma Dynamics Laboratory, Massachusetts Institute of Technology,[1981], 1981.

[13] T Fransson. *Aeroelasticity in axial flow turbomachines*. Von Karman Institute for Fluid Dynamics, Brussels , Belgium, 1999.

[14] RAM Galbraith, MW Gracey, and E Leith. Summary of pressure data for thirteen aerofoils on the university of glasgow's aerofoil database. *GU Aero report 9221, University of Glasgow*, 1992.

[15] Chandra Shekhar Prasad and Luděk Pešek. Efficient prediction of classical flutter stability of turbomachinery blade using the boundary element type numerical method. *Engineering Analysis with Boundary Elements*, 113:328 – 345, 2020.

EURODYN 2020
XI International Conference on Structural Dynamics
M. Papadrakakis, M. Fragiadakis, C. Papadimitriou (eds.)
Athens, Greece, 23–26 November 2020

GEOMETRICALLY NON-LINEAR FREE AND FORCED VIBRATION OF C-F-C-F RECTANGULAR PLATE AT LARGE TRANSVERSE AMPLITUDES

A. MAJID[12], E. ABDEDDINE[12], Kh. ZARBANE[2] and Z. BEIDOURI[2]

[1]Centre d'Etude Doctorale, Ecole Nationale Supérieure de l'Electricité et de Mécanique, Hassan II University of Casablanca
Km7 Route El Jadida, Casablanca, Morocco
e-mail: {a.majid,e.abdeddine}@ensem.ac.ma

[2] Laboratoire Mécanique, Productique et Génie Industriel (LMPGI), Ecole Supérieure de Technologie (ESTC), Hassan II University of Casablanca,
BP 8012 Oasis, Casablanca, Morocco
e-mail: khalid.zarbane@univh2c.ma, zbeidouri@gmail.com

Keywords: Rectangular plate, Geometrically non-linear, Lagrange's equations, Non-linear transverse vibration.

Abstract. *The main purpose of the paper is to investigate the effect of geometrically non-linear first mode shape free and force transverse vibration of "Clamped-Free-Clamped-Free rectangular plate", denoted as 'C-F-C-F RP', at large vibration amplitudes. Lagrange's equations and the harmonic balance method are used in order to formulate the problem that lead to obtain a non-linear algebraic equations. These later can be used to determine the dependency of displacement amplitudes, excitation frequencies, and the deflection associated to the first mode shape. In addition, it exhibits the contribution coefficients of higher mode shapes that contribute on the first mode shape. The obtain equations are solved via explicit solution which is an approximate method and which is used and compared previously in the case of free and forced vibration. The numerical obtain results can be used to predict the influence of the excitation frequencies and the level of applied forces on the dynamic response of thin C-F-C-F flat isotropic structures.*

Nomenclature

(x, y)	Point co-ordinates of RP.	a, b	Length, width of the plate.
$*$	The star exponent indicates non-dimensional parameters.	a_i	Basic function contribution.
α	The plate aspect ratio $\alpha = b/a$.	D	Bending stiffness.
$\mathrm{W}(x, y)$	Transverse displacement at point (x, y) on the plate.	E	Young's modulus.
$\mathrm{w}_{ij}(x, y)$	Basic function obtained as product of the i^{th} Clamped–Clamped and j^{th} Free–Free beam functions in the x and y directions.	F^c	Concentrated harmonic force.
		f_i^c	Generalized force corresponding to concentrated force F^c.
		H	Thickness of the plate.
ρ	Mass density per unit volume of the plate.	q_i	Teneralized co-ordinate.
		S	Dimensional surfaces of RP.
ϑ	Poisson ratio.	T	Knitecs energy.
		V_f, V_a	Bending and axial strain respectively.

1 INTRODUCTION

The thin structures encounter a large amplitude of deflections when they are subject to large external loads; in other words, these structures present geometrically non-linear vibrations. In aircraft skin panels, geometric non-linearity often occurs when the aircraft is subject to high aerodynamic forces [1]. This non-linearity is usually produced by the membrane stresses in the structure and results in an increase of resonance frequencies (hardening or softening resonance) and mode shape changes with regard to level of applied forces on the structure at large vibration amplitudes [2].

The literature on isotropic plate shows a variety of configurations and approaches which are listed and presented in the references [3, 4, 5, 6]. These configurations were numbered at 21 boundary conditions cases and created by Clamped, Free and Simply supported at the plate's edges that were investigated previously. These configurations have been changed from 21 to 55 cases by adding the fourth boundary condition named as Guided. Referring again, to the literature, it could be observed that there is a broad use of plates in various engineering fields and in different structural components because of their flexibility [7].

In the context of non-linear vibrations of thin plates at large deflections, many researchers have studied this type of non-linearity by using different methods [8, 9, 10, 11]. In the last few years, there has been a growing interest in geometrically non-linear using a model that was applied in beams [8] and plates [12] which has known an experimental validation in reference [13]. This model was based on Hamilton's equations and spectral analysis that aim to illustrate the dynamic response of system in order to determine the contribution coefficients of the mode non-concerned on the given mode shape. Furthermore, the model led to prove the dependency of displacement amplitudes, frequency, mode shape and associated bending stress, and is was used and applied in different continue (plates, beams, shell, etc.) ([14, 15, 16, 17]) and discrete (mass and spring) ([18, 19, 20]) structures.

The purpose of this paper is to investigate numerically free and forced vibration of C-F-C-F[1] RP[2] (see Figure 1) with a ratio equals to 0.66 (α=0.66) at large vibration amplitudes. The adopted model is an extend of the model presented in [12]. The non-linear algebraic equations are obtained using Lagrange's equations and the harmonic balance method, in order to illustrate the effect of large deflection on thin mechanical structures (C-F-C-F RP).

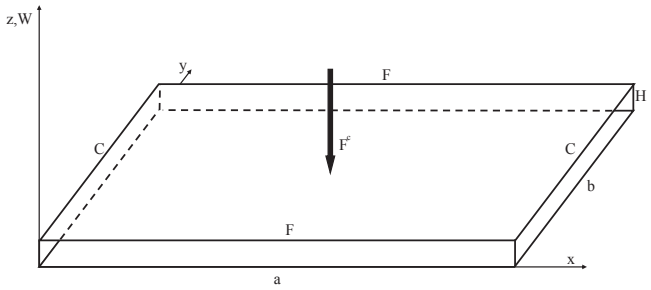

Figure 1: Rectangular plate notations of C-F-C-F

2 Theoretical formulation based on Lagrange's equations and the harmonic balance method

The isotropic thin RPs figured in Figure 1 have the bending stiffness D:

$$D = \frac{EH^3}{12\left(1-\vartheta^2\right)} \tag{1}$$

For such plates, the total strain energy denoted V is given as the sum of the strain energy due to the bending V_f and the membrane strain energy V_a induced by large deflections of structure ($V = V_a + V_f$). These terms can be written as follow without taking into account the in-plane displacements:

$$\mathrm{V_f} = \frac{1}{2}D\int_S \left[\left(\frac{\delta^2 W}{\delta x^2}\right)^2 + \left(\frac{\delta^2 W}{\delta y^2}\right)^2 + 2(1-\vartheta)\left(\frac{\delta^2 W}{\delta x \delta y}\right)^2 + 2\vartheta\left(\frac{\delta^2 W}{\delta x^2}\frac{\delta^2 W}{\delta y^2}\right)\right] dS \tag{2}$$

$$V_a = \frac{3D}{2H^2}\int_S \left[\left(\frac{\delta W}{\delta x}\right)^2 + \left(\frac{\delta W}{\delta y}\right)^2\right]^2 dS \tag{3}$$

And T is the kinetic energy of plate as given by:

$$T = \frac{1}{2}\rho H\int_S \left(\frac{\delta W}{\delta t}\right)^2 dS \tag{4}$$

Where the S is the surface of RP and W is the deflection function.

In the three later equations, terms involving the in-plane displacements and their derivatives have been omitted. This assumption, which simplifies considerably the theory and leads to obtain good results for reasonable ranges of vibration amplitudes, has been adopted and justified in many previous papers.

[1]Clamped-Free-Clamped-Free

[2]Rectangular Plate

The C-F-C-F RP have been discretized from i^{th} C-C and j^{th} F-F beam mode shapes in the x and y directions, respectively. Furthermore, the deflection function is assumed harmonic, which is extended as a series of n basic spatial functions $\mathrm{w}_k(x,y)$:

$$\begin{aligned} W(x,y,t) &= q_k(t)\mathrm{w}_k(x,y) \\ &= a_k\mathrm{w}_k(x,y)\sin(\omega t) \\ &= \alpha_{ij}\mathrm{w}_{ij}(x,y)\sin(\omega t) \end{aligned} \tag{5}$$

with $k = n(i-1)+j$

The rearranging and substitution of the equation (5) into the equations (2), (3) and (4), respectively, leads to obtain the following equations:

$$V_f = \frac{1}{2}q_i q_j k_{ij} \tag{6}$$

$$V_a = \frac{1}{2}q_i q_j q_k q_l b_{ijkl} \tag{7}$$

$$T = \frac{1}{2}\dot{q}_i \dot{q}_j m_{ij} \tag{8}$$

where m_{ij}, k_{ij} and b_{ijkl} are the mass, the linear and non-linear rigidity tensors, respectively. With the indices i, j, k and l are varying from 1 to n. The expressions for these tensors are given by:

$$m_{ij} = \rho H \int_S \mathrm{w}_i \mathrm{w}_j dS \tag{9}$$

$$k_{ij} = D\int_S \left[\frac{\partial^2 \mathrm{w}_i}{\partial x^2}\frac{\partial^2 \mathrm{w}_j}{\partial x^2} + \frac{\partial^2 \mathrm{w}_i}{\partial y^2}\frac{\partial^2 \mathrm{w}_j}{\partial y^2} + 2(1-\vartheta)\frac{\delta^2 \mathrm{w}_i}{\delta x \delta y}\frac{\delta^2 \mathrm{w}_j}{\delta x \delta y} + 2\vartheta\frac{\delta^2 \mathrm{w}_i}{\delta x^2}\frac{\delta^2 \mathrm{w}_i}{\delta y^2}\right] dS \tag{10}$$

$$b_{ijkl} = \frac{3D}{2H^2}\int_S \left[\left(\frac{\partial \mathrm{w}_i}{\partial x}\frac{\partial \mathrm{w}_j}{\partial x} + \frac{\partial \mathrm{w}_i}{\partial y}\frac{\partial \mathrm{w}_j}{\partial y}\right)\left(\frac{\partial \mathrm{w}_k}{\partial x}\frac{\partial \mathrm{w}_l}{\partial x} + \frac{\partial \mathrm{w}_k}{\partial y}\frac{\partial \mathrm{w}_l}{\partial y}\right)\right] dS \tag{11}$$

The dimensionless parameters were used in this paper to simplify the interpretation of the obtained results as used in [14, 16], and we can put:

$$\begin{aligned} \mathrm{w}_i(x,y) = H\mathrm{w}_i^*\left(\frac{x}{a},\frac{y}{b}\right) = H\mathrm{w}_i^*\left(x^*,y^*\right), \quad \frac{\omega^2}{\omega^{*2}} = \frac{D}{\rho H b^4}, \\ \frac{k_{ij}}{k_{ij}^*} = \frac{DaH^2}{b^3}, \quad \frac{m_{ij}}{m_{ij}^*} = \rho H^3 ab, \quad \frac{bijkl}{b_{ijkl}^*} = \frac{DaH^2}{b^3} \end{aligned} \tag{12}$$

2.1 Application to free vibration of C-F-C-F RP

Lagrange's equations have been employed to describe the non-linear dynamic behavior for a conservative system (C-F-C-F RP), that can be written as follow:

$$-\frac{\partial}{\partial t}\left(\frac{\partial T}{\partial \dot{q}_r}\right) + \frac{\partial T}{\partial q_r} - \frac{\partial V}{\partial q_r} = 0, \qquad r = 1-n \tag{13}$$

The q_i is assumed to be harmonic, as used in equation (5) we get:

$$q_i(t) = a_i \sin \omega t, \qquad i = 1 - n$$

In the equation (13), V and T are replaced by their expressions given above in (6), (7), and (8), and their derivatives are calculated with respect to the $a_i's$. The following set of non-linear algebraic equations are obtained by applying the harmonic balance method and non-dimensional parameters:

$$\frac{3}{2} a_i a_j a_k b^*_{ijkr} + a_i k^*_{ir} - a_i \omega^{*2} m^*_{ir} = 0, \qquad i, j, k, r = 1 - n \tag{14}$$

The later can be written in matrix form as following:

$$\left([K^*] - \omega^{*2} [\mathbf{M}^*] \right) \{\mathbf{A}\} + \frac{3}{2} [\mathbf{B}^*(\mathbf{A})] \{\mathbf{A}\} = \{\mathbf{0}\} \tag{15}$$

The column vector of basic function (contribution coefficients) $\{\mathbf{A}\}$, which can be written as $\{\mathbf{A}\}^{\mathrm{T}} = [a_1 a_2 \dots a_n]$.

In addition ω^* is the non-dimensional non-linear frequency response that can be obtained through (14) as:

$$\omega^{*2} = \frac{a_i a_j k^*_{ij} + \frac{3}{2} a_i a_j a_k a_l b^*_{ijkl}}{a_i a_j m^*_{ij}} = \frac{k_{ij}}{m_{ij}} + \frac{3}{2} \frac{a_k a_l b_{ijkl}}{m_{ij}} \tag{16}$$

In order to obtain the numerical solution for the non-linear problem in the neighborhood of the first mode shape, the contribution of this mode is chosen and others of higher modes are calculated numerically via explicit method (first formulation) of the remaining $(n-1)$ non-linear algebraic equations. Furthermore, the dynamic response free vibration can bee obtained the following equations:

$$3 a_i a_j a_k b^*_{ijkr} + 2 a_i k^*_{ir} - 2 a_i \frac{a_i a_j k^*_{ij} + a_i a_j a_k a_l b^*_{ijkl}}{a_i a_j m^*_{ij}} m^*_{ir} = 0, \qquad r = 1 - n \tag{17}$$

2.2 Forced vibration application in C-F-C-F RP

Considering the RP exhibited in Figure 1 which is excited harmonically with a concentrated forces applied at the plate's center (x_0, y_0), In this way we can write:

$$F(x_0, y_0) = F^c \delta(x - x_0) \delta(y - y_0) \sin(\omega t) \tag{18}$$

The corresponding generalized force F^c is given by:

$$F^c_i(t) = F^c \mathrm{w}_i (x_0, y_0) \sin \omega t = f^c_i \sin(\omega t) \qquad i = 1 - n \tag{19}$$

The dimensionless of generalized forces f^{c*}_i that is applied on the RP can be obtained from the following equation:

$$f^{c*}_i = \frac{b^3 F^c}{aDH} \mathrm{w}^*_i(x^*_0, y^*_0), \qquad i = 1 - n \tag{20}$$

Assuming that equation (5) holds for q_i which is supposed to be harmonic, we get:

$$q_i(t) = a_i \sin \omega t, \qquad i = 1 - n \tag{21}$$

The problem of forced vibration was reduced to a non-linear algebraic equation of C-F-C-F RP by applying Lagrange's equations and harmonic balance method as used in the previous subsection:

$$-\frac{\partial}{\partial t}\left(\frac{\partial T}{\partial \dot{q}_r}\right)+\frac{\partial T}{\partial q_r}-\frac{\partial V}{\partial q_r}=F_r, \qquad r=1-n \tag{22}$$

The non-linear algebraic equations have been obtained by substituting the terms of V_f, V_a, T into the later equation and by applying the harmonic balance method that yield to:

$$\frac{3}{2}a_i a_j a_k b^*_{ijkr}+a_i k^*_{ir}-a_i\omega^2 m^*_{ir}=f^*_r, \qquad i,j,k,r=1-n \tag{23}$$

where ω^* is the dimensionless excitation frequency. Hence, the equation (23) can be written in matrix form as:

$$\left([K^*]-\omega^{*2}\left[\mathbf{M}^*\right]\right)\{\mathbf{A}\}+\frac{3}{2}\left[\mathbf{B}^*(\mathbf{A})\right]\{\mathbf{A}\}=\{\mathbf{F}^*\} \tag{24}$$

3 Explicit procedure of solution

3.1 Free vibration

The explicit method or the first formulation as used in [14], leads to obtain the solution in the neighborhood of the first non-linear mode shape, and the basic functions vector $\{\mathbf{A}\}$ can be written as: $\{\mathbf{A}\}^{\mathrm{T}}=[a_1\varepsilon_2\ldots\varepsilon_6]$, with the contribution coefficients indice is varying from 2 to 6. Indeed, $\varepsilon_2\ldots\varepsilon_6$ can be considered small compared to a_1.

This method is based on an approximation that leads to neglect the second and third terms in the expression $a_i a_j a_k b^*_{ijkr}$. With respect to ε_i, the remaining term can be reduced to $a_1^3 b^*_{111i}$.

$$\frac{3}{2}a_1^3 b^*_{1111}+a_1 k^*_{11}-a_1\omega^2 m^*_{11}=0 \tag{25}$$

which gives :

$$\omega^2=\frac{k_{11}}{m_{11}}+\frac{3}{2}a_1^2\frac{b_{1111}}{m_{11}} \tag{26}$$

The i^{th} basic functions of the contributions (ε_i) is explicitly calculated from the i^{th} approximate equation of system (14):

$$\frac{3}{2}a_1^3 b^*_{111i}+\left(k^*_{ii}-\omega^2 m^*_{ii}\right)\varepsilon_i=0 \qquad i=2-6 \tag{27}$$

Then, the last equation allows to the following analytical expression for i^{th} contributions that contribute to the first mode shape:

$$\varepsilon_i=\frac{-\frac{3}{2}a_1^3\overline{b}^*_{111i}}{\overline{k}^*_{ii}-\omega^{*2}_{nl}\overline{m}^*_{ii}}=\frac{-\frac{3}{2}a_1^3\overline{b}^*_{111i}}{\overline{k}^*_{ii}-\left[\frac{\overline{k}_{11}}{\overline{m}_{11}}+\frac{3}{2}\frac{a_1^2\overline{b}_{1111}}{\overline{m}_{11}}\right]\overline{m}^*_{ii}} \qquad i=2-6 \tag{28}$$

The non-linear dynamic response free vibration is described in the equation below:

$$\mathrm{W}^*_{nl}(x^*,y^*)=\frac{-\frac{3}{2}a_1^3 b^*_{1111}}{(k^*_{11}-\omega^{*2}m^*_{11})}\mathrm{w}^*_{11}(x^*,y^*)+\frac{-\frac{3}{2}a_1^3 b^*_{1112}}{(k^*_{22}-\omega^{*2}m^*_{22})}\mathrm{w}^*_{12}(x^*,y^*)+\cdots+\frac{-\frac{3}{2}a_1^3 b^*_{1116}}{(k^*_{66}-\omega^{*2}m^*_{66})}\mathrm{w}^*_{16}(x^*,y^*)) \tag{29}$$

3.2 Forced vibration

The non-linear algebraic equations obtained from (23) were solved using the explicit method. In order to obtain a multi-dimensional non-linear frequency response, this structure has been subjected to high levels of applied forces amplitudes and harmonic excitation. The C-F-C-F RP is excited harmonically in the neighbourhood of the first mode shape, which is generated only by the first basic function w_{11} and that is the predominant in the dynamic response, then the equation (23) is reduced to:

$$\frac{3}{2}a_1^3 b_{1111}^* + \left(k_{11}^* - \omega^2 m_{11}^*\right) a_1 = f_1^* \tag{30}$$

where b_{1111}^*, k_{11}^*, and m_{11}^* are respectively the non-dimension terms of the non-linear, the linear rigidity, and the mass tensor corresponding to the first mode shape of C-F-C-F RP. After rearranging the above equation, we obtain:

$$\left(\frac{\omega^*}{\omega_{1L}^*}\right)^2 = 1 + \frac{3}{2}\overline{a}_1^2 \frac{\overline{b}_{1111}^*}{\overline{k}_{11}^*} - \frac{\overline{f}_1^*}{a_1 k_{11}^*} \tag{31}$$

As mentioned above, the explicit method and harmonic balance method have been applied to deduce ε_i:

$$\frac{3}{2}a_1^3 b_{111i}^* + \left(k_{ii}^* - \omega^2 m_{ii}^*\right) \varepsilon_i = f_i^* \qquad\qquad i = 2 - 6 \tag{32}$$

The last equation allows to the following analytical expression for i^{th} contributions that contribute on the first mode shape:

$$\varepsilon_i = \frac{f_i^* - \frac{3}{2}a_1^3 b_{111i}^*}{k_{ii}^* - \omega^{*2} m_{ii}^*}, \qquad\qquad i = 2 - 6 \tag{33}$$

Then, the first mode of the non-linear steady state periodic forced response function of C-F-C-F RP can be expressed as following:

$$\mathrm{W}_{nl}^*(x^*, y^*) = \frac{f_1^* - \frac{3}{2}a_1^3 b_{1111}^*}{(k_{11}^* - \omega^{*2} m_{11}^*)} \mathrm{w}_{11}^*(x^*, y^*) + \frac{f_2^* - \frac{3}{2}a_1^3 b_{1112}^*}{(k_{22}^* - \omega^{*2} m_{22}^*)} \mathrm{w}_{12}^*(x^*, y^*) + \cdots + \frac{f_6^* - \frac{3}{2}a_1^3 b_{1116}^*}{(k_{66}^* - \omega^{*2} m_{66}^*)} \mathrm{w}_{16}^*(x^*, y^*)) \tag{34}$$

4 Results and discussions

In this section, we will discuss the results obtained in the numerical simulations of free and forced vibration, in order to show the effect of geometrically non-linear on C-F-C-F RP at large vibration amplitudes with the plate's ratio equals to 0.66 ($\alpha = 0.66$). These simulations were carried out on RP made from aluminium alloy with a thickness of 0.6 mm. The dimensions of this plate are 240 x 360 mm (width x length), that gives 0.66 in the ratio. According to the commercial catalog, the density, Young modulus, and the Poisson's ratio of this plate are $2140 Kg/m^3$, 7x$10^{10} N/m^2$, and 0.34, respectively.

Dynamic response of a C-F-C-F rectangular plate is calculated using the first, six, and nine first linear modes shape ($\mathrm{w}_{11}, \mathrm{w}_{12}, \mathrm{w}_{13}, \ldots, \mathrm{w}_{19}$) in equation 29 and 34.

4.1 Free vibration

The non-dimensional terms of mass, linear and non-linear rigidity tensors were computed numerically by using the software "MATLAB".

The linear analysis was obtained by neglecting the term of geometrical nonlinearity; this assumption leads us to obtain the values of the fundamental frequency parameter of various plate's ratio which are included in Table 1. Furthermore, the later linear frequencies have been determined by Leissa in [3] using Symmetric-Antisymmetric Modes of C-F-C-F rectangular plates and are compared with those obtained by our present study which shown a good convergence of solutions. The backbone curves forced vibration in the case of C-F-C-F RP were not found in the literature.

Table 1: Comparison of the first fundamental frequency parameters of a C-F-C-F RP, with various α.

Aspect ratio α	Present study	Leissa[3]	Percentage error (%)
1	25.54	26.40	3.26
0.9	22.70	22.10	-2.71
0.66	13.32	-	-

The values of contribution coefficients corresponding to the first mode shape was calculated by explicit solution from the equation (28) with a given assignment contribution (a_1), and the results are listed in Table (2). From this table, the five contributions show their contribution on the first mode shape and these values become important when the (a_1) increase.

Table 2: Contribution coefficients corresponding to the first mode shape free vibration.

a_1	a_2	a_3	a_4	a_5	a_6	ω/ω_l
0.02	1.38305E-06	-3.88254E-07	1.29696E-07	-7.46271E-08	3.42673E-08	1.0260
0.12	2.98739E-04	-8.38629E-05	2.80144E-05	-1.61194E-05	7.40174E-06	1.0323
0.22	1.84084E-03	-5.16766E-04	1.72625E-04	-9.93286E-05	4.56098E-05	1.0477
0.32	5.66497E-03	-1.59029E-03	5.31235E-04	-3.05672E-04	1.40359E-04	1.0716
0.42	1.28084E-02	-3.59562E-03	1.20112E-03	-6.91121E-04	3.17350E-04	1.1035
0.52	2.43085E-02	-6.82396E-03	2.27954E-03	-1.31165E-03	6.02282E-04	1.1427
0.72	6.45276E-02	-1.81144E-02	6.05110E-03	-3.48180E-03	1.59878E-03	1.2403
0.92	1.34621E-01	-3.77911E-02	1.26241E-02	-7.26390E-03	3.33544E-03	1.3587
1.02	1.3463E-01	-5.15023E-02	1.72043E-02	-9.89935E-03	4.54559E-03	1.4241
1.12	2.42886E-01	-6.81836E-02	2.27767E-02	-1.31057E-02	6.01789E-03	1.4929
1.32	3.97621E-01	-1.11622E-01	3.72871E-02	-2.14550E-02	9.85172E-03	1.6390
1.52	6.07126E-01	-1.70434E-01	5.69335E-02	-3.27595E-02	1.50425E-02	1.7942
1.62	7.35009E-01	-2.06334E-01	6.89258E-02	-3.96599E-02	1.82111E-02	1.8745
1.72	8.79697E-01	-2.46951E-01	8.24940E-02	-4.74670E-02	2.17959E-02	1.9562
1.82	1.04223	-2.92577E-01	9.77352E-02	-5.62368E-02	2.58229E-02	2.0393
1.92	1.22363	-3.43502E-01	1.14747E-01	-6.60252E-02	3.03175E-02	2.1236

Figure 5 represents the corresponding curve of fundamental resonance (F = 0 N) obtained by plotting the equation (29). The first non-linear mode shape of C-F-C-F RP with $\alpha = 0.66$ is depicted in Figure 5 and the dependence of the non-linear frequency on the non-dimensional vibration amplitudes is shown. As may expected, a hardening type of non-linearity of C-F-C-F RP is observed.

The amplitudes mode shape dependence are investigated, which allow to illustrate the effect of large transverse vibration amplitudes on the first mode shape. The normalized sections along the x an y directions, corresponding to $y^* = 0.5$ and $x^* = 0.5$ of the non-linear fundamental mode shape were obtained from equation (29) are plotted in Figure 2 (a) and (b). The later, show respectively the increase of all curvatures near the free edges and decrease for the clamped edges. These curves obtained for the large, medium, and low displacement amplitudes which are corresponding to 4.91, 0.98, and 0.4 at the plate's center, respectively.

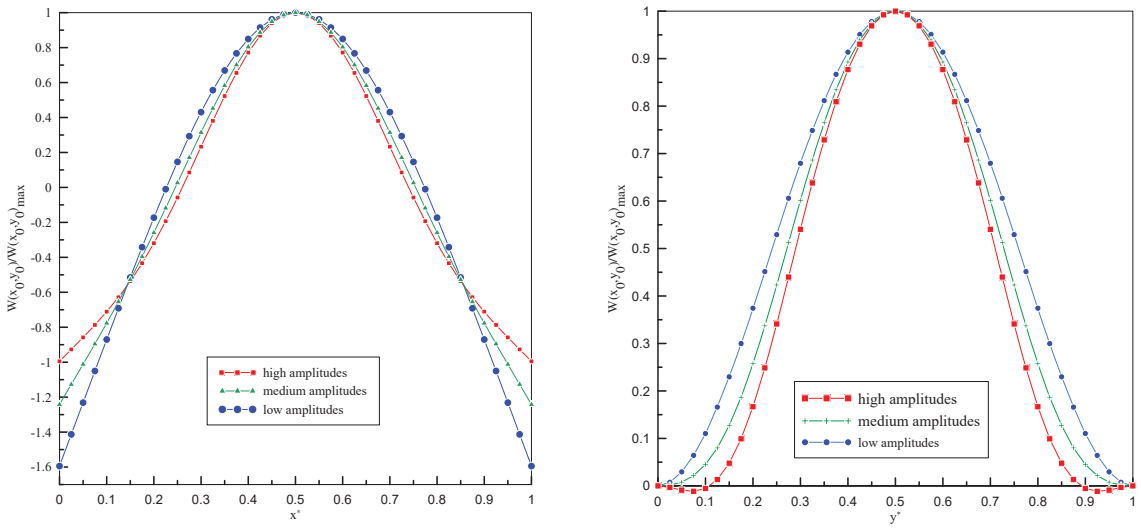

(a) (F-F) (b) (C-C)

Figure 2: Amplitudes deflections in x and y direction of the first mode shape of a RP corresponding to (a): $y^* = 0.5$ and (b): $x^* = 0.5$, respectively.

4.2 Forced vibration

The present subsection aims to treat the transverse steady state periodic forced response of thin C-F-C-F isotropic RP with the $\alpha = 0.66$, which the geometric and mechanical characteristics were presented above.

The equation (32) holds to obtain (33), which allows to an analytical expression for ε_i with $i = 2 - 6$ to be derived in terms of a_1, and the results are listed in Table 3. These results are obtained with a given typical values of a_1 in order to calculate the first six basic functions varying from 0.3 to 2.

The thin C-F-C-F isotropic RP was excited with a concentrated harmonic forces at the plate's center. The non-linear algebraic equations (23) have been reduced to single-mode approach, that assumed to neglect all co-ordinates except a single resonant co-ordinate as obtained in equation (30) and (31). The convergence of the solution was studied using the first mode shape which is the predominant (single mode approach), the first six and nine mode shapes (multimode solution) in the two equations (31) and (34), respectively, with 1 N of forcing vibration amplitude.

Table 3: Contribution coefficients corresponding to the first mode shape forced vibration, $F^c = 1N$

a_1	a_2	a_3	a_4	a_5	a_6	ω/ω_l
0.30	0.00322822	-0.00712518	0.00042405	-0.00125437	0.00011480	0.484975
0.35	0.00523468	-0.00787544	0.00067479	-0.00140170	0.00018239	0.597414
0.40	0.00794480	-0.00885931	0.00100893	-0.00159734	0.00027236	0.672148
0.45	0.01146892	-0.01011443	0.00143847	-0.00184833	0.00038792	0.727486
0.50	0.01591960	-0.01167769	0.00197545	-0.00216168	0.00053227	0.771300
0.55	0.02141195	-0.01358563	0.00263195	-0.00254439	0.00070862	0.807696
0.60	0.02806402	-0.01587472	0.00342006	-0.00300346	0.00092018	0.839069
0.65	0.03599711	-0.01858148	0.00435189	-0.00354589	0.00117015	0.866921
1.00	0.13846239	-0.05233845	0.01592585	-0.01026664	0.00426587	1.018605
1.20	0.24706054	-0.08662607	0.02759709	-0.01702517	0.00737621	1.094426
1.30	0.31956203	-0.10889450	0.03513883	-0.02138498	0.00938139	1.132057
1.40	0.40645169	-0.13502586	0.04395471	-0.02647495	0.01172127	1.169896
1.50	0.50967663	-0.16536841	0.05414880	-0.03235280	0.01442197	1.208102
1.80	0.94096357	-0.28533444	0.09406229	-0.05529619	0.02495135	1.325703
1.90	1.13491984	-0.33626483	0.11083904	-0.06491010	0.02935816	1.365996
2.00	1.35997236	-0.39335470	0.12953718	-0.07560623	0.03425769	1.406839

These latter are plotted in Figure 3 and showed the convergence of the results that can be reached for six modes shape via multimode solution. In addition, these curves show a slight difference for the dimensionless displacements less than 1.5 and the difference becomes clearer for the remains results.

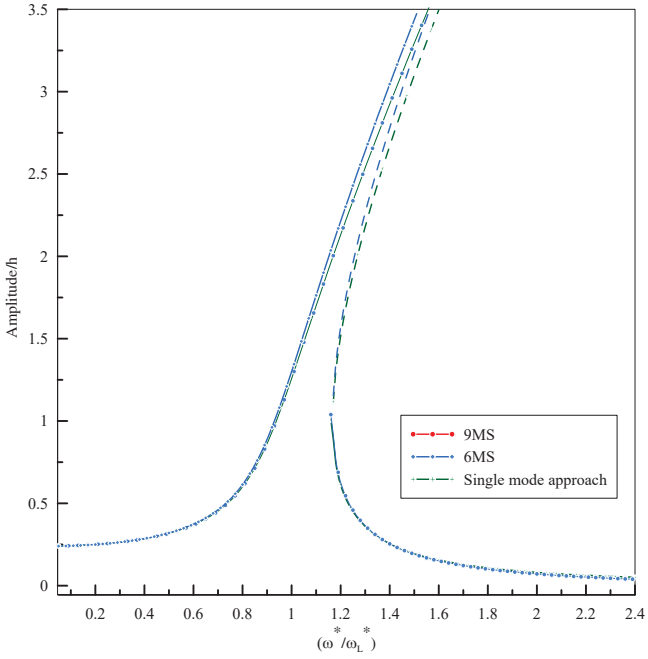

Figure 3: Backbone curve corresponding to the single mode approach and multi-mode solution.

In Figure 4 the linear and nonlinear frequency response curves are given in term of the

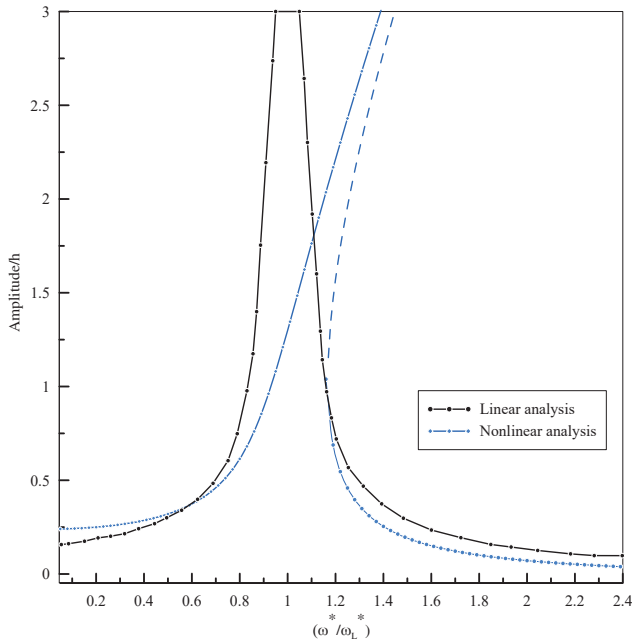

Figure 4: Linear and nonlinear analysis forced vibration response of C-F-C-F RP.

amplitudes and the frequency parameter. The results corresponding to this excitation correspond to the classical response in the forced linear model that obtained by neglecting the nonlinear term (b_{ijkl}) in equation (34).

Furthermore, forced responses of RP under different concentrated amplitude forces (F^c= 0, 0.25, 0.5, and 1 N) are shown in Figure 5 using first six modes shape. These three curves show the hardening type resonance for all considered excitation levels and the jump phenomena was observed near 0.6, 0.8, and 1.1 dimensionless displacements, respectively.

5 Conclusion

The geometrically non-linear dynamic free and steady state periodic forced response of thin and isotropic C-F-C-F RP were investigated via a theoretical model which was developed in this paper. The effect of large vibration amplitudes was studied in order to determine the amplitudes frequency dependence and associated first mode shape free and forced vibrations.

The model used is based on Lagrange's equations and the harmonic balance method that were used to reduce the problem to non-linear algebraic equations without tacking into account the in-plane displacements and their derivatives. These later, gave the terms of mass tensor, linear and non-linear rigidity due to the geometrical non-linearity which were computed numerically. In addition, the non-linear dynamic, response in free and forced vibration, were investigated by using the first six plate functions. These functions were obtained as products of the first six beam functions in the x and y directions that were used to discretize the C-F-C-F RP.

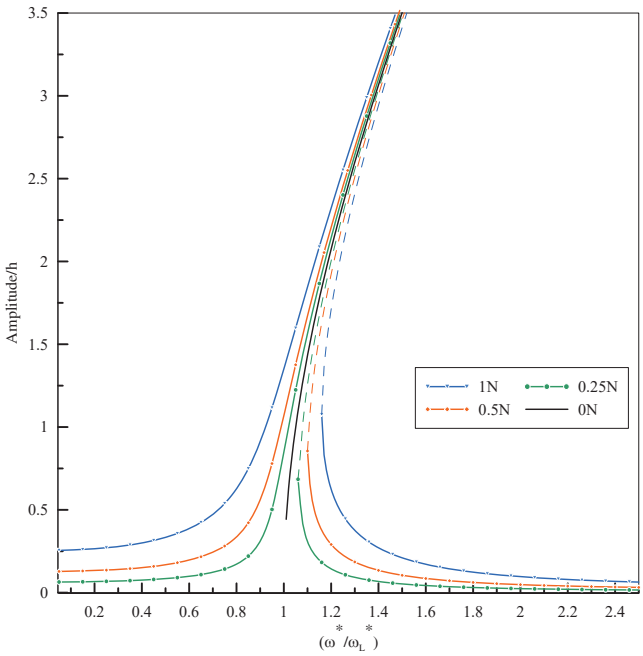

Figure 5: Resonance curves for 0, 0.25, 0.5 and 1 N of forcing vibration.

The RP's α=0.66 was chosen, the amplitudes frequency dependence were studied and presented for free vibration case. The results obtained showed that the frequency response increases with the increase of the amplitude, which led as to exhibit the hardening type of resonance as expected. In addition, when the amplitude increases, the deflection of the first mode shape increases at the Free-Free edges and decreases in the vicinity of plate's center, and an increase of the mode shape of C-C edges when the amplitudes increase.

The steady state periodic forced response was studied and the hardening non-linearity was obtained as in the free case using the same structure. Furthermore, the single-mode approach and the multi-mode solution were studied and plotted, illustrating a correlation between them for 1.5 in dimensionless displacements. The effect of applied harmonic forces (0, 0.25, 0.5 and 1N) and the excitation frequency on the dynamic response of C-F-C-F RP were illustrated. These results show the jump phenomena near 0.6, 0.8, and 1.1 dimensionless displacements, respectively for 0.25 , 0.5 and 1 N, forcing vibration.

Based on the obtained results, it can be concluded that the research into geometrically non-linear dynamic on thin and isotropic C-F-C-F RP has been very successful. Furthermore, these investigation are require to taking into account of the in-plane displacements. Thus, the future works will concerning to carry out an experimental studies to compare with the obtained numerical results.

REFERENCES

[1] L. Salvatore L., P. Dale M., T. Michael J., G. Nicholas, Air Vehicle Integration and Technology Research (AVIATR). Delivery Order 0013: Nonlinear, Low-Order/Reduced-Order Modeling Applications and Demonstration (2011) 269.

[2] Nayfeh, Ali H. and Pai, P.F., Linear and Nonlinear Structural Mechanics, Meccanica 40 (2) (2005) 221–222.

[3] A.W. Leissa, Vibrations of plates, 1969. NASA SP-160, U.S. Government Printing Office, Washington, D.C., Washington, 1969.

[4] A. Leissa, The free vibration of rectangular plates, Journal of Sound and Vibration 31 (3) (1973) 257–293.

[5] M. Eisenberger, A. Deutsch, Solution of thin rectangular plate vibrations for all combinations of boundary conditions, Journal of Sound and Vibration 452 (2019) 1–12.

[6] B. Wu, A. Pagani, M. Filippi, W. Chen, E. Carrera, Large-deflection and post-buckling analyses of isotropic rectangular plates by Carrera Unified Formulation, International Journal of Non-Linear Mechanics 116 (2019) 18–31.

[7] E. Carrera, Historical review of Zig-Zag theories for multilayered plates and shells, Applied Mechanics Reviews 56 (3) (2003) 287–308.

[8] R. Benamar, M. Bennouna, R. White, The effects of large vibration amplitudes on the mode shapes and natural frequencies of thin elastic structures part I: Simply supported and clamped-clamped beams, Journal of Sound and Vibration 149 (2) (1991) 179–195.

[9] O. Thomas, C. Touzé, A. Chaigne, Asymmetric non-linear forced vibrations of free-edge circular plates. Part II: experiments, Journal of Sound and Vibration 265 (5) (2003) 1075–1101.

[10] J. Noël, G. Kerschen, Nonlinear system identification in structural dynamics: 10 more years of progress, Mechanical Systems and Signal Processing 83 (2017) 2–35.

[11] J. Lee, T. Detroux, G. Kerschen, HARMONIC BALANCE COMPUTATION OF THE NONLIN- EAR FREQUENCY RESPONSE OF A THIN PLATE (2017) 6.

[12] R. Benamar, M. Bennouna, R. White, The Effects Of Large Vibration Amplitudes On The Mode Shapes And Natural Frequencies Of Thin Elastic Structures, Part II: Fully Clamped Rectangular Isotropic Plates, Journal of Sound and Vibration 175 (3) (1992) 377–395.

[13] R. Benamar, M. Bennouna, R. White, The Effects Of Large Vibration Amplitudes On The Mode Shapes And Natural Frequencies Of Thin Elastic Structures, Part III: Fully Clamped Rectangular Isotropic Plates—Measurements Of The Mode Shape Amplitude Dependence And The Spatial Distribution Of Harmonic Distortion, Journal of Sound and Vibration 175 (3) (1993) 377–395.

[14] M. El Kadiri, R. Benamar, Improvement of the semi-analytical method, based on Hamilton's principle and spectral analysis, for determination of the geometrically non-linear response of thin straight structures. Part III: steady state periodic forced response of rectangular plates, Journal of Sound and Vibration 264 (1) (2002) 1–35.

[15] K. El Bikri, R. Benamar, M. Bennouna, Geometrically non-linear free vibrations of clamped simply supported rectangular plates. Part I: the effects of large vibration amplitudes on the fundamental mode shape, Computers & Structures 81 (20) (2003) 2029–2043.

[16] Z. Beidouri, R. Benamar, M. El Kadiri, Geometrically non-linear transverse vibrations of C–S–S–S and C–S–C–S1 rectangular plates, International Journal of Non-Linear Mechanics 41 (1) (2006) 57–77.

[17] E. Merrimi, K. El Bikri, R. Benamar, Geometrically non-linear forced vibrations of a clamped-clamped beam with an edge crack: a single mode approach, Proceedings of the 8th International Conference on Structural Dynamics, EURODYN 2011 Leuven, Belgium,, 2011, p. 8.

[18] Z. Beidouri, A. Eddanguir, R. Benamar, Geometrically nonlinear free transverse vibration of 2-dof systems with cubic nonlinearities, 7th European Conference on Structural Dynamics, EURODYN 2008, Southampton, United Kingdom, 2008.

[19] A. Adri, Z. Beidouri, R. Benamar, Geometrically non linear mode shapes and resonant frequencies of multi-span beams, 8th International Conference on Structural Dynamics, EURODYN 2011, Leuven; Belgium, 2011.

[20] A. Rahmouni, R. Benamar, A discrete model for geometrically non-linear transverse free constrained vibrations of beams carrying a concentrated mass at various locations, 9th International Conference on Structural Dynamics, EURODYN 2014, Porto; Portugal, 2014, pp. 2093–2099.

EURODYN 2020
XI International Conference on Structural Dynamics
M. Papadrakakis, M. Fragiadakis, C. Papadimitriou (eds.)
Athens, Greece, 23–26 November 2020

NONLINEAR LONGITUDINAL FREE VIBRATION OF UNIFORM RODS AND RODS WITH SECTIONS VARYING EXPONENTIALLY (EURODYN 2020)

E. ABDEDDINE[12], A. MAJID[12], Z. BEIDOURI[2] and Kh. ZARBANE[2]

[1]Centre d'Etude Doctorale, Ecole Nationale Supérieure de l'Electricité et de Mécanique, Hassan II University of Casablanca
Km7 Route El Jadida, Casablanca, Morocco
e-mail: {e.abdeddine,a.majid}@ensem.ac.ma

[2] Laboratoire Mécanique, Productique et Génie Industriel (LMPGI), Ecole Supérieure Technologie (ESTC), Hassan II University of Casablanca
BP 8012 Oasis, Casablanca, Morocco
e-mail: khalid.zarbane@univh2c.ma, zbeidouri@gmail.com

Keywords: Non-Linear Longitudinal Vibration, Lagrange's equations, Linearized Approach, Harmonic Balance Method, Geometrically Non-linear.

Abstract. *The present study aims to investigate the problem of linear and non-linear longitudinal free vibration of uniform rods and rods with sections varying exponentially. This problem is reduced to a non-linear algebraic equation which is based on the Lagrange's equations and the harmonic balance method. In fact, these methods were applied previously to study the non-linear transverse vibration of the different continuous structures (beams, plates, and shells) and discrete structures (2-dof and multi-dof systems). However, the present model leads to obtain a solution of a non-linear algebraic system using numerical method. The non-linear frequencies corresponding to the first, second and third non-linear mode shapes of Clamped-Free uniform and non-uniform rods are treated via the Linearized Approach. Therefore, the obtained numerical results exhibit the geometrically non-linear effect. The dependencies of the amplitude on the slope of exponential function coefficient, the frequency and on the non-linear mode shape are applied for the first, second and third mode shapes, in order to examine the used method in the case of Clamped-Free non-uniform rods longitudinal free vibration at large amplitudes.*

Nomenclature

δ	Slope of exponential function coefficient	k_i	linear rigidity of spring i
ω	frequency parameters	k_{ij}	General terms for the linear rigidity tensor
*	the asterisk indicates non-dimensional parameters	L	Length of the rod
ρ	Mass per unit volume	m_i	i^{th} mass of 2-dof system
A	Mode amplitude	m_{ij}	General terms for the mass tensor
A_i	Amplitude of the displacement u_i	S	Area of the cross section
a_i	Contribution coefficient of i^{th} linear mode shape	S_0	Maximum section of rods
a_i	contribution coefficient	T	kinetic energy
b_{ijkl}	General terms for the nonlinearity tensor	$U(x,t)$	The longitudinal displacement
C	Velocity of propagation	u_i	Displacement of mass m_i
E	Young's modulus	U_l	Linear potential energy
		U_{nl}	non-linear potential energy
		x	Axial position coordinate

1 Introduction

The longitudinal vibration analysis of rods is an important issue in structural engineering applications, such as high-rise buildings, long-span bridges, aerospace machines and many other industrial usages. Longitudinal and torsional vibrations are significant in these structures and their natural frequencies have to be considered in the design process. The determination of both linear and nonlinear natural frequencies, with associated mode shapes and bending stress, are essential in structural dynamic analysis in order to design efficient machines. The external vibrations loading and services condition may cause large displacements and rotations that lead to considerable pre-stress states in the structure. Consequently, the modal behavior of structures is evidently a property of the equilibrium state and natural frequencies are subject to change.
The exact solutions and the numerical techniques for linear longitudinal vibration of homogeneous rods can be found in literature [16, 13], while analytical studies on inhomogeneous rods are scarce. Eisenberger [11], Matsuda and al [15], Bapat [4], Abrate [1], Kumar and Sujith [12], Anil Raj , Sujith [18] and Xu and al [19] studied the linear longitudinal vibration of rods with variable sectional area and they obtained the exact solutions for certain functional forms of an involved parameter.
The present work devotes to the non-linear longitudinal vibration of rods using a model based on Lagrange's formulation and harmonic balance method. This structure is reduced to a non-linear algebraic system, which can be solved by numerical procedures (iterative, linearized or explicit). These methods have been developed and used to examine the non-linear behavior of continuous structures and discrete systems [8, 7, 9, 10, 17, 2], longitudinal, transverse vibration of 2-dof systems [6]. In our case, an application is made using the linearized procedure [8]

leading to the fundamental non-linear longitudinal mode shape of C-F[1] rods.

2 Theoretical formulation

Actually, the main objective of the present paper is to determinate the dynamic response of C-F rods with section varying exponentially at large vibration amplitudes, in order to illustrate the non-linear longitudinal mode shapes and natural frequencies of C-F rods with section varying exponentially. We start by presenting in the first subsection the formulas for the natural frequencies, mode shapes and displacements of linear C-F rods. Then in the second one the formulation of the basic theory of geometrically non-linear longitudinal free vibration of rods are presented.

2.1 Linear Model

The uniform rods having the following characteristics: E: Young's modulus, ρ: mass per unit volume, L: length of the rod, S: area of the cross section, $U(x,t)$: the longitudinal displacement which is assumed to be harmonic, i.e. $U(x,t) = u(x)\sin(\omega t)$, and are well-known by the equation of longitudinal vibrations of rods, this can be written by:

$$\frac{\partial}{\partial x}\left(S\frac{\partial u}{\partial x}\right) = \frac{S}{C^2}\frac{\partial^2 u}{\partial t^2} \tag{1}$$

where C is the velocity of propagation of the displacement or stress waves in the rod, and it is given by:

$$C = \sqrt{\frac{E}{\rho}} \tag{2}$$

Considering now the longitudinal vibrations of the rods with exponential sections which are illustrated in Figure 1, taking into account the same geometrical characteristics presented earlier. These sections can be written as below and S_0 is the maximum section of rods:

$$S(x) = S_0 \exp(\delta x) \tag{3}$$

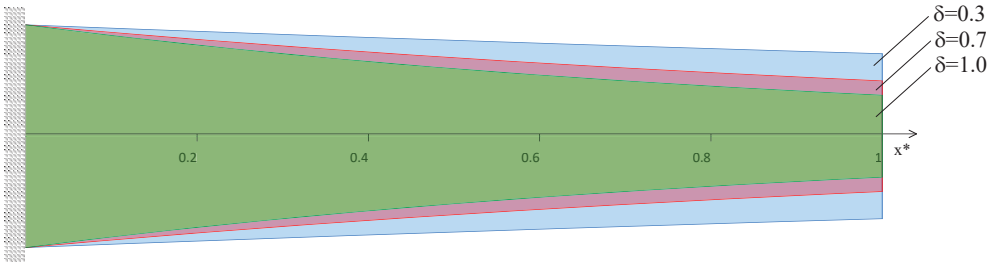

Figure 1: Notation of rods with sections varying exponentially (blue: $\delta = 0.3$, red: $\delta = 0.7$, green: $\delta = 1.0$)

[1]Clamped-Free

By substituting the equation (3) into (1) and by using the classical method of separation of variables, we obtain a differential equation we the solution gives the following mode:

$$u_n(x) = \left(\sin \frac{n\pi}{L} x\right) e^{-\frac{\delta}{2}x} \tag{4}$$

with the frequencies expression written as:

$$\omega_n = \frac{1}{2}\sqrt{\frac{E}{\rho}}\sqrt{\left(\frac{4\pi^2 n^2}{L^2} + \delta^2\right)} \tag{5}$$

2.2 Non-Linear Model

The method presented in this subsection is based on a semi-analytical approach. The dynamic behavior is obtained by using Lagrange's equations for a conservative system, which leads to:

$$-\frac{\partial}{\partial t}\left(\frac{\partial T}{\partial \dot{q}_r}\right) + \frac{\partial T}{\partial q_r} - \frac{\partial V}{\partial q_r} = 0, \quad r = 1, \ldots, n \tag{6}$$

In the above equation, T is the kinetic energy of the rod given by:

$$T = \frac{1}{2}\int_0^L \rho S \left(\frac{\partial u}{\partial t}\right)^2 dx \tag{7}$$

V is the total strain energy, which can be written as the sum of the linear strain energy V_l and the non linear strain energyV_{nl}:

$$V = V_l + V_{nl} = \frac{1}{2}\int_0^L ES\left(\frac{\partial u}{\partial x}\right)^2 dx + \frac{1}{2}\left[\int_0^L ES\left(\frac{\partial u}{\partial x}\right)^3 dx + \frac{1}{4}\int_0^L ES\left(\frac{\partial u}{\partial x}\right)^4 dx\right] \tag{8}$$

The large displacement U is assumed to be harmonic which is expanded in the form of a finite series, one obtains:

$$U(x,t) = q_i(t)u_i(x) = a_i u_i(x)\sin \omega t \tag{9}$$

where the usual summation convention for the repeated index i varies from 1 to n. After substituting the expression given in equation (9) ,for the displacement function U, in the energy expressions (7) and (8) and performing the discretization,we obtain the following expressions for the potential and kinetic energies that can be written as:

$$T = \frac{1}{2}\dot{q}_i \dot{q}_j m_{ij} \tag{10}$$

$$V_l = \frac{1}{2} q_i q_j k_{ij} \tag{11}$$

$$V_{nl} = \frac{1}{2} q_i q_j q_k q_l b_{ijkl} + \frac{1}{2} q_i q_j q_k c_{ijk} \tag{12}$$

where k_{ij} denotes the classical rigidity tensor due to V_l; b_{ijkl} and c_{ijk} represent the nonlinearity tensors due to V_{nl} and m_{ij} stands for the mass tensor attributable to T. The expressions for the general terms of these tensors are given by :

$$m_{ij} = \int_0^L \rho S u_i u_j dx \tag{13}$$

$$k_{ij} = \int_0^L ES \frac{\partial u_i}{\partial x} \frac{\partial u_j}{\partial x} dx \tag{14}$$

$$b_{ijkl} = \int_0^L \frac{ES}{4} \left(\frac{\partial u_i}{\partial x} \frac{\partial u_j}{\partial x} \frac{\partial u_k}{\partial x} \frac{\partial u_l}{\partial x} \right) dx \tag{15}$$

$$c_{ijk} = \int_0^L ES \left(\frac{\partial u_i}{\partial x} \frac{\partial u_j}{\partial x} \frac{\partial u_k}{\partial x} \right) dx \tag{16}$$

Referring to [7], we put The non-dimensional parameters as follow:

$$u_i(x) = L u_i^* \left(\frac{x}{L} \right) = L u_i^* \left(x^* \right); \frac{\omega^2}{\omega^{*2}} = \frac{E}{\rho L^2}; \frac{m_{ij}}{m_{ij}^*} = \rho S L^3; \frac{k_{ij}}{k_{ij}^*} = ESL; \frac{b_{ijkl}}{b_{ijkl}^*} = ESL \tag{17}$$

The amplitudes a_i are the unknown parameter that should to be determined as well as the frequency ω. Replacing T and V into equation (6) by their expressions given above, and applying the harmonic balance method we obtain:

$$2 a_i k_{ir}^* + 3 a_i a_j a_k b_{ijkr}^* - 2 \omega^{*2} a_i m_{ir}^* = 0; \qquad r = 1, \ldots, n \tag{18}$$

the later can be written in matrix form as:

$$2 \left[K^* \right] \{A\} + 3 \left[B^* (\{A\}) \right] \{A\} - 2 \omega^{*2} \left[M^* \right] \{A\} = 0 \tag{19}$$

where ω^* is the non-dimensional non-linear frequency parameter. The expression of the later can be obtained by pre-multiplying equation (19) by $\{A\}^T$ from the left hand side, and written as:

$$\omega^{*2} = \frac{\{A\}^T [K^*] \{A\} + \frac{3}{2} \{A\}^T [B^* (\{A\})] \{A\}}{\{A\}^T [M^*] \{A\}} \tag{20}$$

By substituting and rearranging the equation (20) into (18), we obtain:

$$3 a_i a_j a_k b_{ijkr}^* + 2 a_i k_{ir}^* - 2 \left(\frac{a_i a_j k_{ij}^* + \frac{3}{2} a_i a_j a_k a_1 b_{ijkl}^*}{a_i a_j m_{ij}^*} \right) a_i m_{ir}^* = 0; \quad r = 1, \ldots, N \tag{21}$$

This obtained equation is a non-linear algebraic system that can be solved using an iterative, explicit and linearized procedure. This later is used in the present work in order to study the amplitude frequency dependence and associated first, second and third nonlinear longitudinal mode shapes of C-F uniform rods and non-uniform rods, respectively.

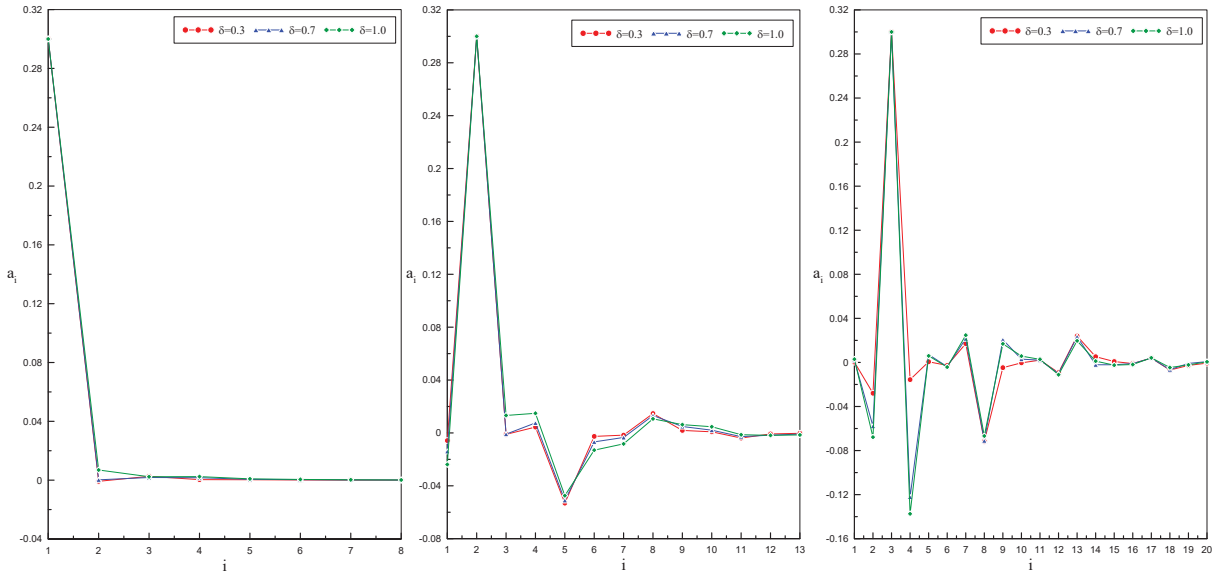

(a) First mode shape (b) Second mode shape (c) Third mode shape

Figure 2: Contribution coefficients value of mode shapes for various values of δ

3 Numerical Details

Various non-linear vibration problems are solved due to the non-linear algebraic system formally similar to equation (19) and having the following form:

$$\left([K_l] + \frac{3}{2}[B(A)]\right)\{A\} - \omega^2[M]\{A\} = \{0\} \tag{22}$$

in which $\{A\}^T$ is the column matrix of the basic function or the linear mode shape contribution coefficients $\{A\}^T = [a_1 a_2 \dots a_N]$.$[M]$, $[K_l]$ and $[B]$ are respectively the mass matrix, the linear rigidity matrix and the non-linear rigidity matrix. Equation (22) can be also written as:

$$\left([K_l] + \frac{3}{2}[K_{nl}]\right)\{A\} = \omega^2[M]\{A\} \tag{23}$$

Each term of the matrix $[K_{nl}]$ is a quadratic function of the column matrix of coefficients $\{A\}$, and is given by $(K_{nl})_{ij} = (3/2)a_k a_l b_{ijlk}$. When the later term is neglected, the non-linear eigenvalue problem (23) is reduced to the classical linear eigenvalue problem as written below:

$$[K_l]\{A\} = \omega^2[M]\{A\} \tag{24}$$

which is the Rayleigh-Ritz formulation of the linear vibration problem. In the linear case, the eigenvalue of the equation (24) leads to a series of eigenvalues and corresponding eigenvectors. In the non-linear case, the solution of the equation (23) should lead to a set of amplitude dependent eigenvectors, with their associated amplitude dependent eigenvalues. The non-linear problem (23) could be solved using incremental-iterative, linearized or approximate solution known as the explicit method that was used previously in [14].

In this paper the linearized method [5] is adopted to solve the equation (23). The purpose is to replace the iterative method of of the non-linear eigenvalue problem (23) solution, by a direct solution of a modified linear eigenvalue problem. The numerical results obtained, generally in similar problems, have shown that the contribution coefficient a_c of the assigned basic function

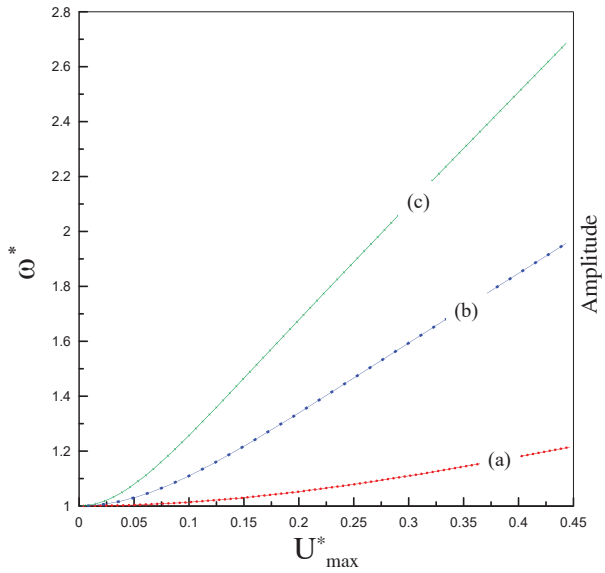

Figure 3: The backbone curves correspond- ing to the first (a), second (b) and third (c) non linear longitudinal mode shapes of a C- F uniform rods.

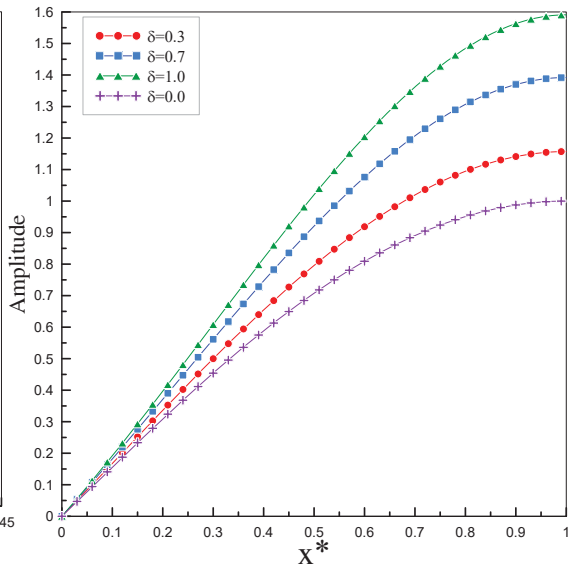

Figure 4: The first linear mode shape of a C- F rods with a section varying exponentially for various values of δ.

remains predominant for a wide range of amplitudes, compared to the other basic functions or linear mode shape contribution coefficients. Based on this result, an assumption is made in the neighborhood of the considered resonance, by writing the general term of the non-linear geometrical stiffness matrix in a simplified form:

$$(K_{nl})_{ij} = \frac{3}{2} a_c^2 b_{ccij} \tag{25}$$

The non-linear eigenvalue problem (23) becomes:

$$[K]\{A\} = \omega^2 [M]\{A\} \tag{26}$$

in which $[K]$ is the modified global stiffness matrix of the structure given by:

$$K_{ij} = (K_l)_{ij} + \frac{3}{2} a_c^2 b_{ccij} \tag{27}$$

Thus, for a given value of the predominant contribution a_c of the mode under consideration, the modified rigidity matrix $[K]$ is constant, and the eigenvalue problem (26) is a classical one. The direct solution of the linear eigenvalue problem (26), for a specified value of a_c and corresponding to a fixed amplitude of vibration of a chosen point, leads to the value of the eigenvalue ω^2 and the corresponding eigenvector $\{A\}$.

The choice of the number of the basic functions was based on the contribution coefficients value a_i assigned of other mode shapes which allow the convergence of the calculation and the time compilation optimization. For this purpose we calculated the contribution coefficients value on the first, second and third mode shapes to determinate the number of the contribution

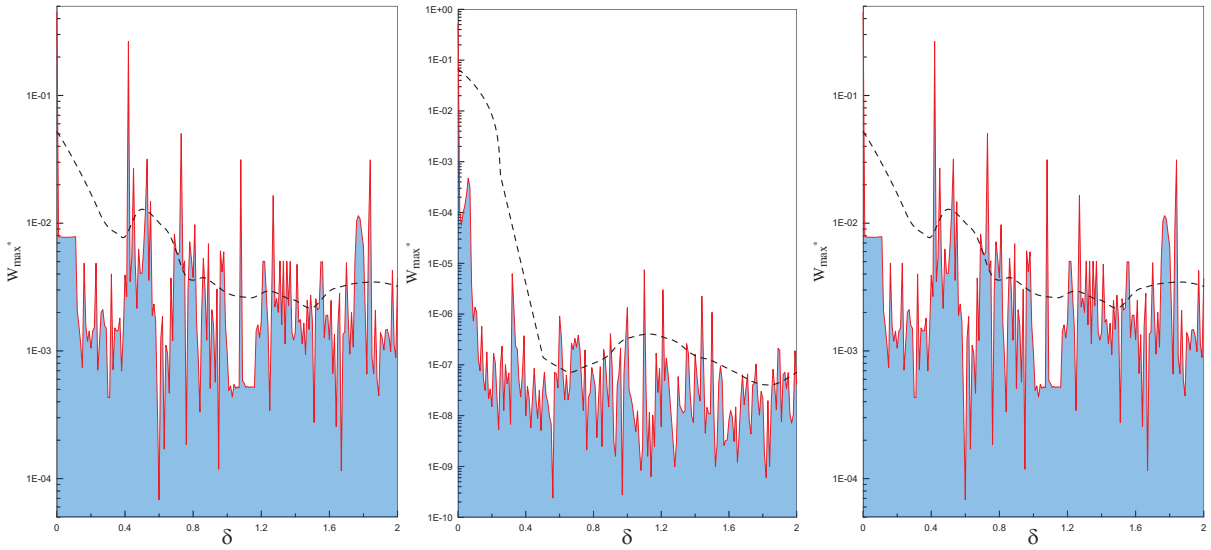

(a) First mode shape (b) Second mode shape (c) Third mode shape

Figure 5: (——) Maximum amplitude versus the slope of exponential function coefficient, (- - -): Locally Estimated Scatterplot Smoothing (LOESS).

coefficients value that contribute significantly. Figure 2 illustrates the value of contribution coefficients for the first, second and third mode shapes for each δ value that increases with the increase of the contribution coefficients. This figure leads us to deduce the choice of the numbers of the basic functions which are 5, 13 and 19, that contribute significantly on the first, second and third mode shapes ,respectively, and which can not be neglected in the process of simulation.

4 Results and Interpretations

To verify the method used in the current paper, non-dimensional frequency is compared with the differential quadrature method employed in the reference [3]. This later consists in approximating the derivative of a function at a sample point to a weighted linear summation of the value of the function at all of the sample points in the domain. The calculations were made using 15 points Differential Quadrature Method for both uniform and non-uniform clamped-free rods. Table 1 shows a clear concordance value of non-dimensional frequency for uniform C-F rods. In order to compare non-uniform rods for $S(x) = (x+1)^2$, presented in the reference [3], with sections varying exponentially, the slope of exponential function coefficient was fixed at a value equals to 1.386 as plotted in Figure 8. Table 2 shows that the method gives acceptable results due to the section difference.

Table 3: First mode shape value of C-F rod with a section varying exponentially for $\delta = 1.0$

X/L	0.000	0.100	0.200	0.300	0.400	0.500	0.600	0.700	0.800	0.900	1.000
Linear	0.000	0.121	0.249	0.382	0.515	0.641	0.757	0.856	0.933	0.983	1.000
Nonlinear	0.000	0.142	0.279	0.413	0.544	0.667	0.779	0.873	0.943	0.986	1.000
Relative difference %		15.092	10.459	7.492	5.308	3.835	2.822	1.948	1.096	0.351	0.000

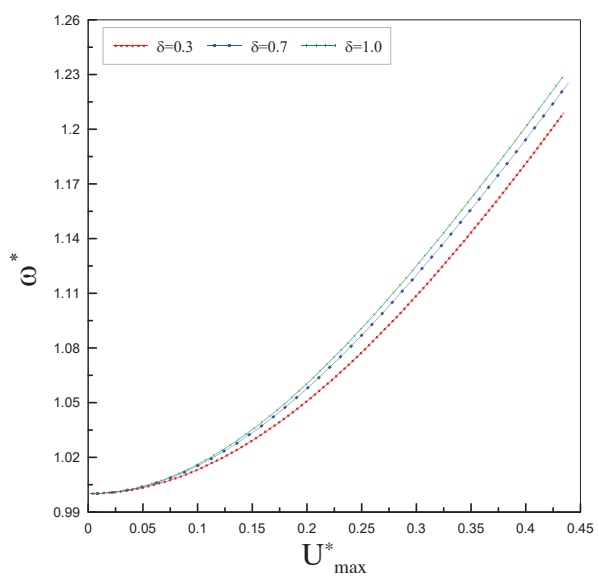

(a) First mode shape

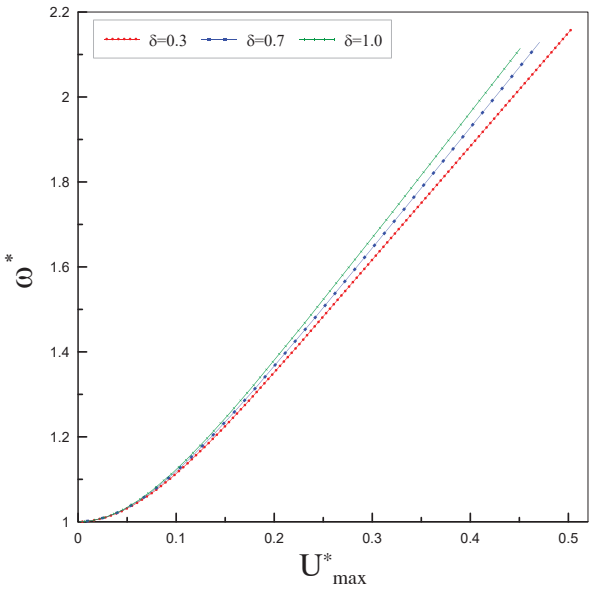

(b) Second mode shape

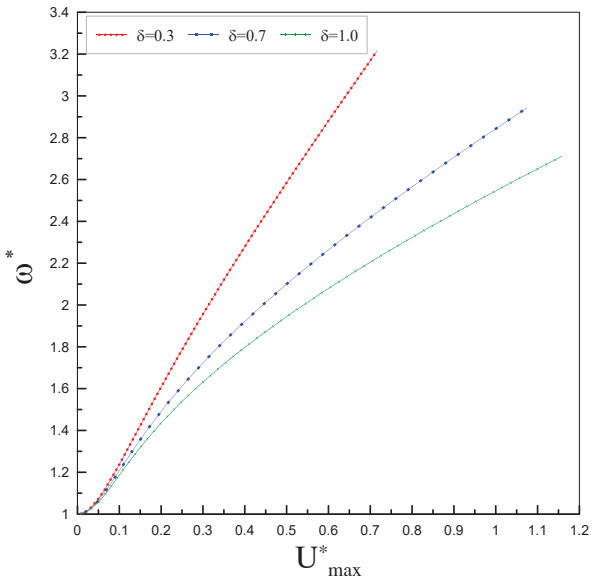

(c) Third mode shape

Figure 6: The backbone curves of the non linear longitudinal mode shapes of a C-F rod with a section varying exponentially for various values of δ.

Table 4: Second mode shape value of C-F rod with a section varying exponentially for $\delta = 1.0$

X/L	0.000	0.100	0.200	0.300	0.400	0.500	0.600	0.700	0.800	0.900	1.000
Linear	0.000	0.297	0.553	0.703	0.698	0.524	0.205	-0.197	-0.594	-0.889	-1.000
Nonlinear	0.000	0.175	0.429	0.696	0.499	0.264	0.059	-0.153	-0.412	-0.754	-1.000
Relative difference %		69.333	29.042	1.046	39.832	98.444	245.171	28.440	44.137	17.814	0.000

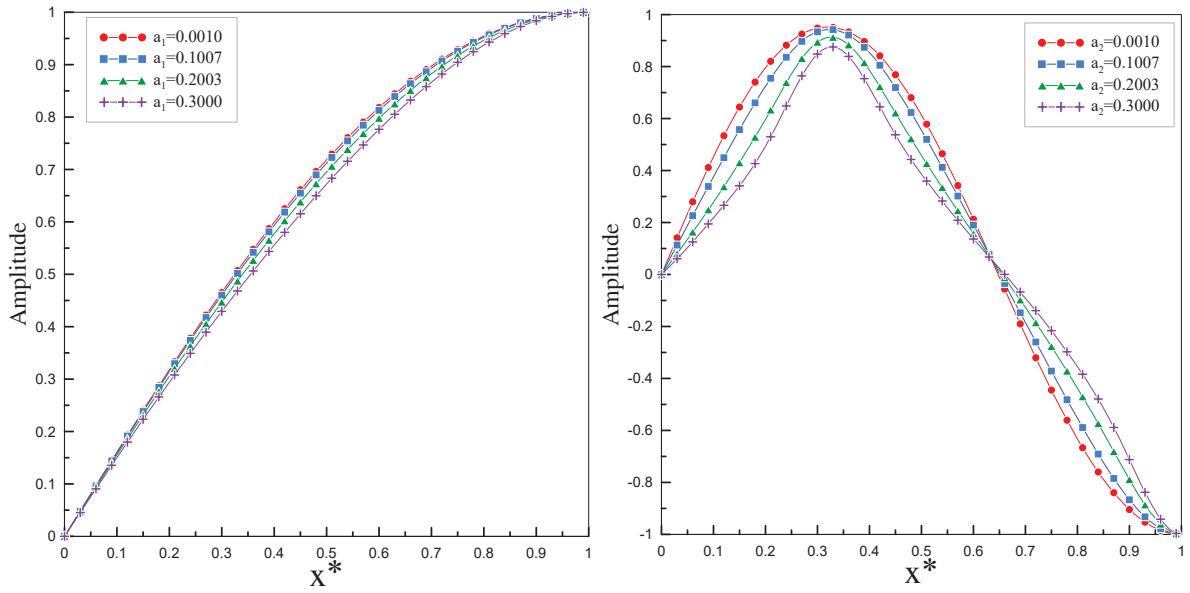

(a) First mode shape

(b) Second mode shape

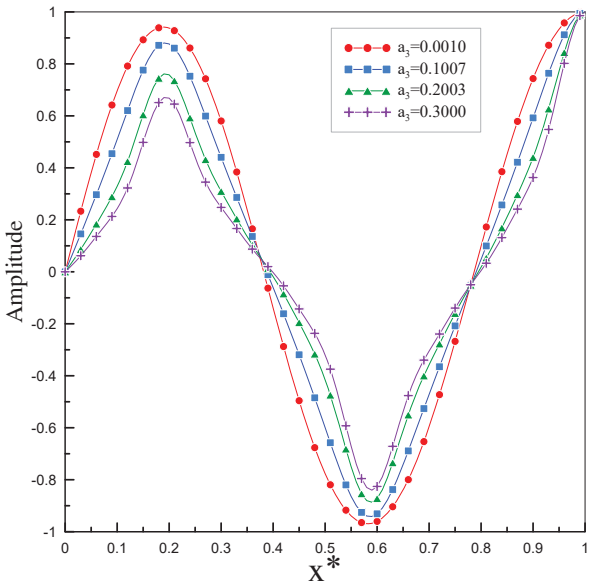

(c) Third mode shape

Figure 7: Amplitude dependence of the non linear longitudinal mode shapes of C-F rod with a section varying exponentially for $\delta = 0.3$

4.1 Uniform rods

Numerical results are obtained for C-F uniform rods. The backbone curves, corresponding to the uniform case for the first three nonlinear longitudinal mode shapes, shows a hardening type of nonlinear dynamic behavior with an increase of the nonlinear frequencies parameters by 12%, 46% and 88%, respectively for the first three nonlinear mode shapes with the maximum non dimensional vibration amplitude equals to 0.16. This can be depicted in Figure 3.

Uniform [3]	Uniform [present]
1.5708	1.570796327
4.7124	4.71238898
7.8540	7.853981634
10.9956	10.99557429

Table 1: Non-dimensional frequency comparison for uniform C-F rods

Non-uniform [3]	Non-uniform [present]
1.1656	1.529084254
4.6042	4.408039122
7.7899	7.373738343
10.9499	10.34303691

Table 2: Non-dimensional frequency comparison for non-uniform C-F rods

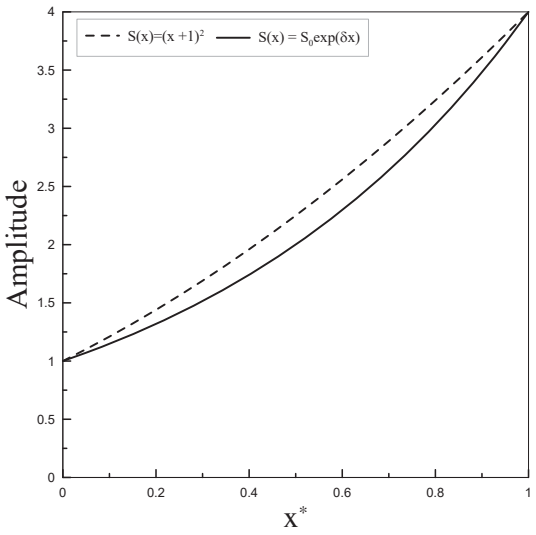

Figure 8: Comparaison of non-uniform rods.

4.2 Rods with section varying exponentially

The first three linear mode shapes of C-F rods with section varying exponentially $S = S_0 e^{\delta x}$ are plotted for various values of δ and shown in Figure 4. These linear modes correspond to the basic functions used in each case within the nonlinear theory.

Figure 5 illustrates the displacement amplitude versus the slope of exponential function coefficient and shows that the amplitude decreases with the increase of exponential slope (δ) due to the decrease of the section at the Free boundary condition.

The backbone curves of a C-F rods with a section varying exponentially for the first three nonlinear longitudinal mode shapes and their geometric non-linearity effect are represented in Figure 6.

Thus, for the first nonlinear mode shape corresponding to the maximum non dimensional vibration amplitude is equal to 0.2, the nonlinear frequencies increase with 5%, 6% and 6.2% respectively for delta equals to 0.3, 0.7 and 1.0. In addition, the second nonlinear mode shape corresponding to the maximum non dimensional vibration amplitude is equal to 0.3, the increase of the nonlinear frequencies is equal to 61.8%, 65% and 67.5% respectively for delta equals to 0.3, 0.7 and 1.0. And finally, the third nonlinear mode shape corresponding to the maximum non dimensional vibration amplitude is equal to 0.4, the nonlinear frequencies increase by 80%, 92% and 128% respectively for delta equals to 1, 0.7 and 0.3.

Figure 7 depicts the amplitude longitudinal mode shapes dependence that can be clearly seen, and shows the importance of the nonlinear effect on our structure which should be taken into account in the calculation. It can be also seen in Table 3 and 4 the difference between the geometrical nonlinearities and the linear case for first and second mode shapes with δ equals to 1.0 , with a relative difference up to 15.092% for the first mode shape and 245.171% for the second mode shape.

5 Conclusion

The model, based on Lagrange's formulation and Harmonic Balance Method, was developed to determine the nonlinear mode shapes of transverse vibration of beams, circular and rectangular plates. The numerical formulation of this model was presented and the expressions of the linear and nonlinear rigidity tensors were developed. The linearized procedure was used to solve the nonlinear algebraic equation obtained by reducing the problem of C-F uniform and non-uniform rods. The numerical results corresponding to the fundamental, the second and the third nonlinear modes shape were presented showing qualitative consistence of the model used. Furthermore, the obtained results showed a nonlinear behavior of the hardening type resonance response.

REFERENCES

[1] Serge Abrate. Vibration of non-uniform rods and beams. *Journal of Sound and Vibration*, 185(4):703–716, aug 1995.

[2] A. Ahmed and B. Rhali. Geometrically nonlinear transverse vibrations of bernoulli-euler beams carrying a finite number of masses and taking into account their rotatory inertia. In *Procedia Engineering*, volume 199, pages 489–494, 2017. Cited By :2.

[3] A. Al Kaisy, Ramadan Esmaeel, and Mohamed Nassar. Application of the Differential Quadrature Method to the Longitudinal Vibration of Non-Uniform Rods. *Engineering Mechanics*, 14(5):303–310, 2007.

[4] C.N. Bapat. Vibration of rods with uniformly tapered sections. *Journal of Sound and Vibration*, 185(1):185–189, aug 1995.

[5] Z. Beidouri, R. Benamar, and M. El Kadiri. Geometrically non-linear transverse vibrations of c-s-s-s and c-s-c-s. *International Journal of Non-Linear Mechanics*, 41(1):57–77, 2006. cited By 9.

[6] Z. Beidouri, A. Eddanguir, and R. Benamar. Geometrically nonlinear free transverse vibration of 2-dof systems with cubic nonlinearities. In *7th European Conference on Structural Dynamics, EURODYN 2008*, 2008.

[7] Zitouni BEIDOURI. *Contribution à une Théorie d'Analyse Modale Non-Linéaire. Application aux Structures Continues et aux Systèmes Discrets à Non-Linéarités Localisées*. PhD thesis, EMI Rabat,, 2006.

[8] R. Benamar, M.M.K. Bennouna, and R.G. White. The effects of large vibration amplitudes on the mode shapes and natural frequencies of thin elastic structures part I: Simply supported and clamped-clamped beams. *Journal of Sound and Vibration*, 149(2):179–195, sep 1991.

[9] R. Benamar, M.M.K. Bennouna, and R.G. White. The Effects of Large Vibration Amplitudes on the Mode Shapes and Natural Frequencies of Thin Elastic Structures, Part II: Fully Clamped Rectangular Isotropic Plates. *Journal of Sound and Vibration*, 164(2):295–316, jun 1993.

[10] R. Benamar, M.M.K. Bennouna, and R.G. White. The Effects Of Large Vibration Amplitudes On The Mode Shapes And Natural Frequencies Of Thin Elastic Structures, Part III: Fully Clamped Rectangular Isotropic Plates—Measurements Of The Mode Shape Amplitude Dependence And The Spatial Distribution Of Harmo. *Journal of Sound and Vibration*, 175(3):377–395, aug 1994.

[11] Moshe Eisenberger. Exact longitudinal vibration frequencies of a variable cross-section rod. *Applied Acoustics*, 34(2):123–130, 1991.

[12] B.M. Kumar and R.I. Sujith. Exact Solutions for the Longitudinal Vibration of Non-Uniform Rods. *Journal of Sound and Vibration*, 207(5):721–729, nov 1997.

[13] Leonard Meirovitch. *Elements of Vibration Analysis*. New York, 2nd editio edition, 1986.

[14] C. L. Lou and D. L. Sikarskie. Nonlinear Vibration of Beams Using a Form-Function Approximation. *Journal of Applied Mechanics*, 42(1):209, 1975.

[15] H. Matsuda, T. Sakiyama, C. Morita, and M. Kawakami. Longitudinal impulsive response analysis of variable cross-section bars. *Journal of Sound and Vibration*, 181(3):541–551, mar 1995.

[16] Philip M. Morse and K. Uno Ingard. *Theoritical Acoustics*. Princeton University Press, first edit edition, 1992.

[17] A. Rahmouni and R. Benamar. A discrete model for geometrically non-linear transverse free constrained vibrations of beams carrying a concentrated mass at various locations. In *Proceedings of the International Conference on Structural Dynamic , EURODYN*, volume 2014-January, pages 2093–2099, 2014.

[18] Anil Raj and R. I. Sujith. Closed-form solutions for the free longitudinal vibration of inhomogeneous rods. *Journal of Sound and Vibration*, 283(3-5):1015–1030, 2005.

[19] D. Xu, J. Du, and Z. Liu. An accurate and efficient series solution for the longitudinal vibration of elastically restrained rods with arbitrarily variable cross sections. *Journal of Low Frequency Noise Vibration and Active Control*, 38(2):403–414, 2019.

EURODYN 2020
XI International Conference on Structural Dynamics
M. Papadrakakis, M. Fragiadakis, C. Papadimitriou (eds.)
Athens, Greece, 23–26 November 2020

DYNAMIC RESPONSE OF TWO INTERACTING EXTENSIBLE BARS IN FRICTIONAL CONTACT

Timo Molenkamp[1], **Athanasios Tsetas**[1], **Apostolos Tsouvalas**[1] **and Andrei V. Metrikine**[1]

[1] TU Delft
Faculty of Civil Engineering
Stevinweg 1, 2628 CN Delft
T.Molenkamp@tudelft.nl

Keywords: Pile Dynamics, Normal modes, Regularized Coulomb friction

Abstract. *In this paper, a new model is developed to describe the nonlinear dynamics of two axially deformable bars sliding relative to each other in which the interaction is governed by friction. The first bar is fixed at one end and is subjected to a distributed normal force perpendicular to its axis to activate friction at the common interface, while the second bar is allowed to slide relative to the fixed one. A semi-analytical solution method is developed in which only the nonlinear interaction is addressed numerically. The dynamic behaviour of the bars is expressed as a summation of vibration modes including the necessary rigid body mode to allow for the permanent sliding of one bar relative to the other. This results in a computationally efficient scheme without compromising the accuracy of the solutions. The developed model can be used in pile driveability studies. In this case the fixed bar resembles the soil column while the second bar describes the dynamics of the driven pile.*

1 INTRODUCTION

In many engineering fields, including the field of pile driving, friction plays an important role. For example, accurate prediction of underwater noise generated in the seawater during the process of pile driving with vibratory devices requires the simultaneous prediction of the pile progression into the soil and, thus, the incorporation of a proper frictional model to describe the pile-soil slip behaviour. State of the art models in underwater noise prediction for impact pile driving all assume perfect contact between pile and soil [1, 2]. Problems including high frequency bands solved with a fixed FE-mesh, need both a fine spatial and time discretization to describe the propagating waves. This results in enormous computational efforts upto insolvable problems [2]. As a first step towards the development of a computational efficient model that predicts noise during vibratory pile driving including slippage of the pile, the dynamics of two elastic bars in frictional contact is studied in this paper.

The inclusion of friction complicates the problem, as it introduces a strong nonlinearity. To describe the forces at a frictional interface an appropriate frictional law should be chosen [3]. Since the focus herein is on noise generated during the driving process of piles with vibratory devices, the interest is in a straightforward frictional model that can describe the sliding between pile and soil. The most common frictional model is based on the Coulomb friction law. Coulomb's friction can be applied in many fields such as in a simplified model for belt driving mechanics, in which the Coulomb's friction law represents the dry friction between belt and support [4]. Variations on Coulomb's friction for multi-body mechanicals systems are described for example by Marques et al. [5]. The Coulomb friction, which is multivalued at zero velocity, can be approximated by alternative methods which deviate from Coulomb's friction below a certain velocity threshold and have a finite slope at zero velocity, e.g. linear velocity-dependent friction at low velocities and an approximation by a hyperbolic tangent [5]. Another alternative is introduced by Threlfall, the method avoids the discontinuity in the transition between positive and negative and it has a higher resemblance with the Coulomb friction law at velocities below a certain threshold [6]. This last friction law fits the problem of vibratory pile driving since it is smooth and the pile is assumed to slide continuously to the soil, while sticking can be neglected.

The model discussed in this work can be seen as a predecessor of a three-dimensional model to be used in pile driving noise prediction including the effect of pile-soil slip. In section 2, the problem statement is explained, including the equations of motions, boundary conditions and Threlfall's friction law. Hereafter, the solution method is described. The solution approach is largely analytical; a numerical scheme is used only to evaluate standard integrals. Section 3 describes the limitations of the method in terms of convergence, including criteria for the truncation of the number of modes that are used in this work. Section 4 shows results for the case of an impact load represented by a block function and a harmonic load. Finally, section 5 contains conclusions regarding the model performance.

2 MATHEMATICAL FORMULATION

2.1 Governing equations

The model under consideration is schematized in Fig. 1. It consists of two bars, which can deform in the axial direction and interact through a frictional interface. The equations of motion

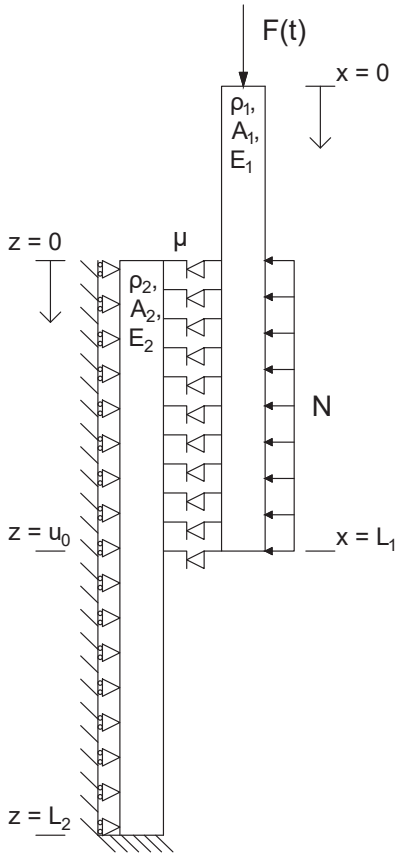

Figure 1: Schematization of the problem statement

describing the dynamics of the two bars read:

$$\rho_1 A_1 \ddot{u}_1(x,t) = E_1 A_1 u_1''(x,t) - T_1(x,t) + F(t)\delta(x) \tag{1}$$

$$\rho_2 A_2 \ddot{u}_2(z,t) = E_2 A_2 u_2''(z,t) - T_2(z,t) \tag{2}$$

in which subscript 1 refers to the forced bar and subscript 2 to the constrained bar, hereafter called bar 1 and 2. The constants ρ, A and E define the density, area and elasticity of the bars respectively. $T_{1,2}(x,t)$ represents the friction that acts on either bar. The driving force $F(t)$ can alternatively be included in a time-dependent boundary [7], however, the interest here lies not in the precise description of the top boundary stresses. A local coordinate system is adopted for bar 1. The progression of the lower end of bar 1 with respect to the upper end of bar 2 is characterized by $u_0(t)$ as shown in Fig. 1. The prime and dot indicate derivatives with respect to spatial coordinates and time, respectively. Threlfall's friction law is adopted, i.e. the signum function that is smoothed around zero velocity:

$$T_1(x,t) = \mu N \operatorname{sgn}(\Delta v_1(x,t)) \left(1 - e^{-k\frac{\Delta v_1(x,t)}{v_{95}}}\right) H(x - L_1 + u_0(t)) \tag{3}$$

$$T_2(z,t) = \mu N \operatorname{sgn}(-\Delta v_2(z,t)) \left(1 - e^{-k\frac{\Delta v_2(z,t)}{v_{95}}}\right) H(u_0(t) - z) \tag{4}$$

with:

$$\Delta v_1(x,t) = \dot{u}_1(x,t) - \dot{u}_2(x - L_1 + u_0(t), t) \tag{5}$$

$$\Delta v_2(z,t) = \dot{u}_2(z,t) - \dot{u}_1(z + L_1 - u_0(t), t) \tag{6}$$

where H is the Heaviside function and v_{95} is a velocity threshold above which the friction behaves almost velocity independent, i.e. at $\Delta v = v_{95}$: $T \approx 0.95 T_{max}$ for $k = 3$. The velocity threshold is based on the maximum modal change of velocity amplitude per time step, derived based on the results of section 2.2 of this paper as:

$$v_{95} = \frac{4\mu N \Delta t}{\pi \rho_1 A_1} \tag{7}$$

The boundary conditions read:

$$u_1'(0,t) = u_1'(L_1,t) = u_2'(0,t) = u_2(L_2,t) = 0 \tag{8}$$

The initial conditions are:

$$u_1(x,t_0) = u_{t_0}, \quad \dot{u}_1(x,t_0) = \dot{u}_{t_0}, \quad u_2(x,t_0) = w_{t_0}, \quad \dot{u}_2(x,t_0) = \dot{w}_{t_0} \tag{9}$$

Eqs. (1) to (9) govern the dynamics of the coupled system in the time domain.

2.2 Solution method

A modal solution approach is adopted, therefore, the displacements are expressed as a summation of modes:

$$u_1(x,t) = \sum_{n=1}^{\infty} \phi_n(x)\eta_n(t), \qquad u_2(z,t) = \sum_{m=1}^{\infty} \psi_m(z)\zeta_m(t) \tag{10}$$

Bar 1 is allowed to slide with respect to bar 2; the relative motion is governed by the rigid body motion of bar 1; relative displacement due to deformation of either bar is neglected. Substitution of Eq. (10) into Eqs. (1) and (2) yields:

$$\sum_{n=1}^{\infty} \phi_n(x)\ddot{\eta}_n(t) + \omega_n^2 \phi_n(x)\eta_n(t) = \frac{F(t)\delta(x) - T_1(x,t)}{\rho_1 A_1} \tag{11}$$

$$\sum_{m=1}^{\infty} \psi_m(z)\ddot{\xi}_m(t) + \omega_m^2 \psi_m(z)\xi_m(t) = -\frac{T_2(z,t)}{\rho_2 A_2} \tag{12}$$

with:

$$\phi_n(x) = \cos\left(\frac{\omega_n x}{c_1}\right), \qquad \omega_n = \frac{n\pi c_1}{L_1} \qquad n = 0,1,2,... \tag{13}$$

$$\xi_m(z) = \cos\left(\frac{\omega_m z}{c_2}\right), \qquad \omega_m = \frac{(2m-1)\pi c_2}{2L_2} \qquad m = 1,2,3,... \tag{14}$$

being the spatial eigenfunctions satisfying Eqs. (8). Eqs. (11) and (12) are multiplied by another mode and integrated over the length of each bar, making use of the orthogonality relation of the modes. After substituting Eqs. (3) and (4) into Eqs. (11) and (12), one obtains:

$$\ddot{\eta}_n(t) + \omega_n^2 \eta_n(t) = \frac{1}{\rho_1 A_1 a_n}\left(F(t) - \mu N \int_{L_1 - u_0(t)}^{L_1} \phi_n(x)\,\mathrm{sgn}(\Delta v_1(x,t)) \times \left(1 - e^{-k\frac{\Delta v_1(x,t)}{v_{95}}}\right)\mathrm{d}x\right) \tag{15}$$

$$\ddot{\xi}_m(t) + \omega_m^2 \xi_m(t) = -\frac{\mu N}{\rho_1 A_1 a_m}\int_0^{u_0(t)} \psi_m(z)\,\mathrm{sgn}(\Delta v_2(z,t))\left(1 - e^{-k\frac{\Delta v_2(z,t)}{v_{95}}}\right)\mathrm{d}z \tag{16}$$

with:

$$a_n = \int_0^{L_1} \phi_n(x)^2 \mathrm{d}x = \begin{cases} L_1 & n = 0 \\ \frac{1}{2} L_1 & n \neq 0 \end{cases}, \quad a_m = \int_0^{L_2} \psi_m(z)^2 \mathrm{d}z = \frac{1}{2} L_2 \tag{17}$$

To facilitate a computationally efficient solution of Eqs. (15) and (16), a straightforward time-stepping scheme is chosen, assuming that the relative velocity, $\Delta v_{1,2}(z,t)$, and the progression $u_0(t)$ are constant during a time step. Under the stated assumptions, Eqs. (15) and (16) act linear during a time step and the modal amplitudes η_n and ξ_m can be found using the Duhamel's integral for each time step. The closed-form solution to Eq. (15) reads:

$$\begin{aligned} \eta_n(t_{i+1}) = {} & A_n \sin(\omega_n t_{i+1}) + B_n \cos(\omega_n t_{i+1}) \\ & + \frac{1}{\omega_n a_n \rho_1 A_1} \int_{t_i}^{t_{i+1}} F(\tau) \sin(\omega_n (t_{i+1} - \tau)) \mathrm{d}\tau - \frac{\mu N \left(1 - \cos(\omega_n \Delta t)\right)}{\omega_n^2 a_n \rho_1 A_1} \\ & \times \int_{L_1 - u_0(t_i)}^{L_1} \phi_n(x) \operatorname{sgn}(\Delta v_1(x,t_i)) \left(1 - e^{-k \frac{\Delta v_1(x,t_i)}{v_{95}}}\right) \mathrm{d}x \end{aligned} \tag{18}$$

in which A_n and B_n are found by the previous time step:

$$\begin{aligned} A_n &= \frac{\sin\left(\omega_n t_i\right) \omega_n \eta_n(t_i) + \cos\left(\omega_n t_i\right) \dot{\eta}_n(t_i)}{\omega_n} \\ B_n &= \frac{\cos\left(\omega_n t_i\right) \omega_n \eta_n(t_i) - \sin\left(\omega_n t_i\right) \dot{\eta}_n(t_i)}{\omega_n} \end{aligned} \tag{19}$$

and in the special case of the initial time step:

$$\eta_n(t_0) = \frac{\int_0^{L_1} u_{t_0} dx}{a_n}, \qquad \dot{\eta}_n(t_0) = \frac{\int_0^{L_1} \dot{u}_{t_0} dx}{a_n} \tag{20}$$

The time derivative of $\eta_n(t)$ is given as:

$$\begin{aligned} \dot{\eta}_n(t_{i+1}) = {} & A_n(t_i) \omega_n \cos(\omega_n t_{i+1}) - B_n(t_i) \omega_n \sin(\omega_n t_{i+1}) \\ & + \frac{1}{a_n \rho_1 A_1} \int_{t_i}^{t_{i+1}} F(\tau) \cos(\omega_n (t_{i+1} - \tau)) \mathrm{d}\tau - \frac{\mu N \sin(\omega_n \Delta t)}{\omega_n a_n \rho_1 A_1} \\ & \times \int_{L_1 - u_0(t_i)}^{L_1} \phi_n(x) \operatorname{sgn}(\Delta v_1(x,t_i)) \left(1 - e^{-k \frac{\Delta v_1(x,t_i)}{v_{95}}}\right) \mathrm{d}x \end{aligned} \tag{21}$$

with $\Delta t = t_{i+1} - t_i$. Similar procedure for ξ_m results in:

$$\begin{aligned} \xi_m(t_{i+1}) = {} & C_m(t_i) \sin(\omega_m t_{i+1}) + D_m(t_i) \cos(\omega_m t_{i+1}) \\ & - \frac{\mu N \left(1 - \cos(\omega_m \Delta t)\right)}{\omega_m^2 a_m \rho_2 A_2} \int_0^{u_0(t_0)} \psi_m(z) \operatorname{sgn}(\Delta v_2(z,t_i)) \left(1 - e^{-k \frac{\Delta v_2(z,t_i)}{v_{95}}}\right) \mathrm{d}z \end{aligned} \tag{22}$$

$$\begin{aligned} \dot{\xi}_m(t_{i+1}) = {} & C_m(t_i) \omega_m \cos(\omega_m t_{i+1}) - D_m(t_i) \omega_m \sin(\omega_m t_{i+1}) \\ & - \frac{\mu N \sin(\omega_m \Delta t)}{\omega_m a_m \rho_2 A_2} \int_0^{u_0(t_i)} \psi_m(z) \operatorname{sgn}(\Delta v_2(z,t_i)) \left(1 - e^{-k \frac{\Delta v_2(z,t_i)}{v_{95}}}\right) \mathrm{d}z \end{aligned} \tag{23}$$

Where C_m and D_m are found similar to A_n and B_n. As mentioned earlier, the spatial integrals including the friction terms need numerical evaluation. The time step needs to be chosen such that it is smaller than a tenth of the smallest period in the system: $\Delta t < 2\pi / \max(\omega_i)/10$.

2.3 Linear equivalent model

The model is compared to a fully linear model that is valid for the case of no sliding. The

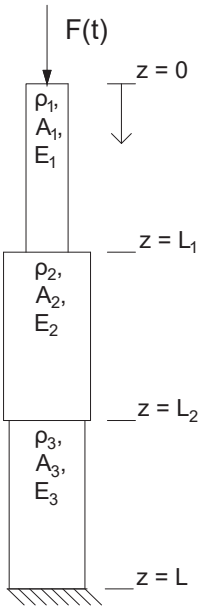

Figure 2: Schematization of the linear equivalent model

linear equivalent problem is composed of three bars as shown in Fig. 2, where the material properties of the second bar are based on the weighted averages of bar 1 and 3. The equation of motion of the whole system for each bar reads:

$$\begin{aligned} \rho_1 A_1 \ddot{u}_1 - E_1 A_1 u_1''(z,t) &= F(t)\delta(z) \qquad 0 < z < L_1 \\ \rho_2 A_2 \ddot{u}_2 - E_2 A_2 u_2''(z,t) &= 0 \qquad\qquad L_1 < z < L_2 \\ \rho_3 A_3 \ddot{u}_3 - E_3 A_3 u_3''(z,t) &= 0 \qquad\qquad L_2 < z < L \end{aligned} \tag{24}$$

The top boundary is stress-free since the applied force is accounted for in the equation of motion and the bottom boundary is fixed, furthermore, the interface conditions describe the continuity of displacements and stresses. The modes of the system can be found by solving the eigenvalue problem that is formed after substituting the general solution for each of the bars in the boundary and interface conditions. The modes are orthogonal with respect to the density and area [8]:

$$\int_0^{L_1} \rho_1 A_1 \phi_m(z)\phi_n(z)dz + \int_{L_1}^{L_2} \rho_2 A_2 \phi_m(z)\phi_n(z)dz + \int_{L_2}^{L} \rho_3 A_3 \phi_m(z)\phi_n(z)dz = a_n \delta_{nm} \tag{25}$$

The modal amplitudes are found analytically by making use of the orthogonality of the modes:

$$\eta_n(t) = A_n \sin(\omega_n t) + B_n \cos(\omega_n t) + \frac{1}{\omega_n a_n} \int_0^t F(\tau) \sin(\omega_n (t-\tau)) \mathrm{d}\tau \tag{26}$$

A_n and B_n are found by the initial conditions at $t = 0$:

$$A_n = \frac{1}{a_n \omega_n} \sum_{i=1}^{3} \int_{L_i} \rho_i A_i \phi_n(z) \dot{u}_i(z,0) dz \tag{27}$$

$$B_n = \frac{1}{a_n} \sum_{i=1}^{3} \int_{L_i} \rho_i A_i \phi_n(z) u_i(z,0) \mathrm{d}z \tag{28}$$

3 RESULTS

Two cases will be examined; the case of a block function load and the case of a high-frequency harmonic excitation. The two load cases are visualized in both time and frequency domain in Fig. 3. The material properties are chosen such that the wave speeds in both bars are

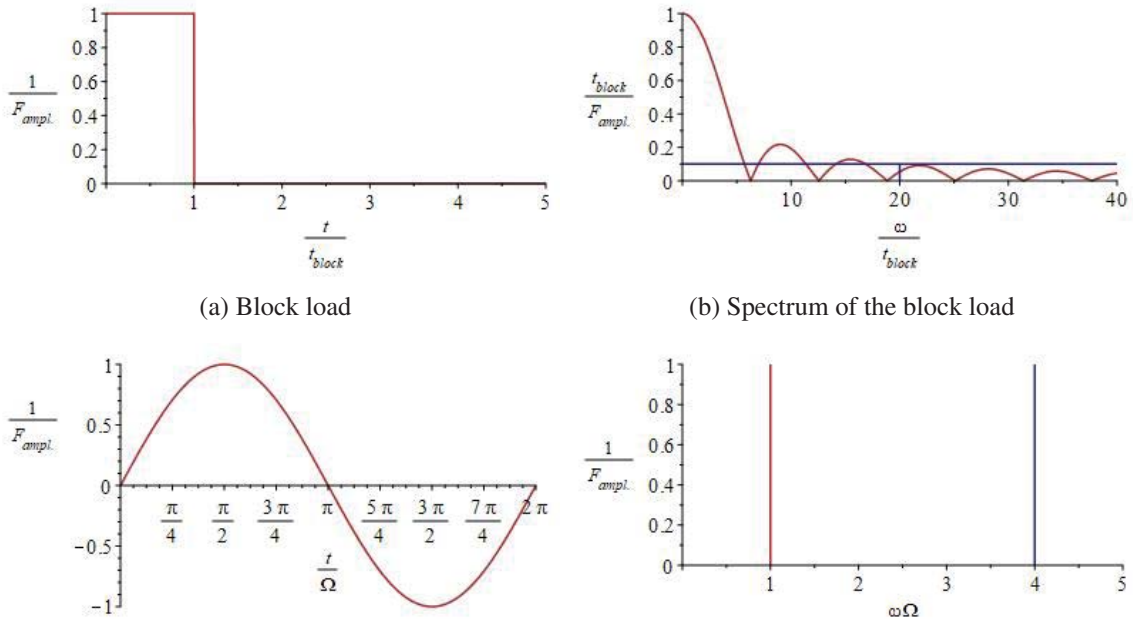

(a) Block load

(b) Spectrum of the block load

(c) Harmonic load

(d) Spectrum of the harmonic load

Figure 3: Load in time and frequency domain (red), and the minimum of frequencies included in the results (blue)

representative for steel and sandy soil. For bar 1 the properties are: $\rho_1 A_1 = 1$, $E_1 A_1 = 5000^2$, $c_1 = 5000$ and $L_1 = 20$, for bar 2: $\rho_2 A_2 = 5$, $E_2 A_2 = 500^2$ $c_2 = 500$ and $L_2 = 20$. In the initial state, the friction interface is half of bar 1, i.e. $u_0(0) = 10$. The duration of the applied block load is $t_{block} = 0.001$. The harmonic load starts at $t = 0$ with $\Omega = 1000$. The amplitude of both loads is 10. The influence of the friction coefficient μN is shown in the graphs, where μN varies from 0.1 to $100 \mu N$. $\mu N = 100$ is chosen sufficient high to approximate the linear case, where both bars move together and no sliding occurs. This case serves as validation of the description of the model with friction. The number of modes that are considered is based on the eigenfrequencies of the modes. At least frequencies excited by the block load, with an amplitude higher than 10% of the maximum amplitude or frequencies up to four times the excitation frequency of the harmonic load are included, as indicated with the blue lines in Figures 3b and 3d. For the block load and harmonic load this result in $\omega_{max} = 20.000$ and $\omega_{max} = 4.000$ respectively. This relates to about 25 and 5 flexible modes of bar 1 and about 250 and 50 modes

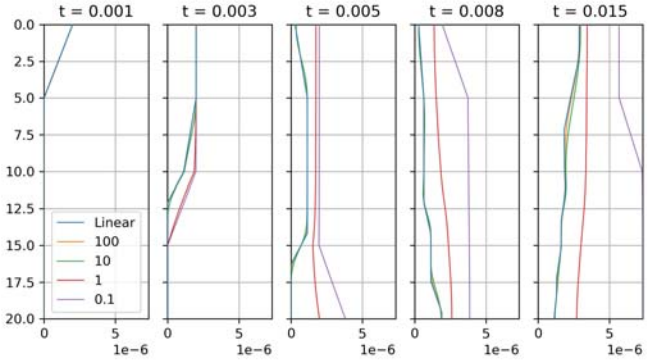

(a) Displacement of bar 1

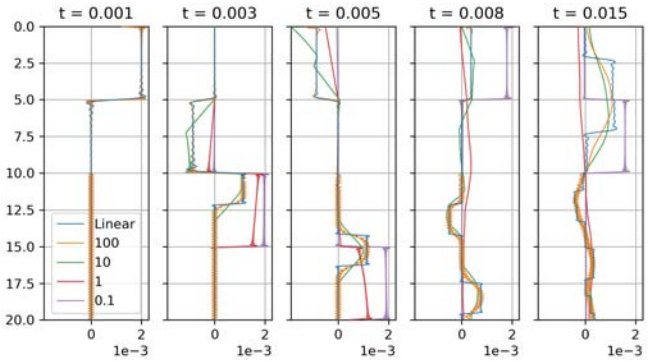

(b) Velocity of bar 1

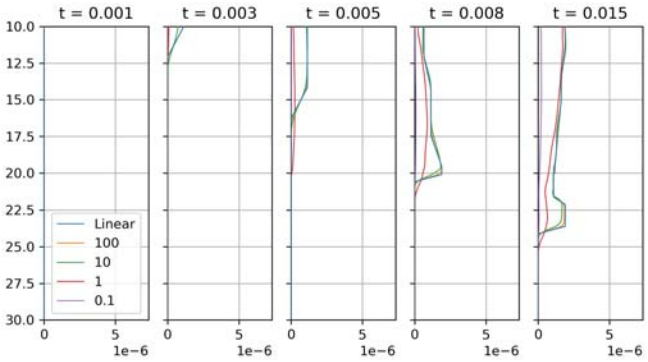

(c) Displacement of bar 2

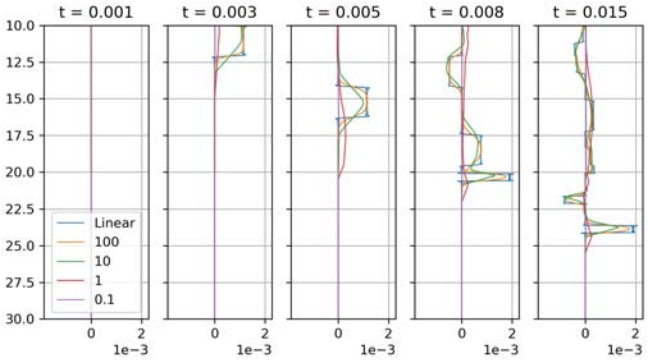

(d) Velocity of bar 2

Figure 4: The dynamic response of the bars when bar 1 is subjected to the block load for different values of μN

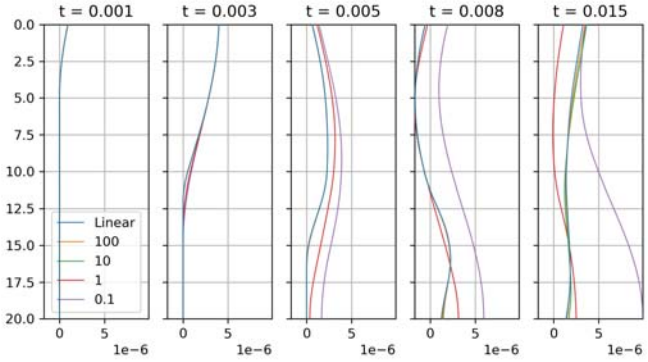

(a) Displacement of bar 1

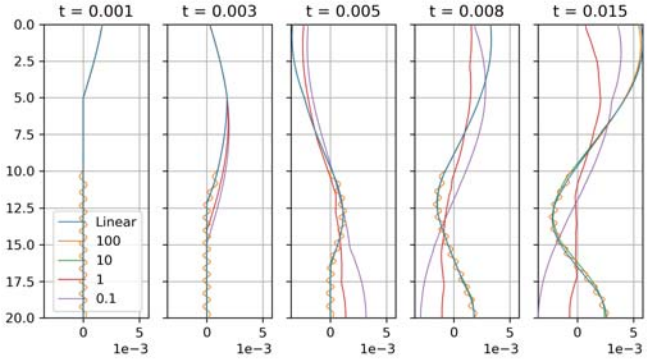

(b) Velocity of bar 1

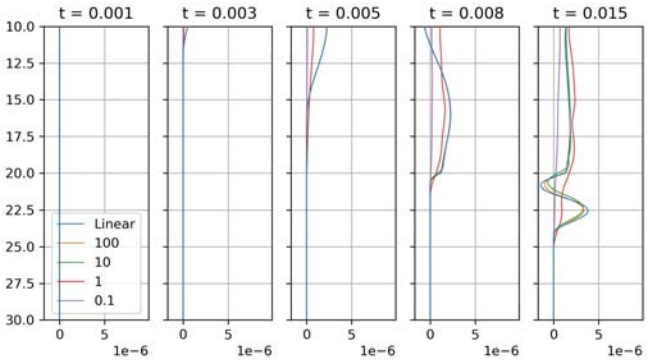

(c) Displacement of bar 2

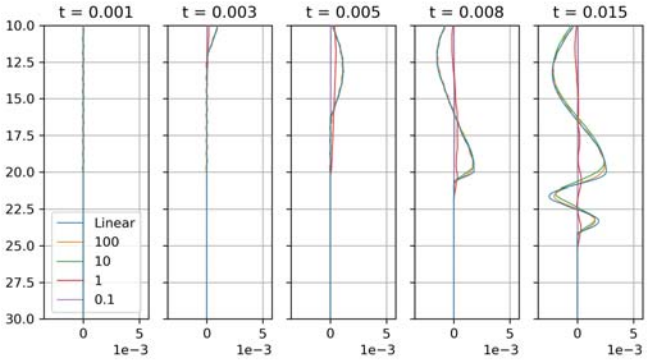

(d) Velocity of bar 2

Figure 5: The dynamic response of the bars when bar 1 is subjected to a sinusoidal load for different values of μN

for bar 2. While the friction force is based on the relative velocity of the bars, the velocities are preferably described with the same accuracy, i.e. the smallest wavelength of both bars is of the same order. Since both bars have the same length, the same number of modes are included in both bars, governed by the highest number required.

Fig. 4 shows the displacement and velocity of both bars due to a block load, representing impact pile driving. It can be seen that the block function is well represented by the summation of modes. Therefore also higher modes are activated along the whole bar. This can be seen in the amplification of higher modes, ahead of the wave-front in Fig. 4a, especially in case of high friction forces. Although present, over time these vibrations cancel out and they do not excite the system. For low friction coefficients, almost no energy dissipates into bar 1. Therefore, the wave reflects back and forth almost undisturbed.

In case of the response to a harmonic load, shown in Fig. 5, higher frequencies are not excited from the beginning, therefore, the results are more smooth. In all cases, the highest friction $\mu N = 100$ is in good agreement with the linear results. Both bars converge to the same displacement and velocity for $\mu N = 100$. Contrary, for low friction amplitudes, the unconstrained bar slides over the constrained bar. Due to that, final displacements are bigger at $t = 0.015$, best shown in Fig. 4a. Generally, the model behaves as expected, e.g. the wave-fronts align for all waves in the first bar upon the moment it starts interacting with the second bar, then for high friction amplitudes, the wave speed of both bars is based on a weighted average, whereas for low-frequency amplitudes, the wave-speed is less affected by the second bar. This is best shown in Figures 4c and 4d, where at $t = 0.004$, the three different wave-fronts are visible.

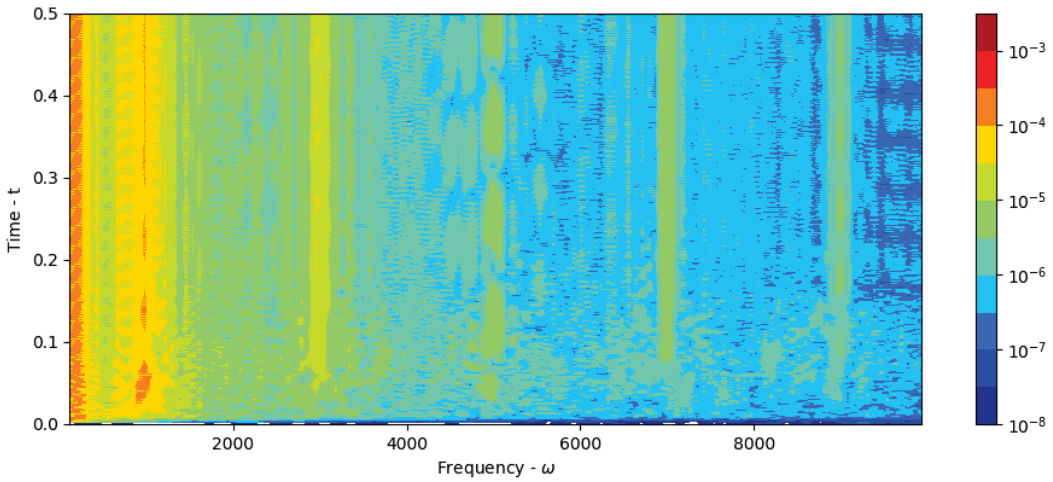

Figure 6: Time-frequency response of bar 2 for μN = 1

Fig. 6 points the importance of including the frictional interface in noise generating models for vibratory pile driving. The time-frequency plot clearly identifies the presence of the odd higher order harmonics that are excited in the system due to the presence of the frictional surface.

4 CONVERGENCE

The convergence of the model is satisfied based on displacements and velocities. The model is not able to describe the stress at the top boundary correctly due to the delta function, but the exact boundary stress at the top is not of interest, with an increasing number of modes, a

good approximation of the stress close to the boundary can be obtained. Since the time step is chosen sufficiently small: $\Delta t < 2\pi/\max(\omega_i)/10$, and depends on the number of modes in the system, the convergence of the solution depends on the truncation of the modes. The truncation criterion is based on the displacement of the bar at the final time step:

$$\delta(x, t_{i_{max}}) = \frac{\left|\sum_{n=1}^{0.9N} u_n(x,t) - \sum_{m=1}^{N} u_m(x,t)\right|}{\left|\sum_{m=1}^{N} u_m(x,t)\right|} < 1\% \tag{29}$$

where N is the number of modes. It needs to be mentioned that the convergence criterion only holds at each point from the time moment onwards when the first wave reaches the point, while before that, the denominator is zero. The convergence over time for the block load case from section 3 and $\mu N = 10$ is studied for both bars. Since the final wavefront just passed half of bar 2, only the upper half of bar 2 is taken into account. The convergence is checked between $N = 225$ and $N = 250$ modes. Fig. 7 shows that the displacements converge directly after the

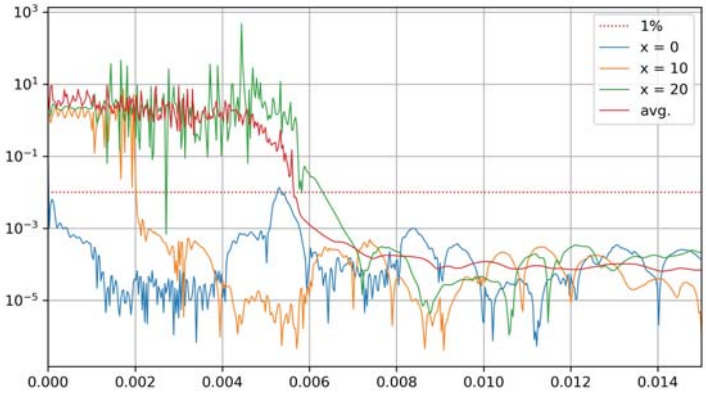

(a) $\delta(x, t_i)$ of bar 1

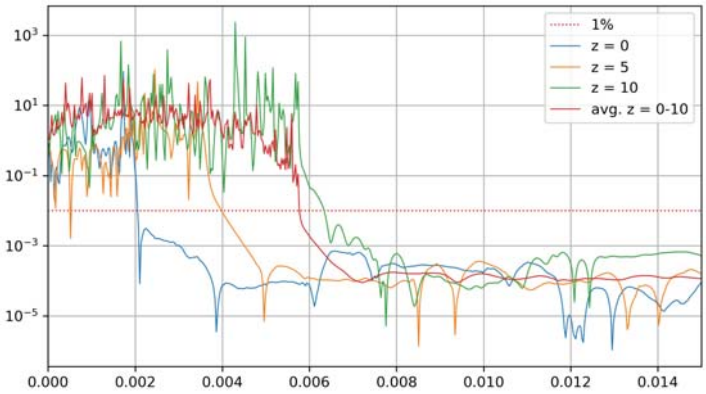

(b) $\delta(z, t_i)$ of bar 2

Figure 7: Relative error between 225 and 250 modes for $t = 0 \rightarrow 0.015$

first wavefront arrives to $\delta < 0.1\%$. It confirms that the number of modes chosen in section 3 is more than sufficient for the convergence of the displacements.

5 CONCLUSIONS

The modelling technique presented in this paper is suitable for describing the interaction of two flexible bars in frictional contact. Although stick is not included in the model, high friction forces approximate the linear model that corresponds to bars under stick condition. The accuracy of the solution increases with the number of modes included. The number of modes included is a trade-off between computational efficiency and accuracy, whereas the length of the time signal is linearly related to the computation time. More modes need to be included to approximate sudden jumps in stress or velocity. This is of major importance in impact excitations but since the work focuses on harmonic excitations, sudden jumps are not expected. Conclusively, the modelling approach seems suitable for the field of application since the excitation is mainly harmonic, the non-linear behaviour of the interface can be included without compromising the computational time compared to linear models.

6 ACKNOWLEDGEMENT

This research is associated with the GDP project in the framework of the GROW joint research program. Funding from "Topsector Energiesubsidie van het Ministerie van Econsomische Zaken" under grant number TEHE117100 and financial/technical support from the following partners is gratefully acknowledged: Royal Boskalis Westminster N.V., CAPE Holland B.V., Deltares, Delft Offshore Turbine B.V., Delft University of Technology, ECN, Eneco Wind B.V., IHC IQIP B.V., SHL Offshore Contractors B.V., Shell Global Solutions International B.V., Sif Netherlands B.V., TNO, and Van Oord Offshore Wind Projects B.V.

REFERENCE

[1] A. Tsouvalas and A. V. Metrikine. A three-dimensional vibroacoustic model for the prediction of underwater noise from offshore pile driving. *Journal of Sound and Vibrationn*, 333 (8):2283–2311, 2014. ISSN 21954364. doi: 10.1007/978-3-642-40371-2_38.

[2] Moritz B. Fricke and Raimund Rolfes. Towards a complete physically based forecast model for underwater noise related to impact pile driving. *The Journal of the Acoustical Society of America*, 137(3):1564–1575, 2015. ISSN 0001-4966. doi: 10.1121/1.4908241.

[3] E. J. Berger. Friction modeling for dynamic system simulation. *Applied Mechanics Reviews*, 55(6):535–577, 2002. ISSN 00036900. doi: 10.1115/1.1501080.

[4] M. J. Leamy, J. R. Barber, and N. C. Perkins. Distortion of a harmonic elastic wave reflected from a dry friction support. *Journal of Applied Mechanics, Transactions ASME*, 65(4):851–857, 1998. ISSN 15289036. doi: 10.1115/1.2791921.

[5] Filipe Marques, Paulo Flores, J. C. Pimenta Claro, and Hamid M. Lankarani. A survey and comparison of several friction force models for dynamic analysis of multibody mechanical systems. *Nonlinear Dynamics*, 86(3):1407–1443, 2016. ISSN 1573269X. doi: 10.1007/s11071-016-2999-3.

[6] D. C. Threlfall. The inclusion of Coulomb friction in mechanisms programs with particular reference to DRAM au programme DRAM. *Mechanism and Machine Theory*, 13(4):475–483, 1978. ISSN 0094114X. doi: 10.1016/0094-114X(78)90020-4.

[7] Josué Aranda-Ruiz and José Fernández-Sáez. On the use of variable-separation method for the analysis of vibration problems with time-dependent boundary conditions. *Proceedings of the Institution of Mechanical Engineers, Part C: Journal of Mechanical Engineering Science*, 226(12):2912–2924, 2012. ISSN 09544062. doi: 10.1177/0954406212442289.

[8] Hsu Chieh Yeh. Solving boundary value problems in composite media by separation of variables and transient temperature of a reactor vessel. *Nuclear Engineering and Design*, 36(2):139–157, 1976. ISSN 00295493. doi: 10.1016/0029-5493(76)90001-7.

EURODYN 2020
XI International Conference on Structural Dynamics
M. Papadrakakis, M. Fragiadakis, C. Papadimitriou (eds.)
Athens, Greece, 23–26 November 2020

NUMERICAL STUDY OF DYNAMIC PROPERTIES OF A SELECTED MATERIAL LAYER OF BULLETPROOF SHIELDS

M. Bocian[1], **K. Jamroziak**[1], **M. Kulisiewicz**[1], **J. Pach**[2], **and D. Pyka**[1]

[1] Department of Mechanics, Materials and Biomedical Engineering, Wroclaw University of Science and Technology
Smoluchowskiego 25 Str., 50370 Wroclaw, Poland
e-mail: miroslaw.bocian@pwr.edu.pl, krzysztof.jamroziak@pwr.edu.pl, maciej.kulisiewicz@pwr.edu.pl, dariusz.pyka@pwr.edu.pl

[2] Department of Lightweight Elements Engineering, Foundry and Automation, Wroclaw University of Science and Technology
Lukasiewicza 7-9 Str., 50371 Wroclaw, Poland
e-mail: joanna.pach@pwr.edu.pl

Keywords: Non-linear dynamics, Impact loads, Analysis and modelling, Dissipation of impact energy

Abstract: *Impact protection systems are currently constructed from several layers of materials with different mechanical properties. The purpose of such a system is to stop the projectile after hitting and also to minimize the damage to the inner layers of the shield caused by the impact. The frontal layer plays a significant role in the deceleration of the impact mass. This layer must be made of a material with appropriate elastic properties. It is necessary to create a suitable theoretical model (mechanical model) and analyze it to design an effective material system. In this test a theoretical dynamic model of the protective structure is adopted for the elastic-damping dynamic system. The model assumes that two parameters are responsible for the projectile braking efficiency in the frontal layer. These are such coefficients as dry friction (h) and viscous friction (η), which occur in a function describing the braking force of an appropriate form. Their values were estimated using a numerical method, where the limiting time of projectile braking in the frontal layer of the analyzed material and the braking distance were determined. These two values obtained by means of numerical simulation methods with the use of ABAQUS program allowed verifying the usefulness of the proposed identification method. The range of calculations was performed on the composite material samples made of rubber material - SBS rubber waste combined with polyurethane resin. The penetration of samples was simulated with M43 7.62 mm projectile core.*

1 INTRODUCTION

Current solutions of anti-impact systems (butts) are based on the search for such solutions that the frontal layer provides safe protection against projectiles ricocheting. A projectile fired from a gun poses two primary threats. The first one is the possibility of piercing the shield behind the target butt, which, in consequence, allows the bullet to continue its flight beyond the designated area. The second threat is a ricochet phenomenon [1]. It consists in that the projectile falling at an appropriate angle to the shield bounces off it and causes a return towards the shooter [2, 3]. Such a shield is to prevent the further flight of the projectile without changing direction and protect against further movement of the reflected projectiles.

The front protective layer of the impact shield (the so-called "front layer") is designed to reduce to the maximum extent possible the velocity of the bullet hitting the specific shield, which is traditionally made of e.g., armored sheet [4]. The design of such a system relates to the development of an appropriate puncture model and its analysis. The authors have presented many works related to the models of the process of piercing the composite shields [5–7]. This issue is frequently solved by employing numerical tools [8–10].

Therefore, this work aims to present an identification method used to determine specific values of constants describing mechanical properties of the frontal layer under conditions of fast velocity that we are dealing with during the piercing of a small-arms projectile. Experimental verification of the model constants was carried out in the ABAQUS program. The obtained results are guidelines for working on useful materials of the frontal layer of anti-ricochet plates.

2 THEORY

2.1 Model and assumptions

In this work, a theoretical dynamic model of the anti-impact construction with the diagram shown in Figure 1 has been adopted.

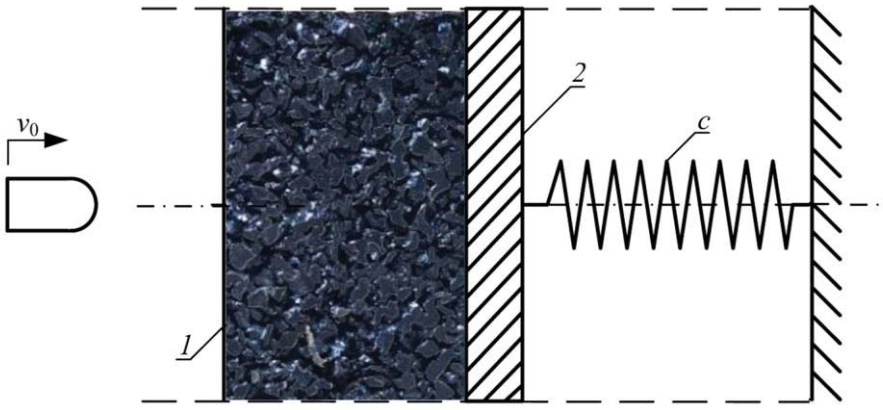

Figure 1: Diagram of the adopted dynamic model: 1 – visco-plastic front layer, 2 – energy-absorbing layer, v_0 – initial velocity of the projectile, c – rigidity of the system.

This model assumes that the central ballistic shield (2) is preceded by a specific frontal layer (1) made of a material capable of absorbing the projectile's kinetic energy as much as possible. Determining the necessary thickness of this protective layer is one of the objectives of this study. In order for this layer to be indestructible, it is envisaged that it is made of a material with viscous-plastic properties (e.g., granulates, dense liquids, gels, sands, muddy soils, etc.). For mechanical properties, such materials give resistance to a body moving in it (e.g., a

projectile). It takes the form of a force dependent on the projectile's speed. It is assumed that the model of such a force is the $S(v)$ function of the form:

$$S(v) = h\,sign(v) + \eta v \tag{1}$$

where h is the constant that determines the so-called dry friction, while η is the constant that defines viscous friction.

2.2 Identification of dynamic properties of the front layer

The model assumes two parameters responsible for the projectile braking efficiency in the front layer. These are constant coefficients h and η, which appear in the function of the form (1).

The method using the angular momentum principle was proposed to determine those values. Assuming two moments of time: t_1 and t_2 (with $t_2 > t_1$), the difference of momentum in these moments, under the principle that the difference of momentum is equal to the force impulse, is calculated from the dependence:

$$p(t_2) - p(t_1) = \int_{t_1}^{t_2} -S(v)dt \tag{2}$$

Provided that in this case the moment $t_1 = 0$ means the time when the projectile of the mass m falls into the material of the protective layer and has an initial velocity of $v(0) = v_0$ and at t_2 the projectile stops (that is $t_2 = t_z$), where $v(t_z) = 0$ and the force $S(v)$ takes the form (1), the above equation will take form:

$$-mv_0 = -\int_0^{t_z} h dt - \int_0^{t_z} \eta v dt \tag{3}$$

hence:

$$mv_0 = ht_z + \eta \int_0^{x(t_z)} dx = ht_z + \eta b \tag{4}$$

where x is the projectile path in the material ($v = dx/dt$), and $b = x(t_z)$ is the braking distance of the projectile in the material. Hence the relationship $t_z(b)$ of the form:

$$t_z = \frac{m}{h} v_0 - \frac{\eta}{h} b \tag{5}$$

Constants:

$$A_1 = \frac{m}{h}, \quad A_2 = \frac{\eta}{h} \tag{6}$$

which can be estimated from the relation (5) if for several different initial velocity values v_0 the corresponding values t_z and t_z are measured and then a known method of regression analysis is used. Once the values A_1 and A_2 have been determined, the parameters of the constants of the function model (1) are of the following form:

$$h = \frac{m}{A_1}, \quad \eta = A_2 h \tag{7}$$

Therefore, the identification should be based on the measurement of the penetration time of the projectile until it stops in the material under investigation for different initial velocities and determining the length of the braking distance of the projectile in the examined material.

3 EXPERIMENTAL VERIFICATION

Simulation tests were carried out in the ABAQUS program. For this purpose, geometric elements of the samples and the projectile were made as volumetric ones. The hybrid method combining the standard finite element method (FEM) [11] with smoothed particle hydrodynamics (SPH) [12] was used as a limiting parameter of the strain ε_{li}.

3.1 Material description

The material accepted for testing, which constituted the surface layer, was a polymer composite obtained from the rubber waste from used car tires. This composite was made up of styrene butadiene rubber (SBR) in combination with polyurethane resin (PUR3), in the 1:1 mixing ratio.

Figure 2 displays an example of basic material characteristics from piercing on a testing machine at the speed of 30 mm/sec.

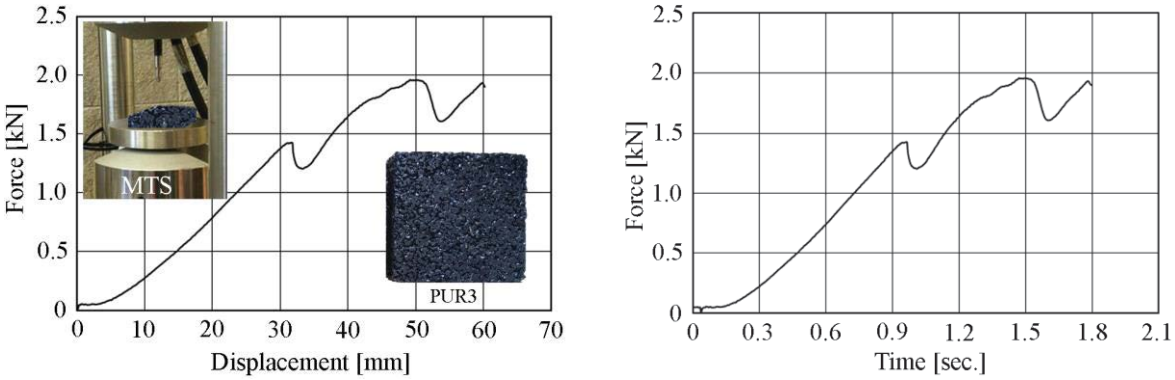

Figure 2: Selected piercing characteristics of the PUR3 sample: (a) displacement, (b) time.

3.2 Assumptions for modeling

In numerical analysis, the system was simplified to one 200 × 200 × 100 mm block and a projectile core. The analysis considered the M43 PS 7.62 mm projectile, the exact characteristics of which are given in the paper [13]. The simplification was made in the projectile model by modeling only its core since the jacket and lead jacket have hardly any effect on the analysis result and could be omitted. The core was volume-modeled with the 0.5 mm Hex-type discretization. The material of the polymer layer (anti-ballistic top layer) was described with 0.8 mm Hex-type elements (Fig. 3).

The Johnson-Cook (J-C) constitutive model was employed to describe the projectile material. This model correctly reproduces the material behavior under high-speed deformation conditions in the elastic-plastic range with the account taken of the material reinforcement and thermal weakening [13, 14]. The shielding material was described using the elastic-plastic model. The boundary conditions were set in such a way that the numerical model reproduces the features of the system during experimental studies to the utmost possible level. The initial velocity v_{0_1} = 715 m/s, v_{0_2} = 665 m/s, v_{0_3} = 615 m/s and v_{0_4} = 565 m/s was assigned to the projectile. The rotational speed was omitted, and its influence on kinetic energy dissipation was assumed to be negligible. The elastic layer of the ballistic shield was fixed on the perimeter. The restraint of the shield was blocked as translations and rotations in the three X, Y and Z axes. The analysis used the default contact model based on the "punishment function" method [15]

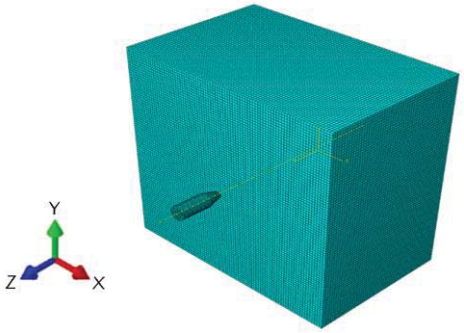

Figure 3: Numerical model of the projectile core and shield material.

Material parameters of the PUR3 composite were specified based on own research (Appendix A), and Table 1 presents the remaining.

	ρ [kg/m^3]	E [GPa]	ν [-]	A [MPa]	B [MPa]	C [-]	n [-]	m [-]
Core	7800	210	0.32	430	820	0.002	0.3	1.03
PUR3	1100	3.7	0.48	-	-	-	-	-

where: ρ – density, E – Young's modulus, ν – Poisson's ratio, A – yield at zero plastic strain, B – hardening constant, C – the strengthening coefficient of strain rate, n – hardening exponent, m – temperature softening constant.

Table 1: Material constants [13, 14].

4 RESULTS AND DISCUSSION

The numerical analysis aimed at determining such parameters as the projectile braking distance in the material (b) and the limiting time (t_z) at which the projectile is decelerated in the material.

The numerical analyses found that the system of 4 PUR3 blocks brakes the projectile, which was also confirmed in preliminary studies on the ballistic track. When the verification had been completed, several series of calculations were carried out. Figure 4 displays the example results.

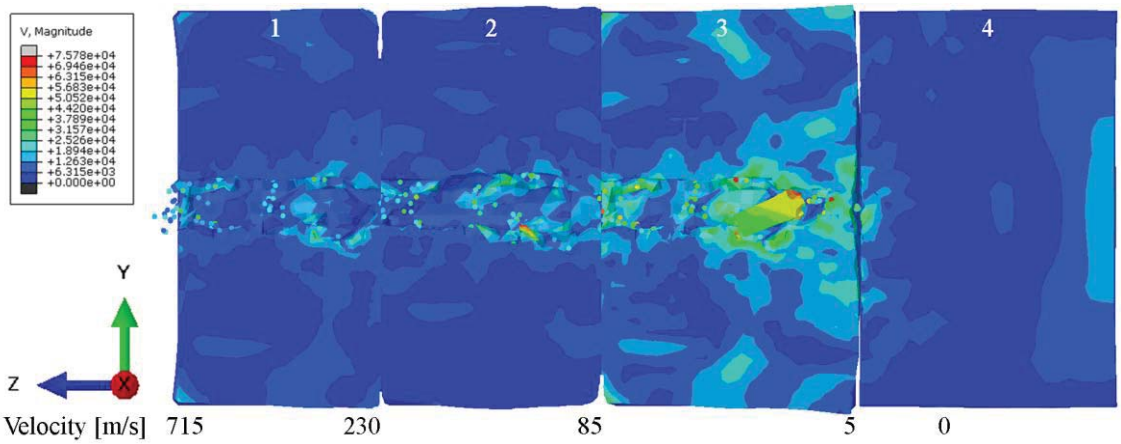

Figure 4: Example of velocity distribution of the impactor in the PUR3 material.

The impactor velocity steps shown in the analyzed system of the anti-ballistic shield front layer made up of four 200 × 200 × 100 mm blocks allow the determination of the projectile path (x) in the material as well as its braking distance $x(t_z)$. The latter was easy to estimate

from the analysis of time steps of the projectile position in the material. Parameters were estimated based on equation (5) for four initial velocities of the projectile. The results are summarized in Figure 5 only for v_{0_1} = 715 m/s.

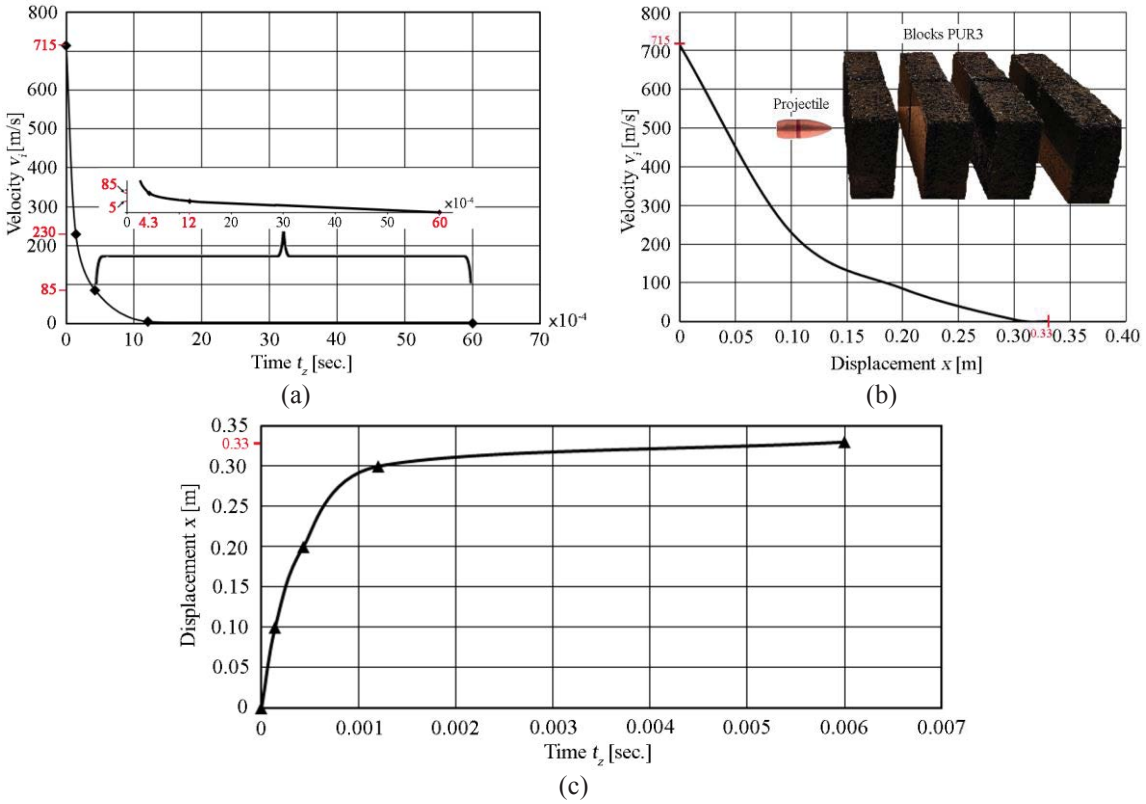

Figure 5: Diagrams of numerical analyses: (a) velocity v_i – time t_z dependence (b) velocity v_i – displacement x dependence, (c) displacement x – time t_z dependence.

After the estimation of the unknowns t_z and b, values A_1 i A_2 were calculated using the regression analysis method. Ultimately, it was possible to estimate the model parameters, i.e., the constant determining the so-called dry friction (h) and viscous friction (η). Example results are presented in Table 2.

Parameter	v_0 [m/s]	t_z [s]	b [m]	A_1 [s²/m]	A_2 [s/m²]	h [kgm/s²]	η [kg/ms]
Value	715	$6.0 \cdot 10^{-3}$	0.330	$1.4 \cdot 10^{-5}$	$1.2 \cdot 10^{-2}$	565.512	6.815
	665	$5.6 \cdot 10^{-3}$	0.290				
	615	$5.2 \cdot 10^{-3}$	0.270				
	565	$4.9 \cdot 10^{-3}$	0.245				

Table 2: Example searched values of the analyzed model.

During the analysis, it could be clearly seen that the higher the dry friction value, the greater was the error in estimating the values of h and η.

5 CONCLUSIONS

The analysis of the proposed model of dynamic estimation of parameters responsible for its effectiveness proved the right direction of work. The proposed method of identification based

on the momentum principle, and then the use of numerical tools in the form of the ABAQUS program can be successfully employed. The method is burdened with some errors resulting from simplifications applied in numerical analysis. However, it enables the adoption of certain conclusions for designing the anti-impact shield layers. Based on the findings obtained, it can be stated that the dry friction value has an impact on the final result. The application of the hybrid methods of the adopted model parameterization can be presumed as promising directions of conducting works on identifying the type of impact resistance systems. The authors intend to perform similar experimental studies, including tests of real systems.

ACKNOWLEDGEMENT

Calculations have been carried out in Wroclaw Centre for Networking and Super-computing (http://www.wcss.pl), grant No. 452.

REFERENCES

[1] Y-E. Yong, A systemic review on ricochet gunshot injuries, *Legal Medicine* 26, 45-51, 2017.

[2] L.C. Haag, Shooting incident reconstruction, ISBN: 9780120884735, 2006.

[3] J. Xue, P. Shen, X. Wang, Research on ricochet and its regularity of projectiles obliquely penetrating into concrete target, *Journal of Vibroengineering* 18, 2754-2770, 2016.

[4] M. Bocian, K. Jamroziak, M. Kulisiewicz, Dynamic identification method for determining the plastic properties of the material used as a front layer of impact shields, *Proceedings of the 15th International Conference: Dynamical Systems - Theory and Applications, DSTA-2019, Theoretical Approaches in Non-Linear Dynamical Systems,* 2019.

[5] M. Bocian, K. Jamroziak, M. Kulisiewicz, An identification of nonlinear dissipative properties of constructional materials at dynamical impact loads conditions, *Meccanica* 49, 1955-1965, 2014.

[6] K. Jamroziak, M. Bocian, Identification of composite materials at high speed deformation with the use of degenerated model, *Journal of Achievements in Materials and Manufacturing Engineering* 28, 171-174, 2008.

[7] K. Jamroziak, M. Bocian, M. Kulisiewicz, Identification of a subsystem located in the complex dynamical systems subjected to random loads, *Journal of Computational and Nonlinear Dynamics* 12(1): 014501, 2017.

[8] J.F. Moxnes, Ø. Frøyland, S. Skriudalen, A.K. Prytz, J.A. Teland, E. Friis, G. Ødegårdstuen, On the study of ricochet and penetration in sand, water and gelatin by spheres, 7.62 mm APM2, and 25 mm projectiles, *Defence Technology* 12, 159-170, 2016.

[9] M. Seidl, T. De Vuyst, N. Djordjevic, Numerical investigations on 7.62x39 mm projectile ricochet off aramid plates, *Proceedings of the Conference: Light Weight for Defense and Security*, 2019.

[10] A. Mackiewicz, D. Pyka, J. Pach, K. Jamroziak, M. Bocian, Comparison of numerical modelling methods of innovative materials for ballistic shields, *Advanced Materials for Defense* 4, 119-127, 2020, https://doi.org/10.1007/978-3-030-34123-7_13.

[11] L. Mazurkiewicz, M. Malachowski, P. Baranowski, Optimization of protective panel for critical supporting elements, *Composite Structures* 134, 493-505, 2015.

[12] Y. Lu, A. Hu, X. Chang, Z. Li, Y. Wei, Grid-free modelling based on the finite particle method for incompressible viscous flow problems, *Shock and Vibration* ID 4610524, 2019, https://doi.org/10.1155/2019/4610524.

[13] A. Kurzawa, D. Pyka, K. Jamroziak, M. Bajkowski, M. Bocian, M. Magier, J. Koch, Assessment of the impact resistance of a composite material with EN AW-7075 matrix reinforced with α-Al_2O_3 particles using a 7.62 × 39 mm projectile, *Materials* 13, 769, 2020, doi:10.3390/ma13030769.

[14] A. Poplawski, P. Kedzierski, A. Morka, Identification of Armox 500T steel failure properties in the modeling of perforation problems, *Materials & Design* 2020, https://doi.org/10.1016/j.matdes.2020.108536.

[15] L. Mazurkiewicz, J. Malachowski, P. Baranowski, Optimization of protective panel for critical supporting elements, *Composite Structures* 134, 493-505, 2015.

Appendix A: Characteristics of the composite material PUR3 as stress - strain

Plastic - Isotropic								
No.	Stress [MPa]	Strain [-]	No.	Stress [MPa]	Strain [-]	No.	Stress [MPa]	Strain [-]
1	40	0.00	**21**	802.31	20.20	**41**	1695.49	40.86
2	55.13	0.71	**22**	862.75	21.24	**42**	1742.46	41.89
3	47.01	1.63	**23**	926.33	22.27	**43**	1782.39	42.92
4	51.58	2.63	**24**	985.63	23.31	**44**	1802.66	43.95
5	60.21	3.66	**25**	1047.24	24.35	**45**	1828.36	44.98
6	82.73	4.68	**26**	1106.45	25.38	**46**	1872.28	46.01
7	107.27	5.72	**27**	1166.72	26.42	**47**	1894.18	47.05
8	143.74	6.75	**28**	1225.59	27.45	**48**	1919.31	48.08
9	182.23	7.79	**29**	1292.07	28.48	**49**	1959.25	49.11
10	220.97	8.82	**30**	1348.33	29.52	**50**	1957.81	50.14
11	266.09	9.85	**31**	1403.36	30.55	**51**	1937.80	51.17
12	315.79	10.89	**32**	1425.06	31.58	**52**	1800.02	52.20
13	366.40	11.92	**33**	1221.80	32.61	**53**	1620.81	53.24
14	415.85	12.96	**34**	1215.01	33.64	**54**	1618.64	54.27
15	466.94	13.99	**35**	1258.36	34.67	**55**	1674.70	55.30
16	518.54	15.03	**36**	1340.30	35.70	**56**	1746.81	56.33
17	572.23	16.07	**37**	1428.75	36.73	**57**	1803.36	57.36
18	627.90	17.10	**38**	1507.80	37.76	**58**	1853.39	58.39
19	682.25	18.14	**39**	1577.03	38.79	**59**	1917.22	59.42
20	739.22	19.17	**40**	1635.68	39.82	**-**	-	-

EURODYN 2020
XI International Conference on Structural Dynamics
M. Papadrakakis, M. Fragiadakis, C. Papadimitriou (eds.)
Athens, Greece, 23–26 November 2020

MEASUREMENTS OF NONLINEAR VIBRATIONS OF A BEAM SUBJECTED TO TWO BROADBAND CORRELATED RANDOM EXCITATIONS

S. TALIK[1,2], M. CLAEYS[1], J-P. LAMBELIN[1], J-J. SINOU[2,3]

[1] CEA/CESTA
CS60001
15 avenue des Salinières, 33116 Le Barp, France
sebastien.talik@cea.fr
maxence.claeys@cea.fr
jean-pierre.lambelin@cea.fr

[2] Laboratoire de Tribologie et Dynamique des Systèmes UMR CNRS 5513
École Centrale de Lyon
36 avenue Guy de Collongue 69134 Écully Cedex, France
jean-jacques.sinou@ec-lyon.fr

[3] Institut Universitaire de France
75005 Paris, France

Keywords: Nonlinear Dynamics. Experiments. Correlated Multipoints Excitation. Numerical Simulation. Harmonic Balance Method for random excitations.

Abstract. *This paper presents experiments of a nonlinear system subjected to two broadband correlated random excitations. The system studied is a steel beam bonded on both sides to a heavy steel block. First of all, correlation between two broadband random excitations is studied. This study analyses and compares the effects of the correlation choice into the apparition and/or attenuation of some symmetric or anti-symmetric modes of the beam. Two different types of correlation are experimentally introduced: in phase and opposite phase. Secondly, nonlinear effects are identified according to the presence of secondary peaks corresponding to the appearance of harmonic components of the first three natural modes (i.e. two symmetric and one anti-symmetric) of the clamped-clamped beam. Then, from experimental output data, the correlation effects added to the nonlinear effects open the discussion about the observation of some combinations of different harmonics from different modes of the nonlinear system under study. Finally, an extension of the classical Harmonic Balance Method (HBM) is proposed for the numerical prediction of the nonlinear dynamic behavior of a mechanical system subjected to two broadband correlated random excitations. Comparison between experiments and numerical simulations validate the numerical strategy for the prediction of the global nonlinear response as well as the contribution of harmonics for a mechanical system subjected to multipoints correlated random excitations.*

1 INTRODUCTION

Nonlinear vibrations in many mechanical systems may have different origins. For instance, nonlinearities can be explained by the constitutive law of the material used in a dynamical structure or by the geometry of the structure itself (such as for example the case of large displacements). Nonlinearities effects are numerous [1]: discontinuities in the frequency response, dependency of eigenfrequencies with input amplitude [2], presence of secondary peaks resulting from the harmonics generated by the primary resonance [3], *etc*. Correlated multipoints excitations and its effects on the linear (or nonlinear) response of a dynamical system have already been studied in the literature [4, 5]. This paper illustrates correlation effects as the amplification and/or the attenuation of some symmetric or anti-symmetric vibrations modes. Numerical methods have been developed to compute the nonlinear response of such structures. Among them, an extension of the classical Harmonic Balance Method (HBM) enables to compute the multi-harmonic frequency response of the clamped-clamped beam with non-ideal boundary conditions and subjected to two broadband random excitations.

This paper is organized as follows: firstly experimental set-up of the clamped-clamped beam is presented with observations of correlation on temporal input data for two different types of correlation (in phase and opposite phase). Correlation effects are experimentally observed on the first three natural modes of the clamped-clamped beam. Then, the presence of secondary peaks corresponding to the harmonics generated by the primary resonance of each mode are studied to point out nonlinear behavior. Finally, numerical simulations based on an extension of the Harmonic Balance Method are performed for the prediction of the nonlinear response of a mechanical system subjected to two broadband correlated random excitations.

2 EXPERIMENTS

2.1 Experimental set-up

The experimental clamped-clamped beam studied in this paper is the same as the one presented in [2, 3]. A new experiment set-up is presented in figure 1a, the structure (beam + blocks) is screwed to a heavy steel block and the whole system has been instrumented with four three-dimensional accelerometers (A1 to A4), two one-dimensional accelerometers (A5, A6) and two cell forces (F1, F2) as depicted in figure 1b. Accelerometers A2, A3 and A4 are present to assure the correct embedding of the whole structure during experiments. The beam is subjected to a bipoints random correlated excitation by two electrodynamic shakers referenced in figure 1b using Multi-Input-Multi-Output (MIMO) control technology [8]. The shakers configuration is designed to excite the modes of the beam within a chosen bandwidth of frequencies. The first correlation is therefore spatial since the position of each shaker is fixed for all the experiments, and symmetrical about the center of the beam.

2.2 Temporal input data

Each shaker is piloted with a Power Spectral Density (PSD) and the correlation between both excitations is defined in the Cross Spectral Density (CSD) with the notions of coherence and phase, according to the equation (1):

$$S_{12}(f) = \sqrt{\gamma_{12}^2(f) S_{11}(f) S_{22}(f)}\, \exp\left(j\phi_{12}(f)\right) \tag{1}$$

where $S_{11}(f)$ and $S_{22}(f)$ are the PSD of temporal excitations $F_1(t)$ and $F_2(t)$, f is the frequency. $\gamma_{12}(f)$ is the coherence between both PSD $S_{11}(f)$ and $S_{22}(f)$, its value experimentally

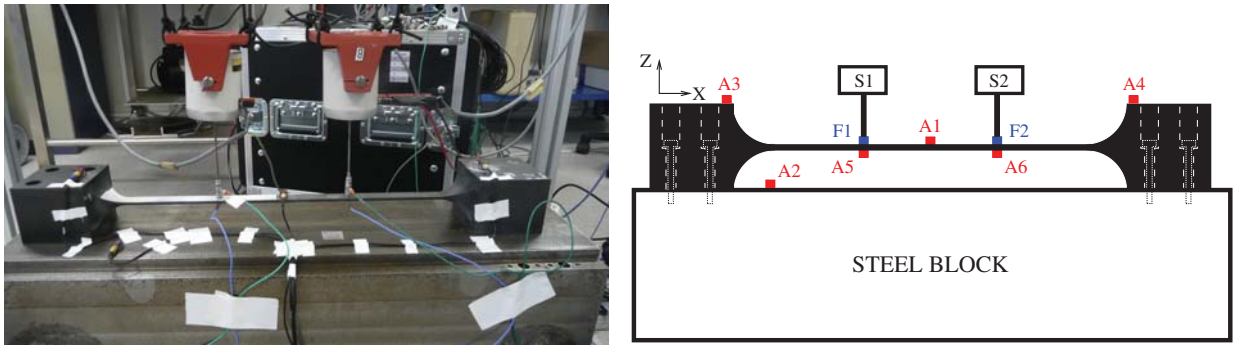

(a) (b)

Figure 1: (a) A picture of the experimental set-up. (b) A schematic of the experimental set-up which includes six accelerometers (A1 to A6) and two cell forces (F1, F2) related to the two electrodynamic shakers S1 and S2.

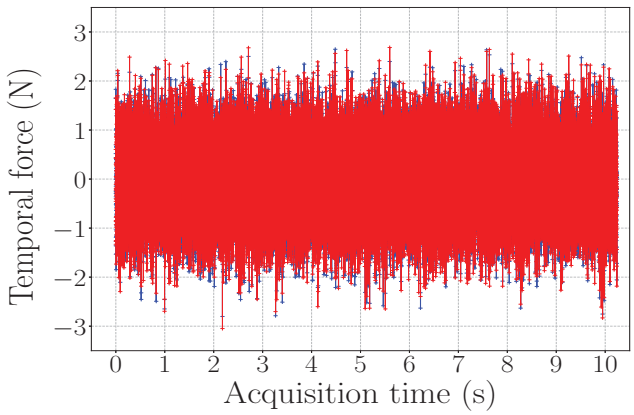

Figure 2: Two experimental random temporal forces F1 (blue) and F2 (red) generated with the MIMO control technology [8], the "in phase" correlation is the one created with a coherence equal to 0.98 and a phase equal to 0° along the whole bandwidth.

varies between 0.05 and 0.98: it is impossible to get two perfectly correlated or uncorrelated multipoints excitations with the electronic devices of this experimental set-up. $\phi_{12}(f)$ is the phase between both temporal excitations $F_1(t)$ and $F_2(t)$. The phases corresponding to the two correlation types studied in this paper are respectively 0° (in phase) and 180° (opposite phase), with a coherence set at 0.98. Other configurations of coherence and phases have been tested, but are not presented is in this paper for the sake of clarity.

The shape of each PSD is a band-limited white noise, *i.e.* the level of excitation is constant along the whole bandwidth, for all experiments. The sampling frequency is 3200 Hz with a desired resolution frequency of 0.098 Hz. The total duration of one experiment is 307.2 s. The output signal is decomposed into 30 temporal blocks of 10.24 s each. A periodogram estimate computes an approximation of the PSD for each of the 30 blocks. Then, the PSD of the output signal is calculated by averaging all the estimates [9]. The input PSD is constant over time to ensure that the response is stationary. Both experimental temporal random inputs of one of the temporal blocks of 10.24 s for two different correlation types (in phase and opposite phase) are plotted in figures 2 and 3. The generation of a bipoints correlated random excitation with the MIMO control technology is validated.

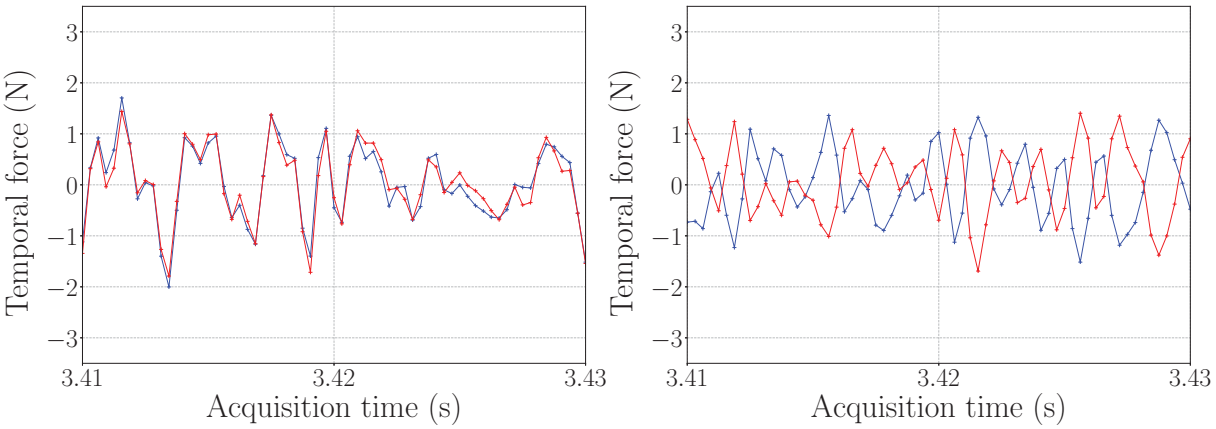

Figure 3: Zoom on two types of correlation (a) in phase (b) opposite phase for two experimental random temporal forces F1 (blue) and F2 (red).

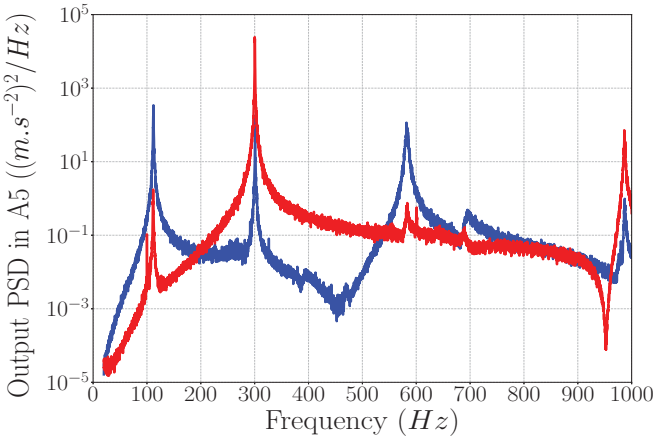

Figure 4: Experimental output PSD of accelerometer A5 with a RMS level of 0.5 N for two different correlation types along the bandwidth $[20 - 1000\,\text{Hz}]$. The correlation types are in phase (blue) and opposite phase (red).

2.3 Results

2.3.1 Correlation effects

Experimental results for one level of excitation (0.5 N RMS) along the bandwidth $[20 - 1000\,\text{Hz}]$ for two different correlation types (in phase and opposite phase) are plotted in figure 4. Correlation effects are observed as the amplification and/or the attenuation of some symmetric or anti-symmetric vibrations modes in the vicinity or their primary resonance. For the "in phase" correlation, as shown in figure 5, symmetric modes are amplified and anti-symmetric modes are attenuated whereas for the "opposite phase" correlation, symmetric modes are attenuated and anti-symmetric modes are amplified.

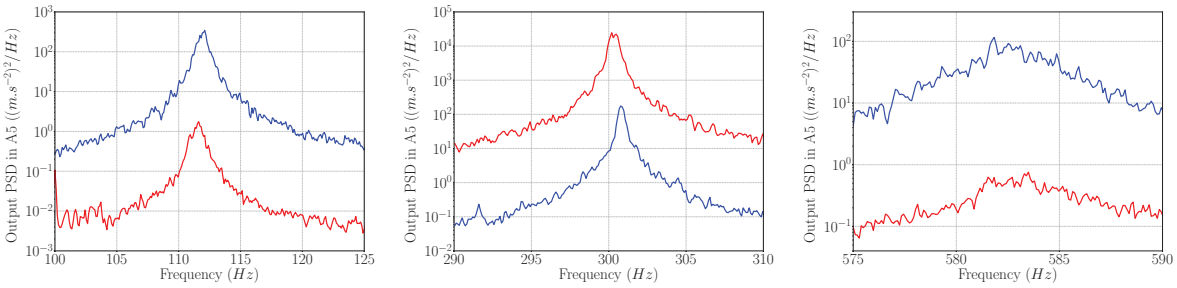

(a) (b) (c)

Figure 5: Zoom on the resonance of each mode: (a) first mode (symmetric) (b) second mode (anti-symmetric) (c) third mode (symmetric). The correlation types are in phase (blue) and opposite phase (red).

2.3.2 Nonlinear effects

As described in [3], an input PSD centered around the frequency of the primary resonance of one mode induces nonlinear effects. This nonlinear behavior is generally characterized by the appearance of secondary peaks corresponding to the harmonics generated by the primary resonance of this mode. Then, in order to study the combination of correlation effects and nonlinear effects, an approach similar to that of [3] is followed and experimental measurements have been realized for one level of excitation (0.5 N RMS) along the bandwidth $[20 - 500$ Hz$]$ *i.e.* where only the first symmetric mode and the first anti-symmetric mode of the clamped-clamped beam are solicited.

Both experimental input and output for one ideal level of excitation (0.5 N RMS) along the bandwidth $[20 - 500$ Hz$]$ for the in phase correlation are plotted in figure 6. The control of the input PSD shows its limitations, as in [3], with the presence of unexpected resonance peaks in the bandwidth $[500 - 1000$ Hz$]$. The output is rich in information. In the bandwidth $[20 - 500$ Hz$]$, the same effects of correlation choice are foreseen in the vicinity of the primary resonance of the first mode and the second mode of the clamped-clamped beam. In the bandwidth $[500 - 1000$ Hz$]$, several peaks of resonance which are not present in the experimental input signal are observed. They reveal a nonlinear dynamic behavior. Moreover some of these peaks are harmonics generated by the primary resonance of the amplified mode (first mode). Figure 7 illustrates closer the nonlinear effects depicted along the bandwidth $[500 - 1000$ Hz$]$. Harmonics of the primary resonance of the first mode situated at approximately $f_1 = 110.28$ Hz are highlighted with vertical lines from $5f_1$ to $9f_1$. Most of the peaks in the figure 7 correspond to an harmonic of f_1, nevertheless other peaks are observed.

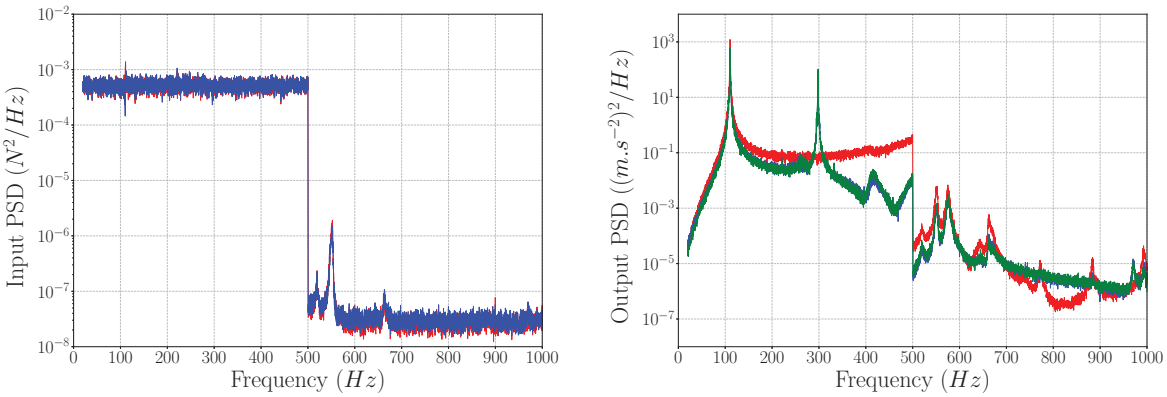

(a) (b)

Figure 6: Experimental input (a) and output (b) PSD for the experiment with a RMS level of 0.5 N along the bandwidth $[20 - 500\,\text{Hz}]$ for the "in phase" correlation. The input PSD are the ones from the two shakers S1 (blue) and S2 (red). The output PSD are the ones from accelerometers A1 (red), A5 (blue) and A6 (green).

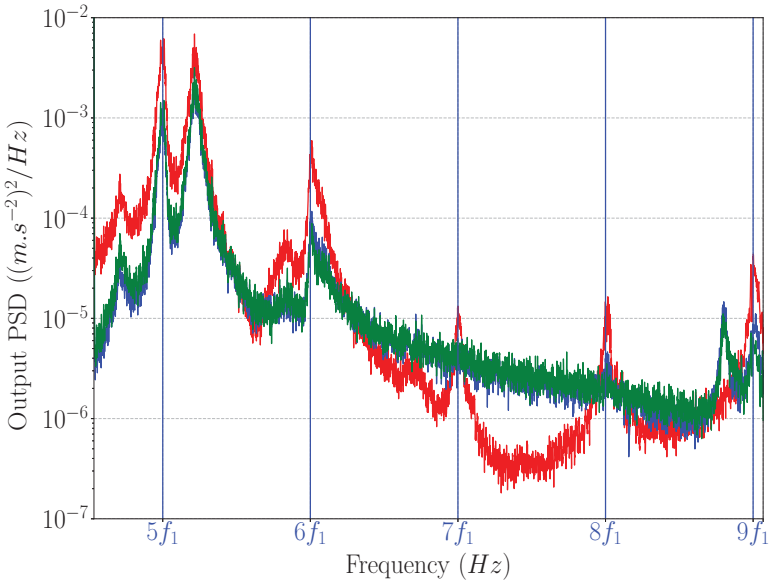

Figure 7: Zoom on the experimental output PSD on the bandwidth $[500 - 1000\,\text{Hz}]$ for the experiment with a RMS level of 0.5 N along the bandwidth $[20 - 500\,\text{Hz}]$ for the "in phase" correlation. The output PSD are the ones from accelerometers A1 (red), A5 (blue) and A6 (green). Vertical lines (blue) represent harmonics of the primary resonance of the first mode situated at $f_1 = 110.28$Hz.

3 HARMONIC BALANCE METHOD (HBM) FOR RANDOM EXCITATIONS

The Harmonic Balance Method enables to solve numerically a discrete problem described as [6] :

$$\mathbf{M\ddot{W}} + \mathbf{D\dot{W}} + \mathbf{KW} = \mathbf{F_1} + \mathbf{F_2} + \mathbf{F_{nl}}(\mathbf{W}) \tag{2}$$

where $\mathbf{M}$, $\mathbf{D}$ and $\mathbf{K}$ are mass, damping and stiffness matrices of a mechanical system.

In the case of a nonlinear system subjected to random excitations, the steady state nonlinear response $\mathbf{W}$, the stochastic excitations $\mathbf{F_j}(t)$ ($j = 1, 2$) and the nonlinear force $\mathbf{F_{nl}}(t)$ are defined as:

$$\begin{aligned}
\mathbf{W}(t) &= \mathbf{B_0} + \sum_{i=1}^{N} \left(\mathbf{A_i} \sin\left(i\Delta f t\right) + \mathbf{B_i} \cos\left(i\Delta f t\right)\right) \\
\mathbf{F_j}(t) &= \mathbf{C_{0,j}} + \sum_{i=1}^{N} \left(\mathbf{S_{i,j}} \sin\left(i\Delta f t\right) + \mathbf{C_{i,j}} \cos\left(i\Delta f t\right)\right) \\
\mathbf{F_{nl}}(t) &= \mathbf{C_0} + \sum_{i=1}^{N} \left(\mathbf{S_i} \sin\left(i\Delta f t\right) + \mathbf{C_i} \cos\left(i\Delta f t\right)\right)
\end{aligned} \tag{3}$$

where Δf is the resolution frequency and N defines the number of harmonic components in order to describe the entire frequency band of interest.

We define $F_1(a_1, t)$ and $F_2(a_2, t)$ as two correlated random forces applied to the structure respectively at abscissas a_1 and a_2 and initiated with the cross-spectral density matrix:

$$\mathbf{S}(f) = \begin{bmatrix} S_{11}(f) & \rho(f)\sqrt{S_{11}(f)S_{22}(f)} \\ \bar{\rho}(f)\sqrt{S_{11}(f)S_{22}(f)} & S_{22}(f) \end{bmatrix} \tag{4}$$

where $S_{11}(f)$ and $S_{22}(f)$ represent PSD of excitations 1 and 2. We define correlation in the off-diagonal term $S_{12}(f)$ as $\rho(f)\sqrt{S_{11}(f)S_{22}(f)}$ where $\rho(f)$ is the spectral correlation coefficient. It can be real or complex and enables to introduce a phase between the two temporal excitations. Equations developed by Shinozuka [11] are used to define two correlated random forces in the time domain. Thanks to Cholesky decomposition, $\mathbf{S}(f)$ can be written as the product $\mathbf{H}(f)\mathbf{H}^*(f)$ where $H_{ij}(f)$ terms are defined as functions of the $S_{mn}(f)$ terms. Finally, $F_1(a_1, t)$ and $F_2(a_2, t)$ can be expressed by:

$$F_1(a_1, t) = \delta(a_1, x)\sqrt{2\Delta f}\ \Re\left[\sum_{i=1}^{N} H_{11}(f_i) \exp\left[j2\pi f_i t + i\phi_{1i}\right]\right] \tag{5}$$

$$\begin{aligned}
F_2(a_2, t) \;=\; & \delta(a_2, x)\ \sqrt{2\Delta f}\ \Re\left[\sum_{i=1}^{N} H_{21}(f_i) \exp\left[j2\pi f_i t + i\phi_{1i}\right]\right] \\
& + \delta(a_2, x)\ \sqrt{2\Delta f}\ \Re\left[\sum_{i=1}^{N} H_{22}(f_i) \exp\left[j2\pi f_i t + i\phi_{2i}\right]\right]
\end{aligned} \tag{6}$$

where $\delta(a_j, x)$ is the Dirac function defined at abscissa a_j. Δf is the resolution frequency. $\Re$ is the real part number. $H_{ij}(f)$ terms are known from Cholesky decomposition of matrix $\mathbf{S}(f)$. f_i is the ith frequency of the frequency domain. The ϕ_{ji} random variables uniformly distributed between 0 and 2π are defined for all the frequencies $i \in [\![1, N]\!]$ and for the two excitations $j \in$

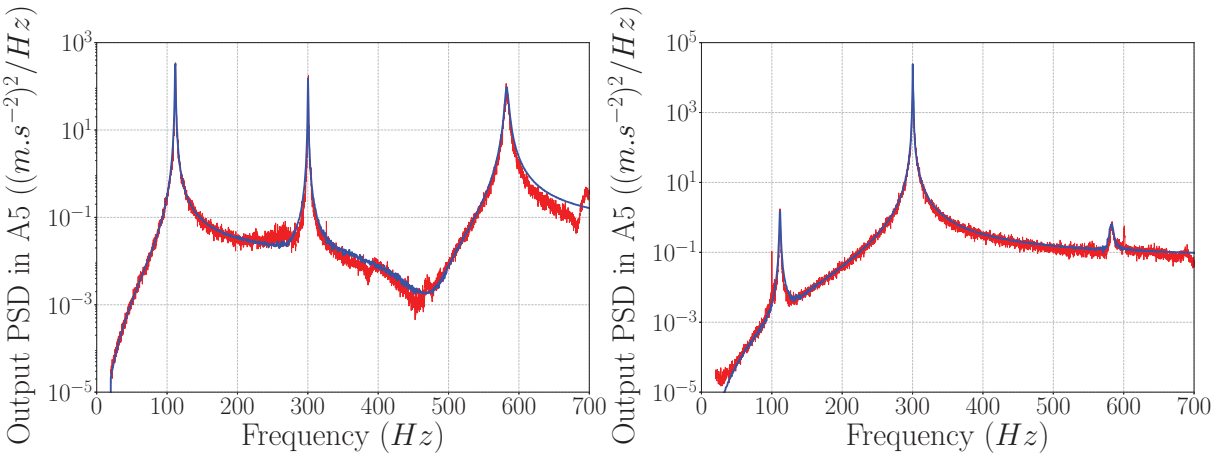

(a) (b)

Figure 8: Experimental output (red) and numerical simulation (blue) based on the extended Harmonic Balance Method for in phase (a) and opposite phase (b) random excitations.

$[\![1, 2]\!]$, they are independent one from each other. It can be noted that the HBM seeks the steady state solution in the form of a truncated Fourier series for nonlinear systems subjected to a deterministic excitation with one fundamental frequency or evenly spaced frequencies [3]. In order to fulfill this objective with two broadband correlated random excitations, the key is to define the parameter Δf in equations (5) and (6) as the fundamental frequency. That choice leads to the fact that the random excitation is now seen as an equivalent deterministic excitation with one fundamental frequency and multiple harmonics. Yet, the method remains random since the numerical output PSD is obtained by averaging the estimates from the individual responses to one multipoints correlated random excitation.

One of the originality of the proposed methodology is to be able to consider the random excitation as a series of cosine functions with weighted amplitudes, evenly spaced frequencies and random phase angles. This new formulation will allow to use the HBM for the prediction of the nonlinear response of a mechanical system subjected to two broadband correlated random excitations. For the interested reader, different versions of HBM adapted to single-point random excitation have been previously studied and compared to a shooting method (based on time integration) in terms of robustness and computional efficiency [3].

As described in [3], if an expression of the nonlinear force $f_{nl}(t)$ is known, Alternate Frequency Time-method is used to determine coefficients $\mathbf{C_i}$ and $\mathbf{S_i}$ as functions of unknowns $\mathbf{A_i}$ and $\mathbf{B_i}$. The final set of equations which needs to be minimized with a continuation technique is given by:

$$\mathbf{H}\left(\mathbf{X}, \mathbf{F1}, \mathbf{F2}\right) = \mathbf{AX} - \mathbf{B}\left(\mathbf{F_1}, \mathbf{F_2}\right) - \mathbf{B_{nl}}\left(\mathbf{X}\right) \tag{7}$$

Figure 8 shows the comparison of simulation and experiments for the in phase and the opposite phase correlations. For each simulation, an ideal input PSD along the bandwidth $[20 - 1000$ Hz$]$ has been created based on the RMS value of each effort (0.5 N RMS) and 100 estimates have been performed in order to reduce the variance of the estimated output PSD. Comparison between experiments and simulation enables to validate the mechanical model of the beam.

4 CONCLUSION

Experiments for a clamped-clamped beam have been performed in order to study the effects of a multipoints correlated random excitation to a nonlinear system. Correlation effects have been observed with the amplification and/or the attenuation of some symmetric or anti-symmetric vibrations modes. Nonlinear effects, as previously observed in [3] for a random excitation centered around the frequency of the primary resonance of one mode, have been pointed out with the presence of secondary peaks corresponding to the harmonics of this mode. In the current study, combination of both correlation and nonlinear effects have been observed.

Once the mechanical model of the beam validated, on going work is focusing on the simulation, using the proposed Harmonic Balance Method for random excitations, of the secondary peaks in the bandwidth $[500 - 1000\,\text{Hz}]$. It will help the understanding of these nonlinear effects and their dependency to the correlation of the random excitations.

ACKNOWLEDGMENTS

The authors gratefully acknowledge the support of the CEA/CESTA teams that helped with this study. J.-J. Sinou acknowledges the support of the Institut Universitaire de France.

REFERENCES

[1] J.P. Noel, G. Kerschen. Nonlinear system identification in structural dynamics: 10 more years of progress. Commun Nonlinear Sci Numer Simulat 83. 2017. pp. 2-35.

[2] M. Claeys, J-J. Sinou, J-P. Lambelin, B. Alcoverro. Multi-harmonic measurements and numerical simulations of nonlinear vibrations of a beam with non-ideal boundary conditions. Commun Nonlinear Sci Numer Simulat 19. 2014. pp. 4196-4212.

[3] T. Roncen, J-P. Lambelin, J-J. Sinou. Nonlinear vibrations of a beam with non-ideal boundary conditions and stochastic excitations - experiments, modeling and simulations. Commun Nonlinear Sci Numer Simulat 74. 2019. pp. 14-29.

[4] M. Shinozuka. Simulation of Multivariate and Multidimensional Random Processes. The Journal of the Acoustical Society of America 49. 1971.

[5] A.K. Sinha. On Digital Simulation of Multicorrelated Random Processes and Its Applications. PhD thesis. Dept. Eng. Sci. Mech. Virginia Poly. Inst. and State U. 1973.

[6] J-J. Sinou. Non-linear dynamics and contacts of an unbalanced flexible rotor supported on ball bearings. Mechanism and Machine Theory 44. 2009. pp. 1713-1732.

[7] A.H. Nayfeh, Nonlinear transverse vibrations of beams with properties that vary along the length, Journal of the Acoustical Society of America 53. 1973. pp. 766-770.

[8] B. Peeters, J. Debille. Multiple-input-multiple-output random vibration control: Theory and practice. Proceedings of the 2002 International Conference on Noise and Vibration Engineering, ISMA. 2002. pp. 507-516.

[9] P. Welch. The use of fast fourier transform for the estimation of power spectra: a method based on time averaging over short, modified periodograms. IEEE Trans Audio Electroacoust. 1967.

[10] P. Ribeiro. The second harmonic and the validity of Duffing's equation for vibration of beams with large displacements. Comput Struct. 2001.

[11] M. Shinozuka. C-M. Jan. Digital simulation of random processes and its applications. The Journal of Sound and Vibration 49. 1972.

EURODYN 2020
XI International Conference on Structural Dynamics
M. Papadrakakis, M. Fragiadakis, C. Papadimitriou (eds.)
Athens, Greece, 23–26 November 2020

VIBRATION POWER FLOW TRANSMISSION BETWEEN NONLINEARLY COUPLED OSCILLATORS WITH DUAL FORCES EXCITATIONS

Baiyang Shi, Chendi Zhu, Jian Yang*

Department of Mechanical, Materials and Manufacturing Engineering, The University of Nottingham Ningbo China, 199 Taikang East Road 315100, P.R. China
*Corresponding author e-mail: jian.yang@nottingham.edu.cn

Keywords: power flow analysis, vibrational energy transfer, nonlinear interface, double external forces

Abstract. *This paper investigates the vibration power flow transmission between nonlinearly coupled oscillators, each subjected to a harmonic excitation force with different phase angles. The harmonic balance method is used for analytical formulations of frequency-response relationship and time-averaged power flows. Numerical integrations are also conducted for validation of the analytical results and for comparison. Time-averaged transmitted power between the oscillators is used as an index to quantify the level of vibration transmission. The effects of the stiffness nonlinearity of the coupling interface on vibration power transmission are studied and revealed. It is found that when the excitation forces are of certain phase difference, the dynamic response of the oscillators and power flow between then may be reduced in the low-frequency range. The relative displacement amplitude between two oscillators may increase with the relative phase angle. It is also found that when the system is excited near resonances, the relative phase angle has little effects on the response amplitudes and time-average input power. It is also shown that time-averaged transmitted power is more sensitive than time-averaged input power to the relative phase angle. These findings lead to better understanding of vibration transmission mechanisms of coupled systems with different excitation forces and thus can facilitate enhanced designs of vibration suppression systems.*

1 INTRODUCTION

There is a growing interest in the vibration behaviour of nonlinear mechanical systems for enhanced understanding and also for better use of nonlinear elements to improve the dynamic performance. Whilst many previous investigations have focused on the response characteristic in terms of the displacement or velocity responses, limited work has been reported on the corresponding vibration energy transmission within nonlinear systems. Correspondingly it is necessary to examine the vibration power flow input, transmission and dissipation mechanisms in nonlinear systems.

The power flow analysis (PFA) is a widely accepted tool for dynamic analysis of vibration systems. Vibration power flow combines the force and velocity amplitudes as well as their phase angle into one quantity, and hence provides a better indication of vibration transmission in oscillating systems. The PFA method is well-established for the linear systems [1-4]. In recent years, the PFA is developed to investigate vibration transmission within nonlinear dynamic systems. Xiong et al. [5] investigated the power flow performance of a nonlinear isolator mounted on a travelling flexible ship. The PFA approach has also been employed to investigate the power flow characteristics of the Duffing oscillator [6], a nonlinear vibration isolation system with negative stiffness mechanism [7], coupled oscillators with a nonlinear interface [8] and power flow between coupled nonlinear oscillators [9]. Work has also been reported on power flow and vibration transmission characteristics of non-smooth oscillating system with bilinear elements [10] and impact oscillators with linear and nonlinear constraints [11]. Most of these investigations consider a single external force, the vibration transmission and power flow behaviour of coupled systems subjected to multiple external excitation forces is not clear and needs investigations.

In this paper, vibration power flow characteristics of nonlinearly coupled oscillators excited by two harmonic forces with the same frequency but different phase angles are investigated. Both analytical harmonic balance method and numerical results are presented to reveal the effects of the relative phage angle between the two forces on the steady-state response amplitudes and on the time-averaged power flows. The remaining content of paper is organised as follows. The modelling and formulation parts are presented in section 2 and section 3, respectively. Section 4 examines the influence of phase angle lag on the vibration power flow transmission. Conclusions are drawn at the end of paper.

2 MODELLING

Figure 1 shows a schematic representation of the system comprising two linear subsystems with a nonlinear interface. Subsystem one consists of a mass m_1 with a linear spring with stiffness coefficient k_1 and a viscous damper with damping coefficient c_1 subjected to an external harmonic force $f_1 \cos \omega t$. Subsystem two comprises a mass m_2 attached to a linear spring with coefficient k_2 and a viscous damper with damping c_2 with another external force $f_2 \cos(\omega t + \varphi)$, where φ is the relative phase angle between the two harmonic forces. The masses oscillate horizontally without friction and their static equilibrium positions, where $x_1 = x_2 = 0$, are taken as the reference. The two subsystems are connected by a nonlinear interface with restoring force $g(\delta) = k_3\delta + k_4\delta^3$, where k_3 and k_4 are the linear and nonlinear spring coefficients at the interface, respectively, $\delta = x_2 - x_1$ is the relative displacement between the two masses.

The governing equations of the coupled system are

$$m_1\ddot{x}_1 + k_1x_1 + c_1\dot{x}_1 - g(\delta) = f_1 \cos \omega t, \tag{1a}$$

$$m_2\ddot{x}_2 + k_2x_2 + c_2\dot{x}_2 + g(\delta) = f_2 \cos(\omega t + \varphi). \tag{1b}$$

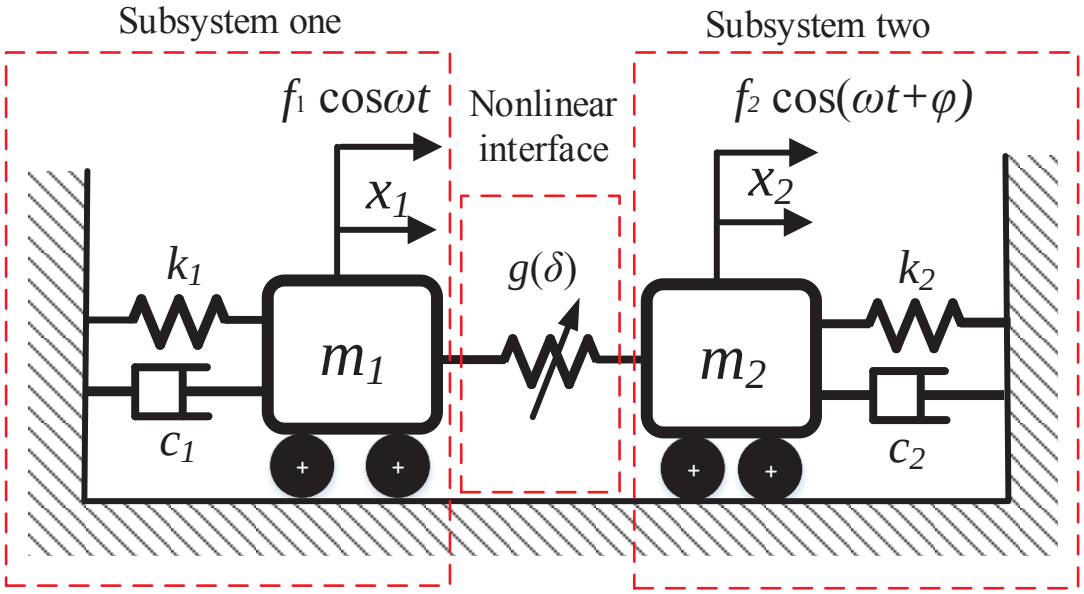

Figure 1: A schematic representation of nonlinearly coupled oscillators excited by two different external forces

Non-dimensional parameters and variables are introduced below to facilitate later calculations,

$$\omega_1 = \sqrt{\frac{k_1}{m_1}}, \omega_2 = \sqrt{\frac{k_2}{m_2}}, \mu = \frac{m_2}{m_1}, \lambda = \frac{k_3}{k_1}, \beta = \frac{k_4 l_0^2}{k_1}, \gamma = \frac{\omega_2}{\omega_1}, X_1 = \frac{x_1}{l_0}, X_2 = \frac{x_2}{l_0},$$

$$Y = X_2 - X_1, \zeta_1 = \frac{c_1}{2m_1\omega_1}, \zeta_2 = \frac{c_2}{2m_2\omega_2}, F_1 = \frac{f_1}{k_1 l_0}, F_2 = \frac{f_2}{k_1 l_0}, \Omega = \frac{\omega}{\omega_1}, \tau = \omega_1 t.$$

where ω_1 and ω_2 are the natural frequencies of subsystems one and two, respectively, μ is the mass ratio, λ and β are the non-dimensional stiffness ratios of the spring at the interface, γ is the natural frequency ratio, l_0 is the un-stretched length of the spring k_1 on the left, X_1 and X_2 are the non-dimensional displacements of masses m_1 and m_2, respectively, Y is the non-dimensional relative displacement of the masses, ζ_1 and ζ_2 are the non-dimensional damping coefficients, F_1 and F_2 are the non-dimensional forcing amplitudes, Ω is the non-dimensional excitation frequency, τ is the non-dimensional time. Using these non-dimensional parameters, the governing equations (1a) and (1b) can be written into a non-dimensional form

$$X_1'' + X_1 + 2\zeta_1 X_1' - \lambda Y - \beta Y^3 = F_1 \cos\Omega\tau, \tag{2a}$$

$$\mu(X_1 + Y)'' + 2\mu\zeta_2\gamma(X_1 + Y)' + \mu\gamma^2(X_1 + Y) + \lambda Y + \beta Y^3 = F_2 \cos(\Omega\tau + \varphi), \tag{2b}$$

where the primes denote differentiation operations with respect to the non-dimensional time τ. Eqs. (2a) and (2b) can be further transformed into first-order ordinary differential equations and solved using a fourth-order Runge-Kutta numerical integration method. Although this method can provide accurate predictions of the response, the computational cost is relatively high. In comparison, the harmonic balance method can be used to obtain he steady-state response at lower computation cost.

Here, a first-order harmonic balance method is used to predict the steady-state response of the system. The displacement, velocity and acceleration of the mass m_1 and the relative displacement between the two masses are assumed to be

$$X_1 = a\cos(\Omega\tau + \phi), X_1' = -a\Omega\sin(\Omega\tau + \phi), X_1'' = -a\Omega^2\cos(\Omega\tau + \phi), \tag{3a-3c}$$

$$Y = b\cos(\Omega\tau + \theta), \quad Y' = -b\Omega\sin(\Omega\tau + \theta), Y'' = -b\Omega^2\cos(\Omega\tau + \theta). \tag{3d-3f}$$

Using Eq. (3) to replace the corresponding terms in Eq. (2a) and (2b) and balancing the coefficients of terms $\cos(\Omega\tau)$ and $\sin(\Omega\tau)$, it follows that

$$-a\Omega^2\cos\phi + a\cos\phi - 2\zeta_1 a\Omega\sin\phi - \lambda b\cos\theta - \frac{3\beta b^3}{4}\cos\theta = F_1, \tag{4a}$$

$$a\Omega^2\sin\phi - a\sin\phi - 2\zeta_1 a\Omega\cos\phi + \lambda b\sin\theta + \frac{3\beta b^3}{4}\sin\theta = 0, \tag{4b}$$

$$\mu(-a\Omega^2\cos\phi - b\Omega^2\cos\theta) + 2\mu\zeta_2\gamma(-a\Omega\sin\phi - b\Omega\sin\theta) + \mu\gamma^2(a\cos\phi + b\cos\theta) + \lambda b\cos\theta + \frac{3\beta b^3}{4}\cos\theta = F_2\cos\varphi, \tag{4c}$$

$$\mu(a\Omega^2\sin\phi + b\Omega^2\sin\theta) + 2\mu\zeta_2\gamma(-a\Omega\cos\phi - b\Omega\cos\theta) + \mu\gamma^2(-a\sin\phi - b\sin\theta) - \lambda b\sin\theta - \frac{3\beta b^3}{4}\sin\theta = -F_2\sin\varphi. \tag{4d}$$

Note that Eq. (4) provides four nonlinear algebraic equations with four unknowns a, b, ϕ and θ. The Newton-Raphson based numerical continuation could be employed to obtain the corresponding solutions for dynamics responses, phase angles and associated vibration power flow variables as formulated in the section below.

3 VIBRATION POWER FLOW ANALYSIS

3.1 Time-averaged input power

The non-dimensional instantaneous power input into the integrated system is the product of external forces and corresponding velocities

$$p_{\text{in}} = X_1' F_1\cos\Omega\tau + X_2' F_2\cos(\Omega\tau + \varphi), \tag{5}$$

where X_1' is the non-dimensional velocity of mass m_1 and X_2' is the non-dimensional velocity of mass m_2. The steady-state time-averaged input power over an excitation cycle is

$$\bar{p}_{\text{in}} = \frac{1}{\tau_s}\int_{\tau_0}^{\tau_0+\tau_s} p_{\text{in}}\ \mathrm{d}\tau \approx -\frac{aF_1\Omega}{2}\sin\phi - \frac{aF_2\Omega}{2}\sin(\phi-\varphi) - \frac{bF_2\Omega}{2}\sin(\theta-\varphi). \tag{6}$$

where τ_0 is the starting time for the averaging and τ_s is the averaging time. The approximation made in Eq. (6) was based on a first-order analytical approximation of the steady state velocities, i.e., $X_1' = -a\Omega\sin(\Omega\tau+\phi)$ and $X_2' = X_1' + Y' = -a\Omega\sin(\Omega\tau+\phi) - b\Omega\sin(\Omega\tau+\theta)$, and an averaging time of one excitation cycle, i. e., $\tau_s = 2\pi/\Omega$.

3.2 Time-averaged transmitted power

The non-dimensional transmitted power transferred from subsystem one to subsystem two through the nonlinear interface is product of transmitted force and non-dimensional velocity $X_2{}'$ of the mass of subsystem two:

$$p_{\text{t}} = F_t X_2' = F_t(X_1{}' + Y'), \tag{7}$$

where $F_t = -\lambda Y - \beta Y^3$ is the non-dimensional transmitted force. The steady-state time-averaged transmitted power from $\tau = \tau_0$ to $\tau = \tau_0 + \tau_s$ is

$$\bar{p}_{\text{t}} = \frac{1}{\tau_s}\int_{\tau_0}^{\tau_0+\tau_s} p_{\text{t}}\,\mathrm{d}\tau \approx -ab\Omega\sin(\theta-\phi)\left(\frac{\lambda}{2} + \frac{3b^2\beta}{8}\right), \tag{8}$$

where first-order approximations of the steady-state displacements and velocities were used as in Eq. (6). In the approximation in Eq. (8), the averaging time τ_s is set to be one excitation period, i.e., $\tau_s = 2\pi/\Omega$.

4 RESULTS AND DISCUSSIONS

The effects of the relative phase angle φ between two external forces on the level of vibration transmission of coupled system is investigated herein. The phase angle φ changes from 0 to $\pi/2$ and then to π with the corresponding analytical results denoted by solid, dashed and dotted lines in Figs. 2 and 3. The squares, circles and triangles represent the direct numerical integration results obtained by the fourth-order Runge-Kutta method for the cases with φ being $0, \pi/2$ and π, respectivley. The other parameters of the system are $\mu = 0.5, \lambda = \gamma = 1, \zeta_1 = \zeta_2 = 0.01, \beta = 0.5, F_1 = F_2 = 0.1$.

Figure 2 examines the effects of phase angle φ on the response amplitude of mass m_1 and relative displacement amplitude under dual forces excitations. Fig. 2 shows that there are two peaks in each displacement amplitude curve of mass m_1 but only one peak in the curve of relative displacement amplitude. It could be explained by modal analysis theory that the masses experience in-phase motion at the first resonance and out-of-phase motion at the second resonant frequency. When the relative phase angle equals π, i.e., two external forces acting in different directions, the first resonant peak of oscillator m_1 disappears. Fig. 2(a) also shows that the response amplitude of mass m_1 decreases as the increase of the relative phase angle φ at a prescribed excitation frequency in the low-frequency range. In contrast, the relative displacement amplitude b between the masses is the largest when $\varphi = \pi$ at a prescribed value of Ω in the low-frequency range. As the excitation frequency Ω becomes large in the high-frequency range, the effects of phase angle on the response amplitude a becomes weak. Fig. 2(b) shows that at a specific value of Ω in the high-frequency range, the relative displacement amplitude b is the largest when $\varphi = \pi$, compared with the other two cases. It is also noted that the relative phase angle φ between two excitation forces has very small effects on the resonant peak frequencies as the resonant peaks of the three considered cases merge.

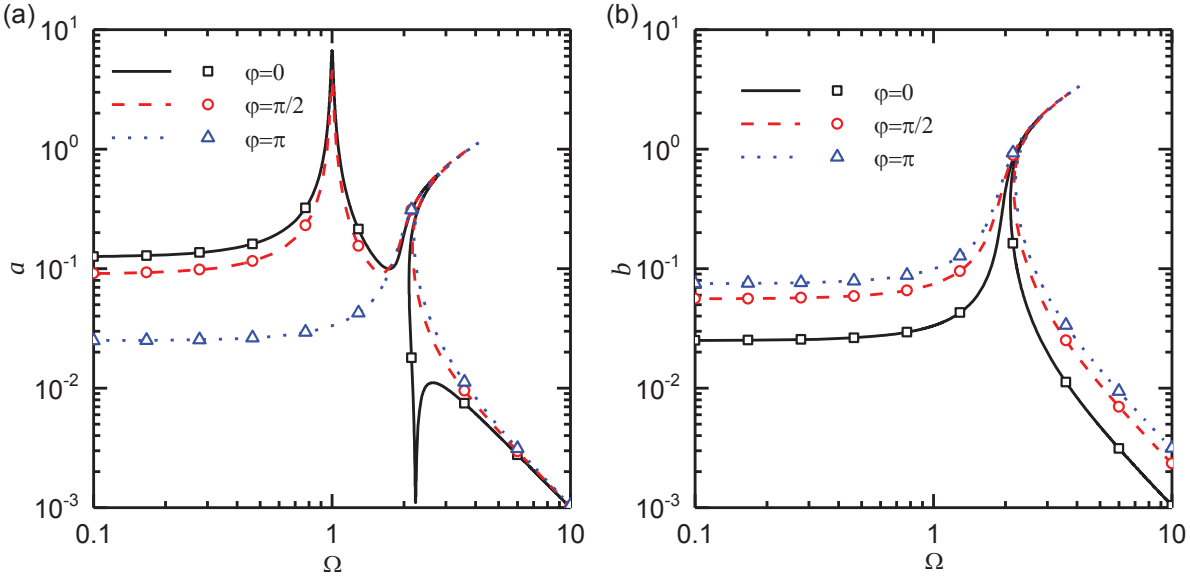

Figure 2: Effects of phase angle lag φ on the response amplitude a and b. Other system parameters are $\mu = 0.5, \lambda = \gamma = 1, \zeta_1 = \zeta_2 = 0.01, \beta = 0.5, F_1 = F_2 = 0.1$.

Figure 3 presents the influence of the relative phase angle φ on the power flow transmission. Two resonant peaks are observed in each curve of both the time-averaged input power $\bar{p}_{\text{in}}$ and the time-averaged transmitted power $\bar{p}_{\text{t}}$, as shown in Fig. 3(a) and 3(b), respectively. Fig. 3(a) shows that there is a larger amount of input power into the coupled system for the $\varphi = 0$ case

when Ω is small, as compared with the other two cases with different values of φ. As the increase of excitation frequencies, the effects of different values of phase angle φ on $\bar{p}_{\mathrm{in}}$ is observed to be small. Fig. 3(b) shows that the phase angle has a significant influence on the time-averaged transmitted power $\bar{p}_{\mathrm{t}}$. Compared with the other two cases, the case with $\varphi = \pi$ (i.e., the forces act in opposite directions) can result in lower power transmission level. It also demonstrated the relative phase angle between the two excitations may significantly change the peak values of the transmitted power behaviour. The results indicate that the phase angle of the excitation forces may have large influence on vibration transmission in nonlinear systems.

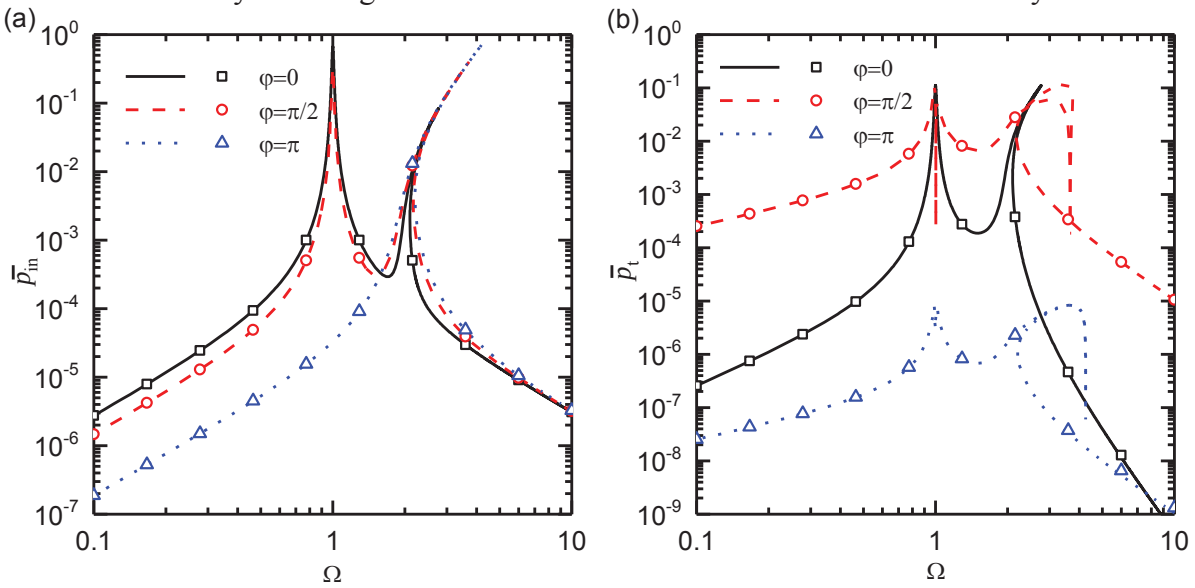

Figure 3: Effects of phase angle lag φ on the time-averaged power flow $\bar{p}_{\mathrm{in}}$ and $\bar{p}_{\mathrm{t}}$. System parameters are $\mu = 0.5, \lambda = \gamma = 1, \zeta_1 = \zeta_2 = 0.01, \beta = 0.5, F_1 = F_2 = 0.1$.

5 CONCLUSIONS

The dynamic response and the time-averaged power flow characteristics of nonlinearly coupled oscillators subject to dual forces excitations with different phase angles are investigated. Both analytical harmonic balance method and numerical Runge-Kutta method are used to explore the effects of the relative phase angle on steady-state response amplitudes and vibration power flow variables. It is found dynamic response and power transmission in the system excited at low frequencies could be reduced by adjusting phase angle difference in dual excitations systems. The relative displacement amplitude between the masses may increase with the relative phage angle when away from the resonance. It is also found that the phase angle of the excitation forces may have small effects on the peaks of dynamic response and the time-averaged input power. It is also shown that the vibration transmission in terms of the time-averaged transmitted power between the two oscillators may be sensitive to the variations of the relative phase angle. The results provide some new insight into vibration transmission and power flow in nonlinear systems with more than one excitation forces. The PFA method may also be used for vibration transmission analysis of more complex nonlinear systems for enhanced design of vibration mitigation devices exploiting nonlinearity.

ACKNOWLEDGEMENTS

This work was supported by National Natural Science Foundation of China (Grant number 51605233) and by Ningbo Science and Technology Bureau under Natural Science Programme (Grant number 2019A610155).

REFERENCES

[1] H.G.D. Goyder, R.G. White, Vibration power flow from machines into built-up structures, *Journal of Sound and Vibration* 68,59–117,1980.

[2] J.T. Xing, W.G. Price, A power-flow analysis based on continuum dynamics, *Proceedings of the Royal Society A* 455,401–36,1999.

[3] Y.P. Xiong, J.T. Xing, W.G. Price, Power flow analysis of complex coupled systems by progressive approaches, *Journal of Sound and Vibration* 239,275–95,2001.

[4] Y.P. Xiong, J.T. Xing, W.G. Price, A general linear mathematical model of power flow analysis and control for integrated structure–control systems, *Journal of Sound and Vibration* 267,301–34,2003.

[5] Y.P. Xiong, J.T. Xing, W.G. Price, Interactive power flow characteristics of an integrated equipment-nonlinear isolator-travelling flexible ship excited by sea waves, *Journal of Sound and Vibration* 287,245–76,2005.

[6] J. Yang, Y.P. Xiong, J.T. Xing, Nonlinear power flow analysis of the Duffing oscillator, *Mechanical Systems and Signal Processing* 45,563–78,2014.

[7] J. Yang, Y.P. Xiong, J.T. Xing, Dynamics and power flow behaviour of a nonlinear vibration isolation system with a negative stiffness mechanism, *Journal of Sound and Vibration* 332,167–83,2013.

[8] J. Yang, B.Y. Shi, C. Rudd, On vibration transmission between interactive oscillators with nonlinear coupling interface, *International Journal of Mechanical Sciences* 137,238–51,2018.

[9] B.Y. Shi, J. Yang, C. Rudd, On vibration transmission in oscillating systems incorporating bilinear stiffness and damping elements, *International Journal of Mechanical Sciences* 150,458-470,2019.

[10] B.Y. Shi, J. Yang, Quantification of vibration force and power flow transmission between coupled nonlinear oscillators, *International Journal of Dynamics and Control* 8, 418-35 2020.

[11] W. Dai, J. Yang, B.Y. Shi, Vibration transmission and power flow in impact oscillators with linear and nonlinear constraints, *International Journal of Mechanical Sciences* 168, 15234, 2020.

EURODYN 2020
XI International Conference on Structural Dynamics
M. Papadrakakis, M. Fragiadakis, C. Papadimitriou (eds.)
Athens, Greece, 23–26 November 2020

STOCHASTIC DYNAMICAL RESPONSE OF A NON-SMOOTH DYNAMICAL SYSTEM UNDER FILTERED WHITE NOISE

Saeed Gheisari Hasnijeh[1] and Arvid Naess[2]

[1]Dept of Mechanical Engineering, University of Isfahan
Isfahan, Iran
e-mail: saeed.gheisari@gmail.com

[2] Dept of Mathematical Sciences, NTNU
Trondheim, Norway
e-mail: arvid.naess@ntnu.no

Keywords: Gear model, Stochastic dynamics, Path integration, Filtered noise

Abstract. *The stochastic dynamic response of a spur gear pair model under filtered noise excitation is investigated. The spur gear pair is modeled as a single degree of freedom (SDOF) system in which nonlinear backlash and time-varying mesh stiffness as well as stochastic excitation are considered. Four cases are addressed, based on how the noise is incorporated in the loading terms. A first order filter is employed to generate various filtered noises with the same energy but different power spectrum. The combination of the SDOF gear model and the shaping filter leads to a three dimensional (3D) Markov model. The numerical path integration (PI) technique is adopted to obtain the probabilistic response of the gear model using an adaptive time-stepping method in order to increase the accuracy of the time integration. To model a narrow band noise excitation, a second order filter is applied to model the excitation, leading to a four dimensional (4D) Markov model. The results are verified by comparing with Monte Carlo simulations. The effect of the noise spectrum on the probabilistic response is evaluated for different loading cases.*

1 INTRODUCTION

Gears are widely used in a variety of different industrial applications. Investigation on the dynamical behavior of gears is important for other fields of related research such as design, tribology, reliability assessment, etc. The first studies of the dynamics of gear systems are from the early 20th century and the topic has continued to be an active research area until now. Early gear models were linear, excluding or neglecting nonlinearities such as backlash [1]. Nonlinear, time-varying (NTV) gear models were developed and investigated in the 90's [2–5]. More recently, researches have focused on multi-degrees of freedom (DOF) modeling of the gear mesh system, which lead to more realistic and complicated models as well [6,7]. All those studies belong to the category of deterministic dynamics.

Stochastic excitation may be prevalent in gear systems due to randomness in the external loading or within internal parameters. In some applications, such as wind turbine drivetrains, ship propulsions and automobile gearboxes, the effect of randomness is significant, which implies the necessity to conduct a stochastic analysis to obtain accurate and realistic results. Moreover, knowledge about the probability density function (PDF) of the response is of key importance for the purpose of reliability assessment and reliability-based design in such systems. This latter can be achieved by considering a stochastic component as part of the excitation. Under suitable modelling assumptions, this would typically lead to a stochastic differential equation (SDE). Although the simplest stochastic excitation is the Gaussian white noise (GWN), which is characterized by a uniform power across the frequency band, real stochastic loadings will invariably have varying spectral distributions. For instance, some wind loadings has a descending power spectral density (PSD) which can be approximated by a first order linear filter [8]. In this work, the random excitation is assumed to be a filtered Gaussian white noise, which leads to an n-dimensional SDE in the state space. The response of such systems is a Markov vector process and its transitional PDF is governed by the Fokker-Planck (FP) equation. However, the analytical solution of the FP equation is restricted to linear systems and a limited class of nonlinear models [9].

Tobe et al. [10,11] considered random excitation in gear systems using a statistical linearization technique. They also experimentally verified their theoretical results. Using statistical linearization leads to inaccurate results for systems with discontinuous nonlinearities. This led Kumar et al. [12] to adopt a direct integration technique to study the dynamic response of a gear pair. Similarly, Neriya et al. [13] investigated a helical gear system which included both backlash and time-varying mesh stiffness, and was also subjected to a random transmission error. The mean value and variance of the response were calculated by the piecewise linearization method. Pfeiffer and Kunert [14] evaluated the rattling problem for a gear system. Wang and Zhang [15] considered the effect of speed-dependent random errors on the stochastic vibration of the gear model.

The path integration (PI) method provides a numerical approach to approximate the solution of FP equations. A basic version is used by Wehner and Wolfer [16] to solve nonlinear FP equations. Subsequently, Naess and Moe [17], Lin and Yu [18], Zhu [19], and others have applied and further developed the PI technique in order to evaluate several engineering problems. An efficient and accurate approach was applied by Naess et al. [20] for solving a SDOF gear model with a non-smooth restoring mechanism under stochastic excitation caused by Gaussian white noise. It is a unique feature of the PI method to deal with non-smooth stochastic dynamics. The dynamical model in [20] was assumed as nonlinear time-invariant (NTI), neglecting the variation of mesh stiffness with contact status. A short time Gaussian approximation (STGA) was adopted to approximate the conditional PDF [21] and captured the evolution of the response PDF using a stepwise solution technique. Later, Mo and Naess [22] showed that for chaotic

response of a gear system, the stochastic and deterministic attractors are very similar by comparing the response PDF with the Poincaré map of the deterministic system in [2]. In both papers, a fixed time step was used in general. However, in order to reduce numerical errors due to non-smooth dynamical behavior, a backward Runge-Kutta time-stepping algorithm combined with a Newton iteration method was used to split the fixed step into two sub-steps. This permits to accurately find out when the deterministic trajectory crosses the boundary between two regimes of nonlinearity. Another similar approach to account for the non-smooth backlash function was proposed by Wen et al. [23], who dealt with a linear dynamic model for each part of the state space. Although an important interaction between time-varying mesh stiffness and backlash nonlinearity in gear meshing systems was reported, a constant averaged stiffness was used in their model. Considering the stochasticity of the system, establishing the exact switching time between different regimes of the dynamical system is not meaningful since there is no deterministic trajectory. Therefore, the aforementioned approach may fail to be sufficiently accurate and efficient, a fact confirmed by the results obtained with Monte Carlo simulations. In order to decrease the calculation error, Hasnijeh et al. [24] applied a novel adaptive time-stepping method. The main idea of this method is to determine the time-step length based on the amount of marginal probability at non-smooth boundaries. They proved the efficiency of the adaptive method relative to the fixed time-stepping for non-smooth systems.

The simplest and usually the most reliable approach to determine the response PDF of SDEs is provided by the Monte Carlo simulation (MCS) method. In this approach, the response statistics are extracted from a large number of response realizations, which are generated using a stochastic integration method. Feng et al. [25] used MCS to investigate a stochastic spur gear model including the effects of sliding friction. MCS is useful as a verification tool for checking results obtained by other more efficient methods. However, it is a rather time-consuming method if highly accurate results are needed, especially for low probability events.

In the present paper, the response PDF of an SDOF nonlinear, time-varying gear model under the excitation of a filtered noise is obtained. The NTV gear model includes both backlash nonlinearity and time-varying mesh stiffness (TVMS). Three main sub-problems are addressed herein. The first assignment consists in proving the capability of the adaptive path integration (API) method to investigate non-smooth dynamical gear systems under the excitation of filtered white noise. A first order filter is used to generate the filtered white noise, extending the Markov property of this second-order system to the 3D state space. The second goal pursued here is to evaluate the effect of uncertain loading parameters on the response PDF. For this purpose, the applied additive noise of the problem is categorized into two different stochastic loading models. Finally, a parametric study is carried out to show the effect of the loading spectrum on different aspects of the response PDF. Three filtered versions of noises are applied with equal energies but different spectrum distributions. To assess the capability of the path integration method in dealing of systems with higher dimensions, a 4D system is also considered by using a second-order filter to generate a narrow-band noise. Results are verified by Monte Carlo simulations for all cases. To the best of the authors' knowledge, the response PDF of a gear model under filtered noise has not been investigated before. The response PDF contains a lot of raw information which can be utilized in different ways depending on the purpose of the analysis, such as mechanical design and reliability analysis. In addition, the effect of the input frequency spectrum on the response PDF is studied for each stochastic excitation case.

2 STOCHASTIC DYNAMICAL MODEL

Fig. 1 depicts the spur gear pair model considered here. The equation of motion for this model is given in dimensionless form in Eq. (1), and its derivation is discussed in [1, 24].

$$\ddot{q}(t) + 2\zeta\dot{q}(t) + k_h(t)f\big(q(t)\big) = F_m + F_{ah}\cos(\Omega t) \tag{1}$$

$$f\big(q(t)\big) = \begin{cases} q(t) - 1 & q(t) > 1 \\ 0 & -1 < q(t) < 1 \\ q(t) + 1 & q(t) < -1 \end{cases} \tag{2}$$

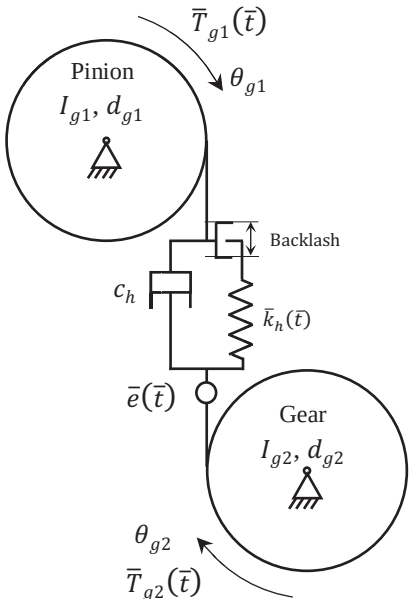

Figure 1: Gear pair model [24]

In Eq. (1), q is the difference between the dynamic transmission error and the static transmission error, ζ denotes damping ratio, k_h is the time-varying mesh stiffness, f represents the nonlinear backlash function, Ω is the excitation frequency, and F_m and F_{ah} are the mean and alternating components of the loading, respectively.

Eq. (1) is a two-dimensional state space NTV problem and may have multi-solutions, depending on the parameter values. The deterministic solution of this system can include no-impact, single-sided or double-sided impact cases, maybe with several subharmonics [2]. In the case of a multi-solution problem, the initial conditions will determine which deterministic solution would occur. As opposed to deterministic dynamics, the probabilistic response of the system may include both solution types simultaneously because of the stochastic essence of the excitation and also due to uncertain initial conditions [3]. In order to evaluate the effect of uncertainty in loading components on the dynamical behavior of the gear system, two separate cases are defined in the following based on an additive noise F_s and intensity parameter λ.

Case A: Uncertainty in the mean component of the loading which may arise from external torque fluctuation

$$\ddot{q}(t) + 2\zeta\dot{q}(t) + k_h(t)f\big(q(t)\big) = (F_m + \lambda F_s) + F_{ah}{\Omega_h}^2\cos(\Omega_h t) \tag{3}$$

Case B: Uncertainty in the alternating component of the loading that may be caused by manufacturing errors [4–6]

$$\ddot{q}(t) + 2\zeta\dot{q}(t) + k_h(t)f\big(q(t)\big) = F_m + (F_{ah} + \lambda F_s){\Omega_h}^2\cos(\Omega_h t) \tag{4}$$

3 FILTERED WHITE NOISE

3.1 First order linear filter

The noise component is assumed to be a stationary process, allowing the use of the shaping filter techniques in order to generate it from a Gaussian white noise [7]. In this study, the stochastic excitation is considered to have a particular power spectral density (PSD) function which can be modeled as follows

$$\dot{F}_s = -\alpha F_s + \gamma N_t \tag{5}$$

where N_t is the standard Gaussian white noise process and, α and γ are filter parameters. Knowing that $N_t dt = dW(t)$ [8] and defining $x_1 = q(t)$, $x_2 = \dot{q}(t)$ and $x_3 = F_s(t)$, the state space form of Eq. (3) can be rewritten as

$$\begin{cases} \mathrm{d}x_1 = x_2 \mathrm{d}t \\ \mathrm{d}x_2 = \left[F_m + F_{ah}{\Omega_h}^2 \cos(\Omega_h t) - 2\zeta x_2 - k_h(t) f(x_1) + \lambda x_3\right] \mathrm{d}t \\ \mathrm{d}x_3 = -\alpha x_3 \mathrm{d}t + \gamma \, \mathrm{d}W(t) \end{cases} \tag{6}$$

where $W(t)$ now denotes a standard Wiener process with stationary and independent increments. Similar forms will be obtained for Eq. (4). The power spectral density function for F_s is,

$$S(\omega) = \frac{\gamma^2}{2\pi(\omega^2 + \alpha^2)} \tag{7}$$

3.2 Second order linear filter

To evaluate the capability of the path integration method in dealing with non-smooth systems of higher dimensions, the gear model in combination with a second order linear filter is also considered. The filter equations are as follows [7]

$$\begin{cases} \dot{G}_s = -\alpha F_s \\ \dot{F}_s = G_s - \beta F_s + \gamma N_t \end{cases} \tag{8}$$

α, β and γ are filter parameters. In the current study, the second order filter is only used for case A. Defining $x_3 = G_s$ and $x_4 = F_s$, the 4D state space model for Eq. (3) can be written as

$$\begin{cases} \mathrm{d}x_1 = x_2 \mathrm{d}t \\ \mathrm{d}x_2 = \left[F_m + F_{ah}{\Omega_h}^2 \cos(\Omega_h t) - 2\zeta x_2 - k_h(t) f(x_1) + \lambda x_4\right] \mathrm{d}t \\ \mathrm{d}x_3 = -\alpha x_4 \mathrm{d}t \\ \mathrm{d}x_4 = (x_3 - \beta x_4) \mathrm{d}t + \gamma \, \mathrm{d}W(t) \end{cases} \tag{9}$$

The power spectral density function for F_s is obtained as follows,

$$S(\omega) = \frac{1}{2\pi} \frac{\gamma^2 \omega^2}{(\alpha - \omega^2)^2 + (\beta\omega)^2} \tag{10}$$

The advantage of being able to use a second order filter is that it allows a study of the effect of narrow band excitation processes on the response of the gear system.

4 THE PATH INTEGRATION METHOD

Eq. (6) can be expressed by the standard Itô SDE form as follows,

$$\mathrm{d}\mathbf{x}(t) = \boldsymbol{\alpha}(\boldsymbol{x}, t)\mathrm{d}t + \boldsymbol{\beta}(t)\mathrm{d}\mathbf{W}(t) \tag{11}$$

Since the main goal of the current study is to investigate 3D problems, the formulation is developed for a 3D state space model. The formulation can be easily generalized to higher dimensions. Therefore, $\mathbf{x}(t) = (x_1, x_2, x_3)^{\mathrm{T}}$ is a 3D state space vector process, $\boldsymbol{\alpha}(\mathbf{x}, t)$ is the drift vector and $\boldsymbol{\beta}(t)$ is the diffusion matrix and the vector $\mathrm{d}\mathbf{W}(t) = \mathbf{W}(t + dt) - \mathbf{W}(t)$ denotes the independent increments of a standard Wiener vector process. The SDE (11) has a unique solution in the strong sense for every set of parameter values [9]. This solution has a joint probability distribution of states for a specific time that can be calculated through application of the numerical PI method.

The response of the dynamical system (11) is a Markov process and the transition probability density function (TPDF), $p(\mathbf{x}, t|\mathbf{x}', t')$, satisfies the Fokker-Planck (FP) equation, which is written as follows

$$\frac{\partial}{\partial x} p(\mathbf{x}, t|\mathbf{x}', t') = -\sum_{i=1}^{3} \frac{\partial}{\partial x_i} \alpha_i(\mathbf{x}, t) p(\mathbf{x}, t|\mathbf{x}', t') + \frac{1}{2} \sum_{i=1}^{3} \sum_{j=1}^{3} \frac{\partial^2}{\partial x_i \partial x_j} \left(\boldsymbol{\beta}(t).\boldsymbol{\beta}^{\mathrm{T}}(t)\right)_{i,j} p(\mathbf{x}, t|\mathbf{x}', t') \quad (12)$$

In addition to several numerical methods presented for solving the FP equation directly, the probabilistic evolution of the state space vector process $\mathbf{x}(t)$ can be captured based on the Markov property of the response using the basic equation of the PI method

$$p(\boldsymbol{x}, t) = \int_{\boldsymbol{\Gamma}} p(\boldsymbol{x}, t|\boldsymbol{x}', t') p(\boldsymbol{x}', t') d\boldsymbol{x}' \quad (13)$$

where $\boldsymbol{\Gamma}$ is the state space and $d\mathbf{x}' = \prod_{i=1}^{3} dx_i'$. In fact, the method consists of evaluating the TPDF core thence determining the PDF $p(\mathbf{x}, t)$ of the state space vector $\mathbf{x}$ at time t from the previous PDF $p(\mathbf{x}', t')$ at time t' through Eq. (13). To implement the PI method, a discrete time approximation is needed. Naess and Moe [17] proposed a fourth-order Runge-Kutta-Maruyama (RKM) for the numerical solution of (11) as follows

$$\mathbf{x}(t) = \mathbf{x}(t') + \mathbf{r}(\mathbf{x}(t'), t', \Delta t) + \beta(t')\Delta\mathbf{W}(t') \quad (14)$$

The deterministic part of Eq. (14) is the explicit fourth-order Runge–Kutta (RK4) approximation $\mathbf{x}(t) = \mathbf{x}(t') + \mathbf{r}(\mathbf{x}(t'), t', \Delta t)$, which represents the time evolution of the deterministic part of (11) with a global error of order $O(\Delta t^5)$, where $\Delta t = t - t'$. Numerical experiments predict that the approximation to the deterministic part outweighs other residues in terms of accuracy in the solution of Eq. (11) [8]. Thus, a fourth-order RKM is applied in the form of $\mathbf{r}(\mathbf{x}(t'), t', \Delta t)$ for the deterministic part of Eq. (11). The Wiener process $\mathbf{W}(t)$ has independent increments, hence $\Delta\mathbf{W}(t') = \mathbf{W}(t) - \mathbf{W}(t')$ is a Gaussian variable and the TPD $p(\mathbf{x}, t|\mathbf{x}', t')$ is a Gaussian PDF for every t'. For sufficiently small Δt, the time sequence $\{\mathbf{x}(t_i)\}_{i=0}^{\infty}$ becomes a Markov chain which can approximate the time-continuous Markov solution of the SDE (11). For the model given by Eq. (6), the conditional PDF $p(\mathbf{x}, t|\mathbf{x}', t')$ follows a degenerate multi-dimensional Gaussian PDF [11],

$$p(\mathbf{x}, t|\mathbf{x}', t') = \delta\left(x_1 - x_1' - r_1(\mathbf{x}(t'), t', \Delta t)\right) \delta(x_2 - x_2' - r_2(\mathbf{x}(t'), t', \Delta t)) \tilde{p}(x_3, t|\mathbf{x}', t') \quad (15)$$

where $\delta(.)$ denotes the Dirac delta function and

$$\tilde{p}(x_3, t|\mathbf{x}', t') = \frac{1}{\sqrt{2\pi\gamma^2\Delta t}} \exp\left\{-\frac{\left(x_3 - x_3' - r_3(\mathbf{x}(t'), t', \Delta t)\right)^2}{2\gamma^2\Delta t}\right\} \quad (16)$$

in which $r_{\mathrm{i}}(\mathbf{x}', t', \Delta t)$ $i = 1,2,3$ are Runge-Kutta increments corresponding to each state. If the initial PDF $p_0(\mathbf{x}^{(0)}) = p(\mathbf{x}, t_0)$ is specified, Eq. (13) can be written in a stepwise format as follows

$$p\left(\mathbf{x}^{(n)}, t_n\right) = \int_{\mathrm{R}^3} \dots \int_{\mathrm{R}^3} \prod_{i=1}^{n} p\left(\mathbf{x}^{(i)}, t_i \middle| \mathbf{x}^{(i-1)}, t_{i-1}\right) p_0\left(\mathbf{x}^{(0)}\right) \mathrm{d}\mathbf{x}^{(0)} \dots \mathrm{d}\mathbf{x}^{(n-1)} \tag{17}$$

Eq. (17) expresses the mathematical formulation of the PI technique as used in this study. A finite region of integration that covers almost the whole probability range of the response should be introduced for evaluating Eq. (17), with consideration that the computational time is dramatically influenced by the state space discretization resolution. If the region of integration is determined appropriately, the probability loss that arises would be negligible. The initial PDF can, in principle, be chosen quite arbitrarily as long as there is nonzero variance in all spatial dimensions. This is necessary for the numerical algorithms to work properly. What determines the choice of the initial PDF depends on the specific problem investigated. For the purpose of this paper, the initial PDF is assumed to be Gaussian, as follows:

$$p_0\left(\mathbf{x}^{(0)}\right) = p\left(\mathbf{x}^{(0)}, t_0\right) = \prod_{i=1}^{n} \frac{1}{\sqrt{2\pi}\sigma_{x_i}^{(0)}} \exp\left(-\frac{1}{2}\left(\frac{x_i - \mu_{x_i}^{(0)}}{\sigma_{x_i}^{(0)}}\right)^2\right) \tag{18}$$

where $\mu_{x_i}^{(0)}, i = 1,2,3$ denote initial mean values and $\sigma_{x_i}^{(0)}$ $(> 0), i = 1,2,3$ represent standard deviations.

A challenging issue in the numerical calculations of non-smooth dynamics is the abrupt change in their behavior. In the deterministic problems, it can be overcome by identifying the transition point between two different dynamical regimes within a time step and splitting it into two sub-steps with different dynamics. However, in the corresponding stochastic dynamic analysis, there is no specific trajectory that would allow the transition points to be identified. In this study, a new adaptive time-stepping scheme is used in order to reduce both the numerical error and calculation runtime in comparison with the fixed time-step method [1]. The main idea behind this adaptive time-stepping method is to decrease the time step proportionally to the magnitude of the marginal probability density at the non-smooth boundaries. In the considered gear system, there are two boundaries $x_1 = -1$ and $x_1 = 1$ that separate three different dynamical zones. The mathematical formulation behind this approach can be written as follows

$$\Delta t_i = t_i - t_{i-1} = \max\left[\left(\left(1 - \frac{\max\left\{p_{x_1}(-1, t_{i-1}), p_{x_1}(1, t_{i-1})\right\}}{p_{x_1}^{(\max)}}\right)\Delta t_{\max}\right), (\Delta t_{\min})\right] \tag{19}$$

where p_{x_1} is the marginal PDF for the state variable x_1 and $p_{x_1}^{(\max)}$ is its maximum value. $\Delta t_{\max}$ is the maximum time step, and a minimum time increment $\Delta t_{\min}$ is introduced in order to avoid a zero length step when the marginal PDF approaches its maximum at the specified boundaries.

5 RESULTS AND DISCUSSION

5.1 Deterministic dynamical behavior

The deterministic dynamics of the model is investigated in order to compare probabilistic response with the deterministic results. A square-wave is considered as follows

$$k_h(t) = \begin{cases} 0.8 & (n-1)t_p \le t < (n-1)t_p + t_p/2. \;\; n = 1.2.3 \cdots \\ 1.2 & (n-1)t_p + t_p/2 \le t < nt_p. \;\; n = 1.2.3 \cdots \end{cases} \tag{20}$$

where t_p is the gear mesh period. It has been reported that the interaction between time-varying mesh stiffness and backlash nonlinearity becomes more pronounced in the multi-solution zone and especially for heavily loaded systems [12]. As a dimensionless case of study, parameters $\zeta = 0.05$, $F_m = 0.3$ and $F_{ah} = 0.1$ are borrowed from references [2,3,12]. This is a heavily loaded gear pair system, since $\hat{F} = F_m/F_{ah} = 3$ [2]. For $\Omega_h = 0.65$ there are two coexisting

solutions, which are named by Kahraman [2] as the no impact and the single-sided impact solutions (Fig. 2-a). The deterministic domain of attraction is shown in (Fig 2-b). The deterministic system will adopt one of the solutions depending on the initial condition. The initial distribution parameters in this paper are chosen as $\mu_{x_1}^{(0)} = \mu_{x_2}^{(0)} = 0$, $\sigma_{x_1}^{(0)} = 0.5$ and $\sigma_{x_2}^{(0)} = 0.25$ which covers both basins of attraction, but mostly the single-sided impact solution. The difference between applying deterministic versus stochastic initial condition is illustrated schematically in Fig. 2-b.

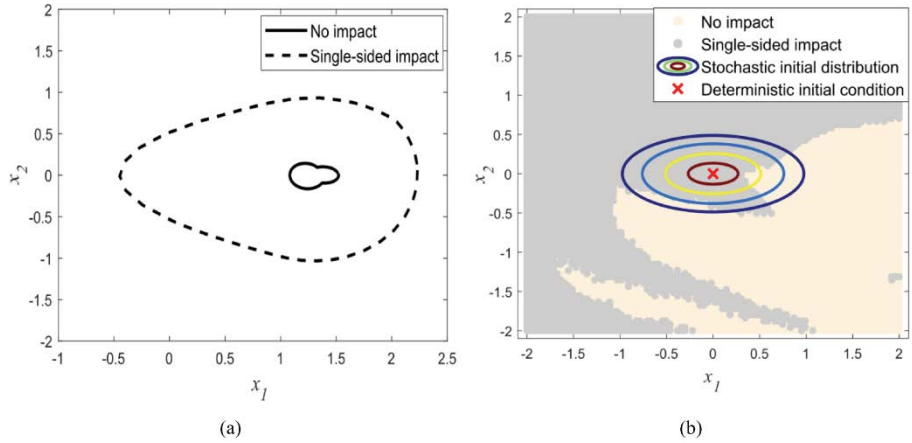

Figure 2: a) Multi-solution system with limit cycles in phase plane. b) Stochastic initial distribution versus deterministic initial condition in the domain of attraction of the system.

5.2 Stochastic dynamics of 3D Problems

In order to investigate the effect of introducing noise spectrum on the probabilistic response of the gear model, three different stochastic excitations are considered here. The filter parameters for the three cases illustrated in Fig. 3 are specified in such a manner that the energy of the noise is kept constant. The intensity of noise for all cases of study is λ=0.05.

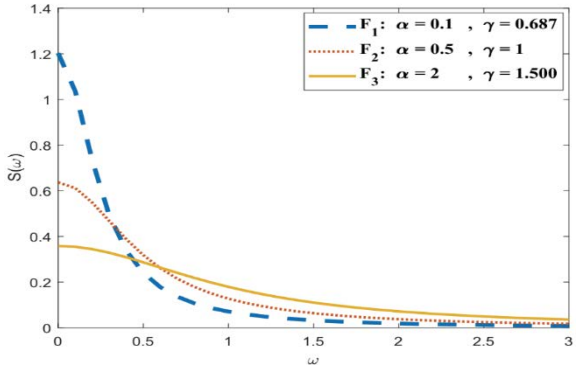

Figure 3: Frequency spectrum for different noises

The first goal of the current study is to show the capability of the adaptive path integration method to obtain accurate response PDF of a non-smooth random dynamical system under filtered noise. The evolution of the response PDF is captured via the PI technique with an adaptive time-stepping approach. Comparisons of the marginal PDFs for t = 10 t_p obtained by Monte Carlo simulations are shown in Figs. 4 and 5 for cases A, B, respectively. The accuracy and precision of the method are confirmed qualitatively for all cases due to good agreement between the PI and MCS results.

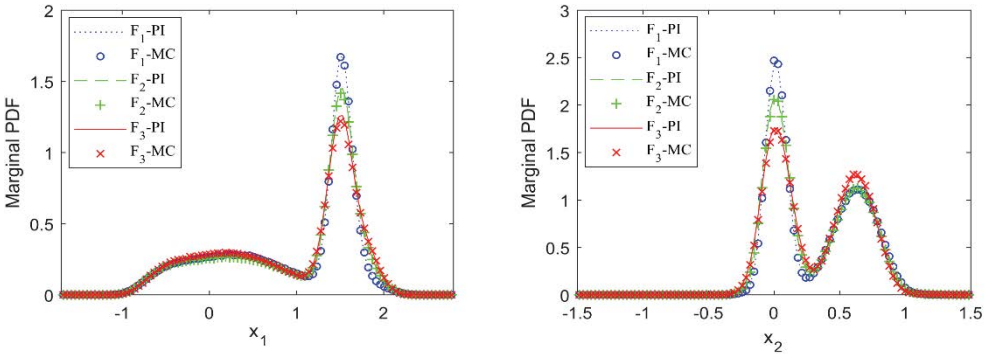

Figure 4: Marginal PDFs of the response for case A after $10t_p$ obtained by the PI method and MC simulation

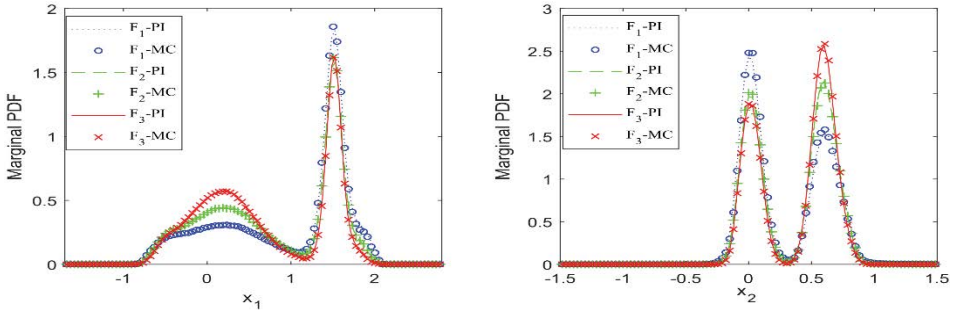

Figure 5: Marginal PDFs of the response for case B after $10t_p$ obtained by the PI method and MC simulation

In order to better illustrate both the effects of noise spectrum and loading uncertainty, the joint PDFs for cases A and B are also plotted in Figs. 6 and 7. In contrast to deterministic dynamic systems which assume a unique solution, the stochastic system response will be characterized by a probability distribution influenced by a nondeterministic distribution of initial conditions as well as an additive stochastic excitation. In this study, the initial distribution covers both basins of attraction of each solution. According to similar studies [18,23], it is expected that both no-impact solutions and single-sided impact solutions coexist. As the effect of uncertainty in these two categories reveals quite different results, the necessity of investigating the source of stochastic excitation in such nonlinear dynamical systems becomes obvious. It is also seen that the spectrum shape of the additive noise partly affects the probabilistic response in cases A and B.

The uncertainty in each component of the loading is basically due to external torque perturbations or manufacturing errors in the real system [26–28], but this matter is not pursued in the context of the current paper. The methodology and results that are presented in this study can have important implications in engineering applications of gear systems under uncertain excitation. The probability distribution function of the gear system response contains subtle information about the system, which is essential for the purpose of reliability-based design of such systems.

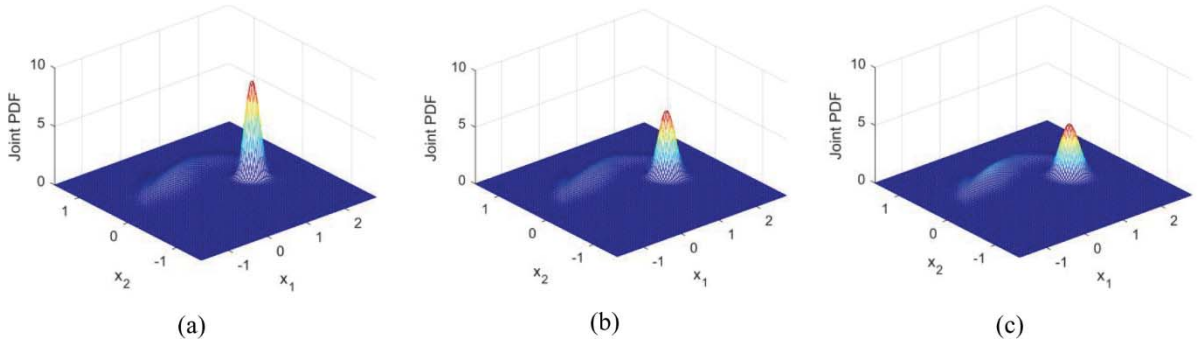

Figure 6: Stationary response Joint PDF of the problem case A under filtered noise excitation of a) F_1, a) F_2 and c) F_3

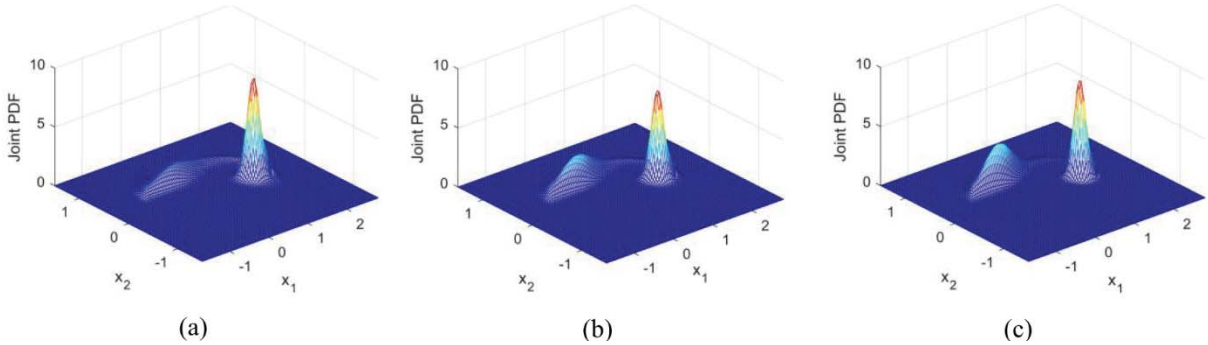

Figure 7: Stationary response Joint PDF of the problem case B under filtered noise excitation of a) F_1, b) F_2 and c) F_3

5.3 Stochastic dynamics of the 4D Problem

Considering parameter values $\alpha = 1.5, \beta = 0.5$ and $\gamma = 1$, the frequency spectrum of the filtered noise is illustrated in Fig. 10. This spectrum can be considered as an approximation of a narrow-band noise. The intensity of the noise for all cases of study is set to λ=0.05.

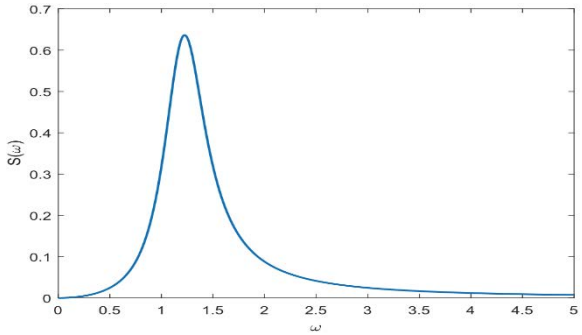

Figure 8: Frequency spectrum of second order filter

The response PDF is calculated by the path integration method and compared with Monte Carlo simulations. Fig. 9 indicates marginal PDFs and Fig. 10 shows joint PDFs for $t = 10t_p$. Although increasing the dimensions of the problem raised the computational cost, the accuracy and precision of the results are satisfactory for the solution of this non-smooth 4D problem. This shows the capability of the path integration method in dealing with higher dimensional problems.

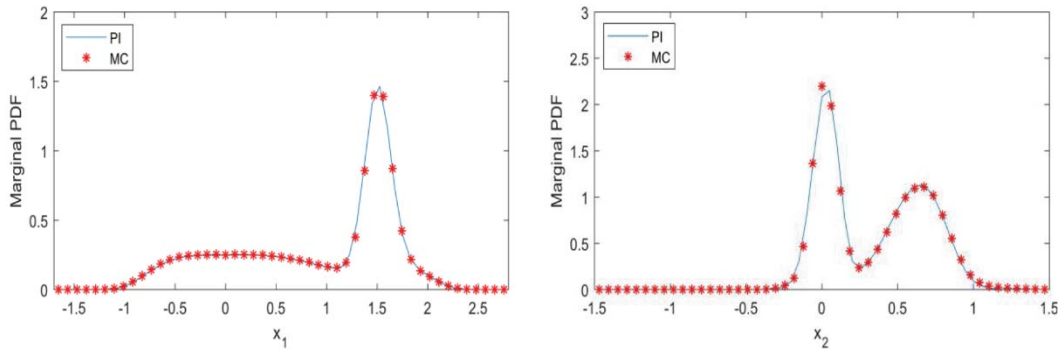

Figure 9: Marginal PDFs of the response for the 4D problem by the PI method and MC simulation

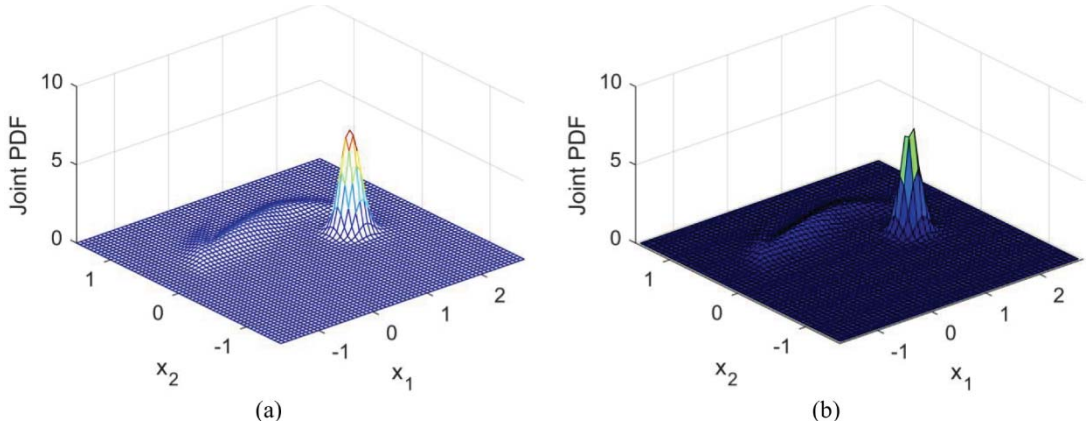

Figure 10: a) Stationary response joint PDF of the 4D problem by the path integration method, b) and Monte Carlo simulations.

6 CONCLUSIONS

In the current study, the probabilistic response of a spur gear pair under uncertain loading is investigated. The single degree of freedom gear model contains both backlash nonlinearity and time-varying mesh stiffness. Based on which component of the loading contains uncertainty, two different sub-problems are defined. The uncertainty is assumed to be represented by a first order filtered white noise, resulting in a 3D state space problem. An efficient numerical path integration technique in combination with a novel adaptive time-stepping scheme is applied in order to capture accurately the evolution of the response PDF. Marginal PDFs calculated via the PI method are compared with those obtained by Monte Carlo simulations for each of the cases that are studied. The comparisons confirm the accuracy and precision of the methodology. The effect of uncertain loading on the stationary response is quite different depending on its origin. This demonstrates the importance of identifying the stochastic source in investigating the dynamics of gear systems. The effect of spectra on the dynamic behavior is also studied by considering three noise representations with equal energies but different frequency spectrum in each case. In addition, an extension of the problem to 4D, combining the gear model with a second order filter is investigated to show the capability of path integration method in dealing with higher dimensional problems. The response PDF contains raw but qualitatively important information that needs further interpretations according to the application.

REFERENCES

[1] H.N. Ozguven, D.R. Houser, Mathematical models used in gear dynamics—A review, J. Sound Vib. 121 (1988) 383–411.

[2] A. Kahraman, R. Singh, Non-linear dynamics of a spur gear Pair, J. Sound Vib. 142 (1990) 49–75.

[3] A. Kahraman, R. Singh, Interactions between time-varying mesh stiffness and clearance non-linearities in a geared system, J. Sound Vib. 146 (1991) 135–156.

[4] G.W. Blankenship, A. Kahraman, Steady state forced response of a mechanical oscillator with combined parametric excitation and clearance type non-linearity, J. Sound Vib. 185 (1995) 743–765. doi:10.1006/jsvi.1995.0416.

[5] R.G. Parker, S.M. Vijayakar, T. Imajo, Non-Linear Dynamic Response of a Spur Gear Pair: Modelling and Experimental Comparisons, J. Sound Vib. 237 (2000) 435–455.

[6] C.G. Cooley, R.G. Parker, A Review of Planetary and Epicyclic Gear Dynamics and Vibrations Research, Appl. Mech. Rev. 66 (2014) 1–15. doi:10.1115/1.4027812.

[7] H. Ma, J. Zeng, R. Feng, X. Pang, Q. Wang, B. Wen, Review on dynamics of cracked gear systems, Eng. Fail. Anal. 55 (2015) 224–245. doi:10.1016/j.engfailanal.2015.06.004.

[8] E. Goβmann, H. Waller., Analysis of multi-correlated wind , excited vibrations of structures using the covariance method, Eng. Struct. 5 (1983) 264–272.

[9] T.K. Caughey, Nonlinear Theory of Random Vibrations, Adv. Appl. Mech. 11 (1971) 209–253.

[10] T. Tobe, K. Sato, N. Takatsu, Statistical analysis of dynamic loads on spur gear teeth: effect of shaft stiffness, Bull. JSME. 19 (1976) 808–813.

[11] T. Tobe, K. Sato, N. Takatsu, Statistical analysis of dynamic loads on spur gear teeth (Experimental Study), Bull. JSME. 20 (1977) 1315–1320.

[12] A.S. Kumar, M.O.M. Osman, T.S. Sankar, On Statistical Analysis of Gear Dynamic Loads, J. Vib. Acoust. Stress. Reliab. Des. 108 (1986) 362–368.

[13] S. V. Neriya, R.B. Bhat, T.S. Sankar, On the Dynamic Response of a Helical Geared System Subjected to a Static Transmission Error in the Form of Deterministic and Filtered White Noise Inputs, J. Vib. Acoust. Stress. Reliab. Des. 110 (1988) 501–506.

[14] F. Pfeiffer, A. Kunert, Rattling models from deterministic to stochastic processes, Nonlinear Dyn. 1 (1990) 63–74.

[15] Y. Wang, W.J. Zhang, Stochastic vibration model of gear transmission systems considering speed-dependent random errors, Nonlinear Dyn. 17 (1998) 187–203.

[16] M.F. Wehner, W.G. Wolfer, Numerical evaluation of path-integral solutions to Fokker-Planck equations, Phys. Rev. A. 27 (1983) 2663–2670.

[17] A. Naess, V. Moe, Efficient path integration methods for nonlinear dynamic systems, Probabilistic Eng. Mech. 15 (2000) 221–231.

[18] J.S. Yu, Y.-K.K. Lin, Numerical path integration of a non-homogeneous Markov process, Int. J. Non. Linear. Mech. 39 (2004) 1493–1500.

[19] H.T. Zhu, Non-stationary response of a van der Pol-Duffing oscillator under Gaussian white noise, Meccanica. 52 (2016) 833–847.

[20] A. Naess, F.E. Kolnes, E. Mo, Stochastic spur gear dynamics by numerical path integration, J. Sound Vib. 302 (2007) 936–950.

[21] J.Q. Sun, C.S. Hsu, The Generalized Cell Mapping Method in Nonlinear Random Vibration Based Upon Short-Time Gaussian Approximation, J. Appl. Mech. 57 (1990) 1018–1025.

[22] E. Mo, A. Naess, Nonsmooth Dynamics by Path Integration: An Example of Stochastic and Chaotic Response of a Meshing Gear Pair, J. Comput. Nonlinear Dyn. 4 (2009) 34501.

[23] Y. Wen, J. Yang, S. Wang, Random dynamics of a nonlinear spur gear pair in probabilistic domain, J. Sound Vib. 333 (2014) 5030–5041.

[24] S.G. Hasnijeh, M. Poursina, B.J. Leira, H. Karimpour, W. Chai, Stochastic dynamics of a nonlinear time-varying spur gear model using an adaptive time-stepping path integration method, J. Sound Vib. 447 (2019).

[25] Y. Fang, X. Liang, M.J. Zuo, Effects of friction and stochastic load on transient characteristics of a spur gear pair, Nonlinear Dyn. 93 (2018) 1–11.

[26] J.H. Kuang, A.D. Lin, Theoretical aspects of torque responses in spur gearing due to mesh stiffness variation, Mech. Syst. Signal Process. 17 (2003) 255–271.

[27] M. Inalpolat, A Computational Model to Investigate the Influence of Spacing Errors on Spur Gear Pair Dynamics, in: Exp. Tech. Rotating Mach. Acoust., Springer, Cham, 2015: pp. 1–10.

[28] E.P. Remmers, Gear mesh excitation spectra for arbitrary tooth spacing errors, load and design contact ratio, J. Mech. Des. 100 (1978) 715–722.

[29] W. Chai, A. Naess, B.J. Leira, Filter models for prediction of stochastic ship roll response, Probabilistic Eng. Mech. 41 (2015) 104–114.
[30] E. Mo, Nonlinear stochastic dynamics and chaos by numerical path integration, PhD thesis, Norwegian University of Science and Technology, 2008.
[31] P.E. Kloeden, E. Platen, Numerical solution of stochastic differential equations, Springer-Verlag, 1992.
[32] A. Naess, J.M. Johnsen, Response statistics of nonlinear, compliant offshore structures by the path integral solution method, Probabilistic Eng. Mech. 8 (1993) 91–106.

EURODYN 2020
XI International Conference on Structural Dynamics
M. Papadrakakis, M. Fragiadakis, C. Papadimitriou (eds.)
Athens, Greece, 23–26 November 2020

A NEW TIME INTEGRATION SCHEME IN MULTIBODY DYNAMICS INVOLVING FRICTIONAL IMPACT BASED ON A RETURN MAP TO NON-FLAT CONFIGURATION MANIFOLDS

E. Paraskevopoulos, P. Passas and S. Natsiavas

Department of Mechanical Engineering, Aristotle University
54 124 Thessaloniki, Greece
e-mail: natsiava@auth.gr

Keywords: Multibody dynamics, impact and friction, return map, augmented Lagrangian, geometric cubic splines.

Abstract. *This work presents a new numerical integration method for determining dynamics of a class of multibody systems with impact and friction. The method is based on the development of a novel return mapping and its proper incorporation into an augmented Lagrangian formulation. Namely, when an impact is detected during a time step, this map is applied at the end of the step to bring the system position back to the configuration manifold of the allowable motions. The novelty of this map is related to the fact that it is performed within a non-flat manifold. Moreover, once an impact is detected, the post-impact state is determined by analytical means. This is achieved by first performing a proper coordinate transformation, bringing the system into a new set of coordinates, which are suitable for describing the impact dynamics. In this coordinate set, the dominant dynamics is governed by a system of three equations of motion only, which are valid during the short contact interval. In this way, the inherent numerical stiffness of the class of systems examined is properly addressed. Finally, the accuracy and efficiency of the new method is demonstrated by applying it to a several mechanical examples.*

1 INTRODUCTION - OBJECTIVES

A new numerical scheme is developed, leading to an accurate and efficient determination of the dynamics of a class of multibody mechanical systems subjected to a single unilateral and a set of bilateral motion constraints. The existing methods can be classified in two categories, known as event-driven or time-stepping methods. When an event-driven method is applied, a standard integrator is employed during an impact free phase of the system up until a contact is detected. The state of the system at the beginning of the next impact free part of the motion is then determined by applying a complementarity formulation or an augmented Lagrangian method [1,2]. When a time-stepping method is used, a temporal discretization of the generalized displacements and velocities is performed by selecting a time step regardless of the presence or absence of switching points [2,3]. These methods evaluate the impulse of both the impulsive and non-impulsive forces over the time step. Eventually, they yield the position and velocity at the end of the time step by solving a complementarity problem or applying an augmented Lagrangian method. Consequently, the time-stepping methods are more efficient for large scale systems, exhibiting a large number of closely spaced events. Their main drawback is that they have a low order of accuracy due to the discontinuities induced by the impacts [4,5].

The main objective of this work is to present a new method for the direct integration of the equations of motion for multibody systems with frictional impacts. For systems with bilateral constraints only, a suitable numerical integration methodology was developed recently, based on an augmented Lagrangian formulation [6]. That methodology is now extended to systems involving a unilateral constraint as well. This task is achieved by developing a suitable return map, which is activated any time an impact event is detected when using a time-stepping integration method. The idea of a return map is similar to that applied earlier to other problems of mechanics, including friction or plasticity effects [7,8]. However, these methods were applied to Euclidean manifolds and were based on a projection to the closest point on the restricting surface. Here, a significant modification is necessary since the configuration space is non-Euclidean. In addition, following the detection of an impact event, the equations of motion are transformed into a set of three equations only, evolving over a much smaller time scale than the others, which are solved separately, until the end of the impact event [9]. This is a key to overcoming numerical stiffness problems in an efficient manner. These advantages are demonstrated in the second part of this study by using some typical mechanical examples.

The material of this paper is organized as follows. First, the essential dynamic characteristics of the class of constrained multibody mechanical systems examined are presented briefly in the following section. Next, the main idea of the return map is introduced. Namely, the basic ingredients of the new numerical algorithm, leading to development of a suitable return mapping process, are presented. Then, selected numerical results are presented for several mechanical examples. Finally, a summary of the main results, together with possible future extensions are included in the last section.

2 CLASS OF SYSTEMS EXAMINED - NUMERICAL INTEGRATION

This work focuses on dynamics of a class of multibody mechanical systems, subject to a set of bilateral constraints and a single frictional contact constraint. The equations of motion were obtained in earlier studies of the authors within the general framework of Analytical Dynamics [6,9]. In brief, the motion is described by a set of generalized coordinates $q = (q^1 \dots q^n)$, locating the position of a point p along a curve of the configuration manifold M for any time t [10,11]. The tangent vector $\underline{v}$ to this curve represents the generalized ve-

locity and belongs to an n-dimensional vector space T_pM, the tangent space of manifold M at p. Consequently, if $\mathfrak{B}_e = \{\underset{\sim}{e}_1 \quad \dots \quad \underset{\sim}{e}_n\}$ is a basis of T_pM, then $\underset{\sim}{v} = v^i \underset{\sim}{e}_i$, by using the common summation convention on repeated indices. Also, each vector is related directly to a covector, by employing the duality pairing $\underset{\sim}{u}^*(\underset{\sim}{w}) \equiv \langle \underset{\sim}{u}, \underset{\sim}{w} \rangle$, $\forall \underset{\sim}{w} \in T_pM$, where $\langle \cdot, \cdot \rangle$ is the inner product of T_pM [12]. Moreover, the elements of the dual (cotangent) space T_p^*M represent generalized momenta with components

$$p_i = g_{ij} v^j, \quad (i, j = 1, \dots, n), \tag{1}$$

where g_{ij} are the components of the metric tensor at point p.

When there are no motion constraints, the solution path on manifold M is determined by Newton's second law

$$\nabla_{\underset{\sim}{v}} \underset{\sim}{p}_M^* - \underset{\sim}{f}_M^* = \underset{\sim}{0}. \tag{2}$$

Covectors $\underset{\sim}{p}_M^* = p_i \underset{\sim}{e}^i$ and $\underset{\sim}{f}_M^* = f_i \underset{\sim}{e}^i$ represent generalized momenta and applied forces, respectively. The covariant differential of covector $\underset{\sim}{p}_M^*$ along a curve with tangent vector $\underset{\sim}{v}$ takes the form

$$\nabla_{\underset{\sim}{v}} \underset{\sim}{p}^*(t) = (\dot{p}_i - \Lambda_{ji}^m p_m v^j) \underset{\sim}{e}^i, \tag{3}$$

where the quantities Λ_{ij}^k are known as affinities [12].

The presence of a contact event is modeled by an inequality of the form

$$\rho(p) \geq 0. \tag{4}$$

Then, the motion of point p is restricted to lie on one side of a hypersurface in M. In this way, the function ρ establishes a new manifold

$$X = \{p \in M \mid \ \rho(p) \geq 0\}, \tag{5}$$

with dimension n. Apart from the boundary ∂X, defined by the equality in expression (4), this manifold possesses an interior $X^o = X \setminus \partial X$. This theoretical setting makes possible the direct application of results from the theory of manifolds with a boundary [13]. Also, the impulse occurs along the direction defined by the convector

$$d\rho = (\partial \bar{\rho} / \partial x^i) \underset{\sim}{e}^i, \tag{6}$$

where $\bar{\rho} = \rho(\varphi^{-1}(x))$ and $x = \varphi(p)$ is a special coordinate set of the manifold employed in the vicinity of a boundary point.

The presence of bilateral motion constraints is signaled by equalities, with general form

$$\dot{\psi}^R \equiv a_I^R(q) v^I = 0, \ (I = 1, \dots, n \ \text{and} \ R = 1, \dots, k). \tag{9}$$

For a holonomic constraint, the corresponding equation can be integrated and put in the form

$$\phi^R(q) = 0. \tag{10}$$

If the constraints are given by Eq. (9), the equations of motion on manifold M are obtained by

$$\underset{\sim}{h}^{*} \equiv \underset{\sim}{h}_{M}^{*} - \underset{\sim}{h}_{C}^{*} = \underset{\sim}{0}, \tag{13}$$

in place of Eq. (2), where

$$\underset{\sim}{h}_{M}^{*} = h_I \underset{\sim}{e}^{I} \text{ with } h_I = (g_{IJ} v^J)^{\cdot} - \Lambda_{LI}^{K} g_{KJ} v^J v^L - f_I \tag{14}$$

and

$$\underset{\sim}{h}_{C}^{*} = \sum_{R=1}^{k} h_R a_I^R \underset{\sim}{e}^{I} \text{ with } h_R = (\bar{m}_{RR} \dot{\lambda}^R)^{\cdot} + \bar{c}_{RR} \dot{\lambda}^R + \bar{k}_{RR} \lambda^R - \bar{f}_R . \tag{15}$$

The convention on repeated indices does not apply to index R. Also, the quantities $\bar{m}_{RR}$ and $\bar{f}_R$ are determined completely by the constraints, while the coefficients $\bar{c}_{RR}$ and $\bar{k}_{RR}$ are also selected in an appropriate manner [14]. Finally, substitution of Eqs. (14) and (15) into Eq. (13) leads to a set of n second order ODEs in the $n+k$ unknowns q^I and λ^R. A complete mathematical formulation is obtained after including the k equations of the constraints, which are expressed originally by Eq. (9) and put eventually in the following second order ODE form

$$g_R = (\bar{m}_{RR} \dot{\psi}^R)^{\cdot} + \bar{c}_{RR} \dot{\psi}^R = 0 \text{ or } g_R = (\bar{m}_{RR} \dot{\phi}^R)^{\cdot} + \bar{c}_{RR} \dot{\phi}^R + \bar{k}_{RR} \phi^R = 0, \tag{16}$$

for a non-holonomic and a holonomic constraint, respectively.

The picture becomes more involved in the presence of friction [9,15]. In general, the complexity of the resulting set of equations of motion precludes application of procedures leading to analytical solutions and makes difficult even the selection and application of appropriate numerical techniques. Consequently, the focus of the present study is to initiate the establishment of a theoretically sound and numerically efficient process for solving these equations. This process involves several challenging tasks. One of them is to set up a suitable algorithm, which leads first to detection of a contact event and then to prediction of a pre-impact state of the system in a sufficiently accurate and efficient manner. This is the main objective of the present study.

3 RETURN MAP

To facilitate the discussion, Fig. 1 is provided. First, at time t_m the system configuration is represented by a point p_m, with coordinates q_m, which lies in the interior X^0 of the corresponding constrained manifold X. However, at the next discrete time t_{m+1}, the new configuration point $p_{m+1}^{(k,1)}$, with $k=1$, is found to lie outside X, indicating that an impact event may have occured. In practice, this is verified by using an appropriate contact detection algorithm [16,17]. The next step is to return to a point on the boundary ∂X, representing the configuration of the system where the impact took place. This is achieved through development and application of a suitable return mapping. In the present work, this step is performed with extra care, since the configuration manifold M is non-Euclidean. First, due to the non-flatness of the configuration space, a special type of curves is employed in performing a spatial discretization. Specifically, these are selected to be the straightest curves, known as autoparallels [12]. In addition, the boundary ∂X is locally convex (i.e., it is a half-space or a corner for a single or multiple contact, respectively [9,18]). Based on the above, the task of returning from $p_{m+1}^{(k,1)}$ back to a point $p_{m+1}^{(j+1,2)}$ on the boundary ∂X in a unique way is reduced to finding the auto-

parallel joining these points, having the shortest length among a family of autoparallels. This leads naturally to construction of suitable Jacobi fields along these curves [19].

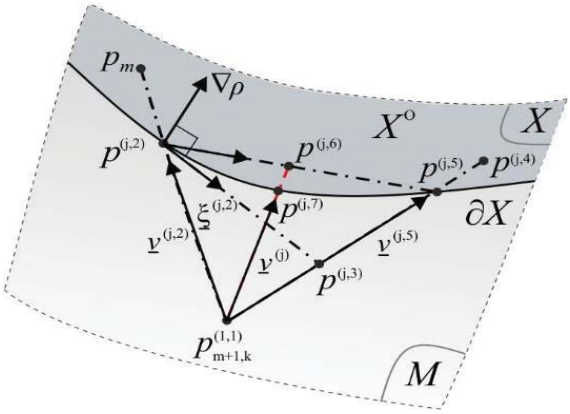

Figure 1: Illustration of the basic steps of the return map.

A complete description of the steps of the return map developed can be found in [18]. With this map, some significant theoretical gains were achieved by exploiting the Lie group nature of the configuration manifolds arising for the class of systems examined. Specifically, the special curve selected by this map to return a point from the outside to the boundary of the constrained manifold, defined by a unilateral constraint, has the shortest length among a special set of curves emanating from the outer point. The length was defined in terms of the kinetic energy of the system. In particular, the kinetic energy associated with the motion of the figurative particle along a natural curve $\gamma(r)$ on the configuration manifold is related to the length of this curve by

$$T(t) = \tfrac{1}{2}\int_0^t \langle \underline{v}(r), \underline{v}(r)\rangle dr\,, \tag{17}$$

where $\underline{v}(r)$ is the tangent vector of $\gamma(r)$ [11,12]. Using this definition as a basis, the energy function

$$L(s) = \tfrac{1}{2}\int_0^1 \langle \underline{v}(r,s), \underline{v}(r,s)\rangle dr \tag{18}$$

is introduced next for each γ^s curve of the two-dimensional surface created around a Jacobi field, parameterized so that $r=0$ at the pole p and $r=1$ at its other end and having tangent vector $\underline{v}(r,s)$ (see Fig. 2). Then, the special value of s, at which this function possesses an extreme value is found by imposing the condition

$$\varphi(s) \equiv L'(s) = \underline{\xi}(L) = 0\,, \tag{19}$$

where $\underline{\xi}(L)$ represents the derivative of L along the direction defined by vector $\underline{\xi}$. In order to check whether this extremum corresponds to a minimum or a maximum value of the energy function $L(s)$, its Hessian should be constructed in an appropriate manner on the configuration manifold [20], according to the following definition

$$H(s) \equiv L''(s) = \underline{\xi}(L'(s))\,. \tag{20}$$

It can be shown that the Hessian function is at least locally positive, rendering the energy function $L(s)$ locally convex [18].

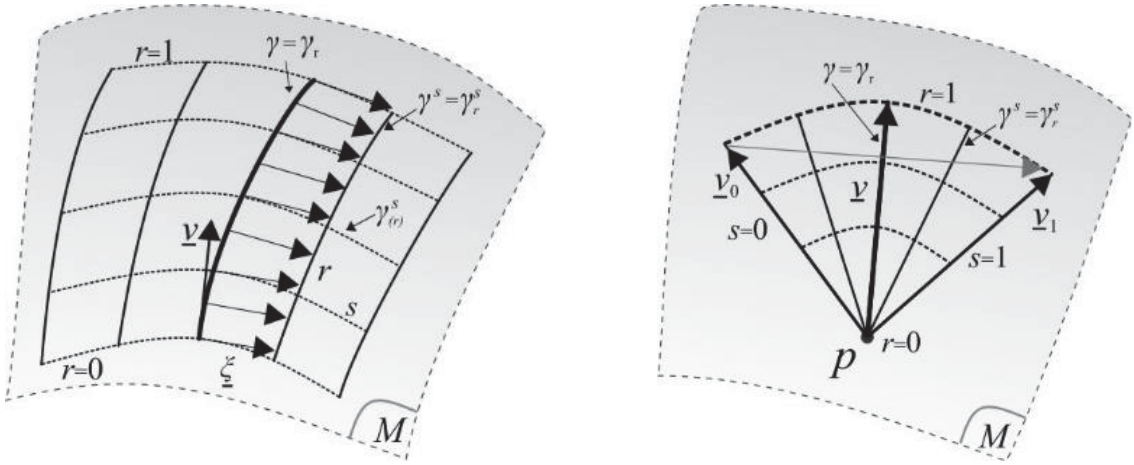

Figure 2: Jacobi fields: (a) without and (b) with a pole p.

In addition, the curve selected crosses the boundary of the allowable motions in a normal way, while the corresponding Jacobi field has no component normal to this autoparallel. In this way, the new return map can be considered as a generalization of the classical orthogonal projection operation performed in Euclidean spaces [8,21,22]. Based on this theoretical foundation, a complete numerical algorithm was set up, providing the means to project points escaping from the constrained configuration manifold during the numerical integration, back to the set of allowable motions [18]. Once this process converges to a point near ∂X, the equations of motion are transformed into a special set of coordinates, where the dominant dynamics is governed by three differential equations only [9]. These equations are then solved until the end of the impact event, where they are transformed back to the original coordinates. In this way, the inherent numerical stiffness problem is treated in an efficient manner.

4 NUMERICAL RESULTS

The set of numerical results presented next focuses on performance of the return map, which plays a central role in the integration scheme developed. This procedure was developed in a way that can fit within any of the available methodologies for the integration of the equations of motion of constrained systems. Here, the equations of motion employed in producing the numerical results form a set of second order ODEs in both the generalized coordinates and the Lagrange multipliers related to the constraint action [14]. For systems with bilateral constraints, these equations were solved by developing a suitable numerical integration methodology, based on an augmented Lagrangian formulation [6].

In all the examples studied next, knowledge of the function ρ, defined as in Eq. (6), permits evaluation of its differential $d\rho$. This is a covector related to vector $\nabla\rho$, the gradient vector of ρ, through Eq. (1). In matrix form,

$$d\rho^T = G\nabla\rho \quad \Rightarrow \quad \nabla\rho = G^{-1}d\rho^T \tag{21}$$

where the (invertible) matrix $G=[g_{ij}]$ includes the components of the metric tensor in the selected basis. In addition, covector $d\rho$ is related to a covector $d\hat{\rho}$ of the physical space by a linear mapping [15], as follows

$$d\rho = d\hat{\rho} D \,. \tag{22}$$

In general, the matrix D in this mapping is established by relating the relative velocity $\underline{V}$ at the contact point in the physical space with the generalized velocities, by

$$\underline{V} = D\,\underline{\dot{q}} \tag{23}$$

Then, combination of Eqs (21) and (22) yields eventually

$$\nabla\rho = G^{-1}(d\hat{\rho} D)^T \,. \tag{24}$$

The gradient vector $\nabla\rho$ is normal to the boundary hypersurface ∂X . In this case, the representative vector of $d\hat{\rho}$ is normal to the local contact surface in the physical space.

4.1 Impact of a particle within a circular ring

The first mechanical system examined is a particle with mass m , moving in the interior of a rigid circular ring of radius R , as shown in Fig. 3a. This example involves a planar translation only, so that the particle position can be determined by two Cartesian coordinates, q^1 and q^2 , while the original configuration space is $M = \mathbb{R}^2$. In this case, the inward normal to the boundary ∂X , consisting of the perimeter of the ring, is

$$\underline{n} \equiv \nabla\rho = \tfrac{1}{m} d\rho^T \tag{25}$$

Moreover, if (q_b^1, q_b^2) are the coordinates of the bisection point $p_{m+1,k}^{(j,2)}$, the normal vector to the boundary ∂X is

$$\underline{n} = -\frac{1}{m\sqrt{(q_b^1)^2+(q_b^2)^2}} \begin{pmatrix} q_b^1 & q_b^2 \end{pmatrix}^T \tag{26}$$

Then, the tangent vector to ∂X at that point is given by

$$\underline{\xi} = \underline{v} - \frac{\underline{v}\,\underline{n}^T}{\underline{n}^T\underline{n}}\,\underline{n} \tag{27}$$

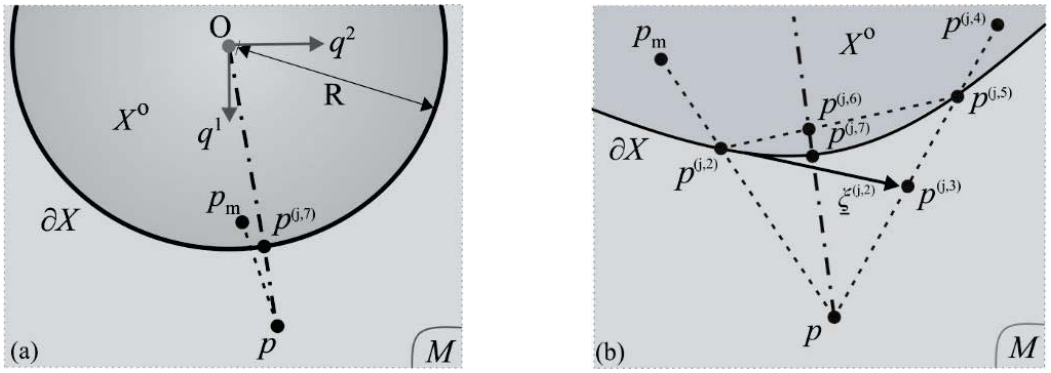

Figure 3: (a) Particle in a circular ring and (b) details of the projection from pole p to boundary ∂X .

The second term in the right hand side of Eq. (27) corresponds to the classical orthogonal projection of vector $\underline{v}$ on vector $\underline{n}$, arising in a flat manifold [21,22].

First, in Fig. 3b are shown details of the projection from the pole p back to ∂X . Next, in Fig. 4 are shown selected numerical results for the example considered, for a particle of unit mass and a ring of radius R=0.74m. The initial position of the particle was at (0.1m, -0.5m),

while its initial velocity was (10m/s, -2m/s). The results presented were obtained for $k=1$, by choosing different initial length steps $s_{m+1,1}^{(j,2)}$ along the direction defined by the tangent vector $\underline{\xi}_{m+1,1}^{(j,2)}$, in order to locate point $p_{m+1,1}^{(j,3)}$, according to the process described earlier. Specifically, the reference length step was selected to coincide with the length of the straight line (autoparallel) joining points $p_{m+1,1}^{(1,1)}$ and $p_{m+1,1}^{(j,2)}$. First, in Fig. 4a are depicted results illustrating the number of iterations needed in order to locate the correct value of coordinate q^1 at impact, for the same pole $p_{m+1,1}^{(1,1)}$. Qualitatively similar results were also obtained for coordinate q^2. Likewise, in Fig. 4b are presented results for the norm of vector $\underline{\xi}_{m+1,1}^{(j,2)}$, normalized by the norm of the velocity vector of the autoparallel joining points $p_{m+1,1}^{(1,1)}$ and $p_{m+1,1}^{(j,2)}$. Obviously, selecting an initial step value close to the characteristic length step s_0 leads to a rapid convergence.

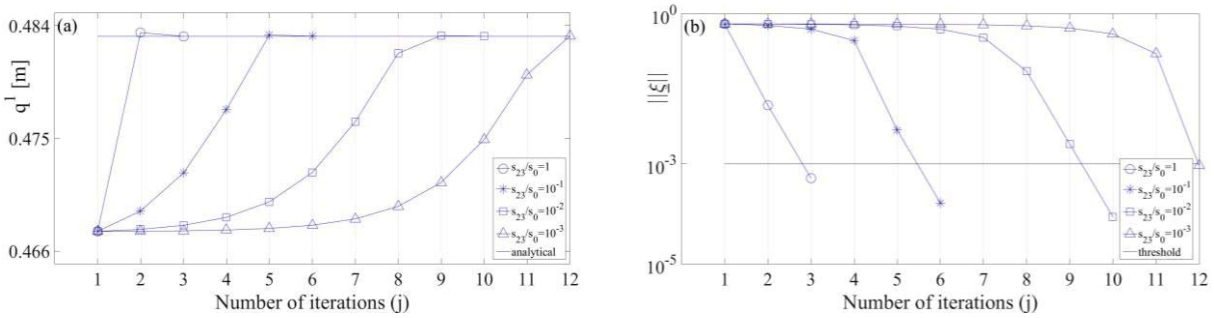

Figure 4: Collision of a particle with a rigid circular ring: (a) convergence in coordinate q^1 and (b) norm of vector $\underline{\xi}$ at the point where the shortest autoparallel crosses the boundary ∂X.

The above numerical results indicate that the smaller the value of s_{23} (compared to s_0) the larger the number of iterations needed for convergence. In such a case, the two-dimensional smooth surface created between the two end autoparallels emanating from the pole and ending at points $p_{m+1,1}^{(j,2)}$ and $p_{m+1,1}^{(j,5)}$ (see Fig. 1) does not include the minimizing autoparallel during the initial iterations. On the other hand, convergence difficulties were also encountered for $s_{23} > s_0$, due to several reasons. The most frequent was the non-intersection of the autoparallel passing through the pole $p_{m+1,1}^{(1,1)}$ and point $p_{m+1,1}^{(j,3)}$ with the boundary ∂X. Cases where point $p_{m+1,1}^{(j,3)}$ was found in the interior X^o or point $p_{m+1,1}^{(j,6)}$ was located out of the constrained manifold X, due to loss of convexity of the boundary ∂X or failure of the contact detection algorithm, were also encountered. In all these cases, the successful remedy to achieve convergence was to reduce the value of s_{23}.

4.2 Impact of a rigid body with a rigid wall

Next, a rigid body hitting a rigid wall is considered, as depicted in Fig. 5. As configuration space of the free body is selected the six-dimensional product $M \equiv \mathbb{R}^3 \times M(3)$ [23]. Then, the position and orientation of the body with respect to an inertial reference frame $\mathbb{F}$ (or $O\chi^1\chi^2\chi^3$) in the physical space is represented by a point on this manifold, with generalized coordinates $\underline{q}(t) = (\underline{q}_C^T \quad \underline{q}_R^T)^T$. Part $\underline{q}_C$ specifies the position of the body center of mass C,

while $\underline{q}_R$ describes the body orientation in the physical space. The tangent vector to the autoparallel curves is also split in a similar form. The first part leads to curves corresponding to segments of straight lines, while the rotational part leads to special curves on the manifold, with each point on these curves related to a 3×3 rotation matrix R, providing the orientation of the body with respect to $\mathbb{F}$. Moreover, for two points along such a curve, located at a distance Δs,

$$R(s+\Delta s) = R(s)\exp(\Delta s\,\tilde{v}_R) \tag{28}$$

where the entity $R(s+\Delta s) = R(s)\exp(\Delta s\,\tilde{v}_R)$ represents a 3×3 skew-symmetric matrix having $\underline{v}_R$ as axial vector [24].

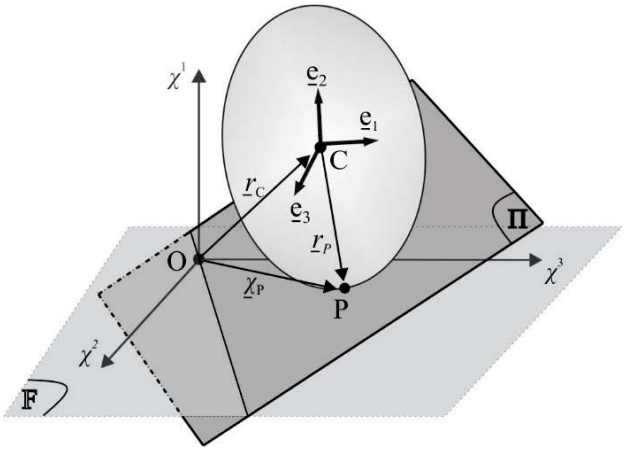

Figure 5: A rigid body hitting a plane rigid wall.

Next, in Fig. 6 are shown numerical results corresponding to impact of a homogeneous solid ellipsoid with a rigid ground. The ellipsoid has a unit mass and principal semi-axes equal to 0.1m, 0.3m and 0.15m, while the position of the rigid plane is determined by selecting $(s_1 \quad s_2 \quad s_3)$=(-0.2 0.1 1.0). Moreover, the initial position of the ellipsoid center of mass is at point (0.3m, 0.4m, 0.2m), while the components of the initial angular velocity of the ellipsoid in the body frame are $\underline{\Omega}$=(0.3 0.1 0.2) rad/sec. Finally, the set of results presented next were obtained for different length steps s_{23} along vector $\underline{\xi}^{(j,2)}_{m+1,k}$, locating point $p^{(j,3)}_{m+1,k}$, as shown in Fig. 1. Also, the reference length step s_0 was selected as in the previous example. Again, all the results presented next were obtained for $k=1$, while similar behaviour was also encountered for $k>1$, when needed.

In the set of results shown in Fig. 6, the motion of the ellipsoid center of mass is restricted by a spherical joint, so that only rotation of the ellipsoid is possible to occur. First, in Fig. 6a is illustrated the convergence obtained in the value of one of the Euler angles for a given pole ($k=1$) and variable j. Similar results were also obtained for the other two Euler angles of the ellipsoid and for other poles. Likewise, in Fig. 6b are presented results for the norm of vector $\underline{\xi}$ obtained at the point where the shortest autoparallel crosses the boundary ∂X. Again, selecting a value of the initial length step along vector $\underline{\xi}^{(j,2)}_{m+1,1}$ close to the characteristic length step s_0 leads to a rapid convergence. In addition, similar convergence difficulties with

those mentioned in the previous example were also encountered for $s_{23} > s_0$, which were overcome by decreasing the value of s_{23}.

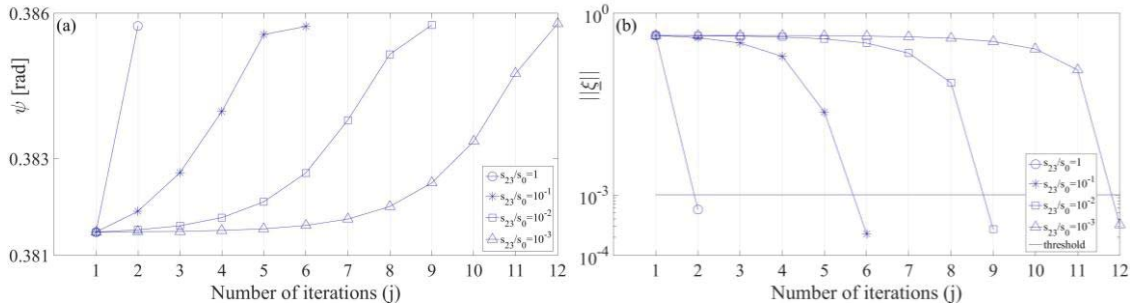

Figure 6: Collision of a rigid ellipsoid (with a pinned center of mass) with a rigid ground: (a) convergence in an Euler angle and (b) norm of vector $\underline{\xi}$ at the point where the shortest autoparallel crosses the boundary ∂X.

4.3 Impact of two solid bodies

The algorithm developed can be applied to general single point collisions, with any combination of solid bodies. For instance, in Fig. 7a is illustrated the convergence obtained in one of the Euler angles of the ellipsoid, while a similar diagram for a translational coordinate of its mass center is shown in Fig. 7b. Then, in Fig. 7c are shown results for one of the box Euler angles. Finally, in Fig. 7d are presented results for the norm of vector $\underline{\xi}$ obtained at the point where the shortest autoparallel crosses ∂X. Once again, selecting a value close to the reference length step s_0 leads to a rapid convergence. Also, convergence was achieved eventually in all cases, by properly adjusting the length step.

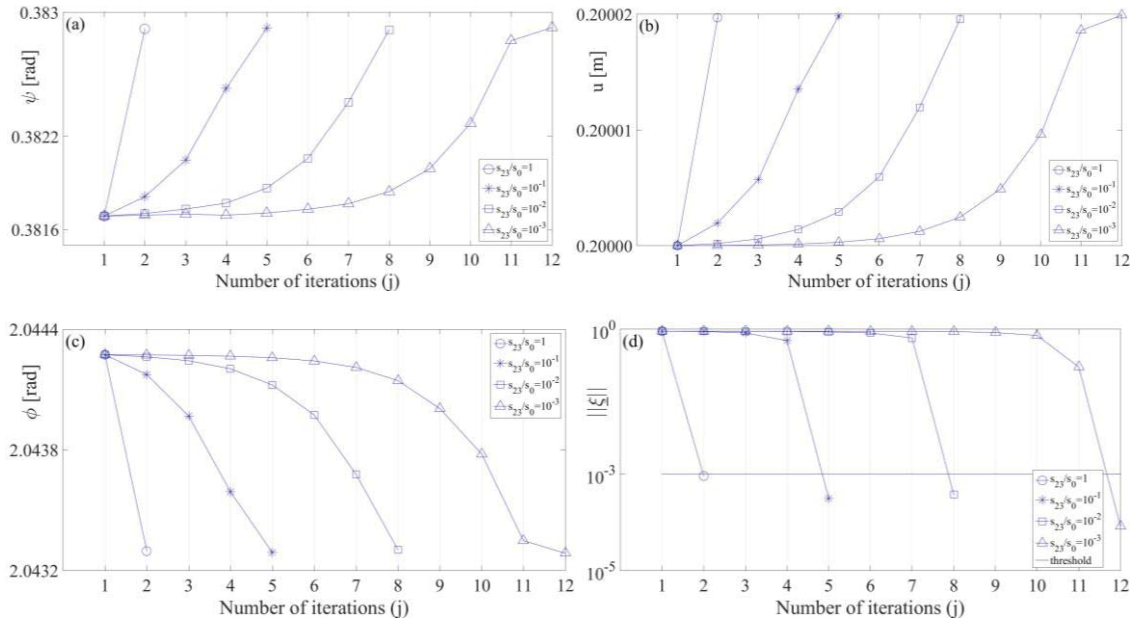

Figure 7: Collision of an ellipsoid with a box: (a) convergence of one Euler angle of the ellipsoid, (b) convergence of one translational coordinate of the ellipsoid, (c) convergence of one Euler angle of the box and (d) norm of vector $\underline{\xi}$ at the point where the shortest autoparallel crosses the boundary ∂X.

Finally, it is noted that the same analysis is also applicable to mechanical systems involving deformable bodies, as well, by assuming that they have been discretized geometrically before. For instance, if the dominant flexibility effects of a free solid body are described by n elastic modes, included in a $3\times n$ matrix Φ, the configuration manifold is represented by an $(n+6)$-dimensional product space, $M \equiv \mathbb{R}^3 \times M(3) \times \mathbb{R}^n$ [24,25]. This implies that the array with the generalized coordinates $\underline{q}(t)$ is now split in parts $\underline{q}_C$, $\underline{q}_R$ and $\underline{q}_F$, with the last part representing the flexibility effects.

4.4 Dice tossing

The time integration method developed can be applied to general single point collisions, with any combination of solid bodies and any geometric shape. For instance, a set of numerical results is presented next, obtained for motion of a die thrown over a rigid ground. This motion is viewed from a coordinate system $Oxyz$, which is fixed on the ground. It is affected by gravity, acting along the negative z-axis and involves frictional impacts. The die considered is a homogeneous rigid cube, with a mass of 0.016 kg and edge length 0.02 m. It starts from a position above the ground, with the cube edges parallel to the axes of the $Oxyz$ coordinate system. Moreover, the initial position and (linear and angular) velocity are chosen to satisfy two scenarios. In the first, the cube executes a planar motion, taking place in the vertical plane Ozx. Namely, it hits the ground with one of four of its eight edges only, so that the motion is equivalent to a square hitting the horizontal line Ox. In the second scenario, the initial conditions are modified so that the cube exhibits a spatial motion and hits the ground with one of its vertices. In all cases, the value of the kinematic restitution parameter was selected as $e = 0.5$. In addition, the value of the coefficient of friction between the die and the ground was chosen as $\mu = 0.05$ or 0.20, while the maximum penetration ratio was selected as $\delta = 0.20$.

The first set of numerical results is presented in Fig. 8. Here, the initial position of the cube center is at (0, 0, 0.3) m, while its initial velocity is (0.5, 0, -0.5) m/s. Moreover, the initial angular velocity of the cube is (0, 10, 0) rad/s. These initial conditions lead to a subsequent plane motion of the cube, which is continued even after the bouncings on the ground due to the symmetry of the cube geometry. First, in Fig. 8a is shown the projection of the trajectory executed by the cube center of mass on the vertical plane Ozx for the two values selected for μ. Likewise, in Fig. 8b is shown the projection of the same trajectory on the horizontal plane Oxy. Then, the histories of the two non-zero velocity components of the mass center are shown in Fig. 8c. Finally, the history of angular velocity of the cube is presented in Fig. 8d. A remarkable result is that, for the case with $\mu = 0.20$, the cube starts moving in the opposite direction than it was thrown after the first impact, as it becomes clear by Figs. 8a and 8c.

Next, in the set of results presented in Fig. 9, the initial position of the cube center and its initial velocity are kept the same as in the previous case. However, an angular velocity component about the x-axis is added, so that the initial cube angular velocity is (10, 10, 0) rad/s. These initial conditions lead to a general spatial motion of the cube. First, in Fig. 9a is shown the projection of the trajectory executed by the cube center of mass on plane Ozx for the two values selected for the coefficient of friction. Likewise, in Fig. 9b is depicted the projection of the same trajectory on plane Oxy.

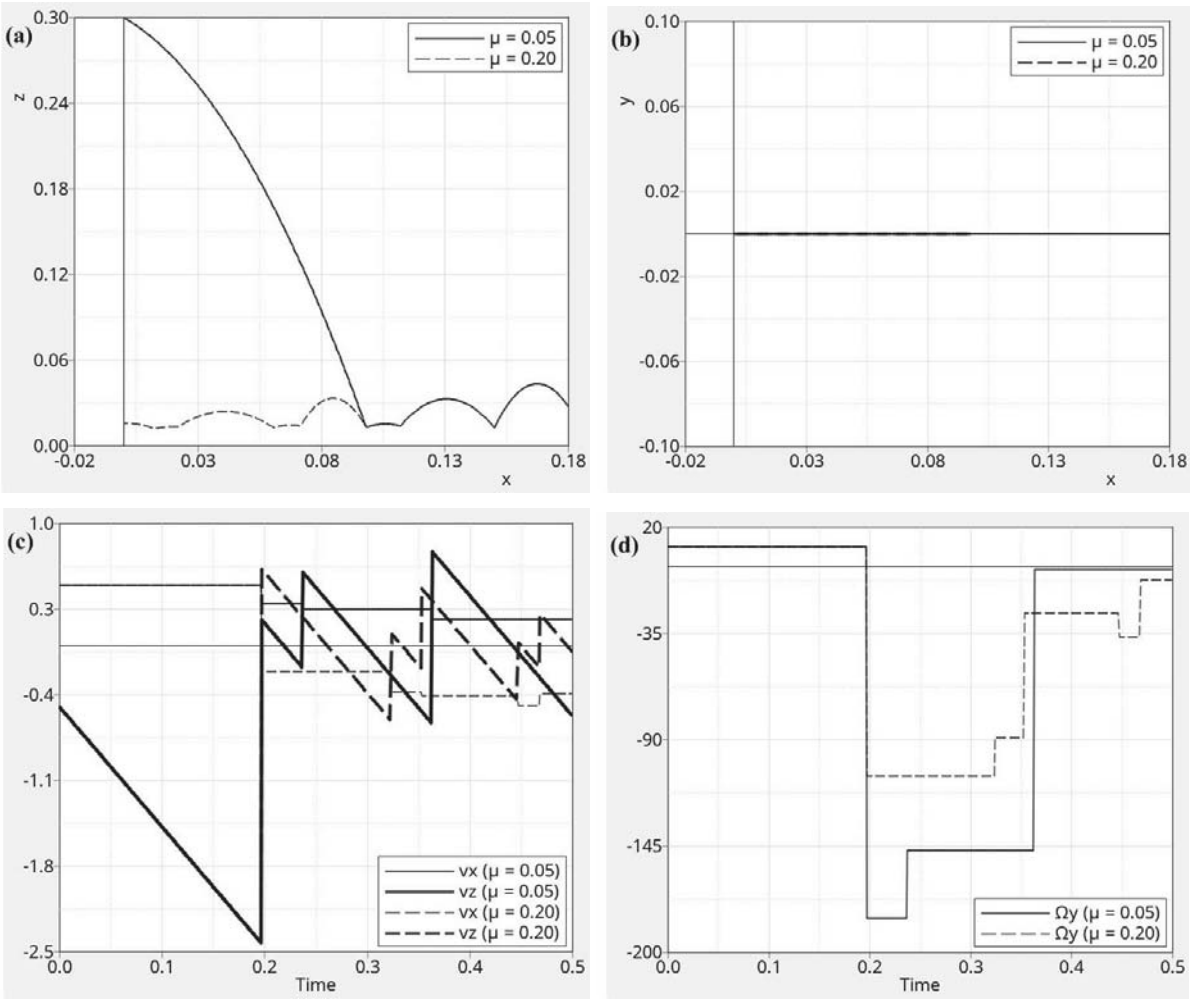

Figure 8: Plane die tossing. Projection of the trajectory of the cube center on: (a) the vertical plane Ozx and (b) the horizontal plane Oxy. Histories of: (c) the velocity components of the mass center and (d) the angular velocity of the cube.

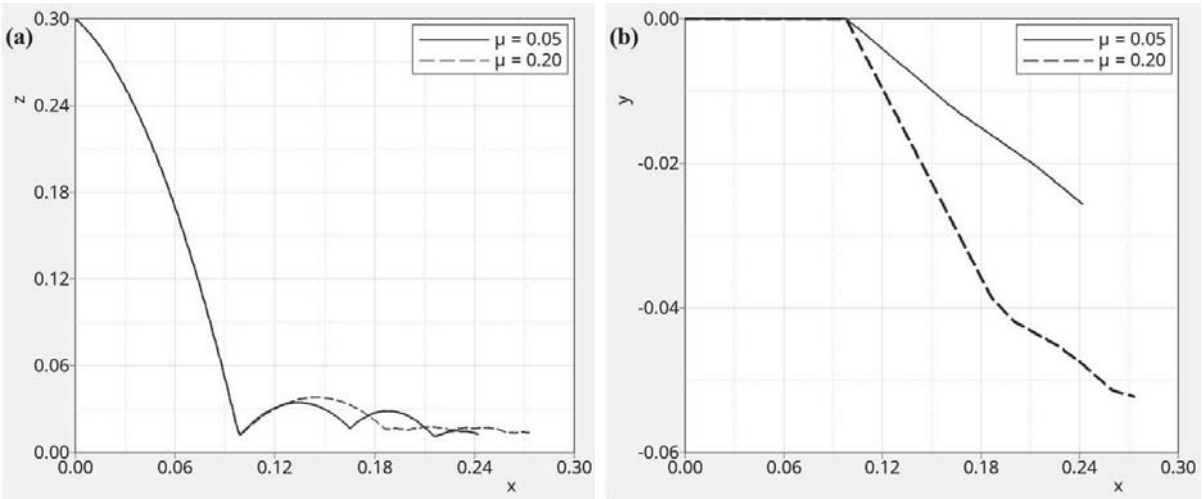

Figure 9: Spatial die tossing. Projection of the trajectory of the cube center on: (a) the vertical plane Ozx and (b) the horizontal plane Oxy.

Finally, the emphasis was placed on the dynamics of the cube during the first impact phase. For this, the velocity components of the cube contact point are shown in Fig. 10. First, the tangential velocity V_x is presented in Fig. 10a, while the corresponding tangential velocity V_y and normal velocity V_z are included Fig. 10b, for the plane motion of the die. Similar results are also included in Figs. 10c and 10d, for the spatial cube motion. In all cases examined, a smooth change is observed to occur in the velocity components throughout the impact phase.

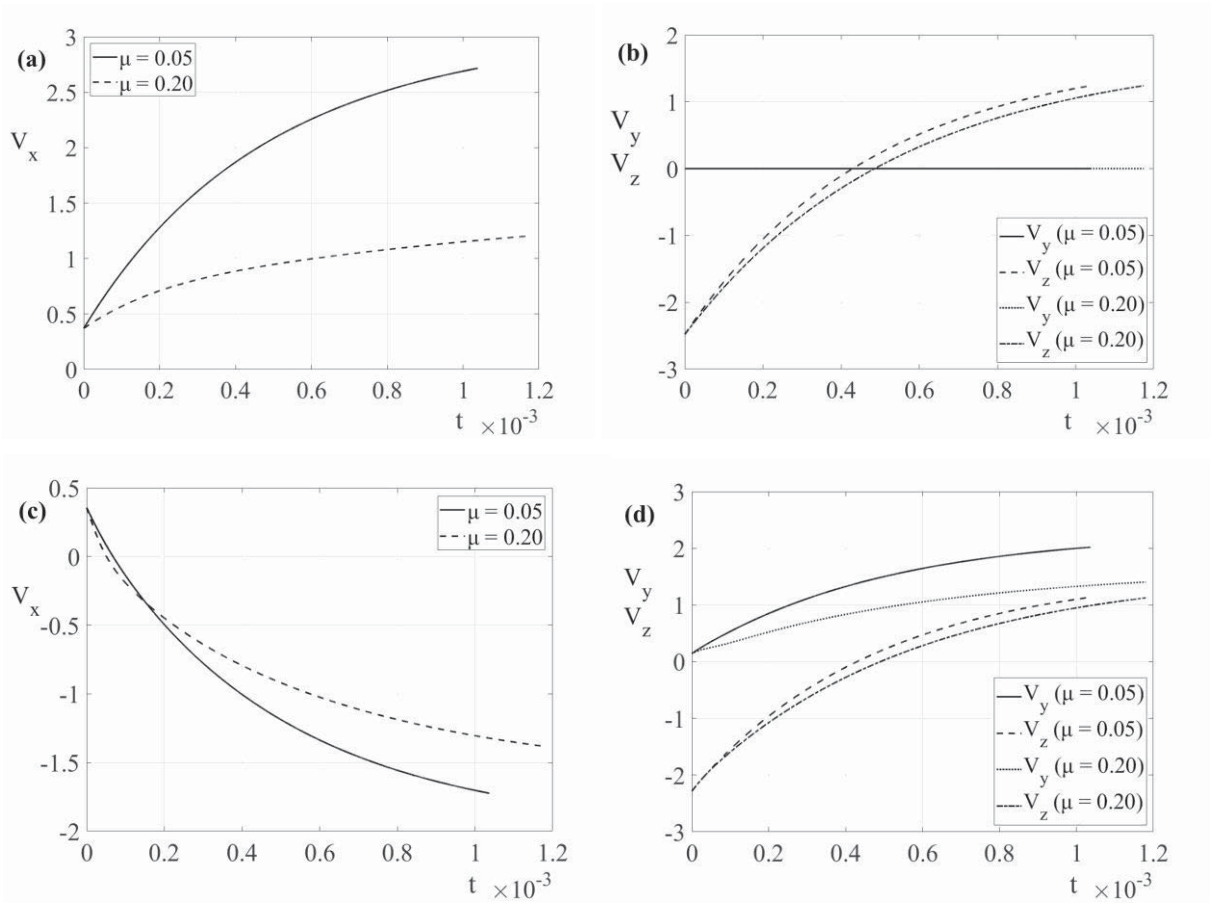

Figure 10: Velocity components of the cube contact point during the first impact phase: (a) tangential component V_x (plane motion), (b) tangential component V_y and normal component V_z (plane motion), (c) tangential component V_x (spatial motion), (d) tangential component V_y and normal velocity component V_z (spatial motion).

5 SUMMARY AND EXTENSIONS

In the first part of this study, the basic steps of a return map, which can be a vital part of any time stepping scheme for capturing dynamics of multibody systems involving impacts, were presented. A theoretical basis for this map was built using concepts of differential geometry, referring to Jacobi fields on manifolds. This need arises from the fact that the configuration space of the class of systems examined is non-Euclidean. Specifically, application of this map in order to return a point from the outside to the boundary of the constrained manifold, defined by a unilateral constraint, leads to a curve with the shortest length among a special set of curves emanating from the outer point. These curves represent the straightest curves on a manifold and are known as autoparallels. In addition, the final curve selected crosses the boundary of the allowable motions in a normal way. In this way, the new return map is a gen-

eralization of the classical orthogonal projection operation performed in Euclidean spaces. Based on these ideas, a complete numerical algorithm was set up, providing the means to project points escaping from the constrained configuration manifold during the numerical integration, back to the set of allowable motions. Finally, these ideas were verified in the second part of this work, by presenting numerical results for a selected set of mechanical examples.

The return map developed can be applied to any discrete mechanical system subject to a set of bilateral motion constraints and a single unilateral constraint. A first possible step is to extend this map for handling cases with multiple impacts. This is a theoretically challenging subject, involving consideration of configuration manifolds with corners, having a large engineering importance [1,3,26]. Another useful extension is to embed this map into a complete time-stepping methodology, employed for the direct integration of the equations of motion of multibody systems with impacts. In particular, violation of a unilateral constraint during time integration is associated with interpenetration, which may occur during the numerical process but is not physically acceptable. In such cases, application of this map can provide appropriate values of the position and velocity, which can then be used as the pre-impact state of the class of dynamical systems examined. This, in turn, is a necessary step for the evaluation of the post-impact state and the subsequent return to a new smooth part of the motion.

REFERENCES

[1] Pfeiffer, F., Glocker Ch. (1996) Multibody Dynamics with Unilateral Contacts, J. Wiley & Sons, New York.

[2] Leine R.I., Nijmeijer H. (2013) Dynamics and Bifurcations of Non-Smooth Mechanical Systems, Springer-Verlag, Berlin.

[3] Acary V., Brogliato B. (2008) Numerical Methods for Nonsmooth Dynamical Systems, *Lecture Notes in Applied and Computational Mechanics*, 35, Springer, Berlin.

[4] Jean, M. (1999) The Non-smooth Contact Dynamics Method. *Comput. Methods Appl. Mech. Engrg*. 177: 235-257.

[5] Moreau, J.J. (1999) Numerical Aspects of the Sweeping Process. *Comput. Methods Appl. Mech. Engrg*. 177: 329–349.

[6] Potosakis N., Paraskevopoulos E., Natsiavas S. (2020) Application of an Augmented Lagrangian Approach to Multibody Systems with Equality Motion Constraints. *Nonlinear Dyn*. 99: 753–776.

[7] Giannakopoulos, A.E. (1989) The Return Mapping method for the Integration of Friction Constitutive Relations. *Comp. Struct*. 32: 157-167.

[8] Simo J.C., Hughes T.J.R. (1998) Computational Inelasticity, Springer-Verlag, New York.

[9] Natsiavas S., Paraskevopoulos E. (2019) A Boundary Layer Approach to Multibody Systems Involving Single Frictional Impacts. *ASME J. Comput. Nonlinear Dyn.* 14: 011002-16.

[10] Greenwood, D.T. (1998) Principles of Dynamics. Prentice-Hall Inc., Englewood Cliffs, New Jersey.

[11] Bloch, A.M. (2003) Nonholonomic Mechanics and Control. Springer-Verlag, New York.

[12] Frankel, T. (1997) The Geometry of Physics: An Introduction. Cambridge University Press, New York.

[13] Melrose, R.B. (1993) The Atiyah-Patodi-Singer Index Theorem. Research Notes in Mathematics, 4, A.K. Peters Ltd., Wellesley, MA.

[14] Natsiavas, S., Paraskevopoulos, E. (2015) A Set of Ordinary Differential Equations of Motion for Constrained Mechanical Systems. *Nonlinear Dyn*. 79: 1911-1938.

[15] Natsiavas, S., Paraskevopoulos, E. (2018) An Analytical Dynamics Approach for Mechanical Systems Involving a Single Frictional Contact Using b-Geometry. *Int. J. Solids Struct*. **148-149**: 140-156.

[16] Gilbert, E.G., Johnson, D.W., Keerthi, S.S. (1988) A Fast Procedure for Computing the Distance Between Complex Objects in Three-dimensional Space. *IEEE J. Robotics Autom.* **4**: 193–203.

[17] Pournaras, A., Karaoulanis, F., Natsiavas, S. (2017) Dynamics of Mechanical Systems Involving Impact and Friction Using a New Contact Detection Algorithm. *Int. J. Non-Linear Mech*. 94: 309-322.

[18] Paraskevopoulos, E., Passas, P., Natsiavas, S. (2020) A Novel Return Map in Non-flat Configuration Spaces of Multibody Systems with Impact. *Int. J. Solids Struct*. **202**: 822-834.

[19] Kobayashi S., Nomizu K. (1969) Foundations of Differential Geometry, Vol. II. Interscience Publishers, New York.

[20] Udriste, C. (1994) Convex Functions and Optimization Methods on Riemannian Manifolds. Mathematics and its Applications, **297**, Kluwer Academic Publishers Group, Dordrecht.

[21] Bayo E., Ledesma R. (1996) Augmented Lagrangian and Mass-Orthogonal Projection Methods for Constrained Multibody Dynamics. *Nonlinear Dyn.* **9**: 113–130.

[22] Dopico, D., Gonzalez, F., Cuadrado, J., Kövecses, J. (2014) Determination of Holonomic and Nonholonomic Constraint Reactions in an Index-3 Augmented Lagrangian Formulation with Velocity and Acceleration Projections. *ASME J. Comput. Nonlinear Dyn*. **9**: p. 041006.

[23] Paraskevopoulos, E., Natsiavas, S. (2013) A New Look into the Kinematics and Dynamics of Finite Rigid Body Rotations Using Lie Group Theory. *Int. J. Solids Struct*. **50**: 57-72.

[24] Geradin, M., Cardona, A. (2001) Flexible Multibody Dynamics. J. Wiley & Sons, New York.

[25] Bauchau, O.A. (2011) Flexible Multibody Dynamics. Springer Science+Business Media, London.

[26] Joyce D. (2016) A Generalization of Manifolds with Corners. *Advances Math.* **299**: 760–862.

EURODYN 2020
XI International Conference on Structural Dynamics
M. Papadrakakis, M. Fragiadakis, C. Papadimitriou (eds.)
Athens, Greece, 23–26 November 2020

COMPUTING BACKBONE CURVES FOR NONLINEAR OSCILLATORS WITH HIGHER ORDER POLYNOMIAL STIFFNESS TERMS

Ayman M. Nasir[1], **Neil D. Sims**[2], **David J. Wagg**[2]

[1] PhD Student – University of Sheffield
Sheffield, S1 3JD, UK
e-mail: amnasir1@sheffield.ac.uk

[2] Prof. in Mechanical Engineering Dep. - University of Sheffield
Sheffield, S1 3JD, UK
e-mail: n.sims@sheffield.ac.uk, david.wagg@sheffield.ac.uk

Keywords: Nonlinear, Vibrations, Normal forms, Backbone curves, Symbolic computations.

Abstract. *Single-degree-of-freedom (SDOF) nonlinear oscillators are widely used for modelling systems with just one degree-of-freedom in addition to single mode approximations to structural elements such as beams and cables, as well as other multi-degree-of-freedom (MDOF) applications. In this work, an investigation of the behavior of SDOF nonlinear oscillators is carried out using the method of direct normal forms. So far, this method has only been considered as a theoretical technique used for solving limited nonlinear dynamical systems in which low orders of nonlinearities appear, involving quadratic and cubic nonlinearities. In this work, thanks to the implementation of symbolic computations, the method of direct normal forms is generalized for solving nonlinear SDOF systems with any order of polynomial (or geometric) weak nonlinearities. Using this new approach, the effect of any higher order nonlinear term, or any combination of nonlinear terms can be investigated. Backbone curve relations are obtained for a selection of example systems representing both hardening and softening systems, and the results are verified by comparing the approximate analytical solutions to numerical solutions generated using COCO numerical continuation toolbox in Matlab.*

1 INTRODUCTION

Nonlinear normal forms method is a well-established technique for obtaining approximate solutions for nonlinear oscillators with various types of weak (typically smooth) nonlinearities. In principle, it can be used for either SDOF or MDOF problems; although for systems with more than a few degrees-of-freedom the algebraic complexity quickly escalates. It is also possible for the analyst to select certain resonant (or non-resonant) cases to study, by making one (or sometimes more) near-identity transforms [3]. The analytical basis of the technique is to use matrix algebra via a series of analytical steps that finally detect the desired resonances and can be used to find approximate solutions, such as so-called backbone curves, for the SDOF or MDOF system being considered.

While this method has the potential to be applied for a wide range of applications, it can generate large and complicated mathematical terms. As a result, it could be helpful to use symbolic packages, which can deal with such complex mathematical expressions and also offer the possibility of enhancing the accuracy of solution by increasing the number of terms truncated in the solution.

Another way to simplify such computations is to reduce the system order prior to computation. This is a pragmatic way to decrease the matrix sizes involved, however the size of the residual terms (i.e. those excluded by the reduction) should be estimated in order to ensure the accuracy of the final solution. Using a computation package, such as Maple software, makes it possible to build a highly structured code that can, in principle, solve for any order of nonlinearity and potentially a large number of nonlinear terms. In this work, the number of terms is limited to two.

The origin of the idea of normal form transformations is attributed to the work of Poincaré. Following this, the application of normal forms method for SDOF and MDOF is discussed widely in the literature. Notably the Hamiltonian normal form (and Birkhoff normal forms) were introduced for conservative dynamical systems [21], and are typically used to model undamped unforced applications in physics and engineering. The work of Arnold [22] did much to extend and promote the idea of normal form transformation in engineering mechanics. The normal form approach was extended to problems of forced and damped systems of coupled nonlinear oscillators by Jezequel and Lamarque, [24], and given recast in a perturbation framework by Nayfeh [25].

Because most mechanical vibration problems are naturally described by sets of second-order differential equations, a variant of the normal forms method applied directly to second order dynamical problems was first introduced by Neild and Wagg in [3]. The authors originally referred to this modified technique as ‘second order normal forms’. This approach will be used during the formulation and discussion in this work.

Compared with other techniques, the primary advantage of the direct normal forms is the ability of inherently computing the harmonics without pre-assuming any specific harmonic components included in trial solutions. Thus, no prior knowledge of the harmonic components in the response of the system is required and no additional complexity is needed when considering the harmonics. Furthermore, the process of direct normal forms can be formulated in a matrix-based manner, which makes its application more appropriate for the computer automation.

The direct normal form technique has been used in a number of conducted research works, investigating nonlinear dynamics of mechanical systems. Xin et al., [9], considered the SDOF nonlinear oscillators of polynomial-type nonlinearities using the direct normal form technique, their work involved investigation of velocities and displacements, whilst illustrating the contributions of the different polynomial nonlinearities in different forms to the system response by the resulting resonance response functions (RRFs).

Shaw et al. [23], studied the performance of the nonlinear vibration isolator using the direct normal form technique. The system was modelled as a SDOF oscillator with cubic and quintic nonlinear terms. The authors estimated a group of backbone curves of the nonlinear vibration isolator by considering its equivalent conservative system. Cammarano et al. [9] investigated the optimal load for the nonlinear energy harvester in the case of purely resistive loads. Their work was carried out both analytically and numerically, and the results showed that analytical solutions obtained using direct normal forms were in very close agreement with the numerical results within the frequency range of interest. The direct normal form technique was also applied to study the nonlinear dynamic behaviors of MDOF systems, see for example [9] and references therein.

However, in order to generalise the applications of direct normal forms, thanks to the implementation of Maple symbolic computations, this work focuses on studying SDOF nonlinear systems with higher orders of geometric nonlinearities. One reason for taking this approach is that, when attempting the direct normal forms analysis of such systems, usual hand calculations, can be extremely difficult as the number of terms included increases.

Due to the inherent nature of nonlinearities, the use of direct normal forms is not limited to nonlinear oscillators; many real-life engineering applications exhibit geometric, or even damping nonlinearities quite naturally. Therefore, the direct normal form technique has been used to study nonlinear beams, cables, shells, plates and multi-storey buildings - see [3] for detailed description of many of these applications. In this work, the direct normal forms method is used to analyse some SDOF oscillators with one, or two, geometric nonlinear terms. The application of this method, with the aid of symbolic computation algorithm, enables a robust computational method for the investigation of the dynamics exhibited by these types of oscillators using backbone curves.

2 DIRECT NORMAL FORMS METHODOLOGY

For the case of unforced vibrating systems, the technique is applied using four main consecutive steps:

Step 1: Linear modal transformation in order to decouple the linear terms.
Step 2: Derivation of the equation of motion for the nonlinear transformation.
Step 3: Applying the near-identity transform.
Step 4: Solving the resulting normal forms equation (or equations).

In addition, studying systems that are externally forced usually requires one further transformation, in which, any non-resonant forcing terms are to be excluded. Finally, damping term (usually viscous damping) is normally included within the nonlinear vector.

2.1 Computation of backbone curves using direct normal forms

Consider the case of nonlinear forced-damped SDOF oscillator, whose equation of motion may be written as

$$M\,\ddot{x}(t)+C\,\dot{x}(t)+K\,x(t)+N_x(x,\dot{x},r)=P_x\mathbf{r},, \tag{1}$$

where the over dots represent derivation with respect to time, x represents the physical displacements, M, C and K denote the mass, damping coefficient and linear stiffness respectively, $N_x(x)$ is the nonlinear restoring force, ε is used to denote smallness of the nonlinear terms, the amplitude of the forcing term is denoted by P_x, and $\mathbf{r}$ is the forcing vector which can be written as $\mathbf{r}=\left\{r_p, r_m\right\}^T=\left\{e^{i\Omega t}, e^{-i\Omega t}\right\}^T$ where the forcing frequency is denoted a by Ω.

As mentioned earlier, direct normal forms analysis is applied using four main steps, for convenience, only key parts of the analysis are to be discussed in this work while the complete detailed analysis of this type of systems is extensively discussed in [3]. Moreover, for the application of the direct normal form technique, the nonlinear terms are assumed to be expressed in a polynomial form in terms of x.

From Eq. (1) all nonlinear terms are gathered in one term, $\overline{N}_x(x)$. Herein, both damping and nonlinear terms are assumed to be efficiently small compared to the linear stiffness and the forcing term, hence, more conveniently Eq. (2) can be rewritten as

$$M\,\ddot{x}(t)+K\,x(t)+\overline{N}_x(x,\dot{x},r)=\mathbf{P_x}\mathbf{r}, \tag{2}$$

where $\overline{N}_x(x,\dot{x},r)=N_x(x,\dot{x},r)+C\,\dot{x}(t)$

Now, the application of direct normal forms begins, by writing Eq. (2) in its *linear modal normal form*, using the transformation $x \to q$, simply by applying $x = \Phi q$, where Φ is the matrix containing the mode shapes, then, Eq. (2) becomes

$$\ddot{q} + \Lambda q + \overline{N}_q(q, \dot{q}, \mathbf{r}) = \mathbf{P_q r}, \tag{3}$$

where $\overline{N}_q(q, \dot{q}, \mathbf{r}) = \left(\Phi^T M \Phi\right)^{-1} \Phi^T \overline{N}_x(\Phi q, \Phi \dot{q}, \mathbf{r})$, $\mathbf{P_q} = \left(\Phi^T M \Phi\right)^{-1} \Phi^T \mathbf{P_x}$

Herein, $q = u + \varepsilon H(u)$ where u and $H(u)$ are the fundamental and harmonic components of q respectively.

The assumed solution has the form

$$u = u_p + u_m = \left(\frac{U}{2} e^{-i\phi}\right) e^{i\omega_r t} + \left(\frac{U}{2} e^{i\phi}\right) e^{-i\omega_r t}, \tag{4}$$

Where U, ϕ and ω_n are the displacement amplitude, phase lag, and response frequency, respectively.

In order to complete the analysis, $\overline{N}_q$, in view of Eq. (4), should be decomposed into two vector $\mathbf{n}^*$ and $\mathbf{u}^*$ where $\mathbf{n}^*$ is a row vector contains the coefficients part and $\mathbf{u}^*$ is a column vector represents the nonlinear functions of u.

For the case of polynomial nonlinear terms (as appears in Eq. 2), the ℓ^{th} element of $\mathbf{u}^*$ may be written as

$$u_\ell^* = u_{pn}^{s_{p,\ell}} u_{mn}^{s_{m,\ell}} \tag{5}$$

Where $s_{p,l}$ and $s_{m,l}$ are exponents of u_p and u_m in the ℓ^{th} element of $\mathbf{u}_{(j)}^*$ respectively. This step is symbolically done in the proposed algorithm for every term in $\mathbf{u}^*$. In order to identify the resonant nonlinear terms retained in $\mathbf{n}_{u(j)}$ from $\mathbf{n}_{(j)}$, a vector $\beta_{(j)}$, is introduced, i.e.

$$\beta_{(j)n,\ell} = \left[\sum_{n=1}^{N} \left(s_{pj,\ell,n} - s_{mj,\ell,n}\right) \omega_{rn}\right]^2 - \omega_{rn}^2 \tag{6}$$

Finding $\boldsymbol{\beta}^*$ matrix is crucially important to complete the analysis, and it is performed symbolically with a series of iterative loops that capture the power indices in Eq. (5) and then substitute the result in Eq. (6).

The procedure discussed above is a short summary of the direct normal forms technique. In the following subsection, two examples of SDOF nonlinear oscillators are studied; the first example represents a SDOF conservative (unforced and undamped) oscillator with two different orders of geometric nonlinearities, whereas the second example is a SDOF oscillator with

viscous damping and harmonic forcing applied away from resonance. Lastly, the frequency response of a general system of a forced damped nonlinear oscillator with two types of geometric nonlinearities is studied. It is important to mention that all manipulations and solutions to be shown are computed using Maple symbolic computation packages with the aid of the COCO toolbox in Matlab for numerical comparisons and verifications.

2.2 SDOF conservative oscillator with various nonlinearities

Considering the following general formula for unforced, un-damped SDOF oscillator,

$$\ddot{x}(t) + \omega_n^2 x(t) + \alpha_1 x^{\mu}(t) + \alpha_2 x^{\nu}(t) = 0, \tag{7}$$

where ω_n is the natural frequency of the system, α_1 and α_2 are arbitrary small coefficients for the nonlinear terms, μ and ν are the lower and higher orders of the nonlinear terms, respectively. Furthermore, in order to achieve stable energy levels, at least one of the nonlinear orders (i.e. μ and ν) should be an odd number, for detailed discussion of the potential functions and how they are used to study the stability level of the system refer to [3].

Using this approach it is possible to compare the results for different configurations of μ and ν. Such systems with different parameters and orders of nonlinearities can be theoretically used for modelling some engineering applications. In principle, the symbolic computations method introduced in this work has the potential to be applied to general SDOF systems with any number of nonlinear terms. In order to test this method we start with two nonlinear terms described by Eq. (7) and increase the order, accordingly, it is possible to understand the capabilities and limitations of this method.

The following procedure illustrates the use of symbolic computations of a normal form method in order to solve Eq. (7) for $\mu = 2$ and $\nu = 7$, nevertheless, following the same procedure, it is possible to solve the equation for any other values, as long as at least one exponent is odd.

Direct normal forms analysis of such systems undergoes a series of transformations that involve complex mathematical manipulations, in this work the most important results are shown, focusing on the utilization of symbolic computation software, i.e. Maple. Rewriting Eq. (7) with $\mu = 2$ and $\nu = 7$, leads to

$$\ddot{x}(t) + \omega_n^2 x(t) + \alpha_1 x^2(t) + \alpha_2 x^7(t) = 0, \tag{8}$$

The first step is using Eq. (3) in view of Eq. (2) to make the linear modal transformation, in this step it should be noticed that for SDOF systems the transform is unity and $x = q$, then

$$\ddot{q} + \Lambda q + N_q(q) = 0, \text{ where } \Lambda = \omega_n^2 \text{ and } N_q(\mathbf{q}) = \alpha_1 q^2 + \alpha_2 q^2 \tag{9}$$

The second step is the near-identity transform, and for $\varepsilon = 1$, rewriting the nonlinear terms using $\mathbf{u}$, one should obtain $N_q(u) = \alpha_1 u_1^2 + \alpha_2 u_1^7$ and $\mathbf{u}_1 = \mathbf{u}_{p1} + \mathbf{u}_{m1}$, thus

$$\mathbf{n}_{(1)}(\mathbf{u}) = \mathbf{n}^* \mathbf{u}^*(\mathbf{u}_p, \mathbf{u}_m) = \alpha_1 \left(u_{p1} + u_{m1}\right)^2 + \alpha_2 \left(u_{p1} + u_{m1}\right)^7 \tag{10}$$

Expanding Eq. (10), $\mathbf{n}_{(1)}(\mathbf{u})$ will contain many terms (11 term in this case), these terms have to be primarily decomposed into coefficients and nonlinear functions vectors $\mathbf{n}^*$ and $\mathbf{u}^*$, respectively.

$$\mathbf{n}^* = \begin{bmatrix} \alpha_1 & \alpha_1 & \alpha_2 & \alpha_2 & 2\alpha_1 & 7\alpha_2 & 21\alpha_2 & 35\alpha_2 & 35\alpha_2 & 21\alpha_2 & 7\alpha_2 \end{bmatrix} \tag{11a}$$

$$\mathbf{u}^* = \begin{bmatrix} u_{m1}^2 & u_{p1}^2 & u_{m1}^7 & u_{p1}^7 & u_{p1}u_{m1} & u_{p1}u_{m1}^6 & u_{p1}^2 u_{m1}^5 & u_{p1}^3 u_{m1}^4 & u_{p1}^4 u_{m1}^3 & u_{p1}^5 u_{m1}^2 & u_{p1}^6 u_{m1} \end{bmatrix}^T \tag{11b}$$

As the number of nonlinear terms and their corresponding orders increase, or when considering higher order accuracy (i.e. ε_2, ε_3, ...) this initial step becomes harder to be manipulated by usual hand calculations. Symbolically, the proposed algorithm can be efficiently completed to do this step and produce $\mathbf{n}^*$ and $\mathbf{u}^*$ matrices.

Using the proposed symbolic algorithm, we have been able to study several SDOF oscillators with two weak nonlinearities of variable orders. The key point in applying direct normal forms, especially for SDOF problems, is the number of terms involved in the matrices. Table 1 shows the number of terms for cases of conservative nonlinear oscillators of various orders of nonlinearities, i.e. for different configurations of μ and ν. Values in the highlighted cells represents the case when only one nonlinear term appears in the EOM.

Table (1): Number of terms involved in matrices for selected values of ν and μ

μ \ ν	3	5	7	9	11	13
2	7	9	11	13	15	17
3	**4**	10	12	14	16	18
4	9	11	13	15	17	19
5	10	**6**	14	16	18	20
6	11	13	15	17	19	21
7	12	14	**8**	18	20	22
8	13	15	17	19	21	23
9	14	16	18	**10**	22	24
10	15	17	19	21	23	25
11	16	18	20	22	**12**	26
12	17	19	21	23	25	27
13	18	20	22	24	25	**14**

The increasing number of terms appearing in Table 1 leads to additional difficulties for hand calculations to be performed. Importantly, more complex systems will lead to a higher number of terms; some examples of more complex cases include:

- the EOM involves viscous damping (in this case two additional terms are to be added to those in Table 1),
- the system contains more than two types of polynomial nonlinearities,
- solving the EOM for a higher order accuracy (i.e. ε_2)
- and when using the direct normal forms technique for MDOF systems,

all of the aforementioned cases can yield to a dramatic increase in the size of the matrices, thus, the mathematical complexity is also increased, these causes can justify turning to symbolic computation method.

In order to complete the analysis, by applying Eq. (6), $\boldsymbol{\beta}^*$ can be written as

$$\boldsymbol{\beta}^* = \begin{bmatrix} 3\omega_{r1}^2 & 48\omega_{r1}^2 & 3\omega_{r1}^2 & 48\omega_{r1}^2 & -\omega_{r1}^2 & 24\omega_{r1}^2 & 8\omega_{r1}^2 & 0 & 0 & 8\omega_{r1}^2 & 24\omega_{r1}^2 \end{bmatrix} \tag{12}$$

It should be emphasized that, according to direct normal forms analysis, any *zero* value in $\boldsymbol{\beta}^*$ matrix indicates the presence of a resonant term; while any *nonzero* value indicates a non-resonant or harmonic term.

The next step, illustrates the resulting coefficients of resonant terms $\mathbf{n}_{\mathbf{u}}^*$ and of harmonic terms $\mathbf{h}^*$ for both resonant and non-resonant cases (refer to [3] for detailed analysis). In symbolic programming, this step is based on conditional loop manipulation for each element in $\boldsymbol{\beta}^*$ with respect to $\mathbf{n}^*$. The results are

$$\mathbf{n}_{\mathbf{u}}^* = \alpha_2 \begin{bmatrix} 0 & 0 & 0 & 0 & 0 & 0 & 0 & 35 & 35 & 0 & 0 \end{bmatrix} \tag{13a}$$

$$\mathbf{h}^* = \frac{1}{\omega_{r1}^2} \begin{bmatrix} \frac{\alpha_1}{3} & \frac{\alpha_1}{48} & \frac{\alpha_2}{3} & \frac{\alpha_2}{48} & -2\alpha_1 & \frac{7\alpha_2}{24} & \frac{21\alpha_2}{8} & 0 & 0 & \frac{21\alpha_2}{8} & \frac{7\alpha_2}{24} \end{bmatrix} \tag{13b}$$

If the analysis is only truncated to ε_1 accuracy, which regularly leads to acceptable inspection of the nonlinear effects of small nonlinearities, the final step is rewriting the transformed equation of motion. For the non-resonant case, Eq. (9) in u-transformed coordinate system becomes

$$\ddot{\mathbf{u}} + \Lambda \mathbf{u} + \mathbf{n}_{\mathbf{u}}^* \mathbf{u}^* = 0,$$

$$\ddot{\mathbf{u}} + \omega_n^2 \mathbf{u} + 35\left(u_{p1}^3 u_{m1}^4 + u_{p1}^4 u_{m1}^3\right) = 0, \tag{14}$$

and the near identity transform is written as

$$\mathbf{q} = \mathbf{u} + \mathbf{h}^{*}\mathbf{u}^{*},$$

$$\mathbf{q} = \mathbf{u} + \frac{1}{3\omega_{r1}^{2}}\left(\begin{array}{l}\alpha_1 u_{m1}^{2} + \dfrac{\alpha_1 u_{p1}^{2}}{16} + \alpha_2 u_{m1}^{7} + \dfrac{\alpha_2 u_{p1}^{7}}{16} - 6\alpha_1 u_{p1}u_{m1} + \dfrac{7\alpha_2 u_{p1}u_{m1}^{6}}{8} + \\ \dfrac{63\alpha_2 u_{p1}^{2}u_{m1}^{5}}{8} + \dfrac{63\alpha_2 u_{p1}^{5}u_{m1}^{2}}{8} + \dfrac{7\alpha_2 u_{p1}^{6}u_{m1}}{8}\end{array}\right) \tag{15}$$

Substituting in the assumed solution Eq. (4), and solving the positive (or negative) complex exponential terms by exact balancing, one can get the equation of the backbone curve for this system, which is

$$\omega_{r1}^{2} = \omega_n^{2} + \frac{35}{64}\alpha_2 U^{6} \tag{16}$$

Following the same aforementioned procedure, one should be able of finding the backbone curve for any values of ν and μ in Eq. (7). One advantage of having a computer pattern in such case is the ability of doing several runs with different conditions. Table 2 shows the backbone curve obtained for the first four values of ν when $\mu = 2$ for the ε_1 expansion. It is clear that a general pattern is repeated for the backbone equation found, so if $\mu = 2$ it could be generalized for any value of ν that

$$\omega_{r1}^{2} = \omega_n^{2} + \eta_i \alpha_2 U^{\nu-1}, \quad \nu = 3, 5, 7, \ldots \tag{17}$$

Where η_i is a constant.

Table (2): Backbone curve equations of ε_1 accuracy for different values of ν while $\mu = 2$

Value of ν	Equation of motion	Backbone curve equation
3	$\ddot{x}(t) + \omega_n^{2}x(t) + \alpha_1 x^{2}(t) + \alpha_2 x^{3}(t) = 0$	$\omega_{r1}^{2} = \omega_n^{2} + \frac{3}{4}\alpha_2 U^{2}$
5	$\ddot{x}(t) + \omega_n^{2}x(t) + \alpha_1 x^{2}(t) + \alpha_2 x^{5}(t) = 0$	$\omega_{r1}^{2} = \omega_n^{2} + \frac{5}{8}\alpha_2 U^{4}$
7	$\ddot{x}(t) + \omega_n^{2}x(t) + \alpha_1 x^{2}(t) + \alpha_2 x^{7}(t) = 0$	$\omega_{r1}^{2} = \omega_n^{2} + \frac{35}{64}\alpha_2 U^{6}$
9	$\ddot{x}(t) + \omega_n^{2}x(t) + \alpha_1 x^{2}(t) + \alpha_2 x^{9}(t) = 0$	$\omega_{r1}^{2} = \omega_n^{2} + \frac{63}{128}\alpha_2 U^{8}$

Practically, for weak nonlinear case, the values of α_1 and α_2 should be small, typically less than unity, Fig. (1) shows the backbone curves for the conservative oscillators appearing in Table 2, using the following numerical values; $\alpha_1 = 0.2$, $\alpha_2 = 0.1$ and $\omega_n = \pi$ rad/s.

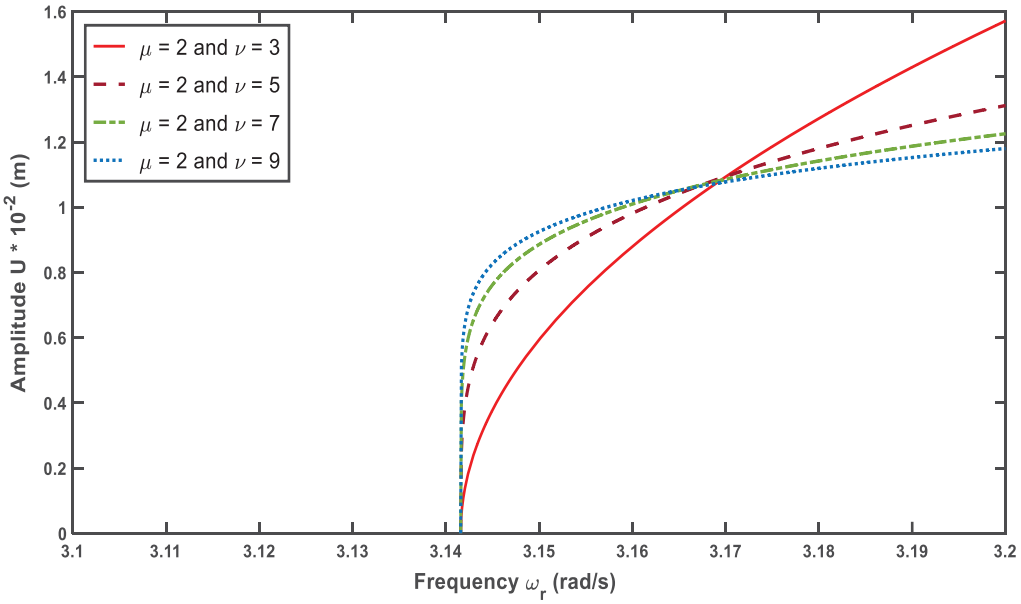

Fig. (1): Conservative backbone curves for different values of ν while $\mu = 2$

Furthermore, we could obtain the backbone curve relation truncated to ε_1 accuracy for any values of ν and μ in Eq. (7). Table 3 shows some examples of these results.

Table (3): Backbone curve equations of ε_1 accuracy for different values of ν and μ

Value of ν	Value of μ	Equation of motion	Backbone curve equation
3	5	$\ddot{x}(t) + \omega_n^2 x(t) + \alpha_1 x^3(t) + \alpha_2 x^5(t) = 0$	$\omega_{r1}^2 = \omega_n^2 + \frac{3}{4}\alpha_1 U^2 + \frac{5}{8}\alpha_2 U^4$
4	7	$\ddot{x}(t) + \omega_n^2 x(t) + \alpha_1 x^4(t) + \alpha_2 x^7(t) = 0$	$\omega_{r1}^2 = \omega_n^2 + \frac{35}{64}\alpha_2 U^6$
5	9	$\ddot{x}(t) + \omega_n^2 x(t) + \alpha_1 x^5(t) + \alpha_2 x^9(t) = 0$	$\omega_{r1}^2 = \omega_n^2 + \frac{5}{8}\alpha_1 U^4 + \frac{63}{128}\alpha_2 U^8$
6	9	$\ddot{x}(t) + \omega_n^2 x(t) + \alpha_1 x^6(t) + \alpha_2 x^9(t) = 0$	$\omega_{r1}^2 = \omega_n^2 + \frac{63}{128}\alpha_2 U^8$
7	11	$\ddot{x}(t) + \omega_n^2 x(t) + \alpha_1 x^7(t) + \alpha_2 x^{11}(t) = 0$	$\omega_{r1}^2 = \omega_n^2 + \frac{35}{64}\alpha_2 U^6 + \frac{231}{512}\alpha_2 U^{10}$

The following findings are noted:

- Any even nonlinearity found in the EOM is removed by the normal form transformation and does not appear in the backbone curve. This phenomenon is found in literature in terms of quadratic nonlinearity, here we generalise this finding for any even nonlinearity.

- Referring to Table 3 and comparing with Table 2, it is clear that the frequency detuning accompanied with direct normal forms resulted in, at least for ε_1 accuracy, a behavior similar to superposition regarding the final backbone curve expression.

- Some of these results are numerically verified using COCO numerical continuation toolbox in Matlab (see Fig. (3)), and acceptable agreement between analytical backbone curves and numerical backbone manifolds is seen.

In conclusion, in order to generalise the ε_1 backbone curve relation for any SDOF nonlinear oscillator with two types of nonlinearities, Eq. (7), in view of Table 1 and Table 2, provided that ν and μ are odd, the following relation can be obtained

$$\omega_{r1}^2 = \omega_n^2 + \eta_1 \alpha_1 U^{\nu-1} + \eta_2 \alpha_2 U^{\mu-1} \tag{18}$$

Where η_1 and η_2 are constants directly related to the order of the nonlinearity, Table 4 shows the values of this constant for several orders of the nonlinear terms. Finally, as mentioned earlier, any even nonlinearity in the EOM will be removed by the normal form and will not appear in Eq. (18).

Table (4): Values of the constant η_i appearing in the backbone curve relation, Eq. (18)

Order of nonlinearity	3	5	7	9	11	13	15	17
η_i	$\frac{3}{4}$	$\frac{5}{8}$	$\frac{35}{64}$	$\frac{63}{128}$	$\frac{231}{512}$	$\frac{429}{1024}$	$\frac{6435}{16384}$	$\frac{12155}{32768}$

Using Eq. (18) and Table 4 it is possible to get the conservative backbone curve relation for any nonlinear oscillator with two different types of polynomial nonlinearities. As an example, if the EOM contains both cubic and quintic nonlinearities, i.e.

$$\ddot{x}(t) + \omega_n^2 x(t) + \alpha_1 x^3(t) + \alpha_2 x^5(t) = 0,$$

then, the conservative backbone curve of ε_1 accuracy will be

$$\omega_{r1}^2 = \omega_n^2 + \frac{3}{4}\alpha_1 U^2 + \frac{5}{8}\alpha_2 U^4$$

2.3 Non-resonant Duffing oscillator with cubic nonlinearity

As an example of a more complex system, we now consider the system of a Duffing oscillator with cubic nonlinearity, viscous damping and forcing away from resonance where the ratio between the driving frequency and the natural frequency is 1/3 (i.e. $a = 1/3$),

$$\ddot{x}(t) + 2\zeta\omega_n \dot{x}(t) + \omega_n^2 x(t) + \alpha\, x^3(t) = R\cos(\Omega t) \tag{19}$$

Using the proposed direct normal forms technique applied symbolically, it is required to generate analytical conservative backbone curve equations for ε_1 accuracy, and compare with forced (and lightly damped) response curves. The step by step procedure involves large matrices and algebraic terms, hence, only the key results are to be shown, while further results for matrix algebra manipulations can be found in Appendix 1. After applying direct normal forms analysis we get

$$\frac{1}{4}\left[3\alpha U_1^3 + \left(24\alpha e^2 + 4\left(\omega_n^2 - \omega_{r1}^2\right)\right)\right]\cos\left(\omega_{r1}t - \phi_1\right) + 2\alpha e^3\cos\left(\omega_{r1}t\right) - 2\zeta\omega_n\omega_{r1}U_1\sin\left(\omega_{r1}t - \phi_1\right) = 0 \tag{20}$$

Where $e = \dfrac{R}{2(\omega_n^2 - \Omega^2)}$.

Applying the suitable trigonometric identities, and then balancing the sines and cosines terms in Eq. (20) we get

$$\zeta\omega_n\omega_{r1}U = -\alpha e^3\sin\left(\phi_1\right) \tag{21a}$$

$$3\alpha e^2 + \frac{3}{8}\alpha U_1^3 + \frac{1}{2}\left(\omega_n^2 - \omega_{r1}^2\right) = -\alpha e^3\cos\left(\phi_1\right) \tag{21b}$$

Hence, it is possible to use Eq. (21) to get an expression for U as a function of ω_{r1}, therefore, computing the forced response curve analytically, this has been previously done in [3] by applying traditional hand calculations. In order to compare with our proposed symbolic computation method, the same problem has been solved in conservative case (unforced-undamped case), and the conservative backbone curve is computed using Eq. (18) and Table (4) and plotted in Fig. (2), along with the analytically computed forced-damped response curves for several values of R using Eq. (21). The numerical values chosen for this figure are $\omega_n = 2$ rad/s, $\zeta = 0.01$ and $\alpha = 0.2$.

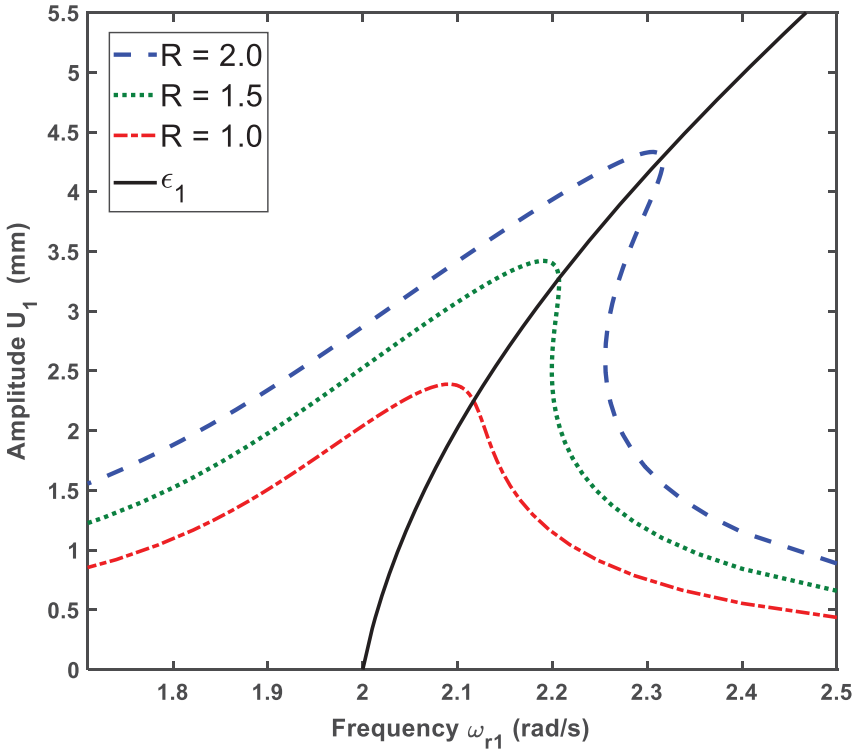

Fig. (2): Backbone curve of damped forced Duffing oscillator with cubic nonlinearity

Figure (2) represents a typical backbone curve and response curves for any forced damped nonlinear system. From this figure, several important observations can be noticed; first of all, as the value of α is positive, hardening behavior is clearly seen, in contrary, if α is negative softening behavior will be noticed. Furthermore, as the figure shows the relation between natural frequency and amplitude, the backbone curves do not perfectly coincide with the manifolds, and this is due to the presence of damping. Finally, as the forcing amplitude *R* becomes higher, more matching between the backbone curves and their manifolds occurs.

Finally, in order to compare the frequency response of several nonlinear terms in combination, recall Eq. (5) in its forced damped case, that is

$$\ddot{x}(t) + 2\zeta\omega_n\dot{x}(t) + \omega_n^2 x(t) + \alpha_1 x^{\nu}(t) + \alpha_2 x^{\mu}(t) = R\cos(\Omega t) \tag{22}$$

Various values of ν and μ can be considered, the corresponding EOM can be studied using direct normal forms and analytical backbone curve relations are then obtained. Three cases are studied, linear oscillator and cubic-quintic oscillator in both hardening and softening cases (3-5 Hardening, 3-5 Softening). Figure 3 represents backbone equation for all previous cases along with their forcing manifolds obtained numerically using COCO. Figure 3 is generated using the numerical data: general parameters for all cases $\omega_n = 2$ Hz, $\zeta = 0.05$ and $R = 1$. In the case of hardening cubic-quintic oscillator $\alpha_1 = 0.2$ and $\alpha_2 = 0.3$. Finally, for softening cubic-quintic oscillator $\alpha_1 = -0.2$ and $\alpha_2 = -0.3$.

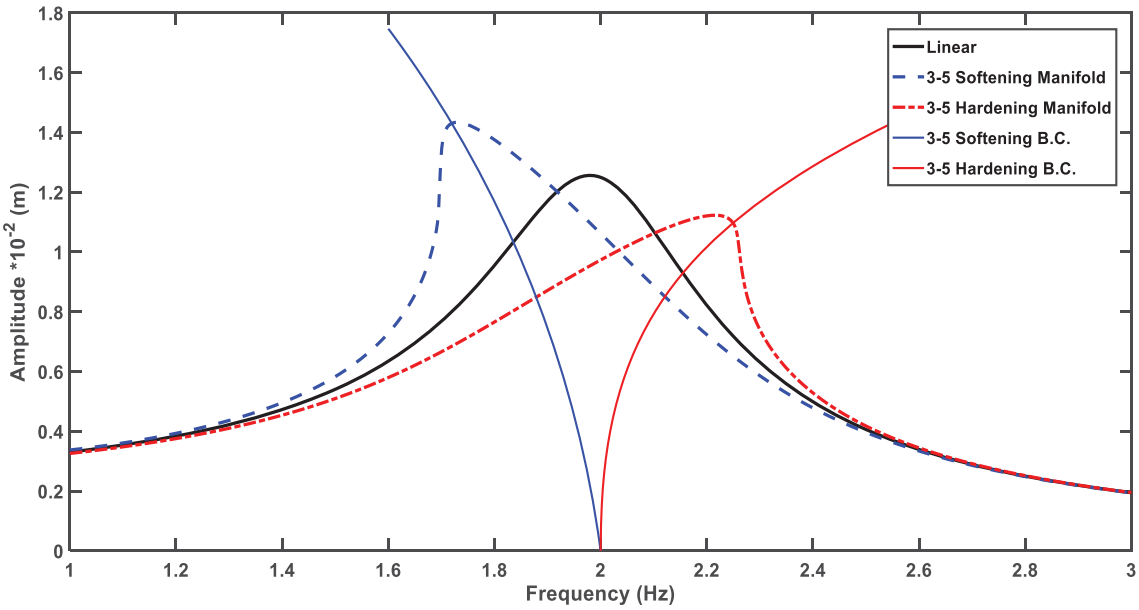

Fig. (3): Frequency response of various types of nonlinearities

Figure 3 illustrates the effect of both hardening and softening nonlinear terms on the frequency response of the system; firstly, compared to the linear case, hardening polynomial nonlinearities the shift the peak to the right whilst minimizing the maximum vibration amplitude of the system. On the other hand, softening nonlinear terms cause shifting to the left and maximizing the vibration amplitude. However, using Eq. (18) along with Table 4 it is possible to obtain the conservative backbone curves for SDOF oscillator with two nonlinear terms, and compare with the forced-damped frequency response computed numerically using COCO toolbox in Matlab.

3 CONCLUSION

In this work, the direct normal forms method is used to study the dynamical behavior of SDOF oscillators with higher orders of polynomial nonlinearities. Symbolic computations using Maple were implemented for the analytical solutions, where backbone curves expressions of ε_1 order were obtained and the results were verified using COCO numerical continuation toolbox in Matlab. A general formula for any SDOF nonlinear oscillator with two polynomial nonlinearities are obtained by computing high number of terms in the solution (refer to Table 1).

The overall truncated analytical results show good agreement with the numerical results, accordingly, extending the direct normal forms using symbolic computations can yield to some desired findings regarding the dynamics of the system. Although the proposed technique overcomes the mathematical complexities and enables fast analysis of SDOF nonlinear oscillators, its limited to weakly nonlinear systems were the nonlinear terms are modelled by polynomial terms in the EOM, so that the direct normal forms technique is applicable.

Overall, the work shows good insight regarding the implementation of symbolic computations when studying SDOF nonlinear oscillators, were we have been able to analytically compute the conservative backbone curves for any SDOF oscillator with two nonlinear terms.

ACKNOWLEDGEMENTS

Ayman M. Nasir has a scholarship funded by Alzaytoonah University of Jordan in order to obtain his PhD degree.

REFERENCES

[1] Jack K Hale. Oscillations in nonlinear systems. *McGraw-Hill*, 1963.

[2] Minoru Urabe. Nonlinear autonomous oscillations: Analytical theory, volume 34. *Academic Press*, 1967.

[3] Wagg D, Neild S. A., Nonlinear vibration with control: for flexible and adaptive structures. *Solid Mechanics and its Applications*, 2nd edition, vol. 218. Berlin, Germany: Springer, 2014.

[4] Nayfeh A., Mook D. Nonlinear oscillations. *New York, NY: Wiley*, 1995.

[5] Everett Minnich Baily. Steady-state harmonic analysis of nonlinear networks. PhD thesis, Department of Electrical Engineering, *Stanford University*, 1968.

[6] JOHN C Lindenlaub, An approach for finding the sinusoidal steady state response of nonlinear systems. In Proc. 7th Ann. Allerton Conf. Circuit and System Theory. Univ. Illinois, 1969.

[7] S. Wang and K. Huseyin. 'Maple' Analysis of nonlinear oscillations, *Mathematical and Computer Modelling*, Vol. 16, No. 11, pp. 49-57, 1992.

[8] Z.F. Xin, S.A. Neild, D.J. Wagg, and Z.X. Zuo. Resonant response functions for nonlinear oscillators with polynomial type nonlinearities. *Journal of Sound and Vibration*, 332 (7): 1777–1788, 2013.

[9] T. L. Hill, A. Cammarano, SA Neild, and DJ Wagg. An analytical method for the optimisation of weakly nonlinear systems. *Proceedings of EURODYN 2014*, pages 1981–1988, 2014.

[10] A. H. Nayfeh, Perturbation Methods, *Wiley, New York*, 1973.

[11] F. Schilder and H. Dankowicz. Recipes for Continuation, *SIAM Computational Science and Engineering*, 2013.

[12] F. Schilder and H. Dankowicz. Continuation core and toolboxes (coco). Available at https://sourceforge.net/projects/cocotools/, 2017.

[13] J. Thomsen, Vibrations and Stability: Order and Chaos, *McGraw Hill*, 1997.

[14] D. Richards, Advanced mathematical methods with Maple, *Cambridge University Press*, 2009.

[15] R. Enns and G. McGuire, Nonlinear physics with Maple for scientists and engineers, *Springer*, 2000.

[16] S. Bellizzi and R. Bouc. A new formulation for the existence and calculation for nonlinear normal modes. *Journal of Sound and Vibration*, 287(3): 545-569, (2005).

[17] X. Lui, Symbolic Tools for the Analysis of nonlinear dynamical systems, PhD thesis, Department of Applied Mathematics, *University of Western Ontario*, London, 1999.

[18] Liu, X., & Wagg, D. J. ε_2- order normal form analysis for a two-degree-of-freedom nonlinear coupled oscillator. *Submitted to appear in Proceedings of the First International Nonlinear Dynamics Conference (2019).*

[19] P. B. Kahn and Y. Zarmi, Nonlinear dynamics: Exploration through normal forms, *Dover Publications*, New York, USA, 2014

[20] T. Breunung and G. Haller, Explicit backbone curves from spectral submanifolds of forced-damped nonlinear mechanical systems. Proc. R. Soc. A 474, 20180083, 2018.

[21] Kenneth Meyer, Glen Hall, and Dan Offin, Introduction to Hamiltonian dynamical systems and the n-body problem: A Mechanised Logic of Computation, volume 90. *Springer Science & Business Media*, 2008.

[22] Vladimir Igorevich Arnold, Geometrical methods in the theory of ordinary differential equations, volume 250. *Springer Science & Business Media*, 2012.

[23] A. D. Shaw, S. A. Neild, and D. J. Wagg. Dynamic analysis of high static low dynamic stiffness vibration isolation mounts. *Journal of Sound and Vibration*, 332:1437–1455, 2012.

[24] Jezequel, L. and Lamarque, C. H. Analysis of nonlinear dynamic systems by the normal form theory. *Journal of Sound and Vibration*, 149(3), 429–459, 1991.

[25] A. H. Nayfeh, Method of normal forms, *Wiley*, New York, 1993.

APPENDIX 1

Matrix manipulation of forced damped Duffing oscillator of cubic order nonlinearity, with forcing away from resonance.

$$\mathbf{u}^* = \begin{bmatrix} r_m^3 \\ r_p^3 \\ u_{m1}^3 \\ u_p^3 \\ r_p r_m^2 \\ r_m r_p^2 \\ u_m r_m^2 \\ u_m r_p^2 \\ r_m u_m^2 \\ r_p u_m^2 \\ u_p r_m^2 \\ u_p r_p^2 \\ u_p u_m^2 \\ r_m u_p^2 \\ r_p u_p^2 \\ u_m u_p^2 \\ u_m r_m r_p \\ u_p r_m r_p \\ u_p u_m r_m \\ u_p u_m r_p \\ r_m \\ r_p \\ u_m \\ u_p^2 \end{bmatrix} \rightarrow \left(\boldsymbol{\beta}^*\right)^T = \omega_{r1}^2 \begin{bmatrix} 0 \\ a^2-1 \\ 0 \\ a^2-1 \\ 0 \\ a^2-1 \\ a^2-1 \\ 0 \\ 8 \\ 8 \\ 0 \\ 0 \\ 9a^2-1 \\ 9a^2-1 \\ a^2-4a+3 \\ a^2-4a+3 \\ 4a(a-1) \\ 4a(a+1) \\ a^2-1 \\ 4a(a-1) \\ a^2+4a+3 \\ 4a(a+1) \\ a^2+4a+3 \\ a^2-1 \end{bmatrix} \xrightarrow{\text{Substitute } a=1/3} \left(\boldsymbol{\beta}^*\right)^T = \omega_{r1}^2 \begin{bmatrix} 0 \\ -\frac{8}{9} \\ 0 \\ -\frac{8}{9} \\ 0 \\ -\frac{8}{9} \\ -\frac{8}{9} \\ 0 \\ 8 \\ 8 \\ 0 \\ 0 \\ 0 \\ 0 \\ \frac{16}{9} \\ \frac{16}{9} \\ -\frac{8}{9} \\ \frac{16}{9} \\ -\frac{8}{9} \\ -\frac{8}{9} \\ \frac{40}{9} \\ \frac{16}{9} \\ \frac{40}{9} \\ -\frac{8}{9} \end{bmatrix} \rightarrow \mathbf{h}^* = \frac{1}{\omega_{r1}^2} \begin{bmatrix} 0 \\ \frac{9}{12} ie\zeta\omega_n \\ 0 \\ -\frac{9}{12} ie\zeta\omega_n \\ 0 \\ -\frac{27}{4}\alpha e \\ -\frac{27}{4}\alpha e \\ 0 \\ \frac{\alpha}{8} \\ \frac{\alpha}{8} \\ 0 \\ 0 \\ 0 \\ 0 \\ \frac{27}{16}\alpha e \\ \frac{27}{16}\alpha e \\ -\frac{27}{8}\alpha e^2 \\ \frac{27}{16}\alpha e^2 \\ -\frac{27}{8}\alpha e^3 \\ -\frac{27}{8}\alpha e^2 \\ \frac{27}{40}\alpha e \\ \frac{27}{16}\alpha e^2 \\ \frac{27}{40}\alpha e \\ -\frac{27}{8}\alpha e^3 \end{bmatrix}$$

EURODYN 2020
XI International Conference on Structural Dynamics
M. Papadrakakis, M. Fragiadakis, C. Papadimitriou (eds.)
Athens, Greece, 23–26 November 2020

TOWARD A SYSTEMATIC CONSTRUCTION OF THE BASIS FOR NONLINEAR GEOMETRIC REDUCED ORDER MODELS

X.Q. Wang[1], **and Marc P. Mignolet**[2]

[1] SEMTE, Faculties of Mechanical and Aerospace Engineering
Arizona State University, Tempe, AZ 85287-6106, USA
e-mail: xwang138@asu.edu

[2] SEMTE, Faculties of Mechanical and Aerospace Engineering
Arizona State University, Tempe, AZ 85287-6106, USA
e-mail: marc03@asu.edu

Keywords: Non-intrusive reduced order modeling, Nonlinear geometric vibration, Basis construction

Abstract. *Reduced order modeling for nonlinear geometric vibrations of thin-walled structures has been an active research subject in the last two decades due, in particular, to its advantage in significantly reducing the computational cost of determining the dynamic response. Two key issues of this modeling are the construction of the basis and the identification of nonlinear stiffness coefficients. The present study focuses on the basis construction and a systematic strategy is proposed to achieve it using data derived from the linear modes of the structure with some general information about the dynamic loading, e.g., cut-off frequency. Thus, the basis is applicable to a broad range of such dynamic loadings. A clamped-clamped straight beam is used to demonstrate the construction of bases according to the proposed strategy. A force distribution mapped from measured aerodynamic pressure distribution is used as loading for which both static and dynamic nonlinear responses are obtained at various levels, from weakly to very strong nonlinear, and from both finite element and reduced order models. This data is used to assess the constructed bases and validate the predictions of the ensuing reduced order models. It is shown that the constructed bases provide a very good representation of the finite element nonlinear structural responses and that the corresponding reduced order model lead to accurate predictions of these responses. The importance of adding out-of-band linear modes in the basis is also demonstrated.*

1 INTRODUCTION

In the last two decades, reduced order modeling methods have been developed for the prediction of the nonlinear geometric vibrations of thin-walled structures [1-14]. As seen below, these methods require a notable number of nonlinear static solutions to be performed as part of the reduced order model (ROM) construction. Thus, they are not computationally efficient for determining the static response of the structure to a few different loads. Rather, the ROMs become valuable when there is a large number of nonlinear solutions needed, either when there are many different static loadings or more likely when determining long duration dynamic computations, e.g., for fatigue life prediction. The ROMs are also very desirable in multi-physics problems, see [15-17] for examples, both because many iterations may be needed between different physics solvers but also because of the ease of implementing the ROM governing equations in a non-structural solver. Reduced order models are also very valuable in uncertainty analyses, see [18-20] for example not only because of their computational efficiency but also because they provide a framework to globally introduce uncertainty which is challenging to do at the finite element level.

Of interest here are non-intrusive nonlinear reduced order models (ROMs), i.e., those built from data extracted from commercial finite element software, e.g., Nastran, Abaqus, etc., see [21] for a recent review. One advantage of non-intrusive reduced order models is the capability to handle complex geometry and boundary conditions of structures in engineering practice. Such reduced order models have been built for a large number of structures and their potential has been demonstrated, e.g., see [13, 22-25].

In the present nonlinear reduced order models, the nonlinear structural displacemens of the finite element model $\underline{u}(t)$ are represented as

$$\underline{u}(t) = \sum_{n=1}^{N} q_n(t)\,\underline{\phi}^{(n)} \,. \tag{1}$$

where $q_n(t)$ are the time-dependent generalized coordinates and $\underline{\phi}^{(n)}$ are the basis functions. Assuming the material is linearly elastic following a Kirchhoff – Saint Venant constitutive equation, the governing equation of the nonlinear reduced order model can be obtained using the Galerkin approach, see [7] for details, as (summation over repeated indices implied)

$$M_{ij}\ddot{q}_j(t) + D_{ij}\dot{q}_j(t) + K_{ij}^{(1)} q_j(t) + K_{ijl}^{(2)} q_j(t) q_l(t) + K_{ijlp}^{(3)} q_j(t) q_l(t) q_p(t) = F_i(t), \qquad i = 1, 2, \ldots, N, \tag{2}$$

where M_{ij} denotes the elements of the mass matrix, $K_{ij}^{(1)}$, $K_{ijl}^{(2)}$, and $K_{ijlp}^{(3)}$ are the linear, quadratic, and cubic stiffness coefficients, and $F_i = \underline{\phi}^{(i)T}\,\underline{F}$ is the modal force associated with mode i. The damping matrix D_{ij} is added to collectively represent various energy dissipation mechanisms. One commonly used damping model, as adopted in the present paper, is the Rayleigh damping model, defined as

$$D_{ij} = \alpha M_{ij} + \beta K_{ij}^{(1)} \,, \tag{3}$$

where α and β are the Rayleigh damping coefficients.

In non-intrusive reduced order models, the ROM matrices in Eq. (2) are identified using data from commercial finite element software. The computation of the linear matrices, i.e., the mass and the stiffness, is straightforward once their finite element counterparts are extracted from the finite element software. Specifically, the matrices M and $K^{(1)}$ are obtained as the projection on the basis $\Phi = \left\{ \underline{\phi}^{(1)}, \underline{\phi}^{(2)}, \ldots, \underline{\phi}^{(N)} \right\}$ of the finite element mass ($M^{(FE)}$) and linear stiffness ($K^{(FE)}$), i.e.,

$$M = \Phi^T M^{(FE)} \Phi \quad \text{and} \quad K^{(1)} = \Phi^T K^{(FE)} \Phi \,. \tag{4}$$

The damping matrix can then be computed using the Rayleigh damping model.

The evaluation of the nonlinear stiffness coefficients has to proceed differently since the global nonlinear stiffness operator is typically not computed/not available in a commercial finite element code. In one proposed approach, the displacement-force method [6,7], a set of designed static displacements are imposed to the structure and the corresponding nonlinear forces are obtained from the finite element code. They are then used to compute the corresponding modal forces F_i. Finally, imposing the same modal displacements and modal forces to the ROM governing equation, Eq. (2), leads to the conditions

$$K_{ij}^{(1)} q_j + K_{ijl}^{(2)} q_j q_l + K_{ijlp}^{(3)} q_j q_l q_p = F_i \tag{5}$$

which can be used to determine the stiffness coefficients $K_{ijl}^{(2)}$ and $K_{ijlp}^{(3)}$. By an appropriate selection of imposed displacements, the coefficients to be identified can be divided into a number of smaller (including up to three modes) groups and identified separately, see [6,7] for details.

When the basis of a ROM is large, this displacement-force method requires a large number of static solutions, i.e., $O(N^3/6)$. To resolve this issue, a method using the tangent stiffness matrix, denoted as $K^{(T)}$, instead of the force in the identification has been developed [13]. This displacement-$K^{(T)}$ method relies on the availability of the tangent stiffness matrix for each imposed displacement. Once this matrix has been obtained, it is projected on the basis, as in Eq. (4), and then matched to its ROM counterpart of *iu* element given by

$$K_{iu}^{(T)} = \frac{\partial F_i}{\partial q_u} = K_{iu}^{(1)} + \left[K_{iju}^{(2)} + K_{iuj}^{(2)} \right] q_j + \left[K_{ijlu}^{(3)} + K_{ijul}^{(3)} + K_{iujl}^{(3)} \right] q_j q_l \,. \tag{6}$$

The advantage of this approach is that an $N \times N$ matrix (the tangent stiffness matrix) is obtained for each solution, thereby leading to a reduction of the computational effort to $O(N^2/2)$.

In principle, the nonlinear stiffness coefficients should be independent of the imposed displacements used to identify them. However, due to difference the nonlinear formulation between the ROM and most commercial finite element software, it is observed that the identified stiffness coefficients exhibit variations with respect to the amplitude of the displacements used. To counteract this dependence, a multi-level identification method has been developed to find the optimal displacement level for each nonlinear stiffness coefficient [26].

The above discussion has focused on the identification of the nonlinear stiffness coefficients but another key issue is the selection of the basis. The basis determines how well the ROM represents nonlinear responses of the structure, while the nonlinear stiffness coefficients dictate

the nonlinear geometric effects due to the large deformation of the structure. Together they determine the accuracy of the ROM predictions.

A significant feature of the nonlinear geometric response of thin-walled structures is the in plane displacements due to the large transverse deformations associated with the "membrane stretching" effect. These in plane displacements, which are typically higher frequency/higher strain than their transverse counterparts, play an important role in the nonlinear stiffening and thus must be properly accounted for by the nonlinear ROM. In this discussion, the transverse direction is formally defined as the direction normal to the thin-wall surface, and the two in plane directions in general are defined as two orthogonal directions on the surface perpendicular to the transverse direction. Thus, the transverse and in plane directions would then change with location on the structure when curvature is present. To avoid this situation, the transverse and in plane directions will here be defined for panels with shallow curvature as those associated with the fixed, flat, mean surface.

In previous non-intrusive nonlinear ROM investigations, two types of approaches have been used to construct the ROM basis, see [21] for discussion. One approach, termed the implicit condensation and expansion method [5], uses a basis composed of linear modes that captures well the transverse component of the displacements. The in plane displacements are not directly modeled, they are assumed statically condensed on the linear modes and thus their effects are accounted for through changes of the nonlinear stiffness coefficients. If desired, e.g., to estimate the stresses, the in plane displacements can be recovered in the expansion component of the method.

The second strategy to construct the ROM basis seeks to represent all components, transverse and in plane, of the displacement field. Such a basis is formed by enriching the linear modes that would be used in the absence of nonlinear effects with a set of additional basis functions, such as dual modes [7], higher order linear modes (see [21]), other modal derivatives [27]. The dual modes, used in the sequel, are extracted from a set of nonlinear static solutions corresponding to loadings that would induce in the linear case displacements that are along one or two of the selected linear modes. The corresponding forces on the finite element mesh are thus of the form

$$\underline{F}_{ij,s}^{(FE)} = K^{(FE)}\left[\pm\alpha_{ij,s}(\underline{\phi}_i + \underline{\phi}_j)\ /\ 2\right], \tag{7}$$

where i and j are the indices of the two modes (the case $i = j$ emulates the single mode case). In this equation, $\alpha_{ij,s}$ are a set of scaling factors selected so that the corresponding structural response spans a given range of levels. Once these responses have all been determined, the transverse components of this data are first removed by making the displacements orthogonal to the linear modes selected. Next, a proper orthogonal decomposition (POD) analysis is carried out and POD eigenvectors with desired features (see section 2) are retained as dual modes.

While the final measure of the appropriateness of a basis is the accuracy in the matching of predictions from the ROM and from the underlying finite element model, this measure is also affected by the estimation of the nonlinear stiffness coefficients, which may be inaccurate, see [28]. An intermediate validation of the basis can be performed by quantifying how well the basis represents the displacement field obtained from the finite element model. This task can be achieved through the representation error defined as

$$\varepsilon_{re} = \frac{\left\|\underline{u}_{basis} - \underline{u}_{FE}\right\|}{\left\|\underline{u}_{FE}\right\|} \times 100\%, \tag{8}$$

where $\underline{u}_{FE}$ is a nonlinear structural displacement predicted by the finite element software, and $\underline{u}_{basis}$ is its best approximation given the basis in the least squares sense, i.e.,

$$\underline{u}_{basis} = \Phi \cdot \underline{q}_{proj}, \tag{9}$$

where $\underline{q}_{proj}$ is the vector of projection coefficients of the finite element displacement on the basis. It should be noted that the representation error can be evaluated for the entire displacement field or any subset thereof. In fact, it will be convenient in the sequel to determine separately representation errors of the transverse and in plane displacement. For such computations, the projection is still performed overall displacements but the computation of ε_{re} is limited to the displacements chosen.

2 SYSTEMATIC PROCEDURE FOR DUAL MODES BASIS CONSTRUCTION

Since its introduction[3], the dual modes methodology has been used to form the ROM basis for 35 different structural models, see [3,4,7,11-13,15-17, 21-26] and references therein, ranging from simple structures to rather complex ones (e.g., the 9-bay panel of [13]. Over the years the methodology has slightly evolved and has been refined. This section presents an up-to-date, detailed nonlinear ROM basis construction procedure, starting with the selection of the linear modes and the determination of the associated duals.

As stated in the introduction, nonlinear ROMs are most valuable for dynamic analyses, multi-physics problems, and/or uncertainty quantification and propagation efforts owing to their overhead in nonlinear static solutions. The latter two situations may require specific considerations on the basis construction and thus are not covered here where the focus is on the dynamic response to a persistent loading in the frequency band [0, f_{cutoff}] where f_{cutoff} is a frequency low enough that (i) the natural frequencies of the linear system are reasonably well separated (this requirement is also applicable for linear ROMs) and (ii) the modes excited are primarily transverse.

As is well known and will be further shown in Section 3, the nonlinear response of structures evolves, and not just by a scaling, as the loading level increases. It is thus desirable to set a limit on what level of displacements the basis will be expected to represent well. If there is no problem specific limit, it is suggested here that the maximum displacement be set from first failure of the structure. Higher levels could be set if the desired application of the ROM is to crack initiation and propagation till ultimate collapse. First failure for clamped thin walled structures that we have considered occurs often when the peak displacement is of the order of a few (say 3-5) thickness.

With the above conditions, the construction of the ROM basis proceeds as follows.

(A) Selection of the Linear Modes

The selection of the relevant linear modes is the first step of the basis construction. At the very least, this set should include the linear modes that would be used in the linear case, i.e., those in the band [0, f_{cutoff}]. This set may not be sufficient however. Energy transfer between in-band and out-of-band modes is well known to exist and can occur in particular "statically" through modal interactions rooted in the nonlinear stiffness coefficients as well as "dynamically", e.g., internal resonances, see section 3 and [29] for ROM-based examples. The former interaction is detectable in particular in the construction of the duals, see step C below, but the latter is more difficult to predict a priori. A safer approach for the latter would then be to include modes in a broader band [0, $p\ f_{cutoff}$] where p is a factor larger than 1. Given the cubic nature of the nonlinearity, the value $p = 3$ is used in section 3. In this regard, note that "strong nonlinear

events", e.g., local buckling, global buckling, snap-through, may necessitate a finer mode selection to be well captured.

(B) Generation of Data for Dual Modes Determination

As discussed in section 2, the dual modes are extracted from static finite element solutions in which the loading is of the form of Eq. (7). In principle, all (non repeating) combinations of *i* and *j* should be considered, including *i* = *j*. Proceeding in this manner will lead to $O(N_t^2/2)$ combinations and sets of static solutions where N_t denotes the number of linear modes selected in step A above. For complex structures/large models, this number of combinations may be excessively large, especially assuming that some dual modes will be taken for each combination.

In seeking a reduction of this effort, it is noted that not all combinations are as important. From the derivation in [7], it is concluded that the combinations that involve the largest responding modes are those producing the most important dual modes. Assuming that such information is available or can be estimated, one could split the linear modes into three groups: group 1 of which all combinations are taken (i.e., "dominant modes"), group 2 which are considered in combination each with a group 1 mode, and group 3 which are not included in any combination.

In the past, the split between these 3 groups has been made based on the linear response and this has worked well except for the beam of [23] and the 9-bay panel of [13] in which a linear mode with very little linear response has a much larger one in the nonlinear case. Such cases could be detected from the set of nonlinear stiffness coefficients of the linear modes only which can already be identified. Such a detection is currently investigated. Another strategy is to check as the dynamic response is computed that the split of modes is indeed correct and to modify the basis if it is found that the assumed split is not appropriate.

In the above spirit, the example of section 3 will consider all modes in-band to belong to group 1 and those out-of-band to belong to group 3 based on the expectation that the in-band modes will contribute notably more than the out-of-band ones. Should an internal resonance involving an out-of-band mode be suspected, this mode should be included in group 1 (see discussion of [29]).

In closing this discussion, it is worthwhile to comment on the factor of 1/2 appearing in Eq. (7). As written, the linear responses induced by the forces of Eq. (7) are

$$\underline{u} = \pm\alpha_{ij,s}(\underline{\phi}_i + \underline{\phi}_j) \ / 2 \tag{10}$$

and thus these displacements involve both significantly (equally) the 2 modes. As time progresses, the ratio of the responses of modes *i* and *j* will vary and thus no fixed number is likely to characterize their relative importance. Assuming them equal, as in Eq. (10), is thus meant as inducing a representative interaction. In fact, an earlier version of Eq. (7) [7] used the finite element mass matrix instead of the stiffness one. This gives rise to static linear displacements

$$\underline{u} = \pm\frac{\alpha_{ij,s}}{2}\left[\frac{\underline{\phi}_i}{\omega_i^2} + \frac{\underline{\phi}_j}{\omega_j^2}\right] \tag{11}$$

which differ from Eq. (10) by the relative scaling of the two modes involved which involves the two linear natural frequencies ω_i^2 and ω_j^2. Very good bases were also constructed from the corresponding nonlinear static responses.

(C) Selection of the Dual Modes

The dual modes are constructed using the above nonlinear displacement data from each combination, one after another in a loop over all combinations. The default order of the

combinations in the loop is determined by sorting the summations of the squares of the natural frequencies of the two modes in each of the combinations, which is an indication of the combined stiffness of the two modes, from the smallest to the largest. The smaller the summation is, the larger the effect of that combination of two modes on the in plane deformation may be expected.

Overall, the dual modes will be selected as eigenvectors of POD analyses of the data generated in step B, each combination in turn, but not necessarily the eigenvectors with largest eigenvalues. Rather the necessary eigenvectors are those that lead to a good capturing of especially the in plane displacements which are significantly larger for nonlinear responses than they are for linear ones owing to the membrane stretching effect. In the past, see for example [7,13,21], this selection was performed based on a strain energy measure associated with each eigenvector based on the expectation that in plane motions are stiffer, typically much stiffer than their transverse components. Then, as many of the large strain POD eigenvectors would be taken for each combination as necessary to capture well each of the responses generated for that combination. A slightly different strategy is described below that effectively leads to the same dual mode selection but is more systematic. It relies on prescribed representation error thresholds for the transverse and in plane displacements, $\varepsilon_{re,thr}^{T}$ and $\varepsilon_{re,thr}^{I}$. In our past investigations, as well as in section 3, these thresholds were set to 1%.

Then, the dual construction is divided in the following sub-steps.

(a) The first sub-step focuses on confirming or completing the linear mode basis. At the beginning of the loop, the basis consists of linear modes only. Then, the response data for each combination is projected on the current set of linear modes and the corresponding representation errors of the transverse displacements, ε_{re}^{T} are computed. If these errors are below the threshold $\varepsilon_{re,thr}^{T}$, then no action is taken. If one or more is above this threshold, then two options are possible. The first one is to add more linear modes to be basis, specifically those that are most present in the transverse components of $\underline{u}_{basis} - \underline{u}_{FE}$. The second option is to enrich the basis during step (c).

(b) For each combination in the loop starting with the first, the set of nonlinear displacements are made orthogonal to the set of linear modes, including those obtained in sub-step (a) if applicable. Then, a proper orthogonal decomposition (POD) of this set of displacement residuals is carried out and step (c) follows.

(c) For all quantities of interest, e.g., total displacement, individual displacement components, the representation error of the set of nonlinear responses for the current combination by the current basis - including transverse modes and dual modes constructed from previous combinations if any - is computed. If any of these errors is larger than its pre-defined threshold, then one or more POD eigenvector will be added to the current basis. To select which one is most appropriate, each POD eigenvector is added to the current basis individually and the representation error of the set of displacements by this temporary new basis is computed. The POD eigenvector which gives the largest reduction of representation error is taken as a dual mode and added to the current basis, which is then updated. This is repeated for the current combination with the rest of the POD eigenvectors until all representation errors are below their respective thresholds. Note that if a threshold is set for the representation error of the transverse displacement, adding appropriate POD eigenvectors to satisfy this threshold is the alternate option to the addition of linear modes discussed in sub-step (a). A comparison of these two options for a beam example is presented in Section 3.

The basis is updated, then sub-steps (b) and (c) are carried out for the next combination. After going through all the combinations, the construction of the basis is finished, and the ROM basis is obtained.

3 BEAM EXAMPLE

3.1 ROM of a clamped-clamped beam

An isotropic straight beam is used to exemplify the systematic procedure described above for the basis construction. Note that the flat character of the beam and its uniform properties through the thickness imply that transverse and in plane set of modes are decoupled from each other which will allow sharper conclusions to be drawn. The beam is of rectangular cross section and clamped at both ends, and its geometric and material properties are listed in Table 1.

Properties	Value
Length	0.2286 m
Width	1.2696e-2 m
Thickness	7.8765e-4 m
Density	7867.3 kg/m^3
Young's modulus	2.05e+11 Pa
Shear modulus	8.00e+10 Pa

Table 1: Properties of the clamped-clamped straight beam.

A finite element model of this beam was constructed in Nastran using 40 beam ("CBEAM") elements. The beam span is along the x-direction, and the transverse direction is the z-direction which is along the thickness of the beam.

For the basis construction, it is assumed that the cut-off frequency of the loading is f_{cutoff} = 500 Hz. For this clamped-clamped beam, the nonlinearity can be measured by its maximum transverse displacement in terms of the beam thickness, h, and the target for the basis is to represent the nonlinear displacements up to $u_{max} = 3h$, which is the failure level for the load defined below, with an error less than or equal to 1% in both transverse and in plane directions.

Following the proposed procedure, the six linear transverse modes within the band of $[0,3\,f_{cutoff}]$ were taken as the initial transverse modes of the basis. Their natural frequencies are listed in Table 2.

Mode	1	2	3	4	5	6
Natural frequency (Hz)	79.1	218.0	427.3	706.2	1054.8	1472.9

Table 2: Properties of the clamped-clamped straight beam.

For the dual modes, the combinations of the first three transverse modes in the excitation band are considered (i.e., they are part of group 1) while the out-of-band modes are not considered at all (they form group 3). Thus, the number of combinations is 6. For each combination, a set of 14 pairs (positive and negative) of forces are generated by Eq. (7), and the corresponding nonlinear static displacements are computed with Nastran. The values of the coefficients $\alpha_{ij,s}$ were selected so that the corresponding displacement fields span the domain $u_{max} \in [-3h,-0.1h] \cup [0.1h,3h]$ as uniformly as possible. The dual modes were constructed by

proceeding through the 6 combinations in the order stated in section 2, i.e., [1-1, 1-2, 2-2, 1-3, 2-3, 3-3], where the numbers are the indices of the transverse modes in Table 2.

From step (1) of the procedure, it is found that the six linear transverse modes are not enough to satisfy the 1% criterion for the representation error in the transverse direction, and the two options as described in sub-steps (Ca) and (Cc) are implemented. With the option of adding more linear transverse modes (Ca), a 20-mode basis is constructed which consists of the initial 6 linear modes, additional 4 linear modes, and 10 duals (Basis 10L10D). With the option of adding POD eigenvectors (Cc), a 18-mode basis is constructed which consists of the initial 6 linear modes and 12 dual modes (Basis 6L12D) where two of the dual modes are accounting for the transverse error. Owing to the decoupling of in plane and transverse basis functions, the 10 in plane duals of the two bases are essentially the same.

Two more bases will be considered which are reductions of ones above. In the first, the 2 transverse dual modes of the 6L12D basis or the 4 additional linear modes of the 10L10D are moved leading to a 6L10D basis. For the final basis, the 3 out-of-band linear modes are removed resulting in a 3L10D basis.

3.2 Load case for basis assessment and ROM validation

The aerodynamic pressure distribution measured on a panel [30], as shown in Fig. 1(a), is mapped on the beam yielding the normalized pressure distribution of Fig. 1(b) and (1c). This spatial distribution was multiplied by a bandlimited white noise of cut-off frequency of 500 Hz scaled to different sound pressure levels to produce the dynamic loading to assess the adequacy of the basis and to validate the ROM predictions.

The modal forces along the six transverse modes selected corresponding to this load are listed in Table 3. All the modes have non-zero modal forces; the first mode has the largest value but modes (in decreasing order) 3, 5, and 2 have large/non-negligible values as well.

Mode	**1**	**2**	**3**	**4**	**5**	**6**
Modal force	127.31	-20.31	-53.08	-3.37	31.16	-0.84

Table 3: Modal forces of the transverse modes.

3.3 Basis assessment

Nonlinear static and dynamic response data was generated from Nastran with the above loading for the assessment of the four bases constructed. For the static data, the force was scaled at 14 different levels to achieve maximum displacements from very small to 4.3 thicknesses. For the dynamic data, three overall sound pressure levels (OASPLs) of 110dB, 125dB, and 130dB, were considered and 5-second response time histories were obtained at the time step of 5×10^{-5} second for a total of 100,000 time steps. The standard deviation of the steady-state response of transverse displacement at the center point of the beam, where the maximum displacement is observed, is about 0.50, 0.88, and 1.85 thicknesses for the three load levels, with corresponding maximum values of 1.34, 3.57, and 5.30 thicknesses, respectively.

For the assessment of the two constructed bases, the representation error of the transverse (ε_{re}^{T}) and in plane (ε_{re}^{I}) displacement components were computed using the static and the dynamic response data.

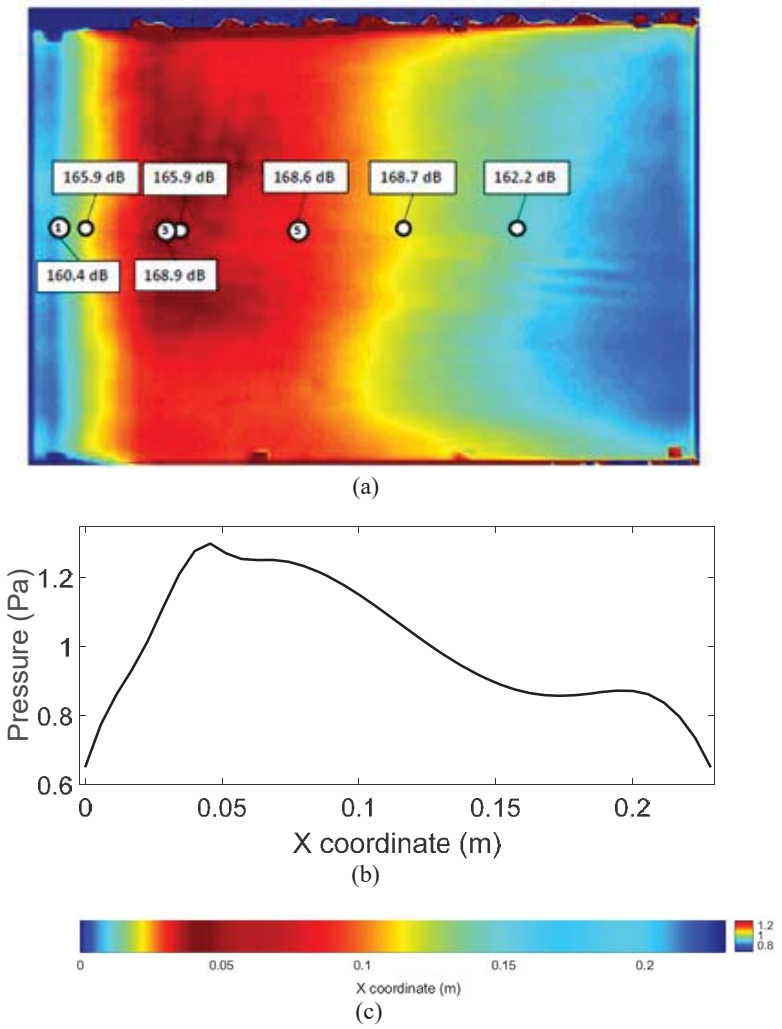

Figure 1. Spatial distribution of the force on the beam, mapped from experimental measurement of aerodynamic pressure distribution on a flexible panel. (a) measured pressure distribution on a panel [24]); (b), (c) mapped force distribution on the beam.

In addition, for the static data, the error in recovering the first eigenvalue of the tangent stiffness matrix of the beam at a deformed position is also computed as

$$\varepsilon^{K_t} = \frac{\left|\lambda_{basis}^{K_t} - \lambda_{FE}^{K_t}\right|}{\lambda_{FE}^{K_t}} \times 100\%, \tag{12}$$

where λ_{FE}^{Kt} and λ_{basis}^{Kt} are the first eigenvalues of the tangent stiffness matrix of the finite element model (directly computed in Nastran) and that of the basis which is obtained by projecting the finite element tangent stiffness matrix on the basis, respectively.

The values of the errors ε_{re}^{T}, ε_{re}^{I}, and ε^{K_t} are shown in Table 4 for all 4 bases described in section 3.1 for static displacement levels of 2.0, 3.0, and 4.1 thicknesses. For each basis, two reduced bases are generated, the first one removing the dual modes or the higher-order linear modes and the second one further removing the three linear modes out of the excitation band

which are common to the two bases. The three error for the reduced bases is then computed and listed in Table 4 as well.

From this data, it is seen that the two "full" bases, 6L12D and 10L10D, both have very good (small) representation errors, even at the displacement level of 4.1 thicknesses which is beyond the 3 thicknesses used as maximum displacement for the basis construction. All errors are below 1%, consistently with the 1% threshold set for the basis construction. This suggests the displacement data used in the basis construction is sufficient.

Consider next the 6L10D basis which has the same in plane basis as the 6L12D and 10L10D models Accordingly, it has the same in plane error ε_{re}^{I} but higher transverse representation and eigenvalue errors exceeding in fact the 1% threshold level for the highest loading. Reducing the number of linear modes to 3, i.e., the 3L10D basis yields further increases in the transverse and eigenvalue errors. This finding is not surprising given the notable modal force on linear mode 5.

	ε_{re}^{T}			ε_{re}^{I}			ε^{Kt}		
$u_{\max}$	*2.0h*	*3.0h*	*4.1h*	*2.0h*	*3.0h*	*4.1h*	*2.0h*	*3.0h*	*4.1h*
6L12D	0.04%	0.05%	0.02%	0.03%	0.04%	0.04%	0.010%	0.001%	0.031%
10L10D	0.03%	0.08%	0.15%	0.03%	0.04%	0.04%	0.059%	0.215%	0.485%
6L10D	0.38%	0.79%	1.27%	0.03%	0.04%	0.04%	0.676%	0.560%	2.315%
3L10D	1.39%	2.51%	3.55%	0.03%	0.04%	0.04%	1.932%	3.345%	4.057%

Table 4: Representation errors of the nonlinear static displacements at various levels by the various bases

Listed in Tables 5 and 6 are listed the comparison of the means and standard deviations of the transverse and in plane representation errors computed from the dynamic data. From this standpoint, both of the full bases perform very well, except for the standard deviation of the in plane displacement at 130dB. However, it should be noted that at this load level the maximum displacement is 5.30 thicknesses, far above the level which the constructed bases are expected to perform well.

The reduced bases have similar behavior to the static data which is actually surprising because one would expect that the out-of-band modes, be it modes 4, 5, 6, or the extra 4 linear modes in the 10L10D model or finally the 2 transverse duals of the 6L12D, would have only a very small effect on the response which is dominated by its in-band behavior. This finding already suggests that the out-of-band modes will play an important role in the dynamic predictions discussed in the ensuing section.

	ε_{re}^{T}			ε_{re}^{I}		
OASPL	*110dB*	*125dB*	*130dB*	*110dB*	*125dB*	*130dB*
u_{std}	*0.50h*	*0.88h*	*1.85h*	*0.50h*	*0.88h*	*1.85h*
6L12D	0.006%	0.020%	0.052%	0.121%	0.331%	0.762%
10L10D	0.002%	0.018%	0.032%	0.121%	0.331%	0.762%
6L10D	0.037%	0.174%	0.337%	0.121%	0.331%	0.762%
3L10D	0.198%	1.051%	1.882%	0.121%	0.331%	0.762%

Table 5: Mean of representation errors of the nonlinear dynamic displacements at various load levels by the various bases.

	ε_{re}^{T}			ε_{re}^{I}		
OASPL	*110dB*	*125dB*	*130dB*	*110dB*	*125dB*	*130dB*
u_{std}	*0.50h*	*0.88h*	*1.85h*	*0.50h*	*0.88h*	*1.85h*
6L12D	0.009%	0.019%	0.175%	0.154%	0.493%	1.231%
10L10D	0.003%	0.015%	0.026%	0.154%	0.493%	1.231%
6L10D	0.050%	0.148%	0.454%	0.154%	0.493%	1.231%
3L10D	0.284%	0.911%	1.666%	0.154%	0.493%	1.231%

Table 6: Standard deviation of representation errors of the nonlinear dynamic displacements at various load levels by the various bases.

3.4 ROM validations

The stiffness coefficients of the two full bases (6L12D and 10L10D) were identified using the multi-level displacement-$K^{(T)}$ method [26]. This effort also provides the stiffness coefficients of the 6L10D and 3L10D by eliminating the coefficients relating to deleted modes. The static and dynamic prediction from these four ROMs were then compared to the corresponding Nastran predictions.

The ROM-Nastran comparisons for the static case are shown in Figs 2 and 3. Shown in Fig. 2 are the transverse displacements at the center of the panel and the in plane displacements at the left and right quarter points. Moreover, shown in Fig. 3 are the entire displacement field at three load levels. Clearly, the matching between the 6L12D or 10L10D ROM predictions and their Nastran counterpart is excellent.

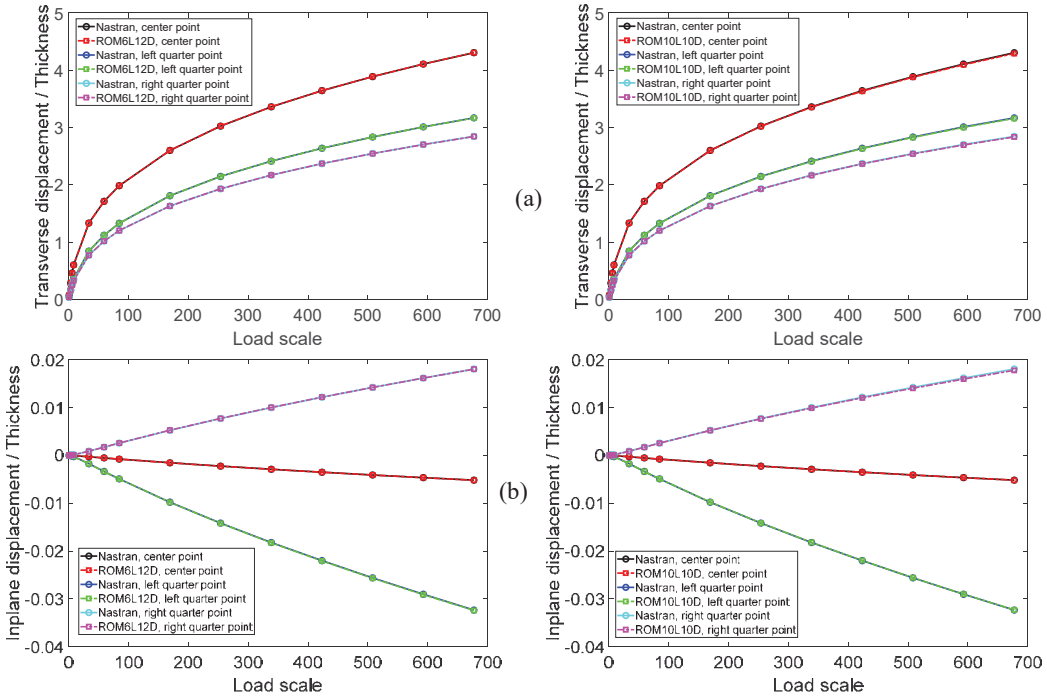

Figure 2. Static displacements at the center and the two quarter points as function of load scale. ROM6L12D (left column), ROM10L10D (right column) vs. Nastran. (a) Transverse and (b) in plane displacement.

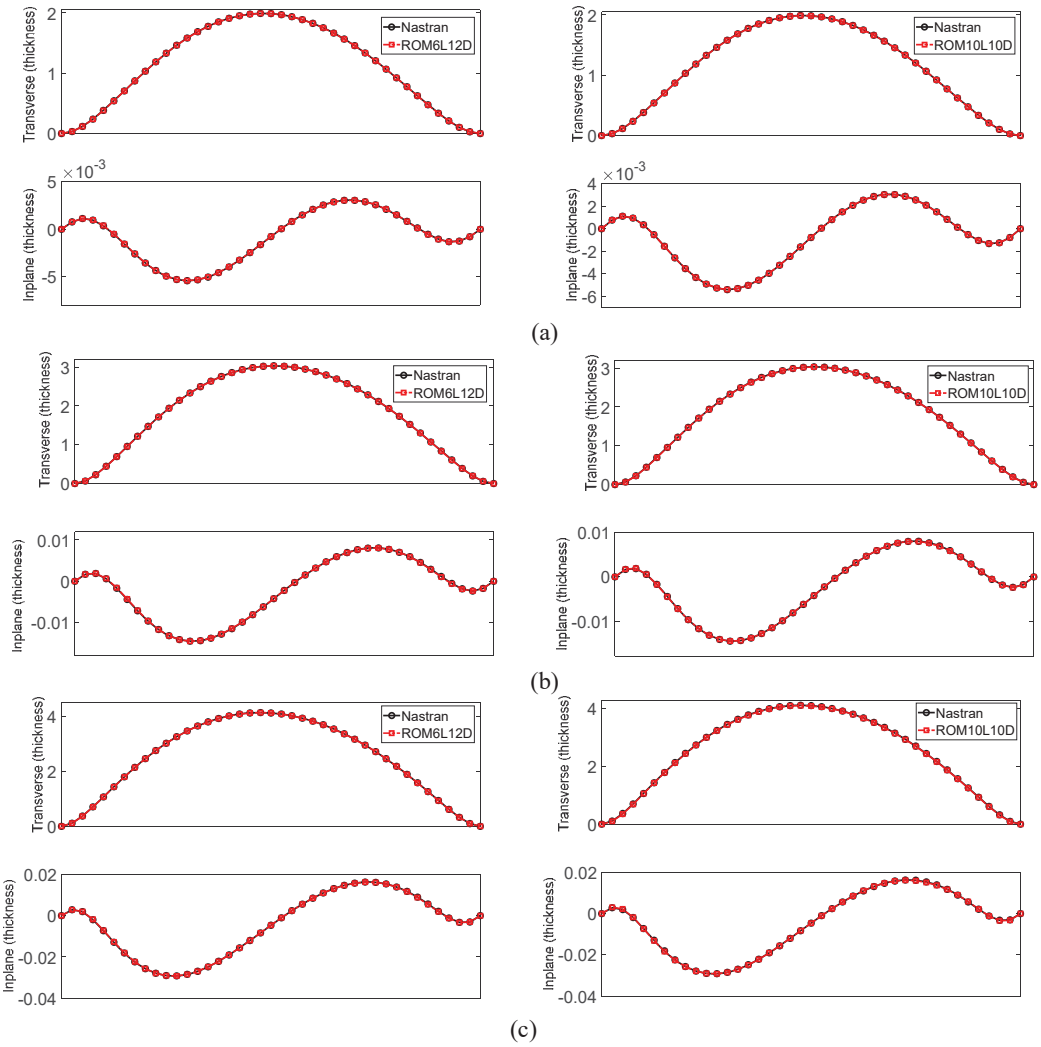

Figure 3. Static validation: whole-field displacements at three displacement levels. ROM6L12D (left column), ROM10L10D (right column) versus Nastran. (a) Displacement level of 2 thicknesses; (b) Displacement level of 3 thicknesses; and (c) Displacement level of 4 thicknesses.

The validation of the ROMs in the dynamic case started with an assessment of the bases to represent the Nastran data. This was done by projecting this data at each time step on the 6L12D and 10L10D bases at the three OASPLs, then summing the modal contributions as in Eq. (9) to reconstruct the full displacement fields. As shown in Figs 4-6, the power spectral densities (PSDs) of the reconstructed displacements labeled as "Basis" in these figures matched nearly identically their Nastran counterparts. These results demonstrate that the bases are very good.

While computing the ROM dynamic responses at the three different sound pressure levels, it was observed that these predictions are sensitive to the identified nonlinear stiffness coefficients, especially those which are known to be usually poorly identified (see [28] for discussion). To minimize, but not eliminate, this sensitivity the ROMs were "cleaned" [28] zeroing out most of the poorly identified coefficients, many of which are expected to be zero by symmetry. This operation allows a good comparison between different bases and, as will be seen below, still leads to an excellent match with the Nastran predictions.

The dynamic responses of the four ROMs were then computed at the three OASPLs of

110dB, 125dB, and 130dB using a Newmark solver with the same time step as Nastran, initially set to 5 10^{-5}s. The corresponding power spectral densities (PSDs) of the transverse displacement at the center point and the in plane displacement at the left quarter point for both the 6L12D and 10L10D bases are first compared to those of the Nastran results in Figs. 4-6.

It is seen that these ROM predictions match their Nastran counterparts very well at the 110dB and 125dB levels but differences are clearly visible at the 130dB level. This trend seems consistent with the representation errors of Tables 5 and 6 but the differences in spectra, e.g., on Fig. 6 appear much more significant that the representation errors which are still barely larger

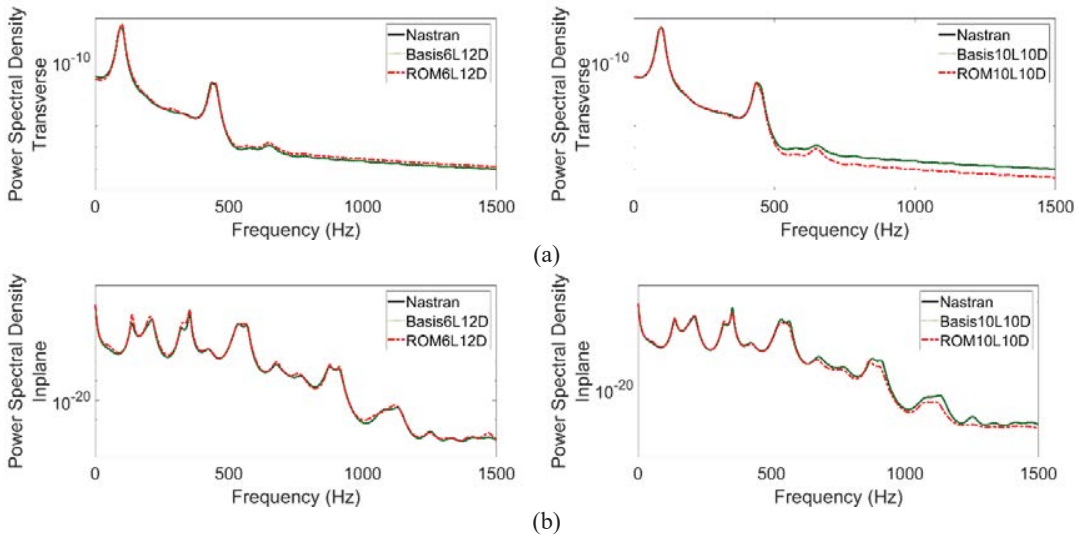

Figure 4. Dynamic validation: power spectral densities (PSD) of displacement at 110dB OASPL (maximum standard deviation of transverse displacement is 0.5 thicknesses). Cleaned ROM6L12D (left column) and ROM10L10D (right column) versus Nastran. (a) Transverse displacement at center point; and (b) In plane displacement at left quarter point.

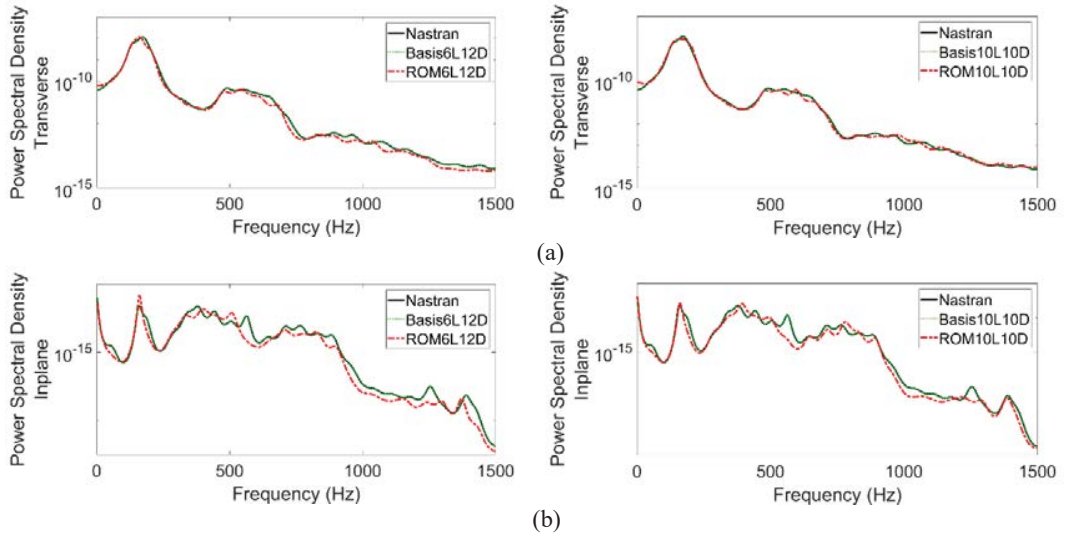

Figure 5. Dynamic validation: power spectral density (PSD) of displacement. Load level 125dB (maximum standard deviation of transverse displacement is 1.5 thicknesses). Cleaned ROM6L12D (left column) and ROM10L10D (right column) versus Nastran. (a) Transverse displacement at center point; and (b) In plane displacement at left quarter point.

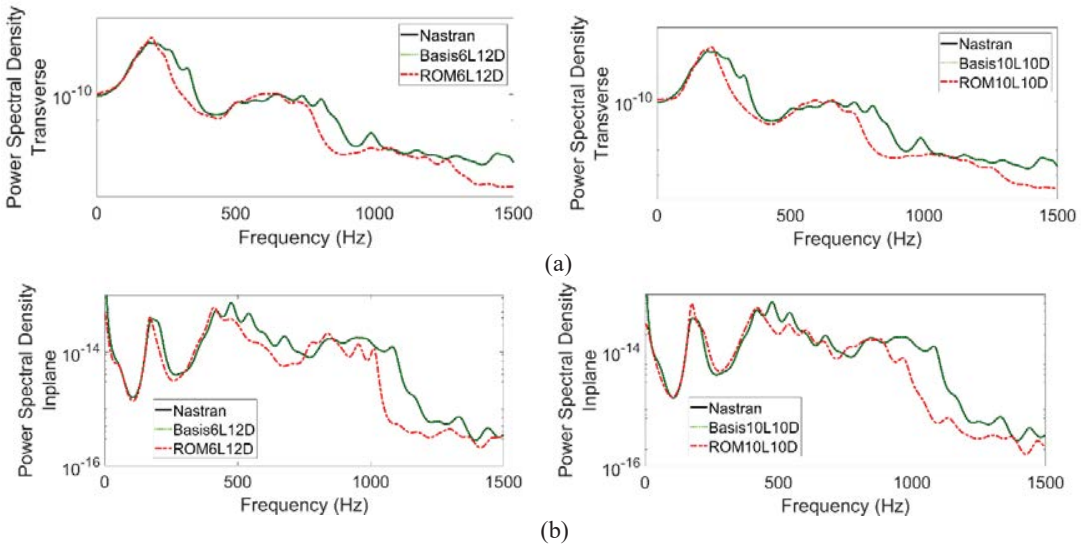

Figure 6. Dynamic validation: power spectral density (PSD) of displacement. Load level 130dB (maximum standard deviation of transverse displacement is 1.9 thicknesses). Cleaned ROM6L12D (left column) and ROM10L10D (right column) versus Nastran. (a) Transverse displacement at center point; and (b) In plane displacement at left quarter point.

than the 1% threshold. An investigation of the 130dB response was carried out and it was found that the time step of $5\ 10^{-5}$s. is not sufficiently small to capture the in plane dynamics. Accordingly, it was reduced to $1\ 10^{-5}$s for both Nastran and ROMs and shown in Fig. 7 are the resulting power spectral densities of the displacements. An excellent matching is observed for both ROMs and in both directions

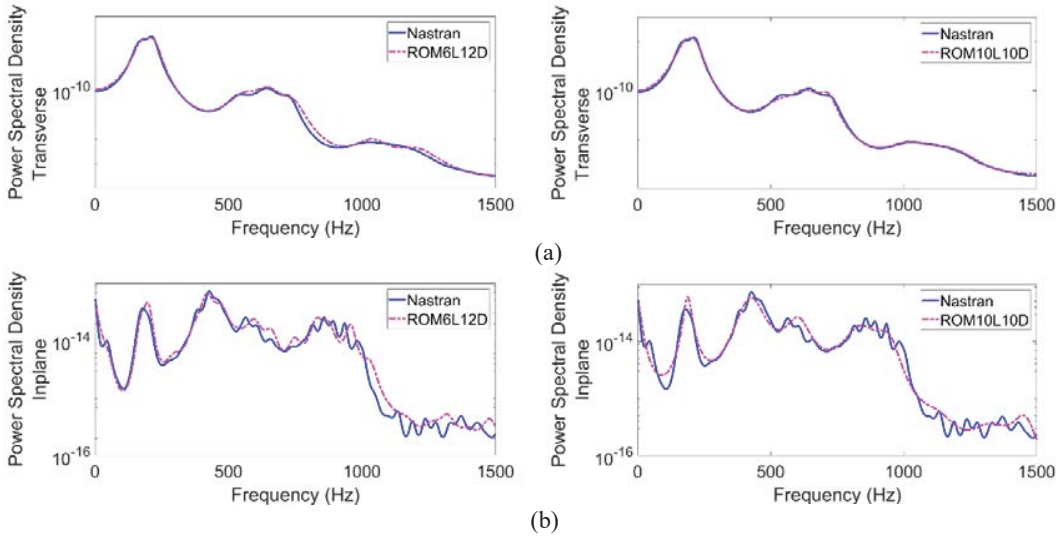

Figure 7. Dynamic validation: power spectral density (PSD) of displacement computed at a smaller time step then resampled back to the original. Load level 130dB (maximum standard deviation of transverse displacement is 1.9 thicknesses). Cleaned ROM6L12D (left column) and ROM10L10D (right column) versus Nastran. (a) Transverse displacement at center point; and (b) In plane displacement at left quarter point.

The final aspect of the present effort focused on assessing the effect of including transverse / linear modes whose natural frequencies are out of the excitation band. To this end, starting from the ROM6L12D the two dual modes which are basically transverse modes were first removed, leading to a ROM6L10D, then three linear modes were also removed, giving rise to a ROM3L10D. Note that all the modes removed have natural frequencies out of the excitation band. Then, the predictions of these two reduced ROMs (cleaned similarly to ROM6L12D) are shown in Figs 8-10 at the same three sound pressure levels of 110dB, 125dB, and 130dB and with time steps of 5 10^{-5}s at the lowest two levels and 1 10^{-5}s at the highest one. While the matching between the ROM and Nastran predictions is still very good at the 110dB level, some differences become visible at 125dB but the predictions can still be considered good. The comparison worsens further at the 130dB level in both transverse and in plane directions, the latter particularly. It is not very easy to assess which of the two models is better. Regardless, the key conclusion drawn from these results is that out-of-band transverse modes play an increasingly important role as the excitation level is increased. Thus, the inclusion of some of these modes in the model is necessary for the accurate prediction of the response especially at high response levels.

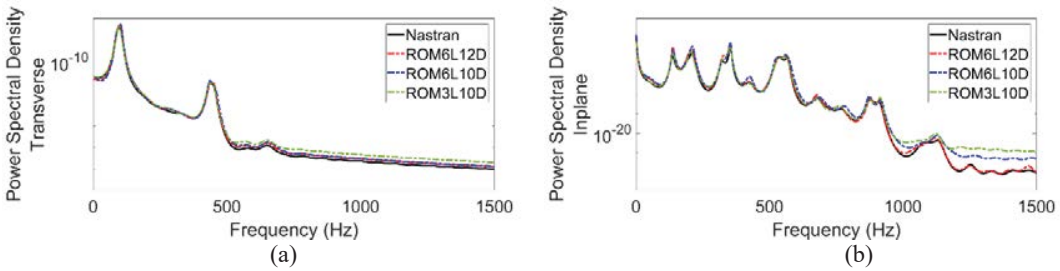

Figure 8. Comparison of the power spectral density (PSD) of displacement predicted by ROM6L12D, ROM6L10D and ROM3L10D, all cleaned, against Nastran. Load level 110dB (maximum standard deviation of transverse displacement is 0.5 thicknesses). (a) Transverse displacement at center point; and (b) In plane displacement at left quarter point.

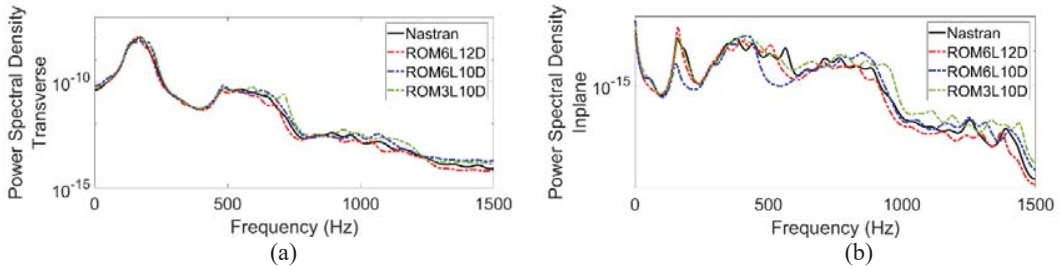

Figure 9. Comparison of the power spectral density (PSD) of displacement predicted by ROM6L12D, ROM6L10D and ROM3L10D, all cleaned, against Nastran. Load level 125dB (maximum standard deviation of transverse displacement is 1.5 thicknesses). (a) Transverse displacement at center point; and (b) In plane displacement at left quarter point.

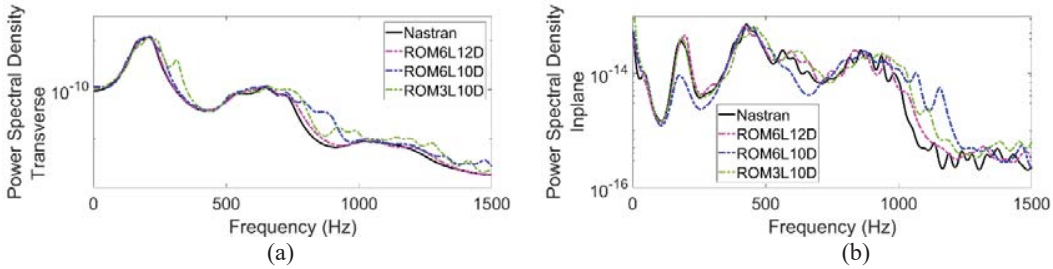

Figure 10. Comparison of the power spectral density (PSD) of displacement predicted by ROM6L12D, ROM6L10D and ROM3L10D, all cleaned, against Nastran. The same smaller time step resampled back to the original as in Figure 7 is used. Load level 130dB (maximum standard deviation of transverse displacement is 1.9 thicknesses). (a) Transverse displacement at center point; and (b) In plane displacement at left quarter point.

4 CONCLUSIONS

A systematic strategy is developed for the construction of a "general" basis for reduced order models of the nonlinear geometric vibration of thin-walled structures. This strategy is an extension/more detailed version of the existing one where some linear modes are selected to represent large transverse displacements and the associated "dual" modes are derived to account for the "in plane" membrane stretching deformations due to the nonlinear geometric effects. Central to this basis construction process is the selection of linear modes of the basis according to the cut-off frequency, f_{cutoff}, of the loading, and the derivation of the dual modes using static nonlinear responses related to the selected linear modes.

Formalizing some recent, limited observations, it is proposed here that the set of linear modes selected at the start of the basis construction includes not only those in the band of excitation but also some out-of-band modes ones. Tentatively, it is suggested that the linear modes selected span the band $[0,3\, f_{cutoff}]$. As in prior investigations, dual modes are added to this basis which are derived from proper orthogonal decompositions (POD) of residuals of projection of specific static nonlinear finite element responses on the linear basis. The process by which POD eigenvectors are selected as dual modes is however fully formalized and is based on the representation error of the data generated by the current basis. The step-by-step implementation procedure of the proposed strategy is presented.

A clamped-clamped straight beam is used to exemplify the approach and two bases are constructed following the implementation procedure. A distributed force mapped from a measured aerodynamic pressure distribution on a panel is used as a good example of loading. For this load, nonlinear static and dynamic response data are obtained from the commercial finite element software Nastran and used to assess the constructed bases. It is shown that the proposed procedure is appropriate, and the constructed bases are excellent in terms of representation errors.

The nonlinear stiffness coefficients of these bases are next identified to permit predictions and their comparisons with the corresponding static and dynamic finite element data. The predictions from the two bases are found to be essentially identical but do not match well the Nastran data at the highest dynamic load. It is argued that these differences are in fact rooted in errors in the identified ROM coefficients, not in shortcomings of the basis. Finally, two reduced bases are obtained from the previous two by removing the out-of-band linear modes/transverse basis functions. It is found that the predictions from these bases is still very good at low response levels but worsens as the peak displacements increase clearly demonstrating the importance of

including out-of-band linear modes/transverse basis functions in sharp contrast with linear problems.

ACKNOWLEDGEMENT

The authors gratefully acknowledge the support of this work by the AFRL-University Collaborative Center in Structural Sciences (Cooperative Agreement FA8650-13-2-2347) with Dr. Ben Smarslok as program manager.

REFERENCES

[1] M.I. McEwan, J.R. Wright, J.E. Cooper, A.Y.T. Leung, A combined modal/finite element analysis technique for the dynamic response of a nonlinear beam to harmonic excitation, *Journal of Sound and Vibration*, 243, 601-624, 2001.

[2] J.J Hollkamp, R.W. Gordon, S.M. Spottswood, Nonlinear modal models for sonic fatigue response prediction: a comparison of methods, *Journal of Sound and Vibration*, 284, 1145-1163, 2005.

[3] M.P. Mignolet, A.G. Radu, X. Gao, Validation of reduced order modeling for the prediction of the response and fatigue life of panels subjected to thermo-acoustic effects, *Proceedings of the 8th International Conference on Recent Advances in Structural Dynamics*, Southampton, United Kingdom, Jul. 14-16, 2003.

[4] A.G. Radu, B. Yang, K. Kim, M.P. Mignolet, Prediction of the dynamic response and fatigue life of panels subjected to thermo-acoustic loading, *Proceedings of the 45th Structures, Structural Dynamics, and Materials Conference*, Palm Springs, California, Apr. 19-22, 2004. Paper AIAA-2004-1557.

[5] J.J. Hollkamp, R.W. Gordon, Reduced-order models for nonlinear response prediction: implicit condensation and expansion, *Journal of Sound and Vibration*, 318, 1139-1153, 2008.

[6] A. Przekop, S.A. Rizzi, A reduced order method for predicting high cycle fatigue of nonlinear structures, *Computers and Structures*, 84, 1606-1618, 2006.

[7] K. Kim, A.G. Radu, X.Q. Wang, M.P. Mignolet, Nonlinear reduced order modeling of isotropic and functionally graded plates, *International Journal of Non-Linear Mechanics*, 49, 100-110, 2013.

[8] A. Przekop, S.A. Rizzi, Nonlinear reduced order random response analysis of structures with shallow curvature, *AIAA Journal*, 44, 1767-1778, 2006.

[9] S.M. Spottswood, J.J. Hollkamp, T.G. Eason, On the use of reduced-order models for a shallow curved beam under combined loading, *Proceedings of the 49th Structures, Structural Dynamics, and Materials Conference*, Schaumburg, Illinois, Apr. 7-10, 2008. AIAA Paper AIAA-2008-1873.

[10] A. Przekop, S.A. Rizzi, Dynamic snap-through of thin-walled structures by a reduced-order method, *AIAA Journal*, 45, 2510–2519, 2007.

[11] S.M. Spottswood, T.G. Eason, X.Q. Wang, M.P. Mignolet, Nonlinear reduced order modeling of curved beams: a comparison of methods, *Proceedings of the 50th Structures,*

Structural Dynamics, and Materials Conference, Palm Springs, California, May 4-7, 2009. AIAA Paper AIAA-2009-2433.

[12] X.Q. Wang, R.A. Perez, M.P. Mignolet, R. Capillon, C. Soize, Nonlinear reduced order modeling of complex wing models, *Proceedings of the 54th Structures, Structural Dynamics and Materials Conference*, Boston, Massachusetts, Apr. 8-11, 2013. AIAA Paper AIAA-2013-1520.

[13] R.A. Perez, X.Q. Wang, M.P. Mignolet, Non-intrusive structural dynamic reduced order modeling for large deformations: enhancements for complex structures, *Journal of Computational and Nonlinear Dynamics*, 9, 031008, 2014.

[14] R.W. Gordon, J.J. Hollkamp, Reduced-order models for acoustic response prediction of a curved panel, *Proceedings of the 52nd Structures, Structural Dynamics and Materials Conference*, Denver, Colorado, Apr. 4-7, 2011. AIAA Paper AIAA 2011-2081.

[15] A. Gogulapati, R. Deshmukh, A.R. Crowell, J.J. McNamara, V. Vyas, X.Q. Wang, M.P. Mignolet, T. Beberniss, S.M. Spottswood, T.G. Eason, Response of a panel to shock impingement: modeling and comparison with experiments, *Proceedings of the AIAA Science and Technology Forum and Exposition (SciTech2014)*, National Harbor, Maryland, Jan. 13-17, 2014. AIAA Paper AIAA 2014-0148.

[16] A. Matney, M.P. Mignolet, A.J. Culler, J.J. McNamara, S.M. Spottswood, Panel response prediction through reduced order models with application to hypersonic aircraft, *Proceedings of the AIAA Science and Technology Forum and Exposition (SciTech2015)*, Orlando, Florida, Jan. 5-9, 2015. AIAA Paper AIAA 2015-1630.

[17] A. Gogulapati, K. Brouwer, X.Q. Wang, R. Murthy, J.J. McNamara, M.P. Mignolet, Full and reduced order aerothermoelastic modeling of built-up aerospace panels in high-speed flows, *Proceedings of the AIAA Science and Technology Forum and Exposition (SciTech2017)*, Dallas, Texas, Jan. 9-13, 2017. AIAA Paper AIAA 2017-0180.

[18] Mignolet, M.P., and Soize, C. "Stochastic Reduced Order Models for Uncertain Geometrically Nonlinear Dynamical Systems," *Computer Methods in Applied Mechanics and Engineering*, Vol. 197, No. 45, 2008, pp. 3951-3963. doi: 10.1016/j.cma.2008.03.032.

[19] Capiez-Lernout, E., Soize, C., and Mignolet, M.P.. "Post-Buckling Nonlinear Static and Dynamical Analyses of Uncertain Cylindrical Shells and Experimental Validation," *Computer Methods in Applied Mechanics and Engineering*, Vol. 271, 2014, pp. 210-230. doi: 10.1016/j.cma.2013.12.011.

[20] Wang, X.Q., Mignolet, M.P., and Soize, C., "Structural Uncertainty Modeling for Nonlinear Geometric Response using Nonintrusive Reduced Order Models," *Probabilistic Engineering Mechanics*, Vol. 60, 103033, pp. 1-9, 2020.

[21] M.P. Mignolet, A. Przekop, S.A. Rizzi, S.M. Spottswood, A review of indirect/non-intrusive reduced order modeling of nonlinear geometric structures, *Journal of Sound and Vibration*, 332, 2437-2460, 2013.

[22] X.Q. Wang, P.J, O'Hara, M.P. Mignolet, J.J. Hollkamp, Reduced order modeling with local enrichment for the nonlinear geometric response of a cracked panel, *AIAA Journal*, 57, 421-436, 2019.

[23] Y. Wang, X.Q. Wang, M.P. Mignolet, Component-centric reduced order modeling for the prediction of the nonlinear geometric response of a part of a stiffened structure, *ASME Journal of Computational and Nonlinear Dynamics*, 13, 121006, 2018.

[24] X.Q. Wang, G.P. Phlipot, R.A. Perez, M.P. Mignolet, Locally enhanced reduced order modeling for the nonlinear geometric response of structures with defects, *International Journal of Nonlinear Mechanics*, 101, 1-7, 2018.

[25] R.A. Perez, X.Q. Wang, M.P. Mignolet, Nonlinear geometric response of panels with localized geometric defects by reduced order models - a notched panel, *Journal of Sound and Vibration*, 333, 6572-6589, 2014.

[26] X.Q. Wang, Jinshan Lin, B.A. Wainwright, M.P. Mignolet, Multiple-level identification of stiffness coefficients in nonlinear reduced order modeling, *Proceedings of the 37th IMAC, Conference and Exposition on Structural Dynamics*, Orlando, Florida, USA, January 28-31, 2019.

[27] Tiso, P, Jansen, E., and Abdalla, M., "Reduction Method for Finite Element Nonlinear Dynamic Analysis of Shells, *AIAA Journal*, Vol. 49, No. 10, pp. 2295-2304, 2011.

[28] Lin, J., Wang, X.Q., and Mignolet, M.P., "Non-Intrusive Identification of Nonlinear Reduced Order Models: Symmetry and Tuning," *Proceedings of the International Modal Analysis Conference, IMAC XXXVIII*, Houston, Texas, Feb. 10-13, 2020.

[29] Wainwright, B. A., Wang, X.Q., and Mignolet, M.P., "Investigation of Out-of-Band Response in Reduced Order Models of Nonlinear Geometric Response," *Proceedings of the International Modal Analysis Conference, IMAC XXXVIII*, Houston, Texas, Feb. 10-13, 2020.

[30] S. Spottswood, T. Eason, T. Beberniss, Influence of shock-boundary layer interactions on the dynamic response of a flexible panel, *Proceedings of the ISMA-2012,* 603-616, Leuven, Belgium, September 17-19, 2012.

EURODYN 2020
XI International Conference on Structural Dynamics
M. Papadrakakis, M. Fragiadakis, C. Papadimitriou (eds.)
Athens, Greece, 23–26 November 2020

NONLINEAR VIBRATIONS OF AN ELASTIC PLATE ON A VISCOELASTIC FOUNDATION MODELLED BY THE FRACTIONAL DERIVATIVE STANDARD LINEAR SOLID MODEL

Marina V. Shitikova[1]*, Anastasiya I. Krusser[2]

[1]Voronezh State Technical University
Research Centre on Dynamics of Solids and Structures
Voronezh 394006
mvs@vgasu.vrn.ru

[2] Voronezh State Technical University
Research Centre on Dynamics of Solids and Structures
Voronezh 394006
an.krusser@yandex.ru

Keywords: nonlinear vibrations, fractional derivative, viscoelastic foundation, standard linear solid model

Abstract. *The interaction between a loaded plate and the soil foundation is a typical problem in civil engineering. To solve the plate-foundation interaction problem, different viscoelastic models of foundations are used, among them fractional derivative Winkler-type or Pasternak-type models [1], since during last decades the fractional calculus plays an important role in dynamic problems of structural mechanics [2]. In the present paper, the dynamic response of a rectangular simply supported nonlinear plate resting on a viscoelastic Winkler-type foundation, the damping features of which are described by the fractional derivative standard linear solid model, is studied using the fractional derivative expansion method [3,4].*

1 INTRODUCTION

Over the last few decades the problems of the interaction between various building structures and soil foundation have been of great interest among researchers. In order to calculate the reaction force of the foundation in dynamic problems, several models were proposed. The first attempt to describe the reaction of foundation was the Winkler model, according to which the foundation is considered to be elastic. The main disadvantage of a linear elastic model is its inconsistency in the representation of the viscoelastic behavior of materials. In this regard, a viscoelastic element was added to the Winkler model. There are many combinations of elastic and viscous elements connected in series or in parallel, therefore, based on the Winkler elastic model, several viscoelastic models of foundation were proposed, such as the Kelvin-Voigt, Maxwell, Zener, Poynting-Thomson and Burgers models, which are reviewed in [5].

Later, the Winkler model was developed and supplemented by several scientists, such as Filonenko-Borodich (1940), Hetényi (1950), Pasternak (1954), Vlasov (1966) and Reissner (1958), as a result of which the so-called two-parameter foundation models appeared [6]. Two-parameter models are known as models, wherein the top layer connects the elements of foundation to each other, therefore, in addition to the vertical component of the foundation reaction force, shear stresses are also taken into account. The Pasternak model was also generalized for a viscoelastic case [5,6]. The dynamic behavior of plates on a viscoelastic foundation was considered in [7] and [8], where the response of a viscoelastic plate and thick plate on viscoelastic foundation was studied, respectively.

Nowadays, fractional derivative Winkler-type or Pasternak-type models of viscoelastic foundations are becoming increasingly widespread [1, 9-14], since during last decades the fractional calculus plays an important role in dynamic problems of structural mechanics [2]. Thus, the Kelvin – Voigt fractional model is used in [9] to describe the time-dependent behavior of the soil foundation under the vertical load. The behavior of a rectangular viscoelastic plate on a viscoelastic foundation, which is described by a two-parameter model with a fractional derivative, is analyzed in [10]. The interaction between a rectangular linear elastic plate and the viscoelastic foundation defined by the fractional derivative standard linear solid model with four parameters, which is the combination the Kelvin-Voigt element and a spring connected in series, was studied in [11]. A rectangular plate subjected to a moving load was considered in [12], in so doing the viscoelastic properties of the foundation were defined by the Winkler-type model. Graphs of the stress on the plate surfaces were numerically constructed for the cases of free (after the termination of the action of a movable load on the plate) and forced vibrations. The fractional derivative Kelvin-Voigt model for a Pasternak-type viscoelastic foundation was utilized in [13], and the equations of motion were derived for an elastic and viscoelastic rectangular loaded plate. Forced vibrations of completely free rectangular orthotropic nanoplate were studied in [14], where the viscoelastic foundation was described via the Kelvin-Voigt model.

In the present paper, the dynamic response of a rectangular simply supported nonlinear plate resting on a viscoelastic Winkler-type foundation, the damping features of which are described by the fractional derivative standard linear solid model, is studied for the case of the one-to-one internal resonance using the fractional derivative expansion method [3,4].

2 PROBLEM FORMULATION

Let us consider nonlinear vibrations of a simply supported elastic plate in a viscoelastic medium, based on a viscoelastic foundation (Fig.1), the dynamic response of which is described by the von Karman equation in terms of the plate's lateral deflection $w = w(x, y, t)$ and the Airy's stress function ϕ:

$$D\nabla^4 w+\rho h\frac{\partial^2 w}{\partial t^2}-\frac{\partial^2 w}{\partial x^2}\frac{\partial^2 \phi}{\partial y^2}-\frac{\partial^2 w}{\partial y^2}\frac{\partial^2 \phi}{\partial x^2}+2\frac{\partial^2 w}{\partial x\partial y}\frac{\partial^2 \phi}{\partial x\partial y}=q-F_1-F_2, \tag{1}$$

$$\nabla^4\phi=Eh\left[\left(\frac{\partial w}{\partial x\partial y}\right)^2-\frac{\partial^2 w}{\partial x^2}\frac{\partial^2 w}{\partial y^2}\right], \tag{2}$$

where $\nabla^4=\partial^4/\partial x^4+2\partial^4/\partial x^2\partial y^2+\partial^4/\partial y^4$ is the biharmonic operator, q is the external load, $D=Eh^3/12(1-\nu^2)$ is the plate's cylindrical rigidity, E and ν are the elastic modulus and Poisson's ratio of the plate's material, respectively, h and ρ are its thickness and density, t is the time, $F_2=\tilde{\lambda}w$ is the reaction force of the viscoelastic foundation, $F_1=æ_1\tau_1^{\gamma_1}D_{0+}^{\gamma_1}w$ is the damping force of the viscoelastic medium possessing the retardation time τ_1 and damping coefficient $æ_1$, which is modeled by the viscoelastic Kelvin-Voigt model with the Riemann-Liouville derivative $D_{0+}^{\gamma_1}$ of the fractional order γ_1 $(0<\gamma_1\le 1)$ [2,15]:

$$D_{0+}^{\gamma}x(t)=\frac{d}{dt}\int_0^t\frac{x(t-t')dt'}{\Gamma(1-\gamma)t'^{\gamma}}\quad(0<\gamma=\gamma_1\le 1), \tag{3}$$

and $\Gamma(1-\gamma)$ is the Gamma function.

Let us assume, following [16], that the compliance operator of a viscoelastic foundation is described by the standard linear solid model with the Riemann-Liouville fractional derivative D_{0+}^{γ} (3) when $\gamma=\gamma_2$:

$$\tilde{\lambda}=\lambda_\infty\left[1-æ_2\nu_\varepsilon\frac{1}{1+\tau_2^{\gamma}D_{0+}^{\gamma_2}}\right], \tag{4}$$

where λ_∞ is the coefficient of instantaneous compliance of the foundation, $\nu_\varepsilon=\Delta\lambda\lambda_\infty^{-1}$, $\Delta\lambda=\lambda_\infty-\lambda_0$ is the defect of the compliance, i.e., the value characterizing the decrease in the compliance operator from its non-relaxed value to its relaxed value, and τ_2 and $æ_2$ are the retardation time and damping coefficient of the viscoelastic foundation, respectively.

Considering a simply supported plate, the following boundary conditions should be added to the set of equations (1) and (2) at each edge:

$$\text{at}\quad x=0\ \text{and}\ a,\quad w=\frac{\partial^2 w}{\partial x^2}=0;\qquad \text{at}\ y=0\ \text{and}\ b,\quad w=\frac{\partial^2 w}{\partial y^2}=0. \tag{5}$$

In order to identify the possibility of the occurrence of the internal resonance during nonlinear vibrations of a plate based on a viscoelastic foundation and to carry out its subsequent analysis, suppose that only two natural modes of vibrations with numbers m_1n_1 и m_2n_2 are excited. Then the deflection of the plate could be represented in the following form:

$$\begin{aligned}w(x,y,t)&=x_1(t)\sin\frac{\pi m_1 x}{a}\sin\frac{\pi n_1 y}{b}+x_2(t)\sin\frac{\pi m_2 x}{a}\sin\frac{\pi n_2 y}{b}\\&=x_1(t)W_{m_1n_1}(x,y)+x_2(t)W_{m_2n_2}(x,y),\end{aligned} \tag{6}$$

where $x_i(t)$ $(i=1,2)$ are generalized displacements, and $W_{m_in_i}(x,y)$ are the eigen functions.

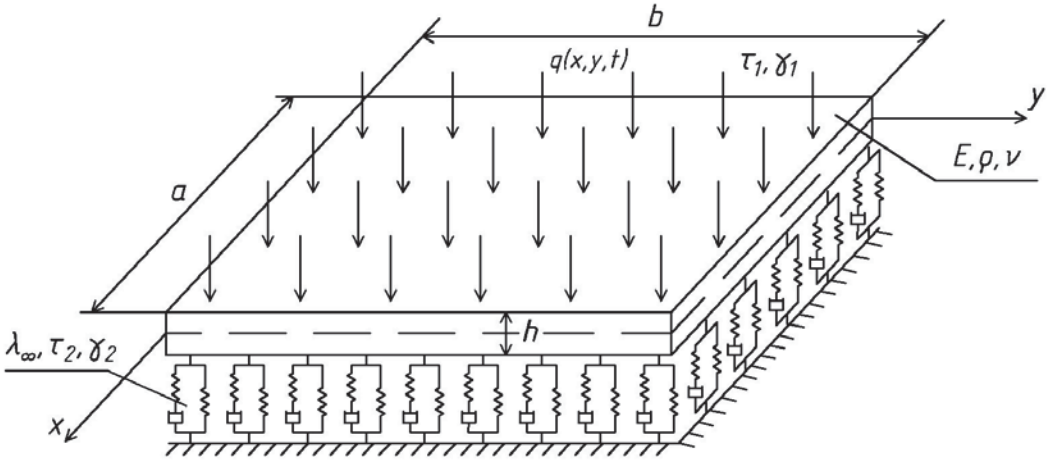

Figure 1: Plate on a viscoelastic foundation modelled by the fractional derivative standard linear solid model

Substituting the proposed solution (6) in (2), taking into account the boundary conditions (5) and integrating with account for the orthogonality conditions of sines, we obtain the stress function in the following form:

$$\begin{aligned}\phi(x,y,t) &= \frac{1}{32\xi^2}\left(\frac{n_1^2}{m_1^2}\cos\frac{2\pi m_1 x}{a}+\xi^4\frac{m_1^2}{n_1^2}\cos\frac{2\pi n_1 y}{b}\right)x_1(t)^2\\ &+\frac{1}{32\xi^2}\left(\frac{n_2^2}{m_2^2}\cos\frac{2\pi m_2 x}{a}+\xi^4\frac{m_2^2}{n_2^2}\cos\frac{2\pi n_2 y}{b}\right)x_2(t)^2\\ &+\frac{1}{4}\left[\left(B^2\cos\frac{\pi(m_1+m_2)x}{a}\cos\frac{\pi(n_1-n_2)y}{b}\right.\right.\\ &\left.+C^2\cos\frac{\pi(m_1-m_2)x}{a}\cos\frac{\pi(n_1+n_2)y}{b}\right)\beta_1^2\\ &-\left(A^2\cos\frac{\pi(m_1+m_2)x}{a}\cos\frac{\pi(n_1+n_2)y}{b}\right.\\ &\left.\left.+D^2\cos\frac{\pi(m_1-m_2)x}{a}\cos\frac{\pi(n_1-n_2)y}{b}\right)\beta_2^2\right]x_1(t)x_2(t),\end{aligned} \tag{7}$$

where $\xi=\frac{b}{a}$, $\beta_1=(m_1n_2+m_2n_1)$, $\beta_2=(m_1n_2-m_2n_1)$,

$$A^2=\frac{\xi^2}{\left[(m_1+m_2)^2\xi^2+(n_1+n_2)^2\right]^2},\qquad B^2=\frac{\xi^2}{\left[(m_1+m_2)^2\xi^2+(n_1-n_2)^2\right]^2},$$

$$C^2=\frac{\xi^2}{\left[(m_1-m_2)^2\xi^2+(n_1+n_2)^2\right]^2},\qquad D^2=\frac{\xi^2}{\left[(m_1-m_2)^2\xi^2+(n_1-n_2)^2\right]^2}.$$

Substituting the assumed two-term expansion for the deflection function of the plate (6) and the stress function (7) in the equation of motion of the plate (1) resting on the viscoelastic

foundation yields the following set of nonlinear differential equations with respect to the generalized displacements:

$$\ddot{x}_1 + \Omega_1^2 x_1 + \frac{\lambda_\infty}{\rho h}\left[1 - æ_2 \nu_\varepsilon \, э_\gamma^* (\tau_2^{\gamma_2})\right] x_1 + \alpha_1 x_1^3 + \alpha_2 x_1 x_2^2 + \frac{æ_1 \tau_1^{\gamma_1}}{\rho h} D_{0+}^{\gamma_1} x_1 = P_1(t), \tag{8}$$

$$\ddot{x}_2 + \Omega_2^2 x_2 + \frac{\lambda_\infty}{\rho h}\left[1 - æ_2 \nu_\varepsilon \, э_\gamma^* (\tau_2^{\gamma_2})\right] x_2 + \alpha_3 x_2^3 + \alpha_4 x_2 x_1^2 + \frac{æ_1 \tau_1^{\gamma_1}}{\rho h} D_{0+}^{\gamma_1} x_2 = P_2(t), \tag{9}$$

where $P_i(t) = \dfrac{\int_0^a \int_0^b q(x,y,t) W_{m_i n_i}(x,y)\, dxdy}{\rho h \int_0^a \int_0^b \left[W_{m_i n_i}(x,y)\right]^2 dxdy}$, α_i are the coefficients depending on the vibration mode numbers which are given in Appendix, Ω_i^2 are the natural frequencies of the linear vibration of the plate defined as

$$\Omega_i^2 = \frac{Eh^2}{12\rho(1-\nu^2)} \nabla^4 W_{m_i n_i}(x,y) = \frac{E\pi^4 h^2}{12\rho(1-\nu^2)b^4}\left(\xi^2 m_i^2 + n_i^2\right)^2, \tag{10}$$

and $э_\gamma^* (\tau_2^{\gamma_2})$ is the Rabotnov dimensionless fractional operator defined as follows [17]

$$э_\gamma^* (\tau_2^{\gamma_2}) = \frac{1}{1 + \tau_2^{\gamma_2} D_{0+}^{\gamma_2}}. \tag{11}$$

Note that in the case of free damped vibrations $P_i(t) = 0$.

3 METHOD OF SOLUTION

In order to solve a set of two nonlinear equations, (8) и (9), the method of multiple time scales [18,19] could be utilized assuming damping coefficients $æ_i$ to be small values of order of ε^2

$$æ_i = \varepsilon^2 \mu_i, \tag{12}$$

where μ_i are finite values.

Then the generalized displacements $x_i(t)$ could be represented via the following expansion in two time scales T_0 and T_2:

$$x_i(t) = \varepsilon X_{i1}(T_0, T_2) + \varepsilon^2 X_{i2}(T_0, T_2) + \varepsilon^3 X_{i3}(T_0, T_2) + \ldots, \tag{13}$$

where $T_n = \varepsilon^n t$ are new independent variables, among them: $T_0 = t$ is a fast scale characterizing motions with the natural frequencies, and $T_2 = \varepsilon t^2$ is a slow scale characterizing the modulation of the amplitudes and phases of the modes with nonlinearity.

Recall that the first and the second time derivatives, as well as fractional derivative could be expanded in terms of the new time scales, respectively, as follows [4, 19]:

$$\frac{d}{dt} = D_0 + \varepsilon^2 D_2 + \ldots, \quad \frac{d^2}{dt^2} = D_0^2 + 2\varepsilon^2 D_0 D_2 + \ldots \tag{14}$$

$$D_+^\gamma = \left(\frac{d}{dt}\right)^\gamma = \left(D_0 + \varepsilon^2 D_2 + ...\right)^\gamma = D_0^\gamma + \varepsilon^2 \gamma D_0^{\gamma-1} D_2 + ..., \tag{15}$$

where $D_0 = \partial / \partial T_0$, and $D_2 = \partial / \partial T_2$.

Note that [15]

$$\left(\frac{d}{dt}\right)^\gamma \varphi = D_+^\gamma \varphi = \frac{d}{dt} \int_{-\infty}^{t} \frac{\varphi(t')dt'}{(t-t')^\gamma \Gamma(1-\gamma)}. \tag{16}$$

But in the present case the process of vibrations starts at the time $t = 0$. Thus, the fractional derivative $D_{0+}^\gamma \varphi$ in the form of (3) should be adopted.

Fractional derivatives (16) and (3) act in a different way on the exponential function $e^{\lambda t}$, which is utilized in further treatment, i.e. [20]

$$D_+^\gamma e^{\lambda t} = \lambda^\gamma e^{\lambda t}, \tag{17}$$

and

$$D_{0+}^\gamma e^{\lambda t} = \lambda^\gamma e^{\lambda t} + \frac{\sin \pi x}{\pi} \int_0^\infty \frac{u^\gamma}{u+\lambda} e^{-ut} du\,. \tag{18}$$

However, as it has been shown in [20], if when utilizing the generalized method of multiple time scales only the zero and first order approximations are considered, then the second term in (18) could be neglected.

Expansion of the Rabotnov dimensionless fractional operator in a Taylor series in terms of a small parameter has the form [21]:

$$\begin{aligned} \text{э}_\gamma^* (\tau^\gamma) &= \frac{1}{1+\tau^\gamma D_{0+}^\gamma} = (1+\tau^\gamma D_{0+}^\gamma)^{-1} = \left[1+\tau^\gamma (D_0^\gamma + \varepsilon^2 \gamma D_0^{\gamma-1} D_2)\right]^{-1} \\ &= (1+\tau^\gamma D_0{}^\gamma)^{-1} - \varepsilon^2 (1+\tau^\gamma D_0{}^\gamma)^{-2} \tau^\gamma \gamma D_0{}^{\gamma-1} D_2 + ... \end{aligned} \tag{19}$$

Substituting expansion (13) with account for relationships (14), (15), and (19), after equating the coefficients at like powers of ε to zero, we are led for the case of free damped vibrations to the following set of recurrence equations to various orders:

to order ε

$$D_0^2 X_{11} + \omega_1^2 X_{11} = 0\,, \tag{20}$$

$$D_0^2 X_{21} + \omega_2^2 X_{21} = 0\,, \tag{21}$$

to order ε^3

$$\begin{aligned} D_0^2 X_{13} + \omega_1^2 X_{13} = &-2D_0 D_2 X_{11} - \left(\overline{\mu}_1 \tau_1^{\gamma_1} D_0^{\gamma_1} - \lambda_\infty \nu_\varepsilon \overline{\mu}_2 (1+\tau_2^{\gamma_2} D_0^{\gamma_2})^{-1}\right) X_{11} \\ &- \alpha_1 X_{11}^3 - \alpha_2 X_{11} X_{21}^2\,, \end{aligned} \tag{22}$$

$$\begin{aligned} D_0^2 X_{23} + \omega_2^2 X_{23} = &-2D_0 D_2 X_{21} - \left(\overline{\mu}_1 \tau_1^{\gamma_1} D_0^{\gamma_1} - \lambda_\infty \nu_\varepsilon \overline{\mu}_2 (1+\tau_2^{\gamma_2} D_0^{\gamma_2})^{-1}\right) X_{21} \\ &- \alpha_3 X_{21}^3 - \alpha_4 X_{21} X_{11}^2\,, \end{aligned} \tag{23}$$

where ω_1 and ω_2 are vibration frequencies of the mechanical system "plate + viscoelastic foundation"

$$\omega_i^2 = \Omega_i^2 + \frac{\lambda_\infty}{\rho h}, \tag{24}$$

and $\overline{\mu}_i = \dfrac{\mu_i}{\rho h}$ $(i = 1, 2)$.

The solution of linear equations (20) and (21) has the form

$$X_{j1} = A_j(T_2)\exp\left(i\omega_j T_0\right) + \overline{A}_j(T_2)\exp\left(-i\omega_j T_0\right), \tag{25}$$

where $A_j(T_2)$ $(j = 1, 2)$ are yet unknown functions and $\overline{A}_j(T_2)$ are conjugate functions with $A_j(T_2)$.

In order to solve the set of equations (22) and (23), it is necessary to define the action of the fractional derivative $D_{0+}^{\gamma_i}$ (3) and the Rabotnov dimensionless fractional operator $э_\gamma^*(\tau_2^{\gamma_2})$ (11) on the functions X_{j1}, i.e., to calculate $D_{0+}^{\gamma_i} e^{i\omega_j t}$ and $\dfrac{1}{1+\tau_2^{\gamma_2} D_{0+}^{\gamma_2}} e^{i\omega_j t}$. It was shown in [2, 21] that these expressions are reduced to the following form:

$$D_{0+}^{\gamma} e^{i\omega_j t} \simeq \left(i\omega_j\right)^{\gamma} e^{i\omega_j t}, \tag{26}$$

$$\frac{1}{1+\tau_2^{\gamma_2} D_{0+}^{\gamma_2}} e^{i\omega_j t} \simeq \frac{1}{1+(i\omega_j \tau_2)^{\gamma_2}} e^{i\omega_j t}. \tag{27}$$

Substituting relationships (25) in equations (22) and (23) with due account for formulas (26) and (27) yields

$$\begin{aligned}
&D_0^2 X_{13} + \omega_1^2 X_{13} = -2i\omega_1 D_2 A_1 \exp\left(i\omega_1 T_0\right) \\
&-\left[\overline{\mu}_1 \tau_1^{\gamma_1} \left(i\omega_1\right)^{\gamma_1} - \lambda_\infty \nu_\varepsilon \overline{\mu}_2 (1 + \tau_2^{\gamma_2} \left(i\omega_1\right)^{\gamma_2})^{-1}\right] A_1 \exp\left(i\omega_1 T_0\right) \\
&-\alpha_1\left[A_1 \exp\left(3i\omega_1 T_0\right) + 3\overline{A}_1 \exp\left(i\omega_1 T_0\right)\right] A_1^2 \\
&-\alpha_2\left\{A_2^2 \exp\left[\left(\omega_1 + 2\omega_2\right) T_0\right] + 2A_2\overline{A}_2 \exp\left(i\omega_1 T_0\right) + \overline{A}_2^2 \exp\left[i\left(\omega_1 - 2\omega_2\right) T_0\right]\right\} A_1 + cc,
\end{aligned} \tag{28}$$

$$\begin{aligned}
&D_0^2 X_{23} + \omega_2^2 X_{23} = -2i\omega_2 D_2 A_2 \exp\left(i\omega_2 T_0\right) \\
&-\left[\overline{\mu}_1 \tau_1^{\gamma_1} \left(i\omega_2\right)^{\gamma_1} - \lambda_\infty \nu_\varepsilon \overline{\mu}_2 (1 + \tau_2^{\gamma_2} \left(i\omega_2\right)^{\gamma_2})^{-1}\right] A_2 \exp\left(i\omega_2 T_0\right) \\
&-\alpha_3\left[A_2 \exp\left(3i\omega_2 T_0\right) + 3\overline{A}_2 \exp\left(i\omega_2 T_0\right)\right] A_2^2 \\
&-\alpha_4\left\{A_1^2 \exp\left[\left(2\omega_1 + \omega_2\right) T_0\right] + 2A_1\overline{A}_1 \exp\left(i\omega_2 T_0\right) + \overline{A}_1^2 \exp\left[i\left(\omega_2 - 2\omega_1\right) T_0\right]\right\} A_2 + cc.
\end{aligned} \tag{29}$$

The analysis of equations (28) and (29) shows that the one-to-one internal resonance is possible in the case when

$$\omega_1 = \omega_2, \quad \text{and therefore,} \quad \Omega_1 = \Omega_2. \tag{30}$$

The condition for eliminating secular terms in equations (28) and (29) with account for equation (30) leads to a set of two governing equations:

$$2i\omega_1 D_2 A_1 + \left[\overline{\mu}_1 \tau_1^{\gamma_1} \left(i\omega_1\right)^{\gamma_1} - \lambda_\infty \nu_\varepsilon \overline{\mu}_2 (1 + \tau_2^{\gamma_2} \left(i\omega_1\right)^{\gamma_2})^{-1} \right] A_1 + 3\alpha_1 A_1^2 \overline{A}_1 + \alpha_2 \overline{A}_1 A_2^2 + 2\alpha_2 A_1 A_2 \overline{A}_2 = 0, \tag{31}$$

$$2i\omega_2 D_2 A_2 + \left[\overline{\mu}_1 \tau_1^{\gamma_1} \left(i\omega_2\right)^{\gamma_1} - \lambda_\infty \nu_\varepsilon \overline{\mu}_2 (1 + \tau_2^{\gamma_2} \left(i\omega_2\right)^{\gamma_2})^{-1} \right] A_2 + 3\alpha_3 A_2^2 \overline{A}_2 + \alpha_4 \overline{A}_2 A_1^2 + 2\alpha_4 A_2 A_1 \overline{A}_1 = 0. \tag{32}$$

Multiplying (31) by $\overline{A}_1$ and (32) by $\overline{A}_2$, adding and subtracting the equations conjugate to them, and also representing functions A_1 and A_2 in their polar form

$$A_i = a_i e^{i\varphi_i} \quad (i = 1, 2), \tag{33}$$

where $a_i = a_i(T_2)$ and $\varphi_i = \varphi_i(T_2)$ are the functions of amplitudes and phases of vibrations, yield the following set of equations:

$$\left(a_1^2\right)^{\cdot} + s_1 a_1^2 = -\omega_1^{-1} \alpha_2 a_1^2 a_2^2 \sin\delta, \tag{34}$$

$$\left(a_2^2\right)^{\cdot} + s_2 a_2^2 = \omega_2^{-1} \alpha_4 a_1^2 a_2^2 \sin\delta, \tag{35}$$

$$\dot{\varphi}_1 = \frac{1}{2}\lambda_1 + \frac{3}{2}\alpha_1 \omega_1^{-1} a_1^2 + \alpha_2 \omega_1^{-1} a_2^2 + \frac{1}{2}\alpha_2 \omega_1^{-1} a_2^2 \cos\delta, \tag{36}$$

$$\dot{\varphi}_2 = \frac{1}{2}\lambda_2 + \frac{3}{2}\alpha_3 \omega_2^{-1} a_2^2 + \alpha_4 \omega_2^{-1} a_1^2 + \frac{1}{2}\alpha_4 \omega_2^{-1} a_1^2 \cos\delta, \tag{37}$$

where $\delta = \varphi_2 - \varphi_1$ is the phase difference,

$$s_i = \overline{\mu}_1 \tau_1^{\gamma_1} \omega_i^{\gamma_1 - 1} \sin\psi_1 + \lambda_\infty \nu_\varepsilon \overline{\mu}_2 \omega_i^{-1} R_i \sin\Phi_i, \quad \lambda_i = \overline{\mu}_1 \tau_1^{\gamma_1} \omega_i^{\gamma_1 - 1} \cos\psi_1 - \lambda_\infty \nu_\varepsilon \overline{\mu}_2 \omega_i^{-1} R_i \cos\Phi_i,$$
$$\psi_i = \frac{1}{2}\pi\gamma_i, \quad R_i = \sqrt{1 + 2(\tau_2\omega_i)^{\gamma_2} \cos\psi_2 + (\tau_2\omega_i)^{2\gamma_2}}, \quad \tan\Phi_i = \frac{(\tau_2\omega_i)^{\gamma_2} \sin\psi_2}{1 + (\tau_2\omega_i)^{\gamma_2} \cos\psi_2} \quad (i = 1, 2). \tag{38}$$

The set of equations (34)-(37) is the determining one for the amplitudes and phases of nonlinear free vibrations of a simply supported elastic plate on a viscoelastic foundation, damping features of which are defined by the fractional derivative standard linear solid model (4), when vibrations occur in a viscoelastic surrounding medium, properties of which are described by the fractional derivative Kelvin-Voigt model (3).

Reference to the governing equations (34)-(37) shows that nonlinear damped vibrations of the mechanical system "elastic plate on a viscoelastic foundation" in a viscoelastic surrounding medium are defined by the damping coefficients s_i (38), which depend on natural frequencies of two coupled modes Ω_i and rheological parameters of the supporting foundation and surrounding medium, involving two fractional parameters γ_1 and γ_2.

4 NUMERICAL ANALYSIS

The resulting set of equations (34)-(37) is solved numerically by using the fourth-order Runge-Kutta method in the «GNU Octave» system. The results of a numerical experiment are shown in Fig. 2 for free vibrations at different magnitudes of fractional parameters γ_1 and γ_2.

A rectangular plate with an aspect ratio $a/b=3$ was considered as an example for the case of $m_1=3, n_1=2, m_2=6, n_2=1$, for which $\Omega_{32}=\Omega_{61}$.

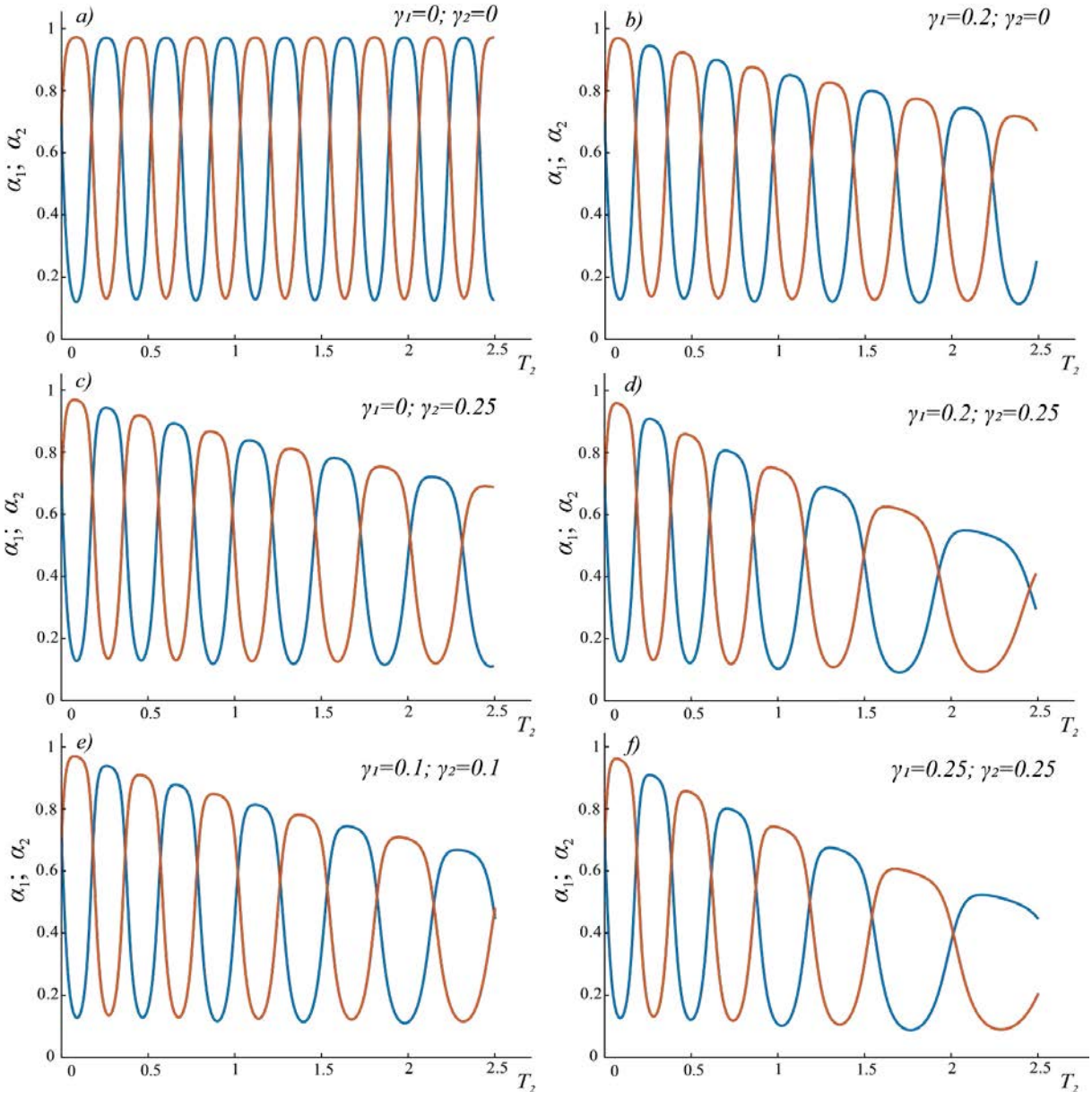

Figure 2: The dimensionless time T_2 dependence of the dimensionless amplitudes of free vibrations in the case of the 1:1 internal resonance for a plate on a viscoelastic viscoelastic foundation, blue line – a_1, orange line - a_2

Reference to Fig. 2 clearly shows the energy exchange between interacting vibration modes for all considered cases: undamped and damped vibrations of an elastic plate on an elastic foundation, respectively, at $\gamma_1=\gamma_2=0$ (Fig. 2a) and $\gamma_1=0.2$, $\gamma_2=0$ (Fig. 2b); vibrations of an elastic plate on a viscoelastic foundation ($\gamma_2\neq 0$) surrounded by an elastic ($\gamma_1=0$) and viscoelastic ($\gamma_1\neq 0$) medium, in Fig. 2c and Figs. 2d-f, respectively. The increase in the fractional parameter of the viscoelastic foundation results in a significant decrease in dimensionless amplitudes of nonlinear vibrations (Fig. 2c). With the appearance of the damping

properties of the environment (Fig. 2d-f), in which the plate vibrates, the damping of vibrations increases.

Figure 3 shows the calculated results of vibration amplitudes of the plate in the elastic medium ($\gamma_1 = 0$) when damping features of the viscoelastic foundation are described by the fractional derivative standard linear solid model (solid lines) and fractional derivative Kelvin-Voigt model (dashed lines) at $\gamma_2 = 0.25$. From Fig. 3 it is seen that the period of vibrations described by the KV-model is more than that described by the SLS-model.

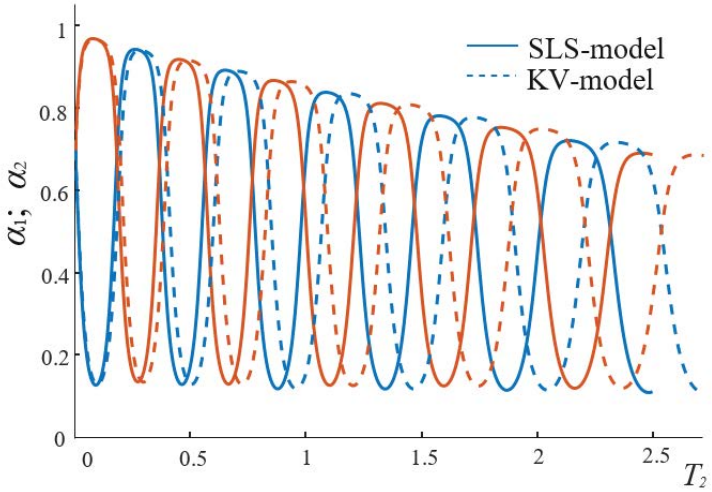

Figure 3: The time T_2 dependence of the dimensionless amplitudes of free vibrations in the case of the 1:1 internal resonance for a plate on a viscoelastic foundation at $\gamma_1 = 0,\ \gamma_2 = 0.25$; blue line – a_1, orange line - a_2

5 CONCLUSION

In the present paper, the problem of nonlinear vibrations of a von Karman simply supported elastic plate based on a viscoelastic foundation is solved. The damping features of the viscoelastic foundation are described by the fractional derivative standard linear solid model, while the damping properties of the environment in which the vibrations occur are described by the Kelvin-Voigt viscoelastic model with the Riemann-Liouville fractional derivative. The governing equations are obtained for determining nonlinear amplitudes and phases in the case of free vibrations, when the natural frequencies of the two dominant vibration modes are close to each other. The resulting set of equations allows one to control the damping properties of the external environment and the foundation by changing the fractional parameters from zero, what corresponds to an elastic medium and/or elastic foundation, to unit, what conforms to the traditional standard linear solid model, resulting in the expansion of the range of applicability of the solution obtained.

The derived set of equations has been solved numerically and could be also generalized for the case of force driven vibrations [22]. The results of numerical investigation have been compared with the case of viscoelastic foundation, the damping features of which are described by the fractional derivative Kelvin-Voigt model. The proposed standard linear solid model is preferable over other models, because it is able to describe both creep and relaxation properties of the viscoelastic materials (soil), while the Kelvin-Voigt model is unsuitable for describing the relaxation of materials and the Maxwell model could not describe the creep of materials. Thus, the obtained results are more accurate in comparison with those based on more simple models of viscoelasticity.

Acknowledgement. This research was supported by the Russian Foundation for Basic Research under the Grant No. 20-01-00443.

APPENDIX

$$\alpha_1 = -\frac{1}{8}\pi^4 \int_0^a \int_0^b \sin^2\left(\frac{\pi m_1 x}{a}\right)\sin^2\left(\frac{\pi n_1 y}{b}\right)\left[\frac{m_1^4}{a^4}\cos\left(\frac{2\pi n_1 y}{b}\right)+\frac{n_1^4}{b^4}\cos\left(\frac{2\pi m_1 x}{a}\right)\right]dxdy\,, \tag{A.1}$$

$$\begin{aligned}
\alpha_2 = \pi^4 \int_0^a \int_0^b \Bigg\{ & -\frac{1}{8}\sin\left(\frac{\pi m_1 x}{a}\right)\sin\left(\frac{\pi n_1 y}{b}\right)\left[\frac{m_1^2 m_2^2}{a^4}\cos\left(\frac{2\pi n_2 y}{b}\right)+\frac{n_1^2 n_2^2}{b^4}\cos\left(\frac{2\pi m_2 y}{b}\right)\right] \\
& -\frac{1}{4}\frac{m_2^2}{a^2 b^2}\sin\left(\frac{\pi m_2 x}{a}\right)\sin\left(\frac{\pi n_2 y}{b}\right)\cos\left(\frac{\pi\left(m_1+m_2\right)x}{a}\right) \\
& \times\left[-A^2\left(n_1+n_2\right)^2\cos\left(\frac{\pi\left(n_1+n_2\right)y}{b}\right)\beta_2^2+B^2\left(n_1-n_2\right)^2\cos\left(\frac{\pi\left(n_1-n_2\right)y}{b}\right)^2\beta_1^2\right] \\
& -\frac{1}{4}\frac{m_2^2}{a^2 b^2}\sin\left(\frac{\pi m_2 x}{a}\right)\sin\left(\frac{\pi n_2 y}{b}\right)\cos\left(\frac{\pi\left(m_1-m_2\right)x}{b}\right) \\
& \times\left[-D^2\left(n_1-n_2\right)^2\beta_2^2\cos\left(\frac{\pi\left(n_1-n_2\right)y}{a}\right)+C^2\left(n_1+n_2\right)^2\beta_1^2\cos\left(\frac{\pi\left(n_1+n_2\right)y}{b}\right)\right] \\
& -\frac{1}{4}\frac{n_2^2}{a^2 b^2}\sin\left(\frac{\pi m_2 x}{a}\right)\sin\left(\frac{\pi n_2 y}{b}\right)\cos\left(\frac{\pi\left(n_1+n_2\right)x}{a}\right) \\
& \times\left[-A^2\left(m_1+m_2\right)^2\beta_2^2\cos\left(\frac{\pi\left(m_1+m_2\right)y}{b}\right)+B^2\left(m_1-m_2\right)^2\beta_1^2\cos\left(\frac{\pi\left(m_1-m_2\right)y}{b}\right)^2\right] \\
& -\frac{1}{4}\frac{n_2^2}{a^2 b^2}\sin\left(\frac{\pi m_2 x}{a}\right)\sin\left(\frac{\pi n_2 y}{b}\right)\cos\left(\frac{\pi\left(n_1-n_2\right)x}{b}\right) \\
& \times\left[-D^2\left(m_1-m_2\right)^2\beta_2^2\cos\left(\frac{\pi\left(m_1-m_2\right)y}{a}\right)+C^2\left(m_1+m_2\right)^2\beta_1^2\cos\left(\frac{\pi\left(m_1+m_2\right)y}{b}\right)\right] \\
& +\frac{1}{2}\frac{m_2 n_2}{a^2 b^2}\cos\left(\frac{\pi m_2 x}{a}\right)\cos\left(\frac{\pi n_2 y}{b}\right)\left(m_1+m_2\right)^2\sin\left(\frac{\pi\left(m_1+m_2\right)x}{a}\right) \\
& \times\left[-A^2\left(n_1+n_2\right)^2\beta_2^2\sin\left(\frac{\pi\left(n_1+n_2\right)y}{b}\right)+B^2\left(n_1-n_2\right)^2\beta_1^2\sin\left(\frac{\pi\left(n_1-n_2\right)y}{b}\right)^2\right] \\
& +\frac{1}{2}\frac{m_2 n_2}{a^2 b^2}\cos\left(\frac{\pi m_2 x}{a}\right)\cos\left(\frac{\pi n_2 y}{b}\right)\left(m_1-m_2\right)^2\sin\left(\frac{\pi\left(m_1-m_2\right)x}{b}\right) \\
& \times\left[-D^2\left(n_1-n_2\right)^2\beta_2^2\sin\left(\frac{\pi\left(n_1-n_2\right)y}{a}\right)+C^2\left(n_1+n_2\right)^2\beta_1^2\sin\left(\frac{\pi\left(n_1+n_2\right)y}{b}\right)\right]\Bigg\} \\
& \times\sin\left(\frac{\pi m_1 x}{a}\right)\sin\left(\frac{\pi n_1 y}{b}\right)dxdy,
\end{aligned} \tag{A.2}$$

$$\alpha_3 = -\frac{1}{8}\pi^4 \int_0^a \int_0^b \sin^2\left(\frac{\pi m_2 x}{a}\right)\sin^2\left(\frac{\pi n_2 y}{b}\right)\left[\frac{m_2^4}{a^4}\cos\left(\frac{2\pi n_2 y}{b}\right)+\frac{n_2^4}{b^4}\cos\left(\frac{2\pi m_2 x}{a}\right)\right]dxdy\,, \tag{A.3}$$

$$\begin{aligned}
\alpha_4 = \pi^4 \int_0^a \int_0^b \Bigg\{ & -\frac{1}{8}\sin\left(\frac{\pi m_2 x}{a}\right)\sin\left(\frac{\pi n_2 y}{b}\right)\left[\frac{m_1^2 m_2^2}{a^4}\cos\left(\frac{2\pi n_2 y}{b}\right)+\frac{n_1^2 n_2^2}{b^4}\cos\left(\frac{2\pi m_2 y}{b}\right)\right] \\
& -\frac{1}{4}\frac{m_1^2}{a^2 b^2}\sin\left(\frac{\pi m_1 x}{a}\right)\sin\left(\frac{\pi n_1 y}{b}\right)\cos\left(\frac{\pi\left(m_1+m_2\right)x}{a}\right) \\
& \times\left[-A^2\left(n_1+n_2\right)^2\beta_2^2\cos\left(\frac{\pi\left(n_1+n_2\right)y}{b}\right)+B^2\left(n_1-n_2\right)^2\beta_1^2\cos\left(\frac{\pi\left(n_1-n_2\right)y}{b}\right)^2\right] \\
& -\frac{1}{4}\frac{m_1^2}{a^2 b^2}\sin\left(\frac{\pi m_1 x}{a}\right)\sin\left(\frac{\pi n_1 y}{b}\right)\cos\left(\frac{\pi\left(m_1-m_2\right)x}{b}\right) \\
& \times\left[-D^2\left(n_1-n_2\right)^2\beta_2^2\cos\left(\frac{\pi\left(n_1-n_2\right)y}{a}\right)+C^2\left(n_1+n_2\right)^2\beta_1^2\cos\left(\frac{\pi\left(n_1+n_2\right)y}{b}\right)\right] \\
& -\frac{1}{4}\frac{n_1^2}{a^2 b^2}\sin\left(\frac{\pi m_1 x}{a}\right)\sin\left(\frac{\pi n_1 y}{b}\right)\cos\left(\frac{\pi\left(n_1+n_2\right)x}{a}\right) \\
& \times\left[-A^2\left(m_1+m_2\right)^2\beta_2^2\cos\left(\frac{\pi\left(m_1+m_2\right)y}{b}\right)+B^2\left(m_1-m_2\right)^2\beta_1^2\cos\left(\frac{\pi\left(m_1-m_2\right)y}{b}\right)^2\right] \\
& -\frac{1}{4}\frac{n_1^2}{a^2 b^2}\sin\left(\frac{\pi m_1 x}{a}\right)\sin\left(\frac{\pi n_1 y}{b}\right)\cos\left(\frac{\pi\left(n_1-n_2\right)x}{b}\right) \\
& \times\left[-D^2\left(m_1-m_2\right)^2\beta_2^2\cos\left(\frac{\pi\left(m_1-m_2\right)y}{a}\right)+C^2\left(m_1+m_2\right)^2\beta_1^2\cos\left(\frac{\pi\left(m_1+m_2\right)y}{b}\right)\right] \\
& +\frac{1}{2}\frac{m_1 n_1}{a^2 b^2}\cos\left(\frac{\pi m_1 x}{a}\right)\cos\left(\frac{\pi n_1 y}{b}\right)\left(m_1+m_2\right)^2\sin\left(\frac{\pi\left(m_1+m_2\right)x}{a}\right) \\
& \times\left[-A^2\left(n_1+n_2\right)^2\beta_2^2\sin\left(\frac{\pi\left(n_1+n_2\right)y}{b}\right)+B^2\left(n_1-n_2\right)^2\beta_1^2\sin\left(\frac{\pi\left(n_1-n_2\right)y}{b}\right)^2\right] \\
& +\frac{1}{2}\frac{m_1 n_1}{a^2 b^2}\cos\left(\frac{\pi m_1 x}{a}\right)\cos\left(\frac{\pi n_1 y}{b}\right)\left(m_1-m_2\right)^2\sin\left(\frac{\pi\left(m_1-m_2\right)x}{b}\right) \\
& \times\left[-D^2\left(n_1-n_2\right)^2\beta_2^2\sin\left(\frac{\pi\left(n_1-n_2\right)y}{a}\right)+C^2\left(n_1+n_2\right)^2\beta_1^2\sin\left(\frac{\pi\left(n_1+n_2\right)y}{b}\right)\right]\Bigg\} \\
& \times\sin\left(\frac{\pi m_2 x}{a}\right)\sin\left(\frac{\pi n_2 y}{b}\right)dxdy.
\end{aligned} \tag{A.4}$$

REFERENCES

[1] W. Cai, W. Chen, W. Xu, Fractional modeling of Pasternak-type viscoelastic foundation, *Mechanics of Time-Dependent Materials* 21, 119–131, 2017.

[2] Yu.A. Rossikhin, M.V. Shitikova, Application of fractional calculus for dynamic problems of solid mechanics: Novel trends and recent results, *Applied Mechanics Reviews* 63, 010801, 2010.

[3] Yu.A. Rossikhin, M.V. Shitikova, New approach for the analysis of damped vibrations of fractional oscillators, *Shock and Vibration* 16, 365–387, 2009.

[4] M.V. Shitikova, The fractional derivative expansion method in nonlinear dynamic analysis of structures, *Nonlinear Dynamics* 99(1), 109-122, 2020.

[5] D. Younesian, Elastic and viscoelastic foundations: a review on linear and nonlinear vibration modeling and applications, *Nonlinear Dynamics* 97, 853–895, 2019.

[6] A.D. Kerr, Elastic and viscoelastic foundation models, *Journal of Applied Mechanics* 31(3), 491-498, 1964.

[7] K.S. Pister, Viscoelastic plate on a viscoelastic foundation, *Journal of the Engineering Mechanics Division* 87, 43–54, 1961.

[8] M. Zaman, M.R. Taheri, A. Alvappillai, Dynamic response of a thick plate on viscoelastic foundation to moving loads, *International Journal for Numerical and Analytical Methods in Geomechanics* 15, 627–647, 1991.

[9] H.H. Zhu, L.C. Liu, H.F. Pei, B. Shi, Settlement analysis of viscoelastic foundation under vertical line load using a fractional Kelvin–Voigt model, *Geomechanics and Engineering* 4, 67–78, 2012.

[10] L. Kou, Y. Bai, Dynamic response of rectangular plates on two-parameter viscoelastic foundation with fractional derivatives, *Journal of Vibration and Shock* 33, 141-147, 2014.

[11] C. Zhang, H. Zhu, B. Shi, L. Liu, Theoretical investigation of interaction between a rectangular plate and fractional viscoelastic foundation, *Journal of Rock Mechanics and Geotechnical Engineering* 6, 373–379, 2014.

[12] T.D. Hien, N.N. Lam, Vibration of functionally graded plate resting on viscoelastic elastic foundation subjected to moving loads, *IOP Conference Series: Earth and Environmental Science* 143, 2018.

[13] A. Zhou, J. Xu, B. Wang, Response for a loaded rectangular plate on viscoelastic foundation with fractional derivative model: *Proceedings of Geo Shanghai 2018 International Conference: Fundamentals of Soil Behaviours,* 2018.

[14] J. Fan, D. Rong, C. Xu, X. Xu, Exact solutions for forced vibration of completely free orthotropic rectangular nanoplates resting on viscoelastic foundation, *European Journal of Mechanics, A/Solids* 73, 22-33, 2019.

[15] S.G. Samko, A.A. Kilbas, O.I. Marichev, Fractional Integrals and Derivatives. Theory and Applications*, English translation by Gordon and Breach Science Publishers*, ISBN: 9782881248641, 1993.

[16] Yu.A. Rossikhin, M.V. Shitikova, Fractional operator models of viscoelasticity, *Encyclopedia of Continuum Mechanics,* 971-982, H. Altenbach, A. Öchsner (eds.), *Springer*, ISBN: 978-3-662-53605-6, 2020.

[17] Yu.A. Rossikhin, M.V. Shitikova, Centennial jubilee of Academician Rabotnov and contemporary handling of his fractional operator, *Fractional Calculus and Applied Analysis* 17, 674-683, 2014.

[18] A.H. Nayfeh, Perturbation Methods, *John Wiley & Sons, Inc.*, ISBN: 9783527617609, 2003.

[19] Yu.A. Rossikhin, M.V. Shitikova, Application of fractional calculus for analysis of nonlinear damped vibrations of suspension bridges, *Journal of Engineering Mechanics* 124, 1029–1036, 1998.

[20] Yu.A. Rossikhin, M.V. Shitikova, On fallacies in the decision between the Caputo and Riemann-Liouville fractional derivatives for the analysis of the dynamic response of a nonlinear viscoelastic oscillator, *Mechanics Research Communications,* 45, 22-27, 2012.

[21] Yu.A. Rossikhin, A.I. Krusser, M.V. Shitikova, Impact response of a nonlinear viscoelastic auxetic doubly curved shallow shell, *Proceedings of the 24th International Congress on Sound and Vibration*, 2017.

[22] M.V. Shitikova, V.V. Kandu, Force driven vibrations of fractionally damped plates subjected to primary and internal resonances, *The European Physical Journal Plus* 134 (9), PaperID 423, 2019.

EURODYN 2020
XI International Conference on Structural Dynamics
M. Papadrakakis, M. Fragiadakis, C. Papadimitriou (eds.)
Athens, Greece, 23–26 November 2020

NONLINEAR HARDENING BEHAVIOR OF A HELMHOLTZ RESONATOR

Emmanuel Gourdon[1], **Alireza Ture Savadkoohi**[1], **and Claude-Henri Lamarque**[1]

[1]LTDS UMR CNRS 5513
Ecole Nationale des Travaux Publics de l'Etat
Rue Maurice Audin 69518 Vaulx en Velin Cedex, FRANCE
e-mail: {emmanuel.gourdon, alireza.turesavadkoohi, claude-henri.lamarque}@entpe.fr

Keywords: Helmoltz resonator, hardening behavior, time multiple scales, subharmonic resonance.

Abstract. *Nonlinear amplitude-frequency response of a Helmholtz resonator is investigated by taking into account nonlinear restoring and damping forces [1]. Method of multiple time scales [2] applied to complexified form [3] of system equations are used for detection of different system dynamics. Several developments are done to obtain hardening behavior allowing targeted energy transfer from an acoustical mode to the nonlinear absorber [4]. Modified geometries of the neck are first considered to decrease the damping and activate cubic nonlinearities. Obtained results for large amplitudes show accelerated amplitude dependency of resonant frequencies of nonlinear geometry resonators compared to classical ones. This nonlinear response can be used as a passive controller system with nonlinear restoring forcing function for having broadband frequency absorption. The time multiple scale method around the 1:1 resonance allows to detect Slow Invariant Manifold (SIM) of the system, its equilibrium and singular points. Analytical predictions are compared with those obtained by direct numerical integration of system equations. Experimental verifications are performed and presented. Then, a two frequency driving (subharmonic resonance) is considered and we show that the phase difference of the driving can modify the classical softening behavior of an Helmholtz resonator. By choosing a phase difference into a certain range we show that it is possible to obtain hardening behavior and an improvement of the nonlinear response with generation of higher amplitude oscillations. The proposed results are mainly obtained by using method of multiple time scales [2] which has been used in thousands of papers and has been proved to be very accurate and very computational efficient. The results have been validated numerically with Runge-Kutta schemes of order four: the errors are less than 1% and the computational time is drastically reduced owing to analytical approximations.*

1 INTRODUCTION

In acoustics, Helmholtz Resonators (HR) [5] are often used to absorb sound, specifically for low frequencies where the classical porous materials are not efficient anymore. A lot of applications are done in buildings [6], aeronautics, industries. However, they are only efficient for a specific frequency. To broadband the frequency range of efficiency of classical mecanical resonators, it is possible to use a nonlinear restoring force [7, 8, 9, 10]. Some authors [11, 12] applied this concept in vibro-acoustics by using a cubic nonlinearity (a viscoelastic membrane). They have shown that it is possible to transfer acoustical energy irreversibly. In the present work, we are interested to use a pure acoustical resonator.

In [1], it was shown that it is possible to obtain nonlinear behavior of HR. Indeed nonlinear damping (due to jet loss) [13] and also nonlinear restoring force with quadratic and cubic term (due to the nonlinear elasticity of the cavity air for high amplitudes excitations) [14] can be taken into account. In [14] they show that it is theoretically possible to obtain a softening behavior.

Moreover, [15] mentioned the frequency dependency of the resonator on the flow velocity and on the resonator geometry. That is why, as underlined by [16], tayloring the neck of the resonator can influence the vortex apparition and dissipation around the neck. This fact allows to go further in the nonlinear domain, in terms of the nonlinear restoring force, if the vortex and dissipation around the neck are minimized. This point has been underlined in [1] and is also shown in the present paper with different neck geometries. By reducing vortex shedding by nonlinear tailoring of the HR neck, it is then possible to obtain hardening behavior for high amplitudes and not only softening behavior as performed by previous papers [14, 17]. Experimental verifications are also provided.

With this hardening behavior of the HR, it has been shown in [4] that it possible and feasible to activate targeted energy transfer. The case of the passive control of an coustical mode (created by a system composed of a tube with coupling boxes) by using a HR having a nonlinear hardening behavior has been treated analytically using method of multiple time scales [2] applied to complexified form [3] of system equations for detection of different system dynamics. In the present paper main results are given. Experimental verification has also been perfomed.

In [1, 4], it was shown that for very high amplitudes it is possible to obtain hardening behavior under certain conditions (neck geometry, decreasing of vortex phenomenon...). So it is not obvious to obtain hardening behavior for classical HR. That is why we propose in the present paper to study the two frequency driving (subharmonic resonance) case for a classical HR. The aim is to show that the phase difference of the driving can modify the classical softening behavior of an HR. By choosing a phase difference into a certain range we show that it is possible to obtain hardening behavior and an improvement of the nonlinear response with generation of higher amplitude oscillations. The proposed results are mainly obtained by using method of multiple time scales [2] which has been used in thousands of papers and has been proved to be very accurate and very computational efficient.

This paper is structured as follows: First, in Section 2, results about hardening behavior of HR with modified neck geometry are shown with experimental verifications of the targeted energy transfer. Then, in Section 3, the response of the two-frequency driving is studied. Finally, in Section 4, we conclude about the results of this work.

2 ONE-FREQUENCY DRIVING WITH MODIFIED GEOMETRY OF HR

In the following we consider HR excited by sound wave as shown in Figure 1. HR consists

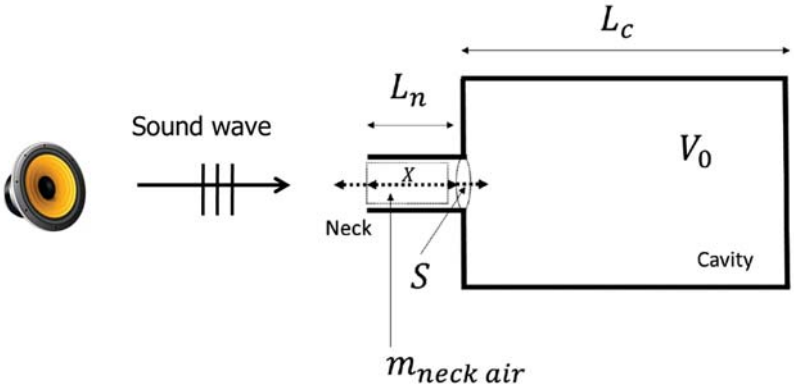

Figure 1: Helmholtz resonator excited by sound wave.

in an air column neck considered as incompressible mass and compressible air in the cavity. For HR physics, following hypothesis are considered: the transformations inside the acoustic resonator are adiabatic; the neck length L_n is considered much smaller than cavity length L_c and the neck air mass $m_{neck\ air}$ is considered as incompressible [18]. The friction due to the air high velocity in the neck will produce damping [13, 14] and the compression of the air in the cavity produces a restoring force. The displacement X of the air in the neck will cause the change of pressure Δp [17, 14]:

$$\Delta p = -\rho L_e \omega_0^2 \left[X - \frac{(\hat{\gamma}+1)\, S}{2V_0} X^2 + \frac{(\hat{\gamma}+1)\,(\hat{\gamma}+2)\, S^2}{6V_0^2} X^3 \right] \tag{1}$$

where ρ is the air density, L_e is the effective length of the neck ($L_e = L_n + (16r/3\pi)$, with r the radius of the cylindrical neck as mentioned in [14]), S is the cross section of the neck, V_0 is the volume in the cavity, $\hat{\gamma}$ is the specific heat ratio and ω_0 is the linear resonance frequency of the resonator.

2.1 Nonlinear behavior of modified HR

In [1] and [19] , different geometries of the neck of HR (as illustrated in Figure 2) have been considred to decrease the vortex phenomenon to be able to activate nonlinear terms of the nonlinear restoring force. Indeed, usually, the cubic term in Equation (1) is not taken into account [17]. However, incorporating here the cubic nonlinearity allows to balance damping term, which is usually of third order. Because of the attenuation of vortex shedding (by tailoring the neck) the nonlinear term will be dominant and the cubic nonlinearity can be activated.
In Figure 2, configurations H_1 and H_2 correspond to cylindrical and conical necks respectively, while configurations H_5 corresponds to quadratic neck with different radius of inlets and outlets. Characteristics of these configurations are given in Table 1.

To measure different acoustic properties of the HR, the test set-up is a classical Kundt tube (described for example in [1]) with different microphone positions to be able to measure the incident pressure on the HR (the HR is inserted as the end of the Kundt tube) and the pressure inside the cavity of the resonator. The used Kundt tube has a diameter of 46 mm. The length of the cavity has been taken as 25mm and the systems are excited by different sinusoidal forces: pressures inside the cavity during resonances are measured and corresponding amplitudes are evaluated. Obtained results are shown in Figure 3. In Figure 3 the behavior of the resonator with cylindrical neck remains almost linear until a high pressure level, i.e. the frequency does

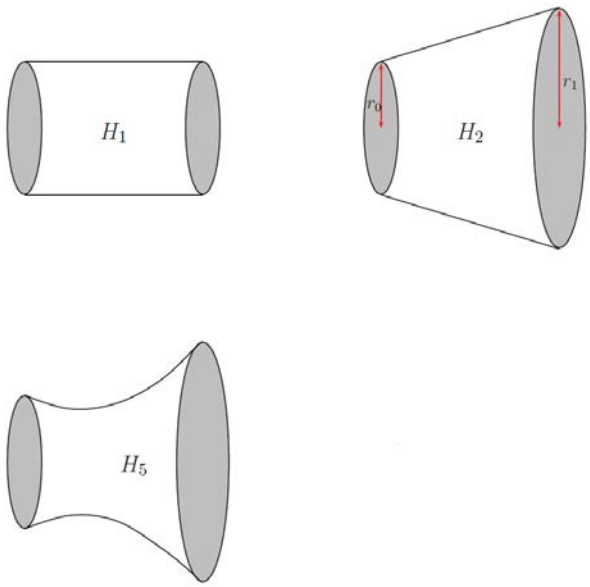

Figure 2: Different geometries of the neck of HR considered in [19].

	H_1	H_2	H_5
$L_n(mm)$	8.5	8.5	8.5
$r_0(mm)$	1.5	1.5	1.7
$r_1(mm)$	1.5	2	3.25

Table 1: Characteristics of different configurations of necks .

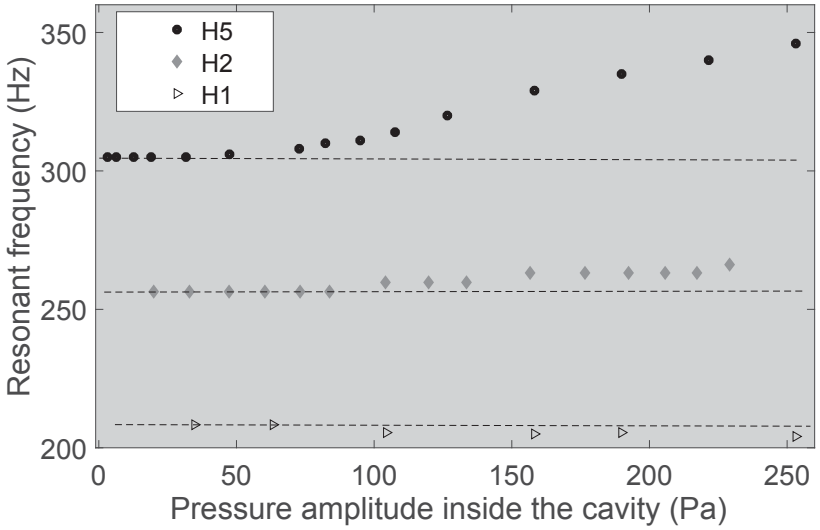

Figure 3: Dependency of the resonant frequency on the pressure amplitude (sinusoidal excitation, different resonators with length of the cavity of 25mm): resonant frequency vs. pressure amplitude inside the cavity.

not vary much in function of amplitude. We can also see a slightly softening behavior already

seen in previous publications [14, 17].
Moreover, Figure 3 shows that geometrical nonlinearity of the neck H_5 makes the resonator experiences a nonlinear behavior that starts at lower pressure level compared to the cylindrical case, i.e. after $P = 31.6Pa$ (with conical neck H_2 the nonlinear behavior starts at $P = 100Pa$). This means that frequency increases in a nonlinear manner with the increase of the amplitude, i.e. hardening behavior. These experimental results show that nonlinear tailored neck of the resonator accelerates considerably the start of the nonlinear response of the system compared to the resonators with cylindrical necks.

Combining all damping, restoring terms and the external pressure increment p^*, we can obtain the governing equation (see for example [1] for more details):

$$\frac{d^2X}{dt^{*2}} + \frac{\xi}{2L_e}\frac{dX}{dt^*}\left|\frac{dX}{dt^*}\right| + 2\delta^*\frac{dX}{dt^*} + \omega_0^2 X\left(1 - \alpha\frac{SX}{V_0} + \beta\left(\frac{SX}{V_0}\right)^2\right) = -\frac{p^*}{\rho L_e} \tag{2}$$

where t^* is the real time,
$\delta^* = (S/2\rho L_e)\, Re\,(Z_{in} + Z_{vis})$, $\alpha = (\hat{\gamma}+1)/2$, $\beta = ((\hat{\gamma}+1)(\hat{\gamma}+2))/6$ and ξ is the total hydraulic-resistance coefficient of the neck. Z_{in} is the acoustic impedance at inlet of HR, Z_{vis} is the friction acoustic impedance. We introduce dimensionless variables, $t = \omega_0 t^*$, $x = \frac{SX}{V_0}$, $\delta = 2\delta^*/\omega_0$, $\sigma = (\xi/2)(V_0/L_e S)$, $p = p^*/\rho c^2$ (c is the sound velocity) we get:

$$\frac{d^2x}{dt^2} + \sigma\frac{dx}{dt}\left|\frac{dx}{dt}\right| + \delta\frac{dx}{dt} + \left(x - \alpha x^2 + \beta x^3\right) = -p \tag{3}$$

In [1], in function of the order of magnitude of the displacement x, small parameter ε was introduced (for example $x = \varepsilon y$, with y of order 1 when x is small) and all parameters have been estimated in function of this ε. It was found that two regimes have to be considered to perfectly modelised the behavior of such HR, i.e. to obtain softening behavior first (for low levels) and then hardening behavior (for high levels).
Classical development by using multiple scales method developped by Nayfeh [2] can be performed to obtain fixed points of the system. This allows to obtain the skeleton curve of the amplitude-frequency (see [1] for more details). Example of results are shown in Figure 4. This nonlinear behavior of the resonator can be used as the nonlinear geometrical restoring forcing function of an oscillator to be coupled to a medium for passively controlling the acoustical energy of that medium via the same principles as in mechanical systems [20]. In the following we present results on the energy transfer from a linear system to modified HR.

2.2 Nonlinear targeted energy transfer by using modified HR

In [4], it has been shown that it is possible to obtain a targeted energy transfer from one acoustical mode to an HR with nonlinear behaviors. For the HR, nonlinear restoring forces and nonlinear damping have been taken into account with modified geometry of the neck. The considered system is represented in Figure 5. A time multiple scale method around a 1:1 resonance has been used to detect slow invariant manifold of the system, its equilibrium and singular points. We denote X_1 the displacement of the air mass in the small diameter tube (acoustical mode created owing to coupling box) and X_2 the displacement of the neck air mass of the modified HR. We can deduce different orders of magnitude of each parameter by taking their realistic values for possible practical applications in acoustics. Some parameters are fixed (for example air properties) and others are adjusted for the experiment within a realistic range. So

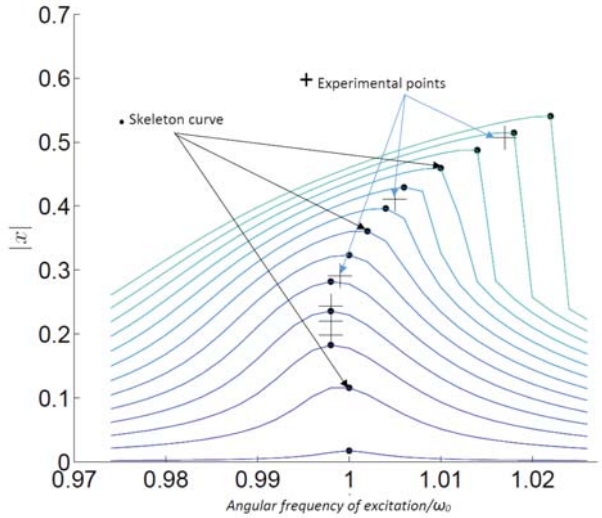

Figure 4: Softening and hardening behavior in function of amplitude of excitation (data taken from [1]).

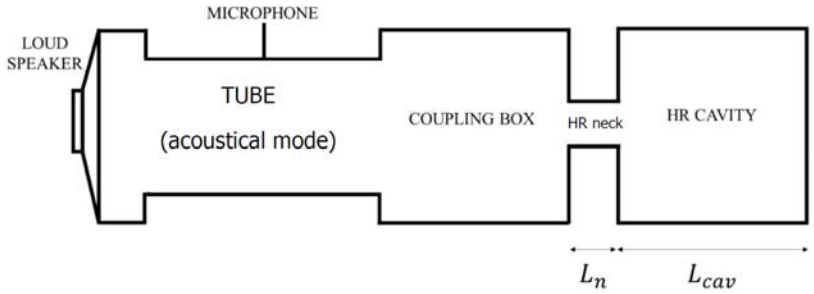

Figure 5: Considered system to obtain targeted energy transfer from one acousticla mode to HR.

we are able to express the govering equations in different orders of magnitudes, using a small parameter, $\varepsilon \ll 1$, considered as the ratio of the secondary system mass to the main system mass and we can also normalize equations with respect to time by considering the following changes of variable: $\tau = \Omega t$, where Ω is the natural angular frequency of the main acoustical mode.
Complex variables of Manevitch [3] can also be used:

$$\begin{aligned} \varphi_1 e^{j\omega_n \tau} &= \frac{dX_1}{d\tau} + j\omega_n X_1 \\ \varphi_2 e^{j\omega_n \tau} &= \frac{dX_2}{d\tau} + j\omega_n X_2 \end{aligned} \tag{4}$$

with $j^2 = -1$ and ω_n is the ratio of the angular frequency of excitation divided by Ω.
A multiple scale method [2] can be performed, where we consider a new scales of time $\tau_k = \varepsilon^k \tau$, $k = 0, 1, ...0$, where τ_0 is the fast time scale and τ_1 and so on are slow time scales.
We study the system around the 1:1 resonance and we replace expressions of X_1 and X_2 as functions of φ_1 and φ_2 in the system of governing equations and we use a Galerkin's technique by keeping first harmonics of the system [21]. As shown in [4], by solving the system of equations at different orders of ε and by using polar expressions

$$\varphi_1 = N_1 e^{j\delta_1} \tag{5}$$

$$\varphi_2 \quad = \quad N_2 e^{j\delta_2}$$

it is possible to find the Slow Invariant Manifold (SIM), that give the relations of N_1 in function of N_2. It is also possible to analyze the behavior of the system at τ_1 time scale around the SIM. This allows to find ordinary fixed points and fold singularities [21]. Stability borders of the SIM as presented in [21] can be provided. When the system possesses fold singularities, in fact equilibrium and singular points coincide on the fold line of the system. In this case, the system presents persisting bifurcations between its stable zones which correspond to extreme energy exchanges between two oscillators [22]. It has been shown in [4] that existence and positions of fold singularities and equilibrium points, for fixed parameters of the HR, depends on characteristics of excitation.

In order to activate nonlinear absorber, the absorber should be designed in a manner that the SIM can present two peaks for given physical parameters. This means that the parameters of HR relevant to nonlinear terms should be tuned. Via setting $\dfrac{\partial N_1}{\partial N_2} = 0$, we impose that the SIM possesses two local maxima which leads to find possible parameters of HR for having two peaks. This gives us a mathematical inequality that some parameters must be satisfied. Results for possible realistic values satisfying this condition are shown in Figure 6 where we can see the superposition of SIM compared to the numerical simulation in terms of N_1 vs N_2 curve (a good analytical prediction is obtained) for a given set of parameters (details are given in [4]). In the Figure 6 we also show the numerical simulation of N_1 versus τ where one can see a better decreasing of N_1 when the HR is coupled. First, after starting from the initial conditions there are nonlinear interactions between energies of the acoustical mode and HR in terms of N_1, N_2, which is accompanied by reduction of N_1 in a nonlinear manner. Then when the system reaches to the stability border of SIM, it faces a bifurcation which corresponds to abrupt energy decrease of N_2 with almost constant level of N_1. Finally, after bifurcation the energy of acoustical mode, N_1 decreases until it reaches to zero. In [4] experimental verifications have also been done. An example of experimental result is given in Figure 7 with the evolutions of energies of the main system, i.e. N_1 with and without coupled HR. We can see that the energy transfer to the HR allows to have faster absorption i.e. sharper slop of the energy decreament of the main system. An energy reduction is shown in a sharp and faster manner followed by a classical exponential decrease. This scenario is typical behavior for targeted energy transfer and has already been underlined by [11].

So, it was shown that for very high amplitudes it is possible to obtain hardening behavior under certain conditions (neck geometry, decresaing of vortex phenomenon...) allowing to activate targeted energy transfer. However it is not obvious to obtain hardening behavior for classical HR. That is why we propose in the next section to study the two frequency driving (subharmonic resonance) case for a classical HR.

3 SUBHARMONIC RESONANCE OF CLASSICAL HR

In this section we consider that the external excitation p of a classical resonator in Equation (3) is a two-frequency driving.

By assuming that displacement x is small, we introduce small parameters to solve this equation. Indeed, we introduce ε such that $x = \varepsilon y$, with y of order 1. So, in function of the orders of magnitude (by looking at physics), we can write $\delta = \varepsilon^2 r_2$, $\sigma = \varepsilon r_1$. For the two frequency driving we choose $p = \varepsilon^3 f_0 \cos(\Omega t) + \varepsilon^2 f_2 \cos(2\Omega t + \phi)$. The linear frequency is expressed

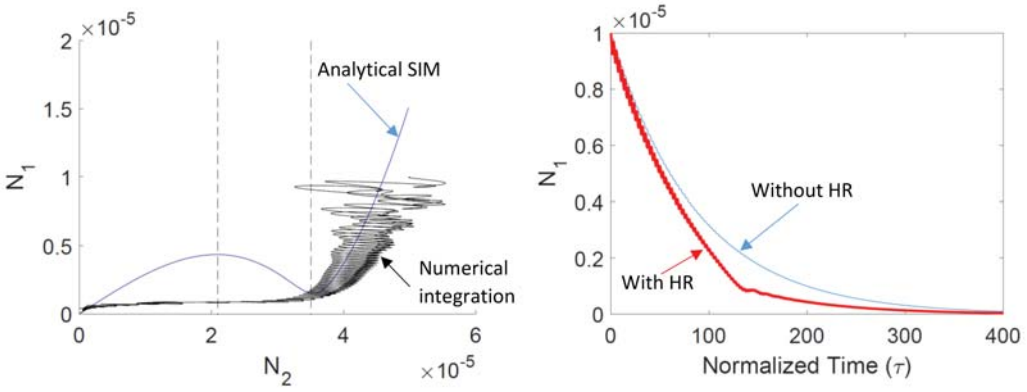

Figure 6: N_1 vs N_2 analytical and numerical for initials conditions ($\tau = 0$) $X_1 = X_2 = 0$, $\frac{dX_1}{d\tau} = 1 \times 10^{-5}$, $\frac{dX_2}{d\tau} = 5 \times 10^{-5}$ (data taken from [4]).

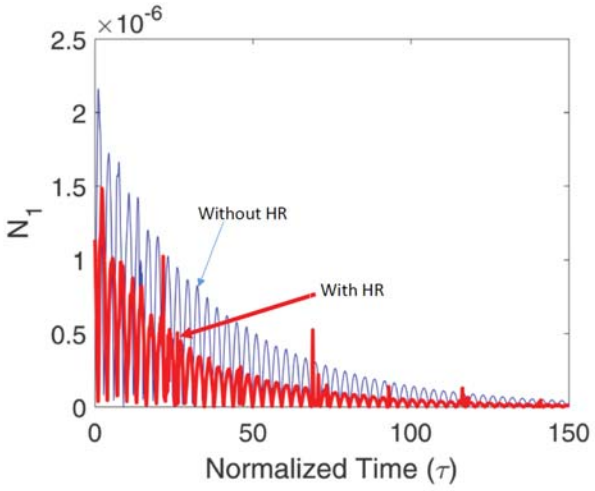

Figure 7: Experimental results showing targeted energy transfer from one acoustical mode to HR (data taken from [4]).

by $\Omega = 1 + \varepsilon^2\mu$ where μ is the frequency detuning.

$$\frac{d^2y}{dt^2} + \varepsilon^2 r_1 \frac{dy}{dt}\left|\frac{dy}{dt}\right| + \varepsilon^2 r_2 \frac{dy}{dt} + y - \varepsilon\alpha y^2 + \varepsilon^2\beta y^3 = -\varepsilon^2 f_0 \cos(\Omega t) - \varepsilon f_2 \cos(2\Omega t + \phi) \quad (6)$$

Then, we apply the multiple time scale method with the expansion of y in the form of: $y = y_0 + \varepsilon y_1 + \varepsilon^2 y_2 + O(\varepsilon^3)$. We develop the time in fast and slow scales: $T_0 = \varepsilon^0 t$, $T_1 = \varepsilon^1 t$ and $T_2 = \varepsilon^2 t$. When we replace these developments in the principal equation (6), we obtain :

$$\varepsilon^0 : \qquad \frac{\partial^2 y_0}{\partial T_0^2} + y_0 = 0 \quad (7)$$

$$\varepsilon^1 : \quad 2\frac{\partial^2 y_0}{\partial T_0 \partial T_1} + \frac{\partial^2 y_1}{\partial T_0^2} + y_1 - \alpha y_0^2 = -\frac{f_2}{2}\left[e^{i(2T_0 + 2\mu T_2 + \phi)} + e^{-i(2T_0 + 2\mu T_2 + \phi)}\right] \quad (8)$$

ε^2 :

$$2\frac{\partial^2 y_0}{\partial T_0 \partial T_2} + \frac{\partial^2 y_0}{\partial T_1^2} + 2\frac{\partial^2 y_1}{\partial T_0 \partial T_1} + \frac{\partial^2 y_2}{\partial T_0^2} + r_1 \frac{\partial y_0}{\partial T_0}\left|\frac{\partial y_0}{\partial T_0}\right| + r_2 \frac{\partial y_0}{\partial T_0} + y_2 - 2\alpha y_0 y_1 + \beta y_0^3 \quad (9)$$

$$= -\frac{f_0}{2}\left[e^{i(T_0+\mu T_2)} + e^{-i(T_0+\mu T_2)}\right]$$

When we follow the development in multiple scales used by Nayfeh [2], we continue eliminating secular terms of the precedent equations (7, 8, 9).
The equation (7) has a solution with the following form:

$$y_0 = A\left(T_1, T_2, T_3, ...\right) e^{iT_0} + A^*\left(T_1, T_2, T_3, ...\right) e^{-iT_0} \tag{10}$$

where .* stands for conjugate of a complex variable.
For the first equation coming from (8):

$$A = A\left(T_2, T_3, ...\right) \tag{11}$$

For the second equation coming from (8):

$$y_1 = -\frac{1}{3}\alpha A^2 e^{2iT_0} + 2\alpha A A^* - \frac{1}{3}\alpha A^{*2} e^{-2iT_0} + \frac{f_2}{6}\left[e^{i(2T_0+2\mu T_2+\phi)} + e^{-i(2T_0+2\mu T_2+\phi)}\right] \tag{12}$$

We introduce (10) and (12) in the expression (9), and we replace A with the complex form: $A = \hat{y}e^{i\gamma}$. The expression is separated in the real part and the imaginary part. After simplifying, using $\Delta = \gamma - \mu T_2$, we obtain the system of two equations:

$$\begin{aligned} \hat{y}\frac{\partial \Delta}{\partial T_2} &= -\ \hat{y}\mu + \frac{f_0}{4}\cos\left(\Delta\right) + \hat{y}^3\left[\frac{3}{2}\beta - \frac{5}{3}\alpha^2\right] - \frac{f_2}{6}\alpha\hat{y}\cos\left(\phi - 2\Delta\right) \\ \frac{\partial \hat{y}}{\partial T_2} &= \frac{f_0}{4}\sin\left(\Delta\right) - \frac{r_2}{2}\hat{y} - r_1\hat{y}^2\left(\frac{8}{3\pi}\right) + \frac{f_2}{6}\alpha\hat{y}\sin\left(\phi - 2\Delta\right) \end{aligned} \tag{13}$$

Fixed points of the system (13) can be obtained by setting $\frac{\partial \Delta}{\partial T_2} = 0$ and $\frac{\partial \hat{y}}{\partial T_2} = 0$. This will allow to obtain the skeleton curve of the amplitude-frequency curve.
It should be underlined that for the special case $f_0 = 0$ and no non linear damping ($r_1 = 0$), we obtain directly from the second equation of System (13) that $\sin\left(\phi - 2\Delta\right) = 3\frac{r_2}{\alpha f_2}$. It means that this is possible only if this value is inferior to 1. So it means that subharmonic resonance, for the case of excitation by just the second harmonic ($f_0 = 0$), is possible only as $3\frac{r_2}{\alpha f_2} < 1$. Physically, this implies that the coefficient of the double frequency term must overcome the coefficient of the damping term, which is a well known result for subharmonic resonance. However, if the two terms (f_0 and f_2) are taken in account, then it is possible to obtain subharmonic resonance even if $3\frac{r_2}{\alpha f_2} > 1$ and very different behaviors can occur.
Indeed, it is then possible to obtain different nonlinear behaviors in function of the phase difference ϕ. For example, we can calculate the amplitude-frequency curve in function of ϕ as shown in Figure 8 by taking the following physical realistic parameters: $\hat{\gamma} = 1.4$ (specific air ratio of air), $r_1 = 0.8$ and $r_2 = 2$ (values very close to litterature values by assuming $\varepsilon = 0.1$), $f_0 = 0.25$ (the case $f_2 = 0$ and $f_0 = 0.25$ corresponds to 122dB by considering sound velocity $c = 343\text{m.s}^{-1}$ and $\rho = 1.2\text{kg.m}^{-3}$) and $f_2 = 0.6$ (this corresponds to 150dB).
In Figure 8, we can clearly see that for a certain range of ϕ it is possible to obtain hardening behavior instead of classical softening behavior when ϕ equals to 0 (softening for $\mu < 0$ and hardening for $\mu > 0$). The dots represent the maximum of amplitude for each curve (one curve for each fixed ϕ) so at the resonance frequency.

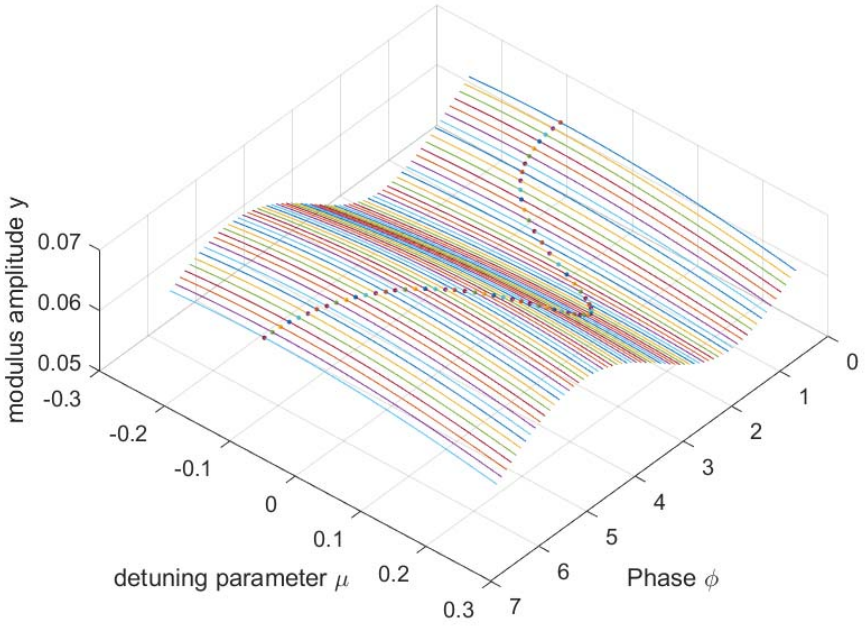

Figure 8: Example of amplitude-frequency curve in function of the phase lag ϕ. The dots represent the maximum of amplitude for each curve (one curve for each fixed ϕ) so at the resonance frequency.

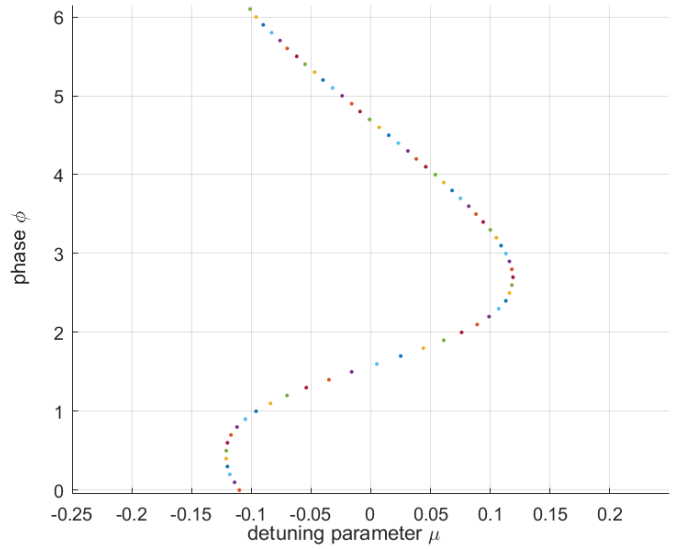

Figure 9: Nonlinear response of ϕ as function of μ (softening for $\mu < 0$ and hardening for $\mu > 0$). The dots represent the maximum of the amplitude-frequency curve (so at the frequency of resonance).

The Figure 9 allows to see that the intervals where the behavior becomes hardening is around $\phi \in [\pi/2; 3\pi/2]$.

Moreover, as shown in Figure 10, the phase ϕ allows to obtain higher amplitudes at resonance, which can be very interesting for some applications. With the given parameters for this figure the case with only the first harmonic (case $f_0 = 0.25$ and $f_2 = 0$) gives an amplitude of

0.06. By considering the two-frequency driving excitation and owing to the phase difference the amplitude can increase at almost 0.0675 for a phase difference near $3\pi/2$. It means that amplitude can increase approximately 12.5% as compared with the single frequency driving. All the results have been validated numerically with Runge-Kutta schemes of order four: the errors are less than 1% and the computational time is drastically reduced owing to analytical approximations.

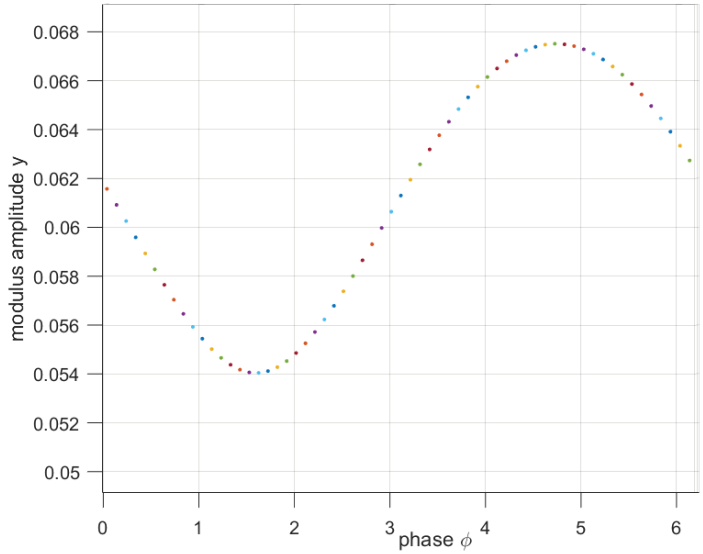

Figure 10: The variation of amplitude at resonance frequency in function of ϕ .The dots represent the maximum of the amplitude-frequency curve (so at the frequency of resonance).

4 CONCLUSIONS

Nonlinear amplitude-frequency responses of an acoustic Helmholtz resonator have been investigated by taking into account nonlinear restoring and damping forces. The objective of the present paper is to show that it is possible to obtain nonlinear hardening behavior of HR either by modifying the geometry of the neck either by using a two-frequency driving with a phase difference. This nonlinear hardening behavior is necessary to active targeted energy transfer phenomenon from an acoustical mode to a pure acoustical resonator. Analytical treatment of governing system equations has been carried on by using time multiple scale method and complexification method to detect slow invariant manifold of the system, its equilibrium and singular points. Owing to the obtained analytical developments, we have shown that it is possible to use all nonlinear characteristics of the HR, including bifurcations and not just its classical damping capacity. Analytical predictions have been compared with those obtained by direct numerical integration of system equations showing good agreement. Experimental verification has also been perfomed for some configurations. The nonlinear response can be increased by using a two-frequency driving for certain phase difference and taking into account the two first harmonics can change the characteristic responses even for situation where the double frequency component does not overcome the damping effect. We have shown that the phase difference has a crucial role to obtain different nonlinear behaviors. It remains to verify

experimentally this last point and apply those last results in practical engineering applications.

REFERENCES

[1] V. Alamo Vargas, V., E. Gourdon, A. Ture Savadkoohi, Nonlinear softening and hardening behavior in Helmholtz resonators for nonlinear regimes, *Nonlinear Dynamics*, **91 (1)**, 217–231, 2018.

[2] A. H. Nayfeh., Nonlinear oscillation. *Wiley*, New York, 1979.

[3] L. I. Manevitch, The description of localized normal modes in a chain of nonlinear coupled oscillators using complex variables, *Nonlinear Dynamics*, **25(1)**, Jul, pp. 95–109, 2001.

[4] E. Gourdon, A. Ture Savadkoohi, V. Alamo Vargas, Targeted energy transfer from one acoustical mode to an helmholtz resonator with nonlinear behavior, *Journal of Vibration and Acoustics, Transactions of the ASME*, **140 (6)**, art. no. 061005, 2018.

[5] H. V. Helmholtz (1863 in German and 1912 in English). On the sensations of tone as a physiological basis for the theory of music, 4th edn. trasnlated to English by A. J. Ellis. Braunschweig, Druck und Verlag von Friedrich Vieweg und Sons, Germany. Longmans, Greens, and Co., London, New York, Bombay and Calcutta.

[6] E. Gourdon, M. El Mankibi, R. Issoglio, P. Stabat, D. Marchio, C.F. Dordelly. Silencer design for awning windows: Modified Helmholtz resonators with perforated foam *Building Simulation*, **10 (5)**, 677–685, 2017.

[7] O. Gendelman, L.I. Manevitch, A.F. Vakakis, R. MCloskey, Energy pumping in nonlinear mechanical oscillators: part i - dynamics of the underlying hamiltonian systems, *Journal of Applied Mechanics*, **68 (1)**, 34–41, 2001.

[8] E. Gourdon, N.A. Alexander, C.A. Taylor, C.-H. Lamarque, S. Pernot, Nonlinear energy pumping under transient forcing with strongly nonlinear coupling: theoretical and experimental results, *Journal of Sound and Vibration*, **300**, 522–551, 2007.

[9] L.I. Manevitch, A.S. Kovaleva, E.L. Manevitch, Limiting Phase Trajectories and Resonance Energy Transfer in a System of Two Coupled Oscillators, *Mathematical Problems in Engineering*, **210**, 1–24, 2009.

[10] A. Ture Savadkoohi, B. Vaurigaud, C.-H. Lamarque, S. Pernot, Targeted energy transfer with parallel nonlinear energy sinks, part II: theory and experiments, *Nonlinear Dynamics*, **67**, 37–46, 2012.

[11] B. Cochelin, P. Herzog, P.-O. Mattei, Experimental study of energy pumping in acoustics. *Comptes Rendus Mecanique*, **334**, 639–644, 2006.

[12] R. Bellet, B. Cochelin, P. Herzog, P.-O. Mattei, Experimental study of targeted energy transfer from an acoustic system to a nonlinear membrane absorber, *Journal of Sound and Vibration*, **329(14)**, 2768–2791, 2010.

[13] D. Kumar Singh, S.W. Rienstra, *A Systematics Impedance Model for Non-Linear Helmholtz Resonator Liner. 19th AIAA/CEAS Aeroacoustics Conference, Berlin, Germany*, 27-29 May 2013.

[14] G.K. Yu, Y.D. Zhang, Y. Shen, Inducing passive nonlinear energy sinks in vibrating systems, *Journal of Vibration and Acoustics*, **123(3)**, 324–332, 2001.

[15] M. Meissner, The response of a Helmholtz resonator to external excitation. Part II: Flow-induced resonance, *Archives of acoustics*, **30 (1)**, 57–71, 2004.

[16] K. Förner, M. Askin Temiz, W. Polifke, I. Lopez Arteaga, *On the non-linear influence of the edge geometry on vortex shedding in the helmholtz resonators. The 22nd International Congress on Sound and Vibration, Florence, Italy*, 12-16 July 2015.

[17] O. Richoux, V. Tournat, T. Le Van Suu, *Comportement non linéaire des bandes interdites dans un réseau acoustique unidimensionnel. Congrès Français d'Acoustique*, 2006.

[18] A. Hersh, B. Walker, Fluid Mechanical Model of the Helmholtz Resonator. *NASA Contractor Report*, Washington, D.C., USA, 1977.

[19] E. Gourdon, A. Ture Savadkoohi, *Nonlinear Structuring of Helmholtz Resonators for Increasing the Range of Sound Absorption, EuroNoise 2015, Maastricht*, 31 May - 3 June 2015.

[20] R.E. Roberson, Synthesis of a nonlinear dynamic vibration absorber, *Journal of the Franklin Institute*, **254 (3)**, 205–220, 1952.

[21] A. Ture Savadkoohi, C.-H. Lamarque, Z. Dimitrijevic, Vibratory energy exchange between a linear and a nonsmooth system in the presence of the gravity, *Nonlinear Dynamics*, **70**, 1473–1483, 2012.

[22] Y. Starosvetsky, O. Gendelman, Strongly modulated response in forced 2dof oscillatory system with essential mass and potential asymmetry, *Physica D*, **237**, 1719–1733, 2008.

EURODYN 2020
XI International Conference on Structural Dynamics
M. Papadrakakis, M. Fragiadakis, C. Papadimitriou (eds.)
Athens, Greece, 23–26 November 2020

EMPIRICAL EXPRESSION PREDICTING SEISMIC DISPLACEMENT OF SANDY SLOPES IN GREECE IN TERMS OF SOIL PROFILE TYPE USING NON-LINEAR DYNAMIC STICK-SLIP ANALYSIS

Loukas C. Katsenis[1], Constantine A. Stamatopoulos[2] and Vassilis P. Panoskaltsis[3]

[1] PhD candidate, Department of Civil Engineering, Demokritos University of Thrace, Greece
e-mail: katsenisloukas@yahoo.gr

[2] Partner, Stamatopoulos and Associates Co; Instructor, Hellenic Open University; 5 Isavron str, Athens, 11471, Greece, e-mail: k.stam@saa-geotech.gr

[3] Professor, Department of Civil Engineering, Demokritos University of Thrace, Greece, e-mail: panoskaltsis@yahoo.com

Abstract

In earthquake analyses, usually the seismic displacement of slopes along slip surfaces is estimated by the sliding-block model, where a rigid block rests on an inclined plane and every time that the applied horizontal acceleration is larger than the critical horizontal acceleration value for relative motion, the block slides. Empirical expressions giving the distance moved by the sliding-block model have been proposed and recently these equations are based on relevant data bases of specific regions. However, level of accuracy of the sliding-block model is limited primarily because of the dynamic response of the soil both above and below the slip surface. Recently a coupled numerical code which predicts the seismic response along slip surfaces by considering the dynamic response both above and below the slip surface has been developed (Katsenis et al, 2019). The code is used to propose empirical expressions relating the seismic displacement along slip surfaces, not only on the predictions of the sliding block model, but also on the soil type category according to Eurocode and the depth of the slip surface. For this purpose, extensive parametric analyses were performed. Different acceleration histories recorded in Greece were applied below the soil layers with a slip surface with varying horizontal critical acceleration value for relative motion and depth. Soil behaves linearly only at very small shear strains, well below the typical shear strains exerted in soil profiles near severe earthquakes. The present work extends previous work for non-linear soils. It was observed that the non-linear effect is more important on loose deposits and the previously developed equations were extended to simulate this effect.

Keywords: slopes, sliding-block model, dynamic response, seismic displacement, constitutive modeling, slip surface, coupled analyses, slopes.

1 INTRODUCTION

Engineers usually assess the seismic safety of slopes using the dynamic factor of safety calculated along slip surfaces by comparing the applied forces to the soil strength [1]. However, evaluations based on the dynamic factor of safety have the serious drawback that they do not consider the seismic displacement, which is directly related to damage [2]. The "conventional" sliding-block model [3] is the most commonly used simplified model predicting the seismic displacement of slopes for given earthquake motions [4]. A rigid block rests on an inclined plane (Fig. 1). The resistance along the block-inclined plane boundary follows the Mohr-Coulomb law. Critical acceleration is defined as the minimum horizontal acceleration which causes movement of the block. Every time where the applied horizontal acceleration is larger than the critical acceleration, the block slides. The total displacement is obtained by the addition of the partial slips. This model is used for the prediction of permanent seismic movement of slopes along a predefined slip surface, by appropriately selecting the equivalent critical and applied acceleration values of the "conventional" sliding-block model [2, 3, 4]. Different empirical expressions have been proposed predicting the seismic displacement of the sliding-block model, in terms, primarily, of the ratio of the maximum acceleration of the applied seismic motion divided by the critical horizontal acceleration for sliding [4-9]. Some of these expressions use other than the maximum acceleration parameters of the seismic motion, such as the maximum velocity or the Arias Intensity, or parameters of the earthquake that produced the seismic motion, such as its earthquake magnitude or its earthquake fault distance [5, 9]. In addition, region-specific empirical expressions have been proposed predicting the seismic displacement of the sliding-block model, as different regions have different earthquake faults and geological profiles conditions, and thus potentially different applied seismic motions characteristics. Region-specific empirical expressions predicting the seismic displacement with the "conventional" sliding-block model for seismic motions in Greece have been proposed by [9].

The conventional sliding-block model described above assumes rigid motion and thus it does not consider the dynamic response of the soil both above and below the slip surface, which affects the seismic displacement along the slip surface. Based on results of simplified dynamic models, expressions have been proposed predicting the seismic displacement along the slip surface in terms of not only the critical acceleration for sliding and characteristics of the applied seismic motion described above, but also characteristics affecting the dynamic response of the sliding mass such as its height and shear wave velocity [10-12]. However, the seismic displacement along a slip surfaces depends not only on the dynamic characteristics of the sliding mass, but also on the dynamic characteristics of the soil profile below the slip surface and above the underlying bedrock [13, 14]. Recently, a new cost-effective method, is proposed predicting the seismic sliding movement of dry slopes in soil profiles along slip surfaces with resistance following the Mohr-Coulomb law. The method models the coupled dynamic response of soils both above and below the slip surface [13]. An advantage of this method is simplicity, which makes it ideal in performing dynamic parametric analyses.

Depending on the geographical locations, National Codes specify the characteristics of the design typical seismic motion, such as the maximum seismic acceleration [15]. This seismic motion typically corresponds at bedrock sites. Furthermore, Eurocode [1] classifies the soil profiles into distinct categories, presumably exhibiting similar dynamic response. Based on the above, it is of interest for practicing engineers, to relate the seismic displacement along slip surfaces, not only to characteristics of the seismic motion and the critical horizontal acceleration for sliding, but also to the soil type category according to Eurocode, as well as, possibly, the depth of the slip surface.

Katsenis et al. [16, 17] proposed empirical expressions relating the seismic displacement along slip surfaces in Greece, in terms of not only characteristics of the acceleration history and the critical horizontal acceleration for sliding, but also to the soil type category according to Eurocode, as well as, the depth and length of the slip surface. In particular, they proposed and validated equations correcting the predictions of the conventional sliding-block model for typical seismic motions of Greece in terms of the soil profile type according to Eurocode and the depth and length of the slip surface. Katsenis et al. [16, 17] assumed a linear soil profile. However, soil behaves linearly only at very small shear strains, well below the typical shear strains exerted in soil profiles near severe earthquakes. It is inferred that for accurate predictions, the linear methods described in the previous chapter must be extended with constitutive equations simulating the non-linear soil response.

The purpose of the present work is to extend the empirical expressions proposed by Katsenis et al. [16, 17] for dry sandy layers considering the non-linear soil response. For this purpose, the following are performed below: (a) ground profile types are selected according to Eurocode, (b) a data base of seismic motions in Greece is collected, (c) numerical analyses are performed using the recently developed numerical code by [13], (d) based on the analyses performed and statistical analysis an empirical equation correcting the seismic displacement predictions of the sliding-block model based on the soil type category according to Eurocode, as well as the depth of the slip surface is derived and validated, (e) the results are discussed and an example practical application of the proposed expression for the prediction of the seismic displacement of an actual slope in Greece is given.

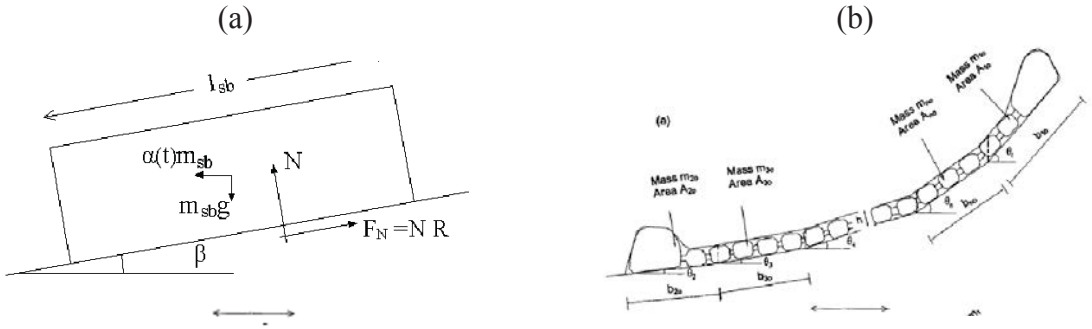

Fig. 1: (a) The conventional sliding block model, (b) the sliding chain model used to derive equation (3b).

2 MODEL SIMULATING THE NON-LINEAR SLIDING DYNAMIC RESPONSE OF SLOPES [13]

2.1 Simulation of sliding dynamic response

As shown in Fig. 2a, the present work models a slope with a slip surface as a continuous dynamic system of height (h_1+h_2) separated by a horizontal slip element at height h_2 above its base. Only horizontal acceleration is applied at the base of the lower body and above and below the slip element different properties exist. Thus, the system is divided in two non-linear elastic bodies. The index "1" is used for the upper body and the index "2" is used for the lower body. The upper body and lower bodies have mass m_i, tangent shear modulus $G_{t\text{-}i}$, viscous material damping ratio λ_i, and density ρ_i where i takes the values 1 and 2 for bodies 1 and 2 respectively. The two bodies move a horizontal distance x_i, velocity x'_i and acceleration x''_i, where i takes the values 1 and 2 for bodies 1 and 2 respectively

(a) (b)

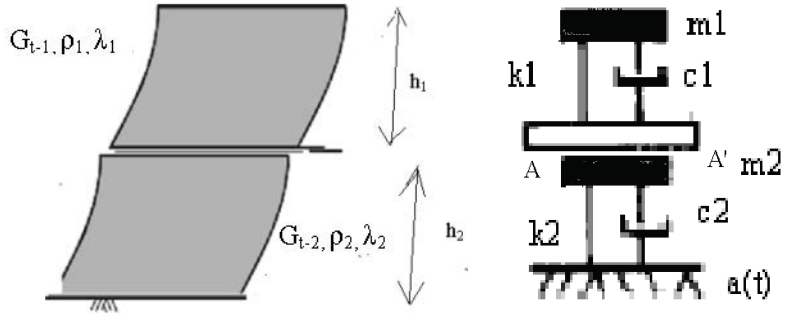

Figure 2: (a) Continuous system dynamic system considered in the present work, (c) the assumed discrete dynamic system approximation.

Fig. 2b gives the assumed equivalent discrete 2-body dynamic system with slip element approximation of the continuous system of Fig. 2a. If no slippage at the slip surface occurs, the equation of motion of the 2-body system of Fig 2b is:

$$\begin{bmatrix} m_1 & 0 \\ 0 & m_2 \end{bmatrix} \begin{bmatrix} x''_1 \\ x''_2 \end{bmatrix} = \begin{bmatrix} k_1(t) & -k_1(t) \\ -k_1(t) & k_1(t)+k_2(t) \end{bmatrix} \begin{bmatrix} x_1 \\ x_2 \end{bmatrix} + \begin{bmatrix} c_1(t) & -c_1(t) \\ -c_1(t) & c_1(t)+c_2(t) \end{bmatrix} \begin{bmatrix} x'_1 \\ x'_2 \end{bmatrix} - a(t) \begin{bmatrix} m_{ef-1} \\ m_{ef-2} \end{bmatrix} \quad (1a)$$

where

$$m_i = \frac{\rho_i \times h_i}{2} \quad (1b)$$

$$m_{ef-i} = \frac{2 \times \rho_t \times h_i}{\pi}$$

$$k_i(t) = \frac{\pi^2 \times m_i \times G_{t-i}(t)}{4 \times h_i^2 \times \rho_t}$$

$$c_i(t) = \frac{\pi \times m_i \times \lambda_i}{h_i} \sqrt{\frac{G_{t-i}(t)}{\rho_t}}$$

where a(t) is the applied acceleration in the base of the system in terms of time t, $k_i(t)$ and $c_i(t)$ are the viscous damping and spring stiffness coefficients of bodies 1 and 2, in terms of time t, m_i are the masses of bodies 1 and 2 and m_i are the equivalent masses of bodies 1 and 2 where the inertia acceleration is applied.

Also, non-linear elasticity and the geometry of Fig. 2b predicts that for any incremental change in horizontal displacement of the two bodies (dx_1, dx_2) the corresponding incremental change in shear stress at time t ($d\tau_1$, $d\tau_2$) at the two bodies equals

$$d\tau_1 = G_{t-1}(t) \frac{dx_1 - dx_2}{h_1} \quad (2a)$$

$$d\tau_2 = G_{t-2}(t) \frac{dx_2}{h_2} \quad (2b)$$

Sliding at the slip element of Fig. 2b occurs when

$$-a_c(t)-\frac{m_{ef-1}}{m_1}x_1''-a(t)>0 \tag{3a}$$

$$-m_1a_c(t)-m_1x_1''-m_1a(t)>0$$

where $a_c(t)$ is the horizontal acceleration for relative displacement of the slip element, in terms of time. In particular, the effect of rotation of the sliding mass above the slip surface is simulated by increasing the critical acceleration of the slip element with the distance moved along the slip element (u) as:

$$a_c(t)=a_{co}+11\frac{u}{L} \tag{3b}$$

where a_{co} is the critical acceleration at u=0 and L is the slip length.

Sliding in only one direction is assumed and the governing equation of motion at the slip element is

$$u''=-a_c(t)-\frac{m_{ef-1}}{m_1}x_1''-a(t)=-a_c(t)-0.64x_1''-a(t) \qquad \text{for} \quad u'>0 \tag{4}$$

where u'' and u' is the relative acceleration and velocity along the slip element.

During sliding, the two bodies move separately. The equations of motion for the upper and lower masses become:

$$m_1x_1''+c_1(t)x_1'+k_1(t)x_1=-m_{ef-1}[a(t)+u''(t)] \tag{5a}$$

$$m_2x_2''+c_2(t)x_2'+k_2(t)x_2=-m_{ef-2}a(t)-u''(t)m_{ef-1} \tag{5b}$$

Sliding stops when the relative velocity of the slip element (u') becomes zero. Then, again equations (1) hold.

The above solution is, according to the terminology used by [4,5], is "coupled". On the other hand, in the approximate "decoupled" case, separation of the two bodies is not simulated and equations (5) are not applied. Furthermore, for the rigid conventional sliding-block case, the above equations do not hold: sliding occurs when

$$-a_c(t)-a(t)>0 \tag{6a}$$

and the governing equation of motion at the slip element is

$$u''=-a_c(t)-a(t) \qquad \text{for} \quad u'>0 \tag{6b}$$

It should be noted that in equations (5) the critical acceleration for relative motion is expressed in terms of $a_c(t)$, and thus the effect of rotation of the sliding mass above the slip surface is simulated by equation (3b).

2.2 Constitutive modeling of the soil profile in the non-linear case

For the non-linear case, at the soil profile bodies i (i=1,2), the tangent shear modulus G_{t-i} is estimated as:

$$G_{t-i}(t) = \frac{G_{o-i}}{T_i(t)} \tag{7a}$$

where

$$G_{o-i} = Vs_i^{\,2}\rho_t \tag{7b}$$

$$T_i(t) = 1 + \left(\frac{1}{\eta a_i} - 1\right)\left|\frac{\tau_t(t) - \tau_{o-t}(t)}{\eta b_i}\right| \tag{7c}$$

where G_{o-i} and Vs_i are the shear modulus and shear wave velocity respectively at very small shear strain, $\tau_i(t)$ and $\tau_{o-i}(t)$ is the shear stress and the shear stress of the last stress reversal at time t of body i and a_i and b_i are model parameters which equal to

$$\eta a_i = 0.5 \tag{8a}$$

for $PI_i(\%) \le 15\%$ $$\eta b_i = 6.4 \cdot 10^{-5}\left(\frac{Go_i}{\sigma'_i}\right) \tag{8b}$$

for $PI_i(\%) > 15\%$ $$\eta b_i = (1.29 \cdot PI_i(\%) - 8.00) \cdot 10^{-5}\left(\frac{Go_i}{\sigma'_i}\right)$$

where PI_i is the plasticity index of body i. Fig. 3b illustrates that equation (8b) fits well the factor $\{\eta b / [Go/\sigma']\}$ in terms of PI.

2.3 Discussion of the proposed equations

Equations (1b), (4a), (5) are identical to those used by Rathje and Bray [5] and the form of equations (1a), (6) and (7) is similar to those used by Lin and Whitman [4]. In addition, equation (4b) has been used by Jafarian and Lashgari [7] based on the sliding chain model of figure 1b [20].

The constitutive model equations (8) predicting shear modulus degradation along of the body above and below the slip element are similar to those proposed by Papadimitriou et al. [19], but adjusted for the dry simpler case. The state-of-art work by Vucetic and Dobry [23], indicates that the decrease of the shear modulus with the shear strain depends as a first approximation only on the Plastisity Index (PI) of the soil, as illustrated in Fig. 3a. In equations (8), the model parameters ηa_i specify the Gs/Gmax ratio where the shear stress-degradation response is fitted, and the model parameter ηb_i fits the value of the actual response at a_i. A typical value of a_i for the problem considered is 0.5. Assuming ηa=0.5, for the simulation of Fig. 3a, $\eta\beta_i$ varies in terms of only Go and PI, as illustrated in equations (8).

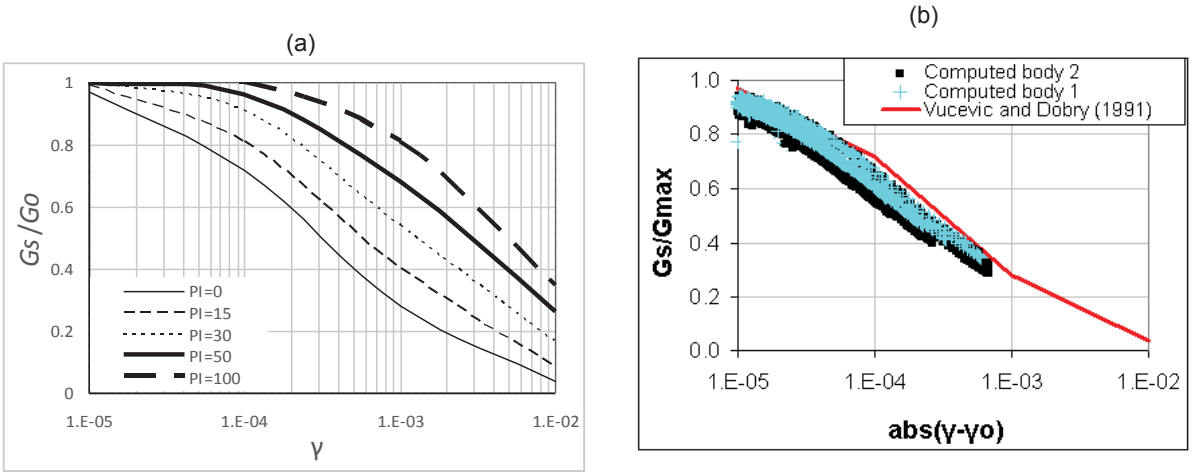

Figure 3: (a) State-of the art shear modulus degradation in terms of shear strain (γ) and Plasticity Index (PI) [23]. (b) simulation for this degradation for the case studied in section 2.4.

2.4 Numerical implementation

Equations (1)-(5), (7) and (8) simulating the non-linear dynamic response of a 2-body system with a slip element with constant strength were solved numerically using the Newmark method with its parameters β and γ taking the values of 0.25 and 0.50 respectively. For the linear case, input at the numerical code is the seismic acceleration history, the critical acceleration a_{co} and the variables h_i, Vs_i, ρ_i, λ_i. Output includes the acceleration time history of the two bodies for the coupled and decoupled cases and the acceleration, velocity and displacement history along the slip element for the coupled, decoupled and rigid cases. For the non-linear dry case, additionally, the value of the Plasticity Index (PI_i) is needed. Additional output of the program in this case is (a) the tangent shear moduli of bodies 1 and 2 versus time, (b) the shear stress-strain response of the two bodies and the (c) the secant modulus degradation with shear strain of the two bodies.

Figures 4 and 3b give typical output results of the proposed method. The case of non-linear sandy soil with $h_1=h_2=15$m, $Vs_1=200$m/s, $Vs_2=300$m/s, $\rho_1=\rho_2=2$t/m^3, $\lambda_1=\lambda_2=0.15$, under the Aegion 1995 earthquake input motion and slip surface with $a_{c0}=0.5$m/s^2 and, L=100m and model parameters $a_1=\alpha_2=0.5$, $\beta_1=\beta_2=1$ is presented. Fig. 3b illustrates that equation (8b) fits well the Vucetic and Dobry [23] curves.

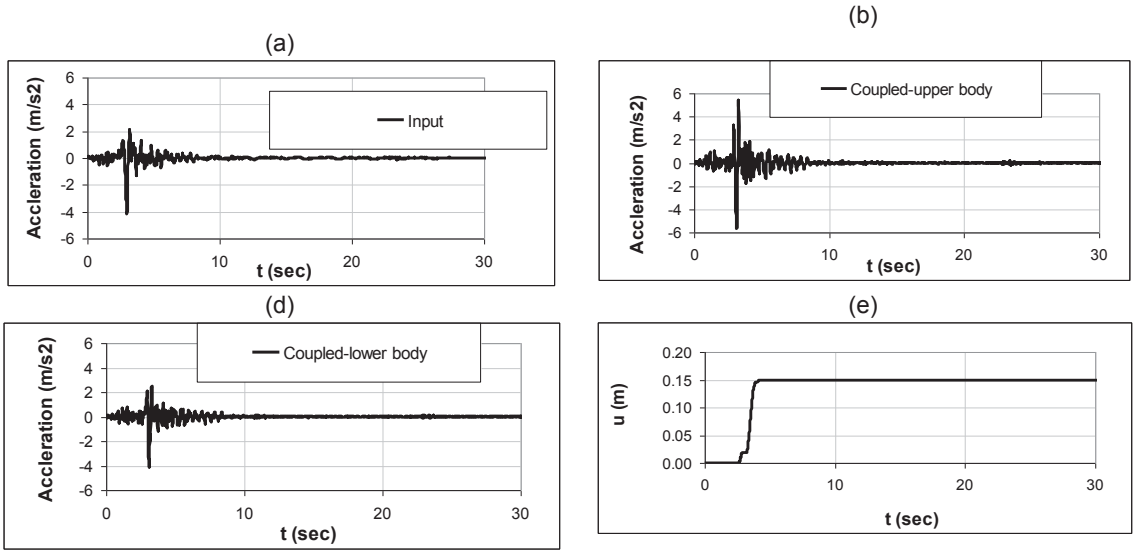

Figure 4: Typical results of the proposed method. The case of non-linear sandy soil with $h_1=h_2=15$m, $Vs_1=200$m/s, $Vs_2=300$m/s, $\rho_1=\rho_2=2$t/m^3, $\lambda_1=\lambda_2=0.15$, under the Aegion 1995 earthquake input motion and slip surface with $a_{c0}=0.5$m/s^2, L=100m and model parameters $a_1=\alpha_2=0.5$, $\beta_1=\beta_2=1$. (a) input acceleration history, (b),(c) acceleration histories of bodies 1 and 2, (d) seismic displacement along the slip surface versus time.

3 GROUND TYPES ACCORDING TO EUROCODE

Eurocode [1] defines ground types A-E, as given in table 1, based on observations by the earthquake engineering community that (a) only the first 30m depth of a soil profile play an important role in the dynamic response, (b) for given soil type, the only soil property that affects considerably the dynamic response is the shear wave velocity and (c) for similar dynamic response, a non-uniform soil profile with n layers may be simplified by an uniform one, with shear velocity Vs_{30}, defined as

$$Vs_{30} = \frac{30\text{m}}{\sum_{i=1}^{n} \frac{h_i}{Vs_i}} \tag{9}$$

where h_i and Vs_i is the thickness in m and elastic shear wave velocity of layer i of the n layers of the soil profile.

Ground type	Description	Vs_{30} (m/s)
A	Rock or other rock-like geological formation	>800
B	Deposits of very dense or medium-dense sand, gravel or stiff clay	360-800
C	Deep deposits of dense or medium-dense sand, gravel or stiff clay	180-360
D	Deposits of loose-to-medium cohesionless soil or of soft-to-firm cohesive soil	<180
E	Soil profile consisting of a surface alluvium layer with Vs values of type C or D and thickness varying between 5-20m, underlain by type A soil	

Table 1: Ground type according to Eurocode [1].

4 DATA BASE OF SEISMIC MOTIONS IN GREECE

In the present work real-time acceleration histories from the most significant recorded seismic events that took place in Greece between 1970 and 2014 were used as a database. Data were obtained from the Internet Site for European Strong-Motion Data (www.isesd.hi.is/). In addition, the seismic recording from the more recent earthquake that occurred in Kefalonia on 03/02/2014 of size M≥6.10 [Argostoli, Lixuri, Chavriata], which were is included until recently in the European Strong-Motion Database (ESD) was used. In particular, the filtered acceleration time histories for the horizontal seismic component xx were obtained. The criteria used to select the Database are the magnitude of the earthquake Mw>5 and the maximum acceleration α max≥0.04g. A total of 50 seismic motions were selected in this manner. Table A1 of the Appendix presents the number of the seismic motion, its name, its station, its date, and its magnitude (Mw). The time histories were analyzed with the seismosignal program [16] the to extract the spectral and temporal parameters. Table A2 of the Appendix presents for each seismic motion, its mean period, its predominant period, its peak acceleration and velocity value (a_{max} and V_{max}), its Arias intensity and its Epicentral distance.

5 PREVIOUS EMPIRICAL EXPRESSION

5.1 Cases considered

The elastic soil profile option of the model [13] was used. and thus equations (7) and (8) were not applied. In addition a very long slip length (L=1000m) was used initially and thus the rotation of the sliding mass effect was not simulated. Then, in order to assess the effect of the rotation of the sliding mass, the above cases were repeated for L=10m, 30m, 100m, 300m. According to Eurocode ground types of table 1, the soil profiles of table 2 were selected. The Vs_1,Vs_2 values correspond to the average ones of each soil profile of table 1, while for the density value, which does not affect considerably the dynamic soil response, the typical value of $\rho=2t/m^3$ was selected. The damping was taken as $\lambda_1=\lambda_2=15\%$, similarly to analyses by [5, 7, 13]. The critical acceleration value a_c was selected in such a way that computed final seismic displacement of the conventional sliding-block case ($u_{f\text{-}sl}$) varies from about 0.05m to about 0.5m. The reason is these are tolerable displacement values for typical structures.

At least five (5) a_c values were applied for each seismic motion and Vs_1,Vs_2 soil profile. For all these cases of soil profiles and a_c values, the 50 seismic motions described in section 2 above were applied and the seismic displacement (u_f) was computed. For comparison reasons, the seismic displacement for a rigid block for the same applied motion and critical acceleration value ($u_{f\text{-}sb}$) was also estimated.

Ground type	Vs (m/s)	h_1	h_1+h_2	$\rho_1=\rho_2$	$\lambda_1=\lambda_2$	a_{co}
S-B	$Vs_1=Vs_2=580$	5, 10, 20m	30m	2t/m3	0.15	In such a way that computed final seismic displacement along the slip surface (uf) varied from a few mm to tens of cm
S-C	$Vs_1=Vs_2=270$					
S-D	$Vs_1=Vs_2=100$					
S-E	Vs_1=200m/s, Vs_2=1000m/s					

Table 2. Soil profiles assumed in the analysis

5.2 Form of equation

As described above, as different regions have unique earthquake faults and geological profiles characteristic conditions, they have seismic motions of different characteristics and thus different empirical expressions predicting seismic dis-placement. Region-specific empirical expressions predicting (uf-rigid) in Greece has been proposed by [9]. For this reason, in order, possibly to omit predicting the effect of factor such as a_c, a_{max}, Arias intensity, earthquake magnitude etc on u_f, we propose just to relate u_f on $u_{f\text{-}rigid\text{-}L=1000m}$, where $u_{f\text{-}rigid\text{-}L=1000m}$ is predicted with previously proposed equations and the u_f incorporates, additional the dynamic effects of the soil profile both above and below the slip surface. Based on the above, we can write

$$u_f = Ra\ R\ u_{f\text{-}rigid\text{-}L=1000m} \tag{10}$$

where the factor RA simulates the dynamic effect for L=1000m and Ra simulates the effect of the rotation of the sliding mass on the rigid case.

Furthermore, preliminary inspections of the obtained results illustrated that RA increases or decreases as a_c decreases, and at small a_c value it tends to 1. However, a_c for the design seismic displacement value varies a lot for different seismic motions: for the typical results for a seismic motion of high and low a_{max} value, a_c varies between 0.01-0.09g and 0.002-0.05g respectively. This variation is eliminated if the factor R is related to $u_{f\text{-}rigid\text{-}L=1000.}$. Fig. 5 gives the ratio RA in terms of ($u_{f\text{-}rigid\text{-}L=1000}$) of soil profiles (a) S-B, (b) S-C, (c) S-D, (d) S-E in terms of ($u_{f\text{-}rigid}$) for seismic motion (i) S3 and (b) S29 of Appendix A. It can be observed that: RA increases or decreases as $u_{f\text{-}rigid\text{-}L=1000}$ increases, and at large $u_{f\text{-}rigid\text{-}L=1000}$ value it tends to 1. Based on the above we propose the following equation:

$$RA = 1 + a1\ (0.1/\ u_{f\text{-}rigid\text{-}L=1000})^{a2} \tag{11a}$$

where a1, a2 are model parameters. In particular, a1 gives the factor (R-1) at $u_{f\text{-}rigid}$=0.1m and a2 gives the manner that the factor R changes in terms of $u_{f\text{-}sb,}$ Further parametric analysis illustrated that as a first approximation a1 depends on both the soil profile and h1, while a2 depends only on the soil profile (Fig. 6). Thus, equation (4) can be adjusted as

$$RA = 1 + [n1 - n2\ (h1\text{-}10m)]\ (0.1/\ u_{f\text{-}rigid\text{-}L=1000}\ )^{a2} \tag{11b}$$

where the parameters n1, n2, a2 depend on the soil type.

After having obtained the effect of soil type and slip surface depth, the effect of slip length is investigated in the present work. We propose the following equation predicting R1:

$$Ra=0.5\ \{1+\tanh\ [\ln(c_2/(\ u_{f\text{-}rigid\text{-}L=1000}\ /L)^{c1}\ )]\ \} \tag{12}$$

where c1, c2 may depend on the seismic motion.

Equation (12) is a modified version of an equation used by Ishibashi and Zhang [12] to simulate a similar effect: the decrease from 1 to zero the ratio of the secant shear modulus to the small strain shear modulus as the shear strain increases. Equation (6) predicts that Ra equals to one when ($u_{f\text{-}rigid\text{-}L=1000}$ /L) takes a very small value and Ra decreases from one to zero as ($u_{f\text{-}rigid\text{-}L=1000}$ /L) increases.

Further analysis illustrated that it was sufficient to keep the c1 factor constant, taking the value 0.8, and varying the factor c_2, which takes a very small value when Ar is very small and then increases as Ar increases (Fig. 7).

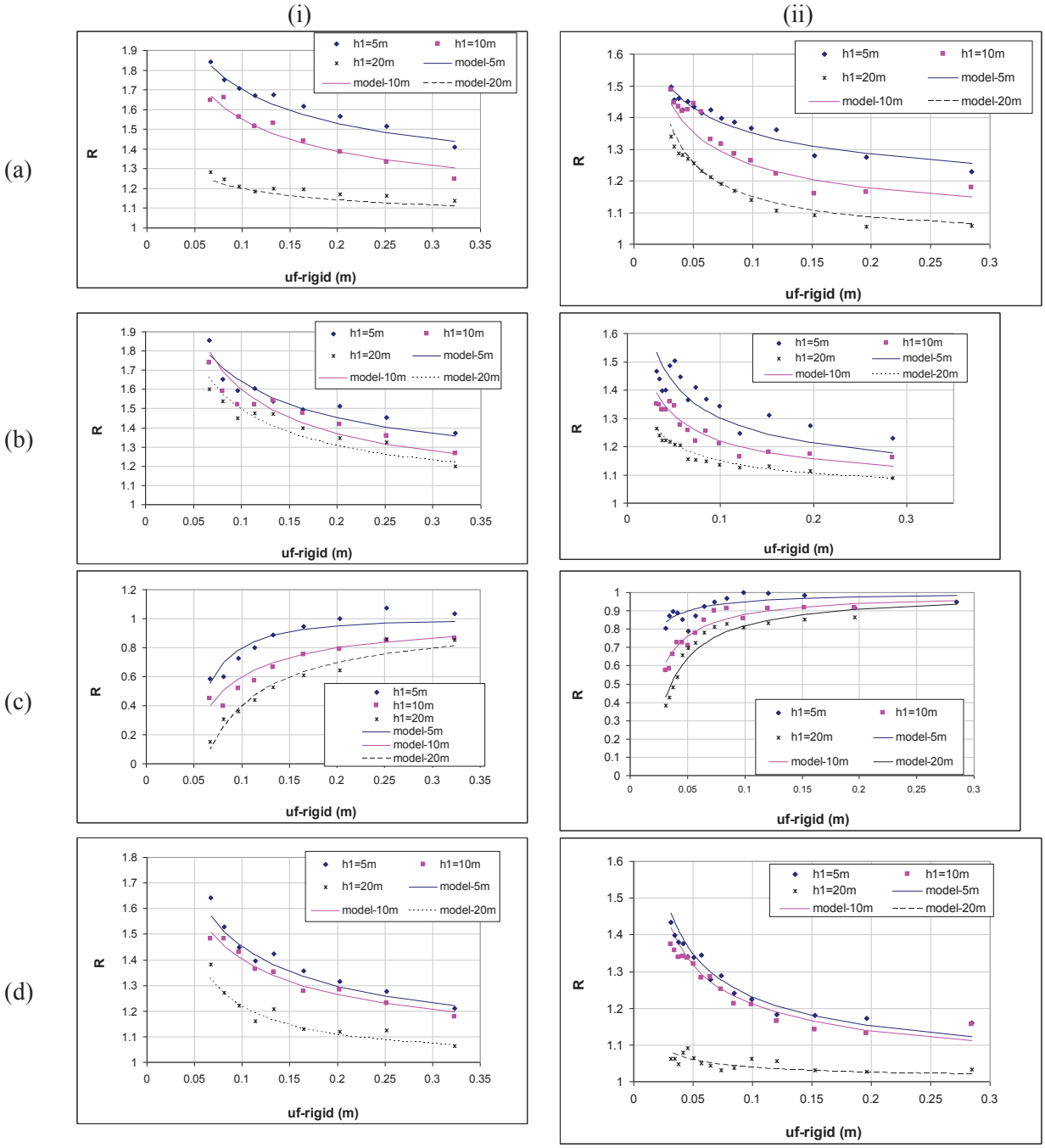

Fig. 5. Ratio RA in terms of ($u_{f\text{-}rigid}$) of soil profiles (a) S-B, (b) S-C, (c) S-D, (d) S-E for seismic motion (i) S3 and (b) S29 of table A1

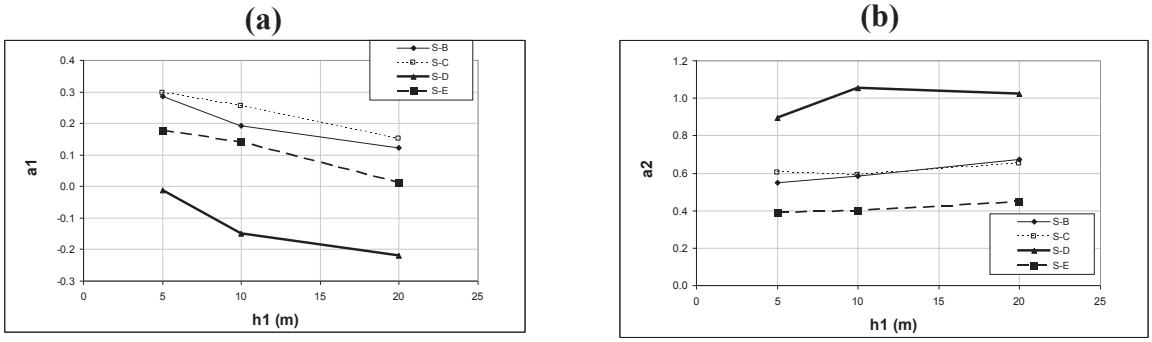

Fig. 6. The average factors (a) a1, (b) a2 in terms of the soil profile type and h1 for DB1.

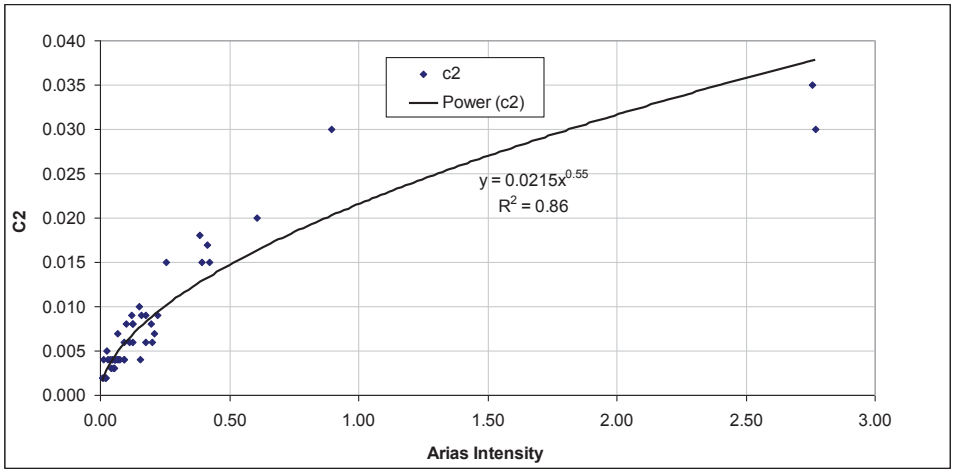

Fig. 7: The factor c2 in terms of Arias intensity and best-`fit trend for all seismic motion cases

5.3 Proposed equation

Based on the previous section results, Katsenis et al. [17] give the following equation predicting the seismic displacement along slip surfaces in terms of (a) the conventional sliding-block predictions **($u_{f\text{-}rigid\text{-}1000m}$)**, (b) soil type category according to Eurocode, (c) the depth (h1) and length (L) of the slip surface:

$$u_f = Ra\ u_{f\text{-}rigid\text{-}1000m}\ \{1+ [n1 - n2\ (h1\text{-}10m)]\ (0.1/\ u_{f\text{-}rigid\text{-}1000m}\ )^{a2}\} \quad (13a)$$

where

$$Ra = 0.5\ \{1+\tanh[\ln((([0.0215Ar^{0.55}]/(u_f/L))^{0.8})]\ \} \quad (13b)$$

and n_1, n_2, a_2 are model parameters given in table 3.

Soil type	n1	n2	a2	n1'
S-B	0.19	0.0093	0.6	0.05
S-C	0.26	0.0101	0.6	-0.63
S-D	-0.15	0.0111	1.0	-0.88
S-E	0.14	0.0118	0.4	0.02

Table 3. Parameters of equations (13) and (15) in terms of soil type

6 EFFECT OF NON-LINEAR RESPONSE

Katsenis et al [13] studied in detail the effect of non-linear response for a particular case: the Aegion 1995 seismic motion with a_{co}=0.5m/s^2, Vs_1= 20 to 5000m/s, Vs_2=Vs_1, h_1=h_2=15m, ρ_1=ρ_2=2t/m3, λ_1=λ_2=0.15, L=1000m, PI_i=0. Fig 8a presents the computed effect of non-linearity: u_f for the linear and nonlinear (coupled) cases versus Ts_1/Tm, where Tm is the mean period of the applied seismic motion and

$$Ts_1 = \frac{4h_1}{Vs_1} \tag{14}$$

Fig 8b gives the corresponding maximum shear strain for the non-linear analyses.

Fig 8a illustrates that the effects of non-linearity on u_f are significant. They can be interpreted by the effect of non-linearity on the representative shear modulus value of the analysis. In particular, as a result of non-linearity, the shear modulus value decreases and therefore, the "equivalent" Ts_1/Tm value is larger than the "elastic one". It is inferred that the u_f versus Ts_1/Tm curves are shifted to the left in the non-linear analyses. More specifically, fig. 8b illustrates that in the non-linear analyses the maximum shear strain takes a very small value at Ts_1/Tm=0 and then gradually increases as Ts_1/Tm increases. The reason is that as Ts_1/Tm increases, Vs_1=Vs_2 decreases and thus the soil becomes softer. Consistently to the above, Fig 8a illustrates that u_f in the non-linear analyses is more-or-less the same at Ts_1/Tm=0, but as Ts_1/Tm increases the u_f versus Ts1/Tm curve is shifted to the left and the shift is more pronounced as Ts_1/Tm increases.

To demonstrate quantitatively the effect of nonlinearity described above, we consider the example case of Fig. 8a and Ts_1/Tm=0.5. According to Fig. 8a, in this case in the linear response u_f=0.25m and according to Fig. 8b in the non-linear dry response the maximum γ_{cyc} value for bodies 1 and 2 equals 0.2 and 1% respectively, or 0.6% in average. Thus, according to Fig. 3a the maximum shear modulus decrease is by about 10 times and thus the average decrease is 5 times. As in these analyses Vs_1=Vs_2, it is inferred that in the nonlinear dry case Ts-av/Tm increases about 2.2 times and thus the "equivalent linear" Ts_1/Tm =Ts-av/Tm value equals 0.5*2.2=1.1 and the corresponding u_f value according to fig 8a is 0.14m. It is inferred that for Ts_1/Tm=0.5, u_f decreases from 0.25m in the linear case to 0.14m in the non-linear dry case. This agrees completely with the numerical results given in Fig. 8a for Ts_1/Tm=0.5.

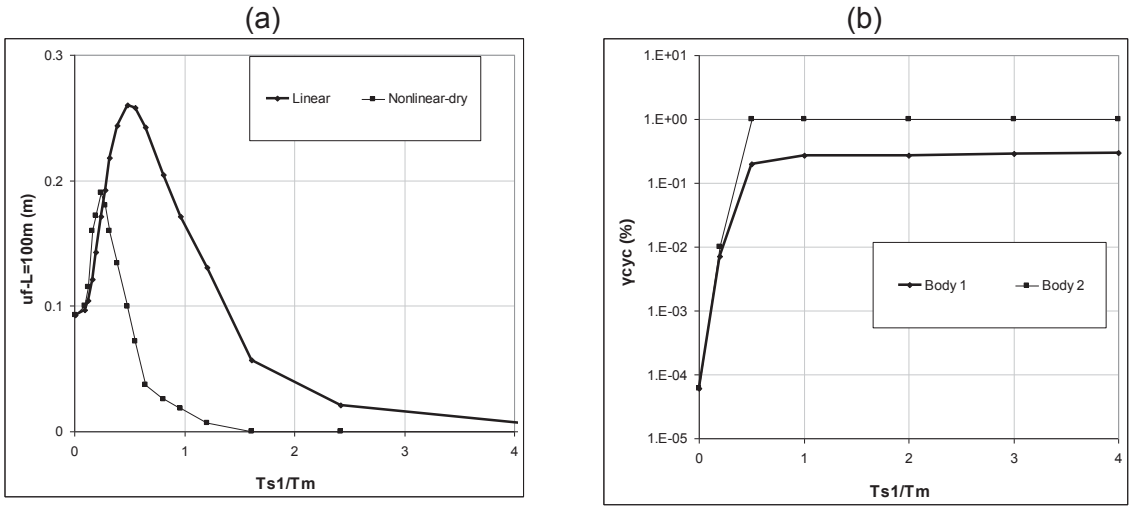

Fig. 8. (a) The computed permanent seismic displacement (u_f) for the linear, nonlinear dry (fa_i= 0) and nonlinear saturated (fa_1=0.3, fa_2=1) coupled analyses versus Ts_1/Tm and (b) the corresponding maximum shear strain for the non-linear analyses. The case of the Aegion 1995 seismic motion with a_{co}=0.5m/s^2, Vs_2=Vs_1, h_1=h_2=15m, ρ_1=ρ_2=2Mg/m^3, λ_1=λ_2=0.15. L=1000m, PI_i=0 is presented.

7 EMPIRICAL EQUATION: PROPOSED MODEL: FORM AND DERIVATION AND VALIDATION PROCEDURE

Based on section above, it is inferred that in non-linear analyses, the shear velocity of the soil layer is modified. As described in section 5, the shear wave velocity in the existing empirical model (13) enters thru the parameters n1, n2, a2. According to table 3, from these three parameters, only the parameter n1 varies dramatically with soil type, taking values ranging from 0.26 to -0.15. It is inferred that, as a first approximation, only this parameter may be modified for the non-linear case. Furthermore, as Vs increases, the shear strain which develops during seismic loading is less and thus the modification needed in the parameter n1 will be less.

Thus, we propose the following equation to estimate the seismic displacement for the non-linear case:

$$u_f = Ra\ u_{f\text{-}rigid\text{-}1000m}\ [1+ [n1 + n1' - n2\ (h1\text{-}10m)]\ (0.1/\ u_{f\text{-}rigid\text{-}1000m}\ )^{a2'}] \quad (15a)$$

where

$$Ra =0.5\ \{1+\tanh[\ln(([0.0215Ar^{0.55}]/(u_f/L))^{0.8})]\ \} \quad (15b)$$

and n_1, n_2, a_2 are the model parameters of the previous equation (13), given in table 3, while the model parameter n1', which simulates the effects of nonlinearity in sandy soils depends on soil type.

In addition, the following procedure is used to evaluate the model parameter n1', defined as

$$n1'= n1_{non\text{-}linear\text{-}PI=0} - n1_{linear} \quad (16)$$

- (a) First, the data base described in section 5.1 is divided in two parts, one to determine the model parameters (DB1), and the other to validate it (DB2). The data base DB1 is the odd number earthquakes and DB2 is the even number of earthquakes.

- (b) Then, for the non-linear case for sands (PI=0), perform parametric analyses identical to those described in section 5.1 for L=1000m.
- (c) Estimate the model parameter n1' by analyzing the results for h1=10m per soil type and taking the average value. In this respect, it can be observed that, as L=1000m, Ra=1 and thus for h1=10m

$$n1' = [u_{f\text{-non-linear}} / u_{f\text{-rigid-1000m}} - 1] / [0.1 / (u_{f\text{-rigid-1000m}})^{a2'}] - n1 \quad (17)$$

- (d) Analyze the error in the estimation of n1' for h1=5m and 20m in terms of soil type. The error of the predictions is defined in the present work as

$$Er = 1 - Predicted/Computed \quad (18)$$

- (e) Once these empirical expressions is derived, use the database DB2 described above to validate the proposed equation. Measure the error (Er) in all 12 cases of the 25 input motions, thus in 12*25=300 cases in total and confirm that the mean and standard deviation of the error are close to zero. Furthermore, analyze the obtained error for all earthquakes in terms of soil type and h_1 (for 12 cases) in order to establish if the accuracy depends on soil type and h_1.

8 EMPIRICAL EQUATION: PROPOSAL AND VALIDATION

Based on the procedure described in section 7, table 3 gives the n1' obtained value per soil type. The standard deviation per soil type and h1 of the error (equation (18)) was in the range of 0.06-0.09, reasonably close to zero. Furthermore, in table 3 it can be observed that the estimated n1' values are larger for the cases of soil types S-C and S-D, consistently to the fact that these two soil types have much lower Vs values and thus the effects of nonlinearity in these soils are greater. Thus, for the non-linear case, equation (15) is proposed with the model parameters of table 3.

Once the empirical equation (15) with the model parameters of table 3 was established using the database DB1, its error in the predictions of this equation was established using DB2. Considering all the data of DB2, the absolute value mean and standard deviation of the error (equation (18)) were estimated as 0.05 and 0.05 respectively. As these values are close to zero, the error is small and acceptable. Furthermore, the obtained error for all earthquakes was obtained in terms of soil type and h_1 as given in table 4. It can be observed that in all cases the error has mean value less than 0.10 and standard deviation less than 0.12.

	Mean Value (Absolute value)			Standard Deviation		
Soil type	h1=5m	h1=10m	h1=20m	h1=5m	h1=10m	h1=20m
S-B	0.08	0.08	0.08	0.07	0.05	0.09
S-C	0.07	0.07	0.09	0.08	0.10	0.11
S-D	0.08	0.08	0.07	0.07	0.08	0.09
S-E	0.09	0.09	0.10	0.06	0.06	0.12

Table 4. Statistical analysis of the error in the predictions of equation (17) with the parameters of table 3 in terms of soil type and h_1

9 EXAMPLE APPLICATION

As an example application, we consider a site in Greece of soil category S-C where the slip surface is at average depth 5m and geotechnical and seismic analysis for bedrock seismic mo-

tion characteristics of the site gave ac=0.01g, and design earthquake of magnitude Mw=7.0 at distance R=1km. Equation (13) by [9] predicts an Arias Intensity Ia=22.0m/s and equation (21) by [9] predicts a corresponding maximum value of seismic displacement with "conventional" sliding-block model $u_{f\text{-}rigid\text{-}L=1000m}$=9.5cm. Application of the empirical expressions (6) with the parameters of table 3 would predict that when considering dynamic effects, Ra=0.98 and u_f=6.3cm. For the elastic case, u_f would equal 12.3cm. Thus, the seismic displacement u_f would increase by about 50% as a result of non-linear response.

10 CONCLUSIONS

- The present work proposes the empirical expression (15) with the parameters of table 3 predicting the seismic displacement of sandy slopes along slip surfaces in Greece, in terms of (a) the conventional sliding-block model predictions, (b) the soil type category according to Eurocode and (c) the depth and length of the slip surface.
- These equations were obtained by extensive parametric analyses using a recently developed dynamic coupled numerical code which predicts the seismic displacement of a ninlinear soil profile along a slip surface at some depth. An extensive data base of seismic motions recorded in Greece was applied below typical soil layers according to Eurocode category type with slip surface at different depths and varying the resistance (as defined by the critical acceleration value) in such a way that computed final seismic displacement of the conventional sliding-block case varies from about 0.05m to 0.5m. The results were analyzed statistically.
- The effects of non-linearity are simulated thru the factor n1', which affects considerably the results for the soft/loose soil profiles S-C and S-D.

REFERENCES

[1] European Standard (2003). Eurocode 8: Design of structures for earthquake resistance, Final Draft, prEN 1998-5, 2003, December.

[2] Whitman R. V. (1993). Predicting earthquake-caused permanent deformations of earth structures, article on “Predictive Soil Mechanics”, Thomas Telford, London, 729-741

[3] Newmark, N. M. (1965). Effects of earthquakes on dams and embankments. Geotechnique, 55 (2), 139-159.

[4] Ambraseys N. and Menu J. (1998). Earthquake induced ground displacements, Earthquake engineering and structural dynamics, 16, 7, 985-1006.

[5] Ambraseys NN, Srbulov M (1994) Attenuation of earthquake-induced displacements. Journal of Earthquake Engineering and Structural Dynamics 23: 467–487

[6] Ambraseys Jibson R. W. Regression models for estimating coseismic landslide displacement

[7] Jibson R. W. Regression models for estimating coseismic landslide displacement Engineering Geology 91 (2007) 209–218.

[8] Rathje EM, Saygili G (2006) A vector hazard approach for Newmark sliding block analysis. Proc.Earthquake Geotech. Engrg. Workshop, University of Canterbury, Christchurch, New Zealand, Nov. 20–23

[9] Chousianitis K., Gaudio V., Kalogeras I, Ganas A. Predictive model of Arias intensity and Newmark displacement for regional scale evaluation of earthquake – induced landslide hazard in Greece , Soil Dynamics and Earthquake Engineering , 2014

[10] Bray J. D. and Travasarou T. (2007). Simplified Procedure for Estimating Earthquake-Induced Deviatoric Slope Displacements, Journal of Geotechnical and Geoenvironmental Engineering, 133 (4), 381-392.

[11] Rathje E. M. and Bray J. D. An examination of simplified earthquake induced displacement procedures for earth structures. Can. Geotech. J. 36: 72–87 (1999)

[12] Jafarian Y. and Lashgari A. (2016). Simplified Procedure for Coupled Seismic Sliding Movement of Slopes Using Displacement-Based Critical Acceleration, International Journal of Geomechanics, Volume 16 Issue 4 - August 2016

[13] Katsenis L. C. Stamatopoulos C. A, Panoskaltsis V. P. , Di B. Prediction of large seismic sliding movement of slopes using a 2-body non-linear dynamic model with a rotating stick-slip element. Soil Dynamics and Earthquake Engineering 129 (2020) 105953

[14] Lin J.-S., and Whitman, R.V. 1983. Decoupling Approximation to the evaluation of earthquake-induced plastic slip in earth dams. Earthquake Engineering and Structural Dynamics, 11: 667–678.

[15] Organization of antiseismic design and protection of Greece (OASP) (1999), Hellenic Seismic Code, September (in Greek).

[16] Katsenis L. C., Stamatopoulos C. A., Panoskaltsis V. P., Thomaidou K. (2019) Seismic sliding displacement of slopes in terms of soil profile type, COMPDYN 2019, 7th International Conference on Computational Methods in Structural Dynamics and Earthquake Engineering, 24-26 June 2019, Crete, Greece

[17] Katsenis L. C., Stamatopoulos C. A, Panoskaltsis V. P., Seismic sliding displacement of slopes in Greece terms of soil profile type and slip surface length, 4th Panhellenic Conference of earthquake engineering and technical seismology, 5-7.09/2019, Athens, Greece

[18] https://www.seismosoft.com/seismosignal

[19] Vucetic M. And Dobry R. “Effect of soil plasticity on cyclic response, Journal of the Geotechnical Division, ASCE, 117 (1). 1991. Bolton M. D. (1986). The strength and dilatancy of sands. Geotecnique 36 (1), 65-78.

[20] Stamatopoulos, C. A. Sliding System Predicting Large Permanent Co-Seismic Movements of Slopes. Earthquake Engineering and Structural Dynamics. 1996. Vol. 25, No, 10, 1075-1093.

Appendix

Table A1. Earthquakes applied

No	Name	Station	Year	M (Mw)
1	Off Cephallonia	Chavriata Chv1	03/02/14	6,10
2	Off Cephallonia	Lixouri Lxr1	03/02/14	6,10
3	Ionian	Lefkada-OTE Building	04/11/73	5,80
4	Pyrgos	Pyrgos-Agriculture Bank	26/03/93	5,40
5	Patras	Patra-San Dimitrios Church	14/07/93	5,60
6	Ano Liosia	Athens-Sepolia (Garage)	07/09/99	6,00
7	Alkion	Korinthos-OTE Building	24/02/81	6,60
8	Kalamata	Kalamata-Prefecture	13/09/86	5,90
9	Ano Liosia	Athens 3 (Kallithea District)	07/09/99	6,00
10	Alkion	Xilokastro-OTE Building	24/02/81	6,60
11	Kalamata	Kalamata-OTE Building	13/09/86	5,90
12	Kozani (aftershock)	Karpero-Town Hall	19/05/95	5,20
13	Off Cephallonia	Argostoli Arg2	03/02/14	6,10
14	Kefallinia (aftershock)	Argostoli-OTE Building	23/03/83	6,20
15	Kefallinia island	Argostoli-OTE Building	23/01/92	5,60
16	Ano Liosia	Athens-Sepolia (Metro Station)	07/09/99	6,00
17	Kozani	Kozani-Prefecture	13/05/95	6,50
18	Komilion	Lefkada-OTE Building	25/02/94	5,40
19	Aigion	Aigio-OTE Building	17/05/90	5,21
20	Patras	Patra-National Bank	14/07/93	5,60
21	Patras	Patra-OTE Building	14/07/93	5,60
22	Ierissos	Ierissos-Police Station	26/08/83	5,09
23	Heraklio	Heraklio-Prefecture	19/03/83	5,60
24	Etolia	Valsamata	18/05/88	5,30
25	Kefallinia island	Argostoli-OTE Building	23/06/92	5,09
26	Kefallinia island	Kefallinia	17/09/72	5,6
27	Kefallinia (aftershock)	Kefallinia	30/10/72	5,36
28	Kozani (aftershock)	Chromio-Community Building	15/05/95	5,20
29	Kyllini	Amaliada-OTE Building	16/10/88	5,90
30	Kyllini	Zakynthos-OTE Building	16/10/88	5,90
31	Ano Liosia	Athens 2 (Chalandri District)	07/09/99	6,00
32	Volvi	Thessaloniki-City Hotel	20/06/78	6,20
33	Arnaia	Poligiros-Prefecture	04/05/95	5,30
34	Preveza	Preveza-OTE Building	10/03/81	5,40
35	Mouzakaiika	Lefkada-OTE Building	13/06/93	5,30
36	Kozani (aftershock)	Chromio-Community Building	17/05/95	5,30
37	Komilion	Lefkada-Hospital	25/02/94	5,40
38	Ano Liosia	Athens-Sygrou-Fix	07/09/99	6,00
39	Strofades	Zakynthos-OTE Building	18/11/97	6,60
40	Alkion	Korinthos-OTE Building	25/02/81	6,30
41	Ano Liosia	Athens 4 (Kipseli)	07/09/99	6,00
42	Lefkada	Lefkada-OTE Building	27/05/81	5,30
43	Kalamata	Koroni-Town Hall	13/10/97	6,40
44	Volvi	Thessaloniki-City Hotel	04/07/78	5,41
45	Pyrgos	Amaliada-OTE Building	26/03/93	5,40
46	Kalamata (aftershock)	Kyparrisia-Agr. Bank	10/06/87	5,30
47	Ierissos	Ouranoupolis	26/08/83	5,10
48	Ano Liosia	Athens-Syntagma	07/09/99	6,00
49	Ierissos	Poligiros-Prefecture	26/08/83	5,10
50	Gulf of Corinth	Nafpaktos- OTE Building	04/11/93	5,30

Table A2. Characteristics of applied earthquakes

No	Mean Period	Predominant Period	a_{max} (m/s^2)	V_{max} (m/sec)	Arias intensity (m/sec)	Epicentral distance (km)
1	0,30729	0,16	7,3360	0,3215	2,76936	7,00
2	0,82566	0,9	6,545	0,7677306	2,75813	7,00
3	0,45012	0,34	5,1459	0,38516	0,89603	15,00
4	0,246	0,08	1,4244	0,06406	0,06707	10,00
5	0,24819	0,08	1,4992	0,07922	0,11386	9,00
6	0,22257	0,16	2,7592	0,21152	0,39398	14,00
7	0,4679	0,34	2,2566	0,14617	0,42166	20,00
8	0,46054	0,3	2,108	0,27389	0,41461	10,00
9	0,26487	0,08	2,6014	0,25544	0,22299	16,00
10	0,4544	0,22	2,8382	0,1593	0,60747	19,00
11	0,43318	0,22	2,3537	0,29092	0,38456	11,00
12	0,25146	0,14	2,601	0,10955	0,25406	16,00
13	0,13857	0,06	2,198	0,0488	0,15636	12,00
14	0,18438	0,1	1,788	0,09629	0,20986	9,00
15	0,21945	0,12	1,249	0,1062	0,07634	14,00
16	0,25703	0,16	2,1698	0,16418	0,17729	14,00
17	0,21054	0,16	2,0388	0,16501	0,19868	17,00
18	0,35851	0,18	1,71620	0,09177	0,12485	16,00
19	0,2101	0,14	1,14910	0,03693	0,02189	20,00
20	0,2754	0,2	1,37730	0,11783	0,09903	10,00
21	0,2702	0,14	1,13720	0,0423	0,09253	10,00
22	0,2295	0,12	1,22820	0,09927	0,05427	8,00
23	0,1989	0,16	0,75026	0,05918	0,0576	40,00
24	0,2261	0,22	1,62380	0,06671	0,09257	23,00
25	0,2124	0,18	1,71720	0,06517	0,09291	16,00
26	0,2016	0,12	1,19270	0,07615	0,0717	31,00
27	0,242	0,18	0,61381	0,05185	0,01451	19,00
28	0,1706	0,08	1,2951	0,06495	0,05646	9,00
29	0,2968	0,18	0,7845	0,08526	0,04902	36,00
30	0,3089	0,34	1,4789	0,07214	0,15926	14,00
31	0,2522	0,08	1,0685	0,07901	0,05804	20,00
32	0,329	0,20	1,3095	0,07733	0,12136	29,00
33	0,1528	0,10	1,4255	0,07613	0,0596	28,00
34	0,2328	0,20	1,4019	0,06422	0,17736	28,00
35	0,2159	0,16	0,4262	0,01477	0,00905	48,00
36	0,1945	0,16	1,2897	0,05671	0,05639	16,00
37	0,3595	0,32	1,2701	0,091	0,12521	15,00
38	0,4444	0,12	0,8329	0,06277	0,02688	19,00
39	0,3493	0,18	1,1944	0,08539	0,20123	38,00
40	0,6177	0,18	1,1714	0,10388	0,14958	25,00
41	0,294	0,3	1,1710	0,08864	0,06613	17,00
42	0,2086	0,16	1,1703	0,05143	0,04701	26,00
43	0,2677	0,12	1,1217	0,07781	0,12713	48,00
44	0,2761	0,2	1,12480	0,05836	0,04483	16,00
45	0,265	0,1	1,1214	0,16299	0,04209	24,00
46	0,2177	0,1	0,6611	0,03294	0,01229	17,00
47	0,1816	0,16	0,8164	0,03718	0,02224	15,00
48	0,3574	0,14	1,0872	0,06552	0,03649	18,00
49	0,1915	0,08	1,0500	0,07606	0,021	42,00
50	0,2863	0,12	0,6532	0,03156	0,03005	10,00

EURODYN 2020
XI International Conference on Structural Dynamics
M. Papadrakakis, M. Fragiadakis, C. Papadimitriou (eds.)
Athens, Greece, 23–26 November 2020

SUPPRESSION OF CLASSICAL FLUTTER OSCILLATIONS IN BLADED WHEEL USING INNER DAMPING EFFECT

L. Pesek[1], **P. Snabl**[1], **and Ch. S. Prasad**[1]

[1]Institute of Thermomechanics of the Czech Academy of Sciences
Dolejskova 5, Prague 8, CZ 182 00
e-mail: pesek@it.cas.cz

Keywords: blade, flutter, travelling wave, Van der Pol model

Abstract. *Inner material damping effect for reduction of self-excited vibrations due to aero-elastic instability is studied on a numerical reduced model of a rotating turbine wheel with 66 blades. The aerodynamic nozzle excitation of the rotating wheel arises from the spatially periodical flow of steam through the stator blade cascade. This excitation causes travelling deformation waves in the wheel. The analysis of forced vibration of the wheel under self-excitation is oriented on the narrow frequency range and therefore the bladed wheel is modelled by a modal synthesis method. The self-excited aero-elastic forces are described by Van der Pol model acting herein independently to the 1th axial flexural mode of each blade of the wheel. Numerical simulations showed a very fast entry of amplitudes increase due to self-excitation. The initial forced vibration mode by nozzle excitation was decisive for the vibration pattern of self-excitation. Its suppression depended on the ratio between the intensity factor of self-excitation and the size of proportional damping describing the inner damping.*

1 INTRODUCTION

Since traditional computational fluid and structural tools are computationally very expensive and required large computational power to simulate fluid-structure problems in machines where the large fluid domain and complex solid bodies need to be discretized, we aim at development and application of reduced-order modeling order modeling (ROM) of flutter oscillations in turbine bladed wheel dynamics. Although such ROM approaches are medium fidelity models yet, they can bring interesting knowledge of their dynamic behavior of a bladed wheel system.

Beside the forced nozzle excitation, the gas flowing through a blade cascade can cause instability and/or increase of self-excited oscillations [1-3]. For determination of critical behavior of self-excited vibration in the blade cascade, the boundary element based panel method as ROAM method is developed to model a flow field around bodies [4]. For description of post-critical dynamic behavior of the bladed wheels, a semi-analytical approach based on the Van der Pol model was proposed [5-7]. For case studies, the different blade systems modeled by mass-spring discretized models with viscous-elastic or dry-friction damping in the blades shroud were analyzed. Van der Pol model advantage is a conversion of negative damping into positive one after the amplitude of self-excited oscillations exceeds prescribed limits.

This contribution is continuation of our study of self-excitation in bladed wheels. In this approach, however, we choose the modal synthesis ROM method for the bladed wheel reduction [8-10]. It shows that the vibration of the turbine wheels occurs in narrow frequency ranges when dominant resonant vibration occurs. In literature Van der Pol model of self-excitation is used in connection with stator blade vortex shedding excitations and “lock-in” phenomena. As the vortex shedding frequency approaches the natural frequency of the body, both frequencies lock-in [11-13]. In our approach, however, we deal with classical flutter phenomena [1] in bladed wheels that is linked with travelling deformation waves and inter-blade-phase-angle (IBPA) initiated by nozzle excitation. If the material and structural damping of the wheel is low, the flutter can cause rapid increase of vibration amplitudes that can lead to high cycle fatigue of the blade. Resonant frequencies and vibration mode shapes does not change significantly due to higher vibration amplitudes in the flutter state. Therefore, if we correctly asses the frequency range for modal reduction, this method could precisely describe the bladed wheel dynamics because the modal properties of the reduced system are properly approximated. The aero-elastic forces are described again by Van der Pol model related to selected eigenmode. As example of possible suppression of this dangerous phenomenon, we introduced a simple proportional damping term which describes inner material damping into the equation of motion.

2 GENERAL SPECIFICATIONS

The homogeneous equation of motion of the undamped original mechanical system can be written in the matrix form as

$$\mathbf{M}\ddot{\mathbf{u}} + \mathbf{K}\mathbf{u} = \mathbf{0}\,, \tag{1}$$

where $\mathbf{M}$ and $\mathbf{K} \in R^{n\times n} \in R^{n\times n}$ are mass and stiffness square matrices of dimension n, $\ddot{\mathbf{u}}$, $\mathbf{u}$ are acceleration, displacement vectors of the DOFs.

That leads to the eigenvalue problem

$$(\mathbf{K} - \Lambda\mathbf{M})\mathbf{X} = \mathbf{0}\,, \tag{2}$$

The solution of (2) yields the matrices of eigenvalues Λ and of eigenvectors $\mathbf{X}$

$$Diag(\mathbf{\Lambda}) = [\lambda_1, \lambda_2, \ \dots \ , \lambda_n], \mathbf{X} = [\mathbf{x}_1, \mathbf{x}_2, \ \dots \ , \mathbf{x}_n] . \tag{3}$$

If the eigenvector matrix satisfies the orthonormal condition then

$$^T\mathbf{XMX} = \mathbf{I}, \mathbf{XKX} = \mathbf{\Lambda} . \tag{4}$$

For simplicity of modal synthesis explanation, let us assume assembly just two identical blade segments (n_r=2). The homogenous equation of motion of uncoupled subsystems is

$$\mathbf{M}_c\ddot{\mathbf{u}}_c + \mathbf{K}_c\mathbf{u}_c = \mathbf{0} , \tag{5}$$

where

$$\mathbf{M}_c = \begin{bmatrix} \mathbf{M} & 0 \\ 0 & \mathbf{M} \end{bmatrix}, \ \mathbf{K}_c = \begin{bmatrix} \mathbf{K} & 0 \\ 0 & \mathbf{K} \end{bmatrix}, \ \mathbf{u}_c = \begin{bmatrix} \mathbf{u}_1 \\ \mathbf{u}_2 \end{bmatrix},$$

with eigenvalue characteristics

$$\mathbf{\Lambda}_c = \begin{bmatrix} \mathbf{\Lambda} & 0 \\ 0 & \mathbf{\Lambda} \end{bmatrix}, \ \mathbf{X}_c = \begin{bmatrix} \mathbf{X} & 0 \\ 0 & \mathbf{X} \end{bmatrix}, \tag{6}$$

where $\mathbf{K}_c, \mathbf{M}_c, \mathbf{X}_c, \mathbf{\Lambda}_c \in R^{nn_r xnn_r}$ (n is number of DOFs of the segment, n_r is number of segments).

Each connection between the blade subsystems can be described by a constraint vector $\mathbf{T}_v$. For example, let $\mathbf{K}$ is a matrix of R^{4x4} and 4th DOF u_{14} of the 1th blade and the 3rd DOF u_{23} of the 2nd blade are connected by spring with stiffness c_1. The constrain is governed by the expression

$$c_1(u_{14} - u_{23}) = F_1 . \tag{7}$$

To create the full modification stiffness matrix in original DOFs, the constrain can be expressed by a constraint vector $\mathbf{T}_v$

$$c_1 \, ^T\mathbf{T}_v\mathbf{u}_c = F_1 , \tag{8}$$

where $^T\mathbf{T}_v = \begin{bmatrix} 0 & 0 & 0 & 1 & 0 & 0 & -1 & 0 \end{bmatrix}$. Then the modification stiffness is constituted as

$$\Delta\mathbf{K} = \mathbf{T}_v \, ^T\mathbf{T}_v c_1 . \tag{9}$$

The full synthesized system can be described by the equation of motion

$$\mathbf{M}_c\ddot{\mathbf{u}}_{cN} + \left(\mathbf{K}_c + \Delta\mathbf{K}\right)\mathbf{u}_{cN} = \mathbf{f}_{cE} , \tag{10}$$

which leads to eigenvalue problem

$$\left(-\mathbf{\Lambda}_{cN}\mathbf{M}_c + \left(\mathbf{K}_c + \Delta\mathbf{K}\right)\right)\mathbf{X}_{cN} = \mathbf{0} . \tag{11}$$

To reduce the full DOF space of the synthesized structure (10) we choose the modal subspace

$$\bar{\mathbf{X}}_c = \begin{bmatrix} \bar{\mathbf{X}} & 0 \\ 0 & \bar{\mathbf{X}} \end{bmatrix},$$

where $\bar{\mathbf{X}} \in R^{n\times m}$ is matrix of arbitrarily chosen m eigenvectors of $\mathbf{X} \in R^{n\times n}$ of the original one-blade subsystem. Introducing the transformation $\mathbf{u}_{cN} = \bar{\mathbf{X}}_c \mathbf{Q}_{cNR}$ and $\ddot{\mathbf{u}}_{cN} = -\bar{\mathbf{X}}_c \mathbf{\Lambda}_{cNR} \mathbf{Q}_{cNR}$ and pre-multiplying by ${}^T\bar{\mathbf{X}}_c$ in (11), when the eigenvector matrix $\bar{\mathbf{X}}_c$ satisfies the orthonormal condition (4) then we get

$$[-\mathbf{\Lambda}_{cNR} + (\mathbf{\Lambda}_{cR} + \Delta\mathbf{K}_{cNR})]\mathbf{Q}_{cNR} = \mathbf{0}, \tag{12}$$

where $\mathbf{Q}_{cNR}$ is reduced synthesized modal matrix, $\Delta\mathbf{K}_{cNR} = {}^T\bar{\mathbf{X}}_c \Delta\mathbf{K} \bar{\mathbf{X}}_c$ is reduced modification matrix of $R^{mn_r \times mn_r}$.

Remark: To avoid the calculations of the eigenvalue problem of the full synthesized system (10) the modal subspace $\mathbf{X}_{cN}$ is approximated by $\mathbf{X}_c$ for expression of $\mathbf{u}_{cN}, \ddot{\mathbf{u}}_{cN}$. Therefore it is necessary to use the same boundary conditions of the uncoupled and synthesized models.

To preserve the solution in modal space, then the external and self-excitation forces has to be expressed in reduced space and equation of motion of synthezised reduced wheel system can be expressed as

$$\mathbf{M}_{cR}\ddot{\mathbf{u}}_R + \beta(\mathbf{K}_{cR} + \Delta\mathbf{K}_{cNR})\dot{\mathbf{u}}_R + \mathbf{G}(\mathbf{u}_{RB}, \dot{\mathbf{u}}_{RB}) + (\mathbf{K}_{cR} + \Delta\mathbf{K}_{cNR})\mathbf{u}_R = \mathbf{f}_{cRE}(t), \tag{13}$$

where $\mathbf{K}_{cR} = {}^T\bar{\mathbf{X}}_c \mathbf{K}_c \bar{\mathbf{X}}_c$, $\mathbf{M}_{cR} = {}^T\bar{\mathbf{X}}_c \mathbf{M}_c \bar{\mathbf{X}}_c$, β is coefficient of proportional damping and $\mathbf{u}_{RB}$ is defined bellow..

In steam turbines the stator blades create so-called nozzle excitation, i.e. spatially periodical flow that acts on the rotor blades with periodic force which frequency is dependent on angular velocity of the rotor and number of stator blades. Number of stator blades is usually chosen lower than number of rotor blades and their difference gives number of NDs which is excited by the nozzle excitation. The excitation force can be described by

$$F_{Ei} = F_b \cos\left[n_s \omega_r t - 2\pi \left(1 - \frac{n_s}{n_r}\right) i \right], \quad i = 1, \ldots, n_r, \tag{14}$$

where F_b is the force amplitude, ω_r the angular velocity of the rotor and n_r and n_s are the numbers of rotor and stator blades. So force vector ${}^T\mathbf{f}_{cRE} = \left[{}^T\mathbf{f}_{cRE1} \quad {}^T\mathbf{f}_{cRE2} \quad . \quad {}^T\mathbf{f}_{cREn} \right]$ is composed of reduced external excitation vectors $\mathbf{f}_{cREi} = \mathbf{p}_{Ei} F_{Ei}$ of each blade (i=1, n_r), where $\mathbf{p}_{Ei} = {}^T\bar{\mathbf{X}}\mathbf{d}_{cEi}$ is participation factor of i-blade. Distribution excitation vector $\mathbf{d}_{cEi}$ of the blade is zeros vector with ones only on positions corresponding to DOFs of the blade where forces act.

In addition to the nozzle excitation, we assumed the self-excitation aerodynamic forces $\mathbf{G}$ that uniformly act on one selected mode of each blade. To study the effect of the self-excited vibrations, Van der Pol model was used as

$$G_i = -\mu\left[1-\left(\frac{u_{RBi}}{r}\right)^2\right]\dot{u}_{RBi}, \quad i=1,\ldots,n_r, \tag{15}$$

where μ is intensity of self-excitation and r is a value of amplitude at which the negative damping changes into positive. This property allows us to study the behavior in this unstable regions because it prevents the amplitude to grow to infinity and stopping the simulations. Displacements u_{RBi} and their velocities $\dot{u}_{RBi}$ are linked with absolute values of selected modal coordinates calculated for each blade at each step of time integration. The construction of vector $\mathbf{G}$ is analogical to $\mathbf{f}_{cRE}$ Due to uniformity distribution assumption its vectors $\mathbf{d}_{ci}$ are unity vector and arising participation vectors of blades are multiplied by function (15). Therefore, the unstable behavior of each blade in selected vibration modes is enabled.

3 STUDY CASE

For demonstration of the blade assembly by modal synthesis and calculations of its dynamic behavior under nozzle excitation and self-excitation, the modified turbine bladed wheel was chosen as a study case (Fig.1). In addition to the modified model, the real structure of the wheel (n_r =66 blades) has interconnections in shrouds and tie-bosses of blades.

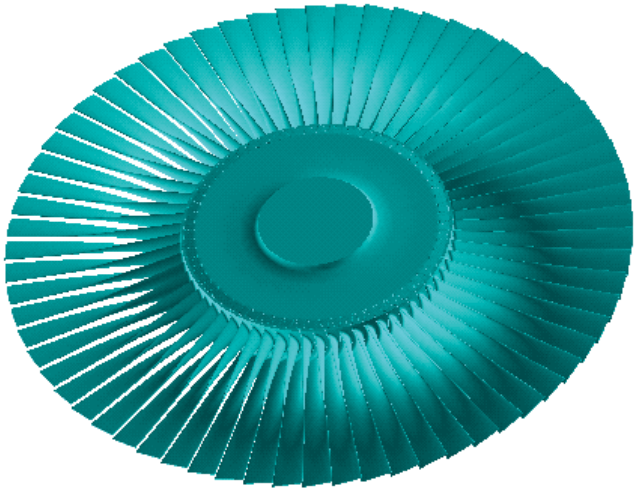

Figure 1: Model of bladed wheel.

The numerical models of the whole wheel with mesh of 1946303 nodes and the one-blade segment used for modal synthesis of 30383 nodes (91149 DOFs) were built in the program ANSYS 19.3. The node topology of one-blade segment including a blade and disk partition is shown in figure 2.

The bottom nodes (light blue marks) of the model (shaft area) were clamped in all DOFs. The nodes (N25201 and N25467) of y-axis nozzle excitation and nodes of ten couplings' pairs between left and right sides of neighboring segments, i.e. pairs N3696-N3185, N3475-N1875, N3546-N1587, N3405-N1980, N3427-N2077, N1109-N3154, N3602-N2408, N3673-N2690, N3273-N1840, N3561-N2515, are depicted in the figure too. All DOFs of the paired nodes were connected by springs with stiffness $c_1 = 1e8 Nm^{-1}$. Then the constrain expressions (9) were used to create modification matrix $\Delta\mathbf{K}_{cR}$. Since the modal matrix $\bar{\mathbf{X}} \in R^{91149\times 3}$ consisted

of flexural (one tangential and two axial) eigenmodes of the first three eigenfrequencies (Tab.1) of the segment, the final dimensions of the global matrices of equation (13) were reduced (198x198).

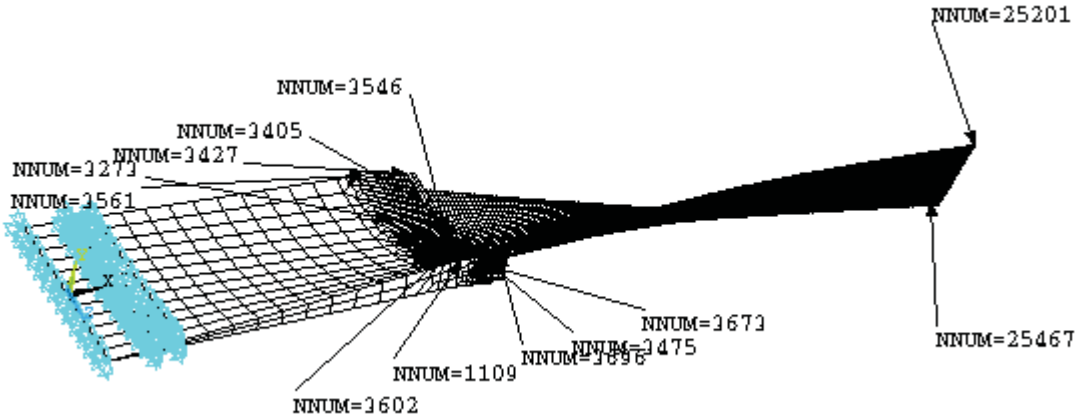

Figure 2 FE model of one-blade segment

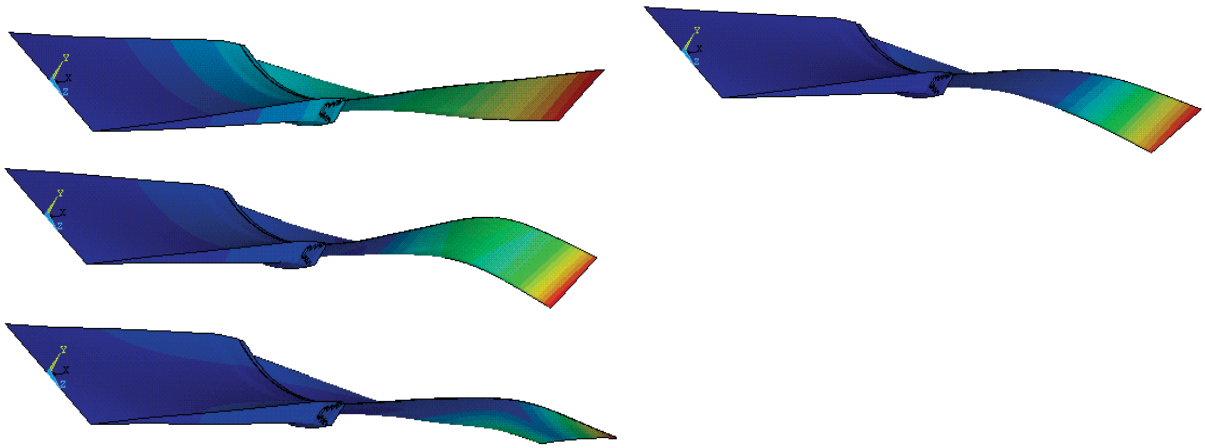

Figure 3: First four eigenmodes: a) 1. Tangential bending, b) 1. Axial bending c), 2. Axial bending, d) 1. Torsional.

By couplings between the 1th and the last 66th blade we create a rotational periodicity of the assembly. These structures are characteristic by double eigenfrequencies of the eigenvalue problem. To assess accuracy of the mode approximation the results of eigenfrequencies ω_{ci} of uncoupled assembly, ω_{cFi} of full unreduced model (as reference) and ω_{cNRi} of modified reduced system are presented in Tab. 2. It can be seen a good agreement between full model and synthesized model results. Small differences between modes with different number of nodal diameters show that the disk is relatively stiff compared to the blades that is demonstrated by small disk displacements of all eigenmodes in Fig. 4. Selected shapes of eigenmodes (2ND and 4ND) associated with their double eigenfrequencies computed by the full wheel FE model are depicted in the figure 4.

i - mode order number	Blade segment	Whole wheel		NDs of wheel modes
	$\omega_{Ri}/2\pi$	$\omega_{cFi}/2\pi$	$\omega_{cNRi}/2\pi$	
1	22.099	35.059	34.6673	1
2	38.519	35.059	34.6673	1
3	91.850	35.075	34.8195	2
4	160.36	35.075	34.8195	2
5	169.55	35.082	34.9142	3
6	182.74	35.082	34.9142	3
7	198.70	35.085	34.9903	4
8	319.72	35.085	34.9903	4
9	364.04	35.088	35.0655	5
10	399.35	35.088	35.0655	5

Table 1: Eigenfrequencies ω_{Ri} of blade segment, ω_{cFi} of full unreduced model (as reference) and ω_{cNRi} of modified reduced system of the bladed wheel.

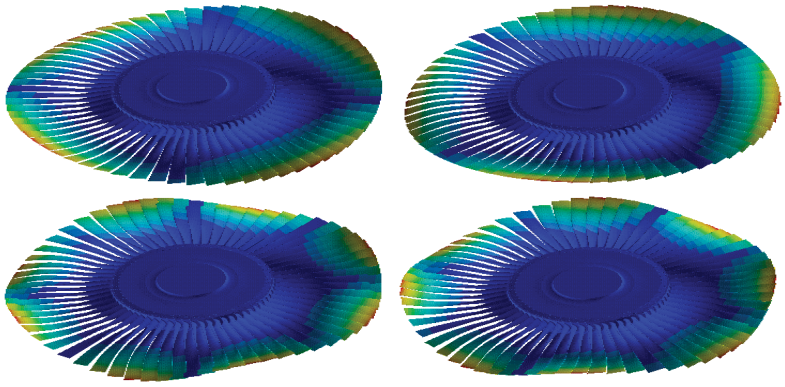

Figure 4: Contour pictures of eigenmodes: a) 2ND; b) 4ND of the wheel.

Selection of modes, modal reduction of one-blade segment and modal synthesis of the wheel were calculated in Matlab after importing full matrices from ANSYS.

4 SIMULATIONS OF WHEEL DYNAMIC BEHAVIOUR - NOZZLE EXCITATION AND SELF-EXCITATION

The simulations of self-excited vibrations on reduced-order model of bladed wheel were realised in Simulink block scheme environment. Simulation time-step was chosen 1e-4 s and the used solver was "ode3". The mode sensitive to self-excitation was selelected the 1th axial flexural mode (Fig. 3). To analyse dynamical response of the wheel with combined nozzle excitation and self-excitation we assumed 62 stator blades (n_s). At this case the vibration mode with 4ND is dominantly excited. When we assume that the revolution speed is 300rpm, the excitation frequency of rotor blades is 5x62 = 310Hz and therefore very far away from resonant vibration of the 4ND mode (cca 35Hz). The force amplitude F_b was 10N. At this

case, the wheel is out of forced resonant vibration and amplitudes are small. However, the vibration level can get to high amplitudes in some conditions due to self-excitation caused by the stator blade wakes. Therefore, we aimed at this study on evolution of vibration amplitudes in time for different values of the intensity of Van der Pol self-excitation (Fig.5).

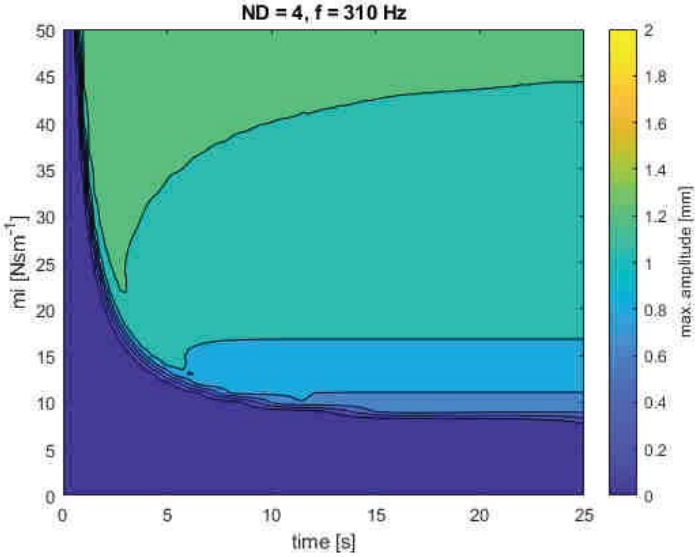

Figure 5: Contour picture of maximal amplitude time dependence versus size of intensity of Van der Pol excitation.

The figure shows evolution of maximal amplitude in time with change of the intensity of Van der Pol self-excitation μ. For small self-excitation intensity, the self-excitation is not able to overcome structural damping and the amplitude of vibration excited by nozzle excitation remains at very small level. When the intensity gets higher, the self-excitation starts to dominate after certain period of time. The higher the intensity is, the shorter time is needed for the self-excitation to start and the higher the final vibration amplitude is. As to the excited vibration mode number of nodal diameters of the running wave it was found out that 4 nodal diameters initially excited stay even when the vibration is dominated by the self-excitation. Therefore, self-excitation does not change the vibration mode determined by number of stator blades.

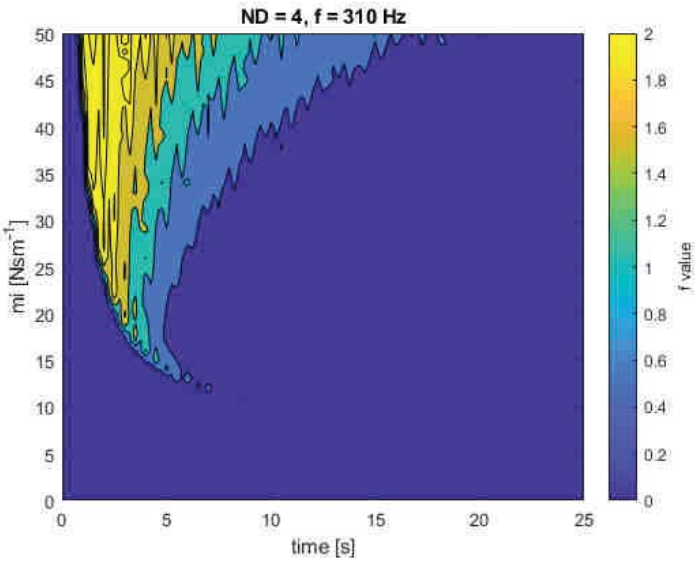

Figure 6: Contour picture of ND's identification error function time dependence versus size of intensity of Van der Pol excitation.

Number of nodal diameters was evaluated in certain time-steps of the simulation by fitting sine function on ordered amplitudes of all blades by minimizing the target function. Amplitude of "f value" is reached minimum of that function (Fig.6). From this figure we can see that when self-excitation starts, a combination of vibration modes is excited before it stabilises during time. Because of the combination a higher error in ND identification occurs.

5 SUPPRESSION OF SELF-EXCITATION BY INNER DAMPING

To study the effect of additional structural damping which could suppress or diminish danger of self-excited vibrations we introduced to our numerical model for self-excitation also proportional damping as described in equation (13). The proportional damping models mainly inner material damping. For describing the effect we chose intensity of self-excitation $\mu = 25$ and calculated dynamic responses of the wheel for different values of coefficient β. The similar graphs (Fig. 7-8) are shown as in the previous paragraph. Instead of intensity μ dependence, however, time development of vibration amplitudes is evaluated for different values of coefficient β.

We can see that due to higher values of β we can suppress effect of self-excitation. For lower values, however, the self-excitation is suppressed just at the beginning and pronounces in few seconds. Again the vibration mode with 4ND prevails, except of short time period and lower values of β, in both forced and self-excited vibration states.

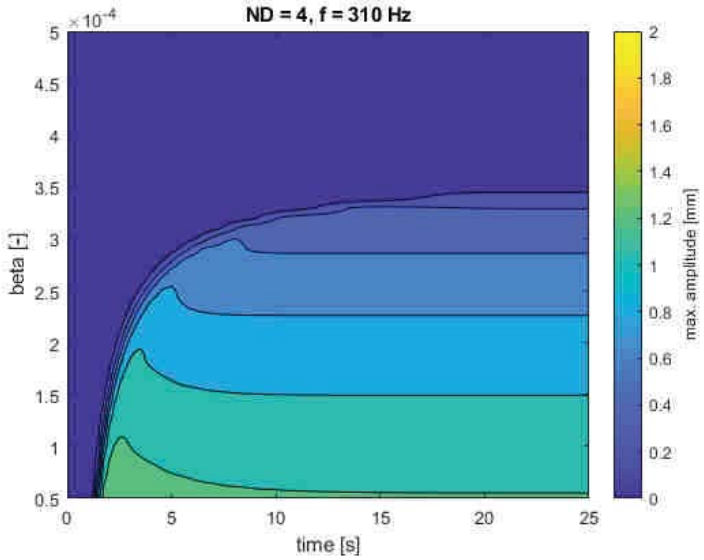

Figure 7: Contour picture of maximal amplitude time dependence (case $\mu = 25$) versus size of coefficient of proportional damping.

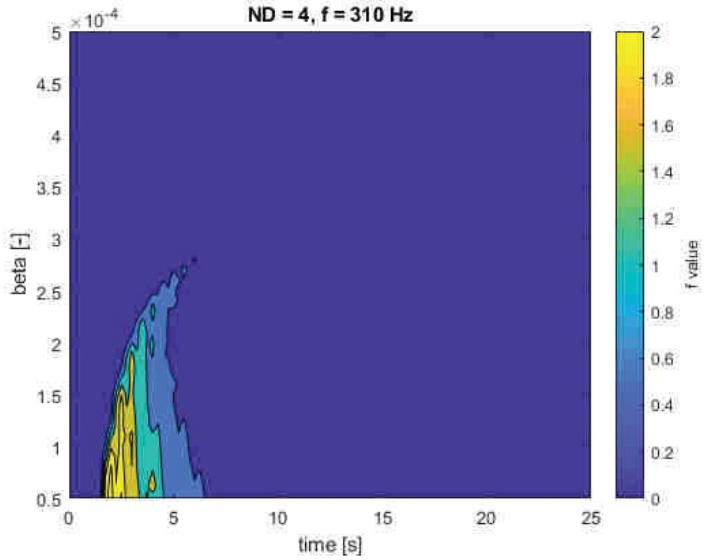

Figure 8: Contour picture of ND's identification error function time dependence (case $\mu = 25$) versus size of coefficient of proportional damping.

6 CONCLUSION

The paper introduced the method of modal synthesis as ROM method for the turbine bladed wheel modelling. It was shown that this approach can lead to efficient DOF reduction with very good approximation of modal characteristics. It brings possibility to calculate fast more realistic deformation patterns of the blades and whole turbine wheels for study of flutter phenomena. Due to high DOF reduction (from tens of thousands to several DOFs), a computational time of time integration of the motion equations decreases from days to minutes and this ratio increases with complexity of non-linearities (e.g. dry-friction contacts) included in the wheel model.

The ascertained results of numerical simulations showed that due to self-excitation the very fast entry of amplitude increase can arise. The slope depends on the ratio between intensity factor of self-excitation and coefficient of proportional damping. At this first study the Van der Pol model was related to the 1th axial flexural mode of vibration. The result leads to logical conclusion since the self-excitation forces and viscous damping forces are dependent both on absolute velocity of blades. On contrary to vortex shedding excitations and "lock-in" effect, the simulations of classical flutter showed that the effect of self-excitation can arise out of resonant frequency and low vibration amplitudes. If it occurs, it is dependent on ratios between damping factor and intensity of self-excitation. In the study case, four nodal diameters mode initiated by nozzle excitation remained even if the vibration was dominated by the self-excitation. So, the initial forced structural mode was decisive for the vibration pattern of self-excitation. The achieved results are in accord qualitatively with our previous studies [5-7] performed on the simplified numerical models.

Next, these simulations will be extent to different types of Van der Pol model, e.g. dependent on relative blade motions, and to suppression of self-excitation by dry-friction damping. Possibilities of more complex distribution of Van der Pol model based on experimental results would be considered, too.

In this study we modelled self-excitation by Van der Pol model, however, this approach can be used for other FSI approaches such as loose coupling structural solver with a ROAM panel method, too.

ACKNOWLEDGEMENT: This research is supported by the research project of Czech science foundation GA19-02288J: Robust reduced-order modelling of fluid-structure interaction problems. The authors are also grateful to Doosan Škoda Power, s.r.o. for providing bladed wheel geometry.

REFERENCES

[1] Fransson T. Introduction to blade flutter in axial flow turbomachinery, Lecture notes, Udine, 1993.

[2] Panovsky J., Kielb R. A design method to prevent low pressure turbine blade flutter, *J Eng Gas Turbine Power*, 122 (1), pp. 89-98, 2000.

[3] Vogt D. Experimental Investigation of Three-Dimensional Mechanisms in Low-Pressure Turbine Flutter, *Ph.D. Thesis*, 2005.

[4] Prasad, C. S., Pešek, L. Estimation of aeroelastic stability parameters of blade cascade using 2D boundary element method, *Engineering Analysis with Boundary Elements*, 113, 2020, pp. 328-345, 2020.

[5] Půst, L. Pešek, L. Blades forced vibration under aero-elastic excitation modeled by Van der Pol, *International Journal of Bifurcation and Chaos*, 27(11), 13 pages, 2017.

[6] Půst, L., Pešek, L., Byrtus, M. Modelling of flutter running waves in turbine blades cascade, *Journal of Sound and Vibration*, 436, pp. 286-294, 2018.

[7] Pešek, L., Půst, L., Šnábl, P. Study of dry-friction damping effect on two simplified models of flutter oscillations, *Advances in Mechanism and Machine Science*, Springer Nature Switzerland, pp. 3419-3428, 2019.

[8] Braun S. G., Ram Y.M. Modal modification of vibrating systems: Some problems and their solution, *Mechanical Systems and Signal Processing*, 15(1), 2001, pp.101-119.

[9] He B. J. Structural modification, *Phil. Trans*,. Royal Society London A, 359, 187-204, 2001.

[10] Nad M. Structural dynamic modification of vibrating systems, *Applied and Computational Mechanics*, 1, 203 – 214, 2007.

[11] Giannini O., Sestieri A. Experimental characterization of veering crossing and lock-in in simple mechanical systems, *Mechanical Systems and Signal Processing*, 72-73, 846-864, 2016.

[12] Hoskoti, L., Misra, A., Sucheendran, M. Frequency lock-in during vortex induced vibration of a rotating blade, *Journal of Fluids and Structures*, 80, 145-164, 2018.

[13] Byrtus M., Dyk S. Influence of friction damping on frequency lock-in in cyclic structure, *Proceedings of ENOC 2020, July 5-10, 2020, Lyon* (to be published), 2020.

EURODYN 2020
XI International Conference on Structural Dynamics
M. Papadrakakis, M. Fragiadakis, C. Papadimitriou (eds.)
Athens, Greece, 23–26 November 2020

THE THEORY OF BODY COLLISIONS IN ROLLING THROUGH GEOMETRY, KINEMATICS AND DYNAMICS OF BILLIARDS

Hedrih (Stevanović) R. Katica[1,2]

[1] Mathematical Institute of Serbian Academy of Sciences and Arts, Belgrade, Serbia

[2] Faculty of Mechanical Engineering at University of Niš, Serbia

e-mail: khedrih@sbb.rs, katicah@mi.sanu.ac.rs

Keywords: Theory of collision, Rolling balls, Billiards.

Abstract. *The elements of geometry, kinematics and dynamics of rolling homogeneous balls along curvilinear lines are defined. The complete theory of the impact and collision of heavy rolling balls, through geometry, kinematics and dynamics of rolling balls, is defined. A new definition of the coefficient of restitution (collision) was introduced, starting from the hypothesis of the conservation of the sum of angular momentum of the balls in rolling, for instantaneous rolling axes, after the collision in relation to the before collision of the bodies. The expressions for the outgoing angular velocities of the ball rolling after the collision have been derived and their rolling paths after the impact or collision have been determined and various possible anchors have been shown. The difference between the content of the term billiards used in mathematical works of many mathematicians, as well as the research that remains in the field of geometry is pointed out. Our theory of ball rolling and collision is based on the examples of the abstraction of real systems of rolling heavy homogeneous billiard balls to a mechanical model.*

1 INTRODUCTION. A BRIEF OVERVIEW OF THE HISTORY OF CLASSICAL IMPACT AND COLLISION THEORY

In 1668, the Royal Scientific Society in London launched a call for a solution to the problem of impact and collision dynamics, and for that call, the well-known scientists Wallis (John Wallis, 1616-1703, Mechanica sive de mote-1688) and Huygens (Christiaan Huygens - De motu corporum ex percusione) submitted their papers. Using the results of the collision, which they submitted to the Royal Scientific Society of Wallis, and the Huygens, and adding their generalizations, Isaac Newton laid down the fundamental foundations of the Theory of Impact, which are still unsurpassed today. Even before Newton, Wallis and Huygens, there was research into the dynamics of impact. Thus, for example, collision problems were addressed by Galileo Galilee, who came to the realization that the impact force was infinitely large in relation to the pressure forces, but did not reach and learn about the relation of the impact impulses and the impact forves of movement. Today's knowledge of collision dynamics has not, in fact, been much advanced than this collision theory, which was founded

by Newton, Wallis, and Huygens. In connection with this competition of the Royal Scientific Society, are submitted Papers which contained the first set of basic eelements of collision theory. The name also mentions Sir Christopher Michael Wren (20 October 1632 - 25 February 1723), who was also the president of the Royal Scientific Society**.**

Figure 1. From left to right scientists: Sir Christopher Michael Wren (20 October 1632 - 25 February 1723), John Wallis (1616-1703), Christian Huygens (14 April 1629 - 8 July 1695) and Gaspard-Gustave de Coriolis, (Paris, May 21, 1792 - Paris, September 19, 1843).

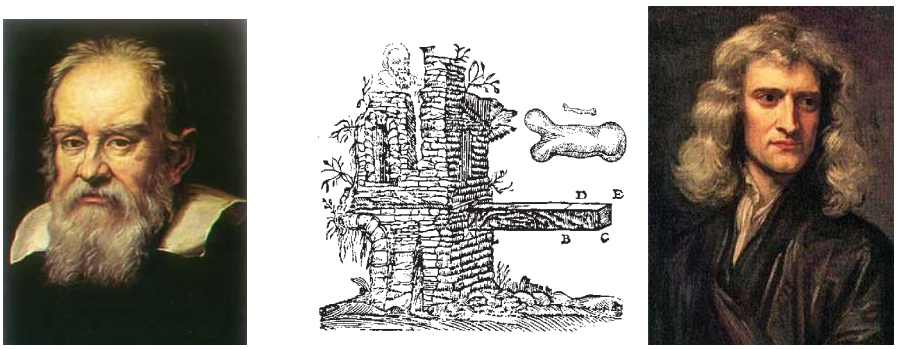

Figure 2. Scientists: author of the original ideas Theoretical and Applied Mechanics: Galileo Galilei (Paris, February 15, 1564 - Florence, January 8, 1642) and author of an authentic and significant work: *"Discorsi e dimostrazioni matematche intorno a due nuove scienze attenti alla mecanica e i movimenti locali" 1638* (left) and Sir Isaac Newton, (Lincolnshire, December 25, 1642 - London, March 20, 1726/7) (right) author of Basic Collision Theory and Works: Mathematical Principles of Natural Philosophy (Lat. Philosophiae Naturalis Principia Mathematica), published in 1687.

The dynamics of collisions between rolling balls occur in many engineering systems, and especially in the dynamics of roller bearings. Even today, no general theory of collisions between rolling balls has been given. Some recent results by the author of this paper present new and original results in support of the classical theory of collisions between rolling balls. These results are presented in the next parts of this article.

In the game of billiards, collisions of rolling equal balls occur. The complexities of billiard dynamics and billiard models and the possibility of observing and noting the complex phenomena and phenomena of collision dynamics were pointed out by Coriolis (fr. Gaspard-Gustave de Coriolis; Paris, May 21, 1792). - Paris, September 19, 1843) and to illustrate this we quote the following quotation (see References [1, 2, 3]):

"In connection with the game of billiards ..... different dynamic tasks occur, the solutions of which are contained in this event. I think that people, who know theoretical mechanics, and even students of the Polytechnic Schools, are interested in learning about the explanations of all the original phenomena, which can be observed with the movement of billiard balls. "

2 AN ELEMENTARY LOGICAL ANALOGY

In the examples of the simplest dynamics of rigid bodies with one degree of freedom of movement, we will present an elementary logical analogy, which should be understandable and easily understood.

Why do we begin with this article, which should be popular but at the same time contain the results of a high scientific domain?

It is well known that the most fundamental breakthroughs in science, which have become a lasting scientific heritage, are in fact elementary learning, which, in the integration of knowledge and conceptual processes, grows into complex scientific disciplines. The aim and answer of the question posed is to show that starting from the simplest dynamics of rigid bodies, translation and rolling, and then determining the elementary logical analogy among these dynamics and abstraction to the model of these dynamics, one can move to qualitative and mathematical analogies.

Then, by abstracting the disparate parameters of the dynamics of two real systems, one can come up with one theoretical model, meaning described by a unique mathematical model with the same elements of mathematical phenomenology, we can use the knowledge of the properties of one to convey it in the knowledge of the properties of the other, logically analogous.

Using logical, structural, qualitative and mathematical analogies, in both directions, we aim to obtain new original results of the theory of collision between bodies in rolling. We base the new results on the well-known theory of collision between bodies in translation. Here, and today the unsurpassed theory of collision between bodies in translational moving, has been formulated by world-renowned scientists Isaac Newton, John Wallis, and Christiaan Huygens.

So, let's start with a logical analogy between the dynamics of the body systems shown in Figure 3. a * and b *.

Figure 3.a* shows two rigid bodies that can move along an ideally smooth horizontal surface in one direction, so that their median plane is always vertical, so it is a planar, translational motion of a rigid body with one degree of freedom of movement, so we can consider it as a material point of concentrated mass in the center of mass. Such a body is exposed to the effect of five constraints (links): two translations are prevented (one in the vertical direction and one in the direction perpendicular to the plane of plane motion) and three rotations about three orthogonal directions (about the direction of the body translation, about the vertical direction and about the direction perpendicular to the previous two).

The kinetic parameters of the motion translation of the rigid body model from Figure 3. a* are: m_k, $k=1,2$, masses,, the velocities of body translation, $\vec{v}_{C1}$ and $\vec{v}_{C2}$, which are the connected vectors for the centers of mass of these bodies C_1 and C_1. Suppose that each of the bodies is loaded by one external force with intensity F_k, $k=1,2$, with a direction collinear with velocity and an attack point at the center of mass of the corresponding body affected.

On the basis of the theorem on the change of the linear momentum of motion (or quantity of motion), we construct the differential equation of translational dynamics of one and the other body, in translator motion, in the form:

$$m_k \dot{v}_{Ck} = F_k \,,\ k = 1,2 \tag{1}$$

The change in the linear momentum of body motion theorem states that this change in time equals the sum of active and reactive forces. The linear momentum of motion in the translation of a rigid body or the impulse of the translational motion of a body is the product between the mass of the body and the velocity $\vec{v}_{Ck}$, $k = 1,2$ of the center of mass: $\vec{\mathbf{K}}_k = m_k \vec{v}_{Ck}$, $k = 1,2$.

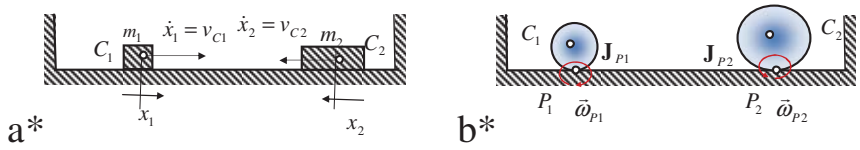

Figure 3. Models of the two simplest dynamics of material bodies, each with one degree of freedom of movement: a * transition dynamics of a rigid body and b* rolling without sliding of a rigid body (with form of homogeneous disk, homogeneous sphere or homogeneous with one axis and one plane of symmetry).

Figure 3 b * shows two bodies, which roll, without sliding, straight along a linear path (guide, trace) through a circular plane contour of the body, a circular shape with a corresponding center at a point, C_1 , and C_2, respectively. These rolling bodies may be spherical balls, cylinders, or disks, but also of other shapes, having one axis of symmetry and one plane of symmetry in which there is a contour of the shape of a circle, by which the legs are to roll.

Such bodies, which roll without sliding, have one degree of freedom of movement. Since each free body has six degrees of freedom of movement, this means that five motion constraints, three translation constraints and two rotations are imposed on the motion of these bodies from Figure 1. b *, that is, five bonds are imposed on each of the bodies. The first limitation is that the median plane of symmetry of the body, in which the center of mass of the body, is at all times in the plane of contour of rolling. This produces the constraints of one translation perpendicular to that rolling plane, and of two rotations about two orthogonal axes in that plane of rolling. The connection with the non-slip rolling route prevented one translation in the direction of the rolling route and one translation directly on the rolling route. All these together represent five links and constraints, leaving only one degree of freedom of movement, which is rolling around the current instantaneous axis of rolling.

Therefore, we direct our further consideration to that class of bodies, which roll without slipping. Figure 3 b * shows two rigid bodies, which roll without sliding at angular velocities $\vec{\omega}_{P1}$ and $\vec{\omega}_{P2}$, at the corresponding instantaneous axes of rolling, passing through the points, P_1 or P_2 respectively, of the contact of the bodies in rolling and the track on which they are rolling, which are directed orthogonal to the plane of the rolling. The axial moments of inertia of the masses of the body in rolling for the instantaneous axes of rolling are $\mathbf{J}_{P1}$ and $\mathbf{J}_{P2}$. As kinetic parameters of the rolling dynamics of each body are the instantaneous angular velocities of rolling $\vec{\omega}_{P1}$ and $\vec{\omega}_{P2}$, which are related to the instantaneous axes of rolling. These axes move translation ally along the rolling path, and the axial moments of inertia of the mass of the body and for the corresponding instantaneous oscillations, for the observed body class, $\mathbf{J}_{P1}$ and $\mathbf{J}_{P2}$ do not change during the rolling dynamics.

Based on the theorem on the change of angular momentum (or kinetic moment) for the instantaneous axis of rolling without sliding, we construct the differential equation of the dynamics of rolling of one and the other body, in the form:

$$\mathbf{J}_{Pk}\dot{\omega}_{Pk} = \mathfrak{M}_{Pk}, \quad k = 1,2 \tag{2}$$

By comparing two analyzes of the dynamics of the bodies on two systems, one in translation and other in rolling, without sliding, from Figure 3. a * and b *, we establish a logical, and at the same time, qualitative analogy and phenomenological mapping of the kinetic parameters of these models of two different dynamics, each with one degree of freedom. The mathematical analogy follows.

3 DYNAMICS OF COLLISION BETWEEB TWO ROLLING BODIES IN NON-SLIP ROLLING

3.1 Basic settings for collision dynamics between two bodies in non-slip rolling

From the previous kinetic analysis, and the conclusions, we have drawn and proved, it follows that to consider the dynamics of collisions of axial symmetric rigid bodies with one plane of symmetry, which are in non-slip rolling, we must start with incoming angular velocities and rolling paths. Then, the axial moment of inertia of rolling body masses for the instantaneous axes of rolling should be included by introducing analogous assumptions, as well as for the case of analogous dynamics of impact and collisions of bodies in translational motions determined by the translational velocities and corresponding masses.

The theory of collision dynamics (and in the special case of impact) is based on the following assumptions:

1* The contact time τ of two bodies in a collision is very short;

2* The impact forces $\vec{F}^{ud}$ and the corresponding impact moments $\vec{\mathfrak{M}}^{ud}$ of the forces are variable and of high intensity, of the order of magnitude $\frac{1}{\tau}$, and of short duration during the contact time τ of two bodies in the collision and during the collision they have attack points at the contact points in the collision;

3* The change of angular momentum of motion of the material two bodies in rolling for the corresponding rolling axes, during the collision is finite.

4* The impulse (linear momentum) and angular momentum of "ordinary forces" compared to the impulse (linear momentum) and angular momentum of instantaneous collision forces, are much much smaller and can be neglected.

3.2 Intensity of outgoing angular velocities in the centrally centric collision of two bodies in the rolling, without sliding, immediately after the collision

We look at two axial symmetric rigid bodies, with one central plane of symmetry, centrally colliding, and making contact at one point of collision, or two balls of different radii, or two disks of different radii, axial moments of inertia of masses of bodies for the corresponding instantaneous axes of rolling $\mathbf{J}_{P1}$ and $\mathbf{J}_{P2}$. These axial moments of inertia of masses do not change for the axial rolling axes in motion.

The bodies are in a non-slip rolling position at the moment t_0 and have angular velocities $\vec{\omega}_{P1}(t_0)$ and $\vec{\omega}_{P2}(t_0)$at an instant t_0 before entering the collision configuration and are referred to as incoming (inlet or impact) angular velocities. At the moment t_0 of collision starting, the two bodies will touch at one point P where both bodies have a tangential plane

in common. We assume that a collision lasts briefly over an interval $(t_0, t_0+\tau)$ of time, which lasts for a short time τ (and realistically tends to zero). After this collision of short-term contact, the bodies are separated and separated by angular velocities $\vec{\omega}_{P1}(t_0+\tau)$ and $\vec{\omega}_{P2}(t_0+\tau)$, which we call the outgoing angular velocities. That it is necessary to determine the intensities of these outgoing angular velocities, $\vec{\omega}_{P1}(t_0+\tau)$ and $\vec{\omega}_{P2}(t_0+\tau)$, and that we have already determined the paths of outgoing rolling velocities and the directions of rolling and directions of those outgoing velocity velocities immediately after the collision.

Imagine that, at the point P of contact of two bodies in a state (configuration) of collision, we have drawn a tangential plane and it's normal $\vec{n}$. This tangential plane is called the touch plane, and the direction of that normal to the touch plane determines the direction of the collision. Since the centers C_1 , and C_2 of mass of the bodies in collision are at this normal, and if the incoming rolling traces of the bodies are at that normal, the collision is called a centric (central) collision, and if not the collision is skew or oblique eccentric. When the incoming angular velocities $\vec{\omega}_{P1}(t_0)$ and $\vec{\omega}_{P2}(t_0)$ of both bodies in the collision are collinear with the tangent plane, that is, direct with the direction of the collision, then it is a true (directional) collision of the rolling bodies, otherwise it is an skew collision of two rolling bodies.

3.3 Hypothesis of conservation of sum of angular momentum for instantaneous axes of rolling of two bodies in rolling before and after collision of two axial symmetric bodies

At the time of the collision, both bodies, which roll immediately before the collision, come into contact at one point, or line-derivatives. In the collision event, although we have made the assumption of models of rigid, axisymmetric bodies with a central plane of symmetry, during the collision they deform locally, in the local contact area. If the contact of the bodies in the collision is at the point of contact (for example, the contact of the spherical surfaces of the balls in the collision, or the rotation ellipsoids), deformation occurs in the immediate vicinity of the contact point. And this deformation lasts until the projections of the angular velocities of rotation of the body in the collision in the direction of the collision (the normal on the tangent equal to both bodies in the contact point of the collision) are equal. Then also the projections of the relative angular velocities of the rolling motion around the instantaneous axes of rolling of the body in the collision, one relative to the other, towards the collision direction became zero. From that moment, zero projections of relative angular velocities in the direction of the collision, begin to restore the state of the body as it was before the collision until the moment when the bodies separate from each other. During this time the projection of the relative velocities of the bodies in the collision of one relative to the other begins to increase and continues until the bodies have, in the part in contact, their original shape. Then there is a moment when we consider that the bodies have practically separated and that there is a period of time after the collision. Therefore, the collision period can be divided into two parts: τ' the compression period in the tangential direction to the body at the point of contact, and τ'' the restitution period in the tangential direction to the body at the point of contact in the collision, with the total short-time duration $\tau = \tau' + \tau''$ of the collision.

Since external active forces and moments of forces of finite intensities have impulses of forces equal to zero, and couplings have kinetic moments equal to zero and, at infinitesimal intervals of time, we consider that two material rigid bodies, which roll with the incoming angular velocities and in collision, are considered as one system. Therefore, the hypothesis of

the conservation of the sum of angular momentum (kinetic momentum) for the instantaneous axes of rolling of the body - the movement before and after the collision, can be applied to the dynamics of the same to in the form:

$$\mathbf{J}_{P1}\vec{\omega}_{P1}(t_0)+\mathbf{J}_{P2}\vec{\omega}_{P2}(t_0)=\mathbf{J}_{P1}\vec{\omega}_{P1}(t_0+\tau)+\mathbf{J}_{P2}\vec{\omega}_{P2}(t_0+\tau). \quad (3)$$

This hypothesis about the conservation of the sum of the angular momentum of motion by rolling in a collision of two bodies, which is analogous to the hypothesis of the conservation of the sum of the linear momentum of motion of two bodies in a collision and in translational motion (see References [4-8, 11-15[).

3.4 Coefficient of restitution or collision of two axisymmetric rolling bodies with one central plane of symmetry

When the incoming angular velocities $\vec{\omega}_{P1}(t_0)$ and $\vec{\omega}_{P2}(t_0)$ of rolling and the axial moments of inertia of mass $\mathbf{J}_{P1}$ and $\mathbf{J}_{P2}$ for the instantaneous axes of rolling of the bodies in a collision, are known, the previous hypothesis relation (3) of conservation of the sum of the angular momentum of motion for the instantaneous axes of rolling bodies, before and after the collision, is not sufficient to determine two unknown outgoing angular velocities $\vec{\omega}_{P1}(t_0+\tau)$ and $\vec{\omega}_{P2}(t_0+\tau)$, after the collision of two bodies, which roll just before and after the collision. We need another relation, an equation, which we will set from the very properties of the body in a collision. As we have already described the collision and contact process of two bodies, in the period of solid body compression, the angular velocity $\vec{\omega}_{P1}(t_0)$ of the first body will decrease by $\vec{\omega}_{P1}(t_0)-\vec{\omega}_{CP}$, and the second increases by $\vec{\omega}_{CP}-\vec{\omega}_{P2}(t_0)$, where $\vec{\omega}_{CP}$ the angular velocity of both bodies in the collision is at the end of the compression at the local environment of the contact point of the bodies in the collision. As both bodies are deformed in the local area around the point of joint contact in the collision, it is apparent that, during the restitution period, the deformations of the body will not be immediately lost and that the angular velocity $\vec{\omega}_{P1}(t_0)$ of the first body will decrease by $k(\vec{\omega}_{CP}-\vec{\omega}_{P2}(t_0))$ another angular velocity and the angular velocity $\vec{\omega}_{P2}(t_0)$ of the second body will increase for size $k(\vec{\omega}_{CP}-\vec{\omega}_{P2}(t_0))$, where k is some coefficient. Based on this analysis we can write that the angular velocities $\vec{\omega}_{P1}(t_0+\tau)$ and $\vec{\omega}_{P2}(t_0+\tau)$ of the bodies that were in the collision are outgoing

$$\vec{\omega}_{P1}(t_0+\tau)=\vec{\omega}_{P1}(t_0)-(1+k)(\vec{\omega}_{P1}(t_0)-\vec{\omega}_{CP})=(1+k)\vec{\omega}_{CP}-k\vec{\omega}_{P1}(t_0), \quad (4)$$

$$\vec{\omega}_{P2}(t_0+\tau)=\vec{\omega}_{P2}(t_2)+(1+k)(\vec{\omega}_{CP}-\vec{\omega}_{P2}(t_0))=(1+k)\vec{\omega}_{CP}-k\vec{\omega}_{P2}(t_0). \quad (5)$$

Subtracting these previous relations (4) - (5) we obtain

$$\vec{\omega}_{P2}(t_0+\tau)-\vec{\omega}_{P1}(t_0+\tau)=k(\vec{\omega}_{P2}(t_0)+\vec{\omega}_{P1}(t_0)). \quad (6)$$

The ratio k of the relative angular velocities of rolling of the axisymmetric bodies after and before the collision is

$$k=\frac{\omega_r(t_0+\tau)}{\omega_r(t_0)}=\frac{\omega_{P2}(t_0+\tau)-\omega_{P1}(t_0+\tau)}{\omega_{P1}(t_0)-\omega_{P2}(t_0)} \quad (7)$$

and *is called the collision coefficient, or the coefficient of restitution, or the coefficient of establishment of rolling bodies in a collision.*

This coefficient k is also newly introduced and represents a new definition of the collision coefficient, or the coefficient of restitution or the coefficient of establishment of rolling bodies in a collision. This new definition (7) is derived by author of this paper.

With the introduction of this new refinement of collision coefficient, we have generalized Newton's definition from the theory of collision between rigid bodies in translator motion to the theory of collision between rigid bodies in rolling motion without sliding by use difference of rolling angular velocities both after and before the collision. If a kinetic state can be defined by one angular velocity about the instantaneous axis of rolling for each of the bodies, in arriving to define the dynamics of the collision, we inject our definition of the coefficient k of restitution over the ratio of the relative angular velocities of the rolling bodies after and before the collision.

3.5 Intensity of outgoing angular velocities of rolling two bodies after a collision

In order to determine the intensities of the outgoing angular velocities of rolling of two bodies after a collision, $\vec{\omega}_{P1}(t_0+\tau)$ and $\vec{\omega}_{P2}(t_0+\tau)$, it is sufficient to eliminate from the previous relations (4) - (5) the unknown angular velocities of both bodies, $\vec{\omega}_{CP}$, in the collision at the end of the compression at the local environment of the point of contact of the bodies in the collision. Then solve the relations by unknown outgoing angular velocities and, which is not difficult to do, so for the outgoing angular velocities, $\vec{\omega}_{P1}(t_0+\tau)$ and $\vec{\omega}_{P2}(t_0+\tau)$, after the collision of the balls, we get the following expressions:

$$\vec{\omega}_{P1}(t_0+\tau)=\vec{\omega}_{P1}(t_0)-\frac{1+k}{1+\frac{\mathbf{J}_{P1}}{\mathbf{J}_{P2}}}(\vec{\omega}_{P1}(t_0)-\omega_{P2}(t_0)) \tag{8}$$

$$\vec{\omega}_{P2}(t_0+\tau)=\omega_{\mathbf{P1}}(t_0)+\frac{1+k}{1+\frac{\mathbf{J}_{P2}}{\mathbf{J}_{P1}}}(\omega_{\mathbf{P1}}(t_0)-\omega_{\mathbf{P2}}(t_0)) \tag{9}$$

By determining these intensities of the outgoing angular velocities $\vec{\omega}_{P1}(t_0+\tau)$ and $\vec{\omega}_{P2}(t_0+\tau)$ of rolling of the balls (axial symmetric bodies each with central plane of symmetry) after the collision, we have solved the complete problem of the theory of collision of axisymmetric bodies in rolling without slipping (see References [4-15[)..

These expressions (3), (7), (8) and (9) can be reached by a logical, qualitative and mathematical analogy, starting from the theory of collisions of bodies in translational motion.

4 MECHANICS OF BILLIARDS I – GEOMETRY AND KINEMATICS

"In connection with the game of billiards .... various dynamic tasks occur, the solutions of which are contained in that event.

I think that people, who know theoretical mechanics, and even students of the Polytechnic School, are interested in explaining all the original phenomena, which can be observed with the movement of billiard balls".

Gaspar-Gustav de Coriolis (1990). *Théorie mathématique des effets du jeu de billard ; suivi des deux celebres memoires publiés en 1832 et 1835 dans le* Journal de l'École Polytechnique*: Sur le principe des forces vives dans les mouvements relatifs des machines & Sur les équations du mouvement relatif des systèmes de corps* (Originally published by Carilian-Goeury, 1835 ed.). Éditions Jacques Gabay. ISBN 2-87647-081-0.

For an introduction to the content of billiard mechanics, which includes content on the geometry, kinematics and dynamics of billiard games, it is most illustrative to rely on a few Coriolis sentences, which we have adopted as the motto of this paper. Obviously, many authors believe that these few sentences point to the complexity of geometry, kinematics and dynamics of billiard games; because the analysis, which we will expose here, reveals that the dynamics of billiards includes many phenomena of dynamics of real systems. Our presentation will be based on our results, but also on the constant, from comparisons with the results achieved today by other authors, both mechanics and mathematicians, and it is evident that our results are original.

Multiple keywords and concepts of kinematics and dynamics, such as: ball dynamics as a rigid body, non-slip rolling, collision, alternation of velocity direction, impact velocity, outgoing velocity, ball rolling path, center of gravity trajectory, central and scew (oblique) collision, force impulse, kinetic energy, impact and collision, collision of two spheres, collision of three spheres, impulse forces, linear momentum of motion, angular momentum of motion, speak about their complexity of dynamics of the system of billiard game elements. This is even when looking at only the movement of one billiard ball, but when more balls are involved, and then we have a really complex system, hybrid structures and dynamic configurations of billiard play.

s*

b*

Figure 4. a * Gaspar-Gustave de Coriolis or Gistav Coriolis (fr. Gaspard-Gustave de Coriolis) (Paris, May 21, 1792 - Paris, September 19, 1843) and b * Jean Victor Ponsele (fr. Jean-Victor Poncelet) (July 1, 1788 - December 22, 1867)

But first let's start with the names of famous scientists who have contributed to the knowledge of certain aspects of the dynamics of billiards.

As we were quoting a few sentences from Gaspar-Gustavo de Coriolis or Gustavo Coriolis at the outset, here is some biographical information about this important scientist, especially in the field of mechanics. He was a mathematician, a mechanical engineer, and a scientist. He is best known for his work on the Coriolis acceleration and Coriolis force. Coriolis was the first to coin the term "work" for the product of force and distance. In 1829, Coriolis published a textbook, *Calcul de l'Effet des Machines*, which presented mechanics in a way that could easily be applied in industry. During this period, the true term for kinetic energy $\mathbf{E_k} = \frac{1}{2}mv^2$ was established, as well as its relation to mechanical work (see References [1, 2,3]).

Coriolis explored the possibilities of generalizing kinetic energy and work on rotating systems and, as a result, produced the work *Sur les équations du mouvement relatif des*

systèmes de corps, presented at the French Academy of Sciences (1832). Coriolis wrote the work *Sur les équations du mouvement relatif des systèmes de corps*,1835. In the 20th century, the terms "*Coriolis acceleration*" and "*Coriolis force*" appeared on systems with coupled transverse rotational motion and relative curvilinear motion.

Beginning with the works of George Birkoff, billiard systems have become a popular topic of study, drawing on a variety of fundamentals, beginning with ergodic Mors theory, KAM theory, and others. Also, the dynamics of billiard systems is interesting because it occurs quite naturally in a number of tasks of mechanics and physics: in the dynamics of vibro-impact systems, diffraction of short waves, dynamics of ball bearings, etc.

The basis of the dynamics of billiards is the theory of dynamics of systems with one-sided constraints. There are essentially various models of theory of impact. The one-sided bond imposed on the system can be replaced by the field of conservative and dissipative forces. Then, the coefficients of elasticity and dissipation by some assumption are introduced to the aspirations of infinity, as Kozlov writes in Reference [10]. It can then be shown that the movement of such a "released" system with fixed initial data, at each finite interval of time, tends to move with an impact (see Reference [10])..

Finally, it is necessary to emphasize again that in the approach to investigating the properties of the billiard game phenomenon, it is necessary to establish the basic models of billiards. These models, under the same keyword "*billiards*", distinguish between defined tasks: geometry, kinematics, and dynamics of billiards, or the totality of all these tasks. For example, starting tasks are about the properties of mathematical billiards. When approached by mathematicians, then it remains in the domain of billiard geometry and the elements are the geometric point and its possible open or closed polygonal paths, that is, polygons inscribed in a certain area by a unilaterally bounded closed contour line. Periodic trajectories are possible, depending on the initial position and the initial direction of the trajectory of the geometric point. Then, the basic determinations are the lengths and angles that determine the directions of the path of the geometric point. Then it works with lengths and angles, and the units of measurement are meters and degrees or radians. This is a rough approximation of the real billiards system and does not take into account the time at which the geometric point is moved along the trajectory. If the basic determination of time in addition to lengths and angles is included, then it moves into the field of kinematics, kinetics, so kinetic parameters, elements of translation velocity and angular velocity of rolling are included.

If we stay only on the mathematical model that we enrich with basic determination over time, with a unit in seconds, then only the kinematic element of the geometric point translation rate, with the unit of meter per second, is included. A mass associated with a geometric point can be added to this model, so we have a model of gross abstraction of a real billiard by a material point that has mass, velocity, and its motion in time is observed. The mass has a unit in pounds. We have already included this in the model in addition to geometry and kinematics and dynamics, and with that we open the questions of determining the impulses of motion, kinetic energy and forces under which the dynamics are realized, including impacts at unilateral holding bonds and collisions between material points. However, for better abstraction of the billiard system to the model of billiard dynamics, it is not a satisfactory model not with a geometric point or with a material point, but with a rolling ball, which has its mass, a certain mass distribution, defined by the axial moment of inertia of the masses for the axis of rolling of the ball, and has a certain the instantaneous angular velocity of rolling about the instantaneous axis of rolling, measured in units of radian per second, or the velocity of translation of the center of mass in units of meters per second, and the angular velocity of rotation about the central eigen axis of self-rotation measured in units of radians per second. It means that if a billiards model is formed as an abstraction of a real

model of billiards with one or more balls rolling, then the elements of the billiard events are studied elements of geometry, kinematics and dynamics of billiards.

Then we have a body of a certain shape and a line along which it rolls, so the definitions of length are used, so we are in the domain of geometry, and when we include the analysis of translational velocities of the center of mass and the angular velocity of rotation of central self rotation axis, then we are in the domain of kinematics, and if we now include masses and moment of inertia of masses, and with it impulses of motion and kinetic moment (angular momentum), kinetic energy and impulse forces, we completed the task of kinetics of billiards or dynamics of the system of billiards. In the following chapters, we will first define the models of billiards and then analyze the elements of geometry, kinematics and dynamics of billiards within the limits of contemporary knowledge of the scientific literature in this field, as well as the original results of the authors of this chapter.

4.1 Billiard geometry in a nutshell

In this section, we also highlight the contributions of the French scientist, engineer and mathematician, Jean-Victor Poncelet (July 1, 1788 - December 22, 1867), who is known for the following works: ''*Traité des propriétés projectives des figures''* (1822) and ''*Introduction à la mécanique industrielle* (1829)''. And here, we will point out a number of his theorems in geometry, which are of importance for investigation of the geometry of billiards and for determining the periodic paths of the rolling of billiard balls in elliptic billiards, as well as in billiards other forms of contours (see References [9,10]).

It is certainly important to find out the properties of ideal mathematical billiards. Today, many researches on this topic are based on a series of basic theorems of Jean-Victor Poncelet, so here we will list the definitions of some of them (see References [9,10])..

Theorem 1. (Poncelet Theorem): Consider two conical sections (conics) C and D, which lie in the plane. Suppose that a polygon is inscribed in a conical section C, and described around a conical section (conics) D. Then there are an infinite number of such polygons inscribed in one conical section, and described around the other conical section, all of which have an equal number of sides. Even more than that, every point of the conical intersection C is the subject of such a broken line.

Theorem 2. (Poncelet Theorem): Suppose that there is such a point on the conical section (conic) Γ that the polygon $\mathbf{T}_0\mathbf{T}_1\mathbf{T}_2\mathbf{T}_3\mathbf{T}_4...\mathbf{T}_{n-2}\mathbf{T}_0\mathbf{T}_{n-1}\mathbf{T}_0$ with the number of sides $n \geq 3$ is inscribed in the conic section (conic) Γ and described around the conic section Γ_u and that the right Γ_u does not tangent the conic section (conic) Γ_u for $i = 2,3,3,...,n-2,n-1$. Then for arbitrary $n \geq 3$ there is some polygon $\mathbf{N}_0\mathbf{N}_1\mathbf{N}_2\mathbf{N}_3\mathbf{N}_4...\mathbf{N}_{n-2}\mathbf{N}_0\mathbf{N}_{n-1}\mathbf{N}_0$ with sides inscribed in a conical section Γ and described around a conical section Γ_u.

Theorem 3. (Poncelet theorem for an area): Suppose that C and D, are two areas in space (on the surface). If there is some closed polygon, inscribed in the area C and described around the area D, it means that there are infinitely many such polygons. In addition, each point of the area C appears as the theme of such a polygon and all polygons have an equal number of sides.

One of the numerous Poncelet theorems is Comprehensive Generalized Poncelet Theorem, but we don't preset it, because in our opinion previous three listed theorems are

good illustration of the content and aims of these series of Poncelet theorems for applications in the geometry of models of billiards as abstraction of real billiards into mathematical billiards, as pre geometrical objects without reality (for more details see mathematical references [9]).

Figure 5 shows the mechanical model as a good abstraction of a real elliptical billiard: Track of the ball rolling along the horizontal plane of the elliptical billiard with the plan of horizontal components of the incoming impact velocities and outgoing velocities after the impact of the ball into a contour elliptical cylindrical surface with vertical derivatives, as well as a detail plan of the velocity of one ball skew impacts.

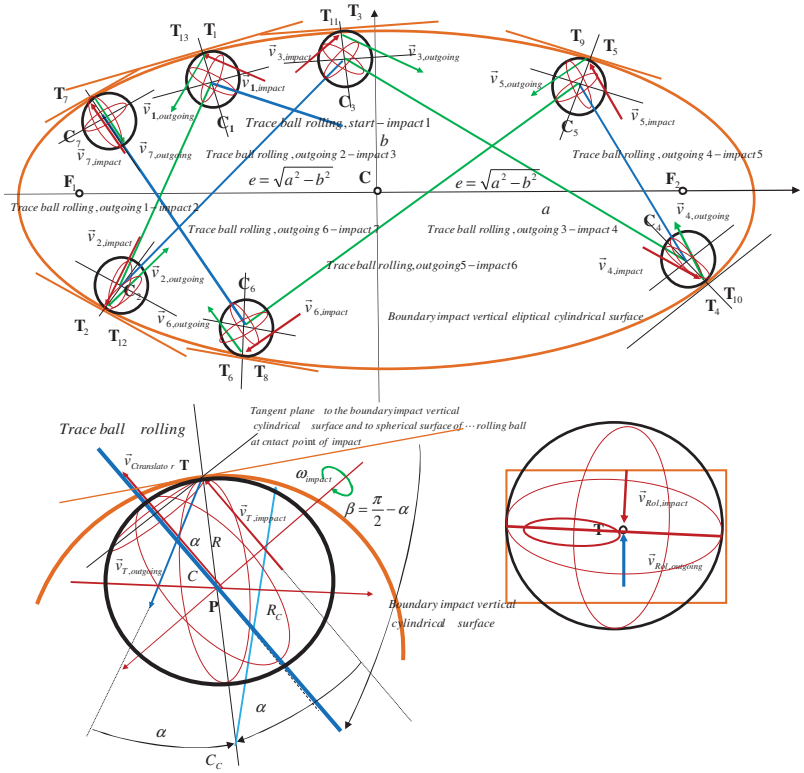

Figure 5. Line-trace of the rolling motion of the ball along the horizontal plane of the elliptical billiards with the plan of horizontal components of the incoming impact velocities and the outgoing velocities of the contact point after the impact of the ball into a contour elliptical cylindrical surface with vertical derivatives (up). Detail of the plan of the velocity of one ball in the configuration of the skew impact (down).

4.2 Elements of billiards kinematics

In the Figure 5, we have presented a model of an elliptical billiard with a rolling one ball, which rolls on a horizontal surface bounded by a single-size contour elliptical-cylindrical surface with vertical derivatives. The billiard balls are of the same dimensions and radius R, which is not negligible with respect to the semiaxis ellipses in the horizontal flat base of the elliptical billiards, which we denote by and a and b, which, according to the semi-axes, has an eccentricity of focus $e = \sqrt{a^2 - b^2}$. With this in mind, the model of elliptical billiards in

Fig. 5 cannot be reduced to mathematical billiards by reducing the billiard sphere to a material or geometric point. Her line-trace of billiard ball rolling, which is a broken polygonal line, open or closed, is a polygon, and its path can be determined purely geometrically using Poncelet theorems, or other results in the field of mathematical billiard models known from the literature, which remain in the domain of pure geometry. It is necessary to first determine the geometric location of the points of centers of ball of the impacts in relation to the contour of the elliptic area of billiards, and in the new contour to determine the paths of rolling the ball centers.

In the observed model of the elliptical billiard from case in Figure 5, we can see that the parts of the track of the roll of the billiard ball in arriving at the point of impact, ball and contour, and leaving it after being hit by the contour elliptical-cylindrical surface are parallel to the corresponding horizontal velocity component just before the impact and by the corresponding horizontal component of the outgoing velocity of the point of impact of the ball after impact. The translational velocities of the center of mass of the sphere, before and after impact in the contour surface, are equal to the horizontal components of the incoming velocity before impact and the outgoing velocity after the collision, the point at which the sphere impact to the contour elliptical-cylindrical surface.

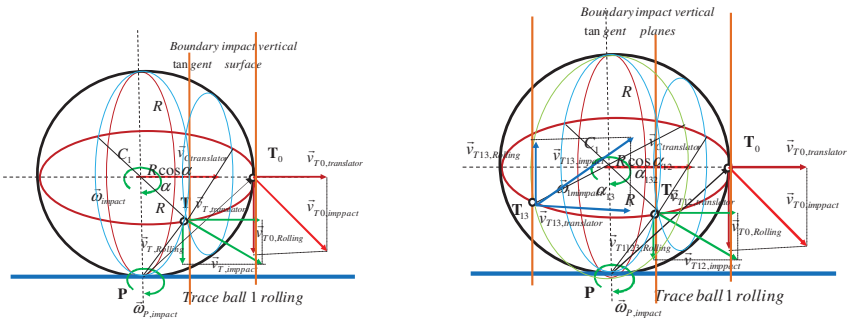

Picture 6. Plan of the velocity of impact of a point on a large circle of a sphere, which rolls along a straight line in a horizontal plane

We will, now, turn to the representation of the kinematic elements of each of the possible impacts of a ball in rolling, to the contour surface, as well as to the kinematic elements of different cases of mutual collision of two balls.

4.2.1. Component velocities of points of impact of billiard balls in rolling. In the picture 6 has shown several points, $\mathbf{T}_0$, $\mathbf{T}$ and $\mathbf{T}_{13}$ which all lie on a large circle in a horizontal plane parallel to the horizontal plane of the billiards, in which lie the lines-traces of rolling the sphere.

At these points, vertical lines corresponding to the vertical derivatives of the contour elliptical-cylindrical surface of the impact of the ball on it are drawn. There are infinitely many such possible points of impact of a ball, as well as collisions with another ball, and we denote them by $\mathbf{T}_k$, $k = 0,1,2,3,4,.....$, and all of them also lie on a large circle in a horizontal plane. The rolling path without sliding the ball is parallel to that plane. The point $\mathbf{P}$ is the point of contact between the ball and the ball rolling path. The axis of instantaneous rotation-rolling of the ball along the track passes through the point $\mathbf{P}$ of the contract. That axis is perpendicular to the route of rolling at all times and moves along that route. With point $\mathbf{P}$, we have indicated the angular velocity of the training rolling when the ball is rolling, without sliding, along the incoming route before impact the ball in the contour cylindrical surface.

From Figure 6 it can be observed that the point at the greatest normal distance from the central instantaneous axis of rotation when rotating the ball along the line-trace and that it is equal to the radius R of the ball, while all other points from the large circle of the sphere, in the horizontal central plane, is at a smaller normal distance, and that this distance equals zero points on the diameter of that circle parallel to the current axis of rotation of the ball rolling along the track. If we denote the angle α_k that the radius of a large circle drawn from the center of that circle to a point $\mathbf{T}_k$, $k=0,1,2,3,4,.....$ on it coincides with the direction of the radius of that circle with the direction of the impact, then the normal distance of a point on the large circle of a billiard ball sphere is $h_{\mathbf{T}_k}=R\cos\alpha_k$ in the range from zero to R.

The incoming velocity by which a billiard ball impacts to a contour cylindrical (polygonal-cylindrical, elliptical-cylindrical or curvilinear-cylindrical) surface with vertical derivatives, corresponding to a point, $\mathbf{T}_k$, $k=0,1,2,3,4,.....$ of impact, has two components: one horizontal parallel to the incoming line of rolling of the ball-sphere surface, equal to the velocity $\vec{v}_{\mathbf{T}_k,impact}=\vec{v}_{\mathbf{C}_k,impact}$ of the center of mass of the ball and one vertical due to the rotation - the ball about the current central axis

$$\vec{v}_{\mathbf{T}_k,Roling,impact}=-\omega_{\mathbf{P}_k,impact}R\cos\alpha_k\vec{k}=-\frac{v_{\mathbf{C}_k,impact}}{R}R\cos\alpha_k\vec{k}=-v_{\mathbf{C}_k,impact}\cos\alpha_k\vec{k} \quad (10)$$

After impacting the ball in a cylindrical (polygonal-cylindrical, elliptical-cylindrical or curvilinear-cylindrical) surface with a vertical derivative, a point $\mathbf{T}_k$, $k=0,1,2,3,4,.....$, by which the ball struck and bounced, has an outgoing velocity with two components: one horizontal parallel to the outgoing track of the ball equal to the outgoing translational velocity $\vec{v}_{\mathbf{T}_k,outgoing}=\vec{v}_{\mathbf{C}_k,outgoing}$ of the center of mass of the ball and one vertical component $\vec{v}_{\mathbf{T}_k,Roling,outgoing}$ due to the outgoing rotation-rolling of the ball:

$$\vec{v}_{\mathbf{T}_k,Roling,outgoing}=\omega_{\mathbf{P}_k,outgoing}R\cos\alpha_k\vec{k}=\frac{v_{\mathbf{C}_k,outgoing}}{R}R\cos\alpha_k\vec{k}=v_{\mathbf{C}_k,outgoing}\cos\alpha_k\vec{k}. \quad (11)$$

The directions of trace rolling and directions of these velocities are determined purely kinematically by the rule that the angles, which are the directions of the horizontal component of the incoming and outgoing velocities of the observed possible contact points $\mathbf{T}_k$, $k=0,1,2,3,4,.....$, are closed with the normal on the contour cylindrical surface of the impact. The same rule applies to the vertical components of the ball rolling, which, with the direction of normal to the contour cylindrical surface into which the ball hits, close the right angles.

A complete prior analysis of the velocity components before and after the impact of a point on a rolling ball by which a ball strikes or collides is valid in the event of a collision, but the specifics of determining the direction of outgoing velocities are shown in each specific case of impact or collision. Therefore, in the following Figures 5 we will show a number of special cases of configuration of a rolling ball and a cylindrical shock, respectively, of two balls in a collision, or of striking a ball on different contour surfaces of the impact. From the previous kinematic analysis of the component incoming and outgoing velocities of the contact-impact points $\mathbf{T}_k$, $k=0,1,2,3,4,.....$ of the individual rolls of the ball in the rolling, before and after the collision, we conclude that it is *sufficient to consider the incoming and outgoing angular rolling velocity* before and after the collision, as well as the corresponding rolling routes. With kinematic elements we can completely define the kinematics of the ball's impact in rolling. We will show this in other cases of billiard ball strikes and collisions.

The answer to the question what are the values of the intensity of the outgoing component angular velocities belongs to the field of impact dynamics and collisions, so we

will answer this question in the chapter dynamics of billiards, taking into account the type and type of impact, ie collision. Although, from the forms (8) and (9), we can obtain that the outgoing angular velocity $\vec{\omega}_{P1}(t_0+\tau)=-k\vec{\omega}_{P1}(t_0)$ of the ball rolling after impact into a fixed contour, in which the coefficient k of restitution. In ideally elastic impact coefficient k of restitution is equal to one, and depending on the type of impact, that is, the properties of the sphere and the contour, it is in the interval $k\in[0,1]$, where we have adopted for the contour, in which the sphere of ball strikes, that the axial moment of inertia of mass is infinite $\mathbf{J}_{P2}\to\infty$ and its incoming angular the rolling velocity $\omega_{P2}(t_0)=0$ "is equal to zero", and it follows that its "outgoing angular rolling velocity" is zero, $\vec{\omega}_{21}(t_0+\tau)=0$, just as it was before the ball struck it, into the boundary surface.

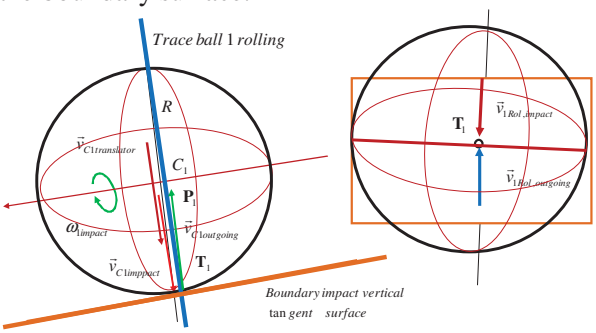

Figure 7. Plan for the incoming and outgoing velocities of the point of impact of a ball at the central impact of a billiard ball, which rolls along a horizontal plane and an impact perpendicular to the vertical contour plane of impact

4.2.2. The central impact of the ball in rolling into a contour vertical plane, as well as into a convex and concave surface.

In the Figure 7 shows a plan of the incoming and outgoing velocities of the contact point of the central impact of a billiard ball in rolling, which rolls along a horizontal plane and a track perpendicular to the vertical contour surface in which it strikes. The horizontal component of the incoming velocity of the ball impact point is equal to the translational velocity of the center of mass of the ball, while the vertical component of the incoming velocity of that ball impact point is equal

$$\vec{v}_{\mathbf{T},Roling,impact}=\vec{v}_{1,Roling,impact}=-\omega_{\mathbf{P},impact}R\vec{k}=-\frac{v_{\mathbf{C},impact}}{R}R\vec{k}=-v_{\mathbf{C},impact}\vec{k} \tag{12}$$

and it has the highest intensity because it is $\alpha=0$, also the point of impact, in this case it is farthest from the current axis of rotation of the ball and equals R, that is, the ball rolling line closes the angle $\alpha=0$, because it is directional to the contour radius of the ball. The angular velocity $\vec{\omega}_{1,impact}$ of rotation of the ball when rolling is parallel to the contour plane, that is, to the direction of rotation of the ball and is denoted by:

$$\vec{\omega}_{P,impact}=\vec{\omega}_{1,impact}=-\frac{v_{\mathbf{C},impact}}{R}\vec{i}\,, \tag{13}$$

if we have adopted the coordinate axis x in the contour plane, the axis y in the normal direction to that plane. So that $\vec{v}_{\mathbf{T},impact} = \vec{v}_{\mathbf{C},impact} = -v_{\mathbf{C},impact}\vec{j}$. The direction and direction of the incoming roll path of a billiard ball before impact is determined by a unit vector $-\vec{j}$, while the outgoing roll path after a impact is determined by a unit vector $\vec{j}$. Immediately after the central impact on the contour vertical plane, the components $\vec{v}_{\mathbf{T},outgoing}$ and $\vec{v}_{\mathbf{T},Roling,outgoing}$ of the outgoing velocity of the point of impact of the ball and the center of mass of the rolling ball, as the angular velocity $\vec{\omega}_{P,outgoing}$ of the outgoing rolling of the ball along the outgoing route are:

$$\vec{v}_{\mathbf{T},outgoing} = \vec{v}_{\mathbf{C},outgoing} = v_{\mathbf{C},outgoing}\vec{j} \tag{14}$$

$$\vec{v}_{\mathbf{T},Roling,outgoing} = \omega_{\mathbf{P},outgoing}R\vec{k} = \frac{v_{\mathbf{T},outgoing}}{R}R\vec{k} = v_{\mathbf{C},outgoing}\vec{k} \tag{15}$$

$$\vec{\omega}_{P,outgoing} = -\vec{\omega}_{P,impact} = -\vec{\omega}_{1,impact} = \frac{v_{\mathbf{T},outgoing}}{R}\vec{i} = \frac{v_{\mathbf{C},outgoing}}{R}\vec{i} \tag{16}$$

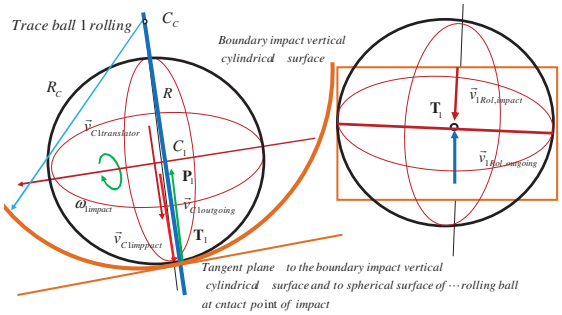

Figure 8. Plan of the incoming and outgoing velocities of the point of impact of a ball at the central impact of a billiard ball, which rolls along a horizontal plane and a track perpendicular to the vertical contour of a curvilinear cylindrical concave surface

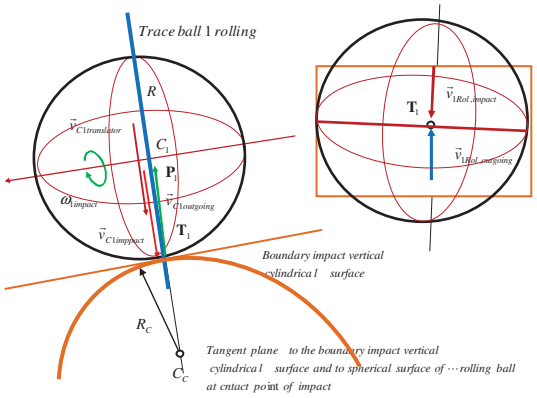

Figyre 9. Plan of the incoming and outgoing velocities of the point of impact of the ball at the central impact of the billiard ball, which rolls along the horizontal plane and the route perpendicular to the vertical contour curved cylindrical convex surface of impact

The central impact of a ball in rolling into a contour concave curvilinear surface with a vertical derivative is presented in Figure 8. In this Figure 8 shows a plan of the incoming and

outgoing velocities of a billiard ball point in the case of a central impact in a tangent plane to a contour concave curvilinear surface with vertical derivatives. This line of incoming ball rolling passes through the center of the curve of the concave line along which the vertical derivative describes that curvilinear cylindrical surface. In order for such an impact, it is necessary that the radius of curvature in the part of the concave curve along the line of the curvilinear contour surface be greater than the radius of the billiard sphere. This is shown in Figure 8. Position the coordinate system so that the coordinate axis x is in a tangent plane to the contour curved cylindrical surface, and the axis y in the normal direction to that plane, so that it passes through the center of the curve of the contour surface, while the axis z is in the direction of its vertical derivative is drawn through the point contact (impacts, strikes) billiard balls into the contour surface. Now, by defining the tangent surface through the point of impact of the billiard ball into the contour surface, for this case we have reduced the central impact of the billiard ball to a plane.

The central impact of a ball in rolling into a contour convex curvilinear surface with a vertical derivative is presented in Figure 9. In the Figure 9 shows a plan of the incoming and outgoing velocities of a ball point in the event of a central impact of a billiard ball in rolling, which rolls on a horizontal plane and a track perpendicular to a vertical tangent plane drawn to a contour convex curvilinear surface with a vertical derivative in which it strikes. This line of incoming rolling trace of the sphere passes through the center of the curve of the convex curve along which the vertical derivative describes that curvilinear surface. In order for such a collision, the ratio of the radius of curvature in the part of the curve to the line of the curvilinear contour surface and the radius of the billiard sphere is irrelevant. This is shown in Figure 9. Position the coordinate system such that the coordinate axis x is in a tangent plane to the contour convex curvilinear cylindrical surface, and the axis y in the normal direction to that plane, so that it passes through the center of the contour surface curvature, while the axis z in the direction of its vertical derivative is drawn through the point strikes billiard ball into a contour convex surface. Now, by defining the tangent surface through the point of impact of the billiard ball into the contour surface, we have reduced the task to the central impact of the billiard ball on a plane.

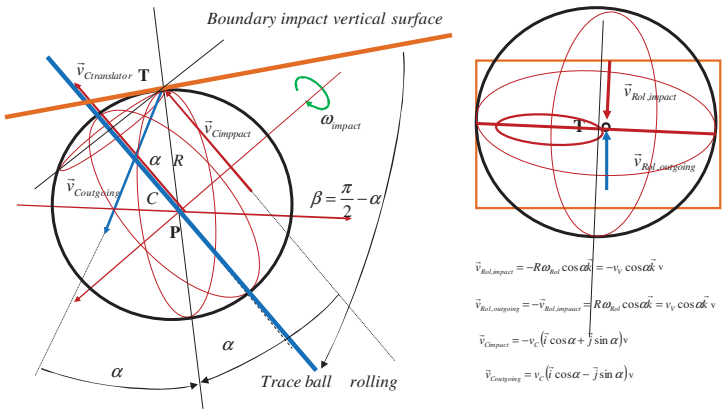

Figure 10. Plan of the incoming and outgoing velocities of the point of impact of a ball at a skew (oblique) impact of a billiard ball, which rolls along a horizontal plane and a track directed at an angle in relation to the normal to the vertical contour plane of the impact

4.2.3. Oblique (skew) impact of a ball in rolling into a contour vertical plane. In the Figyre 10 shows a plan of the incoming and outgoing velocities of a billiard ball point in

the event of an oblique (skew) roll of a billiard ball in rolling, before and after it strikes a vertical plane. The ball rolls along a horizontal plane and slopes obliquely at a sharp angle to the vertical contour plane of impact. We set up the coordinate system so that the coordinate axis x is in the contour plane of impact, and the axis y in the normal direction to that plane, while the axis z in the direction of its vertical derivative is drawn through the point of impact of the billiard ball into the contour plane. The unit vector orientation of the direction and direction of the ball rolling path before impact is: $\vec{n}_{impact} = -\left(\vec{i}\sin\alpha + \vec{j}\cos\alpha\right)$. The incoming velocity components are:

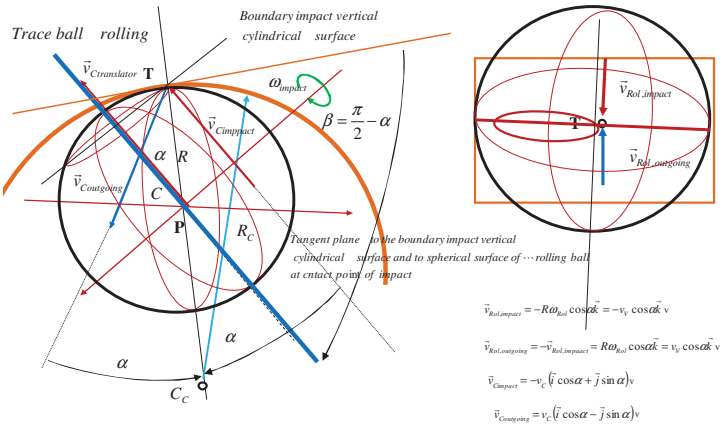

Figure 11. Plan of the incoming and outgoing velocities of the contact point of impact of a ball at an oblique impact of a billiard ball, which rolls along a horizontal plane and a line directed at an angle relative to the normal to a vertical contour curved cylindrical concave surface

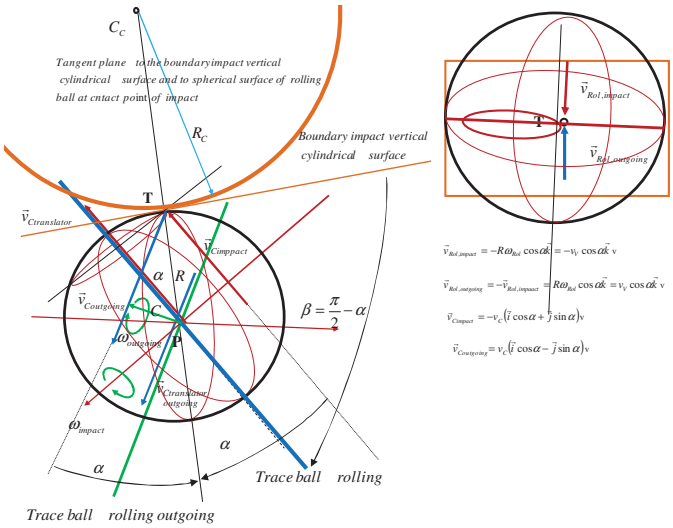

Figure 12. Plan of the incoming and outgoing velocities of the contact point of impact of a ball at an oblique impact of a billiard ball, which rolls along a horizontal plane and a line directed at an angle in relation to the normal to the vertical contour curved cylindrical concave impact surface

The translational velocity of the center **C** of mass of the ball just before impact is:

$$\vec{v}_{C,impact} = -v_C\left(\vec{i}\sin\alpha + \vec{j}\cos\alpha\right) \tag{17}$$

The instantaneous angular velocity $\vec{\omega}_{P,impact}$ of rotation due to the ball rolling along the route immediately before impact is:

$$\vec{\omega}_{impact} = \vec{\omega}_{P,impact} = \omega_{P,impact}\left(-\vec{i}\cos\alpha + \vec{j}\sin\alpha\right) = \frac{v_{C,impact}}{R}\left(-\vec{i}\cos\alpha + \vec{j}\sin\alpha\right) \tag{18}$$

The horizontal component $\vec{v}_{\mathbf{T},hor,impact}$ of the velocity of the ball point $\mathbf{T}$ by which the ball strikes the vertical contour plane is equal to the translational velocity $\vec{v}_{C,impact}$ of the center $\mathbf{C}$ of mass of the ball:

$$\vec{v}_{\mathbf{T},hir,impact} = \vec{v}_{C,impact} = -v_C\left(\vec{i}\sin\alpha + \vec{j}\cos\alpha\right) \tag{19}$$

The vertical component $\vec{v}_{\mathbf{T},Rol,impact}$ of the velocity $\vec{v}_{\mathbf{T},impact}$ of the ball point $\mathbf{T}$, by which the ball hits the vertical contour, is planar due to the rolling of the ball along the horizontal line-trace by the angular velocity $\vec{\omega}_{P,impact}$ of rolling about momentary avis and is equal to:

$$\vec{v}_{\mathbf{T},Rol,impact} = -R\omega_{\mathbf{P},Rol}\cos\alpha\vec{k} = -v_{\mathbf{C},impact}\cos\alpha\vec{k} \tag{20}$$

The horizontal component $\vec{v}_{\mathbf{T},hor,outgoing}$ of the velocity $\vec{v}_{\mathbf{T},outgoing}$ of the ball point $\mathbf{T}$ with which the ball leaves after hitting the vertical contour plane is equal to:

$$\vec{v}_{\mathbf{T},hor,outgoing} = v_{\mathbf{T},hormoutgoing}\left(-\vec{i}\sin\alpha + \vec{j}\cos\alpha\right) \tag{21}$$

The velocity $\vec{v}_{C,outgoing}$ of translation of the center $\mathbf{C}$ of mass of the ball immediately after impact is a horizontal component $\vec{v}_{\mathbf{T},hor,outgoing}$ of the departure velocity $\vec{v}_{\mathbf{T},outgoing}$ of the ball point $\mathbf{T}$ after the impact of the ball into the contour plane:

$$\vec{v}_{C,outgoing} = v_{C,outgoing}\left(-\vec{i}\sin\alpha + \vec{j}\cos\alpha\right) = \vec{v}_{\mathbf{T},hor,outgoing} = v_{\mathbf{T},hor,outgoing}\left(-\vec{i}\sin\alpha + \vec{j}\cos\alpha\right) \tag{22}$$

The instantaneous angular velocity $\vec{\omega}_{\mathbf{P},outgoing}$ of rotation due to the ball rolling along the track immediately after impact is:

$$\vec{\omega}_{outgoing} = \vec{\omega}_{\mathbf{P},outgoing} = \omega_{P,outgoing}\left(\vec{i}\cos\alpha + \vec{j}\sin\alpha\right) = \frac{v_{\mathbf{T},hor,outgoing}}{R}\left(\vec{i}\cos\alpha + \vec{j}\sin\alpha\right) \tag{23}$$

The vertical component $\vec{v}_{\mathbf{T},Rol,outgoing}$ of the velocity of the ball point $\mathbf{T}$, by which the ball leaves after striking the vertical contour plane, is the cause of the continuous rolling of the ball along the horizontal line at angular velocity $\vec{\omega}_{\mathbf{P},outgoing}$ and is equal to:

$$\vec{v}_{\mathbf{T},Rol,outgoing} = R\omega_{\mathbf{P},outgoing}\cos\alpha\vec{k} = -v_{\mathbf{T},Rol,impact}\vec{k} \tag{24}$$

The unit vector orientation of the direction and direction of the ball rolling path after impact is: $\vec{n}_{outgoing} = \left(-\vec{i}\sin\alpha + \vec{j}\cos\alpha\right)$.

4.2.4. An oblique (skew) impact of a ball in rolling into a contour concave or convex curvilinear surface with a vertical derivative. In Figures 11 and 12 show the plans of the incoming and outgoing velocities of the contact point $\mathbf{T}$ of a billiard ball in the case of an oblique impact, before and after the impact of the contour concave or the convex curvilinear surface with vertical derivatives. The ball rolls on a horizontal plane and slants obliquely at a sharp angle with respect to the tangent plane to the contour convex or concave curvilinear surface at the contact point $\mathbf{T}$ of impact of the sphere into it. Then, the incoming ball rolling path does not collinear with normal to the tangent plane through contact point $\mathbf{T}$ and do not cross the center $\mathbf{C}_0$ of its curve before the impact. Position the coordinate system so that the coordinate axis x is in a tangent plane to the contour surface of the impact, and the axis y in the normal direction to that tangent plane, so that it passes through the center of its curve $\mathbf{C}_0$, as well as into centre of ball $\mathbf{C}$, while the axis z in the direction

of its vertical derivative is drawn through the contact point $\mathbf{T}$ of impact of the billiard ball in the contour surface. The snow velocities for both of these cases are as analogous as in the case of an oblique impact in the plane contour-boundary, where in the tangent plane is analogous to the occupational impact from the previous example of an oblique collision into the plane.

4.2.5. Central collision between two billiard balls in rolling. If the rolling paths of the stock exchange slides of the two billiard balls are in one rolling line and are directed towards each other or the first one roll at a slower velocity so that the second one can catch up, a central collision between two balls can be realized. The configuration of the between two billiards balls is shown in Figure 13.

Now, at the point $\mathbf{T}_1 \equiv \mathbf{T}_2 \equiv \mathbf{T}_{12}$ of collision of the two balls, we place an imaginary common tangent plane, which are tangent to both and the other sphere at the contact point $\mathbf{T}_1 \equiv \mathbf{T}_2 \equiv \mathbf{T}_{12}$ of their collision. We set up a coordinate system such that the coordinate axis x is in their common tangent plane through the collision-contact point $\mathbf{T}_1 \equiv \mathbf{T}_2 \equiv \mathbf{T}_{12}$, and the axis y in the normal direction to that tangent plane, while the axis z in the vertical direction lies in the tangent plane in which the paths of the balls rolling are drawn through the collision point of the billiards balls.

The unit vectors of orientation of the direction $\vec{n}_{1,impact} = -\vec{j}$ and $\vec{n}_{2,impact} = \vec{j}$ direction of the paths of the ball rolling before the collision are in the opposite directions, respectively. The components of the incoming velocities of the rolling balls before the collision are $\vec{v}_{C1,impact} = -v_{C1}\vec{j}$ or $\vec{v}_{C2,impact} = v_{C2}\vec{j}$: The translation velocities of the centers of mass, $\mathbf{C}_1$, or $\mathbf{C}_2$ the balls immediately before their collision, are $\vec{v}_{C1,impact} = -v_{C1}\vec{j}$ and $\vec{v}_{C2,impact} = v_{C2}\vec{j}$: respectively. The angular velocities of the rolling billiard balls without slipping immediately before their collision, are $\vec{\omega}_{P1,impact}$ and $\vec{\omega}_{P2,impact}$: respectively are:.

$$\vec{\omega}_{1,impact} = \vec{\omega}_{P1,impact} = -\vec{i}\,\omega_{P1,impact} = -\frac{v_{C1,impact}}{R}\vec{i}$$

$$\vec{\omega}_{2,impact} = \vec{\omega}_{P2,impact} = \vec{i}\,\omega_{P2,impact} = \frac{v_{C2,impact}}{R}\vec{i} \tag{25}$$

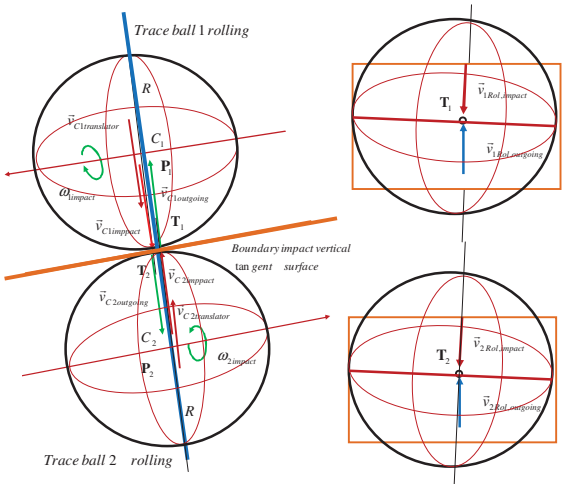

Figure 13. Plan the incoming and outgoing velocities of the collision points of two balls at their central collision

The horizontal components $\vec{v}_{\mathbf{T}1,hor,impact}$ and $\vec{v}_{\mathbf{T}2,hor,impact}$ of the velocities $\vec{v}_{\mathbf{T}1,impact}$ and $\vec{v}_{\mathbf{T}2,impact}$ of the points $\mathbf{T}_1$ and $\mathbf{T}_2$ the balls that the balls collide with are equal to the velocities $\vec{v}_{C1,impact}$ or $\vec{v}_{C2,impact}$ of the corresponding centers of mass, $\mathbf{C}_1$, or $\mathbf{C}_2$ the corresponding balls:

$$\vec{v}_{\mathbf{T}1,hor,impact} = \vec{v}_{C1,impact} = -v_{C1}\vec{j}\text{, respectively } \vec{v}_{\mathbf{T}2,hor,impact} = \vec{v}_{C2,impact} = v_{C2}\vec{j}\ , \quad (26)$$

Vertical components $\vec{v}_{\mathbf{T}1,Rol,impact}$ and $\vec{v}_{\mathbf{T}2,Rol,impact}$ of velocities of points $\mathbf{T}_1$ and $\mathbf{T}_2$ of the balls that collide with the balls are velocities due to the rolling of the balls along the horizontal track by the incoming angular velocities $\vec{\omega}_{P1,impact}$ and $\vec{\omega}_{P2,impact}$ are defined as:

$$\vec{v}_{\mathbf{T}1,Rol,impact} = -R\omega_{\mathbf{P}1,Rol}\vec{k} = -v_{\mathbf{C}1,impact}\vec{k} \quad (27)$$

respectively

$$\vec{v}_{\mathbf{T}2,Rol,impact} = -R\omega_{\mathbf{P}2,Rol}\vec{k} = -v_{\mathbf{C}2,impact}\vec{k} \quad (28)$$

The horizontal components $\vec{v}_{\mathbf{T}1,hor,outgoing}$ and $\vec{v}_{\mathbf{T}1,hor,outgoing}$ of the velocities of the points $\mathbf{T}_1$ and $\mathbf{T}_2$ of the balls with which the balls leave after the collision are:

$$\vec{v}_{\mathbf{T}1,hor,outgoing} = v_{\mathbf{T}1,hor,outgoing}\vec{i}\ \text{, respectively } \vec{v}_{\mathbf{T}2,hor,outgoing} = -v_{\mathbf{T}2,hpr,outgoing}\vec{i} \quad (29)$$

The velocities $\vec{v}_{C1,outgoing}$ and $\vec{v}_{C2,outgoing}$ of translation of the centers of mass, $\mathbf{C}_1$, or $\mathbf{C}_2$ the corresponding sphere immediately after the mutual collision, is equal to the corresponding horizontal components $\vec{v}_{\mathbf{T}1,hor,outgoing}$ and $\vec{v}_{\mathbf{T}1,hor,outgoing}$ of the departure velocities of the corresponding contact point $\mathbf{T}_1$ and $\mathbf{T}_2$ sphere after the collision:

$$\vec{v}_{C1,outgoing} = v_{C1,outgoing}\vec{j} = \vec{v}_{\mathbf{T}1,hor,outgoing} = v_{\mathbf{T}1,hoe,outgoing}\vec{j}$$
$$\vec{v}_{C2,outgoing} = -v_{C2,outgoing}\vec{j} = -\vec{v}_{\mathbf{T}2,hoe,outgoing} = -v_{\mathbf{T}2,hor,outgoing}\vec{j} \quad (30)$$

The instantaneous angular velocities $\vec{\omega}_{\mathbf{P}1,outgoing}$ and $\vec{\omega}_{\mathbf{P}2,outgoing}$ of ball rolling due to the outgoing rolling of each of the balls per track immediately after the collision are:

$$\vec{\omega}_{1,outgoing} = \vec{\omega}_{\mathbf{P}1,outgoing} = \omega_{P1,outgoing}\vec{i} = \frac{v_{\mathbf{T}1,hor,outgoing}}{R}\vec{i}$$

$$\vec{\omega}_{2,outgoing} = \vec{\omega}_{\mathbf{P}2,outgoing} = \omega_{P2,outgoing}\vec{i} = -\frac{v_{\mathbf{T}2,hor,outgoing}}{R}\vec{i} \quad (31)$$

The vertical component $\vec{v}_{\mathbf{T}1,Rol,outgoing}$ and $\vec{v}_{\mathbf{T}2,Rol,outgoing}$ of the departure velocities of contact points $\mathbf{T}_1$ and $\mathbf{T}_2$ of the balls, by which each of the balls leaves after each other's central collision, is the cause of the outgoing rolling of each of the balls along the horizontal track at angular velocity, respectively, and is determined by the following expressions:

$$\vec{v}_{\mathbf{T}1,Rol,outgoing} = R\omega_{\mathbf{P}1,outgoing}\vec{k} = v_{\mathbf{T}1,Rol,impact}\vec{k}$$
$$\vec{v}_{\mathbf{T}2,Rol,outgoing} = R\omega_{\mathbf{P}2,outgoing}\vec{k} = v_{\mathbf{T}2,Roll,impact}\vec{k} \quad (32)$$

The unit vectors of orientation of the direction and orientation of the outgoing lanes of the outgoing roll of the balls in the outlet after the collision are: $\vec{j}$ and $-\vec{j}$, respectively.

4.2.6. An oblique collision of two billiard balls in a non-slip roll. If the rolling traces of two billiard balls on rolling without slipping intersect, and the balls simultaneously reach the position that they can collide, then such a collision is said to be an oblique collision of two balls. Figures 14 and 15 shown the plans of the component incoming $\vec{v}_{C1,impact}$ and $\vec{v}_{C2,impact}$ and outgoing $\vec{v}_{C1,outgoing}$ and $\vec{v}_{C2,outgoing}$ velocities of ball center mass $\mathbf{C}_1$ and $\mathbf{C}_2$ of

an oblique collision of two billiard balls rotating horizontally relative to a common vertical tangent plane at a common point of collision.

Their velocities $\vec{v}_{C1,impact}$ and $\vec{v}_{C2,impact}$ of the centers of mass $\mathbf{C}_1$ and $\mathbf{C}_2$, are non-collinear and we are using the collision model decomposition to subsystems presented in Figure14. In the following Figure 15 shows a plan of the component of incoming $\vec{v}_{C1,impact}$ and $\vec{v}_{C2,impact}$, and outgoing $\vec{v}_{C1,outgoing}$ and $\vec{v}_{C2,outgoing}$ velocities of an oblique collision of two billiard balls, rolling along a horizontal plane, relative to a common vertical tangent plane at a common impact point of oblique collision when their translational velocities of their centers $\mathbf{C}_1$ and $\mathbf{C}_2$ of ball mass are no collinear, using a complex system model.

When asked how many such positions in the collision configuration can be insulated, how to define using the distance of the centers of mass of the two balls. Here is the conclusion of the theorem.

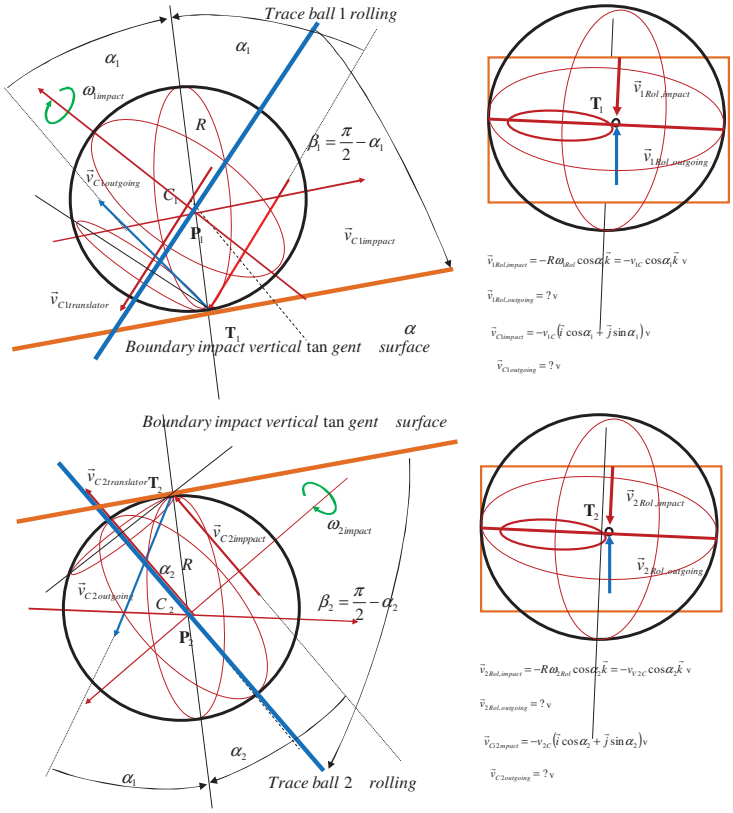

Figure 14. Decomposed system of two equal billiard balls in configuration of a oblique (skew) collision. Plan of the incoming and outgoing velocities of the collision contact points of each of the two balls at their oblique collision.

4.2.7. The theorem of the feasibility of the collision of two billiard balls. *Two billiard balls, of equal radius, in rolling without slipping, and rolling along the intersecting tracks, can reach the configuration of the collision, and the realization of the same, only if only if their centers* $\mathbf{C}_1$ *and* $\mathbf{C}_2$ *of mass are located at the corresponding distance* $\overline{\mathbf{C}_1\mathbf{C}_2} = 2R$ *at points, which are at the translational velocities of their centers of mass* $\mathbf{C}_1$ *and* $\mathbf{C}_2$ *, and*

are directed and oriented to the point of intersection of their rolling paths. There are infinitely many such configurations of the collision feasibility of two balls. A collision is possible before both balls pass the point of intersection of the tracks, and also in the condition that one has not reached the position of the section of the tracks and that the other ball has passed through that section of the tracks, but so that the intensities of the velocities allow the first round to cross the position of cross sections of the tracks.

We shall now give one analysis and explanation of the plan of the component velocities $\vec{v}_{\mathbf{T}1,hor,outgoing}$ and $\vec{v}_{\mathbf{T}1,hor,outgoing}$, as well as $\vec{v}_{\mathbf{T}1,Rol,outgoing}$ and $\vec{v}_{\mathbf{T}2,Rol,outgoing}$ of the points $\mathbf{T}_1$ and $\mathbf{T}_2$ of balls in which the balls collide, using quoted Figures 14 and 15 respectively. If there was a collision through the points $\mathbf{T}_1$ and $\mathbf{T}_2$ at the collision point $\mathbf{T}_1 \equiv \mathbf{T}_2 \equiv \mathbf{T}_{12}$, then the two balls, set up an imaginary common tangent plane, which is tangent to both sphere surface at the point of their collision $\mathbf{T}_1 \equiv \mathbf{T}_2 \equiv \mathbf{T}_{12}$. Let us set the coordinate system so that the coordinate axis x is in their common tangent plane through the collision point, and the axis y in the normal direction to that tangent plane and passes through both cents of the mass $\mathbf{C}_1$ *and* $\mathbf{C}_2$ of billiard balls in the collision configuration, while the axis z is in the tangent plane and in the vertical direction in the plane in which the tracks of rolling balls lie and are pulled through the collision point of billiard balls.

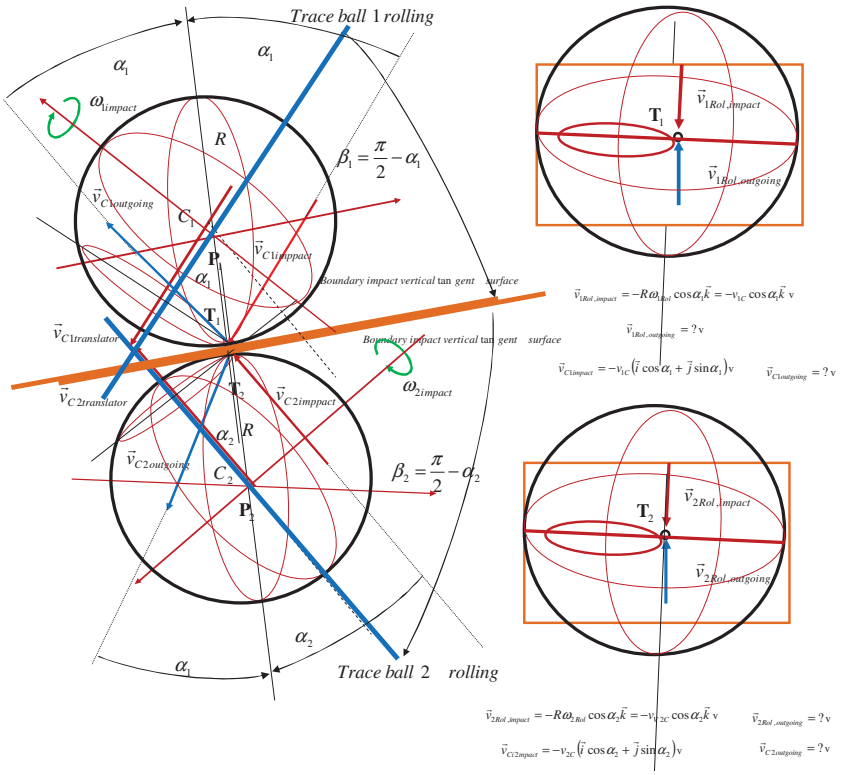

Figure 15. A system of two equal billiard balls that roll on rolling tracks in a oblique (skew) collision configuration. Plan the incoming and outgoing velocities of the collision points of each of the two balls at their oblique collision

The unit vectors of orientation of the direction and focusing of the incoming ball rolling paths, just before the oblique collision, are defined by the unit orientation vectors:

$$\vec{n}_{1,impact}=-\left(\vec{i}\sin\alpha_1+\vec{j}\cos\alpha_1\right),\ \text{and}\ \ \vec{n}_{2,impact}=-\vec{i}\sin\alpha_2+\vec{j}\cos\alpha_2. \tag{33}$$

in which the angles α_1 and α_2 of the rolling path of each of the balls are locked by the direction of the normal to the tangent plane to the sphere surfaces of the balls at the contact point of their collision, that is, by the direction of the line passing through the centers $\mathbf{C}_1$ and $\mathbf{C}_2$ of mass and both balls.

The components of the incoming velocities of the balls in rolling before the collision are:

The translation velocities $\vec{v}_{C1,impact}$ and $\vec{v}_{C2,impact}$ of the centers of mass $\mathbf{C}_1$ and $\mathbf{C}_2$, or of the balls just before their collision, are:

$$\vec{v}_{C1,impact}=v_{C1}\vec{n}_{1,impact}=-v_{C1}\left(\vec{i}\sin\alpha_1+\vec{j}\cos\alpha_1\right),$$

and

$$\vec{v}_{C2,impact}=v_{C2}\vec{n}_{2,impact}=v_{C2}\left(-\vec{i}\sin\alpha_2+\vec{j}\cos\alpha_2\right) \tag{34}$$

The instantaneous angular velocities $\vec{\omega}_{P1,impact}$ and $\vec{\omega}_{P2,impact}$ of rolling due to the rolling of balls on the corresponding incoming traces immediately before their collision are:

$$\vec{\omega}_{1,impact}=\vec{\omega}_{P1,impact}=\omega_{P1,impact}\left(\vec{i}\cos\alpha_1+\vec{j}\sin\alpha_1\right)=\frac{v_{C1,impact}}{R}\left(\vec{i}\cos\alpha_1+\vec{j}\sin\alpha_1\right)$$

$$\vec{\omega}_{2,impact}=\vec{\omega}_{P2,impact}=\omega_{P2,impact}\left(\vec{i}\cos\alpha_2-\vec{j}\sin\alpha_2\right)=\frac{v_{C2,impact}}{R}\left(\vec{i}\cos\alpha_2-\vec{j}\sin\alpha_2\right) \tag{35}$$

The horizontal components $\vec{v}_{\mathbf{T}1,hor,impact}$ and $\vec{v}_{\mathbf{T}2,hor,impact}$ of the velocities of the points $\mathbf{T}_1$ and $\mathbf{T}_2$ the balls that the balls collide with are equal to the velocities of the corresponding centers $\mathbf{C}_1$, and $\mathbf{C}_2$ of mass, of the corresponding balls:

$$\vec{v}_{\mathbf{T}1,hor,impact}=\vec{v}_{C1,impact}=v_{C1}\vec{n}_{1,impact}=-v_{C1}\left(\vec{i}\sin\alpha_1+\vec{j}\cos\alpha_1\right)$$

and

$$\vec{v}_{\mathbf{T}2,hor,impact}=\vec{v}_{C2,impact}=v_{C2}\vec{n}_{2,impact}=v_{C2}\left(-\vec{i}\sin\alpha_2+\vec{j}\cos\alpha_2\right) \tag{36}$$

Vertical components $\vec{v}_{\mathbf{T}1,Rol,impact}$ and $\vec{v}_{\mathbf{T}2,Rol,impact}$ of velocities of the contact points $\mathbf{T}_1$ and $\mathbf{T}_2$ balls that collide with the balls are velocities due to the rotation of the balls along the horizontal track by the incoming angular velocities and are defined as:

$$\vec{v}_{\mathbf{T}1,Rol,impact}=-R\omega_{\mathbf{P}1,Rol}\vec{k}=-v_{\mathbf{C}1,impact}\vec{k}$$

and

$$\vec{v}_{\mathbf{T}2,Rol,impact}=-R\omega_{\mathbf{P}2,Rol}\vec{k}=-v_{\mathbf{C}2,impact}\vec{k} \tag{37}$$

The horizontal components $\vec{v}_{\mathbf{T}1,hor,ougoing}$ and $\vec{v}_{\mathbf{T}2,hor,outgoing}$ of the velocities of contact points $\mathbf{T}_1$ and $\mathbf{T}_2$ balls, with which each of the balls leaves after the mutual collision are:

$$\vec{v}_{\mathbf{T}1,hor,ougoing}=\vec{v}_{C1,outgoing}=v_{C1}\vec{n}_{1,outgoing}=v_{C1}\left(-\vec{i}\sin\alpha_1+\vec{j}\cos\alpha_1\right)$$

and

$$\vec{v}_{\mathbf{T}2,hor,outgoing}=\vec{v}_{C2,outgoing}=v_{C2}\vec{n}_{2,outgoing}=-v_{C2}\left(\vec{i}\sin\alpha_2+\vec{j}\cos\alpha_2\right) \tag{38}$$

The outgoing velocities $\vec{v}_{C1,outgoing}$ and $\vec{v}_{C2,outgoing}$ of translation of the centers $\mathbf{C}_1$ and $\mathbf{C}_2$ of mass, or the corresponding sphere, immediately after the mutual collision of the billiard balls are equal to the corresponding horizontal component $\vec{v}_{\mathbf{T}1,hor,ougoing}$ and $\vec{v}_{\mathbf{T}2,hor,outgoing}$ of the outgoing velocity of the corresponding contact points $\mathbf{T}_1$ and $\mathbf{T}_2$ sphere after the collision:

$$\vec{v}_{C1,outgoing} = v_{C1}\vec{n}_{1,outgoing} = \vec{v}_{\mathbf{T}1,hor,ougoing} = v_{\mathbf{T}1,hor,ougoing}\left(-\vec{i}\sin\alpha_1 + \vec{j}\cos\alpha_1\right)$$

and

$$\vec{v}_{C2,outgoing} = v_{C2}\vec{n}_{2,outgoing} = \vec{v}_{\mathbf{T}2,hor,outgoing} = -v_{\mathbf{T}2,hor,outgoing}\left(\vec{i}\sin\alpha_2 + \vec{j}\cos\alpha_2\right) \quad (39)$$

The instantaneous angular velocities $\vec{\omega}_{\mathbf{P}1,outgoing}$ and $\vec{\omega}_{\mathbf{P}1o,utgoing}$ of the rolling and due to the outgoing rolling of each of the balls per track immediately after the collision are:

$$\vec{\omega}_{1,outgoing} = \vec{\omega}_{\mathbf{P}1,outgoing} = \omega_{P1,outgoing}\left(\vec{i}\cos\alpha_1 + \vec{j}\sin\alpha_1\right) = \frac{v_{\mathbf{T}1,hor,outgoing}}{R}\left(\vec{i}\cos\alpha_1 + \vec{j}\sin\alpha_1\right)$$

$$\vec{\omega}_{2,outgoing} = \vec{\omega}_{\mathbf{P}2,outgoing} = \omega_{P2,outgoing}\left(-\vec{i}\cos\alpha_2 + \vec{j}\sin\alpha_2\right) = \frac{v_{\mathbf{T}2,hor,outgoing}}{R}\left(-\vec{i}\cos\alpha_2 + \vec{j}\sin\alpha_2\right) \quad (40)$$

The vertical components $\vec{v}_{\mathbf{T}1,Rol,outgoig}$ and $\vec{v}_{\mathbf{T}2,Rol,outgoig}$ of the departure velocities of contact points $\mathbf{T}_1$ and $\mathbf{T}_2$ of balls, by which each of the balls leaves after each other's oblique collision, are the cause of the outgoing rolling of each of the balls along the horizontal track at angular velocities, $\vec{\omega}_{P1,outgoing}$ respectively $\vec{\omega}_{P2,outgoing}$, and are determined by the following expressions:

$$\vec{v}_{\mathbf{T}1,Rol,outgoing} = R\omega_{\mathbf{P}1,outgoing}\cos\alpha_1\vec{k} = v_{\mathbf{T}1,impact}\cos\alpha_1\vec{k}$$

$$\vec{v}_{\mathbf{T}2,Rol,outgoing} = R\omega_{\mathbf{P}2,outgoing}\cos\alpha_2\vec{k} = v_{\mathbf{T}2,impact}\cos\alpha_2\vec{k} \quad (41)$$

The unit vectors of orientation of the direction and focusing of the outgoing traces of the outgoing roll of each ball of the balls in the outlet after the collision are:

$$\vec{n}_{1,outgoing} = -\vec{i}\sin\alpha_1 + \vec{j}\cos\alpha_1 ,$$

respectively

$$\vec{n}_{2,outgoing} = -\vec{i}\sin\alpha_2 + \vec{j}\cos\alpha_2 \quad (42)$$

Conclusion-Theorem: *If the incoming paths of the balls in the rolling block equal angles with the common tangent plane to the balls at the contact points of collision of the balls, then the horizontal components of the outgoing velocities of those points close the same angles with that tangent plane. Also, the outgoing paths of one or the other ball, as well as the translational velocities of the centers of mass of the ball, close the same angles with this common tangent plane of collision.*

4.2.8. A special case of an oblique collision of two billiard balls in rolling along parallel rolling tracks. In Figures 16 and 17 shown the plan of incoming and outgoing velocities of an oblique collision of two billiard balls, rolling along parallel tracks in one horizontal plane, relative to the common vertical tangent plane when their velocities are collinear – decomposition, in Figure16, of the system into subsystems at the time of the collision. This is a special case of the previous general case of the configuration of an oblique collision of two billiard balls. Figure 17 shows that velocity plan on a complex, unrecompensed system. For such a collision to be possible, the necessary condition is that the maximum normal distance between the incoming traces of rolling of the balls before the collision is less than the diameter of the balls, respectively $h_{\max} \le 2R$.

Here, we will not list the expressions for the component velocities of the contact point of the balls in the collision configuration, since it is only obvious how to determine them according to the velocity plans from Figures 16, 17 and 17, and the order from the pre-description in the general case of the oblique collisin.

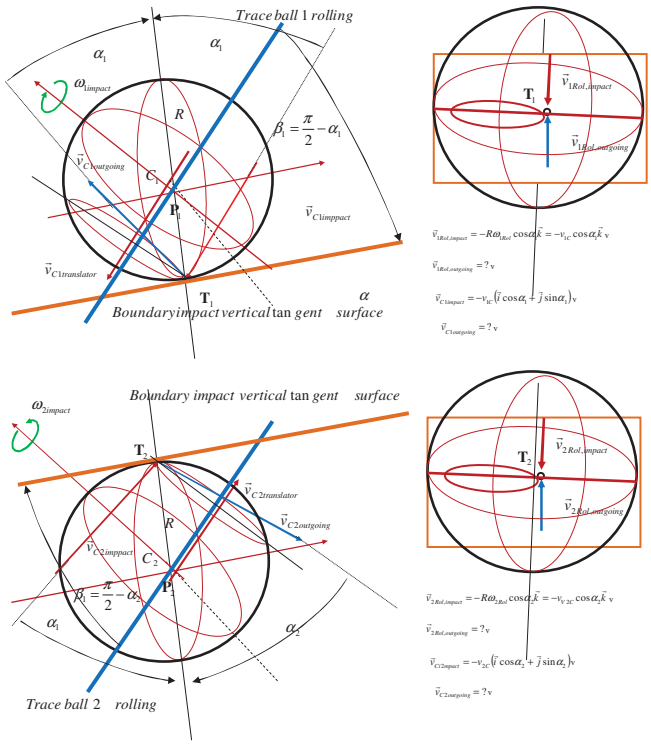

Figure 16. Decomposed system of two equal billiard balls rolling along parallel tracks in a collision configuration - Plan for the incoming and outgoing velocities of the collision points of each of the two balls, at their oblique collision and parallel incoming tracks, but parallel and outgoing treks

We, only, give the expressions for the instantaneous angular velocities $\bar{\omega}_{\mathbf{P}1,outgoing}$ and $\bar{\omega}_{\mathbf{P}1o,utgoing}$ of rolling and due to the outgoing rolling of each of the balls on the track immediately after the collision, which are:

$$\bar{\omega}_{1,outgoing} = \bar{\omega}_{\mathbf{P}1,outgoing} = \omega_{P1,outgoing}\left(\vec{i}\cos\alpha_1 + \vec{j}\sin\alpha_1\right) = \frac{v_{\mathbf{T}1,hor,outgoing}}{R}\left(\vec{i}\cos\alpha_1 + \vec{j}\sin\alpha_1\right)$$

respectively

$$\bar{\omega}_{2,outgoing} = \bar{\omega}_{\mathbf{P}2,outgoing} = -\omega_{P2,outgoing}\left(-\vec{i}\cos\alpha_1 + \vec{j}\sin\alpha_1\right) = -\frac{v_{\mathbf{T}2,hor,outgoing}}{R}\left(-\vec{i}\cos\alpha_1 + \vec{j}\sin\alpha_1\right) \quad (43)$$

The unit vectors of orientation of the direction and focusing of the outgoing traces of the outgoing rolling of the balls in departure immediately after the collision are:

$$\vec{n}_{1,outgoing} = -\vec{i}\sin\alpha_1 + \vec{j}\cos\alpha_1 ,$$

respectively

$$\vec{n}_{2,outgoing} = -\left(-\vec{i}\sin\alpha_1 + \vec{j}\cos\alpha_1\right) \quad (44)$$

Conclusion-Theorem: *In the case of an oblique collision of balls with parallel incoming rolling paths, the outgoing rolling paths of the balls following the collision are also parallel, and the horizontal components of the incoming velocities of the collision points are in a straight line, while the horizontal components of the outgoing velocities of the collision points after the collision are at to another real one. These rights are crossed at the collision*

point in the collision configuration. The departure velocities of the center of mass after the collision are also parallel.

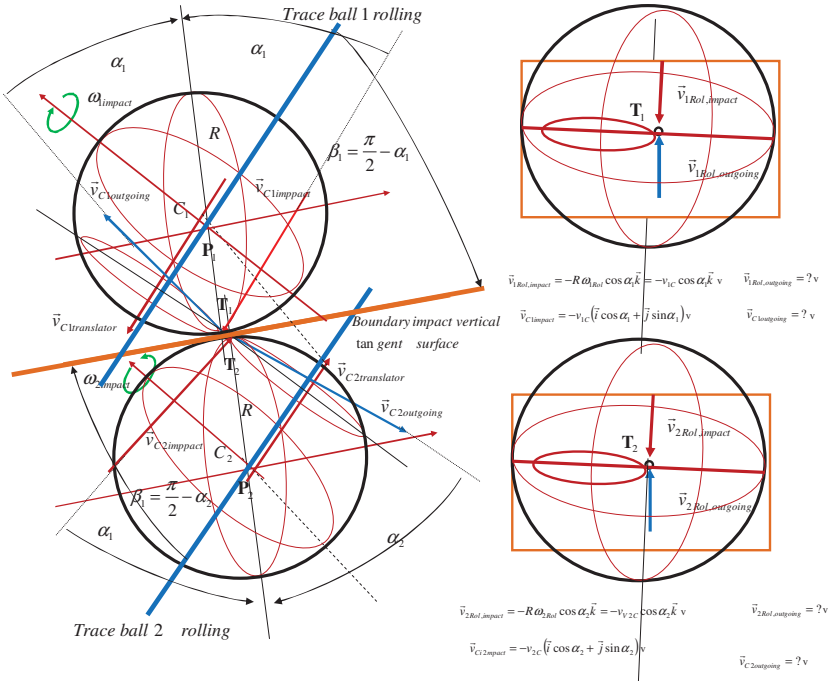

Picture 17. A system of two equal billiard balls rolling along parallel tracks in a collision configuration-Plan the incoming and outgoing velocities of the collision points of each of the two balls at their oblique collisions and parallel incoming traces, but parallel and outgoing traces of rolling

Main conclusion-Main Theorem: *The complete analysis of the component velocities of the collision points - the contact points of the balls in rolling was aimed to show that in the collision theory there is a ball of billiards in rolling, and more generally in the theory of collisions of axisymmetric bodies with one central plane of symmetry in which there is a circular contour by which the body can be rolled, it is sufficient to use only the angular velocity of rolling of the body around the instantaneous rolling axis, to describe the complete geometry, kinematics, and dynamics of the collision of the body in rolling.*

5 MECHANICS OF BILLIARDS II - THE DYNAMICS OF BILLIARDS

5.1 Basic elements of the dynamics of collision and impact of the rolling homogeneous rigid material balls

In order to describe the basic phenomena of the dynamics of billiards, we start from some basic definitions and definitions in the dynamics of the rolling of a material homogeneous rigid billiard ball with sphere surface, which we have presented at the beginning of this article, in the section on logical, qualitative and mathematical analogies.

Moving to the dynamics of billiards, in addition to the lengths and times, we also introduce the materiality of billiard balls. When rolling a ball, which is performed by rolling about the current axis of rotation or by translating at the velocity of the center of mass and rotating about its own central axis at some instantaneous angular velocity, we have two

approaches for description billiard ball dynamics. To describe such motion, materiality is calculated using the mass M of the ball and the axial moments of inertia of the mass of the ball for the instantaneous axis of rotation or for the central axis of rotation. For a material ball of mass M and radius R, the mass of the ball is: $M = \rho\frac{4}{8}R^3\pi$, ρ is the mass density of the ball or the mass per unit volume of the ball, the axial moment of inertia of the mass of the billiard ball for the center axis is $\mathbf{J}_C=\frac{2}{5}MR^2$, and the axial moment of inertia of the mass of the billiard ball for the axis tangent to the ball in any the point of its surface corresponding to the instantaneous axis of rolling of the ball when rolling is $\mathbf{J}_P=\mathbf{J}_C+MR^2=\frac{2}{5}MR^2+MR^2=\frac{7}{5}MR^2$, and is equal to the sum of the axial moment of mass inertia for the parallel central axis and the position moment of inertia of mass (which is equal to the product of mass of the ball and the square of the distance of the instantaneous axis of rolling from its parallel center axis of rotation of the sphere). These axial moments of inertia of the mass of a material sphere represent the inertial coefficients of the dynamics of the ball, which is rolling, and as the mass of the ball is the inertial coefficient for the case of translational motion of the ball, so the axial moments of inertia of the mass of the ball for rotation or rolling are its corresponding inertial coefficients! *Billiard balls with equal radiuses can be with different axial moments of inertia of their masses depending of the mass density of ball's material.*

When the paths of two material points meets at some point and if they reach the same point of their paths at different velocities and accelerations, then the dynamics of the collision of those two material points is achieved. The reciprocal dynamic effect of one material point on another material point is called a collision, and their dynamics in that short time interval are *the dynamics of a collision*.

If one material sphere (ball) is stationary and the other is moving, and in the movement of the rolls, it encounters a sphere in speace, one, moving, material sphere strikes (impacts) another, immobile material sphere. Since rest is a special case of the dynamics of a material sphere (ball), then we can say that the *concept of collision is more general than the concept of impact.*

An impact and collision can occur between one material sphere (ball) and a system of material balls, a collision with one of the material balls of a system of material balls, which is transmitted instantaneously to the other material balls of the system or body. Likewise, a collision of a material sphere-ball can be achieved by collision with a material rigid or deformable body. Collision is also possible in various combinations between material balls, material ball systems, and rigid and or deformable bodies. According to the properties and character of the material systems - participants in the collision event, collisions can be divided into several different types or groups: ideally elastic collision, ideally plastic collision and collision with a coefficient of restitution between zero and one.

It is very important to be aware of the phenomenon and the inherent elements of the collision, in other words the dynamics of the collision and its *vector and scalar invariants.* In the dynamics of billiards, as we can conclude from the preceding chapters, there is an impact of a billiard ball into a contour cylindrical surface, as well as a collision between two balls or a number of billiard balls in rolling.

Characteristic of a collision is that two solid spheres-balls come into contact at one common point at which one point of the spherical surfaces of the spheres in the collision reach simultaneously.

That point is the contact point of the collision of the masses of both balls, in which their dynamics interact, and thus the instantaneous, short-term duration, dynamic effect of one

rolling ball on the other at the contact of the current (very short interval) time is observed whereby the occurrence of a jump (discontinuous) changes in the kinetic parameters of the dynamics of both in the arrival of both rolling balls. This is primarily manifested in the change of direction and intensity of the velocity of motion of both material balls, which collided with respect to the intensities and directions of their velocities before their collision. In the collision of two material balls, *instantaneous forces of high intensity* and *short-time-action* occur in a short time interval in which the material balls are in contact during the dynamics of the collision, which disappear upon the separation of the system immediately after the collision.

The forces created by the collision of two material balls and in the state of contact of these two balls are also called *high-intensity impact forces*, of *short duration* and of final impulse. It should be emphasized that, by moving to the study of the dynamics of collisions, we have introduced, in addition to the length and time, the mass, or materiality, of billiard balls.

When studying collisions, and even material balls, some basic assumptions are made, which allow the model of collision dynamics of two rolling billiard balls to be assembled, and the task is simplified, but satisfactory models of real dynamics of collision of two balls are obtained. In the first part of this article we have presented the latest results of the authors of this article, which contribute to the extension of the theory of collision, geometry, kinematics and dynamics of collisions of the body in the rolling, which we will not repeat here but only to determine the outgoing angular velocities of the roll of billiard balls immediately after the collision.

5.2 Impact forces $\vec{F}(t)$ and impact moments $\vec{\mathfrak{M}}(t)$ in the collision of two material balls in rolling. Instantaneous impulse and momentum of motion of a ball in rolling before and after a collision

When it comes to systems of two bodies moving by rolling without sliding and in the dynamics of billiards, we have two or more balls, which are in rolling around the corresponding instantaneous axis of rolling, so the angular momentum difference of motion of the balls for the instantaneous axis of rotation is:

$$d\vec{\boldsymbol{p}}(t) = \vec{\mathfrak{M}}(t)dt = d\vec{\mathfrak{L}}_{\mathfrak{M}}(t) \tag{45}$$

where by $\vec{\mathfrak{L}}_{\mathfrak{M}}$ is denoted the impulse angular momentum and $\vec{\mathfrak{M}}(t)$ is the moment of impact impulse forces. If we integrate the previous differential relation, we obtain the following expression for the coupling angular momentum $\vec{\mathfrak{L}}_{\mathfrak{M}}$ of the body in rolling:

$$\vec{\mathfrak{L}}_{\mathfrak{M}} = \vec{\mathfrak{L}}(t) - \vec{\mathfrak{L}}(0) = \int_0^t \vec{\mathfrak{M}}(t)dt = \mathbf{J}_{\mathbf{P}}\vec{\omega}_{\mathbf{P}}(t) - \mathbf{J}_{\mathbf{P}}\vec{\omega}_{\mathbf{P}}(0) = \mathbf{J}_{\mathbf{P}}\vec{\omega}_{\mathbf{P}} - \mathbf{J}_{\mathbf{P}}\vec{\omega}_{\mathbf{P}0} \tag{46}$$

This previous vector expression should be considered conditionally, taking into account the discontinuity of the velocity direction in the impact configuration, as well as the discontinuity of the direction of movement occurring between the configuration immediately before and after the collision of two balls, as well as the interaction of rolling traces of the balls at the moment of impact. Also, it should be taken into account that the moment of the oscillating impact force, that is, the angular momentum of motion for the rolling axis, is also scalar, as opposed to the angular momentum of the moment for the point, which will be discussed in the case of rolling without sliding along the track, where the current the axis moves translation.

The increment $\Delta\vec{\mathfrak{L}}(t)$ of kinetic momentum or angular momentum $\vec{\mathfrak{L}}_{\mathfrak{M}}(t)$ of the motion for a finite time interval is equal to the momentum of an impulse impact force $\vec{\mathfrak{M}}(t)$ or coupling acting on a rolling ball, along its rolling path, at that short time.

Since both the linear momentum $\vec{K}_F(t)$ of the impulse impact force and the angular momentum $\vec{\mathfrak{L}}_{\mathfrak{M}}$ of the coupling are vector integrals, these in the general case do not coincide with the direction of the force $\vec{F}(t)$ or coupling $\vec{\mathfrak{M}}(t)$.

The mean value of the instantaneous coupling $\vec{\mathfrak{M}}_{sr}(t)$ can be determined from the previous relation (46) as:

$$\vec{\mathfrak{M}}_{sr}(\tau)=\frac{\vec{\mathfrak{L}}_{\mathfrak{M}}(\tau)}{\tau}=\frac{1}{\tau}\int_{t_0}^{t_0+\tau}\vec{\mathfrak{M}}(t)_{ud}\,dt \tag{47}$$

In the event that the coupling $\vec{\mathfrak{M}}(t)$ or moment of constant forces $\pm\vec{F}(t)=\vec{const}$, the angular momentum $\vec{\mathfrak{L}}_{\mathfrak{M}}(t)$ of coupling or moment of forces, though a vector integral, is collinear with coupling:

$$\vec{\mathfrak{L}}_{\mathfrak{M}}(t)=\vec{\mathfrak{L}}(t)-\vec{\mathfrak{L}}(t_0)=\int_{t_0}^{t}\vec{\mathfrak{M}}dt=\vec{\mathfrak{M}}(t-t_0)=\mathbf{J}_{\mathbf{P}}\vec{\omega}_{\mathbf{P}}(t)-\mathbf{J}_{\mathbf{P}}\vec{\omega}_{\mathbf{P}}(0)=\mathbf{J}_{\mathbf{P}}\vec{\omega}_{\mathbf{P}}-\mathbf{J}_{\mathbf{P}}\vec{\omega}_{\mathbf{P}0} \tag{48}$$

It means that the impulse $\vec{\mathfrak{L}}_{\mathfrak{M}}(t)$ of the coupling $\vec{\mathfrak{M}}(t)$ or moment of force, acting on the material ball via the point of impact, along its trajectory of motion when rolling the ball, at a finite time interval $\Delta t=t-t_9=\tau$, is equal to the increment of the angular momentum $\Delta\vec{\mathfrak{L}}(t)$ of the motion (kinetic moment) for that finite time interval.

When the coupling $\vec{\mathfrak{M}}(t)$ or moment of force is finite, the impulse $\vec{\mathfrak{L}}_{\mathfrak{M}}(t)$ of that coupling or torque in a small time interval, when $\Delta t=t-t_9=\tau\to 0$, equals zero. If the change in angular velocity $\Delta\vec{\omega}=\vec{\omega}(t)-\vec{\omega}(t_0)=\vec{\omega}-\vec{\omega}_0$ is finite in magnitude and occurs in a very short time $\Delta t=t-t_0=\tau\to 0$, then the impulse $\vec{\mathfrak{L}}_{\mathfrak{M}}(t)$, of the coupling $\vec{\mathfrak{M}}(t)$, ie the moment of forces must be finite, but that coupling $\vec{\mathfrak{M}}(t)$, or moment of the forces $\vec{F}(t)$, must be infinitely large. Such couplings $\vec{\mathfrak{M}}(t)$ or moments of forces $\vec{F}_{ud}(t)$ that occur in the short time and give a finite impulse $\vec{\mathfrak{L}}_{\mathfrak{M}}(t)$ (angular momentum) of the coupling are called the instant coupling or the momentary impact moment of the momentary impact forces of the finite impulse.

From the relation of the theorem on the change of kinetic energy and its relation to the coupling power, that is, the moment of forces, which performs work along the trajectory of motion of a material sphere-ball in rolling, it is valid:

$$\frac{dE_k}{dt}=P=\left(\vec{\mathfrak{M}}(t),\vec{\omega}(t)\right) \tag{49}$$

we can write:

$$dE_k=Pdt=\left(\vec{\mathfrak{M}}(t),\vec{\omega}(t)\right)dt \tag{50}$$

Upon approximate integration of the last relation we obtain:

$$E_k-E_{k0}=\int_{t_0}^{t}\left(\vec{\mathfrak{M}}(t),\vec{\omega}(t)dt\right)=\int_{t_0}^{t}\left(\vec{\mathfrak{M}}(t)dt,\vec{\omega}(t)\right)=\int_{t_0}^{t}\left(\vec{\omega}(t),d\vec{\mathfrak{L}}_{\mathfrak{M}}(t)\right)$$

$$E_k - E_{k0} \approx \frac{1}{2}\left(\vec{\omega}(t) + \vec{\omega}(t_0), \vec{\mathfrak{L}}_{\mathfrak{M}}(t - t_0)\right) \tag{51}$$

whereby we assumed that the approximate value of the integral could be determined assuming the mean value of the instantaneous angular velocity $\vec{\omega}_{sr} = \frac{1}{2}[\vec{\omega}(t) + \vec{\omega}(t_0)]$ during the impact process in a short time interval.

Based on the foregoing approximate relation (51), we can conclude that for infinitely short intervals the increments of the "*live force*" (*kinetic energy*) of the material sphere-ball in the rolling and in the collision dynamics, as well as the operation of the instantaneous impact forces, have finite values.

Moving by rotating about the current axis of rolling by an angle $\vec{\vartheta}_{\mathbf{P}} = \vec{\vartheta}$, or around the current pole, on a track of rolling a material ball, which by rolling has reached the collision configuration, is infinitesimal $\Delta t = t - t_0 = \tau \to 0$ and tending to zero during a small increment of time $\Delta t = t - t_0 = \tau \to 0$. Since the angular velocity $\vec{\omega} = \dot{\vec{\vartheta}}$ of rolling around the current axis of rolling, the angular momentum of the rolling pulse is the same:

$$\vec{\mathfrak{L}}_{\mathfrak{M}}(t_0 + \tau) = \vec{\mathfrak{L}}(t_0 + \tau) - \vec{\mathfrak{L}}(t_0) = \int_{t_0}^{t_0+\tau} \vec{\mathfrak{M}} dt = \vec{\mathfrak{M}}(t_0 + \tau - t_0) \tag{52}$$

$$\vec{\mathfrak{L}}_{\mathfrak{M}}(t_0 + \tau) = \mathbf{J}_{\mathbf{P}} \vec{\omega}_{\mathbf{P}}(t_0 + \tau) - \mathbf{J}_{\mathbf{P}} \vec{\omega}_{\mathbf{P}}(t_0) = \mathbf{J}_{\mathbf{P}} \dot{\vec{\vartheta}}_{\mathbf{P}} - \mathbf{J}_{\mathbf{P}} \dot{\vec{\vartheta}}_{\mathbf{P}0} \tag{53}$$

respectively

$$\mathbf{J}_{\mathbf{P}} \dot{\vec{\vartheta}}_{\mathbf{P}} = \vec{\mathfrak{L}}_{\mathfrak{M}}(t_0 + \tau) + \mathbf{J}_{\mathbf{P}} \dot{\vec{\vartheta}}_{\mathbf{P}0} \tag{54}$$

which after integration gives:

$$\mathbf{J}_{\mathbf{P}}\left[\vec{\vartheta}_{\mathbf{P}}(t_0 + \tau) - \vec{\vartheta}_{\mathbf{P}}(t_0)\right] = \int_{t_0}^{t_0+\tau} \vec{\mathfrak{L}}_{\mathfrak{M}}(t) dt + \mathbf{J}_{\mathbf{P}} \dot{\vec{\vartheta}}_{\mathbf{P}0}(t_0 + \tau - t_0) = \int_{t_0}^{t_0+\tau} \vec{\mathfrak{L}}_{\mathfrak{M}}(t) dt + \mathbf{J}_{\mathbf{P}} \dot{\vec{\vartheta}}_{\mathbf{P}0}(t_0)$$

$$\mathbf{J}_{\mathbf{P}}\left[\vec{\vartheta}_{\mathbf{P}}(t_0 + \tau) - \vec{\vartheta}_{\mathbf{P}}(t_0)\right] = \int_{t_0}^{t_0+\tau} \vec{\mathfrak{L}}_{\mathfrak{M}}(t) dt + \mathbf{J}_{\mathbf{P}} \dot{\vec{\vartheta}}_{\mathbf{P}0}(t_0) \tag{55}$$

where the mean value $\vec{\mathfrak{L}}_{\mathfrak{M},sr}$ of the angular momentum of the instantaneous coupling or moment of force in a short time interval $\Delta t = t - t_0 = \tau \to 0$.

As $t \to t_0$ there will be an increase in the angle of rolling, that is $\Delta \vec{\vartheta}_{\mathbf{P}} = \left[\vec{\vartheta}_{\mathbf{P}}(t_0 + \tau) - \vec{\vartheta}_{\mathbf{P}}(t_0)\right]_0 \approx 0$, the rolling of the ball during the impact or the collision, on the basis of which, we can conclude that the material sphere during the short-lived effect of the instantaneous coupling, or the moment of the instantaneous force in the dynamics of the collision is immobile.

We can, now also, define the term impact in terms of action.

The action which gives to a body the instantaneous forces $\vec{F}_{impact}$ and instantaneous couplings $\vec{\mathfrak{M}}_{impact}$ of a finite impulse, that is, angular momentum of moment short-lived action in the interval $\Delta t = t - t_0 = \tau \to 0$ is called a *stroke-impact*.

The vector invariants $\vec{\omega}_{\mathbf{P}}(t_0 + \tau)$ and $\vec{\omega}_{\mathbf{P}}(t_0)$, the instantaneous angular velocities before and after the impact always refer to the same material ball that rolls, $\vec{\omega}_{\mathbf{P}}(t_0)$, and $\vec{\omega}_{\mathbf{P}}(t_0 + \tau)$ are called the instantaneous angular velocities of the observed material sphere-ball to impact, before and, after, the collision (or impact). If the material ball at the moment of

impact on the motionless material of another system has an instantaneous angular velocity $\vec{\omega}_{\mathbf{P}}(t_0)=\vec{\omega}_{\mathbf{P},impact}$ then we say that it is the *incoming angular velocity of the rolling ball* or *the angular velocity of impact.* This currently produced angular velocity during a collision by which a material ball rolls out of contact with another system with $\vec{\omega}_{\mathbf{P}}(t_0+\tau)=\vec{\omega}_{\mathbf{P},outgoing}$ which it collided is called *the outgoing angular velocity.*

As we have shown in the previous analysis, we must bear in mind that in the short time of collision contact, the positions of the material balls in collision contact, when the impact forces or shocks are acting, change very little and slowly. These infinitesimal changes in the position of the material balls by rolling, or by changing the rolling angle, are in the order of magnitude of the small interval of time during which the collision takes place. Therefore, it is justified that changes in position during a short interval in which a collision occurs are neglected.

In the case of impact of a material ball into a fixed material or a limiter or a unilaterally restraining bond, the following relation can be written:

$$\vec{\omega}_{\mathbf{P},outgoing}-\vec{\omega}_{\mathbf{P},impact}=\Delta\vec{\omega}_{\mathbf{P}}=\frac{1}{\mathbf{J}_{\mathbf{P}}}\vec{\mathfrak{L}}_{\mathfrak{M}}(t_0+\tau)=\frac{1}{\mathbf{J}_{\mathbf{P}}}\int_{t_0}^{t_0+\tau}\vec{\mathfrak{M}}_{impact}(t)dt \tag{56}$$

5.3 Outgoing angular velocities, translational velocities, momentum of coupling impulses, and motion of rolling balls after an oblique ideally elastic collision of two balls

In Figures 15 and 18 show the configuration of the balls and the plan of the incoming and outgoing translational velocities and the angular rolling velocities of both balls in the case of an oblique (skew) collision of two equal balls, moving in opposite directions along the intersecting tracks. In order to determine the intensities of the outgoing angular velocities of the balls after the oblique collision, we will make an analogy with the central centric collision of two balls moving towards each other known angular velocities, for which the relations between the incoming and outgoing angular velocities are known.

In the case of ideally elastic oblique collision between balls, which we consider, the intensities of the component outgoing velocities after their collision, and in accordance with the previous decomposition analyzes of the kinematics of the balls in the collision into simple motions, when we consider that the masses of the balls are $m_1=m_2=M$ equal and the coefficient of restitution $k=1$, for ideal elastic collision, are:

1* The intensities of the horizontal components $v_{T1,trabslator,outgoing}$ and $v_{T2,translator,outgoing}$ of the outgoing velocities of the ball points due to translation after an oblique collision are:

$$v_{T1,trabslator,outgoing}=v_{T1,translator,impact}-\frac{2}{1+\dfrac{\mathbf{J}_{P1}}{\mathbf{J}_{P2}}}\left(v_{T1,translator,impact}-v_{T2,translator,i,pact}\right) \tag{57}$$

$$v_{T1,trabslator,outgoing}=v_{T2,translator,impact}=v_{T1,hor,outgoing}$$

$$v_{T2,translator,outgoing}=v_{T2,translator,impact}+\frac{2}{1+\dfrac{\mathbf{J}_{P2}}{\mathbf{J}_{P1}}}\left(v_{T1,translator,impact}-v_{T2,translator,impact}\right) \tag{58}$$

$$v_{T2,translator,outgoing}=v_{T1,translator,impact}=v_{T2,hor,outgoing}$$

The directions of these outgoing velocities are shown in figures 15 and 18, as in Figure 20. In the Figure 20 shows a complete plan of the incoming and outgoing angular velocities of rolling both balls with their rolling paths before and after an oblique collision.

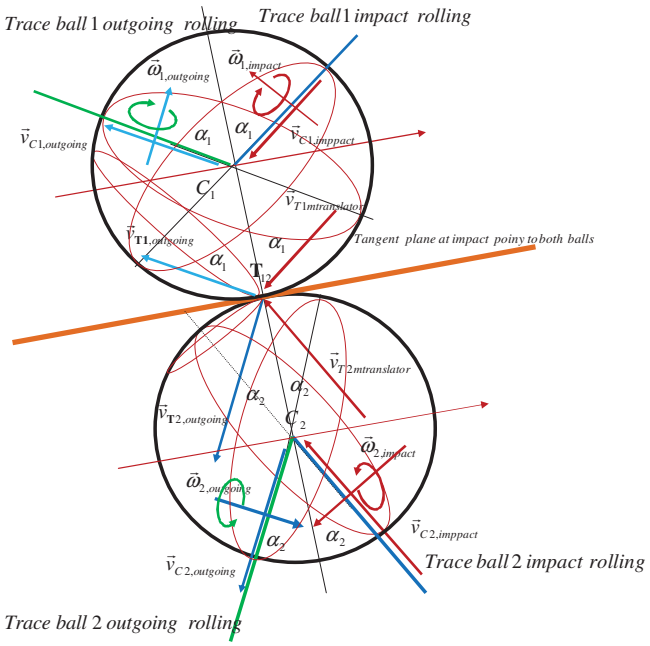

Figure 18. Collision of two rolling balls: Plan of incoming and outgoing angular velocities of rolling balls with their rolling paths before and after an oblique collision

2* The intensities of the outgoing angular velocities $\omega_{\mathbf{P}1,,outgoing}$ and $\omega_{\mathbf{P}2,outgoing}$ of rolling of the balls after a collision are determined by the following expressions:

$$\omega_{\mathbf{P}1,,outgoing} = \omega_{\mathbf{P}1,impact} - \frac{1+k}{1+\frac{\mathbf{J}_{P1}}{\mathbf{J}_{P2}}}\left(\omega_{\mathbf{P}1,impact} - \omega_{\mathbf{P}2,impact}\right) = \omega_{\mathbf{P}2,impact} = \frac{v_{\mathbf{C}2,impact}}{R} \tag{59}$$

$$\omega_{\mathbf{P}2,outgoing} = \omega_{\mathbf{P}2,impact} + \frac{1+k}{1+\frac{\mathbf{J}_{P2}}{\mathbf{J}_{P1}}}\left(\omega_{\mathbf{P}1,impact} - \omega_{\mathbf{P}2,impact}\right) = \omega_{\mathbf{P}1,impact} = \frac{v_{\mathbf{C}1,impact}}{R} \tag{60}$$

which are identical to expressions (8) and (9) for the case of a central collision of balls, in which this applies only to the intensities of the outgoing angular velocities, but whose directions of traces are different and depend on the type of collision and the configuration of the incoming angular velocities of the balls in with respect to their tangent plane at the point of impact, tangent to both balls at their common point of contact in the collision configuration.

Intensity of vertical components $v_{T1,Rolling,outgoing}$ and $v_{T2,Rolling,outgoing}$ of the velocity of the point of impact on the spherical surface of the sphere after impact due to the rolling of the balls in a horizontal plane, for ideal elastic collision, are:

$$v_{T1,Rolling,outgoing} = v_{T1,Rolling,impact} - \frac{2}{1+\frac{\mathbf{J}_{P1}}{\mathbf{J}_{P2}}}\left(v_{T1,Rolling,impact} - v_{T2,Rolling,impact}\right) = v_{T2,Rolling,impact} \tag{61}$$

$$v_{T2,Rolling,outgoing} = v_{T2,Rolling,impact} + \frac{2}{1+\frac{\mathbf{J}_{P2}}{\mathbf{J}_{P1}}}\left(v_{T1,Rolling,impact} - v_{T2,Rolling,impact}\right) = v_{T1,Rollin,impactg} \tag{62}$$

For an oblique impact of a collision of two balls, we cannot use a vector relation to change the angular momentum of the motion of one or the other sphere-ball in rolling because these are moments of impulses for different axes directions, but we must go to scalars, since the moments of the impulse of motion for axes are scalars. So now, to change the angular momentum intensity of the rolling motion of the first rolling ball, from the kinetic state just before the collision to the kinetic rolling state of the first ball after the oblique collision and the angular momentum of the coupling momentum as a result of the interaction of the collision of the second ball with the first due to the oblique collision, we can write the forces:

$$\left|\vec{\mathfrak{L}}_{\mathfrak{M},12}\right| = \left|\vec{\mathfrak{L}}_1(t)\right| - \left|\vec{\mathfrak{L}}_1(0)\right| = \left|\int_0^t \vec{\mathfrak{M}}_{12}(t)dt\right| = \mathbf{J}_{\mathbf{P},1}\left[\left|\vec{\omega}_{\mathbf{P}1}(t)\right| - \left|\vec{\omega}_{\mathbf{P}1}(0)\right|\right]$$

$$\left|\vec{\mathfrak{L}}_{\mathfrak{M},12}\right| = \left|\vec{\mathfrak{L}}_1(t)\right| - \left|\vec{\mathfrak{L}}_1(0)\right| = \mathbf{J}_{\mathbf{P}1}\left[\left|\vec{\omega}_{P1,outgoing}\right| - \left|\vec{\omega}_{P1,impact}\right|\right] \tag{63}$$

$$\left|\vec{\mathfrak{L}}_{\mathfrak{M},12}\right| = \left|\vec{\mathfrak{L}}_1(t)\right| - \left|\vec{\mathfrak{L}}_1(0)\right| = \left|\int_0^t \vec{\mathfrak{M}}_{12}(t)dt\right| = \frac{\mathbf{J}_{\mathbf{P}1}}{R}\left(v_{\mathbf{T}1,outgoing} - v_{C1,impact}\right)$$

$$\left|\vec{\mathfrak{L}}_{\mathfrak{M},12}\right| = \left|\vec{\mathfrak{L}}_1(t)\right| - \left|\vec{\mathfrak{L}}_1(0)\right| = \frac{7}{5}MR\left(v_{C2,outgoing} - v_{C1,impact}\right) \tag{64}$$

Then, now, to change the angular momentum intensity of the motion of the second rolling ball, from the kinetic state just before the collision to the kinetic rolling state of the second ball after the oblique collision and the momentum coupling resulting from the interaction of the collision of the first ball with the second due to the oblique collision, we can write the forces as:

$$\left|\vec{\mathfrak{L}}_{\mathfrak{M},21}\right| = \left|\vec{\mathfrak{L}}_2(t)\right| - \left|\vec{\mathfrak{L}}_2(0)\right| = \left|\int_0^t \vec{\mathfrak{M}}_{21}(t)dt\right| = \mathbf{J}_{\mathbf{P},2}\left[\left|\vec{\omega}_{\mathbf{P}2}(t)\right| - \left|\vec{\omega}_{\mathbf{P}2}(0)\right|\right]$$

$$\left|\vec{\mathfrak{L}}_{\mathfrak{M},21}\right| = \left|\vec{\mathfrak{L}}_2(t)\right| - \left|\vec{\mathfrak{L}}_2(0)\right| = \mathbf{J}_{\mathbf{P}2}\left[\left|\vec{\omega}_{P2,outgoing}\right| - \left|\vec{\omega}_{P2,impact}\right|\right] \tag{65}$$

$$\left|\vec{\mathfrak{L}}_{\mathfrak{M},21}\right| = \left|\vec{\mathfrak{L}}_2(t)\right| - \left|\vec{\mathfrak{L}}_2(0)\right| = \left|\int_0^t \vec{\mathfrak{M}}_{21}(t)dt\right| = \frac{\mathbf{J}_{\mathbf{P}2}}{R}\left(v_{\mathbf{T}2,outgoing} - v_{C2,impact}\right)$$

$$\left|\vec{\mathfrak{L}}_{\mathfrak{M},21}\right| = \left|\vec{\mathfrak{L}}_2(t)\right| - \left|\vec{\mathfrak{L}}_2(0)\right| = \frac{7}{5}MR\left(v_{C1,outgoing} - v_{C2,impact}\right) \tag{66}$$

The sum of these changes is the angular momentum intensity of motion of the first and second balls by rolling from the kinetic state just before the oblique collision to the kinetic state of rolling the balls after the oblique collision relative to the kinetic state before the oblique collision is:

$$\left|\vec{\mathfrak{L}}_{\mathfrak{M},21}\right| - \left|\vec{\mathfrak{L}}_{\mathfrak{M},21}\right| = 0 \tag{67}$$

which gives *the condition of conservation of the sum of the angular momentum intensity of* the angular momentum of motion during the oblique collision of the balls in rolling, and which was introduced by hypothesis (3) in the first part of this paper:

$$\left|\vec{\mathfrak{L}}_{\mathfrak{M},1}(0)\right| + \left|\vec{\mathfrak{L}}_{\mathfrak{M},2}(0)\right| = \left|\vec{\mathfrak{L}}_{\mathfrak{M},1}(t)\right| + \left|\vec{\mathfrak{L}}_{\mathfrak{M},2}(t)\right| \tag{68}$$

$$\mathbf{J}_{\mathbf{P},1}\left|\vec{\omega}_{\mathbf{P}1}(0)\right| + \mathbf{J}_{\mathbf{P},2}\left|\vec{\omega}_{\mathbf{P}2}(0)\right| = -\left(\mathbf{J}_{\mathbf{P},1}\left|\vec{\omega}_{\mathbf{P}1}(t)\right| + \mathbf{J}_{\mathbf{P},2}\left|\vec{\omega}_{\mathbf{P}2}(t)\right|\right) \tag{69}$$

This means that the sum of the angular momentum magnitudes of the two balls rolling at the moment just before the ideally elastic oblique collision is equal to the sum of the angular momentum intensities of their motion immediately after the ideally elastic and central and oblique collision.

The kinetic energy of the system, consisting of the first and second balls, which roll to each other, in the kinetic state and moment just before the ideally elastic of their oblique collision, is:

$$\mathbf{E}_{Kin,impact} = \mathbf{E}_{1,Kin,impact} + \mathbf{E}_{2,Kin,impact} = \frac{1}{2}\left[\mathbf{J}_{\mathbf{P}1}\omega^2_{\mathbf{P}1,impact} + \mathbf{J}_{\mathbf{P}2}\omega^2_{\mathbf{P}2,impact}\right] \tag{70}$$

$$\mathbf{E}_{Kin,impact} = \frac{1}{2}\left[\mathbf{J}_{C1}\omega^2_{1impact} + M_1 v^2_{C1impact}\right] + \frac{1}{2}\left[\mathbf{J}_{C2}\omega^2_{2,impact} + M_2 v^2_{C2impact}\right]$$

$$\mathbf{E}_{Kin,impact} = \frac{M}{2}\left(\mathbf{i}^2_C + 1\right)\left(v^2_{C2,impact} + v^2_{C1,impact}\right) \tag{71}$$

where the coefficient $\kappa = \left(\mathbf{i}^2_C + 1\right) = \frac{7}{5}$ of rolling without sliding the balls along the track.

The kinetic energy of the system, consisting of first and second balls, which rolls away from each other, in the kinetic state and the moment immediately after their ideally elastic skew collision is:

$$\mathbf{E}_{Kin,outgoing} = \mathbf{E}_{1,Kin,outgoing} + \mathbf{E}_{1,Kin,outgoing} = \frac{1}{2}\left[\mathbf{J}_{\mathbf{P}1}\omega^2_{\mathbf{P}1,outgoing} + \mathbf{J}_{\mathbf{P}2}\omega^2_{\mathbf{P}2,outgoing}\right] \tag{72}$$

$$\mathbf{E}_{Kin,outgoing} = \frac{1}{2}\left[\mathbf{J}_{C1}\omega^2_{1,outgoing} + M_1 v^2_{C1outgoing}\right] + \frac{1}{2}\left[\mathbf{J}_{C2}\omega^2_{2,outgoing} + M_2 v^2_{C2outgoing}\right] \tag{73}$$

$$\mathbf{E}_{Kin,impact} = \frac{M}{2}\left(\mathbf{i}^2_C + 1\right)\left(v^2_{C2,impact} + v^2_{C1,impact}\right) \tag{74}$$

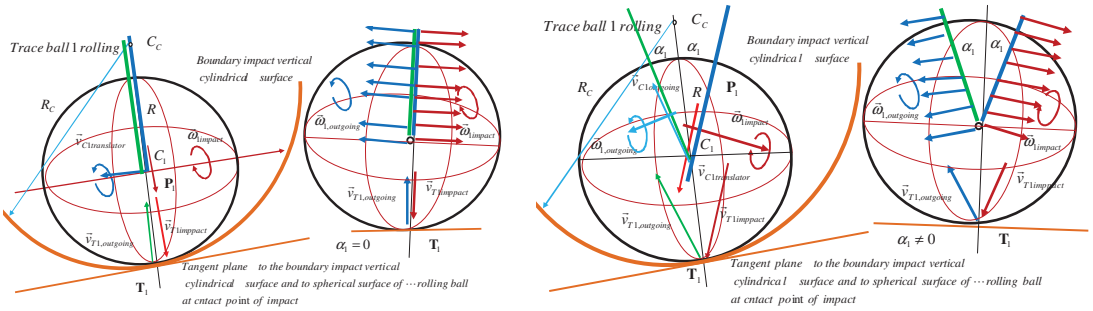

a* b*

Figure 19. Partial analogies between central and oblique collisions of a rolling ball into a cylindrical curvilinear surface with vertical derivatives: opening of the trace od a rolling ball for an oblique collision (b *) with respect to the central impact (a *)

So it is

$$\mathbf{E}_{Kin,outgoing} = \mathbf{E}_{Kin,impact}$$

$$\mathbf{E}_{1,Kin,outgoing} + \mathbf{E}_{2,Kin,outgoing} = \mathbf{E}_{1,Kin,impact} + \mathbf{E}_{2,Kin,impact} \tag{75}$$

and that *there is no loss of kinetic energy* in an *obliquely elastic collision of two equal balls.*

In Fig. 19 shows the configuration of the ball and the plan of incoming and outgoing velocities of translation of the point of impact and angular velocities of rolling with incoming and outgoing rolling paths for different cases of impact of the ball into fixed cylindrical concave or convex surfaces, and for cases of central and oblique-skew collisions respectively.

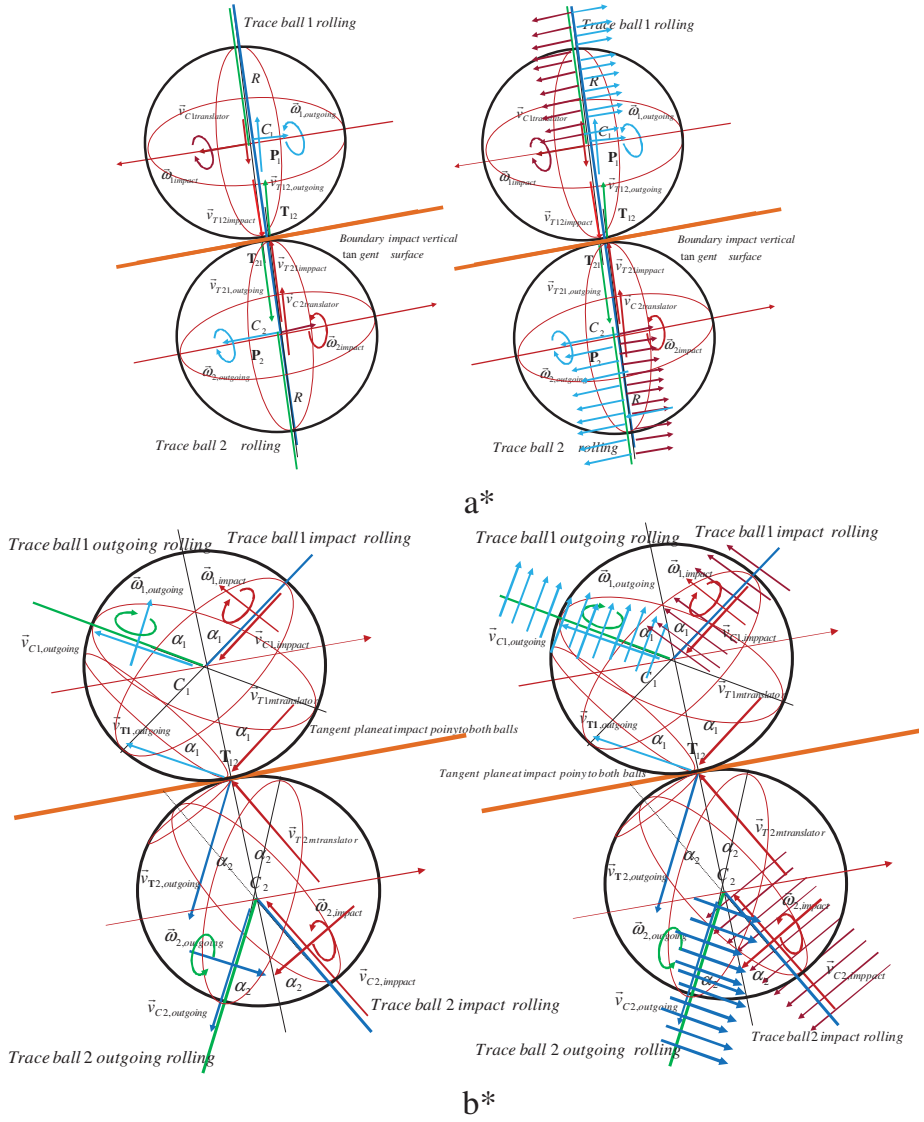

Figure 20. Partial analogies between the central and oblique collisions of two rolling balls: the opening of the traces of ball rolling in oblique (skew) collision (b *) with respect to the central collision of the balls (a *).

In the Figure 20 shows the configuration of two balls with corresponding plans of the incoming and outgoing translation velocities of the point of their contact and angular rolling velocities with incoming and outgoing rolling paths for different cases of mutual collision of these balls, and for cases of centric central as well as oblique collisions.

In this, as in the previous cases of different types of ball collision configurations, when ideally elastic collisions occur, there is no loss of kinetic energy, and the expressions for kinetic energy before and after collision will not be cited because they are identical to the terms written in the previous first section.

6 CONCLUDING CONSIDERATIONS

Using the analysis of the elements of geometry, kinematics and dynamics of impact (see Figure 19) and collision of balls (see Figure 20), which we have given in the previous parts of this paper, it is possible to draw some conclusions and generalizations.

Here we can imagine that the route-traces of rolling both balls, by which the balls are rolling "*corrected*" into straight lines and that each ball is rolling along the corresponding "*corrected straight route*" until the configuration is impact by an appropriate incoming angular velocity, and from the configuration of the collision by the outgoing angular velocities along *"broken traces with break",* as if a central collision had occurred, but we should take into account that at the point of collision on the route "a fracture" of the route occurs and that the angular velocity discontinuity occurs with the alternations of the angular velocity direction and orientation. The same goes for the other ball. This practically means that there is *a jump in the intensity of the angular velocity of rolling in the kinetic state of the collision*, and that the "*breaking*" *of the rolling path changes and the direction of the instantaneous angular velocity of the roll-out after the collision changes*. The "fracture of the rolling path" depends on the angle at which the rolling path comes from the normal tangent plane to the balls at the point of impact.

This consideration returns us to the central collision of two balls. So the task comes down to a central collision of two balls from which to determine the intensities of the translational outgoing velocities and the outgoing angular velocities of rolling about the current axis, or around it parallel to its own central axis of each of the balls, and then the "*track legs expand*" as corner angles with the apex in the point of collision configuration and set at angles with respect to the normal of the tangent plane at the collision-contact points of the rolling traces of the balls, depending on the angles that the incoming balls rolling paths close to that normal. This leads us to the conclusion that it is, also, possible to use a central collision to determine the intensities of the angular velocity of rolling and to change the angular momentum of motion, and in the case of oblique collision of rolling balls of different radii and masses, and to use appropriate analogies. It should be emphasized that it is necessary to determine the outgoing rolling routes after a collision taking into account the incoming routes.

In the dynamics of billiards, there is a simultaneous collision of several balls, so the problem of determining the directions of the components of the outgoing velocities after the collision is not difficult to determine, but even today the question of determining the intensity of the individual components of the outgoing angular velocities of rolling formed in the collision of several balls is open.

Acknowledgement. Parts of this research were supported by the Ministry of Education, Sciences and Technology of Republic Serbia trough Mathematical Institute SANU Belgrade Grants OI 174001" Dynamics of hybrid systems with complex structures. Mechanics of materials", and Faculty of Mechanical Engineering University of Niš.

REFERENCES

[1] Coriolis G., (1990). *Théorie mathématique des effets du jeu de billard ; suivi des deux celebres memoires publiés en 1832 et 1835 dans le* Journal de l'École Polytechnique*: Sur le principe des forces vives dans les mouvements relatifs des machines & Sur les équations du mouvement*

relatif des systèmes de corps (Originally published by Carilian-Goeury, 1835 ed.). Éditions Jacques Gabay. ISBN 2-87647-081-0.

[2] Coriolis G., (1832). "Sur le principe des forces vives dans les mouvements relatifs des machines". *J. De l'Ecole royale polytechnique* **13**: 268–302.

[3] Coriolis G., (1835). "Sur les équations du mouvement relatif des systèmes de corps". *J. De l'Ecole royale polytechnique* **15**: 144–154.\

[4] Hedrih (Stevanović) KR., (2019), Rolling heavy ball over the sphere in real Rn3 space, Nonlinear Dynamics, Springer, (2019) 97:63–82, https://doi.org/10.1007/s11071-019-04947-1. ISSN: 0924-090X (print version) ISSN: 1573-269X (electronic version)

[5] Hedrih (Stevanović) K.R, (2019**),** Vibro-impact dynamics of two rolling heavy thin disks along rotate curvilinear line and energy analysis, **Journal** Nonlinear Dynamics, 98(4), 2551-2579, **DOI** 10.1007/s11071-019-04988-6; Springer; ISSN: 0924-090X (print version) ISSN: 1573-269X (electronic version); http://link.springer.com/article/10.1007/s11071-019-04988-6;

[6] Hedrih (Stevanović) KR., (2018**),** Non-linear phenomena in vibro-impact dynamics: Central collision and energy jumps between two rolling bodies, Dedicated to memory of Professor and important scientist Ali Nayfeh (December 21, 1933-March 27, 2017). **Nonlinear Dynamics,** February 2018, Volume 91, Issue 3, pp 1885–1907. https://doi.org/10.1007/s11071-017-3988-x. ISSN: 0924-090X (print version) ISSN: 1573-269X (electronic version)

https://link.springer.com/article/10.1007/s11071-017-3988-x
http://www.springer.com/engineering/mechanics/journal/11071?detailsPage=pltci_1888917

[7] Hedrih (Stevanović) KR., (2017), Central collision of two rolling balls: theory and examples, Advances in Theoretical and Applied Mechanics, Vol. 10, 2017, no. 1, 33-79. https://doi.org/10.12988/atam.2017.765.

[8] .Hedrih (Stevanović) KR.,(2017), Dynamics of Impacts and Collisions of the Rolling Balls, Dynamical Systems: Theoretical and Experimental Analysis, Springer Proceedings in Mathematics & Statistics, Volume Number: 182, Chapter 13, pp. 157-168. © Springer, Part of Springer Science+Business , ISBN 978-3-319-42407-1. ISSN 2194-1009 ISSN 2194-1017 (electronic).

[9] Dragović V. and Radnović M., (2010), Integriruemie biliardi, kvadriki i mnogomernie porizmi Pomsele ; Miskva Iževsl, 2010, str. 336.

[10] Козлов ВВ., Трєв ДВ., Билиардì-Генетическое ббедение динамику систем с ударами, Издателство Московского университета, 1991. Москва, стр. 192.

[11] Hedrih (Stevanović) KR., Jović S., *„Energy of the vibro-impact systems with Coulomb's type frictions"*, ESMC Lisbon 2009 Minisymosium MS-24 Kinetics, Control and Vibrorheology KINCONVIB-2009, 7-11 Septembar 2009. pp. 43-47.

[12] Hedrih (Stevanović) KR., Jović S., *„Energy of the vibroimpact system dynamics: Heavy material particle oscillations along rough circle with one side impact limit"*, 6-th IFAC INTERNATIONAL WORKSHOP on Knowledge and technology transfer in/to developing countries: automation and infrastructure, Hotel Metropol Resort, Ohrid Republic of Macedonia, Septembar 26-29, 2009 (is uploaded to the DECOM-TT 2009 web site with ID number D65).

[13] Hedrih (Stevanović) KR., Jović S., *„Vibroimpact system dynamics: Heavy material particle oscillations along rough circle with one side impact limit"* , 10th Conference

on Dynamical systems- theory and applications (DSTA) Lodz, Decembar 7-10, 2009 Poland. Procedings Volume 1, pp.213-220

[14] Hedrih (Stevanović) KR., Jović S., *Models of Technological Processes on the Basis of Vibro-impact Dynamics*, Scientific Technical Review, Vol.LIX,No.2,2009, pp.51-72, M52=1,5 boda.

[15] Hedrih (Stevanović) KR., Raičević V. and Jović S., Phase Trajectory Portrait of the Vibro-impact Forced Dynamics of Two Heavy Mass Particles Motions along Rough Circle, Communications in Nonlinear Science and Numerical Simulations, 2011 16 (12):4745-4755, DOI 10.1016/j.cnsns.2011.05.027. ISSN: 1007-5704

EURODYN 2020
XI International Conference on Structural Dynamics
M. Papadrakakis, M. Fragiadakis, C. Papadimitriou (eds.)
Athens, Greece, 23–26 November 2020

THE EFFECT OF BUILDING'S RESPONSE ON THE FRAGILITY OF FREESTANDING SYMMETRIC OR ASYMMETRIC CONTENTS

S. Diamantopoulos, and M. Fragiadakis

School of Civil Engineering, National Technical University of Athens
9 Iroon Polytechniou, 15780, Athens, Greece
e-mail: sdiamadop@central.ntua.gr; mfrag@mail.ntua.gr

Keywords: Building contents, RC building, Fragility assessment, Asymmetric rigid blocks.

Abstract. *The seismic response of freestanding building contents that are hosted in different stories of a structure has not received yet the appropriate attention in the literature, despite the fact that the possible damage of the contents may result to excessive losses. Considering that valuable objects, e.g. artefacts, hospital equipment, computer servers, among others, are hosted in multistorey buildings and are freestanding on a rigid base, there is urgent need for seismic fragility and risk assessment methods in order to prioritize seismic protection measures. The paper discusses, a performance-based fragility assessment framework using either acceleration or velocity-based demand parameters. The structure's capacity is assessed using the Multiple Stripe Analysis (MSA) method. The fragility curves of the building contents are obtained using appropriate Engineering Demand Parameters (EDPs) and Intensity Measures (IMs) for the problem at hand. The paper aims to shed light on the fragility assessment of freestanding rigid blocks investigating how the behavior of the structure affects the block's response. A second goal is the comparison of the seismic response of symmetric and asymmetric freestanding contents hosted in a multistorey shear RC building.*

1 INTRODUCTION

Earthquake losses may be due to structural damage, damage of non-structural components and also due to the damage of the structure's contents. Recent guidelines, e.g. FEMA P-58 [1], FEMA E-74 [2], ATC-120 [3], address the problem of the seismic response of building contents, acknowledging that the losses are comparable, or may exceed, those of structural damage. Non-structural damage can be due to damage of components attached, or anchored, to the hosting building, or due to damage on the freestanding inventory of the building. In the latter case, there is a huge variability of systems and configurations hampering the systematic study of the problem and the recommendation of generally-applicable guidelines. The risk assessment of building contents is a complicated task since the response of the contents depends also on the behaviour of the hosting structure. As a result, there may be cases where a strong earthquake does not overturn an object but strongly damages the structure, while more benign ground motions may leave the structure intact causing losses due to damage on the building's contents. The paper focuses on the seismic performance, fragility and risk assessment of freestanding building contents that can be assumed rigid and are either symmetric or asymmetric. Freestanding building contents are usually treated as rocking rigid blocks and thus are modelled using Housner's theory [4]. The Multiple Stripe Analysis (MSA) method is adopted in order to assess the structure and its contents considering that the structural collapse implies also collapse/overturning of the contents. The latter observation was first implemented and discussed in detail by Fragiadakis and Diamantopoulos [5] by only for symmetric rectangular blocks. A second point of interest is the derivation of fragility curves and the calculation of the Mean Annual Frequency (MAF) of the rocking building contents.

Despite the significance of the problem at hand, there are relatively few past studies on the seismic response assessment of freestanding contents. Recent research examines, for example, the seismic behaviour of artefacts or hospital equipment. Spyrakos *et al.* [6] proposed predictive models for artefacts assuming that they form systems of one, or two, rocking blocks, while Di Sarno *et al.* [7] performed shake table tests on hospital equipment. In this direction, Wittich and Hutchinson [8, 9] studied the seismic response of human-formed artefacts that are either standing on a pedestal [8] or are asymmetric [9]. Both configurations are common for freestanding building contents and therefore the numerical tools developed are quite useful for their seismic performance assessment.

One of the first studies that focus on the fragility of rocking systems is the work of Purvance *et al.* [10]. They showed that objects with multiple rocking points are more fragile than predicted. Konstantinidis and Makris [11] studied the seismic response of laboratory equipment using analytical solutions and experimental results, while Konstantinidis and Nikfar [12] studied the sliding motion of stocky freestanding equipment and contents located at base-isolated buildings. Dimitrakopoulos and Paraskeya [13] proposed dimensionless fragility curves for the rocking response of rectangular blocks under near-fault excitations of their base. Their work was the first that proposed dimensionless Intensity Measures (IMs) for rocking blocks, while Giouvanidis *et al.* [14] discussed the fragility assessment of rocking frames. Petrone *et al.* [15] focused on the efficiency of different intensity measures in predicting the damage states of the rigid block, while alternative intensity measures for rocking systems were also investigated by Pappas *et al.* [16] and Kavvadias *et al.* [17]. Furthermore, Fragiadakis and Diamantopoulos [5] examined the fragility assessment of building contents that are hosted in a four-storey RC building proposing an early-stage risk framework for non-anchored contents. The main interest of the paper focuses on the probabilistic response assessment of the contents without neglecting

the structure's response. Some years earlier Fragiadakis *et al.* [18] and Fragiadakis and Diamantopoulos [19] had presented preliminary results on handling building contents assuming either elastic response of the structure or omitting the effect of structure's collapse on the fragility assessment. Recently, Fragiadakis *et al.* [20] completed an extensive experimental campaign on the seismic response of artefacts, with emphasis on statues and busts, which are asymmetric, Vlachos *et al.* [21] proposed compact solutions for handling asymmetric museum exhibits that are freestanding on a pedestal and Masi *et al.* [22] examined the resistance of museum artefacts against blast loading.

The paper presents a performance-based seismic fragility and risk assessment framework for freestanding building contents which has been discussed in Fragiadakis and Diamantopoulos [5] for symmetric rectangular blocks only. An extension of the methodology in case of asymmetric building contents is presented here concerning blocks whose distance of the center of mass is different from the two pivot points. Contrary to previous works on the seismic fragility assessment of rocking contents, the proposed methodology discusses how the response of the hosting building and that of the contents are coupled and also the effect of different stories. In order to consistently study the effect of increasing seismic intensity in a performance-based setting, a modified version of the Multiple Stripe Analysis method is adopted. It is shown that the EDP that should "drive" the MSA simulations is that of the building rather than that of the contents and also that the collapse of the building should not be neglected. Moreover, the calculation of fragility and risk are discussed. Existing fragility assessment methodologies are adopted showing that the IM of the building should be adopted (instead of that of the contents), while a procedure that uses the total probability theorem in order to calculate the MAFs combining fragilities that were separately generated for the structure and for the contents is investigated. Overall it is shown that the problem is not as simple, as it may initially seem, and that various tools should be appropriately combined in order to accurate and efficiently calculate the risk of freestanding contents. Essentially, the paper is based on the work of Fragiadakis and Diamantopoulos [5] extending the fragility and risk assessment of symmetric building contents to the planar investigation of non-symmetric cases, which is usual for museum artefacts.

2 THE DYNAMICS OF A ROCKING BLOCK

2.1 Symmetric freestanding rocking block

In order to study the seismic response of freestanding building contents that are subjected to an earthquake ground motion, it is firstly assumed that the bodies are orthogonal (i.e. symmetric) rocking blocks. Following the pioneering work of Housner [4], the problem of rocking and overturning of freestanding blocks has been the subject of intense analytical and experimental research. Despite its apparent simplicity, the rocking problem has been proven difficult, since the blocks behave nonlinearly and also due to the occurrence of many impacts between the rocking bodies and their base. Previous studies have revealed the complex response, including certain counter-intuitive trends [23]. Planar models are adopted in this work. This is an often made approximation, which may leads to unconservative results when applied to three-dimensional objects. Nevertheless, the two-dimensional, planar modelling, which is adopted here, offers some simplicity and was found adequate for the purpose of this work.

The fundamentals of rocking theory are briefly summarized in order to allow studying the seismic behaviour of freestanding rocking blocks and also the transition to the asymmetric case to be straightforward for the reader. Figure 1a shows a rigid block of dimensions $2b \times 2h$ that oscillates about point O (or O'). The block has weight W and moment of inertia I_0 about point

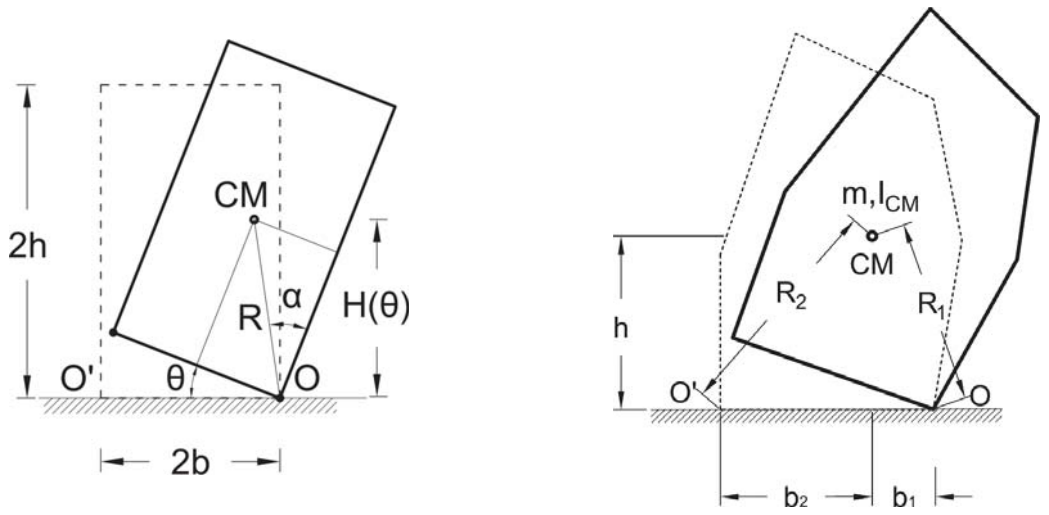

(a) (b)

Figure 1: Geometry of: (a) the symmetric rocking block and (b) the asymmetric rocking block.

O. Assuming that the block is homogeneous and thus the center of gravity is located at height h, the block's slenderness angle is equal to $\alpha = atan(b/h)$. The slenderness angle α together with the size parameter $R = \sqrt{b^2 + h^2}$ define fully the geometry of the block. Consequently, the equation of motion of the rocking block as first proposed by Housner[4] is:

$$I_o\ddot{\theta}(t) + mgR\sin\left[\alpha\text{sgn}\theta(t) - \theta(t)\right] = -m\ddot{u}_g(t)\,R\cos\left[\alpha\text{sgn}\theta(t) - \theta(t)\right] \tag{1}$$

where the rotation θ is the only degree of freedom. The sign function is used to define the pivot point (O or O'), i.e. when O' is the pivot point, the angle θ is negative. The fact that the equation of motion changes when the rotation changes sign makes the behaviour of the system nonlinear. For rectangular blocks, the moment of inertia is $I_0 = (4/3)mR^2$ and Eq. 1 can be written:

$$\ddot{\theta}(t) = p^2\left[-\sin\left(\alpha\,\text{sgn}\left(\theta(t)\right) - \theta(t)\right) - \frac{\ddot{u}_g(t)}{g}\cos\left(\alpha\,\text{sgn}\left(\theta(t)\right) - \theta(t)\right)\right] \tag{2}$$

where p denotes the characteristic frequency parameter of the rocking block, defined as:

$$p = \sqrt{\frac{WR}{I_0}} = \sqrt{\frac{3g}{4R}} \tag{3}$$

Following Figure 1a, in the static case, when $\theta \geq \alpha$ the block will overturn since the self-weight becomes an overturning force instead of a restoring force. Under dynamic loading, this is not strictly true since there may be cases where the block does not overturn for θ/α values that slightly exceed one. Therefore, the rotation is normalized with the slenderness angle in order to obtain the metric θ/α that provides an estimate of how close to overturning is the block. Moreover, when the block is at rest ($\theta = 0$), omitting the inertia term in Eq. 1, we find that it will start rocking motion if the ground acceleration $\ddot{u}_g$ exceeds a threshold value, i.e. when:

$$|\ddot{u}_g| \geq (b/h)g \Leftrightarrow |\ddot{u}_g| \geq g\tan\alpha \tag{4}$$

On the other hand, a body will slide if the seismic force $F_{eq} = m\ddot{u}_g$ exceeds the static friction:

$$F_{eq} \geq \mu_{st}W \Leftrightarrow |\ddot{u}_g| \geq \mu_{st}g \tag{5}$$

where μ_{st} is the static coefficient of friction. Therefore, the inequality of Eq. 5 implies that typically an acceleration above $0.60g$ is required for sliding to occur if the $\mu_{st} = 0.60$. Comparing Eq. 4 with Eq. 5, sliding will precede rocking only if $tan\alpha$ is less than μ_{st}. This is possible for small friction conditions, or for stocky blocks, i.e. for small μ_{st} or for large $tan\alpha$ values. When neither conditions of Eq. 4 or Eq. 5 are met, the body will remain at rest in its initial position. Assuming that μ_{st} are large and that the buildings contents considered here are slender, the effect of sliding is omitted. Therefore, the freestanding building contents are examined considering that their response concerns pure rocking motion.

The seismic response assessment of rocking structures is a complicated task. Various alternative ways to model and solve rocking systems that are subjected to real ground motion records are discussed in Diamantopoulos and Fragiadakis[24]. Furthermore, damping is event-based, meaning that energy is lost only when the angle of rotation θ reverses, indicating an impact of the block at a non-deformable base. The conservation of angular momentum just before and right after each impact defines the coefficient of restitution η, which is calculated with the formula proposed by Housner[4]:

$$\eta = \frac{\dot{\theta}_2}{\dot{\theta}_1} = 1 - \frac{3}{2}\sin^2\alpha \tag{6}$$

where $\dot{\theta}_1$ and $\dot{\theta}_2$ are the angular velocities before and after the impact, respectively.

2.2 Asymmetric freestanding rocking block

Considering the dynamics of a symmetric freestanding block, that have been discussed in the previous subsection, the extension of the theory to asymmetric cases is presented here. Thus, the asymmetric rocking block of Figure 1b is assumed. The block's width is $b = b_1 + b_2$, the center's of mass height is h while the total mass and the rotational moment of inertia with respect to the center of mass are m and I_{CM}, respectively.

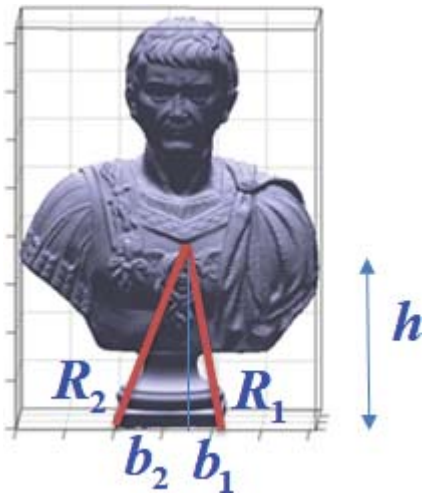

Figure 2: Implementation of the asymmetric rocking block theory to a freestanding bust.

.

The rocking motion of an asymmetric rocking block (e.g. the bust of Fig. 2), that can be assumed as rigid, is described by a modified equation of motion that has been introduced by

Wittich and Hutchinson [9]:

$$\left(I_{CM}+mR_i^2\right)\ddot{\theta}\left(t\right)+mgR_i\sin\left[\alpha_i\text{sgn}\theta\left(t\right)-\theta\left(t\right)\right]=-m\ddot{u}_g\left(t\right)R_i\cos\left[\alpha_i\text{sgn}\theta\left(t\right)-\theta\left(t\right)\right] \tag{7}$$

where the subscript i denotes the positive or negative rotation of the block and $sgn(\theta)$ is the signum function that corresponds to rocking motion with respect to the critical or the noncritical side. It is assumed that $i=1$ when the block rotates with respect to O and $i=2$ when the pivot point is the O'.

When an impact occurs, the kinetic energy is reduced and this reduction is derived through conservation of momentum with reference to the rocking point immediately before and just after the impact. This yields to a velocity ratio, known as the coefficient of restitution, which for the rigid block of interest is given by the following formulas for the positive to negative rotation (η^{+-}) and the negative to positive transition (η^{-+}), respectively:

$$\eta^{+-}=\frac{1}{I_{CM}+mR_1^2}\left[I_{CM}+mR_2^2-m(b_1+b_2)R_2sin\alpha_2\right] \tag{8}$$

$$\eta^{-+}=\frac{1}{I_{CM}+mR_2^2}\left[I_{CM}+mR_1^2-m(b_1+b_2)R_1sin\alpha_1\right] \tag{9}$$

3 FRAGILITY AND RISK ASSESSMENT

3.1 Fragility analysis

The seismic risk assessment of building contents requires the prior knowledge of the fragility of both the building and the contents. For building contents, the fragility provides the probability of overturning as a function of the seismic excitation (i.e. seismic intensity). Past research on fragility assessment focuses on the risk assessment of the structure itself [25], while the contents are examined separately and, usually, neglecting the effect of the hosting structure. Usually, fragility curves of building contents are empirical and are targeted to specific component types (e.g. cladding panels, masonry parapets). The direct fragility calculation that is here adopted through simulations allows to consider additional sources of uncertainty (e.g. related to the shape of the object, its mass distribution) and has been discussed in detail by Fragiadakis and Diamantopoulos [5]. A brief summary of the methodology is presented in the lines below.

The fragility function is the conditional limit-state exceedance probability, given by the expression:

$$F_R=P(EDP>edp|IM) \tag{10}$$

The structure is first examined. There will be simulations that the building collapses (denoted as "C") and simulations where no collapse occurs (denoted as "NC"). Making this separation and dropping the conditioning term in order to simplify the notation, i.e.: $P(EDP)=P(EDP>edp|IM)$, the probability of Eq. 10 is calculated using the total probability theorem (TPT):

$$F_R^{(s)}=P(EDP^{(s)}|NC)(1-P_C)+P_C \tag{11}$$

Focusing on the rocking body, when an object is subjected to a seismic ground motion there are three possible types of response: (i) the object may not rock and remain at rest, (ii) it may rock, or (iii) it may overturn. Using the TPT for the block, the fragility function becomes:

$$F_R^{(b)}=P(EDP^{(b)}|NoRock)P_{NoRock}+P(EDP^{(b)}|Rocking)P_{Rocking}+P(EDP^{(b)}|Ovtn)P_{Ovtn} \tag{12}$$

where $P(EDP^{(b)}|NoRock)$, $P(EDP^{(b)}|Rocking)$ and $P(EDP^{(b)}|Ovtn)$ are the probabilities that $EDP^{(b)} = \theta/\alpha$ exceeds a threshold value $edp^{(b)}$ and P_{NoRock}, $P_{Rocking}$ and P_{Ovtn} are the corresponding probabilities of no rocking, rocking and overturning, respectively. The superscripts "s" and "b" are used in order to distinguish the quantities that refer to the structure and the block, respectively. Blocks that will not rock, will not exceed any $edp^{(b)}$ value and thus $P(EDP|NoRock) = 0$, while the overturning blocks always exceed the limit-state threshold and consequently $P(EDP|Ovtn) = 1$. The conditional limit-state probability (fragility) is further simplified to:

$$F_R^{(b)} = P(EDP^{(b)} \geq edp|Rocking)(1 - P_{Ovtn} - P_{NoRock}) + P_{Ovtn} \tag{13}$$

The calculation of Eq. 13 is discussed in the sections that follow. A fundamental assumption of our derivation is that: "the simulations that collapse the building also overturn/collapse the freestanding contents".

3.2 Risk assessment

The risk is expressed as the mean annual frequency (MAF) of a limit-state being exceeded. Adopting the PEER's formula, the limit-state MAF for the structure and for a rigid block are calculated with the aid of the following expressions:

$$\lambda_{EDP}^{(s)} = \int_{IM^{(s)}} P(EDP^{(s)}|IM^{(s)}) \, |d\lambda_{IM^{(s)}}| \tag{14}$$

$$\lambda_{EDP}^{(b)} = \int_{IM^{(b)}} P(EDP^{(b)}|IM^{(b)}) \, |d\lambda_{IM^{(b)}}| \tag{15}$$

where $\lambda_{EDP}^{(s)}$, $\lambda_{EDP}^{(b)}$ is the mean annual frequency of the engineering demand parameter ($EDP^{(s)}$ or $EDP^{(b)}$) exceeding threshold level and $d\lambda_{IM}^{(s)}$, $d\lambda_{IM}^{(b)}$ is the slope of the seismic hazard curve. The limit-state MAFs are easily obtained convolving the site hazard curve, expressed as function of the IM, with the fragility curve obtained with respect to the EDP of interest. For the structure, the IM of interest is always available, e.g. spectral acceleration $S_a(T_1, 5\%)$, but for the block this information is available only at the ground floor. For assets located at a storey, the calculation of $d\lambda_{IM}^{(b)}$ has no meaning and thus their fragility should be calculated as function of $IM^{(s)}$ instead of $IM^{(b)}$:

$$\lambda_{EDP}^{(b)} = \int_{IM^{(s)}} P(EDP^{(b)}|IM^{(s)}) \, |d\lambda_{IM}| \tag{16}$$

Conditioning the block's fragility to $IM^{(s)}$, i.e. using Eq. 16 instead of Eq. 15, is also conceptually preferable since the MAF is directly calculated from the site's hazard. The superscript "s" has been dropped from $d\lambda_{IM^{(s)}}$, since $d\lambda_{IM}$ always refers to the site and thus the structure.

A simplified and more generic methodology for the seismic risk of structure's contents is possible if we apply the TPT, using the block's intensity measure $IM^{(b)}$ as an intermediate variable. This allows to expand Eq. 16 and obtain the MAF using the expression:

$$\lambda_{EDP}^{(b)} = \int_{IM^{(s)}} \int_{IM^{(b)}} P(EDP^{(b)}|IM^{(b)}) \, dP(IM^{(b)}|IM^{(s)}) \, |d\lambda_{IM}| \tag{17}$$

where $P(IM^{(b)}|IM^{(s)}) = P(EDP^{(s)}|IM^{(s)})$ is the building's fragility curve. Eq. 17 can be used in order to calculate separately the fragilities using Eqs. 14 and 15, thus bypassing the need for performing building simulations and storing the response acceleration histories for the stories of interest. This approach has been examined by Fragiadakis and Diamantopoulos [5] and is not adopted in the current work.

4 MULTIPLE STRIPE ANALYSIS

The Multiple Stripe Analysis (MSA) method can be used for calculating the limit-state fragilities for both the structure and its contents. Multiple Stripe Analysis (MSA) method [26, 27] has conceptual similarities to the IDA method. In MSA instead of scaling separately all ground motions, every record is scaled to the same IM level. IDA involves subjecting the structure, or the block, to a suite of ground motion records, each scaled to multiple levels of intensity. After incrementally scaling every ground motion, single record capacity curves are produced in terms of demand versus seismic intensity [5].

Since for every scaling level the ground motions have the same IM value, the EDP values form a "stripe" which allows to directly calculate the median (50% percentile) and the 16% and 84% percentile capacity curves conditional on the IM. In IDA the scaling factors will be different, but stripped data can be easily obtained with interpolation. Below we first discuss how the MSA method is applied for the cascading problem at hand. We first examine the structure and in the subsection that follows we discuss how the fragilities of the freestanding contents are obtained from the floor response histories.

The four-storey RC building (Fig. 3), that adopted in Fragiadakis and Diamantopoulos [5], is also considered here. For the building every MSA curve can be plotted in the EDP-IM plane. The median curve (50% percentile) provides an estimate of the expected value and the fractile curves can be used to measure the dispersion as it is discussed in Vamvatsikos and Fragiadakis[28]. The MSA capacity curves plot the $S_a(T, 5\%)$ vs the $EDP^{(s)}$ [5]. In the most common form of MSA $EDP^{(s)}$ is the maximum interstorey drift ratio. However, a different EDP has to be adopted for studying building contents. The $EDP^{(s)}$ is either the normalised peak floor acceleration (PFA), or the peak floor velocity (PFV). Summarizing the data to EDP-IM plots [5] allow to directly calculate $P(EDP_j^{(s)}|NC)$ and P_C (Eq. 11) for every IM stripe. If the $EDP_j^{(s)}$ values are lognormally distributed, the buildings fragility for the j^{th} storey is calculated as follows:

$$P(EDP^{(s)} \geq edp^{(s)}) = 1 - P(EDP^{(s)} < edp^{(s)}) = \Phi\left(\frac{\mu_{logEDP} - edp^{(s)}}{\sigma_{logEDP}}\right) \tag{18}$$

where μ_{logEDP} and σ_{logEDP} are the mean and the standard deviation of the logarithm of the demand, always conditional on the $IM^{(s)}$. Regardless the IM, the fragility of the building should be obtained combing Eq. 18 with Eq. 11:

$$F_R^{(s)} = \Phi\left(\frac{\mu_{logEDP} - edp^{(s)}}{\sigma_{logEDP}}\right)(1 - P_C) + P_C \tag{19}$$

where P_C is the percentage of collapsed simulations. Obviously different fragilities will be obtained depending on the EDP of interest.

A very efficient alternative for calculating the fragilities using MSA, is to fit the CDF (cumulative distribution function) of a lognormal distribution on the striped EDP-IM data as discussed by Baker [27]. The fragility function can be simply seen as the lognormal CDF:

$$F_R^{(s)} = P(EDP^{(s)} \geq edp) = \Phi\left(\frac{log(EDP^{(s)}/\theta_a)}{\beta_a}\right) \tag{20}$$

where θ_a and β_a are the parameters that we need to determine. θ_a is the "median" of the fragility function, i.e. the IM value corresponding to limit-state probability equal to 0.5 and β_a is the

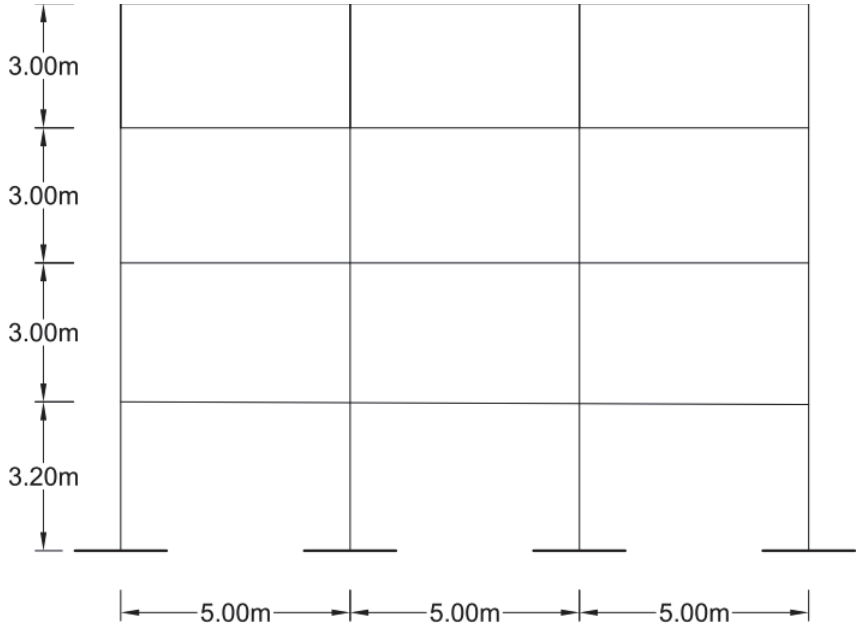

Figure 3: Four storey RC building.

dispersion (standard deviation of $\log(IM)$). The values of θ_a and β_a are obtained from the whole data using a Maximum Likelihood Estimation (MLE) approach [27] that is briefly summarized in the lines below. Eq. 20 should not be confused with Eq. 19; the latter concerns a single stripe and thus provides a single point of the fragility curve, while the former is the lognormal CDF that represents the whole fragility curve.

MSA provides at discrete IM levels (stripes), the number of successes n_{suc}, i.e. the number of simulations that the limit-state has been exceeded after n_{tot} simulations. Using the binomial distribution on the data of a single stripe, the probability of having exactly n_{suc} successes after n_{tot} simulations, will be:

$$P(Success = n_{suc}) = \left(\begin{array}{c} n_{tot} \\ n_{suc} \end{array} \right) P(EDP^{(s)})^{n_{suc}} (1 - P(EDP^{(s)}))^{n_{tot} - n_{suc}} \tag{21}$$

If there are k stripes, substituting Eq. 20 to Eq. 21, we obtain the MLE function as:

$$\mathcal{L} = \prod_{i=1}^{k} \left(\begin{array}{c} n_{tot,i} \\ n_{suc,i} \end{array} \right) \Phi \left(\frac{log(EDP^{(s)}/\theta_a)}{\beta_a} \right)^{n_{suc,i}} \left(1 - \Phi \frac{log(EDP^{(s)}/\theta_a)}{\beta_a} \right)^{n_{tot,i} - n_{suc,i}} \tag{22}$$

The only unknowns are θ_a and β_a which are found as the values that maximise the likelihood function $\mathcal{L}$ of Eq. 21, or preferably its natural logarithm. This can be achieved easily with a spreadsheet or with a simple computer script. The MLE approach uses the whole EDP-IM data of the stripe and thus it is not necessary to separate them according to Eq. 12. This approach produces always smooth fragility curves.

Figure 4 shows the EDP-IM plots of a freestanding block with $R = 1.0m$ and $\alpha = 0.2$. The hosting structure was subjected to the MSA simulations as it has been discussed in Fragiadakis and Diamantopoulos [5] and then the simulations are transferred to the $EDP^{(b)} - IM^{(b)}$ (Fig. 4a), or the $EDP^{(b)} - IM^{(s)}$ plane (Fig. 4b). In both plots the collapsed simulations appear as dots just right to the vertical line at $EDP^{(b)} = 1$. The dots below the horizontal line at

$IM^{(b)} = 1$ (Fig. 4a) correspond to the no rocking simulations. As already discussed in Section 3.1, the $EDP^{(b)} - IM^{(b)}$ is the natural EDP-IM representation, but is not the easiest choice when it comes to the calculation of MAF $\lambda_{EDP}^{(b)}$. Moreover, as shown in Figure 4a, the data in the $EDP^{(b)} - IM^{(b)}$ form a cloud, while if they are plotted in the $EDP^{(b)} - IM^{(s)}$ plane they are already conditional on the $IM^{(s)}$.

Both EDP-IM representations allow to calculate the fragility of the blocks, but with respect to a different IM. Defining the fragility conditional on the IM of the structure, i.e. $F_R^{(b)} = P(EDP^{(b)}|IM^{(s)})$ can be used for directly calculating the MAF using Eq. 16. On the other hand, the intuitive definition $F_R^{(b)} = P(EDP^{(b)}|IM^{(b)})$ provides the storey fragilities with respect to the block's IM and for the storey of interest. Another major difference is that when $IM^{(b)}$ is adopted, the EDP-IM data appear as a "cloud" (Fig. 4a), while when $IM^{(s)}$ is adopted instead, they appear in stripes (Fig. 4b). The MSA method can be directly applied to the striped data, while the cloud data require a different post-processing in order to derive the fragility curve. In the case of Figure 4b, the data form stripes and hence they can be post processed as was already shown for the building:

$$F_R^{(b)} = \Phi\left(\frac{\mu_{logEDPb} - edp^{(b)}}{\sigma_{logEDPb}}\right)(1 - P_{Ovtn} - P_{NoRock}) + P_{Ovtn} \tag{23}$$

Since the $F_R^{(b)}$ is calculated at every stripe P_{NoRock}, P_{Ovtn} are simply obtained as the percentage of simulations where no-rocking and overturning was observed, respectively. The fitting of Eqs.20-22 is also very efficient in the case of the freestanding contents. If the data are not stripped, as in Figure 4a, the cloud analysis method, discussed in the next section, should be used instead.

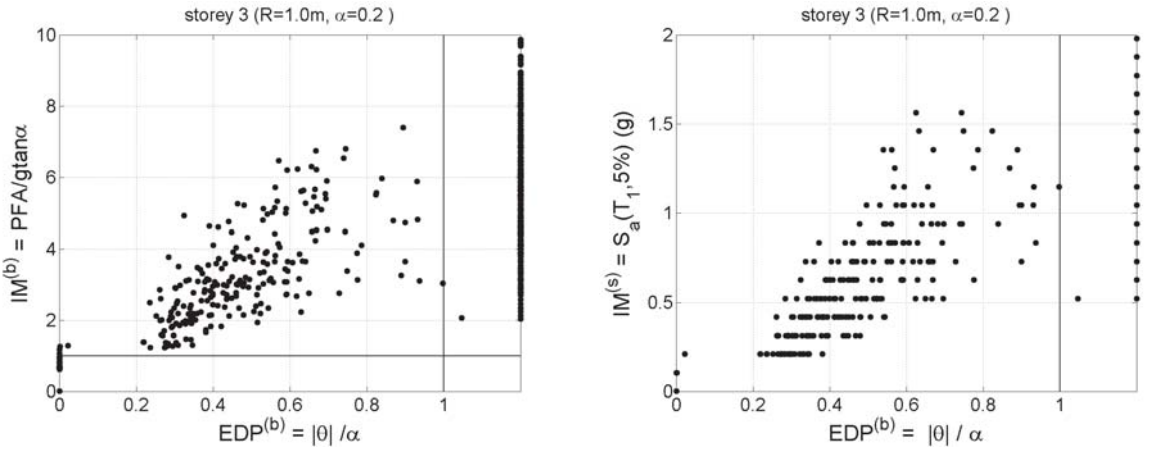

(a) (b)

Figure 4: Seismic response of a freestanding building content with $R = 1.0m$ and $\alpha = 0.2$: (a) plotting $EDP^{(b)} - IM^{(b)}$ results to cloud data, (b) plotting $EDP^{(b)} - IM^{(s)}$ results to data in stripes.

Cloud analysis is a common method when the data are scattered in the EDP-IM plane (e.g. Fig. 4a). This occurs when the ground motions are left unscaled, or when they have all been scaled with the same factor. In cloud analysis a least-squares straight line is usually fitted on the $log(EDP^{(b)})$ - $log(IM^{(b)})$ data [5]. The linear fit provides the mean of the logarithms (μ_{logEDP}) and a single constant value for the dispersion σ_{logEDP}. Knowing μ_{logEDP} and σ_{logEDP}, it is

possible to calculate the fragility of the rocking simulations using Eq. 23. This requires the knowledge of the no-rocking P_{NoRock} and overturning P_{Ovtn} probabilities over the whole IM range. These probabilities are calculated using a logistic regression model (logit) which yields a probability estimate that is function of the $IM^{(b)}$ [29]. Therefore, for the overturning case:

$$P_{Ovtn} = \frac{1}{1 + e^{-(b_1 + b_2 log(IM^{(b)}))}} \tag{24}$$

where the constants b_1, b_2 are the parameters of the logistic regression model, obtained with binomial-based, generalized linear model (GLM) regression.

The fitting of Eqs.20-22 is a robust method also for cloud analysis. The fitting is possible assuming stripes with a single simulation. Thus, in Eq. 22, k is equal to the total number of simulations of the cloud and in Eq. 21, n_{suc} is either 0 or 1 and always $n_{tot} = 1$. Attention should be paid on applying the MLE formula on the complete set of simulations that consists of no-rocking, rocking and overturning simulations. The fragility curves produced by the rocking data will considerably differ from the curves of the full dataset giving unsafe results [5]. The problem can be amended applying the MLE fitting to the rocking data only and combining the resulting fragilities with the no-rocking and the overturning fragilities P_{NoRock} and P_{Ovtn} of the logistic regression model (Eq. 24). The combination is achieved with the total probability theorem (TPT) (Eq. 13) and, as shown in Fragiadakis and Diamantopoulos [5], it gives exactly the same curve with that obtained from all the data.

5 NUMERICAL INVESTIGATION

The case study building adopted is the four-storey RC building that has been discussed in detail by Fragiadakis and Diamantopoulos [5]. This planar building is considered as a simplification and is used as a case study. The building is subjected to a suite of thirty far-field ground motion records and the response time-histories are used as input for the response assessment of the contents. The work aims to shed light on the fragility and risk assessment of building contents that are hosted in different stories of a structure and are considered as symmetric or asymmetric. The asymmetry of a rocking block leads to different equation of motion and the energy dissipation depends on the pivot point. Also, it has been shown in Vlachos *et al.* [21] that the sign of the ground motion also affects the response.

Considering the fragility and risk assessment two blocks, a symmetric and an asymmetric, are assumed. The symmetric block has slenderness angle $\alpha = 0.20$ and size parameter $R = 1.0m$ and the asymmetric slenderness angles $\alpha_1 = 0.212$, $\alpha_2 = 0.182$ and size parameters $R_1 = 1.003m$, $R_2 = 0.997m$. Three limit-states are identified for each block. The corresponding $EDP^{(b)} = \theta/\alpha$ threshold values are assumed as 0.3, 0.5 and 1, respectively. Figure 5a shows the fragility curves of a rectangular block on the 2^{nd} storey of the RC building considered and Figure 5b compares the fragility curves of the symmetric and the asymmetric block in each limit-state. The curves were produced with respect to $IM^{(s)} = S_a(T_1, 5\%)$, a practice that allows convolving the fragility curve with the hazard curve in order to obtain the mean annual frequency (MAF) (Eq. 16). As shown in Figure 5, both chainsaw-like and smooth fragilities can be obtained depending on the post-processing method. Both curve types are acceptable, although intuitively the reader will be more comfortable with the smooth curves offered by the MLE fitting of Eq. 20. The smooth fragility curves are shown in rest of the manuscript. Figure 6 shows the block overturning fragilities using PFA as the intensity measure $IM^{(b)}$ of the block. The solid lines refer to the block subjected to the storey response time-history and assuming that the structure's collapse means overturning of the blocks, while the dashed

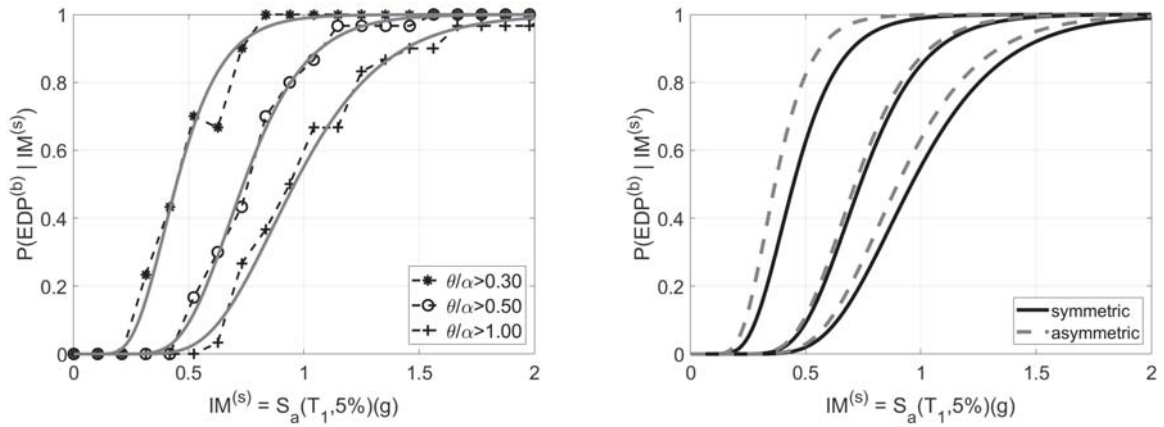

(a) (b)

Figure 5: Fragility curves for a block located at the 2^{nd} storey of the building: (a) slender block ($R = 1.0m, \alpha = 0.2$), (b) comparison between the symmetric and the asymmetric block considered.

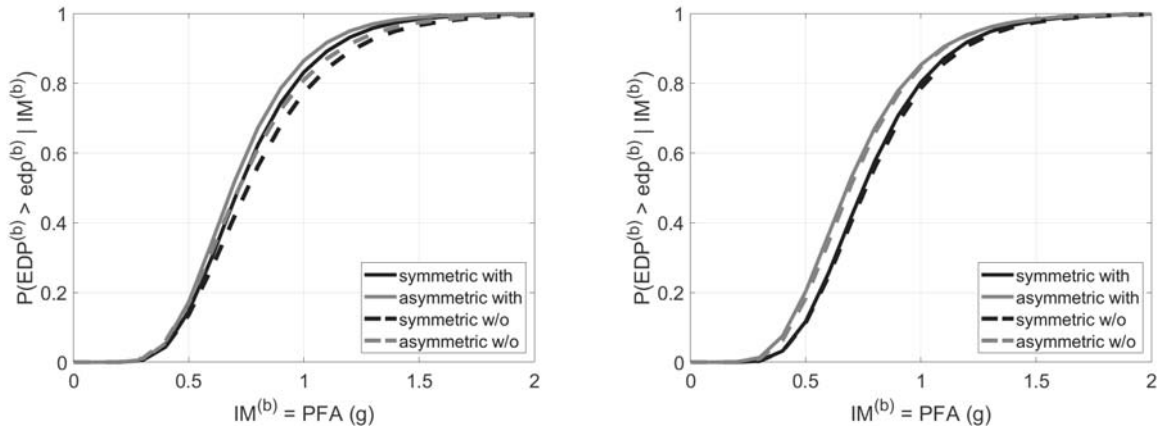

(a) (b)

Figure 6: Overturning fragility curves of a slender block assuming it as symmetric or asymmetric: (a) the block is considered at the 1^{st} storey of the structure, (b) the block is considered at the 4^{th} storey of the structure.

lines were obtained omitting the structure's collapse. Also, the dark lines correspond to the symmetric block and the grey to the asymmetric. As expected, the asymmetric block is always more vulnerable, while the building affects the fragilities especially when the block is hosted in the lower storeys of the building (Fig. 6a vs Fig. 6b). Figure 7 presents for all stories of the structure the block overturning fragilities assuming $IM^{(b)} = PFA/gtan\alpha$. For both blocks, the storey fragilities practically coincide. In principle, the fragility curves should coincide since they provide a property of the system that should not be sensitive to the ground motion set. However, due to the substantially different frequency content of the ground motions this in not always the rule. Of interest is also to show the fragilities obtained using as $IM^{(b)}$ the PFV instead of the PFA (Fig. 8). Adopting the PFV, the storey fragilities appear more dispersed compared to the $PFA/gtan\alpha$, which is more profound for the symmetric block. It is noted that the value of $tan\alpha$ is obtained from the symmetric block. As a general conclusion, although qualitatively our conclusions are not affected by the $IM^{(b)}$, the fragility curves will differ and

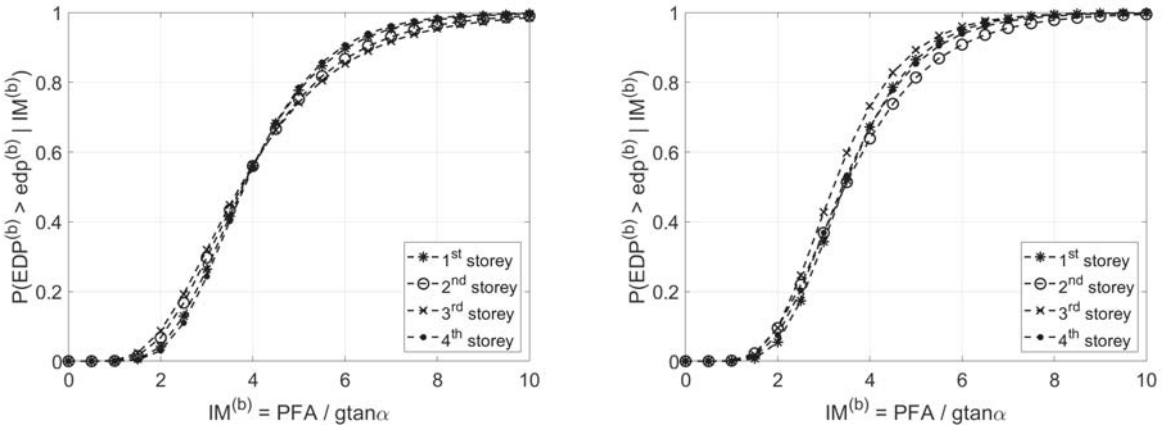

(a) (b)

Figure 7: Storey overturning fragility curves: (a) slender symmetric block ($R = 1.0m, \alpha = 0.2$), (b) slender asymmetric block. The structure's collapse has been adopted in both cases.

their interpretation requires attention.

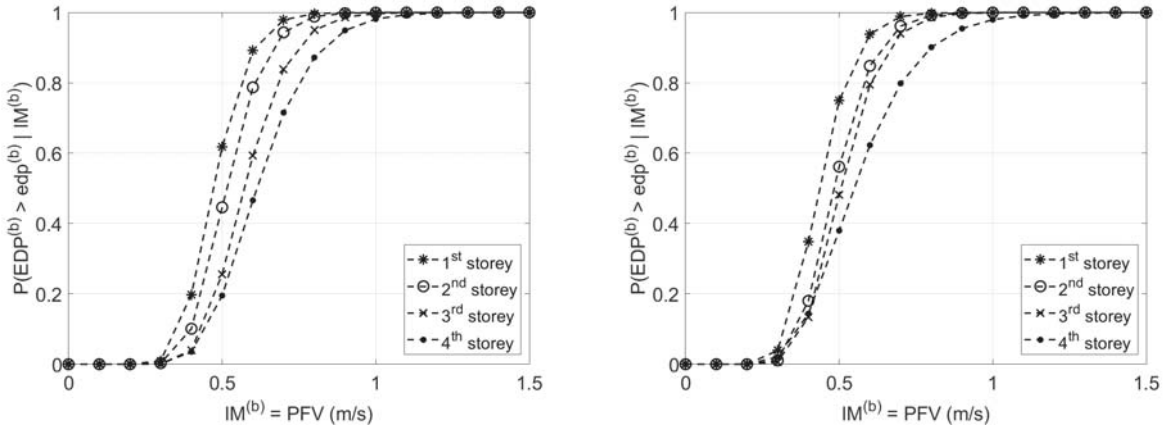

(a) (b)

Figure 8: Storey overturning fragility curves using PFV as the IM of the block: (a) slender symmetric block ($R = 1.0m, \alpha = 0.2$), (b) slender asymmetric block. The structure's collapse has been adopted in both cases.

In order to calculate the limit-state mean annual frequencies (MAF) of the block, we adopt the hazard curve that has been adopted in Fragiadakis and Diamantopoulos [5] and corresponds to a site in the island of Crete, Greece. As discussed in Section 3.2, the limit-state MAFs are "exactly" calculated with Eq. 16. Alternatively, the MAFs can be calculated with Eq. 17 finding separately the fragility of the block and of the structure. The calculation of Eq. 17 requires the derivative of the block's fragility, which essentially is the probability density function (PDF) for a number of discrete limit-states. This alternative has been discussed in Fragiadakis and Diamantopoulos [5] showing that the PFV leads to more stable solutions in comparison with the PFA. For the blocks considered, the MAFs of Eq. 16 are shown in Table 1 for the first and the fourth storey of the RC building considered. From the values of the MAFs it is obvious that a symmetric block is more stable than an asymmetric is all storeys of the structure. Especially, in the fourth storey the differences become important while the values of the MAFs in the first

storey are close comparing the symmetric and asymmetric case.

storey	$(\theta/\alpha \leq 0.3)$	$(\theta/\alpha \leq 0.5)$	$(\theta/\alpha \leq 1.0)$
$1^{st} symmetric$	1353 years	3427 years	5280 years
$1^{st} asymmetric$	1230 years	2838 years	4933 years
$4^{th} symmetric$	170 years	808 years	2478 years
$4^{th} asymmetric$	105 years	538 years	1226 years

Table 1: Limit-state MAFs obtained for a rocking block using the exact (Eq. 16) approach.

6 CONCLUSIONS

A fragility assessment framework for freestanding building contents has been discussed. The building contents were modelled as rigid, symmetric or asymmetric, blocks and it was assumed that they are hosted in a four-storey RC building [5]. It has been shown that the problem addressed is complicated since the response of the structure and the contents are coupled. The problem becomes more complicated when the contents are asymmetric because the response depends also on the sign of the record and the side of the asymmetry. The findings of the study have been obtained using a two-dimensional, four-storey building and two-dimensional simulations for the contents. Hence, the reults cannot be always generalized. Further research is required in order to fully understand the effect of the structure on the fragility of freestanding contents. In conclusion, the authors would like to mention that the work presented should be considered as an attempt to offer some first guidelines on how the rocking problem can be handled for freestanding objects that can be assumed asymmetric and are hosted in a building. Some of the major conclusions of the paper are briefly summarized as follows:

- An MSA-based (Multiple Stripe Analysis) fragility-assessment methodology, tailored to freestanding building contents, is presented. The vulnerability of the contents depends on their geometry and the dynamic characteristics of the structure. Moreover, the fragility of the blocks should not be calculated independently of the collapse, or damage, of the building.

- Depending on the post-processing of the results, cloud or multiple-stripe data are obtained. The proper post-processing in order to consistently handle rocking, non-rocking and overturned blocks should be considered; otherwise the fragilities will be underestimated.

- A symmetric and an asymmetric block have been considered, showing that the geometry of the block is critical. It is found that symmetric blocks are more safe because the asymmetry affects the response. Of course this observations refers to the four-storey structure considered, but it clearly shows the importance of both building and block properties and also the fact that the fragility of freestanding contents is very different from that of anchored contents that are expected to behave as elastically deforming structures.

REFERENCES

[1] FEMA, FEMA P-58-1: Seismic Performance Assessment of Buildings - Volume 1, Methodology, 2012.

[2] FEMA, FEMA E-74: Reducing the Risks of Nonstructural Earthquake Damage - A Practical Guide, 2012.

[3] NIST, ATC-120: Seismic Analysis, Design, and Installation of Nonstructural Components and Systems – Background and Recommendations for Future Work. GCR 17-917-44, prepared by the Applied Technology Council for the National Institute of Standards and Technology, Washington, D.C., USA, 2017.

[4] G.W. Housner, The behavior of inverted pendulum structures during earthquakes, *Bulletin of the Seismological Society of America*, **53(2)**, 404–417, 1963.

[5] M. Fragiadakis, S. Diamantopoulos, Fragility and risk assessment of freestanding building contents, *Earthquake Engineering & Structural Dynamics*, **49(10)**, 1028–1048, 2020.

[6] C.C. Spyrakos, C.A. Maniatakis, I.M. Taflampas, Application of predictive models to assess failure of museum artifacts under seismic loads, *Journal of Cultural Heritage*, **23(1)**, 11–21, 2016.

[7] L. DiSarno, C. Petrone, G. Magliulo, G. Manfredi, Dynamic properties of typical consultation room medical components, *Engineering Structures*, **100**, 442–454, 2015.

[8] C.E. Wittich, T.C. Hutchinson, Shake table tests of unattached, asymmetric, dual-body systems, *Earthquake Engineering & Structural Dynamics*, **46(9)**, 1391–1410, 2017.

[9] C.E. Wittich, T.C. Hutchinson, Shake table tests of stiff, unattached, asymmetric structures, *Earthquake Engineering & Structural Dynamics*, **44(14)**, 2425–2443, 2015.

[10] M. Purvance, A. Anooshehpoor, N. Brune, Freestanding block overturning fragilities: Numerical simulation and experimental validation, *Earthquake Engineering & Structural Dynamics*, **37**, 791–808, 2008.

[11] D. Konstantinidis, N. Makris, Experimental and analytical studies on the response of freestanding laboratory equipment to earthquake shaking, *Earthquake Engineering & Structural Dynamics*, **38**, 827–848, 2009.

[12] D. Konstantinidis, F. Nikfar, Seismic response of sliding equipment and contents in base-isolated buildings subjected to broadband ground motions, *Earthquake Engineering & Structural Dynamics*, **44**, 865–887, 2015.

[13] E. Dimitrakopoulos, T. Paraskeya, Dimensionless fragility curves for rocking response to near-fault excitations, *Earthquake Engineering & Structural Dynamics*, **44(12)**, 2015–2033, 2015.

[14] A.I. Giouvanidis, M. Fragiadakis, E.G. Dimitrakopoulos, *Vulnerability assessment of flag-shaped hysteretic rocking bridge bents, Proceedings of the 6th International Conference on Computational Methods in Structural Dynamics and Earthquake Engineering (COMPDYN 2017)*, 15-17 June, 2017.

[15] C. Petrone, L. DiSarno, G. Magliulo, E. Consenza, Numerical modelling and fragility assessment of typical freestanding building contents, *Bulletin of Earthquake Engineering*, **15(4)**, 1609–1633, 2017.

[16] A. Pappas, A. Sextos, F. Da Porto, C. Modena, Efficiency of alternative intensity measures for the seismic assessment of monolithic free-standing columns, *Bull Earthquake Eng*, **15**, 1635–1659, 2017.

[17] I. Kavvadias, A. Papachatzakis, K. Bantilas, L. Vassiliadis, Rocking spectrum intensity measures for seismic assessment of rocking rigid blocks, *Soil Dynamics and Earthquake Engineering*, **101**, 116–124, 2017.

[18] M. Fragiadakis, M. Kolokytha, S. Diamantopoulos, Seismic risk assessment of rocking building contents of multistorey buildings, *Procedia Engineering: X International Conference on Structural Dynamics, EURODYN 2017*, **199**, 3534–3539, 2017.

[19] M. Fragiadakis, S. Diamantopoulos, *Risk assessment of rocking contents in Multistorey buildings , 16th European Conference on Earthquake Engineering*, 18-21 June, 2018.

[20] M. Fragiadakis, L. DiSarno, A. Saetta, M.G. Castellano, I. Rocca, S. Diamantopoulos, V. Crozet, I. Politopoulos, T. Chaudat, S. Vasic, I.E. Bal, E. Smyrou, I. Psycharis, T.C. Hutchinson, L. Berto, *Experimental seismic assessment and protection of museum artefacts , XI International Conference on Structural Dynamics (EURODYN 2020)*, 23-25 November, 2020.

[21] N. Vlachos, S. Diamantopoulos, M. Fragiadakis, *Seismic response assessment of artefacts freestanding on a solid pedestal , 4th Hellenic National Conference on Earthquake Engineering and Engineering Seismology*, 5-7 September, 2019.

[22] F. Masi, I. Stefanou, P. Vanucci, V. Maffi-Berthier, Resistance of museum artefacts against blast loading, *Journal of Cultural Heritage*, 2020.

[23] M. Fragiadakis, I. Psycharis, G.P. Mavroeides, *Parametric Investigation of The Dynamic Response of Rigid Blocks Subjected to Synthetic Near-Source Ground Motion Records, ECCOMAS Congress 2016: VII European Congress on Computational Methods in Applied Sciences and Engineering*, 5-10 June, 2016.

[24] S. Diamantopoulos, M. Fragiadakis, Seismic response assessment of rocking systems using single degree of freedom oscillators, *Earthquake Engineering & Structural Dynamics*, **48(7)**, 689–708, 2019.

[25] M. Fragiadakis, D. Vamvatsikos, M.G. Karlaftis, N.D. Lagaros, M. Papadrakakis, Seismic assessment of structures and lifelines, *Journal of Sound and Vibration*, **334**, 29–56, 2015.

[26] F. Jalayer, Direct probabilistic seismic analysis: Implementing non-linear dynamic assessments, *Department of Civil and Environmental Engineering, Stanford University, CA*, 2003.

[27] JW. Baker, Efficient Analytical Fragility Function Fitting Using Dynamic Structural Analysis, *Earthquake Spectra*, **31(1)**, 579–599, 2015.

[28] D. Vamvatsikos, M. Fragiadakis, Incremental dynamic analysis for estimating seismic performance sensitivity and uncertainty *Earthquake Engineering & Structural Dynamics*, **39(2)**, 141–163, 2010.

[29] F. Jalayer, H. Ebrahimian, A. Miano, G. Manfredi, H. Sezen Incremental dynamic analysis for estimating seismic performance sensitivity and uncertainty *Earthquake Engineering & Structural Dynamics*, **46(15)**, 2639–2663, 2017.

EURODYN 2020
XI International Conference on Structural Dynamics
M. Papadrakakis, M. Fragiadakis, C. Papadimitriou (eds.)
Athens, Greece, 23–26 November 2020

PARAMETRIC INSTABILITY OF PULTRUDED FIBER-REINFORCED POLYMER COLUMNS UNDER AXIAL HARMONIC FORCING

Julio C. Coaquira[1], Daniel C. T. Cardoso[1], Paulo B. Gonçalves[1] and Diego Orlando[2]

[1] Department of Civil Engineering and Environmental Engineering, Pontifical Catholic University of Rio de Janeiro, PUC-Rio
Rua Marquês de São Vicente, 225, Gávea, 22451-900, Rio de Janeiro, RJ, Brazil
e-mail: jccoaquira@gmail.com, dctcardoso@puc-rio.br, paulo@puc-rio.br

[2] Department of Mechanics and Energy – FAT, State University of Rio de Janeiro, UERJ
Rodovia Presidente Dutra, km 298, 27537-000, Resende, RJ, Brazil
e-mail: dgorlando@gmail.com

Keywords: Parametric instability, Thin-walled column, Local buckling, FRP column

Abstract. *The parametric instability of pultrude fiber-reinforced polymer columns with a channel section under harmonic axial load is investigated in this paper. The three plates of channel section (web and two flanges) are modelled using von Kármán nonlinear plate theory. The Ritz method is used to discretize the continuous structure resulting in coupled nonlinear equations of motion, which are solved numerically. Bifurcation diagrams obtained by continuation methods and Floquet theory are used to obtain the transition curves between trivial and nontrivial solutions and to study the nonlinear oscillations of the column in the unstable regions.*

1 INTRODUCTION

The use of structural elements made of fiber reinforced polymers (FRP) has significantly increased in recent years. The increased interest lies in the advantages over traditional construction materials, such as high strength-to-weight ratio, corrosion resistance and the ease of transportation and erection. Structural elements with thin-walled and open sections are commonly found in metal structures and, more and more often, in structures designed with new materials such as FRP profiles and other composite materials. FRP structural shapes have shown to provide efficient and economical applications in buildings, bridge decks, retaining walls, airport facilities, storage structures exposed to salts and chemicals, reinforcing members of casings or fuselages as, salt storage sheds, bridge superstructures, among others. Short thin-walled bars under compressive loads may fail due to a local instability buckling mode with the critical load controlling their design [1, 2]. Under dynamic loads the column may buckle due to parametric instability at load levels much lower than the static critical load and exhibit a complex nonlinear behavior. Parametric resonances are often encountered in mechanics (e.g., dynamic buckling of columns, plates and shells, water waves in vertically forced containers, stability of general motions) and in various areas of physics. However, little is known on their behavior and stability under dynamic loads. In the present work a short column with a channel cross-section under harmonic forcing is analyzed. The channel section is discretized as three thin-walled plates described by the von Kármán nonlinear plate theory and appropriate continuity conditions are prescribed at the web-flange intersections [3]. A consistent modal solution is used together with the Ritz method to obtain the coupled nonlinear equation of motions, which are solved by the Runge-Kutta method and bifurcation diagrams are obtained by the brute-force method and continuation techniques. A parametric analysis, considering different materials, shows the influence of the column length, section geometric dimensions and elastic constants of the material on the parametric instability boundaries in the force control space and bifurcation scenario of the structure.

2 PROBLEM FORMULATION

The present work considers a thin-walled column of length L having a channel cross-section with web width b_w, web thickness t_w, flange width b_f and flange thickness t_f, as illustrated in Fig. 1(a). Since many commercially-available pultruded shapes have constant thickness, it is hereafter assumed that $t_w = t_f = h$. For the local buckling analysis, the flanges and web are modelled using the von Kármán nonlinear plate theory [4].

The displacement field is given by,

$$\bar{u} = u + z\beta_x; \quad \bar{v} = v + z\beta_y; \quad \bar{w} = w; \quad \beta_x = -w_{,x}; \quad \beta_y = -w_{,y} \tag{1}$$

where $\bar{u}$ and $\bar{v}$ are the in-plane displacement components in the x and y directions, respectively, $\bar{w}$ is the transversal displacement in the z direction of an arbitrary point (x, y, z) of the plate, u, v and w are the corresponding displacements at a point $(x, y, z = 0)$ situated in the middle surface of the plate (see Fig. 1(b)) and β_x and β_y are the rotations around the x and y axes, respectively.

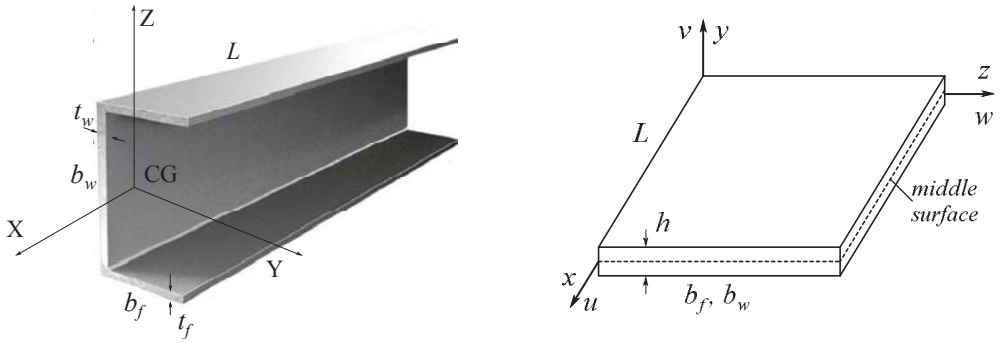

Figure 1: (a) C-profile geometry and global coordinate system. (b) Plate element (web and flange), local coordinate system and displacement field (the global and local *x* axes have the same direction).

The strain–displacement relations and changes of curvature of the middle-surface are given by:

$$\begin{gathered}\varepsilon_x = u_{,x} + \frac{1}{2}w_{,x}^2;\ \varepsilon_y = v_{,y} + \frac{1}{2}w_{,y}^2; \\ \gamma_{xy} = \left(u_{,y} + v_{,x} + w_{,x}w_{,y}\right);\ k_x = \beta_{x,x}; \\ k_x = \beta_{y,y};\ k_{xy} = (\beta_{x,y} + \beta_{y,x})/2\end{gathered} \tag{2}$$

Considering the constitutive equations of a typical orthotropic elastic material obeying Hooke's law, with the principal directions coinciding with the direction of the fibers and its transversal direction in the *x*-*y* plane, and the strain-displacement relations, the expression relating internal forces and moments to the strains of the FRP profile can be written as [5]:

$$\begin{Bmatrix} N_x \\ N_y \\ N_{xy} \\ M_x \\ M_y \\ M_{xy} \end{Bmatrix} = \begin{bmatrix} A_{11} & A_{12} & 0 & 0 & 0 & 0 \\ A_{12} & A_{22} & 0 & 0 & 0 & 0 \\ 0 & 0 & A_{66} & 0 & 0 & 0 \\ 0 & 0 & 0 & D_{11} & D_{12} & 0 \\ 0 & 0 & 0 & D_{12} & D_{22} & 0 \\ 0 & 0 & 0 & 0 & 0 & D_{66} \end{bmatrix} \begin{Bmatrix} \varepsilon_x \\ \varepsilon_y \\ \gamma_{xy} \\ \kappa_x \\ \kappa_y \\ \kappa_{xy} \end{Bmatrix} \tag{3}$$

where N_x, N_y and N_{xy} are the normal and shear in-plane stress resultants per unit length, M_x, M_y and M_{xy} are the flexural and torsional moment resultants per unit length, as illustrated in Fig. 2, and:

$$A_{ij} = \int_{-\frac{h}{2}}^{\frac{h}{2}} Q_{ij}\, dz; \qquad D_{ij} = \int_{-\frac{h}{2}}^{\frac{h}{2}} Q_{ij}\, z^2\, dz \quad (i,j = 1,2,6) \tag{4}$$

where

$$\begin{gathered}Q_{11} = \frac{E_{11}}{(1-v_{12}v_{21})}; \\ Q_{22} = \frac{E_{22}}{(1-v_{12}v_{21})}; \\ Q_{12} = \frac{v_{21}E_{11}}{(1-v_{12}v_{21})};\ Q_{66} = G_{12}\end{gathered} \tag{5}$$

The x direction coincides with the main direction of the material parallel to the fibers, direction 1, the y direction coincides with the main direction of the material perpendicular to the fibers, direction 2, and the z direction coincides with the direction perpendicular to the thickness.

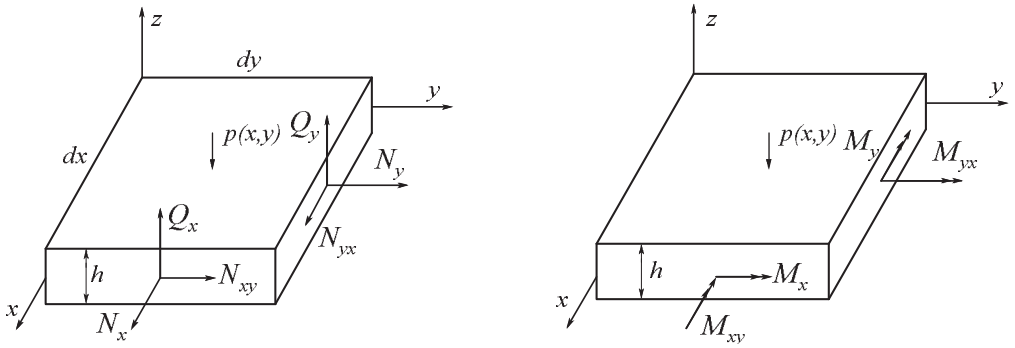

Figure 2: Plate element and internal force resultants per unit length in the local coordinate system (positive directions [6]).

The strain energy, U, is given by [4-6]:

$$U = \frac{1}{2}\iint \left(A_{11}\varepsilon_x^2 + 2A_{12}\varepsilon_x\varepsilon_y + A_{22}\varepsilon_y^2 + A_{66}\gamma_{xy}^2\right) dx\, dy + \frac{1}{2}\iint \left(D_{11}\kappa_x^2 + 2D_{12}\kappa_x\kappa_y + D_{22}\kappa_y^2 + D_{66}\kappa_{xy}^2\right) dx\, dy \tag{6}$$

For the axially compressed plate the potential energy of the applied loads is given by:

$$\Omega = -\frac{\bar{N}_x}{2}\int_0^b \int_0^L w_{,x}^2 dxdy \tag{7}$$

where $\bar{N}_x$ is the applied axial load per unit length at $x = 0$ and $x = L$.

The kinetic energy T of the plate, considering only the transversal inertia, is:

$$T = \frac{\rho h}{2}\int\int \dot{w}^2\, dxdy \tag{8}$$

where $\left(\dot{}\right)$ denotes the derivative with respect to time and ρ is the density of the material.

The Lagrangian of the three plates of the C profile is given by:

$$L = \sum_{i=1}^{3} T_i - \mathrm{U}_i - \Omega_i \tag{9}$$

To use the Ritz method, appropriate shape functions taking into account the boundary and continuity conditions for the displacements need to be prescribed. The following expressions are adopted for the web:

$$\begin{aligned} (x,y,t) &= U(t)sin\left(2\frac{m\pi x}{L}\right)cos\left(2\frac{\pi y}{b_w}\right); \\ v(x,y,t) &= V(t)cos\left(2\frac{m\pi x}{L}\right)sin\left(2\frac{\pi y}{b_w}\right) \\ w(x,y,t) &= W(t)sin\left(\frac{m\pi x}{L}\right)sin\left(\frac{\pi y}{b_w}\right) \end{aligned} \tag{10}$$

where $U(t)$, $V(t)$, $W(t)$, $X(t)$ and $Y(t)$ are the time dependent modal amplitudes and m is the number of axial half-waves. By imposing the compatibility conditions along the web-flange connection the displacements for the flange are given by (connection at $y = 0$)

$$u(x,y,t) = U(t)sin\left(2\frac{m\pi x}{L}\right)\left[1-\left(\frac{y}{b_w}\right)^2\right];$$
$$v(x,y,t) = V(t)cos\left(2\frac{m\pi x}{L}\right)\frac{y}{b_w} + y^3 \quad (11)$$
$$w(x,y,t) = W(t)sin\left(\frac{m\pi x}{L}\right)\frac{\pi y}{b_w}$$

They satisfy the simply-supported boundary conditions at $x = 0$ and $x = L$ and the continuity conditions along the web-flange interface.

3 RESULTS

In the present numerical analysis, a thin-walled column of length L having a channel cross-section with web width $b_w = 200\text{mm}$, flange width $b_f = 100\text{mm}$ and uniform thickness $t_w = t_f = 5\text{mm}$ is considered. As a reference an isotropic material (ISO) with Young's modulus $E_1 = E_2 = 28\text{kN/mm}^2$, in-plane shear modulus $G_{12} = 11.38\text{kN/mm}^2$ and Poisson ratio $v_{12} = v_{21} = 0.23$ is assumed. A FRP profile´s with Young's modulus in the longitudinal direction $E_1 = 28\text{kN/mm}^2$, Young's modulus in transverse direction $E_2 = 19.3\text{kN/mm}^2$, in-plane shear modulus $G_{12} = 2.6\text{kN/mm}^2$, major Poisson's ratio $v_{12} = 0.23$ and minor Poisson's ratio $v_{21} = 0.1585$, based on catalog values, is adopted. For the mass density is equal to $\rho = 1850\text{kg/m}^3$ and the viscous damping ratio is $\xi = 1.45\%$. Similar to a plate [6], the channel profile buckle with m half-waves in the longitudinal direction, with m increasing with L. For each value of m, the load reaches a minimum value which is usually taken as the critical load of the structure [6]. The minimum static critical load for the isotropic material is 239.3kN/m, while for the pultruded column it is equal to 115.5kN/m, a decrease of 52% in the load capacity. Also, the fundamental frequency is highly dependent on the material constants decreasing from 1982rad/s to 1255rad/s. This affects the parametric instability boundaries in the forcing frequency versus forcing magnitude plane, as illustrated in Fig. 3, decreasing the parametric instability transition boundary and moving the resonant regions to the lower frequency range. These boundaries are obtained by solving the nonlinear equation of motion of the damped system by continuation techniques in conjunction with Floquet theory for a large number of forcing frequencies [7] and by increasing slowly the forcing magnitude while holding the frequency constant. The dashed horizontal black lines correspond to the static critical load. Again, there is a palpable decrease in the dynamic critical load compared with the isotropic material. The principal parametric resonance region occurs in the neighborhood of $\Omega_f = 2\omega_o$, while second instability region to the left corresponds to $\Omega_f = \omega_o$, and is referred to as fundamental resonance region. These two regions are the most significant in structural dynamics, since in these two regions the critical dynamic buckling load can be considerably lower than the static buckling load. These results evidence the dangerous consequences of parametric instability in lightly damped structural systems.

Figure 4 compare the nonlinear frequency-amplitude relations of the two materials. They are obtained by the shooting method starting at $2\omega_o$ [8]. Here ω_{nl} is the amplitude-dependent nonlinear frequency. Both structures exhibit a hardening behavior with the FRP column exhibiting a higher degree of nonlinearity. This influences the bifurcations connected with each tongue in the force control space. The principal parametric resonance region is bounded on the left by a supercritical period-doubling bifurcation, as illustrated for the bifurcation diagrams of the two materials for $\Omega_f = 2\omega_o$ in Fig. 5(a), and on the right by a subcritical period-doubling bifurcation, while fundamental resonance region is bounded on the left by a supercritical pitchfork bifurcation and on the right by a subcritical pitchfork bifurcation.

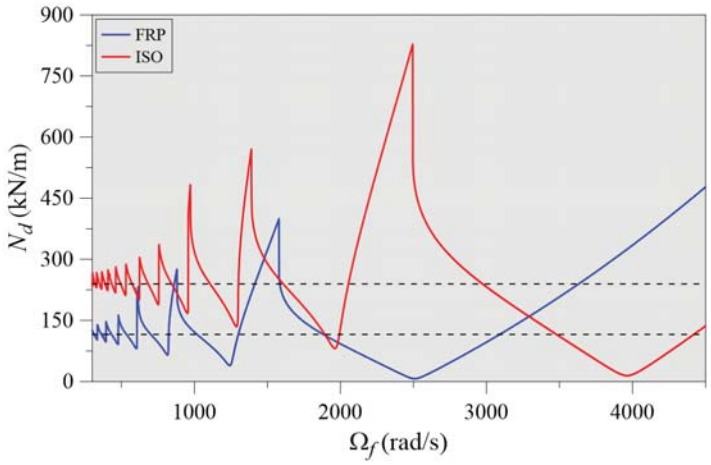

Figure 3: Parametric instability boundaries of the isotropic and pultrude profiles in the force control space.

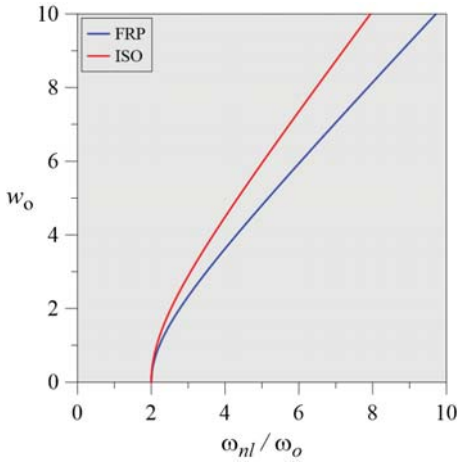

Figure 4: Nonlinear frequency-amplitude relation.

The effect of a static pre-load is to decrease the fundamental frequency and the dynamic buckling mode. Additionally, it leads to an increasing number of bifurcations at low load levels, leading to various coexisting solutions. Figure 5(b) shows the bifurcation diagram obtained considering a static load level equal to 75% of the static critical load ($Q_s = N_s/N_{cr} = 0.75$, compare with Fig. 5(a)). For this static load level, Fig. 6(a) shows the basin of attraction, while Fig. 6(b) shows the associated four coexisting solutions for $\Omega_f = 2\omega_o$ and $Q_d = 0.76$ (the dots are the fixed points of the Poincaré map of each solution). There are two large amplitude period-one attractors and two medium amplitude period-two attractors, but most initial conditions converge to one of the two large amplitude attractors. Fig. 6(c) shows the Poincaré map of the chaotic attractor obtained for $\Omega_f = 2\omega_o$ and $Q_d = 1.50$.

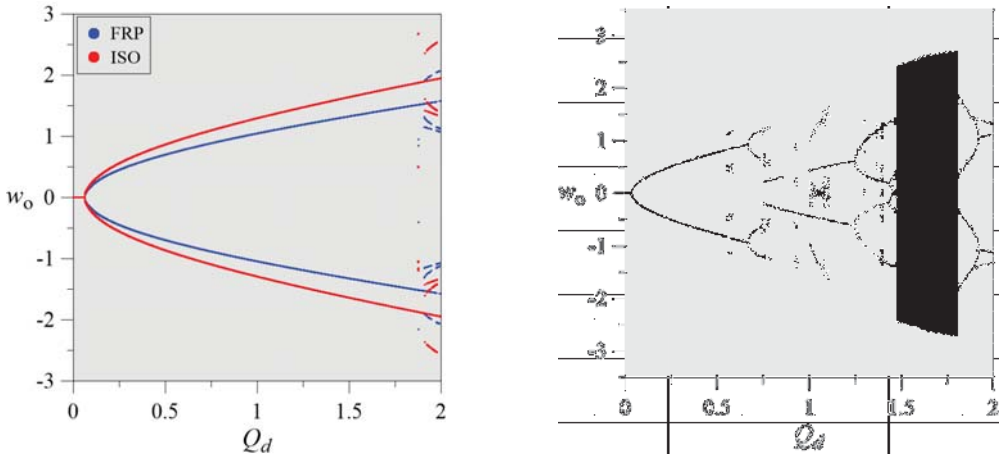

Figure 5: (a) Bifurcation diagram of the Poincaré map for the two material considering $\Omega_f = 2\omega_o$. $Q_d = N_d/N_{cr}$. (b) The effect of a static preload $Q_s = N_s/N_{cr} = 0.75$ on the bifurcation diagram of the FRP profile considering $\Omega_f = 2\omega_o$.

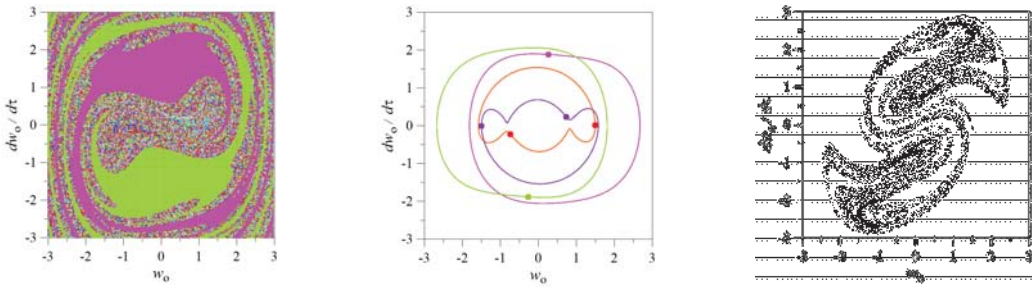

Figure 6: (a-b) Basin of attraction and associated attractors for $\Omega_f = 2\omega_o$ and $Q_d = 0.76$. (c) Poincaré map for $\Omega_f = 2\omega_o$ and $Q_d = 1.50$.

4 CONCLUSIONS

The results evidence that the static buckling loads, natural frequencies and parametric instability load are highly dependent on the orthotropy of the FRP material. There is a palpable decrease in static and dynamic the critical load and fundamental frequency when compared with the isotropic material. This decrease is due to the FRP low resistance in the transversal direction and low shear modulus. Within the parametric instability tongues, the nonlinearity leads to a qualitatively rich dynamics with several coexisting periodic and chaotic solutions, leading to basins of attraction with a complex topology. The parametric instability of the pultruded column is important because it causes the stable vertical equilibrium position to bifurcate into large-amplitude solutions and initiates a process that may lead the failure and the loss of load carrying capacity.

REFERENCES

[1] G.G. Cintra, D.C. Cardoso, J.D. Vieira, Parameters affecting local buckling response of pultruded GFRP I-columns: Experimental and numerical investigation, *Composite Structures* 222, 110897, 2019.

[2] D.C. Cardoso, K.A. Harries, E.D.M. Batista, Closed-form equations for compressive local buckling of pultruded thin-walled sections, *Thin-Walled Structures* 79, 16–22, 2014.

[3] D.C. Cardoso, G.C. De Salles, E.D.M. Batista, P.B. Gonçalves, Explicit equations for distortional buckling of cold-formed steel lipped channel columns, *Thin-Walled Structures* 119, 925-933, 2017.

[4] M. Amabili, Nonlinear vibrations and stability of shells and plates, ISBN: 9781107435421, 2008.

[5] J.N. Reddy, Mechanics of laminated plates and shells theory and analysis, *Theory and Analysis*, ISBN: 9780849315923, 2004.

[6] D.O. Brush, B.O. Almroth, Buckling of bars, plates, and shells, ISBN: 9780070085930, 1975.

[7] D. Orlando, P.B. Gonçalves, G. Rega, S. Lenci, Influence of modal coupling on the nonlinear dynamics of Augusti's model, *Journal of computational and nonlinear dynamics* 6(4), 041014, 2011.

[8] R. Seydel, From Equilibrium to Chaos: Practical Bifurcation and Stability Analysis, ISBN: 978-0444012500, 1988.

EURODYN 2020
XI International Conference on Structural Dynamics
M. Papadrakakis, M. Fragiadakis, C. Papadimitriou (eds.)
Athens, Greece, 23–26 November 2020

EFFECTS OF INITIAL GEOMETRICAL IMPERFECTIONS ON DYNAMIC STABILITY OF CIRCULAR CYLINDRICAL PANELS

Frederico M. A. Silva[1], Wanclaine A. Vaz[1], Paulo B. Gonçalves[2]

[1] School of Civil and Environmental Engineering, Federal University of Goiás
Av. Universitária 1488, Goiânia - GO, Brazil
e-mail: silvafma@ufg.br, wanclainealmeida@gmail.com

[2] Department of Civil Engineering, Pontifical Catholic University of Rio de Janeiro
Rua Marquês de São Vicente, 255, Gávea, Rio de Janeiro - RJ, Brazil
paulo@puc-rio.br

Keywords: geometrical imperfection, cylindrical panel, internal resonances.

Abstract. *This work evaluates the influence of initial geometric imperfections on a slender cylindrical panel nonlinear response, considering the three following cases of internal resonances: 1:1, 1:3 or 1:1:2. Nonlinear Donnell shallow shell theory is used to obtain the nonlinear equations of motion. Based on previous works, a consistent modal solution for the transverse displacement field is derived from a perturbation technique, considering the modal coupling and interaction in a simply supported cylindrical panel. Then, the standard Galerkin method is applied to reduce the problem to a system of differential equations in time domain. The backbone curves, resonance curves, phase-portraits and basin of attraction are obtained to evaluate the influence of the initial geometrical imperfection on the stability of transversally excited circular cylindrical panels. The numerical results indicate that the presence of an initial geometrical imperfection changes strongly the resonance curves, creating news stable paths and dynamic jumps and increases the nonlinearity and complexity of the panel response for each case of internal resonance, leading to fractal basins of attraction in the main resonance region.*

1 INTRODUCTION

Thin-walled cylindrical panels are used in several engineering areas, with emphasis in naval, aeronautical and civil engineering applications. They are circular sectors of cylindrical shells and are usually described by the shallow shell theory. Despite a simple geometry, the slenderness of this element makes it susceptible to loss of stability and excessive vibrations when subjected to static and dynamic loads, which can lead the structure to collapse. For these reasons, efforts should be employed to understand the nonlinear phenomena and instabilities of these structures. Among the non-linear phenomena, due to the geometric nonlinearities, strong modal coupling and interaction are inherent phenomena of slender shell structures. Another phenomenon is the modal interaction that occurs when different buckling or vibration modes have same critical load or some natural frequencies are commensurate (internal resonance) [1-3]. Therefore, this study aims to contribute to the understanding of the phenomena: modal coupling and modal interaction in simply supported cylindrical panels. To consider both phenomena, the transverse displacement field is deduced from a perturbation technique [4-6], leading a reduced order model that converges for vibration amplitudes up to the order of the thickness of the panel.

2 PROBLEM FORMULATION

Consider a simply supported cylindrical panel subjected to a time-dependent transversal load made by a linear, homogeneous and isotropic material. The transversal equation of motion and the compatibility equation, based on Donnell's non-linear shallow shell theory, are given in terms of the transversal displacement w and Airy stress function f respectively by:

$$\begin{aligned}\rho h\ddot{w}+2\eta_1\rho h\Omega_0\,\dot{w}+D(w_{,xxxx}+\frac{2}{R^2}w_{,\theta\theta xx}+\frac{1}{R^4}w_{x\theta\theta\theta})-f_{,\theta\theta}(w_{,x}+w_{0,x})_{,x}\\ +R\,f_{,xx}-f_{,xx}(w_{,\theta}+w_{0,\theta})_{,\theta}-2\,f_{x\theta}(w_{,\theta x}+w_{0,\theta x})-p(t)=0\end{aligned} \tag{1}$$

$$\frac{\nabla^4 f}{E\,h}=\frac{1}{R^4}\left(w_{,x\theta}{}^2-w_{,xx}w_{,\theta\theta}+R\,w_{,xx}+2\,w_{,x\theta}w_{0,x\theta}-w_{,xx}w_{0,\theta\theta}-w_{,\theta\theta}w_{0,xx}\right) \tag{2}$$

where D [$=Eh^3/12(1-\nu^2)$] is the flexural stiffness, R is the radius of curvature, h is the cylindrical panel thickness, ρ is the mass density, $p(t)$ is the transversal load distributed along the domain, η_1 is the viscous damping parameter, E is the Young's modulus, ν is the Poisson ratio and Ω_0 is the natural frequency of the perfect cylindrical panel.

The transversal harmonic pressure load, distributed along the domain, is given by:

$$p(t)=pl\sin(n\,r)\sin(m\,q)\cos(\Omega t) \tag{3}$$

where $r=\pi\theta/\Theta$, $q=\pi x/L$, pl is load magnitude, Ω is the excitation frequency, Θ is the angle width of the cylindrical panel and m and n are the number of axial and circumferential half-wave, respectively.

The initial geometrical imperfection is described by a pre-defined function w_0 in the shape of the fundamental vibration modes [6]:

$$w_{01}=C_1\sin(q)\sin(r) \tag{4}$$

where C_1 is the imperfection magnitude.

3 NUMERICAL RESULTS

Based on the analytical results of the vibration frequencies of a simply supported perfect panel, obtained by the use their classical vibration modes of a simply supported cylindrical panel [5, 6], three different geometries displaying different types of internal resonance are selected. Table 1 presents the basic geometric dimensions of the selected cylindrical panels that exhibits 1:1, 1:3 and 1:1:2 internal resonance as well as the natural frequencies and modes involved in the internal resonances. From Table 1, it is observed that small changes in the angle the panel's length or opening angle lead to different types of internal resonances.

Θ (rad)	L (m)	Internal resonance	Axial half-wave	Circumferential half-wave	Natural frequency (Hz)
0.1658	0.1	1:1	$m = 1$	$n = 1$	686.29
			$m = 1$	$n = 2$	686.29
0.0577	0.1	1:3	$m = 1$	$n = 1$	992.05
			$m = 3$	$n = 2$	2976.16
0.1658	0.091	1:1:2	$m = 1$	$n = 1$	741.88
			$m = 1$	$n = 2$	741.88
			$m = 2$	$n = 1$	1483.75

Table 1: Geometries of cylindrical panel with internal resonance and their natural frequencies and vibration modes (R = 1m, h = 0.001m, $E = 2.06\text{x}10^{11}$ N/m², ρ = 7800kg/m³ and $\nu = 0.3$).

For the nonlinear analysis, the transversal displacement field is obtained by applying the perturbation technique described in [2-6]. To start the perturbation procedure, it is necessary to consider a seed solution, which in this work is the sum of the linear vibration modes involved in the internal resonance (Table 1) [2-3, 6]. The perturbation procedure leads to a modal solution that considers naturally all modal coupling and interaction concerning these modes. However the obtained general modal solution is extremely long and for easy understanding only the considered modes are shown here.

The modal solution for the cylindrical panel with 1:1 internal resonance is given by:

$$\begin{aligned} w=&\left[A1_{11}(t)\,\sin(r)+A1_{13}(t)\,\sin(3r)+A2_{11}(t)\,\sin(2r)+A2_{13}(t)\,\sin(6r)\right]\sin(q)\\ &+\left\{A3_{22}(t)\left[3/4-\cos(2r)+1/4\cos(4r)\right]+A4_{22}(t)\left[3/4-\cos(4r)+1/4\cos(8r)\right]\right\}\\ &\left[3/4-\cos(2q)+1/4\cos(4q)\right] \end{aligned} \tag{5}$$

while for the cylindrical panel with 1:3 internal resonance the obtained modal solution is given by:

$$\begin{aligned} w=&\left[A1_{11}(t)\,\sin(q)+A1_{13}(t)\,\sin(3q)+A1_{15}(t)\,\sin(5q)+A1_{17}(t)\,\sin(7q)\right]\sin(r)\\ &+\left\{A1_{22}(t)\left[3/4-\cos(2q)+1/4\cos(4q)\right]+A2_{22}(t)\left[3/4-\cos(6q)+1/4\cos(12q)\right]\right\}\\ &\left[3/4-\cos(2r)+1/4\cos(4r)\right] \end{aligned} \tag{6}$$

and for the case with 1:1:2 internal resonance the considered modal solution is:

$$
\begin{aligned}
w=&\left[A1_{11}(t)\sin(r)+A2_{11}(t)\sin(2r)+A2_{13}(t)\sin(6r)+A3_{13}(t)\sin(3r)\right]\sin(q)+\\
&\left[A3_{11}(t)\,\sin(r)+A3_{13}(t)\,\sin(3r)\right]\sin(2q)+\left\{A4_{22}(t)\left[3/4-\cos(2r)+1/4\cos(4r)\right]\right.\\
&\left.+A5_{22}(t)\left[3/4-\cos(4r)+1/4\cos(8r)\right]\right\}\left[3/4-\cos(2q)+1/4\cos(4q)\right]\\
&+A6_{22}(t)\left[3/4-\cos(2r)+1/4\cos(4r)\right]\left[3/4-\cos(4q)+1/4\cos(8q)\right]
\end{aligned}
\tag{7}
$$

These modal solutions, Eqs. (6)-(7), ensure the convergence of the backbone and resonance curves up to vibration amplitudes of the same order as the shell thickness [6]. These expressions satisfy the following transversal boundary conditions:

$$
\begin{aligned}
&w(0,\theta)=w(L,\theta)=w(x,0)=w(x,\Theta)=0\\
&M_x(0,\theta)=M_x(L,\theta)=M_\theta(x,0)=M_\theta(x,\Theta)=0
\end{aligned}
\tag{8}
$$

To obtain the Airy stress function f, the modal expansion in Eq. (5-7), depending on the case, is substituted into Eq. (2), together with the geometrical imperfection, Eq. (4), and the compatibility equation is solved analytically. The obtained stress function and the chosen modal expansion are then substituted into equation of motion, Eq. (1), and discretized by using the standard Galerkin method.

Figure 1 shows the variation of the natural frequency of imperfect cylindrical panel, normalized with respect the natural frequency of perfect cylindrical panel, with the magnitude of geometrical imperfection. It is observed from Fig. 1a that for negative values of C_1/h the natural frequency of both vibration modes diverge and the 1:1 internal resonance is destroyed. On the other hand, for positive values of C_1/h the 1:1 the two frequencies remain sufficiently close to ensure the 1:1 internal resonance. In the 1:3 and 1:1:2 internal resonances cases, the amplitude of the geometrical imperfection in the analyzed range maintain the natural frequencies remains nearly commensurate, so that the influence of the internal resonance is always observed.

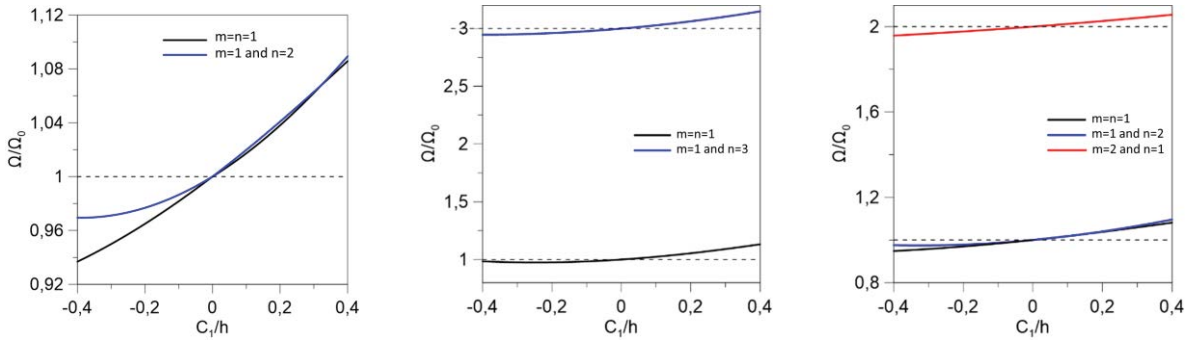

(a) 1:1 internal resonance (b) 1:3 internal resonance (c) 1:1:2 internal resonance

Figure 1: Variation of the normalized natural frequency with the amplitude of initial geometric imperfection for the different cases of internal resonance.

When an initial geometrical imperfection in the shape of fundamental vibration mode with amplitude C_1/h is considered, it is observed in Fig. 2 that the resonance curves are dependent of magnitude and sign of the geometric imperfection. For a positive value of imperfection (blue curve), the resonance curve moves to the right compared with the perfect case (black curve) due to the increase of the natural frequency of imperfect panel (see Fig. 1). On the other hand, for negative value of imperfection (purple curve) the resonance curve moves to the left due to the decreasing value of the natural frequency according with Fig 1.

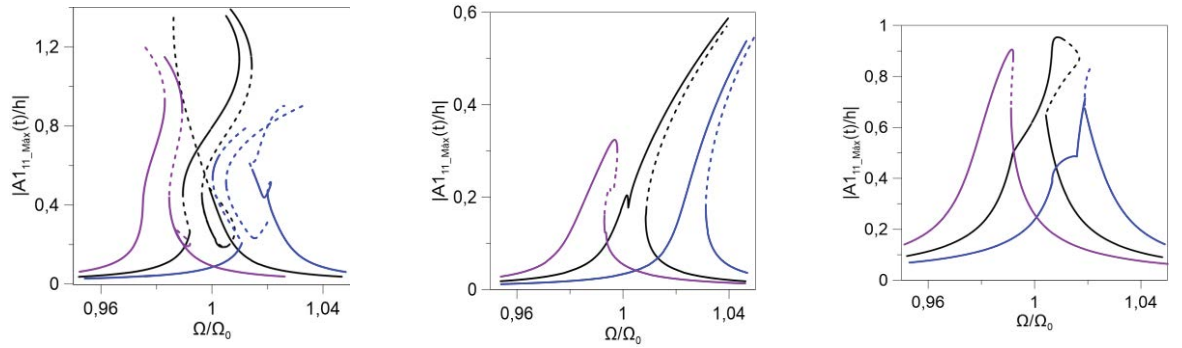

(a) 1:1 internal resonance (b) 1:3 internal resonance (c) 1:1:2 internal resonance

Figure 2: Resonance curves of perfect and imperfect panel – amplitude of driven mode and imperfection in the shape of driven mode. (pl = 0.5 kN/m²; η_1 = 0.001; —— C_1/h = -0.10; ---- C_1/h = 0.0; —— C_1/h = 0.10).

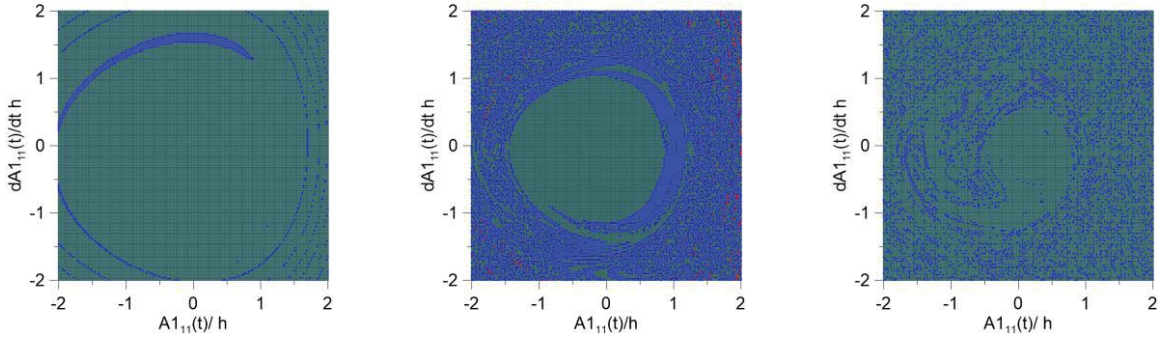

(a) C_1/h = -0.10 - Ω/Ω_0 = 0.98 (b) perfect panel - Ω/Ω_0 = 1.005 (c) C_1/h = 0.10 - Ω/Ω_0 = 1.005

Figure 3: Basin of attraction for 1:1 internal resonance case considering selected values of frequency of excitation. (pl = 0.5 kN/m²; η_1 = 0.001)

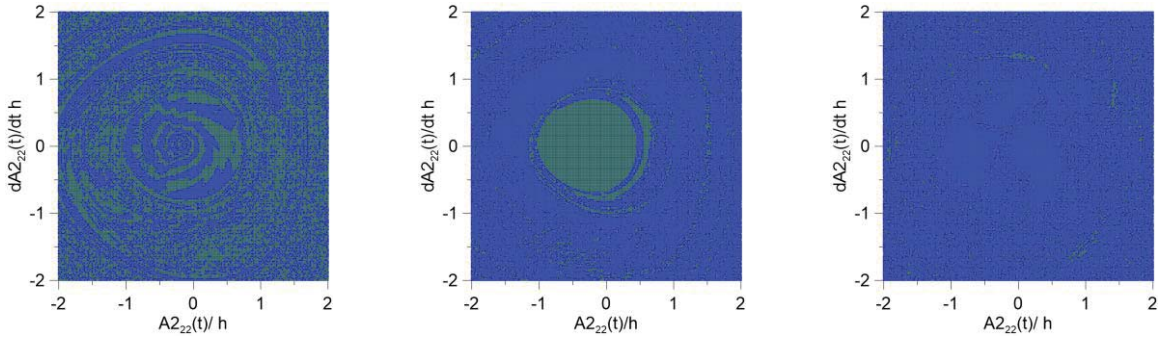

(a) C_1/h = -0.10 - Ω/Ω_0 = 0.98 (b) perfect panel - Ω/Ω_0 = 1.005 (c) C_1/h = 0.10 - Ω/Ω_0 = 1.021

Figure 4: Basin of attraction for 1:1:2 internal resonance case considering selected values of frequency of excitation. (pl = 0.5 kN/m²; η_1 = 0.001)

The presence of an initial geometrical imperfection changes strongly the resonance curves, creating news stable paths and dynamic jumps and increases the nonlinearity and complexity of the panel response for each evaluated internal resonance as illustrated by, for example, the basins of attraction given by Figs. 3 and 4 for the 1:1 and 1:1:2 internal resonance cases, respectively. The competition between the resonant and non-resonant attractors lead to large fractal regions and sensitivity to initial conditions. The presented basins of attractions in Figs.

3 and 4 agree with the resonance curves in Fig. 2 with respect the number of detected attractors for the chosen values of excitation frequency.

4 CONCLUDING REMARKS

A new consistent modal solution, that takes into account the modal interaction between two, or three, different vibration modes, previously developed by the authors, is applied in this work to investigate the influence of an initial geometrical imperfections on the resonance curves of a cylindrical panel displaying three distinct cases of internal resonance. It is verified in free vibration analysis that positive geometric imperfection in the form of the fundamental mode increases the stiffness of the cylindrical panel, and, consequently its natural frequencies, while negative imperfections causes a decrease in the natural frequencies involved in the internal resonance. The forced vibrations of the cylindrical panel with an initial geometrical imperfection in the shape of fundamental mode modifies the vibration amplitudes, the dynamic stability and bifurcation scenario of the resonance curves, leading to strong competition between the resonant and the non-resonant attractors which in its turn leads to highly intertwined fractal basins of attraction in the main region of resonance.

ACKNOWLEDGEMENTS

This work was made possible by the support of the Brazilian Ministry of Education, CAPES, CNPq, FAPERJ and FAPEG.

REFERENCES

[1] P. B. Gonçalves, Z. J. G N Del Prado, Effect of non-linear modal interaction on the dynamic instability of axially excited cylindrical shells, *Computers and Structures* 82, pp. 2621-2634, 2004.

[2] L. Rodrigues, F. M. A. Silva, P. B. Gonçalves, Z. J. G. N. Del Prado, Effects of modal coupling on the dynamics of parametrically and directly excited cylindrical shells, *Thin-walled structures* 81, pp. 210-224, 2013.

[3] L. Rodrigues, P. B. Gonçalves, F. M. A. Silva, Internal resonances in a transversally excited imperfect circular cylindrical shell, *Procedia Engineering* 199, pp. 838-843, 2017.

[4] P. B. Gonçalves, R. C. Batista, Non-linear vibration analysis of fluid-filled cylindrical shells, *Journal of Sound and Vibration* 127, pp. 133-143, 1988.

[5] F. M. A. Silva, H. A. R. Sattler, P. B. Gonçalves, Z. J. G. N. Del Prado, Influence of modal coupling on the nonlinear vibration of simply supported cylindrical panels, *Applied Mechanics and Materials* 849, pp. 106-118, 2016.

[6] F.M.A. Silva, W.A. Vaz, P.B. Gonçalves, Internal resonances in an imperfect circular cylindrical panel. In: Lacarbonara W., Balachandran B., Ma J., Tenreiro Machado J., Stepan G. (eds) *Nonlinear Dynamics of Structures, Systems and Devices.* Springer, Cham, ISBN: 978-3-030-34712-3, 2020.

EURODYN 2020
XI International Conference on Structural Dynamics
M. Papadrakakis, M. Fragiadakis, C. Papadimitriou (eds.)
Athens, Greece, 23–26 November 2020

ON THE WAVE DYNAMICS OF MICROSCALE BISTABLE TENSEGRITY STRUCTURES

A. Micheletti[1], Z. Vangelatos[2], N. Singh[3], C.P. Grigoropoulos[2] and F. Fraternali [3]

[1]Deptt. of Civil and computer Science Engineering
University of Rome, Tor Vergata, Italy
e-mail: micheletti@ing.uniroma2.it

[2] Dept. of Mechanical Engineering, University of California
UC, Berkeley, USA
e-mail: {zacharias_vangelatos, cgrigoro}@berkeley.edu

[3] Dept. of Civil Engineering, University of Salerno
Salerno, Italy
e-mail: {snarinder, f.fraternali}@unisa.it

Keywords: Bistable units, Tensegrity architecture, Multiphoton lithography, Lattice metamaterials

Abstract. *This work deals with the design, the mechanical modeling and the experimental testing of microscale lattice structures tessellating bistable tensegrity prisms. The analyzed units have only one internal mechanism and one self-stress state, and can be transformed into bistable structures, by replacing the cables with bars, and suitably adjusting the members' lengths. We experimentally validate the theoretical prediction of the response of spatial assemblies of such units, through mechanical tests on physical models fabricated by multiphoton lithography. We also numerically show that the examined structures support the propagation of compact compression waves under impact loading, which paves the way to their use for the fabrication of novel acoustic lenses with tensegrity architecture.*

1 INTRODUCTION

In the past several years, the advancement in additive manufacturing (AM), and especially in nano and micro scale printing, has taken a big leap, opening a new era for futuristic materials and material sciences. Research on metamaterials is one of the most focused area because of their unprecedent properties arising from the physical structure of the lattices. Generally, materials in their original and/or traditional form do not show better properties as compared to those shown by the same material but in a designed architected shape. Due to their particular architecture, which can confer them high strength to weight ratio, frequency bandgaps, negative overall moduli and negative mass density, they possess highly stable physical characters [**?**, **?**]. Success in producing metamaterials with extraordinary properties has been achieved at the macroscale level. However, due to their usually complex geometry, it is quite difficult to produce micro- and nanoscale metamaterials with AM techniques [**?**]. Tensegrity architectures represent some of the most complex forms, making them difficult to produce as well. Nevertheless, due to their nonlinear properties they are one of the most suitable candidates for morphing structures [**?**]. Tensegrities have originally been used for producing free-standing prestressed systems with cables in tension and bars in compression. In addition, since they exhibit various non-linear static and dynamic properties, arising from their connectivity, geometry and internal mechanisms, tensegrity systems have become more popular and subject of research [**?**]- [**?**]. Various stable configurations are possible only with change in stress levels and in the lengths of cables and bars. In this way it becomes possible to have bi-stable tensegrity structures, and some of the recent studies have found bi-stable tensegrities at macroscopic scale. This commendable property can be highly inspirational in producing reconfigurable metamaterials and structures based on tunable tensegrity structures [**?**]. One paradigmatic example presented by Calladine [**?**] can be examined to understand the behavior of tensegrity structures, this is shown in Figure **??**. In

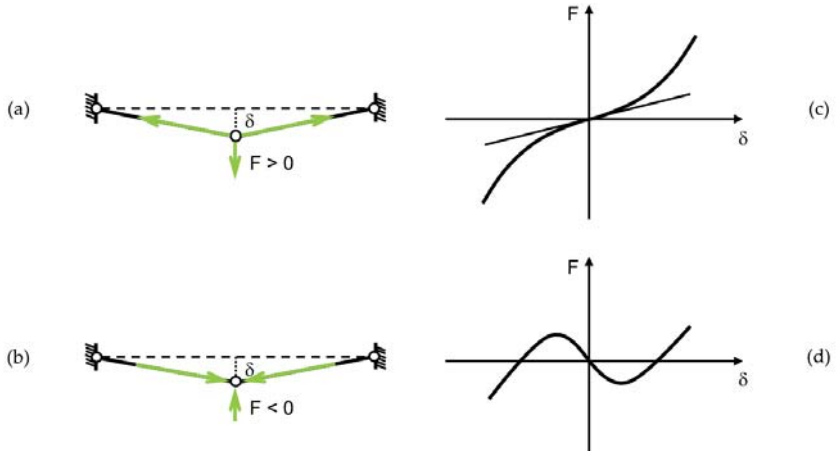

Figure 1: Behavior of the two-element system in various prestress states.

Figure **??** (a) two pre-stressed elements are hinged at three points placing the mechanism in equilibrium state when the pre-stress is positive (cables in tension). The same configuration can be turned into an unstable equilibrium one if the sign of the stress is changed as shown in the Figure **??** (b). The resulting nonlinear behaviour under load is related to the sign of pre-stress is as shown in Figure **??** (c, d). It has been observed that if the rest length of the elements is increased slightly with respect to the lengths in the equilibrium state, then system becomes

bi-stable by showing the two different stable configurations. It is worth noticing that, the AM of cables poses a challenge because present day technologies are not yet capable of manufacturing such elements, while the manufacturing of bars are feasible with various AM processess. One option to overcome this challenge is to manufacture corresponding lattice structures by keeping nodal positions the same, allowing for bending stresses to be present in the structure. Bending stresses can be mitigated by manufacturing the ends of the bars in a tapered way or by introducing flexible hinges. The limitation of this procedure is that hinges does not behave in a perfect manner. However, lattice structures obtained from tensegrity systems can still inherit some of their nonlinear properties, included the bistable behavior.

2 Materials and methods

2.1 Bi-stable configuration from monostable tensegrity structures

A method to obtain bi-stable system based on tensegrity systems can be devised by following the analogy with the system shown in Figure **??**. When the system has only one stable configuration, then it is termed as monostable and if it has two stable configurations, it is termed as bi-stable system. It is possible for such a system to have a stable self-stress state when the two elements are in tension, introducing first-order stiffness to internal mechanism. In a system consisting of two linearly elastic member, the load-displacement relationship can be approximated by a cubic-polyomial equation. In such a system, the slope of the curve in the origin is always directly proportional to the self-stressing forces. By changing the sign of the self-stress the system can be turned into an unstable one. In addition, when the elements are unstressed, the systems is placed in either one of two stable configurations. The load-displacement curve in this case is similar to that shown in Figure **??** (d). Two example in three dimensions are

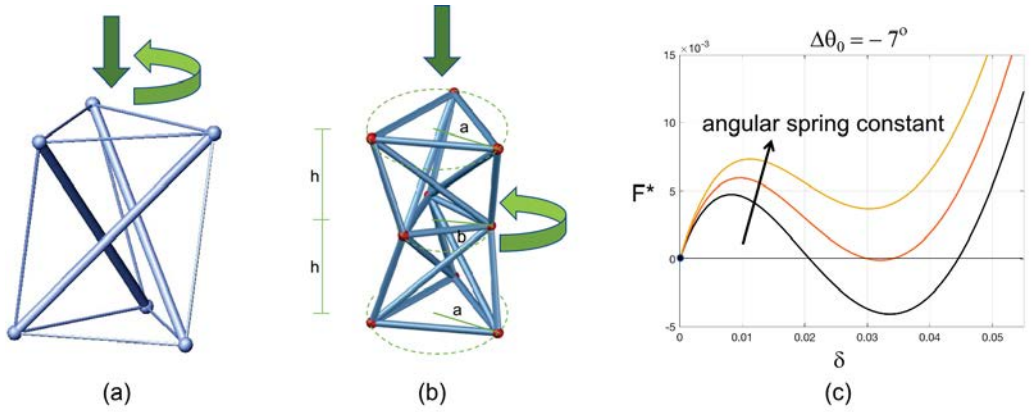

Figure 2: Tensegrity prism (a). Dual tensegrity prism (b). Examples of force-displacement diagrams for the dual tensegrity prism subjected to a vertical load (c). The three $F^* \, vs \, \delta$ curves correspond to increasing values of the angular spring constant k_s, with the black curve corresponding to $k_s = 0$, the orange (dark grey) curve corresponding to $k_s = 0.8 \mu N \mu m$, and the yellow (light grey) curve corresponding to $k_s = 1.6 \mu N \mu m$ (see the other model parameters in the text). The force parameter $F^* = F/(dk_a)$ is given by the applied vertical force F divided by the bars' diameter d and by an axial spring constant equal to $k_a = 99.07 \mu N/\mu m$, while the displacement parameter δ is the ratio between the vertical displacement and $2h$.

presented in Figure **??** (a) and (b). The first one is the classical-tensegrity triangular prism (See Figure **??** (a)), while the second one is a dual tensegrity prism, realized with bars only, obtained by superposition of two mirror copies of a same tensegrity prisms. When a verti-

cal load is applied to the tensegrity prims, it causes a roto-translation of the top triangle with respect to the bottom triangle (see green arrows in Figure **??**, a). When a vertical load is applied on the dual tensegrity prism, it causes a roto-translation of the middle triangle, and just a relative translation of the top triangle, with respect to the bottom one. Bi-stable structures can be obtained by following these steps: (i) a pre-stressed stable tensegrity structure should be found with one independent self-stress state and one internal mechanism, (ii) a slightly displaced, unstressed configuration of the same structure should be considered, (iii) a numerical model should be adopted to obtain bi-stable response under static loading, (iv) the geometry and material properties cab be adjusted according to the available fabrication methods and experimentation conditions, (v) fabricated structures should be subjected to the experimental tests in order to confirm the designed behaviour the model. To this purpose, a dual bistable lattice have been considered, as shown in Figure **??** (b), and corresponding force-displacement diagrams have been computed (see Figure **??** (c)). A Stick-and-Spring model has been adopted in such computation [**?**, **?**], where the elements of the structure are considered as axial springs, and angular springs responds to change in angles between certain pairs of adjacent bars. While the stable configuration of a tensegrity prism corresponds to a relative rotation between top and bottom triangles of $\theta_0 = 150$ degrees, in the dual tensegrity prism the initial relative rotation between bases in each prism is $\theta_0 = 150 + \Delta\theta_0$. The plots in Figure **??** (c) are obtained considering an elastic material of Young's modulus $E = 1.2GPa$ (typical of polymers used in multiphoton lithography), members' diameter $d = 0.75\mu m$, top and bottom base radius $a = 5\mu m$, middle base radius $b = 3.5\mu m$, prism height $h = 10\mu m$. The three $F^* \, vs \, \delta$ curves correspond to increasing values of the angular spring constant k_s, with the black curve corresponding to $k_s = 0$, the orange (dark grey) curve corresponding to $k_s = 0.8\mu N\mu m$, and the yellow (light grey) curve corresponding to $k_s = 1.6\mu N\mu m$. The force parameter $F^* = F/(dk_a)$ is given by the applied vertical force F divided by the bars' diameter d and by an axial spring constant equal to $k_a = 99.07\mu N/\mu m$ (obtained considering a nominal member length of $5.35\mu m$). The displacement parameter δ is the ratio between vertical displacement and $2h$.

2.2 Fabrication by multiphoton lithography (MPL) technology

The structure in Figures **??** (a), composed of three dual prisms, has been considered for fabrication. The specimen shown in Figures **??** (b) has been fabricated with the help of the multiphoton lithography (MPL) technology. The material used was obtained by mixing of several organic-inorganic constituents: Zr-DMAEMA consisting of 70 wt % zirconium propoxide, 10 wt% (2-dimethylaminoethyl) methacrylate (DMAEMA) (Sigma-Aldrich), and 20 wt% ASTM type II deionized, distilled water. First, 1.4 ml of 3-(trimethoxysilyl)propyl methacrylate (MAPTMS) (Sigma-Aldrich) were mixed with 0.14 gr of hydrochloric acid into a vial. Afterwards, 137.7 μl of DMAEMA were mixed with 0.66 ml of zirconium (IV) propoxide solution containing 70 wt% 1-propanol in another vial. Then the two mixtures have been added together and diluted with 0.2 ml of distilled water and 0.016 gr of photoinitiator consisting of 4,4-bis(diethylamino)benzophenone (Sigma-Aldrich). Fabrication was performed 24 hour after placing it on glass substrate in vacuum. Multi-level experimentation was performed to ensure the least experimental error. After preparation of samples as shown in Figure **??** (b), samples were subjected to the multiple tests by nano-indentation.

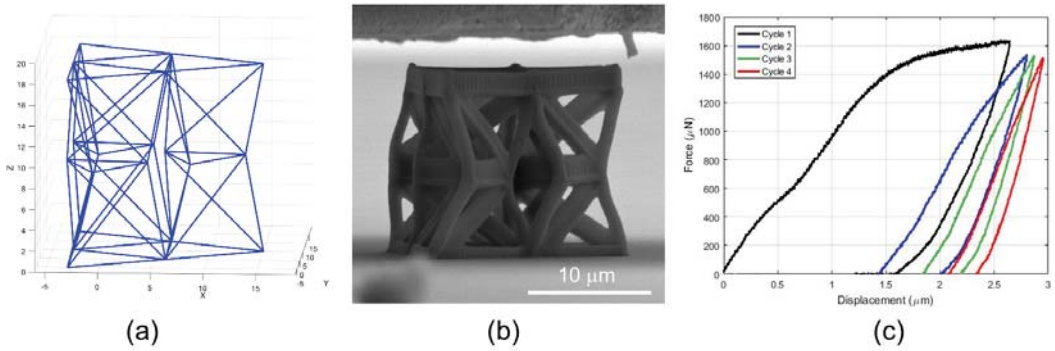

Figure 3: Model of fabricated structure (a). Sample fabricated by MPL and subjected to a compression test (b). Force-displacement curve for a cyclic loading-unloading compression test (c).

3 Compression test

After fabrication of the samples with the help of MPL, multi unit array compression tests were performed at the minuscule scale shown in Figure **??** (b) to analyze the behaviour of the fabricated samples in order to understand the major effects and experimental accuracy of MPL fabrication technology. The obtained force-displacement relationship are shown in Figure **??** (c). Twisting of the middle triangle during testing has been observed. In the force-displacement graph the softening behavior of the system has been seen and at the same time residual deformation has been seen after unloading. The elastic model developed earlier shows a behavior consistent with that depicted in Figure **??** (c). In addition, material behaves in slight viscoelastic manner when loading-unloading cycles were applied. An estimate of the critical damping factor that can be associated to our force-displacement curves in Fig. **??**(c) gives a damping ratio greater than 10% in the first cycle, reducing to few percents in the fourth cycle.

4 Wave dynamic applications

A major application of the nano lattice structures is in wave dynamics. The response of the bistable structure exhibiting the single soft mode can also be used in carrying mechanical energy through compact solitary waves. Figure **??** shows the design of a chain of tensegrity-based

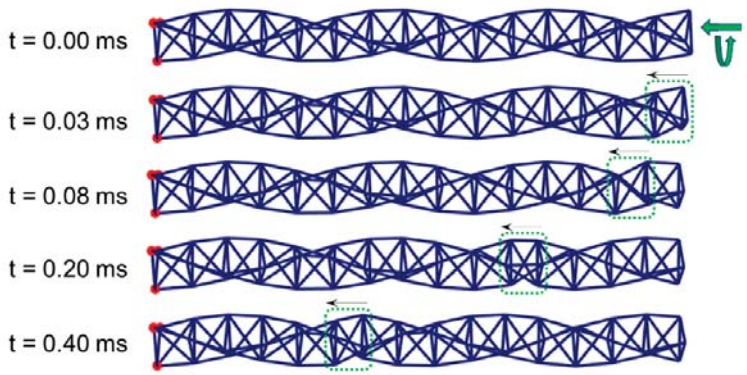

Figure 4: Various stages of motion of a column of fifteen bistable prisms.

units, fixed at the one end, which can be useful in wave dynamic applications and in the area of

non-linear mechancal metamaterials. The concept design of the bistable tensegrity architecture shown in Figure **??** can be very helpful to formulate the mechanical metamaterials. This design, which is fixed at one end and free at other end, can be tested for wave dynamic applications according to the procedure given in refs. [**?**,**?**], which shows that the design is capable of forming compression waves when impulsive load is applied at the free end. The Figure **??** shows the behavior of such system at discrete times, after being impacted with initial horizontal speed of v_0 and angular speed ω of the end triangle so that the bistable mechanism get activated. The dimensions of such system comprises of *a/h* = 0.5, $\Delta\theta_0$ = -3, $v_0(\mathrm{E}/\rho)^{0.5}$= 0.3609, $v_0/\omega_0 = a^2/h$, $k_s/(a^2 k_a)$= 0.0041, with a the circumscribed radius of the base triangle, h the height of a prism, E the Young's modulus, k_a and k_s the axial and angular spring constant respectively, and ρ denoting the mass density of the material. In this system localization of compression waves was observed at one unit in the chain, while almost no movement in rest of the system has been observed. This 'localized' behavior of such system can be highly useful in designing the revolutionary acoustic lenses, which can be used in non-invasive scalpel to accurately locate the defects in various biological or engineering materials. In addition, the highly non-linear structures can be used to generate compact solitary waves in tensegrity acoustic lenses. Further studies will be focused on the generation of such bistable unit cells.

5 Concluding remarks

In this research work the bistable mechanical response of microlattice structures with nanoscale features and tensegrity architecture has been studied. The MPL technology has been employed to additively manufacture physical models of the investigated structures.These models have been tested under compression loading, and their bistable response, combined with viscoelastic behavior, has been experimentally verified. Numerical simulations have shown that the examined lattices support the propagation of compression compact waves under the application of compression forces and twisting moments at one end. Such a behavior can be profitably employed to fabricate novel acoustic lenses that are able to focus the mechanical energy in very narrow regions of space within a host body.

Acknowledgements

This research is partially supported by the National Science Foundation (NSF) under the Scalable 475 Nanomanufacturing (SNM) Program, grant number 1449305. A.M. acknowledges financial support from the Italian Ministry of Education, University, and Research (MIUR) under the PRIN 2017 National Grant '3D printing: a bridge to the future' (grant number 2017L7X3CS_004). N.S. and F.F. acknowledge financial support from MIUR under the PRIN 2017 National Grant 'Multiscale Innovative Materials and Structures'(grant number 2017J4EAYB).

REFERENCES

[1] Z. Liu, X. Zhang, Y. Mao, Y. Y. Zhu, Z. Yang, C. T. Chan, P. Sheng, Locally resonant sonic materials. *Science*, **289**, 1734-1736, 2000.

[2] L.R. Meza, S. Das, J.R. Greer, Strong, lightweight, and recoverable three-dimensional ceramic nanolattices, *Science*, **345**, 1322-1326, 2014.

[3] S. Walia, C.M. Shah, P. Gutruf, H. Nili, D.R. Chowdhury, W. Withayachumnankul, M. Bhaskaran, and S. Sriram, Flexible metasurfaces and metamaterials: A review of mate-

rials and fabrication processes at micro-and nano-scales. *Applied Physics Reviews*, **2(1)**, 011303, 2015

[4] A. Iscen, A.Agogino, V.SunSpiral, and K.Tumer, Controlling tensegrity robots through evolution. *In Proceedings of the 15th annual conference on Genetic and evolutionary computation*, 1293-1300, 2013

[5] R.E., Skelton, F., Fraternali, G. Carpentieri, and A., Micheletti, 2014. Minimum mass design of tensegrity bridges with parametric architecture and multiscale complexity. *Mechanics Research Communications*, **58**, 124-132, 2014.

[6] D.E., Ingber, Tensegrity-based mechanosensing from macro to micro. *Progress in biophysics and molecular biology*, **97(2-3)**,163-179, 2008.

[7] D.E., Ingber, Tensegrity I. Cell structure and hierarchical systems biology. *Journal of cell science* , **116(7)**,1157-1173, 2003.

[8] I., Stern, Harris Corp, Deployable reflector antenna with tensegrity support architecture and associated methods. U.S. Patent 6,542,132, 2003.

[9] J. Quirant, M.N. Kazi-Aoual, and, R., Motro, Designing tensegrity systems: the case of a double layer grid. *Engineering structures*, **25(9)**,1121-1130, 2003.

[10] B. Jenett, S. Calisch, , D. Cellucci, N. Cramer, N. Gershenfeld, S. Swei, and K.C. Cheung, Digital morphing wing: active wing shaping concept using composite lattice-based cellular structures. *Soft robotics* , **4(1)**, 33-48, 2017.

[11] C.R. Calladine, Buckminster Fuller's "Tensegrity" Structures and Clerk Maxwell's Rules for the Construction of Stiff Frames, *International Journal of Solids and Structures*, **14(2)**, 161-172, 1978.

[12] F. Fraternali, L. Senatore, C. Daraio, Solitary waves on tensegrity lattices. *Journal of the Mechanics and Physics of Solids*, **60**, 1137-1144, 2012.

[13] F. Fraternali, G. Carpentieri, A. Amendola, R.E. Skelton, V.F. Nesterenko, Multiscale tunability of solitary wave dynamics in tensegrity metamaterials. *Applied Physics Letters.*, **105**, 201903, 2014.

[14] C. Davini, A. Micheletti, P. Podio-Guidugli, On the impulsive dynamics of T3 tensegrity chains, *Meccanica*, **51**, 2763-2776, 2016.

[15] A. Micheletti, G. Ruscica, F. Fraternali, On the compact wave dynamics of tensegrity beams in multiple dimensions. *Nonlinear Dynamics*, **98**, 2737-2753, 2019.

[16] A. Favata, A. Micheletti, P. Podio-Guidugli, A Nonlinear Theory of Prestressed Elastic Stick-and-Spring Structures, *International Journal of Engineering Sciences*, **80**, 4-20, 2014.

[17] A. Amendola, A. Favata, A. Micheletti, On the mechanical modeling of tensegrity columns subject to impact loading. *Frontiers in Materials*, **5**, 1-22, 2018.

EURODYN 2020
XI International Conference on Structural Dynamics
M. Papadrakakis, M. Fragiadakis, C. Papadimitriou (eds.)
Athens, Greece, 23–26 November 2020

PIECEWISE CONSTRUCTION OF WAVE DISPERSION CURVES IN ELASTIC PERIODIC NETWORKS BY ASYMPTOTIC MULTI-SCALE APPROACH

A. Rallu, C. Boutin, S. Hans[1]

[1]ENTPE
LGCB/LTDS CNRS UMR 5513 ENTPE, Vaulx-en-Velin
e-mail: antoine.rallu@entpe.fr

Keywords: Periodic media; Dispersion curve; modulation; high frequency; multi-scale method

Abstract. *Dynamics at low frequencies of periodic heterogeneous media is conventionally described by the method of homogenization of periodic media, when it exists a scale separation between displacements and the characteristic size of a cell irreducible from the media. At higher frequency, this separation of scales is lost and the homogenization method becomes obsolete. In order to cross this barrier, we propose to consider periodic modes over a period composed of several irreducible cells. Around the eigenfrequencies of these multicells periods with periodic boundary conditions, large evolution situations emerge. A new separation of scales is therefore defined between the amplitude of the mode and the characteristic size of the period. The equations governing the modulation are thus obtained, and their nature differs if the mode considered is single or multiple.*

From the macroscopic modulation equations we can extract an approximation of the fundamental dispersion curve, in the vicinity of the periodic eigenmodes of the multi-cells period. Consequently, a construction by parts of the fundamental dispersion curve is provided.

1 Introduction

This paper falls within the study of macroscopic dynamic behaviour of periodic media. In most cases, analytic description is not reachable and the problem is solved via a numeric computation of the dispersion curves, which carry all the dynamic properties of the system. We propose in this paper an analytic method for reaching parts of the dispersion curves via an asymptotic multi-scale method. This method is first full described on a periodic network of spring-mass, for which the dispersion curve is well-known. In a second time, we evidence the power of this methodology to periodic reticulated beams, which present a more complex behaviour.

At low frequency, when there is a large scale separation between the length of the cell and the characteristic size of the vibrations, the classical homogenization method allows efficiently to establish the continuous equivalent description. This scale separation is lost for frequencies higher than the diffraction frequency. However, instead of considering the amplitude of the mean displacement in a unit cell, it appears that the concept of scale separation may still be used when considering the amplitude of periodic eigenmodes defined on (multi-)cells. Thus, the same principle of asymptotic multi-scale method enables to describe the large scale modulations around the eigenfrequencies of the mono- and/or multi-cells period. Finally, the properties of the modulation are straightforwardly related to the dispersion curves at the considered frequencies.

2 Exact dispersion relations in 1D spring-mass chains.

Exact wave dynamics of a spring-mass chain is well known for harmonic waves at any frequency in such systems. However a new point of view is provided by the modulation analysis as initially proposed in Daya *et al.* (2002), Craster *et al.* (2010), or in (Boutin *et al.*, 2012) using a multi-cells approach.

2.1 Classical analysis

Consider a periodic 1D spring-mass system whose irreducible period Ω is constituted by a massless spring of stiffness k, length ℓ, and a rigid mass m. Studying harmonic wave propagation at the angular frequency ω, the balance of forces on the n^{th} mass (i.e. on the n^{th} cell Ω), reads

$$(v_{n+1} - 2\,v_n + v_{n-1}) + \chi_\omega\, v_n = 0, \quad \chi_\omega = (\omega/\omega_0)^2, \quad \text{and} \quad \omega_0 = \sqrt{\frac{k}{\mathrm{m}}} \tag{1}$$

Then the motion v_n of n^{th} mass is on the form : $v_n = V_0 e^{i(\omega\, t - \mathrm{k}_\omega\, n\, \ell)}$ where k_ω is the wave number. Thus (1) leads to the dispersion relation:

$$4\sin^2\left(\frac{\mathrm{k}_\omega\,\ell}{2}\right) = \chi_\omega = \left(\frac{\omega}{\omega_0}\right)^2 \tag{2}$$

Consequently $2\omega_0$ corresponds to the absolute cut-off angular frequency, separating propagating and non propagating waves. That is in the angular frequency range $\omega \leq 2\omega_0$, the waves can propagate with the wave number k_ω defined by the dispersion relation (2). Long wavelengths correspond to $\mathrm{k}_\omega\ell \to 0$ so that successive masses follow almost the same motion. From the dispersion relation (2), this situation is reached at low angular frequency, $\omega \ll \omega_0$. Furthermore, expanding (2) near zero gives :

$$|\mathrm{k}_\omega|\ell \simeq \frac{\omega}{\omega_0}$$

thus $|\mathrm{k}_\omega| \simeq \omega/\sqrt{k\ell^2/\mathrm{m}}$ when $\omega \ll \omega_0$, i.e the dispersion relation matches the usual description of long wave propagation in a 1D medium of lineic elastic modulus $k\ell$ and lineic mass m/ℓ.

2.2 Multi-cells analysis

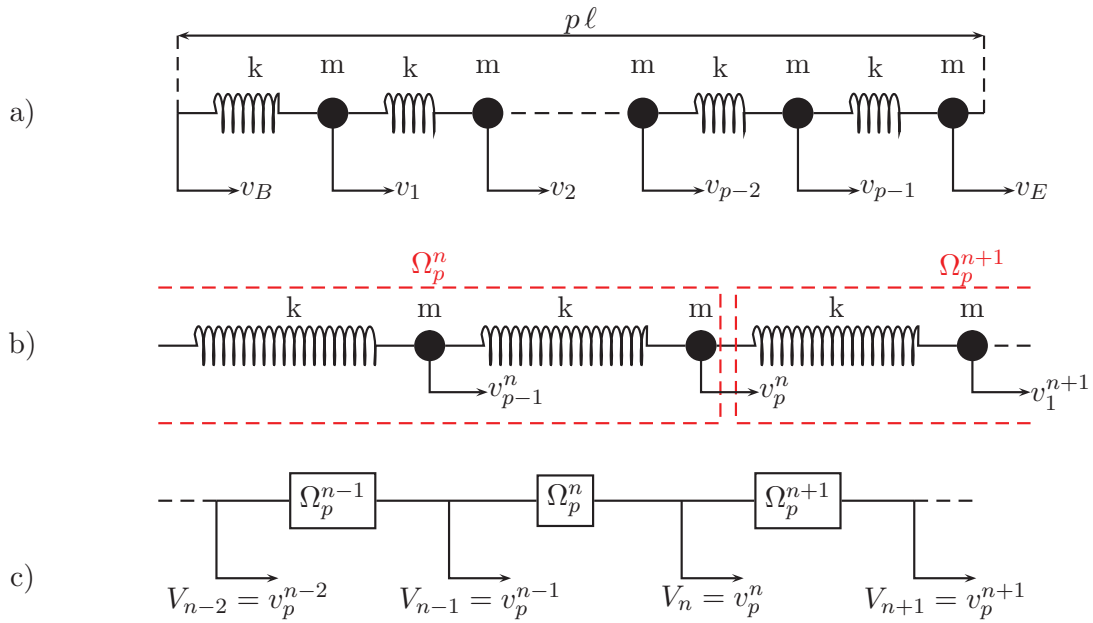

Figure 1: Multi-cells approach. a) A multi-cells period Ω_p made of p spring-mass (length ℓ, stiffness k, mass m) with extremity motions v_B and v_E as limit conditions. b) The two last masses of n^{th} multi-cells Ω_p and the first mass of $(n+1)^{th}$ Ω_p. c) Macroscopic viewpoint : the displacement of the p^{th} mass of the n^{th} multi-cells Ω_p defines the leading displacement $V(x_n)$ of this period.

Dispersion equation (2) shows that the only situation presenting an evolution at large scale is found in the vicinity of $\omega \simeq 0$. In order to find other situations, we now investigate the same spring-mass chain, but with a period Ω_p made of p irreducible cell Ω, that is $\Omega_p = \bigcup_p \Omega$. We denote $V_n = v_{np}$ the motion of an edge the n^{th} period Ω_p, and $v_{np+m}, 0 < m < p$ the motion of inner masses of Ω_p, which can be liked to V_n and V_{n+1} by the following expression :

$$v_{np+m} = \frac{(\beta_\omega^{p-m} - \beta_\omega^{m-p})\, V_n + (\beta_\omega^m - \beta_\omega^{-m})\, V_{n+1}}{\beta_\omega^p - \beta_\omega^{-p}} \quad ; \quad 0 \leq m \leq p \tag{3}$$

By construction, expression (3) insures that the dynamic balance is satisfied for the inner masses of Ω_p, with $\beta_\omega^p + \beta_\omega^{-p} = 2 - \chi_\omega$

$$V_{n-1} - \left(\beta_\omega^p + \beta_\omega^{-p}\right)\, V_n + V_{n+1} = 0 \tag{4}$$

When $\beta_\omega^p = 1$ then $V_n = V_{n+1}$ which means that motions are Ω_p-periodic. In other words the p^{th} roots of the unity lead to large scale evolution. The expression of these roots are (Int(.) stands for the Integer part)

$$\left\{ \beta_{\omega\,\frac{q}{p}} = \exp(\pm i \frac{q}{p} 2\pi) \qquad \forall q \in [\![0; \mathrm{Int}(\frac{p}{2})]\!] \right\}$$

Moreover, as $\beta_\omega = \exp(i\mathrm{k}_\omega \ell)$ we can express the wavenumbers and angular frequencies corresponding to the latter expression of $\beta_{\omega_{\frac{q}{p}}}$, see (2) :

$$\left\{ \mathrm{k}_{\omega_{\frac{q}{p}}} = \frac{q}{p}\frac{2\pi}{\ell} \quad ; \quad \omega_{\frac{q}{p}} = 2\omega_0 \sin(\frac{q}{p}\pi) \qquad \forall q \in [\![0; \mathrm{Int}(\frac{p}{2})]\!] \right\} \tag{5}$$

We can now rewrite (3) as :

$$v_{np+m} = a\Phi_m^{\frac{q}{p}} + b\Psi_m^{\frac{q}{p}} \quad \forall 0 \leq m < p\,;\, 0 \leq q \leq \mathrm{Int}(\frac{p}{2}) \text{ with } \begin{cases} \Phi_m^{\frac{q}{p}} = \cos(\mathrm{k}_{\omega_{\frac{q}{p}}} m\ell) \\ \Psi_m^{\frac{q}{p}} = \sin(\mathrm{k}_{\omega_{\frac{q}{p}}} m\ell) \end{cases}$$

where the set of eigenmodes $\{\Phi^{\frac{q}{p}}, \Psi^{\frac{q}{p}}\}$ respects the periodic boundary conditions of Ω_p. Moreover, since Ω_p owns p degrees of freedom, there are p modes. Note that $\Psi^0 = 0$ and, for p even, $\Psi^{\frac{1}{2}} = 0$. Hence the only single modes are Φ^0 and $\Phi^{\frac{1}{2}}$ (for p even) which are respectively associated with the zero frequency and the cut-off angular frequency $2\,\omega_0$, and lead to an identical (respectively opposite) motion of consecutive masses, independently of Ω_p. For $\frac{q}{p} \neq \{0, 1/2\}$, $\Phi^{\frac{q}{p}}$ and $\Psi^{\frac{q}{p}}$ are double modes associated with the angular eigenfrequency $\omega_{\frac{q}{p}}$ given by (5).

3 Wave dispersion curves derived through asymptotic multi-scale method

3.1 Large modulation of high frequency waves in a periodic network of resonators

The motions of a period Ω_p are periodic exactly at the periodic angular eigenfrequencies $\omega_{\frac{q}{p}}$ and, despite these motions vary at a scale ℓ, the amplitudes of the modes are constant over the whole Ω_p. Hence, in the vicinity of these angular frequencies, the mode amplitudes are no longer constant but present a large-scale evolution, compared to the size of the period. This allows to introduce the scale ratio $\varepsilon_p = \ell_p/L = p\,\ell/L$ where L reprents the modulation length. The macroscopic description is derived using the homogenization of discrete periodic media Caillerie *et al.* (1989), Hans et Boutin (2008), Sanchez-Palencia (1980) adapted to multi-cells period and high frequencies Rallu *et al.* (2018) :

- The first step is to introduce a continuous variable $V(x)$, as $V(x_n = n\ell_p) = V_n$. This variable represents the mode amplitude;
- Then, because of the small variation of $V(x)$ between x_n and x_{n+1}, a Taylor expansion is performed for the consecutive reference masses :

$$V_{n\pm1} = V\left(x_n \pm \ell_p\right) = V\left(x_n\right) \pm \ell_p \partial_x V\left(x_n\right) + \frac{\ell_p^2}{2}\partial_x^2 V\left(x_n\right) + \ldots$$

- The spatial and frequency variables are assymptotically exanded in powers of ε_p, for example

$$V(x) = V^{(0)}(x) + \varepsilon_p\, V^{(1)}(x) + \mathcal{O}(\varepsilon_p^2) \quad ; \quad \omega = \omega^{(0)} + \varepsilon_p\, \omega^{(1)} + \mathcal{O}(\varepsilon_p^2) \text{ with } \omega^{(0)} = \omega_{\frac{q}{p}}$$

  Note that the angular frequency is expanded around the periodic angular eigenfrequencies $\omega_{\frac{q}{p}}$;

- These three developments are then introduced in the balance equation (4);
- Finally, sort and collect the differents terms in ε_p powers. The dominant terms yield a non trivial equation that provides the macroscopic description at the leading order.

Applying this process leads to the following macroscopic descriptions at the leading order:

Low-frequency range i.e $q = 0, \omega \approx 0 + \varepsilon_p\, \omega^{(1)}$.

$$k\, \ell\, \partial_x^2 V + \frac{\mathrm{m}}{\ell}\, \omega^2\, V = \mathcal{O}\left(\varepsilon_p\right) \tag{6}$$

This case corresponds to the usual assumption of scale seration, where the variation of motion of two consecutive masses is very small. Note that in this case the mode amplitude matches the motion of the masses. This macroscopic equation describes the modulation the (simple) static mode.

Frequencies close to the cut-off frequency for p even, that is, $q = p/2$ and $\omega \approx 2\,\omega_0 + \varepsilon_p^2\, \omega^{(2)}$.

$$k\, \ell\ \partial_x^2 V + \frac{\mathrm{m}}{\ell}\left(-\omega^2 + \left(2\,\omega_0\right)^2\right)\, V = \mathcal{O}(\varepsilon_p) \tag{7}$$

This equation describes the modulation of a simple mode where two consecutive masses have opposite motions.

Frequencies close to the double eigenmodes frequencies i.e. $0 < q < \mathrm{Int}(p/2)$ and $\omega \approx \omega_{\frac{q}{p}} + \varepsilon_p\, \omega^{(1)}$

$$k\, \ell\, \partial_x^2 V + \frac{\mathrm{m}}{\ell}\, \frac{\left(\omega - \omega_{\frac{q}{p}}\right)^2}{\cos^2(\frac{q}{p}\pi)}\, V = \mathcal{O}\left(\varepsilon_p\right) \tag{8}$$

Note that contrary to (7), (i) this case correspond to the modulation of a *double* mode, (ii) the frequency term is always positive and (iii) this macroscopic description depends on p. Morevover, the modulation frequency is not an edge of the Brillouin zone, and could not be derived with antiperiodic conditions used in Craster *et al.* (2010).

3.2 Approximation of the dispersion equations

Drawing a parallel with the wavenumber $\pm\mathrm{k}_\omega$ describing wave propagation in the spring-mass system, we can introduce the *modulation number* κ_ω in order to describe the harmonic modulation :

$$V(x) = V_0\, \exp(\pm i\, \kappa_\omega\, x) \tag{9}$$

In the vicinity of the periodic angular eigenfrequencies, an approximation of the fundamental dispersion curve can be built as a perturbation of the periodic mode. Consequently the modulation number is the angular frequency increment divided by the group velocity :

$$\mathrm{k}_\omega = \mathrm{k}_{\omega_{\frac{q}{p}}} + \kappa_\omega + \mathcal{O}\left(\varepsilon\right) \quad ; \quad \kappa_\omega = \frac{\omega - \omega_{\frac{q}{p}}}{C_{\omega_{\frac{q}{p}}}} \quad ; \quad C_\omega = \frac{d\omega}{dk_\omega}$$

Introducing (9) in the three modulation equations at the leading order (6), (8), (7) yields the dispersion relation for modulation. Moreover, modulation numbers are straightforwardly linked to the scale ratio ε_p

$$\varepsilon_p = |\kappa_\omega| \ell_p$$

Consequently, at a given ε_p, an estimation of the validity frequency range around the periodic angular eigenfrequency is possible.

Low frequency range $\omega \approx 0$ $(q = 0)$:

$$|\kappa_\omega| = \frac{1}{\ell}\frac{\omega}{\omega_0} + \mathcal{O}(\varepsilon) = k_\omega + \mathcal{O}(\varepsilon)$$

Thus in low-frequency range, the modulation number κ_ω matches the wavenumber k_ω at the leading order. An estimation of the validity frequency range is :

$$\frac{|\Delta\omega|}{\omega_0} = \frac{|\omega - 0|}{\omega_0} \approx \frac{\varepsilon_p}{p} \tag{10}$$

Frequencies close to the cut-off frequency ($\omega \approx 2\,\omega_0$ and p even), the dispersion relation of modulation is determined from (7) as:

$$|\kappa_\omega| = \frac{1}{\ell}\sqrt{4 - \left(\frac{\omega}{\omega_0}\right)^2} + \mathcal{O}(\varepsilon) = \frac{2}{\ell}\sqrt{\frac{2\omega_0 - \omega}{\omega_0}} + \mathcal{O}(\varepsilon)$$

Then the frequency range of validity is given by

$$\frac{|\Delta\omega|}{\omega_0} = \frac{|2\omega_0 - \omega|}{\omega_0} \approx \left(\frac{\varepsilon_p}{2p}\right)^2 \text{ if } \omega < 2\omega_0 \tag{11}$$

Frequencies close to the double eigenmode eigenfrequencies $\omega \approx \omega_{\frac{q}{p}}$, $0 < q < \mathrm{Int}(p/2)$) the modulation number given by (8) reads

$$|\kappa_\omega| = \frac{1}{\omega_0\,\ell}\frac{|\omega - \omega_{\frac{q}{p}}|}{\cos\left(\frac{q\,\pi}{p}\right)} + \mathcal{O}(\varepsilon)$$

corresponding to a frequency range of :

$$\frac{|\Delta\omega|}{\omega_0} = \frac{|\omega - \omega_{\frac{q}{p}}|}{\omega_0} \approx \frac{\varepsilon_p}{p\cos(\frac{q}{p}\pi)} \tag{12}$$

Note that when $\omega > \omega_{\frac{q}{p}}$ (respectively $\omega < \omega_{\frac{q}{p}}$) then k_ω and κ_ω have identical (respectively opposite) signs. Consequently, the wave and the modulation propagate in the same (respectively opposite) direction, see Figure 2.

In the Figure 3, we build (a) the fundamental dispersion curve in the first half of the Brillouin area, and then piecewise parts of the dispersion curve, near the periodic eigenfrequencies of :

- (b) the specific periodic modes of Ω ($\omega \approx 0$, dashed blue lines), Ω_2 ($\omega \approx 2\omega_0$, dashed red lines) and Ω_3 ($\omega \approx \sqrt{3}\omega_0$, dashed cyan lines)
- (c) in adding the specific modes of Ω_4 ($\omega \approx \sqrt{2}\omega_0$, dashed magenta lines) and Ω_5 ($\omega \approx 2\sin(\frac{\pi}{5})\omega_0$ and $\omega \approx 2\sin(\frac{2\pi}{5})\omega_0$, dashed green lines).

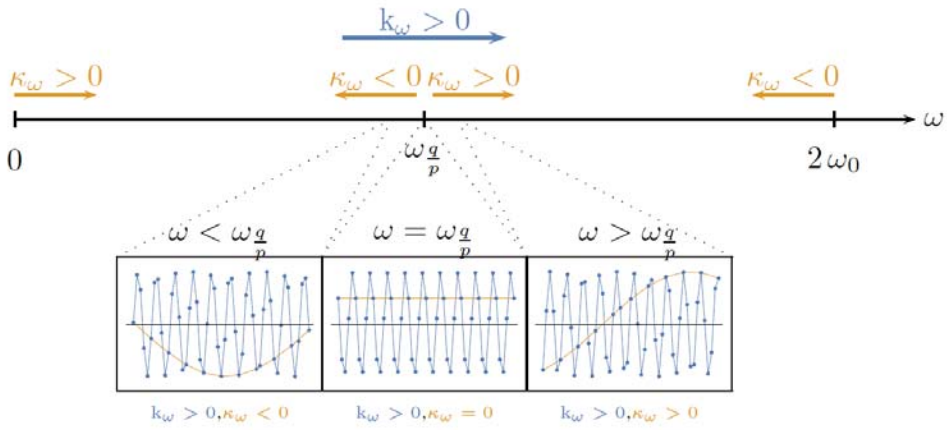

Figure 2: Direction of propagation of the wave (in blue) versus the direction of propagation of the modulation of the wave (in orange). As an illustration, a period Ω_5 is considered and both the wave and modulation direction of propagation are indicated for frequencies around the first angular eigenfrequency $\omega_{\frac{1}{5}}$.

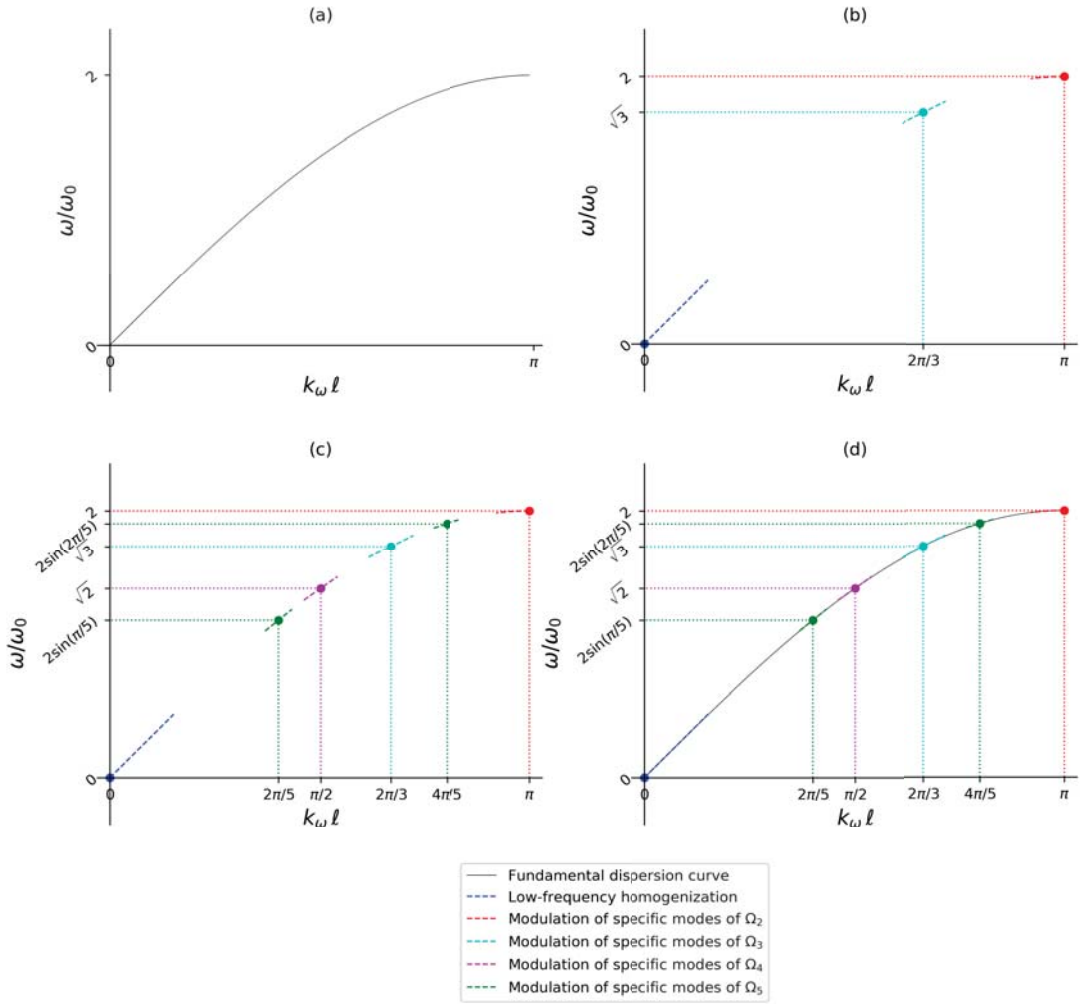

Figure 3: (a) Fundamental dispersion curve in the first half of the Brillouin zone. This dispersion curve can be rebuilt in part from the modulation number: (b) with the specific modes of $\{\Omega_p\}_{0<p\leq 3}$ and (c) with the specific modes of $\{\Omega_p\}_{0<p\leq 5}$. (d) an overlay of fundalental and piecewise parts of the dispersion curve.

The frequency ranges of validity of the macroscopic descriptions have been taken with a value of $\varepsilon_p = 0.5$. Because of the term ε_p^2, the frequency validity range (11) is much less wide than (10) and (12). In the Figure (d), the fundamental dispersion curve is overlayed on its piecewise approximations. In the Figure 4, the dispersion curve of the spring-mass system is built piecewise in varying the value of ε_p : (a) $\varepsilon_p = 0.5$, (b) $\varepsilon_p = 1$, (c) $\varepsilon_p = 1.5$ and (d) $\varepsilon_p = 2.5$. These great values of ε_p are not mathematically justifiable, because the homogenization process requires that $\varepsilon_p \to 0$. Nevertheless, we can see this as an extrapolation of the osculated curves around the Bloch modes : hence, the more the value of ε_p is great and the more the fundamentable dispersion curve is accuratly built thanks to piecewise approximations around the Bloch modes. Moreover, in the case where $\varepsilon_p = 2.5$, the successive approximations pass from their origin almost to the next Bloch mode, allowing a rebuilt by successive secant osculation curves.

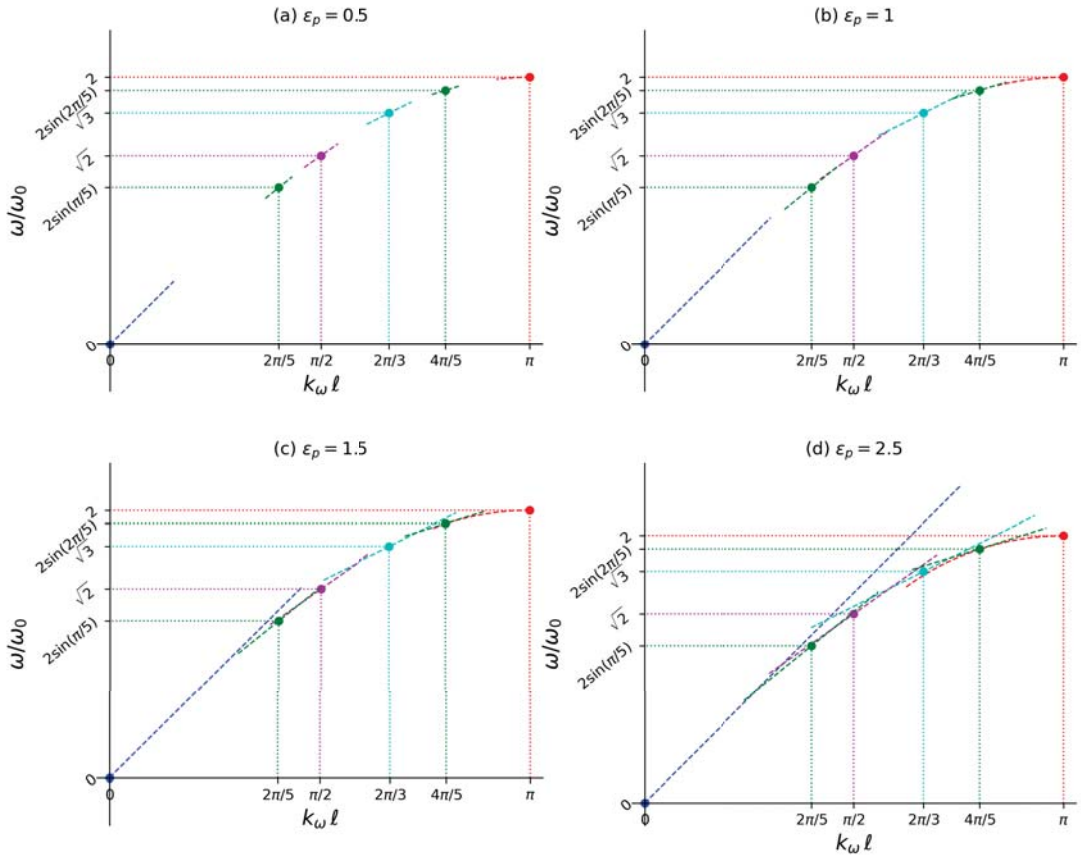

Figure 4: Dispersion curve build piecewise thanks to modulation curves as in the Figure 3, but in varying the value of ε_p from 0.5 to 2.5.

4 Application to discrete lattices

The latter methodology, developped on a well-known spring-mass system, is now applied to a network made of a stack of symetric elastic frames (see Figure 5) constituted by three identical rigidly and mass-less connected bending beams. This structure departs from the spring-mass system because in the reticulated beams (i) stiffness and mass are continuously distributed in the local beams, therefore an irreducible cell Ω owns an infinite number of periodic eigenmodes, and (ii) the 2D nature of the structure involves an enriched kinematics. Each cell owns two

nodes then six degrees of freedom. Each local beam is characterized by (i) its geometrical parameters : length ℓ, width a, depth h, cross section A and inertia regarding its longitudinal axis $I = a^3 h/12$, and (ii) its mechanical elastic parameters : elastic modulus E, mass density ρ.

Due to the symmetry of the considered structures, the local variables can be reorganized in two sets of uncoupled variables linked to (i) the transversal kinematic of the reticulated beam (namely V_n the average transversal displacement, θ_n the average rotation of the nodes and α_n the rotation of the n^{th} cell) and (ii) to the longitudinal kinematic of the reticulated beam (U_n the average longitudinal displacement, Δ_n the transversal dilatation and Φ_n the differential rotation of the nodes). In this paper we illustrate the piecewise building of dispersion curve only on

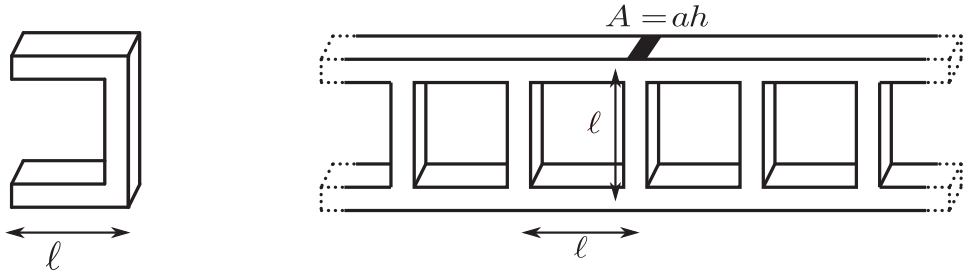

Figure 5: Left : Cell Ω of the reticulated beam. Right : periodic framed beam.

transversal kinematics. The chosen geometrical and mechanical parameters of local frames are:

$$E = 210\text{GPa}\,;\ \nu = 0.2\,;\ \rho = 7800\text{kg/m}^3\,;\ \ell = 1\text{cm}\,;\ a = 0.5\text{mm} \tag{13}$$

which corresponds to a slenderness of a local beam : $\ell/a = 20$.

Denoting by $\underline{\mathcal{V}}_n =^T \left(\frac{1}{2}\,\alpha_n\,\ell, V_n, \theta_n,\right)$ the transversal generalized displacements of the n^{th} cell, the force and momentum balances of the n^{th} cell involves the generalized displacements of the neighboring cell $n-1$ and $n+1$ and take the matrix form:

$$\underline{\underline{H}}.\,\underline{\mathcal{V}}_{n-1} + \underline{\underline{\mathcal{H}}}_T.\,\underline{\mathcal{V}}_n +^T \underline{\underline{H}}.\,\underline{\mathcal{V}}_{n+1} = \underline{0} \tag{14}$$

$$\underline{\underline{H}} = \begin{bmatrix} \frac{EA}{\ell} g_2(\chi) & 0 & 0 \\ 0 & \frac{12\,EI}{\ell^3} f_4(\gamma) & \frac{6\,EI}{\ell^2} f_6(\gamma) \\ 0 & -\frac{6\,EI}{\ell^2} f_6(\gamma) & -\frac{2\,EI}{\ell} f_5(\gamma) \end{bmatrix}$$

$$\underline{\underline{\mathcal{H}}}_{\mathrm{T}} = \begin{bmatrix} a_{\mathrm{T}} & 0 & b_{\mathrm{T}} \\ 0 & c_{\mathrm{T}} & 0 \\ b_{\mathrm{T}} & 0 & d_{\mathrm{T}} \end{bmatrix} \text{ with } \begin{cases} a_{\mathrm{T}} = -\dfrac{12\,EI}{\ell^3}\left(f_1(\gamma) + f_4(\gamma)\right) - \dfrac{2\,EA}{\ell} g_1(\chi) \\ b_{\mathrm{T}} = \dfrac{6\,EI}{\ell^2}\left(f_3(\gamma) + f_6(\gamma)\right) \\ c_{\mathrm{T}} = \dfrac{EA}{\ell}\left(g_2(\chi) - g_1(\chi)\right) - \dfrac{24\,EI}{\ell^3} f_1(\gamma) \\ d_{\mathrm{T}} = -\dfrac{2\,EI}{\ell}\left(f_5(\gamma) + 2\,f_2(\gamma)\right) - \dfrac{8\,EI}{\ell_{\mathrm{w}}} f_2(\gamma) \end{cases}$$

where $\chi = \sqrt{\frac{\rho\,\omega^2}{E}}\,\ell$ and $\gamma = \sqrt[4]{\frac{\rho\,A\,\omega^2}{E\,I}}\,\ell$ are two dimensionless parameters describing the local regime of the beam respectively in compression and in bending. The elasto-inertial functions f_i

and g_i are defined by :

$$\begin{cases} g_1(x) = x\cot(x) \\ g_2(x) = \dfrac{x}{\sin(x)} \\ f_1(x) = \dfrac{\cosh(x)\,\sin(x)+\sinh(x)\,\cos(x)}{1-\cos(x)\,\cosh(x)}\,\dfrac{x^3}{12} \\ f_2(x) = \dfrac{\cosh(x)\,\sin(x)-\sinh(x)\,\cos(x)}{1-\cos(x)\,\cosh(x)}\,\dfrac{x}{4} \end{cases} \qquad \begin{cases} f_3(x) = \dfrac{\sinh(x)\,\sin(x)}{1-\cos(x)\,\cosh(x)}\,\dfrac{x^2}{6} \\ f_4(x) = \dfrac{\sinh(x)+\sin(x)}{1-\cos(x)\,\cosh(x)}\,\dfrac{x^3}{12} \\ f_5(x) = \dfrac{\sinh(x)-\sin(x)}{1-\cos(x)\,\cosh(x)}\,\dfrac{x}{2} \\ f_6(x) = \dfrac{\cosh(x)-\cos(x)}{1-\cos(x)\,\cosh(x)}\,\dfrac{x^2}{6} \end{cases}$$

4.1 Dispersion equations

The dispersion relation $\mathcal{E}\,(\omega, \mathrm{k}_\omega) = 0$ of harmonic transversal waves can be found considering $\underline{\mathcal{V}}_n =^T \left(\frac{1}{2}\,\alpha_n\,\ell, V_n, \theta_n, \right)$ in the form (the time dependence $e^{i\omega t}$ is omitted) :

$$\underline{\mathcal{V}}_n = \underline{\mathcal{V}}_0\, e^{i\,\mathrm{k}_\omega\, n\,\ell} \qquad k_\omega \in [0, \frac{\pi}{\ell}[\tag{15}$$

Introducing (15) in (14) yields :

$$\underline{\underline{\mathbb{D}}}_{\mathrm{T}}.\underline{\mathcal{V}}_0 = \begin{bmatrix} \tilde{a}_{\mathrm{T}} & 0 & b_{\mathrm{T}} \\ 0 & \tilde{c}_{\mathrm{T}} & \tilde{e}_{\mathrm{T}} \\ b_{\mathrm{T}} & -\tilde{e}_{\mathrm{T}} & \tilde{d}_{\mathrm{T}} \end{bmatrix}.\underline{\mathcal{V}}_0 = \underline{0} \text{ where } \begin{cases} \tilde{a}_{\mathrm{T}} = a_{\mathrm{T}} + \dfrac{2\,EA}{\ell_{\mathrm{w}}}\,g_2(\chi)\,\cos\left(\mathrm{k}_\omega\,\ell\right) \\ \tilde{c}_{\mathrm{T}} = c_{\mathrm{T}} + \dfrac{24\,EI}{\ell^3}\,f_4(\gamma)\,\cos\left(\mathrm{k}_\omega\,\ell\right) \\ \tilde{d}_{\mathrm{T}} = d_{\mathrm{T}} - \dfrac{4\,EI}{\ell}\,f_5(\gamma)\,\cos\left(\mathrm{k}_\omega\,\ell\right) \\ \tilde{e}_{\mathrm{T}} = \dfrac{12\,EI}{\ell^2}\,f_6(\gamma)\,i\sin\left(\mathrm{k}_\omega\,\ell\right) \end{cases}$$

The roots of the determinant of $\underline{\underline{\mathbb{D}}}_{\mathrm{T}}$ yield the dispersion equation of the transversal waves in the reticulated structure :

$$\det\left(\underline{\underline{\mathbb{D}}}_{\mathrm{T}}\right) = \left(\tilde{a}_{\mathrm{T}}\,\tilde{d}_{\mathrm{T}} - \tilde{b}_{\mathrm{T}}^2\right)\,\tilde{c}_{\mathrm{T}} + \tilde{a}_{\mathrm{T}}\,\tilde{e}_{\mathrm{T}}^2 = \mathcal{E}_{\mathrm{T}}\,(\omega, \mathrm{k}_\omega) = 0$$

Then, the corresponding kernel of $\underline{\underline{\mathbb{D}}}_{\mathrm{T}}$ provides the kinematics associated to set $\{\omega_I, \mathrm{k}_{\omega I}\}_I$ solutions of $\mathcal{E}_{\mathrm{T}}\,(\omega, \mathrm{k}_\omega) = 0$. Application of this method is illustrated on Figure 6:

The first quasi-linear branch clearly shows that at low frequencies the transversal dynamics is driven by the average transversal displacement V. The second branch, strongly non-linear corresponds at low wavenumbers to the gyration mode. The latter, driven by the rotation of the section $\alpha\,\ell$, is activated after a cut-off frequency (around 4,4 kHz). Note however that for wavenumbers greater than $\mathrm{k}_\omega = 0.2\pi/\ell$ the dynamics activated in this branch, moves from $\alpha\,\ell$ to the average rotation of the nodes $\theta\,\ell$. As for the third branch, that appears at higher frequencies (around 37kHz), the kinematics is firstly driven by V, and by θ at larger wavenumbers. The two next branches are dominated by nodes rotation θ, the rigid body motion of the two nodes being negligible, consistently with the inner resonance mechanism within the framed beams. This shows that a given branch is not associated with a specific kinematics.

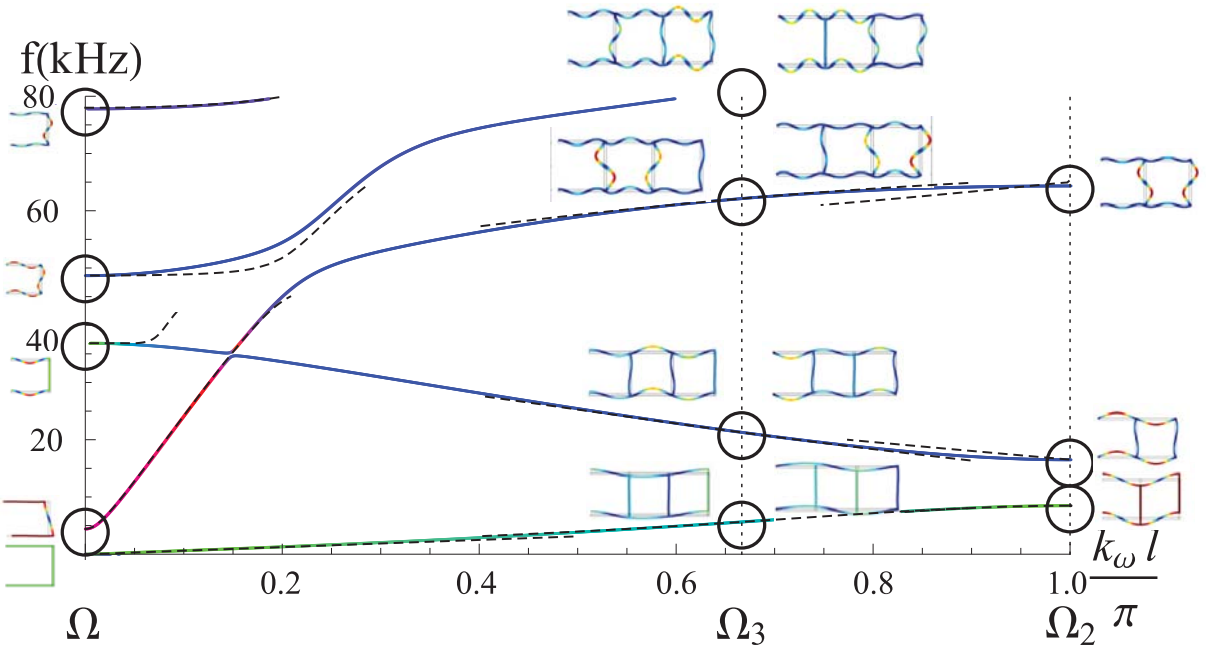

Figure 6: Dispersion curve in the half on the first Brillouin zone for the transversal kinematics : $\alpha\,\ell$,V,$\theta\,\ell$. Black circles correspond to the Bloch modes for periods made of one cell (Ω), two cells (Ω_2) and three cells (Ω_3). In dashed lines the asymptotic description of the dispersion curves derived by modulation analysis.

4.2 Bloch modes

Let a period $\Omega_p = \bigcup_p \Omega$, constituted by a stack of p irreducible cells Ω. When $\mathrm{k}_\omega \ell/2\pi = q/p \in [0, 1/2[$, then the eigenmodes of Ω_p with periodic boundary conditions are emerging. This leads to the associated periodic angular eigenfrequencies thanks to the dispersion relation :

$$\mathcal{E}\left(\omega, \frac{q2\pi}{p\ell}\right) = 0 \quad \text{where} \quad q = 0, ..., \mathrm{Int}(p/2) \tag{16}$$

Finally, the Bloch mode is given by the kernel of $\underline{\underline{\mathbb{D}}}_T$, given at the couple $(\omega, \frac{q2\pi}{p\ell})$ solutions of (16).

On the figure 6, the first solutions corresponding to periods Ω, Ω_2 and Ω_3 are depicted by black circles. The corresponding modal shapes (taking account of their multiplicity) are calculated by finite element on these three periods with periodic boundary conditions.

4.3 Modulation approach

This asymptotic approach is closely related to the HPDM method Caillerie *et al.* (1989) and the asymptotic method for modulation analysis of framed beams is full described in Rallu *et al.* (2018). The procedure is splitted into the following key steps. 1. Reduce the studied structure to an equivalent discrete model. This is obtained by condensing the balance equations of the beam elements within the period at the nodes of the period. 2. Establish an exact recurrence equation by expressing the balance of the edges nodes of the considered (multi-)cells period. 3. Identify the periodic eigenmodes and eigenfrequencies of the (multi-)cell. 4. Consider frequencies close to a given eigenfrequency and assume a large scale modulation. Then rewrite the recurrence equation in terms of Taylor expansions of the continuous variables that describe the amplitude of the eigenmode. 5. Introduce the asymptotic expansions of the variables and rescale the physical parameters of the element constituting the period. Here, all the local frames

are identical, and we consider a slenderness contrast of the local fram as $\ell/a = O(\varepsilon^{-1})$. The geometrical values chosen in (13) are consistent with this contrast. 6. Deduce the various envelope models that apply close to the eigenfrequencies of the considered (multi-)cells.

This approach applied on the transversal kinematics allows to extract the approximation of dispersion curve around the periodic eigenmodes of periods made of one, two and three irreducible cells. All the equations are detailed in Rallu *et al.* (2019). These approximations are given in dashed lines on Figure 6.

In the figure 6 are represented in parallel of the dispersion curves determined from a direct calculus and the asymptotic dispersion curves derived from the analytical expressions given by the modulation analysis. This figure clearly shows that the asymptotic model for quasi-static "V"-mode fits the exact dispersion curve related to the bending of the reticulated beam in a large wave number range, namely up $k_\omega = 0.5\pi/\ell_{\rm w}$, which is much larger than its theoretical validity domain $k_\omega \ell_{\rm w} \ll 1$.
On the contrary the asymptotic model for the dynamic "V"-mode fits the exact solution in a limited range of wavenumbers. This relies on the fact that the dominant kinematic variable of this branch change from variable V for $k_\omega \leq 0.05\,\pi/\ell_{\rm w}$, to θ for $k_\omega \geq 0.05\,\pi/\ell_{\rm w}$. As for the asymptotic dispersion curves identified considering Ω_2 and Ω_3, one notices a large range of good matching between the asymptotic and exact results.

5 Conclusion

The goal of this paper is to describe the methodology of construction of parts of the dispersion curve of periodic elastic networks. This process is full and clearly described on a a periodic network of elastic resonators : First, a multi-cells approach is presented in order to identify the situation of large scale evolutions, which correspond to the frequency ranges around the eigenfrequencise of the multi-cells period Ω_p with periodic boundary conditions. Then, in these situations, the framekork of asymptotic analysis of high-frequency modulation in periodic systems is a applied and yields the equations governing the large scale modulations. At low frequencies, the modulation approach matches the classical homogenization method. But at higher frequencies, the nature of the descriptions departs from the usual macroscopic formulation : (i) the macroscopic operator is applied on the amplitude of the periodic eigenmodes, (ii) instead of an unique equivalent model, a family of descriptions is derived for modulation phenomena; this family is associated to the modes of the irreducible or the multiple cells, (iii) the nature of the modulation equations is different whether the mode is simple or multiple. Thanks to these macroscopic descriptions, a piecewise built of the dispersion curve is possible in the vicinity of the periodic eigenfrequencies of Ω_p. Finally, compared to Floquet-Bloch theory, the specificity of the modulation approach is to extract the frequency bands where the large scale modulations are allowed and to determine their governing equations.

As an illustration, we applied this methodology to reticulated beams, whose the enriched kinematics and the continuous distribution of mass and stiffness involve wave dispersion curves with several branches. The main outcomes are (i) a given dispersion branch may involves different kinematics, (ii) the modulation analysis performed on multi-cell around rational Bloch number allows to build by parts the dispersion curves and to relate them to an effective analytical description, (iii) these approximations are reliable in a range such that the kinematics do not significantly changed. These results established on a particular beam lattices may be extended to more complexe periodic structures and clarify the physics behind the dispersion curves.

References

BOUTIN, C., RALLU, A. et HANS, S. (2012). Large scale modulation of high frequency acoustic waves in periodic porous media. *The Journal of the Acoustical Society of America*, 132(6): 3622–3636.

CAILLERIE, D., TROMPETTE, P. et VERNA, P. (1989). Homogenisation of periodic trusses. *In IASS Symp. 10 Years Prog. Shell Spat. Struct.*, Madrid.

CRASTER, R. V., KAPLUNOV, J. et PICHUGIN, A. (2010). High-frequency homogenization for periodic media. *In Proceedings of the Royal Society of London A: Mathematical, Physical and Engineering Sciences*, page rspa20090612. The Royal Society.

DAYA, E. M., BRAIKAT, B., DAMIL, N. et POTIER-FERRY, M. (2002). Continuum modeling for the modulated vibration modes of large repetitive structures. *Comptes Rendus - Mec.*, 330:333–338.

HANS, S. et BOUTIN, C. (2008). Dynamics of discrete framed structures: A unified homogenized description. *Journal of Mechanics of Materials and Structures*, 3(9):1709–1739.

RALLU, A., BOUTIN, C. et HANS, S. (2019). Wave dispersion curves in discrete lattices derived through asymptotic multi-scale method. *In Journal of Physics: Conference Series*, volume 1264, page 012012. IOP Publishing.

RALLU, A., HANS, S. et BOUTIN, C. (2018). Asymptotic analysis of high-frequency modulation in periodic systems. analytical study of discrete and continuous structures. *Journal of the Mechanics and Physics of Solids*, 117:123 – 156.

SANCHEZ-PALENCIA, E. (1980). *Non-Homogeneous Media and Vibration Theory*, volume 127. Lecture Notes in Physics, Berlin Springer Verlag.

EURODYN 2020
XI International Conference on Structural Dynamics
M. Papadrakakis, M. Fragiadakis, C. Papadimitriou (eds.)
Athens, Greece, 23–26 November 2020

DEVELOPMENT OF FREQUENCY CURVES FOR CROSS-LAMINATED TIMBER (CLT) FLOORS USING DYNAMIC STIFFNESS METHOD

Miroslav S. Marjanović[1], Verica Lj. Jugović[1], and Marija T. Nefovska-Danilović[1]

[1] Faculty of Civil Engineering, University of Belgrade
Bulevar kralja Aleksandra 73, 11000 Belgrade, Serbia
e-mail: mmarjanovic@grf.bg.ac.rs, 563_19@student.grf.bg.ac.rs, marija@grf.bg.ac.rs

Keywords: Cross-laminated timber, Dynamic stiffness method, Floor, Natural frequency

Abstract. *Cross-laminated timber (CLT) panels have an increasing market share and extensive application in civil engineering practice, as full size walls or floor structures. CLT provides a compelling alternative to the concrete and steel (as conventional building materials), providing a low carbon footprint and comfortable living conditions. However, the orthotropic elastic material behavior of wood and the crosswise lay-up yield a relatively complex kinematics of CLT, characterized by high shear deformation across the thickness. This complicates the appropriate and accurate kinematic description of CLT and further prolongs the design phase of the real engineering structure.*

Due to the relatively low weight, CLT floors are particularly prone to human-induced vibrations, causing vibration serviceability issues such as annoyance to human occupants and dysfunction of vibration sensitive equipment. Therefore, for the accurate response prediction of CLT under dynamic loading, its fundamental dynamic properties should be derived first.

In the paper, dynamic stiffness-based FREEVIB software, previously developed by the authors, has been used for modeling and prediction of the free vibration characteristics of CLT floor structures. Frequency curves taking into account: (i) span-to-thickness (a/h) ratio, (ii) plate aspect (a/b) ratio and (iii) different combinations of end constraints, have been developed using FREEVIB and systematized to be easy for use in engineering practice, especially in the conceptual design phase of CLT-based buildings. The results have been compared against the current CLT design recommendations.

1 INTRODUCTION

Recent technological advances and new construction techniques have led to the development of new natural composite material called cross-laminated timber (CLT) - a multilayer composite made of several thin wooden layers bonded together in a crosswise manner. It has outstanding structural strength, stiffness and aesthetic properties, a high level of prefabrication, fire resistance and construction speed. Finally, it is highly sustainable material that represents a compelling alternative to the traditional concrete, steel and masonry structures [1].

Due to the relatively low weight, CLT floors are prone to human-induced vibrations, causing vibration serviceability issues such as annoyance to human occupants and dysfunction of vibration sensitive equipment. Therefore, for the accurate response prediction of CLT under dynamic loading, its fundamental dynamic properties should be derived first.

The aim of this paper is to provide the practical guidelines for design of CLT floors by means of their dynamic properties. FREEVIB [2] software developed by the authors, based on the dynamic stiffness method (DSM) [3] in conjunction with the higher-order shear deformation theory (HSDT) [4], has been used for modeling and prediction of the free vibration characteristics of CLT floors. Key feature of the DSM is the dynamic stiffness element and the corresponding dynamic stiffness matrix derived from the exact (strong form) solution of the governing equations of motion. So far, the FREEVIB's library includes several rectangular dynamic stiffness element formulations, capable to describe the complex kinematics of laminar composites. It allows for the application of arbitrary combinations of edge conditions and, like in the conventional FEM, implies the effective assembly procedure.

By using FREEVIB, frequency curves taking into account: (i) span-to-thickness (*a/h*) ratio, (ii) plate aspect (*a/b*) ratio and (iii) different combinations of end conditions, have been developed and systematized to be easy for use in engineering practice. The results have been compared against the current CLT design recommendations from CLT Handbook Canada [5], CLT Structural design – proHolz Austria [6], or the exact solution based on classical laminated plate theory (CLPT) [7], in order to highlight the influence of transverse shear deformation on dynamic properties of the panel.

2 DYNAMIC STIFFNESS METHOD FORMULATION

The dynamic stiffness matrix of the considered HSDT-based plate element is obtained through several steps. The first one is derivation of Euler-Lagrange equations of motion for the HSDT, by using the Hamilton's principle in terms of the displacements. After that, the equations of motion are transformed into the frequency domain by assuming a harmonic representation of the displacement/rotation field:

$$u(x,y,t) = \hat{u}(x,y,\omega)e^{i\omega t} \tag{1}$$

In. Eq. (1), $\hat{u}(x,y,\omega)$ are the amplitudes of the displacement or rotation $\hat{u}(x,y,t)$ in the frequency domain. Having in mind that Eq. (1) is valid for all angular frequencies ω in the considered frequency range, the argument ω will be omitted in further representations. After the substitution of the above transformation into the governing equations of motion, they are transformed into the following set of partial differential equations:

$$\mathbf{L}\hat{u}(x,y) = 0, \tag{2}$$

where **L** is the matrix of the differential operators [8, 9] defined in terms of the plate stiffness coefficients, the mass moments of inertia and the angular frequency ω. Displacement or rotation amplitudes of a rectangular plate element are then represented as a superposition of four symmetry contributions: both symmetric (SS), symmetric - anti-symmetric (SA), anti-

symmetric - symmetric (AS) and both anti-symmetric (AA). It is now possible to analyze only one quarter of a rectangular plate, which significantly reduces the size of the corresponding dynamic stiffness matrix. By using the method of separation of variables, the general solution for each symmetry contribution can be represented in the Fourier series form as:

$$\tilde{u}^{ij}(x,y) = \sum_{m}^{\infty} {}^{1}U_m^{ij}(x)\, {}^{1}f_m^{ij}(y) + \sum_{m}^{\infty} {}^{2}U_m^{ij}(y)\, {}^{2}f_m^{ij}(x) \tag{3}$$

In Eq. (3), $\tilde{u}^{ij}(x,y)$ is the corresponding displacement or rotation function, ${}^{1}U_m^{ij}(x)$ and ${}^{2}U_m^{ij}(y)$ (ij = SS, SA, AS or AA) are the unknown displacement or rotation functions, while $f_m^{ij}(y)$ and $f_m^{ij}(x)$ are the base trigonometric functions, depending on the symmetry case. In practical calculations, the infinite Fourier series must be truncated. Thus, the accuracy of solution depends on the number of terms in the general solution.

With the aid of the projection method [10], the following relation is obtained:

$$\tilde{\mathbf{Q}}^{ij} = \tilde{\mathbf{F}}_D^{ij} \left(\tilde{\mathbf{D}}_D^{ij} \right)^{-1} \tilde{\mathbf{q}}^{ij} = \tilde{\mathbf{K}}_D^{ij} \tilde{\mathbf{q}}^{ij}, \tag{4}$$

where $\tilde{\mathbf{q}}^{ij}$ is the vector of projections of displacement components $\hat{u}^{ij}$ along plate boundaries, $\tilde{\mathbf{Q}}^{ij}$ is the corresponding force projection vector, and $\tilde{\mathbf{K}}_D^{ij}$ is the dynamic stiffness matrix for the ij symmetry contribution. The dynamic stiffness matrix for a completely free dynamic stiffness element is obtained by using the transformation matrix $\mathbf{T}$ (for details see [8, 9, 11]).

The size of the dynamic stiffness matrix $\tilde{\mathbf{K}}_D$ depends on the number of terms in the general solution M, the type of the vibration problem (in plane or transverse) and applied plate theory (CPT, FSDT, HSDT).

Considering that transverse and in-plane vibrations of a single plate represent two independent states, the dynamic stiffness matrix of the single plate is derived by combining the dynamic stiffness matrices for the transverse and in-plane vibration, respectively. The assembly procedure is then performed as in the conventional FEM.

In the analysis, arbitrary combinations of boundary conditions can be applied by removing the rows and columns of the global dynamic stiffness matrix that correspond to the components of the constrained displacement projections. After that, the natural frequencies can be computed from the assembled global dynamic stiffness sub-matrix (related to the unknown generalized displacement projections), using some of the search methods. Finally, after the natural frequencies have been computed, the i^{th} mode shape corresponding to the natural frequency ω_i is obtained in the usual manner.

Formulated dynamic stiffness elements served as basis for the development of object-oriented computational framework FREEVIB [2] for free vibration analysis of plate-like structures. FREEVIB is written in Python [12]. For input parameters related to the geometry, material and number of terms in trigonometric series (M), simple text file may be created in the prescribed format, or generated using the existing graphical pre-processors. Using the procedure described in the previous sections, a variety of plate-like structural problems can be analyzed.

3 CALCULATION OF FUNDAMENTAL DYNAMIC PROPERTIES OF CLT PANELS AND DEVELOPMENT OF FREQUENCY CURVES

In this section, fundamental frequencies of different CLT panels have been calculated using FREEVIB, taking into account: (i) span-to-thickness (*a/h*) ratio, (ii) plate aspect (*a/b*) ratio and (iii) different combinations of boundary conditions (BC). They are then systematized to be easy for use in engineering practice (this is of special importance in the conceptual design phase of CLT-based buildings).

Current models for design of CLT panels mainly emerged from the long tradition of using only simple beam-like elements in timber structures. Gamma method is based on the procedure for design of mechanically jointed beams according to Eurocode 5, Annex B [13]. The stiffness properties are defined using the effective moment of inertia $I_{0,ef}$, and the connection efficiency factors γ_i which account for the shear flexibility of the cross layers. The Gamma method accounts for the influence of transverse load-bearing effect and different static systems using the $k_{transverse}$ and k_e coefficients, respectively. The above method is based on the Bernoulli's hypothesis and linear stress-strain relationship, without accounting for the transverse shear deformation.

However, this approach is not able to accurately account for the 2D load transfer and, therefore, cannot reflect the load carrying mechanism of a plate. To overcome this, classical exact solutions for composite laminates could be successfully applied for thin CLT panels, simply supported along all sides. However, this limits the possible area of application by means of edge conditions.

FREEVIB tends to overcome the above issues, by: (i) accurately accounting for the transverse shear deformation, (ii) taking into account the cross-lamination of layers and, (iii) considering arbitrary combinations of boundary conditions.

3.1 Frequency curves for rectangular simply supported CLT panels

To validate the model and highlight the influence of transverse shear deformation on fundamental dynamic properties of CLT panel, the study of simply supported (SSSS) 3- and 5-layers rectangular CLT panels is performed by using the HSDT-based dynamic stiffness elements using FREEVIB. All layers are of equal thickness. C24 strength class according to [6] is used (see Table 1), which is common in the production of CLT. The outer layers are oriented in the *a*-direction (longitudinal), while the cross layers are oriented in the *b*-direction (lateral).

Different plate side to thickness ratios have been considered, varying from thick ($a/h = 5$) to thin ($a/h = 30$) plate situation. The calculations have been performed by using M=9 terms in the series expansion. Plates were discretized using only one dynamic stiffness element.

In the first phase, the model is validated against the results based on the following CLT design recommendations:

- CLT Handbook Canada [5], based on the Bernoulli-Euler beam theory, without accounting for the transverse shear deformation and neglecting the transverse load-bearing effect,
- CLT Structural design – proHolz Austria [6], based on the Gamma method [13],
- the exact (2D) solution based on classical laminated plate theory (CLPT) [7]).

E_0	E_{90}	G_0	G_r	ν_{12}	ρ
11000 N/mm^2	370 N/mm^2	690 N/mm^2	50 N/mm^2	0.44	420 kg/m^3

Table 1: Mechanical properties for C24 timber class of CLT panels

The results for dimensionless frequencies $\Omega = \omega\left(a^2 / h\right)\left(\rho / E_{90}\right)^{1/2}$ are plotted in Figure 1.

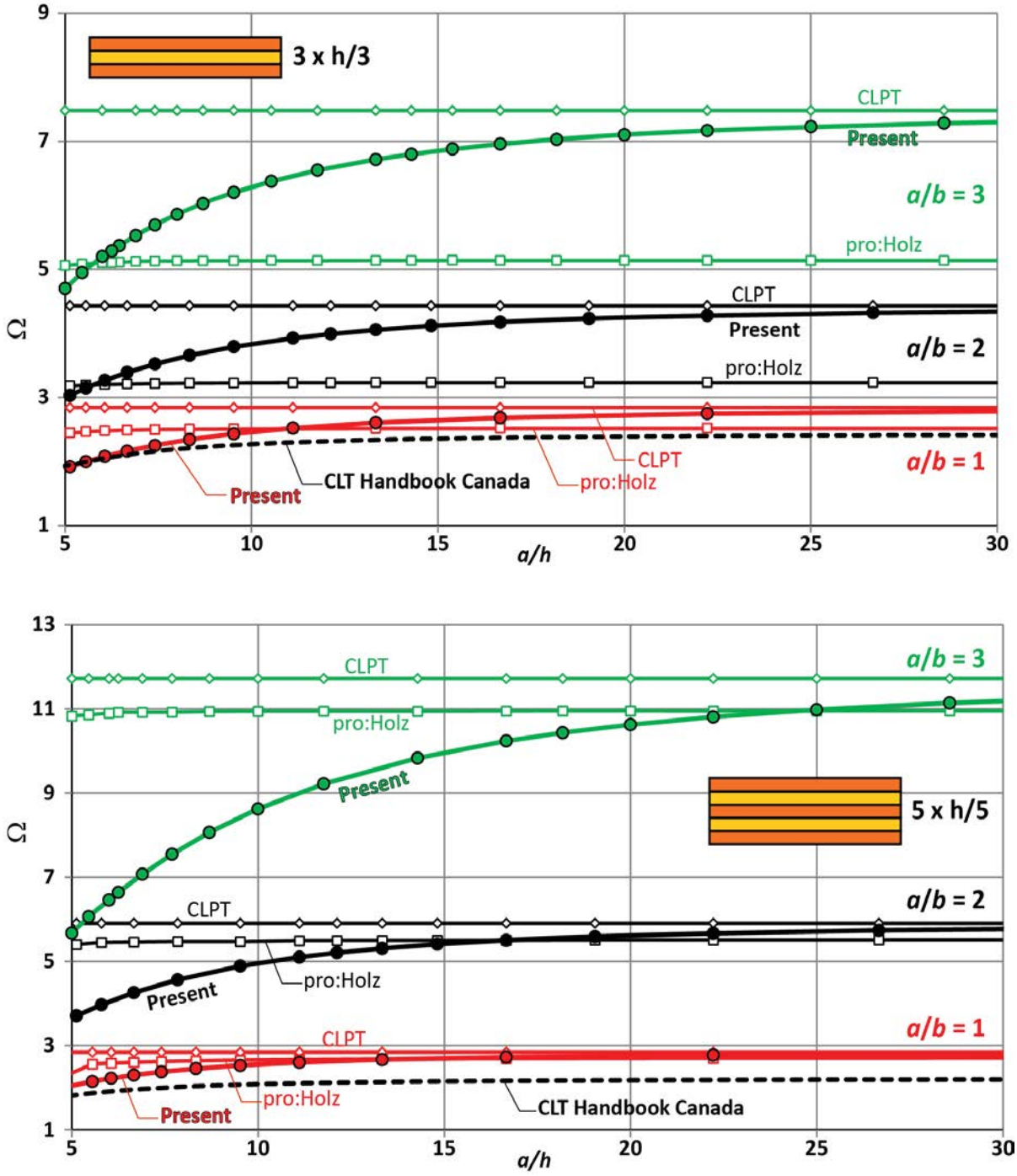

Figure 1: Frequency curves for rectangular simply supported (SSSS) CLT panels (C24), considering different numerical models, stacking sequences, span-to-thickness (*a*/*h*) and plate aspect (*a*/*b*) ratios

The dimensionless natural frequencies presented in Figure 1 are not completely practical for the application in engineering practice. Having in mind that the HSDT-based models accounts for the transverse shear deformation, cross-lamination and arbitrary boundary conditions, the frequency curves will be systematized in a more logical way, to be applicable in preliminary engineering design of CLT floors.

The results are shown in Figure 2, for the simply supported (SSSS) 3- and 5-layers panels.

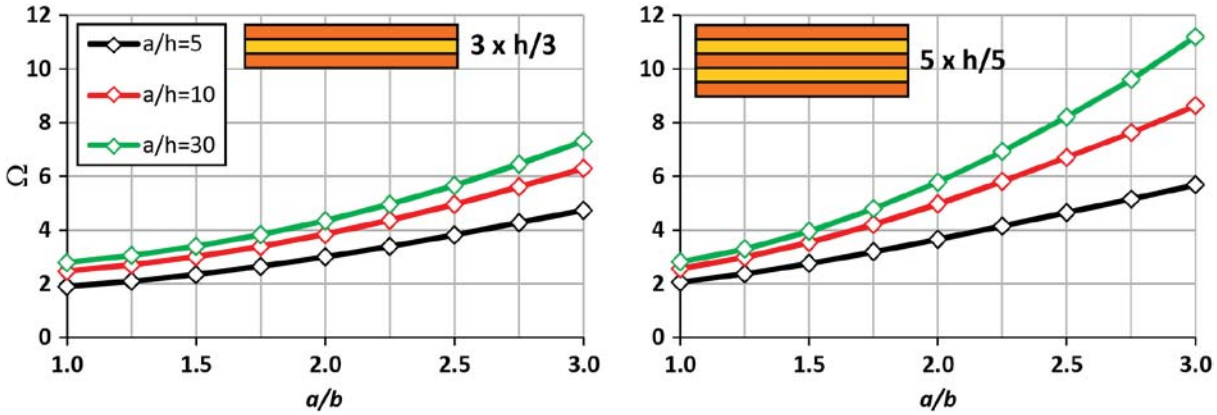

Figure 2: Frequency curves from FREEVIB for rectangular simply supported (SSSS) CLT panels (C24)

3.2 Frequency curves for rectangular CLT panels with different combinations of BC

In this section, we provide the frequency curves for CLT panels with non-classical boundary conditions. This is applicable in engineering practice, where different combinations of boundary conditions may occur. The panels with SSSF and SFSF boundary conditions (see Figure 3 for details) are considered.

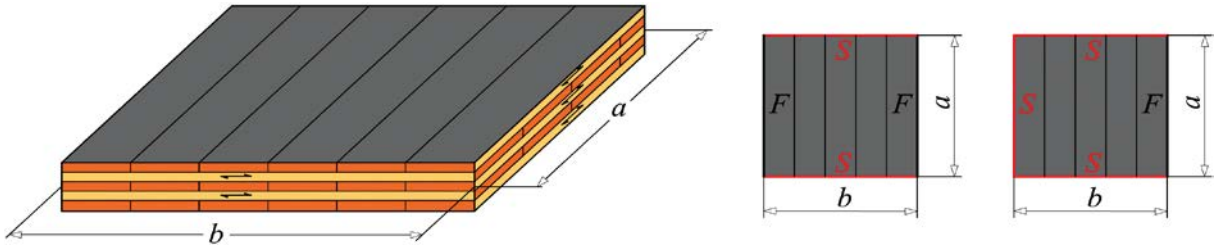

Figure 3: SFSF and SSSF CLT panels with marked grain orientation of the layers

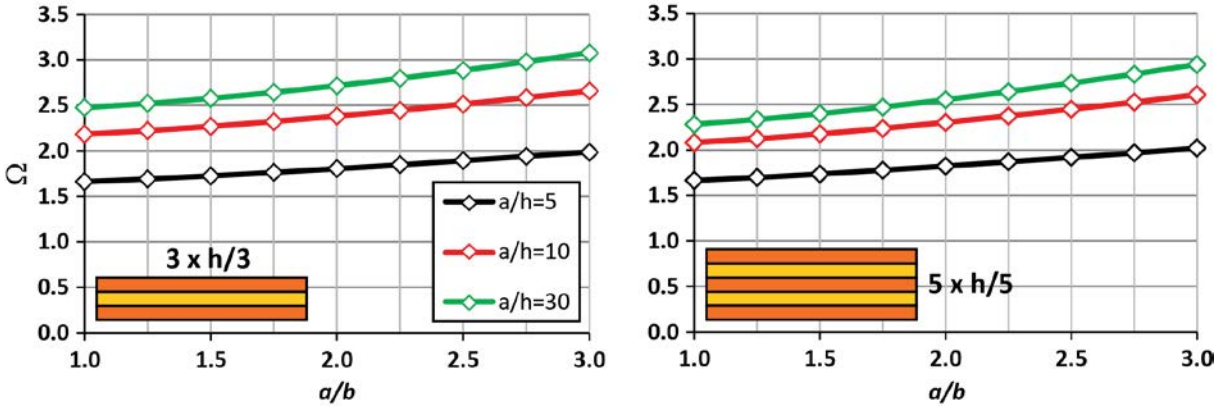

Figure 4: Frequency curves from FREEVIB for rectangular SSSF CLT panels (C24)

For both considered boundary conditions (Figures 4 and 5), the lower *a/h* ratio expectedly yields the lower values of dimensionless frequencies. With increasing *a*/*b* for the fixed *a*/*h*, dimensionless frequencies are slightly increased for the SSSF boundary conditions. This is due to the influence of constraints along the *a*-side (Figure 4), which is more pronounced for lower values of length *b*.

Finally, the SFSF model (Figure 5), which is in fact the beam-like structure, the influence of *a*/*b* does not exist, because only single (longitudinal) load-bearing direction is activated.

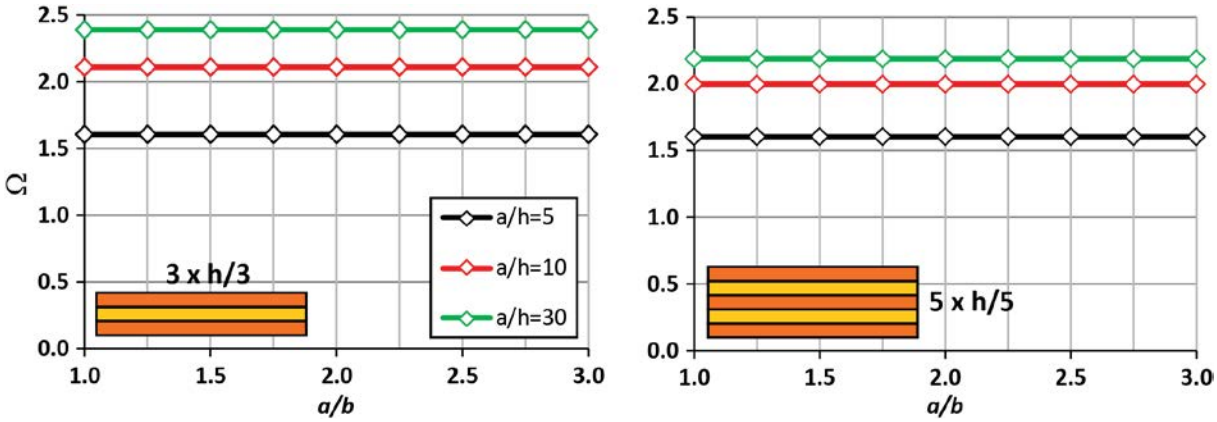

Figure 5: Frequency curves from FREEVIB for rectangular beam-like SFSF CLT panels (C24)

4 CONCLUSIONS

From the performed analyses and constructed frequency curves, some conclusions are derived:

- When calculating the fundamental frequencies of the SSSS panels, both the CLPT-based model [7] and the one based on proHolz recommendations [6] are insensitive to the change of *a/h* ratio, due to the simplifications of transverse shear deformation.
- The difference in Ω between these two models is higher for the 3- than for the 5-layers panels, because the influence of the cross layers is higher for the 3-layers case, which cannot be completely accounted for by using the relatively simple model from [6].
- On the contrary, FREEVIB results are accurately accounting for the transverse shear deformation. Therefore, the fundamental frequency expectedly decreases with the lower values of *a*/*h* (thick plate situation). When the *a*/*h* ratio approaches the slender panel limit, the obtained results from the FREEVIB converge to the CLPT solution.
- The increasing of the *a*/*b* ratio for the fixed *a*/*h*, results in the increased dimensionless frequency Ω for the SSSS panel. This scenario means that value for *b* is decreasing for the fixed values of *a* and *h*, which yields the higher frequency because of the fact that all sides are simply supported.
- The results from the CLT Handbook Canada [5] are not taking into account the *a/b* ratio, because they treat the panel as a 1m wide beam, simply supported on two sides, without any additional treatment of the transverse load-bearing mechanism.
- The FREEVIB also accurately predicts the fundamental frequencies of the CLT panels with non-classical boundary conditions. The lower *a/h* ratio expectedly yields the lower values of dimensionless frequencies. With increasing *a*/*b* for the fixed *a*/*h*, dimensionless frequencies are slightly increased.

Beside the presented analyses, FREEVIB [2] could be successfully applied for the 7-layers panels, as well as for the prediction of fundamental frequencies of panels with openings.

ACKNOWLEDGMENTS

The financial support of the Ministry of Education, Science and Technological Development of the Republic of Serbia and the Science Fund of the Republic of Serbia, is acknowledged.

REFERENCES

[1] I. Sustersic, M. Fragiacomo, B. Dujic, Seismic analysis of cross laminated timber buildings using code prescribed methods, *Proceedings of the World Conference on Timber Engineering WCTE 2016*, Vienna, Austria, 3421-3429, 2016.

[2] M. Marjanović, M. Nefovska-Danilović, E. Damnjanović, Framework for dynamic-stiffness-based free vibration analysis of plate-like structures, *Shock and Vibration,* Paper 1369235, 2019.

[3] J. F. Doyle, Wave propagation in structures, *Springer-Verlag*, New York, 1997.

[4] J. N. Reddy, A simple higher-order theory for laminated composite plates, *Journal of Applied Mechanics*, Vol. 51, 745-752, 1984.

[5] G. Sylvain, P. Ciprian, CLT Handbook - Canadian Edition, *FPInnovations*, Special publications SP-528E, Quebec, 2011.

[6] N. Markus, J. Koppelhuber, K. Pock, CLT Structural design: Basic design and engineering principles according to Eurocode, *proHolz Austria*, 2014.

[7] J. N. Reddy, Mechanics of laminated composite plates and shells: theory and analysis, *CRC Press*, Boca Raton, Florida, USA, 2003.

[8] M. Marjanović, N. Kolarević, M. Nefovska-Danilović, M. Petronijević, Free vibration study of sandwich plates using a family of novel shear deformable dynamic stiff-ness elements: limitations and comparison with the finite element solutions, *Thin-Walled Structures*, Vol. 107, 678-694, 2016.

[9] M. Nefovska-Danilović, N. Kolarević, M. Marjanović, M. Petronijević, Shear deformable dynamic stiffness elements for a free vibration analysis of composite plate assemblies – Part I: Theory, *Composite Structures*, Vol. 159, 728-744, 2017.

[10] J. B. Casimir, S. Kevorkian, T. Vinh, The dynamic stiffness matrix of two-dimensional elements: application to Kirchhoff's plate continuous elements, *Journal of Sound and Vibration*, Vol. 287, No. 3, 571–589, 2005.

[11] M. Nefovska-Danilović, M. Petronijević, In-plane free vibration and response analysis of isotropic rectangular plates using the dynamic stiffness method, *Computers & Structures*, Vol. 152, 82-95, 2015.

[12] Python Software Foundation. Python Language Reference, version 2.7. Available at http://www.python.org.

[13] EN 1995-1-1: Eurocode 5: Design of timber structures - Part 1-1: General - Common rules and rules for buildings, *CEN - European Committee for Standardization*, 2004.

EURODYN 2020
XI International Conference on Structural Dynamics
M. Papadrakakis, M. Fragiadakis, C. Papadimitriou (eds.)
Athens, Greece, 23–26 November 2020

ANALYTICAL SOLUTIONS FOR THE FLEXURAL NATURAL VIBRATION OF THE COMPOSITE GIRDERS WITH CORRUGATED STEEL WEBS

Li Yunsheng[1], Liu Chaoxing[1], Dai Qingnian[1], and Zhang Yanling[1*]

[1] School of Civil Engineering, Shijiazhuang Tiedao University, Shijiazhuang 050043, China
e-mail: Liysh70@163.com

Keywords: Composite girder, Corrugated steel web, Natural vibration, Analytical solution, Numerical analysis

Abstract. *To study the dynamic performance of the composite box-girders with corrugated steel webs (CBGCSWs), three CBGCSWs with different cross-sections (single-cell, double-cell, and triple-cell cross-sections) were taken as the research objects respectively to study their dynamic characters. Considering the shear lag effect and the shear deformation of the corrugated steel webs, the governing differential equations and boundary conditions of the natural vibration were derived based on the energy variation principle and Hamilton principle. The theoretical natural flexural vibration frequencies of the CBGCSWs were obtained and compared with the numerical results by ANSYS software. A parametric analysis was conducted including the wave shape and the thickness of the corrugated steel web, the ratio of the section width to the calculating span B/L, and the ratio of the section height to the calculating span H/L. The results show that the shear lag effect and the shear deformation of the web have a great influence on the vertical flexural vibration of the CBGCSWs. The vertical flexural frequencies increase slightly with the increasing of B/L, the increasing of the web thickness, and the decreasing of the corrugated angle of the steel web, but apparently with the increasing of the height of the girder.*

1 INTRODUCTION

The composite box-girders with corrugated steel webs (CBGCSWs) have been used widely due to their great advantages such as lighter structural self-weight, faster construction speed, higher efficiency of prestressing, better solution for avoiding the problem of web cracking, and so on [1,2]. The static properties of the CBGCSWs including bending, shear, and torsional behaviors have been researched rather deeply at present [3-6]. There are also some studies on the dynamic performance of the CBGCSWs by using theoretical, numerical and experimental methods, but most of them were about the single-cell box section [7-11].

In this paper, a theoretical derivation about the vertical flexural vibration characters was performed on single-cell, double-cell, and triple-cell CBGCSWs respectively. The analytical solutions were compared with the numerical results by ANSYS software, and some key parameters were analyzed by using the theoretical model.

2 THEORETICAL ANALYSIS

2.1 Assumptions

The cross-sections and ordinate used in this paper are shown in figure.1, where b_1, b_3 are the half width of the top and bottom inner flanges, respectively; b_2, b_4 are the width of the top and bottom cantilever flanges, respectively; t_t, t_b are the thickness of the top and bottom flanges, respectively; h_w is the height of the steel girder; z_t, z_b are the distance from the top and bottom flanges to the gravity axis of the section, respectively.

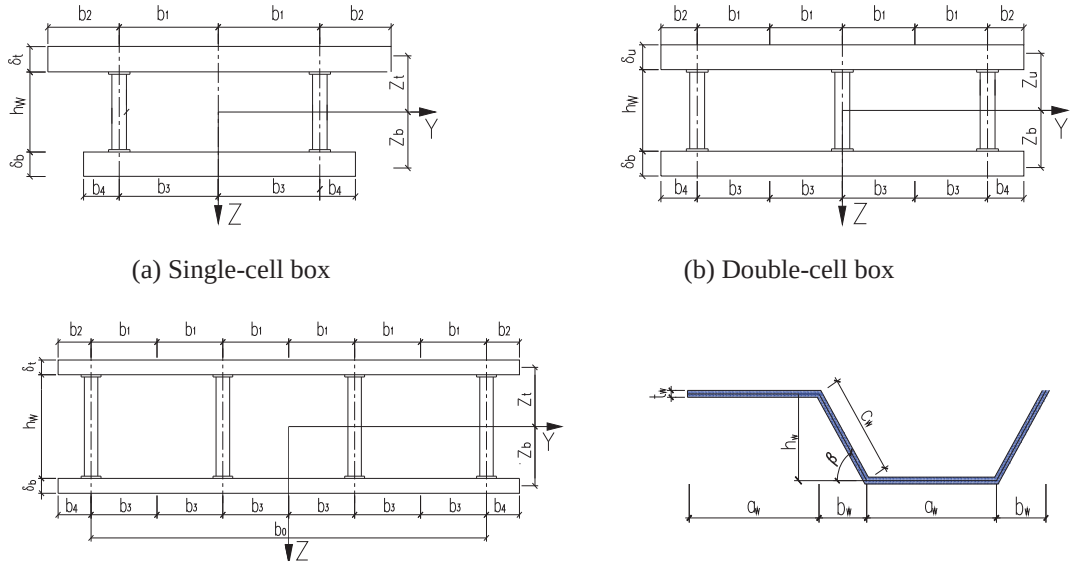

(a) Single-cell box

(b) Double-cell box

(c) Triple-cell box

(d) Wave shape of the corrugated steel web

Figure 1: Cross-sections and ordinate.

The assumptions in the subsequent derivation are as follows:

(1) Both the corrugated steel web and the concrete flange are in the elastic stage and there is no relative slip between them.

(2) The section remains quasi-plane under flexural deformation.

(3) The flexural rigidity of the corrugated steel web is neglected. The bending moment is only resisted by the top and bottom concrete flanges, while the shear force is only resisted by the corrugated steel webs.

(4) Only the in-plane shear strain and the longitudinal normal strain of the concrete flanges are considered, the vertical and lateral normal strain in the concrete flanges and all of the out-plane shear strain are neglected, namely, $\varepsilon_x \neq 0$, $\varepsilon_y = \varepsilon_z = 0$, $\gamma_{xy} \neq 0$, $\gamma_{yz} = \gamma_{xz} = 0$.

2.2 Warp shape function of the shear lag

In the flexural vibration of the CBGCSWs, the longitudinal displacement in the cross-section is induced not only by the bending deformation which obeys the plane-section law, but also by the shear lag effect, so the generalized longitudinal dynamic displacement in the flexural vibration $U(x,y,t)$ can be expressed as follows,

$$U_{\mathrm{t(b)}}(x,y,t) = -z_{\mathrm{t(b)}} \cdot \varphi(x,t) + g(y)u(x,t) \tag{1}$$

Where the subscript t and b represent the top and bottom flanges respectively; $\varphi(x,t)$ is the dynamic slope in the bending deformation; $g(y)$ is the warp shape function of the shear lag; $u(x,t)$ is the dynamic displacement function of the maximum difference of the shear deformation in the concrete slab.

The cosine function is used for the warp function of the shear lag in this paper as follows,

$$g_i(y)=\begin{cases} -\alpha_1\left|\cos\dfrac{\pi y}{2b_1}\right| + D & \text{Top inner flange} \\ -\alpha_2 \cos\dfrac{\pi(|y|-ib_1-b_2)}{2b_2} + D & \text{Top cantilever} \\ -\alpha_3\left|\cos\dfrac{\pi y}{2b_3}\right| + D & \text{Bottom inner flange} \\ -\alpha_4 \cos\dfrac{\pi(|y|-ib_3-b_4)}{2b_4} + D & \text{Bottom cantilever} \end{cases} \tag{2}$$

Where i is the number of the cells, i=1,2,3⋯, and when i is an even number, the variable y in the top and bottom flanges should be replaced by $\bar{y}=|y|-b_1$; α_j (j=1,2,3,4) is the coefficient to consider the warp difference between the top and bottom flanges and can be given by,

$$\alpha_j = \frac{\left[l^2 + 8b_1^2(1+\nu)\right]}{\left[l^2 + 8b_j^2(1+\nu)\right]} \cdot \frac{b_j^2}{b_1^2} \cdot \beta \quad (j=1,2,3,4) \tag{3}$$

Where l is the calculating span; μ is the Poisson ratio; β is a coefficient, when j=1,2, β=1; and when j=3,4, $\beta=z_b/z_t$.

To satisfy the self-equilibrium condition of the axial force in the overall section, let $\int g(y)dA = 0$, then,

$$D=\left(\alpha_1 A_1 + \alpha_2 A_2 + \alpha_3 A_3 + \alpha_4 A_4\right) \Big/ \left(2\pi A_f\right) \tag{4}$$

Where A_f is the total area of the top and bottom flanges; A_1, A_3 are the areas of the top and bottom inner flanges, respectively; A_2, A_4 are areas of the top and bottom cantilevers.

2.3 Vibration equations

In the following derivation, the first, second and third-order partial derivatives of an arbitrary function $F(x,t)$ will be written as $F'(x,t)$, $F''(x,t)$ and $F'''(x,t)$ on the variable x, and $\dot{F}(x,t)$, $\ddot{F}(x,t)$ and $\dddot{F}(x,t)$ on the variable t.

(1) The dynamic flexural strain energy of the concrete flanges

From equation (1), the longitudinal dynamic normal strain of the flanges should be,

$$\varepsilon_{xt(b)}(x,y,t)=\frac{\partial U_{t(b)}(x,y,t)}{\partial x}=-z_{t(b)}\varphi'(x,t)+g(y)u'(x,t) \tag{5}$$

Then the total flexural dynamic strain energy of the top and bottom flanges can be given by,

$$\begin{aligned} V_{fb}(t)&=\frac{1}{2}\int_A t_t E_c \varepsilon_{xt}{}^2(x,y,t)dA+\frac{1}{2}\int_A t_b E_c \varepsilon_{xb}{}^2(x,y,t)dA \\ &=\frac{1}{2}E_c\int_0^l\left\{I_y[\varphi'(x,t)]^2+A_y[u'(x,t)]^2-2S_y\varphi'(x,t)u'(x,t)\right\}dx \end{aligned} \tag{6}$$

Where t_t, t_b are the thickness of the top and bottom flanges, respectively; E_c is the elastic module of concrete; I_y is the total inertia moments of the top and bottom flanges about the axis y, $I_y=\int_A z^2dA=z_t^2(A_1+A_2)+z_b^2(A_3+A_4)$; A_y is the total warp area of the shear lag of the top and bottom flanges, $A_y=\int_A g^2(y)\,dA=\sum_{j=1}^{4}\left(\alpha_j^2/2-4\alpha_j D/\pi+D^2\right)A_j$; S_y is the warp area moment of the shear lag, $S_y=\int_A zg(y)dA=z_t\sum_{j=1}^{2}A_j(D-2\alpha_i/\pi)+z_b\sum_{j=3}^{4}A_j(D-2\alpha_i/\pi)$.

(2) The dynamic shear strain energy of the concrete flanges induced by the shear lag

From equation (1), the dynamic shear strains of the flanges induced by the shear lag are,

$$\gamma_{ft(b)}(x,y,t)=\frac{\partial U_{t(b)}(x,y,t)}{\partial y}=g'(y)u(x,t) \tag{7}$$

Then the total dynamic shear strain energy of the top and bottom flanges can be given by,

$$V_{fs}(t)=\frac{1}{2}\int_A t_t G_c\gamma_{ft}(x,y,t)^2dA+\frac{1}{2}\int_A t_b G_c\gamma_{fb}(x,y,t)^2dA=\frac{1}{2}\int_0^l G_c k_u u^2(x,t)dx \tag{8}$$

Where G_c is the shear module of concrete, $G_c=E_c/[2(1+\nu_c)]$, ν_c is the Poisson ratio of concrete; k_u is the warp coefficient of the shear lag, $k_u=\int_A[g'(y)]^2dA$.

(3) The dynamic shear strain energy of the corrugated steel webs

The dynamic shear strain of the steel web is the difference between the first-order derivative of the vertical dynamic deflection $W(x,t)$ and the dynamic slope $\varphi(x,t)$ of the girder, namely, $\gamma_w(x,t)=W'(x,t)-\varphi(x,t)$, so the dynamic shear strain energy of the corrugated steel web can be given by,

$$V_w(t)=\int_0^l\frac{G_e A_s}{2}\gamma_w^2(x,t)dx=\frac{1}{2}\int_0^l G_e A_s\left[W'(x,t)-\varphi(x,t)\right]^2dx \tag{9}$$

Where G_e is the equivalent shear module of corrugated steel web due to the corrugation effect, $G_e=G_s(a_w+c_w)/(a_w+b_w)$, a_w, b_w, c_w are shown in figure 1; G_s the shear module of steel, $G_s=E_s/[2(1+\nu_s)]$, ν_s is the Poisson ratio of steel; A_s is the total shear area of the steel web.

(4) The total dynamic strain energy of the CBGCSWs

The total dynamic strain energy of the CBGCSWs $\Pi(t)$ is the summation of the $V_{fb}(x,t)$, $V_{fs}(x,t)$, and $V_w(x,t)$, namely,

$$\begin{aligned} \Pi(t)&=V_{fb}(t)+V_{fs}(t)+V_w(t)=\frac{1}{2}E_c\int_0^l\left\{I_y[\varphi'(x,t)]^2+A_y[u'(x,t)]^2-2S_y\varphi'(x,t)u'(x,t)\right\}dx \\ &+\frac{1}{2}\int_0^l G_c k_u u^2(x,t)dx+\frac{1}{2}\int_0^l G_e A_s\left[W'(x,t)-\varphi(x,t)\right]^2dx \end{aligned} \tag{10}$$

(5) The kinetic energy of the CBGCSWs

In the vertical flexural vibration, the kinetic energy of the CBGCSWs can be expressed as,

$$T(t)=\frac{1}{2}\int_0^l \dot{W}(x,t)^2\bar{m}dx \tag{11}$$

Where $\bar{m}$ is the mass of the girder per unit length, $\bar{m}=\rho_c A_f+\rho_s A_s$, ρ_c, ρ_s are the density of the concrete and the steel, respectively.

2.4 The solution of the vibration equations

According to the Hamilton principle, for a structure in elastic and small deformation state, in the time interval t_1 to t_2, only the real movement can make the first-order variation of the total energy function be zero, namely, $\delta\int_{t_1}^{t_2}\left[\Pi(t)-T(t)\right]dt=0$. Substitute equations (10) and (11) into it, the flexural vibration controlling differential equations and boundary conditions of the CBGCSWs can be obtained as follows,

$$\bar{m}\ddot{W}(x,t)+G_e A_s\left[\varphi'(x,t)-W''(x,t)\right]=0 \tag{12}$$

$$G_e A_s\left[\varphi(x,t)-W'(x,t)\right]+E_c S_y u''(x,t)-E_c I_y\varphi''(x,t)=0 \tag{13}$$

$$G_c k_u u(x,t)-E_c A_y u''(x,t)+E_c S_y\varphi''(x,t)=0 \tag{14}$$

$$E_c\left[I_y\varphi'(x,t)-S_y u'(x,t)\right]\delta\varphi\Big|_0^l=0 \tag{15}$$

$$\left[E_c A_y u'(x,t)-E_c S_y\varphi'(x,t)\right]\delta u\Big|_0^l=0 \tag{16}$$

$$G_e A_s\left[W'(x,t)-\varphi(x,t)\right]\delta W\Big|_0^l=0 \tag{17}$$

The vertical dynamic deflection $W(x,t)$ in flexural vibration of a simply supported girder can be expressed by,

$$W(x,t)=\sum_{n=1}^{\infty}W_n(x)\sin(\omega_n t+\alpha_n) \tag{18}$$

Where $W_n(x)$ is the vibration function of a simply supported girder, $W_n(x)=A_n\sin(n\pi x/l)$ [9], $(n=1、2、3、4.....\infty)$; ω_n is the circular frequency of the flexural vibration; α_n is the initial phase angle.

Substitute equation (18) into equation (12), (13), and (14), and consider $\sin(\omega_n t+\alpha_n)$ will not always be zero, therefor,

$$\begin{aligned}&\bar{m}\omega_n^2\left[G_e G_c A_s k_u W_n(x)-E_c\left(G_c k_u I_y+G_e A_s A_y\right)W_n''(x)+E_c^{\,2}\left(I_y A_y-S_y^2\right)W_n^{(4)}(x)\right]\\&=G_e G_c A_s k_u E_c I_y W_n^{(4)}(x)+E_c^{\,2}G_e A_s\left(I_y A_y-S_y^2\right)W_n^{(6)}(x)\end{aligned} \tag{19}$$

From equation (19), the circular frequency of the flexural vibration can be obtained as,

$$\omega_n=\beta_n\left(\frac{n\pi}{l}\right)^2\sqrt{\frac{E_c I_y}{\bar{m}}} \tag{20}$$

$$\beta_n=\frac{\sqrt{1+\left(\frac{n\pi}{l}\right)^2\frac{E_c\left(S_y^2-I_y A_y\right)}{G_c k_u I_y}}}{\sqrt{1+\left(\frac{n\pi}{l}\right)^2\frac{E_c I_y}{G_e A_s}+\left(\frac{n\pi}{l}\right)^2\frac{E_c A_y}{G_c k_u}+\left(\frac{n\pi}{l}\right)^4\frac{E_c^{\,2}\left(I_y A_y-S_y^2\right)}{G_e G_c A_s k_u}}} \tag{21}$$

$$f_n=\omega_n/2\pi \tag{22}$$

From equation (21) it can be seen, when the shear lag effect and the shear deformation of the web are neglected, the coefficient β_n=1, and ω_n, f_n will be the solutions of a Euler-Bernoulli beam.

3 EXAMPLES

3.1 Analytical Solutions

The flexural natural frequencies of three 4.4m-span simply-supported CBGCSWs with single-cell, double-cell, and triple-cell cross-sections respectively are calculated herein. The sections of each girder are shown in figure 1, and the dimensions and some sectional characters are shown in table 1. For each girder, the concrete is C40 with an elastic modular of E_c=3.25×10^{4}MPa, a Poisson ratio of v_c=0.1667, and a shear modular of G_c=1.39×10^{4}MPa; the steel web is Q235 with an elastic modular of E_s=2.06×10^{5}MPa, a Poisson ratio of v_s=0.3, a shear modular of G_s=7.92×10^{4}MPa and an equivalent shear modular of G_e=9.81×10^{4}MPa. The wave shape of the corrugated steel web shown in figure 1 is same for each girder, with a h_w of 200mm, a a_w of 64mm, a b_w of 24mm, and a c_w of 45mm.

Section	b_1	b_2	b_3	b_4	t_t	t_b	I_y	A_y	S_y	k_u	$\bar{m}$
	(mm)						(10^9mm^4)	(10^4mm^2)	(10^7mm^3)		(g/mm)
Single-cell	400	200	400	100	80	80	2.15	6.23	0.90	3.90	332.38
Double-cell	400	100	400	100	80	80	3.14	6.50	1.14	4.20	493.68
Triple-cell	400	100	400	100	80	80	4.39	9.70	1.71	6.17	696.57

Table 1: Dimensions and some sectional characters of the examples.

From equations (20)-(22), the flexural natural frequencies can be obtained in table 2.

Section	f_{1E}(Hz)	ω_1	f_1(Hz)	error	f_{2E}(Hz)	ω_2	f_2(Hz)	error
Single-cell	38.32	208	33.18	13.4%	153.30	632	100.67	34.3%
Double-cell	37.97	207	32.99	13.1%	151.90	631	100.52	33.8%
Triple-cell	37.83	205	32.69	13.6%	151.31	622	99.02	34.6%

Note: f_{1E} and f_{2E} are the frequencies of a Euler beam with the same section and dimensions with the CBGCSWs.

Table 2: Flexural natural frequencies of the examples.

From table 2 it can be seen,

- There is little difference among the vertical flexural frequencies of the three girders, which is because the vertical flexural frequency is mainly influenced by the flexural rigidity and the mass of the girder by increasing with the former and decreasing with the latter. With the larger of the cell number, the increasing magnitude of the mass is a little higher than that of the flexural rigidity, so the vertical flexural frequencies have no increase but a little decrease.
- There are great errors between the solutions of the Euler-Bernoulli beam and the results of equation (22), which means the shear lag effect and the shear deformation of the web have a great influence on the vertical flexural vibration of the CBGCSWs.

3.2 Comparison with numerical results

The FE models of the three examples were built by using ANSYS software. The concrete flanges were simulated by element solid65, and the steel webs were simulated by element shell63. The Multipoint Constrain function was employed to realize the connection between the concrete flanges and the steel webs. The natural vertical flexural frequencies and the comparison between the theoretical and numerical results are shown in table 3.

Section	The first-order			The second-order		
	$f_{theoretical}$(Hz)	$f_{numerical}$(Hz)	error(%)	$f_{theoreticla}$(Hz)	$f_{numerical}$(Hz)	error(%)
Single-cell	33.18	30.66	-7.59	100.67	92.03	-8.58
Double-cell	32.99	30.2	-8.45	100.52	90.19	-10.27
Triple-cell	32.69	29.14	-10.8	99.02	87.14	11.99

Table 3: Comparison between the theoretical and numerical results.

From table 3 it can be seen that the numerical results are satisfied well with the theoretical solutions with the errors all below 5%, which can prove the correction of the analytical derivation process and the FE model.

4 PARAMETRIC ANALYSIS

Based on the theoretical and FE model, a parametric analysis including the wave shape and the thickness of the corrugated steel web, the ratio of the section width to the calculating span *B*/*L*, and the ratio of the section height to the calculating span *H*/*L* were performed.

4.1 The wave shape and the thickness of the corrugated steel web

Based on the section and dimension of the double-cell CBGCSWs, remain a_w=64mm and b_w=24mm in figure 1(d) and change c_w and d_w of the corrugated steel web to the values shown in table 4, then the first and second-order vertical flexural frequencies are shown in figure 2(a).

Based on the double-cell CBGCSWs, change the web thickness to 1mm, 2mm, 3mm, 4mm, 5mm, 6mm and 7mm, then the results can be obtained and shown in figure 2(b).

Corrugated angle β（°）	0	10	20	30	40	50	60	70
c_w（mm）	24.0	24.3	25.7	27.3	31.2	36.9	48.4	69.3
d_w（mm）	0	4	9	13	20	28	42	65

Table 4: Dimensions of the corrugated steel web.

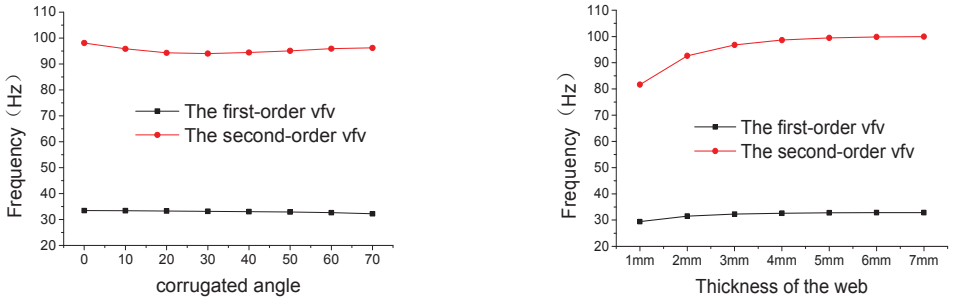

(a) Wave shape (b) Thickness

Figure 2: Effect of the wave shape and the thickness of the corrugated web.

From figure 2 it can be seen that,

- The largest vertical flexural frequency appears when the corrugated angle β=0 (namely, straight web), and then with the increase of β, the frequencies decrease slightly, which means the larger of the β, the smaller of the axial rigidity of the steel webs and subsequently the flexural rigidity of the CBGCSWs.
- The vertical flexural frequencies increase with the web thickness, but the increasing magnitude is small, especially for the first-order one, which means that the vertical flexural rigidity is mainly supplied by the top and bottom concrete flanges, and only increasing the web thickness cannot improve the vertical flexural rigidity apparently.

4.2 The ratio of the section width to the calculating span *B*/*L* and the ratio of the section height to the calculating span *H*/*L*

Based on the section and dimension of the double-cell CBGCSWs, change the width of the flange to 0.6m, 0.8m, 1.0m, 1.2m, 1.4m, 1.6m and 1.8m (*W*/*L*=0.136, 0.181, 0.227, 0.272, 0.318, 0.363, and 0.409, respectively), then the results are shown in figure 3(a).

Also based on the double-cell CBGCSWs, change the height of the section to 0.28m, 0.32m, 0.36m, 0.40m, 0.44m, 0.48m and 0.52m (*H*/*L*=0.063, 0.073, 0.082, 0.091, 0.100, 0.110, and 0.118, respectively), then the results are shown in figure 3(b).

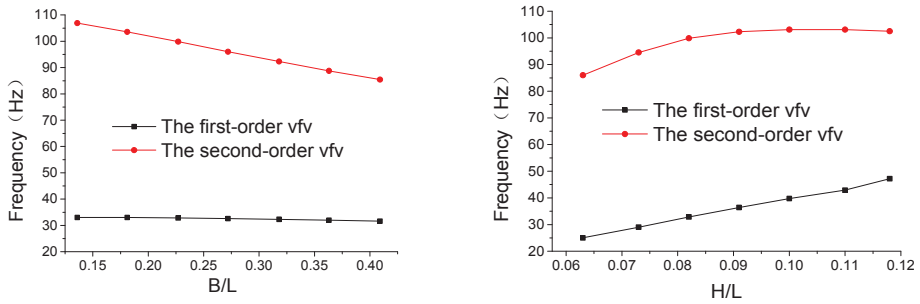

(a) *B*/*L* (b) *H*/*L*

Figure 3: Effect of *B*/*L* and *H*/*L* on the natural frequencies of the CBGCSWs.

From figure 3 it can be seen that,

- The vertical flexural frequencies decrease with the increasing of *B*/*L* due to the increasing magnitude of the mass exceeding that of the vertical flexural rigidity;
- The flexural frequencies increase with the increasing of *H*/*L* in a linear tendency for the first-order one and a curved tendency for the second-order one, which means the height of the section is a predominant factor to enlarge the vertical flexural rigidity of the girder.

5 CONCLUSIONS

- The shear lag effect and the shear deformation of the web have a great influence on the vertical flexural vibration of the CBGCSWs.
- There is little difference among the vertical flexural frequencies of the single-cell, double-cell, and triple-cell CBGCSWs due to the increasing magnitude of the mass exceed-

ing that of the vertical flexural rigidity, and for the same reason, the vertical flexural frequencies decrease with the increasing of *B*/*L*.

- The vertical flexural rigidity is mainly supplied by the top and bottom concrete flanges, and only increasing the web thickness or reducing the corrugated angle cannot improve the vertical flexural rigidity apparently.
- The height of the section is a predominant factor to enlarge the vertical flexural rigidity of the girder.

6 ACKNOWLEDGEMENT

This study is sponsored by the National Natural Science Foundation of China(51508348, 51778377) and the Natural Science Foundation of Hebei Province (E2018210149).

REFERENCES

[1] J. He, Y. Liu, A. Chen, T. Yoda, Mechanical behavior and analysis of composite bridges with corrugated steel webs: state-of-the-art, *International Journal of Steel Structures* 12 (3), 321-338, 2012.

[2] R.J. Jiang, K.F.T. Au, Y.F. Xiao, Prestressed concrete girder bridges with corrugated steel webs: review, *Journal of Structural Engineering* 141 (2), 4014108, 2015.

[3] D. H. Lee, J. Y. Oh, H. Kang., K. S. Kim, H. J. Kim, H. Y. Kim, Structural performance of prestressed composite girders with corrugated steel plate webs, *Journal of Constructional Steel Research* 104, 9-21, 2015.

[4] M. Zhou, J. D. Zhang, J. T. Zhong, Y. Zhao, Shear stress calculation and distribution in variable cross sections of box girders with corrugated steel webs, *Journal of Structural Engineering* 142(6): 1-10, 2016

[5] K.J. Shen, S. Wan, Y.L. Mo, A. Song, X.Y. Li, Behavior of single-box multi-cell box-girders with corrugated steel webs under pure torsion. Part I: Experimental and numerical studies, *Thin-Walled Structures* 129, 542-557, 2018.

[6] K.J. Shen, S. Wan, Y.L. Mo, Z.W. Jiang, X.Y. Li, Behavior of single-box multi-cell box-girders with corrugated steel webs under pure torsion. Part II: Theoretical model and analysis, *Thin-Walled Structures* 129, 558-572, 2018.

[7] H. B. Chen, B. D. Liu, H. W. Ren, Research on dynamic characteristic of concrete box-girder with corrugated steel webs, *Journal of Highway and Transportation Research and Development* 2(2), 63-66, 2007.

[8] W. Ji, S. Z. Liu, P. Z. Lin, Experiment and analysis for vibration frequency of composite box girder with corrugated steel webs, *China Journal of Highway and Transport* 26(5), 102-107, 2013 (in Chinese).

[9] L. Cao, J.P. Liu, Y. F. Chen, Theoretical and numerical study on the natural frequencies of bridges with corrugated steel webs, *Structures* 15, 224-231, 2018.

[10] Y. J. Zhang, P. M. Huang, J. Di, X. H. Zhou, Free vibration characteristics and experimental study of composite box girder with corrugated steel webs. *Journal of Traffic and Transportation Engineering* 8(5):76–80, 2008.

[11] W. Ji, S. Z Wei, Liu PZ Lin. Analysis and experimental study on nature vibration frequencies of PC continuous box girder bridge with corrugated steel webs. *Journal of Central South University (Science and Technology)* 47(4), 1297-1304, 2016.

EURODYN 2020
XI International Conference on Structural Dynamics
M. Papadrakakis, M. Fragiadakis, C. Papadimitriou (eds.)
Athens, Greece, 23–26 November 2020

METAMATERIALS WITH FIBERS OF ELLIPTIC CROSS SECTION

Guy Bonnet[1], and Vincent Monchiet[1]

[1]Université Paris Est
Laboratoire Modélisation et Simulation Multi-Echelle UMR 8208 CNRS 5 boulevard Descartes
77454 Marne la Vallée Cedex
e-mail: {guy.bonnet,vincent.monchiet}@univ-paris-est.fr

Keywords: Composite, Metamaterial, Elastodynamics, Elliptic fibers.

Abstract. *The paper presents the study of elastic composites acting as resonant metamaterials. The composites are made of long fibers of elliptic cross section. The condition for obtaining resonant metamaterials is presented in the context of homogenization by using asymptotic expansion. It is shown that inner resonance occurs in the case of soft inclusions embedded within a stiffer matrix, both components having mass densities of the same order of magnitude. The localization problem coming from the asymptotic expansion is solved in the case of fibers with elliptic cross sections, leading to the dynamic density of the material. The dynamic density is characterized by resonance frequencies and the related eigenfunctions of the inclusions, that are obtained by using an expansion along Mathieu functions. The method allows us to obtain the (orthotropic) dynamic density related to various cases of elliptic cross section, recovering the extreme cases of circular cross-sections and nearly plate inclusions.*

1 INTRODUCTION

Numerous works were performed during the last decades on metamaterials, firstly in the field of electromagnetism and more recently in the field of acoustics. This field of research can be traced back to 1968 paper of Veselago [1] on electromagnetism, as explained in [2]. There are different ways to produce acoustic metamaterials and this work is restricted to inclusion-matrix elastic composites.

This work rests on results obtained by asymptotic homogenization in elastodynamics. Homogenization methods extending the ones used in elastostatics have been indeed used since a few decades[3]. These methods produce two kinds of effective behaviours:

- When the elastic properties of constituents are of the same order within the composite, the effective behaviour is essentially non local in space: this is characterized by effective parameters expressed with the use of wave vectors and this type of behaviour is often studied by using Bloch waves.

- For composites containing soft and massive inclusions, the dynamic behaviour is characterized by inner resonance. The effective properties are local in space, but some effective physical parameters, the components of the "effective dynamic density" are frequency dependent: the behaviour is non-local in time[4, 5].

This work produces results on a locally resonant fiber-matrix composite containing fibers of elliptic cross section. In a first step, we recall the results of homogenization theory showing the conditions to produce locally resonant inclusion matrix composites and the general expression of the dynamic density induced by the inner resonators. This expression uses the resonance frequencies of the inclusions and the participation factors of each resonance frequency. In a second step, a fiber-matrix composite containing elastic fibers is studied. The resonance frequencies within the elastic fibers are produced for different components of the motion at the macroscopic scale. Finally, it is shown that the metamaterial is in fact an acoustic polarizer: it allows us to cancel preferentially some components of the dynamic motion around specific frequencies.

2 CONDITIONS FOR INNER RESONANCE

One considers a periodic composite containing two species: matrix ($s = m$) and inclusions ($s = i$), each phase being characterized by Lamé coefficients $\lambda_{(s)}, \mu_s, s = m, i$ and densities $\rho_{(s)}$. The dynamic equation in each phase is given for an harmonic motion by

$$\mathbf{div}(\boldsymbol{\sigma}_{(s)}) + \rho_{(s)}\omega^2\mathbf{u}_{(s)} = 0, \tag{1}$$

where $\boldsymbol{\sigma}_{(s)}$ is the stress tensor, $\mathbf{u}_{(s)}$ the displacement field and ω the radial frequency. The components $\sigma_{ij(s)}$ of the stress tensor are related to the components of linearized strain tensor $\epsilon_{ij(s)}$ by

$$\sigma_{ij(s)} = 2\mu_{(s)}\epsilon_{ij(s)} + \lambda_{(s)}\epsilon_{kk(s)}\delta_{ij}. \tag{2}$$

Homogenization theory can be used if the size of the periodic cell l is small compared with the size L of the composite volume under consideration, allowing us to introduce the scaling factor $\varepsilon = l/L$. As shown in [4], the inner resonance occurs when the elasticity parameters comply with the following condition:

$$\frac{\lambda_{(i)} + 2\mu_{(i)}}{\lambda_{(m)} + 2\mu_{(m)}} = O(\varepsilon^2), \tag{3}$$

$\rho_{(m)}$ and $\rho_{(i)}$ being of the same order.

Under these conditions and if the radial frequency leads to a wavelength within the matrix being of order of L, the material has an effective behaviour characterized by a (static) effective elasticity tensor obtained by considering that the inclusions are void (negligible elasticity tensor of the inclusions) and a dynamic density $\rho_{eff}(\omega)$ obtained by studying the displacement within the inclusion.

The relative displacement $\mathbf{w} = \mathbf{u}_{(i)} - \mathbf{u}_{(m)}$ within the inclusion is obtained from the solution of

$$\begin{aligned} \mu_{(i)}\mathbf{\Delta w} + (\lambda_{(i)} + \mu_{(i)})\mathbf{grad}(div(\mathbf{w})) + \rho_{(i)}\omega^2\mathbf{w} \\ = -\rho_{(i)}\omega^2\mathbf{u}_{(m)}, \end{aligned} \tag{4}$$

its value being null at the boundary between matrix and inclusion. The displacement $\mathbf{u}_{(m)}$ of the matrix around the inclusion is considered as nearly constant, its fluctuations being negligible due to the large stiffness of the matrix.

Due to the homogeneous boundary condition, the solution of this problem can be obtained from the related eigenfunctions and eigenvalues. For a periodic cell with three planes of symmetry, the dynamic density is a second order diagonal tensor in the axes of symmetry and its components are given by :

$$\rho_{jj(eff)} =< \rho > +n_{(i)}\rho_{(i)}h_{jj}, \tag{5}$$

where the components h_{jj} are given from the radial eigenfrequencies $\omega_p, p = 1..\infty$ by:

$$h_{jj}(\omega) = \sum_{p=1}^{\infty} K_{jj}^p \frac{\omega^2}{\omega_p^2 - \omega^2}, \tag{6}$$

K_{jj}^p being the participation factors obtained from the eigenfunctions $\mathbf{u}^p$ by:

$$K_{jj}^p = \frac{(< \mathbf{u}^p >_{(i)} .\mathbf{e}_j)^2}{< ||\mathbf{u}^p||^2 >_{(i)}}, \tag{7}$$

$\mathbf{e}_j$ being the unit coordinate vectors.

In theory, the sum in the previous expression is infinite. However, the only acceptable frequency contents of the waves crossing the composite are those complying with the condition for the wavelength in the matrix to be large compared with the size of the cell. Therefore, the sum must be restricted to the eigenfrequencies meeting this condition. The eigenfunctions are obtained for the three directions $j = 1, 2, 3$ of the macroscopic acceleration. For each direction of $\mathbf{e}_j$, one obtains a set of eigenfunctions and eigenvectors characterized by a specific symmetry, the three sets being independent.

3 SOLUTION BY SEPARATION OF VARIABLES FOR ELLIPTIC FIBERS

The solution by separation of variables is used to obtain the eigenfrequencies and eigenfunctions in cylinders of elliptic cross section, as shown in Fig. 1.

3.1 LONGITUDINAL MOTION

For a longitudinal motion, the motion is antiplane with $\mathbf{w} = w_3\mathbf{e}_3$, where w_3 is solution of

$$\mu\Delta w_3 + \rho\omega^2 w_3 + f_3 = 0, \tag{8}$$

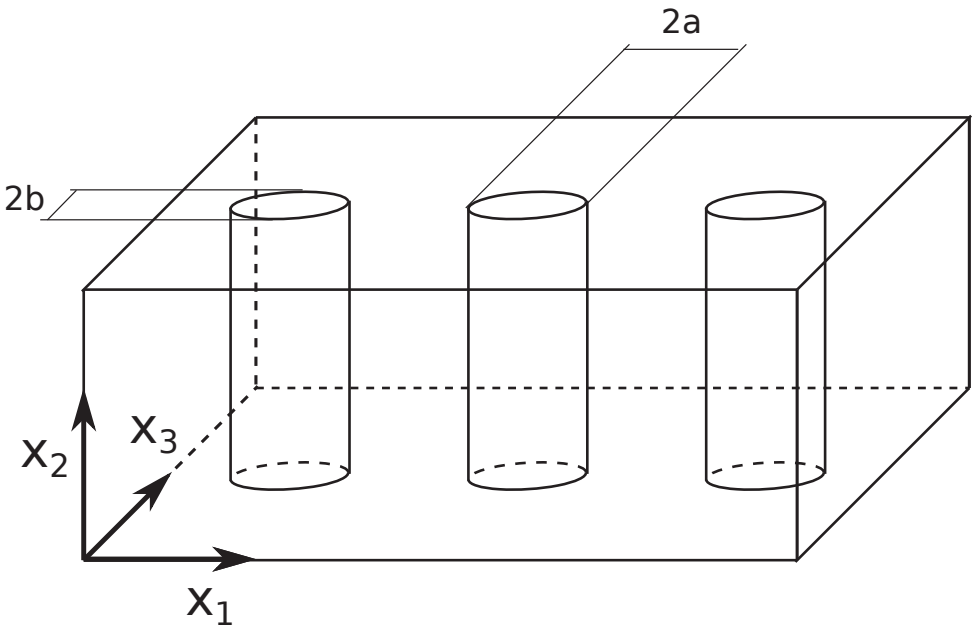

Figure 1: Geometry of the composite: fibers with elliptic cross section characterized by radii a and b.

where $\mu = \mu_{(i)}, \rho = \rho_{(i)}, f_3 = \rho_{(i)}\omega^2 u_{3(m)}$. The motion is characterized by the celerity of shear waves $v_s = \sqrt{\mu/\rho}$ within the inclusions. For an elliptic cross-section, the separation of variables is achieved by using $x_1 = c\cosh\xi\cos\eta, x_2 = c\sinh\xi\sin\eta$. ξ is the radial coordinate ($0 \leq \xi < \infty$) and η is the angular coordinate ($0 \leq \eta < 2\pi$), $2c$ being the focal length of the ellipse. For the interior of the ellipse, ξ is restricted to $\xi \leq \xi_e$, where ξ_e corresponds to points located on the elliptic contour. Taking into account that w_3 must be symmetric with respect to $0x_1$ and $0x_2$, the solution in elliptic coordinates is given by:

$$w_3(\eta,\xi) = \sum_{p=0}^{\infty} D_p ce_{2p}(\eta, q_s) Mc_{2p}(\xi, q_s) \tag{9}$$

where D_p are constant, ce_{2p} are Mathieu functions characterized by the previously defined symmetry, Mc_{2p} are the related radial Mathieu functions. q_s is function of the wave number $k_s = \omega/v_s$ given by: $q_s = \frac{1}{4}c^2k_s^2$. Mathieu functions are obtained under the form of Fourier series

$$ce_{2m}(\eta, q_s) \quad = \quad \sum_{r=0}^{\infty} A_{2r}^{(2m)}(q_s)\cos 2r\eta$$

where the Fourier coefficients $A_{2r}^{(2m)}(q_s)$ are functions of q_s. Obtaining these coefficients has been the subject of numerous works. A finite set of these coeffficients can be obtained by computing the eigenvalues and eigenvectors of a matrix function of q_s[6]. Then, the radial Mathieu functions Mc_{2p} are also expressed by using the set of Fourier coefficients. A recent work [7] gives the best way to obtain the set of Fourier coefficients. Using the orthogonality property of Mathieu functions and the boundary condition allows us to compute the eigenfunctions by solving: $Mc_{2p}(\xi_e, q_s) = 0$ for different values of p. This gives a set of values of q_s which provide the set of eigenfrequencies. Then, the eigenfunction related to each eigenfrequency is $ce_{2p}Mc_{2p}$, which provides the related participation factor.

3.2 TRANSVERSAL MOTION

For a transversal motion, the solution is given by a plane displacement in plane x_1, x_2. It is obtained by decomposition into scalar and vector potentials φ, $\mathbf{\Psi}$ by $\mathbf{u} = \mathbf{grad}\varphi + \mathbf{curl}\mathbf{\Psi}$, with $\mathbf{\Psi} = \psi.\mathbf{e}_3$. Both potentials φ, ψ can be again expanded along Mathieu functions, using q_p for φ and q_s for ψ. This leads to an expression of the displacement from Mathieu functions and their derivatives. The eigenfunctions are again obtained by the homogeneous boundary condition along the elliptic contour and the participation factors are given by a suitable integration within the contour.

4 NUMERICAL RESULTS

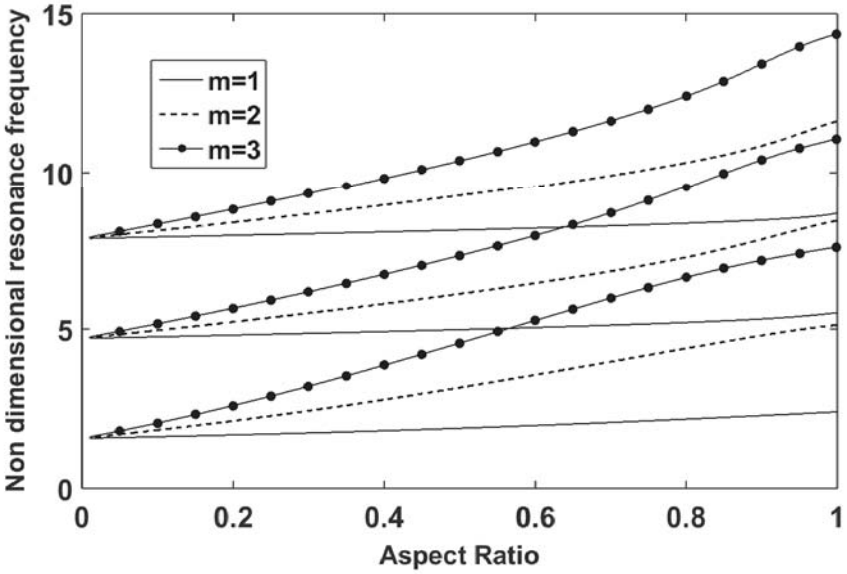

Figure 2: Resonance frequencies for a longitudinal motion as a function of the aspect ratio: modes related to the first three eigenfrequencies for Mathieu functions of first three orders ($m = 1, 2, 3$).

For the longitudinal motion, the solution does not involve compressional waves. As a consequence, the eigenfrequencies are functions of the shear modulus μ and of the radii a and b of the fibers. All results can be expressed by looking for the non-dimensional resonance frequency $\omega^{(p)*} = b\omega/v_s$ as a function of the aspect ratio $f = b/a$. The length introduced into the non dimensional frequency is the smaller radius b of the ellipse. The aspect ratios related to decreasing values of f correspond to ellipses of the same smaller radius and increasing values of the larger radius.

As explained previously, the modes related to Mathieu functions of different orders are decoupled. So, for each value of order m, one can find a set of eigenfrequencies which cancel the value of the radial Mathieu function at the surface of the fiber.

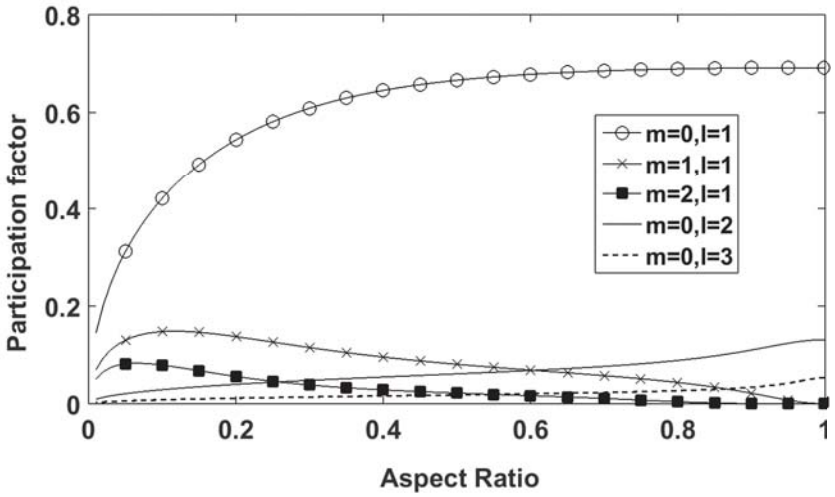

Figure 3: Participation factors for a longitudinal motion as a function of the aspect ratio: modes related to the 9 cases of Fig. 2 which have a significant contribution.

Fig. 2 presents the first three eigenfrequencies related to the first three values of m. It has been checked that, for the limit case of circular cross sections ($f = 1$), the results recover the values of eigenfrequencies for $m = 1$ obtained in [8]. In the case of circular fibers, the solution is expressed by using Bessel functions J_{2m}. The values for $m > 1, f = 1$ recover also the ones obtained for circular fibers and higher indices of Bessel functions. The limit case of small aspect ratio is also of interest. It can be seen that the first eigenfrequencies for $m = 0, 1, 2$ tend to $\pi/2$ while the second (resp. third) eigenfrequencies tend to $3\pi/2$ (resp.$5\pi/2$), these limit values correspond to the case of very flat fibers, whose eigenfunctions can be obtained explicitly. All eigenfrequencies increase with f, due to the fact that the section of the ellipse decreases with f when b is constant.

The participation factors that have a significant contribution related to the eigenfrequencies of Fig. 2 are reported in Fig. 3. It can be seen for almost circular sections that the participation factors are null for $m > 0$ and are not null for $m = 0$, which corresponds to the results obtained in [8]. However, the curves show that the participation factors increase for smaller aspect ratios, the contribution for the first eigenfrequencies related to $m > 0$ becoming significative. In the case of transversal motion, along x_1 or x_2, the results (not reported here) are functions of compressional and shear waves, v_p and v_s and therefore functions of the Poisson's ratio.

As explained in the previous section, the components of the dynamic density are negative near the resonance frequencies. As an example, the three components of dynamic density are reported in Fig. 4 for a composite containing fibers of plastified PVC ($E_i = 112MPa, \nu_i = 0.38, \rho_i = 1500kg/m^3$) within an aluminium matrix ($E_m = 72GPa, \nu_m = 0.34, \rho_m = 2500$). The three stopping bands sb_i corresponding to the first

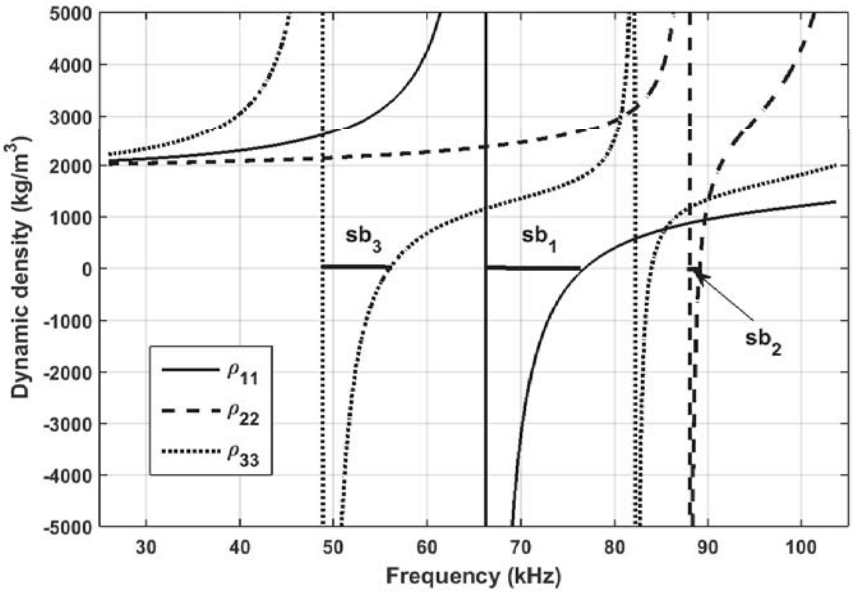

Figure 4: The three components of dynamic density for a composite of aluminium matrix and PVC fibers with an aspect ratio of 0.5. The first stop band for each direction i is reported by sb_i

eigenfrequencies along the three directions are distinct contrarily to the case of cylindrical fibers (2 identical stopping bands) or spherical inclsions (3 identical stopping bands. It means that one of the components of motion for plane waves crossing the composite is cancelled: the composite acts as a full polarizer, as do the well known linear optical polarizers.

5 CONCLUSIONS

The conditions for inclusion matrix composites to produce inner resonance have been recalled: the elasticity constants of inclusions must be significantly smaller than the ones of the matrix, the densities of both components being of the same order. In this case, the dynamic density is a function of the resonance frequency of the inner inclusions and of the eigenfunctions obtained at resonance. The dynamic density becomes negative near each eigenfrequency and the effect of the related eigenfunction on the dynamic density is characterized by a participation factor. A composite containing soft elliptic fibers embedded within a significantly stiffer matrix has been studied. The dynamic motion within the fiber is studied by using Mathieu functions and the eigenfrequencies and eigenfunctions were computed. For this configuration, the dynamic density is orthotropic, the motion along the three axes being characterized by components of the dynamic densities that are

all different, which is not the case for spherical inclusions or circular cylindrical fibers. As a consequence, the composite acts as a polarizer, which can extinct one component of the motion near the related eigenfrequency.

REFERENCES

[1] V.G. Veselago, The electrodynamics of substances with simultaneously negative values of ϵ and μ, *Soviet Physics Uspekhi*, **28**, 509-514,1968 .

[2] E. Shamonina and L. Solymar, Metamaterials: How the subject started, *Metamaterials*, **1**, 12-18,2007 .

[3] J.R. Willis, Variational principles for dynamic problems for inhomogeneous elastic media, *Wave Motion*, **3**, 1-11,1981 .

[4] J.L. Auriault and G.Bonnet, Dynamique des composites élastiques périodiques. (Dynamics of periodic elastic composites), *Arch. Mech.*, **37**, 269-284,1985 .

[5] J.L. Auriault and C. Boutin, Long wavelength inner-resonance cut-off frequencies in elastic composite materials, *International Journal of Solids and Structures*, **49**, 3269-3281,2012 .

[6] M. Abramowitz and I.A. Stegun, Handbook of Mathematical Functions with Formulas, Graphs, and Mathematical Tables, *Dover*, N.Y., 1972.

[7] M.M. Bibby and A.F. Peterson, Accurate computation of Mathieu functions, *Morgan and Claypool*, San Rafael, California, 2013.

[8] G. Bonnet and V. Monchiet, Dynamic mass density of resonant metamaterials with homogeneous inclusions., *Journal of the Acoustical Society of America*, **142-2**, 890-901,2017 .

EURODYN 2020
XI International Conference on Structural Dynamics
M. Papadrakakis, M. Fragiadakis, C. Papadimitriou (eds.)
Athens, Greece, 23–26 November 2020

A TWO MODE NON-UNIFORM APPROXIMATION FOR AN ELASTIC ASYMMETRIC SANDWICH

Mohammed Alkinidri, Julius Kaplunov, and Ludmila Prikazchikova

Keele University
Staffordshire, UK, ST5 5BG
e-mail: m.o.s.alkinidri@keele.ac.uk, j.kaplunov@keele.ac.uk, l.prikazchikova@keele.ac.uk

Keywords: Asymptotic, contrast, laminate, two-mode, wave, non-uniform.

Abstract. *An elastic asymmetric sandwich is considered under the assumption that the stiffness and density of thin skin layers are much greater than those of a core layer. It is shown that for typical values of problem parameters the lowest shear resonance frequency appears to be asymptotically small, while the rest of thickness resonances do not belong to a low-frequency range. As an example, a scalar antiplane problem in linear elasticity is studied. A polynomial long-wave low-frequency approximation of the full dispersion relation is derived. It governs two vibration modes including the fundamental one and the lowest harmonic. Without asymmetry the dispersion relation splits into two parts corresponding to symmetric and antisymmetric modes [1], simplifying analysis drastically. It is remarkable that for the chosen set of problem parameters the derived approximation is not asymptotically uniform and is only valid over narrow non-overlapping vicinities of zero and the lowest shear thickness resonance frequencies. This is in contrast to the earlier considered setup of a similar laminate with the thick skin layers, for which the associated asymptotic behaviour is uniform [2]. The same observation is also true for in-plane motion of a symmetric laminate, see [3] for further detail.*

1 Introduction

Asymmetric sandwich plates become increasingly important as components of ultra-light multifunctional structures in various fields of engineering, see for example [4, 5, 6] and references therein. Many of these structures might also demonstrate high contrast in material and geometric properties of the layers, for example lightweight photovoltaic panels [7] and new models of windscreens [8].

Asymptotic analysis of an asymmetric sandwich structure with a light core and stiff skin layers is conducted in [2] for anti-plane shear motion. As shown in this paper, an additional small cut-off frequency might arise depending on the choice of the contrast material parameters of the layers. A two-mode long-wave asymptotic approximation, constructed in [2] is uniform, i.e. valid for the whole low-frequency range. At the same time, despite the presence of a small cut-off frequency, it might not always be the case. There are some setups of contrasting problem parameters resulting in non-uniform asymptotic behaviour, e.g. see [3] considering a plane problem for a symmetric sandwich plate. In this case, the associated asymptotic behaviour appears to be composite, i.e. it is valid only over narrow non-intersecting vicinities of zero and lowest cut-off frequencies. The concept of composite expansions is based on tackling limiting cases only without a special care of the less important intermediate region, e.g. see [10] and [11]. Recently, composite wave models have been constructed for thin and periodic structures in [12, 13, 14]. An asymptotic methodology for three-layered plates with contrast parameters of the layers was earlier adapted in [15] mainly concerned with static deformation. Among the publications on the subject, we also mention [16, 17, 18, 19, 20].

In this paper we investigate the anti-plane problem for a three-layered asymmetric plate with very light core layer and stiff thin skin layers of different thickness. A two-mode long-wave low-frequency approximation of the exact dispersion relation is constructed and shown to be non-uniform. The asymptotic results are compared with the exact solution.

2 Statement of the problem

Consider a three-layered asymmetric elastic laminate, comprised of isotropic layers of thickness h_l, $l = 1, 2, 3$, see Figure 1. The axis x_1 of the Cartesian coordinate system passes through the mid-plane of the core layer, while the axis x_2 is orthogonal to the mid-plane. For the sake of simplicity we assume that the two outer layers have the same material parameters.

Consider antiplane shear motion, for which the only non-zero displacement component is orthogonal to the plane x_1x_2. The equations of motion for each of the layers is then given by

$$\Delta u_l - \frac{1}{c_{2l}^2}\frac{\partial^2 u_l}{\partial t^2} = 0, \qquad l = 1, 2, 3, \tag{1}$$

where $\Delta = \partial^2/\partial x_1^2 + \partial^2/\partial x_2^2$ is the Laplace operator, $u_l = u_l(x_1, x_2, t)$ are out of plane displacements, t is time, and

$$c_{2l} = \sqrt{\frac{\mu_l}{\rho_l}},$$

are the shear wave speeds, with μ_l and ρ_l standing for the Lamé elastic moduli and volume mass densities, respectively. As mentioned above, $\mu_1 = \mu_3$ and $\rho_1 = \rho_3$.

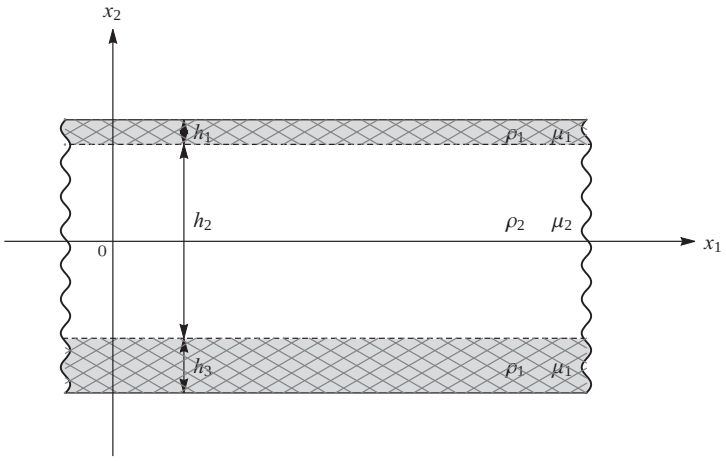

Figure 1: A three-layered asymmetric laminate

For traction-free faces and perfect bonding between the layers, the dispersion relation may be derived in the form

$$\mu\alpha_1\alpha_2\big(\tanh(h_{12}\alpha_1)+\tanh(h_{32}\alpha_1)\big)+\mu^2{\alpha_2}^2\tanh(\alpha_2)+ \\ +{\alpha_1}^2\tanh(h_{12}\alpha_1)\tanh(h_{32}\alpha_1)\tanh(\alpha_2)=0 \tag{2}$$

where

$$\alpha_1=\sqrt{K^2-\frac{\mu}{\rho}\Omega^2},\qquad \alpha_2=\sqrt{K^2-\Omega^2}$$

and

$$K=kh_2,\quad \Omega=\frac{\omega h_2}{c_{22}},\quad \mu=\frac{\mu_2}{\mu_1},\quad \rho=\frac{\rho_2}{\rho_1},\quad h_{12}=\frac{h_1}{h_2},\quad h_{32}=\frac{h_3}{h_2}.$$

3 Asymptotic approach

Consider an asymmetric laminate of a sandwich type, with the outer layers being stiff, thin and very heavy compared to the inner core layer. Hence, the ratio of parameters in the layers are taken as

$$\mu\ll 1,\quad \rho\sim\mu^2,\quad h_{12}\sim\mu,\quad h_{32}\sim\mu. \tag{3}$$

Setting K = 0 in (2) we obtain as expected $\Omega=0$, and also a small non-zero cut-off frequency given by

$$\Omega_{sh}\approx\sqrt{\frac{(h_{12}+h_{32})\rho}{h_{12}h_{32}}}\sim\sqrt{\mu}\ll 1. \tag{4}$$

Next, expanding the trigonometric functions in (2) in Taylor series about $\Omega=K=0$ and assuming (3), an approximate polynomial dispersion relation may be obtained in the form

$$\gamma_1K^2+\gamma_2\Omega^2+\gamma_3K^4+\gamma_4K^2\Omega^2+\gamma_5\Omega^4+\gamma_6K^6 \\ +\gamma_7K^4\Omega^2+\gamma_8K^2\Omega^4+\gamma_9\Omega^6+\cdots=0, \tag{5}$$

where the coefficients γ_i, $i=1,2,\ldots 9$ have been presented in [2] (cf. formula [14] in the cited paper).

Now, in view of (3), leading order coefficients γ_i become

$$\begin{aligned}
\gamma_1 &= \gamma_1^0\mu^2, \qquad & \gamma_1^0 &= 1 + h_{12}^0 + h_{32}^0,\\
\gamma_2 &= \gamma_2^0\mu + O\left(\mu^2\right), \qquad & \gamma_2^0 &= -\frac{h_{12}^0 + h_{32}^0}{\rho_0},\\
\gamma_3 &= \gamma_3^0\mu^2 + O\left(\mu^4\right), \qquad & \gamma_3^0 &= h_{12}^0 h_{32}^0 - \frac{1}{3},\\
\gamma_4 &= \gamma_4^0\mu + O\left(\mu^2\right), \qquad & \gamma_4^0 &= -\frac{2h_{12}^0 h_{32}^0}{\rho_0},\\
\gamma_5 &= \gamma_5^0 + O\left(\mu^2\right), \qquad & \gamma_5^0 &= \frac{h_{12}^0 h_{32}^0}{\rho_0^2},\\
\gamma_6 &= \gamma_6^0\mu^2 + O\left(\mu^4\right), \qquad & \gamma_6^0 &= \frac{2}{15} - \frac{h_{12}^0 h_{32}^0}{3},\\
\gamma_7 &= \gamma_7^0\mu + O\left(\mu^2\right), \qquad & \gamma_7^0 &= \frac{2h_{12}^0 h_{32}^0}{3\rho_0},\\
\gamma_8 &= \gamma_8^0 + O\left(\mu\right), \qquad & \gamma_8^0 &= -\frac{h_{12}^0 h_{32}^0}{3\rho_0^2},\\
\gamma_9 &= \gamma_9^0 + O\left(\mu\right), \qquad & \gamma_9^0 &= \frac{h_{12}^0 h_{32}^0}{3\rho_0^2},
\end{aligned} \tag{6}$$

where $\rho_0 = \rho/\mu^2$, $h_{12}^0 = h_{12}/\mu$ and $h_{32}^0 = h_{32}/\mu$. These results are summarised in Table 1, allowing comparison of asymptotic orders of the terms in approximation (5) both in the vicinity of zero and the lowest cut-off frequency (4).

Order of γ_i	Terms	Fundamental mode $\Omega^2 \sim \mu K^2$	First harmonic $\Omega_{sh}^2 \sim \mu$
$\gamma_1 \sim \mu^2$	$\gamma_1 K^2$	$\mu^2 K^2$	$\mu^2 K^2$
$\gamma_2 \sim \mu$	$\gamma_2 \Omega^2$	$\mu^2 K^2$	μ^2
$\gamma_3 \sim \mu^2$	$\gamma_3 K^4$	$\mu^2 K^4$	$\mu^2 K^4$
$\gamma_4 \sim \mu$	$\gamma_4 K^2\Omega^2$	$\mu^2 K^4$	$\mu^2 K^2$
$\gamma_5 \sim 1$	$\gamma_5 \Omega^4$	$\mu^2 K^4$	μ^2
$\gamma_6 \sim \mu^2$	$\gamma_6 K^6$	$\mu^2 K^6$	$\mu^2 K^6$
$\gamma_7 \sim \mu$	$\gamma_7 K^4\Omega^2$	$\mu^2 K^6$	$\mu^2 K^4$
$\gamma_8 \sim 1$	$\gamma_8 K^2\Omega^4$	$\mu^2 K^6$	$\mu^2 K^2$
$\gamma_9 \sim 1$	$\gamma_9 \Omega^6$	$\mu^3 K^6$	μ^3

Table 1: Asymptotic behaviour at $\mu \ll 1, \quad \rho \sim \mu^2, \quad h_{12} \sim h_{32} \sim \mu$

Using this Table, the leading order shortened approximate dispersion relation may be constructed, incorporating the fundamental mode along with the lowest harmonic with the asymptotically small cut-off frequency (4). It may be expressed as

$$\mu^2\gamma_1^0 K^2 + \left(\mu\gamma_2^0 + \gamma_5^0\Omega^2\right)\Omega^2 + \mu\gamma_4^0 K^2\Omega^2 + \gamma_8^0 K^2\Omega^4 + \gamma_9^0\Omega^6 = 0. \tag{7}$$

In this formula all the terms are of the same order μ^3 at $\Omega - \Omega_{sh} \sim \mu^{3/2}$, $K \sim \sqrt{\mu}$. The local asymptotic approximation for the fundamental mode is given by

$$\mu\gamma_1^0 K^2 + \gamma_2^0 \Omega^2 = 0. \tag{8}$$

At the same time, the local expansion for the first harmonic becomes

$$\mu^2\gamma_1^0 K^2 + \left(\mu\gamma_2^0 + \gamma_5^0\Omega^2\right)\Omega_{sh}^2 + \mu\gamma_4^0 K^2\Omega_{sh}^2 + \gamma_8^0 K^2\Omega_{sh}^4 + \gamma_9^0\Omega_{sh}^6 = 0, \tag{9}$$

where Ω_{sh} is given by (4). The associated typical near cut-off expansion, e.g. see [21, 22] for further details, is

$$\Omega^2 - \Omega_{sh}^2 = -K^2\frac{1}{\gamma_5^0}\left(\mu^2\frac{\gamma_1^0}{\Omega_{sh}^2} + \mu\gamma_4^0 + \gamma_8^0\Omega_{sh}^2\right) - \frac{\gamma_9^0\Omega_{sh}^4}{\gamma_5^0}. \tag{10}$$

Note that the long-wave assumption $K \ll 1$ dictates that the approximation (8) for the fundamental mode is valid only for $\Omega \ll \sqrt{\mu}$, whereas (10) is associated with $\Omega \sim \sqrt{\mu}$. Thus, the approximation (7) is non-uniform, in line with previous considerations in [3].

Numerical illustrations of the derived approximations are given in Figures 2-3. In Figure 2 two-mode approximation (7) (dotted lines) is compared numerically with the exact solution of the dispersion relation (2) (solid lines). A characteristic gap where the asymptotic formula (7) is not applicable is shown in Figure 2.

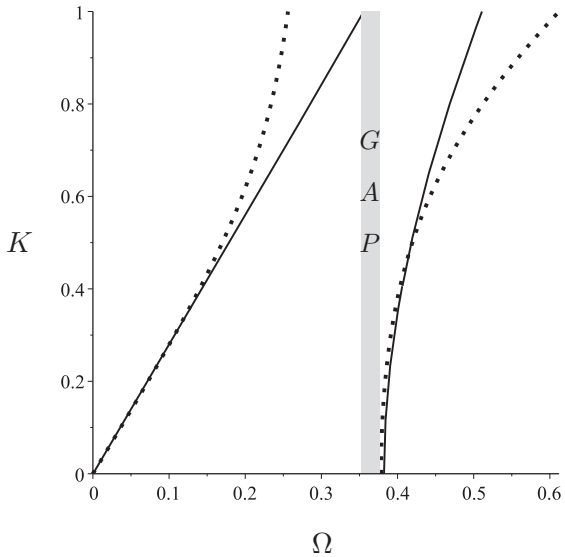

Figure 2: Dispersion curves (2) (solid lines) together with approximation (7) (dotted lines) for $h_{12} = 0.1$, $h_{32} = 0.2$, $\mu = 0.1$, and $\rho = 0.01$.

In Figure 3 exact dispersion curves (2) (solid lines) are shown together with approximations for the fundamental mode (8) and for the lowest harmonic (10) (dotted lines), demonstrating high accuracy of asymptotic predictions.

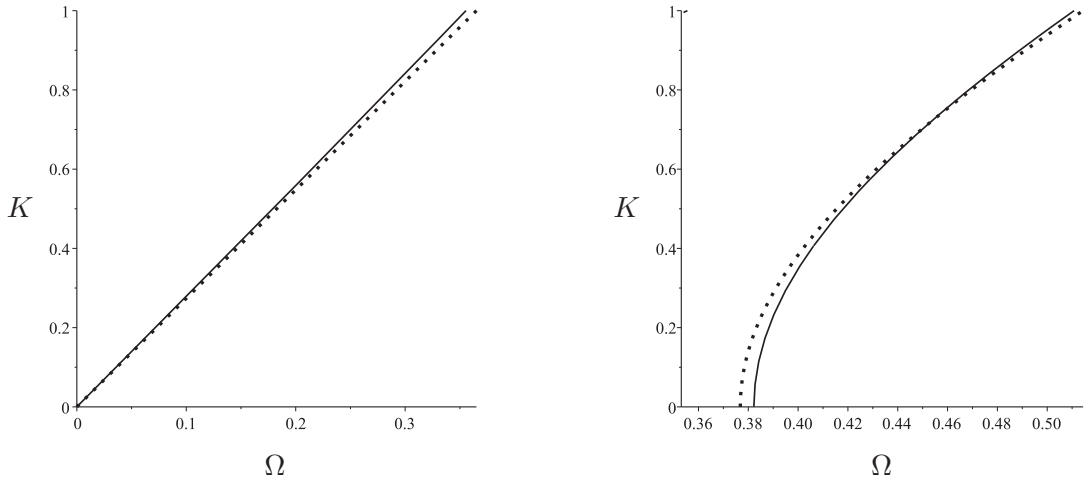

(a) Fundamental mode (b) First harmonic

Figure 3: Dispersion curves (2) (solid lines) together with approximations for a) the fundamental mode (8) and b) the lowest harmonic (10) (dotted lines) for $h_{12} = 0.1$, $h_{32} = 0.2$, $\mu = 0.1$ and $\rho = 0.01$

4 Conclusion

The present analysis complements the previous results for an asymmetric layered plate in [2]. Two-mode approximate dispersion relation has been derived for a chosen scenario for which the outer layers are relatively stiff, thin and very heavy compared to the inner layer. In contrast to [2], in which the two-mode long-wave low-frequency approximation was asymptotically uniform, the approximation obtained in the paper is of composite nature, being only valid over non-overlapping vicinities of the origin and the first cut-off frequency. Thus, the effect of high contrast does not always result in a uniform two-mode approximation as might be expected. The proposed research may be expanded to the derivation of the related two-mode differential equations of motion, based on the same scaling.

Acknowledgement

The work was supported by the grant J2-9224 from the Slovenian Research Agency. M.Alkinidri acknowledges PhD Scholarship from Saudi Arabian Government.

REFERENCES

[1] L. Prikazchikova, Y. Ece Aydin, B. Erbaş, J. Kaplunov, Asymptotic analysis of an anti-plane dynamic problem for a three-layered strongly inhomogeneous laminate, *Mathematics and Mechanics of Solids*, 1081286518790804, 2018.

[2] M. Alkinidri, J. Kaplunov, L. Prikazchikova, Two-mode long-wave low-frequency approximations for anti-plane shear deformation of a high-contrast asymmetric laminate. *Springer Proceedings in Mathematics and Statistics, DSTA 2019, in press.*

[3] J. Kaplunov, D. Prikazchikov, L. Prikazchikova, Dispersion of elastic waves in a strongly inhomogeneous three-layered plate, *International Journal of Solids and Structures*, **113**, 169–179, 2017.

[4] B. Castanié, J-J. Barrau, J-P. Jaouen, Theoretical and experimental analysis of asymmetric sandwich structures, *Composite Structures*, **55** (3), 295–306, 2002.

[5] J. Kim, S.R. Swanson, Effect of unequal face thickness on load resistance of sandwich beams, *Journal of Sandwich Structures and Materials*, **6** (2), 145–166, 2004.

[6] J. Rion, Y. Leterrier, J.A.E. Månson, J.M. Blairon, Ultra-light asymmetric photovoltaic sandwich structures, *Composites Part A: Applied Science and Manufacturing*, **40** (8), 1167–1173, 2009.

[7] M. Weps, K. Naumenko, H. Altenbach, Unsymmetric three-layer laminate with soft core for photovoltaic modules, *Composite Structures*, **105**, 332–339, 2013.

[8] M. Ulizio, D. Lampman, M. Rustagi, J. Skeen, C. Walawender, Practical design considerations for lightweight windshield applications, *SAE International Journal of Transportation Safety*, **5** (1), 47–57, 2017.

[9] M. Aßmus, K. Naumenko, H. Altenbach, Mechanical behaviour of photovoltaic composite structures: influence of geometric dimensions and material properties on the eigenfrequencies of mechanical vibrations, *Composites Communications*, **6**, 59–62, 2017.

[10] M. Van Dyke, Perturbation methods in fluid mechanics/Annotated edition. *NASA STI/Recon Technical Report A 75.Research supported by the U.S. Air Force.Stanford, CA: Parabolic Press*, 1975.

[11] I.V. Andrianov, J. Awrejcewicz, L.I. Manevitch, Asymptotical mechanics of thin-walled structures, *Springer Science & Business Media*, 2013.

[12] B. Erbaş, J. Kaplunov, E. Nolde, E., M. Palsü, Composite wave models for elastic plates, *Proceedings of the Royal Society A: Mathematical, Physical and Engineering Sciences*, **474** (2214), 20180103, 2018.

[13] B. Erbaş, J. Kaplunov, M. Palsü, A composite hyperbolic equation for plate extension, *Mechanics Research Communications*, **99**, 64–67, 2019.

[14] D.J. Colquitt, V.V. Danishevskyy, J. Kaplunov, Composite dynamic models for periodically heterogeneous media, *Mathematics and Mechanics of Solids*, 1081286518776704, 2018.

[15] V.L. Berdichevsky, An asymptotic theory of sandwich plates, *International Journal of Engineering Science*, **48** (3), 383–404, 2010.

[16] P. Lee, N. Chang, Harmonic waves in elastic sandwich plates, *Journal of Elasticity*, **9** (1), 51–69, 1979.

[17] C.O. Horgan, Saint-Venant end effects for sandwich structures, *In Fourth International Conference on Sanwich Construction. EMAS Publishing UK*, **1**, 191–200, 1998.

[18] M.Y. Ryazantseva, F.K. Antonov, Harmonic running waves in sandwich plates, *International Journal of Engineering Science*, **59**, 184–192, 2012.

[19] C. Boutin, K. Viverge, Generalized plate model for highly contrasted laminates, *European Journal of Mechanics-A/Solids*, **55**, 149–166, 2016.

[20] K. Viverge, C. Boutin, F. Sallet, Model of highly contrasted plates versus experiments on laminated glass, *International Journal of Solids and Structures*, **102**, 238–258, 2016.

[21] J.D. Kaplunov, D.G. Markushevich, Plane vibrations and radiation of an elastic layer lying on a liquid half-space, *Wave Motion*, **17** (3), 199–211, 1993.

[22] M.I. Lashhab, G.A. Rogerson, L.A. Prikazchikova, Small amplitude waves in a pre-stressed compressible elastic layer with one fixed and one free face, *Zeitschrift für angewandte Mathematik und Physik*, **66** (5), 2741–2757, 2015.

EURODYN 2020
XI International Conference on Structural Dynamics
M. Papadrakakis, M. Fragiadakis, C. Papadimitriou (eds.)
Athens, Greece, 23–26 November 2020

MODELING OF CFRP STRUCTURES USING MODEL UPDATING TECHNIQUES AND EXPERIMENTAL MEASUREMENTS

I. Zacharakis[1], D. Giagopoulos[*1], I. Zyganitidis [1], A. Arailopoulos[1], O. Markogiannaki [1]

[1]Department of Mechanical Engineering
University of Western Macedonia
Kozani, GR-50100, Greece
e-mail: dgiagopoulos@uowm.gr; web page: http://lvmd.mech.uowm.gr

Keywords: Structural Dynamics, Model Updating, Optimal Modeling, Winded Carbon Fibers

Abstract. *An optimal computational modeling approach of CFRP (Carbon Fiber Reinforced Composite) structures is presented using cylindrical tubes parts produced on a spinning axis by winded carbon fibers in various angles and directions. First, appropriate specimens and experimental structures are being produced for testing procedures under static and dynamic load conditions for the examination of the mechanical material properties and comparison with numerical models. Discreet FE models of the specimens and the examined structures are developed consisting of mainly shell elements, simulating each carbon fiber ply and resin matrix, and solid elements for other parts such as connectors and glue that interacting with the composite. Due to the two-phase heterogeneous nature of the composite material appropriate micromechanical modeling is being applied to extract the mechanical properties parameters under the homogenization process of one layer of carbon-fiber composite of the FE model. To minimize the error between the physical structure and the FE model due the original assumptions of the homogenizations, in combination with commercial finite element analysis software an update methodology framework is being developed and used to acquire the optimal FE model. This is achieved through combining measured and numerical time-histories of strains. Single objective structural identification strategies without the need of sub-structuring methods, are used for estimating the parameters (material properties in each deformation plane) of the finite element model, based on minimizing the deviations between the experimental and analytical characteristics. A stochastic optimization evolution strategy is applied in parallel computing, to solve the single-objective optimization problem. The effect of model error and finite element model parameterization on the optimal models along with and their variability, are examined.*

1 INTRODUCTION

Carbon fiber reinforced polymer (CFRP) composites have gained much attention in recent years through their industrialized implementation and use, as a structural material for static and dynamic load bearing as well as resistance to accidental excitations and actions. Due to its low-density, low thermal expansion and high strength, stiffness and corrosion resistance, applications from aerospace and automotive industry to building reinforcement and retrofit, as well as cryogenic fuel storage tanks are emerging rapidly [1–6]. Plain-woven CFRPs are the most popular carbon fiber-reinforced composites and have been extensively investigated by researchers and are widely used in numerous applications. However, composite materials produced by filament winding manufacturing technique despite disadvantages, such as geometry limitation and need of a mandrel, has been extensively used for its low cost and speed of production with applications on pressure vessels, natural gas vehicle tanks, power transmission shafts and sporting equipment [7]. Being inherently sensitive to manufacturing treatment and due to its material variability, filament winded CFRPs strongly require certification results through numerical verification and hybrid (numerical - experimental) validation [8].

The mechanical properties of long-fiber composites show large variations [9,10] their prediction for unidirectional or woven laminated composites has been extensively discussed in the literature [11–15], but due to the complexity of the fiber paths in the layers of filament winding, these properties cannot accurately describe the behavior of filament wound pipes. The lamina properties can vary between different positions of a single filament wound tube. Thus, not only the behavior of the structure cannot be modeled efficiently, but also the failure may start prior, at an unexpected point at the weakest areas of the pattern that is being produced by the winding.

From the engineer's perspective, in order to successfully and accurately design a Carbon Fiber Reinforced Polymer (CFRP) structure, the lamina mechanical properties need to be used in combination with robust Finite Element Analysis (FEA) approaches. Other common isotropic materials might have small deviations from their nominal values in terms of mechanical properties, thus a great percentage of error at the response of a structure can be accredited at the CFRP components.

The main goal of this work is to acquire the optimal lamina mechanical properties of a CFRP composite with an efficient procedure minimizing the time-consuming experimental tests that usually required. More specifically, a simple tension test is executed first to acquire the experimental strain data. Next, a homogenization method at the fiber-matrix level using a micromechanical model is applied in order to acquire the nominal mechanical properties of the lamina. From the wide variety of micromechanical models that have being proposed [11], [13], [16], Huang's model [17] will be used as it has also being applied in similar tubes made of Glass Fiber Reinforced Polymer composites [18]. Next, the nominal values of layer properties are tuned taking full advantage of a state-of-the-art stochastic single objective optimization algorithm, alongside with experimental strain measurements of the tension test and a high-fidelity numerical finite element model (FEM). For the updating process, Covariance Matrix Adaptation – Evolution Strategy (CMA-ES) coupled with MSC Nastran Finite Element Analysis (FEA) software is applied. CMA-ES stochastic optimization algorithm is a general purpose method, that has demonstrated rapid convergence capabilities, particularly when searching for a single global optimum and has been successfully applied to linear and non-linear FE updating problems, involving large and complex models and cases [19–23]. The results are validated in different experimental tests with different types of loading and different specimen thickness, fiber orientation angles and diameter size.

The present work has the following organization. First the theoretical formulation of the

materials homogenization (Section 2.1) and the finite element model update (Section 2.2) are briefly presented. At Section 3 the experimental test to characterize the material and the application of the finite element model update procedure is presented. Section 4 presents the experimental validation on static and dynamic loads and at last Section 5 the conclusions are summarized.

2 LAMINA PROPERTIES AND FINITE ELEMENT MODEL UPDATING STRATEGIES

2.1 Nominal Lamina Properties

To acquire the nominal lamina mechanical properties from the variety of micromechanical models that have been proposed [11], [13], [16], Huang's [17] model is used, which shows acceptable results [14] for unidirectional composites and has being applied ta similar tubes formed by Glass Fiber Reinforces Polymer composite [18]. Most of the fiber and matrix properties are being provided by the manufacturer and the remaining can be found from material databases such as [24,25].

The major equations needed to calculate the nominal lamina mechanical properties are listed below:

$$E_1 = V^f E_1^f + V^m E^m \tag{1}$$

$$E_2 = \frac{(V^f + V^m a_{11})(V^f + V^m a_{22})}{(V^f + V^m a_{11})(V^f S_{22}^f + a_{22} V^m S_{22}^m) + V^f V^m (S_{21}^m - S_{21}^f) a_{12}} \tag{2}$$

$$v_{12} = V^f v_{12}^f + V^m v^m \tag{3}$$

$$G_{12} = G^m \frac{(G_{12}^f + G^m) + V^f (G_{12}^f - G^m)}{(G_{12}^f + G^m) - V_f (G_{12}^f - G^m)} \tag{4}$$

$$G_{23} = \frac{0.5(V^f + V^m a_{22})}{V^f (S_{22}^f - S_{23}^f) + V^m a_{22} (S_{22}^m - S_{23}^m)} \tag{5}$$

With: $a_{11} = \frac{E^m}{E_1^f}$ $a_{22} = a_{33} = a_{44} = 0.5(1 + \frac{E^m}{E_2^f})$ $a_{55} = a_{66} = 0.5(1 + \frac{G^m}{G^f})$

$$S_{22}^f = \frac{1}{E_2^f} \quad S_{21}^f = \frac{-v_{12}^f}{E_1^f} \quad S_{23}^f = \frac{-v_{23}^f}{E_2^f} \quad S_{22}^m = \frac{1}{E^m} \quad S_{21}^m = \frac{-v^m}{E^m} \quad S_{23}^m = \frac{-v^m}{E^m}$$

The variables E, ν, and G are the Youngs modulus, Poisson's ratio and shear modulus respectively expressed for the additional material and direction, with f, m to represent the fiber and matrix properties and direction 1 to be parallel to the fiber direction, 2 in-plane perpendicular to 1 and 3 perpendicular to both 1,2. While α_{ij} and S_{ij} correspond at elements of row i and column j of the bridging matrix and elastic-plastic compliance matrix respectively of the Huang's model [17].

2.2 Model Updating Framework

The Covariance Matrix Adaptation – Evolution Strategy (CMA-ES) is a general-purpose stochastic algorithm and together with a simple experiment is used to acquire the optimal lamina mechanical properties.

Let M be a parameterized class of structural dynamic models, that simulates the structural system and will be used to estimate desired quantities of interest. Consider $\underline{\theta}_m \in R^{N_\theta}$ be the set

of free structural model parameters to be adjusted using the measured data and let $g(\underline{\theta}_m \mid M_m)$ be the model predictions given the values of the parameter set $\underline{\theta}_m$. In this work, parameter estimation is based on response time history measurements of strains. This formulation has the advantage of applicability over both linear and non-linear systems; it compares the measured raw data of the experimental arrangement to the equivalent predictions of the numerical model. In this way, all available information is preserved, and systematic errors of the identification procedure are alleviated.

The difference between the measured response time histories and the model predicted response time histories, take the form [26]:

$$J(\underline{\theta};M)=\frac{1}{m}\sum_{i=1}^{n}\frac{\sum_{j=1}^{m}\left(\underline{g}_{ij}(\underline{\theta}_m \mid M)-\hat{y}_{ij}\right)^2}{\sum_{j=1}^{m}\left(\hat{y}_{ij}\right)^2} \tag{6}$$

where $\underline{g}_{ij}(\underline{\theta}_m \mid M)$ is the numerical time-history of the introduced FE model and $\hat{y}_{ij}$ is the respective experimental signal. Subscripts i correspond to the sensor location and measurement direction, and j corresponds to the time-step instant. n is the total number of measured sensor locations and directions, whereas m is the total number of measured time-steps (number of observations).

The measure of fit as introduced in equation (6) is consisted for strains equally weighted, expanding to the following equation (7), where $s\left(\underline{\theta}_m \mid M\right)_{ij}$ are the numerical time-histories of strains of the introduced FE model and $\widehat{s_{ij}}$ are the respective experimental strain signal. At the present experimental setup only one sensor is present resulting in equation (7).

$$J(\underline{\theta};M)=\frac{1}{m}\frac{\sum_{j=1}^{m}\left(s(\underline{\theta}_m \mid M)_{ij}-\hat{s}_{ij}\right)^2}{\sum_{j=1}^{m}\left(\hat{s}_{ij}\right)^2} \tag{7}$$

CMA-ES is applied to update the developed FE model minimizing the objective function of equation (7). The flow chart of the complete framework is presented at Figure 1 presents the flow chart of the applied framework. The flow of the framework is distinguished in two separate parts the homogenization of the material parameters and the FE model updating. The homogenization of the material parameters takes place once and considers the carbon fiber and matrix properties in order to produce the lamina properties introduced to the FE model. Independently the experimental strain response time histories are collected. The model-updating framework utilizes experimental data and the developed numerical FE model. It begins by sampling a set of material parameters from a Multivariate Normal Distribution using given means and variances based on initial lower and upper bounds. Then the FEA solver is invoked in order to compute strain response time histories at matching excitation – response locations regarding the experimental measurements. The objective function of equation (7) is calculated and the upon completion of a set of function evaluations (iteration) CAM-ES collects the minimum values in order to create new means and variances and begin a new iteration until convergence criterion is fulfilled. In this work convergence was set the difference of the best values of two consecutive iterations to be less than $\Delta J(\underline{\theta})<10^{-3}$. CMA-ES ends when convergence is met and the material parameters that correspond to the minimum objective function value pertain to the optimal updated values.

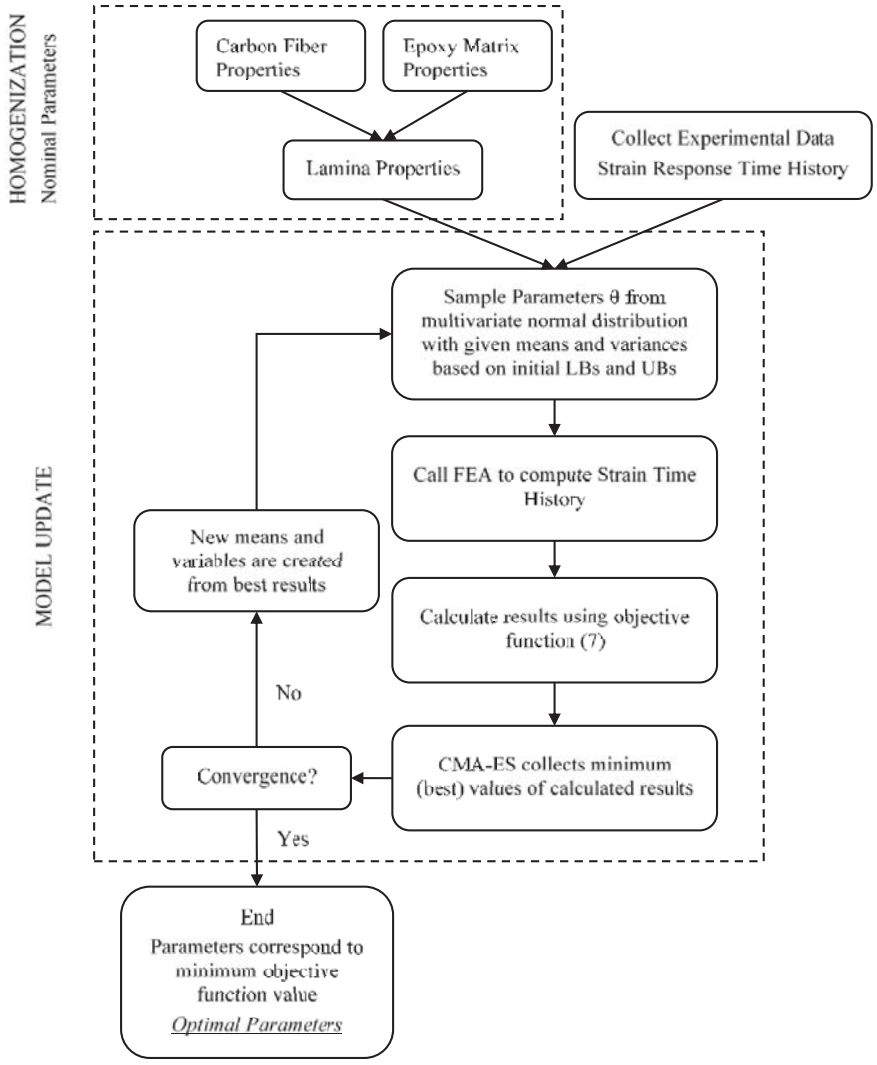

Figure 1. Flow chart of the applied CMA-ES framework based on the linear FE model updating scheme.

3 EXPERIMENTAL APPLICATION-MATERIAL CHARACTERIZATION TEST

3.3 Optimal lamina mechanical properties

A uniaxial tension experiment per ASTM 3039 [27] standard is selected for the CFRP tube with lamina properties presented in Table 1. Single-axis strain gauges were placed at the middle of each specimen and appropriate 3D printed PLA patches were glued at the edges to match the curvature of the specimen so the testing machine would not damage the specimen on installation as presented in Figure 2.

Table 1. Tensile Test Specifications.

Specimen properties				
Layer Orientation	(+/-55º)/(+/-55º)/(+85º)/(+/-55º)/(+/-55º)/(+/-55º)			
Tube Internal Diameter	220 mm			
Layer Thickness	+/- 55º	0.35 mm	**Free Height**	122 mm
	85º	0.16 mm	**Width**	22 mm

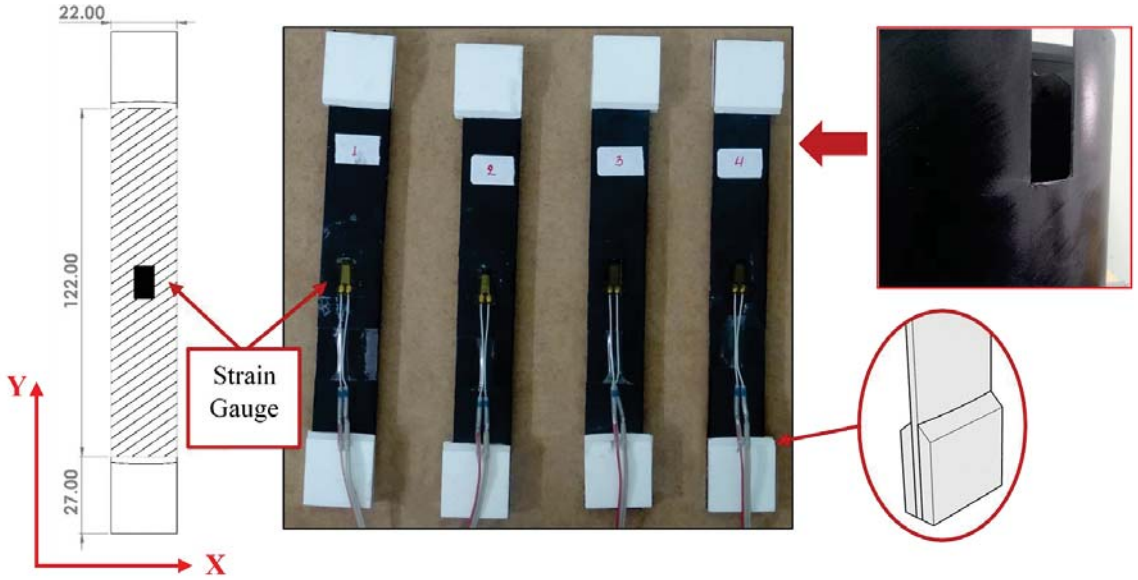

Figure 2. Tensile specimens and test setup for uniaxial tensile.

Figure 3. Experimental uniaxial tensile setup with the corresponding finite element model.

All the specimens were manufactured with the same raw materials, Toray T700S fiber and Epikote 828LVEL matrix.

The model updating methodology is conducted by parameterizing the FE model resulting in six parameters that correspond to the material lamina properties. As the material can be characterized as transversally isotropic the shear modulus at directions 1-2 and 1-3 are equal thus limiting the parameters to E_1, E_2, ν_{12}, $G_{12}=G_{13}$, G_{23}. At Table 3 the nominal values from the micromechanical model are presented along with the model update procedure results, the lower (LB) and upper (UB) bounds selected and the difference between optimal and nominal values.

A direct comparison of the strain along the Y direction is presented at Figure 4a between the nominal model and the measured experimental strain until the moment of first ply failure. The blue continuous line (labeled as Experimental) in Figure 4a represents the average of all experimentally measured tensile specimens, while the red-dotted line (labeled as ST2) and purple dash-dotted line (labeled as ST4) corresponds to the upper and lower outlines respectively, in means of strain time response, enveloping all specimens tested. The dashed line although corresponds to the numerical predictions from the nominal FE model.

Table 2. Updated design variables and updated design bounds (Lower Bound and Upper Bound) of Lamina Mechanical Properties.

	Parameters	Lower Bound	Nominal Value	Upper Bound	Updated Optimal Value	Difference (%)
1	$E_1\ [MPa]$	120000	161900	165000	138945	14.17
2	$E_2\ [MPa]$	5000	9456	12000	6615.4	30.03
3	ν_{12}	0.22	0.272	0.35	0.278	2.20
4	$G_{12}, G_{13}\ [MPa]$	3000	5908.7	6500	3387	42.67
5	$G_{23}\ [MPa]$	2000	3308.4	4500	2286.41	30.89

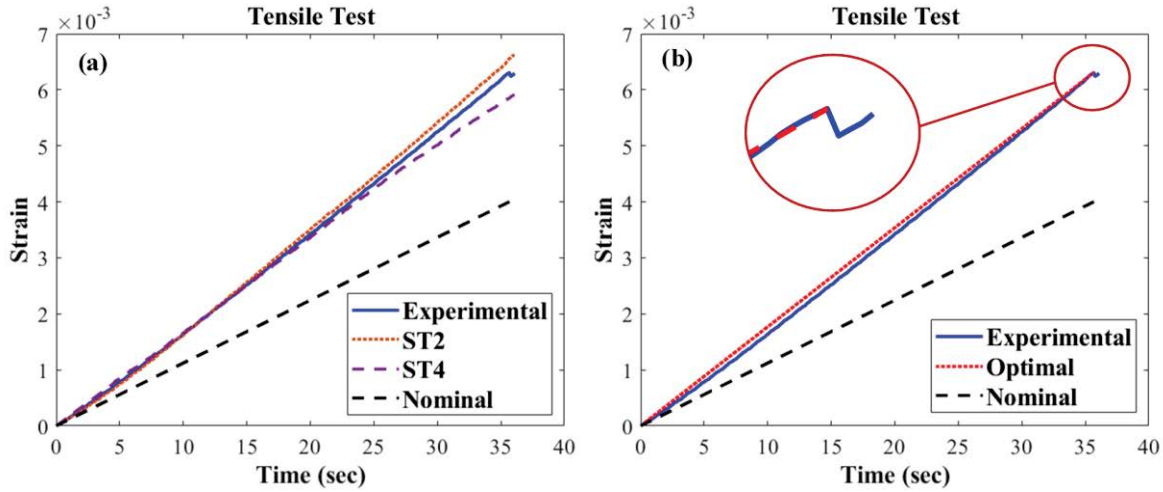

Figure 4. (a) Comparison of experimental strain with nominal FE model (b) Comparison of experimental strain with FE optimal and FE nominal models.

At last on Figure 4b the strain time response by the optimal FE model (red dotted line) is compared to the nominal predictions (black dashed line) and to the averaged experimental data, while the magnified area presents the response at the time of failure.

4 VALIDATION

In order to validate the previous results further experimental test were executed in more complex loading conditions and structures.

4.1 Three Point Bending

A straight strip with 220 mm length (180mm free length) and 36 mm width was removed from the same tube used to collect the specimens in the previous tensile test described in section **Error! Reference source not found.**. In a three-point bending test, the strip is placed at the testing machine as presented in Figure 5a, with a force control motion of the machine's head. Two strain gauges, SG1 in the transverse direction (X-axis) and SG2 in the longitudinal direction of the specimen (Y-axis) were placed to measure the induced deformations. During the experiment the machine's head was moving against the middle of the simply supported strip, up to a maximum displacement measuring time histories of head's displacement and strains developed as presented in Figure 5b.

Figure 5c presents the corresponding non-linear contact model developed in MSC Marc in the initiation state while Figure 5d presents the numerical results at the state of maximum

bending of the strip.

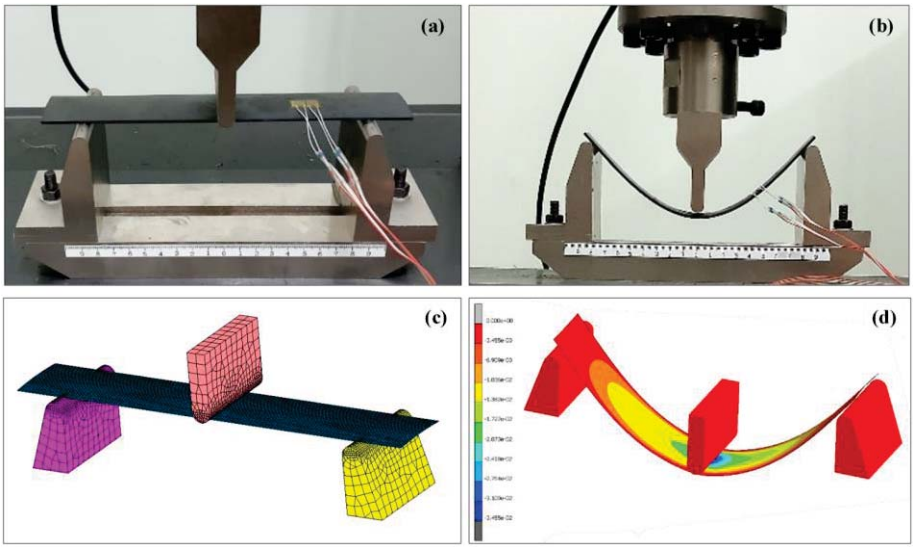

Figure 5. Three-point bending experimental set up and numerical model, (a), experimental initial state, (b) experimental max bending, (c) Non-linear FE model initial state, (d) Numerical strains along Y direction at t=335sec - max bending.

Figure 6a and Figure 7b present a comparison of the strain time responses for the strain gauge locations SG1 and SG2 respectively, between optimal FE model (red dotted line), nominal FE model (black dashed line) and experimentally measured data (blue continuous line). It is clear that the optimal model gives a far better approximation of the physical specimen. The magnified areas on Figure 8b correspond at first ply failure and a random ply failure during the experiment accordingly. While at the end of the experiment no visible damage could be detected, a plastic deformation occurred at the specimen by delamination phenomena or fault lines within the matrix of the CFRP specimen.

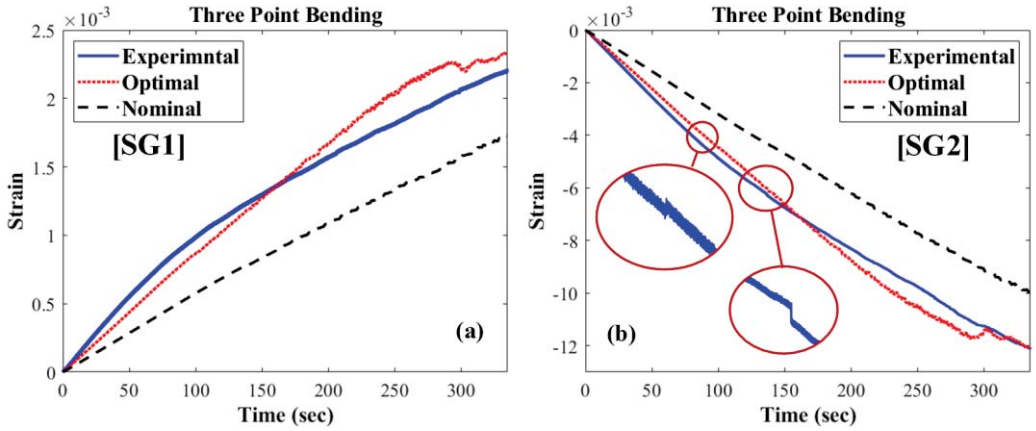

Figure 9. Comparison of experimental, FE optimal and FE nominal models for (a) SG1 (X-transverse axis) and (b) SG2 (Y-longitudinal axis).

4.2 Cylinder on Radial Deformation

The second validation test introduces a CRFP cylindrical specimen under radial deformation. The specimen's material properties are presented in Table 3. The experimental set-up was comprised of a cylindrical CFRP tube and two internal steel cylinders, properly connected to two hook-like heads and accordingly placed at the Universal Testing Machine (UTM) as presented in Figure 10.

Two cases were examined, Case 1 limited only at the linear elastic area of the material and

Case 2 until total material failure occurred. In both cases two strain gauge sensors are placed on the specimen, at an angle of 90 degrees with the axis passing through the center of the machine's grips, i.e. SG1 in the transverse direction (direction along the X-axis of the cylinder) and SG2 in the longitudinal direction of the specimen (direction in the tube perimeter, Y-axis).

The corresponding non-linear numerical model was developed using shell composite elements for the CFRP specimen, while the steel cylinders were modeled with solid elements as shown in Figure 10b.

Table 3. CFRP Specimen Properties

Specimen properties				
Layer Orientation	(+/-55º)/ (+/-55º)/(+86º) /(+/-55º) (+/-55º)/ (+/-55º)			
Tube Internal Diameter	150mm		**Width**	50mm
Layer Thickness	+/- 55º	0.35 mm		
	85º	0.16 mm		

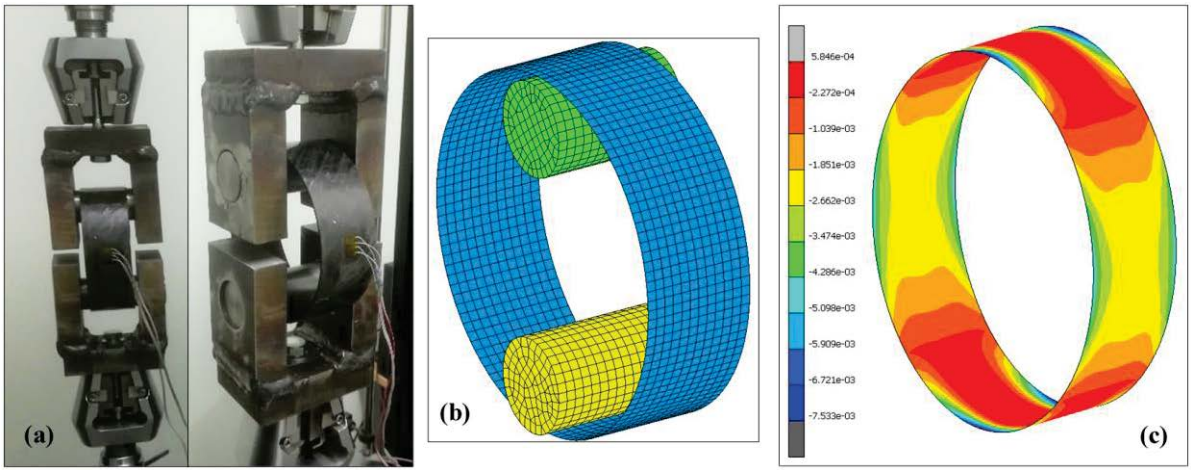

Figure 10. (a) Experimental set-up, (b) Numerical model at MSC Marc, (c) Strain at Y direction for t=23sec.

Figure 10c presents the Y-axis strain distribution on the optimal FE model of the cylindrical CFRP specimen at the point in time of maximum displacement (t=23sec) for Case 1. Regarding this Case limited at the linear area of the material, Figure 11a and Figure 11b present a comparison of the strain time responses at the strain gauge locations SG1 and SG2, between the optimal FE model (red dotted line), the nominal FE model (black dashed line) and the experimental measured data (blue continuous line).

Regarding the Case 2, until the total failure of the material, Figure 12a and Figure 12b presents a comparison of strain time responses at the strain gauge locations SG1 and SG2, between the optimal FE model (red dotted line) and the experimental measured data (blue continuous line). The magnified area of Figure 12b corresponds at the first ply failure of the experimental test. Furthermore, the three highlighted areas as the same figure represent a different state at the specimen condition. The first represent the state just before the material fail all across the width of the specimen at the contact areas for the FE optimal model. While the second state represent the state after the failure across the width of the specimen and the third the moment just before the total failure of the material and separation of the specimen.

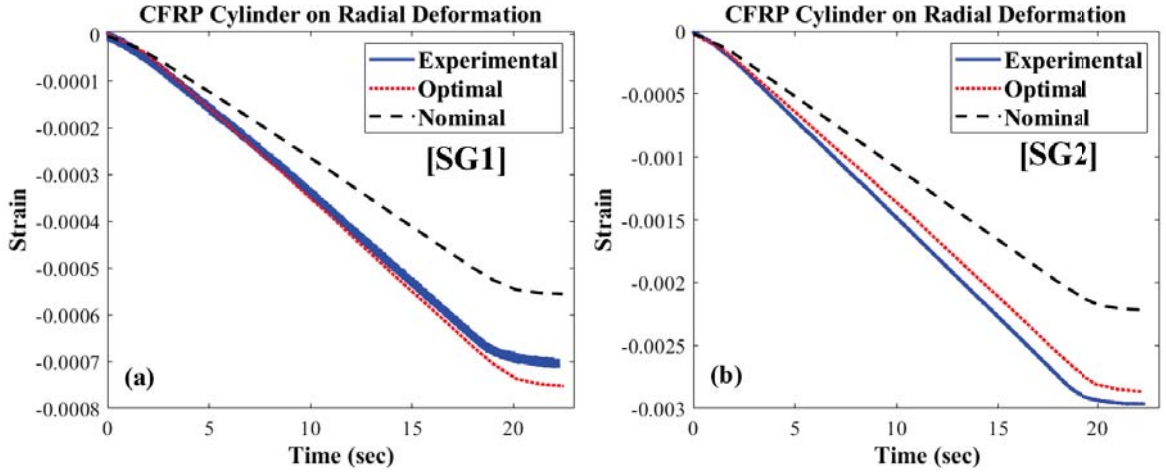

Figure 11. Comparison of experimental, FE optimal and FE nominal models for case 1, (a) SG1 (X-transverse axis) and (b) SG2 (Y-longitudinal axis).

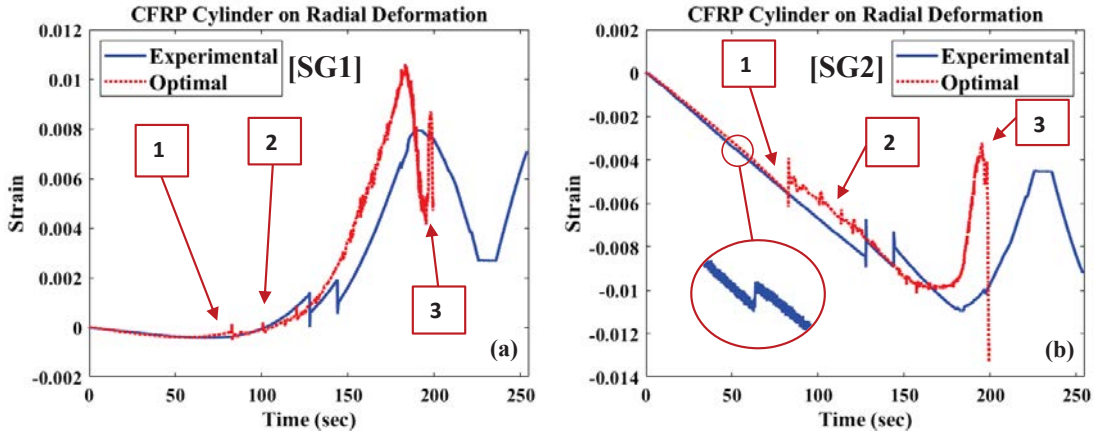

Figure 12. Comparison of experimental and FE optimal model for Case 2, (a) SG1 (X-transverse axis) and (b) SG2 (Y-longitudinal axis).

4.3 Cantilever CFRP tube

Dynamically induced excitation tests were conducted at a cantilever CFRP tubular beam as presented in Figure 13. A small radius CFRP tube along with two tri-axial accelerometers, a strain gauge sensor and a load cell at the free end of the cantilever beam, where an electromagnetic shaker device is mounted. The tubes properties are presented at Table 4 while aluminum joints were glued at the tube's edges which can be seen at Figure 14 along with the corresponding FE model in MSC Nastran.

Table 4. CFRP tube properties

CFRP properties				
Layer Orientation	(+/-8º)/ (+/-8º)/(+86º) /(+/-8º) (+/-8º)			
Tube Internal Diameter	25mm		**Length**	1m
Layer Thickness	+/- 8º	0.26 mm		
	86º	0.16 mm		

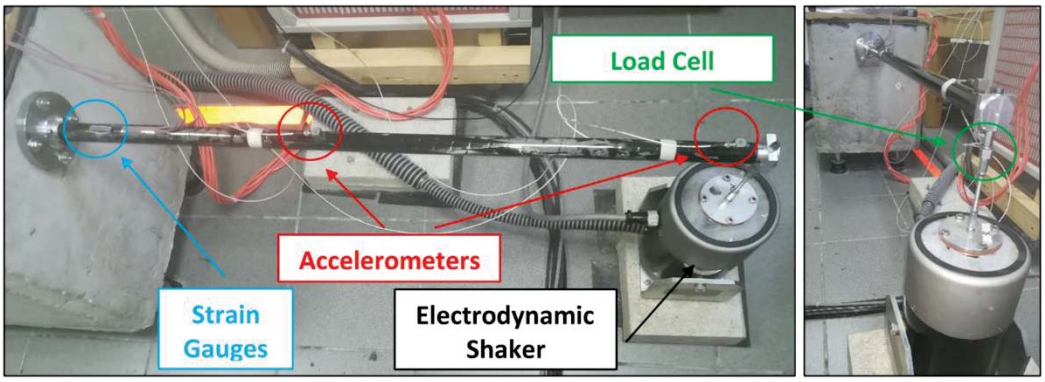

Figure 13. Experimental setup of cantilever CFRP tube under dynamic load excitation.

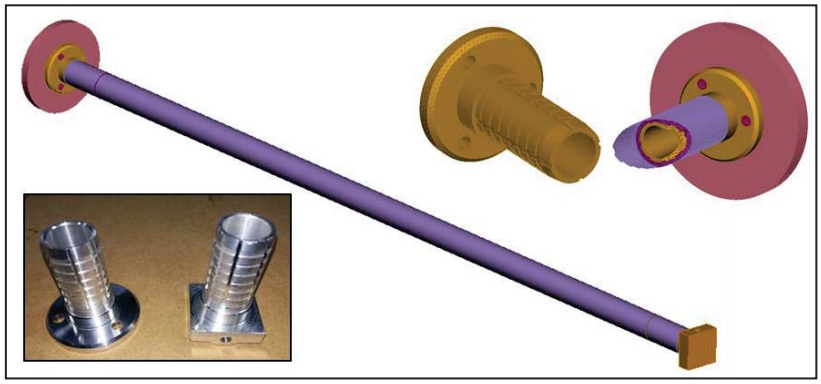

Figure 14. FE model of cantilever CFRP tube along with aluminum drop-outs.

An experimental modal analysis procedure of the CFRP cantilever beam was performed in order to quantify the dynamic characteristics of the examined structure. The measured frequency range of the test was 0-600 Hz. An initial investigation indicated that the beam has seven (7) natural frequencies in this frequency range. At Table 5 the comparison of experimentally identified natural frequencies with the numerical natural frequencies of the nominal and optimal FE model.

Table 5. Comparison between identified, nominal and optimal FE predicted modal frequencies

Mode	Identified Experimental	Nominal Numerical		Optimal Numerical	
	Frequency (Hz)	Frequency (Hz)	Error (%)	Frequency (Hz)	Error (%)
1	18.16	15.54	16.86	18.48	1.73
2	18.18	16.62	11.79	19.12	2.82
3	149.45	137.23	8.9	147.53	1.3
4	167.51	144.22	16.15	168.8	0.76
5	414.32	408.12	1.52	415.34	0.25
6	436.14	428.12	1.87	435.54	0.14
7	531.36	472.35	12.49	524.87	1.24

4.4 Small-scale pin-jointed CFRP structure

At last a complex structure (Figure 15) is presented. CFRP tubes similar to the one of Section 4.3 glued and mounted with aluminum joints were used. Four tri-axial accelerometers were placed on the pin-joined CFRP frame structure, which was anchored on flat plate parallel to the ground, on a vertical concrete column. An electromagnetic shaker was mounted on a free end of the frame where a load cell sensor was placed to record imposed forces under dynamic

excitation load.

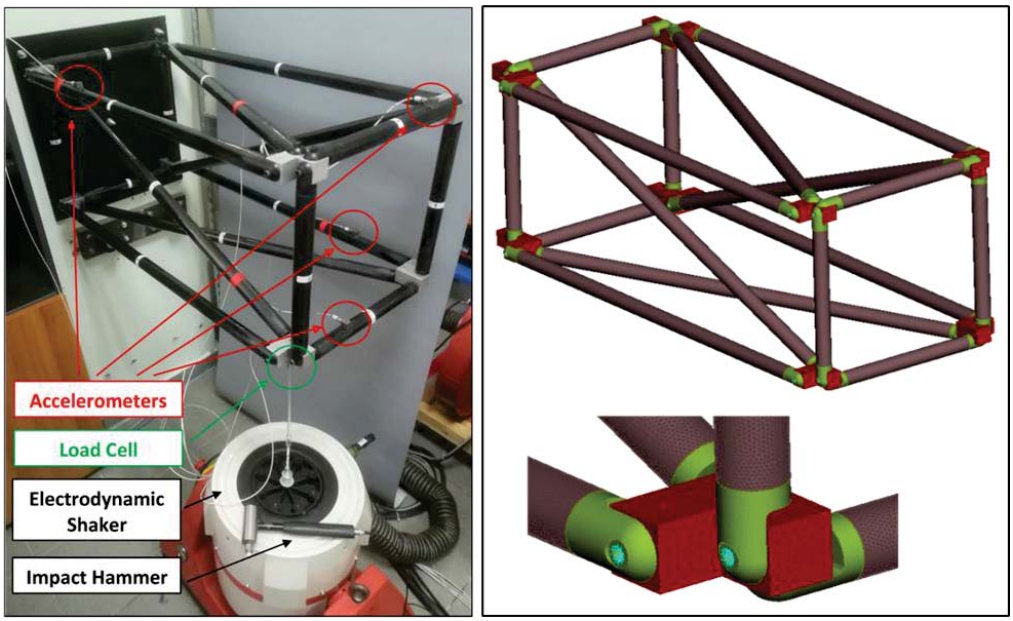

Figure 15. Experimental setup and FE model of small-scale CFRP pin-joined structure.

The corresponding optimal FE model was created in MSC Nastran (Figure 15), the geometry of the structure is discretized with composite shell and solid elements. For a harmonic excitation a comparison between the experimental and numerical acceleration time histories of two measured locations is presented at Figure 16 . The experimental acceleration is represented with black continuous line while with red continuous line is the equivalent response of the optimal FE model. As it is obvious the optimal model can predict the response of the physical structure.

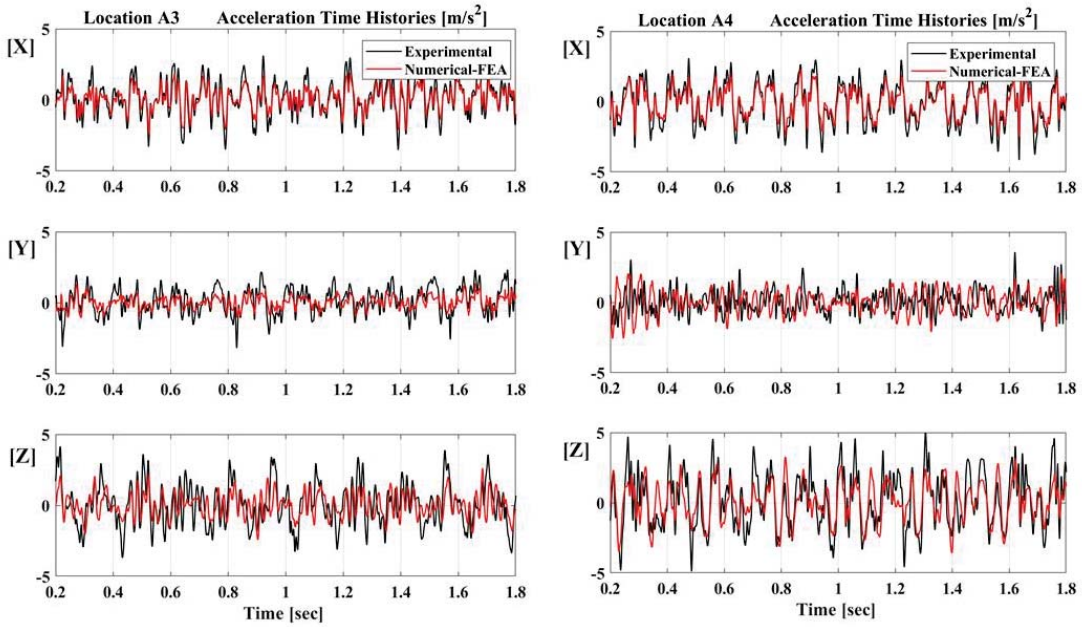

Figure 16. Comparison between experimental and numerical acceleration time histories in X, Y and Z local directions at a random force excitation.

As it is obvious the optimal model can predict the response of the physical structure. The remaining error can be addressed at the mechanical properties and uncertainties during the manufacturing of the other parts of the assembly.

5 CONCLUSIONS

In this work a modeling procedure of structures that include filament wound CFRP tubes parts is presented. From a simple tensile experiment and with the use and a stochastic single objective optimization algorithm (CMA-ES) coupled with a commercial finite element software the optimal lamina mechanical properties can be acquired with precision. These properties show a great range between different raw materials and manufacturing methods and are crucial for the prediction of material failure but also at the dynamic response of a structure. The presented methodology has been experimentally validated with different loading types and in simple and more complex structures at the linear area of the material but also until the material's failure. It is able to predict with the structure's response and the materials behavior until failure thus reducing the error that a micromechanical model produces.

6 ACKNOWLEDGEMENT

This research has been co-financed by the European Regional Development Fund of the European Union and Greek national funds through the Operational Program Competitiveness, Entrepreneurship and Innovation, under the call RESEARCH – CREATE – INNOVATE (project code: T1EDK:05393).

7 REFERENCES

[1] Soutis C. Carbon fiber reinforced plastics in aircraft construction. Mater Sci Eng A 2005;412:171–6. https://doi.org/10.1016/j.msea.2005.08.064.

[2] Suresh Kumar M, Ambresha M, Panbarasu K, Kishore I, Ranganath VR. A comparative study of failure features in aerospace grade unidirectional and bidirectional woven CFRP composite laminates under four-point bend fatigue loads. Materwiss Werksttech 2015;46:644–51. https://doi.org/10.1002/mawe.201400278.

[3] Tao W, Liu Z, Zhu P, Zhu C, Chen W. Multi-scale design of three dimensional woven composite automobile fender using modified particle swarm optimization algorithm. Compos Struct 2017;181:73–83. https://doi.org/10.1016/j.compstruct.2017.08.065.

[4] Yang Y, Wu X, Hamada H. Application of fibre-reinforced composites beam as energy absorption member in vehicle. Int J Crashworthiness 2013;18:103–9. https://doi.org/10.1080/13588265.2012.756309.

[5] Robinson M, Stolzfus J, Owens T. Composite material compatibility with liquid and gaseous oxygen. 19th AIAA Appl. Aerodyn. Conf., Reston, Virigina: American Institute of Aeronautics and Astronautics; 2001. https://doi.org/10.2514/6.2001-1215.

[6] Zheng H, Zeng X, Zhang J, Sun H. The Application of Carbon Fiber Composites in Cryotank. Solidification, InTech; 2018. https://doi.org/10.5772/intechopen.73127.

[7] ASM International. ASM Handbook Volume 21 Composite. 2001.

[8] Zhu C, Zhu P, Liu Z. Uncertainty analysis of mechanical properties of plain woven carbon fiber reinforced composite via stochastic constitutive modeling. Compos Struct 2019;207:684–700. https://doi.org/10.1016/j.compstruct.2018.09.089.

[9] Lekou DJ, Philippidis TP. Mechanical property variability in FRP laminates and its effect on failure prediction. Compos Part B Eng 2008;39:1247–56. https://doi.org/10.1016/j.compositesb.2008.01.004.

[10] Philippidis TP, Lekou DJ, Aggelis DG. Mechanical property distribution of CFRP filament wound composites. Compos Struct 1999;45:41–50.

https://doi.org/10.1016/S0263-8223(99)00012-4.

[11] Chamis CC, Sendeckyj GP. Critique on Theories Predicting Thermoelastic Properties of Fibrous Composites. J Compos Mater 1968;2:332–58. https://doi.org/10.1177/002199836800200305.

[12] Carvelli V, Poggi C. A homogenization procedure for the numerical analysis of woven fabric composites. Compos - Part A Appl Sci Manuf 2001;32:1425–32. https://doi.org/10.1016/S1359-835X(01)00041-0.

[13] Crookston JJ, Long AC, Jones IA. A summary review of mechanical properties prediction methods for textile reinforced polymer composites. Proc Inst Mech Eng Part L J Mater Des Appl 2005;219:91–109. https://doi.org/10.1243/146442005X10319.

[14] Kriz RD, Stinchcomb WW. Elastic moduli of transversely isotropic graphite fibers and their composites. Exp Mech 1979;19:41–9. https://doi.org/10.1007/bf02324524.

[15] Sharifi S, Gohari S, Sharifiteshnizi M, Vrcelj Z. Numerical and experimental study on mechanical strength of internally pressurized laminated woven composite shells incorporated with surface-bounded sensors. Compos Part B Eng 2016;94:224–37. https://doi.org/10.1016/j.compositesb.2016.03.020.

[16] Aboudi J. Micromechanical Analysis of Composites by the Method of Cells. Appl Mech Rev 1989;42:193–221. https://doi.org/10.1115/1.3152428.

[17] Huang Z ming. Micromechanical prediction of ultimate strength of transversely isotropic fibrous composites. Int J Solids Struct 2001;38:4147–72. https://doi.org/10.1016/S0020-7683(00)00268-7.

[18] Toh W, Tan L Bin, Tse KM, Giam A, Raju K, Lee HP, et al. Material characterization of filament-wound composite pipes. Compos Struct 2018;206:474–83. https://doi.org/10.1016/j.compstruct.2018.08.049.

[19] Giagopoulos D, Arailopoulos A. Computational framework for model updating of large scale linear and nonlinear finite element models using state of the art evolution strategy. Comput Struct 2017;192:210–32. https://doi.org/10.1016/j.compstruc.2017.07.004.

[20] Arailopoulos A, Giagopoulos D. Nonlinear constitutive force model selection, update and uncertainty quantification for periodically sequential impact applications. Nonlinear Dyn 2020;99:2623–46. https://doi.org/10.1007/s11071-019-05444-1.

[21] Giagopoulos D, Arailopoulos A, Chatziparasidis I, Sapidis NS. Optimum design of large-scale systems considering material nonlinearities and uncertainties. Comput Struct 2019;223:106102. https://doi.org/10.1016/j.compstruc.2019.106102.

[22] Giagopoulos D, Arailopoulos A, Natsiavas S. A model-based fatigue damage estimation framework of large-scale structural systems. Struct Heal Monit 2019. https://doi.org/10.1177/1475921719871953.

[23] Giagopoulos D, Arailopoulos A, Dertimanis V, Papadimitriou C, Chatzi E, Grompanopoulos K. Structural health monitoring and fatigue damage estimation using vibration measurements and finite element model updating. Struct Heal Monit 2019;18:1189–206. https://doi.org/10.1177/1475921718790188.

[24] MSC Software. Digimat 2017.

[25] Altair Engineering. ESA Comp 2018.

[26] Zapico-Valle JL, Alonso-Camblor R, González-Martínez MP, García-Diéguez M. A new

method for finite element model updating in structural dynamics. Mech Syst Signal Process 2010;24:2137–59. https://doi.org/10.1016/j.ymssp.2010.03.011.

[27] ASTM. ASTM D3039M/D3039M-14, Standard test method for tensile properties of polymer matrix composite materials. Annu B ASTM Stand 2013;15:1–13. https://doi.org/10.1520/D3039.

EURODYN 2020
XI International Conference on Structural Dynamics
M. Papadrakakis, M. Fragiadakis, C. Papadimitriou (eds.)
Athens, Greece, 23–26 November 2020

VIBRATION ANALYSIS OF LAMINATED COMPOSITE CYLINDRICAL SHELLS WITH VARIOUS FIBRE ORIENTATIONS

Chendi Zhu, Baiyang Shi, Chen Zhou and Jian Yang*

The University of Nottingham Ninbo China, Ningbo 315100, P.R. China
chendi.zhu@nottingham.edu.cn
*Corresponding author email: jian.yang@nottingham.edu.cn

Keywords: laminated composite, cylindrical shells, natural frequencies, vibration analysis.

Abstract. *This paper investigates the vibration behaviour of simply-supported laminated composite cylindrical shells with various fibre orientations. For some specific fibre orientations, theoretical wave propagation approach based on Love's theory is used for free vibration analysis of the laminated orthotropic composite cylindrical shells. The circumferential natural frequencies have been obtained and compared with numerical finite element results for validation and comparison. The finite element method is employed for the forced vibration analysis of laminated composite cylindrical shells with various fibre orientations subjected to harmonic loading. The results show that natural frequencies, mode shapes and the steady-state response at prescribed points can be tailored by properly designing fibre orientations for vibration mitigation. It is found that fibre orientations may have significant influence on the circumferential natural frequencies of the first few circumferential modes. For the first two circumferential modes, the associated natural frequencies may increase with fibre orientation angle. In comparison, the natural frequencies of larger circumferential modes may decrease with fibre orientation angle. The steady-state responses of cylindrical shells under a harmonic concentrated force are obtained. The variations of the resonance frequencies and corresponding peak value of steady-state response with fibre orientations have been investigated. The findings could improve the understanding of dynamic behaviour of the laminated composite cylindrical shells, and benefits optimisation of the fibre orientations for vibration suppression purpose.*

1 INTRODUCTION

There has been much research interest in the vibration transmission behaviour of mechanical systems and engineering structures for possible vibration suppression [1-6]. Laminated composite structures are increasingly used in various engineering applications including aircrafts, rockets, submarines and pipes due to their superior performance such as high stiffness-to-weight and strength-to-weight ratios, and flexibility in design, compared to traditional metallic structures. The circular cylindrical shells have been one of the most important and basic structural elements in engineering structures [7-8]. In the practical applications, those engineering components may exhibit severe vibrations when the frequencies of the external force are close to one of the natural frequencies. As a result, vibration problems of this type of structures have been a subject of great interest. Various laminated shell theories have been proposed and developed through different assumptions and simplifications such as Reissner-Naghdi's linear shell theory, Donnell-Mushtari-Vlasov's theory, Sanders' theory and Flugge's theory [9]. Among the numerous theories, the classical shell theory based on the Kirchhoff-love hypothesis is widely used. The detailed comparison studies can be found in monographs on vibration of shells, which has been done by Leissa [9], Qatu [10] and Reddy [11]. To conclude, vibration analysis of this type of structures has been of great significance, from which insight may be gained into dynamic characteristics and optimal design of such laminated composite structures.

There have been some methods developed and used to study the vibration behaviour of cylindrical shells [12-17]. For example, Lam and Loy [12-13] compared the natural frequencies of rotating laminated cylindrical shells with different shell theories, namely Donnell's, Flugge's, Love's and Sanders' and then employed the Ritz method to study the effects of boundary conditions and fibre orientation on the natural frequencies of thin orthotropic laminated cylindrical shells based on Love's theory. The free vibration of laminated cylindrical shells using differential quadrature method was conducted by Shu and Du [14]. Zhang [15] developed wave propagation approach for vibration analysis of cross-ply laminated composite shells base on Love's shell theory. Liu et al. [16] derived exact characteristic equations for free vibration of thin orthotropic circular cylindrical shells based on Donnell-Mushtari shell theory. Jin et al. [17] employed Rayleigh-Ritz method based on Reissner-Naghdi's theory to obtain the exact solution based on the energy functions of the shell, which is applicable to a variety of boundary conditions.

Most of the previous studies have focused on the development of analytical methods to investigate the free vibration analysis of cross-ply laminated composite cylindrical shells according to different shell theories in confined boundary conditions and exact solutions for the shells with a variety of boundary conditions. There is much less research work on the detailed vibration characteristics of laminated composite cylindrical shells with arbitrary lamination schemes. The free and force vibration characteristics of submerged finite elliptic cylindrical shell has been investigated [8]. The vibration analysis of the laminated composite plates has been conducted and the influence of the lamination schemes on the vibration characteristics has been investigated [18-19]. It is of great significance to develop an accurate and efficient method that can be used to investigate the vibration characteristics of laminated composite cylindrical shells with complex lamination schemes. It has been revealed that the wave propagation method based on Love's theory is feasible and of high accuracy for cross-ply laminated composite cylindrical shell. For the cylindrical shell with complex lamination schemes, the FEA method may be used for the vibration analysis of composite structures and it also can be employed to verify the analytical results. In this study, the natural frequencies and mode shapes of the laminated composite cylindrical shells with different lamination schemes and geometric parameters are obtained by using both the wave propagation method and the FEA for comparison. The dynamic

responses of the cylindrical shells under harmonic excitation are investigated and obtained. The effects of fibre orientations on the vibration behaviour are examined.

2 METHMATICAL MODELLING

2.1 Model description

Figure 1 shows the schematic diagram of a thin laminated composite cylindrical shell having length L, thinckness h and radius R, and arbitrary number of layers. The cylindrical coordinate system (x, θ, z) is fixed at the middle surface of the cylindrical shell. The components of the displacement field (u, v, w) in this coordinate system are defined such that u is the displacement in the axial direction of x, v in the circumferential direction of θ and w in the radial direction of z. The fibres of laminates in each layer follows helix lines on the cylindrical shell, and the helix angle for the i-th layer is denoted by θ_i. A harmonic force is applied to the point (x_e, θ_e, R) on the cylindrical shell. The circumferential modal shapes with different circumferential modal numbers have been shown in Fig. 1(b) [15]. Fig. 1(c) shows the geometry of the cylindrical shells composed of N layers.

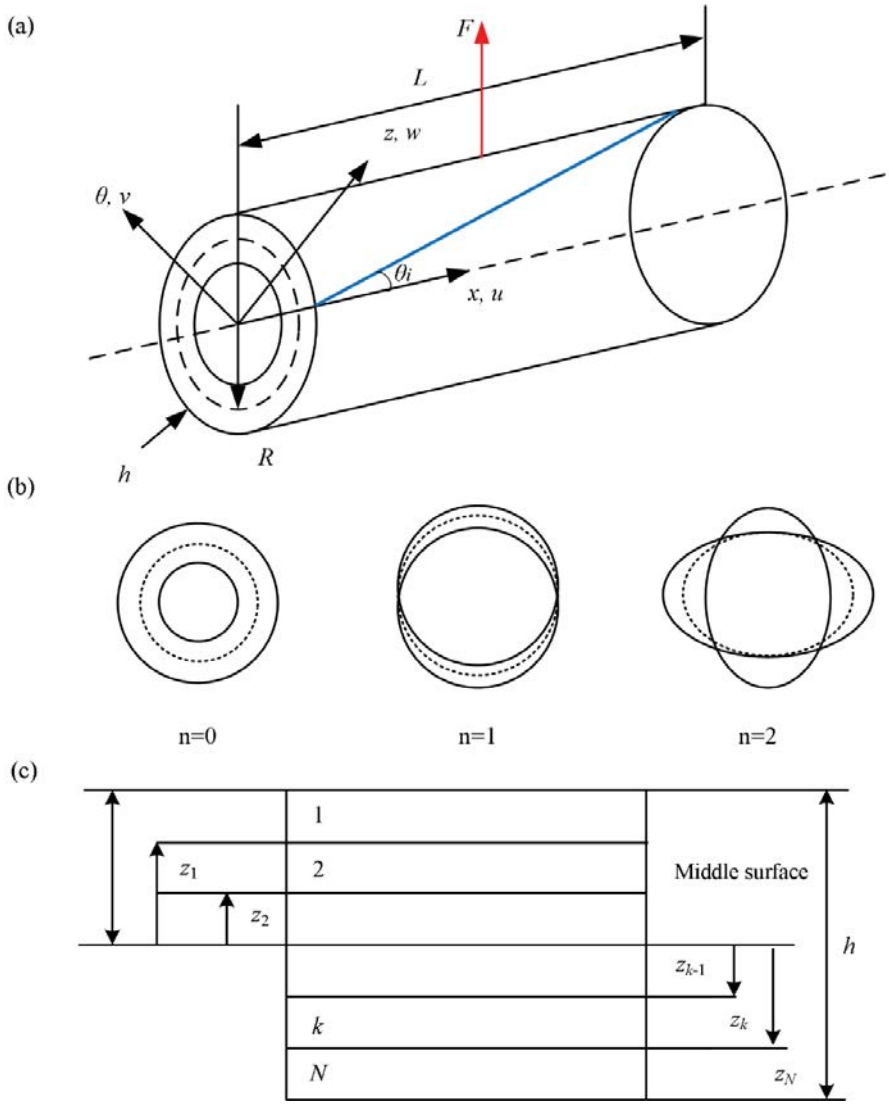

Figure 1: (a) The geometry of a laminated composite cylindrical shell; (b) circumferential modal shapes and (c) Geometry of an N-layered laminated composite cylindrical shell.

2.2 Theoretical solution of free vibration analysis

The classical shell theory is employed to establish the theoretical model. The displacement field for the shell is described by

$$u(x,\theta,z,t) = u_0(x,\theta,t) - z\frac{\partial w_0(x,\theta,t)}{\partial x},$$
$$v(x,\theta,z,t) = v_0(x,\theta,t) - z\frac{\partial w_0(x,\theta,t)}{R\partial\theta},$$
$$w(x,\theta,z,t) = w_0(x,\theta,t), \tag{1}$$

where u_0, v_0 and w_0 represent the middle surface displacement of the laminated composite cylindrical shell in axial, circumferential and radial directions, respectively.

The cylindrical shell under consideration is with constant thickness h, mean radius R, axial length L. here the respective displacements in the axial, circumferential and radial directions are denoted by $u(x,\theta,t)$, $v(x,\theta,t)$ and $w(x,\theta,t)$. The strain-displacement relations for thin circular cylindrical shells are

$$\varepsilon_x = \frac{\partial u}{\partial x}, \quad \varepsilon_\theta = \frac{\partial v}{R\partial\theta} + \frac{w}{R}, \quad \varepsilon_{x\theta} = \frac{\partial u}{R\partial\theta} + \frac{\partial v}{\partial x},$$
$$\chi_x = -\frac{\partial^2 w}{\partial x^2}, \quad \chi_\theta = \frac{1}{R^2}\left(\frac{\partial v}{\partial\theta} - \frac{\partial^2 w}{\partial\theta^2}\right), \quad \chi_{x\theta} = \frac{2}{R}\left(\frac{\partial v}{\partial x} - \frac{\partial^2 w}{\partial x\partial\theta}\right).$$

The relationship between the stress resultants and the internal forces and moments is

$$\begin{bmatrix} N_x \\ N_\theta \\ N_{x\theta} \\ M_x \\ M_\theta \\ M_{x\theta} \end{bmatrix} = \begin{bmatrix} A_{11} & A_{12} & A_{16} & B_{11} & B_{12} & B_{16} \\ A_{12} & A_{22} & A_{26} & B_{12} & B_{22} & B_{26} \\ A_{16} & A_{26} & A_{66} & B_{16} & B_{26} & B_{66} \\ B_{11} & B_{12} & B_{16} & D_{11} & D_{12} & D_{16} \\ B_{12} & B_{22} & B_{26} & D_{12} & D_{22} & D_{26} \\ B_{16} & B_{26} & B_{66} & D_{16} & D_{26} & D_{66} \end{bmatrix} \begin{bmatrix} \varepsilon_x \\ \varepsilon_\theta \\ \varepsilon_{x\theta} \\ \chi_x \\ \chi_\theta \\ \chi_{x\theta} \end{bmatrix}, \tag{2}$$

where N_x, N_θ and $N_{x\theta}$ are membrane forces, M_x,,M_θ and $M_{x\theta}$ are bending and torsion moments, and A_{ij} , B_{ij} and D_{ij} denotes the stiffnesses expressed by $A_{ij} = \sum_{k=1}^{N} \bar{Q}_{ij}\,(z_{k+1} - z_k)$, $B_{ij} = \frac{1}{2}\sum_{k=1}^{N} \bar{Q}_{ij}\,(z^2{}_{k+1} - z^2{}_k)$ and $D_{ij} = \frac{1}{3}\sum_{k=1}^{N} \bar{Q}_{ij}\,(z^3{}_{k+1} - z^3{}_k)$,where $i,j = 1,2$ or 6. For a specially orthotropic laminated composite shell, some stress stiffness coefficients are zero, i.e. $B_{ij} = 0$ and $A_{16} = A_{26} = D_{16} = D_{26} = 0$.

The governing equations of motion for thin cylindrical shells according to the love's theory in terms of the force and moment resultants are expressed as,

$$\frac{\partial N_x}{\partial x} + \frac{\partial N_{x\theta}}{R\partial\theta} = \rho h\frac{\partial^2 u}{\partial t^2},$$
$$\frac{\partial N_{x\theta}}{\partial x} + \frac{\partial N_\theta}{R\partial\theta} + \frac{\partial M_{x\theta}}{R\partial x} + \frac{\partial M_\theta}{R^2\partial\theta} = \rho h\frac{\partial^2 v}{\partial t^2},$$
$$\frac{\partial^2 M_x}{\partial x^2} + \frac{2\partial^2 M_{x\theta}}{R\partial x\partial\theta} + \frac{\partial^2 M_\theta}{R^2\partial\theta^2} - \frac{N_\theta}{R} = \rho h\frac{\partial^2 w}{\partial t^2}. \tag{3}$$

The governing equations can be rewritten in the matrix form,

$$\begin{bmatrix} L_{11} & L_{12} & L_{13} \\ L_{21} & L_{22} & L_{23} \\ L_{31} & L_{32} & L_{33} \end{bmatrix} \begin{Bmatrix} u(x,\theta,t) \\ v(x,\theta,t) \\ w(x,\theta,t) \end{Bmatrix} = \begin{bmatrix} 0 \\ 0 \\ 0 \end{bmatrix}. \tag{4}$$

where the coefficients are defined as follows,

$$L_{11} = A_{11}\frac{\partial^2}{\partial x^2} + \frac{A_{66}}{R^2}\frac{\partial^2}{\partial\theta^2}\ , \qquad L_{12} = \left(\frac{A_{12}}{R} + \frac{A_{66}}{R}\right)\frac{\partial^2}{\partial x\partial\theta}\ , \qquad L_{21} = \left(\frac{A_{12}}{R} + \frac{A_{66}}{R}\right)\frac{\partial^2}{\partial x\partial\theta}\ ,$$

$$L_{13}=\frac{A_{12}}{R}\frac{\partial}{\partial x},\quad L_{22}=\left(A_{66}+\frac{2D_{66}}{R^2}\right)\frac{\partial^2}{\partial x^2}+\left(\frac{A_{22}}{R^2}+\frac{D_{22}}{R^4}\right)\frac{\partial^2}{\partial\theta^2},$$
$$L_{23}=\left(\frac{A_{22}}{R^2}\frac{\partial}{\partial\theta}-\left(\frac{D_{12}+2D_{66}}{R^2}\right)\frac{\partial^2}{\partial x^2\partial\theta}-\frac{D_{22}}{R^4}\frac{\partial^3}{\partial\theta^3}\right),\ L_{31}=-\frac{A_{12}}{R}\frac{\partial}{\partial x},$$
$$L_{32}=\left(\frac{D_{12}+4D_{66}}{R^2}\right)\frac{\partial^3}{\partial\theta\partial x^2}+\frac{D_{22}}{R^4}\frac{\partial^3}{\partial\theta^3}-\frac{A_{22}}{R^2}\frac{\partial}{\partial\theta},$$
$$L_{33}=-D_{11}\frac{\partial^4}{\partial x^4}-2\left(\frac{D_{12}+2D_{66}}{R^2}\right)\frac{\partial^4}{\partial x^2\partial\theta^2}-\frac{D_{22}}{R^4}\frac{\partial^4}{\partial\theta^4}-\frac{A_{22}}{R^2}.$$

Based on the wave propagation approach [15], for the case of the shell simply supported at both ends, the explicit form of the solution can be assumed as

$$u(x,\theta,t)=\sum_{n=1}^{\infty}U_{mn}\cos(\beta\theta)\,e^{\mathrm{i}\omega t-\mathrm{i}k_m x},$$
$$v(x,\theta,t)=\sum_{n=1}^{\infty}V_{mn}\sin(\beta\theta)\,e^{\mathrm{i}\omega t-\mathrm{i}k_m x},$$
$$w(x,\theta,t)=\sum_{n=1}^{\infty}W_{mn}\cos(\beta\theta)\,e^{\mathrm{i}\omega t-\mathrm{i}k_m x},\tag{5}$$

where U_{mn}, V_{mn}, W_{mn} are the maximum amplitudes in the axial, circumferential and radial directions, respectively, $k_m=m\pi/L$, $\beta=n/R$ and, m and n are the axial and circumferential wavenumbers, respectively. Substituting Eq. (5) into Eq. (4) leads to

$$\begin{bmatrix}L_{11}-\Omega & L_{12} & L_{13}\\ L_{21} & L_{22}-\Omega & L_{23}\\ L_{31} & L_{32} & L_{33}-\Omega\end{bmatrix}\begin{Bmatrix}U_n\\V_n\\W_n\end{Bmatrix}=0.\tag{6}$$

Expansion of the determinant for the coefficient matrix of Eq. (6) in terms of $\rho h\omega^2=\Omega$ leads to a cubic equation for Ω:

$$\Omega^3+C_1\Omega^2+C_2\Omega+C_3=0,\tag{7}$$

which can be used to obtain the natural frequencies of the laminated composite shell. It has been demonstrated that the three positive roots are the angular natural frequencies of the cylindrical shell in the axial, circumferential and radial directions. The lowest value of the three positive roots is for the flexural vibration, and the other two represent in-plane vibrations.

3 RESULSTS AND DISCUSSSIONS

The theoretical formulations that were presented in the previous section is used firstly to obtain the free vibration behaviour. The structure considered are three-layered composite laminates cylindrical shells. The thickness of each layer is one third of the shell thickness. The cylindrical shell is constructed of different layers of orthotropic materials with different fibre orientations and the relevant properties are as the same as that given in literature [15] for verification of results. The geometrical and material properties parameters are set as $h/R=0.002$, $L/R=20$, $E_{22}=7.6\mathrm{GN/m^2}$, $E_{11}/E_{22}=2.5$, $G_{12}=4.1\mathrm{GN/m^2}$, $\nu_{12}=0.26$ and $\rho_0=1643\mathrm{kg/m^2}$. According to the Love's theory, it is assumed that layers are perfectly bonded. There is no flaw or gap between the layers, and no slipping between the layers. For the cylindrical shells with orthotropic laminates, different cases with the fibre orientation reducing from 90° to 0° at the interval of 15°.

The natural frequencies of laminated composite cylindrical shell with fibre orientation of $[90^\circ/0^\circ/90^\circ]$, $[90^\circ]_3$ and $[0^\circ]_3$ can be obtained based on theoretical approach as presented previously. For the other cases, the FEA are used to obtain the results. In ANSYS FEA modelling, the element 281 is employed to model the cylindrical composite laminated shell. The whole model contains 24080 nodes and 8000 elements. Each element has 8 nodes, each with six degrees of freedom. The number of integration points for each layer is set as three. There is one point located on the top surface, one on the bottom surface, and the third point is located at the

midpoint between the previous two points. The ANSYS Shell281 element is based on the first order shear deformation theory. The calculations have been carried out for the axial wavenumber *m*=1. A comparison of the natural frequencies of laminated composite cylindrical shells with various fibre orientations with different circumferential mode numbers *n* has been presented in the Table 1. For the composite laminate cylindrical shell with cross-ply $[90^\circ/0^\circ/90^\circ]$ lamination scheme, Table 1 shows that the theoretical results from wave propagation approach have great agreement with the those obtained from the FEA method and those are obtained by the Newton-Raphson procedure theoretically in the literature [12]. It is also found that theoretical results of the natural frequencies of laminated composite shells in $[90^\circ]_3$ and $[0^\circ]_3$ are close to those obtained from numerical FEA method. The FEA is therefore verified and employed for free vibration analysis of the cylindrical shells with other fibre orientations.

Fibre angle	Source	Mode number				
		n=1	n=2	n=3	n=4	n=5
$[90^\circ/0^\circ/90^\circ]$	Ref [15]	0.023590	0.007904	0.005869	0.009020	0.014236
	Theoretical	0.023597	0.008046	0.006338	0.009591	0.014819
	FEA	0.023590	0.007894	0.005770	0.008788	0.014108
$[90^\circ]_3$	Theoretical	0.026080	0.008874	0.006482	0.009406	0.014444
	FEA	0.026074	0.008749	0.006017	0.008775	0.013753
$[75^\circ]_3$	FEA	0.024612	0.008239	0.005924	0.008922	0.014046
$[60^\circ]_3$	FEA	0.021785	0.007296	0.005906	0.009497	0.015064
$[45^\circ]_3$	FEA	0.019426	0.006577	0.006217	0.010583	0.016867
$[30^\circ]_3$	FEA	0.017953	0.006196	0.006754	0.011915	0.019058
$[15^\circ]_3$	FEA	0.017207	0.006048	0.007239	0.013009	0.020891
$[0^\circ]_3$	Theoretical	0.017011	0.006460	0.008363	0.014472	0.022727
	FEA	0.016986	0.006014	0.007431	0.013433	0.021615

Table 1: Comparison of non-dimensional frequency parameter $\bar{\omega} = \omega\sqrt{\rho R^2/E_{22}}$ for three-layered cylindrical shells with different lamination sequences with simply supported-simply supported boundary conditions (h/R=0.002 and L/R=20).

Fig. 2 presents the circumferential mode shapes of the three-layered cross-ply cylindrical shells in $[\theta]_3$ with different fibre orientations while the axial wavenumber is kept to be *m*=1 and circumferential number is *n*=2. It is found that when the circumferential number is 2, the natural frequencies increase with the increase of the fibre orientations. It is observed that the circumferential modal shapes vary significantly with the change of fibre orientations. The position on the circumferential mode with the maximum displacement rotates with the change the fibre orientations. When the fibre orientation is changed from 0° to 90°, the maximum position for modal displacement changes from left side to right side, as shown in Fig. 2. It reveals that excited mode can be changed by tailoring fibre orientations.

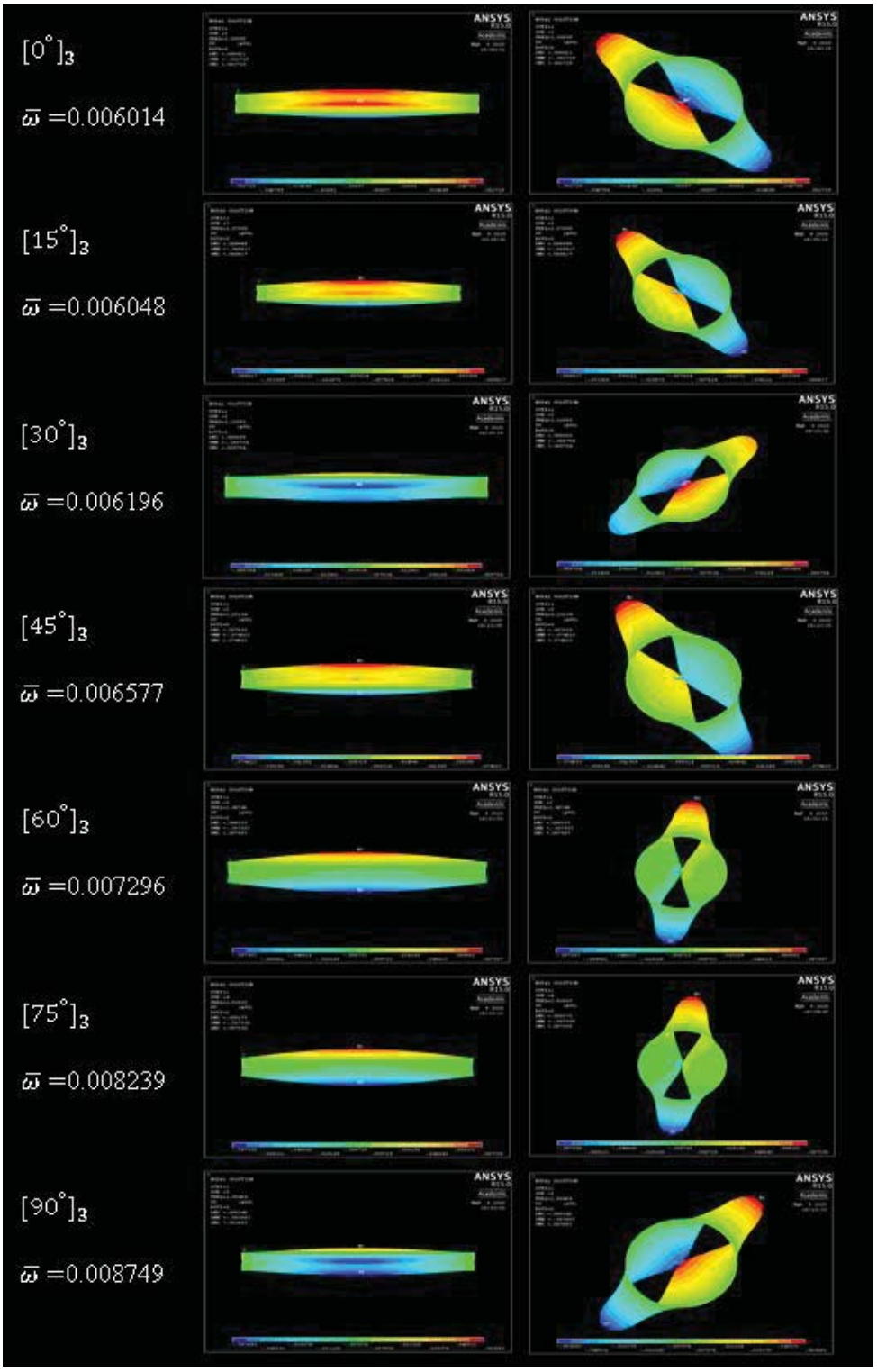

Figure 2: Mode shape of three-layered cross-ply cylindrical shells in $[\theta]_3$ with different fibre orientations with mode shape circumference number of n=2.

Fig. 3 shows the effects of fibre orientation on the circumferential natural frequencies with the mode sequence number n changing from 1 to 5. It is found that the influence of fibre orientations on circumferential natural frequencies is more significant at small circumferential mode n. The circumferential natural frequencies increase with the increase of fibre orientation angle when n=1 and 2. When $n = 1$, the principal mode shape is described as the bending mode. The

main reason can be that when the fibre orientation is increased to 90°, the stiffness along the circumferential directions reaches the maximum, leading to the increase of natural frequencies. In comparison, when n=3, 4 and 5, the natural frequencies decrease with fibre orientation. When the fibre orientation angle is larger than 30°, the circumferential natural frequencies corresponding to n=1 for each case are larger than those associated with large circumferential modes.

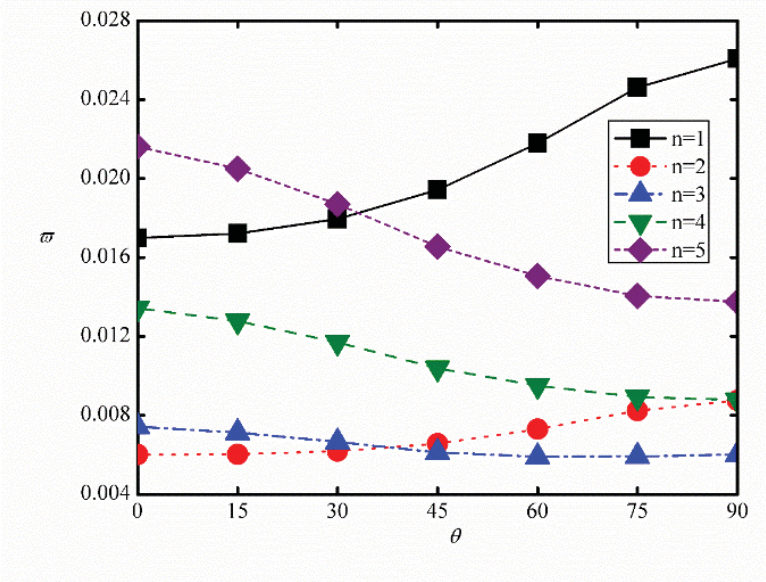

Figure 3: Variations of the non-dimensional frequencies of the shells in $[\theta]_3$ against the fibre orientations.

The theoretical wave propagation method can be employed for the free vibration of the composite laminate cylindrical shells in $[0^{\circ}]_3$ and $[90^{\circ}]_3$ to investigate the effects of the geometric ratios L/R on the natural frequencies, respectively. Four cases with different values of L/R being 1, 5, 10 and 20 are considered. Table 2 shows that for the case of L/R=1, the natural frequencies generally decrease with the increase of n. For other cases, the natural frequencies decrease first and then increase with the increase of n. It is found that natural frequency of the composite laminate cylindrical shells in $[0^{\circ}]_3$ with n=1 is the largest. It is found that when the stacking sequence is changed to the $[90^{\circ}]_3$, the natural frequencies with different circumferential number n are reduced but changing the stacking sequence from $[90^{\circ}]_3$ into $[0^{\circ}]_3$ could effectively increase the natural frequencies associated with n=1 and 2.

Table 2 has showed that the natural frequencies for the case L/R=1 decrease with the increase of n from 1 to 7. In the current case study, the forced vibration analysis of the cylindrical composite laminate shell with length L of 1m, thickness h of 0.002m and radius R of 1m is conducted. A harmonic excitation force is applied to the middle point $(0.5m, 0^{\circ}, 1m)$ of the shell structure. The fibre orientation of the cylindrical shells is set as 0°, 45° and 90°, respectively. Fig. 4. presents the dynamic response on the middle point of the cylindrical shells of different lamination schemes with the variation of the excitation frequencies. It is found that due to the superposition of the modal responses, there are a large number of the resonant peaks in a narrow frequency band. It is found that the change of the fibre orientation could effectively change the resonance frequencies and the corresponding amplitudes of the dynamic response. At specific excitation frequencies such as $\bar{\omega}$ =0.2, there is resonance peak of the shell in $[45^{\circ}]_3$ but a trough for the shell in $[0^{\circ}]_3$. At some resonance frequencies, the displacement may increase with the fibre orientation angle. These findings provide some evidence that the dynamic response could be reduced at some specific frequencies by changing the fibre orientations. More

detailed study of the vibration characteristics and effects of the fibre orientation on the dynamic behaviour may then be done for the optimization of the cylindrical shells to achieve reduced vibration level.

Fibre angle		Mode number			
	n	L/R=1	L/R=5	L/R=10	L/R=20
$[\mathbf{0}^\circ]_3$	1	1.236213	0.206763	0.063306	0.017011
	2	0.843835	0.081142	0.021841	0.006460
	3	0.577349	0.040869	0.013017	0.008364
	4	0.406315	0.027521	0.015580	0.014472
	5	0.296260	0.027386	0.023036	0.022727
	6	0.224422	0.034598	0.032991	0.032884
	7	0.177559	0.045613	0.044950	0.044905
$[\mathbf{90}^\circ]_3$	1	0.911537	0.259599	0.090962	0.026080
	2	0.740182	0.116127	0.033199	0.008874
	3	0.578831	0.060523	0.016847	0.006482
	4	0.450674	0.037151	0.013050	0.009406
	5	0.353995	0.027740	0.015600	0.014444
	6	0.282155	0.026713	0.021231	0.020822
	7	0.228989	0.031020	0.028579	0.028411

Table 2: Comparison of non-dimensional frequency parameter $\bar{\omega} = \omega\sqrt{\rho R^2/E_{22}}$ for three-layered cylindrical shells in $[0^\circ]_3$ and $[90^\circ]_3$ with different geometric ratios L/R with simply supported-simply supported boundary conditions (h/R=0.002).

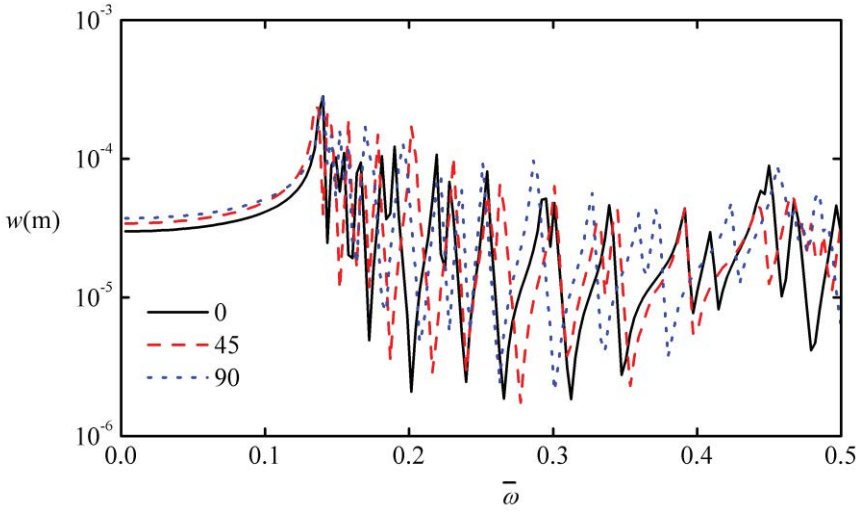

Figure 4: Dynamic response on the middle point of the three-layered cylindrical shells with different lamination sequences with simply supported-simply supported boundary conditions (h/R=0.002 and L/R=1).

4 CONCLUSIONS

The vibration behaviour of laminated composite cylindrical shells simply-supported at both ends with various fibre orientations has been investigated. For specific fibre orientations, theoretical wave propagation approach based on Love's theory has been used for free vibration analysis of the laminated orthotropic composite cylindrical shells. The circumferential natural frequencies were obtained and compared with numerical finite element results for validation. The FEA was also employed for the forced vibration analysis of laminated composite cylindrical shells with various fibre orientations subjected to harmonic loading. The results showed that natural frequencies, mode shapes and the steady-state response at prescribed points can be tailored by properly designing fibre orientations for vibration mitigation. It was found that fibre orientation angle of the shell structure has significant influence on the natural frequencies associated with the first few circumferential modes. It was shown that for different circumferential modes, the fibre angles have distinctly different effects on the corresponding natural frequencies associated. The steady-state responses of cylindrical shells under a harmonic concentrated force were obtained for comparison. It was shown that the fibre angle can effectively vary the resonance frequencies and corresponding peak value of steady-state response.

ACKNOWLEDGEMENT

This work was supported by National Natural Science Foundation of China (Grant number 51605233) and by Ningbo Science and Technology Bureau under Natural Science Programme (Grant number 2019A610155).

REFERENCES

[1] J. Yang, YP. Xiong, JT. Xing, Power flow behaviour and dynamic performance of a nonlinear vibration absorber coupled to a nonlinear oscillator, *Nonlinear Dynamics* 80(3), 1063-1079, 2015.

[2] J. Yang, YP. Xiong, JT. Xing, Vibration power flow and force transmission behaviour of a nonlinear isolator mounted on a nonlinear base, *International Journal of Mechanical Sciences* 115–116, 238-252, 2016.

[3] BY. Shi, J. Yang, C. Rudd, On vibration transmission in oscillating systems incorporating bilinear stiffness and damping elements, *International Journal of Mechanical Sciences*, 150, 458-270, 2019.

[4] BY. Shi, J. Yang, Quantification of vibration transmission between coupled nonlinear oscillators, *International Journal of Dynamics and Control*, 2019, 2019.

[5] J. Yang, JZ. Jiang, S. Neild, Dynamic analysis and performance evaluation of nonlinear inerter-based vibration isolators, *Nonlinear Dynamics* 99, 1823-1839, 2020.

[6] W. Dai, J. Yang, BY. Shi, Vibration transmission and power flow in impact oscillators with linear and nonlinear constraints, *International Journal of Mechanical Sciences* 168, 105234, 2020.

[7] HS. Chen, TY. Li, X. Zhu, J. Yang, Analysis of Dispersion Characteristics of an Infinite Cylindrical Shell Submerged in Viscous Fluids Considering Hydrostatic Pressure, *Journal of Vibration and Acoustics* 137 (021018), 1-14, 2015.

[8] GJ. Zhang, TY. Li, X. Zhu, J. Yang, YY. Miao, Free and forced vibration characteristics of submerged finite elliptic cylindrical shell. *Ocean Engineering* 129, 92-106, 2017.

[9] AW. Leissa, Vibration of shells, *US Government Printing Office*, 1973.

[10] MS. Qatu, Vibration of laminated shells and plates, *Elsevier*, 2004.

[11] JN. Reddy, Mechanics of laminated composite plates and shells: theory and analysis, *CRC press*, 2003.

[12] KY. Lam, CT. Loy, Analysis of rotating laminated cylindrical shells by different thin shell theories, *Journal of Sound and Vibration* 186(1), 23-35, 1995.

[13] KY. Lam, CT. Loy, Influence of boundary conditions and fibre orientation on the natural frequencies of thin orthotropic laminated cylindrical shells, *Composite Structures* 31(1), 21-30, 1995.

[14] C. Shu, H. Du, Free vibration analysis of laminated composite cylindrical shells by DQM, *Composites Part B: Engineering* 28(3), 267-274, 1997.

[15] XM. Zhang, Vibration analysis of cross-ply laminated composite cylindrical shells using wave propagation approach, *Applied Acoustics* 62(11), 1221-1228, 2001.

[16] B. Liu, YF. Xing, MS. Qatu, AJM. Ferreira, Exact characteristic equations for free vibrations of thin orthotropic circular cylindrical shells. *Composite Structures* 94, 484-93, 2012.

[17] GY. Jin, TG. Ye, YH. Chen, Z. Su, YQ. Yan, An exact solution for the free vibration analysis of laminated composite cylindrical shells with general elastic boundary conditions. *Composite Structures* 106, 114-127, 2013.

[18] CD. Zhu, J. Yang, Free and forced vibration analysis of composite laminated plates, Proceedings of the 26th International Congress on Sound and Vibration 2019 (ICSV26), IIAV, Montreal, Canada, 2019.

[19] CD. Zhu, J. Yang, Vibration analysis of harmonically excited antisymmetric cross-ply and angle-ply composite laminated plates, Proceedings of the 18th Asia Pacific Vibration Conference (APVC2019), Sydney, Australia, 2019.

EURODYN 2020
XI International Conference on Structural Dynamics
M. Papadrakakis, M. Fragiadakis, C. Papadimitriou (eds.)
Athens, Greece, 23–26 November 2020

ACOUSTIC WAVES IN HOMOGENIZED FLUID-SATURATED DEFORMING PERIODIC SCAFFOLDS UNDER PERMANENT FLOW

Eduard Rohan[1], **Robert Cimrman**[1], **and Salah Naili**[2,3]

[1] Department of Mechanics and European Centre of Excellence, NTIS – New Technologies for Information Society, Faculty of Applied Sciences, University of West Bohemia, Czech Republic, e-mail: rohan@kme.zcu.cz

[2] Univ Paris Est Creteil, CNRS, MSME, F-94010 Creteil, France, e-mail: naili@u-pec.fr

[3] Univ Gustave Eiffel, MSME, F-77447 Marne-la-Vallée, France

Keywords: Acoustic waves, Homogenization, Porous media, Fluid-structure interaction, Advection, Wave dispersion

Abstract. *Acoustic waves in a poroelastic medium with periodic structure are studied with respect to permanent seepage flow which modifies the wave propagation. The homogenization method provides the macroscopic equations governing the dynamic response of an effective medium. whose the properties are determined by the characteristic responses. We consider a Newtonian slightly compressible fluid under the barotropic acoustic approximation. In contrast with usual simplifications, the advection phenomenon of the Navier-Stokes equations is accounted for. The homogenization results are based on the periodic unfolding method combined with the asymptotic expansion technique. The dynamic permeability depends on the fluid flow properties including the advection effects associated with an assumed stationary perfusion of the porous structure. Numerical results show influence of the advection velocity on the strong dispersion of the quasi-shear modes*

1 INTRODUCTION

We consider acoustic wave propagation in periodic elastic, or viscoelastic scaffolds saturated by Newtonian slightly compressible fluids under the barotropic acoustic approxiamtion. The aim is to derive and analyze an effective medium model of acoustic waves superimposed to a permanent steady seepage flow through the porous material. To analyze the wave dispersion, the homogenization has been employed to upscale the Navier-Stokes equations in the context of deforming pores. This procedure leads to an effective porous medium model which captures the wave propagation for wave lengths significantly larger than the characteristic porosity size corresponding to the one period of the lattice.

The model equations were obtained in [9] using the periodic unfolding method [3], *cf.* [1] combined with the asymptotic expansion technique. Local problems for corrector functions provide the effective model parameters of the macroscopic wave propagation model which is coherent with the Biot model, yielding the two pressure modes referred to as P1 and P2. The local characteristic responses of the solid and fluid parts are decoupled even in the dynamic interactions including the wall shear stress on the periodic interfaces. A modified Darcy law is obtained; the frequency-dependent dynamic permeability tensor consisting of two parts one of which is associated with the steady advection at the pore level heterogeneity. The model has been implemented using the finite-element method and dispersion curves were obtained for different flow parameters, scaffold geometries and frequencies. Also extension for viscoelastic solid materials was elaborated [9]. The homogenized poroviscoelastic model involves the time convolutions related to the skeleton viscoelasticity and the fluid viscosity. While the macroscopic fading memory phenomena associated with the skeleton viscoelasticity are determined by the relaxation and creep functions of the pure solid phase, the seepage-associated memory effects depend on the fluid, the micropore geometry and the permanent flow perfusion.

In this paper, we record the homogenization result obtained recently in [9] and explore the dispersion properties of plane waves propagating in the homogenized medium. The aim is to illustrate the influence of the advection on the effective permeability and on the wave speed.

Basic notations

Through the paper, we shall adhere to the following notation. A point position in a Cartesian frame is specified by $x = (x_1, x_2, x_3) \in \mathbb{R}^3$, where $\mathbb{R}$ is the set of real numbers. The boldface notation for vectors $\boldsymbol{a} = (a_i)$ and second-order tensors $\boldsymbol{b} = (b_{ij})$ is used. The second-order identity tensor is denoted by $\boldsymbol{I} = (\delta_{ij})$. The fourth-order elasticity tensor is denoted by $\mathbb{D} = (D_{ijkl})$. The superposed dot denotes a derivative with respect to time. The gradient, divergence and Laplace operators are denoted by $\nabla, \nabla\cdot$ and ∇^2, respectively. When these operators have a subscript referring to the space variable, it is for indicating that the operator acts relatively at this space variable, for instance $\nabla_y = (\partial_i^y) = (\partial/\partial y_i)$. The symbol dot '$\cdot$' denotes the scalar product between two vectors and the symbol colon ':' stands for scalar (inner) product of two second-order tensors, *e.g.* $\boldsymbol{A} : \boldsymbol{B} = A_{ij}B_{ij} = \mathtt{tr}[\boldsymbol{A}^T\boldsymbol{B}] = A_{ki}B_{kj}\delta_{ij}$, where $\mathtt{tr}[\star]$ is the trace of a tensor and superscript T in $\star^T$ is the transposition operator. Operator $\otimes$ designates the tensor product between two vectors, *e.g.* $\boldsymbol{a} \otimes \boldsymbol{v} = (a_i v_j)$. Standard notations for functional spaces are adhered. Throughout the paper, x denotes the global ("macroscopic") coordinates, while the "local" coordinates y describe positions within the representative unit cell $Y \subset \mathbb{R}^3$. The normal vectors on a boundary of domains Ω_α (or Y_α) are denoted by $\boldsymbol{n}^\alpha$, $\alpha = s, f$, to distinguish their orientation outward to Ω_α (or Y_α) when dealing with the solid-fluid interfaces. By $\boldsymbol{e}(\boldsymbol{w}) = 1/2(\nabla\boldsymbol{w} + (\nabla\boldsymbol{w})^T)$ we denote the strain of a vector field $\boldsymbol{w}$ (displacements, or

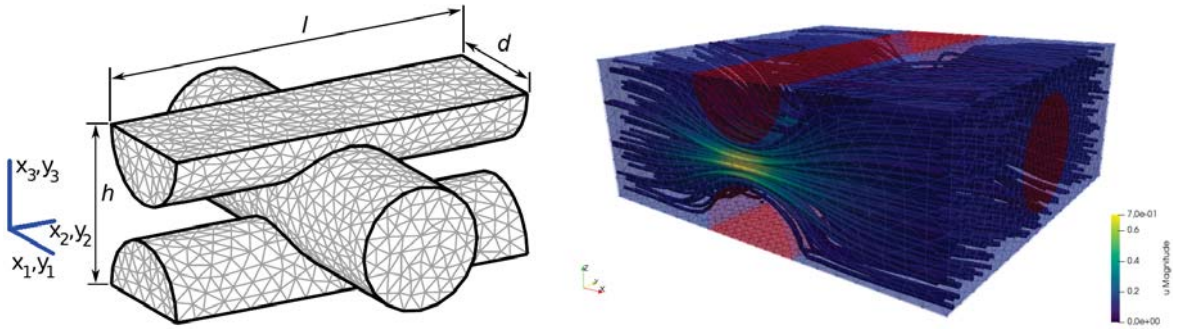

Figure 1: The periodic cell of solid fibres (left, from [4]) and the 3D periodic cell (right) consisting of the deformable solid scaffolds (red) and the fluid domain, where the flow streamlines for the mean advection velocity $\bar{w}^0 = 0.1$ m/s are shown.

velocities). The "tilde"-notation can have various meanings which are explained through the text and are clear within the particular context. The following standard functional spaces are used: by $L^2(\Omega)$ we refer to square integrable functions defined in an open bounded domain Ω; by $H^1(\Omega)$ we mean the Sobolev space $W^{1,2}(\Omega) \subset L^2(\Omega)$ formed by square integrable functions including their first generalized derivatives.Bold notation is used to denote spaces of vector-valued functions, e.g. $\mathbf{H}^1(\Omega)$; by subscript $_\#$ we refer to the Y-periodic functions.

2 Formulation of the acoustic problem

2.1 Periodic microstructure

The microstructure size is expressed by the scale parameter $\varepsilon = \ell/L$ defined by the ratio of the micro- and macroscopic characteristic lengths, denoted by ℓ and L, respectively. We consider a periodic structure of channels Ω_f^ε saturated by one homogeneous fluid. Due to the assumed periodicity of Ω_f^ε, a representative periodic cell $\mathcal{Z}_f^\varepsilon$ can be defined, which generates the fluid domain, see Fig. 1.

A periodic cell $\mathcal{Z}^\varepsilon = \prod_{i=1}^3]0, \varepsilon \ell^i[$ can be introduced, such that $\mathcal{Z}^\varepsilon = \mathcal{Z}_f^\varepsilon \cup \mathcal{Z}_s^\varepsilon \cup \partial_s \mathcal{Z}_f^\varepsilon$, where $\mathcal{Z}_s^\varepsilon \subset \mathcal{Z}^\varepsilon$ is the solid skeleton and $\partial_s \mathcal{Z}_f^\varepsilon$ is the fluid-solid interface. By $\partial_\# \mathcal{Z}_f^\varepsilon = \partial \mathcal{Z}_f^\varepsilon \setminus \partial_s \mathcal{Z}_f^\varepsilon$ we denote the "periodic part" of the boundary. For the purpose of the homogenization we consider the "unit periodic cell" $Y = \varepsilon^{-1} \mathcal{Z}^\varepsilon$ which consists of the fluid and solid parts accordingly the decomposition of $\mathcal{Z}^\varepsilon$, thus, $Y = Y_f \cup Y_s \cup \Gamma$.

The stress tensors of fluid and solid phases are respectively denoted by $\tilde{\boldsymbol{\sigma}}_f^\varepsilon$ and $\tilde{\boldsymbol{\sigma}}_s^\varepsilon$. The fluid phase is characterized by its mass density ρ_0, the bulk modulus k_f and the viscosity tensor $\mathbb{D}^{f,\varepsilon}$, see (5), whilst the solid phase is characterized by its density ρ_s and elasticity tensor $\mathbb{D}^{s,\varepsilon}$.

2.2 Acoustic wave decomposition

To treat the nonlinearity associated with fluid advection, we introduce a decomposition of the model responses into the steady part and the acoustic fluctuations, The total fields $\boldsymbol{w}$, p and the mass density of the fluid, ρ, are split into the "flow" parts $\bar{\boldsymbol{w}}$, $\bar{\rho}$ and $\bar{p}$ and the "acoustic fluctuation" parts $\tilde{\boldsymbol{w}}$, $\tilde{\rho}$ and $\tilde{p}$, so that

$$\boldsymbol{w} = \bar{\boldsymbol{w}} + \tilde{\boldsymbol{w}} \,, \quad p = \bar{p} + \tilde{p} \,, \quad \rho = \bar{\rho} + \tilde{\rho} \,. \tag{1}$$

Since the stationary fluid flow is assumed incompressible, $\bar{\rho} = \rho_0$ is a constant. Below, we assume that the steady-state flow is periodic in terms of the velocity $\tilde{\boldsymbol{w}}$. Essentially, because of the dissipation, pressure $\bar{p}$ cannot be described by a periodic function.

Concerning the solid displacement filed $\boldsymbol{u}$, the deformed configuration for the steady-state is taken as the reference one, so that $\boldsymbol{u}$ will only be associated with acoustic fluctuations (one can put $\bar{\boldsymbol{u}} \equiv \boldsymbol{0}$).

2.3 Acoustic problem formulation

The weak formulation of the acoustic problem at the pore level relies on the acoustic decomposition (1), so that the steady state response $(\bar{\boldsymbol{w}}^\varepsilon, \bar{p}^\varepsilon, \bar{\boldsymbol{u}}^\varepsilon)$ is assumed to be known.

Let $\hat{V}^\varepsilon(\Omega_f^\varepsilon), Q^1(\Omega_f^\varepsilon)$ and $\hat{U}^\varepsilon(\Omega_s^\varepsilon)$ be three admissible function spaces of the unknown fields $(\widetilde{\boldsymbol{w}}^\varepsilon, \widetilde{p}^\varepsilon, \widetilde{\boldsymbol{u}}^\varepsilon)$ of the problem constituted by the sufficiently differentiable complex-valued functions.

For almost all $t > 0$, the three fields $(\widetilde{\boldsymbol{w}}^\varepsilon, \widetilde{p}^\varepsilon, \widetilde{\boldsymbol{u}}^\varepsilon)$ such that $\widetilde{\boldsymbol{w}}^\varepsilon(t,\cdot) \in \hat{V}^\varepsilon(\Omega_f^\varepsilon)$, $\widetilde{p}^\varepsilon(t,\cdot) \in Q^1(\Omega_f^\varepsilon)$, and $\widetilde{\boldsymbol{u}}^\varepsilon(t,\cdot) \in \hat{U}^\varepsilon(\Omega_s^\varepsilon)$ satisfy

$$
\begin{aligned}
&\rho_0 \int_{\Omega_f^\varepsilon} \boldsymbol{\theta}^\varepsilon \cdot \Big(\dot{\widetilde{\boldsymbol{w}}}^\varepsilon + \ddot{\widetilde{\boldsymbol{u}}}^\varepsilon + \bar{\boldsymbol{w}}^\varepsilon \cdot \nabla(\widetilde{\boldsymbol{w}}^\varepsilon + \dot{\widetilde{\boldsymbol{u}}}^\varepsilon) + (\widetilde{\boldsymbol{w}}^\varepsilon + \dot{\widetilde{\boldsymbol{u}}}^\varepsilon) \cdot \nabla \bar{\boldsymbol{w}}^\varepsilon \Big) \\
&- \int_{\Omega_f^\varepsilon} \widetilde{p}^\varepsilon \nabla \cdot \boldsymbol{\theta}^\varepsilon + \int_{\Omega_f^\varepsilon} \mathbb{D}^{f,\varepsilon} \boldsymbol{e}(\widetilde{\boldsymbol{w}}^\varepsilon + \dot{\widetilde{\boldsymbol{u}}}^\varepsilon) : \boldsymbol{e}(\boldsymbol{\theta}^\varepsilon) = \int_{\Omega_f^\varepsilon} \tilde{\boldsymbol{f}}^f \cdot \boldsymbol{\theta}^\varepsilon + \int_{\partial_\sigma \Omega_f^\varepsilon} \tilde{\boldsymbol{g}}^{f,\varepsilon} \cdot \boldsymbol{\theta}^\varepsilon \,, \\
&\int_{\Omega_f^\varepsilon} q^\varepsilon \Big(\dot{\widetilde{p}}^\varepsilon + \bar{\boldsymbol{w}}^\varepsilon \cdot \nabla \widetilde{p}^\varepsilon + k_f \nabla \cdot (\widetilde{\boldsymbol{w}}^\varepsilon + \dot{\widetilde{\boldsymbol{u}}}^\varepsilon) \Big) = 0 \,,
\end{aligned}
\tag{2}
$$

for all $\boldsymbol{\theta}^\varepsilon \in V_0^\varepsilon(\Omega_f^\varepsilon)$ and $q^\varepsilon \in Q^0(\Omega_f^\varepsilon)$, and

$$
\int_{\Omega_s^\varepsilon} \rho_s \ddot{\widetilde{\boldsymbol{u}}}^\varepsilon \cdot \boldsymbol{v}^\varepsilon + \int_{\Omega_s^\varepsilon} \mathbb{D}^{s,\varepsilon} \boldsymbol{e}(\tilde{\boldsymbol{u}}^\varepsilon) : \boldsymbol{e}(\boldsymbol{v}^\varepsilon) - \tilde{\mathcal{I}}^\varepsilon(\tilde{\boldsymbol{\sigma}}_f^\varepsilon, \boldsymbol{v}^\varepsilon) = \int_{\Omega_s^\varepsilon} \tilde{\boldsymbol{f}}^s \cdot \boldsymbol{v}^\varepsilon + \int_{\partial_\sigma \Omega_s^\varepsilon} \tilde{\boldsymbol{g}}^{s,\varepsilon} \cdot \boldsymbol{v}^\varepsilon \,,
\tag{3}
$$

for all $\boldsymbol{v}^\varepsilon \in U_0^\varepsilon(\Omega_s^\varepsilon)$, where $\tilde{\mathcal{I}}^\varepsilon$ represents the fluid stress virtual power on interface Γ_{fs}^ε,

$$
\begin{aligned}
\tilde{\mathcal{I}}^\varepsilon(\tilde{\boldsymbol{\sigma}}_f^\varepsilon, \boldsymbol{v}^\varepsilon) &= \int_{\Gamma_{fs}^\varepsilon} \boldsymbol{n}^s \cdot \tilde{\boldsymbol{\sigma}}_f^\varepsilon \cdot \boldsymbol{v}^\varepsilon \,, \\
\tilde{\boldsymbol{\sigma}}_f^\varepsilon(\tilde{p}^\varepsilon, \boldsymbol{w}^\varepsilon + \dot{\tilde{\boldsymbol{u}}}^\varepsilon) &= -\boldsymbol{I}\tilde{p}^\varepsilon + \mathbb{D}^{f,\varepsilon} \boldsymbol{e}(\boldsymbol{w}^\varepsilon + \dot{\tilde{\boldsymbol{u}}}^\varepsilon) \,.
\end{aligned}
\tag{4}
$$

3 Homogenized model

An effective model of the two-phase medium was derived using in the asymptotic analysis $\varepsilon \to 0$ of the micro-model (2) and (4). The following scaling by powers of ε is used for the fluid viscosity μ^ε and the steady flow advection $\bar{\boldsymbol{w}}^\varepsilon$ to adjust them to the microstructure, namely to the pore size proportional to ε,

$$
\begin{aligned}
\text{viscosity:} \quad & \mu^\varepsilon = \varepsilon^2 \bar{\mu} \,, \quad \mathbb{D}^{f,\varepsilon} = \varepsilon^2 2\bar{\mu}(\mathbb{I} - \frac{1}{3}\boldsymbol{I} \otimes \boldsymbol{I}) \,, \\
\text{advection velocity:} \quad & \bar{\boldsymbol{w}}^\varepsilon(x) = \varepsilon \bar{\boldsymbol{w}}(y) \,,
\end{aligned}
\tag{5}
$$

where $\mathbb{I}$ is the fourth-order identity tensor and $\bar{\boldsymbol{w}}(y)$ with $y = x/\varepsilon$ is the Y-periodic advection velocity field, as represented in Y_f. It is worth noting that the periodic structure is retained if all the material parameters constituting the microstructure and also the advection velocity $\bar{\boldsymbol{w}}$ are constant with respect to the macroscopic position in the medium. In a general situation, the velocity field describing the steady flow in the microstructure can be established for a given macroscopic velocity $\boldsymbol{w}^0$ by means of the Forchheimer law, see *e.g.* [2], *cf.* [9], so that $\bar{\boldsymbol{w}}(x,y)$ is a two-scale function satisfying the incompressibility constraint $\nabla_y \cdot \bar{\boldsymbol{w}}(x,y) = 0$.

3.1 Characteristic responses

The asymptotic analysis (2) and (4) yields the limit equations involving macroscopic fields and two-scale fields. Due to the linearity, the latter fields can be expressed using multiplicative split into the macroscopic and the characteristic responses. However, to do so, the Laplace transformation, $\mathcal{L}\{f\} \mapsto \underset{\sim}{f}(\lambda)$, where λ is a complex variable representing the angular frequency, must be employed, since the two-scale functions are coupled with the macroscopic functions in time. In what follows, we employ the following bilinear and trilinear forms, defined in terms of the inner product and and the averaging integral,

$$\begin{aligned} \langle \boldsymbol{u},\, \boldsymbol{v}\rangle_{Y_f} &= \fint_{Y_f} \boldsymbol{u}\cdot\boldsymbol{v}\ , \\ \fint_D \star &= \frac{1}{|Y|}\int_D \star\ , \qquad \text{for any } D\subset Y\ , \\ a_f\left(\boldsymbol{w},\, \boldsymbol{v}\right) &= \langle \nabla_y \boldsymbol{w},\, \nabla_y \boldsymbol{v}\rangle_{Y_f}\ , \\ b_f\left(\bar{\boldsymbol{w}},\, \boldsymbol{w},\, \boldsymbol{v}\right) &= 2\,\langle \bar{\boldsymbol{w}}\otimes\boldsymbol{w},\, \boldsymbol{e}_y(\boldsymbol{v})\rangle_{Y_f}\ , \end{aligned} \tag{6}$$

where D can be a subdomain, or a manifold in Y. We employ the spaces of Y-periodic functions: we define $H^1_{\#}(Y)\subset W^{1,2}(Y)$ and $\mathbf{H}^1_{\#}(Y)\subset \boldsymbol{W}^{1,2}(Y)$ for scalar and vectorial fields, respectively; space $\widetilde{\mathbf{H}}^1_{\#}(Y_s)\subset \mathbf{H}^1_{\#}(Y_s)$ is restricted to functions with zero mean values in Y_s; admissible flow velocities belong to the space

$$\mathbf{H}^1_{\#0}(Y_f) = \{\boldsymbol{v}\in \mathbf{H}^1_{\#}(Y_f)|\ \boldsymbol{v}=\boldsymbol{0} \text{ on } \partial Y_f\setminus\partial Y\}\ . \tag{7}$$

In order to introduce the local autonomous problems for characteristic flow responses, we establish the following tensor operator attaining two alternative forms,

$$\boldsymbol{A} = (A_{ij})\ , \quad A_{ij} = \left\{ \begin{array}{l} \delta_{ij}\ , \\ G_{ij} = \partial^y_j \bar{w}_i \end{array}\right. . \tag{8}$$

Note that $(\boldsymbol{A}\mathbf{1}_k)_i = A_{ik}$, whereby $(\mathbf{1}_k)_j = \delta_{jk}$, thus, $(\boldsymbol{G}\mathbf{1}_k)_i = (\nabla_y \bar{\boldsymbol{w}}\mathbf{1}_k)_i = \partial^y_k \bar{w}_i$.

The characteristic responses $(\boldsymbol{w}^{\boldsymbol{A},k}, \pi^{\boldsymbol{A},k})$, where $\underset{\sim}{\boldsymbol{w}}^{\boldsymbol{A},k}\in \mathbf{H}^1_{\#0}(Y_f)$ and $\underset{\sim}{\pi}^{\boldsymbol{A},k}\in L^2(Y_f)$, satisfy

$$\begin{aligned} \lambda\left\langle \underset{\sim}{\boldsymbol{w}}^{\boldsymbol{A},k},\, \boldsymbol{v}\right\rangle_{Y_f} - b_f\left(\bar{\boldsymbol{w}},\, \underset{\sim}{\boldsymbol{w}}^{\boldsymbol{A},k},\, \boldsymbol{v}\right) \\ +\frac{1}{\bar{\nu}} a_f\left(\underset{\sim}{\boldsymbol{w}}^{\boldsymbol{A},k},\, \boldsymbol{v}\right) - \left\langle \underset{\sim}{\pi}^{\boldsymbol{A},k},\, \nabla_y\cdot\boldsymbol{v}\right\rangle_{Y_f} = \frac{1}{\lambda}\left\langle \boldsymbol{A}\mathbf{1}_k,\, \boldsymbol{v}\right\rangle_{Y_f}\ , \\ \left\langle q,\, \nabla_y\cdot \underset{\sim}{\boldsymbol{w}}^{\boldsymbol{A},k}\right\rangle_{Y_f} = 0\ , \end{aligned} \tag{9}$$

for all $\boldsymbol{v}\in\mathbf{H}^1_{\#0}(Y_f)$ and $q\in L^2(Y_f)$, where $\bar{\nu}=\rho_0/\bar{\mu}$ is the rescaled kinematic viscosity.

The poroelastic coefficients of the Biot model are expressed in terms of time-independent characteristic responses $\boldsymbol{\omega}^{ij}$ and $\boldsymbol{\omega}^*(y)$. Using the elastic bilinear form,

$$a_s\left(\boldsymbol{u},\, \boldsymbol{v}\right) = \fint_{Y_s} \mathbb{D}_s \boldsymbol{e}_y(\boldsymbol{u}) : \boldsymbol{e}_y(\boldsymbol{v})\ , \tag{10}$$

two standard autonomous problems are introduced.

(i) Find $\boldsymbol{\omega}^{ij} \in \widetilde{\mathbf{H}}^1_{\#}(Y_s)$, such that

$$a_s\left(\boldsymbol{\omega}^{ij}, \boldsymbol{v}\right) = -a_s\left(\boldsymbol{\Pi}^{ij}, \boldsymbol{v}\right) \ , \quad \forall \boldsymbol{v} \in \mathbf{H}^1_{\#}(Y_s) \ , \tag{11}$$

where $\boldsymbol{\Pi}^{ij} = (\Pi^{ij}_k)$ with $\Pi^{ij}_k = y_j \delta_{ik}$.

(ii) Find $\boldsymbol{\omega}^* \in \widetilde{\mathbf{H}}^1_{\#}(Y_s)$, such that

$$a_s\left(\boldsymbol{\omega}^*, \boldsymbol{v}\right) = -\oint_{\Gamma} \boldsymbol{v} \cdot \boldsymbol{n}^s \ , \quad \forall \boldsymbol{v} \in \mathbf{H}^1_{\#}(Y_s) \ . \tag{12}$$

3.2 Effective material parameters

Two homogenized tensors $\widehat{\underset{\sim}{\mathcal{K}}} = (\widehat{\underset{\sim}{\mathcal{K}}}_{ij})$ and $\widehat{\underset{\sim}{\mathcal{G}}} = (\widehat{\underset{\sim}{\mathcal{G}}}_{ij})$ constituting the effective Darcy law are determined by the characteristic responses $\underset{\sim}{\boldsymbol{w}}^{\boldsymbol{I},i}$ and $\underset{\sim}{\boldsymbol{w}}^{\boldsymbol{G},i}$,

$$\widehat{\underset{\sim}{\mathcal{K}}}_{ij}(\lambda) = \lambda \oint_{Y_f} \underset{\sim}{w}^{\boldsymbol{I},j}_i \ , \quad \widehat{\underset{\sim}{\mathcal{G}}}_{ij}(\lambda) = \lambda \oint_{Y_f} \underset{\sim}{w}^{\boldsymbol{G},j}_i \text{ for } i,j = 1,\dots,3. \tag{13}$$

Using the $\boldsymbol{\omega}^{ij}$ and $\boldsymbol{\omega}^*(y)$, the effective poroelastic coefficients of the Biot model are computed,

$$\begin{aligned} D^H_{ijkl} &:= a_s\left(\boldsymbol{\omega}^{ij} + \boldsymbol{\Pi}^{ij}, \boldsymbol{\omega}^{kl} + \boldsymbol{\Pi}^{kl}\right) \ , \\ B^H_{ij} &:= -a_s\left(\boldsymbol{\omega}^*, \boldsymbol{\Pi}^{ij}\right) = a_s\left(\boldsymbol{\omega}^*, \boldsymbol{\omega}^{ij}\right) = -\oint_{\Gamma} \boldsymbol{\omega}^{ij} \cdot \boldsymbol{n}^s \ , \\ N^H &:= \oint_{Y_f} \nabla_y \cdot \widetilde{\boldsymbol{\omega}}^* = a_s\left(\boldsymbol{\omega}^*, \boldsymbol{\omega}^*\right) \ , \end{aligned} \tag{14}$$

recalling that $\widetilde{\boldsymbol{\omega}}$ is a smooth extension of $\boldsymbol{\omega}$ to entire Y. Above, the alternative expressions can be derived due to the local problems (11) and (12). The following properties of the homogenized poroelastic coefficients hold: the Biot compressibility modulus $M^H > 0$, the elasticity coefficients are symmetric, $D^H_{ijkl} = D^H_{klij} = D^H_{jikl}$, and positive definite, *i.e.* $D^H_{ijkl}\xi_{ij}\xi_{kl} > 0$ for any $\xi_{ij} \in \mathbb{R}$, and the analogous properties hold also for Biot stress-coupling coefficients $B^H_{ij} = B^H_{ji}$ satisfying $\widehat{B}^H_{ij}\zeta_i\zeta_j > 0$ for any $\zeta_i \in \mathbb{R}$.

Upon introducing coefficients involving the porosity ϕ_f,

$$\widehat{\boldsymbol{B}}^H := \boldsymbol{B}^H + \phi_f \boldsymbol{I} \ , \quad M^H := N^H + \frac{\phi_f}{k_f} \ , \quad \text{with } \phi_f = \oint_{Y_f} \ , \tag{15}$$

we recover the Biot model of the poroelastic material; the total effective stress $\boldsymbol{\sigma}^{\text{eff}}$,the local pore fluid content increase $\dot{\mathcal{J}}_f = -\nabla_x \cdot (\phi_f \boldsymbol{w}^0)$, and the effective seepage velocity $\phi_f \underset{\sim}{\boldsymbol{w}}^0$ are given by

$$\begin{aligned} \boldsymbol{\sigma}^{\text{eff}} &= \mathbb{D}^H \boldsymbol{e}_x(\boldsymbol{u}^0) - p^0 \widehat{\boldsymbol{B}}^H \ , \quad \dot{\mathcal{J}}_f = \widehat{\boldsymbol{C}}^H : \boldsymbol{e}_x(\boldsymbol{u}^0) + M^H \dot{p}^0 \ , \\ \phi_f \underset{\sim}{\boldsymbol{w}}^0 &= -\widehat{\underset{\sim}{\mathcal{K}}} \frac{1}{\rho_0} (\nabla_x \underset{\sim}{p}^0 + \rho_0 \lambda^2 \underset{\sim}{\boldsymbol{u}}^0 - \underset{\sim}{\widehat{\boldsymbol{f}}}^f) + \widehat{\underset{\sim}{\mathcal{G}}} \lambda \underset{\sim}{\boldsymbol{u}}^0 \ . \end{aligned} \tag{16}$$

While the dynamic permeability $\widehat{\underset{\sim}{\mathcal{K}}}$ constitutes the Darcy law (16), as in the case of a rigid porous medium, tensor $\widehat{\underset{\sim}{\mathcal{G}}}$ presents a coupled effect of the advection $\bar{\boldsymbol{w}}$ and the macroscopic skeletom velocity $\lambda \underset{\sim}{\boldsymbol{u}}^0$.

3.3 Permeability and the visco-dynamic operator

In many works (see *e.g.* [6] and [5]) the dynamic permeability is introduced using the second-order tensor $\eta[\boldsymbol{k}(\lambda)]^{-1} := \lambda\boldsymbol{\rho} + \eta\boldsymbol{K}^{-1}$ which presents the "low-frequency approximation" (*i.e.* for small $\lambda := \mathrm{i}\omega$, given by the frequency ω and $\mathrm{i} = \sqrt{-1}$) of the visco-dynamic operator, defined by the static permeability $\boldsymbol{K}$, the dynamic fluid viscosity, η, and the tortuosity $a_\tau \geq 1$: $\boldsymbol{\rho} \approx \boldsymbol{I}\rho_a$ with $\rho_a = \rho_f a_\tau/\phi_f$. We consider $\widetilde{\boldsymbol{\mathcal{K}}}(\lambda) := [\lambda\boldsymbol{\rho} + \boldsymbol{K}^{-1}]^{-1}$ and compare it with the permeability $\widehat{\boldsymbol{\mathcal{K}}}(\lambda)$ just introduced above.

Let $\boldsymbol{\Lambda} = \mathrm{diag}_k(\Lambda_k)$ is the diagonal tensor formed by the eigenvalues Λ_k, $k = 1, 2, 3$ of the static permeability $\boldsymbol{K}$, thus, $\boldsymbol{K}\boldsymbol{X} = \boldsymbol{\Lambda}\boldsymbol{X}$. The following holds:

$$\widetilde{\boldsymbol{\mathcal{K}}}(\lambda) = \boldsymbol{X}\mathrm{diag}_k(\xi_k)\boldsymbol{X}^T\ , \quad \xi_k = \frac{\Lambda_k}{1+\lambda\Lambda_k\rho_a} = \frac{\Lambda_k(1+\lambda^*\Lambda_k)}{1+(|\lambda|\Lambda_k\rho_a)^2}\ , \tag{17}$$

where λ^* is the complex conjugate of λ and $|\lambda| = \sqrt{\lambda\lambda^*}$. The obvious asymptotics yields $\xi_k \to \Lambda_k$ for $|\lambda| \to 0_+$ and $\xi_k \to 0$ for $|\lambda| \to \infty$. It is easy to see that

$$\widetilde{\boldsymbol{\mathcal{K}}}^{-1}(\lambda) = \boldsymbol{X}\mathrm{diag}_k\left(\lambda\rho_a + \Lambda_k^{-1}\right)\boldsymbol{X}^T\ , \tag{18}$$

noting that eigenvalues Λ_k are independent of λ. By virtue of the approximation $\widehat{\boldsymbol{\mathcal{K}}}(\lambda) \approx \widetilde{\boldsymbol{\mathcal{K}}}(\lambda)$ the above asymptotics and (17),(18) reveal also the variation of $(\widehat{\boldsymbol{\mathcal{K}}}(\lambda))^{-1}$ with frequency λ.

4 Poroelastic model in the frequency domain

To study the wave propagation in the homogenized medium, the Biot model with the dynamic Darcy law will be presented in the frequency domain. We shall consider monochromatic harmonic waves of a given circular frequency ω. Further, we employ $\mathrm{i}^2 = -1$; note the relationship with the preceding section by putting $\lambda = \mathrm{i}\omega$. The Fourier transform $\mathcal{F}(\omega) : u(t,x) \mapsto \mathring{u}(\omega,x)$ is applied, replacing formally the Laplace transformation employed above. In what follows, for the sake of simplicity, we keep unchanged notation for the unknown fields, just dropping the superscript ^{0}. Since the reference fluid density ρ^0 is a constant, it is useful to introduce the following notation:

$$\begin{aligned}
\boldsymbol{u} &:= \mathring{\boldsymbol{u}}\ , & \widehat{\mathbb{D}}^H &:= \mathbb{D}^H/\rho^0\ ,\\
p &:= \mathring{p}/\rho^0\ , & \widehat{M}^H &:= \rho^0 M^H\ ,\\
\boldsymbol{w} &:= \phi_f\mathring{\boldsymbol{w}}\ , & \widehat{\mathring{\boldsymbol{\mathcal{K}}}} &:= \rho^0\mathring{\boldsymbol{\mathcal{K}}}\ ,\\
\widehat{\mathring{\boldsymbol{f}}} &:= \widehat{\mathring{\boldsymbol{f}}}/\rho^0\ , & \widehat{\mathring{\boldsymbol{\mathcal{G}}}} &:= \rho^0\mathring{\boldsymbol{\mathcal{G}}}\ ,\\
\widehat{\mathring{\boldsymbol{f}}}^f &:= \widehat{\mathring{\boldsymbol{f}}}^f/\rho^0\ , & \mathring{\boldsymbol{g}}^s &:= \mathring{\boldsymbol{g}}^s/\rho^0\ ,\\
\hat{r} &= \bar{\rho}/\rho_0\ , & \text{where } \bar{\rho} &= \bar{\rho}_s + \phi_f\rho_0 = \fint_{Y_s}\rho_s + \phi_f\rho_0\ ,
\end{aligned} \tag{19}$$

thus, $\bar{\rho}$ is the mean density. The visco-dynamic operator, *cf.* [6] and [5], is represented by the inverse dynamic permeability $\widehat{\mathring{\boldsymbol{\mathcal{K}}}}^{-1}$. Within assumptions of the acoustic fluctuations, the dynamic response of the homogenized poroelastic medium is governed by the following set of

differential equations

$$
\begin{aligned}
-\omega^2 \hat{r}\boldsymbol{u} + \mathrm{i}\omega\boldsymbol{w} - \nabla\cdot\left(\widehat{\mathbb{D}}^H \boldsymbol{e}_x(\boldsymbol{u}) - p\widehat{\boldsymbol{B}}^H\right) &= \widehat{\underset{\circ}{\boldsymbol{f}}}\,, \\
\mathrm{i}\omega\widehat{\boldsymbol{B}}^H : \boldsymbol{e}_x(\boldsymbol{u}) + \nabla\cdot\boldsymbol{w} + \mathrm{i}\omega\widehat{M}^H p &= 0\,, \\
\widehat{\underset{\circ}{\boldsymbol{\mathcal{K}}}}^{-1}(\boldsymbol{w} + \mathrm{i}\omega\widehat{\underset{\circ}{\boldsymbol{\mathcal{G}}}}\boldsymbol{u}) - \omega^2\boldsymbol{u} + \nabla_x p &= \widehat{\underset{\circ}{\boldsymbol{f}}}^f\,,
\end{aligned}
\tag{20}
$$

where $\widehat{\underset{\circ}{\boldsymbol{f}}}^f$ and $\widehat{\underset{\circ}{\boldsymbol{f}}}$ are the effective volume forces in the fluid phase and in the bulk mixture material; however, these forces are not involved in the dispersion analysis studied below. It is worth to note that the extra term $\mathrm{i}\omega\widehat{\underset{\circ}{\boldsymbol{\mathcal{K}}}}^{-1}\widehat{\underset{\circ}{\boldsymbol{\mathcal{G}}}}\boldsymbol{u}$ in the last equation emerges due to the advection phenomenon of the permanent fluid flow given by the advection Y-periodic velocity field $\bar{\boldsymbol{w}}$.

Remark 1. It is worth noting that the computed permeability $\widehat{\underset{\circ}{\boldsymbol{\mathcal{K}}}}$ is usually represented by the visco-dynamic operator $[\boldsymbol{k}(\omega)]/\eta$, see *e.g.* [6], such that $\widehat{\underset{\circ}{\boldsymbol{\mathcal{K}}}}^{-1} \approx \eta[\boldsymbol{k}(\omega)]^{-1} := \mathrm{i}\omega\boldsymbol{\rho} + \eta\boldsymbol{K}^{-1}$ presents the low-frequency Biot's approximation of the visco-dynamic operator, where $\boldsymbol{K}/\eta$ is the static permeability.

4.1 Wave dispersion analysis

The wave propagation in the heterogeneous two-phase medium is analyzed using the model of the homogenized medium. In what follows, the volume forces are disregarded, since we are interested in the free wave propagation, thus $\widehat{\underset{\circ}{\boldsymbol{f}}} = \widehat{\underset{\circ}{\boldsymbol{f}}}^f \equiv \boldsymbol{0}$.

4.2 Plane waves in homogenized medium

We look for a monochromatic harmonic plane wave propagating in direction $\boldsymbol{n}$, such that it can be written in the form

$$
\begin{aligned}
\tilde{\boldsymbol{u}}(x,t) &= \boldsymbol{u}\exp\left(-\mathrm{i}\boldsymbol{\kappa}\cdot\boldsymbol{x}\right)\exp\left(\mathrm{i}\omega t\right)\,, \\
\tilde{p}(x,t) &= p\exp\left(-\mathrm{i}\boldsymbol{\kappa}\cdot\boldsymbol{x}\right)\exp\left(\mathrm{i}\omega t\right)\,, \\
\tilde{\boldsymbol{w}}(x,t) &= \boldsymbol{w}\exp\left(-\mathrm{i}\boldsymbol{\kappa}\cdot\boldsymbol{x}\right)\exp\left(\mathrm{i}\omega t\right)\,,
\end{aligned}
\tag{21}
$$

where the triplet $(\boldsymbol{u}, p, \boldsymbol{w})$ denotes the plane wave amplitudes, ω is the circular frequency and $\boldsymbol{\kappa} = \varkappa\boldsymbol{n}$ is the wave vector. In the Fourier space, transformed (21) substituted in (20) yields

$$
\begin{aligned}
-\omega^2\hat{r}\boldsymbol{u} + \mathrm{i}\omega\boldsymbol{w} + \varkappa^2\boldsymbol{n}\cdot\widehat{\mathbb{D}}^H : \boldsymbol{n}\otimes\boldsymbol{u} - \mathrm{i}\varkappa\widehat{\boldsymbol{B}}^H\boldsymbol{n}p &= \boldsymbol{0}\,, \\
\varkappa\omega\widehat{\boldsymbol{B}}^H : \boldsymbol{n}\otimes\boldsymbol{u} - \mathrm{i}\varkappa\boldsymbol{n}\cdot\boldsymbol{w} + \mathrm{i}\omega\widehat{M}^H p &= 0\,, \\
\widehat{\underset{\circ}{\boldsymbol{\mathcal{K}}}}^{-1}(\boldsymbol{w} + \mathrm{i}\omega\widehat{\underset{\circ}{\boldsymbol{\mathcal{G}}}}\boldsymbol{u}) - \omega^2\boldsymbol{u} - \mathrm{i}\varkappa\boldsymbol{n}p &= \boldsymbol{0}\,.
\end{aligned}
\tag{22}
$$

Let us recall the approximate expression (18) of $(\widehat{\boldsymbol{\mathcal{K}}}(\mathrm{i}\omega))^{-1}$ which reveals that $(22)_3$ is well defined.

The dispersion analysis yields an implicit mapping $\omega \mapsto \varkappa$ within an interval of frequencies, $\underline{\omega} \le \omega \le \overline{\omega}$, $\underline{\omega}, \overline{\omega} \in \mathbb{R}$ for a specified direction $\boldsymbol{n}$. To compute $\varkappa$ for a given $\omega \in \mathbb{R}$, an eigenvalue problem (EVP) must be solved. The straightforward formulation (22) involving all the three variables $(\boldsymbol{u}, p, \boldsymbol{w})$, as well as the reduced formulation in $(\boldsymbol{u}, p)$, both lead to a quadratic EVP, cf. [10]. By eliminating the pressure from (22), the formulation in $(\boldsymbol{u}, \boldsymbol{w})$ is obtained, which leads to a linear EVP. Therefore, we pursue this approach of performing the dispersion analysis.

4.3 Formulation $(\boldsymbol{u}, \boldsymbol{w})$

The pressure can be eliminated from (22),

$$\begin{aligned} p &= \frac{-1}{\mathrm{i}\omega\widehat{M}^H}\left(\varkappa\omega\widehat{\boldsymbol{B}}^H : \boldsymbol{n}\otimes\boldsymbol{u} - \mathrm{i}\omega\boldsymbol{n}\cdot\boldsymbol{w}\right) \\ &= \frac{\mathrm{i}\varkappa}{\widehat{M}^H}\widehat{\boldsymbol{B}}^H : \boldsymbol{n}\otimes\boldsymbol{u} + \frac{\varkappa}{\omega\widehat{M}^H}\boldsymbol{n}\cdot\boldsymbol{w}\ , \end{aligned} \tag{23}$$

Upon substituting (23) in (22), we get

$$\begin{aligned} \varkappa^2\left(\boldsymbol{n}\cdot\widehat{\mathbb{D}}^H : \boldsymbol{n}\otimes\boldsymbol{u} + (\widehat{M}^H)^{-1}(\widehat{\boldsymbol{B}}^H\boldsymbol{n})\otimes(\widehat{\boldsymbol{B}}^H\boldsymbol{n})\boldsymbol{u}\right) - \omega^2\hat{r}\boldsymbol{u} \\ + \left(\mathrm{i}\omega\boldsymbol{I} - \varkappa^2\mathrm{i}(\omega\widehat{M}^H)^{-1}\widehat{\boldsymbol{B}}^H\boldsymbol{n}\otimes\boldsymbol{n}\right)\boldsymbol{w} = 0\ , \\ \left(\mathrm{i}\omega\widehat{\mathcal{K}}^{-1}\widehat{\mathcal{G}} - \omega^2\boldsymbol{I} + \varkappa^2(\widehat{M}^H)^{-1}(\boldsymbol{n}\otimes\boldsymbol{n})\widehat{\boldsymbol{B}}^H\right)\boldsymbol{u} + \left(\widehat{\mathcal{K}}^{-1} - \varkappa^2\mathrm{i}(\omega\widehat{M}^H)^{-1}\boldsymbol{n}\otimes\boldsymbol{n}\right)\boldsymbol{w} = 0\ , \end{aligned} \tag{24}$$

where the following substitutions (abbreviations) can be applied:

$$\begin{aligned} \widehat{\mathbb{D}}^U &= \widehat{\mathbb{D}}^H + \widehat{\boldsymbol{B}}^H\otimes\widehat{\boldsymbol{B}}^H/\widehat{M}^H\ , \\ \mathcal{A}^{U,n}_{ij} &= \widehat{D}^U_{ikjl}n_kn_l\ , \\ \boldsymbol{\mathcal{N}}^n &= \boldsymbol{n}\otimes\boldsymbol{n}\ , \end{aligned} \tag{25}$$

To proceed, (25) is substituted in (24) which then yields

$$\begin{aligned} \varkappa^2\left(\boldsymbol{\mathcal{A}}^{U,n}\boldsymbol{u} - \mathrm{i}(\omega\widehat{M}^H)^{-1}\widehat{\boldsymbol{B}}^H\boldsymbol{\mathcal{N}}^n\boldsymbol{w}\right) - \omega^2\hat{r}\boldsymbol{u} + \mathrm{i}\omega\boldsymbol{w} = 0\ , \\ \varkappa^2\left((\widehat{M}^H)^{-1}\boldsymbol{\mathcal{N}}^n\widehat{\boldsymbol{B}}^H\boldsymbol{u} - \mathrm{i}(\omega\widehat{M}^H)^{-1}\boldsymbol{\mathcal{N}}^n\boldsymbol{w}\right) + \left(\mathrm{i}\omega\widehat{\mathcal{K}}^{-1}\widehat{\mathcal{G}} - \omega^2\boldsymbol{I}\right)\boldsymbol{u} + \widehat{\mathcal{K}}^{-1}\boldsymbol{w} = 0\ . \end{aligned} \tag{26}$$

Now, $(26)_1$ and $(26)_2$ are multiplied by $1/\omega^2$ and i/ω^3, respectively. The modified equations can be expressed upon introducing matrices $\mathbb{M}(\omega)$ and $\mathbb{K}(\omega)$, where

$$\begin{aligned} \mathbb{M}(\omega) &= \begin{pmatrix} \hat{r}\boldsymbol{I}\ , & -\frac{\mathrm{i}}{\omega}\boldsymbol{I} \\ \frac{\mathrm{i}}{\omega}\boldsymbol{I} + \frac{1}{\omega^2}\widehat{\mathcal{K}}^{-1}\widehat{\mathcal{G}}\ , & -\frac{\mathrm{i}}{\omega^3}\widehat{\mathcal{K}}^{-1} \end{pmatrix}\ , \\ \mathbb{K}(\omega) &= \begin{pmatrix} \boldsymbol{\mathcal{A}}^{U,n}\ , & -\frac{\mathrm{i}}{\omega\widehat{M}^H}\widehat{\boldsymbol{B}}^H\boldsymbol{\mathcal{N}}^n \\ \frac{\mathrm{i}}{\omega\widehat{M}^H}\boldsymbol{\mathcal{N}}^n\widehat{\boldsymbol{B}}^H\ , & \frac{1}{\omega^2\widehat{M}^H}\boldsymbol{\mathcal{N}}^n \end{pmatrix}\ , \end{aligned} \tag{27}$$

The dispersion analysis consists in solving the following eigenvalue problem: Given $\omega\in\mathbb{R}$, find $\gamma = \varkappa/\omega\in\mathbb{C}$, such that a nontrivial $\mathbf{q} = [\boldsymbol{u};\boldsymbol{w}] \not\equiv \boldsymbol{0}$ satisfies

$$\mathbb{M}(\omega)\mathbf{q} = \lambda\mathbb{K}(\omega)\mathbf{q}\ , \qquad \text{where } \lambda := \gamma^2\ . \tag{28}$$

Recall that both $\mathcal{K}$ and $\mathcal{G}$ depend of the frequency $\omega > 0$.

In 3D, (28) provides 6 eigenvalues $\lambda = \gamma^2$. It is clear that $\mathrm{Ker}\,(\mathbb{K}) \neq \emptyset$; Let $\boldsymbol{n}_\perp$ is any unit vector, such that $\boldsymbol{n}_\perp\cdot\boldsymbol{n} = 0$. Then $\mathbf{q}_\perp = [\boldsymbol{0};\boldsymbol{n}_\perp]\in\mathrm{Ker}\,(\mathbb{K})$, noting that $\boldsymbol{\mathcal{N}}^n\boldsymbol{n}_\perp = \boldsymbol{0}$. Hence $\mathrm{card}\,(\mathrm{Ker}\,(\mathbb{K})) = 2$. As the consequence, there are two $\lambda_5 = \lambda_6 = \infty$. The remaining eigenvalues $\lambda_1,\ldots,\lambda_4$ represent four modes which can be identified as the quasi-shear (qS) and quasi-compressional, usually called quasi-pressure modes (qP), depending on the cosinus $\approx \boldsymbol{u}\cdot\boldsymbol{n}$ of the angle between the solid displacement polarization.

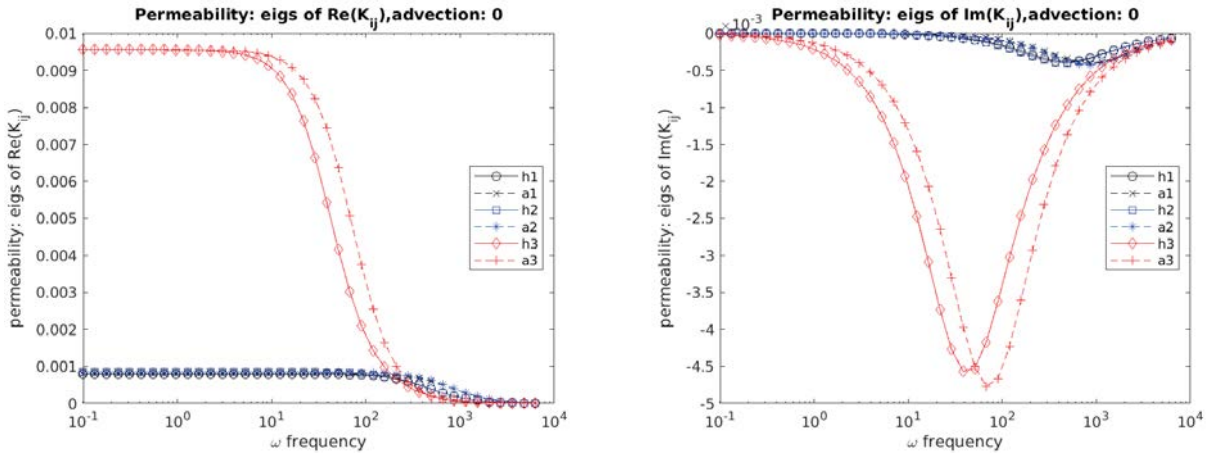

$\Re$ parts ($\bar{w}^0 = 0$ m/s) $\Im$ parts ($\bar{w}^0 = 0$ m/s)

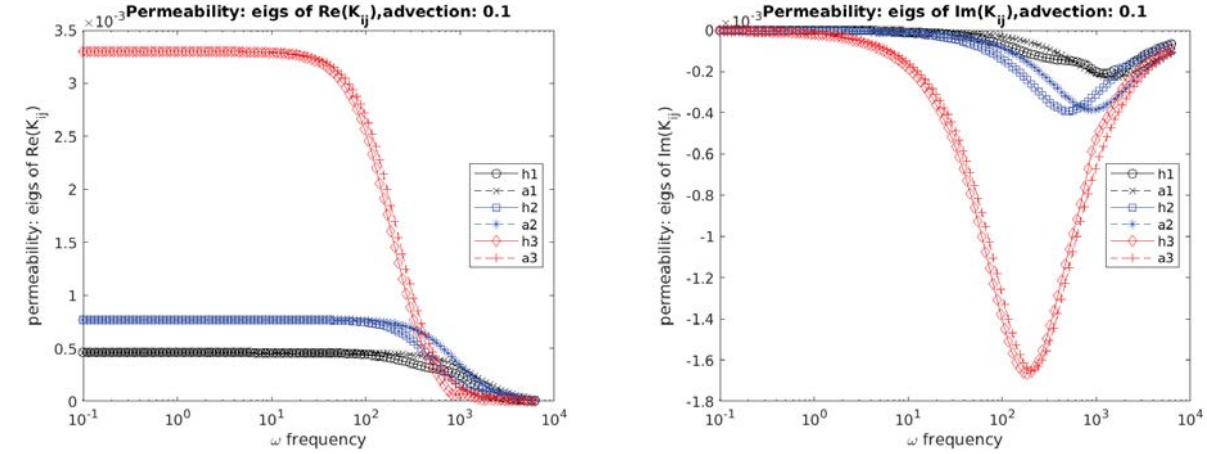

$\Re$ parts ($\bar{w}^0 = 0.1$ m/s) $\Im$ parts ($\bar{w}^0 = 0.1$ m/s)

Figure 2: Eigenvalues of the permeability tensors $\widehat{\boldsymbol{\mathcal{K}}}(\omega)$ (computed by homogenization, labels $h1, h2, h3$) and $\widetilde{\boldsymbol{\mathcal{K}}}(\omega)$ (the Biot's visco-dynamic operator approximation, labels $a1, a2, a3$). Steady advection: $\bar{w}^0 = 0$ (top figures), $\bar{w}^0 = 0.1$ (bottom figures).

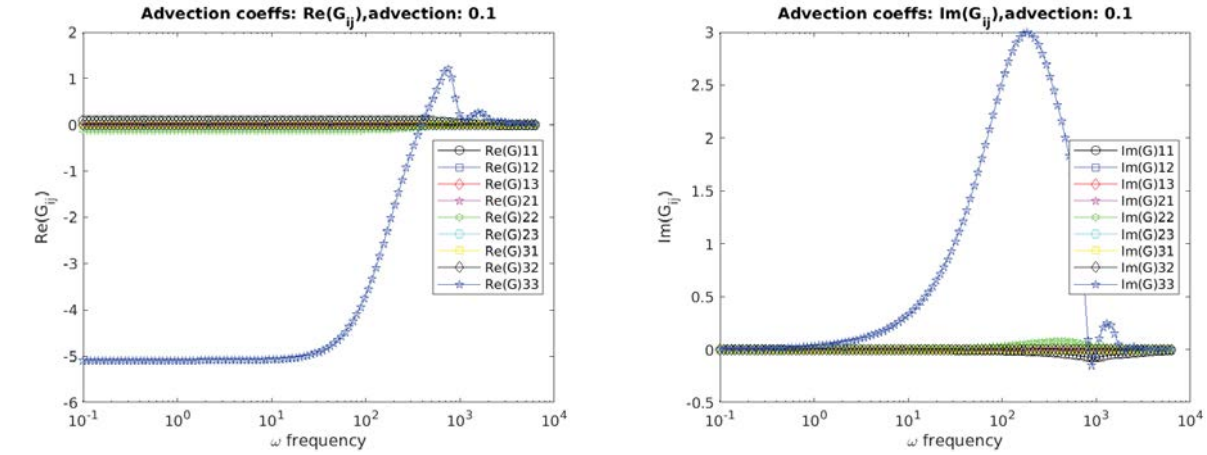

$\Re$ parts $\Im$ parts

Figure 3: The components of the tensors $\widehat{\boldsymbol{\mathcal{G}}}(\omega)$. Steady advection: $\bar{w}^0 = 0.1$ (note that $\widehat{\boldsymbol{\mathcal{G}}}(\omega) \equiv 0$ for $\bar{w}^0 = 0.0$).

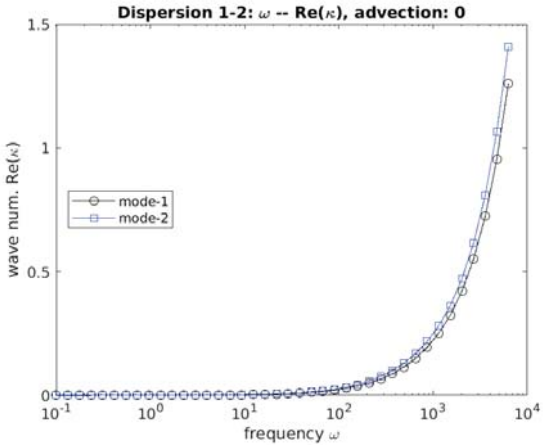

$\Re(\varkappa)$ – wave propagation

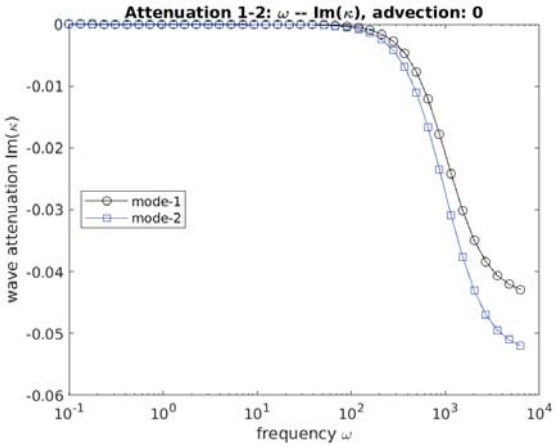

$\Im(\varkappa)$ – wave attenuation

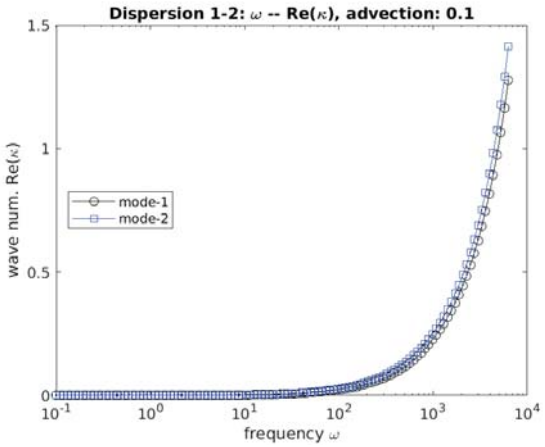

$\Re(\varkappa)$ – wave propagation

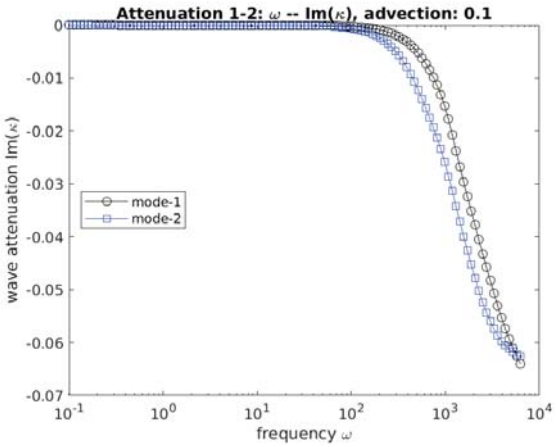

$\Im(\varkappa)$ – wave attenuation

Figure 4: Wave numbers $\varkappa_1$ (mode 1, qP1 mode) and $\varkappa_2$ (mode 2, qS1 mode). Steady advection: $\bar{w}^0 = 0$ (top figures), $\bar{w}^0 = 0.1$ (bottom figures).

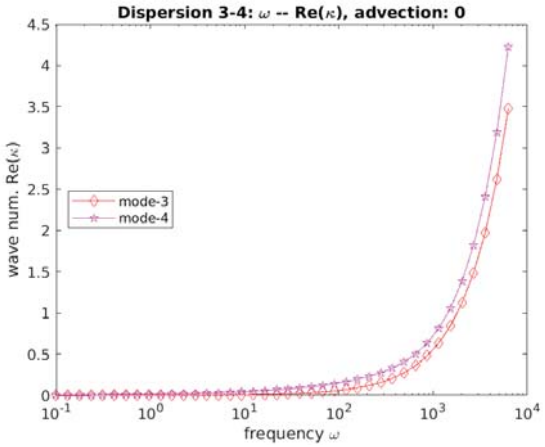

$\Re(\varkappa)$ – wave propagation

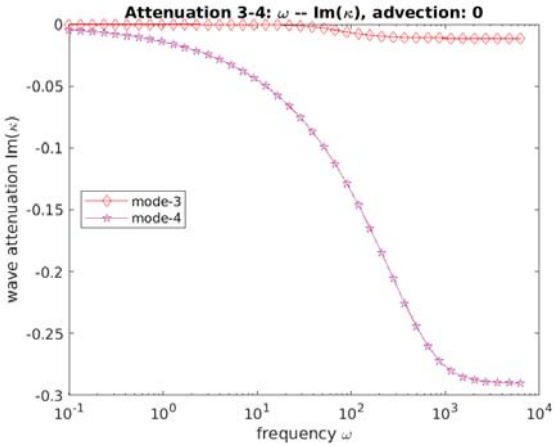

$\Im(\varkappa)$ – wave attenuation

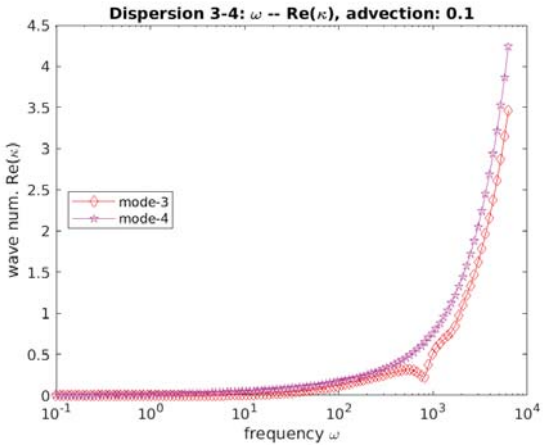

$\Re(\varkappa)$ – wave propagation

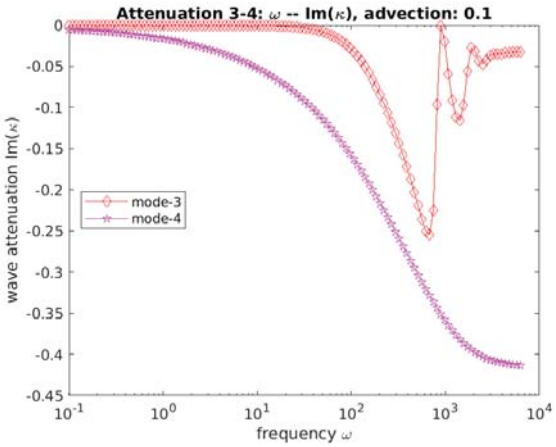

$\Im(\varkappa)$ – wave attenuation

Figure 5: Wave numbers $\varkappa_1$ (mode 3, qS2 mode) and $\varkappa_2$ (mode 4, qP2 mode). Steady advection: $\bar{w}^0 = 0$ (top figures), $\bar{w}^0 = 0.1$ (bottom figures).

5 Numerical illustrations

We shall illustrate the wave dispersion using a 3D geometry shown in Fig. 1, representing the periodic elastic scaffolds saturated by viscous fluid. Acoustic waves propagating in an inviscid fluid saturating this particular structure, but considered as rigid, were analyzed in [7, 8]. In Fig. 1, right, the elastic skeleton Y_s is indicated by the red color, while the flow streamlines of the advection flow $\bar{\boldsymbol{w}}$ are depicted in the fluid domain Y_f. Note that the mean velocity $\bar{w}^0 = 0.1$ m/s represents the microscopic advection field $\bar{\boldsymbol{w}}(y)$ defined in Y_f, such that $\bar{\boldsymbol{w}}^0 = \boldsymbol{\nu}\bar{w}^0 = \fint_{Y_f} \bar{\boldsymbol{w}}$ is the mean advection vector with $\bar{w}^0 = |\bar{\boldsymbol{w}}^0|$.

We aim to demonstrate the influence of the permanent fluid flow given by the macroscopic velocity $\bar{\boldsymbol{w}}^0$ on the wave dispersion. For this, compute the permeability, analyze the wave numbers obtained by solving the eigenvalue problem (28) which yiled phase velocities and attenuations of the four propagating modes. We consider two values of the advections velocity: a) $\bar{w}^0 = 0$ m/s (zero advection), b) $\bar{w}^0 = 0.1$ m/s, whereby the overall flow direction is $\boldsymbol{\nu} = \boldsymbol{e}^1 = [1,0,0]^T$. The incident wave direction $\boldsymbol{n} = \frac{1}{\sqrt{2}}[1,1,0]^T$ is not aligned with the permanent flow direction $\boldsymbol{\nu}$. The dimensions of the periodic cell shown in Fig. 1 (right) were 7.5×10^{-4} m (x_1 axis), 6.5×10^{-4} m (x_2 axis), 2.75×10^{-4} m (x_3 axis), with the fibre diameters 2×10^{-4} m. The solid fibres domain had the Al_2O_3 material parameters ($E = 300$ GPa, $\nu = 0.27$, and $\rho = 3900$ kg/m^3) while the fluid domain was filled with water ($\mu = 1.02 \times 10^{-3}$ Pa·s, $k_f = 2.25$ GPa, and $\rho_0 = 1000$ kg/m^3).

In response to the varying frequency ω, we compute eigenvalues of the dynamic permeability tensors, *i.e.* $\widehat{\boldsymbol{\mathcal{K}}}(\omega)$ and its approximation $\widetilde{\boldsymbol{\mathcal{K}}}(\omega)$, see Section 3.3. To characterize the wave propagation in such porous media, for a given direction $\boldsymbol{n}$, the classical dispersion curves $\omega \mapsto \varkappa$ are computed which yield phase velocities $\omega \mapsto c(\varkappa)$, where $c = \omega/\Re\varkappa$. It is worth noting, that the four modes can be classified as the quasi-pressure and quasi-pressure modes. For this, however, computing the projections of the complex polarization vectors $\boldsymbol{u}$ to $\boldsymbol{n}$ may yield ambiguous interpretations. Therefore, we prefer to use mode indices 1,2,3, and 4 which are assigned according to the speed of sound ordering, *i.e.* $c_1 \geq c_2 \geq c_3 \geq c_4$. Obviously, on one hand, mode switching may appear, so that this classification is not universally relevant. On the other hand, there is a correlation between prevailing model polarization and the sound speed value. In our example, modes 1 and 4 and the fast (qP1) and the slow (qP2) modes, whereas modes 2,3 describe the qS modes.

To illustrate the dynamic permeability and the advection phenomenon influence, the eigenvalues of the dynamic permeability tensors are displayed in Fig. 2; there the curves labelled by $h1, h2, h3$ represent the eigenvalues of $\widehat{\boldsymbol{\mathcal{K}}}(\omega)$ given by $(13)_1$ as the result of the homogenization of problem (2). The curves labelled by $a1, a2, a3$ are the eigenvalues of the Biot's visco-dynamic operator approximation determined using the static permeability $\boldsymbol{K} = \widehat{\boldsymbol{\mathcal{K}}}(0)$ and the isotropic tensor $\boldsymbol{\rho}$ with the tortuosity $a_\tau = 1$. The influence of the steady advection velocity $\bar{\boldsymbol{w}}^0$ is manifested both in the eigenvalue magnitudes and in differences between the eigenvalues 1, 2 for the nonzero velocity. The components of the tensors $\widehat{\boldsymbol{\mathcal{G}}}(\omega)$ are shown in Fig. 3. Since $\widehat{\boldsymbol{\mathcal{G}}}(\omega) \equiv 0$ for $\bar{w}^0 = 0.0$, only the curves for $\bar{w}^0 = 0.1$ are depicted.

The dispersion curves are $\omega \mapsto \Re(\varkappa)$ and attenuation $\omega \mapsto \Im(\varkappa)$ curves are presented in Fig. 4 (modes 1-2) and Fig. 5 (modes 3-4). The flow advection influences more the attenuation properties expressed by $\Im(\varkappa)$, rather than the wave propagation speed corresponding to $\Re(\varkappa)$. This phenomenon is even more pronounced when the phase velocities $\omega/\Re(\varkappa_k)$ of the four modes are inspected in Fig. 6. Namely the oscillations of the shear mode $qS2$ in the interval $500 \div 1500$ Hz induced by the advection are remarkable.

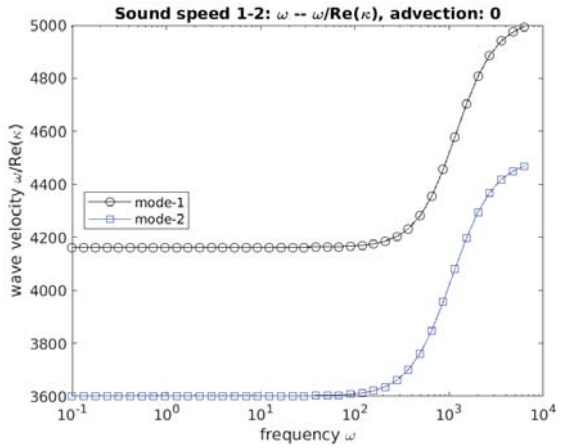

phase velocity $c_{1,2}$ (modes 1,2) for $\bar{w}^0 = 0$

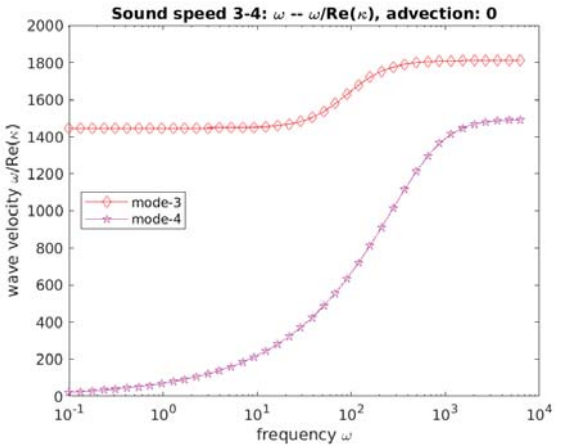

phase velocity $c_{3,4}$ (modes 3,4) for $\bar{w}^0 = 0$

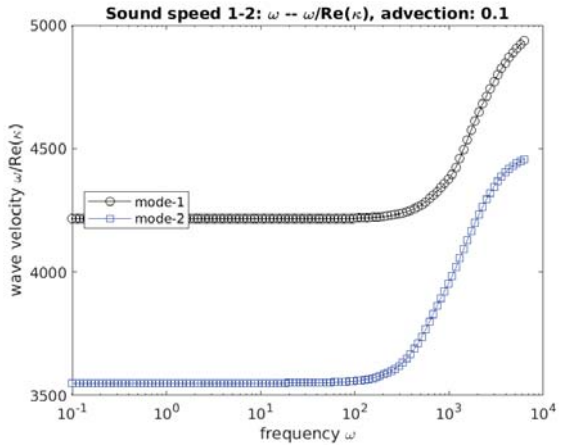

phase velocity $c_{1,2}$ (modes 1,2) for $\bar{w}^0 = 0.1$

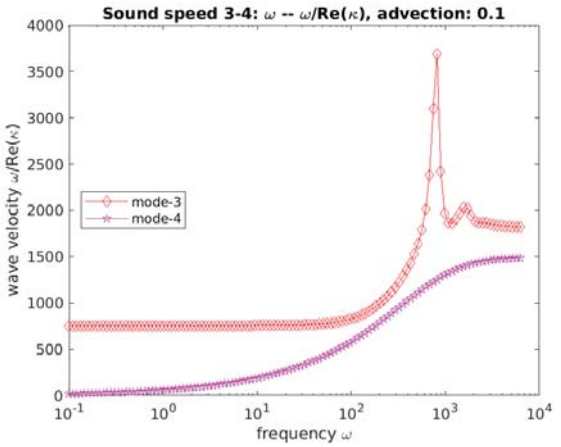

phase velocity $c_{3,4}$ (modes 3,4) for $\bar{w}^0 = 0.1$

Figure 6: Phase velocity $c_k = \omega/\Re(\varkappa_k)$, $k = 1, \ldots, 4$ of the compressional qP1 and qP2 modes (labelled by indeces 1 and 4, respectively), and the shear modes qS1, qS2 (labelled by indeces 2 and 3, respectively). Steady advection: $\bar{w}^0 = 0$ (top figures), $\bar{w}^0 = 0.1$ (bottom figures).

6 Conclusion

In this paper, we presented the effective model of the acoustic wave propagation in a periodic poroelastic medium perfused by a viscous fluid. To respect an influence of the permanent flow component on the acoustic fields, the model was derived using the asymptotic homogenization applied to a linearized problem relying on the acoustic perturbations of all the involved fields. This approach enables to retain the advection phenomenon manifested by the macroscopic steady flow velocity $\bar{\boldsymbol{w}}^0$ in the limit homogenized model. As a consequence, a new generalized Darcy law governing the macroscopic seepage velocity of the acoustic waves is constituted by a modified dynamic permeability and another new tensor which introduces a coupling effect between macroscopic fluctuations of the seepage velocity and the skeleton velocity. Both these tensors are nonsymmetric when $\bar{\boldsymbol{w}}^0 \neq \boldsymbol{0}$ and depend on the advection associated with the permanent flow. This is a new ingredient in the model. The reported numerical example illustrates the strong influence of the advection phenomenon on the wave dispersion and namely the attenuation properties in specific frequency intervals in which possible oscillations of the dispersion curves are encountered. Further numerical results and a deeper analysis of the dispersion phenomenon influenced by the permanent flow in porous media will be reported in a forthcoming paper.

Acknowledgments This research was supported by project GACR 19-04956S of the Scientific Foundation of the Czech Republic and due to the European Regional Development Fund-Project "Application of Modern Technologies in Medicine and Industry" (No. CZ.02.1.01/0.0/0.0/17 048/0007280), and in part by project LO 1506 of the Czech Ministry of Education, Youth and Sports.

REFERENCES

[1] G. Allaire. Homogenization of the unsteady Stokes equations in porous media. In C. Bandle, J. Bemelmans, M. Chipot, M. Grüter, and J. Saint Jean Paulin, editors, *Progress in Partial Differential Equations: Calculus of Variations, Applications*, volume 296 of *Pitman Research Notes in Mathematics Series*, pages 109–123. Longman Scientific & Technical, 1992.

[2] Z. Chen, L. Lyons, and G. Qin. Derivation of the Forchheimer law via homogenization. *Transport in Porous Media*, 44:325–335, 2001.

[3] D. Cioranescu, A. Damlamian, and G. Griso. The periodic unfolding method in homogenization. *SIAM Journal on Mathematical Analysis*, 40(4):1585–1620, 2008.

[4] A. Kruisová, M. Ševčík, H. Seiner, P. Sedlák, B. Román-Manso, P. Miranzo, M. Belmonte, and M. Landa. Ultrasonic bandgaps in 3d-printed periodic ceramic microlattices. *Ultrasonics*, 82:91–100, Jan 2018.

[5] V.-H. Nguyen, E. Rohan, and S. Naili. Multiscale simulation of acoustic waves in homogenized heterogeneous porous media with low and high permeability contrasts. *International Journal of Engineering Science*, 101:92–109, 2016.

[6] A.N. Norris. On the viscodynamic operator in Biot's equations of poroelasticity. *J. Wave-Material Interaction*, 1:365–380, 1986.

[7] E. Rohan, R. Cimrman, *Wave dispersion in fluids saturating periodic scaffolds; Homogenization and Floquet-Bloch wave decomposition*, Proc. of the ICSV 2019, the 26th Int. Congr. on Sound and Vibration, Montreal, 2019.

[8] E. Rohan, R. Cimrman, Modelling wave dispersion in fluid saturating periodic scaffolds. *(submitted 2020)*.

[9] E. Rohan, S. Naili, Homogenization of the fluid-structure interaction in acoustics of porous media perfused by viscous fluid. *(submitted 2020)*.

[10] E. Rohan, V.-H. Nguyen, and S. Naili. Analysis of wave propagation in heterogeneous fluid-saturated porous media – Floquet-Bloch decomposition and homogenization approaches. *(submitted 2020)*

EURODYN 2020
XI International Conference on Structural Dynamics
M. Papadrakakis, M. Fragiadakis, C. Papadimitriou (eds.)
Athens, Greece, 23–26 November 2020

A NEW ANALYTICAL METHOD FOR FREE VIBRATION ANALYSIS OF SANDWICH BEAMS

Lhoucine BOUTAHAR[1], Zakaria IBNORACHID[1], and Khalid EL BIKRI[1]

[1] Affiliation Mohammed V University of Rabat, ENSET- Rabat, M2SM, B.P.6207, Rabat Instituts 10100, Rabat, Morocco
lhoucine.boutahar@um5s.net.ma , Ibnorachid@gmail.com and k.elbikri@um5s.net.ma

Keywords: Sandwich beam, Zig-Zag model, Analytical method.

Abstract. *This work provides a bending free vibration analysis of sandwich beams with three layered, using a proposed new analytical method based on energy approach and spectral analysis. Zig-zag displacement model is used to define the face and core layers displacements. The upper and lower layers are assumed to be Euler-Bernoulli beams, while the central layer is considered to be a Timoshenko beam. Two boundary conditions (Simply supported and clamped ends) are assumed. Assuming a harmonic motion, the governing equations of the sandwich beam are derived by applying Hamilton's principle. Two differential equations coupled in axial and transverse deformations are obtained. The present model is validated by comparing the obtained results with those available in the literature. A parametric study is done to show the effects of some parameters such as face/core thickness ratio and face/core density ratio on the natural frequencies of sandwich beams.*

1 INTRODUCTION

Sandwich structures have spread in automotive, aerospace and marine industries due to their lightness, excellent acoustic absorption and their im-pact and heat resistance. Heavy use of this type of structure in several industries required the research of new theories adapted to the study of their behavior in bending, buckling and vibrations.

Numerous of publications concerning sandwich beams, plates and shells are cited by Vinson [1] who presented characteristics and advantages of sandwich structures. Grigolyuk and Chulkov [2] provided the first hypotheses on the deformations of sandwich structures. Wang et al. [3] provided the higher-order hypotheses which include shearing of beams and plates. Zigzag hypotheses for multilayered plates were formulated by Carrera [4].

The earliest to provide the basic theory of sandwich structures were Plantema [5] and Allen [6]. Free vibration analysis of Sandwich beams has been performed by many scientists. Some references which are directly related to this work are briefly reviewed as follows. The first studies on the free vibrations of sandwich beams were carried out by Di Taranto [7] Mead and Marcus [8] using classical theory. Mead [9] developed a model which supposes that the upper and lower faces of a sandwich beam are deformed according to the theory of the Bernoulli-Euler beam, while the core deforms only in shear and shear. This model has been validated by comparing it to the different models adopted in several studies to analyze the free vibration of sandwich beams. Iaccarino et al. [10] investigated the core geometry effect on bending behavior of sandwich beam.

Solutions based on the finite elements used to analyse the vibrations of the sandwich beams are available in the Refs [11, 12]. This model based on a higher order theory using zigzag displacement field has been developed by Chakrabarti et al. [13] for static analysis of laminated soft-core sandwich beams. Sakiyama et al. [14] presented free vibration analysis of sandwich beam with both elastic and viscoelactic core for arbitrary conditions. They introduced a green function to obtain the characteristic equation which allows to computing modes and natural frequencies. It is a discrete solution to the differential equation governing the bending behavior of a sandwich beam.

Dynamic Stiffness Method (DSM) allows better results with a minimum number of elements. This has prompted scientists in recent years to use this method to study the free vibrations of sandwich beams. For example, Banerjee [15] used DSM to investigate the free vibrations of symmetrical sandwich beams. In this study, the governing motion equations are derived by ignoring mass of the nucleus with respect to those of the both faces. Howson and Zare [16] studied the vibratory behavior of the sandwich beam by taking into account the acceleration of flexion of the beam with the nucleus and ignoring the axial acceleration of the beam by deriving the equations of motion governing. They used DSM for various boundary conditions and elastic supports. Khalili et al. [17] investigated the free vibration of three-layered symmetric sandwich beam consists of sprung masses using the finite element formulation and DSM. Numerical examples are used for discussing the finite element formulation and dynamic stiffness matrix. Frostig and Baruch [18] investigated the free vibrations of sandwich beams with flexible core based on higher order theory. They presented different model for sandwich beams analysis. Amirani et al. [19] investigated the bending vibration of a sandwich beam with a core layer made in FGM. They used the Galerkin method to derive equations of motion. Natural frequencies are obtained by using the finite element analysis. A quasi-two-dimensional finite element formulation was developed by Bekuit et al [20] to analyze dynamic and static behavior of sandwich beams. The assumed model is three-layered and the longitudinal and transverse displacements are considered. In this study the formulations were independent of the flexibility of the central layer.

The main purpose of this research is to validate the new approach proposed here to analyze vibrational responses of a sandwich beam. Then, a parametric study is carried out to show the effects of some parameters such as face/core thickness ratio and face/core density ratio. First, the displacement field at face and core layers, is defined by using Zig-zag model. Then, assuming a harmonic motion, the both displacements are extended as finite series of basic functions, and kinetic and total strain energies are expressed in discretized forms. Finally, Hamilton's principle is applied to obtain the motion equations for both boundary conditions. Differential equations system is reduced to an eigenvalue problem, which is solved by the Rayleigh-Ritz formulation. Natural frequencies are therefore easy to determine.

2 GENERAL FORMULATION

2.1 Problem definition

The structure studied here is shown in Fig 1. It is a sandwich beam of length "*l*" l and width "*b*" b. "h_f" and "h_c" are the face sheet and core thickness respectively h_c. As shown in this figure, the beam deformations are considered to be in (x, z) plane.

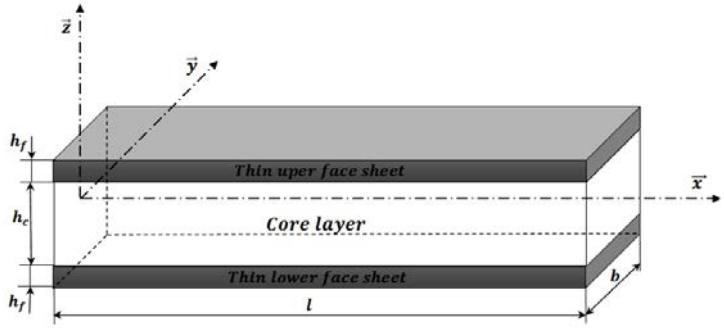

Figure 1: Geometry and coordinate system of the sandwich beam.

2.2 Displacement field

The proposal of the zig-zag model is explained by the fact that the core and sheets are made of different materials and have different thickness. This leads to a discontinuity of mechanical properties through the thickness of the beam. This does not allow to use the same theory for the core and sheets, and to treat them independently.

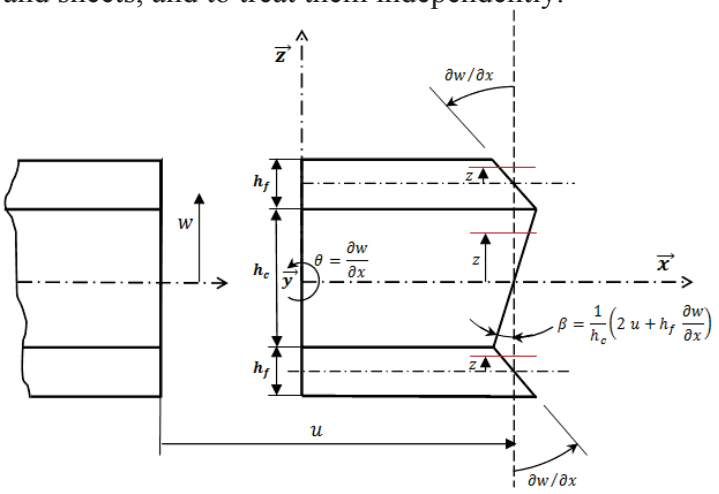

Figure 2: Geometry and coordinate system of the sandwich beam.

Motion equations of a sandwich beam elementare are derived on the basis of the following assumptions:

- Sandwich beam elementare behavior is assumed in the linear elasticity case;
- Normal deformations in z-axis direction are negligible on the core and faces $\varepsilon_z = 0$.
- No slippage and no delamination between core and sheets.
- Uper and lower thin face sheets are assumed to be deformed according to the Euler-Bernoulli beam theory, and the core is assumed to be deformed only in shear.
- Transverse displacement $w(x,t)$ is considered the same for the three layers.
- Axial displacements of the median lines of the uper and lower face sheets are $u_u(x,t)$ and $u_l(x,t)$ respectively.
- Symmetric deformation$\rightarrow u_u(x,t) = -u_l(x,t)$. $u_u(x,t) = -u_l(x,t)$ are axial displacements of the median lines of the uper and lower face sheets respectively. Therefore, $u_u = -u_l = u$

The beam displacement field is derived from the compatibility conditions for deformations.

$$U(x,t) = \begin{cases} u - z\dfrac{\partial w}{\partial x} & \textit{Uper layer} \quad -\dfrac{h_f}{2} \le z \le \dfrac{h_f}{2} \\ \left(2u + h_f \dfrac{\partial w}{\partial x}\right)\dfrac{z}{h_c} & \textit{Core layer} \quad -\dfrac{h_c}{2} \le z \le \dfrac{h_c}{2} \\ -u - z\dfrac{\partial w}{\partial x} & \textit{Lower layer} \quad -\dfrac{h_f}{2} \le z \le \dfrac{h_f}{2} \end{cases} \tag{1}$$

$$W(x,t) = w \qquad \textit{All layer} \qquad \forall\, z$$

2.3 Governing equation

To obtain the sandwich beam motion equation, Hamilton's principle Hamilton principle is applied. It is symbolically written for a period 0 to $\pi/2\omega$ as:

$$\partial \int_0^{\pi/2\omega} (T - \mathrm{U})\, dt = 0 \tag{2}$$

where, U and T are strain and kinetic energy respectively.

o Kinetic and strain energy calculation

By neglecting the axial motion, the beam kinetic energy is expressed as follows:

$$\begin{aligned} T &= \frac{1}{2}\iiint_{d\mathrm{V}} \rho \left(\left(\frac{\partial U}{\partial t}\right)^2 + \left(\frac{\partial W}{\partial t}\right)^2 \right) d\mathrm{V} = \\ &= \frac{1}{2}\iiint_{d\mathrm{V_f}} \rho_f \left[\left(\left(\frac{\partial u}{\partial t}\right) - z\left(\frac{\partial^2 w}{\partial t \partial x}\right)\right)^2 - \left(\left(\frac{\partial u}{\partial t}\right) + z\left(\frac{\partial^2 w}{\partial t \partial x}\right) + 2\left(\frac{\partial w}{\partial t}\right)^2 \right)^2 \right] d\mathrm{V_f} = \\ &+ \frac{1}{2}\iiint_{d\mathrm{Vc}} \rho_c \left[\frac{z^2}{h_c{}^2} \left(2\left(\frac{\partial u}{\partial t}\right) + h_f \left(\frac{\partial^2 w}{\partial t \partial x}\right)\right)^2 + \left(\frac{\partial w}{\partial t}\right)^2 \right] d\mathrm{V_c} = \end{aligned} \tag{3}$$

ρ_f, ρ_c are mass density of sheet-face and core respectively, with $m_f = \rho_f \mathrm{A}_f$; $m_c = \rho_c \mathrm{A}_c$.

Calculation of the integrals of Eq (3), leads to the following kinetic energy expression:

$$T=\frac{1}{2}\int_0^l\left(2m_f\left(\frac{\partial u}{\partial t}\right)^2+\left(2m_f+m_c\right)\left(\frac{\partial w}{\partial t}\right)^2+\frac{m_c}{12}\left(2\left(\frac{\partial u}{\partial t}\right)+h_f\left(\frac{\partial^2 w}{\partial t\partial x}\right)\right)^2\right)dx \tag{4}$$

Taking into account the previous assumptions, the beam strain energy is given by:

$$\mathrm{U}=\frac{1}{2}\left[\iiint_{d\mathrm{V}_f}\sigma_x\varepsilon_x d\mathrm{V}_f+\iiint_{d\mathrm{V}_c}\tau_{xz}\gamma_{xz}d\mathrm{V}_c+\iiint_{d\mathrm{V}_f}\sigma_x\varepsilon_x d\mathrm{V}_f\right] \tag{5}$$

$$\sigma_x=E\varepsilon_x \quad ; \quad \tau_{xz}=G\gamma_{xz} \tag{6}$$

$$\mathrm{U}=\frac{1}{2}\left[\iiint_{d\mathrm{V}_f}E_f\varepsilon_x^2 d\mathrm{V}_f+\iiint_{d\mathrm{V}_c}G_c\gamma_{xz}^2 d\mathrm{V}_c+\iiint_{d\mathrm{V}_f}E_f\varepsilon_x^2 d\mathrm{V}_f\right] \tag{7}$$

The integrals in the Eq. (7) are calculated by substituting the values of the strains, to obtain the following expression of the strain-energy:

$$\mathrm{U}=\frac{1}{2}\int_0^l\left(2E_fA_f\left(\frac{\partial u}{\partial x}\right)^2+2E_fB_f\left(\frac{\partial^2 w}{\partial x^2}\right)^2+G_cA_c\left[\frac{4}{h_c}u^2+\left(\left(1+\frac{h_f}{h_c}\right)\frac{\partial w}{\partial x}\right)^2+\frac{4}{h_c}\left(1+\frac{h_f}{h_c}\right)u\frac{\partial w}{\partial x}\right]\right)dx \tag{8}$$

$$d\mathrm{V}_f=\mathrm{A}_f\,dx \;;\; \mathrm{A}_f=bdz \tag{9}$$

$$\left(A_f,B_f\right)=\frac{1}{2}\int_{-h_f/2}^{+h_f/2}\left(z,z^2\right)bdz \quad ; \quad A_c=\frac{1}{2}\int_{-h_c/2}^{+h_c/2}d\mathrm{A}_c \tag{10}$$

- **Kinetic and Strain energy discretization.**

Assumptions:

- The motion is assumed to be harmonic;
- The space-functions and time are assumed to be separable.

With these assumptions, the transverse and in-plane displacements can be written respectively as:

$$\begin{cases}w(x,t)=w(x)\cos(\omega t)\\ u(x,t)=u(x)\cos^2(\omega t)\end{cases} \tag{11}$$

Space-functions $w(x)$ and $u(x)$ are expanded in the form of finite series of n basic functions $w_i(x)$ and $u_i(x)$ respectively as:

$$\begin{cases}w(x)=a_iw_i & i=1,2,3.....p\\ u(x)=b_iu_i & i=1,2,3.....q\end{cases} \tag{12}$$

It can be demonstrated by a convergence study of spectral expansions used for this model that $p=q=6$ are sufficient to obtain precise results concerning frequencies and stresses.

Discretization of the strain and kinetic energy expressions is made by substituting the expression given in Eqs. (11) into Eqs. (4) and (8), and rearranging. This leads to the following expressions:

$$\mathrm{U}=\frac{1}{2}\left[a_ia_jK_{ij}^w\cos^2(\omega t)+b_ib_jK_{ij}^u\cos^4(\omega t)+a_ib_jC_{ij}^{uw}\cos^3(\omega t)\right] \tag{13}$$

$$T=\frac{1}{2}\left[a_ia_j\omega^2M_{ij}^w\sin^2(\omega t)M_{ij}^w+b_ib_j\omega^2M_{ij}^u\sin^2(\omega t)+a_ib_j\omega^2M_{ij}^{uw}\sin(\omega t)\sin(2\omega t)\right] \tag{14}$$

where,

K_{ij}^u, K_{ij}^w : Rigidity tensors associated with u and w respectively.

M_{ij}^u, M_{ij}^w : Mass tensors associated with u and w respectively.

C_{ij}^{uw}, M_{ij}^{uw} : Coupling tensors.

$$
\begin{aligned}
K_{ij}^{w} &= \int_0^l \left[G_c A_c \left(1+\frac{h_f}{h_c}\right)^2 \frac{\partial w_i}{\partial x}\frac{\partial w_j}{\partial x} + 2E_f B_f \frac{\partial^2 w_i}{\partial x^2}\frac{\partial^2 w_j}{\partial x^2} \right] dx \\
K_{ij}^{u} &= \int_0^l \left[\frac{4G_c A_c}{hc^2} u_i u_j + 2E_f A_f \frac{\partial u_i}{\partial x}\frac{\partial u_j}{\partial x} \right] dx \\
C_{ij}^{uw} &= 4G_c \frac{A_c}{h_c}\left(1+\frac{h_f}{h_c}\right)\int_0^l u_i \frac{\partial w_j}{\partial x} dx \\
M_{ij}^{w} &= \int_0^l \left(2m_f + m_c\right) w_i w_j + \frac{m_c h_f^2}{12}\frac{\partial w_i}{\partial x}\frac{\partial w_j}{\partial x} dx \\
M_{ij}^{u} &= \int_0^l u_i u_j dx, \quad M_{ij}^{uw} = \frac{m_c h_f}{3}\int_0^l u_i \frac{\partial w_j}{\partial x} dx
\end{aligned}
\tag{15}
$$

Replacing U and T by their discretized expressions and integrating the time functions with respect to a_i's and b_i's, leads to the following coupled system of linear algebraic equations:

$$
\begin{cases}
2a_i K_{ir}^{w} + \dfrac{8}{3\pi} b_i K_{ir}^{uw} - 2\omega^2 \left(a_i M_{ir}^{w} + \dfrac{4}{3\pi} b_i M_{ir}^{uw} \right) = 0 \ , \qquad r = 1.....p \\
\dfrac{3}{2} b_i K_{is}^{u} + \dfrac{8}{3\pi} a_i K_{is}^{uw} - 2\omega^2 \left(b_i M_{is}^{u} + \dfrac{4}{3\pi} a_i M_{is}^{uw} \right) = 0 \ , \qquad s = 1.....q
\end{cases}
\tag{16}
$$

To simplify the analysis and the numerical treatment of the linear equations system, non-dimensional formulation has been considered by putting the spatial displacement functions as:

$$
x^* = x/l, \quad w_i(x) = H w_i^*(x^*), \quad u_i(x) = \lambda H u_i^*(x^*), \quad \lambda = H/l \tag{17}
$$

Eqs (16) can be written in a dimensionless form as:

$$
\begin{cases}
2a_i K_{ir}^{w*} + \dfrac{8}{3\pi} b_i K_{ir}^{uw*} - 2\omega^{*2} \left(a_i M_{ir}^{w*} + \dfrac{4}{3\pi} b_i M_{ir}^{u*} \right) = 0 \quad (1) \ , \quad r = 1.....p \\
\dfrac{3}{2} b_i K_{is}^{u*} - 2\lambda^2 \omega^2 b_i M_{is}^{u*} + \dfrac{8}{3\pi} a_i \left(K_{is}^{uw*} - \omega^{*2} M_{is}^{uw*} \right) = 0 \quad (2) \ , \quad s = 1.....q
\end{cases}
\tag{18}
$$

Axial inertia designated by the term λ^2 and coupling mass tensor M_{ir}^{uw*} can be neglected. The second set of Eq (18) can be then solved for b_i's leading to:

$$
b_i = a_j D_{ji}^*, \qquad D_{ij}^* = -\frac{16}{9\pi} K_{jl}^{u*-1} K_{il}^{uw*} \tag{19}
$$

And, $K_{ij}^{w*}, K_{ij}^{u*}, M_{ij}^{w*}, M_{ij}^{u*}, K_{ij}^{uw*}$ are non-dimensional tensors expressed as:

$$
\begin{aligned}
K_{ij}^{w*} &= \int_0^1 \alpha \frac{\partial w_i^*}{\partial x^*}\frac{\partial w_j^*}{\partial x^*} + \frac{\partial^2 w_i^*}{\partial x^{*2}}\frac{\partial^2 w_j^*}{\partial x^{*2}} dx^*, \qquad K_{ij}^{u*} = \gamma \int_0^1 \lambda u_i^* u_j^* + \frac{\partial u_i^*}{\partial x^*}\frac{\partial u_j^*}{\partial x^*} dx^* \\
M_{ij}^{w*} &= \int_0^1 w_i^* w_j^* + \eta \frac{\partial w_i^*}{\partial x^*}\frac{\partial w_j^*}{\partial x^*} dx^*, \ M_{ij}^{u*} = \int_0^1 u_i^* u_j^* dx^*, \ K_{ij}^{uw*} = \zeta \int_0^1 u_i^* \frac{\partial w_j^*}{\partial x^*} dx^*
\end{aligned}
\tag{20}
$$

$$
\begin{aligned}
\alpha &= \frac{G_c A_c l^2}{2E_f B_f}\left(1+\frac{h_f}{h_c}\right)^2, \ \gamma = \frac{A_f}{B_f} H^2, \ \lambda = 2\left(\frac{G_c A_c}{E_f A_f}\right)\left(\frac{l}{h_c}\right)^2 \\
\eta &= \frac{m_c}{12\left(m_c + 2m_f\right)}\left(\frac{h_f}{l}\right)^2, \ \zeta = 2\left(\frac{G_c A_c H l^2}{E_f B_f h_c}\right)\left(1+\frac{h_f}{h_c}\right)
\end{aligned}
\tag{21}
$$

Replacing expressions in Eq (19) into the first set of Eqs (16) leads to a decoupled set of linear algebraic equation in terms of a_i 's coefficients only:

$$a_i\left(K_{ir}^{w*}+\frac{4}{3\pi}D_{il}^{*}K_{lr}^{uw*}\right)-a_i\omega^{*2}M_{ir}^{w*}=0 \tag{22}$$

The linear algebraic Eq (22) also called the amplitude equation, can be written in the matrix form as:

$$\left[K^*\right]\{A\}-\omega^{*2}\left[M^*\right]\{A\}=\{0\} \tag{23}$$

where,

$\left[M^*\right]$ and $\left[K^*\right]$ are the dimensionless mass and stiffness matrixes respectively.

$\{A\}=\left[a_1,a_2,a_3,.....a_p\right]^T$ is the column matrix of coefficients a_i

ω^* is dimensionless natural frequency of beam defined as:

$$\omega^{*2}=\frac{\left(2m_f+m_c\right)l^4}{2E_fB_f}\omega^2 \tag{24}$$

By assuming harmonic variation, the transverse $w_i\left(x^*\right)$ and in-plane $u_i\left(x^*\right)$ basic functions are expressed as follows:

- For a simply supported sandwich beam

$$\begin{cases}w_i\left(x^*\right)=\sin\left(p_i\pi x^*\right)\\ u_i\left(x^*\right)=\cos\left(q_i\pi x^*\right)\end{cases},\quad i=1,2,3,.....,6 \tag{25}$$

- For a sandwich beam with clamped ends

$$\begin{cases}w_i\left(x^*\right)=\dfrac{ch(p_ix^*)-\cos(p_ix^*)}{ch(p_i)-\cos(p_i)}-\dfrac{sh(p_ix^*)-\sin(p_ix^*)}{sh(p_i)-\sin(p_i)}\\ u_i\left(x^*\right)=\sin\left(q_i\pi x^*\right)\end{cases},\quad i=1,2,3,.....,6 \tag{26}$$

The first six modes of transversal displacements are plotted in figure 3 for simply supported sandwich beam and sandwich beam with clamped ends.

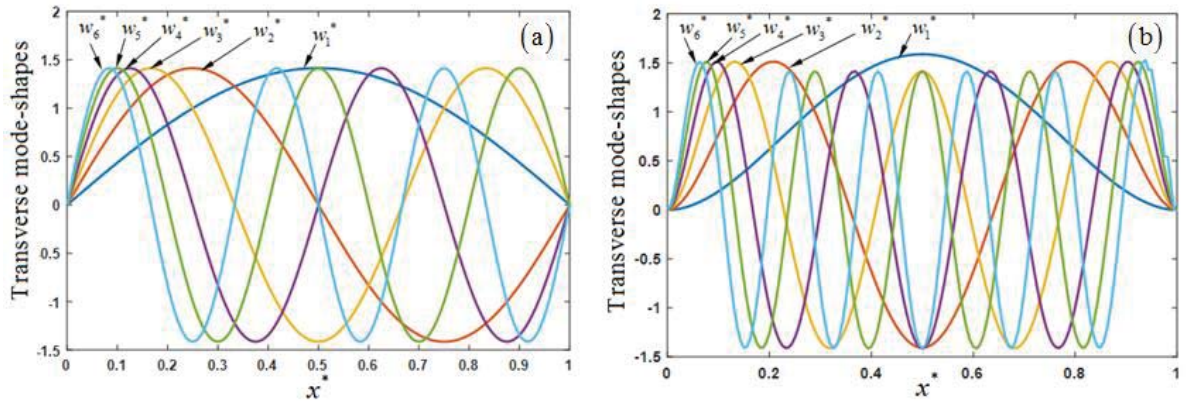

Figure 3: The first six transverse basic functions of: (a) Simply supported sandwich beam, (b) Sandwich beam with clamped ends

3 RESULTS AND ANALYSIS

Validation of the approach used in this work and the impact of some parameters such as density and thickness for various boundary conditions on sandwich beam natural frequency, are presented in this paragraph. To validate the present theory, two models are considered: Sakiyama et al. [6] and Howson and Zare [8]. The characteristics of the sandwich beams used here are shown in Table 1.

	E_f (MPa)	G_c (MPa)	ρ_f (Kgm^{-3})	ρ_c (Kgm^{-3})	h_f (mm)	h_c (mm)	b (mm)	L (mm)
Sandwich beam N°1	68900	82.68	2680	32.8	0.4572	12.7	25.4	914.4
Sandwich beam N°2	68900	68.9	2687.3	119.7	0.4062	6.35	25.4	1218.7

Table 1: Characteristics of sandwich beam.

Results obtained here in the first case, concerning three natural frequencies are summarized in Table 2. These results are compared with those found by the authors [8, 6], who used different methods for simply supported sandwich beam N°1. Howson and Zare [8] studied flexural vibration behavior of sandwich beams by applying DSM (Dynamic stiffness Method), while Sakiyama et al. [6] used the Green's function as solution to analyse free vibration of sandwich beams.

It can be confirmed from this table, that the obtained results are in good agreement with the results of DSM used by Howson and Zare [8], with an acceptable accuracy.

Methods	Ω_1 (Hz)	Ω_2 (Hz)	Ω_3 (Hz)
Green's function [14]	56,159	215,820	457,220
DSM [16]	57,135	219,585	465,172
Present method	57,132	219,522	465,015

Table 2: Natural frequencies of simply supported sandwich beam.

Results obtained in the second case concerning three natural frequencies of sandwich beams N°2 with clamped ends are summarized in Table 3. These results are compared with those found by Sakiyama et al. [6] and Howson and Zare [8], who used different methods to derive motion equations. Results of these works, here again, agree perfectly with the obtained results in this study. The little differences in the results are due to approximations made and the assumptions assumed here.

Methods	Ω_1 (Hz)	Ω_2 (Hz)	Ω_3 (Hz)
Green's function [14]	33.5630	90.3640	172.0700
DSM [16]	34.5965	93.1000	177.1550
Present method	34.6055	93.1102	177.1561

Table 3: Natural frequencies of sandwich beam with clamped ends.

The plot in Fig.4 represented fundamental natural frequency variation versus thickness ratio (h_f /h_c) for two boundary conditions. This figure shows that, increase the thickness ratio leads to an increase of fundamental natural frequency in the simply supported sandwich

beams case, whereas in the case of sandwich beam with fixed ends, this frequency increases at first then decreases gradually.

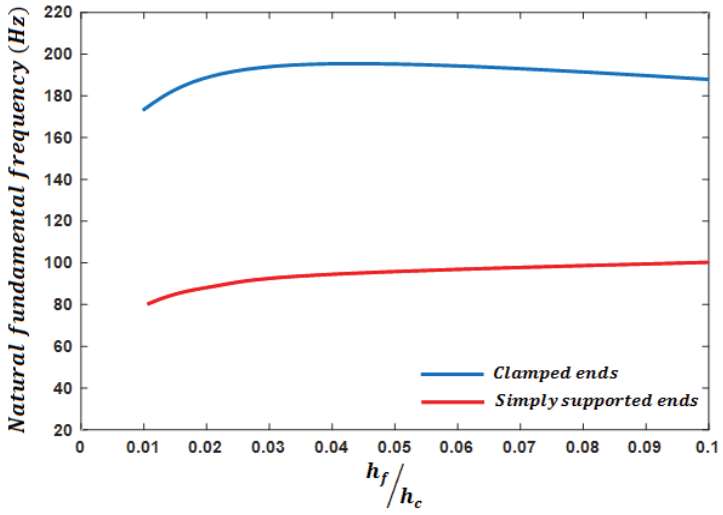

Figure 4: Effect of the thickness ratio on fundamental frequency of a sandwich beam.

The fundamental natural frequency variation versus core/face density ratio (ρ_c / ρ_f) is plotted in Fig.5. The smallest value of density ratio is corresponded the low core density. As shown in this figure, the increase of density ratio leads to a decrease of fundamental natural frequencies, whatever the boundary conditions.

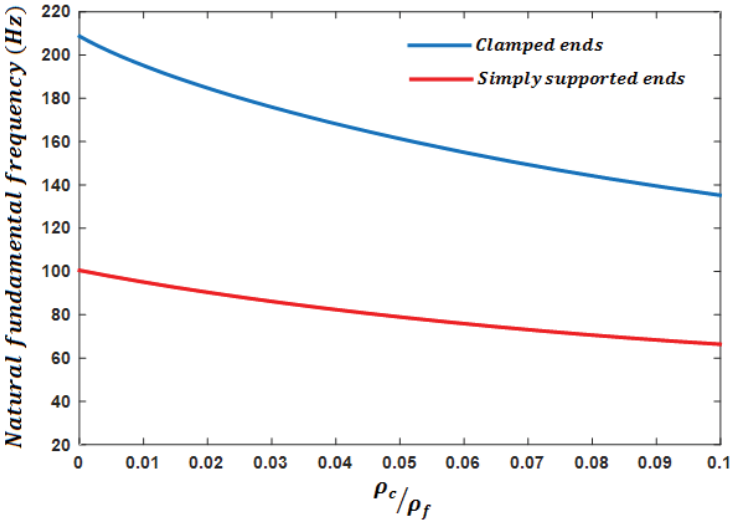

Figure 5: Effect of the density ratio on fundamental natural frequency of a sandwich beam.

4 CONCLUSION

The subject of this work is studying and analysing the bending behavior of a sandwich beam by a model based on energy approach and a spectral analysis. Various boundary conditions are assumed. Motion equations are derived by applying Hamilton's principle. Two differential equations coupled in axial and transverse deformations are obtained. These equations are decoupled by neglecting the axial inertia of the beam, and a single differential equation is formed. Natural frequencies are then computed and validated. The results obtained in present work using the new method are in good agreement with obtained results by the published theories.

The effects of thickness and density of sandwich beam are analyzed by a parametric study. This revealed that regardless of boundary conditions, the natural frequencies of the sandwich beam increase with the increase of the face/core thickness ratio, but it decrease when the core/face density ratio increases.

REFERENCES

[1] Vinson J.R. "Sandwich Structures: Past, Present, and Future". Sandwich Structures 7: Advancing with Sandwich Structures and Materials 2005 : 3-12

[2] E.I. Grigolyuk, P.P. Chulkov. "Stability and vibrations of three layers shells". Moscow, Mashinostroene (in Russian), 1973.

[3] 3. C.M. Wang, J.N. Reddy, K.H. Lee. "Shear deformable beams and plates". Elsevier: Amsterdam, Laussane, New York, Oxford, Shannon, Singapore, Tokyo, 2000.

[4] E. Carrera. "Historical review of Zig-Zag theories for multilayered plates and shells". Applied Mechanics Reviews, 56, 3, 287–308, 2003.

[5] F.J. Plantema. "Sandwich construction". John Wiley & Sons: New York, London, Sydney, 1966.

[6] H.G. Allen. "Analysis and design of structural sandwich panels". Pergamon Press: Oxford, London, Edinburgh, New York, Toronto, Sydney, Paris, Braunschweig, 1969.

[7] Di Taranto RA. "Theory of vibratory bending for elastic and viscoelastic layered finite length beams". J Appl Mech 1965; 87:1–6.

[8] Mead DJ, Markus S."The forced vibration of a three-layer damped sandwich beam with arbitrary boundary condition". J Sound Vib 1969; 10:63–75.

[9] Mead DJ. "A comparison of some equations for the flexural vibration of damped sandwich beams". J Sound Vib 1982; 83:63–77.

[10] P. Iaccarino, C. Leone, M. Durante, G. Caprino, A. Lamboglia. "Effect of a thin soft core on the bending behavior of a sandwich with thick CFRP facings". Journal of Sandwich Structures and Materials, 13, 2, 159–175, 2010.

[11] Ahmed KM. "Free vibration of curved sandwich beams by the method of finite elements". J Sound Vib 1971; 18:61–74.

[12] Ahmed KM. "Dynamic analysis of sandwich beams". J Sound Vib 1972; 21: 263–76.

[13] A. Chakrabarti, H.D. Chalak, Mohd. Ashraf Iqbal, Abdul Hamid Sheikh. "A new FE model based on higher order zigzag theory for the analysis of laminated sandwich beam with soft core". Composite Structures, 93, 2, 271–279, 2011.

[14] Sakiyama T, Matsuda H, Morita C. "Free vibration analysis of sandwich beam with elastic or viscoelastic core by applying the discrete Green function". J Sound Vib 1996; 191:189–206.

[15] Banerjee JR. "Free vibration of sandwich beams using the dynamic stiffness method". J Comput Struct 2003; 81:1915–22.

[16] Howson WP, Zare A. "Exact dynamic stiffness matrix for flexural vibration of three-layered sandwich beams". J Sound Vib 2005; 282:753–67.

[17] Khalili. “Free vibration analysis of sandwich beam carrying sprung masses”. Int. J. Mech. Sci. 52 (2010) 1620-1633.

[18] Frosting Y, Baruch M. “Free vibration of sandwich beams with a transversely flexible core: a hight order approach”. J Sound Vib 1994; 176:195–208.

[19] M. Chehel Amirani. “Free vibration analysis of sandwich beam with FG core using the element free Galerkin method”. Composite Structures 90 (2009) 373–379.

[20] J.-J.R.B. Bekuit, D.C.D. Oguamanam, O. Damisa. “Aquasi-2D finite element formulation for the analysis of sandwich beams”. Finite Elements in Analysis and Design 43 (2007) 1099– 1107.

EURODYN 2020
XI International Conference on Structural Dynamics
M. Papadrakakis, M. Fragiadakis, C. Papadimitriou (eds.)
Athens, Greece, 23–26 November 2020

HOMOGENIZED MODEL OF UNCONVENTIONAL DYNAMIC BEHAVIOUR OF PERIODIC PLATES AND EXPERIMENTAL COMPARISONS

P. Fossat[1], C. Boutin[2], and M. Ichchou[1]

[1]École Centrale de Lyon, LTDS, UMR-CNRS 5513,
36 Avenue Guy de Collongue 69134 Ecully, France e-mail: pascal.fossat,
mohamed.ichchou@ec-lyon.fr

[2] École Nationale des Travaux Publics de l'État, Université de Lyon
LTDS/LGCB UMR-CNRS 5513, Rue Maurice Audin, 69518, Vaulx-en-Velin, France
e-mail: claude.boutin@entpe.fr

Keywords: asymptotic homogenization, ribbed plates, inner resonance media, Inhomogeneous Wave Correlation

Abstract. *This paper deals with the dynamic behavior of periodic orthogonally ribbed plates. Theoretical results describing the out-of-plane behavior of cellular plates involving inner resonance phenomena are derived using the periodic homogenization approach. These theoretical results are successfully compared to Wave Finite Element computations together with a mock-up of orthogonally ribbed plate with aluminium stiffeners and polycarbonate plate. The good agreement between analytical predictions and experimental measurements over the whole frequency range in terms of frequency and amplitude confirms the ability of the homogenized model to capture the locally resonant nature of the plate.*

1 INTRODUCTION

The classical plates models are well suited for homogeneous or moderately heterogeneous plates. However, difficulties appear when attempting to extend classical theories to composite structures with significantly contrasted properties. When considering ribbed plates with stiffeners of similar flexural rigidity than that of the plate, then the global behavior is that of a classical but anisotropic plate. If the stiffeners are much stiffer than the plate, the global behavior will be that of a beam lattice. In-between situations with specific beam grid/plate coupled behavior should exist. The present paper focuses on this specific situation in dynamic regime, in which the stiffener/plate contrasts induces inner resonance phenomena.

In dynamics, numerical approaches as finite elements method formulated in the framework of Floquet-Bloch theory has been developed to determine the wave dispersion of periodic media. As for ribbed plates, such a WFEM (Wave Finite Element Method) [14] has been used to determine, the free-wave propagation in plate stiffened by a grid of orthogonal beams. This method can be improved with modal reduction techniques as demonstrated by [8] in the case of orthogonally ribbed plates. Advanced numerical procedure have also been applied to the identification of propagation parameters in composite structures from experimental measurements. For example, the IWC (Inhomogeneous Wave Correlation) method introduced by [4] allows extracting the wavenumber from the experimental data and yields the empirical dispersion curve(s), as presented in [11] for several applications to ribbed panels and plates. These different numerical approaches provide accurate numerical results provided that he micro-structure is given, but fail to identify the underlying model that arises from the physics involved within the cell.

Among the theoretical approaches, the homogenization of periodic media [15, 3] is a rigorous asymptotic method for up-scaling the physics at micro-scale into a macroscopic model. This method has been extensively applied to develop advanced plate theories, and one may refer to [13, 12] for reviews on composite plates, structured plates, corrugated plates, heterogeneous shells, etc. Recently, the asymptotic approach have been applied to highly contrasted mono directionally ribbed plates [9]. This study explains theoretically that the unconventional behavior with singular dispersion and possible band-gap are straightforwardly related to inner resonance phenomena. The latter corresponds to situations where dynamic regimes co-exist at both the micro-scale of the period and the macro-scale of the structure [1, 2] that may results into negative effective mass over bands centered around the inner resonance frequencies [1, 5, 7].

The purpose of the present work is to extend the previous analysis of unidirectional ribbed plate [9] to periodic bidirectional ribbed plates.The main outcomes of this study are an analytical formulation of the equivalent model of orthogonally ribbed plates involving inner resonance phenomena, and the experimental validation of these new theoretical results.

The paper is structured as follows. The Section 2 focuses on the flexural behavior of 2D-ribbed plates. The out-of-plane model of beam grids accounting for local bending and torsion is first established through the method of asymptotic homogenization of periodic discrete media, initiated by [17], and applied to in-plane behavior in [6], [7]. Then, the coupling between the beam grid and the internal plates is detailed. From this, the equivalent plate model is established, and the unconventional features of the flexural wave dispersion is presented. Section 3 is devoted to the numerical and experimental validations of the homogenized model. The theoretical results are successfully compared to numerical calculations conducted using WFEM. Finally, the experiments performed on a prototype of ribbed plate evidences the ability of the homogenized model to describe their complex dynamic behavior.

2 Homogenization of the flexural behavior of 2D-ribbed plates

2.1 Investigated structures

The periodic orthogonally ribbed plate (hereafter called 2D-ribbed plates for simplicity and denoted $\mathcal{RP}$) under study is depicted in Fig. 1. It comprises identical "micro"-plate elements (denoted $\mathcal{P}$) connected to an orthogonal beam grid (denoted $\mathcal{G}$), both made of isotropic elastic materials. The beams of the grid are assumed significantly stiffer than the "micro"-plate (in a sense precised latter on). We focus on the dynamic range such that the size of the cell (or the width of $\mathcal{P}$) is small in regards to the wavelength in the beam grid. The referential frame of unit vectors $(\underline{e}_x, \underline{e}_y, \underline{e}_z)$ is such that $\underline{e}_x$ and $\underline{e}_y$ are the in-plane vectors along the orthogonal ribs, while $\underline{e}_z$ is the out-of-plane vector.

The two families of perpendicular beams (or stiffeners) define the ortho-beam grid $\mathcal{G}$. The stiffeners oriented along x (resp. y) are identical and spaced periodically by the length ℓ_y (resp. ℓ_x). However, the two families may differ from one another. These stiffeners intersect on perfectly stiff and mass-less nodes. This defines the rectangular periodic mesh, which is constituted by the portions of the two orthogonal stiffeners that join at a node. The period of surface $S = \ell_x \ell_y$ is characterized by the length $\ell = \sqrt{\ell_x \ell_y}$, and $O(\ell_x) = O(\ell_y) = \ell$. We will also use in the sequel the dimensionless quantities $\ell_x^\star = \ell_x/\ell$; $\ell_y^\star = \ell_y/\ell$ so that $\ell_x^\star \ell_y^\star = 1$ and $O(\ell_x^\star) = O(\ell_y^\star) = O(1)$.

Each segment of stiffeners between two consecutive nodes is modeled as an Euler-Bernoulli

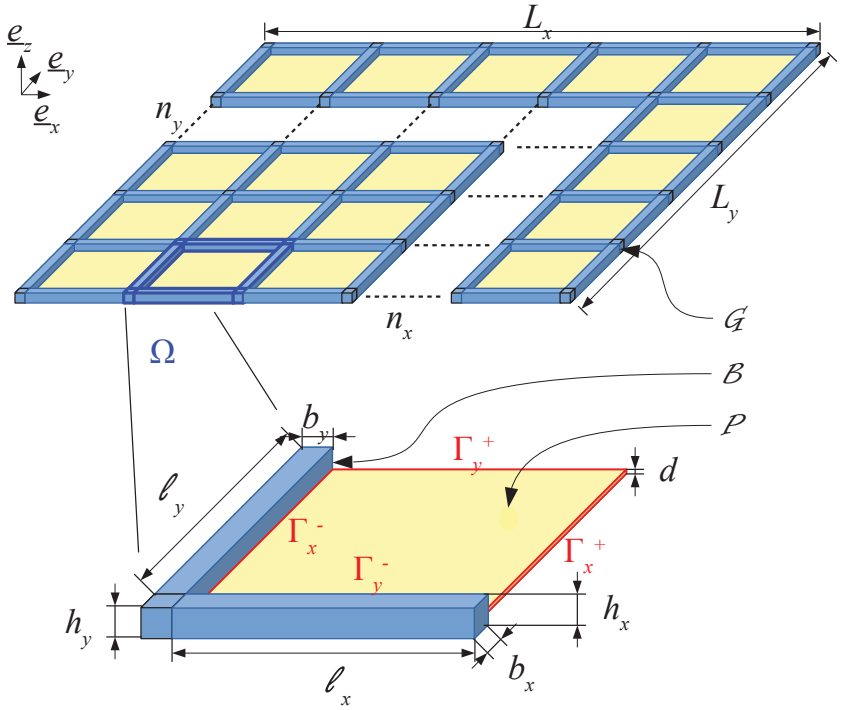

Figure 1: Orthogonally ribbed plate $\mathcal{RP}$ under study with notations associated with macro-beams constituting the beam grid $\mathcal{G}$, and focus on the unit cell Ω made of micro-beams $\mathcal{B}$ and internal micro-$\mathcal{P}$-plate

"micro"-beam (denoted $\mathcal{B}_x$, $\mathcal{B}_y$). The geometrical parameters of $\mathcal{B}_j$, with $j = x, y$, are (ℓ_j, h_j, b_j, A_j)

which stand respectively for their length, $\underline{e}_z$-thickness, width with $b_j = O(h_j)$ and section area $A_j = h_j b_j$. The mechanical parameters $(E_j, I_j = b_j h_j^3/12, G_j, \mathcal{I}_j, \rho_j, \Lambda_j = \rho_j A_j, \rho_j J_j)$ denote respectively the Young Modulus, the bending inertia, the torsional modulus and torsional inertia, the density, the linear mass, and the polar moment. The dimensions of the sections $\sqrt{A_j}$ are assumed small with respect to the lengths ℓ_j so that the behavior of the inter-node elements can be effectively modeled as Euler-Bernoulli beams. It is further assumed that the geometrical and the mechanical parameters of both types of beams $\mathcal{B}_j$ are of the same order of magnitude.

The material of the micro-plates $\mathcal{P}$ of area $\ell_x \ell_y$ and thickness d, have a Young's modulus E_p, a Poisson's ratio ν_p (the "plate modulus" is $E'_p = E_p/(1-\nu_p^2)$) and a density ρ_p. The plate bending inertia is denoted $I'_p = d^3/12$ and the surface mass $\Lambda'_p = \rho_p d$.

2.2 Homogenization of the ortho-beam grid

We aim at building a model for large transverse flexural vibrations in small deformations. The up-scaling process of the out-of plane dynamics of the ortho-grid is performed through the HPDM method (namely Homogenization of Periodic Discrete Media) [17, 10]. The developments follow the same guidelines as for the in-plane behavior studied in [7] and proceed into three steps, namely (i) the discretization of the dynamic balance, then (ii) the homogenization procedure itself through scale separation assumption and normalization, leading (iii) to the equivalent continuous model. This method applies under the key assumption of scale separation. This means that the wavelength $O(L)$ is much larger than the period size $O(l)$ and consequently $\epsilon = l/L << 1$. The macroscopic description of the grid, valid at the dominant order, is the limit behavior reached for $\varepsilon = \ell/L \to 0$. After these few steps, we are left with the following macroscopic description of the grid at the leading order :

$$\frac{E_x I_x}{\ell_y}\frac{\partial^4 U}{\partial x^4} + \frac{E_y I_y}{\ell_x}\frac{\partial^4 U}{\partial y^4} + \left(\frac{G_x \mathcal{I}_x}{\ell_y} + \frac{G_y \mathcal{I}_y}{\ell_x}\right)\frac{\partial^4 U}{\partial x^2 \partial y^2} + \omega^2\left(\frac{\rho_y J_y}{\ell_x}\frac{\partial^2 U}{\partial x^2} + \frac{\rho_x J_x}{\ell_y}\frac{\partial^2 U}{\partial y^2}\right) = \omega^2\left(\frac{\Lambda_x}{\ell_y} + \frac{\Lambda_y}{\ell_x}\right)U \quad (1)$$

The governing equation (1) is expressed with the properties of the micro-beams constituting the cell. This equation can be recast in the classical form of orthotropic plate equations, by defining

- the transverse forces $T_x^{\mathcal{G}}\underline{e}_z$, $T_y^{\mathcal{G}}\underline{e}_z$ exerted on the faces of normal $\underline{e}_x$, $\underline{e}_y$ and the in-plane vector $\underline{T}^{\mathcal{G}} = T_x^{\mathcal{G}}\underline{e}_x + T_y^{\mathcal{G}}\underline{e}_y$
- the momentum matrix $\underline{\underline{M}}^{\mathcal{G}}$ that involves the bending and torsion effects

Thus (1) is rewritten equivalently as (the differential operators operates in the (x, y) plane):

$$\begin{cases} \mathrm{div}(\underline{T}^{\mathcal{G}}) + \omega^2 \Lambda_{\mathcal{G}} U = 0 \quad ; \quad \Lambda_{\mathcal{G}} = \dfrac{\Lambda_x}{\ell_y} + \dfrac{\Lambda_y}{\ell_x} \\ \underline{\mathrm{div}}(\underline{\underline{M}}^{\mathcal{G}}) - \underline{T}^{\mathcal{G}} - \omega^2 \underline{\underline{J}}^{\mathcal{G}}.\underline{\mathrm{grad}}(U) = 0 \\ \underline{\underline{M}}^{\mathcal{G}} = \begin{pmatrix} M_{xx} = -\frac{E_x I_x}{\ell_y}\partial_x^2 U & M_{xy} = -\frac{G_y J_y}{\ell_x}\partial_x\partial_y U \\ M_{yx} = -\frac{G_x J_x}{\ell_y}\partial_y\partial_x U & M_{yy} = -\frac{E_y I_y}{\ell_x}\partial_y^2 U \end{pmatrix} \quad ; \quad \underline{\underline{J}}^{\mathcal{G}} = \begin{pmatrix} \rho_y J_y & 0 \\ 0 & \rho_x J_x \end{pmatrix} \end{cases} \quad (2)$$

The grid model (2) explicitly shows the coupling between the flexural and torsional behaviors. Note that in statics, i.e. $\omega \to 0$, (2) is identical to the grid model of [16]. Remind also that

the inertial terms containing the polar moments $\underline{\underline{J}}^{\mathcal{G}}$ may be neglected in regards to those related to the linear masses Λ. Note also that the description could be improved by considering the correctors constituted by the higher order terms of the expansions. They will not be explored here but their contribution could be appreciable when dealing with poor scale separation.

At this stage, (2) applies to the beam grid only free of external loading. The following section aims at introducing the contribution of the internal plates.

2.3 Conditions for inner dynamics of 2D-ribbed plates

We investigate 2D-ribbed plates presenting inner resonance phenomena, i.e., the stiff ortho-beam grid conveys the large wavelength, while the soft internal plate experiences a local resonance. Such a mixed regime within the cell results into (i) an inhomogeneous kinematics where the plate and grid displacements differ at the leading order and (ii) an asymmetrical coupling where the grid is forcing the soft plate. Let us specify the conditions for the occurrence of such a co-dynamic regime.

2.3.1 The co-dynamic condition

In inner resonance regime, the grid $\mathcal{G}$ and $\mathcal{P}$-plate fundamental resonances are of same order i.e., $O(\omega_{\mathcal{G}}) = O(\omega_p)$, so that :

$$O\left(\frac{E'_p I'_p}{\Lambda'_p \ell^4}\right) = O\left(\frac{EI}{\Lambda L^4}\right) \qquad \text{i.e.} \qquad \frac{E'_p}{E}\frac{\rho}{\rho_p} = O\left(\frac{h^2}{d^2}\frac{\ell^4}{L^4}\right) = O\left(\varepsilon^4 \frac{h^2}{d^2}\right) \tag{3}$$

This relation highlights the significant contrasts of mechanical properties of the constituting materials of the beam grid $\mathcal{G}$ and $\mathcal{P}$-plate.

2.3.2 Asymmetric coupling

As above stated, in presence of inner resonance, the grid acts as the forcing system that imposes its displacement to the forced $\mathcal{P}$-plate, in turn, the latter exerted forces on the grid. Considering the transverse balance of the grid loaded by the internal plates, such an asymmetric coupling requires :

$$\mathrm{div}(\underline{T}_{\mathcal{G}}) = O(T_p) \tag{4}$$

where $\underline{T}_{\mathcal{G}}$ relates to the transverse shear force (unit kN) in the grid $\mathcal{G}$ and T_p is the transverse linear shear force in the internal $\mathcal{P}$-plate (unit kN/m). The plate and beam displacements are identical at their junction, and consequently we have $w = O(U)$. Thus, from (4) and recalling that $b_k = O(h_k)$ one deduces the following requirement

$$O\left(E\frac{bh^3}{L^4}\right) = O\left(E'_p \frac{d^3}{\ell^3}\right) \qquad \text{i.e.} \qquad \frac{E'_p}{E} = O\left(\frac{\ell^3}{d^3}\frac{\ell^4}{L^4}\right) = O\left(\varepsilon^4 \frac{h^2}{d^2}\right) \tag{5}$$

In practice, $\rho/\rho_p = O(1)$ and the two conditions (3)-(5) reduces to $\frac{E'_p}{E} = O\left(\varepsilon^4 \frac{h^2}{d^2}\right)$. For ribbed plate made of a single material $E'_p = E$, and the inner-resonance arises when $d/h = O(\ell^2/L^2)$, i.e. for plates $\mathcal{P}$ significantly thinner than the beams of the grid $\mathcal{G}$. If the $\mathcal{P}$-material is much softer that the $\mathcal{G}$-material, namely $E'_p = O(\varepsilon^4 E)$ then $d/h = O(\ell/L)$ enables the inner-resonance to occur. Note that in these realistic cases, the bending stiffness of the plate is much smaller than that of the grid, in accordance with the asymmetry of the coupling. The case of inverted material properties so that the plate exhibits stiff properties and beam grid soft properties is not assessed here.

2.3.3 Beam grid loaded by internal plates

From the above analysis, provided that the conditions (3)-(5) are fulfilled, the action of internal plates is introduced in the beam grid model (2) in the form an external loading constituted by a shear force $\mathcal{F}\underline{e}_z$ and a couple $\underline{\mathcal{C}}$ resulting from the contact forces. This yield :

$$\begin{cases} \mathrm{div}(\underline{\underline{T}}^{\mathcal{G}}) + \Lambda_{\mathcal{G}}\omega^2 U + \mathcal{F} = 0 \\ \underline{\mathrm{div}}(\underline{\underline{M}}^{\mathcal{G}}) - \underline{T}^{\mathcal{G}} + \underline{\underline{J}}^{\mathcal{G}}\omega^2 \underline{\mathrm{grad}}(U) + \underline{\mathcal{C}} = 0 \end{cases} \tag{6}$$

where the coupling terms $\mathcal{F}$ and $\underline{\mathcal{C}}$ averaged on the cell are given either in terms or contact stresses on the grid or of efforts in the plate, by

$$\mathcal{F} = \frac{1}{\mathcal{S}} \int_\Gamma \underline{\underline{\sigma}}.\underline{n}\,\mathrm{ds} = -\frac{1}{\mathcal{S}} \int_{\partial\mathcal{P}} \underline{T}^{\mathcal{P}}.\underline{n}^{\mathcal{P}}\,\mathrm{dl} \tag{7}$$

$$\underline{\mathcal{C}} = \frac{1}{S} \int_\Gamma \underline{x} \times \underline{\underline{\sigma}}.\underline{n}\,\mathrm{ds} = -\frac{1}{\mathcal{S}} \int_{\partial\mathcal{P}} \underline{\underline{M}}^{\mathcal{P}}.\underline{n}^{\mathcal{P}}\,\mathrm{dl} + \frac{1}{\mathcal{S}} \int_{\partial\mathcal{P}} \frac{1}{2}(b_n^\perp \underline{n}^{\mathcal{P}})(\underline{T}^{\mathcal{P}}.\underline{n}^{\mathcal{P}})\,\mathrm{dl} \tag{8}$$

(where $b_n^\perp$ stands for the "oriented micro-beam width", i.e., $\pm b_y$, resp. $\pm b_x$, when $\underline{n}^{\mathcal{P}} = \pm\underline{e}_x$ resp. $\pm\underline{e}_y$). It remains now to express explicitly these coupling terms induced by the resonating internal plates. This is the aim of the next section.

2.4 Dynamics of the internal plates fully or partially connected to the beam grid

The out-of-plane motion w of the internal plates will be modeled as a Kirchhoff plate. Furthermore, the dynamic of the plate depends on the nature of its connections with the grid. We will consider the following configurations illustrated in Fig. 2 :

- $CCCC$ (Clamped-Clamped-Clamped-Clamped) i.e., the plate is clamped along its four edges,
- $CFCF$ (Clamped-Free-Clamped-Free) i.e., the plate is clamped along two opposite edges and free on the two others opposite edges, that implies a cylindrical bending as in a bi-clamped beam,
- $CFFF$ (Clamped-Free-Free-Free) i.e., the plate is clamped along one edge and free on its three others edges as a cantilever plate,
- In addition, we will also consider the case of additional masses attached on $\mathcal{P}$. To maximize its effect the mass is located at the center of the plate in the $CCCC$ and $CFCF$ configurations, whereas for $CFFF$ configuration, it is located at the outboard side of the clamped edge,

Independently of the specific type of the above listed boundary conditions, the elasto-dynamic plate problem is a 2D ($CCCC$ configuration) or 1D ($CFCF$ and $CFFF$ configurations) linear problem where the deflection $U(x,y)$ of the beam grid is the forcing term, which is *uniform* at the $\mathcal{P}$-plate scale. It results that the plate deflection takes the form

$$w(x,y,\underline{\xi}) = U(x,y)\phi_\omega^{bc}(\underline{\xi}) \tag{9}$$

where $\underline{\xi} = \xi_x\underline{e}_x + \xi_y\underline{e}_y$ stands for the local position within each $\mathcal{P}$-plate and $\phi_\omega^{bc}(\underline{\xi})$ is the frequency dependent deflection, for a unitary displacement of the grid. Hence, $\phi_\omega^{bc}(\underline{\xi})$ is the solution of the $\mathcal{P}$-problem in the configuration specified by the boundary conditions (^{bc}).

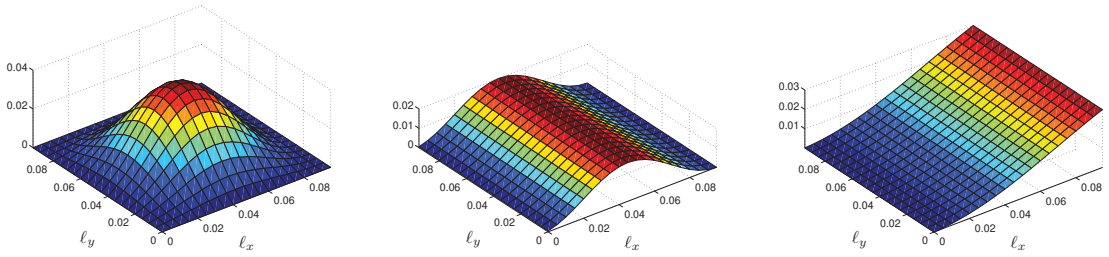

(a) (b) (c)

Figure 2: Shape of the fundamental mode associated with boundary conditions considered for the internal plates $\mathcal{P}$: (a) $C_xC_yC_xC_y$, (b) $C_xF_yC_xF_y$, (c) $C_xF_yF_xF_y$.

2.5 Homogenized flexural behavior of 2D-ribbed plate

The effect of internal plates on the grid is contained in the force $\mathcal{F}$, (7), and couple $\underline{\mathcal{C}}$, (8) and can be deduced from the knowledge of deflection in the plate $\phi_\omega^{bc}(\underline{\xi})$.

Regarding the force $\mathcal{F}$: Using the transverse force balance of $\mathcal{P}$, $\mathcal{F}$ can be re-expressed as

$$\mathcal{S}\mathcal{F}(x,y) = -\int_{\partial\mathcal{P}} \underline{T}^{\mathcal{P}}.\underline{n}^{\mathcal{P}}\,\mathrm{dl} = -\int_{\mathcal{P}} \mathrm{div}(\underline{T}^{\mathcal{P}})\,\mathrm{ds} = \omega^2\Lambda_p'\int_{\mathcal{P}} w\,\mathrm{ds}$$

i.e., introducing the following notation $\langle - \rangle = \frac{1}{\mathcal{S}}\int_{\mathcal{P}} -\mathrm{ds}$ for the mean value on the plate

$$\mathcal{F}(x,y) = \Lambda_p' \left\langle \phi_\omega^{bc} \right\rangle \omega^2 U(x,y) \tag{10}$$

Regarding the couple $\underline{\mathcal{C}}$: After integrating the transverse force balance of $\mathcal{P}$ multiplied by the local coordinate $\underline{\xi}$, one derives that

$$\mathcal{S}\underline{\mathcal{C}} = \omega^2\Lambda_p'\int_{\mathcal{P}} \underline{\xi} w\,\mathrm{ds} + \int_{\partial\mathcal{P}} \frac{1}{2}(\ell_n + b_n)\underline{n}^{\mathcal{P}}(\underline{T}^{\mathcal{P}}.\underline{n}^{\mathcal{P}})\,\mathrm{dl}$$

Furthermore, since $\underline{T}^{\mathcal{P}} = T_x^{\mathcal{P}}\underline{e}_x + T_y^{\mathcal{P}}\underline{e}_y$ we are left with

$$\underline{\mathcal{C}}(x,y) = \underline{K_\omega^{bc}} U(x,y) \qquad ; \qquad \underline{K_\omega^{bc}} = \omega^2\Lambda_p'\underline{H_\omega^{bc}} - \frac{E'I_p'}{\mathcal{S}}\underline{C_\omega^{bc}} \tag{11}$$

where $\underline{K_\omega}^{bc}$ is an elasto-inertial effective parameter that involves the frequency dependent dimensionless vectors $\underline{H_\omega^*}$ and $\underline{C_\omega^*}$. The components of the latter read explicitly

$$H_{\omega_x}^{bc} = \langle \xi_x \phi_\omega^{bc}(\underline{\xi}) \rangle \quad ; \quad C_{\omega_x}^{bc} = \frac{\ell_x + b_y}{2}\int_{-\frac{\ell_y}{2}}^{\frac{\ell_y}{2}} \left(\partial_{\xi_x}^3 \phi_\omega^{bc}|_{-\frac{\ell_x}{2},\xi_y} + \partial_{\xi_x}^3 \phi_\omega^{bc}|_{\frac{\ell_x}{2},\xi_y} \right) \mathrm{d}\xi_y \tag{12}$$

with similar expressions of the y-components by switching x and y.

Reporting expressions (7) and (8) into (6) yield the effective model of the 2-D ribbed plate that describes the grid behavior enriched by for the locally resonant internal plates.

$$\begin{cases} \mathrm{div}(\underline{T}) + \omega^2(\Lambda_{\mathcal{G}} + \Lambda_p'\langle\phi_\omega^{bc}\rangle)U = 0 \qquad ; \qquad \Lambda_{\mathcal{G}} = \dfrac{\Lambda_x}{\ell_y} + \dfrac{\Lambda_y}{\ell_x} \\ \underline{\mathrm{div}}(\underline{\underline{M}}) - \underline{T} - \omega^2\underline{\underline{J}}.\underline{\mathrm{grad}}(U) + \underline{K_\omega^{bc}}U = 0 \\ \underline{\underline{M}} = -\begin{pmatrix} \frac{E_xI_x}{\ell_y}\partial_x^2 U & \frac{G_yJ_y}{\ell_x}\partial_x\partial_y U \\ \frac{G_xJ_x}{\ell_y}\partial_y\partial_x U & \frac{E_yI_y}{\ell_x}\partial_y^2 U \end{pmatrix} \qquad ; \qquad \underline{\underline{J}} = \begin{pmatrix} \rho_y J_y & 0 \\ 0 & \rho_x J_x \end{pmatrix} \end{cases} \tag{13}$$

The inner resonance effect appears through the frequency dependent effective parameters $\langle \phi_\omega^{bc} \rangle$, and $\underline{K_\omega}^{bc}$ both associated with the dynamic motion of the internal plate. Let us first estimate the relative order of magnitude of the two non-conventional terms. From the expression (12) of $\underline{K_\omega^{bc}}$ it appears that

$$\frac{|K_\omega^{bc}||\nabla U|}{\Lambda'_p \langle \phi_\omega^{bc} \rangle U} = O\left(\frac{|K_\omega^{bc}|}{L\Lambda'_p \langle \phi_\omega^{bc} \rangle}\right) = O(\ell/L) \ll 1$$

Consequently, the effect of the non conventional torque is of one order smaller than the effect of non conventional inertia. Let us now explicit the effective mass term according to different boundary conditions :

CFCF plates : In that case the local plate problem and the corresponding field is identical to that of a clamped-clamped beam. Thus one has, when the $\mathcal{P}$-plates are clamped on the y-oriented micro beams, as in Fig.2-b (and similar expression switching x and y if the clamping is on $\mathcal{B}_x$)

$$\langle \phi_\omega^{C_x F_y C_x F_y} \rangle = \frac{2}{\delta \ell_x} \frac{1}{\coth(\delta \ell_x) + \cot(\delta \ell_x)} \qquad \delta = \sqrt[4]{\frac{\Lambda'_p \omega^2}{E'_p I'_p}} \tag{14}$$

Note that according to the above analysis $\langle \phi_\omega^{C_x F_y C_x F_y} \rangle \to \pm\infty$ when $\coth(\delta \ell_x) + \cot(\delta \ell_x) = 0$, i.e., at the eigenfrequencies of the y-bi-clamped $\mathcal{P}$-plate symmetric modes. These frequencies are accurately approximated by $(2n - \frac{1}{2})^2 \left(\frac{\pi}{\ell_x}\right)^2 \sqrt{\frac{E_p I_p}{\Lambda_p}}$, $n = 1, 2, 3, \ldots$.

$$\langle \phi_\omega^{C_x F_y F_x F_y} \rangle = \frac{1}{\delta \ell_x} \frac{\cosh(\delta \ell_x)\sin(\delta \ell_x) + \cos(\delta \ell_x)\sinh(\delta \ell_x)}{\cos(\delta \ell_x)\cosh(\delta \ell_x) + 1} \tag{15}$$

As expected, $\langle \phi_\omega^{C_x F_y F_x F_y} \rangle \to \pm\infty$ when $\cos(\delta \ell_x)\cosh(\delta \ell_x) + 1 = 0$ which corresponds to the eigenfrequencies of the y-clamped cantilever $\mathcal{P}$-plate, which are accurately approximated by $(n + \frac{1}{2})^2 \left(\frac{\pi}{\ell_x}\right)^2 \sqrt{\frac{E_p I_p}{\Lambda'_p}}$, $n = 1, 2, 3, \ldots$.

CCCC plates : For a plate clamped on its four sides there is no explicit expression of the local field. However, an analytical solution is available for circular clamped plate. This provides an approximated value for a square plates of side ℓ by matching its first eigenfrequency with that of a circular plate of radius a. The corresponding approximation reads where J_k and I_k are the Bessel and modified Bessel functions of the first kind.

$$\langle \phi_\omega^{Csquare} \rangle \approx \langle \phi_\omega^{Ccircle} \rangle = \frac{4}{\delta a}\left(\frac{J_0(\delta a)}{J_1(\delta a)} + \frac{I_0(\delta a)}{I_1(\delta a)}\right)^{-1} \qquad \text{where} \qquad a \approx 0.53\ell \tag{16}$$

2.5.1 Dispersion features in the orthogonally ribbed plate

Consider a flexural harmonic wave $U(\underline{x}) = \exp(i(k_\theta \underline{n}_\theta . \underline{x})$ propagating in the direction $\underline{n}_\theta = \cos(\theta)\underline{e}_x + \sin(\theta)\underline{e}_y$. Taking into account the facts that (i) the terms associated with polar moments are of weak magnitude compared to the translational inertia, and (ii) the terms of non conventional torque are of one order smaller that those associated with the non conventional inertia, these two terms can be disregarded at the leading order. Consequently, the flexural

$n_x = n_y = 5$	E [Pa]	ρ [kg.m^{-3}]	dimensions [m]	weight [kg]
Beam grid	69×10^9	2700	$h_y = h_x = b_y = b_x = 0.01,$	1.78
Plate	3×10^9	1200	$\ell_y = \ell_x = 0.1,\ d = 0.001$	0.363
Global structure			$L_x = L_y = 0.56$	2.14

Table 1: Geometrical and mechanical parameters of the 2D-ribbed plate $\mathcal{RP}_1$ considered for the numerical validation.

wavenumber $k_\theta(\omega)$ is given by :

$$k_\theta^4 \left(\frac{E_x I_x}{\ell_y} \cos^4(\theta) + \frac{E_y I_y}{\ell_x} \sin^4(\theta) + \left(\frac{G_x \mathcal{I}_x}{\ell_y} + \frac{G_y \mathcal{I}_y}{\ell_x} \right) \cos^2(\theta) \sin^2(\theta) \right) - \omega^2 \left(\frac{\Lambda_x}{\ell_y} + \frac{\Lambda_y}{\ell_x} + \Lambda'_p \langle \phi_\omega^{cb} \rangle \right) = 0 \quad (17)$$

The inner resonance of $\mathcal{P}$-plate accounted by $\langle \phi_\omega \rangle$, lead to dispersion features that differs notably from the classical bending case in which $k \sim \sqrt{\omega}$ in the whole frequency range. Significant changes are expected in the neighborhood of the internal plate's eigenmodes.

3 Numerical and experimental validation

We perform direct WFEM simulations of a 2D-ribbed plate designed so that resonance frequencies of the inner plate matches with that of the beam grid. The considered system denoted hereafter by $\mathcal{RP}_1$ is a square panel made up of 5×5 cells whose the stiffeners are in aluminium and internal plates in perspex, much softer than aluminium. With the geometric and mechanical parameters given on Table 1 the co-dynamic condition (3) $\omega_b = \omega_p$ is satisfied. Typical structural damping coefficients for aluminium and perspex are respectively $\eta_k = 5/1000$ and $\eta_i = 1/100$ and are included into the model as an imaginary part of the Young's modulus. Then, the effective parameters previously defined analytically and the wavenumbers are calculated for different boundary conditions on the internal plates, and compared to the results obtained by WFEM simulations.

Grid without internal plates. A first validation is achieved on the beam grid model itself. On Fig. 3-a one notices an excellent agreement between the wavenumbers along the x direction ($\theta = 0$), and along the oblique direction $\theta = \pi/4$ predicted by the homogenized model and those computed.

Grid with $CCCC$, $CFCF$ and $CFFF$ internal plates. The fundamental frequency of a $CCCC$ plate can be estimated using by Galin's formula. For a square plate : $\omega_p = (36/\ell^2)\sqrt{EI/\rho d}$, that gives here 277 Hz (the three first eigenfrequencies calculated by 3D finite element are 275 Hz, 562 Hz, 1009 Hz). The Fig. 3-b shows that the theoretical and numerical approaches provide very close results. The classical flexural dispersion is notably modified by the singularity induced by the resonance of the symmetric modes of the inner plates.

Further, the first resonance frequencies for the $CFCF$ plate are 170 Hz, 470 Hz, 921 Hz (respectively 27 Hz, 168 Hz for the $CFFF$ plate). The comparison between numerical and theoretical dispersion presented on Fig. 3-c, -d are also very satisfactory on those cases.
On Fig.3-c the singularity in the numerical results that are not predicted by the theoretical results arises at the antisymmetric resonance of the $\mathcal{P}$-plate. The latter are associated with torsional kinematics that are inhibited at the leading order in 2D-ribbed plate. Nevertheless, a slight torsion exists and the singularity generated numerically by the antisymmetric resonance

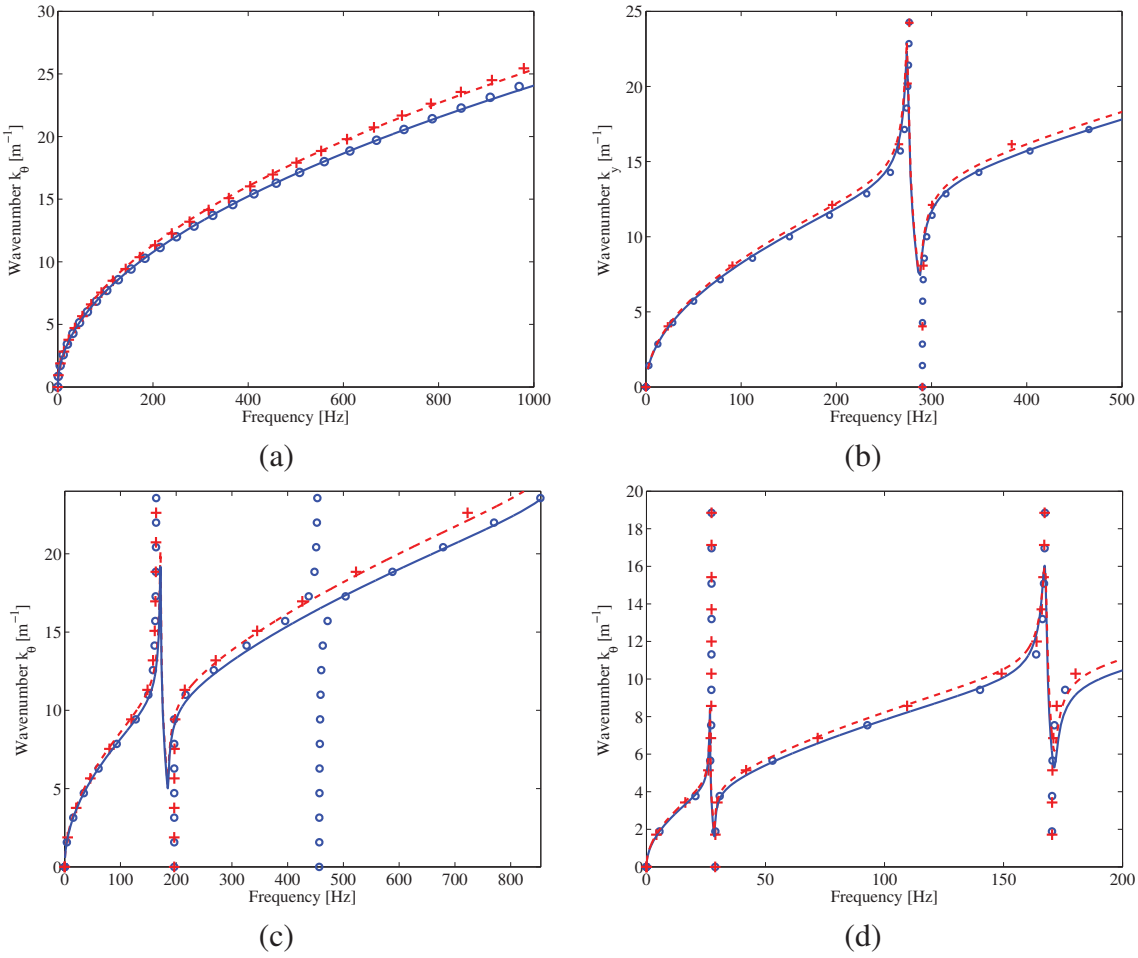

Figure 3: Wavenumbers predicted by the homogenized model in the directions $\theta = 0$ ($-$), $\theta = \pi/4$ ($--$), and by WFEM computation , $\theta = 0$ ($\circ$), and $\theta = \pi/4$ ($+$). a) Top left : Grid without internal plates, b) Top right : Grid with $CCCC$, plates. c) Bottom left : Grid with $CFCF$ plates, d) Bottom right : Grid with $CFFF$ plates.

magnifies the effects and results in a sharp and very tight singularity in the calculated wave numbers.

3.1 Experiments on 1D and 2D-ribbed plates

The panels are freely suspended and excited by a shaker that delivers a wide band random noise, The excitation point is located on the central stiffener and an impedance head gives the input force and acceleration. The velocity field is measured by a scanning Laser vibrometer. The scan is performed on a line along the excited stiffener. Measurements are performed in the frequency range 0-2kHz.

The IWC method is used to extract the wavenumber from the experimental data. For each scanned point, the frequency response function is recorded with its coherence functions. Hereafter, the flexural dispersion curves recovered from the experiments are compared to the analytical and/or the numerical ones.

The Fig. 5 shows that the experimental flexural dispersion of the grid compares satisfactorily with that given by the homogenized model of the grid. The damping results presented in Fig.5 are not investigated in more details in this paper. However they will be compared to that of Fig. 6, 7, 8 where it is clear that the local resonance introduces significant damping on the wave propagation.

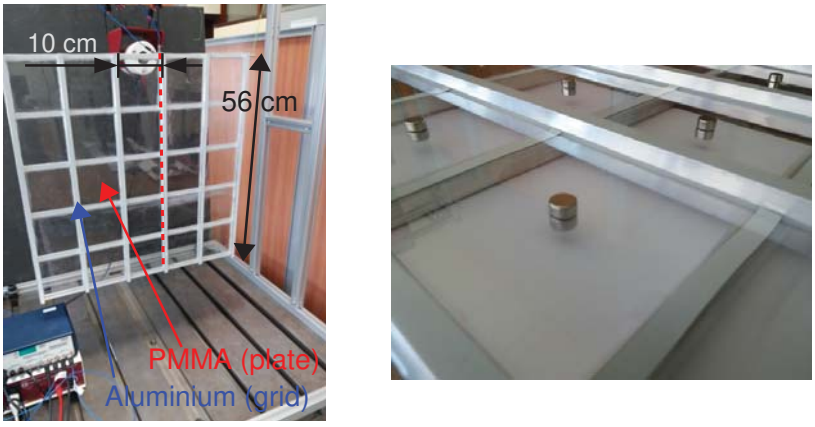

(a) (b)

Figure 4: Experimental setup for the freely suspended ribbed plate : (a) orthogonally ribbed plate ; (b) plate with added mass in the center in $CCCC$ configuration

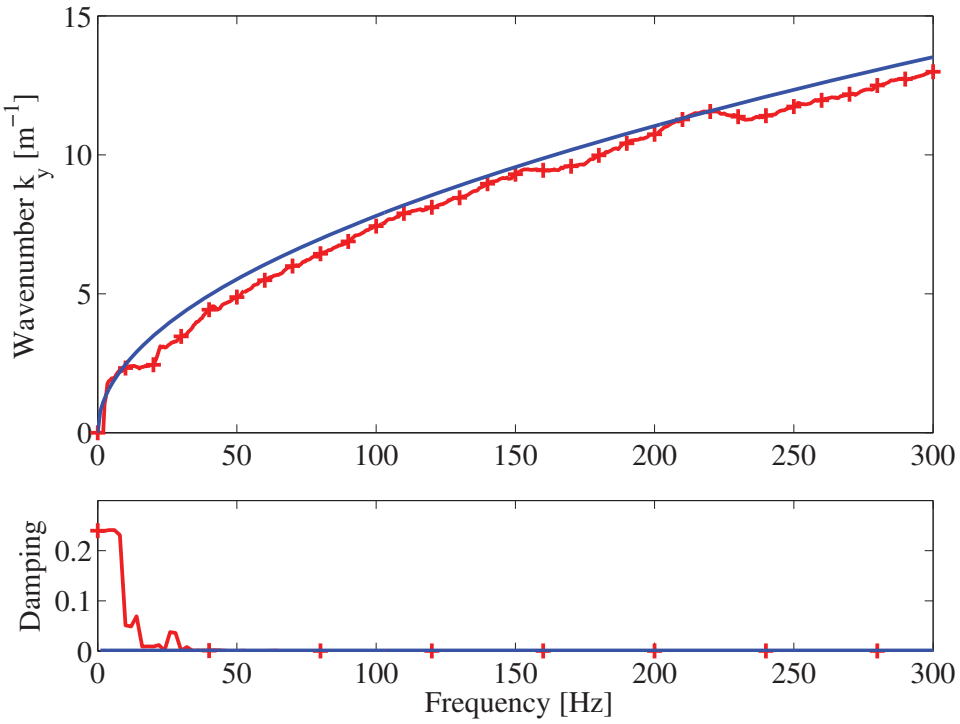

Figure 5: Flexural dispersion curve, analytical ($-$) and experimental ($-+-$) in the beam grid

2D-ribbed plate with $CCCC$ plates : The experiment/model comparison presented in Fig. 6 clearly show that the singularities predicted by the model actually occur in practice. Note that the phase enables to identify significant fluctuations associated with inner resonance of the plate.

2D-ribbed plate with $CFCF$ plates : The same experiments has been performed in the $CFCF$ configuration and the results presented on Fig. 7 (without mass) lead to similar comments as above.

2D-ribbed plate with $CFFF$ plates : The results gained on the $CFFF$ configuration without mass are presented in Fig. 8.

To sum up this section, the numerical simulations and the experimental results gained on

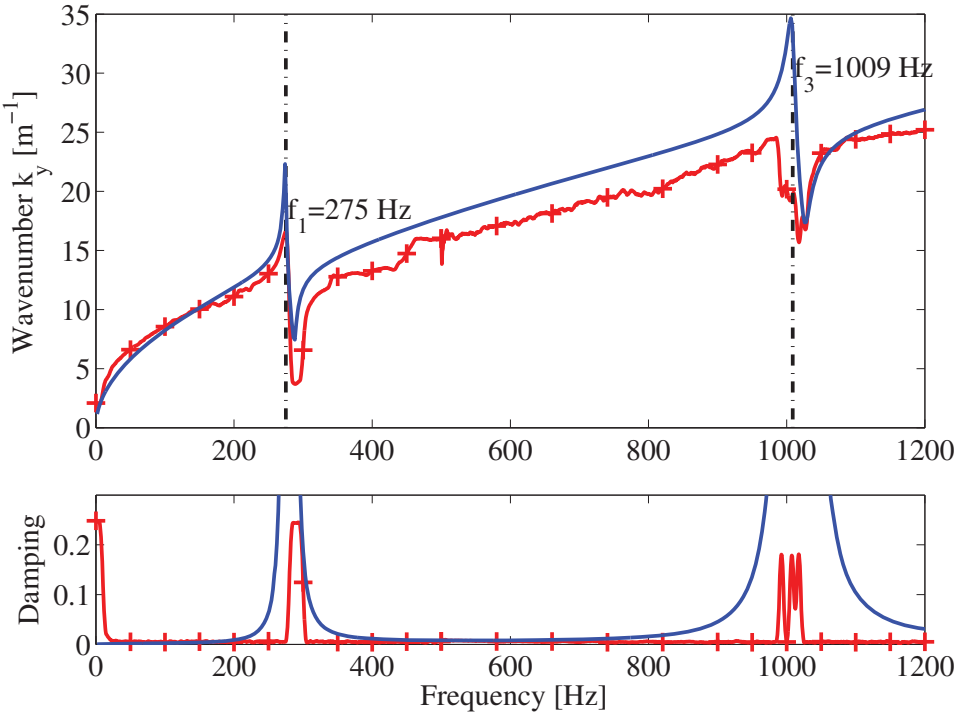

Figure 6: 2D ribbed plate with $CCCC$ internal plates : Flexural wavenumber, homogenized model ($-$), experimental data ($-+-$). The theoretical resonance frequencies are indicated by vertical dotted lines

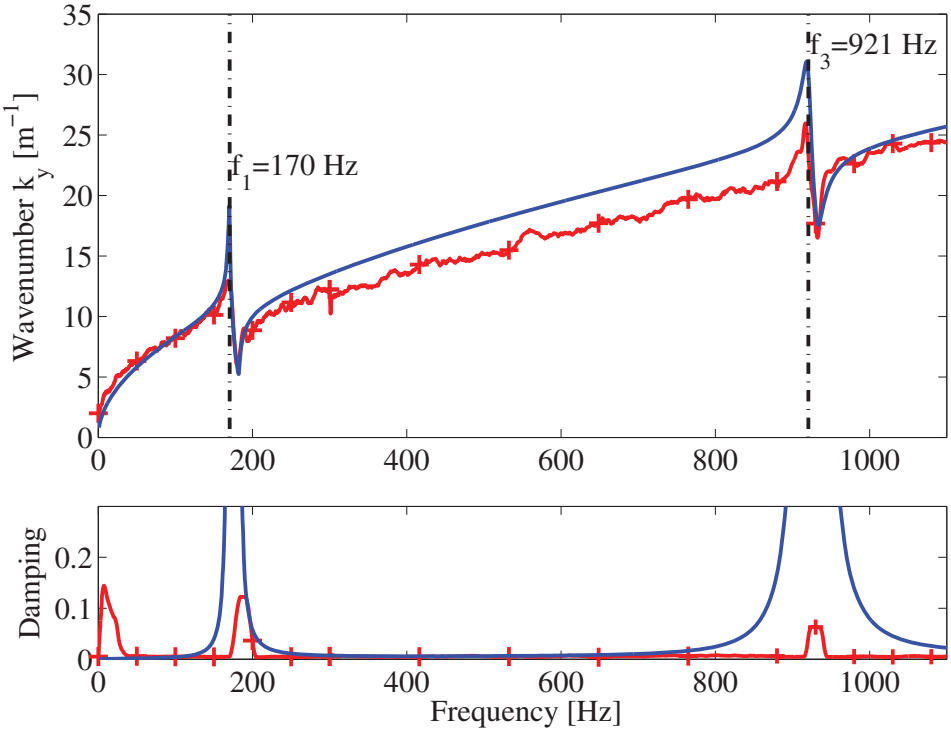

Figure 7: 2D-ribbed plates with $CFCF$ internal plates. Flexural wavenumber, homogenized model ($-$), experimental data ($-+-$), The theoretical resonance frequencies are indicated by vertical dotted lines

various configurations are all very consistent with the theoretical modeling.

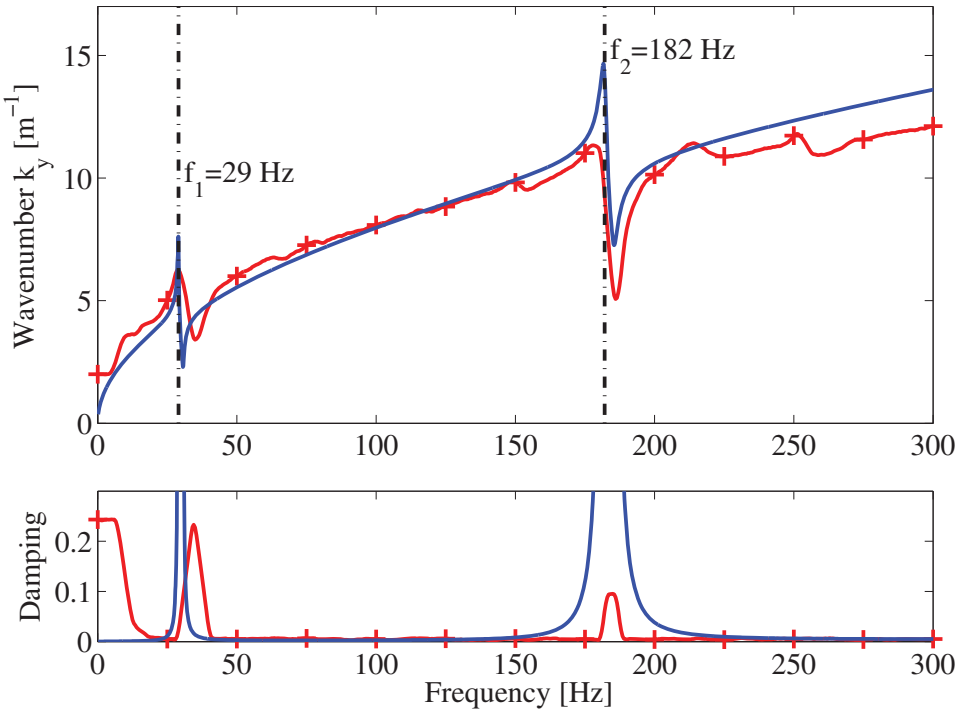

Figure 8: 2D ribbed plate with $CFFF$ internal plates. Flexural wavenumber, from homogenized model ($-$), from experimental datum ($-+-$). The theoretical resonance frequencies are indicated by vertical dotted lines

4 ACKNOWLEDGEMENTS

This work was supported by the LabEx CeLyA (Centre Lyonnais d'Acoustique, ANR-10-LABX-0060) of Université de Lyon, within the program "Investissements d'Avenir" (ANR-11-IDEX-0007) operated by the French National Research Agency (ANR).

5 CONCLUSIONS

The homogenization method applied to periodic orthogonally ribbed plates with contrasted geometrical and/or mechanical parameters allowed to determine their unconventional macroscopic behavior. The model is established within the scale separation assumption, and its effective parameters are explicitly determined from the geometrical and mechanical properties of the plate and stiffeners. The complex dynamic behavior encompasses the atypical flexural dispersion associated with the enriched local kinematics induced by the inner resonance. As a consequence, the flexural waves are affected by the frequency dependent positive or negative effective mass of the moving inner plates. Hence, around the inner plate's eigenfrequencies (that depends on the boundary conditions as $CCCC$, $CFCF$, $CFFF$ or added masses) the wave dispersion presents singularities, namely strong velocity variations together with frequency bands of strong attenuation. These outcomes are successfully compared with WFEM computations for realistic examples of contrasted cellular plates and with experiments performed on two prototypes in different configurations. This shows that the homogenized model correctly captures the phenomena, that the study yields reliable design rules to tailor cellular panels.

REFERENCES

[1] J.-L. Auriault and G. Bonnet. Dynamique des composites élastiques périodiques. *Arch Mech.*, 37(4-5):269–284, 1985.

[2] J.-L. Auriault and C. Boutin. Long wavelength inner-resonance cut-off frequencies in elastic composite materials. *International Journal of Solids and Structures*, 49(23–24):3269 – 3281, 2012.

[3] Jean-Louis Auriault, Claude Boutin, and Christian Geindreau. *Homogenization of Coupled Phenomena in Heterogenous Media (ISTE)*. Wiley-ISTE, 1 edition, 8 2009.

[4] J. Berthaut, M.N. Ichchou, and L. Jezequel. K-space identification of apparent structural behaviour. *Journal of Sound and Vibration*, 280(3–5):1125 – 1131, 2005.

[5] C. Boutin. Microstructural effects in elastic composites. *International Journal of Solids and Structures*, 33(7):1023 – 1051, 1996.

[6] C. Boutin and S. Hans. Homogenisation of periodic discrete medium: Application to dynamics of framed structures. *Computers and Geotechnics*, 30(4):303 – 320, 2003.

[7] Céline Chesnais, Claude Boutin, and Stéphane Hans. Effects of the local resonance on the wave propagation in periodic frame structures: Generalized newtonian mechanics. *The Journal of the Acoustical Society of America*, 132(4):2873–2886, 2012.

[8] C. Droz, C. Zhou, M.N. Ichchou, and J.-P. Lainé. A hybrid wave-mode formulation for the vibro-acoustic analysis of 2d periodic structures. *Journal of Sound and Vibration*, 363:285 – 302, 2016.

[9] P. Fossat, C. Boutin, and M. Ichchou. Dynamics of periodic ribbed plates with inner resonance: Analytical homogenized model and dispersion features. *International Journal of Solids and Structures*, 152-153:85 – 103, 2018.

[10] Stephane Hans and Claude Boutin. Dynamics of discrete framed structures : A unified homogenized description. *Journal of Mechanics of Materials and Structures*, 3(9):1709–1739, 2008.

[11] M.N. Ichchou, J. Berthaut, and M. Collet. Multi-mode wave propagation in ribbed plates. part ii: Predictions and comparisons. *International Journal of Solids and Structures*, 45(5):1196 – 1216, 2008.

[12] Alexander Kalamkarov, Igor Andrianov, and Vladyslav Danishevs'kyy. Asymptotic homogenization of composite materials and structures. *Applied Mechanics Reviews*, 62(3):030802–1–030802–20, 2009.

[13] T. Lewiński and J.J. Telega. *Plates, Laminates, and Shells: Asymptotic Analysis and Homogenization*. Series on advances in mathematics for applied sciences. World Scientific, 2000.

[14] D.J. Mead. A general theory of harmonic wave propagation in linear periodic systems with multiple coupling. *Journal of Sound and Vibration*, 27(2):235 – 260, 1973.

[15] Enrique Sanchez-Palencia. *Non-Homogeneous Media and Vibration Theory (Lecture Notes in Physics)*. Springer, spi edition, 6 1980.

[16] S. Timoshenko and S. Woinowsky-Krieger. *Theory of plates and shells*. Engineering societies monographs. McGraw-Hill, 1959.

[17] H. Tollenaere and D. Caillerie. Continuous modeling of lattice structures by homogenization. *Advances in Engineering Software*, 29(7):699 – 705, 1998.

EURODYN 2020
XI International Conference on Structural Dynamics
M. Papadrakakis, M. Fragiadakis, C. Papadimitriou (eds.)
Athens, Greece, 23–26 November 2020

A DISCRETE-TO-CONTINUUM APPROACH TO FREQUENCY BANGAPS IN 1D BIATOMIC METAMATERIALS

L. Placidi[1], A. Amendola[2*], M. Miniaci[3] and F. Fraternali [2]

[1]International Telematic University Uninettuno,
00186 Rome
Italy
e-mail: luca.placidi@uninettunouniversity.net

[2] Dept. of Civil Engineering
University of Salerno
Salerno, Italy
e-mail:{adaamendola1, f.fraternali}@unisa.it

[3] CNRS-UMR 8520
Institute of Electronics, Microelectronics and Nanotechnology
Lille, FR
e-mail: marco.miniaci@gmail.com

Keywords: Discrete-to-continuum, frequency bandgaps, lattice metamaterials, tensegrity structures.

Abstract. *We formulate a discrete-to-continuum approach to the dispersion relation of one-dimensional lattice metamaterials. With reference to a generic lattice structure that can be described as a biatomic mass-spring chain, we formulate a higher order gradient continuum theory of the competent dynamical problem using a homogenization approach. The proposed theory allows us to obtain an analytic description of the bandgap-type response of the homogenized chain, and to estimate the frequency boundary region that is affected by the full transmission of mechanical waves. Numerical applications of the proposed discrete-to-continuum approach are given with reference to tensegrity metamaterials, which exhibit a prestress-tunable bandgap response over a wide range of frequencies.*

1 Introduction

Recently, researchers have focused on exploring the bandgap-type response of lattice metamaterials, e.g. [1–4]. These materials are artificial periodic structures with potential variations in density and/or geometry (refer, e.g., to [4], [5], [6] and references therein). They are characterized by unusual mechanical properties. It has been shown that such systems support phononic bandgaps, and have frequency ranges with inhibited wave propagation.
This study refers to mass-spring tensegrity lattices for which it has been demonstrated that the dispersion relation can be tuned by varying the applied internal self-stress induced by prestretching the cables forming the tensegrity units, and/or the global prestress induced by the application of compression forces to the terminal bases [7]. This paper addresses the bandgap-type response of the homogenized chain. Previous homogenization methods have been illustrated for both low and high frequency regimes, e.g. in [8], [9], in [10] and [11]. In contrast to these studies, the present work approaches the problem from the point of view of the theory of mixtures. The sense is that, for thermodynamic reason, the existence of bandgap in elastic continuum materials, at least two kinematical descriptors are necessary. The first is that on which it is evident the attenuation in the prohibited frequency band. The second is that on which the energy is stored. Thus, in a bi-atomic chain the kinematical descriptors correspond to the position of those masses and one side of the stiffer spring and on the same side of the softer spring. It is a matter of facts that if the springs have the same rigidity, no band gap is possibile.

In the first part of the paper, we develop a discrete-to-continuum approach to the dispersion relation of 1D periodic arrays, both for monoatomic and biatomic chains. Then, we apply the developed theory to tensegrity metamaterials, and we compare the results with those obtained using the discrete approach [7]. Our key findings are summarized in Sect. 4, where we also propose future research lines for the manufacturing and testing of bandgap metamaterials with tensegrity architecture.

2 Discrete-to-continuum models of bandgap systems

The present section studies continuous mathematical models able to describe the behavior of both monoatomic and biatomic systems. It is a matter of facts that a standard continuous model is not sufficient to represent an intrinsically discrete system. The reason is inside the continuous approximation, that is however attenuated by the use of non standard models. In order to provide a well-posed system of Partial Differential Equations for such models, the use of variational procedure is suggested, see e.g. [12]. Thus, an Action functional $\mathcal{A}$ is defined in terms of kinetic $\mathcal{K}$, internal $\mathcal{U}_{int}$ and external $\mathcal{U}_{ext}$ energies,

$$\mathcal{A} = \int_{t_1}^{t_2} \mathcal{K} - \mathcal{U}_{int} + \mathcal{U}_{ext}, \tag{1}$$

where t_1 and t_2 are two instants of time and where the action $\mathcal{A}$ is a functional of the fundamental kinematical fields of the continuum. We will see in Subsection 2.1 that for the continuous model of monoatomic chain we need only a single placement field χ and in Subsection 2.2 that for the continuous model of biatomic chain we need two placement fields χ_1 and χ_2. For the sake of simplicity, we consider for both cases a one dimensional continuous body of length L and an abscissa X, in the straight reference configuration, such that $X \in [0, L]$.

Once the set of kinematical fields and their admissible variation have been defined, the equation of motion are achieved by imposing that the variation of the action, among all the admissible variation of the kinematical fields, is null, i.e., $\delta\mathcal{A} = 0$

2.1 Monoatomic systems

Kinetic energy of the microstructural continuum representing the monoatomic chain contains not only the standard contribution in terms of the mass density ρ but also a non standard one in terms of the microinertia η,

$$\mathcal{K} = \int_0^L \frac{1}{2}\rho\dot{\chi}^2 + \frac{1}{2}\eta\dot{\chi}'^2, \tag{2}$$

where dot $\dot{a}$ and prime a' represents, respectively, the derivatives with respect to time t and position X.

Analogously, the internal energy contains not only the standard contribution in terms of the strain $\epsilon = u'$ but also in terms of the strain gradient $\epsilon' = u''$, where $u = \chi - X$ is the displacement field,

$$\mathcal{U}_{int} = \int_0^L \frac{1}{2}k_{el1}u'^2 + \frac{1}{2}k_{el2}u''^2, \tag{3}$$

and where k_{el1} is the standard axial stiffness and k_{el2} is the non-standard strain gradient axial stiffness.

The definition of an external energy should provide the necessary ingredients for solving boundary value problems. For the sake of simplicity, here we assume no external energy, i.e. $\mathcal{U}_{ext} = 0$.

Both standard arguments for the derivation of the variation of the action and imposing that its variation among all the admissible variation $\delta\chi$ of the fundamental kinematical field χ is null, i.e. $\delta\mathcal{A} = 0$, yields the Partial Differential Equation of the problem,

$$\rho\ddot{u} - \eta\ddot{u}'' = k_{el1}u'' - k_{el2}u''''. \tag{4}$$

By assuming a plane wave solution for the displacement field u in terms of the real part (i.e. Re) of complex exponential form,

$$u = Re\left(u_0 \exp i\left(\omega t - kX\right)\right), \tag{5}$$

where u_0, ω and k are, respectively, the complex amplitude, the angular frequency and the wave number, we obtain the following dispersion relation

$$\omega = \omega_c\left(k\right) = k\sqrt{\frac{k_{el1} + k_{el2}k^2}{\rho + \eta k^2}}, \tag{6}$$

where the function $\omega_c\left(k\right)$ has been introduced for the present continuous system. A comparison between the dispersion relations for discrete [7] and and for continuous (18) systems can be done only for large wave length $\lambda = 2\pi/k$, that means for small wave number k. Thus, it is reasonable to perform a Taylor's series expansion of both functions $\omega_d\left(k\right)$ and $\omega_c\left(k\right)$,

$$\omega_d\left(k\right) = ka\sqrt{\frac{K_{el}}{M}}\left(1 - \frac{\left(ka\right)^2}{24}\right) + o\left(k^3\right). \tag{7}$$

$$\omega_c\left(k\right) = k\sqrt{\frac{k_{el1}}{\rho}} + k^3\sqrt{\frac{k_{el1}}{\rho}}\frac{k_{el1}\eta - k_{el2}\rho}{2k_{el1}\rho} + o\left(k^3\right), \tag{8}$$

An identification of the two dispersion relations (7) and (8) yields

$$\rho = \frac{M}{a}, \quad k_{el1} = aK_{el}, \quad \eta = \rho\left(\frac{a^2}{12} + \frac{k_{el2}}{k_{el1}}\right) = \frac{M}{a}\left(\frac{a^2}{12} + \frac{k_{el2}}{aK_{el}}\right) \tag{9}$$

Eqns. $(27)_1$ and $(27)_2$ are the standard and intuitive identifications of both continuous mass density ρ and standard axial rigidity k_{el1} in term of the constitutive parameters of the discrete model M, K_{el} and a. Eq. $(27)_3$ gives a relation between the two strain gradient parameters η and k_{el2}. It is worth to be noted that the identification of null microinertia $\eta = 0$ is forbidden by the thermodynamic assumption $k_{el2} \geq 0$, that is implied by positive definiteness of the internal energy (3).

2.2 Biatomic systems

We now examine a continuous model for biatomic chains. As we have already pointed out, the fundamental kinematical fields of the continuum model of biatomic systems are the two placements χ_1 and χ_2.

Kinetic energy of such a continuum is not only the standard contribution in terms of a quadratic form of the two velocity fields $\dot{\chi}_1$ and $\dot{\chi}_2$ but also a non standard one in terms of a quadratic form of the two velocity gradient fields $\dot{\chi}'_1$ and $\dot{\chi}'_2$,

$$\mathcal{K} = \int_0^L \frac{1}{2} \begin{pmatrix} \dot{\chi}_1 & \dot{\chi}_2 \end{pmatrix} A \begin{pmatrix} \dot{\chi}_1 \\ \dot{\chi}_2 \end{pmatrix} + \frac{1}{2} \begin{pmatrix} \dot{\chi}'_1 & \dot{\chi}'_2 \end{pmatrix} B \begin{pmatrix} \dot{\chi}'_1 \\ \dot{\chi}'_2 \end{pmatrix}, \tag{10}$$

where the two matrixes A and B,

$$A = \begin{pmatrix} \rho_1 & \rho_{12} \\ \rho_{12} & \rho_2 \end{pmatrix}, \qquad B = \begin{pmatrix} \eta_1 & \eta_{12} \\ \eta_{12} & \eta_2 \end{pmatrix}, \tag{11}$$

are positive defined.

Analogously, the internal energy contains not only the standard contribution in terms of a quadratic form of the two axial strains $\epsilon_1 = u'_1$ and $\epsilon_2 = u'_2$ but also in terms of the two axial strain gradient $\epsilon'_1 = u''_1$ and $\epsilon'_2 = u''_2$, where the two displacements $u_1 = \chi_1 - X$ and $u_2 = \chi_2 - X$ are defined. Besides, a contribution in terms of the square of the difference between the two displacements u_1 and u_2 is objective and is conceived as follows,

$$\mathcal{U}_{int} = \int_0^L \frac{1}{2} k_{el0} \left(u_1 - u_2\right)^2 + \frac{1}{2} \begin{pmatrix} u'_1 & u'_2 \end{pmatrix} C \begin{pmatrix} u'_1 \\ u'_2 \end{pmatrix} + \frac{1}{2} \begin{pmatrix} u''_1 & u''_2 \end{pmatrix} D \begin{pmatrix} u''_1 \\ u''_2 \end{pmatrix}, \tag{12}$$

where the two matrixes C and D,

$$C = \begin{pmatrix} k_{el1} & k_{el12} \\ k_{el12} & k_{el2} \end{pmatrix}, \qquad D = \begin{pmatrix} k_{2el1} & k_{2el12} \\ k_{2el12} & k_{2el2} \end{pmatrix}, \tag{13}$$

are positive defined. For the sake of simplicity we assume $D = 0$. Besides, we assume no external energy, i.e. $\mathcal{U}_{ext} = 0$.

Both standard arguments for the derivation of the variation of the action and imposing that its variation among all the admissible variation $\delta\chi_1$ and $\delta\chi_2$ of the fundamental kinematical fields χ_1 and χ_2 are null, i.e. $\delta\mathcal{A} = 0$, yields the following system of Partial Differential Equations of the problem,

$$\rho_1 \ddot{u}_1 + \rho_{12} \ddot{u}_2 - \eta_1 \ddot{u}''_1 - \eta_{12} \ddot{u}''_2 = k_{el1} u''_1 + k_{el12} u''_2 - k_{el0}(u_1 - u_2) = 0 \tag{14}$$

$$\rho_2 \ddot{u}_2 + \rho_{12} \ddot{u}_1 - \eta_2 \ddot{u}''_2 - \eta_{12} \ddot{u}''_1 = k_{el2} u''_2 + k_{el12} u''_1 + k_{el0}(u_1 - u_2) = 0 \tag{15}$$

By assuming plane wave solutions for the displacement fields u_1 and u_2 in terms of the real part of complex exponential form,

$$u_1 = Re\left(u_{10} \exp i\left(\omega t - kX\right)\right), \quad u_2 = Re\left(u_{20} \exp i\left(\omega t - kX\right)\right), \tag{16}$$

where u_{10} and u_{20} are the complex amplitudes, we obtain the following dispersion relation

$$\det\begin{pmatrix} \rho_1\omega^2+\eta_1k^2\omega^2-k_{el1}k^2-k_{el0} & \rho_{12}\omega^2+\eta_{12}k^2\omega^2-k_{el12}k^2+k_{el0} \\ \rho_{12}\omega^2+\eta_{12}k^2\omega^2-k_{el12}k^2+k_{el0} & \rho_2\omega^2+\eta_2k^2\omega^2-k_{el2}k^2-k_{el0} \end{pmatrix}=0, \tag{17}$$

that in the explicit form is

$$\omega=\omega_{cc}\left(k\right)=\frac{E\left(k\right)\pm\sqrt{E\left(k\right)^2-4F\left(k\right)}}{2G\left(k\right)}, \tag{18}$$

where

$$\begin{aligned} E\left(k\right) &= k^4\left(k_{el1}\eta_2+k_{el2}\eta_1-2k_{el12}\eta_{12}\right)+ \\ &\quad k^2\left(k_{el1}\rho_2+k_{el2}\rho_1-2k_{el12}\rho_{12}+k_{el0}\left(\eta_1+\eta_2+2\eta_{12}\right)\right)+ \\ &\quad k_{el0}\left(\rho_1+\rho_2+2\rho_{12}\right) \end{aligned} \tag{19}$$

$$F\left(k\right) = k^2\left(k_{el0}\left(k_{el1}+k_{el2}+2k_{el12}\right)+k^2\left(k_{el1}k_{el2}-k_{el12}^2\right)\right)G\left(k\right) \tag{20}$$

$$G\left(k\right) = k^4\left(\eta_1\eta_2-\eta_{12}^2\right)+k^2\left(\rho_1\eta_2+\rho_2\eta_1-2\eta_{12}\rho_{12}\right)+\rho_1\rho_2-\rho_{12}^2 \tag{21}$$

and the function $\omega_{cc}\left(k\right)$ has been introduced for the present continuous system. A comparison between the dispersion relations for discrete and for continuous systems can be done only for large wave length $\lambda=2\pi/k$, that means for small wave number k. Thus, it is reasonable to perform a Taylor's series expansion of both functions $\omega_{dd}\left(k\right)$ and $\omega_{cc}\left(k\right)$, that we perform with the assumption

$$\rho_1=\rho,\quad \rho_2=\rho,\quad \eta_1=\eta,\quad \eta_2=\eta, \tag{22}$$

that yields,

$$\omega_{dd1}\left(k\right)^2 = \left(ka\right)^2\frac{K_1K_2}{2M\left(K_1+K_2\right)} \tag{23}$$

$$\omega_{dd2}\left(k\right)^2 = 2\frac{K_1+K_2}{M}-\left(ka\right)^2\frac{K_1K_2}{2M\left(K_1+K_2\right)} \tag{24}$$

$$\omega_{cc1}\left(k\right)^2 = k^2\frac{k_{el1}+k_{el2}+2k_{el12}}{2\left(\rho+\rho_{12}\right)}, \tag{25}$$

$$\omega_{cc2}\left(k\right)^2 = 2\frac{k_{el0}}{\rho-\rho_{12}}+k^2\left[\frac{k_{el1}+k_{el2}-2k_{el12}}{2\left(\rho-\rho_{12}\right)}-2\frac{k_{el0}\left(\eta-\eta_{12}\right)}{\left(\rho-\rho_{12}\right)^2}\right] \tag{26}$$

An identification of the four dispersion relations (23), (24), (25) and (26) yields

$$\rho=\frac{M}{a},\quad k_{el0}=\frac{K_1+K_2}{a},\quad k_{el1}+k_{el2}=a\frac{K_1K_2}{K_1+K_2},\quad \eta=\frac{MaK_1K_2}{2\left(K_1+K_2\right)^2} \tag{27}$$

with the assumption

$$\rho_{12}=\eta_{12}=k_{el12}=0 \tag{28}$$

3 Numerical results

We shall now apply the theory outlined above to a biatomic tensegrity chain modeled as a mass-spring chain and featuring linear springs with two alternating stiffness constants K_1 and K_2 (where $K_1<K_2$) [7]. This section includes a numerical validation of the approach

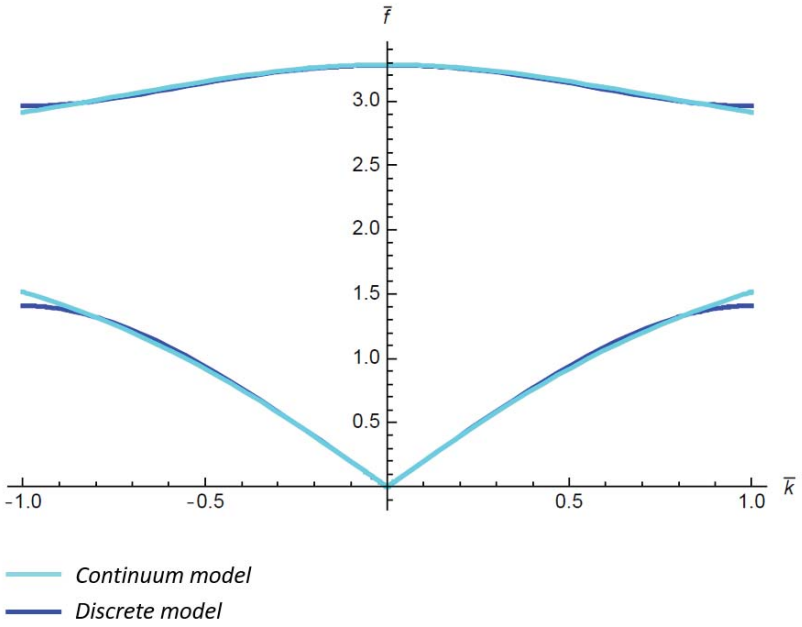

Figure 1: Dispersion relation in the first Brillouin zone for a biatomic chain under $F_0 = 4.21$ N and $\bar{p} = 0.00$, obtained by applying the discrete and continuous models.

presented in Section 2. Our results are compared with those obtained by applying Bloch-Floquet theory to a biatomic tensegrity chain, as illustrated in [7], Subsection 2.2.
We focus on a chain that is uniformly axially loaded with an initial static precompression force $F_0 = 4.21$ N applied to the terminal bases of the structure. Each unit presents an initial self-stress (internal prestress) $\bar{p} = 0.00$.

Fig. 1 compares the dispersion relation of a biatomic tensegrity chain obtained via the discrete model [7] and the continuous model (Section 2), highlighting a good overall agreement between the two approaches.
Here, $\bar{f}$ denotes the normalized frequency $\bar{f} = f\sqrt{\frac{M}{K^*}}$ where K^* is the tangent stiffness of Unit 1 (taken as a reference) in the globally prestressed configuration and M is the total mass of a unit cell. Meanwhile, $\bar{\kappa}$ denotes the normalized wavenumber $\kappa\, \pi/a$ where a is the unit cell size.

It is worth noticing that the identification of the constitutive paramenters of the continuum model in (27-28) has been done assuming small values of the wave number κ and therefore for large wave length $\lambda = 2\pi/\kappa$. Thus, from one hand this is the range in which the continuum approximation is possibile and the comparison that is done in Fig. 1 is relaiable. From the other hand, an investigation in other ranges of wave length for the continuum model still need to be done.

4 Concluding remarks

In this paper, we have analyzed the frequency band structure of a 1D monoatomic and biatomic mass-spring chain. The study led us to formulate a continuum model for these structures based on a higher order gradient continuum theory. In contrast to standard continuous models, this theory allows us to efficiently describe intrinsic discrete systems.

A numerical application of the proposed discrete-to-continuum approach has been presented with reference to tensegrity metamaterials, which exhibit a prestress-tunable bandgap response

over a wide range of frequencies while the material properties of the unit cells remain unchanged. A comparison was made between the dispersion relations for discrete and continuous systems in order to validate the mathematical homogenization theory presented.

Possible engineering applications of tensegrity metamaterials may include bandgap systems [13, 14], waveguiding [15, 16], impact protection gear [6, 17], and/or acoustic lenses [18, 19].

This study paves the way for a number of relevant extensions and generalizations that we will address in future work. These may include, for example, the 3D printing [20] and experimental dynamic analysis of tensegrity metamaterial structures at different scales.

Acknowledgements

FF acknowledges financial support from the Italian Ministry of Education, University and Research (MIUR) under the P.R.I.N. 2017 National Grant‘ Multiscale Innovative Materials and Structures’ (Project Code 2017J4EAYB).

References

REFERENCES

[1] Lu, M.H., Feng, L., Chen, Y.F., 2009. Phononic crystals and acoustic metamaterials. Mater. Today 12, 34-42.

[2] Maldovan, M., 2013. Sound and heat revolution in phononics. Nature 503, 209-217.

[3] Theocharis, G., Boechler, N., and Daraio C., 2013. Nonlinear phononic structures and metamaterials. P.A. Deymier (ed.) Acoustic Matematerials and Phononic Crystals. Springer Series in Solid State Sciences. 173, 217-251. doi: 10.1007/978-3-642-31232-8 7.

[4] Phani, A.S., Hussein, M.I., (eds) 2017. Dynamics of Lattice Materials, John Wiley & Sons, Ltd, Chichester, UK.

[5] Fraternali, F., Senatore, L., Daraio, C., 2012. Solitary waves on tensegrity lattices. J. Mech. Phys. Solids. 60, 1137-1144. doi: 10.1016/j.jmps.2012.02.007.

[6] Fraternali, F., Carpentieri, G., Amendola, A., Skelton, R.E., Nesterenko, V.F., 2014. Multiscale tunability of solitary wave dynamics in tensegrity metamaterials. Appl. Phys. Lett. 105, 201903. doi: 10.1063/1.4902071.

[7] Amendola, A., Krushynska A., Daraio C., Pugno N.M., Fraternali F., 2018. Tuning frequency band gaps of tensegrity metamaterials with local and global prestress, Int. J. Solids Struct., 155, 47–56.

[8] Modeling phononic crystals via the weighted relaxed micromorphic model with free and gradient micro-inertia A Madeo, M Collet, M Miniaci, K Billon, M Ouisse, P Neff Journal of Elasticity 130 (1), 59-83 (2018)

[9] Comi, C., Marigo, J.J., 2020. Homogenization approach and Bloch-Floquet theory for band-gap prediction in 2D locally resonant metamaterials, Jù. Elast. 139, 61–90.

[10] El Sherbiny, M.G., Placidi, L., 2018. Discrete and continuous aspects of some metamaterial elastic structures with band gaps Arch. Appl. Mech. 88:1725–1742.

[11] High-frequency homogenization for periodic media, R. V. Craster, J. Kaplunov and A. V. Pichugin, Proceedings of the Royal Society A: Mathematical, Physical and Engineering Sciences, 466, 2120, 2010

[12] Dell'Isola, Francesco, and Luca Placidi. "Variational principles are a powerful tool also for formulating field theories." Variational models and methods in solid and fluid mechanics. Springer, Vienna, 2011. 1-15.

[13] Theocharis, G., Boechler, N., Daraio, C., 2013. Nonlinear phononic structures and metamaterials, in P.A. Deymier (ed.) Acoustic Matematerials and Phononic Crystals, Springer Series in Solid State Sciences, 173, Springer-Verlag, Berlin-Heidelberg, Germany.

[14] Herbold, E. B., Kim, J. , Nesterenko, V. F., Wang, S. Y., Daraio, C., 2009. Pulse propagation in a linear and nonlinear biatomic periodic chain: effects of acoustic frequency band-gap. Acta Mech 205, 85-103. DOI 10.1007/s00707-009-0163-6.

[15] Ruzzene, M., Scarpa, F., 2005. Directional and band gap behavior of periodic auxetic lattices. Phys. Status Solidi B 242(3), 665-680.

[16] Casadei, F., Rimoli, J. J., 2013. Anisotropy-induced broadband stress wave steering in periodic lattices. Int. J. Solids Struct. 50(9), 1402-1414.

[17] Fraternali, F., Porter, M., Daraio, C., 2010. Optimal design of composite granular protectors. Mech. Adv. Mat. Struct. 17. 1-19.

[18] Spadoni, A., Daraio, C., 2010. Generation and control of sound bullets with a nonlinear acoustic lens. Proc. Natl. Acad. Sci. U.S.A. 107(16), 7230-7234. doi: 10.1073/pnas.1001514107.

[19] Donahue, C., Anzel, P.W.J., Bonanomi, L., Keller, T.A., Daraio, C., 2014. Experimental realization of a nonlinear acoustic lens with a tunable focus. Appl. Phys. Lett. 104, 014103. doi: 10.1063/1.4857635.

[20] Amendola A., Hernández-Nava E., Goodall R., Todd I., Skelton R.E., Fraternali, F. (2015). On the additive manufacturing, post-tensioning and testing of bi-material tensegrity structures. Compos. Struct., 131, 66–71.

EURODYN 2020
XI International Conference on Structural Dynamics
M. Papadrakakis, M. Fragiadakis, C. Papadimitriou (eds.)
Athens, Greece, 23–26 November 2020

INDUCING DISPERSION CURVES WITH NEGATIVE GROUP VELOCITY IN INERTIALLY AMPLIFIED PHONONIC CRYSTALS THROUGH THE APPLICATION OF AN EXTERNAL STATE OF PRESTRESS

M. Miniaci[1], M. Mazzotti[2], A. Amendola[3] and F. Fraternali [3]

[1]CNRS, Centrale Lille, ISEN, Univ. Lille, Univ. Valenciennes, UMR 8520 - IEMN
F-59000 Lille, France
e-mail: marco.miniaci@univ-lille.fr, marco.miniaci@gmail.com

[2] Department of Mechanical Engineering, CU Boulder
Boulder, CO 80309, USA e-mail: matteo.mazzotti@gmail.com

[3] Department of Civil Engineering, University of Salerno
Salerno, Italy
e-mail:{adaamendola1, f.fraternali}@unisa.it

Keywords: Phononic Crystals and Metamaterials, Prestress / Prestrain, Band Diagram Tunability, Inertial Amplification Mechanism.

Abstract. *In this paper, we report about the effect of the application of a state of prestress on the band structure of a periodic phononic crystal characterized by an inertial amplification mechanism. Through a numerical example, we show the possibility of inducing negative group velocity in an isolated branch of the dispersion diagram.*
A 2-step Updated Lagrangian scheme is adopted to calculate the dispersion diagram of the structure. The proposed method include (i) the static geometrically nonlinear analysis of a representative unit cell undergoing the action of an applied external load and (ii) the Bloch-Floquet decomposition applied to the linearized equations of the acousto-elasticity for the unit cell in the deformed configuration. The dispersion analysis is performed in terms of small amplitude motions superimposed on a deformed state, once the desired load has been applied.

1 Introduction

Controlling the propagation of elastic waves in solids has always attracted the interest of physicists and engineers. Considerable progress has been made in this area thanks to the introduction in the last decades of the so called *phononic crystals* and *elastic metamaterials*, i.e., artificial periodic structures with variations in density / stiffness / geometry, exhibiting unconventional dynamic properties, such as for instance frequency regions where the propagation of waves is inhibited, referred to as phononic bandgaps, or negative group velocity of their branches [1], allowing for negative refraction [2].
Since their introduction, a plethora of innovative applications relying on frequency filtering [3], topological protection [4, 5] and wave splitting [6] have been proposed in the most disparate fields ranging from the infrasonic to the ultrasonic frequency regime [7–11].
However, one of the main limitations of these structures is represented by the fact that once designed, their unusual dynamic properties are fixed in terms of operational frequency. For example, a metamaterial designed and manufactured to attain specific unconventional properties in a certain frequency range (for instance attenuating the propagation of elastic waves or exhibiting negative group velocity) cannot be modified to operate in a different frequency range. This implies poor versatility and adaptability to external variations, often essential for various practical applications.
In this context, periodic systems with adaptive elastic properties have been proposed tuning the dispersion diagrams through the piezoelectric effect [12, 13], inducing temperature variation [14], or exployting magneto- and light-based approaches [15, 17], as well as applying external mechanical loads [18–22].
The majority of the aforementioned investigations focused their attention on the bandgap shift / widening / reduction, whereas here, we report about the possibility of inducing negative group velocity in an isolated branch of the dispersion diagram of an inertially amplified phononic crystals. This is achieved through the application of an external state of prestress. A phononic crystal exhibiting inertial amplification mechanism has been chosen because it has been shown that the large inertial forces generated by amplifying the motion of a mass increases the inertia of the overall system and lowers its resonance frequency, allowing thus for sub-wavelength phenomena, while keeping the structure lightweight [25, 26]. As a consequence of this, the inertial amplification allows for a more remarkable curve shifts, if compared to the cases of Bragg scattering [21, 22] and / or ordinary local resonant metamaterials.
We consider the static deformation induced by the prestress to be in the linear elastic regime so to have a complete reversibility of the phenomena (tunability). The analysis is performed in terms of small amplitude motions superimposed on a deformed state once the desired load has been applied.
The paper is organized as follows: in section 2, the calculation method (referred to as a *2-step Updated Lagrangian scheme*) is briefly recalled. Both the static geometrically nonlinear analysis of a representative unit cell undergoing the action of an applied external load and the Bloch-Floquet decomposition applied to the linearized equations of the acousto-elasticity for the unit cell in the deformed configuration, are recalled. Section 3 provides a numerical example showing the concrete possibility of altering the dispersion band diagram through the application of an external state of prestress in a periodic structure exhibiting inertial amplification mechanism. Finally, section 4 synthesizes the principal results and provides future perspectives.

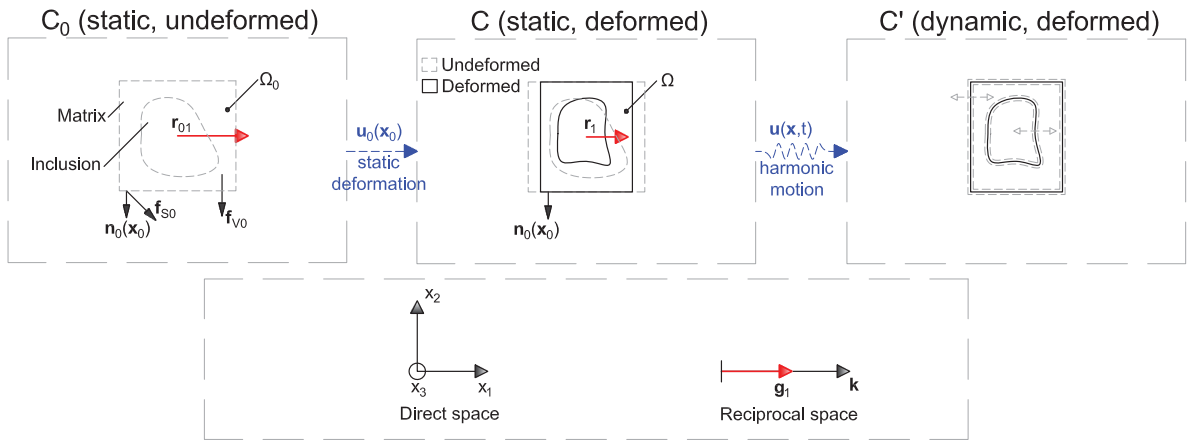

Figure 1: On the top panel, the undeformed configuration C_0, i.e. the initial unit cell (delimited by dashed lines) used to calculate the displacement and stress fields introduced by the external mechanical load (left panel), the static deformed configuration C, resulting from the application of the external mechanical load (middle panel) and the dynamic configuration C' undergoing a harmonic motion (right panel) are reported, respectively. In the bottom panel, the reference systems in the direct and reciprocal spaces are reported as well, for the sake of completeness.

2 Numerical formulation: a brief recall of the 2-step Updated Lagrangian scheme

We here recall the main steps for the band diagram calculation adopting a Bloch-Floquet finite element method which takes into account the effect of the prestress in a formulation called 2-step Updated Lagrangian scheme. Refer to [21, 22] for the full description of the approach. Synthesizing, the numerical procedure includes two principal computational steps:

1) a nonlinear static analysis involving large strains and displacements;

2) a *small-on-large* dynamic analysis, in which small vibrations are superimposed to the statically deformed unit cell.

2.1 Static analysis

Let's consider the unit cell Ω_0 represented on the top left panel of Fig. 1 by the gray dashed line. The unit cell is identified by the position vector $\mathbf{x}$ and represented by the lattice vector $\mathbf{r}_0 = \{r_{01}, 0\}^{\mathrm{T}}$ (periodicity only in the x direction is considered) and its reciprocal vector $\mathbf{g}_0 = \{g_{01}, 0\}^{\mathrm{T}} = \{r_{01}/2\pi, 0\}^{\mathrm{T}}$. If the unit cell is subjected to the application of a static volume load $\mathbf{f}_{V0}$, or surface load $\mathbf{f}_{S0}$, it undergoes a displacement $\mathbf{u}_0$, which causes a change of configuration from the undeformed state C_0 to the static deformed state C.
It is possible to write the relation between $\mathbf{r}_0$ and $\mathbf{r}$ as $\mathbf{r} = \mathbf{F}_L\mathbf{r}_0$, where $\mathbf{F}_L$ defines the affine component of the deformation gradient. Making use of the variational statement, it is possible to derive the equilibrium equations with respect to the undeformed configuration C_0:

$$\int_{\Omega} \left(\mathbf{S}(\mathbf{x}) : \delta\mathbf{E}(\mathbf{x}) - \mathbf{f}_{V0} \cdot \delta\mathbf{u}_0\right) da = \int_{\partial\Omega} \mathbf{f}_{s0} \cdot \delta\mathbf{u}_0 ds, \tag{1}$$

subjected to the Dirichlet boundary conditions:

$$\mathbf{u}_0(\mathbf{x} + \mathbf{r}_0) = \mathbf{u}_0(\mathbf{x}). \tag{2}$$

Assuming a hyperelastic material according to the Murnaghans model [27–29] and specifying the density of the unit cell as ρ_0, the elastic energy density can be defined as:

$$\psi = \frac{1}{2}\left(\lambda + 2\mu\right) I_1^2(\mathbf{E}) - 2\mu I_2(\mathbf{E}) + \frac{1}{3}\left(l + 2m\right) I_1^3(\mathbf{E}) - 2m I_1(\mathbf{E}) I_2(\mathbf{E}) + n I_3(\mathbf{E}), \tag{3}$$

in which λ and μ denote the first and second Lamé parameters, respectively, (l, m, n) the third order Murnaghan parameters, and $I_1(\mathbf{E})$, $I_2(\mathbf{E})$ and $I_3(\mathbf{E})$ the first, second and third invariants of the Green-Lagrange strain tensor, respectively.
The application of a standard Galerkin approach to Eq. (1) leads to the generalized system of equations:

$$\left[\mathbf{\Gamma}_0^{\mathrm{T}} \mathbf{K}(\mathbf{Q}_0) \mathbf{\Gamma}_0\right] \mathbf{Q}_0(\mathbf{X}) = \mathbf{P}_0(\mathbf{X}), \tag{4}$$

where $\mathbf{K}(\mathbf{Q}_0)$ is the static stiffness matrix, $\mathbf{P}_0$ the global vector of nodal forces, $\mathbf{Q}_0$ the global vector of independent nodal displacements and $\mathbf{\Gamma}_0$ the mapping operator resulting from Eq. (2) and realizing the condition $\mathbf{U}_0 = \mathbf{\Gamma}_0 \mathbf{Q}_0$. This will allow us to update the reference configuration from C_0 to C, which will be used, once properly re-meshed, as the basis unit cell for the dispersion curve calculation.

2.2 Floquet-Bloch Analysis

Under the assumption of *small-on-large analysis approach* [28, 30–32], the small harmonic perturbation $\mathbf{u}(\mathbf{x})$ can be expressed as [33]:

$$\mathbf{u}(\mathbf{x}) = \tilde{\mathbf{u}}(\mathbf{x}) \exp(\mathrm{i}kx) \exp(-\mathrm{i}\omega t), \tag{5}$$

in which the Ω-periodic displacement amplitude is taken into account (t denotes the time, ω the angular frequency, and $k \in \Lambda$ the Bloch wavenumber, being Λ the reciprocal unit cell defined in C by the reciprocal lattice vector.
The solution of the elastodynamic problem for free vibrations of the unit cell in C subjected to an initial stress $\boldsymbol{\sigma}_0$ and subjected to the Dirichlet boundary condition proceeds by first generating a new mesh for the deformed geometry of the unit cell in C and then applying a Galerkin approach [34]. The band diagrams of the phononic structure can be computed from the eigenvalue problem (the mathematical expressions of the mapping operator implementing the Dirichlet boundary condition, $\mathbf{K}_3$, $\mathbf{K}_2$, $\mathbf{K}_1$ and $\mathbf{M}$ are not reported in the present paper for the sake of brevity and can be found in Refs. [21, 22]):

$$\left\{\mathbf{\Gamma}^{\mathrm{T}} \left[k^2 \mathbf{K}_3 + \mathrm{i}k \left(\mathbf{K}_2 - \mathbf{K}_2^{\mathrm{T}}\right) + \mathbf{K}_1 - \omega^2 \mathbf{M}\right] \mathbf{\Gamma}\right\} \tilde{\mathbf{Q}}(\omega) = \mathbf{0}. \tag{6}$$

3 Numerical results

In this section, the potential of an applied external mechanical load to alter the dispersion diagram of a periodic structure characterized by an inertial amplification mechanism is shown. Specifically, the switching from positive to negative group velocity of an isolated dispersion curve is reported.
To this aim, the band diagram is calculated for the unit cell reported in Fig. 2A (proposed for the first time by Acar and Yilmaz [26]) through the numerical procedure recalled in section 2. The structure is supposed to be in epoxy with the following material parameters: $\rho = 1540$ kg/m^3, $\lambda = 2.59$ GPa, $\mu = 1.34$ GPa, $l = -18.94$, GPa, $m = -13.36$ GPa and $n = -9.81$ GPa. The geometrical dimensions can be derived from Fig. 2A knowing that $t_2 = 0.4$ mm has been assumed.

Once the deformation induced in the unit cell by an initial state of stress / strain applied to the structure has been calculated according to the steps reported in section 2.1, the band structures are computed considering the unit cell to infinitely duplicate in a periodic linear array, and assuming the epoxy in its linear elastic regime and under the hypothesis of small displacements (see section 2.2). Both a compression and a traction condition of load are considered by applying a displacement $\mathbf{u}_0(\mathbf{x}_0) \cdot \mathbf{n}_0(\mathbf{x}_0)$ normal to the external vertical faces of the unit cell (highlighted in blue in Fig. 2A).
Figure 2B reports the plots of the the reduced wavenumber k^* along the $\Gamma - X$ irreducible path as a function of the frequency ([$0 - 900$ Hz range]) for $+130$ μm (left panel), 0 μm (central panel) and -360 μm (right panel) assigned prestrains. We focus our attention on the dispersion branch highlighted in purple, which, in contrast to the other branches reported in gray, besides a general shift, undergoes a group velocity inversion for some values of the reduced wavenumber k^*. Specifically, if inducing a pre-solicitation state of traction, the inflexion point is achieved around $k^* \simeq 0.5\pi/a$, whereas, when inducing a state of pre-compression, the transition occurs for $k^* \simeq 0.65\pi/a$ (black arrows in Fig. 2B). To gain further insight on this phenomenon, the corresponding mode shape evaluated at the high symmetry points Γ and X are inspected and reported in Fig. 2C. From the comparison it emerges that while the vibration pattern is practically the same for low values of k^* (the 3 mode shapes denoted by the star symbol deform comparably), as the k^* increases, the deformation induced by the states of prestress alter the overall deformation mechanism with respect to the non-prestressed case (compare the 3 modes denoted by the circular dot). This change in the deformation mode happens only for this branch. As a consequence, for the other branches reported in gray in the diagram the effect of the prestress is to solely shift their frequencies. This allows us to infer that the prestress is differently felt from the deformation modes of the phononic crystal.
Finally, it is worth noticing that in the first pre-solicitation case (traction), a region in which solely the negative group velocity part of the dispersion branch can be isolated in frequency (see the orange dashed line and the orange arrow in Fig. 2B) from 525 to 550 Hz.
These results suggest that a deformation of the unit cell geometry induced by a compressive / tensile prestress state, already in the elastic regime, can lead to significant changes in the dynamic behaviour of a periodic structure, especially if the structure is dominated by an inertial amplification mechanism.

4 Concluding remarks

In this paper, we have reported about the effect of the application of a state of prestress on the band structure of a periodic phononic crystal characterized by an inertial amplification mechanism. Specifically, through a numerical example, we have shown the possibility of inducing negative group velocity in an isolated branch of the dispersion diagram.
The dispersion curves are calculated through a *2-step Updated Lagrangian scheme* within the which both the static geometrically nonlinear analysis of a representative unit cell undergoing the action of an applied external load and the Bloch-Floquet decomposition applied to the linearized equations of the acousto-elasticity for the unit cell in the deformed configuration, are implemented. The dispersion analysis is performed in terms of small amplitude motions superimposed on a deformed state, once the desired load has been applied. It is worth mentioning that we have considered the static deformation induced by the prestress to be in the linear elastic regime, so to guarantee a complete reversibility of the phenomena, once the load removed.
This study may represent a practical solution for reducing one of the limitations of phononic crystals / metamaterials, represented by the fact that once designed, their unusual dynamic prop-

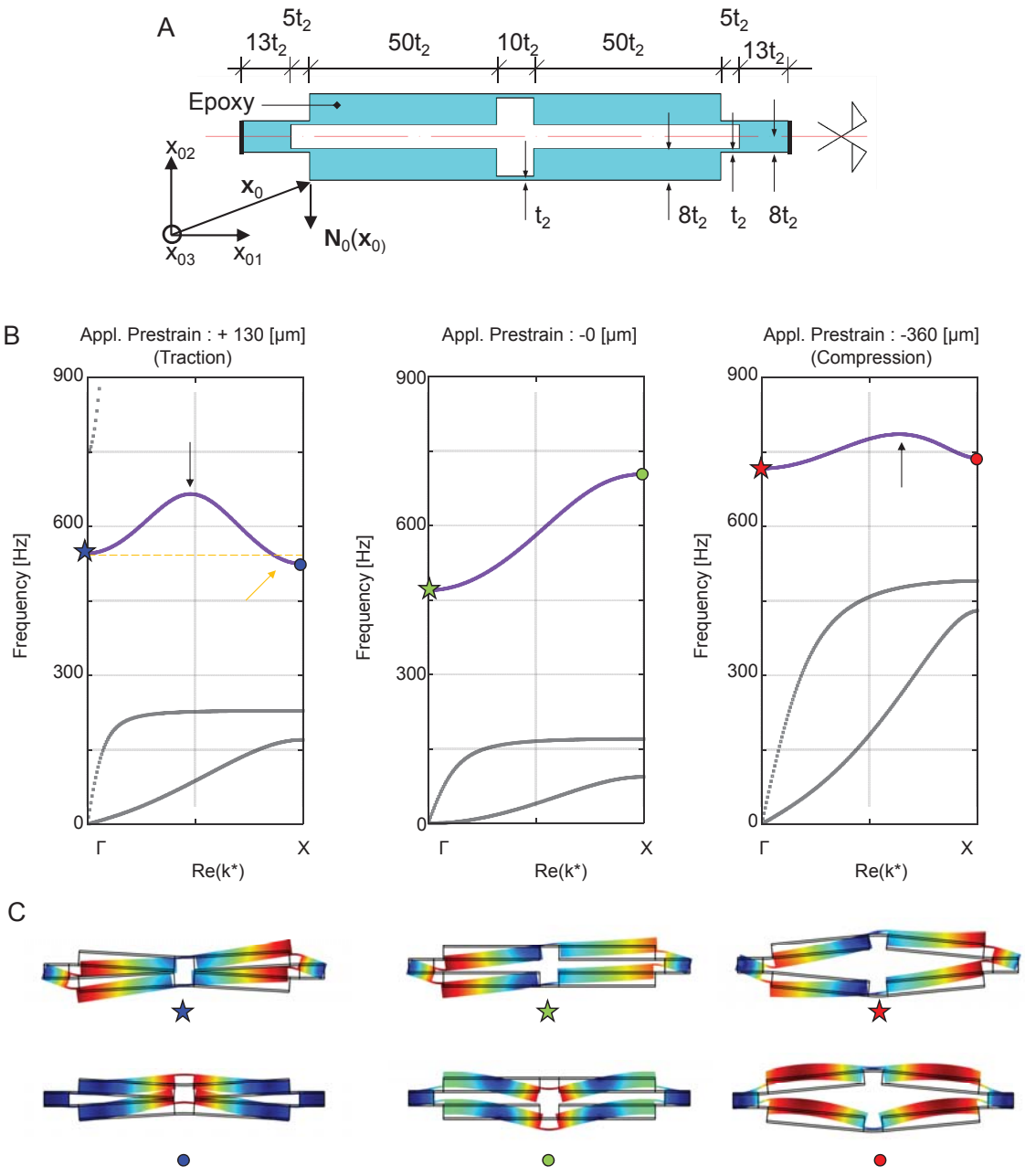

Figure 2: (A) Schematic representation of the considered unit cell along with its position $\mathbf{x}_0$ with respect to the original reference systems x_{0i}, with i = 1,2,3. (B) Plots of the the reduced wavenumber k^* along the $\Gamma - X$ irreducible path as a function of the frequency for $+130$ μm (left), 0 μm (centre) and -360 μm (right) prestrain conditions. (C) Mode shapes at the edges of the $\Gamma - X$ irreducible path.

erties are fixed in terms of operational frequency.
Future research may include the application of additional internal state of prestress (for instance exploiting the tensegrity paradigm) to foster the application of phononic crystals and metamaterials in engineering problems such as waveguiding / filtering of elastic waves, impact protection, and the design of tunable acoustic lenses.

Acknowledgements

FF acknowledges financial support from the Italian Ministry of Education, University and Research (MIUR) under the P.R.I.N. 2017 National Grant‘ Multiscale Innovative Materials and Structures’ (Project Code 2017J4EAYB).

REFERENCES

[1] Deymier P. A., (eds) 2013. Acoustic Metamaterials and Phononic Crystals, Springer Series in Solid-State Sciences (Springer Berlin Heidelberg).

[2] Morvan, B., Tinel, A., Hladky-Hennion, A.-C., Vasseur, J.O., Dubus, B., 2010. Experimental demonstration of the negative refraction of a transverse elastic wave in a two-dimensional solid phononic crystal Appl. Phys. Lett. 96, 101905.

[3] Hussein, M.I., Leamy, M.J., Ruzzene, M., 2014. Dynamics of phononic materials and structures: Historical origins, recent progress, and future outlook, Applied Mechanics Reviews 66, 040802.

[4] Mousavi, H., Khanikaev, A.B., Wang, Z., 2015. Topologically protected elastic waves in phononic metamaterials, Nat. Commun. 6, 8682.

[5] Miniaci, M., Pal, R.K., Morvan, B., Ruzzene, M., 2018. Experimental observation of topologically protected helical edge modes in patterned elastic plates, Phys. Rev. X 8, 031074.

[6] Miniaci, M., Pal, R.K., Manna, R., Ruzzene, M., 2019. Valley-based splitting of topologically protected helical waves in elastic plates, Phys. Rev. B 100, 024304.

[7] Miniaci, M., Gliozzi, A.S., Morvan, B., Krushynska, A.K., Bosia, F., Scalerandi, M., Pugno, N.M., 2017. Proof of concept for an ultrasensitive technique to detect and localize sources of elastic nonlinearity using phononic crystals, Phys. Rev. Lett. 118, 214301.

[8] Brûlé, S., Javelaud, E.H., Enoch, S., Guenneau, S., 2014. Experiments on seismic metamaterials: Molding surface waves, Phys. Rev. Lett. 112, 133901.

[9] Miniaci, M., Krushynska, A., Bosia, F., Pugno, N.M., 2016. Large scale mechanical metamaterials as seismic shields, New Journal of Physics 18, 083041.

[10] Fraternali, F., Amendola, A., Benzoni, G., 2018. Innovative seismic isolation devices based on lattice materials: A review, Ing. Sismica 4, 93–113.

[11] Misseroni, D., Colquitt, D.J., Movchan, A.B., Movchan, N.V., Jones, I.S., 2016. Cymatics for the cloaking of flexural vibrations in a structured plate, Scientific Reports 6, 23929.

[12] Bergamini, A., Delpero, T., De Simoni, L., Di Lillo, L., Ruzzene, M., Ermanni, P., 2014. Phononic crystal with adaptive connectivity, Advanced Materials 26, 1343–1347.

[13] Kherraz, N., Haumesser, L., Levassort, F., Benard, P., Morvan, B., 2016. Controlling Bragg gaps induced by electric boundary conditions in phononic piezoelectric plates, Applied Physics Letters 108, 093503.

[14] Jim, K.L., Leung, C.W., Lau, S.T., Choy, S.H., Chan, H.L.W., 2009. Thermal tuning of phononic bandstructure in ferroelectric ceramic/epoxy phononic crystal, Applied Physics Letters 94, 193501.

[15] Robillard, J.-F., Bou Matar, O., Vasseur, J.O., Deymier, P.A., Stippinger, M., Hladky-Hennion, A.-C., Pennec, Y., Djafari-Rouhani, B., 2009. Tunable magnetoelastic phononic crystals, Applied Physics Letters 95, 124104.

[16] Bou Matar, O., Robillard, J.-F., Vasseur, J.O., Hladky-Hennion, A.-C., Deymier, P.A., Pernod, P., Preobrazhensky, P., 2012. Band gap tunability of magneto-elastic phononic crystal, Journal of Applied Physics 111, 054901.

[17] Gliozzi, A.S., Miniaci, M., Chiappone, A., Bergamini, A., Morin, B., Descrovi, E., 2020. Photo-responsive tunable elastic metamaterials, Nat. Commun. (in press).

[18] Bordiga, G., Cabras, L., Piccolroaz, A., Bigoni, D., 2019. Prestress tuning of negative refraction and wave channeling from flexural sources, Applied Physics Letters 114, 041901.

[19] Bigoni, D., Gei, M., Movchan, A.B., 2008. Dynamics of a prestressed stiff layer on an elastic half space: filtering and band gap characteristics of periodic structural models derived from long-wave asymptotics, Journal of the Mechanics and Physics of Solids 56, 2494–2520.

[20] Gei, M., 2010. Wave propagation in quasi-periodic structures: stop/pass band distribution and prestress effects, International Journal of Solids and Structures 47, 3067–3075.

[21] Mazzotti, M., Bartoli, I., Miniaci, M., 2019. Modeling Bloch waves in prestressed phononic crystal plates, Frontiers in Materials 6, 74.

[22] Miniaci, M., Mazzotti, M., Amendola, A., Fraternali, F., 2020. Effect of prestress on phononic band gaps induced by inertial amplification, (in revision)

[23] Amendola, A. Carpentieri, G., de Oliveira, M., Skelton, R., Fraternali, F., 2014. Experimental investigation of the softening / stiffening response of tensegrity prisms under compressive loading, Composite Structures 117, 234–243.

[24] Slesarenko, V., Galich, P.I., Li, J., Fang, N.X., Rudykh, S., 2018. Foreshadowing elastic instabilities by negative group velocity in soft composites, Applied Physics Letters 113, 031901.

[25] Yilmaz, C., Hulbert, G.M., Kikuchi, N., 2007. Phononic band gaps induced by inertial amplification in periodic media, Physical Review B - Condensed Matter and Materials Physics 76.

[26] Acar, G., Yilmaz, C., 2013. Experimental and numerical evidence for the existence of wide and deep phononic gaps induced by inertial amplification in two-dimensional solid structures, Journal of Sound and Vibration 332, 6389–6404.

[27] Murnaghan, F.D., 1937. Finite deformations of an elastic solid, American Journal of Mathematics 59, 235–260

[28] Pau, A., Lanza di Scalea, F., 2015. Nonlinear guided wave propagation in prestressed plates, The Journal of the Acoustical Society of America 137, 1529–1540.

[29] Dubuc, B., Ebrahimkhanlou, A., Salamone, S., 2017. The effect of applied stress on the phase and group velocity of guided waves in anisotropic plates, The Journal of the Acoustical Society of America 142, 3553–3563.

[30] Mazzotti, M., Marzani, A., Bartoli, I., Viola, E., 2012. Guided waves dispersion analysis for prestressed viscoelastic waveguides by means of the SAFE method, International Journal of Solids and Structures 49, 2359–2372.

[31] Mazzotti, M., Miniaci, M., Bartoli, I., 2017. Band structure analysis of leaky Bloch waves in 2D phononic crystal plates, Ultrasonics 74, 140–143.

[32] Mazzotti, M., Bartoli, I., Miniaci, M., Marzani, A., 2016. Wave dispersion in thin-walled orthotropic waveguides using the first order shear deformation theory, Thin-Walled Structures 103, 128–140.

[33] Collet, M., Ouisse, M., Ruzzene, M., Ichchou, M., 2011. Floquet-Bloch decomposition for the computation of dispersion of two-dimensional periodic, damped mechanical systems, International Journal of Solids and Structures 48, 2837–2848.

[34] Mazzotti, M., Bartoli, I., Marzani, A., 2014. Ultrasonic leaky guided waves in fluid-coupled generic waveguides: hybrid finite-boundary element dispersion analysis and experimental validation, Journal of Applied Physics 115, 143512.

EURODYN 2020
XI International Conference on Structural Dynamics
M. Papadrakakis, M. Fragiadakis, C. Papadimitriou (eds.)
Athens, Greece, 23–26 November 2020

SUSCEPTIBILITY OF U-PROFILES WITH DIFFERENT GEOMETRY AND POROSITY TO GALLOPING

Stanislav Hračov[1] **and Michael Macháček**[1]

[1] Institute of Theoretical and Applied Mechanics of the Czech Academy of Sciences
Prosecká 76, CZ-19000, Prague, Czech Republic
{hracov,machacek}@itam.cas.cz

Keywords: U-profile, aeroelastic instability, galloping, wind tunnel test, rectangular cylinder

Abstract. *The proposed paper deals with the experimental investigation of the susceptibility of the set of slender beams having different U-shaped cross-sections typical, e.g., for footbridges and bridge decks with railings or with wind barriers, to the classical galloping. In particular, the influence of the depth of U-shaped profiles having constant side ratio equal to 2 onto aerodynamic drag and lift coefficients was tested in the wind tunnel. Moreover, the effect of the porosity of the vertical sides of U-shaped cross-sections on these coefficients and galloping stability was also studied. The analysis of the proneness of investigated non-porous U-beams to galloping based on the classical quasi-steady theory indicates that the influence of the depth is minimal. On the other hand, when the vertical sides of U-profiles are porous, the depth represents an important factor influencing the size and angular range of positive slope of the transversal force coefficient. The comparison with the outcomes from the tests of the prisms with rectangular cross-sections is also presented and the differences are discussed in detail.*

1 INTRODUCTION

The long slender structures with bluff cross-section, that are exposed to the wind, e.g. the power line cables, towers, tall buildings, can be prone to self-excited motion classified as transverse galloping [1]. The transverse galloping is characterized as almost harmonic oscillation of the structure with high amplitudes and low frequency, which is normal to the wind direction and emerges after reaching the critical wind velocity. The amplitudes of the vibration steadily grow by increasing the flow speed above the critical value due to negative damping, thus the system is instable and the motion is divergent. The susceptibility to the galloping is usually assessed using the quasi-steady theory [2]. The necessary condition is given by the positive slope of the transverse force [3], i.e. when the negative slope of lift coefficient is higher than the drag coefficient. Both lift and drag coefficients are obtained from the static force measurements of the analyzed body in the wind tunnel. The galloping onset wind velocity estimated on basis of the quasi-steady approach is inversely proportional to the slope of transversal force coefficient and proportional to Scruton number, which characterizes mass and damping properties of the structure or structural element [4].

The loss of aerodynamic stability of prismatic bodies with orthogonal cross-section was extensively studied in the last decades, especially with the focus on rectangular and square cross-sections. For the smooth flow conditions, Parkinson [5] observed the proneness to galloping for rectangular bodies with side ratio, *SR*, between 0.75 and 3. Using force oscillation experiment Washizu et. al. [6] found out, that transverse galloping can occur for prismatic bars with the rectangular section with side ratio, *SR*, smaller than 2.5. The stability parameter related to galloping of rectangular cylinders were also investigated by Ruscheweyh et. al [7]. The authors recommended to use more precise aero-elastic model and indicated the sensitivity to galloping for rectangular with $SR < 3$. Furthermore, the analysis of the sensitivity of other bluff cross-sections such as triangular section [8], L-shaped, T-shaped and cross-shaped sections [9] and D – shaped section [10, 11] typical for ice-coated conductors were also recently published.

This article presents the analysis of the susceptibility of a set of cylinders with various U- shaped cross-sections to galloping based on the results of static wind tunnel tests and quasi-steady hypothesis. In particular, the prisms with various U-shaped cross sections associated with side ratio, $SR = 2$, were tested in detail under the smooth flow conditions. The individual U-profiles have identical outer basic geometry and differ only by their inner depth. For zero depth the U-profile transforms to the rectangle with $SR = 2$, which is prone to galloping. The differences between the aerodynamic coefficients and their trends with varying angle of wind attack related to this rectangle and individual U-profiles are presented and discussed in detail. In addition, the influence of porosity of the vertical sides onto the coefficients and the proneness to galloping instability is also studied.

2 WIND TUNNEL TEST DESCRIPTION

The experimental testing of a set of cylinders with various U-shaped cross-sections was carried out in the wind tunnel of Institute of Theoretical and Applied Mechanics of the Czech Academy of Sciences. All tested specimens were made from wood and were 160 cm long. All have identical $SR = 2$ and identical main along and across wind dimensions $B = 30$ cm and $D = 15$ cm, respectively see Figure 1. The individual U-shaped profiles differ only by their depth, *Db*. The influence of the depth upon the values of the aerodynamic drag and lift coefficient were investigated in detail in terms of dimensionless ratio, *B/Dr*. In particular, the U-profiles with ratios $B/Dr = 2.5$, 3, 4 and 6 were analyzed. In addition, also the effect of the relatively high porosity of the vertical sides (barriers), $p = 75\%$, was studied. Each barrier was built from two plastic nets with a thickness of 1 mm having an axial 5 mm square grid with a

specific degree of fill. The nets were glued onto the frontal and rear sides of a tiny plastic frame in order to secure a sufficient stiffness of the barrier. In particular, the frame consisted from columns with rectangular cross-section of 4 mm × 2 mm and axial distance equal to 5 cm connected together at the top with a horizontal bar having also the rectangular cross-section of 4 mm × 1 mm. The total thickness of the complete barriers, t_b, was 6 mm.

Moreover, the models of prisms with rectangular cross-sections given by all side ratios *B/Dr* were also built and tested for comparison with individual U-profiles.

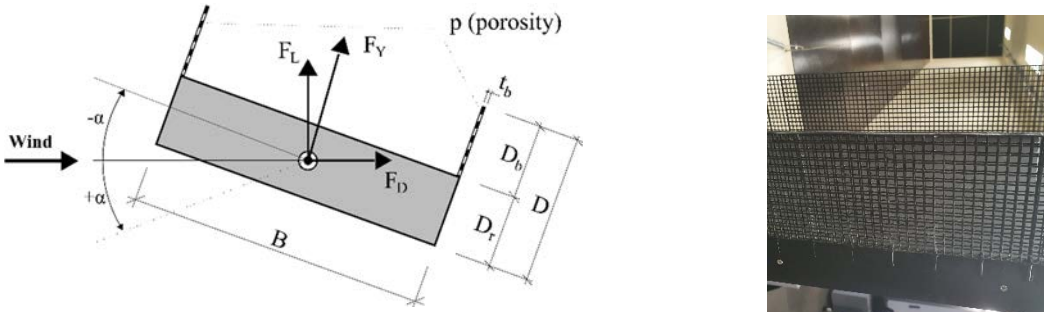

Figure 1: U-profile layout (left) and a snapshot of the vertical barrier with porosity p = 75% (right).

The models were placed vertically into the measuring part of the aerodynamic section of the wind tunnel and were enclosed between wooden and plastic end-plates, that eliminate the 3D influences and assure the homogenous flow conditions. The aerodynamic forces for the angle of attack, α, in the range from -15° to +15° were measured using two load cells ATI Industrial Automation sensors Mini 40, one at each end of the model. Each force/torque sensor was placed between the individual end of the wooden model and a specially designed rotation mechanism, which was fully fixed to metallic frame of a ceiling at the top and to a table of the floor of the wind tunnel at the bottom. The synchronized rotation of both upper and lower mechanisms enables to swivel the model with the very small angle step, $\Delta\alpha$ = 0.2°. Thus, the alternation of aerodynamic coefficients character with the changing angle, α, can be described very precisely. In our case, this small step was used for α in the range from -2.5°to 2.5°. The larger step $\Delta\alpha$ = 0.5° was used for α up to ±5° and finally for even higher α > 5° the step $\Delta\alpha$ = 1° was adopted. The data from the sensors were recorded with a sampling frequency fs = 1000 Hz for 60 seconds, which is sufficient with respect of the ergodicity and stationarity of the process.

All of the tests were performed under smooth flow conditions, i.e. with minimum turbulence intensity around 1%. Wind speed was measured by the Prandtl-Pitot tube at 400 mm above the floor before the model in place of the undisturbed stream, see the photo in Figure 2. At first, the models were loaded with the speeds in the range of 10 % - 70 % of the fan power, which is 3,0 m/s to 20 m/s, in order to determine the interval of independence of the aerodynamic coefficients on the Reynolds number, *Re*. The tests were finally carried out at a velocity of about 14 m/s corresponding to $Re = 2.8e^5$ normalized using along-wind dimension *B*.

Figure 2: Specimen installed in the aerodynamic section of the wind tunnel (left); picture of the load cell with the rotation mechanism fixed to the frame of the ceiling of the tunnel (upper right) and detailed photo of the connection of the model with the sensor at the ceiling (bottom right).

3 PROCEDURE FOR EVALUATION OF PRONENESS TO GALLOPING FROM WIND TUNNEL DATA

In order to assess the susceptibility of the individual tested profiles to the transversal galloping according to quasi-steady theory the coefficient of the static drag and lift forces have to be determined for a various angle of attack, α. The drag and lift coefficients, C_D and C_L, respectively were calculated from the measured forces according to their definitions in the forms

$$C_D(\alpha) = \frac{2 \cdot F_D(\alpha)}{\rho \cdot U^2 \cdot D \cdot L} \quad , \qquad C_L(\alpha) = \frac{2 \cdot F_L(\alpha)}{\rho \cdot U^2 \cdot D \cdot L} \quad , \tag{1}$$

where F_D and F_L are measured drag and lift forces, respectively, ρ is air density, U is the mean wind speed, D is the cross-wind dimension and L represents the length of the model.

The proneness to galloping of the particular cross-section was subsequently assessed based on the Glauert-den Hartog instability criterion [3]

$$\frac{dC_L}{d\alpha} + C_D < 0 \quad , \tag{2}$$

for a neighborhood of the zero angle of attack, i.e., $\alpha = 0°$. Den Hartog criterion was derived from a solution of one degree of freedom system loaded by transverse force *Fy*, see Figure 1, given by the transverse force coefficient [4]

$$C_{FY}(\alpha) = -C_D(\alpha) \cdot \sin(\alpha) - C_L(\alpha) \cdot \cos(\alpha). \tag{3}$$

The course of C_{FY} against the angle of attack is also presented in this paper, since it could serve for, e.g. numerical evaluation of the expected level and character of the response. It must be noted, that the approximate solution of the first derivative of C_{FY} with respect to α for $\alpha = 0°$ gives the galloping stability parameter a_g

$$a_g = \left.\frac{dC_{FY}}{d\alpha}\right|_{(\alpha=0°)} = -\left.\left(\frac{dC_L}{d\alpha} + C_D\right)\right|_{(\alpha=0°)}, \quad (4)$$

which is provided in Eurocode [12] for determination of the critical wind velocity of unstable profiles. This stability parameter was calculated for each of the tested U-profiles for a comparison with the data in existing databases or their extensions. Measurement of the static forces was expected to be slightly distorted by the effect of the higher blockage around 8.5 %. The correction based on a comparison of the results of CFD simulations carried out for a profile placed in almost unbounded space and in the confined space simulating the actual cross-section of the wind tunnel was incorporated.

4 RESULTS OF WIND TUNNEL TESTS

4.1 Beams with rectangular cross-sections

The initial static tests were aimed to determine the drag and lift coefficients for prism with the rectangular cross-section with $SR = 2$, which represents a reference case for all other measurements. The drag coefficient $C_D = 1.48$ for $\alpha = 0°$ and the slope of lift coefficient $dC_L/d\alpha = -11.29$ around the zero angle were calculated from the mean values of measured aerodynamic forces in accord to Eq. (1). The slope of C_L was obtained from a linear regression of values related to angles α from -1° to +1°. The stability parameter $a_g = 9.81$ corresponding to the above mentioned C_D and slope of C_L is significantly higher than $a_g = 2$ provided by Eurocode [12]. Nevertheless, it was confirmed by the tests of many authors, that this value does not appear as conservative at all [13]. The most similar values to the present case can be found e.g., in [6] or [14], where the stability parameter $a_g = 8.8$ and $a_g = 8.6$, respectively were stated.

The results of subsequent measurements of rectangular prisms with higher side ratio revealed, that only for $SR = 2.5$ the slope of C_L is negative and this cylinder is prone accord to Eq.(2) to galloping. The rest of prisms with $SR = 3$, 4 and 6 was determined as stable in relation to this type of instability. The drag coefficient, C_D, and slope of C_L for zero angle of attack together with the stability parameter a_g for all rectangular prisms are summarized in Table 1. In Table 1, also the angular interval, $\Delta\alpha$, where the coefficient C_{FY} has positive slope, is presented. The boundaries of interval $\Delta\alpha$, i.e., angles α_{IP}^- and α_{IP}^+ are presented in the last column of Table 1 and their two illustrative examples are graphically shown in Figure 4.

Cross section	SR [/]	C_D [/]	$dC_L/d\alpha$ [/]	a_g [/]	$\Delta\alpha$ [°]	$\langle\alpha_{IP}^-; \alpha_{IP}^+\rangle$ [°]
	2.0	1.48	-11.29	9.81	12.4	⟨-6.2; 6.2⟩
	2.5	1.32	-17.17	15.85	9.2	⟨-4.6; 4.6⟩
	3	1.14	6.63	-	-	-
	4	1.09	39.22	-	-	-
	6	0.98	67.07	-	-	-

Table 1: The drag coefficient, C_D, and the slope of the lift coefficient, $dC_L/d\alpha$, for zero angle of attack, the stability parameter, a_g, and angular interval, $\Delta\alpha$, of the positive slope of C_{FY} of the tested rectangular prims

The tests indicated higher a_g for $SR = 2.5$ than for $SR = 2$, however, the angular range $\Delta\alpha$ of the positive slope of C_{FY} is smaller. The aerodynamic coefficients and transverse force coefficient against the angle of attack is also graphically presented in Figures 3 and 4, respectively. It must be noted, that in these figures the curves related to the coefficients of rectangular cross-sections are normalized to the height $D = 150$ mm in order to be better comparable with U - beams, while in Table 1 they are normalized with respect to their real across-wind dimensions.

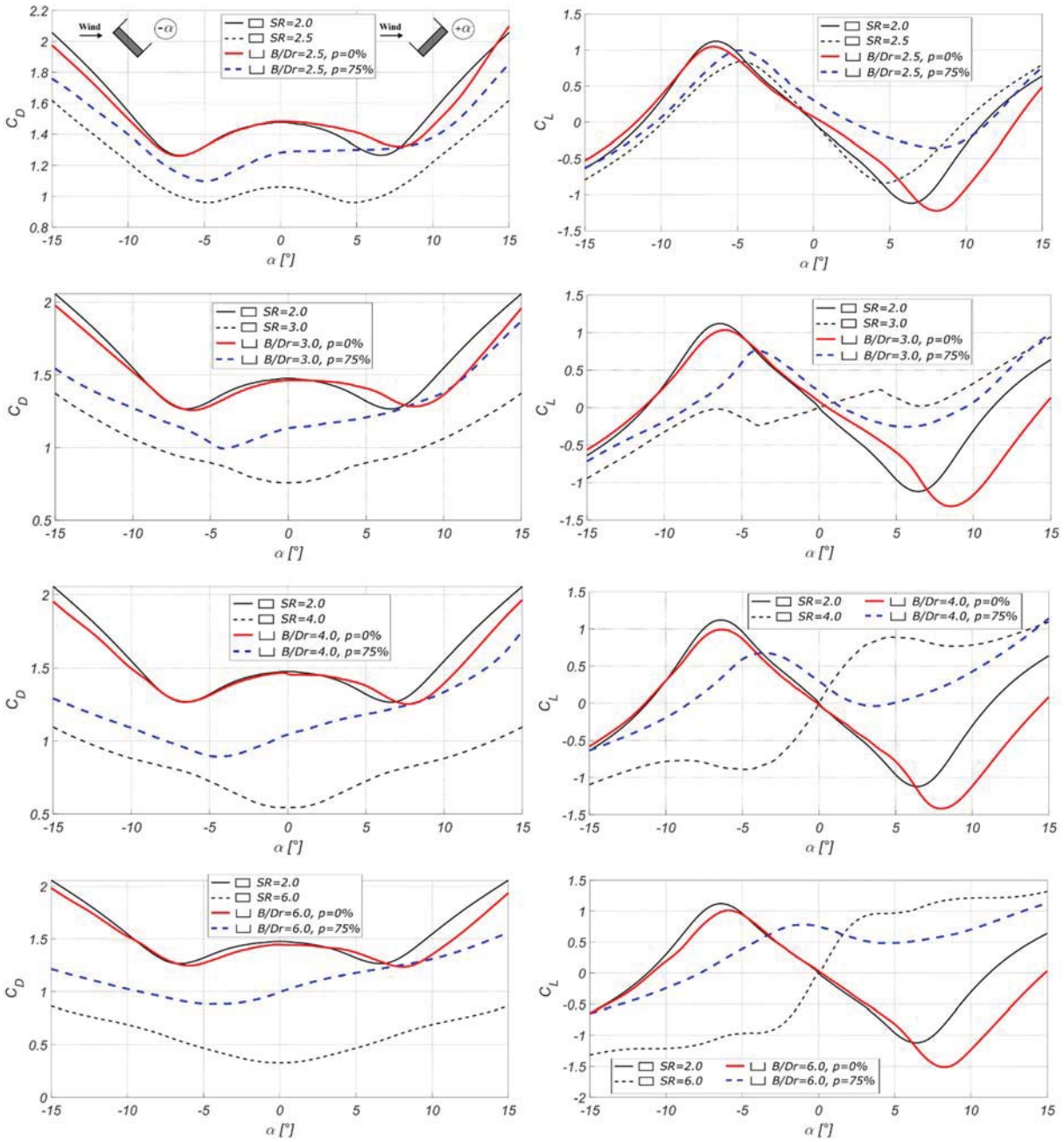

Figure 3: The drag coefficient (left column) and lift coefficient (right column) of the cylinders with rectangular and U-shaped cross sections given by side ratio *B/Dr*

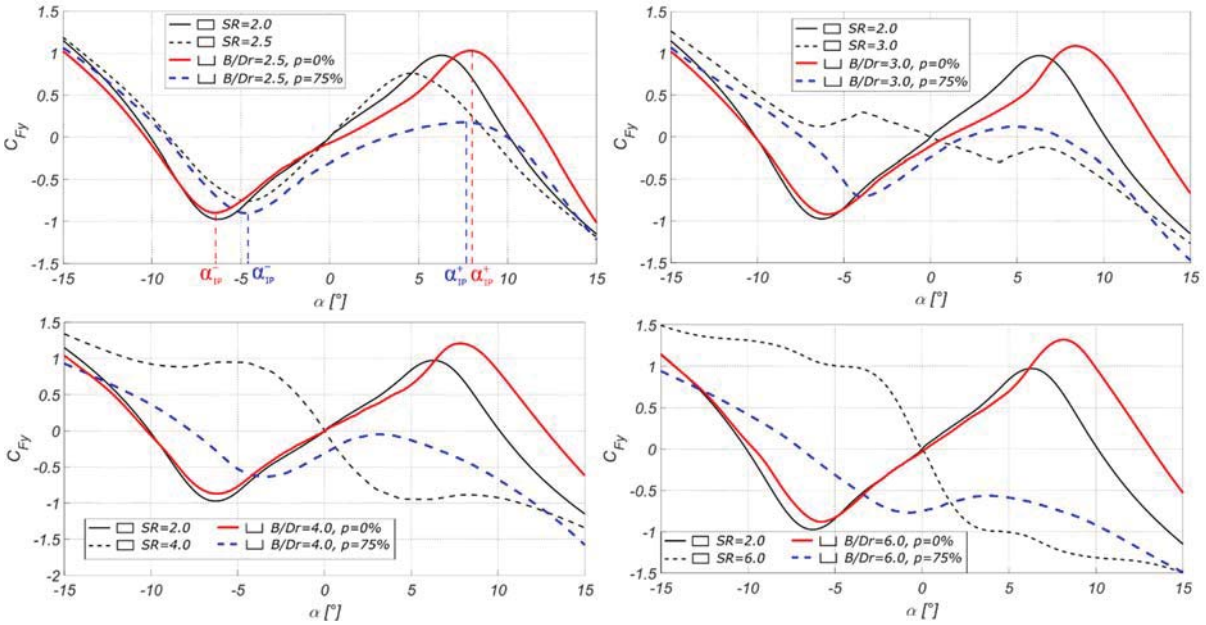

Figure 4: The transverse force coefficient of the tested cylinders with rectangular and U-shaped cross-sections

4.2 Beams with U-shaped cross-sections having non-porous vertical sides

All U-shaped prisms with zero porosity of the front and rear vertical sides (barriers) were identified as unstable. Table 2 presents the relevant aerodynamic parameters for various ratio *B/Dr*, i.e., various inner depth of the U-profile for the vicinity of zero angle of attack. The drag coefficient C_D for all *B/Dr* is almost identical to C_D of the rectangular cross-section with *SR* = 2. The slope of C_L for all *B/Dr* is negative and decreasing with the increasing inner depth, *Db*. On the other hand, the stability parameter a_g is increasing with the increase in *B/Dr*. However, a_g is in all cases smaller than a_g of the reference rectangular prism with *SR* = 2.

Cross section	B/Dr [/]	Porosity [%]	C_D [/]	$dC_L/d\alpha$ [/]	a_g [/]	$\Delta\alpha$ [°]	$\langle\alpha_{IP}^-; \alpha_{IP}^+\rangle$ [°]
⌴	2.5	0	1.48	-7.02	5.54	14.4	⟨-6.3; 8.1⟩
⌴	3	0	1.45	-8.52	7.06	14.4	⟨-6.0; 8.4⟩
⌴	4	0	1.46	-8.99	7.53	14.1	⟨-6.2; 7.9⟩
⌴	6	0	1.45	-9.59	8.14	14.0	⟨-5.7; 8.3⟩

Table 2: The aerodynamic parameters related to U-beams with zero porosity of the vertical sides

The global character of coefficients C_D, C_L and C_{FY} related to U-beams with zero porosity is illustrated in Figures 3 and 4, where they are reported against the angle of attack, α.

For negative angles up to approx. α = -8°, the minima and courses of C_D for all *B/Dr* are very similar to the minimum and the course corresponding to the reference rectangle. The same conclusion can be stated for the lift coefficient, where the coincidence is almost in the whole investigated interval of negative angles. Only the maxima of C_L are a bit lower than maximum of the reference prism.

On the contrary, the differences for positive angles exist for both C_D and C_L. In particular, the minima of C_D and C_L for all *B/Dr* lie at higher angles around α = 8.2°, which is about 2° greater value than for the rectangular prism with SR = 2. The value of the minimum of C_D is increasing with an increase in depth, D_b. On the other hand, with increasing D_b the value of the

minimum of C_L is decreasing and the slope of C_L is approaching to the slope of the reference case.

The character of the course, slope and magnitudes and positions of minima of transversal force coefficient, C_{FY}, is very similar to identical parameters of C_L. This fact holds for all tested ratios *B/Dr* and in the whole interval of investigated angles of attack. Special attention should be paid to the extension of interval Δα of the positive slope of C_{FY}, which is almost independent on depth D_b, see and compare values of $\Delta\alpha$ in Tables 1 and 2.

4.3 Beams with U-shaped cross-sections having highly porous vertical sides

The tests of U-beams with 75% porosity of vertical barriers revealed their different susceptibility to galloping. For ratios *B/Dr* = 2.5, 3 and 4 the values of stability parameter a_g indicate a comparable susceptibility, which is also very similar to non-porous U-beams, see Tables 2 and 3. Nevertheless, the angular ranges $\Delta\alpha$ of the positive slope of C_{FY} are in comparison with the non-porous prisms significantly narrowed. This reduction of $\Delta\alpha$ is increasing with the increase in the inner depth of the U-profile, i.e., in the increase in *B/Dr*.

For the highest ratio *B/Dr* = 6, not only expected decrease in C_D similar to the rest *B/Dr* due to the effect of the higher porosity occurs, but also a substantial decrease in the a_g in comparison with the same non-porous profile was determined. The interval Δα is in this case narrowed down most of all *B/Dr*. The range Δα was shifted toward the positive angles of attack, and thus the slope of C_L was in this case evaluated from data corresponding to angles from -0.4° to 0.4°. Due to the above mentioned facts, this U-beam with the highest *B/Dr* is expected to behave only weakly unstable profile when considering galloping.

Cross section	B/Dr [/]	Porosity [%]	C_D [/]	$dC_L/d\alpha$ [/]	a_g [/]	Δα [°]	$\langle\alpha_{IP}^-; \alpha_{IP}^+\rangle$ [°]
⌊⌋	2.5	75	1.28	-7.93	6.65	12.2	⟨-4.5; 7.7⟩
⌊⌋	3	75	1.10	-8.70	7.60	8.8	⟨-4.0; 4.8⟩
⌊⌋	4	75	1.00	-8.64	7.64	6.6	⟨-3.5; 3.1⟩
⌊⌋	6	75	1.00	-3.25	2.25	4.4	⟨-0.5; 3.9⟩

Table 3: The aerodynamic parameters related to U-beam with the porosity of the vertical sides p = 75%.

From Figure 3 it is evident, that curves of C_D of all prisms with vertical barriers of higher porosity have in the investigated interval of angles of attack only one minimum close to α = - 5°. The results also indicated, that at around α = 8°, there exists the angle for which the equality of C_D of both porosities related to the same ratio *B/Dr* is reached. The negative slopes of C_L around zero angle are almost identical with the corresponding slopes of C_L for zero porosity. The only exception represents the highest ratio *B/Dr*, for which the slope is significantly smaller. The angular range of negative slope of C_L is significantly reduced similarly to C_{FY} and is narrowing with the increasing *B/Dr*.

5 CONCLUSIONS

The paper presents an analysis of a proneness of a set of U-beams with constant side ratio equal to 2 to the transverse galloping. The assessment of the susceptibility of these beams that differ in the inner depth and porosity of their vertical sides was based on the quasi-steady theory and experimentally obtained drag and lift coefficients. These aerodynamic coefficients were determined for a wide range of angles of wind attack by static wind tunnel testing.

The results of analysis indicate, that the depth of the non-porous U profile has only a minor effect on the increase in the observed susceptibility to galloping. The slopes of the transversal

force coefficient related to all depths and zero angle of attack do not differ substantially. All these slopes are smaller but very close to the slope of the rectangular cross-section with identical side ratio. On the other hand, the ranges of angles of attack for which the slope of this coefficient is positive were found wider than range of the rectangular case for all depths.

The influence of the high porosity of the vertical sides of U-profile onto the aerodynamic coefficients and overall proneness to galloping was also investigated in detail. The tests for the porosity of about 75 % revealed, that in this case the depth plays an important role affecting the magnitude and the range of positive values of transversal force coefficient. In our case, especially the significant reduction of this angular range with increasing depth was observed.

ACKNOWLEDGEMENTS

The research was supported by the project No. 19-21817S of the Czech Science Foundation (GAČR).

REFERENCES

[1] R. D. Blevins, Flow-Induced Vibration, *Krieger Pub Co*, ISBN: 978-1575241838, 2001.

[2] J.P. Den Hartog, Transmission line vibration due to sleet, *Trans. AIEE* 51, 1074-1086, 1934.

[3] M.P. Paidoussis, S. J. Price, E. de Langre. Fluid-structure Interactions: cross-flow induced instabilities, *Cambridge University Press*, 2014.

[4] C. Mannini,, A. M. Marra, G. Bartoli,. Experimental investigation on VIV-galloping interaction of a rectangular 3:2 cylinder, *Meccanica, 50 (3)*, 841-853, 2015.

[5] G.V. Parkinson, Aeroelastic galloping in one degree of freedom. Wind effects on buildings and structures. *Proceedings of the conference held at the National Physical Laboratory*, 581–609, Teddington, UK, 1963.

[6] K. Washizu, A. Ohya, Y. Ostuki, K. Fujii, Aeroelastic instability of rectangular cylinders in heaving mode, *Journal of Sound and Vibration, 59(2),* 195-210, 1978.

[7] H. Ruscheweyh, M. Hortmanns, C. Schnakenberg, Vortex-excited vibrations and galloping of slender elements, *Journal of Wind Engineering and Industrial Aerodynamics,* Volume 65, Issues 1–3, 347-352,1996.

[8] G. Alonso, J. Meseguer, I. Pérez-Grande, Galloping stability of triangular cross-sectional bodies: A systematic approach, *Journal of Wind Engineering and Industrial Aerodynamics,*Volume 95, Issues 9–11, 928-940, 2007.

[9] Y. Nakamura, Y Tomonari. The aerodynamic characteristics of D-section prisms in a smooth and in a turbulent flow. *Aeronautical Quarterly* 32, 153–168. 1981.

[10] A. Okajima, et al., Study on aerostatic characteristics and aeroelastic instability of structural L-shaped,T-shaped and cross-shaped sections. *Proceedings of 12th National Symposium on Wind Engineering,* 1992.

[11] J. Lu, Q. Wang, L. Wang, H. Mei, L. Yang, X. Xu, L. Li, Study on wind tunnel test and galloping of iced quad bundle conductor, Cold Regions Science and Technology, Volume 160, 273-287, 2019.

[12] EN 1991-1-4 (2010) Eurocode 1 – Actions on structures – Part 1-4: General actions – Wind actions

[13] C. Mannini, A.M. Marra, G. Bartoli, VIV–galloping instability of rectangular cylinders: Review and new experiments, *Journal of Wind Engineering and Industrial Aerodynamics*, Volume 132, 109-124, 2014.

[14] S.O. Hansen, Wind loading design codes, Fifty Years of Wind Engineering—Prestige Lectures from the Sixth European and African Conference on Wind Engineering. University of Birmingham, pp. 35–68. 2013

EURODYN 2020
XI International Conference on Structural Dynamics
M. Papadrakakis, M. Fragiadakis, C. Papadimitriou (eds.)
Athens, Greece, 23–26 November 2020

THE EFFECT OF FOLDING WINGTIPS ON THE FLIGHT DYNAMICS OF AN AIRCRAFT WITH ELASTIC WING

Davide Balatti[1], Hamed Haddad Khodaparast[1], Michael I. Friswell[1], Marinos Manolesos[1], and Mohammadreza Amoozgar[2]

[1]Swansea University, College of Engineering,
Bay Campus, Fabian Way, Crymlyn Burrows, Swansea, SA1 8EN, UK
996702@swansea.ac.uk
h.haddadkhodaparast@swansea.ac.uk
m.i.friswell@swansea.ac.uk
marinos.manolesos@swansea.ac.uk

[2] University of Huddersfield, School of Computing and Engineering,
Huddersfield HD1 3DH, UK
m.amoozgar@hud.ac.uk

Keywords: Aeroelasticity, gust load alleviation, folding wingtip, passive control

Abstract. *In recent years, the development of lighter and more efficient transport aircraft has led to an increased focus on gust load alleviation. A recent strategy is based on the use of folding wingtip devices that increase the aspect ratio and therefore improves the aircraft performance. Moreover, numerical studies have suggested such a folding wingtip solution may incorporate spring devices in order to provide additional gust load alleviation ability in flight. It has been shown that wingtip mass, stiffness connection and hinge orientation are key parameters to avoid flutter and achieve load alleviation during gusts.*

In this paper, after defining a simplified aeroelastic model representative of an symmetric aircraft, considers the case of adding movable wingtips. The effects of hinge position, orientation and spring stiffness will be considered in order to evaluate the potential of this technique for gust load alleviation. Moreover, is studied the longitudinal flight dynamics of a rigid aircraft with elastic wing and folding wingtips.

1 Introduction

Atmospheric gusts and turbulence can significantly affect aircraft ride quality and increase airframe loads. The turbulence is caused by the movement of the air through which the aircraft passes. The gust velocity is the velocity of the air perpendicular to the flight path. The calculation of the responses to gusts and turbulence is important in the design and development of aircraft because they determine the most extreme levels of stress [1]. For this purpose, loads corresponding to gusts and manoeuvres are applied to detailed linear aeroelastic models to determine the worst-case values for various quantities of interest (e.g., bending moments, shear forces, torques, and load factors) [1] [2][3].

In aircraft design a fundamental aspect is the performance optimization, and nowadays many efforts have been made to find techniques that reduce aerodynamic drag. A considerable contribution, usually 30%-40% of the overall drag, is lift induced drag, which could be reduced by increasing the wingspan. However, such a design solution has some limitations related to the increase in bending moments along the wing and also to the maximum aircraft dimensions allowed at airports. A possible solution to the second problem is to use a folding wing that can be employed on the ground. An example of this technique is the latest version of the B-777, which has a folding wing capability. Recent work has shown the possibility to use a flexible wingtip device for load alleviation. This technique is based on a hinge that allows the wingtip to rotate. A key parameter to enable successful load alleviation is the presence of a relative angle between the hinge line and the airflow [4] [5][6].

In this work two aeroelastic models of a simplified symmetric aircraft have been developed. In the first model a classical straight wing is considered, while the second model is straight wing with a folding wingtip. Dimensions and total mass between the two models is maintained constant. The main goal of this work is to analyse the effect of folding wingtip's parameters on the longitudinal flight dynamics and gust load alleviation of the aircraft [7].

2 Aeroelastic model

In this section the aeroelastic model of the aircraft with a straight wing will be presented (model one) and subsequently the wingtip will be introduced (model two). In the two aeroelastic models the following degrees of freedoms are considered: heave (z_c) and pitch (α) of the aircraft centre of gravity and the torsional (q_t) and the bending (q_b) modes of the wing [3]. The wingtip's span is assumed to be 20% of the half span and there is a relative angle (γ) between the hinge axis and the free stream velocity. The two aeroelastic models of the symmetric aircraft have been obtained through the Lagrange formulation and considering strip theory as the aerodynamic model. Figure 1 shows model one and Figure 2 shows model two.

2.1 Structural and aerodynamic model of model one

The simplified flexible aircraft consists of a uniform, untapered, unswept flexible wing of chord c and semi-span s, plus a rigid fuselage and tailplane, as shown in Figure 1. The wing is assumed to have a uniform mass distribution and the wing mass axis (WM) lies at distance l_{WM} ahead of the aircraft centre of mass. The wing elastic axis (WE) is assumed to lie at distance l_E ahead of the wing mass axis (WM). The wing aerodynamic axis (WA) is at the wing quarter chord and is at distance l_W ahead of the center of mass and at distance l_A ahead of the elastic axis. In order to minimize any coupling between the rigid body modes and the flexible mode equations, the mean axis reference frame has been used [3].

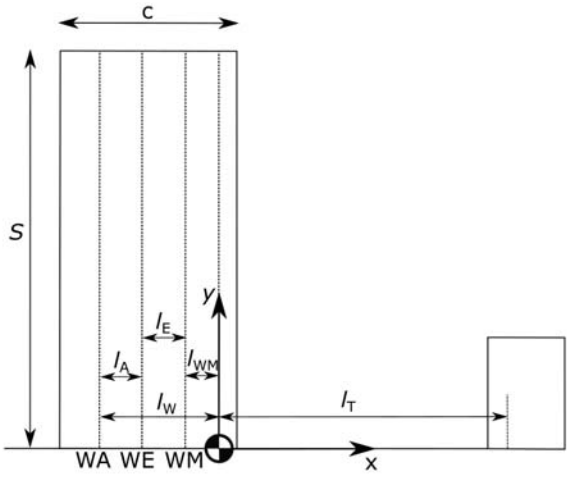

Figure 1: *Model one*

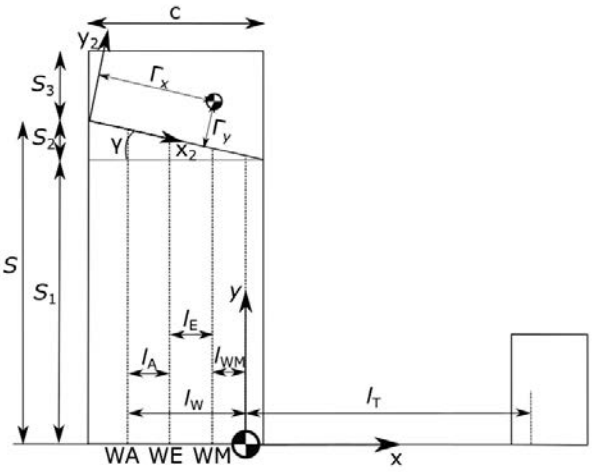

Figure 2: *Model two*

The displacement $z_{WA}(y,t)$ (downwards positive) of the wing aerodynamic axis is

$$z_{WA}(y,t) = z_c(t) - l_W\alpha(t) + k_{e_0}\left(1 + A\left(\frac{y}{s}\right)^2\right)q_b(t) - l_A\gamma_{e_0}\left(1 + B\left(\frac{y}{s}\right)\right)q_t(t) \tag{1}$$

where A and B are unknown constants defining the amount of bending and twist present along the wing span and k_{e_0} and γ_{e_0} are constants defining the wing root displacement and twist deformation. The displacement $z_T(t)$ (downwards positive) of the tailplane aerodynamic center is

$$z_T(t) = z_c(t) + l_T\alpha(t) \tag{2}$$

The aerodynamic terms due to the wing and the tailplane have to be determined. To this aim the tailplane is considered has as a rigid part, while the wing contribution involves integration using a strip dy because of the flexibility. The lift of a strip dy at the position y along the wing span is

$$dL = \frac{1}{2}\rho V^2 c dy a_w\left[\alpha - \alpha_0 + \gamma_{e_0}\left(1 + B\left(\frac{y}{s}\right)\right)q_t + k_{e_0}\left(1 + A\left(\frac{y}{s}\right)^2\right)\frac{\dot{q}_b}{V} + \frac{\dot{z}_c}{V}\right] \tag{3}$$

where a_W is the sectional wing lift curve slope. There is also a zero lift pitching moment for the wing

$$M_{0W} = \frac{1}{2}\rho V^2 S_W c C_{M_{0W}} \tag{4}$$

The tailplane lift considering the contribution of the downwash k_ϵ, the effective incidence due to the nose up pitch rate and the increment of lift due to a rigid vertical displacement, is

$$L_T = \frac{1}{2}\rho V^2 S_T\left\{a_T\left[k_\epsilon\alpha_0 + (1-k_\epsilon)\alpha + \frac{\dot{\alpha}l_T}{V} + \frac{\dot{z}_c}{V}\right] + a_E\eta\right\} \tag{5}$$

where η is the elevator angle and has been included to provide trim.

The effect of the vertical gust on the aerodynamics is a change of angle of attack. Thus on the elastic wing the increment of lift on a strip dy is given by

$$dL_{W_g} = \frac{1}{2}\rho V^2 c dy a_w\frac{w_g(t)}{V} \tag{6}$$

while on the tailplane the gust will act with a delay given by the ratio between the distance between the wing aerodynamic centre and the tailplane aerodynamic centre and the free stream velocity. Hence

$$L_{T_g} = \frac{1}{2}\rho V^2 S_T a_T \frac{w_g(t - \frac{l_W + l_T}{V})}{V} \tag{7}$$

The kinetic energy due to the rigid motion and the dynamic motion is

$$T = \frac{1}{2}m\dot{z}_c + \frac{1}{2}I_y\dot{\alpha} + \frac{1}{2}m_b\dot{q}_b + \frac{1}{2}m_t\dot{q}_t \tag{8}$$

The elastic potential energy corresponds to the strain energy in bending and torsion, such that

$$U = \frac{1}{2}k_b q_b^2 + \frac{1}{2}k_t q_t^2 \tag{9}$$

Finally, the virtual work done by lift forces and moment and gravitational field force

$$\delta W_A = \int_0^s -dL\delta z_{AC} - L_T\delta z_T + \int_0^s -dL_{W_g}\delta z_{AC} - L_{T_g}\delta z_T + M_{0W}\delta\alpha + mg\delta z_c \tag{10}$$

Exploiting the Lagrange formulation the full aeroelastic equation in the classical second order form is obtained as

$$\mathbf{A}\begin{Bmatrix}\ddot{q}_b\\ \ddot{q}_t\\ \ddot{\alpha}\\ \ddot{z}_c\end{Bmatrix} + \Big(\rho V\mathbf{B} + \mathbf{D}\Big)\begin{Bmatrix}\dot{q}_b\\ \dot{q}_t\\ \dot{\alpha}\\ \dot{z}_c\end{Bmatrix} + \Big(\rho V^2\mathbf{C} + \mathbf{E}\Big)\begin{Bmatrix}q_b\\ q_t\\ \alpha\\ z_c\end{Bmatrix} = \mathbf{f}_\eta\eta + \mathbf{f}_0 + \mathbf{f}_g + \mathbf{f}_{W_g}w_g(t) + \mathbf{f}_{T_g}w_g(t - \frac{l_W + l_T}{V}) \tag{11}$$

where **A**, **D** and **E** are the structural inertia, damping and stiffness matrices, **B** and **C** are the aerodynamic damping and stiffness matrices, **q** are the generalised coordinates and the force vector **f** on the right hand side of the equation has contributions due to the elevator, zero incidence, gravitational field, gust on the wing and gust on the tailplane.

2.2 Structural and aerodynamic model of model two

As mentioned above the difference between the two models is the presence of the movable wingtip. The model of the aircraft with the folding wingtip can be obtained from the equations of model one considering the additional contributions coming from the wingtip and taking into account that the elastic wing is composed of two contributions from wingspan s_1 and wingspan s_2, as shown in Figure 2. It is important to note that in the region of s_2 the chord is not constant, but it is function of the flare angle γ and of the span position y. The geometric relation is

$$c(y) = \frac{s_1 + s_2 - y}{\tan(\gamma)} \tag{12}$$

The wingtip is considered as a rigid body with a centre of mass at $\mathbf{\Gamma} = (\Gamma_x, \Gamma_y)$ defined in a reference system with the origin at the leading edge of the elastic wing tip and with the x-axis parallel to the hinge axis, as shown in Figure 2. θ is the degree of freedom related to the wingtip rotation and it is defined such that a positive angle variation produces a downwards displacement.

Assuming the aerodynamic centre of the wingtip is at the quarter chord and halfway along the wingspan its vertical displacement is

$$z_{AC_{wt}} = k_{e_0}\Big(1+A\Big)q_b - l_A\gamma_{e_0}\Big(1+B\Big)q_t - l_w\alpha + z_c + \frac{s_3}{2}\theta \tag{13}$$

The wingtip centre of mass is at position $\mathbf{\Gamma} = (\Gamma_x, \Gamma_y)$, and so its vertical displacement is

$$z_\Gamma = k_{e_0}\Big(1+A\Big)q_b - \Big(x_f - \frac{\Gamma_x}{\cos(\gamma)}\Big)\gamma_{e_0}\Big(1+B\Big)q_t - \Big(l_W + \frac{c}{4} - \frac{\Gamma_x}{\cos(\gamma)}\Big)\alpha + z_c + \Gamma_y\theta \tag{14}$$

where x_f is the longitudinal position of the elastic axis measured from the wing leading edge. The wingtip lift is given by

$$L_{wt} = \frac{1}{2}\rho V^2 S_{WT} a_w \left[k_{e_0}\Big(1+A\Big)\frac{\dot{q}_b}{V} + \gamma_{e_0}\Big(1+B\Big)q_t + \alpha - \alpha_0 + \frac{\dot{z}}{V} + \theta\cos(\gamma) + \frac{S_{wt}}{2}\frac{\dot{\theta}}{V} + \frac{w_g(t)}{V}\right] \tag{15}$$

The kinetic energy due to the rigid and dynamic motion is

$$T_{wt} = \frac{1}{2}m_{wt}|\dot{z}_\Gamma|^2 \tag{16}$$

and the potential energy corresponding to the strain energy of the spring at the hinge between the elastic wing and the wingtip is

$$U_{wt} = \frac{1}{2}k_{wt}\theta^2 \tag{17}$$

The total work done by the external force of the wingtip is

$$\delta W_{wt} = -dL\delta z_{ac}(y) + m_{wt}g\delta z_\Gamma \tag{18}$$

The Lagrange formulation is used to obtain the aeroelastic equation of motion as

$$\mathbf{A}\begin{Bmatrix}\ddot{q}_b\\ \ddot{q}_t\\ \ddot{\alpha}\\ \ddot{z}_c\\ \ddot{\theta}\end{Bmatrix} + \Big(\rho V\mathbf{B} + \mathbf{D}\Big)\begin{Bmatrix}\dot{q}_b\\ \dot{q}_t\\ \dot{\alpha}\\ \dot{z}_c\\ \dot{\theta}\end{Bmatrix} + \Big(\rho V^2\mathbf{C} + \mathbf{E}\Big)\begin{Bmatrix}q_b\\ q_t\\ \alpha\\ z_c\\ \theta\end{Bmatrix} = \mathbf{f}_\eta\eta + \mathbf{f}_0\alpha_0 + \mathbf{f}_g + \mathbf{f}_{W_g}w_g(t) + \mathbf{f}_{T_g}w_g(t - \frac{l_W + l_T}{V}) \tag{19}$$

In contrast to the previous case, Eq.11, an extra degree of freedom related to the wingtip rotation has been introduced.

2.3 Excitation gust

A '1 - cosine' gust disturbance is introduced at different frequencies and a constant amplitude of 5 m/s. A gust length (l_g) is considered in the range of 20-200 m in order to have a wide spectrum of excitation. The results will show that a short gust length will excite mostly the elastic modes while a long gust length will excite the rigid body modes.

3 Results

In order to analyse the models a numerical example found in literature for the gust analysis of a flexible aircraft is considered [3]. The airplane and wingtip main parameters are reported in Tables 1 and 2. All the analysis considers an equivalent airspeed of 150 m/s. The coefficients A, B, γ_{e0}, k_{e0}, the bending and the torsion modal masses have been obtained through a minimization process exploiting the orthogonality condition between the elastic modes and the rigid modes. The bending and torsional modal stiffnesses are determined to obtain the respective modal frequencies [3]. Due to the linearity of the model the analysis have been done without considering the static contribution due the initial trim in order to analyse only the dynamic response to the gust.

Total mass	5000 kg
Half span	7.5 m
l_W	0.6 m
l_T	7 m
l_A	0.25 m
l_E	0.25 m
l_{WM}	0.1 m

Table 1: *Aircraft parameters*

Mass	150 kg
Span	1.5 m
γ	20 deg
Γ_x	$\cos(\gamma)(c/4 + l_A + l_E)$
Γ_y	$\cos(\gamma)s_3/2$

Table 2: *Wingtip parameters*

3.1 Validation

The model validation compares the results of the model outline in this paper with the one obtained using a reference model with three degrees of freedoms, the vertical displacement and the pitch angle of the aircraft centre of gravity and the torsional mode of the wing [3]. In order to have a proper comparison, the natural frequencies of the elastic modes not considered in the reference model have been set to a high value and the torsional frequency is the same as the reference model.

The gust response in terms of vertical displacement of the trailing edge of the tip of the wing (z_{TE}), angle of incidence (α) and vertical displacement of the center of gravity (z_c) are simulated for gusts of different lengths. Figures 3 and 4 compare the results of, respectively, model one (coloured lines) and the reference model (black dash lines) and model two (coloured lines) and the reference model (black dash lines). In both models the torsional mode frequency is set at 8.5 Hz, the bending mode at 56 Hz and the flapping mode at 61 Hz in model two. The results show that the models give similar results.

3.2 Model two gust response

This section presents the dynamic response of model two for different gust lengths and for various wingtip parameters. The modal stiffness has been set in order to obtain the frequency of the bending mode at 5 Hz and the frequency of the torsional mode at 8.5 Hz when an high value of the wingtip stiffness connection is considered.

Figures 5, 6, 7 and 8 show the gust response in the case of low and high value of the stiffness connections between the wing and the wingtip. These two extreme cases represent the cases when the wingtip is free to rotate at the hinge ($k_\theta = 0$ Nm/rad) and wingtip is rigidly attached to the wing ($k_\theta = 10^8$ Nm/rad). When the wingtip is free to rotate at the hinge, the heave mode is less exited and the pitch mode is more exited with respect to the case when the wingtip

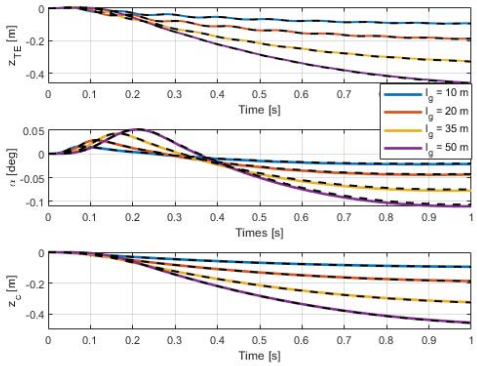

Figure 3: *Comparison between model one (continuous line) and the reference model (dash lines)*

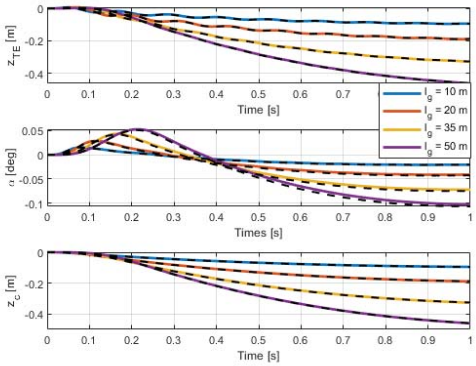

Figure 4: *Comparison between model two (continuous line) and the reference model (dash lines)*

is rigidly attached to the wing. It is also possible to see that the zero value of the stiffness connection reduces the torsional and bending mode responses.

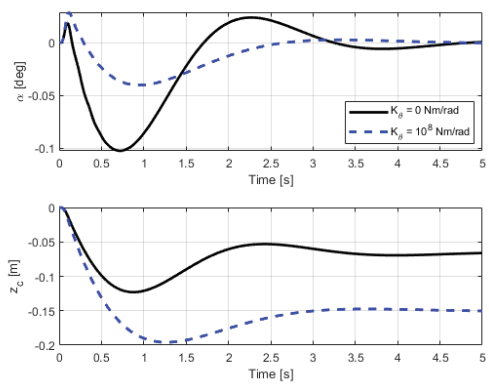

Figure 5: *Gust response of the fuselage degrees of freedom (gust length 20 m)*

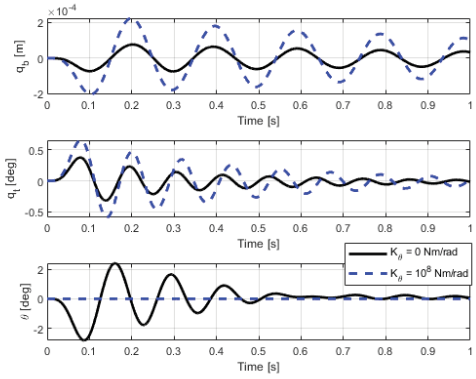

Figure 6: *Gust response of the elastic degrees of freedom (gust length 20 m)*

Figures 9, 10 and 11 show the maximum and minimum values of the wing bending and torsional modes for values of the gust length between 20 m to 200 m. Figure 9 considers different cases of wingtip stiffness connection, Figure 10 considers different cases of the flare angle (γ) and Figure 11 considers different positions, along the chordwise direction, of the wingtip centre of mass (Γ_x).

The hinge with zero torsional stiffness and the introduction of a larger flare angle are able to reduce the wing bending and the wing torsional mode response for all gust lengths. Furthermore for gusts at high frequency, if the centre of mass position is towards the trailing edge of the wingtip the torsional mode has larger positive and negative peaks, but for gusts at low frequency the torsional mode response has smaller peaks.

4 Conclusions

Two aeroelastic models representative of a symmetric aircraft have been developed, considering a straight wing and a straight wing with a folding wingtip. The validation, with respect to a similar model, has shown that the introduction of a wingtip rigidly connected to the wing gives, in terms of gust response, negligible difference with respect to the classical wing. The gust re-

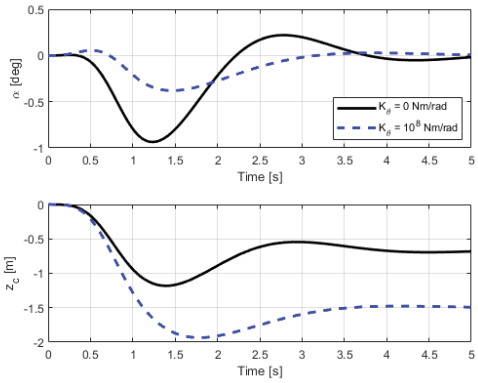

Figure 7: *Gust response of the fuselage degrees of freedom (gust length 200 m)*

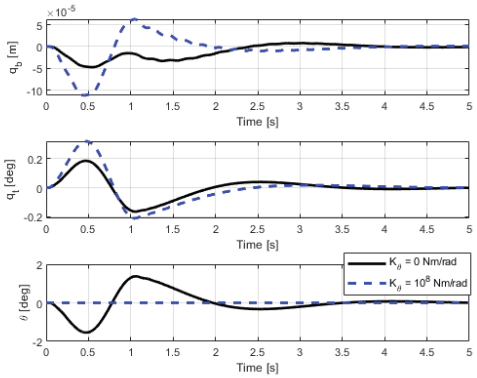

Figure 8: *Gust response of the elastic degrees of freedom (gust length 200 m)*

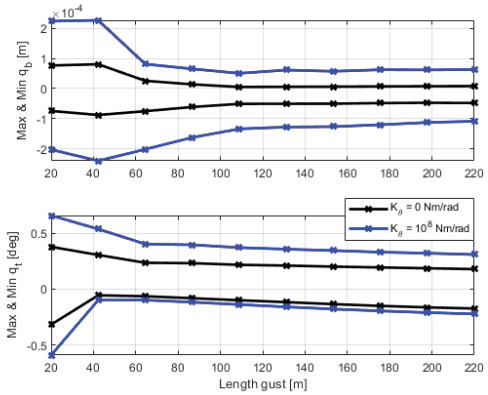

Figure 9: *Gust response for different gust lengths and values of stiffness connection*

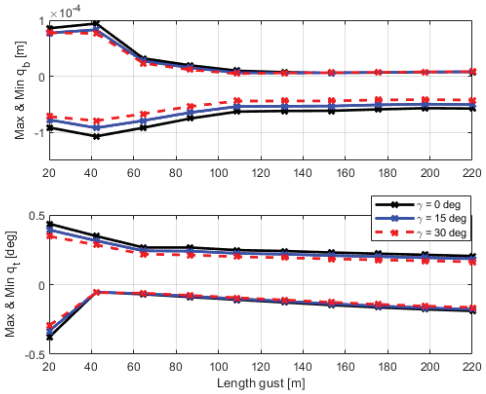

Figure 10: *Gust response for different gust lengths and flare angle ($k_\theta = 0$ Nm/rad)*

sponse analysis considering different stiffness connections of the folding wing have shown that if the wingtip is free to rotate at the hinge it is possible to reduce the bending and torsional deflection and consequently reduce the moment transmitted from the wing to the fuselage. Moreover in this configuration the aircraft will be subjected to a smaller vertical displacement during and after the gust. Finally the flare angle and wingtip centre of mass have shown to be sensitive parameters of the model.

The results have shown that, by a proper selection of the parameters, a folding wingtip could reduce the loads due to gusts with respect to a rigid wingtip. Further investigations are needed in order to better understand, in the case of large span aircraft, the effect of the geometrical nonlinearity related to the large deflections of the wingtip. Moreover experimental tests will be necessary in order to validate the models.

Acknowledgments

The research leading to these results has received funding from the Engineering Physical Science Research Council (EPSRC) through a programme grant EP/R006768/1.

REFERENCES

[1] Hoppe S.M., *Gust Alleviation Using Direct Gust Measurement*, 2000

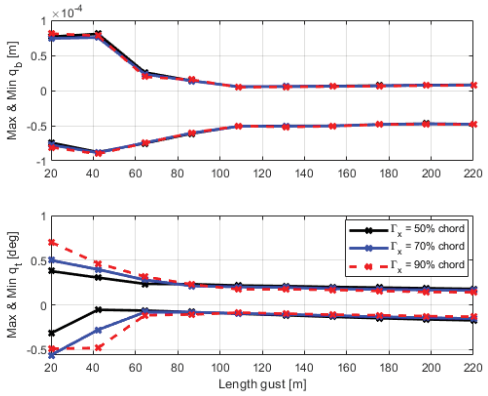

Figure 11: *Gust response for different gust lengths and positions of the wigtip center of mass ($k_\theta = 0$ Nm/rad)*

[2] H. Haddad Khodaparast, S. Coggon, M.I. Friswell, J.E. Cooper *The effects of structural nonlinearity on the dynamic response to aeroelastic gust models*, 27th International Conference on Noise and Vibration Engineering, Paper ISMA 2016

[3] Wright, J.R. and Cooper, J.E., *Introduction to aircraft aeroelasticity and loads* John Wiley & Sons, 2017

[4] A. Castrichini, V. Siddaramaiah, D. Calderon, J. Cooper, T. Wilson, Y. Lemmens, 2017. *Preliminary Investigation of Use of Flexible Folding Wing-Tips for Static and Dynamic Loads Alleviation*, Aeronautical Journal, 121(1235), pp.73-94.

[5] Castrichini, A., Hodigere Siddaramaiah, V., Calderon, D.E., Cooper, J.E., Wilson, T. and Lemmens, Y., *Nonlinear folding wing tips for gust loads alleviation*, Journal of Aircraft, 53, 5, 1391–1399, 2016

[6] Wilson T., Castrichini A., Azabal A., Cooper J. E., Ajaj R., Herring M., *Aeroelastic Behaviour of Hinged Wing Tips*, International Forum on Aeroelasticity and Structural Dynamics, Paper IFASD-2017-216

[7] Cook M. V., *Flight dynamics principles: a linear system approach to aircraft stability and control*, Butterworth-Heinemann, 2012

EURODYN 2020
XI International Conference on Structural Dynamics
M. Papadrakakis, M. Fragiadakis, C. Papadimitriou (eds.)
Athens, Greece, 23–26 November 2020

NONLINEAR STRUCTURAL BEHAVIOUR OF AN ARCH DAM UNDER STATIC AND DYNAMIC LOADS

Carla Ferreira[1], **Helena Barros**[2]

[1,2] Department of Civil Engineering, Faculty of Sciences and Technology University of Coimbra
INESC-C, Rua Luís Reis Santos - Pólo II da Universidade, 3030-788 Coimbra, Portugal
{carla,hbarros}@dec.uc.pt

Keywords: Arch dams stability, Interaction fluid-structure, Concrete Cracking, Alto Lindoso Dam.

Abstract. *The present work deals with the analysis of the structural behaviour of the Alto Lindoso arch dam under static and dynamic loads, considering fluid-structure interaction with the evaluation of service and ultimate capacity. The analysis of the maximum stresses in the super structure is obtained with undeformable foundation, since the development of the nonlinear model to evaluate these stresses, seems not to be influenced by the boundary conditions in the case of the ultimate load capacity.*

The fluid-structure interaction is formulated by the discretisation of the reservoir with infinite elements that gives a simple accommodation to complex geometries and reduced computing time in the case of concrete large dams.

The nonlinearity of the material becomes from the concrete cracking. Under tensile stresses the cracking behaviour is approximated by the smeared crack model within a small band. The width of the band may coincide with the dimension of the element. After cracking a softening behaviour control the release of the tensile stresses and the crack opening dependent on the fracture energy according to the softening behaviour. Since the dimension of the mesh affects the results of the structural analysis the independence of the mesh is obtained in this case considering linear elastic fracture mechanics.

The Alto Lindoso double curvature dam, constructed in 1992 and owned by EDP (Eletricidade de Portugal), is used as an example of the application of the model and compared to other results.

1 INTRODUCTION

A double-curvature arch dam is a very efficient structure with total volume of concrete significantly less than the conventional gravity dams. However, their geometrical complexity hinders the preliminary and final designs. Software to support the decision, to advance with a project in a specific place, giving a preliminary geometrical design with stochastic calculation performance has developed by D. J. Vicente et al [1]. The accuracy and quickness of the analysis are relevant either in the preliminary design as in final verification of the stress and strain states under static or dynamic loads. As pointed out by Chopra [2], to analyse the stress/strain state of an arch dam the structure must be correctly described, with the surrounding foundation, the concrete nonlinearities, the interaction structure-rock foundation-compressible fluid and selecting a low time step for the integration of the dynamic response. To analyse the Morrow Point Dam, Chopra [2] used 20,000 brick elements to model the body dam, 100,000 to the rock foundation, 20,000 to the fluid, and an integration time step of the order of 10−6 s for dynamic analysis. Considering the same factors, J. T. Wang [3] proceeded the analysis of Pacoima Dam, and Hariri [4, 5, 6] add the elastoplastic behaviour of the foundation, also with a large nonlinear finite-element system. These computer solutions are very time consuming, both in data preparation and computer implementation. Other authors [7-12] investigate the behaviour and stability of dams using large finite-element systems, including the relevant factors pointed out by the previous authors [2-6]. One of these factors is the concrete cracking.

The cracking of the concrete is very relevant in the design and analysis of dams in general and particularly in arch dams. The discrete crack models show advantages in the simulation of joint dams interface, as demonstrated by Zhou et al [13], with experiments in more than 20 models of high arch dams, namely under earthquakes where the joints affect the dynamic response. The models based in continuum are convenient because the dissemination and crack orientation are not known in advance. Considering the two models of this category, the damage and the smeared crack models, the smeared crack models do not involve re-meshing, the material degradation is modelled in average way and it is the option in this work by analysing the cracking formation and propagation under both static and dynamic loads. Espandar et al [7] uses a fixed smeared crack with non-orthogonal cracking in the analysis of arch dams, Mirzabozorg et al [9], Calayr et al [8] and Zhong at al [14] resort a rotating smeared crack model with, respectively a linear, exponential and bi-linear strain softening after crack starting. The stability of the smeared crack model was achieved by Li [10] increasing the mesh density and adjusting the elastic modulus according the Weibull distribution in cracking zones. The objectivity of the finite element mesh can be achieved localising the microcracking in the finite element within a small band [15, 16], keeping constant the density of fracture energy [4, 15-17].

As it was referred by Vicente [1], the procedure for the establishment of a dam includes the preliminary design, the structural performance for simplified load cases, followed by good fulfilment for the loading scenarios prescribed by regulations. A suitable solution usual requires the absence of tensile stress in the concrete. This requires to perform numerical computations from the begin to the final design procedure. Moreover, dams constructed before 1990s were designed with a pseudo-static analysis method and the actual seismic safety criteria [18] may not be satisfied. As pointed out by Wieland [19], it is needed a systematic earthquake analysis to evaluate the safety of the dams which have not been designed against earthquakes.

The authors of the present paper believe that a less time consuming model than the founded in the literature, either in data preparation and computer implementation, without loss of quality results, is relevant. This is the objective of the present work - to present a light finite element model that: discretises the structure in a few Ahmad [20] finite elements divided in

thickness layers [21]; discretises the reservoir in infinite elements to consider the fluid-structure interaction [22]; the nonlinearity of the concrete approximated by the smeared crack band model with constant energy density [15]; for dynamic analysis the displacements, velocities or accelerations are directly introduced at the borders and the Newmark-β method is used for direct integration of the equation of motion.

The model was applied to analyse the seismic behaviour of the Alto Lindoso arch dam. The results are compared with other authors. This application shows the good performance of the model.

2 CONSTITUTIVE MODEL FOR CONCRETE DAM

2.1 Title Compressed concrete

The finite element software is fit to approximate the behaviour of concrete through the elastoplastic law with the Ottosen [25] yield function and Von Mises plastic potential. However, in the study of the behaviour of arch dams the values of the compressed stresses are very low and the effect of the plasticity can be neglected.

2.2 Smeared crack band under tensile stresses

In concrete arch dams, the object of the present study, the relevant nonlinearity is due to the concrete cracking. The model used was developed and presented in [15] and it was formulated in terms of global stresses and strains. It is resumed here because it is the most relevant material nonlinearity in the dam analysis and it can highly influence the results.

The microcraking appears in a surface normal to the principal maximum tensile stress σ_t, when their value attains the concrete tensile strength f_{ct}, with the strain ε_{ct}. Being h_t the length of the element in t direction, the damage zone occurs in a length w, within the total length h_t of the element orthogonal to the crack.

In an element of volume V, there are an intact volume V_i and a damage V_d. At direction n, with no cracks, the compatibility condition imposes, $\varepsilon_n = \varepsilon_n^i = \varepsilon_n^d$, and the equilibrium gives the following integration:

$$\sigma_n = \frac{1}{V}\int_{V_i} \sigma_n^i \, dv + \frac{1}{V}\int_{V_d} \sigma_n^d \, dv \tag{1}$$

As the stresses are constant within the element at each Gauss point, the previous equation establishes the stress σ_n by

$$\sigma_n = v^i \, \sigma_n^i + v^d \, \sigma_n^d \tag{2}$$

with $v^i = V_i/V$ and $v^d = V_d/V = w/h_t$, meaning that $v^i + v^d = 1$. It can be asserted that an element has an intact volume v^i, with a strain ε_t^i given by Hook law, and a damage volume v^d, with a strain ε_t^d given by strain softening concrete behaviour.

In the t direction, normal to the crack, the axial equilibrium condition is $\sigma_t = \sigma_t^i = \sigma_t^d$ and the compatibility one is $\varepsilon_t = v^i \, \varepsilon_t^i + v^d \, \varepsilon_t^d$. For tangential stress and angular strain it is also considered $\tau_{nt} = \tau_{nt}^i = \tau_{nt}^d$ for equilibrium equation and $\gamma_t = v^i \, \gamma_{nt}^i + v^d \gamma_{nt}^d$ for deformation compatibility condition.

When the value of ε_t exceed the strain ε_{ct} ($\varepsilon_t \geq \varepsilon_{ct}$) the constitutive relation σ-ε, in terms of local coordinates n and t, can be described by:

$$\begin{Bmatrix} \varepsilon_n \\ \varepsilon_t \\ \gamma_{nt} \end{Bmatrix} = \begin{bmatrix} 1/E & 0 & 0 \\ 0 & 1/E_r & 0 \\ 0 & 0 & 1/G_r \end{bmatrix} \begin{Bmatrix} \sigma_n \\ \sigma_t \\ \tau_{nt} \end{Bmatrix} \tag{3}$$

In the previous expression, E is the Young modulus, E_r, the reduced Young modulus, and G_r the shear reduced modulus, are given by:

$$E_r = \left[\frac{1-v^d}{E} + v^d \frac{de(\sigma_t)}{d\sigma_t}\right]^{-1} ; \quad G_r = \frac{\beta G}{(1-v^d)\beta + v^d}, \tag{4}$$

where β is the decrease in tangential stiffness, varying linearly between 1, when the crack starts, to zero when the crack is opened without tensile stress.
The most common expressions for $e(\sigma_t)$ are linear, multilinear or exponential. In the present model for application to arch dams, the linear softening law is considered with the unidimensional constitutive law $\sigma - \varepsilon$, represented figure 1, and it is written by the following:

$$\sigma = \frac{f_{ct}}{\varepsilon_{ct} - \varepsilon_{tu}}(\varepsilon - \varepsilon_{tu}) \tag{5}$$

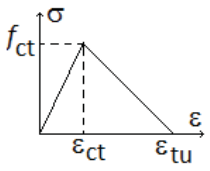

Figure 1: Stress-strain relation for concrete under tension.

The area defined by the diagram (see figure 1) is the energy deformation per unit volume G_f. According to the fracture mechanics concepts, the energy for crack propagation per unit of crack area, G_F, is a property of the concrete that can be defined using the damage length w by $G_F = w f_{ct} \varepsilon_{tu}/2$. The ultimate strain ε_{tu} can be computed and the descending branch of the stress written in function of the material parameter G_F:

$$\sigma = \frac{f_{ct} E}{w f_{ct}^{\ 2} - 2EG_F}(w f_{ct} \varepsilon - 2G_F), \tag{6}$$

that gives

$$\frac{d\sigma}{d\varepsilon} = \left[\frac{1}{E} - \frac{2G_F}{w f_{ct}^{\ 2}}\right]^{-1} \tag{7}$$

The reduced Young modulus, E_r, is obtained substituting $de(\sigma_t)/d\sigma_t$ by the inverse of the previous expression. The band width, w, is function of maximum dimension of the aggregates. In particular case it can be equal to the width of the element $w = h_t$, as suggested by Ozbalt and Bazant [23] the energy density is given by $G_f = G_F/w = G_F/h_t$ and E_r by:

$$E_r = \left[\frac{1}{E} - \frac{2G_f}{f_{ct}^{\ 2}}\right] \tag{8}$$

The material parameters, G_F and w, were evaluated experimentally by Wender et al [24] in order to be used in the numerical simulations.

The model can be extended to more than one crack, as in references [4-7,11, 16,17] but in the arch dam studied by the authors there was no case of two principal tensile stresses at the same Gauss point.

3 INTERACTION FOUNDATION-DAM-RESERVOIR

The foundation was modelled by Hariri [5] using infinite elements and he found that the results are more conservative in term of dam stresses when compared to a solution considering rigid foundation. Similar conclusion is given by Chopra [2] that to neglect the foundation mass, the stresses may be overestimated by a factor of 2 to 3. Since the objective is to develop a model less time consuming allowing a reliable behaviour of the dam under seismic loads, the rock mass foundation is neglected. It must be noted that considering the flexibility of the rock mass the period of vibration increases and influences the results.

Pressure-based infinite elements are used for simulating the reservoir domain with the same number of elements employed in dam discretization. The mid-points of the infinite elements are located at a distance from the dam equal to the height. According to Chopra [2], to neglect water compressibility may underestimated the stresses in some cases and overestimated in other cases. In the present model the water is considered incompressible by the infinite elements.

4 APPLICATION TO THE DAM-RESERVOIR SYSTEM OF ALTO LINDOSO

4.1 Geometrical characteristics of the dam

The model is applied to the Alto Lindoso dam and results are compared to other references. The dam is founded in a granite bedrock, located at the Lima river, with the following main characteristics: 309000 m^3 concrete volume; reservoir capacity of 347,8 hm^3; maximum height above foundation of 110 m; crest length of 298 m. Figure 2 represents the hydroelectric power plant [27] and figures 3 a), b), c) establish the geometrical characteristics [26] given by the planned projection of the dam, horizontal arch at depth z and the crown cantilever that has a five degree polynomial thickness variation with 4 m at the top and 21 m at the base. The arch guideline at depth z comply the equation

$$y = \frac{x^2}{2P_z} - a_z \tag{9}$$

where a_z and P_z are given by:

$a_z = 0.1867834\ z + 0.00223080\ z^2 - 0.00009865876\ z^3 + 0.000001102495\ z^4 - 0.000000004727742\ z^5$

$P_Z = 113 - 0.5703572\ z + 0.003874011\ z^2 - 0.0001736113\ z^3 + 0.000001624506\ z^4 - 0.000000004216277\ z^5$ (10)

The thickness at depth z and ordinate x is given by

$$e = e_f\left[1 + A\left(\frac{x}{100}\right)^2\right] \tag{11}$$

with e_f and A computed by:

$$e_f = 4 + 0.2081566\ z - 0.002679505\ z^2 + 0.00008034516\ z^3 - 0.0000009022521\ z^4 + \\ +0000000003209177\ z^5\ ;$$

$$A = 0.03573173\ z - 0.0008548716\ z^2 + 0.000008962299\ z^3 - 0.00000001278656\ z^4 + \\ 0.000000000005023905\ z^5\ . \tag{12}$$

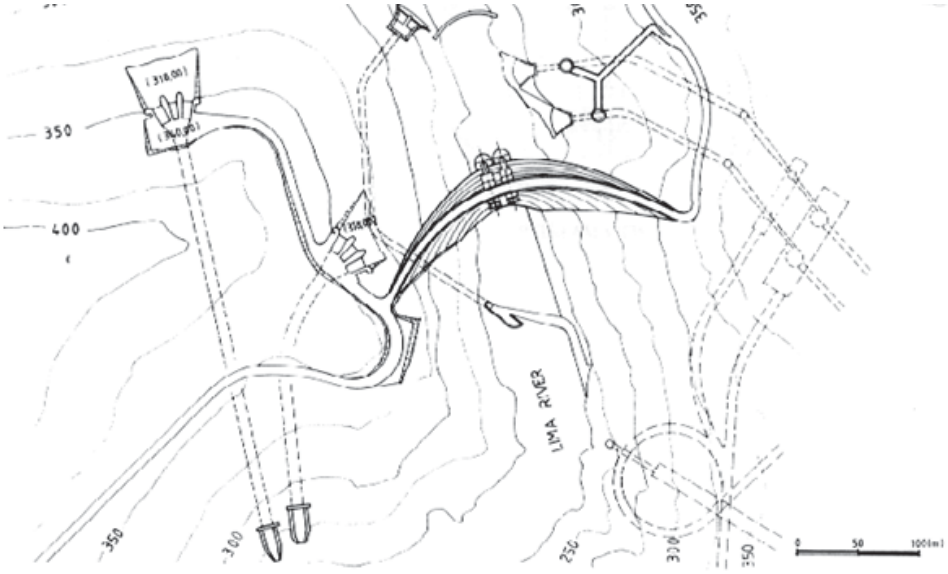

Figure 2: Hydroelectric power plant.

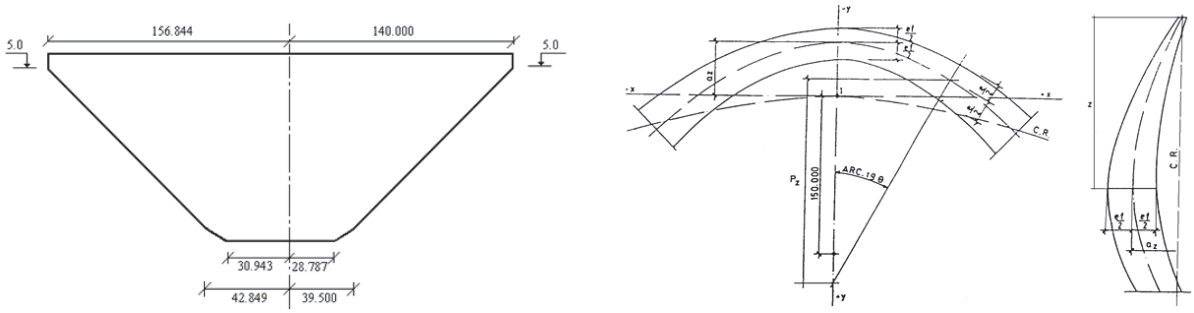

a) planned projection b) arch at depth z c) crown cantilever

Figure 3: Geometrical characteristics of Alto Lindoso arch dam.

4.2 Material parameters

The material parameters used in the analysis are summarized in table 1.

Modulus of elasticity, E	Coeficient of Poisson, ν	Conc. specific weight, γ_g	Water specific weight, γ_a	Conc. tensile strength, f_{ct}	Fracture energy $G_f=f^2_{ct}/2E$
20 GPa	0.22	24.5 kN/m^3	10 kN/m^3	1.8 / 3.65MPa	0/2/20 kN/m^2

Table 1: Material parameters.

The concrete tensile strength of f_{ct}=1.8MPa is the usual value in this kind of structure, but the value of f_{ct}=3.65MPa was also used. Values of twice or triple of the characteristic tensile strength of the concrete are usual to employ in dynamic analysis [26] and, in this case, both are used in order to compare its influence in the behaviour of the structure.

The zero value considered of the fracture energy density G_f corresponds to the σ-ε diagram without tensile retention. The other values are used to define the linear strain softening laws. The values of the fracture energy density G_f are function of the fracture energy G_F and the crack band width w. For dams usual values of G_F= 100 - 200 N/m and w=3 - 5 times the maximum aggregate dimension are generally accepted. To avoid limitations in the finite element mesh dimensions and to ensure objectivity of the analysis, an adjustment of the σ-ε diagram is made, as described above.

4.3 Analysis of the dam under static loads

In the analysis of the behaviour of the structure, in order to compute the stress distribution, the deformed shape and the maximum displacements under static and dynamic loads are relevant issue to test the model. The reliability of the model was proved using a set of analysis whose results were compared with those of the literature. Table 2 resumes the different analysis performed, all of them considering the dead load and the hydrostatic pressure in the upper stream. The foundation was considered with infinite stiffness.

		Linear elastic	Non linear – band crack model		
			G_f=0	G_f=2 kN/m^2	G_f=20 kN/m^2
Mesh A (see fig.3)	f_{ct} = 3.65MPa	ST1	-	ST2	-
	f_{ct} = 1.80MPa		-	ST3	-
Mesh B (see fig.3)	f_{ct} = 3.65MPa	ST4	ST7	ST5	ST9
	f_{ct} = 1.80MPa		ST8	ST6	ST10

Table 2: Static analysis.

The two finite element discretizations for the body dam, used in the analysis related in table 2 are represented in figure 4. The thickness of the Ahmad element is discretized in ten layers.

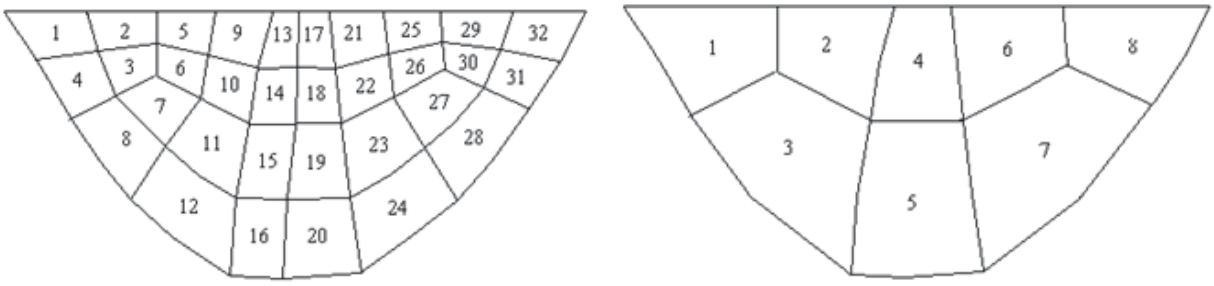

Figure 4. Discretization into 32 (mesh A) and 8 elements (mesh B) used in the analysis.

The dam reservoir was discretized in infinite elements with the intermediate nodes located at 110 m far from the medium surface of the dam, corresponding to a global of 336.9 MN of water. Figures 5 and 6 represent respectively the arch stress, σ_x, and vertical stress σ_y, along the upstream and downstream of the central cantilever, obtained with the analysis ST1e, ST2e and ST3e. The results of EDP and R. Delgado [26] are also plotted.

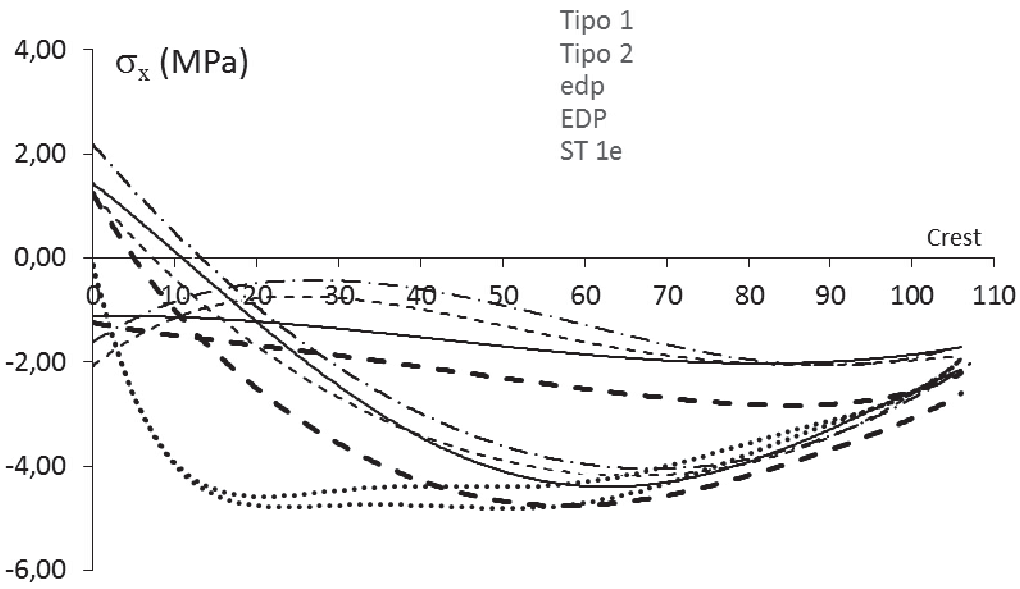

Figure 5. Arch stress σ_x, through the central cantilever.

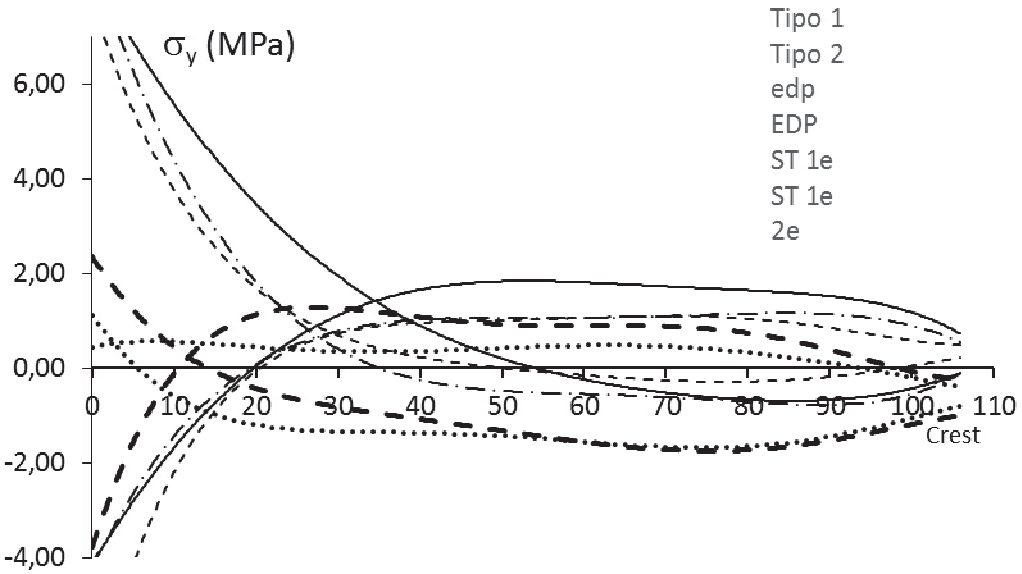

Figure 6. Arch stress σ_y, through the central cantilever.

The results of EDP were computed with a fine mesh of triangular elements and Vogt coefficients to simulate the flexibility of the foundation and R. Delgado uses 18 shell elements appealing to the symmetry of the structure [26]. Table 3 resumes maximum stresses and displacements and figure 7 shows the deformed shape of the crest.

Analysis	Maximum principal stresses (MPa)				Displacements of the midpoint of the crowning (cm)		
	Upstream		Downstream		δ_x	δ_z	δ_y
ST 1e	4.46	-6.15	1.50	-3.57	-0.39	0.98	2.71
ST 2e (f_{ct}=3.65MPa)	2.85	-4.90	1.93	-2.80	-0.40	1.06	3.02
ST 3e (f_{ct}=1.8MPa)	0.32	-2.06	0.30	-2.51	-1.04	2.11	3.29

Table 3. Maximum principal stresses and displacements.

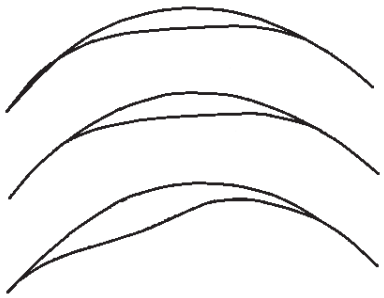

Figure 7. Deformation of the crest.

Figures 8 and 9 show the location of the cracks with the number of layers cracked at each location. In analysis ST 2e the cracks appear only at upstream (figure 8) and considering f_{ct}=1.8MPa both surfaces are cracked (see figure 9).

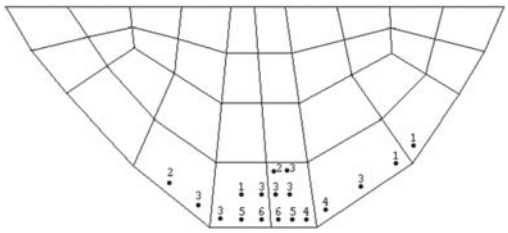

Figure 8. Crack´s location for ST 2e analysis at the upstream (f_{ct}=3.65MPa).

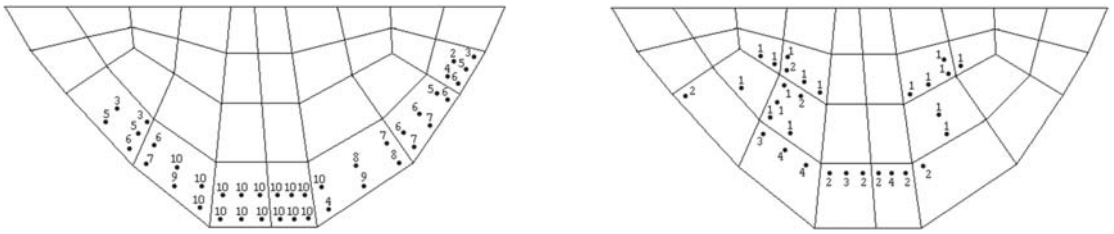

a) Upstream b) Downstream

Figure 9. Crack´s location for ST 3e analysis (f_{ct}=1.8 MPa).

The three analysis performed show: the cracking induces a stress redistribution with relevance only for the tractions at the upstream surface near de foundation; the stress distribution, the values and directions of the principal stresses and the maximum displacements are not significantly changed when the concrete tensile strength is reduced to a half; the concrete tensile strength influences the shape of the deformation and it is not convenient to consider half of the structure even in this case of slight asymmetry of the valley.

The maximum compressive (-) and tensile (+) stresses and corresponding locations, with the number of the element in parentheses, as well the displacements of the midpoint of the crowning are resumed for the analysis ST 4e to 10e in table 4.

Analysis	Maximum principal stresses (MPa)				Displacements of the midpoint of the crowning (cm)		
	Upstream		Downstream		δ_x	δ_z	δ_y
ST 4e	4.03 (5)	-3.23 (6)	2.58 (5)	-2.62 (6)	-0.38	0.97	2.57
ST 5e	1.72 (6)	-1.45 (6)	1.78 (5)	-2.80 (6)	-0.38	0.97	2.64
ST 6e	1.76 (5)	-4.80 (3)	1.79 (5)	-3.60 (6)	-0.34	0.08	2.59
ST 7e	3.44 (4)	-6.03 (6)	3.64 (5)	-6.94 (3)	-0.65	1.10	2.85
ST 8e	1.08 (1)	-8.76 (6)	1.06 (2)	-8.56 (3)	-1.85	6.50	1.60
ST 9e	2.99 (5)	-4.66 (6)	2.03 (5)	-2.93 (4)	-0.38	0.96	2.62
ST 10e	1.76 (5)	-3.01 (4)	1.80 (5)	-3.90 (4)	-0.84	1.87	2.59

Table 4. Maximum principal stresses and displacements for ST 4e to 10e analysis.

Figure 10 shows the location of the cracks with the number of layers cracked at each location.

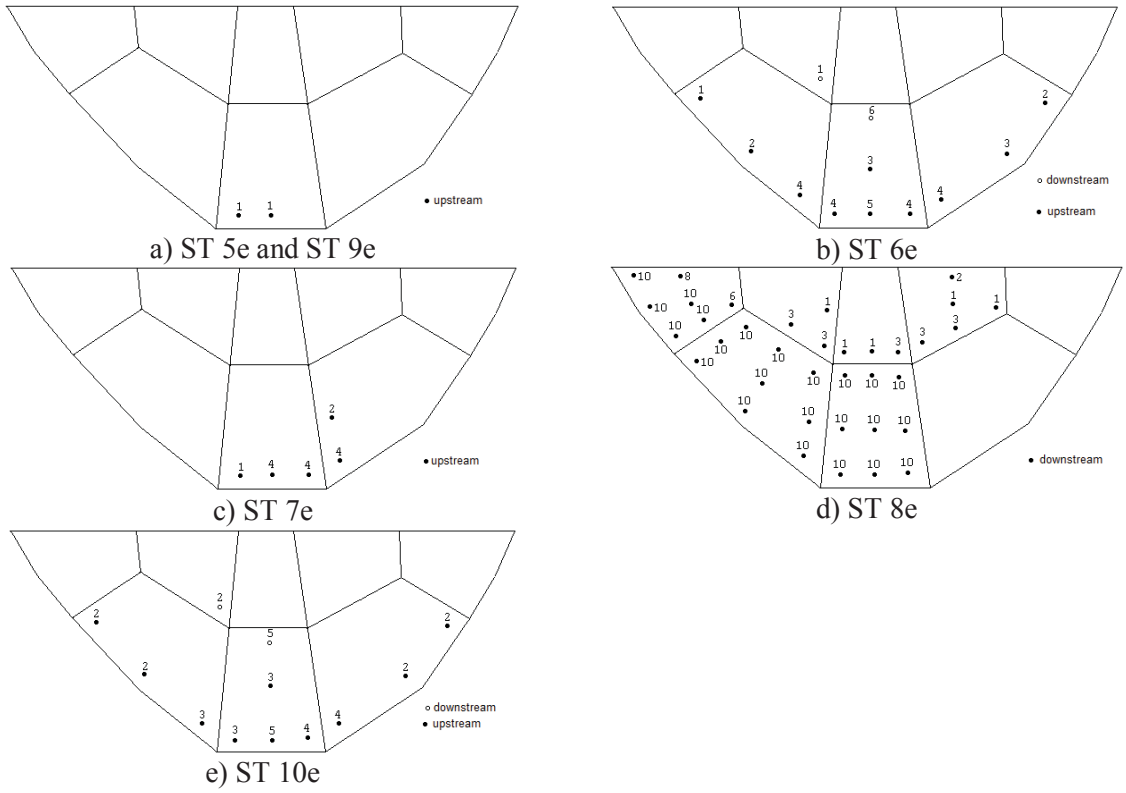

a) ST 5e and ST 9e

b) ST 6e

c) ST 7e

d) ST 8e

e) ST 10e

Figure 10. Crack´s location for ST 5e to 10e analysis.

It is clear the increment in the cracking in ST 6e, 8e and 10e relatively to ST 5e, 7e e 9e, because of the decrease of the tensile strength. The increasing in tensile retention related to the increase of G_f reduces the depth of the cracks (analysis 6e and 10e). The absence of tensile retention with, simultaneously, the tensile strength of f_{ct}=1.8MPa, induces a generalized cracking.

4.4 Analysis of the dam under constant acceleration, a=0.1g

Two groups of analysis are presented. The first group has the objective to compare the results of the present study with those of the existent literature and the second group analyses

the nonlinear behaviour of the dam under seismic loads.
Figure 11 compares the displacement increasing, relatively to the static analysis, of the crest midpoint obtained in linear analysis with mesh A and B and the results obtained by R. Delgado [26] that takes the fluid compressible and meshes of 10 and 18 finite elements for the half body dam. In these analysis the integration time is T/10, where T is the vibration period of 0.4s. The dynamic load is a constant acceleration of 0.1g applied from downstream to upstream and corresponds to the action of a moderate earthquake, traditionally considered in Portugal.

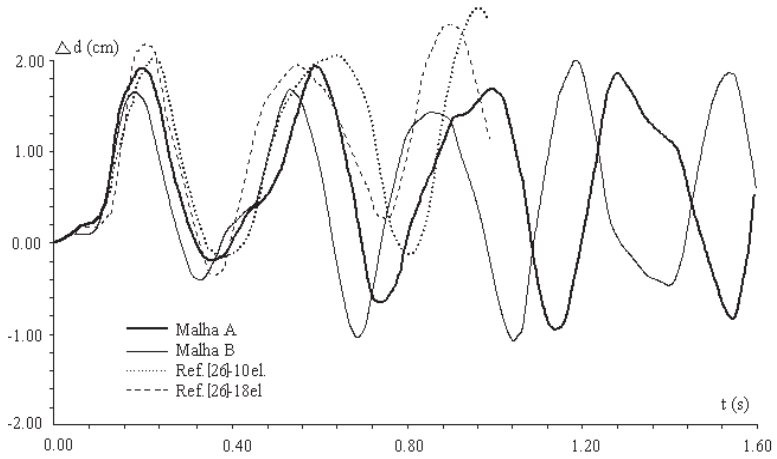

Figure 11. Horizontal displacement variation of the top of the central cantilever for a=0.1g.

The good approximation between all results in figure 11 reveals that: it is enough to consider the hydrodynamic pressures by the infinite element reservoir discretization instead of the use of 3D finite elements in a length equal to 3 times the dam height as in reference [26]; it is not relevant to consider the compressibility of the water as in reference [26]. The differences in the results can be attributed to the differences in the discretization.

The analysis were also performed for both meshes A and B considering the concrete cracking, with the tensile concrete strength of f_{ct}=3.65MPa and a density of energy G_f=2 kN/m^2. The maximum displacements of the midpoint of the crest obtained in both linear and nonlinear analysis are all in the downstream direction movements and they are resumed in table 5.

Total maximum displacements	Mesh A		Mesh B	
	t = 0.21 s		t = 0.19 s	
	Linear	Nonlinear	Linear	Nonlinear
δ_x (cm)	-0.38	-0.05	-0.50	-0.49
δ_y (cm)	4.61	5.03	4.28	4.55
δ_z (cm)	0.88	1.18	0.83	0.82

Table 5. Maximum displacements of the top of the central cantilever for a=0.1g.

At time t=0.21s, all cracks are concentrated upstream, near the support, as it can be seen in figure 12, where the number of layers cracked are indicated.

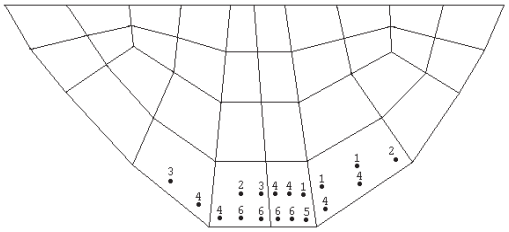

Figure 12. Crack´s location at t=0.21s for a=0.1g.

The stress variation over time can be analysed through the stress variation of two representative points located at the upstream surface of the central cantilever. One of them, placed on half height of the dam, representing the maximum compression σ_x in the arch direction. The other is the Gauss point nearest the support representing the maximum tensile stresses σ_y in the cantilever direction. In figures 13 and 14 are plotted the stresses over time, respectively, σ_x and σ_y, for the two representative points.

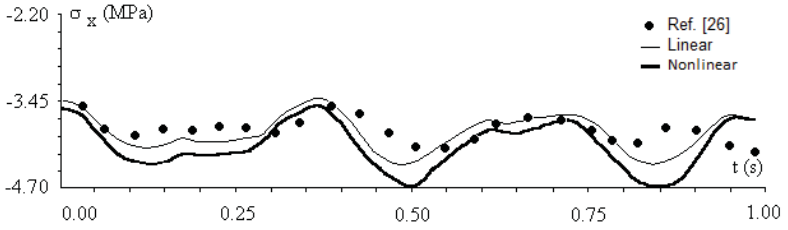

Figure 13. Stress σ_x over time at upstream half height point, for a=0.1g.

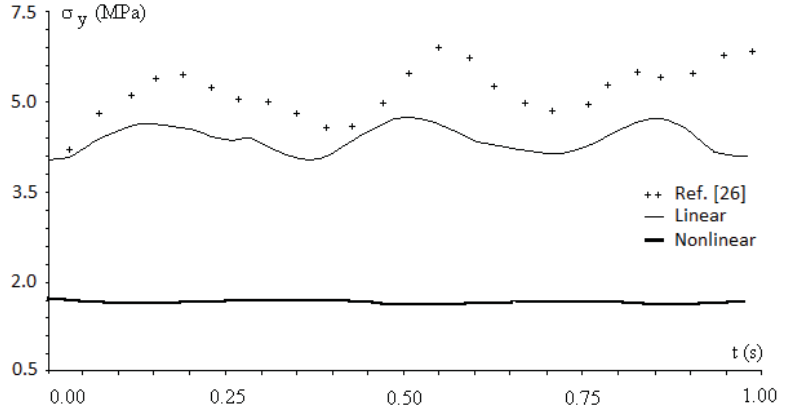

Figure 14. Stress σ_y over time at upstream near the support, for a=0.1g.

For this load case, the nonlinearity due to the cracking does not induce a relevant variation of the displacements because the cracked zone is limited to the vicinity of the support at the base (see figure 12) and simultaneously with the decrease of tensile stresses (see figure 14) the compressed stresses in the arches rise (see figure 13).

4.5 Analysis of the dam under an allowable earthquake

Due to the absence of real seismic registration close to the dam placement, an artificial ac-

celerogram generated from the ground acceleration response spectrum Se(w), as predicted in reference [28] is used. The response spectrum used is plotted in figure 15. It represents an earthquake acting during 10 s with high frequencies. This kind of earthquake is being used in the security check of arch dams and it is usually more conditioning, for typical frequencies of concrete arch dams, than other kind of long duration and low frequencies earthquake [29]. The accelerogram corresponding to the response spectrum is indicated in figure 16.

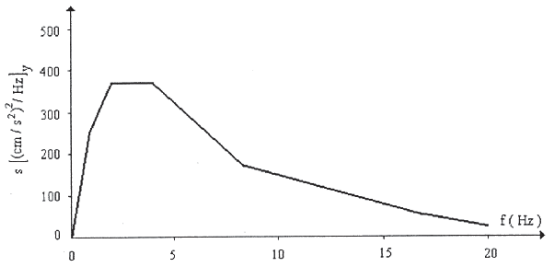

Figure 15. Response spectrum used in the generation of the accelerogram.

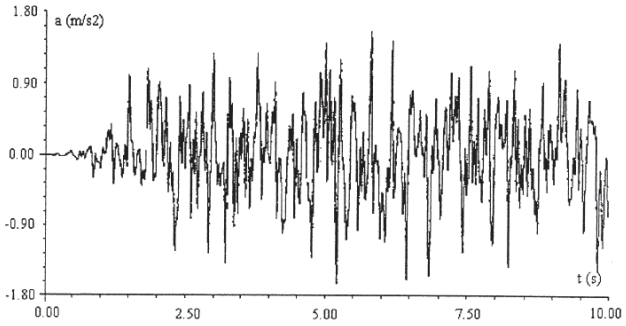

Figure 16. Accelerogram of the earthquake.

It was previously demonstrated, for dynamic load of a constant acceleration a=0.1g, that mesh B represents with good approximation the strain configuration, revealing interest for intensive simulations under seismic loads. The previous material characteristics are used in this application, with concrete strength of f_{ct}=3.65MPa and a density of energy G_f=2 kN/m^2 in nonlinear analysis with mesh B.

The displacements over the time of the midpoint of the crest are plotted in figure 17. The nonlinear analysis is represented in red and the linear in black. The upstream and downstream maximum displacements and occurring time are indicated in table 6. The figure 17 and table 6 indicate that as the effect cracking is to decrease the horizontal displacements, but it is observed an increase in the vertical displacement.

Total maximum displacements	Linear		Nonlinear	
	Upstream	Downstream	Upstream	Downstream
	t = 9.91 s	t = 7.79 s	t = 5.58 s	t = 8.20 s
δ_y (cm)	7.3	13.4	4.7	10.0

Table 6. Maximum displacements of the top of the central cantilever the earthquake.

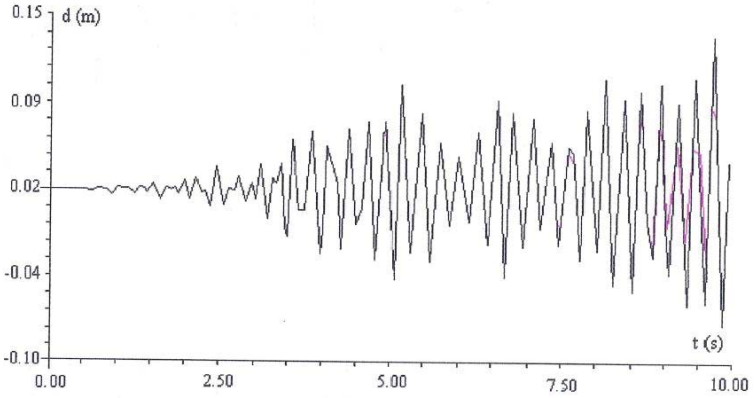

Figure 17. Horizontal displacement of the top of the central cantilever for the earthquake.

The stress variation over time can be analysed through the stress variation of two representative points located at the upstream surface of the central cantilever. One for the arch stresses, indicated in figure 18, and stresses in the cantilever direction in figure 19.

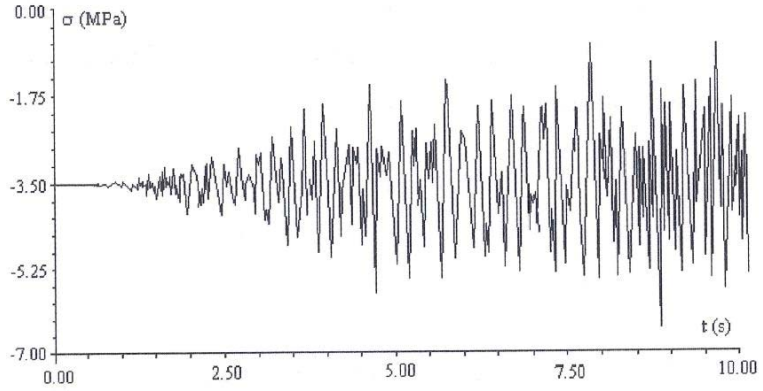

Figure 18. Arch stress, σ_x, variation over time at upstream half height point for the earthquake.

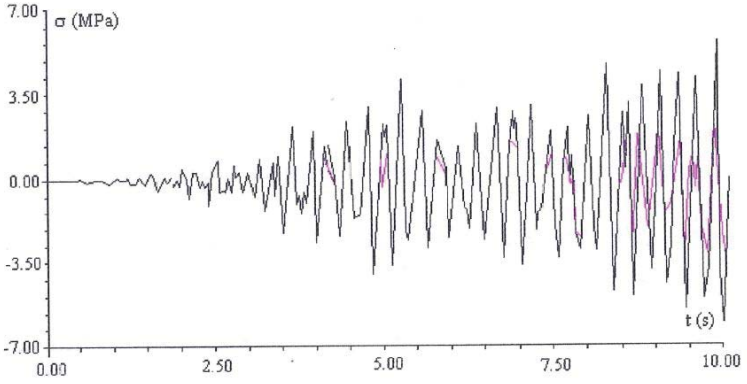

Figure 19. Stress variation, σ_y, over time at upstream near the support, for the earthquake.

The maximum stresses σ_y in the cantilever, at the upstream, vary from 6.44MPa to -4.92MPa, if cracking is disregarded, and from 2.60MPa to -3.67MPa if cracking is considered. The maximum arch stresses σ_x, downstream, vary from 5.80MPa to -0.90MPa, if cracking is disregarded, and from -6.50MPa to -0.92MPa if cracking is considered. Cracking results in a reduction of the stresses σ_y and increase in the compression stresses σ_x downstream.

5 CONCLUSIONS

The The following conclusions can be indicated:

- The present model spends little computer time, either in data preparation and computer implementation, without losing quality in the results;
- The model uses a discretisation of the structure into few finite elements with layers in the thickness;
- The model discretises the reservoir into infinite elements considering the fluid-structure interaction;
- The nonlinearity of the concrete is approximated by the smeared crack band model with constant energy density to obtain the objectivity of the finite element mesh;
- The model consider dynamic analysis of the displacements, stresses and cracking with direct integration of the equation of motion.
- The model is applied to the analysis of the seismic behaviour of an arch dam.
- The results are compared to other analysis showing the good performance of the model.

6 ACKNOWLEDGEMENTS

The financial support of ACIV-Associação para o Desenvolvimento da Engenharia Civil is gratefully acknowledged.

REFERENCES

[1] D. J. Vicente, J. San Mauro, F. Salazar, C. M. Baena, “An interactive tool for automatic predimensioning and numerical modeling of arch dams”. Mathematical Problems in Engineering, Hindawi Pub. Corp., Vol 2017, Article ID 9856938, 2017.

[2] A. K. Chopra, “Earthquake Analysis of Arch Dams: Factors to Be Considered”, Journal of Structural Engineering, ASCE, Vol 138 (2), 2012.

[3] J. T. Wang, Dan-Dan Lv, Feng Jin, Chu-Han Zhang, “ Earthquake damage analysis of arch dams considering dam-water-foundation interaction”, Soil Dynamic and Earthquake Engineering, Elsevier, Vol 49, 64-74, 2013.

[4] M. A. Hariri-Ardebili, S. M. Seyed-Kolbady, H. A. Mirzabozorg, “A smeared crack model for seismic failure analysis of concrete gravity dam considering fracture energy effects”, Structural Engineering Mechanics, 48 (1): 17-39, 2013.

[5] M. A. Hariri-Ardebili, H. A. Mirzabozorg,” A comparative study of the seismic stability of coupled arch dam-foundation-reservoir system using infinite elements and viscous boundary models”, International Journal of Structural Stability and Dynamics, 13(6), 2013.

[6] M. A. Hariri-Ardebili, “Impact of Foundation Nonlinearity on the Crack Propagation of High Concrete Dams”, Soil Mechanics and Foundation Engineering, 51(2): 72-82, 2014.

[7] R. Espandar, V. Lofti, “Comparison of non-orthogonal smeared crack and plasticity models for dynamic analysis os concrete arch dams”, Computers and Structures, 81:1461-1474, 2003.

[8] Y. Calayr, M. Karaton, “Seismic fracture analysis of concrete gravity dams including dam-reservoir interaction”, Computers and Structures, 83:1595-1606, 2005.

[9] H. A. Mirzabozorg, M. Ghaemian, "Nonlinear behaviour of mass concrete in three-dimensional problems using smeared crack approach", Earthquake Engineering Structural Dynamics, 34:247-269, 2005.

[10] Lin P., Ma T., Liang Z., An Tang C., Wang R, "Failure and overall stability analysis on high arch dams based on DFPA code". Engineering Failure Analysis, 45:164-184, 2014.

[11] M. A. Hariri-Ardebili, S. N. Seyed-Kolbadi, "Seismic cracking and instability of concrete dams: smeared crack approach", Engineering Failure Analysis, 52: 45-60, 2015.

[12] Shi Z, Nakano M, Nakamura Y, Lui C. "Discrete crack analysis of concrete gravity dams on the known inertia force field of linear response analysis" Engineering Fracture Mechanics,Vol. 115: 122 -136, 2014.

[13] J. Zhou, G. Lin, T. Zhu, A. D. Jefferson, F. W. Williams, "Experimental investigations into seismic failure of arch dams", Journal of Structural Engineering, ASCE, 2000; 126(8): 926-35.

[14] H. Zhong, Lin G., Li X., J. Li, "Seismic failure modelling of concrete dams considering heterogeinty of concrete", Solid Dynamic Earthquake Engineering, 31(12): 1678-1689, 2011.

[15] M. H. F. M. Barros, R. A. F. Martins, C. C. Ferreira, "Tension stiffening model with increasing damage for reinforced concrete", Engineering Computation,18(5-6):759-785, 2001.

[16] Wu Xu, A. M. Waas, "Modeling damage growth using the crack band model; effect of different strain measures", Engineering Fracture Mechanics, 152: 126-138, 2016.

[17] T. Okabe, S. Onodera, Y. Kumagai, Y. Nagumo, "Continuum damage mechanics modelling of composite laminates including transverse cracks", International Journal of Damage Mechanics, 27(6): 877-895, 2018.

[18] International Commission on Large Dams (ICOLD), *Selecting seismic parameters for large dams*, Committee on Seismic Aspects of Dam Design, Bulletin 137, Paris, 2009.

[19] Wieland M., "Seismic hazard and seismic design and safety aspects of large dams projects", Perspectives on European Earthquake Engineering and Seismology, A. Ansal Ed., Geotechnical, Geological and Earthquake Engineering, 34:627-650, 2014.

[20] S. Ahmad, B. M. Irons, O. C. Zienkiewicz, "Analysis oh thick and thin shells structures by curved finite elements", International Numerical Methods in Engineering, 2(3):419-451, 1970.

[21] J. A. Figueiras, Ultimate load analysis of anisotropic and reinforced concrete plates and shells, PhD Thesis, University of Swansea, 1983.

[22] G. Beer, J. L. Meek, "Infinite domain elements", International Numerical Methods in Engineering,17(1): 43-52, 1981.

[23] Bazant, Z., Ozbolt, J., "Numerical smeared fracture analysis: nonlocal microcrack interaction approach" INME, Vol. 39, 1996.

[24] R. Wender, J. Vorel, J. Smith, C. G. Hoover, Z. Bazant, G. Cusatis, "Characterization of concrete failure behavior: a comprehensive experimental database for the calibration and validation of concrete models", Material and Structures, 48:3603-3626, 2015.

[25] N. S. Ottosen, “A failure criterion for concrete”, Journal of the Engineering Mechanics Division, ASCE,103(4): 527-535, 1977.

[26] E.D.P., “Anteprojecto do Alto Lindoso. Desenho nº14, Barragem-Definição”, July, 1977.

[27] R. Delgado, *O método dos elementos finitos na análise dinâmica de barragens*, PhD Thesis, FEUP, University of Oporto, (in Portuguese), 1984.

[28] R.S.B. *Regulamento de segurança de barragens*, D.L. nº11/90 (in portuguese), 1990.

[29] R. Faria, Avaliação do comportamento sísmico de barragens de betão através de um modelo de dano contínuo, PhD Thesis, FEUP, University of Oporto, (in Portuguese), 1994.

EURODYN 2020
XI International Conference on Structural Dynamics
M. Papadrakakis, M. Fragiadakis, C. Papadimitriou (eds.)
Athens, Greece, 23–26 November 2020

A NEW OPEN SOURCE SOLVER FOR MODELLING FLUID-STRUCTURE INTERACTION: CASE STUDY OF A POINT-ABSORBER WAVE ENERGY CONVERTER WITH POWER TAKE-OFF UNIT

Bonaventura Tagliafierro[1], Rosario Montuori[1], Ioannis Vayas [2], Pablo Ropero[3], Alejandro Crespo [3], José Domìnguez[3], Corrado Altomare[4], Giacomo Viccione[1], Moncho Gòmez Gesteira [3]

[1]University of Salerno
Via Giovanni Paolo II, 132, 84084 Fisciano SA, Italy
e-mail: btagliafierro@unisa.it, r.montuori@unisa.it, gviccion@unisa.it

[2]National Technical University of Athens, Institute of Steel Structures
Iroon Politexneiou 9, 15780 Zografos, Greece
e-mail: vastahl@central.ntua.gr

[3]Universidade de Vigo
CIM-Uvigo, Ourense, Spain
e-mail: roperogiralda@gmail.com, alexbexe@uvigo.es , jmdominguez@uvigo.es, mggesteira@uvigo.es

[4]Universitat Politecnica de Catalunya
Barcelona, Catalunya, Spain
e-mail: corrado.altomare@upc.edu

Keywords: wave energy converter, numerical modelling, SPH, DualSPHysics, point absorber, efficiency

Abstract. *In this work, the capabilities of the open source code DualSPHysics coupled with the multiphysics library Project Chrono are shown. The framework is validated through an experimental campaign performed on a wave energy converter, which consists of a cylindrical heaving-buoy and a power take-off unit. The numerical model proves to correctly reproduce the hydrodynamic response of the wave energy converter under regular waves, and with three different damping coefficients of the power take-off. With this validated setup, the sensitivity of a wave energy converter to the lateral stiffness of the anchoring system is investigated. The outcomes of this numerical campaign show that the correct design of the anchoring structure should develop along with the design of the system. Enough lateral stiffness is able to avoid excessive displacements to limit the loss of efficiency. DualSPHysics is a toolbox ready to manage complex simulations, including mechanical constraints, high energetic sea states. Various scenarios along the lifespan of a floating structure can be investigated. More importantly, the model supports the preliminary studies that are of vital importance to design a test campaign.*

1 INTRODUCTION

The process of shifting our primary energy source from fossil fuel to renewable energy seems to be driven by the increased worldwide awareness about climate change. However, many other driving forces are behind the events of the past decades, such as the economic benefit. Along with solar and wind energy, a more energy-dense source with comparable availability is represented by ocean wave energy [1]. Wave energy converters (WECs) are devices that can capture the wave energy and turn it into electricity using a power take-off (PTO) system. The movement of a floating body is often the input for any system that turns mechanical energy into electric one. Point-absorbers are representative of the most widely applied class of WECs. The floating bodies of such devices are smaller than others, and easier to produce and install [2]. On top of this, they can harvest energy irregardless of the wave directionality.

Along with physical tests, the design and optimisation of such devices can be approached via numerical modelling. A range of models is available to face this problem, such as potential flow based, boundary element method, and computational fluid dynamic (CFD) models. The first two methods—to name some implementations, WAMIT [3] and WEC-Sim [4]—are well suited to tackle the design of WECs, with a particular focus on energy efficiency. However, these approaches ground on over-relaxed conditions when it comes to model fluid, waves, and the buoy mechanics. On this account, such models cannot be used when the device is under operational sea states, where the ability of simulating nonlinearities is strictly advised to obtain reliable predictions. Very energetic sea states may represent more stressing scenarios for both buoys and structures used to restrain their movement [5]. On the other hand, CFD methods can guarantee a wider field of application.

Some meshless methods have appeared over the last decade and grown in popularity as they can be applied to highly nonlinear problems in arbitrarily complex geometries — difficult to be solved by mesh-based methods instead [6]. Among the others, Smoothed Particle Hydrodynamics (SPH) meshless technique is the most popular, having attained the required level of maturity to be used for engineering purposes [7]. Being Lagrangian, SPH can be conveniently adopted to simulate free-surface flows and for capturing highly nonlinear behaviour of wave-structure interactions, or fluid-driven objects. DualSPHysics has been already used, with outstanding outcomes, to simulate WECs [8], such as an oscillating water column [9, 10], an oscillating wave surge converter [11], and a point-absorber device [12], based on the device shown in [13].

In this work, the DualSPHysics code is used to simulate a WEC under regular sea states and with different PTO systems. The energy efficiency dependence on the anchoring-structure stiffness is investigated accounting for different configurations. A simplified model is used to mimic the effect of the structure on the buoy's dynamics.

2 DUALSPHYSICS CODE

2.1 SPH Method

This section introduces the SPH formulation implemented in DualSPHysics code, and important functionalities that are required to simulate the interaction between regular waves and a heaving cylinder.

Smoothed Particle Hydrodynamics (SPH) is a mesh-less method that discretises a volume of fluid into *particles*, whose motion is given by the governing dynamics. These *particles* represent the nodal points where physical quantities (e.g. position, velocity, density, pressure) are approximated with an interpolation of the values of the neighbouring particles on a short-ranged compact support [14, 15]. It is recognised that for free surface flows, the Lagrangian

nature of the SPH method allows multiple connections among the particles, without special treatments of any surface, for the definition itself of free surface loses all meanings. Hence, the technique is ideal for studying irregular and violent flows. SPH has been used to describe a variety of free-surface flows (wave propagation over a beach, plunging breakers, impact on structures and dam breaks [16, 17]).

The mathematical fundamental of SPH is based on the approximation of any quantities by convolution integrals. Any function F can be computed by:

$$F(\boldsymbol{r}) = \int F(\boldsymbol{r'})W(\boldsymbol{r} - \boldsymbol{r'})d\boldsymbol{r'} \tag{1}$$

where W is the kernel function [18], $\boldsymbol{r'}$ is the position of a generic computational point. This function F can approximated by interpolating particle contributions; the summation is performed over all the particles within an influence region of the compact support of the kernel:

$$F(\boldsymbol{r_a}) \approx \sum_b F(\boldsymbol{r_b})W(\boldsymbol{r_a} - \boldsymbol{r_b}, h)\frac{m_b}{\rho_b} \tag{2}$$

where a is the interpolated particle, b is a neighbouring particle, m and ρ being the mass and the density, respectively, m_b/ρ_b the volume associated to the neighbouring particle b. The kernel functions W fulfils several properties, such as positivity inside the area of interaction, compact support, normalisation and monotonically decreasing with distance [19]. One option is the piecewise polynomial Quintic Wendland kernel [20]:

$$W(q) = \alpha_D(1 - \frac{q}{2})^4(2q + 1) \qquad 0 \leq q \leq 2 \tag{3}$$

where α_D is a real number that accounts for the nature of the formulation, r is the distance, and h is the smoothing length.

The code used in this work uses the weakly compressible SPH (WCSPH) for modelling fluid. The Navier-Stokes (NS) equations are solved on account of that assumption. Hence, the differential form of the NS equations are written in a discrete version using the kernel function.

$$\frac{d\boldsymbol{v_a}}{dt} = -\sum_b m_b(\frac{P_a + P_b}{\rho_a\rho_b} + \Pi_{ab})\nabla_a W_{ab} + \boldsymbol{g} \tag{4}$$

$$\frac{d\boldsymbol{\rho_a}}{dt} = \rho_a \sum_b \frac{m_b}{\rho_b}\boldsymbol{v_{ab}}\nabla_a W_{ab} + 2\delta hc\sum_b(\rho_b - \rho_a)\frac{\boldsymbol{v_{ab}}\nabla_a W_{ab}}{\boldsymbol{r_{ab}^2}}\frac{m_b}{\rho_b} \tag{5}$$

where t is the time, $\boldsymbol{v}$ is the velocity, P pressure, Π_{ab} is the artificial viscosity [19], $\boldsymbol{g}$ is the gravitational acceleration, and W_{ab} the kernel function, whose value depends on the distance $a - b$. The system of equations is bonded by a relationship between density and pressure. For the WCSPH formulation, Tait's equation of state is used to determine fluid pressure based on particle density.

$$P = \frac{c^2\rho_0}{\gamma}\left(\left(\frac{\rho}{\rho_0}\right)^\gamma - 1\right) \tag{6}$$

where c is the speed of sound, ρ_0 is the reference fluid density, γ is the politropic constant. The fluid compressibility is adjusted so that the c can be artificially lowered to assure reasonable values for the timesteps. The Symplectic time integration algorithm [21] is used in the present work and a variable time step is calculated, involving the CFL (Courant-Friedrich-Lewy) condition, the force terms and the viscous diffusion term.

2.2 Rigid body dynamics and Coupling with Project Chrono

Fluid-driven body can be easily implemented into a SPH domain. The movement of objects interacting with fluid particles in DualSPHysics is handled with different techniques. A full SPH model can deal with a rigid body by summing the total force contributions of the surrounding fluid. By assuming that a body is rigid, the net force on each boundary particle is computed according to the designated kernel function and smoothing length. Each boundary particle k experiences a force per unit mass given by:

$$\boldsymbol{f_k} = \sum_{b \in fluid} \boldsymbol{f_{kb}} \tag{7}$$

where f_{kb} is the force per unit mass exerted by the fluid particle b on the boundary particle k. For the motion of a rigid body, the basic equations of rigid body dynamics can then be used:

$$\boldsymbol{M}\frac{d\boldsymbol{V}}{dt} = \sum_k m_k \boldsymbol{f_k} \tag{8}$$

$$\boldsymbol{I}\frac{d\boldsymbol{\Omega}}{dt} = \sum_k m_k(\boldsymbol{r_k} - \boldsymbol{r_0}) \wedge \boldsymbol{f_k} \tag{9}$$

where $\boldsymbol{M}$ is the mass of the object, $\boldsymbol{I}$ is the moment of inertia, $\boldsymbol{V}$ is the velocity, $\boldsymbol{\Omega}$ the angular velocity, and $\boldsymbol{r_0}$ the centre of mass. Equations 8 and 9 are integrated in time in order to predict the values of $\boldsymbol{V}$ and $\boldsymbol{\Omega}$ at the beginning of the next time step. Each boundary particle within the body has a velocity given by:

$$\boldsymbol{v_k} = \boldsymbol{V} + \boldsymbol{\Omega} \wedge (\boldsymbol{r_k} - \boldsymbol{r_0}) \tag{10}$$

Finally, the boundary particles within the rigid body are moved by integrating 10 in time. This approach has been checked out by Monaghan et al. (2003) [22], which shows that linear and angular momentum are conservative properties. Validations about buoyancy-driven motion are performed in Dominguez et al. (2019) [23], where DualSPHysics is tested for solid objects larger than the smallest flow scales and with various densities.

Mechanical restrictions among rigid bodies, within the DualSPHysics framework, can be handled by the solvers provided by Project Chrono [24]. The Chrono-Engine library has been implemented into the original framework, creating an integrated interface for simulating structure-structure interaction as well. In fact, the library is primarily developed to handle very large systems of 3D rigid bodies [25]. The coupling allows for arbitrarily shaped bodies to be considered, and the solver is capable of integrating externally applied forces and torques, and the effects of kinematic-type restrictions, dynamic-type restrictions and internal collisions [26]. The problem is described using a Differential Variational Inequality (DVI), cast in Cone Complementary Problem (CCP) form and solved with a novel fixed point iterative method [27]. To mimic the PTO system under study, a spring-damper system is employed (see also [28]). Such element is able to apply a force according to:

$$F(t) = b\dot{z} + kz \tag{11}$$

where b is the viscous damping, k is the stiffness, and z is the displacement.

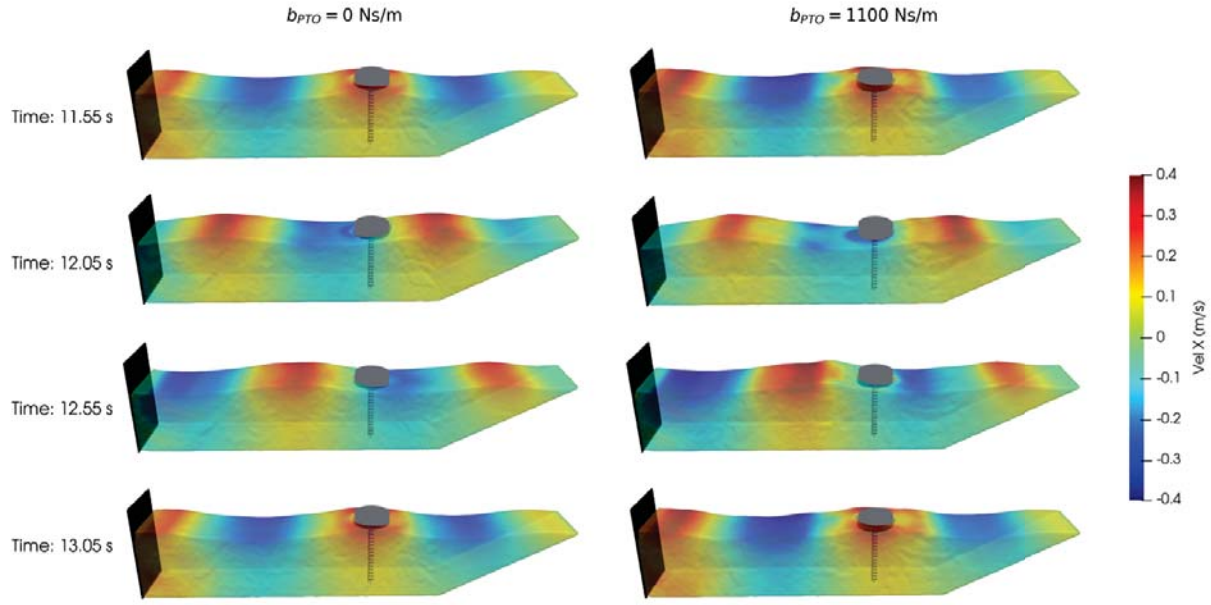

Figure 1: Snapshots of the simulations of the point-absorber for different values of the damping coefficient of the PTO.

3 VALIDATION

The specimen used for validation purposes is the wave energy converter studied by Zang et al.(2018) [29], which consists of a cylindrical heaving-buoy ($D = 0.50$m, $m = 21.6$kg, and $draft = 0.11$m) attached to a PTO system at its bottom. Rather than relying on a real device, a linear air-damper is put in its stead. This is advantageous since it allows to tune the damping coefficient and it guarantees a small variability of its value with velocity. The validation is performed by comparing the hydrodynamic response of the WEC under regular waves ($H = 0.16$m and $T = 1.50$s), and with three different damping coefficients of the PTO (b_{PTO} [Nsm^{-1}]). Different instants of the simulations can be observed in Figure 1 for two different values of b_{PTO}.

The numerical domain is modelled in the same fashion of the experimental geometries involved in (Figure 3). The flume is replicated into its exact geometries but the length. This is necessary to reduce the computational effort needed to perform the numerical analyses. A length proportional to the wave length L is used, specifically $1.50L$, and the centre of the buoy is located at 1L from the piston. This distance guarantees an optimum location, for it is far enough to allow local effects from the wave paddle, and, at the same time, close enough to avoid disturbances in the wave profile. To avoid excessive drag due to the lateral walls, periodic boundary conditions are used in place of solid boundaries. The anti-reflective structure is replaced with a dissipative beach, whose effectiveness is boosted by an additional numerical damping. Figure 1 proposes several snapshots of the numerical model, with the buoy heaving under regular waves.

Figure 2 compares the times series of the experimental and numerical vertical velocities. Each test is repeated with two different inter-particle distances, namely $dp = 0.01$m and $dp = 0.02$m, which represent the resolution of the model. As shown in past research with SPH method [30], a value of dp of around $H/10$, being H the wave height, provides accurate results. However, for a 3D environment, this may pose a limitation to the physical time to be simulated. The two investigated resolutions are respectively representative of $H/16$ and $H/8$.

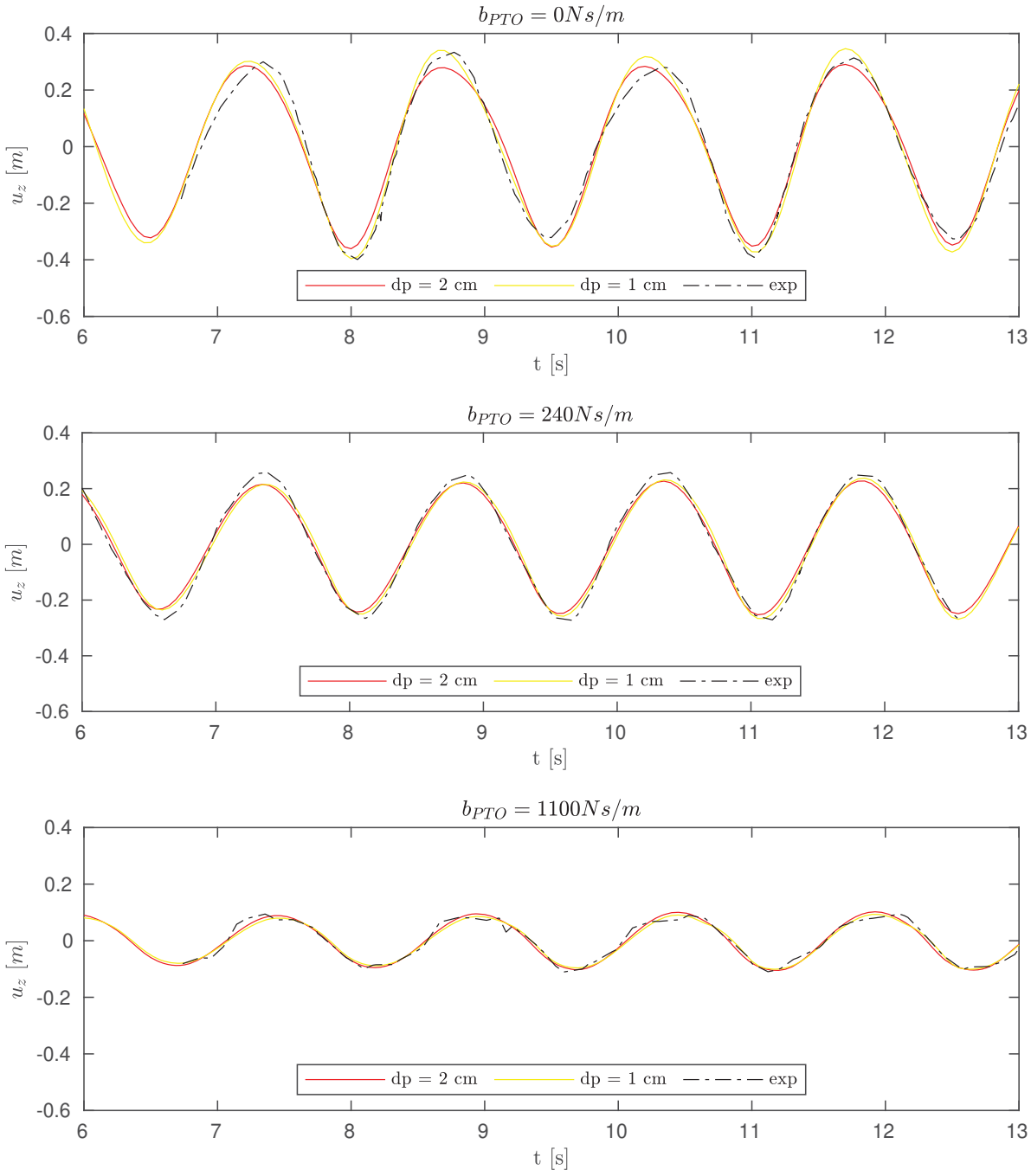

Figure 2: Comparison of the numerical and experimental time series for the vertical velocity with three different values of the damping coefficient of the PTO.

The agreement shown in Figure 2 is rather satisfying for both resolutions. For validation purposes, the time required to perform 15.00s of physical time is of around 20h for $dp = 0.01$m, and 2h for $dp = 0.02$m. These short runtimes are achieved thanks to a GTX2080 GPU card. Even though the finer mesh adheres more closely to the reference solution, the improvement is not as noticeable as the increment of runtime. Overall, the results collected in this section prove the capability of the SPH method to reproduce accurately the fluid dynamics and as well as the wave-structure interaction, which result in a correct prediction of the buoy's motion.

4 EFFICIENCY SENSITIVITY TO STRUCTURAL STIFFNESS

Test models provide researchers with a tool to investigate the physics of a natural phenomena. More than often, the model is a *scaled* reproduction of the specimen to be studied, and the scaling procedure has to be skilfully set up, taking in mind the trade off between feasibility and unavoidable scale effects. Tests in the range 1:10 and 1:20, whose parameters are given by Froude similarity, are deemed to be reliable on account of hydrodynamics. The tests presented by [29] are performed at 1:10 scale. The structure that takes in place the buoy, as it can be observed in Figure 3, may be assumed stiff enough to assume that the dynamics of the buoy develops only along the z-axis (Figure 3a)). However, the same structure can hardly be put in place just by solely scaling the model up. It is necessary to design a proper structure, which should guarantee the same degree of constraint.

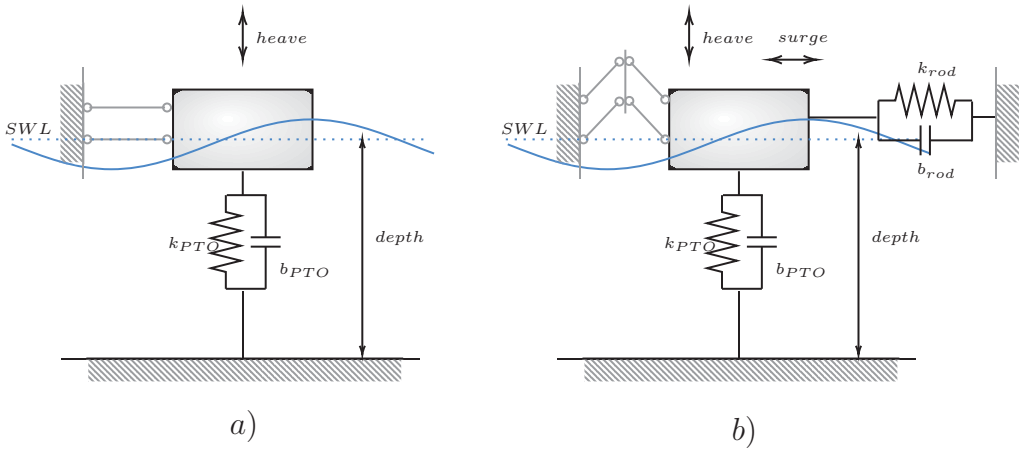

Figure 3: Structural models for the validation case *a)* and the modified one *b)*

Herein, along with the vertical spring-damper element, the submerged structure is modelled as a spring-damper element able to mimic its *lateral* damping and stiffness (Figure 3b)). It is assumed that the structure is clamped at the sea-bottom level and a hollow circular steel cross section makes up the beam. Its properties are given by:

$$k_{rod} = \frac{E\frac{\pi t_n d^3}{8}}{L} \quad \& \quad b_{rod} = 2m_{rod}\xi\sqrt{\frac{k_{rod}}{m_{rod}}} \tag{12}$$

where E is the elastic modulus, t_n is the thickness, d is the diameter, L is the length (0.890m), ξ is the damping ratio that is associated to the beam ($\xi = 0.10$), and m_{rod} is the mass of the beam. Note that the mass of the beam is considered lumped at its top. Additionally, the mass could be neglected due to its low impact on the overall kinematic.

Table 1: Geometric and mechanical properties of the profiles used for the anchoring structure.

	$d\ [mm]$	$t\ [mm]$	m	$k_{rod}\ [N/m]$	$b_{rod}\ [Ns/m]$
flexible	30	2.5	1.1	6 185	14
quasi flexible	40	3.2	1.4	18 766	32
quasi rigid	40	4.0	1.7	23 457	40
rigid	60	5.0	3.2	98 960	112

The dependence on the structural stiffness of the PTO's efficiency is investigated comparing the results obtained for the stiff structure (*rigid* in Table 1) with the results for the remaining

cases presented in Table 1. The wave height is the same used before, $H = 0.16$m, with wave periods ranging in $0.97 - 3.30$s, for a grand total of fourteen cases. In accordance with the tests presented for validation scope, the setup of the numerical domain is consistent: the length of the flume is $1L$, the width is twice the width of the device, the depth is the same. The four different viscous damping coefficients are used $[60,\ 240,\ 480,\ 720]$Ns/m.

The average power absorbed P is the quantity used as a proxy of the performance of the system. It is given by:

$$P = \frac{1}{T}\int_{t_0}^{t_0+T} b_{PTO}\, \dot{v}^2 dt \tag{13}$$

In general, heaving-buoy dynamics is highly affected by the wave conditions. This can be easily understood from the following equation:

$$\omega_0 = \sqrt{\frac{\rho g S}{m_a(\omega) + m}} \tag{14}$$

where ω_0 is the natural frequency of vibration, ρ is the buoy density, g is the gravity acceleration, S is the cross section of the heaving buoy, m_a is the added mass. For a heaving cylinder the excitation force and thus the added mass are given in an analytic form in Ref. [31]. The complex amplitude of the excitation force acting on a generic device is made up of two contributions: the Froude-Krylov force and the diffraction force. Under the assumption that the dimensions of the buoy are small in comparison with the wave length, the following holds:

$$F_e^* \approx (1 - khA^*)e^{-kh} \tag{15}$$

where F_e^* is the dimensionless amplitude of the excitation force, $k = 2\pi/L$ is the wave number, and h is the height of the cylinder. A numerical solution for the added mass, which can by found in [31], is given by:

$$m_a(\omega) = \frac{\rho S}{k}\left(1 - \frac{1.089 e^{-(0.669 k\frac{d}{2})^{0.604}} e^{-kh}}{e^{-kh}}\right) \tag{16}$$

Figure 4 collects the results of the analyses as performed on the model as described in Figure 3b). Each chart depicts the results for a value of the damping in the range above mentioned, while the four values of stiffness are compared (Table 1). Please note the dynamics of the *rigid* structure perfectly match the dynamics of the structure as shown in Figure 3a). The trend displayed by the charts is quite apparent: the less the stiffness of the system, the less the efficiency. Comparing the optimum points, the point at which the maximum power is harvested, it can be seen that there are no substantial differences between stiff and flexible structures. Though there is no difference in frequencies where the maxima are achieved, the average harvested power is sensibly lower, up to 40% in the case of the flexible structure. This trend appears to be quite consistent moving from *rigid* to *flexible* structures. The overall loss of efficiency shown in the four charts can be explained considering that the floating buoy, when free to surge, is prone to exhibit lateral displacements, according to the development of the free surface. However, for the way this PTO system works, this movement is not converted into harvested power.

5 CONCLUSIONS

This piece of research has shown that an SPH framework can presently deal with multi-physics phenomena effectively. The coupling DualSPHysics - Project Chrono library has sky-rocketed the engineering applications that can be studied with this code. Many relevant features

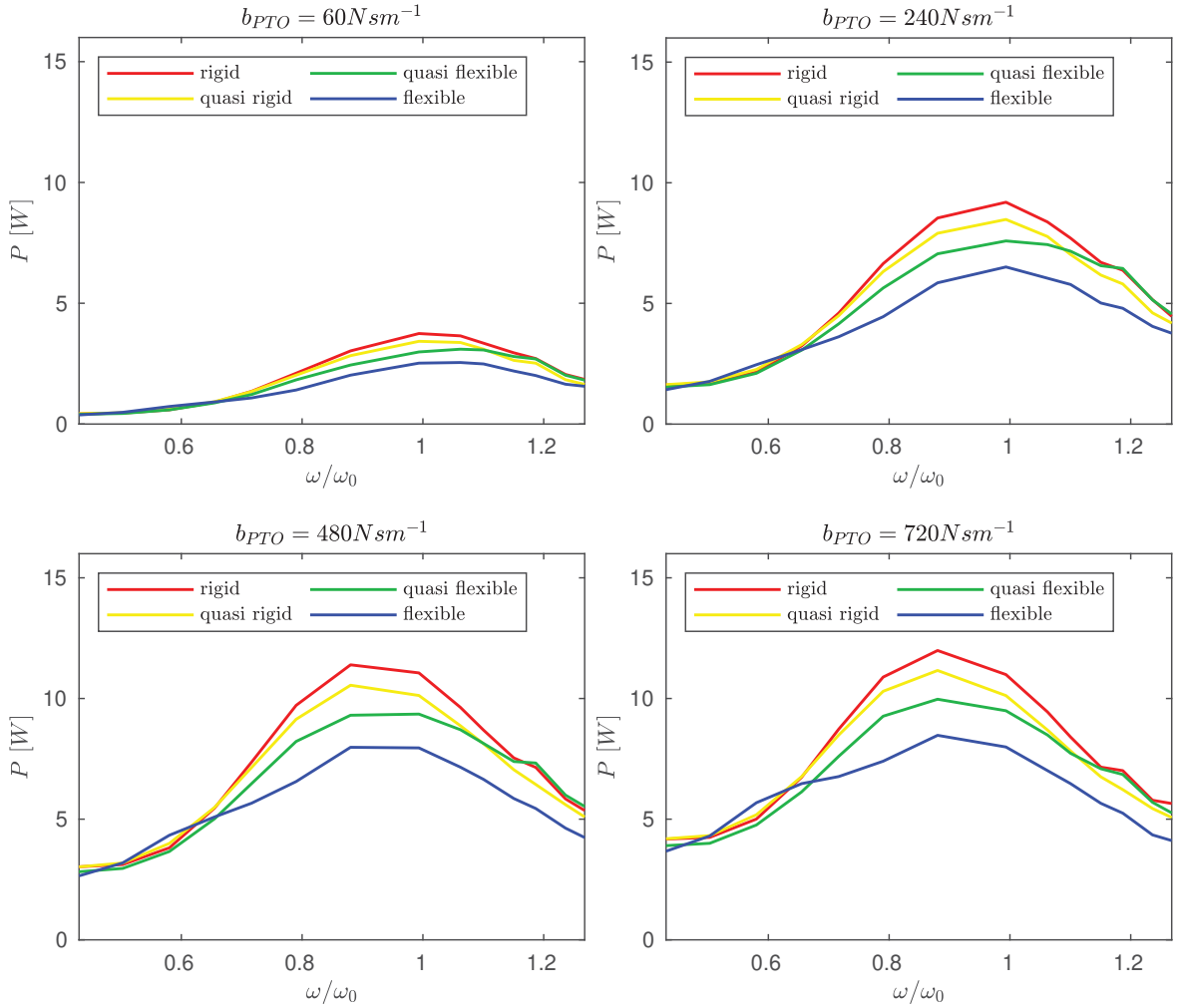

Figure 4: Absorbed power with the relative period of the buoy. Different values of the damping are presented. Each panel presents the results for a different lateral stiffness.

of a complex system can be modelled, allowing to account for the fully nonlinearities that are inherent in any natural phenomena. However, the importance of introducing flexible elements for simulating fluid-structure is not negligible. The structure can be indeed directly model into the simulation, hence considering its interaction with fluid without further assumptions on its behaviour. Indeed this feature would allow for more comprehensive survivability analyses of wave energy converters.

The validation of the numerical model has shown that, for this specific case, it is possible to achieve a high degree of reliability. The model indeed predicts the response of the fluid-driven buoy with accuracy and the runtime is reasonable for a fully 3D simulation. Therefore, the sensitivity to the structural stiffness shows that it is important to include the anchoring structure, even in a simplified way, from the preliminary phases of the design process.

Further implementations are needed to still widen the field of application of the code. It is already ongoing the implementation of Euler-Bernoulli elements, and isogeometric analyses (IGA), which a quite novel approach for finite elments analyses (FEAs).

6 ACKNOWLEDGEMENTS

The first author's Ph.D. scolarship is granted by the Italian Ministry for Education, University and Research (MIUR) as part of the program "Dottorati Innovativi a caratterizzazione industriale", ID DOT 1328490–3, funded by the European Union (Structural Funding ERDF-ESF for "Research and Innovation" 2014-2020). The authors are grateful for the support.

REFERENCES

[1] K. Gunn and C. Stock-Williams. Quantifying the global wave power resource. *Renewable Energy*, 44:296 – 304, 2012. ISSN 0960-1481. doi: https://doi.org/10.1016/j.renene.2012.01.101.

[2] B. Drew, A. Plummer, and M. Sahinkaya. A review of wave energy converter technology. *Proceedings of The Institution of Mechanical Engineers Part A-journal of Power and Energy - PROC INST MECH ENG A-J POWER*, 223:887–902, 12 2009. doi: 10.1243/09576509JPE782.

[3] C-H. Lee. Wamit theory manual, 1995.

[4] Y.H. Yu, M. Lawson, K. Ruehl, and C. Michelen Strofer. Development and demonstration of the wec-sim wave energy converter simulation tool. In *2nd Marine Energy Technology Symposium, Seattle*, 2014.

[5] A. Kolios, L.F. Di Maio, L. Wang, L. Cui, and Q. Sheng. Reliability assessment of point-absorber wave energy converters. *Ocean Engineering*, 163:40 – 50, 2018. ISSN 0029-8018. doi: https://doi.org/10.1016/j.oceaneng.2018.05.048.

[6] A. Amicarelli, S. Manenti, R. Albano, G. Agate, M. Paggi, L. Longoni, D. Mirauda, L. Ziane, G. Viccione, S. Todeschini, A. Sole, L.M. Baldini, D. Brambilla, M. Papini, M.C. Khellaf, B. Tagliafierro, L. Sarno, and G. Pirovano. Sphera v.9.0.0: A computational fluid dynamics research code, based on the smoothed particle hydrodynamics mesh-less method. *Computer Physics Communications*, 250:107157, 2020. ISSN 0010-4655. doi: https://doi.org/10.1016/j.cpc.2020.107157.

[7] D. Violeau and B.D. Rogers. Smoothed particle hydrodynamics (sph) for free-surface flows: past, present and future. *Journal of Hydraulic Research*, 54(1):1–26, 2016. doi: 10.1080/00221686.2015.1119209.

[8] T. Verbrugghe, J.M. Domínguez, A.J.C. Crespo, C. Altomare, V. Stratigaki, P. Troch, and A. Kortenhaus. Coupling methodology for smoothed particle hydrodynamics modelling of non-linear wave-structure interactions. *Coastal Engineering*, 138:184 – 198, 2018. ISSN 0378-3839. doi: https://doi.org/10.1016/j.coastaleng.2018.04.021.

[9] A.J.C. Crespo, C. Altomare, J.M. Domínguez, J. González-Cao, and M. Gómez-Gesteira. Towards simulating floating offshore oscillating water column converters with smoothed particle hydrodynamics. *Coastal Engineering*, 126:11 – 26, 2017. ISSN 0378-3839. doi: https://doi.org/10.1016/j.coastaleng.2017.05.001.

[10] D. Kisacik, V. Stratigaki, M. Wu, L. Cappietti, I. Simonetti, P. Troch, A. Crespo, C. Altomare, J.M. Domínguez, M. Hall, M. Gómez-Gesteira, R. Canelas, and P.K. Stansby.

Efficiency and survivability of a floating oscillating water column wave energy converter moored to the seabed: An overview of the esflowc marinet2 database. *Water*, 12:992, 04 2020. doi: 10.3390/w12040992.

[11] M. Brito, R.B. Canelas, O. García-Feal, J.M. Domínguez, A.J.C. Crespo, R.M.L. Ferreira, M.G. Neves, and L. Teixeira. A numerical tool for modelling oscillating wave surge converter with nonlinear mechanical constraints. *Renewable Energy*, 146:2024 – 2043, 2020. ISSN 0960-1481. doi: https://doi.org/10.1016/j.renene.2019.08.034.

[12] B. Tagliafierro, A. Crespo, J.M. Domínguez, O. García Feal, M. Gómez-Gesteira, R. Canelas, R. Coe, G. Bacelli, H. Cho, S. Spencer, and G. Viccione. Numerical modelling of a point-absorbing wec model using dualsphysics coupled with a multiphysics library. In *Proceedings of the 13$^t h$ European and Tidal Energy Conference (EWTEC2019), Naples, Italy*, volume 1672, page 8, 1-6 September 2019. ISBN 2309-1983.

[13] R. Coe, G. Bacelli, D. Wilson, and D. Patterson. System identification of a heaving point absorber: Design of experiment and device modeling. *Energies*, 10:472, 04 2017. doi: 10.3390/en10040472.

[14] G. Viccione, V. Bovolin, and E. Pugliese Carratelli. Defining and optimizing algorithms for neighbouring particle identification in sph fluid simulations. *International Journal for Numerical Methods in Fluids*, 58(6):625–638, 2008. doi: 10.1002/fld.1761.

[15] J. M. Domínguez, A. J. C. Crespo, M. Gómez-Gesteira, and J. C. Marongiu. Neighbour lists in smoothed particle hydrodynamics. *International Journal for Numerical Methods in Fluids*, 67(12):2026–2042, 2011. doi: 10.1002/fld.2481.

[16] E. Pugliese Carratelli, G. Viccione, and V. Bovolin. Free surface flow impact on a vertical wall: a numerical assessment. *Theoretical and Computational Fluid Dynamics*, 30, 03 2016. doi: 10.1007/s00162-016-0386-9.

[17] D. De Padova, M. Meftah, F. De Serio, M. Mossa, and S. Sibilla. Characteristics of breaking vorticity in spilling and plunging waves investigated numerically by sph. *Environmental Fluid Mechanics*, 06 2019. doi: 10.1007/s10652-019-09699-5.

[18] J J Monaghan. Smoothed particle hydrodynamics. *Reports on Progress in Physics*, 68(8): 1703–1759, jul 2005. doi: 10.1088/0034-4885/68/8/r01.

[19] J. J. Monaghan. Smoothed particle hydrodynamics. *Annual Review of Astronomy and Astrophysics*, 30(1):543–574, 1992. doi: 10.1146/annurev.aa.30.090192.002551. URL `https://doi.org/10.1146/annurev.aa.30.090192.002551`.

[20] H. Wendland. Piecewise polynomial, positive definite and compactly supported radial basis functions of minimal degree. *Advances in Computational Mathematics*, 4(1):389–396, December 1995. doi: 10.1007/BF02123482. URL `http://sro.sussex.ac.uk/id/eprint/24323/`.

[21] B. Leimkuhler, S. Reich, K. Zentrum, H. Str, and R. Skeel. Integration methods for molecular dynamics. 82, 02 1995. doi: 10.1007/978-1-4612-4066-2_10.

[22] J.J. Monaghan, A. Kos, and N. Issa. Fluid motion generated by impact. *Journal of Waterway, Port, Coastal, and Ocean Engineering*, 129(6):250–259, 2003. doi: 10.1061/(ASCE)0733-950X(2003)129:6(250).

[23] J.M. Domínguez, A.J.C. Crespo, M. Hall, C. Altomare, M. Wu, V. Stratigaki, P. Troch, L. Cappietti, and M. Gómez-Gesteira. Sph simulation of floating structures with moorings. *Coastal Engineering*, 153:103560, 2019. ISSN 0378-3839. doi: https://doi.org/10.1016/j.coastaleng.2019.103560.

[24] Project Chrono Development Team. Chrono: An Open Source Framework for the Physics-Based Simulation of Dynamic Systems. `https://github.com/projectchrono/chrono`. Accessed: 2020-05-07.

[25] M. Brito, R. Canelas, R. Ferreira, O. García Feal, J.M. Domínguez, A. Crespo, and M. Neves. Coupling between dualsphysics and chrono-engine: towards large scale hpc multiphysics simulations. In *SPHERIC 2016, Munich, Germany*, 01 2016.

[26] R.B. Canelas, M. Brito, O.G. Feal, J.M. Domínguez, and A.J.C. Crespo. Extending dualsphysics with a differential variational inequality: modeling fluid-mechanism interaction. *Applied Ocean Research*, 76:88 – 97, 2018. ISSN 0141-1187. doi: https://doi.org/10.1016/j.apor.2018.04.015.

[27] A. Tasora and M. Anitescu. A matrix-free cone complementarity approach for solving large-scale, nonsmooth, rigid body dynamics. *Computer Methods in Applied Mechanics and Engineering*, 200(5):439 – 453, 2011. ISSN 0045-7825. doi: https://doi.org/10.1016/j.cma.2010.06.030.

[28] M. Penalba, G. Giorgi, and J. V. Ringwood. Mathematical modelling of wave energy converters: A review of nonlinear approaches. *Renewable and Sustainable Energy Reviews*, 78:1188 – 1207, 2017. ISSN 1364-0321. doi: https://doi.org/10.1016/j.rser.2016.11.137.

[29] Z. Zang, Q. Zhang, Y. Qi, and X. Fu. Hydrodynamic responses and efficiency analyses of a heaving-buoy wave energy converter with pto damping in regular and irregular waves. *Renewable Energy*, 116:527 – 542, 2018. ISSN 0960-1481. doi: https://doi.org/10.1016/j.renene.2017.09.057.

[30] C. Altomare, J.M. Domínguez, A.J.C. Crespo, J. González-Cao, T. Suzuki, M. Gómez-Gesteira, and P. Troch. Long-crested wave generation and absorption for sph-based dualsphysics model. *Coastal Engineering*, 127:37 – 54, 2017. ISSN 0378-3839. doi: https://doi.org/10.1016/j.coastaleng.2017.06.004.

[31] I. Tejado, M. Alves, and D. Valerio. Excitation force and added mass of a heaving cylinder. In *Proceedings of the 2013 International Conference on Fractional Signals and Systems (FSS2013)*, 01 2013.

EURODYN 2020
XI International Conference on Structural Dynamics
M. Papadrakakis, M. Fragiadakis, C. Papadimitriou (eds.)
Athens, Greece, 23–26 November 2020

SPEED DISTRIBUTION ON ROAD TEST SECTIONS FOR THE NEED OF PROFILE GROUND TESTING OF SPECIAL WHEELED VEHICLES

Mariusz Kosobudzki

Wroclaw University of Science and Technology

Department of Off-Road Machine and Vehicle Engineering

50-371 Wrocław, Łukasiewicza Str. 7/9

e-mail: mariusz.kosobudzki@pwr.edu.pl

Keywords: high mobility wheeled vehicle, speed distribution, road test sections

Abstract. *The required mobility of military sub-units (including logistics sub-units) is achieved due to the widespread use of appropriate means of transport. This is especially important in land forces. The basic means of transport there are high mobility wheeled vehicles with low (up to 4 tons), medium (up to 7 tons) and high (over 7 tons) payload. Often the chassis of these vehicles are designed taking into account some additional requirements for base chassis for military equipment (e.g. as mobile radar stations, mobile rocket launchers, recovery vehicles, etc.). Before taking a decision about accepting a new vehicle to equip army sub-units, a number of studies and tests are conducted, including qualification tests [1,2,3,4]. Their goal is to collect the required data characterizing the vehicle and check to what extent it meets the initial requirements[5]. Such tests are conducted in laboratory and operational conditions (profile ground tests). To model the laboratory and operation conditions, it is necessary to know their Life Cycle Profile [4]. The simplified Life Cycle Profile (containing basic data in the form of predicted road conditions, mileage, maximum and average speeds) is specified at the beginning of the design and construction process. However, more detailed data are required for qualifying tests on a new vehicle, including distribution of speed characteristic in given road conditions and the required test duration. The paper presents the method of determining the speed distribution over mileage and driving time to assumed road conditions using statistical tools. As a result, detailed preliminary data is obtained for planning experiments, selection of measurement equipment, or indication of appropriate road test sections [6]. In addition, an analysis was made of how the determined traffic parameters correlate with the possible driving speeds of a 4x4 military vehicle.*

1 INTRODUCTION

Military vehicles, including non-combat vehicles, are constructed in such a way as to best meet the requirements in the concept of operations (CONOPS). This paper compares all relevant requirements and characterizes the future operating environment of the vehicle, including minimum requirements for the logistics security system as well as user competence and capability. Vehicles such as these end up in the system for utilization for an extended period of time (even 30 years), therefore complex and long-term qualifying tests (Environmental Tests) are carried out before a decision is made about their ultimate acceptance [1,2,3,4]. The aforementioned tests should model future operating conditions correctly. Tests that are too stringent can cause problems such as oversizing of vehicle components (increase in total mass). Relaxing testing conditions can lead to future rapid wear of the vehicle and an increase in its failure rate. In the testing concept presented in [1], scenarios for the operational use of the vehicle are constructed using individual and distinct operational events. These scenarios are repeated until, based on the data collected, it is possible to characterize the trends of changes in critical vehicle parameters describing its durability, reliability, repairability, etc. [2]. The relevant operational events used in the respective scenarios must be modeled so that the collected data are reliable and unambiguous, and the conclusions drawn on their basis apply to the veritable future conditions of vehicle use. To that end, for test drives including, but not limited to normalized road sections, representing road surfaces on which the vehicle will operate (the length of test roads are proportional to their share in the given test run), while traveling speeds and the load carried are determined based on the postulates included in the concept of operational use (maximum and average speed). An alternative to conducting this research is used in a situation where the aforementioned standardized road test sections are not available [6,7]. Testing being conducted on selected sections of public roads is anticipated. This is a great simplification, however, when compared to the use of test sections, because the selected road sections are not standardized, causing recorded loads to be difficult to consider as a statistical representation of the operating conditions for the entire collection of vehicles. In such a case, proper modeling of the vehicle's crucial driving parameter, in this situation its speed, is of particular importance. Establishing exemplificatory statistical distributions of vehicle speed on selected sections of test roads improves the reliability of collected measurement data, and using comparative indicators in the form of pseudo damage as an example, [8] allows for modeling the required test scenarios based on other (but those of the same class) road measuring sections.

2 MODELLING THE ENVIRONMENTAL PROFILE OF VEHICLE USAGE

The choice of road section types for vehicle testing should meet the general guidelines contained in the relevant standards [6]. The basic types of roads for testing vehicles are presented there, along with the percentage of distance of these sections in the total vehicle mileage over its life cycle. From the concept of the vehicle's operational use, conclusions can be drawn regarding the expected vehicle speed (maximum and average speed). This is the basis for the compilation of statistical distributions of vehicle operation speed to the identified types of roads. For an example scenario of vehicle use, the case of a technical support vehicle was chosen when it was created from the combination of a universal high-mobility wheeled chassis with a container body complete with appropriate tools and equipment that would provide technical assistance to combat vehicles [9]. It is assumed that in such a situation the vehicle can cover a distance of approximately 60 km over 24 hours in cross-country conditions with speeds equaling V_{max}= 10 km/h and V_{avg}= 5 km/h. If the vehicle is used in tactical displace-

ment, it will travel about 20-25 km per day at speeds of V_{max}= 40 km/h and V_{avg}= 20÷25 km/h for off-road and secondary roads. If the vehicle is used for technical closing of the marching column, it can travel at speeds of V_{max}= 80 km/h and V_{avg}= 50 km/h on asphalt and paved roads which are in average and poor technical condition. However, during an individual vehicle drive as part of an operational march, operating speeds may have a value of V_{max}= 90 km/h and V_{avg}= 60 km/h on main and secondary roads. A summary of the anticipated speeds for selected vehicle use scenarios is presented in Table 1.

No.	Surface type	Estimated average speed [km/h]	Estimated maximum speed [km/h]
1	asphalt, concrete (e.g. motorways, expressways) - good surface quality	60	90
2	asphalt, concrete, cobblestone (e.g. district roads, commune roads) - medium and low surface quality	50	80
3	off-roads	25	40
4	cross-country	5	10

Table 1. Properties of Vehicle Traffic Conditions

3 STATISTICAL DISTRIBUTION OF VEHICLE'S SPEED

To prepare representative speed distributions for the indicated vehicle use scenarios, a beta statistical distribution was used, as seen in [10]:

$$f(x) = \frac{\Gamma(\alpha+\beta)}{\Gamma(\alpha)\Gamma(\beta)} x^{\alpha-1}(1-x)^{\beta-1} \tag{1}$$

where: Γ - gamma function, α, β - parameters of shape of distribution, x - width of accepted sub-range speed.

If the entire speed range is divided into a finite number of equal subranges, the formula (1) can be simplified and presented as:

$$f(x) = \frac{(\alpha+\beta-1)!}{(\alpha-1)!(\beta-1)!} x^{\alpha-1}(1-x)^{\beta-1} \tag{2}$$

where: α, β - parameters of shape of distribution, x - width of accepted sub-range speed.
For the initial determination of the value of the parameter α, the data presented in Table 2 [2] can be used.

V_{avg}/V_{max} [%]	10	20	30	40	50	60	70	80	90
α	0,2	0,5	0,75	1,25	2	3	4	6	13

Table 2. The value of α parameter.

The following equations can be used to determine the value of parameter β [10]:

$$\beta = \frac{\alpha \cdot \vartheta_{max}}{\vartheta_{avg}} - \alpha \tag{3}$$

The width of the sub-range can be posited to make it possible to maintain a set speed during tests, e.g. for cross-country driving ΔV=1.5÷4 km/h, and for main roads ΔV=5÷10 km/h. The final selection of ΔV depends on the technical capabilities of the tested vehicle. Examples of the speed distribution of the analyzed vehicle driving on a main road and driving off-road are presented in Tables 3 and 4 and in Figures 1 and 2. Table 3 presents the vehicle speed distribution (V_{max}= 90 km/h and V_{avg}= 60 km/h) where these roads represent 20% of the total test run (200km for every 1000km test).

Represented speed V_{rep} [km/h]	V_{min} [km/h]	V_{max} [km/h]	V_{avg} [km/h]	Driving time [%]	Driving time [min]	Sectional mileage [%]	Sectional mileage [km]
-	0	10	5	0,05	0,1	0,004	0,01
10	5	15	10	0,3	0,6	0,05	0,1
20	15	25	20	1,7	3,3	0,6	1,1
30	25	35	30	4,4	8,9	2,2	4,4
40	35	45	40	8,5	17,0	5,7	11,4
50	45	55	50	13,4	26,7	11,1	22,3
60	55	65	60	18,1	36,1	18,1	36,1
70	65	75	70	21,2	42,4	24,7	49,5
80	75	85	80	20,6	41,2	27,5	55,0
90	85	95	90	12,3	24,6	18,4	36,9
				100,0	**200,9**	**108,0**	**216,7**

Table 3. The beta distribution of speed (V_{max}= 90 km/ h i V_{avg}=60 km/h, distance 200 km).

The proportions of compositional speeds in the test is shown in Figure 1.

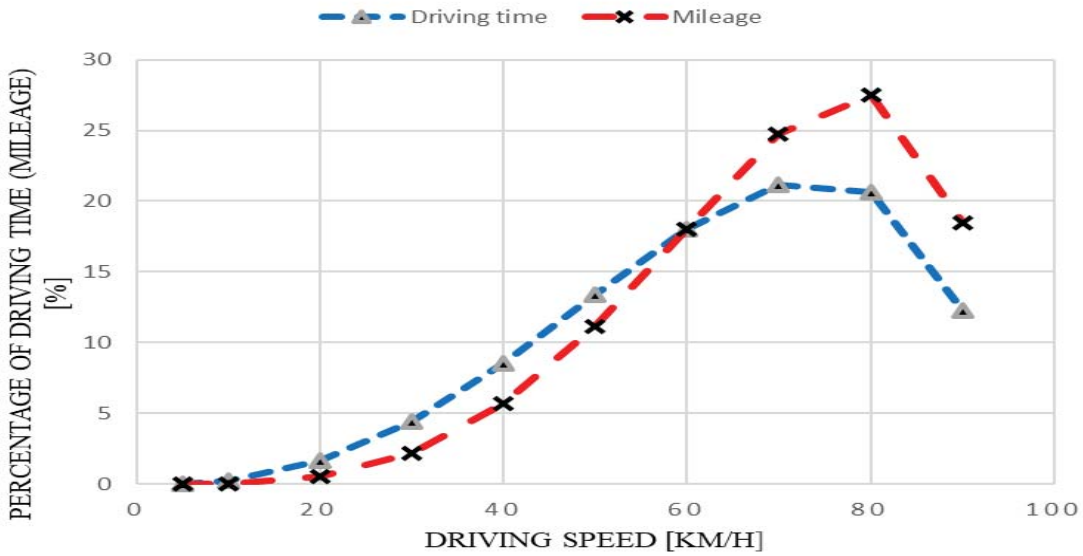

Figure 1. The beta distribution of speed (V_{max}= 90 km/ h i V_{avg}=60 km/h, distance 200 km).

Figure 1 shows that, e.g. speed V= 40 km/h, 8.5% of the driving time (17 minutes in total) should be maintained over a 5.7% distance of 200 km (11.4 km in total). Another case is presented in Table 4 concerning the distribution of vehicle speed in cross-country conditions

(V_{max}= 10 km/h and V_{avg}= 5 km/h), when these roads constitute 20% of the total mileage in the test (200km for every 1000km test).

Represented speed V_{rep} [km/h]	V_{min} [km/h]	V_{max} [km/h]	V_{avg} [km/h]	Driving time [%]	Driving time [min]	Sectional mileage [%]	Sectional mileage [km]
-	0	2	1	8,3	200,0	1,7	3,3
2	1	3	2	15,0	360,0	6,0	12,0
4	3	5	4	23,3	560,0	18,7	37,3
6	5	7	6	25,0	600,0	30,0	60,0
8	7	9	8	20,0	480,0	32,0	64,0
10	9	11	10	8,3	200,0	16,7	33,3
				100,0	**1200,0**	**105,0**	**210,0**

Table 4. The beta distribution of speed (V_{max}= 10 km/ h i V_{avg}=5 km/h, distance 200 km).

The proportions of compositional speeds in the test is shown in Figure 2.

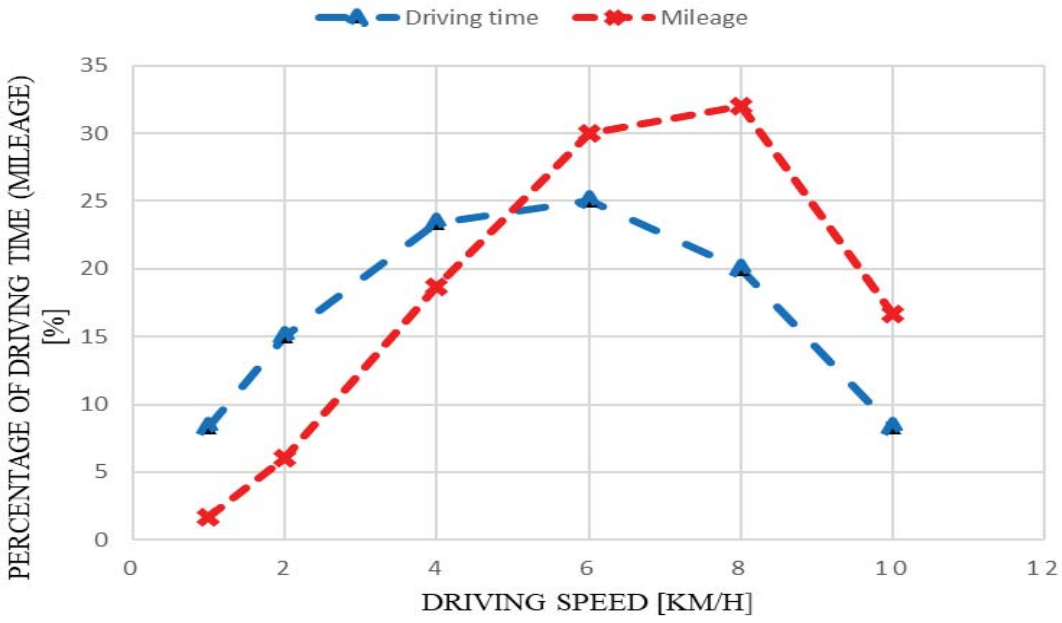

Figure 2. The beta distribution of speed (V_{max}= 10 km/ h i V_{avg}=5 km/h, distance 200 km).

The figure shows that given a speed of V= 4 km/h as an example, it is necessary to maintain 23.3% of the driving time (for a total of 560 minutes) on the 18.7% section of 200 km (37.3km in total).

4 TECHNICAL LIMITATION OF VEHICLE'S SPEED

The determined compositional speeds in vehicle tests should be achievable by the vehicle. In order to check these possibilities, a preliminary analysis of the vehicle speed resulting from the properties of the propulsion system should be carried out. Detailed information for an example of a 4x4 vehicle with a 5000kg payload is provided in Table 5. It was assumed that during the test the engine crankshaft revolutions per minute were to be kept between maxi-

mum torque and maximum power. High mobility wheeled vehicles are equipped with tires adapted for driving with variable air pressure. This causes a change in tire deflection U and a change in the vehicle speed, as shown in Table 5. Deflection U can be calculated as follows:

$$U = \frac{H'}{H} \tag{4}$$

where: H' – height of a loaded tire by reduced air pressure, H – height of loaded tire by nominal air pressure.

Max. engine torque:			Nominal engine power:			Tire:	**14.00R20 164/160J**			
1300 [Nm]	**1200÷1600** [1/min]		**240** [kW]	**2200** [1/min]		Cross-country speed correction based on tire deflection:				
Road speed [km/h]			**Cross-country** speed [km/h]			U=0,86 (nominal deflection)	U=0,8	U=0,7	U=0,6	U=0,5
Gear	**V** (n=1700 [1/min])	**ΔV** (Δn=±500 [1/min])	Gear	**V** (n=1700 [1/min])	**ΔV** (Δn=±500 [1/min])	$\Delta V_{0,86}$	$\Delta V_{0,8}$	$\Delta V_{0,7}$	$\Delta V_{0,6}$	$\Delta V_{0,5}$
C	6,9	2,0	C	3,4	1,0	0,0	-0,1	-0,2	-0,3	-0,4
1	9,9	2,9	1	4,9	1,5	0,0	-0,1	-0,3	-0,4	-0,6
2	13,9	4,1	2	6,9	2,0	0,0	-0,2	-0,4	-0,6	-0,8
3	18,7	5,5	3	9,3	2,7	0,0	-0,3	-0,5	-0,8	-1,1
4	24,8	7,3	4	12,4	3,6	0,0	-0,4	-0,7	-1,1	-1,5
5	34,4	10,1	5	17,2	5,1	0,0	-0,5	-1,0	-1,6	-2,1
6	48,2	14,2	6	24,1	7,1	0,0	-0,7	-1,4	-2,2	-2,9
7	65,0	19,1	7	32,5	9,6	0,0	-0,9	-1,9	-2,9	-3,9
8	86,7	25,5	8	43,4	12,8	0,0	-1,2	-2,6	-3,9	-5,3
R	7,2	2,1	R	3,6	1,1	0,0	-0,1	-0,2	-0,3	-0,4

Table 5. Technical characteristic of 4x4 high mobility special wheeled vehicle with payload 5000 kg (example).

The data presented in Table 5 show that low speeds (see Table 4) are achievable and maintainable if a central tire inflation system is used and the tire pressure is lowered.

5 SUMMARY

The speed distributions presented to established road sections within the adopted scenarios of vehicle utilization can be used directly (during tests, maintaining the set speeds for a specified driving time or distance) or can be used as a benchmark to compare the speed properties of the tests. This approach should provide a statistical representation of the speed of vehicles of a given category in the anticipated scenarios for their use on different roads (belonging to a certain group of roads). The error in determining the compositional speed values (approximately 5%) results from the simplifying assumptions that were made, which seems to be acceptable for this type of research.

REFERENCES

[1] MIL-STD-810H – Environmental Engineering Considerations and Laboratory Tests.

[2] AECTP-240-1 – Allied Environmental Conditions and Test Publication.

[3] DEF-STAN 00-35 – Environmental Handbook for Defence Materiel. Part 3. Environmental Test Methods.

[4] Decyzja Nr 141/MON Ministra Obrony Narodowej z dnia 5 lipca 2017 r. w sprawie systemu pozyskiwania, eksploatacji i wycofywania sprzętu wojskowego Sił Zbrojnych Rzeczpospolitej Polskiej, Dz. Urz. MON z dn. 06.07.2017, poz. 149, (in Polish).

[5] NO-23-A200 - Military automotive vehicles – High mobility cars – Requirements, (in Polish).

[6] PDNO-23-A503 – Military vehicles – Reliability tests, (in Polish).

[7] NO-06-A106 – Armament and Military Equipment – General Technical Requirements Methods – Reliability Test Methods, (in Polish)

[8] M. Kosobudzki, T. Smolnicki, Generalized vehicle durability index for different traffic conditions, AIP Conference Proceedings 2078, 020017 (2019); https://doi.org/10.1063/1.5092020.

[9] DD4. Organizacja i zadady działania pododdziałów technicznych. Inspektorat Wsparcia Sił Zbrojnych, MON, Bydgoszcz, 2013, (in Polish).

[10] R. Zieliński, *Statystyka matematyczna stosowana. Elementy*, ISBN: 978-83-61993-03-2, 2011, (in Polish).

EURODYN 2020
XI International Conference on Structural Dynamics
M. Papadrakakis, M. Fragiadakis, C. Papadimitriou (eds.)
Athens, Greece, 23–26 November 2020

TMEASY 6.0 – A HANDLING TIRE MODEL THAT INCORPORATES THE FIRST TWO BELT EIGENMODES

Georg Rill

OTH Regensburg
Galgenbergstr. 30, 93053 Regensburg, Germany
e-mail: georg.rill@oth-regensburg.de

Keywords: TMeasy Tire Model, Tire Force Dynamics, Virtual Test Rig, Real-time Simulation, Frequency Analysis.

Abstract. *TMeasy 6.0, an extension to the standard TMeasy tire model of version 5.3, takes the relevant first two rigid body eigenmodes of the belt into consideration. These modes represent the in plane longitudinal and rotational movements of the belt relative to the rim. The dynamics of the longitudinal force is of higher order then and reproduces the tire wheel vibrations, required for indirect tire-pressure monitoring systems (iTPMS), sufficiently well. A tailored implicit solver, which takes the stiff coupling between the longitudinal force and the belt motions into account, still provides real-time performance in addition. Simulation examples show that a rigid body vehicle model equipped with TMeasy 6.0 makes it possible to investigate second generation indirect tire-pressure monitoring systems.*

1 INTRODUCTION

Passenger car models consisting of rigid bodies are usually supplemented by handling tire models, which include a first order dynamics. This kind of vehicle models are valid up to approximately 20 Hz and provide sufficient accuracy with comparatively low computational effort. They are used to study the handling performance up to the limit range and the basics of ride comfort in offline and online simulations. In addition, modern control systems, which improve safety and comfort in general, assist the driver, or even provide automated driving, can be tested, enhanced or developed from the scratch [1]. However, indirect tire-pressure monitoring systems (iTPMS) of second generation analyze a wheel tire vibration of more than 100 Hz, which is sensitive to the tire inflation pressure, [2]. Structural tire models, like CDTire or FTire, as well the three-dimensional rigid belt approach, realized in the SWIFT tire model, incorporate the corresponding eigenmodes of course. Yet, these models are rather complex, require measurements for parameterization, and are not entirely suitable for real-time applications. That is why, the TMeasy handling tire model [3] was supplemented by the first two rigid body eigenmodes of the belt. This version is capable to reproduce rim and tire belt eigen-modes which occur in the range of 100 to 200 Hz for typical passenger car tires.

2 TMEASY TIRE MODEL

2.1 Standard Approach

TMeasy represents a handling tire model based on a semi-physical model. A smooth transition from stand still to normal driving situations is provided by a three-dimensional slip approach which includes a rather simple but very effective dynamic parking torque model in addition, [3]. In a sophisticated but quite simple contact calculation the geometric contact point is shifted at first to the static contact point and then to the dynamic contact point, [4]. These shifts take the shape of the tire cross section, the camber angle, and the tire compliance into account. TMeasy enables a skilled engineer to estimate appropriate parameter by just knowing or estimating the size, the payload of the tire, as well as the friction property of the tire road combination, [5]. Of course, the TMeasy parameter can be adjusted to tire or vehicle dynamics measurements by curve fits or just by inspection, [6].

The standard model incorporates a first order tire dynamics, which is based on the tire deflections, Figure 1. Due to this deflections the sliding velocities v_x and v_y as well as the bore angular velocity ω_n change to

$$v_x \longrightarrow v_x + \dot{x}_e, \quad v_y \longrightarrow v_y + \dot{y}_e, \quad \omega_n \longrightarrow \omega_n + \dot{\psi}_e \tag{1}$$

where $\dot{x}_e$, $\dot{y}_e$, and $\dot{\psi}_e$ describe the time derivatives of the tire deflections in the longitudinal, lateral, and torsional directions. As a consequence the normalized longitudinal slip for example is then provided as

$$s_x^N = \frac{-(v_x + \dot{x}_e - r_D\,\Omega)}{r_D\,|\Omega|\,\hat{s}_x + v_N} \tag{2}$$

where r_D names the dynamic rolling radius and Ω the angular velocity of the wheel or the rim respectively. The terms $\hat{s}_x$ and v_N denote a slip normalization factor and a small fictitious velocity which are part of the TMeasy model approach discussed in [7]. TMeasy generates the dynamic tire force in the longitudinal direction by

$$F_x^D = f_G\,\frac{-(v_x + \dot{x}_e - r_D\,\Omega)}{r_D\,|\Omega|\,\hat{s}_x + v_N} \tag{3}$$

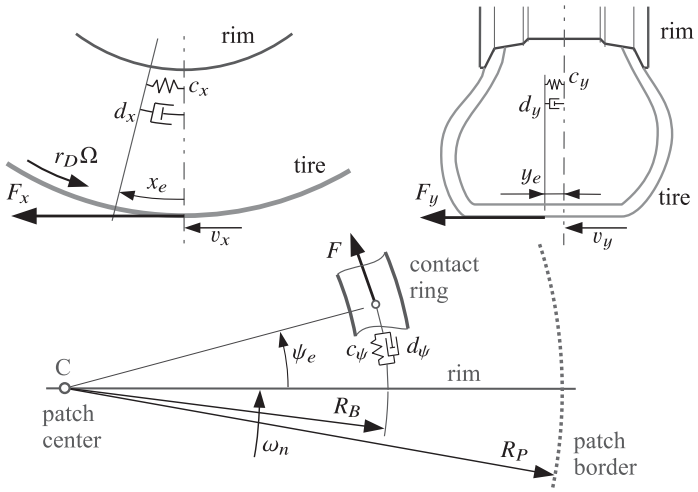

Figure 1: Tire deflections in the longitudinal, lateral, and torsional directions

where f_G represents the global derivative of the generalized force characteristics, which depends on the generalized and three-dimensional slip and processes the steady-state tire characteristics in longitudinal and lateral directions. On the other hand, the tire compliance provides the dynamic force in the longitudinal direction as

$$F_x^D = c_x\, x_e + d_x\, \dot{x}_e, \tag{4}$$

where c_x, and d_x represent the overall stiffness and damping properties of the sidewall and the tread particles in the longitudinal direction. Combining Equations (3) and (4) finally results in a first order differential equation

$$((r_D\,|\Omega|\,\hat{s}_x + v_N)\,d_x \;+\; f_G\,)\;\dot{x}_e \;=\; -\,(r_D\,|\Omega|\,\hat{s}_x + v_N)\,c_x\,x_e \;-\; f_G\,(v_x - r_D\,\Omega) \tag{5}$$

defining the dynamics of the tire deflection x_e in the longitudinal direction and via Equation (4) the first order dynamics of the longitudinal force F_x^D in addition. Similar approaches deliver the first order dynamics of the lateral force and the first order dynamics of the bore or turn torque.

The experimental validation of the lateral tire dynamics showed that in this case the first order approach realized in TMeasy already results in a quite good performance, [8]. However, braking scenarios or just rides on rough roads invoke eigen-modes of the belt that will result into a higher order dynamics of the longitudinal tire force.

2.2 In-Plane Belt Dynamics

Complex structural tire models, also provide the eigen-modes of an unloaded tire with a fixed rim, Fig. 2. The eigen-modes 1 and 2 of a freely vibrating tire correspond quite well to motions, where the rigid belt performs a rotation about the wheel rotation axis and a translation into the longitudinal direction. These two modes remain nearly unchanged if the tire is in contact with the road, which in vehicle dynamics is the most common and important case. All other modes incorporate already belt deformations or rigid belt like modes of a freely vibrating tire, like the modes 3 and 4 in Fig. 2, will be distorted significantly by the contact forces and torques.

That is why TMeasy 6.0 just takes mode 1 and 2 into account, because these first two eigen-modes influence the sliding velocity at the contact point into the longitudinal direction and hence strongly affect the longitudinal tire force. A model extension, where the wheel is split into a rigid rim and a rigid belt, takes the corresponding belt motions into account, Fig. 3.

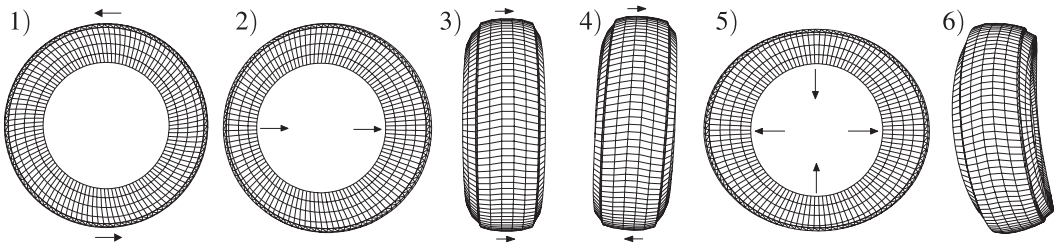

Figure 2: First six eigen-modes from left to right of a standard passenger car tire taken from [9]

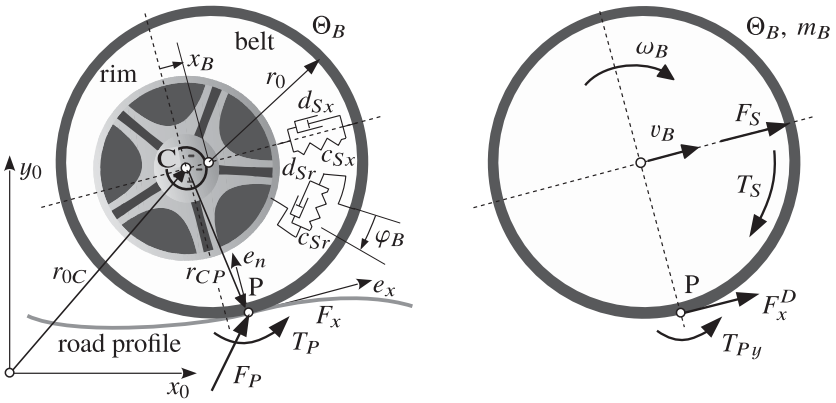

Figure 3: Rotating wheel split into rim and belt and free body diagram of the belt

The belt performs relative to the rim the rotation φ_B about the wheel rotation axis and the motion x_B into the longitudinal direction defined by the unit vector e_x, which is perpendicular to the local road normal e_n. The corresponding absolute belt velocity v_B and the absolute belt angular velocity ω_B together with the deflection of the tread particles x_T and the tire deflection y_e into the lateral direction, as well as the tire torsional deflection γ_e about the road normal e_n accomplish the internal tire states of the extended model. Whereas the standard model of version 5.3 just gets along with $n = 3$ internal states, Table 2.2.

TMeasy standard version 5.3 ($\mathbf{n = 3}$)		**TMeasy extendend version 6.0** ($\mathbf{n = 7}$)	
x_e	longitudinal tire deflection (tire sidewall + tread particles)	x_T	tread particle deflection in longitudinal direction
y_e	lateral tire deflection (tire sidewall + tread particles)	y_e	lateral tire deflection (tire sidewall + tread particles)
γ_e	torsional tire deflection (tire sidewall + tread particles)	γ_e	torsional tire deflection (tire sidewall + tread particles)
	—	x_B	translational belt motion (relative to rim)
	—	φ_B	rotational belt motion (relative to rim)
	—	v_B	absolute belt velocity (in longitudinal direction)
	—	ω_B	absolute angular belt velocity (about wheel rotation axis)

Table 1: Internal tire states of the TMeasy tire models of version 5.3 and version 6.0

The natural frequencies f_0^x and f_0^r of the first two tire eigen-modes provide the stiffness of the tire sidewall in longitudinal and torsional directions

$$c_{Sx} = m_B \left(2\pi f_0^x\right)^2 \quad \text{and} \quad c_{Sr} = \Theta_B \left(2\pi f_0^r\right)^2 \tag{6}$$

where Θ_B defines the belt inertia and the fictitious belt mass is simple provided by

$$m_B = \Theta_B / r_0^2 \tag{7}$$

because the belt is simply considered as a thin ring with the radius r_0 which corresponds to the unloaded tire radius. The corresponding damping parameter are computed via

$$d_{Sx} = 2\,\zeta_{Sx}\,\sqrt{m_B\,c_{Sx}} \quad \text{and} \quad d_{Sr} = 2\,\zeta_{Sr}\,\sqrt{\Theta_B\,c_{Sr}} \tag{8}$$

where ζ_{Sx} and ζ_{Sr} specify the viscous damping parameter for the tire sidewall in longitudinal and torsional directions.

In extension to Equation (3) the dynamic longitudinal tire force is now provided by

$$F_x^D \;=\; f_G\,\frac{-\left(v_x + \dot{x}_T + \dot{x}_B - r_D\dot{\varphi}_B - r_D\,\Omega\right)}{r_D\,\left|\Omega + \dot{\varphi}_B\right|\,\hat{s}_x + v_N} \tag{9}$$

The time derivative of the overall displacement $\dot{x}_e$ is replaced here by the time derivative of the displacement of the tread particles $\dot{x}_T$ and the rigid belt motions relative to the rim contribute to the transport velocity $r_D\,|\Omega| \;\rightarrow\; r_D\,|\Omega + \dot{\varphi}_B|$ and with the term $\dot{x}_B - r_D\dot{\varphi}_B$ to the contact point sliding velocity in longitudinal direction. By approximating the compliance of the tire tread particles by the stiffness c_{TP} and the damping parameter d_{TP} the dynamic tire force in longitudinal direction is also defined by

$$F_x^D \;=\; c_{TP}\,x_T \;+\; d_{TP}\,\dot{x}_T \tag{10}$$

Combining these Equations finally results in the first order differential equation

$$\left(d_{TP}\,v_{tnx} + f_G\right)\dot{x}_T \;=\; -v_{tnx}\,c_{TP}\,x_T \;-\; f_G\left(v_x + \dot{x}_B - r_D\dot{\varphi}_B - r_D\,\Omega\right) \tag{11}$$

where the abbreviation $v_{tnx} = r_D\,\left|\Omega + \dot{\varphi}_B\right|\,\hat{s}_x + v_N$ shortens the result. Now, the time derivatives $\dot{x}_B$ and $\dot{\varphi}_B$ of the translational and rotational belt motions are required in addition.

The belt equations of motion read as

$$m_B\,\dot{v}_B \;=\; F_x^D + F_S \quad \text{and} \quad \Theta_B, \dot{\omega}_B \;=\; T_y + T_S \tag{12}$$

where v_B describes the absolute velocity of the belt center into the longitudinal direction defined by the unit vector e_x and ω_B denotes the absolute angular velocity of the belt about the wheel or respectively rim rotation axis defined by the unit vector e_{yR}.

Equation (10) delivers the the dynamic longitudinal tire force F_x^D and the tire sidewall compliance provides the corresponding force and torque

$$F_S = -\left(c_{Sx}\,x_B + d_{Sx}\,\dot{x}_B\right) \quad \text{and} \quad T_S = -\left(c_{Sr}\,\varphi_B + d_{Sr}\,\dot{\varphi}_B\right) \tag{13}$$

Finally, the component of the resulting tire torque about the wheel rotation axis is provided by

$$T_y \;=\; e_{yR}^T\left(\,T_P + r_{CP} \times F_P\,\right) \;=\; e_{yR}^T\,T_T \tag{14}$$

The vectors F_P and T_P collect the tire forces and torques acting at the contact point P on the wheel (rim and belt) and the vector r_{CP} points from the rim center C to the contact point P. Then, the vector T_T represents the resulting torque which is applied to the wheel center C.

The time derivatives of the translational and rotational belt motions required in Equation (11) are defined by the kinematic differential equations

$$\dot{x}_B = v_B - e_x^T v_{0C} = v_B - v_x \quad \text{and} \quad \dot{\varphi}_B = \omega_B - e_{yR}^T \omega_{0C} = \omega_B - \Omega \tag{15}$$

where v_{0C} and ω_{0C} are vectors describing the absolute velocity of the rim center and the angular velocity of the rim and v_x and Ω denote the corresponding components into the longitudinal direction and about the wheel rotation axis.

The forces and torques applied to the rim are then given by

$$F_R \;=\; F_T - e_x^T \left(F_x^D + F_S\right) \quad \text{and} \quad T_R \;=\; T_T - e_{yR}^T \left(T_y + T_S\right) \tag{16}$$

where the torque vector T_T and the torque about the wheel rotation axis T_y are defined in Equation (14).

The TMeasy tire model of version 6.0 incorporates the unconstrained rotation of the rigid belt about the wheel or respectively rim rotation axis e_{yR}. That is why, the belt inertia Θ_B must be split off from the wheel body inertia tensor according to

$$\Theta_W \;\rightarrow\; \Theta_W - e_{yR}\,\Theta_B\,e_{yR}^T \tag{17}$$

The movements of the belt mass relative to the rim is restricted to a motion into the longitudinal direction defined by the unit vector e_x which is perpendicular to the local road normal e_n. The main motions of the wheel center, made possible by the suspension system of a vehicle, are in general performed nearly perpendicular to the road surface. Hence, the contribution of the belt mass inertia forces to the overall wheel motions is negligible within the TMeasy 6.0 model approach. The belt mass m_B is therefor considered just as a fictitious modal mass, which is used to describe the higher order dynamics of the longitudinal tire force, but will have no significant impact to the translational wheel motions.

3 PARTLY IMPLICIT SOLVER

The differential equations (11) and (12) are strongly coupled and stiff. Hence, a real time solution requires an appropriate implicit approach. At first, the differential equations (11) and (12) are combined with the kinematic differential equations (15) and grouped to a system

$$\underbrace{\begin{bmatrix} \dot{x}_T \\ \dot{v}_B \\ \dot{\omega}_B \\ \dot{x}_B \\ \dot{\varphi}_B \end{bmatrix}}_{\dot{x}} = \underbrace{\begin{bmatrix} -\left(v_{tnx}\,c_{TP}\,x_T \;+\; f_G\left(v_B - r_D\,\omega_B\right)\right) / \left(d_{TP}\,v_{tnx} + f_G\right) \\ \left(F_x^D + F_S\right)/m_B \\ \left(T_y + T_S\right)/\Theta_B \\ v_B - v_x \\ \omega_B - \Omega \end{bmatrix}}_{f(x)} \tag{18}$$

where $v_{tnx} = r_D\,|\omega_B|\,\hat{s}_x + v_N$ holds in addition. A trapezoid like integration step of size h delivers at first

$$x^{k+1} = x^k + \frac{h}{2}\left(f(x^k) + f(x^{k+1})\right) \tag{19}$$

where $x^k = x(t)$ and $x^{k+1} = x(t+h)$ denote the state vectors at time t and $t+h$. A truncated Taylor-expansion delivers

$$f(x^{k+1}) \approx f(x^k) + \frac{df}{dx}\left(x^{k+1} - x^k\right) \tag{20}$$

and Equation (19) yields

$$x^{k+1} = x^k + h\, f(x^k) + \frac{h}{2}\frac{df}{dx}\left(x^{k+1} - x^k\right) \tag{21}$$

which finally results in

$$x^{k+1} = x^k + \left(I - \frac{h}{2}\frac{df}{dx}\right)^{-1} h\, f(x^k) \tag{22}$$

where I is the identity matrix which fits to the Jacobian df/dx. If the step size h is not too large, the global derivative of the generalized tire characteristic f_G, the longitudinal velocity of the wheel center v_x, and the angular velocity of the rim Ω can be considered as nearly constant in the interval $t \rightarrow t+h$. Then, the last two equations in (22) can be solved straight away

$$x_B^{k+1} = x_B^k + \frac{h}{2}\left(v_B^k - v_x \;+\; v_B^{k+1} - v_x\right) = x_B^k - h\, v_x - \frac{h}{2}\left(v_B^{k-1} - v_B^k\right) \tag{23}$$

$$\varphi_B^{k+1} = \varphi_B^k + \frac{h}{2}\left(\omega_B^k - \Omega \;+\; \omega_B^{k+1} - \Omega\right) = \varphi_B^k - h\,\Omega - \frac{h}{2}\left(\omega_B^{k-1} - \omega_B^k\right) \tag{24}$$

In addition, the elements of the remaining 3×3 Jacobian can be calculated analytically, which speeds up the computation significantly. The partly implicit solver provided in Equation (22) produces rather accurate and stable results up to step sizes of $h = 1$ ms which corresponds to the sampling rate applied in common vehicle control systems.

4 A VIRTUAL TEST RIG

The virtual tire test rig represents a quarter car model, Figure 4. It consists of the corresponding chassis mass and the wheel. The latter is suspended at the chassis mass such that it can perform an up and down motion as well as steer and camber movements. The chassis mass

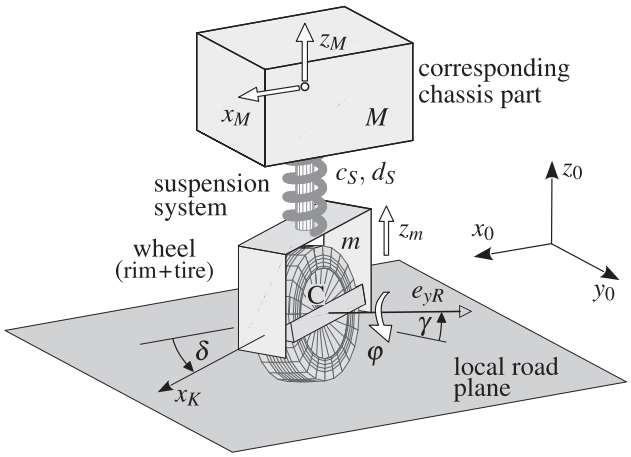

Figure 4: A virtual tire test rig represented by a quarter car model

M is supposed to move in longitudinal and vertical directions only. The generalized coordinates x_M and z_M characterizes these movements. The vector

$$r_{0M,0} \begin{bmatrix} x_M \\ 0 \\ r_0 + h_0 + z_M \end{bmatrix} \quad \text{and} \quad v_{0M,0} = \dot{r}_{0C,0} = \begin{bmatrix} \dot{x}_M \\ 0 \\ \dot{z}_M \end{bmatrix} \tag{25}$$

describes the momentary position of the chassis center with respect to the earth-fixed reference frame 0 and its velocity. The comma separated index 0 indicates that the vectors are expressed in the earth-fixed frame 0, the parameter h_0 represents the height of the chassis center above the wheel center in design position, and r_0 names the unloaded wheel radius.

The suspension system allows the wheel to perform the hub motion z_m, the steer motion δ about the vertical z_0-axis, the camber motion γ about the knuckle fixed x_K-axis, and the rotation φ about the rim fixed y_R-axis. In this model approach the wheel center C is located on the steering axis. Then, its momentary position and its velocity are provided by

$$r_{0C,0} = \begin{bmatrix} x_M \\ 0 \\ r_0 + z_m \end{bmatrix} \quad \text{and} \quad v_{0C,0} = \dot{r}_{0C,0} = \begin{bmatrix} \dot{x}_M \\ 0 \\ \dot{z}_m \end{bmatrix} \tag{26}$$

The momentary position of the wheel rotation axis and the angular velocity of the wheel or rim respectively are defined by

$$e_{yR,0} = \begin{bmatrix} -\sin\delta\cos\gamma \\ \cos\delta\cos\gamma \\ \sin\gamma \end{bmatrix} \quad \text{and} \quad \omega_{0R,0} = \begin{bmatrix} \dot{\gamma}\cos\delta - \dot{\varphi}\sin\delta\cos\gamma \\ \dot{\gamma}\sin\delta + \dot{\varphi}\cos\delta\cos\gamma \\ \dot{\delta} + \dot{\varphi}\sin\gamma \end{bmatrix} \tag{27}$$

Then

$$\Omega \;=\; e_{yR,0}^T\,\omega_{0R,0} \;=\; \dot{\varphi} + \dot{\delta}\sin\gamma \tag{28}$$

describes the absolute angular velocity of the wheel/rim about the wheel rotation axis.

The equations of motion for the virtual test rig are provided by

$$M\,\ddot{x}_M = F_D + e_{x,0}^T\,F_{T,0} \tag{29}$$

$$M\,\ddot{z}_M = F_S - M\,g \tag{30}$$

$$m\,\ddot{z}_m = -F_S - m\,g + e_{z,0}^T\,F_{T,0} \tag{31}$$

$$\Theta_W\,\dot{\Omega} = T_{D/B} + e_{yR,0}^T\,T_{T,0} \tag{32}$$

The fictitious force F_D applied to the chassis mass and provided by an appropriate controller makes it possible to accelerate or decelerate the vehicle without driving or braking the wheel. The TMeasy tire model delivers the contact forces and torques collected in the force vector $F_{T,0}$ and the torque vector $T_{T,0}$ which is related to the wheel center. The suspension force

$$F_S \;=\; F_0 - c_S\,(z_M - z_m) - d_S\,(\dot{z}_M - \dot{z}_m) \tag{33}$$

is modeled by a linear spring-damper-element, where c_S, d_S characterize its stiffness and damping properties and $z_M - z_m$ represents the suspension travel. The preload $F_0 = M\,g$ compensates the chassis weight. The torque $T_{D/B}$ makes it possible to apply a driving or braking torque to the wheel.

The maneuver driving straight ahead on a random road is characterized by vanishing steer and camber angles $\delta = 0$ and $\gamma = 0$ when potential steer and camber changes due to the suspension kinematics are neglected in this basic study. A nearly constant driving velocity is maintained either by a controlled drive force F_D acting at the chassis mass or a controlled drive torque $T_{D/B} = T_D$ applied via the half-shaft to the wheel. The former models a not driven the latter a driven wheel.

5 RESULTS

5.1 Model Parameter

The TMeasy tire model is characterized by 58 parameter in the standard version 5.3. The extended version 6.0 requires six more parameter which specify the belt inertia, the natural eigen-frequencies and viscous damping rates of the belt, as well as the stiffness of the tread particles. Table 2 collects the main parameter of the virtual test rig which characterize a standard midsize passenger car in a quarter car model approach.

Vehicle/Tire				Tire/Belt			
chassis mass	M =	312.2	kg	tire unloaded radius	r_0 =	0.2930	m
wheel mass	m =	44.6	kg	tire dynamic radius$^{(*)}$	r_D =	0.2815	m
susp. stiffn.	c_S =	17 750	N/m	belt inertia	Θ_B =	0.6868	kgm^2
susp. damp.	d_S =	2354	N/(m/s)	nat. freq. belt long.	f_{0x} =	120	Hz
rim inertia	Θ_R =	0.462	kgm^2	nat. freq. belt rad.	f_{0r} =	90	Hz
tire vert. stiffn.	c_T =	190 000	N/m	tread part. stiffn.$^{(*)}$	c_{TP} =	10	kN/mm
tire vert. damp.	d_T =	500	N/(m/s)	tread part. damp.$^{(*)}$	d_{TP} =	9 000	N/(m/s)

Table 2: Main parameter of virtual test rig and TMeasy tire model where $(*)$ holds at the tire payload of 3500 N

Equation (7) delivers a fictitious modal belt mass of

$$m_B = 8 \text{ kg} \tag{34}$$

and Equation (6) produce the stiffness properties of the sidewall as

$$c_{Sx} = 4\,500\,000 \text{ N/m} \quad \text{and} \quad c_{Sr} = 220\,000 \text{ Nm/rad} \tag{35}$$

A pressure loss in the tire is modeled by reducing the sidewall and the vertical tire stiffness to

$$c_{Sx}^{red} = 3\,000\,000 \text{ N/m} \quad \text{and} \quad c_{Sr}^{red} = 150\,000 \text{ Nm/rad} \quad \text{as well as} \quad c_T^{red} = 155\,000 \text{ N/m} \tag{36}$$

The corresponding damping parameters were kept unchanged. The reduced vertical tire stiffness lowers the dynamic rolling radius of the tire at steady-state to $r_D^{red} = 0.2789$ m as a consequence.

5.2 Driving straight ahead on random road

At first, the vehicle model is driven with a constant velocity of $v = 120$ km/h $= 33.3$ m/s on a horizontal and nearly flat road which just contains small randomly distributed irregularities. Hence, a distance of $s = 33.3$ m is covered in the interval $0 \leq t \leq 1$ s of the time histories plotted in Figure 5. The TMeasy contact model processes the road profile by an effective local road plane, which results in a slightly smoother time history of the effective contact point compared to the road roughness, Figure 5 top graph.

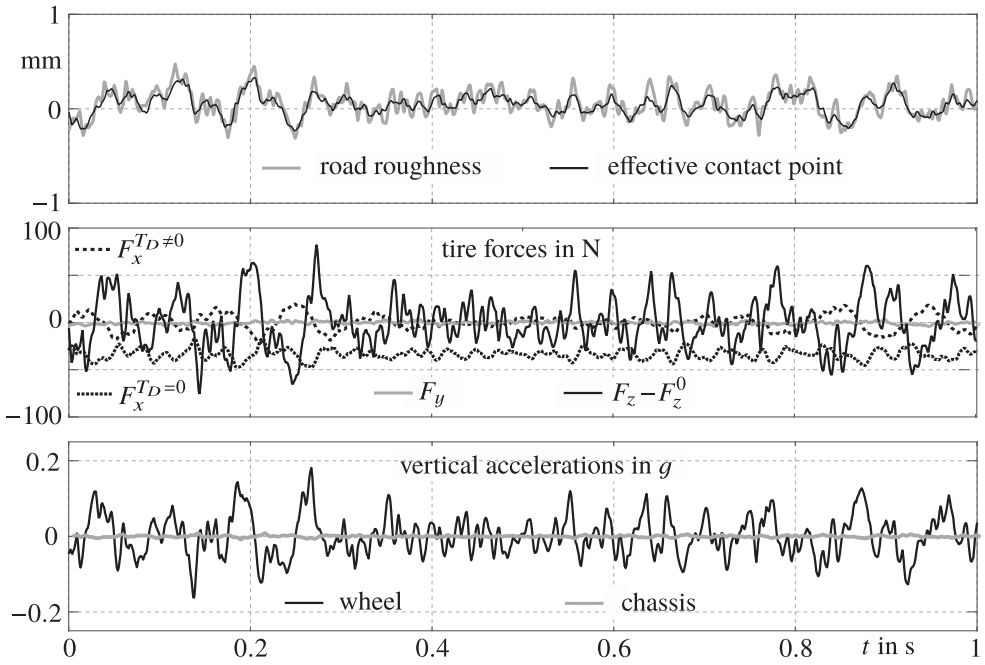

Figure 5: Virtual tire test driven straight ahead with constant velocity on random road

The spatial road profile induces small tire force fluctuations not only in the vertical but also in the longitudinal and the lateral directions, Figure 5 center graph. The longitudinal force $F_x = F_x(t)$ oscillates about zero if the wheel is driven ($T_D \neq 0$) and about a small negative value if the wheel is not driven ($T_D = 0$). In the former case the drive torque compensates the rolling resistance at the wheel and just very small longitudinal forces are required to keep the wheel rotating. In the latter case a drive force $F_D \neq 0$ applied to the chassis mass maintains the constant velocity and a certain amount of negative longitudinal tire forces is required to counteract the rolling resistance of the wheel.

The vertical tire forces F_z deviates from the steady-state value F_z^0 and generates rapidly oscillating vertical accelerations of the wheel mass, black line in bottom graph of Figure 5. The suspension system filters these excitation and results in a very smooth and comfort ride, because the vertical accelerations of the chassis mass, gray line in bottom graph of Figure 5, are hardly noticeable.

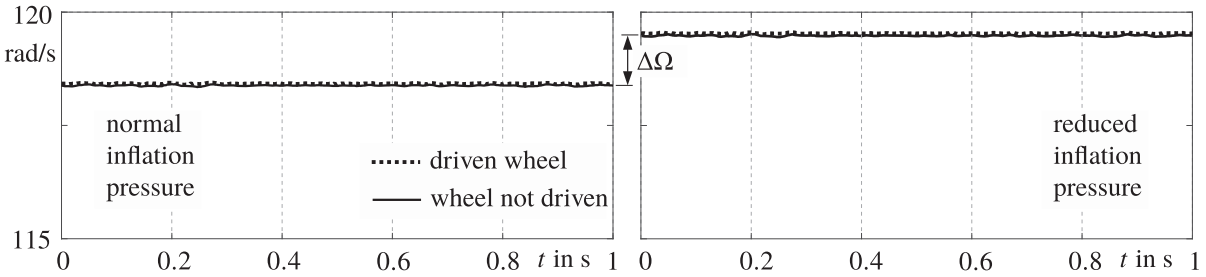

Figure 6: Rim angular velocity with normal and reduced inflation pressure

The mean value of the wheel or rim angular velocity Ω increases when the tire inflation pressure is reduced, Figure 6. Some indirect tire-pressure monitoring systems (iTPMS) take advantage of this effect. A pressure loss is detected if one wheel angular velocity deviates

significantly from the others. However, no detection is possible if all tires loose pressure at the same time.

Sophisticated iTPMS perform a frequency analysis of the angular wheel or respectively rim velocities. Induced by the road irregularities the rotating rim performs oscillations. Inspecting the angular velocity $\Omega(t)$ in the interval $0 \leq t \leq T$ a corresponding, but shifted and normalized signal is obtained by

$$y(t) = \Omega(t) - \text{mean}(\Omega(t)) \quad \text{and} \quad s(t) = \frac{2\,y(t)}{\max(y(t)) - \min(y(t))} \tag{37}$$

where $T = 1$ s was used in this basic study. This signal $s(t)$ is then transformed into the frequency domain. To eliminate any FFT processing errors, it is approximated by

$$\sigma(t) = p + q\,t + \sum_{i=1}^{i=N} A_i \,\sin\left(2\pi f_i\,t + \phi_i\right) \tag{38}$$

where $N = 200$ frequencies are predefined by $f_i = 1(1)201$ Hz and the $2 + 2N$ parameter p, q, A_i, and ϕ_i are obtained by a least square curve fit. The signal $s(t)$, its approximation $\sigma(t)$, as well as the absolute values of the amplitudes A_i are plotted in Figure 7 for different tire inflation pressures. In both cases (normal pressure and reduced pressure) the approximation

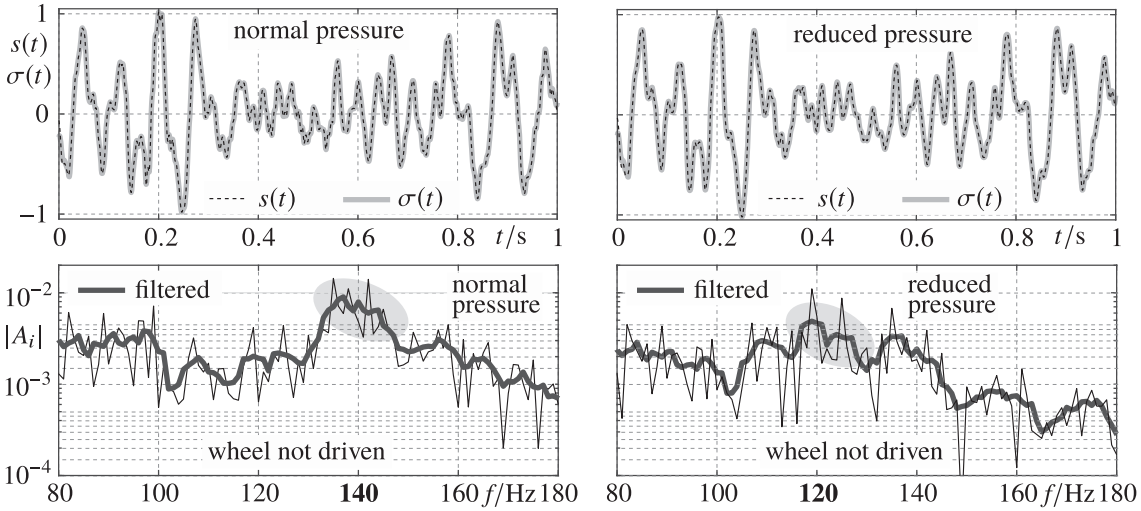

Figure 7: Frequency analysis of shifted and normalized rim angular velocity with normal and reduced inflation pressure for a not driven wheel of the virtual test rig

$\sigma(t)$ matches the signal $s(t)$ perfectly, which confirms the quality of this approach.

For a more convenient comparison the frequency responses are smoothed by a moving-average filter which operates as

$$\begin{aligned}
&\left|\hat{A}_1\right| = |A_1|\,, \quad \left|\hat{A}_2\right| = \tfrac{1}{3}\left(|A_1| + |A_2| + |A_3|\right) \\
&\left|\hat{A}_j\right| = \tfrac{1}{5}\sum_{k=j-2}^{k=j+2} |A_k| \quad \text{for} \quad 2 \leq j \leq N-2 \\
&\left|\hat{A}_{N-1}\right| = \tfrac{1}{3}\left(|A_{N-2}| + |A_{N-1}| + |A_N|\right), \quad \left|\hat{A}_N\right| = |A_N|
\end{aligned} \tag{39}$$

Practically no difference is noticeable between the time histories of the signals at normal and reduced pressure. But, the corresponding frequency responses differ in a characteristic manner. Rim and belt incorporate an eigen-mode where the rotational motion of the belt is in phase with its translational motion and out of phase with the rim rotation.

At normal pressure this eigen-mode is excited at a frequency of approximately 140 Hz which results in the resonance phenomena indicated by a grey ellipse in the lower left plot of Figure 7. This resonance frequency is slightly larger than the natural eigen-frequencies specified in Table 2, because the former occurs when the tire is in contact with the road whereas the latter hold for free tire vibrations.

A reduced inflation pressure lowers these eigen-frequencies. In this particular case, the natural eigen-frequencies of the free vibrating tire were reduced by the factor $\sqrt{2/3}$ which results in an adjustment factor of $2/3$ for the corresponding stiffness parameter. As a consequence, the resonance phenomena in the frequency response is shifted accordingly, lower right plot of Figure 7.

Figure 8 demonstrates that the characteristic shift of the resonance phenomena is also present when the wheel is driven.

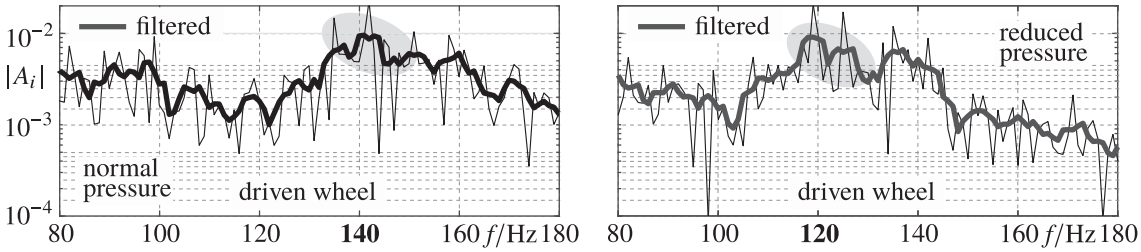

Figure 8: Frequency analysis of shifted and normalized rim angular velocity with normal and reduced inflation pressure for a driven wheel of the virtual test rig

The shift of the resonance phenomena is also observed at low ($v = 60$ km/h) and high ($v = 180$ km/h) vehicle velocities, Figure 9. The maximum resonance magnification may be

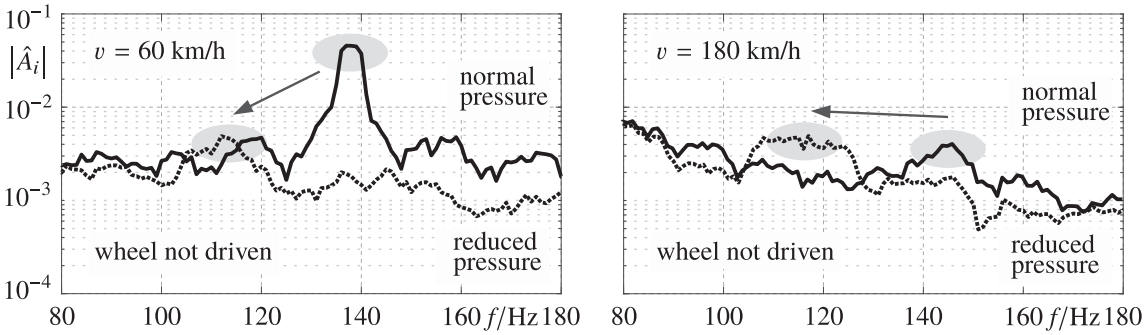

Figure 9: Frequency analysis of shifted and normalized rim angular velocity with normal and reduced inflation pressure for a driven wheel of the virtual test rig at different driving velocities

different because of specific stochastic properties of the road irregularities. But in both cases the maximum is shifted significantly to lower frequencies when the tire inflation pressure is lowered. In this particular case, it is reduced by the factor $\sqrt{2/3}$ and the shift takes place from $f \approx 140$ Hz to $f \approx 120$ Hz.

Hence, the frequency response of the angular wheel or respectively rim angular velocity, which is automatically measured in any modern passenger car, clearly indicates a pressure loss. Indirect tire-pressure monitoring systems (iTPMS) based on this concept are able to detect a simultaneous pressure loss at all tires in addition.

5.3 TMeasy standard versus TMeasy extended

The first order tire dynamics applied in the standard TMeasy 5.3 just holds in the lower frequency range. This model is suitable for all kind of driving situations but does not cover the higher frequencies of the rim and tire belt eigen-modes which are modeled in addition in the extended TMeasy version 6.0.

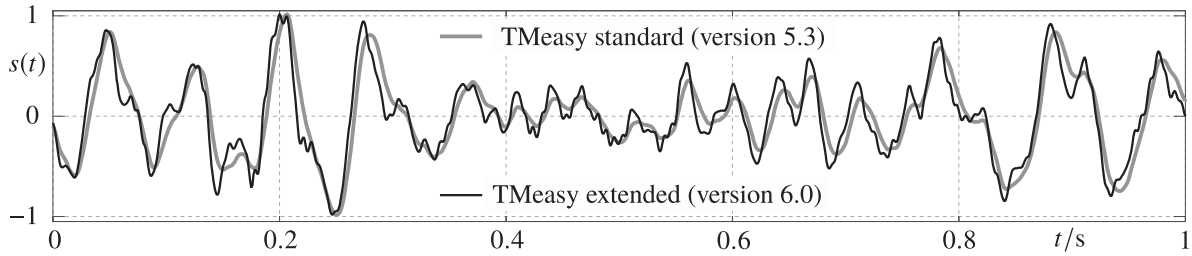

Figure 10: Time histories of shifted and normalized rim angular velocity computed for a not driven wheel of the virtual test rig with TMeasy standard and extended

Figure 10 illustrates the difference between TMeasy 5.3 and Tmeasy 6.0 by the computed time histories of the shifted and normalized rim angular velocity. The time history of the extended TMeasy version 6.0 clearly shows high-frequency components which are responsible for the resonance phenomena in the corresponding frequency range.

6 CONCLUSIONS

Some indirect tire-pressure monitoring systems (iTPMS) process higher frequent vibrations of the rim and the tire belt which are excited by road irregularities and which are sensitive to the tire inflation pressure. The extended tire model TMeasy 6.0 takes the corresponding vibration modes oft the belt into account and makes it possible to investigate such kind of iTPMS. Just the first two belt eigen-modes have to be considered which keeps the tire model TMeasy as simple as possible. A tailored partly implicit solver, which takes the coupling between the longitudinal force and the belt motions into account, provides a fast and stable numerical solution which is required in real-time applications.

REFERENCES

[1] Peter Lugner (Editor), Vehicle Dynamics of Modern Passenger Cars, Springer International Publishing, 2019.

[2] Wenrui Han, Günther Prokop, et al. , Model-based development of iTPMS (indirect Tire Pressure Monitoring System, in: 10th International Munich Chassis Symposium 2019, 775–794, Springer, Wiesbaden 2020.

[3] Georg Rill, TMeasy – The Handling Tire Model for all Driving Situations, in: DINAME 2013 – Proceedings of the XV International Symposium on Dynamic Problems of Mechanics, M.A. Savi (Editor), ABCM, Buzios, RJ, Brazil, February 17–22, 2013.

[4] Georg Rill, Sophisticated but quite simple contact calculation for handling tire models, Multibody System Dynamics 45, 131–153 (2019).

[5] Georg Rill, An Engineer's Guess on Tyre Parameter made possible with TMeasy, in: Proceedings of the 4th International Tyre Colloquium, Guildford, U.K., 2015, http://epubs.surrey.ac.uk/807823 (access at 18.01.2020).

[6] Wolfgang Hirschberg, Frantisek Palcak, et al., Reliable vehicle dynamics simulation in spite of uncertain input data, in: Proceedings of 12th EAEC European Automotive Congress, (Bratislava), 2009.

[7] Georg Rill and Abel Arrieta Castro, Road Vehicle Dynamics: Fundamentals and Modeling with MATLAB®, 2nd Edition, Taylor & Francis, Boca Raton, 2020.

[8] Andreas Hackl, Wolfgang Hirschberg, et al.,Experimental validation of a non-linear first-order tyre dynamics approach, in: Proceedings of 24th International Symposium on Dynamics of Vehicles on Roads and Tracks (J. Bernasch and M. Rosenberger, eds.), (Graz, Austria), IAVSD, VIRTUAL VEHICLE Research Center, 2015.

[9] Michael Gipser, FTire, a New Fast Tire Model for Ride Comfort Simulations, available at https://www.cosin.eu/wp-content/uploads/ftire_eng_1.pdf (access at 18.01.2020).

EURODYN 2020
XI International Conference on Structural Dynamics
M. Papadrakakis, M. Fragiadakis, C. Papadimitriou (eds.)
Athens, Greece, 23–26 November 2020

OPTIMIZATION OF NONLINEAR QUARTER CAR SUSPENSION-DRIVER SEAT MODEL USING GA BASED PID CONTROLLER

Omar El-Mezayen[1], Mustafa Qasem[1], Hesham Ibrahim[1], Nora Merabet[2], and Zakaria Elnaggar[3]

[1] German University in Cairo
Mechatronics Department, Cairo, Egypt.
e-mail:{omar.almzayen, mustafa.kalieb}@student.guc.edu.eg

e-mail: hesham.hamed-ahmed@guc.edu.eg

[2] Emirates Aviation University
School of Mathematics, Statistics & Computing, Dubai, UAE
e-mail: nora.merabet@emirates.com

[3] Cairo University
Faculty of Engineering, Giza, Egypt
e-mail: Zakaria.elnaggar@bag-eg.com

Keywords: Quarter car, Suspension, Optimal seat design, Car-driver model, Genetic algorithm, PID controller.

Abstract. *This paper investigates the optimal active/passive system parameters of a nonlinear quarter car suspension-driver seat model. The mathematical model of the system has four degrees of freedom (4-DoF), with quadratic and cubic stiffness nonlinearities in suspension springs and tires, respectively. The comfort, the stability and the behavior of the suspension system are simulated using Matlab Simulink. Multi-objective genetic algorithms (GA) are used to tune the PID controller and to optimize the head acceleration, the crest factor, and the suspension and tire deflection. The numerical results show that the proposed GA-tuned parameters of the PID controller, as well as GA-tuned design parameters in the quarter car model are more efficient than those of Ziegler-Nicholas and Matlab auto-tuner techniques. The numerical results also demonstrate that active suspension systems are more efficient compared to passive systems.*

1 INTRODUCTION

The main component responsible for the dynamic behavior of a vehicle is its suspension system. The suspension system isolates the vehicle's occupants from strong vibrations induced by road surface irregularities, and enables wheels to maintain contact with the road, which provides the vehicle's stability and control. This paper investigates both passive and active vehicle suspensions. A passive suspension system uses conventional springs and dampers with no feedback action to absorb the road disturbances, while an active suspension system uses force actuator elements in a closed loop control, to provide adequate control force to the system, as a response to the input from the various sensors associated with the vehicle's vertical dynamics. Suspension systems, vehicle handling and stability as well as driver comfort and safety have been extensively studied in the literature. A wide range of global optimization techniques have been investigated to determine the optimum design and control parameters that enhance vehicle stability and passengers' safety. Wael Abbas et al [5] presented a 4-DoF human-body model, with linear seat suspension, for half car model. In this model, the seated human-body was constructed as four separate mass segments interconnected by five sets of springs and dampers, with a total human mass of 60.67 kg. O. Gundogdu [1] solved an optimization problem of a 4-DoF quarter car seat and suspension system model using genetic algorithm, to determine parameters that achieve best comfort. The quarter car and the seat, with the driver's body were modeled as a 4-DoF damped spring-mass system. Du et al [2] presented an integrated vehicle seat and suspension control strategy for a quarter car model, to improve suspension impact on ride comfort. A 4-DoF lumped parameter human model is suggested by Boileau and Rakheja [3]. The selection of the design parameters defines the constitutive relationship for nonlinear stiffness and damping while the 4-DoF driver model is linear. The reported data on biodynamic responses of the seated and standing human body exposed to whole-body vibration along different directions and the associated experimental conditions are reviewed by Rakheja et al. [4], in an attempt to identify datasets that are likely to represent comparable and practical postural and exposure conditions. A 7-DoF vehicle and seat suspension design was presented by Abbas el al. [5]. A genetic algorithm is applied to search for the optimal parameters of the seat, in order to minimize seat suspension deflection, driver's body acceleration, and achieve the best ride comfort. The simulation results were compared with the ones of the passive suspensions, subject to different road profiles. A generalized nonlinear model is formulated by Bouazara et al. [6], for the dynamic analysis of the seat suspension system with passive, semi-active and active dampers. It was concluded that the comfort performance of a seat suspension with semi-active and active dampers was enhanced by 20 to 30%. The spring and damper settings that ensure optimal ride comfort, on different road profiles and at different speeds, have been investigated by Uys et al. [7]. It is found that combining driver and rear passenger's seats weighted root mean square (RMS) and vertical acceleration, as the objective function of the optimization problem returns better results compared to the case when only one seat value is used. Genetic algorithm is employed to search for the parameters, such as damping ratio and springs constants that achieve an optimum trade-off between ride comfort and handling quality, under random road input. Genetic algorithm is also used to obtain the seat suspension system controller parameters. The results showed that an active suspension using genetic algorithm improved the dynamic performance parameters of the seat with minimum actuator force. Baumal et al. [8] also investigated both active control and passive mechanical parameters of a vehicle suspension system, that minimize the passenger's seat acceleration, under the required road-holding ability and suspension working space constraints. An analytical study along with experimental

validation, on lumped parameter models for seated human subjects, without backrest support, under vertical vibration excitation, have been carried out by Liang and Chiang [9]. Kuznetsov et al. [10] investigated a quarter car design, as a 3-DoF seat suspension system, with the driver represented by 1-DoF. Ride comfort criteria as per ISO 2631-1 were used as constraints in the algorithm for global optimization problems. Badran et al. [11] optimized a quarter car system using genetic algorithm. A weighted average of seat acceleration and head acceleration was used as a single objective function, and suspension working space as constraints.

Control of active suspension systems has been extensively covered in the literature, and span a wide range of techniques such as PID, linear quadratic regulator, adaptive sliding control, H control, sliding mode control, fuzzy logic, preview control, optimal control and neural network. However, these methods need refined mechanisms and some are difficult to implement in applications. PID and linear quadratic regulator controllers were investigated by Nagarkar et al [14] to control a nonlinear quarter car along with a human model. The quarter car model includes quadratic tire stiffness and cubic stiffness in suspension springs. The active system gives minimum head acceleration, crest factor, amplitude ratio at head and upper torso, thus providing comfort and meeting health criteria. Mahesh et al [14] ,[13] investigated a multi-objective genetic algorithm to optimize an active nonlinear quarter car suspension system, with PID and fuzzy logic control. Simulation results show that GA-based fuzzy logic and PID controller give better ride comfort.

In this paper a 4-DoF quarter car seat and suspension system model for both passive and active suspension systems subject to an excitation from a road profile is investigated. Genetic algorithm is used to determine the optimal design and control parameters that maximize ride comfort and vehicle stability. Enhanced suspension parameter values are extracted from multiple genetic algorithm runs. Dynamics of the system is simulated using Matlab/Simulink. A PID controller is tuned using Ziegler-Nicholas method to identify parameter boundaries, then tuned again using genetic algorithm, to select the best gains. These values are fed into genetic algorithm to compute enhanced design parameters. Results show an improvement in comfort. Further details will be discussed in the following sections.

2 MODEL DEVELOPMENT

The vehicle model investigated in this paper is an improvement of the linear model in [1]. It is a 4-DoF quarter car model in which the driver is represented by the upper 2-DoF lumped mass system. In this study, both linear and nonlinear models are considered. The quarter car model is set using interconnections of masses, springs and dampers, as illustrated in (Fig. 1), where M_s is the sprung mass, M_u is the un-sprung mass, K_s is the spring stiffness constant, C_s denotes dashpot. Z_r is the road or step input to the tire, Z_s and Z_u are the displacements of masses M_s and M_u respectively. The nonlinearities consist of quadratic and cubic tire stiffness and spring stiffness. The lower springs and damper represent the tire stiffness, with coefficients K_y for linear model and K_{y_1}, K_{y_2} and K_{y_3} for nonlinear model. Similarly C_s is the damping coefficient for linear model and C_{s_1}, C_{s_2} for non-linear model. The un-sprung mass is impacted by the road surface data Z_r through the tires' contact. Elastic properties of the cushion are also modeled as a spring and a dashpot with respective constants of K_c and C_c. The driver is represented by a 2-DoF lumped mass system. The upper body is also connected to the lower part through a spring and a dashpot combination with constants K_t and C_t respectively. The variables Z_t and Z_p are displacements of the thorax and pelvis from their static equilibrium positions [1]. It is assumed that the system does not vibrate in lateral and longitudinal directions, only oscillates in vertical direction (vertical to road surface). Furthermore, the tires are assumed

not losing the contact with the road surface. The motion in other directions is assumed small and hence neglected.

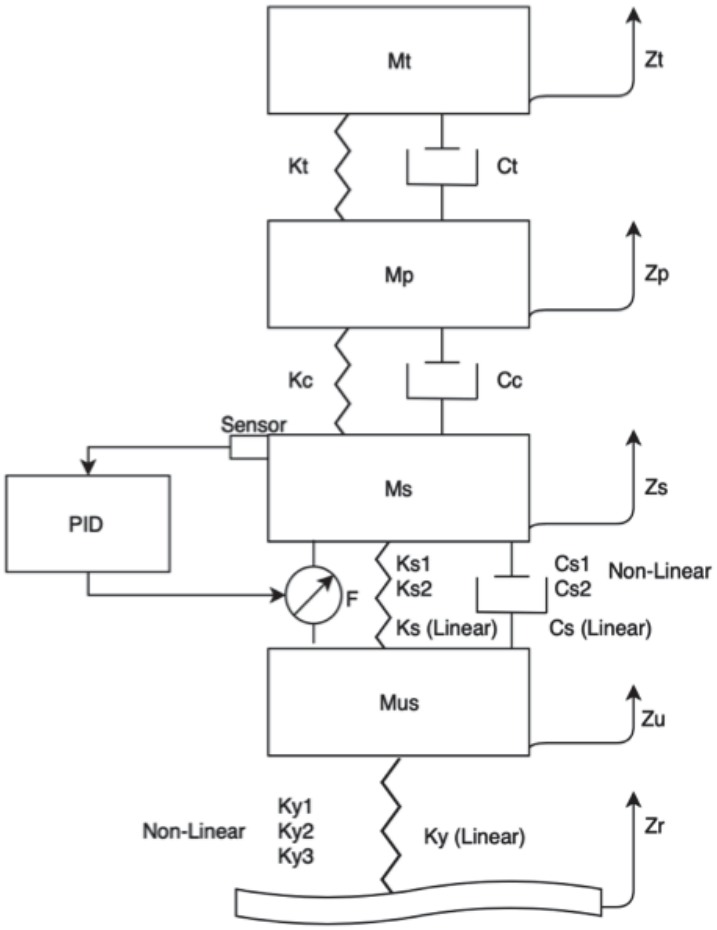

Figure 1: Model Development

The mathematical model of the quarter car model is described by the following set of equations of motions from their static equilibrium positions. The systems are solved for four state variables Z_t, Z_p, Z_s and Z_u given the road excitation Z_r.

Equations of motions for linear model

$$\begin{aligned} M_t Z_t^{''} &= -K_c \,.\, (Z_t - Z_p) - C_t \,.\, (Z_t^{'} - Z_p^{'}) \\ M_p Z_p^{''} &= K_t \,.\, (Z_t - Z_p) + C_t \,.\, (Z_t^{'} - Z_p^{'}) - K_c \,.\, (Z_p - Z_s) - C_c \,.\, (Z_p^{'} - Z_s^{'}) \\ M_s Z_s^{''} &= K_c \,.\, (Z_p - Z_s) + C_c \,.\, (Z_p^{'} - Z_s^{'}) - K_s \,.\, (Z_s - Z_u) - C_s \,.\, (Z_s^{'} - Z_u^{'}) + F \\ M_u Z_u^{''} &= K_s \,.\, (Z_s - Z_u) + C_s \,.\, (Z_s^{'} - Z_u^{'}) - K_y \,.\, (Z_u - Z_r) - F \end{aligned} \tag{1}$$

Equations of motions for non-linear model

$$
\begin{aligned}
M_t Z_t^{''} &= -K_t \,.\, (Z_t - Z_p) - C_t \,.\, (Z_t^{'} - Z_p^{'}) \\
M_p Z_p^{''} &= K_t \,.\, (Z_t - Z_p) + C_c \,.\, (Z_t^{'} - Z_p^{'}) - K_c \,.\, (Z_p - Z_s) - C_c \,.\, (Z_p^{'} - Z_s^{'}) \\
M_s Z_s^{''} &= K_c \,.\, (Z_p - Z_s) + C_c \,.\, (Z_p^{'} - Z_s^{'}) - K_{s_1} \,.\, (Z_s - Z_u) - K_{s_2} \,.\, (Z_s^{'} - Z_u^{'}) \\
&\quad -C_{s_2} \,.\, (Z_s^{'} - Z_u^{'})^2 + F \\
M_u Z_u^{''} &= K_{s_1} \,.\, (Z_s - Z_u) + K_{s_2} \,.\, (Z_s - Z_u)^3 + C_{s_1} \,.\, (Z_s^{'} - Z_u^{'}) + C_{s_2} \,.\, (Z_s^{'} - Z_u^{'})^2 \\
&\quad -K_{y_1} \,.\, (Z_u - Z_r) - K_{y_2} \,.\, (Z_u - Z_r)^2 + K_{y_3} \,.\, (Z_u - Z_r)^3 - F
\end{aligned}
\tag{2}
$$

The above models are simulated in Matlab-Simulink, with the following values for the equations' coefficients:

Suspension Parameter	**Symbol**	**Value**
Linear Spring Stiffness Coefficient	K_{s_1}	15302
Non-Linear Spring Stiffness Coefficient	K_{s_2}	2728
Linear Spring Damping Coefficient	C_{s_1}	3482
Non-Linear Spring Damping Coefficient	C_{s_2}	580
Linear Tire Stiffness Coefficient	K_{y_1}	60063
Non-Linear Square Tire Stiffness Coefficient	K_{y_2}	42509
Non-Linear Cube Tire Stiffness Coefficient	K_{y_3}	22875
Sprung Mass	M_s	295
Un-sprung Mass	M_u	39
Upper Body Mass	M_t	18.6
Lower Body Mass	M_p	46.4
Spring Stiffness Coefficient	K_s	9015
Spring Damping Coefficient	C_s	2031
tire Stiffness Coefficient	K_y	41815
Thorax Stiffness Coefficient	K_t	45005.3
Thorax Damping Coefficient	C_t	1360
Cushion Stiffness Coefficient	K_c	2500
Cushion Damping Coefficient	C_c	131.59

Table 1: Suspension parameters' values

The aim is to analyze the dynamic behavior of the active car-driver system, and determine the seat and the suspension system design parameters (coefficients in the equations of motion above) that maximize rider's comfort. This is done by minimizing the vertical displacements and acceleration of the driver's head and upper body, while maximizing the vehicle's stability and control.

A Proportional, Integral and Derivative PID controller has been used for the active suspension system (Fig.1):

PID controller design

PID control is a feedback control design. The three terms operate on the error signal to produce a control signal. If $u(t)$ is the control signal which is sent to the system, $y(t)$ the actual output, $r(t)$ the desired output, and $e(t)$ the tracking error then a PID control law is expressed as

$$u(t) = k_p\, e(t) + k_i \int_0^t e(\tau)\, d\tau + k_d\, e'(t).$$

The desired closed loop dynamics can be obtained by adjusting the three parameters k_p, k_i and k_d. Model's stability can often be obtained using only the proportional term. The integral term permits the rejection of a step disturbance. The derivative term provides damping or shaping of the response. Both the suspension system design parameters and PID controller parameters were tuned using genetic algorithm, in the next sections.

3 METHODOLOGY AND SIMULATION

3.1 Objective functions

The optimization problem is stated as a multi-objective minimization problem, solved using multi-objective genetic algorithm from Matlab toolbox. The objective function to be minimized **J** is defined as a vector function with four components, head acceleration (J_{HA}), crest factor (J_{CF}), suspension deflection (J_{S}), and tire Deflection (J_{TD}), as follows:

$$\mathbf{J} = \begin{bmatrix} J_{\text{HA}} & J_{\text{CF}} & J_{\text{S}} & J_{\text{TD}} \end{bmatrix}^t \tag{3}$$

The function J_{HA} is the root mean square of head acceleration (RMS_h) , (with $T = 5$ sec, in simulations), given by:

$$J_{\text{HA}} = \text{RMS}_h = \left\{ \frac{1}{T} \int_0^T [Z_t'']^2\, dt \right\}^{\frac{1}{2}} = \left\{ \frac{1}{T} \int_0^T \left[-\frac{k_t}{m_t} (Z_t - Z_p) - \frac{c_t}{m_t} (Z_t' - Z_p') \right]^2 dt \right\}^{\frac{1}{2}}$$

The function CF_h is the crest factor of the head acceleration and it is a ratio of the maximum acceleration to J_{HA}.

$$J_{\text{CF}} = \frac{\max Z_t''}{\text{RMS}_h}$$

The function J_{S} is the RMS value of the suspension deflection.

$$J_{\text{S}} = \left\{ \frac{1}{T} \int_0^T (Z_s - Z_u)^2\, dt \right\}^{\frac{1}{2}}$$

The function J_{TD} is the RMS value of the tire deflection.

$$J_{\text{TD}} = \left\{ \frac{1}{T} \int_0^T (Z_u - Z_r)^2\, dt \right\}^{\frac{1}{2}}$$

3.2 Genetic algorithm for suspension system

Multi-objective genetic algorithm is used to optimize the suspension parameters C_c, K_c, K_s, C_s in the linear model and C_c, K_c, K_{s_1}, K_{s_2}, C_{s_1}, C_{s_2} in the nonlinear model. In simulation,

boundary conditions are imposed on the parameters, as per the industry standards and from the literature. The Genetic algorithm minimizes the objective function given by (3), subject to equations of motion (1), (2), as nonlinear constraints and boundary conditions on the parameters. The genetic algorithm settings were selected as follows: The population size $= 30$, crossover probability, $P_c = 0.001$, and mutation probability rate, $P_m = 0.002$.
Graphs representing the state variables are generated using Simulink. Optimized parameters are given in Table 2 for linear model and Table 3 for nonlinear model.

Suspension Parameters	Symbol	Value
Cushion Damping Coefficient	C_c	128.006
Cushion Stiffness Coefficient	K_c	1414.24
Spring Stiffness Coefficient	K_s	6033.23
Spring Damping Coefficient	C_s	1750.68

Table 2: Optimized parameters (Linear case)

Suspension Parameters	Symbol	Value
Cushion Damping Coefficient	C_c	194.82
Cushion Stiffness Coefficient	K_c	1314.22
Linear Spring Stiffness Coefficient	K_{s_1}	9374.97
Non-Linear Spring Stiffness Coefficient	K_{s_2}	2338.56
Linear Spring Damping Coefficient	C_{s_1}	3459.68
Non-Linear Spring Damping Coefficient	C_{s_2}	700.07

Table 3: Optimized parameters (Nonlinear case)

3.3 Tuning PID control using genetic algorithm

PID controller was designed to ensure the displacement of the system can be controlled and minimized when the road disturbance occurs. PID parameters are randomly initialized and objective functions are determined using Ziegler-Nicholas Method and Auto-Tuner Methods in order to set the bounds for the Genetic Algorithm. GA parameters were chosen according to trial and error method. Genetic algorithm parameters are as follows: Population size $=$ 50; Crossover Fraction $= 0.8$; Mutation rate $= 0.2$; Maximum generation $= 100$; Crossover Function is arithmetic; Mutation Function is Adaptive feasible; Bounds of Parameters From 0 to 5000. In active nonlinear suspension system, the PID tuning was done using genetic algorithm, after linearizing the nonlinear system using Linearization in Simulink.

k_p	k_i	k_d
4813	54	630

Table 4: Optimized PID parameters for linear model

k_p	k_i	k_d
6810	329	947

Table 5: Optimized PID parameters for nonlinear model

4 RESULTS and ANALYSIS

In this section, simulation results of different displacements and accelerations are presented in Tables and graphs for both linear and nonlinear models. The resulting head acceleration, head displacement, sprung accelerations and displacements of the system with the optimized parameters, the classical ones and the controlled ones are compared in figures 2-5 for linear model, and in figures 6-9 for nonlinear system. In the simulations, a step height of 0.02 m is used. The color-coded legend is as follows: classical parameters are in blue, optimized parameters are in red, and GA-tuned PID controller in green.

4.1 Linear Model

System	Passive	Optimized	Optimized PID	Variation (Passive-Optimized)	Variation (Passive-PID Optimized)
Settling Time	4.71	4.6	2.32	2.34%	50.1%
Overshoot	0.0254	0.0243	0.024	4.33%	5.51%

Table 6: Results for Sprung Displacement

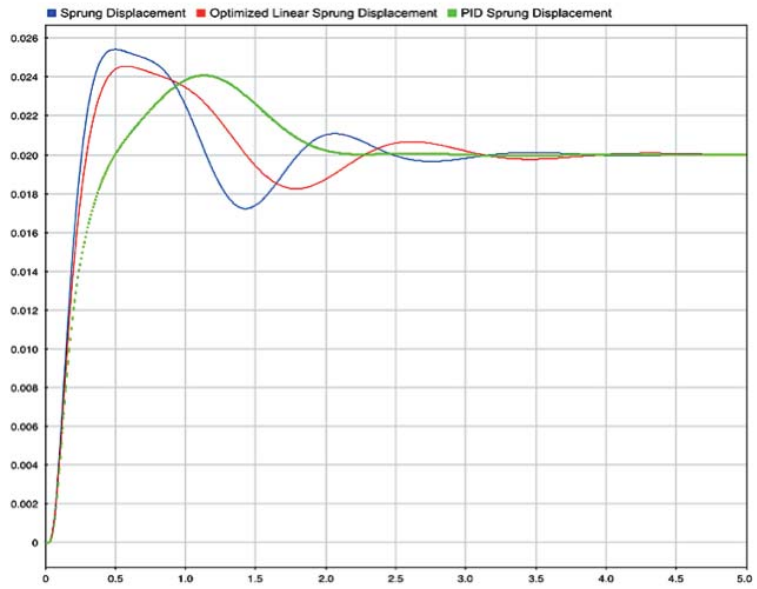

Figure 2: Linear Sprung Displacement

Figure 2 shows the sprung displacement versus time for the passive, optimized-passive and

the active suspension systems. Overshoots and settling times are extracted from the plots to show the variation between the three systems. The response of the passive suspension system is compared with both the optimized-passive and active suspension systems, which shows a variation of 2.34% in settling time values and 4.33% in overshoot values for (Passive-Optimized). While, a variation of 50.1% in settling time values and 5.51% in overshoot values are shown for (Passive-PID Optimized).

System	Passive	Optimized	Optimized PID	Variation (Passive-Optimized)	Variation (Passive-PID Optimized)
Settling Time	5+ (6.1)	4.8	4.5	21.31%	26.22%
Overshoot	0.0388	0.0365	0.0319	5.92%	17.78%

Table 7: Results for Head Displacement

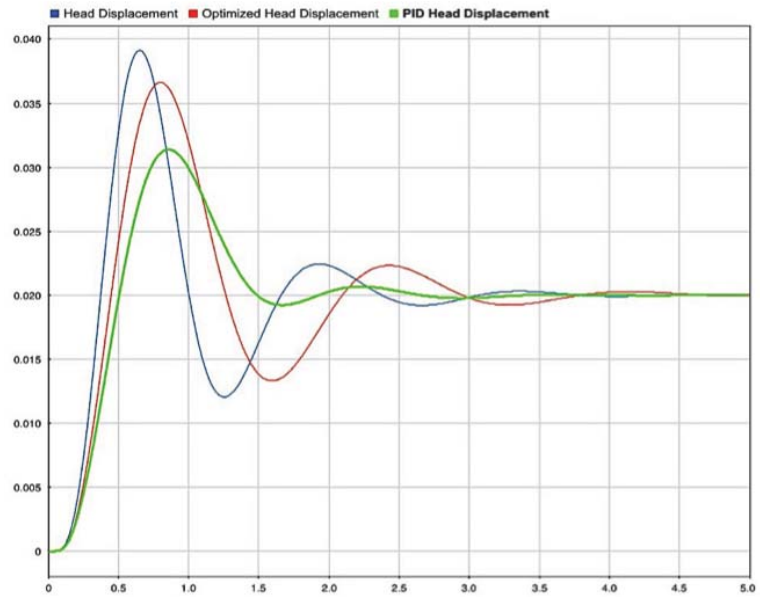

Figure 3: Head Displacement

Figure 3 shows the head displacement versus time for the passive, optimized-passive and the active suspension systems. There is a variation of 21.31% in settling time values and 5.92% in overshoot values for (Passive-Optimized) while a variation of 26.22% in settling time values and 17.78% in overshoot values are shown for (Passive-PID Optimized).

Figure 4 shows the head acceleration versus time for the passive, optimized-passive and the active suspension systems. There is almost no variation in settling time values and 40% in overshoot values for (Passive-Optimized). While, a variation of 14.15% in settling time values and 46.29% in overshoot values are shown for (Passive-PID Optimized).

Figure 5 shows the linear sprung acceleration vs time for the passive, optimized-passive and the active suspension systems. There is a variation of 13.57% in settling time values and

System	Passive	Optimized	Optimized PID	Variation (Passive-Optimized)	Variation (Passive-PID Optimized)
Settling Time	4.31	4.32	3.7	0%	14.15%
Overshoot	0.54	0.324	0.29	40%	46.29%

Table 8: Results for Head Acceleration

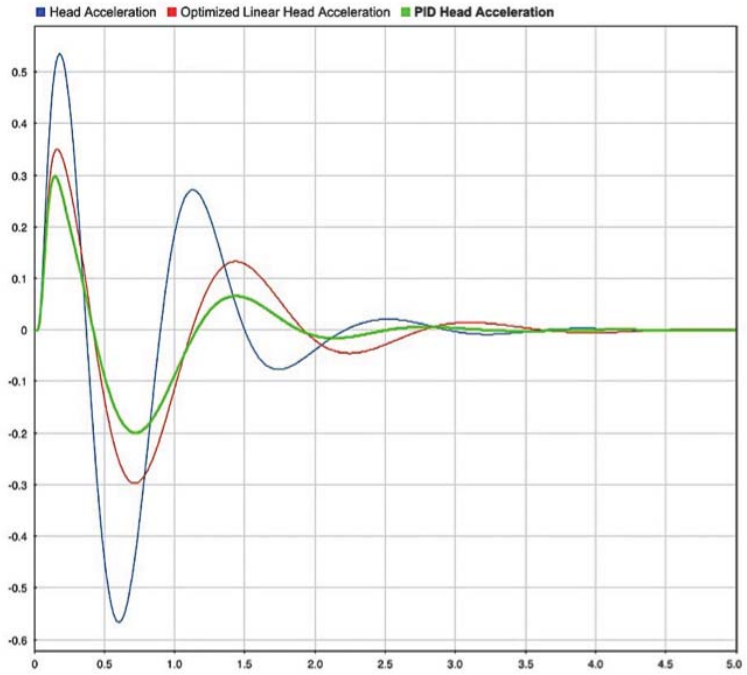

Figure 4: Head Acceleration

System	Passive	Optimized	Optimized PID	Variation (Passive-Optimized)	Variation (Passive-PID Optimized)
Settling Time	3.61	3.12	2.28	13.57%	36.84%
Overshoot	1.83	1.72	1.54	6.01%	15.84%

Table 9: Results for Sprung Acceleration

6.01% in overshoot values for (Passive-Optimized). While, a variation of 36.84% in settling time values and 15.84% in overshoot values are shown for (Passive-PID Optimized).

4.2 Nonlinear Model

Figure 6 shows the non-linear sprung displacement vs time for the passive, optimized-passive and the active suspension systems. There is a variation of 32.6% in settling time values and 6.22% in overshoot values for (Passive-Optimized). While, a variation of 47.39% in settling time values and 14.39% in overshoot values are shown for (Passive-PID Optimized).

Figure 7 shows the non-linear head displacement vs time for the passive, optimized-passive and the active suspension systems. There is a variation of 22.81% in settling time values and

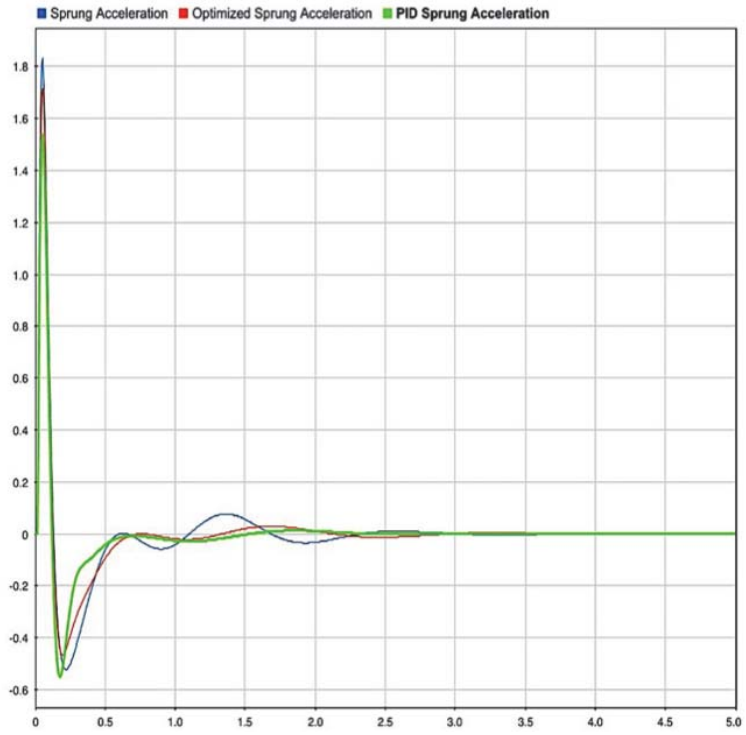

Figure 5: Sprung Acceleration

System	Passive	Optimized	Optimized PID	Variation (Passive-Optimized)	Variation (Passive-PID Optimized)
Settling Time	4.6	3.1	2.42	32.6%	47.39%
Overshoot	0.0257	0.0241	0.022	6.22%	14.39%

Table 10: Results for Non Linear Sprung Displacement

System	Passive	Optimized	Optimized PID	Variation (Passive-Optimized)	Variation (Passive-PID Optimized)
Settling Time	4.78	3.69	2.92	22.81%	38.91%
Overshoot	0.038	0.032	0.0275	15.78%	27.63%

Table 11: Results for Non Linear Head Displacement

15.78% in overshoot values for (Passive-Optimized). While, a variation of 38.91% in settling time values and 27.63% in overshoot values are shown for (Passive-PID Optimized).

Figure 8 shows the non-linear sprung acceleration vs time for the passive, optimized-passive and the active suspension systems. there is a variation of 34.37% in settling time values and 3.21% in overshoot values for (Passive-Optimized). While, a variation of 50.93% in settling time values and 20.35% in overshoot values are shown for (Passive-PID Optimized).

Figure 9 shows the non-linear head acceleration vs time for the passive, optimized-passive and the active suspension systems. There is a variation of 26.53% in settling time values and

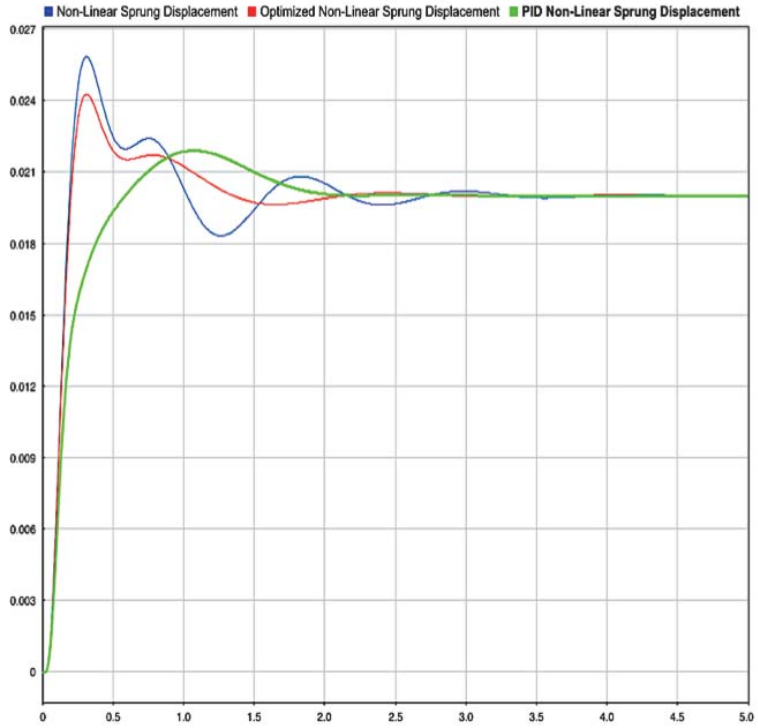

Figure 6: Non Linear Sprung Displacement

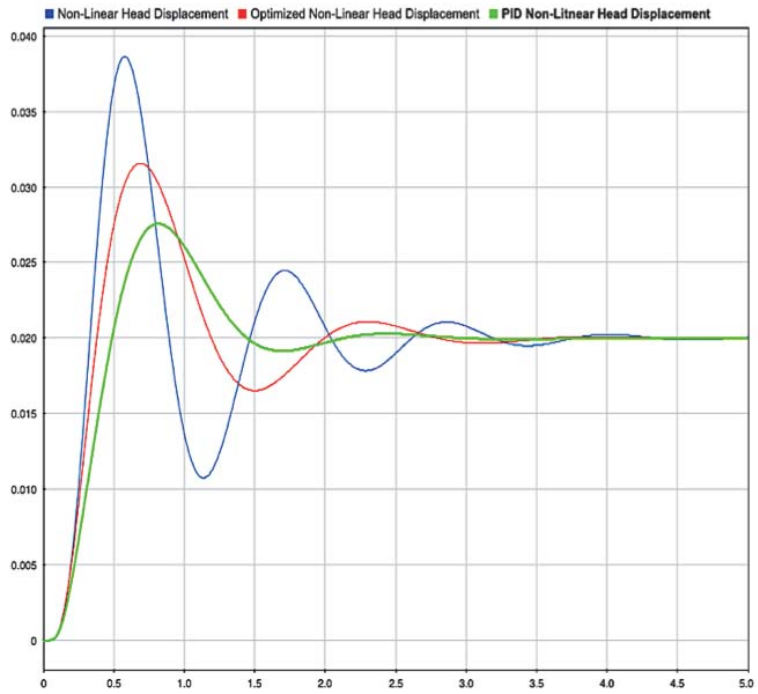

Figure 7: Non Linear Head Displacement

System	Passive	Optimized	Optimized PID	Variation (Passive-Optimized)	Variation (Passive-PID Optimized)
Settling Time	3.2	2.1	1.57	34.37%	50.93%
Overshoot	2.8	2.71	2.23	3.21%	20.35%

Table 12: Results for non-linear sprung acceleration

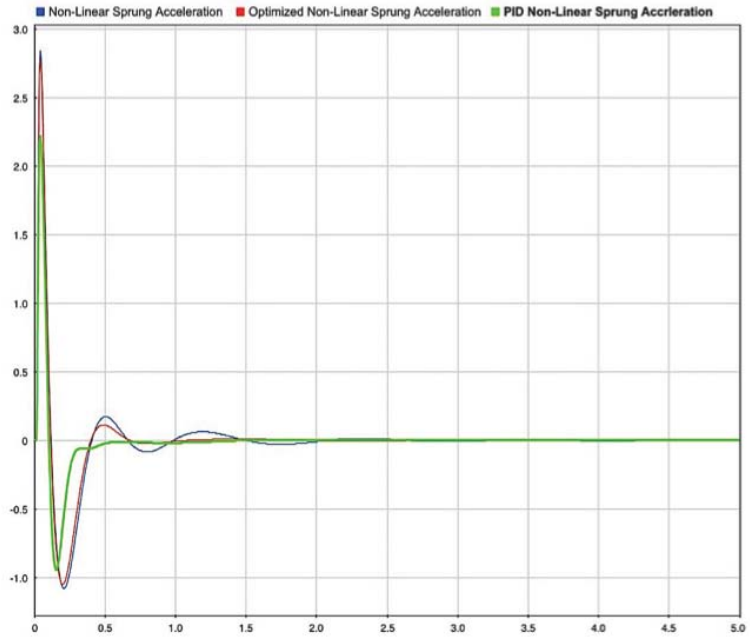

Figure 8: non-linear sprung acceleration

System	Passive	Optimized	Optimized PID	Variation (Passive-Optimized)	Variation (Passive-PID Optimized)
Settling Time	4.9	3.6	2.78	26.53%	46.08%
Overshoot	0.72	0.57	0.42	20.83%	41.67%

Table 13: Results for non-linear head acceleration

20.83% in overshoot values for (Passive-Optimized). While, a variation of 46.08% in settling time values and 41.67% in overshoot values are shown for (Passive-PID Optimized).

5 CONCLUSIONS

In this paper, a nonlinear quarter car model with a driver seat and driver, as a 4-DoF system with PID controller is investigated and compared with the passive linear system version. The model is designed to have four masses that are attached with linear and nonlinear springs and dampers. The methodology was developed to design and compare passive and active suspension systems using a classical PID controller and GA-tuned PID controller. Genetic algorithm is used to determine optimum values for the suspension design parameters and PID controller, to achieve the best performance of the system in terms of driver's comfort and vehicle's stabil-

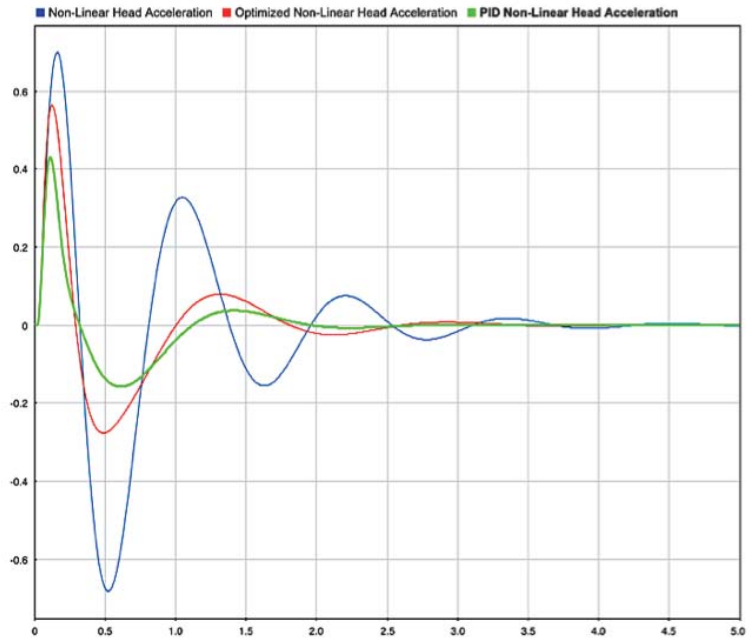

Figure 9: non-linear head acceleration

ity. Genetic algorithms showed optimum results. The optimal solutions are less oscillatory and have lower values of maximum overshoots and settling times, which results in lower HA and CF, that are directly proportional to the driver's health and comfort. Both linear and non-linear active suspension models with PID Controller were tuned by using different methods of tuning such as GA, Ziegler-Nicholas Method, and the Auto Tuner in Matlab-Simulink Toolbox. Simulation results show that implementing a GA-tuned PID controller gives better ride comfort and health criterion. The study shows a significant improvement for the active suspension system compared to the passive suspension system.

REFERENCES

[1] O. Gundogdu, Optimal seat and suspension design for a quarter car with driver model using genetic algorithms, *International Journal of Industrial Ergonomics*, **37**, 327–332, 2007.

[2] Du, H., Li, W. & Zhang, N. Integrated seat and suspension control for a quarter car with driver model, *IEEE Transactions on Vehicular Technology*, **61(9)**, 3893–3908, 2012.

[3] P. Boileau, & S. Rakheja, Whole-body vertical biodynamic response characteristics of the seated body biodynamic response under vertical vibration, *J Sound Vib*, **215(4)**, 841–62, 1998.

[4] R.G. Rakheja, S. Dong, P.E. Patra, P. Boileau, Marcotte, & C. Warren, Biodynamics of the human body under whole-body vibration- synthesis of the reported data, *International Journal of Industrial Ergonomics*, **40**, 710–732, 2010.

[5] Wael Abbas, Ossama B. Abouelatta, Magdy S. El-Azab, & Adel A. Megahed, Application of Genetic Algorithms to the Optimal Design of Vehicle's Driver-Seat Suspension Model, *Proceedings of the World Congress on Engineering, London, UK* 1630–1635, 2010.

[6] M. Bouazara, M.J. Richard, & S. Rakheja, Safety and comfort analysis of a 3-D vehicle model with optimal non-linear active seat suspension, *Journal of Terramechanics*, **43**, 97–118, 2006.

[7] P.E. Uys, P.S. Els, & M. Thoresson, Suspension settings for optimal ride comfort of off-road vehicles traveling on roads with different roughness and speeds, *Journal of Terramechanics*, **44**, 163–175, 2007.

[8] A.E. V Baumal, J.J. McPhee, & P.H. Calamai, Application of genetic algorithms to the design optimization of an active vehicle suspension system, *Computer Methods Appl. Mech. Engrg*, **163**, 87–94, 1998.

[9] C.C Liang, & C.F. Chiang, A study on biodynamic models of seated human subjects exposed to vertical vibration, *International Journal of Industrial Ergonomics*, **36**, 869–890, 2006.

[10] A. Kuznetsov, M. Mammadov, I. Sultan, E. Hajilarov, Optimization of a quarter car suspension model coupled with driver bio-mechanical effects, *J. Sound Vib.*, **46**, 330–2937, 2011.

[11] S. Badran, A. Salah, W. Abbas, O. Abouelatta, Design of optimal linear suspension for quarter car with human model using genetic algorithms, *Res Bull Jordan ACM*, **2**, 42–51, 2012.

[12] MP. Nagarkar, Dr. YJ Bhalerao, Dr. GJ Vikhe Patil, RN. Zaware Patil, Multi- Objective Optimization of nonlinear quarter car suspension system, PID and LQR control, *Procedia Manufacturing*, **20**, 420–427, 2018.

[13] P. Mahesh Nagarkar, J. Gahininath, Vikhe Patil, N. Rahul, Zaware Pati, Optimization of nonlinear quarter car suspension-seat-driver model, *Journal of Advanced Research*, **7**, 991–1007, 2016.

[14] P. Mahesh Nagarkar, J. Yogesh Bhalerao, J. Gahininath Vikhe Patil and N. Rahul Zaware Patil, GA-based multi-objective optimization of active nonlinear quarter car suspension system, PID and fuzzy logic control, *Int J Mech Mater Eng*, **13**, 10, 2018.

EURODYN 2020
XI International Conference on Structural Dynamics
M. Papadrakakis, M. Fragiadakis, C. Papadimitriou (eds.)
Athens, Greece, 23–26 November 2020

ENHANCING ROAD – VEHICLE BEHAVIOR BY IMPLEMENTING ACTIVE - CONTROLLED DRIVER SEAT COMBINED WITH SEMI-ACTIVE GROUND HOOK SUSPENSION SYSTEM

Mohamed Ezzat[1], Hesham H. Ibrahim[2], , Zakaria Elnaggar[4] , Nora Merabet[3], and Mohamed Salama[1]

[1]Research Assistant, Mechatronics Department, German University in Cairo,
New Cairo, Egypt.
mohamed.ezzatmahmoud@student.guc.edu.eg, mohamed.abdelatif@student.guc.edu.eg

[2]Associate Professor
Mechatronics Department, German University in Cairo,
New Cairo, Egypt
hesham.hamed-ahmed@guc.edu.eg

[3]Assistant Professor
Faculty of Engineering, Cairo University,
Giza, Egypt
zakaria.elnaggar@aucegypt.edu.eg

[4]Associate Professor
School of Mathematics, Statistics & Computing, Emirates Aviation University,
Dubai, United Arab Emirates
nora.merabet@emirates.com

Keywords- Half-Car Model, Active Driver-Seat, Ground Hook Control

Abstract- *This paper investigates the worthiness of implementing an active PID control on the driver seat alongside with semi-active ground-hook control on the suspension system in order to compensate the down side of the ground-hook control in terms of driving comfort. The suspension - driver seat model is derived using half car model with five degrees of freedom and Matlab Simulink is utilized to simulate the Active/Semi-active stability and comfort of the different proposed setups of the suspension system. Binary and continuous ground-hook control are attempted separately while the optimum combination between them is presented using the Matlab optimization toolbox. Finally, it was deduced that implementing semi-active controlled car seat doesn't provide any significant improvement, in terms of comfort, when combined with semi-active controlled suspension system. It is also found that implementing an active controlled car seat could significantly restore or even improve the deteriorated comfort caused by ground hook controlled suspension while maintaining its superior performance in terms of stability.*

1. INTRODUCTION

The dynamic behavior of a car can be evaluated in many different ways; one of which, is its suspension system behavior. The main components of a conventional suspension system are springs, shock absorbers (or dampers), control arm, steering knuckle, ball joints and control arm brushing. The interest of the current study is to focus on the role of the springs and dampers, in the suspension system which absorbs the noise and shock, induced by the road irregularities or bumps, and isolates the wheel-suspension assembly from the rest of the vehicle. Drivers are usually subjective in judging their vehicles and their evaluation is manly dominated by the vehicle dynamic characteristics including ride and handling. Therefore, the vehicle's subjective evaluation originates from its perceived comfort level and ride stability which are considered two of the most important performance features. The design process of a conventional suspension system boils down to a tradeoff between ride comfort and vehicle handling which are conflicting processes in nature. When suspension system is designed to optimize the handling and stability of the vehicle, the passenger often perceives the ride to be rough and uncomfortable. On the other hand, when it is designed to optimize the comfort level, the vehicle is less stable during maneuvers. Car manufacturers always strive to design suspension systems of acceptable level of both stability and comfort.

Various chassis control systems have been developed, to enhance vehicle dynamic performance and driving safety. Vehicle dynamics are characterized by three motions, namely roll, pitch, and yaw, which are strongly coupled and thus affect the vehicle dynamics and control in a very complex manner. Skreekar [1] worked on reducing the vibrations transmitted to the passenger in order to improve the ride comfort. An experimental design was used to obtain the modeling equations and a genetic algorithm was then introduced to optimize the model's parameters. Crolla [2] presented a comprehensive review of vehicle dynamics theories and their contributions to practical vehicle design. In particular, the review focused on actively controlled components, like active suspension and four wheel steering and their impact on vehicle performance and safety. Rauh [3] introduced the recent advances in simulation technologies, explaining their available potentials and limitations. It was highlighted that advanced simulation technologies enabled the development of complex mechatronic chassis systems, like active suspensions, in relatively short periods of time. Gordon [4] provided a new dual model methodology of steering, throttle and braking near-optimal control inputs to simulate the closed-loop linear and nonlinear vehicle handling dynamics. Tener [5] introduced a cockpit adjustable air suspension system to either improve handling or to increase ground clearance. In addition, the spring rate can be either decreased to enhance isolation or increased to promote handling performance. Zhang [6] used a linear switched reluctance actuator (LSRA) in his active suspension and took into consideration multiple force dependent variables like the force ripple minimization and adaptive force distribution function. Funde [7] implemented sky-hook semi active control which helped increase the comfort and reduce the suspension working space and implemented ground-hook control which increased the stability on a quarter car. Darus [8] developed a mathematical model to simulate the passive and active suspension systems using full car model. A linear quadratic control technique is selected to represent the active suspension system. Florin et al. [9] utilized a quarter car model, of two degrees of freedom, to simulate the handling and ride performance of a vehicle with passive suspension system. A scheme, using Matlab Simulink, was developed and was compared to the state space model. Hassan and Mohammed [10] developed a mathematical model, using Lagrange's equation, for a full vehicle

dynamic system of ten degrees of freedom. Vassal et.al [11] Introduced design stability requirement that have been used as guidelines in this paper. Sammier et.al [12] compared between H-infinity and skyhook control for semi-active suspension systems, H-infinity performed better than the skyhook control but skyhook control required less parameters and was easier to implement. Geweda [13] also used the genetic algorithm on a seven degrees on freedom system and compared his results to the PID controlled model.
The current work implements a different combinations of active/semi-active controls, applied to the sprung mass and the driver seat, in attempt to promote comfort without compromising the stability.

2. Formulation

In the current study, a half-car model with car seat is implemented using five degrees of freedom. These degrees of freedom are represented as two unsprung mass vertical displacement, sprung mass vertical displacement, pitching rotation and driver-seat displacement. Figure 1 presents a schematic for the implemented model.

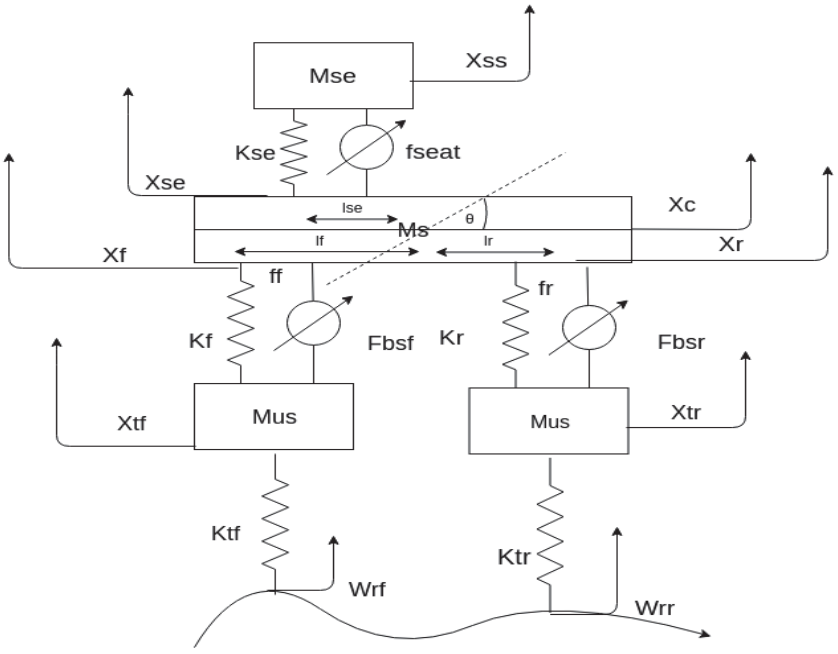

Figure 1: Half-car Model Schematic

Parameter	Symbol
Spring force	F_{ksi}
Damper force	F_{bsi}
Force quarter car	f_i
Sprung mass	M_{se}
Sprung mass moment of inertia	I_{se}
Unsprung mass front and rear	M_{us}
Stiffness tire front and rear	K_{tf} , K_{tr}
Stiffness spring front	K_f
Stiffness spring rear	K_r
Stiffness spring seat	K_{se}
Passive damping front	F_{bsf}
Passive damping rear	F_{bsr}
Passive damping seat	F_{seat}
Semi-active damper	$C_{(I)}$
Length between sprung mass center of mass and front	L_f
Length between sprung mass center of mass and rear	L_r
Length between sprung mass center of mass and car seat	L_{se}

Table 1: Car parameters abbreviation i ∈ {f,r}.

The current model was built as two independent quarter car models which were coupled together to simulate the dynamic behavior of a half-car. The following equations represent the modelling equations used in Matlab. For i ∈ {f,r}

Quarter car force:

$$f_i = F_{ksi} + F_{bsi} \tag{1}$$

Tire spring force:

$$F_{kti} = K_{ti} \times [x_{ti} - w_i] \tag{2}$$

Tire damping force:

Passive damper: $$F_{bti} = C_{ti} \times [\dot{x}_{ti} - \dot{w}_i] \tag{3}$$

Sprung mass spring force:

$$F_{\mathrm{ki}}=\mathrm{K}_i \times [x_{\mathrm{ti}} - x_i] \tag{4}$$

Sprung damping force:

Passive damper: $$F_{\mathrm{bsi}}=\mathrm{C}_i \times [\dot{x}_{\mathrm{ti}} - \dot{x}_i] \tag{5}$$

Semi-active damper: $$F_{\mathrm{bsi}}=\mathrm{C}(I)_i \times [\dot{x}_{\mathrm{ti}} - \dot{x}_i] \tag{6}$$

Active PID actuator: $$F_{\mathrm{bsi}}=\mathrm{k}_p \mathrm{e(t)}+\mathrm{k}_i \int \mathrm{e(t)}\,\mathrm{dt}+\mathrm{k}_d \frac{\mathrm{de(t)}}{\mathrm{dt}} \tag{7}$$

Car seat force:

$$f_{\mathrm{seat}} = (x_{\mathrm{ss}} - x_{\mathrm{se}}) \times K_{\mathrm{se}} + (\dot{x}_{\mathrm{ss}} - \dot{x}_{\mathrm{se}}) \times C_{\mathrm{se}} \tag{8}$$

Half car coupling equations:

$$x_f=\mathrm{x}_c - l_f \sin(\theta) \tag{9}$$

$$\dot{x}_f = \dot{x}_c - l_f \dot{\theta} \cos(\theta) \tag{10}$$

$$x_r=\mathrm{x}_c+\mathrm{l}_r \sin(\theta) \tag{11}$$

$$\dot{x}_r = \dot{x}_c+\mathrm{l}_r \dot{\theta} \cos(\theta) \tag{12}$$

$$x_{\mathrm{se}}=\mathrm{x}_C - l_{\mathrm{se}} \sin(\theta) \tag{13}$$

$$\dot{x}_{\mathrm{se}} = \dot{x}_C - l_{\mathrm{se}} \dot{\theta} \cos(\theta) \tag{14}$$

Three control methods were used to improve the passive performance of the suspension system, namely Sky-hook control, Ground-hook control as a semi-active technique, and PID active control. The Ground-hook is a control method that hooks the tires of the car to the ground to add more stability that is achieved by adjusting the damping coefficient.
Ground-hook semi-active control is given as follows:

$$C(i) = \begin{cases} C_{min}, & -\dot{x}_{ti}\dot{x}_{def} \le 0 \\ C_{max}, & -\dot{x}_{ti}\dot{x}_{def} > 0 \end{cases} \quad \text{for } i \in \{\mathrm{f,r}\}. \tag{15}$$

The second control type used is PID active control. This control was used due to the limitations of the semi-active suspension system. When semi-active suspension was implemented and didn't provide good results, active PID control was implemented as it can deliver pure force output on demand and it isn't constrained by states of the system (displacement, velocity, and acceleration). It is true that the active actuator consumes higher energy to provide such forces but when the control is applied only on one seat, we can safely assume lower energy consumption compared to fully active suspension system.

3. RESULTS AND DISCUSSION

Table.2 presents the car parameters used in the simulations as acquired from [14].

Parameter	Value
Sprung Mass (M_{se})	580 Kg
Sprung mass moment of inertia (I_{se})	1100 Kg.m^2
Unsprung Mass front and rear (M_{us})	40 Kg
Stiffness tire front and rear (K_{tf},K_{tr})	190 kN/m
Stiffness spring front (K_f)	23500
Stiffness spring rear (K_r)	23500
Stiffness spring seat (K_{se})	15 kN/m
Passive damping front (F_{bsf})	1500 N/m.s
Passive damping rear (F_{bsr})	1500 N/m.s
Passive damping seat (F_{seat})	500 N/m.s
Semi-active damper ($C_{(I)}$)	$C_{(I)} \in$ [900,3000]N/m.s
Length between sprung mass center of mass and front (L_f)	1 m
Length between sprung mass center of mass and rear (L_r)	1.5 m
Length between sprung mass center of mass and car seat (L_{se})	0.5 m

Table 2: Suspension system parameters.

In the following sections, several control configurations in suspension systems will be presented and compared to the passive system performance, in an attempt to analyze the improvement in terms of stability and comfort.

3.1 Passive car seat and semi-active ground-hooked car suspension

This section analyzes the semi-active ground-hook control (GH) suspension system performance compared to the passive suspension system performance. In the following, the two systems are denoted by “GH-Passive System” and “Passive system” in Figure 2. GH-Passive system stands for the system as described in Figure 1, with GH controlled applied to the unsprung mass while both the seat and the sprung mass are represented using a passive system. The other system denoted by Passive System stands for the system without any control applied to it.

Figure 2 presents the car seat and sprung mass displacements and accelerations and car tire displacement graphs in response to a step input of 0.05 meter, car speed is 60km/h. Step input was chosen as it excites multiple frequencies in the system, thus gives a complete picture of the system. The seat acceleration, depicted in Figure 2. (A), shows higher peak acceleration of the car seat in GH-Passive system compared to passive system due to the presence of GH controller on the unsprung mass.

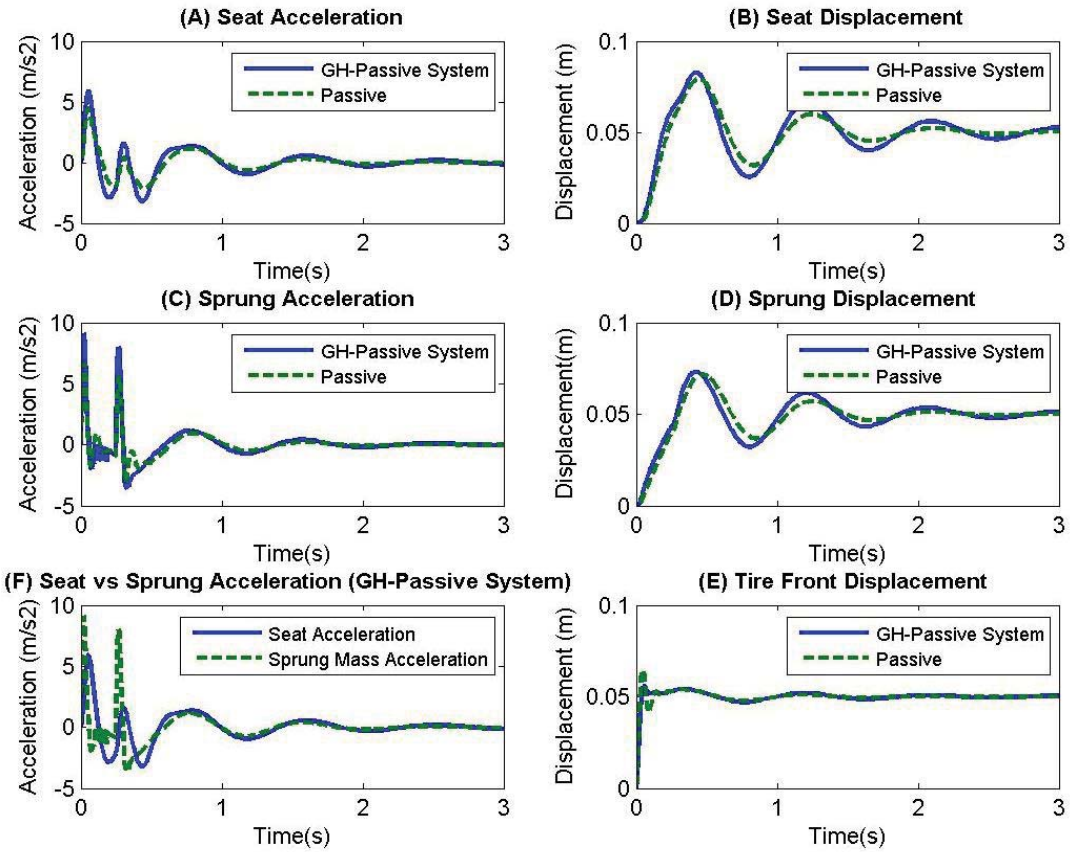

Figure 2: Ground Hook suspension/ Passive Seat.

The front tire displacement, depicted in Figure 2. (E), shows a 62.5% improvement in the overshoot value and a 47.5% less settling time compared to the passive system, note that the system starts oscillating again at 0.25s as this is the time when the back wheel hits the step input. The sprung acceleration, depicted in Figure 2. (C), shows higher peak and higher RMS acceleration in the GH system relative to the passive system. Figure 2. (F) shows that the implementation of a passive system on the car seat improves the comfort with 45% lower peek than the one of the sprung mass acceleration, and an improvement of 15% in the RMS value with respect to the sprung mass.

The implementation of GH-Passive system gives a seat RMS acceleration of 0.608, and a sprung mass RMS acceleration of 0.72. The passive system seat RMS acceleration is 0.49 and the passive

system Sprung mass RMS acceleration is 0.45. The values presented in this section will be used as a reference to compare to, in the following sections, where other combinations of different controls are applied.

3.2 Semi-active Ground-hook binary suspension and Sky-Hook Controlled seat

This section present the dynamic behavior of Sky-hooked seat (SH) alongside with the ground-hook control compared to the performance of the passive system. Figure 3 presents the car seat and sprung mass displacements and accelerations and car tire displacement, in response to a step input of 0.05 meter, car speed is 60km/h. Figure 3. (A) shows higher peak acceleration than the passive system, while Figure 3. (C) shows performance similar to that of Figure 2. (C). Figure 3. (F) shows a decline in performance as the improvement of seat peak acceleration in the first peak was reduced to 25.3% only relative to 45% in the passive system.

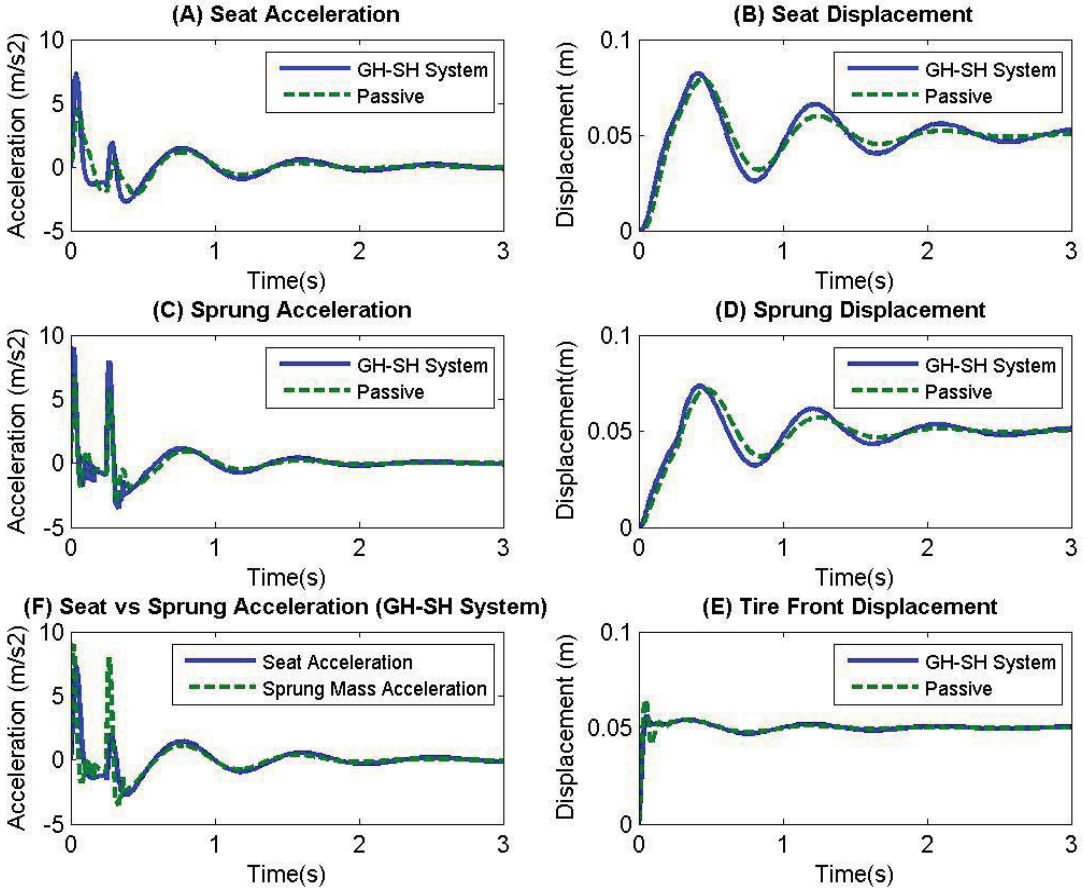

Figure 3: Ground Hook suspension/ Passive Seat.

This system resulted in seat RMS acceleration of 0.607 and sprung mass RMS acceleration of

0.6805. The RMS accelerations and the performance of the sky-hooked seat doesn't encourage the usage of a SH seat when GH is implemented and suggests that the implementation of a passive system on the car seat would be enough.

3.3 Semi-active Ground-hook binary suspension and active PID Controlled seat

In the following, the response of a system denoted by "GH-PID System" is depicted in Figure 3, which stands for GH controlled unsprung mass while a PID control is applied to the driver seat. This system is compared to the Passive System. PID controller parameters were optimized to minimize the following error expressed in terms of sprung mass displacement ant seat acceleration:

$$e(t) = \ddot{x}_{se} + (x_{ss} - x_{se}) \quad (16)$$

The auto-tuner of the PID controller in Matlab resulted in an integral controller without any proportional nor differential parameters, as shown in Table 3: PID controller parameters.

It is suggested to use a conditional parameter so that the deflection doesn't cross a certain value but that wasn't implemented here.

Parameter	Value
Kp	0
Ki	3124.23
Kd	0

Table 3: PID controller parameters.

Figure 4 presents the car seat and sprung mass displacements and accelerations in addition to car tire displacement in response to a step input of 0.05 meter and a vehicle speed of 60km/h.
The car seat acceleration Figure 4. (A) shows an improvement of 70% relative to the passive system seat. The car seat displacement of graph Figure 4. (B) shows a better displacement graph on the active seat compared to the passive seat. Figure 4. (F) shows the accelerations of both the sprung mass and the car seat, in which car seat acceleration is found to be smoother and with a lower peak; while the peak acceleration of the sprung mass is 8.6 m/s^2 while the one of the car seat is 1.86 m/s^2, this is an improvement in peak accelerations of 78.37%. This indicates that the active system managed to suppress most of the acceleration peaks applied to the sprung mass.

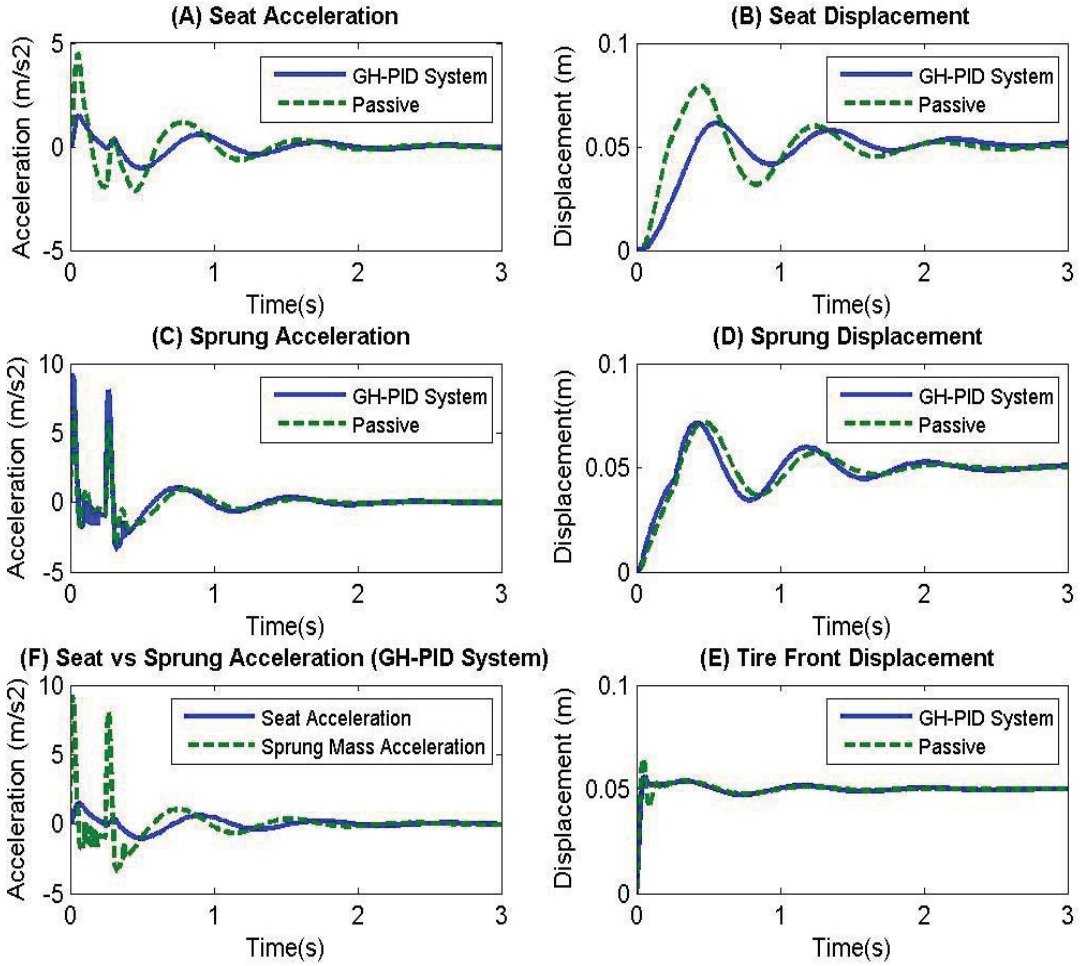

Figure 4: GH Suspension system/Active PID seat

The tire displacement shown in Figure 4. (E) is found to be similar to the tire displacement of the GH-Passive system displayed in Figure 2. (E), which means that the active seat didn't adversely affect the Ground-hook performance. Therefore, the stability using the ground-hook control was maintained while providing much better comfort performance using the active control seat. This setup resulted in a seat RMS acceleration of 0.26 and sprung RMS acceleration of 0.608, which reflects an improvement of 54.3% using the setup of active seat and semi-active ground-hook suspension system over the semi-active ground-hook suspension and passive seat setup. This is a good improvement considering that the active seat will use much less power to achieve such comfort, relative to applying PID control on the whole system. The semi-active GH system also uses very low power achieving both low power consumption and high comfort and stability performance. Both of Figure 4. (A) and Figure 4. (B) show smoother and lower peaks in displacement and acceleration respectively in the implemented hybrid system.

3.4 Semi-active Ground-hook continuous suspension and active PID Controlled seat

An attempt to improve the GH-PID binary system was to implement a GH-PID continuous system to improve the system performance and to check the overall effect of the GH continuous system.

$$C(I) = \begin{cases} C_{min}, & -\dot{x}_{ti}\dot{x}_{def} \leq 0 \\ \dfrac{\propto * C_{max} * (\dot{X}\imath - X\dot{r}\imath) + (1-\propto)Cmax * \dot{W}r\imath}{(\dot{X}\imath - X\dot{r}\imath)}, & -\dot{x}_{ti}\dot{x}_{def} > 0 \end{cases} \quad (17)$$

The factor $\propto$ determines the percentage of continuous system versus the percentage of the binary system. When $\propto = 1$ the system is reduced to a binary system and when $\propto = 0$ the system is continuous only. Genetic algorithm was implemented to find the optimum value for the parameter $\propto$ that minimizes the seat RMS acceleration and the tire max displacement. The optimum value obtained using genetic algorithm is $\propto = 0.75$.

Figure 5 presents the car seat and sprung mass displacements and accelerations and car tire displacement graphs response to a step input of 0.05 meter (5 cm), car speed is 60km/h.

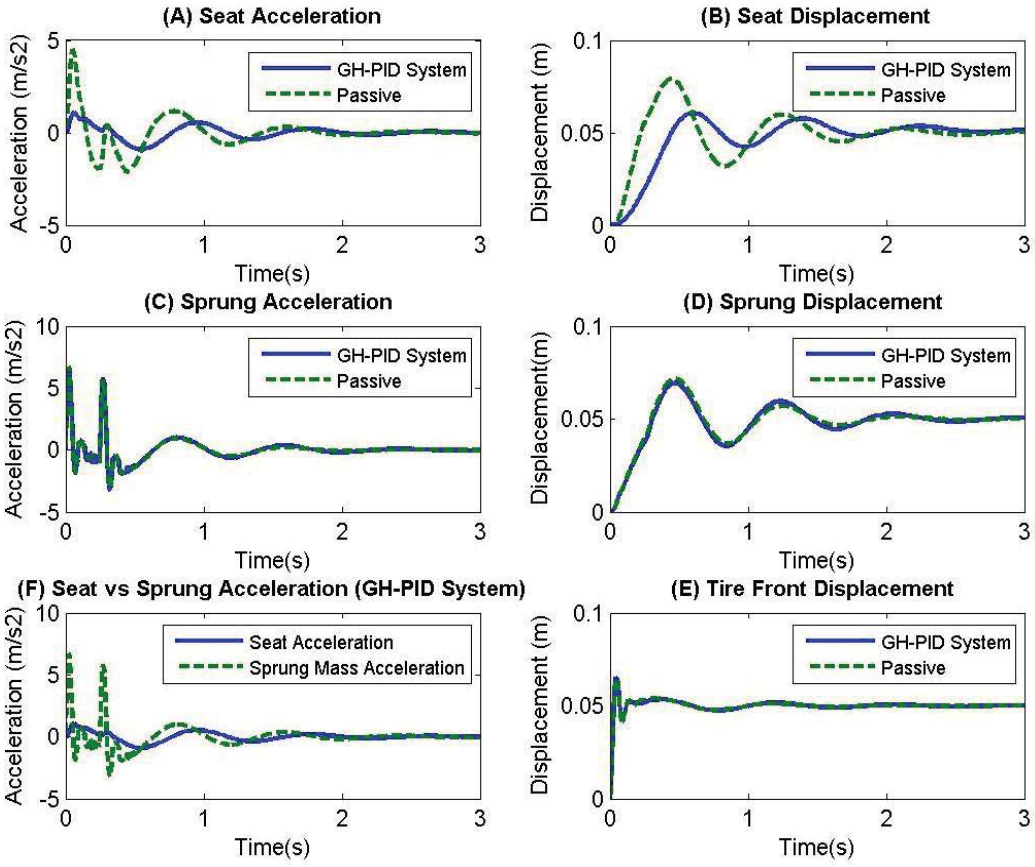

Figure 5: Continuous GH Suspension / Active PID Seat.

As shown in Figure 5. (A), the peak acceleration improved 7% compared to the GH-PID binary system presented in Figure 4. (A) and the seat displacement in Figure 5. (B) is slightly better than the seat displacement shown in Figure 4. (B). However Figure 5. (E) shows that the stability is reduced compared to that of the passive system. In addition, the performance displayed in Figure 5. (C, D) are almost identical to those of the passive system. The seat RMS acceleration is 0.24 and the sprung RMS acceleration is 0.5. The RMS acceleration was reduced, but this came at the cost of losing the improvement of the stability previously achieved in the GH binary system.

4. Conclusion

This paper investigated the worthiness of implementing an active PID control on the driver seat alongside with semi-active ground-hook control on the suspension system in order to compensate the downside of the ground-hook control in terms of driving comfort. The suspension driver seat model was derived using half car model with five degrees of freedom and Matlab Simulink is utilized to simulate the Active/Semi-active stability and comfort of the different proposed setups of the suspension system. It was found that applying semi-active ground hook control could significantly promote vehicle stability on the expense of deteriorated riding comfort. The implementation of sky-hook control of the driver-seat alongside with ground-hook control was investigated in an attempt to compensate the loss of comfort, but this type of control was of no added value. However, active PID control, when implemented in the driver-seat model has successfully fixed the downside of the ground-hook control and this set up has noticeable enhancement in both of stability and comfort.

5. References

[1] C. Poussot-Vassal, O. Sename, L. Dugard, R. Ramirez-Mendoza, F. Leonardo. Optimal Skyhook Control for Semi-active Suspensions. 4. 608-613. 10.3182/20060912-3-DE-2911.00106 (2006).

[2] D. Baumal, A., McPhee, J., & Calamai, P. (1998). Application of Genetic Algorithms to the Design Optimization of an Active Vehicle Suspension System. *Computer Methods in Applied Mechanics and, 163*, 87-94.

[3] Crolla, D. (2010). Vehicle dynamics - theory into practice, IMechE Part D. *Journal of Automobile Engineering*, 83-94.

[4] DARUS, R. B. (2008). *Modeling and control active suspension system for a full car model.* University Teknologi Malaysia, Faculty of Electrical of Engineering. Malaysia: IEEE.

[5] Florin, A., 2, M.-R. I.-C., & Liliana, P. (2013). Passive suspension modeling using MATLAB, quarter car model, input signal step type. *TEHNOMUS, 1*, 258-263.

[6] Gordon, T., & Best, M. (2006). On the synthesis of driver inputs for the simulation of closed-loop handling maneuvers. *International Journal of Vehicle Design*(40), 52-76.

[7] Hassaan, G. A., & Mohammed, N. A.-A. (2015). Frequency Response of 10 Degrees of Freedom Full-Car Model For Ride Comfort. *IJSRET, 4*(1), 43-49.

[8] Kazemi, R., Hamedi, B., & Javadi, B. (2000). Improving the Ride & Handling Qualities of a Passenger Car via Modification of its Rear Suspension Mechanism. *SAE Technical Paper 2000-01-1630*.

[9] Mechanical vibration and shock - Evaluation of human exposure to whole-body vibration Part 1: General requirements, ISO 2631-1:1997. (n.d.). ISO 2631-1, 1997.
[10] Rauh, J. (2003). Virtual development of ride and handling characteristics for advanced passenger cars. *Vehicle System Dynamics*, 135-155.
[11] Sharma, S., Pare, V., Chouksey, M., & Rawal, B. (2016). Numerical studies using full car model for combined primary and cabin suspension. *Procedia Technology, 23*, 171 – 178.
[12] Tener, D. (2004). Overcoming the Ride/Handling Compromise – A Cockpit Adjustable Suspension System. *SAE Technical paper 2004-01-1078*.

EURODYN 2020
XI International Conference on Structural Dynamics
M. Papadrakakis, M. Fragiadakis, C. Papadimitriou (eds.)
Athens, Greece, 23–26 November 2020

AUTO-SAPIENS, AN EXPERIMENTAL AUTONOMOUS DRIVING SYSTEM

M. Laurenza[1], **G. Pepe**[1], **and A. Carcaterra**[1]

[1] [1]Department of Mechanical and Aerospace Engineering of Sapienza University of Rome, Italy
via Eudossiana, 18
e-mail: {maicol.laurenza,gianluca.pepe,antonio.carcaterra}@uniroma1.it

Keywords: Autonomous car, Collision avoidance, Optimal feedback control, Nonlinear control

Abstract. *This paper presents self-driving control experiments applied to a standard vehicle equipped with an autonomous driving kit. The Auto Sapiens project is an experimental platform to test different control strategies and develop new obstacle avoidance algorithms. The Smart Fortwo vehicle is equipped with steering, thrust and brake actuators, and proprioceptive and exteroceptive sensors to identify both real-time vehicle attitude and obstacles on the track. The vehicle is controlled by a hardware in the loop system, in which innovative nonlinear control logics, called Feedback Local Optimality Principle FLOP, are implemented to achieve high performance in maintaining the stability of the vehicle during avoidance abrupt maneuvers. Tests were carried out through an ad-hoc vehicle-to-vehicle (V2V) communication system to share location, speed, heading and size information between the obstacle and the controlled vehicle. Eventually, a performance analysis of the system is made in terms of crash probability.*

1 INTRODUCTION

One of the interesting tasks of control theories is to develop new strategies devoted to the vehicle control in complex scenarios. The present investigation is in the context of safe autonomous driving in presence of obstacles [1-4]. The Society of Automotive Engineers – SAE defined different levels of automation in self-driving vehicles [5], describing systems ranging from an auxiliary assistance to the driving operations, up to a complete exclusion of the human driver. This paper is devoted to the development of level 3-4 automated driving systems, in which even if the driver is careless or absent-minded, the vehicle manages to avoid obstacles. The achievement of this goal needs to overcome several intrinsic problems, such as the management of high-speed maneuvers, which requires nonlinearities in the vehicle's model, and fast response control logics.

The standard predictive controls are one the most used strategies in the field of autonomous driving. Despite the many advantages of being able to include nonlinearities, of using general forms for constraints and cost functions, they have as negative counterpart a high computational cost, not feasible for many online processing [6], unless explicit laws [7-9] and fast approximated optimization algorithms [10] are introduced.

A new control strategy, based on the optimal control theory, is under the name of *Feedback Local Optimality Principle – FLOP*. The great advantage of this algorithm relies on its capabilities of dealing with strong nonlinearity that are the cases to which the LQR does not apply. FLOP allows feedback control laws, under general cost function, at low computational cost [11-13]. As a further result, FLOP is able to deal with obstacle avoidance strategies, as the ones developed by the authors based on the Velocity Obstacle approach [14, 15], further improved for including environmental constraints, such as the road boundaries for lane keeping. The enhanced performances achieved through FLOP control logic are demonstrated, for instance, in terms of ability to handle different and simultaneous tasks, thanks to a proper choice of a nonlinear cost function [12] and in terms of identification of a more effective optimal trajectory, obtained via a nonlinear dynamic model [11].

Auto-Sapiens is an experimental platform of the Mechatronics and Vehicle Dynamics Lab of Sapienza University of Rome, a car equipped with exteroceptive and proprioceptive sensors, steering wheel, throttle and braking actuators. Results show the avoidance maneuver performed under high-speed conditions against a virtual obstacle.

After a brief presentation of the FLOP control logic, and the related nonlinear vehicle models, Section 2 shows how to implement lane keeping and obstacle avoidance. The Auto-Sapiens platform described in Section 3 is detailed and tested is Section 4. Eventually, in Section 5, the conclusions are drawn.

2 AUTO-SAPIENS CONTROL SYSTEM

The Auto-Sapiens driving system consists of two nested control blocks. The first is the main trajectory planner to maintain or change lanes or avoid potential obstacles, compatibly with the free space available. The second is the actuators management controller, which manages the thermal engine, braking and acceleration operations to achieve the trajectory objectives stated by the planner block. The general scheme is in Figure 1 where, after the identification of the vehicle state through sensors and environmental identification, the guidance control returns a control vector in terms of desired wheel torque and steering angle. Traction and braking control The torque of the wheels is processed by the traction and braking control. If an increase of the engine torque is required, the control reads the engine speed and the gear engaged and computes the equivalent percentage of the accelerator and/or shifting to lower gears. In case of a braking

torque, the braking control comes into play. Eventually, the steering angle transforms into a wheel steering angle, according to the linear relations resulting from the kinematic steering linkage (rack and pinion steering).

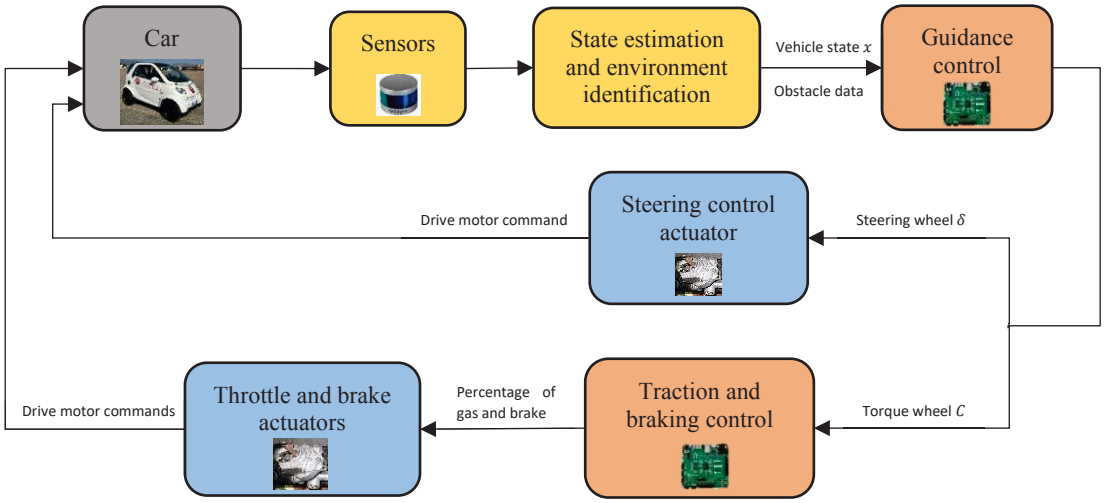

Figure 1: Auto-Sapiens control system scheme.

The control algorithms driving the guidance and traction-braking control are part of a recently developed method by the authors, called Feedback Local Optimality Principle, FLOP [11-16]. FLOP uses the classical variational approach, based on minimization of a performance index J under nonlinear constraints. Unlike excellent predictive controllers, often used to drive autonomous vehicles, the FLOP is a purely feedback control that, by incorporating nonlinear constraints and assigning custom objective functions, works in real-time at low computational costs compared to predictive controls.

The FLOP is aimed at minimizing J, a functional depending on the function $E(\boldsymbol{x},\boldsymbol{u})$, that is non-quadratic in the state variable $\boldsymbol{x}$ and quadratic in the control variable $\boldsymbol{u}$, subjected to an affine differential equation, a constraint introduced into the functional by using the Lagrangian multiplier $\boldsymbol{\lambda}$:

$$J = \int_0^T E(\boldsymbol{x},\boldsymbol{u}) + \boldsymbol{\lambda}^T\left(\dot{\boldsymbol{x}} - (\boldsymbol{\phi}(\boldsymbol{x}) + \boldsymbol{B}\boldsymbol{u})\right) dt \qquad (1)$$

$$E(\boldsymbol{x},\boldsymbol{u}) = \frac{1}{2}\boldsymbol{u}^T\boldsymbol{R}\boldsymbol{u} + g(\boldsymbol{x})$$

where $g(\boldsymbol{x})$ is any differentiable function, $\boldsymbol{\phi}(\boldsymbol{x})$ is a generic nonlinear function, $\boldsymbol{B}$ depends on the available actuators, and $\boldsymbol{R}$ is a tuning matrix. The FLOP decomposes integral (1) into $N = T/\Delta h$ sub-integrals, where Δh is the time horizon of each integral:

$$J \approx \sum_{i=1}^{N} J_i = \sum_{i=1}^{N} \int_{LB_i}^{UB_i} E(\boldsymbol{x},\boldsymbol{u}) + \boldsymbol{\lambda}^T\left(\dot{\boldsymbol{x}} - (\boldsymbol{\phi}(\boldsymbol{x}) + \boldsymbol{B}\boldsymbol{u})\right) dt \qquad (2)$$

$$\min(J_i)\ \forall\ i$$

where UB_i and LB_i limits are the upper bound and lower bound for each time interval, respectively. Moreover, for each integral, the transversality conditions hold:

$$\boldsymbol{x}_{LB_i} = \boldsymbol{x}_{UB_{i-1}} \quad ; \quad \boldsymbol{\lambda}_{UB_i} = \boldsymbol{0} \tag{3}$$

Applying the optimality principle through a finite difference technique with a time step equal to the integration step Δh, leads to the explicit control law [13]:

$$\boldsymbol{u}_{LB_i} = \boldsymbol{R}^{-T}\boldsymbol{B}^T \left[\nabla_{\boldsymbol{x}}\boldsymbol{\phi}^T|_{LB_i} - \frac{1}{\Delta h}\boldsymbol{I}\right]^{-1} \nabla_{\boldsymbol{x}} g|_{LB_i} \tag{4}$$

where $\boldsymbol{I}$ is the identity matrix. Equation (4) represents the basis of the two driving system controllers, described in detail below.

2.1 Guidance control system

Driving safely through the road traffic requires two main capabilities: being able to identify a feasible trajectory to reach a given target, and avoid any obstacle during the motion. The guidance control system, illustrated in Figure 2, consists of a decision-making logic that, analyzing external information such as lanes and obstacle position, proprioceptive data, defines a target trajectory $\boldsymbol{x}_t$ and the penalty function $g(\boldsymbol{x})$.

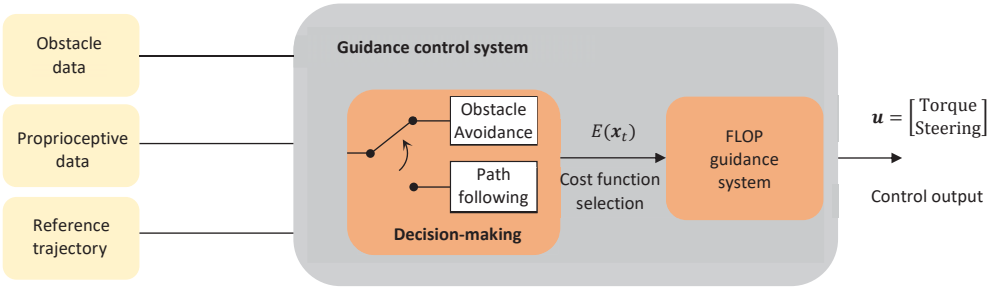

Figure 2: Auto-Sapiens guidance control system.

When detecting an obstacle, the system introduces the penalty function $g_{Obst}(\psi, \omega, V)$ to avoid the crash. For example:

$$g_{Obst}(\psi, \omega, V) = \frac{1}{2}k_1(\psi - \psi_t)^2 + \frac{1}{2}k_2\omega^2 + \frac{1}{2}k_3(V - V_t)^2 \tag{5}$$

The penalty function drives the speed of the vehicle, in terms of the its modulus V and direction ψ towards the target vector $P_t(\psi_t, V_t)$ using the penalty terms $\frac{1}{2}k_1(\psi - \psi_t)^2 + \frac{1}{2}k_3(V - V_t)^2$. They allow the safest avoidance maneuver in term of distance between the obstacle and the road boundaries (see Figure 3, a). The heading rate ω, through the penalty term $\frac{1}{2}k_2\omega^2$, slows down the steering wheel maneuvers, and the $k_i s$ are tuning parameters.

The strategy uses the Velocity Obstacle approach [14, 15], identifying a set of safe (green) and unsafe regions (red) in the velocity field.

Instead, if the road is obstacle-free, assuming a pre-assigned lane, the algorithm uses the penalty function g_{Path} (Figure 3, b):

$$g_{Path}(\psi, \omega, V, d) = \frac{1}{2}k_1(\psi - \psi_t)^2 + \frac{1}{2}k_2\omega^2 + \frac{1}{2}k_3(V - V_t)^2 + \frac{1}{2}k_4 d^2 \tag{6}$$

The vehicle trajectory to follow minimizes the distance d between the CoG (centre of gravity) and the nearest point P on the target trajectory. Then, the point P_h defines a target for the vehicle heading ψ, considering a time horizon h_t that allows to anticipate the maneuver to better chase the trajectory due to the delay of the actuators. A control for the heading rate ω is still present, and for the $k_i s$ different settings are used.

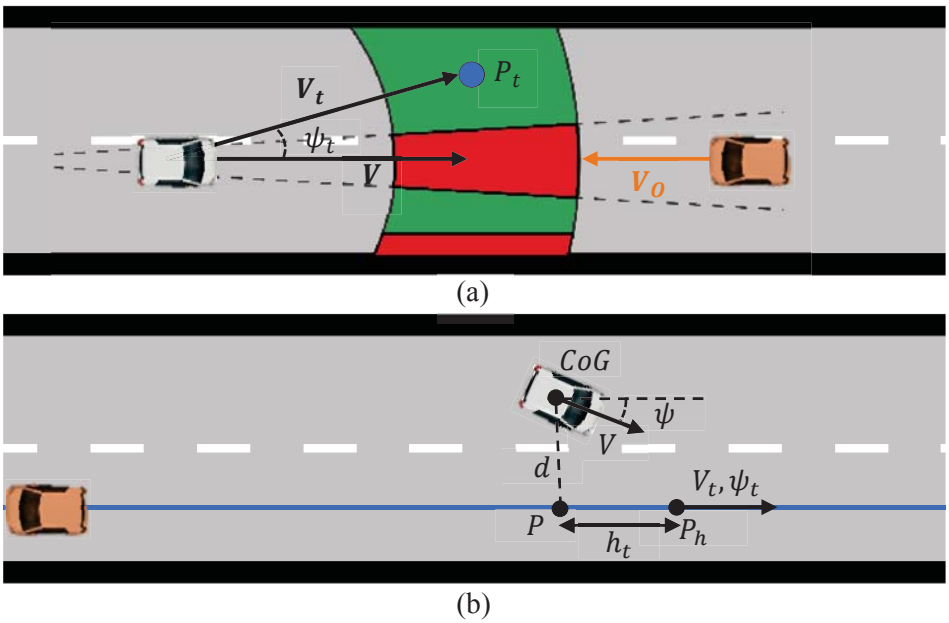

Figure 3: Autonomous driving strategies: (a) Obstacle Avoidance, (b) Lane keeping

The chosen dynamic model $\dot{\boldsymbol{x}} = \boldsymbol{\phi}(\boldsymbol{x}) + \boldsymbol{B}\boldsymbol{u}$ to control the car is based on the classical bike model [14] with rotating wheels (see Figure 4). The state $\boldsymbol{x} = [\boldsymbol{\nu}, \boldsymbol{\eta}]$ of the system is arranged as: (i) the speed field $\boldsymbol{\nu} = [u, v, \omega, \omega_r, \omega_f]$, with u, v the longitudinal and the lateral velocity in the mobile reference frame, ω is the yaw rate, ω_f and ω_r are rotational speed of frontal and rear wheel; (ii) the position and heading in the fixed frame $\boldsymbol{\eta} = [X, Y, \psi]$. The control vector $\boldsymbol{u} = [\delta, C]$ is composed by the steering angle δ and the rear wheel torque C. The $\boldsymbol{M}$, $\boldsymbol{C}(\boldsymbol{\nu}), \boldsymbol{J}$ are the inertia, Coriolis and rotational matrixes while $\boldsymbol{T}_{Pac}(\boldsymbol{\nu}, \delta), \boldsymbol{T}_{roll}(\boldsymbol{\nu}), \boldsymbol{T}_{aer}(\boldsymbol{\nu})$ and $\boldsymbol{T}_{wheel}(C)$ are forces and moment of Pacejka contact action, rolling, aerodynamic and the internal actions.

$$\begin{aligned} \boldsymbol{M}\dot{\boldsymbol{\nu}} + \boldsymbol{C}(\boldsymbol{\nu})\boldsymbol{\nu} &= \boldsymbol{T}_{Pac}(\boldsymbol{\nu}, \delta) + \boldsymbol{T}_{roll}(\boldsymbol{\nu}) + \boldsymbol{T}_{aer}(\boldsymbol{\nu}) + \boldsymbol{T}_{wheel}(C) \\ \dot{\boldsymbol{\eta}} &= \boldsymbol{J}(\psi)\boldsymbol{\nu} \end{aligned} \tag{7}$$

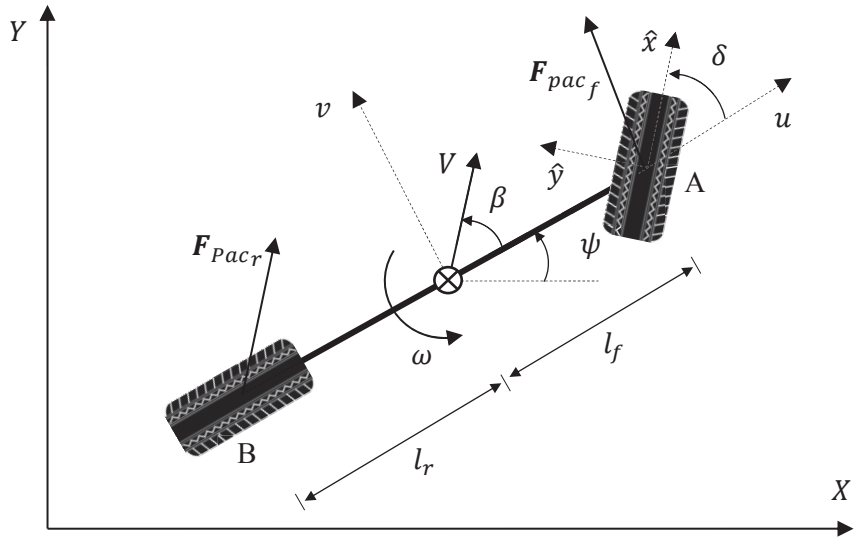

Figure 4: Bike model.

The Pacejka contact actions $\boldsymbol{T}_{Pac}$ are forces compositions $\boldsymbol{F}_{Pac}(k, \beta, F_z)$ based on the Magic Formula [17] widely used to describe the dynamic characteristics of tires. The forces depend on longitudinal and lateral slip, k and β, and the vertical load of each wheel F_z (Figure 5).

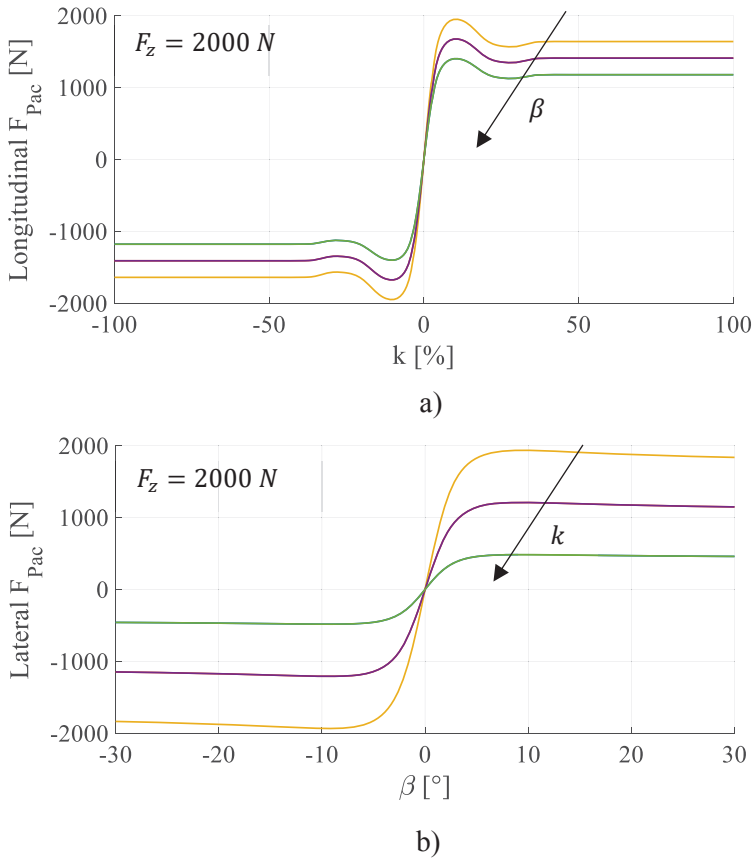

Figure 5: Longitudinal and lateral Pacejka forces.

Finally, in order for the system (7) to be included into the FLOP control, equations transform to a first order differential system, linearizing the part relating to the control actions, i.e. steering and torque. The linearization is updated to the step close to the previous conditions, such that the FLOP can consider all the nonlinearities of the bike model in terms of $\boldsymbol{v}$ and $\boldsymbol{\eta}$, ensuring a good control even of sudden maneuvers typical of obstacle avoidance. Pacejka coefficients were estimated performing empirical tests according to [18].

2.2 Traction and braking control

The traction and braking control aims at defining the percentage of throttle u_{gas} and brake u_{brake} commands to convey to the actuators. When the guidance control system returns a driving torque, $C > 0$, a second FLOP provides the control u_{gas}, considering the entire vehicle driveline up to the thermal engine (Figure 6). On the other hand, in case of a braking torque $C < 0$, the brake pedal is pressed proportionally to the value of C, up to a maximum empirical value that the braking system can provide.

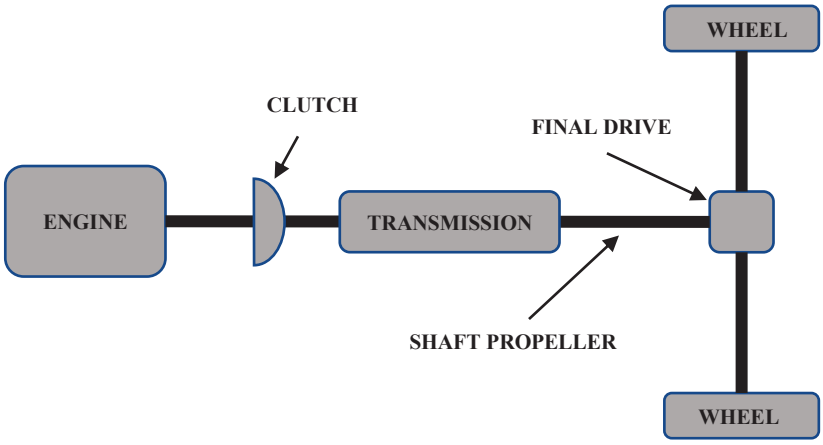

Figure 6: Driveline scheme.

The considered driveline consists by the engine, characterized by its torque curve, the flying wheel with its equivalent moment of inertia, the gearbox with its transmission ratio, the clutch, the wheels and the mass of the vehicle as shown in (Figure 6). The FLOP objective function is defined to meet two requirements: maintaining the target speed V_t, defined a priori by the guidance control system, and defining a target throttle u_t that is as much as possible close to the target control that we are going to describe below:

$$E(\omega_e, u_{gas}) = \frac{1}{2} k_1 \left(\omega_e - \tau(i) \frac{V_t}{R_{wheel}} \right)^2 + \frac{1}{2} k_2 \left(u_{gas} - u_t \right)^2 \tag{8}$$

where $\tau(i)$ is the transmission ratio between the engine and the wheel as a function of the engaged gear pair (denoted by i), coming from the on-board control unit; the R_{wheel} is the radius of the wheel; ω_e the engine revolution rate and the $k_i s$ tuning parameters.
The engine torque $C_e\left(u_{gas}, C_{e_{max}}, C_{e_{min}}\right)$ is a linear function of the u_{gas} command percentage between the maximum and minimum engine torque, as depicted in Figure 7. Therefore, the control target u_t is defined by assigning the desired torque C and the V_t:

$$u_t = \frac{\frac{\tau(i)C}{\eta} - C_{e_{min}}\left(\tau(i)\frac{V_t}{R_{wheel}}\right)}{C_{e_{max}}\left(\tau(i)\frac{V_t}{R_{wheel}}\right) - C_{e_{min}}\left(\tau(i)\frac{V_t}{R_{wheel}}\right)} \tag{9}$$

where η is the efficiency of the driveline.

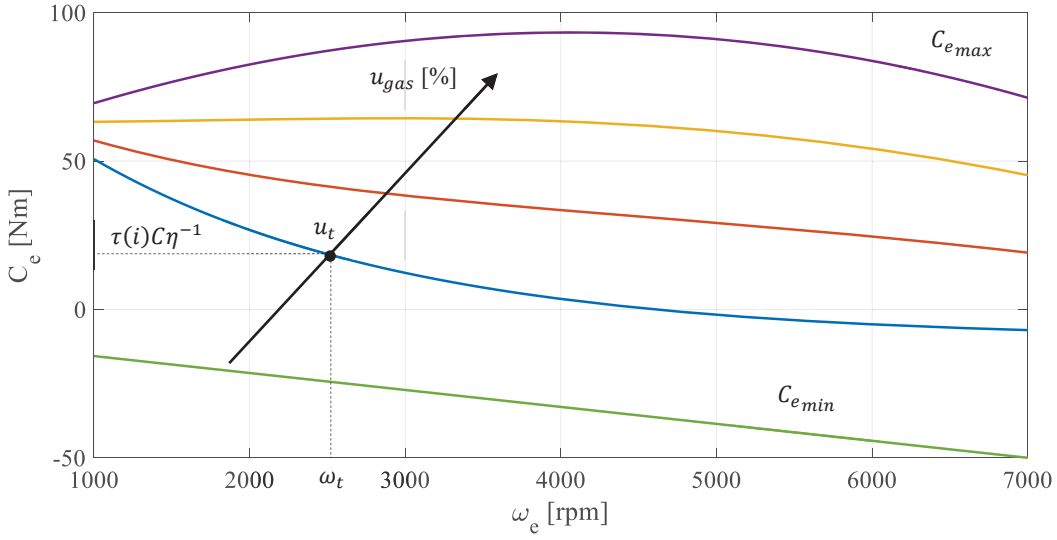

Figure 7: Engine torque curve.

The FLOP's dynamic function $\dot{\boldsymbol{x}} = \boldsymbol{\phi}(\boldsymbol{x}) + \boldsymbol{Bu}$ models the driveline of Figure 6:

$$\dot{\omega}_e = \frac{1}{I_{tot}(i)}\Big(\big(C_{e_{max}}(\omega_e) - C_{e_{min}}(\omega_e)\big)u_{gas} + C_{e_{min}}(\omega_e) - C_{res}(i)\Big) \tag{10}$$

where I_{tot} is the driveline inertia depending on the –*th* gear pair engaged, and on the efficiency η, and C_{res} is the total resistance torque related to rolling resistance, the gravity force, etc.

Also in this case, according to the FLOP formulation, it is necessary to linearize the term related to the control variable u_{gas}. When the required torque is negative and the motor is no longer able to deliver enough braking torque, the brake actuator comes into action.

3 AUTO-SAPIENS EQUIPMENT

The autonomous vehicle of the Mechatronics and Vehicle Dynamics Lab, at Sapienza University of Rome, named Auto-Sapiens is a Smart ForTwo City-Coupe, suitably modified for scientific autonomous driving experiments (Figure 8). This section describes the overall architecture of the vehicle and the hardware changes to transform it into an autonomous platform. The car has been equipped with: (*i*) proprioceptive sensors as 9DOF inertial measurement unit, GPS SKYTRAQ with 50Hz frequency, four wheels encoders; (*ii*) exteroceptive sensors as a LIDAR Velodyne, long-range radar AWR1243, short-range radar AWR1642, and ultrasonic sensors MB7040-200 Maxbotix. A central control unit manages all the data from sensors and sends the inputs from the control system to the actuators through different digital IO physical connections as I2C, P-MOD, USB 2.0, Gigabit Ethernet and Can-Bus as shown in Figure 9.

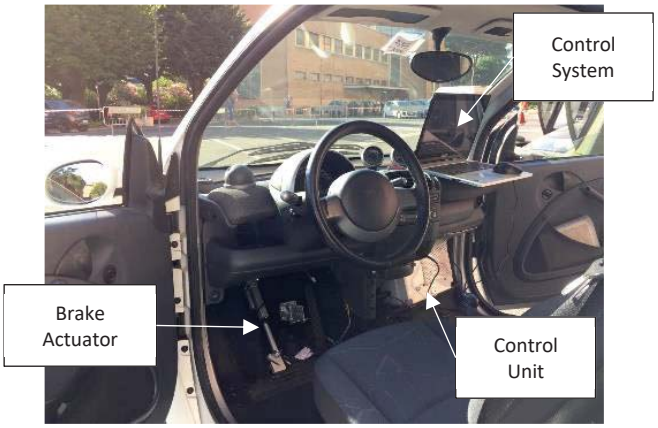

Figure 8: Autonomous kit on the *Auto-Sapiens* platform

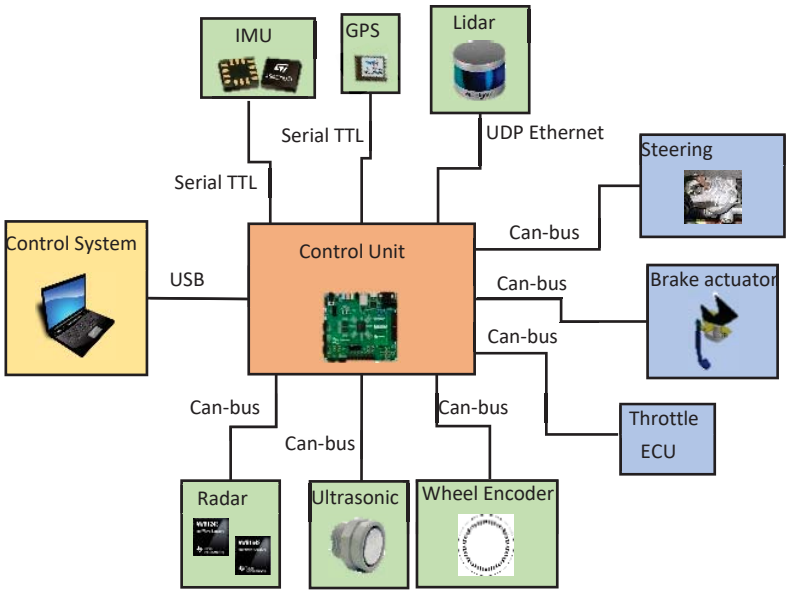

Figure 9: Hardware connection scheme

The actuators handle the steering, brake and throttle systems. The wheels are steered by the electric power unit, the same equipping the power steering of the car. A sensor to evaluate the rotation angle of the steering wheel has been set directly to the steering wheel. An ECU-Electronic Control Unit manages the throttle valve, with two potentiometers to evaluate the position of the pedal. An electrodynamic linear actuator controls the brakes applying a direct force to the pedal linkage acting on the brake pump. The Table 1 shows the most important characteristics of the vehicle.

The tests are aimed at analyzing the behavior of the car with respect to the control inputs, so the obstacle recognition is performed via V2V (Vehicle-To-Vehicle) communication, in which a virtual obstacle sends his position and attitude to the controlled vehicle (Figure 10). A local network, 30 Hz, receives the data through an UDP protocol, thanks to which the control system manages the control inputs connected to the central unit via USB with an update frequency of 20 Hz.

Parameters	Values
Mass	950 Kg
Yaw Inertia (supposed)	2000 Kg*m^2
Wheelbase	1.83 m
Distance between front wheel and CoG	1.03 m
Distance between rear wheel and CoG	0.8 m
Track	1.24 m
Wheel radius	0.2 m
Wheel inertia (supposed)	1 Kg*m^2
Max torque	92 Nm at 4500 rpm
Max Power	52 kW at 5800 rpm
0 - 100 km/h	15.5 s
Steering ratio	22:1

Table 1: Car parameters.

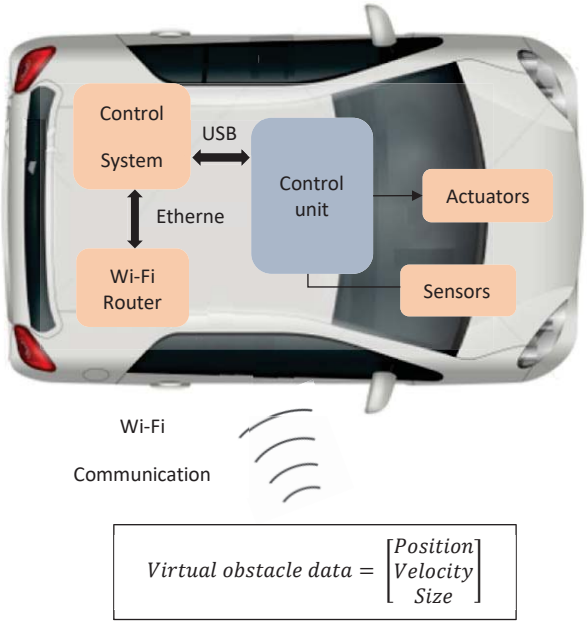

Figure 10: Auto-Sapiens communication system

4 STATE ESTIMATION

Vehicle system dynamic state estimation is a widely subject of investigation in automotive technology [19-22]. A well-known approach is the model-based estimation, which consists of two categories: kinematic and dynamic. In this framework, the Auto-Sapiens use the well-known EKF-Extended Kalman Filter applied to nonlinear dynamic models.

Writing in a compact form equation (7), the Extended Kalman filter is applied to the equations:

$$\begin{aligned} \dot{\boldsymbol{x}}(t) &= \boldsymbol{f}(\boldsymbol{x},\boldsymbol{u}) + \boldsymbol{w}(t) \\ \boldsymbol{z} &= \boldsymbol{h}(\boldsymbol{x}) + \boldsymbol{v}(t) \end{aligned} \tag{11}$$

where $\boldsymbol{w}(t)$ and $\boldsymbol{v}(t)$ represent process and measurement noise respectively and $\boldsymbol{z}$ is the observed state:

$$h = \begin{bmatrix} X \\ Y \\ \psi + \beta \\ V_X(\psi) \\ V_Y(\psi) \\ \omega \\ \omega_r \\ \omega_f \end{bmatrix} \qquad z = \begin{bmatrix} X_{Odo} \\ Y_{Odo} \\ \psi_{GPS} \\ V_{X_{GPS}} \\ V_{Y_{GPS}} \\ \omega_{IMU} \\ \omega_{r_{Odo}} \\ \omega_{f_{Odo}} \end{bmatrix} \tag{12}$$

The estimation of the position of the vehicle is possible via different methods, like simultaneous localization and mapping (SLAM), visual odometry etc. In the present case, the position $[X_{Odo}, Y_{Odo}]$ is estimated through the odometry technique which makes use of a kinematic bike-model with the velocity of the wheels, coming from the ABS, to compute the trajectory covered [22]. This approach is quite reliable if the distance and the velocities involved are not large. Vehicle heading ψ_{GPS} information coming from GPS sensor, can be used to correct the yaw prediction ψ, since the heading is the sum of the yaw and slip angle β. Moreover, from the GPS we get the speed information in the fixed reference $[V_{X_{GPS}}, V_{Y_{GPS}}]$. The yaw rate ω_{IMU} is measured by the IMU and, as mentioned before, the speed of the wheels $[\omega_{r_{Odo}}, \omega_{f_{Odo}}]$ is taken from the ABS.

5 RESULTS

The several tests performed in a controlled environment, involve the analysis of a frontal crash scenario, in which the controlled vehicle has to maintain its pre-assigned lane. Figure 11 shows that a virtual obstacle performs random generated trajectories that pass through a specific region A at a specific time, such that it will crash against the controlled vehicle.

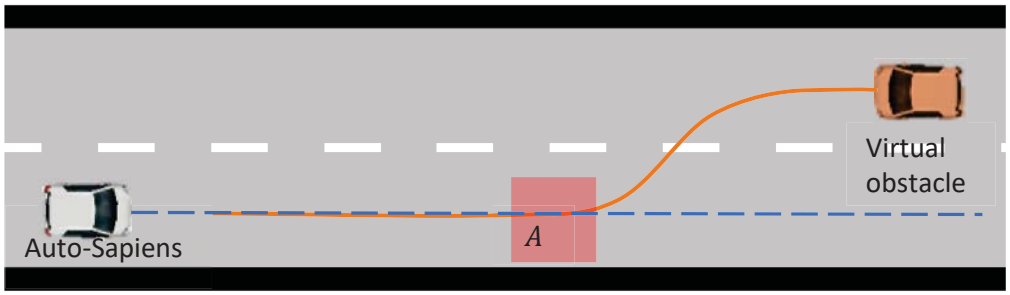

Figure 11: Crash scenario for experimental tests

The tests velocities belong to the range of 40-60 Km/h. Figure 12 shows the trajectory of the vehicle in blue, and the one in red is the obstacle: the controlled vehicle manages to evade the virtual obstacle and return to the assigned trajectory. The maneuver of obstacle avoidance starts at t_{start} with the switch-on of the penalty (5), followed by the switch-off of (5) and activation of penalty (6) till to the end, at t_{end}.

Along this time interval, the evolution of the actuators commands and that of the longitudinal velocity u are investigated. In Figure 13, the longitudinal velocity has a small decrease while the obstacle avoidance strategy is engaged, then the velocity is increasing to the target value which is the speed before the obstacle avoidance intervention.

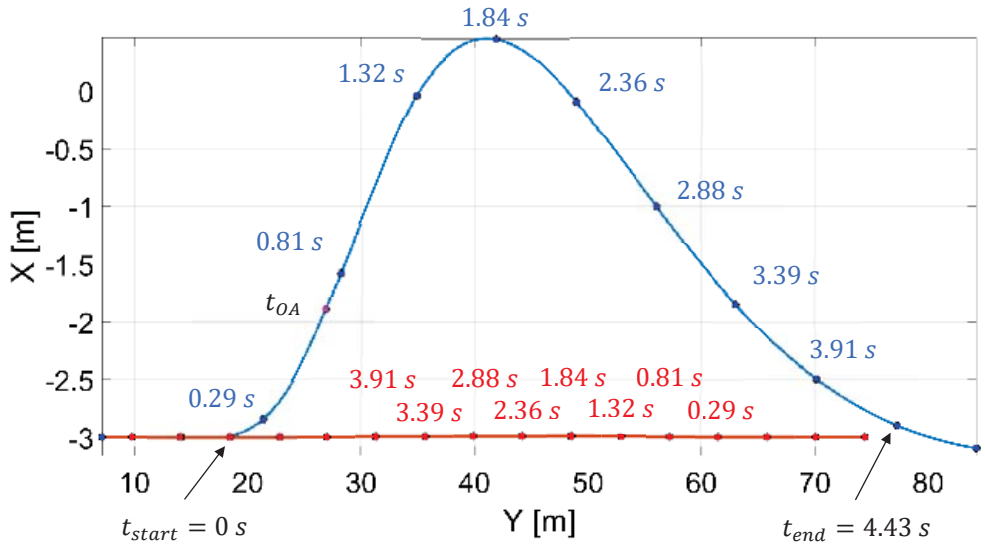

Figure 12: Trajectory of the vehicle in blue and obstacle in red with time

Alongside this, the throttle shown in Figure 14 is zero when the obstacle is engaged. This happens because the intervention threshold for the obstacle avoidance strategy to intervene is chosen for safety purposes and has a value of 2s. The control, having enough time, prefers to do a stable maneuver without braking and steering at the same time. Finally, the steering wheel of Figure 15 behaves according to the maneuver depicted in Figure 12.

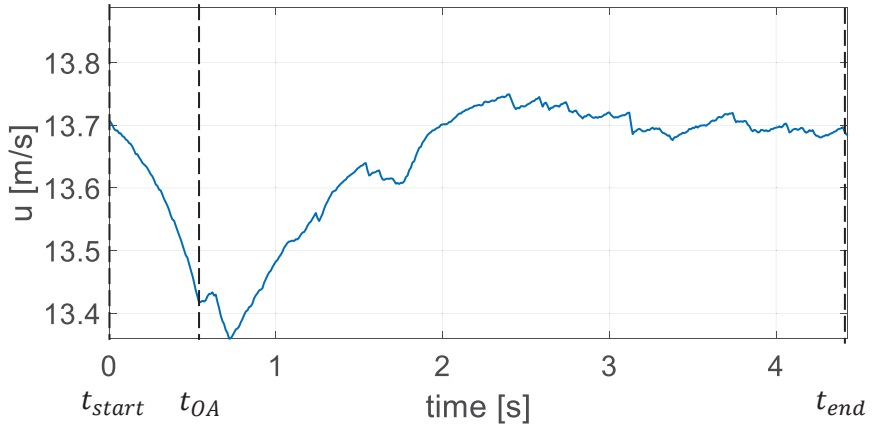

Figure 13: Longitudinal speed between t_{start} and t_{end}

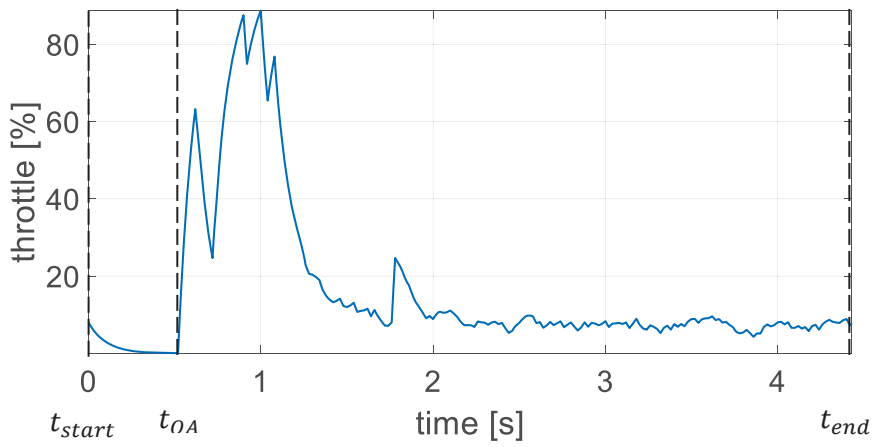

Figure 14: Throttle between t_{start} and t_{end}

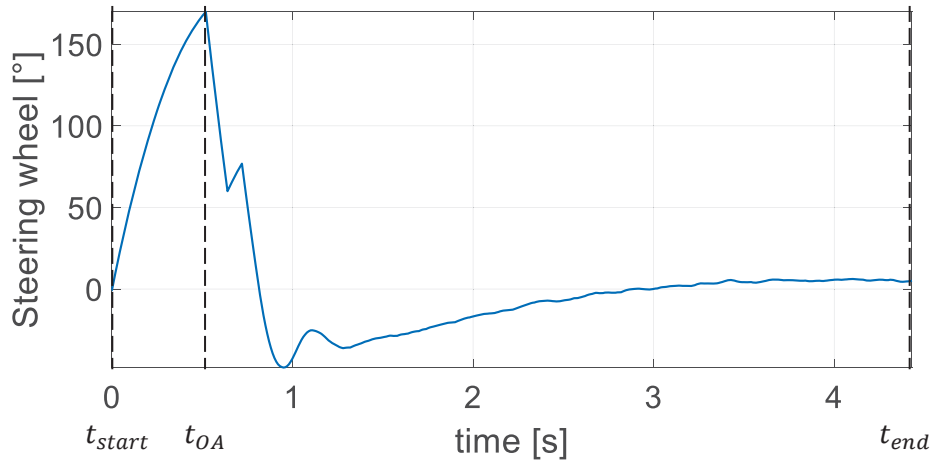

Figure 15: Steering wheel angle between t_{start} and t_{end}

An interesting analysis investigates the performance of the car in terms of accident probability. Figure 16 shows the number of successful crash-avoidance maneuvers compared to the failed maneuvers leading to the crash, classified according to a quality parameter ρ (within the range 0 to 1). In the range between 0 to 0.5, the quality of the successful avoidance maneuver is assessed through the measure of the minimum distance between the road boundaries and the virtual obstacle: at 0 the vehicle is equally distant between the boundaries and the obstacle, while at 0.5 the vehicle brushes against them. Between 0.5 and 1, the quality of the crash maneuver are assessed in terms of kinetic energy released in the collision: at 0.5 the kinetic energy involved is very low, due to the vehicle brushing against the road boundaries or obstacle, while at 1 the kinetic energy is at his maximum value between all the tests. Figure 16 shows all the experimental tests and can be noted that most of them resulted in successful maneuvers with a peak at $\rho = 0.3$, while few scenarios resulted in a crash.

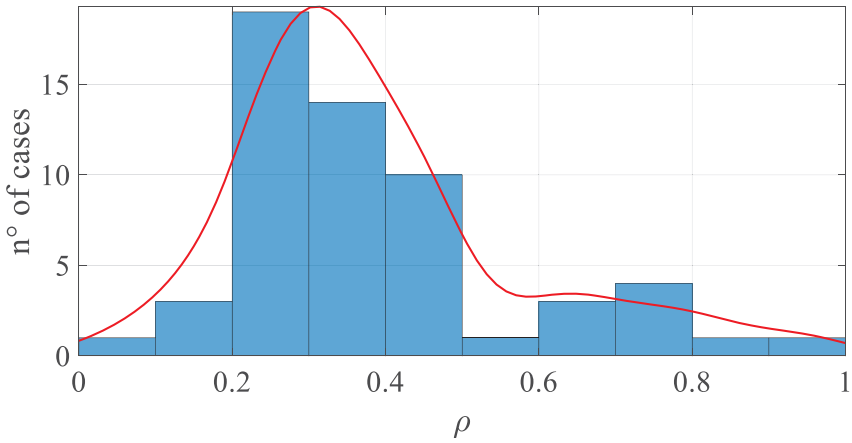

Figure 16: Performance of the system in different frontal crash scenarios: number of successful cases ($0 < \rho < 0.5$) and which ended with a crash ($0.5 < \rho < 1$).

6 CONCLUSIONS

The authors presented the first experimental tests on the *Auto-Sapiens* platform of a new autonomous driving system. The use of a new nonlinear feedback control, named *FLOP* and a new obstacle avoidance strategy, developed by the authors, shows good results in terms of performance with random scenarios under high-speed conditions. Further tests will be the subject of further investigation performed to check the robustness against more challenging scenarios, i.e. multiple obstacles, crossroads, including models of sensors to keep the environment reconstruction and obstacle detection, such as Lidar, Camera and Radar.

REFERENCES

[1] M. Aria, "A Survey of Self-driving Urban Vehicles Development," *IOP Conference Series: Materials Science and Engineering,* vol. 662, p. 042006, 2019/11/20 2019, doi: 10.1088/1757-899x/662/4/042006.

[2] H. Okuda, N. Sugie, and T. Suzuki, "Realtime collision avoidance control based on continuation method for nonlinear model predictive control with safety constraint," in *2017 Asian Control Conference, ASCC 2017*, 2018, vol. 2018-January, pp. 1086-1091, doi: 10.1109/ASCC.2017.8287322. [Online]. Available: https://www.scopus.com/inward/record.uri?eid=2-s2.0-85047534529&doi=10.1109/ASCC.2017.8287322&partnerID=40&md5=8dbe7e5e04cb631030035b10833dc1a1

[3] M. J. Kim and J. W. Jang, "A study on avoidance technique for autonomous avoidance of unmanned vehicle," *Journal of Engineering and Applied Sciences,* Article vol. 12, no. 11, pp. 2861-2866, 2017, doi: 10.3923/jeasci.2017.2861.2866.

[4] Y. Jin, S. Li, J. Li, H. Sun, and Y. Wu, "Design of an Intelligent Active Obstacle Avoidance Car Based on Rotating Ultrasonic Sensors," in *8th Annual IEEE International Conference on Cyber Technology in Automation, Control and Intelligent Systems, CYBER 2018*, 2019, pp. 753-757, doi: 10.1109/CYBER.2018.8688326. [Online]. Available: https://www.scopus.com/inward/record.uri?eid=2-s2.0-85064973415&doi=10.1109/CYBER.2018.8688326&partnerID=40&md5=5e30879213501abe6d34e3f5e33190e3

[5] A. Taeihagh and H. S. M. Lim, "Governing autonomous vehicles: emerging responses for safety, liability, privacy, cybersecurity, and industry risks," *Transport Reviews,* vol. 39, no. 1, pp. 103-128, 2019/01/02 2019, doi: 10.1080/01441647.2018.1494640.

[6] A. Swief, A. El-Zawawi, and M. El-Habrouk, "A Survey of Model Predictive Control Development in Automotive Industries," in *2019 International Conference on Applied Automation and Industrial Diagnostics (ICAAID)*, 25-27 Sept. 2019 2019, vol. 1, pp. 1-7, doi: 10.1109/ICAAID.2019.8934974.

[7] C. N. Jones and M. Morari, "Approximate explicit MPC using bilevel optimization," in *2009 European Control Conference (ECC)*, 23-26 Aug. 2009 2009, pp. 2396-2401, doi: 10.23919/ECC.2009.7074764.

[8] M. Canale, L. Fagiano, and M. Milanese, "Set Membership approximation theory for fast implementation of Model Predictive Control laws," *Automatica,* vol. 45, no. 1, pp. 45-54, 2009/01/01/ 2009, doi: https://doi.org/10.1016/j.automatica.2008.06.015.

[9] J. Lee and H.-J. Chang, "Analysis of explicit model predictive control for path-following control," *PLOS ONE,* vol. 13, no. 3, p. e0194110, 2018, doi: 10.1371/journal.pone.0194110.

[10] Y. Wang and S. Boyd, "Fast Model Predictive Control Using Online Optimization," *IEEE Transactions on Control Systems Technology,* vol. 18, no. 2, pp. 267-278, 2010, doi: 10.1109/TCST.2009.2017934.

[11] D. Antonelli, L. Nesi, G. Pepe, and A. Carcaterra, "A novel approach in Optimal trajectory identification for Autonomous driving in racetrack," in *2019 18th European Control Conference (ECC)*, 25-28 June 2019 2019, pp. 3267-3272, doi: 10.23919/ECC.2019.8795637.

[12] D. Antonelli, L. Nesi, G. Pepe, and A. Carcaterra, "A novel control strategy for autonomous cars," in *2019 American Control Conference (ACC)*, 10-12 July 2019 2019, pp. 711-716, doi: 10.23919/ACC.2019.8814944.

[13] G. Pepe, D. Antonelli, L. Nesi, and A. Carcaterra, "*Flop: feedback local optimality control of the inverse pendulum oscillations*," presented at the ISMA, Leuven, 2018.

[14] M. Laurenza, G. Pepe, D. Antonelli, and A. Carcaterra, "Car collision avoidance with velocity obstacle approach: Evaluation of the reliability and performace of the collision avoidance maneuver," in *5th International Forum on Research and Technologies for Society and Industry: Innovation to Shape the Future, RTSI 2019 - Proceedings*, 2019, pp. 465-470, doi: 10.1109/RTSI.2019.8895525. [Online]. Available: https://www.scopus.com/inward/record.uri?eid=2-s2.0-85075634772&doi=10.1109/RTSI.2019.8895525&partnerID=40&md5=4ec5929c8f72e43dd57245de1e7efdb1

[15] G. Pepe, M. Laurenza, D. Antonelli, and A. Carcaterra, "A new optimal control of obstacle avoidance for safer autonomous driving," in *2019 AEIT International Conference of Electrical and Electronic Technologies for Automotive (AEIT AUTOMOTIVE)*, 2-4 July 2019 2019, pp. 1-6, doi: 10.23919/EETA.2019.8804549.

[16] D. Antonelli, L. Nesi, G. Pepe, and A. Carcaterra, "Mechatronic control of the car response based on VFC," *Proceedings of the ISMA2018, Leuven, Belgium,* pp. 17-19, 2018.

[17] H. B. Pacejka, "Chapter 4 - Semi-Empirical Tire Models," in *Tire and Vehicle Dynamics (Third Edition)*, H. B. Pacejka Ed. Oxford: Butterworth-Heinemann, 2012, pp. 149-209.

[18] D. Arosio, F. Braghin, F. Cheli, and E. Sabbioni, "Identification of Pacejka's scaling factors from full-scale experimental tests," *Vehicle System Dynamics,* vol. 43, pp. 457-474, 01/01 2005, doi: 10.1080/00423110500229683.

[19] D. Chindamo, B. Lenzo, and M. Gadola, "On the Vehicle Sideslip Angle Estimation: A Literature Review of Methods, Models, and Innovations," *Applied Sciences,* vol. 8, no. 3, 2018, doi: 10.3390/app8030355.
[20] H. Guo, D. Cao, H. Chen, C. Lv, H. Wang, and S. Yang, "Vehicle dynamic state estimation: state of the art schemes and perspectives," *IEEE/CAA Journal of Automatica Sinica,* vol. 5, no. 2, pp. 418-431, 2018, doi: 10.1109/JAS.2017.7510811.
[21] Jin, Yin, and Chen, "Advanced Estimation Techniques for Vehicle System Dynamic State: A Survey," *Sensors,* vol. 19, p. 4289, 10/03 2019, doi: 10.3390/s19194289.
[22] H. Min, Wu, Cheng, and Zhao, "Kinematic and Dynamic Vehicle Model-Assisted Global Positioning Method for Autonomous Vehicles with Low-Cost GPS/Camera/In-Vehicle Sensors," *Sensors,* vol. 19, p. 5430, 12/09 2019, doi: 10.3390/s19245430.

EURODYN 2020
XI International Conference on Structural Dynamics
M. Papadrakakis, M. Fragiadakis, C. Papadimitriou (eds.)
Athens, Greece, 23–26 November 2020

IDENTIFICATION OF NONLINEAR ROAD-VEHICLE DYNAMIC BEHAVIOR USING AUTOREGRESSIVE TECHNIQUE

Mohab Anwar[1], Mostafa Tamer[1], Mohamed Tawfik[2], and Hesham H. Ibrahim[3]

[1]Research Assistant
Mechatronics Department, German University in Cairo
New Cairo, Egypt
mostafa.tamer@student.guc.edu.eg, mohab.alkhayat@student.guc.edu.eg

[2] Director
Academy of Knowledge
Cairo, Egypt
mohamed.tawfik@academyofknowledge.org,

[3]Associate Professor
Mechatronics Department, German University in Cairo
New Cairo, Egypt
hesham.hamed-ahmed@guc.edu.eg

Keywords: Full car model, Autoregressive System, Active suspension

Abstract. *This work presents an identification technique for the suspension dynamics of a nonlinear full car model by implementing an autoregressive system with exogenous input (ARX). The ARX model was proposed as a simple and powerful tool, in terms of accuracy and computational time, compared to the complexity and significant computational cost involved with the neural networks approach which is commonly used. Firstly, the training data is provided through a full car model simulated by Matlab/Simulink. Then the training data is fed into the autoregressive algorithm, which in turn provided an autoregressive model for the suspension dynamic behavior, while this model was calibrated using another data set grabbed from the same Simulink model. Several RMS values of noise were added to different types of road excitation in order to assess the efficiency of the proposed ARX system in terms of noise filtration. Finally, the active response the autoregressive system is simulated, using a PID controller, and compared with those of the Simulink model. The proposed system identification technique proved it's efficiency in terms of accuracy in the light of its very fast computational speed.*

1 INTRODUCTION

A suspension system plays a crucial role in maintaining an automobile's stability and passenger comfort during the drive. The suspension system can be divided into three types, passive, semi-active and active suspension. The passive model is an open-loop control system that is not acted upon by any control system. It only contains springs and dampers, allowing the system to passively store energy by the springs and dissipate energy through the dampers. Changing the damper on the existing passive suspension into variable damper, transforms the system into a semi-active suspension, adapting to changing road conditions. The addition of an actuator to the system transforms the system into active suspension, adding external controlling energy that is presented as a closed-loop system. This allows the system to take action against road change, it calculates and adds the required energy to keep the tires intact on the road, improving the overall driving stability and passenger comfort.

M. Savaresi et $al.$ [1] have created a black box Non-linear autoregressive with exogenous input (NARX) model for a magneto-rheological (MR) damper for vehicle control. A. Suebsomran [2] has developed an approximate linear model for a non-linear electromagnetic suspension system as well as Linear state feedback control, adaptive neural network control and a hybrid of linear state feedback and adaptive neural network control on the plant system. I.Ö. Bucak et $al.$ [3] have done vibration control on a non-linear quarter-car suspension system by reinforcement learning method . D. Hanafi et $al.$ [4] have developed a NARX model for quarter-car suspension system using neural network technique, data used were real data obtained by automobile driving on a special road. D. Hanafi. [5] implemented a PID controller on NARX model for a semi-active quarter car suspension system. M.N.Howell et $al.$ [6], developed a reward-intaction based reinforcement learning algorithm to minimize the RMS of four-wheel car body acceleration. Z. Saad et $al.$ [7], have developed a NARX model and RLS learning algorithm as a black box model for car speed forecasting. B. C. Ng et $al.$ [8], have developed a NARX model to model the dynamic behavior of an automobile air conditioning system. S. Inagaki et $al.$ [9], have developed a SS-ARX model in the purpose of human driving behavior recognition. H. Luo et $al.$ [10], have developed a Dual-Tree Complex Wavelet enhanced Convolutional Long Short- Term Memory neural network (DTCWT-CLSTM), a method aimed to be a structural health monitoring tool for an automotive suspension. Y. Mao et $al.$ [11], have proposed two estimation algorithms for Hammerstein controlled autoregressive systems. V. Krishnaswami et $al.$ [12], presented a NARMAX model to detect a failure in actuators of an internal combustion engine. W. Pawlus et $al.$ [13], proposed a NAR model parameters estimated by feed-forward neural networks the NAR model is derived from a more general NARMA model, NAR model was proposed for calculating vehicle crashworthiness. S. Barone et $al.$ [14], have developed a CAR model as a statistical tool for improving the reliability of a pre-equipped OBD system in a passenger car. C. Debes et $al.$ [15], proposed an autoregressive algorithm to process the signal with added non-Gaussian noise. C. A. Aliza et $al.$ [16], proposed a prototype model for a passive quarter car suspension. C. Kim et $al.$, Y. Qin et $al.$ [17], proposed a classification method for a semi-active suspension system based on deep neural networks, evaluation done through computer simulation. X. Q. Sun et $al.$ [18], have used hybrid system theory to model the continuous and discrete dynamics of the height adjustment process of a vehicle. X. Xu et $al.$ [19], developed a non-linear parallel interlinked air half-car suspension system, then the model was linearized by Taylor expansion. E. Ilkonen et $al.$ [20], proposed a non-linear dynamic model for a MacPherson active suspension system as well as state control and estimation using Makrov models. E. Asadi et $al.$ [21], proposed a model for an adaptive electromagnetic hybrid damper.

M. F. Aly et $al.$ [22], have carried out a design and optimization for a vehicle suspension system with passive variable stiffness and active damping, using a genetic algorithm. A. H. Tesfay et $al.$ [23], designed and modeled a variable stiffness air spring semi-active suspension system.

ARX is an abbreviation for autoregressive system with exogenous input. Unlike any system identification method, ARX models aim to find direct relation between the systems' degrees of freedom, system inputs, and output. The current work presents an attempt to generate an autoregressive model for a full-car suspension system. Training data will be given in the form of time domain data for the displacement of each sprung and unsprung masses of each wheel as well as the road input all given as learning data. All of the training data were generated by a model for a full car suspension developed on Simulink and the same Simulink model will be used afterwards for validation purposes.

2 The Full Car Mathematical Model

2.1 Full Car Suspension Parameters

The current full car suspension system has seven degrees of freedom, as shown in the illustrative figure (1) below, which represents the vertical displacement of each wheel, the vertical displacement of the unsprung mass, the pitch of the unsprung mass and the roll of the unsprung mass. The current study implements the same car model presented by Darus et $al.$ [24], and table (1) presents the definitions of the model's notations.

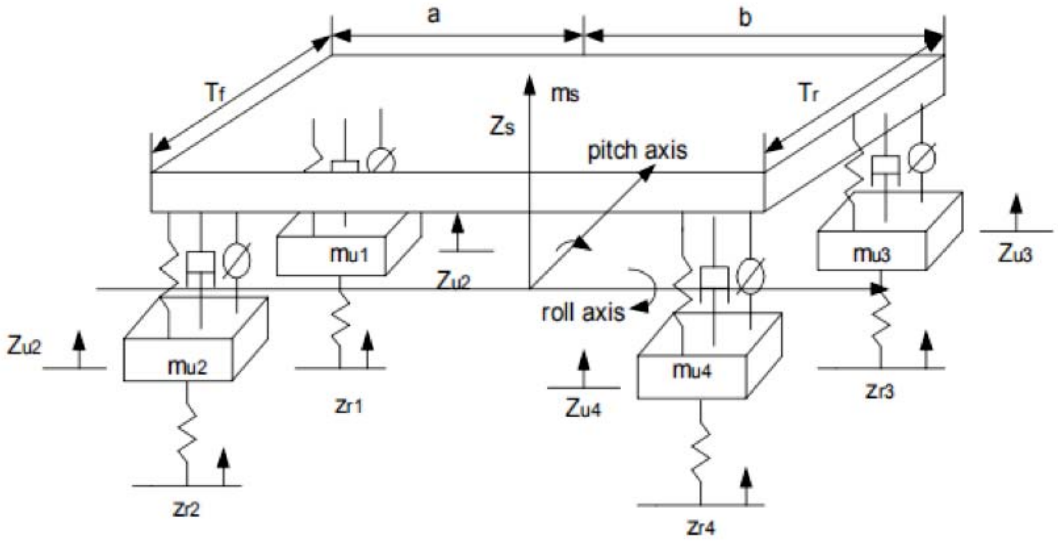

Figure 1: Full car mathematical model

Table 1: Table of notations.

Variables	Definitions
Z_s	Vertical displacement of the center of mass of the sprung mass
Z_{u1}	Vertical displacement of the front right wheel
Z_{u2}	Vertical displacement of the front left wheel
Z_{u3}	Vertical displacement of the rear right wheel
Z_{u4}	Vertical displacement of the rear left wheel
θ_s	Sprung mass of the pitch angle
ϕ_s	Sprung mass of the roll angle
f_i	Force due to actuation on wheel i
i	Index reference to each wheel (1,2,3,4)

From the above model the equations of motion for the sprung mass parts connecting with each unsprung mass $(Z_{s1}, Z_{s2}, Z_{s3}, Z_{s4})$ can be stated as follows

$$Z_{s1} = T_f\phi_s + a\theta_s + Z_s \tag{1}$$

$$Z_{s2} = -T_f\phi_s + a\theta_s + Z_s \tag{2}$$

$$Z_{s3} = -T_r\phi_s - b\theta_s + Z_s \tag{3}$$

$$Z_{s4} = -T_r\phi_s - b\theta_s + Z_s \tag{4}$$

3 Autoregressive Full Car Model

The autoregressive process aims to predict the following states Z_{si}, Z_{ui}, Z_{ri} by using the data extracted from the Simulink model as an input training data. Once Z_{si} is acquired from each wheel. θ_s, ϕ_s, Z_s can be computed from the relations mentioned before.

$$Z_{St+\delta t} = \begin{pmatrix} Z_{S2} \\ Z_{S3} \\ \vdots \\ Z_{S999} \end{pmatrix}, Z_{St} = \begin{pmatrix} Z_{S1} \\ Z_{S2} \\ \vdots \\ Z_{S998} \end{pmatrix}, Z_{St-\delta t} = \begin{pmatrix} Z_{S0} \\ Z_{S1} \\ \vdots \\ Z_{S997} \end{pmatrix} \tag{5}$$

Similarly, for Z_u and Z_r, the above procedure was implemented to get their corresponding time vectors.
The solution of the system was assumed to be as follows:

$$Z_{si(t+\delta t)} = a_0 Z_{si(t)} + a_1 Z_{si(t-\delta t)} + a_2 Z_{ui(t)} + a_3 Z_{ui(t-\delta t)} + a_4 Z_{ri(t)} + a_5 Z_{ri(t-\delta t)} + b_0 f_{i(t)} + b_1 f_{i(t-\delta t)} \tag{6}$$

In order to calculate Z_s, a matrix "A" is formulated as shown in equation (7). The "A" matrix was formulated using the same order of the terms in equation (6) where $b_0, b_1 = zero$ in case of the passive suspension system.

$$A = \left[Z_{s(t)} \left| Z_{s(t-\delta t)} \right| Z_{u(t)} \left| Z_{u(t-\delta t)} \right| Z_{r(t)} | Z_{r(t-\delta t)} \right] \tag{7}$$

$$\{a\} = \left([A]^T [A]^{-1} \right) [A]^T \left\{ Z_{s(t+\delta t)} \right\} \tag{8}$$

By solving for the vector a gives the coefficients $a_0, a_1, a_2, a_3, a_4, a_5$ which are used later in the formulation of the polynomial representing the displacement of the sprung mass Z_s as in equation (6).

Similarly for Z_u, the same procedures were implemented as follows:

$$A = \left[Z_{u(t)} \left| Z_{u(t-\delta t)} \right| Z_{s(t)} \left| Z_{s(t-\delta t)} \right| Z_{r(t)} | Z_{r(t-\delta t)} \right] \tag{9}$$

$$\{a\} = \left([A]^T [A]^{-1} \right) [A]^T \left\{ Z_{u(t+\delta t)} \right\} \tag{10}$$

$$Z_{ui(t+\delta t)} = a_0 Z_{ui(t)} + a_1 Z_{ui(t-\delta t)} + a_2 Z_{si(t)} + a_3 Z_{si(t-\delta t)} + a_4 Z_{ri(t)} + a_5 Z_{ri(t-\delta t)} + b_0 f_{i(t)} + b_1 f_{i(t-\delta t)} \tag{11}$$

By solving equations (1), (2), (3), and (4) simultaneously, we can get the following: θ_s, ϕ_s, Z_s:

$$\phi_s = \frac{Z_{s1} - Z_{s2} + Z_{s3} - Z_{s4}}{2T_f + 2T_r} \tag{12}$$

$$\theta_s = \frac{Z_{s1} + Z_{s2} - Z_{s3} - Z_{s4}}{2a + 2b} \tag{13}$$

$$Z_s = Z_{s1} + Z_{s2} + Z_{s3} + Z_{s4} + \frac{(2b - 2a)\theta_s}{4} \tag{14}$$

It can be seen that these three degrees of freedom are functions of the other four ones, thus, the first four degrees of freedom $(Z_{s1}, Z_{s2}, Z_{s3}, Z_{s4})$ can be used to calculate the other three which will save computational time spent on applying regression techniques to model them.

In order to improve the accuracy and to account for the coupling between the four wheels, some difference and product terms were added as follows:

$$(Z_{u1} \cdot Z_{u2}, Z_{u3} \cdot Z_{u4}, Z_{u1} \cdot Z_{u3}, Z_{u2} \cdot Z_{u4}, Z_{u1} \cdot Z_{u4}, Z_{u2} \cdot Z_{u3})$$

and the difference terms added were:

$$(Z_{u1} - Z_{u2}, Z_{u3} - Z_{u4}, Z_{u1} - Z_{u3}, Z_{u2} - Z_{u4}, Z_{u1} - Z_{u4}, Z_{u2} - Z_{u3})$$

where:

$$Z_{u1} \cdot Z_{u2} = Z_{u1}(t_i)\, Z_{u2}(t_i) \; and \; Z_{u1} - Z_{u2} = Z_{u1}(t_i) - Z_{u2}(t_i)$$

The choice of the non-linear terms was biased to symmetrical terms and was subject to trial and error. Each vector that represents its corresponding non-linear term is concatenated in each $[A]$ matrix, and each corresponding term is included in the regression polynomial in equations (6) and (11).

The approach used in the addition of a PID controller to the autoregressive model generated was by solving the system in two steps, the first step was by applying the autoregressive technique on a passive model, then by using this model generated to predict the effect of the force outputted from the PID controlled actuator in the following manner; in the same manner in equation (10), the passive model was generated, then the same regression technique will again be applied but with as follows:

$$Z_s(t + \delta t) - \{a\}[A] = b_0 f(t) + b_1 f(t - \delta t) \tag{15}$$

$$\{b\} = \left([B]^T [B]^{-1} \right) [B]^T \left\{ Z_{s(t+\delta t)} - \{a\}[A] \right\} \tag{16}$$

where B is a matrix containing the time steps of the generated PID force as illustrated in figure (2). By substituting the values of b_0 and b_1, extracted from equation (16), into equation (6).

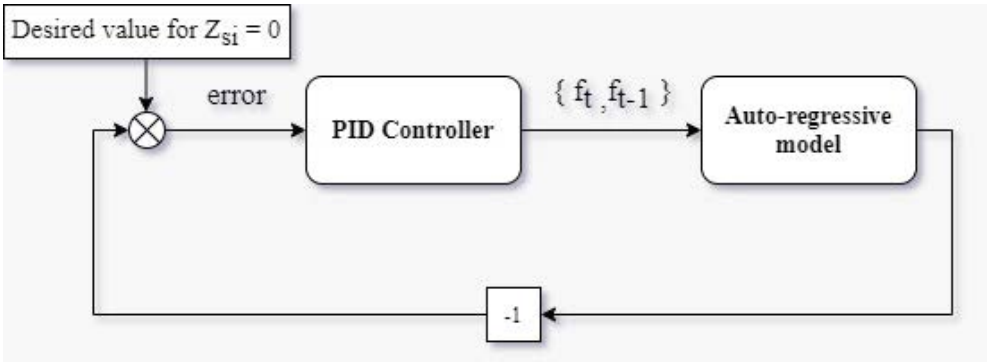

Figure 2: Block diagram showing the active suspension model

4 Results and Discussion

In order to test the predicted model, several road input types were introduced to the system and the response calculated from the auto-regressive system polynomial was compared to that extracted from the Simulink model. The types of input introduced to the system were sinusoidal input, step input, road bumps, and random excitation.

4.1 Sinusoidal input

A sinusoidal input, of 0.06 m amplitude and 10 $\frac{rad}{sec}$ frequency, has been applied to all wheels, while those applied to wheels 1 and 4 have a phase shift of $\frac{\pi}{2}$ which can be expressed as [24]:

$$Z_{r1}(t), Z_{r4}(t) = 0.06sin(10t + \frac{\pi}{2}) \tag{17}$$

$$Z_{r2}(t), Z_{r3}(t) = 0.06sin(10t) \tag{18}$$

The same road input excitation applied to the predicted model was applied to the Simulink model and the results were compared and shown as follows in figures (3), (4), and (5).

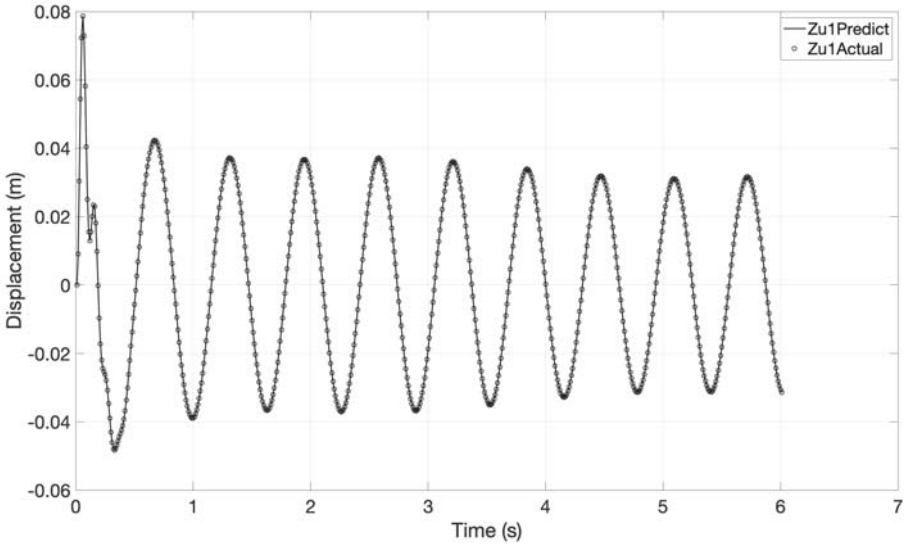

Figure 3: Unsprung mass Zu1 response

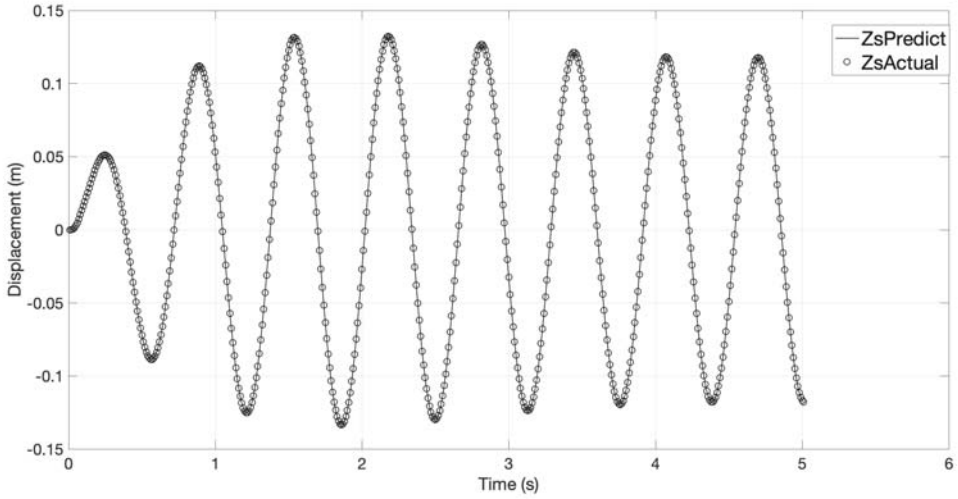

Figure 4: Center of mass Zs response

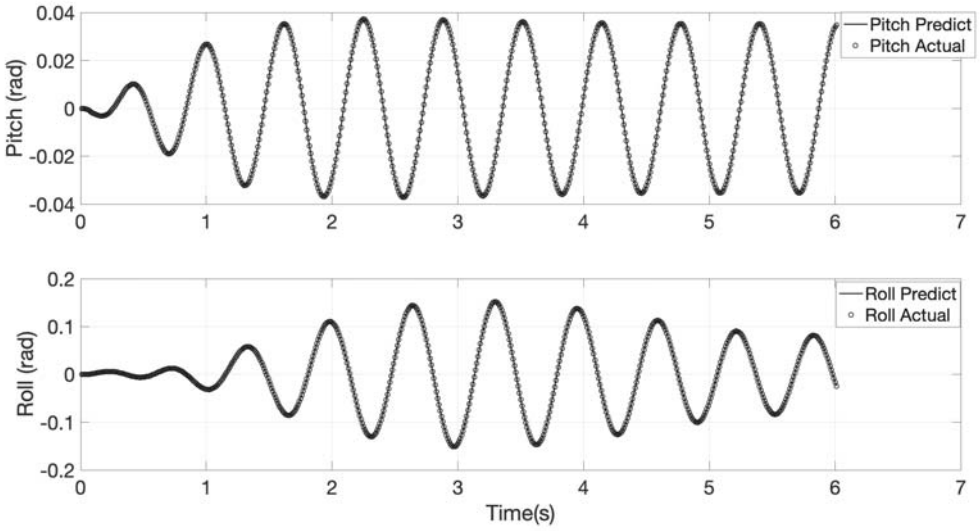

Figure 5: Sprung mass Pitch and Roll

It is shown in the above figures (3), (4), and (5) that the results of Z_{u1},Z_s, $Pitch$, and $Roll$ show that the predicted model responses are in a very good agreement with their corresponding states obtained from the Simulink model.

4.2 Model Robustness

While building the model, the assessment of the model robustness was a crucial issue. Therefore, in order to test the robustness of the model, two different types of data sets were implemented in training the autoregressive model. The first one was an input with a training data set of monotonic nature like, for example, step input or sinusoidal, applied seperately as shown in figure. The second one was a mixed type of input presented as a combination of two different road excitations, for example, sinusoidal and step applied in sequence.

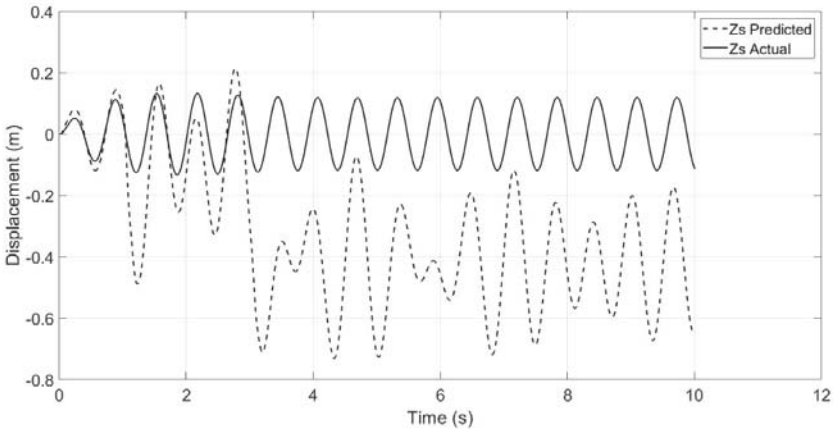

Figure 6: Sprung mass response, subjected to sinusoidal input and trained by step input

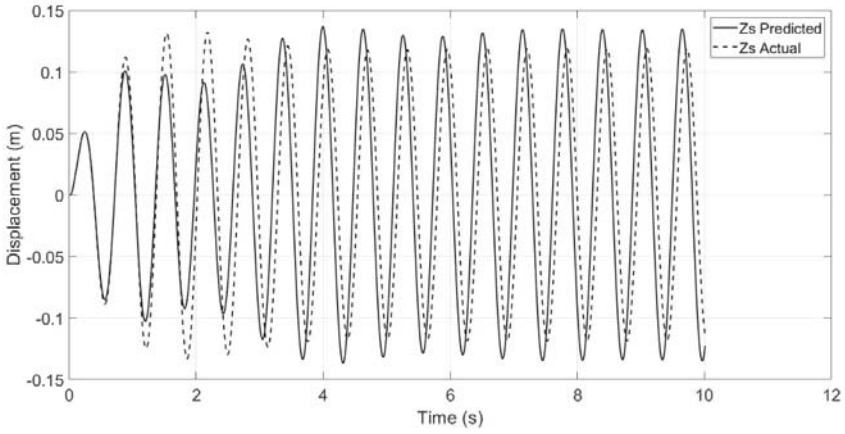

Figure 7: Sprung mass response, subjected to sinusoidal input and trained by mixed input

Figure (6) represents the sprung mass repsonse, subjected to sinusoidal input when it was trained by only step input, while figure (7) represents the sprung mass reponse, subjected to the same sinusoidal input when it was trained by a multiple inputs, which was simulated as a step input followed by a random excitaion. It's found that using single-type input, utilised in training data sets, fell short in training the autoregressive model which was reflected by a very poor prediction of the sprung mass displacement in response to sinusoidal input as depicted in figure (6), while, the usage of multi-type input proved efficient in training the autoregressive model as depicted in figure (7).

4.3 PID controller implementation

In order to test the active performance, of the trained autoregressive model, compared to it's passive response to the same sinusoidal input mentioned above in equations (17) and (18). The active response of the sprung mass, using a PID controller following the procedure detailed equations (15) and (16), is presented in figures (8) and (9).

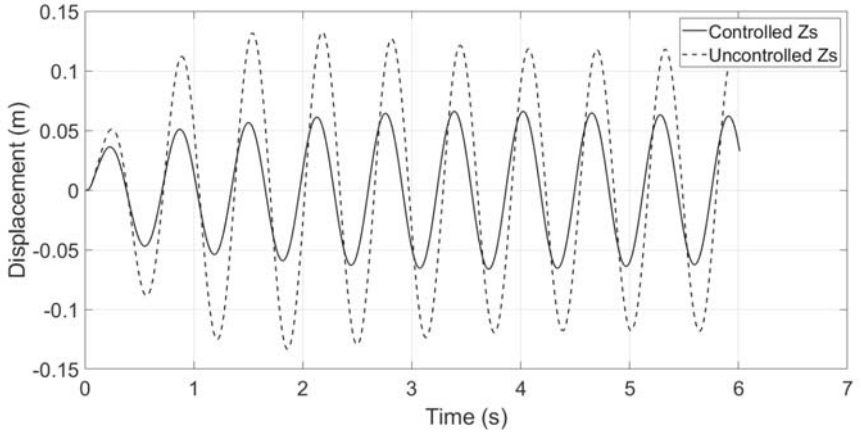

Figure 8: Sprung mass response after adding PID controller

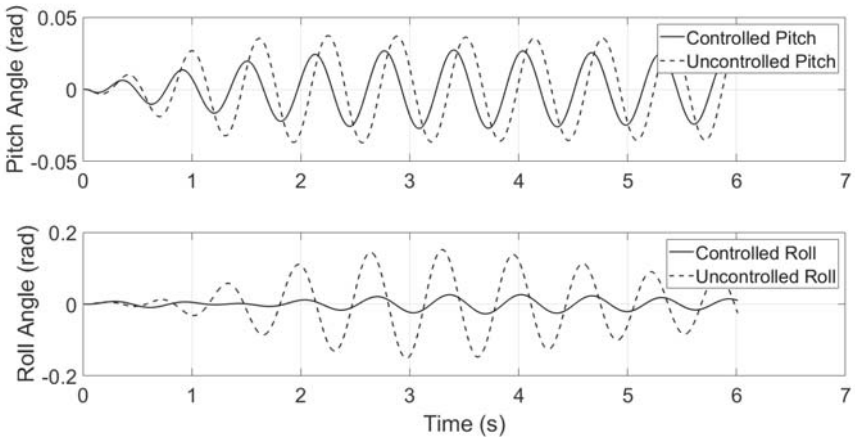

Figure 9: Sprung mass Pitch and Roll after adding PID controller

It's found in the figures 8 and 9, as expected that the PID control can add significant effect in mitigating the vertical displacement, pitch, and roll amplitudes.

4.4 Noise Filtration Capacity of Autoregressive systems

In order to test the ability of the autoregressive model to generate a stable model in spite of being in a noisy environment, the approach used was adding noise to the inputs used to build the autoregressive model through adding a random signal to the signals from Unsprung and Sprung masses of each wheel. Firstly, a noise of Variance of *0.0005 m* and the mean value of *zero* was added to the sinusoidal input mentioned above in equations (17) and (18). The results of the wheel number 1 "Z_{u1}" and Sprung mass "Z_s" are shown below in Figures (10) and (11) respectively.

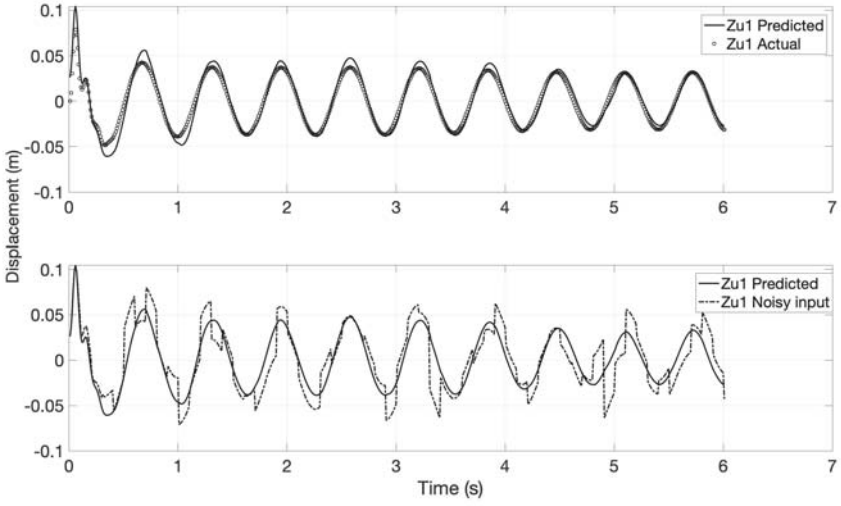

Figure 10: Wheel number 1 displacement in response to noisy sinusoidal excitation

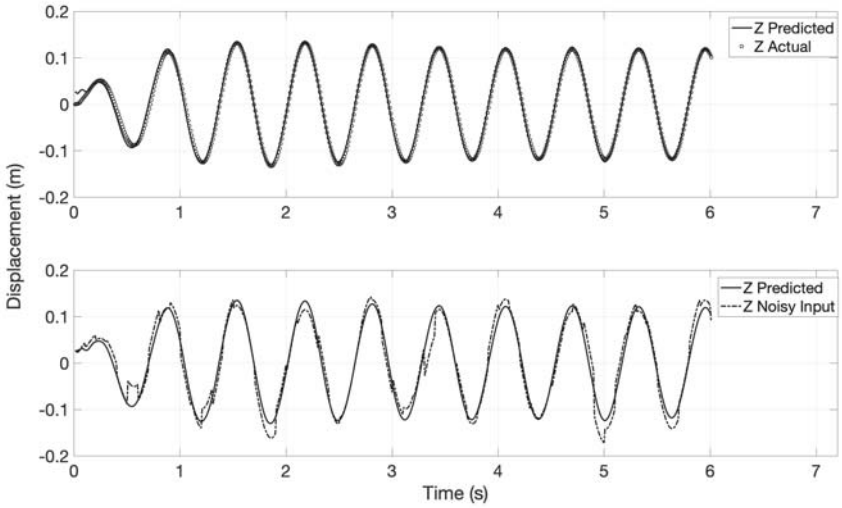

Figure 11: Sprung mass displacement in response to noisy sinusoidal excitation

The above figures (10), and (11) show the predicted model responses of different degrees of freedom Z_{u1}, and Z_s compared to the training data with and without the inclusion of noise to the training set. This shows the model's capability to filter the noise. For further testing of the model, it was tested with no inputs and only with an initial excitation, the initial conditions applied to the system were:

$$Z_{u1}(0) = Z_{u2}(0) = Z_{u3}(0) = Z_{u4}(0) = Z_s(0) = 0.1, \text{ and } \dot{Z}_s(0) = 1$$

The response for the Unsprung and sprung masses to the above initial excitation is shown below in figures (12) and (13) respectively.

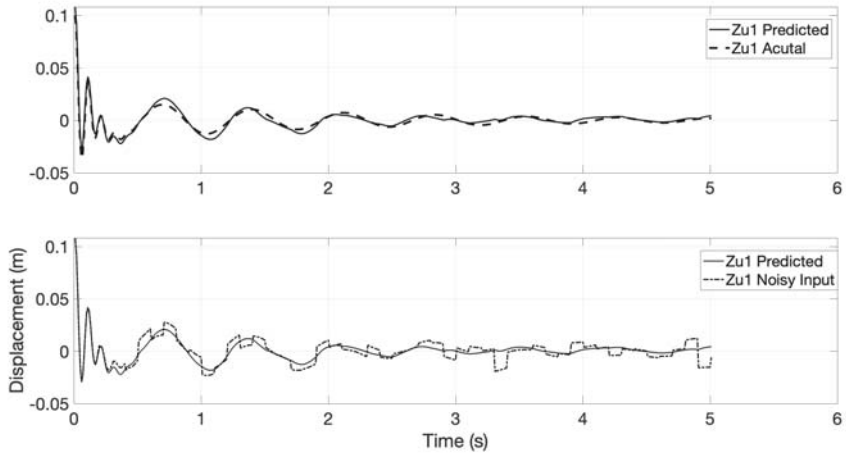

Figure 12: Wheel number 1 displacement in response to noisy initial condition

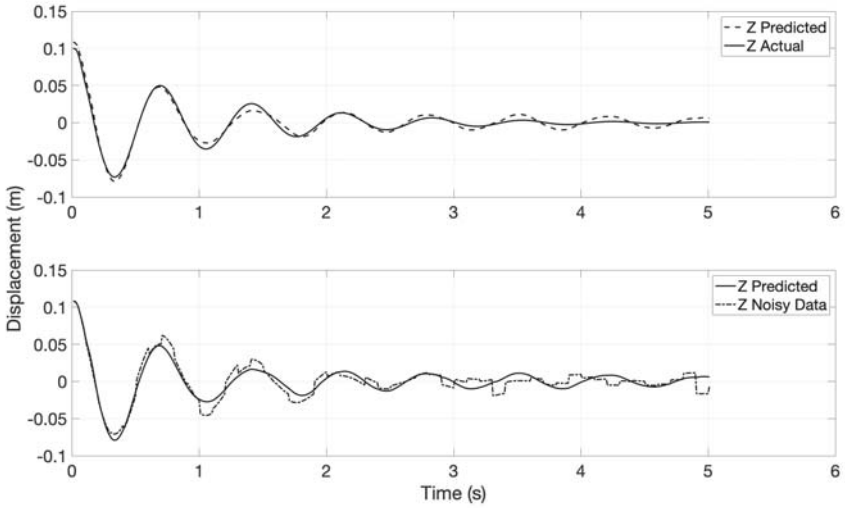

Figure 13: Sprung mass displacement in response to the noisy initial condition

Figures 12 and 13 show that the autoregressive model was able to be trained with noise added to the data sets and to give accurate predictions of the data excluding the effect of the noise.

4.5 Conclusion

- While testing the generated autoregressive model, it was noticed that the model has a higher capability of capturing the actual system dynamics when various types of inputs were used in the training phase. It was found that the predictions can be improved significantly if the system is trained with two types of inputs, for example, sinusoidal and random, it can provide much better predictions to the step response rather than when it was built only using single input; sinusoidal or random.

- The autoregressive model was able to be trained with noise added to the data sets and to give accurate predictions of the data excluding the effect of the noise.

- Autoregressive models could come up with unacceptable results once being trained, using a training data set which contains a constant value for a relatively long duration.

References

[1] Sergio M Savaresi, Sergio Bittanti, and Mauro Montiglio. Identification of semi-physical and black-box non-linear models: the case of mr-dampers for vehicles control. *Automatica*, 41(1):113–127, 2005.

[2] Anan Suebsomran. Adaptive neural network control of electromagnetic suspension system. *International Journal of Robotics and Automation*, 29(2):144–154, 2014.

[3] İhsan Ömür Bucak and Halil R Öz. Vibration control of a nonlinear quarter-car active suspension system by reinforcement learning. *International Journal of Systems Science*, 43(6):1177–1190, 2012.

[4] Dirman Hanafi, Mohd Fua'ad bin Rahmat, Zainal Abidin bin Ahmad, and Amran bin Mohd Zaid. Intelligent system identification for an axis of car passive suspension system using real data. In *2009 6th International Symposium on Mechatronics and its Applications*, pages 1–7. IEEE, 2009.

[5] Dirman Hanafi. Pid controller design for semi-active car suspension based on model from intelligent system identification. In *2010 Second International Conference on Computer Engineering and Applications*, volume 2, pages 60–63. IEEE, 2010.

[6] Mark N Howell, Geoff P Frost, Timothy J Gordon, and Qing H Wu. Continuous action reinforcement learning applied to vehicle suspension control. *Mechatronics*, 7(3):263–276, 1997.

[7] Z Saad and MY Mashor. Model structure selection for speed forecasting with nonlinear autoregressive with an exogenous input. In *2013 4th International Conference on Intelligent Systems, Modelling and Simulation*, pages 290–293. IEEE, 2013.

[8] Boon Chiang Ng, Intan Zaurah Mat Darus, Hishamuddin Jamaluddin, and Haslinda Mohamed Kamar. Dynamic modelling of an automotive variable speed air conditioning system using nonlinear autoregressive exogenous neural networks. *Applied Thermal Engineering*, 73(1):1255–1269, 2014.

[9] Shogo Sekizawa, Shinkichi Inagaki, Tatsuya Suzuki, Soichiro Hayakawa, Nuio Tsuchida, Taishi Tsuda, and Hiroaki Fujinami. Modeling and recognition of driving behavior based on stochastic switched arx model. *IEEE Transactions on Intelligent Transportation Systems*, 8(4):593–606, 2007.

[10] Huan Luo, Miaohua Huang, and Zhou Zhou. A dual-tree complex wavelet enhanced convolutional lstm neural network for structural health monitoring of automotive suspension. *Measurement*, 137:14–27, 2019.

[11] Yawen Mao and Feng Ding. Multi-innovation stochastic gradient identification for hammerstein controlled autoregressive autoregressive systems based on the filtering technique. *Nonlinear Dynamics*, 79(3):1745–1755, 2015.

[12] V Krishnaswami, G Luh, and G Rizzoni. Nonlinear parity equation based residual generation for diagnosis of automotive engine faults. *Control Engineering Practice*, 3(10):1385–1392, 1995.

[13] Witold Pawlus, Hamid Reza Karimi, and Kjell G Robbersmyr. Data-based modeling of vehicle collisions by nonlinear autoregressive model and feedforward neural network. *Information Sciences*, 235:65–79, 2013.

[14] Stefano Barone, Paolo D'Ambrosio, and Pasquale Erto. A statistical monitoring approach for automotive on-board diagnostic systems. *Quality and Reliability Engineering International*, 23(5):565–575, 2007.

[15] Christian Debes and Abdelhak M Zoubir. Bootstrapping autoregressive plus noise processes. In *2007 2nd IEEE International Workshop on Computational Advances in Multi-Sensor Adaptive Processing*, pages 53–56. IEEE, 2007.

[16] Che Amran Aliza, Fen Ying Chin, Mariam Md Ghazaly, Shin Horng Chong, and Vasanthan Sakthivelu. Development of passive quarter car suspension prototype. In *Applied Mechanics and Materials*, volume 761, pages 238–244. Trans Tech Publ, 2015.

[17] Yechen Qin, Reza Langari, Zhenfeng Wang, Changle Xiang, and Mingming Dong. Road excitation classification for semi-active suspension system with deep neural networks. *Journal of Intelligent & Fuzzy Systems*, 33(3):1907–1918, 2017.

[18] XiaoQiang Sun, Long Chen, ShaoHua Wang, and Xing Xu. Vehicle height control of electronic air suspension system based on mixed logical dynamical modelling. *Science China Technological Sciences*, 58(11):1894–1904, 2015.

[19] Xing Xu, Nan-Nan Zou, Long Chen, and Xiao-Li Cui. Modelling and analysis of parallel-interlinked air suspension system based on a transfer characterisation. *International Journal of Vehicle Noise and Vibration*, 12(1):1–23, 2016.

[20] Enso Ikonen, Kaddour Najim, and Alfonso García-Cerezo. Macpherson suspension system modeling and control with mdp. In *2016 IEEE Symposium Series on Computational Intelligence (SSCI)*, pages 1–8. IEEE, 2016.

[21] Ehsan Asadi, Roberto Ribeiro, Mir Behrad Khamesee, and Amir Khajepour. A new adaptive hybrid electromagnetic damper: modelling, optimization, and experiment. *Smart Materials and Structures*, 24(7):075003, 2015.

[22] Mohamed F Aly, Ashraf O Nassef, and Karim Hamza. Multi-objective design of vehicle suspension systems via a local diffusion genetic algorithm for disjoint pareto frontiers. *Engineering Optimization*, 47(5):706–717, 2015.

[23] AH Tesfay and VK Goel. Analysis of semi-active vehicle suspension system using air-spring and mr damper. In *IOP Conference Series: Materials Science and Engineering*, volume 100, page 012020. IOP Publishing, 2015.

[24] Rosheila Darus and Yahaya Md Sam. Modeling and control active suspension system for a full car model. In *2009 5th International Colloquium on Signal Processing & Its Applications*, pages 13–18. IEEE, 2009.

EURODYN 2020
XI International Conference on Structural Dynamics
M. Papadrakakis, M. Fragiadakis, C. Papadimitriou (eds.)
Athens, Greece, 23–26 November 2020

EFFICIENT METHODS TO ASSESS LINEAR AND NON-LINEAR AUTOMOTIVE PLATOON CONTROL STABILITY AND PERFORMANCE

Christian Kalteis[1], **Sebastian Thormann**[1], **Alexander Schirrer**[1] **and Stefan Jakubek**[1]

[1]Technical University Vienna
Karlsplatz 13, 1040 Vienna
e-mail: christian.kalteis@student.tuwien.ac.at
{sebastian.thormann,alexander.schirrer,stefan.jakubek}@tuwien.ac.at

Keywords: String stability, Automated driving, Co-simulation, Platooning control.

Abstract. *This work proposes a set of methods and tools to analyse and quantify key performance aspects of controlled automotive platoons. These methods assess classical stability and string stability properties in both analytical and empirical settings. An automotive platoon consists of multiple tightly spaced vehicles which aim to follow a desired velocity or distance profile safely, autonomously, and efficiently. Cooperative vehicular platooning can greatly improve traffic efficiency and safety, while increasing traffic throughput and fuel efficiency. One difficulty for establishing a stable platoon, besides classical stability of individual vehicles, is known as "string stability". Essentially, in a string stable platoon, disturbances of any individual vehicle are not amplified along the platoon. In addition to stability, the performance of a platoon control structure must be quantified, for example by measuring disturbance rejection bandwidth / control error decay rate. Most of the proposed platoon control architectures developed in the past guarantee platoon stability/string stability only under restrictive assumptions. In this work tools and methods are proposed to analyse classical stability, error signal measures, as well as analytical and empirical string stability. This allows the user to evaluate platoon safety and performance for given control structures and conduct parameter studies at various levels of system complexity. To investigate platoon behaviour under realistic conditions, test scenarios are empirically evaluated in a co-simulation of multiple instances of the commercial simulation software IPG TruckMaker.*

1 INTRODUCTION

As heavy duty vehicle (HDV) road traffic is rising steadily through growing freight transportation, increasing road capacity is gaining importance. One way to address this issue is to reduce the distance between consecutive vehicles, as shown in [1]. For safety reasons, however, safe driving by human drivers requires a time-headway of about 2 seconds as typically laid down in legal regulations. Driving at small inter-vehicular distances also comes with benefits in fuel efficiency due to reduction of air resistance [2]. To safely reduce the distance, longitudinal control architectures are added. To further improve performance of a string of longitudinal controlled semi-autonomous vehicles following each other, thereby forming a platoon, vehicle-to-vehicle (V2V) communication is added. This allows the platoon to react cooperatively according to desired trajectories in a situation-aware manner [3].

To achieve this goal, each individual vehicle must show stable dynamics with respect to injected disturbances. Essentially, a desired time headway policy must be reliable. Single-vehicle control structures, for example adaptive cruise control (ACC) systems, were developed in the past. However, these did not consider error propagation along a platoon of vehicles. It has been shown that in many commercially available ACC systems, errors are actually amplified from one vehicle to its follower [4]. To assess this problem, the concept of string stability is introduced. In a string stable platoon, disturbance propagation does not increase along the platoon. Multiple definitions for string stability were proposed in the past as surveyed in [5].

Intensive research has been done before on linear platoon dynamics. Due to high expenses of testing platoon dynamics in real world settings though, only few experiments were executed. To allow an efficient assessment and analysis of platoon behaviour in arbitrary simulation settings, this work provides the following main contributions:

- methods formulated to assess
  - stability properties,
  - string stability analysis and
  - performance indicators,
- implemented into tools to evaluate these aspects in
  - linear dynamics,
  - non-linear high-fidelity co-simulation settings.

Using the proposed methods and tools allows to evaluate platoon performance in realistic settings in an efficient and reproducible way.

2 LINEAR AND NON-LINEAR MODELS

In this first section, the chosen platoon model, classical linear stability as well as string stability are described.

2.1 Linear platoon dynamics model

The position of each vehicle is denoted as x_i wherein the index $i \in \mathbb{Z}$ refers to the i-th vehicle. Hence, x_{i-1} denotes the predecessor's position, and x_{i+1} as the follower's as depicted in Fig. 1. The distance between one vehicle and its predecessor is given by

$$d_i = x_{i-1} - x_i - L_{i-1}, \tag{1}$$

where L_i denotes the length of the i-th vehicle. Starting from x (index i dropped in the following when referring to the ego vehicle i only), the velocity v and the acceleration a are given by the differential equations $v = \dot{x}$ and $a = \dot{v}$. For simplicity (to measure error propagation) homogeneous vehicle platoons are assumed below. With the controller input $u := a_{desired}$ and by approximating the vehicle behaviour with the simplified linear time invariant (LTI) dynamics

$$\dot{a} = -\frac{1}{\tau}a + \frac{1}{\tau}u, \tag{2}$$

as well as using the state vector $\mathbf{x} = \begin{bmatrix} x & v & a \end{bmatrix}^T$, the general vehicular system in discrete state-space form can be written as

$$\mathbf{x}_{k+1} = \mathbf{A}_d \mathbf{x}_k + \mathbf{b}_d u_k \tag{3}$$

where $\mathbf{A}_d$ and $\mathbf{b}_d$ are the corresponding discrete equivalents of $\mathbf{A}$ and $\mathbf{b}$ with T_s as sampling time. The time constant $\tau = \tau(v)$ represents the engine dynamics, which depends on the current vehicle's velocity. Due to this dependence, a constant value of τ can only be assumed for a specific operating point at velocity v_0. Furthermore, to focus on control parameter studies, wireless communication is assumed flawless.

2.2 Non-linear platoon dynamics

With knowledge of linear vehicle dynamics behaviour, more sophisticated results are obtained using the non-linear high fidelity simulation software IPG TruckMaker®[7]. The co-simulation structure is depicted in Fig. 2, taken from [3].

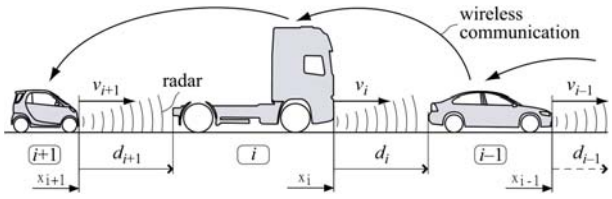

Figure 1: CACC-equipped string of vehicles, adopted from [6]

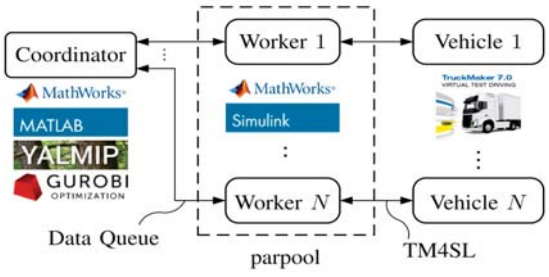

Figure 2: Structure of the co-simulation setup taken from [3]

3 STABILITY PROPERTIES

In general two aspects of stability are considered. First one to be addressed is individual vehicle stability. On one hand, direct evaluation of classical stability exists in linear time-invariant systems, in which one vehicle is linearly modelled as mentioned in Sec. 2.1. In this work absolute and relative stability criteria are used to assess linear dynamics stability.

3.1 Combined criterion of absolute and relative stability

The absolute stability criterion of the Laplace transformed system $G(s)$ is given by

$$\max(\Re(s_j)) < -\alpha, \qquad \forall j = 1, ..., n, \quad \alpha \geq 0, \tag{4}$$

where $\max(\Re(s_j))$ denotes the real part of the slowest pole, α is the value which corresponds to the desired absolute stability (decay rate of envelope) and n is the order of the denominator polynomial of $G(s)$. With (4) fulfilled, any error response in the system decays faster than $\exp(-\alpha t)$. Classical stability corresponds to fulfilling (4) with $\alpha = 0$. Relative stability is fulfilled if all poles at least show damping ratio ζ_{min}, that is, they lie to the left of the rays

$$\mathrm{s} = \omega_n \left(-\zeta_{\min} + j\sqrt{1 - \zeta_{\min}^2} \right) \qquad \omega_n \in \mathbb{R}^+ \cup \{0\} \tag{5}$$

with $\zeta_{\min}$ as the desired damping factor and ω_n as the natural frequency of the oscillation.

If both criteria (4) and (5) are met, the system is considered as stable under the stability requirements α and ζ_{min}.

3.2 String stability criteria

String stability, on the other hand, is one special problem in autonomous platoon control. For example, the fact that adaptive cruise control (ACC) systems as they are implemented in modern autonomous vehicles are stable and robust, does not imply a damping effect on error propagation between vehicles. Such controllers are thus generally not string stable for an autonomous platoon as shown in [4]. There are numerous definitions for string stability as surveyed in [5]. The original verbal definition from [8] reads

Def. *A string of vehicle is stable if, for any set of bounded initial disturbances to all the vehicles, the position fluctuations of all the vehicles remain bounded and these fluctuations approach zeros as* $t \to \infty$

However, to assess string stability mathematically, one common criterion for string stability, taken from [5], is given by the system p-norm

$$\|G_i(s)\|_p \leq \|G_{i-1}(s)\|_p \qquad p = 1, 2, \infty, \tag{6}$$

where $G_i(s)$ is a chosen closed-loop error transfer function in the case of linear platoon dynamics. An empirical formulation based on error signal $\mathcal{L}_p$-norms, also from [5], reads

$$\text{a)} \quad \frac{\|e_i\|_p}{\|e_{i-1}\|_p} \leq 1 \qquad \text{b)} \quad \frac{\|e_i\|_p}{\|e_2\|_p} \leq 1 \qquad i = 3, ..., m \qquad p = 1, 2, \infty, \tag{7}$$

where e_i denotes the spatial error signal, see Sec. 4.1, and m is the number of vehicles in the platoon. Essentially, equation (7, a) requires that the selected error signal norm decays along the platoon. A weaker formulation is formulated by (7, b) which means that the error signal norm is bounded behind the second vehicle.

Note that even in a string stable platoon, collisions can happen if the spatial error exceeds the required distance d_i. Therefore the $\mathcal{L}_\infty$-norm of the spatial error needs to be bounded as

$$\|e_i\|_\infty \leq r + hv_i \qquad i = 2, \ldots, m, \tag{8}$$

to assure string stability and collision avoidance. In turn, the $\mathcal{L}_1$ or $\mathcal{L}_2$-norms are less relevant if they are not strictly decaying along the platoon, however, further investigation is required in this case. Furthermore a performance indicator can be defined for each vehicle by quantifying the ratio of eqn. (7, a). Taking the average ratio across the platoon (9, b) is one possible measure of the performance of the platoon.

$$\text{a)} \quad PI_{p,i}^{string} = \frac{\|e_i\|_p}{\|e_{i-1}\|_p} \qquad \text{a)} \quad PI_{p,avg}^{string} = \frac{1}{m-1}\sum_{i=2}^{m} \frac{\|e_i\|_p}{\|e_{i-1}\|_p}. \tag{9}$$

4 PLATOON CONTROL STRUCTURES

In this work, close attention is paid to the cooperative adaptive cruise controller (CACC) derived in [6] as well as the model predictive controller (MPC) used in [3].

4.1 Cooperative adaptive cruise control (CACC)

Starting from a constant time headway spacing policy the position error is given by

$$e_i(t) = (x_{i-1}(t) - x_i(t) - L_{i-1}) - (r + hv_i(t)) \tag{10}$$

with the time headway h and the desired standstill distance r. The control law is designed for the error dynamics as

$$\dot{u}_i = -\frac{1}{h}u_i + \frac{1}{h}(k_p e_i + k_d \dot{e}_i + k_{dd}\ddot{e}_i) + \frac{1}{h}u_{i-1}, \qquad i = 2, \ldots, m,$$

with the adjustable controller parameters $\mathbf{K} = \begin{bmatrix} k_p & k_d & k_{dd} \end{bmatrix}^T$ and the desired acceleration u_i of vehicle i. Note that the leader vehicle in position $i = 1$ is controlled differently. The block diagram of the controlled system is depicted in Fig. 3 with the controller parameter vector $K(s)$ and the vehicle actuation transfer function $G(s)$

$$K(s) = k_p + k_d s + k_{dd} s^2, \qquad G(s) = \frac{1}{\tau s + 1} \tag{11}$$

4.2 Model predictive controller (MPC)

A more sophisticated controller is given by the distributed platooning MPC with safety guarantees as detailed [3]. In that concept, predicted ego vehicle trajectories are being communicated to the follower in order to inform the follower's predictive control problem. This communication is done event-triggered based on a predefined tolerance which is a key design parameter.

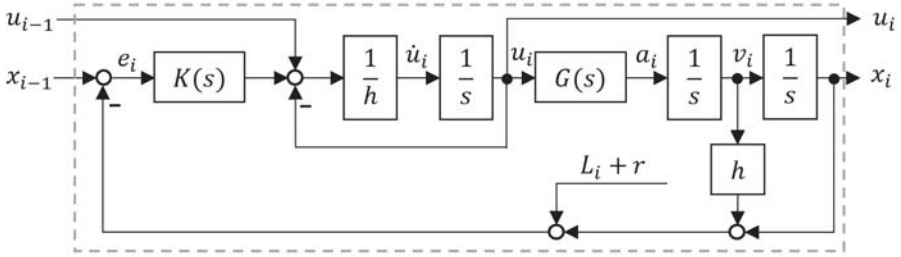

Figure 3: Block diagram of a CACC controlled vehicle adopted from [6].

5 METHODS AND TOOLS

In this section, the developed methods and tools are presented. With the listed mathematical criteria, a platoon can be tested for classical stability as well as string stability.

5.1 Parametrization of the controller

For the CACC control structure of Sec. 4.1, the platoon closed loop dynamics is parametrized via the parameter vector $\mathbf{K}$ given by

$$\mathbf{K} \in \mathcal{K}_p \times \mathcal{K}_d \times \mathcal{K}_{dd} \tag{12}$$

wherein $\mathcal{K}_p = \{k_{p,\min}, \ldots, k_{p,\max}\}$ (with $\mathcal{K}_d$ and $\mathcal{K}_{dd}$ defined analogously) are sets which contain all investigated parameter values. The platoon analyses are carried out on the whole cartesian parameter space. Depending on which values are tested, the parameter vector $\mathbf{K}$ can be defined analogously for any control architecture.

5.2 Stability analysis of individual vehicles

Starting out, a linear model has to be checked if the required classical stability criteria are met. This is achieved by calculating the poles of the resulting discrete system which correspond to the eigenvalues of $\mathbf{A}_d$, see equation (3). As these poles are in the discrete z-domain they are converted back to the continuous time s-domain by $s = \frac{1}{T_s}\ln(z)$, with the sampling time T_s. Absolute and relative stability are then checked with equations (4) and (5). Thus irrelevant parameter combinations are sorted out rapidly.

5.3 Platoon string stability

With knowledge about linear individual vehicle stability, string stability can be assessed via simulation of the platoon with predetermined manoeuvres (see Sec. 5.6). The resulting error signal norms are then used in criteria (7, a or b) to assess string stability. As linear analysis requires only small effort, a large range of parameter combinations can be tested efficiently.

The non-linear co-simulation setup is then used to compare with linear analysis on a subset of the parameter combinations and receive high-fidelity results via the software IPG TruckMaker®.

5.4 Performance indicator

To further investigate non-linear platoon behaviour a performance indicator (PI) is evaluated via eqn. (9), which is the averaged quantification of the error decay along vehicles $2, \ldots, m$ along the platoon.

Note: Although these methods are described with the CACC architecture, they can readily be used for other control architectures (such as the distributed MPC from [3]) as well.

5.5 Implementation of analysis methods and tools

The developed set of methods and tools have been implemented in MATLAB as described in the following section. First, the goal is to obtain knowledge of relevant parameter ranges in which basic individual vehicle stability is present. Then, string stability has to be assessed only if each individual vehicle is stable. The second part is responsible to test one specific combination of parameters with either the linear or non-linear dynamics (TruckMaker co-simulation). To run the second part for all relevant configurations from part 1, the third code part is developed. Finally the simulation results are assessed for performance properties. A summarized overview is given in Fig. 4.

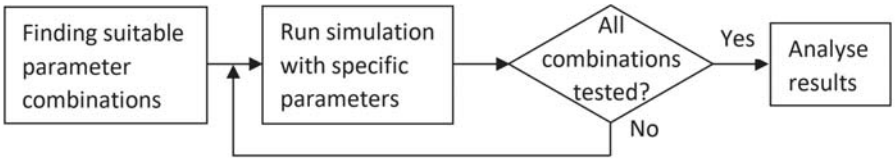

Figure 4: Flow-chart of the algorithm

5.6 Platoon simulation

Starting out, a suitable value for the time constant τ, used in the linear model, has to be set. By simulating an acceleration step of $a = 0.2\,\mathrm{m/s^2}$ starting from $v = 50\,\mathrm{km/h}$, a time constant of $\tau = 0.3\,\mathrm{s}$ is chosen as an appropriate approximation the drivetrain dynamics by comparing against the detailed TruckMaker co-simulation.

It shows that the linear model can produce too large control signals which is not directly comparable to the non-linear situation, where the maximum acceleration is significantly limited by the power of the vehicle's engine. Thus, for the linear simulation, maximum acceleration bounds $a_{\max}(v)$ are implemented as a lookup table, clipping acceleration and deceleration with respect to the current velocity v. The used data for the clipping bounds are typical values of realistic HDVs.

To efficiently obtain the desired information, three different test manoeuvres are implemented. First, an acceleration step response is tested for one individual vehicle, which allows to estimate the time constant τ used in the linear model. The second manoeuvre is set up to assess string stability. The platoon is required to drive at a constant velocity while at time t_M the leader performs a short sudden braking action followed by acceleration to the desired velocity again. This allows to examine error propagation empirically. Finally, a velocity reference step is investigated to further understand the behaviour of the platoon.

As all relevant parameter combinations need to be tested, a result matrix $\mathcal{M}^{string}(PI^{string}_{p,i})$ is defined to store the results with parametrization $\mathbf{K}$ as mentioned in section 5.1. To keep the result memory requirements small, only the number of decaying p-norms is stored.

In this study, 3 different error signal p-norms ($\|\cdot\|_1,\ \|\cdot\|_2,\ \|\cdot\|_\infty$) are evaluated. These are then normalized by the value of the second vehicle. Thus an direct evaluation of string stability can be done as given by equation (7, left).

6 RESULTS

As mentioned above, special attention is given to the selected CACC and MPC architectures. Results obtained via the above derived methods and tools are presented in this section.

6.1 Cooperative adaptive cruise control

Three parameters are tested for the CACC architecture as mentioned in Sec. 5.1. The comparison of string stable and string unstable behaviour is depicted in Fig. 5. 2D-slices of the resulting matrix $\mathcal{M}^{string}$ are depicted in Fig. 6. Although the majority of the linear system configurations meet the stability requirements, only a few parameter configurations of the non-linear system lead to all three error signal norms decaying.The performance indicator shows decaying $\mathcal{L}_\infty$ error norms for a string stable system as depicted in Fig. 7.

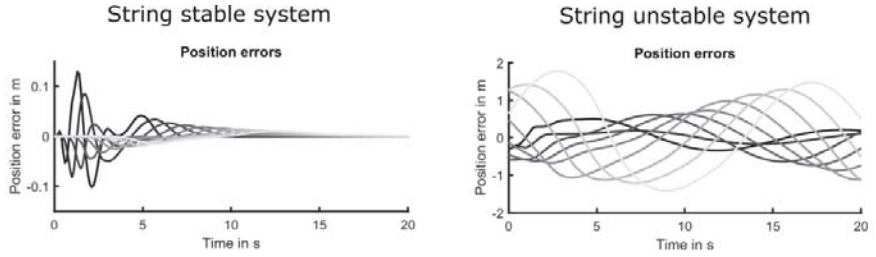

Figure 5: Example of a string stable and a string unstable parameter configuration. Starting from the second vehicle in black, following vehicles getting brighter in colour.

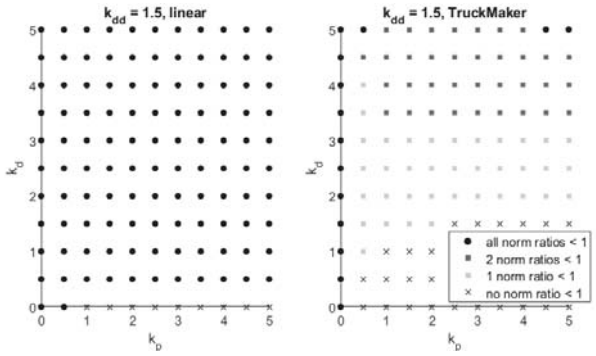

Figure 6: String stability map for parametrization $\mathbf{K}$ with linear simulation results left and non-linear co-simulation results right.

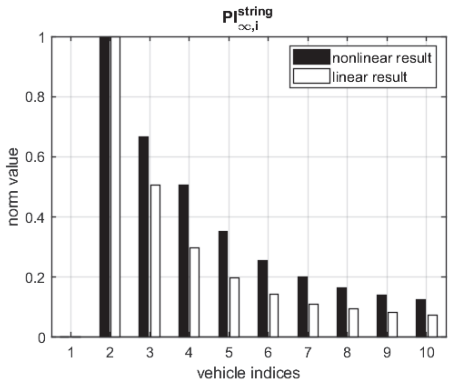

Figure 7: $PI_{\infty,i}^{string}$ (eqn. (9)) resulting from CACC parameters: $k_p = 5$, $k_d = 5$ and $k_{dd} = 1.5$.

6.2 Model predictive control

For the MPC architecture the varied parameters are the corridor width r (defining the event trigger tolerance to send predictive information along the platoon) and the tolerance time samples n_{tol} (affecting control robustness) (see [3] for details). The chosen manoeuvre consists of a platoon of 10 vehicles driving at a speed of $v = 50\,\mathrm{km/h}$ which approach a slower car driving at $v = 30\,\mathrm{km/h}$. The controlled platoon slows down to avoid a collision. Fig. 8 shows the parameter result map (left) as well as the performance indicator for a string stable system (middle) and a string unstable system (right).

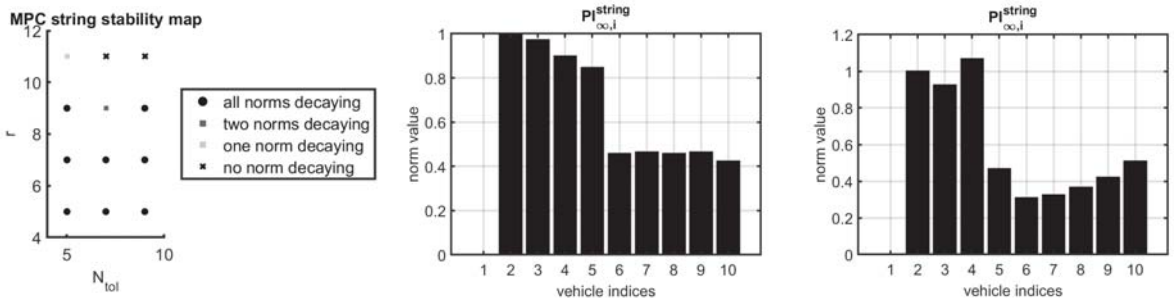

Figure 8: Results from the MPC with the string stability map (left) and $PI_{p,i}^{string}$ for a stable system ($r = 9, N_{tol} = 5$, middle) as well as for an unstable system ($r = 11, N_{tol} = 7$, right) with $p = \infty$

7 CONCLUSIONS

In this work, methods and tools are proposed to efficiently assess and quantify stability and performance aspects of semi-autonomous vehicular platoons. These allow to compare results from linear investigations with results gained from a high-fidelity co-simulation, here based on detail simulations with the commercial software IPG TruckMaker®. A short overview of investigated aspects is given in Table 1. These proposed tools can directly be applied to assess the performance of other control architectures.

Evaluated Aspect	CACC	MPC
Individual stability	✓	
Linear string stability	✓	
Non-linear string stability	✓	✓
Performance	✓	✓

Table 1: Overview of investigated aspects of CACC and MPC architectures.

ACKNOWLEDGMENTS

This work has been supported by the Austrian Lead Project Connecting Austria (FFG grant no. 865122).

REFERENCES

[1] J. Lioris, R. Pedarsani, F. Y. Tascikaraoglu, and P. Varaiya, "Platoons of connected vehicles can double throughput in urban roads," 2017. [Online]. Available: http://arxiv.org/abs/1511.00775

[2] D. R. Lopes and S. A. Evangelou, "Energy savings from an Eco-Cooperative Adaptive Cruise Control: A BEV platoon investigation," in *2019 18th European Control Conference (ECC)*. IEEE, 2019, pp. 4160–4167.

[3] S. Thormann, A. Schirrer, and S. Jakubek, "Safe and Efficient Cooperative Platooning," *IEEE Transactions on Intelligent Transportation Systems*, 2020, accepted for publication.

[4] G. Gunter, D. Gloudemans, R. E. Stern, S. McQuade, R. Bhadani, M. Bunting, M. L. D. Monache, R. Lysecky, B. Seibold, J. Sprinkle, B. Piccoli, and D. B. Work, "Are commercially implemented adaptive cruise control systems string stable?" 2019. [Online]. Available: http://arxiv.org/abs/1905.02108

[5] S. Feng, Y. Zhang, S. E. Li, Z. Cao, H. X. Liu, and L. Li, "String stability for vehicular platoon control: Definitions and analysis methods," 2019.

[6] J. Ploeg, B. T. M. Scheepers, E. van Nunen, N. van de Wouw, and H. Nijmeijer, "Design and experimental evaluation of cooperative adaptive cruise control," in *2011 14th International IEEE Conference on Intelligent Transportation Systems (ITSC)*, 2011, pp. 260–265.

[7] "IPG automotive website," accessed on 28.11.2019. [Online]. Available: https://ipg-automotive.com/de/

[8] K.-c. Chu, "Decentralized control of high-speed vehicular strings," vol. 8, no. 4, pp. 361–384, 1974.

EURODYN 2020
XI International Conference on Structural Dynamics
M. Papadrakakis, M. Fragiadakis, C. Papadimitriou (eds.)
Athens, Greece, 23–26 November 2020

ANALYSIS OF AUTOMOBILE BRAKE CREEP GROAN VIBRATIONS: TEST RIG EXPERIMENTS IN COMPARISON TO FINITE ELEMENT SIMULATIONS

Manuel Pürscher[1], **Severin Huemer-Kals**[1] **and Peter Fischer**[1]

[1] Institute of Automotive Engineering
Graz University of Technology
Inffeldgasse 11/2, 8010 Graz, Austria
e-mail: m.puerscher@tugraz.at

Keywords: Creep groan, Disk brake, Test rig, Transient simulation, Vibration analysis

Abstract. *Vibro-acoustic brake emissions impair a vehicle's comfort and quality. In this context, self-excited brake creep groan phenomena gain in relevance. The non-linear low-frequency vibrations of creep groan potentially appear during an overlap of moderate brake pressures with slow velocities near standstill. Electrified cars with semi-autonomous driving functionalities are especially prone. To treat creep groan already at early stages of the brake development process, reliable investigation and evaluation methods must be available. On that account, this paper deals with test rig experiments and equivalent transient simulations. Both approaches are considered at vehicle corner level which involves axle and suspension components, brake assembly and wheel of one front side of a passenger car. The observed creep groan phenomena have fundamental stick-slip intervals at approximately 90 or 20 Hz. To analyse measured and/or computed time series data in a deterministic way, different rating criteria are specified. These relate to physically reasonable, purely synthetic or statistical metrics. Thereby obtained abstract number values allow the identification, categorisation and validation of brake creep groan vibrations in experiment and/or simulation.*

1 INTRODUCTION

1.1 Vibro-acoustic brake emissions

Noise, vibration and harshness (NVH) phenomena of technical products have a long-term relevance, see trend curves in Figure 1. As discussed by Barden [1], haptical characteristics and audible properties evolve into the most important subconscious criteria after a few month after purchase.

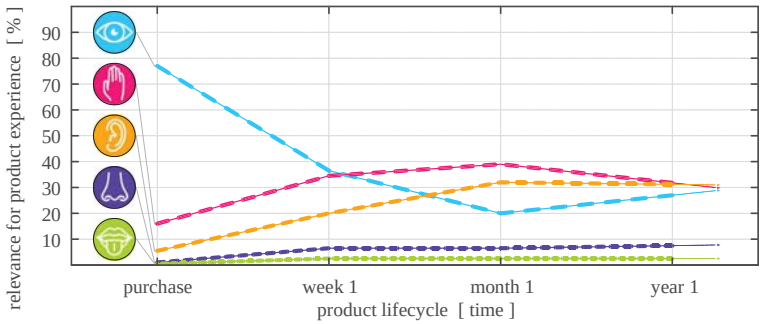

Figure 1: Product experience over time, adapted from [1].

Vibro-acoustic phenomena are critical in automotive fields. Abendroth et al. [2] discussed this issue with respect to friction brake systems. Haptical and audible brake NVH problems impair a vehicle's comfort and quality. Moreover, vibro-acoustic brake emissions pretend a brake system malfunction.

North American market studies from 2011 [3] and 2014 [4] indicated brake NVH phenomena as a top-three complaint reason about passenger cars newer than six months and as a top-five complaint reason about passenger cars newer than three years. A survey from 2017 [5] revealed vibro-acoustic brake emissions as major inconvenience for roughly 2 % of Japanese customers.

Warranty claims against the manufacturers are caused by multiple possible brake NVH problems, see terminology in Figure 2 and remarks in [6].

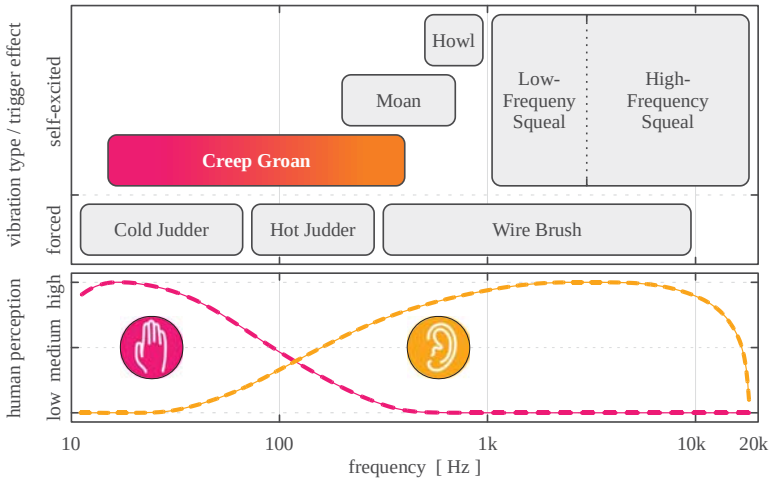

Figure 2: Typical classification and human perception of disk brake NVH phenomena.

1.2 Brake creep groan

According to literature [7 - 21] and the authors' works [22 - 26], disk brake creep groan can be described as follows:

Creep groan refers to periodic non-linear brake and chassis vibrations which are relevant in a low-frequency range from approximately 15 to 400 Hz.

Creep groan phenomena mainly occur at brake pressures below 30 bar in conjunction with vehicle velocities below 0.3 km/h.

It occurs if drive torque and brake torque are at similar levels. The friction contacts between linings and disk potentially have two alternating tribological states, namely stick or slip. The macroscopic stick causes a system pretension with large elastic deflections. The macroscopic slip leads to a relaxation of the system. Alternating stick-slip is enabled by different coefficients of static and dynamic friction. Depending on the situation, self-excited stick-slip persists up to some seconds.

Each abrupt transition from stick to slip excites resonances of the auxiliary vehicle corner components. These inherent oscillations significantly contribute to the impulsive non-linear vibrations.

Creep groan mainly appears for cars with automated gearboxes or electrified automobiles if the service brake is released for a slow move-off. Creep groan also appears for vehicles with any powertrain architecture if the service brake is released for a slow roll-off at inclines or if the service brake is activated during steering at standstill. Moreover, semi-autonomous driving functionalities such as remote-controlled-parking often lead to creep groan, see Figure 3.

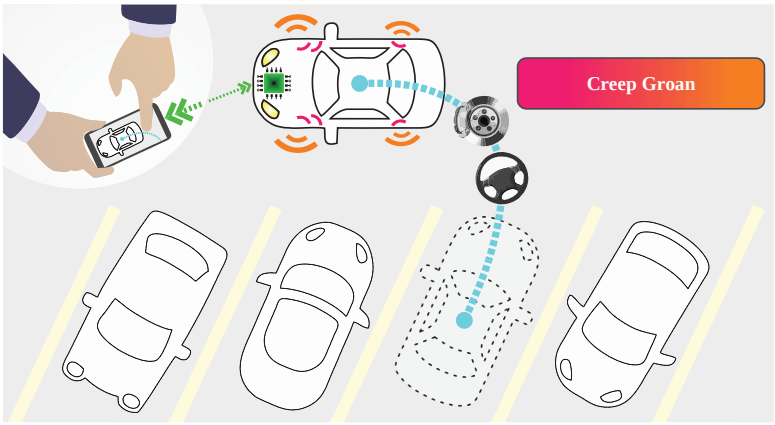

Figure 3: Remote-controlled-parking with creep groan during slow move-off or during steering at standstill.

To avoid further expensive warranty claims against the manufacturers, creep groan robust brake systems must be designed based on improved brake NVH development processes. As outlined by Abendroth et al. [2] and Abdelhamid [6], the manufacturers require more standardised investigation methods as well as more homogenous data analysis techniques.

1.3 Existing investigation (data generation) methods for brake creep groan

Early industrial publications, e.g. the work of Schwartz et al. [7], rather focussed on basic road tests. Papers of the 1990s, e.g. [8 - 10], comprised more detailed full vehicle measurements and/or simple dynamometer test bench investigations. These studies also included a 1-d rigid body model [8] and a 2-d finite element (FE) model [9]. Then, a 3-d multi-body system (MBS) model [11] and a sophisticated lumped torsional model [12] of the vehicle driveline were presented.

More recent publications from industry and academia often involve road tests, test rig experiments at different subsystem levels and/or friction pair benchmarks, e.g. [13 - 21]. Simulative investigations of diversified complexity can also be found, compare with [15, 16, 20, 21].

Several previous works of the authors have dealt with subsystem test procedures and equivalent simulative methods. An experimental creep groan screening approach is discussed in [22]. It is performed on a drum driven suspension and brake test rig. A transient simulation strategy for the computation of creep groan vibrations is discussed in [24, 26]. It relates to a 3-d corner FE model.

In current brake NVH development processes, full vehicle road tests such as the recommendation VDA 314 [27] are state-of-the-art. No creep groan experiments at component level are performed by the manufacturers. No approach for a reliable simulative prediction of creep groan is established.

1.4 Remarks on established data evaluation techniques for brake squeal

To evaluate brake squeal at component level, experimental and simulative techniques are widely applied in current brake NVH development processes.

On the experimental side, one can find the recommendation SAE J2521 APR2013 [28], see discussion in [2, 6]. This established dynamometer test matrix procedure involves more than thousand operational parameter combinations. A spectral algorithm analyses the A-weighted sound pressure level (SPL). If a certain deciBel (dB) threshold is exceeded within two given frequency limits, any acoustic event is quantitatively rated as squeal noise. All measurements can be cumulated to one objective noise index (ONI) according to directives of an acceptance chart. This chart has adaptable rating scales, e.g. values from 1 to 9 with 1 as worst case. The ONI correlates with the subjective human perception.

On the simulative side, one can find the complex eigenvalue analysis (CEA), see mathematical description in [23]. This established quasi-static linear FE approach calculates the natural mid- to high-frequency oscillation behaviour of the operated brake system. The complex eigenvalues calculated by the CEA are analysed. Negatively damped eigenmodes appear if the real parts of the complex eigenvalues have positive signs. This case refers to dynamically unstable modal coupling and squeal noise respectively.

1.5 Existing data evaluation techniques for brake creep groan

The full vehicle road test procedure VDA 314 [27] consists of separated creep groan test sessions. Subjective annoyance ratings from 1 to 10 are determined by the test driver. Averaged and maximum A-weighted SPL of at least one cabin microphone are documented as well. Accelerometers at each brake calliper are optional. Exemplary raw data is shown in Figure 4.

The measured sound pressure next to the driver’s ear is an incoherent superposition of 85 Hz creep groan at both front brakes of the tested car. However, there is also significant background noise from the internal combustion engine of the passenger car.

In general, sound pressure analyses are more challenging for creep groan than for squeal due to reasons such as reduced low-frequency microphone sensitivity and harsh noise composition of creep groan including super-harmonics. Bader [13] applied a discrete wavelet transformation including its inverse equivalent. His method relates to the kurtosis which describes the fourth moment of the signal. It is increased during creep groan. Abdelhamid and Bray [14] used a signal whitening filter to improve the results. Moreover, they applied tonality and loudness to obtain psycho-acoustic evaluations. Augsburg et al. [19] calculated the radiated sound power based on microphone data, but the outcome of this method was not discussed.

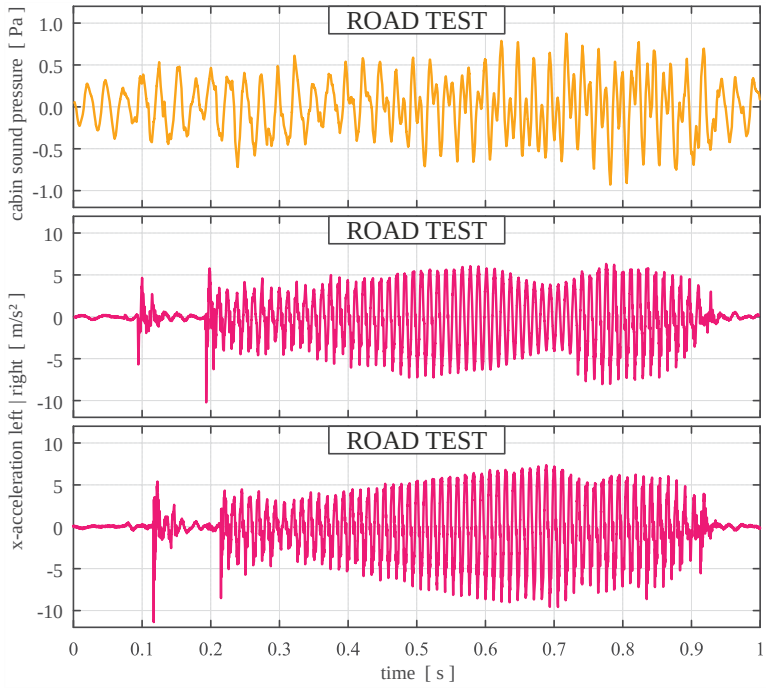

Figure 4: Cabin microphone signal and both front brake calliper x-acceleration signals of exemplary 85 Hz creep groan during road tests.

In general, acceleration analyses regarding creep groan are challenging as well. To detect creep groan, Crowther and Singh [12] examined time domain metrics such as duration of creep groan, dynamic acceleration range and two different quadratic sum definitions. Neis et al. [17] used a root mean square (RMS) expression akin to these quadratic sums. A similar method was presented by Augsburg et al. [19]. This group calculated an averaged overall vibration emission by the RMS in the frequency domain. Rösner and Özdil [18] applied modulation principles, e.g. a low-pass filter or a peak hold algorithm. They found correlations between cumulative energy as well as time domain peak hold areas with purely subjective ratings. Zhao et al. [21] used the acceleration's kurtosis to detect creep groan.

The authors elaborated two techniques to analyse and classify creep groan based on acceleration signals, see [22, 25]. A spectral algorithm is described in [22]. If an adjustable dB threshold is exceeded by several equidistant peaks within two adaptable frequency limits, any brake NVH event is quantitatively rated as creep groan. Moreover, the fundamental stick-slip frequency is identified by logical inquiries. An artificial neural network (ANN) framework is treated in [25]. It rests on millions of emulated acceleration spectra. Inputs and outputs during training of the ANN framework were created according to the spectral algorithm's logic. Based on both techniques, the systematic test matrix measurements lead to a creep groan map (CGM) and a cumulated creep groan index (CGI), see [22]. The CGI indicates excellent to poor creep groan performance with values from 0 to 1000. Certainly, these analyses can be applied to simulative data alike.

Transient simulation offers great potentials to gain deeper insight to the mechanisms of creep groan vibrations. To evaluate simulative data, time series of disk to linings relative motions are often used, compare with [11, 20, 23, 24, 26]. System energy quantities, e.g. dissipative energy [11, 20], or friction contacts associated quantities, e.g. local coefficient of friction [9, 20], are also suitable to evaluate creep groan vibrations.

1.6 Outline of this paper

Firstly, experiments and simulations at vehicle corner level are discussed. Then, comparison metrics are introduced. These are used for the identification, categorisation and validation of typical brake creep groan vibrations. Lastly, conclusions are drawn.

2 TEST RIG EXPERIMENTS

A vehicle corner including its wheel is according to Augsburg et al. [19] a suitable subsystem to perform creep groan experiments. In terms of complexity, corner test rigs are situated in between inertia type brake dynamometers and roller type chassis dynamometers, see differentiations in [2, 18].

The authors have access to a drum driven suspension and brake test rig. It is placed in an air-conditioned chamber. A hydraulically adjusted loading unit maintains a defined in-situ height of the test setup to guarantee the correct vertical pretension of axle and suspension components. The wheel is driven against a brake torque exclusively by the drum. Therefore, brake pressure and drum velocity are under control. Further information on the corner test rig is provided in [22 - 26].

The relevant test setup is a MacPherson suspension strut assembly of the left front side including its 17” wheel. It has a front-mounted single-piston floating calliper brake system. The friction couple consists of a ventilated 330 mm cast iron monobloc disk and pad linings which are designed for the European market. This test setup, which has a mass of roughly 55 kg, is mounted to the test rig’s attachment plate, see photograph in Figure 5.

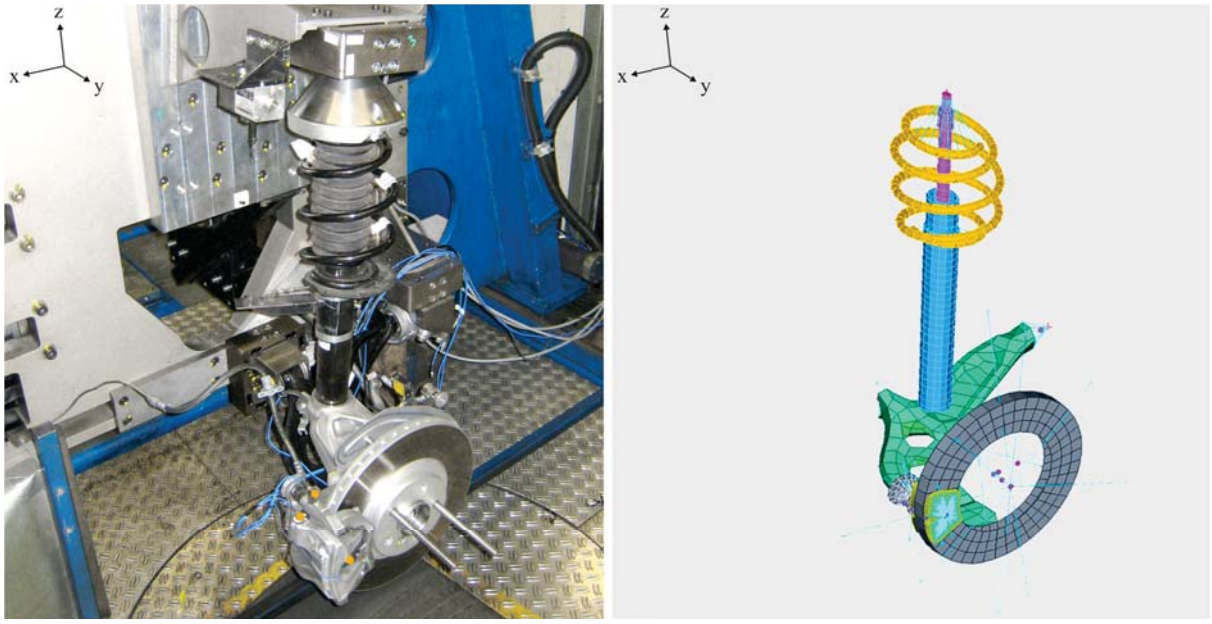

Figure 5: Left: Drum driven corner test rig including lifted MacPherson setup (wheel removed) with front-mounted floating calliper brake system. Right: Pre-processor representation of corner FE model (wheel included) at in-situ height.

The installed sensor equipment is listed in Table 1. Signals were sampled at 10 kHz. In particular, two axis directions from the triaxial accelerometer at the calliper anchor as well as the y-force from the load cell behind the hydro bushing are relevant in this paper.

subject	component; location	sensor type
acceleration	floating calliper; top middle	triaxial accelerometer ‘PCB 356A01-HT’
-‖-	calliper anchor; top middle	triaxial accelerometer ‘PCB 356A02’
-‖-	outer pad; backing plate centre	triaxial accelerometer ‘PCB 356A01-HT’
-‖-	knuckle with hub; rear centre	triaxial accelerometer ‘PCB 356A02’
force	control arm; hydro bushing	triaxial load cell ‘ME K3D160-20kN’
-‖-	control arm; rubber bushing	triaxial load cell ‘ME K3D160-20kN’
-‖-	suspension strut; top support	triaxial load cell ‘ME K3D160-50kN’
rotation	wheel; rim well middle	rotational encoder ‘SCANCON SCA24-5000’ with rubber ring pulley
temperature	disk; inner friction surface	sliding K-thermocouple ‘THERMA MST-20347’

Table 1: Sensor equipment in corner test rig experiments.

Systematic test matrix measurements were carried out for brake pressures from 4 to 40 bar and drum velocities from 0.04 to 0.40 km/h. A cooling airstream stabilised the friction pair temperature between 20 and 35°C.

The analysis of calliper acceleration signals leads to a CGM, see Figure 6. Regions with creep groan are clearly separated from rather uncritical vibration-free sections. Large coloured circles indicate creep groan as well as its fundamental stick-slip frequency. Note that regions with multiple possible creep groan phenomena can be identified, e.g. for 15 bar at 0.14 km/h. Basic explanations on these vibration bifurcations are provided in [21].

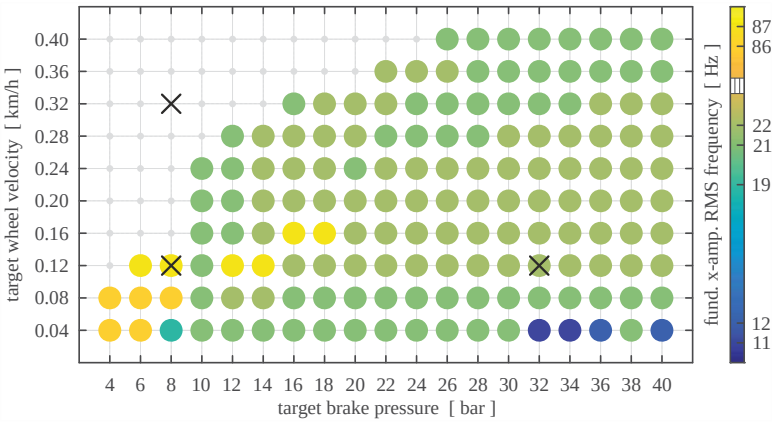

Figure 6: Exemplary CGM of fundamental creep groan frequencies.

Three representative experimental examples, which are marked with a cross in Figure 6, are chosen to apply different comparison metrics:

- **no creep groan for 8 bar at 0.32 km/h**
- **87 Hz creep groan for 8 bar at 0.12 km/h**
- **22 Hz creep groan for 32 bar at 0.12 km/h**

3 FE SIMULATIONS

A 3-d FE model was presented in [24]. It was used in [26] as well. An improved version of this initial 3-d FE model is relevant here. The improvements relate to the contact stiffness definition, the suspension strut discretisation, the coordinate system alignment and the system's velocity excitation as well as its longitudinal pretension. A pre-processor snapshot of this improved corner FE model is shown in Figure 5. Vehicle corner parts and FE model implementations are listed in Table 2. An overview of topology, elements, constraints as well as other descriptive subjects is given in Table 4 (Appendix).

vehicle corner part	FE model implementation
tyre 17"	linear spring-damper elements + point inertia
5-spoke rim	kinematic couplings + point inertia
monobloc disk	rigid shells + point inertia
pad lining	solid continuum elements
pad backing plate	kinematic couplings + point inertia
hydraulic piston	rigid shells + kinematic couplings + point inertia
floating calliper	rigid shells + kinematic couplings + point inertia
calliper anchor	kinematic couplings + point inertia
knuckle with hub	kinematic couplings + point inertia
control arm	shell continuum elements
track rod	rigid elements + point inertia
hydro bushing (y)	non-linear spring-damper element
other bushings (xyz)	linear spring-damper elements
strut damper tube	Timoshenko beams
strut damper rod	Timoshenko beams
strut coil spring	Timoshenko beams

Table 2: MacPherson setup with floating calliper brake system versus FE model.

The corner FE model has a mass of almost 53 kg. It involves 3438 nodes and 2449 elements which have a minimum length of 1.50 mm. Each lining consists of 792 first-order solid elements which have an averaged length of 4.39 mm. The disk is considered by rigid shells. The two structural components of the floating calliper subsystem are simplified by lumped masses in kinematic relations. More attention was paid to the suspension strut assembly including coil spring because this subsystem strongly participates in the non-linear vibration patterns during creep groan. Rubber bushings and hydro bushings also strongly contribute to quasi-static displacements and dynamic deflections of the vehicle corner, see [24, 26].

Four boundary nodes provide fixed positions similar to the attachment points at the corner test rig. Since the FE model is positioned at in-situ height, no loading according to the car's mass is applied. Longitudinal and rotational pretension of the axle and suspension components is achieved by imposing brake pressure as well as ground velocity. Further information on the application of both operational parameters is provided in [24, 26].

The exponential expression according to Equation 1 is relevant for the tangential friction interaction of disk to linings, compare with [15, 16, 20]. The specific coefficient of friction μ at any lining node depends on the local relative speed $\dot{c}_r$. Two exemplary curves were defined, see [24, 26]. The coefficient of static friction μ_s was set to 0.5 respectively. The coefficient of dynamic friction μ_k was set to 0.45 for 8 bar and it was set to 0.42 for 32 bar. The decay factor d_c was set to 0.1609 for 8 bar and it was set to 0.0208 for 32 bar.

$$\mu = \mu_k + (\mu_s - \mu_k) e^{-d_c \dot{c}_r} \tag{1}$$

ABAQUS was used for transient FE simulations. Two solution schemes of direct time integration were considered, namely explicit and implicit. Initial and minimum time increment of the implicit algorithm were manually set to 1e-3 and 1e-12 s. Based on the FE model's properties, e.g. size, density and stiffness of each element, the stable time increment for the explicit scheme was automatically set to 3.612e-7 s. Computations were performed on four cores of a 2 GHz processor with access to 96 GByte main memory.

The result correlation of both solution schemes appeared quite well, but the calculation effort was clearly different. In case of macroscopic stick-slip, the ratio between computation time and simulation time was at least 58e3 for the best-performing implicit scheme, but it was always roughly 19e3 for the explicit algorithm. These ratios are valid for 2 s simulation time and output data sampled at 10 kHz. Results calculated by the explicit scheme are presented in this paper.

In analogy to the three representative experimental examples, comparable simulative examples are chosen to apply different comparison metrics:

- **no creep groan for 8 bar at 0.32 km/h**
- **89 Hz creep groan for 8 bar at 0.12 km/h**
- **23 Hz creep groan for 32 bar at 0.12 km/h**

4 DEFINITION OF COMPARISON METRICS

4.1 Spectral contents - various signals

The overall RMS value y_{RMS} for n values of a digitised field quantity signal y_i reads as Equation 2. This physically reasonable definition reflects the original signal's energy equivalent. The overall dB level $\mathrm{L}_{y_{\mathrm{RMS}}}$ in reference to a predefined or standardised value y_0 reads as Equation 3.

$$y_{\mathrm{RMS}} = \sqrt{\frac{1}{n}\sum_{i=1}^{n}|y_i|^2} \tag{2}$$

$$\mathrm{L}_{y_{\mathrm{RMS}}} = 10\lg\frac{y_{\mathrm{RMS}}^2}{y_0^2} \tag{3}$$

Time series data sampled at 10 kHz is relevant. Frequency spectra are calculated from 1 Hz to 2.5 kHz in a constant 1 Hz interval. Therefore, a Hanning window Fast Fourier Transform (FFT) algorithm is used. It splits any digitised signal into a finite number of sine functions with corresponding frequency, amplitude and phase. If this is done for n values of y_i, a separate $y_{\mathrm{RMS}}(f_j)$ is available for each discrete frequency f_j. The incoherent spectral dB level sum $\mathrm{L}_{y[f_a, f_b]}$, which includes each $y_{\mathrm{RMS}}(f_j)$ within two frequencies $[f_a, f_b]$, is for a constant interval Δf as written in Equation 4. It represents an incoherent superposition of certain spectral components of the original signal. Two identical incoherent summands would achieve a 3 dB increase.

$$\mathrm{L}_{y[f_a, f_b]} = 10\lg\frac{y_{\mathrm{RMS}}^2(f_a) + y_{\mathrm{RMS}}^2(f_a+\Delta f) + \cdots + y_{\mathrm{RMS}}^2(f_b)}{y_0^2} \tag{4}$$

If an energy size signal Y_i is analysed, the overall arithmetic mean value $\mathrm{Y}_{\mathrm{amv}}$ according to Equation 5 is used instead of Equation 2. Nevertheless, it also reflects the original signal's energy equivalent. The overall dB level $\mathrm{L}_{\mathrm{Y}_{\mathrm{amv}}}$ in reference to Y_0 reads as Equation 6.

$$\mathrm{Y_{amv}} = \frac{1}{n}\sum_{i=1}^{n} Y_i \tag{5}$$

$$\mathrm{L_{Y_{amv}}} = 10\lg\frac{\mathrm{Y_{amv}}}{Y_0} \tag{6}$$

After the Hanning window FFT is performed, the spectral dB level sum $\mathbf{L_{Y[f_a, f_b]}}$ includes each relevant $\mathbf{Y_{amv}}(f_j)$. It is calculated according to Equation 7. Again, a superposition of two equally valued spectral summands would achieve a 3 dB increase.

$$\mathrm{L_{Y[f_a, f_b]}} = 10\lg\frac{\mathrm{Y_{amv}}(f_a) + \mathrm{Y_{amv}}(f_a + \Delta f) + \cdots + \mathrm{Y_{amv}}(f_b)}{Y_0} \tag{7}$$

4.2 Orbital indices - motion signals

In the following, the estimation of the border area $\mathbf{A_{P_v|Q_h}}$ of an exemplary 2-d orbit face is explained, see Figure 7. This synthetic metric is shaped by two digitised signals which are denoted as P_v and Q_h here. The signals' subscripts indicate vertical and horizontal axis assignments. To estimate $\mathbf{A_{P_v|Q_h}}$, two synchronous calculation threads are executed.

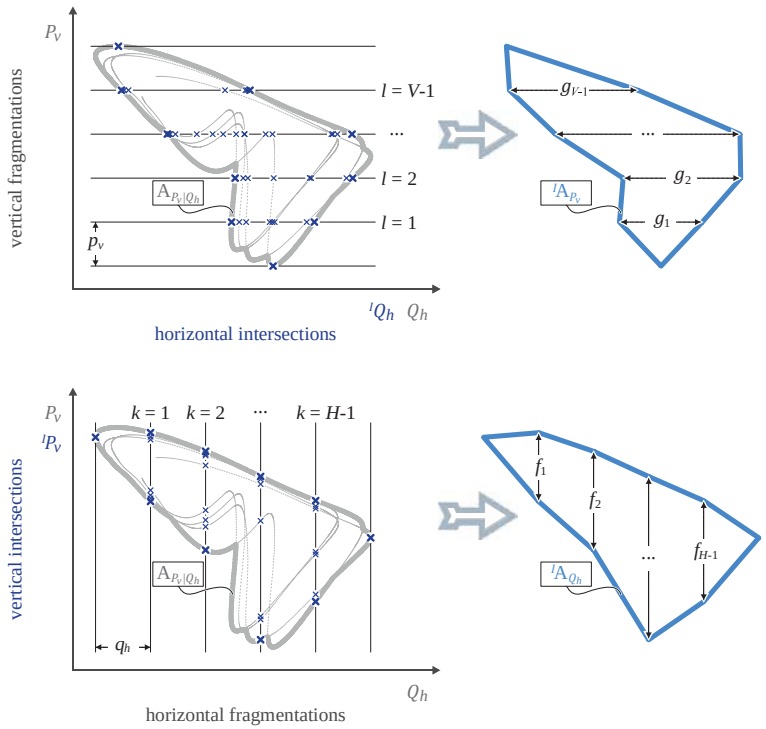

Figure 7: Synchronous calculation threads for the border area of an exemplary 2-d orbit face.

Firstly, a number of V equidistant fragments of height p_v and a number of H equidistant fragments of width q_h are used to discretise the 2-d orbit face. Height p_v and width q_h are defined by Equation 8 and Equation 9 with respect to 50 equidistant fragments respectively.

$$p_v = \frac{\max(P_v) - \min(P_v)}{V} \tag{8}$$

$$q_h = \frac{\max(Q_h) - \min(Q_h)}{H} \tag{9}$$

Secondly, P_v and Q_h are replaced by coarser signal equivalents ${}^{I}P_v$ and ${}^{I}Q_h$ which have data points exclusively at grid line intersections. Local vertical and horizontal spreadings f_k and g_l at each grid line are obtained by Equation 10 and Equation 11.

$$f_k = \max\left({}^{I}P_{v_k}\right) - \min\left({}^{I}P_{v_k}\right) \quad \text{for } k = 1, \cdots, H-1 \tag{10}$$

$$g_l = \max\left({}^{I}Q_{h_l}\right) - \min\left({}^{I}Q_{h_l}\right) \quad \text{for } l = 1, \cdots, V-1 \tag{11}$$

Thirdly, two border areas ${}^{I}\mathbf{A}_{P_v}$ and ${}^{I}\mathbf{A}_{Q_h}$ of the 2-d orbit face are calculated. Triangles at the outer fragments lead to simplified trapezoidal formulas as written in Equation 12 and Equation 13.

$${}^{I}\mathrm{A}_{P_v} = q_h \sum_{k=1}^{H-1} f_k \tag{12}$$

$${}^{I}\mathrm{A}_{Q_h} = p_v \sum_{l=1}^{V-1} g_l \tag{13}$$

Lastly, Equation 14 is applied to estimate $\mathbf{A}_{P_v|Q_h}$ of the exemplary 2-d orbit face, see Figure 7.

$$\mathrm{A}_{P_v|Q_h} \approx \frac{{}^{I}\mathrm{A}_{P_v} + {}^{I}\mathrm{A}_{Q_h}}{2} \tag{14}$$

4.3 Statistical characteristics - various signals

The arithmetic mean value is calculated according to Equation 5. The range is defined similar to Equation 10 or Equation 11. The sample standard deviation reads as Equation 15.

$$\mathrm{Y}_{\mathrm{std}} = \sqrt{\frac{1}{n-1}\sum_{i=1}^{n}(Y_i - \mathrm{Y}_{\mathrm{amv}})^2} \tag{15}$$

Based on an empirical approach, two additional customised statistical metrics $\mathbf{Y}_{\mathbf{mtr1}}$ and $\mathbf{Y}_{\mathbf{mtr2}}$ are considered. These are defined by Equation 16 and Equation 17.

$$\mathrm{Y}_{\mathrm{mtr1}} = 2 \times \mathrm{Y}_{\mathrm{std}} + \mathrm{Y}_{\mathrm{rng}} \tag{16}$$

$$\mathrm{Y}_{\mathrm{mtr2}} = \frac{2 \times \mathrm{Y}_{\mathrm{std}} + \mathrm{Y}_{\mathrm{rng}}}{\mathrm{Y}_{\mathrm{amv}}} \tag{17}$$

5 DISCUSSION OF RESULTS

5.1 Comparison of spectral contents

- **component acceleration (experiment / simulation)**

Two combined FFT spectra are shown in Figure 8, Figure 9 and Figure 10 respectively. These xz-acceleration spectra relate to the sensor at the calliper anchor or its equivalent mesh node in the corner FE model. To combine x- and z-direction, the incoherent sum is calculated separately for each frequency. This is done based on Equation 4. Spectral contents from 50 to 500 Hz and 5 to 1000 Hz are summed alike.

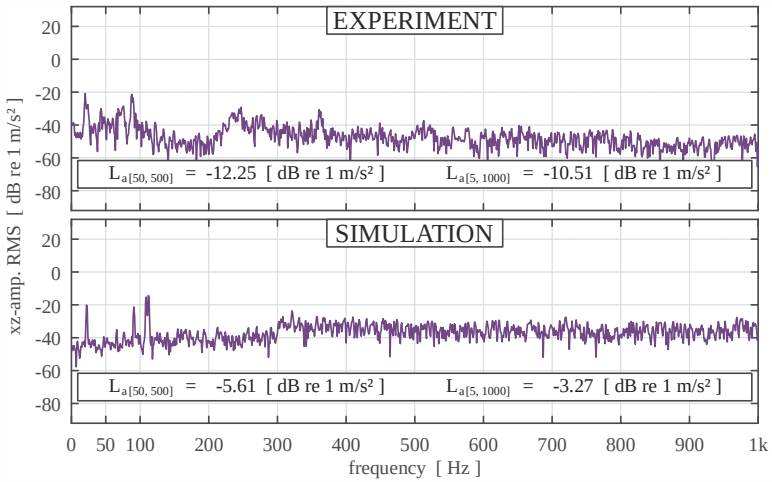

Figure 8: Both no creep groan / summed spectrum of calliper anchor xz-acceleration signals for 1 s.

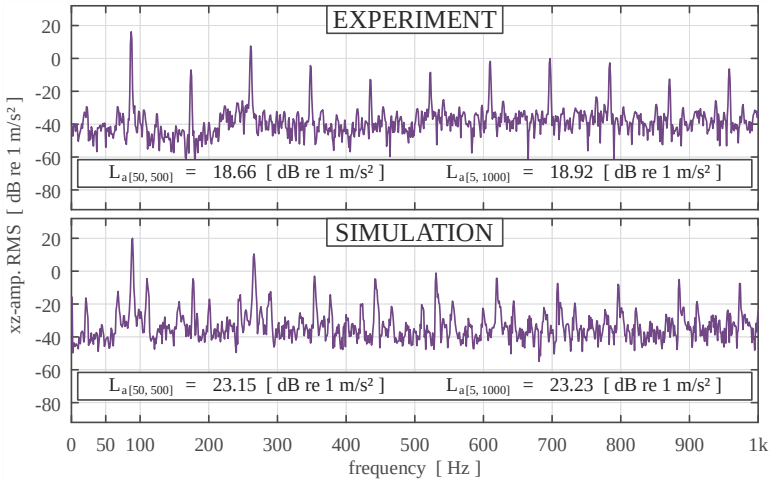

Figure 9: 87|89 Hz creep groan / summed spectrum of calliper anchor xz-acceleration signals for 1 s.

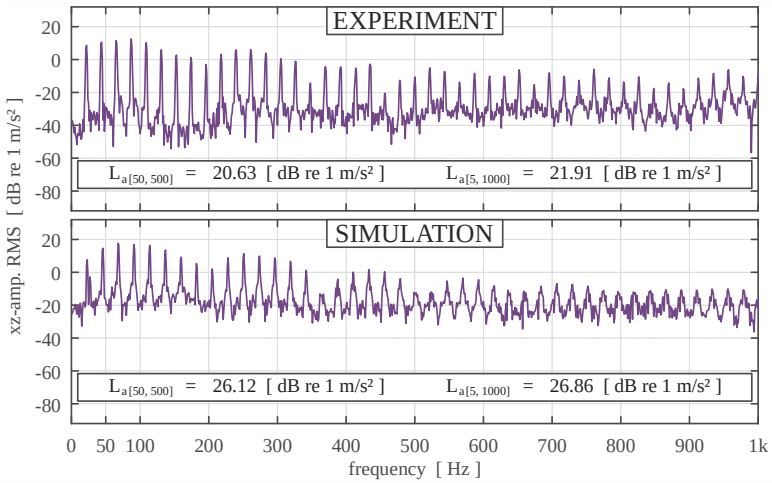

Figure 10: 22|23 Hz creep groan / summed spectrum of calliper anchor xz-acceleration signals for 1 s.

Both xz-acceleration spectra in Figure 8 reflect low and flat broadband vibration characteristics. This is expectable for any almost vibration-free example. All four spectra in Figure 9 and Figure 10 show typical patterns of creep groan vibrations, compare with [7, 10, 11, 12, 17,

19, 20]. The fundamental peak indicates the major stick-slip interval. Its super-harmonics reflect non-linear vibration characteristics.

In case of creep groan, the spectral acceleration dB level sum is approximately 30 dB increased, see Table 5 (Appendix). Hence, this physically reasonable acceleration metric enables a recognition of creep groan vibrations and an assessment of the general low-frequency NVH criticality. However, the differences between the creep groan phenomena with fundamental stick-slip intervals around 90 or 20 Hz are just roughly 3 dB. Thus, a distinction between the two types is uncertain.

- **system energy (simulation)**

Purely simulative results are shown in Figure 11, Figure 12 and Figure 13. These FFT spectra relate to the overall kinetic energy of the corner FE model. Spectral contents from 50 to 500 Hz and 5 to 1000 Hz are calculated based on Equation 7.

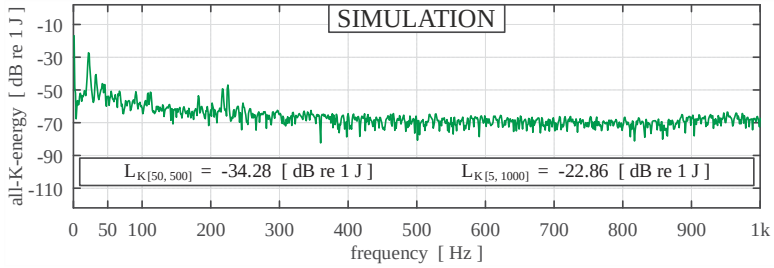

Figure 11: No creep groan / spectrum of computed overall kinetic energy signal for 1 s.

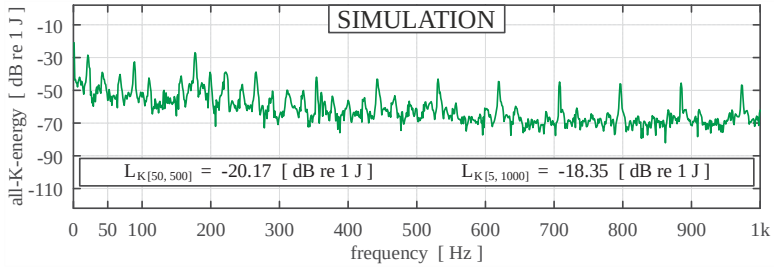

Figure 12: 89 Hz creep groan / spectrum of computed overall kinetic energy signal for 1 s.

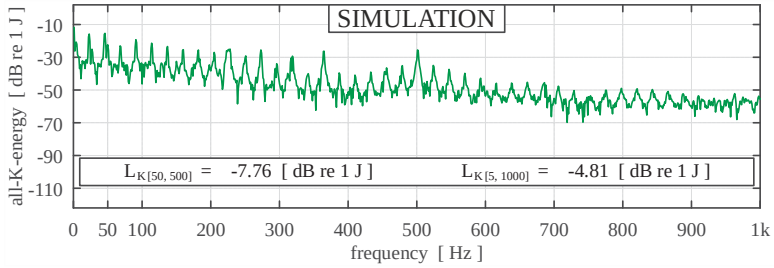

Figure 13: 23 Hz creep groan / spectrum of computed overall kinetic energy signal for 1 s.

These kinetic energy spectra show characteristics akin to the three simulative xz-acceleration spectra, but the amplitudes at higher frequencies are lower due to the velocity dependency of the kinetic energy. Note that a constant rotation of the wheel assembly including disk contributes to the 0 Hz amplitude.

Both energy dB level sums enable a detection of macroscopic stick-slip, see Table 5 (Appendix). In particular, spectral contents from 50 to 500 Hz are suitable for a reliable distinction between the two types. The 23 Hz stick-slip vibration achieves at least a 10 dB higher

spectral dB level sum than the 89 Hz stick-slip vibration. A disadvantage of this physically reasonable energy metric is its purely simulative applicability.

5.2 Comparison of orbital indices

- **time integral of component acceleration (experiment / simulation)**

To estimate velocity and displacement from experimental or simulative acceleration data, a trapezoidal time integral formula is used. Concerning 0.18 s time segments, operating deflection shape (ODS) patterns, 2-d orbit faces and phase portraits are shown in Figure 14, Figure 15 and Figure 16. Border area indices are calculated for x- and z-direction of the sensor at the calliper anchor or its equivalent mesh node in the corner FE model, see Table 5 (Appendix).

Each example contains four quadrants. The brake ODS graph on the bottom right indicates substantial vibration patterns of the floating calliper subsystem including disk, compare with [9, 10]. The graph on the top left shows the clockwise-rotating displacement-displacement orbit face concerning x- and z-direction. A coloured bar indicates the absolute xz-velocity. The graphs on lower left and upper right show clockwise-rotating phase portraits which are shaped by different displacement-velocity combinations.

Figure 14 refers to 8 bar at 0.32 km/h. This combination does not cause creep groan in experiment and simulation. Based on marginal motions and low surface velocities, border areas and orbital indices are very small.

Figure 15 refers to 8 bar at 0.12 km/h. Creep groan appears with a fundamental stick-slip interval around 90 Hz respectively. Thus, both examples show roughly 16 repetitive cycles with comparable signatures. The border areas lead to similar orbital indices of medium size. Distinctive rotational motions of the calliper subsystem about the disk's axis occur with high surface velocities. These vibration patterns are enabled by a first-order bending deflection of the MacPherson suspension strut assembly, see [24, 26]. Maximum surface velocities are reached shortly after a macroscopic transition from stick to slip.

Figure 16 refers to 32 bar at 0.12 km/h. Creep groan appears with a fundamental stick-slip interval around 20 Hz respectively. Thus, both examples show roughly four repetitive cycles. The orbital indices are relatively high. The vibration patterns involve two relevant contributors, see [24, 26]. Firstly, large longitudinal displacements of the wheel assembly including disk. These motions, which relate to the fundamental stick-slip interval, are mainly enabled by elastic deformations of the lower control arm bushings. Secondly, fast rotational deflections of the floating calliper subsystem. These motions, which relate to superposed natural eigenmodes of higher frequency, occur similar in Figure 15. The highest surface velocities appear shortly after a macroscopic transition from stick to slip.

Since the orbital indices depend on the observed vibration patterns, a recognition and distinction of creep groan is possible. Moreover, the general low-frequency NVH criticality can be determined.

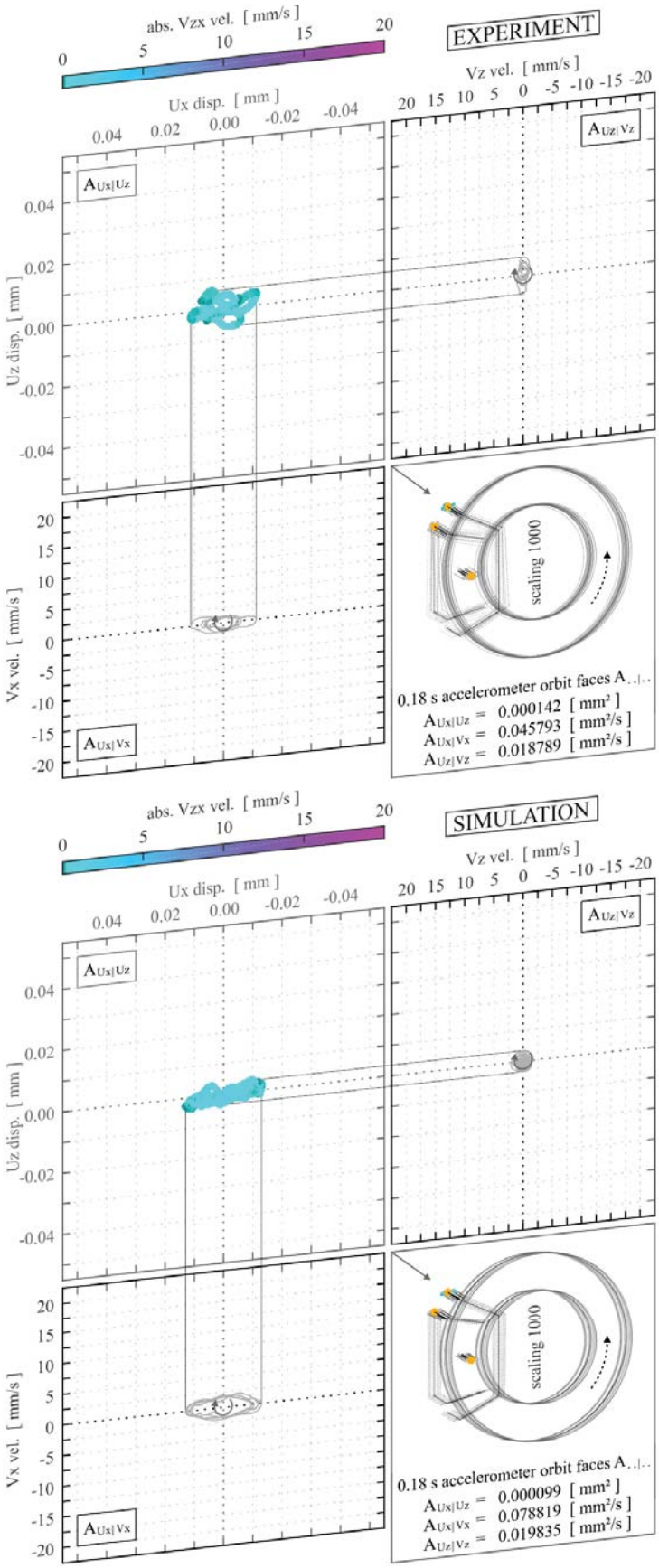

Figure 14: Both no creep groan / disp.-disp. and disp.-vel. patterns of calliper anchor x- and z-acceleration signal time integrals for 0.18 s.

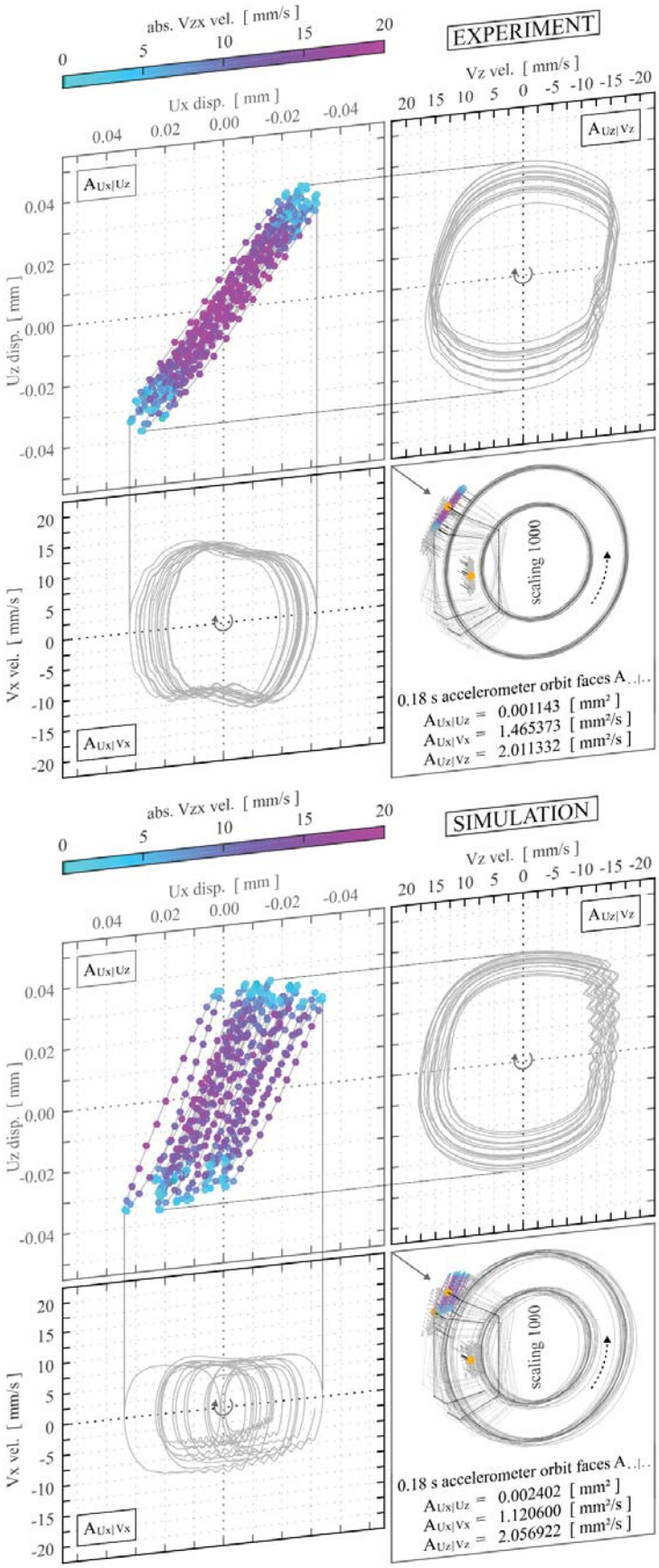

Figure 15: 87|89 Hz creep groan / disp.-disp. and disp.-vel. patterns of calliper anchor x- and z-acceleration signal time integrals for 0.18 s.

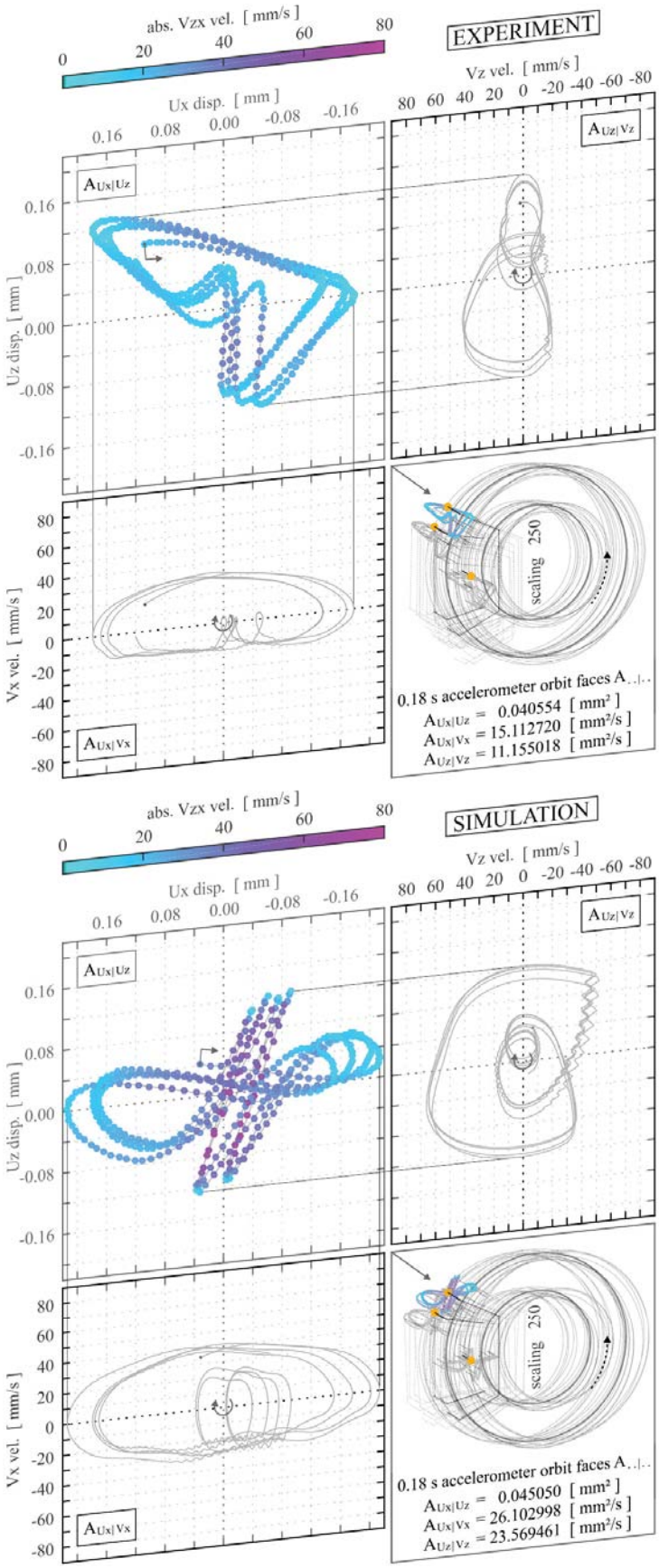

Figure 16: 22|23 Hz creep groan / disp.-disp. and disp.-vel. patterns of calliper anchor x- and z-acceleration signal time integrals for 0.18 s.

5.3 Comparison of statistical characteristics

- **interface force (experiment / simulation)**

Different creep groan phenomena favour different characteristics of the dynamic forces between lower control arm bushings and vehicle body, see [24, 26]. In the following, the y-force at the hydro bushing is analysed. Its quasi-static proportion relates to the system pretension which depends on brake pressure and coefficient of friction. The dynamic proportion of this y-force relates to the vibration behaviour.

Figure 17, Figure 18 and Figure 19 show results for 0.18 s time segments. The y-force associated values of arithmetic mean, range and sample standard deviation as well as the values of both empirical metrics are listed in Table 5 (Appendix).

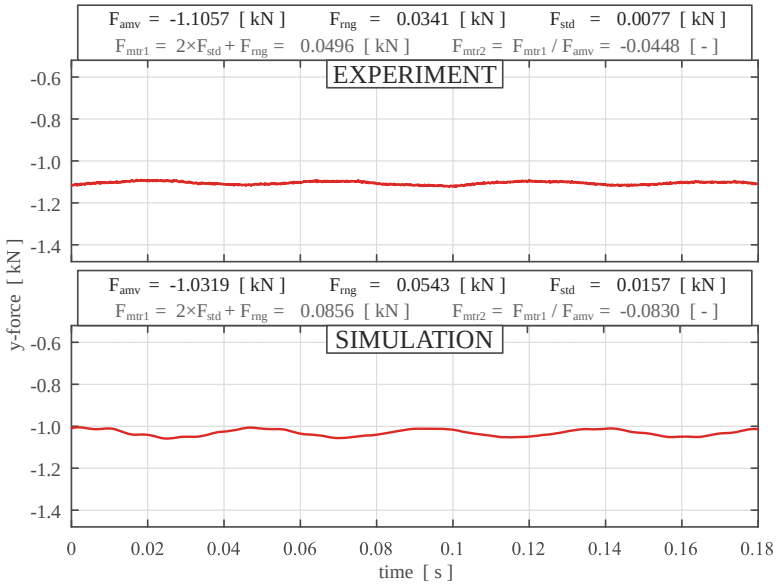

Figure 17: Both no creep groan / hydro bushing y-force signal for 0.18 s.

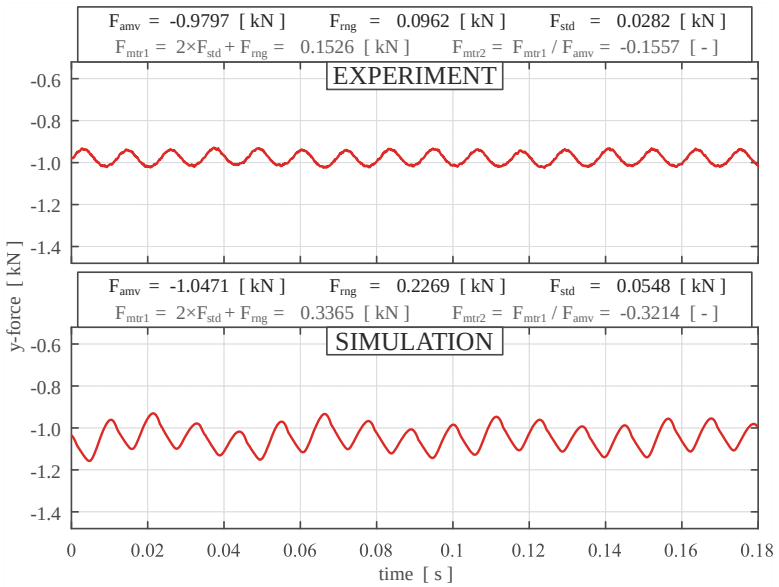

Figure 18: 87|89 Hz creep groan / hydro bushing y-force signal for 0.18 s.

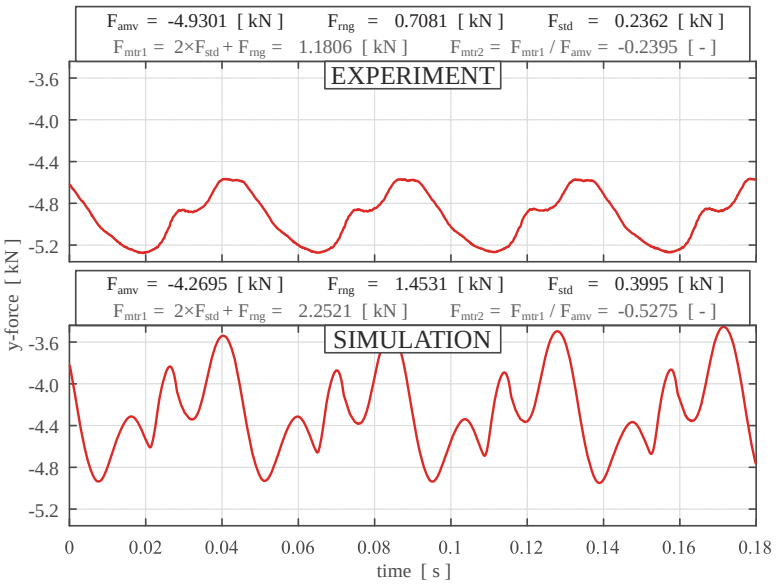

Figure 19: 22|23 Hz creep groan / hydro bushing y-force signal for 0.18 s.

Both almost vibration-free examples in Figure 17 reveal a sinusoidal oscillation of low amplitude. In case of creep groan, the y-force signal reflects the first-order bending deflection of the suspension strut assembly. This elastic deformation is mainly involved in the 87 and 89 Hz examples, see Figure 18. However, it also appears for the 22 and 23 Hz examples which are dominated by elastic hydro bushing deformations, see Figure 19. Either way, the highest absolute y-force appears shortly prior to each macroscopic transition from stick to slip. Different y-force characteristics in experiment and simulation most likely indicate weaknesses of the hydro bushing's FE model implementation.

Creep groan leads to an increased y-force range and an increased y-force sample standard deviation. A distinction between the two types in Figure 18 and Figure 19 is probably possible. The y-force arithmetic mean depends on brake pressure and coefficient of friction. It is used to normalise one of the empirical metrics. Based on this normalised value, a recognition and distinction of creep groan can be achieved if integer numbers of stick-slip vibration cycles or sufficiently long time series data are considered.

- **averaged friction pair condition (simulation)**

The contact status is relevant for 231 mesh nodes per lining. The optional specific states are defined as gap, slip and stick. These have freely chosen number values of 0, 1 and 2, compare with [20]. All additional mesh nodes at the lining chamfer are always in specific gap status.

An exemplary post-processor snapshot of continuous macroscopic slip is shown in Figure 20. Accordingly, mesh nodes in specific stick status and mesh nodes in specific slip status appear simultaneously.

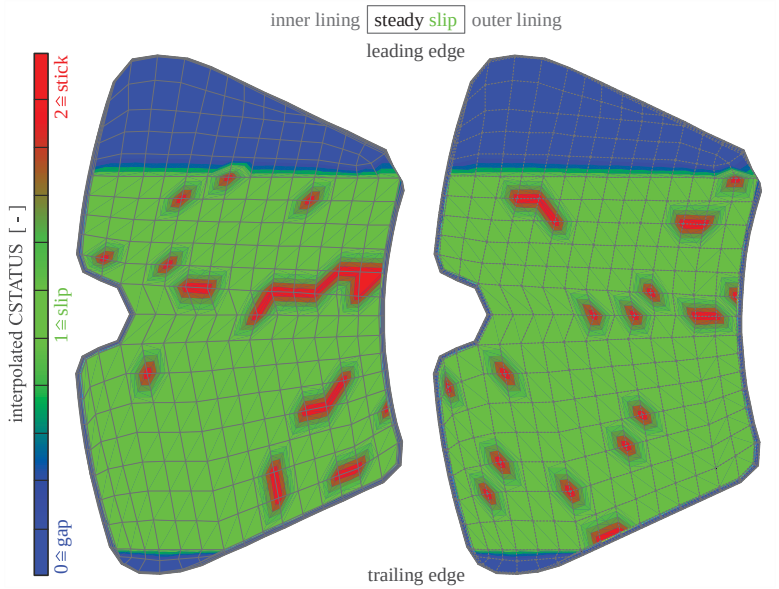

Figure 20: No creep groan / contact status (gap / slip / stick) specific node assignment example of continuous macroscopic slip.

In the following, the averaged contact status is analysed. It is shown for 0.18 s time segments in Figure 21, Figure 22 and Figure 23. Again, each calculated value is listed in Table 5 (Appendix).

The upper part of Figure 21 confirms the absence of macroscopic stick-slip. The lower part of Figure 21 represents Figure 20. Note that mesh nodes in specific stick status at this arbitrary point in time also change to specific slip status during the 0.18 s time segment. Certainly, these changes appear vice versa as well.

The averaged contact status in Figure 22 clearly indicates the 89 Hz stick-slip vibration. The four exemplary node assignments show typical transitions. These transitions have no detectable macroscopic pattern. A comparable random transition behaviour of all mesh nodes also occurs for the 23 Hz stick-slip vibration, see Figure 23.

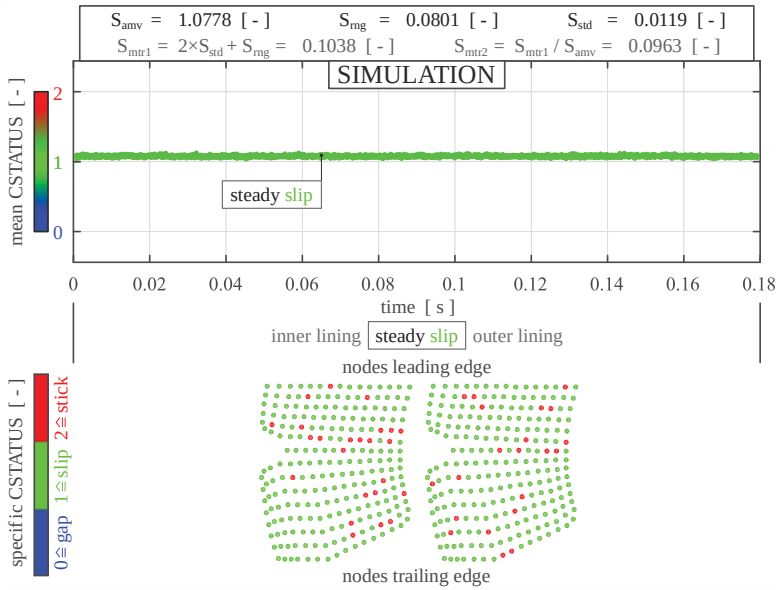

Figure 21: No creep groan / averaged friction pair contact status signal for 0.18 s and specific node assignment example.

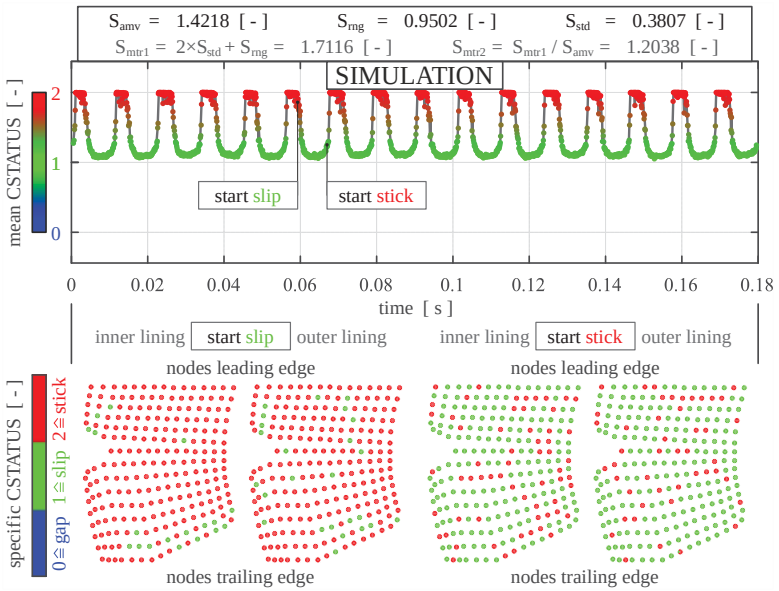

Figure 22: 89 Hz creep groan / averaged friction pair contact status signal for 0.18 s and specific node assignment example.

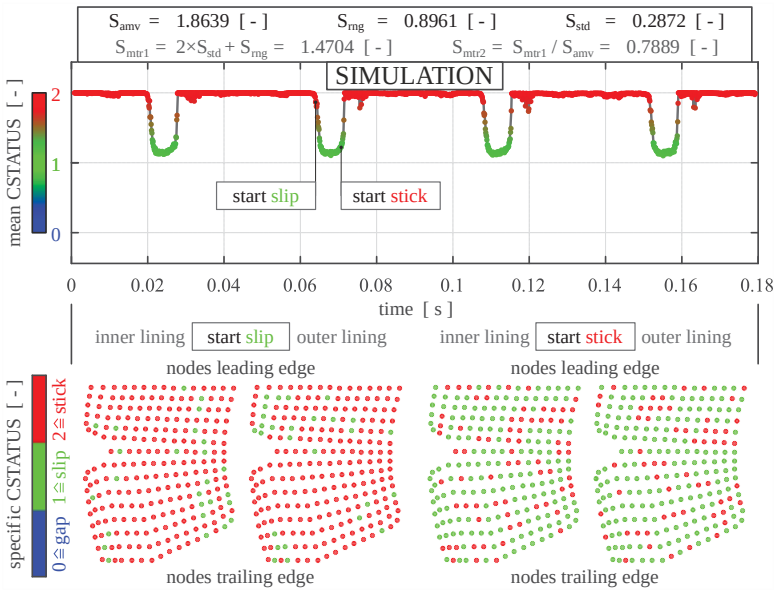

Figure 23: 23 Hz creep groan / averaged friction pair contact status signal for 0.18 s and specific node assignment example.

Based on the freely chosen number values of 0, 1 and 2 for the averaged friction pair contact status, macroscopic stick-slip leads to an increase of arithmetic mean, range and sample standard deviation. The empirical metric according to Equation 17 can be used for a simulative distinction between the two most relevant types of stick-slip vibrations. Again, integer numbers of stick-slip vibration cycles or sufficiently long time series data have to be considered.

6 CONCLUSIONS

Suitable subsystem investigation methods and efficient data analysis techniques are necessary to reveal problematic creep groan already at early stages of the brake development pro-

cess. For this purpose, experimental and simulative approaches at vehicle corner level as well as different rating criteria are discussed in this paper.

Concerning an exemplary MacPherson setup with floating calliper brake system, two different creep groan phenomena were identified. Depending on the applied operational parameter combinations in experiment and simulation, fundamental stick-slip intervals were at roughly 90 or 20 Hz. Certainly, vibration-free conditions were identified as well.

To objectively compare experiments and/or simulations in terms of creep groan, three kinds of metrics were calculated in MATLAB based on time series data. These are physically reasonable, purely synthetic and statistical metrics. Thereby obtained absolute quantities are listed in Table 5 (Appendix). These abstract number values are helpful for efficient data evaluations and large-scale result validations.

A normalised summary of the most promising rating criteria is given in Table 3. Concerning each comparison metric, the smallest value relates to 0 % and the largest value represents 100 %. This normalisation is done separately for experiment and simulation. Similar creep groan phenomena lead to comparable percentage spans. Thus, the identification, categorisation and validation of typical brake creep groan vibrations is possible.

norm. comparison metric		**experiment: .. Hz**			**simulation: .. Hz**		
symbol	**norm. unit**	**no**	**87**	**22**	**no**	**89**	**23**
rel. spectral contents (no lg)							
$L^N_{a[50,500]}$	ms²/ms² in %	0	64	100	0	50	100
$L^N_{K[50,500]}$	J/J in %	×	×	×	0	6	100
rel. orbital indices							
$A^N_{Ux\|Uz}$	mm²/mm² in %	0	2	100	0	5	100
$A^N_{U\|V}$	mm²s/mm²s in %	0	13	100	0	6	100
rel. statistical characteristics							
F^N_{mtr2}	kN/kN in %	100	43	0	100	46	0
S^N_{mtr2}	-/- in %	×	×	×	0	100	63

Table 3: Summary of relativised quantities of suitable comparison metrics in experimental and/or simulative validation.

To confirm or improve the proposed comparison metrics, a next step might be an extended operational parameter study. Attention might be given to situational weighting factors depending on the most common real-world operational parameter combinations. Modified psycho-acoustic evaluation metrics might be applicable as well.

REFERENCES

[1] Barden, P.: Decoded: The Science Behind Why We Buy. Hoboken, U.S.: John Wiley & Sons (2013). ISBN-13: 978-1118345603.

[2] Abendroth, H., Haverkamp, M., Hoffrichter, W., Blaschke, P. et al.: Current and New Approaches for Brake Nosie Evaluation and Rating. SAE Int. J. Passeng. Cars - Mech. Syst. 2 (2), 32-45 (2009). https://doi.org/10.4271/2009-01-3037.

[3] Csere, C.: The Trouble with J.D. Power's Initial Quality Study (IQS) with Focus on the 2011 U.S. Survey. Boone, U.S.: Car and Driver Magazine (2011). https://www.caranddriver.com/features/a15122465/the-trouble-with-jd-powers-initial-quality-study-feature, Accessed 19 July 2018.

[4] Youngs, J.: Top-10 Problems in 3-Year-Old Vehicles according to J.D. Power's 2014 U.S. Vehicle Dependability Study (VDS). Westlake Village, U.S.: J.D. Power (2014). https://www.jdpower.com/cars/articles/jd-power-studies/vehicle-dependability-study-top-10-problems-3-year-old-vehicles, Accessed 19 July 2018.

[5] Davies, G.O.: Vehicle Dependability in Japan Declines, J.D. Power's 2017 Study (VDS) finds. Penarth, U.K.: Automotive World Ltd (2017). https://www.automotiveworld.com/news-releases/vehicle-dependability-japan-declines-j-d-power-finds, Accessed 19 July 2018.

[6] Abdelhamid, M.K.: Filling the Gaps in Brake NVH Development. SAE Technical Paper 2010-01-1684 (2010). https://doi.org/10.4271/2010-01-1684.

[7] Schwartz, H.W., Hays, W.D., Tarter, J.H.: A Systematic Approach to the Analysis of Brake Noise. SAE Technical Paper 850990 (1985). https://doi.org/10.4271/850990.

[8] Abdelhamid, M.K.: Creep Groan of Disc Brakes. SAE Technical Paper 951282 (1995). https://doi.org/10.4271/951282.

[9] Brecht, J., Hoffrichter, W., Dohle, A.: Mechanisms of Brake Creep Groan. SAE Technical Paper 973026 (1997). https://doi.org/10.4271/973026.

[10] Vadari, V., Jackson, M.: An Experimental Investigation of Disk Brake Creep-Groan in Vehicles and Brake Dynamometer Correlation. SAE Technical Paper 1999-01-3408 (1999). https://doi.org/10.4271/1999-01-3408.

[11] Xu, J.J.: Disc Brake Low Frequency Creep Groan Simulation Using ADAMS. In: Proceedings of International ADAMS User Conference, Orlando, U.S. (2000).

[12] Crowther, A.R., Singh, R.: Identification and Quantification of Stick-Slip Induced Brake Groan Events Using Experimental and Analytical Investigations. Noise Control Eng. J. 56 (4), 235-255 (2008). https://doi.org/10.3397/1.2955772.

[13] Bader, D.: Entwicklung einer flexiblen akustischen Messmethode zur Detektierung von verzahnungstechnischen Qualitätsproblemen: Dissertation Thesis. Technical University, Illmenau, Germany (2006).

[14] Abdelhamid, M.K., Bray, W.: Braking Systems Creep Groan Noise: Detection and Evaluation. SAE Technical Paper 2009-01-2103 (2009). https://doi.org/10.4271/2009-01-2103.

[15] Wu, G., Jin, S.: Combination of Test with Simulation Analysis of Brake Groan Phenomenon. SAE Int. J. Passeng. Cars - Mech. Syst. 7 (3), 1119-1127 (2014). https://doi.org/10.4271/2014-01-0869.

[16] Suetti, A.G.L., Pederiva, R.: Phase Plane Analysis and Determination of Damping Limit in Mechanical Systems with Stick-Slip. SAE Technical Paper 2015-36-0026 (2015). https://doi.org/10.4271/2015-36-0026.

[17] Neis, P.D., Ferreira, N.F., Poletto, J.C., Matozo, L.T. et al.: Quantification of Brake Creep Groan in Vehicle Tests and its Relation with Stick-Slip Obtained in Laboratory Tests. J. Sound Vib. 369, 63-76 (2016). https://doi.org/10.1016/j.jsv.2016.01.036.

[18] Rösner, D., Özdil, R.: A Standardized Methodology for Creep Groan Investigation on a Dynamometer: EB2016-SVM-009. In: Proceedings of EuroBrake Conference and Exhibition, Milan, Italy (2016).

[19] Augsburg, K., Hauschild, P., Beierlieb, C.: Basic Investigations for the Evaluation of the Creep Groan Phenomenon: EB2017-FBR-017. In: Proceedings of EuroBrake Conference and Exhibition, Dresden, Germany (2017).

[20] Meng, D., Zhang, L., Xu, J., Yu, Z.: A Transient Dynamic Model of Brake Corner and Subsystems for Brake Creep Groan Analysis. J. Shock Vib. 2017, 18 pp (2017). https://doi.org/10.1155/2017/8020797.

[21] Zhao, X., Gräbner, N., von Wagner, U.: Theoretical and Experimental Investigations of the Bifurcation Behavior of Creep Groan of Automotive Disk Brakes. J. Theor. App. Mech.-Pol. 56 (2), 351-364 (2018). https://doi.org/10.15632/jtam-pl.56.2.351.

[22] Pürscher, M., Fischer, P.: Systematic Experimental Creep Groan Characterization Using a Suspension and Brake Test Rig. SAE Technical Paper 2017-01-2488 (2017). https://doi.org/10.4271/2017-01-2488.

[23] Huemer-Kals, S., Pürscher, M., Fischer, P.: Application Limits of the Complex Eigenvalue Analysis for Low-Frequency Vibrations of Disk Brake Systems. SAE Technical Paper 2017-01-2494 (2017). https://doi.org/10.4271/2017-01-2494.

[24] Pürscher, M., Huemer-Kals, S., Fischer, P.: Experimental and Simulative Study of Creep Groan in Terms of MacPherson Axle Bushing Elasticities: EB2018-SVM-011. In: Proceedings of EuroBrake Conference and Exhibition, The Hague, Netherlands (2018).

[25] Pürscher, M., Schöpf, S., Fischer, P.: NVH Signal Analysis via Pattern Recognition ANNs: Automotive Brake Creep Groan as Case Study. In: Proceedings of Alps Adria Acoustic Association Congress, Zagreb, Croatia (2018).

[26] Pürscher, M., Huemer-Kals, S., Fischer, P.: Investigations on Creep Groan Concerning Static and Dynamic Axle Bushing Properties: EB2019-SVM-001. In: Proceedings of EuroBrake Conference and Exhibition, Dresden, Germany (2019).

[27] Verband der Automobilindustrie - Expertenkreis Bremsgeräusche: Acoustic Evaluation of Brake Creep Groan Noise in Vehicle Tests. Recommendation VDA 314 (2016).

[28] Brake NVH Standards Committee: Disk and Drum Brake Dynamometer Squeal Noise Test Procedure. Surface Vehicle Recommended Practice SAE J2521 APR2013 (2013). https://doi.org/10.4271/J2521_201304.

APPENDIX

input file keyword	classification (...) / purpose	∑
NODE	/ mesh	3438
SOLID	C3D8 (linear 8-node hexa)	1512
-‖-	C3D6 (linear 6-node penta)	60
-‖-	C3D4 (linear 4-node tetra)	12
RIGID	R3D4 (3-d with 4 nodes)	332
SHELL	S4 (linear 4-node)	257
-‖-	S3R (linear 3-node reduced integration)	59
BEAM	B31 (linear 3-d Timoshenko)	217
CONNECTOR	BUSHING (2 nodes) / elasticity; damping	14
-‖-	SLIDE-PLANE / calliper anchor to pad backing plates	2
-‖-	CYLINDRICAL / calliper anchor to sliding pins and floating calliper to piston	2
-‖-	SLIPRING + RETRACTOR / wheel rotation including torque and force	1
MASS	/ point inertia	21
COUPLING	KINEMATIC	21
ROTARY	/ point inertia	16
BOUNDARY	DISPLACEMENT / control arm bushings; strut top support; track rod	4
-‖-	VELOCITY (amplitude) / longitudinal ground excitation	1
RIGID BODY	SHELL / disk; calliper; piston	3
DLOAD	DSLOAD (amplitude) / hydraulic brake pressure application	2
CONTACT	GENERAL CONTACT (finite sliding tracking; default penalty method; surface to surface / disk (master) to linings (slave)	2
SURFACE INTERACTION	FRICTION (exponential decay function) / disk to linings	2

Table 4: Appendix: FE model subjects with quantities.

comparison metric		experiment: .. Hz creep groan			simulation: .. Hz creep groan			observed system; measurand; time span Δt
symbol	**unit**	**no**	**87**	**22**	**no**	**89**	**23**	**value description**
spectral contents								calliper anchor top; xz-acceleration;1 s
$L_{a[50,500]}$	dB re 1 m/s²	-12.25	18.66	20.63	-5.61	23.15	26.12	xz-amp. RMS sum (incoherent) from 50 to 500 Hz
$L_{a[5,1000]}$	dB re 1 m/s²	-10.51	18.92	21.91	-3.27	23.23	26.86	xz-amp. RMS sum (incoherent) from 5 to 1000 Hz
spectral contents								corner FE model; all kinetic energy;1 s
$L_{K[50,500]}$	dB re 1 J	×	×	×	-34.28	-20.17	-7.76	kinetic energy sum from 50 to 500 Hz
$L_{K[5,1000]}$	dB re 1 J	×	×	×	-22.86	-18.35	-4.81	kinetic energy sum from 5 to 1000 Hz
orbital indices								calliper anchor top; xz-acceleration; 0.18 s
$A_{Ux\|Uz}$	mm²	0.000142	0.001143	0.040554	0.000099	0.002402	0.045050	disp.-disp. face area U_x by U_z
$A_{Ux\|Vx}$	mm²/s	0.045793	1.465373	15.112720	0.078819	1.120600	26.102998	disp.-vel. portrait area U_x by V_x
$A_{Uz\|Vz}$	mm²/s	0.018789	2.011332	11.155018	0.019835	2.056922	23.569461	disp.-vel. portrait area U_z by V_z
$A_{U\|V}$	mm²/s	0.064582	3.476705	26.267738	0.098654	3.177522	49.672459	synthetic portrait area sum: $A_{U\|V} = A_{Ux\|Vx} + A_{Uz\|Vz}$
statistical characteristics								hydro bushing boundary interface; y-force; 0.18 s
F_{amv}	kN	-1.1057	-0.9797	-4.9301	-1.0319	-1.0471	-4.2695	arithmetic mean of y-force
F_{rng}	kN	0.0341	0.0962	0.7081	0.0543	0.2269	1.4531	range of y-force
F_{std}	kN	0.0077	0.0282	0.2362	0.0157	0.0548	0.3995	sample standard deviation of y-force
F_{mtr1}	kN	0.0496	0.1526	1.1806	0.0856	0.3365	2.2521	empirical sum: $F_{mtr1} = 2 \times F_{std} + F_{rng}$
F_{mtr2}	kN	-0.0448	-0.1557	-0.2395	-0.0830	-0.3214	-0.5275	norm. empirical sum: $F_{mtr2} = F_{mtr1} / F_{amv}$
statistical characteristics								disk surface to linings; averaged contact status; 0.18 s
S_{amv}	-	×	×	×	1.0778	1.4218	1.8639	arithmetic mean of averaged contact status
S_{rng}	-	×	×	×	0.0801	0.9502	0.8961	range of averaged contact status
S_{std}	-	×	×	×	0.0119	0.3807	0.2872	sample standard deviation of averaged contact status
S_{mtr1}	-	×	×	×	0.1038	1.7116	1.4704	empirical sum: $S_{mtr1} = 2 \times S_{std} + S_{rng}$
S_{mtr2}	-	×	×	×	0.0963	1.2038	0.7889	norm. empirical sum: $S_{mtr2} = S_{mtr1} / S_{amv}$

Table 5: Appendix: absolute quantities of all applied comparison metrics in experimental and/or simulative validation.

abbreviation	meaning
ANN	artificial neural network
CEA	complex eigenvalue analysis
CGI	creep groan index
CGM	creep groan map
CSTATUS	contact status of lining nodes
F	force
FE	finite element
FFT	fast fourier transform
K	kinetic
L	dB level
MBS	multi-body system
N	normalisation
NVH	noise, vibration, harshness
ODS	operating deflection shape
ONI	objective noise index
RMS	root mean square
S	status
SPL	sound pressure level
U	synthetic sum component of Ux and Uz
Ux	displacement in x-direction
Uz	displacement in z-direction
V	synthetic sum component of Vx and Vz
Vx	velocity in x-direction
Vxz	geometric sum of Vx and Vz
Vz	velocity in z-direction
a	acceleration
abs.	absolute
amp.	amplitude
amv	arithmetic mean value
dB re	deciBel (decadic logarithm) regarding
disp.	displacement
fund.	fundamental
mtr1, mtr2	customised statistical metrics
norm.	normalised
rel.	relative
rng	range
std	sample standard deviation
vel.	velocity
1- / 2- / 3-d	1- / 2- 3-dimensional

Table 6: Appendix: nomenclature.

EURODYN 2020
XI International Conference on Structural Dynamics
M. Papadrakakis, M. Fragiadakis, C. Papadimitriou (eds.)
Athens, Greece, 23–26 November 2020

VIBRATIONS FOR ESTIMATING BOLTED JOINT INTEGRITY (VEBJI) PROJECT: CHALLENGES AND RESULTS

Dmitri Tcherniak[1], **Jon J. Thomsen**[2], **and Marie Brøns**[2]

[1] Brüel & Kjær
Skodsborgvej 307, 2850 Nærum, Denmark
e-mail: dtcherniak@bksv.com

[2] Department of Mechanical Engineering, Technical University of Denmark
Nils Koppels Allé, Building 404, 2800 Kgs. Lyngby, Denmark
{jjt,maribr}@mek.dtu.dk

Keywords: Bolt, Tension, Vibration, Estimation,

Abstract. *Bolted joints are one of the oldest and widely-used means of connecting parts of technical installations. For mission-critical and expensive assets, periodic inspection of bolted joints is the conventional way of ensuring the assets' structural integrity, and hence their safe operation. Currently, the inspections require hours of physically demanding and monotonic work, as in practice it often means re-tightening the bolts. Thus, the asset maintenance units will benefit from a simpler and less demanding technique, which would allow checking the correct bolt tightening and notifying if a bolt is loose.*

For the last three years, a joint research team led by the Technical University of Denmark in collaboration with Brüel & Kjær and Karlsruhe Institute of Technology was conducting a project, where vibrations, artificially induced in a bolted joint, were utilized for estimation of the static axial force acting in the bolt. The presented paper provides an overview of the project, lists the numerous challenges the project had to deal with and describes what was learned and achieved.

1 INTRODUCTION

Bolted joints are one of the most used means of connecting parts of technical installations. For mission-critical assets, held together by bolted joints, regular inspections of proper bolt tightness are mandatory for certification and safe operation. As the bolt tension is impossible to measure and check in-situ, most of such inspections today are performed using a torque wrench. This procedure could potentially lead to the overtightening of bolts, which is undesirable. With large structures and heavy bolts, using a torque wrench, the bolt inspection procedure becomes a monotonous and physically demanding work, often conducted in tough environments. That is why a simpler and less demanding technique of checking bolt tightness is on high demand in many industries.

The abovementioned became a motivation for establishing the VEBJI project, a collaborative work between Technical University of Denmark (DTU), Brüel & Kjær and Karlsruhe Institute of Technology. VEBJI stands for Vibration for Estimating Bolted Joints Integrity. As it follows from the title, the project aims in utilizing vibrations, artificially induced in a bolt, as the source of information regarding its tension. As a starting point, we used an observation that, when impacted, a well-tightened bolt sounds differently from a loose one [1]. An impact excites different types of vibrations in the bolt, and some of them cause acoustic waves in the audible range, which a human being can perceive and judge. Thus, it was suggested to study how the bolt tension affects its vibrations, and possibly propose a technique for detecting loose bolts, based on the analysis of bolt transient vibrations, excited, for example, by impacting the bolt with a hammer.

There are alternative methods for bolt tightening check, a review can be found in [2]. Besides torque wrench and hydraulic tensioners, which are used for controllable bolt tightening, the most developed technique for controlling bolt tension is by check bolt elongation utilizing ultrasonic transducers. Commercial solutions employing this technology exist, for example, i-Bolt® by ERREKA [3] can be named as one of them. The drawbacks of the technique are the sensitivity to temperature and special requirement to machining of the bolts' butt-ends.

Two pilot studies, conducted by DTU students as master projects [4], [5], demonstrated that indeed the vibration patterns of tightened and loose bolts are different. Comparing a tightened / loose bolt with a differently tightened guitar string, it is natural to expect the difference in the pitch of the radiated sound. However, in the bolt case, audibly, the difference in pitch is hardly distinguishable. But in contrast, the tightened bolt produces a clear ringing sound, whilst the sound from a loose bolt is rather dull, i.e. decaying faster and containing less high-frequency content. The idea of the pilot projects was to find some properties in the measured vibration signal that can be utilized to characterized bolt tension. In structural health monitoring literature, these properties are often called *features*. Farrar and Worden in [6] provide the following definition: "A damage sensitive feature is some quantity extracted from the measured system response data that indicates the presence (or not) of damage in a structure". Alongside with the abovementioned natural frequencies and damping, other vibration features and / or their combinations are possible, for example, the ratio of natural frequencies, modal interaction, attack time, amplitudes of nonlinear harmonics, etc.

However, it was not straightforward to find the features of the measured vibration signals that could in a robust way indicate if the bolt is well-tightened or not. As bolt tightening features, [4] attempted the natural frequencies and damping of the lowest transverse modes, and in [5] the authors attempted psychoacoustic metrics, the vibration energy decay rate, and spectral centroids. Generally, the results of the two projects were not satisfactory, however, the projects indicated that the experimental work needs to be promoted to a much higher quality level to ensure the experiments being more controllable and reproducible. Alongside that, it became

clear that a better understanding of bolt vibrations is required to explain what was observed during the experiments. These altogether became the groundwork for the VEBJI project.

The paper is built as follows: Section 2 describes the extensive measurement campaign, followed by Section 3, which introduces a model of a single-bolt joint. Section 4 concerns multi-bolt joints. Section 5 touches practical considerations for real-life scenarios. Finally, section 6 introduces the on-going research.

2 EXPERIMENTAL WORK

It was decided to start the project with an extensive measurement campaign, in an attempt to experimentally study the vibration patterns of differently tightened bolts in well-controlled environments and examine the vibration features that are correlated with the bolt tension. The results of the test campaign were thought to initiate the theoretical studies aimed to understand and explain what was observed during the experiments, and theoretically check the applicability of the found vibration features to different bolt sizes and bolted joint configurations.

During the pilot projects, the bolts were tightened using a torque wrench. It was suspected that the torque wrench was the main source of the observed variability. Indeed, applying the wrench in numerous tightening/untightening circles deforms the threads of the bolt and the nut, and damages the mating surfaces of the bolt, washers and the test rig. To retain the geometric and material properties of the test setup, it was decided to replace the torque wrench with a hydraulic tensioner. During the tightening process, the tensioner is pressurized using a hand pump, causing the bolt elongation. Then the nut is finger tightened. After the pressure release, the bolt contracts and compresses the test rig [7].

It is known that a torque wrench is a highly inaccurate tool with the variation of torque-to-tension up to 30% [8]. In the initial experiments conducted in the frame of the pilot studies, a strain gauge mounted on the bolt body was used to estimate its tension. This arrangement was proved to be impractical as the strain gauge is a very delicate sensor, and it requires a special test rig design to allow cabling. Subsequently, the strain gauge was replaced by a force washer directly measuring the compressing force, which is proportional to the bolt's tension.

Considering bolt excitation, it was decided to employ impact excitation as the most practical one. The pilot studies demonstrated that transverse vibrations can be easily excited by impacting the bolt at any point and in any direction. Even an impact in axial direction could excite transverse vibrations (this was later investigated in [9]). For the experiments, the excitation in the transverse direction was chosen.

To catch a possible nonlinear behavior of the bolt, it is necessary to excite the bolt by a well-controllable excitation force with increasing strength. To achieve this, a special pendulum-hammer was designed, where the impact strength was controllable by the initial inclination of the pendulum, and the impact force was measured by a force transducer.

In contrast to the pilot studies, in the VEBJI test campaign, the vibration signal was measured by two miniature accelerometers mounted on the bolt head. One accelerometer was aligned to measure in the direction of the impact, and another in the direction perpendicularly to the first one. This improvement allowed measuring bolt vibration in both transverse directions.

The experiment (the setup is shown in Figure 1), is described in full detail in [10], [11], [12], here a brief overview is given. It was a rather extensive test campaign, two types of bolts were tested, M12x260 and M12x140; the bolt was tightened in 10 load steps, in the range from approximately 0.07 of the yield stress σ_y to approximately 0.8 σ_y (the nominal bolt tension for this class of bolts is 0.7 σ_y). At each tension level, the bolt was impacted with four increasing impact strengths, and each measurement was conducted three times. To ensure repeatability, the experiment was repeated three times, including the full disassembly of the test rig. During

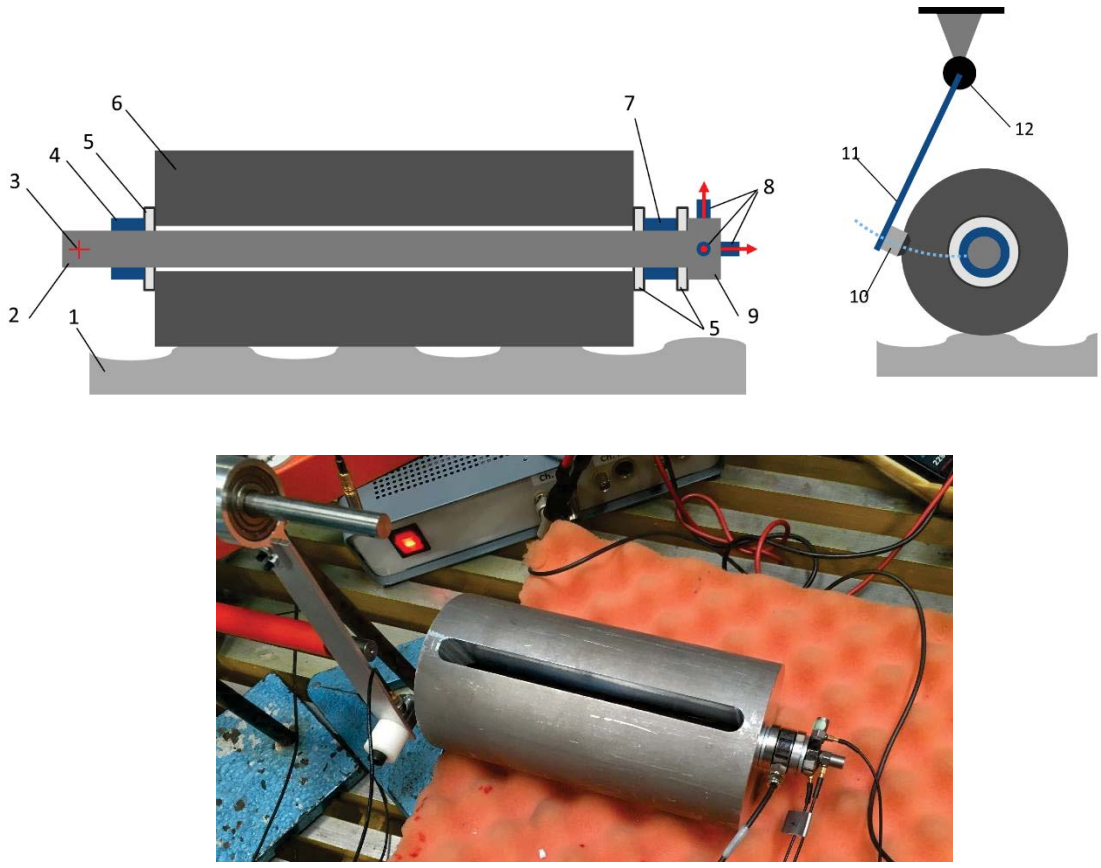

Figure 1. Experimental setup, sketch and photo (from [11]). 1. Foam supporting the structure; 2. Bolt; 3. Impact point; 4; Nut; 5. Washers; 6. Structure; 7. Force washer; 8 – Three monoaxial accelerometers; 9 – Bolt head; 10 – Force transducer; 11 – Pendulum hammer; 12 – Ball bearing holding the hammer.

the experiments, 720 time-histories were acquired with a high sampling rate, each time history consisted of two acceleration signals and the impact force signal.

2.1 Overview of the measurement campaign results

A typical acceleration signal is shown in Figure **2**a. As the bolt is a nearly symmetrical structure, one can expect the pairs of transverse modes of vibration with almost identical natural frequencies. The spectra in Figure **2**b show the peaks corresponding to the first pair of modes (just below 1 kHz) and the second pair of modes (above 2.5 kHz). The double peaks are (sometimes) distinguishable in the zoomed view (as shown). Applying a narrow band-pass filter (BPF) around the natural frequencies of the modes' pairs, it was possible to separate the pairs in the time domain; the resulting filtered signals $a_1(t)$ and $a_2(t)$ measured in the direction of the impact and the perpendicular direction, respectively, are shown in Figure **2**c, together with their envelopes and the envelope of $a_\Sigma(t) = \sqrt{a_1(t)^2 + a_2(t)^2}$.

The amplitudes of the measured signals in Figure **2**c is slowly modulated, which is a characteristic of a beating, the phenomenon which appears when two sinusoidal signals with slightly different frequencies are added together. The frequency of the modulation is then equal to the difference between the frequencies of the sinusoids. In [13], the likely explanation is provided: both modes of the first pair are excited by the hammer impact, and the modal response is the exponentially decaying sinusoidal oscillation at the damped natural frequencies of the mode. The system is effectively linear, and the two modes do not interact but the accelerometers pick up the mixture of both sinusoids, resulting in the observed beating. Another plausible

a)

b)

c)

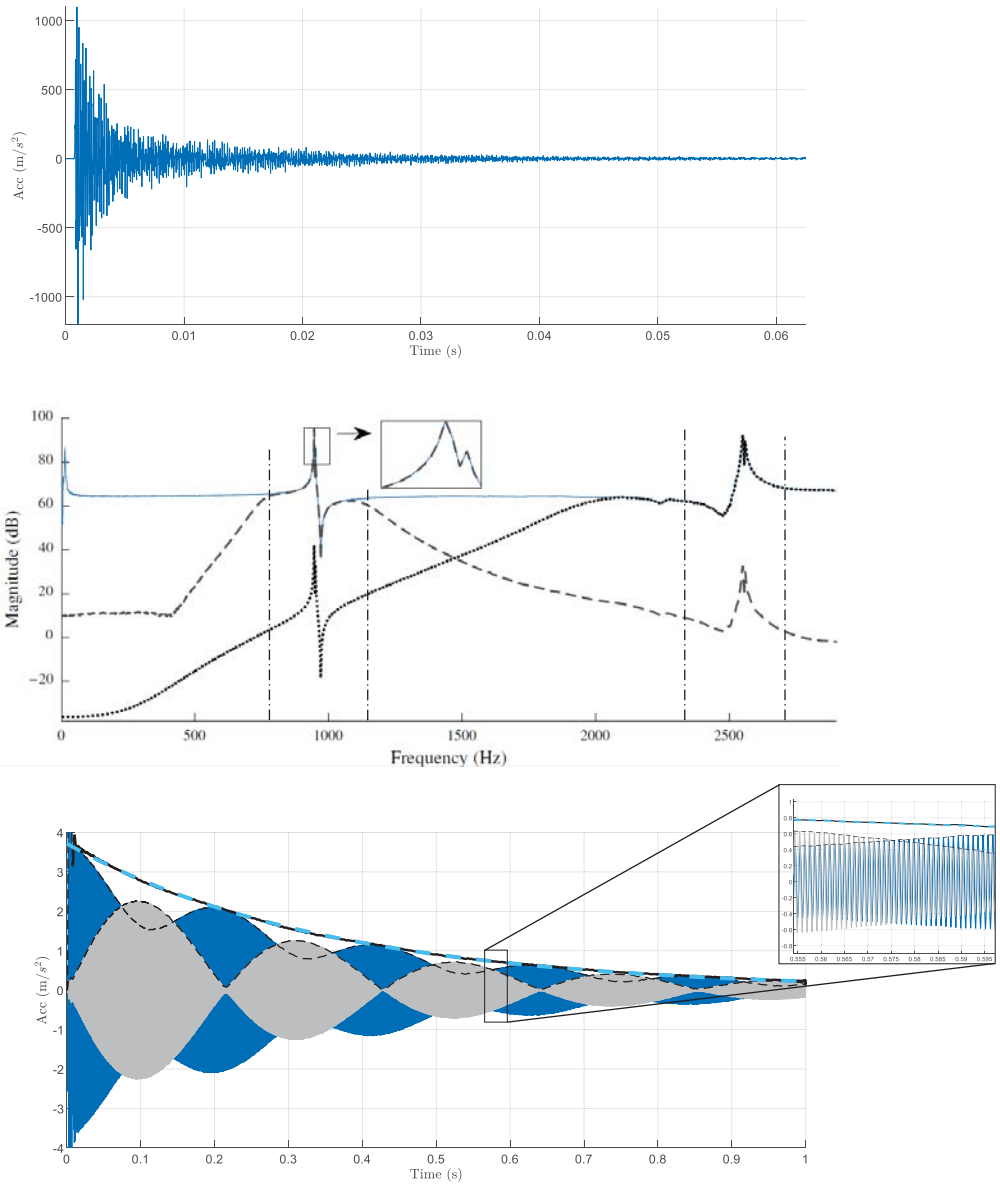

Figure 2. Measure signal and signal processing (from [11]). a) Raw acceleration signal measured in the impact direction. b) Spectra: blue - the spectrum of the raw signal, dash line – after applied BPF around the first natural frequency, dot-line – after applying BPF around the second natural frequency. Vertical dot-dash lines – the cut-off frequencies of the applied BPF. c) Two transverse acceleration signals $a_1(t)$ and $a_2(t)$, after applying BPF around the first transverse resonant frequency. Thin dash lines – their envelopes. Thick dash line – the envelope of $a_\Sigma(t) = \sqrt{a_1(t)^2 + a_2(t)^2}$.

explanation involves a non-linear interaction (i.e. energy exchange) between the two transverse modes, as explained in [14].

Based on the observations during the experiment, numerous vibration characteristics were considered as potential features [12], including natural frequencies, modal damping, modes interaction inside and outside the pairs, variation in time of the instantaneous natural frequencies and damping, input/output linearity, impact duration, etc. These characteristics were correlated with bolt's tension and their reproducibility was checked using available time histories. Based on the analysis, two characteristics were studied in detail, as they demonstrated solid correlation

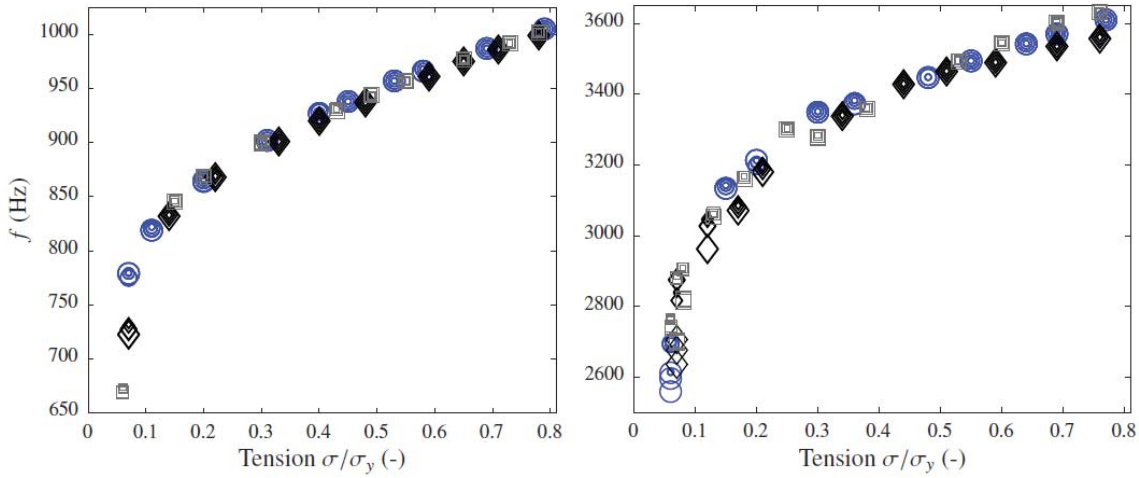

Figure 3. Measured first natural frequency as a function of the bolt tension: long bolt (left) and short bolt (right). The different markers indicate the test series, the marker size denotes the impact strength (from [11], [12]).

with the bolt tension: the natural frequency of the transverse vibrations and the corresponding modal damping. The other attempted potential featues did not demonstrate the sufficient correlation with bolt tension or were not sufficiently reproducible.

2.2 Selected features

Natural frequencies

The natural frequencies obtained by zero-cross counting of the filtered signal are shown in Figure 3. As expected, there is a strong correlation between the natural frequencies and the bolt tension, observed for both long and short bolts.

Damping ratio

The effective linear damping ratio of the first mode was estimated by fitting the exponential decay to the envelope of the filtered signal a_Σ (Figure **2**c). The damping ratio decreases with increasing bolt tension, as shown in Figure **4**, [11] and [12]. In absolute values, the damping ratios

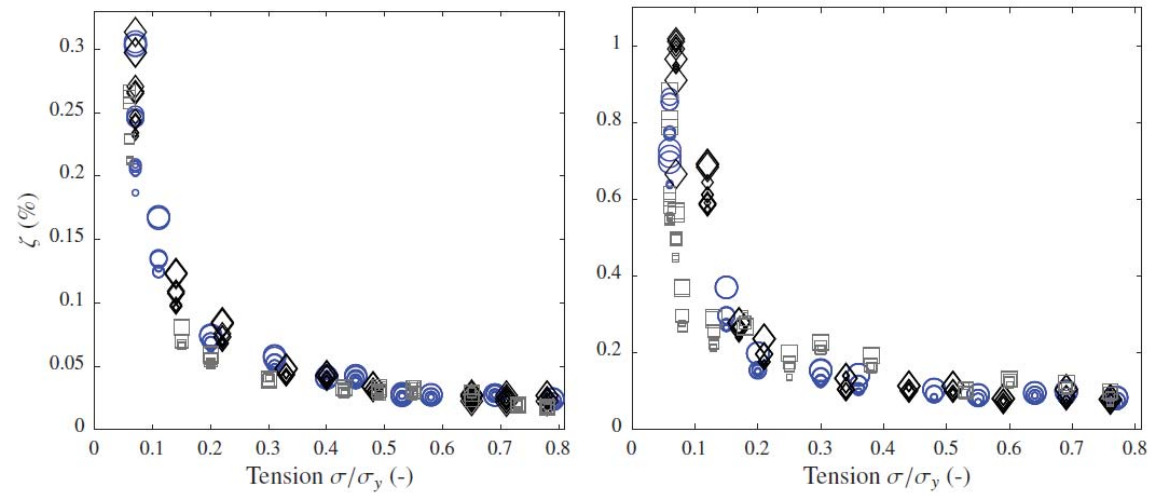

Figure 4. The damping ratio of the first mode as a function of the bolt tension for the long (left) and short (right) bolts (from [11], [12]). Legend is the same as in Figure 3.

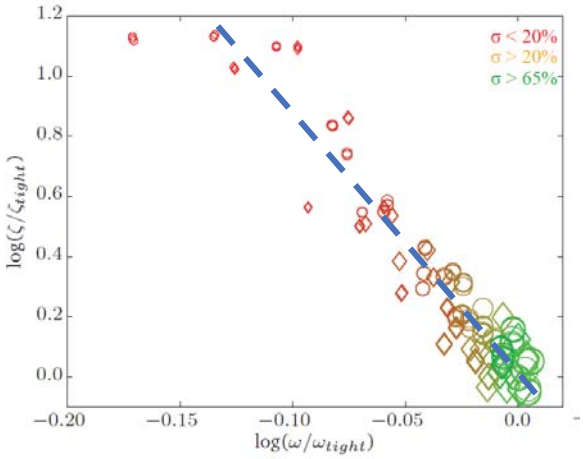

Figure 5. Distribution of the points with coordinates (normalized frequency; normalized damping) (from [12]). The markers' color and size correspond to the tension of the bolt.

differ for the long and short bolt, however, if scaled with the bolt slenderness ratio, the damping ratio becomes invariant to bolt sizes. The slenderness ratio is defined as $s = l/\sqrt{I/A}$, where l, I and A are bolt's length, the moment of inertia of bolt's section and area of bolt's section, respectively. The theoretical explanation of this interesting observation is provided in [12].

Combined frequency and damping feature

The combination of the normalized natural frequency and damping ratio into a single bolt tension feature was suggested in [12] and is shown in Figure 5 for both long and short bolts. The frequency and damping are normalized by the respective characteristics of the nominally tightened bolt. In Figure 5 the points corresponding to the well-tightened bolts are concentrated in the bottom-right corner, whilst those of the relatively loose bolts are spread along the dashed line leading towards the upper-left corner of the plot.

Discussion

During the experiments, it became clear that the frequency and damping, either separately or combined, can be considered as reliable qualitative indicators of bolt tension. The next natural step would be suggesting a model explaining the experimentally observed phenomena and providing a quantitative relation between the measured vibration properties and the unknown bolt tension.

3 MODELLING A SINGLE-BOLT JOINT

From the first glance, it is natural to model a tightened bolt as a pre-stressed clamped-clamped beam. For such a beam the dependence of the i-th transverse natural frequencies from the tension is well-known [15],

$$\omega_i = \frac{\lambda_i}{l\,s}\sqrt{\frac{E}{\rho}\left(1+\frac{\sigma}{E}\left(\frac{K_i\,s}{\lambda_i^2}\right)^2\right)}, i = 1,2\ldots \tag{1}$$

where l is the length of the beam, s is the slenderness ratio, σ is the axial stress, E and ρ are beam's material Young's modulus and density, respectively and K_i and λ_i are non-dimensional constants, depending on the i-th mode shape.

As it follows from (1), the square of the natural frequencies is directly proportional to the axial stress σ, and thus to the bolt tension. Figure 6 shows the corresponding line on top of the experimental results (adjusting the length l to fit the high values of σ). Apparently, for the long

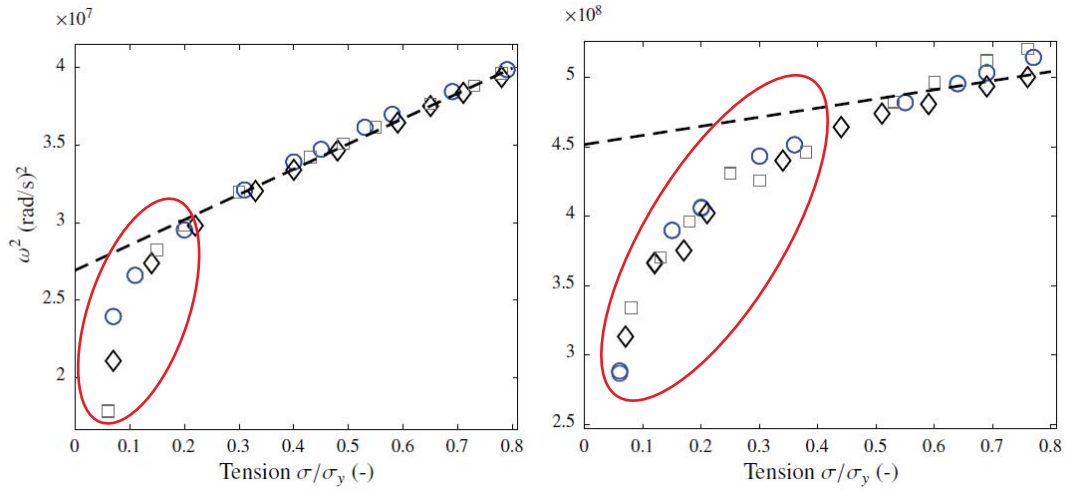

Figure 6. Square of the first natural frequency $\boldsymbol{\omega_1}$ as function of bolt tension $\boldsymbol{\sigma}$. The markers denote experimental results; dashed line is the model according to (1). Left – long bolt, right – short bolt. The red ovals indicate the region where the clamped-clamped beam model is not suitable (from [10]).

bolt, the fit is good for a wide range of σ, and less for the short bolt. Common for both cases, the fit is not good for low tension levels (circled), indicating that the clamped-clamped beam model does not reflect reality at low levels of tension.

The study [10] suggested an extended model that could explain the observed behavior at the full range of the tension levels. The model (Figure **7**) consists of a Bernoulli-Euler beam, subjected to an axial tensile force σA, and supports at both ends, which both have translational and rotational stiffnesses, k_u and k_θ, respectively. To reflect reality, where the bolt tension affects the contact stiffness, in the model, these stiffnesses are functions of the axial force. For high levels of σA, the stiffness values approach infinity, and the beam boundary conditions become clamped-clamped.

With the model in hand, the next task is to obtain the stiffness parameters and their dependence on tension. In [16] it was demonstrated that it is possible to estimate the stiffness parameters from the measured natural frequencies of the beam. Another approach was taken in [10], where the model of the contact between the mating surfaces was introduced. It was noticed that the contact surfaces in real structures are rough, which is manifested as a distribution of tiny asperities at a micro-scale level, whose interactions can be thought of as springs connecting the mating surfaces. It was observed that the normal (interfacial) stiffness increases with the increase of the contact pressure. Using the asperities-based contact model (Figure 8), it was possible to obtain the values of k_u and k_θ, which resulted in quite good agreement with the measured data, for the full range of tension (Figure 9).

The study [17] extended the model suggested in [10] (Figure 8), by the damping elements, which were added to all springs. It was shown that assuming the damping linearly proportional to the rotational and translational stiffnesses, one can get quite a good agreement with the experimental results shown in Figure **4**. Apparently contradicting though, is that the underlying

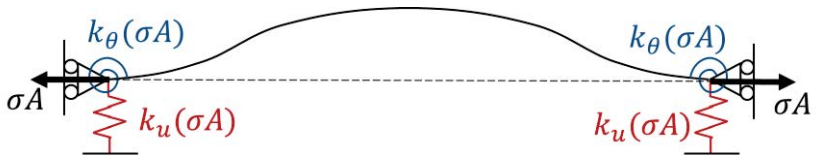

Figure 7. The model suggested in [10].

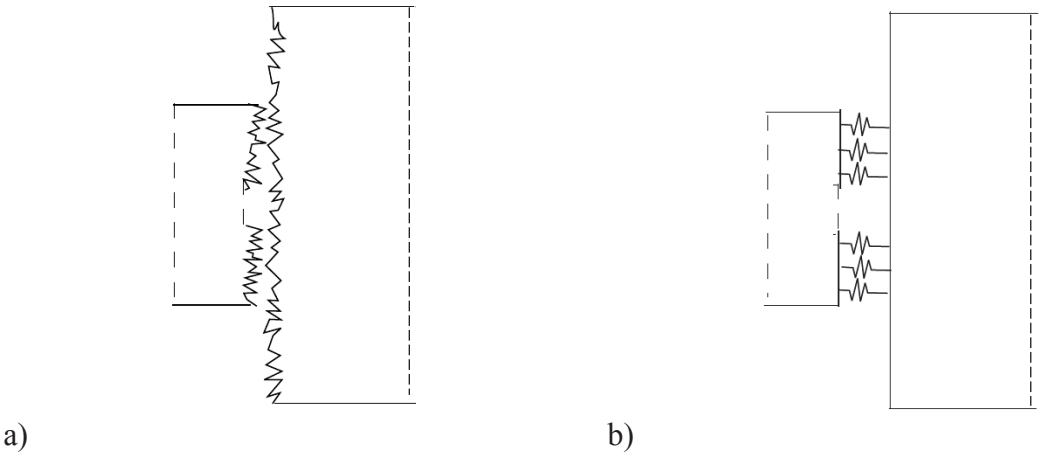

Figure 8. Modeling of the contact between the mating surfaces. a) Micro-level, with the roughness presented as asperities; b) modeling as springs connecting the surfaces (from [10]).

microscale damping mechanism is essentially nonlinear, whilst the collective macroscale behavior is linear. The study [17] suggested a model, which demonstrated that the non-linear multi-degree-of-freedom asperities-based model can be effectively converted to a single-degree-of-freedom model with a cubic nonlinearity, and further showed that the nonlinear term vanishes as the number of asperities increase, thus validating the observed effective linearity in damping.

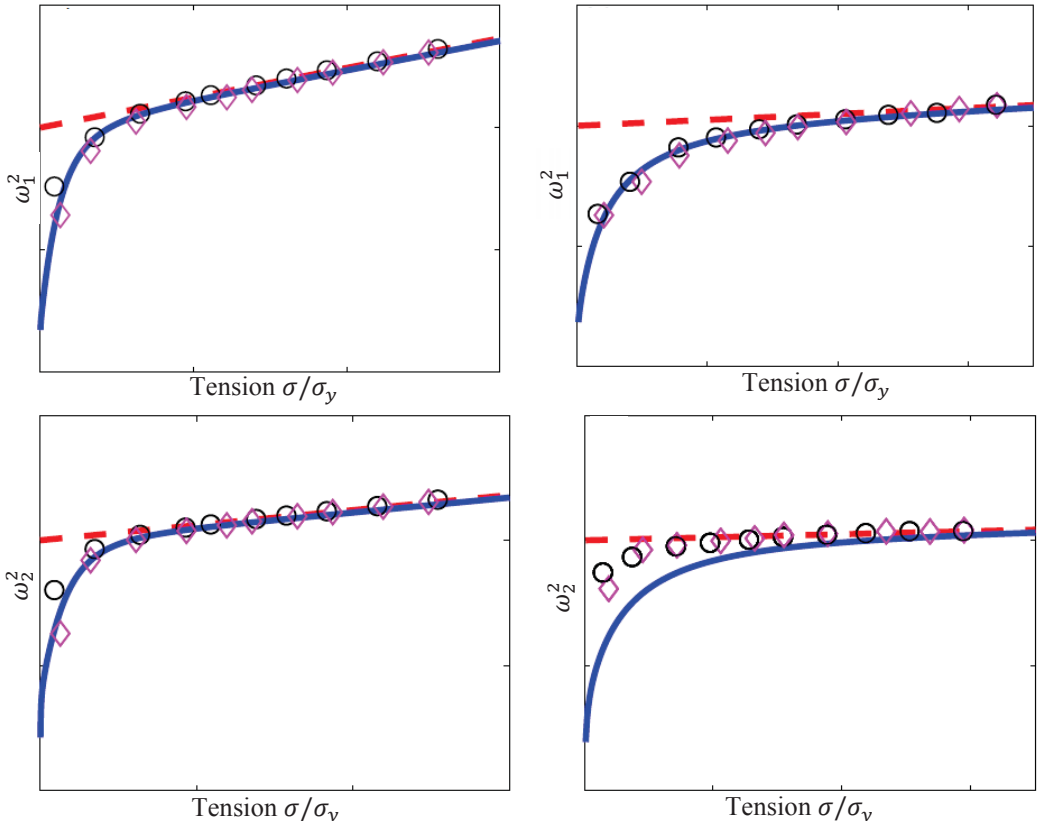

Figure 9. Qualitative comparison of the experimental results (markers), the clamped-clamped model (1) (red dashed line) and the extended model (Figure 7) (blue curve). Left / right columns – long / short bolts; Top / bottom rows – first / second natural frequencies (from [17]).

4 MODELLING MULTI-BOLT JOINT

In studies [18], [19], another aspect of the bolt tension estimation problem was investigated. As the most bolted joints consist of many nearly identical bolts tightened to almost identical levels, the bolts will have very similar boundary conditions and thus almost identical natural frequencies. In a likely case of very light damping, a frequency response measured on one bolt after an impact might include the vibrational response of other bolts. So, a question arises, if it is possible to separate which frequencies belong to which bolt. To start with, analytical, numerical and experimental models of a structure with two identical bolts were established (Figure 10).

It was found that, if the bolts have identical or very similar tension, the system behaves as a whole, and it is impossible to assign natural frequencies to a single bolt, as the global in-phase and anti-phase modes arise. However, if the bolts' tensions are different, their modes can be considered as local, the bolts can be considered separately, and the single-bolt model is fully applicable.

5 PRACTICAL CONSIDERATIONS

One of the aims of the VEBJI project was to explore feasible methods for estimating bolt tension having potential for industrial application. It is apparent (Figure 5), that the studied vibration features are suitable for distinguishing a nominally tightened bolt ($0.7\ \sigma_y$) from a very loose one ($< 0.3\ \sigma_y$). However, the ambition of the project was to be able to distinguish a nominally tightened bolt from the slightly under- and over-tightened ones, for example, to be able to find the tension within $\pm 0.1\sigma_y$ around the nominal tension $0.7\ \sigma_y$. In this region the vibration-based features have a low sensitivity to the tension (Figure 3, Figure **4**), i.e. the value of the feature changes little with the significant change of the tension level. As the vibration features are obtained from noisy measurements, it makes it challenging to develop a robust technique for estimating the tension with the desirable precision.

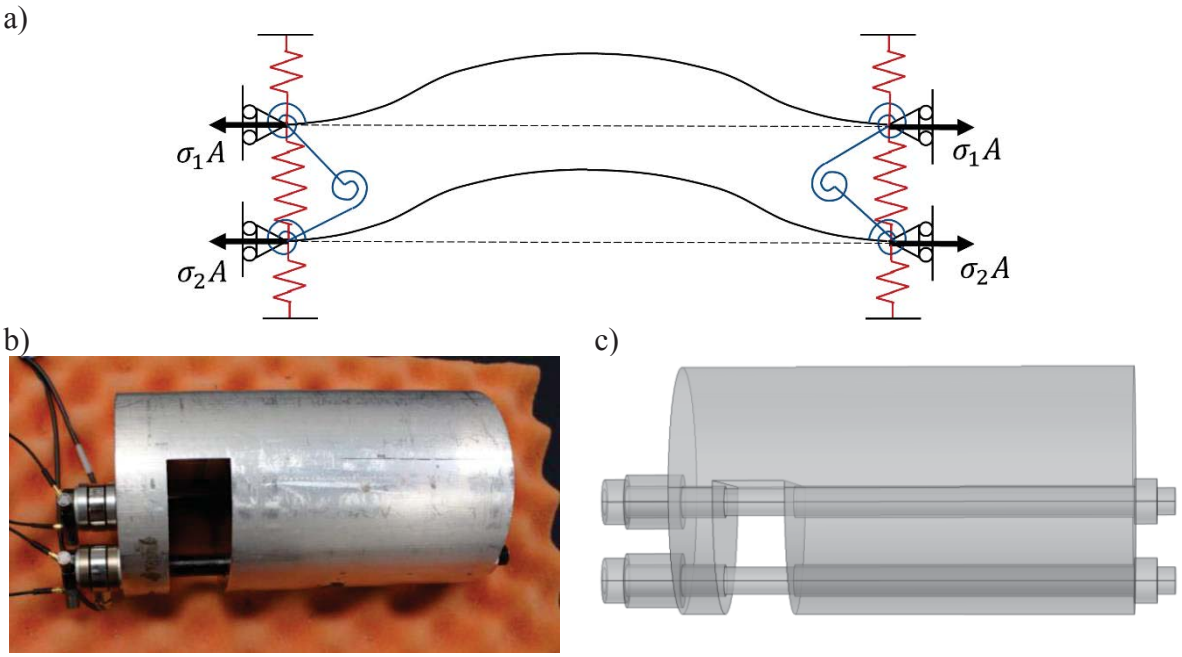

Figure 10. Two bolts structure from [19]: a) Analytical model; b) Experimental setup; c) COMSOL model

The study [20] attempted to suggest and test the algorithm that employs the first transverse natural frequency as the vibration feature, and then takes the next step towards classification, i.e. distinguishing the loose bolts from the tightened ones. The algorithm uses the gradient of the first natural frequency with respect to the tension from the clamp-clamp beam model (1). Also, the algorithm assumes that initially the bolt was tightened to the nominal tension value. The latter is used as the reference for the subsequent tension checks. The propagation of the uncertainty of the measured vibration feature to the uncertainty of the estimated bolt tension was conducted following the Delta method [21]. The variability of the vibration features was estimated by measuring the first transverse natural frequency of a big number of similar bolts holding a wind turbine blade on the test rig (Figure 11). It was concluded that the described above approach is not readily feasible, and it was suggested that the following can potentially improve the technique: 1) Improvements of the excitation/measurement/signal processing procedures; 2) Employing more sensitive features; 3) Combining several vibration features.

6 ON-GOING RESEARCH

The study [9] paved a way to another promising technology developed in the frame of VEBJI, which is currently patent pending [22]. In [9], it was analytically shown and numerically demonstrated that the boundary stiffnesses parameters (Figure 7) can be estimated from measured transverse natural frequencies. However, the method requires identification of a high number of modes, which is difficult to measure in practice (with hammer excitation only the first two transverse modes can be reliably identified). The new method suggests changing the dynamic properties of the bolt in a controllable way, by adding a known mass to the threaded end

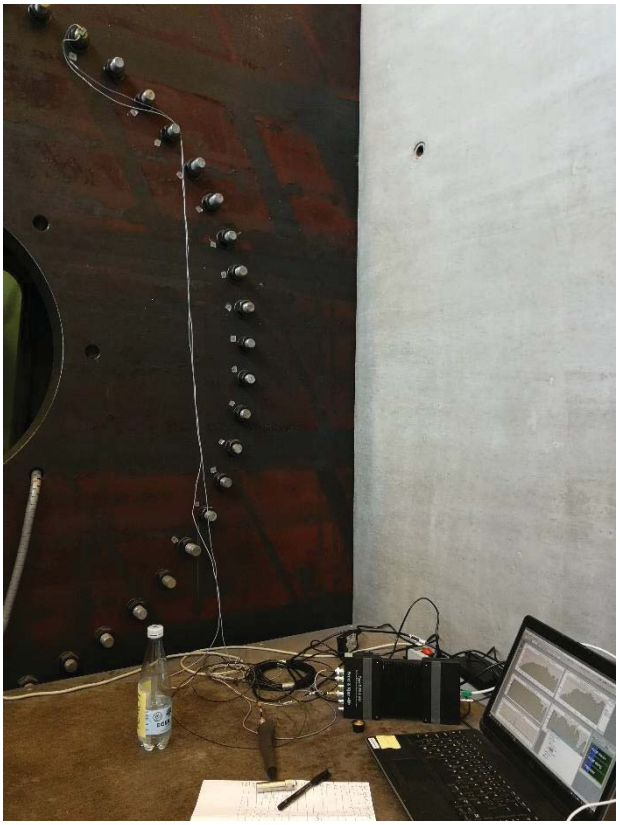

Figure 11. A test rig (wind turbine blade test bench) used to test the classification algorithm suggested in [20].

of the bolt. Thus, adding one or two masses to the bolt and measuring the first few natural frequencies, it is possible to estimate the tensional force acting in the bolt; the details of the method are presented in [23].

In the multi-bolt scenario, it is also anticipated that adding mass to the bolt end will make its dynamics different from the dynamics of the surrounding bolts; this will facilitate distinguishing the response of the tested bolt from the others (see Section 4).

As it was observed during the experiments, with hammer excitation employed, it is only possible to reliably identify the first two transverse modes, mainly due to the lack of excitation energy at the higher frequency range. The attempt to use the method in a real-life scenario, described in Section 5, also called for the improvement of the applied excitation and signal processing procedures. An approach to deal with this problem is to replace the hammer impacts with excitation by piezoelectric elements [24], which are generally more efficient at higher frequency ranges.

CONCLUSION

The paper describes the challenges, learnings, and achievements of the VEBJI project, whose aim was to generate knowledge and potentially develop a technique for estimating bolt tension using vibrations artificially excited in a bolt.

The study demonstrated that it is rather straightforward to distinguish a well-tightened bolt from a loose one, which could be done using the natural frequency and damping of the first transverse mode. However, it is more difficult to distinguish a nominally tightened bolt (characterized by axial stress σ_n) from slightly under- or overtightened ones ($< 0.9\ \sigma_n$ and $> 1.1\ \sigma_n$, respectively). Though the added mass method (Section 6) produces promising results, it still needs to be tested for multi-bolt joints scenarios.

ACKNOWLEDGMENT

This work is financially supported by Independent Research Fund Denmark, grant DFF-6111-00385.

REFERENCES

[1] J. S. Knudsen, "Hit Sound From Tightened Bolts 35 vs. 70 perc yield stress," 2013. [Online]. Available: https://youtu.be/gDl6C2k2jdU.

[2] T. Wang, G. Song, S. Liu, Y. Li and H. Xiao, "Review of bolted connection monitoring," *International Journal of Distributed Sensor Networks,* vol. 2013, no. 2, pp. 1-8, 2013.

[3] "i-Bolt® by ERREKA," 2020. [Online]. Available: http://www.errekafasteningsolutions.com/en/ibolt/.

[4] J. S. Knudsen, "Vibration-based Testing of Bolt Tightening," Technical Univ. of Denmark, MSc thesis, Dept. of Mech. Eng., Kgs.Lyngby, Denmark, 2013.

[5] E. Vind and S. Jespersen, "Estimating Bolt Tension from Transient Vibrations," MSc thesis, Technical Univ. of Denmark, Dept. of Mech. Eng., Kgs.Lyngby, Denmark, 2014.

[6] C. R. Farrar and K. Worden, Structural health monitoring: A machine learning perspective, Chichester, UK: John Wiley & Sons, Ltd, 2013.

[7] S. Chaki, G. Corneloup, I. Lillamand and H. Walaszek, "Combination of longitudinal and transverse ultrasonic waves for in situ control of the tightening of bolts," *Journal of Pressure Vessel Technology,* vol. 129, no. 3, pp. 383-390, 2007.

[8] J. H. Bickford, Introduction to the Design and Behavior of Bolted Joints, Non-Gasketed Joints, CRC Press, 2007.

[9] S. M. Sah, J. J. Thomsen and D. Tcherniak, "Transverse vibrations induced by longitudinal excitation in beams with geometrical and loading imperfections," *Journal of Sound and Vibration,* vol. 444, pp. 152-160, 2019.

[10] S. M. Sah, J. J. Thomsen, M. Brøns, A. Fidlin and D. Tcherniak, "Estimating bolt tightness using transverse natural frequencies," *Journal of Sound and Vibration,* vol. 431, pp. 137-149, 2018.

[11] M. Brøns, J. J. Thomsen, A. Fidlin, D. Tcherniak and S. M. Sah, "Modal impact testing for estimating bolted joint," in *International Conference on Noise and Vibration Engineering (ISMA2018)*, Leuven, Belgium, 2018.

[12] M. Brøns, J. J. Thomsen, S. M. Sah, D. Tcherniak and A. Fidlin, "Estimating bolt tension from vibrations: transient features, nonlinearity, and signal processing.," *Mechanical Systems and Signal Processing,* 2019, Submitted.

[13] S. M. Sah, J. J. Thomses and D. Tcherniak, "Linearly coupled transverse vibrations of tensioned bolts," no. In preparation, 2020.

[14] S. S. Sorokin, J. J. Thomsen and M. Brøns, "Coupled longitudinal and transverse vibrations of tensioned Euler-Bernoulli beams with general boundary condiitions," *Journal of Sound and Vibrations,* no. Submitted, 2019.

[15] A. Bokaian, "Natural frequencies of beams under tensile axial loads," *Journal of Sound and Vibration,* vol. 142, no. 3, pp. 481-498, 1990.

[16] M. H. Hermansen and J. J. Thomsen, "Vibration-based estimation of beam boundary parameters," *Journal of Sound and Vibration,* vol. 429, pp. 287-304, 2018.

[17] S. M. Sah, J. J. Thomsen and A. Fidlin, "Transverse vibrations of tightened bolts: Simplified modeling of tension-dependent boundary stiffness and damping," *Engineering Structures,* vol. 205, 2020.

[18] A. Plaugmann, "Vibration-based estimation of bolt tension: The multi-bolt crosstalk problem," Technical Univ. of Denmark, Dept. of Mech. Eng., BSc thesis, Kgs.Lyngby, Denmark, 2019.

[19] M. Brøns, A. Plaugmann, J. J. Thomsen and A. Fidlin, "Vibration-based bolt tension estimation for multi-bolt joints," in *International Modal Analysis Conference (IMAC-2020)*, Houston, Texas, USA, 2020.

[20] D. Tcherniak and J. J. Thomsen, "On the feasibility of utilizing vibrations for bolted joint assessment," in *9th Europaen Workshop on Structural Health Monitoring*, Manchester, UK, 2018.

[21] Y. M. M. Bishop, S. E. Fienberg and P. W. Holland, Discrete Multivariate Analysis Theory and Practice, New York: Springer, 2007.

[22] M. Brøns and J. J. Thomsen, "A METHOD AND A SYSTEM FOR ESTIMATING THE TENSION OF A TENSION MEMBER". Europe Patent 20154878.1, 01 2020.

[23] M. Brøns and J. J. Thomsen, "Vibrations-based estimation of boundary stiffness and axial tension in beams using added mass," *Journal of Sound and Vibration,* no. Submitted, 2020.

[24] M. Brøns, D. Tcherniak and J. J. Thomsen, "Estimating tension in multi-bolt joints from piezo-electric excitation," in *Conference on Noise and Vibration Engineering (ISMA)*, Leuven, Belgium, 2020.

EURODYN 2020
XI International Conference on Structural Dynamics
M. Papadrakakis, M. Fragiadakis, C. Papadimitriou (eds.)
Athens, Greece, 23–26 November 2020

NONPARAMETRIC NONLINEAR RESTORING FORCE AND EXCITATION IDENTIFICATION WITH LEGENDRE POLYNOMIAL AND DATA FUSION

Bin Xu[1, 2], Ye Zhao[1], Baichuan Deng [3]

[1] College of Civil Engineering, Huaqiao University, Xiamen 361021, China;

[2] Key Laboratory for Intelligent Infrastructures and Monitoring of Fujian Province (Huaqiao University), Xiamen 361021, China

[3] College of Civil Engineering, Hunan University, Changsha 410082, China;

*Corresponding author: binxu@hqu.edu.cn

Keywords: Nonparametric identification, nonlinear restoring force, Legendre polynomial, extended Kalman filter with unknown input, limited acceleration measurement, data fusion

Abstract. *Identification of nonlinear restoring force (NRF) and dynamic loadings provides useful information for structural damage prognosis (DP). Due to higher complexity of structural nonlinearities, it is difficult to establish an exact parametric mathematical model in prior to describe the nonlinear behavior of a structural member or a substructure under strong dynamic loadings in practice. Moreover, external dynamic loading applied on an engineering structure is usually unknown and only acceleration responses at limited degrees of freedom (DOFs) of the structure are monitored. In this study, a nonparametric NRF and excitation identification approach combining Legendre polynomial and extended Kalman filter with unknown input (EKF-UI) is proposed using limited acceleration measurements fused with displacement measurement for the purpose of eliminating drift problem. The performance of the proposed approach is illustrated via numerical simulation with a multi-degree-of-freedom (MDOF) frame structure equipped with an MR damper mimicking nonlinearity under different unknown loading scenarios. Partial acceleration measurement of the structure polluted by intensive measurement noises is employed for the identification. The parameter identification convergency procedure and the effect of initial estimation errors of structural parameters on the final identification results are investigated. Identified results demonstrate that the proposed approach is capable of identifying structural nonlinear behavior, excitation and dynamic response measurement in a nonparametric way with acceptable accuracy.*

1 INTRODUCTION

Structural identification for the purpose of structural health monitoring (SHM) and damage evaluation using vibration measurements has attracted extensive attentions in structural engineering field in the last decades [1, 2]. Generally speaking, structural damage usually results

in changes in structural parameters such as stiffness and damping. Because structural vibration frequencies and modal shapes extracted from dynamic response measurement depend on stiffness, lots of vibration-based structural damage detection approaches have been proposed, where structural damage is represented by a stiffness decrease identified from the extracted structural frequencies and/or modal shapes [3]. Strictly speaking, most of the identification approaches based on eigenvalues and/or modal shapes are only applicable for linear elastic systems. However, structural nonlinearity is a common phenomenon encountered in engineering structures subjected to severe dynamic loading and should be considered during the vibration analysis and the identification for structures [4-6]. Representing damages in a nonlinear dynamic system using the changes in stiffness identified with eigenvalues or modal shapes extracted from dynamic response time history of the system experiencing nonlinearity is doubtful and questionable. Structural nonlinear restoring force (NRF) is a direct director describing the initiation and development of structural nonlinearity and can be used directly to determine the energy consumption during the whole procedure of vibration, which provides more helpful information for damage prognosis (DP) compared with stiffness.

Since it is usually hard to measure structural responses at all degrees of freedom (DOFs) of a structure with lots of sensors, structural identification with only partial structural response measurements has received more attention [7]. A simultaneous NRF and mass identification approach is developed by Xu. et al. [8] for multi-degree-of-freedom (MDOF) structures using the EKF with weighted global iteration (EKF-WGI) based on limited absolute acceleration response. However, the conventional EKF approach works well when the information of external inputs to structures is available. Because all external excitations to a structure are not always available in practice, it is important to develop structural nonlinearity and excitation identification algorithms for engineering structures experiencing nonlinearity under dynamic excitations. Yang et al. [9] proposed an adaptive EKF with unknown input (AEKF-UI) approach for the identification of time-varying parameters and unknown external excitations. Lei et al. [10] proposed an algorithm based on sequential application of an extended Kalman estimator (EKE) for the extended state vector of a structure and least-squares estimation (LSE) of its unknown external excitations to detect structural damage with limited input and output measurement signals. This approach is applied for the identification of linear structures where structure damage is described as the decrease in stiffness. For the identification of non-linear structural parameters under limited input and output measurements, an algorithm based on the sequential application of EKE for the parameters of a parametric model describing nonlinearity and the LSE for the unmeasured excitation is proposed [11]. More recently, Liu et al. [12] proposed a data fusion based EKF with unknown inputs (EKF-UI) approach for simultaneously identifying structural parameters and unknown excitations. A general system and unknown inputs simultaneous estimation using EKF-UI approach was proposed by Pan et al. [13] to meet the challenges coming with the unavailability of dynamic response and excitation information. A General Extended Kalman filter with unknown inputs (GEKF-UI) is proposed to estimate the structural parameters and the unknown excitations (inputs) simultaneously to overcome the limitations of the existing EKF methods for the identification of both time-invariant and time-varying systems. In all of the above studies, the parametric models describing the nonlinearity of the structure are assumed and the parameters of the parametric models are identified.

In this paper, a nonparametric structural NRF, excitation, unmeasured dynamic response identification approach based on the Legendre polynomial model and EKF-UI is proposed for nonlinear structure composed of a linear structure and a nonlinear member of a magnetorheological (MR) damper. Data fusion is used to eliminate the drift problem in dynamic responses identification. The proposed approach was numerically validated with MDOF structures

equipped with a MR damper mimicking nonlinear behavior under different excitation forms. The parameter identification convergency procedure and the effect of initial estimation errors of structural parameters on the final identification results are investigated. Identification results show that the proposed method is effective to identify NRF and the unknown excitations when no parametric models describing the nonlinearity of the structure are employed.

2 NONPARAMETRIC NRF AND EXCITATION IDENTIFICATION APPROACH

In physical science and mathematics, the Legendre polynomial is a system of orthogonal polynomials, with a vast number of beautiful properties and innumerable applications. Any piecewise continuous function $z(x,y)$ with finitely many discontinuities in the interval of [-1, 1] can be expressed by the sequence of sums of a number of Legendre polynomials shown as follows,

$$z(x,y) \approx \sum_{n=0}^{N}\sum_{m=0}^{M} c_{nm} L_n(x) L_m(y) \tag{1}$$

where c_{nm} is the coefficient of the Legendre polynomials of $L_n(x)$ and $L_m(y)$, N and M are integrals.

The recursive relationship of Legendre polynomials is shown in the following equation,

$$L_n(x) = \sum_{m=0}^{\left[\frac{n}{2}\right]} (-1)^m \frac{(2n-2m)!}{2^n m!(n-m)!(n-2m)!} x^{n-2m} \quad (n=0,\ 1,\ 2,\ \cdots\cdots) \tag{2}$$

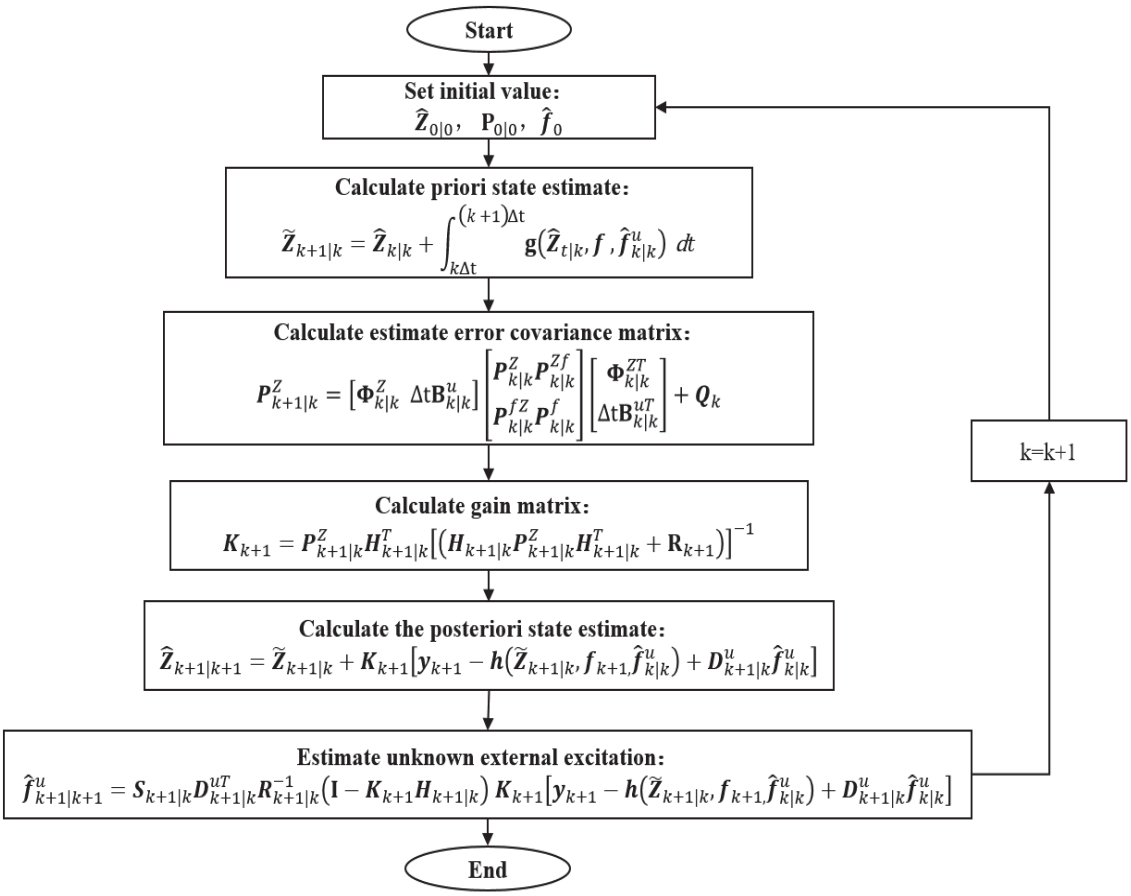

Figure 1: Flowchart of the presented algorithm for identifying structural parameters and unknown excitations

In this study, without using any parametric models describing structural nonlinear behavior, the structural NRF could be described in the form of Legendre polynomial of structural relative velocity, relative displacement as shown in the equation (3),

$$R_{i,i-1}[\dot{x}(t), x(t), \theta] \approx \sum_{h=0}^{k} \sum_{j=0}^{q} c_{i,i-1,h,j}^{non} L_h(v'_{i,i-1}) L_j(s'_{i,i-1}) \tag{3}$$

where $R_{i,i-1}[\dot{x}(t), x(t), \theta]$ is the NRF between the ith DOF and the i-1th DOF, $v_{i,\,i-1}$ and $s_{i,\,i-1}$ are relative velocity and relative displacement vectors, $c_{i,i-1,h,j}^{non}$ is the coefficient of the polynomial, k and q are integers which depend on the nature and extent of the nonlinearity. $L_h(v'_{i,i-1})$ and $L_j(s'_{i,i-1})$ are Legendre polynomial. The identification flowchart of the proposed method is shown in details in Figure 1, where $\boldsymbol{Z}$, $\boldsymbol{P}$, $\boldsymbol{f}$, $\boldsymbol{g}$, $\boldsymbol{K}$ and $\boldsymbol{y}$ are extended state vector, the covariance matrix of error, external excitation, state equation, Kalman gain matrix and observation vector, respectively.

3 NUMERICAL SIMULATION VALIDATION CONSIDERING DIFFERENT EXCITATION SCENARIOS

To verify and validate the effectiveness of the proposed approach for the state of the structure, the unknown inputs and NRF identification with only partial measurements of acceleration and displacement, numerical studies with a four-story shear frame equipped with a MR damper on the fourth floor to mimic nonlinear behavior of structure under two different excitation scenarios including the direct point excitation and earthquake excitation are carried out. The mass, inter-story stiffness and damping coefficients corresponding to each story of the four-story shear frame are $m_i = 400kg$, $k_i = 320kN/m$, and $c_i = 0.24kN \cdot s/m$ (i=1,…, 4), respectively.

In the direct analysis of the dynamic response of the nonlinear structure, a parametric model for the employed MR damper is required even it is unnecessary in the identification approach proposed in this study. Here, the modified Dahl model described in the following equation is used [14].

$$f_{non}^{MR} = K_0 s_{i,i-1} + C_0 v_{i,i-1} + F_d Z - f_0 \tag{4}$$

where f_{non}^{MR} is the NRF provided by the MR damper, K_0 and C_0 is the stiffness coefficient and damper coefficient of the MR damper, F_d represents the coulomb frictional force determined by the current intensity, $s_{i,i-1}$ and $v_{i,i-1}$ represent the displacement and velocity of the MR damper installed on the i-1th floor, f_0 is the initial force, and Z is a constant determined by the following equation:

$$\dot{Z} = \sigma v_{i,i-1}(1 - Z\,\mathrm{sgn}(v_{i,i-1})) \tag{5}$$

where σ is the hysteresis coefficient of the MR damper. Here, the parameters take the following values, $\sigma = 50s/m$, $K_0 = 0.05kN/\mathrm{m}$, $C_0 = 1.995kN \cdot \mathrm{s/m}$, $F_d = 0.035kN$, and $f_0 = 0$.

Only acceleration responses at the first, third, and fourth floors are used in identification. Simultaneously, the displacement responses on the second and fourth floors are used for data fusion. The acceleration responses are polluted with white noises with 3% noise-to-signal ratio in root mean square. In the iterative process, in order to consider the effect of the initial

values of stiffness and damping coefficients on the identification results. A -20% and a -40% initial estimation error for both stiffness and damping coefficients are considered.

A normalized root-mean-square error (NRMSE) is defined to evaluate the accuracy of the unmeasured dynamic responses as well as the unknown excitation identification results. The NRMSE is defined as follows,

$$\mathrm{NRMSE} = \sqrt{\frac{\sum_{k=1}^{np}\left(\gamma_k^i - \gamma_k^a\right)^2}{\sum_{k=1}^{np}\left(\gamma_k^a\right)^2}} \times 100\% \tag{6}$$

in which *np* is the number of sampling points; γ_k^i and γ_k^a are the identified unknown dynamic responses, NRF and unknown excitation and their actual value of the *k*-th sample time step.

3.1 Case1: A point excitation

The nonlinear shear frame structure is subjected to a sinusoidal excitation applied on the third floor. Based on the proposed approach, the inter-story stiffness and the damping coefficients of the corresponding linear part of the structure are identified and the identified results compared with the real values are shown in Table 1. The maximum of the relative errors corresponding to the inter-story stiffness and damping coefficients are 0.62% and 5.42%, respectively.

Structural parameters	Real value	Identified value	Error	Structural parameters	Real value	Identified value	Error
$k_1\left(kN\cdot m^{-1}\right)$	320	319	0.31%	$c_1\left(N\cdot s\cdot m^{-1}\right)$	240	227	5.42%
$k_2\left(kN\cdot m^{-1}\right)$	320	319	0.31%	$c_2\left(N\cdot s\cdot m^{-1}\right)$	240	239	0.42%
$k_3\left(kN\cdot m^{-1}\right)$	320	318	0.62%	$c_3\left(N\cdot s\cdot m^{-1}\right)$	240	242	0.83%
$k_4\left(kN\cdot m^{-1}\right)$	320	320	0.00%	$c_4\left(N\cdot s\cdot m^{-1}\right)$	240	240	0.00%

Table 1: Identified structural parameters (-20% initial parameter error)

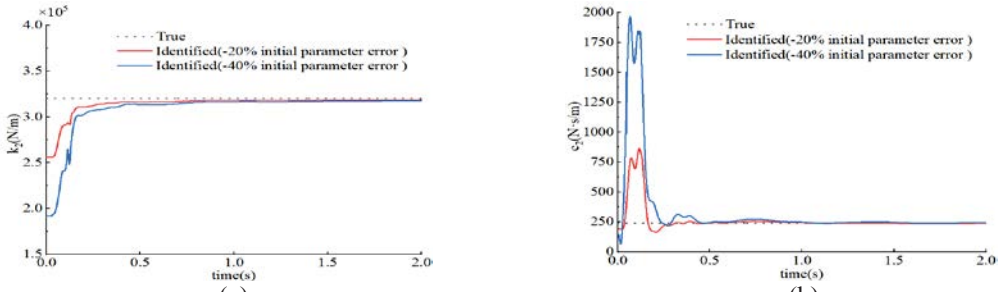

(a) (b)

Figure 2: Iterative identification process compared with the true values: (a) stiffness on the second floor (b) damping coefficient on the second floor

Further investigation on the effect of different initial estimation errors of structural stiffness and damping coefficients on the iterative processes of the identified parameters and their identification accuracy is carried out and the corresponding results are plotted in Figure 2, whereas the dashed curves are the actual ones for comparison. It is obvious that the identified parameters are able to stably converge to their theoretical values. Figure 3 demonstrates the comparison of the identified displacement on the third floor and the acceleration response on the

second floor with their true results determined by integration. Figure 4 shows the comparison of identified excitation force on the third floor and the MR damper force on the fourth floor with their true results when the initial estimation errors for stiffness and damping coefficients are -20%. From Figures 3 and 4, it can be found the identified results have a good agreement with the true values.

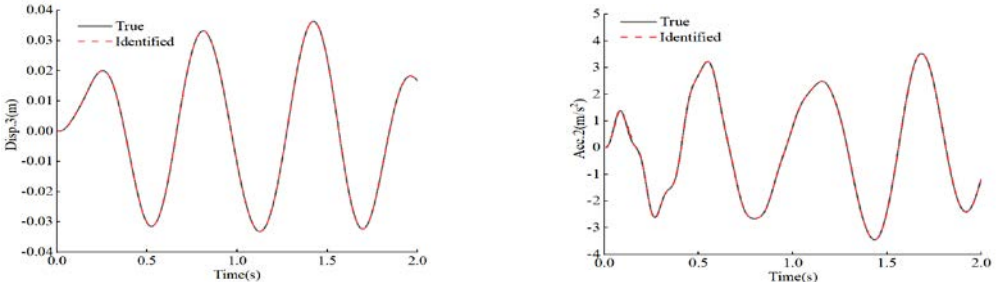

Figure 3: The comparison of identified dynamic response with their true values (-20% initial parameter error): (a) displacement on the third floor, (b) acceleration on the second floor

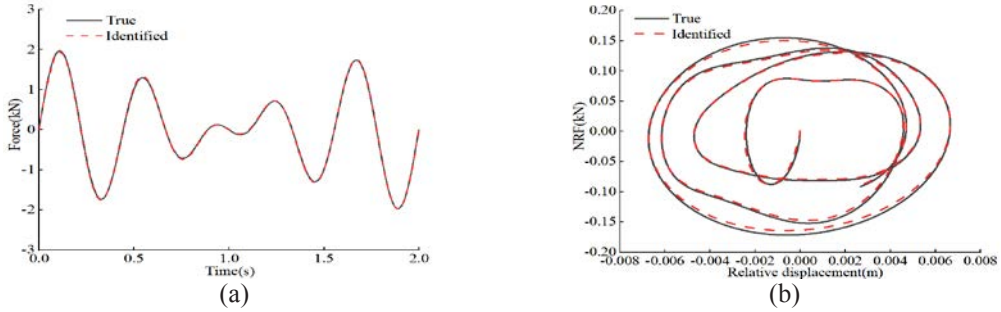

Figure 4: The comparison of identified excitation force and the MR damper force with their true results (-20% initial parameter error): (a) unknown excitation, (b) the hysteretic of MR damper on the fourth floor

Identified quantifies (-20% initial parameter error)	NRMSE(%)	Identified quantifies (-40% initial parameter error)	NRMSE(%)
Displacement on the 3rd floor	0.001	Displacement on the 3rd floor	0.001
Acceleration on the 2nd floor	0.014	Acceleration on the 2nd floor	0.099
Excitation on the 3rd floor	0.048	Excitation on the 3rd floor	0.175
NRF on the 4th floor	0.086	NRF on the 4th floor	0.817

Table 2: NRMSE results corresponding to the identified dynamic response, excitation and NRF

The NRMSE results for the identified numerical model are shown in Table 2. It can be clearly seen from Table 2 that the values of NRMSE are very small, which indicates the identified results are close to their actual ones. However, different initial parameter estimation errors have no obvious negative influence on the identified results.

3.2 Case 2: Earthquake excitation

A further case where the nonlinear shear frame model is subjected to an earthquake excitation with an acceleration peak value of 0.3g is investigated considering the fact that the nonlinear behavior identification for engineering structures after the exciting of earthquake is

critical. Based on the proposed approach, the inter-story stiffness and damping coefficients of the linear part of the nonlinear structure can be identified and compared with their true values as shown in Table 3. It can be found that the inter-story stiffness can be identified with a very high accuracy even noise-contained acceleration response is employed. The maximum relative error for damping coefficients is 3.33% but is still acceptable.

Structural parameters	Real value	Identified value	Error	Structural parameters	Real value	Identified value	Error
$k_1\left(kN\cdot m^{-1}\right)$	320	320	0.00%	$c_1\left(N\cdot s\cdot m^{-1}\right)$	240	232	3.33%
$k_2\left(kN\cdot m^{-1}\right)$	320	320	0.00%	$c_2\left(N\cdot s\cdot m^{-1}\right)$	240	231	3.75%
$k_3\left(kN\cdot m^{-1}\right)$	320	320	0.00%	$c_3\left(N\cdot s\cdot m^{-1}\right)$	240	235	2.08%
$k_4\left(kN\cdot m^{-1}\right)$	320	320	0.00%	$c_4\left(N\cdot s\cdot m^{-1}\right)$	240	239	0.42%

Table 3: Identified structural parameters (-20% initial parameter error)

Iterative process comparison of the identified parameters when different initial estimation errors are considered are shown in Figure 5. Similar to parameter identification results under sine excitation, the identified parameters can converge to their theoretical values with very small error.

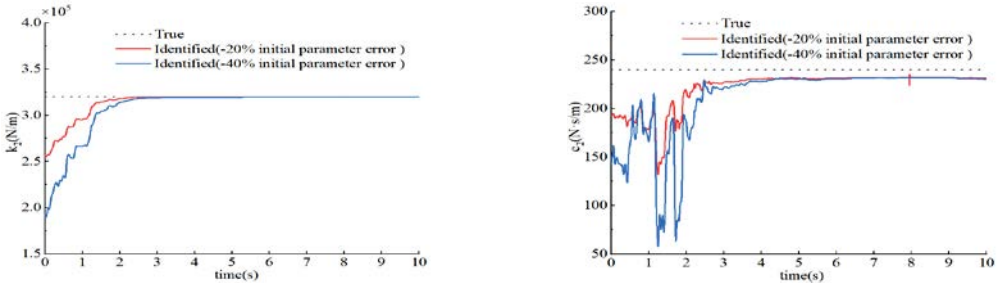

Figure 5: Iterative process comparison of the identified parameters of shear frame structure: (a) stiffness on the second floor (b) damping coefficient on the second floor

Figure 6 gives the comparison of the identified displacement response on the third floor and the acceleration response on the second floor with their corresponding actual results. Figure 7 shows the comparison of identified base excitation acceleration and the hysteretic of the MR damper on the fourth floor with their true values. It can be easily observed from Figures 6 and 7 that the identified unknown dynamic response, earthquake acceleration and the damping force of MR damper meet their true values very well.

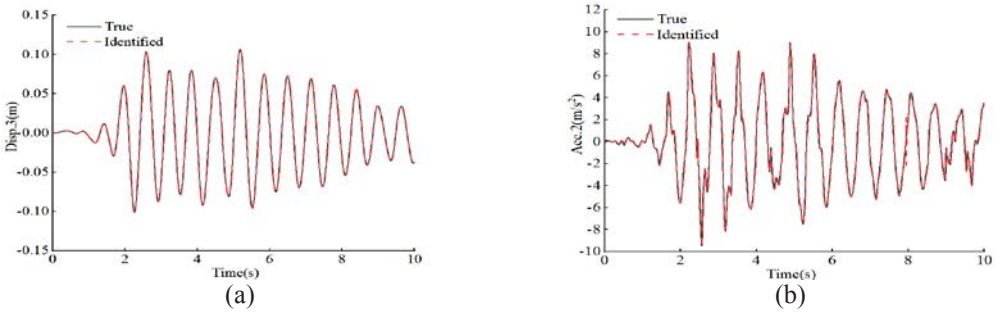

Figure 6: The comparison of identified dynamic response with their true values (-20% initial parameter error): (a) displacement on the third floor, (b) acceleration on the second floor

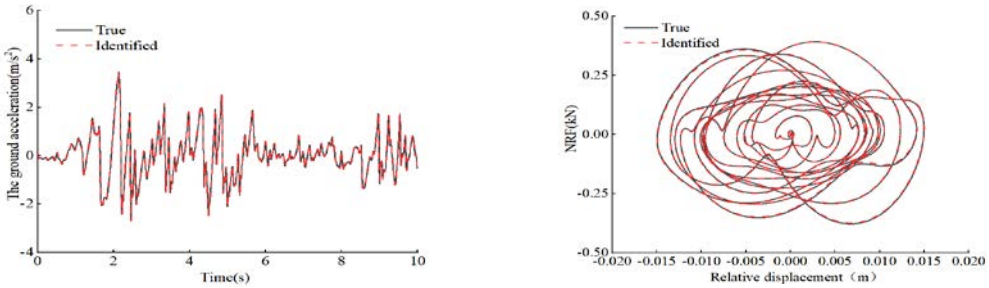

(a) (b)

Figure 7: The comparison of identified results with its true values (-20% initial parameter error): (a) unknown excitation, (b) the MR damper force on the fourth floor

The NRMSE results for the identified unknown responses are shown in Table 4. It can be seen from Table 4 that the values of NRMSE are smaller, which indicates the proposed method can accurately identify the unknown dynamic response, earthquake acceleration and NRF with high accuracy. Moreover, the initial estimation errors for stiffness and damping coefficients have no obvious negative effect on the identification results.

Identified quantifies (-20% initial parameter error)	NRMSE(%)	Identified quantifies (-40% initial parameter error)	NRMSE(%)
Displacement on the 3rd floor	0.001	Displacement on the 3rd floor	0.002
Acceleration on the 2nd floor	0.019	Acceleration on the 2nd floor	0.015
Excitation on the 3rd floor	0.028	Excitation on the 3rd floor	0.018
NRF on the 4th floor	0.021	NRF on the 4th floor	2.195

Table 4: NRMSE results corresponding to the identified dynamic response, excitation and NRF

4 CONCLUDING REMARKS

In this paper, a nonparametric MR damper force identification approach based on a Legendre polynomial and an extended EKF with unknown input is proposed. Numerical simulation results with a MDOF frame structure equipped with a MR damper under both point excitation and based earthquake excitation show that the proposed method is capable of identifying structural responses, MR damper force and unknown input with acceptable accuracy in a nonparametric way, where no parametric models for the MR damper are required.

The proposed approach is potential for structural nonlinearity identification, which plays key roles in post-event damage prognosis and remaining load-carrying capacity and remaining service life forecasting for engineering structures where structural nonlinear behavior and loading profiles should be considered.

REFERENCES

[1] J. Ou and H. Li, Structural health monitoring in mainland China: review and future trends. *Structural Health Monitoring* 9, 219–231, 2010.

[2] W. Fan and P. Qiao, Vibration-based damage identification methods: a review and comparative study. *Structural Health Monitoring* 9, 83–111, 2011.

[3] Z. Wu, B. Xu, and T. Harada, Review on Structural Health Monitoring for Infrastructure. *Journal of applied mechanics* 6, 1043–1054, 2003.

[4] T. Jan, Non-parametric simultaneous identification of both the nonlinear damping and restoring characteristics of nonlinear systems whose dampings depend on velocity alone. *Mechanical Systems and Signal Processing* 25:1159–1173, 2011.

[5] Y. Lei and M. He, Identification of the nonlinear properties of rubber-bearings in base-isolated buildings with limited seismic response data. *Science China Technological Sciences* 56, 1224–1231, 2013.

[6] B. Xu, J. He and S. Masri, Data-based model-free hysteretic restoring force and mass identification for dynamic systems. *Computer-Aided Civil and Infrastructure Engineering* 30, 2–18, 2015.

[7] B. Xu, B. Deng, J. Li and J. He, Structural nonlinearity and mass identification with a nonparametric model using limited acceleration measurements. *Advances in Structural Engineering* 24, 1018-1031, 2018.

[8] B. Xu, J. Li, Shirley. Dyke, B. Deng and J. He, Nonparametric identification for hysteretic behavior modeled with a power series polynomial using EKF-WGI approach under limited acceleration and unknown mass. *International Journal of Non-Linear Mechanics* 119, 103324:1-11, 2020.

[9] J. Yang, S. Pan, and H. Huang, An adaptive extended Kalman filter for structural damage identifications II: unknown inputs, *Structural Control Health Monitoring* 14, 497-521, 2007.

[10] Y. Lei, Y. Jiang, and Z. Xu, Structural damage detection with limited input and output measurement signals, *Mechanical Systems and Signal Processing* 28, 229-243, 2012.

[11] Y. Lei, Y. Wu, and T. Li, Identification of non-linear structural parameters under limited input and output measurements, *International Journal of Nonlinear Mechanics* 47, 1141-1146, 2012.

[12] L. Liu, Y. Su, J. Zhu, and Y. Lei, Data fusion based EKF-UI for real-time simultaneous identification of structural systems and unknown external inputs. *Measurement* 88, 456-467, 2016.

[13] S. Pan, D. Xiao, S. Xing, S.S. Law, P. Du, and Y. Li, A general extended Kalman filter for simultaneous estimation of system and unknown inputs, *Engineering Structure* 109, 85-98, 2016.

[14] Q. Zhou and W. Qu, Two mechanic models for magneto-rheological damper and corresponding test verification, *Earthquake Engineering and Engineering Vibration* 22, 144-150, 2002.

EURODYN 2020
XI International Conference on Structural Dynamics
M. Papadrakakis, M. Fragiadakis, C. Papadimitriou (eds.)
Athens, Greece, 23–26 November 2020

REDUCTION OF QUANTIZATION AND CLIPPING ERRORS USING BAYESIAN VIRTUAL SENSORS

Jyrki Kullaa

Metropolia University of Applied Sciences
P.O. Box 4071, 00079 Metropolia, Finland
e-mail: jyrki.kullaa@metropolia.fi

Keywords: Virtual sensing, Bayes' rule, Quantization, Clipping, Overload error, Sensor network

Abstract. *In vibration monitoring of structures, quantization and overload errors may be significant when measuring vibrations with highly variable magnitudes. In analog-to-digital (A/D) conversion, each data value must be expressed by a finite number of bits. Therefore, a finite number of levels are available to approximate an infinite number of analog values. This A/D conversion results in a round-off error, or quantization error. The signal-to-noise ratio can be increased by setting the dynamic range so that the analog signal occupies it as much as possible. If the dynamic range is too small, it can result in overload error due to signal clipping. Both aforementioned errors can be reduced using Bayesian virtual sensing. Each data point can be estimated using the data from the whole sensor network on the structure. The variance of the quantization error is known, which can be used in the likelihood and prior estimation. The resulting posterior mean is more accurate than the quantized signal. The clipped sensors are estimated using the conditional probability of the clipped sensors given the remaining unclipped sensors. In a numerical experiment of a bridge structure with 28 accelerometers, the reduction of the quantization error and the reconstruction of the clipped sensors were studied using the response data only. The main requirement is that the number of sensors must be greater than the number of active modes to ensure redundancy of the sensor network. The signal-to-noise ratio was used as a performance measure. Virtual sensors outperformed the quantized data and an optimal dynamic range of the A/D converter was found.*

1 INTRODUCTION

In monitoring of structural vibrations, different magnitudes of vibration occur. For example, a bridge may vibrate under the excitation of different types of vehicles, variable wind levels, small ground tremor, or different magnitudes of earthquakes. In some applications, it is important to measure all vibration levels, for example in rainflow analysis for fatigue monitoring.

An issue in measuring a wide range of vibration levels is the quantization error. In analog-to-digital (A/D) conversion, each data value must be expressed by a finite number of bits. Therefore, a finite number of levels are available to approximate an infinite number of analog values. This A/D conversion results in a round-off error, quantization error. The signal-to-noise ratio can be increased by setting the dynamic range so that the analog signal occupies it as much as possible. If the dynamic range is too small, it can result in clipping due to overload. Both of these errors may be significant when measuring vibration with highly variable magnitudes.

Quantization has been studied in communication and a typical problem is how to optimally quantize analog signals [1]. In the present study, however, the objective is to reconstruct the already quantized signals in order to reduce the quantization error. A uniform quantizer is assumed with a user-defined dynamic range. The signal-to-noise ratio (SNR) is used as a performance measure, because it is also very important in the detection theory [2] used in structural health monitoring.

Noise reduction is done by applying Bayesian virtual sensing [3]. It is assumed that a sensor network with simultaneous sampling is installed on the structure. If the network is redundant, each sensor's signal can be estimated using all the signals in the network. It has been shown that the Bayesian virtual sensors are more accurate than the actual measurement [3]. It is assumed that quantization is done properly and quantization error is the only source of error. With this assumption, it is possible to concentrate on the research question whether quantization error can be reduced after digitization. The analog-to-digital converter (ADC) is, however, a nonideal device and exhibits a variety of errors, for example linearity error, gain error, and offset error [4]. It should be mentioned that with modern equipment, other measurement errors may be considerably higher than the error in the A/D conversion [5]. If at least a 12-bit ADC is used, the other sources of error in the data acquisition and processing procedures are more significant in practice [6]. However, even with modern equipment, quantization errors can be significant when different levels of magnitudes are measured with a fixed dynamic range.

The paper is organized as follows. Quantization is introduced in Section 2 with two types of errors, granular noise and overload noise. Bayesian virtual sensors are designed in Section 3 to reduce the quantization error. A numerical experiment of a bridge deck is performed in Section 4, in which three different magnitudes of vibration are measured with 28 accelerometers at different points of the structure. The measurements are quantized and then reconstructed using virtual sensing. Finally, concluding remarks are given in Section 5.

2 QUANTIZATION

Vibration data are continuous both in time and amplitude. Sampling results in time discretization. Resulting samples are still continuous in amplitude. When the samples are digitized in the analog-to-digital converter (ADC), rounding error occurs. Quantization is the process of approximating the continuous range of values with a finite number of bits. The output values are referred to as output levels, output points, or reproduction values [7]. The number of bits determines the number of levels L:

$$L = 2^R \tag{1}$$

where R is the word size, resolution, or code rate. For example, for 8-, 12-, and 16-bit ADCs, the number of levels are 256, 4096, and 65536, respectively.

The quantizer divides the real line into L cells. Figure 1 shows the quantizer characteristics of a uniform 3-bit quantizer with $L = 2^3 = 8$ possible levels. The mapping $y = Q(x)$ in Figure 1a is a staircase function and the quantization error is shown in Figure 1b. Each bounded cell is called a granular cell and a cell that is unbounded is called an overload cell. Together all of the overload cells are called the overload region [7]. The range of the quantizer is defined as the total length of the granular cells.

In a uniform quantizer, the quantized signal $\mathbf{y}(t_i)$ is obtained from the sampled continuous-amplitude data $\mathbf{x}(t_i)$ using the following.

$$\mathbf{y}(t_i) = \Delta x \cdot \mathrm{floor}\left(\frac{\mathbf{x}(t_i)}{\Delta x}\right) + \frac{1}{2} \tag{2}$$

where t_i is the sampling instant and Δx is the quantization interval. The function floor(x) rounds x to the nearest integer less than or equal to x. An analog signal and the corresponding quantized signal with a 3-bit ADC are plotted in Figure 2.

In order to study the quantization error, it is assumed that no other errors occur and quantization is done properly. It should be noted that other sources of error (noise) can be more serious than the quantization error, e.g. aperture error, jitter, and nonlinearities [6].

Uniform quantization is assumed, in which the intervals Δx are of the same length. The true value at each sampling instant is approximated by the quantized level closest to it. The quantization error

$$w(n) = \mathbf{y}(n) - \mathbf{x}(n) \tag{3}$$

thus varies between $-\Delta x/2$ and $\Delta x/2$. A uniform probability density function of the quantization error is assumed [6]:

$$p(w) = \begin{cases} \dfrac{1}{\Delta x} & -\dfrac{1}{2}\Delta x \le w \le \dfrac{1}{2}\Delta x \\ 0 & \text{otherwise} \end{cases} \tag{4}$$

The mean value of the error is zero, and the variance is

$$\sigma_w^2 = \int_{-\infty}^{\infty} w^2 p(w) dw = \frac{1}{\Delta x}\int_{-0.5\Delta x}^{0.5\Delta x} w^2 dw = \frac{\Delta x^2}{12} \tag{5}$$

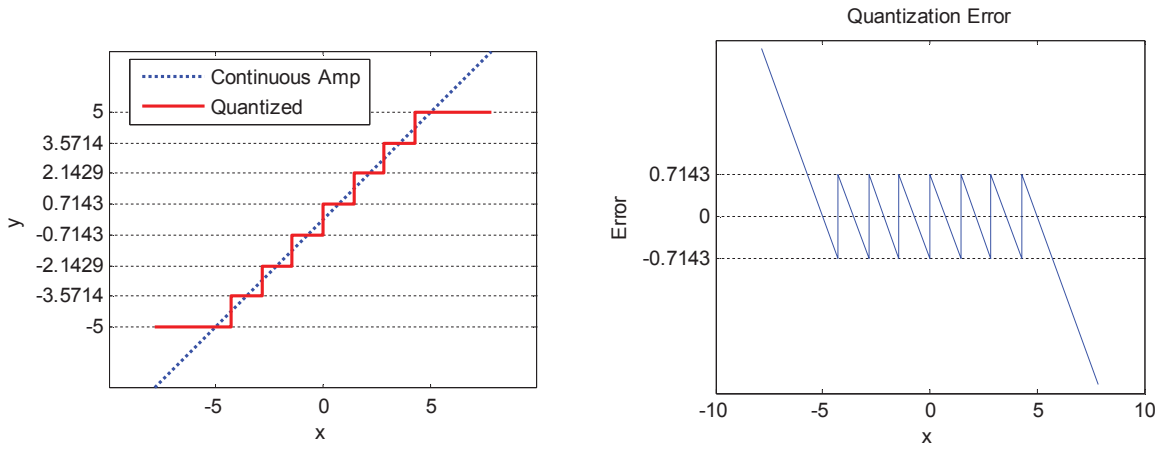

(a) (b)

Figure 1: (a) Mapping of a 3-bit uniform quantizer and (b) the quantization error.

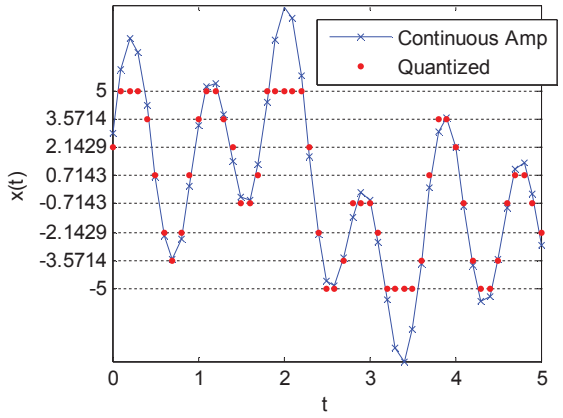

Figure 2: An example of a quantized signal with a 3-bit ADC.

2.1 Granular and overload noise

The quantization error (3) is often denoted as noise introduced by the quantizer. Granular noise occurs for an input that lies within the bounded cells of the quantizer. The overload noise is introduced if the input lies in the overload region i.e. in an unbounded cell. Therefore, granular error is relatively small while overload noise can be very large (Figure 1b and Figure 2) [7].

The performance of the quantizer is often specified in terms of a signal-to-noise ratio (SNR). It should be mentioned that the SNR is also important in the detection theory [2]. Structural health monitoring (SHM) utilizes measured vibration signals in damage detection. Therefore, a quantizer with a large SNR is advantageous [8].

The SNR is defined as [7]

$$SNR = 10\log_{10}\frac{E(X^2)}{D} \tag{6}$$

where D is the average distortion, which for a uniform quantizer is given in (5) if the input signal is bounded in the granular region.

In practice, most of the signals are unbounded, and the maximum error is infinite. Therefore, the overload region should be avoided. On the other hand, for the best signal-to-noise

ratio (SNR), the measured signal must occupy as much of the available ADC range as possible. The ADC setting is therefore a trade-off between the maximal SNR and a small probability of overload.

If the ADC range is adjusted to the extreme events, the SNR of the small events may become small. On the other hand, if the ADC range is adjusted to small amplitudes, the large vibrations can result in overload error due to signal clipping. Clipping occurs if the measured signal exceeds the ADC range. These overload errors can be unbounded. The quantizer approximates the values in the overload region to the maximum (or minimum) quantization level, which is the overload amplitude. In the signal plot, it looks like the signal peaks have been clipped (Figure 2).

The clipped channels may be useless due to a large error. Fortunately, clipping is easy to detect. It may be possible to reconstruct clipped data, if there exist unclipped channels at the same data point. The reconstruction can be done using Bayesian virtual sensing introduced in the next section and applied to both granular and overload errors.

3 BAYESIAN VIRTUAL SENSING

Bayesian virtual sensing is used to estimate sensor data that are more accurate than the quantized signals. A sensor network with simultaneous sampling is required. The objective is to reduce the quantization error of each signal using all the quantized response data in the network.

The main requirement is that the number of sensors in the network is large enough to make the system redundant. In practice, the number of sensors should be larger than the number of active modes.

There are two different quantization errors discussed in Section 2. The granular error is reduced with a different algorithm than the overload error. In order to reduce granular noise, all channels can be used in estimation excluding the clipped data. For granular error, the sensor's own quantized value can be also utilized, because its error variance is known. To reduce overload error and reconstruct the clipped data, the remaining unclipped channels should be only used for estimation. The data from the clipped sensor cannot be used, because its noise variance is unknown. Another option is to assign an infinite error variance to all clipped sensors. This would allow the development of a unified algorithm.

Notice that no mathematical model (e.g. a finite element model) is needed. The virtual sensors are estimated based on quantized measurement only. Also, the excitation is unknown.

Empirical virtual sensing is applied to the current measurement. Consider a sensor network measuring p simultaneously sampled responses $\mathbf{y} = \mathbf{y}(t_i)$ at time instant t_i. An additive noise model of quantization is assumed [7]. Each measurement $\mathbf{y}$ includes measurement error $\mathbf{w} = \mathbf{w}(t_i)$ (3):

$$\mathbf{y} = \mathbf{x} + \mathbf{w} \tag{7}$$

where $\mathbf{x} = \mathbf{x}(t_i)$ are the exact values of the measured degrees of freedom (DOF). All vectors are divided into predicted DOFs $\mathbf{u}$ and remaining DOFs $\mathbf{v}$:

$$\mathbf{y} = \begin{Bmatrix} \mathbf{y}_u \\ \mathbf{y}_v \end{Bmatrix} \qquad \mathbf{x}_m = \begin{Bmatrix} \mathbf{x}_u \\ \mathbf{x}_v \end{Bmatrix} \qquad \mathbf{w} = \begin{Bmatrix} \mathbf{w}_u \\ \mathbf{w}_v \end{Bmatrix} \tag{8}$$

For simplicity but without loss of generality, assume zero-mean variables $\mathbf{y}$. The partitioned data covariance matrix $\mathbf{\Sigma}_y$ is

$$\boldsymbol{\Sigma}_y = \mathrm{E}\left[\mathbf{y}\mathbf{y}^T\right] = \begin{bmatrix} \boldsymbol{\Sigma}_{y,uu} & \boldsymbol{\Sigma}_{y,uv} \\ \boldsymbol{\Sigma}_{y,vu} & \boldsymbol{\Sigma}_{y,vv} \end{bmatrix} = \begin{bmatrix} \boldsymbol{\Gamma}_{y,uu} & \boldsymbol{\Gamma}_{y,uv} \\ \boldsymbol{\Gamma}_{y,vu} & \boldsymbol{\Gamma}_{y,vv} \end{bmatrix}^{-1} = \boldsymbol{\Gamma}_y^{-1} \tag{9}$$

where the precision matrix $\boldsymbol{\Gamma}_y$ is defined as the inverse of the data covariance matrix $\boldsymbol{\Sigma}_y$ and is also written in partitioned form. E(·) denotes the expectation operator.

The objective is to find a linear estimator for the virtual sensors. It is well known that linear estimator is derived if the variables are normally distributed. Therefore, even if the granular error is uniformly distributed, a normal distribution is assumed in this paper with the same mean and variance as the true distribution.

A linear minimum mean square error (MMSE) estimate for $\mathbf{y}_u \mid \mathbf{y}_v$ ($\mathbf{y}_u$ given $\mathbf{y}_v$) is obtained by minimizing the mean-square error (MSE) and can be computed either using the covariance or precision matrix [9, 10]. The expected value, or the conditional mean, of the predicted variable is:

$$\hat{\mathbf{y}}_u = \mathrm{E}(\mathbf{y}_u \mid \mathbf{y}_v) = -\boldsymbol{\Gamma}_{y,uu}^{-1}\boldsymbol{\Gamma}_{y,uv}\mathbf{y}_v = \mathbf{K}\mathbf{y}_v \tag{10}$$

where $\mathbf{K} = -\boldsymbol{\Gamma}_{y,uu}^{-1}\boldsymbol{\Gamma}_{y,uv}$. The error covariance MSE is

$$\mathrm{cov}(\mathbf{y}_u \mid \mathbf{y}_v) = \boldsymbol{\Gamma}_{y,uu}^{-1} \tag{11}$$

Measurement error $\mathbf{w}$ is assumed to be granular noise only and independent of $\mathbf{x}$, with a covariance matrix (see Equation 5)

$$\boldsymbol{\Sigma}_w = E\left[\mathbf{w}\mathbf{w}^T\right] = \begin{bmatrix} \boldsymbol{\Sigma}_{w,uu} & \boldsymbol{\Sigma}_{w,uv} \\ \boldsymbol{\Sigma}_{w,vu} & \boldsymbol{\Sigma}_{w,vv} \end{bmatrix} = \frac{\Delta x^2}{12}\begin{bmatrix} \mathbf{I}_{uu} & \mathbf{0} \\ \mathbf{0} & \mathbf{I}_{vv} \end{bmatrix} \tag{12}$$

where $\mathbf{I}_{uu}$ and $\mathbf{I}_{vv}$ are unity matrices with proper dimensions.

Using Equation 7 and the assumed noise model, the conditional means of $\mathbf{y}$ and $\mathbf{x}$ are equal:

$$E(\mathbf{y}_u \mid \mathbf{y}_v) = E(\mathbf{x}_u \mid \mathbf{y}_v) + E(\mathbf{w}_u) = E(\mathbf{x}_u \mid \mathbf{y}_v) \tag{13}$$

Using Equations 7 and 12, the MMSE error covariance contains both the estimation error and noise:

$$\mathrm{cov}(\mathbf{y}_u \mid \mathbf{y}_v) = \mathrm{cov}(\mathbf{x}_u \mid \mathbf{y}_v) + \boldsymbol{\Sigma}_{w,uu} \tag{14}$$

The objective is to find a better estimate for $\mathbf{x}_u$ than the actual measurement $\mathbf{y}_u$ utilizing the noisy measurements $\mathbf{y}$ from the sensor network. From Bayes' rule,

$$p(\mathbf{x}_u \mid \mathbf{y}) = p(\mathbf{x}_u \mid \mathbf{y}_u, \mathbf{y}_v) = \frac{p(\mathbf{y}_u \mid \mathbf{x}_u, \mathbf{y}_v)\, p(\mathbf{x}_u \mid \mathbf{y}_v)}{p(\mathbf{y}_u \mid \mathbf{y}_v)} \tag{15}$$

where the likelihood is

$$p(\mathbf{y}_u \mid \mathbf{x}_u, \mathbf{y}_v) = p(\mathbf{y}_u \mid \mathbf{x}_u) = N(\mathbf{y}_u \mid \mathbf{x}_u, \boldsymbol{\Sigma}_{w,uu}) \tag{16}$$

and the prior is

$$p(\mathbf{x}_u \mid \mathbf{y}_v) = N(\mathbf{x}_u \mid \mathbf{K}\mathbf{y}_v, \boldsymbol{\Sigma}_{\text{prior}}) \tag{17}$$

and the prior covariance is obtained from (11) and (14):

$$\boldsymbol{\Sigma}_{\text{prior}} = \text{cov}(\mathbf{x}_u \mid \mathbf{y}_v) = \boldsymbol{\Gamma}_{y,uu}^{-1} - \boldsymbol{\Sigma}_{w,uu} \tag{18}$$

The denominator $p(\mathbf{y}_u \mid \mathbf{y}_v)$ in (15) is a Gaussian with mean (10) and covariance (11), and can be easily evaluated. However, it is merely a normalizing factor, which does not depend on $\mathbf{x}_u$, and its computation is not necessary.

The posterior distribution (15) is obtained by some manipulation, resulting in

$$\begin{aligned} p(\mathbf{x}_u \mid \mathbf{y}) &\propto p(\mathbf{y}_u \mid \mathbf{x}_u) p(\mathbf{x}_u \mid \mathbf{y}_v) \\ &\propto \exp\left[-\frac{1}{2}(\mathbf{y}_u - \mathbf{x}_u)^T \boldsymbol{\Sigma}_{w,uu}^{-1}(\mathbf{y}_u - \mathbf{x}_u) - \frac{1}{2}(\mathbf{x}_u - \mathbf{K}\mathbf{y}_v)^T \boldsymbol{\Sigma}_{\text{prior}}^{-1}(\mathbf{x}_u - \mathbf{K}\mathbf{y}_v) \right] \\ &= \exp\left\{ -\frac{1}{2}\left[\mathbf{x}_u - \boldsymbol{\Sigma}_{\text{post}}(\boldsymbol{\Sigma}_{w,uu}^{-1}\mathbf{y}_u + \boldsymbol{\Sigma}_{\text{prior}}^{-1}\mathbf{K}\mathbf{y}_v) \right]^T \boldsymbol{\Sigma}_{\text{post}}^{-1} \left[\mathbf{x}_u - \boldsymbol{\Sigma}_{\text{post}}(\boldsymbol{\Sigma}_{w,uu}^{-1}\mathbf{y}_u + \boldsymbol{\Sigma}_{\text{prior}}^{-1}\mathbf{K}\mathbf{y}_v) \right] \right\} \end{aligned} \tag{19}$$

where the posterior covariance $\boldsymbol{\Sigma}_{\text{post}}$ is

$$\boldsymbol{\Sigma}_{\text{post}} = \text{cov}(\mathbf{x}_u \mid \mathbf{y}) = (\boldsymbol{\Sigma}_{w,uu}^{-1} + \boldsymbol{\Sigma}_{\text{prior}}^{-1})^{-1} \tag{20}$$

and the posterior mean is

$$\hat{\mathbf{x}}_u = E(\mathbf{x}_u \mid \mathbf{y}) = \boldsymbol{\Sigma}_{\text{post}}(\boldsymbol{\Sigma}_{w,uu}^{-1}\mathbf{y}_u + \boldsymbol{\Sigma}_{\text{prior}}^{-1}\mathbf{K}\mathbf{y}_v) \tag{21}$$

Notice that the posterior mean (21) is a weighted sum of all sensor readings in the network. Equation (21) can also be written in the following matrix form.

$$\hat{\mathbf{x}}_u = \left[\boldsymbol{\Sigma}_{\text{post}}\boldsymbol{\Sigma}_{w,uu}^{-1} \quad \boldsymbol{\Sigma}_{\text{post}}\boldsymbol{\Sigma}_{\text{prior}}^{-1}\mathbf{K} \right] \begin{Bmatrix} \mathbf{y}_u \\ \mathbf{y}_v \end{Bmatrix} = \mathbf{a}_u^T \mathbf{y} \tag{22}$$

where the coefficient row vector $\mathbf{a}_u^T$ is

$$\mathbf{a}_u^T = \left[\boldsymbol{\Sigma}_{\text{post}}\boldsymbol{\Sigma}_{w,uu}^{-1} \quad \boldsymbol{\Sigma}_{\text{post}}\boldsymbol{\Sigma}_{\text{prior}}^{-1}\mathbf{K} \right] \tag{23}$$

For each single sensor u, a corresponding vector $\mathbf{a}_u^T$ is computed. All these vectors can be assembled in a coefficient matrix $\mathbf{A}$ to compute all estimates simultaneously:

$$\hat{\mathbf{x}} = \begin{bmatrix} \mathbf{a}_1^T \\ \mathbf{a}_2^T \\ \bullet \\ \mathbf{a}_p^T \end{bmatrix} \mathbf{y} = \mathbf{A}\mathbf{y} \tag{24}$$

where each row u of matrix $\mathbf{A}$ represents the corresponding sensor. Notice that both $\mathbf{u}$ and $\mathbf{v}$ represent the unclipped sensors only. Reconstruction of clipped sensors is discussed in the next section.

3.1 Reduction of overload error

A different algorithm is proposed to reduce overload error. The reconstruction of the clipped sensors in a single data point can be done simultaneously using the prior mean (17) and prior covariance matrix (18). The posterior mean is not used, because the noise variances of the clipped sensors are not known. Sensors $\mathbf{u}$ include all clipped sensors at the data point,

while sensors **v** include the remaining unclipped sensors. Clipped sensors are easy to detect; their values are equal to the overload amplitude.

It is important to have training data with granular error only. The data covariance matrix is estimated from the training data. Also the covariance matrix of the quantization error (12) is formed using the known ADC settings.

4 NUMERICAL EXPERIMENT

A numerical simulation was performed using a finite element model of a stiffened bridge deck (Figure 3). The structure was 30 m long and 11 m wide. It had four longitudinal and three lateral stiffeners. The slab was made of concrete with a Young's modulus of $E = 40$ GPa, Poisson ratio of $\nu = 0.15$, density of $\rho = 2500$ kg/m^3, and thickness of 250 mm. The stiffeners were made of steel ($E = 207$ GPa, $\nu = 0.30$, $\rho = 7850$ kg/m^3). The longitudinal stiffeners had a web with a thickness of $t = 16$ mm and a height of $h = 1.4$ m. The bottom flange had a thickness of $t = 50$ mm and a width of $b = 700$ mm. The lateral stiffeners were 1.4 m high and 30 mm thick plates.

The modelling was done using four-node discrete Kirchhoff quadrilateral shell elements with a diagonal mass matrix. The nodes of the bottom flanges were simply supported at both ends of the bridge. Longitudinal displacements were fixed only at one end of the bridge. The corners of the concrete deck were supported in the lateral and vertical directions.

Seven lowest modes were included in the analysis with natural frequencies of 3.95 Hz, 5.35 Hz, 13.7 Hz, 15.4 Hz, 18.0 Hz, 24.1 Hz, and 24.8 Hz. Modal damping was assumed with damping ratios of $\zeta_1 = \zeta_2 = 0.01$, $\zeta_3 = \zeta_4 = 0.02$, and $\zeta_5 = \zeta_6 = \zeta_7 = 0.03$.

Two independent unknown random loads were applied at nodes 774 and 872 in the vertical direction (the green squares in Figure 3). Three load cases were simulated with different standard deviations of the random excitations: (1) medium excitation with $\sigma_{F1} = 100$ N and $\sigma_{F2} = 150$ N, (2) small excitation with $\sigma_{F1} = 10$ N and $\sigma_{F2} = 15$ N, and (3) large excitation with $\sigma_{F1} = 1000$ N and $\sigma_{F2} = 1500$ N. Because ambient excitation was assumed, the steady state response was computed. For the steady state analysis, periodic pseudorandom excitations in the frequency range between 0 and 8.25 Hz with random amplitudes and phases were generated [11], and the analysis was performed in the frequency domain [12]. The excitation was not measured.

The response was computed with a modal superposition algorithm using the first seven modes. The analysis period was 20.48 s with a sampling frequency of 50 Hz. One measurement period then included 1024 samples from each sensor.

Vertical accelerations were measured at 28 points shown in Figure 3. Each channel was quantized with a 12-bit ADC, $L = 4096$. The dynamic range was the same in all channels. It was set so that a prescribed maximum number of channels overloaded simultaneously. The quantization interval Δx was thus known and the variance of the quantization error σ_w^2 was computed and used in estimating the empirical Bayesian virtual sensors from the physically measured and digitized 28 accelerations. The training data were all data points with no clipping.

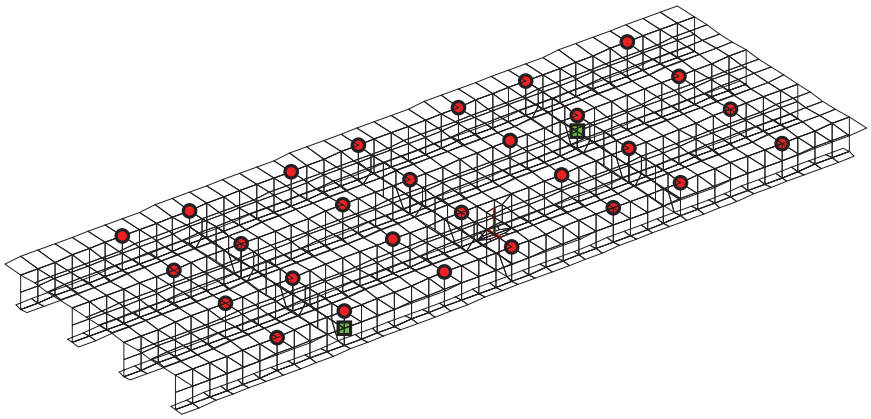

Figure 3: Finite element model of the bridge deck. The accelerometers are shown with red circles and the excitation points with green squares.

4.1 Reduction of granular noise

First, quantization error due to granular noise was only studied. Overload was not allowed, so that the only measurement error was due to granular noise. The dynamic range was set to ± 0.132 m/s^2, $\Delta x = 1.29 \cdot 10^{-4}$ m/s^2, and the standard deviation of the quantization error was $\sigma_w = 3.72 \cdot 10^{-5}$ m/s^2, which was known. Figure 4 shows that the actual quantization error was equal to the theoretical value (5), or $\sigma_w = \Delta x / \sqrt{12} \approx 0.289 \Delta x$. The theoretical value was used in Bayesian virtual sensing, which resulted in virtual sensors having less noise than the actual measurement as shown in Figure 4. It can be seen that all virtual sensors were more accurate than the actual hardware. However, the errors in the virtual sensors were no longer equal but varied between sensors.

The signal of sensor 8 is shown in Figure 5a. The three measurements with different magnitudes can be clearly distinguished. The number of quantization levels in measurement 2 with very small acceleration amplitudes was between 6 (sensor 8) and 29 (sensor 4). A detail of the signal of sensor 8 is shown in Figure 5b. It can be seen that the quantization error was significant resulting in a low SNR. Also in the same plot is the virtual sensor data, which is very close to the exact data.

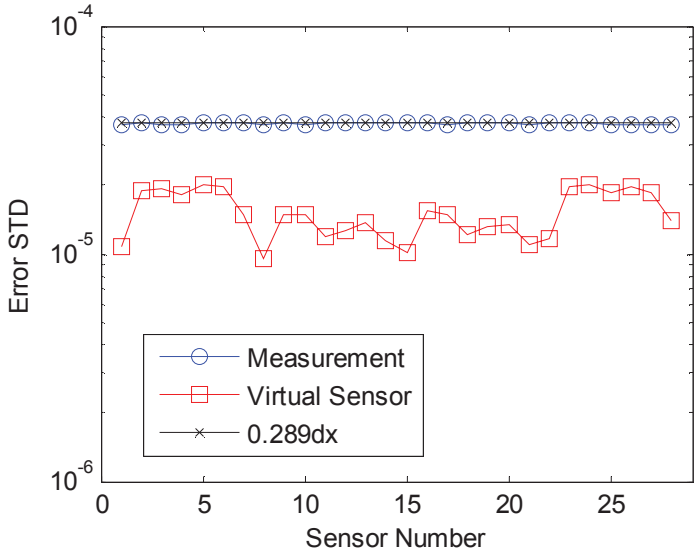

Figure 4: Standard deviation (STD) of the quantization error (actual 'O' and theoretical 'x') and STD of the error in the virtual sensors (squares).

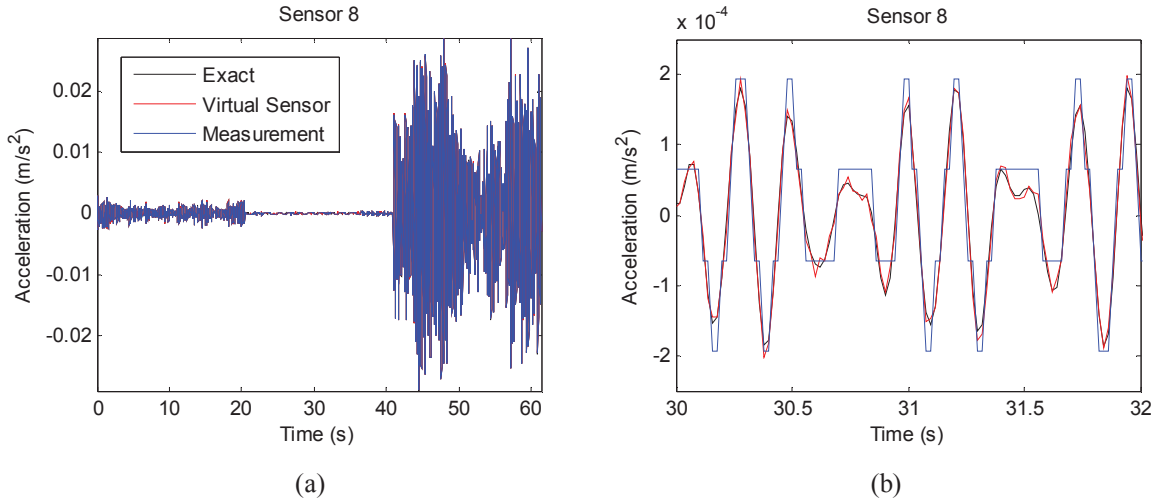

Figure 5: (a) Acceleration of sensor 8 in all three measurements with no clipping. A comparison of the quantized signal, virtual sensor, and exact values. (b) A detail of measurement 2 with only four quantization levels. The virtual sensor and the exact values are also shown.

4.2 Overload error in maximum of 60% sensors

The dynamic range of the ADC was adjusted so that the maximum number of channels in the overload region was 17 (60% of the total number of sensors). The dynamic range was set to ± 0.059 m/s^2, $\Delta x = 5.75 \cdot 10^{-5}$ m/s^2, and the standard deviation of the quantization error was $\sigma_w = 1.66 \cdot 10^{-5}$ m/s^2. The signal of sensor 4 is shown in Figure 6. It can be seen that clipping occurred several times during measurement 3. However, the clipped sensors could be reconstructed using the data of the unclipped sensors.

The estimation error of the virtual sensors 4 and 8 are plotted in Figure 7 together with the estimated 3σ limits. Notice that the estimation error is larger for the data points having clipped sensors. This is because a smaller number of sensors could be used in the estimation.

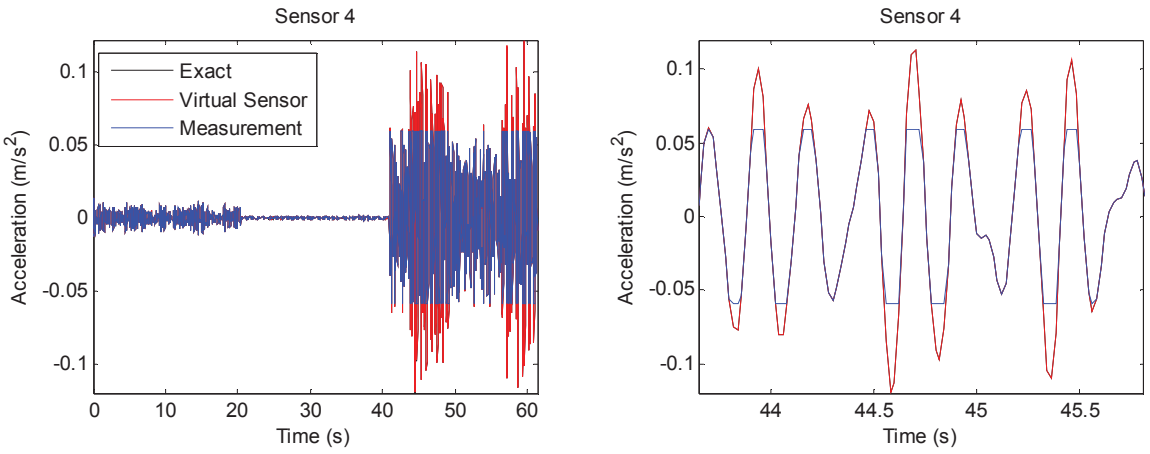

(a) (b)

Figure 6: (a) Signal of sensor 4 and (b) a detail. Overload error (clipping) is clearly seen. The difference between the exact and virtual sensor signals cannot be visually distinguished.

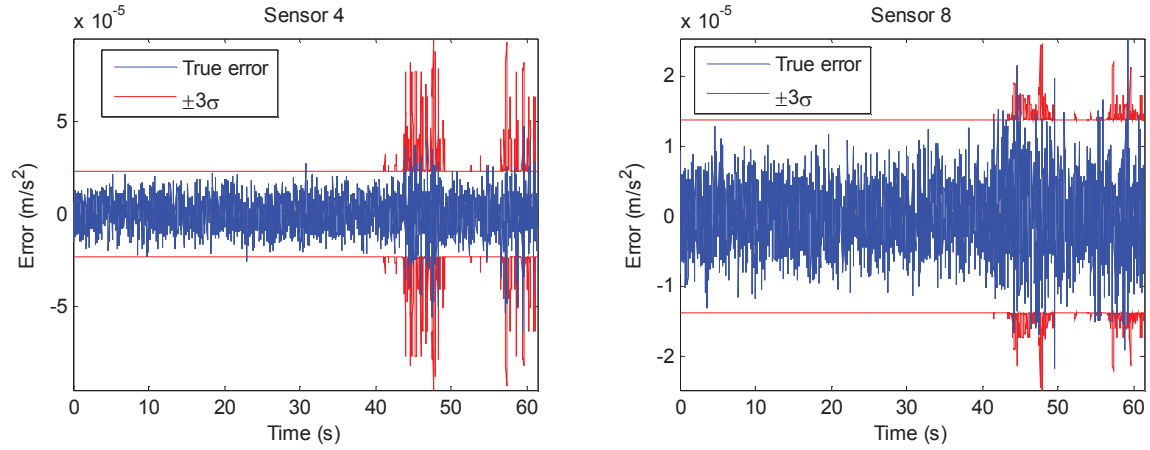

(a) (b)

Figure 7: Estimation errors of (a) virtual sensor 4 and (b) virtual sensor 8. The estimated 3σ limits are also shown.

4.3 The effect of the dynamic range of the ADC

The objective is to maximize the SNR. This can be done by fully utilizing the dynamic range of the ADC. However, the excitation levels can vary considerably and the maximum is unknown. This can result in overload error due to clipping.

The SNRs of the three measurements were studied by varying the dynamic range of the ADC. In the first case, all measurements were within the granular regions and no clipping occurred (Section 4.1). In the next three cases, the maximum number of clipped signals in a single data point was 9, 17 (Section 4.2), and 26 corresponding to respectively 30%, 60%, and 90% of the total number of sensors in the network. The histograms showing the number of data points versus the number of overloaded channels are plotted in Figure 8.

The SNR was computed for each case and separately for each measurement. Because the noiseless signal was known, the SNR values are accurate. The SNRs of each physical and virtual sensor in all three measurements are plotted in Figure 9. First, it can be seen that the virtual sensors provided higher SNRs than the physical sensors in all cases.

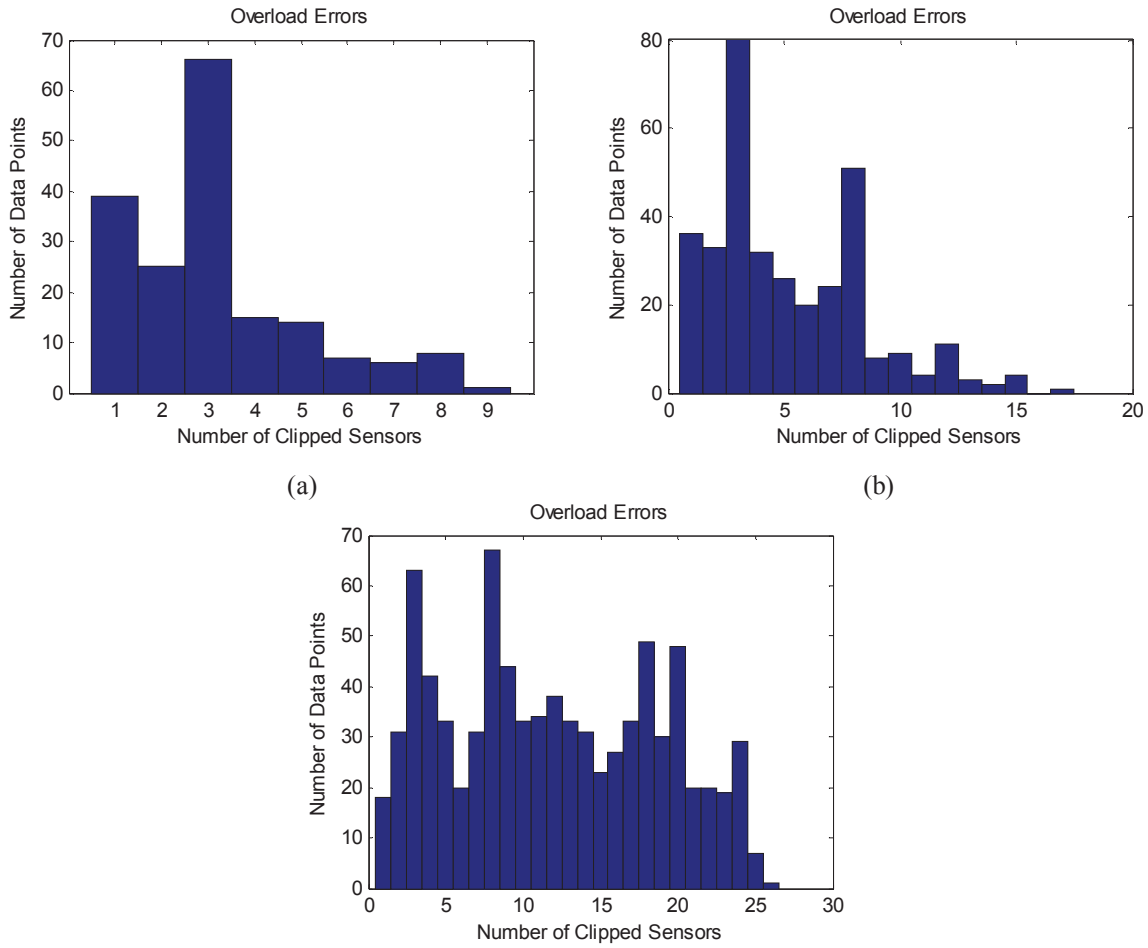

Figure 8: Histograms showing the number of data points with different number of clipped sensors. The maximum number of clipped sensors in a single data point was (a) 9 (30%), (b) 17 (60%), and (c) 26 (90%).

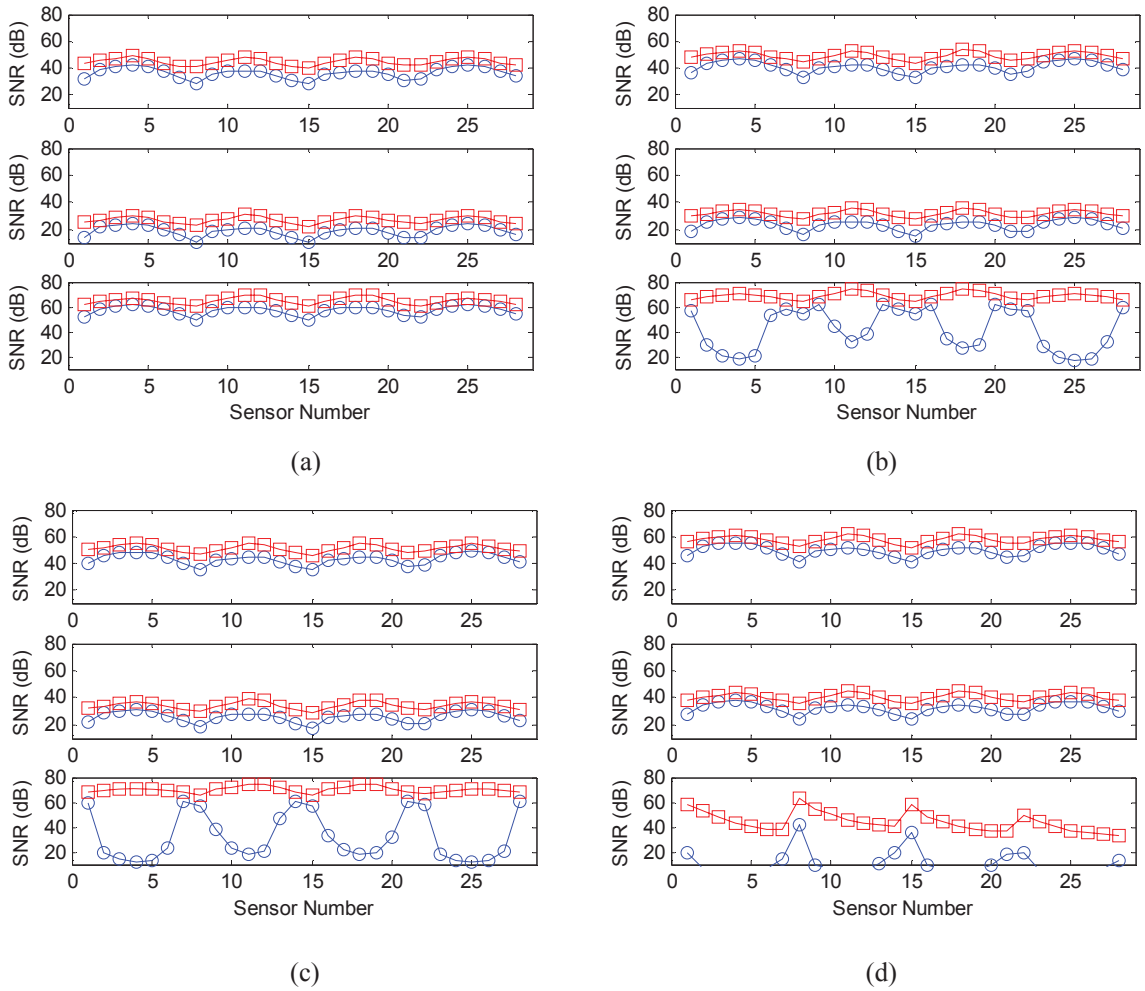

Figure 9: Signal-to-noise ratios (SNR) of physical (blue circles) and virtual (red squares) sensors in each measurement (top: measurement 1, middle: measurement 2, and bottom: measurement 3). In measurement 3, the maximum number of clipped sensors in a single data point was (a) 0 (no clipping), (b) 9 (30%), (c) 17 (60%), and (d) 26 (90%).

Second, the SNRs of measurements 1 and 2 increased when the dynamic range of the ADC was decreased. This is because the two measurements occupied a larger dynamic range of the ADC and no clipping occurred in any channels. All data points of measurements 1 and 2 could therefore been used as training data.

The most interesting is the measurement 3, in which different number of overload errors occurred. With physical sensors, the SNR decreased considerably due to overloading. However, the virtual sensors exhibited an increasing SNR up to the case with a maximum of 17 channels (60%) clipping simultaneously. Beyond that, reconstruction of the clipped signals became inaccurate.

The maximum and minimum SNR of the physical sensors in each case and separately for each measurement are listed in Table 1. Table 2 shows the corresponding data for the virtual sensors. The SNR of the physical sensors decreased considerably in measurement 3 due to clipping. On the other hand, the SNR of the virtual sensors increased with a decreasing dynamic range of the ADC up to the point in which a maximum of 17 sensors (60%) clipped simultaneously. This could be considered optimal from these four possible settings.

Meas No		Max number (%) of clipped sensors			
		0	9	17	26
		0%	30%	60%	90%
1	Max	41.7	46.3	48.5	**55.3**
	Min	27.6	32.5	34.7	**41.2**
2	Max	23.9	28.4	31.0	**37.8**
	Min	10.7	15.6	17.6	**24.6**
3	Max	61.5	**61.8**	61.1	42.3
	Min	**49.8**	16.9	11.9	4.8

Table 1: Maximum and minimum SNRs of the physical sensors. The highest values are shown bolded.

Meas No		Max number (%) of clipped sensors			
		0	9	17	26
		0%	30%	60%	90%
1	Max	48.6	53.3	55.2	**61.6**
	Min	39.7	43.7	45.5	**51.8**
2	Max	30.7	36.1	38.6	**45.2**
	Min	22.4	27.3	28.8	**35.5**
3	Max	69.7	74.0	**74.5**	63.4
	Min	60.3	64.3	**65.4**	33.4

Table 2: Maximum and minimum SNRs of the virtual sensors. The highest values are shown bolded.

5 CONCLUSION

Quantization of measured vibration signals results in granular or overload noise. Bayesian virtual sensing can be used to reduce those errors. If quantization is the only source of error, the variance of the granular noise is known and can be used in estimation.

For a large SNR, it is recommended to adjust the dynamic range of the ADC so that the measured signal occupies the most of it. Quantization error can be an issue in monitoring applications, in which a large range of amplitudes can occur. For very small amplitudes, the SNR may be small, because the signal level is low compared to the granular error. With very large amplitudes, overload error may be large resulting in a low SNR. Both effects are issues in damage detection, because detection performance depends on the SNR.

In order to maximize the SNR of very variable vibration amplitudes, it was shown that it is possible to allow overloading in a subset of channels. It is then possible to reconstruct the clipped channels using the remaining unclipped channels. Also, the granular error can be reduced using virtual sensing.

The very same approach can be used also for a more practical case, in which there exist also other sources of error than quantization. Overload noise is nevertheless always relevant in practice, because the amplitudes are typically unbounded.

ACKNOWLEDGEMENT

This work was supported by Metropolia University of Applied Sciences.

REFERENCES

[1] N.S. Jayant, P. Noll, *Digital coding of waveforms. Principles and applications to speech and video*, Prentice-Hall, Englewood Cliffs, New Jersey, 1984.

[2] S.M. Kay, *Fundamentals of statistical signal processing. Detection theory*, Prentice-Hall, Upper Saddle River, NJ, 1998.

[3] J. Kullaa, Bayesian virtual sensing in structural dynamics, *Mechanical Systems and Signal Processing* 115, 497–513, 2019.

[4] S.K. Mitra, *Digital signal processing. A computer-based approach*, McGraw-Hill, Singapore, 1998.

[5] D.E. Newland, *An introduction to random vibrations, spectral and wavelet analysis.* 3rd edition, Longman Scientific & Technical, Singapore, 1993.

[6] J.S. Bendat, A.G. Piersol, *Random data. Analysis and measurement procedures*. 3rd edition. New York, Wiley, 2000.

[7] A. Gersho, R.M. Gray, *Vector quantization and signal compression*, Kluwer Academic Publishers, Norwell, Massachusetts, USA, 1992.

[8] J. Kullaa, Robust damage detection using Bayesian virtual sensors, *Mechanical Systems and Signal Processing* 135 (2020), 106384.

[9] J. Kullaa, Sensor validation using minimum mean square error estimation, *Mechanical Systems and Signal Processing* 24 (2010) 1444–1457.

[10] C.M. Bishop, *Pattern recognition and machine learning*, Springer, New York, 2006.

[11] A. Brandt, *Noise and vibration analysis: Signal analysis and experimental procedures*, Chichester, Hoboken, N.J., Wiley, 2011.

[12] R.W. Clough, J. Penzien, *Dynamics of structures*. 2nd edition, McGraw-Hill, New York, 1993.

EURODYN 2020
XI International Conference on Structural Dynamics
M. Papadrakakis, M. Fragiadakis, C. Papadimitriou (eds.)
Athens, Greece, 23–26 November 2020

VIBRATION-BASED DAMAGE LOCALIZATION USING THE DENSITY RATIO ESTIMATION METHOD

Yulong. Zhang[1], John. H.G. Macdonald[1], Paul. Harper[1], and Song. Liu[2]

[1]Department of Civil Engineering, University of Bristol
Queen's Building, University Walk, Bristol, BS8 1TR, England, UK
e-mail: {yulong.zhang, john.macdonald, paul.harper}@bristol.ac.uk

[2]School of Mathematics, University of Bristol
Fry Building, Woodland Road, Bristol, BS8 1UG, England, UK
e-mail: song.liu@bristol.ac.uk

Keywords: Damage localization, Density Ratio Estimation method, Kullback–Leibler divergence, Non-parametric estimation.

Abstract. *A machine learning technique, the Density Ratio Estimation method is applied for the first time to detect structural damage, using test data from a scale model of a three-storey building structure under random excitation as a case study. The method detects damage by comparing the Probability Density Functions (PDFs) of measured vibration signals from an undamaged state and a potentially damaged state. Since the vibration signals from one sensor are not independent over time, instead of applying the vibration signals directly, the sequences of signals are used to train the model in order to account for the signal dependence, leading to multi-dimensional PDFs. To enhance model robustness, non-parametric models are applied for structural health monitoring problems. One limited way to detect damage is to estimate the non-parametric PDFs under the undamaged state and potentially damaged state separately, and then compare them. However, this method is very difficult to apply when the dataset has many dimensions, and can often be intractable. The method applied in the current study estimates the PDF change directly, without estimating individual PDFs. Moreover, the damage indices in conventional methods are generally heuristic. In contrast, the damage index in the current study is Kullback–Leibler divergence, which has a clear statistical meaning; a measure of difference between two PDFs. To demonstrate the capability of the method, it is applied to data from a laboratory test which was previously conducted by Los Alamos National Lab. It is shown that the method can detect damage locations successfully.*

1 INTRODUCTION

Structural Health Monitoring (SHM) is used to automate the assessment of damage in civil infrastructure, allowing the cost-effective management of maintenance activities. As part of the SHM problem, vibration-based damage detection has gained widespread interest as the vibration signal measurement and acquisition technology is mature and reasonably low-cost [1]. The underlying idea of vibration-based damage detection is that damage will significantly change the physical properties of a structure, which consequently change the measured vibration response of the structure [2].

Following the framework of Farrar et al. [3], the SHM process can be summarized as (a) operational evaluation, (b) data acquisition and cleansing, (c) feature extraction, and (d) statistical model development. Features are extracted from the measured data and used to develop a statistical model. Commonly used features include the first four statistical moments (mean, standard deviation, skewness, and kurtosis) [4, 5, 6], autoregressive model coefficients [7, 8, 9, 10], and modal parameters (natural frequencies [11, 12, 13], mode shapes [14, 15], and modal damping [16, 17]). Other examples of extracted features can be found in Astroza [18].

A statistical model can be developed by comparing the Probability Density Functions (PDFs) of the extracted features from the undamaged and damaged structures [3, 4]. In this paper, we apply a method which excludes any feature extraction and uses raw data directly to train the statistical model. The main idea is to detect damage by comparing PDFs of measured data from an undamaged state and potentially damaged state. To the authors' knowledge, only Figueiredo et al. [19] have used a similar method to detect damage by comparing PDFs of accelerations. In their work, the measured data from the undamaged state was assumed to be normally distributed, while the PDFs of measured data under nonlinear damaged states deviated from a normal distribution. However, because samples in vibration signals are not independent over time, they need not have specific PDFs. Instead of applying the vibration signals directly, the sequences of signal samples can be used to train the model in order to account for the time dependence of the signal samples relative to each other. This leads the PDFs to be multi-dimensional.

As the PDF type is not known beforehand, the PDF is estimated with non-parametric methods for the sake of algorithm robustness. Two most widely used non-parametric techniques are histogram analysis and kernel methods [20]. Then the damage can be detected by comparing the two PDFs, from the undamaged state and potentially damaged state respectively. However, this approach is very difficult to apply for multi-dimensional PDFs, and can often be intractable, since high dimensional non-parametric density estimation is known to be a hard problem [21]. Therefore, estimating two PDFs separately may be ineffective. Essentially, for the aim of detecting damage, what matters is only the change in the PDFs between the undamaged and damaged states, rather than the PDFs themselves; therefore it is potentially more computationally efficient to directly estimate this PDF change.

On this basis, this paper applies the method presented by Kawahara and Sugiyama [22] to detect damage in structures. Instead of separately estimating the two PDFs, of measured data from the undamaged and potentially damaged structure, this method estimates the change between the two PDFs directly, in the form of a density ratio. The method uses a sequence of signals to train the model in order to account for the time dependence of signal samples relative to each other. The density ratio is then estimated in a non-parametric form to enhance the robustness of the model.

In the remainder of the paper, the theoretical principles behind the damage detection al-

gorithm are presented (Section 2) before an explanation of its application to the case study structure and the key results (Section 3). Finally, the main conclusions and areas of future work are highlighted (Section 4).

2 DAMAGE DETECTION USING DENSITY RATIO ESTIMATION

In this section, the key theoretical principles behind the applied method [22] are briefly summarised.

2.1 Problem formulation

Let y_i be a signal at time step i, for example the acceleration signal from a sensor. Since signals of dynamic response are not independent over time, we consider sequences of them. This is a common practice in subspace identification since it allows us to implicitly take time correlation into consideration to some degree [23]. Let $\boldsymbol{y}(i)$ be the sequence of length k starting at time i:

$$\boldsymbol{y}(i) = [y_i, y_{i+1}, \cdots, y_{i+k-1}]. \tag{1}$$

$\boldsymbol{y}(i)$ is also refered as 'sequence' in the rest of this paper. Similarly, the $\boldsymbol{y}(i+1)$ is

$$\boldsymbol{y}(i+1) = [y_{i+1}, y_{i+2}, \cdots, y_{i+k}]. \tag{2}$$

In this way, a set of sequences $\boldsymbol{y}(i+1)$, $\boldsymbol{y}(i+2)$, $\cdots$, $\boldsymbol{y}(i+n)$ can be generated from the original signal. To estimate the density ratio, we need two sets of sequence samples from the undamaged state and a potentially damaged state, respectively,

$$\{\boldsymbol{y}_{\text{und}}(i+1), \boldsymbol{y}_{\text{und}}(i+2), \cdots, \boldsymbol{y}_{\text{und}}(i+n_{\text{und}})\} \sim p_{\text{und}}(\boldsymbol{y}) \tag{3}$$

$$\{\boldsymbol{y}_{\text{dam}}(i+1), \boldsymbol{y}_{\text{dam}}(i+2), \cdots, \boldsymbol{y}_{\text{dam}}(i+n_{\text{dam}})\} \sim p_{\text{dam}}(\boldsymbol{y}) \tag{4}$$

where $\boldsymbol{y}_{\text{und}}(i+1)$, $\boldsymbol{y}_{\text{und}}(i+2)$, $\cdots$, $\boldsymbol{y}_{\text{und}}(i+n_{\text{und}})$ are the sequence samples for the undamaged structure, which follow (represented by $\sim$) the PDF $p_{\text{und}}(\boldsymbol{y})$. n_{und} is the number of sequence samples. The Eq.(4) is defined likewise for the damaged structure.

The damage is detected by comparing the difference between $p_{\text{und}}(\boldsymbol{y})$ and $p_{\text{dam}}(\boldsymbol{y})$, which is quantified by the Kullback–Leibler (KL) divergence [24]:

$$\begin{aligned} \text{DI} &= \text{KL}(p_{\text{und}}(\boldsymbol{y}) \parallel p_{\text{dam}}(\boldsymbol{y})) \\ &= \int p_{\text{und}}(\boldsymbol{y}) \log\left(\frac{p_{\text{dam}}(\boldsymbol{y})}{p_{\text{und}}(\boldsymbol{y})}\right) \mathrm{d}\boldsymbol{y} \\ &\approx \frac{1}{n} \sum_{i=1}^{n_{\text{und}}} \log\left(\frac{p_{\text{dam}}(\boldsymbol{y})}{p_{\text{und}}(\boldsymbol{y})}\right) \end{aligned} \tag{5}$$

where DI is the Damage Index, and $\mathrm{d}\boldsymbol{y}$ is used as a shorthand for $\mathrm{d}y_1 \mathrm{d}y_2 \cdots \mathrm{d}y_k$ in Eq.(5). If the DI for a sensor location is larger than a predetermined threshold, the corresponding component will be believed to be damaged. Otherwise, the component is believed to be undamaged. The threshold is defined in Section 2.3.

The remaining question is how to estimate the density ratio,

$$r(\boldsymbol{y}) := \frac{p_{\text{dam}}(\boldsymbol{y})}{p_{\text{und}}(\boldsymbol{y})} \tag{6}$$

Of course, $r(\boldsymbol{y})$ can be estimated by estimating the two PDFs $p_{\text{und}}(\boldsymbol{y})$ and $p_{\text{dam}}(\boldsymbol{y})$ with non-parametric models, separately. However, non-parametric PDF estimation is known to be a hard problem, and estimating two PDFs separately may be ineffective. It is suggested that it is more efficient to directly estimate $r(\boldsymbol{y})$.

2.2 Density ratio modelling and estimation

The density ratio is assumed to be a non-parametric form:

$$\hat{r}(\boldsymbol{y}) = \sum_{l=1}^{n_{\text{dam}}} \alpha_l K_\sigma(\boldsymbol{y}; \boldsymbol{y}_{\text{dam}}(l)) \tag{7}$$

where $\{\alpha_l\}_{l=1}^{n_{\text{dam}}}$ are parameters to be learned from the data samples and $K_\sigma(\boldsymbol{y}, \boldsymbol{y}_{\text{dam}}(l))$ is a kernel function. $\hat{r}(\boldsymbol{y})$ is an estimate of the true $r(\boldsymbol{y})$. In this paper, the widely used Gaussian kernel function is applied,

$$K_\sigma(\boldsymbol{y}; \boldsymbol{y}_{\text{dam}}(l)) = \exp(-\frac{\|\boldsymbol{y} - \boldsymbol{y}_{\text{dam}}(l)\|^2}{2\sigma^2}) \tag{8}$$

where the kernel width σ is an open tuning parameter and needs to be chosen appropriately for better estimation.

Once the density ratio is modelled, our next aim is to estimate it. Using the definition of $\hat{r}(\boldsymbol{y})$, we can approximate $p_{\text{dam}}(\boldsymbol{y})$ by

$$\hat{p}_{\text{dam}}(\boldsymbol{y}) = \hat{r}(\boldsymbol{y}) p_{\text{und}}(\boldsymbol{y}) \tag{9}$$

To estimate the ratio $\hat{r}(\boldsymbol{y})$, the method fits the approximated $\hat{p}_{\text{dam}}(\boldsymbol{y})$ to the true $p_{\text{dam}}(\boldsymbol{y})$ using the parameters $\{\alpha_l\}_{l=1}^{n_{\text{dam}}}$. We use the Kullback-Leibler divergence as a goodness of fit measure and the objective is to minimize

$$\begin{aligned}
\text{KL}(p_{\text{dam}}(\boldsymbol{y}) \parallel \hat{p}_{\text{dam}}(\boldsymbol{y})) &= \text{KL}(p_{\text{dam}}(\boldsymbol{y}) \parallel \hat{r}(\boldsymbol{y}) p_{\text{und}}(\boldsymbol{y})) \\
&= \int p_{\text{dam}}(\boldsymbol{y}) \log (\frac{p_{\text{dam}}(\boldsymbol{y})}{\hat{r}(\boldsymbol{y}) p_{\text{und}}(\boldsymbol{y})}) d\boldsymbol{y} \\
&= \underbrace{\text{KL}(p_{\text{dam}}(\boldsymbol{y}) \parallel p_{\text{und}}(\boldsymbol{y}))}_{\text{constant}} - \int p_{\text{dam}}(\boldsymbol{y}) \log \hat{r}(\boldsymbol{y}) d\boldsymbol{y} \\
&= \text{constant} - \sum_{i=1}^{n_{\text{dam}}} \log(\sum_{l=1}^{n_{\text{dam}}} \alpha_l K_\sigma(\boldsymbol{y}_{\text{dam}}(i), \boldsymbol{y}_{\text{dam}}(l)))
\end{aligned} \tag{10}$$

Meanwhile, an additional constraint is introduced, since $\hat{p}_{\text{dam}}(\boldsymbol{y}) = \hat{r}(\boldsymbol{y}) p_{\text{und}}(\boldsymbol{y})$ must be a valid PDF and as such should satisfy,

$$\begin{aligned}
1 = \int \hat{p}_{\text{dam}}(\boldsymbol{y}) d\boldsymbol{y} = \int \hat{r}(\boldsymbol{y}) p_{\text{und}}(\boldsymbol{y}) d\boldsymbol{y} &\approx \frac{1}{n_{\text{und}}} \sum_{j=1}^{n_{\text{und}}} \hat{r}(\boldsymbol{y}(j)) \\
&= \frac{1}{n_{\text{und}}} \sum_{j=1}^{n_{\text{und}}} \sum_{l=1}^{n_{\text{dam}}} \alpha_l K_\sigma(\boldsymbol{y}_{\text{und}}(j), \boldsymbol{y}_{\text{dam}}(l))
\end{aligned} \tag{11}$$

Now the optimization problem is summarised as

$$\begin{cases} \underset{\{\alpha_l\}_{l=1}^{n_{\text{dam}}}}{max} & \sum_{i=1}^{n_{\text{dam}}} \log(\sum_{l=1}^{n_{\text{dam}}} \alpha_l K_\sigma(\boldsymbol{y}_{\text{dam}}(i), \boldsymbol{y}_{\text{dam}}(l))), \\ s.t. & \frac{1}{n_{\text{und}}} \sum_{j=1}^{n_{\text{und}}} \sum_{l=1}^{n_{\text{dam}}} \alpha_l K_\sigma(\boldsymbol{y}_{\text{und}}(j), \boldsymbol{y}_{\text{dam}}(l)) = 1, \\ & \text{and } \alpha_1, \ldots, \alpha_{n_{\text{dam}}} \geq 1. \end{cases} \tag{12}$$

This is a convex optimization problem and the global solution can be obtained, e.g., by simply performing gradient ascent and feasibility satisfaction iteratively. The pseudo code can be found in Kawahara and Sugiyama [22].

2.3 Damage index threshold

For different sensors, distinct DI values can be obtained. The DI is essentially a measure of the change between the undamaged and damaged structure. Therefore, the DI values from the sensors around the damage should be larger compared with those from the other sensors. To distinguish these outliers caused by local damage, a threshold needs to be set up. In previous studies, the measured data of undamaged structures are commonly assumed to be normally distributed [7, 25, 26]. Similarly, the DI of the undamaged structure is assumed to be normally distributed in this paper. The threshold is defined as the upper bound of the 95% confidence, which is calculated by

$$\xi = \bar{x} + \frac{\sigma}{\sqrt{s}} t_{95\%}(s-1) \tag{13}$$

where $\bar{x}$ and σ are the mean and standard deviation of the DI values from all sensors, s is the number of sensors. For the case of this paper, $s = 4$. Therefore, $t_{95\%}(4-1) = 2.353$ is obtained from a statistical table. If a DI value is larger than the threshold ξ, it means the DI value is larger than 95% of the DI values from a certain state, which indicates it is an outlier. Hence it is likely to indicate damage.

3 EXPERIMENTAL DATA AND DAMAGE DETECTION

In order to assess the efficacy of the proposed method for damage detection, a detailed study was carried out on an already published dataset from laboratory tests [19].

3.1 Test structure description

The tests were conducted at Los Alamos National Lab [19], on a three-storey aluminium structure (Figure 1), consisting of plates connected by columns. Different 'damage' states were induced by adding mass to plates or reducing the stiffnesses of columns. The different states are listed in Table 1. State 1 is the baseline condition, where no damage was present. The PDF for State 1 corresponds to the $p_{\text{und}}(\boldsymbol{y})$ in the algorithm. In States 2 and 3, 'damage' was simulated by adding mass on certain floors. For the States 4 - 9, damage was induced by stiffness reduction of different columns. The PDFs for States 2 - 9 correspond to the $p_{\text{dam}}(\boldsymbol{y})$ in the algorithm. The column locations are represented by storey numbers (1, 2, 3) and plates side labels (A, B, C, D), which are shown in Figure 1. For example, 1BD means the column located between the base and first floor at the intersection of plane B and D.

The structure was excited by an electro-dynamic shaker through its base. For each test, a band-limited random excitation in the range of 20 - 150 Hz was used to excite the structure,

with the excitation level approximately 20N RMS measured at Sensor 1. With accelerometers mounted on each plate, acceleration-time series under different structural states were collected. For each state, ten time-series were measured in order to consider the variability in the data. Each time-series includes 8,192 data points and was sampled with a sampling frequency of 320 Hz (the natural frequencies of the structure are approximately 30 Hz, 55 Hz and 70 Hz). The acceleration-time series of States 1, 3, 5, 7, and 9 from Sensors 2 to 5 are plotted in Figure 2. The test data and more information on the structure are accessible from Los Alamos National Lab [27].

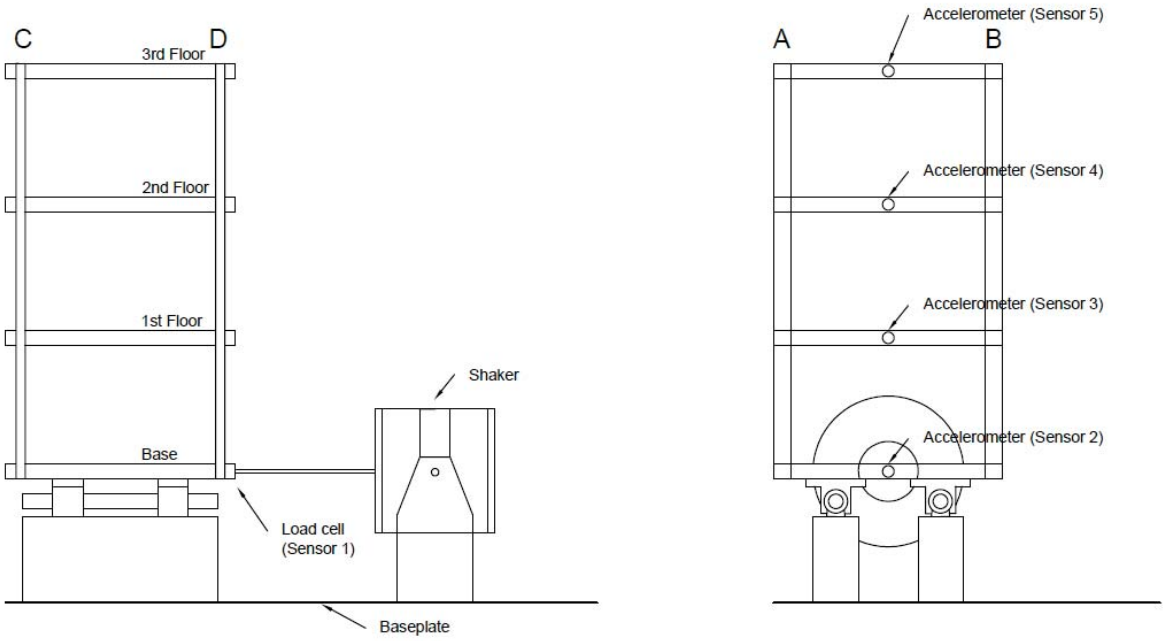

Figure 1: Diagram of laboratory structure (redrawn from [19])

Label	Description
State 1	Baseline condition
State 2	Mass = 1.2 kg at the base
State 3	Mass = 1.2 kg on the 1st floor
State 4	87.5% stiffness reduction in column 1BD
State 5	87.5% stiffness reduction in column 1AD and 1BD
State 6	87.5% stiffness reduction in column 2BD
State 7	87.5% stiffness reduction in column 2AD and 2BD
State 8	87.5% stiffness reduction in column 3BD
State 9	87.5% stiffness reduction in column 3AD and 3BD

Table 1: Structural states tested (after [19])

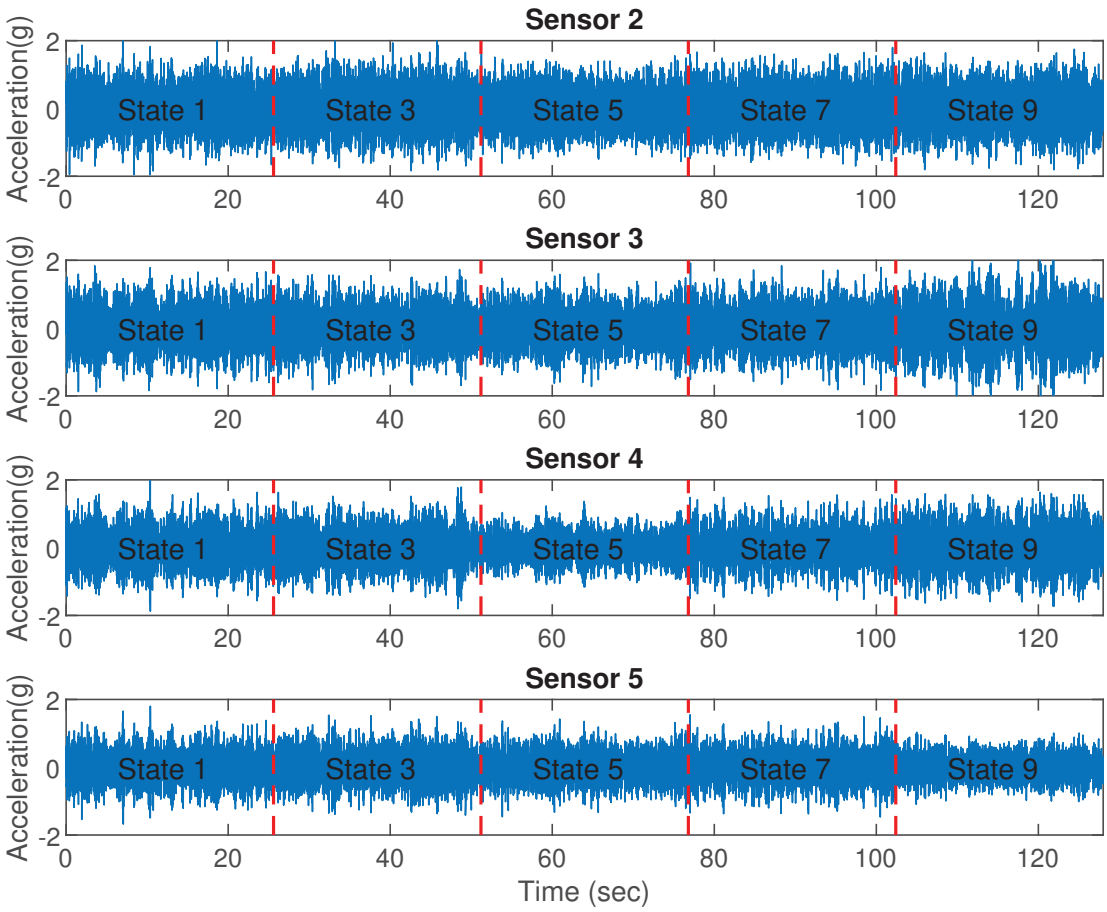

Figure 2: Acceleration-time series of various state conditions from Sensors 2 to 5 (redrawn from [19]).

3.2 Damage detection and localization

For the proposed algorithm, the sequence length is set as $k = 5$. The DI values of States 2 - 9 are obtained by feeding the data from one of the States 2 - 9 and the data from State 1 to the algorithm, respectively. However, because of the variability of the signals, the DI from any two records in State 1 are not zeros, but some small values. To account for this variability, the DI values of State 1 were deducted from the DI values of States 2 - 9. The final results are shown in Figure 3, where blue columns represent DI values for different sensors and red dot lines represent thresholds.

For damage detection, it can be seen that each state except State 4 has one DI above the corresponding threshold, which indicates the state has been identified as damaged. The reason why State 4 has not been detected may be because it contains only a relatively small amount of damage.

For damage localization, it is shown that in State 2, where a mass is added to the base floor, only Sensor 2 has a DI value larger than the threshold, indicating damage is in the base floor. Similarly, for State 3, only Sensor 3 has a larger value than the threshold. From State 4 to State 9, the damage is induced by stiffness reduction of columns at different locations. For States 4 and 5, the DI for Sensor 3 is close to or exceeds the thresholds, indicating the 1st floor is damaged. For the States 6 and 7, the detected location is the 2nd floor. The results for States

8 and 9 indicate that the 3rd floor is detected as damaged. Overall, the model has detected the damage location successfully for all 7 damage states other than State 4.

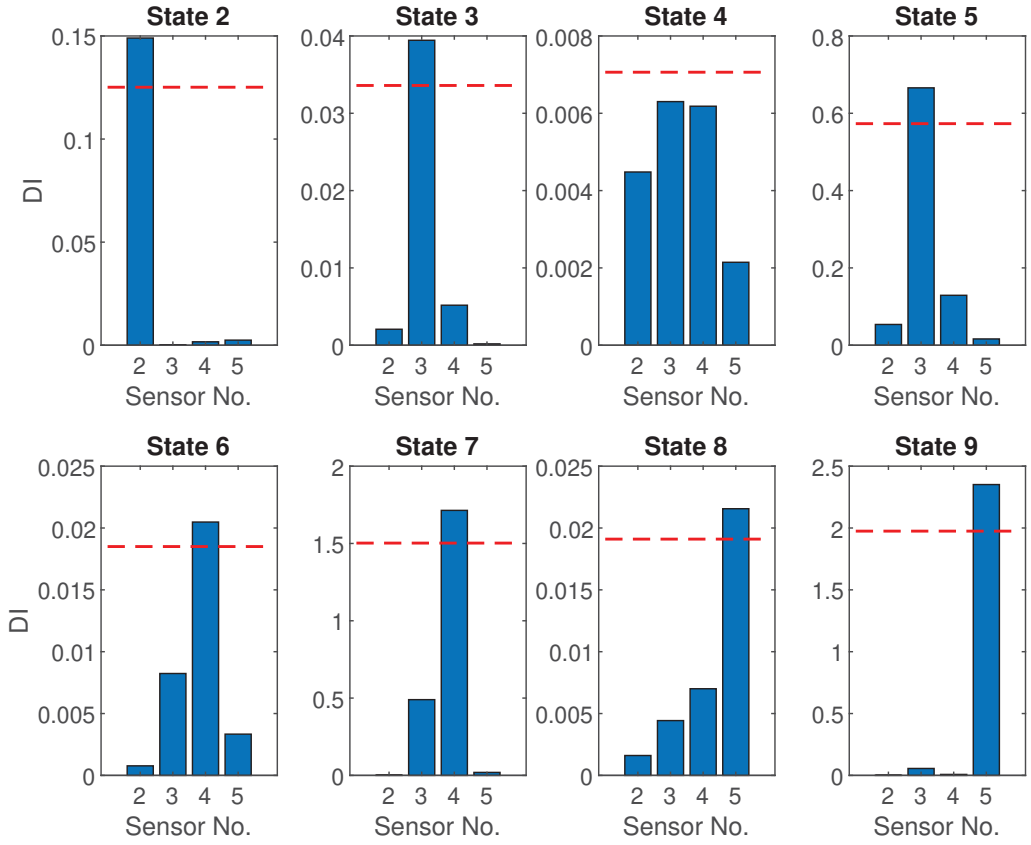

Figure 3: Damage Index for different locations for different states

4 CONCLUSIONS

In this paper, a vibration-based damage localization algorithm is presented. Sequences of acceleration signals are applied as input for model training, to account for the time dependence of samples relative to each other. The KL divergence, between the PDFs of measured vibration signals from an undamaged state and a potentially damaged state, is used as a Damage Index to indicate damage. The difficulty of estimating multi-dimensional PDFs with a non-parametric method is overcome by applying the Density Ratio Estimation method. The method has been demonstrated on experimental data from a scale model of a three-storey building structure under random excitation from Los Alamos National Lab. The results show that the algorithm is able to detect and localize damage in the model. These initial results are very encouraging, but further studies are needed to test the validity of the algorithm, such as on other structures or for less severe damage.

REFERENCES

[1] K. Vamvoudakis-Stefanou, J. Sakellariou, and S. Fassois, Vibration-based damage detection for a population of nominally identical structures: Unsupervised multiple model (mm) statistical time series type methods, *Mechanical Systems and Signal Processing*, **111**, 149–171, 2018.

[2] C. R. Farrar and K. Worden, An introduction to structural health monitoring, *Philosophical Transactions of the Royal Society A: Mathematical, Physical and Engineering Sciences*, **365**, 303–315, 2006.

[3] C. R. Farrar, S. W. Doebling, and D. A. Nix, Vibration–based structural damage identification, *Philosophical Transactions of the Royal Society of London. Series A: Mathematical, Physical and Engineering Sciences*, **359**, 131–149, 2001.

[4] H. Sohn and C. R. Farrar, Damage diagnosis using time series analysis of vibration signals, *Smart Materials and Structures*, **10**, 446, 2001.

[5] M. Todd, J. Nichols, L. Pecora, and L. Virgin, Vibration-based damage assessment utilizing state space geometry changes: Local attractor variance ratio, *Smart Materials and Structures*, **10**, 1000, 2001.

[6] I. Trendafilova, Vibration-based damage detection in structures using time series analysis, Proceedings of the Institution of Mechanical Engineers, Part C: *Journal of Mechanical Engineering Science*, **220**, 261–272, 2006.

[7] C. Bao, H. Hao, and Z.-X. Li, Integrated arma model method for damage detection of subsea pipeline system, *Engineering Structures*, **48** , 176–192, 2013.

[8] A. A. Mosavi, D. Dickey, R. Seracino, and S. Rizkalla, Identifying damage locations under ambient vibrations utilizing vector autoregressive models and mahalanobis distances, *Mechanical Systems and Signal Processing*, **26** , 254–267, 2012.

[9] K. K. Nair, A. S. Kiremidjian, and K. H. Law, Time series-based damage detection and localization algorithm with application to the asce benchmark structure, *Journal of Sound and Vibration*, **291**, 349–368, 2006.

[10] H. Nandan, E. Abrahamson, X. Wang, and C. Brinkmann, *Time series based damage detection and localization in an offshore platform using wireless sensor networks, ASME 2014 33rd International Conference on Ocean, Offshore and Arctic Engineering, American Society of Mechanical Engineers Digital Collection*, San Francisco, California, USA, June 8–13, 2014.

[11] N. Bicanic and H.-P. Chen, Damage identification in framed structures using natural frequencies, *International Journal for Numerical Methods in Engineering*, **40**, 4451–4468, 1997.

[12] O. Salawu, Detection of structural damage through changes in frequency: A review, *Engineering Structures*, **19**, 718–723, 1997.

[13] F. Vestroni and D. Capecchi, Damage detection in beam structures based on frequency measurements, *Journal of Engineering Mechanics*, **126**, 761–768, 2000.

[14] A. Pandey, M. Biswas, and M. Samman, Damage detection from changes in curvature mode shapes, *Journal of Sound and Vibration*, **145** , 321–332, 1991.

[15] A. B. Siddique, L. D. Wegner, and B. F. Sparling, *Identifying damage on a bridge deck using vibration-based damage indices derived from limited measurements, Nondestructive Evaluation and Health Monitoring of Aerospace Materials, Composites, and Civil Infrastructure V*, San Diego, CA, United States, 20 March 2006.

[16] R. Curadelli, J. Riera, D. Ambrosini, and M. Amani, Damage detection by means of structural damping identification, *Engineering Structures*, **30**, 3497–3504, 2008.

[17] G. Kawiecki, Modal damping measurement for damage detection, *Smart Materials and Structures*, **10** , 466, 2001.

[18] R. Astroza, Vibration-Based Health Monitoring and Mechanics-Based Nonlinear Finite Element Model Updating of Civil Structures (Doctoral dissertation, University of California, San Diego, United States), 2015. Retrieved from `https://escholarship.org/uc/item/75r661d1`.

[19] E. Figueiredo, G. Park, J. Figueiras, C. Farrar, and K. Worden, *Structural health monitoring algorithm comparisons using standard data sets*, No. LA-14393. Los Alamos National Lab (LANL), Los Alamos, NM, United States, 2009.

[20] M. Markou, and S. Singh, Novelty detection: a review—part 1: statistical approaches, *Signal processing*, **83**, 2481-2497, 2003.

[21] W. K. Härdle, M. Muller, S. Sperlich, and A. Werwatz, Nonparametric and semiparametric models. *Springer Science & Business Media*, ISBN: 9783642171468, 2012.

[22] Y. Kawahara and M. Sugiyama, Sequential change-point detection based on direct densityratio estimation, *Statistical Analysis and Data Mining: The ASA Data Science Journal*, **5**, 114–127, 2012.

[23] P. Van Overschee and B. De Moor, Subspace identification for linear systems: Theory-Implementation-Applications, *Springer Science & Business Media*, ISBN: 9781461304654, 2012.

[24] S. Kullback, Information theory and statistics. *Courier Corporation*, 1997.

[25] K. Worden, G. Manson, and N. R. Fieller, Damage detection using outlier analysis, *Journal of Sound and Vibration*, **229**, 647–667, 2000.

[26] A.-M. Yan, G. Kerschen, P. De Boe, and J.-C. Golinval, Structural damage diagnosis under varying environmental conditions—Part I: A linear analysis, *Mechanical Systems and Signal Processing*, **19**, 847–864, 2005.

[27] Los Alamos National Laboratory, SHM Data Sets and Software, Available: `https://www.lanl.gov/projects//national-security-education-center/engineering/software/shm-data-sets-and-software.php`. (accessed: 01.02.2020).

EURODYN 2020
XI International Conference on Structural Dynamics
M. Papadrakakis, M. Fragiadakis, C. Papadimitriou (eds.)
Athens, Greece, 23–26 November 2020

PARAMETRIC SPECTRAL ESTIMATION AND DYNAMICS IDENTIFICATION FOR TRAVELING SURFACE VEHICLES

Ilias A. Iliopoulos, Spilios D. Fassois and John S. Sakellariou

Stochastic Mechanical Systems & Automation (SMSA) Laboratory
Department of Mechanical Engineering & Aeronautics
University of Patras, 26504 Patras, Greece
ilias.iliopoulos@upnet.gr; {fassois,sakj}@upatras.gr

Keywords: Surface vehicle dynamics, wheelbase filtering, spectral estimation, dynamics identification

Abstract. *The problems of effective parametric spectral estimation for random vibration signals and dynamics identification for traveling surface vehicles are addressed. Wheelbase Filtering effects, including the induced periodic modulation, on measured random vibration signals are explored, leading to special–structure AutoRegressive Moving Average (ARMA) models which are referred to as Wheelbase Filtering ARMA (WF–ARMA) models. Compared to their conventional counterparts, the postulated models avoid potential model structure mismatch and lack of statistical parsimony, potentially leading to excellent parametric spectral estimation accuracy. Furthermore, exploring their fundamental structural relationships with the stationary (non–moving) vehicle dynamics allows for the postulation of a method for the identification of the latter through the former, thus permitting effective output–only stationary dynamics identification from in–motion random vibration signals. The high achievable accuracy of the postulated estimators is assessed via Monte Carlo numerical experiments with a basic half–vehicle vertical model. The superiority of the postulated WF–ARMA approach is also demonstrated via comparisons with classical Welch based, AR based, and conventional ARMA based spectral estimators.*

1 INTRODUCTION

Random vibration response based, also referred to as *output–only*, modeling and analysis for traveling surface vehicles is of high interest as: (a) It is practical, not requiring unavailable road or rail excitation signals, and (b) may offer valuable insights into the vehicular dynamics under actual operating and boundary conditions, precise dynamical models, and also lead to effective Health Monitoring and Condition Based Maintenance (CBM) for automobiles and rail vehicles [1–4]. Yet, the problem is challenging due to various factors affecting the response of a traveling surface vehicle, including the so–called Wheelbase Filtering (WF) effect [5, p. 168].

Wheelbase Filtering (WF) arises in all wheeled surface vehicles, as the *same* road surface or rail excitation is applied to all wheels on one side of the vehicle with time delays that depend upon the vehicular geometry (distances among axles) and the traveling speed. These delays induce a modulation on the vibration response characteristics, specifically sharp periodic troughs in its Power Spectral Density (PSD), which not only render spectral estimation challenging, but also 'mask' the fundamental (*stationary*) vehicular dynamics (such as resonances and antiresonances). Therefore, the identification of the stationary vehicular dynamics under actual traveling conditions constitutes a challenging problem [6].

Although Wheelbase Filtering is well known in the field of vehicle suspension design [7, 8], its effects on spectral estimation and vehicular dynamics identification have yet to be studied. A recent exception is reference [6], focusing on vehicular dynamics identification via subspace identification techniques under specific conditions, including measurement of the leading wheel excitation.

The present study *aims* at addressing random vibration response modeling and analysis for traveling surface vehicles in two steps: First Wheelbase Filtering is studied and, based upon it, a proper representation and corresponding parametric spectral estimation for in–operation random vibration response signals are postulated. Second, based upon the former, stationary vehicular dynamics identification is explored.

The main idea is based upon considering the effects of Wheelbase Filtering on a random vibration signal and the subsequent introduction of special–structure AutoRegressive Moving Average (ARMA) models fully capturing the induced modulation, and thus allowing for proper signal representation. These models, currently referred to as *Wheelbase Filtering ARMA (WF–ARMA) models*, are characterized by two important *structural characteristics* when compared to their conventional counterparts as employed for modeling the random vibration response on a stationary (non–traveling) vehicle or structural system [9–11]. These constraints pertain to the model's MA polynomial structure, which is shown to be characterized by: (i) Order higher than its AutoRegressive (AR) counterpart, and, (ii) a certain sparsity, due to a number of potentially missing terms. These characteristics offer further insights into the effects of Wheelbase Filtering, as they are demonstrated to lead to zeros close to the unit circle (discrete–time case) which are, in turn, responsible for the periodic troughs appearing in the modulated Power Spectral Density.

The special structure of WF–ARMA models reveals, in particular structural characteristic (i) above, the *model structure misspecification* (mismatch) problem introduced through the use of conventional ARMA models in the context of parametric spectral estimation. In addition, characteristic (ii) above is instrumental in ensuring *statistical parsimony* (model economy) which is, in turn, essential for achieving the highest possible estimation accuracy [12, pp. 491–492].

Furthermore, exploring the relationships between a WF–ARMA model with the stationary vehicular dynamics, allows for the identification of the latter through the former. While this may

be achieved in a simple manner under proper constraints on the time delay between the axles, it is shown that it may be also achieved unconditionally at the expense of employing vibration signals measured under more than one traveling speeds.

In order to effectively demonstrate the concepts, the study makes use of a basic 2 DOF (Degree Of Freedom) vehicle model, that is a two–wheeled (bi–axial) half–vehicle vertical model with front and rear suspension elements, which is capable of describing the bounce and pitch motions. Spectral estimation and vehicular dynamics identification effectiveness is then examined via Monte Carlo numerical experiments with white noise road/rail displacement profiles. Interesting comparisons with non–parametric, Welch–based [12, pp. 186–187], and parametric, conventional AR and ARMA based [13, pp. 172–188], spectral estimators are also presented.

The rest of the article is organized as follows: The Wheelbase Filtering effects on the random vibration response Power Spectral Density are briefly discussed in section 2. The special structure and estimation of Wheelbase Filtering ARMA models are discussed in section 3, and the identification of the stationary vehicular dynamics in section 4. Performance assessment for the postulated methods, along with interesting comparisons, are presented in section 5, and concluding remarks are summarized in section 6.

2 WHEELBASE FILTERING EFFECTS ON THE VIBRATION RESPONSE POWER SPECTRAL DENSITY

Consider the simple, linear (small displacement), 2 DOF, two–wheeled (bi–axial) half–vehicle vertical model of Figure 1, which includes front and rear suspension elements with massless wheels. The vehicle is assumed to travel on a straight track/road under *constant speed*, with the excitation being provided by the vertical rail/road stochastic displacement profile, which is, for simplicity, currently assumed to be uncorrelated (white).

Let the bounce and pitch chassis (center of mass) displacements be designated as $z(t)$ and $\phi(t)$, respectively, and the vertical acceleration at a certain point, say A, on the vehicle by $y(t)$. Also let $u_1(t)$ and $u_2(t)$ represent the excitation (track displacement profile) acting on the front and rear wheel, respectively. The geometrical characteristics of the model are presented in

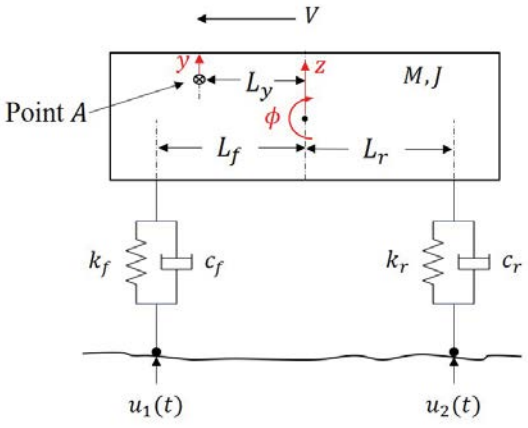

Figure 1: The 2 DOF two–wheeled half–vehicle vertical model.

Figure 1, while its mathematical representation (for small values of $\phi(t)$) is:

$$M\ddot{z}(t) + C_b\dot{z}(t) + K_b z(t) = c_f\dot{u}_1(t) + k_f u_1(t) + c_r\dot{u}_2(t) + k_r u_2(t) \tag{1a}$$

$$J\ddot{\phi}(t) + C_p\dot{\phi}(t) + K_p\phi(t) = c_f L_f\dot{u}_1(t) + k_f L_f u_1(t) - c_r L_r\dot{u}_2(t) - k_r L_r u_2(t) \tag{1b}$$

$$\ddot{y}(t) = \ddot{z}(t) + L_y\ddot{\phi}(t) \tag{1c}$$

with: $K_b := k_f + k_r \qquad C_b := c_f + c_r \qquad K_p := k_f L_f^2 + k_r L_r^2 \qquad C_p := c_f L_f^2 + c_r L_r^2$

Note that the 3rd equation above describes the vertical acceleration at Point A, while M, J stand for the car body mass and pitch moment of inertia, respectively, and k_f, c_f and k_r, c_r stand for the front and rear, respectively, suspension stiffness and viscous damping coefficients. The geometrical parameters L_f, L_r, L_y are defined in Figure 1 with respect to the body center of mass (c.m.).

Based on these equations the relationship between the excitations $u_1(t)$ and $u_2(t)$ and the response $\ddot{y}(t)$ may, in the Laplace (s) domain, be expressed as:

$$\ddot{Y}(s) = H_1(s)U_1(s) + H_2(s)U_2(s) \tag{2}$$

It should be noted that $H_1(s)$ and $H_2(s)$ designate the transfer functions between the track displacement profile acting on the 1st and 2nd wheel, respectively, and the vibration acceleration response at Point A, and as such represent the *stationary* Multiple–Input Single–Output (MISO) vehicular dynamics.

Observing that $u_2(t)$ is identical to $u_1(t)$ but delayed by time delay $\tau = (L_f + L_r)/V$ (see Figure 1; V designating the vehicle traveling speed):

$$u_2(t) = u_1(t - \tau) \tag{3}$$

Equation 2 then yields:

$$\ddot{Y}(s) = \underbrace{\left[H_1(s) + e^{-\tau s}H_2(s)\right]}_{H_{eq}(s)} U(s) \tag{4}$$

with $u(t) := u_1(t)$. Equation 4 clearly suggests that the MISO representation of Equation 2 may be expressed as a Single–Input Single–Output (SISO) system with *equivalent* ('phenomenal') transfer function $H_{eq}(s)$.

The *modulation* induced by Wheelbase Filtering [5, p. 169] may be observed in the frequency domain by examining the Power Spectral Density $S_{\ddot{y}\ddot{y}}(\omega)$ (ω designating frequency in rad/s) of the random vibration acceleration $\ddot{y}(t)$ signal at Point A as follows:

$$\begin{aligned} S_{\ddot{y}\ddot{y}}(\omega) = |H_{eq}(j\omega)|^2 S_{uu}(\omega) = |H_1(j\omega) + e^{-j\omega\tau}H_2(j\omega)|^2 \cdot S_{uu}(\omega) \implies \\ \implies S_{\ddot{y}\ddot{y}}(\omega) = \Big\{|H_1(j\omega)|^2 + |H_2(j\omega)|^2 + \\ +2\Big[\cos(\omega\tau)\,\mathrm{Re}\{H_1(j\omega)H_2^\star(j\omega)\} + \sin(\omega\tau)\,\mathrm{Im}\{H_1(j\omega)H_2^\star(j\omega)\}\Big]\Big\} \cdot S_{uu}(\omega) \end{aligned} \tag{5}$$

with $S_{uu}(\omega)$ designating the track excitation displacement Power Spectral Density, j the imaginary unit, $|\cdot|$ complex magnitude, and * complex conjugation. $\mathrm{Re}\{\cdot\}$ and $\mathrm{Im}\{\cdot\}$ designate real and imaginary part, respectively. The trigonometrical terms in the above expression indicate periodic modulation with period:

$$\Omega_{mod} = 2\pi/\tau \qquad \text{(rad/s)}$$

Parameter	Symbol	Value
Chassis mass (kg)	M	2 880
Pitch moment of inertia ($kg \cdot m^2$)	J	1 440
Front suspension stiffness (N/m)	k_f	1.7×10^6
Rear suspension stiffness (N/m)	k_r	1.7×10^6
Front suspension damping coefficient (Ns/m)	c_f	2.4×10^4
Rear suspension damping coefficient (Ns/m)	c_r	2.4×10^4
Distance between c.m. and the front suspension (m)	L_f	1.25
Distance between c.m. and the rear suspension (m)	L_r	1.25
Distance between c.m. and point $\mathcal{A}$ (m)	L_y	0.50

Table 1: The 2 DOF vehicle model parameters.

introduced by Wheelbase Filtering. It is obvious that for $L_y \neq 0$ (for $L_y = 0$ only bounce motion occurs) the extrema of $S_{\ddot{y}\ddot{y}}(\omega)$ do *not* generally coincide with those of the individual Frequency Response Function (FRF) magnitudes $|H_1(j\omega)|$ and $|H_2(j\omega)|$ which entail the resonances associated with the bounce and pitch motions.

The effects of Wheelbase Filtering on the vibration response Power Spectral Density are demonstrated in the following illustrative case study.

Illustrative Case Study: Consider the basic vehicle model of Figure 1, with parameter values as in Table 1, traveling at $V = 80\ km/h$ with resulting time delay $\tau = 0.1125\ s$. The road/rail vibration displacement excitation is independently identically distributed as normal with zero mean and unit variance. The model is discretized with sampling frequency $f_s = 80\ Hz$ via the impulse invariance method [14, pp. 206–209], with the time delay translated into $d = 9$ sampling periods (samples).

The vehicle's Frequency Response Function (FRF) H_1 and H_2 magnitudes are, along with the vibration acceleration response Power Spectral Density at Point A, $S_{\ddot{y}\ddot{y}}$, depicted in Figure 2. Two resonant frequencies are evident in the two FRF magnitudes, while the Wheelbase Filtering effect, with the introduced periodic modulation with period $F_{mod} = 1/\tau \approx 8.888\ Hz$, heavily distorting the response PSD and 'masking' the original model characteristics, including the resonant frequencies. Further insight may be gained by examining the vehicle model stationary poles and zeros (of the discretized transfer functions H_1 and H_2), along with those of the equivalent (phenomenal) transfer function, H_{eq}, as indicated in Figure 3. Evidently, Wheelbase Filtering introduces (additional) zeros into H_{eq} (hence into the PSD $S_{\ddot{y}\ddot{y}}$), yet none of the equivalent transfer function zeros coincides with those of H_1 or H_2. Furthermore, one complex zero pair (designated as r_1) introduces the first (barely observable) trough in the response PSD (Figure 2), while four additional pairs (designated as r_i for $i = 2, \ldots, 5$) are distributed closely to the unit circle and introduce four subsequent sharp troughs in the response PSD.

Based on the above, it is evident that vibration response spectra are heavily influenced by Wheelbase Filtering effects, which are 'masking' the vehicle's stationary dynamical characteristics, including resonant frequencies. This may have detrimental consequences on signal based modeling, analysis, and condition monitoring.

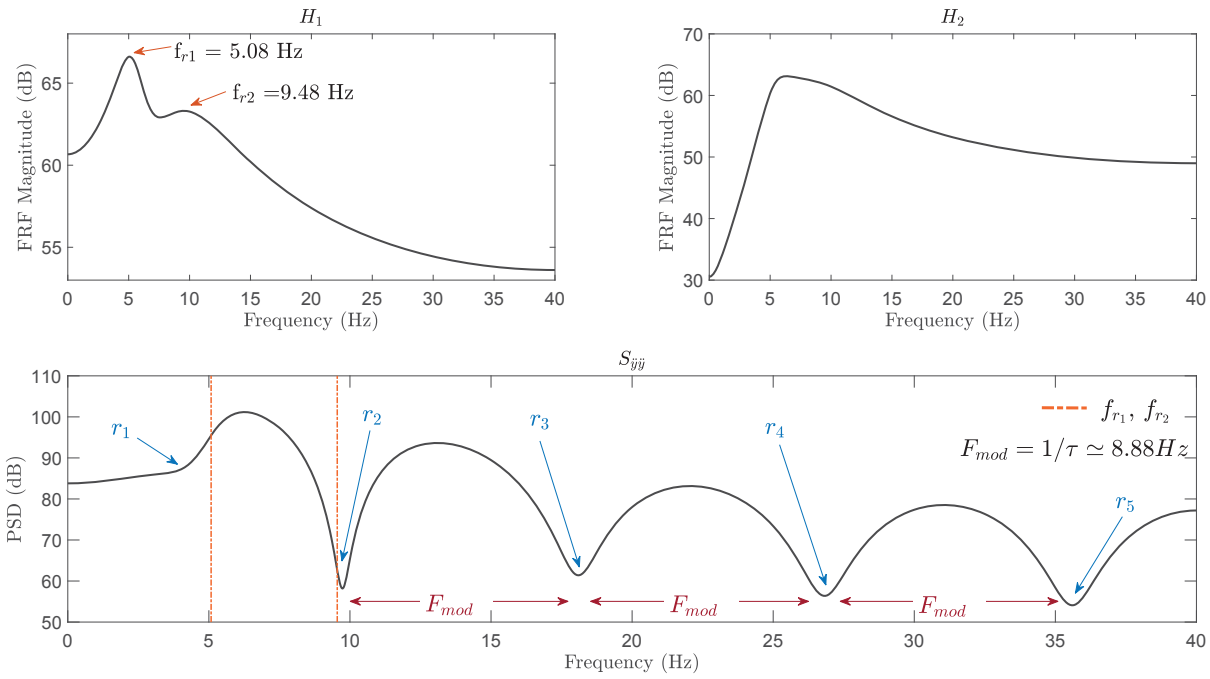

Figure 2: Stationary Frequency Response Function (FRF) magnitude curves for H_1 (a), H_2 (b), and the vertical vibration acceleration response (Point A) Power Spectral Density (c). [Illustrative case study.]

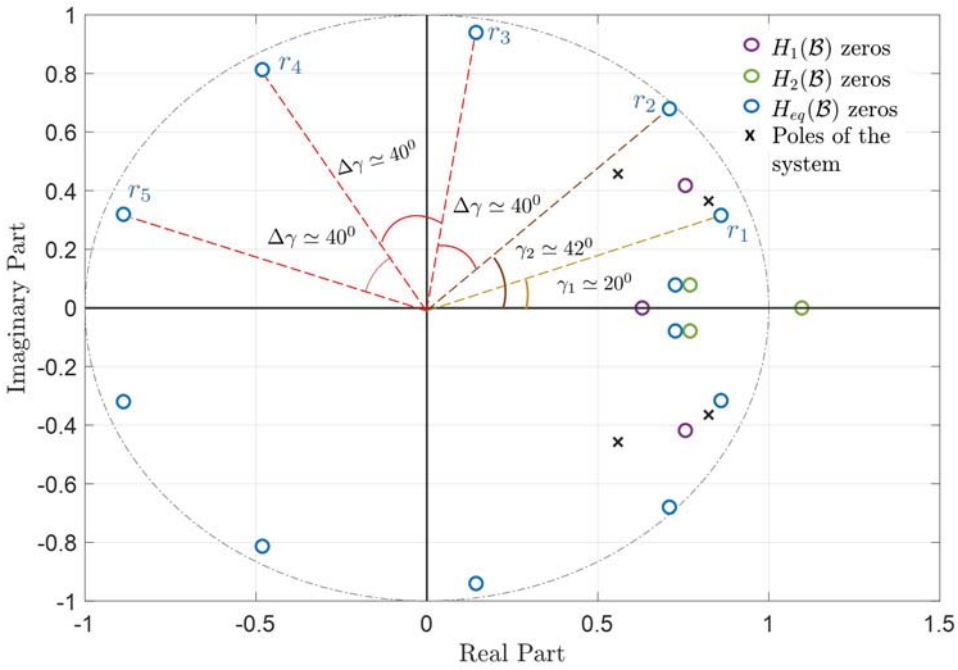

Figure 3: The poles and zeros of the discretized H_1, H_2 and H_{eq} transfer functions. [Illustrative case study.]

3 PARAMETRIC REPRESENTATION AND POWER SPECTRAL DENSITY ESTIMATION FOR THE RANDOM VIBRATION RESPONSE

3.1 The special–structure ARMA model for random vibration response signal representation

The discrete–time H_1 and H_2 stationary transfer functions (Equation 2) may be parameterized as:

$$H_1(\mathcal{B}) := \frac{C_1(\mathcal{B})}{A(\mathcal{B})} \qquad H_2(\mathcal{B}) := \frac{C_2(\mathcal{B})}{A(\mathcal{B})} \tag{6}$$

through the polynomials:

$$\begin{aligned} A(\mathcal{B}) &:= 1 + a_1\mathcal{B} + a_2\mathcal{B}^2 + \ldots + a_{na}\mathcal{B}^{na} \qquad \text{(monic)} \\ C_1(\mathcal{B}) &:= c_{1,0} + c_{1,1}\mathcal{B} + c_{1,2}\mathcal{B}^2 + \ldots + c_{1,nc}\mathcal{B}^{nc} \\ C_2(\mathcal{B}) &:= c_{2,0} + c_{2,1}\mathcal{B} + c_{2,2}\mathcal{B}^2 + \ldots + c_{2,nc}\mathcal{B}^{nc} \end{aligned}$$

with $\mathcal{B}$ (also known as q^{-1}) designating the *backshift operator* defined such that $\mathcal{B}^i u[t] := u[t-i]$ (t within brackets designating discrete time normalized by the sampling period T, that is $t = 0, 1, 2, \ldots$). na, nc designate the corresponding polynomial degrees – obviously na is also the *system order*. Substituting Equation 6 into the discretized version of Equation 2 leads to the following representation of the equivalent SISO model:

$$A(\mathcal{B})y[t] = \Big[C_1(\mathcal{B}) + C_2(\mathcal{B}) \cdot \mathcal{B}^d\Big]u[t], \quad u[t] \sim \text{i.i.d. } \mathcal{N}(0, \sigma^2) \tag{7}$$

with $d := \tau/T$ designating the *time delay* in terms of number of samples (presently assumed to be an integer) and $u[t]$, $y[t]$ standing for the discretized versions of the road/track profile displacement excitation and random vibration response, respectively. As previously stated, $u[t]$ is assumed identically independently distributed (i.i.d.) Gaussian with zero mean and variance σ^2.

Upon re–arrangement and absorption of $c_{1,0}$ into $u[t]$, the equivalent model of Equation 7 may be written as:

$$A(\mathcal{B})y[t] = \bar{C}(\mathcal{B})\bar{u}[t] \qquad \bar{u}[t] = c_{1,0} \cdot u[t] \sim \text{i.i.d. } \mathcal{N}(0, c_{1,0}^2\sigma^2) \tag{8}$$

with the *normalized* MA polynomial being (the normalization is to warrant monic polynomial):

$$\bar{C}(\mathcal{B}) := \frac{1}{c_{1,0}}\Big[C_1(\mathcal{B}) + C_2(\mathcal{B}) \cdot \mathcal{B}^d\Big] := \bar{C}_1(\mathcal{B}) + \bar{C}_2(\mathcal{B}) \cdot \mathcal{B}^d := 1 + \bar{c}_1\mathcal{B} + \cdots + \bar{c}_{nc+d}\mathcal{B}^{nc+d}$$
$$\bar{C}(\mathcal{B}) : \text{monic} \qquad \bar{C}_1(\mathcal{B}) : \text{monic} \qquad \bar{C}_2(\mathcal{B}) : \text{non–monic} \tag{9}$$

and the corresponding normalized versions of $H_1(\mathcal{B})$, $H_2(\mathcal{B})$:

$$\bar{H}_1(\mathcal{B}) := \frac{\bar{C}_1(\mathcal{B})}{A(\mathcal{B})} \qquad \bar{H}_2(\mathcal{B}) := \frac{\bar{C}_2(\mathcal{B})}{A(\mathcal{B})} \tag{10}$$

Notice that in all of the above expressions the overbar designates that the indicated polynomial (or the numerator polynomial in a transfer function) is normalized via division by $c_{1,0}$ (Equation 9).

The representation of Equation 8 is an AutoRegressive Moving Average (ARMA) model of orders $(na, nc + d)$, that is an ARMA$(na, nc + d)$ model, with two structural conditions distinguishing it from conventional ARMA models typically employed for representing the random vibration response on a stationary (non–traveling) vehicle or other structural systems [11]:

(i) The MA order $nc + d$ is, in general, *higher* than its AR counterpart na.

(ii) For $d > nc$ (typical under *low traveling speed*), the MA polynomial is characterized by a certain *sparsity* (missed intermediate terms).

Because of these, and for easy distinction, this model is subsequently referred to as a *Wheelbase Filtering ARMA model of orders* $(na, nc+d)$, with d designating the delay, or in short as a WF–ARMA$(na, nc + d)$ model. The following comments regarding the importance of structural conditions (i) and (ii) are now in order.

Comments:

(a) Structural condition (i) is instrumental for proper modeling, as potential violation (for instance by following the usual AR and MA order equality or MA order being equal to its AR counterpart minus one [11]) would imply *model structure misspecification* (mismatch), causing serious representation deficiency and model accuracy degradation.

(b) Structural condition (ii) is also instrumental because it warrants *statistical parsimony* (model economy), which is essential for achieving the highest possible estimation accuracy [12, pp. 491–492].

(c) As already indicated (illustrative case study in section 2), these structural conditions lead to the introduction of pairs of zeros close to the unit circle, which are responsible for the troughs in the vibration response Power Spectral Density.

(d) The zeros proximity to the unit circle also implies that pure AutoRegressive (AR) models, which are commonly employed in applications due to their estimation simplicity, are inappropriate (especially in the presence of very sharp troughs), as their use is expected to lead to poor approximations and/or very high model orders (see section 5).

(e) Evidently, in the 'very high' traveling speed case, $d \approx 0$ and the WF–ARMA$(na, nc+d)$ model degenerates to a conventional ARMA(na, nc) counterpart.

3.2 Remarks on WF–ARMA model estimation

Estimation of the WF–ARMA$(na, nc + d)$ model of Equation 8, that is determination of the AR/MA parameter vector $\boldsymbol{\theta} := [\ \boldsymbol{a} \vdots \bar{\boldsymbol{c}}\ ]^T$ (^{T} designating transposition) and the white noise variance ($c_{1,0}^2\sigma^2$) from a measured vibration response signal $y[t]$ ($t = 1, 2, \ldots, N$), may be based on the Prediction Error (PE) principle [12, pp. 199–201] subject to the provision that, in accordance to structural feature (ii), for $d > nc$ the pseudo–regression vector should have the form (notice the missing terms between the second and third groups):

$$\boldsymbol{\psi}[t, \boldsymbol{\theta}] := \big[y[t-1] \ldots y[t-na] \vdots e[t-1, \boldsymbol{\theta}] \ldots e[t-nc, \boldsymbol{\theta}] \vdots e[t-d, \boldsymbol{\theta}] \ldots e[t-(nc+d), \boldsymbol{\theta}]\big]^T$$

with $e[t, \boldsymbol{\theta}]$ designating the model–based one–step–ahead prediction error [12, pp. 68–70]. Of course, this is a function of the parameter vector $\boldsymbol{\theta}$, thus leading to a Nonlinear Least Squares optimization problem which may be tackled via *Gauss–Newton* and *Levenberg–Marquardt* procedures [12, pp. 326–329].

Model order estimation may be based on direct computation of d (for given traveling speed) and na, nc selection via the Bayesian Information Criterion (BIC) [12, pp. 505–507].

Once the WF–ARMA$(na, nc + d)$ model has been estimated, the random vibration response model based Power Spectral Density may be obtained as (T designates the sampling period):

$$S_{\ddot{y}\ddot{y}}(\omega) = \left|\frac{\bar{C}(e^{-j\omega T})}{A(e^{-j\omega T})}\right|^2 \cdot \left(c_{1,0}^2\sigma^2\right) \tag{11}$$

4 VEHICULAR DYNAMICS IDENTIFICATION

Vehicular dynamics identification depends upon the delay d (in samples) compared to the stationary MA order nc. As, in turn, d depends on the traveling speed, the cases of 'low' and 'high' traveling speeds are separately considered.

4.1 'Low' traveling speed ($d > nc$) case

In this case the terms of the $\bar{C}_1(\mathcal{B})$ and $\bar{C}_2(\mathcal{B})$ polynomials are, in the $\bar{C}(\mathcal{B})$ expression of Equation 9, non–interlaced and thus clearly separated (by the missing terms) among themselves, so that they may be accurately recovered from the obtained estimate of $\bar{C}(\mathcal{B})$. Using the estimate of $A(\mathcal{B})$, estimates of $\bar{H}_1(\mathcal{B})$ and $\bar{H}_2(\mathcal{B})$ may be then obtained through Equation 10.

Observe that the normalized versions, $\bar{H}_1(\mathcal{B})$ and $\bar{H}_2(\mathcal{B})$, are obtained instead of their original counterparts, or, in other words, the H_1 and H_2 transfer functions are recovered to a constant multiplier (constant multiplier uncertainty). Likewise the excitation variance is obtained as $(c_{1,0}^2 \cdot \sigma^2)$, instead of the actual σ^2 of Equation 7. Frequency Response Function (FRF) estimates may be also readily obtained from the transfer functions via the substitution $\mathcal{B} = e^{-j\omega T}$.

4.2 'High' traveling speed ($d \leq nc$) case

Unlike in the previous case, this is slightly more complex, as the terms of the polynomials $\bar{C}_1(\mathcal{B})$ and $\bar{C}_2(\mathcal{B})$ are interlaced in producing $\bar{C}(\mathcal{B})$ (Equation 9). The precise relationships between the coefficients of the three polynomials may be readily obtained as:

$$\bar{c}_i = \begin{cases} \bar{c}_{1,i} & i = 1, \cdots, d-1 \\ \bar{c}_{1,i} + \bar{c}_{2,i-d} & i = d, \cdots, nc \\ \bar{c}_{2,i-d} & i = nc+1, \cdots, nc+d \end{cases} \tag{12}$$

Evidently, the coefficients of the $\bar{C}_1(\mathcal{B})$ and $\bar{C}_2(\mathcal{B})$ polynomials cannot be uniquely recovered, implying that vehicular dynamics identification is not possible.

Yet, this may be overcome by employing *two* measured random vibration response signals, say $y^p[t]$, $y^q[t]$ $(t = 1, 2, \ldots, N)$ corresponding to *two* distinct traveling speeds V^p and V^q (and thus delays d^p and d^q), respectively. Assume, without loss of generality, that $d^q < d^p < nc$. Based on the available vibration response signals two models, a WF–ARMA$(na, nc + d^p)$ and a WF–ARMA$(na, nc + d^q)$, are estimated:

$$A^p(\mathcal{B})y^p[t] = \bar{C}^p(\mathcal{B})\bar{u}^p[t] \qquad \bar{u}^p[t] = c_{1,0}^p \cdot u^p[t] \sim \mathcal{N}(0, (c_{1,0}^p \sigma^p)^2) \tag{13a}$$

$$A^q(\mathcal{B})y^q[t] = \bar{C}^q(\mathcal{B})\bar{u}^q[t] \qquad \bar{u}^q[t] = c_{1,0}^q \cdot u^q[t] \sim \mathcal{N}(0, (c_{1,0}^q \sigma^q)^2) \tag{13b}$$

Evidently, the AR polynomials should be identical, that is $A^p(\mathcal{B}) \equiv A^q(\mathcal{B})$ (apart from estimation errors), so the AR parameters may be obtained as simple averages of the individual estimates.

On the other hand, the MA polynomials $\bar{C}^p(\mathcal{B})$, $\bar{C}^q(\mathcal{B})$ should be distinct, due to $d^p \neq d^q$, but interrelated due to their internal structure, that is common $\bar{C}_1(\mathcal{B})$ and $\bar{C}_2(\mathcal{B})$ stationary polynomials (Equation 9):

$$\bar{C}^p(\mathcal{B}) := \bar{C}_1(\mathcal{B}) + \bar{C}_2(\mathcal{B}) \cdot \mathcal{B}^{d^p} \qquad \bar{C}^q(\mathcal{B}) := \bar{C}_1(\mathcal{B}) + \bar{C}_2(\mathcal{B}) \cdot \mathcal{B}^{d^q} \tag{14}$$

These relationships lead to the following set of equations:

$$
\begin{array}{ll}
\underline{\bar{C}^p(\mathcal{B}):} & \underline{\bar{C}^q(\mathcal{B}):} \\
\left.\begin{array}{r} \bar{c}_{1,1} = \bar{c}^p_1 \\ \vdots \\ \bar{c}_{1,d^p-1} = \bar{c}^p_{d^p-1} \end{array}\right\} (d^p-1) \text{ eqs} & \left.\begin{array}{r} \bar{c}_{1,1} = \bar{c}^q_1 \\ \vdots \\ \bar{c}_{1,d^q-1} = \bar{c}^q_{d^q-1} \end{array}\right\} (d^q-1) \text{ eqs} \\
\left.\begin{array}{r} \bar{c}_{1,d^p} + \bar{c}_{2,0} = \bar{c}^p_{d^p} \\ \vdots \\ \bar{c}_{1,nc} + \bar{c}_{2,nc-d^p} = \bar{c}^p_{nc} \end{array}\right\} (nc-d^p+1) \text{ eqs} & \left.\begin{array}{r} \bar{c}_{1,d^q} + \bar{c}_{2,0} = \bar{c}^q_{d^q} \\ \vdots \\ \bar{c}_{1,nc} + \bar{c}_{2,nc-d^q} = \bar{c}^q_{nc} \end{array}\right\} (nc-d^q+1) \text{ eqs} \\
\left.\begin{array}{r} \bar{c}_{2,nc+1-d^p} = \bar{c}^p_{nc+1} \\ \vdots \\ \bar{c}_{2,nc} = \bar{c}^p_{nc+d^p} \end{array}\right\} (d^p) \text{ eqs} & \left.\begin{array}{r} \bar{c}_{2,nc+1-d^q} = \bar{c}^q_{nc+1} \\ \vdots \\ \bar{c}_{2,nc} = \bar{c}^q_{nc+d^q} \end{array}\right\} (d^q) \text{ eqs}
\end{array}
\tag{15}
$$

which may be then used to set up an overdetermined linear system of equations with the coefficients of $\bar{C}_1(\mathcal{B})$ and $\bar{C}_2(\mathcal{B})$ as unknowns ($2nc + d^p + d^q$ equations in $2nc + 1$ unknowns). This system may be solved in a Least Squares sense in order to provide estimates of the coefficients of $\bar{C}_1(\mathcal{B})$ and $\bar{C}_2(\mathcal{B})$. The identification of the stationary vehicular dynamics, in terms of the transfer functions $\bar{H}_1(\mathcal{B})$, $\bar{H}_2(\mathcal{B})$, is then complete.

5 PERFORMANCE ASSESSMENT AND COMPARISONS VIA MONTE CARLO EXPERIMENTS

Performance assessment is based on the illustrative case study of section 2. The traveling speed is $V = 80\ km/h$, resulting into a time delay $\tau = 0.1125\ s$, which for sampling frequency $f_s = 80\ Hz$ is equivalent to $d = 9$ samples long. The road/rail vibration displacement excitation is independently identically distributed with normal distribution having zero mean and unit variance, that is $u[t] \sim$ i.i.d. $\mathcal{N}(0, 1)$.

Estimation results are based on $1\ 000$ Monte Carlo runs, with the random vibration vertical acceleration signal in each run being $\Delta t = 250\ s$ ($N = 20\ 000$ samples) long. Each obtained vibration signal is pre–processed by having its sample mean removed and its sample standard deviation normalized to unity (the latter for purely numerical reasons).

Parametric spectral estimation results for the observed random vibration signal are presented first, followed by vehicular dynamics identification results.

5.1 WF–ARMA model based random vibration parametric spectral estimation

For the 2 DOF model treated, a WF–ARMA$(4, 3{+}9)$ model (that is $na = 4$, $nc = na-1 = 3$, $d = 9$) is appropriate [11]. WF–ARMA$(4, 3 + 9)$ based parametric spectral estimation is thus pursued, while interesting comparisons with the non–parametric Welch method [12, pp. 186–187], the pure AR based method, as well as ARMA$(4, 12)$ based spectral estimation [13, pp. 172–188], are also made. These comparisons are of particular interest, as the non–parametric Welch and the AR based methods are quite popular due to their implementation simplicity and low computational complexity. The comparison with ARMA$(4, 12)$ based spectral estimation – notice that this model is order–wise equivalent to its WF–ARMA$(4, 3 + 9)$ counterpart – is performed in order to isolate and assess the benefits of imposing structural condition (ii) related

Estimated Model	Estimation Method	MATLAB function
Non–parametric PSD	Welch	`pwelch.m`
AR(57)	Ordinary Least Squares (OLS)	`ar.m`
ARMA(4,12)	Nonlinear Least squares (NLS)	`armax.m`
WF–ARMA(4,3+9)		`custom function`
Random vibration signal length: $N = 20\,000$ samples		
Welch method details: Hamming window, segment length 512 samples, overlap 90%, $\delta f \simeq 0.15Hz$		

Table 2: Spectral estimation details.

to sparsity (see subsection 3.1) even when structural condition (i) is met. Estimation details are, for all cases, provided in Table 2, while Monte Carlo estimation results are presented in Figure 4.

Based on the obtained results, WF–ARMA$(4, 3 + 9)$ spectral estimation is evidently excellent, exhibiting no bias and minimal variability. Welch based spectral estimation is adequate, but characterized by significantly increased variability. AR based spectral estimation employs AR(57) models, selected via the BIC criterion [11]. This high order is expected and due to the pure AR approximation of the ARMA based dynamics, while it is aggravated by the first, sharp, spectral trough. Yet, estimation accuracy is still not very good for the specific trough, while ripples and considerable variability are observed across the bandwidth. Finally, ARMA$(4, 12)$

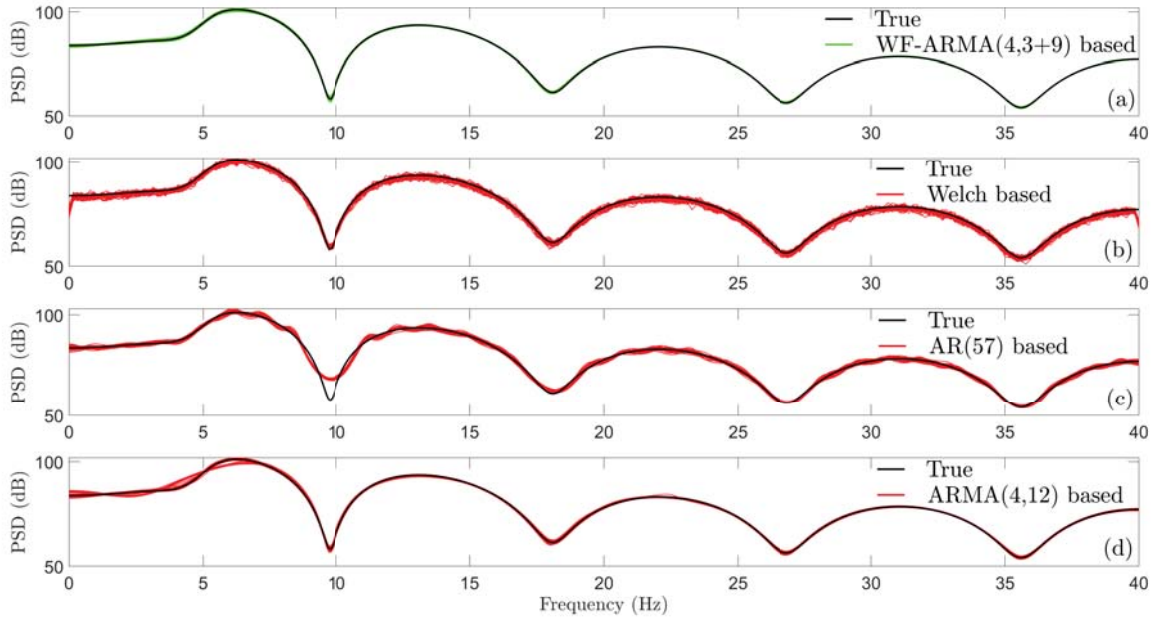

Figure 4: Spectral estimation assessment via the illustrative case study: (a) WF–ARMA based method, (b) Welch based method, (c) AR based method, and (d) ARMA based method with true orders. [In each case the true Power Spectral Density is shown in black; Traveling speed $V = 80\ km/h$; 1 000 Monte Carlo runs per method.]

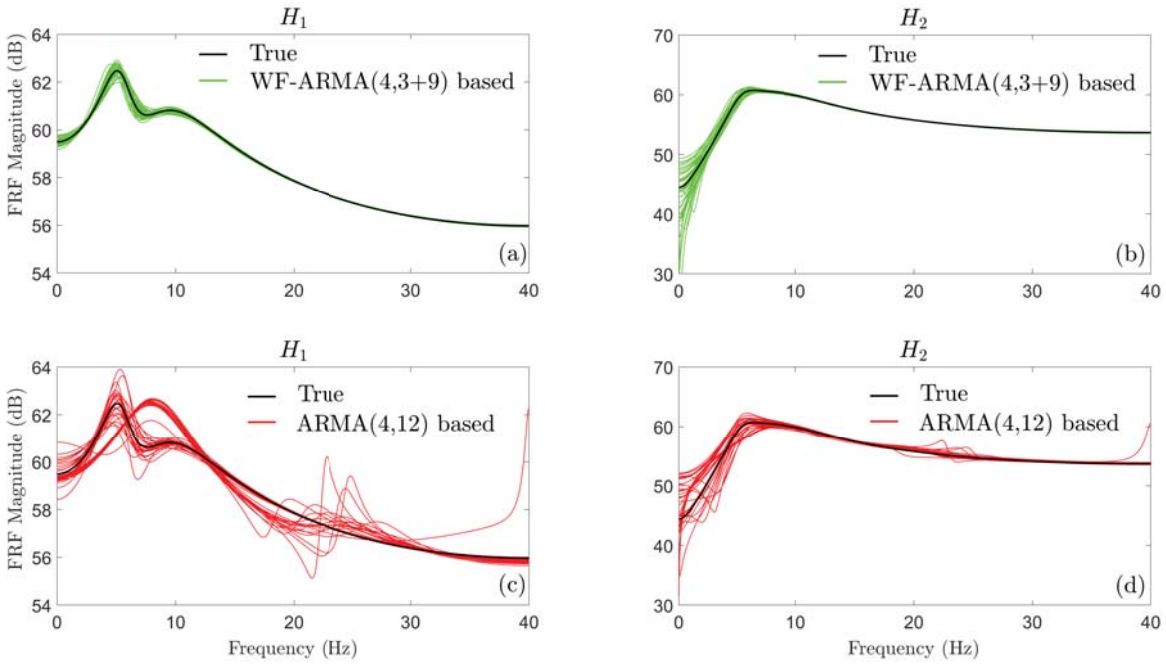

Figure 5: Vehicular dynamics estimation assessment via the illustrative case study under a single traveling speed: Stationary Frequency Response Function (FRF) H_1 and H_2 magnitude estimates obtained by the WF–ARMA (a,b) and ARMA (c,d) based methods. [The true FRF magnitudes are shown in black; Traveling speed $V = 80\ km/h$; 1 000 Monte Carlo runs per method.]

based estimation is adequate, but exhibiting certain bias at low frequencies and somewhat increased variability compared to that attained via the WF–ARMA$(4, 3 + 9)$ model.

Overall, the presented results illustrate the effectiveness and advantages of the postulated WF–ARMA model based spectral estimation approach.

5.2 WF–ARMA model based vehicular dynamics identification

'Low' traveling speed case ($V = 80\ km/h$, $d = 9 > nc = 3$) In this case the procedure of subsection 4.1 is applied based on the WF–ARMA$(4, 3 + 9)$ model. For comparison, in particular for observing the benefits of imposing structural condition (ii) related to sparsity, the procedure is also applied based on an ordinary ARMA$(4, 12)$ model. This is accomplished by a–posteriori setting to zero the parameters that ought to be omitted. Monte Carlo dynamics identification results by both methods are, in terms of stationary Frequency Response Functions (FRF) magnitudes for H_1 and H_2, presented in Figure 5, while corresponding modal parameter estimates obtained by the WF–ARMA$(4, 3 + 9)$ method are presented in Table 3.

The stationary FRF magnitudes estimated by the WF–ARMA based method (in this case without scaling uncertainty, as $\sigma^2 = 1$ so that $c_{1,0}$ is estimated) are very good, while those obtained by the ARMA based method exhibit serious problems in terms of both high variability and (in several cases) wrongly estimated modes. The benefits of imposing structural condition (ii) are thus confirmed as significant. The modal parameter estimates obtained by the WF–ARMA based method are also very good, with small standard deviations.

'High' traveling speed case ($d \leq nc = 3$) In this case the procedure of subsection 4.2 is

Mode	Natural Frequency f_n (Hz)		Resonant Frequency f_r (Hz)		Damping Ratio ζ (%)	
	True	Estimate (mean $\pm$ std)	True	Estimate (mean $\pm$ std)	True	Estimate (mean $\pm$ std)
Bounce	5.47	5.47 ± 0.18	5.08	5.09 ± 0.15	0.24	0.24 ± 0.02
Pitch	9.67	9.66 ± 0.23	9.48	9.47 ± 0.26	0.42	0.43 ± 0.01

Table 3: Vehicular modal parameter estimation for the illustrative case study: Natural frequency, resonant frequency and damping ratio estimates by the WF–ARMA method versus true counterparts. [Traveling speed $V = 80$ km/h; 1 000 Monte Carlo runs.]

applied based on two traveling speeds, $V^p = 240$ km/h and $V^q = 360$ km/h. The resulting models are WF–ARMA$(4, 3+3)$ and WF–ARMA$(4, 3+2)$, respectively.

The estimated H_1 and H_2 stationary FRF magnitudes are contrasted to their theoretical counterparts in Figure 6. The estimates are quite good, with some bias present at very low frequencies. Similarly to the 'low' traveling speed case, the stationary FRF magnitudes are estimated without scaling uncertainty, as $(\sigma^p)^2 = (\sigma^q)^2 = \sigma^2 = 1$ so that $c_{1,0}$ is obtained as a simple average of the individual $c^p_{1,0}$ and $c^q_{1,0}$ estimates [refer to Equation 13, Equation 8 and observe that $c^p_{1,0}$ and $c^q_{1,0}$ do not depend upon the delay d, thus speed, and should be both equal to $c_{1,0}$].

6 CONCLUDING REMARKS

The problems of effective parametric spectral estimation for random vibration signals and dynamics identification for traveling surface vehicles, in view of Wheelbase Filtering effects on measured random vibration signals, have been addressed. Special–structure AutoRegressive Moving Average (ARMA) models, referred to as Wheelbase Filtering ARMA (WF–ARMA) models, have been postulated for the precise representation, estimation, and spectral analysis of random vibration signals. A method for stationary vehicular dynamics identification based on in–motion random vibration signals (output–only identification) has been also developed. The main conclusions from the study may be summarized as follows:

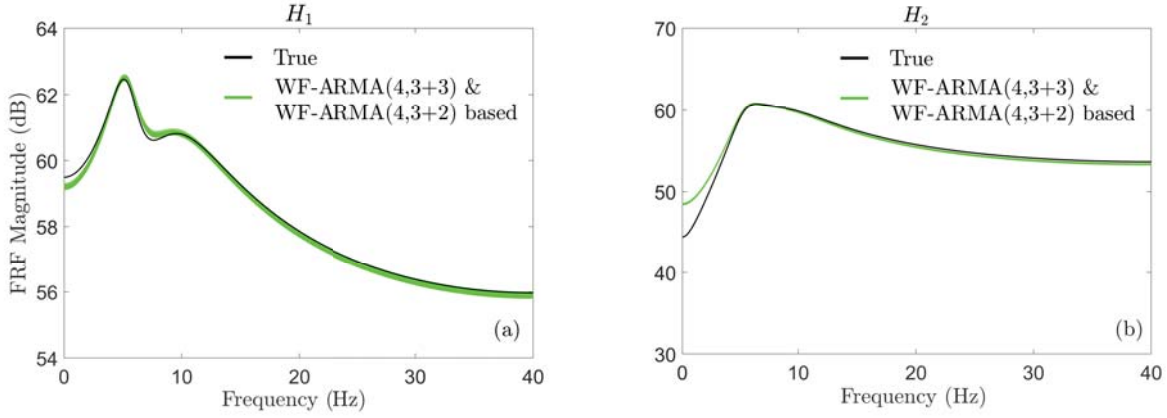

Figure 6: Vehicular dynamics estimation assessment via the illustrative case study under two traveling speeds: Stationary Frequency Response Function (FRF) H_1 and H_2 magnitude estimates obtained by the two WF–ARMA models. [The true FRF magnitudes are shown in black; Traveling speeds $V^p = 240$ km/h and $V^q = 360$ km/h; 1 000 Monte Carlo runs per speed.]

- Wheelbase Filtering effects lead to special–structure ARMA (WF–ARMA) models for the representation and parametric spectral estimation of random vibration signals for traveling surface vehicles.
- The special structure of WF–ARMA models is instrumental for achieving high accuracy. Indeed, compared to their conventional counterparts, WF–ARMA models avoid the detrimental effects of model mismatch and lack of statistical parsimony.
- The stationary vehicular dynamics may be properly identified via in–motion random vibration signals under a single or multiple nominal speeds.
- The superiority of the postulated WF–ARMA based approach has been demonstrated via Monte Carlo comparisons with classical Welch based, AR based, and conventional ARMA based spectral estimators.

ACKNOWLEDGEMENT

This research has been partly financed by the European Union and Greek national funds through the Operational Program Competitiveness, Entrepreneurship and Innovation, under the call RESEARCH–CREATE–INNOVATE (project MAIANDROS; project code: T1EDK–01440).

REFERENCES

[1] T.-C.I. Aravanis, J.S. Sakellariou and S.D. Fassois, Spectral analysis of railway vehicle vertical vibration under normal operating conditions, *International Journal of Rail Transportation*, **4**(4), 193–207, 2016.

[2] T.X. Mei, X.J. Ding, Condition monitoring of rail vehicle suspensions based on changes in system dynamic interactions,*Vehicle System Dynamics*, **47**(9), 1167–1181, 2009.

[3] U.A.U. Rajib, A. Waiz, R. Subhash, Dynamic analysis of railway vehicle–track interactions due to wheel flat with a pitch–plane vehicle model, *Journal of Mechanical Engineering*, **39**(2), 86–94, 2008.

[4] J.S. Sakellariou, K.A. Petsounis, S.D. Fassois, Vibration based fault diagnosis for railway vehicle suspensions via a functional model based method: a feasibility study, *Journal of Mechanical Science and Technology*, **29**(2), 471–484, 2015.

[5] T.D. Gillespie, Fundamentals of Vehicle Dynamics, Pennsylvania: Society of Automotive Engineers Inc., 1992.

[6] L.M. Erviti, J.G. Gimenez, A. Alonso, Influence of repeated and delayed excitations in combined subspace identification, *Vehicle System Dynamics*, **55**(12), 1884–1908, 2017.

[7] D.J. Cole, Fundamental issues in suspension design for heavy road vehicles, *Vehicle System Dynamics*, **35**(4-5), 319–360, 2001.

[8] D. Gong, J. Zhou, W. Sun, On the resonant vibration of a flexible railway car body and its suppression with a dynamic vibration absorber, *Journal of Sound and Vibration*, **19**(5), 649–657, 2012.

[9] S.M. Moore, J.C.S. Lai, K. Shankar, ARMAX modal parameter identification in the presence of unmeasured excitation – I: Theoretical background, *Mechanical Systems and Signal Processing*, **21**(4), 1601–1615, 2007.

[10] E. Reynders, System identification methods for (operational) modal analysis: Review and comparison, *Archives of Computational Methods in Engineering*, **19**(1), 51–124, 2012.

[11] S.D. Fassois, MIMO–LMS identification of vibrating structures – Part I: The method, *Mechanical Systems and Signal Processing*, **15**(4), 723–735, 2001.

[12] L. Ljung, System Identification: Theory for the User, Second ed., New Jersey: Prentice-Hall, 1999.

[13] S.L. Marple, Digital Spectral Analysis with Applications, First ed., New Jersey: Prentice-Hall, 1987.

[14] T.W. Parks, S.C. Burrus, Digital Filter Design, First ed., New York: John Wiley and Sons, 1987.

EURODYN 2020
XI International Conference on Structural Dynamics
M. Papadrakakis, M. Fragiadakis, C. Papadimitriou (eds.)
Athens, Greece, 23–26 November 2020

SYSTEM IDENTIFICATION AND DAMAGE DETECTION FRAMEWORK USING SIMULATED EXPERIMENTS AND MACHINE LEARNING TECHNIQUES

P. Seventekidis[1], D. Giagopoulos[2], A. Arailopoulos[1] and O. MArkogiannaki[1]

[1] Department of Mechanical Engineering
University of Western Macedonia, Kozani GR-50100, Greece
e-mail: dgiagopoulos@uowm.gr

Keywords: FE updating, System Identification, Structural Health Monitoring, Deep Learning, Damage Identification

Abstract. *The present study focuses on the implementation of a methodology to bridge the gap between SHM models with numerically generated data and correspondence with measurements from the real structure to provide reliable damage predictions. In the proposed novel methodology, numerically generated data from simulation models are integrated with measurements from the corresponding real structure to achieve high accuracy in identifying and predicting potential structural damages. A truss structure consisting of composite carbon fiber tubes, aluminum elements and steel bolts for the connections is used for the application of the proposed approach. The process begins with the three-dimensional finite element (FE) models of the examined cylindrical parts, developed in robust finite element analysis software simulating each carbon fiber ply and resin matrix. The real structure and FE models are analyzed in dynamic loading to identify their response. After, the complete assembly FE models are updated based on the data from experimental tests that correspond to the conducted analysis tests on composite cylindrical parts. The potential damage of the structure, set as loose bolts defining a multiclass damage identification problem, is then simulated with the optimal models through a series of stochastic FE load cases for different excitation characteristics. The simulated acceleration time series are then be fed in for the training of a supervised Convolutional Neural Network (CNN) classifier. The trained CNN is finally validated on experimentally measured structural states of the truss. Reliable results prove that optimal FE modeling may be used with machine learning techniques to synthesize a damage identification tool despite the uncertainties, which are tackled by the inherent advantage of numerical generated results to simulate arbitrary number of load cases in small amount of type and minimal effort.*

1 INTRODUCTION

Damage detection methods and Structural Health Monitoring (SHM) is increasingly attracting attention in prognosis and maintenance planning of various structural and mechanical systems. Vibration measurements for damage indexing [1] and SHM [2,3] have been the traditional way of building mathematical classification models that have as task to detect and identify potential damage in systems. More recently, the promising Machine Learning (ML) subcategory known as Artificial Neural Networks (ANN) has entered the SHM field showing great potential in damage detection tasks [4,5]. The advantages that ANNs may offer for SHM against the traditional mathematical models are highlighted as the minimal user preprocessing to input data and the automatic learning of damage features in vibration signals [6]. Usually, ANNs are applied in a multilayer form to achieve that and their architecture and training methods form the wide field of Deep Learning (DL).

Even though new models and methods have been proposed so far for SHM, such as ANNs, the problem of acquiring adequate and appropriate data still exists and is of most importance. All SHM methods go through the so called "training" or model building phase where data of different structural health states is used to "teach" the classifier how to separate a healthy from a damaged condition. The data needs to as representative as possible of the candidate structure for future damage or fault identification, therefore most training data is derived from experimentally measured sources. Experimentally measured data for damaged states could be difficult to get however in most of the cases of real structural systems, since it would require expensive or dangerous to measure damages [7]. Examples in the literature are sparse for data acquisition on damaged states of real structures [8,9].

A novel method was proposed recently with simulated experiments derived from optimal FE models for the data generation [6] in order to bypass difficulties that arise from damaged state measurements and various ambient conditions consideration. The requirement is that the candidate system for SHM to be identified properly on the healthy state and that the damaged are adequately defined to be simulated by FE. Various load cases, ambient conditions and damages may then be simulated and the extracted data can be fed directly with minimal pre-processing in a CNN classifier.

In this work, the potential of the promising system identification and damage detection framework by simulated experiments, is explored further for complex structures. A carbon fiber reinforced polymer (CFRP) truss structure is used as a benchmark. The novel damage detection framework includes a system identification and model updating for the material parameters or the structure and in turn a stochastic FE simulation for generation of labeled health statues. A CNN is trained by the simulated data and validated afterwards by measurements on the real structure. The physical benchmark structure and the imposed damages are described in Section 2, along with the workflow of the complete framework. The system identification and FE model updating is shown in Section 3. Results on the data generation, CNN training and evaluation on the health status of the real structure are shown in Section 4. The performance of the framework is finally discussed in the Conclusions section.

2 CARBON FIBER REINFORCED POLYMER BENCHMARK TRUSS STRUCTURE

Purpose of this work is to test the proposed simulated experiments framework against large and complex structures. The benchmark truss case shown in Figure 1, comprises of CFRP tubes connected on aluminum parts which are bolted on solid aluminum edges [10].

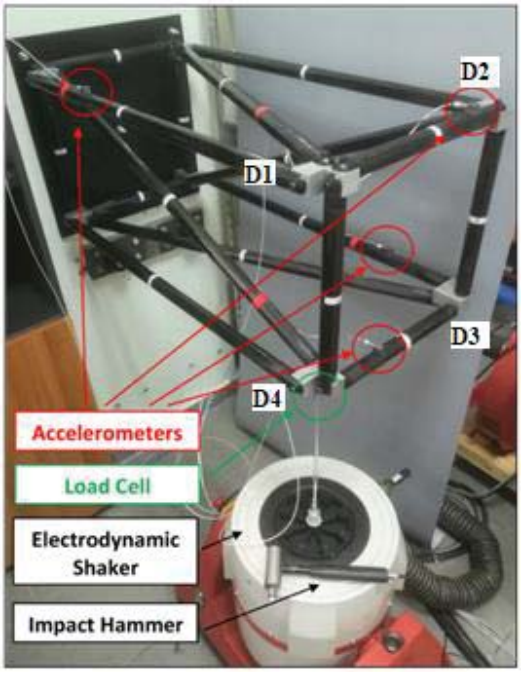

Figure 1 Experimantal setup of the CFRP pin-joined benchmark structure (left). Rubber interface for stiffness reduction of the bolted connection (right)

The benchmark structure poses challenges against the effective identification of the composite material parameters and the effective FE modeling of the bolted connections. The artificial damage to be studied is considered compromised bolts between the aluminum to carbon connection and the solid aluminum edges. Four bolts in total are the candidate damage positions every time as noted in Figure 1 as D1, D2, D3 and D4. The damaged cases bolts are left untightened in order to reduce connection stiffness. Impact loading is used for all SHM tests in this work. The proposed SHM framework proceeds as shown in Figure 2, starting with the FE model building and identification.

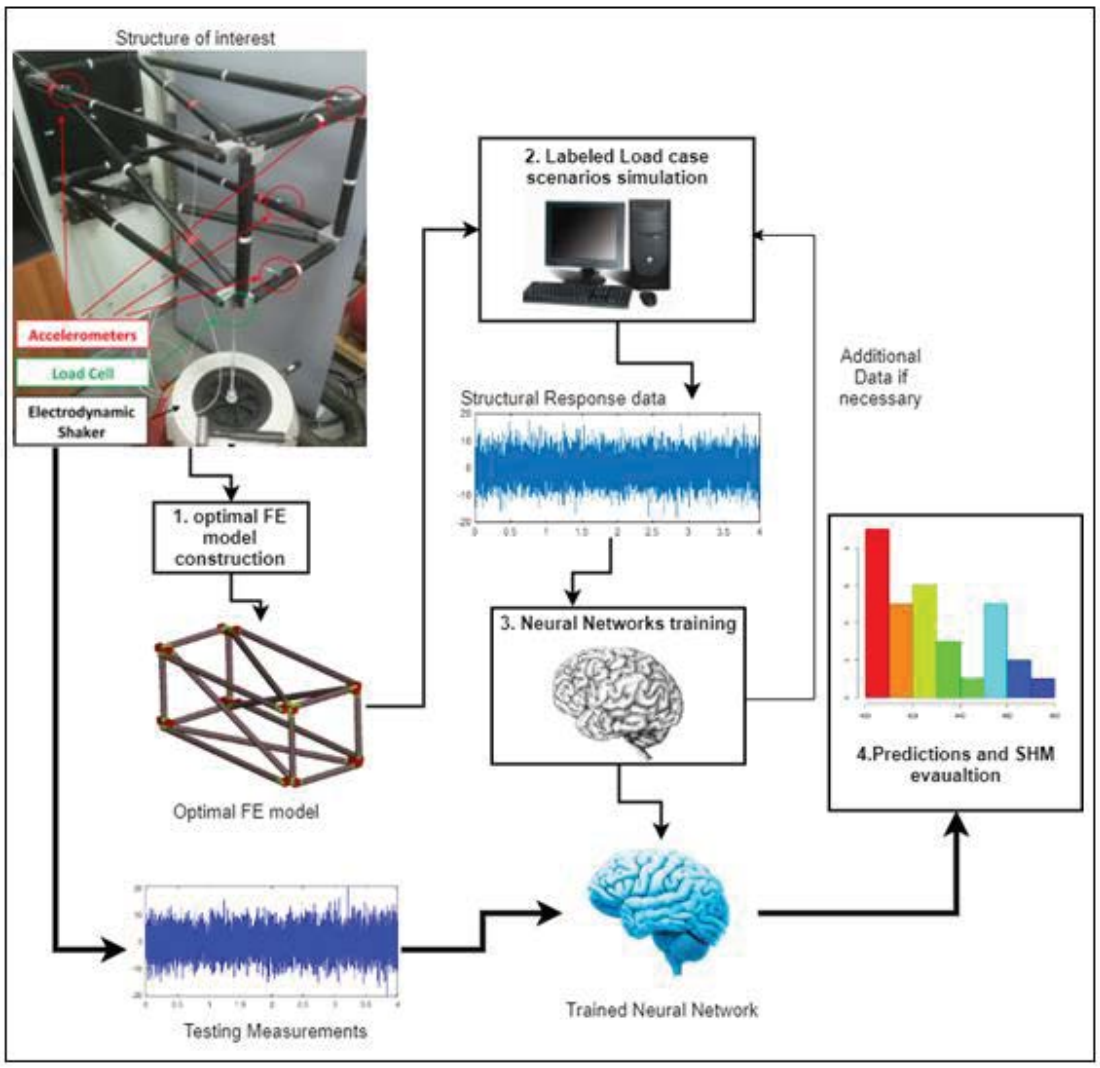

Figure 2 Workflow of the proposed SHM framework

3 SYSTEM IDENTIFICATION AND FINITE ELEMENT MODEL UPDATING OF PARAMETERS

The FE model of the truss structure is constructed using a total of 205.240 triangular shell elements for the CFRP tubes and 1.730.616 tetrahedra elements for the metallic parts and glue that connects them with the tubes. The bolts are modeled as rigid elements that connect the truss sections. In parallel, identification of the truss structure system is performed by extracting the experimental frequency response functions (FRF) with impact loading, shown in Figure 3. The CMA-ES stochastic optimization algorithm [11] is used after to update the FE model CFRP and metallic part material properties on the identified system, based on the experimental FRFs.

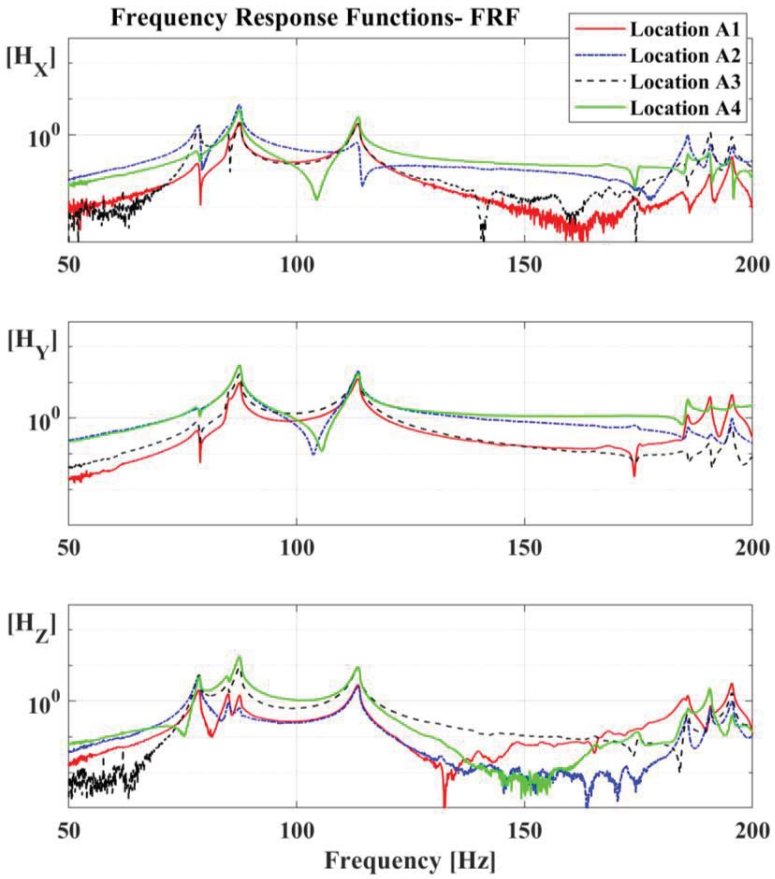

Figure 3 Frequency response functions for impact loading of the truss structure

Prior to update the FE model is divided in parts as shown in Figure 4, according to the material type of each. Results for the first 7 frequencies of the updated FE model are shown in Table 1 in comparison with the identified experimental ones

	Identified Frequency [Hz]	Frequency Updated FE [Hz]	Frequency Error (%)
1	78.456	77.2	1.6
2	84.932	82.85	2.45
3	87.651	91.7	4.619
4	113.542	114.71	1.028
5	185.584	188.91	1.79
6	190.736	189.6	0.59
7	195.502	194.66	0.43

Table 1: Comparison between identified and updated FE frequencies

For damping values, CMA-ES was used again with a starting point the previously updated material values, converging after to the values of 0.0099, 0.00989 and 0.00933 for frequency ranges between 0-100, 100-120 and 120-2000 Hz respectively. The complete updated FE model is after validated on impact excitation and the time histories of

accelerations at the node locations are compared between experimental and numerical results. The results are shown in Figure 5.

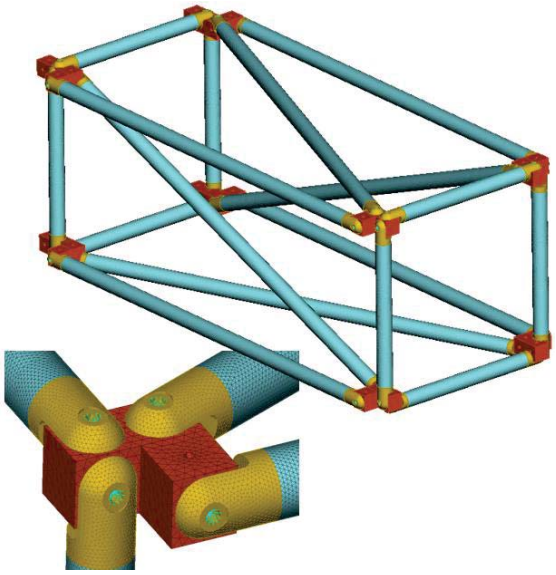

Figure 4 Grouped FE model parts (according to color) with repsect to their material properties

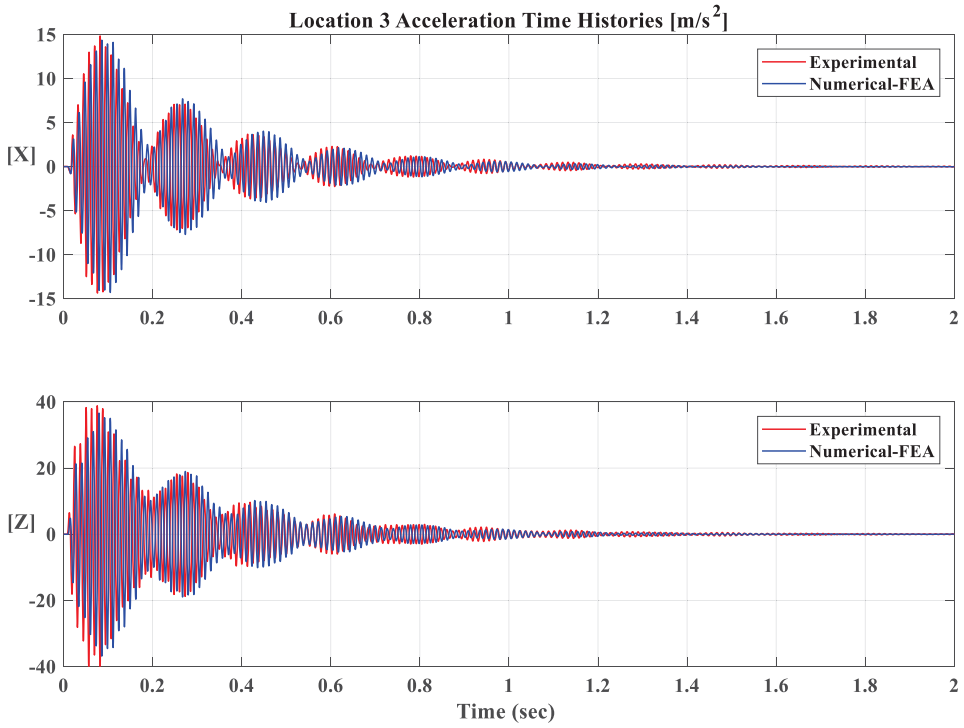

Figure 5 Identified numerical vs experimental acceleration time response for impact load

The acceleration comparison shows a good correspondance between the real and the numerical structure. With the updated FE model at hand now, the data generation step may proceed with the subsequent CNN training, described in Section 4.

4 DATA GENERATION, TRAINING AND EXPERIMENTAL VALIDATIONS

The SHM data generation is performed with the identified FE model of the truss structure which is used to simulate the Healthy the four damaged states D1, D2, D3 and D4. The bolted connections are modeled as rigid bodies for the Healthy status and removed according to the damage type. Random sampling in order to promote classifier generalization is used for the material and model parameters through a repetitive load case scheme [6] on the FE equations of motion:

$$\mathbf{M}(\rho)\mathbf{A} + \mathbf{C}(\mathbf{K},\mathbf{M},\alpha,\beta)\mathbf{V} + \mathbf{K}(E)\mathbf{U} = \mathbf{F} \tag{1}$$

Where $\mathbf{A},\mathbf{V}$ and $\mathbf{U}$ are global the acceleration, velocity and displacement vectors respectively. $\mathbf{M},\mathbf{C}$ and $\mathbf{K}$ represent the global mass, damping and stiffness matrices of the structure that depend on the model physical parameters of density ρ, damping α and β and elasticity E. The data generation algorithm is shown in Algorithm 1. Uniform random distribution is used for all values with a $\pm 10\%$ range from the identified material values. Impact loading was used as excitation.

Algorithm 1: Numerical model data generation algorithm

Input: Number of load cases n and statistical bounds for each quantity ρ, α, β, E

Output: n number of labeled acceleration vectors at preselected FE nodes

1. **for** $i = 1:n$ **do**
2. define Health status y according to FE model $\rightarrow \mathbf{Y}$
3. *sample* $E \rightarrow \mathbf{K} = \mathbf{K}(E)$
4. *sample* $\rho \rightarrow \mathbf{M} = \mathbf{M}(\rho)$
5. *sample* $\alpha, \beta \rightarrow \mathbf{C} = \mathbf{C}(\mathbf{K},\mathbf{M},a_i,\beta_i)$
6. **Solve** $\mathbf{MA} + \mathbf{CU} + \mathbf{KU} = \mathbf{F}$
7. **return A and Y**
8. **end**

The extracted accelerations and health label status after 400 load cases for each 5 statuses are completed form the SHM training data set (2):

$$Train\_set = \{(\mathbf{A}_1, \mathbf{Y}_1), (\mathbf{A}_1, \mathbf{Y}_2), ...(\mathbf{A}_n, \mathbf{Y}_n)\} \tag{2}$$

The CNN is trained after on the examples of set (2) in order to learn to identify damage. A "Deep" and "multiheaded" averaging form [6] is used that comprises of different 1D signal convolutional filters. Next 10 experimental measurements of each state are input in the trained CNN to check its predictions. Results are shown for a binary damage identification case, meaning a Healthy class and a single Damaged class containing D1, D2, D3 and D4. The predictions on the experimental Health status are shown in Figure 6. The class predictions come in values between 0 and 1, with 0.5 being the class threshold. Blue is used for the Healthy class score that the network predicts and red for the Damaged. The sum of the blue and red column is always equal to 1 in the network output. The histograms are read as follows. From 1-10 the histograms show the predictions scores for inputs from

Healthy experimental states. From 11-20, 21-30, 31-40, 41-50 the histograms show the predictions scores for inputs from D1, D2, D3 and D4 experimental states respectively which all together form the Damaged class in this binary damage identification problem. The validations scores come to 100% on the real states with only D1 and D2 predicting the state with 90% and 80% accuracy respectively. The trained CNN can be therefore regarded as reliable for the given problem.

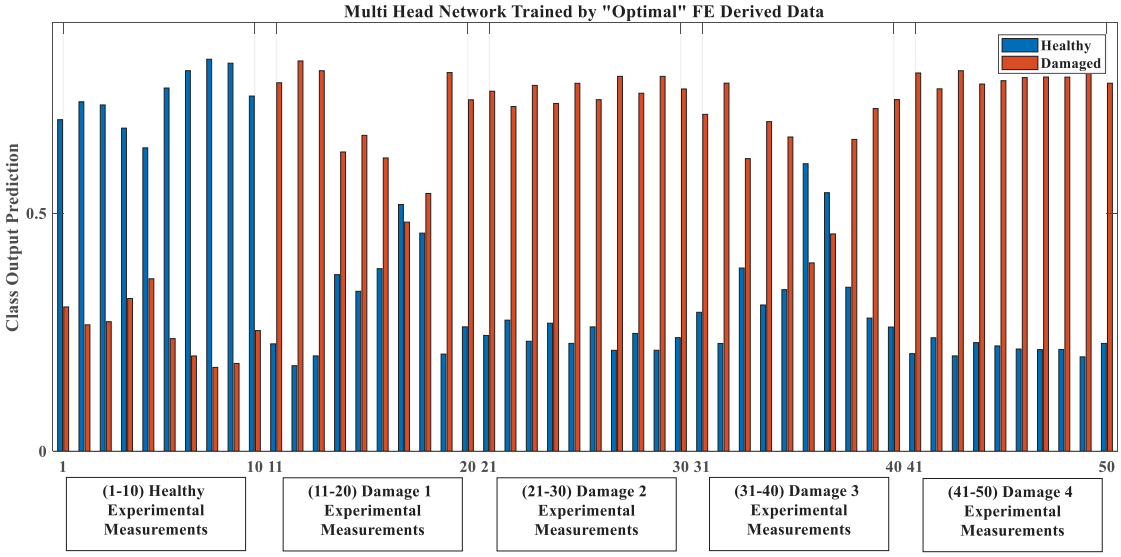

Figure 6 Predictions of the numerically trained CNN on the experimental status

5 CONCLUSIONS

In this work a system identification and damage detection framework was present for a CFRP truss structure. The damage cases for truss structure SHM benchmark test were applied as loose bolts. After the system identification of material parameters, a FE model was developed and served as the SHM training data source in order to feed in a Deep CNN classifier. The numerically trained CNN was finally validated on experimental states of the benchmark and showed close to 100% accuracy in a binary damage identification problem, meaning separating the Healthy from different Damaged conditions. The presented framework on the benchmark structure shows great potential for future SHM tools and further testing is planned such as damage cases of less magnitude and damage detection combing with damage location.

Acknowledgment: *This research has been co-financed by the European Union and Greek national funds through the Operational Program Competitiveness, Entrepreneurship and Innovation, under the call* "Aquaculture" - "Industrial Materials" - "Open Innovation in Culture" *(project code: T6YBII-00478)*

REFERENCES

[1] W. R. Wickramasinghe, D. P. Thambiratnam, T. H. T. Chan, and T. Nguyen, *Vibration characteristics and damage detection in a suspension bridge*, Journal of Sound and Vibration, 2016. **375**: p. 254–274

[2] S. D. Fassois and F. P. Kopsaftopoulos, *Statistical Time Series Methods for Vibration Based Structural Health Monitoring*, New Trends in Structural Health Monitoring, 2013. **542**: p. 209–264.

[3] D. Tcherniak and L. L. Mølgaard, Active vibration-based structural health monitoring system for wind turbine blade: Demonstration on an operating Vestas V27 wind turbine, Structural Health Monitoring, 2017. **16**(5): p. 536–550

[4] O. Abdeljaber, O. Avci, S. Kiranyaz, M. Gabbouj, and D. J. Inman, *Real-time vibration-based structural damage detection using one-dimensional convolutional neural networks*, Journal of Sound and Vibration, 2017. **388**: p. 154–170

[5] R. Zhao, R. Yan, Z. Chen, K. Mao, P. Wang, and R. X. Gao, *Deep learning and its applications to machine health monitoring*, Mechanical Systems and Signal Processing, 2019. **115**: p. 213–237

[6] Panagiotis Seventekidis, Dimitrios Giagopoulos, Alexandros Arailopoulos, Olga Markogiannaki, *Structural Health Monitoring using deep learning with optimal finite element model generated data*, Mechanical Systems and Signal Processing, 2020. 145, 106972

[7] F. Ksica, Z. Hadas, and J. Hlinka, *Integration and test of piezocomposite sensors for structure health monitoring in aerospace*, Measurement, 2019. **147**: p. 106861

[8] M. Döhler, F. Hille, L. Mevel, and W. Rücker, *Structural health monitoring with statistical methods during progressive damage test of S101 Bridge*, Engineering Structures, 2014. **69**: p. 183–193

[9] D. Giagopoulos, A. Arailopoulos, V. Dertimanis, C. Papadimitriou, E. Chatzi, and K. Grompanopoulos, *Structural health monitoring and fatigue damage estimation using vibration measurements and finite element model updating*, Structural Health Monitoring, 2019. **18**(4): p. 1189–1206

[10] Ilias Zacharakis, Alexandros Arailopoulos, Olga Markogiannaki, Dimitrios Giagopoulos, *Vibration based Structural Health Monitoring of Composite Carbon Fiber Structural Systems*, UNCECOMP 2019, International Conference on Uncertainty Quantification in Computational Sciences and Engineering, Crete, Greece, 24–26 June 2019

[11] D. Giagopoulos and A. Arailopoulos, *Computational framework for model updating of large scale linear and nonlinear finite element models using state of the art evolution strategy*, Computers and Structures, 2017. **192**: p. 210–232

EURODYN 2020
XI International Conference on Structural Dynamics
M. Papadrakakis, M. Fragiadakis, C. Papadimitriou (eds.)
Athens, Greece, 23–26 November 2020

AN IN-SITU EXPERIMENTAL SETUP FOR DAMAGE LOCALIZATION AND MECHANICAL PARAMETER ESTIMATION

M. Vollmering[1], I. Dolbonosov[1], A. Lenzen[1]

[1]Institute for Statics, Structural Dynamics, System Identification, and Simulation (I4S)
Leipzig University of Applied Sciences, Karl-Liebknecht-Straße 132, 04277 Leipzig
e-mail: Armin.Lenzen@htwk-leipzig.de

Keywords: Output-only identification, Damage localization, H-infinity estimation, Mechanical parameter estimation, Mass perturbation methods, Projection techniques in state space

Abstract. *A new in-situ experimental setup for damage localization and mechanical parameter estimation has been built at two test fields, outdoors at a rooftop and in a laboratory at Leipzig University of Applied Sciences. Excited by wind, the structure can be identified by output-only methods. In this contribution current progress on the development of damage localization and scaling output-only systems from a general operator notation is shown. At the beginning damage localization based on $\mathcal{H}_\infty$-estimation is briefly shown. Modifying this theory, system scaling and mechanical parameter estimation is discussed afterwards. Finally, experimental results are shown and analysed.*

1 Introduction

In structural dynamics the parametrization of a mechanical model allows to analyse system properties and predict structural responses in certain load cases. To parametrize real life structures, a *linear-elastic* mechanical model is often a well-suited approximation at an operation point, which is modelled by mass, stiffness, and damping ($\bar{M}$, $\bar{K}$, and $\bar{D}$). To avoid a priori model errors and a possible huge numerical effort, *system identification* allows a straightforward alternative parametrization of a mechanical model, which the authors focus in this contribution. Directly based on measurements, the identified system has a considerably smaller model order. Here, the parametrization of a *linear, time-invariant state space system* is very advantageous, as this allows to subsequently apply identified parameters in other techniques.

Stochastic system identification. Because deterministic excitations are cost-intensive, elaborate, and sometimes impossible to apply at large-scale civil engineering structures, identification methods based on *ambient excitations* (e.g. wind, traffic, waves, microseism) should be applied instead [1]. Some stochastic system identification methods are a) stochastic realization [2], b) stochastic subspace identification (SSI) [3], c) canonical correlation analysis (CCA) [4], and so on. Because ambient excitations are in general unmeasurable, state space parameters A and C can be determined only based on structural response measurements. Hence, the physical interpretation of the identified system is an important issue. A widespread approach is the identification of modal data (free scaled mode shapes), named operational modal analysis (OMA) [5–7]. However, without the necessity of numerical computations based on (real or complex-conjugated) mode shapes, we focus on the development of a general, system theoretic identification approach.

Motivation: Mechanical parameter estimation and damage localization. A new in-situ experimental setup for damage localization and mechanical parameter estimation has been built at two test fields, outdoors at a rooftop and in a laboratory at Leipzig University of Applied Sciences (see figure 1 and section 4). Excited by wind, the structure can be identified by output-

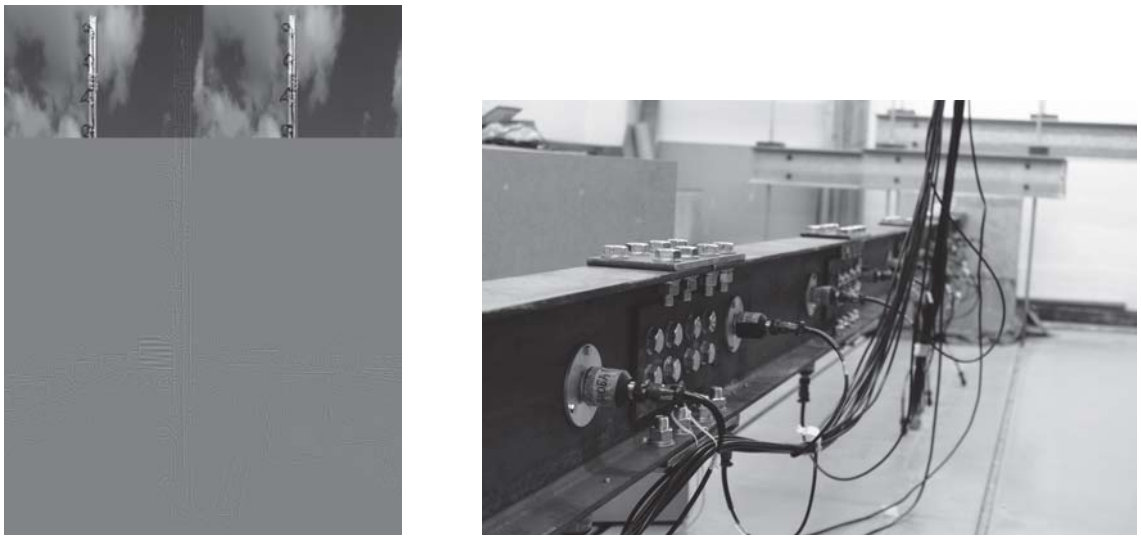

(a) Wind-exposed structure at a rooftop (b) Laboratory structure

Figure 1: Experimental structures

only methods. The authors aim to develop and verify a damage localization method based on the *state projection estimation error* (SP2E) [8–11], which is insensitive to environmental and operational conditions (EOC). While first attempts based on principal component analysis were analysed [12], a system theoretic approach may be advantageous.

In this contribution, current progress on the development of damage localization and scaling output-only systems from a general operator notation is shown. To begin with in section 2, damage localization based on SP2E is briefly shown. Modifying this theory, the novel *state projections for system scaling* (SP2S) method and subsequent mechanical parameter estimation is discussed afterwards, which is based on output-only measurements and the mass perturbation technique (repetition of measurement with known additional mass Δ_M, section 3). Finally, experimental results are shown and analysed in section 4.

Some notes on the used nomenclature. Because structural alterations are a key element of this contribution (e.g. stiffness modifications $\Delta_{K,i}$ and/or *mass perturbations* $\Delta_{M,i}$), the definition of structural state i is introduced: $i = 0$ defines the reference and $i > 0$ the altered structural state.

We focus on the application of estimation/control approaches in structural dynamics. Hence, a more general system theoretic notation is used: The map to y from u is denoted by T_{yu}. By using a linear, time-invariant state space system, T_{yu} may be written in frequency domain as

$$\left.\begin{aligned} \sigma x(\sigma) &= Ax(\sigma) + Bu(\sigma) \\ y(\sigma) &= Cx(\sigma) + Du(\sigma) \end{aligned}\right\} \sigma = (s, z) \ .$$

Based on state space parameters A, B, C, and D, the frequency response matrix function follows:

$$T_{yu}(\sigma) = \left[\begin{array}{c|c} A & B \\ \hline C & D \end{array}\right] \overset{\sigma}{=} C\big(\sigma I - A\big)^{-1} B + D \ .$$

2 Damage localization based on $\mathcal{H}_\infty$-estimation: State projection estimation error (SP2E)

2.1 Basis: Output-only identification

As mechanical system parameters ($\bar{M}$, $\bar{K}$, and $\bar{D}$) and structural excitations are unknown for real large-scale structures, we use the SSI [3] to parametrize discrete-time state space parameters A and C. These matrices are applied to define a *discrete-time system*

$$\begin{bmatrix} x_{k+1} \\ y_k \end{bmatrix} = \left[\begin{array}{c|cc} A & I & 0 \\ \hline C & 0 & I \end{array}\right] \begin{bmatrix} x_k \\ w_k \\ v_k \end{bmatrix}, \quad n_k = \begin{bmatrix} w_k \\ v_k \end{bmatrix} \quad \text{with } \big\langle n_k, n_k \big\rangle := \begin{bmatrix} Q & S \\ S^* & R_v \end{bmatrix} \ . \tag{1}$$

2.2 $\mathcal{H}_\infty$-estimation: Worst-case analysis

$\mathcal{H}_\infty$-theory leads to estimators, which are less susceptible to *disturbance uncertainties*. A key element for that is to consider the so-called worst-case. Hence, one uses the $\mathcal{H}_\infty$-norm to bound a system $T_{\tilde{s}n}$ by γ, which is equivalent to bound the largest singular value of matrix function $T_{\tilde{s}n}$, namely

$$\|T_{\tilde{s}n}\|_{\mathcal{H}_\infty} = \sup_n \frac{\|\tilde{s}\|_2}{\|n\|_2} = \max_\omega \bar{\sigma}\Big(T_{\tilde{s}n}(e^{j\omega})\Big) \ < \gamma \ , \quad \tilde{s} = s - \hat{s} = L\big(x - \hat{x}\big) = L\tilde{x} \ . \tag{2}$$

Although $\mathcal{H}_\infty$-theory may lead to over-conservative estimators, they outperform Kalman filters ($\mathcal{H}^2$ estimators), when the disturbances are unknown [13]. An important difference to Kalman filtering is the usage of weighting parameter L, allowing different applications in $\mathcal{H}_\infty$-estimation [13]. For the case of *filtering signals in additive noise* [14] one uses $L = C$.

There are plenty $\mathcal{H}_\infty$-theory approaches [13–17]. A powerful, theoretical approach is the derivation of estimation as *a special case of control* by using the lower linear fractional transformation (LLFT, see figure 2) [18]:

$$\begin{bmatrix} x_{k+1} \\ \tilde{s}_k \\ y_k \end{bmatrix} = \underbrace{\left[\begin{array}{c|cc|c} A & I & 0 & 0 \\ \hline L & 0 & 0 & -I \\ C & 0 & I & 0 \end{array}\right]}_{P} \begin{bmatrix} x_k \\ w_k \\ v_k \\ \hat{s}_k \end{bmatrix}, \qquad \begin{bmatrix} \hat{x}_{k+1} \\ \hat{s}_k \end{bmatrix} \underbrace{\left[\begin{array}{c|c} A - K_p C & K_p \\ \hline L & 0 \end{array}\right]}_{K} \begin{bmatrix} \hat{x}_k \\ y_k \end{bmatrix} . \tag{3}$$

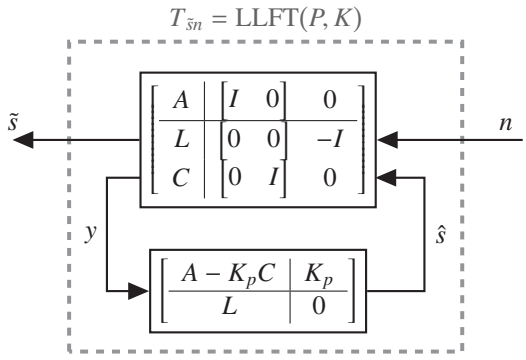

Figure 2: Estimation as a special case of control

LMI based $\mathcal{H}_\infty$-estimation. Linear matrix inequality (LMI) methods are widespread to determine $\mathcal{H}_\infty$-controllers [19, 20]. Based on the bounded real lemma, a γ-optimal controller K exists in discrete-time (see equation (2)) in both equivalent expressions

$$\left\| T_{\tilde{s}n}\big(\mathcal{A}_{cl}, \mathcal{B}_{cl}, \mathcal{C}_{cl}, \mathcal{D}_{cl}\big) \right\|_{\mathcal{H}_\infty} < \gamma, \quad \mathcal{H} = \begin{bmatrix} -\mathcal{X}^{-1} & \mathcal{A}_{cl} & \mathcal{B}_{cl} & 0 \\ \mathcal{A}_{cl}^T & -\mathcal{X} & 0 & \mathcal{C}_{cl}^T \\ \mathcal{B}_{cl}^T & 0 & -\gamma^2 I & \mathcal{D}_{cl}^T \\ 0 & \mathcal{C}_{cl} & \mathcal{D}_{cl} & -I \end{bmatrix} < 0 , \tag{4}$$

if the above inequality is feasible for $\mathcal{X} > 0$. Hence, an *optimization problem* follows, namely the minimization of γ under the above constraints, which may be solved numerically (see [21, 22]). A numerical minimum for γ^2 can be found by *semidefinite programming* (SDP), which may lead to the strictly proper form

$$\begin{bmatrix} \hat{x}_{k+1} \\ \hat{y}_k \end{bmatrix} = \underbrace{\left[\begin{array}{c|c} A_f & K_f \\ \hline C & 0 \end{array}\right]}_{K_{\text{LMI}}} \begin{bmatrix} \hat{x}_k \\ y_k \end{bmatrix} . \tag{5}$$

Riccati recursion/equation based $\mathcal{H}_\infty$-estimation. Besides the LMI solution, the application of indefinite metric spaces for $\mathcal{H}_\infty$-estimation [14] is a remarkable theory. Based on the

minimization of an indefinite quadratic form [23], this theory leads to a Riccati recursion

$$P_{k+1} = AP_k\left(I - \begin{bmatrix}L\\C\end{bmatrix}^*\left(\begin{bmatrix}L\\C\end{bmatrix}P_k\begin{bmatrix}L\\C\end{bmatrix}^* + \begin{bmatrix}-\gamma^2 I & 0\\0 & I\end{bmatrix}\right)^{-1}\begin{bmatrix}L\\C\end{bmatrix}P_k\right)A^* + Q \tag{6a}$$

$$= A\Big(P_k^{-1} - \gamma^{-2}L^*L + C^*C\Big)^{-1}A^* + Q\ . \tag{6b}$$

To determine an $\mathcal{H}_\infty$-estimator, a convergent solution $P = P_{k+1} = P_k$ must be computed and important existence conditions are taken into account

$$\forall k: \quad \tilde{P}_k^{-1} = P_k^{-1} - \gamma^{-2}L^*L > 0, \quad P_k^{-1} - \gamma^{-2}L^*L + C^*C > 0\ . \tag{7}$$

Because a direct recursive computation is numerically imprecise [24], one can solve a *discrete-time algebraic Riccati equation* (DARE) instead. To get a solution, the eigenvectors of an extended symplectic pencil are used to numerically determine matrix P [25], which leads to the *a priori* $\mathcal{H}_\infty$-estimator

$$\begin{bmatrix}\hat{x}_{k+1}\\ \hat{y}_k\end{bmatrix} = \underbrace{\left[\begin{array}{c|c}A_p & K_p\\ \hline C & 0\end{array}\right]}_{K_{\text{DARE}}}\begin{bmatrix}\hat{x}_k\\ y_k\end{bmatrix} \quad \text{with } K_p = A\tilde{P}C^*\big(C\tilde{P}C^* + I\big)^{-1}, \quad A_p = A - K_pC\ . \tag{8}$$

As $\gamma \to \infty$, the estimator in equation (8) becomes the well-known Kalman filter (an $\mathcal{H}_2$-optimal estimator) [13].

2.3 Damage localization by state projection estimation error (SP2E) method

A difference process has been proposed for damage localization by the authors [9–11]. Process d follows the introduced system in discrete-time

$$\begin{bmatrix}\hat{x}_{0,k+1}\\ \hat{x}_{i,k+1}\\ x_{i,k+1}\\ d_k\end{bmatrix} = \underbrace{\left[\begin{array}{ccc|cc}A_{p,0} & 0 & K_{p,0}C_i & 0 & K_{p,0}\\ 0 & A_{p,i} & K_{p,i}C_i & 0 & K_{p,i}\\ 0 & 0 & A_i & I & 0\\ \hline -C_0 & C_i & 0 & 0 & 0\end{array}\right]}_{T_{dn}}\begin{bmatrix}\hat{x}_{0,k}\\ \hat{x}_{i,k}\\ x_{i,k}\\ w_k\\ v_k\end{bmatrix}\ . \tag{9}$$

Using state projections, a Sylvester equation must be solved, which leads to the following:

$$\begin{bmatrix}A_{p,0} & 0\\ 0 & A_{p,i}\end{bmatrix}\bar{\Theta} - \bar{\Theta}A_i = -\begin{bmatrix}K_{p,0}\\ K_{p,i}\end{bmatrix}C_i\ , \quad \bar{\Theta} = \begin{bmatrix}Y\\ Z\end{bmatrix} \tag{10a}$$

$$\begin{bmatrix}\hat{x}_{0,k+1}\\ \hat{x}_{i,k+1}\\ x_{i,k+1}\\ d_{V,k}\end{bmatrix} = \underbrace{\left[\begin{array}{ccc|cc}A_{p,0} & 0 & 0 & -Y & K_{p,0}\\ 0 & A_{p,i} & 0 & -Z & K_{p,i}\\ 0 & 0 & A_i & I & 0\\ \hline -C_0 & C_i & C_iZ - C_0Y & 0 & 0\end{array}\right]}_{T_{dVn}}\begin{bmatrix}\hat{x}_{0,k}\\ \hat{x}_{i,k}\\ x_{i,k}\\ w_k\\ v_k\end{bmatrix}\ . \tag{10b}$$

The SP2E difference process approach is a form of *model reduction*, namely the truncation of estimator poles. This has been discussed by the authors [9–11] and allows to define

$$\begin{bmatrix}x_{k+1}\\ d_{V,k}\end{bmatrix} = \underbrace{\left[\begin{array}{c|cc}A_i & I & 0\\ \hline C_T & 0 & 0\end{array}\right]}_{T_{dVn}}\begin{bmatrix}x_k\\ w_k\\ v_k\end{bmatrix}\ , \quad C_T = \begin{bmatrix}-C_0 & C_i\end{bmatrix}\begin{bmatrix}Y\\ Z\end{bmatrix} = C_iZ - C_0Y\ . \tag{11}$$

As a result one determines the difference process d_V taking state projections into account. The average process power of d_V can be analysed for damage localization:

$$\bar{P}_{dV} = \operatorname{diag}\big(R_{dV}\big) \quad \text{with} \quad R_{dV} = \big\langle d_{V,k}, d_{V,k} \big\rangle \ . \tag{12}$$

The SP2E method has been verified based on experimental data and the study of damage localization results can be found in [9–11].

3 System scaling and mechanical parameter estimation based on output-only identification and mass perturbations

3.1 Relation of structural states in general operator notation

In this section some brief notes on the novel *state projections for system scaling* (SP2S) method and mechanical parameter estimation are given (for details see [26]). To find a relation for that, the constitutive equation of motion in structural dynamics is reordered to

$$a_i \stackrel{s}{=} T_{af,i} f : \qquad \bar{M} a_i(t) + \bar{D} v_i(t) + \bar{K} d_i(t) = f(t) - \Delta_{M,i} a_i(t) \ . \tag{13}$$

The mechanical system in reference structural state $T_{af,0}$ has the response of state i due to input $f - \Delta_{M,i} a_i(t)$ after a settling time (steady state vibrations). Omitting initial values, this may be expressed in Laplace domain by

$$a_i(s) = T_{af,0}(s)\Big(f(s) - \Delta_{M,i} a_i(s)\Big), \qquad T_{af,i} \stackrel{s}{=} T_{af,0}\big(I_p - \Delta_{M,i} T_{af,i}\big) \ . \tag{14}$$

In equation (14) we presuppose the same average excitation spectrum (in a stochastic sense) for both structural states $T_{af,0}$ and $T_{af,i}$. Equation (14) is very important to relate *reference and altered structural states in one framework* and a system description for the structural states is necessary to apply the found relation, which is shown below.

3.2 State projections for system scaling method (SP2S)

A state space approach is focused below, because this allows to apply standard system analysis techniques afterwards. Hence, by applying state space parameters A_i, B_i, C_i, and D_i in equation (14), one concludes the following in continuous-time:

$$\left[\begin{array}{c|c} A_i & B_i \\ \hline C_i & D_i \end{array}\right] \stackrel{s}{=} \left[\begin{array}{c|c} A_0 & B_0 \\ \hline C_0 & D_0 \end{array}\right] \left[\begin{array}{c|c} A_i & B_i \\ \hline -\Delta_{M,i} C_i & I_p - \Delta_{M,i} D_i \end{array}\right] \tag{15a}$$

$$\stackrel{s}{=} \left[\begin{array}{cc|c} A_0 & -B_0 \Delta_{M,i} C_i & B_0 (I_p - \Delta_{M,i} D_i) \\ 0 & A_i & B_i \\ \hline C_0 & -D_0 \Delta_{M,i} C_i & D_0 (I_p - \Delta_{M,i} D_i) \end{array}\right] \tag{15b}$$

$$a_i \stackrel{s}{=} T_{af,i} f : \qquad \begin{bmatrix} \dot{x}_0 \\ \dot{x}_i \\ a_i \end{bmatrix} = \left[\begin{array}{cc|c} A_0 & -B_0 \Delta_{M,i} C_i & B_0 (I_p - \Delta_{M,i} D_i) \\ 0 & A_i & B_i \\ \hline C_0 & -D_0 \Delta_{M,i} C_i & D_0 (I_p - \Delta_{M,i} D_i) \end{array}\right] \begin{bmatrix} x_0 \\ x_i \\ f \end{bmatrix} \ . \tag{15c}$$

In equation (15b) the state space system on the right-hand side has a considerably larger model order than the left-hand side. Applying the state projection technique of equation (10), a block diagonal form is determined:

$$A_0 \Theta_i - \Theta_i A_i = B_0 \Delta_{M,i} C_i \tag{16a}$$

$$\left[\begin{array}{c|c} A_i & B_i \\ \hline C_i & D_i \end{array}\right] \stackrel{s}{=} \left[\begin{array}{cc|c} A_0 & 0 & B_0 (I_p - \Delta_{M,i} D_i) - \Theta_i B_i \\ 0 & A_i & B_i \\ \hline C_0 & C_0 \Theta_i - D_0 \Delta_{M,i} C_i & D_0 (I_p - \Delta_{M,i} D_i) \end{array}\right] \ . \tag{16b}$$

Therefore, constraints are introduced to find a solution in accordance to state projection results:

$$-B_0\Delta_{M,i}C_i = \Theta_i A_i - A_0\Theta_i \tag{17a}$$
$$C_i = C_0\Theta_i - D_0\Delta_{M,i}C_i \tag{17b}$$
$$0 = B_0(I_p - \Delta_{M,i}D_i) - \Theta_i B_i \tag{17c}$$
$$D_i = D_0(I_p - \Delta_{M,i}D_i)\ . \tag{17d}$$

Using above, this leads to a solution to the model order problem of equation (15). A numerical efficient algorithm to solve the described problem is unknown to the authors so far. Hence, a rather theoretical approach based on the Kronecker product $\otimes$ is applied instead:

$$\mathcal{A}\mathcal{X}\mathcal{B} = \mathcal{C} \quad \longrightarrow \quad \Big(\mathcal{B}^T \otimes \mathcal{A}\Big)\mathrm{vec}\big(\mathcal{X}\big) = \mathrm{vec}\big(\mathcal{C}\big)\ . \tag{18}$$

The first two constraints of equation (17) are applied above, while the third and fourth are not used in the following. Using the Kronecker product approach, the set of constraints is reordered:

1. Constraint $-B_0\Delta_{M,i}C_i + A_0\Theta_i - \Theta_i A_i = 0$:

$$-\Big(C_i^T\Delta_{M,i}^T \otimes I_{n_0}\Big)\mathrm{vec}\big(B_0\big) + \Big((I_{n_i}\otimes A_0) - (A_i^T \otimes I_{n_0})\Big)\mathrm{vec}\big(\Theta_i\big) = 0\ . \tag{19}$$

2. Constraint $-D_0\Delta_{M,i}C_i + C_0\Theta_i = C_i$:

$$-\Big(C_i^T\Delta_{M,i}^T \otimes I_p\Big)\mathrm{vec}\big(D_0\big) + \Big(I_{n_i}\otimes C_0\Big)\mathrm{vec}\big(\Theta_i\big) = \mathrm{vec}\big(C_i\big)\ . \tag{20}$$

Because equations (19) and (20) are defined for i, both constraints can be used multiple times. Using A_i, C_i, and $\Delta_{M,i}$ ($i = 0,\ 1,\ \ldots$), both constraints are stacked together in a *system of linear equations*

$$\begin{bmatrix} \mathrm{vec}\big(B_0\big) \\ \mathrm{vec}\big(D_0\big) \\ \mathrm{vec}\big(\Theta_1\big) \\ \mathrm{vec}\big(\Theta_2\big) \\ \vdots \end{bmatrix} = \begin{bmatrix} -C_1^T\Delta_{M,1}^T\otimes I_{n_0} & 0 & (I_{n_1}\otimes A_0)-(A_1^T\otimes I_{n_0}) & 0 & \cdots \\ -C_2^T\Delta_{M,2}^T\otimes I_{n_0} & 0 & 0 & (I_{n_2}\otimes A_0)-(A_2^T\otimes I_{n_0}) & \\ \vdots & \vdots & \vdots & \vdots & \ddots \\ 0 & -C_1^T\Delta_{M,1}^T\otimes I_p & I_{n_1}\otimes C_0 & 0 & \cdots \\ 0 & -C_2^T\Delta_{M,2}^T\otimes I_p & 0 & I_{n_2}\otimes C_0 & \\ \vdots & \vdots & \vdots & \vdots & \ddots \end{bmatrix}^{\dagger} \begin{bmatrix} 0 \\ 0 \\ \vdots \\ \mathrm{vec}\big(C_1\big) \\ \mathrm{vec}\big(C_2\big) \\ \vdots \end{bmatrix}\ . \tag{21}$$

This system of linear equations can be solved to estimate B and D of the structural reference state (e.g. by Tikhonov regularization). The described method is called *state projections for system scaling* (SP2S) and details can be found in [26].

3.3 Mechanical parameter estimation based on identified state space parameters

Using a Markov parameter approach, one may estimate mechanical properties based on continuous-time state space parameters A, B, and C [27]:

$$\hat{M} = \Big(C_0A_0^{1-m}B_0\Big)^{-1}\ , \quad \hat{K} = -\Big(C_0A_0^{-1-m}B_0\Big)^{-1}\ , \quad \hat{D} = -\hat{M}\Big(C_0A_0^{2-m}B_0\Big)\hat{M}\ . \tag{22}$$

Parameter m refers to the measurement type: Displacements $m = 0$, velocities $m = 1$, and accelerations $m = 2$.

3.4 Comparison to the mode shape based approach

Two important eigenvalue problems arise from the equation of motion in structural dynamics [28], which are briefly discussed below. To understand the real mode shape based mechanical parameter estimation problem, the eigenvalue problem

$$\big(- \bar{M}_i \omega_{i,l}^2 + \bar{K} \big) \phi_{i,l} = 0 \tag{23}$$

is shown first, which leads to real mode shapes $\Phi_i = [\phi_{i,1} \quad \phi_{i,2} \quad \ldots]$, $\Phi_i \in \mathbb{R}^{N_{dof} \times N_{dof}}$. A scaling factor α can be used to compute mass-normalized mode shapes $\bar{\phi}_l = \phi_l \alpha_l$. Based on identified real eigenvectors (e.g. by frequency domain decomposition), one needs scaled mode shapes to estimate mechanical parameters by

$$\hat{M}_i = \left[\sum_{l=1}^{n} \bar{\phi}_{i,l} \bar{\phi}_{i,l}^T \right]^{-1}, \quad \hat{K} = \left[\sum_{l=1}^{n} \frac{\bar{\phi}_{i,l} \bar{\phi}_{i,l}^T}{\omega_{i,l}^2} \right]^{-1}, \quad \hat{D} = \left[\sum_{l=1}^{n} \frac{\bar{\phi}_{i,l} \bar{\phi}_{i,l}^T}{2 \zeta_{i,l} \omega_{i,l}} \right]^{-1} . \tag{24}$$

Because real structures always have damping $\bar{D} > 0$, the eigenvalue problem in equation (23) may be generalized to

$$\begin{bmatrix} \bar{D} & \bar{M}_i \\ \bar{M}_i & 0 \end{bmatrix} \begin{bmatrix} \psi_{i,l} \\ \psi_{i,l} \lambda_{i,l} \end{bmatrix} \lambda_{i,l} + \begin{bmatrix} \bar{K} & 0 \\ 0 & -\bar{M}_i \end{bmatrix} \begin{bmatrix} \psi_{i,l} \\ \psi_{i,l} \lambda_{i,l} \end{bmatrix} = 0 \, . \tag{25}$$

The theoretical necessary number of mode shapes is doubled, hence $\Psi_i = [\psi_{i,1} \quad \psi_{i,2} \quad \ldots]$, $\Psi_i \in \mathbb{C}^{N_{dof} \times 2N_{dof}}$. This leads to *complex conjugated* eigenvalues, for i denoted by $\Lambda_i = \mathrm{diag}(\lambda_{i,1}, \lambda_{i,1}, \ldots)$ with $\lambda_{l,l+1} = -\zeta_l \omega_l \pm j \omega_l (1 - \zeta_l^2)^{0.5}$. Again a factor β may be used, which allows to determine scaled mode shapes $\bar{\psi}_l = \psi_l \beta_l$. In contrary to the mass-scaling approach, complex mode shapes can be scaled to $-45°$. Then, mechanical parameters are estimated by analysing the sum of outer products (e.g. based on SSI):

$$\hat{M}_i = \left[\sum_{l=1}^{n} \bar{\psi}_{i,l} \lambda_{i,l} \bar{\psi}_{i,l}^T \right]^{-1}, \quad \hat{K} = \left[- \sum_{l=1}^{n} \frac{\bar{\psi}_{i,l} \bar{\psi}_{i,l}^T}{\lambda_{i,l}} \right]^{-1}, \quad \hat{D} = - \sum_{l=1}^{n} \hat{M} \bar{\psi}_{i,l} \lambda_{i,l}^2 \bar{\psi}_{i,l}^T \hat{M} \, . \tag{26}$$

Several methods have been developed to scale mode shapes based on the mass perturbation technique [29–34]. To estimate mechanical parameters, an important rank problem must be considered: If $\hat{F}$ is full-rank with $n \geq p$, the inverse $\hat{F} \hat{K} = I_p$ exists. Very importantly, the rank deficient case $\hat{K} = \hat{F}^\dagger$ with $n < p$ leads to $\hat{F} \hat{F}^\dagger \neq I_p$.

4 Experimental results of a real structure

4.1 The experimental study

This section covers experimental results of mechanical parameter estimation of the laboratory structure (see figure 1b). The proof of damage localization by SP2E has been given before (see [10]). In this contribution the authors discussed several methods to estimate corresponding mechanical parameters (table 1), which will be applied below. All three methods are based on output-only measurements and mass perturbations (repetition of measurement with known additional mass Δ_M).

Abbreviation	Approach	Equation
<Kronecker>	Kronecker product based method applying state projections.	(22)
<Mode I>	Modal approach based on real eigenvectors.	(24)
<Mode II>	Modal approach employing complex eigenvectors.	(26)

Table 1: Discussed methods to estimate corresponding mechanical parameters

The experimental structure. To apply techniques described above, a cantilever arm (length $6.15\,\mathrm{m}$) in a laboratory at Leipzig University of Applied Sciences was analysed. The modular structure consists of six beam elements with $1\,\mathrm{m}$ length each (cross section IPE200, DIN EN 10 034) and were connected by bolted steel plates. Therefore, stiffness and mass alterations can be applied using additional steel plates. Using a wind excitation by wind machines (random, stationary ambient excitation), structural acceleration responses were measured in lateral direction by twelve uniaxial, piezoelectric accelerometers (equally spaced $100\,\mathrm{cm}$, measurement position $\mathrm{M}_1 \ldots \mathrm{M}_6$, see figure 3).

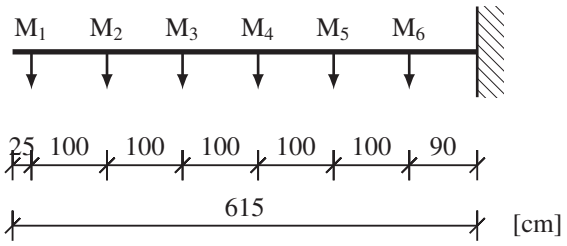

Figure 3: Mechanical system: Cantilever arm

Data processing Measured accelerations had a duration of $30\,\mathrm{min}$ ($f_s = 2\,\mathrm{kHz}$) and were analysed by Welch's method first. For a sufficient statistical population we applied approximately 215 averages by Hanning window ($L = 2^{15}$). The estimated spectrum was used to identify the output-only system: An inverse Fourier transform of spectrum S_y led to covariance matrix function R_y, which was applied in the stochastic subspace identification method. SSI results A and C eventually identified noise poles, which had been suppressed by model reduction techniques afterwards. This led to the identification of six natural frequencies (bending modes in lateral direction).

4.2 Results: Corresponding mechanical parameter estimates

4.2.1 Corresponding mass estimate

In this study all discussed methods led to a mass estimate $\hat{M}$ with a dominant main diagonal, which corresponds to the laboratory structure. Because, corresponding mass estimates are elaborate to analyze (e.g. interpretation of off-diagonal elements), the trace of $\hat{M}$ is used below.

Simulated mass [kg]

17	0	0	0	0	0
0	32	0	0	0	0
0	0	32	0	0	0
0	0	0	32	0	0
0	0	0	0	32	0
0	0	0	0	0	30

<Kronecker> Estimated mass [kg]

1	12.6	1.2	0.4	0.9	-1.4	-4.3
2	3.9	29.8	-4	-1.6	-1.6	-7.9
3	-2.4	1.7	30.9	0.4	0.4	-3.3
4	0.6	2.9	5.4	32.3	1.2	-3.2
5	-0.5	2.4	-3	0.5	32.4	0.7
6	1.2	0.6	-4.8	0.8	0.7	30.5
	1	2	3	4	5	6

<Mode I> Estimated mass [kg]

13.3	3.9	-2.6	0.7	-1.1	0.6
3.9	31.2	-0.1	-0.1	-0.6	-0.2
-2.6	-0.1	31.3	0.9	0.1	0
0.7	-0.1	0.9	31.2	1.2	0.1
-1.1	-0.6	0.1	1.2	30.6	1.3
0.6	-0.2	0	0.1	1.3	29

<Mode II> Estimated mass [kg]

1	13.3	3.9	-2.6	0.7	-1.1	0.6
2	3.9	31.2	-0.1	-0.1	-0.6	-0.3
3	-2.6	-0.1	31.4	1	0.1	-0
4	0.7	-0.1	1	31.2	1.2	0.1
5	-1.1	-0.6	0.1	1.2	30.7	1.3
6	0.6	-0.3	-0	0.1	1.3	29
	1	2	3	4	5	6

Figure 4: Estimated corresponding mass $\hat{M}$, for abbreviations see table 1

The results of corresponding mass estimates is given in figure 4. The Kronecker product based method leads to trace$(\hat{M}) = 168.7\,\mathrm{kg}$. Besides that, both modal approaches lead by definition to symmetric parameter matrices with a similar trace of $\hat{M}$, trace$(\hat{M}) = 166.8\,\mathrm{kg}$. The experiments have been repeated two times and structural mass of the laboratory set-up has been repeatedly estimated.

4.2.2 Corresponding stiffness estimate

Stiffness $\bar{K}$ is a central parameter to describe mechanical systems (e.g. relation between external static forces and measured displacements). Corresponding stiffness estimates are given in figure 5. Although all three methods lead to a similar result in comparison to the simulated, analytical stiffness parameters, differences between simulation and real laboratory structure must be emphasized. Possible explanations may be: a) The real stiffness of laboratory clamping end is not infinite, which was presupposed in the Euler-Bernoulli beam simulation, and b) the used Euler-Bernoulli beam equation assumes a constant flexural rigidity EI, which is not exact considering the bolted steel plate connections (figure 1b).

Essentially, the corresponding mass and stiffness estimates can be evaluated similarly. In the results of all methods one may recognize a band parameter matrix. However, the Kronecker

Simulated stiffness [MN/m]

0.5	-1.1	0.8	-0.2	0.1	-0
-1.1	2.9	-2.8	1.2	-0.3	0.1
0.8	-2.8	4.2	-3.2	1.3	-0.4
-0.2	1.2	-3.2	4.3	-3.2	1.5
0.1	-0.3	1.3	-3.2	4.4	-3.8
-0	0.1	-0.4	1.5	-3.8	6.7

1 2 3 4 5 6

<Kronecker> Estimated stiffness [MN/m]

1	0.6	-1.6	1.6	-1	1	-1.1
2	-1.1	3	-3	1.1	0.5	-1.4
3	0.7	-2.8	4.3	-3.7	2.2	-1.4
4	-0.3	1.3	-3.2	4.3	-3.1	1.1
5	-0	-0.1	1.2	-3.6	5.1	-4.4
6	-0.2	0.8	-1.7	2.9	-4.8	6.8
	1	2	3	4	5	6

<Mode I> Estimated stiffness [MN/m]

0.5	-1	0.8	-0.3	0.1	-0
-1	2.9	-2.9	1.5	-0.6	0.2
0.8	-2.9	4.4	-3.5	1.7	-0.7
-0.3	1.5	-3.5	4.8	-3.7	2
0.1	-0.6	1.7	-3.7	4.9	-4.1
-0	0.2	-0.7	2	-4.1	6.2

<Mode II> Estimated stiffness [MN/m]

1	0.5	-1	0.8	-0.3	0.1	-0
2	-1	2.9	-2.9	1.5	-0.5	0.2
3	0.8	-2.9	4.4	-3.5	1.7	-0.7
4	-0.3	1.5	-3.5	4.8	-3.7	2
5	0.1	-0.5	1.7	-3.7	4.9	-4.1
6	-0	0.2	-0.7	2	-4.1	6.2

Figure 5: Estimated corresponding stiffness $\hat{K}$, for abbreviations see table 1

product based method leads to a non-symmetric parameter matrix. In summary, the estimation of corresponding stiffness has been estimated successfully.

5 Conclusions

In this contribution the current progress on the development of damage localization and scaling output-only systems from a general operator notation is shown. At first damage localization based on the *state projection estimation error* (SP2E) method is briefly presented. Modifying this theory, system scaling and mechanical parameter estimation is discussed afterwards. Based on output-only measurements and a mass perturbation technique, this allows to define a mechanical parameter estimation method, which is afterwards compared to two well-known modal approaches using real and complex eigenvectors. Finally, experimental results are shown and analysed. Identifying a real mechanical system, the applicability of the novel *state projections for system scaling* (SP2S) method is confirmed. More results can be found in [9–11, 26]. Some theoretical and practical issues are still open, which should be analysed in the future. These studies may focus on an application at large-scale structures taking varying environmental and operational conditions into account.

Acknowledgements

This research has been financed by the German Research Foundation (grant number 350257805) and Leipzig University of Applied Sciences (grant number K-7531.20/544-9). The authors acknowledge gratefully the granted support.

References

[1] A. Cunha, E. Caetano, F. Magalhães, and C. Moutinho. Recent perspectives in dynamic testing and monitoring of bridges. *Structural Control and Health Monitoring*, 20(6):853–877, 2013.

[2] P.L. Faurre. Stochastic realization algorithms. *System Identification: Advances and Case Studies*, 126:1–25, 1976.

[3] P. Van Overschee and B. De Moor. *Subspace Identification for Linear Systems: Theory, Implementation, Applications*. Kluwer Academic Publishers, 1996.

[4] T. Katayama. Realization of stochastic systems with exogenous inputs and subspace identification methods. *Automatica*, 35(10):1635–1652, 1999.

[5] B. Peeters and G. De Roeck. Reference-based stochastic subspace identification for output-only modal analysis. *Mechanical Systems and Signal Processing*, 13(6):855–878, 1999.

[6] F. Ubertini, C. Gentile, and A.L. Materazzi. Automated modal identification in operational conditions and its application to bridges. *Engineering Structures*, 46:264–278, 2013.

[7] E. Reynders, K. Maes, G. Lombaert, and G. De Roeck. Uncertainty quantification in operational modal analysis with stochastic subspace identification: validation and applications. *Mechanical Systems and Signal Processing*, 66:13–30, 2016.

[8] A. Lenzen and M. Vollmering. A new technique for damage localisation using estimates in Krein spaces. *Proceedings of the 6th International Operational Modal Analysis Conference*, 2015.

[9] A. Lenzen and M. Vollmering. An output-only damage identification method based on $\mathcal{H}_\infty$ theory and state projection estimation error (SP2E). *Structural Control and Health Monitoring*, 2017.

[10] A. Lenzen and M. Vollmering. On experimental damage localization by SP2E: Application of $\mathcal{H}^\infty$ estimation and oblique projections. *Mechanical Systems and Signal Processing*, 104:648–662, 2018.

[11] M. Vollmering and A. Lenzen. Theory and numerical application of damage localization method state projection estimation error (SP2E). *Structural Control and Health Monitoring*, 25(10):e2237, 2018.

[12] S. Wernitz, D. Pache, T. Grießmann, and R. Rolfes. Damage localization with SP2E under changing conditions. *The 12th International Workshop on Structural Health Monitoring*, 2019.

[13] D. Simon. *Optimal State Estimation: Kalman, H_∞, and Nonlinear Approaches*. Wiley, 2006.

[14] B. Hassibi, A.H. Sayed, and T. Kailath. *Indefinite-Quadratic Estimation and Control: A Unified Approach to H^2 and H^∞ Theories*. SIAM Studies in Applied Mathematics. Society for Industrial and Applied Mathematics, 1999.

[15] R.N. Banavar. *A game theoretic approach to linear dynamic estimation*. PhD thesis, Texas University, Austin, 1992.

[16] K. Takaba and T. Katayama. Discrete-time H_∞ algebraic riccati equation and parametrization of all H_∞ filters. *International Journal of Control*, 64(6):1129–1149, 1996.

[17] R.S. Mangoubi. *Robust Estimation and Failure Detection: A Concise Treatment*. Advances in Industrial Control. Springer London, 2012.

[18] K. Zhou, J.C. Doyle, and K. Glover. *Robust and Optimal Control*. Feher/Prentice Hall Digital and. Prentice Hall, 1996.

[19] P. Gahinet and P. Apkarian. A linear matrix inequality approach to $\mathcal{H}_\infty$ control. *International journal of robust and nonlinear control*, 4(4):421–448, 1994.

[20] T. Iwasaki and R.E. Skelton. All controllers for the general $\mathcal{H}_\infty$ control problem: LMI existence conditions and state space formulas. *Automatica*, 30(8):1307–1317, 1994.

[21] C. Scherer, P. Gahinet, and M. Chilali. Multiobjective output-feedback control via LMI optimization. *IEEE Transactions on automatic control*, 42(7):896–911, 1997.

[22] H. Gao and X. Li. *Robust Filtering for Uncertain Systems: A Parameter-Dependent Approach*. Communications and Control Engineering. Springer International Publishing, 2014.

[23] A.H. Sayed, B. Hassibi, and T. Kailath. Inertia conditions for the minimization of quadratic forms in indefinite metric spaces. *Recent Developments in Operator Theory and Its Applications*, pages 309–347, 1996.

[24] V. Sima. *Algorithms for Linear-Quadratic Optimization*. Chapman & Hall/CRC Pure and Applied Mathematics. Taylor & Francis, 1996.

[25] V. Ionescu, C. Oară, and M. Weiss. *Generalized Riccati Theory and Robust Control: A Popov Function Approach*. Wiley, 1999.

[26] A. Lenzen and M. Vollmering. Mechanical system scaling based on output only identification and mass perturbations by state projections. *Mechanical Systems and Signal Processing*, Special Issue in Honor of Professor Lothar Gaul:106863, 2020.

[27] C. Ebert. *Systemidentifikation zur Modellierung mechanischer Strukturen: Markovparameter zur experimentellen Schadenserfassung*. Dissertation, Universität Siegen, 2013.

[28] E. Balmès. New results on the identification of normal modes from experimental complex modes. *Mechanical Systems and Signal Processing*, 11(2):229–243, 1997.

[29] E. Parloo, P. Verboven, G. Guillaume, and M. van Overmeire. Sensitivity-based operational mode shape normalisation. *Mechanical Systems and Signal Processing*, 16(5):757–767, 2002.

[30] R. Brincker and P. Andersen. A way of getting scaled mode shapes in output only modal testing. In *Proc. 21st Int. Modal Analysis Conference, Kissimmee, FL*, 2003.

[31] D. Bernal. Modal scaling from known mass perturbations. *Journal of engineering mechanics*, 130(9):1083–1088, 2004.

[32] D. Bernal. A receptance based formulation for modal scaling using mass perturbations. *Mechanical systems and Signal processing*, 25(2):621–629, 2011.

[33] M.M. Khatibi, M.R. Ashory, A. Malekjafarian, and R. Brincker. Mass–stiffness change method for scaling of operational mode shapes. *Mechanical Systems and Signal Processing*, 26:34–59, 2012.

[34] D. Bernal. Complex eigenvector scaling from mass perturbations. *Mechanical Systems and Signal Processing*, 45(1):80–90, 2014.

EURODYN 2020
XI International Conference on Structural Dynamics
M. Papadrakakis, M. Fragiadakis, C. Papadimitriou (eds.)
Athens, Greece, 23–26 November 2020

SUB-WAVELENGTH DAMAGE DETECTABILITY ASSESSMENT IN PERIODIC ASSEMBLIES USING A BLOCH MODELLING FRAMEWORK

Christophe Droz[1,2,*], Regis Boukadia[1,2], Elke Deckers[1,2] and Wim Desmet[1,2]

[1] KU Leuven, Belgium
[*]e-mail: christophe.droz@kuleuven.be

[2] DMMS Lab, Flanders Make, Belgium

Keywords: Piecewise periodic, guided wave, meta-structure, damage detection, unit-cell modeling, vibroacoustics

Abstract. *In this work, we develop a numerical framework for analyzing Bloch waves and their interactions with localized damages. A reduced Bloch expansion technique is first used to sub-structure the waveguide's healthy part, while a detailed finite element description of the damaged regions can be applied. A remarkable strength of this modelling technique lies in the possibility to compute the dynamic response of the overall structure (finite or infinite) subjected to harmonic or transient loads. The damage model and its location on the waveguide can both be updated with almost negligible additional computational effort. The performances compared with standard finite element analysis of a similar problem are outstanding (i.e. faster by at least 3 orders of magnitude). Two types of indicators can therefore be computed over a large number of possible waveguide-damage configurations: (i) the local transmission, reflection and conversions of Bloch waves at the interfaces of the damaged region, and (ii) the global harmonic or transient response of a loaded waveguide. This approach is used to extend the detectability of small-scaled damages in large-scaled periodic waveguides by exploiting the frequency-conversions of the Bloch scattering coefficients. These so-called 'diffusion features' are eventually used to improve sub-wavelength damage quantification and localization.*

1 INTRODUCTION

Guided wave testing (GWT) is a reliable, long-range and highly sensitive damage inspection technique. It is already well documented and extensively used for structural health assessment of various transportation, aerospace and offshore components. Although embedded GWT solutions are still seldom in the transportation industry, the upcoming IoT revolution will undoubtedly stimulate this field and replace many periodic maintenance inspections by embedded monitoring devices. On the other hand, many structural parts are becoming increasingly complex in this industry, to tackle combined needs for lightweight structures and enhanced vibroacoustic performances. Despite their many advantages, these lightweight structures exhibit various scattering behaviors (e.g. local resonances, Bragg effects, frequency-conversion) which considerably alter the broadband dispersion features and overall applicability of GWT strategies. The question addressed in this work states as follows: how can advanced waveguide modelling techniques be used to detect small damages in large-scaled periodic assemblies?

If the structure has a canonical form, explicit homogenized models can be used to describe the local dynamics (for stiffened plates, see Fossat et al. [1]). In more complex assemblies such as typical lightweight structures, numerical methods (or semi-analytical [2]) are needed, generally involving a refined finite element description of the structure and associated with model order reduction schemes [3–5] to reduce the computational cost involved. Since it was shown that that high-order guided resonances tend to have a superior sensitivity to small scaled damages [6], the selective generation of guided resonances (or any form of Floquet solutions [7, 8]) can be seen as a possible way to perform multi-modal pre-assessment of a damage's scattering properties. These indicators have already been used in axisymmetric structures (see for ex. [9–11]), however such analyses require extensive computation efforts and wave-based methodologies. This paper presents a computationally efficient modeling scheme able to predict both the wave dispersion characteristics, the finite or semi-infinite dynamic response and local damage scattering properties.

2 METHOD

2.1 Wave Finite Element Method

Consider a waveguide made of identical consecutive sub-structures of length d. Denoting $\mathbb{M}$, $\mathbb{C}$, $\mathbb{K}$ the generalized finite element mass, damping and stiffness matrices of the structure and $\mathbf{u}$ the displacements, the governing equation of the free waveguide writes:

$$(\mathbb{K} + j\omega\mathbb{C} - \omega^2\mathbb{M})\mathbf{u} = \mathbf{0}. \tag{1}$$

The Floquet theory gives the form of the solutions $U(x)$ of a linear differential equation $H(x)U(x) = 0$ where H is a periodic operator such as $H(x + d) = H(x)$. The solution can therefore be written as a superposition of Floquet vectors using a d-periodic invertible matrix $\mathbb{V}$ and a constant matrix κ as:

$$U(x) = \mathbb{V}(x)e^{\kappa x} \tag{2}$$

Defining the complex propagation constants $\lambda = e^{\kappa d}$, the Floquet theory gives the relation between the displacements of two consecutive unit-cells as $u_{i+1} = \lambda u_i$. In the direct WFEM form, the generalized dynamic stiffness matrix is decomposed into its left and right-sided DOFs located at the junction between the unit-cells, while the inner DOFs can be condensed. Introducing the Floquet theory in the force equilibrium equation yields the direct form of the dispersion

relation as the following quadratic eigenvalue problem:

$$\left(\lambda\mathbb{D}_{LR} + (\mathbb{D}_{LL} + \mathbb{D}_{RR}) + \frac{1}{\lambda}\mathbb{D}_{RL}\right)\phi = \mathbf{0}.$$

Alternatively, the dispersion relation can be written without dynamic condensation with the form:

$$\mathbf{D}(\lambda)\begin{Bmatrix}\mathbf{u}_L\\ \mathbf{u}_I\end{Bmatrix} = \begin{Bmatrix}\mathbf{0}\\ \mathbf{0}\end{Bmatrix},$$

where:

$$\mathbf{D}(\lambda)\ :\ \mathbf{D} \longrightarrow \begin{bmatrix}\mathbf{D}_{RL} & \mathbf{D}_{RI}\\ \mathbf{0} & \mathbf{0}\end{bmatrix}\frac{1}{\lambda} + \begin{bmatrix}\mathbf{D}_{RR}+\mathbf{D}_{LL} & \mathbf{D}_{LI}\\ \mathbf{D}_{IL} & \mathbf{D}_{II}\end{bmatrix} + \begin{bmatrix}\mathbf{D}_{LR} & \mathbf{0}\\ \mathbf{D}_{IR} & \mathbf{0}\end{bmatrix}\lambda.$$

The wave-mode WFEM reduction was used to reduce the computational effort (e.g. [4, 5] for details). The propagating solutions are selected among the complex solutions $\lambda = e^{-jkd}$. Solutions are discriminated into positive Ψ^+ and negative Ψ^- wave amplitudes. A wavematching procedure is used to track frequency-dependent waves and plot the dispersion curves.

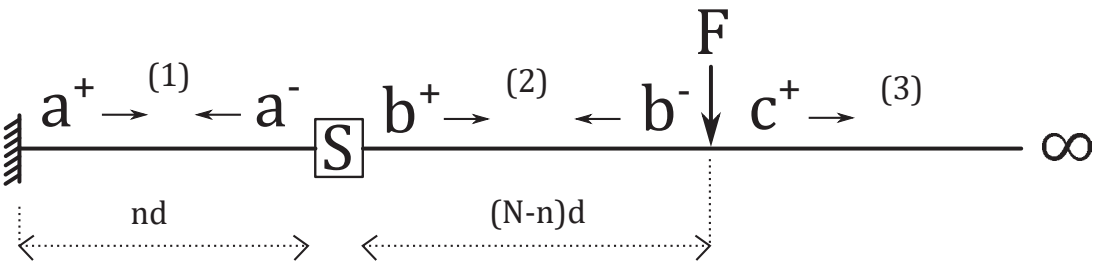

Figure 1: Semi-infinite piece-wise periodic waveguide configuration.

2.2 Diffusion properties

The presence of a coupling region, defined by the scattering matrix $\mathbb{S}$ in the waveguide results in the introduction of two coupling conditions at both sides of the coupling element. Using the above mentioned Floquet expansion gives, for any incident wave source terms (α^+, β^+) [12], the reflection and transmission coefficients as:

$$\begin{Bmatrix} R\\ T\end{Bmatrix} = -\begin{bmatrix}\mathbb{D}_{RL}\Psi^-\Lambda + (\mathbb{D}_{RR}+\mathbb{S}_{LL})\Psi^- & \mathbb{S}_{LR}\Psi^+\\ \mathbb{S}_{RL}\Psi^- & (\mathbb{S}_{RR}+\mathbb{D}_{LL})\Psi^+ + \mathbb{D}_{LR}\Psi^+\Lambda\end{bmatrix}^{-1}\begin{Bmatrix}\alpha^+\\ \beta^+\end{Bmatrix}$$

The above relation allows the computation of diffusion coefficients from a single incident wavetype for any given scattering section $\mathbb{S}$.

2.3 Forced response of the piecewise periodic structure

The following configuration is considered: the piecewise waveguide is composed of three sections as shown in Figure 1. Section 1 contains N_1 cells. It is clamped on the left side and connected to section 2 by a scattering region described by matrix $\mathbb{S}$. An external load is applied at a distance N_2 from the coupling region and defines the semi-infinite section 3. Using

the Floquet expansion, the generalized governing equation can be rewritten under the reduced form:

$$\mathcal{H} \begin{Bmatrix} \mathbf{a}^+ \\ \mathbf{a}^- \\ \mathbf{b}^+ \\ \mathbf{b}^- \\ \mathbf{c}^+ \end{Bmatrix} = \begin{Bmatrix} 0 \\ 0 \\ 0 \\ F \\ 0 \end{Bmatrix},$$

where $\mathcal{H} = \mathcal{H}(\mathbb{D}, \mathbb{S}, \Psi^+, \Psi^-, \{\Lambda^k\}_{k=[0..N]})$ is a Floquet decomposition of the dynamic stiffness matrix projected on the extremities of each waveguide section (interested readers are refered to [13] for detailed methodology). Note that the maximal dimension of this sparse linear problem is equal to the number of DOFs in a single unit-cell's edge. In general, a reduction to a few propagating and evanescent waves can provide an additional reduction of the dimension by several orders of magnitude. In the example below, the total number of DOFs in sections (1) and (2) is 100k DOFs including the scattering element. The Floquet expansion yields a reduced system of size 250.

3 APPLICATION

The methodology is then used to compute the diffusion indicators, displayed as a set of three frequency-dependent coefficients: the Transmission (T) and Reflection (R), as well as a Diffusion (D) term defined as in [12].

3.1 Description of the model

The considered waveguide is an aluminium framed structure of unit-cel's length l_x=5 cm meshed using 3D block elements and involving three different internal damages as described in fig. 2. The loading and boundary conditions are the ones of an attempted inspection of the region between the actuated region and the clamped end, considering a semi-infinite part on the other side (no reflected waves). The configuration therefore corresponds the one shown in fig. 1. The damage model is parametrized and consists in a local reduction of the stiffness on the walls of the damaged unit-cell along three possible direction (see fig. 2).

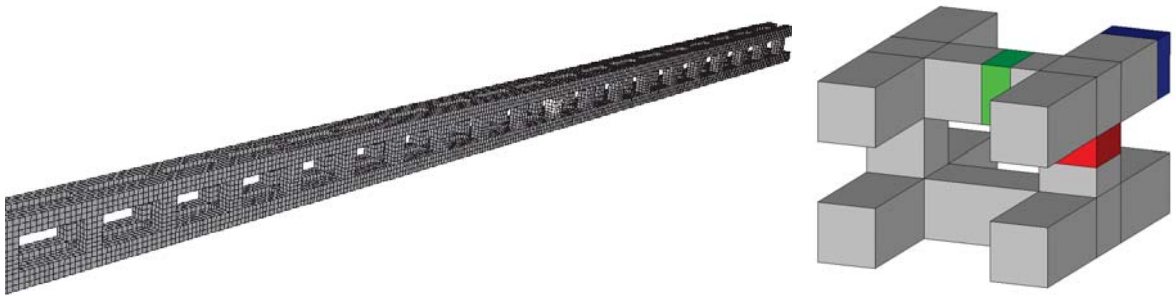

Figure 2: (a) FEM of a finite section of the framed structure. (b) Example of damage scenario along x (blue), y (green) and z (red).

3.2 Diffusion features

The diffusion of all propagating waves produced by a x-oriented damage are computed using Eq. 2.2. The dispersion curves of the first 9 propagating waves is shown in fig. 4. One

can identify the Bragg bandgap affecting most transverse waves between 8-13 kHz. The three coefficients displayed in fig. 3 over frequency for each wave indicate the expected sensitivity of the wave to a given damage. It can be assumed that the more sensitive the wave to the damage is, the more altered the overall dynamic response will be once subjected to this wavetype's loading. For a sake of clarity, the non-propagative regions (e.g. bandgaps) are hidden, based on the wave's spatial attenuation criterion (i.e. above 5% amplitude decay per unit-cell).

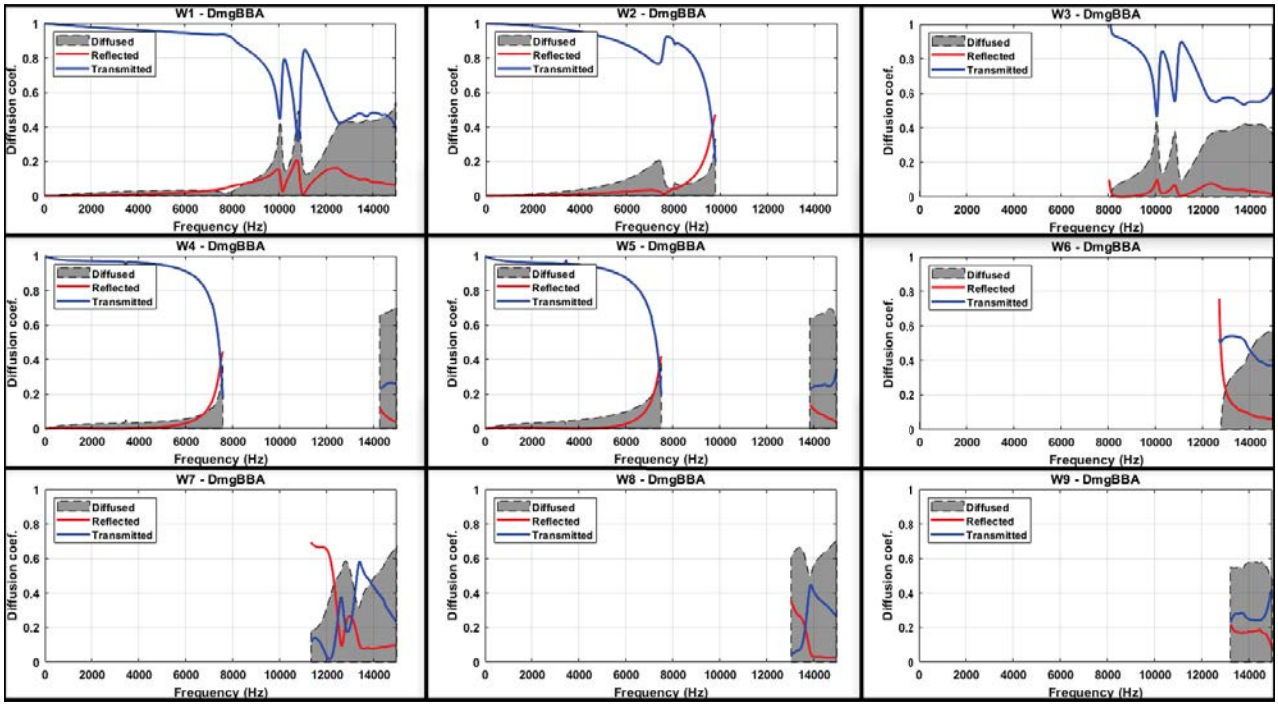

Figure 3: Transmission, Reflection, and Diffusion coefficients of all propagating waves in the considered bandwidth, for a damage of type 'longitudinal'.

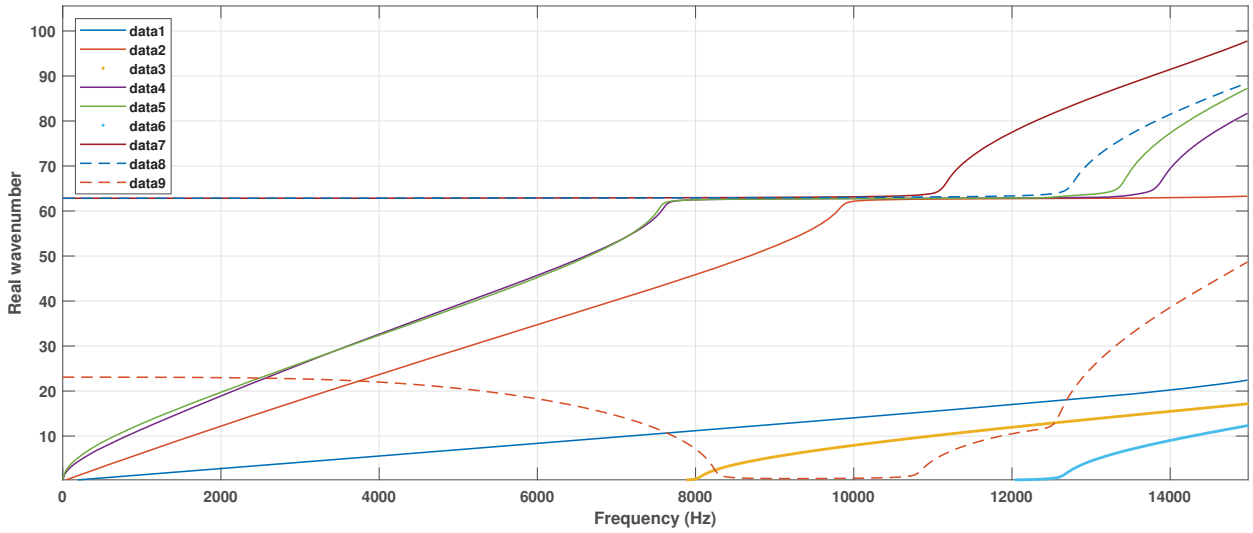

Figure 4: Dispersion curves in the framed structure.

Note that the sensitivities tend to increase close to the non-propagating regions (cut-on, Bragg, local resonances etc.). For illustration purpose, one can compare the diffusion plots of waves 5 (middle) and 7 (bottom left). It is clearly visible that wave 5 is almost insensitive to the damage, except near the bandgap, and is mainly diffused above 14 kHz. On the other hand, wave 7 cuts-on at 12 kHz but exhibits a higher reflection (above 60%) between 12 and 13 kHz.

3.3 Forced response

The hypothesis that the overall dynamic response of the semi-infinite structure will be more sensitive by applying wave 7 than wave 5 is tested in the below. In the loading region, a guided mode actuation is assumed to produce a frequency-dependent edge unit-cell forced appropriation of a selected wave. The co-localized forced response is calculated in fig. 5 for both wavetype actuations, each comparing the healthy and damaged cases. It shows that the diffusion analysis gave a fair prediction, as the dynamic response is more sensitive under normalized load to wave 7 than wave 5, despite its reduced propagative bandwidth. In addition, the reduced wave model described above gives the full dynamic response solution to a given loading case in less than a second.

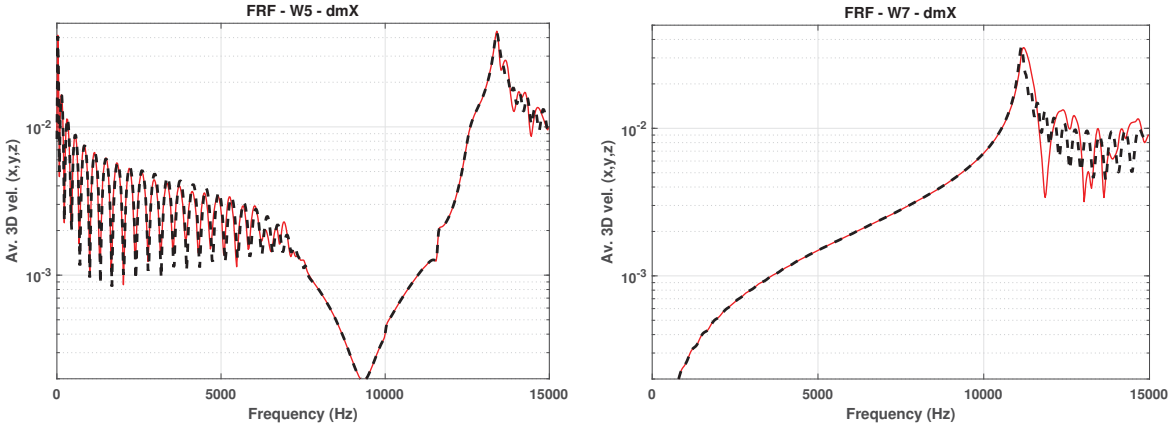

Figure 5: Forced response of the semi-infinite structure under wave-mode appropriation index 5 (a) and (7). The co-localized response is computed considering an healthy (dashed) and damaged (continuous) region with a longitudinal damage type.

4 CONCLUSIONS

The conclusions of this work can be stated as follows:

- A generalized Floquet decomposition was used to derive the dispersion characteristics, the damage scattering information and the forced response from a single unified numerical framework.
- The method was coupled with a model order reduction scheme, providing outstanding computation performances.
- These methodologies were proved of remarkable efficiency to model and predict the detectability of small-scaled damages in a framed structure using both dynamic response and diffusion analysis.

ACKNOWLEDGEMENTS

The research of C. Droz is funded by the European Union's Horizon 2020 research and innovation programme (WIDEA) under the individual Marie Skłodowska-Curie fellowship grant agreement No. 797034. The research of E. Deckers is funded by a postdoctoral grant from the Research Foundation – Flanders (FWO). The Research Fund KU Leuven (IOF) is also gratefully acknowledged for his support.

REFERENCES

[1] P. Fossat, C. Boutin, and M. Ichchou, "Dynamics of periodic ribbed plates with inner resonance: Analytical homogenized model and dispersion features," *International Journal of Solids and Structures*, vol. 152, pp. 85–103, 2018.

[2] M. Gallezot, F. Treyssède, and L. Laguerre, "Numerical modelling of wave scattering by local inhomogeneities in elastic waveguides embedded into infinite media," *Journal of Sound and Vibration*, vol. 443, pp. 310–327, 2019.

[3] C. Droz, J.-P. Lainé, M. Ichchou, and G. Inquiété, "A reduced formulation for the free-wave propagation analysis in composite structures," *Composite Structures*, vol. 113, pp. 134–144, 2014.

[4] R. F. Boukadia, C. Droz, M. N. Ichchou, and W. Desmet, "A bloch wave reduction scheme for ultrafast band diagram and dynamic response computation in periodic structures," *Finite Elements in Analysis and Design*, vol. 148, pp. 1–12, 2018.

[5] A. Palermo and A. Marzani, "A reduced bloch operator finite element method for fast calculation of elastic complex band structures," *International Journal of Solids and Structures*, 2019.

[6] C. Droz, O. Bareille, J.-P. Lainé, and M. N. Ichchou, "Wave-based shm of sandwich structures using cross-sectional waves," *Structural Control and Health Monitoring*, vol. 25, no. 2, p. e2085, 2018.

[7] C. Droz, O. Bareille, and M. N. Ichchou, "Generation of long-range, near-cut-on guided resonances in composite panels," *Journal of Applied Physics*, vol. 125, no. 17, p. 175109, 2019.

[8] V. Serey, N. Quaegebeur, P. Micheau, P. Masson, M. Castaings, and M. Renier, "Selective generation of ultrasonic guided waves in a bi-dimensional waveguide," *Structural Health Monitoring*, vol. 18, no. 4, pp. 1324–1336, 2019.

[9] W. Wang, L. Li, Y. Fan, and Z. Jiang, "Piezoelectric transducers for structural health monitoring of joint structures in cylinders: A wave-based design approach," *Sensors*, vol. 20, no. 3, p. 601, 2020.

[10] W. Yan, D. Chronopoulos, C. Papadimitriou, S. Cantero-Chinchilla, and G.-S. Zhu, "Bayesian damage characterization based on probabilistic model of scattering coefficients and hybrid wave finite element model scheme," in *Proceedings of the 7th International Conference on Computational Methods in Structural Dynamics and Earthquake Engineering*, vol. 2, pp. 2952–2958, 2019.

[11] E. El Masri, N. Ferguson, and T. Waters, “Wave propagation and scattering in reinforced concrete beams,” *The Journal of the Acoustical Society of America*, vol. 146, no. 5, pp. 3283–3294, 2019.

[12] C. Droz, R. Boukadia, M. Ichchou, and W. Desmet, “Diffusion-based design of locally resonant sub-systems using a reduced wave finite element framework,” in *Proceedings of ISMA 2018-International Conference on Noise and Vibration Engineering*, pp. 3071–3083, 2018.

[13] Y. Yong and Y. Lin, “Propagation of decaying waves in periodic and piecewise periodic structures of finite length,” *Journal of Sound and Vibration*, vol. 129, no. 1, pp. 99–118, 1989.

EURODYN 2020
XI International Conference on Structural Dynamics
M. Papadrakakis, M. Fragiadakis, C. Papadimitriou (eds.)
Athens, Greece, 23–26 November 2020

IDENTIFICATION OF DAMAGE TO A TWO-STORY HISTORIC MASONRY BUILDING IN NEPAL DUE TO THE 2015 GORKHA EARTHQUAKE USING NATURAL FREQUENCIES & MODE SHAPES

A. Furukawa[1], J. Kiyono[1], and K. Toki[2]

[1] Department of Urban Management, Graduate School of Engineering, Kyoto University
C cluster, Kyotodaigaku-katsura, Nishikyo-ku, Kyoto, Japan
e-mail: furukawa.aiko.3w@kyoto-u.ac.jp

[2] Ritsumeikan University, Kinugasa Research Organization
58 Komatsubara-Kitamachi, Kita-ku, Kyoto, Japan

Keywords: Damage identification, Two-story building, Nepal, Gorkha earthquake, Natural frequencies, Mode shapes

Abstract.

On April 25, 2015, a Mw 7.8 earthquake struck the Gorkha district of Kathmandu, Nepal. Several masonry structures such as temples and monuments collapsed in Patan Durbar Square. A 300-year-old two-story masonry building in Patan that is the subject of this study is about a 5-minute walk from Patan Durbar Square. Although the building did not collapse, cracks were confirmed in several places. Since the vibrational characteristics of the building had been measured prior to the Gorkha earthquake, the vibrational characteristics of the building were measured again after the Gorkha earthquake.

Since the building is two stories high, it was modelled using a two degree-of-freedom (DOF) system and structural damage was modelled as stiffness reduction of each story. Two damage identification techniques for the two DOF system were proposed which identifies stiffness reduction of each story using modal data. The first method utilises the natural frequencies of the first and second modes and mode shapes of the first mode before and after the earthquake. The second method utilises the natural frequencies and mode shapes of the first and second modes before the earthquake and the natural frequencies of the first and second mode after the earthquake. The mode shape after the earthquake is not utilised in the second technique.

Using the proposed techniques, the stiffness reduction ratio for each story was identified. A comparison of the results of the first and second techniques was conducted and the results of the second technique were superior. During the microtremor observation after the earthquake, the accelerometers were unexpectedly plated at a different location from that before the earthquake. The first technique utilises the mode shapes before and after the earthquake and the mode shapes at the different locations are different. Therefore, the second technique possibly showed better results. Based on the results of the second technique, it was estimated that the stiffness of each story was reduced about 11.5% to 15.5% due to the earthquake.

1 INTRODUCTION

In the Kathmandu Valley, there are seven World Heritage Sites, including dozens of monuments and hundreds of historic private and public buildings that were constructed in the seventeenth and eighteenth centuries. Given that the region lies within the Himalayan orogenic belt, earthquake activity is frequent. Therefore, many historic buildings have been damaged by or collapsed because of earthquakes over the centuries [1),2)]. For example, in 1934, the Bihar earthquake with a magnitude of 8 or more struck Kathmandu, destroying temples, shrines and monuments of significant cultural heritage[3),4)].

The Kathmandu Valley was designated a World Heritage Site by UNESCO in 1979. However, as industrialisation and commercialisation proceeded in this region, numerous historic masonry structures with tiled roofs and composite buildings of masonry and timber were demolished, and low-quality concrete buildings were constructed. Therefore, the Kathmandu Valley was registered in a list of endangered Cultural Heritage sites in 2003. Due to the subsequent efforts of the World Heritage Committee and associated Nepalese ministries, it was unlisted in 2007[5)]. However, efforts to protect these sites from earthquake disasters have been severely lacking.

Against this background, we conducted research to understand the seismic safety of existing historic masonry buildings in Kathmandu [6),7),8),9)]. A 300-year-old, two-story masonry building located in Jhatapol within the Patan district was selected as a target building, and its vibrational characteristics were investigated through microtremor observations in 2009[8)]. Following these researches, the M_w 7.8 Gorkha earthquake struck the region of Kathmandu on April 25, 2015. The earthquake was the most disastrous to strike Nepal since the 1934 Bihar earthquake[10),11),12)]. The total number of completely damaged buildings was determined to be 498,852, with the number of partially damaged buildings being 256,697. Among them, low-strength masonry buildings accounted for 95% of the completely damaged building (474,025) and 67.7% of the partially damaged buildings (173,867)[12)].

After the Gorkha earthquake, we visited Kathmandu to investigate structural damage in the target building, which was categorised as a low-strength masonry building. Even though several monuments and buildings in Patan Durbar Square had been damaged and some had collapsed, the target building survived the earthquake. It was difficult to evaluate the severity of damage to this building by visual inspection alone. Therefore, microtremor observations of the building were conducted in 2016 to search for changes in vibrational characteristics.

The results of this work are presented here as follows. First, the vibrational characteristics, especially the first- and second-mode natural frequencies, the shape of the first mode and the damping ratios of the first mode of the translational motion in the longitudinal and transverse directions, are evaluated for the buildings before and after the earthquake. Second, structural parameters are modelled with a two degree-of-freedom (DOF) system and an identification method for the structural parameters from these vibrational characteristics is proposed. Then, structural parameters are identified from the vibrational characteristics of the buildings before and after the earthquake. Assuming that the mass is unchanged, the structural damage due to the earthquake is estimated as the stiffness reduction of the first and second floors.

2 TARGET BUILDING

The target building is a 300-year-old, two-story brick masonry building located in Jhatapol in the Patan district. It is a public building located near Patan Durbar Square, a World Heritage Site. The distance between the epicentre and the target building is about 78 km. The distance between the target building and the United States Geological Survey (USGS) strong-motion

station (KATNP) is about 4.3 km. The peak ground accelerations at KATNP for the NS, EW and UD components are 162 gal, 155 gal and 184 gal, respectively.

Photos of the building before and after the earthquake are shown in Fig. 1. A plan view of the building is shown in Fig. 2. The building has two stories and lateral dimensions of 16.5 × 5.6 m. The heights of the lower and upper stories are 2.4 and 2.1 m, respectively. The maximum height of the building is 6.5 m. Each wall has openings, with the western wall having the largest openings. The walls are composed of mortared bricks. The roof consists of corrugated galvanised iron sheets resting on wooden beams and battens.

(a) Before earthquake (Nov. 3, 2009) (b) After earthquake (March 5, 2016)

Figure 1: Target building before and after the 2015 Gorkha earthquake (left: south side, right: west side)

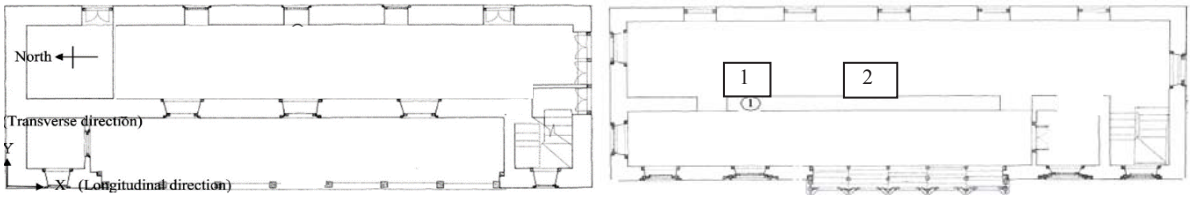

(a) Plan view of the ground floor (b) Plan view of the upper floor

Figure 2: Plan view of the target building with numbered measurement locations

3 NATURAL FREQUENCIES AND MODE SHAPES BEFORE AND AFTER EARTHQUAKE

3.1 Microtremor Observation

Figure 2(a) shows the orientation of the structures and measurement locations where the accelerometers were placed. The acceleration responses were measured at Point 1 before the earthquake and at Point 2 after the earthquake as shown in Fig. 2(b). The measurements at the same locations were not possible due to human error. One accelerometer was placed on the first floor and the other accelerometer was placed on the second floor (roof floor), denoted by F1 and F2, respectively. The sampling interval of measurement data was 0.01 s. From the measured data, 10 sets of 4096 data points were extracted, and the average of their Fourier amplitudes was computed. For smoothing, the Parzen window with a frequency band of 0.4 Hz was applied.

3.2 Natural frequencies and mode shape

Figure 3 compares the Fourier amplitudes of the responses on the first and second floors in the longitudinal (x, NS) and transverse (y, EW) directions before and after the earthquake. Clear peaks can be seen at 6.87 Hz and 10.2 Hz before the earthquake and 6.43 Hz and around 9.56 Hz after the earthquake in the longitudinal direction. Clear peaks can be seen at 4.33 Hz

and 7.13 Hz before and 4.02 Hz and 6.68 Hz after the earthquake in the transverse direction. Peaks at 5.78 Hz in the transverse direction before the earthquake are torsional motion, so these were disregarded.

The mode shape is defined as the ratio of the amplitude of the first floor to the amplitude of the second floor around natural frequencies considering the shapes of the Fourier amplitudes around the natural frequencies. The shape of the first mode in the longitudinal direction then is estimated as 0.368 before and 0.367 after the earthquake. The shape of the first mode in the transverse direction is estimated as 0.269 before and 0.324 after the earthquake. The shape of the second mode before the earthquake was also read.

Comparisons of the natural frequencies of the first and second translational modes, the shape of the first translational mode and the damping ratio of the first translational mode are shown in Table 1. The natural frequencies decreased because of the earthquake by about 6.27% to 7.16%. The reduction ratio in the transverse direction was larger than that in the longitudinal direction. Assuming that the mass of the structure was unchanged by the earthquake, the decrease in the natural frequencies indicates a reduction in stiffness, i.e., the occurrence of structural damage.

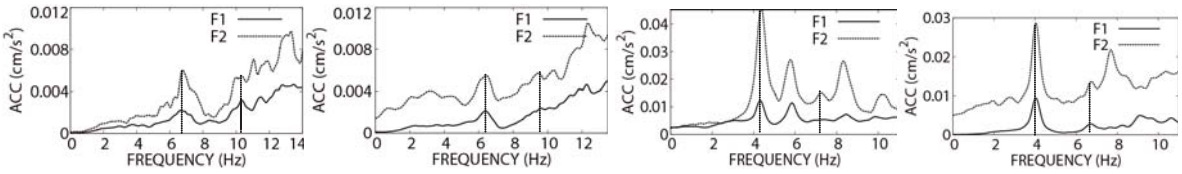

(a) Longitudinal (*x*, NS) direction (b) Transverse (*y*, EW) direction

Figure 3: Fourier amplitudes of the responses on the first and second floors before and after the 2015 Gorkha earthquake (left: Before earthquake (Nov. 3, 2009), right: After earthquake (March 5, 2016))

Table 1: Natural frequencies and mode shape before and after the 2015 Gorkha earthquake

(a) Longitudinal (*x*, NS) direction

	Before earthquake	After earthquake	Change ratio
Natural frequency of the first mode	6.87Hz	6.43Hz	−6.27%
Natural frequency of the second mode	10.2Hz	9.56Hz	−6.28%
Mode shape of the first mode (amplitude ratio of the first to second floors)	0.368	0.367	-0.272%
Mode shape of the second mode (amplitude ratio of the first to second floors)	-0.64	-	-

(b) Transverse (*y*, EW) direction

	Before earthquake	After earthquake	Change ratio
Natural frequency of the first mode	4.33Hz	4.02Hz	−7.16%
Natural frequency of the second mode	7.13Hz	6.68Hz	−6.31%
Mode shape of the first mode (amplitude ratio of the first to second floors)	0.269	0.324	+20.618%
Mode shape of the second mode (amplitude ratio of the first to second floors)	-0.327	-	-

$$* \text{Change ratio} = \frac{\text{value before earthquake} - \text{value after earthquake}}{\text{value before earthquake}}$$

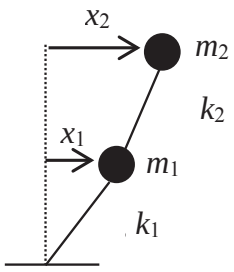

Figure 4: Two DOF system

4 IDENTIFICATION OF STIFFNESS REDUCTION USING FIRST AND SECOND NATURAL FREQUENCIES AND FIRST MODE SHAPE BEFORE AND AFTER EARTHQUAKE

4.1 Identification of stiffness-to-mass ratio using first and second natural frequencies and first mode shape

Since the target building has two stories, the building is modeled with a two degree-of-freedom (DOF) system as shown in Fig.4.

In this section, an identification technique of the stiffness-to-mass ratio used natural frequencies of the first and second modes and the mode shape of the first mode. This method directly identifies the stiffness-to-mass ratio of the building before and after an earthquake. By comparing the stiffness-to-mass ratio before and after the earthquake assuming that the mass is constant before and after the earthquake, structural damage is identified as stiffness reduction.

Let us assume that ω_j is the natural circular frequency and $\phi_j = \{\phi^j{}_1 \ \phi^j{}_2\}^T$ is the shape of the j-th mode. The natural circular frequency can then be obtained from the frequency f_j of the j-th mode by $\omega_j=2\pi f_j$.

ω_j and ϕ_j are the solutions of the eigenvalue problem as follows,

$$\begin{bmatrix} -m_1\omega_j^2 + k_1 + k_2 & -k_2 \\ -k_2 & -m_2\omega_j^2 + k_2 \end{bmatrix} \begin{Bmatrix} \phi_1^j \\ \phi_2^j \end{Bmatrix} = \begin{Bmatrix} 0 \\ 0 \end{Bmatrix}. \tag{1}$$

where m_i and k_i are mass and stiffness of the i-th floor. From the second equation of Eq. (1), the ratio of structural parameters can be correlated with the natural circular frequency and mode shape,

$$\frac{k_2}{m_2} = \frac{\omega_j^2}{1-(\phi_1^j/\phi_2^j)}. \tag{2}$$

In this study, the structural parameter k_2/m_1 is obtained by the natural circular frequency and mode shape of the first mode since the mode shape of the second mode is not estimated in the previous section,

$$\frac{k_2}{m_2} = \frac{\omega_1^2}{1-(\phi_1^1/\phi_2^1)}. \tag{3}$$

Next, to obtain the solution $\phi_j \neq 0$, the determinant of the matrix should be 0 in Eq. (1). Therefore,

$$m_1m_2\omega_j^4 - (m_1k_2 + m_2k_1 + m_2k_2)\omega_j^2 + k_1k_2 = 0. \tag{4}$$

Since ω_1 and ω_2 are the solutions of Eq. (4),

$$\omega_1^2 + \omega_2^2 = \frac{m_1 k_2 + m_2 k_1 + m_2 k_2}{m_1 m_2} = \frac{k_2}{m_2} + \frac{k_1}{m_1} + \frac{k_2}{m_1}, \tag{5}$$

$$\omega_1^2 \omega_2^2 = \frac{k_1 k_2}{m_1 m_2}. \tag{6}$$

By substituting Eq. (3) with Eq. (6), the structural parameter k_1/m_1 is obtained as

$$\frac{k_1}{m_1} = \omega_2^2 \{1 - (\phi_1^1 / \phi_2^1)\}. \tag{7}$$

By substituting Eqs. (3) and (7) with Eq. (5), the structural parameter k_2/m_1 is obtained as

$$\frac{k_2}{m_1} = \omega_1^2 + \omega_2^2 - \frac{\omega_1^2}{1 - (\varphi_1^1 / \varphi_2^1)} - \omega_2^2 \{1 - (\varphi_1^1 / \varphi_2^1)\} = \left\{ - \frac{\omega_1^2}{1 - (\varphi_1^1 / \varphi_2^1)} + \omega_2^2 \right\} (\varphi_1^1 / \varphi_2^1). \tag{8}$$

By taking the ratio of Eqs. (7) and (8), structural parameter m_2/m_1 is obtained as

$$\frac{m_2}{m_1} = \left[-1 + (\omega_2^2 / \omega_1^2) \{1 - (\phi_1^1 / \phi_2^1)\} \right] (\phi_1^1 / \phi_2^1). \tag{9}$$

Therefore, three independent parameters are obtained as shown in Eqs. (7), (8) and (9).

4.2 Results

By substituting the natural frequencies of the first and second translational modes and the mode shape of the first translational mode before and after damage, structural parameters were estimated as shown in Table 2.

The stiffness of the second floor, k_2, is much smaller than that of the first floor, k_1. The mass of the second floor, m_2, is also smaller than that of the first floor, m_1. This is because the ceiling of the upper floor consists of a small number of light timber beams, while the ceiling of the lower floor consists of dense timber beams and heavy bricks.

The mass ratio, m_2/m_1, remains unchanged at 0.146 for the longitudinal direction which supports the assumption that the mass was unchanged by the earthquake. However, the mass ratio was changed from 0.264 to 0.281 for the transverse direction. This is because the measurement location is different before and after the earthquake as shown in Fig.2. The measurement location for the longitudinal direction is almost the middle for both the pre- and post-earthquake conditions and this is why the mass ratio is unchanged before and after the earthquake. On the contrary, the measurement location for the transverse direction is different and this is why the mass ratio changed before and after the earthquake.

Hence, it is possible to assume that the mass is unchanged by the earthquake for the longitudinal direction. Then the reduction of stiffness, k_1 and k_2, can be obtained as the reduction of k_1/m_1 and k_2/m_1, as shown in Table 2 (a). The stiffness reduction ratios of the first and second stories were 12.0% and 12.1% for the longitudinal direction.

As stated before, the mass ratio was different before and after the earthquake for the transverse direction. However, we obtained the reduction of k_1/m_1 and k_2/m_1, as shown in Table 2 (b). The stiffness reduction ratios of the first and second stories were 18.9% and 0.856% for the transverse direction which is different from those for the longitudinal direction. One of the reasons is the different measurement location before and after the earthquake and comparing the mode shapes of the first mode at the different measurement locations is inappropriate.

Table 2 Comparison of structural parameters before and after the 2015 Gorkha earthquake

(a) Longitudinal (x, NS) direction

	Before earthquake	After earthquake	Change ratio
m_2/m_1 [-]	0.146	0.146	0.237%
k_1/m_1 [1/s^2]	2595.4	2283.6	-12.0%
k_2/m_1 [1/s^2]	429.7	377.8	-12.1%

(b) Transverse (y, EW) direction

	Before earthquake	After earthquake	Change ratio
m_2/m_1 [-]	0.264	0.281	6.31%
k_1/m_1 [1/s^2]	1467.7	1190.7	-18.9%
k_2/m_1 [1/s^2]	267.3	265.0	-0.856%

5 IDENTIFICATION OF STIFFNESS REDUCTION USING FIRST AND SECOND NATURAL FREQUENCIES MODE SHAPES BEFORE EARTHQUAKE AND FIRST AND SECOND NATURAL FREQUENCIES AFTER EARTHQUAKE

5.1 Identification of stiffness-to-mass ratio reduction using first and second natural frequencies and mode shapes before earthquake and first and second natural frequencies after earthquake

Since the measurement locations before and after the earthquake are different due to human error, it is better not to compare the mode shapes before and after the earthquake observed at different locations. Therefore, in this section, we propose a different technique. We use the natural frequencies of the first and second modes for both the pre- and post-earthquake conditions, but only use the mode shapes of the first and second modes in the pre-earthquake conditions. We do not use the mode shape in the post-earthquake conditions.

The eigenvalue problem of the model before the earthquake is written as follows.

$$(-\lambda_j[M]+[K])\{\varphi_j\}=0 \tag{10}$$

where $[M]$ is the mass matrix, $[K]$ is the stiffness matrix, λ_j and $\{\phi_j\}$ are the j-th eigenvalue and eigenvector, respectively, of the model before the earthquake. The j-th eigenvector λ_j is the square of the natural frequency ω_j.

The eigenvalue problem of the model after the earthquake is expressed as

$$\left\{(-\lambda_j-\delta\lambda_j)[M]+([K]-[\delta K])\right\}\left(\{\varphi_j\}+\{\delta\varphi_j\}\right)=0 \tag{11}$$

where $[K]$-$[\delta K]$ is the stiffness matrix before the earthquake. The j-th eigenvalue and eigenvector of the model after the earthquake are λ_j -$\delta\lambda_j$ and $\{\phi_j\}$+$\{\delta\phi_j\}$, respectively. $[\delta K]$ is the reduction of the stiffness matrix due to the earthquake, $\delta\lambda_j$ is the reduction of the j-th eigenvalue and $\{\delta\phi_j\}$ is the increment of the j-th eigenvector due to the reduction of the stiffness matrix.

Expanding Eq. (11) and disregarding higher terms yields

$$(-\lambda_j[M]+[K])\{\varphi_j\}+(\delta\lambda_j[M]-[\delta K])\{\varphi_j\}+(-\lambda_j[M]+[K])\{\delta\varphi_j\}=0 \tag{12}$$

Since the first term of Eq. (12) becomes 0 from Eq. (10), Eq. (12) becomes

$$(\delta\lambda_j[M]-[\delta K])\{\varphi_j\}+(-\lambda_j[M]+[K])\{\delta\varphi_j\}=0 \tag{13}$$

After multiplication of each term from the left by $\{\phi_j\}^T$, Eq. (13) becomes

$$\{\varphi_j\}^T(\delta\lambda_j[M]-[\delta K])\{\varphi_j\}+\{\varphi_j\}^T(-\lambda_j[M]+[K])\{\delta\varphi_j\}=0 \tag{14}$$

Since the mass and stiffness matrices are symmetric, the second term of Eq. (14) becomes

$$\begin{aligned}&\{\varphi_j\}^T(-\lambda_j[M]+[K])\{\delta\varphi_j\}=\{\varphi_j\}^T(-\lambda_j[M]^T+[K]^T)\{\delta\varphi_j\}\\&=\left\{(-\lambda_j[M]+[K])\{\varphi_j\}\right\}^T\{\delta\varphi_j\}=0^T\{\delta\varphi_j\}=0\end{aligned} \tag{15}$$

Therefore, Eq. (14) becomes

$$\{\varphi_j\}^T(\delta\lambda_j[M]-[\delta K])\{\varphi_j\}=0 \tag{16}$$

The difference of the eigenvalues can be obtained as

$$\delta\lambda_j=\frac{\{\varphi_j\}^T[\delta K]\{\varphi_j\}}{\{\varphi_j\}^T[M]\{\varphi_j\}} \tag{17}$$

The equation of motion of free vibration of the two DOF system is written as follows,

$$\begin{bmatrix}m_1 & 0\\ 0 & m_2\end{bmatrix}\begin{Bmatrix}\ddot{x}_1(t)\\ \ddot{x}_2(t)\end{Bmatrix}+\begin{bmatrix}k_1+k_2 & -k_2\\ -k_2 & k_2\end{bmatrix}\begin{Bmatrix}x_1(t)\\ x_2(t)\end{Bmatrix}=\begin{Bmatrix}0\\ 0\end{Bmatrix} \tag{18}$$

where $x_i(t)$ is the displacement response of the i-th floor. By dividing the first and second equations by m_1, Eq. (18) is rewritten as,

$$\begin{bmatrix}1 & 0\\ 0 & m_2/m_1\end{bmatrix}\begin{Bmatrix}\ddot{x}_1(t)\\ \ddot{x}_2(t)\end{Bmatrix}+\begin{bmatrix}k_1/m_1+k_2/m_1 & -k_2/m_1\\ -k_2/m_1 & k_2/m_1\end{bmatrix}\begin{Bmatrix}x_1(t)\\ x_2(t)\end{Bmatrix}=\begin{Bmatrix}0\\ 0\end{Bmatrix}. \tag{19}$$

From Eq. (19), we substitute Eq. (20) with Eq. (17)

$$[M]=\begin{bmatrix}1 & 0\\ 0 & m_2/m_1\end{bmatrix}\quad\{\varphi_i\}=\begin{Bmatrix}\varphi_1^j/\varphi_2^j\\ 1\end{Bmatrix}\quad[\delta K]=\begin{bmatrix}1 & 0\\ 0 & 0\end{bmatrix}(\delta k_1/m_1)+\begin{bmatrix}1 & -1\\ -1 & 1\end{bmatrix}(\delta k_2/m_1). \tag{20}$$

Then we obtain

$$\delta\lambda_j=\frac{\{\varphi_1^j/\varphi_2^j\quad 1\}\begin{bmatrix}1 & 0\\ 0 & 0\end{bmatrix}\begin{Bmatrix}\varphi_1^j/\varphi_2^j\\ 1\end{Bmatrix}}{\{\varphi_1^j/\varphi_2^j\quad 1\}\begin{bmatrix}1 & 0\\ 0 & m_2/m_1\end{bmatrix}\begin{Bmatrix}\varphi_1^j/\varphi_2^j\\ 1\end{Bmatrix}}(\delta k_1/m_1)+\frac{\{\varphi_1^j/\varphi_2^j\quad 1\}\begin{bmatrix}1 & -1\\ -1 & 1\end{bmatrix}\begin{Bmatrix}\varphi_1^j/\varphi_2^j\\ 1\end{Bmatrix}}{\{\varphi_1^j/\varphi_2^j\quad 1\}\begin{bmatrix}1 & 0\\ 0 & m_2/m_1\end{bmatrix}\begin{Bmatrix}\varphi_1^j/\varphi_2^j\\ 1\end{Bmatrix}}(\delta k_2/m_1) \tag{21}$$

where δk_i is the reduction in the stiffness of the i-th floors.

$$\delta\lambda_j=\frac{(\varphi_1^j/\varphi_2^j)^2}{(\varphi_1^j/\varphi_2^j)^2+m_2/m_1}(\delta k_1/m_1)+\frac{(\varphi_1^j/\varphi_2^j)^2-2(\varphi_1^j/\varphi_2^j)+1}{(\varphi_1^j/\varphi_2^j)^2+m_2/m_1}(\delta k_2/m_1) \tag{22}$$

By using the first and second eigenvalues and eigenvectors of the model before the earthquake, we obtain the correlation between the reduction of eigenvalues and the reduction of the stiffness.

$$\begin{Bmatrix}\delta\lambda_1\\ \delta\lambda_2\end{Bmatrix}=\begin{bmatrix}\dfrac{(\varphi_1^1/\varphi_2^1)^2}{(\varphi_1^1/\varphi_2^1)^2+m_2/m_1} & \dfrac{(\varphi_1^1/\varphi_2^1)^2-2(\varphi_1^1/\varphi_2^1)+1}{(\varphi_1^1/\varphi_2^1)^2+m_2/m_1}\\ \dfrac{(\varphi_1^2/\varphi_2^2)^2}{(\varphi_1^2/\varphi_2^2)^2+m_2/m_1} & \dfrac{(\varphi_1^2/\varphi_2^2)^2-2(\varphi_1^2/\varphi_2^2)+1}{(\varphi_1^2/\varphi_2^2)^2+m_2/m_1}\end{bmatrix}\begin{Bmatrix}\delta k_1/m_1\\ \delta k_2/m_1\end{Bmatrix} \tag{23}$$

By solving Eq. (23), we finally get the stiffness reduction of each floor.

$$\begin{Bmatrix} \delta k_1 / m_1 \\ \delta k_2 / m_1 \end{Bmatrix} = \begin{bmatrix} \dfrac{(\varphi_1^1 / \varphi_2^1)^2}{(\varphi_1^1 / \varphi_2^1)^2 + m_2 / m_1} & \dfrac{(\varphi_1^1 / \varphi_2^1)^2 - 2(\varphi_1^1 / \varphi_2^1) + 1}{(\varphi_1^1 / \varphi_2^1)^2 + m_2 / m_1} \\ \dfrac{(\varphi_1^2 / \varphi_2^2)^2}{(\varphi_1^2 / \varphi_2^2)^2 + m_2 / m_1} & \dfrac{(\varphi_1^2 / \varphi_2^2)^2 - 2(\varphi_1^2 / \varphi_2^2) + 1}{(\varphi_1^2 / \varphi_2^2)^2 + m_2 / m_1} \end{bmatrix}^{-1} \begin{Bmatrix} \delta\lambda_1 \\ \delta\lambda_2 \end{Bmatrix} \tag{24}$$

The necessary parameters in this technique are the mode shapes of the first and second modes before the earthquake ($\varphi_1^1 / \varphi_2^1$, $\varphi_1^2 / \varphi_2^2$), mass ratio before the earthquake (m_2 / m_1), and reduction of eigenvalues due to the earthquake ($\delta\lambda_1$, $\delta\lambda_2$). The mass ratio is estimated using the technique in the previous section and the reduction of the eigenvalue is computed from the natural frequencies before and after the earthquake.

5.2 Results

The results are shown in Table 3. The stiffness reduction of the first and second stories for the longitudinal direction is about 12.6% and 13.0%, which is almost the same as the results in the previous section. The stiffness reduction of the first and second stories for the transverse direction is about 11.5% and 15.5%, which is different from the results in the previous section. In the previous section, the stiffness reduction ratio for the longitudinal and transverse directions differs significantly which is perplexing. Therefore, the result of this section provides a better solution.

Table 3 Comparison of structural parameters before and after the 2015 Gorkha earthquake

(a) Longitudinal (*x*, NS) direction

	Before earthquake	Reduction after earthquake	Change ratio
k_1/m_1 [1/s^2]	2595.4	327.8	−12.6%
k_2/m_1 [1/s^2]	429.7	55.7	−13.0%

(b) Transverse (*y*, EW) direction

	Before earthquake	Reduction after earthquake	Change ratio
k_1/m_1 [1/s^2]	1467.7	169.3	−11.5%
k_2/m_1 [1/s^2]	267.3	41.4	−15.5%

6 CONCLUSIONS

This paper presented a study of a two-story historic masonry building in the Patan district of Kathmandu that survived the 2015 Gorkha earthquake. Since the vibrational characteristics of the building had been measured before the earthquake (in 2009), microtremor observations were conducted after the earthquake (in 2016), then vibrational characteristics such as natural frequencies and mode shape could be compared before and after the earthquake.

The natural frequencies of the first and second translational modes decreased by 6.27% and 6.28% in the longitudinal direction and by 7.16% and 6.31% in the transverse direction, indicating that damage had occurred.

The translational motion of the building was modeled by a two degree-of-freedom system, and an identification method for the stiffness-to-mass ratio based on the first and second natural frequencies and first mode shape was proposed. Through the application of the proposed identification method, structural parameters were identified, and the stiffness of the first and second stories decreased by 12.0% and 12.1% in the longitudinal direction and by 18.9% and 0.856% in the transverse direction. The stiffness reduction in the transverse direction is differ-

ent from that in the longitudinal direction because of the use the mode shapes observed at the different measurement locations before and after the earthquake.

Therefore, the technique using only mode shapes before the earthquake was proposed. Through the application of the second proposed identification method, the stiffness reduction of the first and second stories for the longitudinal direction is about 12.6% and 13.0% which is almost the same as the results in the first proposed method. The stiffness reduction of the first and second stories for the transverse direction is about 11.5% and 15.5%.

Although the target building did not collapse during the M_w 7.8 Gorkha earthquake, one should not assume that the building could survive another earthquake of the same magnitude. The stiffness of the building was reduced about 11.5% to 15.5% which is quite a large reduction.

ACKNOWLEDGEMENTS

The authors deeply thank the late Prof. Hitoshi Taniguchi for his kind encouragement and warming support during the research.

REFERENCES

[1] Preparedness Network Nepal, Earthquake, http://www.dpnet.org.np/index.php?pageName=earthquake [Last accessed June 1, 2016].

[2] Bilham R, Ambraseys N: Apparent Himalayan slip deficit from the summation of seismic moments for Himalayan earthquakes 1500-2000, Current Science, Vol.88(10), pp.1658–1663, 2005.

[3] Amatya S: Monument conservation in Nepal, Vajra Publications, 2008.

[4] Rana BSJR: Nepal's Great Earthquake 1934, Sahayogi Press, Tripureshwor, Kathmandu (in Nepali), 1935.

[5] Rohit KR: Heritage homeowner's preservation handbook, UNESCO, 2007.

[6] Parajuli HR, Kiyono J, Ono Y, Tsutsumiuchi T: Design earthquake ground motions from probabilistic response spectra: Case study of Nepal, Journal of Japan Association for Earthquake Engineering, Vol.8(4), pp.16–28, 2007.

[7] Parajuli HR, Kiyono J, Taniguchi H, Toki K, Furukawa A, Maskey PM: Parametric study and dynamic analysis of an historical masonry building of Kathmandu. Journal of Disaster Mitigation of Cultural Heritage and Historic Cities, Vol.4, pp.149–156, 2010.

[8] Parajuli HR, Kiyono J, Tatsumi M, Suzuki Y, Umemura H, Taniguchi H, Toki K, Furukawa A, Maskey PM: Dynamic characteristic investigation of an historical masonry building and surrounding ground in Kathmandu. Journal of Disaster Research, Vol.6(1), Dr6-1-4522, 2011.

[9] Furukawa A, Kiyono J, Taniguchi H, Toki K, Tatsumi M, Parajuli HR: Detailed modeling and seismic behavior analysis of existing historic masonry building in Patan District, Kathmandu Valley, Nepal, Journal of Disaster Mitigation of Cultural Heritage and Historic Cities, Vol.6, pp.53–60, 2012.

[10] Parajuli RR, Kiyono J: Ground motion characteristics of the 2015 Gorkha Earthquake, Survey of damage to stone masonry structures and structural field tests, Front Built Environ, Vol.1(23), 2015, http://dx.doi.org/10.3389/fbuil.2015.00023.

[11] Goda K, Kiyota T, Pokhrel RM, Chiaro G, Katagiri T, Sharma K, Wilkinson S: The 2015 Gorkha Nepal earthquake: Insights from earthquake damage survey. Front Built Environ, Vol.1(8), 2015, http://dx.doi.org/10.3389/fbuil.2015.00008.

[12] National Planning Commission: Government of Nepal, Post disaster needs assessment, Vol. A: Key findings, 2015.

[13] Google maps, https://www.google.co.jp/maps?hl=ja [Last accessed: June 1, 2017].

[14] CESMD (Combined Strong-Motion Data), Earthquakes recorded by station KATNP, http://www.strongmotioncenter.org/cgi-bin/CESMD/StaEvent.pl?stacode=NPKATNP [Last accessed: June 1, 2017].

EURODYN 2020
XI International Conference on Structural Dynamics
M. Papadrakakis, M. Fragiadakis, C. Papadimitriou (eds.)
Athens, Greece, 23–26 November 2020

DEMINING WAR SCENARIOS: A PROJECT BASED ON NEW TECHNOLOGIES

Federica Mezzani[1], Gianluca Pepe[1], Nicola Roveri[1], Antonio Carcaterra[1] and Stefano Solferini[1]

[1] Department of Mechanical and Aerospace Engineering, Sapienza, University of Rome
via Eudossiana 18, 00184, Rome, Italy
e-mail: {federica.mezzani, gianluca.pepe, nicola.roveri, antonio.carcaterra}@uniroma1.it, solferini.1659909@studenti.uniroma1.it

Keywords: Demining, Ground Penetrating Radar, Deep Learning, Convolutional Neural Network, Symbolic Data Analysis.

Abstract. *This work has the ambition generate an algorithm able to clearly identify buried antipersonnel mines from GPR data acquisitions. The algorithm is generated as a combination of a convolutional neural network (CNN) and a symbolic data analysis (SDA) process. The CNN is a powerful tool to automatically detect buried objects with even small metal content; the SDA reduces the probability of false positives, i.e. objects identified as mines, even though they are not and has the great advantage of not requiring a predefined dataset. Experimental campaign, conducted on real terrain, has proven the validity of the presented algorithm.*

1 INTRODUCTION

With more than 90 million mines spread in more than 10 countries all over the world, the demining problem is far to be solved. Despite the ban produced by the Ottawa Treaty in 1997, mines still contaminate several countries. The number of victims overcomes 6000 per year including children. More than human lives also the agricultural sector and the economic development of those countries are at stake. Public health costs, psychological effects as post-traumatic stress disorder and depression represent the major example of the produced social impact. Military forces and humanitarian volunteers devote their efforts to mine detection, and to demining. Trained animals, metal detectors and mechanical devices are the most employed strategies. However, they can be excessively time-consuming and expensive, and, as they might fail at detecting all the mines, they can be dangerous. Advanced sensors have been introduced as possible solutions to this problem, as Ground Penetrating Radar (GPR) [1], tomography [2, 3] and X-rays [4], in addition to the more conventional infrared [5], metal detector [6], acoustic waves [7, 8], ultrasounds [9, 10]. Among these technologies, the GPR has often been introduced in subsoil investigations, given its enhanced ability to discriminate even small metal fragments [11]; besides, its least invasiveness, safety and speed mark it as a rather perfect tool for mine clearance exploration and UXOs (unexploded ordnance) detection [12]. Despite the practical advantages, mine detection via GPR is often affected by clutter contamination due to antenna coupling, ground reflection, and other possibly hidden objects [13], which harm the easy implementation of an automatic detection procedure. The clutter phenomenon is here mainly related to the ground reflections: the magnitude of the ground reflections depending upon the surface roughness [14], the small metal content of antipersonnel mines and the modest depth of burial generate a signature of the target hardly discernible, unless clutter mitigation methods are introduced [15].

This work, based on GPR data acquisition, is part of a larger research project, named MINOR, MINe Overall Recognition, aimed at providing the exact real-time location of antipersonnel mines. It introduces a two-step strategy combining algorithms to accurately detect the presence of a mine and tell the difference between a mine and other hidden objects. Eventually, an experimental campaign has been carried out as first attempt to validate the strategy.

2 MINE DETECTION ALGRITHMS

An offline algorithm auto-generates data to train and tune a deep learning neural network able to select those windows identified by characteristic mine reflection signature; a second algorithm based on Symbolic Data Analysis (SDA) is employed to automatically cluster the data and classify the mines from other objects. A convolutional neural network is theoretically able by itself to appropriately cluster the signals in the radargrams; however, a high accuracy level can be achieved only through an extremely broad and various database. Such database can be considered reliable only if the elements of the dataset are produced by experimental acquisitions, implying a time consuming and costly experimental campaign. SDA, being an unsupervised process, does not require a pre-established database and represents one of the most powerful tools for the reduction of false positive detection, namely objects which are not mines but identified as if they were.

2.1 Numerical data generation

Convolutional neural networks (CNN) are regularized versions of multilayer perceptrons, namely a fully connected networks where each neuron in one layer is connected to all neurons

of the following layer. The "fully-connectedness" of these networks results in a data overfitting. A CNN takes advantage of the hierarchical patterns in data and assembles more complex patterns using smaller and simpler ones; a description of the aforementioned techniques is found in [16-19].

AlexNet is an already existing CNN trained on over a million of images, able to recognize 1000 different objects. The reason of employing an existing network stands in the large amount of time and data set needed to train from scratch a new CNN. AlexNet has an input layer and an output layer constituted of 1000 output neurons for the classification and 23 hidden layers that compute convolutional processes. The application of this CNN to this context considers a first training aimed at distinguishing possible targets from free areas, clean by any buried object; indeed, the CNN has been modified so that the last layer returns only two classification outputs. For this purpose, the network has been trained so to recognize the hyperbolic shape, typical of buried objects, inside a radargram. Hence, two kind of radargrams, shown in Figure 1, have been used: one “Target”, namely a hyperbola produced by defining a detailed model of the mine in terms of geometry, dimensions and density of the composing materials, and one “Free area”, which only contains the terrain interface signal. The aspect ratio of the images is such that the dimensions of the image are proportional to the spatial grid of the experimental radargram.

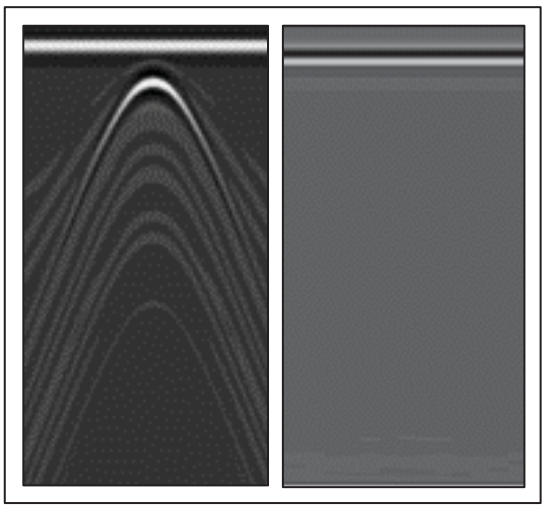

Figure 1: Simulated radargram frames for the neural network training: target on the left and free area on the right.

The training radargrams have been obtained using a Georadar simulation software, GprMax [20], a Finite-Difference Time-Domain software that emulates the propagation of an electromagnetic wave inside a medium. The medium is discretized in a grid of points and every point has assigned physical parameters of the medium (dielectric constant, magnetic permeability). The trend of the electromagnetic field is computed in time in correspondence of the grid points. A total of 2400 radargrams have been generated: 1200 with a target buried in various positions and depths, and 1200 without target, namely free area.

Once the convolutional neural network has been trained, it can be used on the radargrams referred to experimental data. The algorithm generates a window translating along the radargram; each selected frame is compared with the simulated radargram frames in Figure 1, and according to the level of match, the network returns the probability the selected portion of the radargram is actually a mine: low values of probability are related to “Free areas”, encircled in green, high values correspond to “Targets”, even though the possibility of false positive is not cancelled yet.

2.2 Symbolic Data Analysis (SDA)

Symbolic analysis belongs to the larger group of data mining techniques, and in particular of data clustering methods. In data clustering, related data are divided into homogeneous groups even with no a priori information about the groups' characteristics [21]. Clusters are generated by gathering in the same group objects with high level of similarity and separating in different groups those objects with the lowest similarity. This approach allows the identification of structures in an unlabelled dataset by organizing data into similar groups. The data can be presented as time-series or, equivalently in the space domain, as space-series. Space series, as well as time-series, are dynamic data, since each value varies with the space coordinate and time coordinate, respectively. By assuming each point of the space-series as an observation sequentially made, it is apparent how a space-series data is high dimensional.

The importance of clustering space-series datasets stands in: i) the chance to unveil the hidden information buried into space-series database; ii) space-series cluster structures are usually displayed as images; this simplifies the understanding of data clusters, the outliers and the structures.

The idea behind space-series clustering is rather straightforward [22]: in the present context of mine identification, assume D a space-series data, namely $D = \{h(x_1), \dots, h(x_s)\}$ is the set of depths at which a buried object is detected, corresponding to the set of space points $\{x_1, \dots, x_s\}$; consider a set of n space-series data $S = \{D_1, \dots, D_n\}$. Space-series clustering is an unsupervised process that redistributes the set S into a new set $G = \{G_1, \dots, G_p\}$, where similar space-series are assembled together into the *i-th* cluster G_i in respect to a suitable similarity measure. G_i is called cluster, and the original dataset S is the union of p- non overlapping clusters $S = \bigcup_{i=1}^{p} G_i$, being $G_i \cap G_k = 0 \; \forall i \neq k$.

There are several clustering algorithms [16,22], such as: hierarchical, partitioning clustering and multi-step clustering algorithm. in the present context, only hierarchical and partitioning clustering are be employed. Hierarchal clustering creates a hierarchy of clusters by adopting either agglomerative or divisive algorithms. The agglomerative algorithm, here used, considers each symbolic element of the data as a cluster and progressively combines the clusters; as a result, nested hierarchy of similar groups is created. A dendrogram, a tree-like diagram that records the sequences of merges [17], exhibits the generated groups. Despite the strong advantage of hierarchal clustering, which does not require any initial information regarding the number of clusters to be generated, this approach unveils limitations because of its quadratic computational complexity, preventing its application to large datasets. Besides, the accuracy of hierarchical algorithms is limited since they cannot adapt the clusters after merging in agglomerative method.

3 EXPERIMENTAL CAMPAIGN

The experimental campaign is devoted to the identification of objects buried in a field through the mean of a GPR sensor. The aim is the validation of the proposed algorithm. For this reason, mine prototypes have been used as well as metallic objects and other objects, to test the capability of the algorithm to find an object buried underground, and to classify the objects in two classes, namely mine and non-mine objects.

3.1 General description of the phases

Prior the GPR survey, few steps are required to prepare the terrain. At first, a metal detector has been used to check the presence of unwanted buried objects. The following decontamination ensures the GPR would acquire only the on-purpose hidden objects. The hidden objects,

targets of the GPR antenna, consists of three types of mine prototype, different in shape and dimensions, and two additional disturbances: a metal container and a brick. The targets have been set on a grid, as in Figure 2, which also shows the origin of the GPR data acquisition reference system and the axes along which data are collected. The dimensions of the grid are reported in Figure 3, together with the different depths at which the objects are buried so to estimate their influence on detection by GPR: h_1, h_2, h_3 range from 15 cm, up to 7 cm.

Figure 2: Experimental grid.

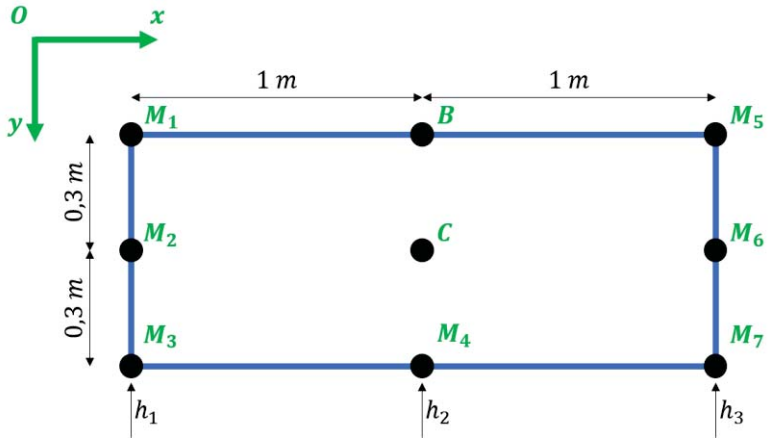

Figure 3: Grid dimensions.

The grid dimensions ensure a wide enough space for the GPR antenna to cross the area in between targets without detecting them. Accordingly, the resulting radargrams should be able to evidently display clear of targets regions and contaminated portions.

3.2 GPR Survey

After the terrain has been left at rest for few days to recreate a semi-undisturbed state, a GPR survey has started. A commercial 1.6-GHz GPR antenna, RIS MF Hi-Mod model, is used to acquire data over a clay mixed with topsoil terrain that simulates woods conditions.

Figure 4 and Figure 5 are examples of the obtained radargrams, related to the longitudinal acquisitions along the y-axis, displayed in Figure 2, of the objects buried at a depth h_1 and h_2, respectively. The green line represents the external boundary of the grid, where the origin of the reference system is set; each red line pinpoints the a priori known position of the targets and, for a resolute acquisition, should correspond to the position identified by the GPR. In

Figure 4, the three red lines correspond to the objects set at h_1 and, accordingly, denote the mines; it is worth to mention the simulated signature in Figure 1 well mimics the experimental ones. There is a clear difference, mainly due to the dimensions of the objects, between the first recorded signal, shown in Figure 4 corresponding to $Y = 0.2m$ and reerring to the largest mine in Figure 2, and the other two, which refer to mines of similar dimensions.

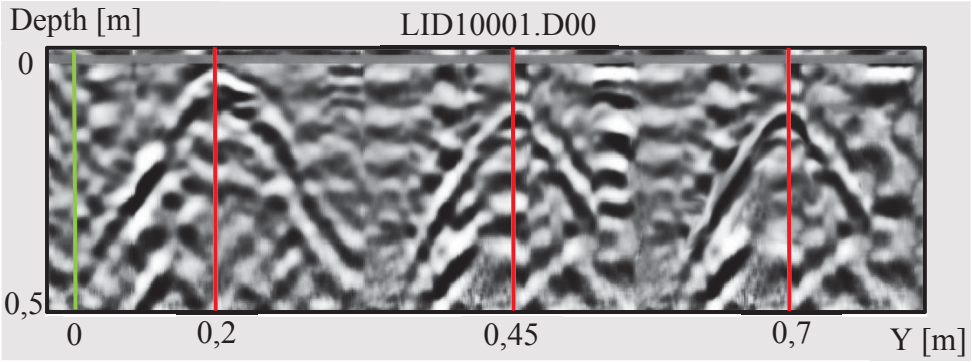

Figure 4: Radargram of the acquisition at $\boldsymbol{h_1}$.

The signatures in Figure 5 are related to the disturbance objects, except for the last one, which refers to the mine M_4 in Figure 3. The first signal is related to the brick and does not show an evident mark because of the type of material; the second identifies the metal can, and given the large amount of metal content, its hyperbola is the most clear one; eventually, the last hyperbola correspond to the mine M_4, and has a rather similar trend with respect to the last hyperbola in Figure 4, which indeed resembles the same type of mine.

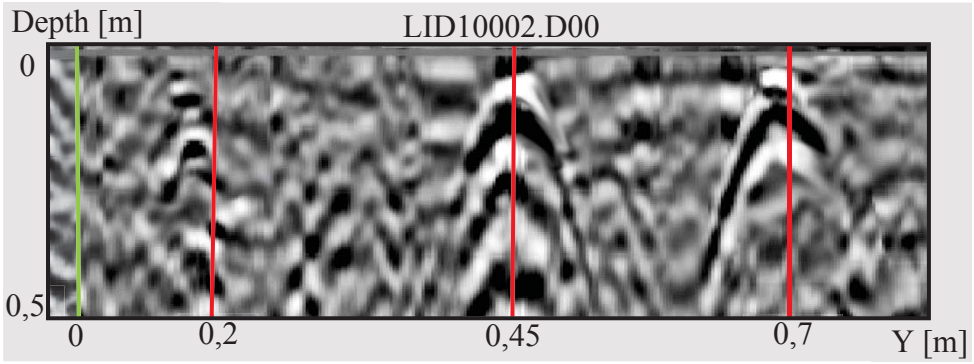

Figure 5: Radargram of the acquisition at $\boldsymbol{h_2}$.

Along the first direction of acquisition, the y axis mines are well detected and provide a rather clear hyperbola, probably due to the good compromise between the dimensions of the mines, the number of metallic pieces and the depth of burial; indeed, the higher the metal content, the clearer the signature, whilst the depth depends upon the frequency of the antenna. Despite the good quality of the acquisition, the signals still appear affected by clutter noise due to the ground reflections. Such a noisy acquisition, which shows a much worse scenario than the several examples present in literature [24,25], can be easily justified. A first reason is related to the terrain composition. Most of the performed experimental campaign have been conducted in different terrains, such as sandy soil; since the resolutions is highly affected by the level of moisture [25], it is apparent how a clayish terrain has less chances to complete dry out with respect to sandy soils, especially during winter days and morning day acquisitions. This

investigation is one of the rarest examples in which a 1.6 GHz antenna is employed in real terrain conditions and, even though the terrain is closer to more realistic situations, it inevitably produces a less defined radargrams with respect to sandy soil, which represents a quite considerable simplification. Eventually, this aspect compromises the neural network training, which should rely on a vast image dataset, hardly acquirable in these conditions. A second issue refers to the employed antenna. 1.6 GHz antenna does not provide an accuracy such that shallow buried objects can be distinctly identified. Indeed, it has high resolution for an, at least, 10 cm depth. This explains the reason why the radargram in Figure 4 is more readable that the one in Figure 5, related to shallow buried objects.

4 RESULTS AND DISCUSSION

The obtained experimental radargram have been used as input for the trained CNN, which should be able to cluster contaminated areas from free areas in a realistic scenario. CNN returns, indeed, the probability the detected object is a mine: the higher the value of the probability, the more likely the target is a mine, and free area should correspond to an almost zero probability. Figure 6 shows the real time application of the proposed algorithm, which is continuously applied to the radargram h_1 in Figure 4 by the use of a suitable sliding window. Starting from the first subplot, the first part of the radargram is framed in a window and processed by CNN, which returns a low probability, of about 34%, of finding a mine. When the window slides rightwards and its position corresponds to the mine position, the probability increases, up to a value of 88 % as in the second subplot; then, when the window progressively overcomes the mine, the probability decreases again.

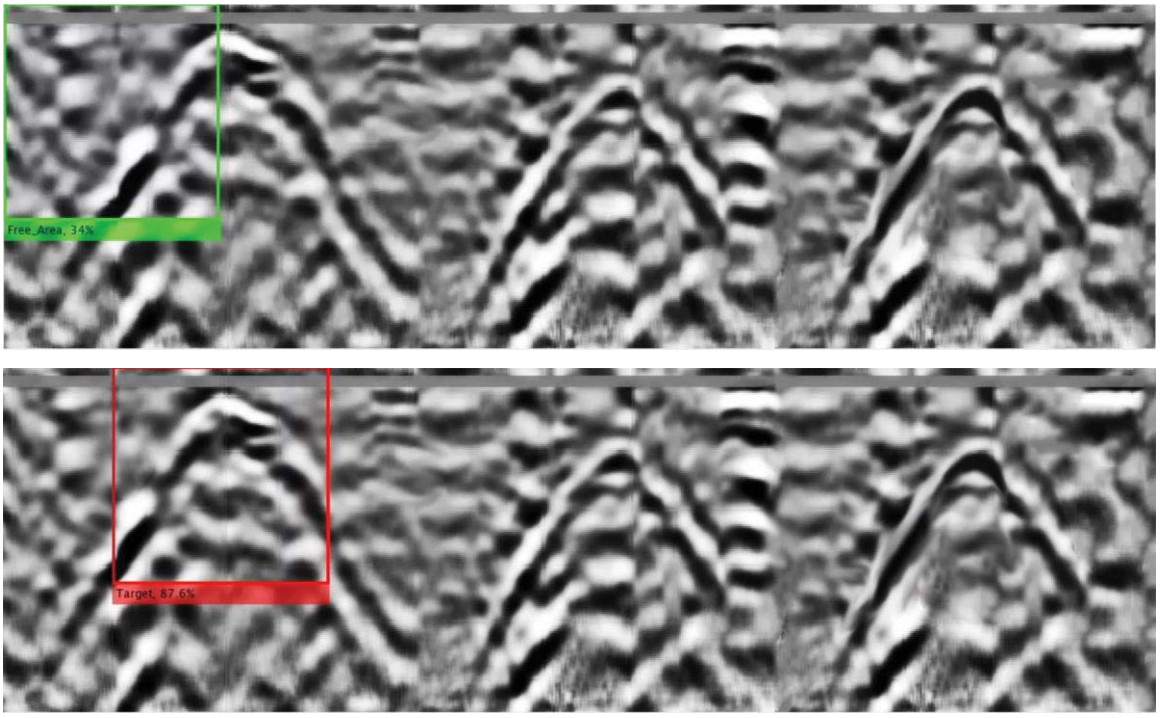

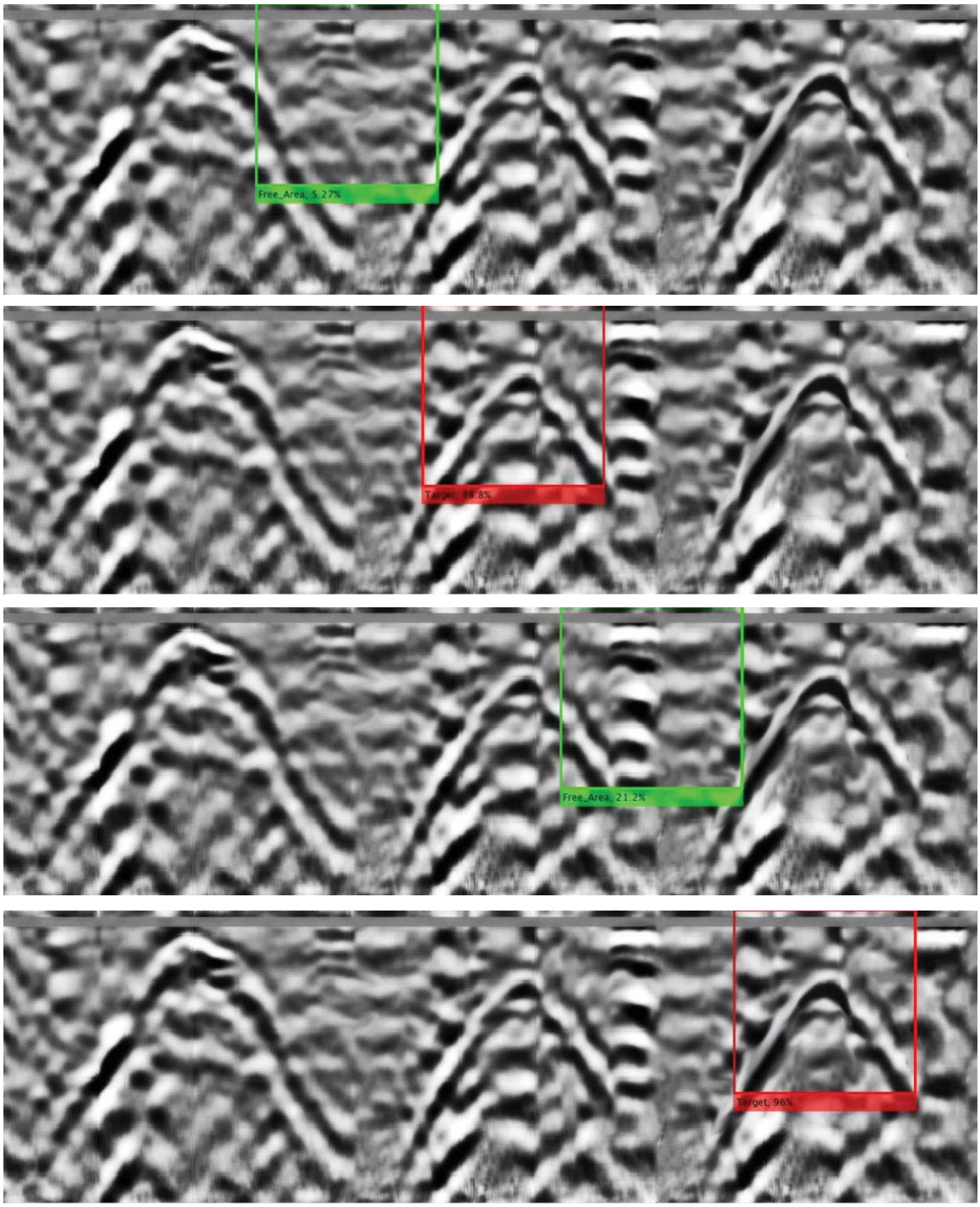

Figure 6: Target estimation of $\boldsymbol{h_1}$ radargram resulting from the neural network clustering.

Figure 7 shows the probability curve generated in output by CNN corresponding to the acquisition h_1 and confirms the reliability of the presented identification procedure.

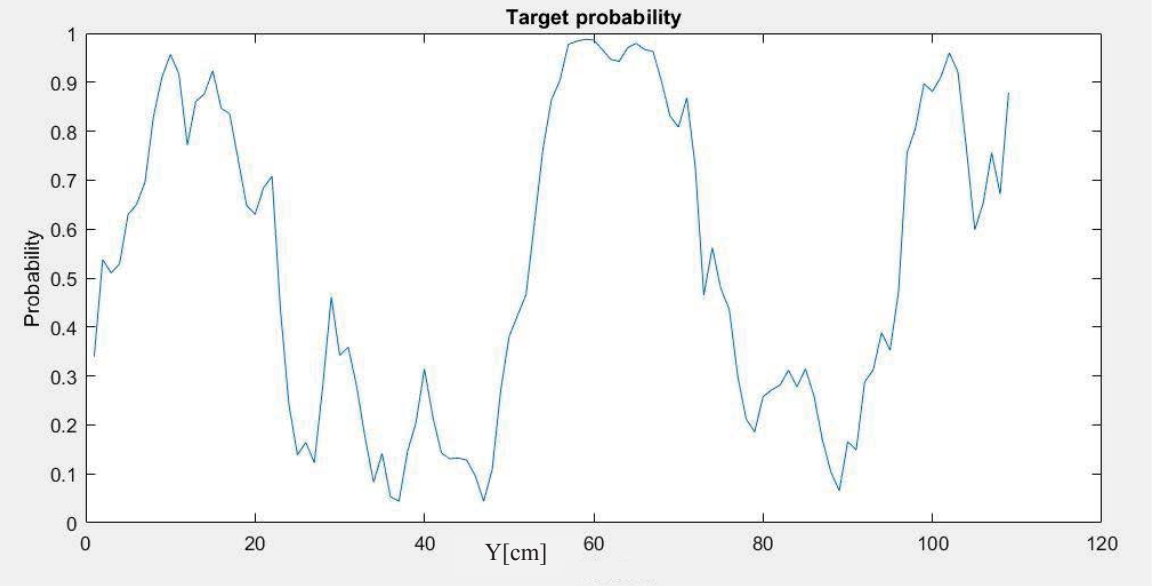

Figure 7: Probability trend corresponding to the $\boldsymbol{h_1}$ acquisition.

Figure 8, analogously to Figure 6, presents the result of the identification algorithm, regarding the acquisition at the depth h_2. Two main aspects are highlighted: i) as shown by the first subplot, the signal related to the brick is not associate to a target and the region is considered as "Free area", with a probability of mine detection of only 21%; ii) on the other hand, the can, given the large amount of metallic parts, is classified as mine, with an extremely high probability of more than 98%, as in the third subplot. This implies the identification algorithm is properly able to cluster "Free areas" and non-metallic objects; however, it is not sufficiently trained to distinguish, among metallic objects, those that are mines. For this purpose, the SDA algorithm must be introduced, even though it is still under test.

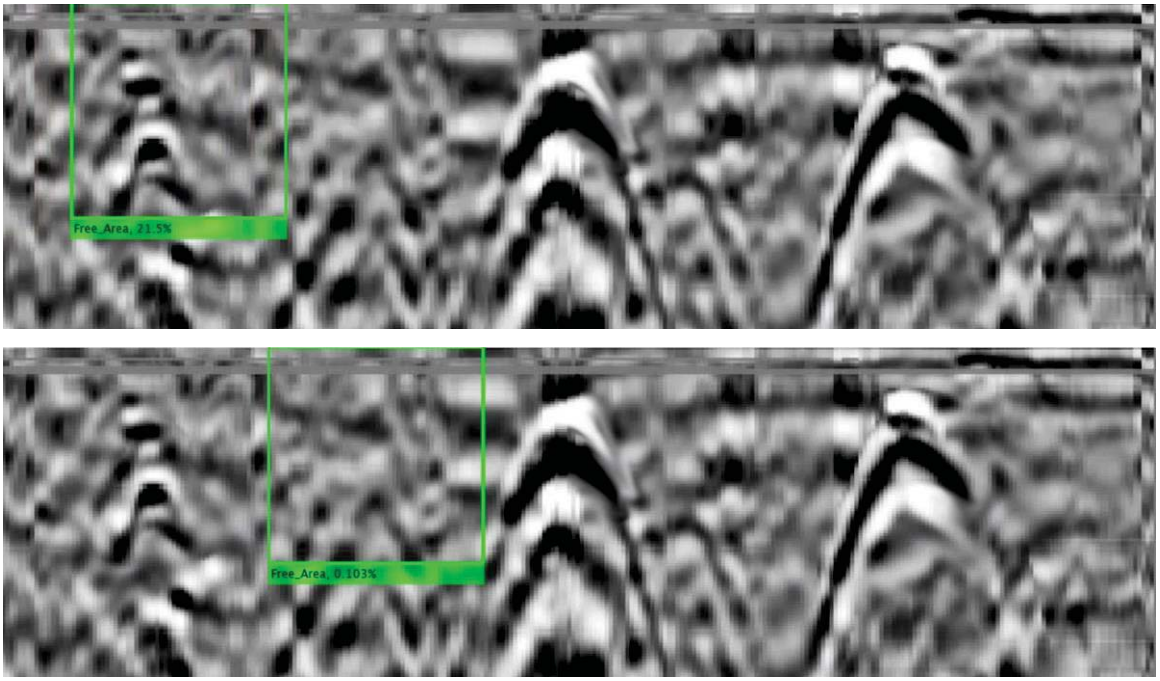

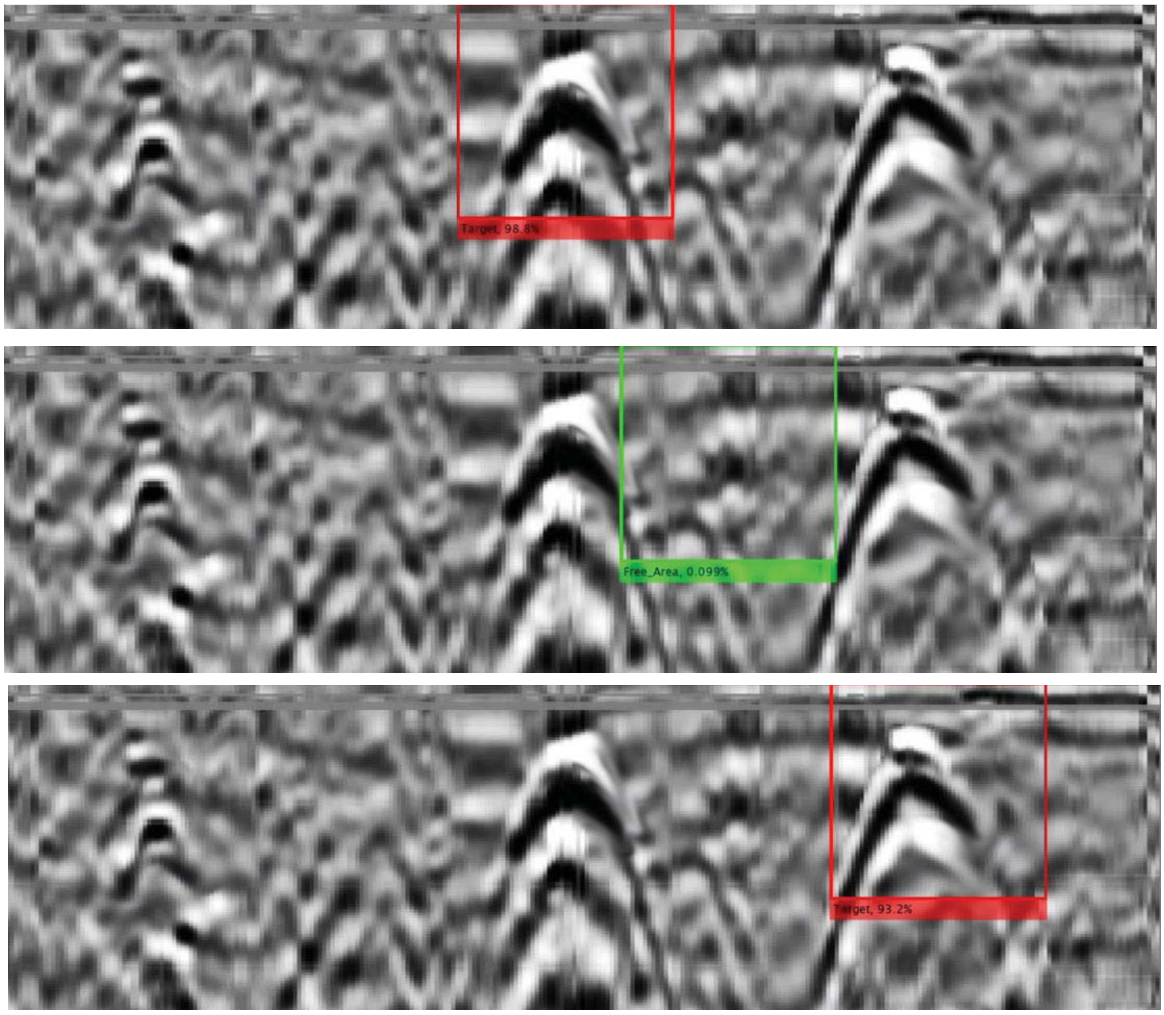

Figure 8: Target estimation of $\boldsymbol{h_2}$ radargram resulting from the neural network clustering.

5 CONCLUSIONS AND FUTURE PERSPECTIVES

The presented work has the ambition generate an algorithm able to clearly identify buried antipersonnel mines from GPR data acquisitions. The algorithm is generated as a combination of a convolutional neural network and a symbolic data analysis process. Despite the experimental measurements are affected by a high level of clutter noise, the two-step algorithm well distinguishes "Free areas" and non-metal objects from mine-like targets. The chance to reduce the probability of false positives, i.e. objects identified as mines, even though they are not, is handled through the SDA, which has the great advantage of not requiring a predefined dataset, but that is still under test.

Part of a larger research project, named MINOR, MINe Overall Recognition, aimed at providing the exact real-time location of antipersonnel mines, the algorithm has shown to be a powerful tool to automatically detect buried objects with even small metal content.

6 ACKNOWLEDGMENTS

The present project has been funded by the L'Oréal-UNESCO Foundation through the "For Women In Science" prize, 2019 edition.

REFERENCES

[1] O.L.L. Tellez, B. Scheers, Ground-Penetrating Radar for Close-in Mine Detection, *Mine Action: The Research Experience of the Royal Military Academy of Belgium*, 51, 2017.

[2] P. Church, J.E. McFee, S. Gagnon, P. Wort, Electrical impedance tomographic imaging of buried landmines, *IEEE Transactions on Geoscience and Remote Sensing*, **44**, 2407–2420, 2006.

[3] M. Metwaly, G. El-Quady, J. Matsushima, Szalai, S´andor, N.S.N. Al-Arifi, Contribution of 3-D electrical resistivity tomography for landmines detection, *Nonlinear Processes in Geophysics*, **15**, 977–986, 2008.

[4] G. Zentai, *X-ray imaging for homeland security, Proceedings of 2008 IEEE International Workshop on Imaging Systems and Techniques*, 2008.

[5] S. Kaya, U.M. Leloglu, Buried and surface mine detection from thermal image time series, *IEEE Journal of Selected Topics in Applied Earth Observations and Remote Sensing*, **10**, 4544–4552, 2017.

[6] K. Takahashi, H- Preetz, J. Igel, Soil properties and performance of landmine detection by metal detector and ground-penetrating radar—soil characterisation and its verification by a field test, *Journal of Applied Geophysics*, **73**, 368–377, 2011.

[7] M.S. Korman, J.M. Sabatier, Nonlinear acoustic techniques for landmine detection, *The Journal of the Acoustical Society of America*, **116**, 3354–3369, 2004.

[8] C. Mc Caffrey, N. Pesonen, I. Marttila, K. Nummila, Towards an Acousto-Ultrasonic Landmine Detector, 2014.

[9] J.S. Martin, D.J. Fenneman, F.T. Codron, P.H. Rogers, W.R Scott Jr, G. Larson, G.S. McCall II, Ultrasonic displacement sensor for the seismic detection of buried land mines, *Ultrasonic displacement sensor for the seismic detection of buried land mines*, **4742**, 606–616, 2002.

[10] A.G. Petculescu, J.M. Sabatier, Doppler ultrasound techniques for landmine detection, *Volume 5415: Detection and Remediation Technologies for Mines and Minelike Targets IX*, 2004.

[11] D.J. Daniels, P. Curtis, Minehound^{TM} trials in Cambodia, Bosnia, and Angola, *Proceedings of 2006 Defence and Security Simposium* 2006.

[12] P.D. Gader, M. Mystkowsky, Y. Zhao, Landmine detection with ground penetrating radar using hidden Markov models, *IEEE Transactions on Geoscience and Remote Sensing*, **36**, 1231–1244, 2001.

[13] V. Kovalenko, A.G. Yarovoy, L.P. Ligthart, A novel clutter suppression algorithm for landmine detection with GPR, *IEEE Transactions on Geoscience and Remote Sensing*, **45**, 3740–3751, 2007.

[14] O. Lopera, E.C. Slob, N. Milisavljevic, S. Lambot, Filtering Soil Surface and Antenna Effects From GPR Data to Enhance Landmine Detection, *IEEE Transactions on Geoscience and Remote Sensing,* **45**, 707–717, 2007.

[15] R. Solimene, A. Cuccaro, A. Dell'Aversano, I. Catapano, F. Soldovieri, Ground Clutter Removal in GPR Surveys, *IEEE Journal of Selected Topics in Applied Earth Observations and Remote Sensing*, **7**, 792–798, 2014.

[16] L. Kaufman, P.J. Rousseeuw, E. Corporation, *Finding groups in data: an introduction to cluster analysis*, 39, Wiley Online Library, Hoboken, 1990.

[17] J.J. Van Wijk, E.R. Van Selow, Cluster and calendar based visualization of time series data, *Proceedings of 1999 IEEE Symposium on Information Vision*, 1999.

[18] H. Sakoe, S. Chiba, Dynamic programming algorithm optimization for spoken word recognition, *IEEE Transactions on Acoustics, Speech and Signal Processing*, 26 (1), 43–49, 1978.

[19] A. Banerjee, J. Ghosh, Clickstream clustering using weighted longest common subsequences, *Proceedings of the Workshop on Web Mining, SIAM Conference on Data Mining* 2001.

[20] C. Warren, A. Giannopoulos, I. Giannakis, Gprmax: Open source software to simulate electromagnetic wave propagation for ground penetrating radar, *Computer Physics Communications*, **209**, 163 – 170, 2016.

[21] P. Rai, S. Singh, A survey of clustering techniques, *International Journal of Computer Applications*, 7 (12), 2010.

[22] H.H. Bock, E. Diday, Analysis of symbolic data, *Springer*, ISBN: 978-3-540-66619-6, 2001.

[23] X. Song, T. Liu, D. Xiang, Y. Su, GPR Antipersonnel Mine Detection Based on Tensor Robust Principal Analysis, *Remote Sensing*, **11**, 984, 2019.

[24] X. Núñez-Nieto, M. Solla, P. Gómez-Pérez, H. Lorenzo, GPR signal characterization for automated landmine and UXO detection based on machine learning techniques, *Remote sensing*, **6**, 9729–9748, 2015.

[25] T.W. Miller, B. Borchers, J.M.H. Hendrickx, S-H. Hong, L.W. Dekker, C.J. Ritsema, Effects of soil physical properties on GPR for landmine detection, *Proceedings of 2001 International Symposium on Technology and the Mine Problem* 2002.

EURODYN 2020
XI International Conference on Structural Dynamics
M. Papadrakakis, M. Fragiadakis, C. Papadimitriou (eds.)
Athens, Greece, 23–26 November 2020

LIE SYMMETRIES, OBSERVABILITY AND MODEL TRANSFORMATION OF NONLINEAR SYSTEMS WITH UNKNOWN INPUTS

X. Shi[1] **and M.N. Chatzis**[2]

[1]Ph.D. Candidate, Department of Engineering Science, University of Oxford, Oxford, UK
e-mail: xiaodong.shi@eng.ox.ac.uk

[2]Associate Professor, Department of Engineering Science, University of Oxford, Oxford, UK
e-mail: manolis.chatzis@eng.ox.ac.uk

Keywords: Nonlinear systems, System identification, Lie symmetries, Observability, Structural Health Monitoring.

Abstract. *This work investigates the use of Lie symmetries for assessing and improving the observability of dynamical systems under examined sensor setups. The framework of Lie symmetry is extended to account for unmeasured and hence unknown inputs. An efficient algorithm is developed to calculate the translation and scaling symmetries of nonlinear systems with unknown inputs. The use of the algorithm to assess the observability of a given nonlinear system is demonstrated, i.e. in theory whether it would be successful to identify the dynamic states, the parameters and the unknown inputs of the system from given measurements. The work further shows the potential application of the calculated symmetries for transforming the model of an unobservable system to an equivalent model with a minimum number of unobservable states and unknown inputs. The proposed method and algorithm are illustrated on the observability properties of a dynamical system with a Bouc-Wen nonlinearity.*

1 Introduction

During a system identification campaign, a priori observability analysis of a dynamical system [1, 2] is used to predict whether it is feasible to infer the state variables and parameters of the system from a given set of input-output measurements [3, 4, 5]. Recent developments of novel identification methods such as [6, 7, 8, 9] allow for estimating the unmeasured and hence unknown inputs of a system reliably as well as its state variables and parameters. To meet the demand of observability analysis when invoking such identification methods, the Observability Rank Condition (ORC) [3] was extended to alleviate the constraint that all inputs need to be measured [10, 11]. Recently the authors achieved efficient automated observability testing of large linear systems with unknown parameters [12], relaxing the significant computational constraints of the default implementations of the ORC.

It has been found in [4, 5, 13, 14] that the observability properties of a system are closely associated with the existence of Lie symmetries in the system. Symmetry was first introduced by Lie [15, 16] to define a way of variable transformations that leaves differential equations invariant. Sedoglavic [4, 5] used the concept of Lie symmetry for dynamical systems with fully known inputs and output measurements, and demonstrated the connections between symmetry and observability. The computational framework of Lie symmetry was explored in [4, 17, 18, 14], resulting in methods for the efficient calculations of certain types of Lie symmetries for a given system.

In this work, the concept of Lie symmetry and the corresponding computational framework are further used and extended for nonlinear systems with partially measured inputs, i.e. where some or potentially all of the inputs are unmeasured. The occurring method, and consequently algorithm, can be used as an alternative tool to assess the observability of such systems. Furthermore, the work illustrates that, relying on the results of symmetries, an unobservable dynamical model can be transformed to an equivalent model with a minimum number of unobservable states and unknown inputs. Such a model, either through the use of a minimal set of assumptions or through re-defining a new state vector of reduced length, can lead to a fully observable model. The proposed method of model transformation will potentially find useful applications in improving the observability and identifiability of dynamical systems under examined sensor setups. In the end of the paper, the proposed algorithm and the idea of model transformation are illustrated through a carefully chosen example.

2 Lie symmetries of nonlinear systems with unknown inputs

This work focuses on nonlinear systems with unknown inputs that can be generally written in the following state space representation:

$$\begin{aligned} \dot{\mathbf{x}} &= \mathbf{f}(\mathbf{x}, \mathbf{u}, \mathbf{w}) \\ \mathbf{y} &= \mathbf{h}(\mathbf{x}, \mathbf{u}, \mathbf{w}) \end{aligned} \tag{1}$$

where $\mathbf{x} = [x_1, x_2, ..., x_n]$ denotes the augmented state vector [1] containing both the dynamic states and the time-invariant parameters of the underlying system. $\mathbf{w} = [w_1, w_2, ..., w_m]$ denotes the unmeasured and hence unknown inputs, $\mathbf{u} \in \mathbb{R}^l$ the vector of measured inputs and $\mathbf{y} \in \mathbb{R}^p$ the vector of output measurements. Assume system (1) contains r groups of Lie symmetries. The $i^{th}(1 \leq i \leq r)$ group of Lie symmetries of system (1) is a one-parameter, $\epsilon_i \in \mathbb{R}$, group of transformations:

$$\begin{aligned} {}^i\boldsymbol{\phi}_{\mathbf{x}}(\mathbf{x}, \mathbf{w}, \epsilon_i) &= [{}^i\phi_{x,1}, {}^i\phi_{x,2}, ..., {}^i\phi_{x,n}] \\ {}^i\boldsymbol{\phi}_{\mathbf{w}}(\mathbf{x}, \mathbf{w}, \epsilon_i) &= [{}^i\phi_{w,1}, {}^i\phi_{w,2}, ..., {}^i\phi_{w,m}] \end{aligned} \tag{2}$$

where the $j^{th}(1 \leq j \leq n)$ component of ${}^i\boldsymbol{\phi}_{\mathbf{x}}$, i.e. ${}^i\phi_{x,j}$, is a Lie symmetry of the j^{th} component of $\mathbf{x}$, i.e. x_j, and it is an analytic funtion of $\mathbf{x}$, $\mathbf{w}$ and the real constant parameter ϵ_i. Similarly, ${}^i\phi_{w,j}(1 \leq j \leq m)$ is a Lie symmetry of w_j and it is also an analytic funtion of $\mathbf{x}$, $\mathbf{w}$ and ϵ_i. A fundamental property of Lie symmetries is that such group of transformations of $\mathbf{x}$ and $\mathbf{w}$ fulfills the equations of system (1) leaving the measured inputs and the output measurements unchanged, i.e.:

$$\begin{aligned} {}^i\dot{\boldsymbol{\phi}}_{\mathbf{x}} &= \mathbf{f}({}^i\boldsymbol{\phi}_{\mathbf{x}}, \mathbf{u}, {}^i\boldsymbol{\phi}_{\mathbf{w}}) \\ \mathbf{y} &= \mathbf{h}({}^i\boldsymbol{\phi}_{\mathbf{x}}, \mathbf{u}, {}^i\boldsymbol{\phi}_{\mathbf{w}}) \end{aligned} \tag{3}$$

where it should be noted that the functions $\mathbf{f}$ and $\mathbf{h}$ between equations (1) and (3) remain the same. Further based on Lie's First Fundamental Theorem [15, 16], the following differential equations hold with known initial conditions of ${}^i\boldsymbol{\phi}_{\mathbf{x}}$ and ${}^i\boldsymbol{\phi}_{\mathbf{w}}$:

$$\begin{aligned} \frac{\partial {}^i\boldsymbol{\phi}_{\mathbf{x}}}{\partial \epsilon_i} &= {}^i\boldsymbol{\xi}_{\mathbf{x}}({}^i\boldsymbol{\phi}_{\mathbf{x}}, {}^i\boldsymbol{\phi}_{\mathbf{w}}), \quad {}^i\boldsymbol{\phi}_{\mathbf{x}}(\mathbf{x}, \mathbf{w}, 0) = \mathbf{x} \\ \frac{\partial {}^i\boldsymbol{\phi}_{\mathbf{w}}}{\partial \epsilon_i} &= {}^i\boldsymbol{\xi}_{\mathbf{w}}({}^i\boldsymbol{\phi}_{\mathbf{x}}, {}^i\boldsymbol{\phi}_{\mathbf{w}}), \quad {}^i\boldsymbol{\phi}_{\mathbf{w}}(\mathbf{x}, \mathbf{w}, 0) = \mathbf{w} \end{aligned} \tag{4}$$

where ${}^i\boldsymbol{\xi}_{\mathbf{x}}$ and ${}^i\boldsymbol{\xi}_{\mathbf{w}}$ are analytic functions. $\frac{\partial {}^i\boldsymbol{\phi}_{\mathbf{x}}}{\partial \epsilon_i}\big|_{\epsilon_i=0} = {}^i\boldsymbol{\xi}_{\mathbf{x}}(\mathbf{x}, \mathbf{w})$ and $\frac{\partial {}^i\boldsymbol{\phi}_{\mathbf{w}}}{\partial \epsilon_i}\big|_{\epsilon_i=0} = {}^i\boldsymbol{\xi}_{\mathbf{w}}(\mathbf{x}, \mathbf{w})$ are called the infinitesimals of the Lie group of transformations.

3 Computations of translation and scaling Lie symmetries

In this section, the computational framework of Lie symmetries of system (1) is derived by extending the works in [18, 13] to account for the existence of the unmeasured inputs. The symmetry computation relies on setting up a system of differential equations whose solution provides the information of ${}^i\boldsymbol{\xi}_{\mathbf{x}}$ and ${}^i\boldsymbol{\xi}_{\mathbf{w}}$ appearing in equations (4). The first differential equation of the system is derived starting from the equation:

$$\frac{\partial(\frac{d^i\boldsymbol{\phi}_{\mathbf{x}}(\mathbf{x},\mathbf{w},\epsilon_i)}{dt})}{\partial \epsilon_i} = \frac{d(\frac{\partial^i\boldsymbol{\phi}_{\mathbf{x}}(\mathbf{x},\mathbf{w},\epsilon_i)}{\partial \epsilon_i})}{dt} \tag{5}$$

Equation (5) is proved to hold for all realizations of $\mathbf{x}$, $\mathbf{w}$ and ϵ_i in Appendix A. The second differential equation is derived based on the property that the measurements remain unchanged with respect to any realization of the value of ϵ_i, and therefore:

$$\frac{d\mathbf{y}}{d\epsilon_i} = \mathbf{0} \tag{6}$$

Applying the chain rule to equations (5) and (6) yields:

$$\begin{cases} \frac{\partial \mathbf{f}}{\partial {}^i\boldsymbol{\phi}_{\mathbf{x}}} {}^i\boldsymbol{\xi}_{\mathbf{x}} + \frac{\partial \mathbf{f}}{\partial {}^i\boldsymbol{\phi}_{\mathbf{w}}} {}^i\boldsymbol{\xi}_{\mathbf{w}} = \frac{\partial {}^i\boldsymbol{\xi}_{\mathbf{x}}}{\partial {}^i\boldsymbol{\phi}_{\mathbf{x}}}\mathbf{f} + \frac{\partial {}^i\boldsymbol{\xi}_{\mathbf{x}}}{\partial {}^i\boldsymbol{\phi}_{\mathbf{w}}}\frac{d^i\boldsymbol{\phi}_{\mathbf{w}}}{dt} \\ \frac{\partial \mathbf{h}}{\partial {}^i\boldsymbol{\phi}_{\mathbf{x}}} {}^i\boldsymbol{\xi}_{\mathbf{x}} + \frac{\partial \mathbf{h}}{\partial {}^i\boldsymbol{\phi}_{\mathbf{w}}} {}^i\boldsymbol{\xi}_{\mathbf{w}} = \mathbf{0} \end{cases} \tag{7}$$

where $\mathbf{f}$ and $\mathbf{h}$ correspond to the functions in (3). It is noted that equations (7) hold for any realization of ϵ_i including $\epsilon_i = 0$. Evaluating equations (7) at $\epsilon_i = 0$ leads to:

$$\begin{cases} \frac{\partial \mathbf{f}}{\partial \mathbf{x}} {}^i\boldsymbol{\xi}_{\mathbf{x}} + \frac{\partial \mathbf{f}}{\partial \mathbf{w}} {}^i\boldsymbol{\xi}_{\mathbf{w}} = \frac{\partial {}^i\boldsymbol{\xi}_{\mathbf{x}}}{\partial \mathbf{x}}\mathbf{f} + \frac{\partial {}^i\boldsymbol{\xi}_{\mathbf{x}}}{\partial \mathbf{w}}\frac{d\mathbf{w}}{dt} \\ \frac{\partial \mathbf{h}}{\partial \mathbf{x}} {}^i\boldsymbol{\xi}_{\mathbf{x}} + \frac{\partial \mathbf{h}}{\partial \mathbf{w}} {}^i\boldsymbol{\xi}_{\mathbf{w}} = \mathbf{0} \end{cases} \tag{8}$$

where $\mathbf{f}$ and $\mathbf{h}$ correspond to the functions in (1). Analytically solving the system of equations (8) yields ${}^{i}\boldsymbol{\xi}_{\mathbf{x}}(\mathbf{x},\mathbf{w})$ and ${}^{i}\boldsymbol{\xi}_{\mathbf{w}}(\mathbf{x},\mathbf{w})$, and the Lie's First Fundamental Theorem ensures ${}^{i}\boldsymbol{\xi}_{\mathbf{x}}(\mathbf{x},\mathbf{w})$ and ${}^{i}\boldsymbol{\xi}_{\mathbf{w}}(\mathbf{x},\mathbf{w})$ contain the essential information for characterizing ${}^{i}\boldsymbol{\xi}_{\mathbf{x}}({}^{i}\boldsymbol{\phi}_{\mathbf{x}},{}^{i}\boldsymbol{\phi}_{\mathbf{w}})$ and ${}^{i}\boldsymbol{\xi}_{\mathbf{w}}({}^{i}\boldsymbol{\phi}_{\mathbf{x}},{}^{i}\boldsymbol{\phi}_{\mathbf{w}})$. Subsequently solving equations (4) allow for obtaining the group of Lie symmetries ${}^{i}\boldsymbol{\phi}_{\mathbf{x}}$ and ${}^{i}\boldsymbol{\phi}_{\mathbf{w}}$.

In general, obtaining the analytical solution of the above system of differential equations is challenging if no assumptions are made for the symmetries [18]. However, if ${}^{i}\boldsymbol{\phi}_{\mathbf{x}}$ and ${}^{i}\boldsymbol{\phi}_{\mathbf{w}}$ are assumed to be certain types of symmetries, such as translations and scalings, the system of differential equations can be solved automatically and efficiently. Section 3.1 and 3.2 discuss in detail the efficient computations of one-parameter translation and scaling types of symmetries of system (1). It is further assumed in the following sections that all the symmetries occuring in the system are related to translation and scaling symmetries and their combinations. This simplifying assumption is often satisfied for a wide range of real world engineering systems. Other types of Lie transformations not studied in this work include affine, quadratic, Mobius and some more general higher-order polynomial symmetries investigated in [18, 14] for systems with fully measured inputs. Efficient computations of those types of symmetries are potentially also available for the system described in (1) and will be the focus of future extensions of this work.

3.1 Translation symmetries

If the i^{th} group of Lie symmetries are translation symmetries then:

$$\begin{aligned}
{}^{i}\phi_{x,1} &= x_1 + \alpha_{i,1}\epsilon_i \\
&\vdots \\
{}^{i}\phi_{x,n} &= x_n + \alpha_{i,n}\epsilon_i \\
{}^{i}\phi_{w,1} &= w_1 + \alpha_{i,n+1}\epsilon_i \\
&\vdots \\
{}^{i}\phi_{w,m} &= w_m + \alpha_{i,n+m}\epsilon_i
\end{aligned} \tag{9}$$

where $\alpha_{i,1},...,\alpha_{i,n+m}$ are constant coefficients to be determined. If the expressions of ${}^{i}\boldsymbol{\phi}_{\mathbf{x}}$ and ${}^{i}\boldsymbol{\phi}_{\mathbf{w}}$ from equations (9) are used in equations (7), consequently equations (8) are simplified to:

$$\begin{cases}
\begin{bmatrix} \frac{\partial f_1}{\partial x_1} & \cdots & \frac{\partial f_1}{\partial x_n} \\ \vdots & \ddots & \vdots \\ \frac{\partial f_n}{\partial x_1} & \cdots & \frac{\partial f_n}{\partial x_n} \end{bmatrix} \begin{bmatrix} \alpha_{i,1} \\ \vdots \\ \alpha_{i,n} \end{bmatrix} + \begin{bmatrix} \frac{\partial f_1}{\partial w_1} & \cdots & \frac{\partial f_1}{\partial w_m} \\ \vdots & \ddots & \vdots \\ \frac{\partial f_n}{\partial w_1} & \cdots & \frac{\partial f_n}{\partial w_m} \end{bmatrix} \begin{bmatrix} \alpha_{i,n+1} \\ \vdots \\ \alpha_{i,n+m} \end{bmatrix} = \mathbf{0} \\
\begin{bmatrix} \frac{\partial h_1}{\partial x_1} & \cdots & \frac{\partial h_1}{\partial x_n} \\ \vdots & \ddots & \vdots \\ \frac{\partial h_p}{\partial x_1} & \cdots & \frac{\partial h_p}{\partial x_n} \end{bmatrix} \begin{bmatrix} \alpha_{i,1} \\ \vdots \\ \alpha_{i,n} \end{bmatrix} + \begin{bmatrix} \frac{\partial h_1}{\partial w_1} & \cdots & \frac{\partial h_1}{\partial w_m} \\ \vdots & \ddots & \vdots \\ \frac{\partial h_p}{\partial w_1} & \cdots & \frac{\partial h_p}{\partial w_m} \end{bmatrix} \begin{bmatrix} \alpha_{i,n+1} \\ \vdots \\ \alpha_{i,n+m} \end{bmatrix} = \mathbf{0}
\end{cases} \tag{10}$$

3.2 Scaling symmetries

If the i^{th} group of Lie symmetries are scaling symmetries then:

$$\begin{aligned} {}^{i}\phi_{x,1} &= e^{\alpha_{i,1}\epsilon_i} x_1 \\ &\vdots \\ {}^{i}\phi_{x,n} &= e^{\alpha_{i,n}\epsilon_i} x_n \\ {}^{i}\phi_{w,1} &= e^{\alpha_{i,n+1}\epsilon_i} w_1 \\ &\vdots \\ {}^{i}\phi_{w,m} &= e^{\alpha_{i,n+m}\epsilon_i} w_m \end{aligned} \tag{11}$$

where $\alpha_{i,1}, ..., \alpha_{i,n+m}$ are constant coefficients to be determined. If the expressions of ${}^{i}\boldsymbol{\phi}_{\mathbf{x}}$ and ${}^{i}\boldsymbol{\phi}_{\mathbf{w}}$ from equations (11) are used in equations (7), consequently equations (8) are simplified to:

$$\begin{cases} \begin{bmatrix} \frac{\partial f_1}{\partial x_1} & \dots & \frac{\partial f_1}{\partial x_n} \\ \vdots & \ddots & \vdots \\ \frac{\partial f_n}{\partial x_1} & \dots & \frac{\partial f_n}{\partial x_n} \end{bmatrix} \begin{bmatrix} \alpha_{i,1} x_1 \\ \vdots \\ \alpha_{i,n} x_n \end{bmatrix} + \begin{bmatrix} \frac{\partial f_1}{\partial w_1} & \dots & \frac{\partial f_1}{\partial w_m} \\ \vdots & \ddots & \vdots \\ \frac{\partial f_n}{\partial w_1} & \dots & \frac{\partial f_n}{\partial w_m} \end{bmatrix} \begin{bmatrix} \alpha_{i,n+1} w_1 \\ \vdots \\ \alpha_{i,n+m} w_m \end{bmatrix} \\ - \begin{bmatrix} \alpha_{i,1} & \dots & 0 \\ \vdots & \ddots & \vdots \\ 0 & \dots & \alpha_{i,n} \end{bmatrix} \begin{bmatrix} f_1 \\ \vdots \\ f_n \end{bmatrix} = \mathbf{0} \\ \begin{bmatrix} \frac{\partial h_1}{\partial x_1} & \dots & \frac{\partial h_1}{\partial x_n} \\ \vdots & \ddots & \vdots \\ \frac{\partial h_p}{\partial x_1} & \dots & \frac{\partial h_p}{\partial x_n} \end{bmatrix} \begin{bmatrix} \alpha_{i,1} x_1 \\ \vdots \\ \alpha_{i,n} x_n \end{bmatrix} + \begin{bmatrix} \frac{\partial h_1}{\partial w_1} & \dots & \frac{\partial h_1}{\partial w_m} \\ \vdots & \ddots & \vdots \\ \frac{\partial h_p}{\partial w_1} & \dots & \frac{\partial h_p}{\partial w_m} \end{bmatrix} \begin{bmatrix} \alpha_{i,n+1} w_1 \\ \vdots \\ \alpha_{i,n+m} w_m \end{bmatrix} = \mathbf{0} \end{cases} \tag{12}$$

Both systems of equations (10) and (12) can be converted to a linear in the coefficients system:

$$\mathbf{M}\boldsymbol{\alpha}_i = \mathbf{0} \tag{13}$$

where $\boldsymbol{\alpha}_i = [\alpha_{i,1}, ..., \alpha_{i,n+m}]$ and $\mathbf{M}$ is a matrix of functions of $\mathbf{x}$, $\mathbf{w}$ and $\mathbf{u}$. $\mathbf{M}$ can be calculated symbolically by:

$$\mathbf{M} = \frac{\partial \mathbf{P}}{\partial \boldsymbol{\alpha}_i} \tag{14}$$

where $\mathbf{P}$ is a vector of the left hand side of equations (10) and (12) that can be commonly expressed in terms of equations (8):

$$\mathbf{P} = \begin{bmatrix} \frac{\partial \mathbf{f}}{\partial \mathbf{x}} {}^{i}\boldsymbol{\xi}_{\mathbf{x}} + \frac{\partial \mathbf{f}}{\partial \mathbf{w}} {}^{i}\boldsymbol{\xi}_{\mathbf{w}} - \frac{\partial {}^{i}\boldsymbol{\xi}_{\mathbf{x}}}{\partial \mathbf{x}} \mathbf{f} \\ \frac{\partial \mathbf{h}}{\partial \mathbf{x}} {}^{i}\boldsymbol{\xi}_{\mathbf{x}} + \frac{\partial \mathbf{h}}{\partial \mathbf{w}} {}^{i}\boldsymbol{\xi}_{\mathbf{w}} \end{bmatrix} \tag{15}$$

The vector of coefficients $\boldsymbol{\alpha}_i$ can then be determined by calculating the kernel of $\mathbf{M}$ symbolically, i.e. $\boldsymbol{\alpha}_i = ker(\mathbf{M})$ giving rise to different bases as groups of realizations of $\boldsymbol{\alpha}_i$. Each basis corresponds to a different parameter ϵ_i. An algorithm was presented in [18] to calculate $\boldsymbol{\alpha_i}$ efficiently for rational nonlinear systems by specializing symbolic variables in $\mathbf{M}$ to random values and performing computations over a finite field.

4 r-parameter group of Lie symmetries, observability and model transformation

4.1 Combination of translation and scaling symmetries

It is often the case that a dynamical system contains multiple one-parameter groups of Lie symmetries. Multiple translation and scaling symmetries of system (1) can be obtained by calculating the kernel of $\mathbf{M}$ for multiple solutions of bases with each basis corresponding to the coefficients of an independent group of translation or scaling symmetries. These obtained groups of translations and scalings can be treated separately, or alternatively they can be combined into a single multi-parameter group of Lie symmetries. The principle behind the way of combination is based on the property that Lie transformations of ${}^i\boldsymbol{\phi}_{\mathbf{x}}$ and ${}^i\boldsymbol{\phi}_{\mathbf{w}}$ are themselves Lie transformations of $\mathbf{x}$ and $\mathbf{w}$ that satisfy the equations of the original system [16]. Assume there exists r one-parameter groups of symmetries including r_t groups of translations and r_s groups of scalings. If one successively applies the translations and scalings in spite of their sequence to transform $\mathbf{x}$ and $\mathbf{w}$ iteratively, the result gives an r-parameter group of Lie symmtries of system (1).

Without loss of generality, it is assumed that all the translation symmetries are combined first. Let $\boldsymbol{\alpha}_1, ..., \boldsymbol{\alpha}_{r_t}$ be the coefficients of the translations, and the j^{th} component of the combination is given by:

$$x_j + \alpha_{1,j}\epsilon_1 + ... + \alpha_{r_t,j}\epsilon_{r_t} \tag{16}$$

Next all the scaling symmtries are combined. Let $\boldsymbol{\alpha}_{r_t+1}, ..., \boldsymbol{\alpha}_r$ be the coefficients of the scalings, and the j^{th} component of the combination is given by:

$$e^{\alpha_{r_t+1,j}\epsilon_{r_t+1}+...+\alpha_{r,j}\epsilon_r} x_j \tag{17}$$

Combining all the one-parameter groups of symmetries using equations (16) and (17) gives:

$$\phi_{x,j} = e^{\alpha_{r_t+1,j}\epsilon_{r_t+1}+...+\alpha_{r,j}\epsilon_r}(x_j + \alpha_{1,j}\epsilon_1 + ... + \alpha_{r_t,j}\epsilon_{r_t}) \tag{18}$$

where $\phi_{x,j}$ is the j^{th} component of $\boldsymbol{\phi}_{\mathbf{x}}$. $\boldsymbol{\phi}_{\mathbf{x}}(\mathbf{x}, \mathbf{w}, \boldsymbol{\epsilon})$ is used to denote the r-parameter group of Lie symmetries with $\boldsymbol{\epsilon} = [\epsilon_1, ..., \epsilon_r]$. $\boldsymbol{\phi}_{\mathbf{w}}(\mathbf{x}, \mathbf{w}, \boldsymbol{\epsilon})$ can be obtained in a similar fashion.

4.2 From Lie symmetries to observability

Same as their one-parameter sub-groups of Lie symmetries, $\boldsymbol{\phi}_{\mathbf{x}}$ and $\boldsymbol{\phi}_{\mathbf{w}}$ as the transformations of $\mathbf{x}$ and $\mathbf{w}$ satisfy the equations of system (1) leaving $\mathbf{u}$ and $\mathbf{y}$ unchanged, i.e.:

$$\begin{aligned} \dot{\boldsymbol{\phi}}_{\mathbf{x}} &= \mathbf{f}(\boldsymbol{\phi}_{\mathbf{x}}, \mathbf{u}, \boldsymbol{\phi}_{\mathbf{w}}) \\ \mathbf{y} &= \mathbf{h}(\boldsymbol{\phi}_{\mathbf{x}}, \mathbf{u}, \boldsymbol{\phi}_{\mathbf{w}}) \end{aligned} \tag{19}$$

This foundamental property builds the relationship between the r-parameter group of Lie symmetries and the observability of system (1). If $\phi_{x,j} \not\equiv x_j$, then x_j is unobservable given the measurements of $\mathbf{u}$ and $\mathbf{y}$. Similarly, if $\phi_{w,j} \not\equiv w_j$, then w_j is unobservable given the measurements of $\mathbf{u}$ and $\mathbf{y}$. On the contrary, if $[\boldsymbol{\phi}_{\mathbf{x}}, \boldsymbol{\phi}_{\mathbf{w}}] \equiv [\mathbf{x}, \mathbf{w}]$, then all the states and unmeasured inputs are observable resulting in a fully observable underlying system.

4.3 Model transformation

The model of an unobservable system can be transformed to an equivalent model with a minimum number of unobservable states and unmeasured inputs utilizing the results of Lie

symmetries. If system (1) was found to contain an r-parameter group of Lie symmetries, then at least a total of r states and unmeasured inputs are unobservable whose symmetries are functions of $\boldsymbol{\epsilon}$. There exist however a set of transformations of the states and unmeasured inputs, $\mathbf{x_T}$, with respect to which the system model can be re-written or transformed such that the transformed model contains up to $n+m-r$ observable states and unmeasured inputs and a minimum number of unobservable variables. In the case where all the unobservable variables could vanish, the model transformation would lead to a fully observable model.

To obtain $\mathbf{x_T}$ in the case of transforming an unobservable model to be observable, if possible, a transformation $\mathbf{S}$ is first sought by combining the components of $\boldsymbol{\phi}_\mathbf{x}$ and $\boldsymbol{\phi}_\mathbf{w}$, i.e. $\mathbf{S}(\boldsymbol{\phi}_\mathbf{x}, \boldsymbol{\phi}_\mathbf{w})$, where the goal is to eliminate all the parameters $\boldsymbol{\epsilon}$. $\mathbf{x_T}$ is then introduced to be identically equal to $\mathbf{S}(\boldsymbol{\phi}_\mathbf{x}, \boldsymbol{\phi}_\mathbf{w})$. This process will be demonstrated through the example where some added properties of this transformation allow for obtaining an observable reduced model.

5 Algorithm

An algorithm is presented as follows to summarize the procedure of computing translation and scaling symmetries of system (1). All the computations involved are symbolic, and the resulting multi-parameter group of Lie symmetries from the algorithm is a combination of all the translations and scalings computed using the methods described in Section 3.1, 3.2 and 4.1.

Algorithm I

Input: state-space and measurement equations of system (1)

Output: an r-parameter group of translation and scaling Lie symmetries

1. Compute $\frac{\partial \mathbf{f}}{\partial \mathbf{x}}$, $\frac{\partial \mathbf{f}}{\partial \mathbf{w}}$, $\frac{\partial \mathbf{h}}{\partial \mathbf{x}}$ and $\frac{\partial \mathbf{h}}{\partial \mathbf{w}}$
2. First compute the translation symmetries. Let ${}^1\boldsymbol{\alpha} = [\alpha_1, ..., \alpha_n]$ and ${}^2\boldsymbol{\alpha} = [\alpha_{n+1}, ..., \alpha_{n+m}]$. Compute $\mathbf{P_1} = \frac{\partial \mathbf{f}}{\partial \mathbf{x}}({}^1\boldsymbol{\alpha})^T + \frac{\partial \mathbf{f}}{\partial \mathbf{w}}({}^2\boldsymbol{\alpha})^T$ and $\mathbf{P_2} = \frac{\partial \mathbf{h}}{\partial \mathbf{x}}({}^1\boldsymbol{\alpha})^T + \frac{\partial \mathbf{h}}{\partial \mathbf{w}}({}^2\boldsymbol{\alpha})^T$
3. Let $\mathbf{P} = [\mathbf{P_1}^T, \mathbf{P_2}^T]^T$, and compute $\mathbf{M} = \frac{\partial \mathbf{P}}{\partial \boldsymbol{\alpha}}$
4. Compute $\boldsymbol{\alpha} = ker(\mathbf{M})$ and obtain r_t bases of $\boldsymbol{\alpha}$
5. Substitute the coefficients to equations (9) to obtain the translations $[{}^1\boldsymbol{\phi}_\mathbf{x}, {}^1\boldsymbol{\phi}_\mathbf{w}]$, ..., $[{}^{r_t}\boldsymbol{\phi}_\mathbf{x}, {}^{r_t}\boldsymbol{\phi}_\mathbf{w}]$
6. Now compute the scaling symmetries. Compute $\mathbf{P_1} = \frac{\partial \mathbf{f}}{\partial \mathbf{x}} diag(\mathbf{x})({}^1\boldsymbol{\alpha})^T + \frac{\partial \mathbf{f}}{\partial \mathbf{w}} diag(\mathbf{w})({}^2\boldsymbol{\alpha})^T - diag({}^1\boldsymbol{\alpha})\mathbf{f}$ and $\mathbf{P_2} = \frac{\partial \mathbf{h}}{\partial \mathbf{x}} diag(\mathbf{x})({}^1\boldsymbol{\alpha})^T + \frac{\partial \mathbf{h}}{\partial \mathbf{w}} diag(\mathbf{w})({}^2\boldsymbol{\alpha})^T$
7. Let $\mathbf{P} = [\mathbf{P_1}^T, \mathbf{P_2}^T]^T$, and compute $\mathbf{M} = \frac{\partial \mathbf{P}}{\partial \boldsymbol{\alpha}}$
8. Compute $\boldsymbol{\alpha} = ker(\mathbf{M})$ and obtain r_s bases of $\boldsymbol{\alpha}$
9. Substitute the coefficients to equations (11) to obtain the scalings $[{}^{r_t+1}\boldsymbol{\phi}_\mathbf{x}, {}^{r_t+1}\boldsymbol{\phi}_\mathbf{w}]$, ..., $[{}^{r}\boldsymbol{\phi}_\mathbf{x}, {}^{r}\boldsymbol{\phi}_\mathbf{w}]$
10. Combine $[{}^1\boldsymbol{\phi}_\mathbf{x}, {}^1\boldsymbol{\phi}_\mathbf{w}]$, ..., $[{}^{r}\boldsymbol{\phi}_\mathbf{x}, {}^{r}\boldsymbol{\phi}_\mathbf{w}]$ to obtain $\boldsymbol{\phi}_\mathbf{x}$ and $\boldsymbol{\phi}_\mathbf{w}$ following equations (16), (17) and (18)

6 Example: a 2 degrees of freedom (DOFs) mass-spring system with a Bouc-Wen element

Consider a 2 DOFs mass-spring system as showin in Figure 1. The displacements of the two masses m are denoted as x_1 and x_2 respectively, and the corresponding velocities are denoted as v_1 and v_2. k_1 and k_1 are the effective stiffness of the springs. The first spring is assumed to be a Bouc-Wen element with the elastic displacement r. The 2 DOFs system is driven by an unmeasured force $F(t)$ applied at the second mass. The state-space equations of the underlying

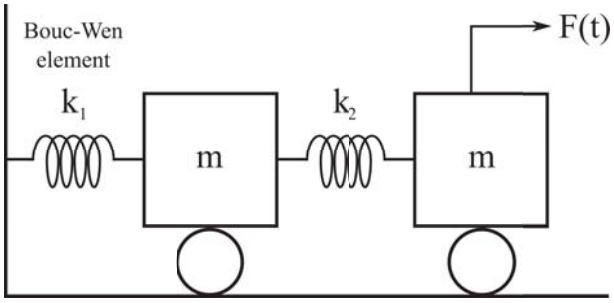

Figure 1: a 2 DOFs mass-spring system with a Bouc-Wen element

system are given by:

$$\frac{d}{dt}\begin{bmatrix} x_1 \\ x_2 \\ v_1 \\ v_2 \\ r \\ k_1 \\ k_2 \\ m \\ \beta \\ \gamma \end{bmatrix} = \begin{bmatrix} v_1 \\ v_2 \\ \big(-k_1 r + k_2(x_2 - x_1)\big)/m \\ \big(k_2(x_1 - x_2) + F\big)/m \\ v_1 - \beta|v_1||r|r - \gamma v_1|r|^2 \\ 0 \\ 0 \\ 0 \\ 0 \\ 0 \end{bmatrix} \tag{20}$$

where β and γ are the Bouc-Wen hysteretic parameters. The parameters k_1, k_2, m, β and γ are unknown and thus are to be identified given measurements. It should be noted that the exponent of the Bouc-Wen model is assumed to be known and equal to 2. This is not due to the limitations of the method suggested in this work which would allow for studying non-rational systems, but for presenting the results within a more concise way. The displacements x_1 and x_2 are measured, and therefore the measurement equations of the system are given by:

$$\mathbf{y} = \begin{bmatrix} x_1 \\ x_2 \end{bmatrix} \tag{21}$$

The proposed method in this work cannot be applied directly to the underlying system because the system is not smooth due to the existence of the absolute value operators. However, as discussed in [1], it can be divided into several smooth branches under different conditions of the states, and these smooth branches are then allowed to be examined separately. The function of $\dot{r}$ for each branch is formulated in the following while the equations of the other states remain the same.

$$\begin{aligned} A &: \dot{r} = v_1 - \beta v_1 r^2 - \gamma v_1 r^2, \quad when \quad v_1 > 0 \quad and \quad r > 0 \\ B &: \dot{r} = v_1 + \beta v_1 r^2 - \gamma v_1 r^2, \quad when \quad v_1 < 0 \quad and \quad r > 0 \\ C &: \dot{r} = v_1 + \beta v_1 r^2 - \gamma v_1 r^2, \quad when \quad v_1 > 0 \quad and \quad r < 0 \\ D &: \dot{r} = v_1 - \beta v_1 r^2 - \gamma v_1 r^2, \quad when \quad v_1 < 0 \quad and \quad r < 0 \end{aligned} \tag{22}$$

For the sake of brevity, only Lie symmetries of branch A are studied, while the detailed discussions on the observability properties of the complete non-smooth system can be referred

in the works [1, 11]. For branch A, Algorithm I gives a 2-parameter group of Lie symmetries that is a combination of a group of translations and a group of scalings:

$$[\boldsymbol{\phi}_{\mathbf{x}}, \boldsymbol{\phi}_{\mathbf{w}}] = [x_1, x_2, v_1, v_2, r, e^{\epsilon_1} k_1, e^{\epsilon_1} k_2, e^{\epsilon_1} m, \beta + \epsilon_2, \gamma - \epsilon_2, e^{\epsilon_1} F] \tag{23}$$

As can be seen from the results of symmetries, the symmetries of x_1, x_2, v_1, v_2 and r are identically equal to themselves, which indicates that those states are observable within branch A. On the contrary, the parameters k_1, k_2, m, β and γ are unidentifiable and the unmeasured excitation F is unobservable. The observability results suggested by the symmetries are in agreement with the results output from the observability algorithm ORC-DF [11].

In the following, a transformation $\mathbf{S}$ is determined for combining the resulting Lie symmetries so as to eliminate all ϵ_1 and ϵ_2:

$$\mathbf{S}(\boldsymbol{\phi}_{\mathbf{x}}, \boldsymbol{\phi}_{\mathbf{w}}) = \begin{bmatrix} x_1 \\ x_2 \\ v_1 \\ v_2 \\ r \\ \frac{e^{\epsilon_1} k_1}{e^{\epsilon_1} m} \\ \frac{e^{\epsilon_1} k_2}{e^{\epsilon_1} m} \\ \beta + \epsilon_2 + \gamma - \epsilon_2 \\ \frac{e^{\epsilon_1} F}{e^{\epsilon_1} m} \end{bmatrix}^T = \begin{bmatrix} x_1 \\ x_2 \\ v_1 \\ v_2 \\ r \\ \frac{k_1}{m} \\ \frac{k_2}{m} \\ \beta + \gamma \\ \frac{F}{m} \end{bmatrix}^T \tag{24}$$

A set of new variables, f_1, f_2, δ and F_m, are then introduced such that:

$$\mathbf{x_T} = \begin{bmatrix} x_1 \\ x_2 \\ v_1 \\ v_2 \\ r \\ f_1 \\ f_2 \\ \delta \\ F_m \end{bmatrix}^T \equiv \begin{bmatrix} x_1 \\ x_2 \\ v_1 \\ v_2 \\ r \\ \frac{k_1}{m} \\ \frac{k_2}{m} \\ \beta + \gamma \\ \frac{F}{m} \end{bmatrix}^T \tag{25}$$

and the model of branch A can be re-written with respect to $\mathbf{x_T}$ as follows:

$$\frac{d}{dt} \begin{bmatrix} x_1 \\ x_2 \\ v_1 \\ v_2 \\ r \\ f_1 \\ f_2 \\ \delta \end{bmatrix} = \begin{bmatrix} v_1 \\ v_2 \\ -f_1 r + f_2(x_2 - x_1) \\ f_2(x_1 - x_2) + F_m \\ v_1 - \delta v_1 r^2 \\ 0 \\ 0 \\ 0 \end{bmatrix} \tag{26}$$

Note in the transformed model (26), $f_1 = \frac{k_1}{m}$ and $f_2 = \frac{k_2}{m}$ are related to the natural frequencies of the system, δ is the new Bouc-Wen parameter and $F_m = \frac{F}{m}$ is a new unmeasured input to the system. Given the same measurements model (26) is observable with all its state variables and parameters as well as the unmeasured input observable, which can be verified by the observability algorithm ORC-DF.

7 Conclusions

This work derives the computational framework of Lie symmetries of nonlinear systems with unmeasured inputs, and proposes an efficient algorithm used to calculate the translation and scaling symmetries of such systems. The computed Lie symmetries find applications in predicting and improving the observability of dynamical systems under examined sensor setups. Furture works will be devoted to extending the algorithm to compute more general forms of Lie symmetries as well as to introducing a systematic methodology of model transformation. Other applications of Lie symmetries in improving models and identification results of engineering systems will be explored.

8 Appendix A: a proof of equation (5)

Applying the chain rule to the left hand side of equation (5), one obtains:

$$\frac{\partial(\frac{d^i\boldsymbol{\phi}_{\mathbf{x}}(\mathbf{x},\mathbf{w},\epsilon_i)}{dt})}{\partial\epsilon_i} = \frac{\partial(\frac{\partial^i\boldsymbol{\phi}_{\mathbf{x}}}{\partial\mathbf{x}}\frac{d\mathbf{x}}{dt} + \frac{\partial^i\boldsymbol{\phi}_{\mathbf{x}}}{\partial\mathbf{w}}\frac{d\mathbf{w}}{dt})}{\partial\epsilon_i} \tag{27}$$

Using the product rule equation (27) is equivalent to:

$$\frac{\partial(\frac{d^i\boldsymbol{\phi}_{\mathbf{x}}(\mathbf{x},\mathbf{w},\epsilon_i)}{dt})}{\partial\epsilon_i} = \frac{\partial^{2i}\boldsymbol{\phi}_{\mathbf{x}}}{\partial\mathbf{x}\partial\epsilon_i}\frac{d\mathbf{x}}{dt} + \frac{\partial^i\boldsymbol{\phi}_{\mathbf{x}}}{\partial\mathbf{x}}\frac{\partial(\frac{d\mathbf{x}}{dt})}{\partial\epsilon_i} + \frac{\partial^{2i}\boldsymbol{\phi}_{\mathbf{x}}}{\partial\mathbf{w}\partial\epsilon_i}\frac{d\mathbf{w}}{dt} + \frac{\partial^i\boldsymbol{\phi}_{\mathbf{x}}}{\partial\mathbf{w}}\frac{\partial(\frac{d\mathbf{w}}{dt})}{\partial\epsilon_i} \tag{28}$$

Since $\dot{\mathbf{x}}$ and $\dot{\mathbf{w}}$ are independent of ϵ_i, $\frac{\partial(\frac{d\mathbf{x}}{dt})}{\partial\epsilon_i}$ and $\frac{\partial(\frac{d\mathbf{w}}{dt})}{\partial\epsilon_i}$ vanish and equation (28) simplifies to:

$$\frac{\partial(\frac{d^i\boldsymbol{\phi}_{\mathbf{x}}(\mathbf{x},\mathbf{w},\epsilon_i)}{dt})}{\partial\epsilon_i} = \frac{\partial^{2i}\boldsymbol{\phi}_{\mathbf{x}}}{\partial\mathbf{x}\partial\epsilon_i}\frac{d\mathbf{x}}{dt} + \frac{\partial^{2i}\boldsymbol{\phi}_{\mathbf{x}}}{\partial\mathbf{w}\partial\epsilon_i}\frac{d\mathbf{w}}{dt} \tag{29}$$

Similarly applying the chain rule to the right hand side of equation (5), one obtains:

$$\frac{d(\frac{\partial^i\boldsymbol{\phi}_{\mathbf{x}}(\mathbf{x},\mathbf{w},\epsilon_i)}{\partial\epsilon_i})}{dt} = \frac{\partial(\frac{\partial^i\boldsymbol{\phi}_{\mathbf{x}}}{\partial\epsilon_i})}{\partial\mathbf{x}}\frac{d\mathbf{x}}{dt} + \frac{\partial(\frac{\partial^i\boldsymbol{\phi}_{\mathbf{x}}}{\partial\epsilon_i})}{\partial\mathbf{w}}\frac{d\mathbf{w}}{dt} \tag{30}$$

Equation (30) simplifies to:

$$\frac{d(\frac{\partial^i\boldsymbol{\phi}_{\mathbf{x}}(\mathbf{x},\mathbf{w},\epsilon_i)}{\partial\epsilon_i})}{dt} = \frac{\partial^{2i}\boldsymbol{\phi}_{\mathbf{x}}}{\partial\epsilon_i\partial\mathbf{x}}\frac{d\mathbf{x}}{dt} + \frac{\partial^{2i}\boldsymbol{\phi}_{\mathbf{x}}}{\partial\epsilon_i\partial\mathbf{w}}\frac{d\mathbf{w}}{dt} \tag{31}$$

Comparing equations (29) and (31), the left and right hand sides of equation (5) coincide and therefore equation (5) is proved to hold.

REFERENCES

[1] M.N. Chatzis, E.N. Chatzi and A.W. Smyth, On the observability and identifiability of nonlinear structural and mechanical systems, *Structural Control and Health Monitoring*, **22**, 574-593, 2015.

[2] L.S. Katafygiotis and J.L. Beck, Updating Models and Their Uncertainties. II: Model Identifiability, *Journal of Engineering Mechanics*, **124(4)**, 463-467, 1998.

[3] R. Hermann and A.J. Krener, Nonlinear Controllability and Observability, *IEEE Transactions on Automatic Control*, **22(5)**, 728-740, 1977.

[4] A. Sedoglavic, A Probabilistic Algorithm to Test Local Algebraic Observability in Polynomial Time, *Journal of Symbolic Computation*, **33(5)**, 735-755, 2002.

[5] M. Anguelova, Observability and identifiability of nonlinear systems with applications in biology, PhD thesis, Chalmers University of Technology and Goteborg University, 2007.

[6] S. Gillijns and B. De Moor, Unbiased minimum-variance input and state estimation for linear discrete-time systems, *Automatica*, **43(1)**, 111-116, 2007.

[7] E. Lourens, E. Reynders, G. De Roeck, G. Degrande and G. Lomaert, An augmented Kalman filter for force identification in structural dynamics, *Mechanical Systems and Signal Processing*, **27**, 446-460, 2012.

[8] S.E. Azam, E.N. Chatzi and C. Papadimitriou, A dual Kalman filter approach for state estimation via output-only acceleration measurements, *Mechanical Systems and Signal Processing*, **60-61**, 866-886, 2015.

[9] K. Maes, F. Karlsson and G. Lombaert, Tracking of inputs, states and parameters of linear structural dynamic systems, *Mechanical Systems and Signal Processing*, **130**, 755-775, 2019.

[10] A. Martinelli, Nonlinear Unknown Input Observability: Extension of the Observability Rank Condition, *IEEE Transactions on Automatic Control*, **64(1)**, 222-237, 2019.

[11] K. Maes, M.N. Chatzis and G. Lombaert, Observability of nonlinear systems with unmeasured inputs, *Mechanical Systems and Signal Processing*, **130**, 378-394, 2019.

[12] X.Shi, M.N. Chatzis and M.S. Williams. Robust computation of the observability of large linear systems with unknown parameters, *Proceedings of the Sixth International Symposium on Life-Cycle Civil Engineering (IALCCE), Ghent, Belgium*, 2018

[13] M. Anguelova, J. Karlsson and M. Jirstrand, Minimal output sets for identifiability, *Mathematical Biosciences*, **239**, 139-153, 2012.

[14] B. Merkt, J. Timmer and D. Kaschek, High-order Lie symmetries in identifiability and predictability analysis of dynamic models, *Physical Review E*, **92**, 2015.

[15] B.J. Cantwell, Introduction to Symmetry Analysis, *Cambridge University Press*, Cambridge, UK, 2002.

[16] F. Oliveri, Lie Symmetries of Differential Equations: Classical Results and Recent Contributions, *Symmetry*, **2**, 658-706, 2010.

[17] E. Hubert and A. Sedoglavic, Polynomial Time Nondimensionalisation of Ordinary Differential Equations via Their Lie Point Symmetries, HAL archive, 2006.

[18] A. Urguplu, Contributions to Symbolic Effective Qualitative Analysis of Dynamical Systems; Application to Biochemical Reaction Networks, PhD thesis, University of Lille, 2010.

EURODYN 2020
XI International Conference on Structural Dynamics
M. Papadrakakis, M. Fragiadakis, C. Papadimitriou (eds.)
Athens, Greece, 23–26 November 2020

VIBRATION TESTING BASED ON EVOLUTIONARY OPTIMIZATION TO IDENTIFY STRUCTURAL FAILURES AND DAMAGE IN GLULAM COMPONENTS

Juan Peña-Lasso[1], Rebeca Sanchez-Ruiz[2], Alvaro Gaute[2], Ignacio Lombillo[2], Ramon Sancibrian[2], Oscar R. Ramos[2]

[1] WSP, Department of Bridges. PCTCAN. Avda. Albert Einstein, 39011 Santander, Spain
e-mail: jupena@louisberguer.com

[2] Department of Structural and Mechanical Engineering, University of Cantabria, Avda. de los Castros s/n, 39005 Santander, Spain
{rebeca.sanchez, alvaro.gaute, ignacio.lombillo, sancibrr, oscar.ramos}@unican.es

Keywords: Damage detection, Structural health, Evolutionary algorithm, Glulam, Optimization.

Abstract. Damage Detection and Structural Health Monitoring use different techniques to diagnose the threat of failure in structures. Vibration-based approaches have demonstrated to be a useful tools in testing and monitoring structures. They use the intrinsic correlation between structural damage and vibration response. Thus, the information provided by vibration sensors defines the health status of the structure allowing to identify the potential cause of failure. Model tuning or updating based methods use an ideal theoretical model (FEM) of the structure and try to minimize the difference with respect to the real system. This difference provides not only a measure of location of the damage but also the intensity. Model updating is performed by means of Evolutionary Algorithms (EA) and other techniques. In this work, Differential Evolution (DE) is used to solve the residual optimization. DE algorithms are the most popular technique within Evolutionary Algorithms. This technique uses an adaptive probabilistic method to mimic the Darwinian evolution in order to find the optimal numerical values of the design variables. This approach uses natural selection, random mutations and crossover to change the values of the variables defining the solution toward the optimal solution. The main goal of the paper is focused on the detection of failures in Glued Laminated Timber (Glulam). To this end, both theoretical and experimental vibrational data are measured and used to perform model updating.

1 INTRODUCTION

The origin of glued laminated timber (Glulam) as a structural element is not new, however, in recent years the use of this material in constructions has experienced a huge increase. Since the 1970s, the evolution of new manufacturing techniques for this material have allowed the construction of curved beams and improved the quality of their performances. Furthermore, due to the capacity to produce large beams Glulam can be used for modern high-volume buildings. Nowadays the manufacturing techniques allow the manufacturing of beams for large spaces, greater than 100 meters, and adopt varied shapes making this material a valuable element in structural applications but also of great aesthetic value. Indeed, Glulam is particularly suitable in situations where a pleasant aesthetic appearance is required, which gives it a very important advantage over other materials commonly used in construction. There are many applications in large spaces such as the construction of auditoriums, sport centers, religious spaces, shopping centers, airports, walkways, etc., which frequently use this material due to the aforementioned properties.

However, it is necessary to highlight an aspect of this material that makes its potential even greater in the future. It is an obvious fact that an ecological and sustainable construction is a growing trend and these facts have an important future in the industrial and economic development of the countries. The use of environmentally responsible and sustainable materials is a fundamental part of this process. The use of wooden structures in construction is one of the best ways to achieve an environmentally friendly activity, since wood is one of the most sustainable resources provided by nature.

Obviously, compared to other traditional materials used in construction the main disadvantage of Glulam is that its mechanical and resistant properties are lower. In addition, a non-homogeneous and anisotropic material, making difficult its numerical modelling and analysis. The safety of wooden structures is controlled and the quality of the wood used and its manufacturing process is certified by means of standards. Technical Building Codes [1] consider timber as a structural material and allows the determination of limit states based on mechanical properties. It is true that these procedures are focused primarily on solid timber and not on Glulam, and fundamentally with laboratory tests in the pre-execution phase [2]. This information allows to know the behavior of the material in a reliable way and to guarantee the safety of the Glulam structures in their calculation and numerical simulation [3]. However, as an organic material, it is exposed to multiple factors that can cause its deterioration and reduce its structural capacity [4].

On the other hand, the analysis of the current situation reveals that there are no general and sufficiently proven techniques for the in-situ structural evaluation of this type of structures [5]–[7]. In fact, until recently the diagnosis of the structural state of this type of construction has been carried out almost exclusively by visual inspections, measurement of humidity and surface density or hardness [8], [9]. The lack of methods for inspection and diagnosis applied over large areas of the structural elements makes necessary the research of the behavior of this material [5]. Despite the preventive treatments to which Glulam is summited, it is exposed to numerous degradation processes that do not have other traditional materials in construction. The causes that could deteriorate the material are abiotic origin (e.g. water, solar radiation, etc.), biotic (e.g. xylophagus fungi, insects, etc.) and mechanical (e.g. wood singularities, deformations, breaks, mechanical overloads, etc,). Due to these peculiarities, the Non-Destructive Testing (NDT) techniques used in other materials cannot be used directly in Glulam, since the possible defects due to the deterioration of the material have particular and generally different characteristics and properties.

In both solid timber and Glulam, these inspection techniques remain an important field of research today[8], [10]. In the case of solid timber, there is a large literature where NDTs and semi-destructive tests (SDT) are investigated [10]–[12]. In the case of laminated wood, the problem is still greater, since there is very little work on this type of test. The problem is accentuated if it is considered that the responsibility of laminated wood structures is greater than those built with solid timber, since these structures are usually of a larger size, which also entails a greater risk and responsibility

As it has been reflected in numerous publications, the dynamic response of the structures provides a rich source of information on the mechanical properties of the structural elements and the defects or degree of deterioration [13]–[16]. Indeed, the vibrational response of a structural component to dynamic excitation depends on its intrinsic characteristics and boundary conditions. In the literature, approaches based on modal analysis have been highlighted above other NDT due to several characteristics that make them very attractive in defining the health status and identifying possible causes of failure. The so-called adjustment by updating EF models uses an intact theoretical model of the system or structural component as a reference[14], [16]–[18]. That is, it takes as reference the theoretical model of finite elements called healthy state. Through experimental measurements on the real system, these tests are compared with the theoretical model. In this way, it is about finding out what modifications have to be made in the theoretical (healthy) model so that the experimental and theoretical response become the same. Modifications in the theoretical model provide information about the defects of the structure under test.

2 MATHEMATICAL BACKGROUND

In this work, modal properties are used for updating finite element model. To this end, modal properties and methods are described in this section. The base of the method is that modal properties are related to the mechanical properties of the structural element. Dynamic behavior of the structures can be described in terms of their distributed stiffness, damping and mass properties. Thus, the modal properties can be related with mass and stiffness matrices. FRF function may be expressed as the summation of the different contribution of each mode. That is,

$$H_{mn}(\omega j) = \sum_{i=1}^{N} \frac{-\omega^2 \varphi_m^i \varphi_n^i}{-\omega^2 + 2\xi_i \omega_i \omega j + \omega_i^2} \tag{1}$$

This equation provides the FRF due to the excitation in position *m* and the response at position *n*. *N* is the number of the mode, ω_i, ξ_i are the i^{th} natural frequency and damping ratio, respectively. The variation of the frequency is considered by means of the parameter ω. The modal properties of the structure depend on the stiffness and mass matrices, therefore, the measured modal parameters can be provided by the finite element model if the correct stiffness and mass are obtained. Thus, the model updating process need to identify the correct dynamic matrices from the measured data. Therefore, it is possible to obtain the correct Young's modulus at different sections of the structural element. The variation of the Young's modulus is related with the presence of defect in the structures. Consequently, the determination of the variation of this modulus in different sections of the structure may help us to find out where a deterioration is produced. In this work, the determination of the correct Young's Modulus is obtained by the following residual function.

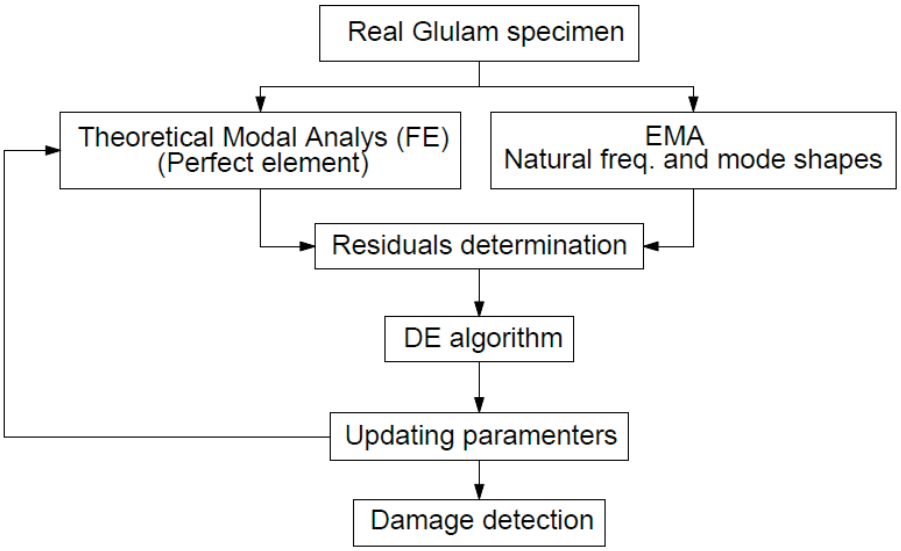

Figure 1: Flowchart of the updating methodology using the Differential Evolution algorithm.

$$\Pi = \sum_{i=1}^{N} \upsilon_i \left(\frac{\omega_i^e - \omega_i^t}{\omega_i^e}\right) + \sum_{i=1}^{N} \tau_i \left[1 - MAC_i\left(\varphi_m^i, \varphi_n^i\right)\right] \quad (2)$$

where the parameter e is for measured and t for theoretical (or calculated). Parameters ν_i and τ_i are the weighting parameters that measures the relative contribution of modes and natural frequencies. The MAC is the Modal Assurance Criterion, which achieves the value of 1 when the evaluated modes are equal and zero when they are completely different. Thus, the first part of Eq.(2) ensures that the natural frequencies obtained by the finite element model are close to those measures experimentally. The second part of this equation measures the correlation between both, theoretical and experimental modes. In this way, by comparing the results the updating method evaluates the changes in the model allowing the evolutionary algorithm to predict the values of the stiffness in each section of the structural element. Thus, the goal of the algorithm is to minimize the Eq.(2). Fig. 1 shows the general procedure where the DE algorithm is included. The basics of this algorithm is described in the following section.

3 DIFFERENTIAL EVOLUTION ALGORITHM

The denomination Evolutionary Algorithms refers to several algorithms that mimic the natural phenomena to optimize a goal function [19], [20]. In this work, Differential evolution is selected because it has been demonstrated in many works that is robust, effective and reliable [21], [22]. This section describes this evolutionary algorithm applied to model updating. The strategy of this algorithm involves the evolution of a population with a size S_{max}. This parameter represents the maximum number of individuals in one generation. It can be formulated as follows,

$$\mathbf{E}_l^g = \mathrm{E}_{l,k}^g; \quad k = 1,2,\ldots, k_{max} \quad (3)$$

where **E** represents the vector of the Young's Modulus parameters at each section. Superscript g stands for the generation number, and l is the index for the individual. Parameter k stands for the dimension of the vector. The size of the population (i.e. k_{max}) does not change during the optimization process. The maximum number of generations is g_{max}, which is established as the convergence criterion of the algorithm. The fitness function is given by Eq.(2) and the

initial vector of the population is chosen to cover a wide range of the space of the variables. A uniform probability function is used to provide the value of the variables in the initial population. However, DE algorithm does not admit the formulation of constraint as local optimization does. Thus, the fitness function should be adapted to include constraints. The method used in this work is Static Penalty. It requires the introduction of the penalty term as follows,

$$\Phi(\mathbf{E}_k^g) = \Pi(\mathbf{E}_k^g) + \sum_{c=1}^{nc} R_c \, max\left[0, g_c\left(\mathbf{w}\mathbf{E}_k^g\right)\right] \tag{4}$$

Where R_c is the penalty coefficient and nc is the number of constraints. In this work, the constraints represent the lowest and highest value of the stiffness.
The mutation operator used in this work is given by the following equation,

$$E_{l,k}^{g+1} = E_{l1,k}^{g} + F\left(E_{l2,k}^{g} - E_{l3,k}^{g}\right); \quad l = 1,2, \ldots, l_{max} \tag{5}$$

where subscripts l_1, l_2 and l_3 refer to three individuals of the actual generation randomly selected. Parameter F is the mutation factor selected by the analyst between 0 and 2. The next operator is Crossover, which is defined as follows,

$$E_{l,m}^{g+1} = \begin{cases} E_{l,m}^{g+1} & if\, A(k) \le Cr \\ E_{l1,m}^{g} & if\, A(k) > Cr \end{cases}; \; k = 1,2, \ldots, k_{max} \tag{6}$$

where Cr is the crossover constant selected by the analyst between 0 and 1. $A(k)$ is a random number. Next, selection operator is applied, which is given by,

$$\boldsymbol{E}_l^{g+1} = \begin{cases} \mathbf{E}_l^{g+1} & if\ \Phi\left(\mathbf{E}_l^{g+1}\right) < \Phi\left(\mathbf{E}_l^{g}\right) \\ \mathbf{E}_l^{g} & if\ \Phi\left(\mathbf{E}_l^{g+1}\right) \ge \Phi\left(\mathbf{E}_l^{g}\right) \end{cases} \tag{7}$$

This equation is repeated for each generation until the maximum number of generations is achieved. Thus, the algorithm requires five parameters defined by the analyst, i.e. population size, l_{max}, constant factor, F, crossover constant, C_r, constraint factor, R_c, and maximum number of generations, g_{max}.

4 EXAMPLE: APPLICATION TO GLULAM BEAMS

Two kind of experiments were carried out in this work. The first test one was done on elements without defects. The main goal of these tests was to obtain the dynamic mechanical properties, obtaining the modal parameters without damage. In order to assess the algorithm in the second kind of experiments, damages were introduced in the elements.

Figure 2: Glulam specimens with two laminas (a and b) and five laminas (c).

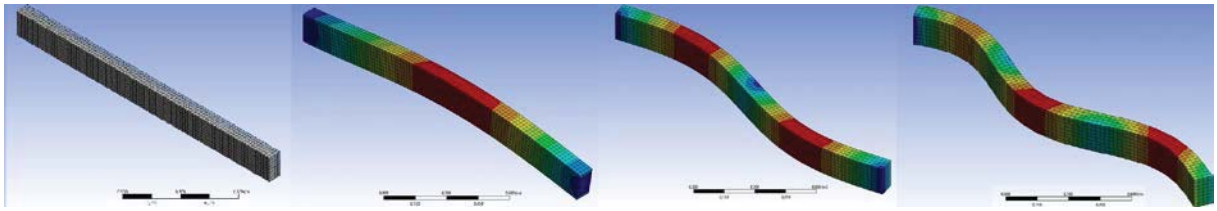

Figure 3: Theoretical model of the glued laminated beam formed by two laminas.

Pinus radiata (GL-24) was the wood specie used for these experiments. The nominal mechanical properties were: MOE = 9.1GPa and Possion ratio = 0.38. The density considered was 336.0 kg/m^3. The adhesive used was melamine-uera 1247 with hardener 2526. The nominal mechanical properties of the adhesive is: MOE = 3.5GPa and Poisson ratio = 0.34.
Three uniform clear beams with any defects were used to determine the dynamic properties of the wood used in Glulam. The dimensions of these elements were L=1.85m (length), d=0.15m (wide) and e=0.04m (thick). These experiments were used to determine the empiric modulus of elasticity (MOE) and Poisson ration of pure wood. After that, three uniform simple Glulam beams formed by two laminas were used to determine the influence of the adhesive between the elements of wood (see Fig. 2a and 2b). Each lamina has a thickness of 0.04m. Finally, Glulam beams formed by five laminas were considered as a general case (see Fig. 2c).
The measurement system consisted of four capacitive accelerometers (Measurement Specialties, model 4610), an impact hammer (Kistler, model 9724A), an acquisition system (HBM, model QuantumX MX1601B, 16 channels). Catman® Software and Matlab® were used to processing the signal and ARTeMIS® software was used to obtain the modal shapes and modal parameters. Each beam was supported at both ends and the accelerometers were located uniformly distributed along its length. The hammer impacted in one point of the beam and the signal was picked up by the four accelerometers to obtain the modal parameters after processing the signal. Commercial finite element package (ANSYS®) was used to generate a 3D-model of the beams. Figure 3 shows the FE model and modes for the model formed by two laminas in a simple beam used in this work. Each lamination was modelled as a separate entity. This modelization allows introducing the material characteristics of each element in order to be modeled individually. A perfect bonded connection was assumed between laminas. The induced damage considered in all cases was a loss of stiffness in some part of the structural element. This effect responds to most of the causes of failures in this type of structures. To modelize the imperfections, the beams were divided in five parts. The stiffness was considered constant in one of each part (see Fig. 3), but they could vary independently in the updating process.

5 RESULTS

Each individual in the DE algorithm is defined by the five variables, which are the Young's Modulus in each section. A damage was induced in the second section of the beams (Section 2 in Fig. 4). The measurement of the FRF provided the natural frequencies and modes of the real system. This information was introduced in the algorithm for updating the finite element model. Therefore, the parameters of the algorithm are the following: size of the population, l_{max}=50, F=2, crossover constant, C_r=1, constraint factor, R_c=1, and maximum number of generations, g_{max}=25.

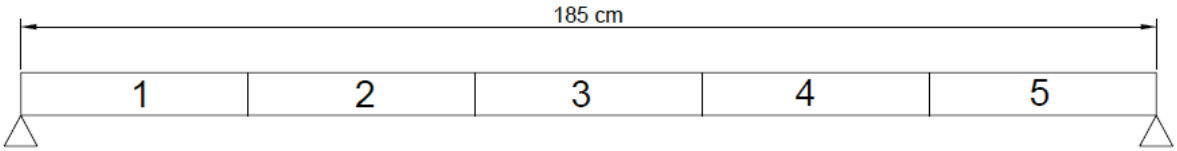

Figure 4: Scheme of the numerical beam with the five part were the stiffness is constant.

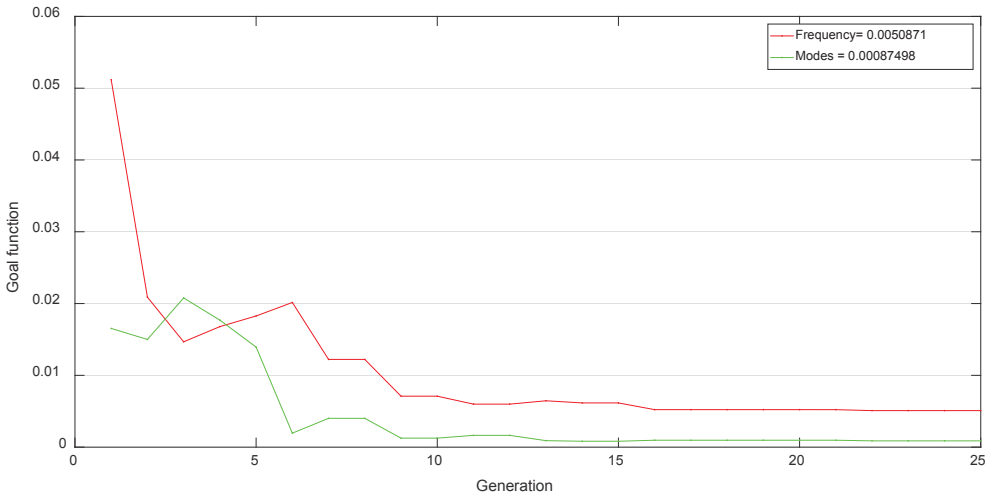

Figure 5: Evolution of the fitness during the updating process.

Fig. 5 shows the evolution of the goal function, i.e. Eq.(2), during the optimization process. In this graph, the two terms of both parts of the formula have been represented (i.e. red = frequency term and green = modes term). It is clear that the trend in the evolution during the 25 generations is good enough. The differences between the two curves is mainly due to the weighting parameters considered in the example. Fig. 6 shows the evolution of the Young's Modulus in each generation. The values of the variables in sections 1, 3, 4 and 5 are very close to the nominal value of the Young's Modulus. However, the value of section 2 is clearly lower due to the damage induced in the beam. Fig. 7 shows the comparison of the theoretical and experimental results with the porcentage of accuracy.

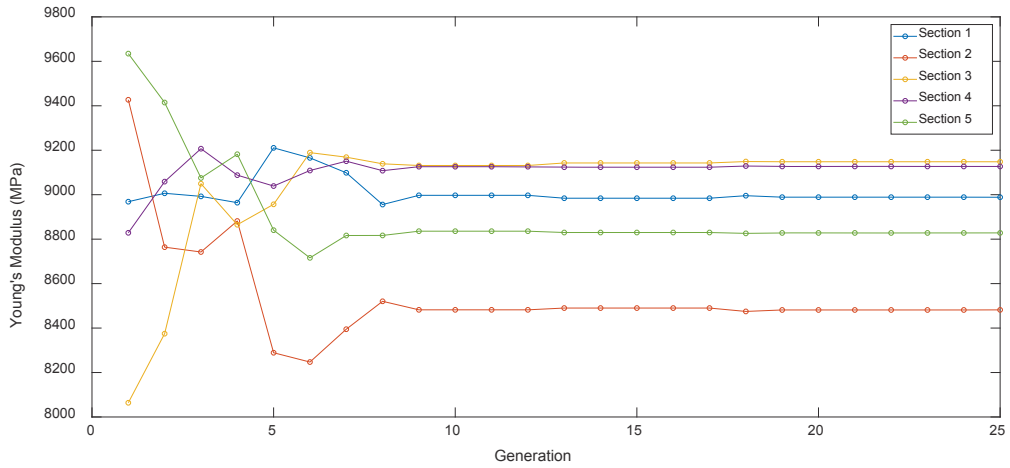

Figure 6: Evolution of the Young's Modulus in each section during the updating process.

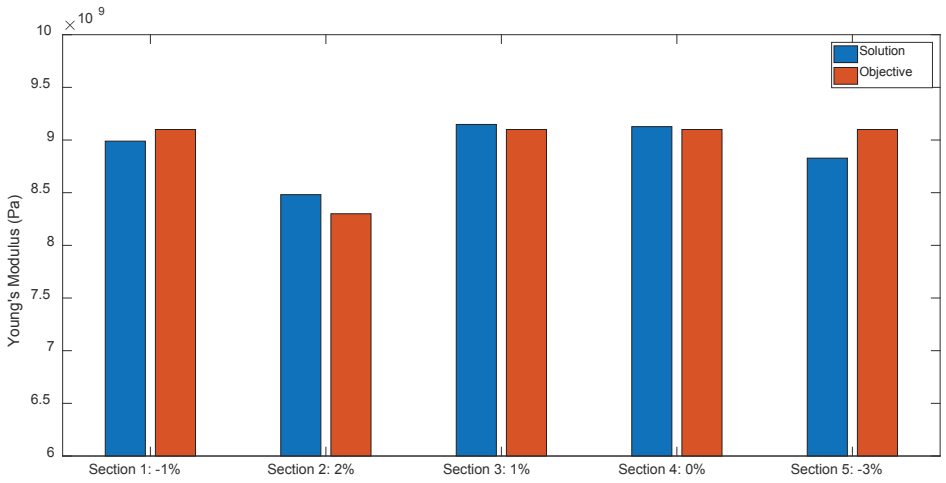

Figure 7: Theoretical values and solution obtained after the updating process.

6 CONCLUSIONS

The use of glued laminated timber is increasing in developed countries due to the several advantages that this material provides. The structural members are used with different size and shapes, which makes this material attractive for architects and users. However, many types of defects that are exclusive to this material have influence on the mechanical properties. This fact makes the evolution of the mechanical properties of this material over time unknown. For this reason, it is necessary to develop methods for the evaluation of the health status of Glulam structural elements. In this study, FE model updating methodology is proposed for the evaluation of damage in structural elements of glued laminated timber. The proposed method was implemented using a DE algorithm for the minimization of the residual function. Experimental and theoretical simulations were compared by means of this residual function. The method demonstrate that it is capable of finding the damage when it is produced by a loss of stiffness. Thus, the algorithm is reliable for the detection of local damage in structural elements made of Glulam.

ACKKOWLEDGEMENT

The authors acknowledge the funding provided from YOFRA S.A., by means of a research project from the Program I+C=+C 2018, Support for R&D Projects, SODERCAN, Government of Cantabria.

REFERENCES

[1] L. Ozola, T. Keskküla, and J. Miljan, “Assessment of timber structures,” *9th World Conf. Timber Eng. 2006, WCTE 2006*, vol. 2, pp. 1462–1469, 2006.

[2] S. Aicher and D. Ohnesorge, “Shear strength of glued laminated timber made from European beech timber,” *Eur. J. Wood Wood Prod.*, vol. 69, no. 1, pp. 143–154, 2011.

[3] T. Bowers, “CORRIM : Report – Module G1 Cradle-to-Gate Life-Cycle assessment of Glued Laminated Timbers US Pacific Northwest Region,” 2017.

[4] J. Dietsch, Philipp; Köhler, “Assessment of timber structures,” *COST Action E55*, vol.

2, pp. 1462–1469, 2010.

[5] S. J. Sanabria, R. Furrer, J. Neuenschwander, P. Niemz, and P. Schütz, "Analytical modeling, finite-difference simulation and experimental validation of air-coupled ultrasound beam refraction and damping through timber laminates, with application to non-destructive testing," *Ultrasonics*, vol. 63, pp. 65–85, 2015.

[6] M. Riggio, J. Sandak, and S. Franke, "Application of imaging techniques for detection of defects, damage and decay in timber structures on-site," *Constr. Build. Mater.*, vol. 101, pp. 1241–1252, 2015.

[7] M. Riggio *et al.*, "In situ assessment of structural timber using non-destructive techniques," *Mater. Struct. Constr.*, vol. 47, no. 5, pp. 749–766, 2014.

[8] F. Cheng and Y. Hu, "Nondestructive test and prediction of MOE of FRP reinforced fast-growing poplar glulam," *Compos. Sci. Technol.*, vol. 71, no. 8, pp. 1163–1170, 2011.

[9] P. Dietsch and H. Kreuzinger, "Guideline on the assessment of timber structures: Summary," *Eng. Struct.*, vol. 33, no. 11, pp. 2983–2986, 2011.

[10] D. Bru, F. J. Baeza, F. B. Varona, J. García-Barba, and S. Ivorra, "Static and dynamic properties of retrofitted timber beams using glass fiber reinforced polymers," *Mater. Struct. Constr.*, vol. 49, no. 1–2, pp. 181–191, 2016.

[11] M. J. Morales Conde, C. Rodríguez Liñán, and P. Rubio de Hita, "Use of ultrasound as a nondestructive evaluation technique for sustainable interventions on wooden structures," *Build. Environ.*, vol. 82, pp. 247–257, 2014.

[12] S. J. Sanabria, C. Mueller, J. Neuenschwander, P. Niemz, and U. Sennhauser, "Air-coupled ultrasound as an accurate and reproducible method for bonding assessment of glued timber," *Wood Sci. Technol.*, vol. 45, no. 4, pp. 645–659, 2011.

[13] A. C. Altunışık, F. Y. Okur, and V. Kahya, "Modal parameter identification and vibration based damage detection of a multiple cracked cantilever beam," *Eng. Fail. Anal.*, vol. 79, pp. 154–170, Sep. 2017.

[14] S. E. Fang and R. Perera, "Damage identification by response surface based model updating using D-optimal design," *Mech. Syst. Signal Process.*, vol. 25, no. 2, pp. 717–733, Feb. 2011.

[15] R. Perera, R. Marin, and A. Ruiz, "Static-dynamic multi-scale structural damage identification in a multi-objective framework," *J. Sound Vib.*, vol. 332, no. 6, pp. 1484–1500, Mar. 2013.

[16] P. G. Bakir, E. Reynders, and G. De Roeck, "An improved finite element model updating method by the global optimization technique 'Coupled Local Minimizers,'" *Comput. Struct.*, vol. 86, no. 11–12, pp. 1339–1352, Jun. 2008.

[17] M. Jeong, J. H. Choi, and B. H. Koh, "Performance evaluation of modified genetic and swarm-based optimization algorithms in damage identification problem," *Struct. Control Heal. Monit.*, vol. 20, no. 6, pp. 878–889, Jun. 2013.

[18] R. Perera, S. E. Fang, and C. Huerta, "Structural crack detection without updated baseline model by single and multiobjective optimization," *Mech. Syst. Signal Process.*, vol. 23, no. 3, pp. 752–768, Apr. 2009.

[19] N. F. Alkayem, M. Cao, Y. Zhang, M. Bayat, and Z. Su, "Structural damage detection using finite element model updating with evolutionary algorithms: a survey," *Neural Comput. Appl.*, vol. 30, no. 2, pp. 389–411, 2018.

[20] A. Greco, D. D'Urso, F. Cannizzaro, and A. Pluchino, "Damage identification on spatial Timoshenko arches by means of genetic algorithms," *Mech. Syst. Signal Process.*, vol. 105, pp. 51–67, May 2018.

[21] F. Kang, J. J. Li, and Q. Xu, "Damage detection based on improved particle swarm optimization using vibration data," *Appl. Soft Comput. J.*, vol. 12, no. 8, pp. 2329–2335, Aug. 2012.

[22] R. Storn and K. Price, "Differential Evolution-A Simple and Efficient Heuristic for Global Optimization over Continuous Spaces," Kluwer Academic Publishers, 1997.

EURODYN 2020
XI International Conference on Structural Dynamics
M. Papadrakakis, M. Fragiadakis, C. Papadimitriou (eds.)
Athens, Greece, 23–26 November 2020

A METHODOLOGY ON INTERPRETABLE NOVELTY DETECTION

Movsessian A.[1], Garcia Cava D.[1], Tcherniak D.[2] and Janeliukstis R.[3]

[1]School of Engineering, Institute for Infrastructure and Environment, University of Edinburgh, Alexander Graham Bell Building, Thomas Bayes Road, Edinburgh EH9 3FG, United Kingdom
e-mail: {Artur.Movsessian,david.garcia}@ed.ac.uk

[2]Brüel & Kjær Sound and Vibration Measurements, Skodsborgvej 307, Nærum 2085, Denmark
e-mail: dmitri.tcherniak@hbkworld.com

[3] Department of Wind Energy, Technical University of Denmark, Frederiksborgvej 399, 4000, Roskilde, Denmark
e-mail: rimja@dtu.dk

Keywords: Decision Trees, Mahalanobis Distance, Damage Detection, Pseudo-Damage Localization.

Abstract. *Vibration-based Structural Health Monitoring (VSHM) systems continuously gather data from an array of sensors mounted on a structure. Features are constructed from the data measured. The aim is to monitor the vibration responses in the search for changes that may hint to damage. The continuous data acquisition generates high-dimensional feature spaces that require Data-Driven approaches to make inferences concerning the integrity of the structure. In recent years, machine learning has played an increasingly important role in VSHM. Data-driven algorithms have been successfully used to construct models capable of detecting anomalies such as damage in the features derived from the vibration signals. Mahalanobis Distance based novelty detection is a common used method to detect damage. Yet, the resulting models have been labelled "black box models" given that they lack interpretability. This becomes a relevant challenge in the presence of high-dimensional feature spaces. Using machine learning algorithms that can be interpreted would enable a more reliable novelty detection process, building trust in these methods and easing the decision-making process. Decision Trees (DT) is a widely used interpretable machine learning algorithm. The hierarchical structure of this algorithm enables the prioritisation of features that are used as predictors in the damage detection models. Furthermore, the nature of the algorithm enables the user to track the decisions and understand the classification process in detail. In this paper, we introduce the complementary use of so-called "black box models" and DT for novelty detection. The proposed damage detection approach is tested on an experimental setup with a 14.3m wind turbine blade (WTB) equipped with 24 accelerometers. A pseudo-damage was simulated by adding masses to several locations of the WTB. The pseudo-damage was detected by means of a semi-supervised novelty-detection. The novelties were later studied in detail with decision-trees to make inferences on their potential causes.*

1 Introduction

Methods to monitor the integrity of a structure have been intensely studied in the past decades [1–5]. Traditionally, researchers have had robust experimental setups and performed reliable measurements to successfully compare the modal parameters of a structure and identify damage [6–8]. However, these methods have limitations given that the confidence interval of features can be exceeded due to environmental factors as shown in [9]. Additionally, such physics-based methods are often impractical due to the high complexity of the structure and the level of expertise that is required for their development [10, 11]. This is where data-driven techniques, and especially machine learning approaches, may become a powerful alternative. In recent years, machine learning techniques have been implemented in research and applied to multiple structures, thus proving their capability to detect damage [12–14]. Semi-supervised algorithms have been of particular interest for damage detection when only the healthy condition of the structure is known. Initially proposed by [15], the use of the Mahalanobis Distance (MD) for novelty detection became a popular method to cluster extracted features from the structure or system response. In [16, 17], the authors used the MD to identify the deviations from a reference state defined from observations from a pristine structure and detect potential damage in a structure or system. Often, this one-dimensional clustering method contains false alarms, i.e., the novelty index is outside the ”healthy” reference cluster but does not correspond to damage. Studies have shown that environmental and operational conditions are one of possible reasons for these false alarms [18, 19].

Decision Trees (DT) are not new to the field of VSHM. For example, [20] localized a point mass on a CFRP plate employing k-nearest neighbors and linear discriminant algorithms such as DTs using strain response data. Similarly, in [21], a problem of localizing an added mass on a plate structure was approached using a modified DT algorithm that also output probabilities of each class. The plate was divided into grids where each zone was assigned to a number. The output of a classifier contained zone numbers as class labels with a probability of point mass being placed in that particular zone. Nevertheless, DTs have been underutilized in VSHM applications by exploding only their classification capability and not its high interpretability and transparency. Therefore, this paper proposes the use of DTs to identify the features and their values responsible for false alarms when identifying novelties while monitoring the condition of a structure. Features related to novelties identified by the semi-supervised MD method proposed by [15] are clustered by means of DTs. Once the novelties are classified, the DTs are used to understand their occurrence. The technique was tested on data gathered from a 14.3m wind turbine blade (WTB) mounted on a test rig. The WTB was equipped with 24 accelerometers and excited by an impulse force of a electromagnetic actuator to force vibration responses. Initially, the vibration response was measured from a pristine WTB. Later, mass was added in different locations to simulate novelties. This is a well-known approach to emulate the local structural changes that are caused by damage. The relevance of each individual feature and the transparent reasons for classification are related to the position and the amount of mass added. By looking into the structure of DTs, it was possible to locate the sensors positioned closer to the mass added.

2 Methodology

The methodology proposed in this study combines the use of MD-based novelty detection and DTs to better understand the occurrence of the novelties.

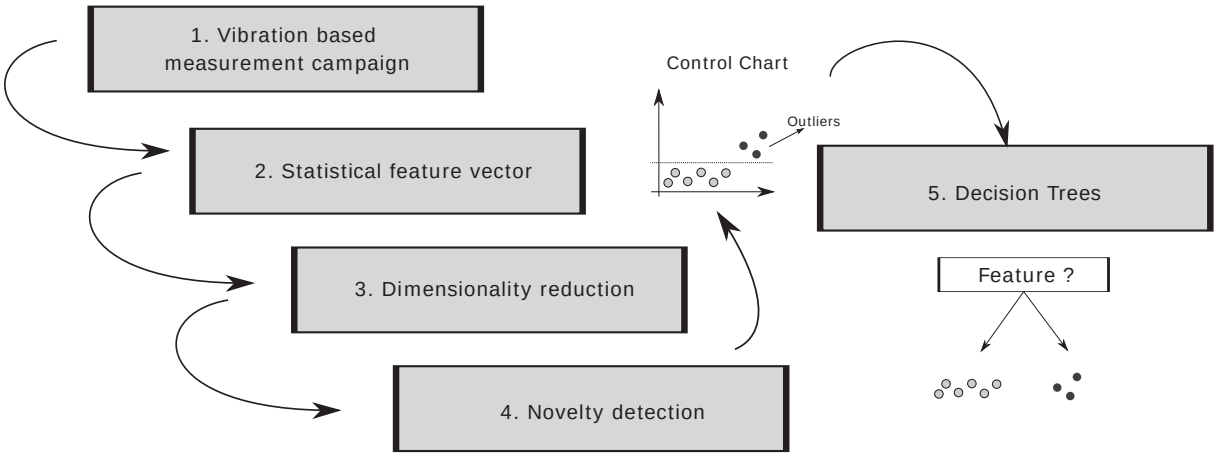

Figure 1: Graphical summary of the methodology followed in this paper

The procedure of DT bases its classification on the best possible split. This allows to understand which features and their values are responsible for the classification of novelties. Fig. 1 summarizes the main steps followed in the methodology suggested in this paper for pseudo-damage detection and interpretation.

2.1 Vibration-based measurement campaign

Vibration responses are measured from a structure when excited by an electromechanical actuator and organised in a matrix as follows,

$$\boldsymbol{V}^k = \begin{pmatrix} v_{11} & v_{12} & \dots & v_{1n} \\ v_{21} & v_{22} & \dots & v_{2n} \\ \vdots & \vdots & \ddots & \vdots \\ v_{m1} & v_{m2} & \dots & v_{mn} \end{pmatrix} = (v_{ij}) \in \mathbb{R}^{m \times n} \tag{1}$$

where v_{ij} is the i^{th} vibration measurement with the length m of the accelerometer j^{th} for the k^{th} observation, i.e, the vibration responses of all the n accelerometers due to an electromechanical actuator on the structure. The details of the measurement campaign are provided later in section 3

2.2 Statistical feature vector

The covariance of the vibration response is used to measure the direct relationship between accelerometers positioned on the WTB. In the context of novelty detection, the covariance is used as a damage sensitive feature (DSF) where a change would enable the identification of

novelties due to changes in vibration response resulting in changes in the covariance feature.

$$\boldsymbol{S}^k = \begin{pmatrix} s_{11} & s_{12} & \cdots & s_{1n} \\ s_{21} & s_{22} & \cdots & s_{2n} \\ \vdots & \vdots & \ddots & \vdots \\ s_{n1} & s_{n2} & \cdots & s_{nn} \end{pmatrix} = (s_{jq}) \in \mathbb{R}^{n \times n} \tag{2}$$

In Eq. 2, $\boldsymbol{S}^k$ is the covariance matrix for the k^{th} observation and stores the covariance s_{jq} between accelerometers j and q and, for $j = q$, s_{jq} represents the variance. Due to the symmetric properties of the covariance matrix, only the upper triangle is used as a feature vector as in Eq. 3.

$$\boldsymbol{f}^k = \begin{bmatrix} s_{11} & s_{12} & \cdots & s_{1n} & \cdots & s_{22} & \cdots & \cdots & s_{nn} \end{bmatrix}^T \tag{3}$$

All feature vectors $\boldsymbol{f}^k$ are arranged in one feature matrix $\boldsymbol{F}$ shown in Eq. (4)

$$\boldsymbol{F} = \begin{bmatrix} \boldsymbol{f}^1 & \boldsymbol{f}^2 & \cdots & \boldsymbol{f}^R \end{bmatrix} \tag{4}$$

where R is the total amount of observations.

2.3 Dimensionality reduction

Prinicipal Component Analysis (PCA) is an orthogonal transformation applied to a set of potentially correlated values into linearly uncorrelated values which are known as the principal components (PC) [22]. The first PCs contain most of the variability from the original dataset leaving each succeeding component with the remaining variability. This procedure allows to reduce the dimension of a dataset while allowing to keep most of the information possible expressed in variability of the data. In this analysis, PCA is applied to reduce the dimension of the feature matrix and account for collinearity between the feature vectors.

2.4 Mahalanobis distance-based novelty detection

The distance between a point and a distribution in a multivariate space can be described by the the Mahalanobis Distance (MD) [23]. Unlike the Euclidean distance, the MD normalizes the features by the inverse covariance matrix taking into account the features trend. A common use for the MD is to cluster multivariate data and detect outliers. In this paper, the MD is used as a novelty detection index. The novelties identified are later correlated to the introduced pseudo-damage created by adding mass in several locations of the blade. The MD is calculated using the following equation:

$$d(\boldsymbol{f}^k, \boldsymbol{Y}) = \sqrt{(\boldsymbol{f}^k - \boldsymbol{\mu_Y})^T \boldsymbol{\Sigma}_{\mathbf{Y}}^{-1} (\boldsymbol{f}^k - \boldsymbol{\mu_Y})} \tag{5}$$

where $d(\boldsymbol{f}_r, \boldsymbol{Y})$ is the MD between the feature vector $\boldsymbol{f}^k$ and the reference state $\boldsymbol{Y} \subseteq \boldsymbol{F}$, $\boldsymbol{\mu_Y}$ is the mean of the samples in $\boldsymbol{Y}$ and $\boldsymbol{\Sigma_Y}$ is the covariance between samples in feature vector $\mathbf{Y}$. To avoid confusion, note that the covariance $\boldsymbol{\Sigma_Y}$ is different from covariance $\boldsymbol{S}^k$. The threshold of the reference state during the training stage is represented by T, consequently $d(\boldsymbol{f}^k, \boldsymbol{Y}) > T$ are considered novelties. In this study, the choice of T is based on the cumulative distribution function of the MD and n^{th} percentile of the data in the training set is allowed to exceed the threshold. For this analysis 2% of training data was allowed to exceed T.

To avoid numerical error by computing the inverse of $\mathbf{\Sigma_Y}$ for the MD, the condition number of $\mathbf{\Sigma_Y}$ are examined and the influence of dimensional reduction by PCA in section 4.1 .

2.5 Decision trees

Decision Trees (DTs) belong to a class of "white box" type supervised learning algorithms [24, p. 1]. DTs make data classification an interpretable and visual process by explicitly representing each decision taken to split the data into their labeled classes. This paper uses DTs mainly to classify the novelties identified by the semi-supervised novelty detection method described in subsection 2.4.

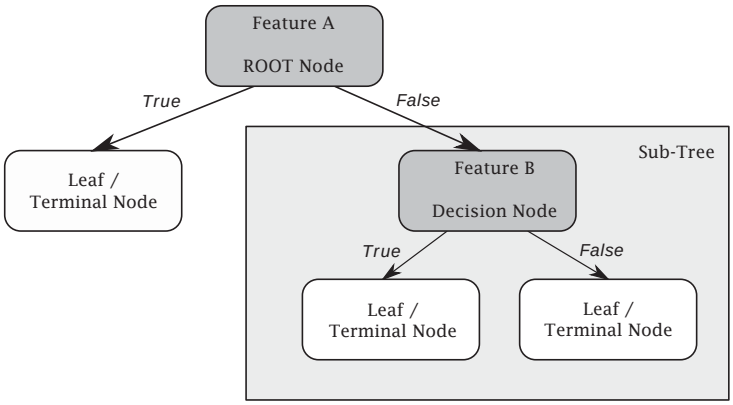

Figure 2: Decision trees principals

DTs are flowchart-like structures, such as the one shown in Fig. 2, that start from a single node, known as the root node and branch into possible outcomes. The algorithm learns to partition and this occurs recursively until no more splits are possible, therefore reaching a terminal node (or leaf node). The aim of the partition is to separate the data-set into its labeled classes.

The key task performed by the DT is the partition. The most effective split of the data-set is based on the selection of appropriate features and characteristics of the feature for comparison and decision-making. There are several attribute selection measures (ASM) that can be used for partitioning such as the information gain, gain ratio, and gini index. The decision as to which ASM to implement is discretionary. As shown in [25], the results from different ASM only differ in 2% of the cases, therefore the choice of ASM does not significantly impact the results. The DTs constructed in this paper use the information gain measure which is based on Shannon's concept of entropy [26], a measurement of the impurity of labeled input-set calculated as per Eq. 6 where p_+ is the proportion of positive examples and p_- the proportion of negative examples. The entropy H of a labeled data-set $\mathbf{S}$ in a decision node describes how well the data is currently split. If the entropy of a node is 0, then the data from this node belongs to its labeled class, i.e., no further partitioning is possible and a terminal node has been reached.

$$H(\mathbf{S}) = -p_+ log_2 p_+ - p_- log_2 p_- \tag{6}$$

Once the data-set is split, e.g., by feature A, the corresponding entropy of the resulting nodes is calculated as in Eq. 7, where $\mathbf{v}$ is a subset corresponding to a class of feature A, $\mathbf{S_v}$ is the size of the subset, and $\mathbf{S}$ the overall number of labeled data in $\mathbf{v}$. That is to say, the entropy of each

of the resulting nodes after the partition are added into a weighted average.

$$H_A(\mathbf{S}) = \sum_{\mathbf{v} \in Values(A)} \frac{|\mathbf{S_v}|}{|\mathbf{S}|} H(\mathbf{S_v}) \tag{7}$$

Since the objective of the information gain measure is to decrease the entropy after the partition, $H(\mathbf{S})$ and $H_A(\mathbf{S})$ are compared by calculating the information gain as per Eq. 8. An iterative process identifies the features that results in a maximum $Gain(\mathbf{S}, A)$.

$$Gain(\mathbf{S}, A) = H(\mathbf{S}) - H_A(\mathbf{S}) \tag{8}$$

Ultimately, the algorithm provides a hierarchical structure, where the root node corresponds to the feature within the data-set with the highest relevance for the classification.

3 Experimental data collection campaign

The proposed method is tested on a 14.3m WTB manufactured by Olsen Wings [27] shown in Fig. 3. The blade is mounted on a test rig and equipped with an electromagnetic actuator such as the one in Fig. 4a and placed close to the root of the blade.

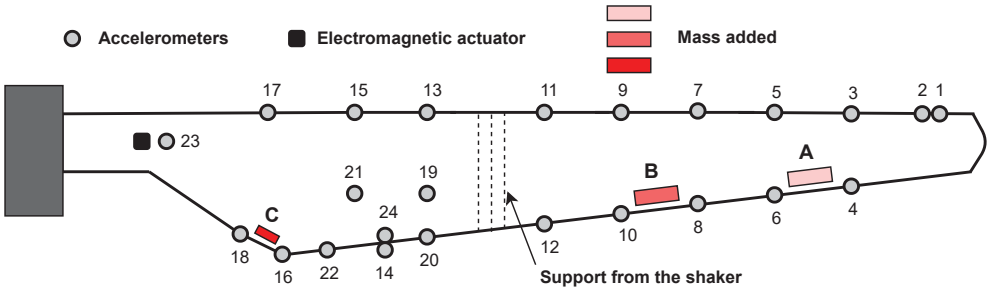

Figure 3: Schematic representation of the experimental set up of the 14.3m wind turbine blade. The WTB is mounted to an additional shaker which is not used for this experiments.

To measure the vibration response of the blade excited by the actuator hit, a total amount of 24 mono-axial accelerometers, Brüel & Kjær Type 4507, were mounted along the blade as shown in Fig. 3. The accelerometers 2 to 22 measure the vibration response in flap-wise direction, accelerometer 1 in edgewise direction.

The measured vibration response was recorded by a data acquisition system with a sampling frequency of 16,384Hz. Using the actuator as a trigger signal, the vibration responses from all accelerometers were aligned and trimmed to 200 samples around the maximum amplitude of accelerometer 23. This sample range was identified as the most sensitive to changes in dynamic response as shown in [19]. An example of the vibration response from accelerometer 8 is shown in Fig 5a and 5b

To simulate novelties, mass in form of heavy bolts, shown in Fig 4b, were placed in different locations marked in red in Fig. 3. The blade was excited 2000 times without mass to create a baseline for novelty detection. Then, in location A, five bolts (each with an approx. weight of 1kg) were place on the blade and the blade was excited ten times. Next, the amount of bolts was increased to 10 and 20 bolts repeating the procedure for each variation of mass and for locations B and C. Masses for each location we placed and measured separately. Table 1 summarizes the damage scenarios simulated with the corresponding mass added and locations.

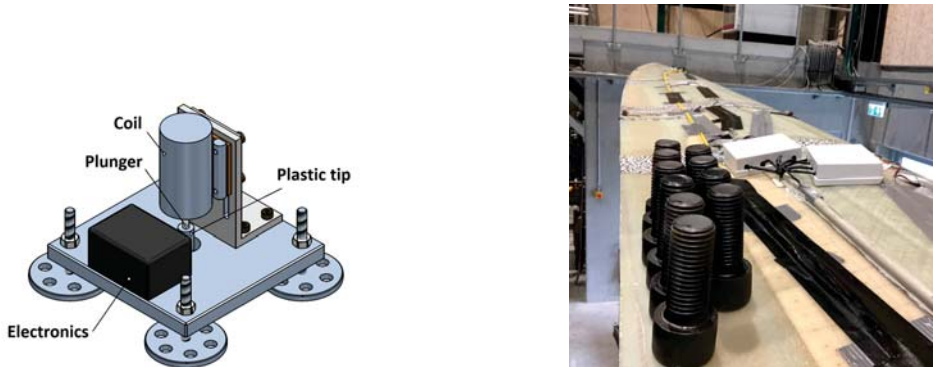

(a) (b)

Figure 4: Experimental set up. (a) Electromechanical actuator and (b) an example of mass added (Photo courtesy of DTU Large Scale Facility).

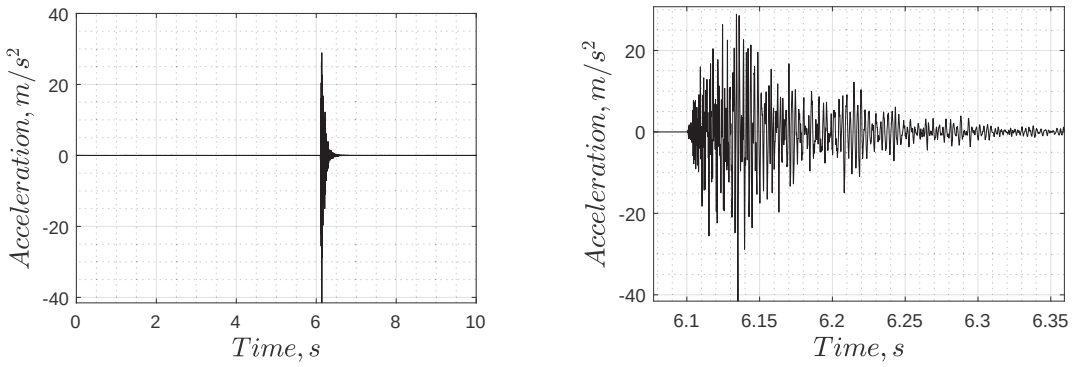

(a) (b)

Figure 5: Vibration response measured by the accelerometer 8. (a) 10s vibration response and (b) Trimmed vibration response

4 Results and discussion

4.1 Novelty detection

The control charts in Fig 6 and 7 illustrate the MD-based novelty index and the necessity to transform the features by dimensional reduction. To highlight the limitations of applying the MD-based novelty index on a large features space of a redundant experiment, the covariance was calculated from the first 22 vibration responses measured in the accelerometers 1 to 22 resulting in a total amount of 253 features per observation. When calculating the MD directly from the features without a transformation, the novelty index strongly deviate from the created reference as shown in Fig. 6.

Comparing the results to Fig. 7, it can be seen that significant deviations occur after the training limit of the first 1500 samples. As shown in Eq. 5, the MD uses the inverse covariance matrix $\mathbf{\Sigma_Y^{-1}}$. To understand the deviations and avoid numerical errors, the condition number of the covariance matrix $\mathbf{\Sigma_Y}$ is calculated after reducing the amount of principal components one by one.

If the condition number is not much larger than 100, the matrix can be considered as well conditioned and non-singular. Given the fact that the blade was excited by the electromechan-

Table 1: Simulated novelties according to location and mass added

Scenario	Mass	Location	Number of Excitations
Blade without mass			
Training		-	1500
Testing		-	500
Blade with mass	5kg	A	10
	10kg	A	10
	20kg	A	10
	5kg	B	10
	10kg	B	10
	20kg	B	10
	5kg	C	10
	10kg	C	10
	20kg	C	10
Total			2090

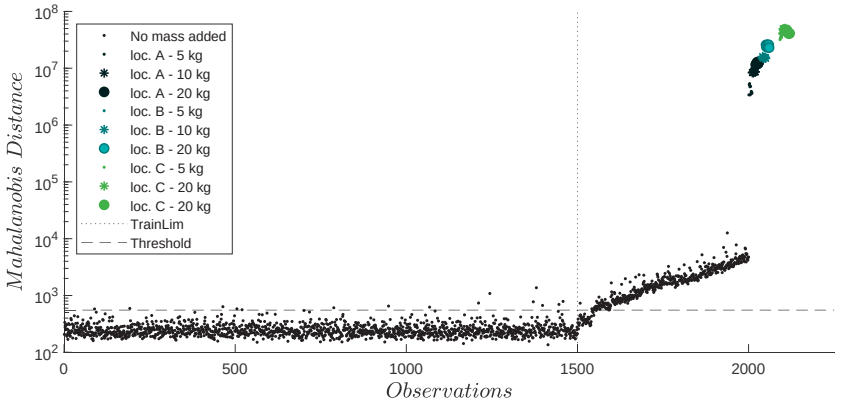

Figure 6: MD-based novelty index without dimensional reduction

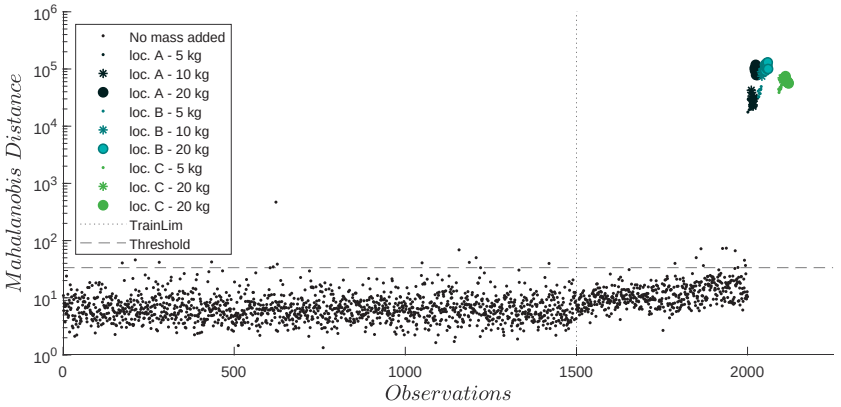

Figure 7: MD-based novelty index with dimensional reduction

ical actuator for 2000 times under the same conditions, small deviation in the excitation or measurement noise will amplify noise in the test data by the factor of the condition number. Therefore, it was crucial for this analysis to avoid high condition numbers. Keeping more then 90% of the explained variance allowed to lower the condition number to 44 and a total amount of 8 components were left.

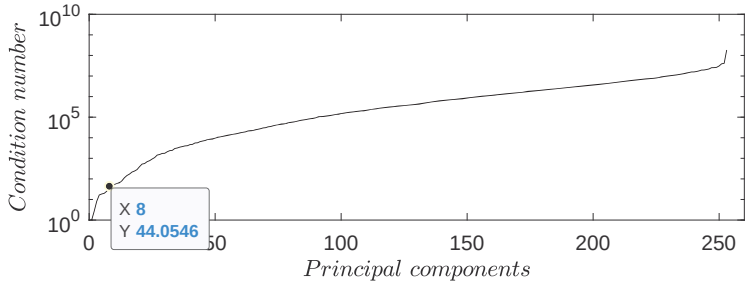

(a)

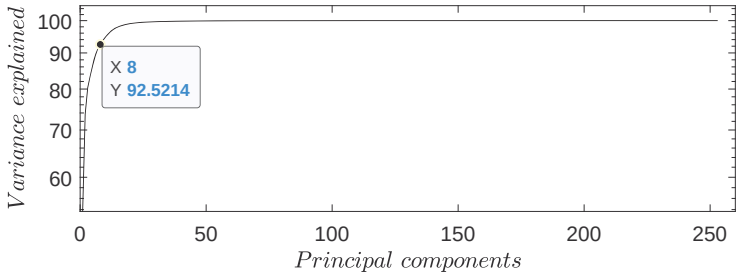

(b)

Figure 8: (a) Condition number. (b) Accumulative variance by principal components

As shown in Fig. 8a, by using a large amount of principal components, the condition number of covariance matrix $\mathbf{\Sigma_Y}$ is over 10^5. Collinearity in the feature matrix can be avoided by reducing the number of principal components. There is no clear answer of how many components to use; nevertheless, the principal components needed can be narrowed down by observing the condition number and variance explained.

4.2 Novelties explained by decision trees

To be able to interpret the DTs, the features used for classification have to be interpretable. Therefore, for analyzing the novelties, the covariance matrix is first reduced to its diagonal using only the variance associated with each accelerometer response. This will simplify the interpretation of the DTs and its complexity. The dimensional reduction by PCA reduced the false alarm rate for novelty detection. Once novelties are detected, features can be used without the dimensional reduction for supervised learning with DT, thereby maintaining the interpretability of the features. Three classification trees were constructed, one for each location of the masses. Locations only along the trailing edge of the WTB were considered. As shown in Table 1, each location has 3 cases (or classes) referring to 3 different masses added. The DT for mass location A is visualized in Fig. 9. The feature in the root of the tree is the variance of sensor 6, which is located right before the added mass. To split the case 1 from the remaining 2, 3 and 4, the variance of the feature had to be below 31.05, i.e., an increase in variance should have occurred

in the vibration signal after the masses were added. To separate the case with 20kg from the ones where 5 and 10kg were added, the variance of accelerometer 6 had to be above 37.02. Data from 5kg and 10kg cases were split by the variance from sensor 4, showing that adding 10kg of mass would increase the variance compared to 5kg. The features chosen by the DT algorithm to separate data recorded from a WTB with mass on it from the ones without mass were those corresponding to the accelerometers positioned next to the mass, thereby pointing the location of the mass placed.

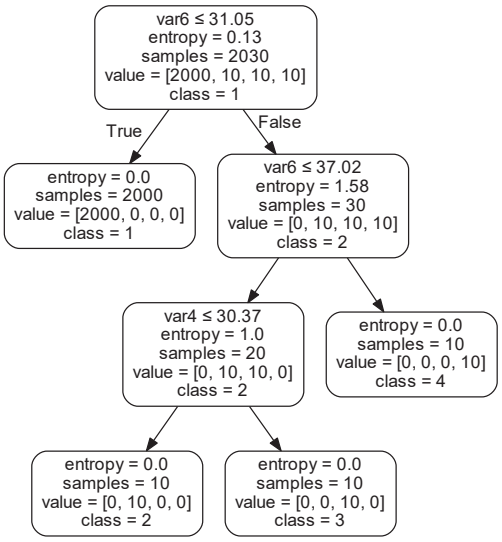

Figure 9: DT for mass location A

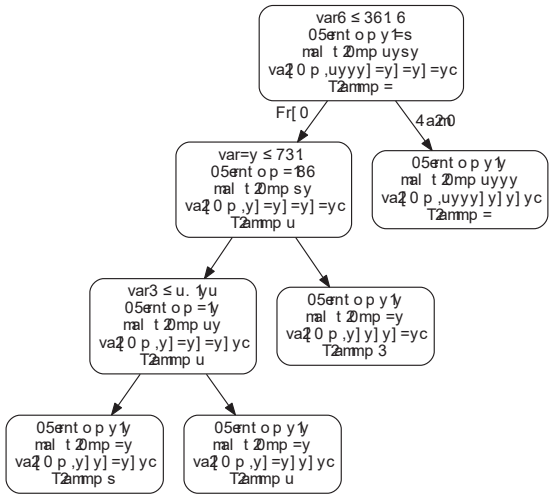

Figure 10: DT for mass location B

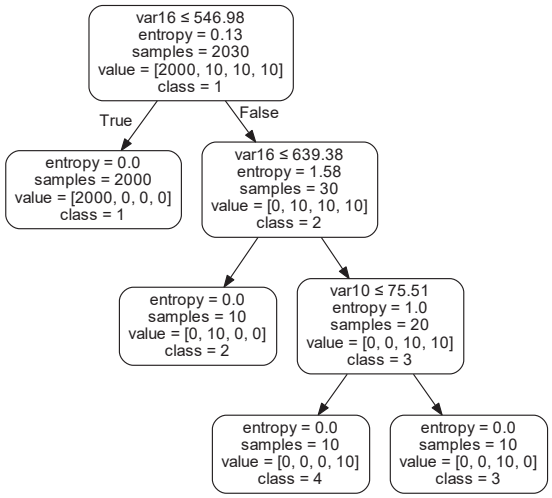

Figure 11: DT for mass location C

For mass location B and C in Fig. 10 and 11, the root nodes of the DTs were able to separate

data from a WTB with and without mass by a single sensor which is located right next to the mass. Nevertheless, by separating the 5kg from 10kg of mass added for location B, the affected sensors were not near the the location of the mass but towards the tip of the blade. The same can be observed for mass location C, where the added mass between sensor 16 and 18 had a significant effect on sensor 10 which is located further down the trailing edge. Detailed information on hyperparameters for the decision trees can be found in Appendix A

5 Conclusions

The work presented in this paper introduces DT as a tool for interpreting and understanding the causes of novelties identified by the MD-based novelty index. The technique was implemented in a large scale WTB with added mass to simulate damage in different locations. The consequences of separating observations from non-added mass and added mass has been studied. Particularly the impact of a collinearity in the feature matrix and its influence on the MD-based novelty index. This was investigated by reducing the dimension of the feature matrix while monitoring the condition number. By avoiding high condition numbers, strong deviations after the training in the control chart were reduced. Once the novelties are identified, DT have been used to understand which features were responsible to cause the novelties in the control chart. The relation of features and accelerometers locations was evaluated. It was found that the accelerometers closer to the location of added mass were at the root of the DT and therefore identifying the importance of a particular feature. Limitations were identified by exploring the separation of different amount of masses. It was observed that the accelerometers further away from the locations were responsible to classify between different amounts of added mass.

This study demonstrated that the occurrence of novelties can be interpreted with the use of DTs. Additional the DTs and their hierarchical structure correlated the location of the mass to the sensor which features were at the root of the tree. Therefore, this could narrow down the location of where the added mass was added and open a further directions to pseudo-locate added masses or in other words damage.

Acknowledgements

The experiments were performed in collaboration with DTU Large Scale Facility, which is a DTU Wind Energy test facility and part of CASMaT - Villum Center for Advanced Structural and Material Testing. The contribution by DTU is partly supported by two projects funded by the Danish Energy Agency through the Energy Technology Development and Demonstration Program (EUDP). The supported projects are BLATIGUE: Fast and Efficient Fatigue Test of Large Wind Turbine Blade (Grant No. 64016-0023) and RELIABLADE: Improving Blade Reliability through Application of Digital Twins over Entire Life Cycle (Grant No. 64018-0068). The financial support is greatly appreciated.

REFERENCES

[1] W. Fan, P. Qiao, Vibration-based damage identification methods: a review and comparative study, Structural health monitoring 10 (1) (2011) 83–111 (2011).

[2] J. J. Moughty, J. R. Casas, A state of the art review of modal-based damage detection in bridges: development, challenges, and solutions, Applied Sciences 7 (5) (2017) 510 (2017).

[3] F. Vestroni, A. Pau, Dynamic characterization and damage identification, in: Dynamical Inverse Problems: Theory and Application, Springer, 2011, pp. 151–178 (2011).

[4] C. S. Sakaris, J. S. Sakellariou, S. D. Fassois, Vibration-based damage precise localization in three-dimensional structures: single versus multiple response measurements, Structural Health Monitoring 14 (3) (2015) 300–314 (2015).

[5] J. Ciambella, A. Pau, F. Vestroni, Modal curvature-based damage localization in weakly damaged continuous beams, Mechanical Systems and Signal Processing 121 (2019) 171–182 (2019).

[6] I. Mekjavić, D. Damjanović, Damage assessment in bridges based on measured natural frequencies, International Journal of Structural Stability and Dynamics 17 (02) (2017) 1750022 (2017).

[7] F. Vestroni, D. Capecchi, Damage detection in beam structures based on frequency measurements, Journal of Engineering Mechanics 126 (7) (2000) 761–768 (2000).

[8] C. Papadimitriou, E. Ntotsios, D. Giagopoulos, S. Natsiavas, Variability of updated finite element models and their predictions consistent with vibration measurements, Structural Control and Health Monitoring 19 (5) (2012) 630–654 (2012).

[9] B. Peeters, G. De Roeck, One-year monitoring of the z24-bridge: environmental effects versus damage events, Earthquake engineering & structural dynamics 30 (2) (2001) 149–171 (2001).

[10] I. Laory, T. N. Trinh, I. F. Smith, Evaluating two model-free data interpretation methods for measurements that are influenced by temperature, Advanced Engineering Informatics 25 (3) (2011) 495–506 (2011).

[11] K. Worden, E. J. Cross, N. Dervilis, E. Papatheou, I. Antoniadou, Structural health monitoring: from structures to systems-of-systems, IFAC-PapersOnLine 48 (21) (2015) 1–17 (2015).

[12] M. H. Rafiei, H. Adeli, A novel machine learning-based algorithm to detect damage in high-rise building structures, The Structural Design of Tall and Special Buildings 26 (18) (2017) e1400 (2017).

[13] R. Ghiasi, P. Torkzadeh, M. Noori, A machine-learning approach for structural damage detection using least square support vector machine based on a new combinational kernel function, Structural Health Monitoring 15 (3) (2016) 302–316 (2016).

[14] J. Xie, Kernel optimization of ls-svm based on damage detection for smart structures, in: 2009 2nd IEEE International Conference on Computer Science and Information Technology, IEEE, 2009, pp. 406–409 (2009).

[15] K. Worden, Structural fault detection using a novelty measure, Journal of Sound and vibration 201 (1) (1997) 85–101 (1997).

[16] K. Worden, H. Sohn, C. R. Farrar, Novelty detection in a changing environment: regression and interpolation approaches, Journal of sound and vibration 258 (4) (2002) 741–761 (2002).

[17] M. Wong, L. Jack, A. Nandi, Modified self-organising map for automated novelty detection applied to vibration signal monitoring, Mechanical systems and signal processing 20 (3) (2006) 593–610 (2006).

[18] T. Bull, M. D. Ulriksen, D. Tcherniak, The effect of environmental and operational variabilities on damage detection in wind turbine blades, in: Proceedings of the 9th European Workshop on Structural Health Monitoring, 2018 (2018).

[19] D. Tcherniak, L. L. Mølgaard, Active vibration-based structural health monitoring system for wind turbine blade: Demonstration on an operating vestas v27 wind turbine, Structural Health Monitoring 16 (5) (2017) 536–550 (2017).

[20] R. Janeliukstis, S. Rucevskis, A. Chate, Condition monitoring with defect localisation in a two-dimensional structure based on linear discriminant and nearest neighbour classification of strain features, Nondestructive Testing and Evaluation (2019) 1–25 (2019).

[21] N. Mechbal, J. S. Uribe, M. Rébillat, A probabilistic multi-class classifier for structural health monitoring, Mechanical Systems and Signal Processing 60 (2015) 106–123 (2015).

[22] S. Wold, K. Esbensen, P. Geladi, Principal component analysis, Chemometrics and intelligent laboratory systems 2 (1-3) (1987) 37–52 (1987).

[23] H. Sohn, C. R. Farrar, N. F. Hunter, K. Worden, Structural health monitoring using statistical pattern recognition techniques, J. Dyn. Sys., Meas., Control 123 (4) (2001) 706–711 (2001).

[24] R. C. Barros, A. C. De Carvalho, A. A. Freitas, et al., Automatic design of decision-tree induction algorithms, Vol. 10, Springer, 2015 (2015).

[25] L. E. Raileanu, K. Stoffel, Theoretical comparison between the gini index and information gain criteria, Annals of Mathematics and Artificial Intelligence 41 (1) (2004) 77–93 (2004).

[26] C. E. Shannon, A mathematical theory of communication, Bell system technical journal 27 (3) (1948) 379–423 (1948).

[27] Olsen Wings A/S manufacturer of small wind turbine blades, `http://olsenwings.dk/`, accessed: 2020-02-25.

[28] scikit-learn developers, sklearn DecisionTreeClassifier, `https://scikit-learn.org/stable/modules/generated/sklearn.tree.DecisionTreeClassifier.html`, accessed: 2020-02-11 (2019).

A Decision Trees and Hyperparameters

This appendix is meant to give some insight on the hyperparameter which were used to train the DTs. The selected values for hyperparameters are shown in 2. The DTs were developed and trained by using the scikit-learn library in Python. Hyperparameters for the DT are selected in a way which does not limit the DTs. The aim is to over-fit the classification in order to understand the novelties. Detailed information about the Hyperparameters can be found in [28].

Table 2: Hyperparameters for Decision Tree IP3 algorithm

Hyper-parameter	Selected value
Split criterion	Entropy
Max depth	None
Max features	None
Max leaf nodes	None
Min impurity decrease	0
Min impurity split	None
Min. samples leaf	1
Min samples split	2
Min weight fraction leaf	0
Presort	False
Splitter	best

For training the DTs the complete labeled dataset was used with the aim to over-fit the data from where interpretation of each class can take place.

EURODYN 2020
XI International Conference on Structural Dynamics
M. Papadrakakis, M. Fragiadakis, C. Papadimitriou (eds.)
Athens, Greece, 23–26 November 2020

INVESTIGATION ON DAMAGE SENSITIVE FEATURES FOR OPTIMAL SENSOR NETWORKS BASED ON REAL-SCALE RECORDINGS

Said Quqa[1], Michelangelo Maria Malatesta[1], Panagiotis Martakis[2], Artur Movsessian[3]

[1]University of Bologna
Department of Civil, Chemical, Environmental and Materials Engineering / Advanced Research Center on Electronic Systems
Viale del Risorgimento 2, 40136 / Viale Carlo Pepoli 3/2, 40123 Bologna
e-mail: {said.quqa2,michelange.malatest2}@unibo.it

[2] ETH Zurich
Chair of Structural Mechanics and Monitoring
Stefano-Franscini-Platz 5, CH-8093, Zurich
e-mail: martakis@ibk.baug.ethz.ch

[3] University of Edinburgh
School of Engineering, Institute for Infrastructure and Environment
Alexander Graham Bell Building, Thomas Bayes Road, Edinburgh EH9 3FG, United Kingdom
e-mail: Artur.Movsessian@ed.ac.uk

Keywords: Damage Sensitive Features, Optimal Sensor Networks, Structural Health Monitoring

Abstract. *Structural health monitoring (SHM) includes a wide range of methods focusing on the improvement of structural reliability and life cycle management of engineered systems. In the past decades, smart maintenance procedures have been proposed and implemented for a large number of civil structures with strategic and monumental relevance. Nowadays, rapid advances in signal processing and sensor technology allow for the implementation of smart maintenance schemes for conventional buildings and infrastructure. Vibration-based SHM techniques are among the most applied in the structural engineering field and become increasingly popular due to their interdisciplinary nature. In this framework, the establishment of reliable damage-sensitive features (DSF) is crucial for the efficient evaluation of structural health. This work comprises an investigation on the effectiveness of data-driven DSFs for the case of a large scale reinforced concrete benchmark under shaking table excitation. Different damage identification techniques are applied to expose the propagation of structural damage during strong ground motions. A discussion on the hardware and algorithmic requirements for reliable wireless smart sensor networks (WSSNs), capable of capturing the desired DSFs, is also included.*

1 INTRODUCTION

Despite the unavoidable costs for installation and supervision, the information obtained through monitoring proves to be invaluable in the aftermath of catastrophic events. The recent disaster of the Morandi bridge exposed the unexploited potential of measurements for the maintenance of aging structures. Considerations regarding the life cycle management consist today a prime part of the design of major infrastructure facilities. Structural health monitoring (SHM) provides the tools and the methodologies that allow for the optimization of the maintenance activities along the operational life of structures with substantial impact on the life cycle costs and the safety of the public.

Rapid advances in hardware and software capabilities allow for the widespread diffusion of SHM techniques in the conventional building stock [1, 2]. In particular, Wireless Smart Sensor Network (WSSNs) are the most promising systems for SHM applications because they don't require long cables leading a significant cost reduction and an easier installation procedure. Moreover, WSSNs are characterized by low cost and feature edge-computing capabilities enabling the decentralization of the monitoring process, by reducing the amount of data transferred and improving the energy efficiency of the monitoring configuration [3]. The energy consumption of a wireless network dictates the maintenance intervals and thus consists the bottleneck for the optimal design of WSSNs. Given that energy consumption is highly related to the network architecture, the choice of a suitable network topology for the studied application is of major importance. Shrestha and Xing [4] discussed the performance of various WSSNs topologies by comparing the reliability, energy–efficiency, network life, scalability, self-organizing capability and data latency. Other parameters that constrain further the design of optimal WSSNs stem from cost and size restrictions.

The recent paradigm of Internet of Things (IoT) [5] allows researchers to vision the Internet of STructures (IoST), where proper indexes could provide information regarding structural health at an urban scale, almost in real time. This information could support substantially both the vulnerability assessment as well as the post earthquake damage estimation, which is currently based on time consuming and inevitably subjective inspections. Despite extensive research in this field, the extraction of robust damage sensitive features (DSFs) from vibrational response still poses challenges, particularly related to damage characterization (location, severity) [6, 7]. A large category of DSFs focuses on changes of the modal properties due to structural damage. Noh and coworkers [8] proposed a DSF criterion, which relies on the ratio of the energy allocated on the first mode over the total energy of the response signal. Other candidate methodologies rely on changes in coherence between different nodes, the wavelet decomposition, Hilbert-Huang transform [9], higher order moments or entropy. Recently, Hwang and Lignos [10] described a framework for estimating story-based engineering demand parameters in instrumented steel frame buildings with steel moment-resisting frames. The proposed framework utilizes wavelet-based damage sensitive features and basic building geometric information to infer the building damage state at a given seismic intensity.

This work comprises the implementation of a wide palette of DSFs for the damage detection of full scale recordings. In section 2, the selected features are presented and the key parameters are described. In section 3, the selected features are applied for the evaluation of the recordings of a 7-storey shear wall benchmark experiment. In section 4 are summarized the results and the comparison of the performance of the studied DSFs. Finally, section 5 includes a discussion on the key issues for the design of a decentralised wireless sensor network in a SHM framework.

2 VIBRATION-BASED DAMAGE IDENTIFICATION

In this section, a brief description and some implementation examples of the selected DSFs are reported. Both modal– and non–modal–based features have been selected. In particular, autoregressive (AR) parameters and principal component analysis (PCA) of the covariance of raw acceleration data are usually referred as non–modal–based methods, as the identified parameters cannot be directly interpreted into a modal or physical domain. On the other hand, the curvature of uniform load lines (ULLs) obtained through the flexibility matrix and the transmissibility function belong to the family of modal–based DSFs. Relevant notions for novelty detection as well as damage indices (DIs) implemented in this study are also reported.

2.1 Autoregressive parameters

Autoregressive (AR) models are among the most popular non–modal–based structural identification tools. It has been shown that, despite the non–intuitive physical interpretation of AR parameters, the features captured by AR models, directly fitted to raw acceleration data, are representative of the structural behavior and can be analyzed to detect changes due to damage or changing environmental conditions [11]. AR parameters are computed following the assumption that each sample of a time series depends linearly on the previous samples and can be reconstructed by adding a residual term, which is usually assumed as Gaussian white noise. After selecting a model order (*i.e.*, how many samples are considered in the description of each element of the time series), the identification of AR parameters can be achieved through solving an ordinary least square problem. The simplicity of this method allowed for various implementation in SHM algorithms, involving different usage of AR parameters for the estimation of structural damage [12, 13].

2.2 Covariance–based DSF

Covariance is a common statistical feature that describes the relationship between two signals in time domain. Assessing the covariance of the vibrational responses of sensors placed in different position along a structure has been established as a valid statistical metric for capturing novelties in the dynamic response [14]. These changes, however, can be attributed not only to structural degradation, but also to changing environmental conditions [15]. Principal component analysis (PCA) [16] has been widely applied to enhance the novelty detection by a consequent algorithm. PCA is a linear transformation which is applied to a potentially correlated feature-set. The principal components (PCs) are sorted by their eigenvalues in a decreasing order, where the first PC has the highest explained variance after the transformation. This procedure can reduce the dimension of the feature-set while maintaining a high remaining variance explained.

2.3 Curvature of the uniform load line

Changes in modal curvature is the basis of various modal-based DSFs in the field of damage identification, as it is proven to be particularly effective to localize structural degradation related to stiffness reduction [17]. Major drawbacks of this this feature include its rather approximate computational scheme (i.e., the central difference method), starting from displacement lines, and the fact that at least three data points are required to evaluate each curvature value. As a result, modal curvature based DSFs tend to be too sensitive to inaccuracies in the identification of modal shapes and require a considerable amount of sensors, placed at equidistant locations.

In this paper, the curvature of the uniform load line (ULL) has been applied. This approach describes the structural behavior in the physical space and is less sensitive to identification errors

for higher modal shapes [18]. In particular, the ULL of a structure represents the deflection shape under the application of a uniform load vector, the entries of which are unitary forces applied at each sensor location. The ULL is generally evaluated through the flexibility matrix of the structure **F**, which can be estimated by the first r vibration modes, as following:

$$\mathbf{F} \cong \sum_{j=1}^{r} \frac{1}{\omega_j^2} \mathbf{\Phi}_j \mathbf{\Phi}_j^T \tag{1}$$

where ω_j and $\mathbf{\Phi_j}$ indicate the j–th natural circular frequency and modal shape, respectively. The ULL can thus be computed as:

$$\mathbf{u} = \mathbf{F}\mathbf{p} \tag{2}$$

where $\mathbf{p} = [1, 1, \ldots, 1]^T$ has the same size as $\mathbf{\Phi}_j$.

It should be noted that, in order to compute the real flexibility matrix, modal shapes must be mass-normalized. In this case, a variation of **u** registered during a monitoring process could also be related to a physical quantification of damage in terms of flexibility increment (*i.e.*, stiffness decrement). In real case studies, however, there is often no precise information regarding the mass distribution, especially for complex structures. As a result, the evaluation of **F** becomes particularly challenging. For the purposes of the present work, a uniform distribution of masses along the height of the building is considered. This assumption coincides with the regular geometry of the studied benchmark experiment. Therefore, modal shapes are normalized with respect to an identity matrix, and **F** is considered as proportional to the real flexibility matrix. In this case, a quantification of damage in absolute terms is not possible, but the method still allows for the localization of damage [19].

2.4 Transmissibility based criteria

Transmissibility based criteria have been recently proposed in an attempt to detect and localize damage based on output-only data [20]. The transmissibility function between points *a* and *b* of an elastic system can be defined as the ratio of the complex amplitude of the system responses in frequency domain, which can be expressed as a fraction of power spectral densities:

$$T_{a,b}(\omega) = \frac{X_a(\omega) \times X_b(\omega)}{X_b(\omega) \times X_b(\omega)} = \frac{G_{a,b}(\omega)}{G_{b,b}(\omega)} \tag{3}$$

By implementing Pearson's correlation coefficient for the transmissibility vectors in different damage states, researchers defined a correlation-based damage indicator (CDI):

$$CDI_{a,b} = |\frac{Cov(T^d, T^u)}{\sigma_{T^d}\sigma_{T^d}}| \tag{4}$$

An additional feature based on the modal assurance criterion was also defined as transmissibility assurance criterion (TAC):

$$TAC_{a,b} = \frac{[(T^d)^T(T^u)]^2}{[(T^d)^T(T^d)][(T^u)^T(T^u)]} \tag{5}$$

where T^d and T^u represent the transmissibility vectors under damaged and healthy conditions. Considering the points *a* and *b* as the recording points along subsequent storeys of a building,

transmissibility based criteria provide information for structural changes between the measuring points. For shear wall concrete buildings with rigid slabs, the earthquake induced damage is expected to concentrate in the lower floor levels. For such cases, transmissibility based criteria for damage detection and localisation are well defined. However, such criteria cannot provide robust estimation for the level of damage since they rely exclusively on low amplitude measurements, where the system is expected to respond in the equivalent elastic regime.

2.5 Mahalanobis Distance

The Mahalanobis distance (MD) is a widely applied multivariate distance metric to highlight novelties or outliers in a feature-set [21]. The MD measures the distance between a point and a distribution. The distribution is commonly calculated for a reference feature-set which is also called the training-set. The MD is described as follows:

$$d(\mathbf{x}^k, \mathbf{Y}) = \sqrt{(\mathbf{x}^k - \boldsymbol{\mu}_\mathbf{Y})^T \boldsymbol{\Sigma}_\mathbf{Y}^{-1} (\mathbf{x}^k - \boldsymbol{\mu}_\mathbf{Y})} \tag{6}$$

where $d(\mathbf{x}^k, \mathbf{Y})$ is the distance between a feature vector $\mathbf{x}^k$ and a reference $\mathbf{Y}$, with k being the k^{th} feature vector in a feature-set. $\boldsymbol{\mu}$ is the mean of features in $\mathbf{Y}$ and $\boldsymbol{\Sigma}$ the covariance of the reference feature-set. This metric is used as DI for the modal-based DSFs investigated in this work.

2.6 Damage indices and novelty detection

For most of the damage identification algorithms the identified parameters are compared to baseline information obtained right after the installation of the monitoring system. This baseline information is considered to represent the undamaged condition. To quantify this comparison, a proper DI has to be selected and a threshold between "damaged" and "healthy" state has to be defined. For the AR and covariance based DSFs the MD has been used as a DI since a statistically significant set of results were evaluated. For the former case, a different set of AR parameters can be identified for each data array (i.e., considering data intervals of user-defined length at each sensor location). In general, damage localization cannot be directly achieved by analyzing local modifications in AR parameters [13]. For this reason, the mean of MDs computed over the set of all recording nodes has been selected as the final DI for the purposes of damage detection. Similarly, the MD-based damage index is evaluated for the covariance and PCA based DSF. A threshold is selected for the reference state and is represented by T_{th}. The choice of T_{th} is based on a cumulative distribution of the damage index where the k^{th} percentile of the data is allowed to exceed the threshold. Consequently, $d(\mathbf{x}^k, \mathbf{Y}) > T_{th}$ are considered as novelties and are potentially correlated to damage.

For the modal-based DSFs longer datasets are required and thus only deterministic DIs can be defined through the analyzed data. For the curvature of the ULL, the percentage variation between local estimates of the DSF in different damage scenarios is considered. For the transmissibility based DSF the identified CDI and TAC metrics are evaluated.

3 DAMAGE DETECTION ON REAL-SCALE RECORDINGS

The DSFs described in Section 2 are evaluated using the data collected during a benchmark experiment on a full-scale RC structure tested on a shaking table at the University of California, San Diego [22, 23]. After a brief description of the case study, the results are reported and discussed.

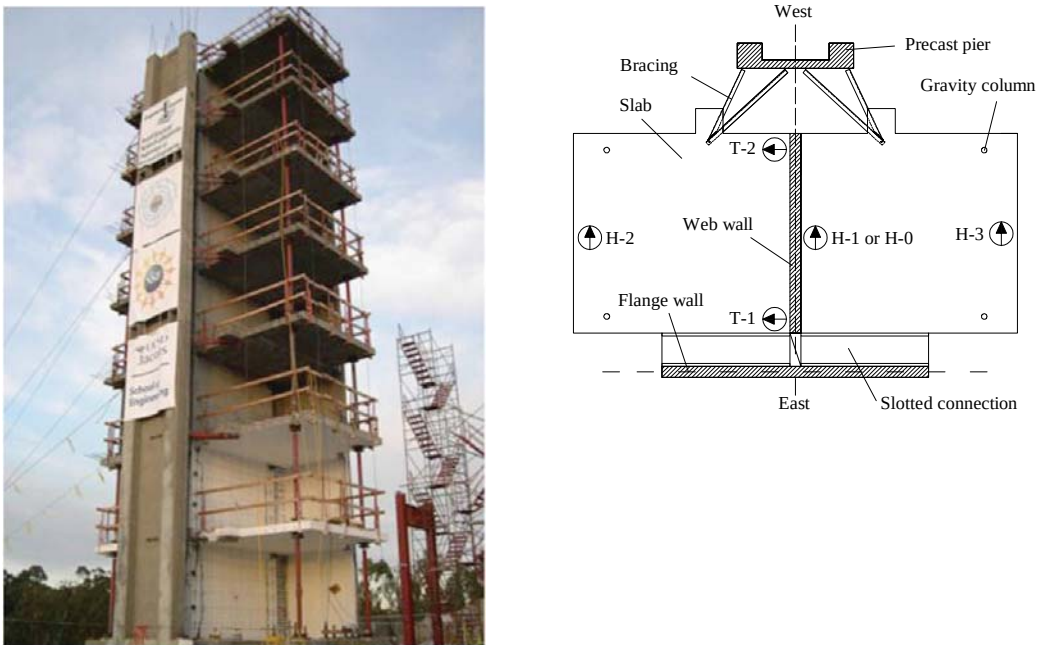

(a) (b)

Figure 1: Picture of the tested structure (a) and ground floor plan of typical storey (b)

3.1 Description of the case study

The specimen, shown in Figure 1a, consists of two perpendicular walls (web and flange wall) and a concrete slab at each storey–level, supported by four gravity columns and an auxiliary post–tensioned column that provides torsional stability to the system (Figure 1b). Shaking table tests were designed to progressively damage the building through the simulation of four historic earthquakes recorded in California, with increasing intensity. Before and after each shaking test, the response of the building was recorded under white noise (WN) excitation, with a root mean square (RMS) amplitude equal to $0.03\,\mathrm{g}$, and low amplitude ambient vibration (AV), as described in detail in [22, 23] and in Table 1. In particular, between tests S3.1 and S3.2, the bracing system between the slabs and the post–tensioned column was stiffened. The present work focuses exclusively on the acceleration response during the white noise excitation before and after the strong shaking events.

The instrumentation of the tested structure includes 45 uniaxial accelerometers: 29 measuring the longitudinal direction (three on each floor slab, one on the web wall at mid-height of each story, and one on the pedestal base), 14 measuring the transversal direction (2 on each floor slab), and 2 nodes measuring the vertical direction (at the base, on the pedestal). In this paper seven different sensor configurations are considered, as described in Table 2, with reference to Figure 1b. The original data are sampled at $240\,\mathrm{Hz}$ and are here downsampled at $100\,\mathrm{Hz}$. More details about the geometry and the instrumentation can be found in [22, 23].

Test	Description
S0	8min WN (0.03%g RMS) + 3min AV
EQ1	San Fernando earthquake, 1971, longitudinal component, Van Nuys station
S1	8min WN (0.03%g RMS) + 3min AV
EQ2	San Fernando earthquake, 1971, transversal component, Van Nuys station
S2	8min WN (0.03%g RMS) + 3min AV
EQ3	Northridge earthquake, 1994, longitudinal component, Woodland Hills Oxnard Boulevard station
S3.1	8min WN (0.03%g RMS) + 3min AV
S3.2	8min WN (0.03%g RMS) + 3min AV
EQ4	Northridge earthquake, 1994, 360°, Sylmar Olive View Med
S4	8min WN (0.03%g RMS) + 3min AV

Table 1: Testing setup

Deployment layout	Description
H-0	SD on the web wall in the horizontal direction, at floor levels and mid-height of storeys
H-1	SD on the web wall in the horizontal direction, at floor levels
H-2	SD on the southern part of the slab in the horizontal direction
H-3	SD on the northern part of the slab in the horizontal direction
T-1	SD on the eastern part of the web wall in the transversal direction, at the floor levels
T-2	SD on the western part of the web wall in the transversal direction, at the floor levels
HT	All sensors described above

Table 2: Sensor deployment layouts

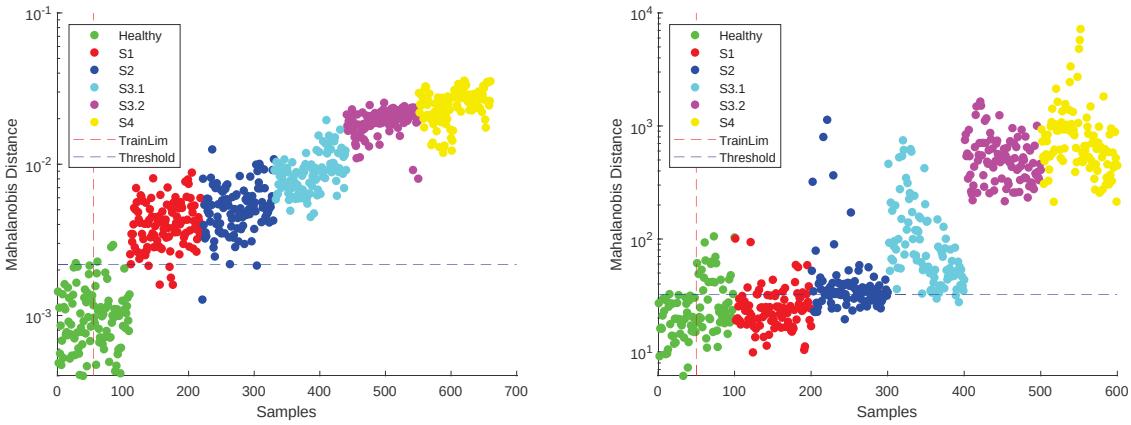

(a) AR Model

(b) Covariance based DSF

Figure 2: Control charts for non-modal-based DSFs

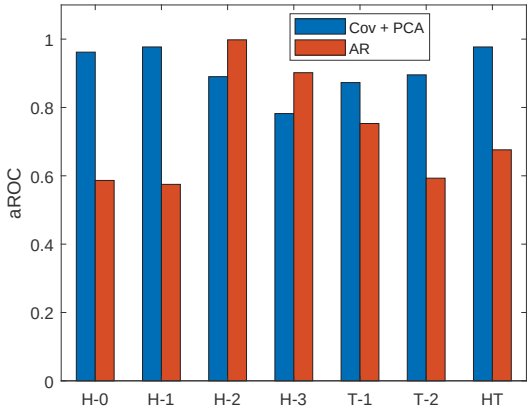

Figure 3: aROC and false alarm rates obtained for the non-modal-based approaches

3.2 Discussion of the results

For non-modal-based DSFs, a control chart approach demonstrates clearly the online novelty detection procedure for damage identification. Response windows of seven minutes, divided into sets of 1000-samples, are considered as separate inspection intervals. The DSF is computed for each inspection interval and compared to the baseline estimation, which is evaluated based on the first 55 intervals for condition S0. In Figure 2, the MD between the feature evaluation on each interval and the baseline is presented. For brevity, only the results for the sensor deployment layout T-1 are reported. The threshold for novelty detection is set in the training set and allows 1% of outliers. A comparison between the control charts of the AR based DSF (Figure 2a) and the covariance based DSF (Figure 2b) demonstrates that, the AR model captures adequately the transition from the healthy state to the first damaged state, while it fails to provide clear boundaries between the subsequent damage states. On the other hand, the covariance based DSF differentiates better significant damage (S4 and S5) from the initial damage states, while indicates minor variations from conditions S1 to S3.1.

Summary results obtained from the evaluation of these DSFs using all the deployment layouts of Table 2 are reported in Figure 3. It can be noticed that, although the false alarm rate of the covariance-based method is generally higher, the area under the ROC curve (indicated

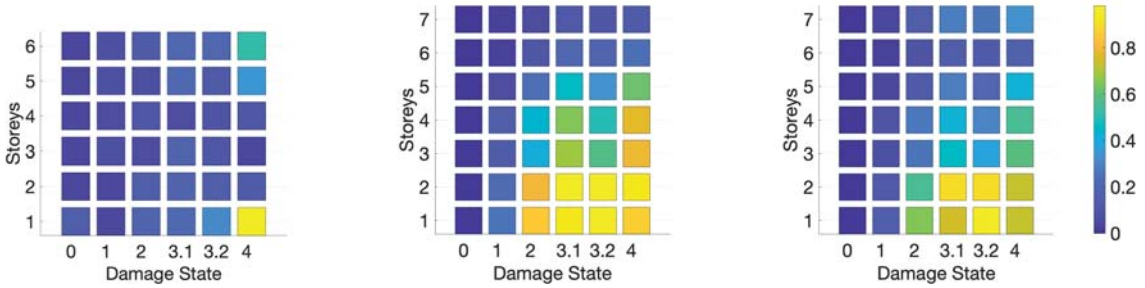

(a) Curvature (b) TAC (c) CDI

Figure 4: Transmissibility-based and curvature-based damage indices evaluated for each damage condition

here as aROC) is greater in most cases, denoting a better discrimination between healthy and damaged conditions. Moreover, it is worthy to note that the AR-based method works better in the transversal direction, showing higher aROC values, while the covariance-based approach performs well in all the deployment layouts.

Figures 4a, 4b and 4c illustrate the damage indices calculate by the curvature-based and the transmissibility based approaches, by considering the sensor deployments H-1. In this work, a deterministic comparison between healthy and damaged conditions is considered. In order to compute curvature, the central difference method is employed, assuming that the base displacement is 0, obtaining 6 curvature values.

While the curvature-based approach is less sensitive to small damages, the transmissibility function appears to detect also small variations in the dynamic behavior, showing an accurate estimation of the damage position and consistent representation of the identified damage degradation due to increasing the excitation amplitude. Moreover, the TAC criterion proves to be more sensitive to damage in comparison to the CDI criterion.

4 CONSIDERATIONS ON WIRELESS SENSOR NETWORK IMPLEMENTATIONS

The considerations reported in this section refer to a star-topology network. This is one of the most commonly used topology due to its simplicity, although Cluster Head and mesh topologies provide a better flexibility, *i.e* network scalability, communication reliability or energy management [4]. In particular, the network was designed to collect n samples of acceleration data at each node location at user-defined inspection intervals. Depending on the feature, DSFs are then partially or fully computed in the central monitoring station (*i.e.*, the sink node), where damage identification takes place. Table 3 summarizes the main characteristics of interest for the implementation of DSFs on a WSSN. While univariate AR parameters and covariance can only identify structural changes due to modifications of the dynamic response in time domain, modal-based parameters can provide information about the position and, under certain assumptions, the extent of damage. The number of channels needed to calculate each DSF reflects the possibility to compute it in a decentralized manner, by performing part of the processing on the nodes. The minimum number of samples to be transferred to the central monitoring station for the evaluation of the DSFs is also considered as a performance index.

AR parameters are identified on single data series, such as the raw acceleration signals recorded by each node. In this case, AR parameters could be identified onboard and the transmission could be reduced to the selected order of the AR model (p). Covariance and trans-

DSF	Id level	Num. of channels	Num. of samples	Complexity
AR parameters	Detection	$\geqslant 1$	p	O(p^2n)
Covariance	Detection	$\geqslant 2$	n	-
Curvature	Loc./Quant.	$\geqslant 3$	n	-
Transmissibility	Localization	$\geqslant 2$	s	O($slog(s)$)

Table 3: Characteristics of the considered DSFs

missibility functions require couples of acceleration channels for their evaluation in time and frequency domain respectively. Truncated spectra can thus be employed to estimate the transmissibility in the band of interest. The number of samples required at the level of central node is therefore equal to the number of points of the truncated frequency spectrum (s), which can be computed on each node before transmission. The curvature based DSF requires recordings of at least three subsequent nodes to be computed. Hence, the identification of this feature has to be performed in a centralized fashion with complete data series, in order to preserve phase information.

Computational complexity is an aspect of utmost importance when decentralized processes are implemented on low-cost smart nodes, since they are generally characterized by small computational capabilities and limited battery life. The identification of AR parameters can be obtained through several algorithms with varying complexity. The ordinary least squares problem yields an asymptotical complexity of O(p^2n), with p denoting the order of AR model and n the number of training samples. Alternatively, through the Yule-Walker method, the complexity becomes O($p^2 + np$), still being strongly dependent on the selected order, which increases with the structural complexity. Among the different Yule-Walker solvers, Dushin and Frolov [24] exploited the Levinson–Dusrbin recursion for extrapolating AR coefficients and monitoring environmental phenomena such as humidity and light. Lynch [25] exploited the Burg's method to solve the Yule-Walker equations which avoids complex matrix inversion operations. In such a case, considering 4000–time samples and the identification of 30 AR coefficients, the WSSN needed $8\,\mathrm{s}$ of computational time with $3\,\mathrm{J}$ of energy consumption.

Covariance and curvature based DSFs are not suitable for decentralization in a simple star-topology network. Hence, the computational complexity at the central node is high, involving the evaluation of all couples of covariance functions for the former feature, and a complete automated modal identification for the latter. The computation of the frequency spectrum for the identification of transmissibility functions can be conducted on the nodes with a complexity of O($slog(s)$), by implementing fast Fourier transform (FFT) with s frequency points. It is worth mentioning that Goertzel's algorithm [26] can also be utilized for frequency analysis with a computational complexity of O(s) for a single bin of the spectrum and exploiting recursion [27].

5 CONCLUSIONS

Despite recent advances in algorithms and hardware related to damage identification, SHM remains an unexploited potential in civil engineering practice. The substantial costs related to the instrumentation and the management of the recorded data undermine the widespread implementation of sensors networks that could provide valuable insights into the structural behaviour of infrastructure and buildings during and after catastrophic events. This work explores the efficiency of various modal-based and data-driven DSFs, implemented on real scale recordings. The applicability of the studied DSFs in low cost WSSNs, in terms of computational complex-

ity, energy efficiency and data transmission, is also discussed.

In the present case, data-driven DSFs estimated by short data series detect accurately damage and could be computed almost in real time in permanent SHM applications. While the AR-based approach proves to be more robust in sensing the transition from healthy to damaged state, the covariance–based approach is more suitable to identify severe structural degradation. The possibility to compute the AR parameters on smart nodes allows for the decentralization of the processing, reducing substantially the volume of the data to be transmitted. For distributed sensor networks, modal–based DSFs can provide information related to both the location and the severity of damage. In the present study, transmissibility–based approaches perform very well in both tasks. Although these indexes can only be assessed in the central node, the required information reduces to truncated spectral coordinates. Finally, the curvature-based approach proves to be sensitive only to severe damage and is not suitable for decentralized configurations.

REFERENCES

[1] B.F. Spencer Jr, J-W. Park, K.A. Mechitov, H. Jo, and G Agha. Next generation wireless smart sensors toward sustainable civil infrastructure. *Procedia Engineering*, 171:5–13, 2017.

[2] F. Zonzini, M. M. Malatesta, D. Bogomolov, N. Testoni, L. De Marchi, and A. Marzani. Heterogeneous sensor-network for vibration-based shm. In *2019 IEEE International Symposium on Measurements & Networking (M&N)*, pages 1–5. IEEE, 2019.

[3] M. Abdulkarem, K. Samsudin, F. Z. Rokhani, and M. F. A Rasid. Wireless sensor network for structural health monitoring: A contemporary review of technologies, challenges, and future direction. *Structural Health Monitoring*, page 1475921719854528, 2019.

[4] A. Shrestha and L. Xing. A performance comparison of different topologies for wireless sensor networks. In *2007 IEEE Conference on Technologies for Homeland Security*, pages 280–285. IEEE, 2007.

[5] C. Scuro, P. F. Sciammarella, F. Lamonaca, R. S. Olivito, and D. L. Carni. Iot for structural health monitoring. *IEEE Instrumentation & Measurement Magazine*, 21(6):4–14, 2018.

[6] F. Casciati and S. Casciati. Structural health monitoring by Lyapunov exponents of non-linear time series. *Structural Control and Health Monitoring*, 13(1):132–146, 2006.

[7] P. Omenzetter and J.M.W. Brownjohn. Application of time series analysis for bridge monitoring. *Smart Materials and Structures*, 15(1):129–138, 2006.

[8] H. Young Noh, K. Krishnan Nair, D. G. Lignos, and A. S. Kiremidjian. Use of wavelet-based damage-sensitive features for structural damage diagnosis using strong motion data. *Journal of Structural Engineering*, 137(10):1215–1228, 2011.

[9] N.E. Huang, Z. Shen, S.R. Long, M.C. Wu, H.H. Snin, Q. Zheng, N.C. Yen, C.C. Tung, and H.H. Liu. The empirical mode decomposition and the Hubert spectrum for nonlinear and non-stationary time series analysis. *Proceedings of the Royal Society A: Mathematical, Physical and Engineering Sciences*, 454(1971):903–995, 1998.

[10] S. H. Hwang and D. G. Lignos. Nonmodel-based framework for rapid seismic risk and loss assessment of instrumented steel buildings. *Engineering Structures*, 156:417–432, 2018.

[11] H. Sohn, J.A. Czarnecki, and C.R. Farrar. Structural health monitoring using statistical process control. *Journal of structural engineering New York, N.Y.*, 126(11):1356–1363, 2000. cited By 280.

[12] R. Yao and S. N Pakzad. Autoregressive statistical pattern recognition algorithms for damage detection in civil structures. *Mechanical Systems and Signal Processing*, 31:355–368, 2012.

[13] G.M. Steven and M.P. Sudhakar. Statistical moments of autoregressive model residuals for damage localisation. *Mechanical Systems and Signal Processing*, 20(3):627 – 645, 2006.

[14] D. Tcherniak and L.L. Mølgaard. Vibration-based shm system: application to wind turbine blades. In *Journal of Physics: Conference Series*, volume 628, page 012072. IOP Publishing, 2015.

[15] D. Tcherniak and L.L. Mølgaard. Active vibration-based structural health monitoring system for wind turbine blade: Demonstration on an operating vestas v27 wind turbine. *Structural Health Monitoring*, 16(5):536–550, 2017.

[16] A.-M. Yan, G. Kerschen, P. De Boe, and J.-C. Golinval. Structural damage diagnosis under varying environmental conditions—part ii: local pca for non-linear cases. *Mechanical Systems and Signal Processing*, 19(4):865–880, 2005.

[17] W. Fan and P. Qiao. Vibration-based damage identification methods: A review and comparative study. *Structural Health Monitoring*, 10(1):83–111, 2011. cited By 1029.

[18] J. Wang and P. Qiao. Improved damage detection for beam-type structures using a uniform load surface. *Structural Health Monitoring*, 6(2):99–110, 2007.

[19] S. Quqa, L. Landi, and P.P. Diotallevi. Instantaneous modal identification under varying structural characteristics: A decentralized algorithm. *Mechanical Systems and Signal Processing*, 142:106750, 2020.

[20] Y.L. Zhou, H. Cao, Q. Liu, and M.A. Wahab. Output-based structural damage detection by using correlation analysis together with transmissibility. *Materials*, 10(8):1–17, 2017.

[21] H. Sohn, C.R. Farrar, N.F. Hunter, and K. Worden. Structural health monitoring using statistical pattern recognition techniques. *J. Dyn. Sys., Meas., Control*, 123(4):706–711, 2001.

[22] B. Moaveni, X. He, J.P. Conte, and J.I. Restrepo. Damage identification study of a seven-story full-scale building slice tested on the ucsd-nees shake table. *Structural Safety*, 32(5):347–356, 2010.

[23] B. Moaveni, X. He, J. P. Conte, J. I Restrepo, and M. Panagiotou. System identification study of a 7-story full-scale building slice tested on the ucsd-nees shake table. *Journal of Structural Engineering*, 137(6):705–717, 2011.

[24] S.V. Dushin and S.A. Frolov. Distributed data compression algorithm for low-power wide-area networks. In *International Conference on Distributed Computer and Communication Networks*, pages 163–173. Springer, 2019.

[25] J.P. Lynch, A. Sundararajan, K.H. Law, A.S. Kiremidjian, and E. Carryer. Embedding damage detection algorithms in a wireless sensing unit for operational power efficiency. *Smart Materials and Structures*, 13(4):800, 2004.

[26] G. Goertzel. An algorithm for the evaluation of finite trigonometric series. *The American Mathematical Monthly*, 65(1):34–35, 1958.

[27] M. Bocca, J. Toivola, L. M. Eriksson, J. Hollmén, and H. Koivo. Structural health monitoring in wireless sensor networks by the embedded goertzel algorithm. In *2011 IEEE/ACM Second International Conference on Cyber-Physical Systems*, pages 206–214. IEEE, 2011.

EURODYN 2020
XI International Conference on Structural Dynamics
M. Papadrakakis, M. Fragiadakis, C. Papadimitriou (eds.)
Athens, Greece, 23–26 November 2020

EXPERIMENTAL ASSESSMENT OF VIBRATION-BASED METHODS FOR DAMAGE LOCALIZATION

Michal Venglár[1], Pier Francesco Giordano[2], Maria Pina Limongelli[2]and Milan Sokol[1]

[1] Slovak University of Technology, Faculty of Civil Engineering, Department of Structural Mechanics
Radlinského 11, SK-810 05 Bratislava, Slovak Republic
e-mail: {michal.venglar,milan.sokol}@stuba.sk

[2] Politecnico di Milano, Department of Architecture, Built environment and Construction engineering
Piazza Leonardo da Vinci 32, IT-201 33 Milan, Italy
{pierfrancesco.giordano, mariagiuseppina.limongelli}@polimi.it

Keywords: direct stiffness calculation, iterative model updating, modal curvature, interpolation error, strain energy, composite beam, comparison

Abstract. *This paper reports results relevant to the experimental comparison of a number of vibration-based methods for damage localization applied using responses recorded during forced vibration tests on a composite beam. Damage is intended herein as a stiffness change. Four methods from the literature were compared: two model-based methods, namely the direct stiffness determination method and the model updating method and two response-driven methods, namely the modal interpolation error method and the modal strain energy method. The tested specimen is a composite beam made of timber and plaster boards, with a total span of 4.0 m and simply supported at the ends. During the forced vibration tests responses in terms of acceleration were measured at 24 points along the beam axis. Responses were recorded in both the reference states and in several modified states in which local variations of bending and shear stiffness were simulated adding a stiffener or unscrewing a number of bolts. Using the accelerometric responses the comparison of the four considered methods was performed in terms of the accuracy of damage localization.*

1 INTRODUCTION

Vibration-based non-destructive testing as part of Structural Health Monitoring (SHM) has become a growing interest of the civil engineering research community due to the increased need of an informed support to decision related to the request for higher safety standards [1], to the large number of structures approaching the end of design life and to the changing of loading conditions due to the increase of traffic [2]. The goal of SHM is to optimize structural management through the identification of structural damage at the earliest stage or the acquisition of data enabling a prognosis of the remaining service life. This can reduce both long-term and emergency management costs [3]–[6]. According to [7], it is expected that in the future SHM will take an important part in the administration of transport infrastructure due to the lack of effectiveness and scarce reliability of visual inspections which are highly dependent on the subjectivity of the operator and do not provide real-time information about the structural state.

Several SHM methods exist in the literature, allowing different levels of damage identification, i.e. damage detection, damage localization, damage quantification and damage prognosis [8]. In this paper the focus in on vibration-based damage localization methods, which uses vibration data, e.g. velocities and accelerations, recorded on instrumented locations of the structure to identify changes in stiffness. In general, they can be classified in model-based methods and response-based methods. Model-based methods need a numerical model of the structure, e.g. Finite Element (FE) model, whereas response-based methods use only data recorded on the structure. Model-based methods are more time consuming and require higher computational effort with respect to response-based methods. However, they usually allow also to quantify the severity of damage beside its existence and location. A comparison of several response-based methods for damage localization applied on a real bridge is provided in the reference [9].

In this paper, four well-known vibration-based methods for damage localization are compared: two model-based methods, namely the direct stiffness determination method and the model updating method and two response-based methods, namely the modal interpolation method and the modal strain energy method. Damage is intended in general as a change in stiffness. The methods are applied to a bridge-like lab specimen using modal parameters provided by experimental modal analysis. The comparison is performed in terms of accuracy of the damage localization. Different scenarios are considered, namely an increase of bending stiffness and two shear damages.

The paper consists of several sections. Section 2 introduces the considered methods; Section 3 describes the experimental specimen and the damage scenarios; Section 4 reports the results of the damage assessment and the comparison of results; conclusions are given in Section 5.

2 THEORETICAL BACKROUND OF USED METHODS

2.1 Model-based methods

2.1.1. Finite Element Model Updating

The Finite Element Model Updating (FEMU) method uses a numerical model of the investigated structure whose parameters are updated minimizing the residual between the model and the structure experimental characteristics. Herein the values of the modal parameters, estimated by means of operational or experimental modal analysis, are used to update the stiffness matrix of the FE model. The stiffness matrix is modelled as a function of the model parameters according to the equation:

$$\mathbf{K}(\theta_{\mathrm{M}}) = \mathbf{K_0} + \sum_{j=1}^{N_M} \theta_{M,j}\mathbf{K_j} \tag{1}$$

where $\mathbf{K_0}$ represents an initial stiffness matrix, $\mathbf{K}(\theta_{\mathrm{M}})$ is the updated stiffness matrix which depends on the parameter vector θ_{M}, $\mathbf{K_j}$ is the contribution of the substructure $j = 1, \dots, N_M$ to the global stiffness matrix and $\theta_{M,j}$ is a scaling parameters representative of its effective stiffness.

The optimal parameters are found by minimizing a cost function [10]. As mentioned in [11], in most practical applications, the cost function is formulated as a sum of squared residuals, as follows:

$$F(\theta_M) = \frac{1}{2}\sum_{k=1}^{m} a_k \frac{\left(\bar{d}_k - y_k(\theta_{\mathrm{M}})\right)^2}{\bar{d}_k^2} \tag{2}$$

where $\bar{d}_k$ is the $k = 1, \dots, m$ experimental data, $y_k(\theta_{\mathrm{M}})$ is the output response of the model and the factor a_k reflects the weight appointed to the normalized residuals. In this paper the components of the modal shapes are used as output model y_{k}.

By minimizing the cost function $F(\theta_M)$, it is possible to find values of the optimal parameter θ^*_{M} that the best match between the model and the experimental data is achieved.

2.1.2. Direct stiffness calculation

The direct stiffness calculation (DSC) method uses the experimental natural frequencies and their corresponding mode-shapes to derive the dynamic stiffness. The method is based on the relation, valid at each section *x* of the beam, between the dynamic bending stiffness *EI*, the bending moment M_b and the corresponding curvature (second derivative of modal shape ϕ_b) [12], [13]:

$$EI(x) = \frac{M_b(x)}{\phi_b''(x)} \tag{3}$$

The bending moments M_b are caused by the inertial forces F_I corresponding to the considered modal shape and can be computed at each section as:

$$F_I(x) = \omega^2 m(x)\phi_b(x) \tag{4}$$

where $m(x)$ represents a mass at each section, ω is the natural frequency and $\phi_b(x)$ is the value at each section of the modal shape connected to the natural frequency ω. In the case of undamped system, the relation between internal forces and inertial forces is:

$$\mathbf{K}\boldsymbol{\phi}_b = \omega^2 \mathbf{M_a}\boldsymbol{\phi}_b \tag{5}$$

where $\mathbf{K}$ is stiffness matrix, $\mathbf{M_a}$ represents a mass matrix (analytically determined) and $\boldsymbol{\phi}_b$ is the vector of the bending modal shape. It represents a pseudo static system. Therefore, the accelerations recorded during the forced vibration tests can be directly multiplied by mass matrix in order to calculate the inertial forces. These pseudo static forces are used in static analysis

(e.g. with a finite element package) in order to calculate modal bending moments M_b. The next step represents calculation of curvature, e.g. using the Finite Difference Method. Because of the occurred inaccuracies, it is recommended to use smoothing function. Therefore, residual penalty-based method is applied and is very similar to FE approach mentioned before. The references [12], [13] describe the method in more detail.

2.2 Response-based methods

2.2.1. Modal strain energy method

The damage index proposed in reference [14] is based on the assumption that damage does not change the fraction of modal strain energy, defined as the ratio between the modal strain energy stored in the *i*-th element and the modal strain energy stored in the structure. In this way, the ratio between the bending stiffness of the *i*-th element in the Undamaged (U) and in the Damaged (D) states can be computed as a function of the modal curvatures retrieved by the SHM system in the two states. Summing up the contributions of all the identified modes, the following expression is obtained for the damage index at the *i*-th location, i.e. one of the $i = 1, \dots, N$ locations where the components of the modal shapes are known that is where sensors are located:

$$\beta_i = \sum_{k=1}^{n_{modes}} \frac{\phi''_{k,i,D}{}^2}{\sum_{i=1}^{N} \phi''_{k,i,D}{}^2} \Big/ \sum_{k=1}^{n_{modes}} \frac{\phi''_{k,i,U}{}^2}{\sum_{i=1}^{N} \phi''_{k,i,U}{}^2} \tag{6}$$

The damage index β_i assumes values higher than one at locations where a reduction of the bending stiffness occurs in the state D.

2.2.2. Modal interpolation error method

The interpolation error method proposed in reference [15] takes advantage of the properties of the cubic spline interpolation of mode-shapes to localize damage on structures. In particular, due to the so-called "Gibbs phenomenon for splines", a sudden increase of the interpolation error is observed at the locations with a curvature discontinuity. Therefore, this property can be used to identify the locations where a change of stiffness occurs. At the i-th ($i = 1, .., N$) instrumented location, the performance of the interpolation is computed for the k-th mode through the interpolation error $E_{k,i}$, defined as the absolute difference between the measured component of the k-th mode-shape at that location $\phi_{k,i}$ and the interpolated value $\hat{\phi}_{k,i}$, i.e. $E_{k,i} = \left|\phi_{k,i} - \hat{\phi}_{k,i}\right|$. The interpolation error at the i-th location is obtained by combining the contributions of all the identified modes as follows:

$$E_i = \sqrt{\sum\nolimits_{k=1}^{n_{modes}} E_{k,i}^2} = \sqrt{\sum\nolimits_{k=1}^{n_{modes}} \left|\phi_{k,i} - \hat{\phi}_{k,i}\right|^2} \tag{7}$$

The interpolation error can be computed in the reference state, E_i^U, and in a possibly damaged state, E_i^D. The increase of the interpolation error at the i-th location with respect to the reference state, $\Delta E_i = E_i^D - E_i^U$, indicates a loss of stiffness at that location and it is assumed as damage indicator. The main advantage of this method is that it does not require the direct computation of modal shapes' curvature. Additional information on the interpolation error method can be found in the references [16], [17].

3 EXPERIMENTAL MODEL

3.1 Description of the lab specimen

The tested lab specimen consisted in a simple bridge-like structure made by a main timber beam coupled with plaster boards, see Figure 1. Three timber boards (each with dimensions of 4000 x 100 x 20 mm) were used to build the main beam. The upper part of the specimen, the "deck", was made of three overlapped plasterboard layers with thickness 12.5mm each. The deck was 300 mm wide and 37.5 mm high. The plasterboard layers were connected by pairs of screws tightened every 170 mm into the main timber beam. The supports are located 50 mm from both ends.

Figure 1: The lab specimen.

Three scenarios have been considered, namely the simulation of a repair and two shear damages. They are displayed in Figure 2. The repair, referred in the following as Scenario 1, was simulated by fixing a timber board (dimensions of 200 x 100 x 20 mm) to the main beam at 1.4 m from the left end of the beam, see Figure 2 (a). The two shear damage scenarios, named Scenarios 2 and 3, were modelled by unscrewing a number of bolts connecting the plaster boards and the main beam: the screws were removed in two stages, four screws for each stage. In Scenario 2, four bolts were removed in the area 0-200 mm from the left support. In Scenario 3, the remain four bolts were removed in the area 200-400 mm from the left support, see Figure 2 (b).

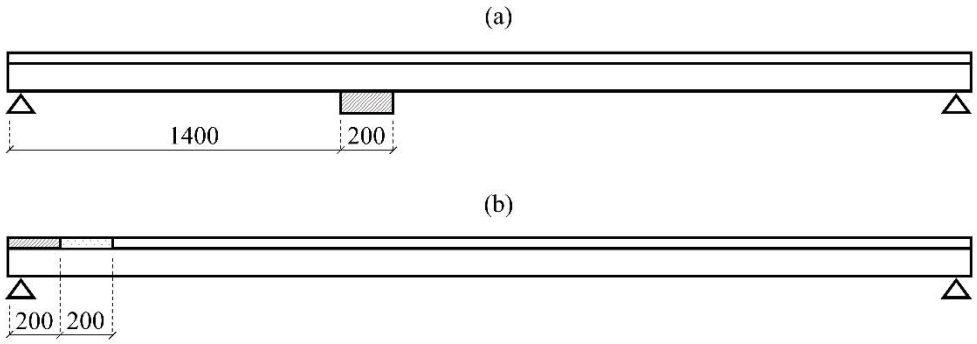

Figure 2: (a) Scenario 1 – the addition of a stiffener; (b) Scenarios 2 and 3 – the shear damage (quotes in mm).

Dynamic tests (forced vibrations test) were carried out using 24 high-sensitivity accelerometers (PCB Piezotronics 393B31) shown in Figure 3 (a). Two electromagnetic exciters were placed 500 mm from both ends of the beam see Figure 3 (b) and synchronized [18] to apply the excitation force as a sine wave. Responses were recorded with a sampling rate of 2048 samples

per second and later down sampled to 100 samples per second. The peak-picking method [19] was applied to perform dynamic identification. Tests were carried out in all scenarios under similar environmental conditions (20°C temperature - 60% humidity). Therefore, the effect of environmental conditions was not taken into account.

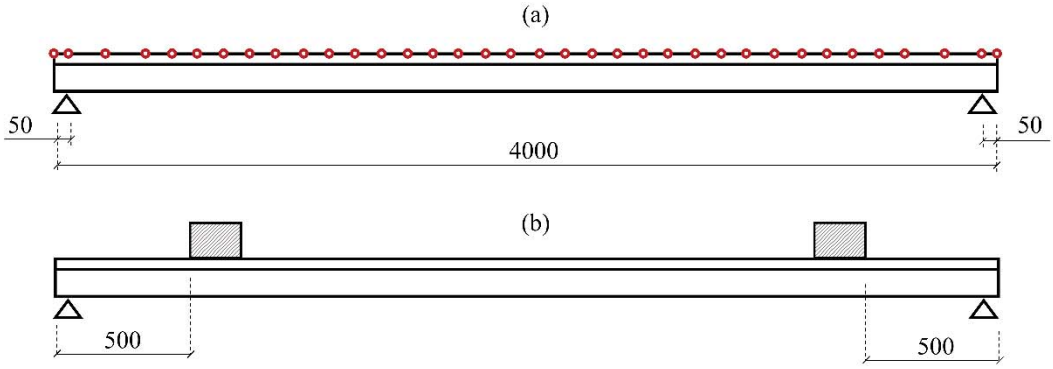

Figure 3: (a) Lateral view of the lab specimen and location of sensors; (b) Location of the exciters (quotes in mm).

4 APPLICATION OF DAMAGE LOCALIZATION MEHTODS

For each scenario, accelerations were measured at 24 locations along the test specimen. The components of the modal shapes were calculated at the same locations and later interpolated using a smooth function according to the method described in [20]. Only the first identified modal shape, reported in Figure 4 for the different scenarios, is used to apply the damage localization methods. It can be observed that in Scenario 1 and Scenario 3 the reference modal shape differs from the modified configuration. Regarding Scenario 2, the modal shapes in the reference and damaged configurations look very similar.

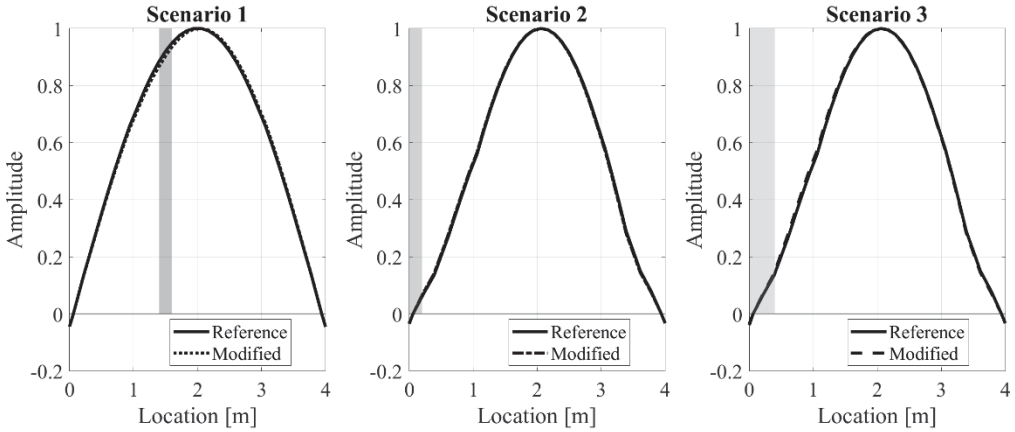

Figure 4: Identified first modal shapes for the considered scenarios

4.1 Results of the model-based methods

The results obtained using the FEMU and the DSC method for Scenario 1, the simulated repair, are displayed in Figure 5. The black line shows the identified values of *EI*. The reference values of this parameter computed from the geometry of the section, are reported with the grey line: EI=274 kNm^2 at the section with the stiffener and EI=145 kNm^2 at all the other sections.

Only the first bending modal shape (shown in Figure 4) was used as input for the two methods. The reason is that the performance of the DSC method decreases when it is applied using higher modal shapes which present multiple nodes, leading to zero by zero division in Equation 3. The bending moments (caused by inertial forces from the first modal shape) at each section were also determined numerically using the FE model. In the application of the DSC method, the curvature was calculated numerically using the Finite Difference Method. According to that, it was possible to calculate the bending stiffness of each section using Equation 3.

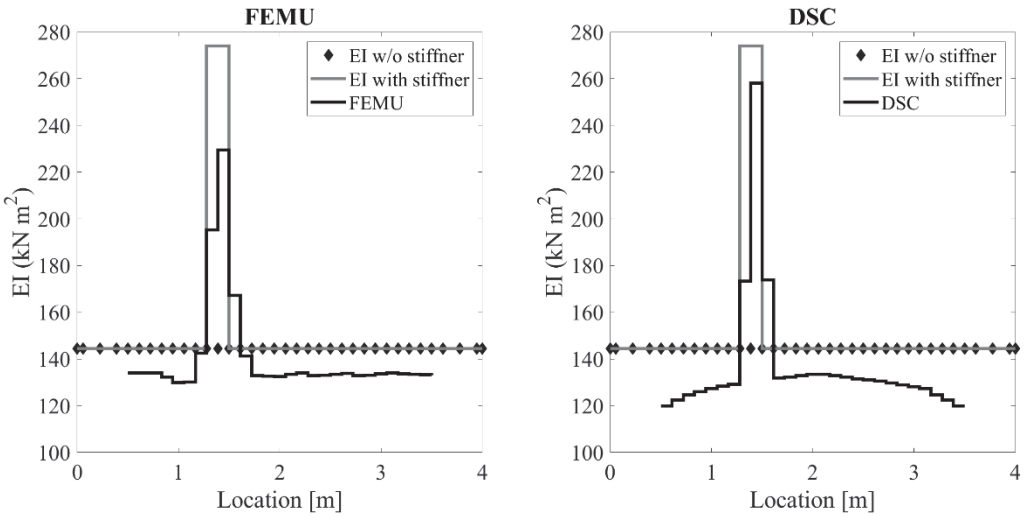

Figure 5: Model based methods: Scenario 1 – repair simulation.

The results of the DSC method are presented only for Scenario 1, since for Scenarios 2 and 3 the method was not able to identify the damage possibly due to its location very close to the boundary where the computation of curvatures is always tricky.

Figure 6 reports the results obtained applying the FEMU method to Scenarios 2 and 3. The reference value computed for the intact beam from its geometry is EI_0=145 kNm^2 marked with a dotted line in Figure 6. The solid line with squares shows the *EI* values identified for the intact structure: the higher values identified in the region close to the left end side of the beam are due to the presence of a higher number of screws with respect to the rest of the beam. The first stage of damage (Scenario 2) was simulated by unscrewing four bolts; additional four bolts were loosened in the second damaged stage (Scenario 3). The values identified for *EI* in the two damage scenarios are reported in Figure 6 and show a decrease around the damaged region with respect to the reference value.

A variation of *EI* (an increase in scenario 2 and a decrease in scenario 3) is mistakenly estimated in the region close to the right end side of the beam, around the section at 3.4 m, from the left end side. This variation is likely to depend on the presence of the shaker at this location that was not modelled as a concentrated mass in the FE model.

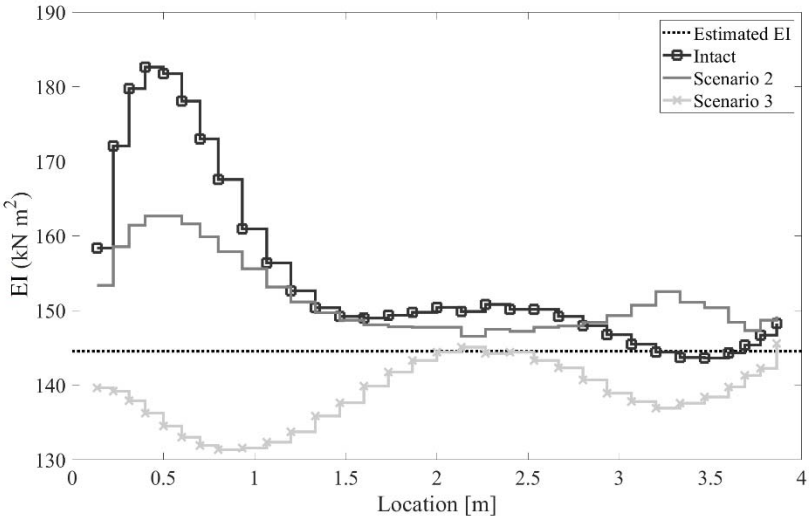

Figure 6: FEMU method: Scenario 2 and 3 – shear damage.

4.2 Response-based methods

The damage indices related to the two response-based damage localization indices are computed according to the formulation described Section 2.2. The curvature, needed to apply the modal strain energy method, is estimated by the Central Difference method. The modal interpolation error method does not require the computation of the curvature. The results are displayed in Figure 7, Figure 8 and Figure 9. The damage indicators in the different positions have been normalized to have the maximum value equal to one. It is observed that both the modal strain energy method and the modal interpolation error method are able to correctly localize changes of stiffness in Scenario 1 and the shear damage simulated in Scenario 2. Note that in the case of the modal strain energy method, the damage indicator reaches the minimum values in correspondence of the added timber board (grey region). In fact, the damage indicator represents the ratio between the bending stiffness between the reference and the "damaged" scenarios. In cases of loss of stiffness, the damage location is associated with a positive peak of the damage indicator.

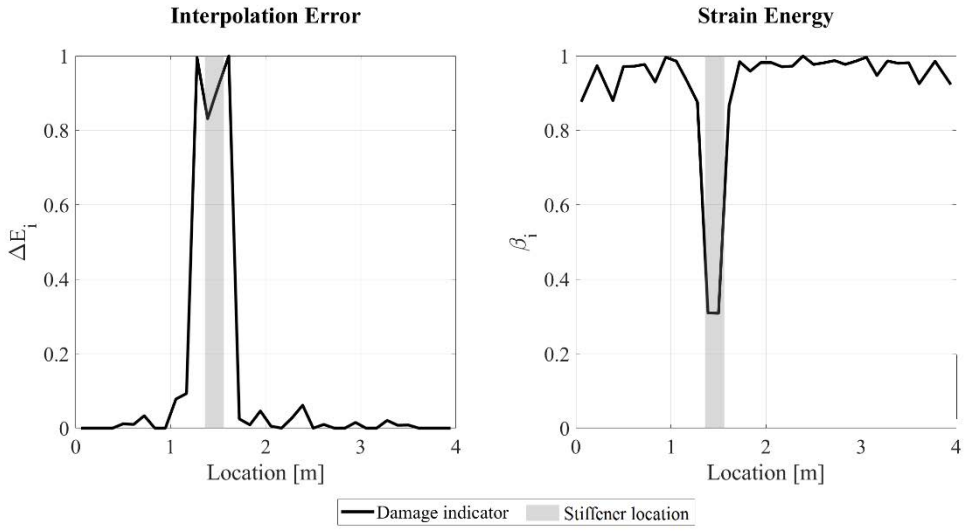

Figure 7 Data-driven methods: Scenario 1 – repair simulation.

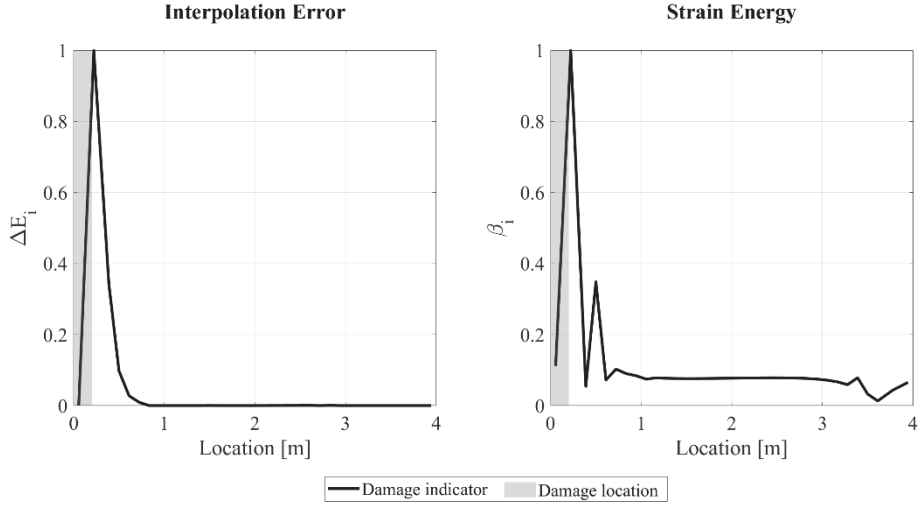

Figure 8: Response-based methods: Scenario 2 – shear damage.

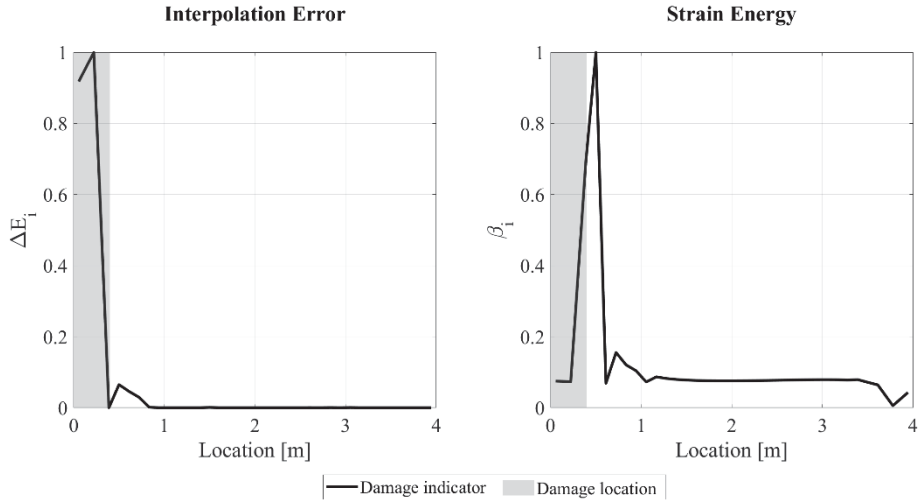

Figure 9: Response-based methods: Scenario 3 – shear damage.

4.3 Comparison of methods

The comparison of the results obtained using the considered methods is performed in terms of the relative error e_L, expressed in percentage, defined in reference [21] as follows:

$$e_L = \frac{x_R - x_I}{L} \times 100 \tag{8}$$

where x_R and x_I are the real and the identified locations, respectively, in which the change of stiffness has occurred and $L = 4\ m$ is the length of the specimen. The relative error can be positive or negative according to the relative locations of x_R and x_I, and it is equal to zero if $x_R = x_I$. The values assigned to x_R are 1. 5 m in Scenario 1, 0.10 m in Scenario 2 and 0.2 m in Scenario 3. The values of the relative errors are displayed in Table 1.

Since a quantification of damage can be achieved by the two model-based methods, a comparison of the two model-based methods is performed in Table 2 in terms of difference of identified and real stiffness achieved in Scenario 1.

Method	Scenario 1	Scenario 2	Scenario 3
DSC	2.78	-	-
FEMU	2.78	-7.23	-4.73
Modal interpolation error	-2.75	-3.05	-0.56
Modal strain energy	0.00	-3.05	-7.50

Table 1: Values of the relative error e_L, in %.

Method	Identified EI [kNm^2]	Reference EI [kNm^2]	Difference [%]
DSC	258	274	-6
FEMU	229	274	-16

Table 2: Comparison of results for Scenario 1.

5 CONCLUSIONS

Four methods for damage localization, two model-based and two response-based are compared in this paper using an experimental case study. Two different damage scenarios were simulated by a) locally changing the bending stiffness of the specimen and b) reducing the shear stiffness gradually in two steps.

The comparison shows that:

- The response-based methods provide the correct identification of damage for the variation of both the bending and the shear stiffness. They are particularly straightforward to apply and do not require a numerical model of the structure. However, these methods do not provide information about damage severity.
- The FEMU - model-based - method provides accurate location and severity of damage for both bending and shear damage scenarios. The DSC while successfully identifies, with higher accuracy with respect to the FEMU, the variation of the bending stiffness, fails to identify a shear damage close to the support of the beam.

ACKNOWLEDGEMENTS

This paper has been supported by the grant No. 1/0749/19 provided by the VEGA Agency of Ministry of Education, Science, Research and Sport of the Slovak Republic and of the Ministry of Education, Science, Research and Sport of the Slovak Republic within the Research and Development Operational Program for the project 'University Science Park of STU Bratislava', ITMS 26240220084. Further support was provided by a grant from the research program of Slovak University of Technology – Excellent teams of young researchers 2018. Part of this work was performed during the stay of Dr Venglar at Politecnico di Milano in the framework of an Erasmus + agreement.

REFERENCES

[1] R. Janeliukstis, S. Rucevskis, M. Wesolowski, and A. Chate, "Damage Identification Dependence on Number of Vibration Modes Using Modal shape Curvature Squares," in *Journal of Physics: Conference Series*, 2016, doi: 10.1088/1742-6596/744/1/012054.

[2] A. Malekjafarian, P. J. McGetrick, and E. J. Obrien, "A review of indirect bridge monitoring using passing vehicles," *Shock and Vibration*. 2015, doi: 10.1155/2015/286139.

[3] Á. Vinkó, "Monitoring and condition assessment of tramway track using in-service vehicle," *Pollack Period.*, 2016, doi: 10.1556/606.2016.11.3.7.

[4] L. Iannacone, P. F. Giordano, P. Gardoni, and M. P. Limongelli, "Quantifying the Value of Information of multiple inspection methods for degrading engineering systems," *Struct. Heal. Monit.*, vol. In Review, 2020.

[5] L. Iannacone, P. Gardoni, P. F. Giordano, and M. P. Limongelli, "Decision making based on the value of information of different inspection methods," in *Structural Health Monitoring 2019: Enabling Intelligent Life-Cycle Health Management for Industry Internet of Things (IIOT) - Proceedings of the 12th International Workshop on Structural Health Monitoring*, 2019, doi: 10.12783/shm2019/32270.

[6] P. F. Giordano, L. J. Prendergast, and M. P. Limongelli, "A framework for assessing the value of information for health monitoring of scoured bridges," *J. Civ. Struct. Heal. Monit.*, vol. In Press, 2020.

[7] Y. An, E. Chatzi, S. H. Sim, S. Laflamme, B. Blachowski, and J. Ou, "Recent progress and future trends on damage identification methods for bridge structures," *Structural Control and Health Monitoring*. 2019, doi: 10.1002/stc.2416.

[8] A. Rytter, "Vibrational Based Inspection of Civil Engineering Structures," 1993.

[9] P. F. Giordano and M. P. Limongelli, "Response-based time-invariant methods for damage localization on a concrete bridge," *Struct. Concr.*, vol. In Review, 2020.

[10] M. P. Limongelli, E. Chatzi, M. Döhler, G. Lombaert, and E. Reynders, "Towards extraction of vibration-based damage indicators," in 8th European Workshop on Structural Health Monitoring, EWSHM 2016, 2016.

[11] E. Simoen, G. De Roeck, and G. Lombaert, "Dealing with uncertainty in model updating for damage assessment: A review," *Mech. Syst. Signal Process.*, vol. 56, pp. 123–149, 2015, doi: 10.1016/j.ymssp.2014.11.001.

[12] J. Maeck and G. De Roeck, "Dynamic bending and torsion stiffness derivation from modal curvatures and torsion rates," *J. Sound Vib.*, 1999, doi: 10.1006/jsvi.1999.2228.

[13] J. Maeck and G. De Roeck, "Detection of damage in civil engineering structures by direct stiffness derivation," *Struct. Dyn. Vols 1 2*, 1999.

[14] N. Stubbs, J. T. Kim, and K. G. Topole, "An efficient and robust algorithm for damage localization in offshore platforms," in *ASCE 10th Structures Congress*, 1992, pp. 543–546.

[15] M. P. Limongelli, "Frequency response function interpolation for damage detection under changing environment," *Mech. Syst. Signal Process.*, 2010, doi: 10.1016/j.ymssp.2010.03.004.

[16] M. P. Limongelli, "The interpolation damage detection method for frames under seismic excitation," *J. Sound Vib.*, 2011, doi: 10.1016/j.jsv.2011.06.012.

[17] M. Dilena, M. P. Limongelli, and A. Morassi, "Damage localization in bridges via the FRF interpolation method," *Mech. Syst. Signal Process.*, 2015, doi:

10.1016/j.ymssp.2014.08.014.

[18] M. Sokol and M. Venglár, "System identification of a composite beam," *Pollack Period.*, 2017, doi: 10.1556/606.2017.12.3.5.

[19] B. Peeters and C. E. Ventura, "Comparative study of modal analysis techniques for bridge dynamic characteristics," *Mech. Syst. Signal Process.*, vol. 17, no. 5, pp. 965–988, 2003, doi: 10.1006/mssp.2002.1568.

[20] M. Sokol and R. Flesch, "Assessment of soil stiffness properties by dynamic tests on bridges," *J. Bridg. Eng.*, 2005, doi: 10.1061/(ASCE)1084-0702(2005)10:1(77).

[21] S. Dincal and N. Stubbs, "Nondestructive damage detection in Euler-Bernoulli beams using nodal curvatures - Part I: Theory and numerical verification," *Struct. Control Heal. Monit.*, 2014, doi: 10.1002/stc.1562.

EURODYN 2020
XI International Conference on Structural Dynamics
M. Papadrakakis, M. Fragiadakis, C. Papadimitriou (eds.)
Athens, Greece, 23–26 November 2020

ON THE PROBLEM OF ON–BOARD VIBRATION–BASED FAULT DETECTION IN RAILWAY SUSPENSIONS UNDER VARYING OPERATING CONDITIONS: A FEASIBILITY STUDY

Georgios Vlachospyros[1], Nikolaos Kaliorakis[1], Ilias A. Iliopoulos[1], Spilios D. Fassois[1], John S. Sakellariou[1], Alexandros Deloukas[2], George Leoutsakos[2], Ilias Chronopoulos[2] and Christos Mamaloukakis[3]

[1]Stochastic Mechanical Systems & Automation (SMSA) Laboratory
Department of Mechanical Engineering and Aeronautics
University of Patras, 26504 Patras, Greece
e-mail: {vlachospyros.g,kaliorakis.n,ilias.iliopoulos}@upnet.gr; {fassois,sakj}@mech.upatras.gr

[2]Attiko Metro S.A.
11525 Athens, Greece
e-mail: {adeloukas,gleoutsakos,ichronopoulos}@ametro.gr

[3]Urban Rail Transport S.A.
10552 Athens, Greece
e-mail: cmamaloukakis@stasy.gr

Keywords: Railway suspension, Fault detection, Health monitoring, Vibration–based methods, Robust methods, Statistical Time Series.

Abstract. *The feasibility of on–board random vibration–based fault detection in railway suspension systems based on a single, car body mounted, vibration sensor and variable nominal traveling speeds (Operating Conditions, OCs) is explored via robust Statistical Time Series (STS) type detection methods. The study is based on field tests performed on an Athens Metro vehicle traveling at* $60, 70, or\ 80\ km/h$*, while two fault scenarios are considered: Air Spring (AS) pressure reduction by* 25% *and Lateral Damper (LD) subject to lubricant loss. The problem is shown to be challenging due to the use of a single sensor, the considerable influence of the OCs (varying nominal speed) on the dynamics, and the minor nature of the LD fault. The study focuses on two Multiple Model type methods: A non–parametric Power Spectral Density based method and a parametric AutoRegressive model based method. The results of the study, based on thousands of test cases, demonstrate perfect detection performance of both methods for the AS fault, but, expectedly, degraded performance (especially by the non–parametric method) for the LD fault. Preliminary comparisons with an alternative method, employing the Multiscale Permutation Entropy (MPE) and Linear Local Tangent Space Alignment (LLTSA), have indicated significant degradation in performance for both fault scenarios.*

1 INTRODUCTION

Health Monitoring for railway vehicle components is important for purposes related to ride comfort and safety, as potential deterioration and faults may have severe implications, including increased derailment risk. Health Monitoring also plays a central role in Condition Based Maintenance (CBM), leading to reduced cost while increasing availability and reliability for railway vehicles [1].

As a result, considerable attention has been devoted to the first important aspect of a Health Monitoring system, which is *detection of faults*, including early–stage faults in railway suspensions which constitute an important part of the vehicles [2].

In this context *on–board vibration–based* methods are particularly important because of a number of advantages, which include the capability of continuous operation without interrupting service, the potential for reliable operation, high detection performance, full automation, operation with a minimal number of sensors (due to the methods' "global" nature), and also the abundant availability of low cost sensors and related equipment [2].

The available methods for this purpose may be divided into two broad categories: *Physics–model–based* and *data–model–based* [1] (broadly referred to as model–based and data–based, respectively). As the name implies, methods in the first category rely on physics–based models of the vehicular suspension dynamics [3]. Fault detection is based on a "consistency" (defined in various ways) check of the measured vibration signals and the model, with the suspension system declared as healthy as long as "consistency" is confirmed [4, 5, 6]. Such methods require the detailed and accurate physics–based modeling of the suspension dynamics, including accurate determination of model parameters, which may be cumbersome or difficult in practice. Moreover, the measurement of a considerable number of signals is also required for parameter determination (estimation) in the "*baseline*" or "*learning phase*"; this may be also needed in the method's normal operation in the "*inspection phase*".

On the other hand, methods within the data–model–based category rely on dynamical models obtained from measured signals via system identification and related techniques [1]. Such approaches are more common and offer various advantages including more realistic and accurate modeling, the use of *partial* models of the dynamics based on only few measured signals (even a single signal may sometimes suffice), and modeling simplicity. The methods typically operate on a proper *feature vector* (or *characteristic quantity*) [7], which conveys information on the dynamics; such feature vectors may consist of time–domain [8, 9], correlation–domain [10, 11], or frequency–domain quantities [12].

For all categories of methods, careful and exhaustive assessment of the achievable detection performance, in particular through field tests, are still limited. Performance assessment with early–stage and incipient faults is also scarce, while the detrimental effects on performance of varying *Operating Conditions (OCs)*, such as traveling speed, payload, track irregularities and so on, have been barely addressed — the reader is referred to [4] for track irregularity effects on performance and to [13] for a method designed to account for varying payload. The issue with varying OCs is particularly serious, as the OCs may have significant effects on the feature vector (representing the suspension dynamics), which may even completely "mask" the effects due to a fault and which need to be captured for effective fault detection [13, 14]. *Robust* methods, aiming at effectively overcoming such issues are thus necessary.

The present study *aims* at examining the feasibility of robust data–model–based vibration methods for overcoming some of the aforementioned critical problems. The following questions are specifically addressed:

- Is it feasible to achieve fault detection for *minor*, early–stage, faults in suspension elements? In particular a Lateral Damper (LD) fault consisting of minor oil leakage is considered, along with a more significant Air Spring (AS) fault consisting of pressure reduction by 25%.

- Is it feasible to achieve *effective* detection with a *single* vibration sensor mounted on the car body (implying a very *partial* model of the dynamics) and under *unsupervised* operation? (Implying use of only healthy system signals in the "*baseline phase*".)

- Is it feasible to maintain high detection performance (that is high correct detection rate combined with a minimal false alarm rate) under *varying nominal speeds* (Operating Conditions)?

In this study these questions are addressed via field measurements on an instrumented Athens Metro rail vehicle under three distinct nominal speeds ($60, 70, 80\ km/h$). Two robust Statistical Time Series (STS) type methods of the Multiple Model (MM) type are employed: A *non-parametric* Unsupervised Multiple Model Power Spectral Density (U-MM-PSD) based method, and a *parametric* Unsupervised Multiple Model AutoRegressive (U-MM-AR) based method. Comprehensive and statistically reliable detection performance assessment results are presented via Receiver Operating Characteristics (ROC) curves using thousands of inspection test cases. Interesting comparisons with an alternative method are also provided.

The rest of this article is organized as follows: The vehicle, the fault scenarios and the field measurements are presented in section 2. Preliminary analysis on the effects of the nominal traveling speed and the faults on the random vibration signals are presented in section 3. The robust Multiple Model (MM) based fault detection methods are outlined in section 4, and fault detection performance assessment is presented in section 5. Concluding remarks are finally summarized in section 6.

2 THE VEHICLE, THE FAULT SCENARIOS, AND THE FIELD MEASUREMENTS

2.1 The railway vehicle, the operating conditions, and the measurement set–up

A typical (locally referred to as "third generation") Athens Metro passenger vehicle, manufactured by Hyundai-–Rotem-–Hanwha and consisting of two motorcars with driver cab ($32.609\ tn$ each), two motorcars ($31.379\ tn$ each) without driver cab, and two trailing cars ($26.788\ tn$ each), is employed (total length $106\ m$, mass $181.551\ tn$). Each car body is supported by two bogies, at its front and rear ends, through secondary suspensions. On the other hand, each bogie is connected to two wheelsets through primary suspensions (Figure 1).

In–operation random vibration acceleration signals are measured during field tests (no passengers on board) on a regular straight track, at one of three nominal traveling speeds ($60, 70, 80\ km/h$; permissible deviations of $\pm 3\ km/h$) which constitute the problem's Operating Conditions (OCs). Signal acquisition is based on a single lightweight accelerometer (PCB $356B21$) mounted on one of the trailing cars, at the car body close to the air spring (Figure 1) and measuring in the lateral (y) direction, and a portable data acquisition unit (NI PXIe-1082 chassis and NI PXIe-4492 module). The total numbers of measured signals and related details are presented in Table 1.

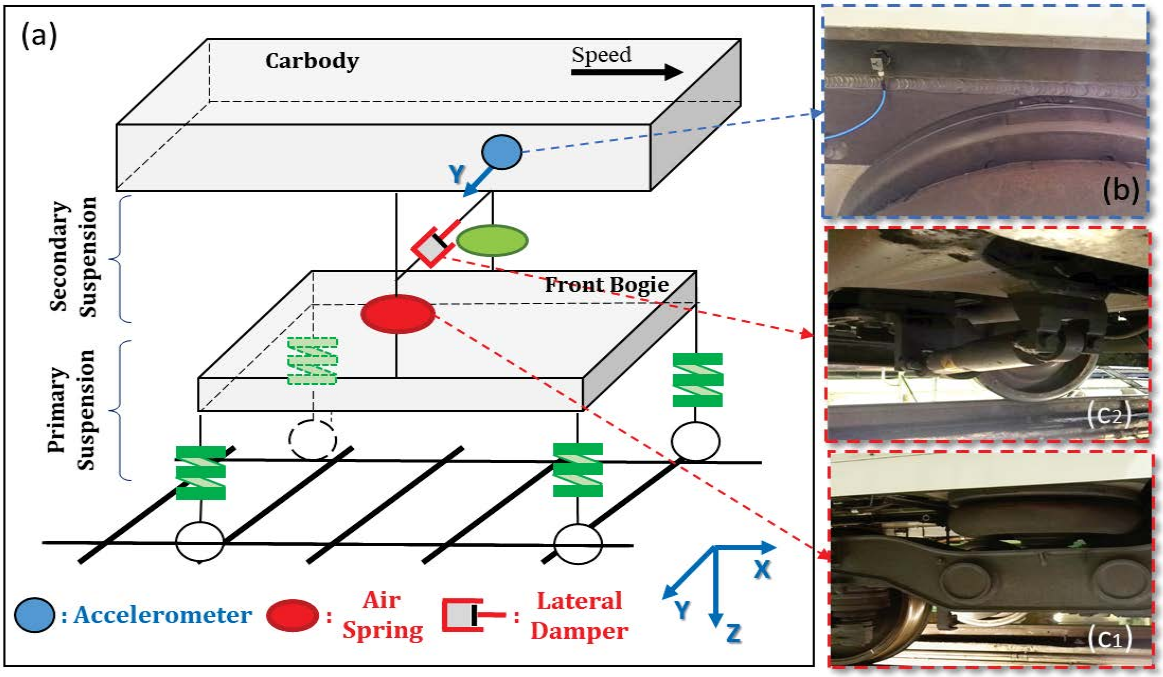

Figure 1: Measurement set–up: (a) Half vehicle schematic, (b) accelerometer position, (c) fault scenarios [(c_1) Air Spring, (c_2) Lateral Damper].

Vehicular health state	# of signals (per speed)	# of signals (all speeds)
Healthy	37	111
Lateral Damper (LD) fault	15	45
Air Spring (AS) fault	12	36
Signal bandwidth $2-490$ Hz; sampling frequency $f_s = 980$ Hz; signal length $N = 8\,000$ samples (8.16 s).		
Nominal vehicular speeds 60, 70, 80 km/h (Operating Conditions).		

Table 1: Numbers of employed signals and their characteristics.

2.2 The fault scenarios and the vibration signals

Two fault scenarios are considered: The 1st corresponds to Air Spring (AS) pressure reduction by 25%, and the 2nd to Lateral Damper (LD) deterioration due to lubricant loss (Figure 1). The measured random vibration signals are pre—processed via Chebyshev Type II high pass filtering (filter order 18, cutoff frequency $f_c = 2\ Hz$) and subsequent normalization by each signal's standard deviation.

3 PRELIMINARY ANALYSIS: EFFECTS OF THE NOMINAL TRAVELING SPEED AND THE FAULTS ON THE RANDOM VIBRATION SIGNALS

The changes in the dynamics induced by a fault are reflected in the measured random vibration signal characteristics, through which fault detection is to be accomplished. Yet, the vibration characteristics (and the corresponding *partial dynamics*) are also influenced by the traveling speed [14]; this is due to the "wheelbase filtering" phenomenon [15] associated with

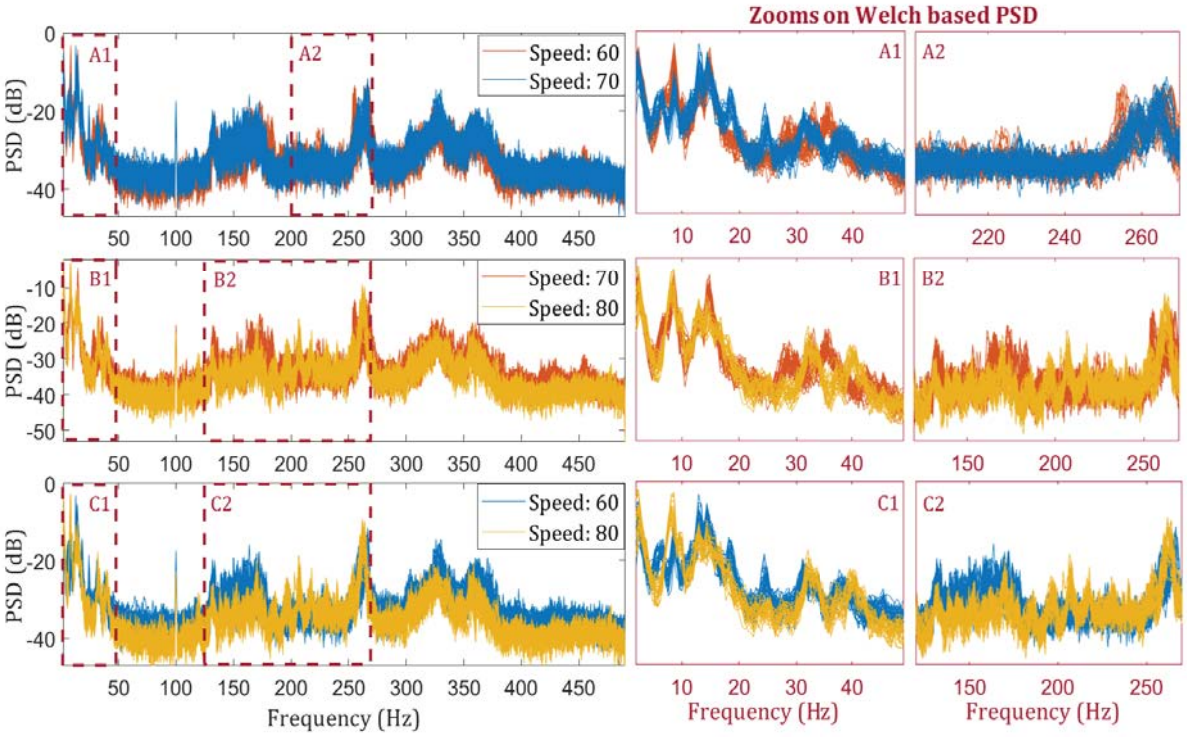

Figure 2: Effects of nominal traveling speed (Operating Condition) on the random vibration PSD for the healthy vehicle. [All 3 nominal speeds; 37 healthy signals per nominal speed; Welch based PSD estimates.]

time delays between any two pairs of wheelsets. The dependence of the random vibration Power Spectral Density (PSD) on the nominal traveling speed ($60, 70, 80\ km/h$) of the healthy vehicle is examined in Figure 2 (Welch PSD estimates [16, pp. 186-187] with Hamming window, segment length of 2048 samples, 85% overlap, frequency resolution $\delta f = 0.47\ Hz$, MATLAB function *pwelch.m*). Based on this, it is evident that the nominal speed has significant effects on the vibration PSD; a fact inevitably challenging fault detection performance.

The effects of faults on the corresponding ("observable") dynamics are, for all three nominal speeds, examined via random vibration PSD comparisons between the healthy and each fault (LD or AS) scenario in Figure 3. Evidently, the Air Spring (AS) fault induces considerable changes in the partial dynamics, which are subsequently reflected on the random vibration PSD, with the healthy and faulty envelopes exhibiting considerable discrepancies at certain frequency ranges. Yet, this is not the case for the Lateral Damper (LD) fault, for which the healthy and faulty envelopes seem to almost coincide. As vibration–based fault detection methods rely on fault–induced changes on the measured signal characteristics (reflecting changes in the corresponding dynamics), the detection of the LD fault is expected to be challenging.

4 THE ROBUST MULTIPLE MODEL BASED FAULT DETECTION METHODS

Fault detection is explored via two *robust* and *unsupervised Multiple Model* (MM) type Statistical Time Series (STS) methods: The first is a *non–parametric* Unsupervised Multiple Model Power Spectral Density (U–MM–PSD) based method and the second a *parametric* Unsupervised Multiple Model AutoRegressive model (U–MM–AR) based method.

At the heart of each method lies a *partial* (based on a single vibration response signal) repre-

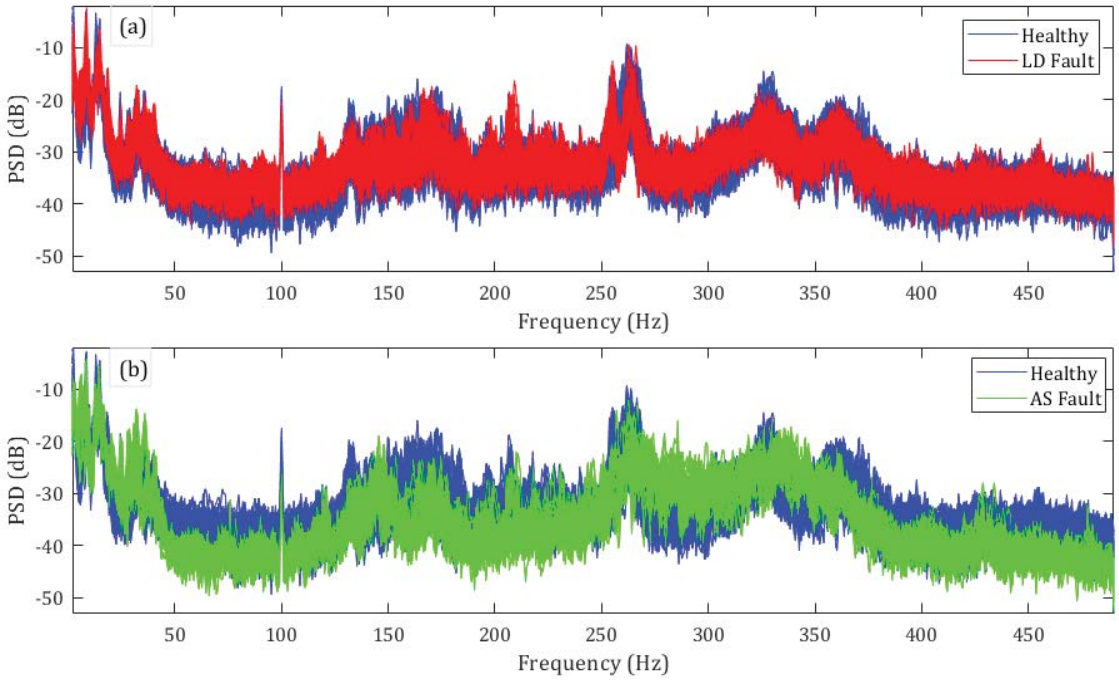

Figure 3: Effects of faults on the vibration PSD under all three nominal speeds: (a) Healthy versus Lateral Damper (LD) fault; (b) Healthy versus Air Spring (AS) fault. [Healthy state 111 signals; LD faulty state 45 signals; AS faulty state 36 signals.]

sentation (*elementary model*) of the vehicular dynamics via the Power Spectral Density (PSD) in the first (U–MM–PSD) method and AutoRegressive (AR) modeling in the second (U–MM–AR). The non–parametric PSD, estimated via the Welch method, and the AR parameter vector thus constitute the *feature* (characteristic quantity) of each method, respectively. AR modeling is based on Linear Least Squares [16, pp. 81-83] (MATLAB function *arx.m*), while model order selection is based on the Bayesian Information Criterion (BIC) and the Residual Sum of Squares normalized by the Signal Sum of Squares (RSS/SSS) [16, pp. 505-507].

Both robust fault detection methods operate within a Multiple Model framework [17], which implies that a multitude of elementary (nominal) models, say $M_{o,i}, i = 1, 2, \ldots, n$ (n designating the MM dimensionality) are used; these collectively constitute the *Multiple Model (MM) representation*, say M_o, of the *healthy* vehicular dynamics under *varying* Operating Conditions and uncertainty (note that the subscript "o" is used for representing the healthy vehicular state). Such a MM representation may be also viewed as a non–parametric description of the "*Healthy Subspace*" within the *Feature Space* (which is the space spanned by the scalar feature components) of a specific method (Figure 4). The Multiple Model representation is built in an *initial baseline (learning)* phase using signals obtained from the healthy vehicular state. In the normal operation of the method (*inspection phase*), a fresh signal is obtained with the vehicle in unknown health state. Based on it, a corresponding elementary (current nominal) model, say M_u (the subscript "u" designates unknown health state), is built, and detection is based on determining whether or not the current nominal model M_u belongs to the healthy subspace M_o. In the positive case the vehicle is declared as "healthy", else as "faulty".

The decision–making mechanism employs a *distance metric* D between the current nominal model M_u and the healthy subspace M_o. This is currently defined as the minimum of individual

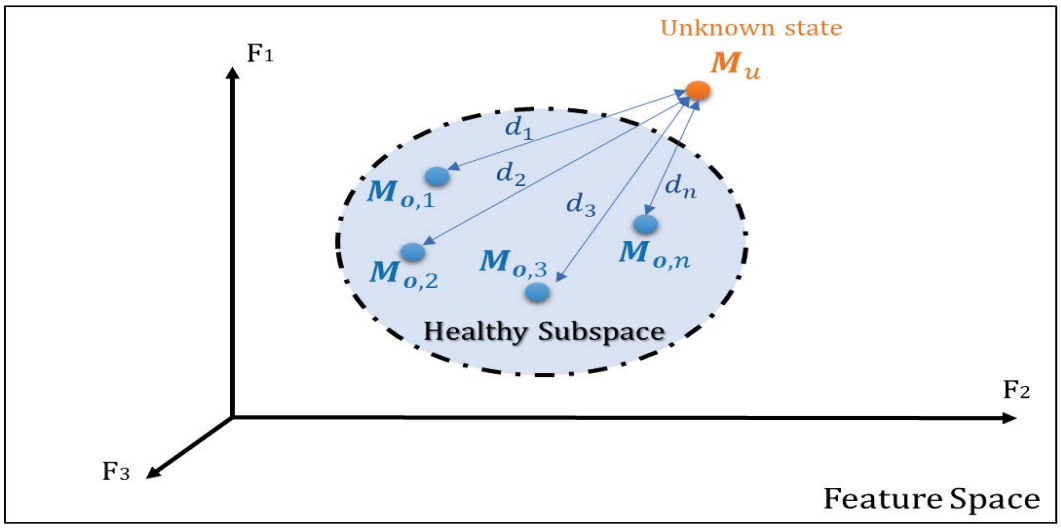

Figure 4: Schematic representation of the MM concept: Within the Feature Space, the Healthy Subspace is non–parametrically modeled via elementary nominal models $M_{o,i}(i = 1, 2, ..., n)$. A model M_u represents the current, unknown, vehicular health state. The current state is then declared as healthy if and only if M_u belongs to the Healthy Subspace.

distances between M_u and all elements of M_o, that is:

$$D := \min_i(d(M_{o,i}, M_u)) \qquad (i = 1, 2, ..., n) \tag{1}$$

with $d(M_{o,i}, M_u)$ designating either the Euclidean distance (U–MM–PSD method) or the Kullback–Leibler (KL) divergence (pseudo-–distance) [18, pp. 756-758] (U-MM-AR method). Fault detection is then declared if and only if D is greater than a user specified threshold l_{lim}, that is:

$$\begin{aligned} D \leq l_{lim} &\rightarrow \textit{Healthy Vehicle} \\ \textit{otherwise} &\rightarrow \textit{Faulty Vehicle} \end{aligned} \tag{2}$$

5 DETECTION PERFORMANCE ASSESSMENT

5.1 Preliminaries and the performance assessment procedure

Based on preliminary analysis, the selections of Table 2 have been made for each method.

The methods' detection performance assessment is then based on a systematic procedure which uses "rotations" in order to warrant consistency and validity of the results by eliminating the dependence of performance on the sample vibration signals selected for use within the baseline phase.

The healthy vehicular state is represented in three "healthy" signal pools, each one corresponding to a different nominal speed $(60, 70, 80\ km/h)$. The vehicle's faulty states are represented in an "AS" and an "LD" signal pool, each one including vibration signals under the Air Spring fault or the Lateral Damper fault and all three nominal speeds. The assessment then consists of the following steps:

Step 1: In the baseline phase, equal numbers of vibration signals are randomly selected from the three "healthy" signal pools. The selected signals form the baseline signal set. The remaining healthy sample signals (from all "healthy" pools) along with the total number of signals

Method	Feature	Feature dimensionality	Distance type
U-MM-PSD	(non-parametric) PSD	1 025	Euclidean
U-MM-AR	AR parameter vector	101	Kullback–Leibler
Multiple Model (MM) dimensionality (# of nominal models) $n = 60$.			
PSD Welch estimation: segment length of 2048 samples; overlap 85%; frequency resolution (δf) 0.47 Hz.			
AR modeling: selected model AR(101); BIC -1.52; RSS/SSS 19%; SPP 79.			
BIC: Bayesian Information Criterion			
RSS/SSS: Residual Sum of Squares normalized by the Signal Sum of Squares			
SPP: (Scalar) Samples Per (estimated scalar) Parameter			

Table 2: Detection method details.

# rotations	# healthy inspection signals	# LD fault inspection signals	# AS fault inspection signals
1	51	45	36
60	3 060	2 760	2 160
No of baseline signals per rotation $n = 60$.			

Table 3: Inspection test cases.

from the "AS" and "LD" signal pools are part of the inspection signal set and reserved for the methods' assessment in the inspection (fault detection) phase.
Step 2: The selection procedure presented in Step 1, which produces the baseline signal set and the inspection signal set respectively, is repeated until all healthy sample signals are selected in at least one baseline signal set. Each such repetition is designated as a "rotation".
Step 3: The fault detection procedure is carried out for all employed sets of baseline signals and the corresponding inspection sets. This leads to a high number of inspection test cases on which fault detection performance is assessed.

The numbers of rotations and baseline and inspection signals are summarized in Table 3.

5.2 Performance assessment

The performance of the fault detection methods is assessed via Receiver Operating Characteristic (ROC) curves, each representing the True Positive Rate (TPR, that is the correct damage detection rate) versus the False Positive Rate (FPR, that is the false alarm rate) for varying decision threshold [19, pp. 34-35]. The obtained results are, for all 7 980 inspection test cases (Table 3), presented in Figure 5 (notice that the distance metric D, normalized in the range $0 - 1$, is also shown for each inspection test case).

Based on these results, it is evident that both methods achieve ideal performance (TPR 100% for FPR 0%) for the Air Spring (AS) fault scenario, despite the variation in the nominal traveling speed. Yet, as expected (see section 3), the performance is less impressive for the Lateral Damper (LD) fault scenario, as the effects of this fault on the partial (single sensor) dynamics presently employed are minimal and "masked" by nominal speed variation and other underlying uncertainties (Figure 3). Indeed, for this scenario the U–MM–PSD method achieves a TPR of 60% for a low ($\approx 5\%$) FPR. The U–MM–AR method is clearly better, achieving a remarkably

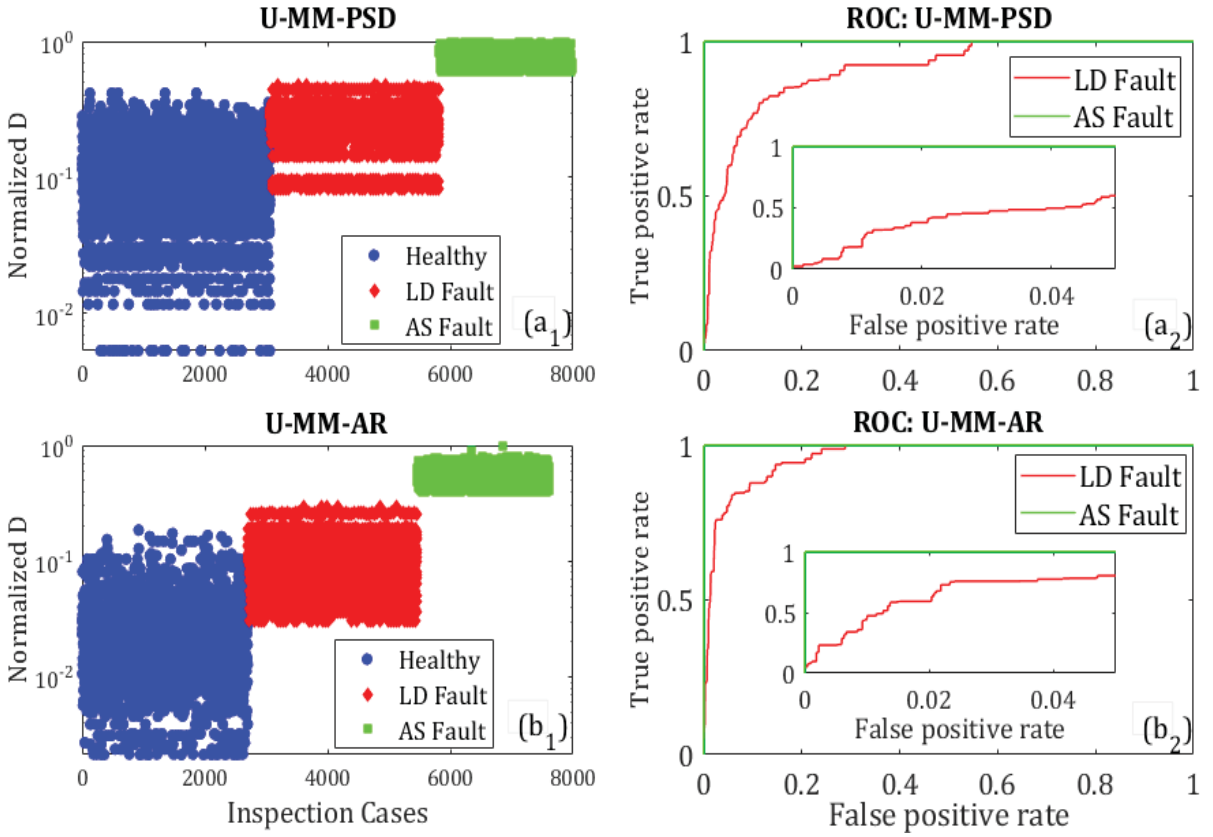

Figure 5: Fault detection performance assessment via the normalized distance metric D and ROC curves: (a_1,a_2) U–MM–PSD method, (b_1,b_2) U–MM–AR method. [All 3 nominal travelling speeds; 7 980 inspection test cases in total for each method.]

higher TPR of 81% for FPR of 5%. This is in line with the results of other studies [17, 20] and may be attributed to the advantages offered by parametric AR models over non–parametric counterparts.

Finally, an interesting, yet preliminary, comparison with an alternative method is presented. This is motivated by a recent study on railway suspension fault detection, employing the Multiscale Permutation Entropy (MPE) as feature and Linear Local Tangent Space Alignment (LLTSA) for feature dimensionality reduction [21]. For the MPE feature, the embedding dimension m, time delay τ, and scale factor s are set to $m = 4$, $\tau = 1$ and $s = 12$ (see [21, pp. 4-5] for definitions and details), respectively. Additionally, for the LLTSA feature dimensionality reduction method, the neighbor number k and intrinsic dimension d are set to $k = 7$ and $d = 3$ (see [21, pp. 5-6] for definitions and details), respectively. These selections are currently embedded into the presented MM framework, giving rise to a U–MM–MPE–LLTSA approach which operates on the raw (no pre–processing) random vibration signal. Details are presented in Table 4 and comparative assessment results are, for all three methods, presented via ROC curves in Figure 6. Based on them, the alternative U–MM–MPE–LLTSA approach offers no improvement in detection performance, as it significantly lags behind the U–MM–PSD and U–MM–AR methods.

Method	Feature	Feature dimensionality	Distance type
U–MM–MPE–LLTSA	Vector of MPE–LLTSA values	3	Euclidean

Table 4: U–MM–MPE–LLTSA detection method details.

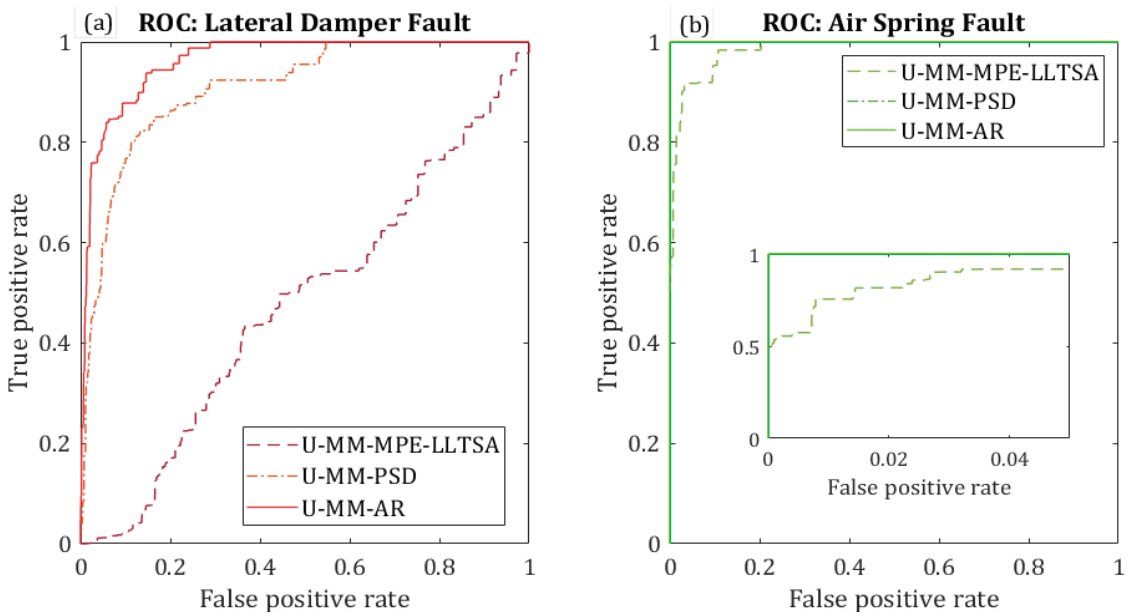

Figure 6: Comparative fault detection performance assessment with an alternative U–MM–MPE–LLTSA method via ROC curves for the: (a) LD fault, and the (b) AS fault. [All 3 nominal traveling speeds; 7 980 inspection test cases in total for each method.]

6 CONCLUDING REMARKS

The feasibility of a *single* random vibration signal based on–board fault detection for railway suspension systems under *varying* nominal traveling speeds (Operating Conditions) has been considered via two Multiple Model (MM) type robust methods: The first is based on *non–parametric* Power Spectral Density (U–MM–PSD method) and the second on *parametric* AutoRegressive modeling (U–MM–AR method). Comparisons with an alternative method have been also presented. All methods are unsupervised, so that only healthy signals are used in the baseline (learning) phase. The study has been based on signals obtained during field tests on an Athens Metro vehicle using a single, laterally–measuring, car body mounted accelerometer. Two fault scenarios have been considered: An Air Spring (AS) fault and an *early–stage* Lateral Damper (LD) fault. The main conclusions from the study may be summarized as follows:

- The use of a *single* vibration sensor (and thus only *partial* system dynamics) has been shown to lead to a challenging detection problem. Yet, it is desirable for reasons of simplicity, as well as reduced maintenance and installation cost.
- The problem is further aggravated by the considerable influence of the *varying* nominal traveling speed (Operating Condition) on the *partial* dynamics.
- While the AS fault is considerable (25% pressure reduction), the LD fault (oil leakage) is minor, with corresponding effects on the *partial* dynamics.

- In spite of the above difficulties, the two *robust* MM methods (U–MM–PSD and U–MM–AR) have achieved perfect performance for the AS fault, but, expectedly, degraded performance for the LD fault.
- Preliminary comparisons with an alternative method employing the Multiscale Permutation Entropy (MPE) and Linear Local Tangent Space Alignment (LLTSA) have indicated significant degradation in performance for both fault scenarios.
- Overall, the study has demonstrated – in a statistically reliable way using thousands of inspection test cases and ROC curves – the potential of single–sensor–based *robust* and *unsupervised* random vibration methods for effective fault detection in railway suspension systems. Work is ongoing on various aspects and will be reported elsewhere.

ACKNOWLEDGEMENTS

This research has been co–financed by the European Union and Greek national funds through the Operational Program Competitiveness, Entrepreneurship and Innovation, under the call RESEARCH–CREATE–INNOVATE (project code: T1EDK - 01440). The authors are grateful to the technicians and volunteers who helped with the field tests.

REFERENCES

[1] R.W. Ngigi, C. Pislaru, A. Ball, F. Gu, Modern techniques for condition monitoring of railway vehicle dynamics, *Journal of Physics: Conference Series*, **364**, 1–12, 2012.

[2] L. Chunsheng, L. Shihui, C. Colin, S. Maksym, An overview: modern techniques for railway vehicle on-board health monitoring systems, *Vehicle System Dynamics*, **55**, 1045–1070, 2017.

[3] S. Strano, M. Terzo, Review on model-based methods for on–board condition monitoring in railway vehicle dynamics, *Advances in Mechanical Engineering*, **11**, 1–10, 2019.

[4] M. Jesussek, K. Ellermann, Fault detection and isolation for a full–scale railway vehicle suspension with multiple Kalman filters, *Vehicle System Dynamics*, **52**, 1695–1715, 2014.

[5] H. Mori, H. Tsunashima, Condition monitoring of railway vehicle suspension using multiple model approach, *Journal of Mechanical Systems for Transportation and Logistics*, **3**, 243–258, 2010.

[6] X. Liu, S. Alfi, S. Bruni, An efficient recursive least square–based condition monitoring approach for a rail vehicle suspension system, *Vehicle System Dynamics*, **54**, 814–830, 2016.

[7] S. Bruni, R. Goodall, X.T. Mei, H. Tsunashima, Control and monitoring for railway vehicle dynamics, *Vehicle System Dynamics*, **45**, 743–779, 2007.

[8] X. Wei, L. Jia, H. Liu, A comparative study on fault detection methods of rail vehicle suspension systems based on acceleration measurements, *Vehicle System Dynamics*, **51**, 700–720, 2013.

[9] R. Melnik, S. Koziak, Rail vehicle suspension condition monitoring – approach and implementation, *Journal of Vibroengineering*, **19**, 487–501, 2017.

[10] D. Mădălina, Fault detection of damper in railway vehicle suspension based on the cross-correlation analysis of bogie accelerations, *Mechanics & Industry*, **20**, 1–14, 2019.

[11] C. Li, S. Luo, C. Cole, M. Spir, Bolster spring fault detection strategy for heavy haul wagons, *Vehicle System Dynamics*, **56**, 1604–1621, 2018.

[12] X. Zhang, X. Wei, G. Zhai, L. Jia, Fault isolation for rail vehicle suspension systems based on PSD distance feature, *Volume 1: Proceedings of 29th Chinese Control And Decision Conference (CCDC)*, 2017.

[13] T.-C.I. Aravanis, J.S. Sakellariou, S.D. Fassois, A stochastic functional model based method for random vibration based robust fault detection under variable non—measurable operating conditions with application to railway vehicle suspensions, *Journal of Sound and Vibration*, **466**, 115006, 2020.

[14] T.-C.I. Aravanis, J.S. Sakellariou, S.D. Fassois, Spectral analysis of railway vehicle vertical vibration under normal operating conditions, *International Journal of Rail Transportation*, **4**, 193–207, 2016.

[15] V. Cossalter, A. Doria, S. Garbin, R. Lot, Frequency–domain method for evaluating the ride comfort of a motorcycle, *Vehicle System Dynamics*, **44**, 339–355, 2006.

[16] L. Ljung, System Identification: Theory for the User, *New Jersey: Prentice-Hall*, ISBN: 9780136566953, 1999.

[17] K.J. Vamvoudakis–Stefanou, J.S. Sakellariou, S.D. Fassois, Vibration–based damage detection for a population of nominally identical structures: unsupervised multiple model (MM) statistical time series type methods, *Mechanical Systems and Signal Processing*, **111**, 149–171, 2018.

[18] W. Press, S. Teukolsky, W. Vetterling, B. Flannery, Numerical Recipes: The Art of Scientific Computing, *New York: Cambridge University Press*, ISBN: 9780521880688, 2007.

[19] R. Duda, P. Hart, D. Stork, Pattern Classification, *New York: John Wiley and Sons*, ISBN: 9788126511167, 2000.

[20] K.J. Vamvoudakis–Stefanou, S.D. Fassois, Vibration–based damage detection for a population of like structures via a MM framework, *6th International Symposium on NDT in Aerospace*, Spain, 2014.

[21] Y. Ye, Y. Zhang , Q. Wang , Z. Wang, Z. Teng, H. Zhang, Fault diagnosis of high–speed train suspension systems using multiscale permutation entropy and linear local tangent space alignment, *Mechanical Systems and Signal Processing*, **138**, 106565, 2020.

EURODYN 2020
XI International Conference on Structural Dynamics
M. Papadrakakis, M. Fragiadakis, C. Papadimitriou (eds.)
Athens, Greece, 23–26 November 2020

SYSTEM IDENTIFICATION OF CODE CONFORMING LOW-RISE RC BUILDING IN LALITPUR, NEPAL

Rajan Dhakal[1], Rajesh Rupakhety[1], Dipendra Gautam[2], Said Elias Rahimi[1]

[1]Earthquake Engineering Research Center, Faculty of Civil and Environmental Engineering,
University of Iceland
Iceland
rad4@hi.is (R.D.), rajesh@hi.is (R.R.), said@hi.is (S.E.)

[2]Department of Civil Engineering, Institute of Engineering, Thapathali Campus,
Nepal
dipendra01@tcioe.edu.np (D.G.)

Keywords: System identification, N4SID, ambient vibration measurement, RC building, brick infill.

Abstract. *System identification of a code conforming low-rise reinforced concrete frame building in Kathmandu, Nepal is reported in this paper. The fundamental vibration period and damping ratio of the building were determined using ambient vibration records taken in three floors of the building. Ambient vibration measurements were taken using three triaxial accelerometers. Two methods of system identification, Welch spectral method and N4SID method, are used to estimate the modal properties. Fundamental vibration periods of the four-storied building estimated from non-parametric Welch spectral method are 0.292s and 0.289s in the two orthogonal directions. The corresponding results from the parametric state-space N4SID method are 0.266s and 0.264s in the orthogonal directions. The corresponding damping ratios are estimated to be 6.3% and 6.9%. These periods are longer than that of a simplified finite element model of the building assumed to be fixed at the supports. This indicates that the flexibility of the soil under the building foundation, plays an important role in the vibration frequencies of the structure.*

1 INTRODUCTION

Civil engineering structures are frequently exposed to dynamic loads in their service lives. Dynamic actions such as earthquake and strong winds can cause severe damage to such structure, or in case of milder actions, impart damages that are not visible immediately, but can accumulate over time. . Also, repeated actions on the structure leads to fatigue of structural elements. These phenomenon cause softening of the structure, which can mean degradation of stiffness and/or strength of its force resisting elements. As a result, the structure becomes more vulnerable to future environmental actions. Identification of such damages, especially those that are not visible on the surface, is important for timely remedial actions so that damage aggravation and accumulation over time can be avoided. Structural system identification and health monitoring is therefore a very important and growing research field in civil engineering.

System identification or an experimental modal analysis is a mathematical framework to identify dynamic properties of a structure from measured vibration and potentially excitation forces. System identification using vibration measurement at different times can reveal potential damage and its accumulation in the structure manifested in the form of change in its dynamic properties. This method has specific advantage over the other methods; they are non-destructive and able to identify damage that is not visible on the surface. Moreover, the structure can remain operational during testing, which can be a continuous process. Also, artificial excitation is often not needed , and ambient vibration induced by traffic or wind actions can be used There are two main genres of mathematical methods for system identification, parametric methods [3] and non-parametric methods [6]. In this study, both methods are used for system identification of a code conforming RC building located in Kathmandu, Nepal.

Finite element modeling based on mechanical properties and geometry of the structural systems can also be used to estimate their modal parameters. Reliability of the numerical results depends on assumption made to create model. There are several uncertainties involved in such modeling, for example in material properties, rigidity of connections, conditions of the soil supporting the foundation, etc., which introduce simplifying assumptions and engineering judgements in finite element modeling. These uncertainties translate to uncertainties in the estimated dynamic behavior of the structure. In addition, as the structure ages, its dynamic properties change. If the structure is subjected to strong loading or repeated moderate loading, it can lose part of its stiffness, which results in change of its dynamic behavior. System identification can be used to identify such changes and calibrate/update finite element models, which can then be used for analyzing its safety and/or designing retrofitting schemes. As dynamic characterization studies are limited in Nepal [9], this study considers a code conforming four-storied residential building located in Lalitpur metropolitan city, Nepal. Sawaki et al. [9] performed system identification of a four-storied residential building using aftershocks and ambient vibration records and concluded that the non-parametric method results in unrealistic damping ratios. To this end, this study incorporates both non-parametric and parametric methods to perform system identification.

2 CASE STUDY BUILDING

The studied residential building is situated in a densely populated area of Kathmandu Valley nearby the Bagmati River. The building is a four-story residential building constructed in 2013. The structural configuration of the building is a reinforced concrete frame with brick infill walls. The moment resisting frame structure consists of concrete columns, beams, and floor slabs. Locally made brick with cement-sand mortar is used as infill walls on the building. The infill walls contribute significantly to the overall stiffness of the building [8].

Figure 1 shows the structural layout of the building showing location of beams and columns. The building is asymmetrical in plan with off grid columns and beams. All the rectangular columns have section size of 300×230mm except the circular columns that have diameter of 230mm. All the beams have section size of 230×355mm including uniform slab thickness of 100mm. Concrete used in the building for casting of primary structural elements is ordinary concrete with mix proportion of 1:2:4 (cement: sand: aggregate) equivalent to M15 grade concrete. The specified characteristics compressive strength of a cube [150mm] in 28days for M15 concrete is 15MPa with modulus of elasticity 19365MPa (IS 456:2000 [2], modulus of elasticity, $E_c = 5000\sqrt{f_{ck}} \approx 19365$MPa). Structural reinforcement used in the building are deformed steel bars of Fe415 grade. The specified minimum 0.2% proof stress or yield strength of corresponding grade steel is 415MPa. The estimated strength of the infill walls is 2.5 MPa with modulus of elasticity 1750 MPa.

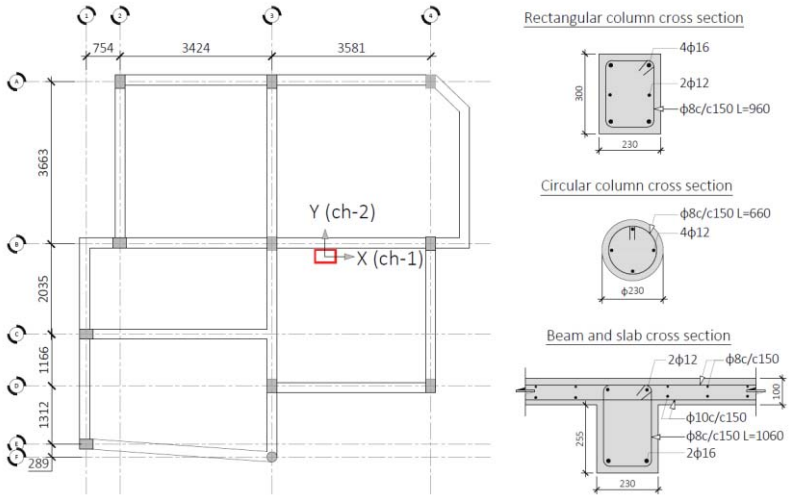

Figure 1: Structural layout of the building showing beams and columns and their cross sections. The red rectangle shows the location of accelerometer and orientation of the instrument sensor axis are indicaed with the arrows.

3 SYSTEM IDENTIFICATION

3.1 Ambient vibration measurement

Three digital accelerometers were installed on three different floors to record ambient vibration of the building. The instruments were located on the first second and third floor. Figure 1 shows the location of instruments (red rectangle) on plan view of the building. All three instruments on different floors were aligned vertically. The accelerometers used are ETNA2 units manufactured by Kinemetrics Inc. Direction of the measurement with respect to accelerometer sensors is indicated by co-ordinate axis shown in Figure 1.

3.2 Welch spectral method

This is a non-parametric method of system identification. This method estimates the frequency response function of the structure based on frequency-domain representations of its excitation and response. Using the Fourier transforms of measured input and output, an empirical estimate of the complex frequency response function, $\hat{H}(\Omega)$, can be obtained. Alternatively, estimates of power spectral densities of the excitation and response can be used as

$$\left|\hat{H}(\Omega)\right|^2 = \frac{\left|S_{yy}(\Omega)\right|}{\left|S_{uu}(\Omega)\right|} \tag{1}$$

where $S_{uu}(\Omega)$ and $S_{yy}(\Omega)$ are the power spectral densities (psd) of excitation and response, respectively, and Ω is the circular frequency.

Because of the inherent variability of Fourier Amplitude Spectra (see, for example, Rupakhety and Sigbjörnsson, 2012 [10]), some form of smoothing needs to be performed on periodogram estimates of psds. The Welch spectra reduces the variation in the psds by dividing the signals into different segments and averaging their spectral estimates. For a stationary signal, the Welch spectra provides an estimate of the true spectra of the random process. In case of ambient vibrations, the excitation can be assumed to be a white noise, and from Equation 1, an estimate of the system transfer function normalized by the variance of the excitation is obtained directly from $S_{yy}(\Omega)$. The natural frequencies can be obtained from the plot of squared amplitude of the complex frequency response function by picking the peaks. For system with small damping values, up to 10% of the critical damping, the peak of the plot occurs close to the natural frequency of the system. The frequencies and most of the power of the response gets concentrated in a narrow band of frequencies around the peak. If the damping ratio of the system is higher, the peak lies away from the natural frequency of the system and the power spectrum becomes wider. Response of a lightly damped structure excited with white noise process can be modelled as a narrow band process. The damping ratio of the structure can be estimated from the half power bandwidth method, which is based on the following equations [4]:

$$\xi = \frac{f_2 - f_1}{2f_n} \tag{2}$$

$$\Delta f = f_2 - f_1 = 2\xi f_n$$

Where, Δf is the half-power bandwidth defined in the frequency band where the power density of the response reduces to half its value at the peak; f_1 and f_2 are linear frequencies at corners of half power and f_n is the linear frequency of the peak which is approximately equal to the undamped natural frequency of lightly damped systems. This method is straightforward when power spectral density function contains one dominant peak, which is the case for damped single degree of freedom systems. For multiple degrees of freedom systems, multiple peaks corresponding to different vibration modes can often be observed. Identification of higher modes can sometimes be difficult due to noise in the measured signal. Identification of higher modes is more difficult when signal to noise ratio is large, which is often the case with ambient vibration measurements.

To apply this method to the case study building, recorded time series data from all the floors channel 1 (ch-1 Figure 1) and channel 2 (ch-2 in Figure 1) were divided into twenty equal segments. Then the signals were filtered using fourth order Butterworth filter to remove noise. The frequency band chosen for the filter was 0.5Hz to 20Hz. Each segment of time series was windowed and tapered with a Tukey window. Power spectral density (PSD) of the filtered signals was estimated using Welch´s algorithm. Figure 2 shows the plot of estimated PSD of the twenty segments with mean PSD for both channels. Figures 2a, 2c, and 2e show plots of PSD from first floor to third floor in the direction of channel 1 with estimated mean PSD. Similarly, Figures 2b, 2d, and 2f show plots of PSD from first floor to third floor in the direction of channel 2. All plots show clear peaks which represents the fundamental frequency of the system in the corresponding direction.

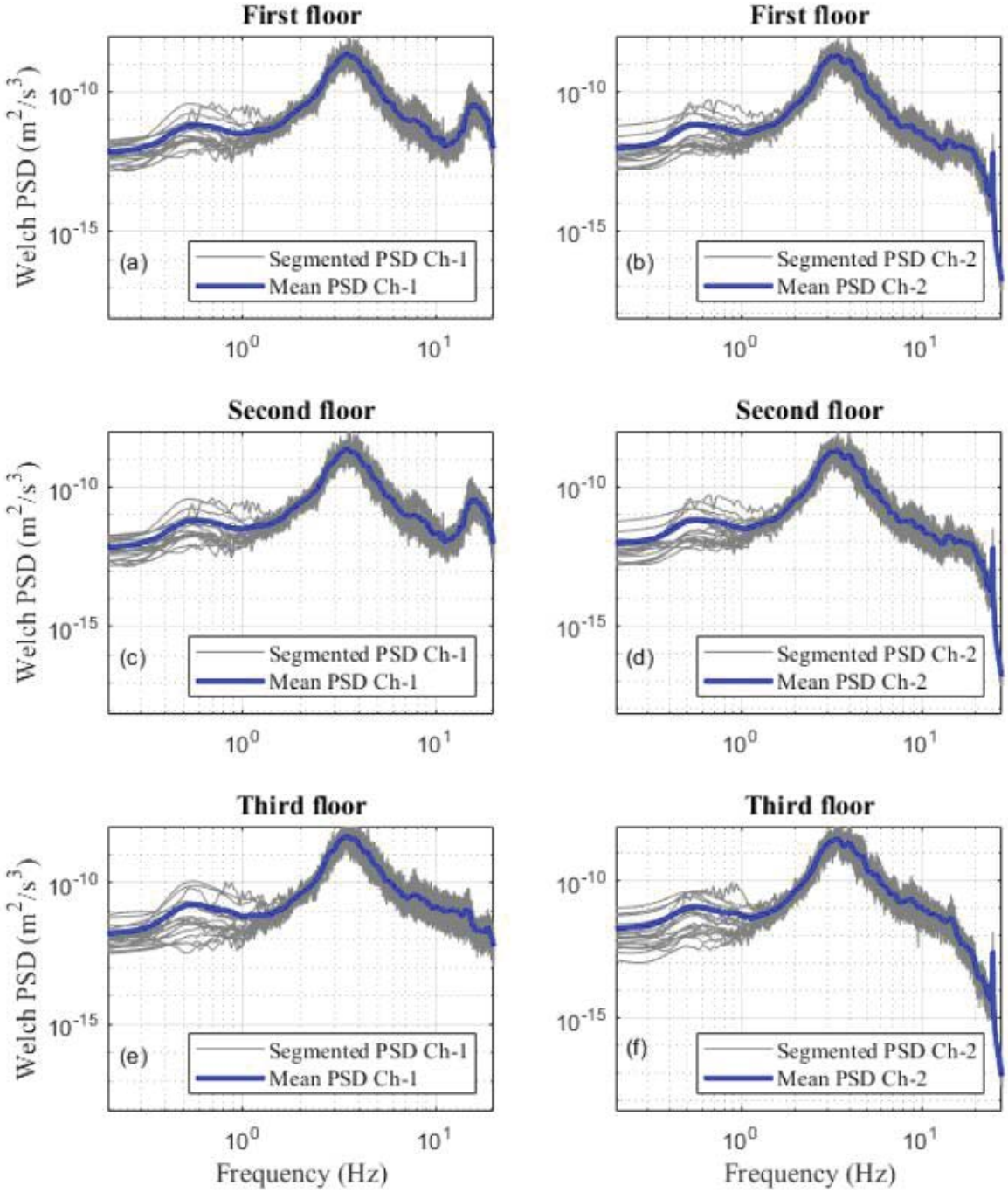

Figure 2: Plot of Welch´s PSD from recorded ambient vibration. The gray lines represent 20 segments of measured acceleration, and the blue lines represent the mean.

Estimated fundamental vibration period and damping ratios from three different floors are tabulated in Table 1. For example, mean vibration period estimated from channel 1 of the first-floor data is 0.290s with standard deviation 0.017s. Similarly, fundamental vibration period obtained from channel 2 is 0.289s with standard deviation 0.028s. Mean natural periods obtained from the second floor and third floor along channel 1 are 0.288s and 0.289s respectively. Mean natural periods obtained from second floor and third floor along channel 2 are 0.296s and 0.291s, respectively. Estimated vibration periods on both principal directions show consistently similar results for different floors. Mean of estimated vibration period along each direction

represents fundamental vibration period of the building along corresponding principal direction. Therefore, it can be concluded that the mean estimated fundamental period of the building along channel 1 is 0.289s and along channel 2 is 0.292s. This concludes that the fundamental periods of the building on both the directions are almost similar. However, mean damping ratios estimated for both the channels from different floors shows more variability with higher standard deviations (range of variation 3 - 6%). Such variation on damping ratio is directly related to the smoothing, window selection and overlap of data during PSD estimation. For example, Smoothing of PSD leads to flattening of the peaks which results in inaccurate estimates of damping ratios [5].

Data	Damping Ratio Ch-1 (%)	Fundamental Period Ch-1 (s)	Damping Ratio Ch-2 (%)	Fundamental Period Ch-2 (s)
First floor	8.126 (3.681)	0.290 (0.017)	11.435 (4.939)	0.289 (0.028)
Second floor	8.389 (3.901)	0.288 (0.017)	9.165 (4.713)	0.296 (0.023)
Third floor	9.148 (4.303)	0.289 (0.016)	11.655 (6.211)	0.291 (0.027)

Table 1: Mean fundamental vibration period and damping ratio with standard deviation estimated from three different floors using Welch spectral analysis.

3.3 N4SID method

N4SID stands for Numerical algorithms for subspace state space system identification and is described in detail in [7]. This method is based on parametric mathematical model called state-space model which consist of a set of input, output and state variables linked together by first order differential equations. The following equations represent a state-space model in continuous time:

$$\left\{\dot{x}(t)\right\} = [A]\{x(t)\} + \{B\}u(t)$$
$$\{y(t)\} = \{C\}\{x(t)\} \tag{3}$$

Where [A] is parametric system matrix, {B} and {C} are parametric vectors. The vector {x(t)} is called the state of the structure. The number of elements of x(t), n, is called the model order. The state space model ([A], {B} and {C}) can be calibrated from measured excitation and response. The model can then be used to estimate vibration periods and damping ratios of the structure. The results are generally sensitive to the selected model order. Selection of suitable model number helps to remove spurious modes and bias of the modes. Spurious modes are either noise modes, that arise due to physical reasons, e.g., excitation and noise or mathematical modes that arise due to over-estimation of the model order. Similarly, bias of the modes can be defined as the combination of different modes (true mode and noise mode) on identified mode which is due to under estimation of model order. The selection of suitable model order is facilitated by stabilization diagrams. A stabilization diagram is made by selecting a wide range of model orders and by plotting all identified modes in a frequency versus model order diagram. Figure 2 shows the stabilization diagram for data segment 5 for channel 1. The plot shows the estimated natural frequencies and damping ratios for model orders 1 to 20. The parameters are estimated by the least squares rational function (LSRF) algorithm. The

figure helps to identify stable and unstable peaks in the frequency response function. The results show that some of the true modes only appear after model order 4. A model order of 6 seems sufficient to identify the two modes of vibration of the structure, and is therefore selected for further analysis.

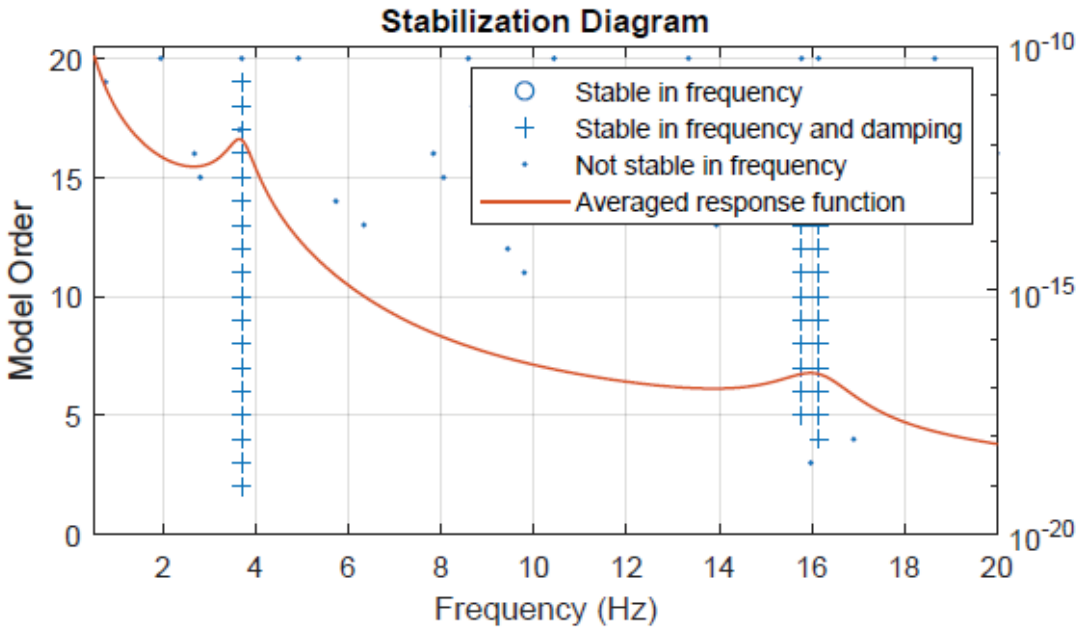

Figure 2: Stabilization diagram showing stable modes and averaged frequency response function for data segment 5 channel -1.

Measured signals from all three floors were aligned in time and divided into twenty segments. Signals were filtered using fourth order Butterworth filter The frequency band chosen for the filter was 0.5Hz to 20Hz. Then N4SID algorithm in MATLAB was used to estimate state-space model with model order of six. No exogeneous input was used in calibrating the model as the excitation is assumed to be a white noise process. Estimated mean fundamental vibration period and damping ratios are presented in Table 2. The mean vibration period for first and second mode obtained from channel 1 data is 0.266s and 0.078s with standard deviation of 0.009s and 0.031s. Similarly, the mean vibration period for first and second mode obtained from channel 2 data is 0.264s and 0.143s with standard deviation of 0.012s and 0.035s respectively. This shows that the variance of period obtained for second mode is higher than that for the first mode. Mean damping ratio obtained from channel 1 data is about 6.3% with standard deviation of 1.3%. Similarly, mean damping ratio obtained from channel 2 data is about 6.9% and standard deviation of 1.1%. Variation in damping ratio estimated from this method is lower than that estimated from the non-parametric method.

Data	Fundamental Period (s)		Damping Ratio (%)
	Mode 1	Mode 2	
Channel 1	0.266 (0.009)	0.078 (0.031)	6.340 (1.265)
Channel 2	0.264 (0.012)	0.143 (0.035)	6.968 (1.140)

Table 2: Mean fundamental vibration period and damping ratio with standard deviation estimated from ambient vibration measurement using N4SID method.

4 DISCUSSION AND CONCLUSIONS

The estimated fundamental period of vibration of the building is around 0.26s. The empirical equation proposed by Guler et al. [1] estimates the fundamental period of reinforced concrete moment resisting frames with brick infill walls with the following equation.

$$T_0 = 0.026H^{0.9} \tag{4}$$

For the building being studied here, this equation results in fundamental vibration period of 0.24s, which is fairly close to the results obtained from system identification. The building being studied is constructed on a site with alluvial deposits, which might affect the vibration frequencies of the structure. Dhakal, 2020 [11] presents finite element models of the building with fixed base and flexible base to account for the effects of soft soils at the site. The finite element models show that the vibration frequencies estimated from the flexible base model matches the results of system identification better. This indicates that system identification using ambient vibration measurement can be used to detect and calibrate the effects of underlying soil in vibration properties of buildings. This is valuable in calibrating and updating finite element models which can be used for detailed seismic analysis. For example, mechanical elements used to model soil in the finite element model of the building can be tuned to match the modal frequencies estimated from ambient vibration measurements.

The results of this study show that system identification using ambient vibrations is a reliable method of estimating the fundamental period of vibration of buildings. The estimated periods are consistent with results presented in the literature and mechanical models of the building. The parametric method seems to be superior to the non-parametric method and is found to be more reliable in identifying higher modes of vibration. In addition, damping ratios estimated from the non-parametric method showed larger variability than those estimated from the parametric method. The degree if smoothing used in the former method is subjective to the analyst and introduces such variability. There is no quantitative guideline on what degree of smoothing is optimal. In the parametric method, some level of subjectivity is introduced by the selection of model order. But unlike in the non-parametric method, the analyst can make use of the stabilization diagram to select a proper model order. In this aspect, the parametric method is found to be more suitable for system identification.

Since ambient vibration measurements are inexpensive and can be performed rapidly, it will be useful to perform similar tests on several buildings in Nepal. By sampling buildings of different construction quality, site conditions, heights, infill walls and opening ratios, effects of these parameters on vibration frequencies of typical reinforced buildings in Nepal can be studied. Furthermore, empirical equations relating these frequencies to parameters such as building height, site conditions, and opening ratios can be calibrated. Such equations will be useful in updating seismic design codes in Nepal.

REFERENCES

[1] Guler K, Yuksel E, Kocak A. Estimation of the fundamental vibration period of existing RC buildings in Turkey utilizing ambient vibration records. Journal of Earthquake Engineering. 2008 May 14;12(S2):140-50.

[2] Indian Standard IS. IS 456: 2000: Plain and Reinforced Concrete. Code of Practice (4th revision). New Delhi. 2000.New Delhi. 2000.

[3] Jenkins GM, Watts DG. Spectral Analysis and Its Applications, San Francisco: HoldenMDay; 1969

[4] Papagiannopoulos GA, Hatzigeorgiou GD. On the use of the half-power bandwidth method to estimate damping in building structures. Soil Dynamics and Earthquake Engineering. 2011 Jul 1;31(7):1075-9.

[5] Peeters B, De Roeck G. Stochastic system identification for operational modal analysis: a review. Journal of Dynamic Systems, Measurement, and Control. 2001 Dec 1;123(4):659-67.

[6] Soderstrom T, Stoica P. System identification prentice hall international. Series in Systems and Contol Engineering. 1989.

[7] Van Overschee P, De Moor B. N4SID: Subspace algorithms for the identification of combined deterministic-stochastic systems. Automatica. 1994 Jan 1;30(1):75-93.

[8] Varum H, Furtado A, Rodrigues H, Dias-Oliveira J, Vila-Pouca N, Arêde A. Seismic performance of the infill masonry walls and ambient vibration tests after the Ghorka 2015, Nepal earthquake. Bulletin of Earthquake Engineering. 2017 Mar 1;15(3):1185-212.

[9] Sawaki Y, Rupakhety R, Olafsson S, Gautam D. System identification of a residential building in Kathmandu using aftershocks of 2015 Gorkha earthquake and triggered noise data. In: Rupakhety R., Olafsson S., Bessason B. (eds) Proceedings of the International Conference on Earthquake Engineering and Structural Dynamics. ICESD 2017. Geotechnical, Geological and Earthquake Engineering, vol 47. Springer, Cham

[10] Rupakhety R, Sigbjörnsson R. Spatial variability of strong ground motion: novel system-based technique applying aprametric time series modelling. Bulletin of Earthquake Engineering, 10:1193-1204

[11] Dhakal R, System identification and seismic analysis of a residential RC building in Kathmandu, Nepal, Master's thesis, Faculty of civil Engineering, University of Iceland. 2020

EURODYN 2020
XI International Conference on Structural Dynamics
M. Papadrakakis, M. Fragiadakis, C. Papadimitriou (eds.)
Athens, Greece, 23–26 November 2020

A DISPERSION-BASED METHODOLOGY FOR THE IN SITU ASSESSMENT OF BENDING STIFFNESS IN BRIDGE CABLES

João Rodrigues[1], Elsa Caetano[1] and João Santos[2]

[1]CONSTRUCT, Faculty of Engineering, University of Porto
Rua Dr. Roberto Frias, 4200-465 PORTO, Portugal
{jmcr, ecaetano}@fe.up.pt

[2]Structural Monitoring Unit, Structures Department, National Laboratory for Civil Engineering
Avenida do Brasil, 101, 1700-066 LISBON, Portugal
josantos@lnec.pt

Keywords: cable dynamics, dispersion, time-frequency analysis, bending stiffness

Abstract. *The assessment of the structural integrity of bridge cables through the identification of axial force has a long tradition in engineering practice. Vibration-based methodologies usually involve fitting a set of measured natural frequencies to a force-frequency relationship, which may take into account the effects of sag-extensibility and non-negligible bending stiffness. However, the accuracy of the results is largely dependent on an adequate characterization of the boundary conditions, namely the effective length of vibration and the rotational restraints at the supports. Moreover, the identification of high-order modes (essential for attaining good estimates of the bending stiffness) may be hampered by the attenuation of small wavelength disturbances before reaching the cable ends, preventing the definition of standing waves.*

This paper presents a novel methodology for the identification of mechanical properties in bridge cables, which does not require any assumption about boundary conditions. Assuming that cables behave as Euler-Bernoulli or Timoshenko beams with a tensile force, analytical expressions for the dispersion relation of transverse waves are derived. As for experimental dispersion relations, they can be obtained by the computation of time-frequency distributions of the response at two different sections of the cable, permitting the identification of arrival times for each frequency component, and of the respective propagation velocities.

The validation of this methodology is conducted on a stay cable from a footbridge, recording the response to an impact hammer excitation with two accelerometers. Mechanical properties are then identified through the fitting of the analytical expressions derived to the experimental dispersion curves. The obtained results for bending stiffness are consistent within a large diversity of experimental setups, regarding the location and type of the external excitation, and the distance between the sensors. This approach can thus provide in situ estimates of the flexural rigidity in bridge cables, unaffected by errors in the characterization of boundary conditions, which will prove useful in the local assessment of damage.

1 INTRODUCTION

The increasing use of cables as load-carrying members in civil engineering structures has generated a need for accurate and reliable methods to evaluate their integrity and identify the installed axial force. Among these, vibration-based techniques are very popular and usually involve fitting a set of measured natural frequencies to force-frequency relationships, which may be exact or approximate, and explicit or implicit. Apart from the simpler taut string model, existing formulations can include the effects of sag-extensibility [1], non-negligible bending stiffness [2], or both [3]. Considering the need to work with large-diameter cables, models that account for flexural rigidity have been the subject of various investigations in recent years, and simultaneous identification of this property and the axial force is now becoming a common practice. Nevertheless, the accuracy of the results depends on the characterization of boundary conditions, particularly the effective length of vibration and the rotational restraints at the edges [4]. Some techniques can already address the problem of non-ideal supports (i.e., besides hinges or clamps) [5] [6] [7], but they require obtaining the cable mode shapes through denser instrumentation, which hampers most in situ applications. In addition to the uncertain boundary conditions, many cables reveal a progression of natural frequencies that is insensitive to the bending stiffness, at least for mode orders typically identified. In fact, small wavelength disturbances (susceptible to the effects of flexural rigidity) are prone to attenuation before reaching the cable ends, preventing the definition of standing waves.

In such a context, this study proposes an identification approach based on the characteristics of transient waves propagating along a cable medium, rather than vibration modes. Dispersion relations for group velocities are derived, assuming that cables behave as Euler-Bernoulli or Timoshenko tensioned beams, and fitted to the ones obtained in situ.

The outline of this paper is as follows: section 2 gathers the theoretical contributions of the study, namely the relevant dispersion characteristics associated with Euler-Bernoulli and Timoshenko models. The methodology for experimental assessment of dispersion relations is described in section 3, and results from an actual scale case study are presented and discussed in section 4. Finally, section 5 synthetizes the main conclusions, pointing out some relevant observations for future work.

2 DISPERSION RELATIONS

2.1 Euler-Bernoulli Model

Assuming that plane sections remain plane after deformation and orthogonal to the neutral axis, the behavior of a cable with constant bending stiffness EI and mass per unit length μ, subject to a tensile force T, is governed by the equation of motion:

$$-c_f^2 \frac{\partial^4 u}{\partial s^4} + c_t^2 \frac{\partial^2 u}{\partial s^2} = \frac{\partial^2 u}{\partial t^2} \tag{1}$$

in which u represents the transverse displacement (as a function of position s and time t), c_t designates the velocity $\sqrt{T/\mu}$ and c_f stands for the quantity $\sqrt{EI/\mu}$.

Harmonic and non-trivial solutions $u(s,t) = Ae^{i(\gamma s - \omega t)}$ for equation (1), with frequency ω and wavenumber γ, exist only if the following characteristic condition is verified:

$$c_f^2 \gamma^4 + c_t^2 \gamma^2 - \omega^2 = 0 \tag{2}$$

Since the group velocity c_g is defined by $d\omega/d\gamma$ [8], one can differentiate implicitly the equation above to obtain:

$$c'_{gt}(\omega) = \sqrt{\frac{2c_t^4 + 8c_f^2\omega^2}{c_t^2 + \sqrt{c_t^4 + 4c_f^2\omega^2}}} \tag{3}$$

This expression corresponds to the dispersion relation for the group velocity of transverse waves in a tensioned Euler-Bernoulli beam and shreds evidence that each frequency component of the response propagates with a distinct velocity. Conversely, if $c_f = 0$ in equations (1) to (3), the non-dispersive model of a taut string is derived, with a constant dispersion relation $c'_{gt}(\omega) = c_t$.

In order to illustrate the previous result, expression (3) is computed for a cable with a cross-sectional area A of 0.015 m^2 and moment of inertia I of 1.25335×10^{-5} m^4, under an axial loading of 7500 kN. As for material parameters, the elastic modulus E and the mass density ρ are assumed equal to 200 GPa and 7.8 ton m^{-3}, respectively. Figure 1(a) reveals that the group velocity approaches c_t when $\omega \to 0$, as anticipated by expression (3); on the other hand, Figure 1(b) illustrates an improper result in a high frequency range, since c'_{gt} grows without limit and, therefore, infinite group velocities are attained.

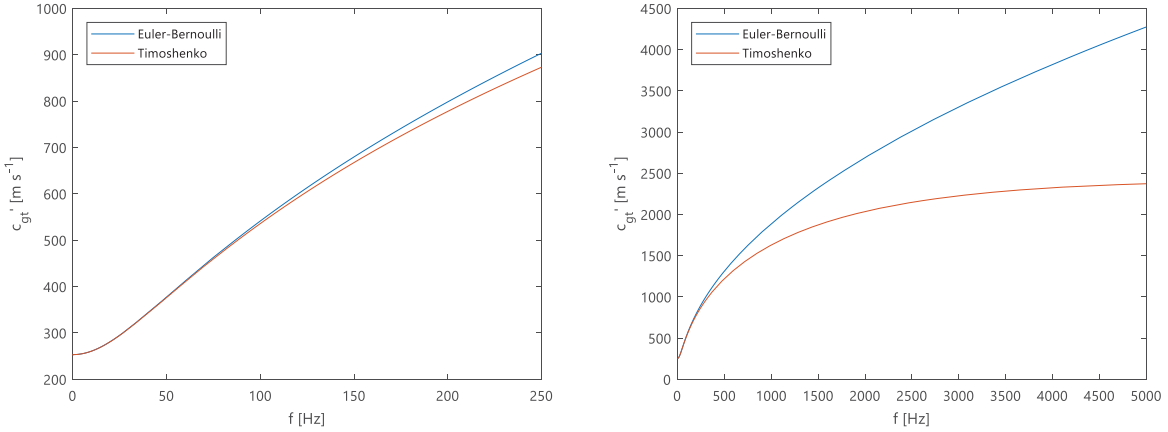

Figure 1: Dispersion relations for c'_{gt} (Euler-Bernoulli and Timoshenko models), up to: (a) 250 Hz; (b) 5000 Hz.

2.2 Timoshenko Model

The correction of the previously obtained result requires introducing the effects of shear deformation and rotary inertia [9]. If φ designates the cross-section rotation, the cable behavior is now expressed by the system of equations:

$$\begin{aligned} \frac{GAK}{\mu}\left(\frac{\partial^2 u}{\partial s^2} - \frac{d\varphi}{ds}\right) + c_t^2\frac{\partial^2 u}{\partial s^2} &= \frac{\partial^2 u}{\partial t^2} \\ \frac{GAK}{\mu}\left(\frac{\partial u}{\partial s} - \varphi\right) + c_f^2\frac{\partial^2 \varphi}{\partial s^2} &= \frac{I}{A}\frac{\partial^2 \varphi}{\partial t^2} \end{aligned} \tag{4}$$

which represents the equilibrium of a tensioned Timoshenko beam [10]; G and K denote the distortion modulus and the shear coefficient, respectively.

The propagation of harmonic waves $u(s,t) = A_1 e^{i(\gamma s - \omega t)}$ and $\varphi(s,t) = A_2 e^{i(\gamma s - \omega t)}$ leads to the characteristic equation:

$$\tau_3\gamma^4 + c_t^2\gamma^2 - (\tau_2\gamma^2 + 1)\omega^2 + \tau_1\omega^4 = 0 \tag{5}$$

where auxiliary parameters τ_1, τ_2 and τ_3 are defined by:

$$\tau_1 = \frac{\mu I}{GA^2K} \tag{6}$$

$$\tau_2 = \frac{I}{A}\left(1 + \frac{T}{GAK} + \frac{E}{GK}\right) \tag{7}$$

$$\tau_3 = \left(1 + \frac{T}{GAK}\right)c_f^2 \tag{8}$$

From equation (5), two dispersion relations for group velocities arise, in accordance with the degrees of freedom of the Timoshenko model. Focusing only on transverse-dominant waves, one can obtain:

$$c'_{gt}(\gamma_t) = \frac{\tau_2\gamma_t + \frac{2\tau_1(2\tau_3\gamma_t^3 + c_t^2\gamma_t) - \tau_2\gamma_t(\tau_2\gamma_t^2 + 1)}{\sqrt{(\tau_2\gamma_t^2 + 1)^2 - 4\tau_1\gamma_t^2(\tau_3\gamma_t^2 + c_t^2)}}}{\sqrt{2\tau_1\left(\tau_2\gamma_t^2 + 1 - \sqrt{(\tau_2\gamma_t^2 + 1)^2 - 4\tau_1\gamma_t^2(\tau_3\gamma_t^2 + c_t^2)}\right)}} \tag{9}$$

with:

$$\gamma_t(\omega) = \sqrt{\frac{\tau_2\omega^2 - c_t^2 + \sqrt{(\tau_2\omega^2 - c_t^2)^2 - 4\tau_3\omega^2(\tau_1\omega^2 - 1)}}{2\tau_3}} \tag{10}$$

Returning to the previous example (and assuming that the material is isotropic, with a Poisson ratio of 0.3), Figure 1 evidences that both models agree in a low frequency range and deviate largely when $\omega \to \infty$; in particular, the new dispersion relation has a horizontal asymptote, of value $\sqrt{c_t^2 + GAK/\mu}$. The validity domain of the Euler-Bernoulli hypothesis is a function of the cable properties; therefore, only the Timoshenko model will be regarded hereinafter.

In order to assess the sensitivity of c'_{gt} to T, EI and GAK, 10% variations in the value of these parameters are now considered and represented in Figure 2. This figure illustrates that group velocity is generally independent of the axial force, except in the low frequency range. On the contrary, shear rigidity controls the value of the horizontal asymptote, while bending stiffness determines the rapidness in the increase of c'_{gt}.

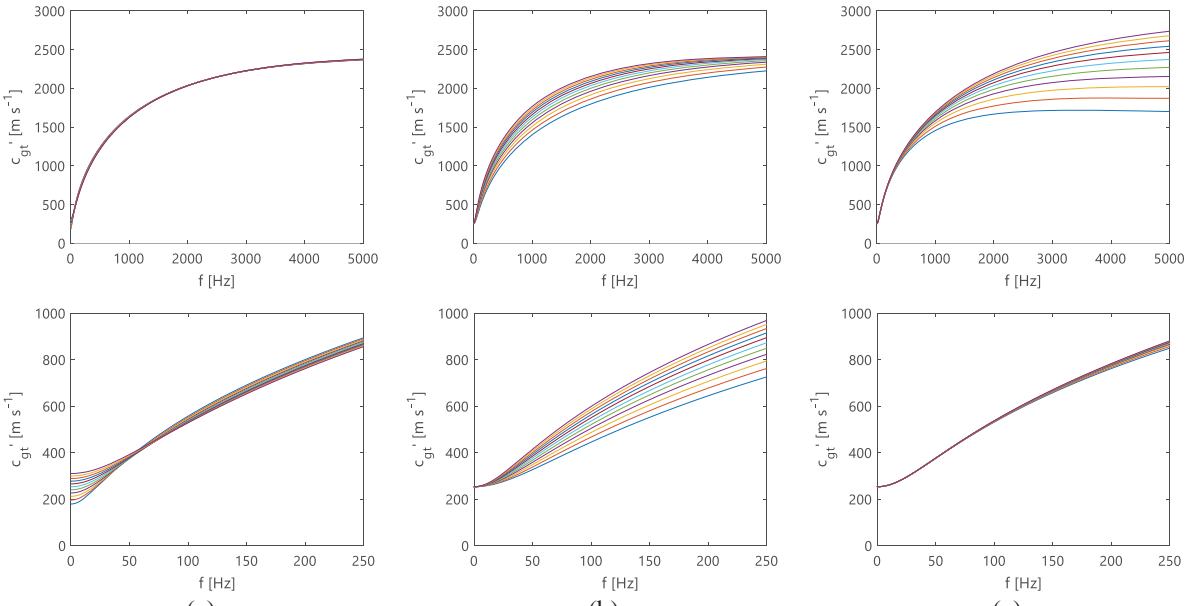

Figure 2: Dispersion relations for c'_{gt} (Timoshenko model), considering 10% variations in the value of: (a) axial force T; (b) bending stiffness EI; (c) shear rigidity GAK.

3 METHODOLOGY

The methodology for the experimental assessment of dispersion relations requires obtaining time-frequency distributions at two sections of a cable. The wavelet transform of the response u is a function $\{\mathcal{W}u\}$, defined by:

$$\{\mathcal{W}u\}(a,b) = \frac{1}{\sqrt{|a|}}\int_{-\infty}^{+\infty} u(t)\psi^*\left(\frac{t-b}{a}\right)dt \tag{11}$$

in which ψ^* denotes the complex conjugate of the mother wavelet ψ, that has an oscillatory nature [11]. Following Apostoloudia *et al.* [12], this study will employ the mother wavelet of Morlet. The scale parameter $a \neq 0$ is responsible for dilating (i.e., stretching or compressing) the function ψ, while b corresponds to a translation parameter. If $\psi(t)$ is localized around $t = 0$ and its Fourier transform around $\omega = \omega_0$, then $\psi((t-b)/a)$ is centered at $t = b$ in the time domain and $\omega = \omega_0/a$ in frequency domain. As such, $\{\mathcal{W}u\}(a,b)$ provides time-frequency information of u around a point $(b, \omega_0/a)$.

Kishimoto *et al.* [13] proved that, for a fixed location s, the peaks in the magnitude of $\{\mathcal{W}u\}$ indicate the arrival time of a frequency component ω that propagates with a group velocity c_g. Accordingly, introducing an external excitation at a section S0 and recording the cable response at S1 and S2, one can identify arrival times t_{S1} and t_{S2} of each frequency ω, by the relative maxima of both time-frequency distributions. Referring to Figure 3(a), the group velocity c'_{gt} is then given by:

$$c'_{gt}(\omega) = \frac{d_{S1,S2}}{t_{S2}(\omega) - t_{S1}(\omega)} \tag{12}$$

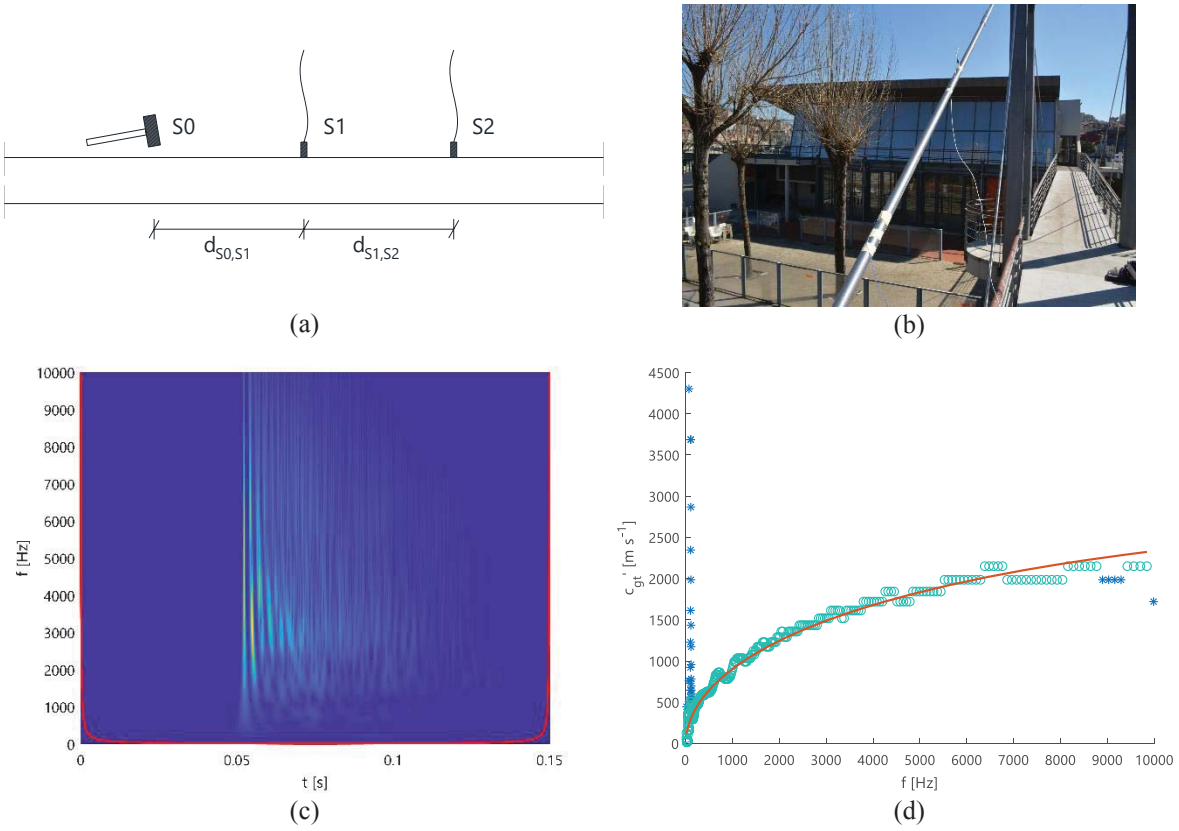

Figure 3: Assessment of dispersion relations in cables: (a) experimental setup; (b) application to the case study; (c) scalogram of the response at S1; (d) experimental and fitted dispersion relation.

The validation of the proposed methodology is performed on a cable from a footbridge, represented in Figure 3(b), using two piezoelectric accelerometers and an impact hammer.

Figure 3(c) illustrates the scalogram of transverse accelerations at S1 (i.e., the magnitude of the respective wavelet transform). This representation reveals that the spectral content is distributed along ridges in the time-frequency plane: the first ridge corresponds to the direct propagation from S0, while the subsequent ones arise from reflections at the cable ends.

In most applications, the sensor position relative to each cable end (and hence the distance covered by the reflected waves) is difficult to assess. As a result, t_{S1} and t_{S2} are here identified by the first ridge in the respective scalograms and the methodology becomes independent of any assumption concerning boundary conditions. Figure 3(d) represents the experimental dispersion curve, calculated according to expression (12); blue markers symbolize outliers, identified through the DBSCAN algorithm [14].

The stay under analysis consists of a solid, stainless steel bar, with a diameter of 28.6 mm and shear coefficient K equal to 0.925 [15]. Assuming that the material is isotropic, only the axial force T and the elastic modulus E remain unknown. These parameters are then estimated by fitting the analytical relation (9) to the experimental curve.

4 RESULTS AND DISCUSSION

Based on the previous methodology, different experimental setups were defined, concerning the impact location and the distance between accelerometers. Red (R), blue (B) and steel (S) hammer tips were used, with increasing hardness of the contact surface and a consequent rise on the excitation's frequency content.

In addition to these experiments, natural frequencies were obtained through an ambient vibration test, which enabled the simultaneous identification of $T = 48.1$ kN and $E = 188.9$ GPa. Table 1 presents the errors in the dispersion-based estimates of E relative to the latter value, and evidences that the obtained results are accurate and consistent within setups, especially for blue and red hammer tips. This methodology appears, however, to be less suitable for extracting adequate estimates of the axial force, since very significant errors are attained in this parameter. In fact, as shown in Figure 2(a), group velocities are generally insensitive to the value of T, except in a low frequency range where arrival times are difficult to identify, because the transient response is concealed in the stationary vibration of the cable.

Setup	S1	S2	S3	B1	B2	B3	R1	R2	R3
$d_{S0,S1}$ [m]	0.564	0.564	0.219	0.564	0.564	0.219	1.120	0.564	0.219
$d_{S1,S2}$ [m]	1.008	1.008	0.487	1.008	0.487	0.487	1.008	1.008	0.487
$\boldsymbol{\delta E}$ **[%]**	**-5.77**	**-4.50**	**-5.19**	**-1.59**	**+2.49**	**-2.75**	**-1.48**	**-2.96**	**+3.39**
RMSE [m s^{-1}]	63.6	76.8	98.2	70.8	103.0	109.6	82.7	63.8	86.6

Table 1: Definition and estimates of E from nine experimental setups.

5 CONCLUSIONS

In this paper, cables were assumed as Euler-Bernoulli or Timoshenko tensioned beams and sag-extensibility effects were neglected. In comparison with the taut string hypothesis, the first model allowed highlighting the dispersive behavior introduced by the bending stiffness, since each frequency component now traveled with a distinct group velocity. The formulation is, however, inadequate for applications involving a wide frequency domain of interest, such as those considered in this study, motivating the corrections for shear deformation and rotary inertia. The Timoshenko model thus derived evidenced that the dynamic behavior of cables is roughly divided into three domains, the first (low frequencies) being governed by the axial force,

the second (increase of c'_{gt}) controlled by the bending stiffness and the last (asymptotic behavior for $\omega \to \infty$) defined by the shear rigidity.

The proposed methodology for experimental assessment of dispersion relations is conceptually independent of boundary conditions and applicable to any cable, regardless of the nature of the progression of natural frequencies. Unlike strategies relying on the characterization of mode shapes, this approach requires only two sensors, from which time-frequency distributions of the transient response are computed. The relative maxima of the scalograms enable the identification of arrival times for each frequency component, and of the respective group velocity.

The results obtained from in situ tests reveal that this dispersion-based methodology provides adequate estimates of the bending stiffness, which will prove useful in the local assessment of damage. In contrast, whether a similar accuracy is attainable for axial force is a subject of ongoing research.

ACKNOWLEDGEMENTS

The first author would like to acknowledge the PhD scholarship SFRH/BD/129183/2017 awarded by FCT.

This work was financially supported by: Base Funding – UIDB/04708/2020 and Programmatic Funding – UIDP/04708/2020 of the CONSTRUCT – Instituto de I&D em Estruturas e Construções, funded by national funds through the FCT/MCTES (PIDDAC); DYNCATLINE – Monitoring and Analysis of the Dynamic Behavior of the Cable/Tower System in Overhead High Voltage Transmission Lines under Wind Excitation (reference POCI-01-0145-FEDER-016877), funded by COMPETE2020 and FCT; SAFESUSPENSE – Safety Control and Management of Long-Span Suspension Bridges (reference POCI-01-0145-FEDER-031054), funded by COMPETE 2020, POR Lisboa and FCT.

REFERENCES

[1] H. M. Irvine, *Cable Structures*. Cambridge: The MIT Press, 1981.

[2] R. Geier *et al.*, "Accurate cable force determination using ambient vibration measurements", *Structure and Infrastructure Engineering*, vol. 2, no. 1, pp. 43-52, 2006. [Online]. Available: https://doi.org/10.1080/15732470500253123

[3] A. B. Mehrabi and H. Tabatabai, "Unified finite difference formulation for free vibration of cables", *Journal of Structural Engineering*, vol. 124, no. 11, pp. 1313-1322, 1998. [Online]. Available: https://doi.org/10.1061/(ASCE)0733-9445(1998)124:11(1313)

[4] E. S. Caetano *et al.*, "Assessment of cable forces at the London 2012 Olympic Stadium roof", *Structural Engineering International: Journal of the International Association for Bridge and Structural Engineering (IABSE)*, vol. 23, no. 4, pp. 489-500, 2013. [Online]. Available: https://doi.org/10.2749/101686613X13627351081713

[5] S. Li *et al.*, "Vibration-based estimation of axial force for a beam member with uncertain boundary conditions", *Journal of Sound and Vibration*, vol. 332, no. 4, pp. 795-806, 2013. [Online]. Available: https://doi.org/10.1016/j.jsv.2012.10.019

[6] C. C. Chen *et al.*, "A novel tension estimation approach for elastic cables by elimination of complex boundary condition effects employing mode shape functions", *Engineering Structures*, vol. 166, pp. 152-166, 2018. [Online]. Available: https://doi.org/10.1016/j.engstruct.2018.03.070

[7] B. Yan *et al.*, "Mode shape-aided tension force estimation of cable with arbitrary boundary conditions", *Journal of Sound and Vibration*, vol. 440, pp. 315-331, 2019. [Online]. Available: https://doi.org/10.1016/j.jsv.2018.10.018

[8] K. F. Graff, *Wave Motion in Elastic Solids*. Mineola: Dover Publications, 1991.

[9] J. D. Achenbach, *Wave Propagation in Elastic Solids*. New York: North-Holland Publishing Company, 1976.

[10] K. Maes *et al.*, "Identification of axial forces in beam members by local vibration measurements", *Journal of Sound and Vibration*, vol. 332, no. 21, pp. 5417-5432, 2013. [Online]. Available: https://doi.org/10.1016/j.jsv.2013.05.017

[11] C. K. Chui, *An Introduction to Wavelets*. San Diego: Academic Press, 1992.

[12] A. Apostoloudia *et al.*, "Time-frequency analysis of transient dispersive waves: A comparative study", *Applied Acoustics*, vol. 68, no. 3, pp. 296-309, 2007. [Online]. Available: https://doi.org/10.1016/j.apacoust.2006.02.002

[13] K. Kishimoto *et al.*, "Time frequency analysis of dispersive waves by means of wavelet transform", *Journal of Applied Mechanics, Transactions ASME*, vol. 62, no. 4, pp. 841-846, 1995. [Online]. Available: https://doi.org/10.1115/1.2896009

[14] E. Schubert *et al.*, "DBSCAN revisited, revisited: Why and how you should (still) use DBSCAN", *ACM Transactions on Database Systems*, vol. 42, no. 3, 2017. [Online]. Available: https://doi.org/10.1145/3068335

[15] J. R. Hutchinson, "Shear coefficients for Timoshenko beam theory", *Journal of Applied Mechanics, Transactions ASME*, vol. 68, no. 1, pp. 87-92, 2001. [Online]. Available: https://doi.org/10.1115/1.1349417

EURODYN 2020
XI International Conference on Structural Dynamics
M. Papadrakakis, M. Fragiadakis, C. Papadimitriou (eds.)
Athens, Greece, 23–26 November 2020

A PSEUDO-INVERSE APPROACH TO THE PHYSICAL MODEL ESTIMATION PROBLEM. CAPACITIES AND LIMITATIONS.

Alvaro Magdaleno[1], **Jose M. Soria**[2], **and Antolin Lorenzana**[1]

[1] ITAP. Universidad de Valladolid
Paseo del Cauce, 59, 47011 Valladolid, Spain
alvaro.magdaleno@uva.es, ali@eii.uva.es

[2] ETSICCP. Universidad Politécnica de Madrid
Calle del Profesor Aranguren 3, 28040 Madrid, Spain
jm.soria@upm.es

Keywords: System identification; structural dynamics; experimental modal analysis

Abstract. *The real dynamic response of any structure, assuming linear behaviour, can be accurately reproduced by means of a modal model issued from an Experimental Modal Analysis (EMA). Natural frequencies, mode shapes and damping ratios, together with some information about the modal masses of the structure, form a complete set of valid information to carry out simulations. However, using that sort of model, no direct information about the physical properties of the structure is available and it may be challenging to try to reproduce the effect of a structural modification like a mass addition, stiffness modification or changes in the boundary conditions. To overcome this, Model Updating techniques have been developed together with the evolution of the Finite Element Method (FEM) paradigm as a way to adapt the computational models to some experimentally estimated properties of a real structure. As a result, the models behave quite similarly to the real structure and, indirectly, some of its physical properties can be estimated and eventually modified according to any simulation requirement. However, the proper application of a Model Updating technique often leads to an iterative and time consuming process which usually rely on accurate enough FEM models and the understanding of relatively sophisticated optimization algorithms to provide meaningful results; otherwise, unrealistic updated properties could be obtained as the best options to reproduce the real structural dynamics and the physical properties estimation or modification is no longer trustworthy.*

In this work, an alternative methodology is proposed to estimate the physical matrices of a structure. We assume that the structure behaves linearly and that a modal model has been previously identified. Then, by using a set of equations like the eigenproblem relationships, the orthogonality equations and symmetry assumptions, the physical matrices elements are calculated by means of the Moore-Penrose pseudo-inverse. This approach provides an exact accomplishment of the equations when there are more unknowns than equations, and an optimal solution in the least squares sense in the opposite situation.

1 INTRODUCTION

During the last decade, advances in the field of microcontrollers and processors have led to the active development of permanent monitoring systems for structures and infrastructures. These systems enable, with a relatively small investment, to continuously track some basic parameters of the structure, like its natural frequencies and damping ratios among others, without the need to deploy large temporary sensor networks for carrying out experimental tests, which usually are more expensive.

This sort of systems is usually associated to structure health monitoring systems (SHM) capable of postprocessing the great amount of measured data with the main aim of assessing the structural integrity. To do so, it is very useful to know the spatial distribution of the structural properties and their relationship with the measured modal parameters. One way to do this requires a Finite Element Method (FEM) model, conveniently updated to represent the same measured structural parameters. However, this presents the problem of having built a detailed enough FEM model, for which the updating process may be very time consuming and lead to unrealistic estimated physical properties, as it can be inferred from [1].

Another way to deal with the modelling problem consists in directly estimating a mathematical reduced model from the measured data, which can be a modal model or a physical model, among others. The modal model is usually easier to estimate, and it enables to simulate different loading scenarios, but it does not directly provide the spatial distribution of the properties, making it difficult to perform potential structural modifications.

Physical models have been estimated since several decades ago, like in [2], where the author proposed a simple orthogonality principle inversion, or [3], who proposed a pseudo-inverse approach for incomplete estimated modal models. Since then, several approaches to this problem have been addressed assuming different types of damping models and various considerations, like [4], [5], [6], [7], [8] or [9]. In this work, a methodology to estimate a physical reduced-order model from experimental data is developed. The procedure is presented as a common framework to deal with both general viscous and general structural damping models, which do not make any proportionality assumption. It is conceived to be programmed in a structural health monitoring system to help with the damage detection and predict the response of the damaged structure to decide if the structure can remain in this way or if maintenance works should be carried out. The model estimation is based on the modal properties, so the proposed procedure happens in two well separated stages: during the first stage, the modal properties are estimated from experimental Frequency Response Functions (FRFs); the second stage is devoted to estimate the physical model from the modal one.

The article first presents the theoretical background needed to settle a nomenclature in Section 2. Section 3 is entirely devoted to developing the methodology and Section 4 shows an example of application. Section 5 is centred on a discussion about the advantages and drawbacks of the proposed methodology finishing the article with a set of conclusions.

2 THEORETICAL BACKGROUND

Every linear system can be described with the system of differential equations of Eq. 1, characterized by the real-valued and symmetric mass (M), damping (D) and stiffness (K) matrices, where q represents the N degrees of freedom of the structure and f stands for the dynamic forces acting on them. According to the chosen damping model, the system of differential equations changes [10]: Eq. 1a represents the system of equations for viscous damping model and Eq. 1b, for structural damping model.

$$M\ddot{q}(t) + D\dot{q}(t) + Kq(t) = f(t) \quad (1a)$$
$$M\ddot{q}(t) + (K + jD)q(t) = f(t) \quad (1b)$$

After transforming Eq. 1 to the frequency domain, Eq. 2 is obtained from which the dynamic stiffness can be defined for each damping model (Eq. 3a for viscous damping and Eq. 3b for structural damping). The inverse of the dynamic stiffness is the commonly known as Frequency Response Functions (FRFs) matrix H(w), whose rows or columns are usually estimated separately by means of experimental tests and it can be demonstrated that only one, well selected, of this rows or columns provides enough information to estimate the modal properties of the tested structure.

$$G(\omega)\, Q(\omega) \;=\; F(\omega) \quad (2)$$

$$G(\omega) = -\omega^2 M + j\omega D + K \quad (3a)$$
$$G(\omega) = -\omega^2 M + K + jD \quad (3b)$$

The modal properties of a structure are defined as a way to solve Eq. 1. Assuming a complex exponential response, the solution to the homogeneous system can be obtained by solving first the eigenproblem of Eq. 4a, for viscous damping, and Eq. 4b, for structural damping, which must be verified for all the *m* pairs of eigenvalues and eigenvectors of the structure. The complex-valued eigenvectors ϕ_r are called mode shapes of the structure and the eigenvalues s_r contain the natural frequency ω_r and damping ratio, ζ_r or η_r, depending on the damping model (see Eq. 5a, viscous damping, and Eq. 5b, structural damping). When the modal information is calculated analytically, the number of obtained modes is equal to the number of degrees of freedom ($m = N$). However, if they are estimated through an experimental modal analysis (EMA), this number is usually lower ($m <= N$) and the model is said to be incomplete.

$$(s_r^2\, M + s_r D + K)\phi_r = 0 \quad (4a)$$
$$(s_r^2\, M + K + jD)\phi_r \;=\; 0 \quad (4a)$$

$$s_r = -\omega_r \zeta_r + j\omega_r \sqrt{1 - \zeta_r^2} \quad (5a)$$
$$s_r^2 = \omega_r^2 (1 + \eta_r) \quad (5b)$$

The mode shapes verify some orthogonality equations respect to the physical matrices. These equations can be divided into two groups, one associated to the mass matrix and another to the stiffness one, as shown in Eqs. 6 (for viscous damping model) and Eqs. 7 (for structural damping model), where $\Phi = [\phi_1 \quad ... \quad \phi_m]$ is the mode shape matrix whose columns contain the mode shapes, S stands for the eigenvalue matrix, a diagonal matrix containing the *m* eigenvalues, and I_m is the $m \times m$ identity matrix. Note that, by definition, mode shapes are not uniquely defined, and they can be scaled arbitrarily. It is common, however, to scale them to make the orthogonality properties have the right sides shown in Eqs. 6 and 7.

$$\Phi^{\mathrm{t}}\, C\, \Phi + S\, \Phi^{\mathrm{t}}\, M\, \Phi + \Phi^{t}\, M\, \Phi\, S = I_m \quad (6a)$$
$$\Phi^{\mathrm{t}}\, K\, \Phi - S\, \Phi^{\mathrm{t}}\, M\, \Phi\, S = -S \quad (6b)$$

$$\Phi^{\mathrm{t}}\, M\, \Phi = I_m \quad (7a)$$
$$\Phi^{\mathrm{t}}\, (K + jD)\, \Phi = S^2 \quad (7b)$$

Thanks to the modal properties, the calculation of FRFs can be simplified to the expressions shown in Eq. 8a, for viscous damping, and Eq. 8b, for structural damping. This represent a huge advantage in terms of computation efficiency in relation with inverting Eq. 3 and makes possible identification techniques like the curve fitting method proposed in the next section.

$$H(\omega) = \Phi \left[diag\left(\frac{1}{j\omega - s_r}\right)\right] \Phi^{\mathrm{t}} \tag{8a}$$

$$H(\omega) = \Phi \left[diag\left(\frac{1}{s_r^2 - \omega^2}\right)\right] \Phi^{\mathrm{t}} \tag{8b}$$

Eq. 8 represent the starting point of the methodology presented in this article and detailed in the next section.

3 METHODOLOGY

The methodology starts by performing a complete modal test to the structure. It is necessary to distribute a set of sensors on the structure and measure both inputs and outputs in *N* well selected degrees of freedom. Then, by means of an estimator like H_1, H_2 or H_v, among others, the FRFs have to be calculated. As stated before, only a well selected row or column of the FRFs matrix H(ω) is needed to completely extract the modal information of the *m* modes inside the measured frequency range.

There are several ways to estimate the modal properties from the FRFs, but the curve fitting method is proposed in this work to estimate at the same time all the required modal information. Also, to make the procedure slightly more independent from the user, a varying order procedure is applied. In this way, the order of the modal model is varied from a minimum value to a maximum, sequentially performing a curve fitting to the expressions in Eq. 8 and enabling to draw a sort of stability diagram like the ones shown in Figure 4. In other words, several modal models are estimated assuming different numbers of modes inside the measured frequency band, each of which differently fits the experimental FRFs. The goodness of fit is evaluated through the sum of squared error between the experimental and the calculated real and imaginary parts of the FRFs, an indicator which should monotonously decrease with the model order. Finally, since the upper bound for the model order can be potentially high, leading to a model with an order unnecessarily high, it can be useful to define an error threshold under which a certain modal model can be "acceptable" for engineering purposes. The value of this threshold should be adapted according to the engineer expertise, the aim of the structure and the kind of the subsequent analysis to be performed with the model. The first order whose modal model meets the error threshold is retained as the identified modal model for the structure.

Once the modal properties have been identified, they are used as inputs to the physical matrix estimation. This technique aims to calculate the full set of physical matrices, M, K and D, that satisfies all the relationships and conditions presented in Section 2. For doing it in the most general way, in this work rewriting Eqs. 4 and 6, for viscous damping, or 7, for structural damping, as a linear system of equations is proposed. The unknowns of such a system are the elements of the physical matrices, as stated in Eq. 9. In this simple equation, x_M contains all the terms of the mass matrix, x_K the terms of the stiffness matrix and x_D the ones corresponding to the damping matrix. Note that the terms in x_M, x_K and x_D can be arranged as desired as long as the columns of A are arranged accordingly.

$$A \begin{bmatrix} x_M \\ x_K \\ x_D \end{bmatrix} = b \tag{9}$$

In the following sections, the different kind of equations are summed up for clarity.

3.1 Eigenproblem equations

Presented in Eq. 4 for each damping model, these equations represent the basic relationship between the modal information and the physical matrices. Since every pair of eigenvalue and eigenvector leads to a column vector of N zeroes, and m pairs have been identified, there are a total of mN eigenproblem equations, shown in Eq. 10. The terms in matrix A_{eig}, of size $mN \times 3N^2$, are composed of eigenvector elements, some of them multiplied by their corresponding eigenvalues. The associated mN terms in vector b_{eig} are equal to 0.

$$A_{eig} \begin{bmatrix} x_M \\ x_K \\ x_D \end{bmatrix} = b_{eig} = 0 \tag{10}$$

3.2 Orthogonality equations

Although derived from the eigenproblem relationship, the orthogonality equations (Eqs. 6 and 7) are linearly independent of them. The corresponding terms in A_{ort} matrix (Eq. 11) are calculated by products of different eigenvectors elements and, in the viscous damping case, some of them are also multiplied by their corresponding eigenvalues. The terms in vector b are not all null, being some of them equal to 1 and other equal to the eigenvalues, according to Eqs. 6 and 7. A priori, there are $2m^2$ orthogonality equations, but thanks to the inherent symmetry of modal matrices this number can be reduced to $2m\,(m+1)/2$.

$$A_{ort} \begin{bmatrix} x_M \\ x_K \\ x_D \end{bmatrix} = b_{ort} \tag{11}$$

3.3 Symmetry equations

Physical matrices are typically symmetric. This means that some of the $3N^2$ variables are equal to some others. This fact can be expressed in a set of $3N\,(N-1)/2$ equations (Eq. 12) containing pairs of 1 and –1 correctly placed in the matrix A_{sym} to take account for this. The corresponding elements in the vector b_{sym} are 0.

$$A_{sym} \begin{bmatrix} x_M \\ x_K \\ x_D \end{bmatrix} = b_{sym} = 0 \tag{12}$$

3.4 Real-valued system of equations

Since matrices A_{eig} and A_{ort} and vectors b_{eig} and b_{ort} are complex valued, the general solution of the system of equations will also be complex. To avoid this and obtain real-valued physical matrices, first split the matrices A_i, vector b_i and variables vector x in real and imaginary parts, obtaining Eq. 13, where i can stand for 'eig' or 'ort' and subscripts 're' and 'im' stand for real and imaginary parts respectively. This expression can be expanded and reorganized to separate real and imaginary parts. Since two complex numbers are equal if, and only if, their real parts are equal and imaginary parts are equal as well, the expression in Eq. 14 must be satisfied, which has been simplified assuming that $x_{im} = 0$, which is the case here.

$$(A_{i,re} + jA_{i,im})(x_{re} + jx_{im}) = b_{i,re} + jb_{i,im} \tag{13}$$

$$\begin{bmatrix} A_{i,re} \\ A_{i,im} \end{bmatrix} x_{re} = \begin{bmatrix} b_{i,re} \\ b_{i,im} \end{bmatrix} \tag{14}$$

This strategy can be applied to the eigenproblem and orthogonality equations before assembly the system of equations (the symmetry equations are real-valued), doubling their number of equations.

3.5 Assembly and solution

Once the different parts of matrix A and column vector b have been built as explained in the previous sections, the complete matrix A can be assembled into one single system of equations of Eq. 15 to be solved for the physical unknowns.

$$\begin{bmatrix} A_{eig,re} \\ A_{eig,im} \\ A_{ort,re} \\ A_{ort,im} \\ A_{sym} \end{bmatrix} \begin{bmatrix} x_M \\ x_K \\ x_D \end{bmatrix} = \begin{bmatrix} 0 \\ 0 \\ b_{ort,re} \\ b_{ort,im} \\ 0 \end{bmatrix} \tag{15}$$

Eq. 15 represents a system of linear equations with $N_{VA} = 3N^2$ variables and a total of $N_{EQ} = 2Nm + 2m\,(m + 1) + 3N\,(N - 1)/2$ independent equations. By comparing N_{VA} and N_{EQ}, three different situations can be found:

- $N_{EQ} = N_{VA}$. The system can be directly solved by traditional means.
- $N_{EQ} > N_{VA}$. The system can be solved using a pseudo-inverse approach, like the Moore-Penrose pseudo-inverse matrix, which provides the best fitting to all equations, minimizing the error in a least squares sense.
- $N_{EQ} < N_{VA}$. The system can be also solved using the Moore-Penrose pseudo-inverse. The obtained solution exactly satisfies all the equations, but it may not be adequate and more equations (restraints) must be imposed.

Although the most desirable situation is the first one, it is quite uncommon to have the same amount of linearly independent equations and variables. Having more equations than variables is a far more common situation if the number of identified modes approaches the number of monitored degrees of freedom. In this case, all the equations should be satisfied at the same time and the closest solution to that situation should be a convenient physical model.

However, the most typical scenario occurs when the number of identified modes is quite lower than the number of monitored degrees of freedom, $N_{EQ} < N_{VA}$. In that case, although all equations are exactly satisfied, they may not be enough for the resulting model to be convenient for further applications and some additional equations should be added to the system. Amongst all the practical options, only the total mass equation is considered in this work. This equation accounts for the total mass of the structure, which can be calculated as the sum of the diagonal terms in the mass matrix and its value should be estimated previously by means of other techniques. The authors have constated that it is only needed a rough estimation of the mass for the methodology to work and the consequences of a bad estimation have not been investigated yet, but it may have important drawbacks when applying any structural modification. Also note that other kind of equations could be also considered, like the nullity of some terms, but they are not covered in this work.

4 CASE STUDY

4.1 Structure and test description

A laboratory-scaled simple-supported beam has been tested for illustrating the methodology described above. It is a 6-meter long aluminium profile with a rectangular hollow section of 100 mm width, 40 mm height and a thickness of 1.5 mm. The supports are conceived in such a way that they can be approximated to perfectly pinned supports and any friction effect can be neglected.

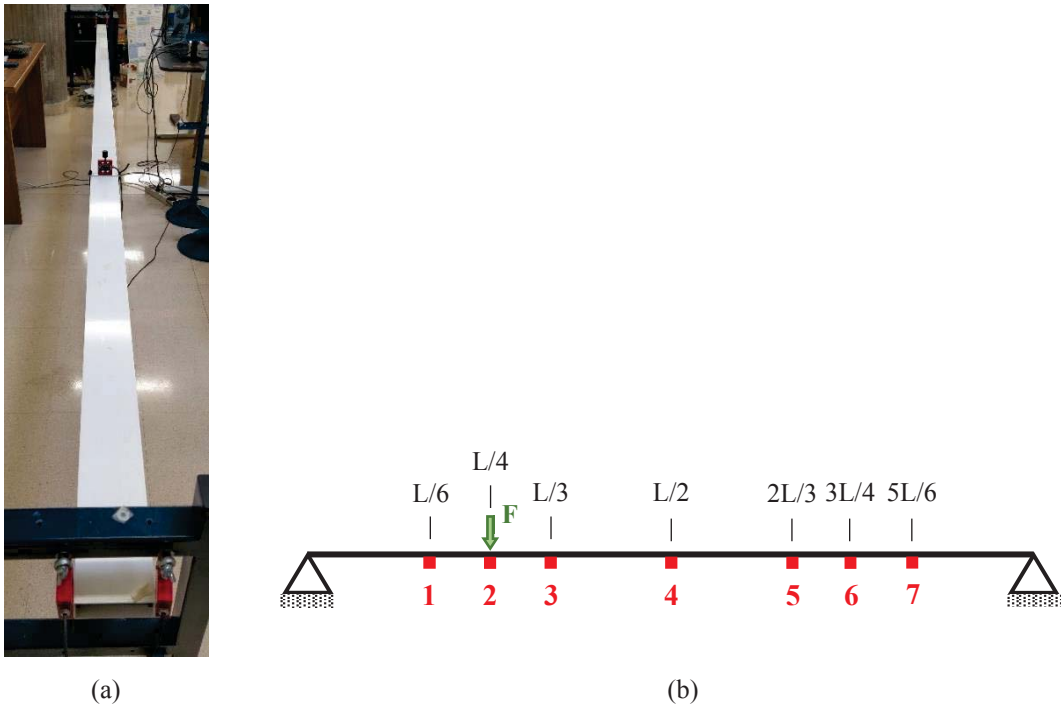

(a) (b)

Figure 1. Experimental set up showing (a) the picture of the beam with the load cell; and (b) the scheme with the position of the sensors, where L is the total length of the beam.

The structure, shown in Figure 1a, is monitored by means of seven accelerometers, some of them being placed on the maxima of the modal shapes for the first three modes, which are expected to be similar to $sin(k\,\pi x/L)$, with k = 1, 2 and 3, and L the total length of the beam. The accelerometers have a sensitivity of 100 mV/g and a measurement range of ±60g. The excitation is induced by means of a hammer, whose force is quantified by using a 2 mV/V, 10 kg load cell attached to the beam at $L/4$ as shown in Figure 1b. For not losing the symmetry caused by the load cell, an equivalent amount of rigid mass has been added at $3L/4$. All the sensors are connected to the acquisition system, a 16 channel SIRIUS® STGS datalogger of the brand Dewesoft. Figure 2 shows an example of recorded force and the corresponding acceleration measurement of the collocated accelerometer.

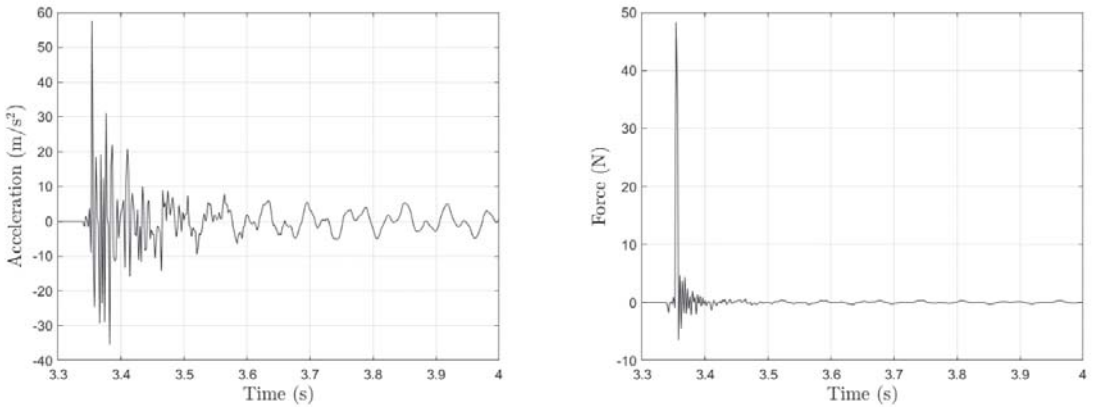

(a) (b)

Figure 2. Example of recording between 3.3 and 4 s: (a) Acceleration at $L/4$; (b) Measured force

4.2 Frequency Response Functions and modal identification

Frequency Response Functions (FRFs) are estimated using the H_v estimator which is defined as the geometric mean of H_1 and H_2 estimators, very common in literature [11]. The magnitude and phase plots of the measured FRFs are shown in Figure 3. The seven FRFs are used as inputs to the modal identification procedure. Both general viscous and structural damping are considered in parallel in this work. Also, the system to be identified corresponds to the beam containing the sensors and their cables and no effort will be devoted in this work to remove their contribution to the modal properties or to the physical matrices.

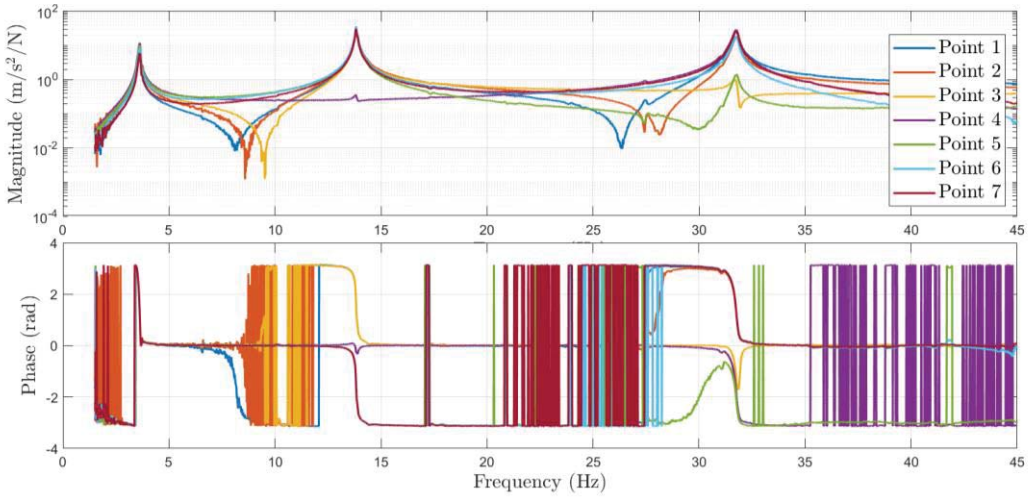

Figure 3. Experimental FRFs

Performing the curve fitting of the FRFs to the expressions in Eq. 8 at the same time applying the variable order technique described in Section 3, leads to the stability diagrams shown in Figure 4, where it can be shown the goodness of the methodology to identify the most evident modes (corresponding to the local maxima). Since there are three evident peaks in the FRFs, the order is set to vary between 1 and 5 modes. As can be seen, the three main peaks are easily identified and, if more modes are considered (4 or 5 in this case), the algorithm places them where it can but very low mode shape amplitudes and high values of damping ratios. In both cases, three modes are enough to represent the dynamic behaviour of the beam. This can be stated also in Figure 5, where the error evolution is shown for every tested model order. From

order three and above, the error remains well under two magnitude orders below the initial error value.

The final modal properties are summed up in Table 1 and the associated mode shapes are depicted in Figure 5. It can be shown that the identified natural frequencies are the same and the viscous damping factors are approximately the half of the structural ones, a relationship that van be assumed for low damped structures. This modal information is now used in the next section to estimate the physical matrices of the beam.

	Viscous damping model		Structural damping model	
	ω_r (Hz)	ζ_r	ω_r (Hz)	η_r
Mode 1	3.61	0.0063	3.61	0.0126
Mode 2	13.84	0.0036	13.83	0.0070
Mode 3	31.72	0.0033	31.72	0.0068

Table 1. Modal properties for both damping models

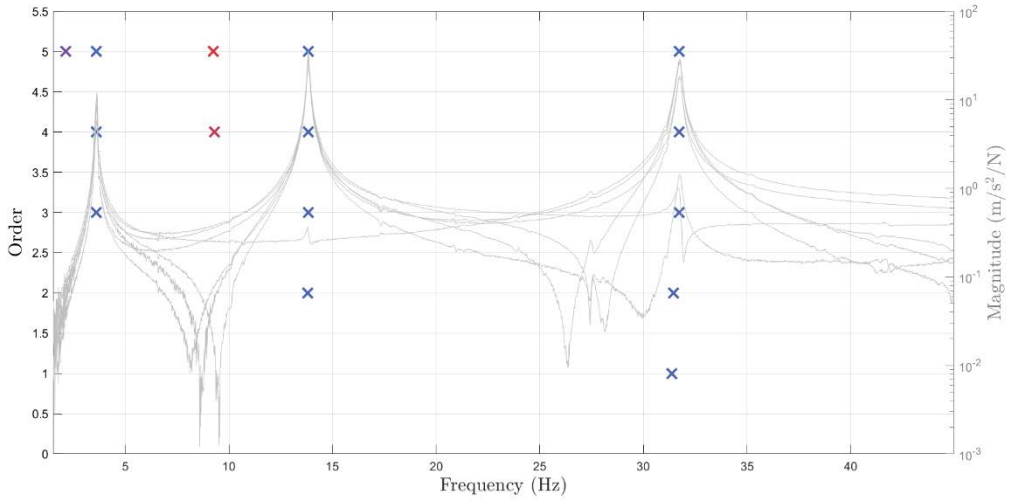

(a)

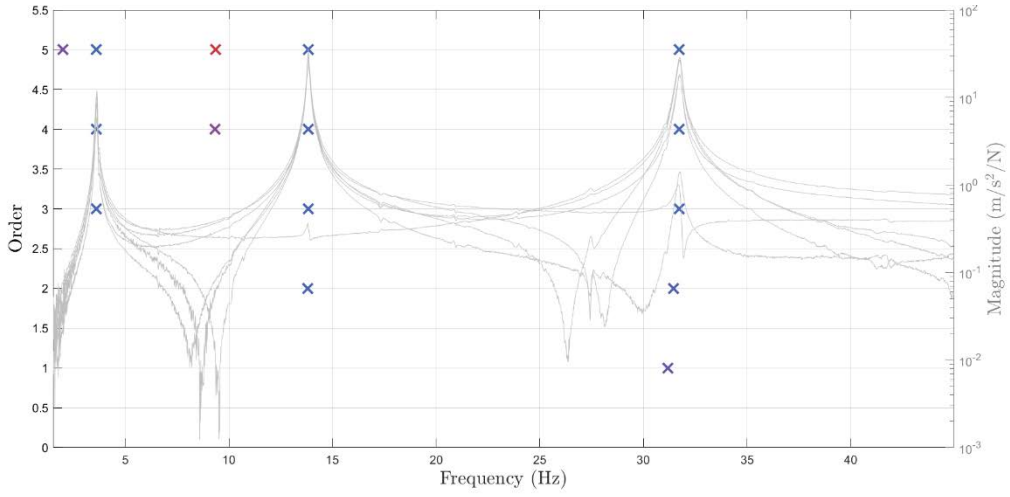

(b)

Figure 4. Stability charts obtained for (a) structural damping model and (b) viscous damping model

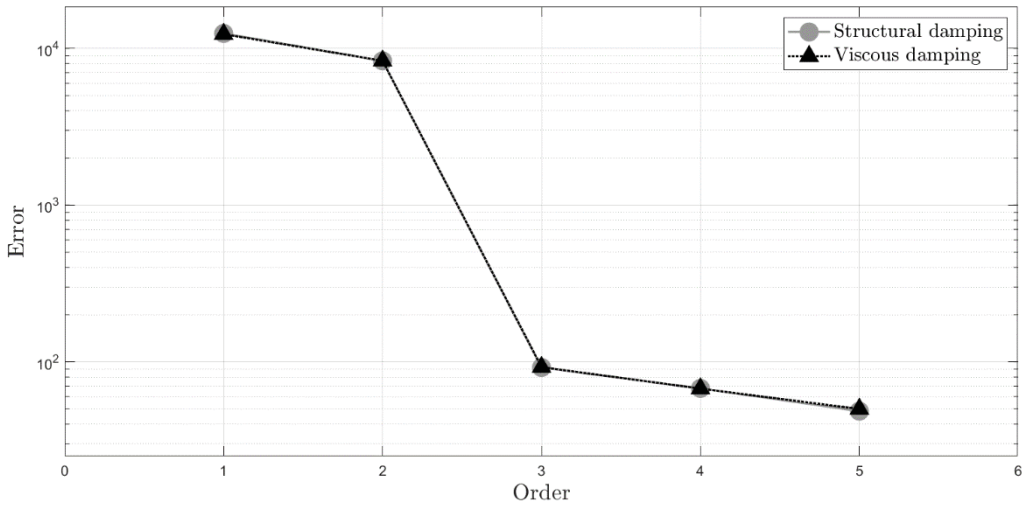

Figure 5. Error evolution for both structural and viscous damping models

4.3 Physical matrices estimation

Using the modal parameters estimated in the previous section it is possible to assemble the system of equations of Eq. 9. For this case, with seven monitored degrees of freedom and three identified modes, the system contains 147 unknowns and a total of 129 equations: 24 orthogonality equations, 42 eigenproblem equations and 63 symmetry equations. Since there are more unknowns than equations, it may be useful to add the mass equation, which is estimated to be 6.5 kg. Solving for that system, matrices in Eq. 16 are obtained for the viscous damping model and in Eq. 17 for the structural damping model. Figure 6 shows an FRF comparison between the experimental one at $L/4$ and the calculated using both obtained physical models.

$$M = \begin{bmatrix} -0.478 & 0.108 & -0.375 & -0.370 & -0.448 & 0.164 & 0.467 \\ & 1.212 & 1.746 & 0.098 & 0.351 & -1.582 & 1.053 \\ & & -0.385 & -0.705 & 1.971 & 0.199 & -1.350 \\ & & & 1.662 & -0.881 & -1.924 & 2.306 \\ & & & & 2.990 & 0.604 & -1.160 \\ & & sym & & & -0.836 & -0.294 \\ & & & & & & 2.336 \end{bmatrix} \quad (16a)$$

$$K = \begin{bmatrix} 0.134 & 0.700 & -0.130 & -0.899 & -0.130 & 0.539 & 0.729 \\ & 1.148 & 0.372 & -0.730 & -0.507 & -0.056 & 0.177 \\ & & -0.028 & -0.085 & -0.020 & 0.032 & 0.034 \\ & & & 1.305 & 0.365 & -0.614 & -0.932 \\ & & & & 0.250 & -0.088 & -0.074 \\ & & sym & & & 0.190 & 0.498 \\ & & & & & & 0.870 \end{bmatrix} \cdot 10^4 \quad (16b)$$

$$D = \begin{bmatrix} -1.262 & -0.390 & -0.057 & 0.662 & 0.071 & -0.322 & -0.506 \\ & 0.974 & -0.019 & -0.296 & -0.200 & 0.030 & 0.028 \\ & & -0.199 & -0.142 & 0.109 & 0.173 & 0.192 \\ & & & 0.806 & 0.402 & -0.412 & -0.611 \\ & & & & 0.032 & -0.284 & -0.363 \\ & & sym & & & 0.284 & 0.331 \\ & & & & & & 0.478 \end{bmatrix} \cdot 10^3 \quad (16c)$$

$$M = \begin{bmatrix} -1.733 & 0.965 & 0.993 & -0.065 & -0.717 & -0.412 & 1.204 \\ & 0.144 & -1.300 & 0.013 & 0.870 & 0.090 & -0.965 \\ & & 0.292 & -0.013 & -0.094 & 0.612 & -0.598 \\ & & & 0.151 & -0.037 & -0.529 & 0.572 \\ & & & & -0.145 & 0.124 & 0.022 \\ & & sym & & & 0.731 & -0.730 \\ & & & & & & 0.565 \end{bmatrix} \cdot 10^3 \quad (17a)$$

$$K = \begin{bmatrix} 7.244 & 0.974 & 1.264 & -2.381 & 3.588 & 5.431 & 5.008 \\ & -2.974 & -0.956 & -1.613 & -1.301 & -1.707 & -2.493 \\ & & 1.099 & 1.293 & 0.205 & 0.530 & -0.643 \\ & & & 2.384 & -3.138 & -3.315 & -4.349 \\ & & & & 1.598 & 2.464 & 2.483 \\ & & sym & & & 1.229 & 1.112 \\ & & & & & & 1.158 \end{bmatrix} \cdot 10^3 \quad (17b)$$

$$D = \begin{bmatrix} -1.122 & 0.477 & 0.258 & 0.584 & -0.515 & 0.033 & 0.166 \\ & -0.152 & -0.035 & -0.382 & 0.098 & 0.014 & 0.017 \\ & & -0.043 & -0.247 & 0.180 & -0.006 & 0.062 \\ & & & 0.086 & 0.138 & 0.058 & -0.309 \\ & & & & -0.072 & -0.037 & 0.104 \\ & & sym & & & 0.004 & -0.040 \\ & & & & & & 0.108 \end{bmatrix} \cdot 10^4 \quad (17c)$$

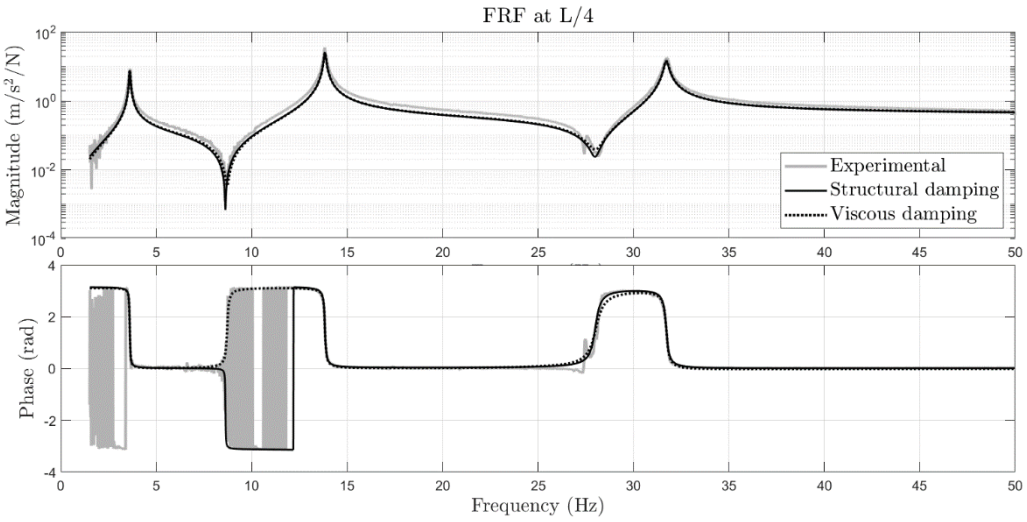

Figure 6. Comparison of FRFs at point L/4

The six presented matrices are full, and no elements can be supposed to be zero as it could be expected for a matrix issued from a finite element assemble. This may be due to several reasons, like the fact that it is a reduced model (a sort of dynamic condensed model) and the effect of the non-measured degrees of freedom have been inherently applied on the measured ones. It is also remarkable the presence of negative terms in the principal diagonals of all matrices. Moreover, it is equally remarkable the difference of magnitude order between both models, specially concerning the mass matrices, being in general the matrices corresponding to the viscous model some magnitude orders above the structural one. Although both facts seem to be counter-intuitive and hard to explain, both combinations of physical matrices lead to the dynamic behaviour represented by the FRFs in Figure 6 and so both models are expected to respond in the same way as the real structure when subjected to actions in the measured frequency band.

5 RESULTS DISCUSSION AND CONCLUSIONS

The proposed methodology is entirely based on the equations that define the modal properties and their relations with the physical matrices. No new equations or results have been extracted in this work and, however, an easy, powerful and fast to apply methodology has been developed. Unlike other methodologies based on optimization and linear programming techniques, that require their time to converge, the pseudo-inverse approach to a rectangular system of equations provides reasonably good results in a very short time lapse, something desirable when it is to be implemented in an automated SHM system.

Although not fully understandable, the two sets of matrices exactly satisfy all the equations presented in Section 3, even the one concerning the total mass of the beam. The systems of equations were, however, under-determined in both cases and the obtained solution via the Moore-Penrose inversion only provided one of the infinite possible solutions. It looks necessary to implement other kind of equations and restrictions for the variables to change this.

Unlike other methodologies based on the pseudo-inversion of some matrices, this procedure does not provide rank-deficient physical matrices. In those cases, this deficiency was caused by the difference between the number of measured degrees of freedom and the number of identified modes. Here, even if that difference exists, its effect is compensated by adding more equations and imposing, for example, the physical terms to be real.

ACKNOWLEDGEMENTS

The authors wish to acknowledge the *Ministerio de Economía y Competitividad, Spanish Government*, for the partial support through the RTI2018-098425 Research Project, the *Ministerio de Educación, Cultura y Deporte, Spanish Government*, for the FPU16/01339 predoctoral grant and the *Universidad de Valladolid* for its financial support to predoctoral students to help attending international conferences.

REFERENCES

[1] S. Sehgal and H. Kumar, "Structural Dynamic Model Updating Techniques: A State of the Art Review," *Arch. Comput. Methods Eng.*, vol. 23, no. 3, pp. 515–533, Sep. 2016.

[2] A. Berman and W. G. Flannelly, "Theory of incomplete models of dynamic structures," *AIAA J.*, vol. 9, no. 8, pp. 1481–1487, 1971.

[3] M. Link, "Theory of a method for identifying incomplete system matrices from vibration test data," *Z. Flugwiss. Weltraumforsch.*, vol. 9, no. 2, pp. 76–82, 1985.

[4] J. A. Fabunmi, "Spectral basis theory for the identification of structural dynamic systems," *AIAA J.*, vol. 26, no. 6, pp. 726–732, 1988.

[5] C.-D. Yang and F.-B. Yeh, "Identification, reduction, and refinement of model parameters by the eigensystem realization algorithm," *J. Guid. Control. Dyn.*, vol. 13, no. 6, pp. 1051–1059, 1990.

[6] J. E. Mottershead and C. D. Foster, "On the treatment of ill-conditioning in spatial parameter estimation from measured vibration data," *Mech. Syst. Signal Process.*, vol. 5, no. 2, pp. 139–154, 1991.

[7] W. J. Ko and C. F. Hung, "Extraction of structural system matrices from an identified

state-space system using the combined measurements of DVA," *J. Sound Vib.*, vol. 249, no. 5, pp. 955–970, Jan. 2002.

[8] A. Srikantha Phani and J. Woodhouse, "Viscous damping identification in linear vibration," *J. Sound Vib.*, vol. 303, no. 3–5, pp. 475–500, Jun. 2007.

[9] K.-S. Kim, Y. J. Kang, and J. Yoo, "Structural parameters identification using improved normal frequency response function method," *Mech. Syst. Signal Process.*, vol. 22, no. 8, pp. 1858–1868, Nov. 2008.

[10] D. J. Ewins, *Modal testing : theory, practice, and application*. Research Studies Press, 2000.

[11] N. M. M. Maia and J. M. M. Silva, *Theoretical and Experimental Modal Analysis*. Research Studies Press, 1997.

EURODYN 2020
XI International Conference on Structural Dynamics
M. Papadrakakis, M. Fragiadakis, C. Papadimitriou (eds.)
Athens, Greece, 23–26 November 2020

MODAL IDENTIFICATION OF STRUCTURES DURING STATIC LOAD TESTING: INTERACTION EFFECTS.

Antolin Lorenzana[1*], Alvaro Magdaleno[1], Tomislav Jarak[2], Roberto Martinez[3], Antonio Balmori[3], Luis-AlfonsoBasterra[3], Lara del Val[4], Juan J. Villacorta[4], Alberto Izquierdo[4]

[1] ITAP. Universidad de Valladolid
Paseo del Cauce, 59, 47011 Valladolid, Spain
alvaro.magdaleno@uva.es, ali@eii.uva.es

[2] Faculty of Mechanical Engineering and Naval Architecture, University of Zagreb
Ivana Lucica 5, 10002 Zagreb
tomislav.jarak@fsb.hr

[3]Research Group of Timber Structures and Wood Technology, University of Valladolid
Avenida de Salamanca, 18, 47014 Valladolid, Spain
(robertomartinez, balmori, basterra)@arq.uva.es

[4]Signal Theory and Communications Department, University of Valladolid
Campus Miguel Delibes, 47011 Valladolid, Spain
(larval, juavil, alberto.izquierdo)@tel.uva.es

Keywords: structural dynamics; experimental modal analysis, solid or liquid live loads.

Abstract. *Structures such as floors or bridges are usually tested, according to some standards, in order to check some of their properties. Stiffness and modal parameters can be obtained through static and dynamic testing. Usually, static testing consists in adding mass to the structure and measuring the additional deflection. For convenience reasons, the added mass is usually implemented with tanks of water. However, if the static testing scenario is used to conclude modal parameters or dynamic serviceability assessment, it is necessary to ensure that the added load is representative of the structure conditions during its life span. Although for static load testing the results do not depend on the nature of the gravitational load, the same does not occur when modal parameters are of interest. Whether the mass is solid (sandbags or concrete blocks), liquid (water in tanks) or other types (as vehicles or people, etc.) greatly affects the damping due to interaction phenomena. These interaction effects appeared in an attempt to evaluate the damping on a wooden floor through traditional techniques (modal analysis using a shaker and some accelerometers). With the floor without any load, the different modes of their girders (one-way slab floor) could be easily identified and their frequencies and damping ratios well quantified. However, when supporting water tanks, the identification procedure was a challenging task. Trying to understand how the nature (solid or liquid) of the added mass affects, six case studies based on a lab-scale structure are presented.*

1 INTRODUCTION

Figure 1 shows a load test on a pedestrian timber bridge. It consists of distributing several water-filled tanks along its length and measuring the increase in deflection to obtain the stiffness of the structure. Taking advantage of the instrumentation carried out, could a modal analysis be made to obtain the modal properties (frequency and damping ratios) of the footbridge in crowded conditions? In the same way, figure 2 shows a full-scale laboratory timber floor. For the same load, the modal properties are very different if the load is just water in a pool (left) or people. Even if people are sitting (center) or standing (right) the results are also very different.

Figure 1. Loading test in a timber footbridge.

Figure 2. Different loading conditions in a timber floor.

Trying to understand how the nature of the added mass affects, figure 3 shows two scale models (a "bridge" and a "2-storey building") on which tests are being carried out by loading these models with water balloons and inducing vertical vibrations (for the bridge) or horizontal vibrations (for the 2-storey building). In both cases, tests can be carried out by means of the standard instrumentation consisting on an impact (over a load cell) and several accelerometers, all the signals been recorded by a proper data-logger. Processing all the data (experimental modal analysis methodology, EMA, [1, 2]), mode shapes, modal damping and natural frequencies can be obtained by identification techniques [3, 4, 5).

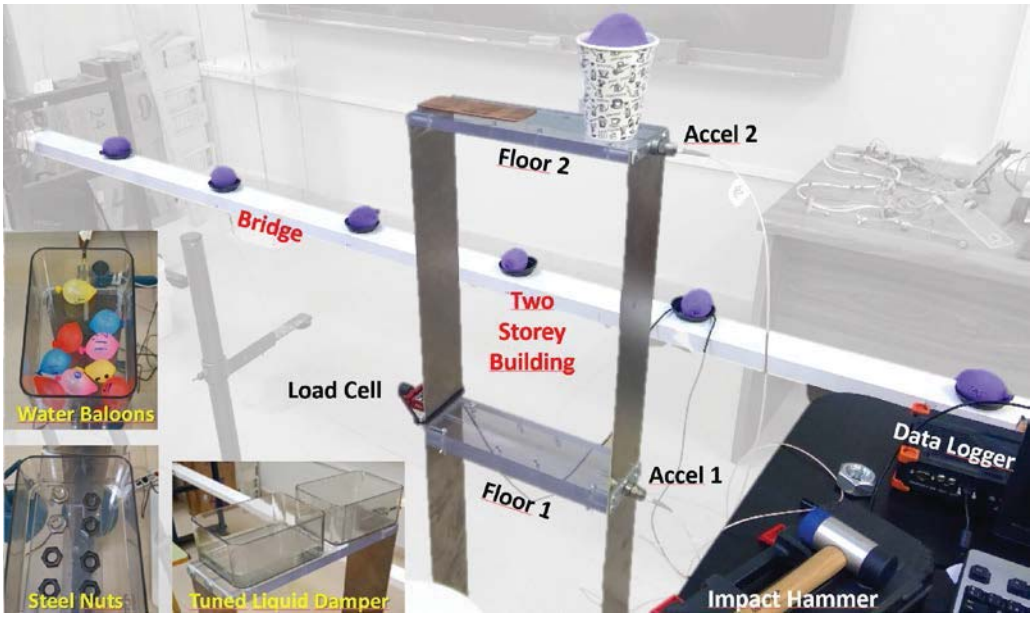

Figure 3. Lab layout.

2 CASE STUDIES DESCRIPTION

In order to design a controlled lab test and to identify the interaction effects, the model of a 2-storey building (figure 3) is used. Each floor consists of a methacrylate plate rigid enough to suppose them to be rigid bodies for the purposes of this work. They are connected to each other and to the ground *via* two aluminium plates. These plates, very stiff in one bending direction with respect to the other, limit the movement of the building model to one horizontal direction.

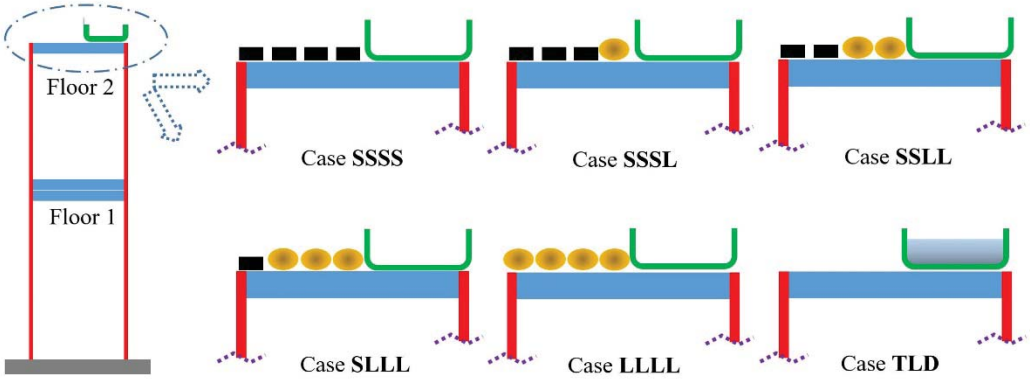

Figure 4. Scenarios under study.

Six case studies are presented (figure 4). As a reference or blank scenario, 16 steel nuts of 0.010 kg each were added on the second floor (accounting for 18% of the total mass of the floor, the first floor weighs twice as much). After that, 4 of the nuts were replaced by 4 balloons

containing the same mass in water. Later, the same with another 4 nuts and so on until the solid masses were all replaced. In the last scenario, nuts and balloons are replaced by a tank containing the same mass in water, constituting a tuned liquid damper (TLD). In figure 3, at left, nuts, balloons and the TLD can be seen. Case SSSS corresponds to the case where all the added mass is solid (nuts). In the SSSL case one quarter of the solid mass is replaced by the equivalent in water (confined in balloons). In the SSLL case half of the added mass is solid and half is liquid. Finally, in the SLLL case the added mass is one-quarter solid and three-quarters liquid and in the case LLLL case all the added mass is liquid.

3 METHODOLOGY

As can be guessed in figure 5, left, two IEPE accelerometers (100 mV/g) are installed on each floor (blue ring), both oriented to measure horizontal accelerations. The excitation consists of an impact applied to the load cell (100 N max.), also installed in floor 1 (red ring). The accelerometers and the load cell are wired to an acquisition system (SIRIUS model of the brand Dewesoft), and data are registered at 400 samples per second. In figure 5 right, FRF (H_1 estimator) are obtained after each impact and several averages (3 or 4) are carried out in order to remove some of noise.

Figure 5. Modal analysis on air.

Both FRFs (the one corresponding to the first floor or auto-FRF and the one of the second floor) (are fitted in magnitude and in phase) to a theoretical system of 2 degrees of freedom (eq. 1), in which a general viscous damping model has been assumed.

$$H_{jk}(\omega) = \sum_{r=1}^{m} \left(\frac{\theta_{rj}\theta_{rk}}{i\omega - s_r} + \frac{\theta_{rj}^{*}\theta_{rk}^{*}}{i\omega - s_r^{*}} \right) \tag{1}$$

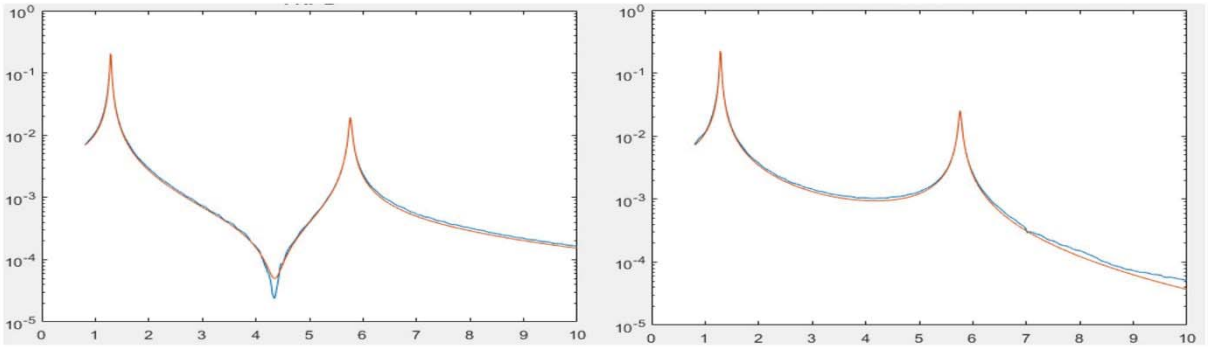

Figure 6. Case SSSS: FRF of the first floor (left) and of the second floor (right)

For the reference case (SSSS), figure 6 shows the experimental FRFs (in blue) and their corresponding fitted curves (in red) when m=2. As can be seen, the system fits perfectly with a two-dof, as intended. After the curve-fitting process, table 1 shows the modal parameters, including the modal coordinates of the two modes, that are plotted in figure 7.

	Frequency **(Hz)**	Damping **(%)**	Modal coordinates **floor1**	**floor2**
Mode 1	1.289	0.0104	-0.0948 + 0.0926i	-0.1042 + 0.0984i
Mode 2	5.764	0.0053	-0.0419 + 0.0393i	0.0593 - 0.0493i

Table 1. Case SSSS after curve fitting and mode shape identification.

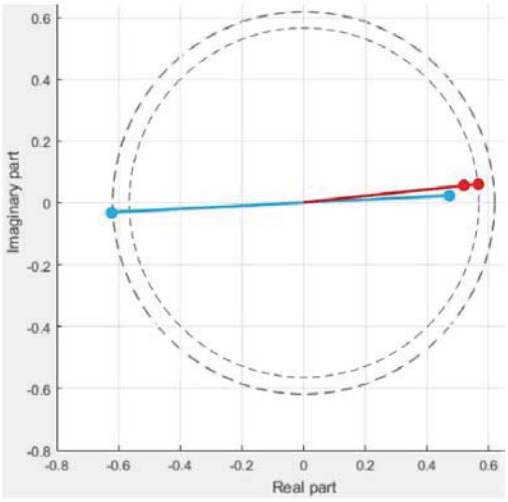

Figure 7. Argand plot for modes 1 (red) and 2 (blue)

	ω1	**Peak_floor1**	**Peak_floor2**	**ξ1**	**ω2**	**Peak_floor1**	**Peak_floor2**	**ξ2**
SSSS	1.289	13.622	14.736	0.0104	5.764	22.638	30.354	0.0053
SSSL	1.297	9.822	11.143	0.0140	5.817	14.329	20.385	0.0081
SSLL	1.301	7.329	8.606	0.0184	5.869	12.166	16.143	0.0100
SLLL	1.306	6.228	7.359	0.0220	5.915	9.746	12.843	0.0129
LLLL	1.298	6.162	6.649	0.0238	5.970	5.683	8.850	0.0195
TLD_a	1.171	1.498	1.906	0.0430	6.000	15.999	32.260	0.0053
TLD_b	1.422	1.536	1.736	0.1211				

Table 2. Modal parameter and accelerance values.

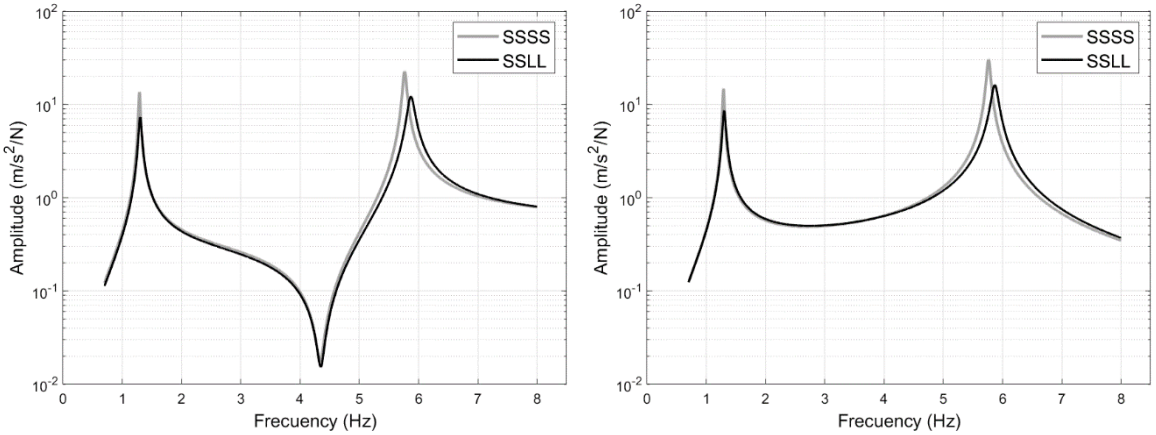

Figure 8. Case SSLL: FRF of the first floor (left) and of the second floor (right)

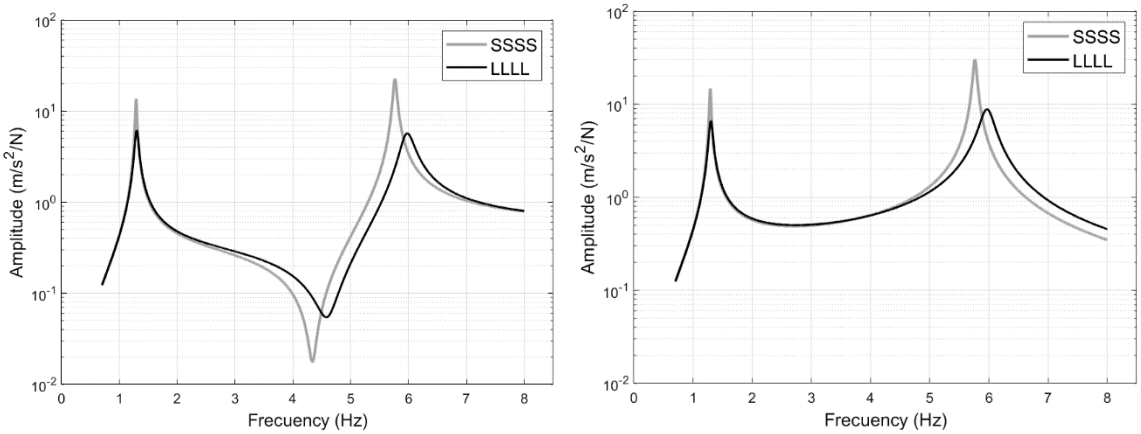

Figure 9. Case LLLL: FRF of the first floor (left) and of the second floor (right)

4 RESULTS

Following a similar procedure for the rest of the cases, results of table 2 and table 3 are obtained. Figure 8 shows the adjusted curves for the SSLL case and figure 9 for the LLLL case. In both cases, the adjusted curves for the SSSS case are shown in grey. Table 2 also shows the values of the accelerance of both FRFs (floor 1 and floor 2) for the peaks corresponding to mode 1 and mode 2. All these values are drawn in the graphs in figure 11.

	Mode shape 1		Mode shape 2	
	floor1	floor2	floor1	floor2
SSSS	-0.0948 + 0.0926i	-0.1042 + 0.0984i	-0.0419 + 0.0393i	0.0593 - 0.0493i
SSSL	-0.0933 + 0.0903i	-0.1069 + 0.1013i	-0.0405 + 0.0389i	0.0610 - 0.0520i
SSLL	-0.0911 + 0.0906i	-0.1110 + 0.1020i	-0.0409 + 0.0403i	0.0572 - 0.0506i
SLLL	-0.0908 + 0.0919i	-0.1136 + 0.1018i	-0.04313 + 0.0409i	0.0568 - 0.0517i
LLLL	-0.0963 + 0.0932i	-0.1069 + 0.0973i	-0.0390 + 0.0375i	0.0624 - 0.0587i
TLD	0.0776 - 0.0097i -0.0692 + 0.1141i	0.0960 - 0.0348i -0.0843 + 0.1115i	0.0341 - 0.0331i	-0.0689 + 0.0650i

Table 3. Modal coordinates.

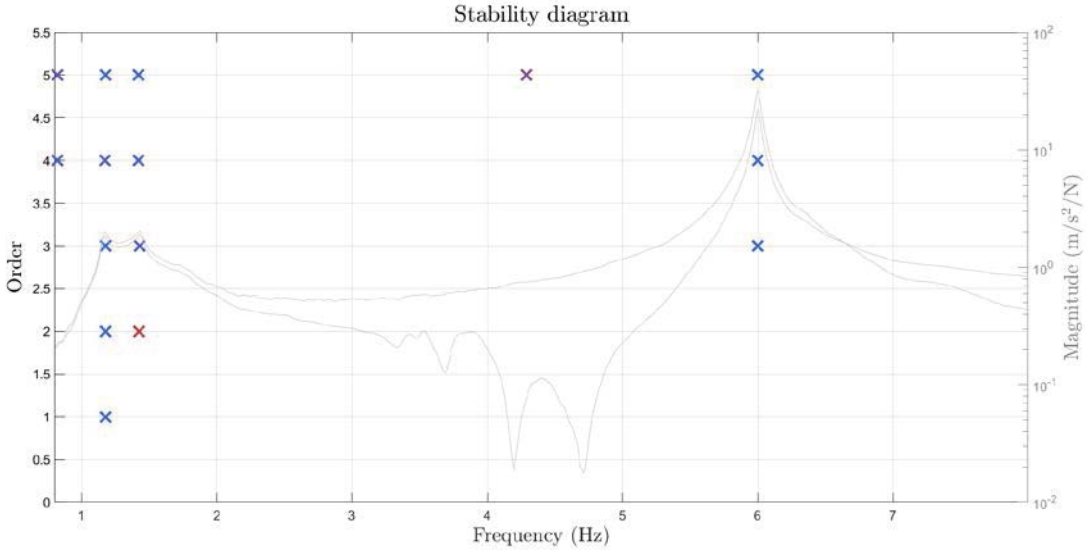

Figure 10a. Case TLD: Stability diagram.

Actually, the adjustment to the TLD case is more complicated. Precisely because of the splitting that occurs in mode 1, a setting of order 3 (m=3 in eq. 1) is necessary. Figure 10a shows the stability diagram together with the fitted FRFs (10b) for this case. The values for the split mode 1 are also shown in the corresponding tables.

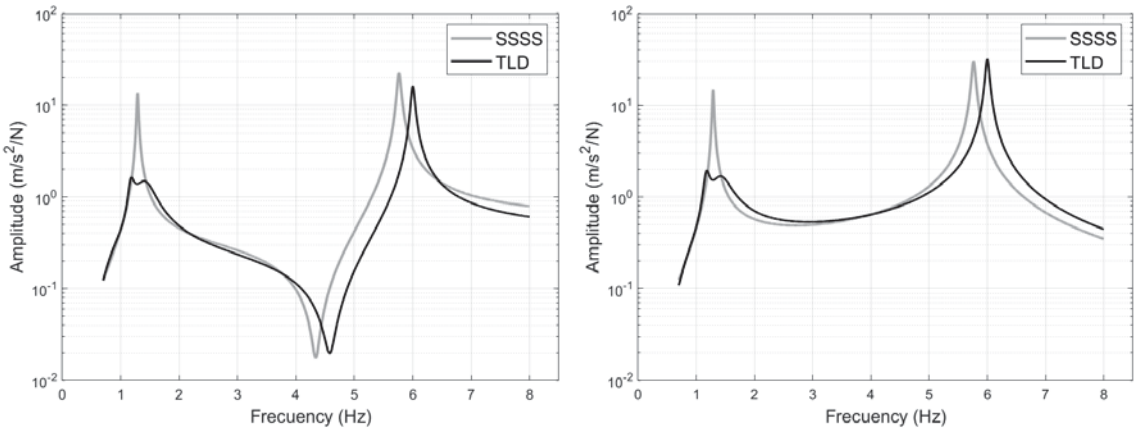

Figure 10b. Case TLD: FRF of the first floor (left) and of the second floor (right)

In order to better observe how the modal parameters evolve through the different cases, Figure 11 shows the accelerances of the first peak (in floor 1 and floor 2) together with the corresponding value of the frequency of the first mode (figure 11 a) and also the modal damping ratio (figure 11b). Similarly, figures 11c and 11d refer to the second mode.

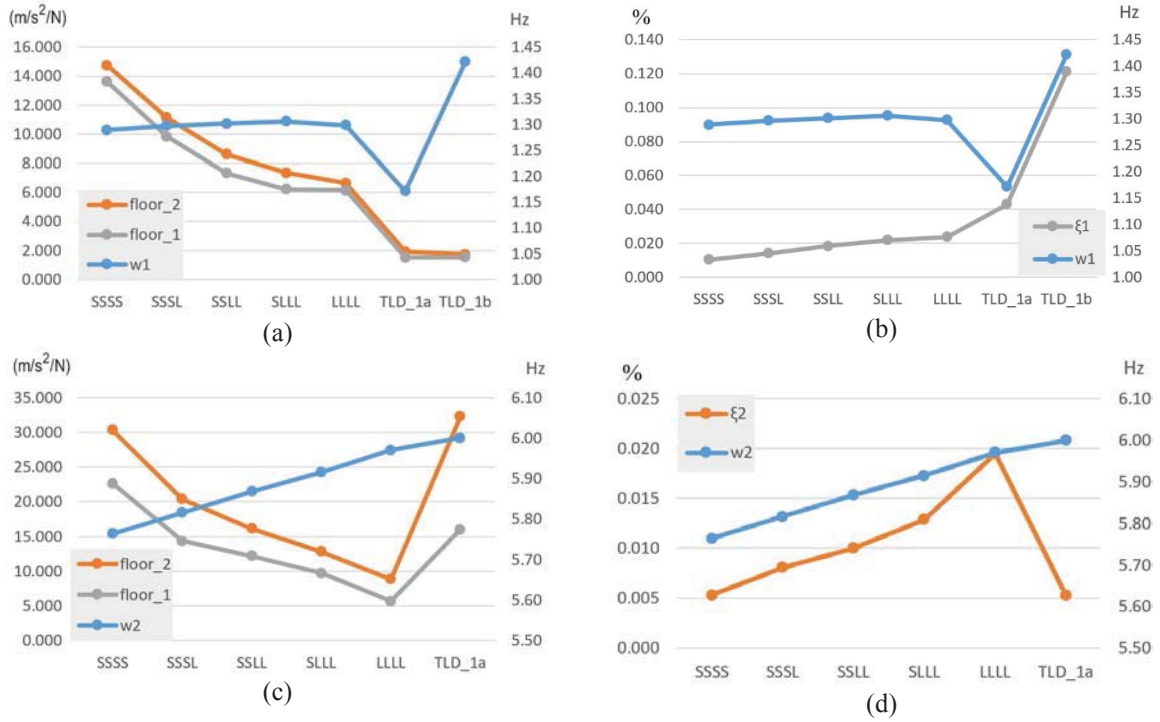

Figure 11. Trends for frequencies, accelerances and dampings

Once known the scaled modal coordinates (table 3) it is also possible to estimate the modal masses of each mode, which is shown in table 4 and plotted in figure 12.

	modal mass 1	modal mass 2
SSSS	3.007	2.323
SSSL	2.828	2.132
SSLL	2.690	2.323
SLLL	2.620	2.281
LLLL	2.936	1.819
TLD	2.867	1.479

Table 4. Modal masses for each case

Figure 12. Trends for modal masses.

5 CONCLUSIONS

As the load changes from solid to liquid, the frequency of the mode 1 remains sensibly constant (except in the split, TMD case) while the frequency of the mode 2 slightly increases (4%). Similarly, the accelerances decrease (55% on average, not counting on the TLD case) and the damping increases (up to 130% for mode 1 and 270% for mode 2, not counting on the TLD case). Modal masses do not have a defined trend.

All these interesting results must be carefully analysed. Similar experiments are proposed for vertical vibrations on the bridge scale model (figure 3). Full scale tests are also pending.

After the analysis of the estimated FRFs for all the scenarios, it will be concluded that the nature (solid or liquid) of the added mass affect the modal properties. It is known that the liquid mass can provide new natural modes. In the case the new modes are close to the ones of the

original model, relevant changes could appear because of the interaction effects, being these phenomena similar to the working principle of the tuned liquid damper (case TLD, included).

Note that more cumbersome scenarios can appear when crowds occupy the floor structure [6, 7]. From the experiments carried out, it should be concluded that the typical static load test scenarios present some limitations when used to perform modal identifications or dynamic tests, since they may not describe the actual conditions of the structure during its normal use (live loading).

Acknowledgements

The authors wish to acknowledge the Ministerio de Economia y Competitividad and the Junta de Castilla y León, Spanish Government, for the partial support through the RTI2018-098425 and VA095P17 Research Projects. Also the Ministerio de Educacion, Cultura y Deporte, Spanish Government, for the FPU16/01339 predoctoral grant.

The third author also wishes to acknowledge the financial support of the Unity through Knowledge Fund (UKF), established by the The Ministry of Science and Education of the Republic of Croatia, obtained in the frame of the UKF grant agreement No. 21/19, that enabled his fruitful collaboration with the researchers at the University of Valladolid.

REFERENCES

[1] D. J. Ewins, Modal testing : theory, practice, and application. Research Studies Press, 2000.

[2] N. M. M. Maia and J. M. M. Silva, Theoretical and Experimental Modal Analysis. Research Studies Press, 1997.

[3] N.J. Bertola and I.F.C. Smith, A methodology for measurement-system design combining information from static and dynamic excitations for bridge load testing. Journal of Sound and Vibration (2019), 463

[4] M. Setareh and S. Gan, Vibration Testing, Analysis, and Human-Structure Interaction Studies of a Slender Footbridge. Journal of Performance of Constructed Facilities (2018), 32(5)

[5] J. A. Fabunmi, Spectral basis theory for the identification of structural dynamic systems, AIAA J., vol. 26, no. 6, pp. 726–732, 1988.

[6] A. Srikantha Phani and J. Woodhouse, Viscous damping identification in linear vibration, J. Sound Vib., vol. 303, no. 3–5, pp. 475–500, Jun. 2007.

[7] K. S. Kim, Y. J. Kang, and J. Yoo, Structural parameters identification using improved normal frequency response function method, Mech. Syst. Signal Process., vol. 22, no. 8, pp. 1858–1868, Nov. 2008.

EURODYN 2020
XI International Conference on Structural Dynamics
M. Papadrakakis, M. Fragiadakis, C. Papadimitriou (eds.)
Athens, Greece, 23–26 November 2020

AN INTEGRATED VIBRATION-IMAGE PROCEDURE FOR DAMAGE IDENTIFICATION IN STEEL TRUSSES

Marianna Crognale [1], Vincenzo Gattulli [1], Salvador Ivorra[2] and Francesco Potenza[3]

[1] DISG, Sapienza University of Rome, Italy
e-mail: {marianna.crognale, vincenzo.gattulli}@uniroma1.it

[2] DIC, University of Alicante, Spain
e-mail: sivorra@ua.es

[3] INGEO, University of Chieti-Pescara, Italy
e-mail: francesco.potenza@unich.it

Keywords: Damage Identification, Steel Structures, Stochastic Subspace Identification, Fatigue Failure.

Abstract. *The paper deals with structural damage identification in steel trusses. Classical procedure based on dynamic measurements able to detect flexibility changes are complemented with data predicting cracks and their evaluating by image processing. The procedure proposes first a damage index, the Stiffness Reduction Factor (SRF), evaluated on the basis of the error between the predictive truss model and the experimental modal model. Then, a nonlinear FEM model is used to determine fatigue cracks in the truss nodes which are compared with the observed ones determined by image processing. A real case study, the Quisi bridge located in Spain, is used to show the potentiality of the procedure.*

1 INTRODUCTION

Steel truss railway bridges are subject to potential damage, mainly due to fatigue phenomena and corrosion. The monitoring of infrastructures' condition becomes a very important issue to our society for detecting their damage. In last years, vibration-based damage identification methods have been proposed in conjunction with other techniques. Even though the matter has strongly exploited in the scientific community, the raising of innovative technologies in mechatronics, robotics and Information and Communication Technology (ICT) opens up new perspectives in facing the classical problems in the management of infrastructures [9]. Related to this topic, two main research fields could have impact in the inspection and monitoring of infrastructures: automated machine vision-based inspection and the classical structural vibration monitoring. In the first area the use of mobile robots and UAV have strongly increased the acquisition of images to sense the spatial characteristics of the environment, permitting the creation of "cloud" of 3D points. The second area consists in a structural health monitoring system to permit visualization and management of sensor data, data interpretation and analysis and interaction with classical finite element model for structural behavior simulation and model updating. Classical vibration-based monitoring acquires the structural dynamic response, and the corresponding analysis obtains knowledge about the actual mechanical behavior of a structure.

To assess the presence of damage in a steel truss railway bridge, a procedure that links information derived by the vibrations of the bridge with image acquisition by means of long-term monitoring system, has been developed. The paper focuses first on the effects of damage on the static and dynamical response of a nominal model of steel truss. For this purpose, damage is described as a reduction of cross section area of one element of the truss. The direct problem is addressed by FEM and the global modes are identified. The procedure for linear damage detection is tested using pseudo-experimental data, that are generated from the model under white noise. The main modal parameters of the dynamic system are evaluated, before and after damage, using Stochastic Subspace Identification (SSI) method [6-8], based on the assumption that the input is a realization of a stochastic process. The damage identification problem is solved by minimizing an objective function.

A global model of the Quisi Bridge case study is made. The aim of the global analysis is the investigation of the bridge structural behavior to evaluate the structural response due to train crossing. Numerical simulations were conducted before and after damage to study the changes in frequencies and mode shapes due to the presence of damage. In order to perform automatic identification of structural modal parameters based on structural response (output) and to calibrate the numerical global model on experimental data by model updating procedures, an Operational Modal Analysis (OMA) procedure is applied with the purpose of achieve an accurate estimation of natural frequencies. Results obtained from numerical analysis and experimental dynamic tests are mixed together to identify critical details most subjected to fatigue-induced cracks.

In particular, this work aimed at obtaining a better and more accurate comprehension of fatigue phenomena which determine fatigue cracks under the application of a large number of cycles. Thus, a local analysis of critical details is performed to assess the local stress induced by load cycles and the resistance of principal elements.

Preliminary studies performed on the Quisi Bridge, are reported.

2 A PROCEDURE FOR DAMAGE DETECTION IN A TRUSS SYSTEM

In order to assess the presence of damage in a truss structure based on vibration measurements, a sensitivity analysis is performed on a planar truss model (Figure 1) to study the defect-induced reduction of stiffness, (combination of damage intensity and extension).

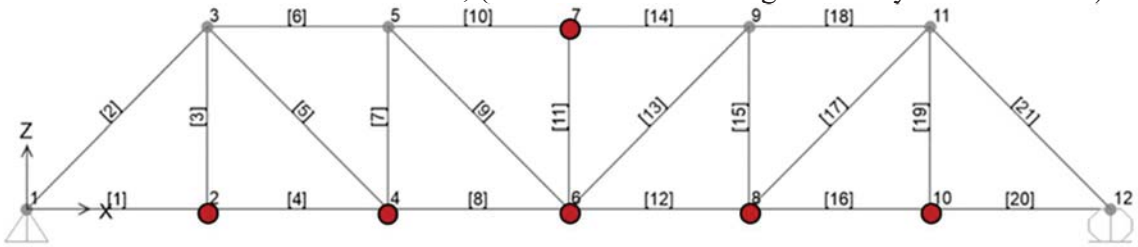

Figure 1: Sketch along with sensor layout in the 2D numerical model.

The damaged truss element is defined and implemented through a classical FEM procedure in which damage is described as a cross-section area reduction and the local stiffness matrix has the following expression:

$$\boldsymbol{K_d^e} = \frac{EA}{L} \cdot \frac{(1-\zeta)(1+\delta\zeta-\zeta)}{[(1-\zeta)(1-\delta)+\delta]^2} \begin{bmatrix} 1 & 0 & -1 & 0 \\ 0 & 0 & 0 & 0 \\ -1 & 0 & 1 & 0 \\ 0 & 0 & 0 & 0 \end{bmatrix} = \frac{EA}{L}(SRF)\boldsymbol{K^e} \tag{1}$$

where the damage intensity ζ and extent δ have been represented in non-dimensional form as:

$$\zeta = \frac{EA-EA_d}{EA},\ \delta = \frac{L_d}{L},\ 0 \le \zeta \le 1, 0 \le \delta \le 1 \tag{2}$$

SRF is the Stiffness Reduction Factor which is a combination of these two parameters affecting the stiffness and consequently the frequencies [10-11]. Several damage scenarios were considered: the damage parameters were applied consecutively to truss element n. 2, 5 and 6 (Figure 1).

The dependence of the frequencies on the SRF is described by numerical evaluation FEM. The procedure uses pseudo-experimental response, generated from the numerical model under white noise. Vertical accelerations of the bridge were evaluated in several nodes of the model, (indicated in red in Figure 1), and based on these measurements a dynamic identification of the modal parameters was made by SSI in time domain. The inverse problem of damage identification is addressed minimizing an objective function $\mathcal{L}(\zeta, \delta)$ based on frequency measurements, that represents the comparison between the numerical and the experimental dynamical response of the truss. The objective function $\mathcal{L}(\zeta, \delta)$ is defined as follows:

$$\mathcal{L}(\zeta, \delta) = \sum_{i=1}^{k} \left| \frac{\omega_{d,i}^{EX} - \omega_{d,i}^{NM}(\zeta,\delta)}{\omega_{u,i}^{EX}} \right|^2 \tag{3}$$

Where $\omega_{d,i}^{EX}$ and $\omega_{d,i}^{NM}(\zeta, \delta)$ are the *i*-th experimental and numerical frequencies of the damaged element respectively, while $\omega_{u,i}^{EX}$ represents the corresponding frequency in the undamaged state. Only an optimum number of modes k are needed to be considered to univocally determine the SRF(δ, ζ) curve in the damage parameter plane (δ, ζ). The number of modes that are necessary to achieve a unique solution in the optimization problem depends on the position of the damaged element in the truss. Figure 2 shows results of the performance of index $\mathcal{L}$ in the detection of curve SRF(δ, ζ) varying the number of modes k. The target point T is indicated with red circle, and the corresponding Γ- curve, in red in Figure 2, is Γ (0.3;0.5) = 0.76923.

Table 1 shows the performance of index $\mathcal{L}$ in the detection of the stiffness reduction factor Γ. The number of modes depends on which damaged truss element is considered and on the effects of the vibrational modes. Considering the first three mode of vibration is enough to determine the stiffness reduction factor for this example.
The sensitivity-based strategy can use different type of objective functions and not only frequencies: a modal assurance criterion (MAC and CoMAC); modal flexibility [5] or a combination of the first options [2]. As reported below, a damage identification based on changes in mode shapes is performed for the Quisi Bridge case study.

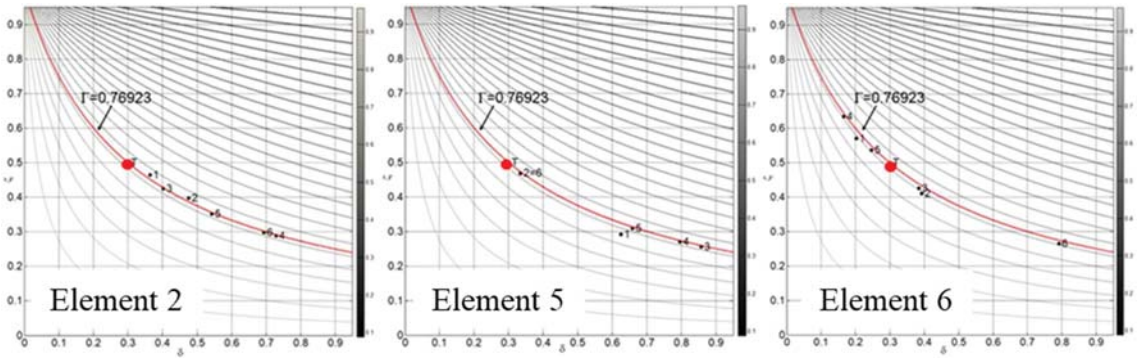

Figure 2: Effects of number of modes in the detection of SRF(δ, ζ) curve respectively in element 2, 5 and 6.

Mode	Element 2		Element 5		Element 6	
	Γ	E_r [%]	Γ	E_r [%]	Γ	E_r [%]
1	0.7596	1.24	0.7958	3.46	0.7879	2.44
2	0.7617	0.90	0.7721	**0.39**	0.7852	2.08
3	0.7709	**0.22**	0.7722	0.40	0.7750	**0.76**
4	0.7714	0.28	0.7725	0.43	0.7766	0.97
5	0.7722	0.39	0.7726	0.44	0.7773	1.05
6	0.7724	0.42	0.7729	0.48	0.7778	1.12

Table 1: Performance of index $\mathcal{L}$.

3 GLOBAL MODEL: QUISI BRIDGE CASE STUDY

The Quisi Bridge located in Benissa (Alicante) is an historic steel truss railway bridge, which is investigated with different techniques to assess the presence of fatigue damages. It is a XX century steel Bridge and it is part of the 9th FGV Railway Line. The structure consists in a top-bearing Pratt type truss. It is 170 m long with six spans of different length (Figure 3).

Figure 3: Quisi Bridge.

A 3D FE model of the main span permits to evaluate frequencies variation due to damage. Two different damage scenarios (DS) are considered: the first one (DS1) affecting one element of the main span with a stiffness reduction factor of 0.3, the second one (DS2) affecting a group of elements of the truss.
The frequency variation for the first four modes in percentage are reported in the Table 2. The frequency variation produced by damage appears to be quite low evidencing the needs of introducing also other type of damage index based on mode shapes.
The changes of mode shape can be evaluated quantitatively using a well-known correlation measure, the modal assurance criteria (MAC) between two modes shape ϕ_i e ϕ_j, as defined as:

$$\boldsymbol{MAC}_{ij} = \frac{\left|\phi_i^d \cdot \phi_j^u\right|^2}{\left|\phi_i^d\right|^2 \left|\phi_j^u\right|^2} \tag{4}$$

Mode	DS 1	DS 2
	$(f_{iu}-f_{id})/f_{iu}$ [%]	$(f_{iu}-f_{id})/f_{iu}$ [%]
1	0.74	1.91
2	0.54	1.15
3	0.46	1.05
4	0.51	0.56

Table 2: Frequency variations due to the presence of different damage scenario (DS).

Scenario	Mode	UN						
		1	2	3	4	5	6	7
DS1	1	**0.984**	0.016	0.000	0.000	0.000	0.000	0.000
	2	0.016	**0.984**	0.000	0.000	0.000	0.000	0.000
	3	0.000	0.000	**0.999**	0.000	0.000	0.000	0.000
	4	0.000	0.000	0.000	**0.999**	0.000	0.000	0.000
	5	0.000	0.000	0.000	0.000	**0.999**	0.000	0.000
	6	0.000	0.000	0.000	0.000	0.000	**1.000**	0.000
	7	0.000	0.000	0.000	0.000	0.000	0.000	**1.000**
DS2	1	**0.8341**	0.1652	0.000	0.000	0.000	0.000	0.000
	2	0.1648	**0.8346**	0.000	0.000	0.000	0.000	0.000
	3	0.000	0.000	**0.9925**	0.072	0.000	0.000	0.000
	4	0.000	0.000	0.071	**0.9925**	0.000	0.000	0.000
	5	0.000	0.000	0.000	0.000	**0.9940**	0.000	0.000
	6	0.000	0.000	0.000	0.000	0.000	**0.8293**	0.1679
	7	0.000	0.000	0.000	0.000	0.000	0.1680	**0.8317**

Table 3: MAC comparing modes from numerical model for damaged and undamaged scenarios. Bold indicates a value calculated with the same mode from the scenario pair.

Table 3 presents MAC values comparing modes obtained by numerical FE model for DS1 and DS2 with the undamaged scenario (UN). The calculated MAC values indicate little change in mode shape for the first damage scenario, with MAC value larger than 0.98 for the first two modes. Marked change in mode shape attributable to the second damage scenario are observed. The most remarkable change occurs in the sixth mode with MAC decreasing to 0.82. A second major change occurs in the first and seventh modes (MAC=0.83). However, in some cases,

MAC fails to reflect the change in mode shape. Another well-known mode shape-derived correlation measure, the coordinate modal assurance criteria (CoMAC), is examined herein. It can be regarded as a point-wise measure of the correlation between two sets of mode shapes and be defined for a measurement point (or degree of freedom) *i* as:

$$\boldsymbol{CoMAC}_i = \frac{\left(\sum_{j=1}^{nm}\left|\phi_{ij}^{d}\phi_{ij}^{u}\right|\right)^2}{\sum_{j=1}^{nm}\left(\phi_{ij}^{d}\right)^2\sum_{j=1}^{nm}\left(\phi_{ij}^{u}\right)^2} \tag{5}$$

The CoMAC between the mode shapes of the damaged and corresponding undamaged scenarios, can be calculated as presented in Figure 4. Although CoMAC is often taken as damage locator for its space information, it might sometimes be affected by its low sensitivity to damage, (as in DS2), and from confusing localization, (as in DS1).

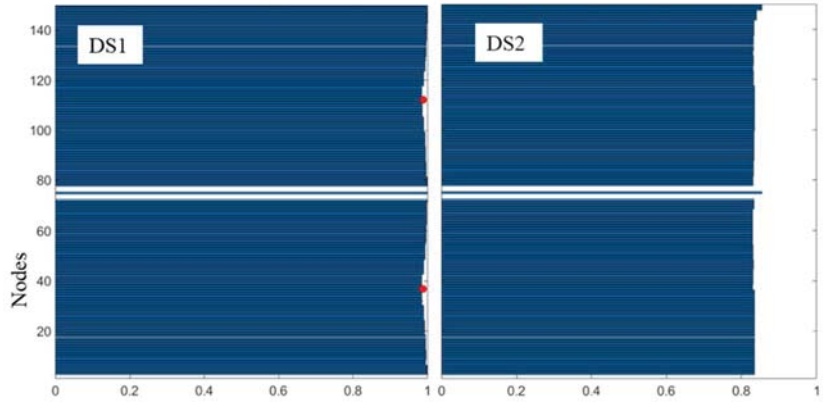

Figure 4: CoMAC comparing modes obtained by numerical model of the main span.

4 EXPERIMENTAL TEST ON THE QUISI BRIDGE

For the Quisi Bridge an experimental dynamic identification of the main features characterizing the dynamic behaviour of the structure, has be performed in order to calibrate the numerical global model on experimental data by updating procedures. Experimental tests constitute a reliable and effective tool for the evaluation of structural dynamic properties. They are composed of experimental acquisitions, obtained recording vibrations of suitable key points of the structure subjected to environmental excitations, and following numerical elaboration of data. Three uniaxial accelerometers were placed on the bridge, one in each mid-span on the right side of the bridge for the first test and on the left side for the second test. Starting from the recorded data, the global modes are identified by Operative Modal Analysis technique (OMA) [4], using the Stochastic Subspace Identification (*SSI*) in the time domain [1]. Data processing, system identification and modal analysis were performed using MACEC, which is a MATLAB toolbox developed for Experimental and Operational Modal Analysis by the Structural Mechanics division of K.U. Leuven [7].
Figure 5 shows the stabilization diagram and the PSD for the main span of the Quisi bridge in the first OMA test. The identified modal frequencies are reported in Table 4. A total of 4 frequencies for the first test, and 3 frequencies for the second test were identified based on measured response only. In general, a very good accordance is achieved. Due to the low number of accelerometers is not possible to also identified mode shapes.

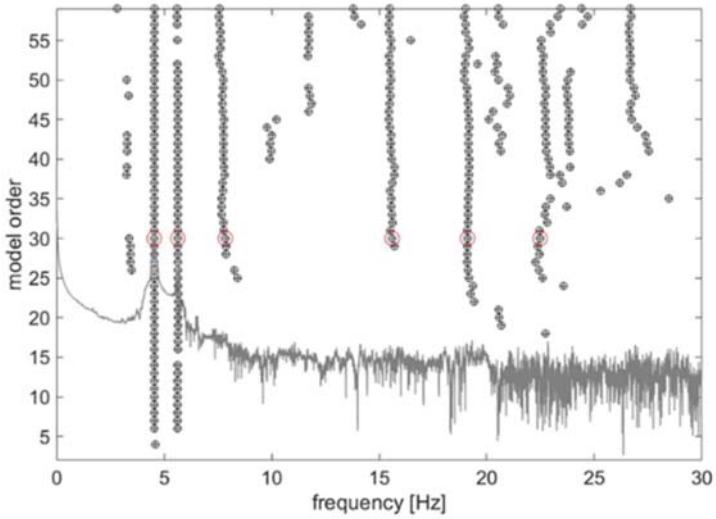

Figure 5: Stabilization diagram and PSD obtained by SSI.

Mode	f_{nm} [Hz]	OMA-test 1		OMA-test 2	
		f_{id} [Hz]	Δ[%]	f_{id} [Hz]	Δ[%]
1	5.05	4.50	10.8	4.50	10.8
2	5.42	5.64	4	5.61	3.5
3	7.30	7.85	7.5	8.42	15
4	15.48	15.60	1	-	-

Table 4: Numerical model frequencies and identified by SSI ones.

5 LOCAL MODEL

The global analysis of the Bridge aimed at the investigation of bridge actual structural performance under train passage, including the assessment of internal forces induced by train into the critical details most subjected to vibration effects. The development of a numerical global model is essential for the identification of the key points that permitting the proper modelling also of critical details. Thus, using forces from the global FE model, it is possible to perform an analysis of the steel connection. There are a lot of benefits of a detailed simulation, first of all the possibility to study system with complex stress distribution, to reproduce correctly local dynamic behaviors, the estimation of action and contact forces, the design of retrofitting for steel connection damaged by corrosion or fatigue cracks. The correct evaluation of local effects generally neglected or simply not consider by standard mechanical modelling is one of the main issues of damage identification. The main effort is the identification of critical details most exposed to damage phenomena, these details can be successful identified by a preliminary analysis of bridge structural behaviour, by means of standard analysis properly refined in order to catch a qualitative indication of local fatigue behaviour.
Once critical details are identified, a nonlinear static analysis can be obtained by means of numerical local models able to represent properly the vibration/distortion phenomena that influence intensity and distribution of stresses. The detailed model using shell FE and links system, is developed by MIDAS-FEA software. The approach to model riveted connection in detailed shell model is made through beam between two surfaces and a system of rigid links between the master node, in the center of the hole, and the slave nodes lying on the circumference of the hole (Figure 6).

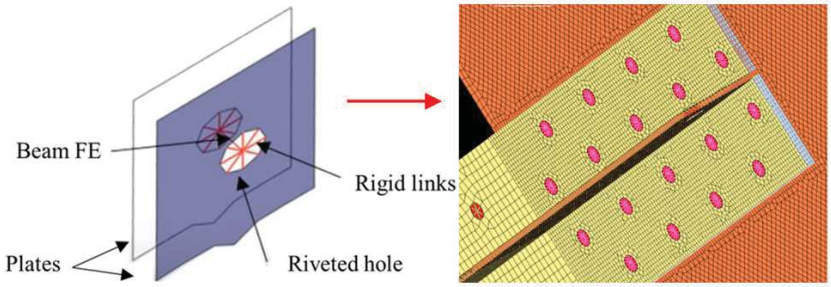

Figure 6: Details of local model.

5.1 Nonlinear static analysis

In this chapter a nonlinear static analysis is carried out. A nonlinear static analysis is a procedure in which the magnitude of the structural loading is incrementally increased in accordance with a certain predefined pattern. With the increase of the magnitude of loading failure mode of the structure are found. Beam element stresses were extracted from the FE global model (Figure 7). For each load step the nonlinear static response of the local model was computed. The stress-strain relation is expressed by an elastic-linear strain hardening law. The elastic-linear strain hardening model supposes that the continuous curve is approximated with two straight lines, the first line has a slope of Young's modulus, while the second straight line presents an idealization for the strain hardening range and has a slope which corresponds to the tangent modulus (E_t), where $E_t < E$. Figure 8 (a-l) shows the distribution of the maximum principal stresses at ten different steps of the incremental static analysis, that are reported in Table 5. The analysis of the figure reveals maximum stress levels in the order of 673 MPa, which represents high values. These maximum stresses are observed on the top of the diagonal member, in the connection plate with the upper chord.

In the Figure 9 (a), the plasticity status obtained by nonlinear static analysis: (a-1) the blue colour indicates the plastic zones that are potential crack locations, (i.e. the connection plate is a plastic region). Figure 9 (a-2) shows a detail of the double strap joint with two rows of rivets in the plate: from a static point of view both rows carry the same load which implies the same stress on the rivets, but from a fatigue point of view the two rows are in a different position, the holes in row B of the plate are loaded by P_B only and in row A the same load P_A is present on the holes but the load already introduced in row B is also passing these holes. The latter load is called a bypass load. Nevertheless, for this case study the holes in row A are more severely loaded than holes in row B and thus will be more fatigue critical. Fatigue cracks will occur in the row A cause of plastic deformation around the holes under static load. In the Figure 9 (b), the flux of the principal stresses is highlighted by blue colour (compression) and red colour (tension) lines with lengths proportional to the stress intensity.

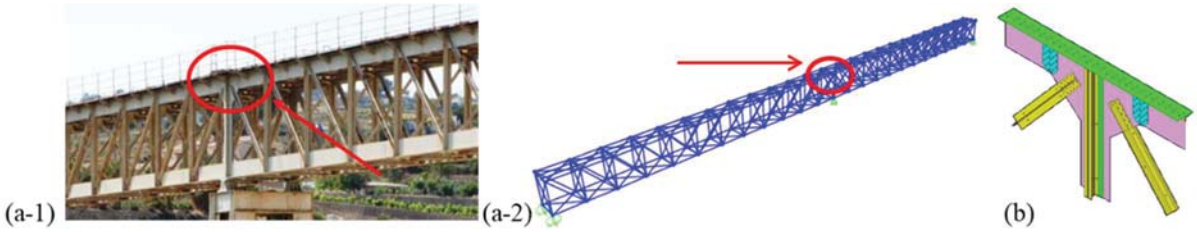

Figure 7: (a-1) Actual photo of the critical point of the Quisi Bridge where fatigue phenomena could arise; (a-2) Location of the potential fatigue critical node; (b) FE local model by MIDAS-FEA.

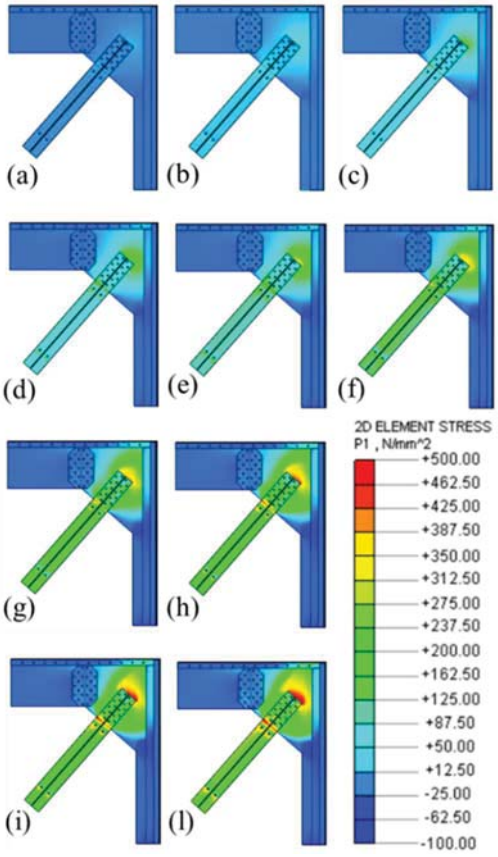

Figure 8: (a-l) Maximum principal stresses obtained by static nonlinear numerical analysis.

Step	T [KN]	σ_I [MPa]
(a)	385	70.21
(b)	770	134.82
(c)	1155	203.13
(d)	1540	270.95
(e)	1925	338.39
(f)	2310	405.26
(g)	2695	472.58
(h)	3080	539.87
(i)	3465	607.17
(l)	3850	673.03

Table 5: Load steps applied and the corresponding maximum principal stress levels, for a finite element of the model located in the upper side of the diagonal member.

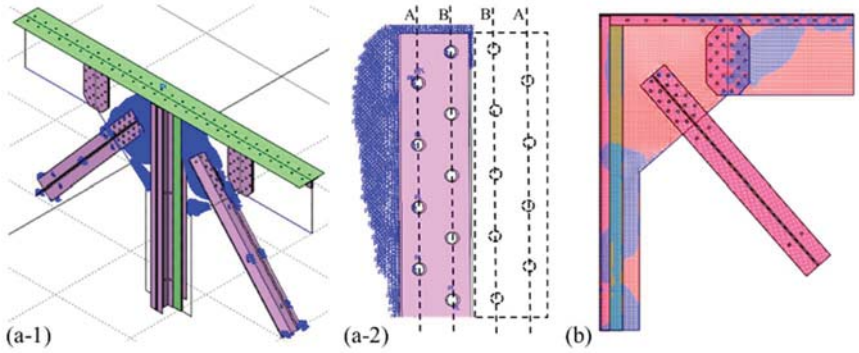

Figure 9: Results obtained by static NL numerical analysis: (a) plasticity element status of the joint: (a-1) the blue colour indicates the plastic zones, (a-2) detail of the double strap joint with two rows of rivets at both side of the joint; (b) flux of the principal stresses: blue colour indicates compression and red colour indicates tension.

5.2 Fatigue analysis

Fatigue failure is defined as the tendency of a material to fracture by means of progressive brittle cracking under repeated alternating or cyclic stresses of an intensity considerably below the normal strength. Although the fracture is of a brittle type, it may take some time to propagate, depending on both the intensity and frequency of the stress cycles. All structures and mechanical components that are cyclically loaded can fail by fatigue. Fatigue failure in structures frequently occurs in joints. Understanding the fatigue mechanism is essential to considering various technical conditions which affect fatigue life and fatigue crack growth.
Fundamental requirements during design and manufacturing to avoid fatigue failure are different for each different case and should be considered during the design phase. Fracture specifically describe the growth or propagation of a crack once it has been initiated and has given rise to many so-called crack growth methodologies. Fatigue analysis can be performed based on stress (stress-life method) and strain (strain-life method).
The stress-life method is mainly used for fatigue analysis under the condition of a low stress level relative to the yield stress. The stress-life method predicts the extent of fatigue under a given loading history using the relationship between the number of loading cycles (N) and stress amplitude (S) at the time when failure occurs from a cyclically applied constant load. The S-N curve shows the relationship between the stress amplitude (S) occurring from a cyclic loading of constant amplitude applied to the structure and the number of cycles to failure (N) when the stress of the corresponding amplitude is repeated. For a fatigue analysis using the stress-life method, a linear elastic analysis on the structure is performed first, and then equivalent stresses (such as principal stresses) are obtained. These stresses are then applied to an S-N curve to predict the number of loading cycles required to reach the fatigue failure in conjunction with detail category tables, to obtain a good estimation of the safety level of each detail on the bridge.
In Eurocode 3 [3], 14 S-N curves, which are equally spaced in log scale, as shown in Figure 10 (a), are defined. Each curve is characterized by the detail category $\Delta\sigma_C$. The slope coefficient m is equal to 3 for stress range above the constant amplitude fatigue limit (CAFL), $\Delta\sigma_D$, at 5 million cycles, and equal to 5 for stress range between the CAFL and the cut-off limit, $\Delta\sigma_L$, at 10 million cycles.
For riveted connections, Italian railways company imposed a value of 71 MPa, corresponding to the detail category 71, see Figure 11 (b), where the nominal stress $\Delta\sigma$ has to be calculated on the net cross-section (gross cross-section minus section of rivet holes in the critical section).

According to Eurocode 3 part 1-9, the fatigue strength value $\Delta\sigma_C$ is divided by γ_{MF}, so obtaining $\Delta\sigma_D = \Delta\sigma_C / \gamma_{MF} = 71/1.35$ MPa = 52 MPa. The fatigue strength curve is defined as follows:

$$(\Delta\sigma_R)^m N_R = (\Delta\sigma_C)^m 2 \cdot 10^6, \quad m = 3 \; for \; N \leq 5 \cdot 10^6 \tag{6}$$

$$(\Delta\sigma_R)^m N_R = (\Delta\sigma_C)^m 2 \cdot 10^6, \quad m = 5 \; for \; 5 \cdot 10^6 \leq N \leq 1 \cdot 10^8 \tag{7}$$

$$\Delta\sigma_L = (5/100)^{1/5} \Delta\sigma_D, \quad (cut - off \; limit) \tag{8}$$

When several stress amplitudes exist, the degree of damage of a material is calculated by accumulating individual damages from each of the stress amplitudes. Using the number of cycles corresponding to a specific stress amplitude, n_i, and fatigue life, N_i, the cumulative damage is calculated using Equation (9). The fatigue life of a structure is the reciprocal of the damage according to Equation (10).

$$Damage = \sum_i \frac{n_i}{N_i} \tag{9}$$

$$Fatigue \; Life = \frac{1}{Damage} \tag{10}$$

The riveted single-track railway Bridge was built in 1917 and was in use until a few years ago. After over 90 years of service, there is a motivation for assessment since the bridge has reached the end of its design working life. Therefore, an assessment is carried out to determine the residual service life of the bridge. Since the bridge has been in use for 94 years, there is a higher probability of failure due to fatigue than due to static overloading.

Data on traffic was collected from the railway's archives. A single type of locomotive has transited this line, (Locomotive series 1000), as sketched in Figure 11.

Results of fatigue analysis performed using MIDAS-FEA are reported in Figures 12 and 13. From the second fatigue result, it is noticed that there is no remaining fatigue life for elements in blue colour, it had expired 4 years before the year in which this assessment was undertaken. The member chosen for the analysis cannot be considered safe anymore. It should be noted that each specific structural element has a different fatigue life.

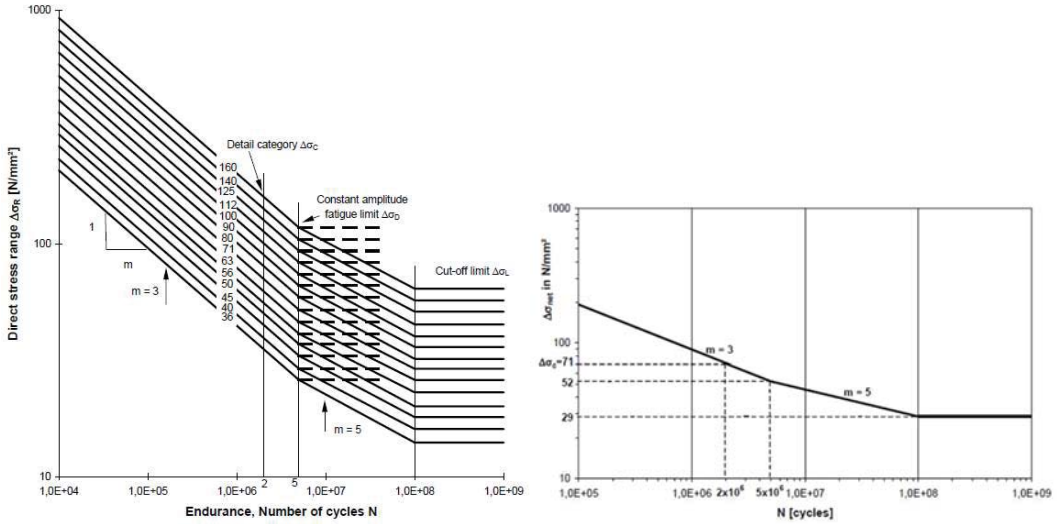

Figure 10: (a) Fatigue strength curves for nominal stress ranges for structural steel components; (b) S/N curve for the fatigue assessment of old riveted steel bridges.

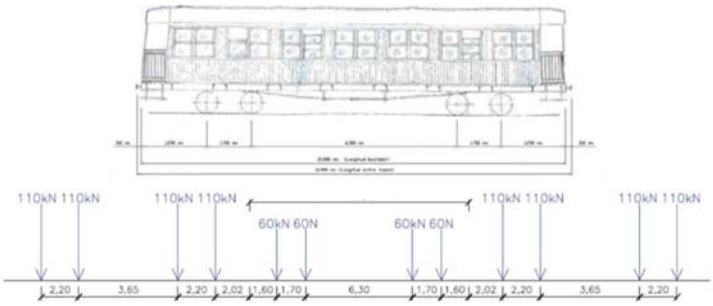

Figure 11: Sketch of Locomotive series 1000 and distance between axles and axle loads.

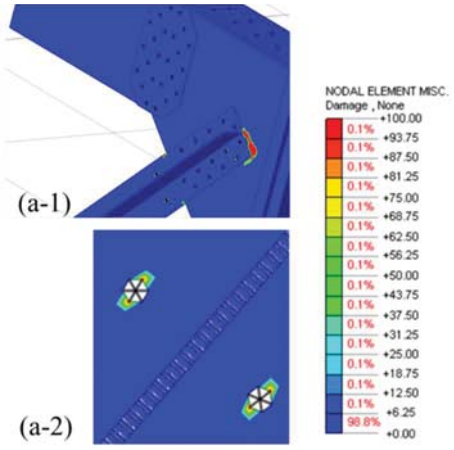

Figure 12: Fatigue analysis results in terms of damage: (a-1) - (a-2) detail views of damage contour.

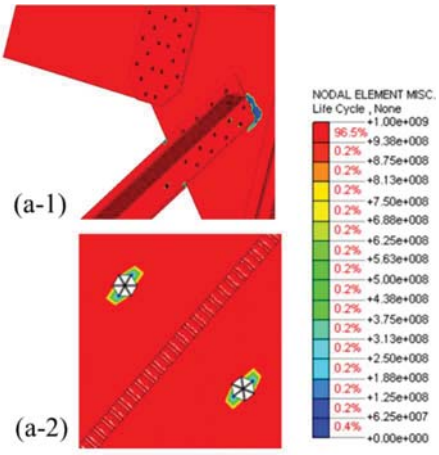

Figure 13: Fatigue analysis results in terms of fatigue life: (a-1) fatigue life of the joint; (a-2) detail of the holes in the diagonal element.

6 LONG-TERM MONITORING

An image acquisition by means of long-term monitoring system on the Quisi Bridge, permits on one hand to improve the procedure and, on the other hand, to obtain the description of current fatigue cracks on the bridge. On-site inspections were carried out by means of non-destructive testing of the connections of the bridge. Gamma radiation radiographs, (gammagraphy), were performed. The tests were performed by the TÜV SÜD ATISAE Laboratory and the test

standard procedure UNE EN ISO 5579 was used. The gammagraphy was carried out in a total of 160 connection geometry of the viaduct. The existence of cracks, cavities, inclusions, fusion and penetration defects, imperfections in shape and dimensions and other types of imperfections have been analyzed. In general, the state of the connections is very acceptable. However, small fissures have been identified in four zones of the bridge, shown in Figure 14, 15 and 16. It is worth noting that the first crack on the first isostatic span (Figure 14) and also the second crack on the iperstatic span (Figure 15) are located down the rivet cap or in the interior of the plate inside the union of several steel sheets. Through visual inspection it is not possible to detect these cracks. The third crack, (Figure 16 (b)), could be an original failure dating back to the stage of fabrication process of the rivet on the bridge; the fourth crack (Figure 16 (c)) is of the same type as the first two. On the isostatic spans the cracks are in a similar position this could be due to the loop effect generated by the train passage. No crack was observed in the position subjected to local modeling. Thus, a second detailed local model is under realization.

The image processing of the crack images has been carried out through segmentation by thresholding. Segmentation in a digital processing is a process of partitioning an image into significant regions and it is used to extract objects from the image. As in Figure 17 the first step is the thresholding that from a grayscale image returns a binary image, subsequently the noise removal, in the third step the assessment of the boundaries of the identified regions, the regions associated with the crack are the regions 3 and 4, and these will be therefore measurable (parameter estimation of the crack). The same procedure is in progress for other crack images, it is requiring pre-processing to highlight the crack from the background (Figure 18).
Based on the information extracted from the images acquisition and the newer local model behavior, it will be possible to update the global model considering the presence of fatigue crack.

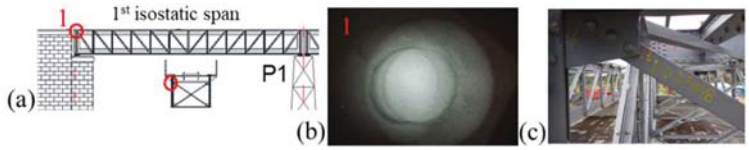

Figure 14: (a) Bridge critical point where crack 1 is observed; (b) Gammagraphy of a crack identified; (c) Cross view where the crack 1 is observed.

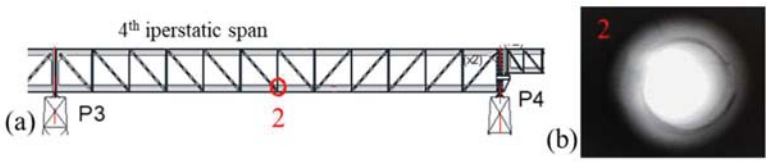

Figure 15: (a) Bridge critical point where crack 2 is observed; (b) Gammagraphy of a crack identified.

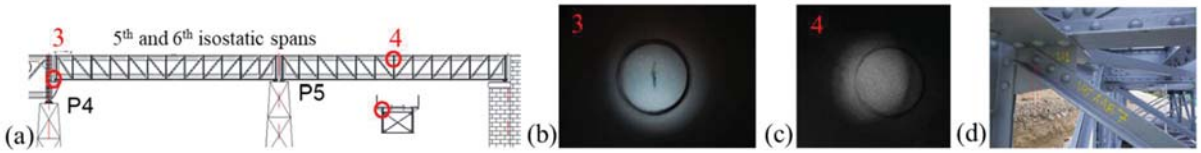

Figure 16: (a) Bridge critical point where cracks 3 and 4 are observed; (b) - (c) Gammagraphies of the two cracks identified; (d) Cross view where the crack 4 is observed.

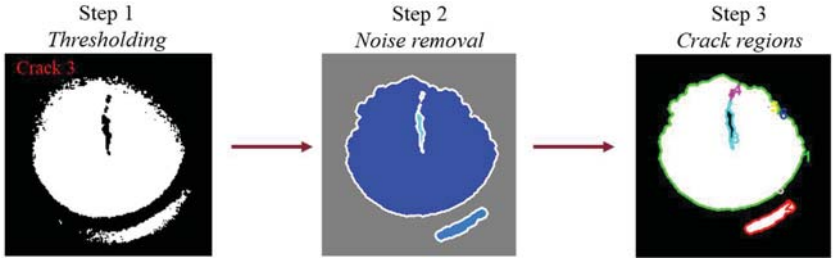

Figure 17: The architecture of image processing based crack detection for crack 3.

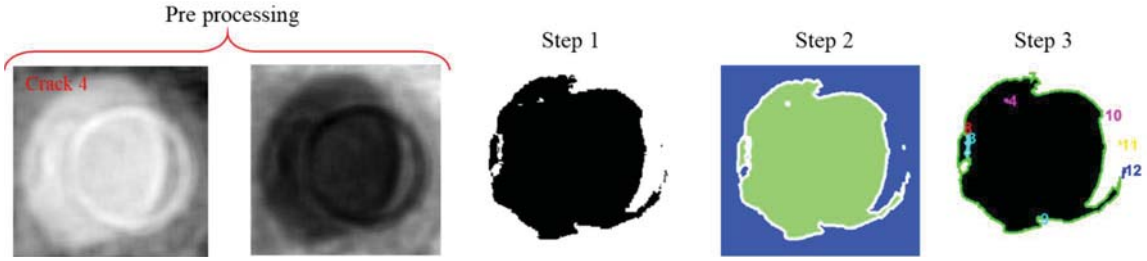

Figure 18: Image preprocessing for crack 4.

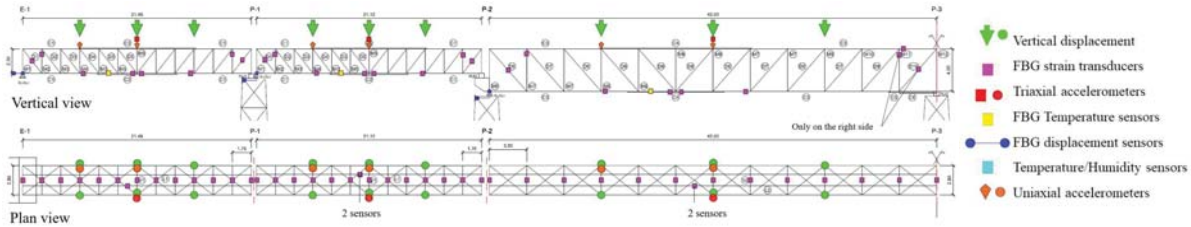

Figure 19: Layout of the permanent monitoring system and types of sensors.

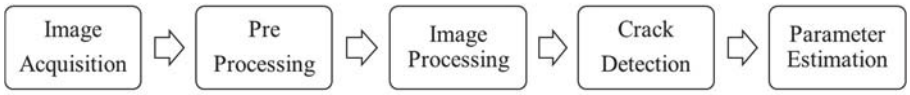

Figure 20: The architecture of image processing based crack detection.

7 CONCLUSIONS

A procedure to identify damage in a steel truss bridge has been proposed. The results obtained through pseudo-dynamic testing and FEM analysis for a simple truss evidences the obtainable resolutions in damage indicator with the increase of a number of modes. For the main span of the Quisi Bridge the damage changes, affected both one single element and then a group of elements, do not affect to the main frequencies of the bridge so, a mode shape based method is performed. Natural frequency changes alone may not be sufficient for a unique identification of the location of structural damage.

From the results of stress intensity obtained in the global model, the critical point is selected to analyze the fatigue phenomena in the local model.

Fatigue damage appears in the form of fatigue cracks and can occur in primary loaded or secondary elements. Since fatigue failure is depending on the load spectra over the service life, consequently, existing steel structures suffer more from fatigue and accumulate more damage the older the bridges are.

Fatigue crack initiation in structural details is generally expected where stress concentrations may occur, such as holes as showed by the presented detailed FEM model of a joint of the Quisi Bridge. These results are comparable with the crack identified by Gammagraphy. More data are expected for the Quisi Bridge in which a permanent monitoring system will be install even with image acquisition. Figure 19 shows the experimental setup with an important number of channels, the data acquisition is done under environmental condition.

Concerning the image-based detection of fatigue cracks, the general architecture of the method is shown in Figure 20 and it includes: an initially collect the image of the structure which will be subjected to the crack detection process (image acquisition), the pre-processing of the images with segmentation, the crack detection using the result of the processed image and finally the crack feature extraction that is the step in which the detected cracks are separated based on the width, depth, area or length of the crack.

The available data will permit to perform a nonlinear model updating through an error criterion based on crack pattern and frequency and modal shape variations.

ACKNOWLEDGMENTS

This paper is a part of a project that has received funding from the Research Fund for Coal and Steel under grant agreement No 800687. (DESDEMONA EU project)

REFERENCES

[1] B. Peeters, G. De Roeck, Reference-based stochastic subspace identification for output-only modal analysis, *Mechanical Systems and Signal Processing*, 1999.

[2] D.J. Ewins, *Modal Testing: Theory and Practice*, New York, John M. Wiley & Sons, 2000.

[3] EN 1993-1-9, *Eurocode 3*: Design of steel structures – Part 1-9: Fatigue, 2004.

[4] L. Zhang, T. Wang, Y Tamura, A Frequency-Spatial Decomposition (FSDD) Technique for Operational Modal analysis. *IOMAC 2005 Procedia: 1st International Operational Modal Analysis Conference,* April 26-27, Copenhagen, Denmark, 2005.

[5] Y. Gao, B. F. Spencer Jr., D. Bernal, Experimental Verification of the Flexibility-Based Damage Locating Vector Method, *Journal of Engineering Mechanics*, 2007.

[6] A. Deraemaeker, E. Reynders, G. De Roeck, J. Kullaa, Vibration-based structural health monitoring using output-only measurements under changing environment. *Mechanical Systems and Signal Processing*, 22, 34-56, 2008.

[7] E. Reynders, M. Schevenels, G. De Roeck, MACEC: A Matlab toolbox for experimental and operational analysis, *Report BWM-2008-07*, April 2008.

[8] D. Foti, V. Gattulli, F. Potenza, Output-Only Identification and Model Updating by Dynamic Testing in Unfavourable Conditions of a Seismically Damaged Building. *Computer-Aided Civil and Infrastructure Engineering*, vol. 29(9), pp 659-675, 2014, doi: 10.1111/mice.12071.

[9] F. Potenza, G. Castelli, V. Gattulli, E. Ottaviano, Integrated process of image and acceleration measurements for damage detection, EURODYN 2017.

[10] M. Crognale, V. Gattulli, S. Ivorra, F. Potenza, Dynamics and damage sensitivity of the Quisi steel truss bridge. Gattulli Vincenzo, Oreste Bursi, and Daniele Zonta, eds. *ANCRiSST 2019 Procedia: 14th International Workshop on Advanced Smart Materials and Smart Structures Technology. Vol. 45*. Sapienza Università Editrice, Agosto 2019.

[11] M. Crognale, V. Gattulli, A. Paolone, F. Potenza, A procedure for damage identification in a steel truss. XXIV Congresso AIMETA 2019, Associazione Italiana di Meccanica Teorica e Applicata15-19 Settembre 2019.

EURODYN 2020
XI International Conference on Structural Dynamics
M. Papadrakakis, M. Fragiadakis, C. Papadimitriou (eds.)
Athens, Greece, 23–26 November 2020

MAXIMUM LIKELIHOOD ESTIMATION OF DAMPING IN THE FREQUENCY DOMAIN DECOMPOSITION METHOD

Javier Cara

[1]ETS Ingenieros Industriales - Universidad Politécnica de Madrid
C/ José Gutiérrez Abascal, 2. 28006 Madrid
e-mail: javier.cara@upm.es

Keywords: Operational Modal Analysis, Frequency Domain Decomposition, Damping Ratios, Maximum Likelihood, EM algorithm.

Abstract. *The Frequency Domain Decomposition (FDD) method consists on identifying natural frequencies and mode shapes of structural and mechanical system as the peaks of a frequency plot. However, the damping ratio is not an output of FDD, but it is calculated in secondary step. In this work a new method is proposed to estimate the damping ratios. The idea is to use maximum likelihood estimation, where the likelihood function is defined in terms of the innovations of the state space model. This is a highly nonlinear and complicated function of the unknown parameters, so a numerical method must be used to find the maximum. In this work, the BFGS algorithm has been chosen. This method also allows quantifying the uncertainty of the parameters using the Hessian matrix. Due to the nature of the method, there are not problems with closely spaced or repeated modes.*

1 INTRODUCTION

The Frequency Domain Decomposition (FDD) algorithm is maybe the most known and used method to estimate modal parameters in Operational Modal Analysis. FDD was introduced as an extension of the classical frequency domain Peak Picking approach [1]. The main advantage of this approach is the fact that engineers and researchers can identify the modes of vibration of their system as the peaks of a frequency plot. On the contrary, other sophisticated techniques like Subspace methods are usually viewed as black boxes where the user looses the physical meaning of the parameters.

Apart from the user-friendlinees of the method, FDD gives reasonable estimates of natural frequencies and mode shapes. However, the damping ratio is not an output of FDD, but it is calculated in secondary step [2]: once the natural frequency and mode shape are computed, the contribution of this mode to the spectral density matrix is isolated and transformed back to the time domain. Then, the damping ratio is computed from the corresponding free decay. This two step method is called Enhanced Frequency Domain Decomposition (EFDD). Reference [3] is an updated review of the most relevant works for damping estimation in the FDD context.

In this work a new method for the estimation of the damping ratio is proposed. Instead of using free decays, the method proposes to estimate the damping ratios using the maximum likelihood method. The likelihood function is defined in terms of the innovations of the state space model. This is a highly nonlinear and complicated function of the unknown parameters, and among all the available numerical algorithms, the BFGS algorithm has been chosen to find the maximum of this function. This method also allows quantifying the uncertainty of the parameters, specifically, the confidence intervals of the estimates can be computed using the Hessian matrix.

2 The FDD method

The vibrations of a mechanical/structural system, $\mathbf{q}(t) \in \mathbb{R}^{n_q}$, are given by the equation:

$$\mathbf{M}\ddot{\mathbf{q}}(t) + \mathbf{C}\dot{\mathbf{q}}(t) + \mathbf{K}\mathbf{q}(t) = \mathbf{F}(t) \tag{1}$$

We can change the coordinate system to modal coordinates by mean of the linear transformation:

$$\mathbf{q}(t) = \mathbf{\Phi}\mathbf{q}_\mathbf{m}(t) \tag{2}$$

where $\mathbf{q}_\mathbf{m}(t)$ is the vibration in modal coordinates and $\mathbf{\Phi}$ is the matrix of modal vectors. Let us assume we are measuring the acceleration of n_y selected points:

$$\mathbf{y}(t) = \mathbf{L}_\mathbf{y}\ddot{\mathbf{q}}(t) \tag{3}$$

We consider the contribution of only n_m modes of vibration:

$$\mathbf{z}_\mathbf{m}(t) = \mathbf{L}_\mathbf{m}\mathbf{q}_\mathbf{m}(t) \tag{4}$$

where $\mathbf{L}_\mathbf{y} \in \mathbb{R}^{n_y \times n_q}$ and $\mathbf{L}_\mathbf{m} \in \mathbb{R}^{n_m \times n_q}$ are selection matrices. Combining these equations we have:

$$\mathbf{y}(t) = \mathbf{L}_\mathbf{y}\ddot{\mathbf{q}}(t) = \mathbf{L}_\mathbf{y}\mathbf{\Phi}\ddot{\mathbf{q}}_\mathbf{m}(t) = \mathbf{L}_\mathbf{y}\mathbf{\Phi}\mathbf{L}_\mathbf{m}^\mathbf{T}\ddot{\mathbf{z}}_\mathbf{m}(t) = \mathbf{\Phi}_\mathbf{e}\ddot{\mathbf{z}}_\mathbf{m}(t) \tag{5}$$

where $\mathbf{\Phi}_\mathbf{e} = \mathbf{L}_\mathbf{y}\mathbf{\Phi}\mathbf{L}_\mathbf{m}^\mathbf{T} \in \mathbb{R}^{n_y \times n_m}$. The auto-correlation matrix of the responses is:

$$\mathbf{C}_\mathbf{y}(\tau) = E[\mathbf{y}(t+\tau)\mathbf{y}(t)^T] = \mathbf{\Phi}_\mathbf{e}E[\ddot{\mathbf{z}}_\mathbf{m}(t+\tau)\ddot{\mathbf{z}}_\mathbf{m}(t)^T]\mathbf{\Phi}_\mathbf{e}{}^T = \mathbf{\Phi}_\mathbf{e}\mathbf{C}_\mathbf{m}(\tau)\mathbf{\Phi}_\mathbf{e}{}^T \tag{6}$$

Applying the Fourier Transform we obtain:

$$\mathbf{G_y}(\omega) = \mathbf{\Phi G_m}(\omega)\mathbf{\Phi}^T \tag{7}$$

where $\mathbf{G_m}(\omega)$ is the matrix of spectral densities in modal coordinates at a given frequency ω. On the other hand, the singular value decomposition of matrix $\mathbf{G_y}(\omega)$ is given by:

$$\mathbf{G_y}(\omega) = \mathbf{UDU}^T \tag{8}$$

where $\mathbf{D}$ is a diagonal matrix and $\mathbf{UU}^T = \mathbf{I}$. The FDD method consists in taking $\mathbf{G_m}(\omega_i) = \mathbf{D}$ and $\mathbf{\Phi} = \mathbf{U}$, where ω_i are the peaks of the spectral densities. Therefore:

- The modal frequencies are the peaks of the spectral densities, $\omega = \omega_i$.
- The modal vectors are the column of the eigenvector matrix $\mathbf{U}$ computed at $\omega = \omega_i$.

The method does not return the damping values. The most known and used approach for computing the damping is the Enhanced FDD [2]. In this work we propose a maximum likelihood approach.

3 PROPOSED METHOD

3.1 The state space model and the likelihood function

Given the acceleration recorded in the structural/mechanical system, $\mathbf{y_{1:n}} = \{\mathbf{y_1}, \mathbf{y_2}, \ldots, \mathbf{y_n}\}$, we model these data using the state space model:

$$\mathbf{x_{t+1}} = \mathbf{A x_t} + \mathbf{w_t} \tag{9}$$

$$\mathbf{y_t} = \mathbf{C x_t} + \mathbf{v_t} \tag{10}$$

where $\mathbf{w_t} \sim N(\mathbf{0}, \mathbf{Q})$ and $\mathbf{v_t} \sim N(\mathbf{0}, \mathbf{R})$. The model parameters are $\boldsymbol{\theta} = \{\mathbf{A}, \mathbf{C}, \mathbf{Q}, \mathbf{R}\}$. Using the Kalman filter, this model can be written in the *innovation form*:

$$\mathbf{x_{t+1|t}} = \mathbf{A x_{t|t-1}} + \mathbf{K e_t} \tag{11}$$

$$\mathbf{y_t} = \mathbf{C x_{t|t-1}} + \mathbf{e_t} \tag{12}$$

where $\mathbf{x_{t|t-1}} = E[\mathbf{x_t}|\mathbf{y_{1:t-1}}]$ are the predicted states, $\mathbf{K} \in \mathbb{R}^{n_s \times n_y}$ is the Kalman gain and $\mathbf{e_t} \in \mathbb{R}^{n_y}$ are the innovations, with distribution $\mathbf{e_t} \sim N(\mathbf{0}, \mathbf{\Sigma})$. Therefore, the likelihood can be written:

$$l_{\mathbf{y}}(\boldsymbol{\theta}) = -\frac{1}{2}\sum_{k=1}^{n}\left[\ln|\mathbf{\Sigma}(\boldsymbol{\theta})| + \mathbf{e_k^T}(\boldsymbol{\theta})\mathbf{\Sigma}(\boldsymbol{\theta})^{-1}\mathbf{e_k}(\boldsymbol{\theta})\right] \tag{13}$$

3.2 Maximum likelihood estimation

Let us consider m natural frequencies $\Omega = \{\omega_1, \omega_2, \ldots, \omega_m\}$ and modal vectors $\mathbf{\Phi} = \{\boldsymbol{\phi_1}, \boldsymbol{\phi_2}, \ldots, \boldsymbol{\phi_m}\}$ computed with the FDD method. The corresponding unknown damping ratios will be called $\mathbf{Z} = \{\varphi_1, \varphi_2, \ldots, \varphi_m\}$. The state space matrices can be defined from them (see [5] for details):

$$\mathbf{A} = \begin{bmatrix} \mathbf{0} & \mathbf{I} \\ -\mathbf{\Omega}^2 & -2\mathbf{Z\Omega} \end{bmatrix}, \quad \mathbf{C} = \mathbf{\Phi}\begin{bmatrix} -\mathbf{\Omega}^2 & -2\mathbf{Z\Omega} \end{bmatrix}. \tag{14}$$

We need to define the matrices $\mathbf{Q}$ and $\mathbf{R}$ for that modal frequencies, damping ratios and modal vectors. We have not found closed formulas for that, so we have used the EM algorithm to estimate them numerically ([6]).

The system matrices, and therefore the likelihood function, are functions of the unknown damping ratios, $\boldsymbol{\theta} = \boldsymbol{\theta}(\mathbf{Z})$. Equation (13) can be written as:

$$l_{\mathbf{y}}(\mathbf{Z}) = -\frac{1}{2}\sum_{k=1}^{n}\left[\ln|\boldsymbol{\Sigma}(\mathbf{Z})| + \mathbf{e}_{\mathbf{k}}^{\mathbf{T}}(\boldsymbol{Z})\boldsymbol{\Sigma}(\mathbf{Z})^{-1}\mathbf{e}_{\mathbf{k}}(\mathbf{Z})\right] \tag{15}$$

This is a highly nonlinear and complicated function of the unknown damping ratios, $\mathbf{Z}$. We have chosen the BFGS algorithm to find the maximum of this function.

4 RESULTS

We have simulated a 4DOF structural/mechanical system defined by the following modal properties:

$$\boldsymbol{\Omega} = \begin{bmatrix} 1.52 & 3.09 & 4.42 & 5.21 \end{bmatrix} \; Hz, \tag{16}$$

$$\mathbf{Z} = \begin{bmatrix} 2.00 & 1.43 & 1.44 & 1.50 \end{bmatrix} \; \%, \tag{17}$$

$$\boldsymbol{\Phi} = \begin{bmatrix} 0.164 & 0.300 & 0.251 & -0.484 \\ 0.357 & 0.353 & -0.050 & 0.608 \\ 0.581 & -0.209 & -0.460 & -0.473 \\ 0.711 & -0.860 & 0.849 & 0.412 \end{bmatrix}. \tag{18}$$

The response of this system to a simulated random force is given in Figure 1.

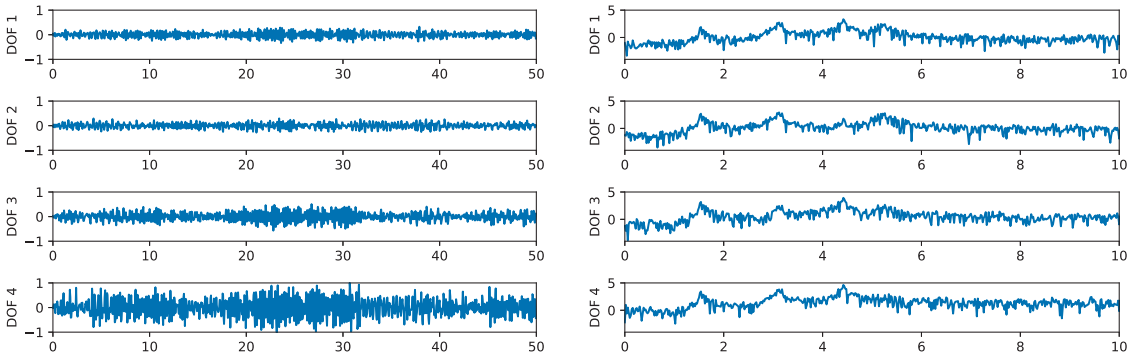

Figure 1: Simulated data.

First, we estimate the modal frequencies and modal vectors using the FDD method, see Figure 2. The results are:

$$\hat{\boldsymbol{\Omega}} = \begin{bmatrix} 1.56 & 3.16 & 4.41 & 5.23 \end{bmatrix} \tag{19}$$

$$\hat{\boldsymbol{\Phi}} = \begin{bmatrix} -0.161 & -0.276 & -0.240 & -0.462 \\ -0.347 & -0.320 & 0.049 & 0.614 \\ -0.580 & 0.221 & 0.434 & -0.465 \\ -0.718 & 0.878 & -0.866 & 0.437 \end{bmatrix} \tag{20}$$

We can check that results obtained with the FDD method are quite good.

The starting point for the BFGS algorithm was a damping ratio of 0.01 for the four modes. We have used the BFGS algorithm included in Scipy 1.4.1. The estimated damping ratios can be found in Table 1. The Table also include a 95% confidence interval computed from the Hessian matrix at the maximum.

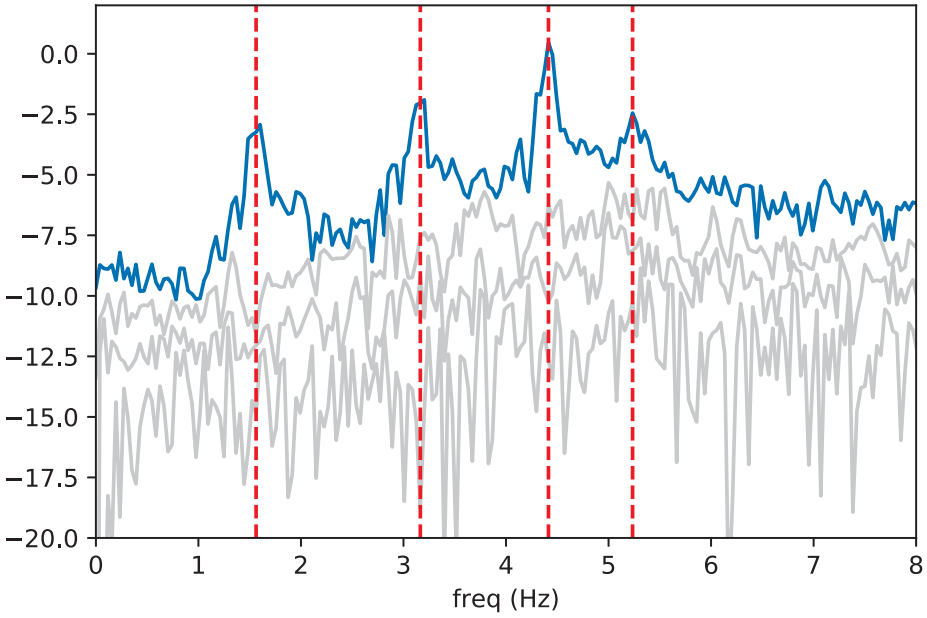

Figure 2: Estimation of modal frequencies using the FDD method.

Theoretical values	2.00	1.43	1.44	1.50
Estimated values	2.20	2.25	1.33	2.06
Standard error	0.66	0.38	0.05	0.07
95% conf. interval				
Lower limit	0.86	1.48	1.22	1.90
Upper limit	3.54	3.02	1.45	2.22

Table 1: Results using the proposed method.

5 CONCLUSIONS

- We have introduced the maximum likelihood estimation of damping in a FDD context.
- First, we have shown the likelihood function.
- The likelihood function is highly nonlinear, so a good algorithm for its maximization is the BFGS.
- In the last section, we have shown the performance of the method with simulated data.

REFERENCES

[1] R. Brincker, L.M. Zhang, P. Andersen, *Modal identification from ambient response using Frequency Domain Decomposition. Proceedings of the 18th IMAC, San Antonio, TX, USA*, 2000

[2] R. Brincker, L.M. Zhang, P. Andersen, *Damping estimation by Frequency Domain Decomposition. Proceedings of the 19th IMAC, Kissimmee, TX, USA,* 2001

[3] M. Danial A. Hasan, Z.A.B. Ahmad, M. Salman Leong, L.M. Hee, Enhanced frequency domain decomposition algorithm: a review of a recent development for unbiased damping ratio estimates, *Journal of Vibroengineering*, Vol. 20, Issue 5, 2018, p. 1919-1936.

[4] S. Gade, N. Moller, H. Herlufsen, H. Konstantin-Hansen, *Frequency Domain Techniques for Operational Modal Analysis, Proceedings of the 21st International Modal Analysis Conference (IMAC-21), 1: 1726, 36*, 2003

[5] J. Cara, Computing the modal mass from the state space model in combined experimental-operational modal analysis, *Journal of Sound and Vibration*, Volume 370, 26 May 2016, Pages 94-110, http://dx.doi.org/10.1016/j.jsv.2016.01.043.

[6] F. J. Cara, J. Carpio, J. Juan, E. Alarcon, An approach to Operational Modal Analysis using the Expectation Maximization Algorithm. *Mechanical Systems and Signal Processing*, Vol. 31, p. 109-129, August 2012, http://dx.doi.org/10.1016/j.ymssp.2012.04.004.

EURODYN 2020
XI International Conference on Structural Dynamics
M. Papadrakakis, M. Fragiadakis, C. Papadimitriou (eds.)
Athens, Greece, 23–26 November 2020

A NUMERICAL INVESTIGATION OF NEW ALGORITHMS FOR THE DRIVE-BY METHOD IN RAILWAY BRIDGE MONITORING

L. Bernardini[1], **M. Carnevale**[2], **C. Somaschini**[1], **K. Matsuoka**[3], **A. Collina**[1]

[1] Politecnico di Milano
Dipartimento di Ingegneria Meccanica
via La Masa 1, 20156 Milano, Italy
e-mail: andrea.collina@polimi.it

[2] Università degli Studi di Pavia
Dipartimento di Ingegneria Industriale e dell'Informazione
via Ferrata 5, 27100, Pavia, Italy
e-mail: marco.carnevale@unipv.it

[3] Railway Technical Research Institute,
Railway Dynamics Division,
2-8-38, Hikari-cho, Kokubunji-shi Tokyo 185-8540 Japan

Keywords: Railway bridges; Drive-by monitoring; Truss structures; Steel structure; Indirect methods for SHM; Continuous wavelet transform (CWT).

Abstract. *Railway Infrastructure Manager increasingly demand for new and effective method for the monitoring of infrastructure health, so that a relevant effort is being placed in the development of condition based monitoring and maintenance techniques for railway infrastructure. This includes track geometry, overhead contact line and the structural health of railway bridges. This paper proposes an algorithm for the bridge monitoring of railway bridges, based on accelerations measured on board train (drive-by method). The diagnostic algorithm is developed and validated based on the results of a 3D numerical model simulating the dynamic interaction of the bridge/track/train structure. The analysis is focused on steel truss bridges, on which the degradation of the connection of one diagonal element is simulated (e.g. lose bolts, deteriorated welding). In comparison with previous research works, this paper tries to overcome the need of comparison to a reference signal corresponding to the healthy bridge, which is the technique on which most of literature papers rely on. This is achieved by exploiting the roll component of the train (difference between right and left acceleration), excited as a consequence of the presence of the defect which generates an asymmetry in the bridge behavior. The numerical results show good accuracy in damage identification and location, good robustness to vehicle speed, to the presence of electrical noise and, in the case of a relevant damage, to track irregularity.*

1 INTRODUCTION

Condition based monitoring and maintenance techniques for railway infrastructure are hot research topics for academies and railway industries, regarding track geometry, overhead contact line, and the structural health of railway bridges [1],[2],[3]. Most of railway bridges were designed several decades ago, in the middle of the last century or even before, when loading conditions and traffic volumes were much different and lighter than today [4],[5]. Some of these bridges may also have undergone deterioration and corrosion during time, and they could now be structurally deficient.

The direct monitoring of a single bridge with dedicated instrumentation [6], which is a common practice in the case of main or high-speed lines, is not a feasible prospective for the entire regional and inter-regional railway lines of a country, due the huge number of bridges and the high costs related. Current bridge maintenance relying on visual inspections can be effective if clear protocols are followed, according to the typology of bridge. The obvious drawback of visual inspection is the dependence on to the experience of the inspector and also on the position of the damage, which often happens to be on a hidden member. Moreover, the time interval between inspections may also depend on the availability of personnel. For these reasons, in the last years, indirect methods have been looked for, relying on measurements acquired on the vehicle which crosses the structure. They are commonly named as drive-by methods [1]. The fundamental concept behind this approach is that a structural damage causes a change in the physical and mechanical properties of the bridge, and the bridge can be directly excited by the train passage. As a consequence, a change in the dynamic behavior of the vehicle interacting with the structure can be observed too. The advantage is that, fitting simple measurement set-up on a normal operating train, it is possible to acquire data in an almost continuous way, so that a proper trend of bridge condition could be in principle obtained for building a data base.

Drive-by methods have been mainly developed for road applications (highway bridges), but in fewer cases to railways too. They can be divided in the following two main categories [1]: *modal parameters* and *non-modal parameters*. The former, consisting in the identification of natural frequencies [7], [8], [9], [10], damping estimation methods [11] and identification of bridge mode shapes [12], [13], are demonstrated to be effective up to limited speeds (maximum 60 km/h) and, in the first two cases, they are not able to identify the exact location of a defects. These techniques are not trivial to be put in practise, and most of them were only demonstrated through numerical simulations. Moreover, their outcome can be affected by environmental conditions like temperature, especially in the case of damping and natural frequencies [14],[15],[16].

Non modal damage detection methods do not explicitly require the computation of bridge dynamic properties, but focuses on the bridge deflection under passing loads (e.g. apparent profile [17], [18] or change of curvature[19],[20]) or on the dynamic response of the vehicle crossing the bridge [21],[22],[3]. This paper focuses on the latter method, which is thought to be more promising and easy-to-implement, even if at the time being it is mostly investigated by numerical analysis. Most of the cases presented in the literature rely on the comparison of accelerations signals, gathered from the train crossing the bridge, to a reference acceleration signal corresponding to the healthy case. Accelerations are low pass filtered to cancel the vehicle and bridge natural frequencies and to isolate the quasi-static component of the signals. The current open points and drawbacks of these methods are related to the small magnitudes of the signals involved, and the need to know the precise position of the train on the bridge to perform the difference against the reference signal [23],[24]. This position may be achieved through balises or transpoder able to identify and transmit on-board train the position of the

bridge. On the other hand, this method seems to be effective even for vehicle speeds close to the common commercial speeds of commuter trains, and not too sensitive to track irregularities [3].
Another possibility to exploit the dynamic response of the vehicle crossing the bridge consists in the comparison of signals measured in the same train's run on different bogies (i.e. leading or trailing), or on different side of the vehicle if the type of defect mainly induces variation on one side of the bridge.
Following the above mentioned research line, and in particular the use of Continuous Wavelet Transform [25], this paper investigates the possibility to overcome the need of comparison to a reference signal corresponding to the healthy bridge. This result is achieved by exploiting the roll component of the bogie (difference between right and left accelerations), excited as a consequence of the presence of a defect which generates an asymmetry in the bridge behavior. The results try to put a step forward with respect to previous research work, all relying on the comparison with a baseline of the healthy bridge [2],[3]. The analysis is performed through numerical simulations carried out with a 3D numerical model for the train/track/bridge interaction [26] of a single span bridge and on a multi-span bridge.

The paper is organized as follows: Section 2 describes the 3D model for the simulation of the bridge/track/train interaction, and the simulation plan. Section 3 describes the proposed algorithm and the results achieved for a single span bridge. Section 4 summarizes the results in the case of a multi-span bridge. Finally, conclusions are drawn in Section 5.

2 NUMERICAL MODEL AND PLAN OF SIMULATIONS

The dynamic simulations of the bridge/track/train interaction are carried out with the software developed at the Department of Mechanical Engineering of Politecnico di Milano [26]. The bridge models considered are steel Warren open truss bridges with medium-span, non-ballasted track, with timber sleepers directly fastened to the girder. This configuration is selected as a first example, since it has more probability to show differences related to the loss of symmetry in the structure. As a first step of the work, a single line bridge is considered, with the track in the middle of the bridge structure. Two cases are analyzed: a single span-bridge (properties in Figure 1), and a multi-span bridge composed of 4 spans with the same properties of the single span model. This second case is investigated to evaluate the possibility of detecting defects on a damaged span by comparison with the records taken on the other spans.

Span length	21.42 [m]
height	3.71 [m]
width	4.5 [m]
1st bending mode	16 Hz
1st torsional mode	19.5 Hz

Span dimensions and natural frequencies

Element	Section area	Polar moment	Torsion constant	Principal moment	Principal moment
	A [m^2]	I_p [m^4]	I_t [m^4]	I_2 [m^4]	I_3 [m^4]
1	0.0143	$3.9\ 10^{-4}$	$1.54\ 10^{-6}$	$2.12\ 10^{-4}$	$1.8\ 10^{-4}$
2	0.0148	$3.5\ 10^{-4}$	$1.91\ 10^{-6}$	$2.14\ 10^{-4}$	$1.4\ 10^{-4}$
3	0.00615	$2.0\ 10^{-4}$	$9.2\ 10^{-7}$	$1.65\ 10^{-4}$	$4.1\ 10^{-5}$
4	0.0013	$1.03\ 10^{-4}$	$4.6\ 10^{-7}$	$8.2\ 10^{-5}$	$2.1\ 10^{-5}$
5	0.0167	$9.1\ 10^{-4}$	$6.6\ 10^{-7}$	$8.97\ 10^{-4}$	$1.9\ 10^{-5}$
6	0.0048	$2.5\ 10^{-4}$	$6.4\ 10^{-7}$	$2.3\ 10^{-4}$	$2.2\ 10^{-5}$

Section properties. Area and moments of Inertia

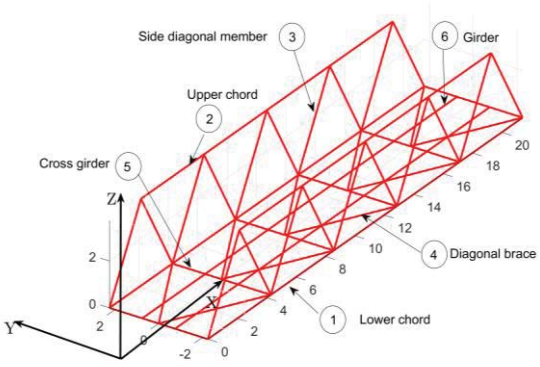

Figure 1: Single span bridge.

Two ballasted modules of length 29.4 m are added before and after the bridge (track properties as in reference [3]), to represent more realistic transients when the train enters and exits the bridge. The damage introduced in the bridge model represents a full or partial degradation of the fastenings in correspondence of the connection between the diagonal member (labelled with 3 in Figure 1) and the lower chord (labelled with 1 in Figure 1). The full damage is modeled by removing the diagonal element from the finite element model and applying a concentrated mass at the connection of the damaged element with the upper chord, to maintain its weight. The partial damage, which represents a more realistic damage condition in practice, is modeled through a reduction of the Young modulus of the damaged diagonal member. This is equivalent to considering a spring at the location of the fastening, in series with the involved diagonal element. Three different defect conditions have been studied, with a reduction of the Young Modulus equal to 30%, 50% and 70% in the damaged diagonal member. Different damage positions along the span are considered, to study whether and how damage location affects the accuracy of its detection.

Simulations of two different commuter trains have been considered, namely CSA and TSR model. They are respectively built with bogies shared between adjacent carbodies (CSA), and with the standard two-bogies configuration for each carbody, double-deck type (TSR). Their properties are described in reference [3], and not repeated here for sake of conciseness. Simulations for each train type are carried out with the train crossing the bridge at four different constant velocities, in the range of 80 km/h-140 km/h. These speeds are near to the maximum commercial speeds of these kind of trains (respectively 140 for TSR and 160 km/h for CSA), so that if satisfactory results are achieved, the desirable result of no traffic delays would result in the line.

The dynamic response of the train is measured at the bogie frame level, on the right and left side, in correspondence of the wheelset. The position of the accelerometer is of primary importance: location on axle box increases the sensitivity to defect, but involves a higher level of acceleration. This higher level of acceleration, requiring a larger full-scale value of the transducer, implies a lower sensitivity [3]. On the other hand, the location of the sensors on the bogie frame takes advantage of the effect of mechanical filtering from the primary suspension, attenuating high frequency components in the acceleration and enabling the use of more sensitive accelerometers. The drawback consists in the fact that sensors on the bogie frame are more distant from the location of the defect, so that the vibration path associated to the defect might be detected with more difficulties. Location on the bogie frame is investigated in the present paper, also considering the advantages in terms of maintenance operation of the train and the measurement set-up itself.

Since the proposed method for damage identification is based on the difference between the right and left hand side accelerations, a different irregularity profile is adopted on left and right rails, so as to simulate a more realistic case. Both vertical and roll track irregularities are considered, the total track profile being a composition of the two contributions. Profiles are obtained starting from the power spectral density functions provided by the standard ORE B176, and obtaining different level of irregularities (the highest level is reported in Figure 2). The level of irregularity is considered to be higher in the ballasted modules before and after the bridge, and it is attenuated along the bridge extension, where a non-ballasted track is present. This is a reasonable assumption considering that on the bridge the only permanent displacement is due to the dimension variation of the timber sleepers.

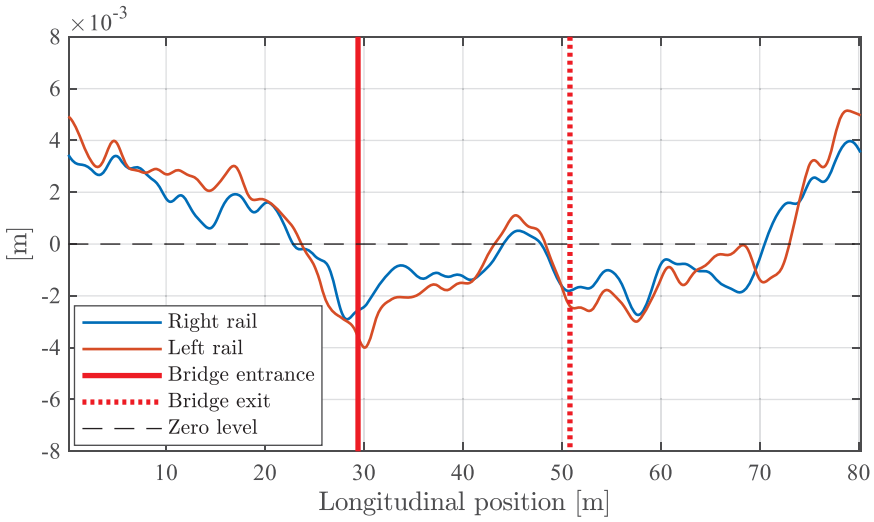

Figure 2: Vertical irregularities on left and right rails.

All the above mentioned parameters are changed individually during the simulations, varying only one parameter at once to investigate its effect on the outcomes of the proposed algorithm.

3 RESULTS FOR THE SINGLE SPAN BRIDGE

The presence of a defect on the bridge side generates an asymmetry in its behavior under the loads of the passing train. Figure 3 shows the deflection of the healthy (Figure 3a) and damaged (Figure 3b) bridges under the train load, with the black arrows highlighting the positions of the two axles of the leading bogie of the CSA train at a specific frame. In Figure 3b the damage is placed on the sixth diagonal member of the right side wall, right in the middle of the two arrows: due to the damage presence, the bridge deflection loses the symmetry characterizing the healthy structure. This asymmetry can be exploited to detect the presence of a defect, by analyzing the difference between the right and left hand side accelerations of the leading bogie.

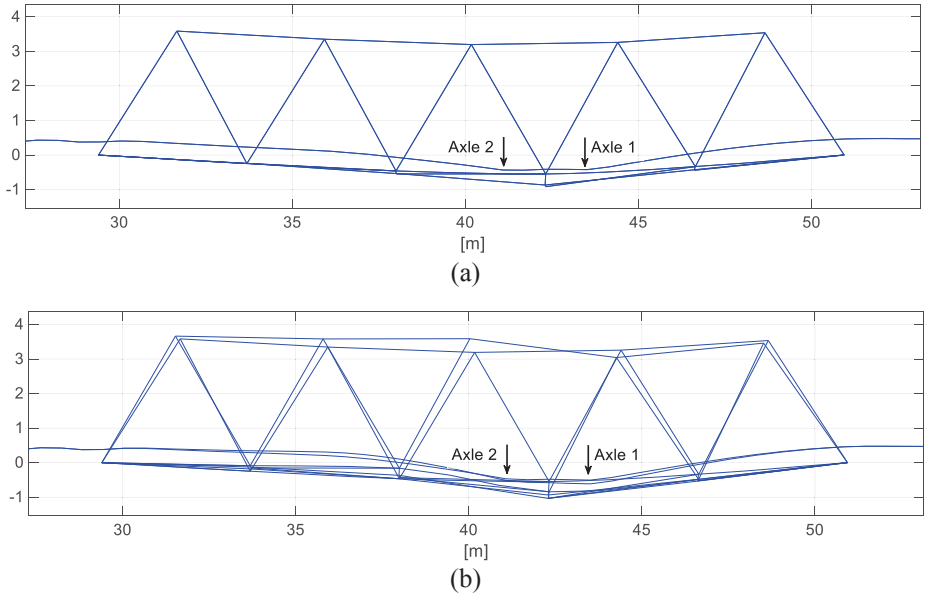

Figure 3: Bridge deflection under the train load (a) Healthy bridge. (b) Damaged bridge.

The processing algorithm consists in the application of the Continuous Wavelet Transform (CWT) to the difference of accelerations measured on the front side of the leading bogie, in correspondence of the right and left axle-boxes. The Huang-Hilbert transform was tested too on the same signal, obtaining consistent results between the two methods. Accelerations on the leading bogie are among the most suitable for diagnostic purposes, for the reason reported in [3]: the leading bogie interacts with an unperturbed bridge, so that differences in accelerations generated by a defect can be identified more precisely; bogie accelerations benefit from the filtering action provided by the primary suspension, which removes disturbances in the higher frequency range, mainly generated by track irregularities.
The possibility to detect a damage on the bridge based on the difference of right and left acceleration can be potentially affected by longitudinal and roll irregularity of the track, which may hide the presence of a damage. In order to assess the robustness of the proposed method in regard to this aspect, a different irregularity profile is adopted for left and right rails, as already described in Figure 2.
Figure 4 reports, as an example, the difference of the right and left side accelerations on the leading bogie of the CSA train at 100 km/h, corresponding to the case of total damage. A random disturbance is added to represent an electric noise, obtained from a Gaussian distribution with standard deviation equal to 10% of the RMS of the original acceleration signal. In the figure, the outer lines represent the start (continuous line) and end (dotted line) of the bridge, whereas the dashed vertical lines in the middle represent the location of the defect. The maximum magnitude of the raw signal is out of the damaged zone, and cannot be of course used as a diagnostic indicator. Wavelet coefficients are therefore computed on this signal, adopting a real-valued Morlet Wavelet.

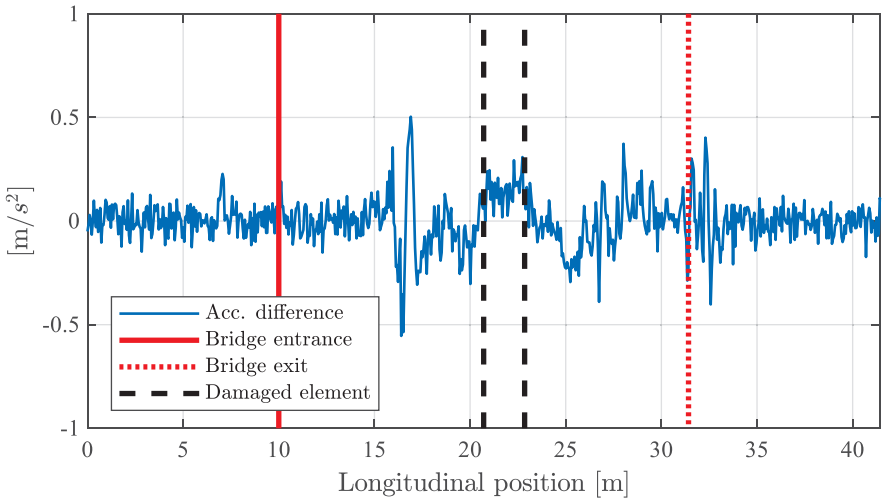

Figure 4: Difference between right and left accelerations on the leading bogie. Train speed 100 km/h.

Figure 5 reports the comparison of the module (absolute value) of the CWT coefficients in the case of the damaged bridge (Figure 5a) and of the healthy bridge (Figure 5b). The presence of the defect can be identified around the pseudo-frequency of 3.85 Hz, which corresponds to the frequency of the first peak obtained by applying a Fast Fourier Transform on the signal of Figure 4. The presence of the defect can be identified in a relatively low frequency range, where the CWT coefficients show peak values which are not present in the case of the healthy bridge. The reported results correspond to the highest level of irregularity adopted, which is the reason why several peaks in the CWT coefficients are visible at higher frequencies. With a reduction of -70% of the Young modulus of the diagonal element the damage is still clearly

identified, whereas for lower entity of the damage (e.g. reduction of 50% of the Young modulus), the presence of irregularity tends to hide the presence of a defect. The exploitability of this method is therefore a compromise between the effect induced by the defect, depending on the defect entity, and the presence of track irregularity.

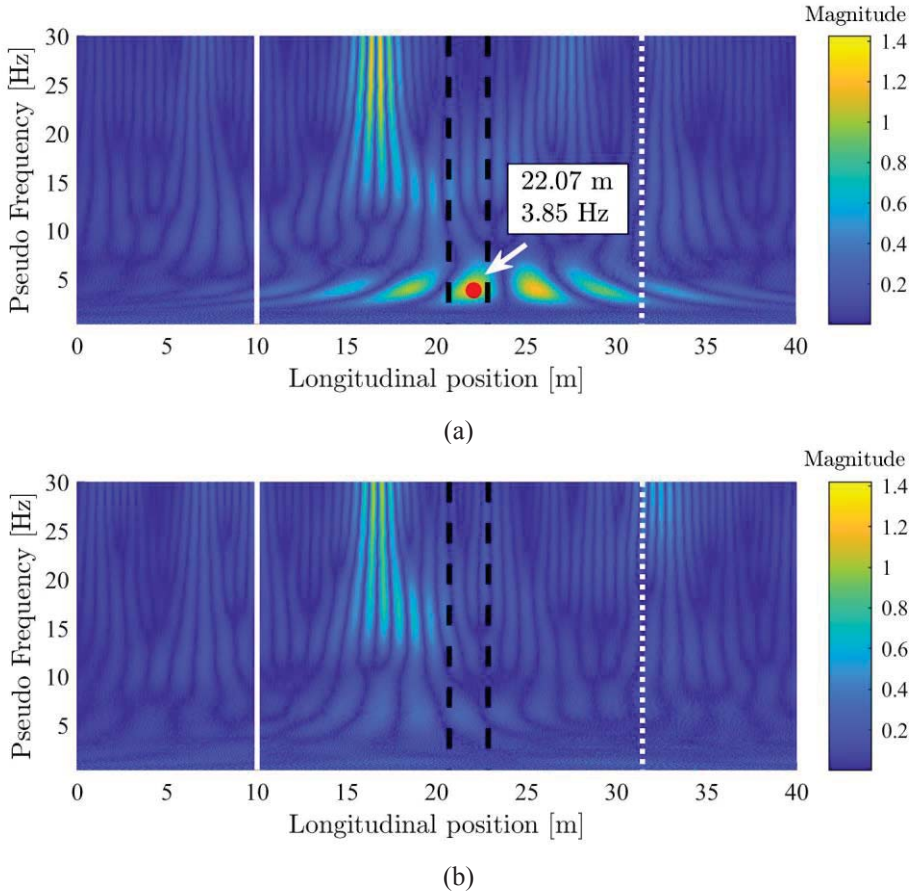

Figure 5: Module of the CWT coefficients, difference between the right and left side bogie accelerations (a) Damaged bridge, total damage. (b) Healthy bridge.

4 SIMULATION RESULTS OF MULTI-SPAN BRIDGE

The previous paragraph described the possibility to detect the presence of a relevant defect by exploiting the asymmetry in the bridge/train behavior. As a further step the case of a multi-span bridge is used to investigate the possibility of identifying a defect through the comparison of indices computed with reference to different spans. Figure 6 represents the scheme of the FEM model developed. The damaged span is highlighted by the black dashed box, whereas the remaining spans are assumed to be healthy. The damage element on span 3 is around the middle span (i.e. from 10.71 m to 12.85 m on a span length of 21.42 m).

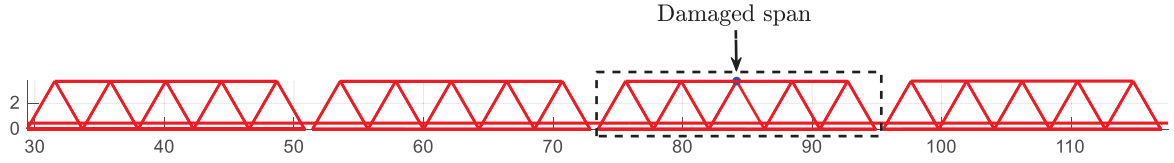

Figure 6: Lateral view of the multi-span bridge simulated.

The irregularity profile adopted is different for each span and for the left and right rails. Figure 7 represents the total irregularity profile on left and right rail, both outside and inside of the bridge area.

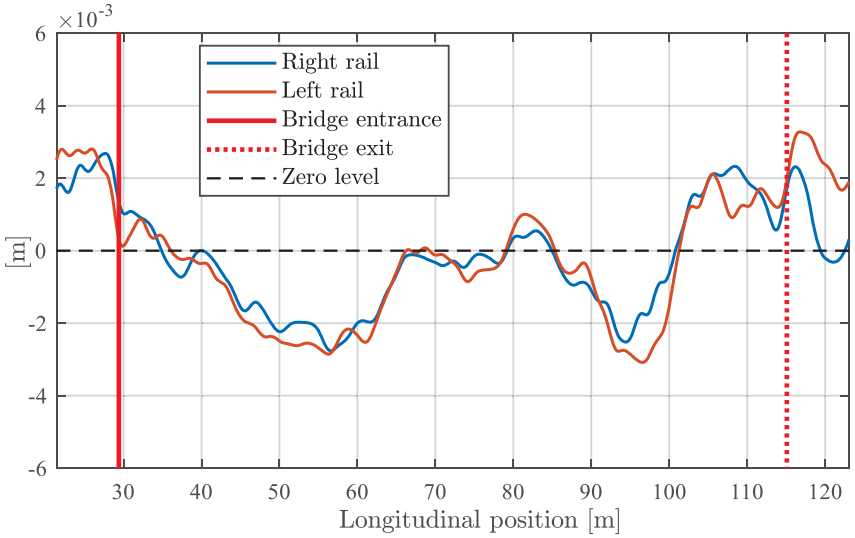

Figure 7: Total irregularity profile for left and right rail.

The acceleration data corresponding to each span can be analyzed separately, assuming to be able to separate the time histories of the four spans by the adoption of a precise GPS signal (e.g. EGNOSS). The difference between right and left bogie accelerations corresponding to each span are reported in Figure 8 for the simulation case with train speed set to 100 km/h and a total damage on the bridge. In the case of the damaged 3rd span it is possible to identify an oscillating shape, which is related to the difference between right and left side accelerations generated by the presence of the defect. The peculiarity of this signal shape can be caught by CWT.

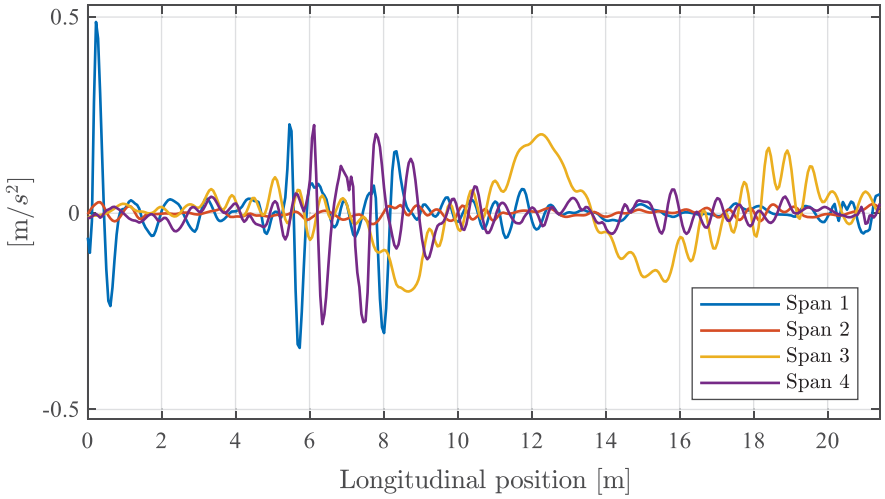

Figure 8: Front bogie accelerations difference, span from 1 to 4.

Figure 9 shows the CWT coefficients obtained with a Morlet wavelet for each single span. Once again it is possible to observe that the defect on the third span is properly caught, also by comparison with the analysis of the other spans. The defect can be properly identified for the total damage, or partial damage with a relevant reduction of the Young modulus in the diagonal element, whereas in the case of small damages it is hidden by track irregularity.

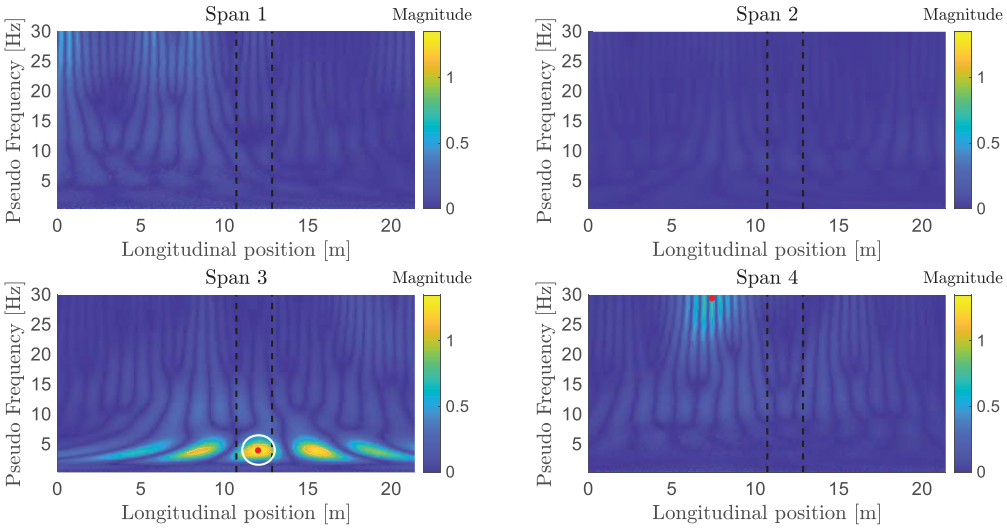

Figure 9: Module of the CWT coefficients evaluated on the difference of right and left hand side bogie accelerations (leading bogie, in correspondence of the front axle-boxes).

5 CONCLUSIONS

The paper focuses on a drive-by method for the diagnostics of railway bridges in commuter lines. It puts forward the idea that the presence of a defect on the bridge may introduce an asymmetry in the structure, which may consequently cause an asymmetry in the dynamic behavior of the train. This asymmetry can be caught by analyzing the difference between the right and left side accelerations measured on the frame of the first bogie of the train, and without the need of comparison with a baseline signal referring to the bridge in healthy condition.

The analysis is carried out through a full 3D model for the simulation of the dynamic behavior of the bridge/track/train system, in the presence of both vertical and roll track irregularity to represent a scenario close to reality. A different profile of the left and right rails may hide indeed the presence of a defect. The defect is inserted by considering the failure, or a percentage ineffectiveness, of the connection of one diagonal member of the side frame in a Warren, open type, medium-span bridge.

The difference between right and left side accelerations corresponding to the leading bogie of the train at the leading axle are analyzed through Continuous Wavelet Transform. The results show that when the simulated defect is relevant (i.e. detachment of one diagonal member in the truss bridge, or strong reduction of its Young modulus) the defect can be properly identified even with a high level of irregularity, but, for lower entities of the damage, the difference of irregularity between right and left track can hide the presence of the defect. The exploitability of this method is therefore dependent on the entity of the defect and on the severity of track irregularity.

REFERENCES

[1] Abdollah Malekjafarian, Patrick J. McGetrick and Eugene J. Obrien (2014), A review of indirect bridge monitoring using passing vehicles (2014), Hindawi Publishing Corporation Shock and Vibration Volume 2015, Article ID 286139.

[2] Amerio, L., Carnevale, M., Collina, A. Damage detection in railway bridges by means of train on-board sensors: A perspective option (2018) The Dynamics of Vehicles on Roads and Tracks, 2, pp. 1215-1220.

[3] Carnevale, M., Collina, A., Peirlinck, T. A feasibility study of the drive-by method for damage detection in railway bridges (2019) Applied Sciences (Switzerland), 9 (1), art. no. 160, DOI: 10.3390/app9010160.

[4] S. L. Davis and D. Goldberg, *The Fix We're In For: The state of our Nation's bridges 2013*, Transportation for America, Washington, DC, USA, 2013.

[5] A. Znidari c,V.Pakrashi, E.O'Brien, andA.O'Connor, "A review of road structure data in six European countries," *Proceedings of the ICE: Urban Design and Planning*, vol. 164, no. 4,pp. 225–232, 2011.

[6] Matsuoka, K., Kaito, K., Sogabe, M. Bayesian time–frequency analysis of the vehicle–bridge dynamic interaction effect on simple-supported resonant railway bridges (2020) Mechanical Systems and Signal Processing, 135, art. no. 106373. DOI: 10.1016/j.ymssp.2019.106373

[7] Y.B. Yang, C. W. Lin, and J. D. Yau, "Extracting bridge frequencies from the dynamic response of a passing vehicle," *Journal of Sound and Vibration*, vol. 272, no. 3-5, pp. 471–493, 2004.

[8] Dionysius M. Siringoringo and Yozo Fujino (2010), Estimating bridge fundamental frequency from vibration response of instrumented passing vehicle: Analytical and Experimental Study, *Advances in Structural Engineering* Vol. 15 No. 3 2012

[9] Y. B. Yang, Y. C. Li, K. C. Chang , Using two connected vehicles to measure the frequencies of bridges with rough surface: a theoretical study, Acta Mech 223, 1851–1861 (2012) DOI 10.1007/s00707-012-0671-7

[10] Chul-Woo Kim, Kai-Chun Chang, Patrick John McGetrick, Shinichi Inoue, and Souichiro Hasegawa (2017), Utilizing moving vehicles as sensors for bridge condition Screening—A Laboratory Verification, *Sensors and Materials*, Vol. 29, No. 2 (2017) 153–163

[11] R. O. Curadelli, J. D. Riera, D. Ambrosini, and M. G. Amani, "Damage detection by means of structural damping identification," *Engineering Structures*, vol. 30, no. 12, pp. 3497–3504, 2008

[12] Y. Zhang, L. Q. Wang, and Z. H. Xiang, "Damage detection by mode shape squares extracted from a passing vehicle," *Journal of Sound and Vibration*, vol. 331, no. 2, pp. 291–307, 2012.

[13] Eugene J. OBrien and Abdollah Malekjafarian A mode shape-based damage detection approach using laser measurement from a vehicle crossing a simply supported bridge, Struct. Control Health Monit. 2016; 23:1273–1286

[14] Eugene J. OBrien, Abdollah Malekjafarian, Arturo González , Application of Empirical Mode Decomposition to drive-by bridge damage detection (2017), European Journal of Mechanics - A/Solids · January 2017

[15] Fan, W., Qiao, P.Z., (2011). Vibration-based damage identification methods: a review and comparative study. Struct Health Monit 10, 83-111.

[16] Qiao, P.Z., Cao, M.S., 2008. Waveform fractal dimension for mode shape-based damage identification of beam-type structures. Int J Solids Struct 45, 5946-5961.

[17] Paraic Quirke, Cathal Bowe, Eugene J. OBrien, Daniel Cantero, Pablo Antolin, Jose Maria Goicolea , Railway bridge damage detection using vehicle-based inertial measurements and apparent profile, Engineering Structures 153 (2017) 421–442

[18] Ahmed Elhattab, Nasim Uddin, Eugene Obrien (2016), Drive-by bridge damage monitoring using Bridge Displacement Profile Difference, J Civil Struct Health Monit DOI 10.1007/s13349-016-0203-6

[19] Eugene J. OBrien, Daniel Martinez, Abdollah Malekjafarian, Enrique Sevillano Damage detection using curvatures obtained from vehicle measurements, Journal of Civil Structural Health Monitoring · July 2017

[20] Abdollah Malekjafarian, Daniel Martinez, and Eugene J. Obrien (2018), The feasibility of using laser doppler vibrometer measurements from a passing vehicle for bridge damage detection, Hindawi Shock and Vibration Volume 2018, Article ID 9385171, 10 pages

[21] David Hester & Arturo González (2015) A bridge-monitoring tool based on bridge and vehicle accelerations, Structure and Infrastructure Engineering, 11:5, 619-637, DOI:10.1080/15732479.2014.890631

[22] González, A.; Hester, D. An investigation into the acceleration response of a damaged beam-type structure to a moving force. J. Sound Vib. 2013

[23] Cathal Bowe, Paraic Quirke, Daniel Cantero, and Eugene J. Obrien , Drive-by structural health monitoring of railway bridges using train-mounted accelerometers, Conference Paper · May 2015 DOI: 10.7712/120115.3490.751

[24] David Hester, Arturo González (2017) A discussion on the merits and limitations of using drive by monitoring to detect localised damage in a bridge, Mechanical Systems and Signal Processing 90 (2017) 234–253

[25] Paul C. Fitzgerald, Abdollah Malekjafariana, Daniel Cantero, Eugene J. OBrien, Luke J. Prendergastc, Drive-by scour monitoring of railway bridges using a wavelet-based approach, Engineering Structures 191 (2019) 1–11

[26] Bruni, S.; Collina, A.; Corradi, R.; Diana, G. Numerical simulation of train-track-structure interaction for high speed railway systems, IABSE Symposium, Antwerp 2003, Belgium.

EURODYN 2020
XI International Conference on Structural Dynamics
M. Papadrakakis, M. Fragiadakis, C. Papadimitriou (eds.)
Athens, Greece, 23–26 November 2020

DAMAGE FEATURE RECOGNITION BASED ON LAMB WAVES DETECTION

Xiaohui. Wang[1], Jinhui. Liang[1], Bin. Zhang[1*], Yeping. Xiong[2] and Jun. Gao[1]

[1] School of Mechanical, Electrical & Information Engineering, Shandong University
180 Wenhuaxi Road, Weihai, China
e-mail: wangxiaohui@mail.sdu.edu.cn
liangjinhui@mail.sdu.edu.cn, bin.zhang@sdu.edu.cn, shdgj@sdu.edu.cn

[2] Faculty of Engineering and Physical Sciences, University of Southampton
Boldrewood Innovation Campus SO16 7QF, Southampton United Kingdom
y.xiong@soton.ac.uk

Keywords: Structural health monitoring, Lamb wave, Damage feature, Damage identification.

Abstract. *Owing to the superiority of lamb waves in the field of Structural Health Monitoring, the Lamb wave-based damage detection and identification technology are widely used. To determine the degree of damage, two damage feature recognitions are proposed in this paper. One is extracted from the time domain, where the lamb wave signals are processed by Hilbert Transform (HT) with the time-domain analysis. According to the law of signal attenuation, the differential signal envelope amplitude procced by the Hilbert Transform is regarded as a damage feature parameter relating to the damage size. The other one is extracted by Fast Fourier transform (FFT) in frequency domain analysis. Two characteristic parameters, the amplitude and probability density in the time domain and the signal roughness parameters in the frequency domain, are defined to characterize the damage size.*

1 INTRODUCTION

With the increase of service time, the plate structure is prone to subject all kinds of damages, such as cracks, delaminations, via holes, corrosion, inclusions, and so on[1]. The Structural Health Monitoring (SHM)[2,3] technology is commonly used in predicting and monitoring structural health conditions. Researchers have been keen to improve the accuracy of determining the damage location[4,5]. Besides the location, the damage size is another important indicator, depending on which different maintenance methods are required. For example, small damage which has little impact on the structure security can be repaired as needed; and the large damage usually needs to be repaired or replaced as soon as possible. Therefore, after confirming the damage location, the relevant characteristic parameters of the damage signal can be extracted and the type/size of the damage can be identified. It will be more beneficial to the long-term use and maintenance of the structure.

Cawley[6,7] studied the effects of notch damage in metals and delamination damage and Lamb waves in composite laminates. In 1992, Wu[8] began to use the Artificial neural network (ANN) to detect structural damage. They explored the application of neural network's self-organization and learning ability in structural damage assessment and trained neural networks to identify damage. Then ANN is widely used to judge the degree of structural damage[9,10]. To accurately identify damage characteristics, it is necessary to select the appropriate damage feature parameters for ANN training and learning. Mares[11] introduced a genetic algorithm into the damage identification and used the residual force method to realize the damage location and quantitative identification. Law[12] selected the sensitivity of wavelet packet transform component energy as damage feature parameter. Li[13] reported a damage identification method based on Lamb wave multi-feature fusion, and determined the damage type by ANN. Sun[14] used energy distribution to identify damage in the structure by ANN. It can be concluded that finding suitable damage feature parameters is the key to improve the success rate of damage recognition.

This work will extract the damage features by analyzing the data based on numerical simulation. The damage size characteristics of the time/frequency domain are analyzed and summarized.

2 ANALYSIS OF ALUMINUM ALLOY PLATE DAMAGE IDENTIFICATION

2.1. Aluminum Alloy Plate Model

The 3D finite element model of the aluminum alloy plate is built with a dimension of 800 mm in length, 800 mm in width and 1 mm in height. The material parameters of the aluminum alloy plate are shown in Table 1, eight PZT sensors are arranged as circular and uniformly distributed with a square damage on the plate. The coordinates of the damage and sensors are as shown in Table 2.错误!未找到引用源。.

Table 1. The material parameters of the aluminum alloy plate

Parameter	Unit	Value
density	kg/m^3	2750
Young's modulus	Gpa	69
Poisson's ratio	--	0.33

Table 2. The coordinate of damage and sensors

	Coordinate		Coordinate
Sensor1	(250，250)	**Sensor2**	(550，250)

Sensor3	(550, 550)	**Sensor4**	(250, 550)
Sensor5	(400, 188)	**Sensor6**	(612, 400)
Sensor7	(400, 612)	**Sensor8**	(188, 400)
Square damage	(425, 340)		

The locations of PZT sensors and damage are shown in Figure 1. Eight sensors served as an actuator to excite Lamb waves in turns while the other PZT sensors act as receivers to collect the Lamb wave signals.

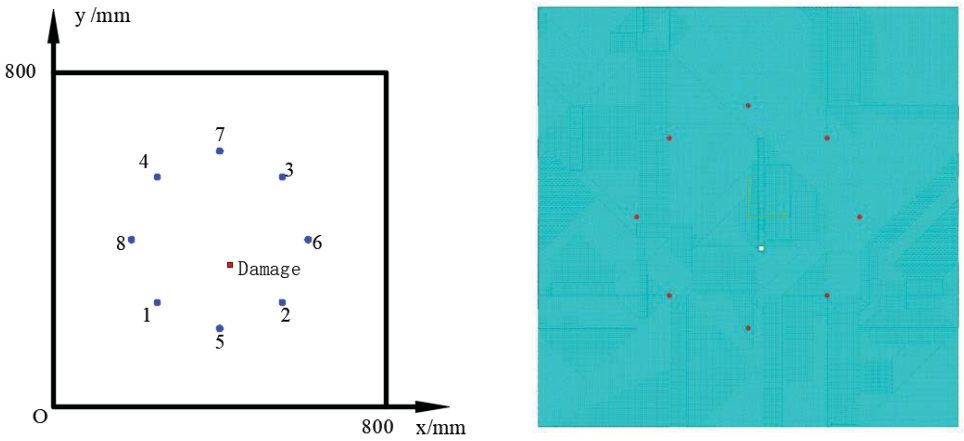

(a) (b)

Figure 1. Finite Element Model of The Aluminum Alloy Plate. (a) Sensor and damage location; (b) Simulation model

2.2. Damage Feature Extraction Based on Time Domain

As shown in Figure 2, when there is a damage in the aluminum plate, the lamb wave signal goes along with the route "exciter 1-damage-receiver 2". The reflection wave can be obtained by subtracting the non-damage signal from the damage signal.

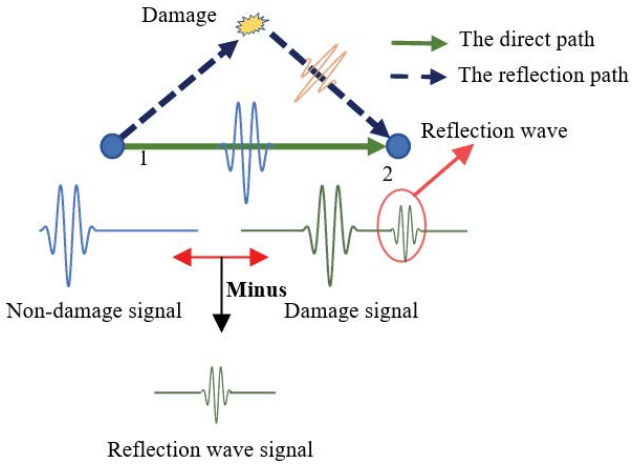

Figure 2. The propagation of damage reflection signal

Taking the square damage as an example, PZT sensor 1 excites a Lamb wave of 200KHz, and PZT sensor 2 receives that signal. The signal is shown in Figure 3.

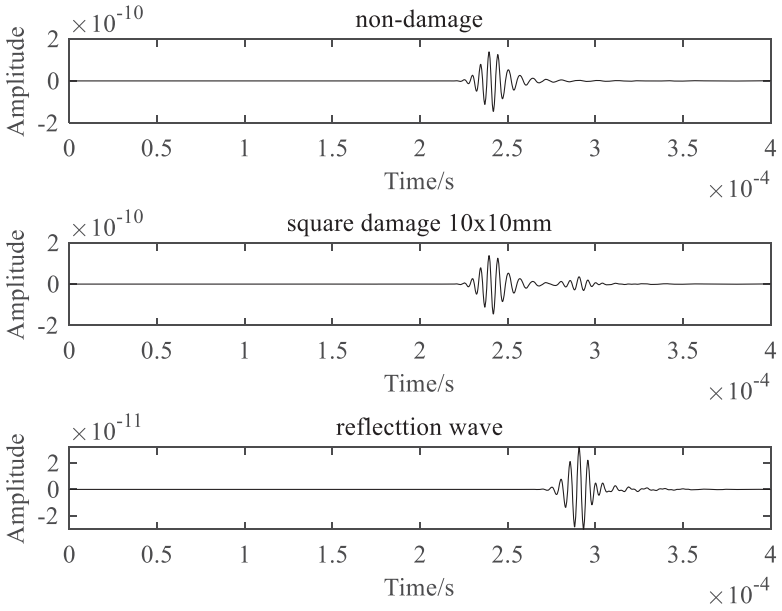

Figure 3. The damage reflection and differential signal

When a wave propagates in medium, its amplitude will gradually decrease with the increase of distance. Generally, the relationship between wave amplitude and propagation distance is

$$A = A_0 e^{\alpha D} \tag{1}$$

where, A_0 denotes the amplitude of excitation, α denotes the attenuation coefficient, and D denotes the propagation distance. To determine the coefficient of the lamb wave, the wave amplitudes in different lengths are collected in the aluminum plate, and the results are shown in Figure 4.

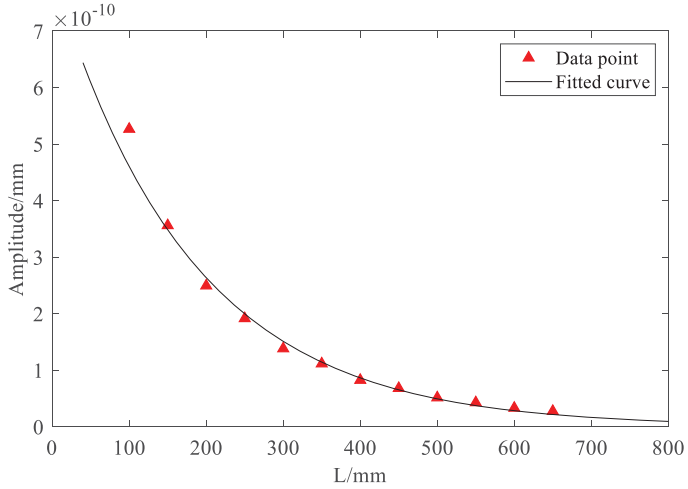

Figure 4. The attenuation of Lamb wave

By use of curve fitting, the attenuation coefficient is obtained as $\alpha = -179.1$. Then the amplitude attenuation function of the lamb wave in the aluminum plate is shown as

$$A = 8.05 \times 10^{-10} e^{\frac{-D}{179.1}} \tag{2}$$

In order to analyze the dynamic regularity of the reflected wave signal with the degree of damage, the envelope processings are performed on the difference signals of various damage size based on Hilbert Transform(HT), as shown in Figure 5-(a). It is easy to observe that the reflection wave gradually stronger as the size of the damage increases. The energy distribution feature of the signal in the time domain is represented by the HT envelope, and the damage characteristic of size is reflected by extracting the amplitude magnitude. The different sizes of damage are simulated, and the amplitude of the reflected wave signal is plotted in Figure 5-(b).

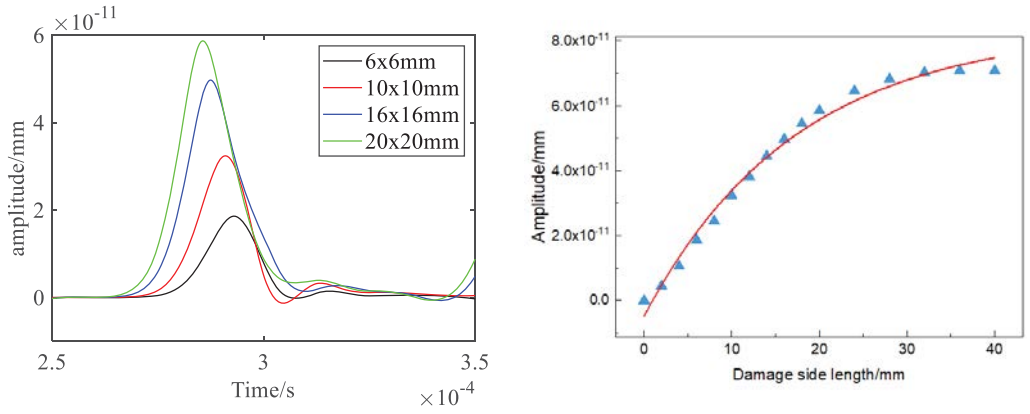

(a) (b)

Figure 5. Lamb wave feature in time domain. (a) The upper envelope of different damage size; (b) The amplitude of the envelope with different damage size

In Figure 5 (b), it can be seen that as the degree of damage increases, the amplitude of the envelope gradually increases to the upper limit value. As the spread of lamb wave energy has limits, the strength of the reflected wave also has a limit and will not increase unlimitedly. Through curve fitting, the functional relationship of the envelope amplitude along with different damage size is

$$y = 8.36\times10^{-11} - 8.83\times10^{-11} e^{\frac{-x}{17.34}} \tag{3}$$

2.3. Damage Feature Extraction Based on Frequency Domain

Based on the frequency domain analysis, the Fast Fourier transform (FFT) is used to extract the frequency domain features from the Lamb waves signal. Frequency components and amplitude characteristics of lamb wave signals are obtained to identify the damage features of an aluminum plate. The amplitude-frequency curve with different damage size are shown in Figure 6.

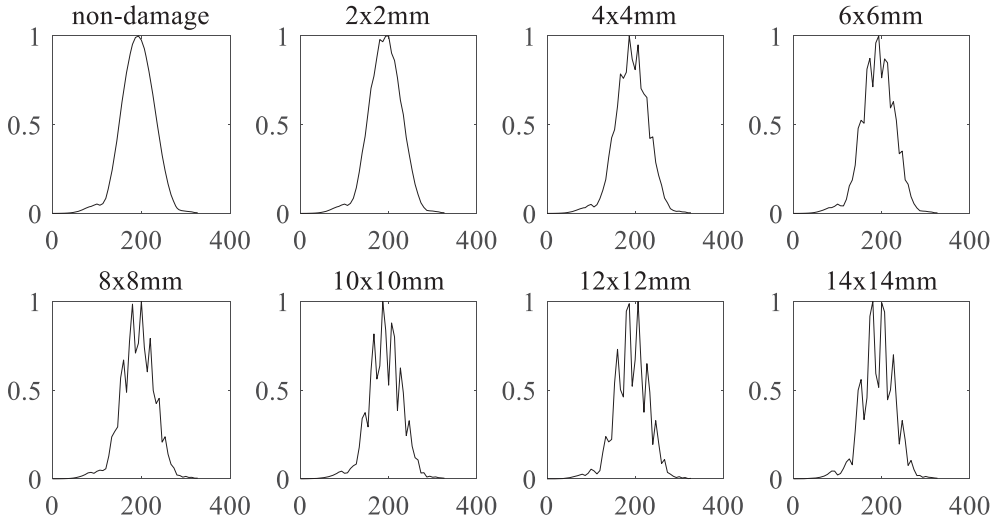

Figure 6. The frequency-domain image of different damage size

In Figure 6, as the damage size increases, the frequency range of the signal becomes decentralized. The larger the damage, the more uneven the frequency distribution. The reason is that when Lamb wave propagates to the position of damage, waveform reflection and modal conversion occur due to the sudden change of structure, which causes the waveform frequency domain signal to fluctuate. The larger the size of the damage, the higher the fluctuation, so the signal concentration level of the frequency-domain image can be used as one of the damage features for determining the damage size.

When there is no damage, the signal received by the receiving sensor is only a 200 KHz Lamb wave signal modulated by the Hanning window. The frequency-domain image of non-damage is similar to the frequency-domain figure of the excitation Lamb wave, and the frequency-domain model conforms to the law of the Hanning window rising first and then falling. Due to the existence of damage, the - reflected wave causes fluctuations in the frequency domain of the received signal. The fluctuations are closely related to the damage size. The above results in multiple frequency peaks in the signal spectrum, as shown in Figure. 5.

In order to characterize the degree of signal decentralization, the signal roughness is introduced in this paper to describe the degree of influence of impairments on frequency-domain signals. The equation of signal roughness is defined as

$$R=\sum_{i=1}^{i=n-2}\left|\frac{y_{(i+2)}-y_{(i+1)}}{\Delta x}-\frac{y_{(i+1)}-y_{(i)}}{\Delta x}\right| \tag{4}$$

where, R denotes the signal roughness and Δx represents a single increment of the frequency-domain signal, y denotes the corresponding amplitude. When the peak value or the sudden change in the graph increases, the signal roughness increases; when the signal gradually concentrates and the sudden change coefficient decreases, the signal roughness decreases.

As shown in Figure 7, the signal roughness of the frequency-domain figure increase with the expansion of damage. Therefore, the signal roughness of the frequency-domain image is a an effective damage feature indicator.

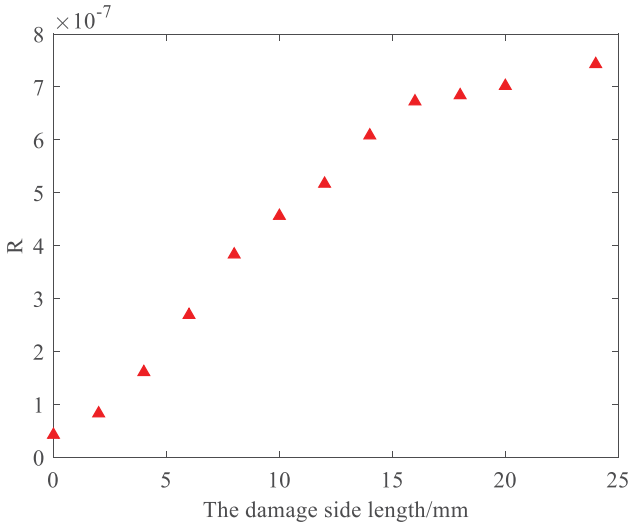

Figure 7. The signal roughness of different damage size

3 THE VERIFICATION OF THE DAMAGE FEATURE PARAMETER

To further verify the damage feature parameters' usabilities, the location of the damage changed while the transmitter and the receiver changed at the same time. As shown in Figure 8, the Lamb signal is excited by the sensor 2 and received by the sensor 3.

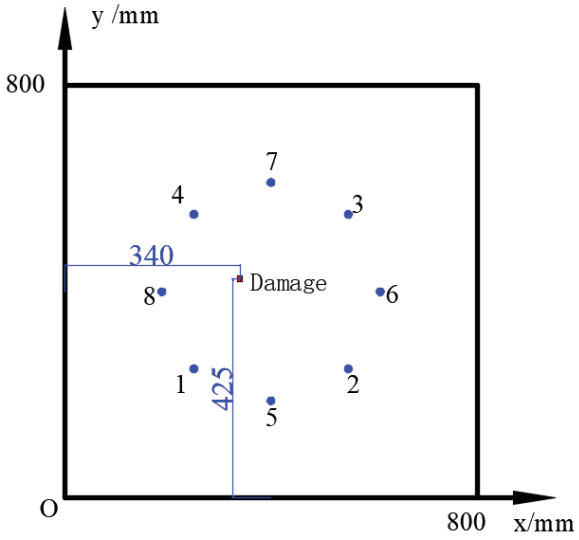

Figure 8. Change the location of the damage

When the lamb wave arrives at the damage location, according to the Huygens-Fresnel principle, the damage will become a new wave source, and the amplitude of the new wave will be lower than the arrival amplitude. The new vibration source wave amplitude is linearly related to the arrival amplitude.

The damage location is shown in Figure 1-(a) and the propagation path length of the reflected wave $L_{1\text{-}D\text{-}2}$ is 322 mm. Another damage location is shown in Figure 8 and the propagation path length of the reflected wave $L_{2\text{-}D\text{-}3}$ is 517 mm. By substituting 322 and 517 into eq. (3), the theoretical amplitude of path $L_{2\text{-}D\text{-}3}$ is 2.9 times that of path $L_{1\text{-}D\text{-}2}$. In Figure 8, the curve-fitting function in Figure 5-(b) is divided by 2.9 so we can get the relationship between the amplitude and the size of the damage as folllows:

$$A_1 = \frac{\left(8.05\times10^{-10}e^{\frac{-L}{179.1}}\right)}{2.9} \tag{5}$$

The relationship between the actual damage size and amplitude is shown in the Figure 9-(a), the simulation damage size coincides with the theoretical predictive value calculated by the eq. (5). Therefore, the amplitude of the reflected wave can be used as a parameter to characterise damagesand the damage size can be successfully predicted.

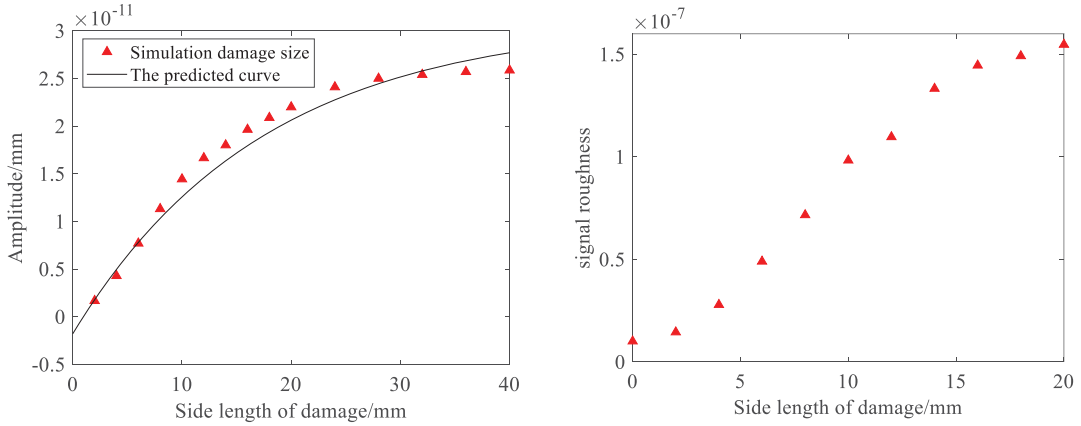

(a) (b)

Figure 9. Simulation verification results. (a) The amplitude of the envelope with different damage size by sensor 2 sensor 3; (b) The signal roughness of different damage size by sensor 2 sensor 3

In Figure 5-(b) and Figure 9-(a), it is clear that the trends of the damage size and the envelope amplitude in the two figures are consistent, which can predict the damage size through simulations. From Figure 7 and Figure 9-(b), it can be concluded that the signal roughness is an important parameter to describe the damage size.

4 CONCLUSIONS

The characteristics of the Lamb wave signal corresponding to the degree of damage are studied in this work. Two parameters are defined to describe the damage degree both in the time-domain and frequency-domain. In the time-domain analysis, the differential signal envelope amplitude extracted from the Hilbert Transform is applied as the damage feature parameter related to the damage size. In the frequency domain analysis, the signal roughness is proposed. It is used as the damage size characteristic parameter. The feasibilities of the envelope amplitude and the signal roughness are verified by numerical simulation. The identification of multiple damages using the proposed approaches is under further investigation.

5 ACKNOWLEDGMENTS:

This project is supported by the Program of National Natural Science Foundation of China (Grant No. 51805298), Natural Science Foundation of Shandong Province (ZR201807090390) and YSPSDUWH.

REFERENCES

[1] H. Yan, H. Jin, R. Yao, Prediction of the damage and fracture of cast steel containing pores. *International Journal of Damage Mechanics,* 29(1), 166-183, 2020.

[2] K. Worden, C R. Farrar, G. Manson, et al. The fundamental axioms of structural health monitoring. *Proceedings of the Royal Society A: Mathematical, Physical and Engineering Sciences*, 463(2082), 1639-1664, 2007.

[3] Y. Tang H, C. Winkelmann, W, Lestari, et al. Composite structural health monitoring through use of embedded PZT sensors. *Journal of Intelligent Material Systems and Structures*, 22(8), 739-755, 2011.

[4] N. Mori, S. Biwa, T. Kusaka. Damage localization method for plates based on the time reversal of the mode-converted Lamb waves. *Ultrasonics*, 91, 19-29, 2019.

[5] A. De Fenza, A. Sorrentino, P. Vitiello. Application of Artificial Neural Networks and Probability Ellipse methods for damage detection using Lamb waves. *Composite Structures*, 133, 390-403, 2015.

[6] N. Alleyne D, P. Cawley. The interaction of Lamb waves with defects. *IEEE transactions on ultrasonics, ferroelectrics, and frequency control*, 39, 381-397, 1992.

[7] N. Guo, P. Cawley. The interaction of Lamb waves with delaminations in composite laminates. *The Journal of the Acoustical Society of America*, 94(4), 2240-2246, 1993.

[8] X. Wu, J. Ghaboussi, H. Garrett Jr J. Use of neural networks in detection of structural damage. *Computers & structures*, 42(4), 649-659, 1992.

[9] C. Su, M. Jiang, S. Lv, et al. Improved damage localization and quantification of CFRP using lamb waves and convolution neural network. *IEEE Sensors Journal*, 19(14). 5784-5791, 2019.

[10] G. Wang. Design of damage identification algorithm for mechanical structures based on convolutional neural network. *Concurrency and Computation: Practice and Experience*, 30(24), e4891, 2018.

[11] C. Mares, C. Surace. An application of genetic algorithms to identify damage in elastic structures. *Journal of sound and vibration*, 195(2), 195-215, 1996.

[12] Law. S S, Li. X Y, Zhu. X. Q, et al. Structural damage detection from wavelet packet sensitivity. *Engineering structures*, 27(9), 1339-1348, 2005.

[13] R. Li, H. Gu, B. Hu, et al. Multi-feature Fusion and Damage Identification of Large Generator Stator Insulation Based on Lamb Wave Detection and SVM Method. *Sensors*, 19(17), 3733, 2019.

[14] D. Sun, Q. Wang, X. Xue, et al. Damage Degree Assessment Based on Lamb Wave and Wavelet Packet Transform. *2019 Chinese Control And Decision Conference (CCDC). IEEE*, 3179-3184. 2019.

EURODYN 2020
XI International Conference on Structural Dynamics
M. Papadrakakis, M. Fragiadakis, C. Papadimitriou (eds.)
Athens, Greece, 23–26 November 2020

DAMAGE ANALYSIS OF STEEL-CONCRETE COMPOSITE BEAMS UNDER STATIC LOADS

Faraz Sadeghi[1], Xinqun Zhu[1], Jianchun Li[1]

[1]Centre for Built Infrastructure Research (CBIR), School of Civil and Environmental Engineering, University of Technology Sydney (UTS), Sydney, NSW 2007, Australia

Faraz.Sadeghi@student.uts.edu.au

{Xinqun.Zhu, Jianchun.Li}@uts.edu.au

Keywords: Damage analysis, Parametric study, Composite structures, Steel-concrete composite beams, Static measurements

Abstract. *This paper presents a study of the static behavior of steel-concrete composite beams with different types of damage. Since the behavior of a composite beam under load is governed by the shear connection, it is important to investigate the overall structural response due to different levels of damage in the interface and composite layers. A finite element (FE) model of a steel-concrete composite beam is developed based on two Euler-Bernoulli beams as the composite layers coupled with a deformable shear connection. Three different damage indices are defined for the concrete slab, the steel girder, and the distributed shear connection and then embedded into the stiffness matrix of the composite beam. This model is validated by comparing its load-displacement behavior with an equivalent FE model developed using the commercial FE software ABAQUS. The impact that the loading location has on the results is then investigated. A convergence study is also carried out in terms of the displacements and strains to determine the number of composite beam FEs. The maximum displacements and strains of composite beams with different types and levels of damage are then investigated. The numerical analysis showed that after an initial reduction when the number of FEs increase, the changes in displacement and strain at each location are very small. Moreover, the bonding slip has almost no effect on the measurements, and the changes in maximum displacement and strain from undamaged to maximum damage are almost the same.*

1 INTRODUCTION

Assessing structural damage through dynamic and static analysis has become increasingly popular because the dynamic and static response of a structure are functions of its physical parameters and therefore any changes in these parameters can be reflected in the structural responses. This is why attempts have been made to evaluate the structural integrity by developing approaches based on dynamic and static measured data. Although few studies can be found in static-based methods, dynamic-based methods have been studied more widely because they are easier to implement [1, 2]. Static-based methods are based on equilibrium equations where the only significant parameter is the stiffness of a structure, which is why any reduction in stiffness due to damage is a significant parameter for damage analysis in terms of the static responses. A large number of measurements are needed to accurately analyse structural damage, which is not practical, however this problem can be solved by changing the loading locations and increasing the number of tests rather than the measurement sensors [3]. There are a number of researches into static-based methods which considered beam structures, and trusses or frames as case studies. For example, Liu and Chian [4] proposed a method to identify the elemental properties of a truss using strain values, Sanayei et al [5] used the deflection and strain data of a steel frame to estimate stiffness parameters, and Laory et al [6] used static measurements to determine the number of sensors. Wang et al [7] examined how partial shear interaction affected the static and dynamic response of steel-concrete composite structures, and found that bond slip and changes to the mode shapes are the effective parameters for identifying damage.

Different models have been developed to investigate the behaviour of steel-concrete composite structures, especially the effect of bond slip. Nie et al [8] studied the effects of bond slip on the deformation of steel-concrete composite beams using its equivalent rigidity, and found that bond slip is an effective contributor to beam deformation. Kumar et al [9] used push out test to determine how the thickness of the adhesive layer affects the capacity of composite connections. Chen et al [10] studied the static and fatigue behaviour of steel-concrete composite beams where the shear connectors had been corroded and found that the corroded studs had reduced the stiffness and load bearing capacity of the beams. Ayoub and Filippou [11] used an inelastic beam element to analyse a steel-concrete composite beam with partial interaction under cyclic loading and considered a shear connection with a distributed force as the interface model. Nguyen et al [12] used an FE model to carry out a linear static analysis of a steel-concrete composite beam with discrete shear bonding. Since no extreme loading conditions had been considered in most of the abovementioned studies, the displacements were very small and therefore the uplift effects were omitted, however, the bonding slip affects the behaviour of two-layer composite beams and must be included [12-14]. Whereas in static-based methods the displacements and/or strains are utilized to analyse structural damage, it is necessary to investigate how these parameters change in terms of different damage types.

In this paper we have developed a steel-concrete composite element with a bonding interface where the layers of concrete and steel are independently interpolated into a displacement based finite element (FE) formulation. Cases with different types of damage are introduced to describe the reduction in stiffness of a concrete slab, a steel girder, and the bonding interface. This model is verified by comparing it with the results obtained from a similar model built using the commercial FE software ABAQUS [15], where the optimal number of FEs are determined through a convergence study. A parametric study is also carried out using displacement and strain measurements. The effects that different levels of damage, and the measurements and loading locations have on the identified results are also discussed.

2 DISPLACEMENT BASED FINITE ELEMENT FORMULATION

2.1 Equilibrium and compatibility

In this section a composite beam with two layers and a deformable shear connection is formulated such that the composite beam element consists of a concrete slab on top of a steel girder with bonding interfaces (Figure 1). The equilibrium equations for each layer are formulated by considering bond slip and the effects of uplift [16]. In Figure 1 the subscripts c and s denote the concrete and steel, N, V, M and h are the axial force, shear force, bending moment, and the distance between the interface and reference axes of each layer, respectively, and D_{sc} and D_t are the shear force (bonding slip) and transverse force (uplift) per unit length. An external distributed load P is applied vertically to the concrete slab. The equilibrium equation for the composite beam section is introduced as [11]

$$\partial^T \boldsymbol{F}(x) - \partial_b^T \boldsymbol{F}_b(x) - \boldsymbol{P}(\boldsymbol{x}) = 0 \tag{1}$$

where $\boldsymbol{F}(x)$, $\boldsymbol{F}_b(x)$ and $\boldsymbol{P}(x)$ are the internal force vectors acting on the cross section, the interface bonding force, and the external load vector, respectively, and ∂ and ∂_b are the differential operators. Although any section of this composite beam has four unknown forces N_c, N_s, M and D_{sc}, there are only three equations of equilibrium for each section, so the compatibility equations should be merged to avoid any indeterminacy with the composite beam.

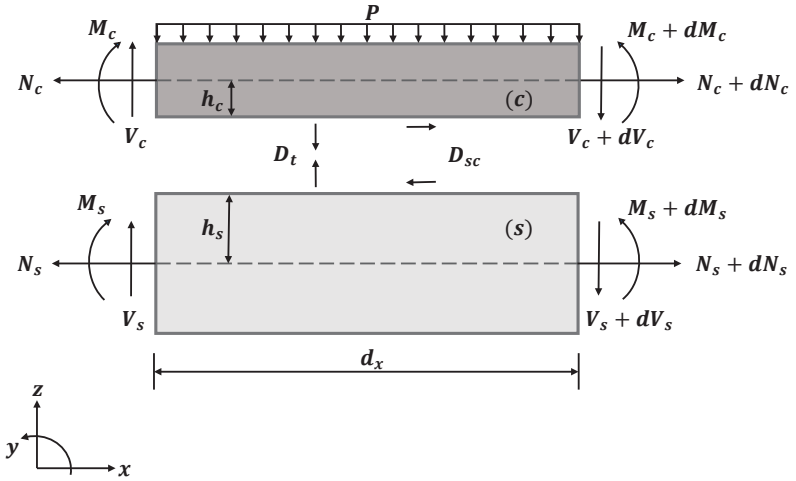

Figure 1: Diagram of a two layered composite beam element where (c) and (s) are the concrete slab and steel girder, respectively.

Since the same transverse displacement (no uplift) is considered for both layers of the composite beam, the curvature and rotation will be the same, even though different axial deformation can occur in the steel and concrete sections. The axial and transverse deformations of the composite beam are handled by the compatibility conditions based on Euler-Bernoulli beam theory. The compatibility conditions define deformation and displacement at the interface between the concrete slab and steel girder [11]. This relative displacement at the interface is known as the bond slip g and can be defined as:

$$g = u_c(x) - u_s(x) + h\partial_x v(x) \tag{2}$$

where $u_c(x)$ and $u_s(x)$ are the axial displacements of the layers of concrete and steel, and $v(x)$ is the transverse displacement. The response of the composite beam subjected to external loads can be obtained with proper boundary conditions.

2.2 Stiffness matrix

The stiffness matrices for the concrete slab, steel girder, and bonding interface are used to define the local and global stiffness matrices of the composite beam element. A continuous spring element is considered as the interface element. The axial displacements of the composite beam are estimated using quadratic polynomial functions, while the transverse displacements are obtained by cubic Hermitian polynomials [17]. Two extra nodes have been added to the middle of the concrete slab and steel girder to provide a continuous bond slip condition along the interface. The vector of elemental nodal displacement is introduced as $\boldsymbol{U} = [u_{c1} \quad u_{c2} \quad u_{c3} \quad u_{s1} \quad u_{s2} \quad u_{s3} \quad v_1 \quad \theta_1 \quad v_2 \quad \theta_2]^T$ where each component represents a degree of freedom (DOF). The composite beam element with bond slip in the interface is handled by ten DOFs including a transverse and rotation in each node, and six axial displacements (Figure 2).

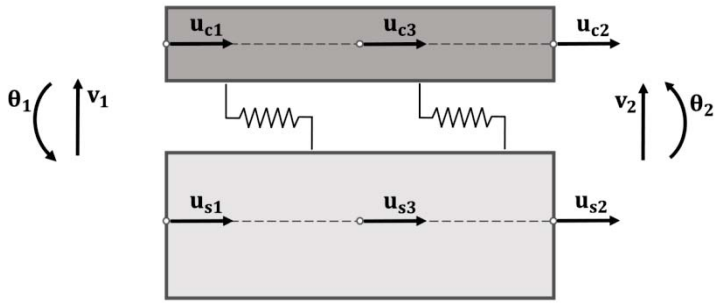

Figure 2: Nodal displacements of a steel-concrete composite element with 10 DOFs

To obtain the stiffness matrices, a small displacement due to an external load is presumed to occur and the amount of work is equal to the amount of residual internal strain energy. Therefore, the elemental stiffness matrices $\boldsymbol{k}_{ec}$ for the concrete, $\boldsymbol{k}_{es}$ for the steel sections, and $\boldsymbol{k}_{eb}$ for the bonding interface are defined as:

$$\boldsymbol{K}_e = \boldsymbol{K}_{ec} + \boldsymbol{K}_{es} + \boldsymbol{K}_{eb} = \begin{bmatrix} [\boldsymbol{K}_{e1}]_{3\times3} & [\boldsymbol{K}_{e2}]_{3\times3} & [\boldsymbol{K}_{e3}]_{3\times4} \\ [\boldsymbol{K}_{e4}]_{3\times3} & [\boldsymbol{K}_{e5}]_{3\times3} & [\boldsymbol{K}_{e6}]_{3\times4} \\ [\boldsymbol{K}_{e7}]_{4\times3} & [\boldsymbol{K}_{e8}]_{4\times3} & [\boldsymbol{K}_{e9}]_{4\times4} \end{bmatrix}_{10\times10} \tag{3}$$

where $\boldsymbol{K}_e$ is the stiffness matrix for the steel-concrete composite element.

2.3 Definition of damage

A damage index is defined as the reduction in elemental stiffness of the composite beam layers where:

$$\alpha = 1 - \frac{E}{\hat{E}} \tag{4}$$

where α is the damage index, and E and $\hat{E}$ are the equivalent Elastic modulus with and without damage, respectively. When damage index is zero, there is no damage in that element ($0 \ll \alpha \ll 1$). While the composite layers are assumed to be damaged, Eq (3) can be updated using the damage indicators as

$$\boldsymbol{K}_e = \boldsymbol{K}_{ec} + \boldsymbol{K}_{es} + \boldsymbol{K}_{eb} = (1 - \alpha_c)\widehat{\boldsymbol{K}}_{ec} + (1 - \alpha_s)\widehat{\boldsymbol{K}}_{es} + (1 - \alpha_b)\widehat{\boldsymbol{K}}_{eb} \tag{5}$$

where $\widehat{\boldsymbol{K}}_{ec}$ and $\widehat{\boldsymbol{K}}_{es}$ are the stiffness matrices of the intact concrete and steel elements, and the subscripts c, s and b denote the damage indices for the concrete, steel, and bonding interfaces. These damage indices are considered individually as scalar values embedded in the elemental damage indices zero vectors with a size that is equal to the composite element FE numbers. A transformation matrix $\boldsymbol{T}$ is used to assemble the global stiffness matrix from the local stiffness matrix presented in Eq (5) as

$$\begin{aligned} \boldsymbol{K} = \boldsymbol{K}_c + \boldsymbol{K}_s + \boldsymbol{K}_b &= \sum_{i=1}^{n} \boldsymbol{T}^T K_{ei} \boldsymbol{T} \\ &= \sum_{i=1}^{n} \boldsymbol{T}^T \boldsymbol{K}_{eci} \boldsymbol{T} + \sum_{i=1}^{n} \boldsymbol{T}^T \boldsymbol{K}_{esi} \boldsymbol{T} + \sum_{i=1}^{n} T^T \boldsymbol{K}_{ebi} \boldsymbol{T} \\ = \sum_{i=1}^{n} \boldsymbol{T}^T (1 - \alpha_{ci}) \widehat{\boldsymbol{K}}_{eci} \boldsymbol{T} + \sum_{i=1}^{n} \boldsymbol{T}^T (1 - \alpha_{si}) \widehat{\boldsymbol{K}}_{esi} \boldsymbol{T} + \sum_{i=1}^{n} \boldsymbol{T}^T (1 - \alpha_{bi}) \widehat{\boldsymbol{K}}_{ebi} \boldsymbol{T} \end{aligned} \tag{6}$$

where n is the number of FEs. $\boldsymbol{K}$, $\boldsymbol{K}_c$, $\boldsymbol{K}_s$ and $\boldsymbol{K}_b$ are the global stiffness matrices of the damaged composite beam, concrete, steel and interface elements, and α_{ci}, α_{si} and α_{bi} are the ith element damage indices of damaged concrete, steel and bonding interfaces, respectively.

3 RESULTS AND DISCUSSION

3.1 Validation of the finite element model

The structural model used in this study is a simply supported 6m long steel-concrete composite beam with a concrete slab sitting on top of an I-shape steel girder with shear connectors. The Young's modulus and density of the concrete and steel are $E_c = 3200\,MPa$, $\rho_c = 2700\ kg/m^3$, $E_s = 210000\,MPa$ and $\rho_s = 7800\ kg/m^3$, respectively. The geometrical characteristics of the beam are shown in Figure 3.

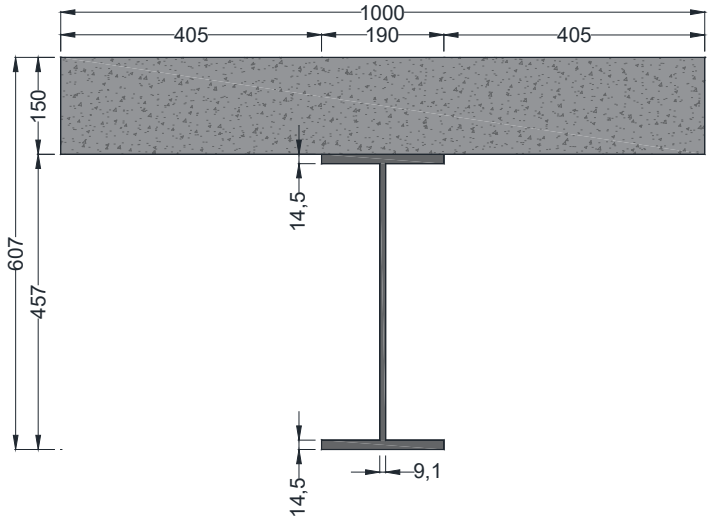

Figure 3: The geometrical characteristics of steel-concrete composite beam cross-section (length in mm)

To develop a reliable baseline FE model that could represent the real structure of interest, two equivalent FE models are constructed and their static response are compared. To this end an FE model of the steel-concrete composite beam is modelled by FE programming in MATLAB. This model is used for the damage identification in terms of different static loading locations, bond interactions, and damage cases. However, to obtain the baseline model, no damage and bond slip are considered in the analysis. Besides, another FE model with the same material and geometrical properties is built using the FE software ABAQUS, as shown in Figure 4.

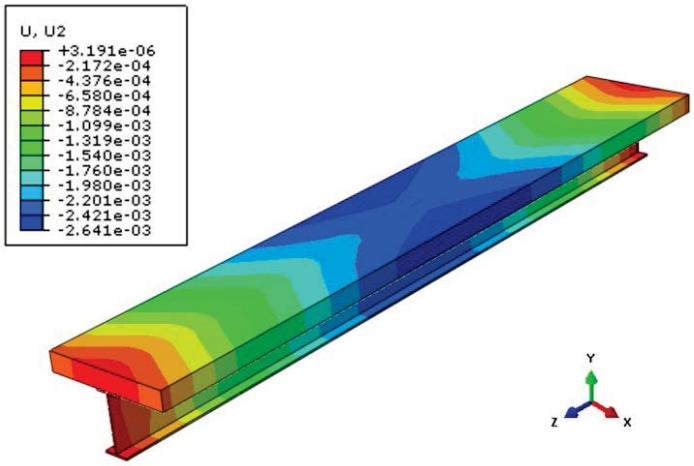

Figure 4: The FE model of steel-concrete composite beam showing displacements along the beam subjected to mid-span point loads

In each case the structure is subjected to a static load where $P = 10000\ N$ at the middle of the beam, and then at $L/3$ from the left support; the analytical displacements are measured from 60 points located equally along the composite beam. The validity of this analysis is enhanced by analysing five models with 12, 24, 36, 48 and 60 FEs for each case and then the displacements due to static loadings are used to compare the two FE models. Table 1 shows the maximum displacements of the steel-concrete composite beam obtained from the FE models developed in MATLAB (FE-M) and ABAQUS (FE-A). These displacements are almost the same for both models, showing how precise the FE model developed is by being programmed in MATLAB.

Measurement		Maximum Displacements				
Number of FEs		12	24	36	48	60
Load applied at L/2	FE-M	$2.89\text{x}10^{-3}$	$2.64\text{x}10^{-3}$	$2.60\text{x}10^{-3}$	$2.58\text{x}10^{-3}$	$2.57\text{x}10^{-3}$
	FE-A	$2.65\text{x}10^{-3}$	$2.64\text{x}10^{-3}$	$2.63\text{x}10^{-3}$	$2.62\text{x}10^{-3}$	$2.61\text{x}10^{-3}$
Load applied at L/3	FE-M	$2.46\text{x}10^{-3}$	$2.27\text{x}10^{-3}$	$2.23\text{x}10^{-3}$	$2.22\text{x}10^{-3}$	$2.21\text{x}10^{-3}$
	FE-A	$2.45\text{x}10^{-3}$	$2.26\text{x}10^{-3}$	$2.24\text{x}10^{-3}$	$2.21\text{x}10^{-3}$	$2.21\text{x}10^{-3}$

Table 1: Maximum displacements (in m) measured from the numerical models in MATLAB (FE-M) and ABAQUS (FE-A)

The differences between the maximum displacements for the model with 12 FEs are greater than those with smaller sized mesh. A convergence study has been carried out using the FE-M in terms of different numbers of FEs, where the FEs are changed from 6 to 60 and the displacement and strain values are measured.

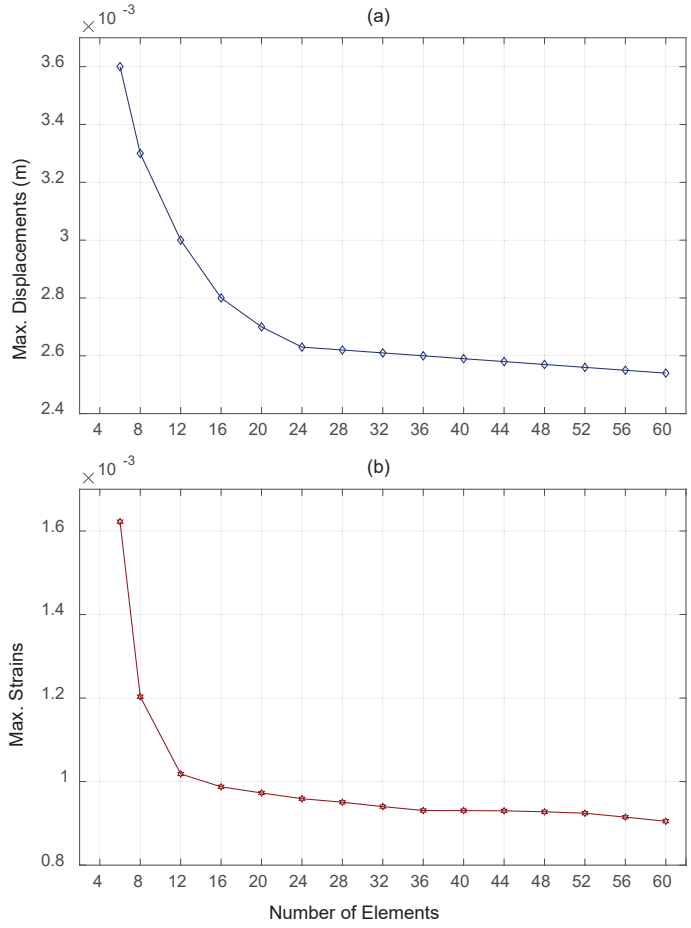

Figure 5: Convergence of maximum (a) displacement, and (b) strain in terms of the number of FEs

Figure 5 shows the convergence of maximum displacement and strain in terms of the number of FEs. While these maximum displacements and strains gradually improve by increments with the number of FEs, in both cases there is an immediate reduction in the models with FE numbers from 6 to 20. Furthermore, since the discrepancies of the model with 24 FEs are very small, 24 elements are used in the following studies.

3.2 Parametric study

A series of parametric studies based on the static responses of the beam have been carried out, and the behavior of the composite beam has been investigated for potential damages in terms of variations in static parameters such as displacement and strain. The parameter that best identifies damage is then selected. The parametric analysis is based on the displacements and strains of the composite beam for six different cases. This consists of three cases of single damage in concrete, steel and interface, two cases of double damage in the concrete-interface, and steel-interface, and one case of triple damage in the concrete-steel-interface. These cases are introduced as a reduction in the stiffness of an element in the composite beam.

Figure 6 shows the changes of maximum displacement and strain of the composite beam with 24 FEs in terms of different cases of damage and reductions in stiffness. Elements number 4 from the support on the left hand side of the composite beam have been considered as the damaged ones and a range of reduction in stiffness is applied from 0% to 90%. The static responses of the composite beam have been obtained for six different cases of damage in ten steps

of the stiffness reductions (intact to maximum damage). Although the maximum displacements increase when the stiffness decrease, these values are very small, particularly in the case of bonding loss. The discrepancies in the strains are almost zero for cases with a loss of bonding. Since the main objective is to analyse the damage on the bonding interface, the case with a single damage on the interface (Case 3 in Figure 6) is used to select the proper parameter. It is found that the loss of bonding interface results a minimum change in the maximum displacement (Figure 6.a) and strain (Figure 6.b) from undamaged to maximum damaged states. Therefore, in order to a reliable damage identification, both parameters could be used because their changes are almost the same.

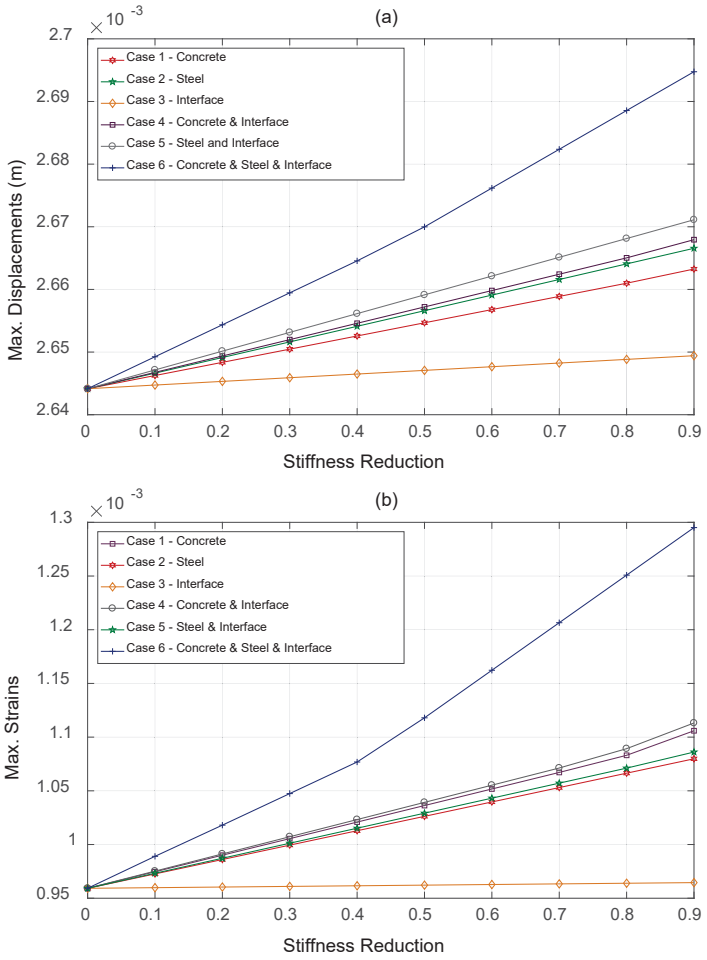

Figure 6: The changes of maximum (a) displacements and (b) strains of the beam with 24 FEs due to reductions in stiffness (from 0% to 90%) in Elements 4 for single damage (cases 1, 2 and 3), double damage (cases 4 and 5), and triple damage (case 6)

4 REVIEW

Peer review under the responsibility of the Scientific committee of Eurodyn 2020.

5 CONCLUSION

In this paper, a numerical analysis of various cases of structural damage has been carried out on a steel-concrete composite beam subjected to static loadings. An FE model of the composite beam is developed by incorporating a distributed shear connection, and then different damage

indices have been embedded into the stiffness matrix of the beam. The results indicate that the model is reliable because the displacements are acceptable in terms of different load locations with a similar FE model built from the commercial FE package ABAQUS. The convergence study established to determine the optimal number of FEs for the composite beam indicates that the discrepancies in the displacements and strains after the model with 24 FEs are very small, and therefore 24 elements are used in the numerical analysis. The maximum displacements and strains in the beam in various cases are also investigated and compared. It is found that the maximum displacements and strains at each loading location remain constant after an initial reduction when the number of FEs increase. Moreover, the bonding slip does not impact the measurements very much, and the change of maximum displacements and strains from undamaged to maximum damage are almost the same.

REFERENCES

[1] Farrar CR, Doebling SW, Nix DA, Vibration–based structural damage identification, *Philosophical Transactions of the Royal Society of London A: Mathematical, Physical and Engineering Sciences*, 359:131-49, 2001.

[2] Fan W, Qiao P, Vibration-based damage identification methods: a review and comparative study, *Structural Health Monitoring*, 10:83-111, 2011.

[3] Choi I-Y, Lee JS, Choi E, Cho H-N, Development of elastic damage load theorem for damage detection in a statically determinate beam, *Computers & Structures,* 82:2483-92, 2004.

[4] Liu P-L, Chian C-C, Parametric identification of truss structures using static strains, *Journal of structural Engineering*, 123:927-33, 1997.

[5] Sanayei M, Imbaro GR, McClain JA, Brown LC, Structural model updating using experimental static measurements, *Journal of structural engineering*, 123:792-8, 1997.

[6] Laory I, Hadj Ali NB, Trinh TN, Smith IF, Measurement system configuration for damage identification of continuously monitored structures, *Journal of Bridge Engineering*, 17:857-66, 2012.

[7] Wang Y, Hao H, Damage identification of slab–girder structures: experimental studies, *J Civ Struct Health Monit*, 3:93-103, 2013.

[8] Nie J, Cai CS. Steel–concrete composite beams considering shear slip effects, *Journal of Structural Engineering*, 129:495-506, 2003.

[9] Kumar P, Patnaik A, Chaudhary S, Effect of bond layer thickness on behaviour of steel-concrete composite connections, *Engineering Structures*, 177:268-82, 2018.

[10] Chen J, Zhang H, Yu Q-Q, Static and fatigue behavior of steel-concrete composite beams with corroded studs, *Journal of Constructional Steel Research*, 156:18-27, 2019.

[11] Ayoub A, Filippou FC, Mixed formulation of nonlinear steel-concrete composite beam element, *Journal of Structural Engineering*, 126:371-81, 2000.

[12] Nguyen Q-H, Hjiaj M, Guezouli S, Exact finite element model for shear-deformable two-layer beams with discrete shear connection, *Finite Elements in Analysis and Design*, 47:718-27, 2011.

[13] Henderson I, Zhu X, Uy B, Mirza O, Dynamic behaviour of steel-concrete composite beams retrofitted with various bolted shear connectors, *Engineering Structures*, 131:115-35, 2017.

[14] Henderson IEJ, Zhu XQ, Uy B, Mirza O, Dynamic behaviour of steel–concrete composite beams with different types of shear connectors, Part I: Experimental study, *Engineering Structures,* 103:298-307, 2015.

[15] ABAQUS. Online documentation help, theory manual: Dassault Systems. V. 6.14 edAccessed on; 2016.

[16] Adekola A, Partial interaction between elastically connected elements of a composite beam, *International Journal of Solids and Structures*, 4:1125-35, 1968.

[17] Amadio C, Fragiacomo M, A finite element model for the study of creep and shrinkage effects in composite beams with deformable shear connections, *Costruzioni Metalliche*, 4:213-28, 1993.

EURODYN 2020
XI International Conference on Structural Dynamics
M. Papadrakakis, M. Fragiadakis, C. Papadimitriou (eds.)
Athens, Greece, 23–26 November 2020

SEISMIC STRUCTURAL HEALTH MONITORING FOR REDUCING LIFE CYCLE COST OF ROAD BRIDGES

Michela Torti[1], **Ilaria Venanzi**[1], **and Filippo Ubertini**[1]

[1]Department of Civil and Environmental Engineering of University of Perugia
Via G. Duranti, 93, 06125 Perugia, Italy
e-mail: michela.torti@collaboratori.unipg.it
e-mail: {ilaria.venanzi,filippo.ubertini}@unipg.it

Keywords: Seismic structural health monitoring, life-cycle cost analysis, seismic hazard curve, sensitivity analysis.

Abstract. *Recent dramatic bridge collapses worldwide have drawn a significant attention on the problem of ageing infrastructural network and highlighted the main failure causes of bridge structures, namely: decay of the mechanical properties due to ageing, increase of traffic loads, subsidence of the soil, earthquakes, and more. Road managers have the great need of acquiring the largest possible information regarding the current health state of the transportation networks that are typically dated and huge in terms of number of bridges. Nowadays, this knowledge is gained through planned inspections to be performed on individual bridges. However, in countries where the seismic risk is high, a special attention must be paid to the seismic response of bridges, as they often constitute the most sensitive and strategic structures for the management of post-earthquake emergencies. Visual inspections are still the most used class of tools to assess the health state of structures after an earthquake. Several efforts have been made to carry out surveys and obtain updated databases on the conditions and the seismic performances of bridges; other efforts have been made to develop automatic procedures for the classification of intervention priorities after seismic events, based on rapid analysis and simplified evaluation forms. The use of seismic structural health monitoring (S^2HM) systems installed on the structure can be an excellent solution to these problems. S^2HM systems allow reducing the uncertainties affecting the assessment of the planned maintenance and allow important economic savings. The present paper proposes a novel methodology for calculating the life cycle costs of road bridges equipped with S^2HM systems. Cost analyses are carried out considering seismic scenarios of the same duration as the life span of the structure, generated through Monte Carlo simulations, based on the mean annual rate values obtained by sampling the seismic hazard curves. The procedure allows to quantify the benefits in terms of structural reliability offered by the S^2HM system, and provides knowledge on the economic advantages of the use of S^2HM that allows avoiding unnecessary traffic closures and interruptions. The cost model allows to investigate the influence of the seismic monitoring systems on life-cycle cost of bridges and to highlight the most sensitive aspects in order to obtain a significant economic return, such as site seismic hazard and lifetime.*

1 INTRODUCTION

The life cycle management of the roadway bridges network is organized with long term plannings of scheduled inspection and maintenance (I&M) that may be defined as ordinary ones. Since these operations are forseen by the design phase of the structure, their execution costs are computable. Ordinary inspections consist of control activities of the global and/or local structural safety made at fixed ranges of time [1, 2]. An Italian regulation from the ministry of public works regarding bridges inspections [3] imposes the obligation to carry out quarterly visual inspections by technicians and more detailed annual visual inspections by engineers. The scopes are to monitor and to update the knowledge of the current health state of the bridges over time in order to perform different levels of ordinary maintenance in time [4]. Ordinary I&M allows proper safety levels regarding the degradation phenomena. Therefore, the maintenance costs can be defined in terms of excpected values, namely as function of a probability of failure [5]. Moreover, to ordinary I&M costs, post-event inspection and maintenance operations (extraordinary I&M) costs must be added. The main Italian road network manager, Anas S.p.A., adds in-depth inspections through the use of special means, such as using an inspection platform, and the execution of non-destructive tests, to be carried out after extraordinary events and, in particular, after earthquakes of sufficiently large intensity. On one hand, extraordinary I&M can produce significant inconvenience to drivers, as disruption and/or diversion of traffic for the time necessary to carry out the operations. On the other hand, post events operations are the most expensive ones due to the uncertainties regarding the damage detection and localization.

Recently, several strategies of post-seismic emergency management were proposed in order to provide priority I&M operations classification methods. O'Reilly [6] and Borzi [7] proposed upadated databases and seismic risk maps for the bridges based on fragility curves to support decision making. Limongelli [8] provided a method based on the value of information of the visual inspections.

In this paper, the use of the results provided by the monitoring system during an earthquake as tool to manage the inspection operations of the monitored bridges is proposed. A life cycle cost model able i) to compute the cost of the post-event operantions when the S^{2}HM data are available [9] and ii) to quantify the obtained gain in comparison to traditional post-seismic emergency strategies is introduced. The results of the cost model application to a case study bridge by Monte Carlo simulations of the seismic scenarios and structural responses are shown. The simulation process allows to compare the total cost values for different strategies by quantitative assessments, in order to quantify the economic benefits and to highlight the most sensitive parameters. In the paper, the effects on the results of seismic hazard and lifetime are investigated.

2 S^{2}HM AND POST-EVENT INSPECTION STRATEGY

The process of implementing the damage detection strategy regarding the structural seismic risk can be defined as Seismic Structural Health Monitoring [10]. The S^{2}HM system operating principle can be different according to the monitored seismic phase [11]: i) before the event, the system processes and stores a huge quantity of data, ii) during the event, the system must be able to record the typical phenomena as exceedence drift, and, finally, iii) after the event, the system must highlight potential behavior anomalies. Each phase requires different architecture features of the system according to the specific purpose.

In this paper, S^{2}HM refers to threshold monitoring systems able to control the structural response during an earthquake and to report it to bridge managers in terms of values above or

below a performance threshold. These values can be used as health state markers of the monitored bridge components. Indeed, each threshold parameter is related to a specific limit state and, hence, to different emergency management activities, such as disruption and/or diversion of traffic, inspections and maintenances. The threshold selection is a prerogative of managers and experts on the basis of i) accuracy of the theoretical/experimental evaluation of the monitored parameters, ii) safety level to ensure, and iii) reliability of the monitoring system result.

In this work, only the ispections operations are managed by seismic monitoring results. Therefore, a condition-based post-event inspection strategy can be defined, and, according to it, the control operations on the bridge components for which an alert is supplied by S^{2}HM are carried out. The strategy is outlined by the following steps:

1) Select the limit states of the bridge to monitor (bearing failure, pier bending, etc.);

2) Identify the level of each limit state (flexural, concrete spalling, bar yelding, ultimate strength, etc.), hereinafter referred to as Damage State DS;

3) Choose and compute the values of damage parameters (pier drift, pier tilt, etc.) and the threshold values referred to the selected DS;

4) Set up the suitable S^{2}HM system to monitor the damage parameter during the eartquake;

5) Outline the extraordinary inspections referred to the exceedance of the DS.

3 LCCA FOR S^{2}HM

The life cycle cost analysis (LCCA) evaluates the total economic benefit of a structure by analyzing initial and discounted future costs [12]. Therefore, the total life cycle cost of a bridge can be defined as the sum of three cost groups: initial, management and final costs. The proposed classification follows the common practice to carry out cost analyses in terms of equivalent present value [12, 13] and, on the other hand, the need to separate the terms supposed as deterministic to the terms affected by uncertaintes and, therefore, described as expected values.

The initial costs, $C_{0,\mathrm{b}}$, include all cost items performed within the year "zero" and, hence, considered as current values. The management costs involve the activities to preserve the performance of the work and all its components. For bridges, the inspection costs, C_{I}, and the maintenance costs, C_{M}, represent the main contributions and, moreover, they must be expressed in terms of expected value, time cumulative and discounted at current value. The last group is the cost of disposal, C_{D}, of the structure at the end of its lifetime to be expressed in terms of present value.

The presence of the monitoring system affects the cost terms at the different stages of the life cycle. First, the initial purchase and installation cost, $C_{0,\mathrm{SHM}}$, and the SHM system management cost, C_{SHM}, must be added to the initial costs and to the discounted future costs, respectively. Hence, the expected total life-cycle cost of a bridge equipped with a seismic monitoring system can be expressed as follows [14]:

$$E[C(t_{\mathrm{L}})]|_{\mathrm{SHM}} = C_{0,\mathrm{b}} + C_{0,\mathrm{SHM}} + \sum_{t=1}^{t_{\mathrm{L}}} \frac{E[C_{\mathrm{SHM}}(t)] + E[C_{\mathrm{I}}(t)]|_{\mathrm{SHM}} + E[C_{\mathrm{M}}(t)]|_{\mathrm{SHM}}}{(1+r)^t} + \\ + \frac{C_{\mathrm{D}}(t_{\mathrm{L}})}{(1+r)^{t_{\mathrm{L}}}} \quad (1)$$

where t_{L} is the lifetime of the bridge expressed in years, $E[.]$ is the expected value of the considered entity, and r is the discount rate.

In a condition-based post-event inspection strategy, the inspection costs at time t can be defined as:

$$E[C_{\mathrm{I}}(t)]|_{\mathrm{SHM}} = \sum_{l=1}^{L(t)} n_{\mathrm{I},l}(t) c_{\mathrm{I},l}^{\mathrm{ord}} + \sum_{n=1}^{N} p_{\mathrm{I},n}^{\mathrm{SHM}}(t) c_{\mathrm{I},n}^{\mathrm{extra}} \tag{2}$$

where L is the total number of ordinary inspection operation types; $n_{\mathrm{I},l}$ the number per year of l-type ordinary inspection; $c_{\mathrm{I},l}^{\mathrm{ord}}$ the l-type ordinary operation, N is the total number of possible extraordinary inspection types (equal to the number of limit states that the monitoring system can detect), $p_{\mathrm{I},n}^{\mathrm{SHM}}$ is the probability that the monitoring system detects the n-th type of damage, $c_{\mathrm{I},n}^{\mathrm{SHM}}$ is the respective inspection cost.

The probability term in Eq. (2), $p_{\mathrm{I},n}^{\mathrm{SHM}}$, is the product of the probability of exceedance of the n-type of Damage State DS_n conditional on the occurrence of an earthquake, IM, and the probability of exceedance of the earthquake in one year:

$$p_{\mathrm{I},n}^{\mathrm{SHM}} = P(DS_n \cap IM) = P(DS_n|IM) \cdot P(IM) \tag{3}$$

When in the design phase, seismic monitoring system data are not available, the expected value of the inspection cost at time t, $E[C_{\mathrm{I}}(t)]$, is again the sum of the costs of ordinary and extraordinary operations, but the probability term corresponds to the probability of occurrence of a seismic event in one year [15]:

$$p_{\mathrm{I}} = P(IM) = 1 - e^{-\lambda} \tag{4}$$

where λ is the annual frequency of exceedance of the event IM, taken from the hazard curve and according to the Poisson distribution.

In order to evaluate the economic gain of the novel post-event inspection strategy compared to the traditional approach, the following cost formulas are considered in the simulation process, for the cases with and without SHM system respectively:

$$E[C(t_{\mathrm{L}})]|_{\mathrm{SHM}} = C_{0,\mathrm{b}} + C_{0,\mathrm{SHM}} + \sum_{t=1}^{t_{\mathrm{L}}} \frac{E[C_{\mathrm{SHM}}(t)] + E[C_{\mathrm{I}}(t)]|_{\mathrm{SHM}}}{(1+r)^t} \tag{5}$$

$$E[C(t_{\mathrm{L}})] = C_{0,\mathrm{b}} + \sum_{t=1}^{t_{\mathrm{L}}} \frac{E[C_{\mathrm{I}}(t)]}{(1+r)^t} \tag{6}$$

The comparison is performed in terms of economic gain, G, defined as the difference of the cumulative cost at t_{L} year between the condition-based and the traditional strategies:

$$G = E[C(t_{\mathrm{L}})] - E[C(t_{\mathrm{L}})]|_{\mathrm{SHM}} \tag{7}$$

and in terms of economically viable cases, n_{evc}, defined as the of number cases for which G is positive, over the total number of simulations, n_{tot}:

$$n_{\mathrm{evc}} = \frac{n_{\mathrm{G>0}}}{n_{\mathrm{tot}}} \tag{8}$$

All inspection costs, ordinary and extraordinary, include both operations direct costs and indirect costs [5] associated with the cost of fatalities and accidents [16], and the traffic delay [13], caused by the operations.

4 SIMULATION METHODOLOGY

In order to apply the described cost model to a case study, a multi-step simulation process is developed. The gaol is to quantify in *occurred*, equal to 1, or *not occurred*, equal to 0, the probability terms of Eqs. (3) and (4) by Monte Carlo simulations.

The starting point of the simulation methodology consists in the realization of seismic scenarios, namely the time distributions of seismic significant intensity events, consistently with the site seismic hazard [4]. The procedure consists of:

1.a) Seismic site hazard curve (PGA-λ) sampling: selection of the number I and PGA_i intensity of the seismic events of interest and evaluation of the corresponding annual frequency of exceedance, λ_i;

1.b) Generation of a sample, of statistically significant size N_{I}, of the random vector $\bar{\mathbf{T}}$ of the I uncorrelated random Earthquakes, IM_i, with Poisson distribution, mean λ_i and intensity PGA_i respectively. Thus, a matrix $I \times N_{\mathrm{I}}$ is the genereted sample where the i-th row represents the distribution on N_{I} years of the arrival times t_{PGA_i} of the i-th earthquake;

1.c) Random extraction of t_{L}-long time windows (seismic scenarios) from the previous matrix. The overlapping of the rows of the resulting $I \times t_{\mathrm{L}}$ matrices represents the time distribution of the seismic events in the interval t_{L}.

The other phases of the multi-step simulation process are:

2) Realization of a Finite Element (FE) model of the case study bridge;

3) Application to the model of accelerograms with PGA_i consistent with the analyzed seismic scenario;

4) Seismic system response relative to each seismic event, namely accelerograms, and comparison with the thresholds DS_n, as described in Sections 2 and 3.

5 CASE STUDY APPLICATION

The results of the life cycle cost analysis according to the proposed cost model in Section 3 are necessarily influenced by the initial parameters, such as input data (examined bridge and site, etc.) and design features (thresholds and inspection operations definition, etc.).

5.1 Case study bridge and S^{2}HM system

The investigated bridge is a continuous steel-concrete composite bridge. It consists of 10 different size spans for a total length of 574 m; the cross-section is made by two I-shaped steel girders and a 32 cm thick concrete slab, and the RC piers have different heights with a bi-hollow rectangular cross-section.

Regarding the condition-based post-event inspection strategy described in Section 2, the following assumptions are made:

1) Limit states: bending of the 10 piers of the bridge;

2) Damage States: cracking and bar yelding of the bottom section of each pier;

Table 1: Comparison of inspection strategies

Strategy	**Type**	**Frequency**
Condition-based post-event inspection	Ordinary level-1 $C_{\text{I-O. level-1}}$	3 months [3], Post-earthquake when $\%\delta_{\text{y},i} \leq \delta_i \leq 0.8\delta_{\text{y},i}$
	Ordinary level-2 $C_{\text{I-O. level-2}}$	Annual [3]
	Extraordinary $C_{\text{I-Extra}}$	Post-earthquake when $\delta_i \geq \%\delta_{\text{y},i}$
Traditional	Ordinary level-1 $C_{\text{I-O. level-1}}$	3 months [3]
	Ordinary level-2 $C_{\text{I-O. level-2}}$	Annual [3]
	Extraordinary $C_{\text{I-Extra}}$	Post-earthquake for each pier

Table 2: Cost items and values for LCCA

Cost item	Cost		
$C_{0,\text{b}}$	2097600 €[design documents]		
$C_{0,\text{SHM}}$	3000 €		
C_{SHM}	10% $C_{0,\text{SHM}}$		
Cost item	**Direct cost**	**Indirect cost**	**Total cost**
$C_{\text{I-O. level-1}}$	297 €/pier [17, 18]	–	297 €/pier
$C_{\text{I-O. level-2}}$	553 €/pier [17, 18]	–	553 €/pier
$C_{\text{I-Extra}}$	975 €/pier [17, 18]	343 €/pier [13, 16, 19, 20, 21]	1318 €/pier

3) Damage parameter and threshold values: relative displacements at the top of the i-th pier, equal to a percentage of the values corresponding to the cracking, $\%\delta_{\text{cr},i}$, and a percentage of the values corresponding to the elastic limit for reinforcement yielding, $\%\delta_{\text{y},i}$;

4) S^{2}HM system: bidirectional low-cost accelerometers placed at the top and at the base sections of each pier (20 accelerometers in total) that record absolute accelerations in the two main directions; relative displacements are evaluated by double integration of the recorded accelerations, with assumed zero initial displacements and velocity;

5) Extraordinary inspections strategy: Table 1 summarizes the implemented inspection strategy with S^{2}HM system; for clarity, also the traditional inspection approach is reported in the same table.

5.2 Cost analysis

Regarding the cost model illustrated at Section 3, Table 2 summarizes the adopted cost items in order to apply the simulation procedure to the case study.

The cost value of the SHM system management, C_{SHM}, is defined as annual cost that has to be discounted; the $C_{\text{I-O. level-1}}$, $C_{\text{I-O. level-2}}$, and $C_{\text{I-Extra}}$ values are reported as unit costs for a single operation and a single pier, to discount and multiply by the occurrence number.

6 SENSITIVITY ANALYSES

The application of the cost model through the simulation process allows to quantify the influence of the initial parameters on the results in terms of economic gain, G, and economically viable cases, n_{evc}.

In this work, the effects of i) the lifetime in which the comparison is performed (t_{L} value) and ii) the site seismic hazard (sampled hazard curve) are investigated. Therefore:

- Variation of lifetime in the range [10, 200] years is analyzed with 2-year step increments;
- Three seismic hazard curves are implemented in the analyses, as shown in Fig. 1.

Any time a seismic scenario is applied to the case study, the corresponding value of the economic gain G is computed. Since the random factors are involved, it is necessary to perform the simulation process a large number of times in order to statistically process the obtained results. Therefore, a first analysis has been performed in order to evaluate the number of simulations, taking into account the computational effort. The following analyses refer to a sample of 2000 scenarios (n_{tot}=2000 in Eq. 8).

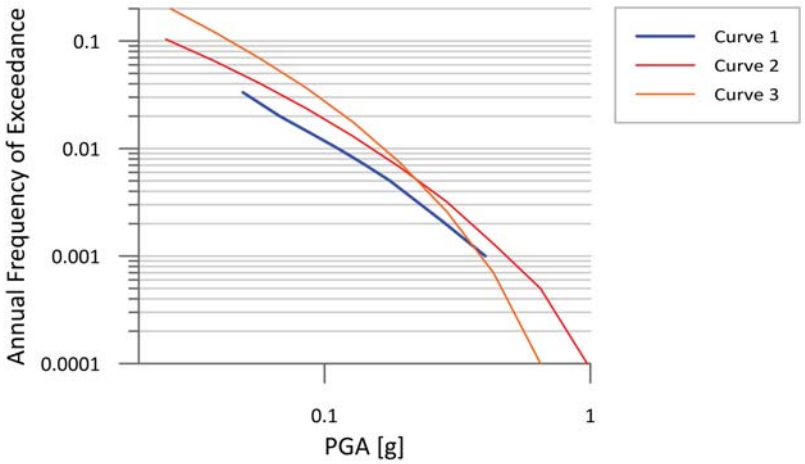

Figure 1: Seismic hazard curve: Curve 1 relative to LAT= 37.1254 LONG= 14.9275 available from [22], Curve 2 relative to LAT= 34.028 LONG= -118.251 available from [23], Curve 3 relative to LAT= 57.048 LONG= -157.236 available from [23].

6.1 Effects of the lifetime

In accordance with a condition-based post-event inspection strategy, the economic gain offered by the monitoring system can be triggered only when a seismic event occurs. Extending the analysis period allows to increase the probability that a higher number of earthquakes may happen in a scenario and, consequently, to raise the probability to obtain greater G values. On the other hand, all future cost items are reduced in terms of the present worth of the investment by the discount rate r and, in accordance with Eq. (1), the reductive effect of r increases exponentially over time. Hence, the added seismic events, as t_{L} increases, cause a progressively lower gain. Therefore, the influence of lifetime in terms of the expected benefits must be assessed in accordance with the adopted value of r.

Sensitivity analyses are performed assuming Curve 1, percentage equal to 80% and r equal to 0.01, 0.03 and 0.05. Table 3 shows the peak ground accelerations and the annual frequencies

PGA [g]	λ
0.0545	0.0284
0.0775	0.0167
0.1350	0.0076
0.2213	0.0032
0.2789	0.0021
0.3364	0.0014
0.4227	0.0009
0.5090	0.0006
0.5666	0.0005
0.6247	0.0004

Table 3: Peak ground accelerations, PGA, and annual frequencies of exceedance, λ, of Curve 1

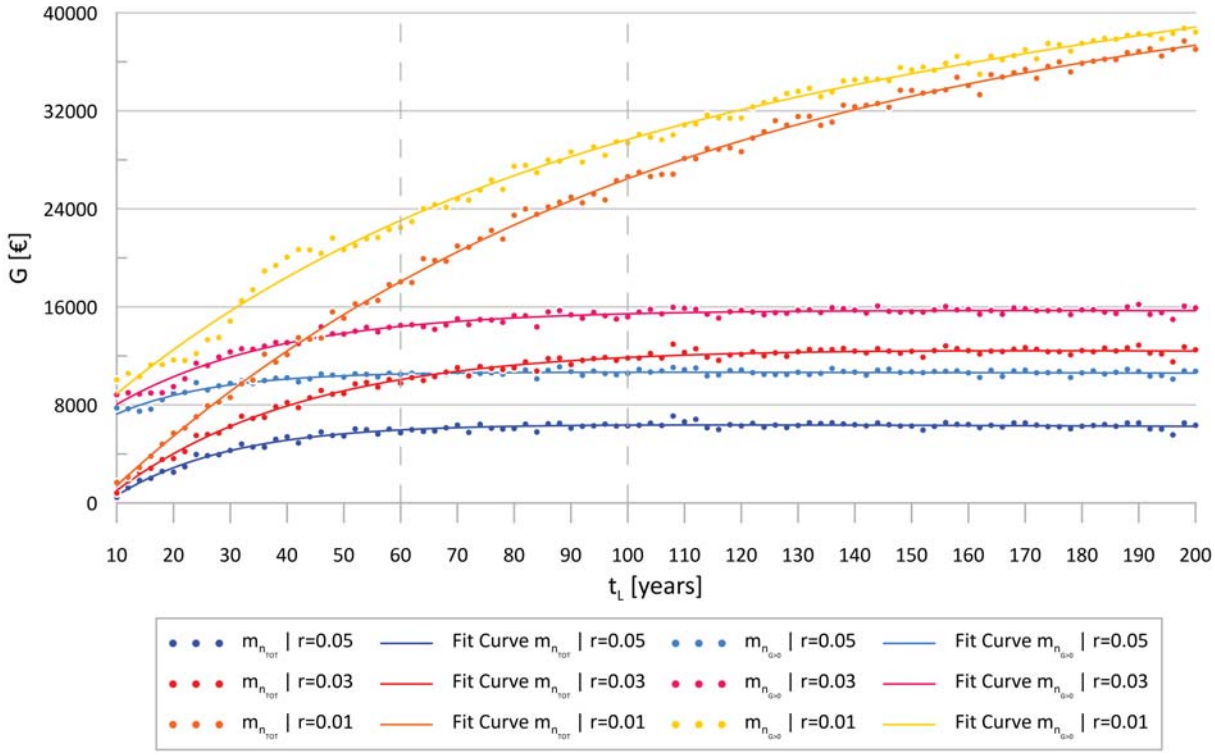

Figure 2: Comparison of $m_{n_{\text{tot}}}$ and $m_{n_{\text{G}>0}}$ function of t_{L} for r = 0.05, r = 0.03, and r = 0.01

of exceedance considered by the sampling of Curve 1 and used for the definition of seismic scenarios. The value of n_{evc}, the mean of the n_{tot} G values, $m_{n_{\text{tot}}}$, and the mean of the $n_{\text{G}>0}$ positive G values, $m_{n_{\text{G}>0}}$, are calculated for each t_{L} of the analysis range. The values of $m_{n_{\text{tot}}}$ and $m_{n_{\text{G}>0}}$ are shown and compared in Fig. 2 and the values of n_{evc} in Fig. 3, as functions of t_{L} for r equal to 0.05, 0.03 and 0.01.

The S^{2}HM benefit increases with the period of analysis with a higher growth rate for minor value of r. For high values of the discount rate, it is possible to identify a limit value of t_{L}, beyond which the gain becomes asymptotic, therefore, the comparison on larger t_{L} provides no further useful information. In the case study, the limit values equal to 60 and 100 years are

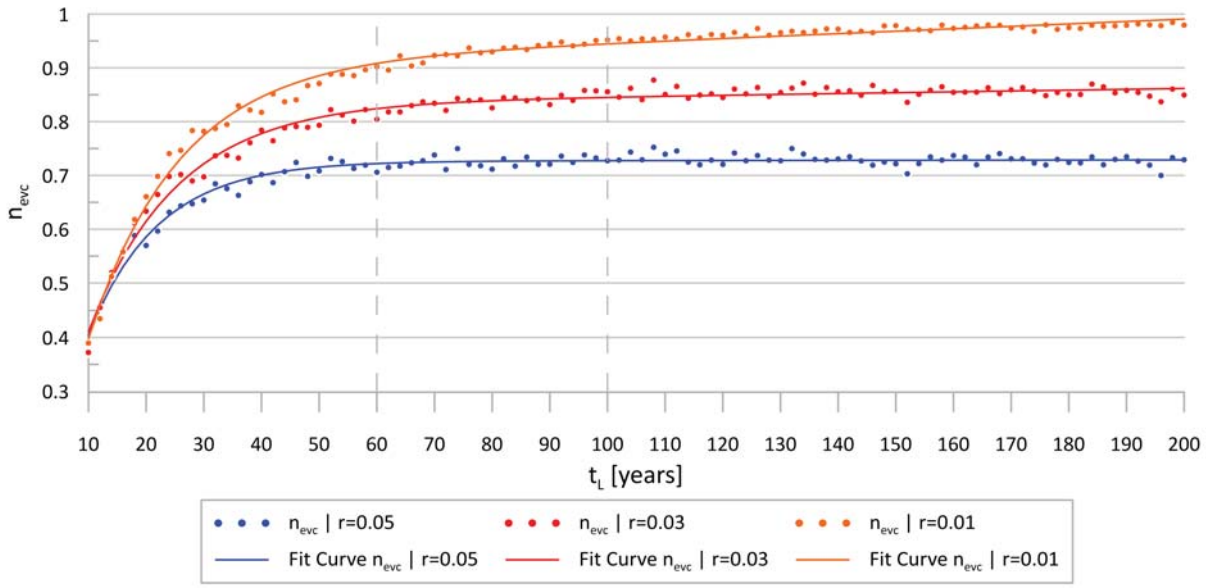

Figure 3: n_{evc} function of t_{L} for r = 0.05, r = 0.03, and r = 0.01

obtained for r=0.05 and r=0.03, respectively. For the initial value of t_{L}, the difference between the values of the pairs $m_{n_{\text{tot}}}$-$m_{n_{\text{G}>0}}$ is maximun and is greater for lower r, because the possible gain provided by single seismic events is more effective, then, it decreases with r and with an increasing t_{L}, because n_{evc} increases with t_{L} and with decreasing r.

6.2 Effects of the seismic hazard

An input parameter determining the number of seismic events that may occur during the lifetime of the bridge is the seismic hazard. A worst site hazard is characterized by bigger annual frequency of exceedance values for the same seismic intensity, therefore, over an equal analyzed lifetime, the number of events of a specific earthquake, obtained by Monte Carlo simulation, may be higher. However, a more severe seismic hazard leads to a higher probability that high intensity seismic events may occur. Severe earthquakes increase the damage probability and, therefore, the probability that more inspections are triggered, reducing the economic benefit of the monitoring system. The selected seismic hazard curves have the following features: Curve 2 is always harder than Curve 1, Curve 3 is harder than the other curves for smaller PGA values, while larger PGA values have lower probabilities.

Sensitivity analyses are performed assuming the same sampling values of PGA. Table 4 compares the annual frequencies of exceedance relative to Curve 1, Curve 2, and Curve3. Moreover, taking into account that the lifetime of a bridge is usually 100 years, the analyses are performed assuming t_{L} equal to 100 years and r equal to 0.03. The adopted percentage value is 80%.

The results are reported in terms of the relative frequency distributions of the n_{tot} G values, Fig. 4, and in terms of n_{evc}, Table 5.

The relative frequency distribution of G relative to Curve 3 is characterized by higher values of G, preceded by the results of Curve 2 and, finally, by Curve 1. The same relationship occurs for n_{evc}.

PGA [g]	λ (Curve 1)	λ (Curve 2)	λ (Curve 3)
0.0545	0.0284	0.0427	0.0737
0.0775	0.0167	0.0268	0.0426
0.1350	0.0076	0.0119	0.0157
0.2213	0.0032	0.0052	0.0051
0.2789	0.0021	0.0034	0.0028
0.3364	0.0014	0.0023	0.0016
0.4227	0.0009	0.0014	0.0008
0.5090	0.0006	0.0009	0.0004
0.5666	0.0005	0.0007	0.0003
0.6247	0.0004	0.0005	0.0002

Table 4: Peak ground accelerations, PGA, and annual frequencies of exceedance, λ, of Curve 1, Curve 2 and Curve 3

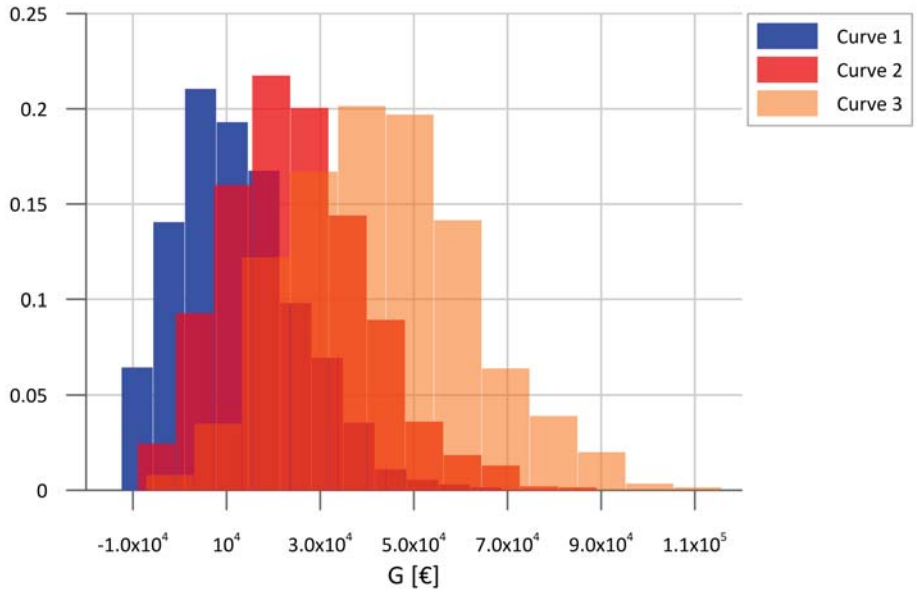

Figure 4: Relative frequency distribution of G for Curve 1, Curve 2 and Curve 3

n_{evc} (Curve 1)	n_{evc} (Curve 2)	n_{evc} (Curve 3)
0.84	0.97	0.99

Table 5: n_{evc} for Curve 1, Curve 2 and Curve 3

7 CONCLUSIONS

The paper proposes a life-cycle cost model of bridges equipped with seismic monitoring systems that allow to implemet post-event inspection strategies alternative to traditional ones. The simulation methodology used in order to compare the expected value of the total cost in cases with and without a monitoring system is illustrated, highlighting the dependence of the results on the most influential parameters.

For a defined discount rate value, the procedure allows to evaluate the most suitable analysis

period, beyond which no additional benefits of the monitoring system can be demonstrated in terms of the present value of the inspection cost. Moreover, it is demonstrated that seismic structural health monitoring systems may produce important economic benefits when site hazard is characterized by high annual frequency of excedance for low PGA.

ACKNOWLEDGMENTS

The authors gratefully acknowledge the support of the "Fondazione Cassa di Risparmio di Perugia" that funded this study through the project "Sviluppo di un modello originale di costo di ciclo di vita per la gestione ottimale di ponti e viadotti con sistema di monitoraggio integrato" (Project Code 2019.0338.029).

REFERENCES

[1] N. Okasha, D. M. Frangopol, Computational platform for the integrated life-cycle management of highway bridges, *Engineering Structures*, **33**, 2145–2153, 2011.

[2] H. Shim, S. Lee, Developing a probable cost analysis model for comparing bridge deck rehabilitation methods, *KSCE Journal of Civil Engineering*, **20**, 68–76, 2015.

[3] Ministero dei Lavori Pubblici, Circolare n° 6736/61/AI del 19.07.1967, "Controllo delle condizioni di stabilità delle opere d'arte stradali", 1967.

[4] D. M. Frangopol, Y. Dong, S. Sabatino, Bridge life-cycle performance and cost: analysis, prediction, optimisation and decision-making, *Structure and Infrastructure Engineering*, **13**, 1239–1257, 2017.

[5] K.M. Lee, H.N. Cho, Y.M. Choi, Life-cycle cost-effective optimum design of steel bridges, *Journal of constructional steel research*, **60**, 1585–1613, 2004.

[6] G. O'Reilly, A. Abarca, R. Monteiro, B. Borzi, C. M. Calvi, Towards Regional Safety Assessment of Bridge Infrastructure *13th International Conference on Applications of Statistics and Probability in Civil Engineering(ICASP13)*, 2019.

[7] B. Borzi, P. Ceresa, P. Franchin, F. Noto, G. M. Calvi, P. E. Pinto, Seismic Vulnerability of the Italian Roadway Bridge Stock, *Earthquake Spectra*, **31**, 2137–2461, 2015.

[8] M. P. Limongelli, S. Miraglia, A. Fathi, The value of visual inspections for emergency management of bridges under seismic hazard, 2018.

[9] M. P. Limongelli, M. Çelebi, Seismic Structural Health Monitoring, *Springer*, ISBN: 978-3-030-13975-9, 2019.

[10] C. R. Farrar, K. Worden, An Introduction to Structural Health Monitoring, *Structural Health Monitoring*, **365**, 303–315, 2007.

[11] M. M. Ettouney, S. Alampalli, Infrastructure Health in Civil Engineering: Applications and Management, *CRC Press*, 2012.

[12] H. Hawk, Bridge life-cycle cost analysis, *Report 483, Washington, DC: National Cooperative Highway Research Program, Transportation Research Board*, 2003.

[13] A. D. Orcesi, A. Feraille, S. Chataigner, Fatigue strengthening of steel structures using high modulus CFRP plates: Development of a life-cycle analysis approach, *Construction and Building Materials*, **227**, 2019.

[14] I. Venanzi, R. Castellani, L. Ierimonti, F. Ubertini, An Automated Procedure for Assessing Local Reliability Index and Life-Cycle Cost of Alternative Girder Bridge Design Solutions, *Advances in Civil Engineering*, 1-17, 2019.

[15] I. Venanzi, O. Lavan, L. Ierimonti, S. Fabrizi Multi-hazard loss analysis of tall buildings under wind and seismic loads, *Structure and Infrastructure Engineering*, **14**, 1295-1311, 2018.

[16] Ministero delle Infrastrutture e dei Trasporti, Studio di valutazione dei Costi Sociali dell'incidentalità stradale, 2012.

[17] Regione Umbria, DELIBERAZIONE DELLA GIUNTA REGIONALE 19 settembre 2018, n. 1027, Elenco regionale dei prezzi e dei costi minimi della manodopera per lavori edili, impianti tecnologici, infrastrutture a rete, lavori stradali e impianti sportivi per l'esecuzione di opere pubbliche - edizione 2018. Elenco regionale dei costi per la sicurezza dei lavoratori - edizione 2018. Approvazione, 2018.

[18] Anas S.p.A., Listino prezzi 2019; Prove, Indagini e Monitoraggio, 2019.

[19] Automobile Club Italia, Localizzazione Incidenti Stradali, `http://www.lis.aci.it/dati/#/localizzati/2017`, 2017.

[20] Ministero dei Lavori Pubblici, Ispettorato generale per la circolazione e la sicurezza stradale, "Definizione dei principali temi di ricerca per il miglioramento della sicurezza delle infrastrutture nel breve, medio e lungo periodo - scheda 8: misure per il miglioramento della sicurezza della circolazione in presenza di cantieri", 2000.

[21] Anas S.p.A., Dati di traffico medio giornaliero annuale, `https://www.stradeanas.it/sites/default/files/Anas%20Dati%20TGMA%202017.pdf`, 2017.

[22] INGV, Mappe interattive di pericolosità sismica, `http://esse1-gis.mi.ingv.it/`.

[23] USGS, Unified Hazard Tool, `https://earthquake.usgs.gov/hazards/interactive/`.

EURODYN 2020
XI International Conference on Structural Dynamics
M. Papadrakakis, M. Fragiadakis, C. Papadimitriou (eds.)
Athens, Greece, 23–26 November 2020

ENGINEERED MODEL FOR THE NUMERICAL INVESTIGATION INTO VIBRATION CHARACTERISTICS OF A NOVEL BRIDGE BEARING UNDER FREE-FREE AND FIXED BOUNDARY CONDITION

Pasakorn Sengsri[1, 2], Charalampos Baniotopoulos[1, 2], and Sakdirat Kaewunruen[1, 2]

[1]Department of Civil Engineering, School of Engineering, University of Birmingham, Birmingham B15 2TT, United Kingdom

[2]Birmingham Centre for Railway Research and Education, School of Engineering, University of Birmingham, Birmingham B15 2TT, United Kingdom

pxs905@student.bham.ac.uk

Keywords: resonance, metastrcutures, free vibration.

Abstract. *One of the most significantly deteriorated causes of bridge bearing failure is the resonance under various vibration conditions. It is important for bridge engineers to prevent the phenomenon, also called resonance, occurs to provide large amplitude vibrations when the bridge is being forced to vibrate at its natural frequency. This may lead to failure of the bridge structure under resonant vibrations. Common bridge bearings cannot well perform when vibrated large for example elastomeric bearings. This is because they do not have adequate mechanical properties to resist extremely various loads. Therefore, the concept of using metastrcutures to gain superior mechanical properties inspired us to generate a novel bridge bearing model. Because of the nature of dynamic forces on bridge structure, the vibration characteristics of a novel bridge bearing are crucial in analysis and design processes. This paper is the world's first to focus on the comprehension of vibration characteristics of a novel bridge bearing under free vibration. Through finite element method using Fusion 360 software, the numerical investigation of the modal parameters under dynamic condition was carried out for the novel bridge bearing. Also, there is a comparison of the free vibration results between the free-free and fixed boundary condition, in order to observe the influence of various boundary conditions responding to fundamental frequencies and mode shapes of a bridge structure. Additionally, to verify and develop a numerical model of bridge element, the free oscillation characteristics of the novel bridge bearing in different loads and boundary conditions are required. It is confirmed that vibration response measurements and parameters of a novel bridge bearing will be useful for bridge engineers to determine the vibration-based deterioration or to remotely monitor the bridge bearing health, since it is obvious that typical bridge bearing damage appears nearly at resonant frequencies of the bearings.*

1 INTRODUCTION

Bridge bearings also called isolators are extensively utilised in bridge engineering. Since 1950s, they have been employed as thermal expansion isolators for highway bridges and seismic base isolation bearings for building applications, especially extreme acoustic environments. Bridge bearings are critical part of the bridge elements in a bridge system. According to a review in [1, 2], the isolation system using these bearings are able to provide an element with high stiffness in one direction and high flexibility in one or more perpendicular directions. Also, the key functions of bearings for building and bridge applications are not only to transmit and accommodate loads and lateral deformations between the superstructure and the superstructure of a bridge, but also they support the weight of the superstructure [3]. Besides, bearings used for bridge application purposes should be more considered in design than those used for building application, due to additionally rotational deformations induced by girders [4].

The concept of combining horizontal flexibility and vertical stiffness is strongly suggested to be used in design of typical bridge bearings [2]. For example, these common bearings consist of rubber pads laminated with reinforcement materials (i.e. steel plates). Over decades, the development of a novel design of bridge bearings with fibre reinforcement has been widely researched. Compared to bridge bearings reinforced by steel-reinforced bearings are relatively heavy because of the steel reinforcement plates [5]. Additionally, the cost of these bearings is high due to the labour severe fabrication process [5]. Therefore, the benefits of utilising fibre reinforcement in bridge bearings are simplicity of installation, lightweight, better damping properties, high base isolation performance and lower stresses in rubber and fibre layers [6].

A main element of a rubber bearing is the rubber pads, based on an investigation in [7]. They can be employed straight without being reinforced (e.g. plain rubber isolators), or the pads can be laminated with reinforcing materials, providing a high tensile capacity for rising the vertical stiffness of the bearing by dominating buckling of the rubber [3]. A review in [8], Caltrans stated that for the entire structure, the selection of seismic rubber isolators with reinforced materials is dependent on the preferred type of an isolator.

According to [2], a rubber bridge isolator can be sensitive to a buckling type of instability identical to that of a common column, but controlled by the low-shear stiffness of an isolator. Reviews in [9, 10], bridge bearings should have adequately vertical stiffness to transfer service loads and besides be capable to facilitate the horizontal or rotational movements occurred in the girders. The bearings having adequate stiffness in vertical direction can well perform to limit the buckling behaviour and also can reduce the risk of leading to accelerated bridge failure to the bridge structure [11]. For instance, damage is not allowed in bridge bearing under any expected actions [3].

One of the most common causes of bridge failure is the resonance phenomenon under highly various vibrations. It is vital to comprehend the modal characteristics of structural bridge elements for designing and to predict the vibrated behaviours of the bridge elements. In terms of general bridge bearings, they should be developed for preventing possibly the resonance by using complex structures to reduce vibration. More recently, the use of metamaterials consisting of metastructures has a great momentum for many applications. Based on studies in [12, 13] a common material having positive Poisson's ratio, PR shows a special situation of swelling in perpendicular to compressive loading. On the other hand, a metamaterial with negative PR exhibits shrink behaviour in a direction transverse to the direction of compression [14, 15]. Negative PR metamaterials express better mechanical properties and appli-

cation prospects regarding lightweight [16], indentation resistance [17], vibration attenuation [18, 19], impact resistance [20, 21], and energy absorption [22, 23].

Our simulation shown in the following chapter was inspired by the development of typical bridge bearings using metastructures under dynamic condition which obtain superior modal properties. Nevertheless, there is no study in the comprehensively numerical modal analysis of novel bridge bearings in free oscillation. This study highlights the outcomes of a sensitivity investigation of free oscillation characteristics of a novel bridge bearing. The simulation of the bearing was investigated dependent on the finite elements, employing Fusion 360 software. The insight into dynamic will be useful for the study on non-destructive testing (NDT) and health monitoring of bridge bearings.

2 THEORETICAL BACKGROUND OF MODAL ANALYSIS

One of the most approaches to determine the dynamic properties of systems in the frequency domain is the modal analysis. In this study, the main objective is to identify the dynamic properties of novel bridge bearing components in terms of fundamental frequencies and mode shapes through the finite element method. The formulas of motion for free vibrations of a bridge bearing can be shown as follows [24-26].

In a dynamic network, the formula of motion of the network can commonly be denoted by:

$$[M]\{\ddot{y}\} + [D]\{\dot{y}\} + [S]\{y\} = \{q\} \tag{1}$$

Where [M] expresses the mass matrix, [D] represents the damping matrix, and [S] denotes the stiffness matrix. The harmonic load applied to the network with magnitude, Q and loading frequency ω is indicated by:

$$\{Q\} = Qsin(\omega t) = Qe^{j\omega t} \tag{2}$$

To be noted, a non-trivial solution to Formula (1) is $\{y\} = \{Y\}e^{j\omega t}$. Substituting the previous solution to Formula (1) and manipulating it with Formula (2), the formula of vibration is obtained as follows:

$$(-\omega^2[M] + j\omega[D] + [S])\{Y\} = \{Q\} \tag{3}$$

With some manipulations, converting Formula (3) employing modal coordinates by employing $\{Y\} = [\Phi]\{W\}$ and the orthogonality principle, and it later yields

$$W_i = \frac{\{\phi_i{}^T\}}{\omega_i^2 - \omega^2 + 2\zeta_i\omega_i\omega j})\{Q\} \tag{4}$$

Recalling $\{Y\} = [\Phi]\{\mathrm{W}\} = W_1\emptyset_1 + \cdots + W_n\emptyset_n$, Formula (4) can be re-written as presented by:

$$\{Y\} = \left(\sum_{i=1}^{n} \frac{\emptyset_i\emptyset_i^T}{\omega_i^2 - \omega^2 + 2\zeta_i\omega_i\omega j}\right)\{Q\} \tag{5}$$

Later, the reacceptance of the network can be determined by:

$$V_{ij}(\omega) = \frac{Y(\omega)}{Q_i(\omega)} = \sum_{i=1}^{n} \frac{\emptyset_i \emptyset_i^T}{\omega_i^2 - \omega^2 + 2\zeta_i \omega_i \omega j} \quad (6)$$

Therefore, ω_i is the resonant frequency, $\emptyset_i$ denotes the mass-normalized mode shape, and ζ_i denotes the modal damping ratio.

In terms of viscous damping (with critical damping c_r), $\zeta_i = \frac{d_i}{d_r}$; for proportional damping $([D] = z[M] + x[S]), \zeta_i = \frac{z}{2\omega_i} + \frac{x\omega_i}{2}$; and for hysteretic damping (η_i), $\zeta_i = \frac{\eta_{ii}}{2}$

3 A FINITE-ELEMENT SIMULATION OF NOVEL BRIDGE BEARING

The dynamic finite element (FE) simulation of a novel bridge bearing in free vibration was developed to investigate its dynamic response (i.e. natural frequency and mode shape). The FE model was generated in Fusion 360 software, using 3.72E+06 linear tetrahedral components with 5.71E+06 nodes. In this paper, we also focus on the free vibration of our model both free-free and fixed boundary condition. In terms of free-free boundary conditions, no excitation force was applied to the model, whilst the upper and lower surface of the model are not fixed because of free-free condition. For fixed condition, it is similar to the free-free condition, but the lower surface of the model is fixed.

Figure 1 demonstrates the three-dimensional finite element model for a novel bridge bearing. The honeycomb structure inspired us to create the engineered model. This is because a honeycomb structure gives a material with a very low density and relatively extreme out-of-plane compressive and out-of-plane shear performance [27-31]. The material and dimensions of the model geometry are based on the STANDARD DRAWINGS for Thai highway design and construction [32]. As given in Table 1, it indicates the material and geometrical properties of the FE model. A range of natural frequency investigations was carried out to evaluate the standard of the FE simulation. It is significant to note that the material utilised in this simulation is merely nitrile rubber, thus it is strongly suggested to use composite materials for this model, in order to acquire superior mechanical properties. Obviously, these components acting a bridge bearing can provide an expected estimation of bridge bearing's vibration in free-free and fixed condition. However, this model should be verified with experimental data in further research for public use in the near future.

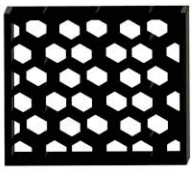

Figure 1: Finite element model of a novel bridge bearing in the free-free and fixed condition.

Parameters		
Material	Rubber	-
Elastic modulus	2	MPa
Poisson's ratio	0.49	-
Density	1.2E-06	kg/mm3
Model weight	5.12	kg
Model volume	4.26E+06	mm3
Model length	300.00	mm

Model width	300.00	mm
Model height	250.00	mm

Table 1: Engineering properties employed in the dynamic simulation.

4 RESULTS

The outcomes of numerical modal analysis for the novel bridge bearing are shown in Table 2 and Table 3 for free-free condition and fixed condition, respectively. For the two bridge bearing models under free vibration with different boundary conditions, it was observed that the fist twisting mode in vertical plane certainly controlled the first resonant mode of oscillation in free-free condition. Whilst appearing the first rolling mode for fixed conditions. For a free-free condition, the first five modes of free vibrations are shown in Table 2. Surprisingly, the minimum harmonic corresponded to the fundamental twisting mode, the second harmonic to the first rolling mode, the third harmonic to the second rolling mode, the fourth harmonic to the first shrinking mode, and lastly the fifth mode to the first buckling mode.

However, it is different to the modes of vibration which were obtained for the bearing model in the fixed condition. Table 3 exhibits the first five modes of free vibration in fixed condition. Surprisingly, the minimum harmonic corresponded to the fundamental rolling mode, the second harmonic to the first torsional mode, the third harmonic to the first shrinking mode, the fourth harmonic to the second shrinking mode, and finally the fifth mode to the third shrinking mode. The most dramatic change in fundamental harmonic between the free-free and fixed condition was the second rolling mode in free-free condition, but the first rolling mode in fixed condition, respectively. The highest frequency decrease was approximately 47.36 percent. It is clear that the fixed support played an important role in decreasing the frequency values of all vibration modes, except the twisting mode due to the increase in the frequency values. In addition, it resulted in all the different mode shapes, especially for the lowest fundamental frequency when compared to free-free condition.

According to a mention in [33], the effect of free vibration, there are several factors affecting the natural harmonics and mode shapes, which are the mass, shape, constraint, stiffness, and applied tensile or compressive loads of material and structure.

On the other hand, the validation of this simulation should be conducted by a comparison between experimental data and numerical results, in order to obtain the improved model and to be safely used in public. It is significant to note that these results are highlighted the dynamic properties because of a development in health monitoring of bridge bearing elements which one typically measures the dynamic behaviours in the bridge system by accelerometers on the bridge bearing surface [34].

Mode no.	Mode shape	Natural frequency (Hz)	Behaviour
1	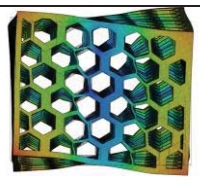	5.756	Twisting

2	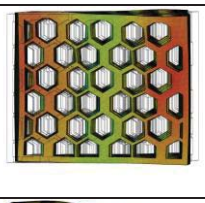	6.996	Rolling
3	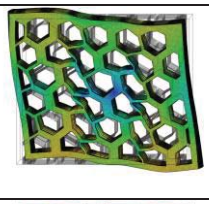	8.308	Rolling
4	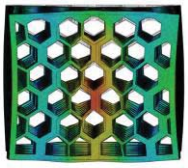	10.110	Shrinking
5	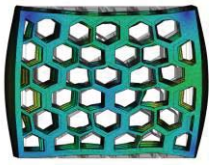	10.280	Buckling

Table 2: Natural frequencies of a conceptually novel bridge bearing (Hz) under the free vibration condition with free-free boundary condition.

Mode no.	Mode shape	Natural frequency (Hz)	Behaviour
1	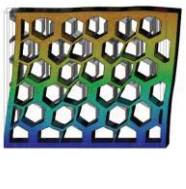	4.373	Rolling
2		7.528	Twisting
3		7.973	Shrinking

4	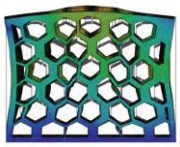	11.080	Shrinking
5	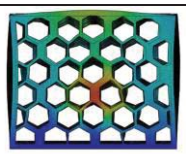	12.120	Shrinking

Table 3: Natural frequencies of a conceptually novel bridge bearing (Hz) under the free vibration condition with fixed boundary condition at the bottom surface.

5 CONCLUSION

Vibration characteristics of a novel bridge bearing play a major role in developing the realistic dynamic simulation of the bearing able to predict its dynamic response. The modal parameters of a novel bridge bearing in bridge system were investigated for modal analysis under free vibration with two different boundary conditions, through the finite element method using 360 Fusion software. The three-dimensional model using a honeycomb structure provides good mechanical properties and lightweight. Obviously, the resonant frequencies connected with the lower mode of oscillation of novel bridge bearing were dramatically influenced by the support boundary condition. Additionally, the mode shapes, which can behave the damaged condition of the novel bridge bearing, were affected by the fixed condition. To sum up, the fixed boundary condition had a particular effect on the vibration mode shapes and natural frequencies of a novel bridge bearing, particularly in the low frequency range. It is suggested that the determined modal parameters of the novel bridge bearing components were utilised to model bridge bearings where the influence of the boundary condition will be calculated. Nevertheless, the model should be created from composite materials that can provide superior mechanical properties. Furthermore, additional research for experiments of the novel bridge bearing fabricated by an additive manufacturing approach should be performed to compare the results between simulation and experiment.

6 ACKNOWLEDGMENTS

The first author wishes to thank Royal Thai Government for his PhD Scholarship at the University of Birmingham. The last author wishes to gratefully acknowledge the Japan Society for Promotion of Science (JSPS) for his JSPS Invitation Research Fellowship (Long-term), Grant No L15701, at the Track Dynamics Laboratory, Railway Technical Research Institute and at Concrete Laboratory, the University of Tokyo, Tokyo, Japan. The JSPS financially supports this work as part of the research project, entitled “Smart and reliable railway infrastructure.” Special thanks to European Commission for H2020-MSCA-RISE Project No. 691135 “RIS-EN: Rail Infrastructure Systems Engineering Net-work” (www.risen2rail.eu). Partial support from H2020 Shift2Rail Project No 730849 (S-Code) is acknowledged. In addition, the sponsorships and assistance from LORAM, Network Rail, RSSB (Rail Safety and Standard Board, UK) are highly appreciated.

REFERENCES

[1] P. Sengsri, M. R. Marsico, S. Kaewunruen, Base isolation fibre-reinforced composite bearings using recycled rubber. *IOP Conference Series: Materials Science and Engineering*, 2019.

[2] JM. Kelly, A. Konstantinidis Dimitrios, Mechanics of Rubber Bearings for Seismic and Vibration Isolation, John Wiley & Sons, Ltd., the edition first published 2011.

[3] AM. Yasser, TJ. Michael, Experimental assessment of utilizing fiber reinforced elastomeric isolators as bearings for bridge applications, Dept. of Civil Engineering, McMaster Univ., 1280 Main St. West, Hamilton, ON, L8S 4L7, Canada.

[4] F. Naeim, J. Kelly, Design of seismic isolated structures: from theory to practice, USA: John Wiley & Sons, 1999.

[5] J. Kelly, D. Konstantinidis, Low-Cost Seismic Isolators for Housing in Highly- Seismic Developing Countries. Istanbul, Turkey: *10th World Conference on Seismic Isolation, Energy Dissipation and Active Vibrations Control of Structures*; 28-31 May 2007.

[6] H. Toopchi-Nezhad, M. Tait, R. Drysdale, Testing and modeling of square carbon fiber reinforced elastomeric seismic isolators. *Struct Control Health Monit* ,15(6), 876-900, 2008a.

[7] J. Kelly, D. Konstantinidis, Mechanics of rubber bearings for seismic and vibration isolation. Chichester, UK: Wiley, 2011.

[8] Caltrans, Bridge memo to designers. Section 7: bridge bearings. Sacramento, California, USA: California Department of Transportation, 1994.

[9] M. Constantinou, I. Kalpakidis, A. Filiatrault, R. Ecker Lay. LRFD-based analysis and design procedures for bridge bearings and seismic isolators. Report No. MCEER-11e0004. Buffalo, New York, USA: Multidisciplinary Center for Earthquake Engineering Research, University at Buffalo, State University of New York, 2011.

[10] Y. Al-Anany, Fiber Reinforced Elastomeric Isolators for Bridge Applications. Ph.D. thesis. McMaster University, 2016.

[11] AASHTO, LRFD Bridge Design Specifications. Washington, DC, USA: American Association of State Highway and Transportation Officials, 2012.

[12] KE. Evans, MA. Nkansah, IJ. Hutchinson, Molecular network design. *Nature* 353,124–125, 1991

[13] KK. Saxena, Das R, EP. Calius, Three decades of auxetics research—materials with negative Poisson's ratio: a review. Adv Eng Mater 18(11), 1847–1870, 2016.

[14] HMA. Kolken, AA. Zadpoor, Auxetic mechanical metamaterials. *RSC Adv* 7(9), 5111–5129, 2017.

[15] J. Robbins, S. J. Owen, BW. Clark, An efficient and scalable approach for generating topologically optimized cellular structures for additive manufacturing. *Addit Manuf* 12, 296–304, 2016.

[16] BG. Compton, JA. Lewis, 3D-printing of lightweight cellular composites. Adv Mater 26(34), 5930–5935, 2014.

[17] LL. Hu, H. Deng, Indentation resistance of the re-entrant hexagonal honeycombs with negative Poisson's ratio. *Mater Res Innov* 19(sup 1), 442-445, 2015.

[18] I. Chekkal, C. Remillat, F. Scarpa, Acoustic properties of auxetic foams. *High Perform Struct Mater* 6, 119–129, 2003.

[19] L. Boldrin, S. Hummel, F. Scarpa, Dynamic behaviour of auxetic gradient composite hexagonal honeycombs. *Compos Struct* 149, 114–124, 2016.

[20] AA. Nia, SB. Razavi, GH. Majzoobi, Ballistic limit determination of aluminum honeycombs-experimental study. *Mater Sci Eng A* 488(1–2), 273–280, 2008.

[21] CJ. Yungwirth, HNG. Wadley, JH. O'Connor, Impact response of sandwich plates with a pyramidal lattice core. *Int J Impact Eng* 35(8), 920–936, 2008.

[22] NA. Fleck, VS. Deshpande, MF. Ashby, Micro-architectured materials: past, present and future. *Proc Mathem Phys Eng Sci* 466(2121), 2495–2516, 2010.

[23] D. Li, J. Yin, L. Dong, Strong reentrant cellular structures with negative Poisson's ratio. *J Mater Sci* 53, 3493–3499, 2018.

[24] DJ. Ewins, Modal Testing: Theory and Practice, Taunton Research Studies Press, 1995.

[25] H. He, Z. Fu, Modal Analysis, Great Britain Butterworth – Heinemann Publishers, 2001.

[26] S. Kaewunruen, AM. Remennikov, Sensitivity analysis of free vibration characteristics of an in-situ railway concrete sleeper to variations of rail pad parameters. *J. SoundVibr.*, 298, 453–461, 2006.

[27] AK. Geim, Graphene: status and prospects, *Science* 324, 1530–1534, 2009.

[28] CN. Rao, AK. Sood, KS. Subrahmanyam, A. Govindaraj, Graphene: the new two-dimensional nanomaterial, *Angew. Chem. Int. Ed.* 48, 7752–7777, 2009.

[29] DR. Dreyer, S. Park, CW. Bielawski, RS. Ruoff, The chemistry of graphene oxide, *Chem. Soc. Rev.* 39, 228–240, 2009.

[30] MJ. Allen, VC. Tung, RB. Kaner, Honeycomb carbon: a review of graphene, *Chem. Rev.* 110, 132–145, 2010.

[31] OC. Compton, ST. Nguyen, Graphene oxide, highly reduced graphene oxide, and graphene: versatile building blocks for carbon-based materials, *Small* 6, 711–723, 2010.

[32] STANDARD DRAWINGS for Thai highway design and construction, Department of Highways, Thailand, 2015.

[33] Fusion 360, Product Document, Modal Analysis. Available at: http://help.autodesk.com/view/fusion360/ENU/?guid=GUID-AA92F5B7-AA22-4CE4-B6EF-F67A9A7D2836.

[34] A. Remennikov, S. Kaewunruen, Experimental investigation on dynamic sleeper/ballast interaction, *Experimental Mechanics* 46, 57–66, 2006.

EURODYN 2020
XI International Conference on Structural Dynamics
M. Papadrakakis, M. Fragiadakis, C. Papadimitriou (eds.)
Athens, Greece, 23–26 November 2020

VIBRATION–BASED ROBUST DAMAGE DETECTION UNDER ASSEMBLY–INDUCED UNCERTAINTY: THE OUTPUT–ONLY CASE

Andreas E. Mastakouris, Georgia P. Andriosopoulou, Kyriakos J. Vamvoudakis-Stefanou and Spilios D. Fassois

Stochastic Mechanical Systems and Automation Laboratory
Department of Mechanical Engineering and Aeronautics
University of Patras, GR 26504 Patras, Greece
E-mails: mead6772@upnet.gr (AEM), mead6698@upnet.gr (GPA),
vamvoudakisk@mech.upatras.gr (KJVS), fassois@upatras.gr (SDF)

Keywords: Robust Detection, Damage Detection, Structural Health Monitoring, Uncertainty

Abstract. *The problem of unsupervised robust vibration based damage detection under assembly–induced uncertainty is considered with a focus on the non–measurable excitation (output–only) case. The study employs a composite aerostructure and damage scenarios based on bolt loosening and characterized by 'minor' effects on the dynamics which are appreciably 'masked' by those of assembly–induced uncertainty. Detection is based on two Statistical Time Series type methods: a Multiple Model (MM) based and a Principal Component Analysis (PCA) based. The results, based on hundreds of test cases, indicate that both methods achieve very good detection performance, with the PCA–based one exhibiting an edge over its MM–based counterpart (99.5% versus 96% correct detection at a 5% false alarm rate). Although the non–measurable nature of the excitation unquestionably increases the problem difficulty, the degradation in performance is quite small, especially for the PCA–based method (from 100% to 99% at 4% false alarm).*

1 INTRODUCTION

Vibration based Structural Health Monitoring (SHM) has received significant attention in recent years as vibration signals are often naturally available and may be measured in a cost effective way and without interrupting the structure's normal operation [1, 2]. Yet, a main difficulty with this technology is related to the fact that most structures operate under varying Environmental and Operating Conditions (EOCs) and uncertainty, factors often inducing significant changes in the dynamics which may appreciably 'mask' those due to damage, thus rendering vibration based Structural Health Monitoring challenging.

Various classes of vibration based SHM methods aiming at overcoming this difficulty by exhibiting *robustness* to varying EOCs and uncertainty have been developed over the past several years. These attempt to 'separate' the effects of minor or incipient damage from those of EOCs and uncertainty, and may be classified as either 'implicit' or 'explicit'. *'Implicit'* methods attempt modeling that portion of the structural dynamics that is not significantly influenced by varying EOCs and uncertainty; they include Principal Component Analysis (PCA) [3, 4] and Factor Analysis (FA) [5] based approaches for damage detection. On the other hand, *'explicit'* methods attempt modeling the complete structural dynamics, explicitly including the effects of varying EOCs and uncertainty, via deterministic or stochastic relations; these include Functional Model (FM) based methods [6, 7], Gaussian or non-Gaussian Random Coefficient (RC) model based methods [8, 9], and Multiple Model (MM) based methods [10, 11].

Robust methods have been assessed in various experimental studies under varying Environmental (usually temperature and humidity) or Operating (such as payload) Conditions [12]. Yet, systematic and statistically reliable performance assessments based on sufficiently high numbers of experiments are relatively scarce. Moreover, damage detection under the practically important assembly–induced uncertainty has been barely considered, with the exception of a recent companion paper by the authors [13]. This has been based on hundreds of laboratory test cases involving re–assembly with a simple composite aerostructure and three distinct bolt loosening damage scenarios. Based on single–excitation trivariate–response signals, it has served to demonstrate that: (i) Detection is challenging, as the effects of damage may be indeed largely 'masked' by those of assembly–induced uncertainty, (ii) the use of robust Statistical Time Series (STS) methods may still lead to high detection performance reaching 100% correct detection at a false alarm rate of 3.5% or higher.

The *aim* of the present study is on addressing the problem of robust damage detection under assembly–induced uncertainty and *non–measurable* random (white noise) excitation (the *output–only* case). This is a case of high practical importance as the excitation is often non–measurable, for instance in flying aircraft, sea vessels, surface vehicles, wind turbines and many more structures under normal operation. Evidently, dropping the excitation signal information renders the damage detection problem more challenging, with the main question thus being on assessing the extent of the resulting degradation in detection performance.

For achieving this goal the present study employs the set–up, damage scenarios, and signals of our companion paper [13], in conjunction with two, properly adjusted, robust Statistical Time Series damage detection methods based on Vector AutoRegressive (VAR) modeling of the trivariate vibration response signal: (a) An Unsupervised Multiple Model VAR (U–MM–VAR) method, and (b) an Unsupervised Principal Component Analysis (PCA) VAR (U–PCA–VAR) method [14]. It is important to note that the *unsupervised* nature of both methods is of high practical importance as well, implying the use of vibration response signals exclusively from the healthy structure in the baseline (training) phase.

The rest of this article is organized as follows: The experimental set–up and the damage scenarios are briefly presented in section 2. The robust output–only damage detection methods are briefly outlined in section 3, while damage detection performance assessment and comparison with the measurable excitation case are presented in section 4. The conclusions drawn are finally summarized in section 5.

2 THE EXPERIMENTAL SET-UP AND THE DAMAGE SCENARIOS

2.1 The structure, the damage scenarios, and the experiments

The experiments are based on the composite aerostructure of our companion paper [13], representing the boom of a Unmanned Aerial Vehicle (UAV). The structure is clamped at its right end simulating the connection to the UAV fuselage, while its left free end is attached to an aluminum mass representing the aircraft tail (Figure 1). Both connections are bolted, with the nominal (corresponding to the healthy state) tightening torques being equal to 2 *Nm* and 4 *Nm*, respectively. The exciting random (white) force is applied at Point X, while the resulting vibration acceleration response signals are measured, at points Y1, Y2 and Y3, via lightweight accelerometers. Further details are provided in [13].

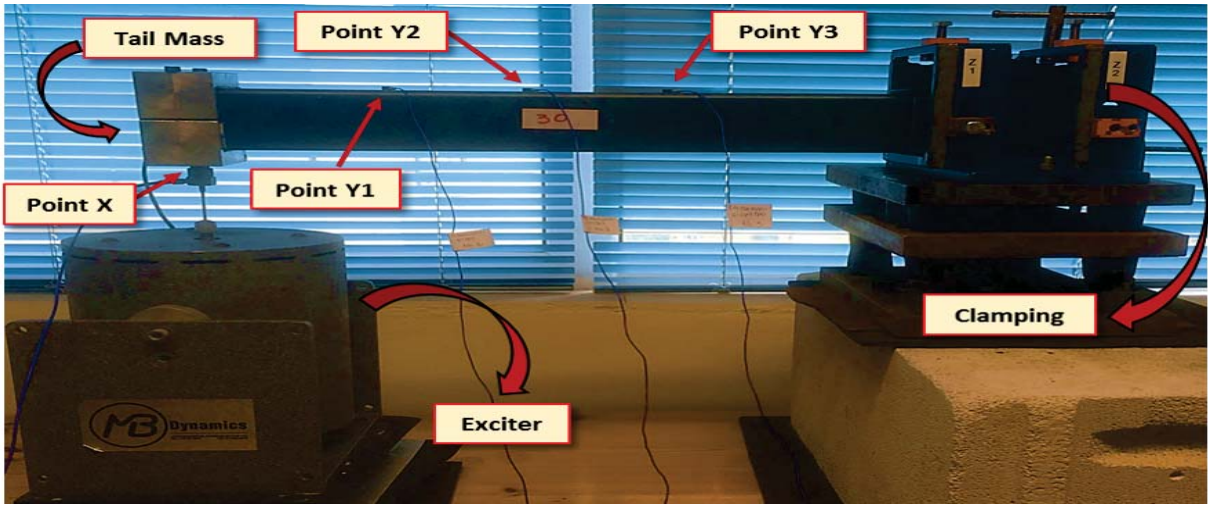

Figure 1: Experimental set–up: A random excitation is vertically applied at Point X and the resulting vertical vibration acceleration is measured at Points Y1, Y2, Y3 [13].

Three distinct damage scenarios are considered, each one characterized by a specific reduction (10%, 30% or 50%) in the tightening torque of its clamped end (fuselage connection). Details and the total number of experiments per health state are provided in Table 1.

Structural Health State	Clamping Torque [N·m]	Tail Mass Torque [N·m]	# of Experiments
Healthy	2	4	600
Damage 1	1.8	4	70
Damage 2	1.4	4	70
Damage 3	1	4	70

Table 1: The three health states and the corresponding numbers of experiments [13].

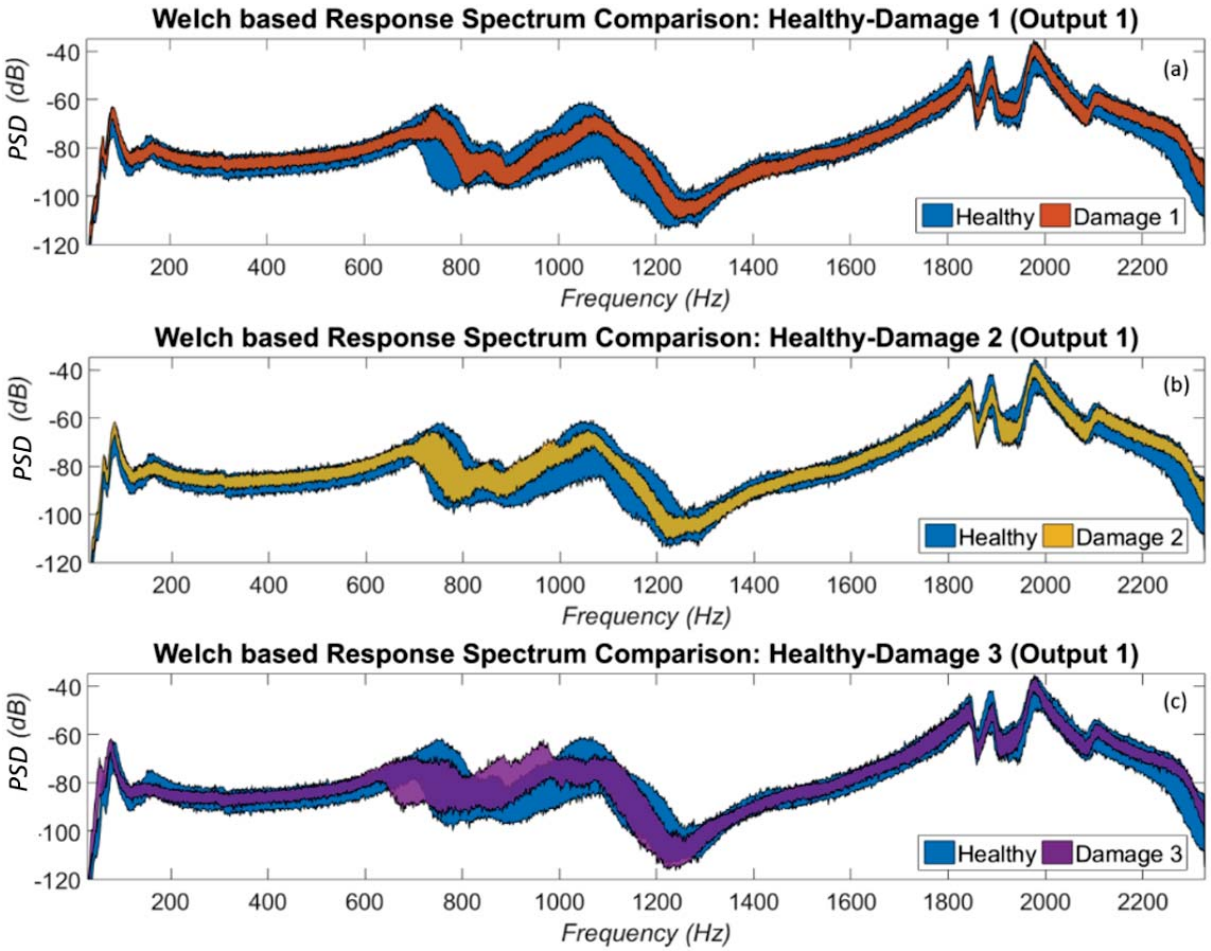

Figure 2: Assessment of the effects of damage and assembly–induced uncertainty on the dynamics: Welch–based vibration response PSD for the healthy structure versus Damage 1 (a), Damage 2 (b), and Damage 3 (c). [Measurement Point Y1; 600 PSDs for the healthy structure, 70 PSDs for each damage scenario; Welch estimation details in Table 2.]

2.2 Assessment of the effects of damage and assembly–induced uncertainty on the dynamics

The effects of each damage scenario, along with those of assembly–induced uncertainty, on the dynamics are demonstrated in Figure 2 via Welch–based Power Spectral Density (PSD) estimates [15, pp. 173-187] for signals measured at Point Y1. Evidently, the assembly–induced variability in the healthy dynamics (blue zone) is quite significant, and, to a very considerable extent, 'masking' that due to each damage scenario (especially for scenarios 1 and 2). These results imply a challenging damage detection problem, especially for the aforementioned two damage scenarios.

3 THE ROBUST OUTPUT–ONLY DAMAGE DETECTION METHODS

3.1 VAR modeling

For uncorrelated (white) force excitation the observed s-dimensional vibration acceleration signal, say $\boldsymbol{y}[t]$ ($t = 1,\ldots,N$ indicating discrete time, with the corresponding analog time being $t \cdot T_s$ with T_s designating the sampling period), may be modeled as an s-variate (presently s=3)

Vector AutoRegressive model of order n, that is a VAR(n) model, of the form [16, 17] (notice that bold face lower/upper case characters indicate vector/matrix quantities, respectively):

$$\begin{aligned} \boldsymbol{y}[t] + \sum_{i=1}^{n} \boldsymbol{A}_i \cdot \boldsymbol{y}[t-i] &= \boldsymbol{e}[t] \\ E\left\{\boldsymbol{e}[t] \cdot \boldsymbol{e}^T[t-\tau]\right\} &= \boldsymbol{\Sigma} \end{aligned} \tag{1}$$

with $\boldsymbol{A}_i\,(s \times s)$ designating the i-th AR matrix, $\boldsymbol{e}[t]\,(s \times 1)$ the model residual (one–step-ahead prediction error) signal characterized by the non–singular (and generally non–diagonal) covariance matrix $\boldsymbol{\Sigma}$, and $E\{\cdot\}$ statistical expectation. Given the vibration signal measurements $\boldsymbol{y}[t]\,(t = 1,\ldots,N)$, the estimation of the VAR parameter vector $\boldsymbol{\theta}$ comprising all AR matrix elements $\boldsymbol{\theta} = \text{vec}([\boldsymbol{A}_1 \ldots \boldsymbol{A}_n]^T)_{(n \times s^2) \times 1}$ and the residual covariance matrix $\boldsymbol{\Sigma}$ is accomplished via linear regression schemes based on minimization of the Ordinary Least Squares (OLS) or the Weighted Least Squares (WLS criterion) [15, p. 206].

3.2 The U–MM–VAR method

This method is based on a MM representation of the *healthy* structural dynamics under uncertainty [18]. This representation consists of a set of VAR(n) models along with their estimated parameters vectors $\boldsymbol{\theta}$. The method operates under two distinct phases: A baseline (training) phase and an inspection (operational) phase.

Baseline phase. $(s \times p)$ (presently $s = 3$) vibration response signals from p different experiments under healthy structural state are obtained. Based on them, a set of p VAR(n) models $m_o = \{m_{o,1},\ldots,m_{o,p}\}$ is estimated, constituting the MM representation of the healthy dynamics.

Inspection phase. Whenever a new set of vibration response signals, obtained under unknown structural state, is obtained, a new VAR(n) model m_u, of the same order as those in m_o, is estimated. A proper pseudo–distance metric, say $D(m_u, m_o)$, between the current model m_u and the MM representation m_o, is then computed.

The unknown health state is then declared as healthy if and only if the pseudo–distance metric $D(m_u, m_o)$ is lower than a user specified threshold l_{lim}, which is taken to imply that m_u belongs to the m_o MM representation; otherwise it is declared as damaged.

In the present study the pseudo–distance metric $D(m_o, m_u)$ employed is defined as:

$$D(m_u, m_o) := \min_k d(m_u, m_{o,k}) \qquad (k = 1,\ldots,p) \tag{2}$$

with $d(m_u, m_{o,k})$ designating the Kullback–Leibler (KL) divergence (pseudo–distance) [19] between two individual VAR(n) models.

3.3 The U-PCA-VAR method

This method employs the centered PCA [20, 21] for defining an n'-dimensional orthogonal coordinate system (where $n' = n \times s^2$, due to the dimension of the estimated VAR(n) parameter vector $\boldsymbol{\theta}$), on which the VAR parameters vector estimates corresponding to the healthy structural state may be projected, forming a set of mutually uncorrelated random variables [14].

Baseline phase. $(s \times p)$ (presently $s = 3$) vibration response signals from p different experiments of the healthy state are initially obtained and then a set of p VAR(n) models $m_o = \{m_{o,1},\ldots,m_{o,p}\}$ and their parameter vectors are obtained. These parameter vectors are sample

mean corrected [22], leading to the parameter vectors $\{\boldsymbol{\theta}_o\} = \{\boldsymbol{\theta}_{o,1}, \ldots, \boldsymbol{\theta}_{o,p}\}$. The sample covariance matrix $\boldsymbol{P} = \frac{1}{p-1}\sum_{k=1}^{p} \boldsymbol{\theta}_{o,k}^T \boldsymbol{\theta}_{o,k}$ $(n' \times n')$ (^{T} designating matrix transposition) is then computed and, via PCA transformation, it is decomposed into $\boldsymbol{P} = \boldsymbol{U}\boldsymbol{S}^2\boldsymbol{U}$, where $\boldsymbol{S}^2$ $(n' \times n')$ is a matrix which includes the squared singular values (positive eigenvalues) of $\boldsymbol{P}$ (arranged in decreasing order) and $\boldsymbol{U}(n' \times n')$ a real unitary matrix containing the corresponding eigenvectors of $\boldsymbol{P}$. The first $q(< n')$ columns (principal components) of the eigenvector matrix $\boldsymbol{U}$ – corresponding to the largest eigenvalues that explain a certain fraction $\gamma(\%)$ of the total parameter vector variability – are then associated with uncertainty, while the remaining m principal components are considered sensitive to damage.

Inspection phase. Whenever a new set of vibration response signals, obtained under unknown structural state, is obtained, a new VAR(n) model m_u and its parameter vector is estimated. Each estimated parameter is then centered by subtracting its sample mean (as obtained in the baseline phase), thus giving rise to the parameter vector $\boldsymbol{\theta}_u$. This is then transformed into the m-dimensional space as $(\bar{\boldsymbol{\theta}}_m)_u = \boldsymbol{U}_m^T \boldsymbol{\theta}_u$. Damage detection may be then based on the Euclidean norm of the transformed parameter vector $(\bar{\boldsymbol{\theta}}_m)_u$, following the decision making mechanism:

$$\begin{array}{rl} D = \|(\bar{\boldsymbol{\theta}}_m)_u\|_{l_2} \leq l_{lim} & \rightarrow \text{ Healthy structure} \\ \text{otherwise} & \rightarrow \text{ Damaged structure} \end{array} \tag{3}$$

where D designating the method's test pseudo–statistic and l_{lim} a user–specified limit.

4 DAMAGE DETECTION RESULTS

4.1 VAR modeling of the vibration response

Based on each set of vibration response signals measured at points Y1, Y2 and Y3 (Figure 1), each one being N=12 000 samples long, the modeling procedure involves the successive fitting of VAR(n) models for increasing AR order n, until an adequate model is reached. Model adequacy is judged via the trace of the estimated residual covariance matrix $\widehat{\boldsymbol{\Sigma}}$ and the Bayesian Information Criterion (BIC) [15, pp. 505-507]. The ratio of the number of signal scalar samples to the number of model parameters (Samples Per Parameter – SPP) should be maintained at sufficient levels (for instance above 20). Final model acceptance is based upon formal verification of the model residual uncorrelatedness (whiteness) hypothesis. This procedure leads to a VAR(55) model for the healthy structural dynamics (details in Table 2).

4.2 Comparative assessment of the methods

Damage detection performance is assessed via Receiver Operating Characteristics, ROC, curves, each representing the True Positive Rate (TPR, that is correct detection rate) versus the False Positive Rate (FPR, that is false alarm rate) for varying decision threshold [23].

$p = 300$ randomly selected experiments with the healthy structure are included in the baseline (learning) phase, while the remaining 300 healthy and 210 damaged (70 per each damage scenario) are reserved for inspection (testing). As p should be greater than the total number n' (presently $n' = 495$) of the estimated model parameters for the PCA (see subsection 3.3), a reduced number of VAR(55) scalar parameters should be employed. Indeed, the first 150 scalar parameters from the diagonals of the VAR(55) model AR matrices are selected, while γ is selected at 99.6% (U–PCA–VAR method). On the other hand 300 conventional VAR(55) models are included in the MM representation (U–MM–VAR method). Details are summarized in Table 3.

Non–Parametric Analysis						
Sampling Frequency (Hz)	Signal Length (samples)	Estimation Method	Window Type / length	Overlap (%)	δf (Hz) / # Segments	Bandwidth (Hz)
4 654.5	120 000	Welch	Hamming / 4 096	80	1.14/ 143	3 - 2 327.25
Matlab function: *pwelch.m* (PSD)						
Parametric (VAR) Analysis						
Signal Length (samples)	Selected Model	# Estimated Parameters	BIC	SPP	Trace of Residual Matrix	Condition No of Inverted Covariance
12 000	VAR(55)	495	-20.95	46.51	10^{-3}	10^{6}
Estimation method: OLS with QR implementation (Matlab function: *armax.m*)						

δf: frequency resolution. BIC, Trace, and Condition number refer to an indicative healthy test case.

Table 2: Non–parametric and parametric estimation details.

Method	VAR Model Order	# Baseline Healthy Exp/s	# Inspection Exp/s	# ROC Points	# VAR Parameters (for detection)	PCA Threshold γ (%)
U–MM—VAR	55	300	510	510	495	-
U–PCA–VAR	55	300	510	510	150†	99.6

Scalar signal length N=12 000 samples.

†The first diagonal AR parameters (U–PCA–VAR).

Table 3: Detection method parameters and numbers of baseline and inspection experiments.

Performance assessment results for both methods are presented in Figure 3, in terms of pseudo–distance metric D and ROC curves, distinctly for each damage scenario. The U–MM–VAR method achieves correct detection rates that, for damage scenarios 1 and 2, approach 91% and 98%, respectively, for 5% or higher false alarm rate. The performance is even better for damage scenario 3, with 100% correct detection achieved for false alarm rate 1.5% or higher. This performance is quite impressive in view of the effects of the damage scenarios and uncertainty on the dynamics! The U–PCA–VAR method achieves even higher performance, as the correct detection rates for damage scenarios 1 and 2 approach 98.6% and 100%, respectively, for 5% or higher false alarm rate, while it achieves 100% correct detection rate for false rates of 0.4% or higher!

4.3 Comparison with the case of measurable excitation

The performance achieved by each method is now compared to that of its counterpart additionally employing the excitation signal (measurable excitation case); the latter methods are based on VAR models with Exogenous excitation (VARX models) and are thus referred to as U–MM–VARX and U–PCA–VARX methods [13]. As expected, the inclusion of excitation signal information leads to somewhat improved performance (Figure 4). This improvement is more evident for the MM–based methods (Figure 4(a)) where the correct detection rate improves from 94% to 100% for false alarm rate of 3.6%. On the other hand, the improvement is less significant for the PCA–based methods, as the correct detection rate improves from 99% to

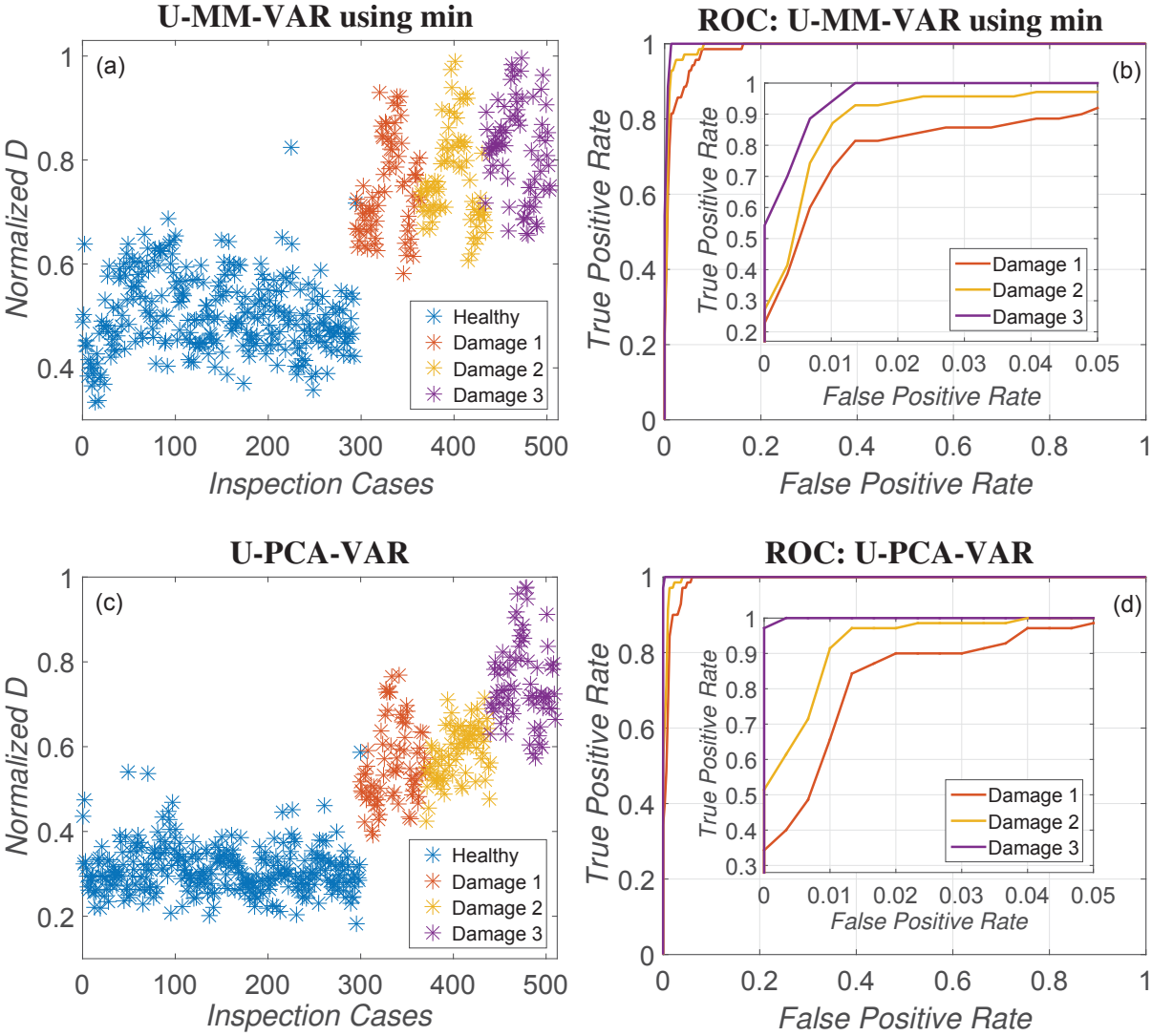

Figure 3: Damage detection performance assessment for each method and each damage scenario: Pseudo–distance metric (left column) and ROC curve (right column) for the U–MM–VAR (a,b) and U–PCA–VAR (c,d) methods (510 inspection experiments).

100% for false alarm rate of 4% (Figure 4(b)).

In general, the results indicate that the deterioration in damage detection performance due to dropping the measurement in the excitation signal is rather small, especially within the context of the PCA–based methods.

5 CONCLUSIONS

The problem of robust vibration damage detection under assembly–induced uncertainty has been considered with the focus set on the practically important non–measurable excitation (output–only) case. For this purpose experiments with a composite aerostructure under repeated assembly operations have been employed under three damage scenarios corresponding to 10%, 30%, or 50% reduction in a clamping bolt tightening torque. The problem has been tackled via two unsupervised and robust Statistical Time Series methods employing Vector AutoRegressive (VAR) modeling: The first is based on Multiple Model (MM) representations (U–MM–VAR

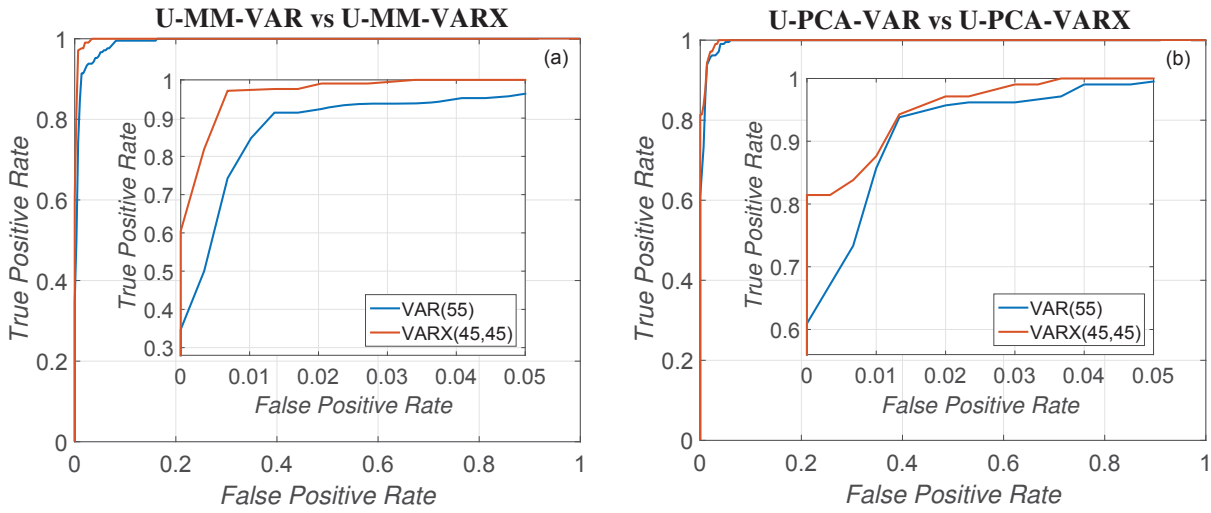

Figure 4: Damage detection performance comparison of the output–only and input–output methods via ROC curves: (a) MM–based methods, (b) PCA–based methods (cumulative curves including all damage scenarios; 510 inspection experiments per damage scenario).

method) and the second on Principal Component Analysis (U–PCA–VAR). Performance assessment has been based on 510 inspection experiments. The main conclusions drawn may be summarized as follows:

1. Despite the relatively 'minor' effects of each damage scenario on the structural dynamics and their appreciable 'masking' by those of assembly–induced uncertainty, both output–only methods lead to very good detection performance.

2. Although the performance characteristics of the two methods are largely similar, the PCA–based method offers an edge over its MM–based counterpart (correct detection rate of 99.5% versus 96% for 5% false alarm when all three damage scenarios are included).

3. As expected, the 1st damage scenario (10% torque reduction) is the most challenging, with scenarios 2 (30% torque reduction) and 3 (50% torque reduction) following in that order.

4. Although excluding the excitation signal from the damage detection procedure unquestionably increases the problem difficulty, the resulting performance degradation is relatively small, that is from 100% to 94% correct detection for the MM–based method (at 3.6% false alarm rate) and from 100% to 99% for the PCA–based method (at 4% false alarm rate).

Overall, the results of the study indicate that the use of proper robust random vibration based methods may effectively overcome the effects of assembly–induced uncertainty and achieve high detection performance even for relatively 'minor' damages and in the absence of measurable excitation.

REFERENCES

[1] A. Deraemaeker, Vibration based structural health monitoring using large sensor arrays: Overview of instrumentation and feature extraction based on modal filters, *Volume 520: A. Deraemaeker, J. Güemes, K. Worden, (Eds.), New Trends in Vibration Based Structural Health Monitoring, CISM Courses and Lectures*, Springer Vienna, 2010. doi.org/10.1007/978-3-7091-0399-9_2.

[2] S.D. Fassois, J. S. Sakellariou, Time–series methods for fault detection and identification in vibrating structures, *Philosophical Transactions of the Royal Society – Series A: Mathematical, Physical and Engineering Sciences*, **365**(1851), 411–448, 2007. doi:10.1098/rsta.2006.1929.

[3] A. Deraemaeker, E. Reynders, G. De Roeck, J. Kullaa, Vibration–based structural health monitoring using output–only measurements under changing environment, *Mechanical Systems and Signal Processing*, **22**(1), 34–56, 2008. doi:10.1016/j.ymssp.2007.07.004.

[4] K.J. Vamvoudakis-Stefanou, J.S. Sakellariou, S.D. Fassois, On the use of unsupervised response–only vibration–based damage detection methods for a population of composite structures, *Proceedings of the 8th European Workshop on Structural Health Monitoring (EWSHM)*, Bilbao, Spain, 2016.

[5] J. Kullaa, Vibration–based structural health monitoring under variable environmental or operational conditions, *Volume 520: A. Deraemaeker, K. Worden (Eds.), New Trends in Vibration Based Structural Health Monitoring, CISM Courses and Lectures*, 107–181, Springer, Vienna, 2010. doi:10.1007/978-3-7091-0399-9_4.

[6] J.D. Hios, S.D. Fassois, Stochastic identification of temperature effects on the dynamics of a smart composite beam: Assessment of multi–model and global model approaches, *Smart Materials and Structures*, **18**(3), 2009. doi:10.1088/0964-1726/18/3/035011.

[7] T.-C.I. Aravanis, J.S. Sakellariou, S.D. Fassois, A stochastic Functional Model based method for random vibration based robust fault detection under variable non–measurable operating conditions with application to railway vehicle suspensions, *Journal of Sound and Vibration*, **446**, 2020. https://doi.org/10.1016/j.jsv.2019.115006.

[8] E. Figueiredo, L. Radu, K. Worden, C. Farrar, A Bayesian approach based on a Markov–Chain Monte Carlo method for damage detection under unknown sources of variability, *Engineering Structures*, **80**, 1–10, 2014. https://doi.org/10.1016/j.engstruct.2014.08.042.

[9] L.D. Avendaño–Valencia, S.D. Fassois, Natural vibration response based damage detection for an operating wind turbine via Random Coefficient Linear Parameter Varying AR modeling, *Proceedings of the 10th International Conference on Damage Assessment of Structures (DAMAS)*, Gent, Belgium, 2015. Also in *Journal of Physics: Conference Series*, **628**(1). doi:http://dx.doi.org/10.1088/1742-6596/628/1/012073.

[10] L.D. Avendaño-Valencia, S.D. Fassois, Robust fault detection based on multiple functional serier TAR models for structures with time-dependent dynamics, *7th European Workshop on Structural Healthy Monitoring (EWSHM)*, 805–814, Nantes, France, 2014.

[11] K.J. Vamvoudakis–Stefanou, J.S. Sakellariou, S.D. Fassois, Assessment of a multiple model based parametric method for output–only vibration–based damage detection for a population of like structures, *Proceedings of the 11th International Conference on Damage Assessment of Structures (DAMAS)*, Gent, Belgium, 2015. Also in *Journal of Physics: Conference Series*, **628** (1). doi:10.1088/1742-6596/628/1/012009.

[12] H. Sohn, Effects of environmental and operational variability on structural health monitoring, *Philosophical Transactions of The Royal Society A Mathematical Physical and Engineering Sciences*, **365** (1851), 539–560, 2007. doi:10.1098/rsta.2006.1935.

[13] G.P. Andriosopoulou, A.E. Mastakouris, K.J. Vamvoudakis–Stefanou, S.D. Fassois, Random vibration based robust damage detection for a composite aerostructure under assembly-induced uncertainty, *Proceedings of the 13th International Conference on Damage Assessment of Structures (DAMAS)*, 775–787, Porto, Portugal, 2019. doi:10.1007/978-981-13-8331-1_61.

[14] K.J. Vamvoudakis–Stefanou, J.S. Sakellariou, S.D. Fassois, Vibration–based damage detection for a population of nominally identical structures: Unsupervised Multiple Model (MM) statistical time series type methods, *Mechanical Systems and Signal Processing*, **111**, 149–171, 2018. https://doi.org/10.1016/j.ymssp.2018.03.054.

[15] L. Ljung, System Identification: Theory for the User, *Prentice Hall PTR, Upper Saddle River*, 1999. https://doi.org/10.1002/047134608X.W1046.pub2.

[16] V. Papakos, S.D. Fassois, Multichannel identification of aircraft skeleton structures under unobservable excitation: A vector AR/ARMA framework, *Mechanical Systems and Signal Processing*, **17**(6), 1271–1290, 2003. doi:10.1006/mssp.2002.1575.

[17] F.P. Kopsaftopoulos, P.G. Apostolellis, S.D. Fassois, Output-–only parametric identification of a scale cable–stayed bridge structure: A comparison of Vector AR and stochastic subspace methods, *4th International Operational Modal Analysis Conference (IOMAC)*, Istanbul, Turkey, 2011.

[18] L.D. Avendaño-Valencia, S.D. Fassois, On multiple–model linear-parameter-varying based SHM for time–dependent structures under uncertainty, *Proceedings of the Surveillance 8 International Conference*, Roanne, France, 2015.

[19] W. Press, S. Teukolsky, W. Vetterling, B. Flannery, Numerical Recipes: The Art of Scientific Computing, 3rd Edition, *Cambridge University Press, New York*, ISBN: 0521880688, 2007.

[20] J. Cadima, I. Jolliffe, On relationships between uncentred and column–centred principal component analysis, *Pakistan Journal of Statistics*, **25** (4), 473–503, 2009.

[21] J. E. Jackson, A User's Guide to Principal Components, *Wiley Series in Probability and Statistics*, ISBN: 9780471725336, 1991. doi:10.1002/0471725331.

[22] A. Yan, G. Kerchen, P. De Boe, J. Golinval, Structural damage diagnosis under varying environmental conditions–Part I: A linear analysis, *Mechanical Systems and Signal Processing*, **19**(4), 847–864, 2005. https://doi.org/10.1016/j.ymssp.2004.12.002.

[23] R. Duda, P. Hart, D. Stork, Pattern Classification, 2nd Edition, *Wiley*, ISBN: 978-0-471-05669-0, 2000.

EURODYN 2020
XI International Conference on Structural Dynamics
M. Papadrakakis, M. Fragiadakis, C. Papadimitriou (eds.)
Athens, Greece, 23–26 November 2020

AUTOMATED OPERATIONAL MODAL ANALYSIS OF A STEEL ARCH BRIDGE FROM DYNAMIC SUB-MICROSTRAIN FIBER BRAGG GRATING DATA

Dimitrios Anastasopoulos[1], **Guido De Roeck**[1], **and Edwin P.B. Reynders**[1]

[1]Structural Mechanics Section, Department of Civil Engineering, KU Leuven
Kasteelpark Arenberg 40, 3001 Leuven, Belgium
e-mail: {dimitrios.anastasopoulos, guido.deroeck, edwin.reynders}@kuleuven.be

Keywords: Modal strains, Fiber Bragg gratings, Operational modal analysis, Structural health monitoring, Railway bridge.

Abstract. *Vibration-Based Monitoring (VBM) can constitute a successful approach for Structural Health Monitoring (SHM) of civil structures, but natural frequencies and displacement mode shapes can exhibit a low sensitivity to certain types of damage when compared to their sensitivity to environmental influences such as temperature. Modal strains are more sensitive to local damage and laboratory experiments have shown that they can also be insensitive to temperature changes. The direct monitoring of modal strains from very small strain levels occurring during ambient, or operational excitation has also become possible thanks to two recently developed optical interrogation techniques. The present work demonstrates for the first time the use of modal strains for VBM purposes through the monitoring a full-size civil structure. A steel railway arch bridge is monitored for a period of more than a year with eighty Fiber-optic Bragg Grating (FBG) strain sensors, multiplexed in four fibers. Thanks to a highly accurate optical interrogation technique, the ambient dynamic sub-microstrains of the monitored bridge are continuously measured with high accuracy and precision. Subsequently, the identification of its modal characteristics (modal strains and natural frequencies) is conducted on hourly basis and in a fully automated manner with the use of hierarchical clustering for the automated interpretation of the obtained stabilization diagrams. Ten modes are systematically identified from dynamic strains with a typical measured root mean square (RMS) strain value of the order of 0.01 micro-strains. The modes are tracked over time as new data are acquired. The influence of the temperature fluctuations on the modal characteristics of the bridge is extensively investigated. The results confirm that, for the achieved temperature range and temperature distribution, the modal strains of the bridge are not influenced by the temperature.*

1 INTRODUCTION

Vibration-Based Monitoring or VBM is a valuable tool for non-destructive damage identification and condition assessment of civil structures [1, 2]. The idea behind VBM is to identify changes in modal characteristics of a structure that are directly related to damage [1, 2]. The main challenge for VBM is to identify characteristics that are as sensitive as possible to structural damage and at the same time as insensitive as possible to measurement noise, loading, and environmental factors such as temperature [3, 4].

Natural frequencies are probably the most commonly used modal characteristics for damage identification [4]. Natural frequencies can be easily obtained with only a few sensors that are placed at proper locations. However, natural frequencies are influenced by environmental factors, such as temperature, and that influence can be high enough to completely mask the presence of even severe damage, necessitating data normalization [1].

Mode shapes consist another modal characteristic that is used for VBM [4]. The advantage of mode shapes over natural frequencies is that they contain local information, facilitating in this way the localization of damage. Mode shapes are also less sensitive to temperature variations, when compared to natural frequencies [4]. However, an array of sensors is required to obtain the mode shapes, which can be difficult and/or uneconomic to install in many civil structures.

Modal strains consist a modal characteristic that can be obtained from strain-based modal analyses, where dynamic strains are used as input [5, 6, 7]. Thanks to two recently developed methods for dynamic sub-microstrain measurements, the dynamic strains that occur on civil structures during ambient or operational excitation can be measured with high accuracy and precision with the use of Fiber Bragg Grating (FBG) sensors [5, 6]. Consequently, the modal strains can be identified from the measured dynamic strains with the use of subspace identification [8, 9]. Several experiments on laboratory tested concrete beams have illustrated that modal strains are highly sensitive to local damage of even moderate severity, while insensitive to temperature changes [6, 10]. Furthermore, modal strains can be obtained in a very dense grid with the use of FBGs. The advantage of FBGs is that multiple sensors can be multiplexed on a single optical fiber, offering valuable local information that facilitates the localization of damage.

The present work demonstrates the use of modal strains for VBM purposes through the long-term monitoring of a steel railway bridge. The monitoring campaign has three main goals. First, to investigate the ability of the strain monitoring method [6] to accurately measure dynamic strains and consequently identify the modal strains of a full-size civil structure under operational excitation. Second, to study the influence that environmental factors and more specifically temperature might have on the modal characteristics of a structure with complex boundary conditions and non-uniform temperature distribution. Third, to use this case study as a proof of concept of the methodology for potential end-users.

2 THE KW51 BRIDGE

The KW51 is an 117 m long railway bridge, located close to the city of Leuven in the Flemish region of Belgium. The bridge is part of the 100 km Line 36 that runs from Brussels to Liége and enables the crossing of two roads and the Leuven-Dijle channel. Line 36 is operated exclusively by passenger Thalys, ICE, Intercity, Suburbain and Omnibus trainsets.

The KW51 is a steel single-span arch bridge with a two-track deck that is suspended from the arch with thirty-two inclined braces (figure 1). The deck consists of two main girders that are stiffened by thirty-three transverse beams. The bridge is supported on four neoprene bearings at its ends, which directly sit on two concrete abutments.

(a) (b)

Figure 1: The KW51 bridge.

3 STRAIN MONITORING

The bridge is monitored with four chains of FBG sensors for more than a year, since 14 February 2019. The temperature of the bridge is also measured with one thermocouple. In the current paper, the results form the first three months of monitoring, up to 15 May 2019 are presented.

3.1 Experimental setup

The four chains of FBG sensors are located at the top surface of the bottom flange of the main girders of the bridge (figures 2 - 4). The fibers are attached to the flanges via a custom clamping system [6], to measure axial dynamic strains (figure 4a). The bottom part or ”base” of a clamping block is directly glued on a strong magnet, which is then placed on its designated location on the flange (figure 4a). Then, the fibers are firmly fixed at the discrete clamping blocks (figure 4b) to ensure the proper transfer of strains from the span to the sensors. The distance between two consecutive clamping blocks varies from 2.3 m to 2.5 m. One sensor exists between two blocks, measuring the average macro-strain between both blocks. Each fiber contains 20 FBGs, except from the northwest one that contains 19 (figure 3b). The fibers are prestressed to ensure that they remain in tension when the corresponding bridge part is being compressed. The gap that exists between the bottom flange of the transverse beams and the bottom flange of the girders (figure 4f), allows the fibers to pass below the transverse beams and get stretched along the girders.

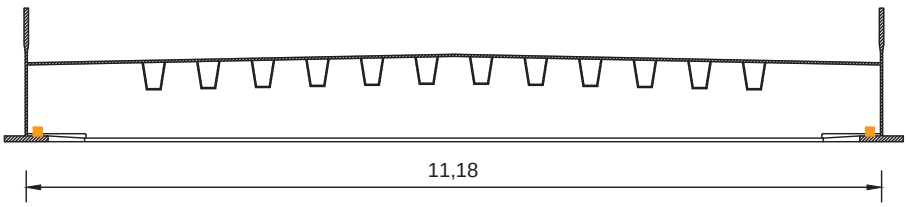

Figure 2: Typical cross-section of the deck of the KW51 bridge. The small cubes represent the clamping blocks (dimensions in m).

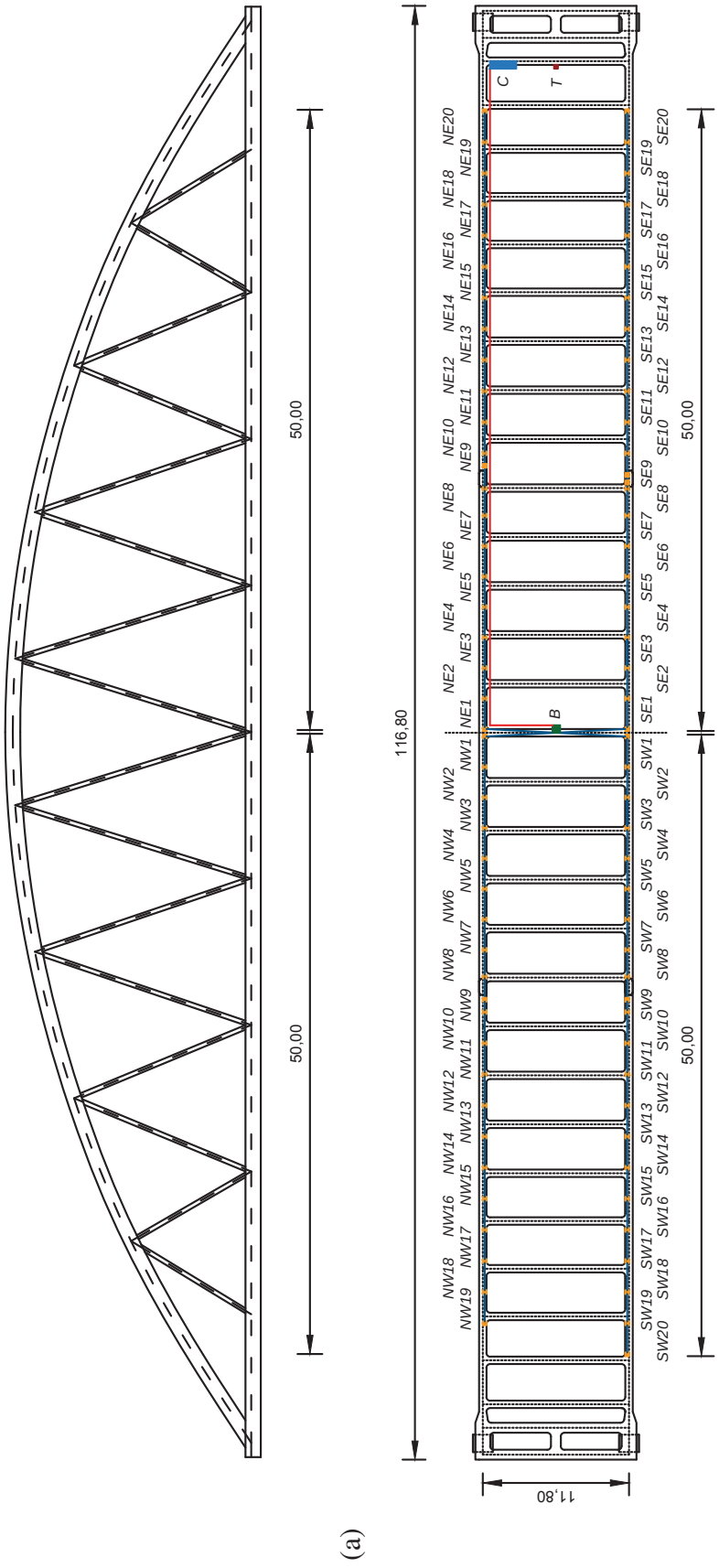

Figure 3: (a) South view of the KW51. (b) Schematic representation of the attachment of the optical fibers. The small cubes represent the clamping blocks and the rectangles the FBGs in between the clamping blocks. All FBGs are labeled; NE stands for northeast, NW for northwest, SE for southeast and SW for southwest. B denotes the box where all fibers are connected to the telecom fiber. C denotes the cabinet that contains the laptop and the acquisition system. T denotes the thermocouple. The telecom fiber is represented with a line connecting B and C (dimensions in m).

Since FBGs are sensitive to both strain and temperature, the fibers are covered with thermal insulation (figure 4c), to ensure that fast temperature fluctuations would not affect the dynamic measurements. Furthermore, the thermal insulation is covered with plastic foils to protect it against the environment. The plastic foils are secured with magnets (figure 4d).

Figure 4: (a) and (b) Photo of mounted clamping blocks and glass fiber. (c) The thermal insulation, covering the clamping box and the fiber. (d) The plastic foil, covering the thermal insulation. (e) One of the steel connection plates. (f) The gap between a transverse beam and a girder.

The strain acquisition is conducted with an interrogator that offers the required high accuracy and precision in dynamic sub-microstrain measurements [5, 6], the FAZ Technologies FAZT-I4. The sampling frequency is f_s = 1000 Hz. The acquisition system and the laptop that is required to operate the acquisition system, perform the measurements and save the data, are placed inside a cabinet that is located close to one end of the bridge and is attached on a transverse beam via magnets. The FBG fibers are connected to the acquisition system through a telecom fiber that spans the distance (≈60 m) between the cabinet and the midspan of the bridge, where all four fibers are connected to the telecom fiber in a wall mount box (figure 3).

The temperature of the bridge is measured throughout the monitoring period with a thermocouple that is used for this purpose [11]. The thermocouple is attached on the same transverse beam as the cabinet that contains the acquisition system (figure 3). The maximum recorded temperature during the first three months of the monitoring is $26°$C and the minimum $4°$C.

4 STRAIN-BASED MODAL ANALYSIS

Dynamic strain data are used for the identification of the modal characteristics of the bridge, i.e. natural frequencies and strain mode shapes. The strain data are obtained from operational excitation tests that were conducted on an hourly basis and had a duration of 900 s each. The strain data are used in strain-based Operational Modal Analyses (OMA), to identify the modal

characteristics of the span under changing temperature conditions and in a repetitive way. In total, 2139 operational excitation tests were conducted during the first three months (table 1).

Period	Tests	Period	Tests	Period	Tests	Period	Tests
14-28/2/19	316	1-31/3/19	743	1-30/4/19	720	1-15/5/19	360
Total 2139							

Table 1: Monthly amount of operational excitation tests recorded during the monitoring period of the KW51 bridge.

4.1 System identification

The data processing and the system identification is conducted with MACEC [12]. First, the static or DC offset is removed from all measured strain signals. Second, the data are low-pass filtered with an 8^{th} order Chebyshev Type I low-pass filter with a cut-off frequency of 16 Hz and then re-sampled at a lower frequency, resulting in a new sampling frequency f_s=40 Hz. Then, a fourth-order Butterworth filter with a high-pass frequency of 0.35 Hz is applied to all channels, in order to remove the influence of temperature fluctuations on the FBGs. The position-averaged RMS strain values among all sensors is in the range of 0.01 $\mu\varepsilon$. The output-only, data-driven stochastic subspace identification (SSI-data) method [8] is employed for identifying a range of state-space models from the strain data. When the time signals include one or more train passages, the data Hankel matrix [8] is modified to exclude them from the identification process, i.e. the columns of the Hankel matrix that contain data from times when a train is on the bridge, are removed. The train passages are automatically identified by an algorithm that tracks peaks in the data with amplitude larger than $1\mu\varepsilon$, which correspond to train bogies. The computed modal characteristics are used for constructing stabilization diagrams (figure 5).

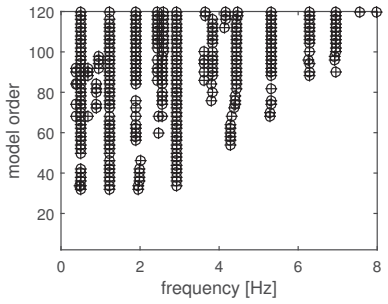

Figure 5: Typical stabilization diagram, as obtained from an ambient excitation test.

4.2 Automatic identification of modal characteristics

Modal analysis consists of four different stages: data collection, data processing, system identification and determination of a validated set of modal characteristics [13, 14]. The first three stages can be easily automated, e.g. with the use of MACEC. The user needs to make some initial choices, e.g. maximum system order, which can be used then for all data sets. The fourth stage, i.e. the determination of the modal characteristics, is also automated here by using the principles of hierarchical clustering, which is a method of cluster analysis [15] and allows to automatically select modes from the constructed stabilization diagrams.

The hierarchical agglomerative clustering is considered as a suitable procedure for clustering the estimated modes of a clear stabilization diagram and automatically obtain the psychical modes of the structure. This procedure has been successfully implemented on the ”Infante D. Henrique” bridge in Porto and it was proved to be very efficient in the identification of the bridge’s first 12 natural frequencies [16]. The implementation of the hierarchical agglomerative clustering for automatically identifying the modal characteristics of KW51 is thoroughly explained in [17]. Ten modes are consistently identified during the considered period. In figure 6, the natural frequencies of these modes are displayed for the period 14/2/19 - 15/5/19.

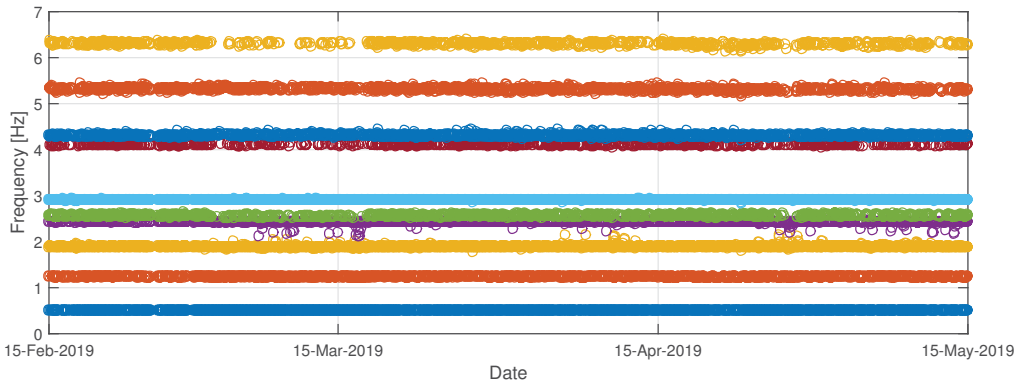

Figure 6: Automatically identified natural frequencies of the modes of KW51, during the period 14/2/19-15/5/19.

The strain mode shapes, natural frequencies and modal damping ratios of the first six modes are displayed in figures 7 and 8. The physical interpretation of the mode shapes is possible thanks to a separate acceleration-based OMA [11]. The modes can be classified as deck or arch modes, depending on which part of the bridge is predominantly excited for every mode.

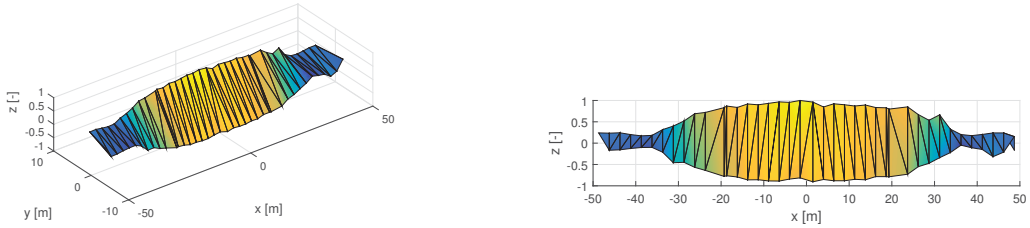

(a) Mode 1 - 1$^{\text{st}}$ lateral mode of the arch ($f_1^{\text{ssi}} = 0.51$ Hz, $\xi_1^{\text{ssi}} = 0.2\%$)

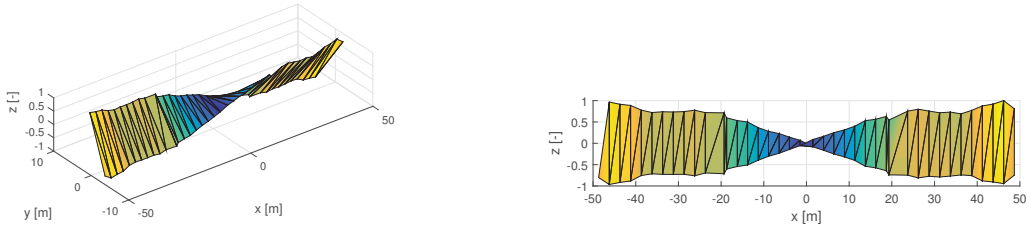

(b) Mode 2 - 2$^{\text{nd}}$ lateral mode of the arch ($f_2^{\text{ssi}} = 1.24$ Hz, $\xi_2^{\text{ssi}} = 0.1\%$)

Figure 7: Strain mode shape, natural frequency and damping ratio of modes 1 and 2 of the KW51 bridge, as identified from strain-based OMA using SSI-data. The left subplots illustrate the 3D view and the right subplots the front (x-z) view of the strain mode shapes.

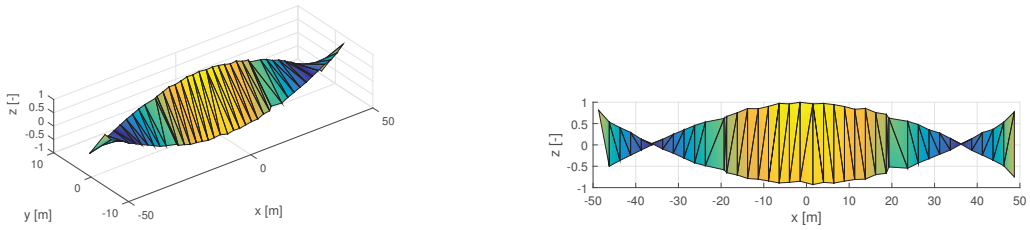

(a) Mode 3 - 1st lateral mode of the deck (f_3^{ssi} = 1.89 Hz, ξ_3^{ssi} = 0.9%)

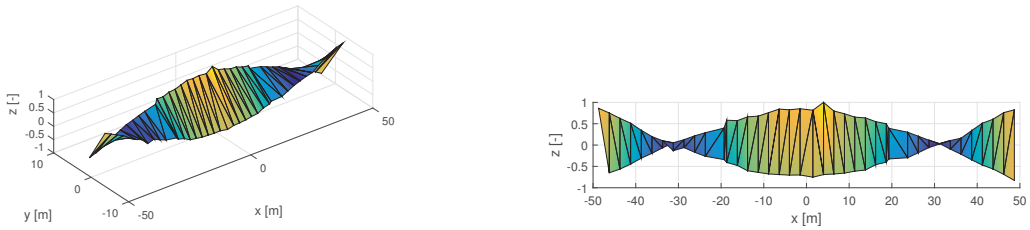

(b) Mode 4 - 3rd lateral mode of the arch (f_4^{ssi} = 2.45 Hz, ξ_4^{ssi} = 0.1%)

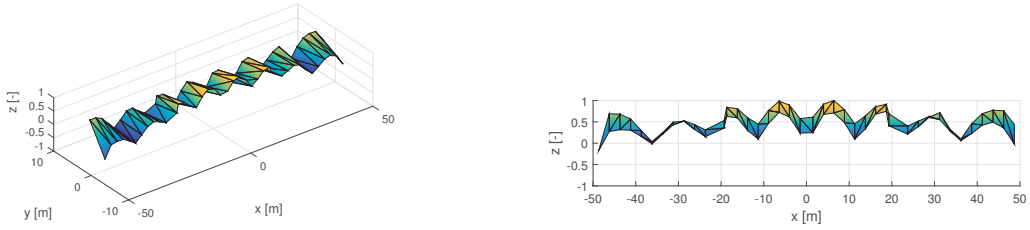

(c) Mode 5 - 1st bending mode of the deck (f_5^{ssi} = 2.54 Hz, ξ_5^{ssi} = 1.8%)

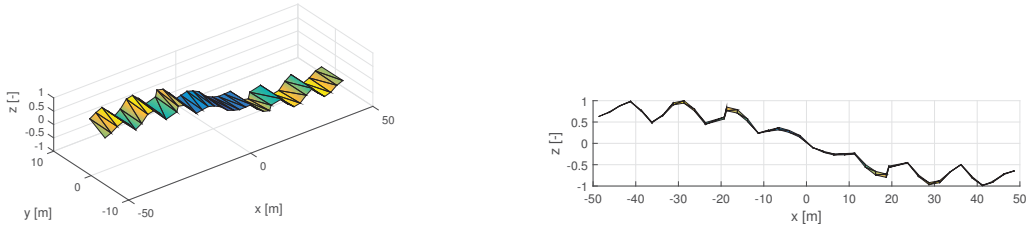

(d) Mode 6 - 2nd bending mode of the deck (f_6^{ssi} = 2.92 Hz, ξ_6^{ssi} = 0.3%)

Figure 8: Strain mode shape, natural frequency and damping ratio of modes 3, 4, 5 and 6 of the KW51 bridge, as identified from strain-based OMA using SSI-data. The left subplots illustrate the 3D view and the right subplots the front (*x*-*z*) view of the strain mode shapes.

4.3 Influence of temperature on modal characteristics

The influence of temperature on the modal characteristics of the bridge, i.e. natural frequencies and strain mode shapes is investigated in the following sections.

4.3.1 Influence of temperature on natural frequencies

The time evolution of the natural frequencies of the ten systematically identified modes of KW51 is displayed in figure 6. In order to investigate the influence of temperature on natural frequencies, the natural frequencies of these modes are plotted as a function of temperature in figure 9. The natural frequencies in figure 9 are plotted within y-axis limits that are defined

based on their mean value $\mu[f_j^{\text{ssi}}]$, to provide with a common relative scaling for all modes. The limits of the y-axis in these figures are defined as $\pm 3\%$ of the mean value $\mu[f_j^{\text{ssi}}]$. The linear regression and the coefficient of determination (R^2) between temperature T and natural frequency f is also computed. Based on the linear regression, the relative change of the natural frequency of each mode $\Delta f[\%]$, for a temperature change of $\Delta T = +10°\text{C}$ can be obtained [17]. The coefficient of determination (R^2) and the relative change of the natural frequency $\Delta f_{10}[\%]$ of each mode are provided in figure 9.

It can be observed in figure 9 that temperature has an insignificant influence on the natural frequency of most of the modes of the deck (modes 3 and 5), while the modes of the arch (modes 1, 2 and 4) and the second bending mode of the deck (mode 6) appear to be more influenced from the temperature changes, for the given temperature range of about $24°\text{C}$ that was achieved during the monitoring period. An increase of $\Delta T = 10°\text{C}$ in temperature results in a relative decrease of about $\Delta f_{10} = 0.2 - 0.25\%$ for the natural frequencies of the arch modes and mode 6. The relationship appears to be relatively consistent among these modes, for the temperature range of $24°\text{C}$. The scattering of natural frequency values for some of the modes, e.g. mode 5 in figure 9e, can be as large as $\pm 2\%$ from the mean value $\mu[f_j^{\text{ssi}}]$, which creates a data "cloud", as it is proved also by their low coefficient of determination (R^2). This data "cloud" poses no correlation with the temperature changes. Such large scattering can be attributed to several factors, such as: influence of other environmental factors than temperature (e.g. solar radiation), the loading amplitude (e.g. wind intensity), the thermal inertia of the structure, identification errors, and others. Similar conclusions are drawn from the rest of the identified modes [17] and thus they are not displayed here.

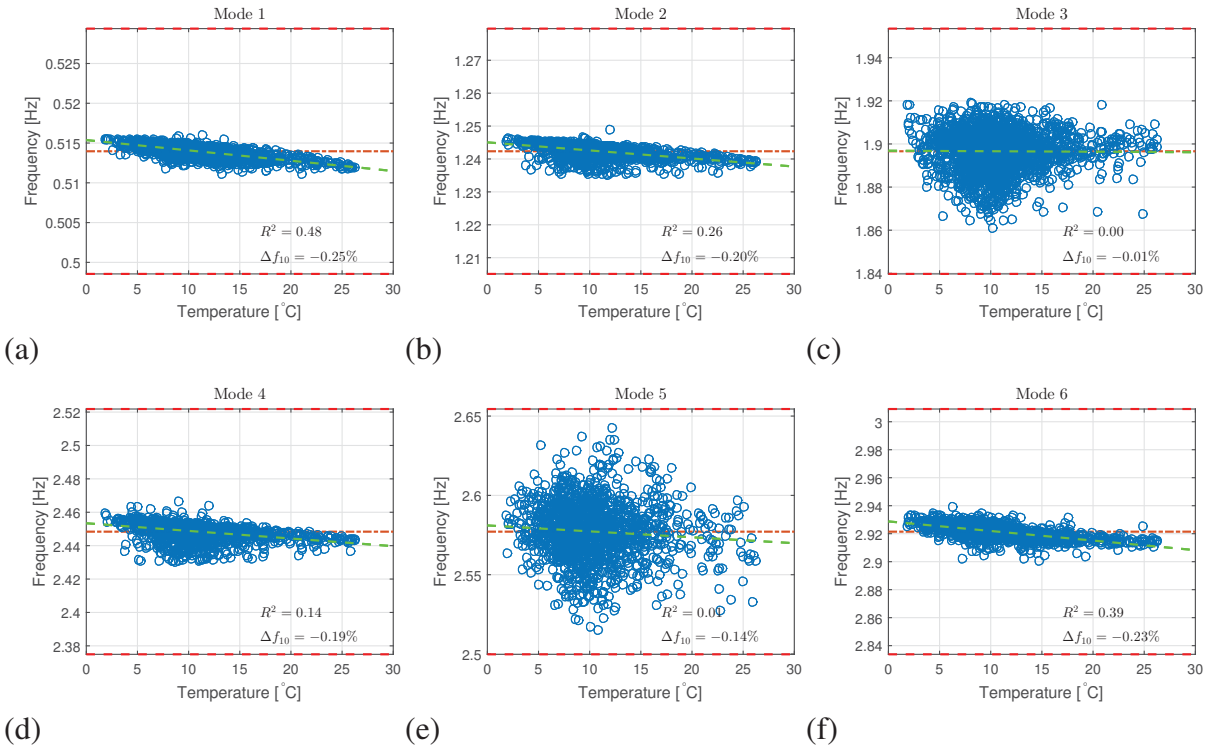

Figure 9: Evolution of the natural frequencies of modes 1 to 6 of the KW51 bridge as a function of temperature, as identified from SSI-data (f_j^{ssi}) and during the period before the retrofitting. The dash-dotted line denotes the mean natural frequency $\mu[f_j^{\text{ssi}}]$, while the dashed line denotes the linear regression of the data $f(T)$. The y-axis limits of the plots, which correspond to $\pm 3\%$ of $\mu[f_j^{\text{ssi}}]$, are also denoted with dashed lines.

4.3.2 Influence of temperature on strain mode shapes

The influence of the temperature fluctuations on the strain mode shapes $\boldsymbol{\psi}_j^{\text{ssi}}$ is investigated. The strain mode shapes obtained from all modal tests are used. First, a normalization scheme [9] is applied which allows for a direct comparison of the strain mode shapes that have been determined at different temperatures [10]. Second, the strain mode shapes are clustered in temperature groups that each have a non-overlapping range of 2°C. Third, for each temperature group k, the sample mean $\mu[\boldsymbol{\psi}_j^{\text{ssi},(k)}]$ of all strain mode shapes in the group is computed, as well as the sample standard deviation $\sigma[\boldsymbol{\psi}_j^{\text{ssi},(k)}]$ and the related $\pm 2\sigma$ confidence interval $\text{CI}[\boldsymbol{\psi}_j^{\text{ssi},(k)}]$, which boils down to a 95% confidence interval when the samples are normally distributed [9, 10]. The mean strain mode shape with its 95% confidence interval for the different temperature groups of the second bending mode of the deck (mode 6) are displayed in figure 10b. It can be clearly observed that the confidence intervals for the different temperature groups overlap completely, and they all have nearly the same width. It can therefore be concluded that, in the present experiment, there is no statistically significant influence of the temperature on the strain mode shapes, for the given temperature range of 24°C. Similar conclusions are drawn from the rest of the strain mode shapes [17] and thus they are not displayed here.

Since temperature does not influence the strain mode shapes, the statistical uncertainty must relate to other causes of variability in the strain mode shapes at a given temperature group, such as identification errors. The fact that the confidence intervals in figure 10b all fall on top of each other, indicates that the identification errors have low bias. This implies that the uncertainty on the identified strain mode shapes can be reduced by averaging. Indeed, the standard deviation *of the sample mean* of the entire set of N_k samples (i.e., identified strain mode shapes) obtained at a given temperature group *k* is related to the standard deviation of the set as:

$$\sigma[\mu[\boldsymbol{\psi}_j^{\text{ssi},(k)}]] = \frac{\sigma[\boldsymbol{\psi}_j^{\text{ssi},(k)}]}{\sqrt{N_k}} \tag{1}$$

and the related $95\,\%$ confidence interval reads:

$$\text{CI}[\mu[\boldsymbol{\psi}_j^{\text{ssi},(k)}]] = [-2\sigma[\mu[\boldsymbol{\psi}_j^{\text{ssi},(k)}]], 2\sigma[\mu[\boldsymbol{\psi}_j^{\text{ssi},(k)}]]] \tag{2}$$

Figure 10c displays, for the second bending mode, the sample mean of the complete set of all the repeatedly identified strain mode shapes $\mu[\boldsymbol{\psi}_j^{\text{ssi},(k)}]$ that are obtained at a given temperature group *k*, together with the 95% confidence interval of *the sample mean of* each set. Note that the sample mean values of figure 10b and figure 10c are identical, but that the width of the confidence intervals in figure 10c are a factor $1/\sqrt{N_k}$ narrower than in figure 10b, because in figure 10c the uncertainty of the averaged, sample mean values is considered. It can be clearly observed that the narrow confidence intervals of *the sample mean of* the different temperature groups overlap completely, and they all have nearly the same width, increasing the confidence that there is no statistically significant influence of the temperature on the strain mode shapes, for the temperature range of 24°C.

5 CONCLUSIONS

The KW51 railway bridge is monitored with four chains of FBGs for a period of more than a year. Modal tests, using ambient excitation as well as the free response of the bridge after train passages are conducted every hour throughout this period. The dynamic strain data from

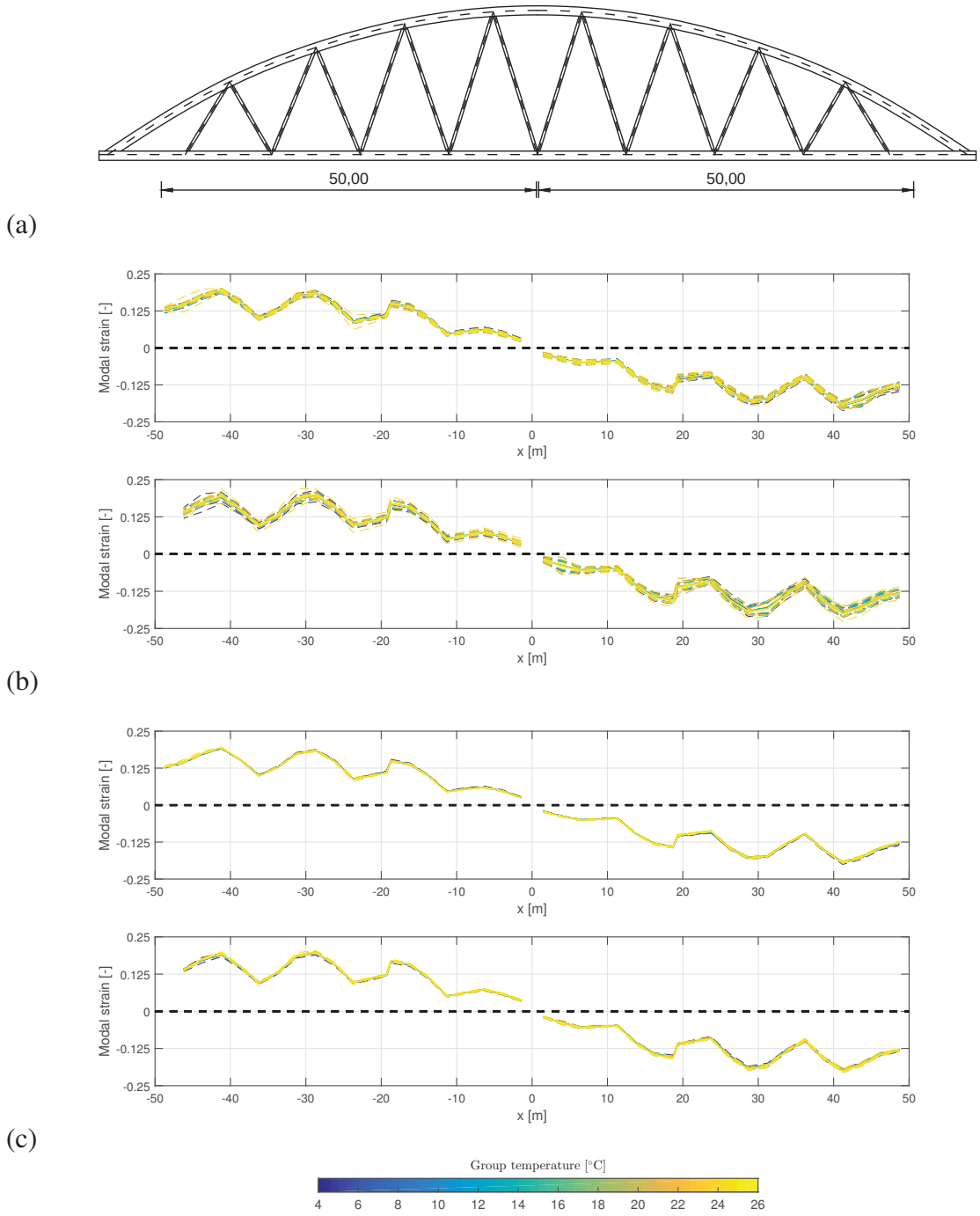

Figure 10: (a) South view of the KW51. (b) Sample mean $\mu[\boldsymbol{\psi}_j^{\mathrm{ssi},(k)}]$ and 95 % CI$[\boldsymbol{\psi}_j^{\mathrm{ssi},(k)}]$ of the strain mode shapes that have been identified in each temperature group k for mode 6. (c) Sample mean $\mu[\boldsymbol{\psi}_j^{\mathrm{ssi},(k)}]$ and 95 % CI$[\mu[\boldsymbol{\psi}_j^{\mathrm{ssi},(k)}]]$ *of the sample mean*, of the strain mode shapes that have been identified in each temperature group k for mode 6. The top and bottom subplots contain the strains at the north and south sides of the bridge, respectively.

these tests are used in operational modal analyses. Results from the first three months of the monitoring are presented in this paper.

The modal characteristics of the bridge are identified in a repetitive and automated way with the implementation of a hierarchical agglomerative clustering algorithm. Ten modes are

successfully and continuously identified throughout the monitoring period. The influence of temperature on the natural frequencies and the strain mode shapes of the bridge is investigated.

A small influence of the temperature on the natural frequency of the arch's modes is identified, while the natural frequency of the deck's modes appears not to be influenced by temperature, for the given temperature ranges.

The strain mode shapes of all identified modes are found to be insensitive to temperature changes, for the given temperature ranges, confirming the observations from past experiments in laboratory tested beams [10]. This is an important conclusion, since a temperature-insensitive dynamic characteristic can be directly used for damage identification, without requiring data normalization.

REFERENCES

[1] J.M.W. Brownjohn, A. De Stefano, Y.-L. Xu, H. Wenzel, and A.E. Aktan. Vibration-based monitoring of civil infrastructure: challenges and successes. *Journal of Civil Structural Health Monitoring*, 1(3–4):79–95, 2011.

[2] S. W. Doebling, C. R. Farrar, and M. B. Prime. A summary review of vibration-based damage identification methods. *The Shock and Vibration Digest*, 30(2):91–105, 1998.

[3] A. Deraemaeker, E. Reynders, G. De Roeck, and J. Kullaa. Vibration based Structural Health Monitoring using output-only measurements under changing environment. *Mechanical Systems and Signal Processing*, 22(1):34–56, 2008.

[4] W. Fan and P. Qiao. Vibration-based damage identification methods: a review and comparative study. *Structural Health Monitoring*, 10(1):83–111, 2010.

[5] D. Anastasopoulos, P. Moretti, T. Geernaert, B. De Pauw, U. Nawrot, G. De Roeck, F. Berghmans, and E. Reynders. Identification of modal strains using sub-microstrain FBG data and a novel wavelength-shift detection algorithm. *Mechanical Systems and Signal Processing*, 86A:58–74, 2017.

[6] D. Anastasopoulos, M. De Smedt, L. Vandewalle, G. De Roeck, and E. Reynders. Damage identification using modal strains identified from operational fiber-optic Bragg grating data. *Structural Health Monitoring*, 17(6):1441–1459, 2018.

[7] J.F. Unger, A. Teughels, and G. De Roeck. Damage detection of a prestressed concrete beam using modal strains. *ASCE Journal of Structural Engineering*, 131(9):1456–1463, 2005.

[8] B. Peeters and G. De Roeck. Reference-based stochastic subspace identification for output-only modal analysis. *Mechanical Systems and Signal Processing*, 13(6):855–878, 1999.

[9] E. Reynders, K. Maes, G. Lombaert, and G. De Roeck. Uncertainty quantification in operational modal analysis with stochastic subspace identification: validation and applications. *Mechanical Systems and Signal Processing*, 66–67:13–30, 2016.

[10] D. Anastasopoulos, G. De Roeck, and E. P. B. Reynders. Influence of damage versus temperature on modal strains and neutral axis positions of beam-like structures. *Mechanical Systems and Signal Processing*, 134:106311, 2019.

[11] K. Maes and G. Lombaert. Geïdentificeerde globale eigenmodes van spoorwegbrug KW51. Report BWM-2019-13, Department of Civil Engineering, KU Leuven, December 2019.

[12] E. Reynders, M. Schevenels, and G. De Roeck. MACEC 3.3: a Matlab toolbox for experimental and operational modal analysis. Report BWM-2014-06, Department of Civil Engineering, KU Leuven, July 2014.

[13] W. Heylen, S. Lammens, and P. Sas. *Modal analysis theory and testing*. Department of Mechanical Engineering, Katholieke Universiteit Leuven, Leuven, Belgium, 2007.

[14] E. Reynders, J. Houbrechts, and G. De Roeck. Fully automated (operational) modal analysis. *Mechanical Systems and Signal Processing*, 29:228–250, 2012.

[15] J. F. Hair, W. C. Black, B. J. Babin, and R. E. Anderson. *Multivariate Data Analysis*. Pearson Education Limited, Essex, UK, 7^{th} edition, 2014.

[16] F. Magalhães, Á. Cunha, and E. Caetano. Online automatic identification of the modal parameters of a long span arch bridge. *Mechanical Systems and Signal Processing*, 23(2):316–329, 2009.

[17] D. Anastasopoulos. *Structural health monitoring based on operational modal analysis from long-gauge dynamic strain measurements*. PhD thesis, Department of Civil Engineering, KU Leuven, 2020.

EURODYN 2020
XI International Conference on Structural Dynamics
M. Papadrakakis, M. Fragiadakis, C. Papadimitriou (eds.)
Athens, Greece, 23–26 November 2020

AN ITERATIVE MULTILEVEL UPDATING SCHEME FOR VIBRATION-BASED DAMAGE ASSESSMENT OF A PRESTRESSED CONCRETE GIRDER BRIDGE

L. He[1], E. Reynders[2], C. Deng[3], G.C. Marano[4], B. Briseghella[4] and G. De Roeck [2]

[1]Sustainable and Innovative Bridge Engineering Research Center (SIBERC), College of Civil Engineering, Fuzhou University and Previously Research Associate at KU Leuven
Nr. 2, Wulongjiang North Road, University Town, 350108, Fuzhou, P.R. China
e-mail: Leqia.He@fzu.edu.cn

[2] Structural Mechanics Section, University of Leuven (KU Leuven)
Kasteelpark Arenberg 40 - box 2448 3001 Leuven Belgium
e-mail: {Edwin.Reynders, Guido.DeRoeck}@kuleuven.be

[3] Department of Structural Engineering, Tongji University
Nr. 1239, Siping Road, Shanghai, P.R. China
e-mail: DengCG@tongji.edu.cn

[4] SIBERC, College of Civil Engineering, Fuzhou University
Nr. 2, Wulongjiang North Road, University Town, 350108, Fuzhou, P.R. China
e-mail: {Marano, Bruno}@fzu.edu.cn

Keywords: Operational modal analysis, FE model updating, Multilevel optimization, Damage assessment.

Abstract. *For vibration-based structural health monitoring, a multilevel optimization scheme is applied to damage assessment of a prestressed concrete bridge. As a linear elastic problem to be addressed, damage was represented by reduction of structural stiffness of the reference model for the elements where the damage occurred. The Finite Element (FE) model updating problem is formulated as a nonlinear least-squares problem, which tries to minimize the differences between the reference model and the real (or simulated) structure with respect to the modal data. Due to the specific structure of the bridge, damage parametrization was introduced both using substructuring and a damage function. Consequently, the optimization variables were divided into global ones and local ones, which leads to the implementation of an iterative multilevel updating scheme. Satisfactory results were obtained for two numerical simulated damage scenarios: one with a single damage and one with multiple damage.*

1 INTRODUCTION

FE model updating has been widely applied to vibration-based structural health monitoring for damage assessment using operational modal data [1, 2, 3]. The damage assessment procedure requires solving an inverse problem based on experimental data to detect, locate, and quantify damage. The model updating technique is generally formulated into a numerical optimization problem, which tries to minimize the differences between the reference model and the real structure with respect to the modal data, such as natural frequencies and mode shapes. The solution procedure often involves a large number of unknown parameters, especially when the structure being investigated is complicate. As a result, the associated numerical problem is usually ill-posed. It might not have an unique solution, or the numerical solution is highly sensitive to small changes of the input data.[4, 5]. For a civil structure, not only the experimental results are effected by noise, but also the numerical models can be inaccurate to reproduce the behaviour of the real structure due to modelling errors. Therefore, several important issues related to FE model updating need to be carefully addressed, such as pramaterization of damage [6], modelling errors [7], objective function [8], regularization [9], environmental effects [10], and numerical optimization algorithms [11, 12, 13].

In practice, the most time consuming part is numerical modal analysis in the model updating process. Modal analysis of the reference model has to be repeated, since the objective function needs to re-evaluated with the updated parameters at every iteration step. Therefore, a simplified model of the bridge or structure is usually preferable as the reference model for the benefits of its computational efficiency [14]. Another practical problem often encountered for a civil structure is the lack of the baseline measurements for the undamaged state. Even though modal properties of the healthy structure can be estimated with a refined FE model [15, 16], the material properties and boundary conditions are influenced by environmental conditions like temperature, which increases the uncertainty of the estimation of damage parameters. In this paper, damage assessment is performed for a prestressed concrete girder bridge. It is a part of a long multispan viaduct, which consisted of a series of simply supported girder bridges. Extensive operational modal analysis was conducted by the Structural Mechanics section of KUL on the viaduct that was associated with corrosion-induced damage. It provided rich information for investigation and evaluation of the aforementioned engineering problems in a very realistic context. When an optimization problem can be divided into a series of smaller problems, an iterative multilevel solution scheme is of specific interest concerning the simplification and robustness of the numerical procedure. The multilevel optimization is a decomposition technique in which the problem is reformulated as several smaller subproblems (local problems) and a coordination problem (global problem) to preserve the coupling among the subproblems. Each span of the viaduct consisted of several main girders connected with transverse trusses. By taking into account the characteristics of the current structure, the multilevel approach described in [17] is adapted to the damage assessment of the bridge.

The paper is organized as follows. In Section 2, the context of the case study is presented regarding the bridge and the operational modal analysis. In Section 3, two different kinds of FE models were built with model calibration. The refined volume model serves as the baseline model. And the simplified plate model is used as the reference model to be updated. Two damage scenarios were simulated by the first model. In Section 4, the solution scheme is described, with the application to the two simulated damage cases. Discussion, conclusions and future perspectives are set forth at the last two sections.

2 BRIDGE DESCRIPTION AND OPERATIONAL MODAL ANALYSIS

2.1 The Boirs viaduct

The Boirs viaduct is a prestressed concrete bridge, which is composed of multiple simply supported spans at around twenty-five meters. The viaduct is a part of the roadway linking Antwerp and Liège in Belgium. There are two parallel bridges to accommodate the transportation in the opposite directions. The viaduct was designed and completed in the 1960s. In 2009, severe corrosion caused damage was found on the viaduct for several spans. Damage was mainly located on the main girders, with cracks, opening of the concrete surface, and exposure of the steel tendons (or even rupture). Humidity and leakage of the rainwater from the bridge deck was found to be the main cause of the damage.

(a) (b)

Figure 1: The Boirs viaduct, pictures taken during the tests: a) top view; b) bottom view.

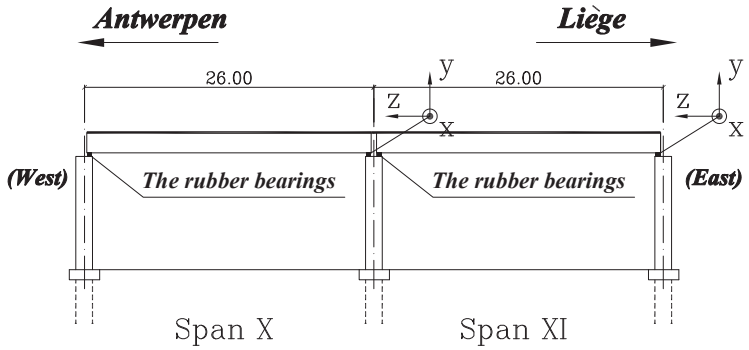

Figure 2: Elevation view of Span X and Span XI (units in meter). Note: the two adjacent Spans were of identical design.

As shown in Fig. 1, there were seven prestressed concrete main girders, simply supported on top of the piers by rubber bearings. The main girders were connected by five transverse trusses. They were assembled by triangle truss components with post-tensioning applied on-site. Extensive ambient vibration tests were performed on one of the mostly damaged spans, labelled as Span X, and the adjacent Span XI, in 2009 and early 2010 before the whole structure was demolished. See Fig. 2. As shown in Fig. 3, each span of the viaduct has similar dimensions

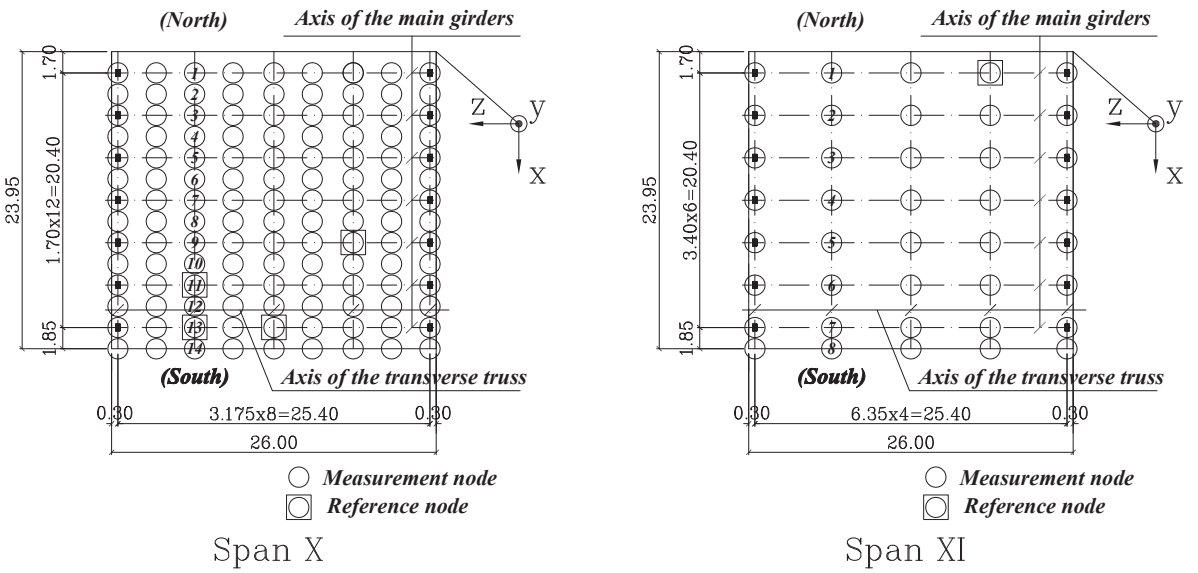

Figure 3: Plan view of Span X and Span XI, with the measurement nodes indicated by circles (units in meter).

in its longitudinal and transverse directions. Hence, the vibration characteristics of the bridge were more close to those of a plate, rather than a simply supported beam.

2.2 Operational modal analysis

Vibration tests of the Boirs viaduct were performed by using either operational modal analysis (OMA) or OMA with eXogenous inputs (OMAX) [18, 19]. Both traditional cabled sensors and latest wireless acquisition system were used to measure the acceleration responses of the deck, while the bridge was under the ambient excitation (e.g., wind and vehicles passing by on the neighbouring viaduct). See, for instance, Fig. 1. Highly reliable experimental modal results were obtained for the Span X, with the very dense sensor grid (9 by 14, equals to 126 nodes) [20]. In detail, nine cross sections of bridge, including those over the supports, were instrumented with fourteen measurement nodes on each. On the adjacent Span XI, operational modal analysis was performed with the less dense sensor grid (5 by 8, equals to 40 nodes) [21]. In detail, five cross sections were instrumented with eight measurement nodes of each. See Fig. 3 for the measurement plan. Both Span X and Span XI were of identical structure. No evident damage was found of Span XI by visual inspection, which was therefore considered almost undamaged. Accordingly, the operational modal data of Span XI could serve as the baseline data for the undamaged state of one span of the viaduct.

The experimental natural frequencies of Span X and Span XI are presented in Table 1. In total, five modes are identified. The corresponding mode shapes are plotted in Fig. 4 for Span X. And those of Span XI were however similar in appearance. Especially, m1 and m5 are not identified for Span XI. It was believed to related to the differences in the testing scheme. Since the number of the measurement nodes exceeds the number of the acquisition channels, the vibration tests had to be divided into several experimental setups concerning the measurement nodes. The incomplete mode shapes identified from each setups were combined lately by considering the predefined reference nodes or the fixed nodes as the basis for linear combination of vectors. For Span X, there were four reference nodes, which were located both at the south side and the middle of the deck, whereas for Span XI there was only one reference node located at

the north edge of the deck. As a result, the experimental modes with the modal displacements mainly on the south side of the deck could not be obtained by the latter scheme, including m1 and m5.

Mode	Span X	Span XI	Vol.(0)	Vol.(d1)	Vol.(d2)	Plate(0)	Plate(d1)	Plate(d2)
m1	5.13	n/a	5.40	5.22	5.13	5.38	5.23	5.16
m2	5.53	5.64	5.64	5.64	5.51	5.65	5.64	5.49
m3	7.83	7.99	7.69	7.65	7.59	7.67	7.62	7.56
m4	12.76	12.99	13.38	13.34	13.32	13.39	13.32	13.25
m5	15.52	n/a	16.99	16.33	16.33	17.04	16.28	16.22

Table 1: Identified natural frequencies f_i of the Boirs viaduct and those predicted by the refined FE volume model and the simplified FE plate model (units in Hz). Note: 0 for undamaged state, d1 and d2 for the simulated damage scenarios.

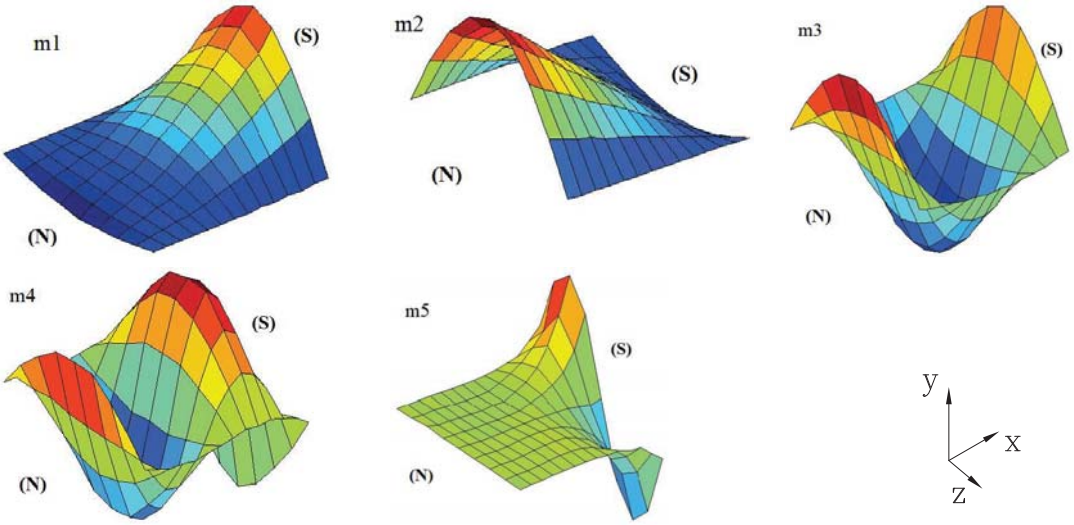

Figure 4: Experimental mode shapes ϕ_i identified from the damaged Span X: m1 to m5.

3 NUMERICAL MODEL OF THE BOIRS VIADUCT

3.1 The refined FE volume model

A refined FE volume model of the viaduct was built in ANSYS mainly with eight-node solid elements, known as Solid45. The geometry of the model strictly follows the design drawings. Even the cantilever part of the deck that served as the side walk had been carefully modelled. See Fig. 5. The rubber bearing supports were modelled with 3-D spring elements, known as Link180. The stiffness of the elements was calculated according to the size of the bearing and its material. Linear elastic properties of the materials are assumed in the FE model. See Table 2. There are in total 91,647 nodes, 71,240 elements and 274,899 DoFs in the refined model.

The intention to build the refined FE volume model is to create an accurate baseline model of the structure, in addition to generate simulated damage scenarios. Operational modal data of the undamaged Span XI were taken as the reference for calibration of the refined FE model.

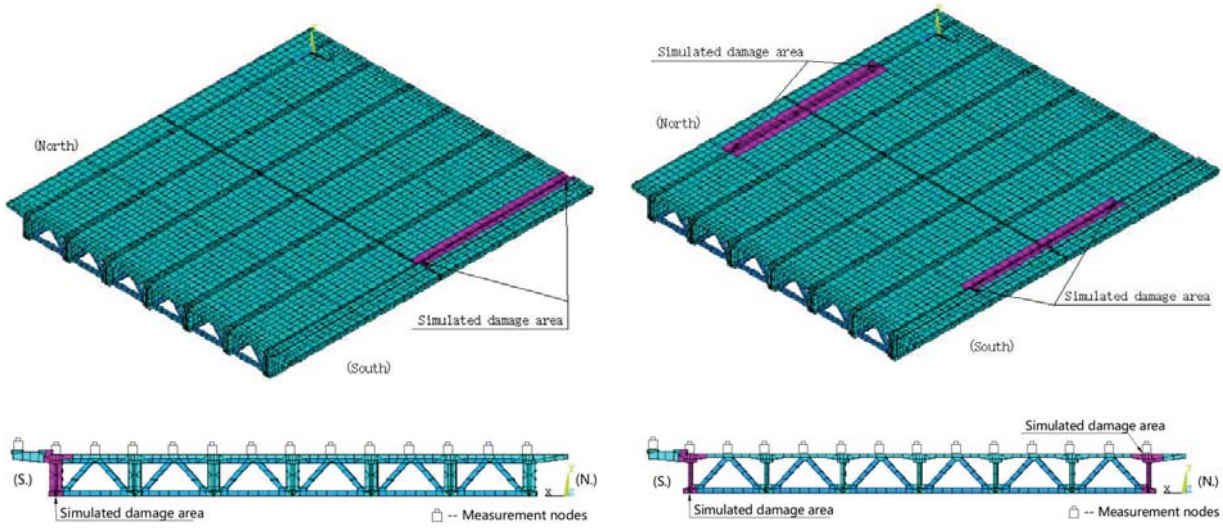

(a) (b)

Figure 5: The refined FE volume model: a) single damage scenario; b) multiple damage scenario. Note: the sensor locations for the measurements on Span X are denoted with symbols on the deck.

Components	E_0(MPa)	E(MPa)	ν	G(MPa)	q(kg/m^3)
Main girder/ Slab	35,000	45,284	0.33	17,024	2,400
Transverse truss	35,000	26,723	0.33	10,046	2,400
	k_x(kN/m)	k_y(kN/m)	k_z(kN/m)		
Boundary spring	5,733	700,000	4,410		

Table 2: Material properties of the refined FE volume model. Note: E for modulus of elasticity, ν for Poisson's ratio, G for shear modulus, q for density and k for equivalent stiffness of springs.

By engineering judgement, the main uncertainties of the FE volume model were the stiffness of the main girders and the transverse trusses. FE model updating was conducted with the Young's modulus E1 and E2 of the main girders (including the slab), and the transverse trusses, respectively, as the updating parameters. Both the residuals of the eigenfrequencies and the mode shapes were included to build the objective function (see the equations below). The three modes, i.e., m2, m3 and m4, identified from Span XI were considered. In a greater detail, the residuals were defined by:

$$\begin{aligned} \varepsilon_{\lambda,i} &= (\lambda_i - \tilde{\lambda}_i)/\tilde{\lambda}_i, \text{ for } i \in \{1,2,...,n_\lambda\} \\ \boldsymbol{\varepsilon}_{\boldsymbol{\phi},i} &= (\boldsymbol{\phi}_i - \tilde{\boldsymbol{\phi}}_i)/\|\tilde{\boldsymbol{\phi}}_i\|_1, \text{ for } i \in \{1,2,...,n_\phi\} \end{aligned} \tag{1}$$

with $\lambda_i = (2\pi f_i)^2$, $\boldsymbol{\phi}_i$ the mode shape vectors, n_λ the number of eigenfrequencies to be considered and n_ϕ the number of mode shape vectors to be considered. Herein, the upper tilde denotes the experimental results and the bold Greek letter denotes a vector. The mode shapes are normalized to the maximum unity with only the real parts being considered. In order to obtain the equivalent magnitude between $\varepsilon_{\lambda,i}$ and $\boldsymbol{\varepsilon}_{\boldsymbol{\phi},i}$, the 1-norm, i.e., the sum of the absolute values of $\tilde{\boldsymbol{\phi}}_i$, had been introduced into the residuals of mode shape. On the basis of the residuals defined

by Eq.(1), the following nonlinear least-squares problem was solved.

$$\min_{\theta} \sum w_{\varepsilon_i}(\varepsilon_i)^2 = \min_{\theta} \boldsymbol{\varepsilon}^T \boldsymbol{W}_{\boldsymbol{\varepsilon}} \boldsymbol{\varepsilon} \tag{2}$$

The initial values of E1 and E2 were taken as 35 GPa and $w_{\varepsilon_i} = 1.$. The problem was solved by the Trust-Region-Reflective Algorithm (lsqnonlin) in MATLAB. The updated values were 45.3 GPa for E1 and 26.7 GPa for E2. Since the trusses were assembled by components with post-tensioning, the updating results were considered to be physically acceptable. The natural frequencies of the updated model Vol.(0) were listed in Table 1.

A single-damage scenario and a multiple-damage scenario were simulated with the calibrated FE volume model. For the single damage scenario, 25% reduction of the Young's modulus was applied to the part of the side main girder at the south edge (Fig. 5(a)). For the multiple damage scenario, the reduction of the Young's modulus was applied to both the middle parts of the side main girders at the north and south edge, but with different amplitudes. In particular, 15% reduction of the north and 25% reduction of the south. See Fig. 5(b). Natural frequencies of the damaged volume models Vol.(d1) and Vol.(d2) are listed in Table 1. The simulated modal data, including also the mode shapes will be used for damage assessment in the later section.

3.2 The simplified FE plate model

A simplified FE plate model of the viaduct was also built by ANSYS mainly with eight-node shell elements (Shell281). The plate model had the same geometry as the bridge deck on the horizontal plane. Each main girder and the adjacent slab was represented with 4 by 19, in total 76 shell elements. See Fig. 6. It was assumed that the plate model had a fixed boundary condition in translational DoFs at the supports. In addition, rotational springs were introduced at the supports to simulate the real constraints of the rubber bearings. Moreover, linear elastic properties were assumed for all the materials in the model.

As the reference model to be updated for damage assessment, the simplified FE plate model should be updated first in order to closely represent the real structure. Since the damage scenarios to be analysed were simulated by the FE volume model, the updating of the plate model took the modal data of Vol.(0) as the target. The model updating procedure followed the same rules as defined in the previous section, except that the dense measurement grid of the five mode shapes as was identified on Span X was considered. In detail, $n_\lambda = 5$, $n_\phi = 5$ in Eq.(1) and $w_{\varepsilon_i} = 1$ in Eq.(2), for which the five modes m1 to m5 as listed in Table 1 were considered. The updating parameters included flexural rigidities D11 and D22, the twisting rigidity D33 and the Poisson's ratio ν of the shell elements. For the cantilever parts of the slab at the north and the south edge, different values of elemental rigidities D should respectively be applied, since the corresponding elements were obviously much more flexible than the others. They were indicated as substructure 1a and 7b in Fig. 6. In addition, the rotational stiffness of the boundary springs was chosen to be updated. In summary, seven parameters were updated for the plate model. The natural frequencies of the updated plate model, which is denoted by Plate(0), can be found in Table 1.

4 ITERATIVE MULTILEVEL UPDATING SCHEME FOR DAMAGE ASSESSMENT

Assessment of the simulated damage scenarios was performed by updating the Plate(0) model as the reference model. As a linear elastic problem to be solved, the structural damage was considered as the reduction of the Young's modulus E in the plate model for the shell

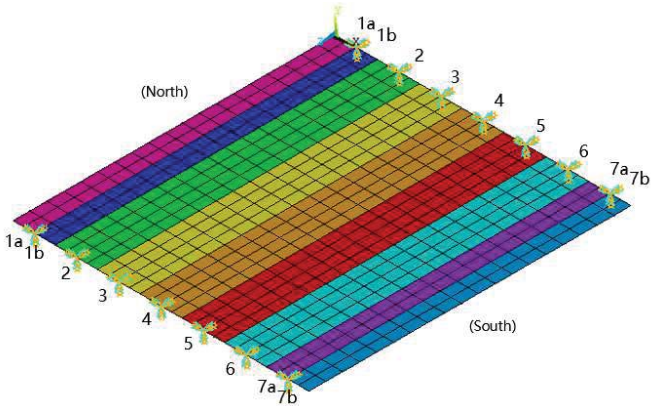

Figure 6: The simplified FE plate model. Note: substructures nr. 1 to 7 correspond to the seven main girders of the bridge.

elements where the damage occurred. The optimization problem as stated in Eq.(2) was solved in order to match the modal data of the plate model as closely as possible to those of the damage scenarios simulated by the volume model.

Modelling errors of the reference model must be addressed carefully, because the optimization method itself could not distinguish the effects of inadequate modelling and the changes of the modal characteristics due to damage. Two approaches have been proposed by the precedent researchers: 1) to update the reference model with respect to the baseline measurement, in order to produce a reliable model (see the previous section); 2) to use the difference between the damage and undamaged modal data in the formulation of the residuals [5]. Herein, the following residuals were considered in FE updating for the damage assessment:

$$\varepsilon_{\lambda,i} = \frac{\lambda_i}{\lambda_{0,i}} - \frac{\tilde{\lambda}_i}{\tilde{\lambda}_{0,i}}, \text{ for } i \in \{1,2,...,n_\lambda\} \tag{3}$$

$$\boldsymbol{\varepsilon}_{\boldsymbol{\phi},i} = \frac{(\boldsymbol{\phi}_i - \boldsymbol{\phi}_{0,i}) - (\tilde{\boldsymbol{\phi}}_i - \tilde{\boldsymbol{\phi}}_{0,i})}{\|\tilde{\boldsymbol{\phi}}_{0,i}\|_1}, \text{ for } i \in \{1,2,...,n_\phi\}$$

where the subscript 0 denotes the undamaged state and again tilde denotes the experimental values or those simulated by the volume model. In order to have the equal amplitude between $\varepsilon_{\lambda,i}$ and $\boldsymbol{\varepsilon}_{\boldsymbol{\phi},i}$, the weighting factors were introduced according to:

$$w_{\varepsilon_\lambda,i} = 1/\sum_i (\varepsilon^0_{\lambda,i})^2, \text{ for } i \in \{1,2,...,n_\lambda\} \tag{4}$$

$$w_{\boldsymbol{\varepsilon}_{\boldsymbol{\phi}},i} = 1/\sum_j (\varepsilon^0_{\boldsymbol{\phi},j})^2, \text{ for } i \in \{1,2,...,n_{\boldsymbol{\phi}}\},\ j \in \{1,2,...,n_{\boldsymbol{\phi}} \times n_{DoF}\}$$

where $\varepsilon^0_{\lambda,i}$ and $\varepsilon^0_{\boldsymbol{\phi},j}$ were obtained from Eq.(3) by replacing λ_i and $\boldsymbol{\phi}_i$ with $\lambda_{0,i}$ and $\boldsymbol{\phi}_{0,i}$, respectively. And n_{DoF} denotes the length of the mode shape vector.

Parametrization of the potential damage was another key issues to be addressed. As an inverse problem, solution of the unknown parameters, e.g., the Young's modulus of the shell elements, through the FE updating procedure was prone to be ill-posed. Modification in stiffness

of two adjacent elements in a FE model has nearly the same influence on the modal characteristics of the structure. As a result, the sensitivity matrix that was calculated between the residuals and the updating parameters was likely to be ill-conditioned, especially when a large number of updating parameters was involved. As a solution, the number of candidate parameters should be reduced by including only those that were more likely to be changed due to damage. Mathematically, it suggests to introduce extract constraints to the optimization problem in order to guarantee an unique, stable and physically acceptable solution. Understanding of the damage mechanism and engineering judgement will play a very important role in this regard.

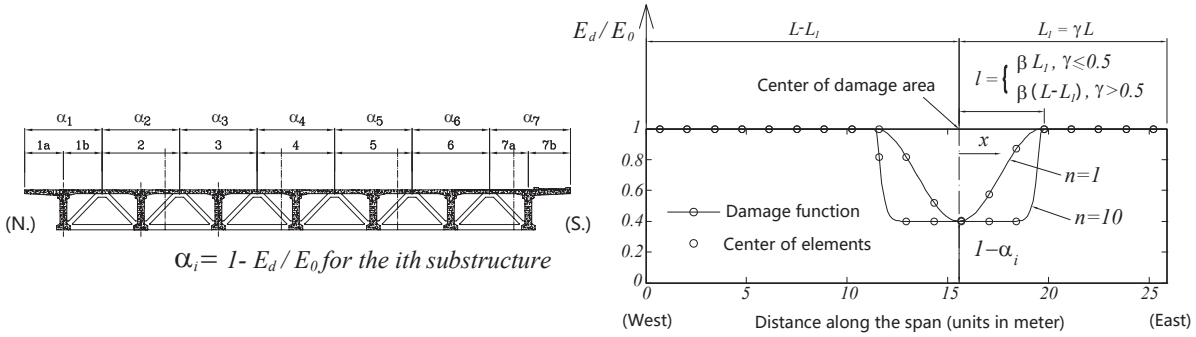

Figure 7: Damage parameterization: the global parameters α_i, and the local parameters β, γ and n for the damaged main girder.

For the current problem, damage parametrization was considered as shown in Fig.7. The reference plate model was divided into seven substructures, labelled from nr. 1 to 7. Each substructure corresponds to one of the main girders. An unique reduction factor α_i of the substructural stiffness, i.e., of the Young's modulus E was applied. This defined the first-level problem, or the global problem to be addressed. Damage localization and quantification of the possibly damaged main girder was the second problem to be solved. Three local parameters β, γ and n were used by following the damage function defined in [6], which helps to characterize a typical damage pattern of a concrete beam. Fig 7 permits the partitioning of the updating parameters into two sets: the global parameters α_i, associated with the global structure and the local parameters β_j, γ_j and n_j, associated with the jth substructure with damage. The optimization problem to be solved however remains unchanged. In detail, the following two-level approach is applied.

First-level (global) Problem. Assuming that the damage area spans across the whole substructure, Eq.(2) is to be solved with the global parameters α_i. It is somehow equivalent to set the local parameters $\beta = 1$, $\gamma = 0.5$ and $n = 100$, or a relatively large number. The damaged main girder is identified by checking $\alpha_i^* > \Delta_d$. Herein, the superscript * denotes the solution and Δ_d is the threshold value.

Second-level (local) Problem. In this stage, Eq.(2) is solved with the local parameters β_j, γ_j and n_j, together with α_j for $j = 1, 2, ..., n_d$, if there were totally n_d substructures identified with damage. Meanwhile, the global parameters α_i, except of α_j for the damaged main girders, remain unchanged. Once the local parameters are found, one proceeds to solve the first-level problem. This process is to be continued until convergence is reached. The iteration can be summarized as follows:

1. Start with an initial local parameter sets such as $\beta = 1$, $\gamma = 0.5$ and $n = 100$ for all the

substructures.

2. Solve the first-level optimization problem by Eq.(2) for the global parameters α_i and find α_i^* and n_d.

3. Solve the second-level optimization problem for α_j and the local parameters β_j, γ_j and n_j, for $j = 1, 2, ..., n_d$ by Eq.(2).

4. Check for the convergence on α_i by $|\alpha_{i,n+1} - \alpha_{i,n}| < \Delta_\alpha(1 + |\alpha_{i,n}|)$ (n for the iteration steps and Δ_α for the step size tolerance).

5. If the process has not converged, go to step 2 but with the newly updated β_j, γ_j and n_j ($j = 1, 2, ..., n_d$) and repeat the process until convergence.

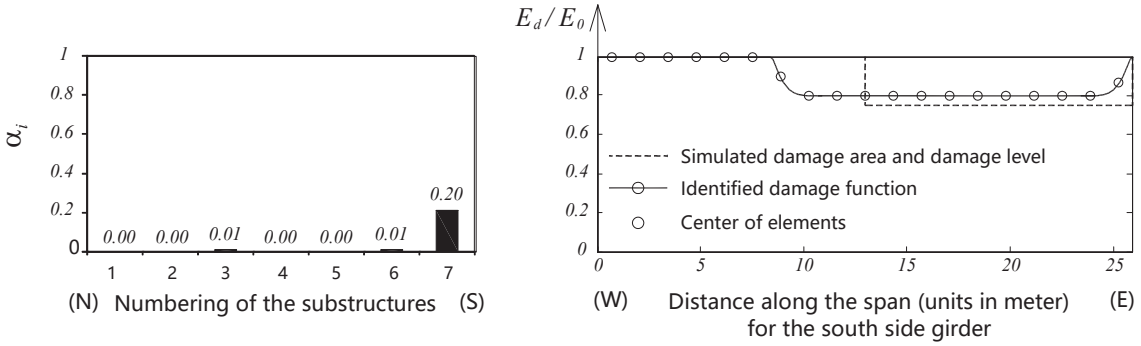

Figure 8: Final solution of the global problem and the identified damage function (the local problem) for the single damage scenario.

The aforementioned multilevel updating scheme was applied to the simulated damage scenario Vol.(d1). The numerical optimization of both the First- and Second-level problems was solved by using the Trust-Region-Reflective Algorithm (lsqnonlin) in MATLAB. Generally, multiple initial points shall be considered in order to obtain the global minimum, instead of the local minimum. Nevertheless, multiple runs could be avoided or at least reduced by choosing appropriate initial points, which should be located in a physically feasible region. In the current case study, use of $\alpha_{i,0} = 0.01$ for the First-level problem leads to the satisfactory result without multiple runs. Similarly, $\beta_{j,0} = 1.0$, $\gamma_{j,0} = 0.5$ and $n_0 = 10$ were considered as the initial values for the Second-level problem. For the substructure identified with damage ($\Delta_d = 1\%$), $\alpha_{j,0}$ took the corresponding solution of α_i^* of the First-level problem. The convergence criteria is on the relative step size with the tolerance $\Delta = 0.1\%$ for lsqnonlin and $\Delta_\alpha = 1\%$ for the multilevel scheme. The modal data of the five modes, m1 to m5 (see Table 1) were used to formulate the objective function of Eq.(2) with the residuals of Eq.(3) and the weighting factors of Eq.(4). Their mode shapes are similar in appearance to the experimental results in Fig. 4. The dense measurement gird of Span X was considered. The updating scheme stopped after three iterations, i.e., First-level, Second-level and then First-level. The respective iteration numbers of the individual problems were 10, 8 and 5. The natural frequencies of the updated plate model are listed in Table 1, denoted by Plate(d1). The final solution of the problem is shown in Fig. 8. The damage function for the south side girder was plotted with the simulated damage area and

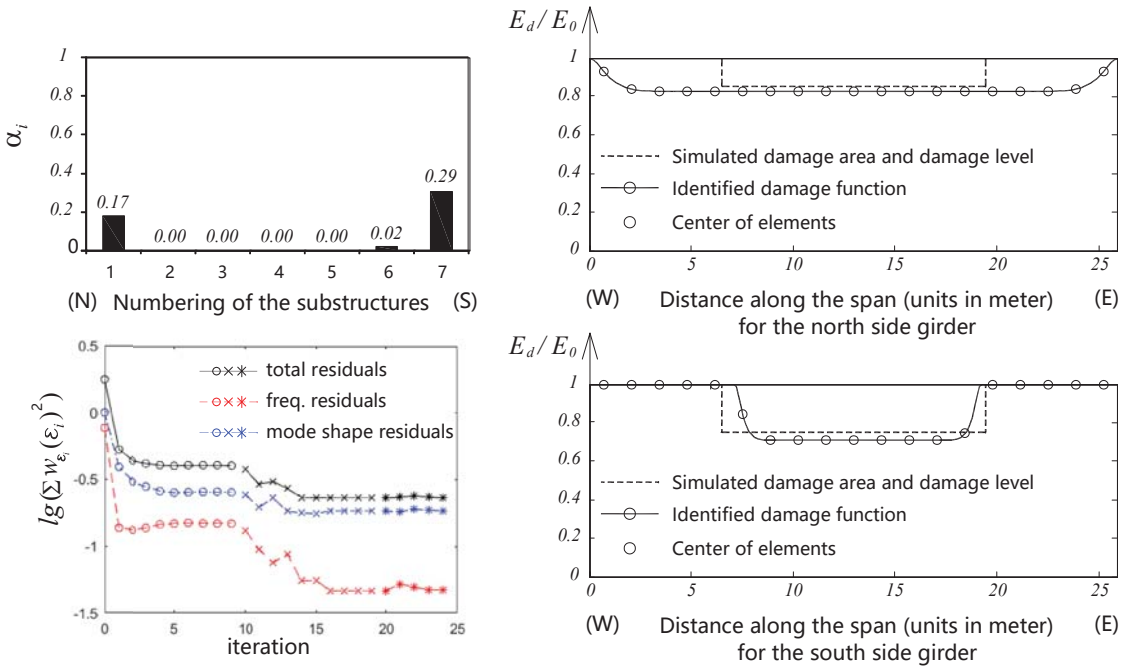

Figure 9: Final solution of the global problem and the identified damage function (the local problem) for the multiple damage scenario, with the convergence plot of the squared norm of the residuals (left below).

damage level. Evidently, the damage location has been identified almost correctly, even though the damage level was a little underestimated.

While applied to the multiple damage scenario Vol.(d2), the multilevel updating scheme used the same settings as previously, except that the threshold of damage $\Delta_d = 2\%$. The natural frequencies of the updated plate model can be found in Table 1, denoted by Plate(d2). The solution of the global and local problems are shown in Fig. 9. The two side girders were correctly identified as the damaged ones. On the south side girder, the damage location was almost properly characterized by the damage function. In comparison, on the north side girder the damage location was overestimated. On both sides, the damage levels were slightly overestimated. It may be explained by the inadequacy of the measurement nodes and the inaccuracy of the reference model. As shown in Fig. 5, the additional sensor array was placed on the cantilever part of the south side (on the side walk). Accordingly, more information about mode shape changes were available on the south side girder, as the objective function was more sensitive to damage on the south side than the north side. In Fig. 9, the convergence plot was also presented. The final solution was achieved after the First-level problem with 10 iterations, the Second-level problem with 10 iterations and the First-level problem with 5 iterations. Both the frequency residuals and the mode shape residuals were mostly smoothly reduced by iterations before the final solution.

5 DISCUSSION

On the basis of the presented case study, several issues related to FE model updating for vibration-based damage assessment of the bridge could be addressed. First, evaluation of the objective function was the most time consuming part during the computation. Since the solution used a gradient-based method, numerical modal calculation by ANSYS had to be repeated with multiple times in order to return the Jacobian matrix. It was found that use of the simplified

plate model greatly improved the computational efficiency. For instance, for each iteration the time consumed for modal analysis of the plate model was around 11 seconds from a Laptop with Intel-Core i5 and 4G Ram. In comparison, that of the volume model was more than ten times on the same device.

Secondly, to formulate the residuals directly on the mode shapes as Eq.(3) rather than the calculated MAC values significantly improved the sensitivity of the objective function to damage. In the current case study, the mode shape residuals have the length of $126 \times 5 = 625$, equals the number of the measurement nodes multiplied by the number of the modes. It is found that the MAC values calculated between the Vol.(d2) and Plate(0) were mostly greater than 0.95 for the five modes. After the updating, they were slightly improved by only around 0.01.

Thirdly, the condition numbers were calculated for the Jacobian matrix $\mathbf{J}$ at the solution points for both the First- and Second-level problems. It is defined as the ratio of the maximum singular value to the minimum singular value of the matrix. For the multiple damage scenario, in the global problem the maximum and the minimum singular values were, respectively, 11.58 and 2.05, of which the ratio was 5.64. In comparison, in the local problem the maximum and the minimum singular value were, respectively, 9.45 and 0.10, of which the ratio was 90.77. The lower the value, the better the conditioning of the Jacobian matrix. Therefore, the local problem is much poorly conditioned than the global problem. It suggests the benefits of the multilevel scheme. By considering the specific structure of the current optimization problem, the division of the variables into global and local variables will improve the robustness of the numerical optimization by solving them separately.

6 CONCLUSIONS AND FUTURE PERSPECTIVES

Based on extensive vibration measurements of the Boirs viaduct, a realistic case study for vibration-based damage assessment using FE model updating is presented. Two damage scenarios were simulated by a refined FE volume model which had been calibrated according to the baseline measurement of an undamaged span. A simplified plate model was taken as the reference model for updating. The multilevel updating scheme leads to the satisfactory results for both the single-damage and multiple-damage scenarios. Further improvement and future work however remain to be done. The influence of the measurement errors has not been investigated in the case study. Moreover, application of the algorithms has to be extended for the real damage on Span X of the Boirs viaduct.

REFERENCES

[1] H. Sohn, C. R. Farrar, F. M. Hemez, and J. J. Czarnecki. A review of structural health review of structural health monitoring literature, 1996-2001. Technical report, Los Alamos National Laboratory, 2002. No. LA-UR-02-2095.

[2] E. P. Carden and P. Fanning. Vibration based condition monitoring: a review. *Structural health monitoring*, 3(4):355–377, 2004.

[3] Keith Worden and Michael I. Friswell. *Encyclopedia of Structural Health Monitoring*, chapter Modal–Vibration-Based Damage Identification. Wiley, 2009.

[4] A. Teughels. *Inverse modelling of civil engineering structures based on operational modal data*. PhD thesis, Structural Mechanics Section, KUL, 2003.

[5] Michael I. Friswell. Damage identification using inverse methods. *Philosophical Transactions of the Royal Society A: Mathematical, Physical and Engineering Sciences*, 365(1851):393–410, 2007.

[6] M.M. Abdel Wahab, G. De Roeck, and B. Peeters. Parameterization of damage in reinforced concrete structures using model updating. 228(4):717–730, 1999.

[7] B. Titurus, M. I. Friswell, and L. Starek. Damage detection using generic elements: Part i. model updating. *Computers and structures*, 81(24):2273–2286, 2003.

[8] E. Reynders, G. De Roeck, P. Gundes Bakir, and C. Sauvage. Damage identification on the tilff bridge by vibration monitoring using optical fiber strain sensors. *Journal of engineering mechanics*, 133(2):185–193, 2007.

[9] B. Titurus and M. I. Friswell. Regularization in model updating. *International Journal for numerical methods in engineering*, 75(4):440–478, 2008.

[10] V. Meruane and W. Heylen. Structural damage assessment under varying temperature conditions. *Structural Health Monitoring*, 11(3):345–357, 2012.

[11] G. Fa, L. He, L. Fenu, E. Mazzarolo, B. Briseghella, and T. Zordan. Comparison of direct and iterative methods for model updating of a curved cable-stayed bridge using experimental modal data. In *Proceedings of the IABSE Conference Guangzhou, China*, pages 538–545, May 2016.

[12] T. Liu, Q. Zhang, T. Zordan, and B. Briseghella. Finite element model updating of canonica bridge using experimental modal data and genetic algorithm. *Structural Engineering International*, 26(1):27–36, 2016.

[13] H. Tran-Ngoc, L. He, E. Reynders, S. Khatir, T. Le-Xuan, G. De Roeck, T. Bui-Tienb, and M. A. Wahab. An efficient approach to model updating for a multispan railway bridge using orthogonal diagonalization combined with improved particle swarm optimization. *Journal of Sound and Vibration*, 476, 2020.

[14] A. Teughels and G. De Roeck. Structural damage identification of the highway bridge z24 by fe model updating. *Journal of Sound and Vibration*, 278(3):589–610, 2004.

[15] A. A. Mosavi, H. Sedarat, S. M. O'Connor, A. Emami-Naeini, and J. Lynch. Calibrating a high-fidelity finite element model of a highway bridge using a multi-variable sensitivity-based optimisation approach. *Structure and Infrastructure Engineering*, 10(5):627–642, 2014.

[16] L He, E Reynders, V Zabel, GC Marano, B Briseghella, and Guido De Roeck. Substructuring-based damage assessment of a steel railway bridge using operational modal data. In *Proceedings of the International Conference on Experimental Vibration Analysis for Civil Engineering Structures*. EVACES 2019, 2019.

[17] Singiresu S. Rao. *Engineering optimization: theory and practice*. Wiley, 5th edition, 2019.

[18] B. Peeters and G. De Roeck. Reference-based stochastic subspace identification for output-only modal analysis. *Mechanical Systems and Signal Processing*, 13(6):855–878, 1999.

[19] E. Reynders and G. De Roeck. Reference-based combined deterministic-stochastic subspace identification for experimental and operational modal analysis. *Mechanical Systems and Signal Processing*, 22(3):617–637, 2008.

[20] Hsu Ting-Yu, Edwin Reynders, Jeroen Houbrechts, and Guido De Roeck. Vibration measurements and operational modal analysis on the boirs viaduct of highway e313. Technical Report bwm-2010-08, Structural Mechanics Section, K.U.Leuven, March 2010.

[21] L. He, E. Reynders, T.-Y. Hsu, and G. De Roeck. Analysis of dynamic coupling between spans of two multi-span bridges using ambient vibration measurements. In G. De Roeck, G. Degrande, G. Lombaert, and G. Müller, editors, *Proceedings of the 8th International Conference on Structural Dynamics EURODYN 2011*, Leuven, Belgium, July 2011.

EURODYN 2020
XI International Conference on Structural Dynamics
M. Papadrakakis, M. Fragiadakis, C. Papadimitriou (eds.)
Athens, Greece, 23–26 November 2020

AN LTE-M OPENTHREAD MESH NETWORK FOR DISTRIBUTED REAL-TIME STRUCTURAL HEALTH MONITORING OF CRITICAL INFRASTRUCTURE IN CANADA

Jason Thornton[1], **Georgios P. Balomenos**[2]

[1] Department of Civil Engineering
McMaster University
1280 Main Street West, Hamilton, ON L8S 4L7, Canada
e-mail: thorntjd@mcmaster.ca

[2] Department of Civil Engineering
McMaster University
1280 Main Street West, Hamilton, ON L8S 4L7, Canada
email: balomeng@mcmaster.ca

Keywords: Structural Health Monitoring, Internet of Things, Mesh Networks, Wireless Sensor Networks, Elastomeric Bridge Bearings, OpenThread, LTE

Abstract. *Structural health monitoring is a vastly manual process that is both costly and time intensive. Implementation of distributed Internet of Things (IoT) sensor networks posits a robust alternative to current discrete-time monitoring techniques. Furthermore, IoT systems allow for long-term analysis to occur in real-time. However, existing IoT solutions for structural health monitoring do not account for remote sensing and often operate under the constraint of a readily available wireless connection. Thus, Wi-Fi-based solutions may not be conducive to remote applications. This study proposes an OpenThread mobile LTE Mesh Network using the Particle IoT development environment. The proposed development platform, in combination with a suite of distributed sensors, allows for the identification of structural degradation in critical infrastructure. In the study carried out herein, piezoelectric sensors are used to determine key salient factors contributing to the decline of overall structural health, particularly that of Canadian bridges and can be adapted for use with MEMS accelerometers or embedded Fiber Bragg gratings. The presented framework is validated through experiments on elastomeric bridge bearings, and is expected to demonstrate real-time, high-fidelity monitoring of critical structural components through a robust mesh network, especially for infrastructure located in remote areas.*

1 INTRODUCTION

Over the past several decades, Canada has experienced accelerated aging of public infrastructure, particularly of crucial transportation arteries, bridges, and trade routes. Of these transportation assets, 40% have been estimated to be in poor condition in comparison to Canadian infrastructure developed over the last 20 years [15]. Specifically, the Gardiner Expressway – a large commuter road connecting the Greater Toronto Area (GTA) with Metropolitan Toronto – is responsible for immeasurable disruptions to commuter vehicles due to persistent retrofitting and repairs [5]. As Canadian transportation infrastructure continues to age and become a hazard on the Canadian public, on-going monitoring and inspection requirements are expected to become more substantial and stringent.

Robust analysis of Canadian infrastructure is – at present – constrained by the periodicity of on-site inspections, and the quantity of aggregate sensor data. Furthermore, the hindrance on the Canadian public is two-fold; as Canadian bridges continue to age, the material consequences manifest as financial and service disruptions to Canadians. Over the next 10 to 11 years, the Canadian government endeavours to mitigate the risk associated with the decline in the condition of its roads and bridges, through the investment of over $180 billion dollars towards advancing Canadian transportation infrastructure [10].

Innovation in real-time Structural Health Monitoring technologies in Canada is stagnant due to constraints pertaining to cost, scalability, and communication protocols (i.e. Wi-Fi, RF, WLAN, or Bluetooth) [1][3][6][11]. Furthermore, innovations in Structural Health Monitoring may benefit from a holistic approach to its design; as such, many existing SHM systems are suited for specific applications and are seldom universally applicable. The study carried-out herein provides a high-level framework for autonomous, real-time monitoring of critical bridge components (i.e. elastomeric bearings). The system architecture is validated experimentally through the instrumentation of elastomeric bridge bearings but can be adapted to suit the needs of alternative applications. The SHM system identified in this study endeavours to address the following objectives through its development:

1. Autonomous, real-time monitoring of critical bridge components through an LTE-based OpenThread Mesh Network;
2. Implementation of real-time Convolutional Neural Networks for robust classification and feature identification of sensor data;
3. Design of a real-time Human-Machine Interface (HMI) for data visualization at an end-user level.

This study addresses the first objective and provides a framework for the overall approach employed in this project; a path for which future developments can be made.

2 THE INTERNET OF THINGS

2.1 Overview

The Internet-of-Things (IoT) comprises all systems composed of autonomous, interrelated devices that communicate via a wireless network. IoT-devices seldom require much human or third-party input, and hence pose promising implications for developments in real-time SHM technologies. At a high-level, IoT systems are defined as the interconnection of wireless sensor nodes with a network gateway (i.e. Wi-Fi, RF, WLAN, Bluetooth, 4G LTE, LTE-M, 5G, etc..), and a network gateway with a cloud service (Figure 1) [3]. IoT systems are typically designed to carry-out tasks that may otherwise *not* occur in real-time. Current monitoring and inspection processes of critical transportation infrastructure is vastly manual, time-intensive, and expensive. The implementation of IoT systems in the context of SHM may alleviate the financial

burden associated with outdated approaches in infrastructure monitoring and is a robust tool for use in risk and hazard mitigation.

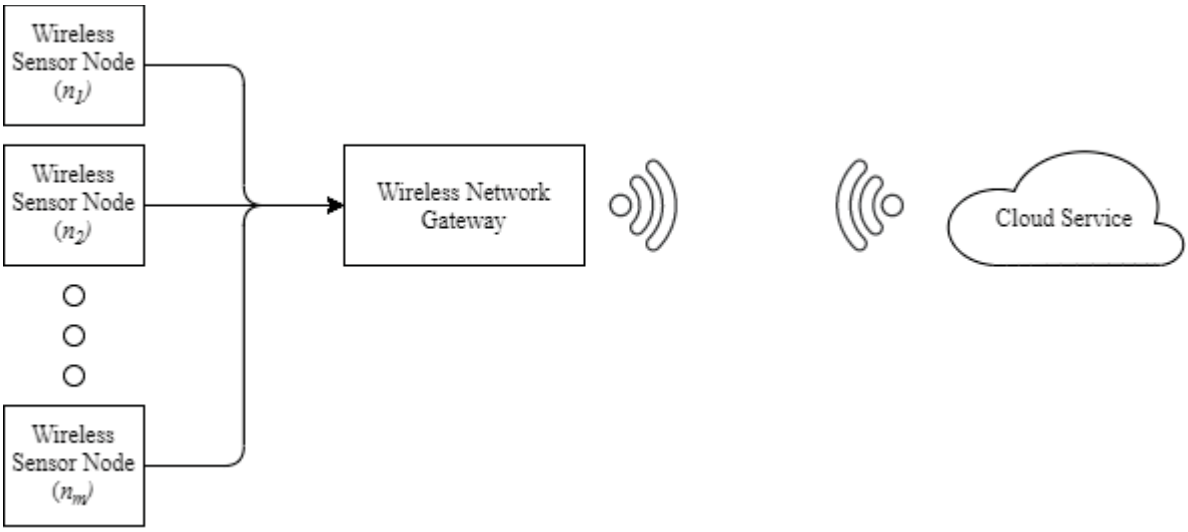

Figure 1: General IoT Architecture

2.2 Shortcomings in Existing SHM Systems

There exists a paradigm-shift in the development of Structural Health Monitoring technologies that is largely driven by the emergence of robust IoT systems. Modern SHM subscribes to a divergence from manual monitoring and inspection processes, and places emphasis on an investment in autonomous, real-time, and wireless replacements.

Network Type

To their detriment, existing solutions in real-time SHM are widely dependent on Wi-Fi or WLAN communication protocols. These networks require substantially more power than their modern counterparts and can provide far less coverage in remote locations where a high-fidelity network may not be readily available. With bandwidth discrepancies becoming narrower between communication protocols, Wi-Fi is no longer as advantageous for use in SHM systems as it may have been in previous decades. LTE networks provide a low-power alternative to Wi-Fi/WLAN with similar bandwidth capabilities, and thus are a compelling alternative for use in SHM systems [2].

Sensor Node Communication

Intercommunication between wireless sensor nodes is *not* ubiquitous among existing IoT systems due to the nature of their network topologies. Star network topologies have substantial penetration in the field of SHM due to their ease of implementation, but are limited by their range of operability, and power requirements. Furthermore, in many applications where star topologies are used, there exists a single point of communication between sensor nodes and the network gateway. This poses limitations not only on the operating range of the SHM system, but on applications where redundancy between sensor nodes is required [8].

Until recently, mesh topologies remained somewhat esoteric in their design and implementation in SHM applications. Mesh networks are an emerging topology in the realm of IoT, that have yet to see extensive application-driven realizations in structural health monitoring. Mesh topologies provide a favorable alternative to traditional SHM systems, most of which are constrained by their security, operating range, and scalability. The mesh network framework

identified herein provides a scalable alternative to existing SHM technologies and aims to address emerging nuances in the field of real-time infrastructure monitoring.

3 MESH NETWORK ARCHITECTURE

3.1 Advantages of a Mesh Network

Mesh network topologies have comparatively less market penetration in the realm of structural health monitoring on account of their once nebulous implementation. The emergence of cost-efficient, high-fidelity mesh development platforms is particularly advantageous for use in industrial structural health monitoring systems. An industrial mesh network poses promising solutions to nuances arising in real-time SHM, particularly in the context of network security, range of operability, and scalability. The framework identified herein was validated through instrumentation of elastomeric bridge bearings.

Network Resilience: Self-Healing and Self-Formation

In traditional wireless sensor network topologies, a single point of communication is established between a sensor node and a network router or gateway. If the connection between a sensor node and the network gateway or router is interrupted, the node may remain offline until human intervention is established. Self-healing capabilities of mesh topologies are two-fold; (1) the network may re-establish the connection to offline nodes, and (2) the network may re-route or reconfigure itself through another router or node in the network so-as-to establish the most reliable connection [11][16]. The ability of a mesh topology to redirect network traffic and data streams is crucial for remote SHM applications, where routine maintenance is infeasible. In general, self-healing algorithms are comprised of three stages:

1. Disconnection – a node is disconnected or removed from the network due to an interrupted connection.
2. Detection – neighbouring nodes in the mesh detect the removal of the node from the network.
3. Reconnection – neighbouring nodes reconnect to the nearest stable nodes in the mesh.

If a node is inserted into the mesh, the network may re-establish its connections in a similar fashion known as self-formation.

Range of Operability and Signal Strength

In mesh topologies, sensor nodes may be configured to behave as repeaters; furthermore, sensor nodes may establish and share a connection between each other to improve the range of operability within a network. Infrastructure monitoring systems have a tendency to span large distances. Specifically, structural health monitoring in the context of bridges necessitates a system with a broad range of operability; hence, such systems may benefit from a network that can operate reliably across long distances. Figure 2 identifies a four node, one gateway mesh network. The four sensor nodes reside within the signal range of the network gateway. In traditional non-mesh wireless sensor networks, if a node is inserted outside of the gateway's range of operability, a connection will not be established. In the case of a mesh network, an inserted node may establish a connection with other sensor nodes, so long as it is in range of a sensor node's shared connection. The inserted node may join the mesh and extend the signal range for subsequent nodes to join the network [9][13].

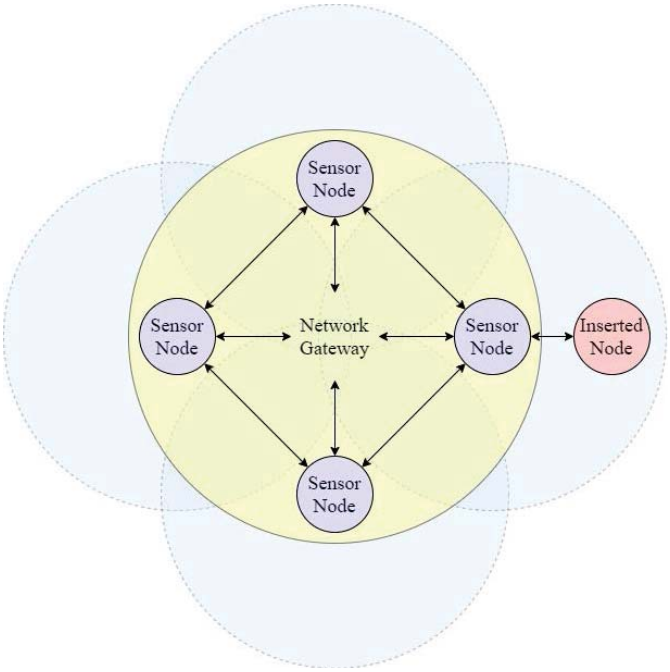

Figure 2: Signal Repeating in Mesh Topologies

3.2 Mesh Framework

The mesh framework identified in this study was founded on the open-source implementation of Thread®, a mesh protocol that facilitates intercommunication between IoT-enabled devices. OpenThread implements all network layers of the Thread protocol (identified in Figure 3), and provides a portable, low-power alternative to traditional non-mesh systems. OpenThread mesh networks support MAC-secure IEEE 802.15.4, a radio frequency communication protocol that enables low-power, short-range interactions between devices. The IEEE 802.15.4 protocol forms the basis for communication between sensor nodes in the overall mesh framework illustrated in Figure 4 [17][18].

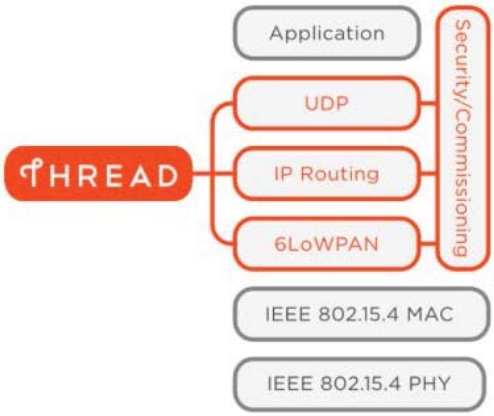

Figure 3: Thread Mesh Framework

The system identified in this study was developed on the LTE-M enabled Particle development platform. The network gateway device utilizes a multi-band LTE Cat M1 modem that enables the mesh to communicate data streams on the nearest cellular network. This is

particularly advantageous in remote applications, where access to a reliable wireless connection may not be readily available. The particle development platform comprises a suite of nodes, routers, and gateways that establish connections with each other via System-on-Chip (SoC) Bluetooth, and proprietary RF communication protocols. The system designed for use in this study is illustrated – in its totality – in Figure 4.

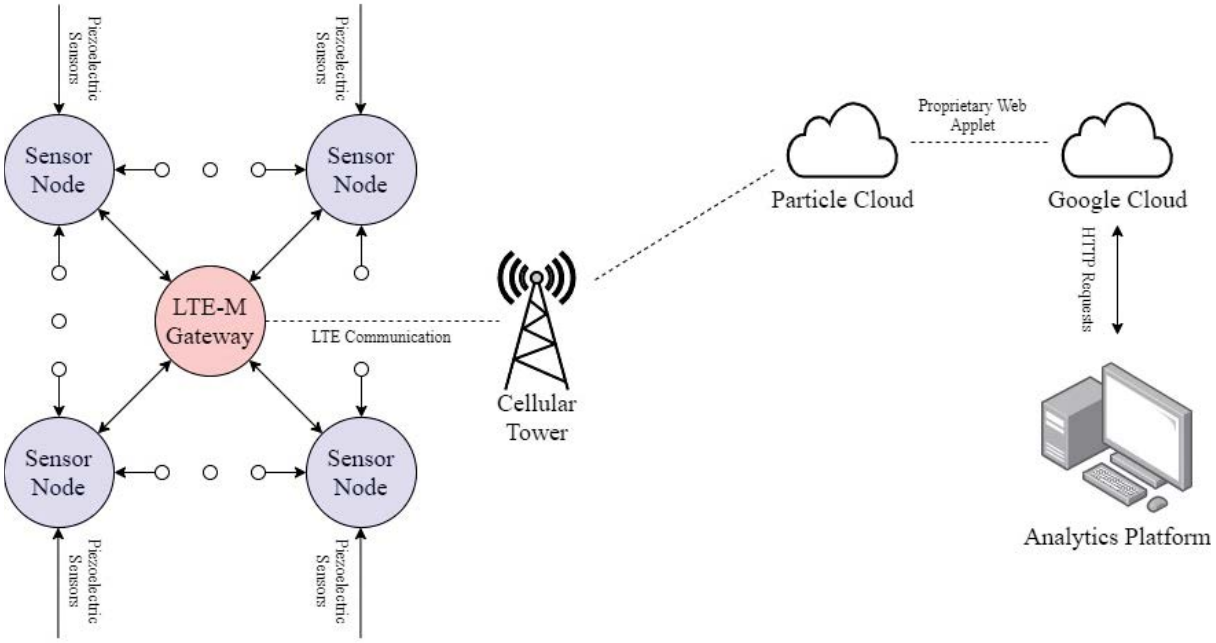

Figure 4: System Architecture

4 EXPERIMENTAL VALIDATION

4.1 Experimental Setup

For demonstrative purposes, a single node single gateway mesh network was established. An elastomeric bridge bearing was instrumented with four Polyvinylidene Fluoride (PVDF) membrane piezoelectric (PZT) sensors. When compressed, the PZT sensors produce a small voltage. To be provided as analog input to the sensor node, a conditioning and level shifting circuit was required. The top-level interconnection between PZT sensors, conditioning circuitry, and sensor node is identified in Figure 5. Per the setup identified in Figure 6, four piezoelectric sensors were placed along the surface of the elastomeric bridge bearing to measure the force (in kN) applied. For demonstrative purposes, a linearly increasing force of up to 20 kN was applied to the elastomeric bearing. It should be noted that these forces are *not* representative; the force applied was limited so-as-to not inflict deliberate damage on the bearing.

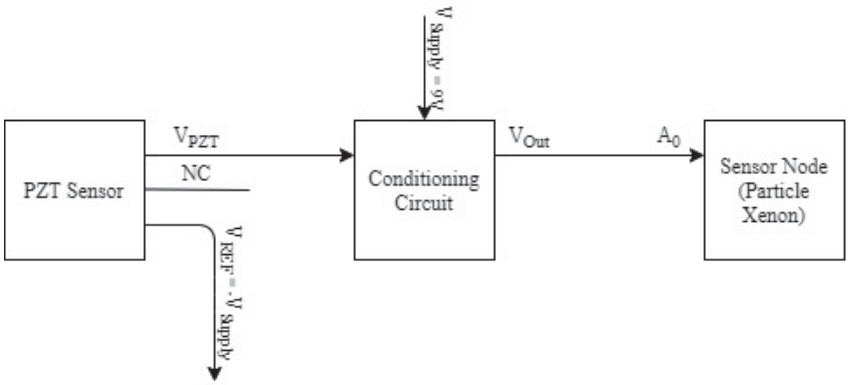

Figure 5: Top-level Sensor Conditioning Block Diagram

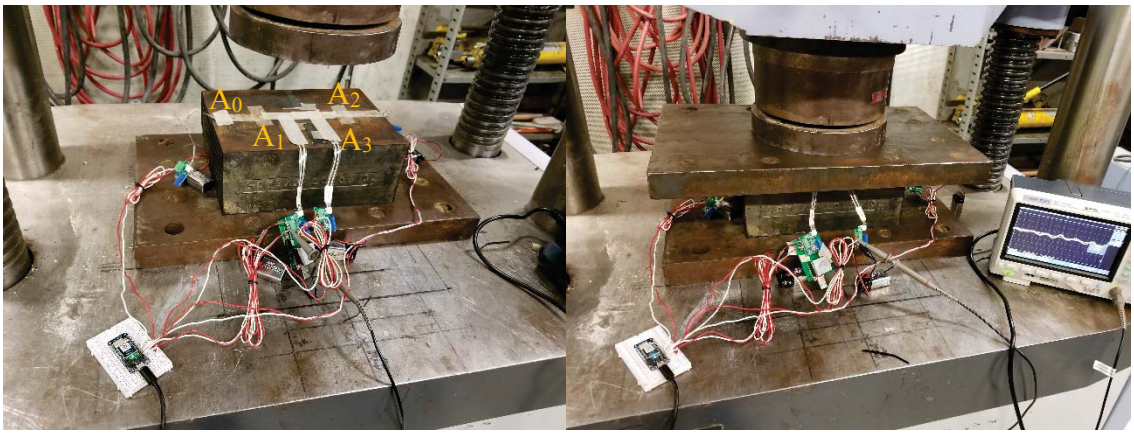

Figure 6: Experimental Setup

4.2 Analysis Methodology

Calibration and Level Shifting

Each sensor was subjected to a 20-point calibration prior to testing. A linear regression was performed to identify the relationship between the response of the sensors (post analog-to-digital conversion) and the applied force in newtons. Due to uneven compression of the sensors from inaccuracies in the distribution of the force applied, sensor pairs A_0 and A_1, and A_2 and A_3 were averaged. An analysis of the high frequency noise intrinsic to the raw signal was performed as a means to identify a model for real-time filtering.

Due to the nature of the SHM system described herein, the convolution of a linear time-invariant (LTI) filter was not sufficient. Data shall not be subjected to analysis at discrete intervals; rather, the data shall undergo real-time analysis. The analysis described herein provides the framework for the design of a linear time-varying filtering model, for use in pre-processing sensor data.

Outlier Identification

Outliers were identified and replaced in the raw data to improve linearity in the response of the sensor data. Outliers were determined through application of a 35-point moving window. Data points that were outside 3 standard deviations of the 35-point moving average were identified as outliers (i.e. datapoints that do not reside within a 99.7% confidence interval).

Preliminary outlier identification was validated through comparison of the Mahalanobis distance with a critical value determined by the chi-square distribution, with 0.3% significance. The Mahalanobis distance is defined as:

$$D_M(x) = \sqrt{(x - \mu)^T S^{-1} (x - \mu)} \tag{1}$$

Where D_M is the computed distance for observations in the dataset, x is the array of observations, μ is the sample mean within the set of observations, and S^{-1} is the inverse of the covariance matrix. Outliers were subsequently determined by computing the cumulative probabilities of the Mahalanobis distances using the chi-square distribution:

$$1 - \varphi(D_M(x), k) \leq 0.03 \tag{2}$$

Where φ is the cumulative distribution function of the chi-square distribution, evaluated for the Mahalobis distances with k degrees of freedom (equal to the number of variates examined in the dataset) [8].

Pre-filtering

An 11-point moving average filter was applied to the dataset to separate the high-frequency noise components from the signal. The moving average filter was defined by:

$$S_{out}[n] = \frac{1}{N} \sum_{i=0}^{N} S_{in}[n - i] \tag{3}$$

Where N is the size of the filter's window, n is sample size, and i is the current data point within the moving window [14]. Note that as the magnitude of the noise intrinsic to the piezoelectric sensor response is increased, the size of the window applied may vary; furthermore, this method is employed for preliminary noise separation only.

High-Frequency Noise Separation

High-frequency noise components of the input signal were separated from the filtered data, by subtracting the filtered data from the raw signal, i.e.:

$$Noise[n] = S_{in}[n] - S_{out}[n] \tag{4}$$

Distribution of Noise

Probability plots were generated to estimate the distribution of high-frequency noise present in the raw sensor data and goodness-of-fit statistics were determined through application of a chi-square test, i.e.:

$$\sum_{i=1}^{k} \frac{(n_i - e_i)^2}{e_i} < C_{1-\alpha,f} \tag{5}$$

k is the number of intervals in the data, n is the observed frequency for k intervals, e is the theoretical frequency of the assumed distribution, and C is the critical value in the chi-square distribution [4].

4.3 Results

Descriptive Statistics

An observation of 1709 data points were sampled from the piezoelectric sensors and were compiled for analysis. No statistical outliers were determined and thus all data points were retained. Descriptive statistics were generated for each of the sensors and are identified in Table 1.

Sensor	Sample Mean (N)	Standard Deviation (N)	Skewness	Kurtosis
Avg (A_0, A_1)	$1.28x10^4$	$4.18x10^3$	-0.1370	1.8644
Avg (A_2, A_3)	$1.27x10^4$	$4.20x10^3$	0.0617	1.8031

Table 1: Raw Data Descriptive Statistics

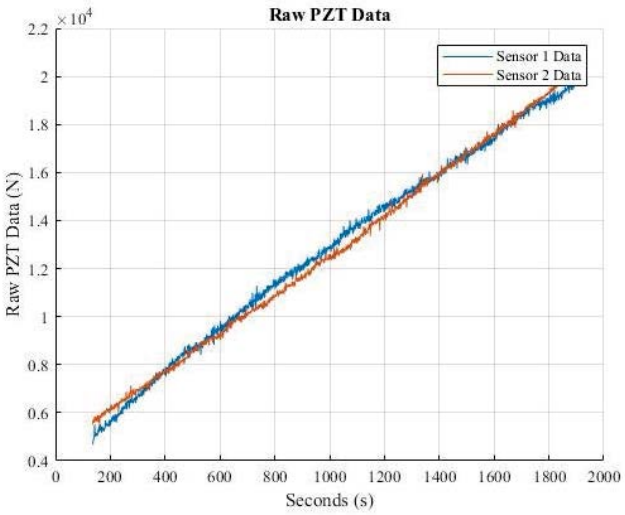

Figure 7: Raw Piezoelectric Sensor Data

Moving Average Filter

Post-application of the moving average filter, descriptive statistics of the filtered data remained within a margin of error of the raw data. The noise-filtered data is identified in Figure 8.

Sensor	Sample Mean (N)	Standard Deviation (N)	Skewness	Kurtosis
Avg (A_0, A_1)	$1.30x10^4$	$4.04x10^3$	-0.1283	1.8600
Avg (A_2, A_3)	$1.29x10^4$	$4.09x10^3$	0.0619	1.8000

Table 2: Filtered Data Descriptive Statistics

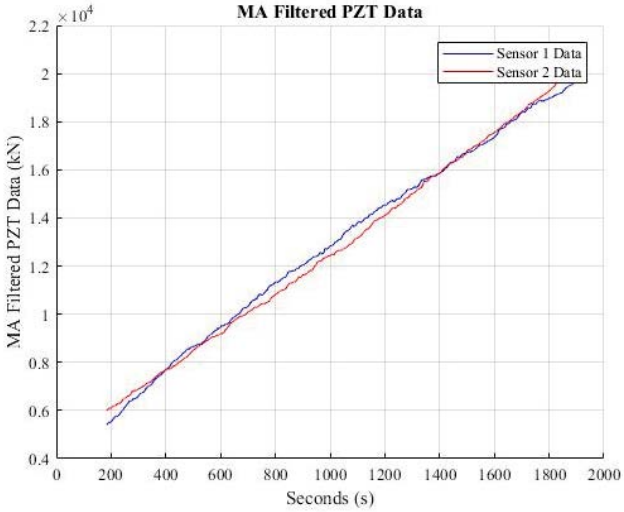

Figure 8: Filtered Piezoelectric Sensor Data

Distribution of Noise

Per the chi-square goodness-of-fit statistics, the null hypothesis is accepted for normally distributed noise, with a significance level of $\alpha = 5\%$. Values within the distribution of high-frequency noise are both positive and negative. For this reason, Rayleigh and lognormal distributions were not tested, as the characteristics of the noise intrinsic to the PZT sensors violates the non-zero, positive nature of these distribution types. The null hypothesis is accepted; the distribution of high-frequency noise is consistent with that of a normal distribution with 95% certainty. The results of the chi-square goodness-of-fit test for an assumed normal distribution are shown in Table 3:

Sensor	DOF	α	$C_{1-\alpha, f}$	X^2
Avg (A_0, A_1)	7	0.05	14.0671	13.2504
Avg (A_2, A_3)	7	0.05	14.0671	12.5474

Table 3: X^2 Goodness-of-Fit Statistics

The chi-square goodness-of-fit statistics for each sensor are below the threshold point indicated by $C_{1-\alpha, f}$, and hence, the null hypothesis is accepted.

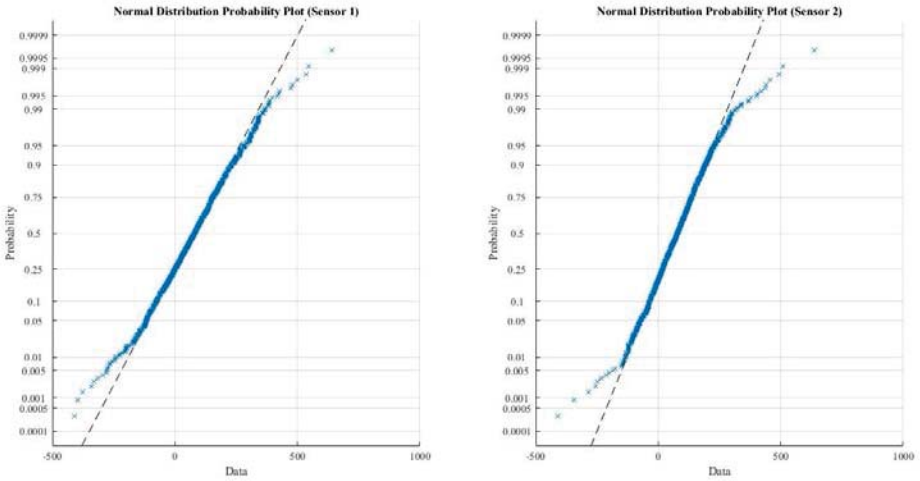

Figure 9: Normal Distribution Probability Plots

Wiener Filtering

Due to the Gaussian nature of the high-frequency noise present in the raw piezoelectric sensor signal, a 1-D linear time-varying Wiener filter was selected for use in this application [7]. The descriptive statistics of the resulting signal are similar to those computed for the moving average filter; furthermore, the difference in signal quality is indiscernible. For the purposes of real-time analysis, a Wiener or moving average filter can be applied in data pre-processing.

Sensor	Sample Mean (N)	Standard Deviation (N)	Skewness	Kurtosis
Avg (A_0, A_1)	1.30×10^4	4.04×10^3	-0.1276	1.8600
Avg (A_2, A_3)	1.29×10^4	4.09×10^3	0.0615	1.8000

Table 4: Wiener-filtered Data Descriptive Statistics

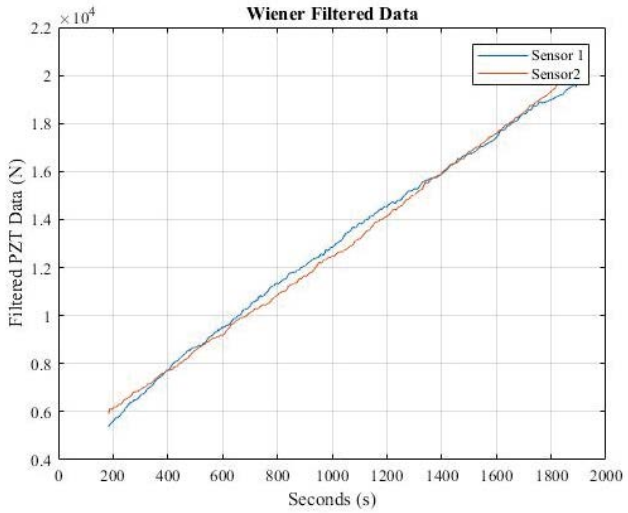

Figure 10: Wiener-filtered Piezoelectric Sensor Data

Monte Carlo Simulations

The signal conditioning methodology described in this study was validated through the iteration of ten thousand Monte Carlo Simulations. These simulations were performed for the addition of programmatically generated Gaussian noise to the original Wiener-filtered signal. A sample of a single iteration of the Monte Carlo simulation, with programmatically generated noise added to the original Wiener-filtered data, is shown in Figure 11. The signal was subsequently subjected to Wiener filtering, the results of which are identified in Figure 12. It was noted that the Wiener filtering algorithm is consistent for gaussian additive noise across all iterations of the Monte Carlo simulation; thus, the chosen filtration methodology is efficient in the removal of gaussian intrinsic to the piezoelectric sensors and is suitable for use in data pre-processing in preparation for deep learning. The mean error across all simulations was 41.3 Newtons or 0.21% of the maximum value in the target signal.

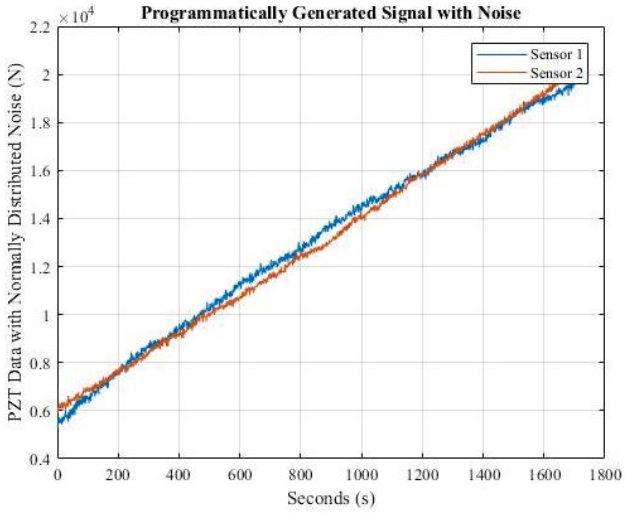

Figure 11: Programmatically Generated Signal with Gaussian Noise

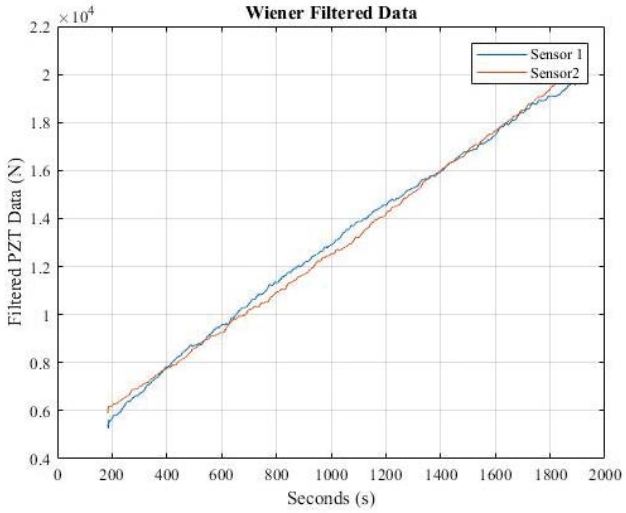

Figure 12: Wiener-filtered Signal

Sensor	Sample Mean (N)	Standard Deviation (N)	Skewness	Kurtosis
Avg (A_0, A_1)	$1.31x10^4$	$4.03x10^3$	-0.1264	1.8600
Avg (A_2, A_3)	$1.30x10^4$	$4.09x10^3$	0.0634	1.8000

Table 5: Wiener-filtered Data Descriptive Statistics

Frequency Spectra Analysis

The efficacy of the chosen filtration methodology was further validated through analysis of the power spectral density (PSD) of each sensor signal. A comparison of each signal's PSD is performed pre and post filtration to determine the extent by which the chosen methodology eliminates high-frequency components from the target signal. It is noted in Figure 13 and Figure 14, the high-frequency n^{th} order harmonics are successfully eliminated from the target signal.

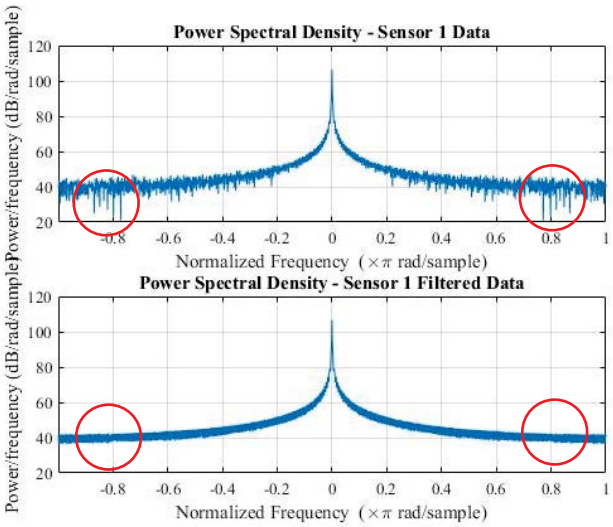

Figure 13: Sensor 1 PSD

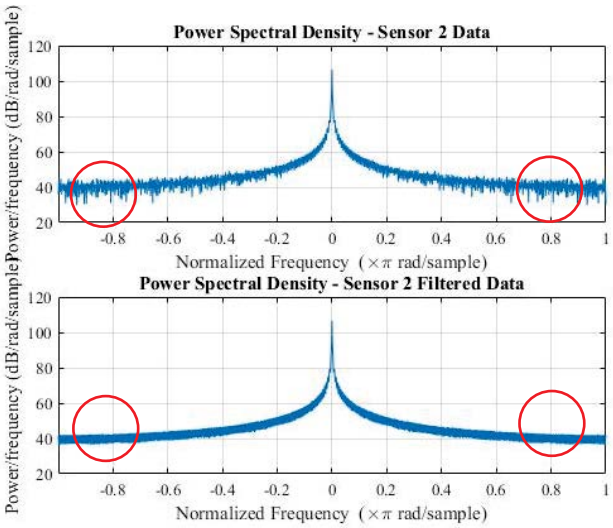

Figure 14: Sensor 2 PSD

5 CONCLUSION AND FUTURE WORKS

The study described herein explores the capabilities and efficacy of OpenThread mesh networks for real-time Structural Health Monitoring (SHM). Through experimental validation on elastomeric bridge bearings, it proposes a linear-time varying filtration model that is applied for pre-processing data for deep learning. The applicability of the proposed approach is investigated experimentally, through the instrumentation of elastomeric bridge bearings subjected to compressive loads. Probability plots and chi-square goodness-of-fit statistics were generated for raw piezoelectric sensor data to estimate the distribution of high-frequency noise intrinsic to the signal of interest. The chosen filtration and signal conditioning methodology was validated through 10000 Monte Carlo Simulations. The simulations were used to identify the efficacy of the chosen filter design for signals with random samples of gaussian noise superimposed on the signal of interest. The results suggest that the LTE-M mesh network identified in this study is a robust tool for long-term and real-time monitoring of elastomeric bridge bearings and provides an alternative for bridge infrastructure located in remote areas, where the use of Wi-Fi/WLAN networks is infeasible.

The proposed network design identified in this study provides a foundation for future developments, including the development of deep learning models for feature identification and classification of real-time data. Future work will examine the efficacy of Convolutional Neural Networks – an emerging deep learning architecture in the field of SHM – for use in pattern recognition, feature identification, and predictive modelling, with the aim to advance infrastructure monitoring capabilities in Canada. Furthermore, with Canada's increasing interest in structural health monitoring and the revitalization of its aging infrastructure, the framework identified in this study poses a compelling solution to intermittent, manual, and time-intensive inspection processes that are currently available.

ACKNOWLEDGEMENTS

The authors gratefully acknowledge the support of this research by a Start-up funding provided by the Faculty of Engineering at McMaster University. Any opinions, findings, and conclusions or recommendations expressed in this material are those of the authors and do not necessarily reflect the views of the sponsor.

REFERENCES

[1] I. Akyildiz, X. Wang, W. Wang, Wireless mesh networks: A survey, *Computer Networks, 47*(4), 445-487, 2005.

[2] A. Striegel, S. Liu, X. Hu, L. Meng, LTE and WiFi: Experiences with Quality and Consumption, *Procedia Computer Science*, *34*, 418–425, 2014.

[3] (n.d.). *AN1142: Mesh Network Performance Comparison.* Retrieved from https://www.silabs.com/documents/public/application-notes/an1142-mesh-network-performance-comparison.pdf.

[4] A-S. Ang, W. Tang, Probability concepts in engineering : emphasis on applications in civil & environmental engineering (2nd ed.), *Wiley,* ISBN: 9780471720645, 2006.

[5] J. Armstrong, Concrete falls from aging Gardiner Expressway, shatters windshield - Toronto, 2005.

[6] *Bluetooth Mesh, Thread, and Zigbee Network Performance Benchmarking - Silicon Labs*. Retrieved from https://www.silabs.com/products/wireless/learning-center/mesh-performance

[7] B. Boashash, Time-Frequency Signal Analysis and Processing (2nd ed.), *Oxford: Academic Press*, ISBN: 9780123984999, 2016.

[8] R. De Maesschalck, D. Jouan-Rimbaud, D. Massart, The Mahalanobis distance, *Chemometrics and Intelligent Laboratory Systems, 50*(1), 1-18, 2000.

[9] S. Bouckaert, E. De Poorter, B. Latré, J. Hoebeke, I. Moerman, P. Demeester, Strategies and challenges for interconnecting wireless mesh and wireless sensor networks, *Wireless Personal Communications*, *53*(3), 443–463, 2010.

[10] Infrastructure Canada - Departmental Plan 2018-19 Horizontal Initiatives, 2019. Retrieved from https://www.infrastructure.gc.ca/pub/dp-pm/2018-19/2018-supp-hi-ih-eng.html

[11] A. Miyaji, K. Omote, Self-healing wireless sensor networks, *Concurrency Computation . 27*, 2547-2568, 2015.

[12] K. Pothuganti, A. Chitneni, A comparative study of wireless protocols: Bluetooth, UWB, ZigBee, and Wi-Fi, 2014.

[13] A. Raniwala, K. Gopalan, T-c, Chiueh, Centralized channel assignment and routing algorithms for multi-channel wireless mesh networks, *ACM SIGMOBILE Mobile Computing and Communications Review, 8*(2), 65, 2004.

[14] S. Smith, Digital Signal Processing: A Practical Guide for Engineers and Scientists, *Elsevier*, ISBN: 9780750674447, 2014.

[15] The 2019 Canada Infrastructure Report Card, 2019. Retrieved from http://canadianinfrastructure.ca/downloads/canadian-infrastructure-report-card-2019.pdf

[16] A. Trehan, Algorithms for Self-Healing Networks, *The University of New Mexico,* 2013.

[17] *What is Thread*. (n.d.). Retrieved from https://www.threadgroup.org/What-is-Thread.

[18] *What is Thread? | OpenThread*. (n.d.). Retrieved from https://openthread.io/guides/thread-primer.

EURODYN 2020
XI International Conference on Structural Dynamics
M. Papadrakakis, M. Fragiadakis, C. Papadimitriou (eds.)
Athens, Greece, 23–26 November 2020

DRIVE-BY RESONANT BRIDGE DETECTION METHOD USING TWO TRACK IRREGULARITIES MEASURED ON THE FIRST AND LAST VEHICLES OF A TRAIN

Kodai Matsuoka[1], Hirofumi Tanaka[2], Kyohei Kawasaki[3], and Kazuhiro Kajihara[4]

[1] Railway Technical Research Institute, Railway dynamics division
2-8-38, Hikari-cho, Kokubunji-shi Tokyo, 185-8540, Japan
matsuoka.kodai.13@rtri.or.jp

[2] Railway Technical Research Institute, Track technology division
2-8-38, Hikari-cho, Kokubunji-shi Tokyo, 185-8540, Japan
tanaka.hirofumi.96@rtri.or.jp

[3] Railway Technical Research Institute, Track technology division
2-8-38, Hikari-cho, Kokubunji-shi Tokyo, 185-8540, Japan
kawasaki.kyohei.96@rtri.or.jp

[4] Railway Technical Research Institute, Track technology division
2-8-38, Hikari-cho, Kokubunji-shi Tokyo, 185-8540, Japan
kajihara.kazuhiro.70@rtri.or.jp

Keywords: On-board measurement, High-speed railway, bridge resonance, track irregularity

Abstract. *The resonance occurring when the excitation frequency of a running train coincides with the frequency of a bridge may considerably affect the safety and comfort of high-speed railway bridges. In Japan, train speed limits have been introduced in bridges operating for over 20 years because the resonance with their frequency has deteriorated. Their detection and monitoring by comprehensive and high-frequency measurements without the need to install sensors are important on many railway bridges. This study proposes a novel and efficient drive-by resonant bridge detection method using two track irregularity measurement devices that are already installed on some commercial high-speed trains. The proposed method enables the estimation of the resonance-induced bridge amplified response by comparing the two track irregularities measured on the first and last train vehicles. The simulation results confirm that the amplified bridge vibration between the passage of the last and first vehicles is accurately detected by the proposed method. In the field tests, the proposed method is applied to two track irregularities measured on the first and last vehicles of a train. The amplified bridge vibration of the resonant bridges validated by in-situ measurements is then detected using the proposed drive-by method.*

1 INTRODUCTION

Resonance inducing a large amplitude vibration of a railway bridge is an inevitable issue in modern high-speed railways [1]. Resonance occurs when the excitation frequency of a running train matches the bridge frequency [2]. The excitation frequency of a running train is determined by the regular wheelset arrangement of its vehicles and the traveling speed. Therefore, resonance is an important issue when the increase of excitation frequency with the acceleration of a high-speed train coincides with the bridge frequency [3]. Moreover, resonance may become an important issue when the bridge frequency decreases because of deterioration and crack propagation associated with aging [4].

Detecting the resonant bridge and measuring the displacement and/or acceleration from the ground are important to confirm the bridge safety and usability at resonance [5]. However, bridges requiring inspection are numerous and involve high human and economic burden for individual ground measurements.

Therefore, efficiently and comprehensively inspecting many railway bridges in one run becomes possible if the condition of high-speed railway bridges can be estimated through on-board data measured by running trains. Moreover, implementing inspections at a high frequency is achievable if using a commercial train is feasible. Therefore, developing a method for evaluating the resonant state of bridges using on-board measurement data for efficient detection and management of resonant bridges is important.

This study introduces a novel drive-by detection method for resonant bridges using the track irregularity data measured on the first and last vehicles in a commercial train on a high-speed railway.

Hester and Gonzales [6] indicated that almost no drive-by bridge performance evaluation method is available for high-speed railways with the train passing through bridges at stages. The fact that a resonant bridge [1–4] in a high-speed railway, which is indirectly but closely related to the bridge performance, is detected by on-board measurements represents the novel and unique engineering contribution of this study. Although many studies involved numerical simulations only, the effectiveness of the proposed method is demonstrated herein by detecting a resonant bridge based on the measured track displacement of a high-speed railway and on-site bridge measurements. This also is another original contribution of this study.

2 DETECTION METHOD

We propose a method for detecting resonant bridges based on the track irregularities measured on the first and last vehicles of a running train. This method assumes that a track irregularity measurement system [7] for commercial trains is present in some high-speed railways in Japan. Details of the instrument and the measurement accuracy are provided in [7]. The track irregularity mentioned herein refers to the track displacement or rail profile, including the bridge's static and dynamic displacement response.

The track irregularity measured at different points in time (two points in a train) includes the bridge's dynamic response, rail irregularities other than the bridge's response, and track structure displacement. Assuming that the track irregularities are unchanged when measured at two points in time, these components are offset by the difference in the two track irregularities measured at different positions, with these converted into functions of the positions. Conversely, when the dynamic response component of a bridge changes (amplifies) as the train passes, only the dynamic response component of the bridge is extracted by the processing difference even if the track irregularity is at the same position.

2.1 Dynamic response of a resonant bridge observed from a moving point

Now, let us consider a case where a concentrated load series at a fixed interval corresponding to a vehicle length L_c runs on a bridge with a span length L_b at a resonance speed v_{res}. Sufficient concentrated loads are assumed to have passed, and a steady state is assumed to have been attained. Here, if the position x_p is a concentrated load and the fundamental frequency of the bridge is f_1, Eq. (1) is satisfied.

$$f_1 = \frac{v_{res}}{L_c} = \frac{x_p}{L_c t} \tag{1}$$

The dynamic response component $z_{b,d}(x,t)$ of the bridge at a position x $(0 \le x \le L_b)$ and time t on the bridge is given by Eq. (2).

$$z_{b,d}(x,t) \approx \xi_{1,d}(t)\sin\left(\frac{\pi x}{L_b}\right) \tag{2}$$

Based on the steady-state assumption, the modal displacement $\xi_{1,d}$ satisfies Eq. (3).

$$\xi_{1,d}(t) = A_{res}\sin(2\pi f_1 t + \theta_{res}) \tag{3}$$

The term A_{res} represents the dynamic response amplitude under the steady state of the resonance. From the resonance condition, $\theta_{res} = \pi(1 - L_b/L_c)$. Equation (4) is obtained by substituting Eq. (3) in Eq. (2) and focusing on the dynamic response $z_{b,d}(x_p)$ of the bridge at the moving concentrated load's position x_p.

$$z_{b,d}(x) \approx A_{res}\sin\left(2\pi\frac{x}{L_c} + \theta_{res}\right)\sin\left(2\pi\frac{x}{2L_b}\right) \tag{4}$$

Equation (4) shows that the track irregularity waveform caused by the resonant bridge's dynamic response component observed at a moving load position during the passage of the resonant bridge can be expressed by multiplying the two waves with the wavelengths representing the vehicle length L_c and twice the bridge length $2L_b$. Figure 1 shows an example when the span length is 50 m. Note that $A_{res} = 1$.

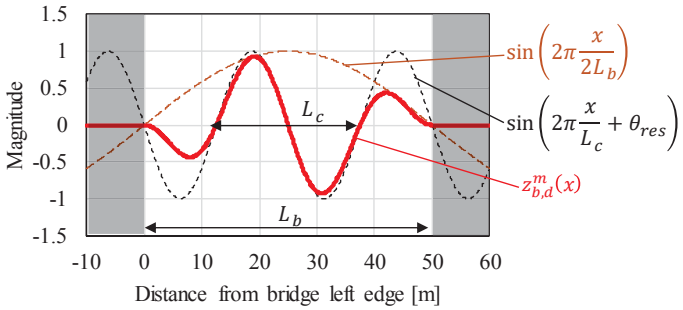

Figure 1: Dynamic response component of a bridge observed at a moving load position during the bridge passage (vehicle length: 25 m; bridge length: 50 m).

2.2 Extraction method for the resonant bridge response

First, a vibration component with a wavelength corresponding to a vehicle length L_c was extracted. A bandpass filter with a passing frequency band equivalent to the vehicle length L_c was used, with bandpass filtering performed on the measured track irregularities. The track irregularities that underwent this processing are termed herein as vehicle length irregularities. Consequently, the track irregularity component, excluding the bridge vibration and the bridge static deflection component, was reduced.

Next, envelope processing, that is, estimating $\sin(\pi x/L_b)$ in Eq. (4), was performed for the vehicle length irregularity. The amplitude of the vibration component with a wavelength equal to the vehicle length L_c was estimated by envelope processing. The track irregularity after this processing is referred to herein as the vehicle length irregularity amplitude. In the resonant bridge, a dominant sinusoidal component corresponding to the bridge span was formed based on the relationship in Eq. (4). By contrast, no dynamic response caused by the resonance existed in non-resonant bridges. The vehicle length irregularity amplitude lacked a dominant component.

Finally, the difference between the vehicle length irregularity amplitudes measured for the first and last vehicles was calculated. The measured track irregularities were assumed to be converted from time to position functions prior to the processing. Determining whether the dominant cause of the vehicle length irregularity in the last vehicle was resonance, static deflection component of the bridge, or irregular component corresponding to the vehicle length by the bandpass filter processing and the envelope processing alone was impossible. The dynamic response of the bridge at resonance gradually increased as the train passes, indicating that the bridge's dynamic component, which was caused by the resonance predominating during the passage of the last vehicle, was hardly generated when the first vehicle passed. Conversely, the static deflection component of the bridge and the track irregularity component corresponding to the vehicle length were almost identical for the first and last vehicles. Common components, such as static deflection and track irregularity, can be removed by subtracting the vehicle length irregularity amplitude of the first vehicle from that of the last. Therefore, if the predominant component corresponding to the bridge length is observed in the irregularities subjected to difference processing, the bridge is said to be resonating.

3 VERIFICATION RESULTS ON THE NUMERICAL SIMULATION

The train speed effect on the proposed method was verified by a numerical simulation for a simply supported bridge. We calculated the bridge displacement component by using a general simulation model [6,8] involving a two-dimensional vehicle with six degrees of freedom (DOF) and a bridge with a three-DOF system. Vehicles are usually based on the multibody system, whereas bridges are based on the beam theory. The train was modeled herein by connecting 12 vehicle models. The vehicle length L_c was 25 m, with a bogie center interval of 17.5 m, an axle interval of 2.5 m, and an axle load of 120 kN. For other parameters and details, please see Ref. [6].

For the actual resonant bridge [4], the span length was 30 m with a unit length mass of 25 t, a natural frequency of 2.8 Hz at which the resonance speed was approximately 250 km/h, and a 2% modal damping ratio.

Considering the track irregularity measurement system, the displacements just below the first/second bogie centers of the last/first vehicle were extracted from the simulation results. When converting the time series response to distance, resampling was performed at 250 mm intervals in accordance with the actual track displacement measurement.

The train speeds were 200, 230, 250, 270, and 300 km/h, which corresponded to ±10% and ±25% of a resonance speed of 250 km/h. Figure 2(a) shows the bridge displacement response at each train speed. Figure 2(b) depicts the bridge displacement responses just below the first/second bogie centers at the last/first vehicle at each train speed. These displacements were assumed to originate from the irregular track measurements. The dynamic response of the bridge was greatly amplified at a resonance speed of 250 km/h, although the track irregularity (bridge displacement) when traversing the bridge, as measured by the first vehicle, was unchanged.

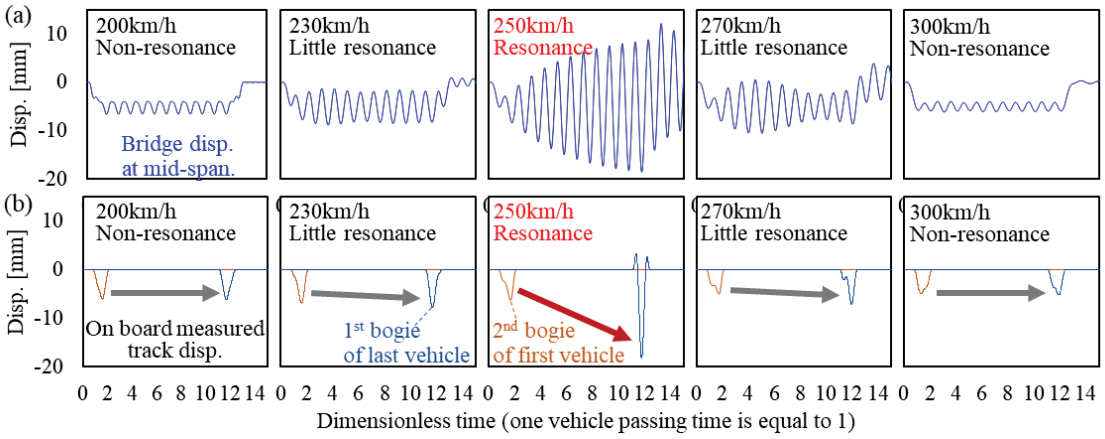

Figure 2: (a) Bridge displacement response at each train speed and (b) bridge displacement response just below the first/second bogie centers at the last/first vehicle at each train speed (vehicle length = 25 m; bridge length = 30 m).

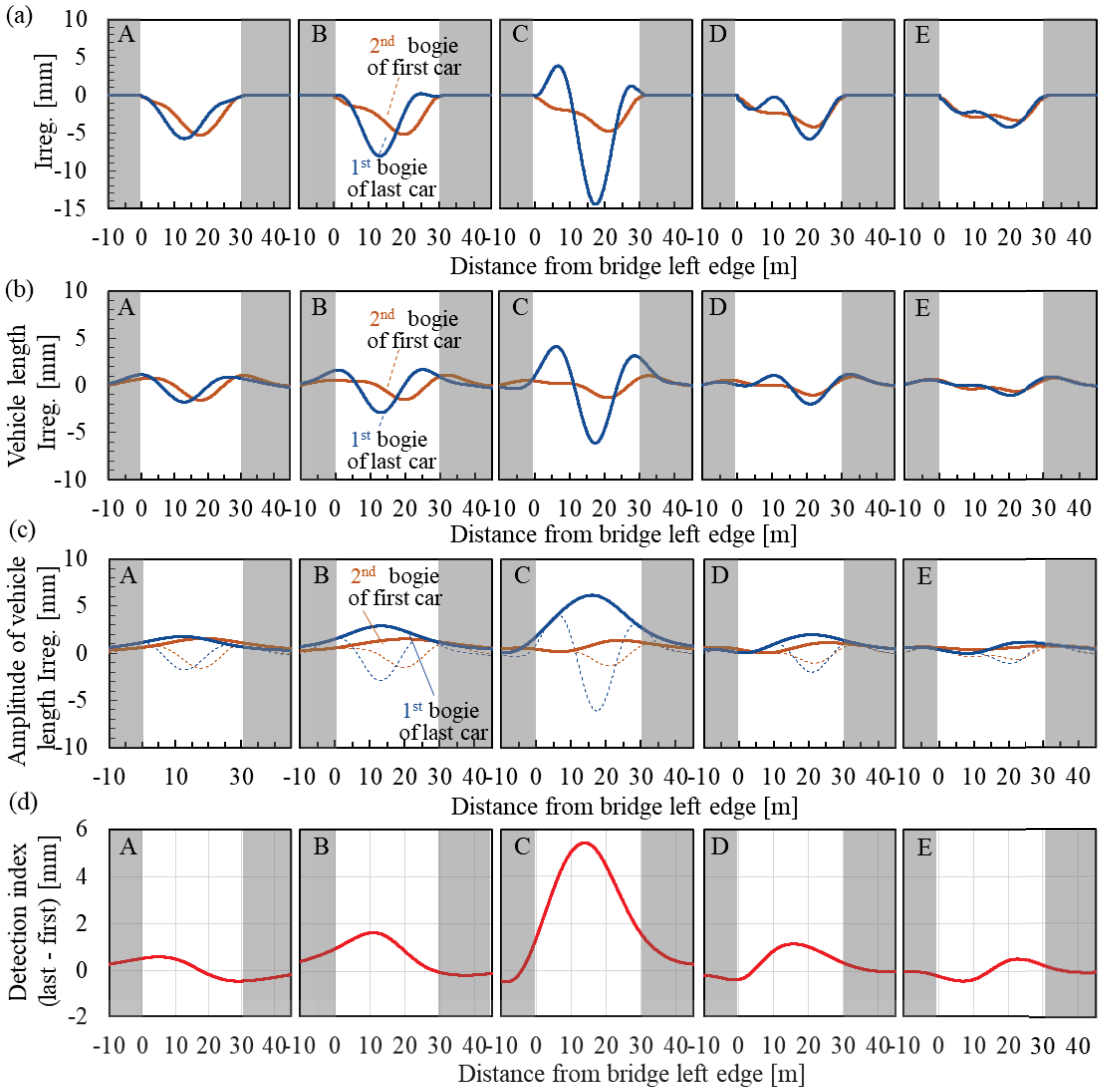

Figure 3: (a) Track irregularity (Irreg) composed of the bridge displacement, (b) vehicle length irregularities, (c) vehicle length irregularity amplitudes, and (d) resonance detection index (A, B, C, D, and E are 200, 230, 250, 270, and 300 km/h, respectively).

Figure 3 illustrates the results of applying the proposed method to the bridge displacement components observed by the first and last vehicles. Figure 3(a) presents the track displacement consisting only of the bridge displacement component obtained by converting Figure 2 into a distance sequence. Figure 3(b) shows the vehicle length irregularities after bandpass filtering. Figure 3(c) displays the vehicle length irregular amplitudes after the envelope processing. Figure 3(d) exhibits the detection indices after the difference processing.

Figures 3(c) and (d) denote that in the resonance state, the vehicle length irregularity amplitude of the last vehicle is higher than that of the first vehicle. Therefore, the detection index forms a convex dominant component in the resonant bridge section.

4 VALIDATION RESULTS ON ACTUAL VEHICLE AND BRIDGE

4.1 Target high-speed railway

A resonant bridge was detected, and the resonance state was verified by an on-site measurement by applying the proposed method to a real high-speed railway. The method was applied to high-speed railway lines, where the first and last vehicles hosting the track displacement measurement devices, including the inertia measurement mounted on a bogie, were run. The train includes eight cars measuring 25 m, a bogie center interval of 17.5 m, an axle interval of 2.5 m, and an axle load of approximately 120 kN when empty. The running speed of the target section was approximately 230–250 km/h. The track irregularity measuring devices were installed at the second and first bogie centers of the first and last vehicles, respectively. The position detection devices were also installed on the first and last vehicles and converted from time to distance function by recording the communication with the ground terminal every 3 km. Furthermore, the relative position of the last vehicle was finely corrected by the cross-correlation based on the measured data of the first vehicle [9]. In this study, the time series response of the track irregularity measured from the vehicle at 2 kHz sampling was converted to a distance series response at 250 mm intervals.

4.2 Detection results of the resonant bridge

Figure 4 shows an example of the application result of the method. From the top, this involves the structure type; structure span; train speed; track irregularities, including the bridge displacement measured at the first and last vehicles; vehicle length irregularities; vehicle length irregularity amplitudes; and resonance detection index (RDI). The train speed was approximately 230 km/h, with six bridges from A1 to A6 in the section. Others frequently involved rigid frame viaducts instead of the embankments on Japanese high-speed railways.

The difference between the first and last vehicles for the measured track irregularities and the vehicle length irregularities is usually very small. However, the vehicle length irregularity of the last vehicle was confirmed to increase in the A3 section of the bridge. Consequently, the vehicle length irregularity amplitude of the last vehicle in the A3 section of the bridge was higher than that of the first vehicle. The RDI of the A3 section of the bridge displayed a dominant convex shape with a primary length almost equal to the bridge span length. This is consistent with the numerical calculation results. Therefore, resonance was determined for bridge A3 at a train speed of 230 km/h. The RDIs of the other bridge sections and the ramen viaduct section were generally less than 1 mm, and the train was not in resonance when running at a speed of 230 km/h.

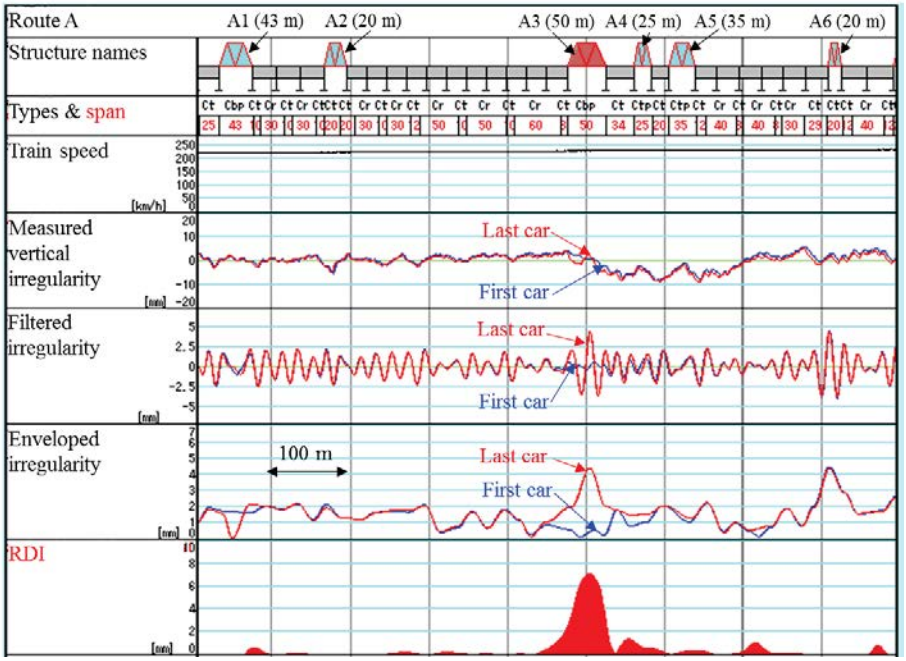

Figure 4: Example of the measured track displacement and application results of the proposed method

4.3 *In-situ* measurement result of the detected bridge

The vertical displacement of bridge A3 during the train passage was measured by using a laser Doppler velocimeter with a self-vibration correction (U-Doppler II, sampling 2 kHz [10]). The details of U-Doppler II are provided in Ref. [10]. The measurement target position was the bridge's mid-span. Figure 5 depicts the field measurements and the equipment used.

Figure 6 shows the time series response of bridge A3 from the *in-situ* field measurements. The dynamic response amplitude of bridge A3 increased as the train passes, with a large free vibration confirmed even after the train has passed. These responses are typical primary resonance waveforms; therefore, the resonance of the bridge detected by the proposed method was proven.

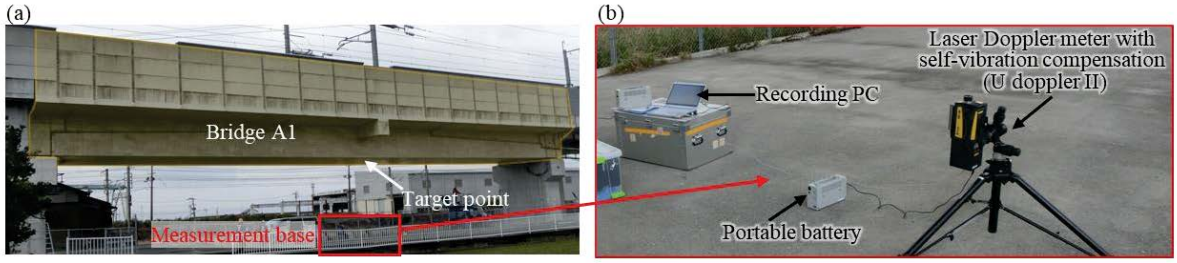

Figure 5: (a) Field test bridge and measurement environment. (b) U-Doppler II and its setup.

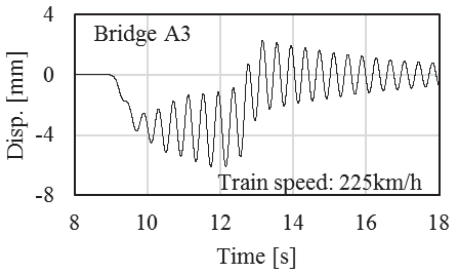

Figure 6: *In-situ* measured time series displacement response of bridge A3 detected by on-board measurement track irregularity data.

5 CONCLUSIONS

In this study, we developed a drive-by system for detecting resonant bridges from the data measured using high-speed railway vehicles. We proposed a novel methodology for detecting a resonant bridge by focusing on the track irregularity differences, including the bridge displacement components measured using the first and last vehicles. After a numerical verification, we applied the proposed method to the measurement data for the track irregularities from high-speed railways of Japan. We proved that resonant bridges were detectable on the track maintenance management system used daily by Japan's railway companies. Our findings are summarized as follows:

- We proposed a bandpass filter and an envelope processing method for estimating the vehicle track length irregularity amplitudes that highlighted unique components of the resonant bridge. The difference between the filtered and enveloped track irregularities measured in the first and last vehicles was used as the resonant bridge detection index. We also proposed a methodology for detecting resonant bridges based on their peaks.
- Through a numerical simulation at different train speeds, the RDI was confirmed to form a convex dominant component, with the dominant length almost identical to the bridge span length only at resonance.
- We applied the proposed method to the track irregularities at the positions of the first and last vehicles measured by the bogie-mounted track irregularity devices installed in Japan's high-speed railway trains. In fact, we detected a resonant bridge based on the RDI. Moreover, the *in-situ* bridge displacement measurements for a detected bridge demonstrated that the detected bridges actually resonated.

Despite these findings, problems associated with the construction of a generalized on-board measurement and diagnosis system still exist. We performed only limited numerical simulations and minimal verification. Therefore, the applications of the proposed method, such as the effects of the track irregularities, excluding the bridge displacement component, effects of the position synchronization errors, and effects of the measurement errors, require detailed studies in the future, especially in terms of the effects of the bridge span length.

REFERENCES

[1] M.D. Martínez-Rodrigo, J. Lavado, P. Museros, Dynamic performance of existing high-speed railway bridges under resonant conditions retrofitted with fluid viscous dampers, *Engineering Structures* 32, 808-828, 2010.

[2] L. Frýba, Vibration of solids and structures under moving loads, *Springer Science & Business Media* 1, 2013.

[3] M. Sogabe, N. Matsumoto, M. Kanamori, H. Wakui, Impact factors of concrete girders coping with train speed-up, *Quarterly Report of RTRI* 46 46-52, 2005.

[4] Junki Nakasuka, T. Mizutani, Y. Yamamoto, M. Uchida, T.N. Di Su, Y. Fujino, Analysis of large amplitude vibration mechanism of Shinkansen PRC girder bridges and the long-term trend of their structural characteristics, *Journal of Structural Engineering A* 62A, 42-49, 2016. (In Japanese).

[5] K. Matsuoka, K. Kaito, M. Sogabe, Bayesian time–frequency analysis of the vehicle–bridge dynamic interaction effect on simple-supported resonant railway bridges, *Mechanical Systems and Signal Processing* 135, 2020.

[6] D. Hester, A. González, A discussion on the merits and limitations of using drive-by monitoring to detect localised damage in a bridge, *Mechanical Systems and Signal Processing* 90, 234-253, 2017.

[7] E. Yazawa, K. Takeshita, Development of measurement device of track irregularity using inertial mid-chord offset method. *Quarterly Report of RTRI* 43, 125-130, 2002.

[8] A. Doménech, P. Museros, M.D. Martínez-Rodrigo, Influence of the vehicle model on the prediction of the maximum bending response of simply-supported bridges under high-speed railway traffic, *Engineering Structure* 72, 123-139, 2014.

[9] H. Tanaka, S. Yamamoto, T. Oshima, M. Miwa, Methods for detecting and predicting localized rapid deterioration of track irregularity based on data measured with high frequency. *Quarterly Report of RTRI* 59, 169-175, 2018.

[10] F. Uehan, Development of the U-Doppler non-contact vibration measuring system for diagnosis of railway structures. *Quarterly Report of RTRI* 49, 178-183, 2008.

EURODYN 2020
XI International Conference on Structural Dynamics
M. Papadrakakis, M. Fragiadakis, C. Papadimitriou (eds.)
Athens, Greece, 23–26 November 2020

CHARACTERIZATION OF VIBRATIONS MEASURED IN THE GRONINGEN BUILDING MONITORING NETWORK

Chris Geurts, Okke Bronkhorst, Davide Moretti, Jitse Pruiksma and Ron Snijders

TNO
Structural Dynamics, Monitoring and Control Services
Delft & Groningen
e-mail: chris.geurts@tno.nl

Keywords: Building vibrations, vibration sources, monitoring network, signal characteristics

Abstract.

A study was undertaken to define which set of signal characteristics can be used to differentiate between various vibration sources in a built environment. Several datasets of vibration measurements on known sources are obtained and analyzed. A set of 11 signal characteristics were determined for all signals. Based on the correlation between these characteristics, 6 signal characteristics (a_{max}, v_{max}, $f_{d,f,a}$, D_s, N_{peak}) were selected for a detailed analysis. This analysis showed that differentiation between vibration sources based on signal characteristics is feasible. Further research should investigate the possibilities and limitations of the dataset and determined whether identification of vibration sources based on the obtained signal characteristics is attainable.

1 INTRODUCTION

Since 2014, a large building vibration monitoring network is in place in the province of Groningen in the North of the Netherlands [1]. The primary objective of this network is to monitor vibrations caused by shallow earthquakes, induced by natural gas production in this region. In approximately 350 buildings vibrations are measured in three orthogonal directions at foundation level in a stiff point near the corner of the building.

After an earthquake with a magnitude M $\geqslant$ 2.5, building inspections are executed for those buildings that experienced a trigger event, i.e. a vibration velocity exceeding a threshold of 1 mm/s [2]. These inspections are performed to obtain information on the occurrence and progression of damage. Besides earthquake vibrations, the threshold is frequently exceeded due to vibrations from other internal and external causes (e.g. traffic, construction work, slamming doors, jumping). To obtain information on the cause of these triggers, building owners are asked to fill in a website-form and specify a reason for the threshold exceedance. The large amount of data collected on all these different types of vibration sources provide for a unique opportunity to obtain a better understanding of their characteristics and the possible influence these sources have on the occurrence of damage to buildings.

The ultimate aim of this research is to develop a method to identify vibration sources in the monitoring network. The goal of this study is to establish a set of signal characteristics and determine to what extent these characteristics can be used to differentiate between various vibration sources in a built environment. To that end, several datasets of vibration measurements on known sources are obtained and analyzed. The following datasets are used to study the set of vibration characteristics:

- Time traces measured in the monitoring network from verified events, i.e. the Garrelsweer earthquake of 9/6/2019 [3] and F16 sonic booms on 6/6/2016 [4].
- A test campaign in the monitoring network with various vibration sources, see report TNO 2019 R11872 [5 for a detailed explanation.
- Data from measurement projects performed in the past by TNO on several external vibration sources (mass pile driving, vibratory pile driving, railway traffic and blasting).

This paper describes the setup of these datasets and discusses the findings of this research. Chapter 2 gives some background information on the monitoring network and discusses the state-of-the-art in vibration source analysis, with a focus on vibration research in the built environment. The datasets used in this research are detailed in Chapter 3; Chapter 4 explains the applied analysis techniques and the determined vibration characteristics. Chapter 5 presents and discusses the results and findings obtained from the various datasets. Chapter 6 gives the conclusions and recommendations of this research.

2 BACKGROUND

2.1 Seismic monitoring networks and seismic noise

Seismic monitoring networks can roughly be grouped in country-scale, urban-scale, and building-scale monitoring networks. Each network has different tasks, but all have a common objective of earthquake risk reduction. According to D'Alessandro et al. [6] the different scale monitoring networks generally have the following purposes:

- National seismic networks are intended for earthquake observation and seismological studies.
- Urban networks are used to map the earthquake intensity and as early-warning system.
- Building networks are applied for structural health monitoring purposes and also as on-site warning systems.

An increasing trend is observed in urban seismic monitoring networks around the world, which are mainly used to characterize the subsurface structure and improve seismic risk management in populated areas [6]. The introduction of low-cost MEMS sensor systems has further contributed to this development [7-9]. Although the original intention of most of these networks was for seismological purposes e.g. [10-13 (see [13] for an extensive reference overview), the data measured for non-natural vibration sources is being studied more thoroughly over the last decades.

Riahi and Gerstoft [14] studied the traffic-generated noise measured by 5200 geophones that covered a 7x10 km area in Long Beach (California, USA). From the seismic noise they were able to extract metro activity, departing and landing aircraft, and traffic movement along the highway at night.

Boese et al. [15] have investigated anthropogenic and natural noise recorded by borehole seismometers installed beneath the Eden Park stadium in Auckland, New Zealand. They observed elevated noise levels (10-15 dB) in records obtained during the 2011 Rugby World Cup matches.

Green et al.[16] studied the recordings of five broadband seismometers, deployed in central London during the summer of 2015. A comparison of power spectra with observatory stations in much less populated areas showed most of the spectrum is dominated by anthropogenic noise. For short periods ($T < 0.4$ s) road traffic was found to have the largest effect. In close proximity to the tracks, railways also generated observable signals for $T < 0.3$ s. At very long periods ($T > 20$ s) the influence of trains was observed across the city. The air movement through the subway also resulted in increased noise levels for periods $T > 30$ s.

Similar observations were made by Diaz et al. [17] through an analysis of the seismic records obtained from a broad-band seismic station located near the center of Barcelona. A spectrogram of the vertical seismic acceleration measured between 1/9/2016 and 13/9/2016 showed the frequency ranges dominated by traffic, ocean activity and subway activity. A decimated timeseries of the same period clearly showed the night/day and working day/weekend variations. Diaz et al. [17] could also relate some peaks in the time series to traffic increases before and after FC Barcelona football games.

Particular relevant for the current study is a statistical analysis performed by Groos and Ritter [18] on 4 hr timeseries for classification purposes. Their classification scheme is based on deviations from the Gaussian distribution. The parameters used in the classification are different ratios of percentile intervals of the vibration signal histogram. Based on these parameters Groos and Ritter [18] defined 10 noise classes, which account for non-corrupt (NC1 – NC6) and corrupt (NC10 – NC13) time series.

The current study investigates the characteristics of signals from vibration sources with frequency content between 1 and 100 Hz (T between 0.01 and 1 second). The studies by for example Green et al. [16] and Diaz et al. [17] show that in this frequency range, the largest contribution generally comes from man-made vibrations. Studies on man-made vibrations have mainly researched the effects on damage, e.g. [19-22], and comfort, e.g. [23-26]. Characteristics that have been extensively studied are the amplitude and frequency of the vibrations, mainly with the purpose of predicting and assessing the risk on damage or nuisance. A detailed discussion of studies into man-made vibrations is provided in chapter 5, where a comparison is made with the results of the current study.

2.2 The monitoring network building vibrations

The monitoring network building vibrations was designed and built with the goal to obtain more insight into the effects of earthquakes on buildings in Groningen. This chapter gives general background on the sensor network; a more detailed description of the monitoring network is provided in report TNO 2015 R10501 [1]. Figure 1 illustrates the approximately 350 locations in the monitoring network where vibrations are measured.

The vibration measurement systems were supplied by GeoSig and consist of a recorder (GMSplus measuring system) and a tri-axial sensor (AC-73 force balance accelerometer). The GeoSig sensors are located near a stiff corner of a building (~0.5 m) on the inside or outside, as illustrated in Figure 2(a) and (b). De X- and Y-direction of each sensor are respectively parallel and perpendicular to the façade, the Z-direction is pointing upwards. The GeoSig sensors continuously sample accelerations at 250 Hz, which are automatically integrated to velocities.

The sensor transmits full resolution (250 Hz) data when a velocity threshold is exceeded. After the exceedance of the threshold level of 1 mm/s in X, Y, or Z-direction, the trigger event is logged with a pre-trigger time of 10 s until 20 s after the last threshold exceedance.

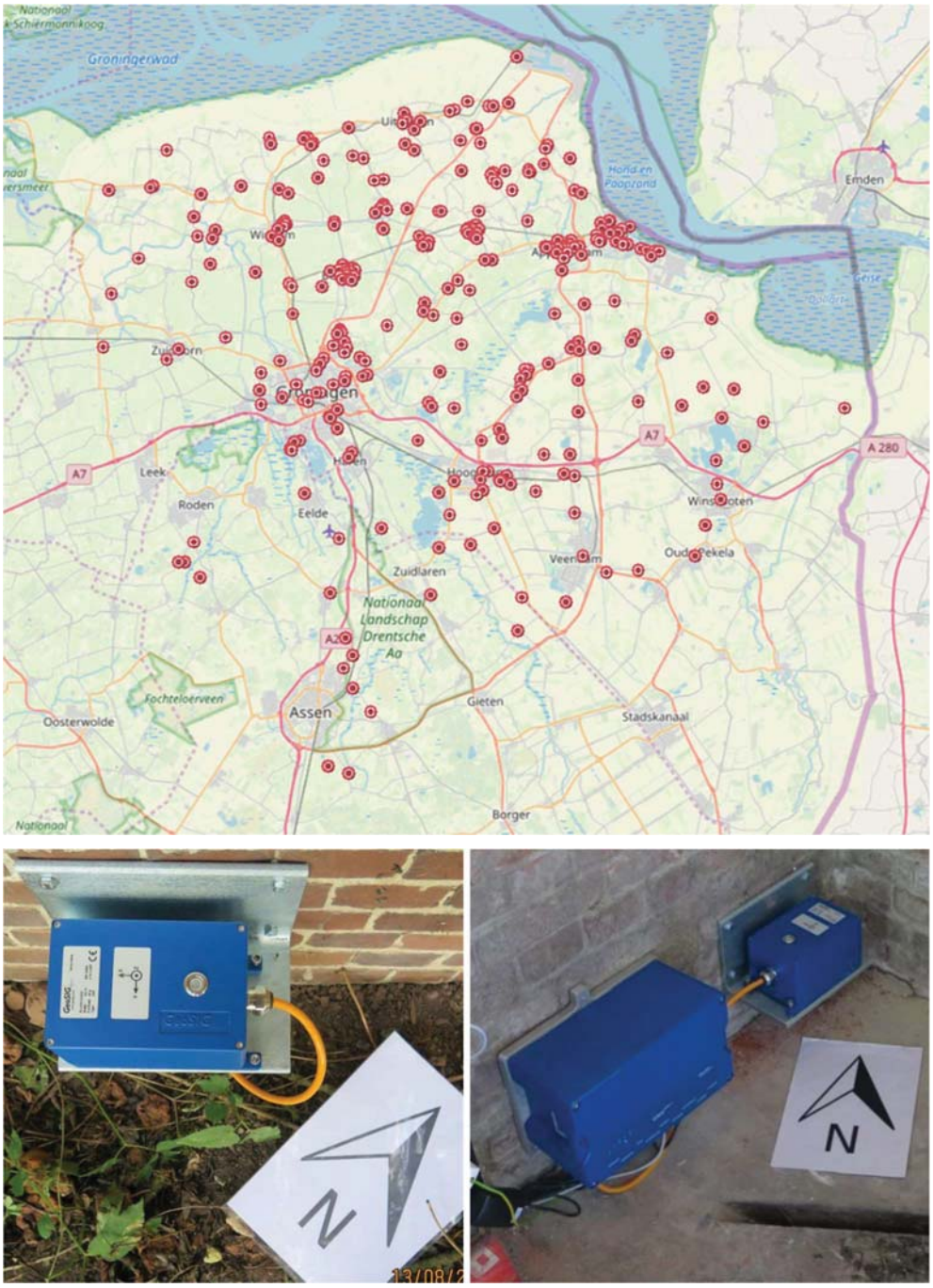

Figure 1: (top) Sensor locations in the building sensor network in Groningen, (bottom left) Geosig sensor near a stiff corner on the outside of a building, and (bottom right) a Geosig sensor near the stiff corner inside, the large box to the left is the recorder, the small box to the right is the sensor.

3 DATA DESCRIPTION

3.1 Earthquake Garrelsweer

On June 9, 2019 an earthquake was measured near Garrelsweer with a magnitude M = 2.5, located at 3 km depth. Figure 2 shows the location of the epicenter as defined by the KNMI [27], and the locations of the triggered and non-triggered sensors.

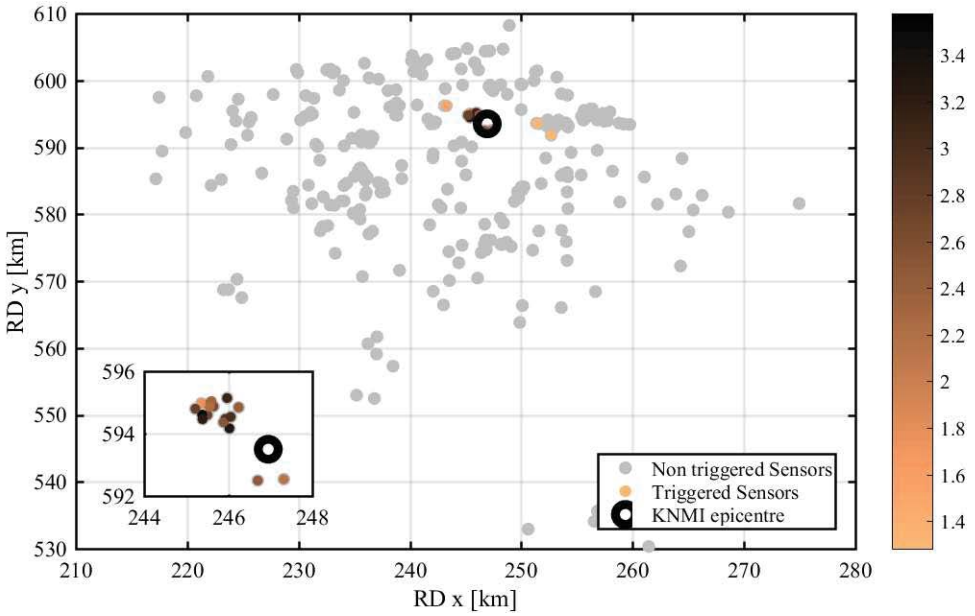

Figure 2: Triggered and non-triggered sensors in the monitoring network during the Garrelsweer earthquake (9-6-2019), taken from [3].

A detailed analysis of the data from the monitoring network can be found in [3]. A total of 257 signals were applied in the current study. The majority of these signals did not result in a trigger, i.e. the maximum observed vibration velocity is lower than 1 mm/s.

3.2 Sonic booms of F16 aircrafts

On the 6th of June 2016 at 15.30 (local time), two F16's crossed the sound barrier above the province of Groningen. The vibrations due to the low-frequency pressure waves were recorded by the monitoring network. Figure 3 shows two snapshots of a movie of the pressure waves due to sonic booms by the F16 aircrafts. These pressure waves were derived from the vibration signals measured by the monitoring network. A total of 271 signals measured in the monitoring network are used in this study to determine the characteristics of building vibrations due to sonic booms caused by supersonic aircrafts.

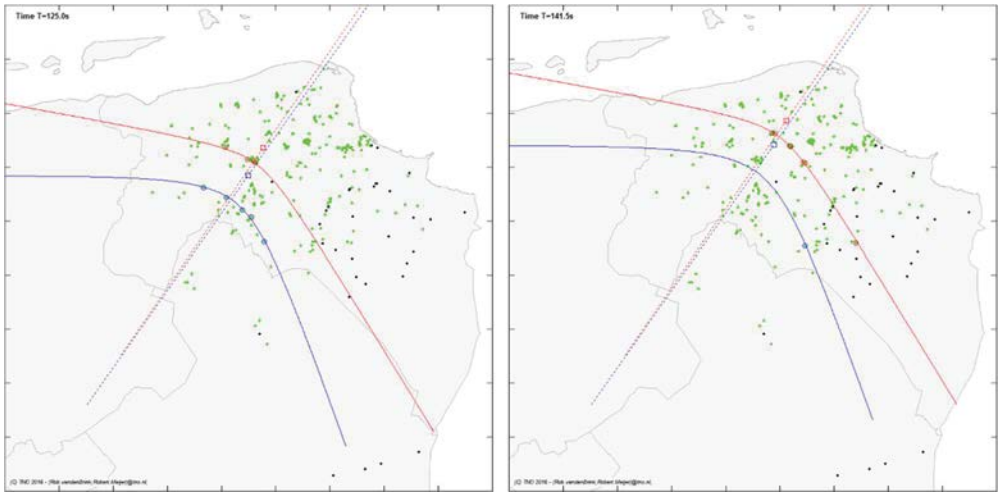

Figure 3: Two snapshots of a movie which shows the movement of the two pressure waves due to the two F16, based on the vibration signals measured in the monitoring network. Taken from [4].

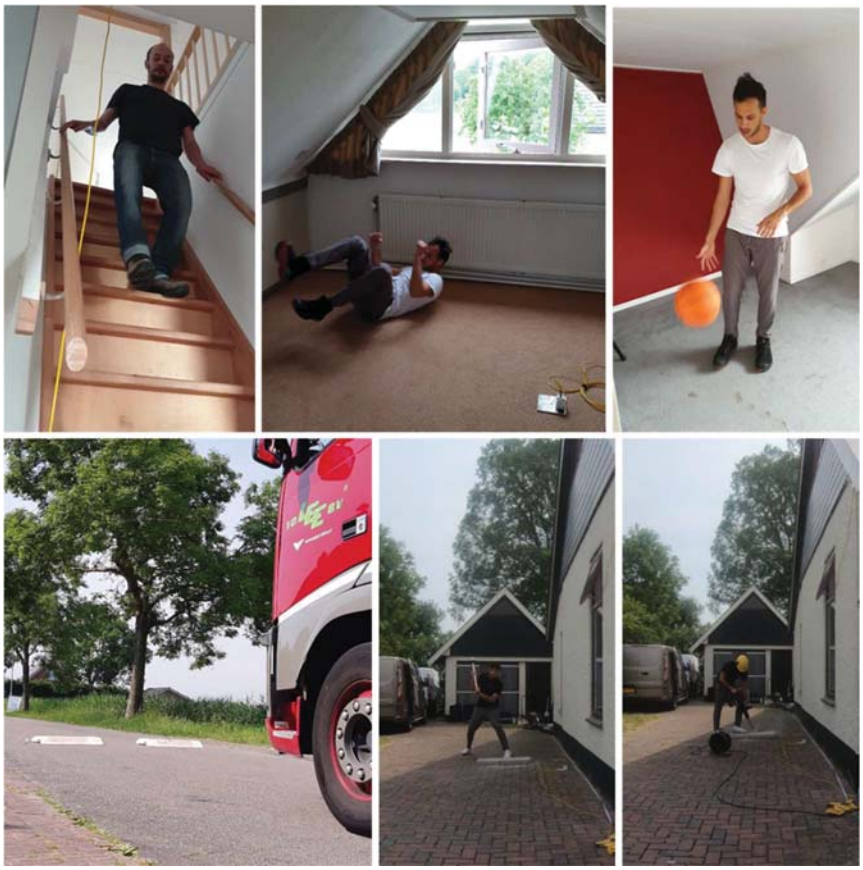

Figure 4: Internal and external vibration sources applied in the test campaign in the monitoring network.

3.3 Test campaign in the building monitoring network

To develop a database with measured vibration signals of internal and external sources, a test campaign was organized and executed, in which known vibrations sources were applied near sensors in the monitoring network. In this campaign two tests were performed:

1. Various internal and external vibration sources were applied in a house in Groningen, while vibrations were measured at various positions in the building.
2. A truck drove twice a predefined route along 17 sensors in the monitoring network.

Figure 4 shows some of the internal and external sources that were tested during this campaign. A detailed description of the tests and the results is given in [5].

3.4 Blasting

A measurement campaign was performed by TNO to assess the influence of blast induced vibrations in buildings around a defense exercise area in the Netherlands. Exercises with 8 different types of explosions were performed in the exercise area, while vibrations were measured at 4 different buildings in the surroundings at distances ranging between 3 and 7.5 km. Measurements were performed with Sundstrand QA-700. The sensors were sampled simultaneously with 2000 Hz. The data of some of these sensors were applied in the current study.

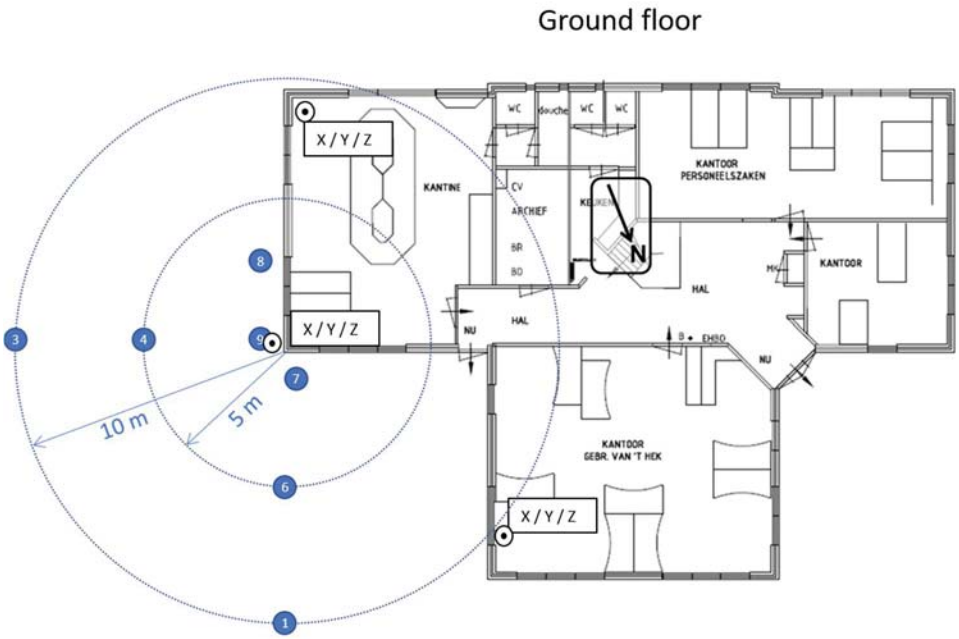

Figure 5: Sensor positions (black circles) and mass pile driving and vibratory sheet pile driving locations (blue circles).

3.5 Mass pile driving and vibratory sheet pile driving

A series of tests were performed with mass pile driving and vibratory sheet pile driving near an office building in the province of North-Holland. Locations of the pile driving and the sensore locations used are specified in Figure 5. Since the building was about to be replaced by a new building, high vibration levels could be induced, and damage initiation was also monitored.

Measurements at these locations were performed with Sundstrand QA-700 sensors; the sensors were sampled at 2000 Hz. The data of the indicated sensors in Figure 5 were used in the current study.

3.6 Railway traffic

Between September and November 2012 measurements were performed by TNO at 3 buildings along the HSL-south track between Amsterdam and Rotterdam. The buildings were located at 125 m, 150 m, and 450 m from the railway track. Only the data of the buildings at 125 m and 150 m that exceeded the background noise were used in this study. The data from the building at 450 m was not clearly distinguishable from background vibration levels.

Accelerations were measured at the foundation, the ground floor, the first floor and outside near the building and 50 m from the track. The accelerations measured at the foundation are used in the current study. The measurements were performed with Sundstrand QA-700 sensors. The data were sampled with 500 Hz. Measurements were performed on Thalys and V250 trains with passage speeds ranging between 160 and 300 km/h.

4 ANALYSIS

Before computation of the various characteristics, some preprocessing is performed on the measured acceleration signals. This preprocessing consists of the following steps:

i. Offsets are removed, such that the acceleration signals have a zero mean value;
ii. A 4th order Butterworth high-pass filter with cut-off frequency of 0.8 Hz is applied to remove trends which might affect the integration to velocities;
iii. The acceleration signals are integrated to obtain velocity signals;
iv. The absolute maximum velocity is determined for the X, Y, and Z-direction;
v. The acceleration and velocity signal of the direction with the largest absolute maximum velocity is selected for further analysis, these are from here on referred to as a(t) and v(t);
vi. The time instance at which the absolute maximum or peak velocity occurs is determined and used to trim the signal;
vii. The acceleration and velocity signal a(t) and v(t) are trimmed from -10 s to +20 s of the peak velocity.

The processed acceleration and velocity signals were analyzed with the Fast Fourier Transform (FFT) and the Short Time Fourier Transform (STFT), and the Arias intensity function of all signals was determined. Finally, the number of peaks in the signals was analyzed through the derivative of the Arias intensity function. The following signal characteristics were determined from the acceleration and velocity signals, a(t) and v(t):

- The absolute maximum acceleration and velocity levels, a_{max} and v_{max};
- The acceleration and velocity peak factor, g_a and g_v;
- The dominant frequencies of the acceleration and velocity FFT spectra, $f_{d,f,a}$ and $f_{d,f,v}$;
- The dominant frequencies of the acceleration and velocity STFT spectra, $f_{d,s,a}$ and $f_{d,s,v}$;
- The Arias intensity, I_a;
- The significant duration, D_s;
- The number of peaks, N_{peak}.

A detailed explanation of the performed analysis is provided in [28].

5 RESULTS AND DISCUSSION

This chapter presents the results of the analysis on the datasets described in chapter 3. Section 5.1 presents and discusses the correlation of the characteristics computed for all vibration signals. Based on these results a set of characteristics is selected, for which detailed results are shown in section 5.2 to 5.6.

5.1 Correlation between determined signal characteristics

Each of the computed characteristics provide some information on the features of the measured signals. However, some characteristics can provide similar information. To filter the characteristics that provide new information, the correlation between each of the characteristics has been computed using the absolute value of the Pearson correlation coefficient, $|\rho_{x,y}|$. If 2 variables are highly correlated then $|\rho_{x,y}|$ tends to 1; if they are poorly correlated, $|\rho_{x,y}|$ tends to 0.

The complete correlation matrix for all the signal characteristics is shown in Figure 6 . This figure shows that the characteristics determined with the acceleration timeseries are highly correlated with those obtained from the velocity timeseries.

The interest of this study is on the signal characteristics that provide new information on a vibration signal, i.e. those signal characteristics that have relatively little correlation with each other (i.e. $|\rho_{x,y}| < 0.6$). The results of the following signal characteristics will be discussed in the next paragraphs:

the maximum acceleration and maximum velocity, a_{max} and v_{max}
the dominant frequency of the acceleration signal, $f_{d,f,a}$
the acceleration peak factor, g_a
the significant duration, D_s
the number of peaks, N_{peak}

Because a relatively large amount of literature can be found on the peak acceleration and velocity these are both discussed in detail in the next paragraph. The results of the other signal characteristics can be found in [28].

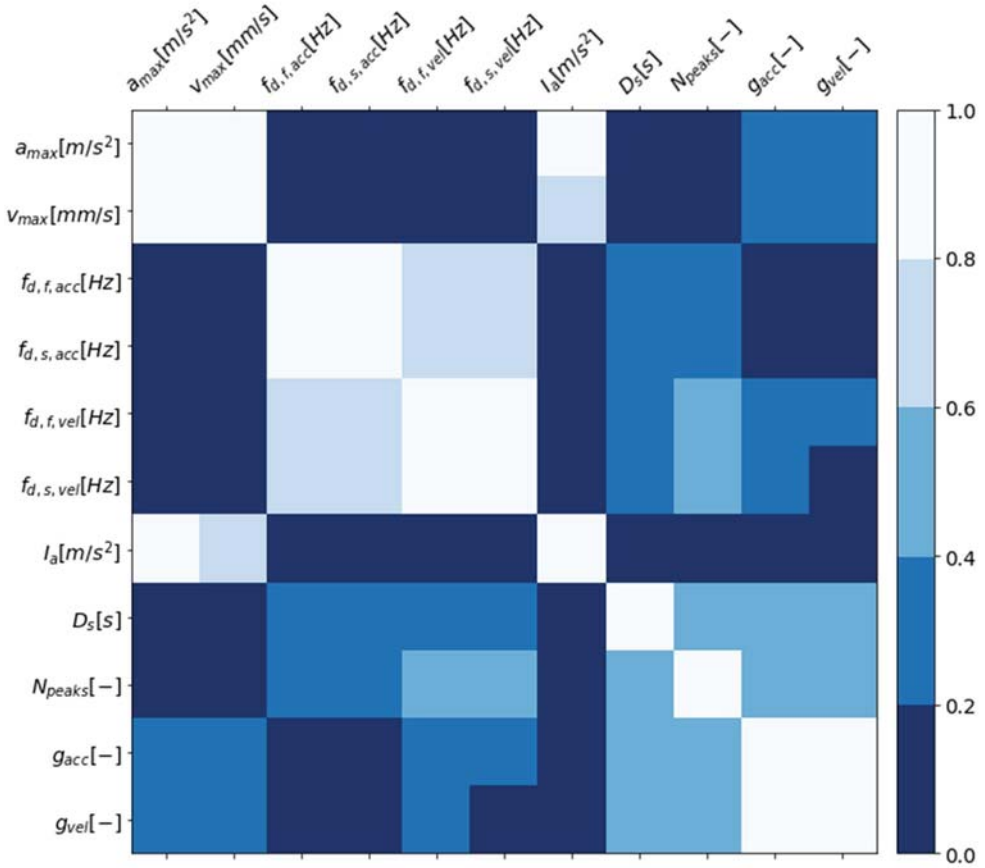

Figure 6: Correlation matrix of all computed signal characteristics. Note that the matrix is symmetric, i.e. the upper half gives the same information as the lower half

5.2 Absolute maximum vibration levels, a_{max} and v_{max}

Figure 6 and Figure 7 show box plots and individual samples of the absolute maximum acceleration and velocity determined per source type. The vibration sources are ranked in order of increasing median value of the boxplots. The background vibration results are placed at the top as reference.

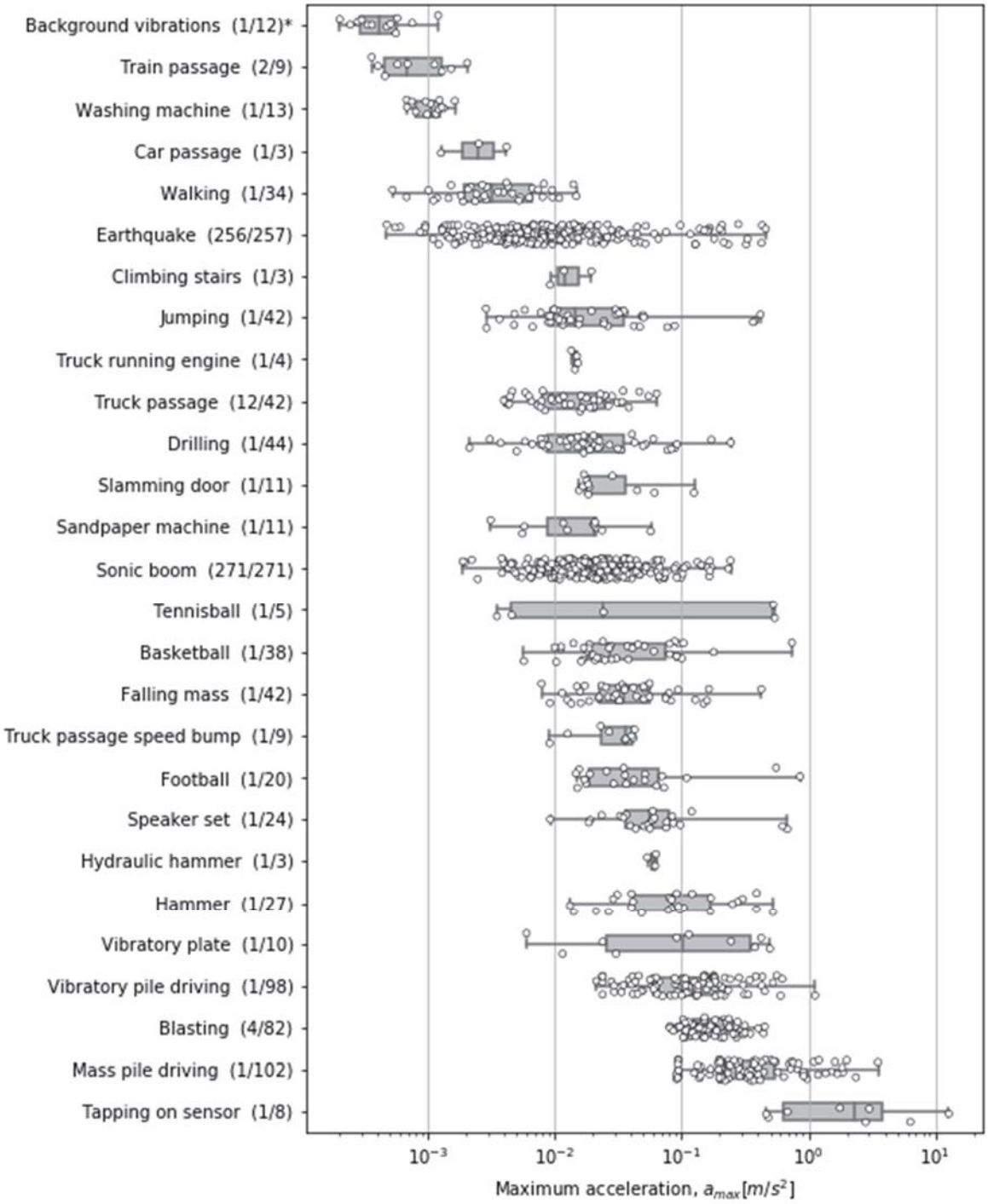

Figure 6: Boxplots and samples for the absolute maximum acceleration a_{max} obtained in all tests.
*(number of buildings/number of measured signals)

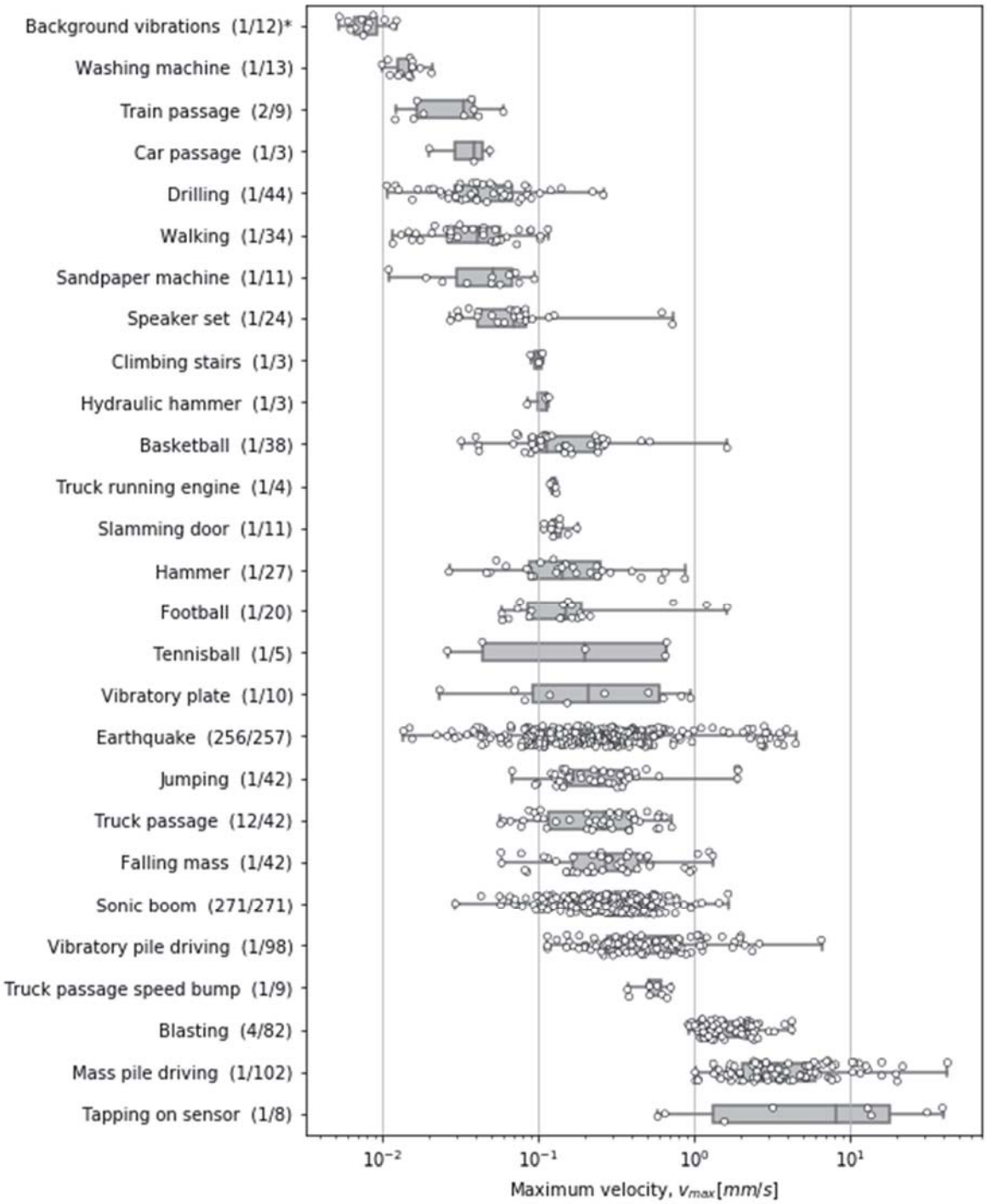

Figure 7: Boxplots and samples for the absolute maximum velocity v_{max} obtained in all tests.
*(number of buildings/number of measured signals)

The smallest maximum vibration levels are observed for the train passages, the washing machine and the car with running engine. In the tests with these sources the vibration levels only just exceeded the measured background vibration levels. The main reason for the low values of the train passages is the large distance between the track and the buildings at which measurements were performed.

Connolly et al. [29] and Kouroussis et al. [30] found peak velocities of 0.1 mm/s and smaller for measurements on vibrations induced by high-speed trains at a distance of 100 m. This matches with the vibration velocities found here for high-speed train passages at distances of 125 m and 150 m. For distances down to 2 m from the track, maximum velocities up to 4 mm/s were measured by Connolly et al. [29].

The vibration levels observed for road traffic, particularly the truck passage, also match well with values found in literature for the range of distances studied here (i.e. between 10 and 30 m). Hao et al [26] observed maximum accelerations of 0.006 – 0.015 m/s^2 for truck passages at a distance of 20 m. Hajek et al. [31] specify that for clay soils the maximum vibration velocities at 10 to 30 m are typically between 0.1 and 2 mm/s. For distances down to 3 m Hajek et al. [31] specify maximum vibrations velocities up to 3 mm/s. Staalduinen and Smits [32] describe maximum velocities ranging between 0.3 and 3 mm/s, based on 12 experimental studies performed by TNO (e.g. [33-36]).

The largest maximum vibration levels are determined for tapping the sensor and mass pile driving. The range of vibration velocities determined for mass pile driving (~1 – 40 mm/s) are similar to those specified by Staalduinen et al. [37] and Jongmans et al. [38]; these studies determined vibration velocities between 3 and 20 mm/s. For the tests performed at 10 m distance, lower values (around 1 mm/s) were found in the current study than in [37] and [38].

For vibratory pile driving Staalduinen et al. [37] found vibrations velocities up to 10 mm/s for distances between 10 and 20 m. Athanasopoulos and Pelekis [39] describe similar vibration levels for these distances. For distances between 1 and 10 m they found vibration velocities up to 25 mm/s. Lower vibration levels are observed for the vibratory pile driving data analyzed in the current study. A possible reason is that these pile driving tests were performed to depths of approximately 16 meter, while the stiff soil layer was at a larger depth.

The maximum accelerations and maximum velocities measured for the 2019 Garrelsweer earthquake range between 5x10-4 and 0.4 m/s^2 and 0.01 and 5 mm/s (see Figure 6.4 and Figure 6.5). During other earthquakes in the Groningen area (see [40]-[45]) vibration velocities up to 27 mm/s and accelerations up to 1.5 m/s^2 were measured by the monitoring network.

The vibrations induced by the air overpressure due to the sonic boom and the blasting exercises had acceleration levels between 0.002 and 0.5 m/s^2 and velocity levels between 0.03 and 4 mm/s. Much larger vibration levels (up to 500-600 mm/s) are described in other studies on blasting induced vibrations [46-48]. The main reason is these data were obtained for much shorter distances between the explosion and the sensor. Not only is the air overpressure larger at shorter distance, but there is also a large contribution of vibrations through the ground.

Few studies describe results of normal household vibrations such as presented in Figure 6.4 and Figure 6.5. Some velocity levels measured of typical building activities are given by Nicholls et al. [46], unfortunately it is not clear at which position in the building these levels were measured. Vibration levels measured by Nicholls et al. [46] for a door closing ranged between 0.1 and 1.4 mm/s. Considering the velocity levels measured in the slamming door tests presented in the current study, a better description is probably closing door tests. For jumping, Nicholls et al. [46] describe velocity levels between 1 and 125 mm/s. The large differences with the levels observed in the current study are probably due to the sensor location, and maybe to some extent due to the intensity of jumping.

In conclusion, the vibration levels observed for the various vibration sources in this dataset fit well with the ranges mentioned in literature. However, they do not give a good representation of the complete range of levels that can occur in the built environment. For most vibration sources the dataset is at the low end of these ranges. Therefore the ranges for a_{max} and v_{max} in Figure 6.4 and Figure 6.5 might not be very useful for differentiation between the studied vibration sources.

5.3 Acceleration dominant frequency, $f_{d,f,a}$

Figure 7 shows the box plots for the dominant frequencies $f_{d,f,a}$ of the acceleration FFT per studied vibration source. The vibration sources are ranked in order of increasing median dominant frequency. The dominant frequencies determined for the background vibrations are placed at the top as reference for the vibration sources.

Figure 7 shows that most signals with dominant frequencies $f_{d,f,a} < 35$ Hz are due to sources producing (repeated) transient vibrations, such as a truck or train passage, mass pile driving, or an earthquake. Sources which generate continuous vibrations, such as drilling, vibratory pile driving, a vibratory plate or a speaker set playing loud music typically have dominant frequencies $f_{d,f,a} > 25$ Hz.

According to Muller [49] the dominant frequency of mass pile driving signals is between 5 and 25 Hz, which is also observed in Figure 7. The dominant frequency $f_{d,f,a}$ determined for vibratory pile driving is concentrated around 37 Hz, which was the driving frequency of the vibratory machine. This frequency is within the range (30 – 40 Hz) for high-frequency pile-driving described by Deckner [22].

In Figure 7 dominant frequencies between 2 and 6 Hz are observed for the train passages. These low values are most likely related to the relative large distances (125 and 150 m) between the buildings and the track. Similar low frequencies were found by Ditzel [50] in measurements at two locations in the Netherlands. Ditzel [50] attributes the relative low dominant frequencies to a low-pass filter behavior of a ditch alongside the track. From measurements on passages of various types of trains, Suhairy [51] found dominant frequencies between 5 and 12.5 Hz. Measurements performed by the Dutch Railways [52] show that the dominant frequencies are generally smaller than 10 Hz.

Based on the previously mentioned studies on the effects of road traffic by TNO, Staalduinen and Smits [32] conclude that the dominant frequency is typically observed around 10 Hz, but can range between 5 and 15 Hz. The dominant frequencies for the car passages in Figure 7 are concentrated at 4-5 Hz, while the dominant frequencies observed for the truck passages are mainly observed between 5 and 15 Hz.

The dominant frequencies for the Garrelsweer earthquake are between 1 and 20 Hz (with one outlier at almost 30 Hz), this corresponds with the dominant frequencies determined for other earthquakes measured in the monitoring network [40-45]. This range is also very similar to that found for truck passages (see Figure 7).

The dominant frequencies for the sonic boom are generally observed between 1 and 25 Hz, which matches well with the range observed for earthquakes and truck passages. However, much larger dominant frequencies were also measured for the sonic boom (up to 95 Hz). For blasting the dominant frequencies were observed between 10 and 25 Hz. Nicholls et al [46] and New [47] found dominant frequencies mainly between 20 and 70 Hz, although they encountered values up to 500 Hz. Aloui et al [48] measured dominant frequencies between 1.5 and 11 Hz. These differences are mainly related to the applied explosion charge and the distances between the source and the sensor. The results of blasting in the current study were obtained for similar distances as applied in Aloui et al [48].

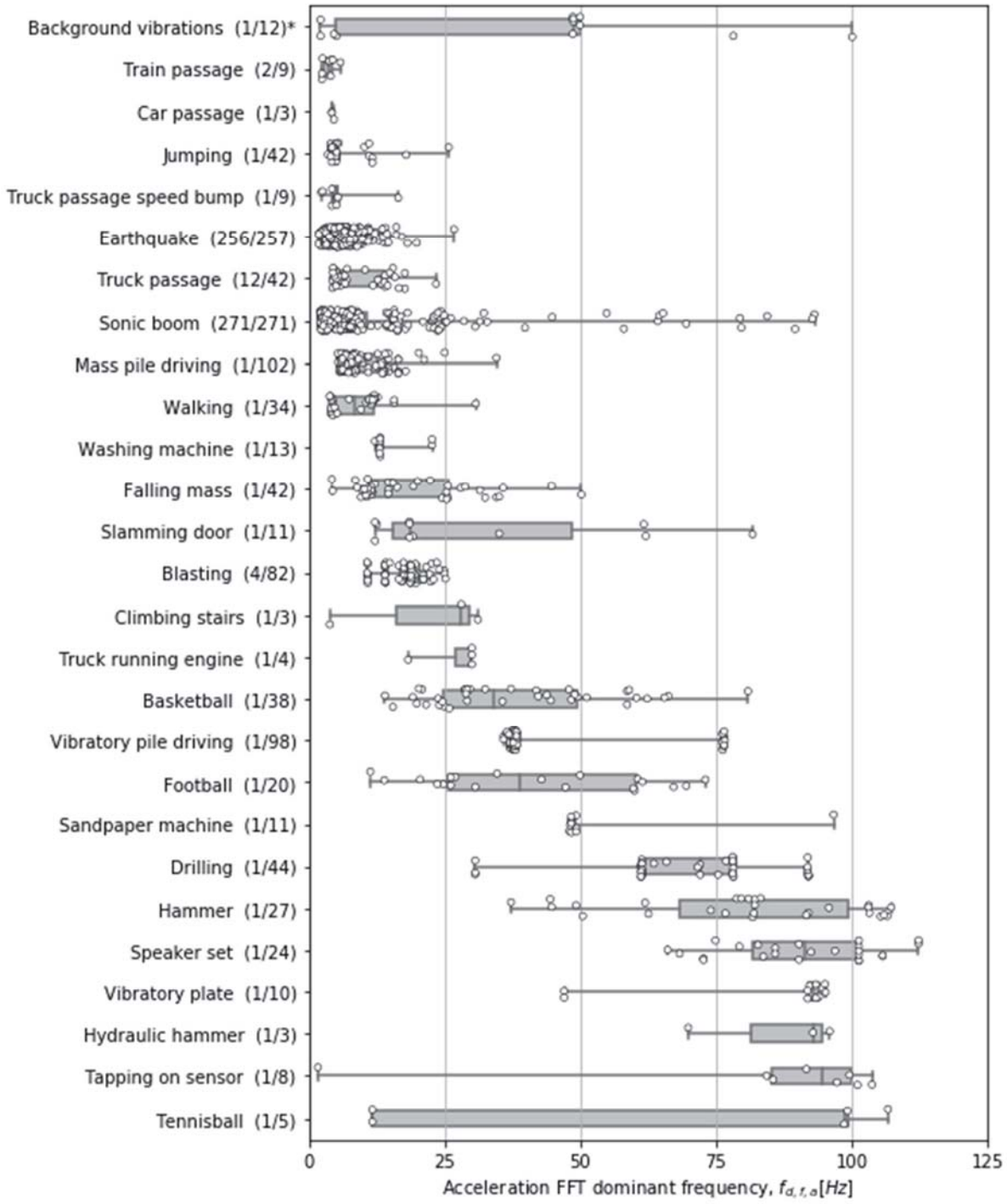

Figure 7: Boxplots and samples for the dominant frequency $f_{d,f,a}$ obtained in all tests.
*(number of buildings/number of measured signals)

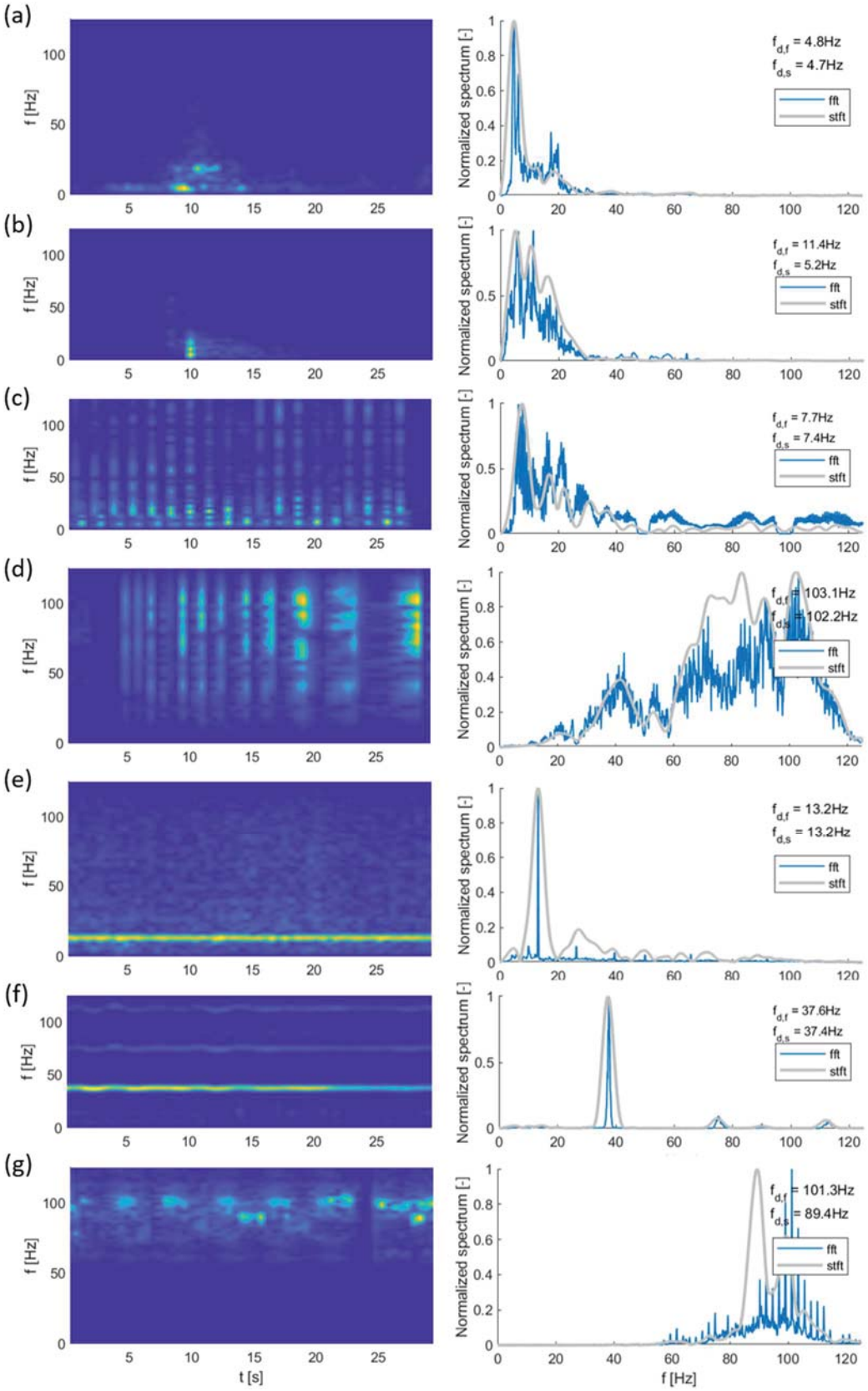

Figure 8: Acceleration spectrograms and spectra of several vibration sources: (a) truck passage, (b) earthquake, (c) mass pile driving, (d) hammer, (e) washing machine, (f) vibratory pile driv-ing, and (g) speaker music.

Figure 8 shows examples of the spectrograms (STFT) and spectra (FFT) of some of the measured acceleration signals. The spectrum of an earthquake and truck passage, Figure 8(a) and (b), are both concentrated in the low frequency range, with most energy content between 0 and 25 Hz. Similar spectra can be observed for a train passage, a sonic boom or blasting.

Similar to the earthquake and truck passage in Figure 8(a) and (b), mass pile driving shown in Figure 8(c), also has a large energy content in the low frequency range. However, for mass pile driving energy content is also found at higher frequencies. The spectral content of the hammer example shown in Figure 8(d) is mainly found above 30 Hz. Another distinguishing feature is the relatively broad spectrum compared to the earthquake, truck passage and mass pile driving.

Figure 8(e), (f), and (g) show STFT and FFT spectra of continuous vibration sources. Both the washing machine and vibratory pile driving have narrow band spectra with harmonic frequencies of the dominant frequency. Similar features are observed in the spectra of other types of machinery, such as the vibratory plate or drilling. The spectrum of the speaker playing music is more broadband, with large peaks at some distinct frequencies.

Based on these FFT and STFT spectra, other spectral features that could prove useful to allow for more differentiation between vibration sources the bandwidth of the spectrum (e.g. the 3 dB bandwidth) or harmonic frequencies (cepstrum analysis).

5.4 Acceleration peak factor, g_a

Figure 9 shows box plots of the acceleration peak factor g_a per studied vibration source. The vibration sources are ranked in order of increasing peak factor; the background vibration results are placed at the top as reference. Figure 10 shows examples of the acceleration signals of some of the tested vibration sources.

The smallest peak factors are observed for signals of sources which produce a (monotonic) continuous vibration, such as a sanding machine or a vibratory hammer used in (sheet) pile driving. The peak factors for these continuous signals are generally even smaller than the peak factors determined for the background vibrations. Vibration signals with peak factors $g_a < 6$ are likely to have been caused by a continuous vibration source, and are unlikely to contain large pulses.

Examples of a monotonic continuous vibration signal from a sanding machine and a background vibration signal are shown in Figure 10(a) and (b). The signal of the sanding machine is much denser due to the high-frequency continuous signal produced by this source, while no large peaks are present. Due to the high-frequency content the standard deviation is larger, which results in a smaller peak factor.

The largest peak factors are observed for signals with a single pulse or small number of pulses or a single short-duration transient. These type of signals are for example caused by hitting the sensor (e.g. by hand or hammer), dropping a hard heavy object (e.g. a stone) or an air pressure wave (e.g. caused by a sonic boom or blasting).

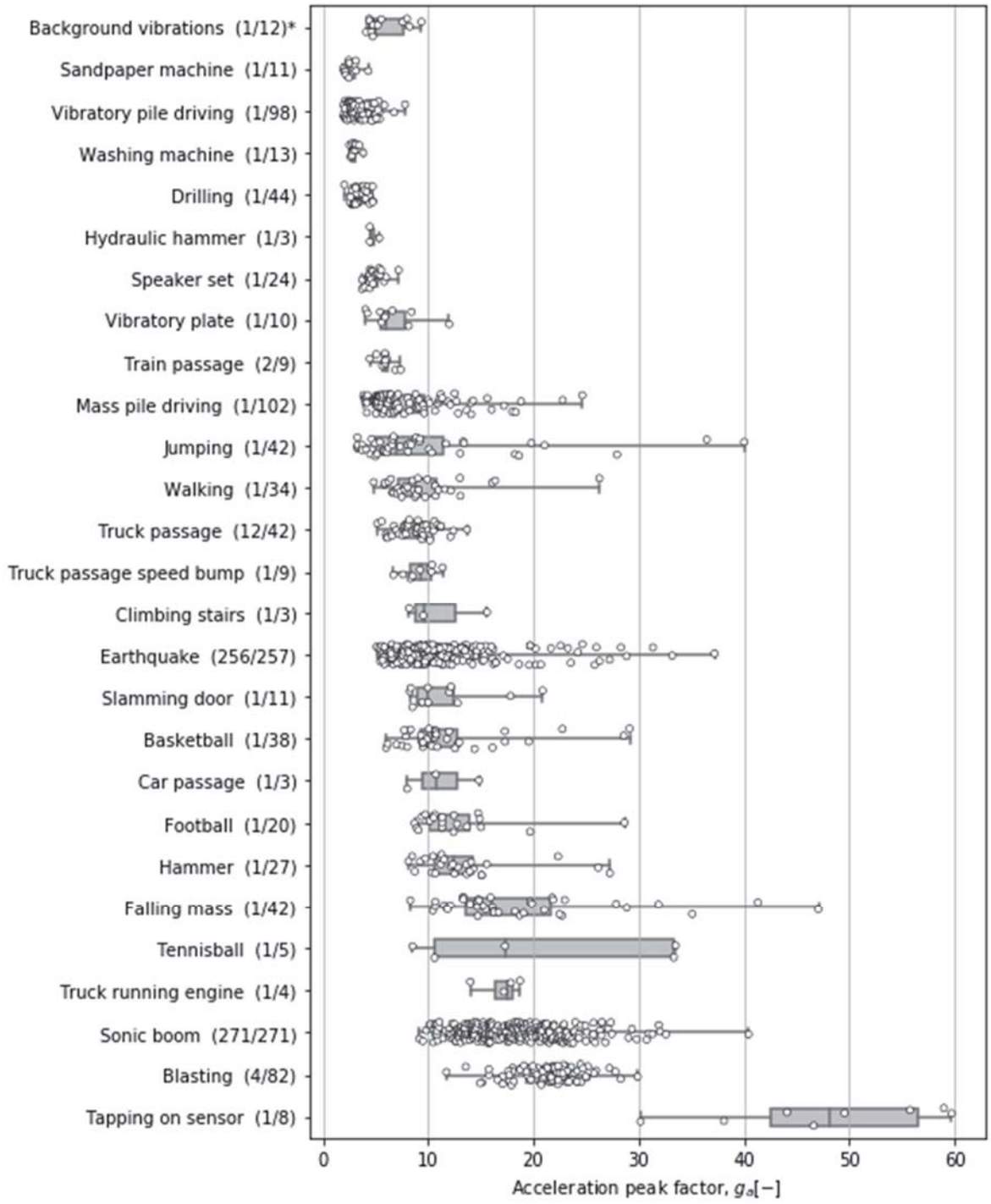

Figure 9: Boxplots and samples for the acceleration peak factor g_a obtained in all tests.
*(number of buildings/number of measured signals)

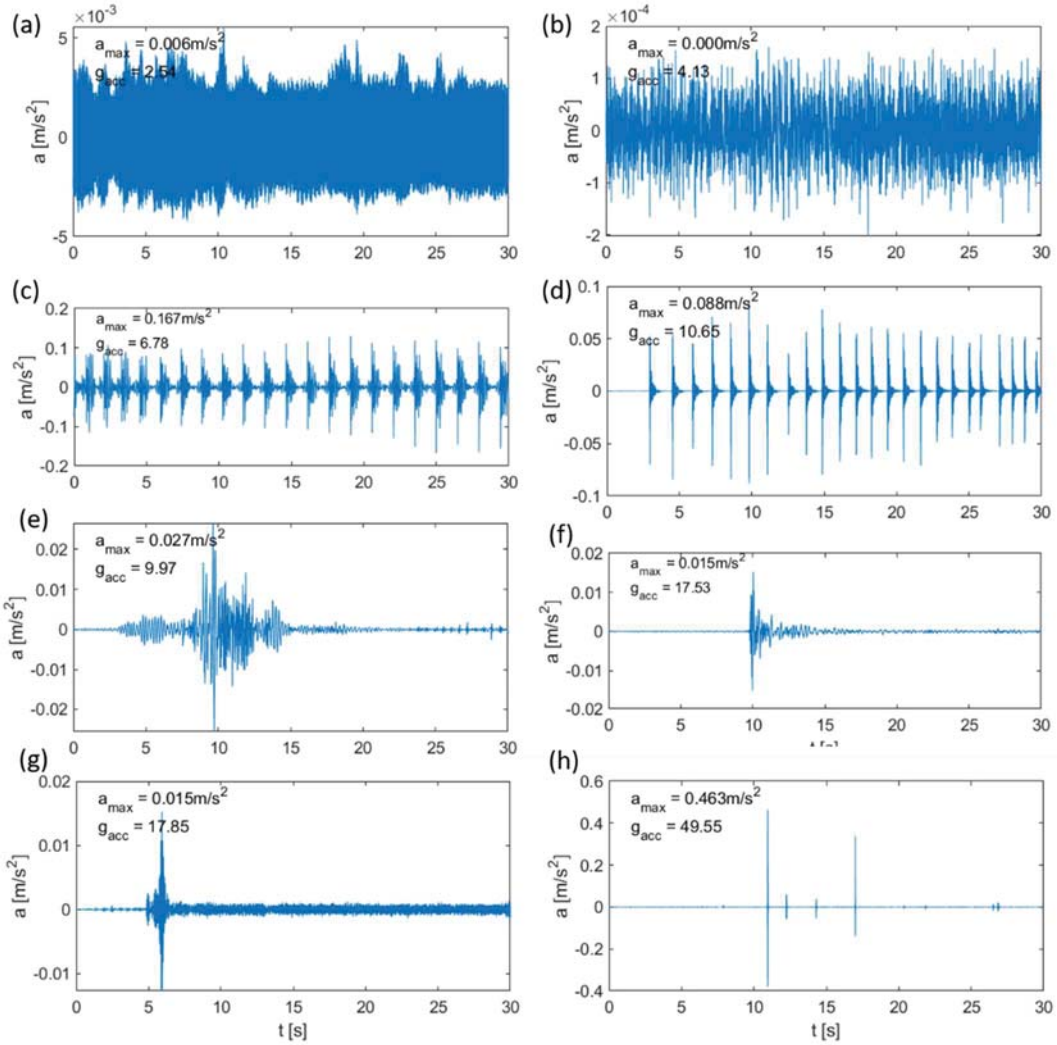

Figure 10: Acceleration signals of vibration sources with varying peak factors: (a) sandpaper machine, (b) background noise, (c) pile driving, (d) basketball against the wall, (e) truck passage, (f) sonic boom, (g) truck starting engine, and (h) hitting the sensor (by hand).

Figure 10(f), (g) and (h) show examples of a single short-duration transient due to a sonic boom, a starting truck engine near a sensor (~2 m) and a signal with several pulses due to hitting the sensor by hand. Signals with peak factors $g_a > 15$ are probably caused by sources which produce pulse-like or short-duration transient vibrations. These signals are unlikely to be the result of a source producing a monotonic continuous vibration. The only exception is the start-up or stopping of a source producing a monotonic continuous vibration, such as the starting truck engine in Figure 10(g).

Signals with $6 < g_a < 15$ are likely to be the result of sources generating repeated transient vibrations or a sustained transient vibration. Figure 10(c), (d) and (e) show examples of repeated transient vibrations (pile driving and throwing a basketball against the wall) and a sustained transient vibration (truck passage).

Several sources (e.g. mass pile driving, jumping, earthquake, and sonic boom) have relatively large ranges for the peak factor. These large ranges are the result of (1) the number of repeated transients over the 30 s period and (2) the distance between the sensor and the source.

Examples of the influence of the number of repeated transients are shown in Figure 11(a) and (b) for pile driving, and in Figure 11(c) and (d) for jumping. For a pile driving signal and a jumping signal with continuous regular transients over the full 30 s period the peak factor is low, whereas the signals with repeated transients over about 10 s has a relatively large peak factor.

Figure 11(e) and (f) show the velocity and acceleration signal of an earthquake measured at ~1 km and ~20 km. The signal at large distance has small peak factors and looks like a sustained transient vibration. At short distance, however, the signal mainly consists of a large pulse and has a large peak factor g_a. A similar effect is seen in Figure 11(g) and (h) for sonic boom signals.

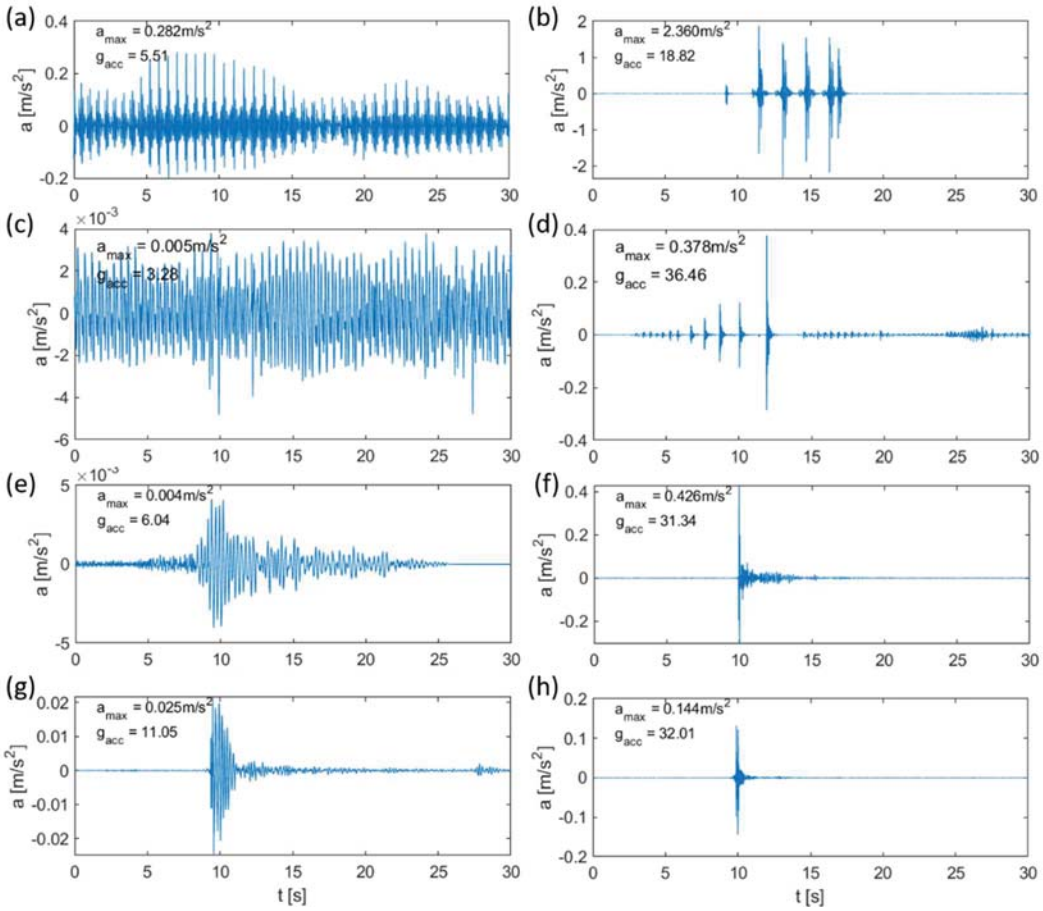

Figure 11: Acceleration signals of various sources which have both small and large peak factors: (a) continuous pile driving, (b) short-period pile driving, (c) continuous jumping, (d) short-period jumping, (e) sustained transient earthquake signal at ~20 km, (f) pulse signal earth-quake signal at ~1 km, (g) transient sonic boom, and (h) pulse signal sonic boom.

5.5 Significant duration, D_s

Figure 12 shows time traces of the acceleration signals and the normalized Arias intensity function. The normalized Arias intensity function shows how the vibration energy is released over the 30 second period. This energy release profile gives useful information about the characteristics of the signal.

Figure 13 shows box plots of the significant duration D_s per studied vibration source. The vibration sources are ranked in order of increasing significant duration, the background vibration results are placed at the top as reference.

Figure 12(a) shows the acceleration signal and normalized Arias intensity function of a hit on the sensor. A single pulse results in a very steep increase in the Arias intensity. The significant duration is therefore very short, i.e. less than 0.1 s. Figure 13 shows that similar short significant durations can occur for blasting, a sonic boom, an earthquake and a falling mass.

Although an earthquake can also have a large peak in the acceleration signal, see Figure 12(b), it is always preceded and followed by low-level vibrations. The resulting Arias intensity function is less steep, which generally gives a significant duration larger than 0.1 s, see Figure 13.

The more sustained the transient vibration becomes, the more gradual is the increase in Arias intensity and the larger the significant duration. Figure 12(c) shows the acceleration signal and Arias intensity function of a truck passage, the significant duration for this signal is close to 4 s. This type of transient vibration signal is for example observed for large road vehicles, trains and earthquakes, and typically has a significant duration larger than 1 s. For larger distance between the source and the sensor, the transient vibration becomes more prolonged and contains less significant peaks. This results in larger significant durations; Figure 13 shows significant durations up to 19 s for train passages. The main reason for these large values are the low vibration levels induced by the train passage, because of the large distance between railway and sensor (125 and 150 m).

A large significant duration can also be the result of a vibration signal consisting of repeated pulses or transients. Figure 12(d) shows a signal of a tennis ball hits against a wall. The repeated pulses result in a stepwise Arias intensity function. Because there are several seconds between each pulse the resulting significant duration is about 4 s, similar to what was observed for the sustained transient signal for the truck passage. This is the main reason for the large variation in significant duration seen in Figure 13 for several sources (e.g. sonic boom, vibratory plate, falling mass, etc.). When a source produces a vibration signal several times in the 30 s period, the significant duration will increase.

A regular repeating transient vibration signal, which can for example be observed for the mass pile driving signal shown in Figure 12(e), results in a regular stepwise Arias intensity function. The significant duration of this signal is ~19 s. A continuous vibration signal gives a similar significant duration. Figure 12(f) shows an example of a continuous vibration signal of a washing machine. The Arias intensity function of this signal increases linearly with time. The sources that are likely to produce these continuous or regularly repeating vibrations typically have significant durations larger than 10 s (see Figure 13). The significant duration for these type of signals is generally smaller than 21 s, i.e. the significant duration of a linearly increasing Arias intensity is 21 s (70% of 30 s).

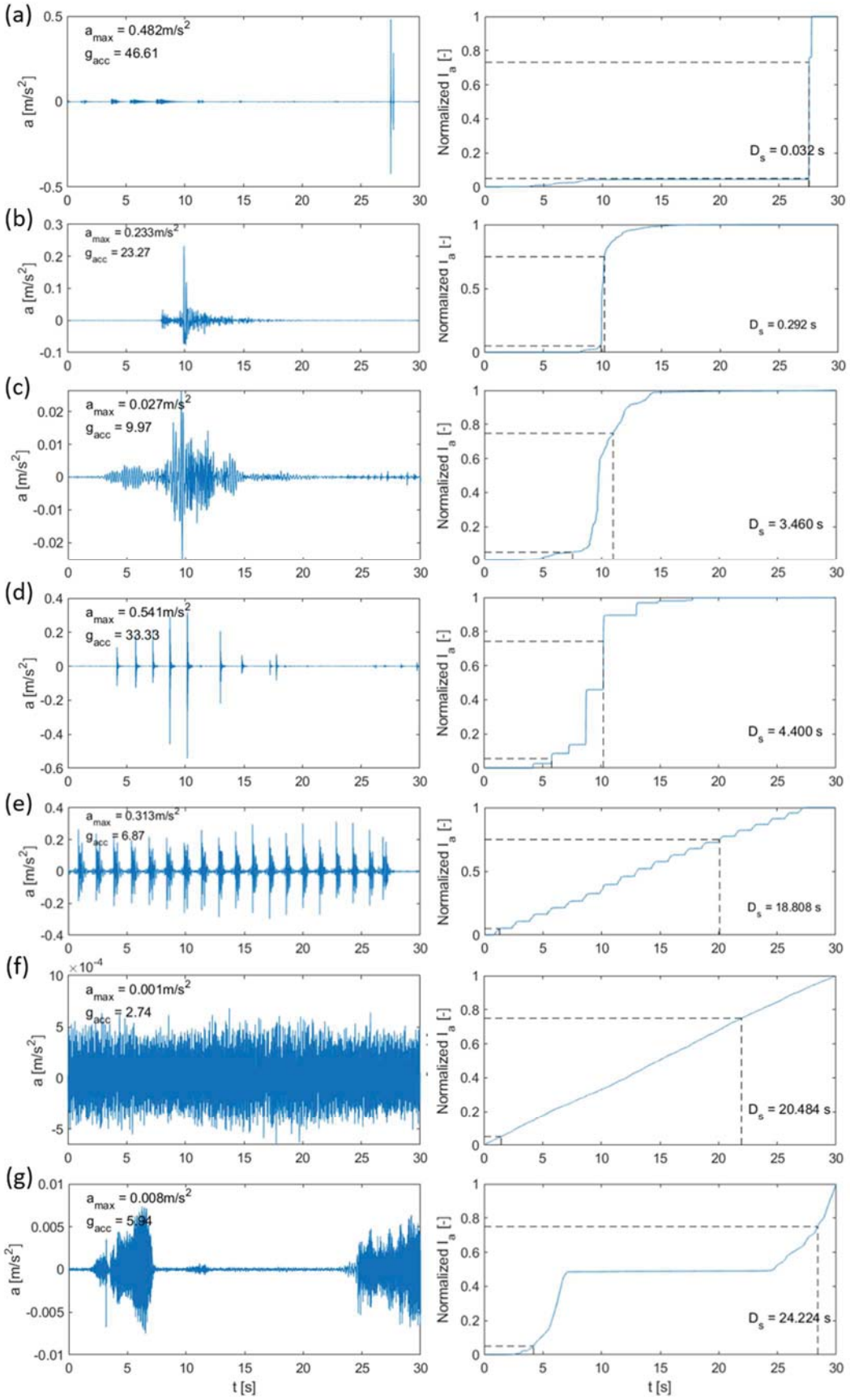

Figure 12: Acceleration signals and the Arias intensity function of various signals: (a) tapping on sensor, (b) earthquake, (c) truck passage, (d) tennis ball, (e) mass pile driving, (f) washing machine, and (g) drilling.

The largest significant durations are found for vibration signals that consist of vibration signals with most energy content at the beginning and end of the 30 s period. Figure 12(g) shows an example of drilling, with two periods of drilling with in-between a 17-18 s period without any significant vibrations. A significant duration larger than 70% of the reference period (in this case 30 s) is an indication that the vibration signal has this particular feature of two separated vibrations at the beginning and end.

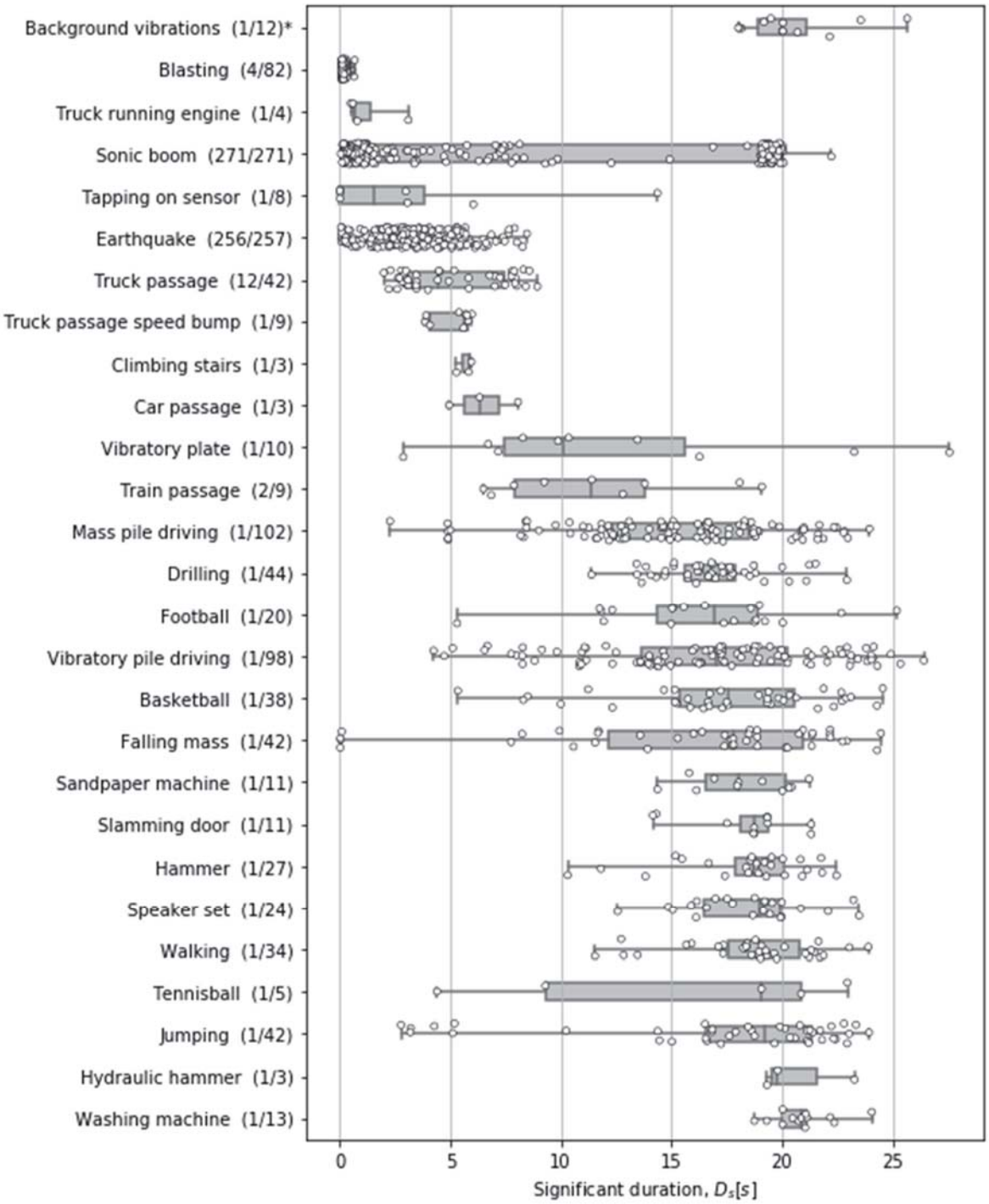

Figure 13: Boxplots and samples for the significant duration D_s obtained in all tests.
*(number of buildings/number of measured signals)

5.6 Number of peaks, N_{peak}

Figure 14 shows the normalized Arias intensity function and the time derivative of the Arias intensity function for some of the signals in Figure 12. Although the time derivative is quite correlated with the Arias intensity function, i.e. $|\rho_{x,y}| \sim 0.5$, it does give some useful additional information on the characteristics of some signals.

Figure 14(a) and (b) show examples of a truck passage and a bouncing tennis ball. Both signals have a significant duration of around 4 s, but the number of peaks of the transient vibration signal of the truck passage is much larger than that of the bouncing tennis ball. This shows that the combination of the significant duration D_s and the number of peaks N_{peak} can in some cases be used to distinguish between a signal with a single transient vibration and a signal with repeated pulses.

A similar difference can be seen for the regular repeated transient and continuous vibration signals in Figure 14(c) and (d). The significant duration of both signals is close to 20 s, while the washing machine vibration signal in Figure 14(d) has a much larger number of peaks than the mass pile driving vibration signal in Figure 14(c).

The drilling vibration signal in Figure 14(e) has a number of peaks much smaller than the washing machine in Figure 14(d). Combined with the large significant duration, the number of peaks is an additional indicator that the vibration signal consists of two separated periods of vibrations at the beginning and end.

The significant duration and the number of peaks are two signal characteristics that mainly provide some quantification of the part of the signal record containing vibrations. Based on the graphs in Figure 14, the periods without (significant) vibration content could also provide useful information on the signal, e.g. the percentage of time the derivative of the Arias intensity function is (close to) zero.

Figure 15 shows box plots of the number of peaks N_{peak} per studied vibration source. The vibration sources are ranked in order of increasing median value, the background vibration results are placed at the top as reference.

Figure 15 shows continuous vibration sources (e.g. a washing machine, drilling or vibratory pile driving) have numbers of peaks which are typically larger than 100.

Repeated or sustained transient vibrations have numbers of peaks which are mostly between 10 and 100. Typical examples are a bouncing ball, hammering, mass pile driving and road or railway traffic.

Vibration signals with a single or small number of pulses have a number of peaks smaller than 10. Sources which are likely to produce these type of vibration signals are tapping on the sensor, blasting or a starting or stopping truck engine.

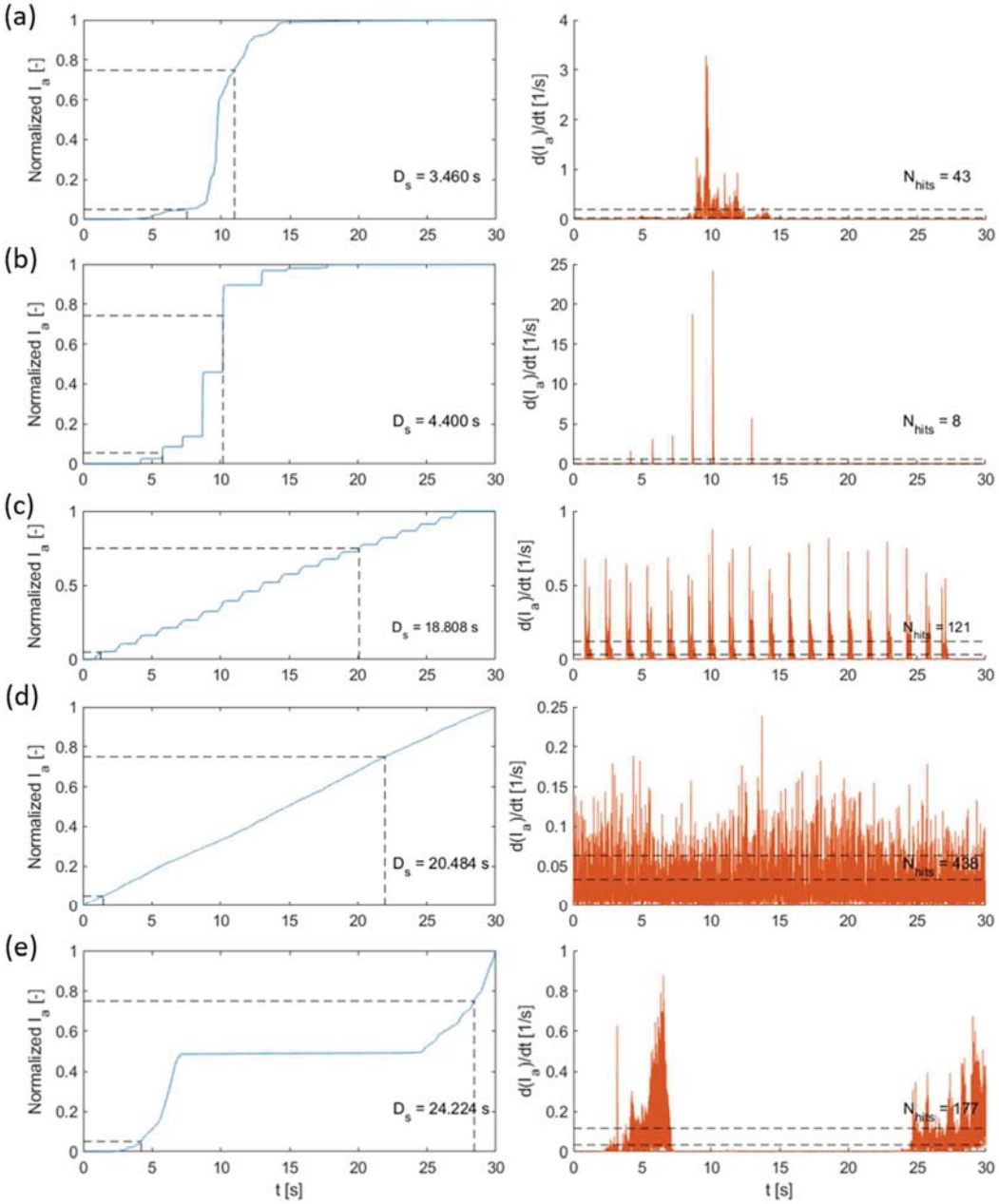

Figure 14: The Arias intensity function and the time derivative of various signals: (a) truck passage, (b) tennis ball, (c) mass pile driving, (d) washing machine, and (e) drilling.

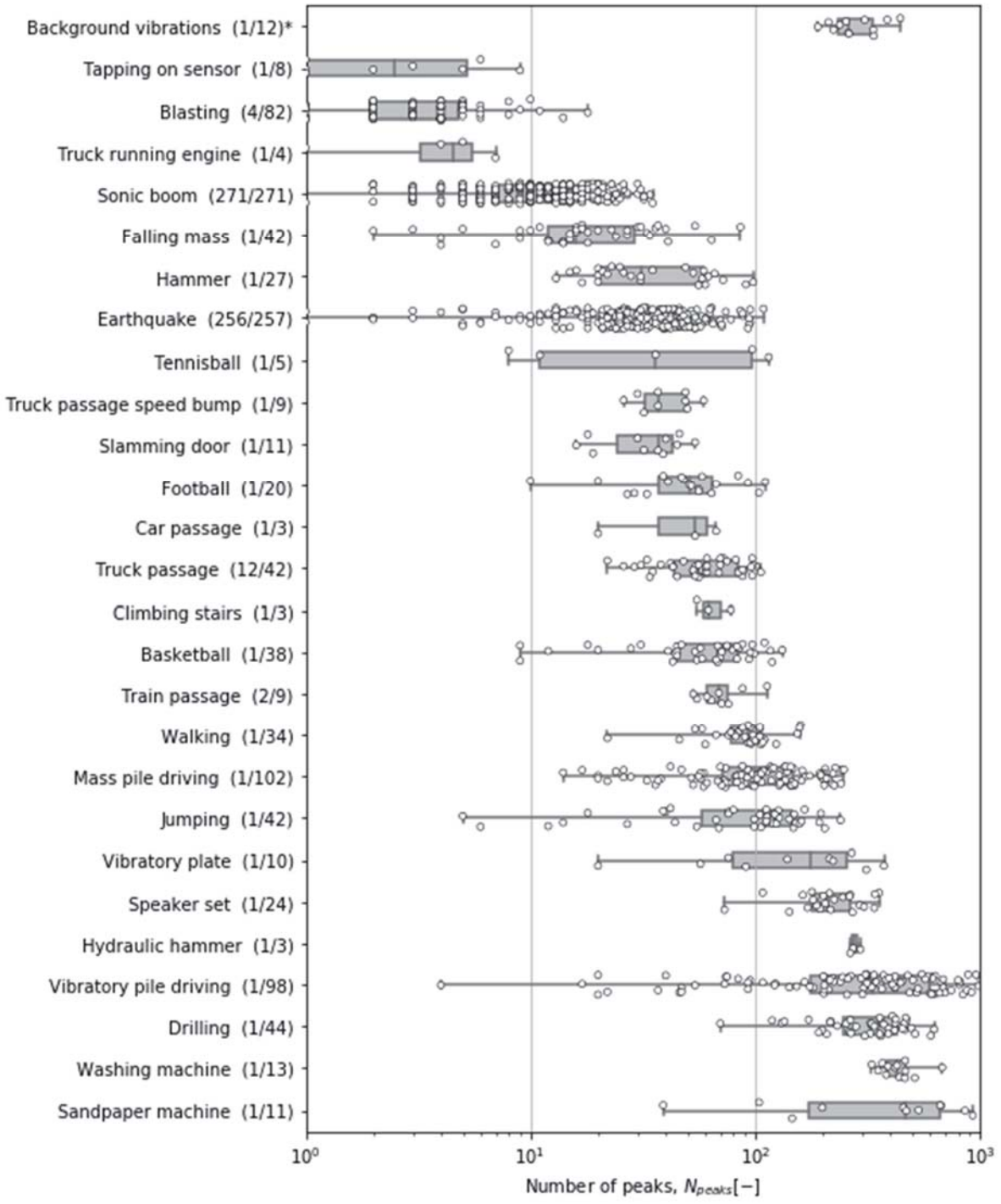

Figure 14: Boxplots and samples for the number of peaks N_{peak} obtained in all tests.
*(number of buildings/number of measured signals)

6 CONCLUSION

This article presented a study on a large dataset of vibration signals from various internal and external vibration sources. The goal of this study was to determine a set of signal characteristics that allow for differentiation between vibration sources in a built environment. The study focused on vibration sources with the main energy content 1 and 100 Hz. The signals in the dataset were trimmed to a period of 30 s. A set of 11 signal characteristics were obtained for all signals in the dataset.

Based on the correlation between these characteristics, 6 signal characteristics were selected for a detailed analysis. Three of these signal characteristics, i.e. a_{max}, v_{max} and $f_{d,f,a}$, are well-established in literature for various vibration sources. The other three characteristics, i.e. g_a, D_s and N_{peak}, have been studied very little for most vibration sources.

The maximum vibration levels a_{max} and v_{max} determined for the various vibration sources fit well with the ranges mentioned in literature. However, for most vibration sources the dataset represents the low end of these ranges; they do not give a good representation of the complete range of levels that can occur in the built environment. Therefore the determined ranges for a_{max} and v_{max} in this study might not be very useful for differentiation between vibration sources.

The results for the dominant frequency $f_{d,f,a}$ also correspond well with literature, and for several sources (e.g. earthquakes, mass pile driving, road traffic) provide a reasonable representation of the mentioned ranges. The results show that vibration signals with dominant frequencies $f_{d,f,a} < 35$ Hz are often due to sources producing (repeated) transient vibrations, such as a truck or train passage, mass pile driving or an earthquake. Sources which generate continuous vibrations, such as drilling or vibratory pile driving typically have dominant frequencies $f_{d,f,a} > 25$ Hz. Other spectral features that could prove useful to allow for more differentiation between vibration sources are the bandwidth of the spectrum (e.g. the 3 dB bandwidth) or harmonic frequencies (cepstrum analysis).

The peak factor g_a provides information on the peakiness of a signal. The smallest peak factors were found for sources with a (monotonic) continuous vibration signal (e.g. vibratory pile driving); these type of signals typically have a peak factor $g_a < 6$. Large peak factors were observed for signals with a single or small number of pulses (e.g. hitting the sensor) or a single short-duration transient (e.g. sonic boom). Signals with peak factors $g_a > 15$ are likely to have been caused by these type of sources. Several sources (e.g. mass pile driving, jumping, earthquake, and sonic boom) have relatively large ranges for the peak factor. These large ranges were found to be the result of the number of repeated transients over the 30 s period or the distance between the sensor and the source, resulting in a prolonged transient vibration.

The significant duration gives information about the length of the period over which a large portion of the vibration energy is released. For a single pulse this gives a very short duration, typically smaller than 0.1 s. This type of duration is typically observed for a (single) hit on the sensor, but can also be observed for blasting, a sonic boom, an earthquake or a falling mass. Large significant durations (> 10 s) are observed for a regular repeated pulse or transient or a continuous vibration signal. The significant duration of these type of signals is generally not larger than 21 s. Signals with $D_s > 21$ s typically have large vibration content at the beginning and end of the 30 s period, with relatively little content in-between.

Although the significant duration D_s and the number of peaks N_{peak} are quite correlated, N_{peak} does give useful additional information on some vibration sources. For example, a signal transient (e.g. truck passage) and a repeated pulse (e.g. tennis ball) a bouncing ball can have the same significant duration, while the number of peaks are generally quite different. A similar behavior was observed for a continuous signal and a repeated transient signal.

The significant duration and the number of peaks are two signal characteristics that mainly provide information on the part of the signal record with vibrations. The periods without (significant) vibration content could also provide useful information on the signal, e.g. the percentage of time the derivative of the Arias intensity function is (close to) zero.

This research presented in this paper indicates that differentiation between vibration sources based on signal characteristics is feasible to a certain extent. Further research should investigate the possibilities and limitations of the dataset and the obtained signal characteristics for identification of vibration sources in the monitoring network. The database with reasons provided by building owners for trigger events is a valuable source to test a first version of an algorithm for vibration source identification.

ACKNOWLEDGMENT

The work presented in this paper was made possible by NAM (*Nederlandse Aardolie Maatschappij*). NAM financed the measurement network and provided for the building in which the tests were carried out.

REFERENCES

[1] H. Borsje, E. Langius, Monitoring Network Building Vibrations, TNO 2015 R10501, 2015.

[2] H. Borsje, J.P. Pruiksma, M. Vasic, Monitoring Network Building Vibrations – Analysis Earthquake 08-01-2018 (Zeerijp), TNO 2018 R10743-B, 2018.

[3] H. Borsje, S.T. Hengeveld, Monitoring Network Building Vibrations – Analysis Earthquake 09-06-2019 Garrelsweer – preliminary draft, 2019.

[4] R.F.M. van den Brink, L. Meijer, Analysis of wide area accelerometer system responses to pressure waves induced by supersonic aircrafts (unpublished), 2016.

[5] D. Moretti, A.J. Bronkhorst, C.P.W. Geurts, Test campaign for characterization of vibration sources in the household monitoring network Groningen, TNO 2019 R11872, 2019.

[6] A. D'Alessandro, A. Costanzo, C. Ladina, F. Buongiorno, M. Cattaneo, S. Falcone, C. La Piana, S. Marzoratti, S. Scudero, G. Vitale, S. Stramondo, C. Doglioni, Urban seismic networks, structural health and cultural heritage monitoring: The National Earthquakes Observatory (INGV, Italy) Experience, Front. Built Environ. 5:127. doi: 10.3389/fbuil.2019.00127, 2019.

[7] S. Horiuchi, Y. Horiuchi, S. Yamamoto, H. Nakamura, C. Wu, P.A. Rydelek, M. Kachi, Home seismometer for earthquake early warning, Geophysical Research Letters, Vol. 36, L00B04, doi:10.1029/2008GL036572, 2009.

[8] R.W. Clayton, T. Heaton, M. Chandy, A. Krause, M. Kohler, J. Bunn, R. Guy, M. Olson, M. Faulkner, M. Cheng, L. Strand, R. Chandy, D. Obenshain, A. Liu, M. Aivazis, Community seismic network, Annals of Geophysics, 6, doi: 10.4401/ag-5269, 2011.

[9] A. D'Alessandro, D. Luzio, G. D'Anna, Urban MEMS based seismic networks for post-earthquakes rapid disaster assessment, Advances in Geosciences, 40, 1-9, doi:10.5194/adgeo-40-1-2014, 2014.

[10] M.A. Ansary, F. Yamazaki, M. Fuse, T. Katayama, Use of microtremors for the estimation of ground vibration characteristics, 3rd Int. Conf. Rec. Adv. Geo. Earth. Eng. Soil Dyn., 2-7 April, 1995.

[11] G. Lombardo, G. Coco, M. Corrao, S. Imposa, R. Azzara, F. Cara, A. Rovelli, Results of microtremor measurements in the urban area of Catania, Italy, Boll. Geo. Teor. Appl., 42, 317-334, 2001.

[12] P. Gerstoft, M.C. Fehler, K.G. Sabra, When Katrina hit California, Geophysical Research Letters, Vol. 33, L17308, doi:10.1029/2006GL027270, 2006.

[13] S. Bonnefoy-Claudet, F. Cotton, P. Bard, The nature of noise wavefield and its applications for site effects studies - A literature review, Earth-Science Reviews 79, 205–227, 2006.

[14] N. Riahi, P. Gerstoft, The seismic traffic footprint: Tracking trains, aircraft, and cars seismically, Geophysical Research Letters, 42, 2674–2681, doi:10.1002/2015GL063558, 2015.

[15] C.M. Boese, L. Wotherspoon, M. Alvarez, P. Malin, Analysis of anthropogenic and natural noise from multilevel borehole seismometers in an urban environment, Auckland, New Zealand, Bulletin of the Seismological Society of America, Vol. 105, No. 1, pp. 285–299, doi: 10.1785/0120130288, 2015.

[16] D.N. Green, I.D. Bastow, B. Dashwood, S.E.J. Nippress, Characterizing Broadband Seismic Noise in Central London. Seism. Res. Lett. 88(1), 113–124, 2016.

[17] J. Diaz, M. Ruiz, P.S. Sánchez-Pastor, P. Romero, Urban seismology: on the origin of earth vibrations within a city, www.nature.com/scientificreports, 7: 15296, doi:10.1038/s41598-017-15499-y, 2017.

[18] J.C. Groos, J.R.R. Ritter, Time domain classification and quantification of seismic noise in an urban environment, Geophysical Journal International, 179, 1213-1231, 179.

[19] K.R. Massarsch, B.B. Broms, Damage Criteria for Small Amplitude Ground Vibrations, Second International Conference on Recent Advances in Geotechnical Earthquake Engineering and Soil Dynamics, St. Louis, Missouri, Vol. 2, 1451 – 1459, 1991.

[20] K.R. Massarsch, Man-made vibrations and solutions, State-of-the-Art Lecture, 3rd Int. Conference on Case Histories in Geotechnical Engineering, St. Louis, Missouri, Vol. II, pp. 1393 – 1405, 1993.

[21] V.S. Hope, D.M. Hiller, The prediction of ground-borne vibration from percussive piling, Can. Geotech. J., 37, 700-711, 2000.

[22] F. Deckner, Ground vibrations due to pile and sheet pile driving – influencing factors, predictions and measurements, PhD thesis, KTH, Royal Institute of Technology Stockholm, 2013.

[23] J.C. Guignard, Human sensitivity to vibration, J. Sound Vib., 15, 1, 11-16, 1971.

[24] M.J. Griffin, E.M. Whitham, Duration of whole-body vibration exposure: its effect on comfort, J. Sound Vib., 48, 3, 333-339, 1976.

[25] M. Sanayei, P. Maurya, J.A. Moore, Measurement of building foundation and ground-borne vibrations due to surface trains and subways, Eng. Struct., 53, 102–111, 2013.

[26] H. Hao, T.C. Ang, J. Shen, Building vibration to traffic-induced ground motion, Building and Environment, 36, 321-336, 2001.

[27] KNMI, Aardbevingen - De meest recente aardbevingen in en rondom Nederland, https://www.knmi.nl/nederland-nu/seismologie/aardbevingen, 2020.

[28] D. Moretti, A.J. Bronkhorst, C.P.W. Geurts, Characterization of vibrations for the Groningen building monitoring network, TNO 2019 R11991, 2019.

[29] D.P. Connolly, G. Kouroussis, W. Fan, M. Percival, A. Giannopoulos, P. Woodward, O. Verlinden, M.C. Forde, An experimental analysis of embankment vibrations due to high speed rail, 12th International Railway Engineering Conference, London, Railway Engineering, 2013.

[30] G. Kouroussis, D. Connolly, M. Forde, O. Verlinden, An experimental study of embankment conditions on high-speed railway ground vibrations, 20th International Congress on Sound and Vibration, ICSV20, Bangkok, 2013.

[31] J.J. Hajek, C.T. Blaney, D.K. Hein, Mitigation of highway traffic-induced vibration, Conf. Transportation Association Canada Charlottetown, 2006.

[32] P.C. van Staalduinen, M.Th.J.H. Smits, Trillingscriteria m.b.t. schade aan gebouwen (Dutch), B-90-822, 1991 (rev. 1993).

[33] J. van Zoest, Meting van trillingen veroorzaakt door het passeren van zwaar verkeer (Dutch), B-84-27, 1984.

[34] H.S. Buitenkamp, P.J. van Brederode, Onderzoek betreffende het verband tussen verkeerstrillingen en scheuren aan een woonhuis te Schellinkhout (Dutch), B-86-240, 1986.

[35] H.S. Buitenkamp, P.J. van Brederode, Onderzoek betreffende het verband tussen verkeerstrillingen en scheuren aan een woonhuis te ’s-Gravenhage (Dutch), B-86-262, 1986.

[36] H.S. Buitenkamp, F.M. Middeldorp, Advies inzake een mogelijke relatie tussen verkeerstrillingen en gebouwschade bij een woning gelegen aan de Gasthuisstraat te Veghel (Dutch), B-86-667, 1986.

[37] P.C. van Staalduinen, M.H.Th.J. Smits, P.H. Waarts, Trillingsonderzoek t.b.v. het handboek ‘damwanden’ Achtergronden (Dutch), B-91-0401, 1991.

[38] D. Jongmans, Prediction of ground vibrations caused by pile driving: A new methodology, Engineering Geology 42, 25 – 36, 1996.

[39] G.A. Athanasopoulos, P.C. Pelekis, Ground vibrations from sheet pile driving in urban environment: measurements, analysis and effects on buildings and occupants, Soil Dynamics and Earthquake Engineering, 19, 371-387, 2000.

[40] TNO, Monitoring network building vibrations – Analysis earthquakes 05-11-2014 (Zandeweer), 30-12-2014 (Woudbloem) and 06-01-2015 (Wirdum), TNO 2015 R11382, 2015.

[41] TNO, Monitoring network building vibrations – Analysis earthquake 30-09-2015 (Hellum), TNO 2016 R10421, 2016.

[42] H. Borsje, J.P., Pruiksma, S.A.J. de Richemont, Monitoring network building vibrations – Analysis earthquakes in 2014 and 2015, TNO 2016 R11323/A, 2016.

[43] H. Borsje, J.P. Pruiksma, M. Vasic, Monitoring network building vibrations – Analysis earthquake 27-05-2017 (Slochteren), TNO 2018 R10275, 2018.

[44] H. Borsje, J.P. Pruiksma, M. Vasic, Monitoring network building vibrations – Analysis earthquake 08-01-2018 (Zeerijp), TNO 2018 R10743-B, 2018.

[45] H. Borsje, S.T. Hengeveld, Monitoring network building vibrations – Analysis earthquake 13-04-2018 (Garsthuizen), TNO 2018 R11093, 2018.

[46] H.R. Nicholls, C.F. Johnson, W.I. Duvall, Blasting vibrations and their effects on structures, Bulletin 656, US Department of Interior, Bureau of Mines, 1971.

[47] B.M. New, Trial and construction induced blasting vibration at the Penmaenbach road tunnel, Transport and Road Research Laboratory, Research report 181, 1989.

[48] M. Aloui, Y. Bleuzen, E. Essefi, C. Abbes, Ground vibrations and air blast effects induced by blasting in open pit mines: Case of Metlaoui mining basin, Southwestern Tunisia, Journal of Geology and Geophysics, 2016.

[49] T.K. Muller, Meten, beoordelen en voorspellen van trillingen in de bouw (Dutch), Geotechniek, pg 40-46, 2007.

[50] A. Ditzel, Train-induced ground vibrations: modelling and experiments, PhD thesis, TU Delft, 2003.

[51] S.A. Suhairy, Prediction of ground vibration from railways, Swedish National Testing and Research Institute, SP Report 2000:25, 2000.

[52] G.W.J. Heijnen, "Basisdocument Trillingen veroorzaakt door treinverkeer (Dutch), Nederlandse Spoorwegen, Centrum voor Technisch Onderzoek, CTO/6/L0.009/074, Utrecht, maart 1990.

EURODYN 2020
XI International Conference on Structural Dynamics
M. Papadrakakis, M. Fragiadakis, C. Papadimitriou (eds.)
Athens, Greece, 23–26 November 2020

MONITORING FATIGUE DAMAGE ACCUMULATION OF WIND TURBINE TOWERS USING LIMITED NUMBER OF OUTPUT-ONLY VIBRATION MEASUREMENTS

Victor Flores Terrazas[1], Omid Sedehi[1], Lambros S. Katafygiotis[1], Costas Papadimitriou[2]

[1] The Hong Kong University of Science and Technology
Department of Civil and Environmental Engineering
Hong Kong, China
vft@connect.ust.hk, osedehi@connect.ust.hk, katafygiotis.lambros@gmail.com

[2]University of Thessaly
Department of Mechanical Engineering
Volos, Greece
costasp@uth.gr

Keywords: Multiaxial Loading, Fatigue Damage Accumulation, Wind Turbines, Bayesian Methods, Input-State Estimation

Abstract. *Fatigue monitoring and remaining fatigue life estimation of structures using output-only vibration measurements has recently garnered increasing attention, producing advances in theoretical, numerical and experimental studies of this phenomenon. The methodology presented in this paper combines methods for estimating stress time histories at the entire body of the structure with fatigue damage accumulation techniques for multiaxial stress state. A novel sequential Bayesian method is employed to estimate both input and state in the modal space and to reconstruct the full-field time-history response in the physical space using output-only vibration measurements. Stress and strain time histories at the finite element level are obtained by using a linear relationship with nodal displacements. Estimated stresses are then used to find the critical plane where the maximum fatigue damage is expected and the shear stress time histories are resolved on this plane. Shear stress cycles are counted by means of the Rainflow Counting Method, and a Modified Wöhler Curve Method is applied to estimate the fatigue damage, whereby normal and shear stress effects are accounted for. This procedure is capable of tackling inherent complexities found in real world applications, such as the multiaxiality of the applied loads and of the resulting stress state. A finite element model of a wind turbine tower was constructed based on reference specifications available from the National Renewable Energy Laboratory and used to illustrate the method presented herein. The results obtained demonstrate the applicability of the methodology as an efficient way to monitor fatigue damage accumulation in the entire body of a steel structure.*

1 INTRODUCTION

Fatigue damage accumulation in ductile materials does not always produce identifiable indicators of damage. Thus, it is important to develop monitoring methods that would enable to diagnose the fatigue state of a metallic structure and to predict the location(s) where high fatigue damage is most likely to accumulate, as well as the remaining fatigue lifetime of the structure, based on output only vibration measurements.

The work by Papadimitriou et al. [1] was the first to promote the use of output-only vibration measurements to estimate fatigue damage accumulation. It introduced the idea of using a Kalman filter to estimate the stress responses of a metallic structure subjected to stationary stochastic loads, thereby estimating the remaining fatigue lifetime. Nevertheless, this approach and subsequent ones [2]–[4] developed to handle non-stationary unknown excitations, considered uniaxial fatigue damage. The present work expands on this idea and applies techniques capable of handling multiaxial stress states.

Thereupon model reduction techniques have been introduced and used in conjunction with SHM methods, e.g., modal decomposition-expansion was employed by Maes et al. [5] to reconstruct the dynamic strain response of an offshore wind turbine tower; Tchemodanova et al. demonstrated in [6] the use of a substructure approach to estimate remaining fatigue lifetime of a section of a rollercoaster; Eftekhar Azam et al. proposed the use of a Dual Kalman in modal space, allowing the use of a modally truncated model [7].

The purpose of this work is to propose a methodology to monitor fatigue damage accumulation on a structural system or its components when subjected to input or interface loads that are unknown. The present work expands on ideas presented in [3], [8] for response reconstruction and fatigue estimation in linear components of structural systems and applies techniques capable of handling multiaxial stress fields. Moreover, it benefits from the latest advances accomplished in the area of joint input-state estimation [7], [9]–[12], adopting a novel sequential Bayesian approach to reconstruct the full-field dynamic responses using sparse output-only measurements.

The organization of this work is as follows. In Section 2, we present pertinent mathematical formulations for the strain/stress response reconstruction of the entire structure by means of the novel sequential Bayesian filtering technique presented in Section 3. In Section 4, we outline the formulations for the full-field multiaxial fatigue damage accumulation. Section 5 shows an illustrative example of the application of the proposed methodology on a FE model of a land-based wind turbine tower structure subjected to wind loads. Lastly, conclusions are put forth in Section 6.

2 MATHEMATICAL FORMULATION FOR STRAIN/STRESS ESTIMATION

2.1 System and observation models

The dynamical response of a linear time-invariant system can be described through Newton's second law of motion:

$$\boldsymbol{M}\ddot{\boldsymbol{x}}(t) + \boldsymbol{C}\dot{\boldsymbol{x}}(t) + \boldsymbol{K}\boldsymbol{x}(t) = \boldsymbol{S}_p\boldsymbol{f}(t) \tag{1}$$

where $\boldsymbol{M} \in \mathbb{R}^{N\times N}, \boldsymbol{C} \in \mathbb{R}^{N\times N}, \boldsymbol{K} \in \mathbb{R}^{N\times N}$, are the mass, damping and stiffness matrices, respectively; N is the number of degrees-of-freedom; $\boldsymbol{f}(t) \in \mathbb{R}^{N_I\times 1}$, is the dynamic force vector comprised of N_I independent components; $\boldsymbol{S}_p(t) \in \mathbb{R}^{N_I\times 1}$ is a matrix characterizing the spatial distribution of external forces; $\ddot{\boldsymbol{x}}(t) \in \mathbb{R}^{N\times 1}$, $\dot{\boldsymbol{x}}(t) \in \mathbb{R}^{N\times 1}$ and $\boldsymbol{x}(t) \in \mathbb{R}^{N\times 1}$ are the

acceleration, velocity, and displacement responses, respectively. When the vibration response is transformed into a truncated modal space, the following equation of motion is obtained [9]:

$$\ddot{\boldsymbol{\zeta}}(t) + \boldsymbol{\Gamma}\dot{\boldsymbol{\zeta}}(t) + \boldsymbol{\Omega}^2\boldsymbol{\zeta}(t) = \boldsymbol{\Phi}^T\boldsymbol{S}_p\boldsymbol{f}(t) \tag{2}$$

where $\boldsymbol{\Phi} \in \mathbb{R}^{N\times N_m}$ is the truncated modal matrix whose columns are filled with N_m mass-normalized mode shape vectors; $\boldsymbol{\zeta}(t) \in \mathbb{R}^{N_m\times 1}$ is the response in the reduced modal space; $\boldsymbol{\Gamma} \in \mathbb{R}^{N_m\times N_m}$ and $\boldsymbol{\Omega}^2 \in \mathbb{R}^{N_m\times N_m}$ are two diagonal matrices with $2\xi_i\omega_i$ and ω_i^2 entries, respectively; ξ_i and ω_i are, correspondingly, the modal damping ratio and modal frequency of the ith dynamical mode. This equation can be written in the state-space form as follows:

$$\dot{\boldsymbol{z}}(t) = \boldsymbol{A}_C\boldsymbol{z}(t) + \boldsymbol{B}_C\boldsymbol{f}(t) \tag{3}$$

where $\boldsymbol{z}(t) = \left[\boldsymbol{\zeta}(t)^T \quad \dot{\boldsymbol{\zeta}}(t)^T\right]^T$ is the state vector; $\boldsymbol{A}_C$ and $\boldsymbol{B}_C$ are the system and feedthrough matrices, computed as:

$$\boldsymbol{A}_C = \begin{bmatrix} \boldsymbol{0} & \boldsymbol{I} \\ -\boldsymbol{\Omega}^2 & -\boldsymbol{\Gamma} \end{bmatrix}, \quad \boldsymbol{B}_C = \begin{bmatrix} \boldsymbol{0} \\ \boldsymbol{\Phi}^T\boldsymbol{S}_p \end{bmatrix} \tag{4}$$

When the responses are discretized in Δt intervals and the variation of input forces is considered to be constant over each interval, the following stochastic state-space model is obtained in the discrete-time:

$$\boldsymbol{z}_k = \boldsymbol{A}\boldsymbol{z}_{k-1} + \boldsymbol{B}\boldsymbol{f}_{k-1} + \boldsymbol{v}_k \tag{5}$$

where $\boldsymbol{A} = e^{\boldsymbol{A}_C\Delta t}$ and $\boldsymbol{B} = (\boldsymbol{A} - \boldsymbol{I})\boldsymbol{A}_C^{-1}\boldsymbol{B}_C$ are the discrete-time system and feedthrough matrices; $\boldsymbol{z}_k$ is the state vector at $t_k = k\Delta t$, $k = \{0,1,2,\dots,n\}$; $\boldsymbol{v}_k$ is the process noise modeled as a Gaussian White Noise (GWN) process.

In a similar manner, the observed output quantities of interest can be written as a function of the state vector and the input forces leading to [7]:

$$\boldsymbol{d}_k \triangleq \begin{bmatrix} \boldsymbol{\varepsilon}_k \\ \boldsymbol{y}_k \\ \dot{\boldsymbol{y}}_k \\ \ddot{\boldsymbol{y}}_k \end{bmatrix} = \boldsymbol{G}\boldsymbol{z}_k + \boldsymbol{J}\boldsymbol{f}_k + \boldsymbol{w}_k \tag{6}$$

$$\boldsymbol{G} = \begin{bmatrix} \boldsymbol{S}_e\boldsymbol{T}\boldsymbol{\Phi} & \boldsymbol{0} \\ \boldsymbol{S}_d\boldsymbol{\Phi} & \boldsymbol{0} \\ \boldsymbol{0} & \boldsymbol{S}_v\boldsymbol{\Phi} \\ -\boldsymbol{S}_a\boldsymbol{\Phi}\boldsymbol{\Omega}^2 & -\boldsymbol{S}_a\boldsymbol{\Phi}\boldsymbol{\Gamma} \end{bmatrix}, \quad \boldsymbol{J} = \begin{bmatrix} \boldsymbol{0} \\ \boldsymbol{0} \\ \boldsymbol{0} \\ \boldsymbol{S}_a\boldsymbol{\Phi}\boldsymbol{\Phi}^T\boldsymbol{S}_p \end{bmatrix} \tag{7}$$

where $\boldsymbol{d}_k \in \mathbb{R}^{N_0\times 1}$ is a vector containing the observed quantities at discrete time t_k, comprised by strains $\boldsymbol{\varepsilon}_k \in \mathbb{R}^{N_e\times 1}$, displacements $\boldsymbol{y}_k \in \mathbb{R}^{N_y\times 1}$, velocities $\dot{\boldsymbol{y}}_k \in \mathbb{R}^{N_{\dot{y}}\times 1}$, and accelerations $\ddot{\boldsymbol{y}}_k \in \mathbb{R}^{N_{\ddot{y}}\times 1}$; the matrices $\boldsymbol{S}_d, \boldsymbol{S}_v, \boldsymbol{S}_a$ and $\boldsymbol{S}_e$ are selection matrices consisting of 0's and 1's used to extract the observed DOF; $\boldsymbol{T}$ is a matrix returning local strains from nodal displacements; $\boldsymbol{w}_k$ is observation noise considered to be GWN.

3 BAYESIAN ESTIMATION OF INPUT AND STATE

We build our method upon the foregoing state-space formulations and the sequential Bayesian method developed in [11], [13]. The reader is referred to [13] for detailed nomenclature and mathematical formulations. This implementation allows estimating the system state and input in real-time based on a limited number of output-only measurements. Another advantage of this novel algorithm is its robust capability to update the process and observation noise covariance matrices in an online manner. On the other hand, a caveat to this method is that, similar to other Kalman-type filters, some initial parameters need to be fine-tuned to

achieve best results; for the sequential Bayesian filter, these parameters are the initial covariance matrices. A good starting point to calibrate the filter is to set the initial state and input covariance matrices equal to identity matrices scaled by a very small number. A more accurate, albeit laborious approach to selecting appropriate initial noise parameters, is to consider different orders of magnitude for the elements the initial estimates for the covariance matrices, in accordance to the modal response quantities (displacement, velocity, acceleration) to which the element corresponds [14].

4 FATIGUE ASSESSMENT

4.1 Maximum Variance Method for locating the critical plane

The so-called critical plane approaches are based on the assumption that fatigue life is mainly dependent on cracks developing along shear planes or tensile planes [15]. Thus, the maximum fatigue damage experienced in an element can be expected to occur at such orientation. To find such orientation, we adopt the use of the Maximum Variance Method (MVM) proposed by Susmel et al. [16]. This method assumes that the critical plane lies along the direction which is anticipated to have the maximum shear stress variation; the rationale stems from the definition of the statistical variance, which measures how much the signal deviates from the mean. Since fatigue damage is caused by cyclic loading, the variance can be an appropriate measure to identify the plane where the signal presents the largest variation range. Therefore, the damage is expected to be the greatest at the aforementioned plane. The advantage of this method lies in that, once the critical plane is found, the shear stress signals can be readily resolved along this orientation by a simple stress transformation.

Lastly, it should be noted that by applying the MVM, the critical plane and its corresponding shear stress are obtained. The latter is a unidimensional parameter, so a cycle counting method, such as the Rainflow Counting Method (RCM), can be used directly with the resolved shear stress signal.

4.2 Modified Wöhler Curve Method for fatigue assessment

In addition to the MVM described above, Susmel et al. [17] formulated the so-called Modified Wöhler Curve Method (MWCM) to be used as a companion method. The motivation behind this method is that the MVM and subsequent cycle counting is based on shear stresses resolved along the critical plane; however, this stress signal alone may fail to account for the multiaxiality of the actual stress state. As such, a modification in the SN-Curve is introduced to account for the level of multiaxiality by considering the stress normal to the critical plane. Ultimately, a modified fatigue lifetime curve is obtained.

For brevity, the detailed formulations of the MWCM are omitted in this paper. The reader is thus referred to [17], [18] for a comprehensive explanation of this method and an illustrative example.

4.3 Fatigue damage accumulation

The last step in the fatigue assessment framework is to use the data generated throughout and to calculate the accumulated damage in the whole structure. The damage accumulation model used herein is the linear Palmgren-Miner's rule, which states that the linear fatigue accumulation damage D is found by [19], [20]:

$$D = \sum_{i=1}^{j} \frac{n_i}{N_{f,i}} \tag{8}$$

where j is the number of different amplitude levels found through RCM; n_i is the number of counted cycles at a given amplitude level, and $N_{f,i}$ is the number of cycles to failure at amplitude level i, found directly in the constructed MWC.

Once the appropriate SN-Curve has been obtained from the MWCM, and the RCM has been applied to the time history of the shear stress relative to the critical plane, this information can then be used to compute the accumulated fatigue damage for each element in the finite element model of the structure. The procedure is repeated for every finite element in the discretized model. The final product is a full-field damage accumulation map.

5 NUMERICAL EXAMPLE

A reference land-based wind turbine tower model was used in this study. Physical and material specifications were obtained from the National Renewable Energy Laboratory (NREL) [21], from which a finite element model (FEM) was constructed. For simplicity, the dynamic response of the rotor nacelle assembly (RNA) was modelled by an equivalent system of forces at the RNA-tower interface, as shown schematically in Figure 1. The model was constructed using four-node shell elements, where at each node, 6 DOF are considered; the varying shell thickness was modeled using the NREL specifications. This type of element was selected due to the type of problem at hand: the structure is, geometrically, a hollow tube constructed by a comparatively thin sheet of steel. The tower model was discretized into 2444 elements, with 2455 nodes, for a total 14,730 degrees of freedom. The elements can be assumed to be in plane strain, which allows performing a reduced order analysis. This assumption also impacts the cost of multiaxial fatigue computations, since the problem reduces to a biaxial problem. Nevertheless, the principles applied still hold for triaxial fatigue computations.

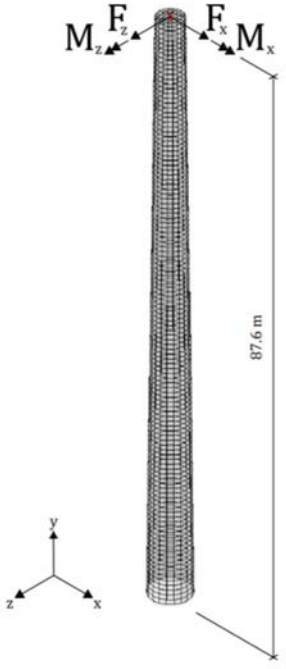

Figure 1. Equivalent system of forces at the RNA-tower interface.

The wind turbine simulation software FAST [22] was employed using the aforementioned tower model specifications. A simulation of 8 s was conducted, recreating operational wind conditions and loads on a tower model with the aforementioned specifications. The time history of the force transmitted through the RNA-tower interface was extracted. The obtained signal time history was subsequently used in the numerical analysis as the system input.

Structural matrices were obtained from the FE model shown in Figure 2, and a modal analysis was performed to obtain the corresponding natural frequencies and mode shape vectors. The dominating dynamic forces at the RNA interface pertaining to the wind loads and rotation dynamics were recorded as 2 concentrated loads and 2 concentrated moments, and frequency analysis was carried out on the input channels. Based on the frequency content of the input, we realized that the first 3 modes predominantly contribute to the system dynamical responses. The natural frequencies are reported in Table 1.

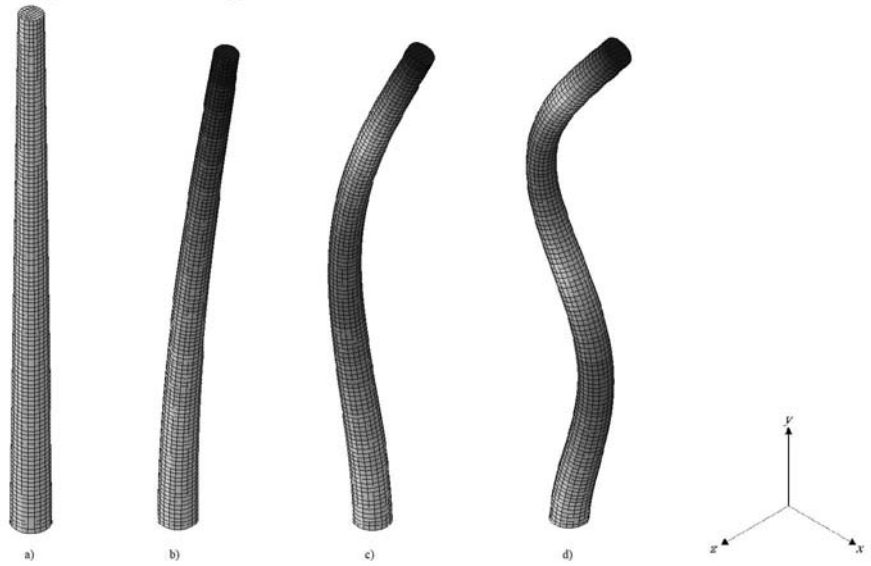

Figure 2: Finite element model of NREL's 5MW land-based wind turbine tower: a) base state, b) first mode, c) second mode, d) third mode.

Mode	Frequency (Hz)
1	0.8761
2	4.1737
3	10.395

Table 1: Finite element model natural frequencies.

The observation model was constructed from a limited number of output measurements; the discussion of stability of an Augmented Kalman Filter (AKF) presented by Lourens et al. [10] pointed out that ill-conditioning in the joint input-state estimator might increase depending on the sensor placement. Additionally, Maes et al. [23] suggested that the number of sensors should at least be equal to the number of forces to be identified. Thus, 2 biaxial acceleration and 4 strain responses were treated as the observed quantities. One set of collocated sensors, comprising 1 acceleration and 2 strain observations, was placed at a height of 86.9 m. from the ground, i.e. in the near-vicinity of the load application point; a similar second set of sensors was placed at a height of 63.5 m. from the ground. Figure 3 shows the locations of the response observations. Noise was introduced to the measurements as 1% of the root-mean-square deviation found in the observed channels, i.e. strains and accelerations.

A dynamic simulation of the first 8 s of operation was conducted. The structure is initially at rest, and the equivalent force system is applied at the beginning of the simulation. The modally-reduced state was estimated using the sequential Bayesian filter, and the full-field system response was reconstructed from the state and input estimation. The stress state time history at the finite element level is computed from a linear relationship between displacements and stresses under static loading cases. Consequently, accuracy in the estimation of nodal displacements is prescribed. Figures 4-5 show the acceleration and displacement, and stress responses, respectively, of an unmeasured near the base of the tower, i.e. a location far from the observations. The response estimates show agreement between the real and estimated responses. Notably, the estimated displacement responses were highly accurate. The stress and strain fields, however, do not display the same level of accuracy; thus, deviations from the real response in the displacement field are amplified in the corresponding stress field.

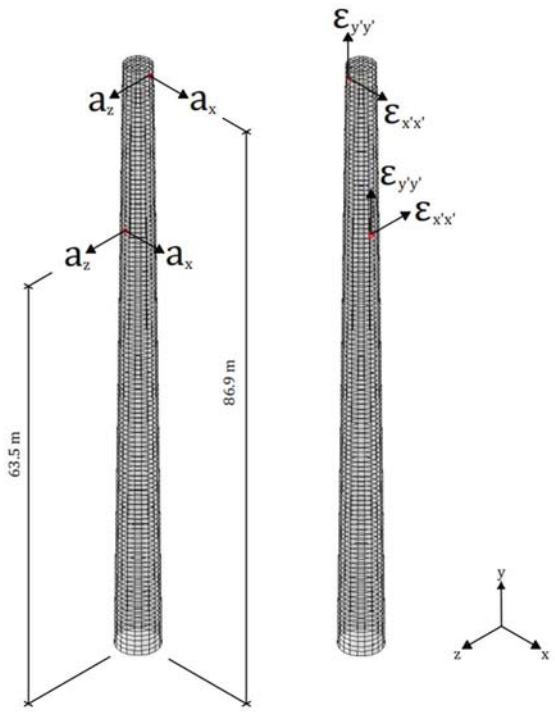

Figure 3: Measurement locations: a) accelerations, b) strains.

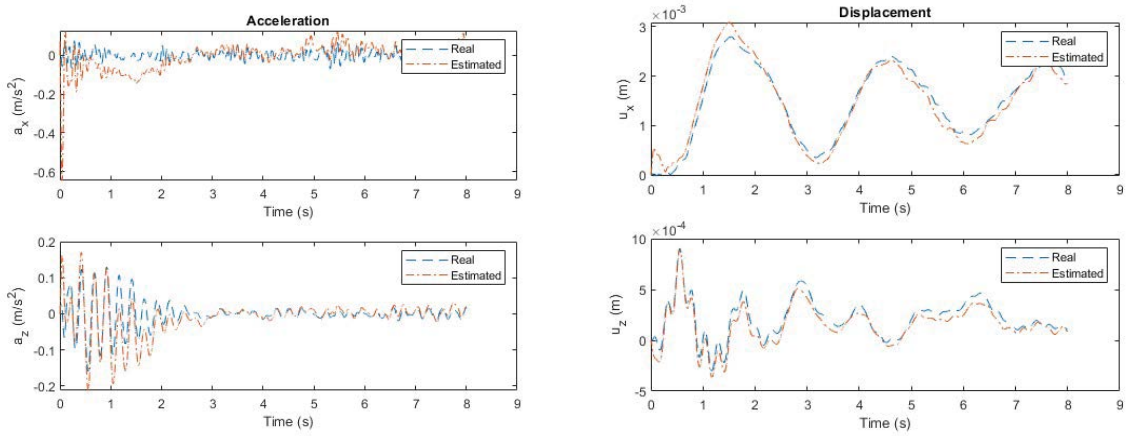

Figure 4: Real vs. estimated acceleration and displacement at unmeasured location near the tower base.

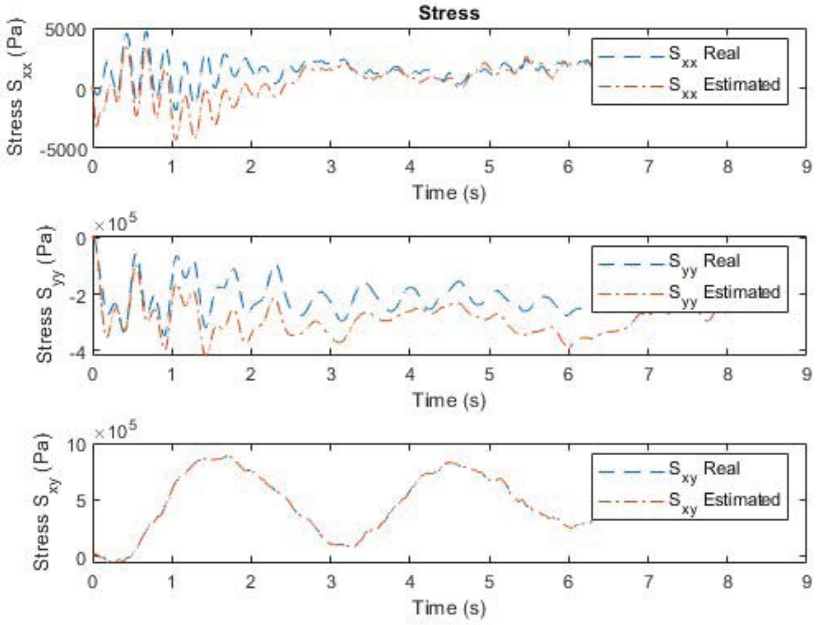

Figure 5: Real vs. estimated responses at unmeasured location near the tower base.

The next step is to identify the critical plane for each finite element by applying the MVM. Figure 6 shows the real and estimated shear stresses resolved along the critical plane. Considering that the shear stress transformation is a function of the stress state, it is evident that the error in the critical plane shear stress depends greatly on the accuracy of the stress tensor estimate. The normal stresses σ_{xx} and σ_{yy} are markedly influenced by the drift in the response estimations. The critical plane shear stress time histories are used to compute the stress amplitude range and the number of cycles at each amplitude range by means of the RCM.

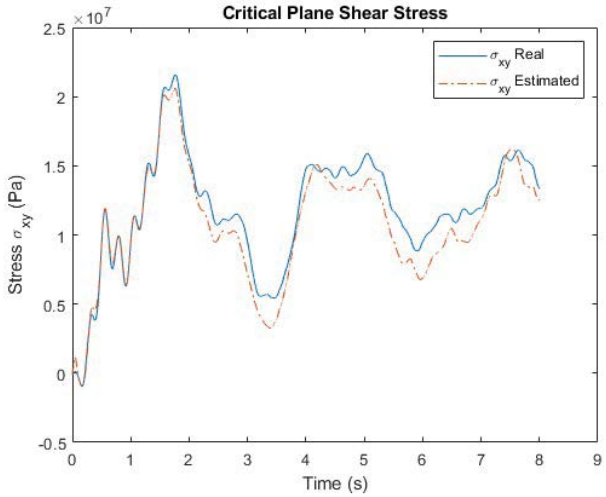

Figure 6: Shear stress resolved along the critical plane.

Lastly, a Modified Wöhler Curve and the linear Palmgren-Miner's rule are applied to compute the accumulated fatigue damage at each finite element. A full-field damage accumulation map and the resulting error are shown in Figures 7-8. The error in the fatigue damage estima-

tion is caused by the deviations in the critical plane shear stress: the error is carried over to the cycle counting, and thence to the damage accumulation computation.

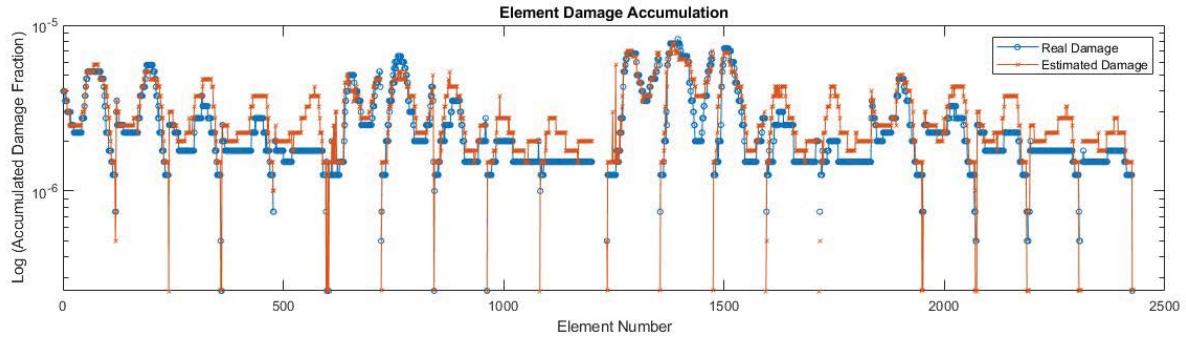

Figure 7: Full-field fatigue damage accumulation.

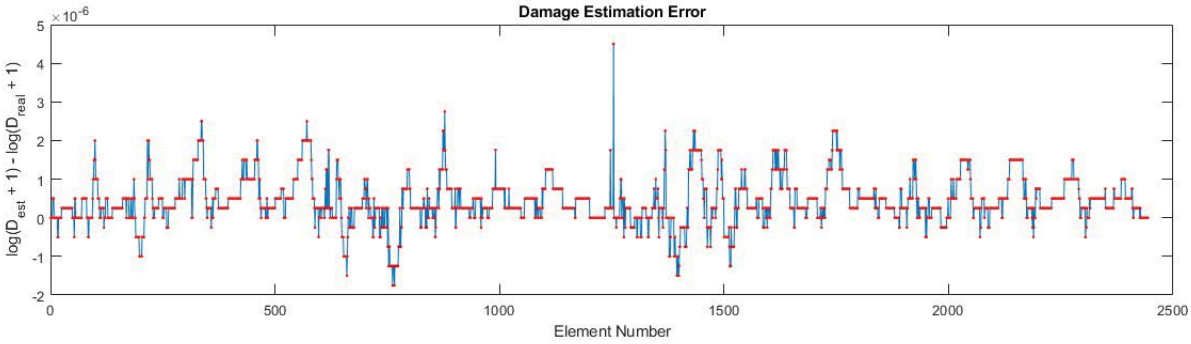

Figure 8: Damage estimation error.

6 CONCLUSION

A framework for computing full-field fatigue damage accumulation from a limited number of output-only measurements was presented. The proposed methodology promises real-world applicability on a variety of structures under unknown excitations, provided the proper calibration of the estimation algorithm is exercised, and an optimal observation location configuration is implemented. Its capability to efficiently produce a full-field fatigue map from limited measurements makes it a powerful tool for monitoring fatigue accumulation in wind turbine tower structures.

7 ACKNOWLEDGEMENTS

Financial support from the Hong Kong Research Grants Council under project No. 16234816, 16212918, and 16211019 is gratefully acknowledged. The first author would like to express his gratitude to the Mexican National Council for Science and Technology CONACYT for its support.

REFERENCES

[1] C. Papadimitriou, C.-P. Fritzen, P. Kraemer, and E. Ntotsios, “Fatigue predictions in entire body of metallic structures from a limited number of vibration sensors using Kalman filtering,” *Struct. Control Heal. Monit.*, vol. 18, no. 5, pp. 554–573, Aug. 2011.

[2] C. Papadimitriou, E. Lourens, G. Lombaert, G. De Roeck, and K. Liu, “Prediction of fatigue damage accumulation in metallic structures by the estimation of strains from

operational vibrations," in *Life-Cycle and Sustainability of Civil Infrastructure Systems: Proceedings of the Third International Symposium on Life-Cycle Civil Engineering (IALCCE'12), Vienna, Austria, October 3-6, 2012*, 2012, p. 103.

[3] K. Tatsis, V. Dertimanis, I. Abdallah, and E. Chatzi, "A substructure approach for fatigue assessment on wind turbine support structures using output-only measurements," *Procedia Eng.*, vol. 199, pp. 1044–1049, Jan. 2017.

[4] N. Noppe, K. Tatsis, E. Chatzi, C. Devrient, and W. Weijtjens, "Fatigue stress estimation of offshore wind turbine using a Kalman filter in combination with accelerometers," in *Proceedings of International Conference on Noise and Vibration Engineering (ISMA 2018), International Conference on Uncertainty in Structural Dynamics (USD 2018)*, 2018, pp. 4693–6701.

[5] K. Maes, A. Iliopoulos, W. Weijtjens, C. Devriendt, and G. Lombaert, "Dynamic strain estimation for fatigue assessment of an offshore monopile wind turbine using filtering and modal expansion algorithms," *Mech. Syst. Signal Process.*, vol. 76–77, pp. 592–611, Aug. 2016.

[6] S. P. Tchemodanova, K. Tatsis, V. Dertimanis, E. Chatzi, and M. Sanayei, "Remaining Fatigue Life Prediction of a Roller Coaster Subjected to Multiaxial Nonproportional Loading Using Limited Measured Strain Locations," in *Structures Congress 2019: Bridges, Nonbuilding and Special Structures, and Nonstructural Components*, 2019, pp. 112–121.

[7] S. Eftekhar Azam, E. Chatzi, and C. Papadimitriou, "A dual Kalman filter approach for state estimation via output-only acceleration measurements," *Mech. Syst. Signal Process.*, vol. 60–61, pp. 866–886, Aug. 2015.

[8] D.-C. Papadioti, "Management of uncertainties in structural response and reliability simulations using measured data," University of Thessaly (UTH), 2015.

[9] E. Lourens, C. Papadimitriou, S. Gillijns, E. Reynders, G. De Roeck, and G. Lombaert, "Joint input-response estimation for structural systems based on reduced-order models and vibration data from a limited number of sensors," *Mech. Syst. Signal Process.*, vol. 29, pp. 310–327, May 2012.

[10] E. Lourens, E. Reynders, G. De Roeck, G. Degrande, and G. Lombaert, "An augmented Kalman filter for force identification in structural dynamics," *Mech. Syst. Signal Process.*, vol. 27, no. 1, pp. 446–460, Feb. 2012.

[11] D. Teymouri, O. Sedehi, L. S. Katafygiotis, and C. Papadimitriou, "A new online Bayesian approach for the joint estimation of state and input forces using response-only measurements," in *13th International Conference on Applications of Statistics and Probability in Civil Engineering, ICASP 2019*, 2019.

[12] V. K. Dertimanis, E. N. Chatzi, S. Eftekhar Azam, and C. Papadimitriou, "Input-state-parameter estimation of structural systems from limited output information," *Mech. Syst. Signal Process.*, vol. 126, pp. 711–746, Jul. 2019.

[13] O. Sedehi, C. Papadimitriou, D. Teymouri, and L. S. Katafygiotis, "Sequential Bayesian estimation of state and input in dynamical systems using output-only measurements," *Mech. Syst. Signal Process.*, vol. 131, pp. 659–688, Sep. 2019.

[14] U. Lagerblad, H. Wentzel, and A. Kulachenko, "Dynamic response identification based on state estimation and operational modal analysis," *Mech. Syst. Signal Process.*, vol. 129, pp. 37–53, Aug. 2019.

[15] D. Socie and G. Marquis, *Multiaxial fatigue*. Warrendale, Pa.: Society of Automotive Engineers, 2000.

[16] L. Susmel, "A simple and efficient numerical algorithm to determine the orientation of the critical plane in multiaxial fatigue problems," *Int. J. Fatigue*, vol. 32, no. 11, pp.

1875–1883, Nov. 2010.
[17] L. Susmel and R. Tovo, “Estimating fatigue damage under variable amplitude multiaxial fatigue loading,” *Fatigue Fract. Eng. Mater. Struct.*, vol. 34, no. 12, pp. 1053–1077, Dec. 2011.
[18] L. Susmel and P. Lazzarin, “A bi-parametric Wohler curve for high cycle multiaxial fatigue assessment,” *Fatigue Fract. Eng. Mater. Struct.*, vol. 25, no. 1, pp. 63–78, Jan. 2002.
[19] A. Palmgren, “Die lebensdauer von kugellargern,” *Zeitshrift des Vereines Duetsher Ingenieure*, vol. 68, no. 4, p. 339, 1924.
[20] M. A. Miner, “Cumulative fatigue damage,” *J. Appl. Mech.*, vol. 12, no. 3, pp. A159–A164, 1945.
[21] J. Jonkman, S. Butterfield, W. Musial, and G. Scott, “Definition of a 5-MW reference wind turbine for offshore system development,” Golden, CO, 2009.
[22] J. Jonkman and B. Jonkman, “NWTC Information Portal (FAST),” 2018. [Online]. Available: https://nwtc.nrel.gov/FAST.
[23] K. Maes, E. Lourens, K. Van Nimmen, E. Reynders, G. De Roeck, and G. Lombaert, “Design of sensor networks for instantaneous inversion of modally reduced order models in structural dynamics,” *Mech. Syst. Signal Process.*, vol. 52–53, no. 1, pp. 628–644, 2015.

EURODYN 2020
XI International Conference on Structural Dynamics
M. Papadrakakis, M. Fragiadakis, C. Papadimitriou (eds.)
Athens, Greece, 23–26 November 2020

DYNAMIC CHARACTERISTICS OF A SIX-STOREY STEEL BUILDING EXAMINED FROM STRONG MOTION AND AMBIENT VIBRATION DATA

Toshihide Kashima[1] **and Hiroto Nakagawa**[2]

[1] Building Research Institute
1 Tachihara, Tsukuba, Ibaraki 305-0802, Japan
e-mail: kashima@kenken.go.jp

[2] Building Research Institute
1 Tachihara, Tsukuba, Ibaraki 305-0802, Japan
e-mail: hiroto-n@kenken.go.jp

Keywords: Steel building, Strong motion, Ambient vibration, System identification

Abstract. *The Building Research Institute (BRI) of Japan is a national institute engaged in research and development in the fields of architecture, building engineering and urban planning. As one of its research activities, the BRI operates a strong motion network that covers buildings in major cities across Japan. As one of the stations in the BRI strong motion network, Miyako City Hall was instrumented in September 2018. More than 80 strong motion records were obtained within 16 months after the installation of the monitoring system.*

The daily natural frequencies and damping ratios in both the horizontal directions of the building were identified from the ambient vibration data recorded on the sixth floor. The natural frequencies decrease slightly for three months after completion but then show stable values. The damping ratios are distributed between 3% and 7%, which are larger than those obtained from the strong motion records.

The fundamental dynamic characteristics of the building are discussed through the analysis of the strong motion data. The natural frequencies in the X-direction vary between 1.6 Hz and 1.9 Hz. It was confirmed that the variation was caused by the amplitude dependence of the natural frequency. The natural frequencies in the Y-direction are close to those in the X-direction and show amplitude dependence as well. The damping ratios in both directions are 3% or less and widely vary.

The seismic monitoring system of the new main building of Miyako City Hall revealed the fundamental dynamic characteristics of the building within 16 months after completion. These results will be useful for structural health assessments of the building in the future.

1 INTRODUCTION

The Building Research Institute (BRI) of Japan is a national institute engaged in research and development in the fields of architecture, building engineering and urban planning. As one of its research activities, BRI operates a strong motion network that covers buildings in major cities across Japan [1]. A great number of strong motion data has been accumulated in the long history of the BRI strong motion network.

As one of the stations in the BRI strong motion network, Miyako City Hall was instrumented in September 2018. The city of Miyako is on the Pacific side of northern Japan and was hit by a tsunami during the 2011 Great East Japan Earthquake (Tohoku Earthquake). The main building of the city hall at that time was inundated to the second floor. The building was restored and used for seven years after the disaster, and then a new office building was built at another location in 2018. BRI had a strong motion instrument in the old city hall building and installed a new system in the new building.

This paper discusses the fundamental dynamic characteristics of the new city hall building using strong motion data and ambient vibration data.

2 TARGET BUILDING

Miyako City Hall was built as a core facility for the central city area development project in 2018. The city hall building is a six-storey steel building and is a complex that combines the functions of a communication and health centre. Table 1 and Figure 1 show the overview and external appearance of the building.

Use	City office, communication centre and health centre
Structure	Steel frame
Number of storeys	6
Building area	4,842.31 m^2
Total floor area	14,068.48 m^2
Height	26.45 m
Foundation	Cast-in-place concrete pile (l=37m)

Table 1: Overview of the target building.

Figure 1: External appearance of the target building.

3 SEISMIC MONITORING SYSTEM

The seismic monitoring system installed in the new building has three triaxial acceleration sensors on the ground, first floor and sixth floor. The sensor configuration is illustrated in Figure 2. The acceleration sensors are installed along the axis of the building, and this paper treats the direction heading north as X and the direction heading west as Y. All acceleration signals are continuously recorded with the logging system placed on the first floor. The system can be accessed via the Internet using the mobile communication network from BRI.

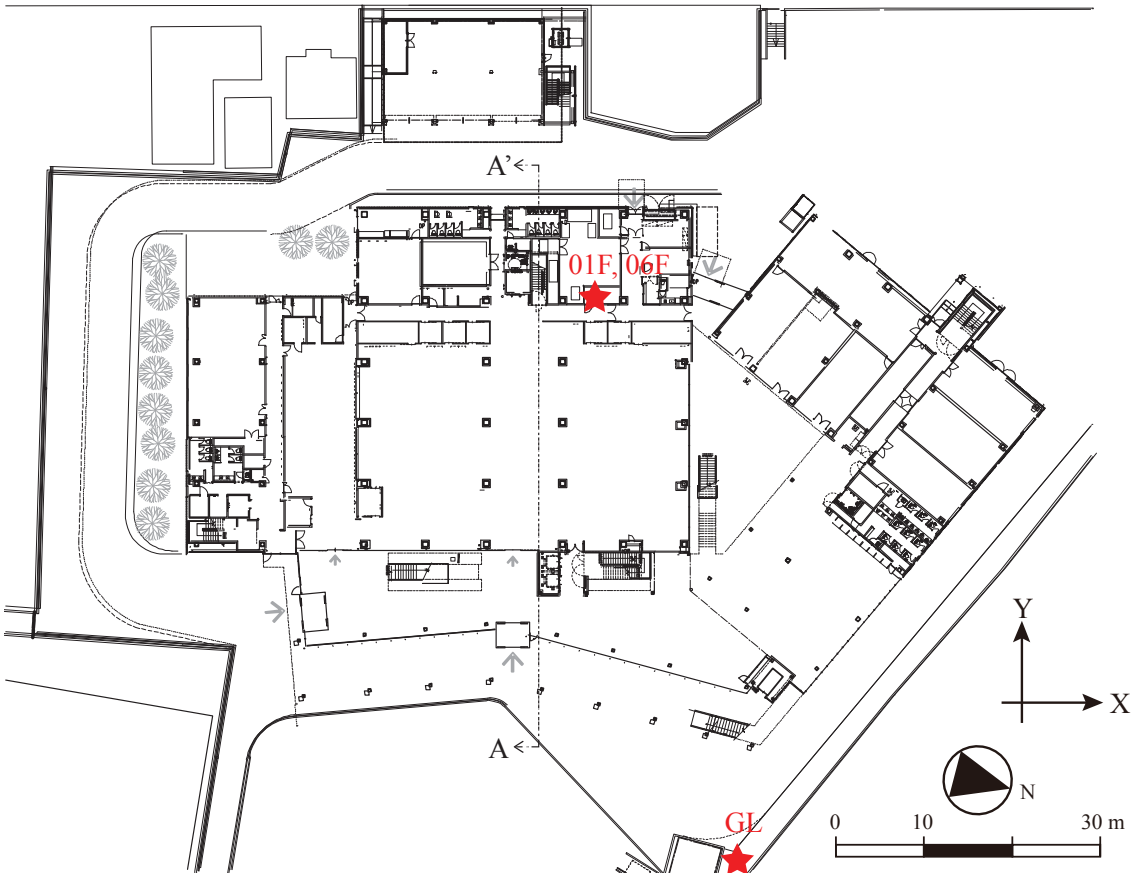

(a) Ground plan

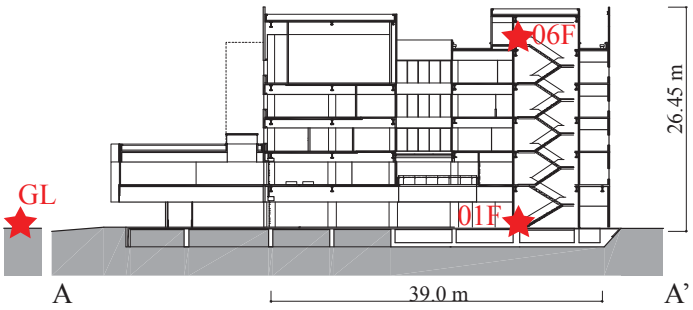

(b) Cross section

Figure 2: Sensor configuration.

4 AMBIENT VIBRATION DATA

The seismic monitoring system stores continuous data as one-hour files. The data files from midnight every day are transferred to BRI manually. The natural frequencies and damping ratios in the X- and Y-directions of the building are identified by the random decrement (RD) technique [2] using the ambient vibration data on the sixth floor ("06F" in Figure 2).

Identified natural frequencies and damping ratios are plotted in Figure 3 as a relation to time. Red circles and blue triangles indicate values in the X- and Y-directions, respectively.

The natural frequencies appear to be stable throughout the monitoring period, and those mean values are 1.88 Hz and 1.79 Hz in the X- and Y-directions as indicated by red and blue dashed lines, respectively. After carefully comparing the daily natural frequencies and mean lines, it was observed that the natural frequencies have been gradually decreasing for a few months after completion.

The damping ratios in both directions widely vary. The mean values are 5.12 % and 4.04 % in the X- and Y-directions, respectively.

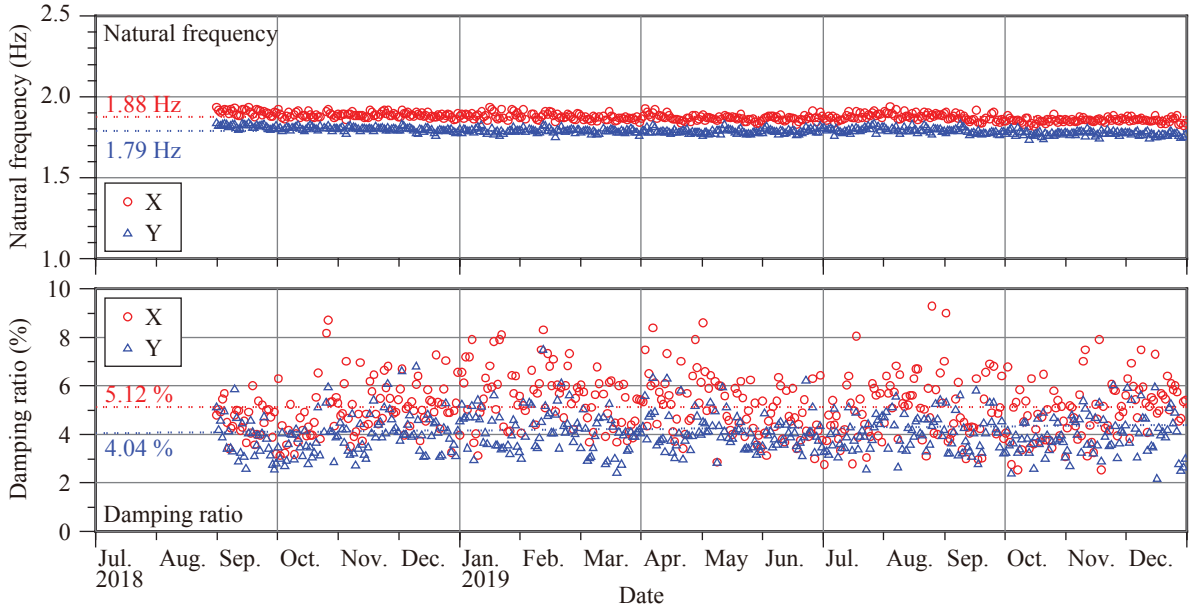

Figure 3: Natural frequencies and damping ratios obtained from ambient vibration data.

5 STRONG MOTION RECORDS

By the end of 2019, more than 80 strong motion records were obtained after the installation of the monitoring system. The amplitudes of the ground motions were small to medium, and the maximum JMA (Japan Meteorological Agency) seismic intensity was 3.

From each strong motion data, the fundamental natural frequencies and damping ratios in two horizontal directions of the building were identified using a parameter optimization technique [3]. With a single-degree-of-freedom system, the natural frequency and damping ratio that had the most fitted response displacement were determined using the grid search. Strong motion data on the first and sixth floors were adopted as the input and output motions, respectively.

Figure 4 indicates changes in the natural frequency and damping ratio of the building with time. Red circles and blue triangles correspond to the X- and Y-directions, respectively. The natural frequencies in both directions are distributed between 1.6 Hz and 1.9 Hz. The damping ratios vary somewhat but are less than 4%, which are smaller than the values obtained from the

ambient vibration data. In the identification using strong motion data, the influence of the soil-structure interaction (SSI) is eliminated by assuming that the first and sixth floors are input and output positions. In contrast, the identification using ambient vibration records is affected by SSI, since it uses only records on the sixth floor. This difference is considered to be one of the causes of difference in damping ratios.

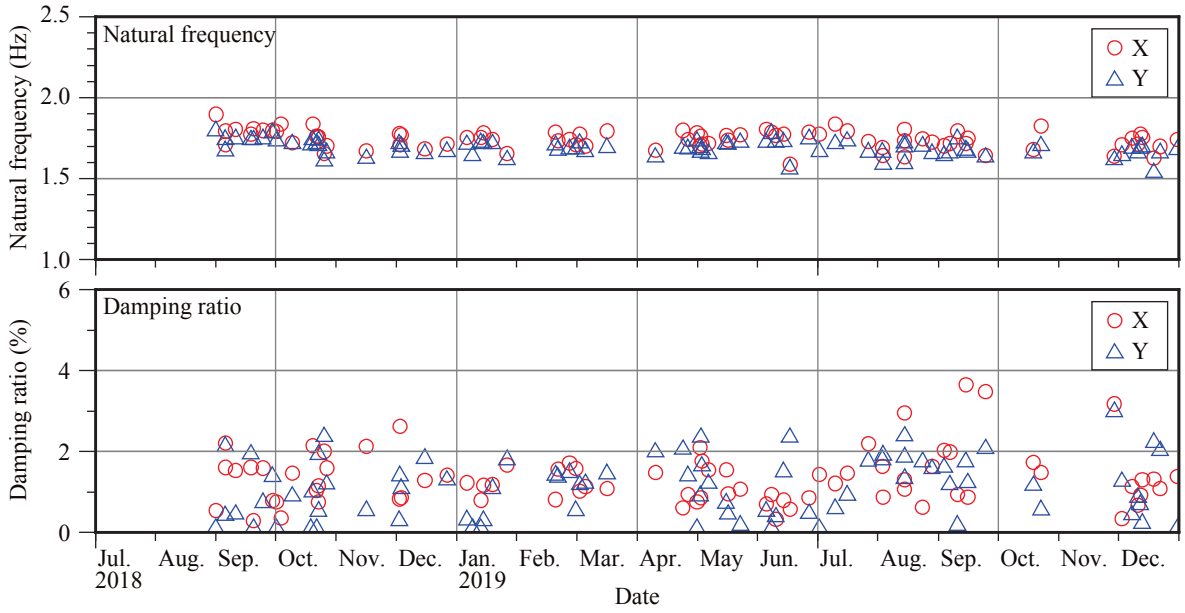

Figure 4: Natural frequencies and damping ratios obtained from strong motion data.

Dependence of dynamic characteristics on response amplitude is examined using the maximum displacement angle $\theta_{\max}$ defined by Eq. (1).

$$\theta_{\max} = |x_{06F}(t) - x_{01F}(t)|_{\max}/H \tag{1}$$

where, $x_{06F}(t)$ and $x_{01F}(t)$ are the time histories of the displacements on the sixth and first floors, respectively, and H is the height of the sixth-floor level from the first-floor level.

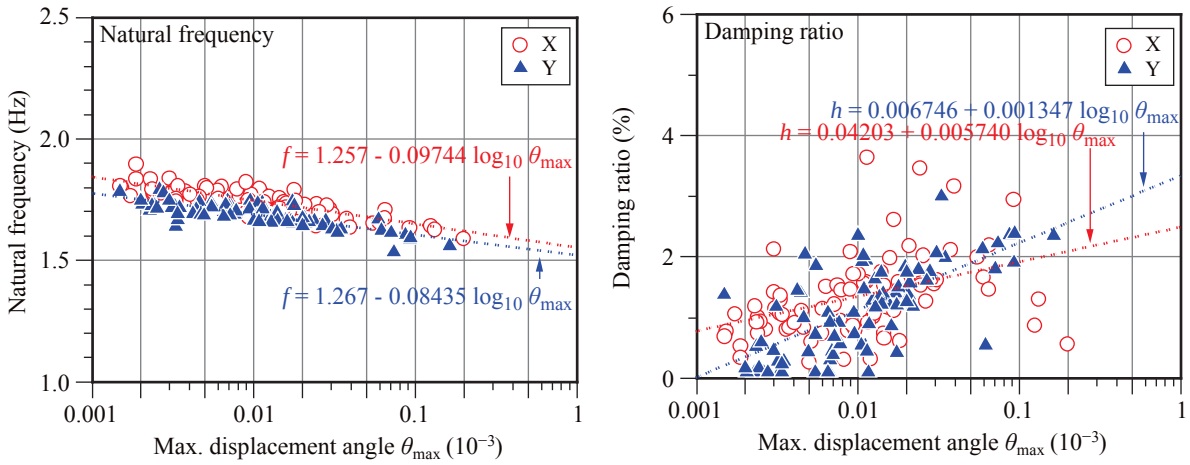

(a) Natural frequency

(b) Damping ratio

Figure 5: Relation of natural frequency and damping ratio to maximum displacement angle.

The relation of the natural frequency and damping ratio to the maximum displacement angle $\theta_{\max}$ is plotted in Figure 5. Hollow red circles and solid blue triangles indicate the values in the X- and Y-directions, respectively.

There is evident amplitude dependence in the natural frequency. Dashed lines represent the results of the regression analysis. When the response amplitude increases ten times, the natural frequencies decrease by 0.1 Hz and 0.08 Hz in the X- and Y-directions, respectively. The damping ratios tend to increase as the response amplitude increases. For reference, the results of the regression analysis are indicated by broken lines in the figure.

6 CONCLUSIONS

As one of the stations in the BRI strong motion network, Miyako City Hall, which is a six-storey steel building, was instrumented in September 2018. This paper discussed the dynamic characteristics of the building using strong motion and ambient vibration data.

The daily natural frequencies in the horizontal directions of the building identified from the ambient vibration data were stable and decreased gradually for a few months from completion. The daily damping ratios widely varied and were 5.12 % and 4.04 % in the X- and Y-directions on average, respectively.

The natural frequencies and damping ratios of the building were estimated from the strong motion data as well. The natural frequencies in both horizontal directions showed apparent amplitude dependence and decreased with the increase of the response amplitude. In the case of this building, the natural frequency decreased by nearly 0.1 Hz when the response amplitude increased tenfold. The damping ratios estimated using the strong motion data varied somewhat and showed smaller values compared with the values obtained from the ambient vibration data.

The damping ratios from strong motion records are obtained by treating records of the first floor as inputs and records of the sixth floor as outputs and do not include the effect of the soil-structure interaction (SSI). On the other hand, the damping ratios from ambient vibration records are obtained only from the records of the 6th floor of the building and are affected by SSI. This can be considered to be one of the causes of the difference in damping ratios. The influence of other factors, such as differences in external force conditions, are also considered, and further investigation is necessary.

REFERENCES

[1] BRI Strong Motion Network, https://smo.kenken.go.jp/, visited on Feb. 25, 2020

[2] Tamura, Y., Sasaki A. and Tsukagoshi, H, Evaluation of Damping Ratios of Randomly Excited Buildings using the Random Decrement Technique, *Journal of Structural and Construction Engineering*, Architectural Institute of Japan, 454, pp.29-38, 1993 (in Japanese).

[3] Kashima, T. and Kitagawa, Y., Dynamic Characteristics of Buildings Estimated from Strong Motion Records, *8th National Conference on Earthquake Engineering*, San Francisco, U.S.A, April 18-22, 2006.

EURODYN 2020
XI International Conference on Structural Dynamics
M. Papadrakakis, M. Fragiadakis, C. Papadimitriou (eds.)
Athens, Greece, 23–26 November 2020

REDUCTION OF TEMPERATURE EFFECTS FOR BRIDGE HEALTH MONITORING

Viet Ha Nguyen[1], Tanja Kebig[1], Jean-Claude Golinval[2], Stefan Maas[1]

[1] University of Luxembourg
6 Rue Richard Coudenhove-Kalergi, Luxembourg 1359
e-mail: vietha.nguyen@uni.lu; tanja.kebig@uni.lu; stefan.maas@uni.lu

[2] University of Liege
9 Allée de la Découverte, Quartier Polytech 1, 4000 Liège 1
e-mail: JC.Golinval@uliege.be

Keywords: temperature compensation, damage detection, eigenfrequency, bridge, Principal Component Analysis

Abstract. *Structural health monitoring of concrete bridges can be achieved by tracking static load-testing results or dynamic properties as for example eigenfrequencies. Deviations from a healthy reference state can be used as damage indicators and even more, help to localize zones of stiffness reduction, i.e. cracking. However, outdoor temperature effects also lead to changes of monitored physical characteristics in the same order of magnitude as damage. Hence, temperature effects need to be removed prior to any condition analysis. The present paper presents a new two-step approach by applying physical compensation first, before using a statistical method based of Principal Component Analysis (PCA) or more exactly on principal vectors and singular values. This technique is here applied to eigenfrequencies, first of a new bridge without damage, but with extreme temperature variation due to thick asphalt layer and special bearing constraints, thus showing strong sensitivity along seasonal temperatures in the intact state. The second object is the Z24 Bridge in Switzerland, which is well documented in literature and where artificial damage was applied prior to demolition. The proposed techniques allow removing noise and temperature effects in a coherent and efficient way. The corrected measurement data can then be used in subsequent steps for its definite purpose, i.e. detection and localization of damage for instance by updating a numerical finite element model which allows assessing a stiffness loss.*

1 INTRODUCTION

Damage diagnosis in civil engineering systems is often based on static or/and dynamic measurements, which allow to detect, localize and quantify stiffness reduction going along with concrete cracking. For instance, for bridge structures, static displacement or strain measurements are typically done along the length at defined positions for a known test-loading in regular time intervals. Alternatively, modal properties like eigenfrequencies, modeshapes, modal masses or damping values can be measured and tracked. However, both static and dynamic characteristics can show high sensitivity to temperature variations, which show important influence on asphalt-, soil- and bearing-stiffness. Variations of the measured characteristics due to temperature can be typically in the same order of magnitude than those caused by real damage. Therefore, prior to further analysis, compensation of measured data regarding temperature effects is mandatory. Furthermore, tests should be performed in similar conditions due to other non-linearities of concrete bridges, e.g. the level of excitation (force, load) either without temperature gradients or local differences in the structure. In real application, bridge temperature cannot be fully controlled due to day-night and seasonal changes, why compensation algorithms are so fundamental prior to further comparison and damage analysis. Lloyd et al. [1] used the bootstrap for temperature compensation of measured frequencies and displacements to assess bending and shear stiffness of a concrete bridge. Temperature and operational effects were removed by Magalhães et al. [2] through multiple linear regression analysis for damage detection in an arch bridge. Cury et al. [3] normalized data of a PSC box girder bridge by a prediction law using non-linear regression based on neural networks.

After temperature compensation, the measured data can be analyzed to evaluate a bridge's current condition. For example, repeating measured static displacements at many points along the length of bridge can be directly taken to draw the deflection line in [4]. Several researchers fit responses of a finite element model to real measured data [5, 6, 7]. The fitting between numerical and experimental characteristics gives good insight to a structure's behavior. But temperature effects must be removed from the raw measurements prior to their use as input for model updating. Schommer et al. [8] compensated static displacement measurements with a 3D finite element model of a prestressed concrete bridge. In the present paper, the same compensation with subsequent noise removal by PCA is applied for eigenfrequencies for two real bridges. Considerable reductions of the scatter are achieved and corrected data may later either be used for direct analysis or for further processing like the mentioned model updating. Finally, a yes-no indicator based on novelty-index is presented and applied to the two bridges with very good results.

2 TEMPERATURE COMPENSATION AND NOISE ELIMINATION

Two subsequent steps are used here for removal of temperature and noise effects: the first consists in shifting the measured characteristics to a reference temperature along a previously identified physical line, while the second step is based on a statistical mathematics with Singular Value Decomposition (SVD) for general noise removal.

2.1 Physical temperature compensation

Nguyen et al. [4] proposed a technique for temperature compensation and applied it to static displacement data. It is based on the projection of measured data along a measured regression line, identified within data from the intact state. Figure 1 illustrates how a set of data A (e.g. eigenfrequency f) from the healthy state of the structure changes versus temperature $t°$. Measurements for other states, possibly in different ranges of temperature, can be traced back

to a reference temperature and compared to the intact state. The comparison is based on linear dependency of the measured quantity *f* versus temperature, which is more or less true, as can be seen in two examples below. Hence, first data are measured at different temperatures in the reference state. Then a linear regression line is determined by its equation's terms; a corresponding standard-deviation σ with respect to this line is also assessed. Once they are known, different sets of data A, B, C can be projected with the slope of the regression line to the reference temperature t_1, referred here as A_1, B_1, C_1. Thus, temperature effects can be reduced based on a physical measured line.

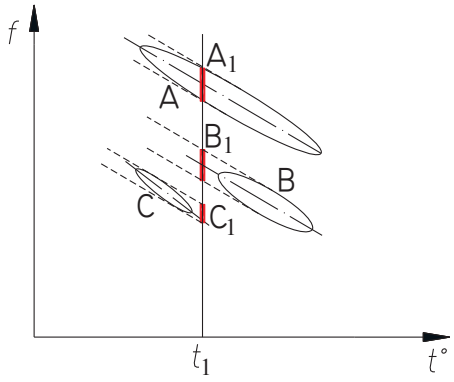

Figure 1: Temperature compensation by data projection

2.2 Principal Component Analysis and Novelty Index

It is known from statistics that Principal Component Analysis (PCA) can be used to remove environmental effects and noise [9]. The Singular Value Decomposition (SVD) of an observation matrix **X** containing *m* records of *N* time samples (e.g. displacements or eigenfrequencies versus time) determines principal vectors and singular values of $\mathbf{X}_{m\times N}$:

$$\mathbf{X} = \mathbf{U}\mathbf{S}\mathbf{V}^T \tag{1}$$

where matrices $\mathbf{U}_{m\times m}$ and $\mathbf{V}_{N\times N}$ are orthogonal; the diagonal matrix $\mathbf{S}_{m\times N}$ contains in decreasing order non-negative singular values while **U** contains column-wise corresponding principal vectors.

When the observation matrix **X** contains for instance *m* eigenfrequencies after temperature compensation, the first singular value in **S** is typically by far larger than subsequent singular values. Hence, there is only a unique dominant singular value and only one principal vector $\mathbf{U}_1$ in **U** has to be considered for reconstruction of the data in order to remove noise:

$$\mathbf{X}_{reconstructed} = \mathbf{U}_1\mathbf{U}_1^T\mathbf{X} \tag{2}$$

By doing so, PCA can be used as additional filter for data processing to clean it from environmental noise.

Furthermore, Novelty Index (*NI*) proposed by YAN et al. in [9] can be used as a damage index, in form of a red-green light index. *NI* sizes up the error of the reconstructed data from the initial observation data through Euclidean norm (Eq. 3) or Mahalanobis norm (Eq. 4):

$$\mathbf{E} = \mathbf{X} - \mathbf{X}_{reconstructed}; \quad NI_k^{Eucl} = \sqrt{\mathbf{E}_k^{\mathrm{T}}\,\mathbf{E}_k} \tag{3}$$

$$NI_k^{Maha} = \sqrt{\mathbf{E}_k^{\mathrm{T}}\mathrm{cov}(\mathbf{X})^{-1}\mathbf{E}_k} \tag{4}$$

where $\mathrm{cov}(\mathbf{X}) = \mathbf{X}\,\mathbf{X}^{\mathrm{T}}$ is the covariance matrix of the features.

Then an actual state can be assessed by two indicators: 1) ratio between the mean values of this actual state and the reference state $\overline{NI}_{actual}/\ \overline{NI}_{reference}$; 2) a statistical threshold as outlier limit e.g. $\overline{NI}_{reference} + 3\sigma$ that σ is the standard deviation of *NI* in the reference (intact) state. A ratio close to unit together a low outlier limit can be assumed no change or damage (i.e. green light); otherwise, statistical relevant changes are very probable (i.e. red light).

3 ANALYSIS

An application of the physical temperature compensation algorithm was presented in [4] with static displacements, which require as reference long-term monitoring without environmental effects and noise. The present work examines eigenfrequencies as characteristic dynamic properties of structure. For bridge systems, the combination of physical and statistical PCA-based temperature compensation can be beneficial as shown below.

First a new composite bridge without damage but with extreme temperature sensitivity is analyzed. Second, an older bridge subjected to multiple artificial damage steps will be dealt with. The data matrix **X** is here frequencies vs. temperature is processed here with the mentioned 2-step procedure. From the reference i.e. initial/ undamaged state, full range of temperature variation is known and a regression line is calculated, i.e. eigenfrequencies f_i versus concrete temperature $t°$. Data from actual measurements are projected with the identified slope of the regression-line to a chosen reference temperature, which is close to the average temperature. The subsequent PCA procedure according to Eq. (2) is also based on the same reference period. For both bridges, the first singular value of matrix **S** is by far larger than the others and occupies more than 95% of the total energy. So only the first principal vector of the reference period $\mathbf{U}_1^{reference}$ is taken into account for data reconstruction.

3.1 Bridge in Useldange, Luxembourg

In 2006 a new bridge was built in Useldange, Luxembourg and then monitored during 4 years. The steel-concrete composite bridge has a very thick asphalt layer, that's why its eigenfrequencies strongly depend on the temperature, e.g. up to 7‰ per °*C* for f_1 [10].

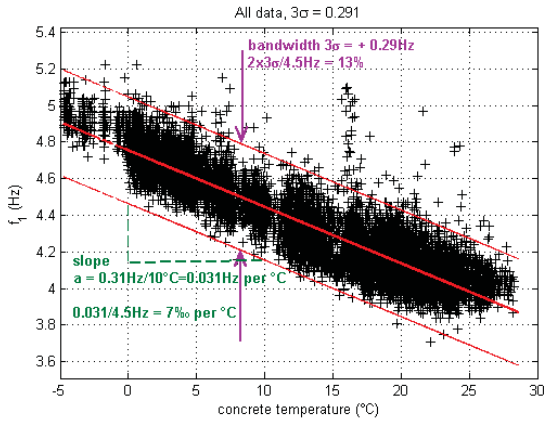

Figure 2: First eigenfrequency f_1 vs. concrete $t°$ for Useldange bridge (Luxembourg - ambient excitation)

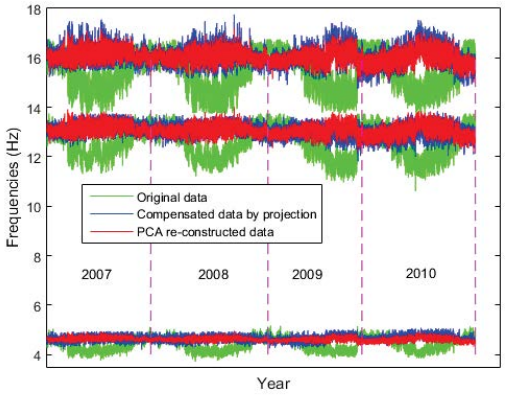

Figure 3: Eigenfrequencies monitored during 4 years- Useldange bridge

Figure 2 show the first eigenfrequency measured from ambient excitation with its regression line. It has an important slope and a quite large scatter of 13%, determined here as 3 times of standard deviation σ. In Figure 3, the data-sets are simply superposed versus time: three classes of data are: original (raw) data in green, data after the physical compensation in

blue and statistical reconstructed data by PCA in red. The original data in green show clearly the seasonal behavior: low stiffness with low frequencies in summer and vice-versa in winter. This behavior is significantly attenuated after the physical temperature compensation and even more after PCA-filtering.

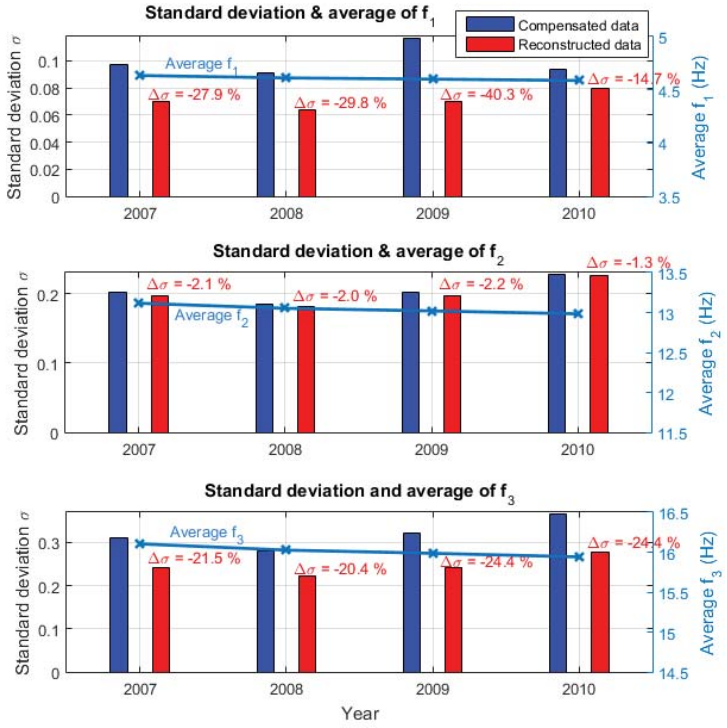

Figure 4: Comparison before and after PCA-filtering for Useldange Bridge

As reported in Figure 4 especially for modes 1 and 3, PCA-filtering reduces the standard deviation σ by approximatively 25% in average even after physical temperature compensation. Also in Figure 4, the mean frequencies are indicated in light blue solid lines with mark "×" referring to the right ordinate axis. It should be noted that for this new bridge without damage, all eigenfrequencies show slight reductions over the first years, which fit well to other studies and other bridges [10], thus confirming the quality of the 2-step compensation.

3.2 Bridge Z24, Switzerland

The Z24-bridge has been studied in several works by Peeters, Teughels, Reynders et al. [11-13]. The bridge was monitored during 1 year and then demolished after about 40 days of testing with progressive damage. Vibration analysis was performed by Peeters et al. [11] together with the measurement of temperature. In Figures 5 and 6, only positive temperatures were selected to avoid freezing periods, where this Z24-Bridge showed quite different behavior.

In Figure 5, the measured eigenfrequencies of 4 modes are plotted against concrete deck temperature. Teughels et al. [12] stated that the first mode is pure bending; while the third and the fourth are coupled bending-torsion modes. They all show decreasing frequencies with increasing temperatures. In contrast, the second is a transversal mode and increases slightly with temperature. Significant differences are noticeable especially for the damaged state, which is shown by red dots.

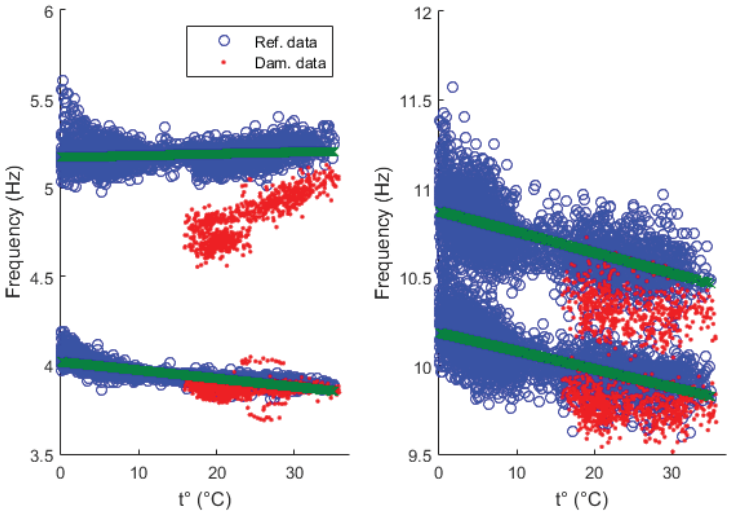

Figure 5: Identified frequencies vs. structural temperature
o - *reference state;* • - *damaged state;*
xxx - *regression line of the reference data*

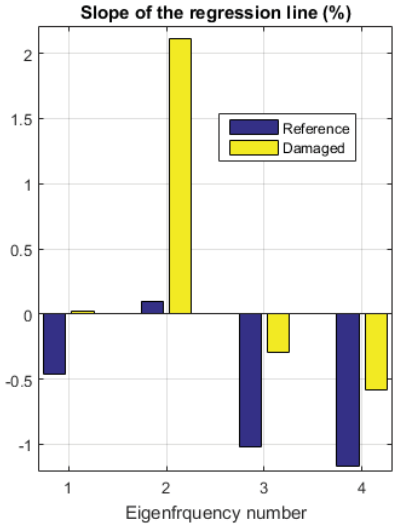

Figure 6: Slopes of the regression lines for the reference and damaged states

Figure 6 highlights the slopes of the regression lines for the reference and the damaged states for each mode. The frequencies f_1, f_3, f_4 show negative gradients whose magnitude decreases with damage. Only f_2 has opposite sign and increases considerably in the damaged state. These are individual characteristics and must be measured at site, i.e. today cannot be ad-hoc simulated.

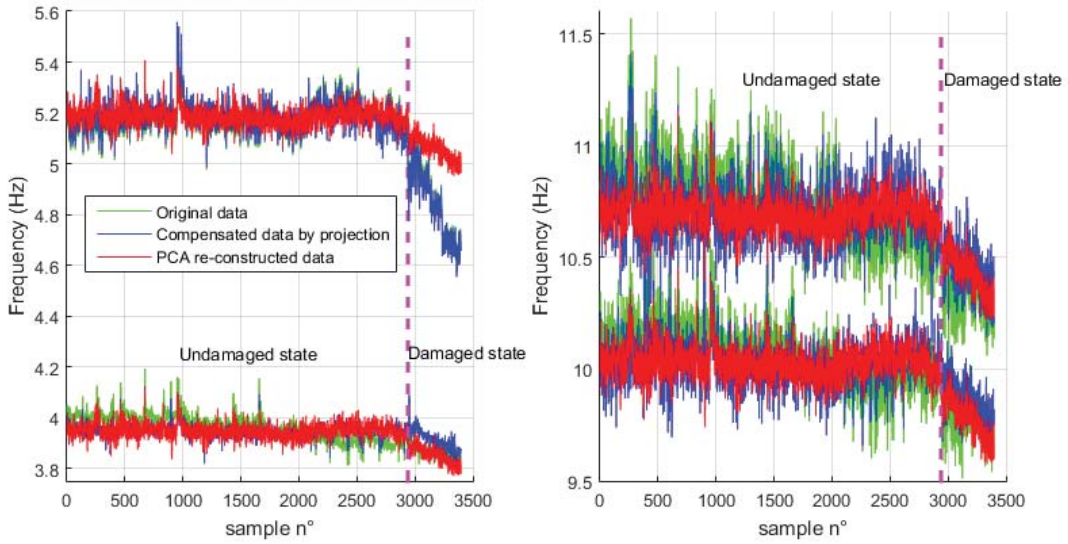

Figure 7: Evolvement of eigenfrequencies during the monitored period

To carry out the physical temperature compensation, all data are projected according to the scheme in Figure 1 to a reference temperature, which is chosen here at medium value $t_{ref} = 20°C$. A PCA-reconstruction step is also performed then the three families of data are presented in Figure 7. Only samples that all the modes could be identified are collected in the observation matrix, in total about 3400 samples. The dashed vertical line separates the intact from the damaged state of the bridge.

For better comparison, eigenfrequencies are analyzed in several small blocks of 150 samples. The scatter of data does not notably differ during the processing and is not presented here. The averaged values of eigenfrequencies are shown on the left of Figure 8, while on the right the relative difference by mean values of each block from the reference state within any family of data is deployed. These results reveal clearly that in the undamaged/reference state, Δf_i can vary up to 2%, but less than 0.5% after the physical temperature compensation. PCA helps additionally a little bit to decrease variation. After introduction of artificial damage, the reduction of eigenfrequencies is much better observed by the proposed compensation procedures. Such processing ensures visibly reliability and thus facilitates comparison between different measurements. Schommer et al. [8] used static deformation data after physical temperature compensation for model-updating and so achieved very good results.

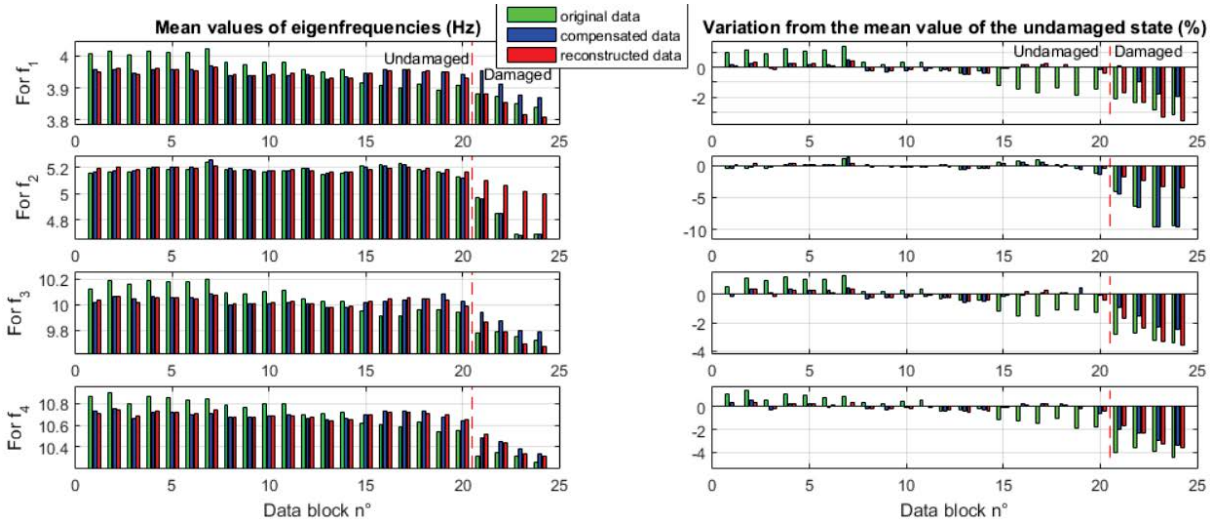

Figure 8: Averaged f_i and Δf_i assessed for each of the 3 families of data

The proficiency of the temperature compensation for damage detection can also be assessed by Novelty Index *NI*, as proposed by Yan et al. [9]. Both initial raw data $\mathbf{X}$ and compensated data - $\mathbf{X}_{reconstructed}$ are used to compute *NI*. Figures 9-10 shows *NI* versus time (or sample number) accordingly to Euclidean and Mahalanobis norms. In each figure, the top image presents the indexes from the original or raw data while the bottom image following to the physical and PCA compensation. Every chart is split into 2 parts, reference and damage states separated around sample n° 2900. An outlier limit is set for instance at $\overline{NI}_{reference} + 3\sigma$. Each state is characterized by its mean value and overshoot counting the percentage of indexes overpassing the outlier limit. By means of Euclidean norm, the ratio between the mean values of the damaged vs. the reference state $\overline{NI}/\ \overline{NI}_r$ weighs 1.9 by the raw data and 2.8 by the compensated data, with overshoot of 16.2% and 41.6% respectively. As for Mahalanobis norm, the ratio is 1.5 with the raw data and doubled to 3.2 after the 2-step compensation, while overshoot grows from 0.6% to 46.6% respectively. So in term of overshoot by the raw data, there is a clear distinction between the two norms but they give quite equivalent outcome based on the compensated data. This confirms the performance and its stability of the proposed compensation technique.

4 CONCLUSIONS

Damage leads to micro-cracking or cracking of concrete and therefore to stiffness loss, which can be detected for instance by reduction of eigenfrequencies. But the stiffness of as-

phalt, bearing pads and subsoil can also be affected by environmental factors, which cause also important perturbation for eigenfrequencies. Hence if eigenfrequencies are used as input for detection, it is necessary to separate temperature from damage effects.

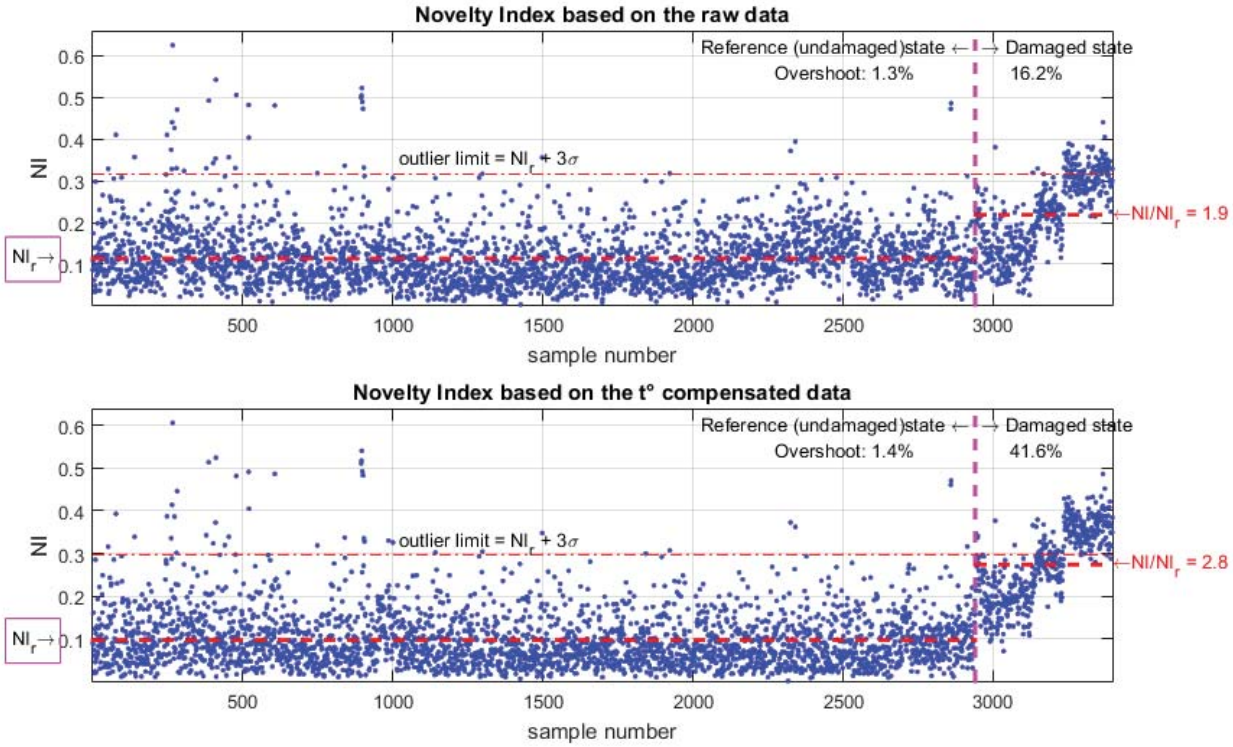

Figure 9: Damage detection by Novelty Index – Euclidean norm, Z24 bridge

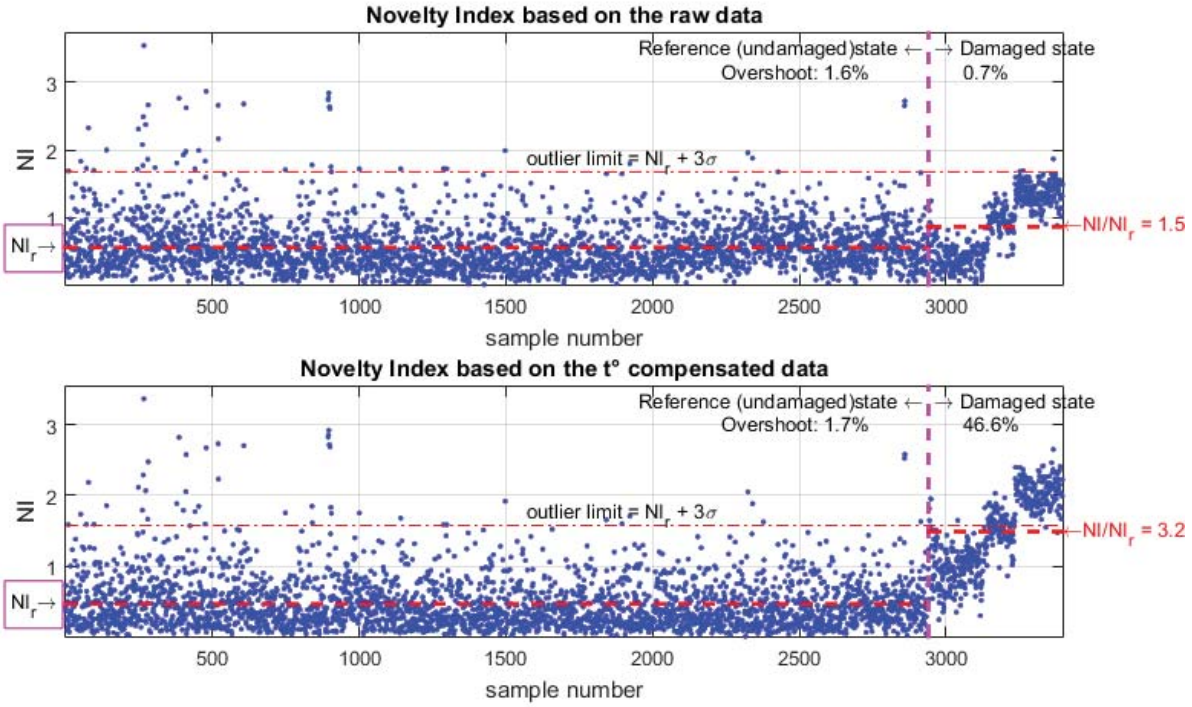

Figure 10: Damage detection by Novelty Index – Mahalonobis norm, Z24 bridge

The present paper does not propose a new damage index, but focuses directly on eigenfrequencies identified from vibrational tests. A two-step procedure is proposed based on measured physical sensitivity and on de-noising by PCA. The technique's efficiency could be proved by its application to two real bridges.

REFERENCES

[1] Lloyd, G.M., Wang, M.L., Wang, X. (2004), Thermomechanical analysis of long-term global modal and local deformation measurement of the Kishwaukee Bridge using the bootstrap, Earthquake engineering and engineering vibration, 05, 3(1), pp.107-115.

[2] Magalhães, F., Cunha, A. A.M.F., De Sa Caetano, E. (2012), Vibration based structural health monitoring of an arch bridge: From automated OMA to damage detection, Mechanical Systems and Signal Processing 28, DOI: 10.1016/j.ymssp.2011.06.011.

[3] Cury, A., Cremona, C., Dumoulin, J. (2012), Long-term monitoring of a PSC box girder bridge: Operational modal analysis, data normalization and structural modification assessment, Mechanical Systems and Signal Processing, Volume 33, pp. 13-37.

[4] Nguyen V. H., Schommer S., Maas S., Zürbes A. (2016), Static load testing with temperature compensation for structural health monitoring of bridges, Engineering Structures 127, pp. 700-718.

[5] Huth, O., Feltrin G., Maeck J., Kilic N. and Motavalli M. (2005), Damage Identification Using Modal Data: Experiences on a Prestressed Concrete Bridge, Journal of Structural Engineering, Volume 131 Issue 12.

[6] Reynders, E., De Roeck G., Bakir, P. G. and Sauvage, C. (2007), Damage Identification on the Tilft Bridge by Vibration Monitoring Using Optical Fiber Strain Sensors, Journal of Engineering Mechanics, Volume 133 Issue 2.

[7] Reynders, E., De Roeck G. (2010), A local flexibility method for vibration-based damage localization and quantification, Journal of sound and vibration, Volume 329, Issue 12, pp. 2367-2383.

[8] Schommer S., Nguyen V. H., Maas S., Zuerbes A. (2017), Model updating for structural health monitoring using static and dynamic measurements, X International Conference on Structural Dynamics, EURODYN 2017, Procedia Engineering.

[9] Yan, A. M., Kerschen, G., De Boe, P., Golinva, J.-C. (2005), Structural damage diagnosis under varying environmental conditions, Part I, Mechanical Systems and Signal Processing 19, pp. 847-880.

[10] Nguyen, V. H., Mahowald, J., Schommer, S., Maas, S. (2017), A study of temperature and aging effects on eigenfrequencies of concrete bridges for health monitoring, Engineering, Volume 9, No.5, 2017.

[11] Peeters, B., Maeck, J., De Roeck, G. (2010), Dynamic Monitoring Of The Z24-Bridge: Separating Temperature Effects From Damage, Proceeding of the European COST F3 Conference on System Identification and Structural Health Monitoring, pp. 377-386.

[12] Teughels, A., De Roeck, G. (2003), Structural damage identification of the highway bridge Z24 by FE model updating, Journal of Sound and Vibration 278, pp. 589-610.

[13] Reynders E. , Wursten G. and De Roeck G. (2014), Output-only structural health monitoring in changing environmental conditions by means of nonlinear system identification, Structural Health Monitoring, 13(1):82-93.

EURODYN 2020
XI International Conference on Structural Dynamics
M. Papadrakakis, M. Fragiadakis, C. Papadimitriou (eds.)
Athens, Greece, 23–26 November 2020

DISCUSSION ON ILL-POSED PROBLEM IN DRIVE-BY PAVEMENT ROUGHNESS IDENTIFICATION

S. Hasegawa[1], C.W. Kim[2], K. C. Chang[2], and N. Toshi[1]

[1] Department of Civil and Earth Resources Engineering, Kyoto University, Japan
e-mail: {hasegawa.soichiro.43c, toshi.naoya.88n}@st.kyoto-u.ac.jp

[2] Department of Civil and Earth Resources Engineering, Kyoto University, Japan
e-mail: {kim.chulwoo.5u, chang.kaichun.4z}@kyoto-u.ac.jp

Keywords: Identification, Pavement roughness, Inverse problem, Accelerometer

Abstract. *Pavement roughness profile is one of the important factors for bridge and road health monitoring and there is a variety of methods to measure pavement roughness profile. Laser displacement sensors have been commonly used for measuring pavement roughness profile and they are attached on a measurement vehicle. However, a laser displacement sensor is relatively expensive than an accelerometer. Therefore, methods to identify pavement roughness profile by using accelerometers attached on the measurement car have been developed and relevant studies become more and more popular in recent years. The identification of pavement roughness profile is a challenging task as an inverse problem, especially which is so-called ill-posed problem. In an ill-posed problem, a slight change in the measurement data has a great effect on identification accuracy. In this paper, the accuracy of several methods for identification of pavement roughness profile using only accelerometers attached on the measurement car is investigated utilizing both data from simulation and experiment.*

1 INTRODUCTION

Pavement roughness profile is one of the important indicators which represents conditions of roads or bridges. If a pavement roughness on a road is very rough, vehicles which run on the pavement are more easily vibrated than on a smooth pavement and would worsen the pavement condition. It is a vicious cycle, and appropriate monitoring and repairment are needed to avoid the vicious cycle. By keeping pavement roughness profile as smooth as possible, not only riding comfortability of cars but also a lifespan of roads and bridges can be increased [1].

There are several methods to measure pavement roughness profile. The basic one is direct and manual measurement, such as a profilometer which measures pavement roughness profile by laser displacement sensors and it needs to be run manually. It is an accurate method but takes much work. Therefore a measurement car, which can measure pavement roughness profile utilizing laser displacement sensors has been developed. There is another method to measure the vehicle axle forces directly and convert them to pavement roughness profile. Those direct measurement methods are reviewed in [2]. The direct method utilizing a measurement car has high accuracy and less labor, though the measurement car is a costly pavement measuring method. In recent years, methods to estimate pavement roughness profile utilizing accelerations on a running vehicle have been studied to reduce labor and cost while satisfying accuracy. The method using acceleration of a running vehicle, which is so-called a drive-by method [3], has been studied not only to estimate pavement roughness profile but also to detect change in dynamic parameters [4 - 6] of bridges. However, it is hard to secure higher accuracy in identification by means of the drive-by method, since the input data is only acceleration data which leads to an ill-posed condition in the inverse problem.

One of the ways to identify pavement roughness profile is to estimate the vehicle dynamic forces first, and next obtain the pavement roughness profile by solving a differential equation which represents a relationship between the vehicle dynamic forces and the pavement roughness profile. The estimated dynamic vehicle forces by the first step are useful information not only for estimating pavement roughness profile but also for bridge damage detection in terms of the drive-by bridge inspection. There are several researches relevant to identification of vehicle dynamic forces. Moving Force Identification algorithm (MFI) [7], especially adapting Tikhonov regularization [8], is one of the effective methods. Some numerical studies have been reported for the MFI using measured acceleration data on a moving vehicle [3], [9]. However, only limit number of studies consider experimental data [10 - 11]. Kalman filter method [12] for vehicle dynamic force identification also has been developed [12 - 14], which is an effective way especially if acceleration and angular velocity of vehicle are measured [13].

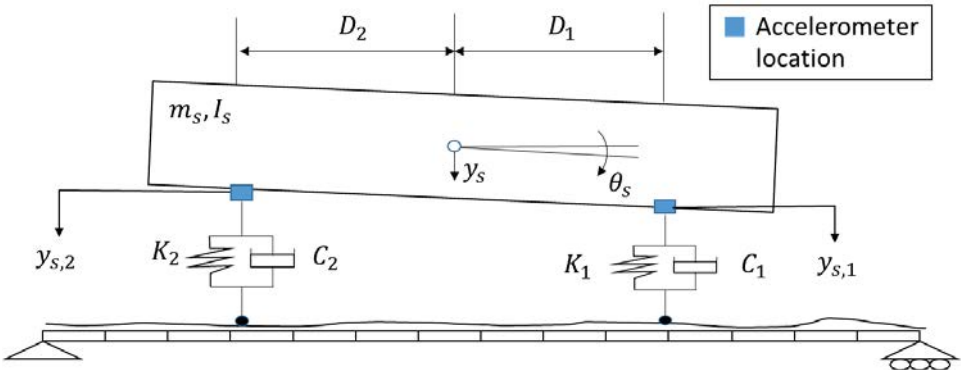

Figure 1: 2 DOF vehicle model scheme.

Geometry (m)	Axle spacing	2.72
	Front axle - centroid	0.8225
	Rear axle – centroid	1.8975
Mass moment of inertia ($kg \cdot m^2$)		3954
Mass (kg)	Total	1994
	Front axle	1391
	Rear axle	603
Suspension spring constant (N/m)	Front axle	75749
	Rear axle	99646
Suspension damping coefficient ($N \cdot s/m$)	Front axle	12535
	Rear axle	3602

Table 1: Vehicle properties.

This study utilizes the method to estimate dynamic vehicle forces in identification of pavement roughness profile. Several methods are investigated and compared focusing on economics of the methods which utilize only accelerometers on the test vehicle. Both numerical and experimental accelerations are considered in the pavement roughness profile identification, and the accuracy of identification results is assessed by an error function and power spectral density (PSD). This paper consists of five sections including Introduction. Identification methods are explained in Section 2 in detail. Section 3 describes pavement roughness profile identification from simulated accelerations and relevant discussions. Pavement roughness profile identification utilizing measured accelerations from a field experiment is discussed in Section 4. Finally, the section of "CONCLUSIONS" summarizes observations.

2 IDENTIFICATION METHOD

2.1 Vehicle model

A vehicle model used in this paper is a two degree-of-freedom half-car model and a scheme of the vehicle model is shown in Figure 1. Properties of the vehicle utilized in pavement roughness profile identification is shown in Table 1. "X-trail" by Nissan Motor Co., Ltd is used during the field experiment as well as in the simulation. A free vibration test was also conducted to determine vehicle properties.

2.2 Method

A pavement roughness profile is identified utilizing accelerations of bounce and pitch motions of the moving vehicle. Here accelerations of bounce and pitch motions at the center of gravity of the vehicle body are estimated utilizing bounce accelerations measured at vehicle floor on the front and rear axles. This study adopts five minimization schemes for the pavement roughness profile identification, and the identification accuracy of each scheme is discussed. Features of those five schemes are summarized in Table 2. Those five schemes are named as DP+LC, PIM+LC, PIM +EM, PIM +LC(L1) and KF, respectively. A least square minimization with L_2 norm regularization, which is so-called Tikhonov regularization, is applied in DP+LC, PIM+LC, and PIM +EM. A least square minimization with L_1 norm as regularization term, which is called as lasso regression, is applied in PIM+LC(L1). A difference between DP and PIM is how to solve the least square minimization. In the DP the least square minimization is solved by dynamic programming [15], and in PIM it is solved by using a pseudo-inverse matrix [16 - 17]. In KF, Kalman filter is applied.

	Basic method	Solution	Regularization parameter determination	Regularization term
DP+LC	Least square minimization	Dynamic programming	L-curve	L_2 norm
PIM+LC	Least square minimization	Pseudo inverse matrix	L-curve	L_2 norm
PIM+EM	Least square minimization	Pseudo inverse matrix	EM algorithm	L_2 norm
PIM+LC (L1)	Least square minimization	Iterative thresholding algorithm	L-curve	L_1 norm
KF	Kalman filter	-	-	-

Table 2: Features of five minimization schemes

In all schemes, vehicle dynamic forces are identified first and in the next step the pavement roughness profile is obtained by solving a differential equation for the relationship between vehicle dynamic forces and pavement roughness profile. Displacements under the front and rear tires of the moving vehicle are estimated by those five schemes. If the vehicle is running on a road, estimated displacements under the tires are equal to estimated pavement roughness profile. Details of each method in Table 2 are explained in the following sub sections.

2.3 DP+LC

Dynamic equation of motion of a vehicle is written as Equation (1).

$$\boldsymbol{M}_v\ddot{\boldsymbol{y}}_v + \boldsymbol{C}_v\dot{\boldsymbol{y}}_v + \boldsymbol{K}_v\boldsymbol{y}_v = \boldsymbol{f}_v \tag{1}$$

where $\boldsymbol{M}_v$, $\boldsymbol{C}_v$ and $\boldsymbol{K}_v$ are matrices of mass, damping and stiffness of 2DOF vehicle respectively. $\boldsymbol{y}_v$ contains vehicle displacements relevant to bounce and pitch motions. Dots above variables stand for derivative. $\boldsymbol{f}_v$ is the force vector applied to vehicle, which is generated by pavement roughness profile and its first derivative, and can be written as Equation (2).

$$\boldsymbol{f}_v = \begin{Bmatrix} \sum_{i=1}^{2}(K_i w_i + C_i \dot{w}_i) \\ -\sum_{i=1}^{2}(-1)^i D_i(K_i w_i + C_i \dot{w}_i) \end{Bmatrix} \tag{2}$$

where w_i, K_i and C_i represent pavement roughness profile, spring constant and damping coefficient respectively. The subscription i is the operator to denote front and rear axles, i.e. i=1 is the front axle and i=2 is the rear axle. D_i is the distance from the centroid of the vehicle body to each suspension. The equation of motion of the vehicle can be rewritten in terms of the state-space representation as Equation (3).

$$\dot{\boldsymbol{X}} = \boldsymbol{A}\boldsymbol{X} + \overline{\boldsymbol{f}_v} \tag{3}$$

$\boldsymbol{X}$, $\boldsymbol{A}$ and $\overline{\boldsymbol{f}_v}$ are defined as shown in Equation (4).

$$\boldsymbol{X} = \begin{Bmatrix} \boldsymbol{y}_v \\ \dot{\boldsymbol{y}}_v \end{Bmatrix}, \quad \boldsymbol{A} = \begin{bmatrix} \boldsymbol{0} & \boldsymbol{I} \\ -\boldsymbol{M}_v^{-1}\boldsymbol{K}_v & -\boldsymbol{M}_v^{-1}\boldsymbol{C}_v \end{bmatrix}, \quad \overline{\boldsymbol{f}_v} = \begin{bmatrix} \boldsymbol{0} \\ \boldsymbol{M}_v^{-1}\boldsymbol{f}_v \end{bmatrix} \tag{4}$$

Equation (4) is converted to time series representation as Equations (5), (6) and (7) by solving the differential equation in Equation (3). *h* is a time step. The subscription *j* stands for a discretized time index.

$$\boldsymbol{X}_{j+1} = \boldsymbol{M}\boldsymbol{X}_j + \boldsymbol{G}\boldsymbol{g}_j \quad ; \; j = 1, \; \ldots, \; N \tag{5}$$

$$\boldsymbol{M} = e^{\boldsymbol{A}h} \tag{6}$$

$$\boldsymbol{G} = \left(\boldsymbol{A}^{-1}(\boldsymbol{M} - \boldsymbol{I})\right)\begin{bmatrix}\boldsymbol{0} \\ \boldsymbol{M}_v^{-1}\boldsymbol{I}\end{bmatrix} \tag{7}$$

where $\boldsymbol{g}_j$ is the vehicle dynamic force vector, which is identification target of dynamic programming. Furthermore, a new state vector and state-space model are defined as Equations (8) and (9) respectively.

$$\widehat{\boldsymbol{X}}_{j+1} = \begin{bmatrix}\boldsymbol{M} & \boldsymbol{G} \\ \boldsymbol{0} & \boldsymbol{I}\end{bmatrix}\widehat{\boldsymbol{X}}_j + \begin{bmatrix}\boldsymbol{0} \\ \boldsymbol{I}\end{bmatrix}\dot{\boldsymbol{g}}_j \quad ; \quad j = 1, \; \ldots, \; N \tag{8}$$

$$\widehat{\boldsymbol{X}}_j = [\boldsymbol{X}_j \quad \boldsymbol{g}_j]^T \tag{9}$$

A least square minimization problem is formulated as Equation (10) using $\widehat{\boldsymbol{X}}_j$ and $\dot{\boldsymbol{g}}_j$.

$$Err\left(\widehat{\boldsymbol{X}}_k, \dot{\boldsymbol{g}}_k\right) = \sum_{k=1}^{m}\left\{\left((\boldsymbol{d}_k - \boldsymbol{Q}\widehat{\boldsymbol{X}}_k), (\boldsymbol{d}_k - \boldsymbol{Q}\widehat{\boldsymbol{X}}_k)\right) + (\dot{\boldsymbol{g}}_k, \boldsymbol{B}\dot{\boldsymbol{g}}_k)\right\} \tag{10}$$

Here $\boldsymbol{d}_j$ is measured acceleration data, $\boldsymbol{Q}$ is a selection matrix to relate $\boldsymbol{d}_j$ and $\widehat{\boldsymbol{X}}_j$. The subscription m stands for bounce and pitch motions. (*x*, *y*) means outer product of *x* and *y*. $\boldsymbol{B}$ contains the regularization parameter as $\mathbf{B} = \lambda\mathbf{I}$ and λ is the regularization parameter which keeps a balance between first and second term's volume. The optimal value of λ can be obtained by the L-curve method [18]. In the L-curve method, candidates of λ are prepared at first. In the next step, E_{norm} and F_{norm} are calculated for each of prepared λ. E_{norm} and F_{norm} can be written as shown in Equations (11) and (12), and they are plotted on a log-log graph, then curvature of L-curve is calculated. At the point which has the maximum curvature, optimal regularization parameter value is obtained. Here E_{norm} and F_{norm} for each λ are obtained by solving Equation (10) by means of dynamic programming. Details on the dynamic programming are shown in [10, 11].

$$E_{norm} = \sqrt{\sum_{k=1}^{m}\left((\boldsymbol{d}_k - \boldsymbol{Q}\widehat{\boldsymbol{X}}_k), (\boldsymbol{d}_k - \boldsymbol{Q}\widehat{\boldsymbol{X}}_k)\right)} \tag{11}$$

$$F_{norm} = \sqrt{\sum_{k=1}^{m}(\dot{\boldsymbol{g}}_k, \dot{\boldsymbol{g}}_k)} \tag{12}$$

By the L-curve method, the optimal λ value, estimated $\widehat{\boldsymbol{X}}_j$ and $\dot{\boldsymbol{g}}_j$ are obtained. $\boldsymbol{g}_j$ is also estimated utilizing $\dot{\boldsymbol{g}}_j$**.** Finally, pavement roughness profile is obtained by solving the differential Equation (2) by means of the 4th Runge-Kutta method, substituting estimated $\boldsymbol{g}_j$ as $\boldsymbol{f}_v$.

2.4 PIM+LC

In PIM+LC, unknown parameters are defined as Equation (13) and measured data are defined as Equation (14). Here $\mathbf{y}_{v,1}$ is a 2×1 matrix and includes displacements for the bounce and pitch motions of the vehicle.

$$\boldsymbol{x} = \begin{bmatrix} \dot{\boldsymbol{g}}_1{}^T & \dot{\boldsymbol{g}}_2{}^T & \cdots & \dot{\boldsymbol{g}}_N{}^T \end{bmatrix}^T \tag{13}$$

$$\boldsymbol{y} = \begin{bmatrix} \boldsymbol{y}_{v,1}{}^T & \boldsymbol{y}_{v,2}{}^T & \cdots & \boldsymbol{y}_{v,N}{}^T \end{bmatrix}^T \tag{14}$$

A least square minimization problem is formulated as Equation (15).

$$L_2 = \min_{\boldsymbol{x}} \{ \|\boldsymbol{y} - \boldsymbol{H}\boldsymbol{x}\|_2^2 + \lambda \|\boldsymbol{x}\|_2^2 \} \tag{15}$$

Here $\boldsymbol{H}$ is a model matrix, which is represented by Equation (16) where K and T are defined as Equation (17).

$$\boldsymbol{H} = \begin{bmatrix} \boldsymbol{QT} & \boldsymbol{0} & \cdots & \boldsymbol{0} & \boldsymbol{0} \\ \boldsymbol{QKT} & \boldsymbol{QT} & \cdots & \boldsymbol{0} & \boldsymbol{0} \\ \vdots & \vdots & \ddots & \vdots & \vdots \\ \boldsymbol{QK}^{N-2}\boldsymbol{T} & \boldsymbol{QK}^{N-3}\boldsymbol{T} & \cdots & \boldsymbol{QT} & \boldsymbol{0} \\ \boldsymbol{QK}^{N-1}\boldsymbol{T} & \boldsymbol{QK}^{N-2}\boldsymbol{T} & \cdots & \boldsymbol{QKT} & \boldsymbol{QT} \end{bmatrix} \tag{16}$$

$$\boldsymbol{K} = \begin{bmatrix} \boldsymbol{M} & \boldsymbol{G} \\ \boldsymbol{0} & \boldsymbol{I} \end{bmatrix}, \quad \boldsymbol{T} = \begin{bmatrix} \boldsymbol{0} \\ \boldsymbol{I} \end{bmatrix} \tag{17}$$

Under the assumption that initial conditions are defined as Equation (18), the solution of the least square minimization is obtained as Equation (19).

$$\boldsymbol{X}_0 = [\boldsymbol{0} \quad \boldsymbol{0} \quad \boldsymbol{0} \quad \boldsymbol{0}]^T, \quad \boldsymbol{g}_0 = [\boldsymbol{0} \quad \boldsymbol{0}]^T \tag{18}$$

$$\boldsymbol{x}_{est,LC} = (\boldsymbol{H}^T\boldsymbol{H} + \lambda \boldsymbol{I})^{-1}\boldsymbol{H}^T\boldsymbol{y} \tag{19}$$

where $\boldsymbol{y}$ indicates measured data. Optimal value of λ is obtained by the L-curve method, and finally pavement roughness profile is obtained by solving Equation (2) by means of the 4th Runge-Kutta method.

2.5 PIM+EM

The PIM+EM is basically same with PIM+LC, but the only difference is how to determine the optimal value of regularization parameter λ. In PIM+EM the optimal λ is determined by the EM algorithm [19] while L-curve method is used in PIM+LC. In the EM algorithm, unknown and measured parameters are treated as random variables which follow a normal distribution. A relationship between $\boldsymbol{x}$ and $\boldsymbol{y}$ are modeled as Equation (20).

$$\boldsymbol{y} = \boldsymbol{H}\boldsymbol{x} + \boldsymbol{\varepsilon} \tag{20}$$

The matrix $\boldsymbol{H}$ is same with Equation (16). $\boldsymbol{\varepsilon}$ indicates a noise which follows a normal distribution as Equations (21) and (22).

$$\boldsymbol{\varepsilon} \sim N(\boldsymbol{\varepsilon}|\boldsymbol{0}, \boldsymbol{\Lambda}^{-1}) \tag{21}$$

$$\boldsymbol{\Lambda} = \beta \boldsymbol{I} \tag{22}$$

$\boldsymbol{\Lambda}$ is inverse covariance matrix of the noise. A prior distribution of $\boldsymbol{x}$ is defined as Equations (23) and (24), which follows normal distribution.

$$f(\boldsymbol{x}) \sim N(\boldsymbol{x}|\boldsymbol{\mu}, \boldsymbol{v}^{-1}) \tag{23}$$

$$\boldsymbol{v} = \alpha \boldsymbol{I} \tag{24}$$

There are two steps in the EM algorithm, which are called E step and M step and these two steps are conducted alternatively until estimated parameters converge. In the E step, estimated unknown parameters are calculated utilizing α and β in Equation (25).

$$\boldsymbol{x}_{est,EM} = \left(\boldsymbol{H}^T\boldsymbol{H} + \frac{\alpha}{\beta}\boldsymbol{I}\right)^{-1}\boldsymbol{H}^T\boldsymbol{y} \tag{25}$$

An inverse covariance matrix of $\boldsymbol{x}_{est,EM}$ is estimated by Equation (26).

$$\boldsymbol{\Gamma} = \alpha\boldsymbol{I} + \beta\boldsymbol{H}^T\boldsymbol{H} \tag{26}$$

In the algorithm, an initial value of $\boldsymbol{\Gamma}$ should be defined before iterative calculation starts. In the M step, α and β values are updated by using $\boldsymbol{x}_{est,EM}$ and $\boldsymbol{\Gamma}$ as Equations (27) and (28).

$$\alpha^{-1} = \frac{1}{N}\left[\left\|\boldsymbol{x}_{est,EM}\right\|_2^2 + tr(\boldsymbol{\Gamma}^{-1})\right] \tag{27}$$

$$\beta^{-1} = \frac{1}{M}[\|\boldsymbol{y} - \boldsymbol{H}\boldsymbol{x}\|_2^2 + tr(\boldsymbol{H}^T\boldsymbol{H}\boldsymbol{\Gamma}^{-1})] \tag{28}$$

Repeating the E step and M step alternatively, we can identify unknown parameters by Equation (25) with converged α and β. Pavement roughness profile is obtained by solving Equation (2) by means of the 4th Runge-Kutta method with identified vehicle forces.

2.6 PIM+LC(L1)

In PIM+LC(L1) unknown parameter $\boldsymbol{x}$, measured data $\boldsymbol{y}$ and initial parameters $\mathbf{X}_0$, $\mathbf{g}_0$ are defined as well as PIM+LC. However, a regularization term of the least square minimization becomes different. In PIM+LC(L1), a least square minimization problem is formulated as Equation (29).

$$L_1 = \min_{\boldsymbol{x}}\{\|\boldsymbol{y} - \boldsymbol{H}\boldsymbol{x}\|_2^2 + \lambda\|\boldsymbol{x}\|_1\} \tag{29}$$

It is difficult to obtain an analytical solution of Equation (29) because a regularization term takes absolute value of unknown parameters. Therefore an iterative thresholding algorithm is adopted in order to obtain an approximated solution. In the iterative thresholding algorithm, the least square minimization which has a form as shown in Equation (30) is newly defined in order to make the solution obtainable.

$$L_{new} = \min_{\boldsymbol{x}}\{\|\boldsymbol{y}_{new} - \boldsymbol{x}\|_2^2 + \lambda\|\boldsymbol{x}\|_1\} \tag{30}$$

Equation (31) is a surrogate function which removes $\boldsymbol{H}$ from Equation (29) and help converting Equation (29) to Equation (30). Equation (31) considers any $\boldsymbol{x}_t$ as an input.

$$G(\boldsymbol{x}, \boldsymbol{x}_t) = L_1(\boldsymbol{x}_t) + \sum_{j=1}^{N}\frac{dL_1(x_{t,j})}{dx_j}(x_j - x_{t,j}) + \frac{\rho}{2}\|\boldsymbol{x} - \boldsymbol{x}_t\|_2^2 \tag{31}$$

where ρ is a learning rate of the iterative calculation. Equation (31) can be rewritten as Equation (32).

$$G(\boldsymbol{x}, \boldsymbol{x}_t) = \frac{\rho}{2}\sum_{j=1}^{N}\left\{\left(x_{t,j} - \frac{1}{\rho}\frac{dL_1(x_{t,j})}{dx_j}\right) - x_j\right\}^2 + const. \tag{32}$$

The support function $G(\boldsymbol{x}, \boldsymbol{x}_t)$ has following two characteristics: $G(\boldsymbol{x}, \boldsymbol{x}_t)$ crosses with $L_1(\boldsymbol{x})$ at $\boldsymbol{x} = \boldsymbol{x}_t$; $L_1(\boldsymbol{x}) \leq G(\boldsymbol{x}, \boldsymbol{x}_t)$ for any $\boldsymbol{x}$.
By using $G(\boldsymbol{x}, \boldsymbol{x}_t)$, a new least square minimization problem is formulated as Equation (33).

$$\boldsymbol{x}_{tu} = \underset{\boldsymbol{x}}{\operatorname{argmin}}(G(\boldsymbol{x}, \boldsymbol{x}_t) + \lambda \|\boldsymbol{x}\|_1) \tag{33}$$

$\boldsymbol{x}_{tu}$ is a solution of the least square minimization. The solution of Equation (33) is shown in Equation (34), which is given by a soft thresholding function S_λ.

$$x_{tu,i} = S_\lambda \left(x_{t,j} - \frac{1}{\rho} \frac{dL_1(x_{t,j})}{dx_j} \right) \tag{34}$$

Equation (34) can be expressed as Equation (35).

$$\boldsymbol{x}_{tu} = S_\lambda \left(\boldsymbol{x}_t + \frac{1}{\rho} \boldsymbol{A}^T (\boldsymbol{y} - \boldsymbol{H}\boldsymbol{x}) \right) \tag{35}$$

The soft thresholding function S_λ is defined as Equation (36) for any p.

$$S_\lambda(p) = \begin{cases} p + \lambda & (p < -\lambda) \\ 0 & (-\lambda \leq p \leq \lambda) \\ p - \lambda & (p > \lambda) \end{cases} \tag{36}$$

Again $1/\rho$ denotes a learning rate of repetitive calculation and the value of $1/\rho$ is defined as Equation (37).

$$\frac{1}{\rho} = \frac{1}{\max_j \sum_i \left| \boldsymbol{H}^T \boldsymbol{H}_{ij} \right|} \tag{37}$$

Until convergence Equation (35) is repetitively calculated and $\boldsymbol{x}$ is updated. Once it converged, estimated $\boldsymbol{x}$ is obtained. Details about all process of iterative thresholding algorithm can be confirmed in [20]. The optimal value of the regularization parameter λ is obtained by the L-curve method as well as DP+LC. Finally pavement roughness profile is obtained by solving Equation (2) by means of the 4th Runge-Kutta method.

2.7 KF

In KF, unknown vehicle dynamic forces are estimated by the Kalman filter. Unknown parameters and state-space model are defined as Equations (38) and (39).

$$\boldsymbol{z}_j = \left[\boldsymbol{y}_{v,j}{}^T \quad \dot{\boldsymbol{y}}_{v,j}{}^T \quad \ddot{\boldsymbol{y}}_{v,j}{}^T \quad \boldsymbol{g}_j{}^T \right]^T \tag{38}$$

$$\boldsymbol{z}_{j+1} = \boldsymbol{S}\boldsymbol{z}_j + \boldsymbol{U}\boldsymbol{\varepsilon}_{s,j} \;\; ; \;\; j = 1, \;\; \ldots, \;\; N \tag{39}$$

$\boldsymbol{S}$ is obtained by applying Wilson-θ method to Equation (1), and how to derive $\boldsymbol{S}$ and $\boldsymbol{U}$ can be confirmed in [21]. The state-space model includes system noise term since unknown parameters and measurement data are treated as random parameters in the Kalman filter. System noise is assumed to follow a normal distribution as Equation (40).

$$\boldsymbol{\varepsilon}_s \sim N(\boldsymbol{\varepsilon}_s | \boldsymbol{0}, \boldsymbol{P}) \tag{40}$$

Here system noise is only applied to 1st derivative of vehicle forces and it is treated as a driving noise of the whole system. Measurement noise is also introduced and a relationship between

unknown parameters and measurement data is defined as Equation (41). Measurement noise follows normal distribution as Equation (42).

$$\boldsymbol{d}_j = \boldsymbol{H}\boldsymbol{z}_j + \boldsymbol{\varepsilon}_{m,j} \tag{41}$$

$$\boldsymbol{\varepsilon}_m \sim N(\boldsymbol{\varepsilon}_m | \boldsymbol{0}, \boldsymbol{R}) \tag{42}$$

At first it is needed to set up initial values of inverse covariance matrices $\boldsymbol{P}$, $\boldsymbol{R}$, and $\boldsymbol{W}$. Here $\boldsymbol{W}$ is an covariance matrix of state vector $\boldsymbol{z}_j$. The main process of the Kalman filter includes two steps as follows.

(a) Prediction step

- Utilizing $\boldsymbol{z}_j$, estimate a state vector of the next step, $\bar{\boldsymbol{z}}_{j+1}$ by Equation (43). (Prior prediction)
- Calculate the inverse covariance matrix of $\bar{\boldsymbol{z}}_{j+1}$ by Equation (44). (Prior distribution)

(b) Modification step

- Calculate Kalman gain $\boldsymbol{K}_g$ by Equation (45).
- Modify the estimated state vector by Equation (46). (Posterior prediction)
- Modify the inverse covariance matrix of the state vector, $\widehat{\boldsymbol{W}}_{j+1}$ as Equation (47). (Posterior distribution)

$$\bar{\boldsymbol{z}}_{j+1} = \boldsymbol{K}\boldsymbol{z}_j \tag{43}$$

$$\boldsymbol{W}_{j+1} = \boldsymbol{S}\boldsymbol{W}_j\boldsymbol{S}^T + \boldsymbol{U}\boldsymbol{P}_j\boldsymbol{U}^T \tag{44}$$

$$\boldsymbol{K}_g = \boldsymbol{W}_{j+1}\boldsymbol{H}^T(\boldsymbol{H}^T\boldsymbol{W}_{j+1}\boldsymbol{H} + \boldsymbol{R})^{-1} \tag{45}$$

$$\hat{\boldsymbol{z}}_{j+1} = \bar{\boldsymbol{z}}_{j+1} + \boldsymbol{K}_g\left(\mathbf{d}_{j+1} - \boldsymbol{H}\bar{\boldsymbol{z}}_{j+1}\right) \tag{46}$$

$$\widehat{\boldsymbol{W}}_{j+1} = \left(\boldsymbol{I} - \boldsymbol{K}_g\boldsymbol{H}\right)\boldsymbol{W}_{j+1} \tag{47}$$

For each step from j=1 to j=N, (a)Prediction step and (b)Modification step are processed and $\hat{\boldsymbol{z}}_{j+1}$ can be obtained step by step. Then estimated $\boldsymbol{g}_j$ is extracted from $\hat{\boldsymbol{z}}_j$. Finally, pavement roughness profile is obtained by solving Equation (2) by means of the 4th Runge-Kutta method with using obtained $\boldsymbol{g}_j$.

3 DISCUSSION FROM SIMULATION

3.1 Setting

Accuracy of each method is compared utilizing simulated accelerations. 100 kinds of pavement roughness profiles are generated randomly, and all of them are categorized as rank A following ISO 8608. First, acceleration data are simulated utilizing generated 100 kinds of pavement roughness profiles and the vehicle whose properties are summarized in Table 1. Those simulated accelerations are assumed as measured data. Vehicle running speed is 10.8 m/s and sampling frequency is 100Hz. The Wilson-θ method was adopted to solve Equation (1) with $\theta = 1.420815$. Acceleration data is contaminated by measurement noise and the noise follows a normal distribution whose mean value is 0 and standard deviation is 1/5 of original measured data's standard deviation. For each of simulated acceleration data, pavement roughness profile is identified utilizing methods introduced in section 2. The range and interval of regularization parameters in the L-curve method are summarized in Table 3. Candidates of regularization parameters are expressed as a form of 10^n and by changing the value of n, an array

of candidates of regularization parameters is set up. An example of L-curve is shown in Figure 2.

For the EM algorithm of PIM+EM, initial values of α and β are defined as 0 and 1 respectively. A number of iterations of the EM algorithm is 300. For the KF, a setting of the parameters is shown in Table 4. Those parameters are determined by trial and error. In order to assess identification accuracy of each method, Effective Error Function (EEF) defined as equation (49) is used.

$$\mathrm{EEF} = \min_{a} \frac{1}{N} \sqrt{\sum_{l=1}^{N} \left(r_{true,l} - r_{est,l} - a \right)^2} \tag{48}$$

where r_{true} and r_{est} are true and estimated pavement roughness profile respectively. The identified pavement roughness profile means the identified displacement under the rear tire of the moving vehicle. Subscript l indicates a discrete distance index in vehicle running direction. Shift parameter a is introduced in order to measure the identification error more precisely than the normal RMSE (Root Mean Square Error). The range of shift parameter is from -10^2 to 10^2 and the interval is 10^{-5}.

3.2 Results and discussion

Table 5 shows average and standard deviation of the EEF for 100 identification results by each identification method. EEF of 100 pavement roughness profiles are shown in Figure 3. KF shows the maximum average EEF and PIM+LC(L1) shows the minimum average EEF among all schemes. An example of the identified pavement roughness profiles is shown in Figure 4.

When comparing EEF between DP+LC and PIM+LC, DP+LC showed smaller EEF value, while theoretically same solutions should be obtained by these two methods. A possible reason is that there are errors related to numerical calculation of inverse matrices and it leads to difference in optimal regularization parameter values. Especially PIM+LC includes a calculation of a large inverse matrix, which may lead to a greater error than DP+LC. In DP+LC, a total cost function is broken down into simpler sub-problems in a recursive manner and the process does not include the large size inverse matrix calculation. In terms of accuracy, DP+LC is better than PIM+LC, while PIM+LC has an advantage on simplicity. As already shown in Equation (19), the solution of PIM+LC is much simpler and easier to understand than that of DP+LC. Therefore, it can be said that PIM has much higher potential to be developed and improved than DP.

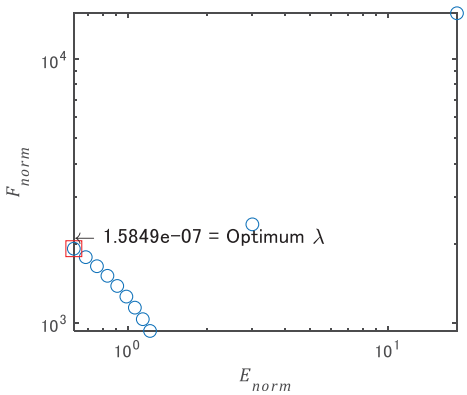

Figure 2: An example of L-curve

Method	Lower edge of n	Upper edge of n	Division interval of n
DP+LC	-7	-6	0.1
PIM+LC	-25	-15	0.1
PIM+LC(L1)	-19	-14	0.1

Table 3: Range of regularization parameter candidates in L-curve method in simulation discussion.

Initial value of state vector	$[0 \quad 0 \quad 0 \quad 0 \quad 0 \quad 0 \quad 0 \quad 0]^T$
Covariance matrix of system noise	$10^{-4} \times \boldsymbol{I_{2\times2}}$
Covariance matrix of measurement noise	$10^{-20} \times \boldsymbol{I_{2\times2}}$
Initial value of covariance matrix of state vector	$10^{-14} \times \boldsymbol{I_{8\times8}}$

Table 4: Initial parameters in KF.

	DP+LC	PIM+LC	PIM+EM	DP+LC(L1)	KF
Average	0.00115	0.00184	0.00183	0.00111	0.00203
Standard Deviation	0.00033	0.00106	0.00106	0.00041	0.00141

Table 5: Average and deviation of EFF of each method.

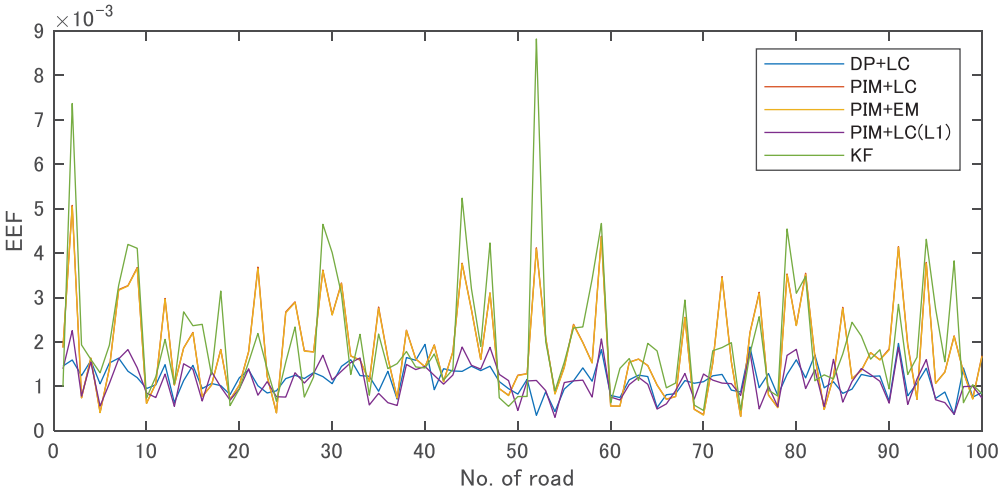

Figure 3 EEF of all methods for 100 pavement roughness profiles in simulation.

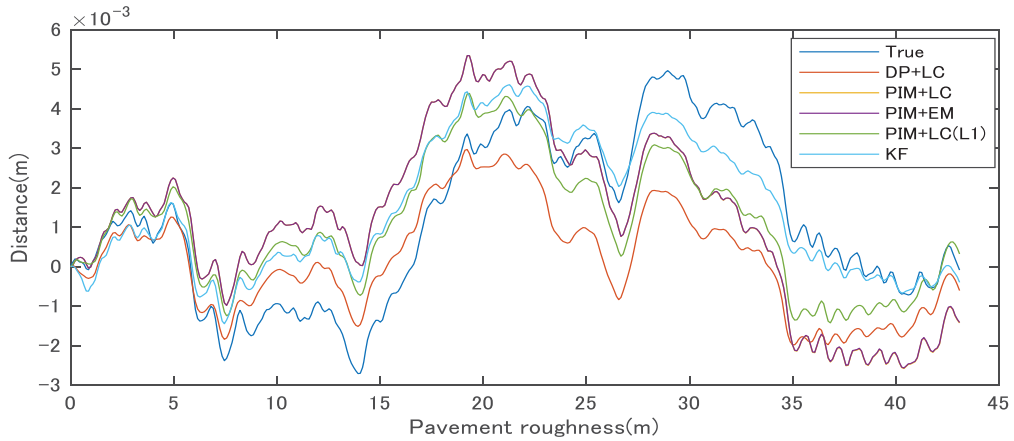

Figure 4: Example of identified pavement roughness profiles by each method.

When comparing EEF between PIM+LC and PIM+EM, little difference on EEF value was observed. The L-curve method needs much less time than the EM algorithm, therefore basically PIM+LC is better than PIM+EM considering calculation time. In comparison of EEFs between

DP+LC and PIM+LC(L1), no clear difference was observed, even though PIM+LC(L1) showed a little smaller EEF. However, PIM+LC(L1) needs more calculation time than DP+LC as PIM+LC(L1) takes an iterative calculation. When comparing EEF between DP+LC and KF, DP+LC resulted in much less EEF than KF. Standard deviation of EEF of DP+LC was smaller than KF. Therefore DP+LC was more accurate and stable method.

4 DISCUSSION FROM EXPERIMENT

4.1 Experimental setting

For further discussion about accuracy of each method, data from a field experiment were examined. In the field experiment, accelerations of the moving vehicle are measured, and then pavement roughness profile under the vehicle passage is identified. Accelerometers were installed at two points in the left side of the test vehicle. The measured acceleration data in the vertical direction are converted to acceleration for the bounce and pitch motions. Quartz sensors (M-A550AC2x by Seiko Epson Corporation) are used in the experiment. The sampling frequency of measurement was 200Hz. The target road was located on a steel plate girder bridge whose span length is 40.5m. An accurate pavement roughness profile is measured by a laser profilometer. This pavement roughness profile measured by the profilometer is called as "True" pavement roughness profile in this paper and compared with identified results. The pavement roughness profile was measured three times during the experiment and called as T1, T2 and T3 respectively.

Identified pavement roughness profiles by DP+LC and KF are compared with the true profile. Two methods were chosen since DP+LC showed higher accuracy and shorter calculation time in simulation based investigations, while KF adopts different concepts comparing to other methods. The range and interval of regularization parameters in the L curve method are shown in Table 6. Those parameters in KF to determine the experimental data are shown in Table 7. Vehicle running speeds for T1, T2 and T3 were about 2.9m/s, 3.2m/s and 3.0m/s respectively.

Method	Lower edge of n	Upper edge of n	Division interval of n
DP+LC	-6.19	-4	0.02

Table 6: Range of regularization parameter candidates in L-curve method in experimental discussion.

Initial value of state vector	$[0 \quad 0 \quad 0 \quad 0 \quad 0 \quad 0 \quad 0 \quad 0]^T$
Covariance matrix of system noise	$10^{-2} \times \boldsymbol{I}_{2\times2}$
Covariance matrix of measurement noise	$10^{-13} \times \boldsymbol{I}_{2\times2}$
Initial value of covariance matrix of state vector	$10^{-14} \times \boldsymbol{I}_{8\times8}$

Table 7: Initial parameters of KF in experimental discussion.

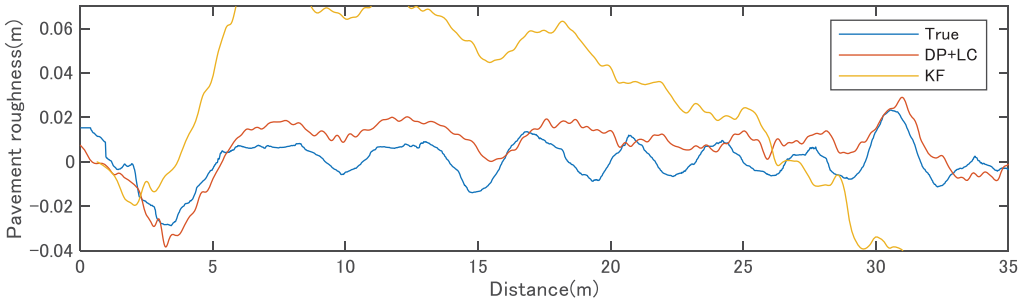

Figure 5: Identified pavement roughness profile in experiment (T1).

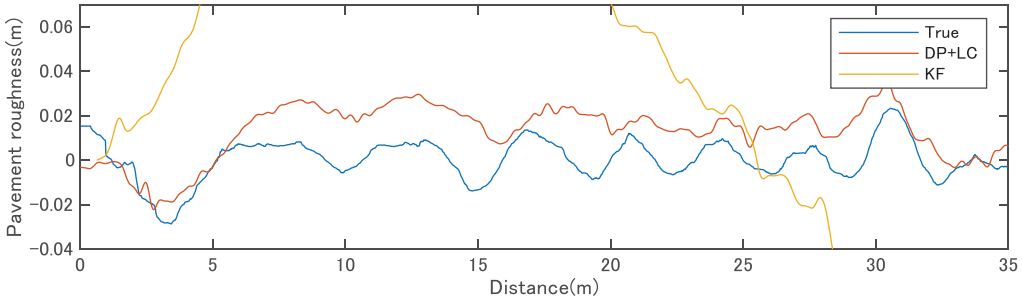

Figure 6: Identified pavement roughness profile in experiment (T2).

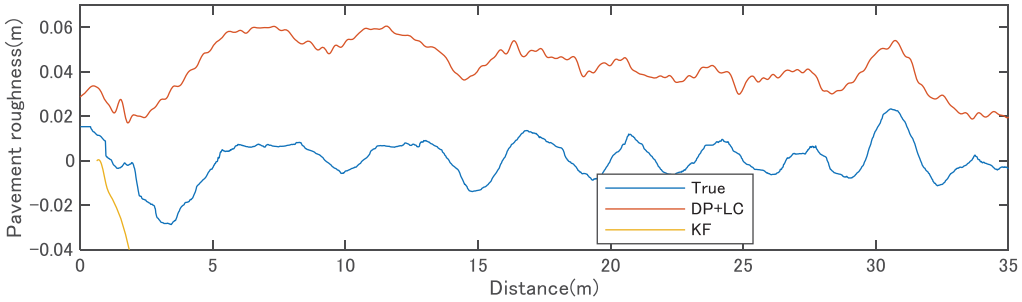

Figure 7: Identified pavement roughness profile in experiment (T3).

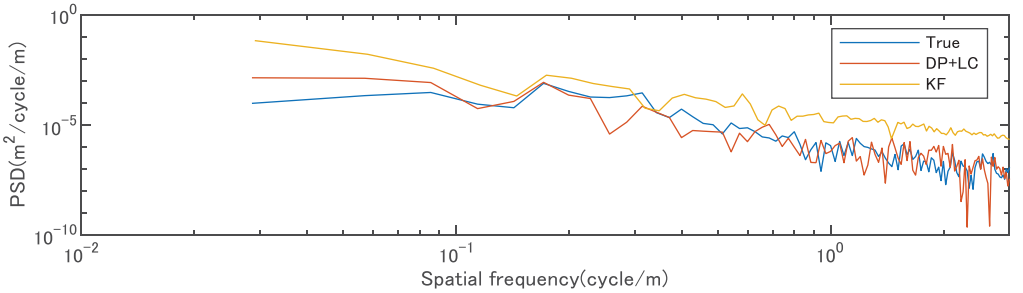

Figure 8: PSD of identified pavement roughness profile in experiment (T1).

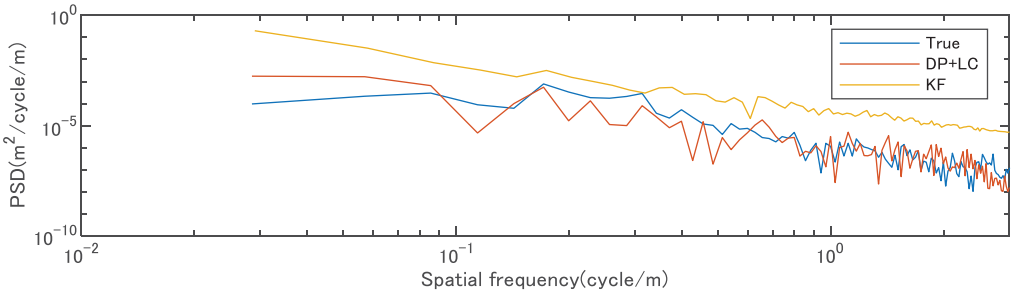

Figure 9: PSD of identified pavement roughness profile in experiment (T2).

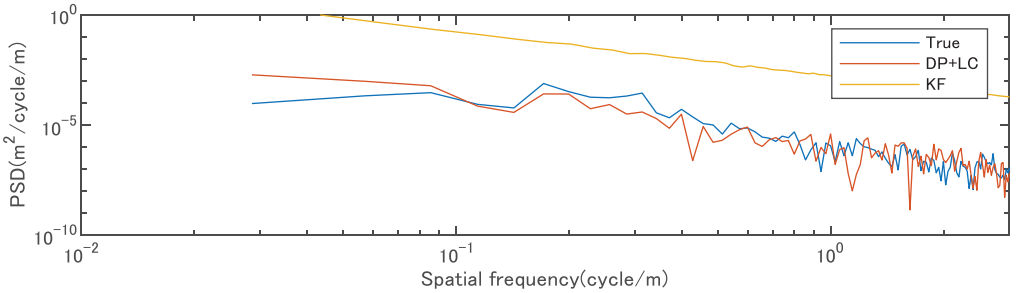

Figure 10: PSD of identified pavement roughness profile in experiment (T3).

4.2 Results and discussion

Identified pavement roughness profiles by DP+LC and KF are shown in Figures 5, 6 and 7 for T1, T2 and T3 respectively. The pavement roughness profiles are identified in good accuracy by DP+LC. However, KF resulted in poor identification of the pavement roughness profile. It is noted that running speeds were not constant during the experiment and as a result the location of true and identified pavement roughness profiles did not coincide with each other. Therefore, power spectral density (PSD) of the identified pavement roughness profiles are examined. PSD curves of identified pavement roughness profiles by DP+LC and KF are shown in Figures 8, 9 and 10 for T1, T2, and T3 respectively. PSD curves show that DP+LC has comparable results with the true one. On the other hand, the PSD of KF is completely different level from the true one. In the simulation, by KF, a rough shape of pavement roughness profile is identified even if the accuracy is worse.

5 CONCLUSIONS

From the discussion utilizing simulation data, observed results are summarized as follows.

- Dynamic Programming (DP) has a less identification error than Pseudo Inverse Matrix (PIM) method as the latter method includes a calculation of large size inverse matrix in the identification process.
- Little difference between L-curve method and EM algorithm was observed for determining the optimal regularization parameter value. It was also observed that the L-curve has less calculation time than EM algorithm.
- The least square minimization with L_1 norm (DP+LC(L1)) showed the most accurate identification result. However, it takes more calculation time than L_2 norm regularization as it needs repetitive calculation until the convergence of parameters.

From the discussion utilizing measured data from the field experiment, observed results are summarized as follows.

- DP+LC shows the reasonable accuracy of pavement roughness profile identification. Identified PSD is also comparable with the true.
- KF resulted in poor identification of the pavement roughness profile, which was far from expectation. The remaining task is to investigate reasons for the poor identification results by means of the Kalman filter.

REFERENCES

[1] M. F. Green and D. Cebon, “Dynamic interaction between heavy vehicles and highway bridges,” *Comput. Struct.*, vol. 62, no. 2, pp. 253–264, 1997, doi: 10.1016/S0045-7949(96)00198-8.

[2] L. Davis and J. Bunker, “Heavy Vehicle Suspensions: Testing and Analysis: A literature review,” *Book*, 2007.

[3] E. J. OBrien, P. J. Mcgetrick, and A. González, “A drive-by inspection system via vehicle moving force identification,” *Smart Struct. Syst.*, vol. 13, no. 5, pp. 821–848, 2014, doi: 10.12989/sss.2014.13.5.821.

[4] A. González, E. J. OBrien, and P. J. McGetrick, "Identification of damping in a bridge using a moving instrumented vehicle," *J. Sound Vib.*, vol. 331, no. 18, pp. 4115–4131, Aug. 2012, doi: 10.1016/J.JSV.2012.04.019.

[5] P. J. McGetrick, A. González, and E. J. OBrien, "Theoretical investigation of the use of a moving vehicle to identify bridge dynamic parameters," *Insight Non-Destructive Test. Cond. Monit.*, vol. 51, no. 8, pp. 433–438, 2009, doi: 10.1784/insi.2009.51.8.433.

[6] Y.-B. Yang, C. W. Lin, and J. D. Yau, "Extracting bridge frequencies from the dynamic response of a passing vehicle," *J. Sound Vib.*, vol. 272, no. 3–5, pp. 471–493, May 2004, doi: 10.1016/S0022-460X(03)00378-X.

[7] S. S. Law and Y. L. Fang, "Moving force identification: Optimal state estimation approach," *J. Sound Vib.*, vol. 239, no. 2, pp. 233–254, 2001, doi: 10.1006/jsvi.2000.3118.

[8] V. Y. A. N., Tikhonov, Arsenin, "Solutions of Ill-posed problems." Wiley, New York, United States, 1977.

[9] A. González, C. Rowley, and E. J. OBrien, "A general solution to the identification of moving vehicle forces on a bridge," *Int. J. Numer. Methods Eng.*, vol. 75, no. 3, pp. 335–354, 2008, doi: 10.1002/nme.2262.

[10] P. J. McGetrick, C.-W. Kim, A. Gonzalez, and E. J. Obrien, "Dynamic Axle Force and Road Profile Identification Using a Moving Vehicle," *Int. J. Archit. Eng. Constr.*, vol. 2, no. 1, pp. 1–16, 2013, doi: 10.7492/ijaec.2013.001.

[11] K. C. Chang, C. W. Kim, S. Hasegawa, S. Nakajima, and P. J. McGetrick, "Estimation of bridge surface profile from moving vehicle accelerations by means of moving force identification - an experimental field study," *Int. J. Lifecycle Perform. Eng.*, vol. 3, no. 3/4, pp. 289–309, 2019, doi: 10.1504/ijlcpe.2019.103698.

[12] R. E. Kalman, "A new approach to linear filtering and prediction problems," *J. Fluids Eng. Trans. ASME*, vol. 82, no. 1, pp. 35–45, 1960, doi: 10.1115/1.3662552.

[13] H. Wang, T. Nagayama, and D. Su, "Estimation of dynamic tire force by measurement of vehicle body responses with numerical and experimental validation," *Mech. Syst. Signal Process.*, vol. 123, pp. 369–385, 2019, doi: 10.1016/j.ymssp.2019.01.017.

[14] J. Dakhlallah, S. Glaser, S. Mammar, and Y. Sebsadji, "Tire-road forces estimation using extended Kalman Filter and sideslip angle evaluation," *Proc. Am. Control Conf.*, pp. 4597–4602, 2008, doi: 10.1109/ACC.2008.4587220.

[15] D. M. Trujillo, "Application of dynamic programming to the general inverse problem," *Int. J. Numer. Methods Eng.*, vol. 12, no. 4, pp. 613–624, 1978, doi: 10.1002/nme.1620120406.

[16] M. Cavacece, P. P. Valentini, and L. Vita, "Identification of modal damping ratios of four- flue chimney of a thermoelectrical plant using pseudo-inverse matrix method," *Struct. Des. Tall Spec. Build.*, vol. 18, no. 2, pp. 203–216, 2009, doi: 10.1002/tal.405.

[17] W. M. To and D. J. Ewins, "The role of the generalized inverse in structural dynamics," *J. Sound Vib.*, vol. 186, no. 2, pp. 185–195, 1995, doi: 10.1006/jsvi.1995.0442.

[18] P. C. Hansen, "Analysis of Discrete Ill-Posed Problems by Means of the L-Curve," *SIAM Rev.*, vol. 34, no. 4, pp. 561–580, 1992, doi: 10.1137/1034115.

[19] C. M. Bishop, *Pattern Recognition and Machine Learning(Information)*. 2011.

[20] I. Daubechies, M. Defrise, and C. De Mol, "An iterative thresholding algorithm for linear inverse problems with a sparsity constraint," *Commun. Pure Appl. Math.*, vol. 57, no. 11, pp. 1413–1457, 2004, doi: 10.1002/cpa.20042.

[21] Y. Fan, C. Zhao, and H. Yu, “Research on dynamic load identification based on explicit Wilson-θ and improved regularization algorithm,” *Shock Vib.*, vol. 2019, 2019, doi: 10.1155/2019/8756546.

EURODYN 2020
XI International Conference on Structural Dynamics
M. Papadrakakis, M. Fragiadakis, C. Papadimitriou (eds.)
Athens, Greece, 23–26 November 2020

DAMAGED DETECTION OF A BELL TOWER THROUGH OMA

Simone Castelli[1], **Andrea Belleri**[1], **Alessandra Marini**[1] **and Babak Moaveni**[2]

[1] Department of Engineering and Applied Sciences, University of Bergamo
Dalmine, Italy
{simone.castelli,andrea.belleri,alessandra.marini}@unibg.it

[2] Department of Civil and Environmental Engineering, TUFTS University
Medfors, USA
babak.moaveni@tufts.edu

Keywords: Bell tower, OMA, FEM update, damaged detection

Abstract. *This document presents the Operational Modal Analysis and finite element update of the bell tower of the church of Castro (BG), in Italy. This procedure was adopted to identify the actual state of structural damage following the widespread carbonation and oxidation of the surface concrete layer and the significant localized damage of the rebars detected by visual inspections. The 39m high structure is a reinforced concrete tower with a hollow section with a double concavity and a tapered section in elevation. Four uniaxial piezoelectric accelerometers were adopted to record environmental vibrations for dynamic identification using the roving technique. After performing dynamic identification, two types of 3D structural models were compared, namely with shell elements and beam elements. Finally, a calibration of the shell finite element model was carried out to identify the boundary conditions and the extension of the damage. The knowledge of the actual state of the structural damage enables the definition and the design of the retrofit strategy aimed at guaranteeing both static and seismic safety, as well as the future preservation of the structure.*

1 INTRODUCTION

The church of San Giacomo (Figure 1), with its adjoining bell tower, is located in the municipality of Castro in the province of Bergamo in the upper area of Lake Iseo at an altitude of about 200m. Located in the old part of the village, near to the lake, it was designed in 1966 by the architect Vittorio Sonzogni and built in 1969 to replace the pre-existing church. The reinforced concrete (RC) bell tower is 37m high and has a square cross-section, with a concavity on the four sides, tapered in elevation. There are also elongated openings alternating on the sides and horizontal joints with a regular pattern.

The bell tower is in a pronounced state of deterioration, with the presence of a significant crack at the third level, probably due to a number of factors: the concavity of the sections and elevations generates a clear washout of the concrete in the central area of each side, revealed by the chromatic alteration of the surfaces; the areas of discontinuity of the surface, such as the openings and the horizontal joints, collect a greater quantity of rainwater percolating from the top. In these areas, there is a greater presence of deterioration due to the corrosion of the reinforcing bars and the spalling of the concrete cover; and poor casting of the conglomerate is revealed by the gravel nests on the worn out surfaces.

Figure 1. View of the church with the adjacent bell tower.

For such reasons dynamic identification was carried out to evaluate the damage extension and provide a reference finite element model to be used in the conceptual design of the retrofit intervention. To record the environmental vibrations, 4 high sensitivity piezoelectric accelerometers (Wilcoxon 731A) were used. The sensors were placed at each floor level according to the scheme depicted in Figure 2: 2 sensors remained in the same position for all the acquisitions (reference) while the others were moved at each registration (roving) and changed in directions according to the Type A and Type B positions. The configuration A allows the identification of flexural and torsional modes at each level, while the configuration B enables the identification of the flexural modes in the orthogonal direction.

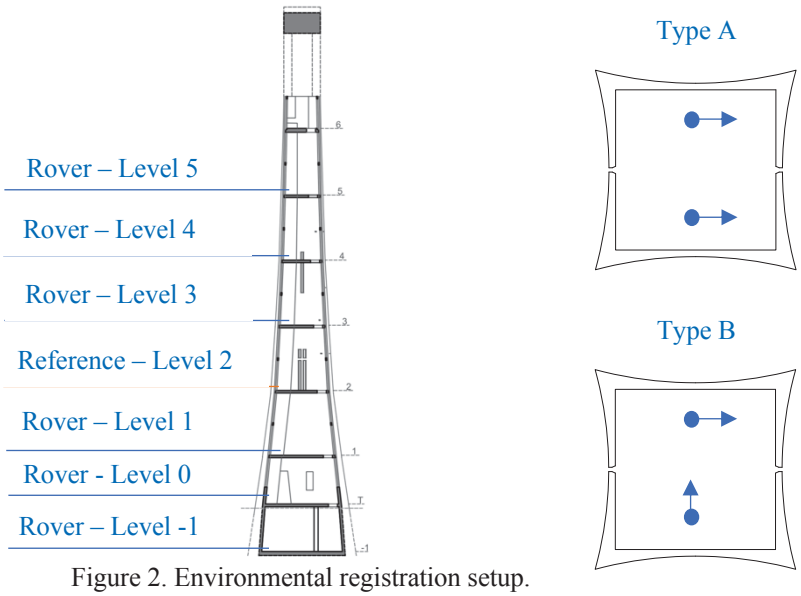

Figure 2. Environmental registration setup.

2 OPERATIONAL MODAL ANALISYS

For the dynamic modal identification, the FDD algorithm was selected [1, 2]. Frequency Domain approaches are based on the processing of a time-correlated signal through a Discrete Fourier Transform (DFT). Frequency Domain Decomposition methods operate a Singular Value Decomposition (SVD) at each line of the frequency spectrum. This procedure separates noisy data from disturbances of various sources and appears to be able to capture close modes of vibration with good accuracy. Typical underlying hypotheses of Frequency Domain Decomposition (FDD) methods are: white noise input, low structural modal damping ratios and geometrically-orthogonal mode shapes of close modes.

The FDD algorithm was used for each recording in order to obtain the modal frequencies and the respective modal forms. A statistical analysis was carried out to obtain mean and variance modal frequencies and the modal forms have been reconstructed starting from the initial knowledge of the eigenvector for each acquisition and the subsequent normalization to the values of the reference sensors [4]. Figure 3 shows the estimated frequencies in a box and whiskers: the central mark indicates the median, and the bottom and top edges of the box indicate the 25^{th} and 75^{th} percentiles, respectively. The whiskers extend to the minimum and to the maximum values excluding the outliers, and the outliers, values that are more than 1.5 times the interquartile range away from the top or bottom of the box, are plotted individually using the '+' symbol. In Figure 3 it is possible to notice the small variance of the estimated frequencies.

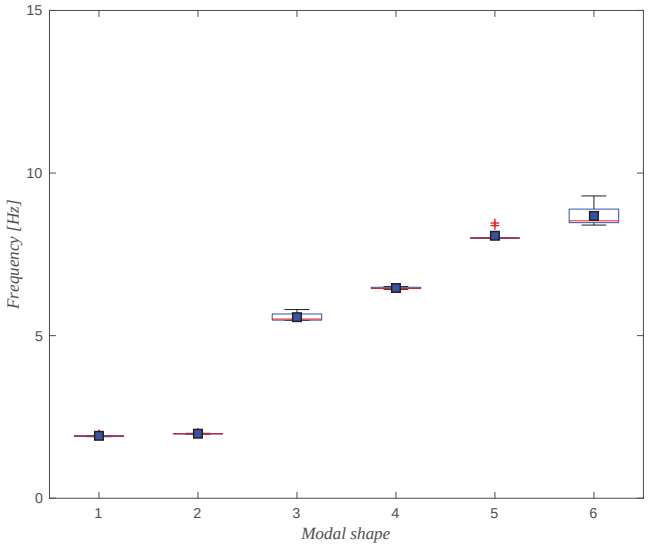

Figure 3. Statistical distribution of the identified modal frequencies.

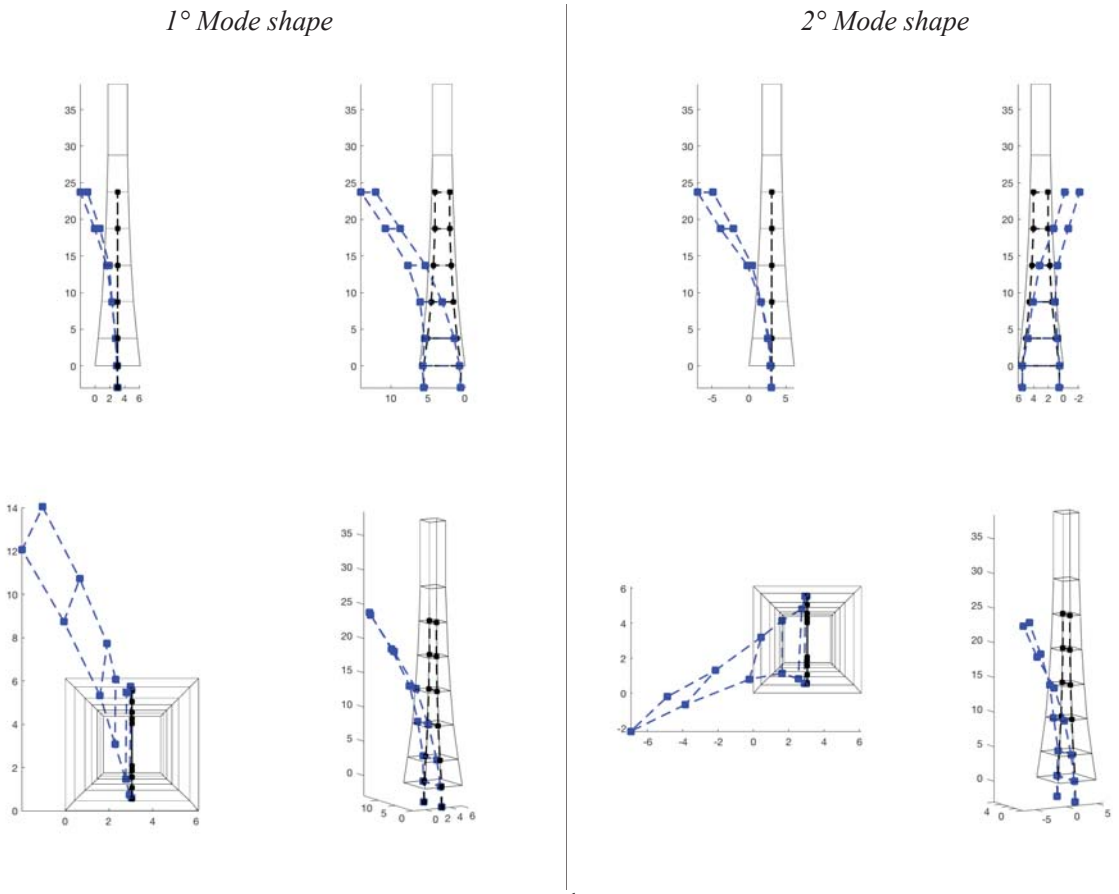

Figure 4. 1st and 2nd modal shapes.

3 FEM CALIBRATION

3.1 FEM Model

A finite element model was built with Midas Gen [3] software using four-node shell elements (Figure 5) connected at the base to a ground point by means of rigid links. To capture the soil-structure interaction, the rotational degrees of freedom of the ground level were released, and two elastic springs were added to simulate rotational stiffness long the principal directions. The model (11412 nodes and 20516 elements) was validated against a brick elements model to check the presence of any geometric locking problem. The mechanical properties of the concrete were calibrated from compressive tests on the bell tower concrete.

Figure 5. FEM model with shell elements.

3.2 Sensitivity analysis

A sensitivity analysis was performed on the parameters that regulate the dynamic behavior: the stiffness of the springs at the base, the percentage and extension of the main crack located at the 3rd level and the Young's modulus of the concrete. The parameters were studied and varied independently from each other to eliminate those that made the matching between OMA and FEM badly conditioned. For example, the stiffness of the spring at the base was found to dominate the curvature of the modal form at the base; so, such stiffness was selected directly looking the modal curvature at the base and it was not further considered in the calibration problem (Figure 6). The elastic modulus of concrete affects mainly the modal frequencies rather than other dynamic properties (Figure 7). Finally, the extent of the main crack at the 3rd level affects the modal form rather than the frequency (Figure 8).

As for the percentage of damage in the crack (evaluated as a reduction of the elastic modulus of the concrete), from a first calibration it resulted in a 98% reduction of the Young modulus, a very high percentage which was confirmed by visual inspections. For such reason, this parameter was kept constant in the calibration problem.

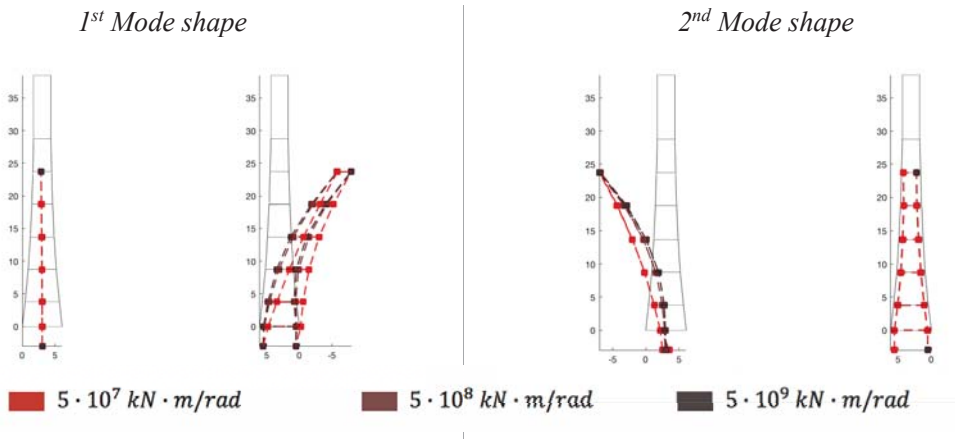

Figure 6. Sensitivity of the 1st and 2nd modal shapes as the stiffness of the rotational base spring.

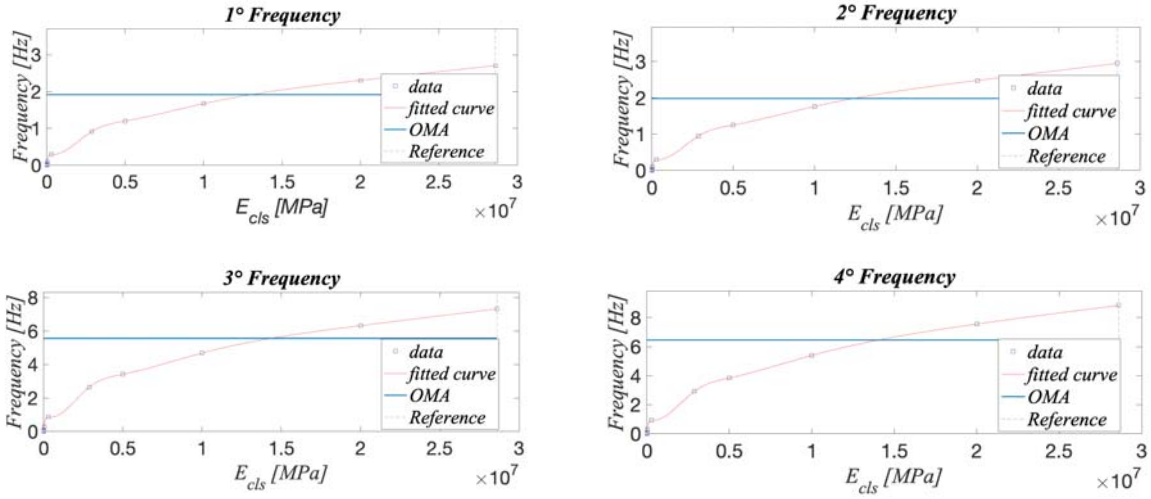

Figure 7. Sensitivity of the modal frequencies as the Young modulus of concrete.

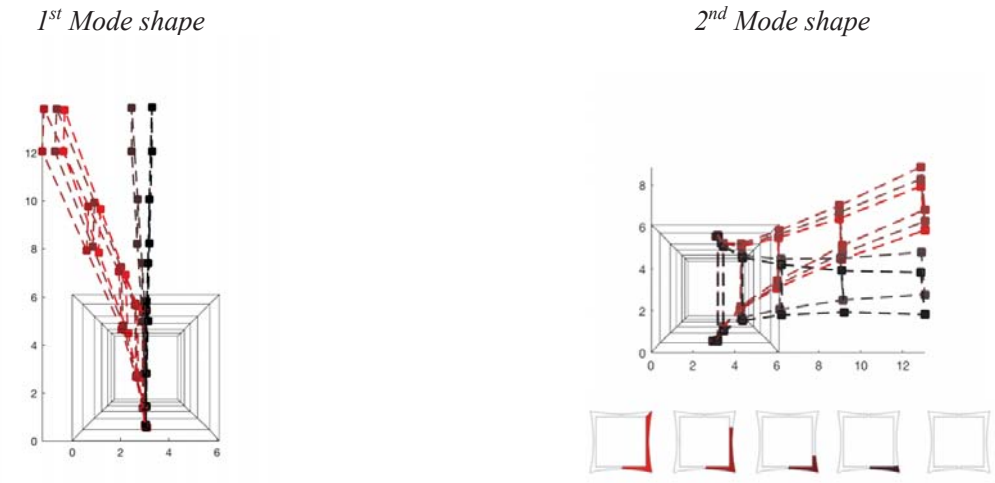

Figure 8. Sensitivity of the 1st and 2nd modal shapes as the extension of damage in the crack at the 3rd level.

3.3 FEM calibration

Starting from the sensitivity analysis, a preliminary manual match on each individual parameter was performed.

Parameter	before calibration	after calibration
Spring Stiffness	500000000 kNm/rad	500000000 kNm/rad
Percentage of damage	0 %	98 %
Young's modulus of concrete	$2.86*10^7$ kN/m^2	$1.7*10^7$ kN/m^2

Table 1: Comparison of parameters before and after calibration.

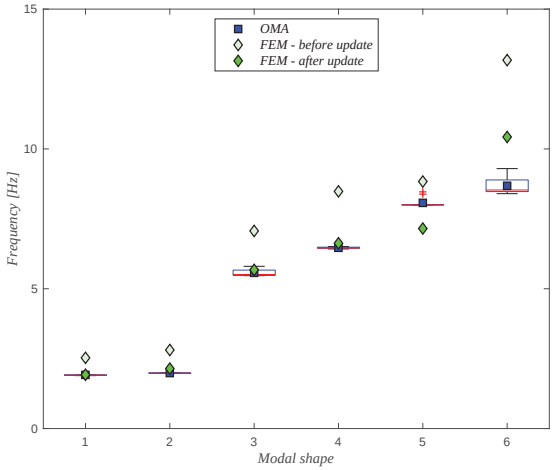

Figure 9. Comparison of modal frequencies before and after calibration.

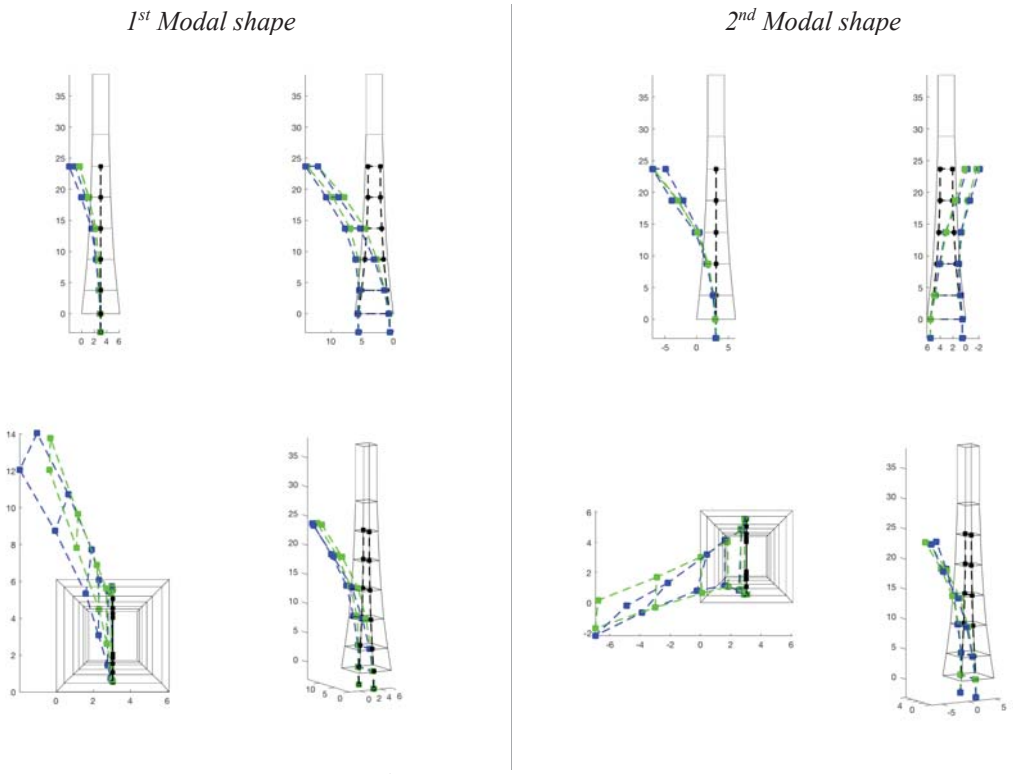

Figure 10. Comparison of 1st and 2nd mode shapes after calibration: OMA (blue) and FEM (green).

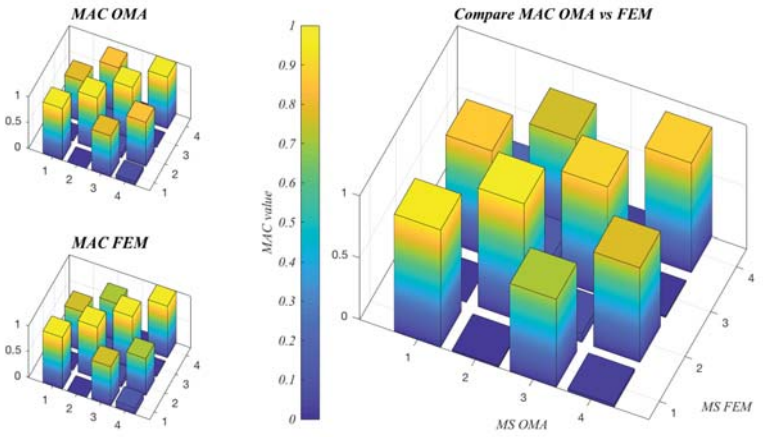

Mode	MAC
1	0.95
2	0.96
3	0.89
4	0.89

Figure 11. Comparison of MAC OMA and FEM post calibration and MAC values.

Figures 9-10-11 show the very accurate matching for the first four modal parameters. This allowed to evaluate, with a good approximation, a first estimate of the state of health of the structure that may be useful for the future retrofit project. It is also interesting to note how the modal forms 1-3 and 2-4 (Figure 11) seem correlated; this is due to the fact that the modal shapes have been calculated only up to the 5th floor (Figures 2-4) and the MAC value of Figure 11 neglects the modal shape above such level.

4. CONCLUSION

The paper presented the dynamic identification of the bell tower of San Giacomo church in the municipality of Castro (Italy). The reinforced concrete tower showed very poor state of preservation with an evident crack extending on the third level. A dynamic identification was performed using the roving technique. The FDD algorithm was applied on each record set and then combined to obtain the full model mode shapes.

A sensitivity analysis was conducted to highlight the influence of a series of parameters on the dynamic properties. In particular, it was found that: damage in the cracked region results in a plan rotation of the modal shapes compatible with the OMA results; the stiffness of the rotational springs at the base can be selected to match the modal curvature at the base of the tower; the concrete modulus of elasticity significantly influences the modal frequencies. Finally, after tuning each parameter, it was possible to obtain a good match of the FE model with the identified OMA properties and quantify the extension of damage in the cracked region.

Acknowledgements

The support of Eng. G. Cottinelli, J. Zanni and Di.Mo.Re. srl in carrying out the experimental campaign is gratefully acknowledged.

REFERENCES

[1] R. Brincker, L. Zhang, P. Andersen, Modal identification of output-only systems using frequency domain decomposition, *Smart Materials and Structures*, 10(3), 441, 2000.

[2] R. Brincker, P. Andersen, Ambient response analysis of the heritage court tower building structure, *Proceedings of the XVII IMAC,* 2000.

[3] MidasGEN 2019, MIDAS Information Technologies Co. Ltd.

[4] A. Belleri, S. Castelli, A. Marini, N. Bettini, B. Moaveni, Operational modal analysis of damaged bell tower, *Proceedings of the 8th IOMAC, International Operational Modal Analysis Conference,* 2019.

EURODYN 2020
XI International Conference on Structural Dynamics
M. Papadrakakis, M. Fragiadakis, C. Papadimitriou (eds.)
Athens, Greece, 23–26 November 2020

TOWARDS STRUCTURAL HEALTH MONITORING BASED RISK BASED INSPECTION PLANNING FOR OFFSHORE WIND TURBINE SUPPORT STRUCTURES

Simon Tewolde[1,2], Rüdiger Höffer[1], and Inka Mueller[3]

[1]Ruhr University Bochum
Bochum, Germany
e-mail: {simon.tewolde,ruediger.hoeffer}@rub.de

[2] Bachmann Monitoring GmbH
Rudolstadt, Germany
e-mail: simon.tewolde@bachmann.info

[3] Bochum University of Applied Sciences
Bochum, Germany
e-mail: inka.mueller@hs-bochum.de

Keywords: offshore wind energy, structural health monitoring, support structure, risk based inspection, reliability analysis.

Abstract. *Almost all offshore wind farms across the world are equipped with a Structural Health Monitoring (SHM) system. Nevertheless, the benefit of using data analysis results for Operation and Maintenance (O&M) optimization is not yet effectively exploited. Reasons for this are manifold but dominated by the fact that usually the development of the SHM system is not integrated from the beginning as part of the project management process. Rather, in most cases, it is mainly implemented to fulfill the minimum requirements by relevant authorities. In addition to this, as the use of monitoring data for possible life time extension is well established, stakeholders miss the benefits for young age wind turbines. However, current research has shown that SHM results are also useful in the early life cycle range to determine healthy state reference parameters and also to optimize the variation of the as-built structure from the designed structure. The information obtained from an SHM system therefore is an added value, which can be estimated before implementing it using value of information concept.*

The main purpose of implementing an SHM system is to reduce uncertainty. This paper makes use of SHM data analysis to reduce the uncertainty of stress ranges when performing reliability analysis for Risk Based Inspection (RBI) planning. For this study, one year strain time history data from four monitored wind turbines in an offshore wind farm in the North Sea is used. The measured stress cycles are counted by Rain Flow Counting (RFC) and grouped into stress range bins. Finally, the distribution of the counted stress cycles are used to fit a Weibull probability distribution function to estimate the parameters and compare them with recommendations from literature and standards. This way, an individual RBI planning for the monitored offshore wind turbines is enabled.

1 INTRODUCTION

In offshore wind energy industry, design optimization and development of innovative construction methods have significantly contributed to cost reduction and increased reliability of wind turbines. However, recently, the focus has shifted towards optimization of Operation and Maintenance (O&M) for further cost reduction. Especially for aging operating offshore wind turbines, with high O&M costs reaching from 25-30% of the energy generation costs [1], [2], [3], making use of this is economically attractive. Corrective maintenance activities are expensive in most cases, as the turbine is usually shutdown for maintenance resulting in loss of revenue from power production. To minimize or avoid corrective maintenance, it becomes necessary to detect faults or damages in their early stage. This can be achieved by having a continuous and reliable information about the performance and condition of the structures through Structural Health Monitoring (SHM). In this paper, one year strain time history data from strain gauges installed in four wind turbines in the North Sea are used. The distribution of the counted stress cycles from the measured stress time history data is fit into a Weibull distribution function to estimate individual Weibull shape parameters and compare them with the values obtained from literature and relevant standards. It is shown that the estimated individual parameters are significantly different from the standard recommendations and using them as an input for RBI planning will result in different inspection plans.

2 STRUCTURAL HEALTH MONITORING AND VALUE OF INFORMATION

The main purpose of implementing a Structural Health Monitoring (SHM) system is to decrease uncertainties and therefore being able to reduce risk. According to ISO 31000 [4], the definition of risk is 'effect of uncertainty on objectives'. In many cases, the objective is the continuous safety and functionality of structures or systems according to design. For the case of offshore wind turbines, the objective is safe and continuous power production with minimum possible unexpected costs.

Vibration-based SHM has been in practice for many decades to monitor bridge structures [5]. The physical properties of a structure are affected by damage or deterioration. Changes in these physical properties (mass, stiffness and damping) of a structure will change its vibration behavior, which can be quantified in terms of the dynamic characteristics such as the Eigenmodes and modal damping or counted stress cycles. These damage and deterioration sensitive performance indicators can be directly measured and/or calculated from the measured quantities of an SHM system.

Earlier monitoring systems were implemented purely from structural engineering point of view for damage detection without Value of Information (VoI) analysis. The term VoI was first used in 1961 by Raiffa and Schlaifer [6] as decision support for selecting the experiment with maximum utility through Bayesian pre-posterior analysis of the experiments. Then, in 2004 VoI analysis was applied by Straub and Faber [7], [8] for inspection optimization of structural systems. Recently, the VoI analysis was applied to SHM [9] and made significant progress as part of the cost action TU1402 project [10], in which pre-posterior decision analysis was used to estimate the expected added value from implementing a monitoring system. Pre-posterior decision analysis is estimation of the VoI before doing the experiment or having any of the expected data [11]. VoI estimates the expected gain from decisions made using the information obtained from the SHM as compared to the decisions made without the SHM and after deducting the cost of the SHM system (or experiment).

The pre-posterior analysis for VoI analysis and comparison is made by Bayesian decision

tree to decide, whether it is beneficial or not to implement a monitoring system. Furthermore, different configurations can also be investigated to optimize for the maximum VOI [12].

$$VoI_{max} = max_{i,j}\{E[C_{T,O}] - E[C_{T,M,i}(d_j)]\} \tag{1}$$

where $E[C_{T,O}]$ is the expected total costs without monitoring and $E[C_{T,M,i}(d_j)]$ is the expected total cost for i^{th} configuration with corresponding j^{th} decision. The benefit from VoI is incorporated to the total cost as a negative component.

VoI also helps to decide when it is most beneficial to start monitoring of a structure. Long et al. [13] investigated the VoI analysis for a truss bridge girder structure by comparing several sensor configuration scenarios. The VoI concept is highly attractive for many industries, which need incorporation of monitoring systems.

In the case of offshore wind industry, during its start the VoI concept was not a well established practice. Also, the pressure to reduce costs has forced the industry to deal with uncharted waters of building bigger wind turbines at deeper waters and far away from the coasts for higher power production. This results in higher uncertainty and made installation of monitoring systems a necessity. As an example, the implementation of a monitoring system on 10% of the wind turbines in an offshore wind farm used to be a BSH (Federal Maritime and Hydrographic Agency) requirement in Germany until 2015 [14]. In 2015, the BSH regulation was revised [15], which gave the wind farm operators more flexibility, concerning the number of monitored turbines, as long as they can prove to the authorities that appropriate safety measures are being taken. After 2015, the operators had a chance to make VoI analysis before implementing a monitoring system and to incorporate the development of a monitoring system as part of their regular project life cycle management. However, still the majority of SHM systems are being implemented based on the outdated BSH recommendation of installing a monitoring system on 10% of the wind turbines in an offshore wind farm. The lack of integrating SHM as part of design and construction process resulted in less interest by the operators to integrate the SHM data analysis results into the O&M decision-making procedures. As a result, the full potential of SHM data analysis results for O&M cost reduction is not yet being effectively exploited.

3 RELIABILITY ANALYSIS AND RISK BASED INSPECTION PLANNING

The expected results of a reliability analysis is estimation of a system's or component's probability of failure (or reliability index). For determination of a failure event it becomes important to formulate a limit state, which can be ultimate, serviceability or fatigue. Violation of the limit state is then considered as a failure event (Melchers and Beck) [16]. In a very simplified form, for a component with a resistance R when exposed to a load S, the probability of failure could be represented by:

$$P_f = P(R \leq S) = P(R - S \leq 0) = P[G(R, S) \leq 0] \tag{2}$$

where G() is a limit state function, for which $G() < 0$ represents a violation. The reliability index (β) can be calculated from the Probability of failure (P_f) as:

$$\beta = -\Phi^{-1}(P_f) \tag{3}$$

with $\Phi()$ assumed as a standard normal distribution function.

Offshore structures are exposed to cyclic loads. As a result, fatigue is the most significant deterioration mechanism. In fatigue reliability analysis, structural failure occurs as a crack growth and the limit state function is violated (failure occurs) when the crack size exceeds the critical crack size. In most cases, failure is considered to occur when crack grows through the steel thickness.

Fatigue analysis is usually done by using Palmgren-Miner rule and S-N curve to estimate fatigue damage. Also, the experiment based Paris law proposed by Paris and Erdogan [17] gives the rate of fatigue crack growth. Fatigue reliability analysis is commonly done by calibrating these both models, the S-N model and the Fracture Mechanics (FM) model [18], [19], [20] to establish the limit state function for crack growth. Furthermore, the calibrated models are also used for inspection planning, see e.g. [8] and [21]. The limit state function involves multiple random variable and is usually solved by making use of First Order Reliability Method (FORM), Second Order Reliability Order (SORM) and recently with the growth of computational capability Monte Carlo Simulation (MCS). The computational time of MCS can further be enhanced using advanced sampling techniques, specially when estimating very low probabilities.

The next step, after reliability analysis (estimating the probability of failure or the reliability index) is Risk Based Inspection Planning (RBIP), which starts by comparison of the estimated reliability index with the acceptance criteria (target reliability index). The central idea of RBIP is to assign the available inspection resources to the structure or component of a structure, where it is mostly needed (with highest risk). For the reliability analysis, input load and structural resistance defining the limit state function need to be analyzed.

Reliability analysis is commonly done using random variables to represent the uncertainty of the input variables to the limit state function. These variables are usually taken from design assumptions. One of the most important inputs is the number and magnitude of stress cycles the structure (hot spot) is exposed to. The probability density function of the stress ranges for offshore structures are commonly represented with a two-parameter (scale and shape) Weibull distribution [22], [23], [24]. The shape and scale parameters represent the distribution and magnitude of the hot spot stress range respectively. ABS (2003) [23] recommends a value which varies from 0.7 to 1.4 for the Weibull shape parameter, while Wirsching and Chen (1988) [25] recommended a value from 0.5 to 1.5. Furthermore, ABS (2003) [23] states that similar offshore fixed platforms structures built in the Gulf of Mexico and the North Sea experience stresses with shape parameter values of 0.7 and more than 1.4 respectively. Figure 1, an example adopted from Straub (2005) [8], shows visualization of stress range ($\Delta\sigma$) Probability Density Function (PDF) for varying shape parameters (γ) of 0.50, 0.75, 1.00, 1.25 and 1.50. A constant scale parameter of 5 MPa is used for all cases.

The Weibull shape parameter is a function of geometry and loading. Generally, an increase in slenderness and dynamic exposure will increase the shape parameter [8], [23]. DNVGL RP-C-210 document [24] illustrates with a graph, that for all S-N curves of varying structure detail, the allowable maximum stress range decreases with increasing Weibull shape parameter. This is obvious from Figure 1, since with increasing of the scale parameter, the contribution of the higher stress ranges become more significant.

The above mentioned Weibull shape parameters recommended in standards are mainly estimated based on wave data [23]. These values are being used for design and reliability analysis of offshore structures. DNVGL RP-C-210 [24] notes that the shape parameter significantly affects the estimated fatigue damage, therefore calibrating these parameter from long term measured stress time history data becomes very important.

For offshore wind turbine structures, there is the benefit of having permanent SHM systems,

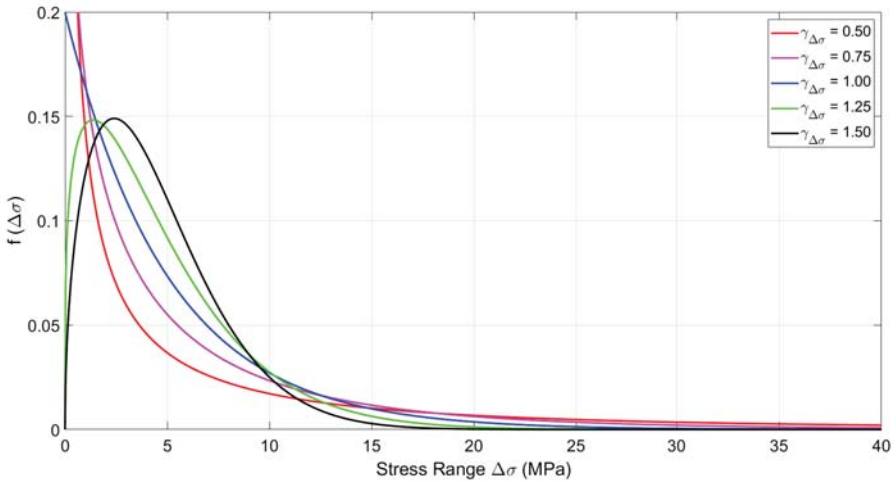

Figure 1: Weibull PDF for varying shape parameter with fixed scale parameter equal to 5MPa

which provide continuous information about the number and magnitude of stresses the structures are exposed to. Moreover, the SHM system measure responses, which represent the collective impact of loads and load combinations on the structure. Comparison of these measured responses against the capacity (resistance) of the structure helps in defining a more realistic limit state function. Experience from many monitored offshore wind turbines showed that most of the offshore wind turbines are built stronger (stiffer) than the design [27].

4 METHODOLOGY

In this section, the analysis procedure of one year strain time history data from four wind turbines in an offshore wind farm in the North Sea is discussed.

The monitoring system installed in all four wind turbines is identical, with eight strain gauges installed at two measurement levels, four sensors at each level at identical positions, in cardinal coordinates. The data is collected with a sampling rate of 100Hz. Before performing Rain Flow Counting (RFC) according to ASTM E1049-85 [28], the raw strain time history data is first pre-processed by removing erroneous data using median filter. Furthermore, the strain data is temperature compensated by removing the apparent strain calculated from the temperature sensors' data installed together with every strain gauge. For calculation of apparent strains relevant manufacturer's temperature compensation curves are used. Finally, the stress time histories are calculated from the corrected strain data by using the relevant young's modulus of steel.

After that, RFC of the stress time history data is done and the counted stress cycles are assigned to predetermined stress range bin sizes. DNVGL recommends a minimum of 20 stress range bins. However, in this study two cases are considered. In case one, uniformly distributed 100 stress bins are used to classify the counted stress cycles. And in the second case, in order to get higher resolution of the bins with very high number of cycles, non-uniform 143 stress bins are used. Finally, for both cases, the counted stress cycles are fitted to Weibull distribution functions for estimation of the scale and shape Weibull parameters. The fitting process is done by using the least square method according to [23].

The estimated Weibull shape parameters are then compared with the values obtained from standards. Furthermore, for the first case, sensitivity analysis of removing the insignificant

stress cycles (the first and second stress range bins) is made. In addition, for both cases, the effect of applying low-pass filters to remove the very small stress cycles before doing RFC is investigated.

5 RESULT

5.1 For uniform sized 100 stress bins

In this subsection, the results obtained from the first case are presented. The stress bins used are 100 uniformly sized stress bins, each with a size of 0.51 MPa. Figure 2 shows the estimated Weibull shape parameters for all four turbines. The x-axis of each subplot indicate the turbine location, for example L-90° means lower level strain gauge at 90°N and U-180° means upper level sensor at 180°N.

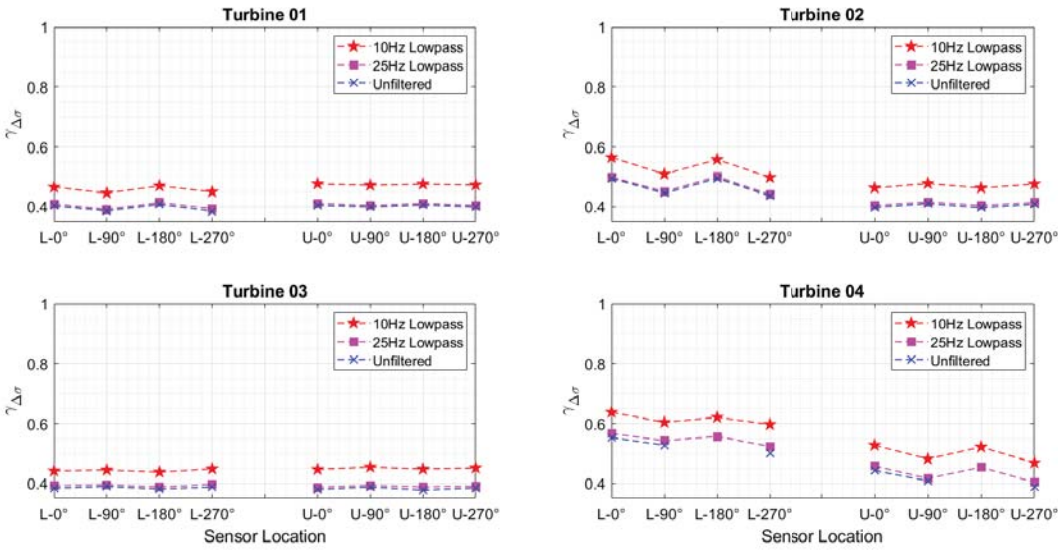

Figure 2: Estimated weibull scale parameter for the 8 sensors in each of the four turbines

The results are generally lower than the recommended value of 1.0 for the North Sea environment [23], [25], [26]. Although all turbines are from the same wind farm, differences between the different wind turbines can be clearly identified, ultimately leading to different risks. The turbines located in the interior of the wind farm (Turbines 02 and 04) have higher shape parameters than those located in the boundary of the wind farm (Turbines 01 and 03). The turbines located in the interior of the wind farm are exposed to higher cyclic loads due to wake effects. In addition, the results for sensors located opposite to each other are of equivalent magnitude and consistent. For example, in every turbine at each measurement level the results for the sensors located at 0°N and 180°N as well as for the sensors at 90°N and 270°N are comparable and consistent.

Furthermore, as expected and shown in all four subplots, the low pass filtering of the small stress cycles before RFC resulted in an increased Weibull scale parameters in all cases. The unfiltered data results in the lowest scale parameter estimation. With decreasing cut-off frequency of the low-pass filter, the magnitude of the scale parameter increases.

To study the effect of removing small stress cycles on the accumulated fatigue damage, the accumulated fatigue damage for every stress bin is calculated using Palmgren-Miner rule and

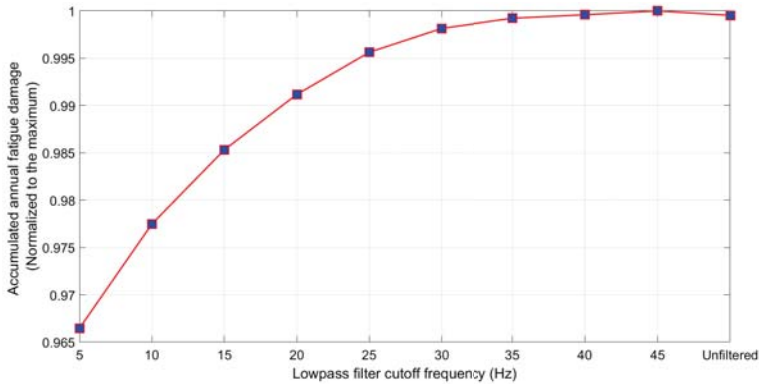

Figure 3: Effect of data low-pass filtering on the accumulated annual fatigue damage

relevant S-N curve. Figure 3 shows the effect of increasing cutoff frequency for the applied low-pass filters. The accumulated annual fatigue damages are normalized to the maximum. This shows that as the sampling frequency decreases the estimated fatigue damage will not be drastically affected as the bigger stress cycles are mainly contributing to the accumulated fatigue damages. For example, using a low-pass filter of 5 Hz will result in an error of 3.35% as compared to the maximum estimate. Although with a very small amount of 0.05%, the fatigue damage estimated from 45 Hz low-pass filter is higher than the estimation from the unfiltered data. This might have something to do with measurement artifact as it was observed in all channels.

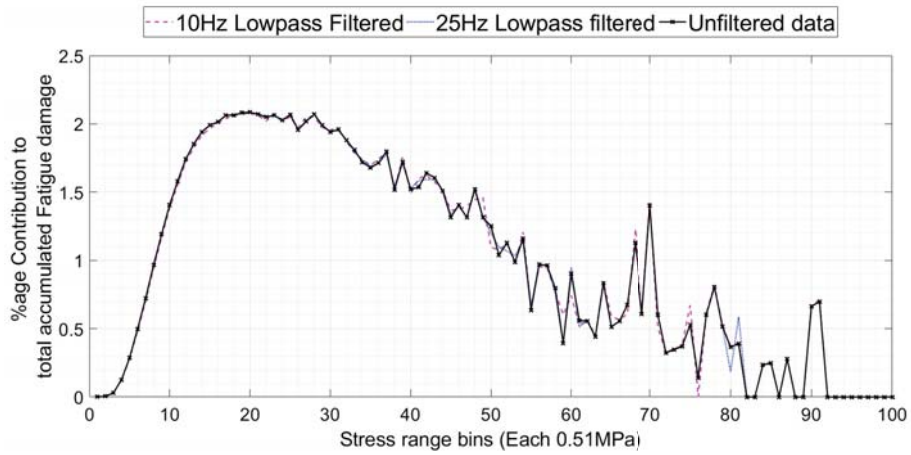

Figure 4: Percentage contribution of each stress bin to the total accumulated Fatigue damage

Furthermore, the fatigue results are used to observe the distribution of the total fatigue damage among the stress bins. Figure 4 show the percentage contribution of all 100 stress bins to the total accumulated fatigue damage. Although the small magnitude stress bins contain a very high number of cycles, they do not contribute to the accumulated fatigue damage. The 100 stress bins have each a size of 0.51 MPa. When the contribution of each stress bin is compared as percentage to the total fatigue damage, the percentage contribution of the first two bins for all three cases are less than 0.004%. The maximum percentage contribution is from stress bin number 20 with appr. 2.08% for all three cases. The third bin has a contribution of appr. 0.03%

in all three cases. From this finding, it might be possible to neglect the first two stress bins to estimate the modified Weibull shape parameter. Also in Figure 4, although not included in order to avoid congestion, the contribution for 45 Hz low-pass filter is higher than for the unfiltered data.

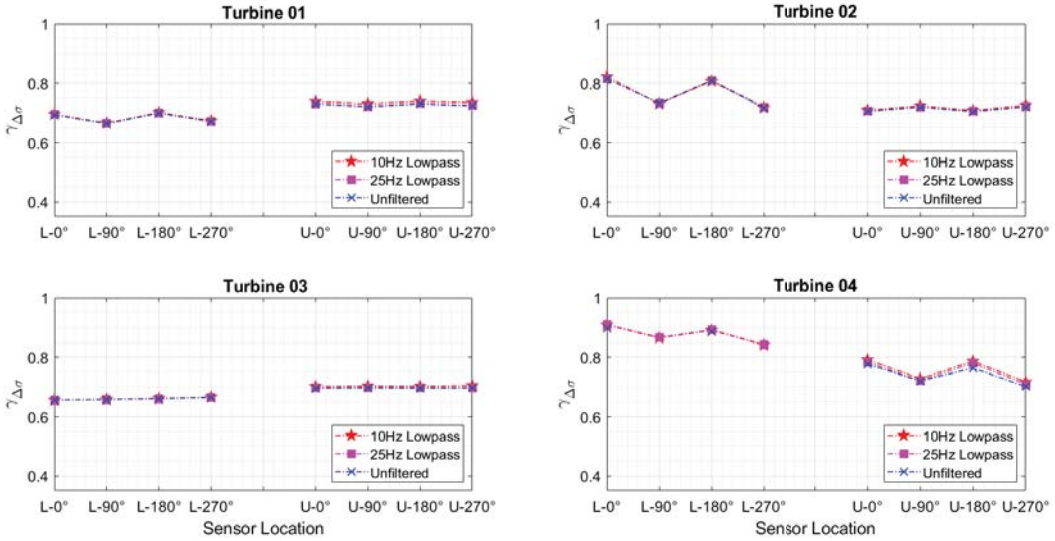

Figure 5: Estimated weibull scale parameter after removing the first stress bin

The estimations in Figure 5 are made by removing only the first stress bin of every sensor in all four turbines. The results plotted in Figure 5 show that all the newly estimated Weibull scale parameters increased, meaning the skewness of the distribution is shifting to the right as the higher stresses are becoming more involved. Another observation is that, that the influence of low pass filtering on the estimated scale parameters is decreased, if the first bin with smallest magnitudes is already removed.

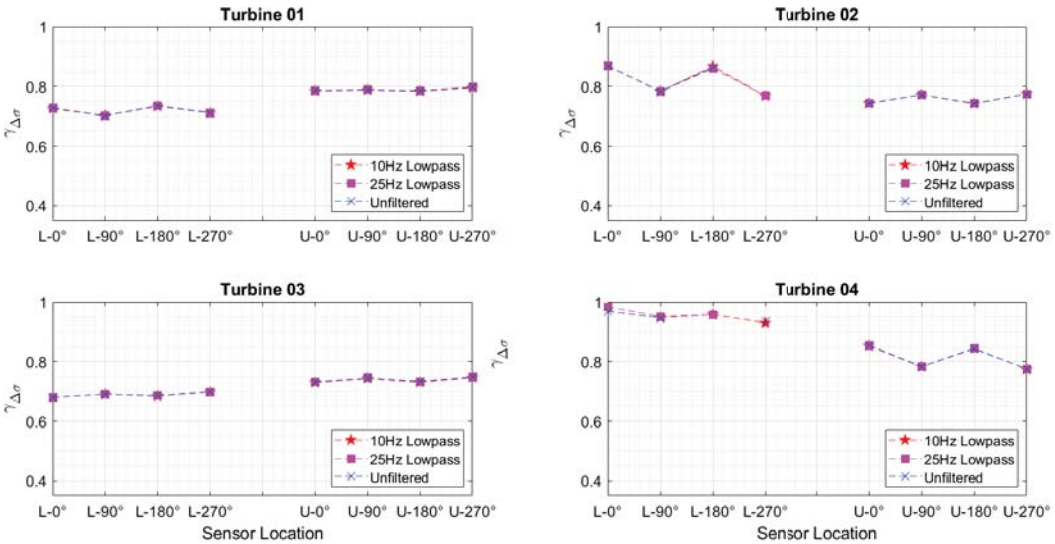

Figure 6: Estimated Weibull scale parameter after removing the first two stress bins

Furthermore, Figure 6 shows the estimated scale parameters after removing the first two stress bins. Again, the estimated scale parameters increased but not very significantly. This indicated that the first stress bin has most effect on the estimated values. Although insignificant on the fatigue damage the number of counted cycles with magnitude less than 0.51 MPa (in the first stress bin) are more than 95% of the total counted number of cycles for all 100 bins. The second bin contains less than 1% number of cycles.

5.2 For non-uniformly sized 143 stress bins

After observing that more than 95% of the total counted cycles belong to the first stress bin, the analysis was repeated by breaking down the first stress bin in to 10 classes. The bin sizes used for the stress ranges between 0 and 0.50 MPa is 0.05, between 0.50 and 2.50 MPa is 0.10, between 2.50 and 10.0 Mpa is 0.25, and for the rest is 0.50 MPa. In this case two, totally 143 non-uniformly sized stress bins are used.

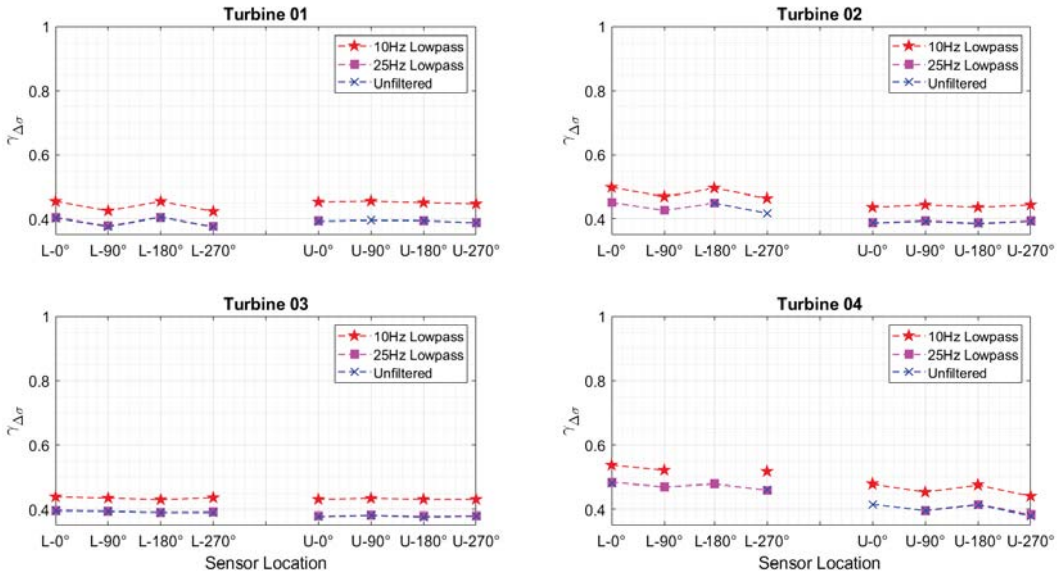

Figure 7: Estimated Weibull scale parameter for 143 stress bins

Figure 7 shows the results for case two. Generally, the results are similar with Figure 2 indicating that increasing the resolution of the stress bins does not significantly affect the estimated Weibull shape parameters.

5.3 Summary of results

Generally, the results show that the Weibull scale parameters estimated from the measured one year strain time history data are less than those recommended by design standards and used for reliability analysis in the North Sea, even when the small value bin is neglected or small cycles are removed by low-pass filters during scale parameter estimation.

The paper shows that, the presence of the lower stress bins does not significantly contribute to the accumulated fatigue damage but significantly affect the estimation of the shape parameter. In addition, removal of high frequency stress cycles with a low-pass filter does not very significantly affect the accumulated fatigue damage and the shape parameter estimation. Furthermore, the wind turbines in the same wind farm have varying shape parameters indicating that they are

exposed to varying risks and can be used as an important input to RBI planning. An important result is also that the wind turbines located in the interior of the wind farm (Turbines 02 and 04) have higher Weibull shape parameters in all estimations than the turbines located at the exterior (boundary) of the wind farm (Turbines 01 and 03). The reason can be that the interior wind turbines are more exposed to cyclic loads from wake effects. This can be important information for extrapolation of the estimated parameters to the unmonitored turbines.

The obtained results, even after removing the lower stress bins are still lower than the recommended values, therefore when used as an input for reliability analysis, more realistic inspection plans can be made. The higher recommended values of scale parameter overestimates the stress cycles the structure is actually exposed to. These results can be considered as one of the added values obtained from incorporating SHM data analysis in the reliability analysis and Risk based inspection planning.

6 CONCLUSION

The paper uses one year strain time history data from four wind turbines in an offshore wind farm located in the North Sea. After pre-processing of the strain data, the corrected strain data is used for calculating the stress time history. Then, Rain Flow Counting (RFC) analysis of the stress time history was made to count the number and magnitude of the stress cycles, the structure is exposed to during the one year monitoring period. The counted stress cycles are first binned in to uniformly sized 100 stress range classes and then for comparison purpose in to a non-uniformly sized 143 classes. For each case, Weibull distribution function is fitted to the counted stress cycles using the least square method. Finally, the stress range Weibull scale parameters are estimated from the fitted Weibull distribution functions. The results obtained from the sensors located opposite to each other (at 0°N - 180°N and at 90°N - 270°N) and at the same measurement level showed good consistency. Furthermore, a sensitivity analysis is made by removing the very small stress cycles which contributed very insignificantly to the total accumulated fatigue damage. The modified scale parameters increased. However, when compared to the stress range scale parameters recommended for North Sea, they are still lower. It is shown that the reliability analysis made using the recommended Weibull shape parameter value of 1.0 for the North Sea would overestimate the stresses the structures are exposed to. In addition, the Weibull shape parameters calculated for the turbines located in the interior of the wind farm are higher than those located in the boundary of the wind farm possibly due to wake effect. This information can also be used for extrapolation of the parameters to the unmonitored wind turbines.

The results contribute as one part of the added values from implementing and analyzing of SHM data. When these results are used to update the scale parameters used for Risk Based Inspection Planning, more realistic inspection plans can be achieved.

REFERENCES

[1] W. Engels, T. Obdam and F. Savenije, Current developments in wind: Going to great lengths to improve wind energy, *ECN: Energy research center of the Netherlands*, 2009.

[2] D. Milborrow, Operation and maintenance costs compared and revealed, *Wind Stats*, **19(3): 3**, 2006.

[3] E. Wiggelinkhuizen, H. Braam, L. Rademakers, J. Xiang,G. Hassan, M. Tipluica, A. MacLean, A. Juhl, E. Becker & D. Scheffler, CONMOW: Condition Monitoring for Offshore Wind Farms. *Project*: CONMOW, 2003

[4] ISO 31000: 2018(en), Risk management - Guidelines, *ISO/TC 262*, International Organization for Standardization. 02.2018

[5] J. Seo, J.W. Hu, J. Lee, Summary Review of Structural Health Monitoring Applications for Highway Bridges, *Performance of Constructed Facilities*, **30: 4**, American Society of Civil Engineers,2016. doi: 10.1061/(ASCE)CF.1943-5509.0000824

[6] H. Raiffa and R. Schlaifer, Applied statistical decision theory, *Studies in managerial economics*, Boston, Division of Research, Graduate School of Business Administration, Harvard University, 1961.

[7] D. Straub and M.H. Faber, System Effects in Generic Risk-Based Inspection Planning, *OFFSHORE MECHANICS AND ARCTIC ENGINEERING*, **126(3)**, 265-271, 2004. doi.org/10.1115/1.1782642

[8] D. Straub, Generic Approaches to Risk Based Inspection Planning for Steel Structures, *Dissertation*, Institute of Structural Engineering, Swiss Federal Institute of Technology, ETH Zürich. 2004

[9] M. H. Faber and S. Thöns, On the Value of Structural Health Monitoring. European Safety and Reliability Conference (ESREL) 2013. Amsterdam

[10] COST Action TU1402, Quantifying the Value of Structural Health Monitoring, EU Framework Program Horizon 2020. 2014 to 2019

[11] M. H. Faber, Statistics and Probability Theory: In Pursuit of Engineering Decision Support, *Springer Netherlands*, 2012. doi.org/10.1007/978-94-007-4056-3

[12] D. Diamantidis, M. Sykora an H. Sousa, Quantifying the Value of Structural Health Monitoring: Guide for practising Engineers, Cost Action TU1402, 2019

[13] L. Long, M. Döhler and S. Thöns, Determination of structural and damage detection system influencing parameters on the value of information. *Structural Health Monitoring*, **1-18**, 2020. doi.org/ 10.1177/1475921719900918

[14] BSH Standard, 2007. Design of Offshore Wind Turbines. Federal Maritime and Hydrographic Agency (BSH). Hamburg and Rostock, Germany.

[15] BSH Standard, 2015. Minimum requirements concerning the constructive design of offshore structures within the Exclusive Economic Zone (EEZ). Standard. Federal Maritime and Hydrographic Agency (BSH). Hamburg and Rostock, Germany.

[16] R. E. Melchers and A. T. Beck, Structural reliability analysis and prediction, Hoboken, NJ : Wiley, 2018.

[17] P. Paris and F. Erdogan, A critical analysis of crack propagation laws, J. Basic Eng. Dec 1963, 85(4): 528-533

[18] H. O. Madsen, R. Skjong, F. Kirkemo, Probabilistic fatigue analysis of offshore structures - reliability updating through inspection results, 3rd International Symposium on Integrity of Offshore Structures (IOS '87), Glasgow, Scotland, 1987.

[19] I. Lotsberg, G. Sigurdsson, and P. T. Wold, Probabilistic Inspection Planning of the Asgard A FPSO Hull Structure with respect to Fatigue. 18th conference OMAE, Newfoundland, Canada, 1999

[20] M. H. Faber, Reliability based assessment of existing structures, *Progress in Structural Engineering and Materials* **2, 247-253**, 2000

[21] NZ Chen, G. Wang and C.G. Soars, Palmgren-Miner's rule and fracture mechanics-based inspection planning, *Engineering Fracture Mechanics*, **78, 3166-3182**, 2011

[22] A. Almar-Naess, Fatigue Handbook - Offshore Steel Structures, Tapir Piblishers, 1985.

[23] ABS (American Bureau of Shipping), COMMENTARY ON THE GUIDE FOR THE FATIGUE ASSESSMENT OF OFFSHORE STRUCTURES, July 2014.

[24] DNVGL-RP-C210 (2015), Probabilistic methods for planning of inspection for fatigue cracks in offshore structures, Det Norske Veritas and Germanischer Lloyd (DNVGL).

[25] Paul H. Wirsching, Y.-N. Chen, Considerations of probability-based fatigue design for marine structures, *Marine Structures*, **Volume 1, Issue 1,1988**, Pages 23-45, doi.org/10.1016/0951-8339(88)90009-3.

[26] Lotsberg, I. (2016). Fatigue Design of Marine Structures. Cambridge: Cambridge University Press. doi:10.1017/CBO9781316343982

[27] S. Tewolde, R. Höffer, H. Haardt and J. Krieger, Structural Health Monitoring results as an input for asset management of offshore wind turbine support structures. 5th International Conference on Smart Monitoring, Assessment and Rehabilitation of Civil Structures (SMAR2019), Potsdam, Germany

[28] ASTM E1049-85 (2017), Standard Practices for Cycle Counting in Fatigue Analysis. West Conshohocken, ASTM International

EURODYN 2020
XI International Conference on Structural Dynamics
M. Papadrakakis, M. Fragiadakis, C. Papadimitriou (eds.)
Athens, Greece, 23–26 November 2020

INVESTIGATION OF EFFICIENT MODAL IDENTIFICATION OF BRIDGES USING BAYESIAN INFERENCE

Yoshinao Goi[1] **and Chul-Woo Kim**[1]

[1] Department of Civil and Earth Resources Engineering, Kyoto University
Kyoto 6158540, Japan
e-mail: {goi.yoshinao.2r, kim.chulwoo.5u}@kyoto-u.ac.jp

Keywords: Modal identification, Bayesian inference, Vector autoregressive model, Uncertainty quantification, Feature extraction.

Abstract. *This study proposes an efficient modal identification method for bridges under operation. The noisy condition caused by the traffic loadings is one of the difficulties involved in the operational modal identification. To cope with the problem, this study quantifies uncertainty involved in the modal properties utilizing Bayesian statistics. The quantified uncertainty enables to determine the reasonable model order and to extract the stably estimated modal properties from the determined model. The proposed method is applied to traffic induced vibration measured from an actual truss bridge. The extracted modal frequencies well correspond to peaks in power spectral density curves. Twelve bending and torsional modes are efficiently extracted by the proposed method. Six modes in the twelve is possibly newly observed modes.*

1 INTRODUCTION

Vibration based structural health monitoring provides a research field for nondestructive evaluation based on physical measurements and computer analyses to complement existing visual inspection methods. Especially for short to medium span bridges, the traffic excites the bridges continuously, and thus vibration monitoring is available without interrupting the traffic. Most of the existing studies examined modal properties such as natural frequencies and mode shapes to assess the bridge condition [1-5].

In actual bridges, however, the noisy condition caused by the traffic loadings is one of the difficulties involved in the operational modal identification. That is because the noisy condition induces spurious estimators of modal properties. In existing methods, it is troublesome to distinguish the physically meaningful estimators from the spurious estimators [6-10]. Aiming at application in noisy condition, several studies provided methodology for uncertainty quantification using Bayesian statistics. For instance, Au [11] proposed a Bayesian modal analysis method using Bayesian inference of modal properties. Several studies investigated the posterior distribution of parameters to assess their variability [12 – 13]. For direct decision-making, Dzunic et al. [14] proposed damage detection and classification methods applying Gibbs sampling. Although the uncertainty is successfully quantified through the previous studies, most of the existing Bayesian methods require computational effort to provide numerical optimization or Monte-Carlo sampling. Aiming at application to on-site damage detection, the difficulty in computation may bother efficient decision making.

To cope with the problem, this study simplifies the uncertainty quantification process using a vector autoregressive (VAR) model. As proposed in an authors' previous study [15], Bayesian inference produce the posterior distribution of regressive parameters of a VAR model without numerical iteration. The posterior distribution is converted to the distribution of poles of the linear system, which related to the modal properties. Uncertainty of the modal properties is quantified through the distribution of the poles. The quantified uncertainty indicates the physically meaningful modal properties among the estimators. The proposed method is applied to traffic induced vibration measured from an actual truss bridge.

2 METHODOLOGY

2.1 Bayesian inference

To formulate a VAR model, first we assume that a synchronized discrete time series of the acceleration measured at *m* measurement locations on a bridge, and assume that the time series includes n time steps. A zero-mean time series is produced by subtracting the mean values from the measured accelerations. Letting $\boldsymbol{y}_k \in \mathbb{R}^{m\times 1}$ $(k = 1 \ldots n)$ denote a column vector of the measured accelerations at the *k*-th time step of the time series whose components corresponding to the measurement locations, then the following VAR model with sufficient model order *p* is known to approximate the time series obtained from a linear structural system excited by white noise [16].

$$\boldsymbol{y}_k = \sum_{i=1}^{p} \boldsymbol{\alpha}_i \boldsymbol{y}_{k-i} + \boldsymbol{e}_k \tag{1}$$

Here, $\boldsymbol{\alpha}_i \in \mathbb{R}^{m\times m}$ denotes the *i*-th AR coefficient matrix and $\boldsymbol{e}_k \in \mathbb{R}^{m\times 1}$ denotes a zero-mean Gaussian white noise vector. Letting $\boldsymbol{\Sigma}$ denote the covariance matrix of $\boldsymbol{e}_k$, the PDF of $\boldsymbol{e}_k$ is given as

$$\mathrm{p}(\boldsymbol{e}_k|\boldsymbol{\Sigma}) = \mathcal{N}(\boldsymbol{e}_k|\boldsymbol{0},\boldsymbol{\Sigma}) = (2\pi)^{-m/2}|\boldsymbol{\Sigma}|^{-1/2}\exp\left\{-\frac{1}{2}\boldsymbol{e}_k{}^{\mathrm{T}}\boldsymbol{\Sigma}^{-1}\boldsymbol{e}_k\right\} \tag{2}$$

where $\mathcal{N}(\boldsymbol{x}|\boldsymbol{\mu},\boldsymbol{\Sigma})$ denotes the PDF of $\boldsymbol{x}$ following the multivariate Gaussian distribution with expectation $\boldsymbol{\mu}$ and covariance matrix $\boldsymbol{\Sigma}$, and where $|\cdot|$ denotes the determinant of a matrix.

The VAR model given in Eq. 1 is a linear regressive model composed of the regressive coefficients $\boldsymbol{\alpha}_1, \ldots, \boldsymbol{\alpha}_p$, input variables $\boldsymbol{y}_{k-1} \ldots \boldsymbol{y}_{k-p}$, and output variables $\boldsymbol{y}_k$. Letting $\mathbf{W} = [\boldsymbol{\alpha}_1, \ldots, \boldsymbol{\alpha}_p] \in \mathbb{R}^{m\times mp}$ and $\boldsymbol{\phi}_k = [\boldsymbol{y}_{k-1}; \ldots; \boldsymbol{y}_{k-p}] \in \mathbb{R}^{mp\times 1}$ for simplicity, Eq. 1 can be rewritten as

$$\boldsymbol{y}_k = \mathbf{W}\boldsymbol{\phi}_k + \boldsymbol{e}_k \tag{3}$$

According to Eqs. 2 and 3, $\boldsymbol{y}_k$ follows the following Gaussian distribution.

$$\mathrm{p}(\boldsymbol{y}_k|\boldsymbol{\phi}_k, \mathbf{W}, \boldsymbol{\Sigma}) = \mathcal{N}(\boldsymbol{y}_k|\mathbf{W}\boldsymbol{\phi}_k, \boldsymbol{\Sigma}) \tag{4}$$

This study presumes that the time series are independently measured l times. Let $\boldsymbol{y}_k^{(i)}$ $(i = 1 \ldots l)$ denote the measured acceleration at k-th time step in i-th time series and n_i denote its data length. Let $\mathbf{Y_i} = \left[\boldsymbol{y}_{p+1}^{(i)}, \ldots, \boldsymbol{y}_{n_i}^{(i)}\right] \in \mathbb{R}^{m\times(n_i-p)}$ and $\boldsymbol{\Phi_i} = \left[\boldsymbol{\phi}_{p+1}^{(i)}, \ldots, \boldsymbol{\phi}_{n_i}^{(i)}\right] \in \mathbb{R}^{mp\times(n_i-p)}$. Because the noise term $\boldsymbol{e}_k$ is white noise, the following PDF is obtained.

$$\mathrm{p}(\mathbf{Y_i}|\boldsymbol{\Phi_i}, \mathbf{W}, \boldsymbol{\Sigma}) = \prod_{k=p+1}^{n} \mathcal{N}(\boldsymbol{y}_k|\mathbf{W}\boldsymbol{\phi}_k, \boldsymbol{\Sigma}) \tag{5}$$

In the proposed method, the PDF in Eq. 5 is regarded as the likelihood function for parameters $\mathbf{W}$ and $\boldsymbol{\Sigma}$. Accordingly, the Bayesian theorem provides the following relationship.

$$\mathrm{p}(\mathbf{W}, \boldsymbol{\Sigma}|\mathbf{Y_i}, \boldsymbol{\Phi_i}) = \mathrm{p}(\mathbf{Y_i}|\boldsymbol{\Phi_i}, \mathbf{W}, \boldsymbol{\Sigma})\mathrm{p}(\mathbf{W}, \boldsymbol{\Sigma})\mathrm{p}(\mathbf{Y_i}|\boldsymbol{\Phi_i})^{-1} \tag{6}$$

For Bayesian inference, this study adopts conjugate priors [17], which produce posterior distributions with invariant functional forms. Aiming at fast computation for in-service damage detection, the conjugate priors are beneficial because they produce the posterior distributions without Monte Carlo sampling. For the VAR model, the conjugate prior for $\mathbf{W}$ and $\boldsymbol{\Sigma}$ is known to be given as the following matrix-normal inverse-Wishart distribution [14].

$$\mathrm{p}(\mathbf{W}, \boldsymbol{\Sigma}) = \mathcal{MN}(\mathbf{W}|\mathbf{M}, \boldsymbol{\Sigma}, \mathbf{L}^{-1})\mathcal{IW}(\boldsymbol{\Sigma}|\boldsymbol{\Psi}, \nu) \tag{7}$$

In that equation, $\mathbf{M} \in \mathbb{R}^{m\times mp}$, $\mathbf{L} \in \mathbb{R}^{mp\times mp}$, $\boldsymbol{\Psi} \in \mathbb{R}^{m\times m}$ and $\nu \in \mathbb{R}$ are hyperparameters, i.e. the parameters composing the PDF for $\mathbf{W}$ and $\boldsymbol{\Sigma}$. $\mathcal{MN}(\mathbf{W}|\mathbf{M}, \boldsymbol{\Sigma}, \mathbf{L}^{-1})$ and $\mathcal{IW}(\boldsymbol{\Sigma}|\boldsymbol{\Psi}, \nu)$ respectively stand for the following matrix-normal and inverse-Wishart distributions as

$$\begin{aligned}&\mathcal{MN}(\mathbf{W}|\mathbf{M}, \boldsymbol{\Sigma}, \mathbf{L}^{-1})\\ &= (2\pi)^{-\frac{mp\times m}{2}}|\mathbf{L}^{-1}|^{-\frac{m}{2}}|\boldsymbol{\Sigma}|^{-\frac{mp}{2}} \times \exp\left\{-\frac{1}{2}\mathrm{tr}[\mathbf{L}(\mathbf{W}-\mathbf{M})^{\mathrm{T}}\boldsymbol{\Sigma}^{-1}(\mathbf{W}-\mathbf{M})]\right\}\end{aligned} \tag{8}$$

$$\mathcal{IW}(\boldsymbol{\Sigma}|\boldsymbol{\Psi}, \nu) = 2^{-\nu m/2}\Gamma_m\left(\frac{\nu}{2}\right)|\boldsymbol{\Psi}|^{\frac{\nu}{2}}|\boldsymbol{\Sigma}|^{-\frac{(\nu+m+1)}{2}} \times \exp\left\{-\frac{1}{2}\mathrm{tr}[\boldsymbol{\Psi}\boldsymbol{\Sigma}^{-1}]\right\} \tag{9}$$

where $\Gamma_m(\cdot)$ is the multivariate gamma function.

The likelihood function in Eq. 5 and Bayesian theorem given in Eq. 6 are known to engender the following posterior distribution [14].

$$\mathrm{p}(\mathbf{W}, \boldsymbol{\Sigma}|\mathbf{Y_i}, \boldsymbol{\Phi_i}) = \mathcal{MN}\left(\mathbf{W}|\mathbf{M}', \boldsymbol{\Sigma}, \mathbf{L}'^{-1}\right)\mathcal{IW}(\boldsymbol{\Sigma}|\boldsymbol{\Psi}', \nu') \tag{10}$$

In the equation above, the following variables are used.

$$\mathbf{L}' = \mathbf{L} + \boldsymbol{\Phi_i}\boldsymbol{\Phi_i}^{\mathrm{T}} \tag{11}$$

$$\mathbf{M}' = (\mathbf{M}\mathbf{L} + \mathbf{Y_i}\boldsymbol{\Phi_i}^{\mathrm{T}})\mathbf{L}'^{-1} \tag{12}$$

$$\nu' = \nu + n_i - p \tag{13}$$

$$\mathbf{\Psi}' = \mathbf{\Psi} + \mathbf{Y_i Y_i}^{\mathrm{T}} + \mathbf{MLM}^{\mathrm{T}} - \mathbf{M}'\mathbf{L}'\mathbf{M}'^{\mathrm{T}} \tag{14}$$

For simplicity, this study adopts uniform prior distribution, i.e. $\mathrm{p}(\mathbf{W}, \mathbf{\Sigma}) \propto Const.$, to represent non-informative prior. That is, we assume the hyperparameters as $[\mathbf{L}]_{ij} = 0\ (i, j = 1 \ldots mp\ ),\ \nu = -(mp + m + 1)$, and $[\mathbf{\Psi}]_{ij} = 0\ (i, j = 1 \ldots m)$. Adopting all of the measured time series, Eqs. 11-14 produces following distribution.

$$\mathrm{p}(\mathbf{W}, \mathbf{\Sigma} | \mathbf{Y_1}, \mathbf{\Phi_1}, \ldots, \mathbf{Y}_l, \mathbf{\Phi}_l) = \mathcal{MN}\left(\mathbf{W} | \mathbf{M}'', \mathbf{\Sigma}, \mathbf{L}''^{-1}\right) \mathcal{IW}(\mathbf{\Sigma} | \mathbf{\Psi}'', \nu'') \tag{15}$$

where

$$\mathbf{L}'' = \Sigma_{i=1}^{l} \mathbf{\Phi}_i \mathbf{\Phi}_i^{\mathrm{T}} \tag{16}$$

$$\mathbf{M}'' = (\Sigma_{i=1}^{l} \mathbf{Y}_i \mathbf{\Phi}_i^{\mathrm{T}}) \mathbf{L}''^{-1} \tag{17}$$

$$\nu'' = -(mp + m + 1) + \Sigma_{i=1}^{l} (n_i - p) \tag{18}$$

$$\mathbf{\Psi}'' = \Sigma_{i=1}^{l} \mathbf{Y}_i \mathbf{Y}_i^{\mathrm{T}} - \mathbf{M}''\mathbf{L}''\mathbf{M}''^{\mathrm{T}} \tag{19}$$

2.2 Model selection

To find optimal model order p, this study adopts following Bayesian information criterion (BIC) [17, 18].

$$BIC = -2 \ln \mathrm{p}\left(\mathcal{D} \middle| \widehat{\boldsymbol{\theta}}\right) + M \ln N \tag{20}$$

where the PDF $\mathrm{p}(\mathcal{D}|\boldsymbol{\theta})$ represents likelihood function of parameters $\boldsymbol{\theta}$ with observed data $\mathcal{D}$, and $\widehat{\boldsymbol{\theta}}$ represents its most likelihood estimators. M denotes the number of parameter, and N denotes total data length.

In this study, the total data length of the observed data $\mathbf{Y}_1, \ldots, \mathbf{Y}_l$ is given as $N = \Sigma_{i=1}^{l} (n_i - p)$. It is known that the most log-likelihood of Gaussian distribution is given as

$$\ln \mathrm{p}\left(\mathbf{Y}_1, \ldots, \mathbf{Y}_l \middle| \widehat{\boldsymbol{\theta}}\right) = -\frac{N}{2} \left(m \ln 2\pi + \ln \left|\widehat{\mathbf{\Sigma}}\right| + m\right) \tag{21}$$

where $\widehat{\mathbf{\Sigma}}$ represents the most likelihood estimator of $\mathbf{\Sigma}$. According to Eqs. 16, 17, and 19, the most likelihood estimator is given as

$$\widehat{\mathbf{\Sigma}} = \mathbf{\Psi}''/N. \tag{22}$$

Therefore the BIC given in Eq. 20 is calculated with the following equation.

$$BIC = N(m \ln 2\pi + \ln|\mathbf{\Psi}''/N| + m) + \left(m^2 p + \frac{m(m+1)}{2}\right) \ln N \tag{23}$$

It is supposed that the less BIC provides the better statistical model.

2.3 Uncertainty quantification

The uncertainty of the each identified mode is derived from Eq. 15 as follows. First, this study assumes $\mathbf{\Sigma}$ is fixed to the most likelihood estimator for simplicity, instead of the inverse-Wishart distribution. Therefore, the posterior distribution of $\mathbf{W}$ is given as follows instead of Eq. 15.

$$\mathrm{p}(\mathbf{W} | \mathbf{Y_1}, \mathbf{\Phi_1}, \ldots, \mathbf{Y}_l, \mathbf{\Phi}_l) = \mathcal{MN}\left(\mathbf{W} | \mathbf{M}'', \widehat{\mathbf{\Sigma}}, \mathbf{L}''^{-1}\right) \tag{24}$$

It is known that the VAR model in Eq. 1 is reproduced to the following state space model [19].

$$\boldsymbol{\phi}_{k+1} = \mathbf{A}\boldsymbol{\phi}_k + \begin{bmatrix} \mathbf{I}_m \\ \mathbf{O} \end{bmatrix} \boldsymbol{e}_k \tag{25}$$

$$\boldsymbol{y}_k = [\mathbf{I}_m \quad \mathbf{O}]\boldsymbol{\phi}_{k+1} \tag{26}$$

where $\mathbf{I}_m$ denotes the eigenmatrix of size m, $\mathbf{O}$ denotes the zero matrix with the appropriate size, and $\mathbf{A} \in \mathbb{R}^{mp \times mp}$ represents the following matrix.

$$\mathbf{A} = \left[\begin{array}{c|c} \mathbf{W} & \\ \hline \mathbf{I}_{m(p-1)} \quad \mathbf{O} & \end{array}\right] \tag{27}$$

The eigenvalue decomposition of the matrix $\mathbf{A}$ is given as follows.

$$\mathbf{A} = \mathbf{P}\boldsymbol{\Lambda}\mathbf{P}^{-1} \tag{28}$$

where $\boldsymbol{\Lambda}$ denotes the diagonal matrix composed of the eigenvalues of matrix $\mathbf{A}$, and $\mathbf{P}$ denotes the matrix composed of the corresponding eigenvectors. It is well known that the eigenvalues represent the poles of the transfer function of the dynamic model given in Eqs. 25-26. That is, letting ω_i and ζ_i respectively represent the i-th natural angular frequency and damping ratio, and λ_i denote the i-th eigenvalue of the matrix $\mathbf{A}$, the following relation is given.

$$\lambda_i = \exp\left[\left(-\zeta_i\omega_i + \jmath\sqrt{1-\zeta_i^2}\omega_i\right)\Delta t\right] \tag{29}$$

where Δt represents the sampling interval of the time series and $\jmath$ represents the imaginary unit.

Because the matrix $\mathbf{W}$ in Eq. 24 is composed of random variables, the random distribution of $\mathbf{W}$ is transformed into the the random distribution of λ_i according to Eq. 28. Accordingly, uncertainty involved in λ_i is quantified through there variables. Because λ_i will be an imaginary number, this study quantifies the uncertainty with the following equation.

$$\mathrm{var}(\lambda_i) = \mathrm{E}[(|\lambda_i - \mathrm{E}[\lambda_i]|^2)] \tag{30}$$

where $\mathrm{E}[\cdot]$ denotes the expectation of a random variable and $|\cdot|$ represents absolute value of an imaginary number. This study refers $\mathrm{var}(\lambda_i)$ in Eq. 30 as "variance of pole."

For efficacy, this study produces approximated closed form solution of $\mathrm{var}(\lambda_i)$ as follows. First, according to Eqs. 24 and 27, the expectation of matrix $\mathbf{A}$ is given as

$$\overline{\mathbf{A}} = \left[\begin{array}{c|c} \mathbf{M}'' & \\ \hline \mathbf{I}_{m(p-1)} \quad \mathbf{O} & \end{array}\right]. \tag{31}$$

Let the eigenvalue decomposition of $\overline{\mathbf{A}}$ represent with the following equation.

$$\overline{\mathbf{A}} = \overline{\mathbf{P}}\overline{\boldsymbol{\Lambda}}\overline{\mathbf{P}}^{-1} \tag{32}$$

And let the deviation of matrices $\mathbf{A}$, $\mathbf{P}$ and $\boldsymbol{\Lambda}$ respectively be represented as $\widetilde{\mathbf{A}} = \mathbf{A} - \overline{\mathbf{A}}$, $\widetilde{\mathbf{P}} = \mathbf{P} - \overline{\mathbf{P}}$ and $\widetilde{\boldsymbol{\Lambda}} = \boldsymbol{\Lambda} - \overline{\boldsymbol{\Lambda}}$. According to Eq. 28, following equation is produced.

$$(\overline{\mathbf{A}} + \widetilde{\mathbf{A}})(\overline{\mathbf{P}} + \widetilde{\mathbf{P}}) = (\overline{\mathbf{P}} + \widetilde{\mathbf{P}})(\overline{\boldsymbol{\Lambda}} + \widetilde{\boldsymbol{\Lambda}}) \tag{33}$$

Ignoring the squared deviations, Eqs. 32-33 approximately produce

$$\widetilde{\boldsymbol{\Lambda}} = \overline{\mathbf{P}}^{-1}\widetilde{\mathbf{A}}\overline{\mathbf{P}} + \overline{\boldsymbol{\Lambda}}\overline{\mathbf{P}}^{-1}\widetilde{\mathbf{P}} - \overline{\mathbf{P}}^{-1}\widetilde{\mathbf{P}}\overline{\boldsymbol{\Lambda}}. \tag{34}$$

Since $\overline{\boldsymbol{\Lambda}}$ is a diagonal matrix,

$$\mathrm{diag}(\overline{\boldsymbol{\Lambda}}\overline{\mathbf{P}}^{-1}\widetilde{\mathbf{P}}) = \mathrm{diag}(\overline{\mathbf{P}}^{-1}\widetilde{\mathbf{P}}\overline{\boldsymbol{\Lambda}}) \tag{35}$$

where $\mathrm{diag}(\cdot)$ represents a vector composed from the diagonal elements of a matrix. According to Eqs. 34-35, the variance of eigenvalues are approximated as follows.

$$\mathrm{diag}(\widetilde{\boldsymbol{\Lambda}}) = \mathrm{diag}(\overline{\mathbf{P}}^{-1}\widetilde{\mathbf{A}}\overline{\mathbf{P}}) \tag{36}$$

Eqs. 27 and 31 ensures that matrix $\widetilde{\mathbf{A}}$ is given as

$$\widetilde{\mathbf{A}} = \begin{bmatrix} \mathbf{W} - \mathbf{M}'' \\ \mathbf{O} \end{bmatrix}. \tag{37}$$

Letting $\widetilde{\mathbf{W}} = \mathbf{W} - \mathbf{M}''$ and $\mathbf{V} = \left(\{\overline{\mathbf{P}}^{-1}\}_{[:,1:m]}\right)^{\mathrm{T}}$, where $\{\cdot\}_{[:,1:m]}$ denotes a submatrix consisting of the first m columns, Eq. 36 is transformed as

$$\mathrm{diag}(\widetilde{\mathbf{\Lambda}}) = \mathrm{diag}(\mathbf{V}^{\mathrm{T}}\widetilde{\mathbf{W}}\overline{\mathbf{P}}). \tag{38}$$

Let the $\tilde{\lambda}_i$ represent the i-th diagonal member of $\widetilde{\mathbf{\Lambda}}$. Eq. 38 produces $\tilde{\lambda}_i = \boldsymbol{v_i}^{\mathrm{T}}\widetilde{\mathrm{W}}\boldsymbol{p_i}$, where $\boldsymbol{v_i}$ and $\boldsymbol{p_i}$ are respectively represent the i-th column of the matrices $\mathbf{V}$ and $\overline{\mathbf{P}}$. Accordingly, the following equation is given.

$$\tilde{\lambda}_i = \boldsymbol{v_i}^{\mathrm{T}}\widetilde{\mathrm{W}}\boldsymbol{p_i} = (\boldsymbol{p_i} \otimes \boldsymbol{v_i})^{\mathrm{T}} vec(\widetilde{\mathbf{W}}) \tag{39}$$

where $\otimes$ denotes the Kronecker product and $vec(\cdot)$ denotes a vectorization of a matrix.

According to the definition, the matrix $\widetilde{\mathbf{W}}$ follows the following matrix normal distribution.

$$\mathrm{p}\left(\widetilde{\mathbf{W}}|\mathbf{Y_1}, \mathbf{\Phi_1}, \dots, \mathbf{Y}_l, \mathbf{\Phi}_l\right) = \mathcal{MN}\left(\mathbf{W}|\mathbf{O}, \widehat{\mathbf{\Sigma}}, \mathbf{L}''^{-1}\right) \tag{40}$$

It is known that the matrix normal distribution is equivalent to the following multivariable Gaussian distribution.

$$\mathrm{p}\left(vec(\widetilde{\mathbf{W}})\middle|\mathbf{Y_1}, \mathbf{\Phi_1}, \dots, \mathbf{Y}_l, \mathbf{\Phi}_l\right) = \mathcal{N}\left(vec(\widetilde{\mathbf{W}})|\mathbf{O}, \mathbf{L}''^{-1} \otimes \widehat{\mathbf{\Sigma}}\right) \tag{41}$$

According to Eqs. 39 and 41, $\mathrm{var}(\lambda_i)$ defined in Eq. 30 is calculated as

$$\begin{aligned} \mathrm{var}(\lambda_i) &= \mathrm{E}\left[|\tilde{\lambda}_i|^2\right] = \left|(\boldsymbol{p_i} \otimes \boldsymbol{v_i})^{\mathrm{T}}\ \mathrm{E}\left[vec(\widetilde{\mathrm{W}})vec(\widetilde{\mathrm{W}})^{T}\right](\boldsymbol{p_i} \otimes \boldsymbol{v_i})^{*}\right| \\ &= (\boldsymbol{p_i} \otimes \boldsymbol{v_i})^{\mathrm{T}}\left(\mathbf{L}''^{-1} \otimes \widehat{\mathbf{\Sigma}}\right)(\boldsymbol{p_i} \otimes \boldsymbol{v_i})^{*} = \boldsymbol{p_i}^{\mathrm{T}}\mathbf{L}''^{-1}\boldsymbol{p_i^*}\boldsymbol{v_i}^{\mathrm{T}}\widehat{\mathbf{\Sigma}}\boldsymbol{v_i^*} \end{aligned} \tag{42}$$

where $\{\cdot\}^*$ represents the conjugate pair. The uncertainty of the each mode are quantified using Eq. 42. This study presumes that the physically meaningful mode produces $\mathrm{var}(\lambda_i)$ with lower value than the others. Thus, physically meaningful modes will be effectively extracted by sorting the calculated $\mathrm{var}(\lambda_i)$ values.

3 CASE STUDY

3.1 Target bridge and preliminary investigation

This study provides a case study for a simply supported truss bridge to assess the feasibility of the proposed method through comparison to an earlier investigation [9]. Field experiments were conducted to the bridge with a moving vehicle. The bridge is a single-lane through-type

Figure 1. Photo of the target bridge.

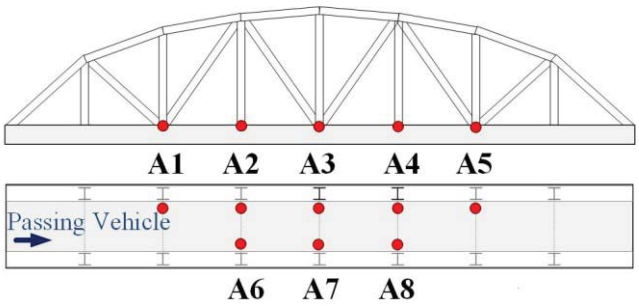

Figure 2. Sensor deployment

Vehicle speed (km/h)	Number of measurement
30	11
40	10
50	5

Table 1. Vehicle speed and number of measurement

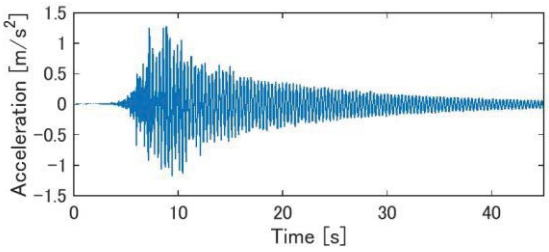

Figure 3. An example of measured acceleration

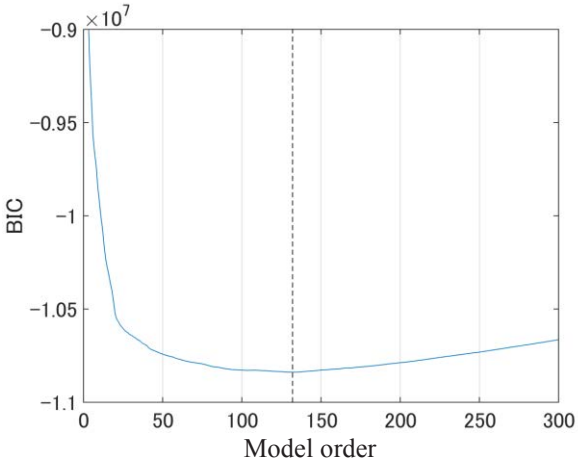

Figure 4. BIC with respect to the model order.

steel Warren truss bridge with 59.2 m span length, 8 m maximum height, and 3.6 m width as presented in Fig. 1. The vehicle used for the experiment is a two-axle recreational vehicle with total weight of about 21 kN. During the experiment, all traffic except the loading vehicle was prohibited. Eight uniaxial accelerometers were installed on the deck of the bridge to measure vertical vibrations as presented in Fig. 2. The sampling rate of each sensor was set as 200 Hz.

Each of the sampled time series is de-trended: the linear trends in the time series are removed in advance. The vehicle was passed over at three speeds: 30 km/h, 40 km/h, and 50 km/h. Table 1 presents the number of vehicle loadings.

Fig. 3 shows a measured time series at A3 accelerometer with vehicle passing by 40 km/h for instance. This case study adopts raw time series data with no pre-processing except the de-trending. BIC in Eq. 23 is calculated using the measured 26 time series as shown in Fig. 4. Fig. 4 indicates that the optimal model order, which produces the minimal BIC, is p=135. This study adopts the optimized model order.

3.2 Identified modes

As mentioned above, the proposed method extract physically meaningful modes by sorting the calculated variance of poles. The proposed Bayesian inference applied to the 26 time series. Fig. 5 shows the sorted variance of poles. In the diagram, the 50 smallest results are displayed. It is observed that 13 poles have smaller variance, i.e. less uncertainty, than the others. This study extracts the 13 poles to identify the physically meaningful modes. In Fig. 5, the vertical dashed line shows the boundary between the extracted and the rest poles. Table 2 shows the 13 smallest variances and corresponding modal frequencies.

Fig. 6 shows comparison between the extracted modal frequencies and power spectral density (PSD) curves obtained from the 8 accelerometers. Fig. 6a provides the PSD curves below

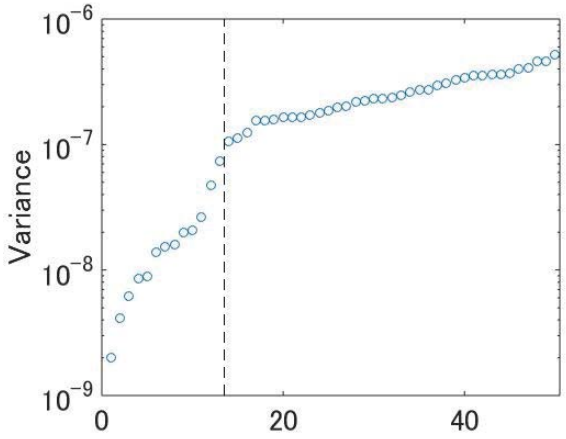

Figure 5. Sorted variance of poles

Variance of Pole	Modal frequency (Hz)
0.200×10 - 8	60.02
0.416×10 - 8	2.97
0.617×10 - 8	6.86
0.851×10 - 8	3.63
0.897×10 - 8	5.19
1.39×10 - 8	10.51
1.53×10 - 8	9.94
1.60×10 - 8	9.59
2.00×10 - 8	6.31
2.09×10 - 8	2.50
2.64×10 - 8	13.41
4.75×10 - 8	22.54
7.40×10 - 8	20.13

Tables 2 Variance of poles and extracted modal frequencies.

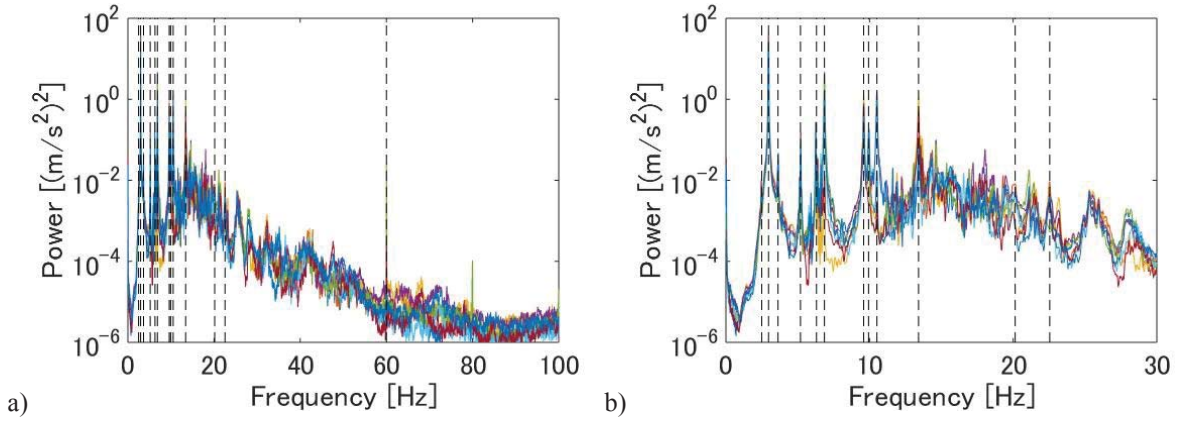

Figure 6. Comparison between the extracted modes and PSD: a) below the Nyquist frequency; b) below 30 Hz.

the Nyquist frequency, i.e. 100 Hz, and Fig. 6b provides the enlarged diagram below 30Hz in Fig. 6a. The PSD curves are estimated from the measured 26 time series as the modified periodograms adopting the Hamming window [20]. The extracted frequencies are depicted as the vertical dashed lines in Figs. 6a and 6b. One of the extracted mode correspond to the peak at 60Hz in Fig. 6a. Apparently, that is signal coming from the power supply in western region of Japan, and thus the mode at 60Hz is not a structural mode. The other 12 modes out of the 13 are below 30 Hz as shown in Fig. 6a. The extracted modes below 30 Hz seem well correspond to the peaks in the PSD curves. This observation describes that the proposed method is comparative to the conventional peak picking for dominant modes. The modes at 3.0 Hz and 3.6 Hz were not identified in the conventional time-domain modal analysis [9]. Fig. 6b also shows that the modes identified at 20.1 Hz and 22.5 Hz are not observed as peaks in PSD diagram. The validity of this result is discussed later considering the mode shapes.

It is well-known that the mode shapes are estimated as a real part of vector $\boldsymbol{v_i}$ [19]. The mode shapes corresponding to the extracted poles are also determined. Fig. 7 shows the extracted mode shapes. In the diagrams, the horizontal axis represents relative location of the sensors along the longitudinal direction on the bridge, and the vertical axis represents relative modal deformation. The markers depicted with blue circles represent the modal deformation from A1 to A5, the markers with orange squares represent the deformation from A6 to A8.

The mode shapes in Fig. 7b), f), g), i), and j) seem to correspond to bending modes because the modal deformations on A1-A5 edge and A6-A8 edge are deforms simultaneously. These results correspond to the previous study by Chang and Kim [9]. Contrarily, it is reasonable to regard the mode shapes in Fig. 7d), h), k), and l) as torsional modes because the both edge deforms alternately. The mode in Fig. 7d) is also observed in the previous study. The other three torsional modes are newly identified in this study. Especially, the modes in Fig. 7k) and l) are not observed in the PSD curves as mentioned above. Also the mode in Fig. 7h) was not observed in the previous study either. That is possibly because the mode is close to the others and Stabilization diagram [19] did not work well in the time-domain analysis. These results suggest that the proposed method has advantage to extract higher modes which is hard to find from the PSD curves.

The mode shapes in Fig. 7a), c), and e) seems like torsional modes also. However, the edges of the bridge do not deform alternately to each other. Further investigation is desired to validate these modes. As mentioned above, the mode shape in Fig. 7m) is derived from the power supply,

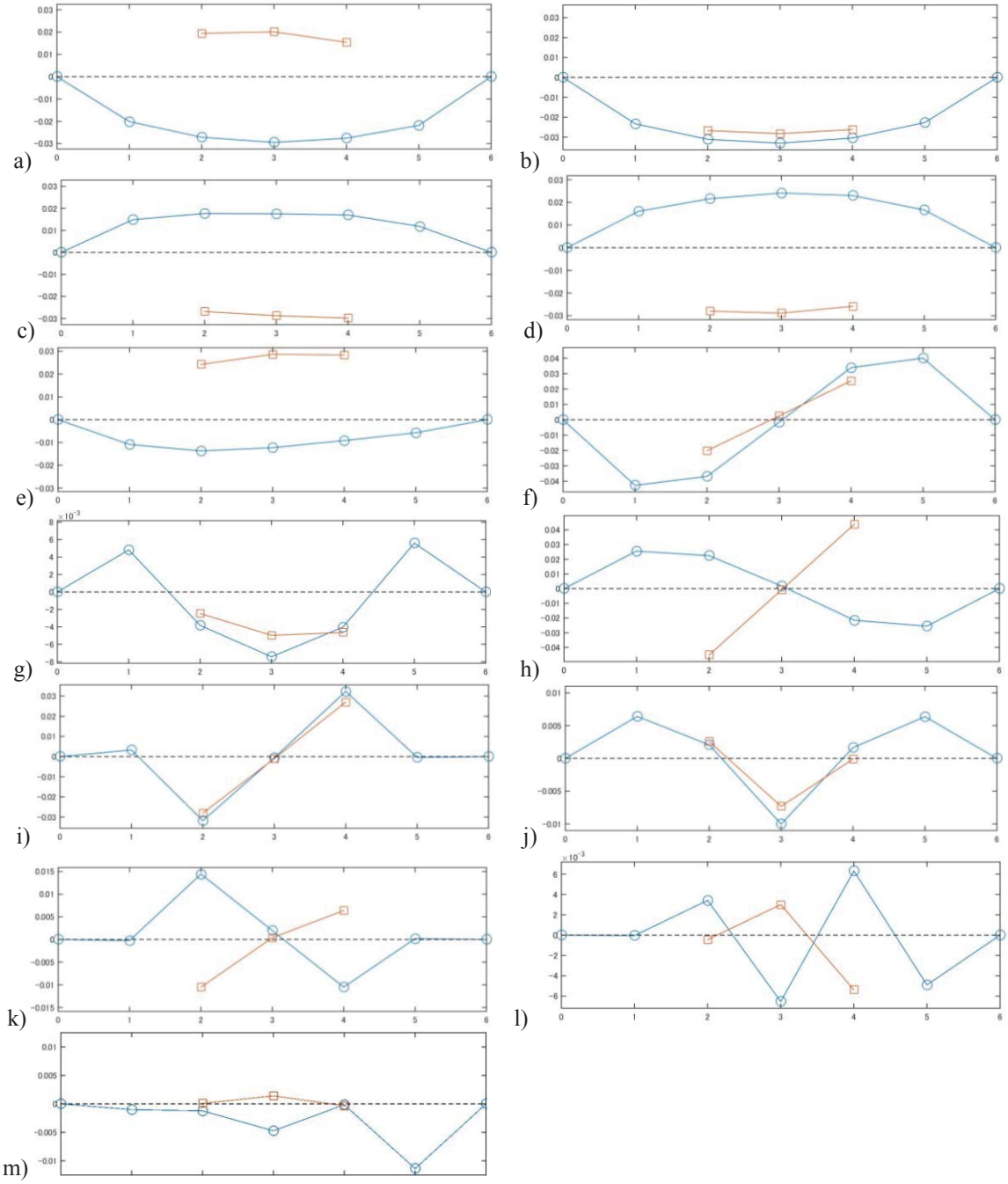

Figure 7. Extracted mode shapes:
a) 2.50Hz； b) 2.97Hz； c) 3.63Hz； d) 5.19Hz； e) 6.31Hz； f) 6.86Hz；
g) 9.59Hz； h) 9.94Hz； i) 10.51Hz； j) 13.41Hz； k) 20.13Hz ; l) 22.54Hz ; m) 60.02Hz.

not from the structural deformation. That is why the mode shapes appear not to correspond to bending or torsional modes.

4 CONCLUSIONS

Aiming to develop effective modal analysis, this study proposed modal identification method applying Bayesian inference. Uncertainty involved modal identification was quantified to extract physically meaningful modes. A vector auto regressive model is applied to produce

posterior distribution of parameters in a dynamical model. Bayesian information criterion is applied to optimize the model order. The uncertainty of the identified modes is quantified evaluating variation of poles of the transfer function of the model.

Time series of acceleration which are actually measured on a simply supported truss bridge are applied for the proposed method. 13 poles produced the variation with lower values than the others. This study investigated the modal properties corresponding to the 13 poles. Power spectrum density curves were compared to the identified modal frequencies. Also, mode shapes were examined to validate the proposed method. One of the identified mode appears to be derived from power supply, and not from structural deformation. Except the one mode, 12 modes seem to correspond to the bending and torsional modes: 5 modes out from the 12 modes correspond to bending modes. 4 modes out from the 12 modes correspond to torsional modes. 5 bending modes and 1 torsional mode were also observed in a previous study [9]. 3 torsional modes were newly observed in this study. This result indicates advantage of the proposed method. The rest 3 modes seem like torsional modes. Further investigation is desired for validation of these 3 modes.

FUNDING

This study was partly sponsored by a Japanese Society for Promotion of Science (JSPS) Grant-in-Aid for Scientific Research (B) under Project No. 16H04398 and for Early-Career Scientists under Project No. 19K15072. That financial support is gratefully acknowledged.

REFERENCES

[1] S.W.S. Doebling, C.R.C. Farrar, M.B.M. Prime, D.W.D. Shevitz, Damage identification and health monitoring of structural and mechanical systems from changes in their vibration characteristics: a literature review. Los Alamos National Laboratory Report LA-13070-MS, 1996.

[2] O.S. Salawu, Detection of structural damage through changes in frequency: a review, *Eng. Struct.,* 19(9), 718–723 1997.

[3] B. Peeters, G. De Roeck, One-year monitoring of the Z 24-Bridge: environmental effects versus damage events, *Earthq. Eng. Struct. Dyn.* 30(2), 149–171, 2001.

[4] Q.W. Zhang, Statistical damage identification for bridges using ambient vibration data, *Comput. Struct.*, 85(7–8), 476–485, 2007.

[5] A. Deraemaeker, E. Reynders, G. De Roeck, J. Kullaa, Vibration-based structural health monitoring using output-only measurements under changing environment, *Mech. Syst. Signal Process.*, 22(1), 34–56, 2008.

[6] R. Brincker, L. Zhang, P. Andersen, Modal identification of output-only systems using frequency domain decomposition, *Smart Mater. Struct.*, 10(3), 441–445, 2001.

[7] C.W. Kim, M. Kawatani, J. Hao, Modal parameter identification of short span bridges under a moving vehicle by means of multivariate AR model, *Struct. Infrastruct. Eng.*, 8(5), 459–472, 2012.

[8] Y.Q. Ni, Y.W. Wang, Y.X. Xia, Investigation of mode identifiability of a cable-stayed bridge: comparison from ambient vibration responses and from typhoon-induced dynamic responses, *Smart Struct. Syst.* 15(2), 447–468, 2015.

[9] K.C. Chang, C.W. Kim, Modal-parameter identification and vibration-based damage detection of a damaged steel truss bridge, *Eng. Struct.*, 122, 156–173, 2016.

[10] Y. Goi, C.W. Kim, Mode identifiability of a multi-span cable-stayed bridge utilizing stabilization diagram and singular values, *Smart Struct. Syst.*, 17(3), 391–411, 2016.

[11] S.K. Au, F.L. Zhang, Y.C. Ni, Bayesian operational modal analysis: Theory, computation, practice, *Comput. Struct*. 126, 3–14, 2013.

[12] L.D. Avendaño-Valencia, E.N. Chatzi, K.Y. Koo, J.M.W. Brownjohn, Gaussian Process Time-Series Models for Structures under Operational Variability, *Front. Built Environ*. 3, 69, 2017.

[13] K. Worden, W.E. Becker, T.J. Rogers, E.J. Cross, On the confidence bounds of Gaussian process NARX models and their higher-order frequency response functions, *Mech. Syst. & Signal Processing* 104, 188–223, 2018.

[14] Z. Dzunic, J.G. Chen, H. Mobahi, O. Büyüköztürk, J.W. Fisher, A Bayesian state-space approach for damage detection and classification, *Mech. Syst. Signal Process.*, 96, 239–259, 2017.

[15] Y. Goi, C.W. Kim, Bayesian outlier detection for health monitoring of bridges, *Proceedia Eng.* 199, 2120–2125, 2017.

[16] X. He, G. De Roeck, System identification of mechanical structures by a high-order multivariate autoregressive model, *Comput. Struct.* 64(1), 341–351, 1997.

[17] C.M. Bishop, Pattern Recognition and Machine Learning, Springer, 2006.

[18] G. Schwarz, Estimating the dimension of a model, *Ann. Stat.*, 6(2), 461–464, 1978.

[19] W. Heylen, S. Lammens, and P. Sas, Modal Analysis Theory and Testing, KU Leuven, 1997.

[20] P.D. Welch The use of fast Fourier transform for the estimation of power spectra a method based on time averaging over short, modified periodograms, *IEEE Trans. Audio Electroacoust.*, 15(2), 70–73, 1967.

EURODYN 2020
XI International Conference on Structural Dynamics
M. Papadrakakis, M. Fragiadakis, C. Papadimitriou (eds.)
Athens, Greece, 23–26 November 2020

VIBRATION-BASED STRUCTURAL HEALTH MONITORING OF A REINFORCED CONCRETE BEAM SUBJECT TO VARYING AMBIENT TEMPERATURES USING BAYESIAN METHODS

P. Simon[1], R. Schneider[1], E. Viefhues[1], S. Said[1], R. Herrmann[1] and M. Baeßler[1]

[1] Bundesanstalt für Materialforschung und -prüfung (BAM)
Unter den Eichen 87, 12205 Berlin, Germany
e-mail: patrick.simon@bam.de (corresponding author)

Keywords: structural health monitoring, Bayesian methods, environmental effects

Abstract. *Inspection and maintenance contribute significantly to the lifetime cost of bridges. There is significant potential in using information obtained through structural health monitoring to update predictive models of the condition and performance of such structures, and thus enable an improved decision-making regarding inspection and maintenance activities. Within the AISTEC project funded by the German Federal Ministry of Education and Research, we develop vibration-based structural health monitoring systems aimed at continuously providing information on the structural condition of bridges. Environmental variations such as changing ambient temperatures can significantly influence the dynamic characteristics of bridges and thus mask the effect of structural changes and damages. It remains a challenge to account for such influences in structural health monitoring. To study the effect of ambient temperatures on the dynamic characteristics of beam structures, we monitor the vibration response of a reinforced concrete beam in the uncracked and cracked state at varying temperatures in a climate chamber. We postulate a set of competing parameterized probabilistic structural models, which explicitly account for the effect of varying ambient temperatures on the mechanical properties of the system. We then combine the information provided by the structural models with the information contained in the recorded vibration data to learn the parameters of the temperature-dependent structural models and infer the plausible state of the beam using Bayesian system identification and model class selection.*

1 INTRODUCTION

As transport infrastructure networks are aging, the efforts and thus the costs for inspection and maintenance of the engineering structures within the networks such as bridges are steadily growing. Structural health monitoring (SHM) has the potential of improving predictions of the condition and performance of such structural systems and can thus enhance decisions on inspection and maintenance activities as well as possible lifetime extensions.

The variability in environmental factors such as ambient temperatures can significantly influence the results of structural health monitoring [1] and consequently increase the uncertainty in the prediction of the structural condition and performance. Two strategies have emerged to address this issue [2]: methods that include a model of the structure's mechanics – here termed *model-based* methods – and methods that don't – termed *model-free* methods. The latter eliminate the environmental effects from the data and/or analysis results [1-4]. In the simplest case, a linear regression on the air temperature can be performed. In any case, predictions of a structure's condition and performance can only be made using model-based methods.

In model-based approaches, mechanical models of the structure – typically finite element (FE) models – are updated with knowledge gained from analyzing static or dynamic data [5]. Two approaches are possible to deal with the issue of environmental effects [2]: (a) eliminate these effects from the data prior to updating the model or (b) explicitly include these effects in the model. The former bears the risk of implicitly incorporating the temperature-dependent loadbearing effect of nominally non-loadbearing members such as ballast or asphalt layers. In the latter approach, the thermal actions on the structure and its effects are modelled and as a result, further knowledge on the structure can be gained.

Previous studies show that the environmental effects on structures can be of complex nature. These effects include – with no claims of comprehensiveness – effects of temperature gradients [6], differences between freezing and thawing periods [7], and non-linear behavior around the freezing point [8].

The updating of models can be accomplished either deterministically or probabilistically. The former employs optimization algorithms, which minimize the difference between model predictions and the measured data. The solution comprises of the optimal set of (deterministic) model parameters. Probabilistic model updating can be done within the Bayesian framework and is referred to as Bayesian model updating or Bayesian system identification [9-11]. This approach provides several advantages: No single *true* solution is identified. Instead, a range of plausible solutions and their relative plausibility in the form of the updated joint probability distribution of the parameters defining the problem. In this way, ill-posed problems with non-unique solution can be addressed. The approach explicitly quantifies the uncertainties in the model parameters, in the models themselves and in the data. Different sources and types of data can be included consistently in the analysis. Any prior knowledge on the structural system including expert judgement is quantified – even in the case where none is available. It is possible to perform the analysis with limited or incomplete data.

Bayesian system identification has been applied to several structural systems. Ntotsios et al. [12] used vibration data from a bridge to determine the plausible states of the structure via Bayesian model class selection [13, 14]. Zonta and Pozzi [15] compared two plausible states of a leaning bell tower. Pioneering work on including temperature-dependent material properties has been conducted by Bemanesh and Moaveni [16], who identified the temperature-dependent elastic modulus of a concrete deck of a footbridge. Recent methodological advances include hierarchical Bayesian frameworks [17-19] and sparse Bayesian learning [20].

In this work, we subject a reinforced concrete (RC) beam to different temperatures inside a climate chamber in a cracked and an uncracked state. We apply Bayesian system identification

and model class selection to determine the plausible states of the system based on modal properties extracted from vibration data. The updated model includes a sub-model of the temperature-dependent material properties and a sub-model of the system mechanics. Finally, a structural health monitoring scenario is created to demonstrate the potential of the proposed method.

2 BAYESIAN FRAMEWORK

2.1 System identification

The aim of system identification is to find a parametric model that adequately describes the physics of a system. Different models may be defined, and the parameters of each model are identified based on data obtained from the real system. The plausibility of the different models is subsequently compared. In Bayesian system identification, the parameters $\boldsymbol{\theta}$ of a model are modelled probabilistically and instead of *identifying* deterministic values of the model parameters, their probability distributions are *learned* from the measured data.

Let $\boldsymbol{q}(\boldsymbol{y}, \boldsymbol{\theta})$ be the prediction that a deterministic model yields for observable quantities $\boldsymbol{z}$ for given parameters $\boldsymbol{\theta}$ and input $\boldsymbol{y}$ of a system. The system input $\boldsymbol{y}$ such as the observed temperature of the structural system is here defined deterministically, but the framework can be extended to also capture the uncertainties in the system input.

The model prediction $\boldsymbol{q}$ and the observable quantities $\boldsymbol{z}$ may be related by means of a multiplicative prediction error $\exp(\boldsymbol{e})$, such that

$$\boldsymbol{z} = \boldsymbol{q}(\boldsymbol{y}, \boldsymbol{\theta}) \odot \exp(\boldsymbol{e}). \tag{1}$$

where $\odot$ denotes the Hadamard (element-by-element) product and the random vector $\boldsymbol{e}$ follows a multivariate Gaussian distribution with zero mean and covariance matrix $\boldsymbol{\Sigma_{ee}}$. The prediction error $\exp(\boldsymbol{e})$ jointly models the uncertainty in the data and the parametric model.

The process of linking the output of a parametric system model with the observable response of the system by means of a prediction error is known as stochastic embedding [9].

A natural logarithm transformation of the quantities in Equation (1) gives:

$$\ln \boldsymbol{z} = \ln[\boldsymbol{q}(\boldsymbol{y}, \boldsymbol{\theta})] + \boldsymbol{e}. \tag{2}$$

The ith dataset $\mathcal{D}_i$ consists of the observed input $\hat{\boldsymbol{y}}_i$ and output $\hat{\boldsymbol{z}}_i$, i.e. $\mathcal{D}_i = (\hat{\boldsymbol{y}}_i, \hat{\boldsymbol{z}}_i)$. In a Bayesian setting, the observed data $\mathcal{D}_i$ is linked to the model parameters $\boldsymbol{\theta}$ by the likelihood function $L(\boldsymbol{\theta}|\mathcal{D}_i)$, which is proportional to the conditional probability density of the data $\mathcal{D}_i$ given that the model parameters take a value $\boldsymbol{\theta}$, i.e.:

$$L(\boldsymbol{\theta}|\mathcal{D}_i) \propto p(\mathcal{D}_i|\boldsymbol{\theta}). \tag{3}$$

Based on the error model introduced in Equations (1) and (2), the likelihood function of $\mathcal{D}_i$ can be formulated as:

$$L(\boldsymbol{\theta}|\mathcal{D}_i) = \frac{1}{\sqrt{(2\pi)^n \det(\boldsymbol{\Sigma_{ee}})}} \exp\left[-\frac{1}{2}[\ln \hat{\boldsymbol{z}}_i - \ln[\boldsymbol{q}(\hat{\boldsymbol{y}}_i, \boldsymbol{\theta})]]^T \boldsymbol{\Sigma}_{\boldsymbol{ee}}^{-1} [\ln \hat{\boldsymbol{z}}_\mathrm{i} - \ln[\boldsymbol{q}(\hat{\boldsymbol{y}}_i, \boldsymbol{\theta})]]\right]. \tag{4}$$

where n corresponds to the number of measurements, i.e. n is equal to the length of $\hat{\boldsymbol{z}}_i$.

When multiple datasets are available and the different datasets are conditionally independent for given model parameters $\boldsymbol{\theta}$, the likelihood function $L(\boldsymbol{\theta}|\mathcal{D})$ describing all available datasets is the product of the likelihood functions of the individual datasets $L(\boldsymbol{\theta}|\mathcal{D}_i)$:

$$L(\boldsymbol{\theta}|\mathcal{D}) = \prod_i L(\boldsymbol{\theta}|\mathcal{D}_i). \tag{5}$$

The plausibility of different realizations of the parameters $\boldsymbol{\theta}$ prior to obtaining data is expressed in terms of the prior distribution $p(\boldsymbol{\theta})$. Following Bayes' rule, the posterior distributions of the parameters $\boldsymbol{\theta}$ conditional on the observed data $\mathcal{D}$ is computed as:

$$p(\boldsymbol{\theta}|\mathcal{D}) = c_E^{-1}\, L(\boldsymbol{\theta}|\mathcal{D})\, p(\boldsymbol{\theta}), \tag{6}$$

whereby the constant c_E is referred to as the model evidence, which is calculated by integrating the likelihood function and prior distribution over the outcome space of the parameters:

$$c_E = \int_{\boldsymbol{\theta}} L(\boldsymbol{\theta}|D)\, p(\boldsymbol{\theta})\, \mathrm{d}\boldsymbol{\theta}. \tag{7}$$

Samples from the posterior distribution $p(\boldsymbol{\theta}|\mathcal{D})$ and an estimate of the model evidence c_E are here obtained using BUS (Bayesian updating with structural reliability methods) with subset simulation introduced by Straub and Papaioannou [21] and improved by Betz et al. [22]. The simulations are performed with conditional probabilities of each intermediate event of 0.1 and 3000 Markov chain Monte Carlo samples per subset level.

2.2 Model class selection

Each parametric system model along with the formulation of the likelihood function and the prior distribution of the parameters $\boldsymbol{\theta}$ form a model class $\mathcal{M}_i$. The evidence of each model class in a set of model classes $\{\mathcal{M}_i\}_{i=1}^m$ is proportional to the probability density of the data $\mathcal{D}$ conditional on the model class $\mathcal{M}_i$:

$$c_{E|\mathcal{M}_i} \propto p(\mathcal{D}|\mathcal{M}_i). \tag{8}$$

For each model class $\mathcal{M}_i$, a prior probability $\Pr(\mathcal{M}_i)$ can be assigned. This probability describes the relative plausibility of each model class within the set prior to obtaining any data from the real system. Applying Bayes' rule anew, the probabilities of the model classes can be updated based on the available data $\mathcal{D}$:

$$\Pr(\mathcal{M}_i|\mathcal{D}) = \frac{p(\mathcal{D}|\mathcal{M}_i)\, \Pr(\mathcal{M}_i)}{\sum_{i=1}^m p(\mathcal{D}|\mathcal{M}_i)\, \Pr(\mathcal{M}_i)}. \tag{9}$$

3 EXPERIMENT

To generate data from a real structural system subject to varying environmental conditions, the vibration response of a simply supported reinforced concrete (RC) beam was measured inside a climate chamber at varying ambient temperatures as shown in Figure 1.

Figure 1: RC beam inside the climate chamber with suspended shaker.

3.1 Setup

The dimensions of the beam are 2.96 m × 0.2 m × 0.4 m (length/height/width). Based on experiments with identical beams and samples from the same concrete batch, the elastic modulus was determined as $E = 33$ GPa [23]. The beam is reinforced with two Ø16mm bars, with an effective distance of 48mm from the bottom and 60mm from the sides of the beam. No shear stirrups were used.

The intended analogy of the experiment is structural health monitoring by means of established operational modal analysis (OMA) methods. Due to its low length to height ratio and hence high eigenfrequencies, the beam is not easily excited by the ambient excitations present in the laboratory. To induce ambient excitation, an electromagnetic shaker was suspended from the beam and insulated from the climatic conditions in the chamber. This shaker generated white noise excitations in the frequency range from 30 Hz to 2000 Hz.

Six geophones – with a layout as illustrated in Figure 2 – were placed on top of the beam to measure vibration velocities. The data were acquired with a sampling rate of 5000 Hz and post-processed with a low-pass Butterworth filter with an order of 6 and a cutoff frequency of 1500 Hz.

The experiment was conducted in three stages: First, the vibration response of the *uncracked* beam was measured at five different temperatures $\{-25\ °C, -5\ °C, 5\ °C, 25\ °C, 40\ °C\}$. Second, the beam was subject to a center point load of $F = 28$ kN to introduce cracks. Third, the vibration response of the *cracked* beam was measured at the same temperatures as in the first test series. Two temperature sensors were placed inside the beam. To ensure that a stationary

temperature field has been reached within the beam, the tests were only conducted when the readings of the temperature sensors inside the beam were within a ±1 K range of the target temperature.

The data acquired for the uncracked beam is referred to as dataset $\mathcal{D}_1$, and the corresponding dataset obtained from the cracked beam is referred to as $\mathcal{D}_2$.

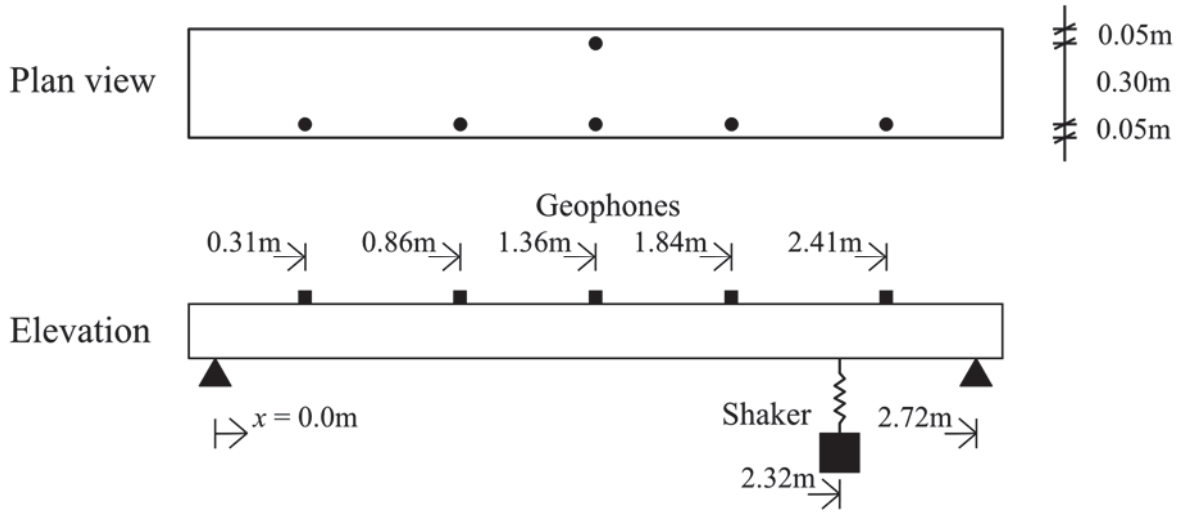

Figure 2: Setup of the experiment with sensor locations and shaker.

3.2 Modal identification

For each run of the experiment, 10 minutes of data were recorded while the beam was excited by the shaker and analyzed with the established frequency domain decomposition (FDD) technique [24]. In Figure 3, the spectrum of the first singular value of the decomposition is shown within a range of 0 Hz to 200 Hz for the test conducted in the uncracked state at -5 °C. The third bending mode, which has been estimated to occur at ~390 Hz, could not be identified from the data. The spectrum of the first singular value is smoothed by applying a gaussian window function with a width of 1001 samples and a standard deviation of 250 samples. At 10 minutes (600 seconds) of data, the frequency resolution is 0.00167 Hz. Thus the window function has a width of 1.668 Hz and a standard deviation of 0.416 Hz in the spectrum.

The distinct double peak at ~40 Hz and ~45 Hz with identical mode shapes corresponds well to a system with a tuned mass damper (TMD). Such a system can be approximated as a two degree of freedom (DOF) system, whereby the two masses correspond to the modal masses of the beam and shaker. In the two closely spaced modes of the double peak, the two masses move in the same and in the opposite direction, respectively. Since only the beam is instrumented, the two identified mode shapes are indistinguishable. The mode shapes of these double-peaked first bending modes and the second bending mode at ~170 Hz of the same test run are displayed in Figure 4.

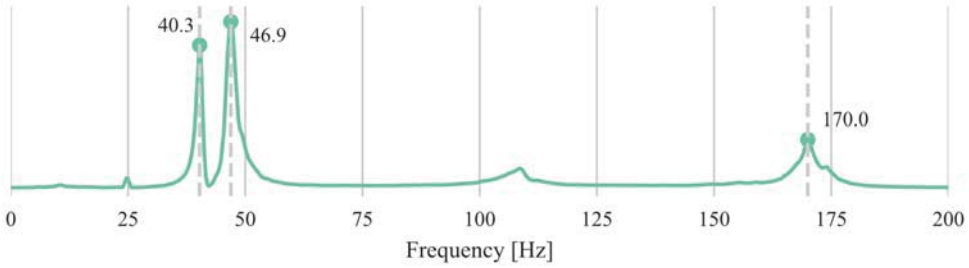

Figure 3: Spectrum (0 ... 200Hz) of the first FDD singular value along with peaks for the uncracked state at -5°C.

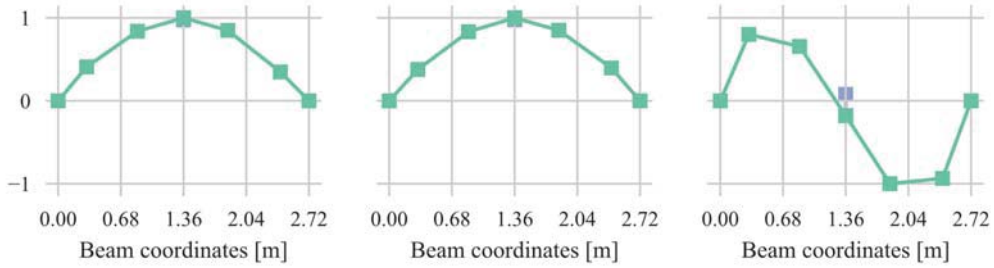

Figure 4: Identified mode shapes (normalized to a maximum amplitude of 1.0) at 40.3 Hz, 46.9 Hz, and 170.0 Hz of the beam in the uncracked state at -5°C.

4 SYSTEM IDENTIFICATION AND MODEL CLASS SELECTION

Structural health monitoring of a structural system can be performed based on Bayesian model class selection in the following steps (see also [15]):

1) A set of m model classes is postulated, where each model class represents a possible state of the structural system. Embedded within the formulation of the likelihood function, these model classes contain deterministic physics-based models of the structural system, and probabilistic models of the model, measurement and statistical uncertainty. In addition, each model class includes the prior knowledge on the model parameters modelled by their prior joint probability distribution.
2) The probability distributions of the model parameters are then updated with observed data from the real system using Bayesian analysis.
3) The relative plausibility of the model classes conditional on the observed data is determined by means of Bayesian model class selection.

4.1 Temperature dependent properties

The proposed model classes consist of a sub-model for the temperature-dependent material properties, a mechanical sub-model, the formulation of the likelihood function based on the prediction error model and prior probability distribution the parameters of the model classes.

In the literature [25-27], the elastic modulus of concrete is modelled as linearly decreasing function of the temperature. Based on these models, a linear model for the temperature-dependent flexural stiffness is applied:

$$EI(T) = EI_0 + \alpha \times T \tag{10}$$

whereby EI_0 is the flexural stiffness at 0°C in [MNm²] and α is the slope in [MNm²/K], while T is the temperature in °C.

4.2 Model class 1: uncracked beam

Model class $\mathcal{M}_1$ represents the temperature-dependent uncracked beam. After the temperature dependent properties of the material – the elastic modulus – have been determined, the observable quantities are calculated with a mechanical sub-model. This mechanical sub-model is implemented via the finite element method (FEM) with the OpenSEES framework [28, 29]. The concrete beam is modelled with linear-elastic Euler-Bernoulli beam elements with a very high spatial resolution of 1cm. The flexural stiffness of these elements is assumed to be constant over the length of the beam with a value determined by Equation (10). To account for the damping effect of the suspended shaker, a single element, which is effectively acting as spring with a linear spring stiffness k, is suspended from the beam at the location of the suspension of the shaker. The mass of the shaker is applied as a point mass m in the lower node of the beam element representing the suspension of the shaker. An illustration of the mechanical model is given in Figure 5.

Geometry and mass of the actual beam can be determined with high certainty and are hence modeled as deterministic values in this model class. The parameters of the temperature-dependency and mechanical sub-model are $\boldsymbol{\theta_{1,sub}} = [EI_0 \quad \alpha \quad k \quad m]^T$.

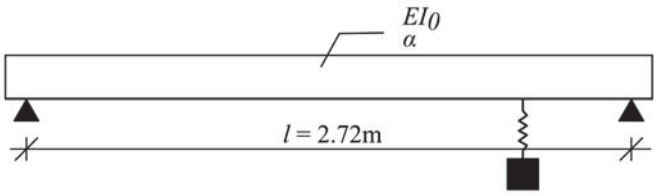

Figure 5: Illustration of the mechanical model embedded in model class $\mathcal{M}_1$

In the current application, only the eigenfrequencies corresponding to the three identified modes are chosen as the observable modal properties of the structural system. Thus, a modal analysis of the finite element model is conducted, and the eigenvalues are expressed in terms of natural frequencies. The model can be parametrized in terms of the known input $y = T$ and written as:

$$\boldsymbol{q}(y, \boldsymbol{\theta_{1,sub}}) = \boldsymbol{q}(T, EI_0, \alpha, k, m) \tag{11}$$

Similar to the model in Equation (1), a multiplicative prediction error is chosen to relate the observable frequencies $\boldsymbol{z} = [f_1 \quad f_2 \quad f_3]^T$ with the frequencies $\boldsymbol{q}$ obtained from the modal analysis of the finite element model:

$$\boldsymbol{z} = \boldsymbol{q}(y, \boldsymbol{\theta_{1,sub}}) \odot \exp(\boldsymbol{e}) \tag{12}$$

The prediction error jointly describes the uncertainty in (a) the vibration data, (b) the method used to extract the modal eigenfrequencies from the vibration data and (c) the eigenvalue analysis based on the FE model. Alternative formulations may adopt an additive error model and/or include information about mode shapes [10, 16-18, 20].

The random vector $\boldsymbol{e}$ is a Gaussian vector with zero mean but covariance matrix $\boldsymbol{\Sigma_{ee}}$. It follows that the prediction errors $\exp(\boldsymbol{e})$ are also correlated. The pairwise correlation coefficient ρ_e for the random variables in $\boldsymbol{e}$ is assumed to be identical. The correlation matrix of $\boldsymbol{e}$ can thus be written as:

$$\boldsymbol{R_{ee}} = \begin{bmatrix} 1 & \rho_e & \rho_e \\ & 1 & \rho_e \\ sym. & & 1 \end{bmatrix} \tag{13}$$

In addition, all random variables in $\boldsymbol{e}$ are assumed to have an identical standard deviation σ_e, so that the vector of standard deviations can be written as $\boldsymbol{\sigma_e} = [\sigma_e \quad \sigma_e \quad \sigma_e]^T$. This assumption simplifies the problem and conceals any possible differences in the prediction errors for the different observable outcomes, but it is justified for multiplicative errors, since higher harmonics of eigenfrequencies are multiples of the base eigenfrequency. If the discrepancy between model predictions and observations is dominated by model errors, the ratio of this discrepancy will be the same for all harmonics, resulting in identical prediction errors.

With these assumptions the covariance matrix $\boldsymbol{\Sigma_{ee}}$ can be determined as:

$$\boldsymbol{\Sigma_{ee}} = \boldsymbol{D_{ee}} \boldsymbol{R_{ee}} \boldsymbol{D_{ee}} \tag{14}$$

where $\boldsymbol{D_{ee}} = \mathrm{diag}(\boldsymbol{\sigma_e})$ is the matrix of standard deviations. This approach effectively parametrizes the covariance matrix. The parameters ρ_e and σ_e of the prediction error model together with the parameters $\boldsymbol{\theta_{1,sub}}$ of the models describing the temperature dependence of the material properties and the mechanical behavior are the parameters of model class $\mathcal{M}_1$ denoted by $\boldsymbol{\theta}_1 = [EI_0 \quad \alpha \quad k \quad m \quad \sigma_e \quad \rho_e]^T$. With the parametrization of the sub-models expressed as $\boldsymbol{q}(y, \boldsymbol{\theta}_1)$ and the parametrization of the covariance matrix as $\boldsymbol{\Sigma_{ee}}(\boldsymbol{\theta}_1)$, the likelihood function $L_1(\boldsymbol{\theta}_1|\mathcal{D}_{i,j})$ describing the relation between the parameters $\boldsymbol{\theta}_1$ and a single sub-dataset $\mathcal{D}_{i,j} = (\hat{y}_{i,j}, \hat{\boldsymbol{z}}_{i,j})$, $i = 1$ (uncracked), 2 (cracked) and $j = 1, \ldots, 5$ can be formulated according to Equation (1):

$$L_1(\boldsymbol{\theta}_1|\mathcal{D}_{i,j}) = \frac{1}{\sqrt{(2\pi)^n \det[\boldsymbol{\Sigma_{ee}}(\boldsymbol{\theta}_1)]}} \times \exp\left[-\frac{1}{2}\left[\ln \hat{\boldsymbol{z}}_{i,j} - \ln\left[\boldsymbol{q}(\hat{y}_{i,j}, \boldsymbol{\theta}_1)\right]\right]^T \boldsymbol{\Sigma_{ee}}(\boldsymbol{\theta}_1)^{-1}\left[\ln \hat{\boldsymbol{z}}_{i,j} - \ln\left[\boldsymbol{q}(\hat{y}_{i,j}, \boldsymbol{\theta}_1)\right]\right]\right]. \tag{15}$$

Given that all five sub-datasets in each dataset $\mathcal{D}_1 = (\mathcal{D}_{1,j})_{j=1}^5$ or $\mathcal{D}_2 = (\mathcal{D}_{2,j})_{j=1}^5$ are conditionally independent for given parameters $\boldsymbol{\theta}_1$, the likelihood function $L_1(\boldsymbol{\theta}_1|\mathcal{D}_i)$ describing the full dataset $\mathcal{D}_i$, $i = 1{,}2$ is given by (see also Equation (5)):

$$L_1(\boldsymbol{\theta}_1|\mathcal{D}_i) = \prod_{j=1}^{5} L(\boldsymbol{\theta}_1|\mathcal{D}_{i,j}) \quad \text{with} \quad i = 1{,}2 \tag{16}$$

Within a Bayesian framework, any prior knowledge on the parameters is quantified by the definition of the prior probability distributions of the parameters. Concerning the flexural stiffness EI_0 at 0 °C, the uncertainty in the geometry is by far outweighed by the uncertainty in the elastic modulus of the concrete. Based on the Probabilistic Model Code [30], the probability density function of the elastic modulus is modelled by a lognormal distribution with a coefficient of variation (c.o.v) 0.15. With a mean cross-sectional area of 0.2 m × 0.4 m and a mean of the elastic modulus of 33 GPa (see Section 3), the mean of the prior distribution of EI_0 is determined as 8.8 MNm².

In the literature [25-27], the slope of the temperature dependent elastic modulus are in the range of -0.3% K^{-1} to -0.8% K^{-1}. For the present system with a flexural stiffness EI_0 of 8.8 MNm², a normal distribution for the slope parameter α with a mean of -0.01 MNm² K^{-1} and a large c.o.v. of 0.5 is chosen.

The mass of the shaker including the construction for suspending the shaker is estimated to be approximately 30 kg. Hence this parameter is modelled with a normal distribution with a mean of 30 kg and a c.o.v. of 0.25.

Since the suspension the shaker does not consist of a single member but a series of members joined by bolted connections, there is a high degree of uncertainty in the value of the equivalent spring constant k, which is expressed through a high c.o.v. Preliminary calculations indicate a range between 2.5 MNm and 4.0 MNm for the value of the spring constant. Negative values are unreasonable, and thus a lognormal distribution with a mean of 3.5 MNm and a c.o.v. of 0.5 is chosen.

The standard deviation σ_e of the prediction errors is assumed to follow a lognormal distribution with a mean of 0.01 and a c.o.v. of 0.25. For the correlation ρ_e of the prediction errors a beta distribution with parameters $\alpha = 5$ and $\beta = 2$ is applied.

All parameters in $\boldsymbol{\theta}_1$ are assumed to be statistically independent. An overview over the prior distributions of the parameters $\boldsymbol{\theta}_1$ is given in Table 1.

Parameter	Distribution	Mean	c.o.v.
EI_0	Lognormal	8.8 MNm²	0.15
α	Normal	-0.01 MNm²/K	0.5
k	Lognormal	3.5 MN/m	0.5
m	Normal	30 kg	0.25
σ_e	Lognormal	0.01	0.25
ρ_e	Beta (5,2)	0.71	0.22

Table 1: Prior probabilistic models of the parameters $\boldsymbol{\theta}_1$ of model class $\mathcal{M}_1$.

4.3 Model class 2: cracked beam

Model class $\mathcal{M}_2$ represents the temperature-dependent cracked beam. It is an extension of model class $\mathcal{M}_1$ where the beam consists of two regions, an uncracked region with material properties $EI_{0,1}$ and α_1, and a cracked region with properties $EI_{0,2}$ and α_2. The transition from the uncracked to the cracked region occurs at symmetric locations of x_D from the supports (see Figure 6). Apart from these assumptions, model class $\mathcal{M}_2$ is analogue to $\mathcal{M}_1$ in the modeling process and formulation of the likelihood function $L_2(\boldsymbol{\theta}_2|\mathcal{D}_i)$, $i = 1,2$. The parameters of model class $\mathcal{M}_2$ is $\boldsymbol{\theta}_2 = [EI_{0,1} \quad \alpha_1 \quad EI_{0,2} \quad \alpha_2 \quad x_D \quad k \quad m \quad \sigma_e \quad \rho_e]^T$. An illustration of the mechanical model of model class $\mathcal{M}_2$ is shown in Figure 6.

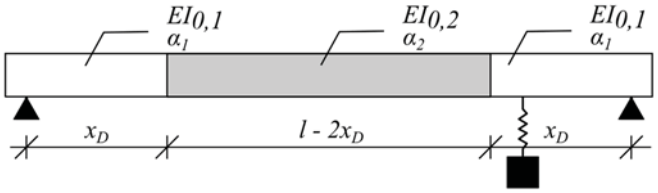

Figure 6: Illustration of the mechanical model embedded in model class $\mathcal{M}_2$

The prior knowledge on the cracked system corresponds to the prior knowledge of the uncracked system. Therefore, the prior distributions of the parameters are identical except for $EI_{0,2}$, α_2, and x_D. It is assumed that the flexural stiffness $EI_{0,2}$ at 0 °C of the cracked region follows a lognormal distribution with a mean of 80% of the mean of $EI_{0,1}$. The prior distribution

of the slope of the linear model of the temperature dependent stiffness is assumed to be alike for the uncracked and cracked region, resulting in identical priors for α_1 and α_2.

A normal distribution is assumed for the location of the transition of the uncracked to the cracked region x_D with a mean located at the quarter points and a standard deviation of 20cm, resulting in a c.o.v. of 0.3. All parameters are assumed to be statistically independent with the exception of the flexural stiffness at 0 °C, $EI_{0,1}$ and $EI_{0,2}$, and the slope of the temperature-dependent stiffness, α_1 and α_2 , which are each correlated with a correlation coefficient of 0.9 . An overview over the prior distributions of the parameters $\boldsymbol{\theta}_2$ is given in Table 2.

Parameter	Distribution	Mean	c.o.v.
$EI_{0,1}$	Lognormal	8.8 MNm²	0.15
α_1	Normal	-0.01 MNm²/K	0.5
$EI_{0,2}$	Lognormal	0.8 × 8.8 MNm²	0.15
α_2	Normal	-0.01 MNm²/K	0.5
x_D	Normal	0.25 * 2.72m	0.3
k	Lognormal	3.5 MN/m	0.5
m	Normal	30 kg	0.25
σ_e	Lognormal	0.01	0.25
ρ_e	Beta (5,2)	0.71	0.22

Table 2: Prior probabilistic models of the parameters $\boldsymbol{\theta}_2$ of model class $\mathcal{M}_2$.

4.4 Results

The data gathered in the experiment are divided into two datasets: A dataset $\mathcal{D}_1$ with data collected from the uncracked beam at all five temperature levels $\{-25\ °C, -5\ °C, 5\ °C, 25\ °C, 40\ °C\}$ and a dataset $\mathcal{D}_2$ with data collected from the cracked beam at the same temperature levels.

The posterior marginal distributions of the parameters $\boldsymbol{\theta}_1$ of model class $\mathcal{M}_1$ conditional on the dataset $\mathcal{D}_1$ are shown in Figure 7 along with their prior distributions. Distinct peaks in the posterior distributions can be seen for the mass m of the shaker and the stiffness k of its suspension, as well as EI_0, the flexural stiffness at 0 °C. These peaks show an information gain through the data while the modest change of the posterior marginal distributions of α, σ_e, and ρ_e compared to their respective prior distributions signify only limited information gain through the data.

The posterior marginal distributions of the parameters $\boldsymbol{\theta}_2$ of model class $\mathcal{M}_2$ conditional on the dataset $\mathcal{D}_2$ are shown in Figure 8 along with their prior distributions. Here, the peaks in the posterior marginal distributions of the parameters are in general less sharp than in the previous case. This is plausible, since the mechanical sub-model with two regions contains more parameters and thus the space of possible solutions is larger. The uncertainty in all the parameters of the mechanical sub-model decreases. The area with the most plausible values of the parameter x_D, which defines the start and extend of the region with reduced stiffness, is between 0.80 m and 1.05 m. Visually observed cracks start at around 1.10 m from the supports from both sides. The observed crack spacing of 0.15 m corresponds to the effective length for the load transfer between reinforcement bars and concrete. The change of flexural stiffness is thus expected to occur at 1.10 m – 0.15 m = 0.95 m, which corresponds to the most plausible values of x_D.

The posterior probabilities of the model classes $\mathcal{M}_1$ and $\mathcal{M}_2$ conditional on the data are shown in Figure 9. A prior probability of $\Pr(\mathcal{M}_1) = \Pr(\mathcal{M}_2) = 0.5$ was assumed for both

model classes. The results show that – as expected – model class $\mathcal{M}_1$ is more plausible for data measured from of the uncracked beam and model class $\mathcal{M}_2$ is more plausible for data obtained from the cracked beam.

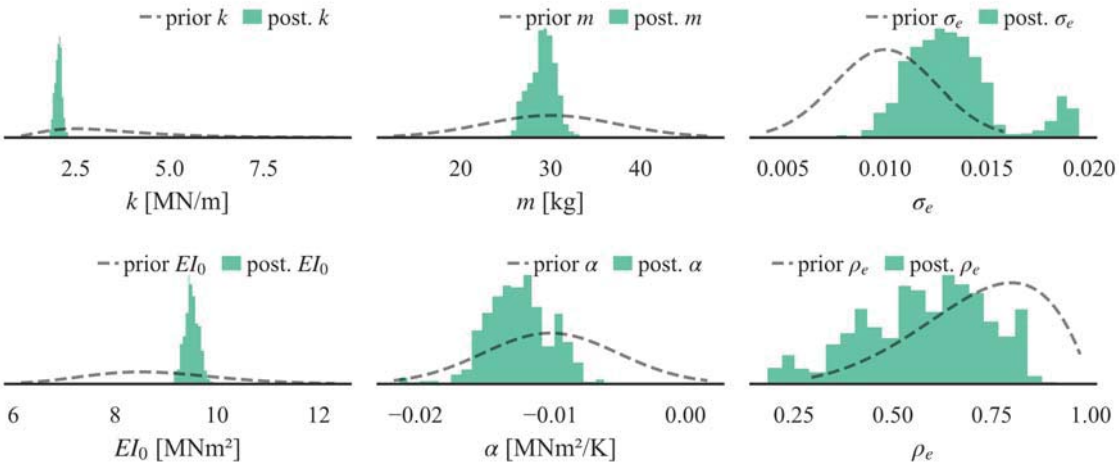

Figure 7: Posterior marginal distributions of the model parameters for model class $\mathcal{M}_1$ conditional on the dataset $\mathcal{D}_1$ (data obtained in the uncracked state).

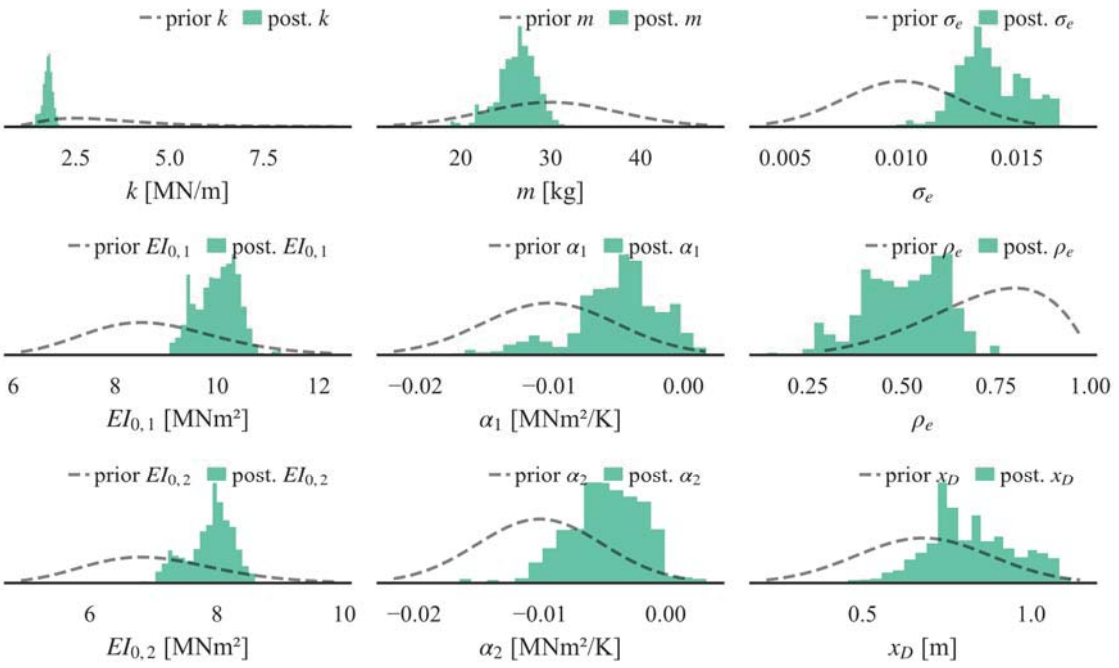

Figure 8: Posterior marginal distributions of the model parameters for model class $\mathcal{M}_2$ conditional on the dataset $\mathcal{D}_2$ (data obtained in the cracked state).

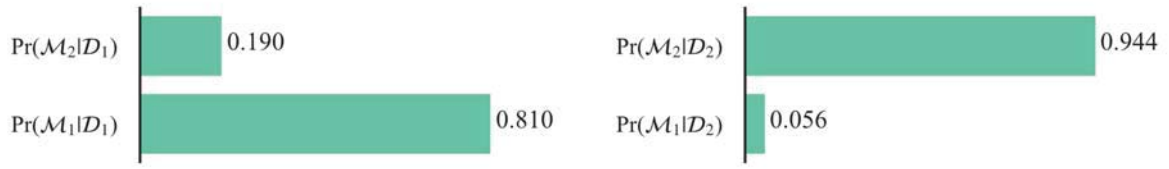

Figure 9: Comparison of the plausibility of the model classes $\mathcal{M}_1$ and $\mathcal{M}_2$ conditional on dataset $\mathcal{D}_1$ measured from the uncracked beam (left) and conditional on dataset $\mathcal{D}_2$ obtained from the cracked beam (right)

5 STRUCTURAL HEALTH MONITORING SCHEME

5.1 Strategy

One of the axioms of structural health monitoring states that damage detection requires the comparison of the current state of a system to an undamaged reference state [31]. To implement this situation, we first split the available data $\mathcal{D}$ into data from the reference state $\mathcal{D}_r$ and data from the current state $\mathcal{D}_c$, which contains all data after the reference state: $\mathcal{D} = (\mathcal{D}_r \quad \mathcal{D}_c)$.

Subsequently, two model classes are introduced: First, a model class is proposed, which assumes that for *both* the data from the current and reference states the beam is in the uncracked state. The likelihood function L_1 is applied to the whole dataset $\mathcal{D}$ and the priors for $\boldsymbol{\theta}_1$ are chosen to be the same as above. This model class is identical with model class $\mathcal{M}_1$.

A second model class denoted as $\mathcal{M}_3$ is proposed, which assumes that the beam is uncracked in the reference state and cracked in the current state. This in effect applies the likelihood function L_1 to the data of the reference state and L_2 to the data of the current state. The parameters of model class $\mathcal{M}_3$ and their prior distributions are identical to those of model class $\mathcal{M}_2$. With $EI_0 \mathrel{\widehat{=}} EI_{0,1}$ and $\alpha_0 \mathrel{\widehat{=}} \alpha_{0,1}$, the parameters $\boldsymbol{\theta}_1$ are a subset of the parameters $\boldsymbol{\theta}_2$ and the likelihood function L_1 can thus also be written as a function of $\boldsymbol{\theta}_2$.

The likelihood functions for the two model classes in this structural health monitoring scheme are formulated as:

$$L_1(\boldsymbol{\theta}_1|\mathcal{D}) = L_1(\boldsymbol{\theta}_1|\mathcal{D}_r) \times L_1(\boldsymbol{\theta}_1|\mathcal{D}_c) \tag{17}$$

$$L_3(\boldsymbol{\theta}_2|\mathcal{D}) = L_1(\boldsymbol{\theta}_2|\mathcal{D}_r) \times L_2(\boldsymbol{\theta}_2|\mathcal{D}_c) \tag{18}$$

5.2 Data

In the current structural health monitoring scenario, the datasets are assembled as follows: The data $\mathcal{D}_r$ obtained in the reference state comprises data measured from of the uncracked beam at five different temperature levels as summarized in Table 3. The data $\mathcal{D}_c$ measured in the current state consists of data measured from the uncracked beam at two temperature levels followed by data obtained from the cracked beam at five different temperature levels as also listed in Table 3.

As the monitoring of a structure progresses, more and more data are accumulated. For this reason, we denote $\mathcal{D}_{1:i}$ as the dataset which includes the individual datasets $\mathcal{D}_1$ to $\mathcal{D}_i$, i.e. $\mathcal{D}_{1:i} = (\mathcal{D}_1 \quad \dots \quad \mathcal{D}_i)$.

	Reference state, $\mathcal{D}_r$					Current state, $\mathcal{D}_c$						
Beam state	uncracked							cracked				
Temperature [°C]	+40	+25	+5	-5	-25	+40	-5	-25	-5	+5	+25	+40
Dataset	$\mathcal{D}_1$	$\mathcal{D}_2$	$\mathcal{D}_3$	$\mathcal{D}_4$	$\mathcal{D}_5$	$\mathcal{D}_6$	$\mathcal{D}_7$	$\mathcal{D}_8$	$\mathcal{D}_9$	$\mathcal{D}_{10}$	$\mathcal{D}_{11}$	$\mathcal{D}_{12}$

Table 3: Datasets for the SHM scenario as a function of the beam state and temperature

5.3 Results

In the same manner as before, a model class selection yields the relative plausibility of the states of the system conditional on the data. Model class $\mathcal{M}_1$ assumes that the beam is uncracked for all available datasets, i.e. it is uncracked in the reference state as well as in the current state. A difference between reference state and current state is made for model class $\mathcal{M}_3$, where the beam is assumed to be uncracked in reference state but cracked in the current state. This means that when – conditional on the data -- $\mathcal{M}_3$ is more plausible than $\mathcal{M}_1$, it is more plausible that the current state of the beam is cracked rather than uncracked.

As before, the prior probabilities of the model classes are assumed to be uniform, representing no prior preference for a specific model class.

With these priors and the evidences obtained from the system identification, for each dataset $\mathcal{D}_{1:i}$ a model class comparison can be conducted, expressing the plausible states of the system for the data acquired at different stages of the monitoring scenario. These model class comparisons are shown in Figure 10. It is apparent that in the reference state, for datasets $\mathcal{D}_{1:1}$ to $\mathcal{D}_{1:5}$, the two model classes are approximately equally plausible.

Datasets $\mathcal{D}_{1:6}$ and $\mathcal{D}_{1:7}$ include additional data from the uncracked beam. In this case, model class $\mathcal{M}_1$, which assumes an uncracked beam for the reference state and current state is far more plausible than model class $\mathcal{M}_3$, which assumes a cracked beam for the current state. For the subsequent datasets $\mathcal{D}_{1:8}$ to $\mathcal{D}_{1:12}$, which also include data from the cracked beam in the current state, model class $\mathcal{M}_3$ gradually becomes more plausible than model class $\mathcal{M}_1$, signifying that a cracked current state is more likely than an uncracked one.

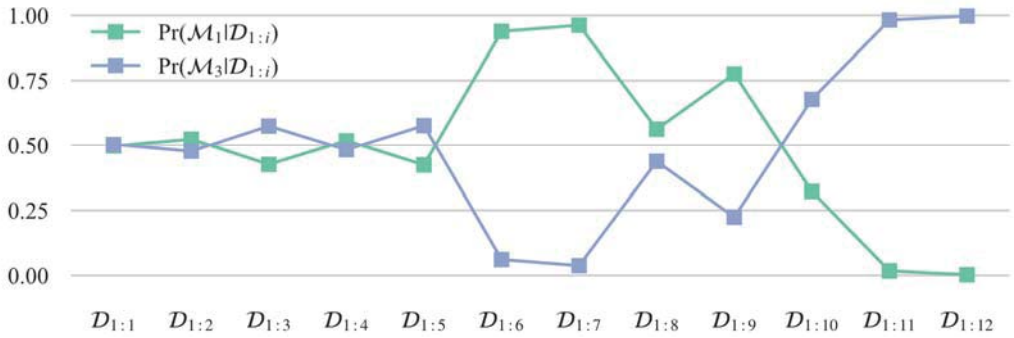

Figure 10: Plausibility of model classes $\mathcal{M}_1$ and $\mathcal{M}_3$ conditional on datasets $\mathcal{D}_{1:i}$.

With the updated parameters of model classes $\mathcal{M}_1$ and $\mathcal{M}_3$ conditional on datasets $\mathcal{D}_{1:12}$, when all observations have been taken into account, the responses of the models can be predicted by using the posterior samples of the parameters as model input. These posterior predictions are shown in Figure 11 for $\mathcal{M}_1$ conditional on datasets $\mathcal{D}_{1:12}$ along with the data. In Figure 12, the posterior predictions for $\mathcal{M}_3$ conditional on datasets $\mathcal{D}_{1:12}$ along with the data.

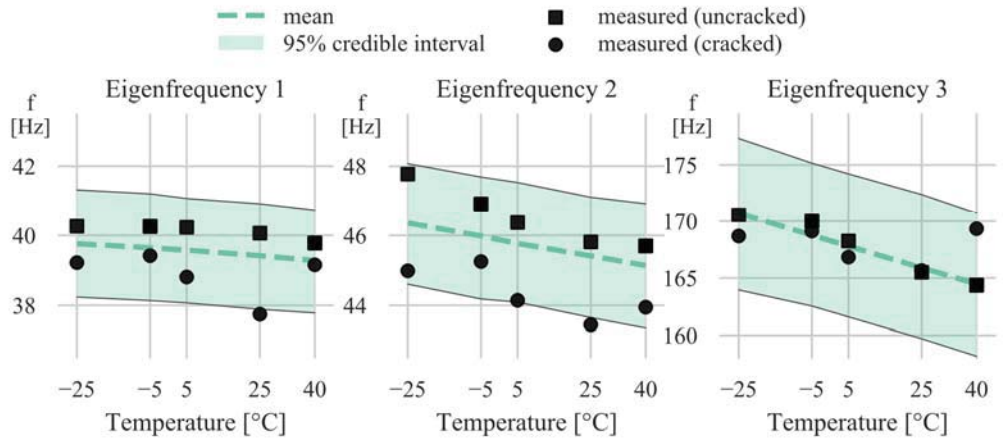

Figure 11: Mean and 95% credible interval for the posterior eigenfrequencies of the beam as well as the identified eigenfrequencies. The statistics of the posterior eigenfrequencies are determined based on model class $\mathcal{M}_1$ conditional on dataset $\mathcal{D}_{1:12}$.

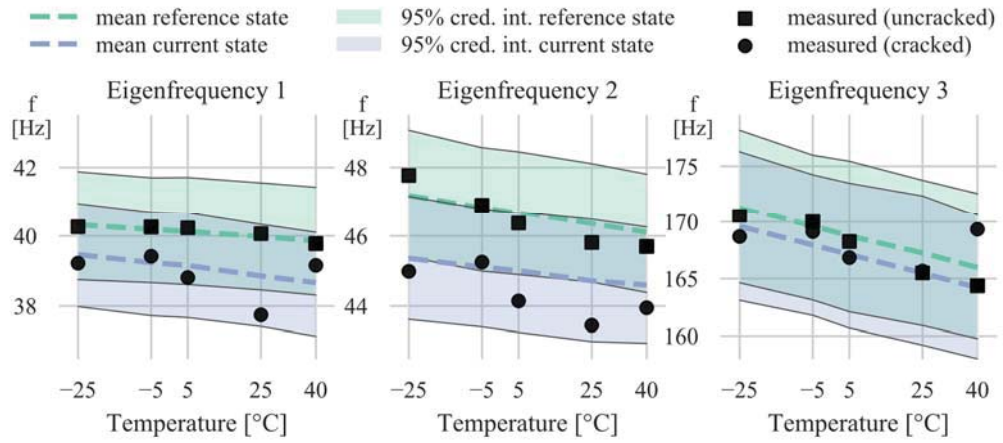

Figure 12: Mean and 95% credible interval for the posterior eigenfrequencies of the beam as well as the identified eigenfrequencies. The statistics of the posterior eigenfrequencies are determined based on model class $\mathcal{M}_3$ conditional on dataset $\mathcal{D}_{1:12}$.

6 CONCLUDING REMARKS

In the current paper, we address the issue of quantifying structural changes in a reinforced concrete beam amid varying environmental conditions based on monitoring data by postulating competing probabilistic models which explicitly describe the temperature-dependency of the structural properties. Each model represents a possible state of the beam. Bayesian model updating is applied based on modal information extracted from vibration data measured from the beam at various temperature levels inside a climate chamber. These updated models include a model of the temperature-dependent material properties and a quantification of the structural changes in the beam. The updated models enable robust predictions of the system responses [32].

By applying Bayesian model class selection, we successfully identify the plausible states of the beam. In a simplistic structural health monitoring scenario, which separates the data into a reference state and a current state and postulates different structural states for the current state, structural changes are detected and quantified.

In the current paper, modal eigenfrequencies were used as data. Additional modal properties such as modes shapes can be included in the analysis and are expected to provide additional information [10, 16-18, 20, 33]. Alternatively, a two-stage approach [34, 35] or time-domain output-only approaches [13, 19, 36] for Bayesian system identification can be applied.

The results presented in this paper are based on limited data and are thus promising for real structural health monitoring applications where more data are typically available. The approach of explicitly modelling the temperature-dependent properties of structural systems is especially beneficial when predicting the performance and condition of structures, which are significantly influenced by the temperature-dependent behavior of nominally non-loadbearing structural components such as ballasted tracks or asphalt layers. Our future work will include structures with nominally non-loadbearing components which (a) exhibit such a strong temperature-dependent behavior and (b) influence the static and dynamic response of the system.

ACKNOWLEDGEMENTS

This work was supported by the German Federal Ministry of Education and Research (BMBF) through grant 13N14658.

REFERECENCES

[1] H. Sohn, Effects of environmental and operational variability on structural health monitoring, *Philosophical Transactions of the Royal Society A: Mathematical, Physical and Engineering Sciences,* **365**(1851), 539-560, 2006.

[2] M. Baeßler, F. Hille, A study on diverse strategies for discriminating environmental from damage based variations in monitoring data, *Maintenance, Safety, Risk, Management and Life-Cycle Performance of Bridges: Proceedings of the Ninth International Conference on Bridge Maintenance, Safety and Management (IABMAS 2018)*, 2018.

[3] C. R. Farrar, K. Worden, *Structural health monitoring: a machine learning perspective*: John Wiley & Sons, 2012.

[4] W. H. Hu, Á. Cunha, E. Caetano, R. G. Rohrmann, S. Said, J. Teng, Comparison of different statistical approaches for removing environmental/operational effects for massive data continuously collected from footbridges, *Structural Control and Health Monitoring,* **24**(8), 2017.

[5] M. Friswell, J. E. Mottershead, *Finite element model updating in structural dynamics*: Springer Science & Business Media, 2013.

[6] J. Mahowald, S. Maas, H. Nguyen, D. Waldmann, A. Zürbes, *Some conclusions from the measurements of temperatures and their gradients on eigenfrequencies of bridges*, 2014.

[7] I. Gonzales, M. Ülker-Kaustell, R. Karoumi, Seasonal effects on the stiffness properties of a ballasted railway bridge, *Engineering Structures,* **57**, 63-72, 2013.

[8] B. Peeters, G. De Roeck, One‐year monitoring of the Z24‐Bridge: environmental effects versus damage events, *Earthquake engineering & structural dynamics,* **30**(2), 149-171, 2001.

[9] J. L. Beck, Bayesian system identification based on probability logic, *Structural Control and Health Monitoring,* **17**(7), 825-847, 2010.

[10] J. L. Beck, S. K. Au, M. V. Vanik, Monitoring structural health using a probabilistic measure, *Computer-Aided Civil and Infrastructure Engineering,* **16**(1), 1-11, Jan, 2001.

[11] J. L. Beck, L. S. Katafygiotis, Updating models and their uncertainties. I: Bayesian statistical framework, *Journal of Engineering Mechanics,* **124**(4), 455-461, 1998.
[12] E. Ntotsios, C. Papadimitriou, P. Panetsos, G. Karaiskos, K. Perros, P. C. Perdikaris, Bridge health monitoring system based on vibration measurements, *Bulletin of Earthquake Engineering,* **7**(2), 469, 2009.
[13] J. L. Beck, K.-V. Yuen, Model selection using response measurements: Bayesian probabilistic approach, *Journal of Engineering Mechanics,* **130**(2), 192-203, 2004.
[14] C. Papadimitriou, K. Christodoulou, Bayesian model selection and updating applied to structural damage identification, *Proc., 9th Int. Conf. on Structural Safety and Reliability*, 2005.
[15] D. Zonta, M. Pozzi, The remarkable story of Portogruaro Civic Tower's probabilistic health monitoring, *Structural Monitoring and Maintenance,* **2**(4), 301-318, 2015.
[16] I. Behmanesh, B. Moaveni, Accounting for environmental variability, modeling errors, and parameter estimation uncertainties in structural identification, *Journal of Sound and Vibration,* **374**, 92-110, 2016.
[17] I. Behmanesh, B. Moaveni, Probabilistic identification of simulated damage on the Dowling Hall footbridge through Bayesian finite element model updating, *Structural Control & Health Monitoring,* **22**(3), 463-483, Mar, 2015.
[18] M. Song, I. Behmanesh, B. Moaveni, C. Papadimitriou, "Hierarchical Bayesian Calibration and Response Prediction of a 10-Story Building Model," *Model Validation and Uncertainty Quantification, Volume 3*, pp. 153-165: Springer, 2019.
[19] O. Sedehi, C. Papadimitriou, L. S. Katafygiotis, Probabilistic hierarchical Bayesian framework for time-domain model updating and robust predictions, *Mechanical Systems and Signal Processing,* **123**, 648-673, May 15, 2019.
[20] Y. Huang, C. Shao, B. Wu, J. L. Beck, H. Li, State-of-the-art review on Bayesian inference in structural system identification and damage assessment, *Advances in Structural Engineering,* **22**(6), 1329-1351, 2019.
[21] D. Straub, I. Papaioannou, Bayesian updating with structural reliability methods, *Journal of Engineering Mechanics,* **141**(3), 2014.
[22] W. Betz, I. Papaioannou, J. L. Beck, D. Straub, Bayesian inference with subset simulation: strategies and improvements, *Computer Methods in Applied Mechanics and Engineering,* **331**, 72-93, 2018.
[23] S. Pirskawetz, G. Hüsken, K.-P. Gründer, D. Kadoke, Damage mechanisms analysis of reinforced concrete beams in bending using non-destructive testing, *Life Cycle Analysis and Assessment in Civil Engineering: Towards an Integrated Vision: Proceedings of the Sixth International Symposium on Life-Cycle Civil Engineering (IALCCE 2018)*, 2019.
[24] R. Brincker, L. M. Zhang, P. Andersen, Modal identification of output-only systems using frequency domain decomposition, *Smart Materials & Structures,* **10**(3), 441-445, Jun, 2001.
[25] fib, *fib Model Code for Concrete Structures 2010*, 2013.
[26] G. Lee, T. Shih, K.-C. Chang, Mechanical properties of concrete at low temperature, *Journal of cold regions engineering,* **2**(1), 13-24, 1988.
[27] S. N. Shoukry, G. W. William, B. Downie, M. Y. Riad, Effect of moisture and temperature on the mechanical properties of concrete, *Construction and Building Materials,* **25**(2), 688-696, 2011.
[28] F. McKenna, OpenSees: A Framework for Earthquake Engineering Simulation, *Computing in Science & Engineering,* **13**(4), 58-66, 2011.
[29] M. Zhu, F. McKenna, M. H. Scott, OpenSeesPy: Python library for the OpenSees finite element framework, *SoftwareX,* **7**, 6-11, 2018.

[30] JCSS, Probabilistic Model Code, *Joint Committee on Structural Safety*, 2001.
[31] K. Worden, C. R. Farrar, G. Manson, G. Park, The fundamental axioms of structural health monitoring, *Proceedings of the Royal Society A: Mathematical, Physical and Engineering Sciences,* **463**(2082), 1639-1664, 2007.
[32] C. Papadimitriou, J. L. Beck, L. S. Katafygiotis, Updating robust reliability using structural test data, *Probabilistic Engineering Mechanics,* **16**(2), 103-113, Apr, 2001.
[33] I. Behmanesh, B. Moaveni, G. Lombaert, C. Papadimitriou, Hierarchical Bayesian model updating for structural identification, *Mechanical Systems and Signal Processing,* **64-65**, 360-376, Dec, 2015.
[34] S.-K. Au, F.-L. Zhang, Fundamental two-stage formulation for Bayesian system identification, Part I: General theory, *Mechanical Systems and Signal Processing,* **66**, 31-42, 2016.
[35] F.-L. Zhang, S.-K. Au, Fundamental two-stage formulation for Bayesian system identification, Part II: Application to ambient vibration data, *Mechanical Systems and Signal Processing,* **66**, 43-61, 2016.
[36] O. Sedehi, C. Papadimitriou, D. Teymouri, L. S. Katafygiotis, Sequential Bayesian estimation of state and input in dynamical systems using output-only measurements, *Mechanical Systems and Signal Processing,* **131**, 659-688, Sep 15, 2019.

EURODYN 2020
XI International Conference on Structural Dynamics
M. Papadrakakis, M. Fragiadakis, C. Papadimitriou (eds.)
Athens, Greece, 23–26 November 2020

MONITORING MONOPILE PENETRATION THROUGH MAGNETIC STRAY FIELD MEASUREMENTS

Peter C. Meijers[1], **Apostolos Tsouvalas**[1], **and Andrei V. Metrikine**[1]

[1]Delft University of Technology,
Faculty of Civil Engineering and Geosciences,
Stevinweg 1, 2628 CN
Delft, the Netherlands
e-mail: {p.c.meijers,a.tsouvalas,a.metrikine}@tudelft.nl

Keywords: Pile penetration monitoring, Non-contact method, Magnetic stray field.

Abstract. *Current methods to infer the penetration of a steel monopile during an offshore installation are rather inaccurate. Since a large number of foundation piles will be installed offshore in the coming years, a reliable technique to infer the penetration depth is vital. This paper proposes a non-contact method to monitor the pile progression into the seabed based on measurements of the magnetic stray field that permeates the air surrounding the structure, eliminating the necessity of a predefined pattern on the pile's surface. A simple magnetisation model for the monopile is proposed from which the relative motion between the moving pile and a stationary magnetic field sensor can be extracted. Comparison between the measured and simulated stray field data show a promising correlation, providing the basis for the new non-contact monitoring technique that is applicable offshore.*

1 INTRODUCTION

In the coming years, a large number of offshore wind farms will be commissioned in the North Sea. The most popular foundation type for wind turbines is the monopile [1], which is a cylindrical shell structure consisting of multiple steel sheets that are welded together. Currently, nearly all of these piles are gradually driven into the seabed by means of hydraulic impact hammers. Real-time knowledge of the pile penetration resulting from each hammer blow is vital to ensure safety during the installation process and to limit the amount of fatigue damage inflicted to the pile, since the energy of the blows can be adjusted accordingly based on the penetration speed. Moreover, after installation, the bearing capacity of the pile is estimated by measuring the pile's response to a single axial impact in a so-called restrike test [2].

Several techniques currently exist to monitor pile penetration. By registering the acceleration with a sensor mounted to the pile, the penetration is computed by integrating the signal twice in time [3]. Disadvantages of this approach include the need to attach the sensor to the surface of the pile, which is a delicate and time-consuming process, and the error in the computed displacement that accumulates due to filtering choices and the integration of the acceleration signal. Alternative techniques rely on optical signals. One such method is to deduce the distance between the top of the pile and a reference level based on the time-of-flight principle [4]. However, in an offshore environment, a steady reference level is not available, since optical signals, instead of reflecting back to the detector, scatter as result of the surface waves at the water level. A different optical approach is to use a camera to track a predefined pattern that is applied to the surface of the pile, e.g. a black and white banded pattern. Several patterns have successfully been administered over the years, especially in the case of restrike tests [5–8]. These approaches share the necessity to prepare the surface of the pile with a distinct predefined visual pattern.

Ideally, a method to register pile penetration is based on a non-contact sensor, simplifying the deployment significantly. Furthermore, such an optimal method does not require any preparation of the pile's surface to operate, i.e. no pattern has to be introduced. A method based on the magnetic stray field generated by a steel structure in the presence of the geomagnetic field could satisfy both of these criteria, since the stray field permeates the space surrounding the monopile. Hence, this paper investigates the feasibility to use the magnetic stray field to monitor the pile's penetration during installation. To this end, first, stray field data measured during a full-scale onshore monopile installation are presented, examining change of the magnetic signature of the structure with increasing penetration depth. Second, the magnetic stray field of the structure is simulated by employing a simple model for the structure's magnetic susceptibility that includes the presence of circumferential welds. Third, the possibility to utilise stray field measurements to determine the relative motion between the pile and a magnetic field sensor is discussed. Finally, the main conclusions of this work are summarised.

2 FULL-SCALE MEASUREMENT CAMPAIGN

During the installation of a steel monopile, the magnetic stray field has continuously been measured by means of a stationary magnetometer, which is mounted on top of a ground-based tripod. Since this concerns an onshore installation, a suitable reference level is available (ground level), allowing for a time-of-flight laser sensor to be employed to measure the pile's penetration in conjunction with the magnetic stray field measurements.

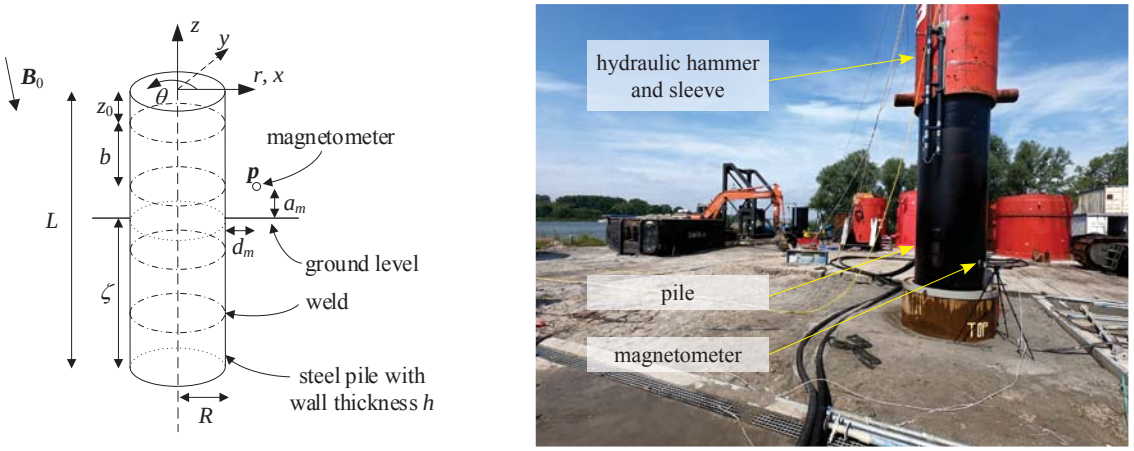

Figure 1: Set-up of the full-scale onshore monopile installation. (a) Schematic indicating the parameters of interest. (b) Photograph of the installation site.

2.1 Description of the set-up

A schematic of the set-up of the pile installation is presented in Figure 1a, which defines two coordinates systems: a cylindrical $r\theta z$-coordinate system—in which r, θ, and z denote the radial, the circumferential, and the axial directions, respectively—and a Cartesian xyz-coordinate system. The coordinate systems share their origin, which is located at the top of the pile. Table 1 lists the numerical values of the relevant parameters of the pile: the radius R, length L, and wall thickness h. The installed pile is composed of cylindrical steel sections with a height b each, which are stacked on top of each other using circumferential welds. Before installation, the pile has been coated for corrosion protection, obscuring the exact locations of the welds. Despite the lack of visible confirmation, their positions relative to the pile top are known *a priori*. The distance z_0 reflects the shorter top segment of pile.

To determine the penetration, a time-of-flight distance sensor is attached to the sleeve of the hydraulic hammer, which is depicted in Figure 1b. The current penetration depth ζ is defined as the distance from lower end of the pile to the ground level, implying that the pile is fully embedded into the soil when $\zeta = L$. The initial penetration depth ζ_0 is also listed in Table 1.

A biaxial magnetometer (type: HMC1022) registers the magnetic stray field while the pile gradually progresses into the soil with each hammer blow. It measures the two dominant components of the stray field: the radial B_r and the axial B_z. Figure 1b shows the magnetometer mounted on top of a tripod. Its position $\boldsymbol{p}$ relative to the ground is given by the offset from the pile's surface d_m, the circumferential position θ_m and the height a_m as specified in Table 1. A final parameter of importance is the direction and intensity of the geomagnetic field, of which the components expressed in the Cartesian xyz-coordinate system are $\boldsymbol{B}_0 = [B_0^x \;\; B_0^y \;\; B_0^z]^T = [15 \;\; 10 \;\; -40]^T\,\mu$T, signalling that it has a predominantly downward component. For the current purpose, the external field is considered to be time and space invariant.

2.2 Magnetic stray field versus penetration depth

Figure 2 shows the magnetic stray field components plotted against the measured penetration depth ζ. Both components of $\boldsymbol{B}$ show a pattern that repeats every 3 m, which is caused by the circumferential welds in the pile. Compared to the fairly homogeneous material in between

Parameter	Value
R	0.6096 m
L	62.0 m
h	0.050 m
b	3.0 m
z_0	0.5 m
ζ_0	48.62 m
a_m	1.5 m
θ_m	300°
d_m	0.2 m

Table 1: Parameters of interest for the pile installed during the measurement campaign.

them, the welds have significantly different magnetic properties, resulting in a local reduction of the magnetic susceptibility, which in turn create distinct markings in the field. Furthermore, it is clear that the magnitude of the radial component B_r increases when the pile penetrates further into the soil, which can be attributed to the sensor approaching the top of the pile. Due to the repeated impacts of the hammer, the pile has become magnetised in the direction of the geomagnetic field. Since that field has a strong downwards component, the top of the pile resembles a magnetic south pole, i.e. a region in space where magnetic field lines appear to converge to. These two observations indicate that the geometry of the pile and the presence of the geomagnetic field create a distinct pattern in the magnetic stray field which might enable one to track the penetration from stray field measurements alone.

3 MODELLING OF THE STRAY FIELD

In this section, the magnetic signature of the pile is simulated to investigate whether the measured data can be captured by a simple model, which would serve as a basis to infer the current penetration depth of the pile from measured magnetic stray field data. To this end, an expression of the magnetic field at an evaluation point $\boldsymbol{B}(\boldsymbol{p})$ generated by the structure's magnetisation $\boldsymbol{M}(\boldsymbol{r})$ is derived, in which $\boldsymbol{r}$ represents all points within the volume of the pile. By applying the same expression to the internal points of the structure in conjunction with a suitable magnetic constitutive equation, the magnetisation induced by the external field is determined. Subsequently, the measured magnetic stray field is reproduced with a proposed simple expression for the magnetic susceptibility.

3.1 The stray field in the presence of an external field

Even though the external field is time and space invariant, the magnetisation of the pile will not be uniform due to the geometry of the structure, which leads to a significant demagnetising field [9]. To compute the magnetic field generated by the structure's magnetisation, a numerical approach applicable to steel sheets is adopted [10], which assumes that the magnetisation component in the normal direction of the sheet (the radial component M_r in the current situation) is negligible.

By evenly subdividing the pile's volume into N_θ elements in the circumferential and N_z elements in the axial direction, the structure is discretised, and the total number of elements equals $N = N_\theta N_z$. Under the assumption that the magnetisation is constant over each element and is concentrated at the element's barycentre $\boldsymbol{r}_i$, i.e. $\boldsymbol{M}(\boldsymbol{r}_i)$, the magnetic field at $\boldsymbol{p}$ is given

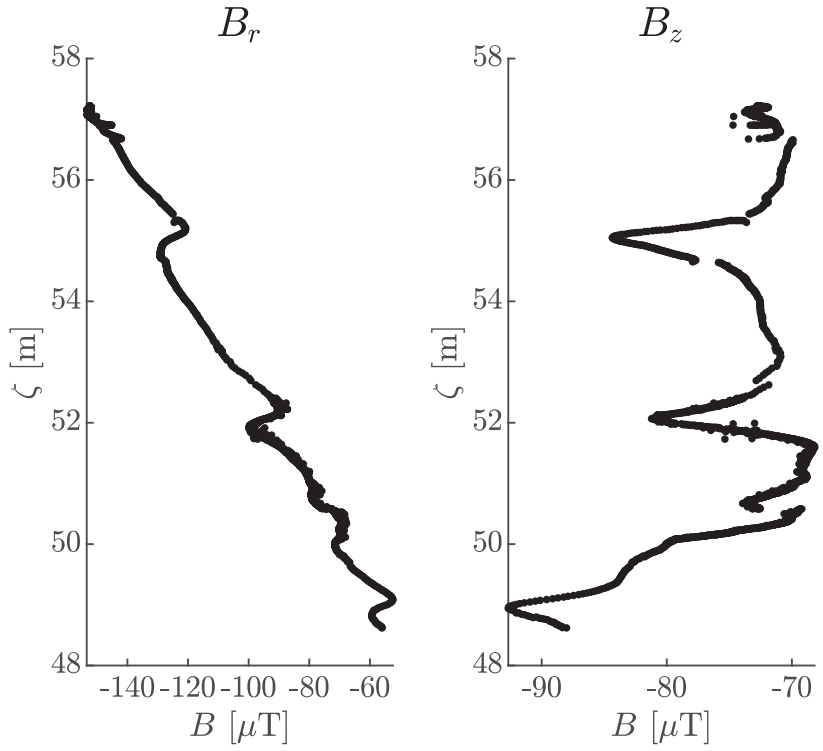

Figure 2: Remanent magnetic stray field versus the penetration depth.

by a summation of the contributions from all elements:

$$\boldsymbol{B}(\boldsymbol{p}) = \frac{\mu_0}{4\pi} \sum_{i=1}^{N} \oint_{\Gamma_i} \boldsymbol{M}(\boldsymbol{r}_i) \cdot \boldsymbol{n}_i \frac{\boldsymbol{p} - \boldsymbol{r}_i}{\|\boldsymbol{p} - \boldsymbol{r}_i\|^3} \, \mathrm{d}\Gamma_i, \tag{1}$$

in which μ_0 denotes the magnetic constant, and $\boldsymbol{n}_i$ is the outward normal to the element's boundary Γ_i. By evaluating the integrals, the expression above is rewritten:

$$\boldsymbol{B}(\boldsymbol{p}) = \mu_0 \sum_{i=1}^{N} \mathbf{G}_i \boldsymbol{M}(\boldsymbol{r}_i) = \mu_0 \mathbf{G}_{\boldsymbol{p}} \boldsymbol{M}, \tag{2}$$

in which $\mathbf{G}_i$ contains the values of the evaluated integrals for each element. In the latter part of the expression, these contributions are condensed into a single matrix $\mathbf{G}_{\boldsymbol{p}}$, and $\boldsymbol{M}$ is a vector incorporating the magnetisation components from all elements. Since the radial magnetisation component is deemed insignificant, $\boldsymbol{M}$ contains $2N$ entries.

To express the magnetisation in terms of the prevailing magnetic field, an appropriate constitutive equation is required. For a (locally) isotropic material, a scalar magnetic susceptibility χ suffices. Hence, the following implicit constitutive equation is employed:

$$\boldsymbol{M} = \chi \left(\frac{\boldsymbol{B}_0}{\mu_0} + \mathbf{G}_{\boldsymbol{r}} \boldsymbol{M} \right), \tag{3}$$

in which $\mathbf{G}_{\boldsymbol{r}}$ is a $2N \times 2N$ matrix representing the non-local interaction of the structure's magnetisation, which is obtained by substituting $\boldsymbol{r}_i$ for each element in Equation (2). Assuming that χ is not a function of the magnetisation itself, rearrangement of the former relation yields

$$\boldsymbol{M} = \chi \left(\mathbf{I} - \chi \mathbf{G}_{\boldsymbol{r}} \right)^{-1} \frac{\boldsymbol{B}_0}{\mu_0}, \tag{4}$$

in which $\mathbf{I}$ is the $2N \times 2N$ identity matrix and $(\cdot)^{-1}$ denotes a matrix inversion. When the susceptibility in known, the structure's magnetisation is computed by means of Equation (4); subsequently, the stray field at $\boldsymbol{p}$ is determined by employing Equation (2).

3.2 Model for the magnetic susceptibility

The experimental stray field data implies that the magnetic properties differ in the vicinity of the circumferential welds. Therefore, the following axial distribution of the magnetic susceptibility is proposed:

$$\chi = \chi_0 - \chi_w \left(\sin\left(\frac{\pi \left(z - z_0 \right))}{b} \right) \right)^n , \tag{5}$$

where χ_0 is the undisturbed susceptibility of the material, χ_w is the reduction of the susceptibility due to the presence of the weld, b is the distance between each weld, z_0 is an offset to correctly position the welds along the pile axis, and n is an even power to localise the reduced susceptibility to a narrow range around the weld's position. In this expression, b and z_0 are determined by the geometry of the pile alone, see Table 1. The numerical values of the remaining parameters have to be calibrated.

3.3 Simulated magnetic signature

To simulate the relative motion between the sensor and the pile, the stray field is evaluated along a line parallel to the axis of the pile, on which the evaluation points $\boldsymbol{p}$ are given in cylindrical $r\theta z$-coordinates by:

$$\boldsymbol{p} = \begin{bmatrix} R + d_m \\ \theta_m \\ \zeta + a_m - L \end{bmatrix} , \tag{6}$$

where $\zeta = [\zeta_0, \zeta_0 + 8.6]\,\mathrm{m}$, which coincides with the recorded penetration range. For these parameters, the corresponding numerical values are presented in Table 1. The volume of pile is discretised in $N_\theta = 25$ and $N_z = 300$ elements. In this case, the penetration is measured independently, and the unknown parameters in the susceptibility can easily be calibrated to match the measured results: $\chi_0 = 2100$, $\chi_w = 1600$, and $n = 20$. Figure 3a shows the susceptibility distribution resulting from these values.

The two components of the simulated magnetic field are presented in Figure 3b along side the measured data. Please note that the modelled values are shifted with a constant to match the measured signal; this shift represents the exact background field at the sensor location. From the figure, it is clear that the trend in the measured data is captured correctly by the simulated data. Only B_z differs for lower values of ζ, which might be attributed to other material inhomogeneities affecting the susceptibility which are not accounted for in the present model. Nonetheless, the simple relation for the magnetic susceptibility that accounts for the presence of circumferential welds is able to reproduce the measured magnetic signature of the pile.

4 DISCUSSION

The correspondence between the simulated magnetic signature and the measurements indicates that the simple susceptibility formulation given in Equation (5) is sufficient to model the magnetic state of the pile after a proper calibration is applied. In this case, the penetration depth is measured, significantly simplifying the calibration, since a fixed reference is present. Normally, however, this reference measurement of the penetration is obviously not available;

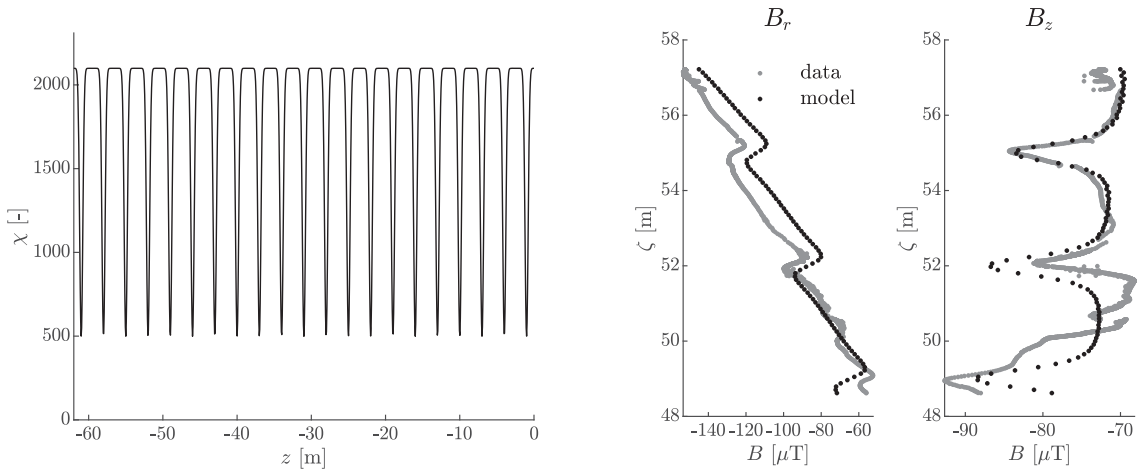

Figure 3: Model results for the magnetic stray field. (a) Modelled magnetic susceptibility along the pile's axis. (b) Modelled magnetic stray field versus the pile penetration compared to the measured data.

only the initial penetration depth is known to some extend. Therefore, the calibration should be founded solely on the measured magnetic field data. Fortunately, the welds create a distinct marking when they pass the sensor, e.g. a peak in the B_z value. Accordingly, as the weld positions are known at the start of the installation, the model can be calibrated based on the passage of one of those fixed markings, perhaps even constantly updating the model while new data is collected.

Once the model is calibrated, the penetration depth can be inferred by comparing the measured stray field to the modelled one. However, the mapping between some values of $\boldsymbol{B}$ and ζ is not unique (Figure 3b). Fortunately, the pile penetrates gradually into the soil; therefore, the penetration depth closest to the previous value should be selected. This additional step to extract the penetration depth from the magnetic data has not been elaborated yet, and it is left for future research.

The proposed method to monitor the pile's penetration has two benefits compared to currently used monitoring techniques; it relies on non-contact measurements, and it does not require an artificial tracking pattern applied to the pile's surface. In its current state, it only considers the magnetic stray field while the pile is unstressed. During the propagation of stress waves in the pile, reversible strain-induced magnetisation changes occur in conjunction to the changes related to the relative motion between the sensor and the pile, complicating the analysis considerably. Thus, the main application of the offered method is to monitor pile penetration during a full installation and not during a single hammer blow, e.g. a restrike test.

5 CONCLUSIONS

Based on magnetic stray field data collected during an onshore pile installation campaign, this paper proposes a new method to monitor the penetration of a steel monopile into the soil during pile driving. Contrary to state-of-the-art techniques, the proposed method is non-contact and does not require the introduction of an artificial pattern onto the surface of the structure. The latter is achieved by taking advantage of the naturally occurring pattern in the magnetic stray field as a result of circumferential welds in the pile. Furthermore, it is shown that this magnetic signature can be simulated by applying simple model for the magnetic susceptibility

proposed in this work. This modelled magnetic signature provides the basis for the method to monitor the penetration of a monopile during installation in real-time.

ACKNOWLEDGEMENTS

This research is part of the EUROS programme, which is supported by NWO domain Applied and Engineering Sciences and partly funded by the Dutch Ministry of Economic Affairs. The authors thank IHC-IQIP for the unique opportunity to perform these measurements at their yard in Sliedrecht, the Netherlands. Furthermore, the technical support provided by Arjan Roest (IHC-IQIP) and Kees van Beek (DEMO, TUDelft) is gratefully acknowledged.

REFERENCES

[1] P. Doherty and K. Gavin. "Laterally Loaded Monopile Design for Offshore Wind Farms". *Proceedings of the Institution of Civil Engineers - Energy* **165**.1 (2012), pp. 7–17. DOI: 10.1680/ener.11.00003.

[2] M. Schallert and O. Klingmüller. "Assessment of Soil Setup from Pile Installation Monitoring and Restrike Tests of Offshore Wind Turbine Foundation Piles". In: *10th International Conference on Stress Wave Theory and Testing Methods for Deep Foundations*. Ed. by P. Bullock, G. Verbeek, S. Paikowsky, and D. Tara. West Conshohocken, PA: ASTM International, 2019, pp. 681–696. DOI: 10.1520/STP161120170190.

[3] E. Wisotzki, R. van Foeken, P. van Esch, and D. Novakovic. "Strain and Acceleration Measurements at Instrumentation Distances to the Pile Head of 0.5 and 1.0 Times the Diameter—Offshore Pile-Monitoring Experience". In: *10th International Conference on Stress Wave Theory and Testing Methods for Deep Foundations*. Ed. by P. Bullock, G. Verbeek, S. Paikowsky, and D. Tara. West Conshohocken, PA: ASTM International, 2019, pp. 506–519. DOI: 10.1520/STP161120170238.

[4] S.-N. Lee, B.-J. You, M.-S. Limb, S.-R. Oh, S.-S. Han, and S. H. Lee. "Visual Measurement of Pile Penetration and Rebound Movement Using a High-Speed Line-Scan Camera". *Proceedings 2002 IEEE International Conference on Robotics and Automation (Cat. No.02CH37292)*. Vol. 4. 2002, 4307–4312 vol.4. DOI: 10.1109/ROBOT.2002.1014436.

[5] M.-S. Lim and J. Lim. "Visual Measurement of Pile Movements for the Foundation Work Using a High-Speed Line-Scan Camera". *Pattern Recognition* **41**.6 (2008), pp. 2025–2033. DOI: 10.1016/j.patcog.2007.10.025.

[6] J. R. M. S. Oliveira, P. R. R. L. Nunes, M. R. L. Silva, D. A. Cabral, A. C. G. Ferreira, L. A. V. Carneiro, and M. T. M. R. Giraldi. "Field Apparatus for Measurement of Elastic Rebound and Final Set for Driven Pile Capacity Estimation". *Geotechnical Testing Journal* **34**.2 (2011), p. 103103. DOI: 10.1520/GTJ103103.

[7] Y. Yeu, Y. S. Kim, and D. Kim. "Development of Safe and Reliable Real-Time Remote Pile Penetration and Rebound Measurement System Using Close-Range Photogrammetry". *International Journal of Civil Engineering* **14**.7 (2016), pp. 439–450. DOI: 10.1007/s40999-016-0053-y.

[8] A. Raza, U. Aqil, U. Baneen, and M. Q. Saleem. "Deep Foundation Testing Using Immunity-Based Displacement Measurement in Successive-Sparse Images". *KSCE Jour-*

nal of Civil Engineering **23**.10 (2019), pp. 4212–4222. DOI: 10.1007/s12205-019-2297-y.

[9] M. Beleggia, D. Vokoun, and M. De Graef. "Demagnetization Factors for Cylindrical Shells and Related Shapes". *Journal of Magnetism and Magnetic Materials* **321**.9 (2009), pp. 1306–1315. DOI: 10.1016/j.jmmm.2008.11.046.

[10] O. Chadebec, J.-L. Coulomb, V. Leconte, J.-P. Bongiraud, and G. Cauffet. "Modeling of Static Magnetic Anomaly Created by Iron Plates". *IEEE Transactions on Magnetics* **36**.4 (2000), pp. 667–671. DOI: 10.1109/20.877537.

EURODYN 2020
XI International Conference on Structural Dynamics
M. Papadrakakis, M. Fragiadakis, C. Papadimitriou (eds.)
Athens, Greece, 23–26 November 2020

MITIGATION OF ENVIRONMENTAL VARIABILITIES IN DAMAGE DETECTION: A COMPARATIVE STUDY OF TWO SEMI-SUPERVISED APPROACHES

A. Movsessian[1], B. A. Qadri[2], D. Tcherniak[3], D. Garcia Cava[1], M. D. Ulriksen[2]

[1]School of Engineering, Institute for Infrastructure and Environment, University of Edinburgh, Alexander Graham Bell Building, Thomas Bayes Road, Edinburgh EH9 3FG, United Kingdom
e-mail: {Artur.Movsessian,david.garcia}@ed.ac.uk

[2]Department of Energy Technology, The Faculty of Engineering and Science, Aalborg University Esbjerg, Niels bohrs vej 8.
e-mail: {baq,mdu}@et.aau.dk

[3]Brüel & Kjær Sound and Vibration Measurements, Skodsborgvej 307, Nærum 2085, Denmark
e-mail: dmitri.tcherniak@hbkworld.com

Keywords: Artificial neural networks, cointegration, damage detection, Mahalanobis distance, environmental variabilities

Abstract. *Vibration-based structural health monitoring (VSHM) employs vibration signals as observables from which inferences are made concerning the integrity of structural systems. More specifically, the premise of this work is to detect damage through changes in a set of features extracted from the vibration signals. A major challenge in this regard is that false positives may arise due to the influence of environmental and operational variabilities (EOVs). Environmental variabilities, e.g. shifts in temperature and humidity, introduce changes in mechanical properties. These changes are reflected in the vibration response and can reduce the probability of detecting damage in a structure. This paper conducts a comparative study between a novel semi-supervised damage detection approach and a well known cointegration-based scheme to deal with EOVs. The novel approach uses the pattern recognition capability of an artificial neural network (ANN) to learn how EOVs affect a Mahalanobis distance-based damage index in a reference state. The cointegration-based scheme seeks to mitigate the EOVs by computing stationary linear combinations of non-stationary output response signals. The merits of the damage detection methods are examined in the context of a mass-spring system, which is exposed to a simulated temperature field that renders the output response non-stationary. The system is analysed in a reference state and a perturbed state in which damage is emulated by reducing a single spring stiffness by 2%. Both methods are evaluated with the area under the curve (AUC) for receiver operating characteristic (ROC) and the false alarm rate. The results show that the ANN-based damage detection approach outperforms the cointegration-based one in this particular example.*

1 Introduction

In most applications, structural health monitoring (SHM) systems consist of a sensor network that continuously collects information from a structure in order to extract damage sensitive features (DSFs) which can be used to assess the structural integrity. The DSFs can be evaluated by statistical or machine learning techniques to detect damage in the structure. Damage detection is a widely researched topic in the field of SHM. Researchers have used both numerical simulations and experimental setups to detect damage in different structures, see for instance [1–4]. One of the prevailing challenges in damage detection is to discriminate between structural damage and environmental and operational variabilities (EOVs) [5]. Environmental parameters that vary over time is for instance the temperature, which causes changes in stiffness, thereby globally affecting the structural response as shown by Alampalli et al. [6]. Sohn et al. [7] demonstrated that EOVs may camouflage the effects of structural damage and tend to increase the false alarm rate in damage detection.

Several methods have been proposed to mitigate the influence of EOVs under the framework of semi-supervised learning. Cross et al. [8] adopted the concept of cointegration, which is widely used in the field of econometrics to identify statistical relationship between non-stationary variables [9]. Within the field of SHM it operates on the premise that the EOVs induce non-stationarities in the DSFs. The concept was tested on a ten degree of freedom (DOF) mass-spring system where EOVs were introduced to render the output response non-stationary. Implementation of a cointegration scheme resulted in DSFs free from the effect of EOVs, and these DSFs were used to detect damage. Qadri et al. [10] applied cointegration to data from an operating Vestas V27 wind turbine blade. Artificial damages were introduced to one of the blades. It was demonstrated that cointegration successfully removed the effects of EOVs on DSFs. This led to detecting the smallest of the introduced artificial damages while the wind turbine was operating. Shi et al. [11] used a four DOF mass-spring system where EOVs were introduced on the stiffness. Additional stiffness variabilities were introduced by letting one spring behave distinctly from the other springs. A regime switching cointegration concept was proposed using the augmented Dickey-Fuller (ADF) test as a tool to detect damage.

Another method to mitigate the influence of EOVs consists of the use of machine learning techniques for vibration-based structural health monitoring (VSHM). Especially the use of artificial neural networks (ANNs) has gained attention among researchers in the field of SHM in the past decade. Nevel et al. [12] highlighted the advantage of using ANNs in a semi-supervised approach for damage detection in a railway bridge. A numerical experiment using a three-dimensional finite element model was set up and two different damage scenarios were simulated. ANNs were trained with acceleration response on the healthy bridge and used in a prediction model. The prediction error was served as a damage index. The resulting indices were compared to a damage detection threshold to discriminate between different levels of structural states.

This paper presents a comparative study between a novel ANN-based damage detection method recently proposed by Movsessian et al. [13] and the cointegration-based damage detection concept proposed by Cross et al. [8]. The two methods are evaluated in the context of a six DOF mass-spring system which is exposed to a stochastic temperature field. Damage is emulated by reducing the stiffness in one of the springs. Additional, random local variabilities (i.e. to simulate discrepancies at different stiffness locations) in two of the six springs are introduced to the system. The paper is organized such that section 2 introduces the two damage detection methods, followed by the case study in section 3. Concluding remarks are provided

in section 4.

2 Methods

2.1 Artificial neural networks

ANN is a mathematical model widely used in the field of artificial intelligence due to its strong pattern recognition capability [14]. The structure is expressed in a mathematical model as shown in Fig. 1. A neuron receives a set of inputs ϑ_j, $j = 1, ..., n$ and this results in a single output. The input values are scaled by weights w_i and summed to be passed through the activation function.

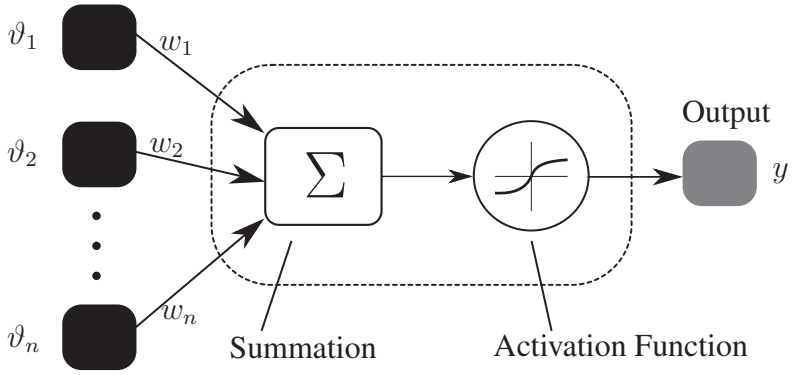

Figure 1: Schematic of an artificial neuron.

The structure shown in Fig. 1 can be expanded to a multilayer ANN by applying Eq. (1) to the next layer of an ANN. In such a system, each node i is connected to each node j in the consecutive layers by a connection with weight w_{ij}. The signals travel through the nodes of each layer in the following manner: in layer k, a weighted summation of all the signals $\vartheta_j^{(k-1)}$ from the preceding layer $k-1$ is calculated, the process is repeated for each node i and results in excitation $z_i^{(k)}$. A non-linear activation function f is applied to $z_i^{(k)}$ and the output of the node $\vartheta_i^{(k)}$ is obtained. Finally, this output is transmitted to the next layer [15].

$$\vartheta_i^{(k)} = f(z_i^{(k)}) = f(\sum_j w_{ij}^{(k)} \vartheta_j^{(k-1)}) \tag{1}$$

The training of an ANN is an adjustment of the connecting weights w_{ij} with the aim to minimize the mean squared error (MSE) between the target and the prediction. The MSE is computed from the output layer backwards. The learning algorithm to reduce the training error is the Bayesian regularization backpropagation as presented by MacKay [16].

2.1.1 Artificial neural networks for mitigating EOVs in damage detection

In the context of continuous monitoring systems, the data from the past and the present is available. To build a regression model by semi-supervised learning for continuous monitoring, DSFs $\boldsymbol{f}_t$ are gathered in a matrix $\boldsymbol{F} = [\boldsymbol{f}_1, \boldsymbol{f}_2, ..., \boldsymbol{f}_t, ..., \boldsymbol{f}_M], \boldsymbol{F} \in \mathbb{R}^{L \times M}$, where L is the length of the DSF vector and M is the number of observations. To provide the ANN regression model

a learning target, the features are labeled by the Mahalanobis distance (MD) Eq. (2):

$$d_t(\boldsymbol{f}_t, \boldsymbol{S}) = \sqrt{(\boldsymbol{f}_t - \boldsymbol{\mu}_{\boldsymbol{S}})^T \boldsymbol{\Sigma}_{\boldsymbol{S}}^{-1} (\boldsymbol{f}_t - \boldsymbol{\mu}_{\boldsymbol{S}})} \tag{2}$$

where $d_t(\boldsymbol{f}_t, \boldsymbol{S})$ is the MD between the observation $\boldsymbol{f}_t$ and the DSF matrix $\boldsymbol{S} \in \mathbb{R}^{L \times E}$ with $E \leq M$, $\boldsymbol{\mu}_{\boldsymbol{S}} \in \mathbb{R}^L$ is the mean of the observations in $\boldsymbol{S}$ and $\boldsymbol{\Sigma}_{\boldsymbol{S}} \in \mathbb{R}^{L \times L}$ is the covariance between observations in $\boldsymbol{S}$. Using the labeled feature matrix, a regression model can be build by training the ANN with the DSF vector $\boldsymbol{f}_t$ and the target $d_t(\boldsymbol{f}_t, \boldsymbol{S})$. For the semi-supervised framework, the ANN function $f_{nn}(\cdot)$ is trained exclusively with observations from a healthy system and their target (label). Let us define the prediction error $\hat{d}_t$ as the new damage index shown in Eq. 3:

$$\hat{d}_t = \frac{f_{nn}(\boldsymbol{f}_t)}{d_t(\boldsymbol{f}_t, \boldsymbol{S})} \tag{3}$$

where the ANN mapping function $f_{nn}(\cdot)$ is learning a unique relationship between the features from the healthy system and its target calculated by the MD metric. If an unlearned relationship between the features and the target occurs, due to e.g. damage in the system, an increased prediction error is expected.

2.2 Cointegration for mitigating EOVs in damage detection

In this study, cointegration is used to compute a linear combination of non-stationary variables in which the EOVs are mitigated. As such, the operating premise is that the EOVs govern the non-stationary behaviour. A brief introduction of cointegration is provided, for a detailed explanation on the method the reader is referred to Cross et al. [8]

The premise of cointegration is to fit a set of non-stationary variables to a p-order vector auto-regressive (VAR) model described as:

$$\boldsymbol{f}_t = \sum_{i=1}^{p} \boldsymbol{A}_i \boldsymbol{f}_{t-i} + \boldsymbol{\epsilon}_t \qquad \boldsymbol{\epsilon}_t \sim \mathrm{NID}(0, \boldsymbol{\Sigma}_\epsilon) \tag{4}$$

where $\boldsymbol{A}_i$, $i = 1, ..., p$ represents the coefficient matrices and p is the number of lags. $\boldsymbol{f}_{t-i}$ is the DSFs that is sought to cointegrate and $\boldsymbol{\epsilon}_t$ is normally and identically distributed (NID) white gaussian noise. The VAR model in Eq. (4) is re-written and formulated as a vector error correction model (VECM) defined by:

$$\Delta \boldsymbol{f}_t = \boldsymbol{\Upsilon} \boldsymbol{f}_{t-1} + \sum_{i=1}^{p-1} \boldsymbol{\Gamma}_i \Delta \boldsymbol{f}_{t-i} + \boldsymbol{\epsilon}_t \tag{5}$$

where $\boldsymbol{\Upsilon} \in \mathbb{R}^{L \times L}$ and $\boldsymbol{\Gamma}_i \in \mathbb{R}^{L \times L}$ are the matrices defined as:

$$\begin{aligned} \boldsymbol{\Upsilon} &= -\boldsymbol{I}_L - \boldsymbol{A}_1 - \boldsymbol{A}_2 - \cdots - \boldsymbol{A}_p \\ \boldsymbol{\Gamma}_i &= \boldsymbol{A}_{i+1} + \boldsymbol{A}_{i+2} + \cdots + \boldsymbol{A}_p \qquad i = 1 \ldots, p-1 \end{aligned}$$

If the DSFs in $\boldsymbol{f}_t$ are cointegrated, then matrix $\boldsymbol{\Upsilon}$ is rank deficient. In that case, the matrix can be decomposed as the product of two matrices:

$$\boldsymbol{\Upsilon} = \boldsymbol{U}\boldsymbol{V}^T \tag{6}$$

where $\boldsymbol{U}$,$\boldsymbol{V} \in \mathbb{R}^{L\times R}$ are matrices spanning the column and row spaces of $\boldsymbol{\Upsilon}$, respectively. The cointegration vectors are found in $\boldsymbol{V}$ and can be used to project the non-stationary variables into stationary residuals by a linear transformation:

$$\boldsymbol{z}_t = \boldsymbol{V}^T \boldsymbol{f}_t \tag{7}$$

where the ADF test is carried out by testing a null hypothesis of the residuals in $\boldsymbol{z}_t$ having a unit-root [17]; if a unit-root is present, then the residual is a non-stationary process and will not be suitable for damage detection. The process is carried out for each residual where the one that constitutes stationarity are used for further examination.

3 Case study

The present section is intended to demonstrate the two aforementioned methods on the six DOF mass-spring system presented Fig. 2. The system consists of six springs that are connected to six masses and fixed at one of the ends.

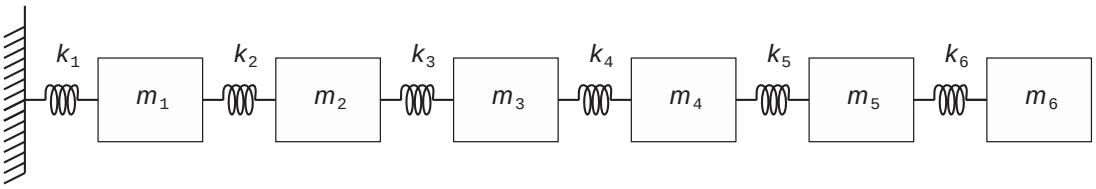

Figure 2: A six DOF mass-spring system.

In this case study, we consider the six natural frequencies of the system as the DSF vector $\boldsymbol{f}_t = [\boldsymbol{s}_1(t), \boldsymbol{s}_2(t), ..., \boldsymbol{s}_6(t)]^T$ where $\boldsymbol{s}_i = \frac{\sqrt{\boldsymbol{\lambda}_i}}{2\pi}$, with the $\boldsymbol{\lambda}$ being the eigenvalues in Eq. 8:

$$(\boldsymbol{K}_\alpha - \boldsymbol{\lambda}\boldsymbol{M})\boldsymbol{\theta} = \boldsymbol{0} \tag{8}$$

with a constant mass matrix where $m_i = 2$. To simulate the effect of EOVs on DSFs, the stiffness of the system is exposed to the temperature field $\boldsymbol{u}(t)$ shown in Fig. 3a. Additionally, stiffness k_2 and k_5 are exposed to random changes. The $\boldsymbol{K}_\alpha$ is the affected stiffness matrix expressed as:

$$\boldsymbol{K}_\alpha = (-\boldsymbol{u}(t) + C)\boldsymbol{K} \tag{9}$$

where C is a random constant value that maps the expression $(-\boldsymbol{u}(t) + C)$ to a positive value. For this study $C = 80$. $\boldsymbol{K}$ is the stiffness matrix that holds the k_i coefficients defined as:

$$k_1 = k_3 = k_4 = k_6 = 2 \tag{10}$$

$$k_2 = 2r_2(t) \tag{11}$$

$$k_5 = 2r_5(t) \tag{12}$$

where $r_2(t) \neq r_5(t)$ are independent and uniformly distributed random values with $r_{2,5}(t)$: $[1 - \alpha > r_{2,5}(t) < 1 + \alpha]$ and $0 \leq \alpha \leq 1$. The eigenvalue problem is then solved M times, where M is the total amount of observations.

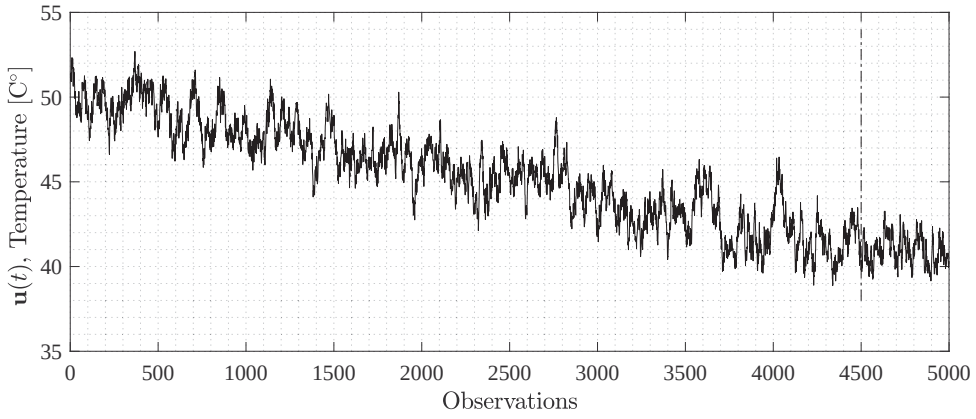

(a)

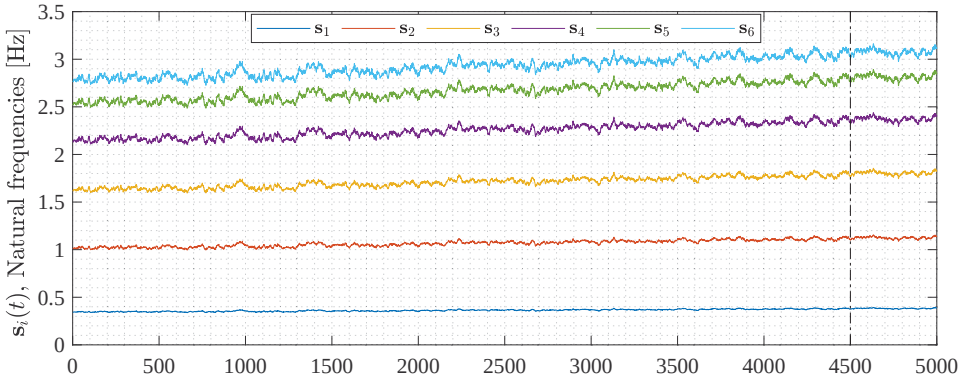

(b)

Figure 3: (a) Simulated temperature field $\boldsymbol{u}(t)$ and (b) the six extracted natural frequencies $\boldsymbol{s}_i$. The dashed vertical line indicates when damage is introduced.

In this case study, the eigenvalue problem is solved for a total of 5000 observations: The first 4500 observations are from a system in a healthy state and the remaining 500 refer to a system in a damaged state. The damage is emulated by decreasing k_3 by 2%. The summary of the number of observations used for semi-supervised learning is presented in table 1. To simulate

Table 1: Summary of observations used for training, testing and damage detection

Scenario	Stiffness reduction	Stiffness parameter	Number of observations
Healthy			
Training		-	1 to 4000
Testing		-	4000 to 4500
Damage	2%	k_3	4501 to 5000
Total			5000

the measurement noise, white Gaussian noise with 90dB signal to noise ratio is added to the natural frequencies. Observations 1 to 4000 were used for training. Both methods, ANN- and cointegration-based damage detection are tested using observations 4001 to 5000; of which the

first 500 are from the healthy state and the remaining from the damaged state. The performance, by means of area under the curve (AUC) of the receiver operating characteristic (ROC) and false alarm rate, of the damage detection methods is evaluated based on observations 4501 to 5000 where the damage is present.

3.1 The effect of EOVs

To illustrate the effects of EOVs, the MD-based damage index $d_t(\boldsymbol{f}_t, \boldsymbol{S})$ is calculated, where $\boldsymbol{S} \in \mathbb{R}^{6\times4000}$ and $\boldsymbol{S}$ is based on the first 4000 observations from a healthy system, see Fig. 4. The damage detection threshold is assigned based on 2% allowed outliers for the first 4000 observations. Evidently, the MD-based damage index follows a trend which hinders the discrimination between damage and EOVs.

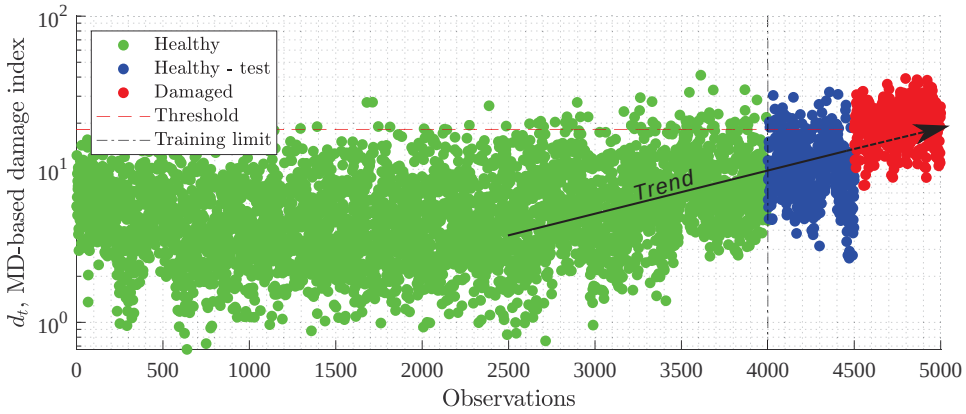

Figure 4: MD-based damage index for $\alpha = 0.15$

3.2 Mitigating the effect of EOVs

To train the ANN the prediction target is calculated by the MD-based damage index with $\boldsymbol{S} \in \mathbb{R}^{6\times500}$ representing the first 500 observations. The ANN is trained with observations from 501 to 4000 which are randomly shuffled. The hyperparameters for the ANN can be found in Appendix A. As shown in Fig. 5 the prediction deviates from the calculated MD once the stiffness reduction is introduced. The prediction error is calculated as per Eq. (3) and used as a new damage index shown in Fig. 6a.

In the cointegration-based approach, the first cointegrating vector that is associated with the highest singular value (i.e. the value that is associated with 'most stationarity') is used to project the natural frequencies into one stationary residual. Evidently the trend is removed as can be observed by comparing Fig. 4 to the cointegration results in Fig. 6b. Due to the additional local variabilities in the stiffness matrix, damage is not clearly separated from observations of the system in a healthy state.

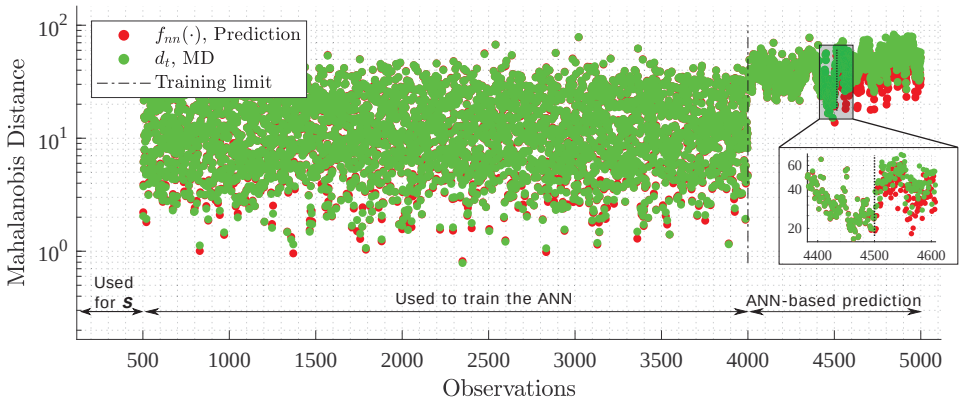

Figure 5: MD and predicted MD by ANN.

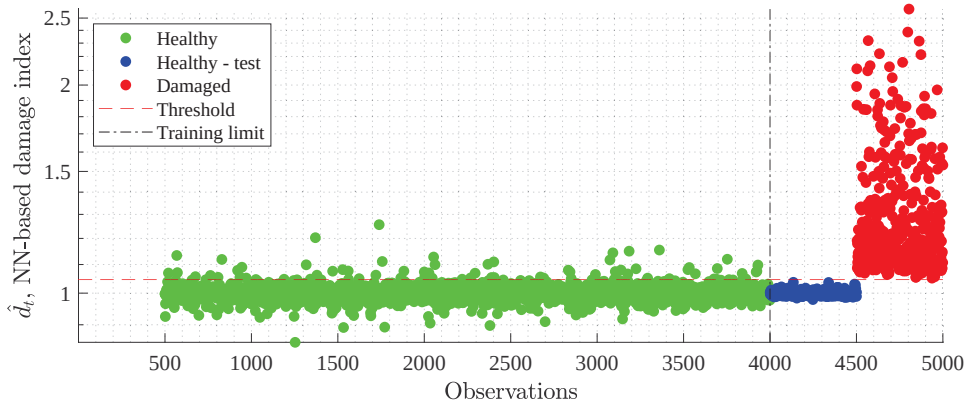

(a)

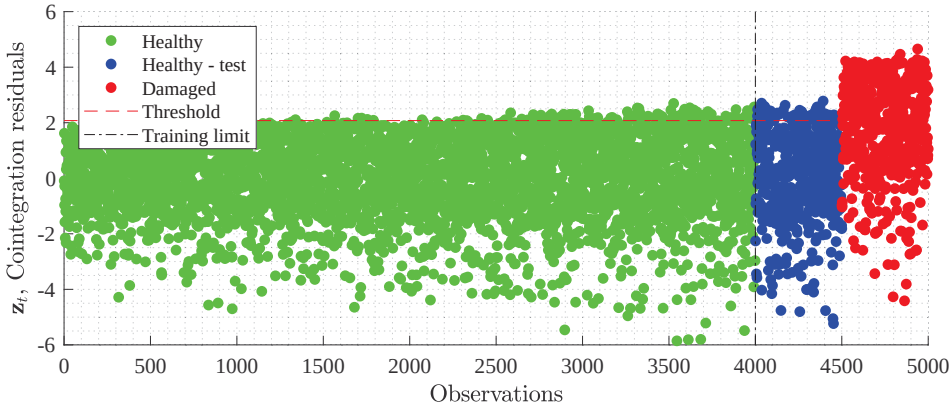

(b)

Figure 6: (a) The prediction error $\hat{d}_t$ using ANN calculated as per Eq. (3). (b) Cointegration residuals $\boldsymbol{z}_t$. Both methods are evaluated for $\alpha = 0.15$.

3.3 Evaluating scenarios with different local variabilities

Eight different scenarios are analysed with α ranging from 0 to 0.35 where $\alpha = 0$ indicates that no local random variabilities are added. By increasing the α value by 0.05 step-wise to 0.35

different scenarios of random variabilities in spring k_2 and k_5 are introduced. The performances of the methods are evaluated for their ability to first detect healthy-test observations, and second to detect damage. False alarm rates are calculated to evaluate the methods' ability to identify new healthy observations as healthy whilst the AUC of ROC is calculated to assess the performance rate of damage detection with respect to the healthy-test observations. The results are presented in Fig. 7.

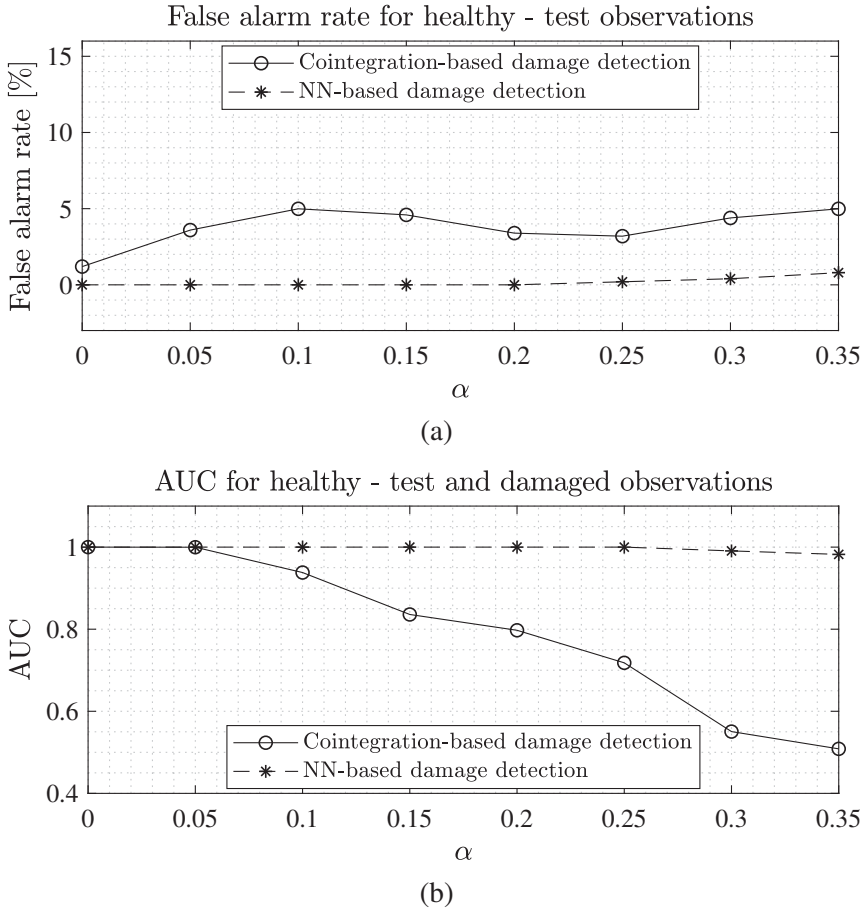

Figure 7: (a) Evaluating performance of the two methods by AUC and (b) false alarm rate for increased α values.

For $\alpha = 0$ the methods perform similar when evaluated by the AUC and false alarm rate. As the α increases, the results indicate a higher or equal performance rate in all cases for the ANN-based damage detection.

4 Discussion

The study demonstrates that both methods are capable of removing environmental trends. Although local variabilities are added to the mass-spring system, the false alarm rate for test observations does not exceed 5% for cointegration-based damage detection and 1% when applying ANN-based damage detection. These results are acceptable considering that 2% false alarm rate is allowed. Nevertheless, the AUC is approaching 0.5 in the case of cointegration when increasing the amount of local variabilities. Increasing the local variabilities does not affect the damage detection performance rate when applying ANN and the AUC is close to 1 in

all cases. The methods show similar results if no additional local variabilities are introduced. For this case, the cointegration approach is preferred due to its interpretability. However, if the mass-spring system is exposed to local variabilities in the stiffness, the ANN-based damage detection yield a higher performance rate by learning the pattern of EOVs for this particular case study. Nevertheless, there is a trade-off with the loss of interpretability inherent in this type of method.

Furthermore, this comparative study is limited to the six DOF mass-spring system defined in section 3 and requires further research. This field could benefit from two streams of research: one where the amount and location of variabilities are further investigated on a simulated system, and another where the methods are tested in real applications.

5 Conclusion

The work presented in this paper compared a novel ANN-based damage detection method in a semi-supervised framework to a well known cointegration approach for mitigating EOVs in damage detection. The methods were tested on a six DOF mass-spring system. The global stiffness of the system was exposed to a stochastic temperature field and additional random variabilities in two of the six springs. Both methods used the natural frequencies as DSFs and were evaluated for their capability to identify healthy-test observations and the emulated damage in the system. Comparing the performance of the two methods on a system exposed to EOVs, the ANN-based damage detection yielded a higher performance rate in terms of AUC and false alarm rate.

REFERENCES

[1] G. Gui, H. Pan, Z. Lin, Y. Li, Z. Yuan, Data-driven support vector machine with optimization techniques for structural health monitoring and damage detection, KSCE Journal of Civil Engineering 21 (2) (2017) 523–534 (2017).

[2] D. Tcherniak, L. L. Mølgaard, Active vibration-based structural health monitoring system for wind turbine blade: Demonstration on an operating vestas v27 wind turbine, Structural Health Monitoring 16 (5) (2017) 536–550 (2017).

[3] M. D. Ulriksen, D. Tcherniak, L. Damkilde, Damage detection in an operating vestas v27 wind turbine blade by use of outlier analysis, in: 2015 IEEE Workshop on Environmental, Energy, and Structural Monitoring Systems (EESMS) Proceedings, IEEE, 2015, pp. 50–55 (2015).

[4] D. García, D. Tcherniak, An experimental study on the data-driven structural health monitoring of large wind turbine blades using a single accelerometer and actuator, Mechanical Systems and Signal Processing 127 (2019) 102–119 (2019).

[5] K. Worden, C. R. Farrar, G. Manson, G. Park, The fundamental axioms of structural health monitoring, Proceedings of the Royal Society A: Mathematical, Physical and Engineering Sciences 463 (2082) (2007) 1639–1664 (2007).

[6] S. Alampalli, Effects of testing, analysis, damage, and environment on modal parameters, Mechanical Systems and Signal Processing 14 (1) (2000) 63–74 (2000).

[7] H. Sohn, M. Dzwonczyk, E. G. Straser, A. S. Kiremidjian, K. H. Law, T. Meng, An experimental study of temperature effect on modal parameters of the alamosa canyon bridge, Earthquake engineering & structural dynamics 28 (8) (1999) 879–897 (1999).

[8] E. J. Cross, K. Worden, Q. Chen, Cointegration: a novel approach for the removal of environmental trends in structural health monitoring data, Proceedings of the Royal Society A: Mathematical, Physical and Engineering Sciences 467 (2133) (2011) 2712–2732 (2011).

[9] P. Kennedy, A guide to econometrics, MIT press, 2003 (2003).

[10] B. A. Qadri, M. D. Ulriksen, L. Damkilde, D. Tcherniak, Cointegration for detecting structural blade damage in an operating wind turbine: An experimental study, in: Dynamics of Civil Structures, Volume 2, Springer, 2020, pp. 173–180 (2020).

[11] H. Shi, K. Worden, E. J. Cross, An exploratory study on removing environmental and operational effects using a regime-switching cointegration method, in: Dynamics of Civil Structures, Volume 2, Springer, 2017, pp. 329–337 (2017).

[12] A. Neves, I. González, J. Leander, R. Karoumi, Structural health monitoring of bridges: a model-free ann-based approach to damage detection, Journal of Civil Structural Health Monitoring 7 (5) (2017) 689–702 (2017).

[13] A. Movsessian, D. García, D. Tcherniak, Artificial neural network approach to mitigate environmental and operational variability's in damage detection (in preparation).

[14] S. Samarasinghe, Neural networks for applied sciences and engineering: from fundamentals to complex pattern recognition, Crc Press, 2016 (2016).

[15] C. R. Farrar, K. Worden, Structural health monitoring: a machine learning perspective, John Wiley & Sons, 2012 (2012).

[16] D. J. MacKay, Bayesian interpolation, Neural computation 4 (3) (1992) 415–447 (1992).

[17] D. A. Dickey, W. A. Fuller, Distribution of the estimators for autoregressive time series with a unit root, Journal of the American statistical association 74 (366a) (1979) 427–431 (1979).

A Artificial neural networks hyperparameters

Table 2: Neural network hyperparameters

Hyperparameters	
Training algorithm	Bayesian Regularization
Hidden layers	10
Neurons per hidden layer	10
Activation function hidden layers	Hyperbolic tangent sigmoid transfer function
Activation function output layer	Linear transfer function
Marquardt adjustment parameter mu	0.005
Increase factor for mu	10
Decrease factor for mu	0.1
Maximum number of epochs to train	3000

EURODYN 2020
XI International Conference on Structural Dynamics
M. Papadrakakis, M. Fragiadakis, C. Papadimitriou (eds.)
Athens, Greece, 23–26 November 2020

IMPLEMENTING A STRUCTURAL HEALTH MONITORING SYSTEM USING DIGITAL MODELS OF THE BAM LARGE DROP TEST FACILITY IN HORSTWALDE

R. Herrmann[1], F. Hille[1], S. Said[1], J. Sterthaus[2], K. Müller[2], T. Quercetti[2], F. Wille[2], J.-A. Paffenholz[3], and M. Baeßler[1]

[1] Federal Institute for Materials Research and Testing (BAM)
Division 7.2 Buildings and Structures
Unter den Eichen 87, 12205 Berlin, Germany
corresponding e-mail: ralf.herrmann@bam.de
e-mail: {firstname.lastname}@bam.de

[2] Federal Institute for Materials Research and Testing (BAM)
Division 3.3 Safety of Transport Containers
Unter den Eichen 44-46, 12203 Berlin, Germany
e-mail: {firstname.lastname}@bam.de

[3] Clausthal University of Technology
Institute of Geotechnical Engineering and Mine Surveying
Erzstraße 18, 38678 Clausthal-Zellerfeld, Germany
e-mail: jens-andre.paffenholz@tu-clausthal.de

Keywords: Drop test, Impact loading, System Identification, Digital Twin, Dynamic Simulation, BIM

Abstract. *At the Bundesanstalt für Materialforschung und -prüfung (BAM) full scale specimens for nuclear transport and storage containers (casks) are tested for their structural integrity in a series of drop tests on the Test Site Technical Safety in Horstwalde, 50 km south of Berlin. These drop tests cause a major stress not only on the casks, but also on the steel tower structure of the test facility, itself. The load pattern makes the structure very interesting for detailed investigation. The focus of the monitoring lies on the bolted joints of the flange connections that are a typical connection for cylindrical elements if welding is technical or economical unfavorable. The definition of the monitoring takes was done by investigating the existing documents and inspection results accompanied by building an initial digital representation of the structure, consisting of two finite element (FE) models and a geometrical 3D point cloud representation. As a first step the structures behavior during static and dynamic loading was analyzed using measurement data and an updated numerical FE Model. The idea behind is to use models for a digital planning and operation/evaluation of the structural health monitoring. A static FE simulation and a dynamic FE simulation are generated, to investigate how the structure behaves under the load conditions.*

1 INTRODUCTION

At the Bundesanstalt für Materialforschung und -prüfung (BAM) full scale specimens for nuclear transport and storage containers are tested for their structural integrity in a series of drop tests on the Test Site Technical Safety in Horstwalde, 50 km south of Berlin. These tests are realized by means of the 200 t drop test facility that was put in operation in 2004 [1]. Since 2004 drop tests were done with varying drop weights up to 180 t. These drop tests cause a major stress not only on the containers to be tested, but also on the steel tower structure of the test facility, itself. During a drop test the tower structure is affected by three load conditions: quasi-static increasing load of the structure until the container left the ground, transient dynamic release of the load and the impact of the container on the target causing ground vibrations with reactions in the tower foundations as well.

The operational loads are below any critical limits for the structure according to the standards that were considered during the design of the structure. However, it is a matter of concern if the unique loading of the drop tests is covered adequately by the considered design procedure, especially for tests with low drop heights. The load regime of the tower is very well known for each drop test. After almost 16 years of operation a details inspection of the structure revealed a loss of the tension in some of the prestressed bolted joints that are fastened with more than 1000 high-strength prestressed bolts of the strength class 10.9. The required scheduled maintenance made it possible to investigate the structures behavior and to start a continuous monitoring by installing a structural health monitoring system (SHM) for the identified deficiencies. The goal of this research is to define a proper workflow for the implementation of a digital twin monitoring task for a well-defined aspect of an existing structure. The focus of the monitoring lies on the bolted joints of the flange connections that are a typical connection for cylindrical elements if welding is technical or economical unfavorable. The definition of the monitoring takes was done by investigating the existing documents and inspection results accompanied by building an initial digital representation of the structure, consisting of two finite element (FE) models and a geometrical 3D point cloud representation. The idea behind is to use models for a digital planning and operation/evaluation of the structural health monitoring. A static FE simulation and a dynamic FE simulation are generated, to investigate how the structure behaves under the load conditions.

The contribution deals with the introduction of this highly interesting dynamically loaded structure, a presentation of test results and related numerical simulation as well as with the conception and implementation of a SHM system.

2 DROP TEST TOWER STRUCTURE AND OCCURRENCES

The large drop test facility consists of a 36 m high drop tower of steel pipe construction; at the top of this tower is a small cabin with a 200 t hoist, with a maximum hook height of 30 m. Below this drop tower is a 24 m x 20 m integrated test hall (steel frame construction independent from the drop tower) with an 80 t portal crane, rolling gates and a roof that can be removed if a cask is connected to the hoist. The impact pad is constructed as an unyielding target realized by reinforced concrete block with dimensions 14 m x 14 m x 5 m depth, with a mass of 2,600 t, and with an impact pad made of steel plates 10 m x 4.5 m x 0.22 m connected to the target with anchor bolts. This construction fulfills the requirements of the International Atomic and Energy Agency (IAEA) [2]. Figure 1 shows the complete drop test facility and the special container detachment device that was designed by BAM to ensure a momentum free release of the specimen. Its construction is based on a hydraulic mechanism rupturing a steel bolt.
The construction of the facility was finished in August 2004 with the static overload test of the whole lifting equipment by lifting weight of 250 t.

Figure 1; BAM Drop Tower at Test Site Technical Safety (left), container detachment device (middle) and overload test (right).

In 2018, after 16 years of operation a regular inspection of the facility found loose bolts at the crane way. For this reason, a detailed inspection of the global structure with specific investigations of the high-strength prestressed bolts at the tower structure was initiated. A selection of seven high-strength prestressed bolts at relevant steel connections of the structure have been examined. The bolts have been unscrewed and the release torque has been measured. Four of the seven bolts showed a reduced released torque. The reasons for the occurrences were not very clear, but dynamic loads induced by more than 150 drop tests performed seem to have an important effect on the prestressed joints of the tower construction. The typical connections at the structure are flange joints and gusset plate joints, see Figure 2.

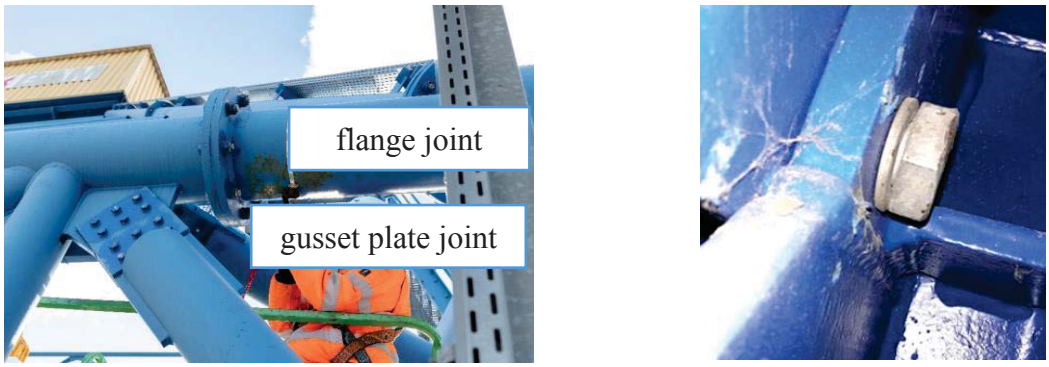

Figure 2: Joints at the tower construction(left) and loosen bolt at one joint (right)

The actions derived from the inspection was to replace the loosened bolts and to develop a monitoring strategy that continuously observes the structure during all operating conditions.

3 DEVELOPMENT OF A MONITORING STRATEGY

The goal for a structural health monitoring is to deliver precise and updated measurements and information of the structure that can be used to asses and predict the current structural condition of the monitored aspect and supports the upcoming inspections with additional insights. The typical process of the design of a monitoring system, like in [3], has been applied but expanded by the implementation of digital models from the start of the design process, see Figure 3.

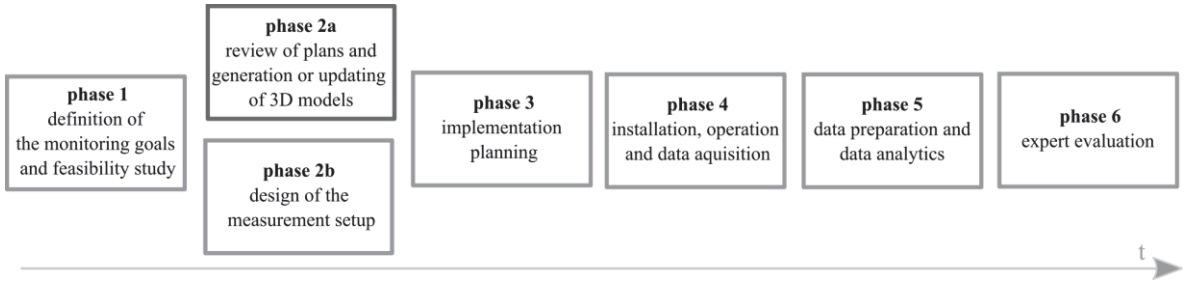

Figure 3: Systematic process of the implementation of a structural health monitoring, according to [3] with an additional process of generating or updating 3D models

In parallel to the design of the measurement concept several digital models of the structure have been developed. The models were several implicit and explicit FE models and BIM model extracted from a 3D point cloud. These models were used to organize the existing data from the visual inspection and from the drawings and to develop a better general understand of the static and the dynamic behavior of the structure and substantial helped to plan the monitoring setup and place sensors. The models were used during the installation phase as planning documents for the monitoring as well as the installation documentation.

The concept of the monitoring covers the following objectives to assess the structure under the testing loads with a long-term monitoring system, see 1. To cover all this monitoring objectives six monitoring tasks with a specific sensor layout has been planned and later realized at the drop tower of BAM, see Table 2.

1	global static behavior	
	1-a	static deflection behavior of the structure under load
	1-b	influence of the temperature distribution on thermal stress
2	pretension losses of the bolts	
	2-a	long term pretension losses
	2-b	pretension losses due to drop tests
	2-c	transient bolt prestress force variation during a drop test
3	dynamic vibration characteristics	
	3-a	structural damage detection based on ambient vibration behavior
	3-b	transient vibration pattern of tower and tower foundation during a drop test
4	comparison to FE models	

Table 1 Identified objectives for the SHM of the BAM drop tower

The monitoring task M covers the metrological conditions of the drop tower. The wind speed, wind direction and the air temperatures at the top and the middle of the tower are continuously measured. On the north facing side of the tower along the southern tower leg, which is full exposed to the sun light, the surface temperature of the steel is measured. In addition, halfway up on all four tower legs, the temperature is measured, too. By the combination of both setups a horizontal and a vertical temperature gradient can be calculated. The detailed temperature measurement is also necessary for an additional temperature compensation of the strain measurements of monitoring task RF and all temperature related effect on the structure, the sensors and the algorithms. The monitoring task RF wants to evaluate the thermal strain at the four corner brackets where the vertical tower legs snap off into the pyramid ridge. This position is

expected to be most influenced by the thermal stress. At each tower leg four strain gauges are installed along the circumference of the steel tube below the corner bracket in longitudinal direction. This setup allows to recognize longitudinal strain due to the test loads but also temperature induced bending strain. The monitoring task RF also deals with the dynamic response of the tower. Together with additional strains gauges at the tower legs near the tower foundations the compression waves that travel through the structure caused by the cask release and the impact on the test foundation during the drop tests will be recorded with a high sampling rate. Especially for low drop heights, the release impulse and the impact impulse can superposition, as the release impulse in independent from the drop height.

monitoring task M (meteorology)	monitoring task G (global deformation)	monitoring task SVD (dynamic bolt pretension)
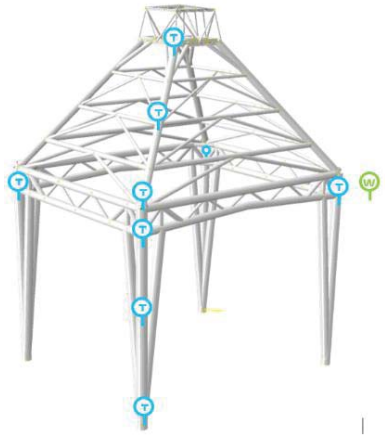	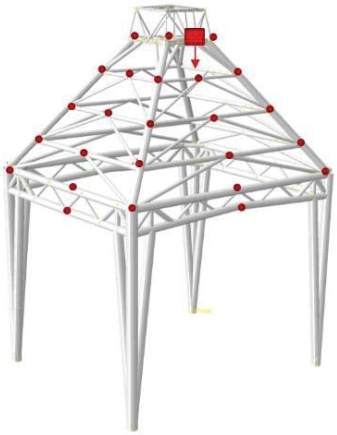	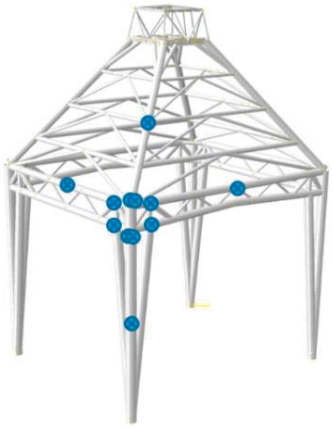
temperature sensor wind speed / direction	position captured by 3D point cloud displacement sensor	force washer
1-a, 1-b, 2-a, 3-a, 4	1-a, 4	2-a, 2-b, 2-c, 4
monitoring task RF (thermal stress)	mon. task SSDD & BD (dynamics & damage detection)	monitoring task SVS (static bolt pretension)
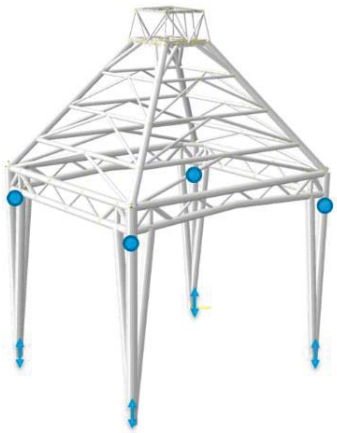	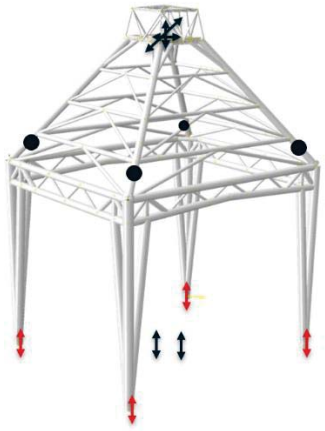	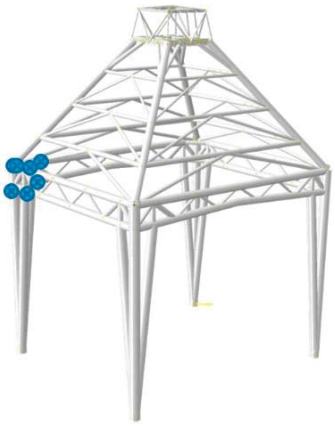
strain gauges setup of 4 single strain gauge	biaxial accelerometer uniaxial accelerometer uniaxial geophone	ultra-sonic force transducer
1-b, 2-a, 3-b, 4	3-a, 3-b, 4	2-a, 2-b, 4

Table 2: Overview of the sensor setup for each monitoring task and the related monitoring objective

The structural dynamics under ambient excitation (e. g. wind) are periodically recorded to identify possible changes in the vibration characteristics that indicate a possible damage by stochastic subspace damage detection, see [4] and with special regard to an uncertain reference, see [5]. The damage detection of monitoring task SSDD relies on four biaxial accelerometers, one at each pyramid ridge. During the drop test additional accelerations are measured in the crane house (triaxial), the test foundation (uniaxial) and vibration velocities at the tower foundations with geophones (monitoring task BD). This data can be evaluated by probabilistic methods, like [6] or robust modal analysis algorithms, like [7].

The main interest based on the observation from the tower inspection is the loss of pretension in the high tensile prestressed bolts. The long-term monitoring is carried out by an ultra-sonic monitoring system that records the tension of eight bolts at the flange joint at the corner bracket every 10 minutes (monitoring task SVS). So, it is possible to compare the bolts condition before and after a drop test and the long-term behavior. The force washers of monitoring task SVD are an independent system for the pretension measurements with a much higher dynamic and time resolution so that the transient forces of the drop test can be recorded. This conventional force measurement has the drawback of a quite large influence of the bolt connection, because much longer bolts are needed and it acks like additional washers in the connection. The ultra-sonic pretension measurement of SVS preserve the native connection that's used in all the flange joints at the corner brackets. Regarding the temperature effects and the prestress development both systems can be compared by symmetrical installed measurement bolds at different tower legs.

The monitoring task G observes the global deformation behavior of the structure in a single measurement campaign, where a laser scanner was used two-fold: First, to obtain point clouds of the whole structure under investigation to yield information to create a digital twin. Therefore, several static positions were used to obtain 3D point clouds, which were in the analysis referenced in a unique coordinate system by means of artificial targets. Second, a 3D point cloud by a single position was acquired during a specific load scenario of the structure. In detail, 3D point clouds for two epochs were acquired: the zero epoch without any load and the epoch under a specific load. This acquisition setup supports the estimation of deflections with a focus on the vertical component to learn about the impact of the load on the behavior of the structure. In literature can be found similar experiments for, e.g., infrastructure objects like bridges, see [8] and [9]. A long-term measurement of the deflection of the tower under test loads and temperature influences by means of an optical distance sensor will follow.

4 DIGITAL TWIN CALIBRATION AND MEASUREMENTS

The concept of a digital twin is multidisciplinary method for a comprehensive physical and functional description of an engineering component, system or network in all phases of the lifecycle beginning from the draft to the dismantling including all information that can be useful in each lifecycle phase. Special interest lies in the operation phase where inspection tasks can be optimized by fusing simulated system behavior and failure predictions with real world input parameters and system responses. For civil engineering the verification of the real operation condition, especially in a probabilistic way, like in [10] is an essential task during the long service lifetime of decades.

An efficient 3D object capturing to yield a digital representation or digital twin of nearly arbitrary objects can be realized by using a laser scanner. Millions of single, spatial closely distributed 3D points represent the object of interest. These so-called 3D point clouds carry next to the spatial information, information about the reflectivity by backscattered intensity values and optional color values obtained by a -nowadays- integrated digital camera.

The working principle of the laser scanner is according to the polar measurement principle. This is characterized by an immediately 3D dimensional, direct centric data acquisition with a high spatial resolution of a few millimeters. The most important characteristics of laser scanner is the area-based object acquisition by a remote position, thus no need to directly access the object under investigation since the range measurement is performed reflectorless. There is not special need for a specific structure on the object as if it is mostly necessary for a photogrammetric data acquisition. Supported by the area-based acquisition a proper data analysis is able to deliver information about deformations ranging up to one digit millimeter level.
The 3D point cloud of an existing structure can be converted into a reduced digital model, which can be a BIM model for a specific BIM platform. Although mainly used for the design, planning and construction in the BIM context the common data environment (CDE) fulfils this requirement of a single source of truth (SSoT) and allows the interchangeability of the model information, and enables continuous updating of information based on a central data hub between all involved specialist, see [11]. The CDE seems to be the data resource for the Digital Twin in civil engineering and can be extended to be used by artificial intelligence for machine learning to generate, train, validate and evaluate machine learning models on the provided data.

Figure 4: Geometrical representation as a 3D point cloud of the drop tower (left) used for planning of the SHM and the modelling of FEM and top view situation of the laser scanner setup (right).

For this monitoring project, the 3D point cloud was prototypical used as a CDE for the drop tower, see Figure 4, to evaluate benefits at the following project phases. At the design phase (2b) of the monitoring setup it reflected the as-built situation of the tower and was used to clarify the geometry for the development of FE models and BIM models. The inspection documentation of the bolts was added to the point cloud to get a better insight. During the implementation planning (3) all installation positions, cable lengths and geometrical constrains were cross-checked. In the installation phase (4) the models helped to locate correct positions and keep installation specific data, which is very beneficial to contribute to high data quality, see [12]. This easily accessible data is relevant for the currently ongoing data preparation and analytics phase (5), where the dynamic response of the structure is simulated by time integration numerical analysis in an optimized complexity. Further motivation for establishing numerical analysis lies in the requirement to identify the locations as well as the magnitude of the peak stress values during drop tests to reliable assess the structural safety of the drop tower (6).

4.1 Model

The numerical analysis of the drop tower was performed using a three-dimensional model, developed in ANSYS® software in its version 2019R2. Figure 5, left shows a global view of the drop towers model. The space frame elements of the tower were modelled with beam elements,

taking the pipe cross-sectional parameters into account. For the gusset plates at the structural connections shell elements were chosen to sustain realistic stiffness relations. All structural dimensions as well as material parameter were taken from construction plans. All six support conditions at each of the four foundations were modelled as springs. Concentrated masses, especially the winch on the top of the tower, were modeled as point masses. The described approach with applying beams for the framework ensures a corresponding limited number of degrees of freedom for a sufficiently accurate image of the global dynamic behavior of the structure as well as a limited computational effort executing time integration analysis.

4.2 Model verification by static load test

Preparing numerical simulations, the quality of the model should be verified, i.e. by assessing the accuracy of simulation results comparing them with measured counterparts. In the case of the analyzed drop tower especially the stiffness parameter should have been under investigation. A simple but effective method for verifying the global structural stiffness is a static load test where measured deflections with the computed ones. Here, as part of a periodic routine examination of the winch braking system a 200 t nominal lift test was executed and used as a load test, see Figure 1. The deflection of the top of the tower just beneath the winch housing was measured using tachymeter. In Figure 5, right the computed deflection of the structure is displayed. For the position of the tachymeter reflector the computed deflection is d = 11.05 mm[1], which is very similar to the measurement, see Table 3. This shows a very good conformity of the model's global stiffness with those of the real structure.

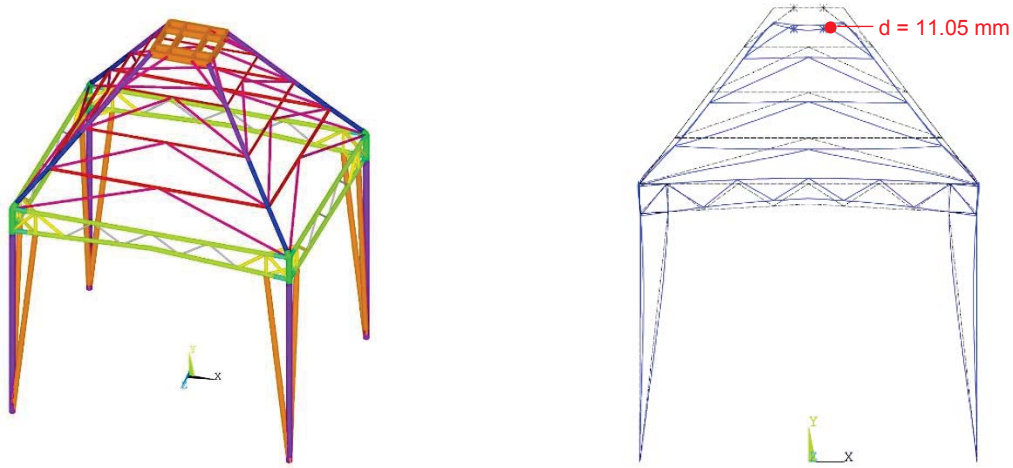

Figure 5: Numerical simulation of the drop tower, left side: ANSYS® model, right side: simulation result of the 200 t load test

test no.	lifted mass [t]	deflection [mm]
1	0	0.0
2	200	11.2
3	195	10.5
4	0	0.0

Table 3 Deflection of the tower in y direction measured with a tachymeter during the load test

[1] For the tachymeter reflector is not applied on a structural member, the simulated deflection is determined by interpolation.

4.3 Model verification by modal values

Besides the stiffness distribution, for numerical simulations of the dynamic structural behavior it is essential to verify the correctness of the dynamic model parameter. The classic approach for analyzing the accuracy of the numerical model consists in the comparison of the modal parameters, representing the dynamic characteristic of the structure and the model alike. Besides comparing measured with computed eigenfrequencies it is especially the mode shapes which emphasizes differences between the model and the real structure. In the scope of this contribution by now the extensive dynamic measurement campaign has not been executed yet, so a distinguished set of mode shapes cannot be presented here. For that reason, the focus of modal analysis lies on the comparison of the eigenfrequencies. Nevertheless, Figure 6 shows a compilation of global mode shapes and the corresponding eigenfrequencies for modes up to 10 Hz.

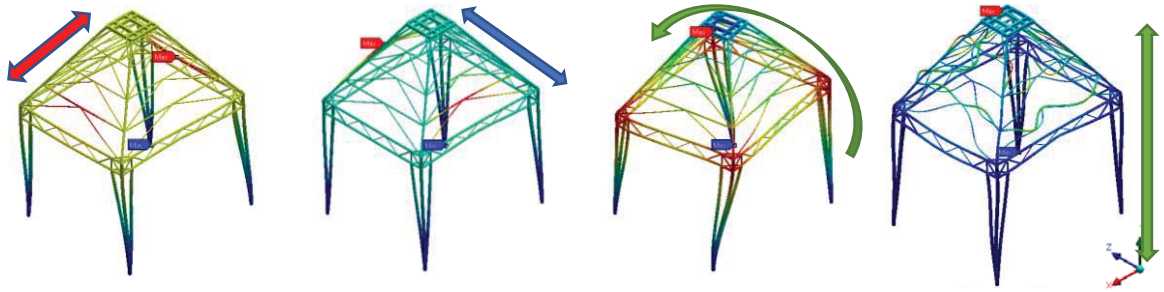

$f_{x,sim}$ = 1.21 Hz	$f_{z,sim}$ = 1.24 Hz	$f_{rot,sim}$ = 2.02 Hz	$f_{y,sim}$ = 10.2 Hz
$f_{x,meas}$ = 1.16 Hz	$f_{z,meas}$ = 1.27 Hz	$f_{rot,meas}$ = 1.98 Hz	$f_{y,meas}$ = 9.96 Hz

Figure 6: Selection of global modes

4.4 Model validation by simulation of drop test

For numerical simulations of the impulse induced dynamic answer of the drop tower, especially in the context of the here described investigations on its damage behavior it is essential to validate the damping and inertial parameter of the model.
Therefore, drop test were simulated using transient (time integration) analysis. For comparison, the measured time histories of accelerations, velocities and deflection during a drop test were used.
Within the validation analysis of the numerical model several parameters where analyzed for their influence on the dynamic answer of the tower impulse loaded by releasing the test body. For comparison, a past drop test with a 182 t test body was chosen. The study confirmed that, beside damping components, especially the duration of the impulse has a major influence on the analysis result. The test body releasing device is designed in a way, that the impulse duration is extremely small. But, the impulse time is also significantly affected by the rope elongation and so by the height of the drop event. Since detailed information about the rope were not at hand, a simple proportional relation between drop test height and impulse time was deployed and used for the model validation.
With the described structural and loading parameters a 182 t drop test was simulated. The sampling (response computing) frequency was set to 200 Hz. Figure 7 shows the simulated acceleration and velocity time history plots. The graphs show an adequate similarity of the magnitudes. For acceleration the values are similar, for velocity the simulated values are slightly higher than the measured and for the deflection magnitudes of both graphs are similar again. Compared to the measured accelerations and the deduced velocities the simulation result

is satisfying. Observing the decay behavior of the vibrational answer, it is obvious, that the damping is significantly higher in nature than in the simulation. Here a more sophisticated consideration of damping parameter in the model will improve the case. Noticeable is a second excitation in the real measurement after approximately 1.5 seconds. This is due to the impact of the test body on the ground plate and the transmission of that impact to the tower foundations.

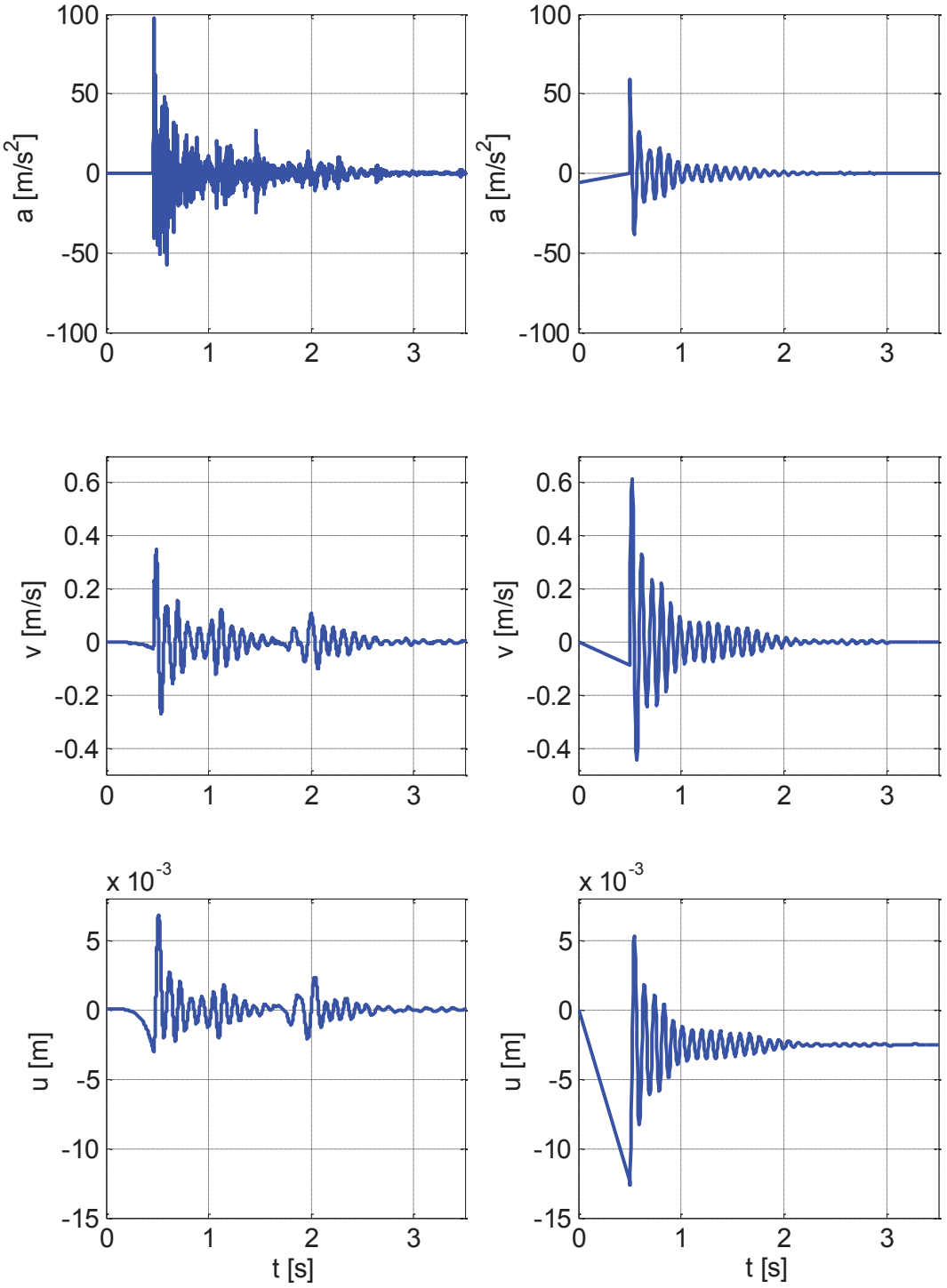

Figure 7: Time history of acceleration, velocity and deflection after a 182 t drop test event, left: measured data and right: simulated data.

5 CONCLUSIONS AND OUTLOOK

In this contribution the planning and the implementation of a structural health monitoring for the large drop tower of BAM by enhancing the standard process with digital models is presented. The models were used in all phases of the structural health monitoring process. The workflows aren't natively implemented in software (BIM, FE, data acquisition software), yet. The quality and the workload can be improved using digital models, especially the traceability, accountability and reproducibility of the results that are valuable for scientific and non-scientific applications. Currently the long-term monitoring of the drop tower just started and results from an upcoming first drop test at the large drop tower will be evaluated, soon.

ACKNOWLEDMENT

The authors would like to thank BAM for its financial support and the BAM personnel for the extraordinary dedication.

REFERENCES

[1] B. Droste, K. Müller, and M. Minack, "New BAM 200 ton drop test facility – construction and operation experiences," *Packaging, Transport, Storage & Security of Radioactive Material*, vol. 17, no. 3, pp. 131–135, Sep. 2006, doi: 10.1179/174651006X130240.

[2] International Atomic Energy Agency (IAEA). Regulations for the Safe Transport of Radioactive Material, 2018 Edition. Specific Safety Requirements No. SSR-6 (Rev. 1), Vienna, 2018.

[3] Deutscher Beton- und Bautechnikverein e.V., Ed., *Brückenmonitoring - Planung, Ausführung, Umsetzung*. Berlin: Eigenverlag, 2018.

[4] F. Hille, „Unterraumbasierte Detektion von Strukturschäden an Jacket-Gründungen von Offshore-Windenergieanlagen", Dissertation, Technische Universität Berlin, Berlin, 2018.

[5] E. Viefhues, M. Döhler, F. Hille, and L. Mevel, "Asymptotic analysis of subspace-based data-driven residual for fault detection with uncertain reference", *IFAC-PapersOnLine*, vol. 51, no. 24, pp. 414–419, 2018, doi: 10.1016/j.ifacol.2018.09.610.

[6] P. Simon; R. Schneider; M. Baeßler, "Bayesian system identification of a reinforced concrete beam subject to temperature variations based on static response data", 10th International Conference on Bridge Maintenance, Safety and Management, IABMAS, Sapporo, 2020 (accepted).

[7] M. Omidalizarandi, R. Herrmann, B. Kargoll, S. Marx, J.-A. Paffenholz, and I. Neumann, "A validated robust and automatic procedure for vibration analysis of bridge structures using MEMS accelerometers" *Journal of Applied Geodesy*, Jun. 2020, doi: 10.1515/jag-2020-0010.

[8] J.-A. Paffenholz; D. Wujanz, "Spatio-temporal monitoring of a bridge based on 3D point clouds - A comparison among several deformation measurement approaches", Proceedings of the 4th Joint International Symposium on Deformation Monitoring (JISDM), Athens, Greece, 2019.

[9] D. Wujanz; M. Burger; F. Neitzel; R. Lichtenberger; F. Schill; A. Eichhorn; U. Stenz; I. Neumann; J.-A. Paffenholz, „Belastungsversuche an einer Mauerwerksbrücke: Terrestrisches Laserscanning zur Verformungsmessung“ In: Jäger, W. (Hrsg.): Mauerwerk-Kalender 2018, Ernst & Sohn: Berlin, 2018, S. 221-239, doi: 10.1002/9783433608050.ch10.

[10] R. Schneider, A. Rogge, S. Thöns, E. Bismut, and D. Straub, “A sampling-based approach to identifying optimal inspection and repair strategies for offshore jacket structures” in *Proceedings of the sixth international symposium on life-cycle civil engineering (IALCCE 2018)*, Ghent, Belgium, 2018, pp. 1081–1088.

[11] R. Hartung, L. Senger, and K. Klemt-Albert, “Linking Building Information Modeling and Structural Health Monitoring for a reliable railway infrastructure” in *Proceedings of the 29th European Safety and Reliability Conference (ESREL)*, Hannover, 2019, pp. 596–603, doi: 10.3850/978-981-11-2724-3 0971-cd.

[12] R. Herrmann; J. Rabe; G. Bolle; S. Marx, „Konzepte für Datenqualität und Datenablage bei Entwurf und Umsetzung von Monitoringsystemen“, Bauingenieur, Vol. 2017, Heft 12, S. 537-545, 2017.

EURODYN 2020
XI International Conference on Structural Dynamics
M. Papadrakakis, M. Fragiadakis, C. Papadimitriou (eds.)
Athens, Greece, 23–26 November 2020

APPLICATION OF A CLASSIFICATION ALGORITHM TO THE EARLY-STAGE DAMAGE DETECTION OF A MASONRY ARCH

Alberto Barontini[1], Maria Giovanna Masciotta[2], Paulo Amado Mendes[3], Luís F. Ramos[1], and Paulo B. Lourenço[1]

[1] ISISE, Department of Civil Engineering, University of Minho - Guimarães, Portugal
Campus de Azurém, Guimarães, 4800-058, Portugal
e-mail: albe.barontini@gmail.com; {lramos,pbl}@civil.uminho.pt

[2] Department of Engineering and Geology, University «G. d'Annunzio» of Chieti-Pescara
Viale Pindaro 42, Pescara, Italy
e-mail: g.masciotta@unich.it

[3] ISISE, Department of Civil Engineering, University of Coimbra - Coimbra, Portugal
R. Luis Reis dos Santos 290, 3030-790 Coimbra, Portugal
e-mail: pamendes@dec.uc.pt

Keywords: Negative Selection Algorithm, Masonry Arch, Damage Detection.

Abstract. *The early-stage identification of structural damage still represents a relevant challenge in civil engineering. Localized damages if not readily detected can lead to disruption or even collapse, involving hazard to people and economical losses. Although the final goal of the identification is to localize and quantify the damage, a reliable discrimination between normal and abnormal states of the structure in the very early stage of the damage onset is not an easy task. In the field of Structural Health Monitoring (SHM) great attention has been paid to the development of damage detection methods based on continuous and automatic registration of the system response to unknown ambient inputs. The numerical algorithms exploited must be: (1) easy to implement and computationally inexpensive, eventually being embedded in the sensors; (2) as much independent on human decision as possible; (3) robust to the many sources of uncertainties affecting the monitoring; (4) able to detect small damage extents in order to provide an early warning; (5) suitable for the application in the case of few and sparse measurements collected only in the normal condition. The performance of a novel version of Negative Selection Algorithm, recently developed by the authors, is here analyzed with attention to these issues. The algorithm is tested against data collected on a segmental masonry arch built in the laboratory of the University of Minho and subject to progressive lateral displacement of one support.*

1 INTRODUCTION

In the context of Structural Health Monitoring (SHM), the Damage Identification (DI) and the early warning in case of damage onset are essential to support any engineered system management. Following the Rytter's hierarchy[1,2], the DI process can be summarized according to five main goals of increasing complexity: (1) Detection of existence; (2) Localization; (3) Classification of the type; (4) Quantification of the extent; (5) Prognosis. Such a hierarchical structure requires that all the lower levels are available before attempting a higher level of information. Thus, the detection of existence is the first basic step that a monitoring strategy must fulfil but, in many cases, it is a complex problem to address.

The SHM theory is based on the existence of a function *f* such that:

$$\boldsymbol{x} = f(\boldsymbol{y}, \boldsymbol{v}) \tag{1}$$

where $\boldsymbol{x} \in \boldsymbol{X}$ is a vector whose elements are all the features of the engineered system (e.g. a structure or infrastructure), $\boldsymbol{y}$ is a vector that describes the condition of this system and $\boldsymbol{v}$ is a vector which accounts for the environmental and operational variables that affect the system features. In damage detection, the state vector $\boldsymbol{y}$ is a binary variable, namely $\boldsymbol{y} \in \{Nonself, Self\}$ or $\boldsymbol{y} \in \{1,0\}$. The goal is the discrimination between a normal '0' and an abnormal '1', potentially damaged, state of the system. Each feature vector $\boldsymbol{x}$ is a point of a multidimensional domain called input space, namely the space of the domain of each single feature of the vector. The DI task aims at assessing the system state by analyzing the values assumed by the features. One of the main issues to tackle consists of the feature selection. Indeed, out of the potentially infinite features of the engineered system, whose domains might also be infinite, the detection is carried out on a scalar valued space called feature space $\boldsymbol{F} \subseteq \boldsymbol{X}$ [3]. Thus, the points $\tilde{\boldsymbol{x}} \in \boldsymbol{F}$ are the projection of the points $\boldsymbol{x} \in \boldsymbol{X}$, from the original input space to a space with reduced dimensionality. This process reduces the time requirement and the complexity of the problem, but also reduces the information content of the feature vector, including its sensitivity to damage. A proper selection should aim at identifying features such that:

$$\tilde{\boldsymbol{x}} = f(\boldsymbol{y}) \tag{2}$$

In other words, the selected features must have a high sensitivity to the system condition $\boldsymbol{y}$ and a negligible sensitivity to operational and environmental variables $\boldsymbol{v}$.

Mathematically, the damage detection can be treated as a classification problem: given a point in the feature space related to a new acquisition of the monitoring system, assess whether the system continues in its normal state or shows an abnormal behavior. Thus, the goal is to define a classifier, namely an approximation of the inverse function:

$$\boldsymbol{y} = f^{-1}(\tilde{\boldsymbol{x}}) \tag{3}$$

This approximation is based on a set of known pairs $\langle \boldsymbol{x}, \boldsymbol{y} \rangle$, i.e. a set of pre-measured samples. The nature of such pairs further complicates the damage detection problem as, normally, the only information available is for the system in normal condition, namely all the pairs are like $\langle \boldsymbol{x}, 0 \rangle$. This is a one-class classification problem which can be addressed only through few machine learning algorithms. The present study aims at discussing how a learning algorithm can be applied to real field testing data. A deterministic version of the Negative Selection Algorithm (NSA), developed by the authors of this work and preliminarily tested on other case studies with simulated data [4–6], is here employed making use of the vibration signals collected during a laboratory experimental campaign. The methodology is applied for the first time to a real case study under progressive damage scenarios. After describing the fundamentals of the algorithm in section 2, the structure object of investigation is presented in section 3.1. Then, the methodology to tailor the algorithm to the specific case study is discussed in section 3.2 followed by the description of the numerical tests used for the algorithm validation.

Based on the results, possible improvements to the methodology are provided in section 3.3. Finally, the main conclusions drawn from the work are summarized in section 4.

2 DETERMINISTICALLY GENERATED NEGATIVE SELECTION ALGORITHM

NSAs are a family of algorithms based on a minimal common framework, initially developed by Forrest et al. [7] and later improved with additional contributions [18,19]. The complete framework of the process underlying the NSAs is composed of several steps that are collected in three main consecutive stages: (1) Representation; (2) Censoring; (3) Monitoring.

The first stage is an overhead operation consisting in the definition of the feature space and the coding of the data set. In this stage, the *n* features are projected onto a unitary space $U=[0,1]^n$. To take into account the emergence of measurements that fall outside the range that is known during the training, such a range is increased by 20%. Future samples that fall outside this enlarged range are automatically labelled as damaged. It is also assumed that the unitary space is divided into two complementary subsets, Self and Nonself, such that:

$$Self \cup Nonself = U \qquad Self \cap Nonself = \emptyset \tag{4}$$

During the so-called censoring stage, the NSA analyses the training data set in the feature space to generate the detectors. The detector set is the tool used for anomaly detection, being a set of elements which covers and identifies the nonself portion of the space. Finally, in the monitoring stage, the new feature values, extracted from the system under analysis, are matched against the trained detectors, which bind to the ones that are likely to belong to an anomalous behavior of the system. The version of NSA used in the present study is called deterministically generated (DNSA), since the detectors are not randomly initialized before being matched against the training samples, but they are placed onto the unitary space according to a regular grid of given size. In order to reduce the time requirement and the complexity, the detection is carried out in a 2-dimensional feature space. Indeed, in Structural Health Monitoring for civil engineering systems, it is common to analyze the structural behavior in terms of correlation between pairs of variables (for instance temperature/first frequency, temperature/second frequency, etc.) [10,11].

3 APPLICATION AND VALIDATION THROUGH REAL VIBRATION DATA

3.1 A masonry arch as case study

The case study used to apply and validate the DNSA algorithm is a small-scale segmental masonry arch (Figure 1) built and tested in the structural laboratory of the Institute of Bio-Sustainability of the University of Minho (Guimarães, Portugal) in order to investigate the effects that support settlements may have on the dynamic behavior of masonry arch bridges. The specimen consists of four rows of 39 brick units (100x75x50 mm3) assembled with staggered lime mortar joints. It has a nominal span of 1900 mm, a springing angle of 40°, a nominal net rise of 430 mm and radial thickness of a 75 mm. Two lime bags of 25 kg each are symmetrically placed on the extrados to simulate the effect of backfill material [12,13].

The structure is supported by two concrete abutments. The left support is fixed to the floor, whereas the other one is allowed to move in horizontal direction through a simple sliding system. Progressive damage is induced by applying, in 5 steps, controlled and uniform increasing displacements to the movable support through a hydraulic jack. After each step, a dynamic identification test is carried out using the ambient noise as source of excitation. The vibration response of the arch is acquired through 8 accelerometers (model PCB 393B12, 0.15 to 1000 Hz frequency range, 10000 mV/g sensitivity, 8μg resolution) of which four are kept fixed and four are moved according to 12 consecutive set-ups, allowing to record the response of 26

measurement points in normal direction and 26 in tangential direction (Figure 2a). This provides a set of 96 acquisitions for each scenario: 48 from the moving accelerometers and 48 from the reference ones. The signals are sampled at 400 Hz for a minimum duration of 180 s, resulting in 72.000 data points per channel.

Figure 1: Configuration of the specimen.

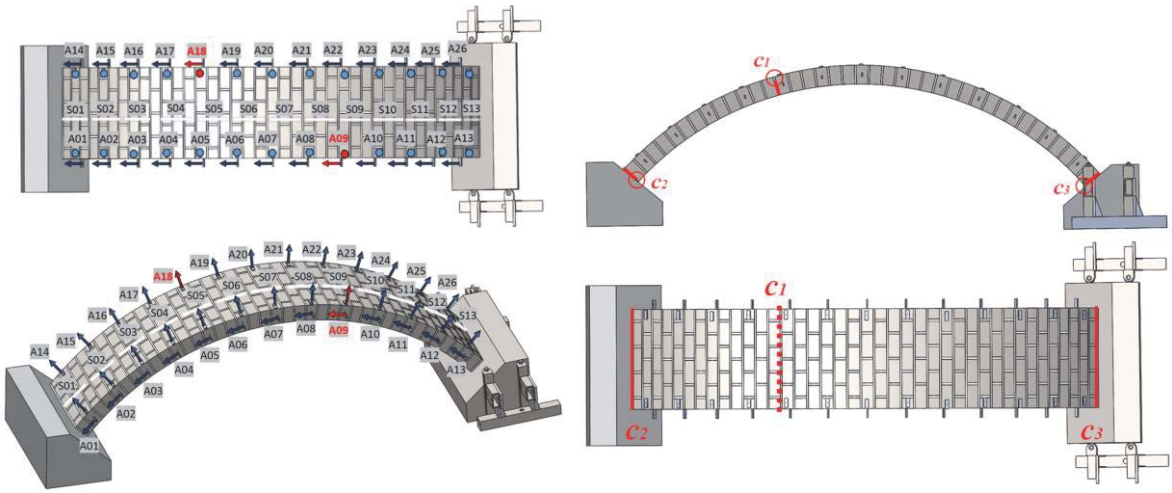

(a) (b)

Figure 2: Test setup and crack pattern: (a) distribution of measurement points and accelerometers (A01 to A26); (b) location of settlement-induced cracks.

Aiming at detecting the damage in the very early stage, only the first two damage scenarios (corresponding to 0.4 and 0.5 mm of incremental displacement, respectively) are considered. After the first step, three cracks start to appear (Figure 2b): *c1* at the intrados, in the left region of the keystone; *c2* at the extrados of the left springing (fixed support) and *c3* at the extrados of the right springing (moving support). The outset of cracks induces a considerable drop of the structural stiffness which is clearly reflected by the downshift of the main natural frequencies of the arch (particularly for modes 1, 4 and 5).

Table 1 reports the dynamic identification results provided by the SSI-UPCX estimator [14] in terms of averaged frequency values for all meaningful vibration modes. In order to test the algorithm in unfavorable conditions, the classification is performed by analyzing the values of the second and third natural frequencies, whose variation between scenarios is the smallest. The test is carried out under constant environmental conditions. For each frequency,

the dataset is composed of 96 values extracted through peak-picking directly from the power spectral density of each acquisition. It is worth noting that the ambient vibrations are weak, and the response signals have a low signal to noise ratio, making the second frequency peak not clearly distinguishable. Nevertheless, it is interesting and reasonable to test the damage detection strategy against a dataset affected by such ordinary sources of uncertainties.

Scenario	Frequencies [Hz]				
	Mode 1	Mode 2	Mode 3	Mode 4	Mode 5
Reference (D0)	30.06	50.95	59.44	95.23	120.62
Damage 1 (D1)	26.31	50.28	59.04	80.47	113.16
Damage 2 (D2)	23.4	48.86	58.14	75.75	111.44

Table 1: Arch eigenfrequencies variation over progressive damage scenarios.

3.2 Training, validation and monitoring

The classifier design and application are divided into three stages: (1) training; (2) validation; (3) monitoring. The latter step is the actual assessment of the system through the analysis of new measurements. The first two steps, instead, are offline preliminary tasks necessary to generate the classifier and tailor it to the specific case study. The training requires a set of samples that are fed to the DNSA to generate the detectors. As mentioned before, in one-class classification problems, the samples belong only to one class (e.g. the self space or normal state). In order to keep some of the collected self data for the validation and the monitoring, out of the 96 records, 50 points are randomly selected to form the training set.

Each algorithm version requires the definition of a set of inner parameters, the so-called parameter setting. Once these parameters' value is fixed, a specific algorithm instance is determined. Different settings lead to different detectors sets and different performances. Thus, the parameter setting consists in comparing different algorithm instances. The parameters are analyzed as controllable variables which assume in their domains different values called levels [15]. The comparison must be cast into a statistical design of the experiment (DOE) and analyzed in terms of a reliable performance metric. Considering the possible outputs of the detection, only two families of errors are possible: false positive (FP), namely normal samples classified as abnormal; and false negative (FN), namely abnormal samples classified as normal. Experience demonstrated that the trend of FPs and FNs for different parameter settings is inverse. Thus, it is not possible to reduce one family of errors without increasing the other and the performance metric should take both into account. When dealing with one-class classification problems, this issue is quite complex because only one type of samples is known, thus the only possible inference is on the number of FPs. In [6] the authors developed a methodology based on the artificial generation of outliers of the normal samples' distribution. The same methodology is here applied, so the classifier can be validated against known self samples and artificial nonself samples, referred as outliers. Three are the main parameters that affect the DNSA performance: (1) number of divisions of the side of the unitary space, which is directly related to the detector radius, r_{det}; (2) self radius, r_{self}; (3) censoring distance, *Cens.dist*. The latter is a qualitative parameter that depends on the values of the other two. Thus, a three-level two-factor full factorial design (3^2 FFD) is used for the experiment, considering the two quantitative parameters (detector and self radii), repeated for three possible formulations of the censoring distance. The validating self set is composed of 23 samples out of the remaining 46 (e.g. 96 minus the 50 used for the training). The validating nonself set is composed of 133 artificial outliers. Figure 3 displays the samples used for both training (D0-T) and validation (D0-V, Outliers) in the unitary feature space.

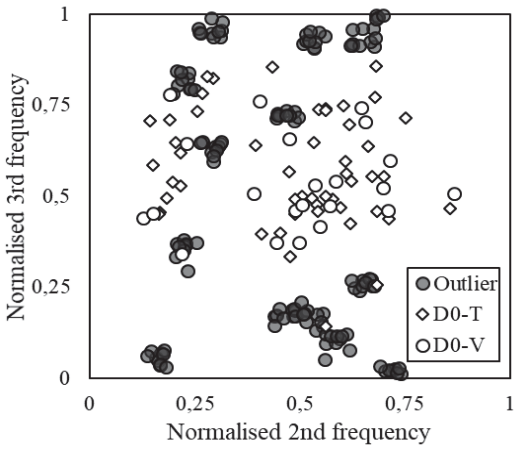

Figure 3: Normalized samples belonging to the training and validating sets.

Table 2 reports the results of the parameter setting together with the performance metric. In the present work, the area under the Reception Operating Characteristic (ROC) curve, called AUC, is used for this purpose. The ROC curve plots, for each classifier, the False Positive Rate (FPR) and the True Positive Rate (TPR). The best combination of parameter levels corresponds to the highest value of the AUC which, for this case study, is: small r_{det}, medium r_{self} and censoring distance equal to $r_{det} + r_{self}$.

Cens.dist=r_{det}			*Cens.dist*=0.5(r_{det}+r_{self})			*Cens.dist*=(r_{det}+r_{self})		
divisions	r_{self}	**AUC**	*divisions*	r_{self}	**AUC**	*divisions*	r_{self}	**AUC**
70	0.01	0.518	70	0.01	0.518	70	0.01	0.576
70	0.035	0.518	70	0.035	0.576	70	0.035	**0.776**
70	0.07	0.518	70	0.07	0.701	70	0.07	0.747
20	0.01	0.626	20	0.01	0.579	20	0.01	0.662
20	0.035	0.626	20	0.035	0.626	20	0.035	0.763
20	0.07	0.626	20	0.07	0.726	20	0.07	0.690
10	0.01	0.678	10	0.01	0.537	10	0.01	0.684
10	0.035	0.678	10	0.035	0.638	10	0.035	0.698
10	0.07	0.678	10	0.07	0.678	10	0.07	0.667
	Avg.	0.607		Avg.	0.620		Avg.	0.696
	Dev.st.	0.071		Dev.st.	0.073		Dev.st.	0.062

Table 2: Results of the parameter setting. In bold the best combination of parameter levels.

The optimized classifier is used to simulate the monitoring of the arch. This means testing the classifier against the samples that it has not met before. The testing self set is composed of the remaining 23 samples, whereas the testing nonself set is composed of just 39 D1 samples and 16 D2 samples, since the others fall outside the unitary space and are automatically classified as damaged. The classifier shows a good performance against the damaged samples with a success rate of 82% for D1 samples and of 94% for D2 samples in terms of correct labelling. However, 48% of the new health samples are wrongly classified.

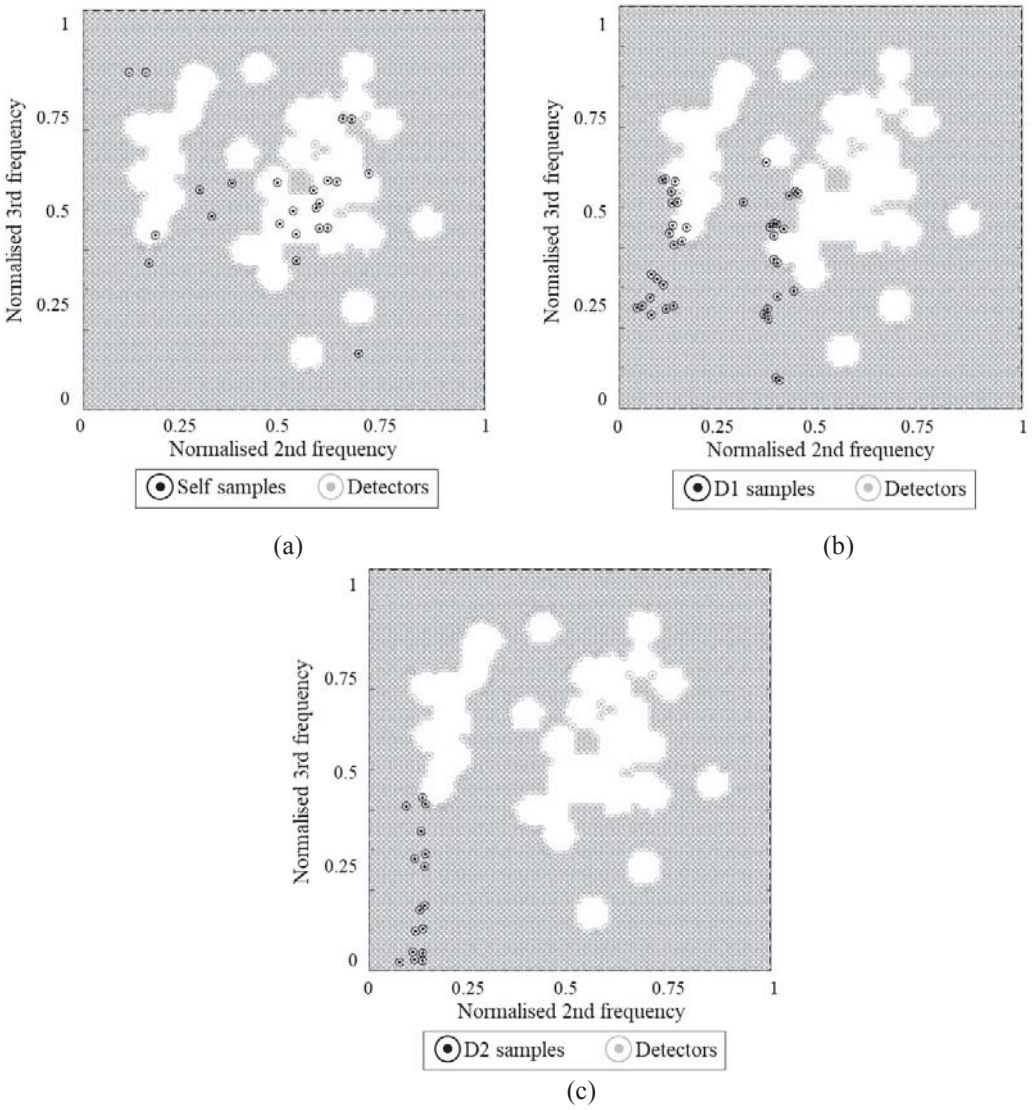

Figure 4: Comparison of the optimized detector set against the testing sets: (a) self samples; (b) D1 samples and (c) D2 samples.

3.3 Improved training

Based on the detector set distribution, the quite "aggressive" behavior highlighted in Figure 4a is likely due to the sparsity of the self samples used for the training. These were mainly distributed in two regions. However, experience supports the idea that frequency values, in conditions similar to the one of the case-study, are continuously distributed over a single region. Thus, new emerging samples are expected to fall in between the two identified areas. Based on this assumption the classifier is improved by artificially generating self points according to a bivariate normal distribution. The mean and the covariance matrices of the 50 training samples are used to define the distribution. Before repeating the training, the new points which fall outside the area within the boundary that envelopes the prior training samples are rejected, assuming that this boundary delimits the known self region. Figure 5 shows the prior and the new training sets. The improved classifier is thus generated keeping the same parameter setting and tested against the same sets. Figure 6 shows the new detector set, compared to the testing sets and Table 3 reports the confusion matrix for the two classifiers. The improved version outperforms the prior one.

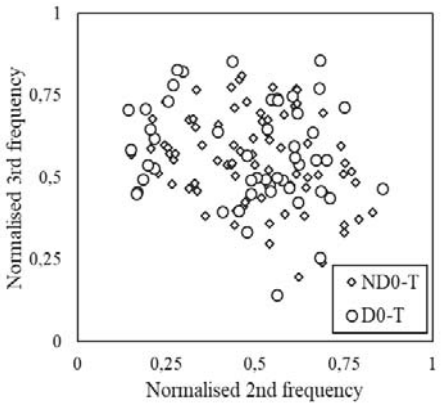

Figure 5: New normalized training samples (ND0-T) compare to the original training set (D0-T).

	TN	FP	Tot. D0 samples	TP1	FN1	Tot. D1 samples	TP2	FN2	Tot. D2 samples
Prior classifier	12	11	23	32	7	39	15	1	16
New classifier	17	6	23	30	9	39	16	0	16

Table 3: Confusion matrix of the prior and the improved classifier over the same testing sets.

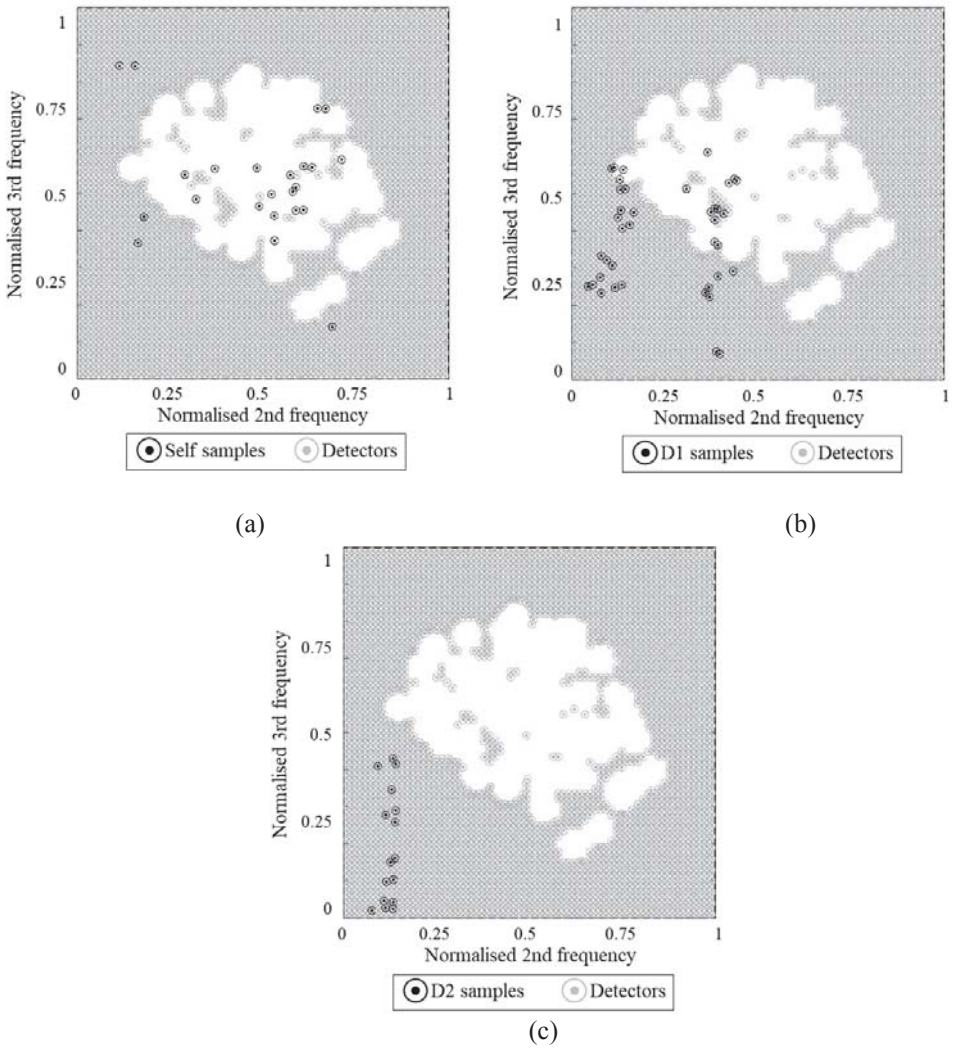

(a) (b)

(c)

Figure 6: Comparison of the new detector set against the testing sets.

4 CONCLUSIONS AND FUTURE SCOPE

The simple discrimination between the normal and the abnormal behavior of an engineered system is a complex task in many real-world applications. The lack of knowledge regarding possible abnormal conditions and the limited knowledge about the normal behavior itself reduce the number of non-model-based numerical methods suitable for damage detection purposes (e.g. one-class classification). In the present work a combination of real and artificial data is proposed to improve the design of a tailored damage detection strategy for real-world applications. The analyzed case study consists of a segmental masonry arch built and tested in the laboratory of the University of Minho and the applied damage detection algorithm is a customized version of the NSA, developed by the authors in a previous work. Hitherto, the following preliminary conclusions can be drawn:

- the performance is robust against the sources of uncertainties, as the noise in the signals or the modal feature extraction through a simplified peak-picking strategy;
- the classification is successful for small damage extent – indeed the frequency downshift estimated for modes 2 and 3 was on the average 1.6% and 0.9% for the first damage scenario (D1), and 1.9% and 2.3% for the second damage scenario (D2);
- the artificial generation of new self and nonself samples, according to the training data distribution, improved the performance facing the reduced and sparse information available;
- the methodology might be suitable for sensor embedment, since the features are extracted from a single sensor acquisition.

To realize the full potential of the algorithm, more research is needed. Indeed, although the cracks after the first displacement stage are barely visible in the arch, the drop in the first frequency value might suggest that the damage is not as small as required for a proper assessment of the algorithm sensitivity. Moreover, the strategy for artificial data generation should be tested on a larger dataset and the analysis should be cast in a statistical framework to infer the behavior of the final classifier in different conditions.

ACKNOWLDGMENTS

This work was supported by FCT (Portuguese Foundation for Science and Technology), within ISISE, scholarship SFRH/BD/115188/2016; it was also financed by FEDER funds through the Competitivity Factors Operational Programme - COMPETE and by national funds through FCT – Foundation for Science and Technology within the scope of the project POCI-01-0145-FEDER-007633.

REFERENCES

[1] C.R. Farrar, K. Worden, An introduction to structural health monitoring, Philos. Trans. R. Soc. A Math. Phys. Eng. Sci. 365 (2007) 303–315. doi:10.1098/rsta.2006.1928.

[2] A. Rytter, Vibrational based inspection of civil engineering structures, (1993).

[3] D. Bernal, 3 - Analytical techniques for damage detection and localization for assessing and monitoring civil infrastructures, in: M.L. Wang, J.P. Lynch, H.B.T.-S.T. for C.I. Sohn (Eds.), Woodhead Publ. Ser. Electron. Opt. Mater., Woodhead Publishing, 2014: pp. 67–92. doi:https://doi.org/10.1533/9781782422433.1.67.

[4] A. Barontini, R. Perera, M.G. Masciotta, P. Amado-Mendes, L. Ramos, P. Lourenço,

Deterministically generated negative selection algorithm for damage detection in civil engineering systems, Eng. Struct. 197 (2019) 109444. doi:https://doi.org/10.1016/j.engstruct.2019.109444.

[5] A. Barontini, M.-G. Masciotta, L.F. Ramos, P. Amado-Mendes, P.B. Lourenço, Application of a Bio-Inspired Anomaly Detection Algorithm for Unsupervised SHM of a Historic Masonry Church, in: Proc. Tenth Int. Mason. Conf., Milan, Italy, 2018: pp. 2259–2272.

[6] A. Barontini, M.G. Masciotta, P. Amado-Mendes, L.F. Ramos, Performance assessment of a bio-inspired anomaly detection algorithm for unsupervised SHM: application to a Manueline masonry church, Int. J. Mason. Res. Innov. (n.d.). https://www.inderscience.com/info/ingeneral/forthcoming.php?jcode=ijmri.

[7] S. Forrest, A.S. Perelson, L. Allen, R. Cherukuri, Self-Nonself Discrimination in a Computer, in: Proc. 1994 IEEE Symp. Secur. Priv., IEEE Computer Society, Washington, DC, USA, 1994: pp. 202--. http://dl.acm.org/citation.cfm?id=882490.884218.

[8] Z. Ji, D. Dasgupta, Applicability Issues of the Real-valued Negative Selection Algorithms, in: Proc. 8th Annu. Conf. Genet. Evol. Comput., ACM, New York, NY, USA, 2006: pp. 111–118. doi:10.1145/1143997.1144017.

[9] D. Dasgupta, S. Yu, F. Nino, Recent Advances in Artificial Immune Systems: Models and Applications, Appl. Soft Comput. 11 (2011) 1574–1587. doi:http://dx.doi.org/10.1016/j.asoc.2010.08.024.

[10] A. Kita, N. Cavalagli, F. Ubertini, Temperature effects on static and dynamic behavior of Consoli Palace in Gubbio, Italy, Mech. Syst. Signal Process. 120 (2019) 180–202.

[11] P.F. Giordano, F. Ubertini, N. Cavalagli, A. Kita, L.F. Ramos, M.G. Masciotta, Diagnostic investigations and structural health state assessment of San Pietro bell tower in Perugia, in: 10th Int. Mason. Conf. IMC 2018, International Masonry Society, 2018: pp. 2273–2291.

[12] M.G. Masciotta, D. Pellegrini, D. Brigante, A. Barontini, P.B. Lourenço, M. Girardi, C. Padovani, G. Fabbrocino, Dynamic characterization of progressively damaged segmental masonry arches with one settled support: experimental and numerical analyses, Frat. Ed Integrità Strutt. 14 (2019) 423–441. doi:10.3221/IGF-ESIS.51.31.

[13] M.-G. Masciotta, D. Brigante, A. Barontini, D. Pellegrini, P.B. Lourenço, G. Fabbrocino, C. Padovani, M. Girardi, Experimental and Numerical Investigations of a Segmental Masonry Arch Subjected to Horizontal Settlements BT - Proceedings of ARCH 2019, in: A. Arêde, C. Costa (Eds.), Springer International Publishing, Cham, 2020: pp. 413–421.

[14] ARTeMIS Modal S 3.1.1 (2018).

[15] R.S. Barr, B.L. Golden, J.P. Kelly, M.G.C. Resende, W.R. Stewart, Designing and reporting on computational experiments with heuristic methods, J. Heuristics. 1 (1995) 9–32. doi:10.1007/BF02430363.

EURODYN 2020
XI International Conference on Structural Dynamics
M. Papadrakakis, M. Fragiadakis, C. Papadimitriou (eds.)
Athens, Greece, 23–26 November 2020

VIBRATION-BASED DAMAGE DETECTION APPLIED TO A CONCRETE ARCH DAM

Sérgio Pereira[1], **Filipe Magalhães**[1], **Álvaro Cunha**[1], **Jorge P. Gomes**[2] **and José V. Lemos**[2]

[1] Construct, ViBest, Faculty of Engineering of the University of Porto
Rua Dr. Roberto Frias, 4200-465 Porto, Portugal
e-mail: {sbp, filipema, acunha}@fe.up.pt

[2] Concrete Dams Department, National Laboratory for Civil Engineering
Avenida do Brasil 101, 1700-066 Lisboa, Portugal
{jgomes, vlemos}@lnec.pt

Keywords: concrete arch dam, continuous dynamic monitoring, operational and environmental effects, data normalization, damage detection

Abstract. *Vibration-based health monitoring systems have been successfully implemented in many different large civil engineering structures such as bridges, wind turbines and belltowers, providing important data about their dynamic behaviour and allowing the establishment of damage detection methodologies based on the evolution of modal properties. Allying this knowledge with the emergence of very sensitive low noise sensors and high-resolution digitizers during the past few decades, an opportunity arose to implement continuously operating dynamic monitoring systems in dams and validate the suitability of these systems to monitor such massive structures with the goal of detecting damage.*

The detection of abnormal structural behaviour, that may indicate the occurrence of damage, can be based on control charts and is associated with shifts in the modal parameters values that are not explained by other physical phenomena but a change in the structure's stiffness. To test these statistical tools, modal parameters obtained from field measured time series may be contaminated with simulated damages.

In this context, the ability of the control charts to identify the emergence of abnormal structural behaviour in dams is studied in this paper using data obtained from the continuous dynamic monitoring of Baixo Sabor arch dam, a concrete dam in Portugal that started operating in late 2015. Since it was not expected to find damage in such a recent structure, a set of plausible damage scenarios were simulated using a numerical model and their influence in the dam dynamic properties was used to contaminate the values of natural frequencies obtained from continuous monitoring.

1 INTRODUCTION

Baixo Sabor hydroelectric development, located in the north of Portugal, is one of the most recent plants in the country. With the aim of studying Baixo Sabor arch dam dynamic properties and their evolution over time, continuous dynamic monitoring of the dam is being carried out, taking into account the variation of ambient and operational conditions [1].

Integrated monitoring systems considering real-time data directly obtained from structures, such as the one implemented in Baixo Sabor dam, are very important for the long-term management of large civil infrastructures [2]. Though health monitoring systems are historically associated with static data, vibration-based systems have already been successfully implemented in different structures such as bridges [3], wind turbines [4], stadia roofs [5] or belltowers [6]. Such vibration-based health monitoring systems rely on operational modal analysis to continuously identify the structures modal properties, which can be used as monitoring features to evaluate the structures health condition evolution over time. Statistical tools such as control charts can be used to detect the occurrence of damage associated with shifts in the modal parameters values that are not explained by other physical phenomena but a change in the structure's stiffness. To test these statistical tools, modal parameters obtained from field measured time series may be contaminated with simulated damages.

In this sense, this paper presents a brief description of the dynamic monitoring system installed in Baixo Sabor arch dam in 2015, and the results obtained during more than three years of continuous dynamic monitoring. The operational and environmental effects that mostly affect the dam's dynamic behaviour are studied and their effects on the natural frequencies are minimized using multiple linear regression models and Principal Components Analysis. Additionally, a numerical model of the dam (developed by the Portuguese National Laboratory for Civil Engineering [LNEC]) is presented and used to simulate damages scenarios. Finally, control charts are used to detect the shifts in natural frequencies evolution due to the simulated damages, and thus evaluate the suitability of these statistical tools for the detection of damages in concrete dams.

1.1 Baixo Sabor arch dam and installed monitoring system

The Baixo Sabor hydroelectric development is located in Sabor river, a tributary of Douro river in the northeast of Portugal. This 123 m high double-curvature concrete arch dam, is 505 meters long and its arch is composed by 32 concrete blocks, separated by vertical contraction joints, and it includes six horizontal visit galleries. The reservoir created by the dam, shown in the aerial picture of the dam presented in the left part of Figure 1, has a capacity of 1095 hm^3 at exploration level (234 m of elevation).

A vibration-based health monitoring system has been working in the dam since December 2015, in order to identify the dam's dynamic characteristics and their evolution over time, while considering the variation of ambient and operational conditions. The continuous dynamic monitoring system consists of 20 uniaxial accelerometers that have been radially disposed in the dam's three upper visit galleries, whose synchronization is achieved using GPS antennas. The right part of Figure 1 shows the position of the accelerometers installed in the dam, marked with red dots in a scheme of the structure. The dynamic monitoring system is configured to continuously record acceleration time series with a sampling rate of 50 Hz and a duration of 30 minutes at all instrumented points, daily producing 48 groups of time series.

To continuously process the data collected by the monitoring system a monitoring software developed at ViBest/FEUP called DynaMo [7] is being used. Besides backing up the original data samples, this monitoring software performs the pre-processing of the acceleration time series, through trend elimination, filtering and re-sampling, it characterizes vibration levels

and it performs the identification of the dam modal properties through automatic operational modal analysis.

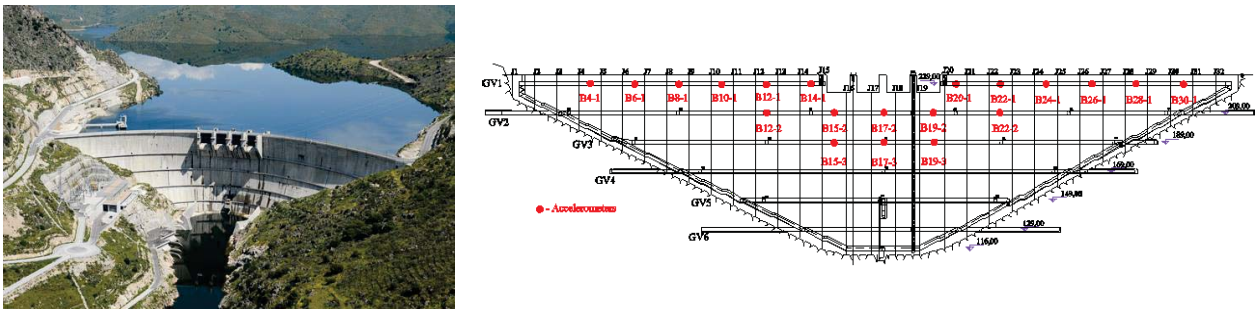

Figure 1: Baixo Sabor arch dam: Aerial view (on the left); position of accelerometers marked with red dots (on the right).

1.2 Modal Tracking

More than three years of data were processed following the steps described in the previous section. The first ten modes of vibration are being identified and natural frequencies, modal damping values and modal configurations tracked over time. The representations of the identified modal configurations can be found in [8]. This work is focused on the evolution of natural frequencies, which are used in the next section to detect novel structural behaviour. In this sense, average natural frequencies (f_{mean}) and their standard deviation (f_{std}) during the studied period are resumed in Table 1 for the first ten vibration modes. It is important to notice the significant standard deviation values verified for all vibration modes, indicating important oscillations during this period.

However, since the evolution of modal properties is easier to understand when graphically depicted, the evolution over three years of the natural frequencies estimates of the first ten modes of vibration of the structure is characterized in Figure 2, where each point corresponds to a 6-hour average. Therefore, two values are presented per day, leading to a figure visually clean, without losing accuracy in the characterization of the modal parameters fluctuations, since their variations are quite slow in very massive structures such as this one. After an initial fast decrease in natural frequency values during the first filling of the reservoir, significant frequency variations due to operational and environmental factors are verified with season succession, indicating the possibility of finding correlation between natural frequencies and these factors.

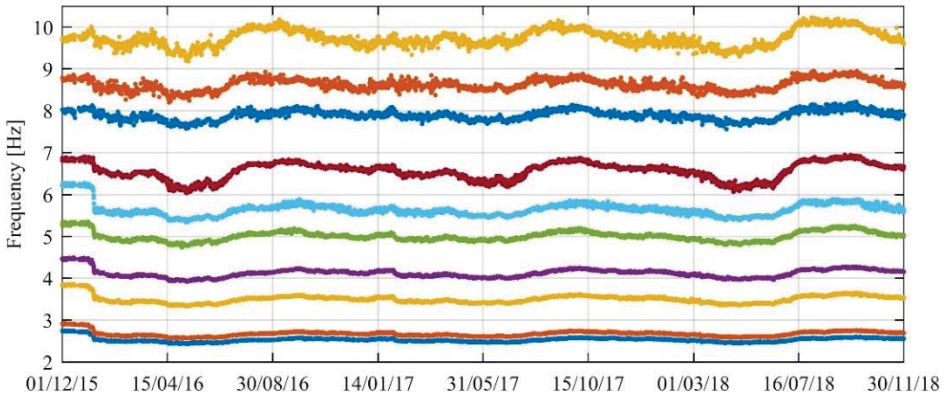

Figure 2: Time evolution of 6-hour average natural frequencies

Mode	1	2	3	4	5	6	7	8	9	10
f_{mean} [Hz]	2.53	2.70	3.50	4.12	5.00	5.62	6.57	7.90	8.63	9.76
f_{std} [Hz]	0.10	0.10	0.14	0.16	0.20	0.25	0.29	0.34	0.38	0.49

Table 1: Statistical characterization of the natural frequencies estimates from 01/12/2015 to 30/11/2018

1.3 Numerical Model

In order to study the static and dynamic behaviour of Baixo Sabor arch dam, the Concrete Dams Department of the National Laboratory for Civil Engineering developed a numerical model of the dam. This model, based on discrete and finite elements, takes into account the dam's contraction joints, the deformability of the foundation and the reservoir [9]. The body of the dam was modelled with 32 vertical blocks, which were discretized into isoparametric 20-node brick finite elements and a simplified representation of the reservoir and foundation was used.

The dynamic dam-reservoir interaction was simulated with Westergaard's added mass technique. The masses had to be scaled since it is known that in arch dams, Westergaard's method overestimates the hydro-dynamic effects [10]. The model was calibrated for several water levels varying from 210 to 234 m, therefore a set of different scaling factors were used to match the first natural frequency estimated with both the results from a forced vibration test performed on the dam [9] and from the continuous dynamic monitoring [11].

The deformability of the foundation was achieved through an elastic joint on the dam's surface of insertion, with stiffness parameters calibrated to provide an approximate deformability of a rock mass with a Young's modulus of 35 GPa, obtained from field tests. A view of the numerical model is presented in Figure 3.

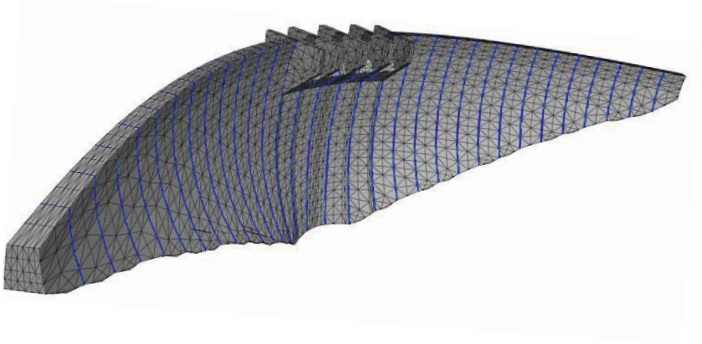

Figure 3: Numerical model of Baixo Sabor arch dam

2 REMOVING THE EFFECTS OF ENVIRONMENTAL AND OPERATIONAL CONDITIONS

In order to detect small variations of the natural frequencies of the structure motivated by structural changes, which may be associated with the occurrence of damages, it is important to minimize the effects of environmental and operational factors, such as reservoir water level and temperature.

Since the factor that more strongly affects natural frequencies is the water level in the reservoir [12], statistical relationships between all the vibration frequencies of the structure and the water level in the reservoir were developed. The representation of the relation between these two variables is presented in Figure 4 (left part of the figure), using the first vibration mode. The adopted quadratic regressions generally provide a good fitting, presenting values for the determination coefficient of the order of 0.95.

The obtained statistical relations were then used to mitigate the effect of water level in the values of natural frequencies and then the process previously described was repeated, now using the values of natural frequencies corrected from the effect of water level and the evolution of ambient temperature. In this case, linear regressions were obtained between ambient temperature and natural frequencies, indicating frequency values increase with the rising of temperature. Lower determination coefficients were obtained, with values between 0.3 and 0.5, depending on the studied vibration mode. The relation between ambient temperature and the frequency of the first vibration mode corrected by the effect of water level is presented in the right part of Figure 4.

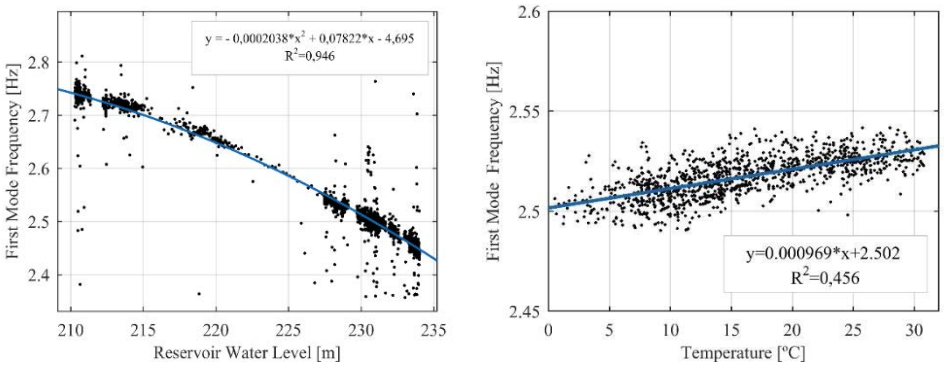

Figure 4: Correlation between the first natural frequency and reservoir water level (on the left); correlation between the corrected first natural frequency and ambient temperature.

Afterwards, multiple linear regression models (MLR) were built using as predictors the evolution of reservoir water level, ambient temperature, concrete temperature and a variable simulating the hardening of concrete over time. Only the first seven vibration modes were considered in this analysis, since modes 8 to 10 presented lower successful identification rates (between 49 and 64 %) that preclude their use in the damage detection process with adequate results.

The experimental natural frequencies were compared to the ones resulting from the regression models and high correlations were verified between them. The values of predicted natural frequencies were subtracted to the values of experimental natural frequencies and the obtained residuals were added to the mean frequency of each mode to obtain a new set of natural frequencies corrected from the effects of operational and environmental factors.

The evolution of the natural frequency of the first two vibration modes after the minimization of operational and environmental effects with the built regression model is presented in Figure 5. A much more stable evolution of natural frequencies around their means was achieved and the sporadic gaps presented are due to missing readings in the predictor variables (mainly ambient temperature).

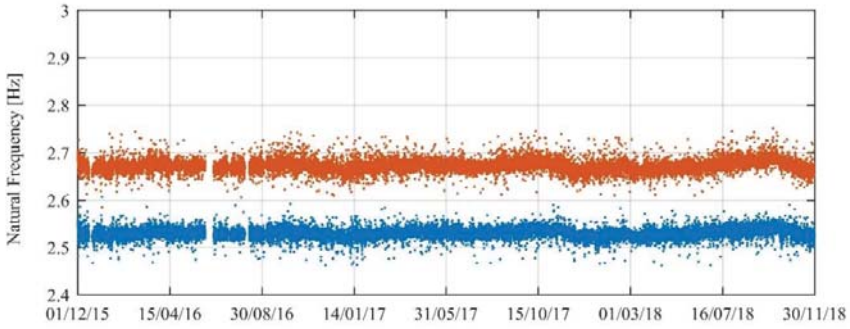

Figure 5: Natural frequency evolution of the first two modes after application of the regression model

To complement the minimization of operational and environmental effects on natural frequencies achieved with the multiple linear regression model, principal components analysis was applied to the residuals previously obtained.

Afterwards, t-statistic control charts based on the obtained residuals were tested to ascertain the quality of the minimization of the effects of external conditions and to define a baseline for damage detection. Data from one entire year was used as reference period (represented in blue) whereas observations between the two following years (represented in orange) were used to build the control part of the chart and verify the quality of the chart associated with the non-damaged situation.

To obtain the upper control limit (UCL) the distribution of the T^2 values during the reference period was considered, thus it was defined as the sum of the average T^2 with two times the T^2 standard deviation (during the reference period), so that approximately 95% of T^2 values would be below the UCL. This approach is only possible as long as the reference period is large enough to confidently define the UCL. Different control charts were tested considering groups from 1 to 96 elements and finally the ones resulting from the consideration of groups with 6 and 96 points, corresponding respectively to 3-hour and 2–day data, are represented in Figure 6.

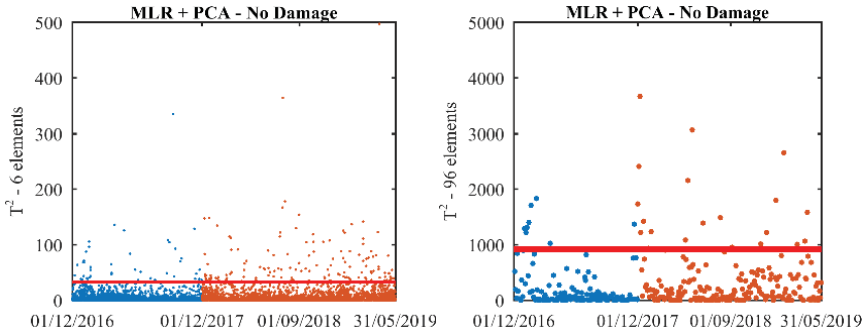

Figure 6: Baseline control charts (no damage) using 6-points (on the left) and 96-points groups (on the right)

3 DAMAGE DETECTION

3.1 Damage Simulation

In the previous section it was shown that it is possible to largely reduce the effects of operational and environmental factors on the identified natural frequencies of an arch dam, to a degree that allows to build stable control charts With the aim of testing the ability of these control charts to identify realistic frequency variations, small damages were simulated with the previously presented finite model of the dam.

Damage in dams may stem from a diversity of occurrences and the accurate numerical modelling of damage scenarios would require the development of very complex non-linear models and a large number of assumptions, resulting only in approximate results. Therefore a simpler approach is followed in this work, namely through reductions of inertia in a few dam components, such as part of concrete blocks, or reduction in stiffness of contraction joints.

In this manner, four different damage scenarios were considered, D1, D2, D3 and D4. The location and extent of each damage considered is presented in Figure 7. The first damage scenario (D1) corresponds to the decrease of the Young's modulus value in a group of 11 elements in the central part of the dam. Only elements in the most upstream layer were considered, which corresponds to a part of the structure that is highly stressed and may be

subjected to cracking. The second damage scenario (D2) is equivalent to the first one, with similar extent, though only 5 elements were damaged in this case, and it is located between the abutment and the central part of the dam. The third scenario (D3) correspond to a more confined damage in the central part of the structure, but it goes from upstream to downstream, through the three layers of elements of the dam model. Finally, in the fourth damage scenario (D4) both the normal and shear stiffness of the six central contraction joints (represented in red in right bottom of Figure 7,) were reduced.

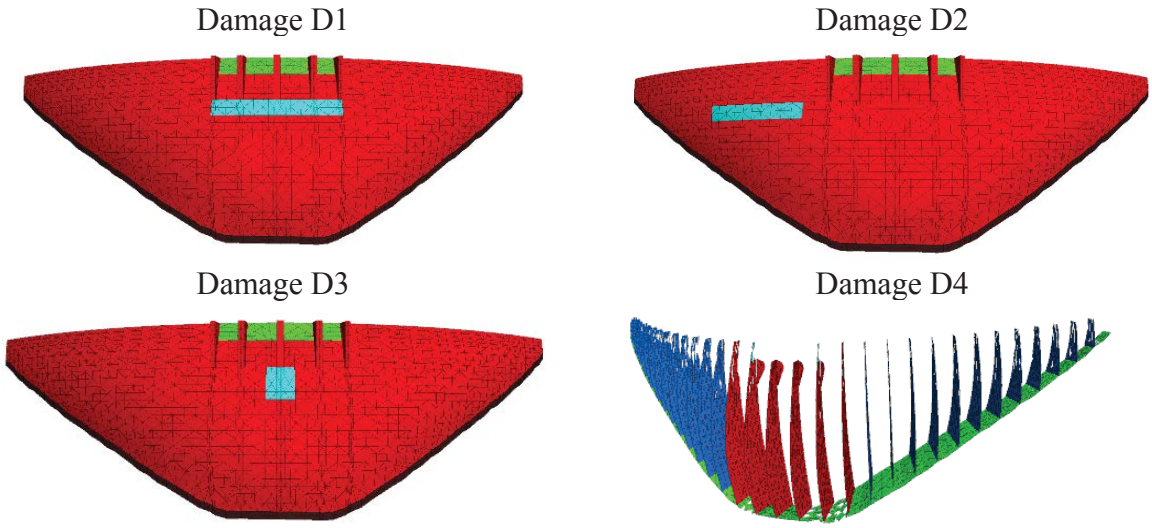

Figure 7: Location, extent and type of simulated damage scenarios.

Natural frequencies obtained after the introduction of each damage were compared with the healthy model and results were obtained for several reservoir water levels between 210 and 234 m. Moreover, five levels of damage intensity were considered, which consisted in the reduction of Young's modulus of selected elements (or normal and shear stiffness in the case of joints) in 10, 30, 50, 70 and 90 %.

The results obtained with full reservoir and damage intensities of just 10 %, which is the most challenging scenario to test the damage detection tools, are presented in Table 2. Frequency reductions between 0.015 and 0.181 % were verified. However, frequency reductions increase to values between 0.1 and 1% when damage intensities rise to 50 %, and to values between 1 and 4 % when 90 % damage intensities are considered. Furthermore, in each damage scenario different frequency reductions were verified for each vibration mode, indicating the possibility of locating damage through the study of the relation of the effect of damages between modes.

Mode	Frequency [Hz]	Δ freq. [%]	Δ freq. [%]	Δ freq. [%]	Δ freq. [%]
1	2.45372	-0.181	-0.014	-0.125	-0.076
2	2.68436	-0.059	-0.052	-0.075	-0.066
3	3.58254	-0.015	-0.122	-0.018	-0.047
4	4.05438	-0.060	-0.076	-0.031	-0.042
5	4.84020	-0.082	-0.073	-0.074	-0.041

Table 2: Natural frequency reductions associated with damage scenarios D1, D2, D3 and D4 (10% of damage intensity) with full reservoir

3.2 Application of damage detection tools

In order to obtain very sensitive control charts, capable of detecting small damages, alternative procedures were tested to minimize the effects of external conditions on natural frequencies, besides the procedure presented in subsection 3, based on the combination of the MLR with PCA. Although good results were achieved with this procedure, it was verified that even better results could be achieved considering just the application of PCA with two principal components. Therefore, this is the procedure considered in this section, and the results that it produces are used as baseline for damage detection.

The damages presented in the previous section were introduced in the estimated natural frequencies obtained from the implemented continuous monitoring processing through the assessed frequency reductions, after which the ability of control charts to detect the presence of such damages is tested.

Since averages of 96 elements were adopted, new points resulting from the collection of new data are only marked in the control charts every two days. As an example, Figure 8 presents two control charts related with the detection of damage, more specifically, the charts obtained considering damage scenario D3 with 30 and 50 % of stiffness reduction. In this case, the healthy state is represented in blue and orange color is used to represent data after he introduction of damages. Damages clearly lead to higher values of T^2, which subsequently increase with the intensity of the damage introduced. In the case of 50 % of stiffness reduction, almost the entire set of T^2 values obtained after the introduction of damage are found above the UCL, thus damage would be unequivocally detected only a few days after its occurrence. A similar situation occurs with the scenario of 30 % of stiffness reduction, which presents the majority of T^2 values clearly above the UCL, thus once again, damage would be detected soon after its occurrence if damage existence is assumed only after a few consecutive points (5 or more) are found above the UCL.

Though not represented, the same conclusions would be achieved for higher damage intensities (70 and 90 % of stiffness reduction), as would be expected. On the other hand, with 10 % of stiffness reduction, the most challenging scenario for the detection algorithms, just a few points are found above the UCL, the average T^2 value increased only marginally and never during the entire tested period is it possible to find five consecutive points above the UCL. In this sense, it would not be possible to detect damage D3 with such low intensity, even if evaluated for several weeks.

This damage detection analysis was repeated with the other three scenarios and similar results were obtained, with the 30 % stiffness reduction scenarios corresponding to the detection threshold. Finally, it is worth noting that damages resulting from 70 % of stiffness reduction, or higher, could be detected just one day after its occurrence, using averages with just 6 points instead of 96.

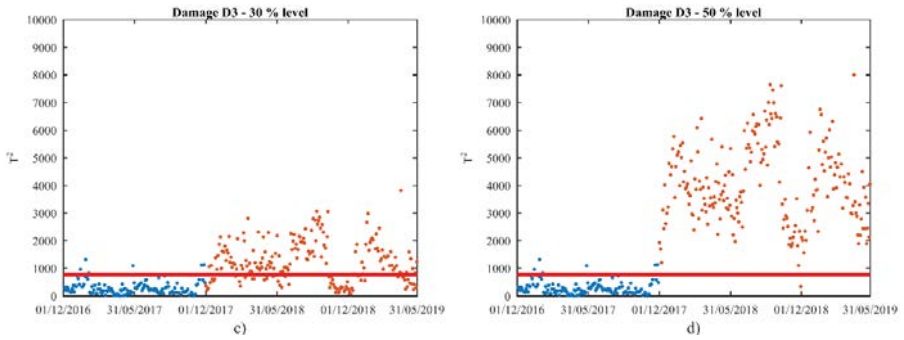

Figure 8: Damage scenario D3 – 30 % to 50 % of stiffness reduction

4 CONCLUSIONS

The dynamic monitoring system installed in Baixo Sabor arch dam has been working almost without failures since it was installed, proving to be an important asset to the long term monitoring and maintenance of the structure.

The time series of accelerations recorded by the monitoring system during the past few years have been used to characterize the structures dynamic behaviour and to study the evolution of natural frequencies over time. It was verified that natural frequency values presented high variability during the monitored period, mostly due to the effects of operational and environmental conditions. The analysis of these effects unveiled an inverse relation between natural frequencies and the level of water in the reservoir, as well as a direct proportionality between air temperature and natural frequencies.

Afterwards, a multiple linear regression model aiming to explain the observed data variability was built and used to minimize the effects of external conditions on natural frequencies. In this particular case study, the application of principal components analysis proved to be more efficient in the delivery of features suitable for damage detection.

The numerical model of the dam developed by LNEC was used to simulate realistic damages that may occur in the dam after strong earthquakes or as the result of long-term material deterioration through ageing and chemical processes. These simulations allowed to ascertain the intensity of the frequency shifts that would be verified in the dam if such damages occurred, after which they were used to manipulate the data obtained from the continuous monitoring.

Finally, it was demonstrated that the construction of control charts with residuals from the application of principal components analysis allows the detection of small frequency shifts due to the numerically simulated damage scenarios.

To conclude, it was verified that a vibration-based monitoring system like the one installed at Baixo Sabor arch dam allows to better understand the dynamic behaviour of concrete arch dams, as well as to prevent the proliferation of small damages through the detection of abnormal structural behaviour.

ACKNOWLEDGMENTS

This work was financially supported by: Base Funding - UIDB/04708/2020 of the CONSTRUCT - Instituto de I&D em Estruturas e Construções - funded by national funds through the FCT/MCTES (PIDDAC); PTDC/ECM-EST/0805/2014|16761 – DAM_AGE - Advanced Online Dynamic Structural Health Monitoring of Concrete Dams, funded by FEDER funds through COMPETE2020 - Programa Operacional Competitividade e Internacionalização (POCI) – and by national funds through FCT - Fundação para a Ciência e a Tecnologia; FCT PhD Scholarship SFRH/BD/100587/2014 provided to the first author. The authors would like also to acknowledge all the collaboration and support provided by EDP Produção.

REFERENCES

1. Pereira, S., F. Magalhães, J. Gomes, Á. Cunha, and J.V. Lemos. *Installation and results from the first 6 months of operation of the dynamic monitoring system of Baixo Sabor arch dam*. in *Procedia Engineering*. 2017.

2. Gomes, J.P., J. Palma, F. Magalhães, S. Pereira, G. Monteiro, and D. Silva Matos. *Seismic monitoring system of baixo sabor scheme for structural dynamic behaviour monitoring and risk management*. in *26th International Congress on Large Dams, 2018*. 2018.
3. Magalhães, F., A. Cunha, and E. Caetano, *Vibration based structural health monitoring of an arch bridge: From automated OMA to damage detection.* Mechanical Systems and Signal Processing, 2012. **28**: p. 212-228.
4. Oliveira, G., F. Magalhães, Á. Cunha, and E. Caetano, *Development and implementation of a continuous dynamic monitoring system in a wind turbine.* Journal of Civil Structural Health Monitoring, 2016. **6**(3): p. 343-353.
5. Martins, N., E. Caetano, S. Diord, F. Magalhães, and T. Cunha, *Dynamic monitoring of a stadium suspension roof: Wind and temperature influence on modal parameters and structural response.* Engineering Structures, 2014. **59**: p. 80-94.
6. Ubertini, F., G. Comanducci, and N. Cavalagli, *Vibration-based structural health monitoring of a historic bell-tower using output-only measurements and multivariate statistical analysis.* Structural Health Monitoring, 2016. **15**(4): p. 438-457.
7. Magalhães, F., S. Amador, Á. Cunha, and E. Caetano. *DynaMo - Software for vibration based structural health monitoring*. in *Bridge Maintenance, Safety, Management, Resilience and Sustainability - Proceedings of the Sixth International Conference on Bridge Maintenance, Safety and Management*. 2012.
8. Pereira, S., *Structural Condition Assessment of Dams based on Continuous Dynamic Monitoring*, in *Civil Engineering Department*. 2019, Faculty of Engineering of University of Porto: Porto. English.
9. Gomes, J. and J.V. Lemos, *Characterization of the dynamic behavior of an arch dam by means of forced vibration tests*, in *1st Meeting of EWG Dams and Earthquakes*. 2016, Balkema: Saint Malo, France.
10. Priscu, R., A. Popovici, D. Stematiu, and C. Stere, *Earthquake engineering for large dams*. John Wiley & Sons. 1985, New York.
11. Pereira, S., F. Magalhães, J.P. Gomes, Á. Cunha, and J.V. Lemos, *Dynamic monitoring of a concrete arch dam during the first filling of the reservoir.* Engineering Structures, 2018. **174**: p. 548-560.
12. Pereira, S., F. Magalhães, A. Cunha, J. Gomes, and J.V. Lemos. *Installation and results from the first 18 months of operation of the dynamic monitoring system of Baixo Sabor arch dam*. in *Life-Cycle Analysis and Assessment in Civil Engineering: Towards an Integrated Vision - Proceedings of the 6th International Symposium on Life-Cycle Civil Engineering, IALCCE 2018*. 2019.

EURODYN 2020
XI International Conference on Structural Dynamics
M. Papadrakakis, M. Fragiadakis, C. Papadimitriou (eds.)
Athens, Greece, 23–26 November 2020

A FULLY AUTOMATED OMA PROCEDURE WITH ADAPTIVE TRACKING OF LONG-TERM MONITORING DATA: AN APPLICATION TO MASONRY TOWERS

G. Zini, M. Betti, and G. Bartoli

Department of Civil and Environmental Engineering (DICEA)
University of Florence
Via di Santa Marta 3, 50139 Florence, Italy
e-mail giacomo.zini@unifi.it,

Keywords: Continuous Structural Health Monitoring (C-SHM), Automated Operational Modal Analysis (AOMA), Cultural Heritage, Masonry towers

Abstract. *During the last decades, the Operational Modal Analysis (OMA) techniques for the dynamic identification have reached a wide application in the large civil structures. Then the focus has been moved on the introduction of the Automated OMA (AOMA) techniques as a component of a wider Structural Health Monitoring (SHM) framework. On the one hand, the automatization of the process is needed to extract the modal properties from huge database of measurements. On the other hand, the methods should be able to minimize the model bias, avoiding the spurious and mathematical modes. Moreover, all the fix thresholds defined a-priori should be carefully set to avoid some tracking errors. This paper presents a new AOMA for the extraction of the modal parameters from long-term monitoring data. The methodology herein discussed aims to minimize the errors that can arise during the modal identification. Moreover, the information obtained during an observation period have been used to define suitable adaptive thresholds. For illustrative purposes, the methodology has been applied to the data acquired from long-term monitoring systems installed on two masonry towers subjected to different operational conditions. The effectiveness of the proposed method has been checked on the extracted modal parameters*

1 INTRODUCTION

Since the beginning of the nineties the long-term monitoring system (LTMS) for the detection of the early stages of damage is an established technique developed for the civil structures. The basic idea was the improvement of the adopted techniques for the inspection of the existing bridges. With the introduction of Vibration Based Inspection (VBI) correlating different extent of damages on a structure with the change in the dynamic properties, a lot of efforts were spent by the researchers. From that pioneering studies, the Structural Health Monitoring framework was fully defined and several examples of full-scale tests on large civil structure have been performed [1–3]. Thanks to the development of the Operative Modal Analysis (OMA) techniques, allowing the extraction of the dynamic properties under operative conditions the attention on the topic was renewed. Moreover, the technology advances in terms of computing and storing information boosts the efforts for the development of effective long-term monitoring techniques. Thus, the challenge has been moved on the definition of automated procedures capable of processing large dataset of measurements. Consequently, in the last years, several Authors have proposed fully or semi-automated OMA procedures [4–9] to extract the modal parameters.

While different strategies have been proposed for the automated extraction of the dynamic properties, not so many studies have investigated the modal tracking phase. Commonly, some fixed thresholds are selected for all the modes and each mode is tracked selecting a reference set of modal parameters usually defined in a preliminary dynamic test. Even if the mode shapes are not sensitive to the changes in the environment [10] like temperature, humidity etc. some changes can occur due to some other effects. Along with that variability in some cases not all the sensors can be online, especially for dense measurements along the time, or if dense spatial grids are used. Moreover, the use of cheap monitoring system with a low-resolution needs a proper selection of the tracking thresholds for each mode. On the top of all that, recently, some Authors have shown how the damage can be detected by the analysis of the outliers of the tracked frequency [11–13] along the time. Hence the definition of suitable automated procedures become crucial point, especially for the application to the cultural heritage buildings [14,15]

In the present paper is introduced an algorithm for the modal tracking of the modal properties of two historic masonry towers with different operational conditions. The accelerations have been collected by a continuous (fifteen minutes of record every hour) wireless monitoring system based on the MEMS technology.

2 THE AOMA PROCEDURE

The AOMA algorithm has been developed considering a Continuous Vibration-Based Structural Health Monitoring (CVB-SHM) approach. As it was stated by Pecorelli [16] with the analysis of the data of a continuous monitoring system in a complex elliptical dome; the input should be selected as those with higher Root Mean Square (RMS) to successfully identify all the modes. Furthermore, Marwitz and Zabel [17] defined a relationship among the quality of the identified modes and the intensity of the input, analyzing the long-term monitoring data of a high-rise telecommunication tower. Hence the presented procedure was developed by introducing some thresholds in the input parameters and in the complexity of the identified modes. That values are defined statistically, considering a suitable observation period where the common operational conditions are present. The full procedure for the extraction of the modal parameters has been fully described in [18].

Here the algorithm to define the adaptive thresholds for each mode is presented and the most relevant operation are described:

1. Selection of one or more calibration periods
2. Definition of a starting thresholds respectively in terms of frequency df_{lim} and mode $d\phi_{lim}$ shapes equal for each mode
3. Random selection of the *b-th* element as a seed of the first cluster
4. Calculate the relative distance d_{bi} in terms of frequency and mode shapes from the *b-th* seed to all the other *i-th* elements of the calibration period
5. The elements within the initial distance d_{lim} are clustered together and the relative distances are saved in the vector
6. For each mode the distance is calculated as the median of the components of d

Thus, the distances in terms of frequency and mode shapes are calculated analyzing the results on the calibration period during the common operational conditions of the structure. Obviously, the initial thresholds d_{lim} should be chosen adequately. For instance, reference values for the MAC can be from 0,05-0,8; while the relative distance in terms of frequency depends on the length of the calibration periods. Anyway, a suitable interval could be between the 1-10 %.

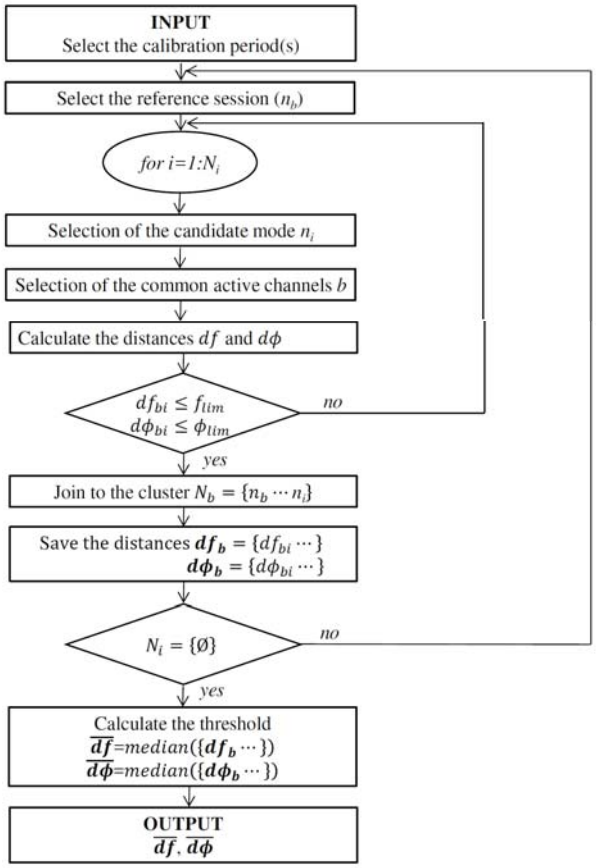

Figure 1: The flowchart of the proposed method.

3 APPLICATION TO TWO HISTORIC MASONRY TOWERS

The two cases of study are the "Torre Grossa" (Tower A) and the "Mastio Matilde" (Tower B). The two towers exhibit different slenderness and different buildings materials: the Tower A made by travertine stones and the Tower B by masonry bricks. Both of them are sorrounded by walls or palaces until a certain level and in an asymettric way. It is worth to

point out that the two towers are subjected to different level of excitations. In one hand, the Tower B arises in the city center of San Gimignano (SI) where the veicular traffic is restricted so the main external dynamic forces are due to the wind. On the other hand, the Tower B is located in the Livorno harbour where the external dynamic excitation level is high and in some cases it is arisen from some colored noise . Hence, these two limits cases for the historic masonry towers seems to be a good test for the proposed automated procedure.

(a) (b)

Figure 2: (a) The "Torre Grossa" in San Gimignano (SI) (b) The "Mastio Matilde" in Livorno (LI).

The two towers have been selected as cases of study for the "Moscardo" project, a project funded by the Tuscany region, aiming to investigate the capability of monitoring the cultural heritage using low invasive techniques. Thus, a wireless network of Micro Electic Mechanic Sensors (MEMS) accelerometers has been adopted and tested for two towers for long-term monitoring purposes. In the next sections, the two networks will be briefly described and the results of the proposed adaptive technique for the modal tracking will be discussed.

3.1 Tower A

The "Torre Grossa" is the tallest medieval tower in the city center of San Gimignano with a height of 55 m and a base square of about 9,5x9,5 m. only two levels at the top have a concrete slabs, while an iron staircase has been fixed to the walls to reach the top level. At the top there is a belfry with three bells, that have no longer been used. A full description of the geometry and of the architectural features can be found in [19].

The installed monitoring system is composed by 12 accelerometers, 2 strain gauges, 2 dispacement transducers and 2 metereological stations: one indoor collecting temperature, humidity and the other outdoor collecting temperature, humidity and the average wind speed and direction.

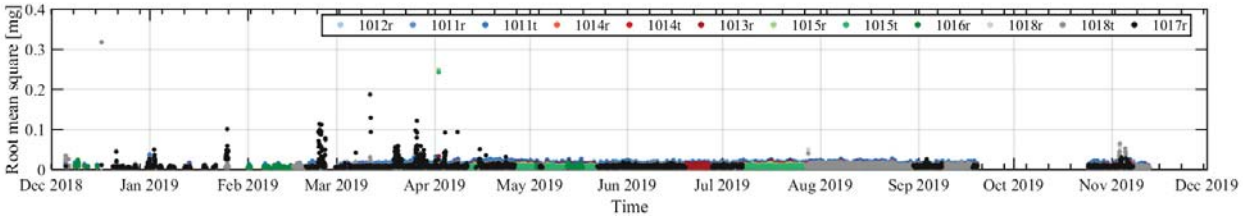

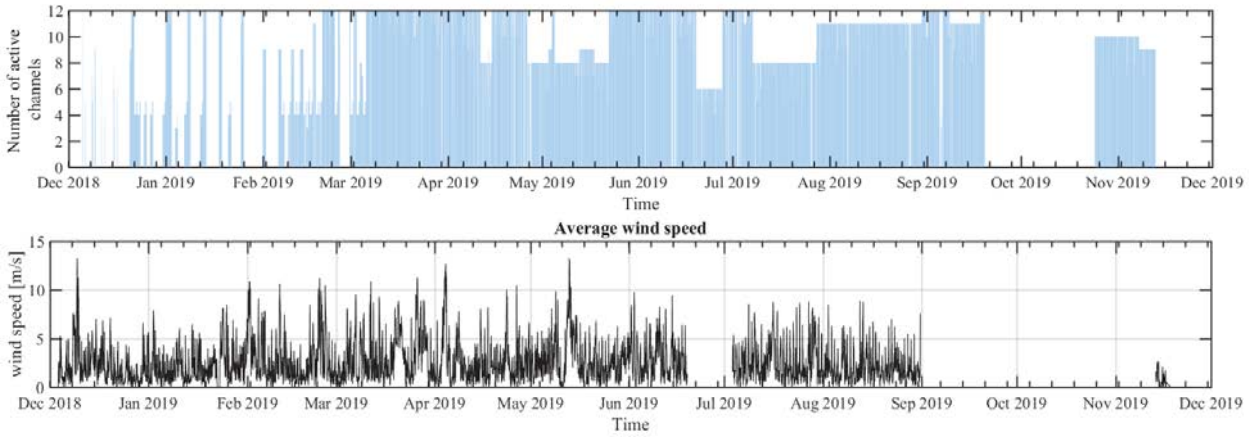

Figure 3: (a) Tower A the rms of the signals collected over the monitoring period, the active channels and the average wind speed recorded in the meteorological station in the last level.

In figure 3 the results of the first year of monitoring are reported in terms of power in the signals and of the measured average wind speed. In the time window from the middle of September to the middle of October the system was off-line. While not all the sensors were working together along the time because of some problems in the network.

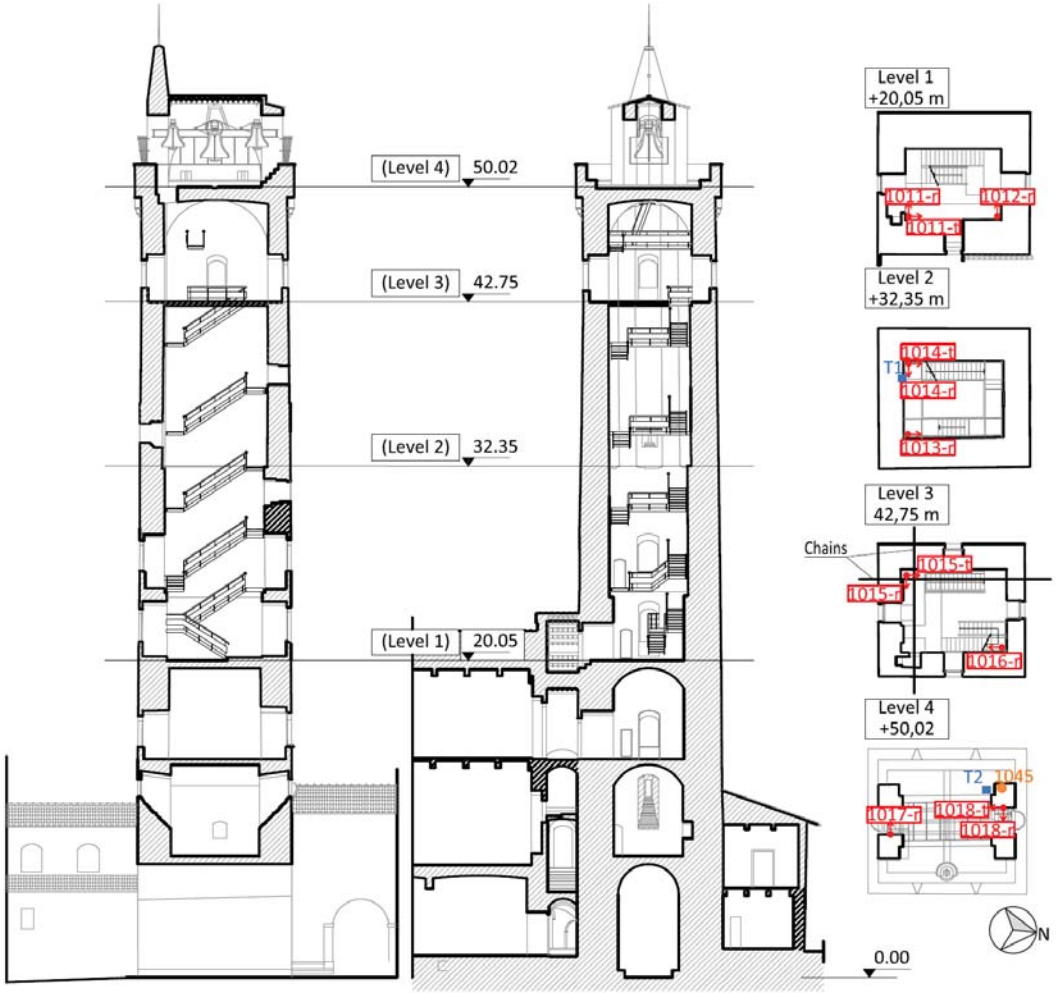

Figure 4: Tower A the long-term monitoring system installed.

3.2 Tower B

The "Mastio Matilde" is an iconic tower of the old fortress in the Livorno harbor. The tower has a round plan with a diameter of 12 m and a total height of about 29 m with four vaulted levels that were retrofitted in the past with steel bars fixed in the vaults. Some more information about the tower can be found in [18].

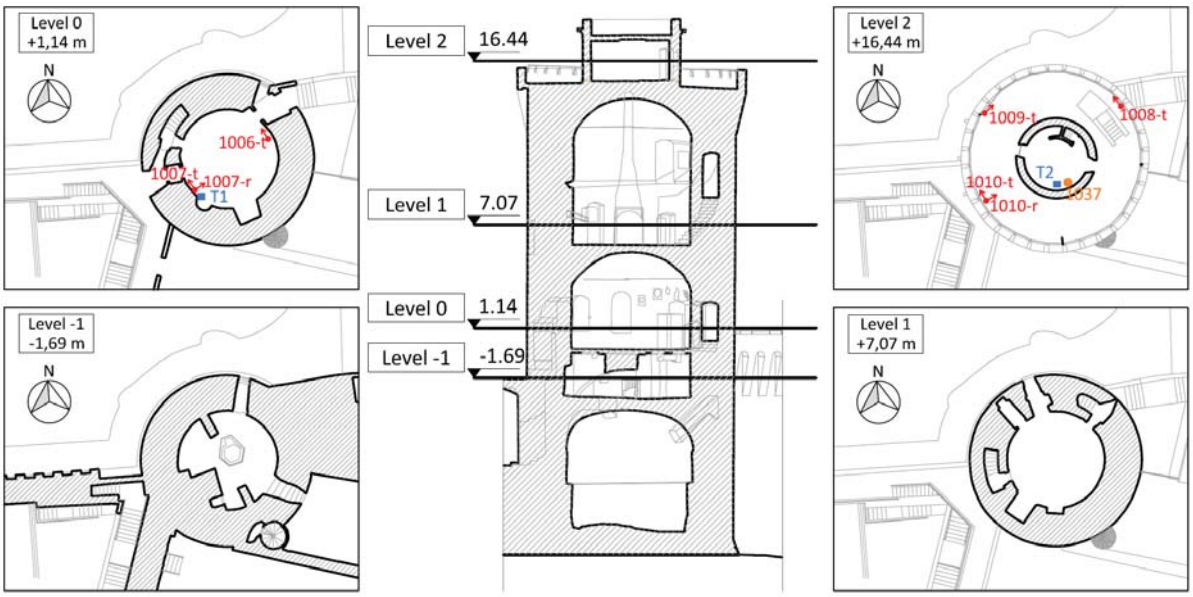

Figure 5: Tower B the long-term monitoring system installed.

Two sections of the tower have been monitored: the top with two mono-axial accelerometers and one biaxial accelerometer; the level 0 with one mono-axial and a biaxial accelerometer. The environmental conditions were monitored with two meteorological stations: one inside and one outside the tower. Both measure the temperature and the humidity, while outside an anemometer measuring the average wind speed and the direction.

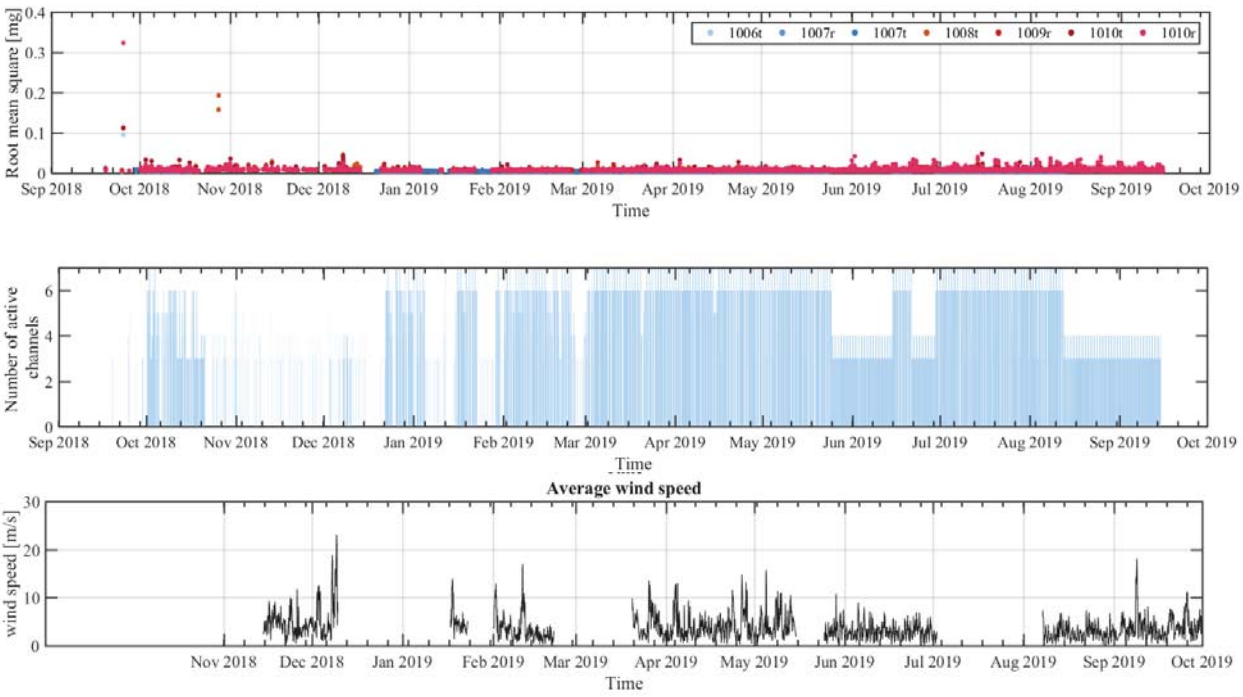

Figure 6: (a) Tower B the rms of the signals collected over the monitoring period, the active channels and the average wind speed recorded in the meteorological station in the last level.

Although also in that case several disconnections of some sensors a large database has been collected (Table 2).

3.3 Observations about the monitoring data

Despite the lacks in the time histories of the recorded signals due to some malfunctioning in the network, is possible to describe the level of vibration of the two cases of study.

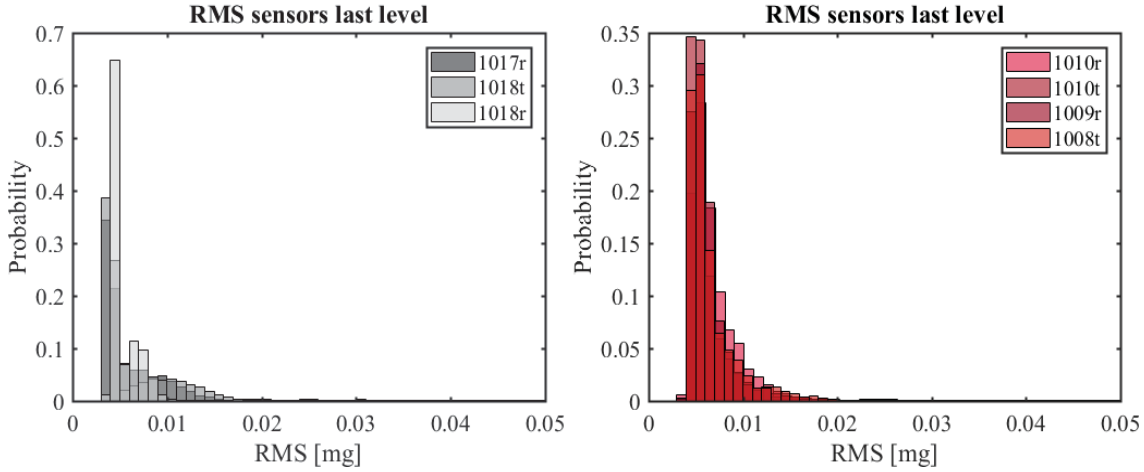

Figure 7: (a) The "Torre Grossa" in San Gimignano (SI) (b) The "Mastio Matilde" in Livorno (LI).

In figure 7 the rms distribution of the last floors of the two towers over the monitoring periods are shown. The level of vibrations of the Tower B is higher of about the 30% than the Tower A, confirming the different operational conditions. For both cases the main dynamic load is the wind and the maximum value has been reached in the Tower B (Figure 6).

	Sensor	Median [mg]	Variance [mg]	Elements
TG	#1017r	0,0045	0,0001	3142
	#1018t	0,0042	0,00003	4382
	#1018r	0,0043	0,00001	4377
MM	#1010r	0,0056	0,0023	2089
	#1010t	0,0057	0,000007	5475
	#1009r	0,0053	0,000009	5471
	#1008t	0,0061	0,00003	5507

Table 1: The rms distribution for the accelerometers in the last floor of the two towers.

4 RESULTS

The two monitoring systems are active from the end of the 2018, but some shutdown of some devices or some errors in the transmission of the data leads to a reduced grid of measuring points (Figures 3b-5b). Hence the adaptive modal tracking procedure proposed herein, considers that issues and the MAC index has been calculated considering the common channels that were recording. Then two suitable calibration periods have been chosen as limit cases of the operational dynamic behavior.

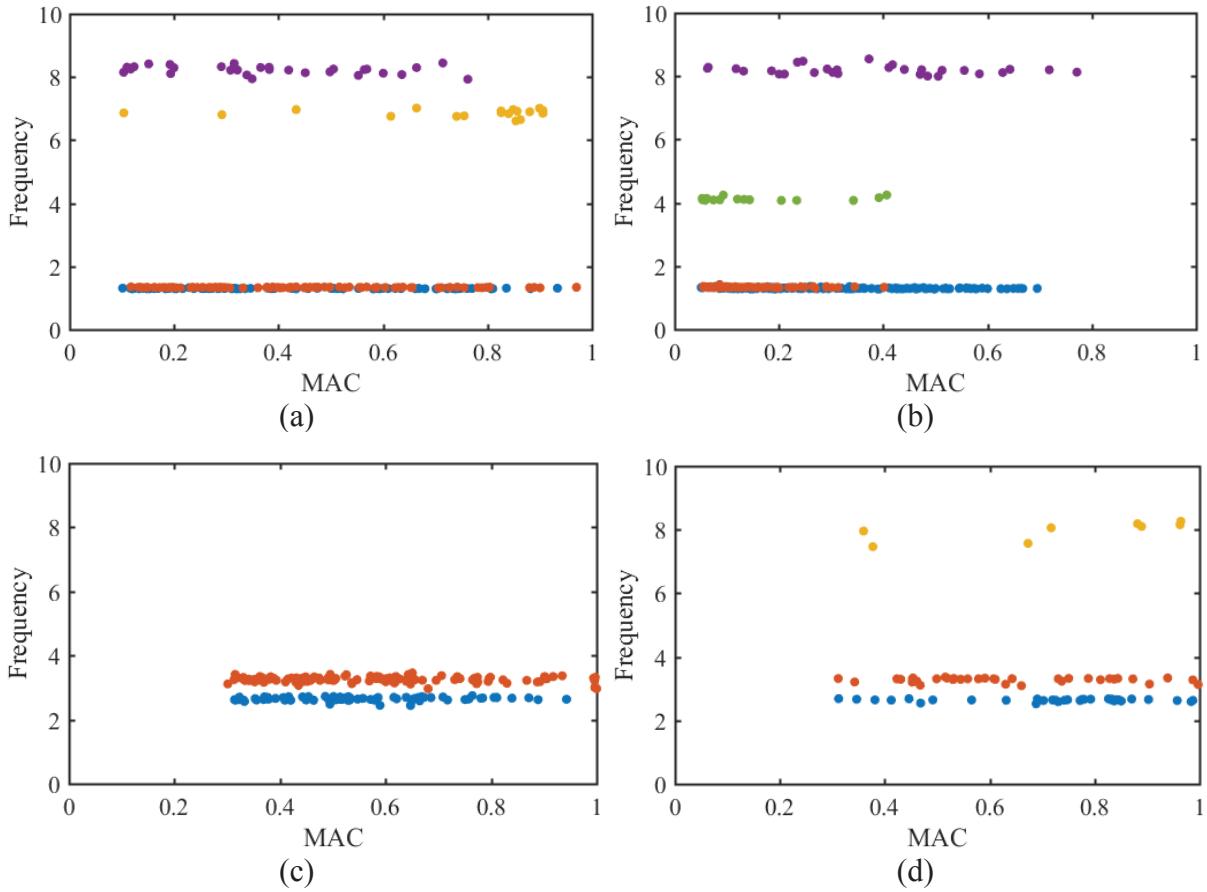

Figure 8: (a) The "Torre Grossa" in San Gimignano (SI) (b) The "Mastio Matilde" in Livorno (LI) (c) (d).

The periods from 10/05/2019-16/05/2019 (#MM1) and from 3/12/2018-9/12/2018 (#MM2) are those where the highest average wind speed has been recorded respectively for the Tower A and Tower B. Meantime, the periods from 1/05/2019-7/05/2019 (#TG1) and from 15/05/2019-21/05/2019 (#TG2) are those where the lowest average wind speed has been recorded respectively for the Tower A and Tower B. Thus, the distances in terms of frequency and mode shapes are calculated with the clustering procedure described in the previous sections.

Lastly, some statistical values of the measured distances for each period can be calculated and the minimum values can be chosen to track the modes. For that cases of study, the median value of the frequency and the third quartile value for the mode shapes.

Period	1st Mode		2nd Mode		3rd Mode	
	f_{lim}	ϕ_{lim}	f_{lim}	ϕ_{lim}	f_{lim}	ϕ_{lim}
#MM1	1,10	0,61	3,65	0,48	-	-
#MM2	3,42	0,83	3,38	0,80	2,48	0,92
#TG1	0,53	0,73	0,56	0,70	1,18	0,78
#TG2	1,04	0,43	1,73	0,65	2,16	0,52

Table 2: Example of the construction of one table.

As a result, the thresholds are not fixed but for each mode are calculated from the observed results in a representative calibration period. The selection of the representative values has been performed statistically analyzing two extreme operative conditions related to the most

relevant dynamic excitation. But the calibration period can be also selected with different approaches that lead to the observation of the operational conditions of the monitored structure.

5 CONCLUSIONS

The paper introduces a novel procedure for the adaptive modal tracking of the modal parameters extracted from long-term monitoring data. That issue is usually underestimated, and it has not been widely deepened by the Authors. This become crucial if the accelerations are measured with low-cost sensors that exhibit a lower resolution. In particular the mode shapes seem to be more sensitive to the background noise than the frequency. Thus, the classical modal tracking approach based on fixed threshold can bring to misleading results.

In addition, the identified modes might be not well excited during the measuring time-window and some channels might be not active.

Consequently, the results show how the tracked modes can exhibit different values based on the level of the ambient vibrations. Therefore, some adaptive threshold for the modal tracking based on the operational conditions should be considered to achieve adequate results.

Here the proposed procedure has been applied to two historic masonry towers monitored with a wireless network system of MEMS devices. That measuring network allows the use of cheaper sensors with a low-visual impact that are highly recommended for the monitoring of cultural heritage structures. Ensuring the use of the structure without compromising the architectonical features.

The proposed method is based on the hierarchical clustering of the modes in a representative observation period. Then the thresholds are selected by a statistical analysis of the results observed in the calibration periods. Nevertheless, the method can be implemented in a fully automated procedure for the modal extraction of the modal properties even if low-cost devices are used. Philosophical Transactions of the Royal Society A: Mathematical, Physical and Engineering Sciences

REFERENCES

[1] J.M.W. Brownjohn, Structural health monitoring of civil infrastructure, *Philosophical Transactions of the Royal Society A Mathematical, Physical and Engineering Sciences* 365 (2007) 589–622.

[2] M. Rizzo, M. Betti, O. Spadaccini, A. Vignoli, Improvement of structural monitoring of jacket platform, *Proceedings of the International Offshore Polar Engineering Conference* (2017).

[3] F. Magalhães, Á. Cunha, E. Caetano, Dynamic monitoring of a long span arch bridge, *Engineering Structures* 30 (2008) 3034–3044.

[4] F. Magalhães, Á. Cunha, E. Caetano, Online automatic identification of the modal parameters of a long span arch bridge, *Mechanical System and Signal Processing* 23 (2009) 316–329.

[5] E. Reynders, J. Houbrechts, G. De Roeck, Fully automated (operational) modal analysis, *Mechanical System and Signal Processing* 29 (2012) 228–250.

[6] R. Cardoso, A. Cury, F. Barbosa, A robust methodology for modal parameters estimation applied to SHM, *Mechanical System and Signal Processing* 95 (2017) 24–41.

[7] E. Neu, F. Janser, A.A. Khatibi, A.C. Orifici, Fully Automated Operational Modal Analysis using multi-stage clustering, *Mechanical System and Signal Processing* 84

(2017) 308–323.
[8] F. Ubertini, C. Gentile, A.L. Materazzi, Automated modal identification in operational conditions and its application to bridges, *Engineering Structures* 46 (2013) 264–278.
[9] A. Cabboi, F. Magalhães, C. Gentile, Á. Cunha, Automated modal identification and tracking: Application to an iron arch bridge, *Structural Control Health Monitoring* 24 (2017).
[10] F. Ubertini, G. Comanducci, N. Cavalagli, A. Laura Pisello, A. Luigi Materazzi, F. Cotana, Environmental effects on natural frequencies of the San Pietro bell tower in Perugia, Italy, and their removal for structural performance assessment, *Mechanical System and Signal Processing* 82 (2017) 307–322.
[11] F. Magalhães, A. Cunha, E. Caetano, Vibration based structural health monitoring of an arch bridge: From automated OMA to damage detection, *Mechanical System and Signal Processing* 28 (2012) 212–228.
[12] F. Ubertini, G. Comanducci, N. Cavalagli, A. Laura Pisello, A. Luigi Materazzi, F. Cotana, Environmental effects on natural frequencies of the San Pietro bell tower in Perugia, Italy, and their removal for structural performance assessment, *Mechanical System and Signal Processing* 82 (2017) 307–322.
[13] N. Cavalagli, G. Comanducci, F. Ubertini, Earthquake-Induced Damage Detection in a Monumental Masonry Bell-Tower Using Long-Term Dynamic Monitoring Data, *Journal Earthquake Engineering* 22 (2018) 96–119.
[14] G. Standoli, E. Giordano, G. Milani, F. Clementi, Model Updating of Historical Belfries Based on Oma Identification Techniques, *International Journal Architectural Heritage* 00 (2020) 1–25.
[15] E. García-Macías, F. Ubertini, Automated operational modal analysis and ambient noise deconvolution interferometry for the full structural identification of historic towers: A case study of the Sciri Tower in Perugia, Italy, *Engineering Structures* 215 (2020) 110615.
[16] M.L. Pecorelli, R. Ceravolo, R. Epicoco, An Automatic Modal Identification Procedure for the Permanent Dynamic Monitoring of the Sanctuary of Vicoforte, *International Journal Architectural Heritage* (2018).
[17] S. Marwitz, V. Zabel, Relations between the quality of identified modal parame- ters and measured data obtained by structural monitoring Description of the Monitoringsystem.
[18] P. Barsocchi, G. Bartoli, M. Betti, M. Girardi, S. Mammolito, D. Pellegrini, G. Zini, Wireless Sensor Networks for Continuous Structural Health Monitoring of Historic Masonry Towers, *International Journal Architectural Heritage* 00 (2020) 1–23.
[19] G. Bartoli, M. Betti, S. Giordano, In situ static and dynamic investigations on the " Torre Grossa" masonry tower, *Engineering Structures* 52 (2013) 718–733.

EURODYN 2020
XI International Conference on Structural Dynamics
M. Papadrakakis, M. Fragiadakis, C. Papadimitriou (eds.)
Athens, Greece, 23–26 November 2020

VIBRATION-BASED ANOMALY DETECTION USING SPARSE AUTO-ENCODER AND CONTROL CHARTS

Rafaelle P. Finotti[1], Carmelo Gentile[2], Flávio S. Barbosa[1] and Alexandre A. Cury[1]

[1]UFJF - Federal University of Juiz de Fora
Faculty of Engineering
Department of Applied and Computational Mechanics
e-mail: {rafaelle.finotti, flavio.barbosa, alexandre.cury}@engenharia.ufjf.br

[2] Politecnico di Milano
Department of Architecture, Built Environment and Construction Engineering (ABC)
e-mail: carmelo.gentile@polimi.it

Keywords: Structural Health Monitoring, Damage Detection, Vibration Signals, Deep Learning.

Abstract. *Several approaches can be found in the scientific literature when the subject is damage detection based on vibration signals. In the last few years, increasing attention has been given to the application of Computational Intelligence algorithms in structural novelty identification. In more details, the powerful data mapping capability of computational deep learning methods has been recently exploited to develop strategies of structural health monitoring through appropriate characterization of dynamic responses. Therefore, the present work is aimed at investigating the capability of a deep learning algorithm called Sparse Auto-Encoder (SAE) to identify structural alterations of the Z24 bridge, a classical benchmark for integrity assessment studies. The main idea is to characterize the Z24 dynamic responses via SAE models and, subsequently, to detect the onset of abnormal behavior through the well-known Shewhart T control chart (T^2-statistic), calculated with SAE extracted features. An advantage of the proposed methodology is that data are processed directly in the time domain, avoiding modal parameters estimation and tracking analysis. Moreover, control charts are considered suitable tools for continuous monitoring due to their relatively simple implementation. The obtained results demonstrate that the proposed strategy based on SAE and Shewhart T control chart has potential to be explored in structural damage detection problems, since it is able to distinguish between the two investigated scenarios (i.e., undamaged and damaged) of Z24 bridge.*

1 INTRODUCTION

The proper functioning of structural systems and the safety of users are among the main concerns of engineers throughout the life cycle of any civil engineering construction. In order to avoid catastrophic failures, it is important to continuously monitor the structural condition and detect any abnormal behavior at an early stage, especially when dealing with large structures, such as bridges, viaducts, tall buildings, and towers.

Among the different methodologies available to identify the occurrence of structural anomalies, vibration-based damage detection has been extensively investigated in the scientific literature (see e.g. [1]). Starting from dynamic time histories obtained through Structural Health Monitoring (SHM) systems, these approaches are applied to investigate novelties in terms of structural behavior. In summary, essential features are extracted from measured data and are successively compared to deduce if a structural change has occurred.

Typically, the structural integrity investigation is performed by employing modal analysis [2, 3]. The degrading process alters the physical properties of the structure, such as mass and stiffness, which influence its natural frequencies, mode shapes, and damping ratios. In the last few years, due to the evolution of computer and information technologies, increasing attention has been given to the application of Computational Intelligence (CI) in structural novelty identification [4, 5, 6]. Among all possible CI algorithms, those based on deep learning appear as promising alternatives to traditional techniques. In this paper, a special highlight is given to the Sparse Auto-Encoder (SAE), a deep neural network algorithm that automatically extracts features from data. The SAE reconstructs its inputs through an internal coding - modeled by linear and nonlinear functions - that transforms them into a "new" group of variables (features) [7]. Auto-encoders are known not only for the ability to deal with large volumes of data but also for their capability to provide optimal solutions, particularly for nonlinear problems, such as structural anomaly detection [8, 9]. Therefore, SAE may be an appropriate method for handling vibration signals. It is important to notice that deep learning algorithms are recent tools in the SHM area, and studies focused on evaluating them to solve novelty detection problems are ongoing.

In this context, the present work is aimed at investigating the performance of the SAE algorithm when applied to the identification of structural alterations. The fundamental idea here is to characterize the structural dynamic responses via SAE models and, subsequently, to detect the onset of abnormal behavior through the well-known Shewhart T control chart (T^2-statistic) [10], calculated with SAE extracted features. The Shewhart chart is a sort of statistical process control technique frequently used in SHM strategies and applied to the residuals between measured and predicted (via regression analysis) quantities. Due to the relatively simple implementation, control charts are considered suitable tools for continuous monitoring. The anomaly detection approach is exemplified using data collected on the Z24 bridge [11], before and after damaging the structure.

An advantage of the proposed methodology is that data are processed directly in the time domain, avoiding modal parameters estimation and tracking. Another interesting aspect of such an approach is the unsupervised analysis, which means that it does not use previously labeled observations or desired output variables. Although many methods in the literature are based on the pre-establishment of different degradation levels (supervised analysis), it is difficult to have prior knowledge of the structure's health condition in actual SHM systems.

2 THEORETICAL BACKGROUND

2.1 Deep Learning and Sparse Auto-Encoder

Deep Learning encompasses a variety of machine learning techniques based on Artificial Neural Network (ANN) theory (see e.g. [12]), mainly characterized by their multiple processing layers. As already stated, the present work is focused on the deep learning algorithm called Sparse Auto-Encoder (SAE). In general terms, an Auto-Encoder (AE) is an Artificial Neural Network (ANN) built to return an approximation of its input. According to Goodfellow *et al.* (2016) [7], this network consists of an internal coding layer described by the function $\mathbf{h} = f(\mathbf{x})$, which learns the characteristics $\mathbf{h}$ of input data $\mathbf{x}$, and a decoding layer defined by $\mathbf{y} = g(\mathbf{h})$, which rebuilds the vector $\mathbf{x}$ from the self-learned vector features $\mathbf{h}$, as suggested by the network architecture shown in Figure 1. Since the cost function evaluates the difference between $\mathbf{x}$ and its own output $\mathbf{y} \approx \mathbf{x}$ ($\mathbf{x}$ reconstructed), the learning of an AE is unsupervised. It is worth mentioning that an AE may have several layers between $\mathbf{x}$ and $\mathbf{h}$, as well as between $\mathbf{h}$ and $\mathbf{y}$ (the AE structure has to be symmetric). However, for didactic purposes, Figure 1 represents an AE with only one encoder and decoder layer.

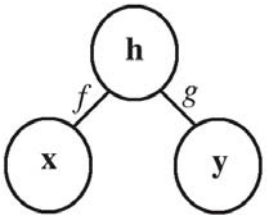

Figure 1: The basic structure of an Auto-Encoder [7].

Nevertheless, the main interest is not in the replicated output of the AE, but in exploring its ability to extract characteristics from "raw data". If the AE is used for data mapping only, without feature reconstruction, it is designed to produce $\mathbf{h}$ with a smaller dimension than $\mathbf{x}$ and is known as Undercomplete Auto-Encoder. The great advantage of reducing the data from $\mathbf{x}$ vector dimension to $\mathbf{h}$ vector dimension is the identification of relevant parameters at a high-level of abstraction, helpful for recognizing patterns in datasets. In this context, the learning of the AE network is accomplished by minimizing a function $Z(\mathbf{x}, g(f(\mathbf{x})))$ that penalizes the differences between $\mathbf{x}$ and $g(f(\mathbf{x}))$. In cases where the coding function is linear, and Z is the mean quadratic error, the Undercomplete Auto-Encoder behaves like the Principal Component Analysis (PCA) [13]. Conversely, when employing nonlinear functions for f and g, the Undercomplete Auto-Encoder may be more powerful than PCA to reduce the dimensionality of a problem [14].

Despite their efficiency in characterizing data, the encoders and decoders may acquire an excessive ability to approximate $\mathbf{y} \approx \mathbf{x}$, resulting in a vector $\mathbf{h}$ with high dimensionality, which many times is not able to provide interesting parameters for modeling the problem. In order to improve the performance of this deep machine learning technique, the Sparse Auto-Encoder (SAE) was proposed. The SAE is an undercomplete auto-encoder where a sparse penalty $\Gamma(f(\mathbf{x}))$ is incorporated into the function Z in the training process. In summary, this penalty allows the AE model to represent large datasets with a small number of $\mathbf{h}$ components, controlling the amount of active neurons in the layers (most weights equal to zero). Consequently, the addition of sparsity-inducing term to auto-encoders usually leads to an increase in the model performance and to a reduction of processing time.

2.2 Shewhart T Control Chart

The Control Chart is a graphical statistical tool used to monitor the variability of a problem's parameters over time. The charts usually depict several data points, which are formed by a specific statistical characteristic and horizontal lines (control limits) responsible for indicating the extreme values of such characteristic when the problem is in-control state. Any point that is beyond these predetermined limits, on the other hand, reveals unusual sources of variability, suggesting an out-of-control situation. [10].

Due to their relatively simple implementation, intuitive interpretation, and effective results, control charts are considered suitable tools for structural on-line monitoring and anomaly detection. The multivariate control technique used herein is the Shewhart T Control Chart. The characteristic plotted in this chart is the Hotelling's T^2-statistic. The T^2-statistic represents the distance between a new data observation and the corresponding sample mean vector - the higher T^2 value, the greater the distance of the new data from the mean. This metric is based on the relationship among the variables and on the scatter of data (covariance matrix). By assuming that matrix $\mathbf{H}_{n\times m}$ represents a dataset during a certain time period (which in this paper are the SAE extracted features), the T^2-statistic may be calculated as follows:

$$T^2 = r(\overline{\mathbf{h}} - \overline{\overline{\mathbf{h}}})^T \mathbf{S}^{-1} (\overline{\mathbf{h}} - \overline{\overline{\mathbf{h}}}) \tag{1}$$

where $\overline{\mathbf{h}}$ is the sample mean vector of the m available features, obtained from a submatrix of $\mathbf{H}$ with r observations ($\mathbf{H}_{r\times m}, r < n$); $\overline{\overline{\mathbf{h}}}$ and $\mathbf{S}$ are the vector of reference averages and the mean of the reference covariance matrices, respectively, both estimated using s preliminary submatrices collected during the in-control state of the problem. In this work, the Upper Control Limit (UCL) is defined as the 95^{th} percentile of the T^2 values of the training data (values greater than UCL may be observed only 5% of the time by chance). The Lower Control Limit (LCL) is zero.

3 THE VIBRATION-BASED ANOMALY DETECTION APPROACH

The present work proposes a structural assessment framework based on SAE models for automatic vibration-data feature learning. Such a framework includes the use of the Hotelling's T^2 control chart applied to SAE extracted characteristics to investigate novelties in terms of structural behavior. Figure 2 shows a general scheme of the suggested anomaly detection methodology.

SHM systems usually comprise a number of accelerometers that record dynamic responses over time. Therefore, it is initially necessary to rearrange the acceleration time histories collected in each measurement point by setting an appropriate window length (duration time) to analyze each measured signal. The vibration measurements are organized in a matrix considering the structural responses of each accelerometer k $(1 \leq k \leq K)$ separately, as illustrated in Figure 3. The rows I indicate each rearranged signal, and the columns J represent the respective dynamic response sampled in time. The definition of the signal duration time should consider the measurements' capacity to represent the current structural condition and the amount of available data. Moreover, since the present approach is focused on continuous monitoring, it is also important to keep the chronological order of the collected signals. In order to make the detection model less sensitive to data scale, after the input matrix is assembled, all data values are divided by the maximum absolute amplitude, leading to acceleration signals between [-1;1].

The developed strategy relies on creating a model with data from the system working in normal conditions, which is named as SAE/T^2-statistic reference model. At this point, the reference matrix previously organized is divided into training and testing data, respecting their

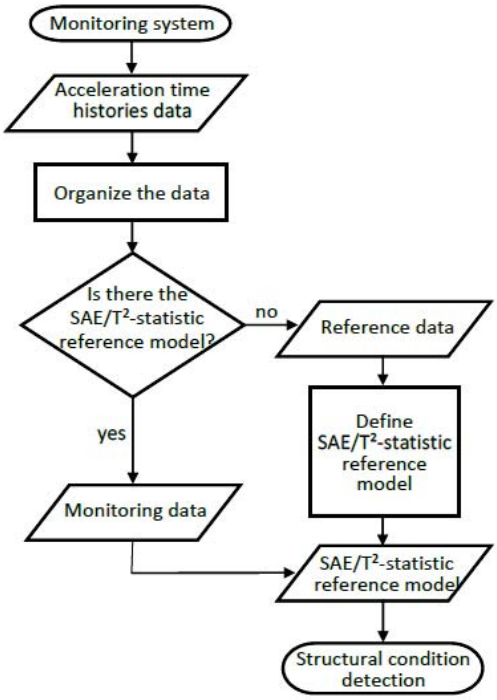

Figure 2: General scheme of the proposed methodology.

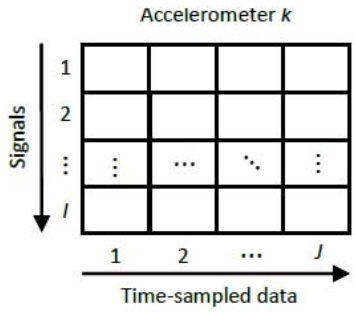

Figure 3: Input data organization for structural anomaly detection approach.

position in time. These two submatrices are used to construct and adjust the SAE/T^2 model through an iterative procedure, described in the following steps:

1. Firstly, the training data are randomized, as usual in algorithms based on ANN theory. This shuffling has the objective of reducing data variance, guaranteeing a greater generalization power for the artificial intelligence model. It is important to emphasize that the randomization is herein performed only on data used to create the artificial intelligence model. After the training task, the data, or rather the SAE extracted features, must be placed in chronological order again;

2. Initial training parameters for the SAE model are defined. These parameters are number of processing layers, number of features to be extracted from time domain responses (number of neurons), optimization method, activation and error functions, maximum number of training iterations (epochs), sparsity proportion ρ and the coefficients β and

λ, related to the sparsity and weights regularization terms of the cost function, respectively. The parameters ρ, β, and λ are related to the sparse penalty function Γ (defined in section 2.1) and assist in the determination of the best solution by the SAE (see e.g. [15]);

3. By using the training data, the SAE model is generated. In the proposed approach, the SAE model is applied to transform the structural signals into a few representative characteristics;

4. The m extracted SAE features are reorganized in chronological sequence (as mentioned in step 1) and used to calculate the T^2-statistic points and the UCL, as shown in Figure 4;

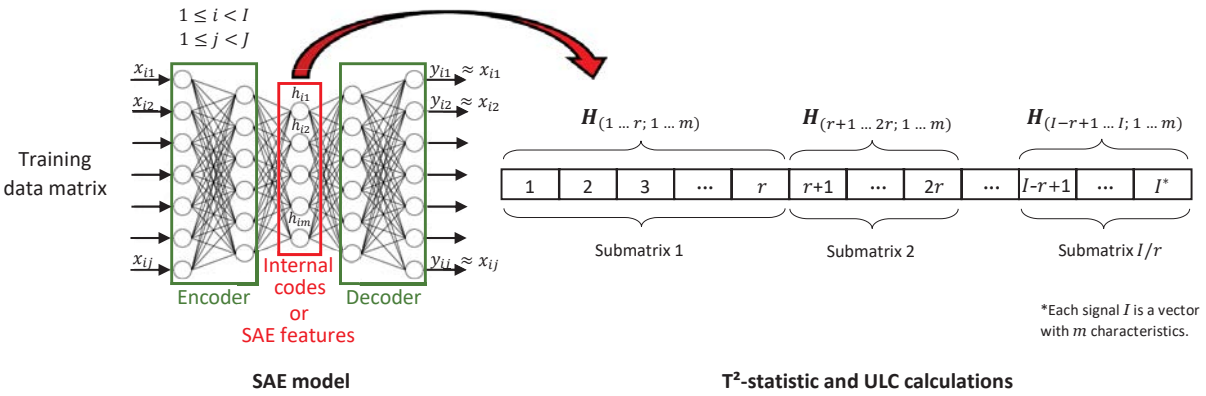

Figure 4: Graphical representation of the T^2-statistic calculation procedure.

5. In order to evaluate the training performance, the SAE/T^2 model is fed with testing data. Since the SAE features are also derived from time measurements collected when the structural system is assumed to be under normal conditions, it is expected that the corresponding T^2-statistic points are below the UCL value. If this statement is not verified, the SAE training parameters are readjusted (empirically), and a new model is created by returning to step 1.

The reference model definition is complete when the SAE/T^2 model developed with the training data is able to correctly represent the current structural behavior by using the testing data. It means that the steps above shall be repeated until all or practically all reference data produce T^2-statistic values bellow the UCL.

Finally, once the SAE/T^2 reference model is properly established, newly acquired data may be classified as being from the normal or abnormal structural condition. SAE features and their T^2-statistics are calculated from monitoring data and plotted in the control chart for comparing the reference structural responses with the newly collected ones. The entire anomaly-detection approach was developed using toolboxes and built-in functions available in Matlab® R2017a.

4 APPLICATION I: Z24 BRIDGE

The Z24 bridge was a highway overpass located at Canton Bern near Solothurn, in Switzerland, built in the early 1960s to connect Koppigen and Utzenstorf. This post-tensioned structure was 58m long composed of three continuous spans with 14m, 30m and 14m, supported on four

piers, as it can be seen in Figure 5. Due to the construction project of a new railway line underneath the highway, the bridge had to be demolished. Therefore, before the structure was completely knocked down, it was instrumented and gradually damaged [11].

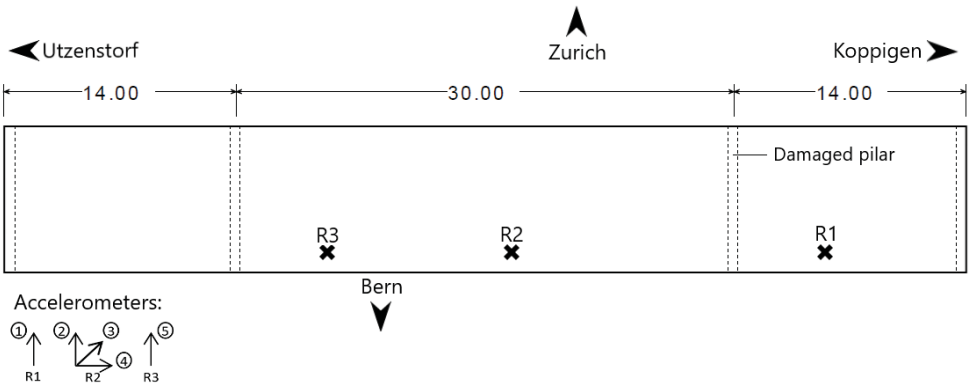

Figure 5: The Z24 bridge - Top view and experimental setup.

The present study evaluates the proposed SHM approach through dynamic signals of forced vibration tests conducted within two structural conditions: undamaged and damaged (settlement of pier - 40mm). Two vertical shakers were used to generate a flat force spectrum excitation with 3-30Hz bandwidth. In each damage scenario, nine dynamic tests were performed considering five accelerometers installed at three measurement points, R1, R2 and R3, as described in Figure 5. Vibration responses have 65535 data points, acquired at a frequency sampling of 100Hz for approximately 11 minutes. The structure's natural frequencies and the temperature variation - before and after the damage - are given in Table 1 for information purposes. The evolution of the eigenfrequencies, as well as the structural modes (see Figure 6), are derived from data of ambient vibration tests by the stochastic subspace identification method [11].

Structural condition	**Temperature**	**1st natural frequency**	**2nd natural frequency**	**3rd natural frequency**	**4th natural frequency**	**5th natural frequency**
Undamaged	17^oC	3.92Hz	5.12Hz	9.93Hz	10.52Hz	12.69Hz
Damaged	29^oC	3.86Hz	4.93Hz	9.74Hz	10.25Hz	12.48Hz

Table 1: Variation of the Z24 eigenfrequencies (values extracted from the work of De Roeck *et al.* (2000) [11]).

For this application, each accelerometer measurement is rearranged into 10-second signals, providing an input matrix [1070×1000]: 1070 dynamic time histories (65 signals per accelerometer × 9 dynamic tests × 2 structural conditions = 1070) composed of 1000 data points (100Hz × 10s = 1000). Henceforth, maintaining its chronological order, the input matrix is subdivided as follows:

- Reference data (undamaged state):

  Training data → matrix [450×1000]

  Testing data → matrix [135×1000]

- Monitoring data (damaged state) → matrix [585×1000]

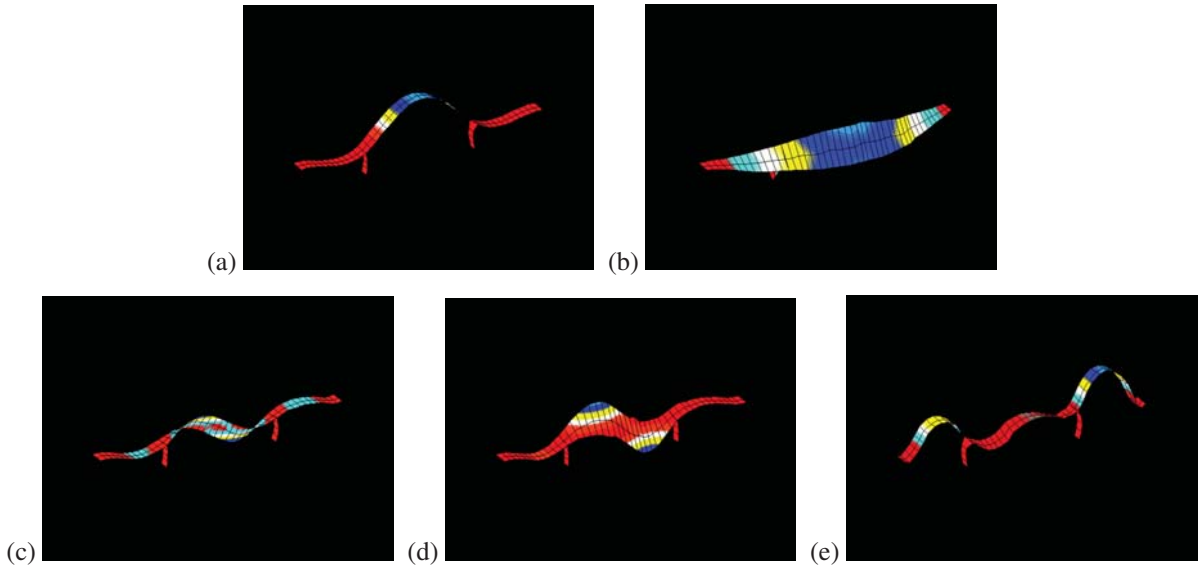

Figure 6: Reference mode shapes of the Z24 bridge - undamaged condition (draws extracted from the work of De Roeck *et al.* (2000) [11]). (a) 1st mode - symmetrical bending mode. (b) 2nd mode - transversal mode. (c) 3rd mode - combined torsional/antisymmetrical bending mode. (d) 4th mode - combined torsional/antisymmetrical bending mode. (e) 5th mode - symmetrical bending mode.

The anomaly detection approach is investigated for each accelerometer channel separately. For all analyses, the achieved SAE model was implemented employing one encoder and decoder layer constituted by 100 neurons (vector $\mathbf{h}$ with 100 components), which reduces the dimensionality of the problem from 1000 data points to 100 features. The other parameters were set to: the sparsity proportion (ρ) $= 0.050$; the sparsity regularization (β) $= 4.000$; the weight regularization (λ) $= 0.001$; the training function = Scaled Conjugate Gradient (SCG) optimization method [16] with gradient maximum value of 1.00×10^{-6}; the encoder and decoder activation functions = logarithmic sigmoid and linear function, respectively; the error metric = mean square; and the maximum number of training epochs $= 1000$. The Hotelling's T^2-statistic was calculated using data subgroups composed of 15 observations ($r = 15$) with the 100 SAE characteristics ($m = 100$). The UCL was estimated considering 30 subgroups of data ($s = 30 = 450$ training examples / 15 observations).

4.1 Results

The results of the proposed approach for the Z24 bridge are shown from Figure 7 to Figure 11. In total, 78 data subgroups were evaluated for each accelerometer channel, considering training (30 subgroups - blue points), testing (9 subgroups - green points), and monitoring data (39 subgroups - red points). In addition to the control chart plotted for one SAE/T^2 model, another control chart was also constructed representing the T^2-statistic for 30 different SAE models. In this case, the UCL is calculated considering the UCL's mean from the 30 models. This practice of examining the performance of various models is usual in ANN-based algorithms. It aims to identify that a specific data ordering (possible correlated samples) is not influencing the model performance.

By analyzing the results, a good performance was achieved for dynamic responses from accelerometers 1 (Figure 7) and 5 (Figure 11). In both cases, during the training and testing periods (undamaged condition), most T^2-statistic values are below the limit line (a small number of false alarms). In the monitoring period (damaged condition), the T^2-statistic abruptly

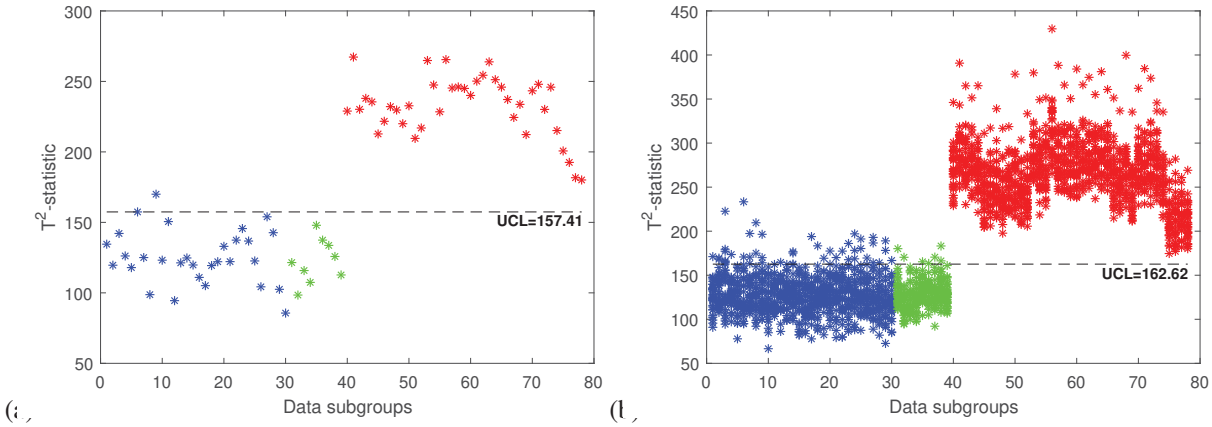

Figure 7: Anomaly detection approach - Output for the accelerometer 1. (a) Control chart for one SAE/T^2 model. (b) Control for 30 SAE/T^2 models.

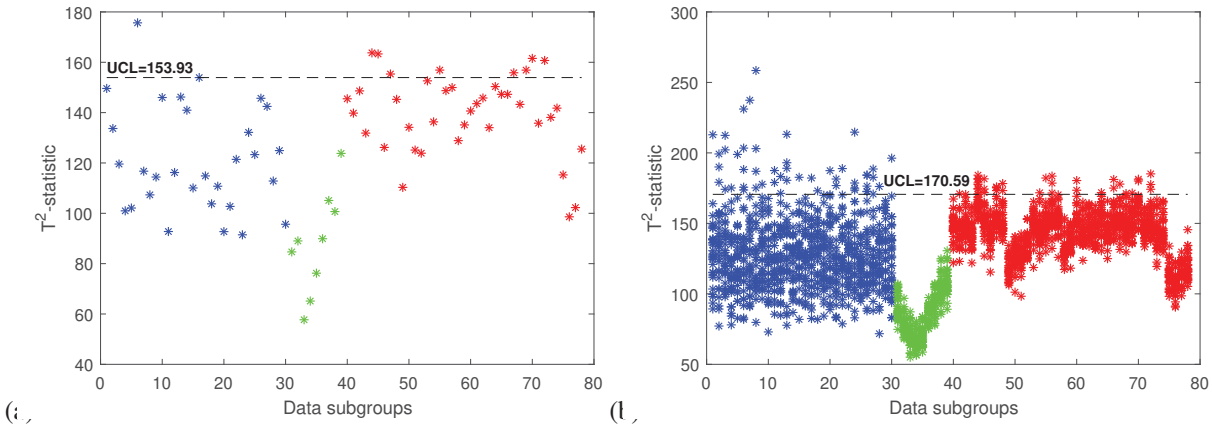

Figure 8: Anomaly detection approach - Output for the accelerometer 2. (a) Control chart for one SAE/T^2 model. (b) Control for 30 SAE/T^2 models.

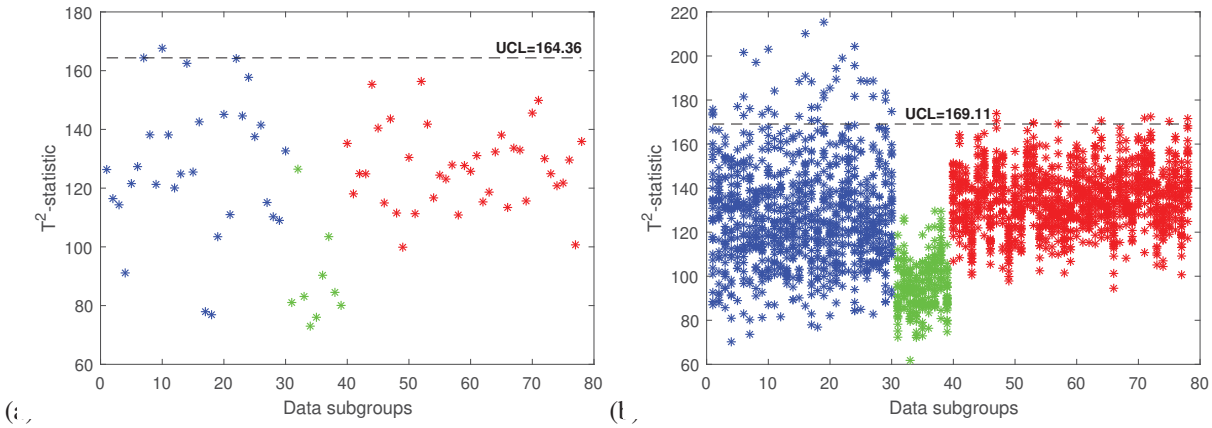

Figure 9: Anomaly detection approach - Output for the accelerometer 3. (a) Control chart for one SAE/T^2 model. (b) Control for 30 SAE/T^2 models.

exceeds the UCL value, laying outside of the in-control region and correctly indicating the presence of the structural anomaly. These outcomes may be attributed to the relation between the position of sensors and the structure's mode shapes. In general, higher natural frequencies are more affected in absolute terms by damage, as seen in Table 1. For this reason, since ac-

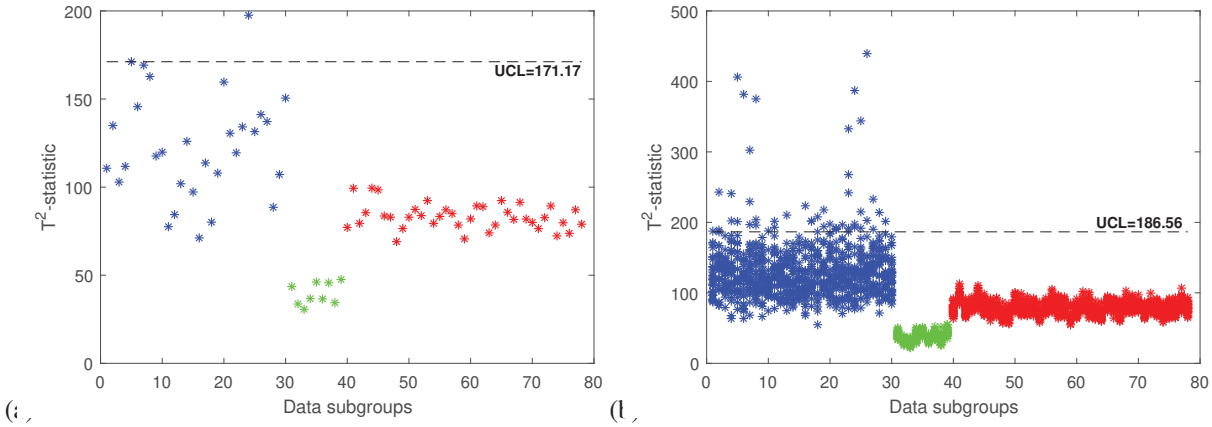

Figure 10: Anomaly detection approach - Output for the accelerometer 4. (a) Control chart for one SAE/T^2 model. (b) Control for 30 SAE/T^2 models.

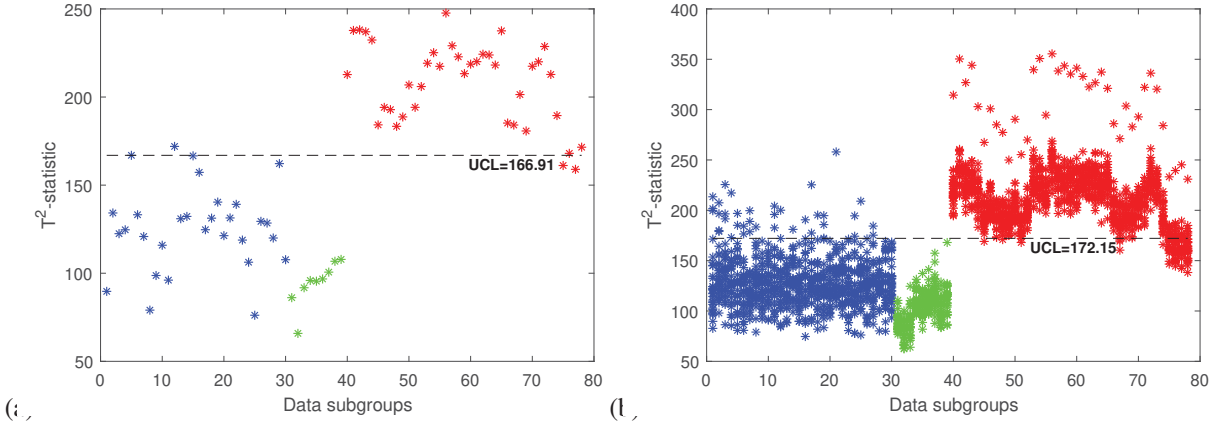

Figure 11: Anomaly detection approach - Output for the accelerometer 5. (a) Control chart for one SAE/T^2 model. (b) Control for 30 SAE/T^2 models.

celerometers 1 and 5 are in positions where the amplitudes related to higher magnitude modes are more significant (absolute difference of 0.27Hz for the 4th frequency and of 0.21Hz for the 5th frequency), they may have had better performance.

The same idea can be used to justify the T^2-statistic of data collected by the accelerometer 2. Even though this channel is more affected by the first vibration mode, due to its location at the midspan, the absolute difference between the natural frequencies is small (0.06Hz), maybe not sufficient for the SAE/T^2 model detects the damage occurrence. Regarding the sensors 3 and 4, they were positioned to capture transversal and longitudinal movements, respectively. Therefore, since the shakers generated components predominantly in the vertical direction and, the structure was considerably rigid on the longitudinal direction, it was expected that the control charts related to these measurement positions would have inconclusive results.

The Mean Square Error (MSE) between original and reconstructed dynamic signals for the 30 SAE models are exhibited in Table 2. It should be noted that the MSE values of training data are smaller than the MSE values of testing and monitoring data, as expected, since the first group of data was used to train the SAE, and the second and third ones were unknown by the created models. Figure 12 displays an example of the SAE reconstructed response in comparison with its respective original signal. Instead of perfectly reconstructs signals, the idea behind the SAE consists of modeling key features of data that are sensitive to structural novelties. Based on

the assumption that lower MSEs are evidence of better signal reconstruction, the slight upward trend in the T^2-statistic verified for testing data of accelerometer 1 may be associated with these values. Table 2 reveals that the responses related to accelerometer 1 have a reconstruction error almost twice as large as the error found for the responses of accelerometer 5, the other channel with good results, where this trend does not appear.

Accelerometer	**1**	**2**	**3**	**4**	**5**
Training data	0.0129	0.0074	0.0057	0.0021	0.0076
Testing and monitoring data	0.0222	0.0120	0.0092	0.0026	0.0138

Table 2: MSE values between original structural responses and corresponding reconstructed signals for the 30 SAE models (units: m^2/s^4).

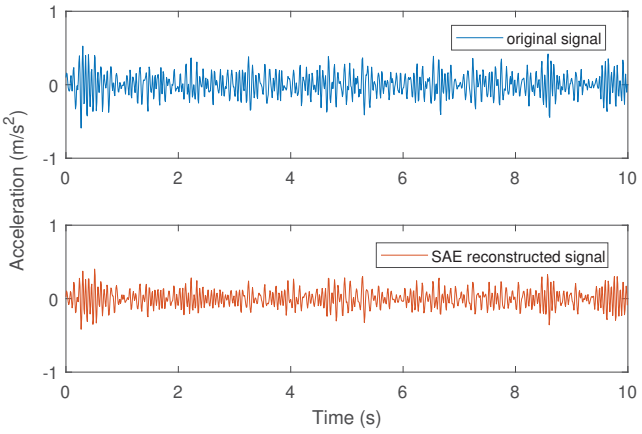

Figure 12: An original response of the Z24 bridge and its respective signal reconstructed by SAE.

5 CONCLUSIONS

The paper presented a structural anomaly detection approach based on Sparse Auto-Encoder and Shewhart T control chart. Features extracted by SAE models, directly from time-domain accelerations, were passed along as input variables of the control chart to detect the onset of abnormal behavior in structures. The developed method was exemplified using experimental data from dynamic tests performed on the Z24 bridge.

According to the obtained control charts, the T^2-statistic calculated with the SAE extracted characteristics were efficient in detecting the two different structural states of the Z24 bridge. The results are in agreement with the respective structural scenarios since the damage imposed on the bridge was clearly identified. Nevertheless, more investigation is required to validate the proposed anomaly detection strategy. In particular, the next steps in this work include analyzing the temperature influence on SAE characteristics and applying the methodology in other structures.

Acknowledgements

The authors would like to thank UFJF (Universidade Federal de Juiz de Fora - Programa de Pós-Graduação em Modelagem Computacional), CAPES (Coordenação de Aperfeiçoamento de Pessoal de Nível Superior), CNPq (Conselho Nacional de Desenvolvimento Científico e Tecnológico), FAPEMIG (Fundação de Amparo à Pesquisa do Estado de Minas Gerais) and Politecnico di Milano.

REFERENCES

[1] S. W. Doebling, C. R. Farrar, M. B. Prime, A summary review of vibration-based damage identification methods, *Shock and Vibration Digest*, 30(2), 91–105, 1998.

[2] A. Alvandi, C. Cremona, Assessment of vibration-based damage identification techniques, *Journal of Sound and Vibration*, 292(1-2), 179–202, 2006.

[3] G. Marrongelli, C. Gentile, A. Saisi, Anomaly detection based on automated OMA and mode shape changes: application on a historic arch bridge, In *Proceedings of ARCH 2019, 9th International Conference on Arch Bridges*, 447–455, Springer, Cham, 2019.

[4] H. Salehi, R. Burgueno. Emerging artificial intelligence methods in structural engineering. *Engineering Structures*, 171, 170–189, 2018.

[5] R. P. Finotti, A. A. Cury, F. S. Barbosa, An SHM approach using machine learning and statistical indicators extracted from raw dynamic measurements, *Latin American Journal of Solids and Structures*, 16(2), e165, 2019.

[6] R. Almeida Cardoso, A. Cury, F. Barbosa, C. Gentile, Unsupervised real-time SHM technique based on novelty indexes, *Structural Control and Health Monitoring*, 26, e2364, 2019.

[7] I. Goodfellow, Y. Bengio, A. Courville. Deep Learning. MIT press, 2016.

[8] C. S. N. Pathirage, J. Li, L. Li, H. Hao, W. Liu, R. Wang. Development and application of a deep learning–based sparse autoencoder framework for structural damage identification. *Structural Health Monitoring*, 18(1), 103–122, 2019.

[9] Y. Bao, Z. Tang, H. Li, Y. Zhang, Computer vision and deep learning–based data anomaly detection method for structural health monitoring, *Structural Health Monitoring*, 18(2), 401–421, 2019.

[10] D. Montgomery, *Introduction to Statistical Quality Control*, John Wiley & Sons, 2009.

[11] G. De Roeck, B. Peeters, J. Maeck, Dynamic monitoring of civil engineering structures, *Computational Methods for Shell and Spatial Structures*, 2000.

[12] J. C. Principe, N. R. Euliano, W. C. Lefebvre, *Neural and adaptive systems: fundamentals through simulations*, John Wiley & Sons, 2000.

[13] P. Baldi, K. Hornik, Neural networks and principal component analysis: learning from examples without local minima, *Neural networks*, 2(1), 53–58, 1989.

[14] Q. Meng, D. Catchpoole, D. Skillicom, P. J. Kennedy, Relational autoencoder for feature extraction, In *2017 International Joint Conference on Neural Networks (IJCNN)*, 364–371, IEEE, 2017.

[15] A. Ng, Sparse autoencoder, *CS294A Lecture Notes*, 72, 1–19, 2011.

[16] M. F. Mϕller, A scaled conjugate gradient algorithm for fast supervised learning, *Neural Networks*, 6(4), 525–533, 1993.

EURODYN 2020
XI International Conference on Structural Dynamics
M. Papadrakakis, M. Fragiadakis, C. Papadimitriou (eds.)
Athens, Greece, 23–26 November 2020

DESIGN OF A MONITORING SYSTEM FOR A LONG-SPAN SUSPENSION BRIDGE: OPTIMAL SENSOR PLACEMENT

Øyvind W. Petersen[1], **Ole Øiseth**[1], **and Gunnstein T. Frøseth**[1]

[1] Norwegian University of Science and Technology
7491 Trondheim
e-mail: {oyvind.w.petersen,o.oiseth,gunnstein.t.froseth}@ntnu.no

Keywords: Optimal sensor placement, structural monitoring, suspension bridge.

Abstract. *The design of systems for structural health monitoring is an exercise that requires careful planning of optimal sensor locations. The number of possible locations usually outnumbers the number of available sensors, which means that solving the problem of optimal sensor placement (OSP) is necessary for a cost-effective network. This paper addresses the design of OSP for a new monitoring system on a long-span suspension bridge. The foremost interest is the response effect of wind loading on the bridge. A finite element model of the bridge is created based on blueprint drawings, and the system model consists of 18 target modes (with frequencies in the range* $[0.05, 0.6]$ *Hz). 22 triaxial force-balance MEMS accelerometers are planned to be deployed. In the design, the sensors are designated into local groups consisting of two or four accelerometers, which are wired to the same data acquisition unit. Two optimization approaches are tried: backward sequential sensor placement and genetic algorithms. The objective metric is the maximization of the determinant of the Fisher information matrix. Six different types of models for the prediction error covariance are tested; one with no correlation and five with varying degrees of error correlation, which is dictated by the sensor distance and a characteristic correlation length. The resulting configurations are compared and discussed.*

1 INTRODUCTION

Structural health monitoring (SHM) of bridges and other civil structures has become a popular method to study the response behavior of structures during the service life. The design of such systems is often subject to cost constraints; thus, it is desired to maximize the information value of the data acquired from the limited available sensors. The problem of optimal sensor placement (OSP) in SHM have been studied widely in the literature, for instance in the in the light of damage detection [1, 2], parameter identification [3, 4], and load reconstruction [5, 6].

The distribution of a small number of sensors in a high number of candidate locations is an OSP problem that cannot be solved by exhaustive searches. Instead, various of optimization methods have been proposed, for instance, backward and forward sequential sensor placement algorithms (FSSP/BSSP) [4], relaxation sequential algorithms [7], genetic algorithms [8], and particle swarm optimization [9]. A review of different methods can be found in [10].

This contribution presents the OSP for a recently opened suspension bridge in the north part of Norway, the Hålogaland bridge. This is a long-span bridge were the wind-induced response is of great importance in both structural reliability and serviceability assessments; thus a SHM system focusing on wind engineering is planned to be deployed to the bridge. The presented OSP design considers the placement of 22 accelerometers. Besides these sensors, it is also planned to install strain gauges, temperature sensors, and several anemometers for wind measurements.

2 OPTIMAL SENSOR PLACEMENT THEORY

This section gives a brief overview of the theory applied in the OSP design. We consider a linear model of the structural vibrations:

$$\mathbf{M}_0\ddot{\mathbf{r}}(t) + \mathbf{C}_0\dot{\mathbf{r}}(t) + \mathbf{K}_0\mathbf{r}(t) = \mathbf{f}(t) \tag{1}$$

Here, the subscript 0 denotes still-air structural properties. This system is modally truncated ($\mathbf{r}(t) = \boldsymbol{\Phi}\mathbf{z}(t)$) using a set of N_m modes:

$$\tilde{\mathbf{M}}\ddot{\mathbf{z}}(t) + \tilde{\mathbf{C}}\dot{\mathbf{z}}(t) + \tilde{\mathbf{K}}\mathbf{z}(t) = \boldsymbol{\Phi}^{\mathrm{T}}\mathbf{f}(t) \tag{2}$$

In this case, the alterations from aeroelastic effects on the mode shapes are not considered, i.e. the modal analysis is performed using still-air vibration modes. We expect that this is reasonable for non-extreme wind conditions. The following linear output model is assumed:

$$\mathbf{y}(t) = \mathbf{S}\boldsymbol{\Phi}\mathbf{z}(t) + \mathbf{S}\boldsymbol{\epsilon}(t) \tag{3}$$

where the binary matrix $\mathbf{S}$ selects the output DOFs of the sensors out of all possible DOFs. It is common to assume that the prediction error $\boldsymbol{\epsilon}(t)$ is a Gaussian stochastic process. This error can be thought to have two independent sources (model errors and measurement noise):

$$\boldsymbol{\epsilon}(t) = \boldsymbol{\epsilon}_{mod}(t) + \boldsymbol{\epsilon}_{meas}(t) \tag{4}$$

These components are associated with their respective covariance matrices:

$$\boldsymbol{\Sigma} = E[\boldsymbol{\epsilon}(t)\boldsymbol{\epsilon}(t)^{\mathrm{T}}] = \boldsymbol{\Sigma}_{mod} + \boldsymbol{\Sigma}_{meas} \tag{5}$$

For the case study presented in Section 3, we expect that errors from the model generally are greater than the measurement noise in Eq. 3-4. This is partly motivated by the fact that currently

available high-quality force-balance MEMS accelerometers have very good noise performance. Previous studies of suspension bridges also indicate that errors from finite element (FE) models are prevailing [11].

When all sensors are of equal type, it is sensible to assume that the latent measurement noise has equal magnitude and is uncorrelated among all outputs, i.e. $\mathbf{\Sigma}_{meas} \propto \mathbf{I}$. Characterizing the model errors, however, is generally more complicated since these usually are propagated from errors on the different physical parameters of the model (stiffness, mass, geometry, etc.). The authors of [12] proposed a correlation structure on the following form:

$$\Sigma_{ij} = \exp(-\delta_{ij}/\bar{\delta}) \tag{6}$$

which penalizes the proximity of two sensors: δ_{ij} is the distance between model DOF i and j, and $\bar{\delta}$ is a characteristic correlation length. Although this model is not physically motivated, it can help avoid problems with sensors clustering close to each other, which can lead to redundant information. An expansion of this model was proposed in [13]:

$$\Sigma_{ij} = \frac{\mathbf{\Psi}_i \mathbf{\Psi}_j^{\mathrm{T}}}{N_m} \exp(-\delta_{ij}/\bar{\delta}) \tag{7}$$

where $\mathbf{\Psi}_i$ and $\mathbf{\Psi}_j$ are scaled rows of the mode shape matrix:

$$\begin{bmatrix} \mathbf{\Psi}_i \\ \mathbf{\Psi}_j \end{bmatrix} = \begin{bmatrix} |\phi_{i\,1}|/\max(|\phi_{i\,1}|,\ |\phi_{j\,1}|) & \dots & |\phi_{i\,N_m}|/\max(|\phi_{i\,N_m}|,\ |\phi_{j\,N_m}|) \\ |\phi_{j\,1}|/\max(|\phi_{i\,1}|,\ |\phi_{j\,1}|) & \dots & |\phi_{j\,N_m}|/\max(|\phi_{i\,N_m}|,\ |\phi_{j\,N_m}|) \end{bmatrix} \tag{8}$$

In essence, the fraction in front of the exponential weighs the similarity in the modal values at model DOF i and j, and assumes a value between zero and one. For instance, if the majority of modes are in orthogonal directions, as often is the case with regular structures that has lateral and vertical bending modes, this weight assigns a low correlation for two DOFs that are orthogonal.

A more advanced idea was proposed in [14], considering the uncertainties in the stiffness matrix $\mathbf{K}$ as the source of the prediction errors. In that case, a first-order perturbation of the mode shapes with respect to uncertain stiffness parameters enters the calculations. A similar approach was proposed in [15], where the robustness of optimal sensor placement under parametric uncertainty was studied. Intervals for parameters were studied in [16].

The present study uses a quite comprehensive FE model of a bridge where the stiffness (or mass) matrix and its derivative are not readily available in a suitable numerical form unless multiple perturbation analysis are performed. For this reason, this contribution mainly uses Eq. 7 as the basis for the error covariance matrix.

Formally, the OSP problem can be cast in a Bayesian framework, see e.g. [3, 4, 8, 17] for details on the theoretical background. In this contribution, we limit the discussion on this topic to defining the Fisher information matrix (FIM) as follows:

$$\mathbf{Q}(\mathbf{S}, \mathbf{\Sigma}) = (\mathbf{S\Phi})(\mathbf{S\Sigma S}^{\mathrm{T}})^{-1}(\mathbf{S\Phi})^{\mathrm{T}} \tag{9}$$

It can be shown that maximizing the determinant of the FIM (or equivalently, minimizing the information entropy) leads to the least uncertainty in the estimate of the modal coordinate vector [12]. Thus, among all possible sensor configurations, the optimal solution is selected as the one that minimizes the following normalized objective function [4]:

$$\mathrm{Obj}(\mathbf{S}, \mathbf{\Sigma}) = \sqrt{\frac{\det(\mathbf{Q}(\mathbf{S}_{ref}, \mathbf{\Sigma}))}{\det(\mathbf{Q}(\mathbf{S}, \mathbf{\Sigma}))}} \tag{10}$$

Figure 1: The Hålogaland bridge (Rendering by Statens Vegvesen).

which is also referred to information entropy index (IEI). Here, $\mathbf{S}_{ref}$ represents a reference configuration where all sensor candidates are included.

3 APPLICATION CASE

3.1 The Hålogaland Bridge

The structure under consideration is the Hålogaland Bridge (Fig. 1), which opened for traffic in March 2019. This suspension bridge has a main span of 1145 m in addition to two side-spans of 240 m and 149 m. The towers are 180 m tall, and the main cable is anchored in bedrock on both sides of the fjord. A cable-supported bridge was chosen for this location due to the high water depths (ca. 340 m) that prohibits short-span bridges with intermediate supports. The main span has a single-box steel girder, which is slenderly designed with two driving lanes and one pedestrian lane. The long span inevitably leads to low natural frequencies, meaning that the structure will be susceptible to excitation from natural wind.

A FE model of the bridge (Fig. 2) is created in the modeling software ABAQUS based on the geometry from technical design drawings. Beam elements are for all structural components. The side-span access roads are discarded from this model as their influence on the dynamic behavior of the main span is deemed negligible.

Typical nominal values are assigned for the structural properties (mass, stiffness, bearing behavior, boundary conditions, etc.). Although there inevitably are uncertainties related to these quantities, the assigned parameter values could later be calibrated in through model updating procedures.

The linearized vibration modes are calculated for the finished state where the structure is in equilibrium under dead loads. The set of selected target modes is chosen as the N_m=18 lowermost vibration modes from the FE model, with natural frequencies ranging from 0.05 Hz and 0.6 Hz. Capturing a higher number of modes would ultimately require a higher number of accelerometers.

As seen from Fig. 3, the different modes can roughly be classified into five types: $i)$ lateral and vertical bending modes, which typically have a $\sin(n\pi x/L)$-type deflection of the bridge deck; $ii)$ torsion modes; $iii)$ cable modes, which mostly have deflects the main cable and hangers; $iv)$ tower modes; $v)$ other combination modes which to some extent excite both the bridge deck and cables. All the mode shapes are normalized so that the maximum amplitude is equal to unity.

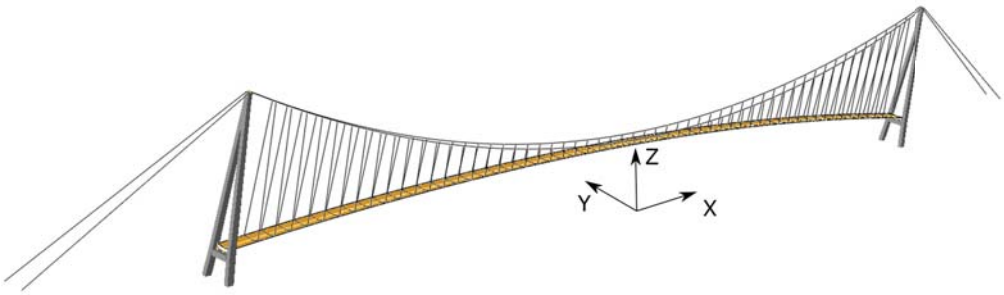

Figure 2: Finite element model of the bridge.

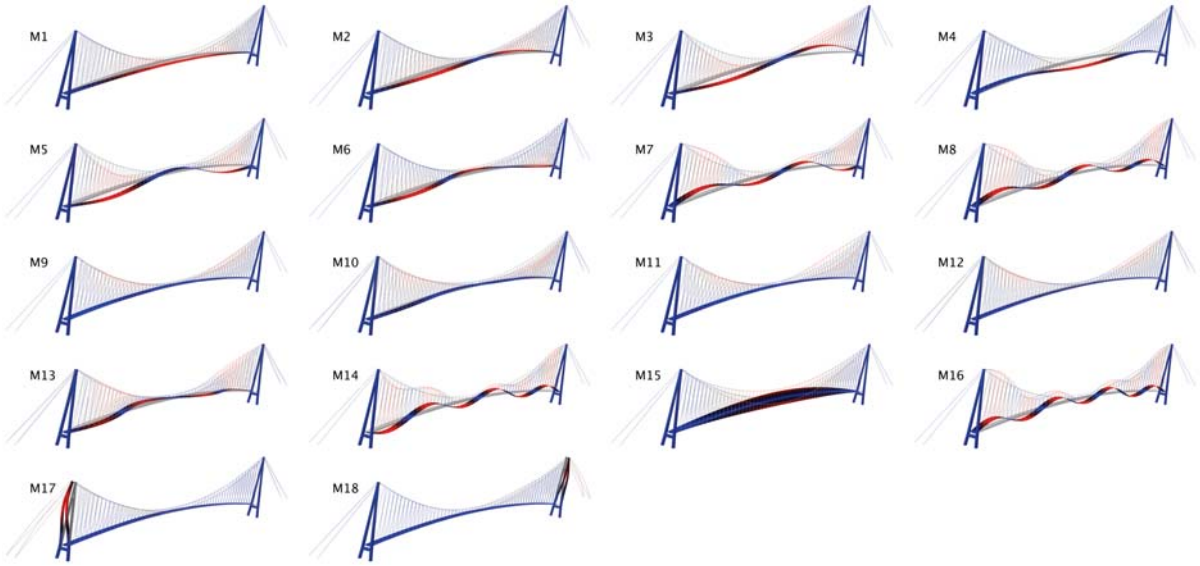

Figure 3: Vibration modes 1-18 from the FE model.

3.2 Strategy of optimal sensor placement

In the OSP, the following strategical points are adopted:

- The sensors are designated into groups of two or four accelerometers in a slice of the box girder, see Fig. 4. The optimization considers the addition or removal of a group of sensors, not individual sensors. This design constraint is adopted for proximity reasons; the sensors in a group must be wired to the same local data acquisition unit (DAU).

- Some output channels are discarded, mainly because the modal deflection is insignificant. Although triaxial accelerometers are used in reality, only the lateral (y) and vertical (z) directions are considered in the for sensors in the main span. For the sensors in the towers, the longitudinal (x) and the lateral (y) directions are included.

- For engineering reasons, some sensors are *a priori* distributed on the bridge. Two accelerometers are chosen to be placed in the mid-span of the bridge since it is desired to have statistics from this location. In addition, one accelerometer is placed in each of the towers.

Two OSP search methods are used in the design: a backward sequential sensor placement (BSSP) algorithm and a genetic algorithm (GA). The BSSP is initiated with sensors in all candi-

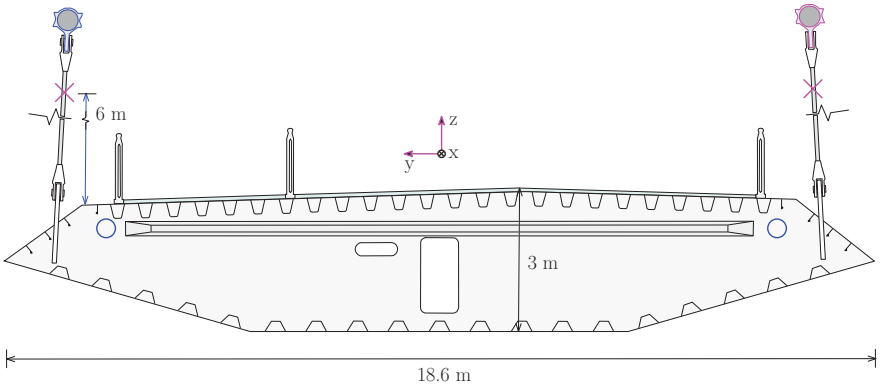

Figure 4: Mounting locations of accelerometers in the box girder (blue circle) and on the hangers (pink cross).

date locations. Then one sensor group is iteratively removed by simply by discarding the group that contributes the least to the objective function in a perturbation analysis. The iterations are stopped when the number of remaining sensors equals the set target of 22 accelerometers. BSSP algorithms are heuristic, and convergence to the optimal configuration (among all possible) is not guaranteed. Therefore, the GA is used to improve the BSSP search, and is given the following rules:

- The population is set to 30 individuals, each corresponding to a sensor configuration. The initial population is chosen to consist of both the obtained BSSP solution and other randomly picked configurations.
- Every iteration, 5 children are generated from 2 parents selected randomly from the population. The sensor locations of a child are a random mix of its parents' locations, with a probability weight of 0.8 and 0.2 assigned to the fittest and least fit parent.
- A child can have random mutations as follows: $i)$ a sensor group can move one or two increments (20 or 40 m) to the left or right with a probability of 0.1; $ii)$ all sensor groups can simultaneously be mirrored about the mid-point of the bridge with a probability of 0.1.
- The next generation is selected as the 30 best configurations among the 35 candidates (30 individuals + 5 children) with respect to the fitness (i.e. the objective function in Eq. 10).
- The iterations are continued for a maximum of 500 generations or until the population is fully homogeneous.

3.3 Optimization resulting

In total, six different optimization cases is performed. The first targets purely measurement errors, where the case of no correlation ($\boldsymbol{\Sigma} = \mathbf{I}$) is tested. The next five cases focuses on model errors using several versions of the covariance model $\boldsymbol{\Sigma}(\bar{\delta})$ from Eq. 7 with $\bar{\delta} = \{10, 100, 250, 500, 1000\}$ m.

For each of these six cases, the BSSP is run first and is next followed by the GA. Compared to the BSSP, the GA is generally found to improve the objective function by 10-20% and only minorly alter the sensor configuration. The resulting sensor locations are shown in Fig. 5. All configurations have 22 accelerometers, and also require 10 local DAUs (8 in the box girder and

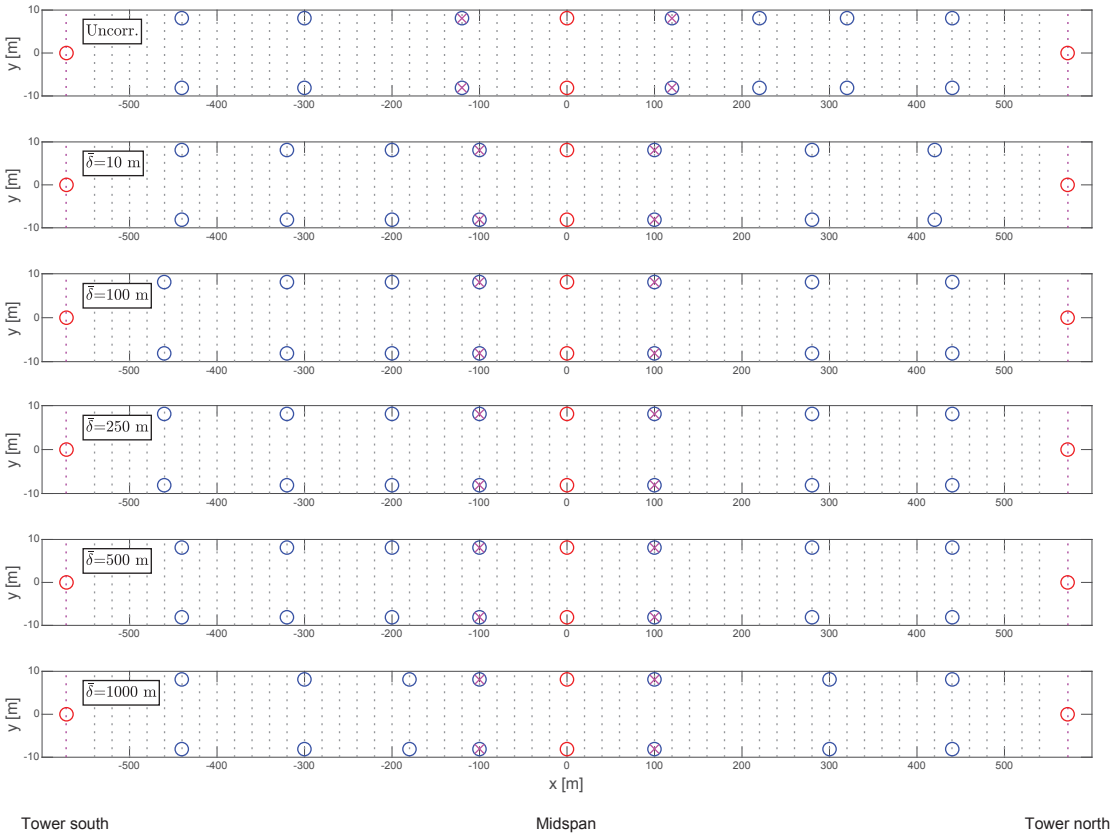

Figure 5: Optimal sensor locations for different covariance models. The black dotted lines indicate the coordinates of the 55 hangers. Blue circles: accelerometer in box girder; pink cross: accelerometer on hanger cable; red circles: apriori chosen locations in the midspan and the towers.

2 in the towers). Notably, all cases (arguably except for the uncorrelated case) display a similar pattern of sensor distribution along the bridge span. Although not shown here, this is only occurring to a lesser extent when instead a lower number of target modes is set ($N_m = 3$ or $N_m = 6$). A plausible explanation for this is that the full target mode selection ($N_m = 18$) contains modes with wavelengths both in the order of 100 and 1000 m, and so a single correlation length variable $\bar{\delta}$ does not highly influence both the higher and lower modes simultaneously.

Since no specific value for $\bar{\delta}$ could be said to be "correct", one can perform a simple robustness check by considering how well the optimal solution from case i performs when evaluated with respect to the objective function from case j. Fig. 6 shows values of the comparative expression:

$$\text{Ratio} = \frac{\text{Obj}(\mathbf{S_i}, \mathbf{\Sigma_j})}{\text{Obj}(\mathbf{S_j}, \mathbf{\Sigma_j})} \tag{11}$$

In Fig. 6, the values on the diagonal ($i = j$) are by definition equal to one, and the others ($i \neq j$) indicate a "cross-performance ratio" larger than one. Not surprisingly, most values in Fig. 6 are close to one. For instance, it could be argued that the optimal solution $\mathbf{S}(\bar{\delta} = 500)$ is attractive since it performs well for all covariance models (1.53 for the uncorrelated case and ≤ 1.05 for the other cases). On the other hand, the sensor configuration for the uncorrelated case does not perform well when it is evaluated using the correlated covariance matrices (ratios ≥ 5).

Besides the FIM and the IEI, the condition number of the matrix $\mathbf{S\Phi}$ has an interest in

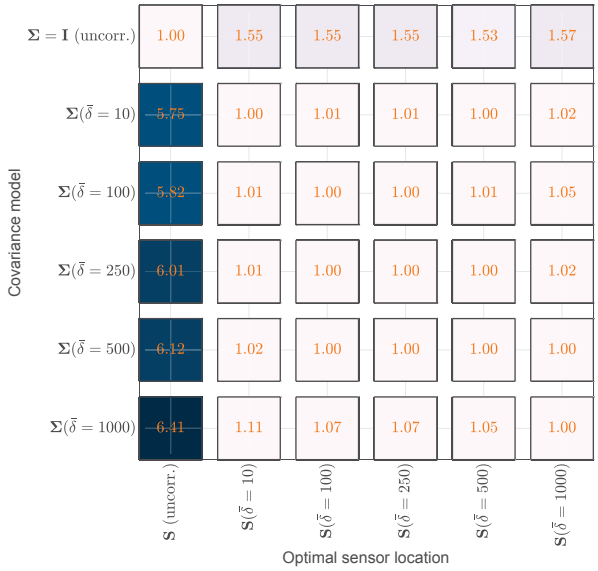

Figure 6: Normalized evaluation of objective functions for different optimal sensor locations (Eq. 11).

applications such as force identification from acceleration data, which is one of the aspirations of this SHM project. Specifically, the matrix rank of $\mathbf{S\Phi}$ plays an important role [5], since this matrix designates the direct influence from the modal loads on acceleration measurements. Generally, it is desired that this matrix has a low condition number, as high condition numbers could lead to numerical rank loss or ill-conditioned pseudo-inversion. Here, it is found that $\text{cond}(\mathbf{S\Phi}) \approx 5.5 \pm 0.5$ for all six cases, which is low and thus very acceptable.

Also the modal assurance criterion (MAC) is a common metric in optimal sensor placement studies [13, 16, 18, 19]. The MAC between mode $\boldsymbol{\phi}_i$ and $\boldsymbol{\phi}_j$ is defined as follows:

$$\text{MAC}_{ij} = \frac{|(\mathbf{S}\boldsymbol{\phi}_i)^{\mathrm{T}}(\mathbf{S}\boldsymbol{\phi}_j)|^2}{(\mathbf{S}\boldsymbol{\phi}_i)^{\mathrm{T}}(\mathbf{S}\boldsymbol{\phi}_i)(\mathbf{S}\boldsymbol{\phi}_j)^{\mathrm{T}}(\mathbf{S}\boldsymbol{\phi}_j)}, \quad 0 \leq \text{MAC}_{ij} \leq 1 \tag{12}$$

As this metric typically is used to distinguish a set of modes, it is desired to have MAC_{ij} close to zero when $i \neq j$. This is particularly important in system identification for structures with close natural frequencies so that that also mode shape information can be effectively utilized for mode matching with FE models. Fig. 7 shows the auto-MAC values for the optimal configuration $\mathbf{S}(\bar{\delta} = 500)$. Although the MAC is not included in the OSP objective, it is reassuring that very low off-diagonal values generally are obtained, except for the single instance $\text{MAC}_{10,13} = 0.59$.

4 SUMMARY

This paper has presented a case study of the OSP with application to the Hålogaland bridge, a long-span suspension bridge. The optimal locations for 22 triaxial accelerometers were designed by maximizing the determinant of the FIM when considering 18 target vibration modes from a FE model. The design was performed by testing several covariance models for the prediction error with different correlation lengths. In this study, it is found the optimal sensor configuration is not very sensitive to the correlation length parameter. This result could be explained by the diversity of characteristic wavelengths in the target modes. In addition, the optimal sensor configurations are found to have low condition numbers (of the mode shape

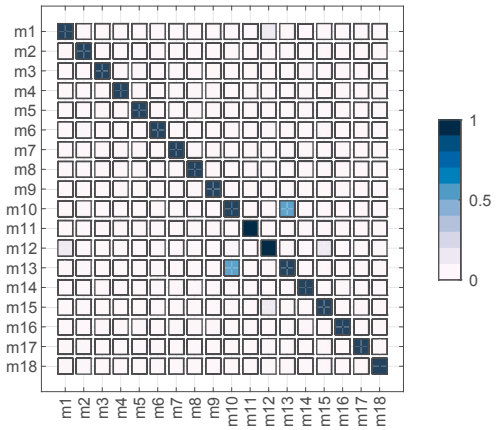

Figure 7: Auto-MAC values for the optimal configuration $\mathbf{S}(\bar{\delta} = 500)$.

matrix), and generally low values for off-diagonal elements in the MAC matrix.

REFERENCES

[1] Z. Shi, S. Law, and L. Zhang. Optimum sensor placement for structural damage detection. *Journal of Engineering Mechanics*, 126(11):1173–1179, 2000.

[2] K. Worden and A. Burrows. Optimal sensor placement for fault detection. *Engineering Structures*, 23(8):885–901, 2001.

[3] C. Papadimitriou, J. L. Beck, and S.-K. Au. Entropy-based optimal sensor location for structural model updating. *Journal of Vibration and Control*, 6(5):781–800, 2000.

[4] C. Papadimitriou. Optimal sensor placement methodology for parametric identification of structural systems. *Journal of Sound and Vibration*, 278(4-5):923–947, 2004.

[5] K. Maes, E. Lourens, K. Van Nimmen, E. Reynders, G. De Roeck, and G. Lombaert. Design of sensor networks for instantaneous inversion of modally reduced order models in structural dynamics. *Mechanical Systems and Signal Processing*, 52:628–644, 2014.

[6] C. Zhang and Y. Xu. Optimal multi-type sensor placement for response and excitation reconstruction. *Journal of Sound and Vibration*, 360:112–128, 2015.

[7] H. Yin, K. Dong, A. Pan, Z. Peng, Z. Jiang, and S. Li. Optimal sensor placement based on relaxation sequential algorithm. *Neurocomputing*, 344:28–36, 2019.

[8] L. Yao, W. A. Sethares, and D. C. Kammer. Sensor placement for on-orbit modal identification via a genetic algorithm. *AIAA journal*, 31(10):1922–1928, 1993.

[9] J. Lian, L. He, B. Ma, H. Li, and W. Peng. Optimal sensor placement for large structures using the nearest neighbour index and a hybrid swarm intelligence algorithm. *Smart Materials and Structures*, 22(9):095015, 2013.

[10] Y. Tan and L. Zhang. Computational methodologies for optimal sensor placement in structural health monitoring: A review. *Structural Health Monitoring*, page 1475921719877579, 2019.

[11] Ø. W. Petersen, O. Øiseth, and E. Lourens. Investigation of dynamic wind loads on a long-span suspension bridge identified from measured acceleration data. *Journal of Wind Engineering and Industrial Aerodynamics*, 196, 2020. doi: https://doi.org/10.1016/j.jweia.2019.104045.

[12] C. Papadimitriou and G. Lombaert. The effect of prediction error correlation on optimal sensor placement in structural dynamics. *Mechanical Systems and Signal Processing*, 28: 105–127, 2012.

[13] L. Vincenzi and L. Simonini. Influence of model errors in optimal sensor placement. *Journal of Sound and Vibration*, 389:119–133, 2017.

[14] X.-Y. Pei, T.-H. Yi, C.-X. Qu, and H.-N. Li. Conditional information entropy based sensor placement method considering separated model error and measurement noise. *Journal of Sound and Vibration*, 449:389–404, 2019.

[15] R. Castro-Triguero, S. Murugan, R. Gallego, and M. I. Friswell. Robustness of optimal sensor placement under parametric uncertainty. *Mechanical Systems and Signal Processing*, 41(1-2):268–287, 2013.

[16] C. Yang, Z. Lu, and Z. Yang. Robust optimal sensor placement for uncertain structures with interval parameters. *IEEE Sensors Journal*, 18(5):2031–2041, 2018.

[17] D. C. Kammer and M. L. Tinker. Optimal placement of triaxial accelerometers for modal vibration tests. *Mechanical Systems and Signal Processing*, 18(1):29–41, 2004.

[18] B. Li, D. Li, X. Zhao, and J. Ou. Optimal sensor placement in health monitoring of suspension bridge. *Science China Technological Sciences*, 55(7):2039–2047, 2012.

[19] T.-H. Yi, H.-N. Li, and M. Gu. Optimal sensor placement for structural health monitoring based on multiple optimization strategies. *The Structural Design of Tall and Special Buildings*, 20(7):881–900, 2011.

EURODYN 2020
XI International Conference on Structural Dynamics
M. Papadrakakis, M. Fragiadakis, C. Papadimitriou (eds.)
Athens, Greece, 23–26 November 2020

COMPARISON OF ALTERNATIVE DYNAMIC VIBRATION MITIGATION APPROACHES FOR WIND TURBINE TOWERS

K. A. Kapasakalis[1], P.O.N. Bollano[1], E. J. Sapountzakis[1], and I. A. Antoniadis[2]

[1] Institute of Structural Analysis and Antiseismic Research, School of Civil Engineering, National Technical University of Athens,
Zografou Campus, GR-157 80 Athens, Greece
kostiskapasakalis@hotmail.com, orfeabollano@hotmail.com, cvsapoun@central.ntua.gr

[2] Dynamics and Structures Laboratory, School of Mechanical Engineering, National Technical University of Athens,
Zografou Campus, GR-157 80 Athens, Greece
antogian@central.ntua.gr

Keywords: Wind turbines; Negative stiffness; Vibration absorption; KDamper; damping;

Abstract. *The application of vibration absorbers to Wind Turbine (WT) towers has the potential to significantly improve the damping of the tower and the nacelle dynamic response, increasing thus the reliability of WTs. The Tuned Mass Damper (TMD) is considered as a benchmark design option for vibration absorption in Wind Turbine towers. However, its effectiveness is limited by the requirement of large masses, in association with its installation location (top of the WT tower). For this reason, two alternative concepts are considered. First, the nacelle is released from the Wind Turbine tower (nacelle isolation concept), using a low stiffness connection. This option is based on the seismic isolation concept of structures with the use of seismic isolation bearings. Alternatively, a novel passive vibration absorption concept is implemented, based on the KDamper concept. The KDamper is essentially based on the TMD, including however an additional negative stiffness element. Instead of increasing the additional mass, the vibration absorption capability of the KDamper can be increased by increasing the value of the negative stiffness element. Thus, the KDamper always indicates better isolation properties than a TMD damper with the same additional mass. In this paper, the performance of these three vibration absorption concepts is examined for increasing the damping of Wind Turbine towers and for the improvement of their dynamic response. Although all methods present a good behavior, the proposed vibration absorption systems present a significant increase of the damping ratio with a minimal value of added mass at the top of the tower.*

1 INTRODUCTION

As wind power continues its rapid growth worldwide, wind farms have a high probability to comprise a significant portion of the total production of wind energy, and can even become a hefty contributor to the total electricity production in some countries. The high-quality wind resource and the closeness to load centers make wind energy a fascinating proposition. The Wind Turbine (WT) is supported by a tower that can experience extreme vibrations caused by both the wind turbine and the wind forces due to its geometry and great height. An accurate analysis of the structural behavior of the tower is of high importance due to its cost, which can represent roughly 20% of the total cost of the system [1]. A lot of researchers have been studying the use of structural control to help overcome the wind-induced vibrations experienced by Wind Turbine towers[2]–[5]. The passive control methods are plain and trustworthy. They do not require an external force, are easy to implement to reduce the structural vibration and are widely used in Wind Turbine technology for the improvement of their damping. They incorporate one or more devices to the main structure to absorb or transfer part of its energy.

The intention with the installation of such devices, for the control of Wind Turbine towers, is the mitigation of their dynamic response because of the fact that the vibrations caused by aerodynamic loads are longstanding and cause fatigue problems to the body of the tower and their foundation.

The installation of a resonant damper like a Tuned Mass Damper (TMD) is the damping concept that has obtained the most consideration in the literature. A Tuned Mass Damper (TMD) is a control device that consists of a mass-spring-dashpot attached to the structure, intending to reduce structural vibration response [6], [7]. The TMD concept was first applied by (Frahm, 1909 [8]). A theory for the TMD was introduced in the paper by (Ormondroyd and Den Hartog, 1928 [9]). A detailed discussion of optimal tuning and damping parameters appears in (Den Hartog, 1956 [10]). Since then, a great number of applications of various forms of TMDs have been reported. Some new examples include vibration absorption in seismic or other forms of excitation of structures (Debnath et al., 2015 [11]). TMDs are available in various physical forms, including solids, liquids, or active implementations (Younespour and Ghaffarzadeh, 2015 [12]). The Active Tuned Mass Damper (ATMD) is a hybrid device comprising of a passive TMD supplemented by an actuator parallel to the spring and damper. It is a well-known concept in structural control and has demonstrated enhanced damping performance compared to the passive TMD [13], [14]. The drawback of such designs is that their performance is directly dependent on the accuracy of the actuator's output, which over time can have alterations in its performance by false estimation of the desired function of the vibration absorption concept. Various forms of Dynamic Vibration Absorbers (DVA) have been used, such as Tuned Liquid Column Damper (TCLD) or a Tuned Mass Damper (TMD). Some of the pioneering work regarding applications in wind turbines include the work by Colwell and Basu [15] in which the damping effect of a TLCD installed in an offshore wind turbine has been examined by assuming correlated wind and wave load conditions. A different geometry of the TMD is the pendulum device [16]. The main structure excites the device, and part of its energy is transferred by its movement and then it is dissipated by the pendulum damper.

In order to be potent, a resonant damper like a TMD should be installed where the absolute motion of the targeted vibration mode is largest, which is at the top of the tower or inside the nacelle. Effective damping by a TMD is correlated with a large damper mass, which forms a major limitation since additional mass is undesirable at the top of the wind turbine.

For this reason, two alternative vibration mitigation concepts are examined in this paper. First, the nacelle is released from the Wind Turbine tower (nacelle isolation concept), using a low stiffness connection. This is the most well-known path to earthquake-resistance designs as

it is based on the concept of reducing the seismic demand instead of increasing the structure's resistant capacity. Modern seismic isolation systems for structures grant horizontal isolation from the seismic effects, by decoupling the structure from its foundation [17]–[21]. Among others, this concept has been shown to behave effectively in bridge decks, supported on flexible piers [22], [23].

Alternatively, the KDamper concept, proposed in Antoniadis et al. 2016 [24], is studied. The KDamper extends the classical Tuned Mass Damper by integrating appropriate negative stiffness elements, rather than increasing the additional mass, which enhances the capability of the KDamper, overcoming the sensitivity problems of TMDs as the tuning is primarily controlled by the negative stiffness element's parameters. Although the KDamper incorporates a negative stiffness element, it is drafted to be both statically and dynamically stable. The KDamper is examined for the protection of bridge structures [25]–[29], Wind Turbines [30], [31] and structural systems [32], [33]. In addition, the KDamper is implemented as an Absorption Base (KDAB) in the bases of structures [34]–[40].

Section 2 of the paper demonstrates the methodology and the modeling procedure for the three approaches. Section 3 presents the method of the optimal selection of the parameters of the three approaches. Section 4 presents a comparison of the approaches with respect to the improvement of the dynamic performance of the Wind Turbine Tower and of the nacelle.

2 METHODOLOGY AND MODELING

The contemporary design of wind turbines requires power rates of more than 5MW which can be accomplished by wider rotors (diameters of more than 120 m); for that reason, a proportionate increase of the tower height is required. However, this height increase has immediate effects on the structural behavior of the wind turbine because of the augmented wind pressure area and the slenderness of the tower. Moreover, considering that both the tower and the foundation are vital components of the wind turbine, reaching a rather large percentage of the overall turbine budget (over 60% including the installation cost) [41], [42] the improvement of the dynamic response of the wind turbine tower is of high importance. In this work, a steel tower of 120 m height that supports the NREL baseline 5-MW nacelle and rotor, is used. The key properties of the wind turbine and the steel tower are listed in Table 1 and Table 2 respectively.

Property	**Value**
Rating	5 MW
Rotor diameter	126 m
Hub diameter	3 m
Cut-in wind speed	3 m/sec
Rated wind speed	11.4 m/sec
Cut-out wind speed	25 m/sec
Cut-in rotor speed	6.9 rpm
Rated rotor speed	12.1 rpm
Nacelle mass	240,000 kg
Rotor mass	110,000 kg
Blade material	Glass-fibre
Blade length	61.5 m
Blade mass	17,740 kg
Blade CM (from blade root)	20.475 m
Blade damping ratio (all modes)	0.48%

Table 1: Key properties of NREL baseline 5 MW wind turbine.

Property	Value
Height	120 m
Base diameter	8.43 m
Base steel thickness	0.048 m
Top diameter	3.87 m
Top steel thickness	0.025 m
Young's modulus	210 GPa
Steel density	8,500 kg/m^3
Total mass	798,640 kg
Location of CM (above base)	43.042 m
Tower damping ratio (all modes)	2%

Table 2: Key properties of the considered steel tower.

2.1 Vibration mitigation concepts considered

Fig. 1 displays the dynamic vibration absorber design options that will be analyzed in this paper. The first vibration absorption concept is based on the classical tuned mass damper (TMD). Figure 1i presents the schematic image of the TMD concept. An additional mass is attached to the top of the wind turbine tower or inside the nacelle, using a positive stiffness element and a linear damper. The main disadvantage is the need for a large additional mass in order for TMD to attain effective damping. Figure 1ii presents the nacelle-isolation vibration absorption concept, where the mass that correlates to the mechanical parts (nacelle, rotor, and blades) is used as an additional mass of a TMD. The additional mass is no more connected rigidly to the steel tower but is accomplished with a stiffness connection and a linear damper, as in the case of the classical TMD concepts. Figure 1iii presents the realization of the KDamper concept [24] in a wind turbine tower. Again, as in the nacelle-isolation concept, the additional mass of the nacelle, rotor, and blades is no longer rigidly attached to the wind turbine tower but through the interference of a KDamper device. This time the additional mass of the vibration absorption concept is connected with the mass that corresponds to the nacelle, rotor, and blades with a positive stiffness element and a linear damper, and with the top of the wind turbine tower with a negative stiffness element.

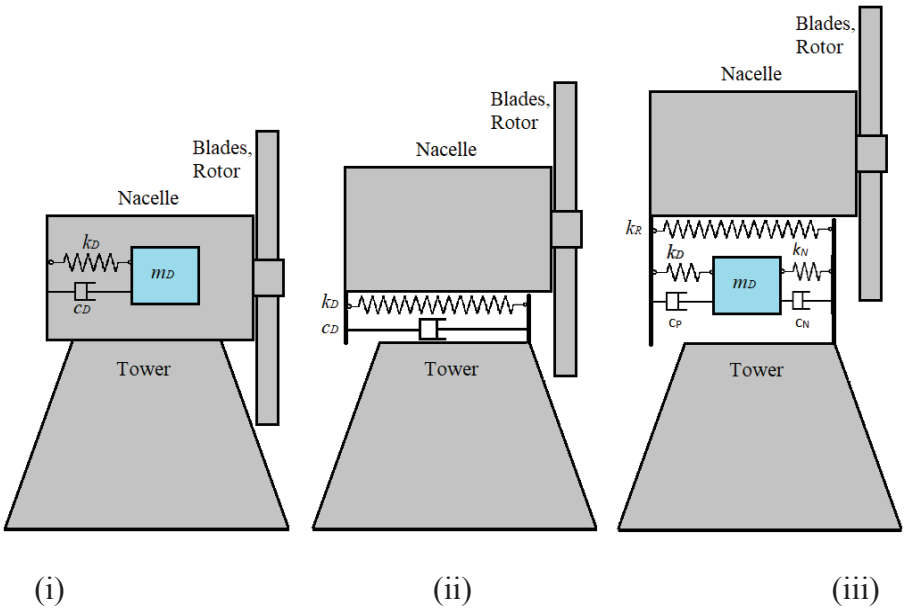

(i) (ii) (iii)

Fig. 1: Schematic representation of the considered vibration absorption concepts, (i) TMD concept, (ii) Nacelle-isolation concept and (iii) KDamper concept.

2.2 Dynamic model of the wind turbine

A wind turbine tower (Table 2) of variable tubular cross-section supporting the NREL baseline 5-MW nacelle and rotor [42] is examined. In order to consider the inertial forces applied by the mechanical parts (nacelle, rotor, and blades), an additional mass concentrated at the top, *mtop*=403.22 tn [42] is added at the top of the tower.

The equations of motion of the wind turbine including the respective vibration mitigation concept to be considered are obtained by analyzing the equilibrium of forces at the location of each degree of freedom as follows:

$$[M_S]\{\ddot{x}_S\}+[C_S]\{\dot{x}_S\}+[K_S]\{x_S\}=[P] \tag{1}$$

Where $[M_S]$, $[C_S]$ and $[K_S]$ are the mass, damping and stiffness matrices of the controlled wind turbine tower, respectively of order $(N+n)$ *x* $(N+n)$. Here, N suggests the degrees of freedom (DoF) for the wind turbine tower and n indicates the DoF of each of the vibration isolation options to be considered. In this paper, the degrees of freedom for the wind turbine tower is N=24. The mass matrix is of order $(N+n)$ *x* $(N+n)$ as follows:

$$[M_S]=\left[\begin{bmatrix}[M_N]_{N\times N} & [0]_{N\times n}\\ [0]_{n\times N} & [0]_{n\times n}\end{bmatrix}+\begin{bmatrix}[M_{n,a}]_{N\times N} & [0]_{N\times n}\\ [0]_{n\times N} & [M_{n,d}]_{n\times n}\end{bmatrix}\right]_{(N+n)\times(N+n)} \tag{2}$$

Where $[M_N]_{NxN}$ is the mass matrix of the uncontrolled wind turbine tower and $[M_n]_{nxn}$ indicates the mass matrix of the vibration isolation concept. The condensed stiffness matrix $[K_N]_{NxN}$ of the uncontrolled wind turbine tower is correlating to the sway degrees of freedom taken as the dynamic DoF. The damping matrix $[C_N]_{NxN}$ is not precisely known but is obtained with the help of the Rayleigh's approach using the same damping ratio in all modes, 2%. The stiffness matrix $[K_N]_{NxN}$ and the damping matrix $[C_N]_{NxN}$ are expressed in agreement to the degrees of freedom associated with the respective vibration isolation system to be considered.

The stiffness and damping matrix of the controlled system are formed as follows:

$$[K_S]=\left|\begin{bmatrix}[K_N]_{N\times N} & [0]_{N\times n}\\ [0]_{n\times N} & [0]_{n\times n}\end{bmatrix}+\begin{bmatrix}\lfloor K_{n,a}\rfloor_{N\times N} & -\lfloor K_{n,b}\rfloor_{N\times n}\\ -[K_{n,c}]_{n\times N} & [K_{n,d}]_{n\times n}\end{bmatrix}\right|_{(N+n)\times(N+n)} \tag{3}$$

$$[C_S]=\left|\begin{bmatrix}[C_N]_{N\times N} & [0]_{N\times n}\\ [0]_{n\times N} & [0]_{n\times n}\end{bmatrix}+\begin{bmatrix}\lfloor C_{n,a}\rfloor_{N\times N} & -\lfloor C_{n,b}\rfloor_{N\times n}\\ -[C_{n,c}]_{n\times N} & [C_{n,d}]_{n\times n}\end{bmatrix}\right|_{(N+n)\times(N+n)} \tag{4}$$

The coupled differential equations of motion (Eq.11111) for t1111he isolated wind turbine tower are thus derived and solved using Newmark's integration method.

The wind turbine tower is modeled as a Generalized Single Degree of Freedom System with a shape function based on the first modal eigenform of the non-isolated wind turbine tower. The additional concentrated mass of 403.22 tn, is placed together with the tower's mass m_B. Therefore, the system's parameters are: m_B = 80.57 tn, k_B = 1977.47 kN/m, c_B = 8kN*s/m. Additional assumptions made for the detailed formulation are: (i) the wind turbine tower is considered to remain within the elastic limit under the aerodynamic loads; and (ii) the effects of soil-structure-interaction (SSI) are not taken into account.

2.3 Aerodynamic load

The loading due to the wind is taken into consideration as follows. The tower is deemed to be subjected to the horizontal force $\overline{F}_N(t)$ due to the wind at its top. Moreover, the horizontal force $F_{Nr}(r, t)$ acting as a position r along the wind turbine blade can be acquired by the following relation [43]:

$$F_{N_r}(\mathrm{r},\mathrm{t}) = \frac{1}{2}\rho_{air} C_N(r) c_{bl}(r)(\overline{V}(t))^2 \tag{5}$$

Where ρ_{air} = 1.225 x 10^{-3} tn/m^3 is the air density and $C_N(r)$ is the coefficient calculated by the corresponding lift $C_L(r)$ and drag $C_D(r)$ coefficients. The values of the latter coefficients depend on the airfoil characteristics of the blades and their distribution with consideration to the "angle of attack" of the wind velocity $\overline{V}(t)$ vector passing through the blade profile can be retrieved from. It is noted that $\overline{V}(t)$ is presumed to have a uniform spatial distribution over the actuator disc. $c_{bl}(r)$, $\beta(r)$ is the chord and the pitch angle of the blade profile fluctuating along the blade length r, the distributions of which are acquired according to the blade type employed to equip the turbine. $C_N(r)$ is given as:

$$C_N(\mathrm{r}) = C_L(r)\cos\varphi(\mathrm{r}) + C_D(r)\sin\varphi(r) \tag{6}$$

Where $\varphi(r)$ is the wind flow angle [43]. In order to calculate $\varphi(r)$ and consequently $C_N(r)$, the blade element momentum theory incorporating Prandtl's tip loss factor and Glauert's correction [43] is utilized with a hypothesis of constant angular velocity of the blades $\boldsymbol{\Omega_{bl}}$. Subsequently, breaking $\overline{V}(t)$ down into a mean component V_m and a fluctuating component $V(t)$, the corresponding mean and fluctuating components of $F_{Nr}(r, t)$ can be obtained as:

$$F_{Nm} = \frac{1}{2}\rho_{air} C_N(r) c_{bl}(r) V_m^2 \tag{7}$$

$$F_N(r,t) = \frac{1}{2}\rho_{air} C_N(r) c_{bl}(r)(2V_m V(t) + V(t)^2) \tag{8}$$

In this work, the mean velocity is gained by using a basic velocity at an altitude of 10 m, V_b and applying the corresponding regulations of EC1, Part1,4 [44]. Moreover, in order to take into consideration the wind velocity fluctuation at the altitude of l_t, an artificial velocity time history is produced applying the procedures presented in References [45]–[47]assuming a value of standard deviation σ. After having established $F_{Nr}(r,t)$, the total concentrated force exerted on the top of the tower can be computed as:

$$\overline{F}_N(t) = 3\int_0^{r_{bl}} \overline{F}_N(r,t)dr \tag{9}$$

Besides the concentrated force applied on the top of the tower because of the operation of the turbine, the distributed loading along the tower height is not taken into account due to the fact that it has a minimal influence on the dynamic response of the tower. The basic wind velocity that is employed has equivalent standard deviations V_b = 27.0 m/s with σ = 3.30 m/s ($V_\mathrm{m}(120)$ = 39.93 m/s). The rotor is presumed to develop a constant angular velocity $\boldsymbol{\Omega_{bl}}$ = 12.1 rpm, while all the necessary blade profile characteristics are retrieved from References [42] and [48] (Fig. 2(i)).

Also, a different type of load (Fig. 2(ii)) is employed for the simulation as described in Shkara et al. [49] so that a proper time history of the aerodynamic loads induced to the tower is

obtained, that accurately depicts the alterations of the aerodynamic load in relation with the motion of the wind turbine blades. The basic wind velocity that is aforementioned is still employed in accordance with the response described in [49]. The figure represents the time history of the load for ten seconds but the simulation is performed for a hundred seconds.

The total force $\overline{F}_N\,(t)$ applied at the top of the wind turbine tower is an instantaneously imposed load that is slowly changing over time. Therefore, for each case separately, in order to properly calculate the maximum permanent displacement of the oscillation of the tower, the first value of the total force $\overline{F}_N\,(t)$ is deducted from all the values of the total force so that the fatigue simulation is conducted without the instantaneous imposing of the load interfering with the response of the tower.

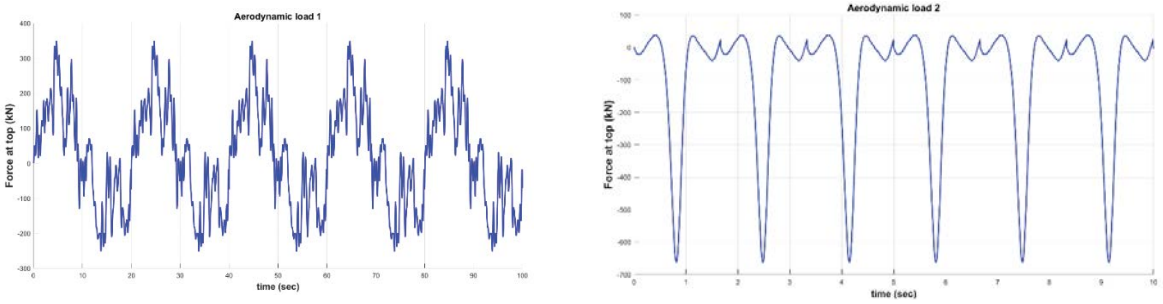

(i) (ii)

Fig. 2: The two different types of loads: (i) Aerodynamic load based on EC1[44], (ii) Aerodynamic load based on Shkara et al. [49].

3 OPTIMIZATION OF THE VIBRATION MITIGATION CONCEPTS

3.1 Harmony search algorithm and optimization process

In this section, the HS metaheuristic algorithm is shortly described and is also presented with a comprehensive example of the recommended optimization procedure. The four key steps of the algorithm are presented below:

Step 1: Initialization of the HS Memory matrix (HM). HM matrix consists of vectors representing potential solutions to the examined optimization problem. The original HM matrix is formed using randomly generated results. For an n-dimension problem, HM has the form:

$$HM = \begin{bmatrix} x_1^1, x_2^1, \ldots, x_n^1 \\ x_1^2, x_2^2, \ldots, x_n^2 \\ \cdot \\ \cdot \\ \cdot \\ x_1^{HMS}, x_2^{HMS}, \ldots, x_n^{HMS} \end{bmatrix} \tag{10}$$

where $[x^1_1, x^1_2, \ldots, x^1_n]$ $(i=1, 2, \ldots, HMS)$ is a result candidate. HMS is generally set to values between 50 and 100. The value of the objective function is determined for every solution vector of the HM matrix.

Step 2: Improvisation of a $[x'_1, x'_1, \ldots, x'_1]$ new result from the HM. Each one of the components of this new result, x'_j, is gained based on the Harmony Memory Considering Rate (HMCR), which is described as the probability of selecting a component from the HM members. 1 – HMCR is, thus, the probability of creating a new component at random. If x'_j is elected from

the HM matrix, it is further altered according to the Pitching Adjusting Rate (PAR), which regulates the probability of a candidate from the HM to be altered.

Step 3: Update of the HM matrix. The value of the objective function of the new result, gained in Step 2, is determined and measured to the ones that correlate to the original HM matrix vectors. If the outcome is a better fitness than that of the worst member in the HM, it will take over that one. If there is more than one member in the HM with bigger values of the objective function that the new solution, the result with the higher value is replaced. Otherwise, the new solution is erased and the HM matrix remains untouched.

Step 4: Repetition of Steps 2 and 3 until a preset termination benchmark is satisfied. A frequently used termination benchmark is the maximum number of total iterations.

The flowchart of the suggested HS algorithm is shown in Fig. 3.

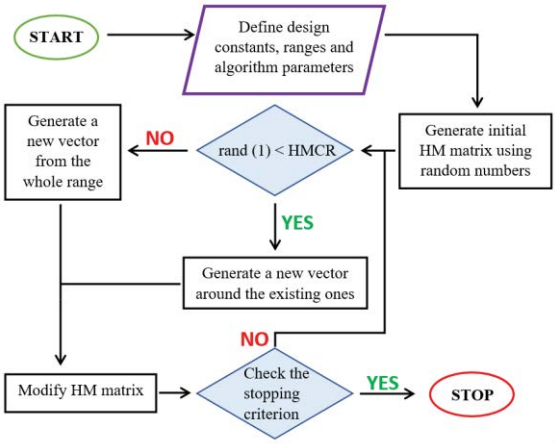

Fig. 3: Flowchart of the proposed HS algorithm.

3.2 Vibration mitigation concepts optimization process

Succeeding the method and flowchart presented above, the features of the inspected optimization problems can be calculated.

First of all, the parameters are selected, whose values shall be optimized for each concept. The KDamper concept has five parameters that control the device's performance and those are k_R, k_D, k_N, c_N, c_p. The additional mass ratio of the KDamper device is selected equal to 1%. The TMD concept has a single parameter ζ_D since the mass ratio is selected equal to 5% and k_D is selected so that the natural period T of the TMD is equal to that of the tower modeled as a Generalized SDOF. The TMD-Nacelle concept has two parameters that control the device's performance, k_D and ζ_D. Furthermore, the restrains of the design variables are decided. Their choice relies on safety, stability and manufacturing parameters that need to be considered. Although these parameters may alter from structure to structure, the restraints presented below produce satisfying results in most cases.

	k_R	k_D(KDamper)	k_N	c_N	c_p	ζ_D(TMD)	k_D(TMD-Nacelle)	ζ_D(TMD-Nacelle)
min	0	0	-40000	0	0	0	0	0
max	120000	120000	0	500	500	1	20000	0.5

Table 3: Variable design limits.

As far as the parameters inherently involved in the HS algorithm are concerned, a common practice is to adopt commonly found values found in relative literature (Table 4). The same is true for the termination criterion, as the maximum number of repetitions is pre-determined.

HMS	HMCR	PAR
75	0.5	0.1

Table 4: Values of the HS algorithm parameters

With the intention of finding the optimum solution for the EC1 [44] aerodynamic load, the top of the tower's displacement is determined as the objective function that needs to be minimized, in each case.

Finally, the constraints and limitations of the inspected optimization problem are specified. Specifically, for the KDamper concept, there are three constraints, the first one demanding that the relative displacement of the additional mass of the KDamper be lower than 1.5 *m*, the second one demanding that the absolute velocity of the nacelle must be lower than 1 *m/sec* and the third one demanding that the relative displacement of the nacelle to the top of the tower be lower than 0.5 *m*. The last two constraints also apply to the other two concepts.

4 COMPARISON OF THE PROPOSED CONCEPTS

The design criterion of the Tuned Mass Damper and KDamper vibration absorption concepts is their mass ratio, which corresponds to the additional mass added to the system, and for the nacelle-isolation concept is that the maximum relative displacement, between the nacelle and the tower, must be under 0.5 m. The mass ratio of the TMD is selected 5% (as a maximum value for constructional reasons), the mass ratio of the KDamper 1% and the relative displacement between the nacelle and the tower, for the nacelle-isolation concept is 0.5 *m*. The exact values derived from the optimization process for each of the employed vibration absorption concepts are the following: (i) KDamper: k_R = 7296 *kN/m*, k_D = 114272 *kN/m*, k_N = -6234 *kN/m*, c_N = 345 *kNs/m*, c_p = 300 *kNs/m*, (ii) TMD: ζ_D = 0.04, (iii) TMD-Nacelle: k_D = 606 *kN/m*, ζ_D = 0.32.

In Table 5 and Table 6, are the results (maximum values) of the controlled wind turbine concerning the dynamic performance of the wind turbine tower for both load cases. In Table 7 are the results (mean values) of the energy dissipated by the dampers of each of the proposed concepts.

	$U_{abs,\,top}$ (m)	$V_{abs,nacelle}$ (m/s)
Initial	0.5851	1.0455
KDamper	0.1607	0.4836
TMD	0.3111	0.5275
TMD-Nacelle	0.1601	0.4920

Table 5: Maximum values of the controlled wind turbine's tower dynamic performance for Aerodynamic load 1.

	$U_{abs,\,top}$ (m)	$V_{abs,nacelle}$ (m/s)
Initial	0.1477	0.2964
KDamper	0.0925	0.3185
TMD	0.1442	0.2825
TMD-Nacelle	0.0960	0.3267

Table 6: Maximum values of the controlled wind turbine's tower dynamic performance for Aerodynamic load 2.

W_d (kW)	Aerodynamic load 1	Aerodynamic load 2
KDamper	8.5373	0.9049
TMD	5.4562	0.1242
TMD-Nacelle	15.6352	2.9603

Table 7: Mean value of the energy dissipated per cycle by the proposed vibration absorption concepts for each aerodynamic load.

In the following figures Fig. 4,Fig. 5,Fig. 6,Fig. 7) are depicted the time-histories of the tower top displacement and the nacelle's velocity for both the aerodynamic loads and for all the vibration absorption concepts so that a more immediate and clear comparison can be made between the proposed concepts. Also in Fig. 8 and Fig. 9 the dissipated energy through the oscillation duration is depicted so that a clear picture can be obtained on whether this energy can be exploited.

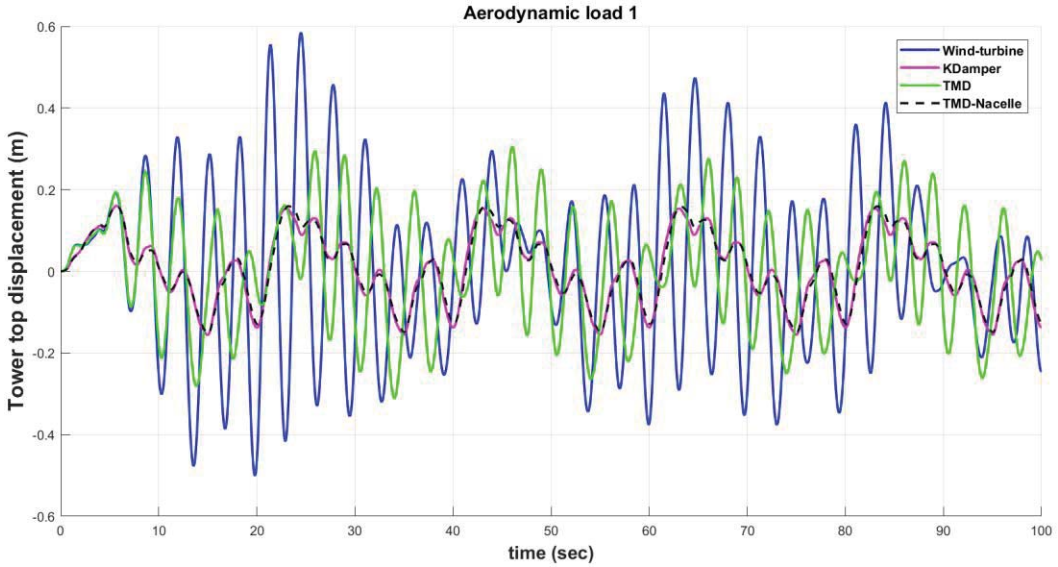

Fig. 4: Time history of tower top displacement for aerodynamic load 1

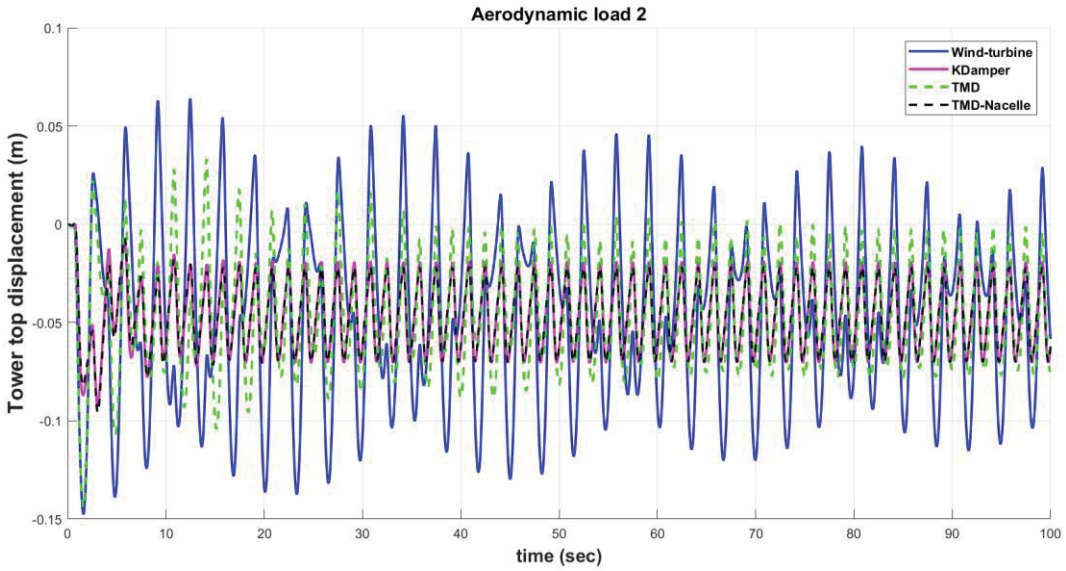

Fig. 5: Time history of tower top displacement for aerodynamic load 2

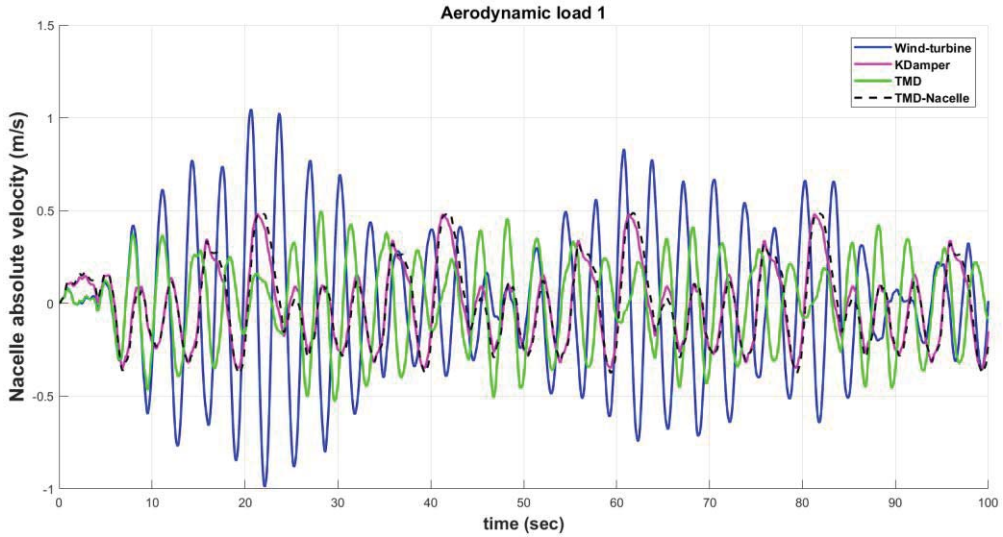

Fig. 6: Time history of nacelle's absolute velocity for aerodynamic load 1

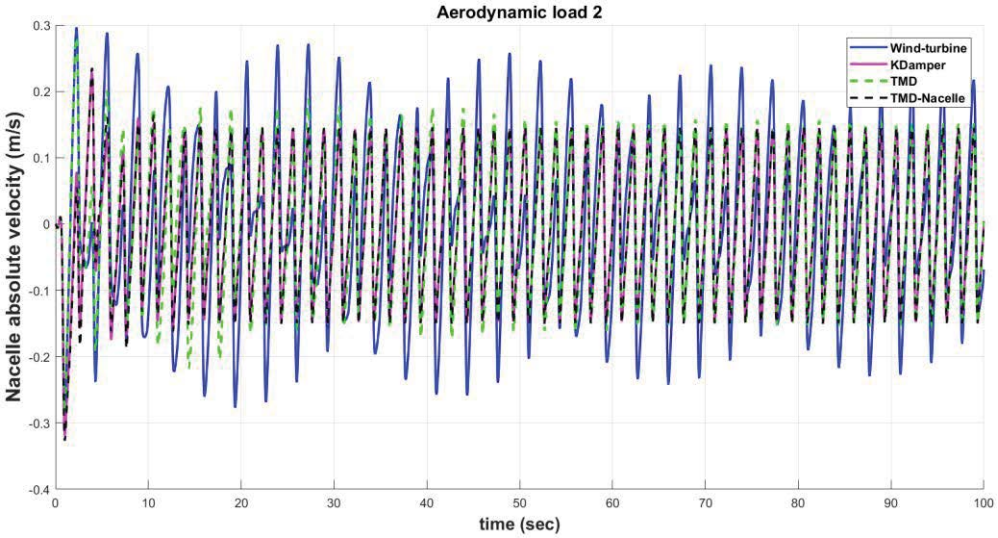

Fig. 7: Time history of nacelle's absolute velocity for aerodynamic load 2

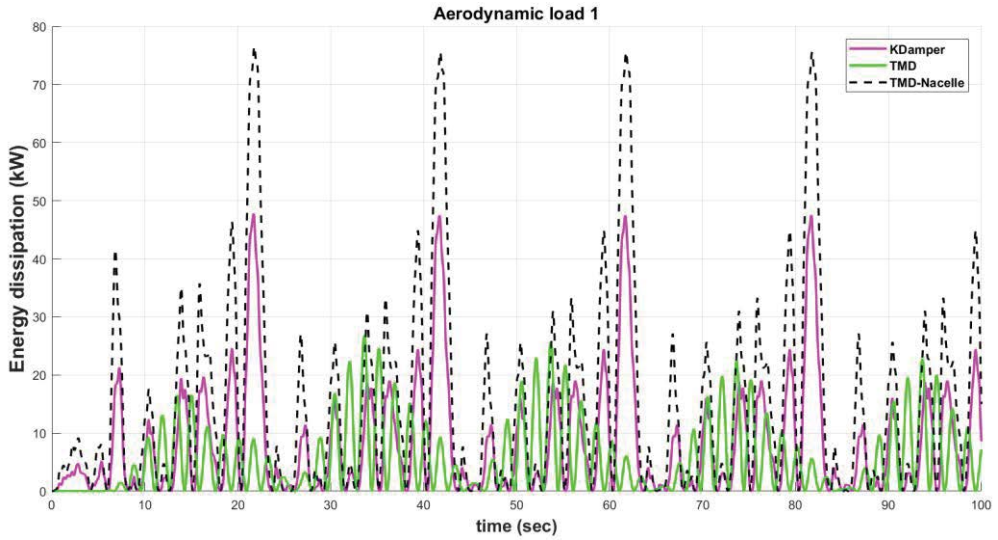

Fig. 8: Energy dissipation for Aerodynamic load 1

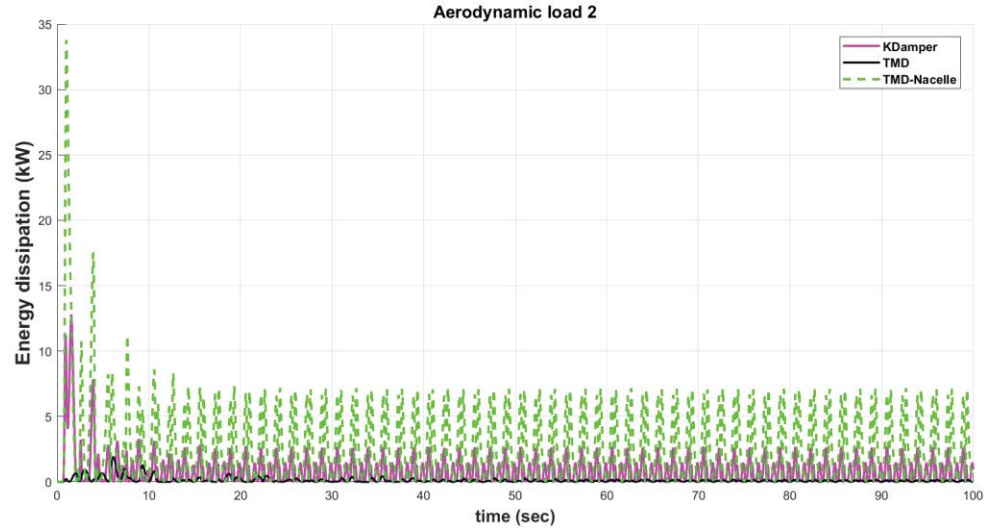

Fig. 9: Energy dissipation for Aerodynamic load 2

5 CONCLUSIONS

In this paper, three dynamic vibration absorber options are examined for improving the wind turbine's dynamic behavior, while also satisfying some certain constraints, the TMD, KDamper and Nacelle-isolation concepts. A wind turbine of 5MW supported by a steel tower of 120 m was analyzed under two different horizontal aerodynamic loads due to the wind. Based on the dynamic analysis and the results collected, the following conclusive observations can be made:

- Concerning the dynamic behavior of the wind turbine tower, the nacelle isolation concept yielded the best results along with the KDamper concept, with which the differences are minimal, followed by the TMD concept.
- Concerning the nacelle's velocity, all three concepts yielded the desirable results, reducing the maximum velocity for the aerodynamic load 1 by roughly 50%. For the aerodynamic load 2, the results can still be considered satisfactory as neither of the proposed concepts produced results close to the 1 *m/s* constraint that was set beforehand.
- The KDamper concept achieves better results than the TMD concepts and roughly the same as the nacelle-isolation concept with only 1/5 of the TMD's additional mass.
- The KDamper shows promising behavior in dissipating the energy of the aerodynamic loads and this energy can be gathered, further increasing the efficiency of the system.

According to the observations made above, the KDamper device can bring a realistic alternative to the existing vibration absorption design options in wind turbine towers, enhancing the dynamic performance both of the nacelle and the tower. The reliability and simplicity of the system are also benefits that render the device appropriate for various technological implementations and competitive against other vibration absorption designs.

REFERENCES

[1] M. Morais, M. Barcelos, S. Avila, M. Szhu, and de C. S. R., "Dynamic behavior analysis of Wind Turbine towers.," in *Congreso de Métodos Numéricos en Ingeniería*, 2009.

[2] S. Nigdeli and G. Bekdas, "Optimum tuned mass damper design in frequency domain for structures.," *KSCE J Civ Eng*, no. 21, pp. 912–922, 2016.

[3] S. Avila, M. Shzu, W. Pereira, L. Santos, M. Morais, and Z. Prado, "Numerical Modeling of the Dynamic Behavior of a Wind Turbine Tower.," *Art Adv Vibr Eng*, no. 4, 2016.

[4] G. Stewart and M. Lackner, "The impact of passive tuned mass dampers and wind-wave misalignment on offshore wind turbine loads.," *Eng Str*, no. 73, pp. 54–61, 2014.

[5] M. Lackner and M. Rotea, "Passive structural control of offshore wind turbines. Wind Energy," *Wind Energy*, no. 14, pp. 373–388, 2011.

[6] T. Soong and G. Dargush, *Passive Energy Dissipation Systems in Structural Engineering*. Wiley, 1997.

[7] F. Casciati and F. Giuliano, "Performance of a multi-tmd in the towers of suspension bridges," *J Vib Con*, no. 15, pp. 821–847, 2009.

[8] H. Frahm, "Device for Damping Vibrations of Bodies," 989958, 1909.

[9] J. Ormondroyd and J. Den Hartog, "The Theory of Dynamic Vibration Absorber," *Trans. ASME*, no. 50, pp. 9–22, 1928.

[10] J. Den Hartog, *Mechanical Vibrations*, 4th ed. McGraw Hill, 1956.

[11] N. Debnath, S. Deb, and A. Dutta, "Multi-modal vibration control of truss bridges with tuned mass dampers under general loading," *J Vib Con*, no. 22, pp. 4121–4140, 2015.

[12] A. Younespour and H. Ghaffarzadeh, "Structural active vibration control using active mass damper by block pulse functions," *J Vib Con*, no. 21, pp. 2787–2795, 2015.

[13] F. Ricciardelli, D. Pizzimenti, and M. Mattei, "Passive and active mass damper control of the response of tall buildings to wind gustiness," *Eng Str*, no. 25, pp. 1199–1209, 2003.

[14] S. Ankireddi and H. Yang, "Simple tmd control methodology for tall buildings subject to wind loads," *J Str Eng*, no. 122, pp. 83–91, 1996.
[15] S. Colwell and B. Basu, "Tuned liquid column dampers in offshore wind turbines for structural control," *Eng Str*, no. 31, pp. 358–368, 2009.
[16] F. Oliveira, A. Gomez, S. Avila, and J. Brito, "Design criteria for a pendulum absorber to control high building vibrations," *Int J IMSE*, no. 1, pp. 82–89, 2014.
[17] R. Skinner, W. Robinson, and G. McVerry, *An Introduction to Seismic Isolation*. New York: John Wiley & Sons, 1999.
[18] S. Deb, "Seismic base isolation – an overview," *Cur Sc*, no. 87, pp. 1426–1430, 2004.
[19] Govardhan, D. Paul, and Y. Singh, "Seismic Base Isolation An- overview," in *National Conference on Trends and Challenges in Structural Engineering and Construction Technique at CBRI*, 2008.
[20] J. Kelly, *Earthquake-Resistant Design with Rubber*, 2nd ed. London: Springer-Verlag, 1996.
[21] Govardhan, D. Paul, R. Jain, and S. Bagchi, "Design and Development of the base isolation system for Seismic protection of buildings," in *7th world congress on Joints, Bearings, and Seismic systems*, 2011.
[22] M. Kunde and R. Jangid, "Seismic behavior of isolated bridges: A-state-of-the-art review," *El J Str Eng*, no. 3, pp. 142–170, 2003.
[23] N. Grant, L. Fenves, and F. Auricchio, "Bridge isolation with high-damping rubber bearings – analytical modeling and system response," in *13th World Conference on Earthquake Engineering*, 2004.
[24] I. A. Antoniadis, S. Kanarachos, K. Gryllias, and I. E. Sapountzakis, "KDamping: A stiffness based vibration absorption concept," *J Vib Con*, no. 24, pp. 1–19, 2016.
[25] I. A. Antoniadis, K. A. Kapasakalis, and E. I. Sapountzakis, "Isolation or Damping? A Soil-dependent approach based on the KDamper concept.," in *ICONHIC*, 2019.
[26] E. I. Sapountzakis, K. A. Kapasakalis, and I. A. Antoniadis, "Negative Stiffness Elements in Seismic Isolation of Bridges.," in *ICONHIC*, 2019.
[27] K. A. Kapasakalis, C.-H. Alamir, I. A. Antoniadis, and E. I. Sapountzakis, "Frequency Base Design of the KDamper Concept for Seismic Isolation of Bridges.," in *ICOVP*, 2019.
[28] P. O. N. Bollano, K. A. Kapasakalis, E. I. Sapountzakis, and I. A. Antoniadis, "Design and Optimization of the KDamper Concept for Seismic Protection of Bridges," *Proc. 14th Int. Conf. Vib. Probl. (ICOVP 2019)*, vol. 1, 2019.
[29] K. A. Kapasakalis, I. A. Antoniadis, and E. I. Sapountzakis, "Implementation of the KDamper Concept for Seismic Protection of Bridges.," *ICOVP*, 2019.
[30] K. A. Kapasakalis, E. I. Sapountzakis, and I. A. Antoniadis, "Implementation of the KDamper concept to wind turbine towers," in *Compdyn*, 2017.
[31] K. A. Kapasakalis, E. I. Sapountzakis, and I. A. Antoniadis, "Optimal Design of the KDamper Concept for Structures on Compliant Supports.," in *ECEE*, 2018.
[32] K. A. Kapasakalis, E. I. Sapountzakis, and I. A. Antoniadis, "KDamper Concept in Seismic Isolation of Multi Storey Building Structures," in *GRACM*, 2018.
[33] K. A. Kapasakalis, E. I. Sapountzakis, and I. A. Antoniadis, "Kdamper concept in seismic isolation of building structures with soil structure interaction.," in *Conf. Comput. Struct. Technol*, 2018.
[34] K. A. Kapasakalis, E. I. Sapountzakis, and I. A. Antoniadis, "Control of Multi Storey Building Structures with a New Passive Vibration Control System Combining Base Isolation with KDamper.," in *Compdyn*, 2019.
[35] K. A. Kapasakalis, E. I. Sapountzakis, and I. A. Antoniadis, "Implementation of the

KDamper Concept for Base Isolation to a Typical Concrete Building Structure.," in *Int. Congr. Mech*, 2019.

[36] K. A. Kapasakalis, I. A. Antoniadis, and E. I. Sapountzakis, "KDamper Concept for Base Isolation and Damping of High-Rise Building Structures.," in *ICOVP*, 2019.

[37] I. A. Antoniadis, K. A. Kapasakalis, and E. I. Sapountzakis, "Advanced Negative Stiffness Absorbers for the Seismic Protection of Structures.," in *Int. Conf. Key Enabling Technol.*, 2019.

[38] K. A. Kapasakalis, I. A. Antoniadis, and E. I. Sapountzakis, "Novel Vibration Absorption Systems with Negative Stiffness Elements for the Seismic Protection of Structures.," in *Natl. Conf. Earthq. Eng. Eng. Seismol*, 2019.

[39] K. A. Kapasakalis, I. A. Antoniadis, and E. I. Sapountzakis, "Performance Assessment of the KDamper as a Seismic Absorption Base.," in *Struct. Control Heal Monit.*, 2019.

[40] K. A. Kapasakalis, I. A. Antoniadis, and E. I. Sapountzakis, "Implementation of the KDamper as a Stiff Seismic Absorption Base: A Preliminary Assessment," *Vib. Acoust. Res. J.*, vol. 1, no. 1, pp. 1–26, 2019.

[41] S. Bhattacharya and S. Adhikari, "Experimental Validation of Soil-Structure Interaction of Offshore Wind Turbines," *Soil Dyn Ear Eng*, no. 31, pp. 805–816, 2011.

[42] A. Quiligan, A. O'Connor, and V. Pakrashi, "Fragility Analysis of Steel and Concrete Wind Turbine Towers," *Eng Str*, no. 36, pp. 270–282, 2012.

[43] M. Hansen, *Aerodynamics of Wind Turbines*, 2nd ed. Earthscan, 2008.

[44] CEN/TC250, "Eurocode 1: Actions on structures-General actions-Part 1-4: Wind actions." 2004.

[45] K. Koulatsou, F. Petrini, S. Vernardos, and C. Gantes, "Artificial Time Histories of Wind Actions for Structural Analysis of Wind Turbines," in *BCCCE*, 2013.

[46] M. Di Paola, "Digital Simulation of Wind Field Velocity," *J Wind Eng Ind Aerodyn*, pp. 74–76, 91–109, 1998.

[47] DNV/Risø, *Guidelines for Design of Wind Turbines*. Denmark, 2002.

[48] J. Jonkman, "Dynamics Modeling and Loads Analysis of an Offshore Floating Wind Turbine," 2007.

[49] Y. Shkara, M. Cardaun, R. Schelenz, and G. Jacobs, "Aeroelastic response of a multi-megawatt upwind HAWT based on fluid-structure interaction simulation," *Wind Energy Sci.*, pp. 10–12, 2019.

EURODYN 2020
XI International Conference on Structural Dynamics
M. Papadrakakis, M. Fragiadakis, C. Papadimitriou (eds.)
Athens, Greece, 23–26 November 2020

AN INTEGRATED MONITORING STRATEGY FOR CURRENT CONDITION ASSESSMENT OF HISTORIC BRIDGES

Gabriele RAVIZZA[1], Rosalba FERRARI[1], Egidio RIZZI[1*], Vasilis DERTIMANIS[2] and Eleni N. CHATZI[2]

[1]University of Bergamo, Department of Engineering and Applied Sciences,
viale G. Marconi 5, I-24044 Dalmine (BG), Italy
*Corresponding Author, e-mail: egidio.rizzi@unibg.it

[2] ETH Zürich, Institute of Structural Engineering,
Department of Civil, Environmental and Geomatic Engineering,
Stefano-Franscini-Platz 5, CH-8093 Zürich, Switzerland

Keywords: Structural Health Monitoring (SHM); Heterogeneous Data Fusion (HDF); Denoising techniques; historic reinforced concrete bridge; acceleration data; displacement data; modal identification.

Abstract. *Nowadays, the need for effective Structural Health Monitoring (SHM) strategies, aiming at preserving the integrity and safety of strategic and historic infrastructures, is increasingly urgent. Within SHM, several vibration-based methodologies have been developed, including those exploiting Heterogeneous Data Fusion (HDF) procedures, as well as Denoising techniques for the treatment of response signals detected through appropriate sensor technologies. In this paper, these two approaches are reconsidered and rejoined, toward developing an innovative signal processing methodology for current condition assessment, specifically referring to historic bridges. In particular, a HDF approach, i.e. the process of combining information from multiple sources, in an effort to enhance the reliability of the monitoring process, and a denoising approach, devoted to the cleaning of spurious noise from the acquired signals, are combined all together, in an integrated strategy. The effectiveness of the proposed platform is tested on data from a real structure (historic bridges). Both dynamic acceleration and displacement response signals, directly detected under operational conditions, can be processed within the proposed methodology, and subsequently employed toward modal dynamic identification purposes and possible model updating of the structure at hand.*

1 INTRODUCTION

This study is motivated by the awareness quest on the critical health conditions that may characterize existing and historical infrastructures, especially those nearing the end of their life cycle. Despite their age, these structures often continue to play a critical role in everyday life, constituting essential connections within the transportation network of several territories and communities. Consequently, a prompt and effective adoption of appropriate and modern strategies and action models toward their conservation and protection shall be set in place. In this scenario, the development of monitoring-based strategies toward structural condition assessment of such important infrastructures, shall constitute a fundamental tool toward the competent analysis.

Accordingly, within the civil engineering context, the Structural Health Monitoring (SHM) research field is becoming increasingly important, since the goal of achieving structural safety is only possible through the possibility to extract more abundant and precise information about the health conditions of a structure to be monitored, for instance by analyzing its current structural dynamic response. As a consequence, within SHM applications, after the signal acquisition stage, to be acquired directly on the structure by predisposing appropriate sensor networks, the subsequent phase of signal processing displays a determinant role, toward the success of the whole monitoring procedure.

In this paper, two complementary and possibly interacting approaches for the post-processing of structural response signals are considered, i.e. a denoising approach, as well as a Heterogeneous Data Fusion (HDF) procedure, aiming at achieving a better screening of real structural response signals, which may be corrupted by some amount of noise, especially in case of a low-cost instrumentation.

In particular, denoising techniques aim at clarifying the signal content, by directly acting on the contaminating noise, reducing its amount, while preserving the useful information embedded in the signal itself. Several denosing-based techniques may be employed for this purpose, including those exploiting Singular Value Decomposition (SVD) or Discrete Wavelet Transform (DWT), as recently investigated in Ravizza et al. [18, 19], where the effectiveness of these approaches has been inspected for both stationary (ambient vibration) and non stationary (seismic excitation) synthetic response signals, and for instances of real vibration signals.

Instead, Heterogeneous Data Fusion (HDF)-based approaches are procedures through which heterogeneous measurements may be combined all together, with the analogous purpose to enhance their quality, by alleviating the amount of noise on the signals and, consequently, reducing the induced uncertainties affecting the monitoring results. Several virtuous examples of HDF applications within the civil engineering field may be found in the literature, as for instance in Chatzi and Fuggini [2, 3], Ferrari et al. [4–6] and in Ravizza et al. [17], where a Kalman Filter (KF) has been involved in a HDF scheme between artificially generated acceleration and displacement response signals, aiming at obtaining enhanced displacement response measurements, for a 3-DOFs numerical dynamic system.

In the present investigation, a denoising-based approach, and a HDF procedure are considered all together and possibly coupled within an integrated monitoring methodology for the purification of real response signals, specifically displacement signals, which usually appear to be affected by higher levels of noise, if compared to accelerations. The obtained post-processed enhanced displacement measurements may then be employed toward modal dynamic identification purposes (see e.g. Pioldi et al. [10–12] and Pioldi and Rizzi [13–16]), and this might result of a crucial interest for real applications related to the SHM context.

Although the proposed methodology aims at a general formulation, as to be suitable for the monitoring of different structural systems, here, a specific real test structure is assumed as a case study for the analysis, in order to highlight the feasibility of the proposed monitoring strategy and show its effectiveness. For this purpose, the historic reinforced concrete (RC) bridge at Brivio (1917), i.e. a strategic infrastructure for some local connections within the northern Italy automotive road notwork, has been considered (Santarella and Miozzi [20], Ferrari et al. [7]).

The multiple goals that this study aims at achieving are:

- to pursue an effective denoising of real acceleration response data, detected on the monitored structure, through appropriate (wireless) acceleration sensors. In fact, although accelerations usually display a good resolution, when the sensor instrumentation employed during the signal acquisition stage is somehow poor, this may become necessary;
- to successfully perform a denoising-based approach on the original (raw) displacement signals, aiming at clarifying their content in the time domain, then resulting in a better representation and reading of the time domain signal features;
- to perform a successful HDF, by involving a KF within the fusion procedure between denoised acceleration and denoised displacement response signals, in order to obtain a further enhancement of the displacement data in the time domain;
- to employ the enhanced displacements, downstream from the HDF processing, toward possible modal dynamic identification purposes within the frequency domain, aiming at estimating the modal characteristics of the considered infrastructure.

To prove that the proposed monitoring methodology is competitive, leading to visible benefits to the structural identification process, the modal natural frequencies identified from post-processed displacements are then compared with the frequencies identified from raw data. The effectiveness of the method is proven, as well as its possible generalization to different typologies of structures.

The paper is organized as follows. In Section 2, a brief description of the structure of interest is outlined, with the reasons behind the choice of taking the Brivio bridge as a benchmark structure for the present analysis. In Section 3, the proposed monitoring strategy is formulated and presented. Then, the obtained results are reported and discussed in Section 4. Finally, last remarks and summary comments are provided within the conclusions reported in Section 5.

2 PRESENTATION OF THE MONITORED STRUCTURE

The peculiar class of structural systems to which this study is addressed to, aims at covering civil engineering structures characterized by a significant and strategic importance, possibly combined with a historical-architectural value. In particular, the monitored structure considered as a case study within the current analysis, is the RC Brivio bridge (1917) (Santarella and Miozzi [20], Ferrari et al. [6]), represented in following Fig. 1.

The bridge, located in northern Italy (Lombardia region), constitutes an important automotive connection between the provinces of Lecco and Bergamo, linking the banks of the Adda river (Brivio (LC) and Cisano Bergamasco (BG)), at an approximate height of 8 m from water.

About its description, the Brivio bridge consists of three spans, each characterized by a couple of parabolic arches, symmetrically located to the mid-longitudinal plane. The two spans

Figure 1: *RC three-span arched Brivio bridge (1917) over the Adda river.*

aside the river banks are 43.4 m long; the central span is 44 m long, for a total length of 130.8 m. The deck is 9.2 m wide and hosts two roadway lanes and two cantilever sidewalks, of a 0.8 m width each. The deck structural frame of each span is constituted by a grid supporting a RC slab of a thickness of 0.15 m. The peculiar parabolic arches of the bridge display a span of 42.80 m and a rise of 8.00 m. The symmetric arches show a cross section that is 0.60 m wide, with a height varying from 1.25 m (at the middle) to 1.37 m (at the ends). Sixteen vertical RC hangers, characterized by a rectangular cross section of sides of 0.32 m and 0.60 m, connect the deck to each arch. The bridge is supported on the river bed through two tapered concrete piers, each one presenting maximum dimensions at the basis equal to 12.8 m (transverse direction) and 3.8 m (longitudinal direction). The piers rest on foundation RC piles driven into the riverbed for a depth of 13 m to 16 m (Froio and Zanchi [9]).

The choice of Brivio bridge being taken as a benchmark structure for this study is motivated by the fact that, despite its age of more than one hundred years, the bridge is still subjected to continuous traffic loading, likely much heavier than that for which it was originally designed way back in 1917. Present use includes daily transit of heavy-duty and various vehicles in both rush hours and all day long. Indeed, similarly to other bridges located in the nearby territories (see e.g. the Paderno d'Adda bridge, Ferrari et al. [8], placed south downstream for just a few kilometers), the Brivio bridge still plays a crucial role in the local transportation network and, for this reason, it may largely benefit from a condition monitoring under operational conditions.

It is worth noting that all signals processed in the present analysis have been acquired during a three-day measurement campaign, performed directly on the Brivio bridge, in June 2014. Further details about such a measurement campaign, as for instance information about the employed measurement instrumentation, as well as on the sensor location, may be found in Ferrari et al. [4–7].

3 MONITORING METHODOLOGY DESCRIPTION

In this section, a comprehensive monitoring strategy for the health condition assessment of historic bridges is presented, by specifically assuming for illustration the case study of the

RC Brivio bridge under operational loading conditions. Both acceleration and displacement response signals, directly detected on the structure as an integrated sensor network are involved within the proposed scheme. In fact, acceleration-based and displacement-based recordings are commonly exploited towards vibration-based monitoring purposes, and the choice of which approach should be preferred, usually depends on the specific monitoring goals to be pursued, as well as on the physical configuration of the analyzed structure.

In particular, acceleration-based monitoring allows to detect changes in the structural health conditions, which may be revealed by identifying variations in the structural modal properties, such as natural frequencies, mode shapes or modal damping ratios, since these quantities may then be employed within damage detection strategies for the current condition assessment of the monitored structure. Displacement-based monitoring, on the other hand, is often exploited both for evaluating the presence of excessive loads under standard service conditions, and for quantifying regular operational loads (e.g. traffic), to serve as reference in bridge design practice.

In this sense, acceleration- and displacement-based monitoring approaches may be considered as complementary, in providing useful tools toward an effective global assessment of historic and strategic infrastructural systems. However, especially due to the increasing demand for the adoption of low-cost monitoring instrumentation during the signal acquisition stage, these measurements may typically be accompanied by a significant amount of noise, which contaminates the structural response itself, by increasing the induced uncertainties and rendering more difficult their employment for SHM purposes. Such a deleterious noise effect is generally more evident on displacement data rather than on acceleration data, due to the intrinsic limits characterizing the present displacement sensor technology.

To address this issue, in the proposed monitoring methodology, a denoising-based approach is possibly integrated with a HDF-based procedure, aiming at exploiting the (more reliable) acceleration measurements for clarifying the dynamic displacement response signal of the bridge, acquired by means of a non-contact QDaedalus system (Bürki et al. [1]). The so obtained purified displacement data may then be employed toward modal identification purposes, e.g. for extracting the natural frequencies and the mode shapes of the monitored structure, and assessing its current structural conditions.

The present methodology combines a time domain analysis and a frequency domain analysis, as illustrated in the flowchart of Fig. 2, representing a global conceptual view of the considered monitoring scheme.

The time domain analysis aims at a better appreciation of the raw displacement recordings, to be later exploited for modal identification purposes. In doing so, the additional availability of acceleration response data, collected by means of wireless MEMS accelerometers, can be taken at a disposal.

Differently from data acquired through wired piezoelectric accelerometers, which may be considered as a rather reliable recording devices, even such raw acceleration data may first need to be purified, by applying appropriate denosing techniques, for reducing the noise level affecting the signal, while preserving the useful information within the recorded signal. To this purpose, a Discrete Wavelet Transform (DWT)-based denoising technique is implemented within the monitoring platform, resulting in the clarification of the detected acceleration response signal. Details about the calibration of the DWT-based denoising settings, adopted within this study, are provided in the next section. It is worth mentioning that also a Singular Value Decomposition (SVD)-based approach might be employed for the denoising of dynamic response signals; however, dealing with non stationary signals, such as those involved in this analysis,

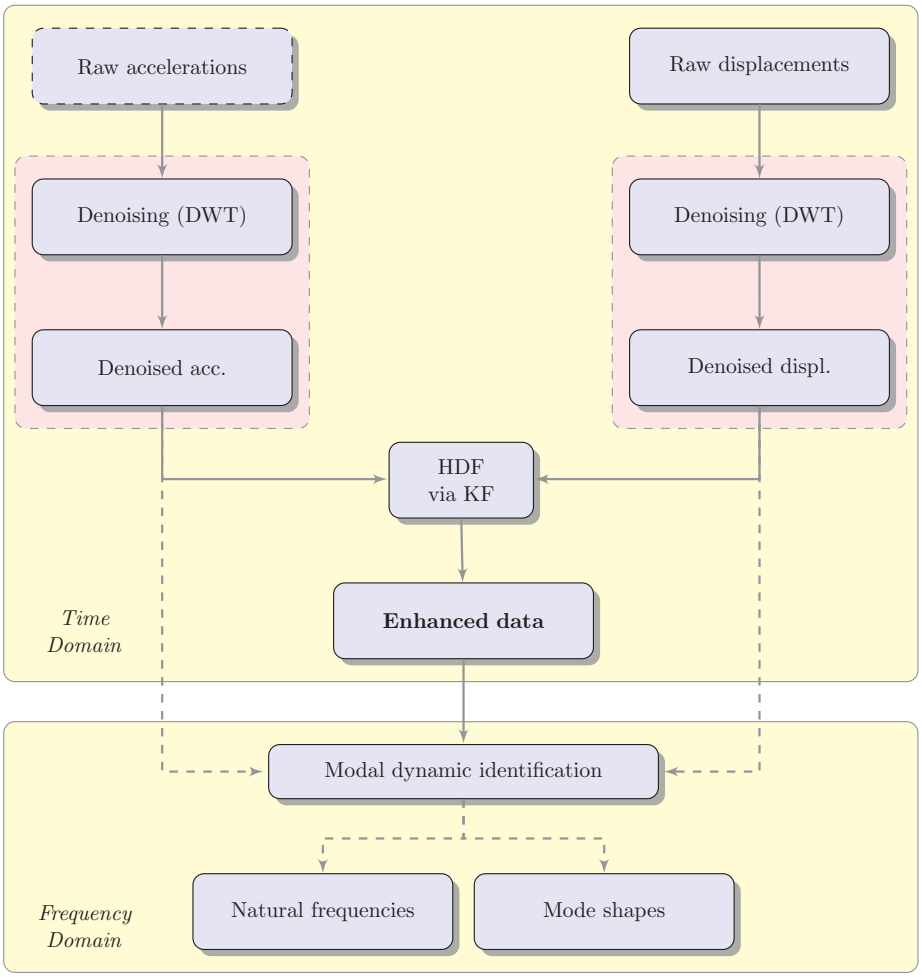

Figure 2: *Flowchart of the proposed monitoring methodology, integrating a denoising-based and a HDF-based approach for the enhancement of response data collected on the structure, and a subsequent structural dynamic identification.*

the DWT-based denoising approach should be preferred, as deeply shown and discussed in Ravizza et al. [18, 19].

In parallel to the (optional) acceleration denoising, a more frequently needed denoising of QDaedalus displacements is also foreseen. The same DWT-based technique is adopted, for the aforementioned reasons, and a preliminary cleaning effect on the signal is made achievable.

The core of the current implementation is now represented by the involvement of a Kalman filter (Chatzi and Fuggini [2]) within the HDF process, resulting in the merge of denoised QDaedalus displacements with acquired denoised accelerations, and an enhanced displacement response signal may be obtained.

A subsequent analysis within the frequency domain is also performed, in which the ambitious goal of successfully performing the modal dynamic identification on displacement data is inspected. In particular, the enhanced displacement response signal is employed for pursuing this purpose and, through an automatic peak-picking procedure performed on the Welch periodogram, the modal natural frequencies of the Brivio bridge may be identified.

It is worth noting that, as it can be appreciated from the flowchart in Fig. 2, the monitoring platform also contemplates the possibility to perform the modal dynamic identification of the structure by solely using either the denoised accelerations or the denoised displacements (dashed arrows in Fig. 2), but the results may be less reliable, especially considering just the displacements. However, they can be exploited for comparative purposes, aiming at highlighting the benefits deriving from a HDF-based methodology in assessing the current health conditions of the specific analyzed bridge, although such a monitoring platform also aims at assuming a more general connotation, being useful for the structural monitoring of any characteristic infrastructure.

4 RESULTS

In this section, some first outcomes obtained by applying the proposed monitoring methodology to the real case of the RC Brivio bridge, are shown. Time domain analysis results are firstly presented, followed by outcomes derived from a subsequent analysis within the frequency domain. Signals are taken from a measurement campaign as acquired and reported in Ferrari et al. [6].

4.1 Time domain analysis

The present analysis (upper box in Fig. 2) aims at purifying a raw displacement signal, making its features to emerge more clearly in the time domain, through an effective HDF with recorded accelerations, supposed to be more reliable. However, in some cases, a preliminary denoising of such acceleration data may also become necessary, e.g. when the sensor instrumentation employed in the signal acquisition phase is not so performing. Therefore, a DWT-based denoising technique is implemented on the detected (original) accelerations (from wireless sensors), and the obtained denoised signal is reported in Fig. 3, as compared with the original one.

Given the non-stationary nature of the response data, a 60 seconds length acceleration response signal from a wireless sensor is denoised, by applying a DWT-based denoising technique, which shall best fit with this signal typology, as shown in Ravizza et al. [18, 19]. In the same study, the optimal calibration of the parameters involved within this technique to deal with non-stationary signals is also inspected, resulting in the adoption of a *Smylet2* mother wavelet, combined with a *Heursure* hard thresholding rule, at decomposition level 2. Thus, the same setting is here assumed.

The effect of the denoising application is visible especially in the time window between 25 s and 40 s, as it may be appreciated in Fig. 3, leading to a signal reduction of 6.58%, in terms of Root Mean Square (RMS). The acceleration peak value is also considered, as it represents one most peculiar time domain signal feature, and a reduction of 9.11% is recorded. Such values are reported in following Table 1, for both the original and the denoised acceleration response signals.

An analogous DWT-based denoising approach is now implemented, for the preliminary clarification of the 60 seconds length QDaedalus displacement response signal, acquired on the Brivio bridge. Despite the very small amplitude of such recordings, which might affect the success of the denoising technique, the denoised estimates appear to be considerably clearer, if compared to the original (raw) data, as represented in Fig. 4.

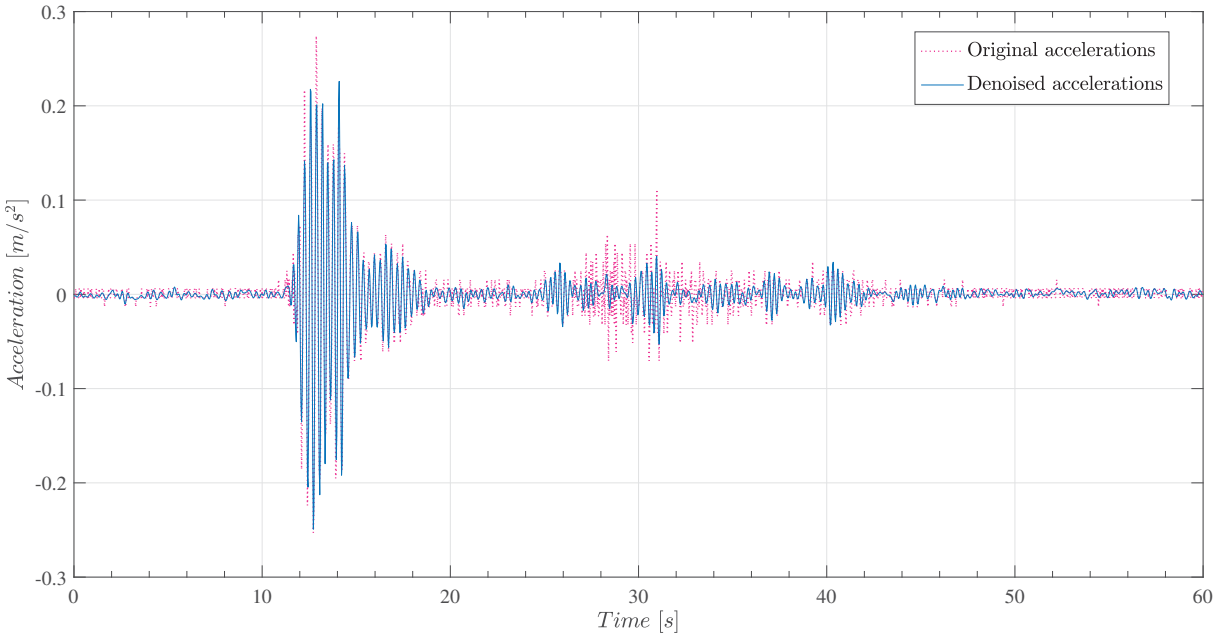

Figure 3: *Brivio bridge (wireless) acceleration response signal, pre and post DWT-based denoising.*

Acceleration signal	**RMS** $[m/s^2]$	Δ [%]	**Peak** $[m/s^2]$	Δ [%]
Original (raw) signal	0.0319		0.2742	
DWT denoised signal	0.0298	-6.58	0.2492	-9.11

Table 1: *Characteristic values of the analyzed acceleration response signals in the time domain and their variation with respect to the original (noise-affected) signal: RMS and peak acceleration values.*

After this preliminary phase, devoted to the pre-treatment of the acquired data, the obtained denoised acceleration and displacement response signals are then processed within a HDF-based implementation, aiming at further enhancing the measured displacements, by enriching them through the information embedded within the denoised accelerations. To this end, a Kalman Filter algorithm is exploited, allowing for the effective merge of the two heterogeneous source signals (Chatzi and Fuggini [2], Ferrari et al. [6], Ravizza et al. [17]). The result is represented by a new enhanced displacement signal, as shown in Fig. 5, which more reliably reflects the response of the monitored bridge.

To complete the time domain analysis, RMS and peak deflection values of the displacement signals are also computed, and summarized in Table 2. A reduction of both values, although lighter than that recorded in the previous acceleration case, is still observable, configuring itself as a peculiar feature of such techniques, as shown for synthetic signals in Ravizza et al. [19].

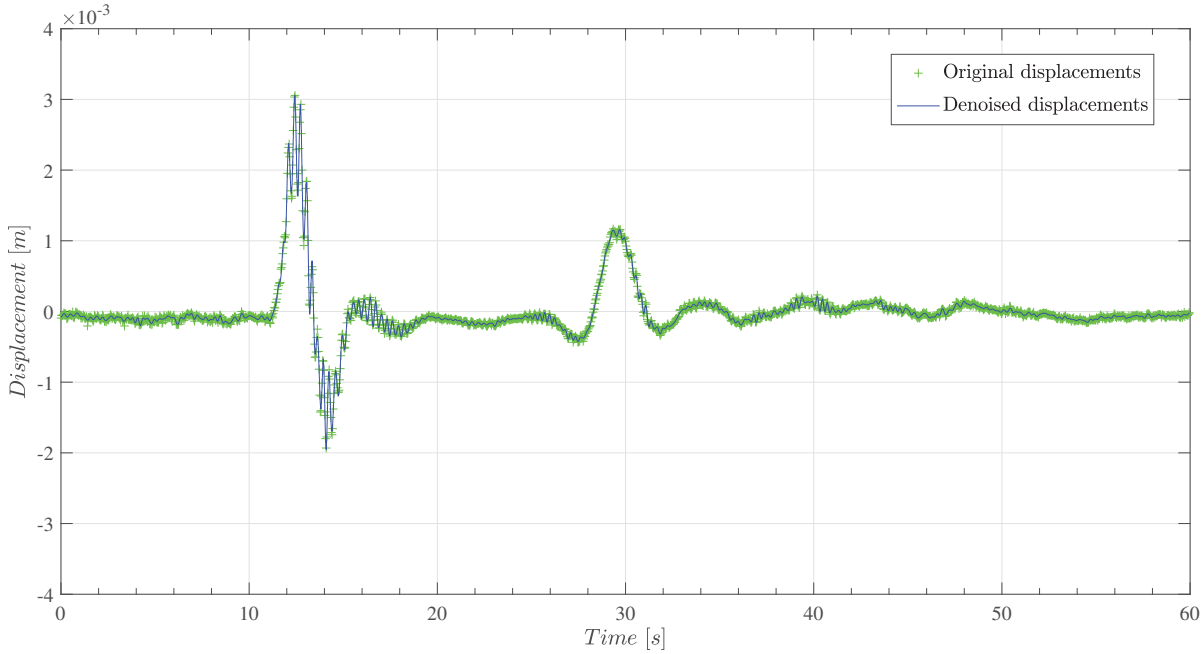

Figure 4: *Brivio bridge (total station) displacement response signal, pre and post DWT-based denoising.*

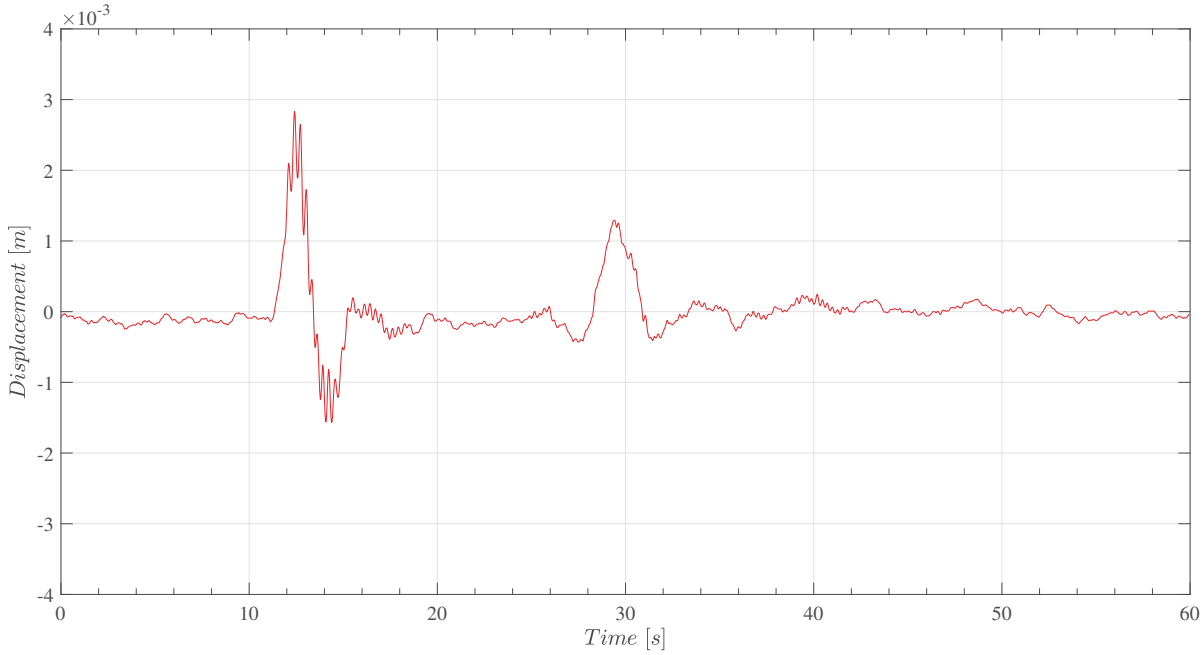

Figure 5: *Enhanced Brivio bridge displacement response signal, obtained by HDF via KF with the denoised acceleration response signal.*

Displacement signal	**RMS** $[mm]$	Δ [%]	**Peak** $[mm]$	Δ [%]
Original (raw) signal	0.4039		3.056	
DWT denoised signal	0.4001	-0.94	3.015	-1.34
HDF enhanced signal	0.3972	-1.66	2.833	-7.30

Table 2: *Characteristic values of the analyzed displacement response signals in the time domain and their variation with respect to the original (noise-affected) signal: RMS and peak deflection values.*

4.2 Frequency domain analysis

The enhanced displacement data, downstream obtained from the HDF procedure with the denoised accelerations, are now employed for performing a modal dynamic identification analysis in the frequency domain. In particular, by applying a Welch method on such displacements, the Power Spectral Density (PSD) function of the signal may be obtained. In following Fig. 6, the response spectrum derived from the HDF displacement signal and from the original (raw) displacement signal are represented and compared.

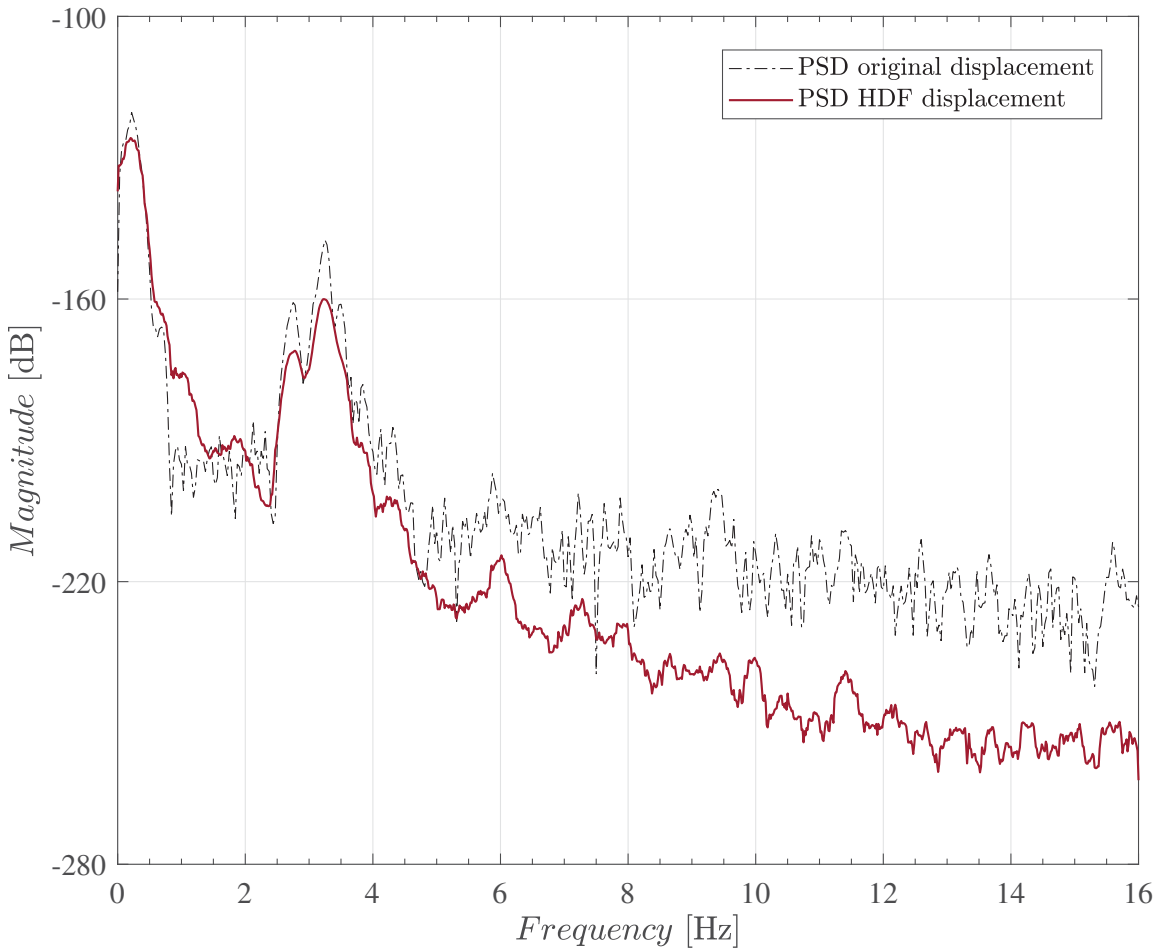

Figure 6: *Brivio Bridge displacement (PSD) response spectrum: original (raw) displacement signal vs. HDF (enhanced) displacement signal.*

The effect of the previously applied time domain filtering techniques (i.e. DWT-based denoising and KF application) is evident, resulting in smoother curves, as well as in the reduction of the signal magnitude, especially within the medium-high frequency region (approximately greater than 6 Hz), where the embedded noise mainly affects the data.

The benefits that the proposed methodology has brought to the identification process emerge by the comparison between the frequency content of the two signals. In fact, whether the original signal allows for the detection of just one frequency peak, corresponding to the first natural frequency of the bridge, the post-processed displacement signal reveals a greater number of frequency response peaks, which were previously indistinguishable, due to the deleterious effect of spurious noise. Consequently, a greater number of natural frequencies may be extracted.

However, due to the limited length of the time window, even the peaks associated to the external loading acting on the bridge (i.e. traffic load) might appear in the response spectrum, making the identification process harder. Thus, to distinguish such peaks from structural modes, an automatic peak-picking procedure is performed on the Welch periodogram, and the first eight natural frequencies of the monitored structure may be identified. To emphasize the benefits that the proposed methodology may bring to the identification process, the same peak-picking technique is performed on the PSD of the original (raw) displacement signal, leading to the identification of the first natural frequency only. Such a comparison is represented in Fig. 7, where the modal natural frequencies are marked by vertical red lines and, then, further reported in Table 3, which coherently compare to analogous results provided in Ferrari et al. [6], namely frequencies identified through a classical FDD method on acceleration signals acquired out of standard wired accelerometer sensors.

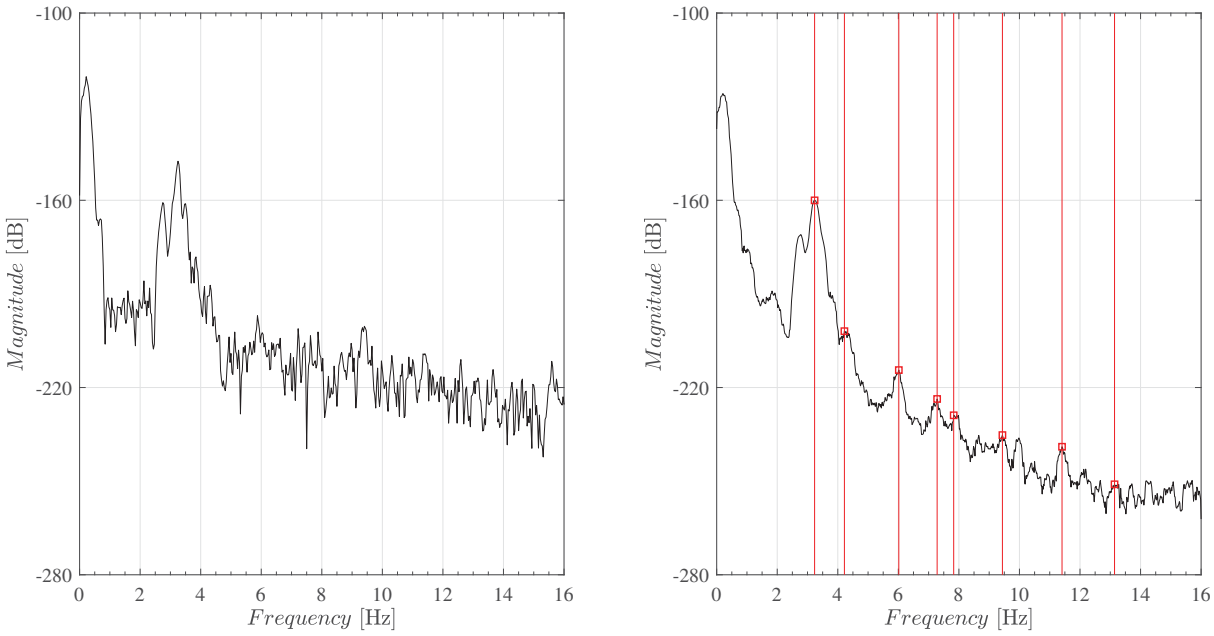

Figure 7: *Brivio bridge identified natural frequencies from displacement signals. Peak-picking procedure on Welch periodogram: original (raw) displacement signal vs. HDF (enhanced) displacement signal.*

Except for the first two and the sixth natural frequencies, which display a not negligible discrepancy with the respective outcomes deriving from a FDD-based inverse analysis on wired

Modes	**I**	**II**	**III**	**IV**	**V**	**VI**	**VII**	**VIII**
$f_{id,WD}$ [Hz]	3.247	4.211	6.016	7.280	7.815	9.378	11.406	13.140
$f_{id,AC}$ [Hz]	3.564	3.857	6.018	7.178	7.690	9.009	11.377	13.086
Δ [%]	−8.89	9.18	−0.03	1.42	1.63	4.10	0.25	0.41

Table 3: *Brivio bridge natural frequencies $f_{id,WD}$ identified from a HDF displacement response signal (wireless sensor), compared to frequencies $f_{id,AC}$ (Ferrari et al. [6]) identified from an acceleration response signal (wired sensor), and their variation.*

accelerations, assumed here as reference, the results show a good agreement, as the percentage variation is in any case below 2%.

Finally, from a FDD analysis (Pioldi et al. [10–12]) on displacement signals (corroborated as above by acceleration data), the bridge first span mode shapes, corresponding to the previously identified frequencies, are obtained and represented in following Fig. 8. In particular, the QDaedalus displacement data, enriched by reliable accelerations, as those acquired through a wireless detection system, represent the selected 8-channel input considered within the current analysis, for the representation of the mode shapes of the monitored structure.

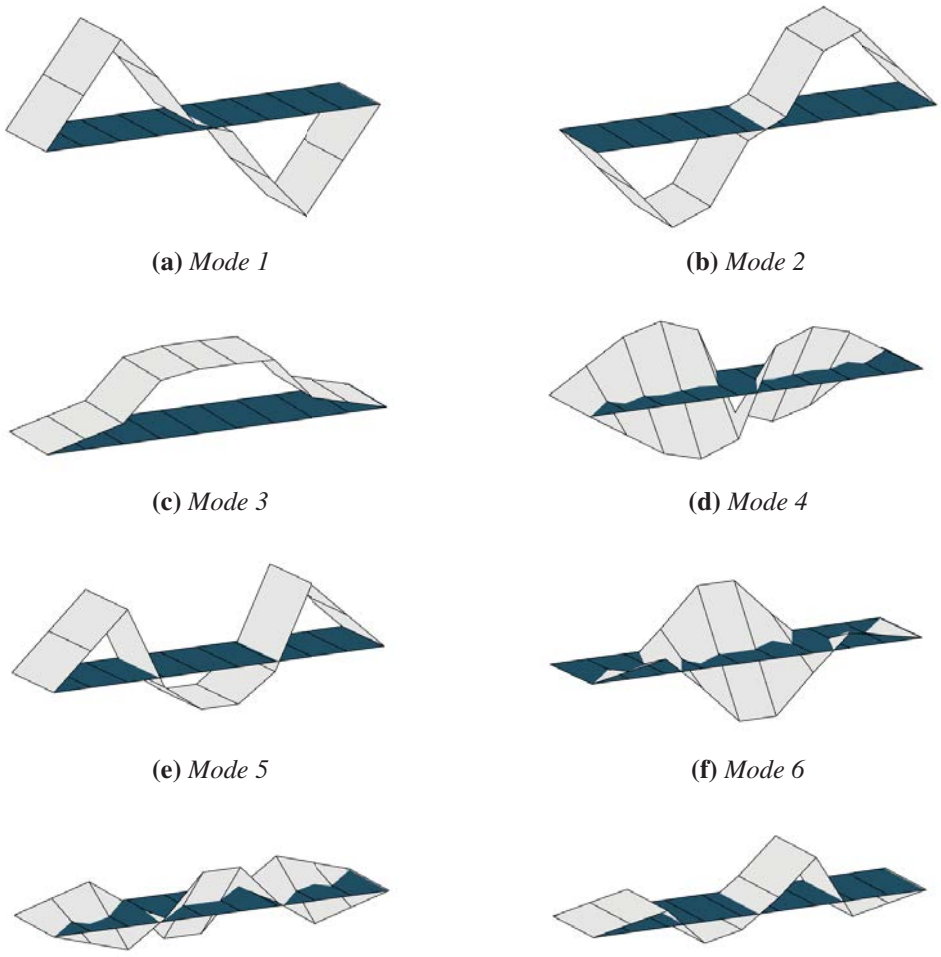

(a) *Mode 1* **(b)** *Mode 2*

(c) *Mode 3* **(d)** *Mode 4*

(e) *Mode 5* **(f)** *Mode 6*

(g) *Mode 7* **(h)** *Mode 8*

Figure 8: *FDD vibration mode shapes of Brivio bridge first span.*

Even concerning the vibration mode shapes, many analogies with the respective results reported in Ferrari et al. [6] may be observed. In particular, mode 1 and mode 2 show a very similar behaviour, although they are related to different natural frequencies. Moreover, most of the modes seem to be regular, characterized by bending or torsion, except for mode 7, in which bending and torsion appear to be coupled.

These similarities between the results may be considered as a further proof of the reliability of the proposed monitoring strategy, which provides an alternative approach aiming at evaluating the structural health condition of a generic civil structural system.

5 CONCLUSIONS

In this paper, an innovative monitoring methodology that integrates a denoising-based approach with a HDF-based strategy is proposed, for the structural health condition assessment of historic and strategic bridges. In particular, the main achievements that the present study has highlighted may be summarized as follows:

- the beneficial effect of the analyzed denoising technique is more pronounced within the time domain, where, after the DWT-based denoising application, the main signal features (i.e. peak value and RMS) may more clearly emerge;
- the acquired Brivio bridge acceleration and displacement response signals have been successfully denoised and, subsequently, involved within a HDF-based implementation, and an enhanced displacement response signal has been obtained;
- the output-only modal identification analysis performed on the enhanced displacement signal reveals the natural frequencies of the investigated structure, proving the effectiveness of the proposed methodology;
- by comparing the obtained results, by effective post-processing of response signals detected through wireless sensors, with those derived from signals acquired through standard wired sensors, no substantial differences emerge: this reinforces the belief that modern wireless sensor technology may become competitive at the signal acquisition stage, if adequately treated as here described, leading to reliable estimates.

In conclusion, the possibility of setting a monitoring platform that integrates a denoising-based approach with a HDF-based strategy may allow the user to achieve a more complete and reliable description of specific response signals, bringing to light their more peculiar characteristics, in both time and frequency domains. In this sense, the post-processing methodology presented in this study, may constitute a useful tool within structural monitoring applications.

Acknowledgments

Public research support from *"Fondi di Ricerca d'Ateneo ex 60%"* and a ministerial doctoral grant and funds at the ISA Doctoral School, University of Bergamo, Department of Engineering and Applied Sciences (Dalmine), are gratefully acknowledged. Prof. Chatzi and Dr. Dertimanis have received funding from Horizon 2020, the EU's Framework Programme for Research and Innovation, under grant agreement number 769373 (Project: FORESEE).

REFERENCES

[1] Bürki, B., Guillaume, S., Sorber, P. and Oesch, H. (2010), DAEDALUS: a versatile usable digital clip-on measuring system for total stations. In: *International Conference on Indoor Positioning and Indoor Navigation*, Zürich, Switzerland, 15–17 September 2010.

[2] Chatzi, E.N. and Fuggini, C. (2012), Structural identification of a super-tall tower by GPS and accelerometer data fusion using a multi-rate Kalman filter. In: *Proceedings of the 3rd International Symposium on Life-Cycle Civil Engineering*, Delft, Netherlands, 3-6 October 2012, 10: 144–151.

[3] Chatzi, E.N. and Fuggini, C. (2015), Online correction of drift in Structural Identification using artificial white noise observations and an Unscented Kalman filter. *Smart Structures and Systems*, 16(2): 296–328.

[4] Ferrari, R., Froio, D., Chatzi, E.N., Gentile, C., Pioldi, F. and Rizzi, E. (2015), Experimental and numerical investigation for the structural characterization of a historic RC arch bridge. In: *COMPDYN 2015, 5th ECCOMAS Thematic Conference on Computational Methods in Structural Dynamics and Earthquake Engineering*, Crete Island, Greece, 25-27 May 2015, 1: 2337–2353, available online in Eccomas Proceedia, www.eccomasproceedia.org/conferences/thematic-conferences/compdyn-2015/3542.

[5] Ferrari, R., Pioldi, F., Rizzi, E., Gentile, C., Chatzi, E.N., Klis, R., Serantoni, E. and Wieser, A. (2015), Heterogeneous sensor fusion for reducing uncertainty in Structural Health Monitoring. In: *UNCECOMP 2015, 1st ECCOMAS Thematic Conference on International Conference on Uncertainty Quantification in Computational Sciences and Engineering*, Crete Island, Greece, 25-27 May 2015, pp. 511–528, available online in Eccomas Proceedia, www.eccomasproceedia.org/conferences/thematic-conferences/uncecomp-2015/4289.

[6] Ferrari, R., Pioldi, F., Rizzi, E., Gentile, C., Chatzi, E.N., Serantoni, E. and Wieser, A. (2016), Fusion of wireless and non-contact technologies for the dynamic testing of a historic RC bridge. *Measurement Science and Technology*, 27(12): 1–19.

[7] Ferrari, R., Froio, D., Rizzi, E., Gentile, C. and Chatzi, E.N. (2018), Model updating of a historic concrete bridge by sensitivity- and global optimization-based Latin Hypercube Sampling. *Engineering Structures*, 179(January 2019): 139–160.

[8] Ferrari, R., Cocchetti, G. and Rizzi, E. (2019), Reference structural investigation on a 19th-century arch iron bridge loyal to design-stage conditions. *International Journal of Architectural Heritage*, Conservation, Analysis, and Restoration. Published online on 05 July 2019: 1-31. DOI: 10.1080/15583058.2019.1613453.

[9] Froio, D. and Zanchi, R. (2014), Finite element modelization and modal dynamic analyses of an historical reinforced concrete bridge with parabolic arches. *MSc Thesis in Building Engineering*, Advisor Rizzi E., Co-Advisor Ferrari R., University of Bergamo, School of Engineering, 232 pages.

[10] Pioldi, F., Ferrari, R. and Rizzi, E. (2015), Output-only modal dynamic identification of frames by a refined FDD algorithm at seismic input and high damping. *Mechanical Systems and Signal Processing*, 68-69(February 2016):265–291.

[11] Pioldi, F., Ferrari, R. and Rizzi, E. (2015), Earthquake structural modal estimates of multi-storey frames by a refined FDD algorithm. *Journal of Vibration and Control*, 23(13):2037-2063.

[12] Pioldi, F., Ferrari, R. and Rizzi, E. (2017), Seismic FDD modal identification and monitoring of building properties from real strong-motion structural response signals. *Structural Control and Health Monitoring*, 24(11):1-20.

[13] Pioldi, F. and Rizzi, E. (2017), Refined Frequency Domain Decomposition modal dynamic identification from earthquake-induced structural responses. *Meccanica*, 52(13):3165-3179.

[14] Pioldi, F. and Rizzi, E. (2017), A refined Frequency Domain Decomposition tool for structural modal monitoring in earthquake engineering. *Earthquake Engineering and Engineering Vibration*, 16(3):627-648.

[15] Pioldi, F. and Rizzi, E. (2018), Assessment of Frequency versus Time Domain enhanced technique for response-only modal dynamic identification under seismic excitation. *Bulletin of Earthquake Engineering*, 16(3):1547-1570.

[16] Pioldi, F. and Rizzi, E. (2018), Earthquake-induced structural response output-only identification by two different Operational Modal Analysis techniques. *Earthquake Engineering and Structural Dynamics*, 47(1):257-264.

[17] Ravizza, G., Ferrari, R., Rizzi, E. and Chatzi, E.N. (2018), Effective heterogeneous data fusion procedure via Kalman filtering. *Smart Structures and Systems*, 22(5): 631–641.

[18] Ravizza, G., Ferrari, R., Rizzi, E., Dertimanis, V. and Chatzi, E.N. (2019), Denoising corrupted structural vibration response: critical comparison and assessment of related methods. In: *Proceedings of the 7th International Conference on Computational Methods in Structural Dynamics and Earthquake Engineering (COMPDYN 2019), An ECCOMAS Thematic Conference, An IACM Special Interest Conference, M. Papadrakakis, M. Fragiadakis (eds.), 24-26 June 2019, Hersonissos, Crete Island, Greece, Institute of Structural Analysis and Antiseismic Research, National Technical University of Athens (NTUA), Conference Proceeding ID: 19291, Category: RS02 - ALGORITHMS FOR STRUCTURAL HEALTH MONITORING*, 12 pages.

[19] Ravizza, G., Ferrari, R., Rizzi, E., Dertimanis, V. and Chatzi, E.N. (2020), Critical assessment of two denoising techniques for purifying structural vibration response signals. *To be submitted.*

[20] Santarella, L. and Miozzi, E. (1948), Ponti Italiani in Cemento Armato. Milano: Hoepli.

EURODYN 2020
XI International Conference on Structural Dynamics
M. Papadrakakis, M. Fragiadakis, C. Papadimitriou (eds.)
Athens, Greece, 23–26 November 2020

APPLICATION OF WAVELET SYNCHRO-SQUEEZED TRANSFORM (WSST) METHOD TO RAILWAY BRIDGE HEALTH MONITORING

N. Mostafa[1], **R. Loendersloot**[1], **D. Di Maio**[1] **and T. Tinga**[1]

[1] University Twente, Drienerlolaan 5 7522 NB Enschede, The Netherlands
e-mail: n.mostafa@utwente.nl

Keywords: Health monitoring, WSST, Vehicle-Bridge interaction

Abstract. *Typically, the identification of resonant frequencies in railway bridges is carried out from free-decay stationary signals as a train leaves the bridge. The same identification proves very challenging when nonstationary vibrations are measured as a train traverses the bridge. Despite the numerous attempts, nonstationary signals with low modulating frequencies are still difficult to be processed. This paper attempts to evaluate the bridge-vehicle first bending resonance by a method known as Wavelet Synchro-Squeezed Transform (WSST). The significant advantage of this signal processing method is to deal with low-frequency modulations, which are typical of long bridges. This research focusses on a Finite Element Model (FEM) of a bridge simulating the nonstationary vibration responses exerted by a spring-mass model traversing the bridge. The paper sets two objectives, and the first one is to investigate how the WSST analyses nonstationary signals generated by the FE model. The instantaneous frequency trace of the bridge-vehicle system will be compared to a similar frequency trace, that is created by performing several modal analyses at different locations of the bridge. The second objective of the paper is to investigate if the instantaneous frequency obtained from WSST is suitable for damage detection, as the FE model is fitted with damages. Both objectives are met, and the results will be presented. The trace of the first natural frequency matches well the one calculated by the WSST, and the instantaneous frequency shows to be capable of detecting damages included in the model.*

1 INTRODUCTION

Understanding the vibration response in Vehicle-Bridge interaction is challenging because the actual instantaneous frequency will depend on the instantaneous location of a moving load. It is therefore understandable that Structural Health Monitoring (SHM) methods, aimed at identifying damage to assess the structural integrity and safety of a structure, have complicated problems to solve. Nevertheless, damage detection techniques have been developed.

In general, the majority of vibration-based damage detection techniques can be grouped into four categories. The first group, the traditional approach, contains the modal-based damage detection techniques [1,2]. These techniques are based on extracting and monitoring the modal properties, which can vary due to the presence of damage. The second group contains structural health monitoring based on Vehicle-Bridge interaction (VBI) response [1-3]. The third one involves model-based techniques which are based on updating the parameters of an analytical or numerical model such that the model matches the real measurements [3,4,5]. The fourth group contains data-driven methods (DDMs). Silva et al. [6,7,8] believe that SHM approaches are in the statistical pattern recognition paradigm.

Most damage detection researches have shown that a singularity appears in the forced vibration signal once damage occurs [9]. Yang et al [10] stated that a discontinuity appears in the acceleration signal when the moving load is in the vicinity of damage. The structure also exhibits non-linear behaviour once the moving load crosses the damage [11]. Therefore, the forced vibration response contains a 'damage event' triggered by the moving load making it more sensitive than the free vibration response. For this reason, a large number of research studies has been devoted to the second group, the vehicle-bridge interaction response.

VBI refers to the dynamic coupling between a bridge and a moving vehicle. VBI has been widely studied in the literature for detecting damage in bridges by analyzing the bridge response (direct methods) or the vehicle response (indirect methods). The focus of the current study is on the damage detection techniques of bridges by analyzing the VBI response measured on the bridge (direct methods). Literature [11,12,13] indicates that the target signal for the majority of the techniques is the bridge mid-span time-deflection response. From a practical point of view, there are motivations to study the bridge acceleration rather than the deflection signal. Firstly, it might not be possible to measure the bridge deflection signal at mid-span directly. Secondly, in comparison with the deflection signal, the bridge acceleration signal is more sensitive to damage [14]. However, the acceleration signal also contains more noise making it challenging to analyze. Continuous Wavelet Transform (CWT) , Discrete Wavelet Transform (DWT) [1], Hilbert Huang Transform (HHT) [4], Empirical Mode Decomposition (EMD) [5] and Ensemble Empirical Model Decomposition (EEMD) [6] have been mostly applied to identify damage [15,16].

Regardless of the applied method, the damage indicators are associated with a singularity. This one does not exist in the healthy bridge and appears in the response of the damaged structures [9]. Furthermore, the singularities are caused by a stiffness change and, therefore, the time-dependent stiffness should be visible in time-dependent resonances (the Instantaneous Frequency: IF). However, IF has only been investigated for the bridge mid-span displacement signal. Roveri et al [11] applied HHT on the mid-span deflection of a modelled bridge. In the first IF of the system, a crest appeared at the instant of damage occurrence. The current paper proposes an approach by applying Synchrosqueezed Wavelet Transform (WSST) on the VBI acceleration response to extract the Instantaneous Frequency (IF) of the system to detect a localized stiffness change. The research work is based on numerical simulations obtained from a Finite Element Model of a real bridge (Boyne Viaduct) located in Ireland. The bridge was refurbished and instrumented with a vibration response monitoring system, which provides many

test data. Considering the healthy conditions of the bridge, the authors decided to investigate the matter numerically and evaluate the WSST technique, as provided in the MATLAB function toolbox.

2 NUMERICAL MODEL AND MODAL SIMULATIONS

Although a large amount of vibration data is available for the Boyne bridge, the measurements are not applicable for the validation of the proposed damage detection approach, because of the recent refurbishments. Hence, to verify the proposed approach, a bridge is modelled numerically.

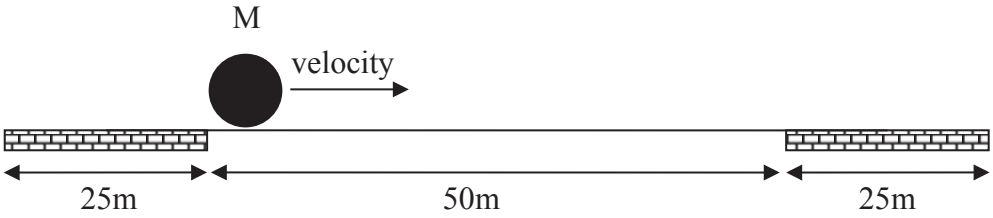

Figure 1: The schematic of the numerical model

All finite element simulations are conducted in a two-dimensional space in ABAQUS where the analysis scheme is chosen to be the implicit time integration. A beam with 50 m of length, 1 m of thickness and 0.5 m of width with Young's modulus of E = 210 GPa and density of ρ = 7860 kg/m3 is implemented as a bridge model. The same geometry has been already used in [17,18] for damage detection. However, the model is modified for the current study due to the moving mass. The forced response of the bridge corresponds to the period during which the mass is moving on the bridge. Achieving free vibrations from the bridge requires the mass should be removed from the bridge. However, the moving mass generates kinetic energy during the forced response analysis, which cannot be removed instantaneously to simulate the free vibration. Hence, approaching and leaving length are added before and after the bridge to properly locate the mass during the forced and free vibrations (see Figure 1).

Three dynamic analysis steps are implemented to calculate the bridge acceleration, corresponding to the mass approaching, crossing and leaving the bridge, as shown in Figure 1. Both approach and leave phases are modelled with beam elements that are clamped in all their nodes. The approaching part is not strictly necessary but is used to provide symmetry to the structure. The bridge model (the centre part of 50 m) has 200 elements, and the benchmark simulation corresponds to a point mass equal to 10% of the bridge mass which slides with a speed of 5 m/s over the bridge. The contact of the mass with the bridge is modelled using a hard node to surface interaction [19]. In the FEM model, the vehicle is considered to be a moving point mass (M) (i) to induce a non-stationarity to the simulated signal [20] and (ii) to investigate the time-varying resonance of the system due to the moving mass.

To implement the damage in the model, the stiffness (or equivalently the elastic modulus E) of a single element at the damage location (mid-span) is reduced [21] to simulate pitting- corrosion or a loose connection. In addition to the benchmark simulation, four groups of simulations are executed to verify the proposed approach for various operational conditions and health states. In the first group, moving masses equal to 5% and 20% of the bridge mass are simulated, and the bridge is considered healthy.

Modal analysis solutions were initially carried out with the mass positioned at specific locations of the bridge. Figure 2 shows the first and second resonances of the bridge as a collection of all the natural frequencies calculated at several locations. Interestingly, the location of the mass on the bridge has a relevant effect on the natural frequencies, which for the first resonance

is very marginal at the extreme locations but more relevant as it is moved towards the mid-span of the bridge. Similarly to the first one, the second shows an equivalent behaviour. The second resonance frequency is unaffected when the mass is positioned mid-span, which as expected as this is a nodal point of the second resonance. This basic modal analysis approach provides a useful insight on what one should expect from the IF recovered by the WSST method, in particular regarding the first bending resonant mode.

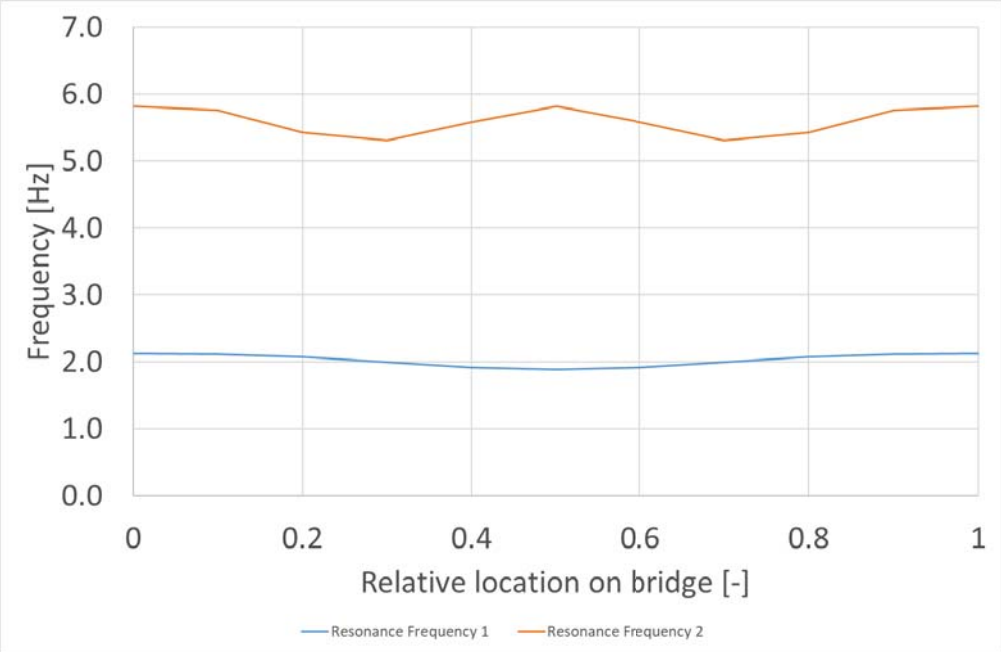

Figure 2: First and Second modal frequencies of the bridge with the mass moved at various locations

3 TIME RESPONSE SIMULATIONS AND RESULTS

A time response simulation of the moving load is carried out in Abaqus with the model earlier introduced. This paper will not focus on any uncertainty deriving from the non-uniform stiffness distribution of the bridge or the non-uniform crossing velocity or the Signal-to-Noise Ratio of typical real acquisitions.

Figure 3 shows the simulated acceleration signal for the undamaged bridge, at the bridge mid-span, where both the forced and the free decay vibration can be appreciated. Despite the simple approach, it was immediately noticed that the very first sample of the vibration vector contained high spikes, as the mass slide from an infinitely rigid surface to a flexible one. Those were removed and not taken into account since most of the vibration energy of those spikes would affect high-frequency modes, not relevant in this paper. Therefore, the signal for the Entrance Phase is a horizontal line at zero acceleration which is not plotted and not used for this study. The Traverse Phase and the Leaving Phase will be analyzed in two steps, such as (i) time series separation and (ii) application of the WSST to each of the time series.

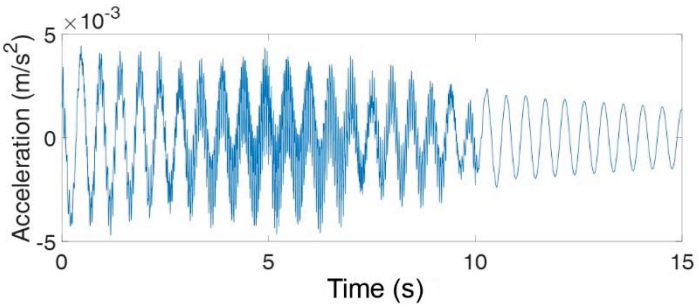

Figure 3: Acceleration simulated during the traversing and leaving phase.

Given the velocity of the moving mass 5 m/s and the length of the bridge, 50 m, the mass leaves the bridge at t = 10 s. The second step is to extract the bridge frequencies by applying WSST to the signal of the Leaving Phase. Figure 4 a&b presents the Instantaneous Frequency of the traversing and leaving (bridge free vibration signal) phases. It can be seen that the Leaving Phase signal only contains the bridge first frequency (2.1 Hz) which is constant in time as expected for a stationary signal. Then, this frequency component should be tracked in the Traverse Phase by again applying WSST. The result is the Synchrosqueezed transform (SST) matrix with the rows and columns corresponding to frequency and time, respectively. The 2D density plot of the SST matrix is shown in Figure 4a in which the IF is displayed as a frequency ridge. This ridge can be extracted as a time-frequency vector by finding the corresponding frequency of the local maxima at each time instant. It is straightforward to observe the similarity between the frequency traces described by the modal solution for the first natural frequency and the one retrieved by processing the time series with the WSST method. Furthermore, Figure 4 shows how the resonance conditions are time-dependent because of the instantaneous location of the moving load.

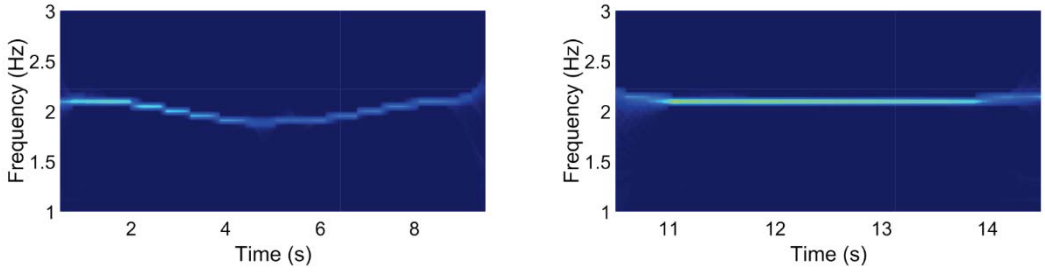

a: Traverse phase *b: Leaving phase*

Figure 4: Ifs of the first resonance frequency in the traversing and leaving phase.

3.1 Simulation results

A set of time response simulations were carried out to observe how the IF changes when the mass ratio is changed, to simulate different operating conditions as different train weight traversing the bridge. Figure 4 displays the bridge first resonance frequency, which varies in time depending on the magnitude and the location of the moving mass. For the benchmark simulation, the bridge frequency reduces to 1.9 Hz due to the added mass of the vehicle when it is located at mid-span (t = 5 s). As expected, IF depends on the different mass ratio, the highest the lowest the resonant frequency. Several papers investigated the dynamic behaviour of a bridge subjected to damage, some of those are referenced in here [22-27].

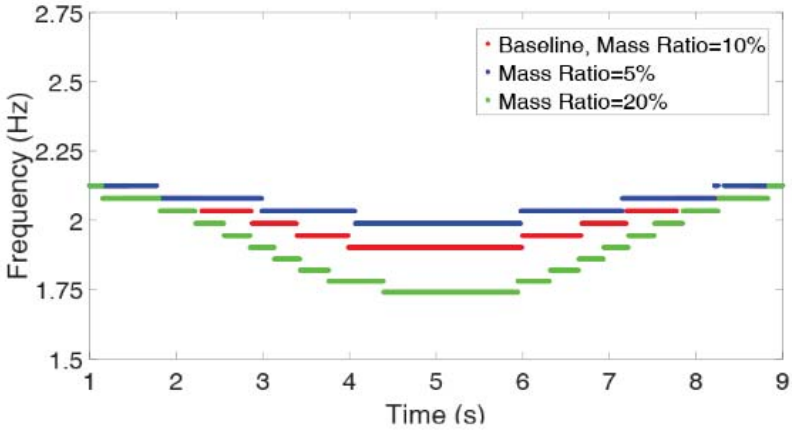

Figure 5: Change of IF caused by various Mass Ratios

The simulations were carried out by changing the mid-span element Young's modulus by 30%, 50% and 70%, respectively, by using the baseline model with mass ratio 10%. Both 50% and 70% are somewhat unrealistic damage conditions for a bridge. However, the purpose is to investigate the sensitivity of the IF to the appearance of damage. Figure 6 shows how the instantaneous resonant frequencies change as the moving load traverses the region where the damaged element was setup. This statement is not difficult to comprehend because the WSST resolves for the highest vibration energy at every point and frequency and, therefore, the instantaneous resonant frequency becomes even lower as the load is near to the weak spot.

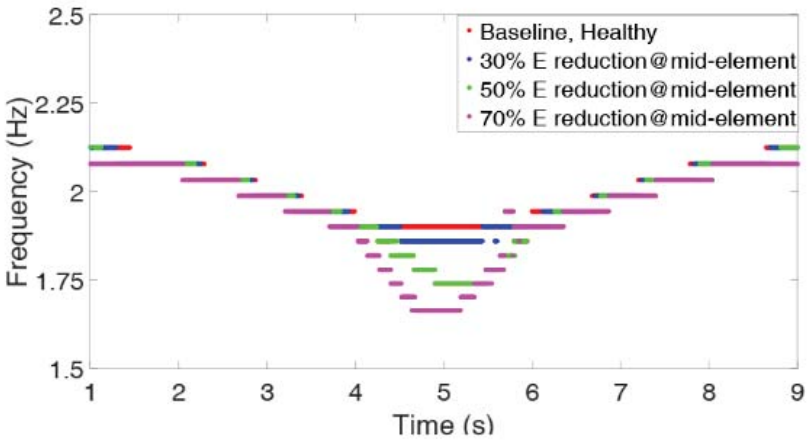

Figure 6: Change of IF caused by element stiffness reduction at the mid-span

As a closing remark of this section, one can appreciate that potential of the WSST as provided by the function toolbox of Matlab. Hence, a much thorough investigation of the system parameters governing the signal processing of the WSST method may increase its capacity beyond this simple simulated case study.

4 CONCLUSIONS

This paper presents for the first time a novel application of the WSST signal processing to the calculation of the instantaneous first resonant frequency of a bridge traversed by a moving mass. The WSST can be potentially exploited in health monitoring where the vibration signals could be processed in a *quasi* real-time as the train has crossed a bridge. It was demonstrated

that the WSST identifies the instantaneous resonant frequency, and which was verified against modal analysis results. Furthermore, it was showed that the IF is sensitive to the presence of damage. This behaviour was demonstrated by fitting the model with damages at the mid-span of the bridge. The IF presented a sudden discontinuity where the damage was set up for all three severity selected for these attempts.

REFERENCES

[1] He, W.-Y. and S. Zhu, Moving load-induced response of damaged beam and its application in damage localization. *Journal of Vibration and Control*, 2016. **22**(16): p. 3601-3617.

[2] Khorram, A., M. Rezaeian, and F. Bakhtiari-Nejad, Multiple cracks detection in a beam subjected to a moving load using wavelet analysis combined with factorial design. *European Journal of Mechanics - A/Solids*, 2013. **40**: p. 97-113.

[3] Zhang, W., et al., Damage detection in bridge structures under moving loads with phase trajectory change of multi-type vibration measurements. *Mechanical Systems and Signal Processing*, 2017. **87**: p. 410-425.

[4] Roveri, N. and A. Carcaterra, Damage detection in structures under traveling loads by Hilbert-Huang transform. *Mechanical Systems and Signal Processing*, 2012. **28**: p. 128-144.

[5] Meredith, J., A. Gonzalez, and D. Hester, Empirical Mode Decomposition of the acceleration response of a prismatic beam subject to a moving load to identify multiple damage locations. *Shock and Vibration*, 2012. **19**(5): p. 845-856.

[6] Aied, H., A. Gonzalez, and D. Cantero, Identification of sudden stiffness changes in the acceleration response of a bridge to moving loads using ensemble empirical mode decomposition. *Mechanical Systems and Signal Processing*, 2016. **66-67**: p. 314-338.

[7] S.W. Doebling, C. R. Farrar, M.B. Prime, A summary review of vibration-based damage identification methods, *The Shock and Vibration Digest*, 1998, 30:91-105

[8] J. J. Moughty, J. R. Casas, A state of the art review of modal-based damage detection in bridges: Development, challenges, and solutions, *Applied Sciences-Base*, 2017, 7(5):510. https://doi.org/10.3390/app7050510

[9] M. I. Friswell, Damage identification using inverse methods, *Philos Trans A Math Phys Eng Sci* 2007, 365:393–410. doi:10.1098/rsta.2006.1930.

[10] R. V. Farahani, D. Penumadu, Damage identification of a full-scale five-girder bridge using time-series analysis of vibration data, Engineering Structures, 2016, 115:129-139. doi:10.1016/j.engstruct.2016.02.008

[11] J. Li, S. S. Law, H. Hao, Improved damage identification in bridge structures subject to moving loads: Numerical and experimental studies, *International Journal of Mechanical Sciences* 2013, 74:99–111. doi:10.1016/j.ijmecsci.2013.05.002.

[12] M. Silva, A. Santos, E. Figueiredo, R. Santos, C. Sales, J. C. W. A. Costa, A novel unsupervised approach based on a genetic algorithm for structural damage detection in bridges, *Engineering Applications of Artificial Intelligence*, 2016, 52:168–180. doi:10.1016/j.engappai.2016.03.002.

[13] G. Comanducci, F. Magalhaes, F. Ubertini, A. Cunha, On vibration-based damage detection by multivariate statistical techniques: Application to a long-span arch bridge, *Structural Health Monitoring*, 2016, 15(5):505–524. doi:10.1177/1475921716650630.

[14] A. Santos, E. Figueiredo, M. Silva, R. Santos, C. Sales, J. C.W. A. Costa, Genetic-based EM algorithm to improve the robustness of gaussian mixture models for damage detection in bridges, *Structural Control & Health Monitoring*, 2017, 24 (3). doi:10.1002/stc.1886.

[15] A. Gonzalez, D. Hester, An investigation into the acceleration response of a damaged beam-type structure to a moving force, *Journal of Sound and Vibration*, 2013, 332:3201-3217. doi:10.1016/j.jsv.2013.01.024.

[16] J. N. Yang, Y. Lei, S. Lin, N. Huang, Hilbert-Huang based approach for structural damage detection, *Journal of Engineering Mechanics*, 2004, 130(1):85–95. doi:10.1061/(Acse)0733-9399(2004)130:1(85).

[17] N. Roveri, A. Carcaterra, Damage detection in structures under traveling loads by hilbert-huang transform, *Mechanical Systems and Signal Processing*, 2012, 28:128–144. doi:10.1016/j.ymssp.2011.06.018.

[18] B.F. Yan, A. Miyamoto, A comparative study of modal parameter identification based on wavelet and Hilbert-Huang transforms, *Computer-Aided Civil and Infrastructure Engineering*, 2006; 21(1):9-23. doi: 10.1111/j.1467-8667.2005.00413.x.

[19] K.V. Nguyen, Comparison studies of open and breathing crack detections of a beam-like bridge subjected to a moving vehicle. *Engineering Structures*, 2013; 51:306-314. doi:10.1016/j.engstruct.2013.01.018.

[20] D. Hester, A. Gonzalez, A wavelet-based damage detection algorithm based on bridge acceleration response to a vehicle, *Mechanical Systems and Signal Processing*, 2012, 28:145–166. doi:10.1016/ j.ymssp.2011.06.007.

[21] Z. Feng, M. Liang, F. Chu, Recent advances in time–frequency analysis methods for machinery fault diagnosis: A review with application examples. *Mechanical Systems and Signal Processing*, 2013; 38(1):165-205. doi:10.1016/j.ymssp.2013.01.017.

[22] H. Aied, A. Gonzalez, D. Cantero, Identification of sudden stiffness changes in the acceleration response of a bridge to moving loads using ensemble empirical mode decomposition, *Mechanical Systems and Signal Processing*, 2016, 66-67:314–338. doi:10.1016/j.ymssp.2015.05.027.

[23] X. Q. Zhu, S. S. Law, Wavelet-based crack identification of bridge beam from operational deflection time history, *International Journal of Solids and Structures*, 2006, 43(7-8):2299–2317. doi:10.1016/j.ijsolstr.2005.07.024.

[24] M. A. Mahmoud, Effect of cracks on the dynamic response of a simple beam subject to a moving load, Proceedings of the Institution of Mechanical Engineers Part F-Journal of Rail and Rapid Transit, 2001, 215(3):207–215. doi:10.1243/0954409011531521.

[25] A. Saleeb, A. Kumar, Automated finite element analysis of complex dynamics of primary system traversed by oscillatory subsystem, *Computational Methods in Engineering Science and Mechanics*, 2011, 12(4):184–202. doi:10.1080/15502287.2011.580830.

[26] A. Poulimenos, S. Fassois, Parametric time-domain methods for nonstationary random vibration modelling and analysis — a critical survey and comparison, Elsevier 20 (4) (2005) 763 – 816. doi:10.1016/j.ymssp.2005.10.003.

[27] W. Zhang, J. Li, H. Hao, H. Ma, Damage detection in bridge structures under moving loads with phase trajectory change of multi-type vibration measurements, *Mechanical Systems and Signal Processing*, 2017, 87:410–425. doi:10.1016/j.ymssp.2016.10.035.

EURODYN 2020
XI International Conference on Structural Dynamics
M. Papadrakakis, M. Fragiadakis, C. Papadimitriou (eds.)
Athens, Greece, 23–26 November 2020

DETECTION OF CLAMPING FORCE LOSS IN BOLTED JOINTS OF RAIL SUPPORTS IN CONSIDERATION OF CHANGING AMBIENT TEMPERATURE

A.-L. Dreisbach[1], V. Yokaribas[1], G. Dietrich[1], D. Sahm[2], D. Pak[2], and C.-P. Fritzen[1,3]

[1] Department of Mechanical Engineering, University of Siegen, 57076 Siegen, Germany
e-mail: anna-lena.dreisbach@uni-siegen.de

[2] Department of Civil Engineering, University of Siegen, 57076 Siegen, Germany
e-mail: pak@bau.uni-siegen.de

[3] Center of Sensor Systems (CESS), University of Siegen, 57076 Siegen, Germany
e-mail: claus-peter.fritzen@uni-siegen.de

Keywords: Rail support, bolted joint, clamping force, electro-mechanical impedance, SHM.

Abstract. *Rail supports are important components of rail construction as their task is to attach rail tracks and transfer occurring loads to the ground. Failure e.g. caused by fatigue cracking or loss of clamping force can cause catastrophic consequences up to derailment. In this work a possible approach for feature detection in order to detect a loss of clamping forces is investigated by applying the electro-mechanical impedance (EMI) method. The EMI method is a high frequency vibration-based structural health monitoring technique which is carried out by piezoelectric wafer active sensors (PWAS) attached to the mechanical structure to be monitored. In order to detect a loss of clamping force in this work two PWAS where attached to the bolted joint of a rail support and the imaginary part of the complex electro-mechanical admittance spectrum (reciprocal of the impedance) was evaluated. As it is known that PWAS measurements are sensitive to variations of ambient temperature a strategy to reduce temperature effects in a range of 0 °C-50 °C is also considered. First experiments show that the investigated technique is promising to distinguish variations of the measured signals which are caused by variations of clamping force from variations caused by changing ambient temperature.*

1 Introduction

The task of Structural Health Monitoring (SHM) is to observe structural properties to ensure the structure's integrity. Its field of application is wide; typical structures to be monitored are aerospace, civil structures or wind energy plants. The monitoring process entails several advantages e.g. the prolongation of service life due to condition-based maintenance and the reduction of inspection time as a consequence of the automated monitoring process [1]. In this study the structures to be monitored are rail supports. These components are an important part of rail construction as their task is to attach rail tracks and transfer occurring loads to the ground. Failure due to the loss of clamping force can cause catastrophic consequences. As real structures like rail supports exist in an environment they are affected by environmental influences like vibrations, humidity, ambient induced noises, etc.. To take changing ambient temperature into account a strategy to reduce temperature effects is investigated. The purpose is to detect variations of clamping forces in the presence of changing temperature by application of the electromechanical impedance method (EMI). As the temperature effects alter the measured signals and can cause 'false alarm' [2, 3] they have to be compensated. There are different methods to remove temperature influences. In [2] it is presented that temperature variations lead to horizontal and vertical shifts of impedance signatures. The efficient frequency shift (EFS) concept based on minimization of the root mean square deviation (RMSD) was introduced in order to shift the signals horizontally for removing the temperature induced shifts. In [4, 5] the authors also utilize EFS based on the maximization of the correlation coefficient (CC).

Table 1: Studies utilized EMI under varying temperatures

Analysed quantity	**Load**	**Damage**	**Publication**
real(Z)	-	X (added mass, hole, cut,..)	[5, 2, 6]
real(Z)	-	X (bolt loosening)	[9]
real(Z)	X	X (bolt loosening)	[10]
real(Z)	X	-	[8]
real(Z), imag(Z)	-	X	[7]
imag(Y)	-	-	[3]
imag(Y)	-	X (detection of clamping force)	this study

The EFS was applied in further studies [6, 7, 2] in order to compensate the temperature effects on the real part of the impedance (real(Z)). In [8] the EFS was used to monitor prestress-loss in prestressed concrete (PSC)-girders and it was found that in presence of varying temperature as well as varying prestress the resonances of the real part of the impedance spectra shift

horizontally. Whereas temperature changes cause approximately the same frequency shifts of

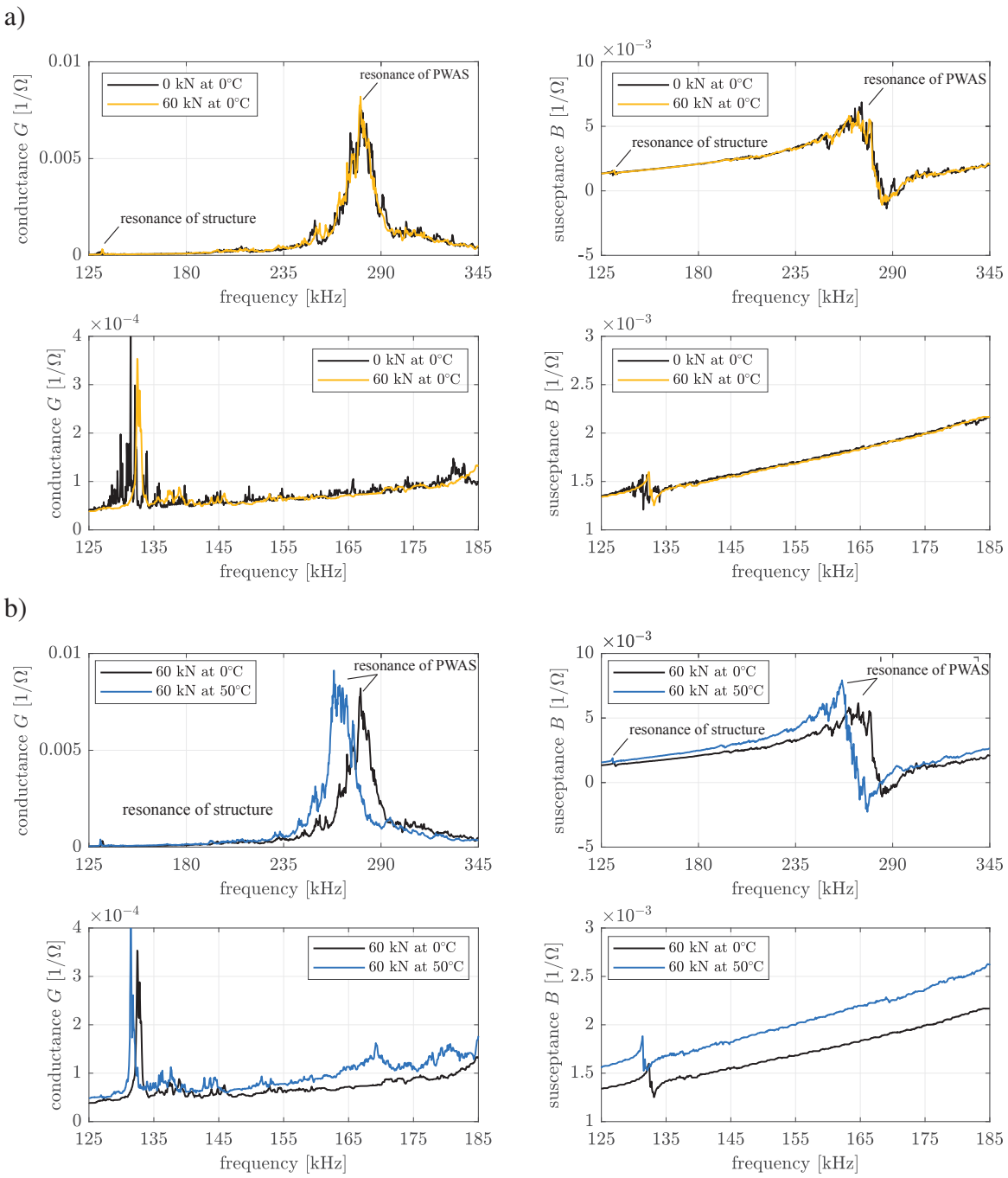

Figure 1: Temperature compensation a) Effects of changing clamping force on conductance and susceptance in a frequency range of 125-185 kHz and 125-345 kHz, respectively b) effects of changing ambient temperature on conductance and susceptance in a frequency range of 125-185 kHz and 125-345 kHz, respectively

the resonant peaks but damage generates different frequency shifts of the resonances. In [9] a bolted steel girder connection was monitored in the presence of varying temperatures. In the damaged cases one or more bolts were loosened from reference torque to a torque of 35 Nm. In [10] also bolt loosening was monitored under varying temperature but also under varying loading. The damage was introduced by loosening one of ten bolts with a half turn. The object to monitor was an aircraft composite wing segment model. An overview of works that applied

the EMI method under varying temperature conditions can be found in table 1. Instead of the real part of the impedance which was used to identify the structural's state in the studys mentioned before, in this work the imaginary part of the admittance Y (reciprocal of impedance), the susceptance (Im(Y)), was used to monitor the loss of clamping force in the presence of temperature variations. As the susceptance also includes resonances of the structure and therefore reflects the structure's state. In [3] it was found that a great effect of temperature influence on the susceptance spectra is the changing signal's slope. At increasing temperature the slope also increases. Furthermore the resonance frequencies move into direction of lower frequencies. These properties and also the EFS concept have been used in this work for reducing the temperature effects on the signals. The purpose of this study is to find an approach for a possible indicator which detects a loss of the clamping force at an incipient state under varying temperature to adjust this defect before failure of the joint occurs.

2 Methodology

In own preliminary studies the effects of temperature and clamping force on conductance and susceptance have been investigated. Exemplary results of these studies are shown in figure 1 which represent the effects of temperature and varying clamping force on the conductance (Re(Y)) and the susceptance (Im(Y)) spectra in the investigated frequency range of 125-185 kHz and additionally 125-345 kHz. The broad frequency range between 125 kHz-345 kHz contains the structural resonances as well as the resonance of the PWAS. In contrast to that the narrow frequency range of 125 kHz-185 kHz only contains the structural resonances but with higher resolution. This is justified by the utilized measurement device which provides a maximum resolution of 1024 points in the defined frequency range. In figure 1 a) the influence of changing clamping force is visible by observing the conductance as well as the susceptance spectra. Whereas in relation to the susceptance this effect is mainly visible in the frequency range very close to the structural resonance. In figure 1 b) the effect of varying temperature is shown. The narrow frequency plot of the conductance shows large changes over the complete displayed frequency range. In contrast to that the susceptance mainly shows a shifting and a changing of the slope. Additionally the height of the peaks at the resonance frequency changes and the signals fluctuate more with rising temperatures (see blue graph at $\approx$ 170 kHz). But apart from that the curve almost remains invariant in the presence of changing ambient temperature. As the temperature effects are easier adjustable it has been As a result of these observations it has been decided to evaluate the susceptance in order to develop a strategy to reduce temperature effects on the signals. The aim of this strategy is to remove the slope as well as the horizontal and vertical shift of the temperature affected signals. The reduction of the temperature effects of the recorded signals was conducted in four steps: First the signal's slopes were determined by means of the linear least squares method. Second the slope and the difference between the offset of the baseline and the x-axis were removed. As a result the signals have horizontal orientation and zero offset. Therefore the peaks at the resonance frequency as well as the surrounding peaks can be easier identified and EFS can be applied. The EFS was carried out by finding the frequency shift $\delta\hat{f}$ were correlation is highest in the third step and shifting the signals horizontally about this distance in the fourth step. In order to detect the differences of clamping forces the RMSD-metric shown in equation 7 was used. For removing the slope of the signals a rotation matrix according to equation 1 was applied in order to rotate the signals about the origin $(0 \mid 0)$:

$$\hat{X_j}^{(k)} = R_{\perp}^{(k)}(\alpha_k) X_j^{(k)} \tag{1}$$

where $\hat{X}_j^{(k)}$ contains the rotated data vectors and $X_j^{(k)}$ the original data of the k'th state.

$R_\perp^{(k)}(\alpha_k)$ is the rotation matrix for computing rotations by the angle α_k about the normal axis. The rotated data matrix $\hat{X}_j^{(k)}$ is given in equation 2:

$$\hat{X_j}^{(k)} = \begin{bmatrix} \text{——} & \hat{f}_j^{(k)T} & \text{——} \\ \text{——} & \hat{B}_j^{(k)T} & \text{——} \end{bmatrix} \tag{2}$$

where $\hat{f}_j^{(k)}$ and $\hat{B}_j^{(k)}$ are the rotated data vectors of the frequency and the susceptance of the k'th state. The original data matrix $X_j^{(k)}$ is given in equation 3:

$$X_j^{(k)} = \begin{bmatrix} \text{——} & f_j^{(k)T} & \text{——} \\ \text{——} & B_j^{(k)T} & \text{——} \end{bmatrix} \tag{3}$$

where $f_j^{(k)}$ and $B_j^{(k)}$ are the original data vectors of the frequency and the susceptance of the k'th state. The rotation matrix is defined as follows:

$$R_\perp^{(k)}(\alpha_k) = \begin{bmatrix} cos(\alpha_k) & -sin(\alpha_k) \\ sin(\alpha_k) & cos(\alpha_k) \end{bmatrix} \tag{4}$$

where α_k is the slope angle of the k'th state signal. Its connection to the slope m_k of a linear function is defined in equation 5:

$$m_k = tan(\alpha_k) \tag{5}$$

Afterwards the converted signals are shifted by the EFS horizontally and vertically by removal of the mean value according to equation 6.

$$\tilde{B}_j^{(k)} = \hat{B}_j^{(k)}(\hat{f} - \delta\hat{f}) - \mu_k \tag{6}$$

where $\delta\hat{f}$ is the EFS and μ_k the mean value of the signal's k'th state. By this operation the signal's offset is 0 and the signals have a comparable range. Which also leads to an approach of the heights of the susceptance peaks of the temperature affected signals. For evaluation the root mean square deviation (RMSD) was applied as follows:

$$RMSD^{(k)} = \frac{\sum_{j=1}^{N}\left[\tilde{B}_j^{(k)} - \tilde{B}_j^{(0)}\right]^2}{\sum_{j=1}^{N}\left[\tilde{B}_j^{(0)}\right]^2} \tag{7}$$

Where $\tilde{B}_j^{(0)}$ is the susceptance signal of the baseline's state and $\tilde{B}_j^{(k)}$ the k'th state. For showing the efficiency of the temperature compensation strategy introduced before the temperature affected original data is compared with the temperature compensated data. The RMSD-algorithm shown in equation 7 is normalized by the baseline. As the baseline is converted by the temperature compensation strategy, too, the RMSD is not suitable for comparing the original and converted data. Therefore only residuals are computed according to equation 8 and 9.

$$R^{(k)}(B_j) = \sum_{j=1}^{N}\left[B_j^{(k)} - B_j^{(0)}\right]^2 \tag{8}$$

$$R^{(k)}(\tilde{B}_j) = \sum_{j=1}^{N}\left[\tilde{B}_j^{(k)} - \tilde{B}_j^{(0)}\right]^2 \tag{9}$$

3 Experimental Setup and Test

In this section the analysed specimen, the experimental setup and data acquisition for performing EMI measurements are briefly described. The experiments were carried out on three specimen.

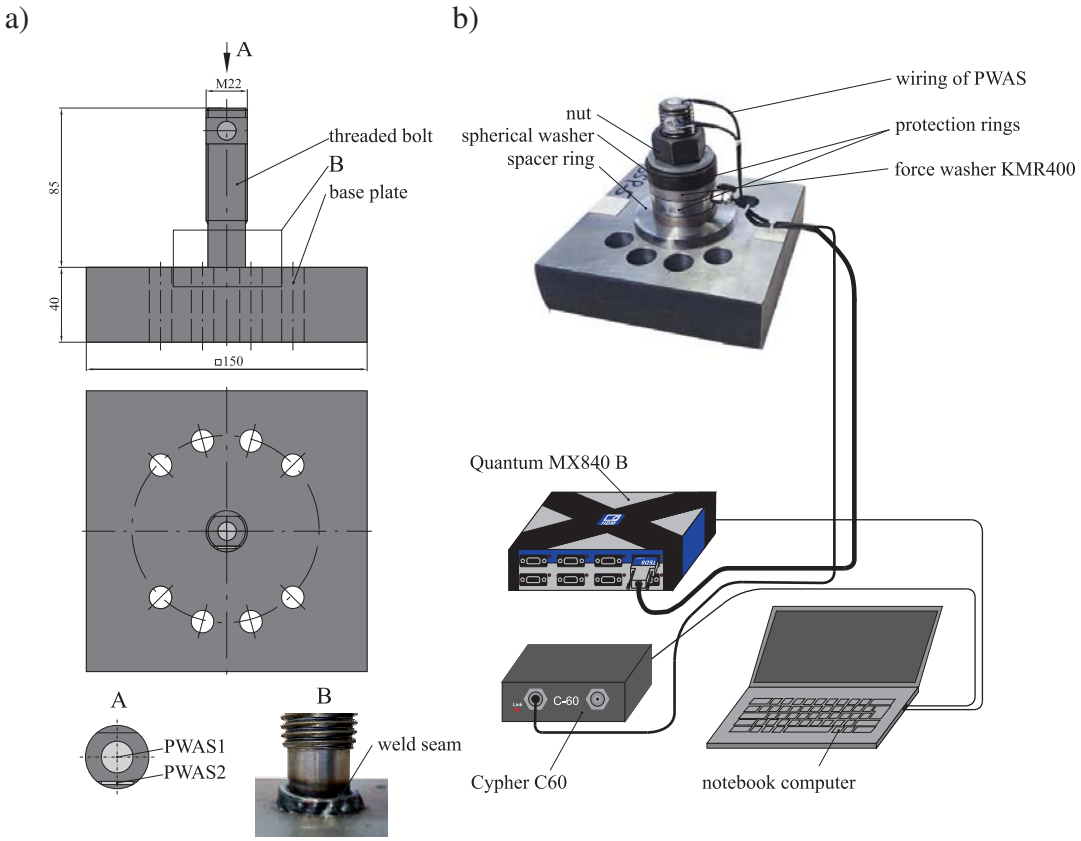

Figure 2: Experiments a) specimen with attached PWAS b) experimental setup

3.1 Specimen and Sensor Technology

The specimen consist of threaded M22-bolts which are welded onto base plates. The welding process is a fusion welding process without filler material. Both parts are composed of structural steel S355. For the experiments the bolts with a length of 85 mm have been welded onto squared 150 $\times$ 150 mm base plates having a thickness of 40 mm. The specimen including the sensors and actors, respectively, is depicted in figure 2a). For EMI measurements two piezoelectric wafer active sensors (PWAS) PI (type *PIC*) with a diameter of 10 mm and a thickness of 0.5 mm were installed according to figure 2. One transducer is positioned at the face side of the bolt (PWAS1). The second one (PWAS2) is arranged laterally at the circumferential surface of the bolt.

3.2 Experiments

For investigating temperature effects under varying clamping force the bolted connection was preloaded in steps of 10 kN starting at 30 kN until the maximum of 60 kN. The clamping force was increased at a temperature of 0°C. At every load step the specimen was heated in steps

of $10°C$ starting at $0°C$ until the maximum of $50°C$. The EMI measurements were carried out at every temperature step with PWAS 1 and PWAS 2 in the frequency range 125-185 kHz. During the experiments the specimen were placed in a *ACS* climatic chamber. The temperature was regulated by the temperature of the specimen with a *PT100* temperature sensor coming along with the *ACS* climatic chamber.

3.3 Measuremental Setup

In figure 2b) the measurement setup is shown. The clamping force was measured by a force washer *KMR400* coming along with two protection rings per flange which was clamped by a nut. Additionally a spherical washer was mounted between the nut and the force washer for compensation of misalignment of the bolt and to transfer the load orthogonal to the force washer. Beneath the bottom of the force washer a spacer ring having a bigger inner diameter than the other parts was mounted because the weld seam at the bottom of the bolt has also a bigger diameter than the bolt itself. The impedance analyser, *Cypher C60*, was used to supply an alternating voltage in the specified frequency range and to measure the corresponding admittance signatures across the two PZT transducers one by one. A notebook computer with Cypher software coming along with the *C60* was used for configuring the measurement settings and recording the admittance spectra. For excitation via *Cypher C60* the set frequency range is divided into 1024 discrete frequencies f_i in order to excite the structure at every single frequency sequentially and to measure the corresponding electro-mechanical impedance and admittance signatures, respectively. The structural response of one state is measured as the impedances Z_i at the single frequencies f_i. The signals of the *KMR400* as well as signals of the *PT100* sensor were measured with the amplifier *Quantum MX840 B* from *HBM*.

4 Results and Discussion

In order to show the efficiency of the temperature compensation strategy described previously in figure 3 the compensation of the temperatures for maximum clamping force are shown.

	frequency with highest amplitudes	evaluated frequency range
first sample	138,3 kHz	142 - 147 kHz
second sample	136,6 kHz	140 - 145 kHz
third sample	136,2 kHz	140 - 145 kHz

Table 2: Overview of frequency with highest amplitudes at $20°C$ and 60 kN clamping force and evaluated frequency ranges for all samples

The original susceptance signals shown in figure 3a) have been measured by PWAS1. The increasing slope and the horizontal shift of the resonance with increasing temperature are apparent. There are two clearly visible resonances. The resonance in the lower frequency range has higher amplitudes than the resonance in the higher frequency range. In figure 3b) the minimization of the temperature effects described previously are visible. This is confirmed by the residuals computed in the diagrams of figure 3c) and d). Note that in both cases the third measurement at $20°C$ was used as baseline and therefore is zero valued. In case of the maximum clamping force the residuals's of the temperature compensated data decreased between 85%

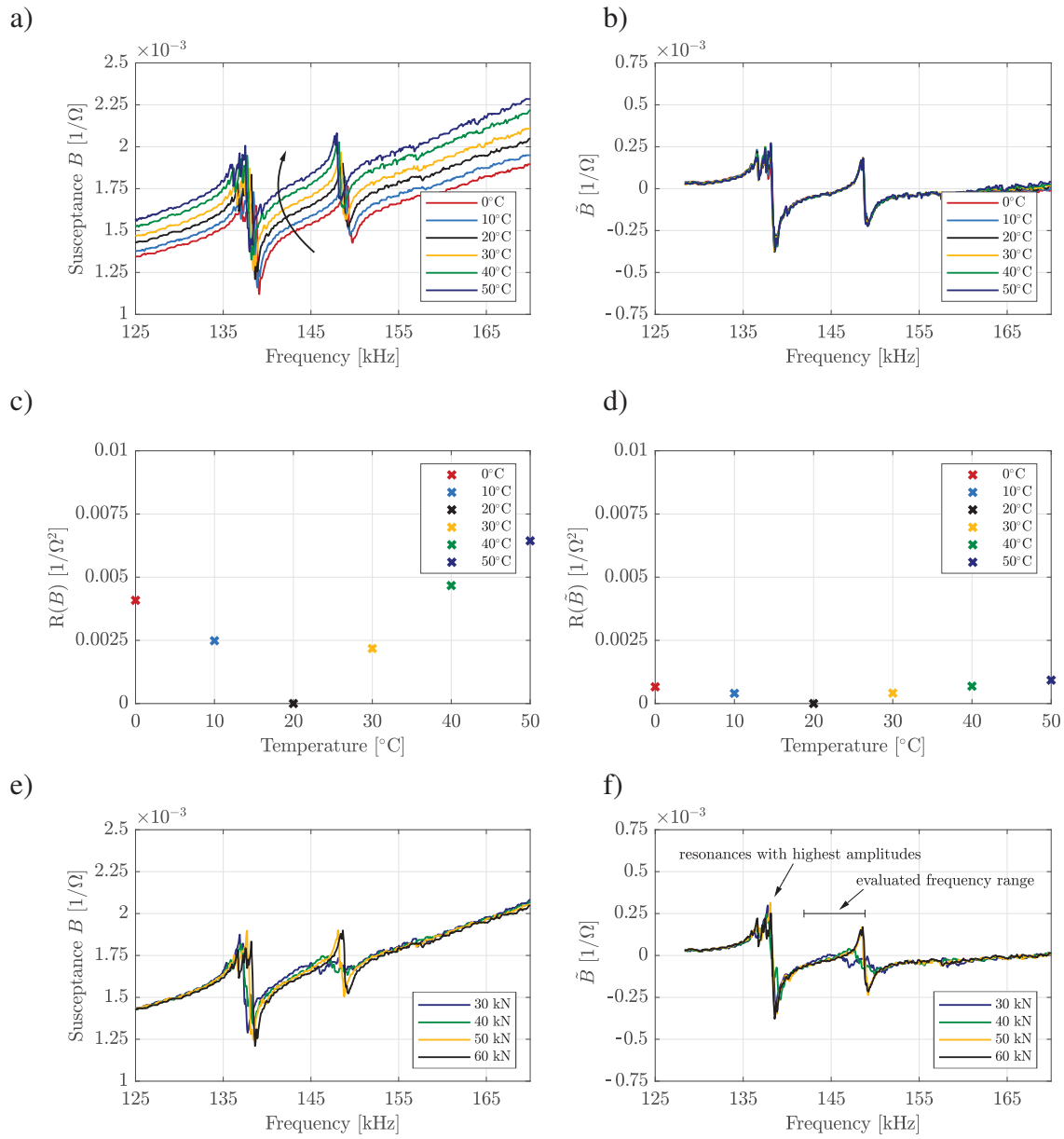

Figure 3: Temperature compensation a) original susceptance signals of 60 kN clamping force and varying temperatures b) temperature compensated signals for 60 kN clamping force c) residuals of original signals for 60 kN clamping force d) residuals for temperature compensated signals for 60 kN clamping force e) original susceptance signals measured at 20°C and variable load states f) temperature compensated signals measured at 20°C and variable load states

and 80% in comparison to the original data. In figure 3e) the original signals measured at 20°C and under variable load states from 30 kN to 60 kN are plotted. The corresponding temperature compensated signals are shown in figure 3f). Because the temperature compensation algorithm is based on maximum correlation, the signals are shifted until the resonances with higher amplitudes coincide. Temperature variation causes approximately the same frequency shift for the two resonances (see figure 3b)) and load variation causes different frequency shifts of the two resonances. Therefore the variation of the load state can be detected by evaluating the frequency range where the second resonances of the four load states are located. This frequency range is labelled in figure 3f). As the several resonance frequencies vary for the three specimen the

evaluated frequency range varies, too. The evaluated ranges are shown in table 2. In figure 4 the RMSD's for three specimen are depicted.

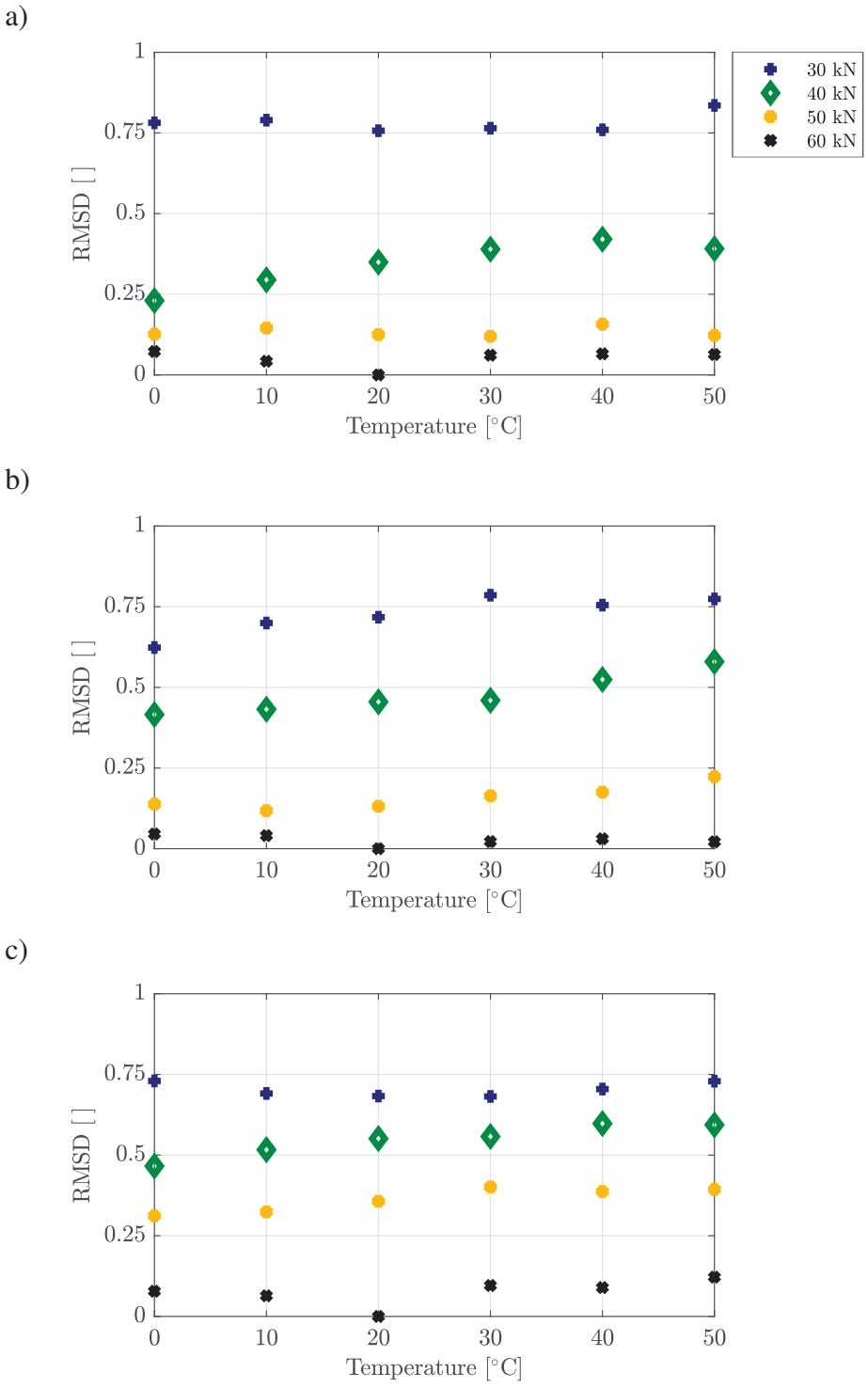

Figure 4: RMSD index for three specimen and seven load states under varying temperatures between 0°C and 50°C in comparison to the baseline at 60 kN load state and 20°C a) evaluated at 142-147 kHz b) evaluated at 142-147 kHz b) evaluated at 140-145 kHz b) evaluated at 140-145 kHz

The diagrams show four load states under varying temperature between $0°C$ and $50°C$. The state of 60 kN at a temperature of $20°C$ was used as baseline state. The load states of 30 kN, 40 kN, 50 kN and 60 kN are separable for each specimen. But the RMSD values for the several load states move in different ranges and fluctuate. A possible explanation regarding the fluctuations for constant load stages and varying temperatures can be made: Due to thermal expansion of the material the contact and tensioning, respectively, between the several components changes. But in total these changes can cancel each other out and as a result they may not be measurable by the force washer. Changing of the clamping force due to thermal expansion or setting behaviour can be precluded because the force washer itself has only shown negligible changes with varying temperatures. For the different behaviour of the indicator in case of the three samples two explanations are possible: As the specimen are manually welded and manual processes are often imprecise the specimen may differ from each other significantly. A further reason can be attributed to the tensioning and contact conditions between the clamped components of the bolted joints which can differ from each other.

5 Summary and Conclusions

In this work a possible feature for detection of the clamping force loss in the presence of varying temperatures in a range of $0°C$ to $50°C$ and a load range of 30 kN to 60 kN has been investigated. The susceptance as the imaginary part of the electromechanical admittance was used to detect changes of the pretension. In order to avoid 'false alarm' caused by temperature effects a temperature compensation strategy had to be applied. Temperature effects on the susceptance have been identified and minimized. First the technique was applied to measurements of one load state at varying temperature. The defined indicator for the assessment of the temperature compensation technique has shown a significant reduction of the discrepancies between the temperature affected signals within 80% and 85%. Afterwards the technique was applied to measurements of varying clamping force and varying temperature. The baseline was defined at the maximum clamping force and a temperature of $20°C$. Fluctuations of the indicator for constant load and under varying temperatures were observed. This behaviour was attributed to changing restraints of the individual clamped components caused by varying temperatures which in total may cancel out each other and therefore can not be registered by the force washer. By application of the proposed technique it may not be possible to detect the exact current load state but it could be used as a possible technique for detection of a significant loss of the clamping force.

REFERENCES

[1] V. Giurgiutiu.Structural Health Monitoring with Piezoelectric Wafer Active Sensors, ISBN:978-0-12-088760-6,2008.

[2] Park, G., Kabeya, K., Cudney, H. and Inman, D.J, Impedance-based Structural Health Monitoring for Temperature Varying Applications, *JSME International Journal*, **42**, 249–258,1999.

[3] I. Buethe, B. Eckstein and C.-P. Fritzen, Model-based detection of sensor faults under changing temperature conditions, *Structural Health Monitoring*, **13**, 109-119, 2013.

[4] S. Bhalla, A.S.K. Naidu and C.K. Soh, *Influence of Structure-Actuator Interactions and Temperature on Piezoelectric Mechatronic Signatures for NDE : Proceedings of SPIE Conference on Smart Materials, Structures,and Systems*, 2003.

[5] K. Y. Koo, S.H. Park, J.J. Lee and C.B. Yun, Automated impedance impedance-based structural health monitoring incorporating effective frequency shift for compensating temperature effects, *Journal of Intelligent Material Systems and structures*, **20**. 367-377.

[6] N. Sepehry, M. Shamshirsaz, F. Abdollahi, Temperature variation effect compensation in impedance-based structural health monitoring using neural networks, *Journal of Intelligent Material Systems and Structures*, **20**, 1-8, 2011.

[7] F. G. Baptista, D. E. Budoya, V. A. D. de Almeida and J. A. C. Ulson, An experimental study on the effect of temperature on piezoelectric sensors for impedance-based structural health monitoring, *Sensors*, **14**, 1208-1227.

[8] T.-C. Huyhn and J.-T. Kim, Compensation of temperature effect on impedance responses of PZT interface for prestress-loss monitoring in PSC girders, *Smart Structures and Systems*, **17**, 881-901, 2016.

[9] D.-S. Hong, K-D. Nguyen, I.-C. Lee, J.-T. Kim, Temperature-Compensated Damage Monitoringby Using Wireless Acceleration-Impedance Sensor Nodes in SteelGirder Connection, *International Journal of Distributed Sensor Networks*, **8**, 2012.

[10] H. J. Lim, M. K. Kim, H. Sohm, C. Y. Park, Impedance based damage detection under varying temperature and loading conditions, *NDTE International*, **44**,740-750, 2011.

EURODYN 2020
XI International Conference on Structural Dynamics
M. Papadrakakis, M. Fragiadakis, C. Papadimitriou (eds.)
Athens, Greece, 23–26 November 2020

NUMERICAL PERFORMANCE EVALUATION OF A BI-DIRECTIONAL ROLLER SEISMIC ISOLATION BEARINGS

Ricardo González[1], Nelson Ortiz-Cano[1], Andrés Nieto-Leal[1] and Carlos Gaviria-Mendoza[1].

[1]Department of Civil Engineering, Universidad Militar Nueva Granada, Cajicá, CU 250247, Colombia.
e-mail: ing.ricardo.gonzalez.olaya@gmail.com, nelson.ortiz@unimilitar.edu.co,
andres.nieto@unimilitar.edu.co, carlos.gaviria@unimilitar.edu.co

Keywords: Seismic isolation, Roller isolation systems, Bi-directional roller bearings.

Abstract. *Base isolation systems (BISs) are devices that mitigate the harmful effects of earthquakes on structures. Nowadays, designers are implementing this technology to bridge and building special projects located in areas of high seismic risk to improve their performance under earthquake excitations. However, high cost, uncertainty and lack of knowledge in the design have limited its massive use, specially in developing countries. According to the mechanical behavior, BISs are clasiffied in elastomeric bearings, sliding bearings and roller bearings. In this work, the performance of a bi-directional roller bearings system was evaluated; thus, the main objective of this publication is to show the efficiency of a bi-directional roller bearing in improving the structural seismic response of multicolumn systems by means of reducing accelerations and displacements. A numerical code in Matlab was written to simulate the response of the structures under base excitations, the finite element method (FEM) in conjunction with frame elements was used to solve the governing equations. The validation of the numerical model was done by direct comparisons between experimental and numerical data.*

1 INTRODUCTION

Various seismic isolation systems have been developed to protect buildings and reduce the potentially harmful effects produced by earthquakes. Isolations systems are commonly grouped into three types: (1) elastomeric bearings, (2) sliding bearings and (3) roller bearings. Jangid and Datta [1], Naeim and Kelly [2], Kunde and Jangid [3] and Harvey and Kelly [4] presented a comprehensive review of the study and use of these systems over the past three decades.

Seismic isolation systems, regardless of their type, partially decouple the horizontal motion between the structure and its base by incorporating a flexible interface with low lateral stiffness at the foundation level. This flexible interface corresponds to the isolation devices or seismic isolators, which allow to avoid that the natural frequencies of the structure coincide with the predominant frequencies contained in the seismic excitation; thus, reducing acceleration and horizontal displacements of the structure [1, 5]. Likewise, it is important to highlight that all types of seismic isolation systems have to return to their initial position, self-centering, after the excitation occurred; in addition, isolation systems should have the capacity of dissipate energy through different mechanisms, typical of each type of system.

Isolation systems have been successfully used since 1969 in 12.720 projects around the world [6]. New construction projects, the retrofitting of structures with insufficient resistance to withstand earthquakes and the updating of structures to current regulations are some examples in which this technology have been implemented [e.g. 2, 7–11]. Spencer Jr. and Nagarajaiah [12] attributed the success of seismic isolation to its reliability, stability, simplicity of design and low cost compared to other seismic protection techniques.

The main objective of this publication is to show the efficiency of a bi-directional roller bearings in improving the structural seismic response of multicolumn systems. This type of isolator was developed by Lee et al. [13] and it is composed of a cylindrical bearing system supported by an inclined V-shaped surface. Initially, this system was studied and implemented in bridges and subsequently studied by Ortiz-Cano et al. [14] to be used in multicolumn structural systems.

Following the work done by Ortiz-Cano et al. [14], in this work a numerical code in Matlab was written to simulate the response of the structures under base excitations, the finite element method (FEM) in conjunction with frame elements was used to solve both the governing equations and boundary conditions. The validation of the numerical model was done by direct comparisons between experimental and numerical data. Finally, a parametric study allowed to verify the efficiency of the isolation system in the control of vibrations under conditions of real earthquake records.

2 MOTION EQUATIONS OF ISOLATED BUILDINGS WITH RB SYSTEM

The equation of motion, in the time domain, that represents the dynamic bahavior of isolated buildings with RB systems under base excitations in a multiple degrees of freedom (MDoF) system is given in Eq.(1),

$$M\ddot{u} + C\dot{u} + Ku + R\left(f_s + f_{dr} + f_{ds}\right) = -M\Gamma\ddot{u}_g \tag{1}$$

Where M, C and K are the mass, damping and stiffness matrices of the MDoF system, respectively. $\ddot{u}$, $\dot{u}$ and u are the acceleration, velocity and displacement vectors.

On the other side, in Eq.(1), $\ddot{u}_g$ is the seismic excitation vector that contains the base accelerations for each direction in which the building can be excited; i.e., 3 translational and 3 rotational DoF's in the Cartesian space. The term Γ is an influence matrix that relates the excited DoF's i with the direction of the seismic excitation j. The elements of the Γ matrix take values of 0 or 1 according to the following expression:

$$\Gamma_{ij} = \begin{cases} 0 & \text{if the DoF } i \text{ isn't excited in the direction } j \\ 1 & \text{if the DoF } i \text{ is excited in the direction } j \end{cases} \tag{2}$$

where, R is a matrix that allocates the forces of restoration f_s, rolling friction f_{dr} and sliding friction f_{ds} developed by the RB system in j direction into a matrix that contains the forces in the DoF's system in i direction. The elements that make up the R vector take values of 0 or 1 as follows.

$$R_{ij} = \begin{cases} 0 & \text{if in the DoF } i \text{ the forces } f_s, f_{dr} \text{ and } f_{ds} \text{ aren't developed in the direction } j \\ 1 & \text{if in the DoF } i \text{ the forces } f_s, f_{dr} \text{ and } f_{ds} \text{ are developed in the direction } j \end{cases} \tag{3}$$

The forces f_s, f_{dr} and f_{ds}, which characterize the RB system, are defined through Equation (4), (5), (6) and (7) as follows,

$${f_s}^{\mathrm{T}} = \{ \ \tfrac{1}{2} m_1 g \sin(\theta_1) f_{H_1}(u) \quad \tfrac{1}{2} m_2 g \sin(\theta_2) f_{H_2}(u) \ \} \tag{4}$$

$${f_{dr}}^{\mathrm{T}} = \{ \ \mu_{r_1} m_1 g f_{H_1}(\dot{u}) \quad \mu_{r_2} m_2 g f_{H_2}(\dot{u}) \ \} \tag{5}$$

$${f_{ds}}^{\mathrm{T}} = \{ \ \mu_{s_1} N_1 f_{H_1}(\dot{u}) \quad \mu_{s_2} N_2 f_{H_2}(\dot{u}) \ \} \tag{6}$$

$$f_H(x) = \begin{cases} 1 & \text{if} \quad x \geq d \\ \frac{1}{d} x & \text{if} \quad -d < x < d \\ -1 & \text{if} \quad x \leq d \end{cases} \tag{7}$$

where m is the mass supported by the isolator, g is the gravitational acceleration, μ_r is the rolling friction coefficient, μ_s is the sliding friction coefficient, N is the normal force applied on the sliding interface, θ is the angle of the inclined V-shape surfaces and f_H is a function governed by a parameter called yield displacement d and a variable auxiliary x associated with the displacement and speed of the base of system (7). Additionally, the subscripts 1 and 2 denote the proper direction of each parameter in the horizontal plane.

In order to solve Eq.(1), the numerical solver of ordinary differential equations (ODE's) `ode23t` implemented by MATLAB was used; it showed greater efficiency and numerical stability compared to others methods offered by MATLAB ODE pack. In general, the algorithm of this solver is an implementation of the trapezoidal rule with an adaptive step-size associated with the use of a "free" interpolant [15]. The use of this solver requires that Eq. (1), which is a second order equation, be rewritten as a two first-order ODE system, as shown in the following expression:

$$\dot{v} = A_1 v(t) + A_2 H(u, \dot{u}) + A_3 \ddot{u}_g \tag{8}$$

with

$$A_1 = \begin{bmatrix} 0 & \mathrm{I} \\ -M^{-1}K & -M^{-1}C \end{bmatrix}; \quad A_2 = \begin{bmatrix} 0 \\ -M^{-1}R \end{bmatrix}; \quad A_3 = \begin{bmatrix} 0 \\ -\Gamma \end{bmatrix} \tag{9}$$

where, A_1 and $v\left(t\right)^{\mathrm{T}} \left(= \left\{u \quad \dot{u}\right\}\right)$ represent the state matrix and state vector of the system. The non-linearity of the system is represented by $H\left(u, \dot{u}\right)$ function, which includes the effects of the RB system previously described.

3 VALIDATION OF THE NUMERICAL SIMULATION ROUTINE

To validate the numerical simulation routine, the results of an experimental evaluation [14] and a numerical simulation of a building with and without RB isolation were compared.

The characteristics of the building model and the numerical simulations that validate the routine are presented in the next subsections.

3.1 BUILDING MODEL

3.1.1 Description of the physical model

The physical model consists of 4 storys supported by columns of polymeric material with rectangular section of $20.0 \times 2.9\, mm$. The model has a total height of $803.4\, mm$ and a rectangular plant with dimensions of $150 \times 200\, mm$. The slabs that make up each story and the story-column connections are constructed of aluminum plates. The base of the building has a thickness of $8.0\, mm$, storys and story-column connections a thickness of $4.0\, mm$. On the other hand, the building supports superimposed masses of $0.50\, kg$ on the second and third storys. A detailed outline of the geometry of the physical model is presented in Figure 1.

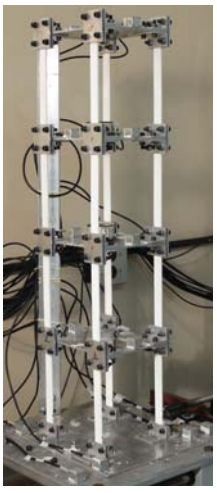

(a) Picture of physical model.

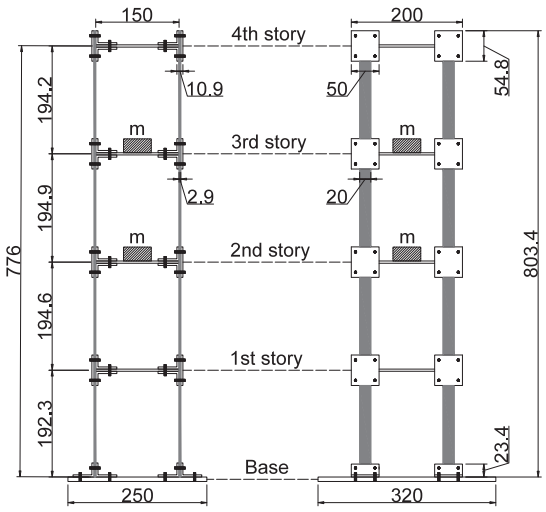

(b) Scheme of physical model, measures in mm.

Figure 1: Physical model.

3.1.2 Modal parameters identified

According to the experimental tests carried out and the analysis methodologies adopted by the author, the modal parameters identified for the fixed-base building model are summarized in Table 1.

Mode	f_{exp} (Hz)	ξ_{exp} (%)
1st flexural (weak direction)	6.82±0.02	0.59±0.03
2nd flexural (weak direction)	20.44±0.03	0.51±0.01
1st torsional	21.55±0.02	2.88±0.03
3rd flexural (weak direction)	31.70±0.02	0.30±0.01
4th flexural (weak direction)	36.65±0.03	0.34±0.02
2nd torsional	77.44±0.02	3.92±0.01

Table 1: Modal parameters identified in the building.

In addition, considering the *Rayleigh* damping, values of the damping constants $\alpha = 4.03 \times 10^{-1}$ and $\beta = 5.58 \times 10^{-5}$ were determined for the first two modes of vibration, which add up to 95% modal participation of the total mass of the building.

3.2 NUMERICAL MODELING

The structural system that makes up the physical model of the building was modelled using three-dimensional frame elements, 68 elements were defined with 56 nodes as presented in Figure 2.

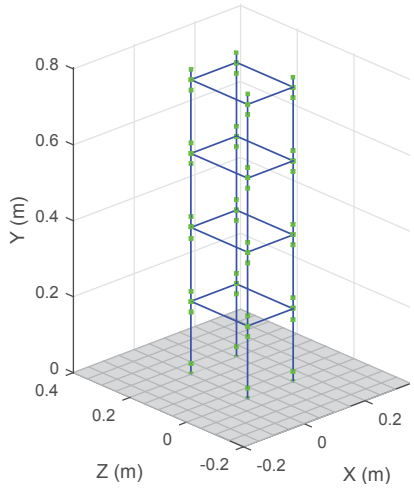

Figure 2: Numerical model raised.

In the numerical model, 3 types of frame elements were used, which are characterized by an elasticity modulus E, a Poisson ratio ν that defines the shear modulus G, a density ρ, a area A, a polar moment of inertia J_x and a moments of inertia I_y and I_z. Table 2 lists the characteristics of the elements used in the numerical representation of the physical model.

Element type	E (GPa)	ν	ρ (Kg/m^3)	A (m^2)	J_x (m^4)	I_y (m^4)	I_z (m^4)
1	28	0.325	1800	5.9×10^{-5}	1.5×10^{-10}	2.0×10^{-9}	4.1×10^{-11}
2	70	0.331	2700	4.0×10^{-4}	7.7×10^{-9}	1.3×10^{-7}	2.5×10^{-9}
3	70	0.331	0	4.0×10^{-4}	7.7×10^{-9}	1.3×10^{-7}	2.5×10^{-9}

Table 2: Mechanical and geometric characteristics of the elements.

The elements type *1* represent the columns constructed in polymeric material, while the elements type *2* and *3* represent the aluminum connections and slabs defined as beams in the numerical model. It is important to highlight that the density of the elements type *3* takes the value of 0 because the slab masses, and other elements that provide mass on each story, were modelled as masses concentrated on the nodes of each story. In this way, concentrated masses of 539.3 g, 196.6 g, 321.2 g, 321.1 g and 196.6 g were incorporated into each of the nodes of the base, 1st, 2nd, 3rd and 4th story.

3.2.1 Building with fixed base

The validation of the numerical model corresponding to the fixed-base building was performed taking in to account both the domain of frequencies and the domain of time; in addition, the frequency response functions (FRFs) and the acceleration response of the model storys were used.

Firstly, the validation in the frequency domain was carried out by direct comparison between the natural frequencies and the FRFs obtained experimentally and numerically.

In Figure 3 the natural frequencies obtained numerically and the vibration modes associated with each frequency are presented, while Figures 4 and 5 show a comparison of the experimental and numerical FRFs of the structure. Accordingly, it is observed that the numerical vibration frequencies are in agreement with the experimental vibration frequencies with a relative difference less than 0.6% in the first four vibration modes (Fig. 3a, b, c, d).

Likewise, using the damping ratios presented in Table 1 the FRF's were computed and then compared with the experimental ones; there is an excellent correlation between experimental and numerical FRFs as shown in Figures 4 and 5. However, it is noteworthy that if the damping ratios given by *Rayleigh* damping model are used (instead of those obtained experimentally) there is a significant difference for high vibration modes.

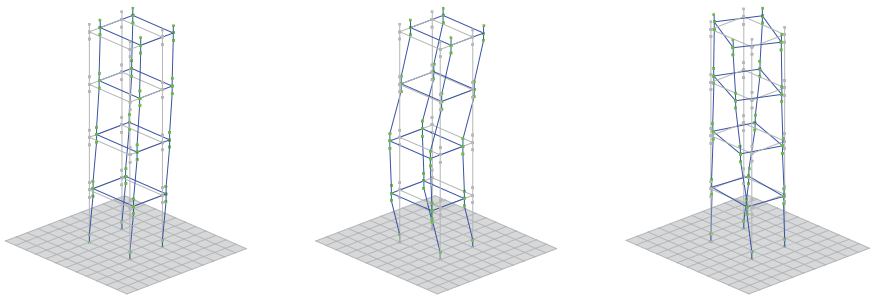

(a) 1st mode, 6.83 Hz. (b) 2nd mode, 20.44 Hz. (c) 3rd mode, 21.55 Hz.

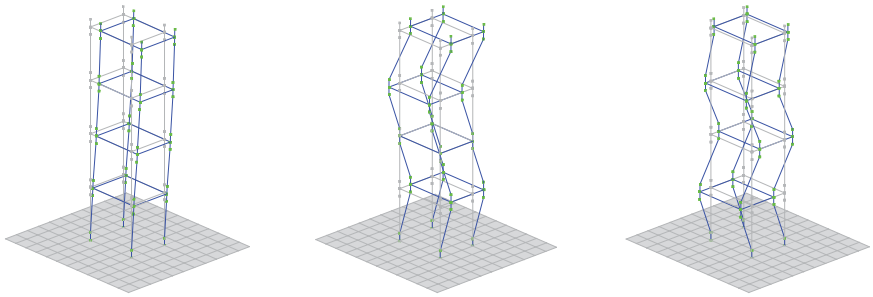

(d) 4th mode, 29.92 Hz. (e) 5th mode, 31.55 Hz. (f) 6th mode, 36.86 Hz.

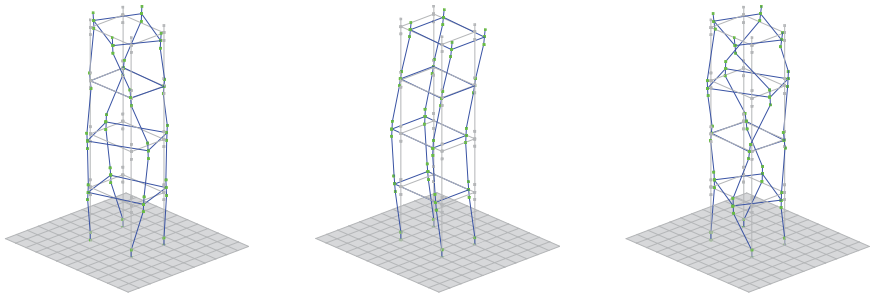

(g) 7th mode, 67.97 Hz. (h) 8th mode, 97.49 Hz. (i) 9th mode, 116.10 Hz.

Figure 3: Vibration modes and vibration frequencies.

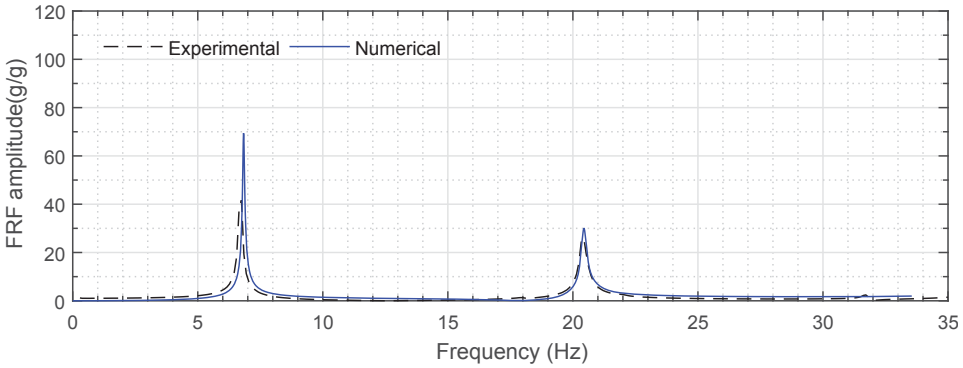

Figure 4: FRFs comparison of the 2nd story with base excitation.

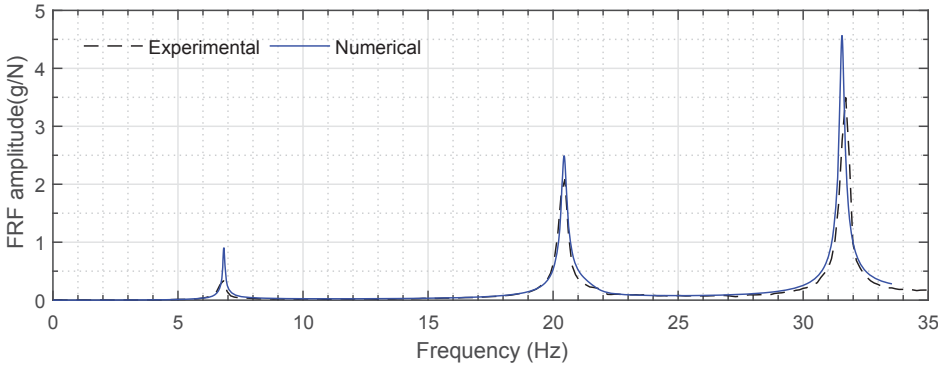

Figure 5: FRFs comparison of the 4th story with impact excitation in the 1st story.

Secondly, in the time domain, the validation of the numerical model was carried out by comparing the numerical and experimental response of the structure when subjected to random base excitation. The comparison of the responses is shown in Figure 6, it is evident that the numerical model represent the response of the fixed-base building.

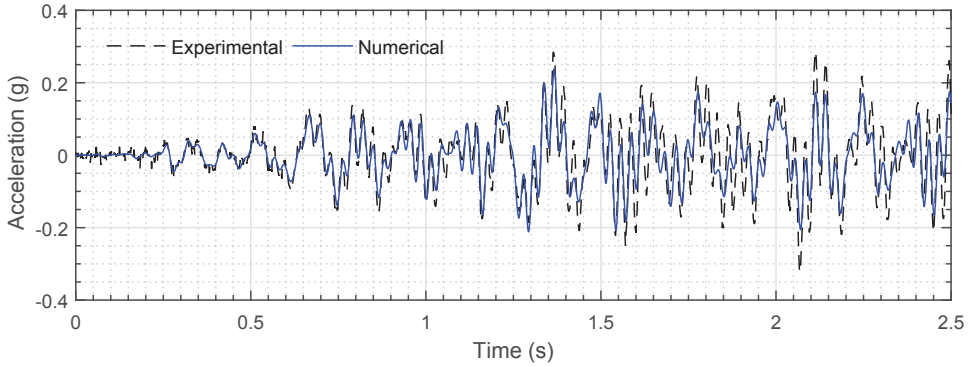

Figure 6: Time series of acceleration response of the 3rd story.

3.2.2 Building with RB system

Turning the attention to the use of roller bearings, the numerical model representing the building with RB was validated by comparing the numerical and experimental response of the structure in both free vibration and base excitation conditions.

To model the building + RB system, the characteristics of the fixed base structure and the RB system parameters $\mu_r = 0.0054$, $d = 1.2 \times 10^{-3}\, m$ and $\theta = 5°$ were used. In the free vibration simulations the initial lateral displacement condition $u_0 = 0.025\, m$ and initial velocity $\dot{u}_0 = 0\, m/s$ were considered, while in the simulations of the building + RB under base excitation initial conditions $u_0 = 0\, m$ and $\dot{u}_0 = 0\, m/s$ were considered in conjunction with a random base excitation record that contained predominant frequencies between 0 and 6 Hz.

In Figures 7 and 8 are shown the comparisons between numerical simulations and experimental responses of the building + RB system in both conditions free vibration and base excitation. In both figures certain degree of dispersion between the responses is noticeable; this dispersion could be related to deficiencies in the isolation system since it is not possible to completely restrict motion in the different directions in which the RB system operates Ortiz-Cano

et al. [14]. However, despite some dispersion, there is a very good agreement between the measured and numerically responses, which prove that the numerical model is able to adequately represent the dynamic behavior of a building + RB system.

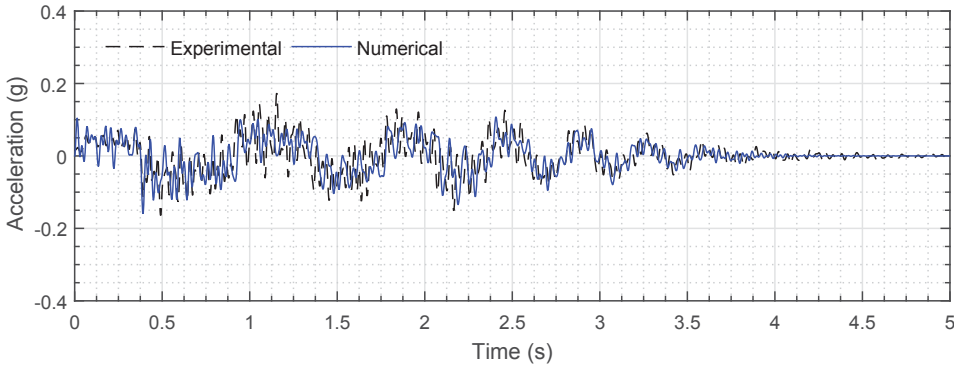

Figure 7: Time series of acceleration response of the 1st story with RB in free vibration.

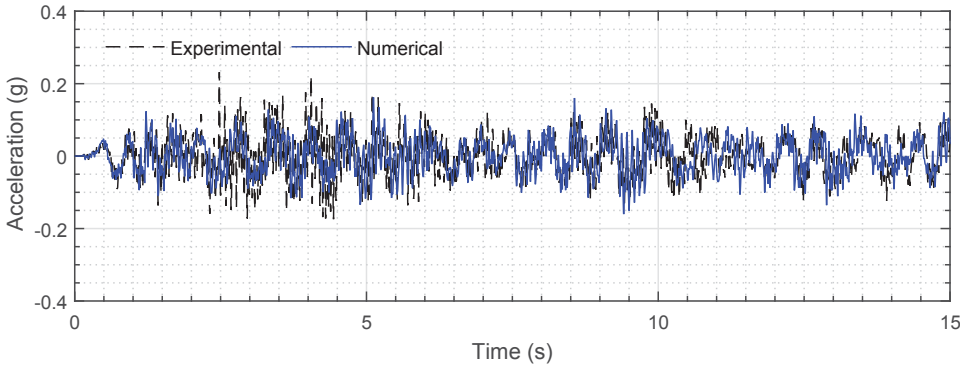

Figure 8: Time series of acceleration response of the 1st story with RB under base excitation.

4 RB SYSTEM PERFORMANCE UNDER BI-DIRECTIONAL SEISMIC EXCITATION

To evaluate the performance of the RB system in structures under base excitations, simulations using the numerical model previously described were carried out employing three earthquake records and four different RB configurations; thus, comparing the response of the fixed-base building with the response of the system when employing the RB system with different configurations. Accordingly, these results let us conclude about the performance of RB systems as seismic isolators in multicolumn structures.

Earthquake records were selected in order to have: I) excitations that produce high velocities at soil surface, II) excitations with both high frequency and high acceleration and III) moderate excitations [2]; in Table 3 are shown the seismic excitations selected for this work.

Earthquake	Station	Component	PGA (g)	PGV (m/s)	PGD (m)
Imperial Valley (1979)	El Centro Array # 6	140	0.339	0.665	0.287
		230	0.437	1.131	0.720
Loma Prieta (1989)	Corralitos	90	0.478	0.475	0.115
		0	0.630	0.552	0.095
Northridge (1994)	Century City	90	0.256	0.214	0.060
		360	0.222	0.251	0.060

Table 3: Seismic excitations.

It is timely to mention that each of the RB system configuration is determined by a different inclination angle θ and a different dissipation force f_{ds}; i.e., first RB configuration corresponds to $\theta = 2.0°$, second one corresponds to $\theta = 3.5°$, third one is given by $\theta = 5.0°$ and the fourth one is defined by $\theta = 5.0°$ + $f_{ds} = 1.14\ N$.

To continue, time series responses of displacement, speed and accelerations were obtained, however, only the responses in displacements will be presented. In Figures 9, 10 and 11 are shown the time series of displacement response at the fourth story obtained in the numerical simulations obtained for each of the earthquake records employing the four different RB configurations. Displacements were normalized by the maximum displacement obtained in the simulation of the fixed-based building u_{max}. Due to the fact that only in the weaker direction of the structure the seismic excitation produced noticeable displacements, the parametric analysis was performed only in that direction. By contrast, the seismic excitation, by means of amplitude and frequencies, did not produced noticeable displacements in the stronger direction of the structure.

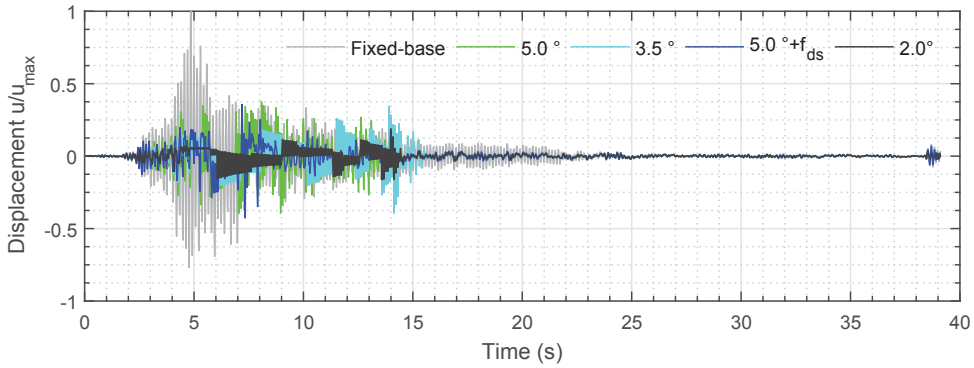

Figure 9: Performance of RB system: Time series of displacement response of the 4st story under base excitation Imperial Valley Earthquake (1979), $u_{\max} = 0.0109\ m$.

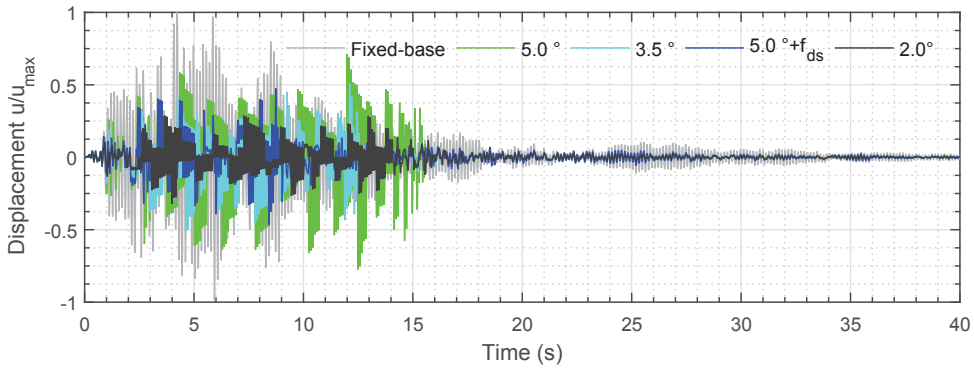

Figure 10: Performance of RB system: Time series of displacement response of the 4st story under base excitation Loma Prieta Earthquake (1989), $u_{\max} = 0.0075\ m$.

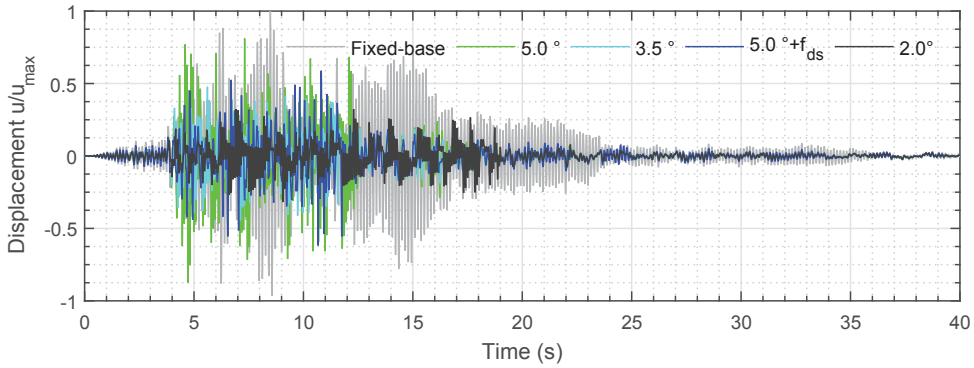

Figure 11: Performance of RB system: Time series of displacement response of the 4st story under base excitation Northridge Earthquake (1994), $u_{\max} = 0.0068\ m$.

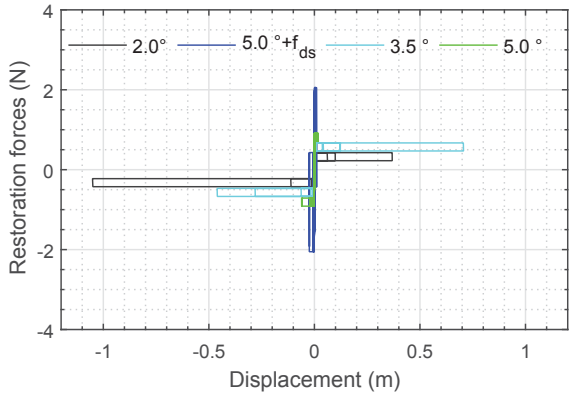

Figure 12: Hysteresis diagrams of isolation devices under base excitation Imperial Valley Earthquake (1979).

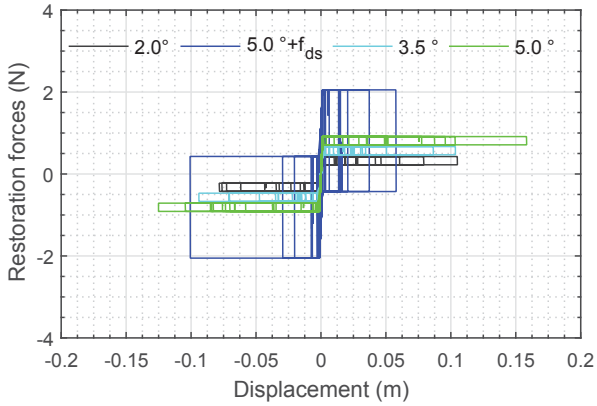

Figure 13: Hysteresis diagrams of isolation devices under base excitation Loma Prieta Earthquake (1989).

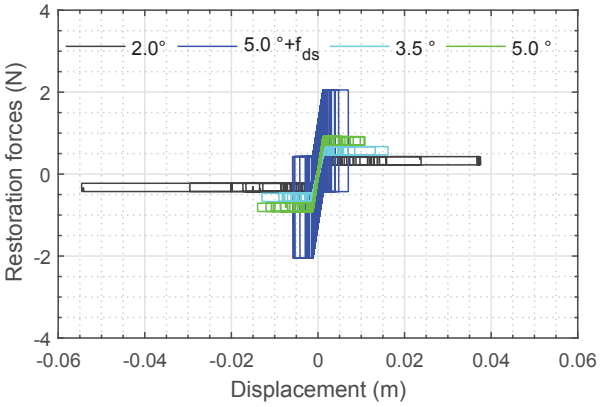

Figure 14: Hysteresis diagrams of isolation devices under base excitation Northridge Earthquake (1994).

Based on the obtained results, it is noticeable that the use of RB system reduce building displacements between 60% to 80% for all three seismic excitations compared with the same results obtained in the simulations without RB systems. The seismic building response improve as θ decreases; however, as θ decreases, large horizontal displacements result at the base of the structure thus limiting the use of RB systems. To avoid this problem, energy dissipation systems must be implemented to control those large displacements at the base of the structure; thus, improving the performance of the whole seismic isolation system (Fig. 12, 13, 14). It is important to mention that the energy dissipation system have to maintain both the decoupling between the structure and the base and the self-centering capability of the isolator device.

5 CONCLUSIONS

The response of a multicolumn structural model employing a Roller Bearing seismic isolation system and the performance of the RB system have been presented. Its performance has been assessed through the simulation of the structural model subjected to seismic excitations. The structural model's response was evaluated by direct comparison between the results of the simulation under fixed-base structure conditions and employing the RB system. It was found that the RB isolation system considerable reduces horizontal displacements relative to the

base for all earthquake records reviewed in this work. Maximum accelerations also decrease by means of the RB systems compared with those ones computed in the fixed-base structure simulations. In addition, it is important to mention that an energy dissipation system reduced the maximum horizontal displacement at the base of the structure improving the overall performance of the seismic isolation system. Finally, a proper relation between parameters θ y f_{ds} will give the best performance to the RB system in different seismic excitations.

ACKNOWLEDGMENT

This research was supported by the Office Vice-Provost for Research at Universidad Militar Nueva Granada under grant number INV-ING-2982, this support is gratefully acknowledged.

References

[1] R. Jangid, T. Datta, Seismic behavior of base-isolated buildings: A state of the art review, Proceedings of the Institution of Civil Engineers, Structures and Buildings 110 (1995) 186–203.

[2] F. Naeim, J. Kelly, Design of seismic isolated structures: From theory to practice, Wiley & Sons, New York, USA, 1999.

[3] M. Kunde, R. Jangid, Seismic behavior of isolated bridges: A state of the art review, Electronic Journal of Structural Engineering 3 (2003) 140–170.

[4] P. Harvey, K. Kelly, A review of rolling-type seismic isolation: Historical development and future directions, Engineering Structures 125 (2016) 521–531.

[5] B. Palazzo, L. Petti, Combined control strategy: base isolation and tuned mass damping, ISET Journal of Earthquake Technology 36 (2012) 121–137.

[6] M. Walters, Seismic isolation: The gold standard of seismic protection, in: Structural Performance, Structure Magazine, 2015.

[7] M. Tsai, S. Wu, K. Chang, G. Lee, Shaking table tests of a scaled bridge model with rolling-type seismic isolation bearings, Engineering Structures 29 (2007) 694–702.

[8] V. Matsagar, R. Jangid, Base isolation for seismic retrofitting of structures, Practice periodical on structural design and construction 13 (2008) 175–185.

[9] M. Hosseini, A. Soroor, Using orthogonal pairs of rollers on concave beds (OPRCB) as a base isolation system Part II: Application to multi-story and tall buildings, The Structural Design of Tall and Special Buildings (2010).

[10] M. Erdik, O. Ülker, B. Şadan, C. Tüzün, Seismic isolation code developments and significant applications in Turkey, Soil Dynamics and Earthquake Engineering 115 (2018) 413–437.

[11] K. Ryan, T. Okazaki, C. Coria, E. Sato, T. Sasaki, Response of hybrid isolation system during a shake table experiment of a full-scale isolated building, Earthquake Engineering and Structural Dynamics 47 (2018) 2214– 2232.

[12] B. Spencer Jr., S. Nagarajaiah, State of the art structural control, Journal of Structural Engineering 129 (2003) 845–856.

[13] G. Lee, Y. Ou, Z. Liag, T. Niu, J. Song, Principles and performance of roller seismic isolation bearings for highway bridges, Technical Report MCEER-07-0019, University at Bufalo, New York, USA, 2007.

[14] N. Ortiz-Cano, C. Magluta, N. Roitman, Numerical and experimental studies of a building with roller seismic isolation bearings, Structural Engineering & Mechanics 54 (2015) 475–489.

[15] L. Shampine, M. Reichelt, J. Kierzenka, Solving Index-1 DAEs in MATLAB and Simulink, SIAM Review 18 (1999) 538–552.

EURODYN 2020
XI International Conference on Structural Dynamics
M. Papadrakakis, M. Fragiadakis, C. Papadimitriou (eds.)
Athens, Greece, 23–26 November 2020

CONTROL LAW AND ACTUATOR CAPACITY EFFECT ON THE DYNAMIC PERFORMANCE OF A HYBRID MASS DAMPER; THE CASE OF ROTTWEIL TOWER

Lefteris Koutsoloukas[1], Nikolaos Nikitas[2], Petros Aristidou[3] and Christian Meinhardt[4]

[1] School of Civil Engineering, University of Leeds
LS2 9JT, Leeds, UK
cn15lk@leeds.ac.uk

[2] School of Civil Engineering, University of Leeds
LS2 9JT, Leeds, UK
N.Nikitas@leeds.ac.uk

[3] Department of Electrical Engineering & Computer Engineering and Informatics,
Cyprus University of Technology
3036 Limassol, Limassol, CY
petros.aristidou@cut.ac.cy

[4] GERB Vibration Control Systems,
Roedernallee 174-176,13407 Berlin, DE
christian.meinhardt@gerb.de

Keywords: Tall Buildings, Active/Hybrid Mass Damper, Model Predictive Control, Structural Dynamics, Vibration Mitigation

Abstract. *This paper considers different vibration control options for a real high-rise tower subjected to real wind loading. To mitigate excessive responses, the tower utilizes a hybrid passive - active control system with a relatively small actuator capacity. Firstly, the methodology for establishing a reduced order numerical model of the tower from a finite element realization is presented. Subsequently, to deal with physical constraints, a Model Predictive Control (MPC) algorithm is employed and compared to a more conventional Linear Quadratic Regulator (LQR). In both cases, the algorithms managed to keep the dynamic displacements within the set desired limit. It was concluded that, the MPC had a better performance when compared to the LQR in terms of peak amplitudes at the expense though of energy.*

1 INTRODUCTION

The technological advancement and increase of cost-efficient computational power , create the ideal conditions for the broader implementation of active control systems. Traditionally, disciplines such as aerospace and automotive, have been utilizing active control schemes in order to enhance performance for a range of applications[1, 2]. Yet, active control is now also growing in disciplines that, it was not popular, or even viable, in the near past. More specifically, the recent trend of building tall and slender structures led to the development of structural control systems that utilize active components for vibration mitigation under extreme loads.

Generally speaking, active and semi-active structural control systems can achieve enhanced control performance when compared to passive equivalents. However, the performance of active control systems may be limited due to various practical and operating constraints. For the case of a mass damper such can be the actuator dynamics, mass stroke, and energy consumption. To this goal, extensive efforts have been made by the structural control research community and smart methods have been developed to minimize, if not eliminate, any performance compromising effects of constraints.

This paper will investigate the application of an active hybrid mass damper system on a real 245m tower subjected to wind loading, without accounting for any aeroelastic effects. For the control of the hybrid system, Model Predictive Control (MPC) algorithm will be used and compared to a more conventional Linear Quadratic Regulator (LQR). Previously, the MPC algorithm was investigated by Mei et al. [3, 4] for the control of the famous 76-storey benchmark building. Moreover, applications of the MPC on different control systems were practiced by Mei et al. [5, 6] for the case of a single and a three-storey structure, by Chen et al. [7] for a ten-storey structure, explaining additionally a more practical implementation of the algorithm, by Peng et al. [8] for two adjacent 20-storey buildings and by Lopez et al. [9] for a six-storey experimental structure.

Herein, the constraint effect of the actuator maximum capacity on the overall performance of the hybrid control system will be examined, and methodologies for minimizing it will be reviewed. More specifically, the actuator that was utilized on the hybrid control system of the 245m tower has a maximum force rating of 35kN, which is relatively low compared to the 180,000t tower mass. For reference and comparison, the actuators deployed for the control of the Nanjing TV tower had a capacity of 100kN [10], for the Shanghai World Financial Center Tower 142.5kN [11], for a 36-storey building reported in [12] 25.4kN, and for a benchmark cable-stayed bridge (Cape Girardeau Bridge, Missouri, USA) up to 7000kN [13] with typical values around reaching 1000kN [14]. For the 76-storey benchmark building, which is of significance to this study, the actuator capacity was limited to lower than 300kN [15], while Mei et al. [3] using the MPC algorithm, found that the maximum actuator force needed was 118kN.

2 APPLICATION DEFINITION

The 245m tower is the Rottweil Tower in Germany and was commissioned with specific requirements for experiencing limited wind-induced vibrations within certain bounds. According to wind tunnel tests, it was expected that wind speeds of the order of 15.3 – 16.7 m/s, referring to ground values at a height of 10m, could excite top floor dynamic response with amplitude of up to 750mm when no added control measure is provisioned. Such vibrations are primarily of vortex shedding type. Associated sway disturbance is anticipated to cause discomfort to the occupants and also impact the structural integrity of the tower particularly in terms of long term fatigue [16].

For ensuring comfort and safety, a limit displacement of up to 200mm was implemented and a hybrid structural control system was designed. The proposed hybrid system combines a

passive Tuned Mass Damper (TMD) with one actuator for each of the two principal directions. In reality, the passive TMD has adjustable stiffness that renders it semi-active; for simplification purposes this adaptiveness will not be considered any further in this study. Based on closed form formulas [17], a mass of 240t was opted for the TMD element of the system; this corresponds to a mass ratio of μ =1.3%. On the sensing side, the system consists of four uniaxial MEMS accelerometers which are able to capture horizontal accelerations at the top of the structure and the TMD mass. The displacements of the actuators are monitored by string pot transducers and an inductive length measuring system integrated within the linear motors [18].

3 PAPER CONTRIBUTIONS

1) Application of the MPC algorithm for the active hybrid control of a real structure and assessment of its performance by comparing it to an LQR controller
2) Optimization of the hybrid control system performance when acting in a passive-active mode of operation, taking into account its limited actuation capacity
3) Presentation of a real case-study that can become a benchmark for subsequent vibration control studies

4 SIMPLIFIED NUMERICAL MODEL DERIVATION

A detailed 3D Finite Element (FE) model of the tower, seen in Figure 1 (b), which falls very close in terms of observed and modelled frequencies, was used as the base for acquiring the reduced 2D lumped mass model shown in Figure 1 (c). In the reduction process, the entire mass of the tower, including the structural and non-structural components, was distributed evenly at the floors of the structure. This method results a diagonal mass matrix **M** of size *n x n* where, *n=34* is the considered number of lumped masses in the reduced model.

To derive the *n x n* stiffness matrix **K**, the methodology described by Qu et al., (2001) [19] was followed. Based on their methodology, the flexibility coefficients δ_{ij} of each floor were determined by evaluating the static responses of the i^{th} floor of the original FE model to unit horizontal forces at each node of the j^{th} floor, with $i,j= 1, 2, 3, \ldots ,n$. Thus, the flexibility matrix was constructed, and the stiffness matrix **K** was obtained by inverting it.

The damping matrix $\hat{\mathbf{C}}$ of size *n x n* for the lumped mass model was determined using the Rayleigh approximation whereby $\hat{\mathbf{C}}$ is described by Eq. 1. Parameters α and β are the mass and stiffness proportional damping coefficients, respectively and were obtained based on critical damping ratio of 1% for modes 1 and 5. For this assumption, α and β are becoming 2.11×10^{-2} and 5.26×10^{-4}, respectively.

$$\hat{\mathbf{C}} = \alpha \mathbf{M} + \beta \mathbf{K} \qquad (1)$$

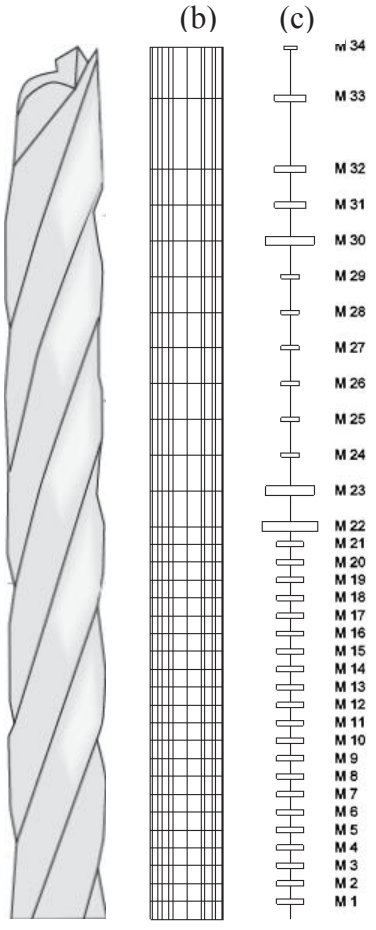

Figure 1: Three models of the tower: (a) architectural model, (b) original 3D FE model, (c) lumped mass model with equivalent masses

5 EQUATIONS OF MOTION FOR THE SYSTEM

The matrix equation of motion for the system in-hand can be expressed by Eq. 2. The nominal properties of the TMD were added to the mass **M**, stiffness **K,** and damping $\hat{\mathbf{C}}$**,** matrices derived in section 4, resulting to matrix sizes n_{tmd} *x* n_{tmd} where, n_{tmd} = 35. **f**(*k*) is an *r*-size vector which contains the external excitations applied on the structure, **u**(*k*) is the active *m*-size control force vector and **s**(*k*) is the n_{tmd} -size displacement vector, all at discrete time *k*. $\hat{\mathbf{D}}$ is the n_{tmd} *x m* matrix that describes how the control force is acting on the system, and **H** is the n_{tmd} *x r* matrix that describes how the excitation inputs are exciting the system.

$$\mathbf{M}\ddot{\mathbf{s}}(k)+\hat{\mathbf{C}}\dot{\mathbf{s}}(k)+\mathbf{K}\mathbf{s}(k)=\hat{\mathbf{D}}\mathbf{u}(k)+\mathbf{H}\mathbf{f}(k) \tag{2}$$

The equivalent spate-space equations are formulated as follows,

$$\dot{\mathbf{x}}(k)=\mathbf{A}\mathbf{x}(k)+\mathbf{B}\mathbf{u}(k)+\mathbf{G}\mathbf{f}(k),\qquad \mathbf{x}(0)=\mathbf{x}_0, \tag{3}$$

$$\mathbf{y}(k)=\mathbf{C}\mathbf{x}(k)+\mathbf{D}\mathbf{u}(k) \tag{4}$$

where **y**(*k*) represents the measured outputs, **C** is the output matrix, **D** is the feedthrough matrix, $\mathbf{x}_0$ is the initial point and,

$$\mathbf{x}(k)=\begin{bmatrix}\mathbf{s}(k)\\ \dot{\mathbf{s}}(k)\end{bmatrix},\ \mathbf{A}=\begin{bmatrix}\mathbf{0} & \mathbf{I}\\ -\mathbf{M}^{-1}\mathbf{K} & -\mathbf{M}^{-1}\hat{\mathbf{C}}\end{bmatrix},\ \mathbf{B}=\begin{bmatrix}\mathbf{0}\\ \mathbf{M}^{-1}\hat{\mathbf{D}}\end{bmatrix},\ \mathbf{G}=\begin{bmatrix}\mathbf{0}\\ \mathbf{M}^{-1}\mathbf{H}\end{bmatrix} \tag{5}$$

6 MPC STATE SPACE FORMULATION

This section includes the general formulation of MPC in state-space form. It is noted that derivation of the LQR controller, used only for comparisons, can be found in [20] and is not shown here for brevity. The MPC is based on an iterative, finite-horizon optimization of a plant. It receives a reference trajectory as the target output of the process. The overview of the algorithm is seen in Figure 2 [21]. The MPC computes a sequence of control actions **u** over a control horizon *q*, that will achieve the optimal behavior of the dependent variables **x** of the system, over a prediction horizon *p* (*p*≥*q*). It then implements only the first computed action **u**(*k*), measures the response of the system **y**(*k*), and repeats the previous process.

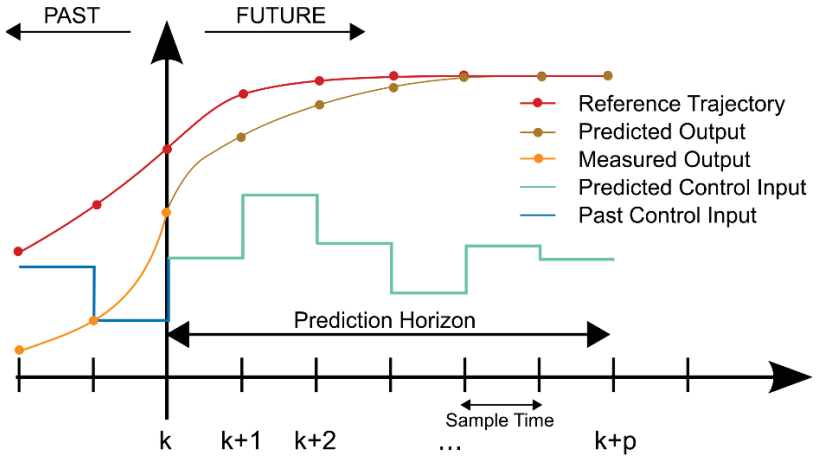

Figure 2: Basic concept for Model Predictive Control with q=p [22]

Since there might be inaccuracies and statistical noise in the measurements received and model used, a Kalman estimator is employed both for estimating the current state $\mathbf{x}(k)$ but also for the predictions needed for the MPC [21]. Eq. 6 describes how the estimates of the current state, $\hat{\mathbf{x}}(k|k-1)$, is generated by the Kalman estimator.

$$\hat{\mathbf{x}}(k \mid k-1) = \mathbf{\Phi}\hat{\mathbf{x}}(k-1 \mid k-2) + \mathbf{\Gamma}\mathbf{u}(k-1) + \mathbf{L}\mathbf{e}(k-1) \tag{6}$$

where, $\mathbf{L}$ the estimator gain matrix, and $\mathbf{C}$ the output matrix. $\mathbf{\Phi}$, $\mathbf{\Gamma}$, and $\mathbf{e}(k)$ are defined in Eq.7 for the control interval T.

$$\mathbf{\Phi} = e^{\mathbf{A}T}, \qquad \mathbf{\Gamma} = e^{\mathbf{A}T}\int_0^T e^{-\mathbf{A}x}dx, \qquad \mathbf{e}(k) = \mathbf{y}(k) - \mathbf{C}\hat{\mathbf{x}}(k \mid k-1) - \mathbf{D}\mathbf{u}(k \mid k) \tag{7}$$

The future state predictions $\hat{\mathbf{z}}(k|k+j)$ for $j=1,2,\ldots p$, are similarly determined by:

$$\hat{\mathbf{z}}(k \mid k+j) = \mathbf{\Phi}\hat{\mathbf{z}}(k+j-1) + \mathbf{\Gamma}\mathbf{u}(k+j-1 \mid k) + \mathbf{L}\mathbf{e}_f(k) \tag{8}$$

where,

$$\hat{\mathbf{z}}(k) = \hat{\mathbf{x}}(k \mid k-1) \tag{9}$$

Unlike the LQR, the constrained MPC is able to take into account bounds on the control actions $\mathbf{u}$ and future states $\hat{\mathbf{z}}$. With the target states and inputs defined by $\mathbf{z}_s$ and $\mathbf{u}_s$, respectively, the MPC objective for time instance k becomes:

$$\underset{\mathbf{u}}{Min}\, J(k) \tag{10}$$

where,

$$J(k) = [\hat{\mathbf{z}}(k+p) - \mathbf{z}_s(k)]^{\mathrm{T}}\mathbf{w}_\infty[\hat{\mathbf{z}}(k+p) - \mathbf{z}_s(k)] + \sum_{j=1}^{p}[\hat{\mathbf{z}}(k+j) - \mathbf{z}_s(k)]^{\mathrm{T}}\mathbf{w}_x[\hat{\mathbf{z}}(k+j) - \mathbf{z}_s(k)] +$$
$$\sum_{j=0}^{q-1}[\mathbf{u}(k+j \mid k) - \mathbf{u}_s(k)]^{\mathrm{T}}\mathbf{w}_u[\mathbf{u}(k+j \mid k) - \mathbf{u}_s(k)] \tag{11}$$

In Eq. 11, $\mathbf{w}_x$ and $\mathbf{w}_u$ are positive definite matrices representing the state error and the input weighting, respectively. $\mathbf{w}_\infty$ represents the terminal state matrix and can be found by solving the discrete Lyapunov equation [21]. The minimization problem is subject to constraints from Eqs. 6-9 (state estimation and predictions), alongside with the control input constraints shown in Eqs. 12-14.

$$\mathbf{u}(k+q \mid k) = \mathbf{u}(k+q+1 \mid k) = \ldots = \mathbf{u}(k+p-1 \mid k) = \mathbf{u}(k+q-1 \mid k) \tag{12}$$

$$\mathbf{u}_{\min} \le \mathbf{u}(k+j \mid k) \le \mathbf{u}_{\max} \qquad j=0, 1, 2 \ldots, q-1. \tag{13}$$

$$\Delta\mathbf{u}_{\min} \le \Delta\mathbf{u}(k+j \mid k) \le \Delta\mathbf{u}_{\max} \qquad j=0, 1, 2 \ldots, q-1. \tag{14}$$

7 PRELIMINARY RESULTS

An MPC and an LQR controller have been designed for the dynamic (response) control of the Rottweil tower, when subjected to real wind loading, using a hybrid mass damper. The passive-active mode of operation implies that, the hybrid mass damper is acting passively, and the actuators are constantly adding forces on top. A Kalman filter was used in both control cases for the state estimation using the four actual sensors located on the structure. Both controllers were designed in Matlab®. The MPC controller was realised based on the YALMIP toolbox, which is mainly used for treating prototype optimization problems [23]. The toolbox can utilize several solvers to carry out the optimization. In this study, the Gurobi optimizer was used [24]. Moreover, a hard constraint was introduced in the optimization procedure for the control input ($\mathbf{u}_k$) where, $\mathbf{u}_{min}$ and $\mathbf{u}_{max}$ were set to -35kN and 35kN respectively, T was set to 100ms and $\mathbf{z}_s$, $\mathbf{u}_s$ and $\mathbf{w}_\infty$ were set to 0. It is noted that the limit for the actuator capacity in the case of the LQR was introduced artificially in the simulation.

To simulate the dynamics of wind loading, a stochastic gust loading based on the Davenport spectrum with a linearly superimposed resonant, vortex shedding-type contribution were used [16]. The wind excitation caused a peak displacement of 248.2mm at the top floor in the case of no TMD installation.

Table 1 summarizes the maximum displacements of the floors of the structure in the uncontrolled and controlled cases. As it can be seen, both algorithms managed to reduce the structural responses at the top of the tower within the desired limit (200mm). However, the MPC had better performance than the LQR in controlling floor displacements throughout.

Floor No.	No control s(mm)	TMD s(mm)	LQR s(mm)	MPC s(mm)
1	1.8	1.6	1.4	1.35
10	53.2	48.3	42.4	40.6
20	160.7	146.1	128.1	122.6
34	248.2	225.7	197.9	189.4

Table 1: Maximum responses for the uncontrolled, TMD, LQR and MPC schemes

Based on the analysis, the maximum force exerted by the TMD without and with the active control component was 135.5kN and 170.5kN, respectively. Figures 3, 4 and 5 show displacement time series of the top floor of the structure with and without control, for the different control variants.

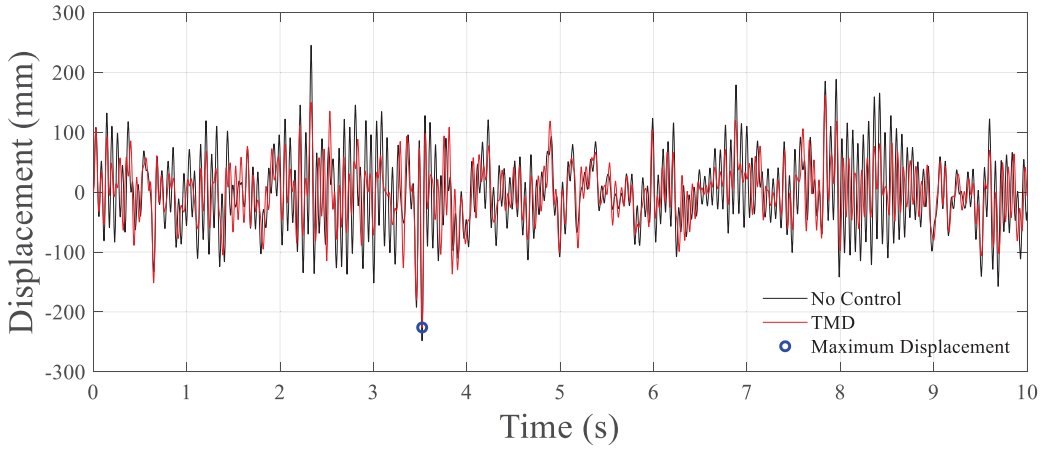

Figure 3: Displacement – Time graph for the uncontrolled case and the structure with a TMD

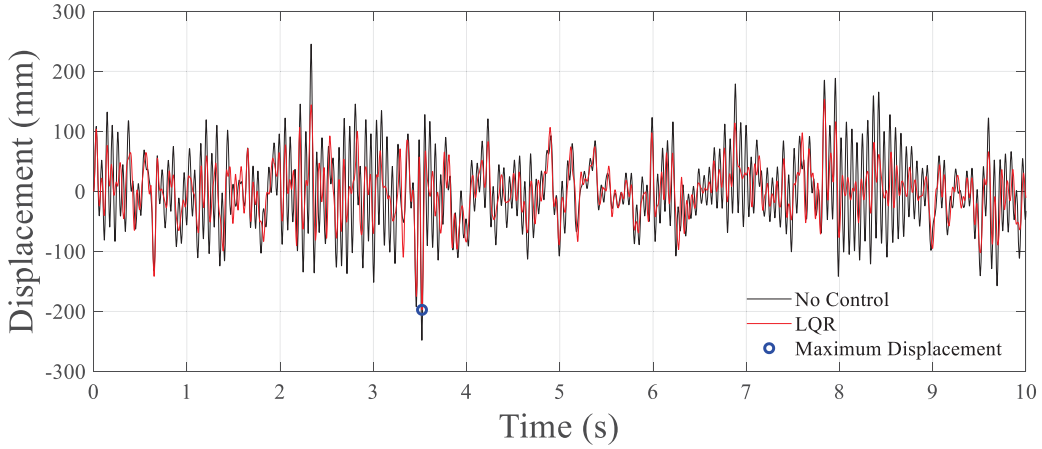

Figure 4: Displacement – Time graph for the uncontrolled case and the structure with active (LQR) control

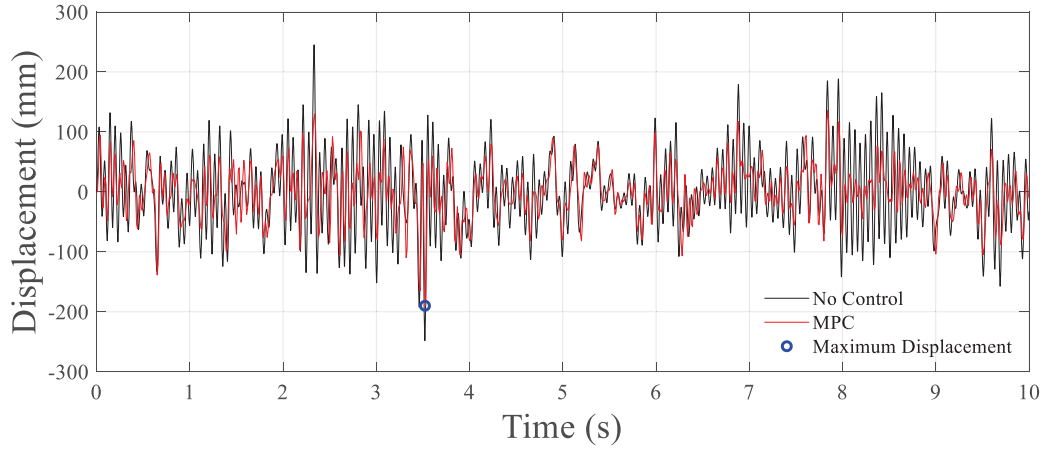

Figure 5: Displacement – Time graph for the uncontrolled case and the structure with active (MPC) control

It is observed that the active control algorithms can limit displacements even when, the actuator capacity is constrained to a fraction of the TMD passive force, as seen in Figures 6. To further asses the relative performance of the two controllers, while on a mixed passive-active

mode of operation, the actuator power, or else the product of actuator force and velocity was considered. It was found that the maximum power needed when using the LQR controller was lower than the equivalent needed for the MPC controller, as seen in Figure 7. When considering the average power the same relation pertains is with differences also in terms of extreme values and positive to negative value balance.

As such, when the hybrid system is acting in the considered passive-active mode, the MPC algorithm had the best performance on limiting dynamic displacements but in the expense of having higher energy demands than the LQR. This makes the consideration of also other modes of operation, (e.g. revised passive-active mode, having the active forces acting only when the passive forces are not sufficient and semi-active – active mode where performance can be gained at lower energy consumption) vital prior to holistically optimising the hybrid mass damper's performance, through control law considerations alone.

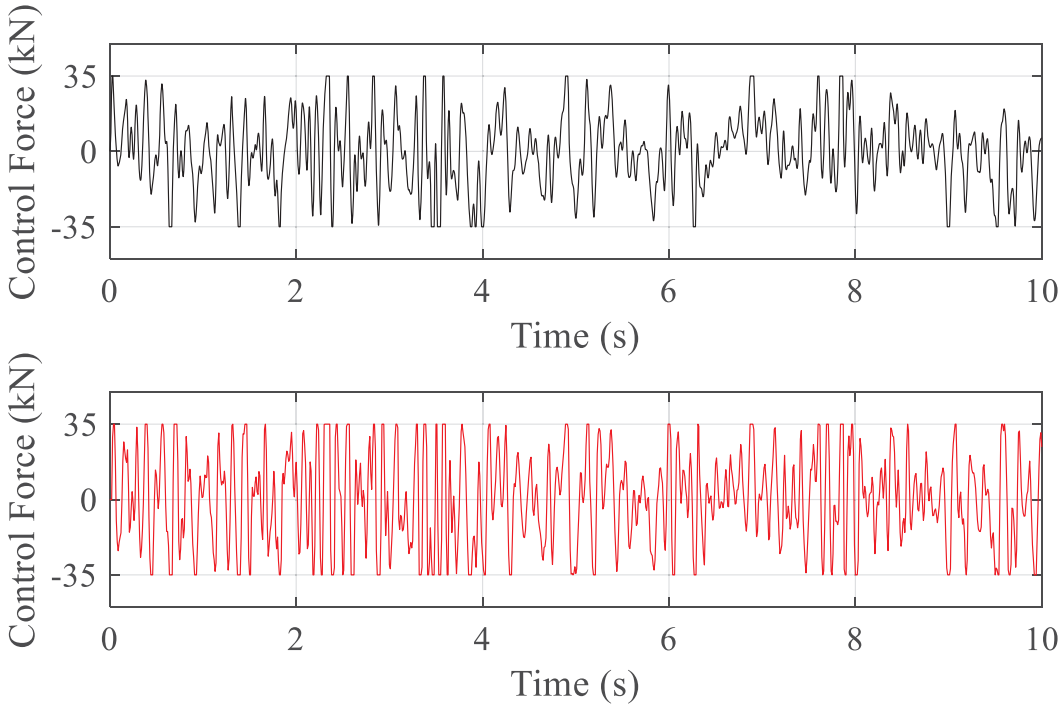

Figure 6: Active control forces when using the LQR (top) and the MPC (bottom) algorithms

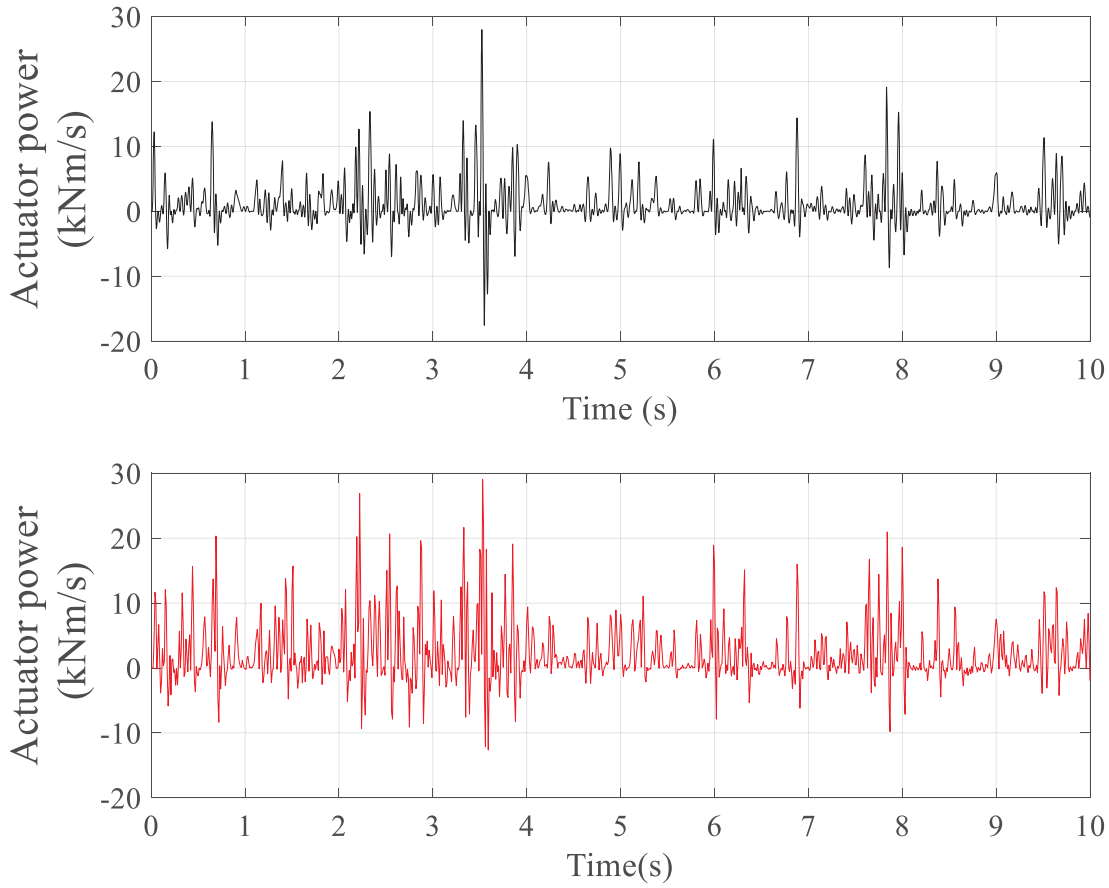

Figure 7: Actuator power when using the LQR (top) and the MPC (bottom) algorithms

8 CONCLUSIONS AND FUTURE RECOMMENDATIONS

This paper presented a real case-study which can introduce a new benchmark problem for structural control purposes. After deriving a reduced order model based on a detailed finite element model of the Rottweil tower, two control laws, namely the LQR and MPC, were applied and their performance was compared, for a passive-active mode of operation of a hybrid mass damper installation.

Based on the analysis it was found that the uncontrolled case-study building, under strong wind excitation developed dynamic displacements with maximum amplitude of 248.2mm at the top floor. When adding a perfectly tuned passive TMD the same displacement reduced to 225.7mm. In both cases, the displacements exceeded a notional serviceability limit that was set at 200mm. When considering active contribution in the control, the LQR algorithm reduced response to 197.9mm whereas, the MPC achieved 189.4mm. It was concluded that, in both cases, the algorithms managed to keep the dynamic displacements within the desired limit however, the MPC had a better dynamic reduction performance than the LQR. Still, the average energy needed for the two controllers was lower for the LQR, leading to the need for holistically optimising performance on mixed objectives.

Future work would involve semi-active – active mass damper devices, consideration of actuator dynamics and different modes-of-operation for the hybrid setup towards achieving a low energy-consumption scheme. Lastly, state-of-the-art data driven controllers, based on Artificial

Intelligence, should also enter the comparison against the presented conventional controllers in order to evaluate any performance gains.

9 ACKNOWLEDGEMENT

The authors would like to thank GERB for providing the hybrid system specifications, the FE models of the tower and the wind loading profiles. Additionally, the authors would like to thank the University of Leeds for providing the scholarship to the 1st author for conducting his PhD studies.

10 REFERENCES

[1] D. Zhao, Z. Lu, H. Zhao, X. Y. Li, B. Wang, and P. Liu, A review of active control approaches in stabilizing combustion systems in aerospace industry, *Progress in Aerospace Sciences*, 97, April 2017, 2018.

[2] P. N. Samarasinghe, W. Zhang, and T. D. Abhayapala, Recent Advances in Active Noise Control Inside Automobile Cabins: Toward quieter cars, *IEEE Signal Processing Magazine*, 33, 6, 2016.

[3] G. Mei, A. Kareem, and J. C. Kantor, Model Predictive Control of Wind-Excited Building: Benchmark Study, *Journal of engineering mechanics*, 2004.

[4] G. Mei, A. Kareem, and J. C. Kantor, Model Predictive Control For Wind Excited Buildings : A Benchmark Problem, *14th Engineering Mechanics Conference*, 2000.

[5] G. Mei, A. Kareem, and J. C. Kantor, Real-time model predictive control of structures under earthquakes, *Earthquake Engineering and Structural Dynamics*, 30, 7, 2001.

[6] G. Mei, A. Kareem, and J. C. Kantor, Model predictive control of structures under earthquakes using acceleration feedback, *Journal of Engineering Mechanics*, 128, 5, 2002.

[7] Y. Chen, S. Zhang, H. Peng, B. Chen, and H. Zhang, A novel fast model predictive control for large-scale structures, *JVC/Journal of Vibration and Control*, 23, 13, 2017.

[8] H. Peng, Y. Chen, E. Li, S. Zhang, and B. Chen, Explicit expression-based practical model predictive control implementation for large-scale structures with multi-input delays, *JVC/Journal of Vibration and Control*, 24, 12, 2018.

[9] F. Lopez-Almansa, R. Andrade, J. Rodellar, and A. M. Reinhorn, Modal predictive control of structures. II: Implementation, *Journal of Engineering Mechanics*, 120, 8, 1994.

[10] H. Cao, A. M. Reinhorn, and T. T. Soong, Design of an active mass damper for a tall TV tower in Nanjing, China, *Engineering Structures*, 20, 3, 1998.

[11] X. Lu, P. Li, X. Guo, W. Shi, and J. Liu, Vibration control using ATMD and site measurements on the Shanghai World Financial Center Tower, *The Structural Design of Tall and Special Buildings*, 23, 2014.

[12] I. Nagashima, R. Maseki, Y. Asami, J. Hirai, and H. Abiru, Performance of hybrid mass damper system applied to a 36-storey high-rise building, *Earthquake Engineering and Structural Dynamics*, 30, 11, 2001.

[13] F. Bontempi, F. Casciati, and M. Giudici, Seismic response of a cable-stayed bridge: Active and passive control systems (benchmark problem), *Journal of Structural Control*, 10, 3–4, 2003.

[14] J. N. Yang, S. Lin, and F. Jabbari, H2-based control strategies for civil engineering structures, *Journal of Structural Control*, 10, 2003.

[15] J. N. Yang, A. K. Agrawal, B. Samali, and J.-C. Wu, Benchmark Problem for Response Control of Wind-Excited Tall Buildings, 130, 2004.

[16] C. Meinhardt, N. Nikitas, and D. Demetriou, Application of a 245 metric ton Dual-Use Active TMD System, *Procedia Engineering*, 199, 2017.
[17] J. P. Den Hartog, *Mechanical Vibrations*, 4th ed. New York, NY, USA: McGraw-Hill, 1956.
[18] ANCO ENGINEERS, Users Guide: GERB TMD Tower Control System, 2017.
[19] W. L. Qu, Z. H. Chen, and Y. L. Xu, Dynamic analysis of wind-excited truss tower with friction dampers, *Computers and Structures*, 79, 32, 2001.
[20] T. Soong, Active Structural Control: Theory and Practice, ISBN: 9780582017825, 1990.
[21] S. C. Patwardhan, A Gentle Introduction to Model Predictive Control (MPC) Formulations based on Discrete Linear State Space Models, 2014.
[22] Wikimedia Commons contributors, File:MPC scheme basic.svg, *Wikimedia Commons, the free media repository*, 2018. [accessed 15 June 2020].
[23] J. Löfberg, YALMIP: A toolbox for modeling and optimization in MATLAB, *Proceedings of the IEEE International Symposium on Computer-Aided Control System Design*, 2004.
[24] Gurobi Optimization, LLC, Gurobi Optimizer Reference Manual, http://www.gurobi.com, 2020. [accessed 15 June 2020].

EURODYN 2020
XI International Conference on Structural Dynamics
M. Papadrakakis, M. Fragiadakis, C. Papadimitriou (eds.)
Athens, Greece, 23–26 November 2020

DOUBLE TUNED MASS DAMPER INERTER FOR SEISMIC RESPONSE REDUCTION OF STRUCTURES

Mahdi Abdeddaim[1], Salah Djerouni[2], Abdelhafid Ounis[2] and Nassim Djedoui[2]

[1] Faculty of science and technology, Biskra University Algeria
P.O.B 145 RP, Biskra, Algeria 07000
e-mail: m.abdeddaim@univ-biskra.dz

[2] LARGHYDE Laboratory, Department of civil engineering and hydraulics, faculty of science and technology, Biskra University Algeria
P.O.B 145 RP, Biskra, Algeria 07000
{s.djerouni,n.dejoudi,a.ounis}@univ-biskra.dz

Keywords: Inerter, Tuned mass damper, Seismic response, Optimization algorithm

Abstract. *The introduction of improved structural control systems is an efficacious solution for reducing the seismic damage induced to structures. Due to the high development in control systems and the growing interest for this research area, multiple control devices were developed, tested and used with a remarkable efficiency. During the last few years, a novel passive damper, called inerter has been introduced, mainly known for its ability to develop a large fictive mass and largely used in combination with tuned mass damper TMD resulting in a TMD-Inerter device. This research work presents a double tuned mass damper inerter DTMDI, which consists of two masses connected with an inerter, this configuration will result in large fictive mass ratio without any retroaction force on the structure. The effectiveness of the double tuned mass damper inerter DTMDI has been demonstrated using a multi-degree of freedom structure submitted to seismic excitations. The results obtained show a significant response reduction compared to simple tuned mass damper inerter TMDI and classical tuned mass damper TMD. The dynamical parameters investigated in this study are the top floor displacement, top floor acceleration, inter-story drift and base shear. The study also underlines optimal parameters for the double tuned mass damper inerter DTMDI.*

1 INTRODUCTION

During the last century earthquakes have been one of the most observed natural phenomena, due to their destructive nature they constituted a main cause of live and economical losses. Hence, earthquakes represent a constant challenge for structural and civil engineers. Aseismic design of structure caught the attention many researchers around the word.

Research, test and experiment of new seismic vibration control strategies lead to the development of many control devices that can be regrouped into three sets, passive, active and semi-active, any combination of two or more control strategies in known as hybrid control [1-3]. Due to their simplicity and efficiency passive devices are the most used around the word, such as base-isolation, viscous dampers and tuned mass damper TMD.

Tuned mass damper (TMD) is a passive device. It is constituted of a moving mass attached to the structure through a spring and a dashpot, the frequency of the TMD as a single degree of freedom system is tuned to the frequency of the main structure, with the participation of it mass inertia the TMD acts as a restoring force to prevent large displacement of the main structure during dynamical loading (wind, earthquake) [4, 5]. Hence, it is obvious that TMD requires relatively a large mass to achieve a response reduction, which may constitute a structural problem in terms of space, vertical load and even cost [6].

During the last year, a new control device was introduced to the civil engineering domain, known as the "inerter" this device uses rotational inertia to produce a force relative to the acceleration between its extremities [7]. The force produced is depending on a factor known as the "inertance" or fictive mass. Therefore, the inerter may produce a large fictive mass if his high inertance is combined with a large relative acceleration [8]. The main use of the inerter in civil engineering is it combination with conventional tuned mass dampers (TMD) to form a new device known as TMDI, this new device attracted the attention of many researchers during the last years. Hence, The performances of these systems were studied by Lazar, Neild [9] for multi-degrees of freedom system subjected to both, sinusoidal and seismic excitations. It was concluded that the optimal location for an inerter based tuned mass damper (TMDI) or a tuned inerter damper (TID) is at the bottom of the structure, where the inerter second terminal can be grounded also known as single terminal inerter. Marian and Giaralis [10] presented an optimal design for inerter based tuned mass damper (TMDI), this design aims to suppress the oscillatory motion of stochastically excited support, hence it was derived from classical tuning methods presented by Den Hartog [11] and Warburton [12]. The damping system was designed for a single degree of freedom undamped system equipped with a TMDI. De Domenico and Ricciardi [13] proposed an optimization procedure for a TMDI tuning, this optimization aims to protect a multi-degree base-isolated system equipped with a grounded TMDI under different seismic records, the optimization was applied on a simple three degree of freedom system composed of a TMDI, a base-isolation level and a superstructure. Further, the procedure was generalized to a five-story model proposed by Xiang and Nishitani [14]. It can be seen that most of the research on the TMDI concluded to the necessity of grounded inerter used (i.e. the second end of the inerter to be fixed to the ground). This is mainly motivated by the retro-action nature of the inerter as a passive device. Hence, if the force of the inerter is to be returned to the structure this will reduce the effect of the TMDI or even increase the response of the structure. This resulted in the limitation of the TMDI for base-isolated and low to mid rise buildings.

In this work, a novel tuned mass damper is proposed and simulated with the aim of using such device into high-rise building, the main idea of this device is to return the force of the inerter two a second mass, this can be achieved by connecting the TMDI mass and the second

mass with the inerter. This structural configuration is herein defined as double tuned mass damper inerter (DTMDI).

2 MATHEMATHICAL FORMULATION

In this study a 10-story fixed base building is equipped with a double tuned mass damper inerter. The system consists of a classical tuned mass damper located at the top floor. The TMD is attached to an adjacent movable mass through an inerter as it can be shown in figure 1. This configuration is denoted double tuned mass damper inerter (DTMDI).

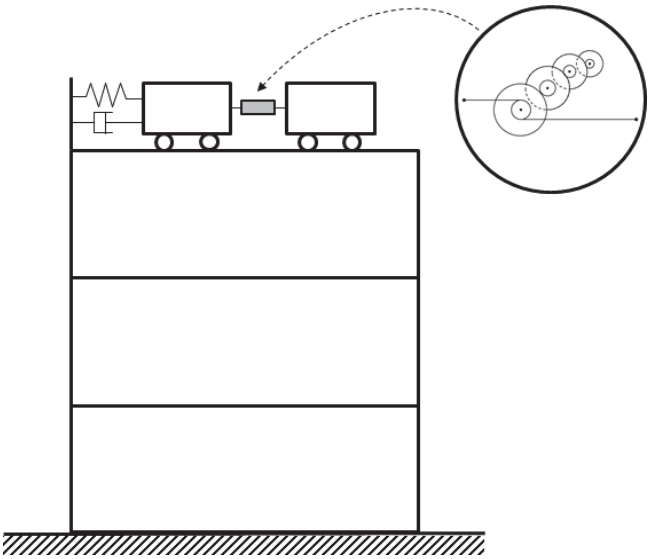

Figure 1. Structural configuration of a double tuned mass damper inerter.

The main motivation behind this configuration is to avoid returning a large amount of force from the second end of the inerter to the main structure. Usually, increasing the inerter fictive mass results in a large force, when returned to the main structure this force may increase the system response, despite the fact that it enhances the total mass of the TMD, thus enhancing it performance. Due to this inconvenience the efficiency of the TMDI remains limited and the amount of fictive mass reached remains low, except for the cases where the second end of the inerter is grounded (fixed to the ground) or connected to lower floors which represents a structural challenge especially for tall buildings .

The general equation of motion of the system shown in figure 1 can be written as follow according to d'Alembert's principle:

$$[M]\{\ddot{x}\}+[C]\{\dot{x}\}+[K]\{x\}=-[\bar{M}]\{r\}\{\ddot{x}_g\} \tag{1}$$

The detailed form of the $[M],[C]$ and $[K]$ matrices can be given as follow

$$\begin{bmatrix} m_1 & 0 & \cdots & \cdots & \cdots & 0 \\ 0 & m_2 & & & & \\ \vdots & & \ddots & & & \\ \vdots & & & m_n & & \\ \vdots & & & & m_{tmdi\ 1}+b & -b \\ 0 & & & & -b & m_{tmdi\ 2}+b \end{bmatrix}_{(n+2)\times(n+2)} \tag{2}$$

$$\begin{bmatrix} c_1+c_2 & -c_2 & \cdots & \cdots & \cdots & 0 \\ -c_2 & c_2+c_3 & & & & \\ \vdots & & \ddots & & & \\ \vdots & & -c_n & c_n+c_{tmdi\ 1} & -c_{tmdi\ 1} & \\ \vdots & & & -c_{tmdi\ 1} & c_{tmdi\ 1} & \\ 0 & & & & & 0 \end{bmatrix}_{(n+2)\times(n+2)} \tag{3}$$

$$\begin{bmatrix} k_1+k_2 & -k_2 & \cdots & \cdots & \cdots & 0 \\ -k_2 & k_2+k_3 & & & & \\ \vdots & & \ddots & & & \\ \vdots & & -k_n & k_n+k_{tmdi\ 1} & -k_{tmdi\ 1} & \\ \vdots & & & -k_{tmdi\ 1} & k_{tmdi\ 1} & \\ 0 & & & & & 0 \end{bmatrix}_{(n+2)\times(n+2)} \tag{4}$$

Where b denotes the additional inerter fictive mass, $m_{tmdi\ 1}$, $c_{tmdi\ 1}$ and $k_{tmdi\ 1}$ denotes the mass, damping and stiffness of the DTMDI, $m_{tmdi\ 2}$ denotes the second mass connected to the first mass through the inerter. $\left[\overline{M}\right]$ denotes the real mass matrix $(b=0)$ and n denoted the degrees of freedom of the structure.

2.1 Governing equations of the inerter

A basic model of the inerter is represented with the scheme shown in the Fig. 2. The inerter comprises of a rack and pinion arrangement rotating about a shaft, represented by the point O. The two extremities of the inerter, represented by *a* and *b* in Fig. 2, are connected to the pinion (of radius ρ) through racks and are responsible for reversing the direction of retro-action (represented by *F(t)*) at both ends. A flywheel having a radius *R* and mass m_i is mounted on the other end of the shaft, to reduce the impact through its higher inertia.

The rotation of the flywheel can be written as:

$$\theta(t)=\frac{x_a(t)-x_b(t)}{\rho} \tag{5}$$

The displacements at the extremities of the inerter element are expressed by x_a and x_b. The dynamic moment equilibrium about the point *O* can be represented by:

$$I_O\theta(t)=F(t)\rho \tag{6}$$

Thus, the moment of inertia of the flywheel rotating about point *O* will be $I_O=(1/2).m.R^2$
Substitution of Eq. (5) and Eq. (6) results in the mechanical linear equation of the inerter

$$F(t)=\frac{1}{2}m\frac{R^2}{\rho^2}\left[\ddot{x}_a(t)-\ddot{x}_b(t)\right] \tag{7}$$

It can be seen from Eq. (7) that the force generated by the inerter is related to the relative acceleration between it extremities. The term multiplied by the relative acceleration is denoted as the inertance b of the device, and is expressed in unit of mass (kg). The inertance of the

device can be enhanced by serially increasing the number of pinions. Hence, the general equation of inerter become

$$F(t) = b\left[\ddot{x}_a(t) - \ddot{x}_b(t)\right] \tag{8}$$

For instance, if a single pinion inerter can produce an inertance of 1440 kg for a device that weights 10 kg [15].

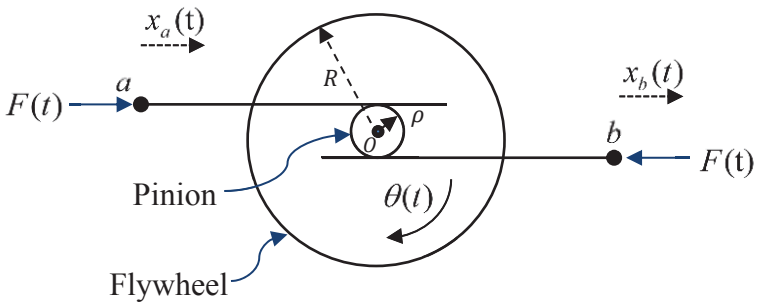

Figure 2. Rheological model of a single flywheel inerter [8].

2.2 Device tuning approach

In order to ensure a maximum efficiency, the DTMDI control strategy formulated in this paper needs a proper tuning, this involves the choice of a proper frequency, stiffness, damping and mass ratio. Hence, a tuning approach proposed by Marian and Giaralis [15] is adopted in this study.

Following the formulation originally proposed by Den Hartog [11] for a classical TMD, Marian and Giaralis [15] proposed an equivalent tuning for TMDI systems. Consider the class of dynamically excited structures amenable to be modelled as single-degree-of-freedom (SDOF) systems equipped with a tuned mass damper inerter as shown in figure 3.

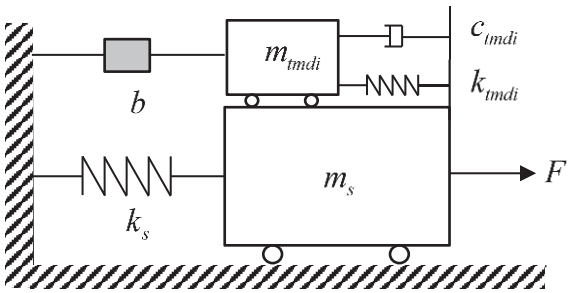

Figure 3. Primary SDOF structure equipped with a TMDI subjected to force excitations

The motion equation of the represented system is figure 3 is given as follow:

$$\begin{bmatrix} m_s & 0 \\ 0 & m_{tmdi}+b \end{bmatrix}\begin{Bmatrix} \ddot{x}_s \\ \ddot{x}_{tmdi} \end{Bmatrix} + \begin{bmatrix} c_{tmdi} & -c_{tmdi} \\ -c_{tmdi} & c_{tmdi} \end{bmatrix}\begin{Bmatrix} \dot{x}_s \\ \dot{x}_{tmdi} \end{Bmatrix} + \begin{bmatrix} k_s + k_{tmdi} & -k_{tmdi} \\ -k_{tmdi} & k_{tmdi} \end{bmatrix}\begin{Bmatrix} x_s \\ x_{tmdi} \end{Bmatrix} = -\begin{Bmatrix} m_s \\ m_{tmdi} \end{Bmatrix} F(t) \tag{9}$$

Equation (9) is elaborated and derived in close form, out of this procedure a TMDI tuning is obtained representing optimal frequency ratio υ_{tmdi} and damping ratio ζ_{tmdi} given in Eq. 10 and 11 respectively.

$$\upsilon_{tmdi} = \frac{1}{1+\beta+\mu} \tag{10}$$

$$\zeta_{tmdi} = \sqrt{\frac{3(\mu+\beta)}{8(1+\mu+\beta)}} \tag{11}$$

Where: β is the inertance ratio defined by $\beta = \frac{b}{m_s}$.

μ: is the TMDI mass ratio, it can be written as $\mu = \frac{m_{tmdi}}{m_s}$, m_{tmdi} and m_s are the masses of the TMDI and the primary structure, respectively.

Regarding the DTMDI tuning, the 2nd mass connected to the inerter can be considered as a floor mass or any other structural part of the structure, hence there will be no difference in the tuning of a classical TMDI or a DTMDI using the approach proposed above. Which will be used during this study.

3 NUMERICAL STUDY AND RESULTS

In order to study the performance of the proposed system four structural configurations are submitted to a set of earthquakes as shown in table 1, the structural configurations can be listed as follow:

- Uncontrolled structure, the structure without any device,
- Structure with a tuned mass damper (TMD) at the top floor,
- Structure with a tuned mass damper Inerter (TMDI) at the top floor, the 2nd extremity of the inerter is fixed to the last floor,
- Structure with a double tuned mass damper inerter (DTMDI) at the top floor (as shown in figure 1).

The mass ratios of the three control devices (*i.e.* TMD, TMDI and DTMDI) are kept equal in order to keep the control devices performance comparable.

The performances of the DTMDI are compared to a classical TMD and a conventional TMDI. In order to achieve the comparison, the structure is submitted to a set of earthquakes.

The structure used in study was presented by Özsarıyıldız and Bozer [16]

N°	Name	Record serial number (RSN)	Component	Fault type	PGA (m/s^2)
1	Northridge	1048	180	Near	4.50
2	Duzce	1605	270	Near	5.05
3	Landers	848	CLW-LN	Far	3.09
4	Kobe	1111	000	Far	4.74

Table 1. Earthquake records used in this study

3.1 Inertance effect on response reduction

In this part the effect of the inertance (ratio of fictive mass to total mass of the structure) is studied for both TMDI and DTMDI. Hence, the inertance will be varied from 0 to 0.1. It is worth noticing that a null inertance is equivalent to a classical TMD. The mass ratio (ratio of the real mass to total mass of the structure) μ is equal to 5% for both TMDI and DTMDI. However, for the DTMDI it will be equally partitioned between the two masses.

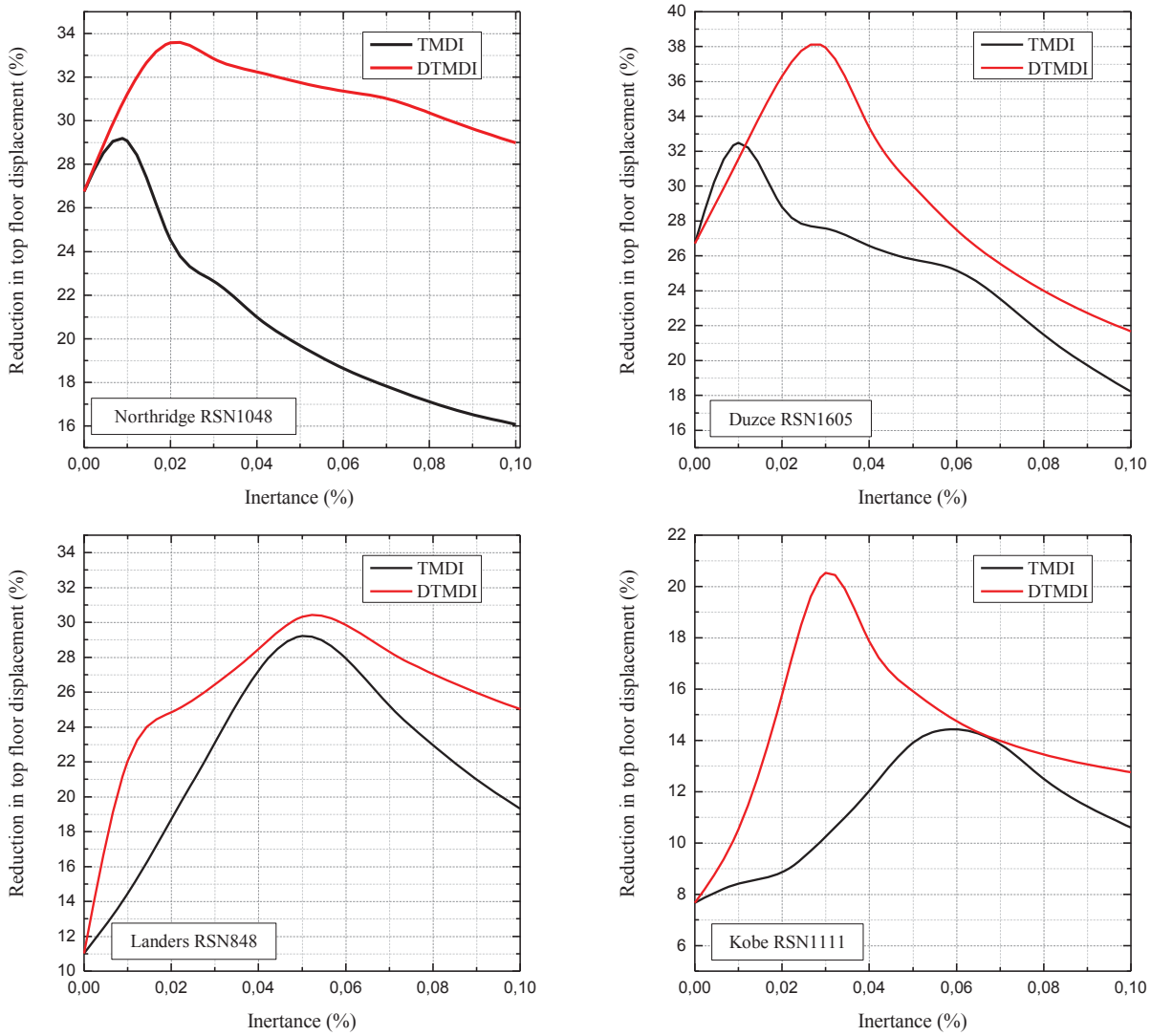

Figure 4. The inertance (β) effect on top floor displacement for both TMDI and DTMDI

From figure 4 it can be clearly seen that the inertance has an important and considerable effect on the response reduction for both TMDI and DTMDI. However, higher inertance involves less response reduction for TMDI; this is mainly due to retro-action force of the inerter being returned to the structure (i.e. the second extremity of the inerter is fixed to the last floor in this case). On the other hand, higher inertance results in more response reduction for the DTMDI, this is mainly motivated by the fact that the retro-action of the inerter is returned to the second mass of the DTMDI. It is also observed that for each earthquake there exists an optimal inertance value for both TMDI and DTMDI. In overall, the performance of DTMDI surpasses the performance of TMDI for the studied earthquakes.

With this in background, an average optimal inertance is defined for both TMDI and DTMDI. The inertance will be set to 1% and 3% of the total mass of the building for both the TMDI and the DTMDI, respectively

3.2 Time history analysis

In order to assess the performances of the proposed DTMDI a time history analysis is performed, for top floor displacement using three control strategies namely, TMD, TMDI and DTMDI, results obtained are shown in figure 5.

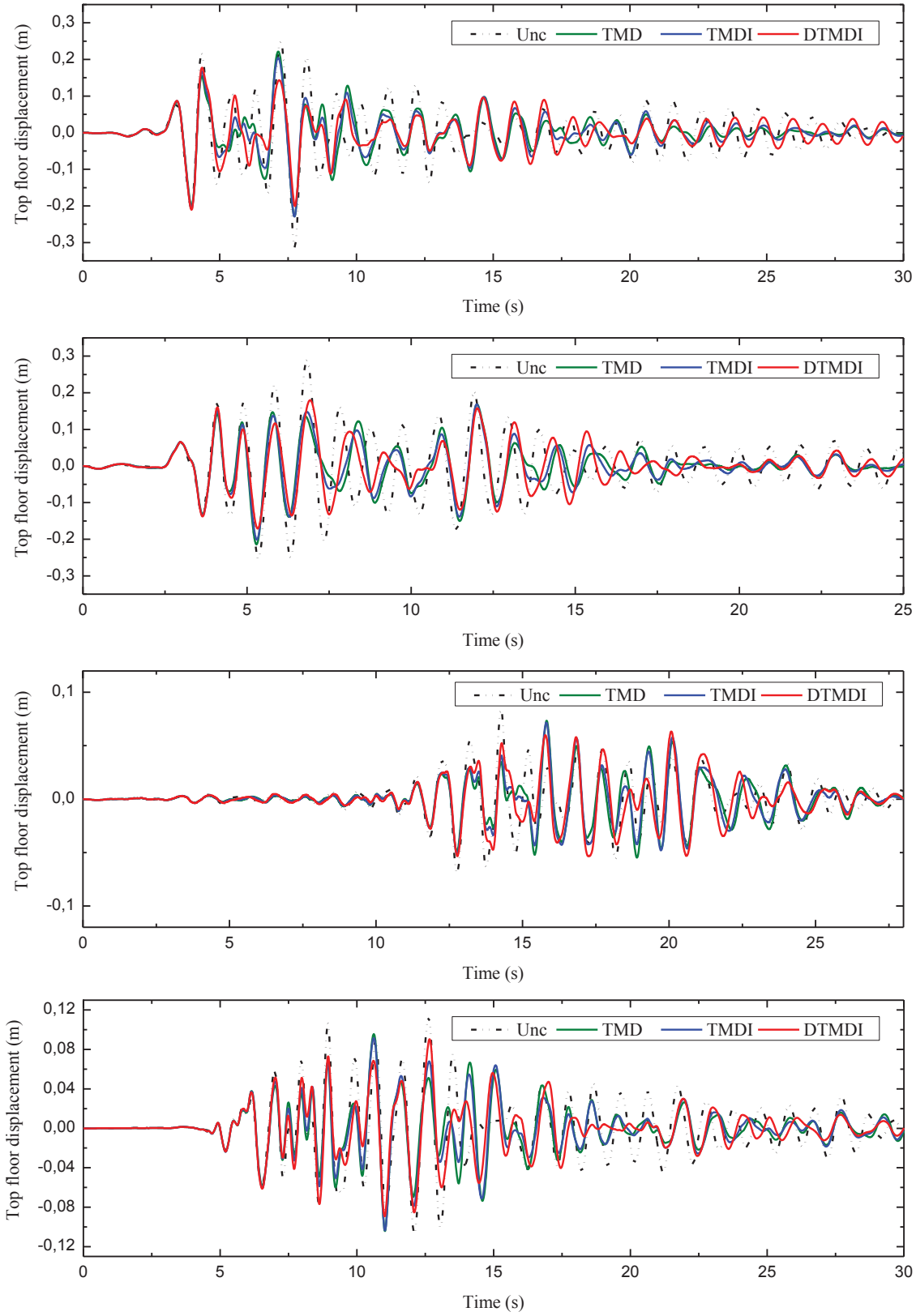

Figure 5. Time history analysis of top floor displacement under three control strategies

As it can be seen from figure 5 the performance of DTMDI is better than both TMDI and TMD, the reduction is clearly visible in peak displacement. The response reduction is achieved for all studied earthquakes. Table 2 shows the top floor maximum displacement for all control devices and also the percentage reduction in brackets.

Earthquake	Uncontrolled	TMD	TMDI	DTMDI
Northridge	0.3131	0.2288	0.2294	0.2106
(RSN1048)	--	(26.95)	(26.75)	(32.73)
Duzce	0.2888	0.2142	0.2010	0.1798
(RSN1605)	--	(25.83)	(30.40)	(37.72)
Landers	0.0837	0.0734	0.0716	0.0634
(RSN848)	--	(12.32)	(14.43)	(24.26)
Kobe	0.1132	0.1042	0.1037	0.0904
(RSN1111)	--	(07.93)	(08.40)	(20.09)

Table 2. Top floor displacement in *[m]* and percentage reduction in (%) under different control strategies

From table 2 it can be seen that performance of TMD and TMDI remain close in terms of top maximum floor displacement reduction. On the other hand, the DTMDI surpasses both the devices in terms of maximum top floor reduction using the same mass ratio μ (which is equal to 5% of the total mass of the structure). The percentage reduction varies from 20 to 32% depending on the earthquake. It is worth noticing that for far-fault earthquake less reduction is obtained due to the small displacements of the building.

3.3 Stroke displacement

One of the performance indexes of the tuned mass damper in the stroke displacement of the damper mass. Hence, in this part of the paper the stroke displacement of the three studied systems will be compared.

Earthquake	TMD	TMDI	DTMDI		
			Mass 1	Mass 2	Sum
Northridge (RSN1048)	0.6252	0.4665	0.4223	0.2357	0.6580
Duzce (RSN1605)	0.5284	0.4476	0.4352	0.3259	0.7611
Landers (RSN848)	0.1381	0.1238	0.1394	0.1516	0.2910
Kobe (RSN1111)	0.2087	0.1992	0.2053	0.1211	0.3264

Table 3. Stroke displacement in *[m]* under different control devices

From table 3 it can be seen that the TMDI achieved the lesser stroke displacement compared to the other devices this is mainly due to the inerter configuration connecting the TMDI mass to the last floor of the structure. Hence limiting the mass displacements. The performance of each mass of the DTMDI remains comparable the TMDI. However, if summed up the total displacement remains high and comparable to a classical TMD. This is directly related to the configuration of the DTMDI device. These large displacements may be reduced by adding a low damping and stiffness devices to the right side of the 2nd mass of the DTMDI.

3.4 Inertance effect on control the control force

In this part the inertance effect on the control force generated by the inerter is examined, for this purpose the inertance β is varied from 0 to 10 percent and the control force generated by the inerter is evaluated for both the TMDI and DTMDI. This can be achieved by multiplying the relative acceleration between the two extremities of the inerter by the inerter parameter b .

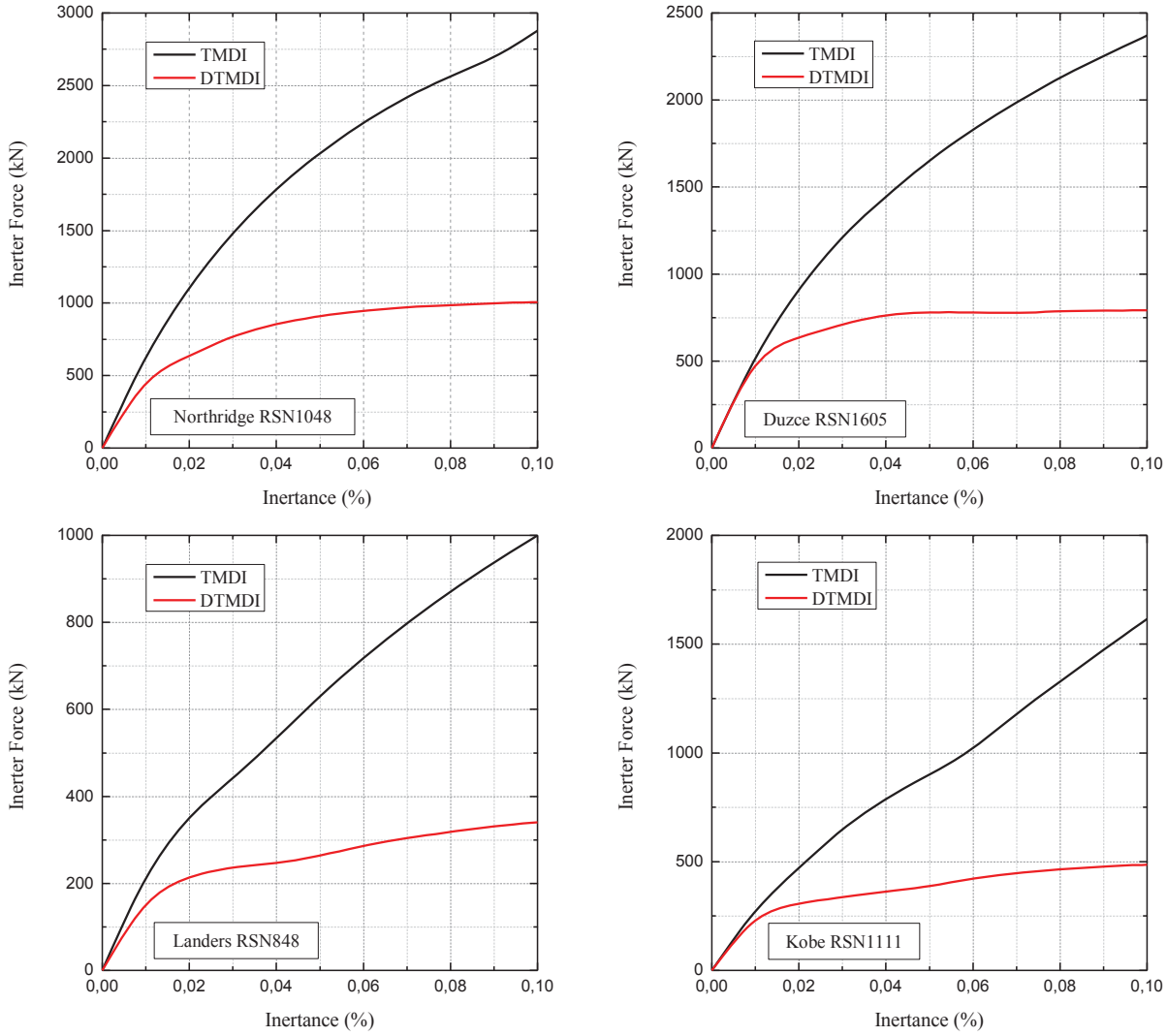

Figure 6. The inertance (β) effect on the inerter force

In figure 6, it can be seen that the inerter force is relative to the inertance. Hence, increasing the inertance results in the augmentation of the inerter force generated. This can be observed for all the studied earthquakes for both TMDI and DTMDI. The force generated by the classical TMDI increases at a higher rate inducing large force to the floor to which the inerter is connected which affects it efficiency at higher inertance values as shown in figure 4. Regarding the DTMDI the curve tends to saturate at high values of inertance, the force generated by the inerter is lower than the classical TMDI case involving less force applied to the secondary mass. It is worth noticing that the DTMDI results in better reduction with less generated force. It can be observed that the force generated by the inerter is relative to the earthquake PGA and fault type.

4 CONCLUSIONS

In this work, a new configuration for tuned mass damper inerter was proposed, the configuration is based on the use of a second mass. This mass will be coupled to the conventional TMDI through an inerter. This disposition will result in a so called double tuned mass damper inerter DTDMI, this later will enhance the performance of the structure by reducing it response to earthquakes compared TMD and TMDI. The main advantage of this configuration is the suppression of the inerter force returned to the structure. Based on the obtained results the following conclusions can be draw:

- Using a second mass connected to a TMDI by an inerter will prevent the application of the inerter retro-action force to the structure. Hence the performance of the DTMDI will reduce the response of the structure to dynamical loading such as earthquakes.
- There exists an optimal inertance parameter for both TMDI and DTMDI for each earthquake. However, the TMDI performs better at low values of inertance while the DTMDI requires higher inertance values to accomplish optimal reduction.
- The response reduction is obtained under four different earthquakes with different fault types.
- The DTMDI performances surpasses both TMD and TMDI despite using the same total mass ratio μ
- The stroke displacement of the TMDI mass is the lesser compared to classical TMD and DTMDI. However, the performance of the DTMDI regarding stroke displacement remains acceptable and comparable to a classical TMD.
- The large stroke displacement of the DTMDI can be limited by adding additional damping and stiffness to the right side of the 2nd mass of the system.
- The DTMDI achieves better reduction with less inerter force generated compared to the TMDI.

REFERENCES

1. Abdeddaim, M., et al., Retrofitting of a weaker building by coupling it to an adjacent stronger building using MR dampers. *Structural Engineering and Mechanics* 62(2), 197-208, 2017.
2. Azimi, M., et al., Improved semi-active control algorithm for hydraulic damper-based braced buildings. *Structural Control and Health Monitoring*, 2016.
3. Azimi, M., et al. Optimal design of active tuned mass dampers for mitigating translational–torsional motion of irregular buildings. in *International Conference on Experimental Vibration Analysis for Civil Engineering Structures*. Springer,2017.
4. Djedoui, N., et al., Hybrid control systems for rigid buildings structures under strong earthquakes. *Asian Journal of Civil Engineering (BHRC)* 18(6), 893-909, 2017.
5. Guenidi, Z., et al., Control of adjacent buildings using shared tuned mass damper. *Procedia Engineering* 199, 1568-1573, 2017.
6. Djedoui, N., A. Ounis, and M. Abdeddaim, Active Vibration Control for Base-Isolated Structures Using a PID Controller against Earthquakes. *International Journal of Engineering Research in Africa* 26, 99-110, 2016.
7. Smith, M.C., Synthesis of mechanical networks: The inerter. *IEEE Transactions on automatic control* 47(10), 1648-1662, 2002.
8. Abdeddaim, M., A.A. Kasar, and N. Djedoui. Seismic vibration control using a novel inerto-elastic damper. in *MATEC Web of Conferences*. EDP Sciences,2018.
9. Lazar, I., S. Neild, and D. Wagg, Using an inerter‐based device for structural vibration suppression. *Earthquake Engineering & Structural Dynamics* 43(8), 1129-1147, 2014.
10. Marian, L. and A. Giaralis, Optimal design of a novel tuned mass-damper–inerter (TMDI) passive vibration control configuration for stochastically support-excited structural systems. *Probabilistic Engineering Mechanics* 38, 156-164, 2014.
11. Den Hartog, J.P., *Mechanical vibrations*. 1985: Courier Corporation.
12. Warburton, G., Optimum absorber parameters for various combinations of response and excitation parameters. *Earthquake Engineering & Structural Dynamics* 10(3), 381-401, 1982.
13. De Domenico, D. and G. Ricciardi, An enhanced base isolation system equipped with optimal tuned mass damper inerter (TMDI). *Earthquake Engineering & Structural Dynamics*, 2017.
14. Xiang, P. and A. Nishitani, Optimum design for more effective tuned mass damper system and its application to base-isolated buildings. *Structural Control and Health Monitoring* 21(1), 98-114, 2014.
15. Marian, L. and A. Giaralis, The tuned mass-damper-inerter for harmonic vibrations suppression, attached mass reduction, and energy harvesting. *Smart Structures and Systems* 19(6), 665-678, 2017.
16. Özsarıyıldız, Ş.S. and A. Bozer, Finding optimal parameters of tuned mass dampers. *The Structural Design of Tall and Special Buildings* 24(6), 461-475, 2015.

EURODYN 2020
XI International Conference on Structural Dynamics
M. Papadrakakis, M. Fragiadakis, C. Papadimitriou (eds.)
Athens, Greece, 23–26 November 2020

OPTIMAL FEEDBACK CONTROL LAW FOR VISCOELASTIC MATERIALS WITH MEMORY EFFECTS

G. Pepe[1], E. Paifelman[2], and A. Carcaterra[1]

[1] Department of Mechanical and Aerospace Engineering Sapienza University of Rome, Italy
e-mail: {gianluca.pepe , antonio.carcaterra}@uniroma1.it

[2]Institute of Marine Engineering of Rome, Italian National Research Council, Italy
e-mail: elena.paifelman@inm.cnr.it

Keywords: Viscoelasticity, Memory effects, Optimal control, Feedback control, Fractional derivatives, Integral-differential equations

Abstract. *Viscoelastic materials have excellent properties of absorbing vibrational energy which makes their use very attractive in structural, aerospace and biomechanics engineering applications. The macroscopic dynamical behaviour of such materials depends on the time history, or memory, of the strain. The stress-strain viscoelastic relation can be described by a convolution integral with a memory kernel, according to Boltzmann's formulation of hereditary elasticity, or by using Caputo or Riemann-Liouville fractional derivatives. In order to emphasize the vibrations damping attitude of these materials, by actively controlling their stress-strain behaviour, novel optimal control logics are required which involve memory effects. This paper deals with a feedback control strategy applied to a structural-dynamic problem described by integral-differential equations. It is shown how to obtain a feedback control, called $PD^{(N)}$, i.e. Proportional-Nth-order-Derivatives control, by using a variational approach. Numerical simulations show how the $PD^{(N)}$ controller is an effective tool to improve the viscoelastic materials performance.*

1 INTRODUCTION

The use of viscoelastic materials is crucially important in many engineering disciplines and there are applications in a wide variety of areas such as aerospace, transport components, biomechanics and civil infrastructures [1-5]. These materials have excellent properties of absorbing vibrational energy which makes their use in engineering applications very attractive, such as the dynamic instabilities and the fluid-structures interaction control.

Often, the macroscopic dynamical behaviour of such materials depends on the time history or memory effects, of the strain response. According to Boltzmann's formulation of hereditary elasticity [6], the stress-strain relation in linear viscoelasticity can be described by a convolution integral with a memory kernel. However, the mathematical form of this kernel is not easily predictable by theoretical tools, but it rather relies on experimental identification.

In the past, combinations of elemental rheological components such as the spring and dashpot, were used to generate a whole family of rheological models, such as Maxwell and Kelvin–Voigt, or the four-parameters Burger's model, generalizing the viscoelastic response, but without including memory effects [7]. Moreover, experimental tests have shown some inconsistencies of viscoelastic materials, especially when the effects of relaxation and creep would be kept into the model [8]. For these reasons in the second part of the last century, many researches have been carried out a more realistic description of creep and/or relaxation given by the use of power law functions with real order exponent [9]. Such formulation captures the creep behaviour and generates the fractional hereditary model. In fact, the constitutive law of viscoelastic materials makes use of the Riemann-Liouville and Caputo's fractional derivative [10, 11]. Due to the high mathematical complexity of such models, which imply integral-differential equations (IDEs), difficulties arise in the formulation of optimal control algorithm.

In recent years the interest in model-based control of mechanical systems incorporating active controlled viscoelastic dampers has been increased in order to improve the mechanical system efficiency. Systems with viscoelastic dampers has been investigated by [12] where the viscoelastic term is approximated by damping terms which are converted into stochastic differential equations solved by a dynamic programming method; meanwhile multi-input and multi-output mechanical systems incorporating viscoelastic dampers are controlled with discrete-time sliding mode control algorithm [13]. Fractal-fractional model are used by [14] where the nonlinear algebraic system is solving by the Gauss-Legendre quadrature rule. Moreover, active control for standard Kelvin-Maxwell viscoelastic structures can be designed accurately with poles and zeros assignment defining an ad-hoc receptance transfer function [15]. Numerical scheme for solving fractional differential equations are proposed by [16] using the approximation of Laguerre integral formula.

In general, the optimal control strategies, applied to viscoelastic model, make use of direct methods. This paper introduces an indirect optimal feedback control algorithm, which is still missing in the literature panorama. Starting from the prototype integral-differential beam equation, the authors show how it is possible to obtain a Proportional-Nth-order-Derivatives control, called PD(N), by using the variational approach. PD(N) algorithm depends on the structure of the kernel and is a sort of hyper-derivative proportional control. The PD(N) control belongs to the category of Variational Feedback Controls-VFC, in the context of which the authors are developing different control architectures [17-19].

The paper consists of three main sections. The first presents the viscoelastic mathematical beam model, using the Caputo's fractional derivatives. The PD(N) feedback optimal control algorithm is derived in the second section, and in the third, numerical results show the effective performance of the proposed control for a bridge deflection control when it is subject to earth-

quake excitation and impulsive disturbances, still maintaining low the cost function in comparison with the LQR method and the implicit Pontryagin solution for IDEs already formulated by authors [20-22].

2 VISCOELASTIC BEAM MODEL

A brief description of the viscoelasticity fractional Kelvin–Voigt model is the premise to obtain the partial differential equations (PDE) of an Euler–Bernoulli viscoelastic beam, of length *L* and subjected to a basement seismic motion z_b (see Figure 1).

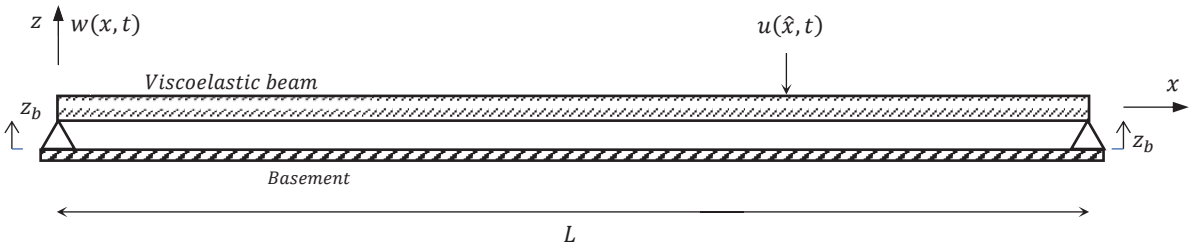

Figure 1: Viscoelastic beam.

The classical Kelvin–Voigt model, using one spring and one viscous pot in parallel, presents a time-varying linear stress-strain relationship $\sigma(\varepsilon)$ which can be expressed by the Caputo's fractional derivative D^{β}:

$$\sigma = E\varepsilon + E_{\beta} D^{\beta}[\varepsilon] \tag{1}$$

with E the Young's modulus, E_{β} the damping modulus and the time varying operator $D^{\beta}[\ \ ]$, with $0 \leqslant \beta \leqslant 1$ depending on material proprieties, defined as:

$$D^{\beta}[\varepsilon] = \frac{1}{\Gamma(1-\beta)} \int_0^t \frac{\dot{\varepsilon}(\tau)}{(t-\tau)^{\beta}} d\tau \tag{2}$$

with $\Gamma(\cdot)$ the Gamma function.

Considering constant ρ density, *A* cross-section area and *I* inertial moment the PDE is derived by defining the conservation of momentum and of moment of momentum:

$$\begin{aligned} \frac{\partial T_z(x,t)}{\partial x} &= \rho A \frac{\partial^2 w_b(x,t)}{\partial t^2} - u(\hat{x},t) - \rho A \ddot{z}_b(t) \\ \frac{\partial M_y(x,t)}{\partial x} &= T_z(x,t) \end{aligned} \tag{3}$$

where $w_b(x,t)$, $T_z(x,t)$, $M_y(x,t)$ and $u(\hat{x},t)$ are the vertical displacement along the z-axis, the shear, the bending moment and the punctual actuation acting on $\hat{x}$, respectively.

The introduction of the kinematic Euler-Bernoulli and the σ stress and bending moment M_y relations

$$\begin{aligned} \varepsilon(x,t) &= -z \frac{\partial^2 w_b(x,t)}{\partial x^2} \\ \sigma(x,t) &= z \frac{M_y(x,t)}{I} \end{aligned} \tag{4}$$

leads to the definition of the viscoelastic beam equation as formulated by [23]:

$$\rho A \frac{\partial^2 w_b(x,t)}{\partial t^2} + EI \frac{\partial^4 w_b(x,t)}{\partial x^4} + E_{\beta} I D^{\beta} \left[\frac{\partial^4 w_b(x,t)}{\partial x^4} \right] = u(\hat{x},t) + \rho A \ddot{z}_b(t) \tag{5}$$

Finally, equation (5) can be expressed in a compact form with the convolution integral term $k * \dot{w}_b^{IV}$ instead of the fractional operator $E_{\beta} D^{\beta}[w_b^{IV}]$ as formulated by Nutting [24]. By using

the derivative convolution properties and considering the supported beam case, the final equation with the associated boundary conditions is:

$$\begin{gathered}\rho A\ddot{w}_b(x,t) + EIw_b^{IV}(x,t) + I\dot{k} * w_b^{IV}(x,t) = \delta(x-\hat{x}\,)u(t) + \rho A\ddot{z}_b(t) \\ w_b''|_0^L = 0 \\ w_b|_0^L = 0\end{gathered} \tag{6}$$

where $\delta(\quad)$ is the Dirac function. In the case of translational base motion, the final transverse displacement w is given by the summation of two contributions:

$$w(x,t) = w_b(x,t) + z_b(t) \tag{7}$$

Decoupling equation (6) by the modal decomposition:

$$w_b(x,t) = \sum_r^{\infty} q_r(t)\phi_r(x) \tag{8}$$

with ϕ_r the eigenfunction of the r-*th* vibration mode, one obtains:

$$\rho A\phi_r\ddot{q}_r + EI{\phi_r}^{IV}q_r + I{\phi_r}^{IV}\,\dot{k} * q_r = \delta(x-\hat{x}\,)u(t) + \rho A\ddot{z}_b(t) \tag{9}$$

With the following normalization:

$$\begin{gathered}\int_0^L \phi_m\rho A\phi_r = \delta_{mr} \quad , \qquad \int_0^L \phi_m EI\phi_r^{IV} = \omega_r^2\delta_{mr} \quad , \quad \widehat{\omega}_r^2 = \frac{\omega_r^2}{E} \\ \gamma_r = \int_0^L \phi_r\,\rho A\end{gathered} \tag{10}$$

equation (9) becomes:

$$\ddot{q}_r + \omega_r^2 q_r + \widehat{\omega}_r^2\,\dot{k} * q_r = \phi_r(\hat{x})u(t) + \gamma_r\ddot{z}_b(t) \tag{11}$$

Finally, equation (11) is a second order integral-differential equation which represents the decoupled dynamic of the controlled viscoelastic Euler-Bernoulli beam when an external basement disturbance is acting on it. In the following section, is investigated a novel optimal control approach to equation (11).

3 THE VISCOELASTIC OPTIMAL CONTROL

For equation (11), it is possible to introduce an optimal feedback control law by using the variational calculus. The control solution is a sort of hyper-derivative proportional control called Proportional-Nth-order-Derivatives, i.e. PD$^{(N)}$ controller, depending on the structure of the kernel [25]. Introducing the new state variable $\boldsymbol{x} = [\boldsymbol{q}, \dot{\boldsymbol{q}}]^T$ and $\boldsymbol{q} = [q_1, \dots, q_r, \dots q_N]^T$ equation (11) takes the space state form:

$$\dot{\boldsymbol{x}} = \boldsymbol{A}\boldsymbol{x} + \boldsymbol{K} * \boldsymbol{x} + \boldsymbol{B}\boldsymbol{u} + \boldsymbol{d} \tag{12}$$

where $\boldsymbol{A} \in \mathbb{R}^{N,N}$ and $\boldsymbol{B} \in \mathbb{R}^{N,1}$ are constant matrixes, $\boldsymbol{u}$ in this example is a scalar control variable, $\boldsymbol{d} \in \mathbb{R}^{N,1}$ the external disturbances vector and $\boldsymbol{K} \in \mathbb{R}^{N,N}$ include the Caputo's fractional derivative.

The optimal control law is based on the minimization of a generic quadratic cost function J which depends on the state and the control variables together with the Lagrange multiplier vector $\boldsymbol{\lambda}$, introduced to account for the system's dynamics expressed by equation (12):

$$J(\boldsymbol{x},\boldsymbol{u},\boldsymbol{\lambda}) = \int_0^T \frac{1}{2}\boldsymbol{x}^T\boldsymbol{Q}\boldsymbol{x} + \frac{1}{2}\boldsymbol{u}^T\boldsymbol{R}\boldsymbol{u} + \boldsymbol{\lambda}^T[\dot{\boldsymbol{x}} - \boldsymbol{A}\boldsymbol{x} - \boldsymbol{K} * \boldsymbol{x} - \boldsymbol{B}\boldsymbol{u} - \boldsymbol{d}]dt \tag{13}$$

The variational calculus finds a solution to the stated problem by using the stationary condition $\delta J(\boldsymbol{x},\boldsymbol{u},\boldsymbol{\lambda}) = 0$. The variations of the term $\boldsymbol{K} * \boldsymbol{x}$ present some nontrivial problems, and a technique to deal with this term is considered in details in [21, 25]. Considering a scalar term

$k * x$, the kernel causality proprieties $k(t-\tau) = 0$ for $t < 0$ and $\tau > t$, produces its variation in the form:

$$\delta \int_0^T x(t) \int_0^t k(t-\tau)x(\tau)d\tau\, dt = \int_0^T \int_t^T k(\tau - t)x(\tau)d\tau\, \delta f dt = \int_0^T k \diamond x\, \delta x\, dt \tag{14}$$

Proceeding with standard variational calculus rules, and using equation (14), the associated extremal conditions are found:

$$\begin{aligned} &\dot{\boldsymbol{\lambda}} = \boldsymbol{Q}\boldsymbol{x} - \boldsymbol{A}^T\boldsymbol{\lambda} - \boldsymbol{K}^T \diamond \boldsymbol{\lambda} \\ &\dot{\boldsymbol{x}} = \boldsymbol{A}\boldsymbol{x} + \boldsymbol{B}\boldsymbol{u} + \boldsymbol{K} * \boldsymbol{x} + \boldsymbol{d} \\ &\boldsymbol{u} = \boldsymbol{R}^{-1}\boldsymbol{B}^T\boldsymbol{\lambda} \\ &\boldsymbol{\lambda}(T) = \boldsymbol{0}\,, \boldsymbol{x}(0) = \boldsymbol{x_0} \end{aligned} \tag{15}$$

Eq. (15) gives the optimal open loop solution to problem (13) and it can be solved with several direct control methods [26]. However, our goal is to obtain an explicit feedback formulation of the control $\boldsymbol{u}(\boldsymbol{x})$, that has tremendous advantages under the engineering application point of view. To this aim, we replace the fractional operator (2) by its approximation by a truncated exponential series. Therefore, the Nutting's kernel $k(t)$ in (11), can be reformulated as:

$$k * x = \frac{E_\beta}{\Gamma(1-\beta)} \int_0^t \frac{x(\tau)}{(t-\tau)^\beta} d\tau \approx \frac{E_\beta}{\Gamma(1-\beta)} \int_0^t \sum_i^N \alpha_i e^{-c_i(t-\tau)} x(\tau) d\tau = \hat{k} * x \tag{16}$$

where α_i and c_i are the N-constants of the exponential series approximation and $\hat{k}$ is introduced to indicate the approximated kernel. In this way, eq. (16) leads to transform the integral-differential equations (15) into the Laplace domain. In fact, both the terms, $\hat{k} * x$ and $\hat{k} \diamond x$ have the corresponding Laplace transform $\mathcal{L}\{\quad\}$ in s as sum of polynomials:

$$\begin{aligned} \mathcal{L}\{\hat{k} * x\} &= X(s) \sum \frac{\alpha_i}{s + c_i} = X(s) \frac{P(N-1)(s)}{D(N)(s)} \\ \mathcal{L}\{\hat{k} \diamond x\} &= X(s) \sum \frac{\alpha_i}{s - c_i} = -X(s) \frac{P(N-1)(-s)}{D(N)(-s)} \end{aligned} \tag{17}$$

where P and D are used to indicate the N-order polynomials.

Then, using the equations (16) and (17) to express the integral terms in the first two of equations (15), setting $\boldsymbol{d} = \boldsymbol{0}$ and eliminating the control $\boldsymbol{u}$ in the equation $\dot{\boldsymbol{x}} = \boldsymbol{A}\boldsymbol{x} + \boldsymbol{B}\boldsymbol{u} + \boldsymbol{K} * \boldsymbol{x}$, using $\dot{\boldsymbol{x}} = \boldsymbol{A}\boldsymbol{x} + \boldsymbol{B}\boldsymbol{R}^{-1}\boldsymbol{B}^T\boldsymbol{\lambda} + \boldsymbol{K} * \boldsymbol{x}$, we can produce the Laplace transform of the obtained equations in terms of $\boldsymbol{X}(s)$ and $\boldsymbol{\Lambda}(s)$ only. Rearranging these equations, and transforming back to time domain, we finally obtain:

$$\begin{aligned} &\sum_{i=0}^{N+1} \boldsymbol{C}_i \boldsymbol{x}^{(i)} + \sum_{i=0}^{N} \boldsymbol{D}_i \boldsymbol{\lambda}^{(i)} = \boldsymbol{0} \\ &\sum_{i=0}^{N+1} \boldsymbol{F}_i \boldsymbol{\lambda}^{(i)} + \sum_{i=0}^{N} \boldsymbol{E}_i \boldsymbol{x}^{(i)} = \boldsymbol{0} \end{aligned} \tag{18}$$

where $\boldsymbol{x}^{(i)} = \frac{d^i \boldsymbol{x}}{dt^i}$, and the problem is reduced to a pure differential equation set, linear and time-invariant. Collecting the variables into $\boldsymbol{\xi} = \left[\boldsymbol{x}^{(N)} \ldots \boldsymbol{x}^{(i)} \ldots \boldsymbol{x}\right]$ and $\boldsymbol{\eta} = \left[\boldsymbol{\lambda}^{(N)} \ldots \boldsymbol{\lambda}^{(i)} \ldots \boldsymbol{\lambda}\right]$, equations (18) can be reduced to a first order normal form differential problem:

$$\begin{cases} \dot{\boldsymbol{\xi}} = \boldsymbol{H}_{\xi\xi}\boldsymbol{\xi} + \boldsymbol{H}_{\xi\eta}\boldsymbol{\eta} \\ \dot{\boldsymbol{\eta}} = \boldsymbol{H}_{\eta\xi}\boldsymbol{\xi} + \boldsymbol{H}_{\eta\eta}\boldsymbol{\eta} \end{cases} \tag{19}$$

Equation (19) is characterized by the matrix $\boldsymbol{H} = [\boldsymbol{H}_{\xi\xi}, \boldsymbol{H}_{\xi\eta}; \boldsymbol{H}_{\eta\xi}, \boldsymbol{H}_{\eta\eta}] \in \mathbb{R}^{2N,2N}$ that is not in general of Hamiltonian type. For this reason, it is not possible to solve the optimal problem by satisfying the Riccati's stationary equation, but a direct solution through the *2N*-eigenvalues and *2N*-eigenvectors is used. By assuring at least *N* negative real part eigenvalues of matrix $\boldsymbol{H}$, one obtains:

$$\begin{aligned} &\boldsymbol{\eta} = \boldsymbol{G}\boldsymbol{\xi} \qquad with \qquad \boldsymbol{G} = \boldsymbol{\Theta}\boldsymbol{\Psi}^{-1} \in \mathbb{R}^{N,N} \\ &\boldsymbol{\Psi} = [\boldsymbol{\psi}_1, \dots, \boldsymbol{\psi}_N] \\ &\boldsymbol{\Theta} = [\boldsymbol{\theta}_1, \dots, \boldsymbol{\theta}_N] \end{aligned} \tag{20}$$

where $\boldsymbol{\psi}_i$ and $\boldsymbol{\theta}_i$ are half of the *2N* eigenvectors of $\boldsymbol{H}$, those associated to negative real part eigenvalues. Finally, since $= \boldsymbol{R}^{-1}\boldsymbol{B}^T\boldsymbol{\lambda}$, extracting from $\boldsymbol{\eta}$ the last sub-vector $\boldsymbol{\eta}_N = \boldsymbol{\lambda}$, the optimal feedback control variable $\boldsymbol{u}$ is:

$$\boldsymbol{u} = \boldsymbol{R}^{-1}\boldsymbol{B}^T \sum_{i=1}^{N+1} \boldsymbol{G}_{ji}\, \boldsymbol{x}^{(i-1)} = \boldsymbol{K}_{\boldsymbol{pdn}}\boldsymbol{\xi} \tag{21}$$

The structure of the solution (21) shows that the optimal control of an integral-differential system is strongly related to the structure of the kernel $\hat{k}(t)$ and contains a combination of state derivatives of order equal to the number of exponential terms of $\hat{k}(t)$. For this reason, (21) is called hyper-derivative proportional control, PD(N). The (21) can also be expressed through a $\boldsymbol{K}_{\boldsymbol{pdn}}$ gain matrix multiplied by the vector $\boldsymbol{\xi}$. The initial state derivatives $\frac{d^i \boldsymbol{x}(0)}{dt^i} = \boldsymbol{x}_0^{(i)}$ for $i > 2$ can be evaluated from the Laplace transformation of (12) in the case of uncontrolled and undisturbed system and replacing the approximated $\hat{k}$ exponential kernel function.

4 NUMERICAL RESULTS

In the following section the numerical results are shown for the deflection control of a bridge when external excitations are acting on it. The bridge has been considered as a three-mode decomposition model. Two different simulations have been performed, considering an impulsive and an earthquake disturbance on the bridge basement. For both cases, we assume the actuator is placed at $\hat{x} = L/2 + 0.2L/4$ in order to control not only the first and third vibrational modes but also the 20% of the second mode. To measure the vibrations of the bridge, three sensors $s1$, $s2$, $s3$, for example accelerometers, have been placed on the structure at $x_{s1} = L/2$, $x_{s2} = L/4$ and $x_{s3} = L/3$, in such a way that it can be easily reconstruct the modal displacements $\boldsymbol{q}$. Table 1 shows the geometrical parameters describing the simulated bridge which has been chosen with a H-beam cross-section.

Description	Parameters	Value
Density [kg/m^3]	ρ	7500
Young modulus [N/m^2]	E	$200 \cdot 10^9$
Length [m]	L	24
Thickness [m]	b	0.18
Height [m]	h	0.4
Momentum of inertia [m^4]	I	$23130 \cdot 10^{-8}$
Cross-sectional area [m^2]	A	$84.46 \cdot 10^{-4}$

Table 1**:** H-beam parameters.

In Table 2 are listed the main dynamic parameters and control settings used to develop numerical simulations in which a kernel function composed by two exponential terms has been considered.

Description	Parameters	Value
Beam eigenfunctions in x_{s1}	$[\phi_1(L/2); \phi_2(L/2); \phi_3(L/2)]$	[0.036; 0; -0.0363]
Beam eigenfunctions in x_{s2}	$[\phi_1(L/4); \phi_2(L/4); \phi_3(L/4)]$	[0.0256; 0.0363; 0.0256]
Beam eigenfunctions in x_{s3}	$[\phi_1(L/3); \phi_2(L/3); \phi_3(L/3)]$	[0.0314; 0.0314; 0]
Beam eigenfunctions in $\hat{x}$	$[\phi_1(\hat{x}); \phi_2(\hat{x}); \phi_3(\hat{x})]$	[0.0358; -0.0112; -0.0323]
Natural frequencies [rad/s]	$[\omega_1; \omega_2; \omega_3]$	[14.6434; 58.6032; 131.8943]
Modal kernel frequencies	$[\widehat{\omega}_1; \widehat{\omega}_2; \widehat{\omega}_3]$	$[0.0327; 0.13; 0.29]\cdot 10^{-3}$
Kernel coefficients	$\left[\frac{\alpha_1 E_\beta}{\Gamma(1-\beta)}; c_1; \frac{\alpha_2 E_\beta}{\Gamma(1-\beta)}; c_2\right]$	$[8\cdot 10^{10}; 100; 2\cdot 10^{10}; 10]$
Control gain	$\mathbf{Q}$; $\mathbf{R}$	$\begin{bmatrix} 10 & 0 & 0 & 0 \\ 0 & 10 & 0 & 0 \\ 0 & 0 & 80 & 0 \\ 0 & 0 & 0 & 80 \end{bmatrix}$; 0.01
Control gain PDN	$\boldsymbol{K_{pdn}}$	$[-102.6;\ 63.7;\ 4.1; -3;\ 1.2; \ldots$ $-0.0117; -0.0833;\ 0.0009]$
Initial displacement [m]	$\boldsymbol{q_0}$	[0; 0; 0]
Initial velocity [m/s]	$\dot{\boldsymbol{q}}_{\boldsymbol{0}}$	[0.1; 0.1; 0.1]

Table 2: Parameters and control settings used for the simulations.

Regarding the first simulation, the impulsive basement disturbance is simulated by considering an initial condition on the modal velocity $\dot{\boldsymbol{q}}_{\boldsymbol{0}}$ different from zero taking into account the first three vibrational modes $r = 1,2,3$ of eq. (11). The performances of the PD(N) controller are compared with the Pontryagin implicit solution, recently proposed by the authors [20, 21], and the benchmarking LQR method by solving eq. (12) neglecting the convolution term.
From Figure 2 to Figure 6 the time evolution of the beam displacement $w(x,t)$, cost function J, power and force actuation, are shown respectively. The bridge deflection has been computed in two different positions x_{s1} and x_{s2} in order to be able to catch the contributions of all the three vibrational modes.

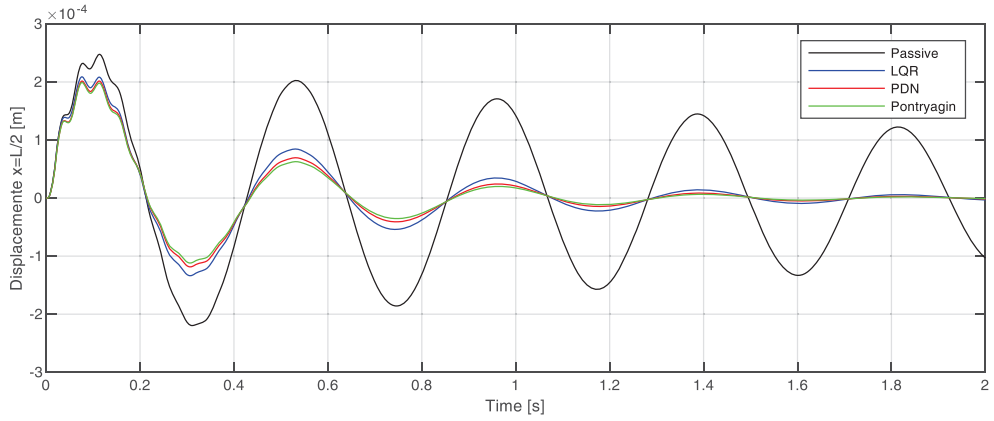

Figure 2: Beam vertical displacement at x_{s1} under impulsive load.

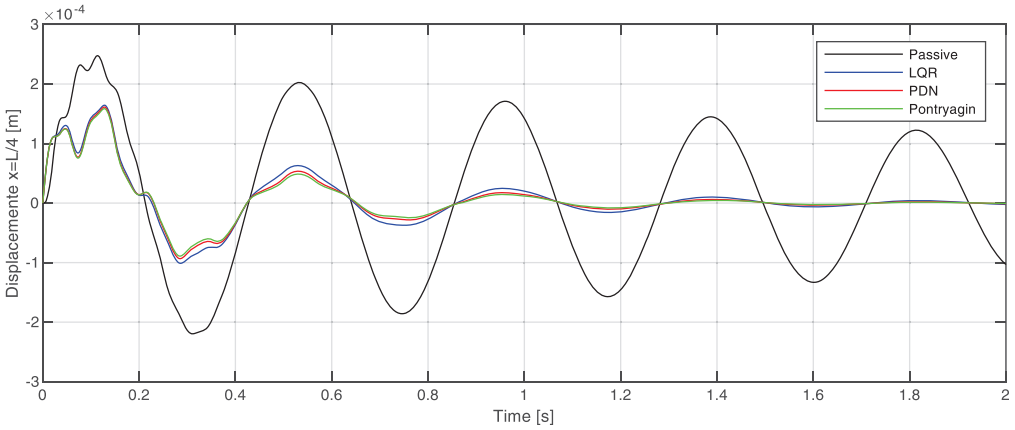

Figure 3: Beam vertical displacement at x_{s2} under impulsive load.

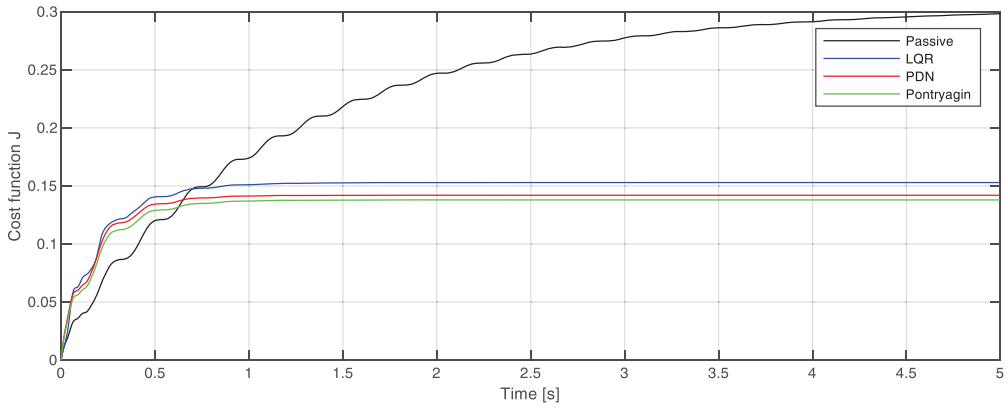

Figure 4: Comparisons of cost functions under impulsive load.

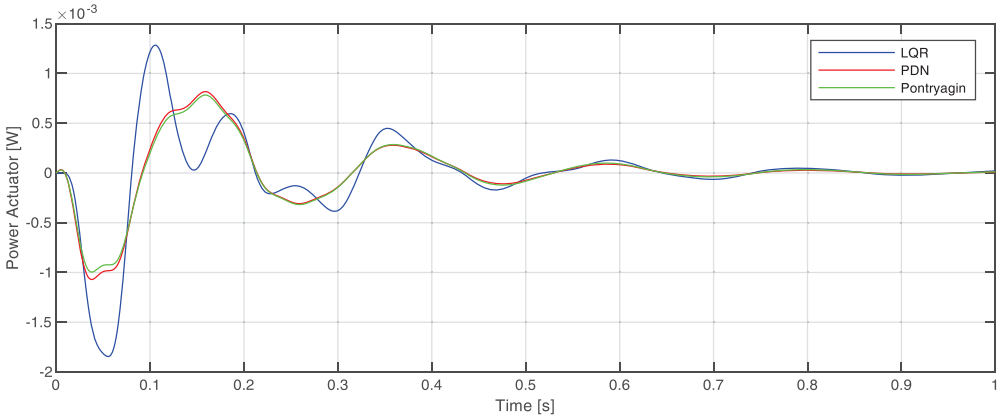

Figure 5: Comparisons of power actuation under impulsive load.

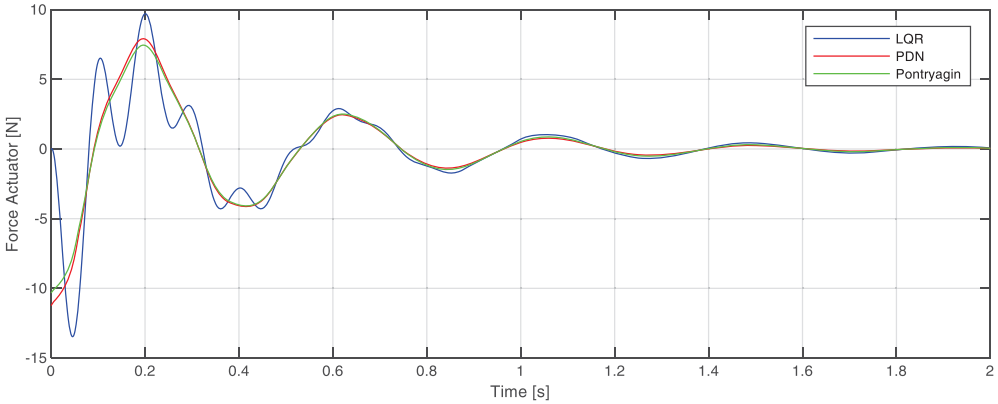

Figure 6: Comparisons of force actuation under impulsive load.

The numerical results show very good performances of the PD(N) algorithm in comparison with the standard LQR method in terms of vibrations minimization. In fact, the LQR, which cannot take into account the viscoelastic memory effects, shows higher values of the actuation force and power in comparison with the PD(N) controller. In fact, the PD(N) algorithm reach half of the actuation power and the 80% of the maximum force reached by LQR, respectively. Moreover, observing Figure 2 and Figure 3 the proposed controller presents lower beam deflection (higher in x_{s2}) and a lower cost function value (Figure 4), stretching its convenience in comparison to the LQR method. The PD(N) performance are at the same level of the Pontryagin implicit solution. Of course, the implicit solution, which is the best optimal solution, presents the lower values of cost function and arrival time.

In the second tested case, the bridge is excited by an earthquake disturb. The Class A earthquake load has been formulated by [27] according to the Eurocode 8 which introduce the possibility to use the stochastic analysis in the design of structures in seismic zone. Figure 7 and Figure 8 describe the earthquake disturbance in term of PSD and acceleration, respectively.

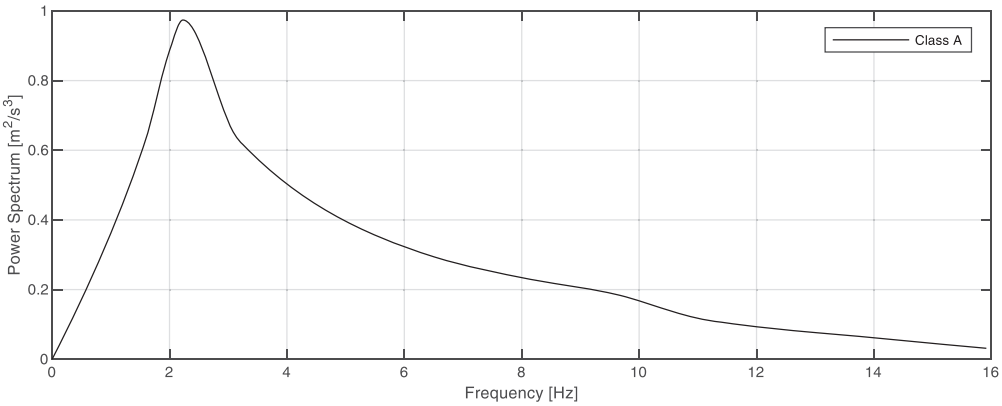

Figure 7: Earthquake PSD

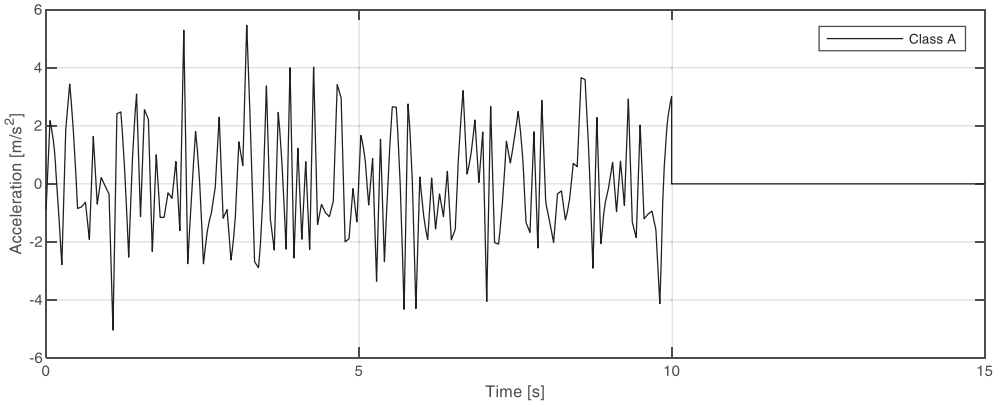

Figure 8: Earthquake acceleration

The class A earthquake PSD amplified the first vibrational mode of the bridge showing a maximum value corresponding to the bridge first natural frequency ($\sim 2Hz$) and on the contrary it does not excite the third mode, because is very far from the spectrum. Moreover, given the symmetry of the noise, even modes are not excited. For all these reasons, the results will be shown only for the position x_{s1}. The earthquake acceleration, $\ddot{z}_b(t)$, in Figure 8 has been generated from the PSD in Figure 7, acting for 10s and in the final 5s the bridge system is free to extinguish its residual vibrations.

In this simulation the performance of the proposed PD(N) controller are only compared with the benchmarking LQR method. In fact, the external disturbance considered in this case is stochastic one, which is impossible to predict and to include in the Pontryagin solution.

From Figure 9 to Figure 12 the time evolution of the bridge deflection in x_{s1}, the cost function J, the power and the force actuation, are illustrated respectively. It is possible to notice that, even when an external random disturbance is acting on the bridge, the proposed PD(N) controller presents better performance respect to the LQR method. The PD(N) algorithm shows a minimization of the bridge deflection requiring a lower force and power of actuation and for these reasons, it is also presenting a lower cost function J.

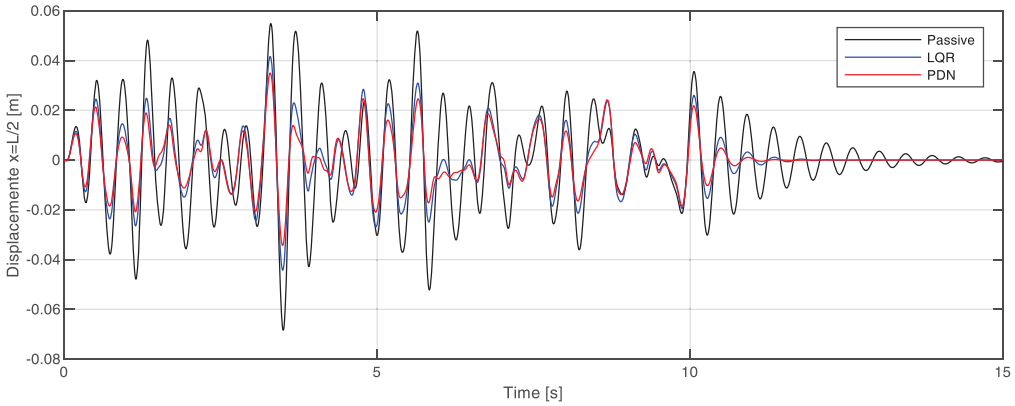

Figure 9: Comparisons of deflection under earthquake load.

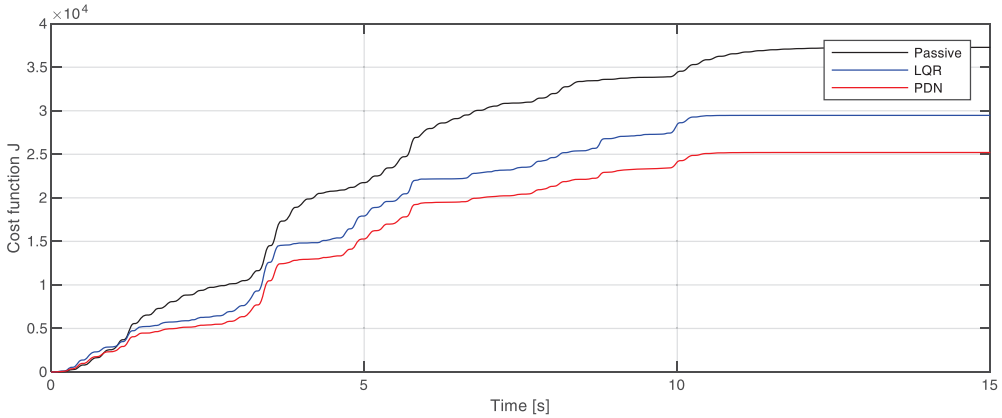

Figure 10: Comparisons of cost function under earthquake load.

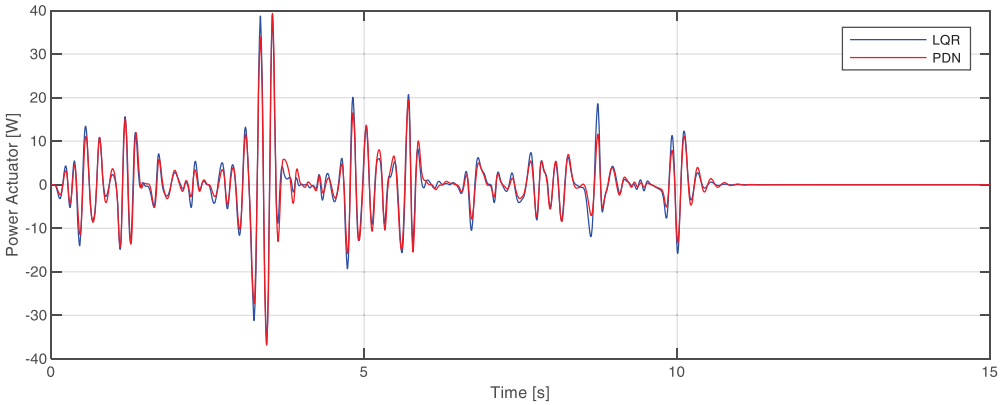

Figure 11: Comparisons of power under earthquake load.

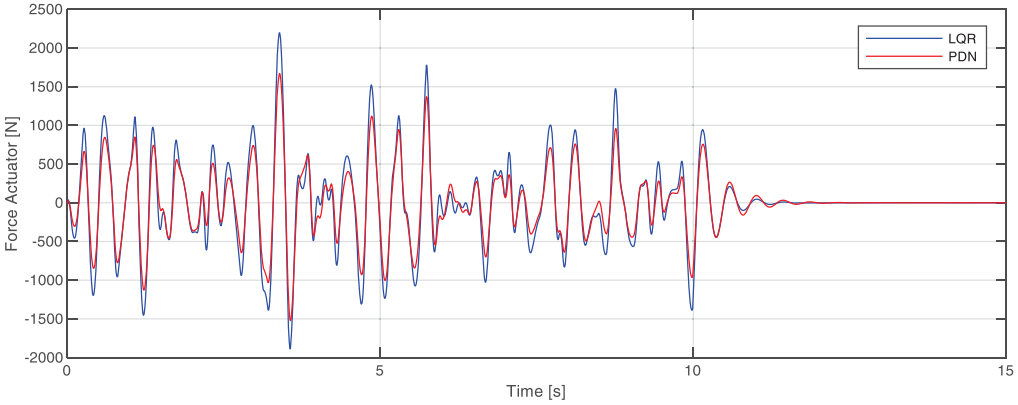

Figure 12: Comparisons of force actuation under earthquake load.

5 CONCLUSIONS

In this paper the authors propose an optimal control algorithm to actively control viscoelastic materials for the structural vibration's minimization.

The proposed algorithm applies to a viscoelastic Euler-Bernoulli beam including Boltzmann hereditary effects by using a Nutting's memory kernel function. The prototype equation is of integro-differential type and requires a non-conventional optimal control strategy, which considers convolution terms (memory effects). In general, the optimal control strategies, applied to

this viscoelastic model, make use of direct methods, while in this paper the authors offer an indirect optimal feedback control algorithm, which is still missing in the literature panorama. The authors show how it is possible to obtain a Proportional-Nth-order-Derivatives control, called PD(N), by using the variational approach. Numerical simulations show very good result of the PD(N) solution compared to the benchmarking LQR and the implicit Pontryagin solution for IDEs, already formulated by the authors in recent works.

Thanks to the hyper derivative properties, the PD(N) controller shows a capability of minimization of beam deflection, in term of force and power of actuation and cost both for different external disturbances acting on the model and also for multiple kernel function compared to the benchmarking optimal control algorithm.

REFERENCES

[1] X. Q. Zhou, D. Y. Yu, X. Y. Shao, S. Q. Zhang, and S. Wang, "Research and applications of viscoelastic vibration damping materials: A review," *Composite Structures,* vol. 136, pp. 460-480, 2016/02/01/ 2016, doi: https://doi.org/10.1016/j.compstruct.2015.10.014.

[2] W. Al Azzawi, M. Herath, and J. Epaarachchi, "15 - Modeling, analysis, and testing of viscoelastic properties of shape memory polymer composites and a brief review of their space engineering applications," in *Creep and Fatigue in Polymer Matrix Composites (Second Edition)*, R. M. Guedes Ed.: Woodhead Publishing, 2019, pp. 465-495.

[3] B. Babaei, A. J. Velasquez-Mao, S. Thomopoulos, E. L. Elson, S. D. Abramowitch, and G. M. Genin, "Discrete quasi-linear viscoelastic damping analysis of connective tissues, and the biomechanics of stretching," *Journal of the Mechanical Behavior of Biomedical Materials,* vol. 69, pp. 193-202, 2017/05/01/ 2017, doi: https://doi.org/10.1016/j.jmbbm.2016.12.013.

[4] A. Carcaterra, N. Roveri, and G. Pepe, "Fractional dissipation generated by hidden wave-fields," *Mathematics and Mechanics of Solids,* Article vol. 20, no. 10, pp. 1251-1262, 2015, doi: 10.1177/1081286513518941.

[5] E. Paifelman, "A comparison between mathematical models of stationary configuration of an underwater towed system with experimental validations for oceans' 17 MTS/IEEE Aberdeen conferences," 2017: IEEE, pp. 1-7.

[6] S. Carillo, "Regular and singular kernel problems in magneto-viscoelasticity," *Meccanica,* vol. 52, no. 13, pp. 3053-3060, 2017/10/01 2017, doi: 10.1007/s11012-017-0722-1.

[7] W. Flugge, "Viscoelasticity, Blaisdell," *Waltham, Mass,* 1967.

[8] M. Di Paola, R. Heuer, and A. Pirrotta, "Fractional visco-elastic Euler–Bernoulli beam," *International Journal of Solids and Structures,* vol. 50, no. 22, pp. 3505-3510, 2013/10/15/ 2013, doi: https://doi.org/10.1016/j.ijsolstr.2013.06.010.

[9] M. Caputo and F. Mainardi, "A new dissipation model based on memory mechanism," *Pure and Applied Geophysics,* vol. 91, no. 1, pp. 134-147, 1971.

[10] M. Caputo and M. Fabrizio, "A new definition of fractional derivative without singular kernel," *Progr. Fract. Differ. Appl,* vol. 1, no. 2, pp. 1-13, 2015.

[11] J. Ahmad and S. T. Mohyud-Din, "Homotopy analysis method with modified Reimann-Liouville derivative for space fractional diffusion equation," *International Journal of Physical Sciences,* vol. 8, no. 43, pp. 1994-1999, 2013.

[12] H. Xiong and W. Q. Zhu, "A stochastic optimal control strategy for viscoelastic systems with actuator saturation," *Probabilistic Engineering Mechanics,* vol. 45, pp. 44-51, 2016/07/01/ 2016, doi: https://doi.org/10.1016/j.probengmech.2016.02.004.

[13] M. R. Homaeinezhad, S. Yaqubi, and H. M. Gholyan, "Control of MIMO mechanical systems interacting with actuators through viscoelastic linkages," *Mechanism and Machine Theory,* vol. 147, p. 103763, 2020/05/01/ 2020, doi: https://doi.org/10.1016/j.mechmachtheory.2019.103763.

[14] M. H. Heydari, "Numerical solution of nonlinear 2D optimal control problems generated by Atangana-Riemann-Liouville fractal-fractional derivative," *Applied Numerical Mathematics,* vol. 150, pp. 507-518, 2020/04/01/ 2020, doi: https://doi.org/10.1016/j.apnum.2019.10.020.

[15] K. V. Singh and X. Ling, "Active Control of Viscoelastic Systems by the Method of Receptance," *Journal of Vibration and Acoustics,* vol. 140, no. 2, 2017, doi: 10.1115/1.4037959.

[16] T. M. Atanackovic and B. Stankovic, "On a numerical scheme for solving differential equations of fractional order," *Mechanics Research Communications,* vol. 35, no. 7, pp. 429-438, 2008/10/01/ 2008, doi: https://doi.org/10.1016/j.mechrescom.2008.05.003.

[17] G. Pepe, D. Antonelli, L. Nesi, and A. Carcaterra, "FLOP: feedback local optimality control of the inverse pendulum oscillations," presented at the ISMA2018, Leuven, 2018.

[18] D. Antonelli, L. Nesi, G. Pepe, and A. Carcaterra, "A novel approach in Optimal trajectory identification for Autonomous driving in racetrack," in *2019 18th European Control Conference, ECC 2019*, 2019, pp. 3267-3272, doi: 10.23919/ECC.2019.8795637. [Online]. Available: https://www.scopus.com/inward/record.uri?eid=2-s2.0-85071599660&doi=10.23919/ECC.2019.8795637&partnerID=40&md5=3a2ef5ec295b9fb6f45c809983b9261e

[19] D. Antonelli, L. Nesi, G. Pepe, and A. Carcaterra, "A novel control strategy for autonomous cars," in *Proceedings of the American Control Conference*, 2019, vol. 2019-July, pp. 711-716. [Online]. Available: https://www.scopus.com/inward/record.uri?eid=2-s2.0-85072275741&partnerID=40&md5=6f43ab309a3722ce43fdcea958deade4

[20] E. Paifelman, G. Pepe, F. La Gala, and A. Carcaterra, "Control of fluctuations of a tethered unmanned-underwater-vehicle," presented at the ISMA2018, Leuven, 2018.

[21] E. Paifelman, G. Pepe, and A. Carcaterra, "An optimal indirect control of underwater vehicle," *International Journal of Control,* pp. 1-15, 2019, doi: 10.1080/00207179.2019.1590737.

[22] E. Paifelman, G. Pepe, and A. Carcaterra, "Optimal control with memory effects: theory and application to wings," 2019: IEEE, pp. 319-324.

[23] J. Freundlich, "Transient vibrations of a fractional Kelvin-Voigt viscoelastic cantilever beam with a tip mass and subjected to a base excitation," *Journal of Sound and Vibration,* vol. 438, pp. 99-115, 2019/01/06/ 2019, doi: https://doi.org/10.1016/j.jsv.2018.09.006.

[24] P. G. Nutting, "A study of elastic viscous deformation," *Proceedings American Soc. for a Testing Materials,* vol. 21, pp. 1162-1171, 1921.

[25] G. Pepe, E. Paifelman, and A. Carcaterra, "Direct feedback control for integral-differential systems and associated Riccati's equation," *International Journal of Control,* Journal paper 2020.

[26] T. J. Böhme and B. Frank, "Hybrid systems, optimal control and hybrid vehicles," *Cham, CH: Springer International,* 2017.

[27] G. Falsone and F. Neri, "Stochastic modelling of earthquake excitation following the EC8: power spectrum and filtering equations," *European Earthquake Engineering,* vol. 14, no. 1, pp. 3-12, 2000.

EURODYN 2020
XI International Conference on Structural Dynamics
M. Papadrakakis, M. Fragiadakis, C. Papadimitriou (eds.)
Athens, Greece, 23–26 November 2020

OPTIMAL DAMPER DISTRIBUTIONS IN SHEAR FRAMES CONSIDERING SOIL CONDITIONS

Ersin Aydin[1], Baki Ozturk[2*], and Osman Sivrikaya[3]

[1] Nigde Omer Halisdemir University
Nigde, Turkey
e-mail: eaydin@ohu.edu.tr

[2*] Hacettepe University
Ankara, Turkey
bakiozturk@hacettepe.edu.tr

[3] Karadeniz Technical University
Trabzon, Turkey
e-mail: osivrikaya@ktu.edu.tr

Keywords: Soil-structure interaction, viscous damping, optimal dampers, sandy soil

Abstract. *When there is an optimal damper application issue, superstructure models are installed and strongly connected to the ground. However; there is no consideration of the ground influences. Within this current research, the influence of sandy soil relative density upon damper issues has been analysed. Assessment has been carried out upon the optimal distribution of viscous dampers along with the influence of sandy soil relative density on the structural dynamic response for the n-storey shear building model. The soil-structure model governing equation has also been derived and the Fourier Transformation is used to present the frequency domain equations. An optimized procedure, which is the Steepest Direction Search Algorithm (SDSA), is applied. Minimization of the objective function, which is the base moment behaviour of structure stated within the frequency domain, is done. The fundamental mode response of structural model has been considered and the El Centro (NS) earthquake ground acceleration record is used to conduct the time history analyses. Investigation has been carried out for the sandy soil relative density influence upon the optimal design of structure responses along with the total damper capacity variation influence applied within the optimization level. Since the optimal design alters due to the base moment, the sandy soil influences have been assessed thoroughly. As compared to no damper at all case, the damped system has taken place with low base moment. At a rigid level, the structural response is lower as compared to a different sandy soil relative density. The structural response is enhanced after dampers are added based on proposed objective function. Furthermore, the damaging influence created by the poor ground conditions has also been reduced.*

1 INTRODUCTION

Since the past few years, the conventional devices have been replaced with passive control devices to reduce vibration and dynamic influences. To attain efficient performance of damping, the regulations have been set to manage the structure design for earthquake resistance through various processes. Recently, many research studies have been carried out upon the tuning of mass dampers applied for the wind and seismic reactions soil-structure collaboration [1-4]. A two-phase soil model has been applied to assess the soil stiffness variations along with the monopile wind turbine foundations offshore damping that is affected by lateral dynamic loads [5]. Two kinds of polypod foundations, ground surface that includes two rigid footings and two flexible embedded piles, have been assessed through the dynamic structure–soil–structure interaction (SSSI) [6].

Civil engineering applications, aerospace, military and other fields make use of a recognized passive damper which is the fluid viscous damper. Building applications have also started making use of this device. Recently, due to globalization, there has been an enhancement in the damper construction and application, specifically for the earthquake-resistant construction design. Keeping these technological aspects in mind, the construction is being carried out within the elastic limits within the seismic and wind loads where they are able to captivate vigorous external consequences. Structural behaviours are enhanced through damping elements. Furthermore, various studies have tried to recognize the optimal damping element placements.

There are various research studies present in the literature upon the structure dynamic response and optimal damper design [7-16]. However, these do not take into account the soil influence. Usually, it is believed that a rigid structure is present within the ground. Hence, the soil influences must be observed to understand how earthquakes affect these structures. Recently, Aydin et al. [17] investigated comparison of optimal damper distributions in shear frames in terms of soil conditions.

The optimal passive structural control has been researched upon in a limited manner even though the literature stated soil structure interaction influences. The objective is upon the optimal control using the tuned mass damper [18-25]. Yet, there are some research studies upon structures that have viscoelastic dampers keeping in mind the soil-structure interaction influence [26, 27]. For the soil structure interaction model, there are research studies which include the tuned mass damper and the viscous damper [28].

Within this current research, the optimal placement of the viscous damper and the structural response would be analysed. This aspect has not been focused upon in earlier research studies. This is why the analysis would be carried out with the help of base moment transfer function as part of the soil structure interaction. For the modelling structural response, the soil influence is taken into account and the optimization procedure is used for the viscous damper placement where no soil influence is present [29]. Furthermore, the viscous damper optimal design for the sandy soil conditions (loose, medium dense and dense) would be analysed and comparison of the results would be made.

2 FORMULATION OF PROBLEM

Figure 1 indicates the model for soil structure interaction and *n*-storey shear building. Horizontal ground acceleration occurs within the system. The assumption present is that the generalized displacement vector is $\boldsymbol{u}$, the system mass matrix is $\boldsymbol{M}$, system stiffness matrix is $\boldsymbol{K}$, structural damping matrix is $\boldsymbol{C}$, and the influence vector is $\boldsymbol{r}$ which is defined as

$\boldsymbol{r} = \{0, \ldots, 0, 1, 0\}^{\mathrm{T}}$. Ground acceleration has been presented using $\ddot{u}_g$ parameter. There are known $\boldsymbol{M}$ and $\boldsymbol{K}$ matrix elements. The stiffness and structural damping matrices are proportional as $\boldsymbol{C} = \alpha \boldsymbol{M}$ where $\alpha = 2\zeta_1\omega_1$. There are known first damping ratio ζ_1 and undamped fundamental natural circular frequency ω_1.

The differential equation of motion within the context of time is presented as follows.

$$\boldsymbol{M}\ddot{\boldsymbol{u}} + \boldsymbol{C}\dot{\boldsymbol{u}} + \boldsymbol{K}\boldsymbol{u} = -\boldsymbol{M}\boldsymbol{r}\ddot{u}_g \tag{1}$$

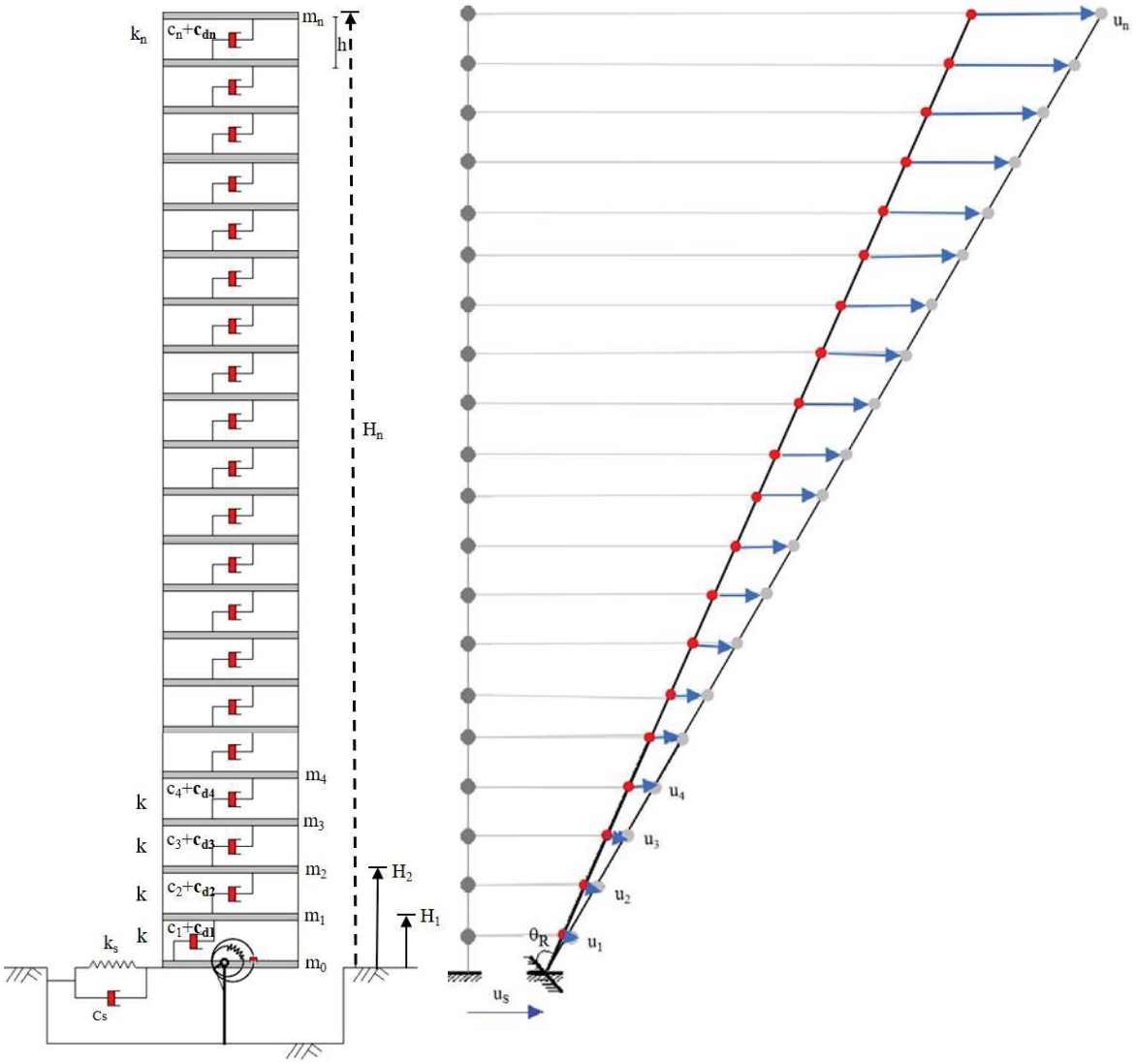

Figure 1: Shear-building soil-structure model and its deformation

The generalized displacements vector is the set $\mathbf{u} = \{u_1, \ldots..u_n\ u_S\ \theta_R\}^{\mathrm{T}}$ in which the u_S and θ_R parameters sway with rocking rotation and displacement. The rocking springs and swaying stiffness are indicated using k_S and k_R. The rocking and swaying dashpots damping coefficients are shown through c_S and c_R.

Hence, the system mass matrix is indicated as following.

$$\boldsymbol{M} = \begin{bmatrix} \boldsymbol{M_B} & \boldsymbol{M_{BS}} & \boldsymbol{M_{BR}} \\ & E_1 & E_2 \\ \text{Sym.} & & E_3 \end{bmatrix} \tag{2}$$

The soil-structure interaction system mass matrix is $\boldsymbol{M}$ and building mass matrix is $\boldsymbol{M_B}$. $\boldsymbol{M_B}$, $\boldsymbol{M_{BS}}$ and $\boldsymbol{M_{BR}}$ matrices are shown below.

$$\boldsymbol{M_B} = \begin{bmatrix} m_1 & 0 & 0 & 0 & 0 \\ 0 & m_2 & 0 & 0 & 0 \\ 0 & 0 & . & 0 & 0 \\ 0 & 0 & 0 & . & 0 \\ 0 & 0 & 0 & 0 & m_n \end{bmatrix} \quad \boldsymbol{M_{BS}} = \begin{bmatrix} m_1 \\ m_2 \\ . \\ . \\ m_n \end{bmatrix} \quad \boldsymbol{M_{BR}} = \begin{bmatrix} m_1 H_1 \\ m_2 H_2 \\ . \\ . \\ m_n H_n \end{bmatrix} \tag{3}$$

From the ground level, the i^{th} floor height is indicated using H_i $(i=1,\ldots,n)$. Considering Equation (2), E_1, E_2 and E_3 are calculated using:

$$E_1 = m_0 + m_1 + \cdots + m_n \tag{4}$$

$$E_2 = m_1 H_1 + m_2 H_2 + \cdots + m_n H_n \tag{5}$$

$$E_3 = m_1 H_1^2 + m_2 H_2^2 + \cdots + m_n H_n^2 + I_{R0} + I_{R1} + I_{R2} + \cdots + I_{Rn} \tag{6}$$

If Equations (3), (4), (5) and (6) are included in Equation (2), it would become Equation (7) as mentioned below.

$$\boldsymbol{M} = \begin{bmatrix} m_1 & 0 & 0 & 0 & 0 & m_1 & m_1 H_1 \\ 0 & m_2 & 0 & 0 & 0 & m_2 & m_2 H_2 \\ 0 & 0 & . & 0 & 0 & . & . \\ 0 & 0 & 0 & . & 0 & . & . \\ 0 & 0 & 0 & 0 & m_n & m_n & m_n H_n \\ m_1 & m_2 & . & . & m_n & \sum_{i=0}^{n} m_i & \sum_{i=1}^{n} m_i H_i \\ m_1 H_1 & m_2 H_2 & . & . & m_n H_n & \sum_{i=1}^{n} m_i H_i & \sum_{i=1}^{n} m_i H_i^2 + \sum_{i=0}^{n} I_{Ri} \end{bmatrix} \tag{7}$$

The following is the system stiffness matrix.

$$\boldsymbol{K} = \boldsymbol{K_B} + \boldsymbol{K_S} + \boldsymbol{K_R} \tag{8}$$

In which,

$$\boldsymbol{K_B} = \begin{bmatrix} k_1+k_2 & -k_2 & 0 & 0 & 0 & 0 & 0 \\ -k_2 & k_2+k_3 & . & 0 & 0 & 0 & 0 \\ 0 & . & . & . & 0 & 0 & 0 \\ 0 & 0 & . & . & -k_n & 0 & 0 \\ 0 & 0 & 0 & -k_n & k_n & 0 & 0 \\ 0 & 0 & 0 & 0 & 0 & 0 & 0 \\ 0 & 0 & 0 & 0 & 0 & 0 & 0 \end{bmatrix} \tag{9}$$

$$\boldsymbol{K_S} = \begin{bmatrix} 0 & 0 & 0 & . & . & 0 & 0 \\ 0 & 0 & 0 & . & . & 0 & 0 \\ 0 & 0 & 0 & . & . & 0 & 0 \\ . & . & . & . & . & 0 & 0 \\ . & . & . & . & . & 0 & 0 \\ 0 & 0 & 0 & 0 & 0 & k_s & 0 \\ 0 & 0 & 0 & 0 & 0 & 0 & 0 \end{bmatrix} \quad \boldsymbol{K_R} = \begin{bmatrix} 0 & 0 & 0 & . & . & 0 & 0 \\ 0 & 0 & 0 & . & . & 0 & 0 \\ 0 & 0 & 0 & . & . & 0 & 0 \\ . & . & . & . & . & 0 & 0 \\ . & . & . & . & . & 0 & 0 \\ 0 & 0 & 0 & 0 & 0 & 0 & 0 \\ 0 & 0 & 0 & 0 & 0 & 0 & k_R \end{bmatrix} \tag{10}$$

In this case, the total system stiffness matrix is denoted by $\boldsymbol{K}$, superstructure stiffness matrix by $\boldsymbol{K_B}$ and the stiffness matrices including only swaying (k_s) and rocking (k_R) springs are $\boldsymbol{K_S}$ and $\boldsymbol{K_R}$, respectively. The following are the system stiffness matrix and the ground stiffness parameters.

$$\boldsymbol{K} = \begin{bmatrix} k_1+k_2 & -k_2 & 0 & 0 & 0 & 0 & 0 \\ -k_2 & k_2+k_3 & . & 0 & 0 & 0 & 0 \\ 0 & . & . & . & 0 & 0 & 0 \\ 0 & 0 & . & . & -k_n & 0 & 0 \\ 0 & 0 & 0 & -k_n & k_n & 0 & 0 \\ 0 & 0 & 0 & 0 & 0 & k_s & 0 \\ 0 & 0 & 0 & 0 & 0 & 0 & k_R \end{bmatrix} \tag{11}$$

$$k_s = \frac{6.77}{(1.79-\mu)} Gr \qquad k_R = \frac{2.52}{(1-\mu)} Gr^3 \tag{12}$$

The soil shear modulus is denoted by G, Poisson's ratio through μ and equivalent circular footing plate radius through r. The structural and ground damping parameters are used for the description of the system damping matrix $\boldsymbol{C}$.

$$\boldsymbol{C} = \boldsymbol{C_B} + \boldsymbol{C_S} + \boldsymbol{C_R} \tag{13}$$

$$\boldsymbol{C} = \begin{bmatrix} c_1+c_2 & -c_2 & 0 & 0 & 0 & 0 & 0 \\ -c_2 & c_2+c_3 & . & 0 & 0 & 0 & 0 \\ 0 & . & . & . & 0 & 0 & 0 \\ 0 & 0 & . & . & -c_n & 0 & 0 \\ 0 & 0 & 0 & -c_n & c_n & 0 & 0 \\ 0 & 0 & 0 & 0 & 0 & c_s & 0 \\ 0 & 0 & 0 & 0 & 0 & 0 & c_R \end{bmatrix} \tag{14}$$

$$c_S = \frac{6.21}{(2.54-\mu)}\rho v_s r^2 \qquad c_R = \frac{0.136}{(1.13-\mu)}\rho v_s r^4 \tag{15}$$

In this case, the system damping matrix is $\boldsymbol{C}$, the structural damping matrix of superstructure is $\boldsymbol{C_B}$ and the ground linear damping matrices including only swaying (c_s) and rocking (c_R) damping coefficients are $\boldsymbol{C_R}$. The shear wave velocity is v_S and mass density of soil is ρ. Takewaki [30] has stated the mass construction, stiffness and damping matrices. The additional damper parameters are not integrated within matrix $\boldsymbol{C}$. If Equation (1) includes the Fourier Transform, then it would be converted to Equation (16).

$$(\boldsymbol{K} + i\omega\boldsymbol{C} - \omega^2\boldsymbol{M})\boldsymbol{U}(\omega) = -\boldsymbol{M}\boldsymbol{r}\ddot{U}_g(\omega) \tag{16}$$

The excitation circular frequency is denoted by ω, i, $\boldsymbol{U}(\omega)$, $\ddot{U}_g(\omega)$ and $\sqrt{-1}$, the Fourier Transform of $u(t)$ and $\ddot{u}_g(t)$. Equation (16) is written as follows, after the structure includes the dampers.

$$(\boldsymbol{K} + i\omega(\boldsymbol{C} + \boldsymbol{C_d}) - \omega^2\boldsymbol{M})\boldsymbol{U_d}(\omega) = -\boldsymbol{M}\boldsymbol{r}\ddot{U}_g(\omega) \tag{17}$$

The displacement vector Fourier Transform is $\boldsymbol{U_d}(\omega)$ and it includes the viscous dampers. The unknown damping matrix is $\boldsymbol{C_d}$ and it is associated with the added damper damping coefficient.

Hence, $\boldsymbol{C_d}$ is stated as:

$$\boldsymbol{C} = \begin{bmatrix} c_{d1}+c_{d2} & -c_{d2} & 0 & 0 & 0 & 0 & 0 \\ -c_{d2} & c_{d2}+c_{d3} & . & 0 & 0 & 0 & 0 \\ 0 & . & . & . & 0 & 0 & 0 \\ 0 & 0 & . & . & -c_{dn} & 0 & 0 \\ 0 & 0 & 0 & -c_{dn} & c_{dn} & 0 & 0 \\ 0 & 0 & 0 & 0 & 0 & 0 & 0 \\ 0 & 0 & 0 & 0 & 0 & 0 & 0 \end{bmatrix} \tag{18}$$

In Equation (19), it is stated as the new parameter.

$$\widehat{\boldsymbol{U}}(\omega) = \frac{\boldsymbol{U_d}(\omega)}{\ddot{U}_g(\omega)} \tag{19}$$

Hence, Equation (17) is written as:

$$\mathbf{A}\widehat{\boldsymbol{U}} = -\boldsymbol{M}\boldsymbol{r} \tag{20}$$

In this case, the displacement transfer function vector is $\widehat{\boldsymbol{U}}$ along with the $\boldsymbol{A}$ matrix and is stated as:

$$\mathbf{A} = (\boldsymbol{K} + i\omega(\boldsymbol{C} + \boldsymbol{C_d}) - \omega^2\boldsymbol{M}) \tag{21}$$

There exists prescription of $\boldsymbol{K}$, $\boldsymbol{M}$ and $\boldsymbol{C}$.

If subtraction is made from Equation (20) for the displacement vector associated with the transfer function, then it would be stated as.

$$\widehat{\boldsymbol{U}} = -\mathbf{A}^{-1}\boldsymbol{Mr} \tag{22}$$

Matrix $\boldsymbol{A}$ represents the unknown c_{di} damping parameters. The $\widehat{\boldsymbol{U}}$ vector includes the top displacement transfer function value. Takewaki [29] includes the governing equations and is applied within the planar building frame which does not have soil influences. Aydin et al. [11] has helped to derive the elastic forces transfer function. Equation (22) includes the displacement transfer vector which would be multiplied by stiffness matrix to attain the elastic forces transfer function vector.

$$\boldsymbol{F} = -\boldsymbol{KA}^{-1}\boldsymbol{Mr} \tag{23}$$

3 OPTIMAL DAMPER PROBLEM

The optimal damper issues can be resolved using the various objective functions. Hence, the several objective functions hold importance in terms of the various kinds of structures. Within the current research, the objective function is the base moment transfer function amplitude that includes the rocking displacement, forces and swaying.

The following is the objective function within the context of the transfer function amplitude for the elastic base moment.

$$f = |M_B| \qquad \text{(Min)} \tag{24}$$

The base moment transfer function amplitude is the following.

$$|M_B| = |F_1| * h_1 + |F_2| * h_2 + \cdots + |F_n| * h_n + |M_R| \tag{25}$$

For the i^{th} storey elastic shear force, the transfer function amplitude is denoted as $|F_i|$ which has been assessed as the undamped fundamental natural frequency. The rocking spring moment transfer function amplitude is $|M_R|$ and the height of the i^{th} storey is h_i (i=1,…,n) as per the base.

The following are the active and passive constraints performed at the sum of the damping coefficients of the added dampers.

$$\sum_{j=1}^{n} c_{dj} = W \tag{26}$$

$$0 \le c_{dj} \le \bar{c}_d \qquad (j = 1,...,n) \tag{27}$$

In this case, the damping coefficients sum for the added dampers (total damper capacity) is W. For each damper, the damping coefficient upper bound is $\bar{c}_d$. The Lagrangian L within the context of objective functions and constraints is indicated by:

$$L(c_d, \lambda, \alpha, \beta) = f + \lambda\left(\sum_{j=1}^{n} c_{dj} - W\right) + \sum_{j=1}^{n} \alpha_j\left(0 - c_{dj}\right) + \sum_{j=1}^{n} \beta_j\left(c_{dj} - \bar{c}_d\right) \tag{28}$$

In this case, the Lagrange Multipliers are λ, $\boldsymbol{\alpha} = \{\alpha_j\}$ and $\boldsymbol{\beta} = \{\beta_j\}$; the objective function is f . For objective function minimization, without the damping coefficient upper and lower bound constraints, the Lagrangian L ($\boldsymbol{\alpha} = 0$, $\boldsymbol{\beta} = 0$) derivatives would be considered within the context of c_{dj} and λ. Then, the following would be Equations (29) and (30).

$$f_{,j} + \lambda = 0 \quad (j = 1,...,n) \qquad 0 < c_{dj} < \bar{c}_d \tag{29}$$

$$\sum_{j=1}^{n} c_{dj} - W = 0 \tag{30}$$

The objective function partial differentiation is denoted by $f_{,j}$ keeping in mind the design variable c_{dj}. It is necessary to make sure that there are no negative damping coefficients for the additional dampers. A physical importance does not hold that there are negative damping coefficients. If there are active damping coefficient upper and lower bound constraints, then modification of Equation (29) occurs as follows.

$$f_{,j} + \lambda \geq 0 \qquad c_{dj} = 0 \tag{31}$$

$$f_{,j} + \lambda \leq 0 \qquad c_{dj} = \bar{c}_d \tag{32}$$

With the help of the Steepest Direction Search Algorithm (SDSA), the optimality criteria have been extracted and the nonlinear Equations (29-32) have been solved [29].

4 DERIVATION OF SENSITIVITIES AND SOLUTION ALGORITHM

Derivation of the first order sensitivities of transfer function vector of displacements [29] and elastic forces [11] are mentioned.

$$\widehat{\boldsymbol{U}}_{,j} = -\boldsymbol{A}^{-1}\boldsymbol{A}_j\widehat{\boldsymbol{U}} \tag{33}$$

$$\boldsymbol{F}_{,j} = -\boldsymbol{K}\boldsymbol{A}^{-1}\boldsymbol{A}_j\widehat{\boldsymbol{U}} \tag{34}$$

Equation (23) quantities of F_i are stated as

$$F_i = Re[F_i] + Im[F_i] \tag{35}$$

The transfer function values are F_i with i^{th} storey elastic forces within a complex form. The quantities of first order sensitivities of F_i are stated as:

$$F_{i,j} = Re\left[F_{i,j}\right] + Im\left[F_{i,j}\right] \tag{36}$$

The absolute value of F_i is stated as:

$$|F_i| = \sqrt{(Re[F_i])^2 + (Im[F_i])^2} \tag{37}$$

The transfer function amplitude first order sensitivity of the absolute value for the i^{th} elastic force is extracted, if the $|F_i|$ are differentiated with respect to the j^{th} damping coefficient c_j.

$$|F_i|_{,j} = \frac{1}{|F_i|}\left\{Re[F_i]\left(Re\left[F_{i,j}\right]\right) + Im[F_i]\left(Im\left[F_{i,j}\right]\right)\right\} \tag{38}$$

The transfer function amplitude for the first order derivative of the base moment is stated as the transfer function sensitivities sum for the story shear forces multiplied with the storey height from the base and rocking moment.

$$|M_B|_{,j} = \sum_{i=1}^{n} |F_i|_{,j} * h_i + M_{R,j} \tag{39}$$

The equation for partial differentiations of Equation (38) within the context of other design parameter c_l

$$|F_i|_{,jl} = \frac{1}{|F_i|^2}\left(|F_i|\left\{Re\left[F_{i,l}\right]Re\left[F_{i,j}\right] + Re[F_i]Re\left[F_{i,jl}\right] + Im\left[F_{i,l}\right]Im\left[F_{i,j}\right] + Im[F_i]Im\left[F_{i,jl}\right]\right\} - |F_i|_{,l}\left\{Re[F_i]Re\left[F_{i,j}\right] + Im[F_i]Im\left[F_{i,j}\right]\right\}\right. \tag{40}$$

With the help of Equation (41), it has been possible to calculate $Re\left[F_{i,jl}\right]$ and $Im\left[F_{i,jl}\right]$ in Equation (40), and this is the second derivative of $\boldsymbol{F}$. For elastic forces, the equations have been integrated with the storey forces by Aydin et al. [11] within Equation (34). The following equation is present for the differentiation of Equation (34) with respect to c_l

$$\boldsymbol{F}_{,jl} = \boldsymbol{K}(\boldsymbol{A}^{-1}\boldsymbol{A}_{,l}\boldsymbol{A}^{-1}\boldsymbol{A}_{,j}\hat{\boldsymbol{U}} - \boldsymbol{A}^{-1}\boldsymbol{A}_{,j}\hat{\boldsymbol{U}}_{,l}) \tag{41}$$

The second order sensitivities of base shear and base moment objective functions have been stated in the form of second derivatives of the transfer function of the storey shear forces in the following manner.

$$|M_B|_{,jl} = \sum_{i=1}^{n} |F_i|_{,jl} h_i + |M_R|_{,jl} \tag{42}$$

There is satisfaction of the constraint $\sum_{i=1}^{n} \Delta c_{di} = \Delta W$ for each design step [29]. Reduction in objective function and direction updates based on index k is observed. Takewaki [29] brought forward this algorithm. Keeping in mind the new objective functions presented in [11] and [13], the algorithm was modified. Within this damper optimization algorithm, the location of additional dampers can be attained through first order sensitivities. Within step 4, if index k is available, and it is corresponding to the design variable, then ΔW and the dampers current damping coefficient is added. Within the next step, there should be an update of the first order sensitivity through the use of second order sensitivity coefficients. If various indices are available $k_1 \ldots k_m$ as stated within the flowchart, there should be a distribution of ΔW within the structure. To satisfy the mentioned formula, it is necessary to attain the ratio within the magnitudes of $\overline{\Delta c_{dk}}$ (k=1,…m).

$$f_{,k1} + \sum_{i=k_1}^{k_m} f_{,k_1 i}\,\overline{\Delta c}_{di} = f_{,k_m} + \sum_{i=k_1}^{k_m} f_{,k_m i}\,\overline{\Delta c}_{di} \tag{43}$$

In Equation (43), the ratio presented within the magnitudes of $\overline{\Delta c_{dk}}$ along with the constraint $\sum_{i=1}^{n} \Delta c_{di} = \Delta W$ helps to attain the value of $\overline{\Delta c_{dk}}$. If various indices are present, $k_1 \ldots k_m$, update should be carried out for the objective function along with the first derivative.

$$f \rightarrow f + \sum_{i=k_1}^{k_m} f_{,i}\, \Delta c_{di} \tag{44}$$

$$f_{,i} \rightarrow f_{,i} + \sum_{i=k_1}^{k_m} f_{,il}\, \Delta c_{dl} \tag{45}$$

5 NUMERICAL EXAMPLE

As an example, a building model with 20 stories would be used. A 20 story structure is observed in Figure 1. For each floor, the masses (m) and mass moment of inertia (I_R) are m_i=30x10^3 kg and I_{Ri}=1.6x10^5 kg.m^2 (i=1,..,20) , respectively. For the ground floor, it is m_0=90x10^3 kg (masses) and I_{R0}=4.8x10^5 kg.m^2 (mass moment of inertia) [30]. Height (h) for each storey is 3.0 m. The structure-ground interaction horizontal motion and angular motion stiffness coefficients (k_S, k_R) and damping coefficients (c_S, c_R) would be extracted using Equations (12) and (15) which have been presented [31]. The uniform selection of structural damping is 2% and story stiffness is 2.5x10^7 N/m. The equivalent circular footing plate radius is 4m and is denoted as r. The total damper capacity (W) of 1x10^7 Ns/m has been taken into account to analyse the damping optimization issue within the context of various sandy soil relative densities. These capacities are within the ranges mentioned in literature [14]. There are three kinds of soil conditions taken into account. Table 1 shows the soil properties that are used for analysis.

Table 1: Soil properties used in analyses [32-34]

Soil type	v_s (m/s)	μ	G (MPa)		ρ (kg/m^3)
			Static	Dynamic	
Loose sand	150	0.25	8	33	1450
Medium dense sand	300	0.30	15	151	1650
Dense sand	550	0.35	24	570	1850

The optimal damper algorithm, mentioned earlier, has been applied to extract the optimal placement of the damper within the soil-structure interaction model. For the analysis, one kind of damper capacity is applied. At the time of optimization, the objective function (f) within the context of step number in case of W=1x10^7 Ns/m and ground conditions (three kinds of soil conditions and rigid case) have been analysed and Figure 2 mentions the variations. The transfer function amplitude is negatively influenced when there are poor soil conditions. There is a general trend for the soil conditions to alter the transfer function amplitude from loose towards medium dense and then dense sand to rigid eventually. As compared to other soil conditions, the loose sand condition has a stronger influence. The dense and medium dense sands maintain similar transfer function amplitudes that are also close to the rigid case. Therefore, when dampers are added at an optimum level to a structure with poor ground condition, the structure behaviour would be close to that of the rigid ground condition. In this

case, when there is an increase in step number, there will be a decrease in the transfer function amplitude, and there is lowest level of response for the rigid case as expected.

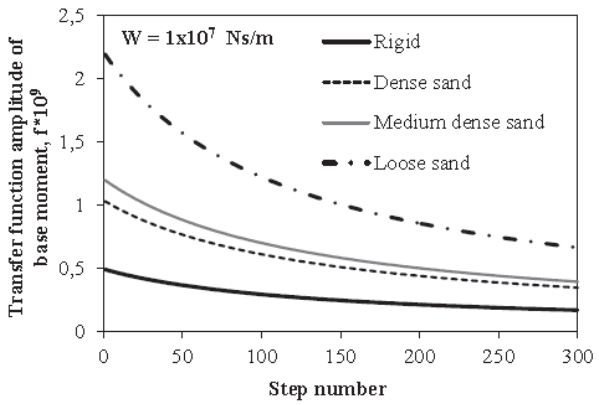

Figure 2: The variations of objective function in terms of ground conditions

Table 2 shows the optimum damper designs that have been extracted using the earlier mentioned optimization method. The objective function found for the optimum design at base moment is also mentioned in Table 2. Force-based designs are extracted through procedures where the base moment is used as the objective function. The table also indicates that the poorness in the ground causes a little change in the floors where the dampers are placed.

Table 2: Optimal damper designs for base shear and base moment

	Optimal Damper Coefficient (Ns/m)*10^6								
Soil Type	c_1	c_2	c_3	c_4	c_5	c_6	c_7	c_8	c_9 - c_{20}
Rigid	2.2	2.1	1.8	1.5	1.1	0.7	0.4	0.1	-
Dense Sand	2.5	2.3	2.0	1.6	1.0	0.5	0.1	-	-
Medium Dense Sand	2.5	2.4	2.0	1.6	1.0	0.4	1.0	-	-
Loose Sand	2.8	2.6	2.2	1.5	0.7	0.2	-	-	-

Additionally, the base moment objective function (f_j) sensitivities within the context of damping coefficients for additional dampers have been assessed for the various sandy soil conditions. Figure 3 indicates the sensitivity of objective function (f_j) variations within the context of step number stated for the objective function and four soil conditions. The objective function first order derivation is denoted by f_j within the context of j^{th} storey damper. In all cases, convergence has taken place. When the negative region is taken into account for their sensitivity values, the objective function first order derivatives indicates the design direction at the initiation of the algorithm. Since the initial stages, derivatives at each step are compared and checking is done for the maximum derivative value. The gradient based procedure is observed and procedure details have already been mentioned. The sensitivity values enhance when soil conditions are subjected to variations from rigid to loose sand case (Figure 3). The total damper capacity is taken as W=1x10^7 Ns/m and comparison is made for rigid and loose sandy ground condition. There is difference in the sensitivity of the numerical values but there is similarity in the design step trends. It is essential to indicate the sensitivity

presentation where the optimal design issue is integrated within the gradient based procedures.

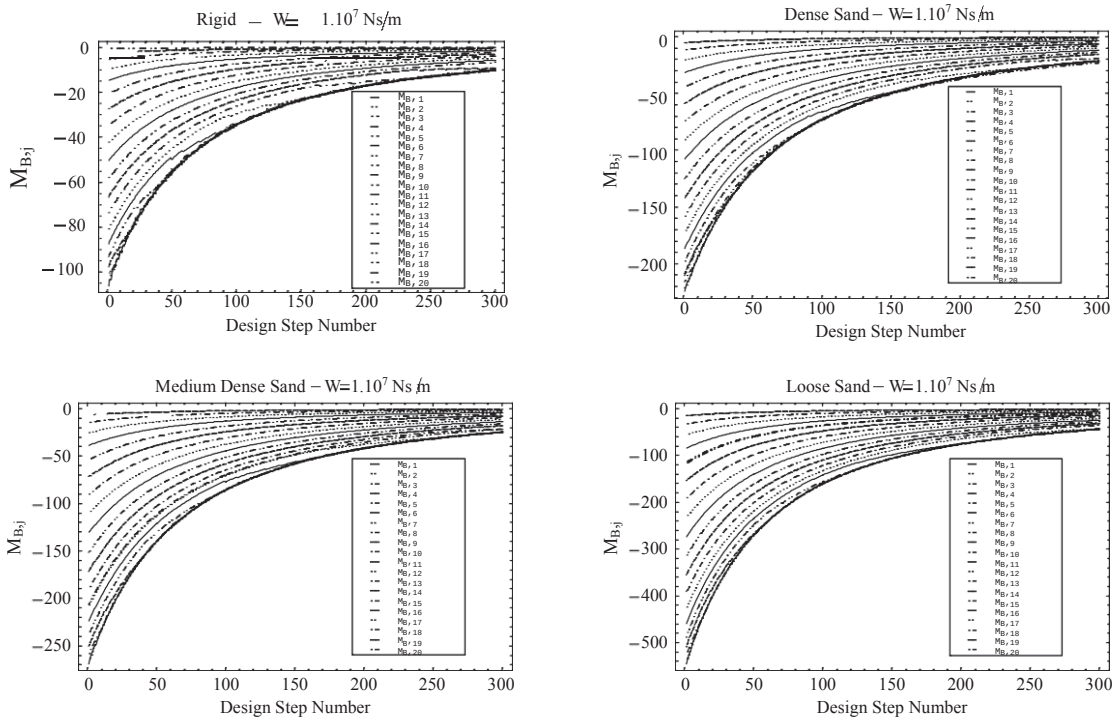

Figure 3: The sensitivities of objective function with respect to ground conditions

For rigid soil and various sandy soil conditions, plotting is carried out through the frequency response of the base moment transfer function amplitude variations in Figure 4. Analysis for frequency behaviours is conducted for $W=1x10^7$ Ns/m. Yet, the structural response is negatively influenced by the soil density conditions. From the rigid to loose sand case, there is an enhancement in the response. Within the context of the transfer function amplitudes, there is a similar behaviour of the medium dense, dense and rigid sand cases. When four kinds of behaviour parameters are applied to assess the frequency behaviour, it is observed that for amplitude, the rigid ground performance is most suitable and worst performance is indicated by loose sand. For ground conditions, the frequency behaviours have been analysed with and without dampers. The amplitudes have also been reduced significantly. When the dampers are added, the rigid and loose sandy soil difference reduces significantly. If optimal dampers are added, the negative influence can be managed. For the current research, this is considered as a significant outcome. The current research also calculates structural behaviours where the structure first mode behaviour indicates that there is minimization of behaviour. Figure 4 indicates that frequency behaviour would be significantly reduced within other higher modes through the first mode optimal dampers. The rigid case can not indicate a structural response, even though there is presence of a comparable optimal damper placement for altered relative sandy soil densities.

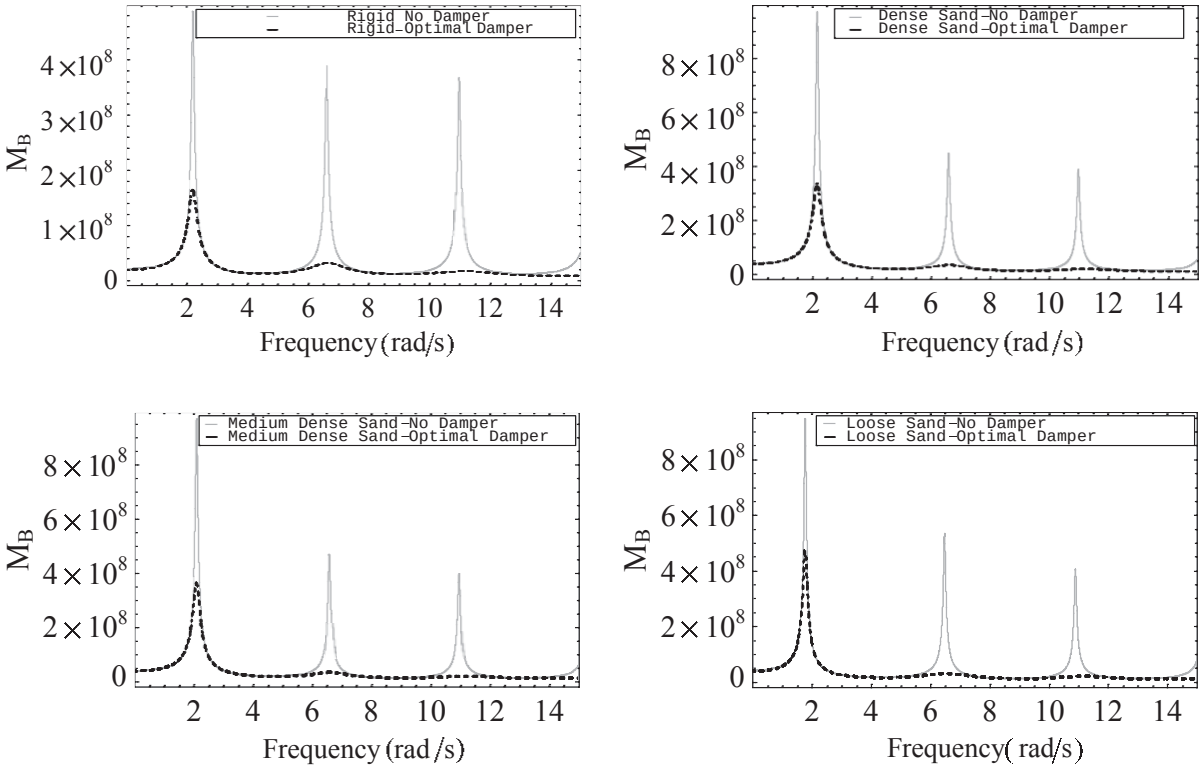

Figure 4: The variations of transfer function amplitude of base moment according to excitation frequency in terms of ground conditions

Within the current research, analysis has been made upon the influence of earthquakes over the structures base moment within the presence of optimal dampers and ground conditions. For the time history analysis, the El Centro earthquake acceleration (NS) record has been implemented. It is observed in Figure 5 that forces are enhanced significantly due to ground weakness within the context of the base moment without damper cases. If dampers are added, the base moment behaviour enhances significantly.

Fig. 5. The variations of transfer function amplitude of base moment according to excitation frequency in terms of ground conditions

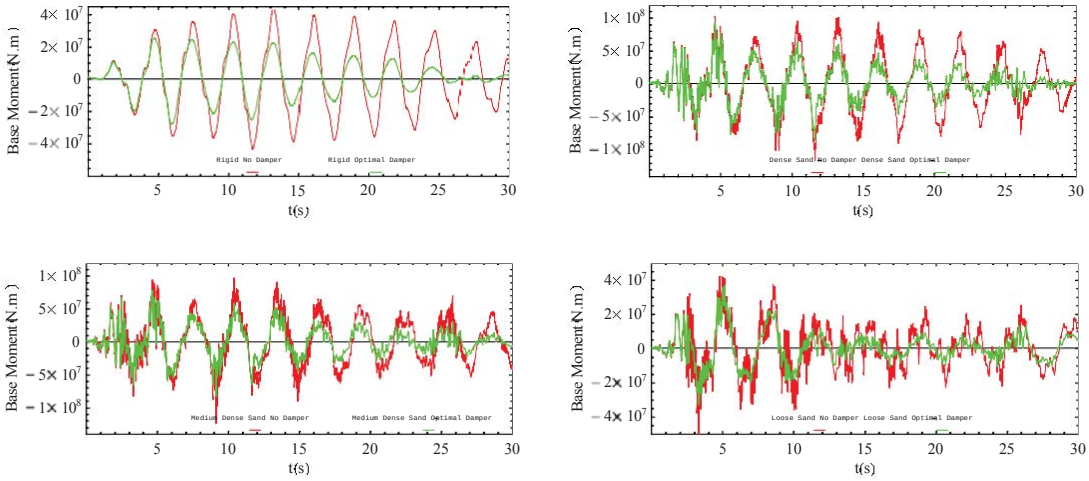

Fig. 9. Time history response of base moment under El Centro earthquake ground motion

Figure 5: Time history response of base moment under El Centro earthquake ground motion

The structure behaviour upon poor ground indicated significant enhancement, when dampers are added. For instance, the loose sand is dependent upon the location and capacity of the damper. The structure can be enhanced using optimal dampers, when there is an issue with the ground conditions keeping in mind the soil-structure interaction issue. For the engineering design, there would be a development, if the adverse situations are prevented through the addition of dampers on the superstructure and the ground conditions are not improved.

6 CONCLUSIONS

Within this current research, the base moment objective function in the case of different sandy soils is studied to investigate the optimal damper distributions and the structural response. Analysis has been carried out upon the objective function sensitivities keeping in mind the design variables of soil structure model frequency and time behaviour. Various sandy soil densities have been investigated within this context. Hence, keeping in mind the above mentioned aspects, the following conclusions are made.

The optimal damper distributions on the floor are influenced by the sandy soil relative densities which are observed through minimization of the structure base moment transfer function amplitude. The analyses of the 20-storey structure showed that dampers are placed on more floors for the rigid state, compared to the sandy ground conditions. As the looseness of the sandy ground increases, the dampers concentrate towards the lower floors. This reveals that if the weakness of the ground increases, the distribution of the dampers concentrates downwards in order to improve the behavior. According to the assessment, the structure behaviour of sandy soils is associated with the rigid ground structure response level at the time when there is optimal addition of the dampers to the poor ground structures.

On the other hand, the sandy soil relative density maintains a large influence upon the structural behaviour parameters that are the transfer function amplitude of four kinds of structural response, its sensitivities, frequencies and time behaviours. For the design steps, within the transfer function amplitude context, there is similar behaviour of the rigid, dense sand and medium dense sand conditions. The highest is of the loose sand which is also different from the rest. When the time domain and frequency were assessed, the relative density influence for sandy soil upon structural response was found. For loose sand, the response structure is not associated with the rigid, dense sand and medium dense sand conditions when the damper is not present. The behaviours for all cases are considered with the addition of the dampers. Within the current research, it is observed that the structural behaviours presented within the poor soil conditions decreased, when the dampers are added without making any soil improvements.

REFERENCES

[1] S. Elias, V. Matsagar, T.K. Datta, Distributed Multiple Tuned Mass Dampers for Wind Response Control of Chimney with Flexible Foundation, *Procedia Engineering*, 199:1641-1646, 2017.

[2] S. Elias, V. Matsagar, Effectiveness of Tuned Mass Dampers in Seismic Response Control of Isolated Bridges Including Soil-Structure Interaction, *Latin American Journal of Solids and Structures*, 14: 2324-2341, 2017.

[3] S. Elias, Effect of SSI on Vibration Control of Structures with Tuned Vibration Absorbers, *Shock and Vibration*, 1-12, https://doi.org/10.1155/2019/7463031, 2019.

[4] S. Elias, V. Matsagar, T.K. Datta, Along Wind Response Control of Chimneys with Distributed Multiple Tuned Mass Dampers, *Struct Control Health Monit.*, 26:e2275, https://doi.org/10.1002/stc.2275, 2019.

[5] M. Bayat, L.V. Andersen, L.B. Ibsen, p-y-ẏ curves for dynamic analysis of offshore wind turbine monopile foundations, *Soil Dynamics and Earthquake Engineering*, 90: 38-51, 2016.

[6] L.V. Andersen, Dynamic soil-structure interaction of polypod foundations, *Computers & Structures*, https://doi.org/10.1016/j.compstruc.2018.07.007, 2018.

[7] I. Takewaki, K. Fujita, K. Yamamoto, H. Takabatake, Smart passive damper control for greater building earthquake resilience in sustainable cities, *Sustain Cities Soc* , 1:3-15, 2011.

[8] M.P. Singh, L.M. Moreschi, Optimal placement of dampers for passive response control, *Earthq Eng Struct Dyn*, 31:955-976, 2002.

[9] R. Levy, O. Lavan, Fully stressed design of passive controllers in framed structures for seismic loadings, *Struct Multidiscipl Optim*, 32(6):485-489, 2006.

[10] G.P. Cimellaro, Simultaneous stiffness-damping optimization of structures with respect to acceleration displacement and base shear, *Eng Struct*, 29:2853-2870, 2007.

[11] E. Aydin, M.H. Boduroglu, D. Guney, Optimal damper distribution for seismic rehabilitation of planar building structures, *Eng Struct*, 29:176-185, 2007.

[12] T. Trombetti, S. Silvestre, Novel schemes for inserting seismic dampers in shear-type systems based upon the mass proportional component of the Rayleigh damping matrix, J Sound Vib, 302(3):486-526, 2007.

[13] E. Aydin, Optimal Damper Placement Based on Base Moment in Steel Building Frames, *JCSR*, 79:216-225, 2012.

[14] J.K. Whittle, M.S. Williams, T.L. Karavasilis, A. Blakeborough, A comparison of viscous damper placement methods for improving seismic building design, *J Earthq Eng*, 16:540-560, 2012.

[15] M. Palermo, S. Silvestri, L. Landi, G. Gasparini, T. Trombetti, Peak velocities estimation for a direct five-step design procedure of inter-storey viscous dampers, *Bull Earthquake Eng*, 14(2):599-619, 2016.

[16] N. Pollini, O. Lavan, O. Amir, Towards realistic minimum-cost optimization of viscous fluid dampers for seismic retrofitting, *Bull Earthquake Eng*, 14:971-998, 2016.

[17] E. Aydin, O. Sivrikaya, B. Ozturk, Comparison of Optimal Damper Distributions in Shear Frames in terms of Soil Conditions, *7th World Conference on Structural Control and Monitoring*, Qingdao, China, 2018.

[18] J.F. Wang, C.C. Lin, Seismic performance of multiple tuned mass dampers for soil irregular building interaction systems, *Int J Solids Struct*, 42:5536-5554, 2005.

[19] C. Li, B. Han, Effect of dominant ground frequency and soil on multiple tuned mass dampers, *The Struct Design of Tall Build*, 20:151-163, 2011.

[20] S.M. Nigdeli, G. Bektas, Optimum Tuned Mass Dampers for Structures at Rock and Soil Sites, *PAMM Proc Appl Math Mech*, 14(1):209-210, 2014.

[21] R.N. Jabary, S.P.G. Madabhushi, Structure-soil-structure interaction effects on structures retrofitted with tuned mass dampers, *Soil Dyn Earthq Eng*, 100:301-315, 2017.

[22] G. Bekdaş, S.M. Nigdeli, Metaheuristic based optimization of tuned mass dampers under earthquake excitation by considering soil-structure interaction, *Soil Dyn Earthq Eng*, 92:443-461, 2017.

[23] F. Khoshnoudian, R. Ziaei, P. Ayyobi, F. Paytam, Effects of nonlinear soil–structure interaction on the seismic response of structure-TMD systems subjected to near-field earthquakes, *Bull Earthquake Eng*, 15:199-226, 2017.

[24] E. Nazarimofrad, S.M. Zahrai, Fuzzy control of asymmetric plan buildings with active tuned mass damper considering soil-structure interaction, *Soil Dyn Earthq Eng*, https://doi.org/10.1016/j.soildyn.2017.09.020, 2017.

[25] F. Kordi, J. Alamatian, Analytical method for designing the tuned mass damper based on the complex stiffness theory, *Iran J Sci Technol Trans Civ Eng*, https://doi.org/10.1007/s40996-018-0222-0, 2019.

[26] Z. Xuefei, W. Shuguang, D.D. Dongsheng, L. Weiqing, Simplified analysis of frame structures with viscoelastic dampers considering the effect of soil-structure interaction, *Earthq Eng & Eng Vib*, 16:199-217, 2017.

[27] Z. Xuefei, W. Shuguang, D.D. Dongsheng, L. Weiqing, Optimal design of viscoelastic dampers in framestructures considering soil-structure interaction effect, *Shock and Vibration*, https://doi.org/10.1155/2017/9629083, 2017.

[28] I. Takewaki, Soil-structure random response reduction via TMD-VD simultaneous use, *Comp. Methods. Apl. Mech. Eng*, 190:677-690, 2000a.

[29] I. Takewaki, Optimum damper placement for planer building frames using transfer functions, *Structural and Multidisciplinary Optimization*, 280-287, 2000b.

[30] I. Takewaki, Probabilistic critical excitation for MDOF elastic-plastic structures on compliant ground, *Earthq Eng Struct Dyn*, 30:1345-1360, 2001.

[31] R.A. Parmelee, The influence of foundation parameters on the seismic response of interaction systems, *The 3rd Japan Earthquake Engineering Symposium*, Tokyo, Japan, 3:49-56, 1970.

[32] J.E. Bowles, Foundation analysis and design, New York: McGraw-Hill, 1996.

[33] M. Carter, S.P. Bentley, Soil properties and their Correlations, 2nd ed. Wiley, 2016.

[34] TEC, Regulation for buildings in seismic areas, *Ministry of Public Works and Housing, Official Gazette* (in Turkish), 2007.

EURODYN 2020
XI International Conference on Structural Dynamics
M. Papadrakakis, M. Fragiadakis, C. Papadimitriou (eds.)
Athens, Greece, 23–26 November 2020

A LOCAL ACTIVE NOISE CONTROL SYSTEM BASED ON A NONLINEAR SENSING TECHNIQUE FOR YACHT APPLICATIONS

Mylonas D., Erspamer A., Paradisiotis A., Yiakopoulos C., Antoniadis I.

National Technical University of Athens, School of Mechanical Engineering, Department of Mechanical Design & Automatic Control, Laboratory of Dynamics and Structures

chryiako@cental.ntua.gr

Keywords: Nonlinear active noise control (NANC), Functional link networks (FLNs), Narrowband noise, Maritime environment.

Abstract. *Active noise control (ANC) is an important subject that plays a central role in many practical problems. In essence, the ANC technique is based on the principle that a noise can be cancelled by another noise with the same amplitude but an opposite phase. Compared with the passive noise control technique, the ANC method is efficient to suppress noise with lower frequency. As an adaptive controller, the filtered-x least mean square (FxLMS) algorithm has gained substantial popularity owing to its simplicity. Unfortunately, in the physical world, many ANC systems exhibit certain degrees of nonlinearity in the primary or secondary path. In such situations, nonlinear ANC (NANC) algorithm is necessary for further implementation. A novel nonlinear filter, which incorporates the concept of exponential sinusoidal models into nonlinear filters based on functional link networks (FLNs) has been applied in this paper. The proposed filter is designed to provide improved convergence characteristics over traditional FLN filters. The conventional trigonometric FLN (TFLN) may be considered as a special case of the proposed adaptive exponential FLN (AEFLN). An adaptive exponential least mean square (AELMS) algorithm has been derived and the same has been successfully applied for identification of a couple of nonlinear plants. This paper investigates the application of active noise control to the attenuation of the noise produced by two asynchronous generators in a luxury yacht, with the specific aim of creating a quiet region in a twin cabin around the sleeping area.*

1 INTRODUCTION

Passive noise control treatments are an effective means of reducing the levels of noise and vibration experienced by humans in a variety of applications. However, due to both weight and size restrictions their performance in practice is generally limited to the control of higher frequency noise and vibration. To overcome this limitation and achieve significant levels of low frequency noise attenuation, active control methods have been widely investigated. Ac-

tive control systems reduce the unwanted primary disturbance by the introduction of secondary sources, which produce either additional noise or vibration to control the original source.

Active control has been successfully demonstrated in a variety of engineering applications where the perception of the acoustic environment is particularly important. For example, in the aircraft environment the low frequency tonal noise induced by the propellers has been successfully controlled using a feedforward active noise control system [1]. In the automotive environment a variety of active control systems have been proposed for both engine [2] and road noise control [3]. More broadly, active control technology has been applied to fan noise [4], active earmuffs [5], noise transmission through windows [6], sound radiation from a helicopter transmission [7] and diesel generator noise in the master cabin of a luxury yacht [8].

Active noise control (ANC) system is an electro-acoustic device based on the principle of destructive interference by generating the signal which has the same amplitude and opposite phase with the undesired noise. Because of the potential industrial applications and digital signal processing advantages, many different kinds of ANC algorithms are developed quickly in recent years [9, 10]. More widely used of them is filtered-x least mean square (FXLMS) algorithm based on linear finite impulse response (FIR) filter [11], which works well in most cases. However, these superiorities are only applied in linear control problem. In other words, when the reference signal measured by the acoustic sensor or the transfer functions of the primary path and secondary path are nonlinear, the ANC system based on FXLMS algorithm performs poorly and even fails to work [12].

In order to solve the nonlinear distortions in ANC system, a variety of nonlinear structures and algorithms are proposed over past fifteen years [13, 14].

Nonlinear filters based on functional link networks (FLNs) have received significant attention owing to its single layer structure, which offers lesser computational complexity and due to the simple learning rule [15]. FLN-based nonlinear system identification by using FLN-based filters has been attempted in [16] and FLN filters have found applications in other areas of nonlinear filtering including channel equalization [17] and echo cancellation [18]. In a traditional trigonometric FLN (TFLN), the input signal is functionally expanded using a set of trigonometric functions, before applying to an adaptive weight matrix. FLNs which employ other functional expansions than trigonometric functions have also been proposed recently. A Chebyshev FLN was presented in [19] for identification of dynamic systems. A Legendre neural network (LeNN), which employs a Legendre functional expansion, has been successfully applied for nonlinear channel equalization in wireless communication systems [20]. The lower computational load offered by TFLN-based nonlinear filters has made TFLN a popular candidate for nonlinear controllers in an ANC scenario also.

Thus, in this work, a nonlinear filter, which is based on an exponentially decaying trigonometric functional expansion has been applied in a yacht environment [21]. The performance of the filter has been enhanced by incorporating an adaptive exponential factor [21]. The effectiveness of the proposed filter has been tested using an extensive real world study. In this work, the filter has been shown to provide an improved noise cancellation in an ANC scenario.

2 DIESEL GENERATOR NOISE CONTROL

The acoustic environment in luxury yachts has become an important consideration for yacht manufacturers. High levels of noise and vibration can result in an uncomfortable environment and, therefore, there is a desire to achieve low levels of noise and vibration. At mid to high frequencies passive noise and vibration control treatments can be employed to achieve a quiet living space on-board. At low frequencies, however, the size and weight of passive treatments becomes too large and is often either impractical or significantly increases the

weight of the yacht, which in turn limits its efficiency. Thus, the occupants are sensitive to the noise produced by the electrical generators whilst moored.

Therefore, focus has been made on controlling the noise produced by the generators in a twin cabin, and especially when the generators are asynchronous.

Fig. 1 shows the yacht and the twin cabin considered in this work. The yacht specification are presented in the Table 1. In order to characterise the noise produced by the asynchronous generators, the sound pressure level has been measured at the head of the bed in the twin cabin using a microphone B&K model 4189 when the diesel generators are running on the mooring. The spectrum of the A-weighted sound pressure level measured by the microphone has been calculated. From the results illustrated in Figs. 6 and 7 it can be seen that the noise signal and its spectrum are characterised by an interference pattern between two sounds of slightly different frequencies, which comprise a series of harmonics of the fundamental engines orders at the mains frequencies of f_o=52 and f_1=55 Hz due to the asynchronous disturbance.

(a) (b)

Figure 1: The ANC has been applied to (a) a luxury yacht and (b) in a twin cabin.

Length (FT)	70
Beam (FT)	24
Draft (FT)	7.3
Engines	MAN 1300 X2
Generators	2X ONAN 21 KW-17 KW
Fuel (LTRS/HR)	400
Cruising Speed (KNOT/HR)	23

Table 1: Yacht specifications.

3 TFLN AND AEFLN BASED NONLINEAR FILTERS

In an FLN, the functionally expanded input signal is multiplied with a set of adaptive weights and then added together to obtain the output signal. Assuming *x(n)* as the input signal, in a TFLN, the functionally expanded signal vector may be written as:

$$f(n) = \{1, x(n), sin[\pi x(n)], \dots, sin[B\pi x(n)], cos[B\pi x(n)], x(n-1), sin[\pi x(n-1)], cos[\pi x(n-1)], \dots, x(n-N+1), sin[\pi x(n-N+1)], cos[\pi x(n-N+1)], \dots, sin[B\pi x(n-N+1)], cos[B\pi x(n-N+1)]\}^T \quad (1)$$

where B is the order of the functional expansion. The output of the TFLN may be written as:

$$y(n) = wf_o(n) + wf_1(n)x(n) + wf_2(n)sin[\pi x(n)] + wf_3(n)cos[\pi x(n)] + \cdots wf_{(M-2)}(n)sin[B\pi x(n)] + wf_{(M-1)}(n)cos[B\pi x(n)] \quad (2)$$

with $\boldsymbol{w_f}(n)=[\, w_{f0}(n), w_{f1}(n), \ldots, w_{f(M-1)}(n)]^T$ as the adaptive weight vector of the TFLN. The weights of the TFLN are usually updated using a gradient descent approach as

$$\boldsymbol{wf}(n+1) = \boldsymbol{wf}(n) + \mu te(n)\boldsymbol{f}(n) \quad (3)$$

where $e(n)$ is the error signal and μ_t is the learning rate.

It may be noted that TFLN attempts to model the nonlinearities in a system using sinusoids. Many of the natural signal-like speech which has fast amplitude variations cannot be effectively modeled using nonlinear filters based on pure sinusoids [22]. It has also been reported that the modeling of such signals can be achieved with better accuracy using sinusoids with exponentially varying amplitudes [23]. In order to overcome this limitation of pure sinusoids-based nonlinear filter like TFLN, we attempt to design a new nonlinear filter, which incorporates exponentially varying sinusoids in the modeling process. The new filter, which is hereafter referred to as AEFLN, is also designed to handle both growing as well as decaying exponential nonlinearities.

Similar to that in a TFLN, in an AEFLN, the tap delayed input signal

$$\boldsymbol{x}(n) = [x(n), x(n-1), \ldots, x(n-N+1)]T \quad (4)$$

of length N is functionally expanded to $M=N(2B+1)+1$ terms. The expanded input signal vector is given by

$$\begin{aligned}\boldsymbol{g}(n) &= \{1, x(n), e^{-\alpha(n)|x(n)|}\sin[\pi x(n)], e^{-\alpha(n)|x(n)|}\cos[\pi x(n)], \ldots, e^{-\alpha(n)|x(n)|}\sin[B\pi x(n)], \\ &e^{-\alpha(n)|x(n)|}cos[B\pi x(n)], x(n-1), e^{-\alpha(n)|x(n-1)|}\sin[\pi x(n-1)], e^{-\alpha(n)|x(n-1)|}\cos[\pi x(n-1)], \ldots, \\ &e^{-\alpha(n)|x(n-1)|}\sin[B\pi x(n-1)], e^{-\alpha(n)|x(n-1)|}\cos[B\pi x(n-1)], \ldots, x(n-N+1), e^{-\alpha(n)|x(n-N+1)|}\sin[\pi x(n-N+1)], \\ &e^{-\alpha(n)|x(n-N+1)|}\cos[\pi x(n-N+1)], \ldots, e^{-\alpha(n)|x(n-N+1)|}\sin[B\pi x(n-N+1)], \\ &e^{-\alpha(n)|x(n-N+1)|}\cos[B\pi x(n-N+1)]\}\end{aligned} \quad (5)$$

where $a(n)$ is an adaptive exponential parameter. The expanded input signal vector $\boldsymbol{g}(n)$ is multiplied by the adaptive weight vector

$$\boldsymbol{w}(n) = [wo(n), w1(n-1), \ldots, wM-1(n)]T \quad (6)$$

to obtain the filter output, which is given by

$$y(n) = w_o(n) + w_1(n)x(n) + w_2(n)sin|\pi x(n)|/\, e^{\alpha(n)|x(n)|} + w_3(n)cos|\pi x(n)|/\, e^{\alpha(n)|x(n)|} + \cdots w_{(M-2)}(n)sin|B\pi x(n)|/\, e^{\alpha(n)|x(n)|} + w_{(M-1)}(n)cos|B\pi x(n)|/\, e^{\alpha(n)|x(n)|} \tag{7}$$

(7) may be written in a compact form as

$$y(n) = \boldsymbol{g}T(n)\boldsymbol{w}(n) \tag{8}$$

The weight vector is updated as

$$\boldsymbol{w}(n+1) = \boldsymbol{w}(n) + \mu we(n)\boldsymbol{g}(n) \tag{9}$$

where μ_w is the step size. In a similar fashion, the adaptive exponential factor *a(n)* is updated as:

$$a(n+1) = a(n) + \mu\alpha e(n)\boldsymbol{z}T(n)\boldsymbol{w}(n) \tag{10}$$

where μ_a is the learning rate of *a(n)* and *z(n)* is an $M\times 1$ vector

$$\boldsymbol{z}(n) = \{0, 0, -|x(n)|\, e^{-\alpha(n)|x(n)|}\sin[\pi x(n)], -|x(n)|\, e^{-\alpha(n)|x(n)|}\cos[\pi x(n)], \ldots, -|x(n)|e^{-\alpha(n)|x(n)|}sin[B\pi x(n)], -|x(n)|e^{-\alpha(n)|x(n)|}cos[B\pi x(n)], \ldots, 0, -|x(n-N+1)|\, e^{-\alpha(n)|x(n-N+1)|}sin[\pi x(n-N+1)], -|x(n-N+1)|\, e^{-\alpha(n)|x(n-N+1)|}cos[\pi x(n-N+1)], -|x(n-N+1)|\, e^{-\alpha(n)|x(n-N+1)|}sin[B\pi x(n-N+1)], -|x(n-N+1)|\, e^{-\alpha(n)|x(n-N+1)|}cos[B\pi x(n-N+1)]\}^T \tag{11}$$

(9) and (10) together forms the adaptive exponential least mean square (AELMS) algorithm. Fig. 2 shows the block diagram of AEFLN updated using an AELMS algorithm.

4 PERFORMANCE ASSESSMENT

The effectiveness of the proposed nonlinear filter has been evaluated through an experimental study a twin cabin of a yacht (Fig. 1). The performance of AEFLN has been compared with that obtained using TFLN.

The mean square error (MSE) has been used as the metric of comparison

$$MSE = 10loog10\{E[e2(n)]\} \tag{12}$$

$$e(n) = d(n) - y(n) \tag{13}$$

where *d(n)* is the output of the system and *y(n)* is the anti-noise signal (Fig. 2).

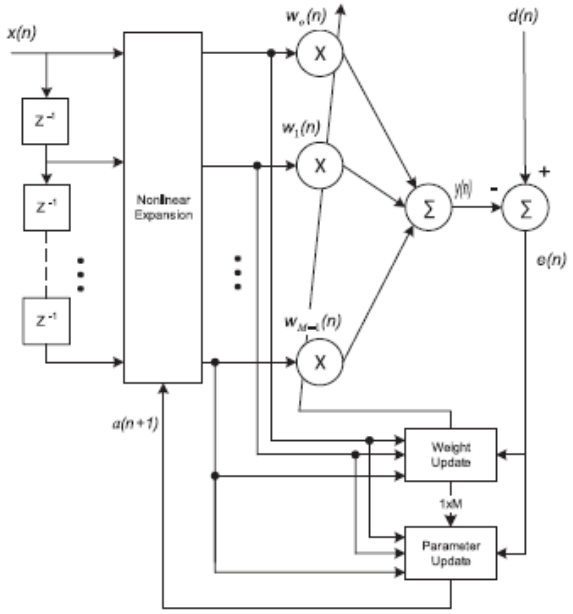

Figure 2: Block diagram of an AEFLN updated using an AELMS algorithm [21].

Initially, an attempt has been made to study the effect of the buffer size *BS* on the performance and the convergence behavior of the AEFLN-based model.

Fig. 3, shows the variations of MSE with respect to the iterations for fixed values of order *ORD*=2, learning rates μ_w=0.01 and μ_a=0.05, and initial value of a=10. As illustrated in Fig. 3, the MSEs computed over the last 3000 iterations are about -36, -28 and -18 dBs for *BS* 30, 20 and 10, respectively. Thus, the AEFLN-based ANC system has been shown to provide a better performance for buffer size greater than 30. The enhanced noise cancellation performance of AEFLN controller with respect to *BS* is confirmed in the Figs. 4 and 5. The error signal *e(n)* measured at the point of interest is presented in Fig. 6, while its spectrum is shown in Fig. 5. From those plots it can been seen that significant levels of narrowband attenuation achieved around the 'beat' components and their harmonics for *BS* greater than 30 samples. In addition to the noise attenuation performance shown in the waveforms of the Fig. 4, it is also interesting to observe the enhanced convergence behavior of the AEFLN controller.

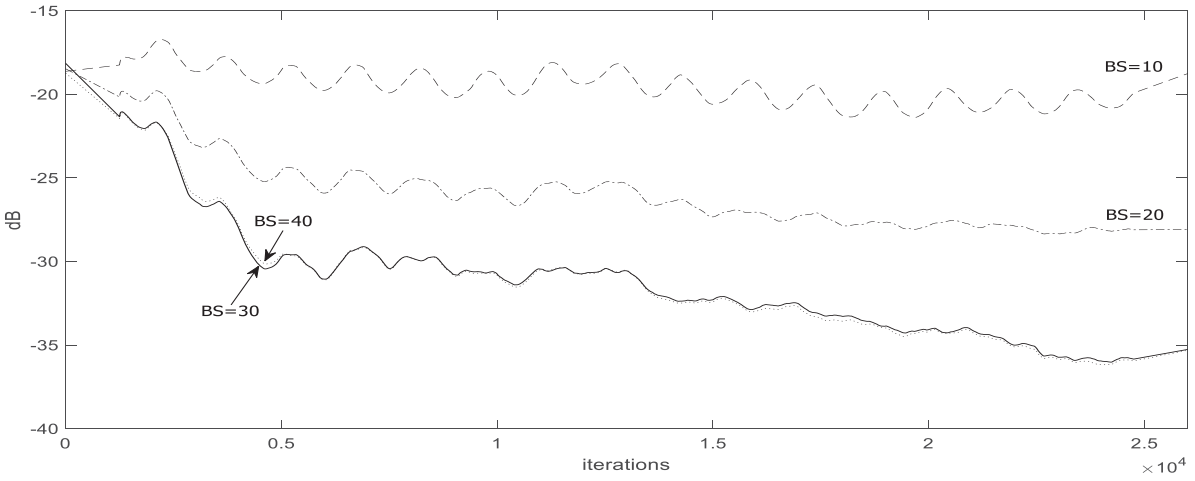

Figure 3: Comparison of convergence characteristics (MSE) obtained for different buffer sizes *BS* and AEFLN order *ORD*=2, a=10, μ_w=0.01 and μ_a=0.05.

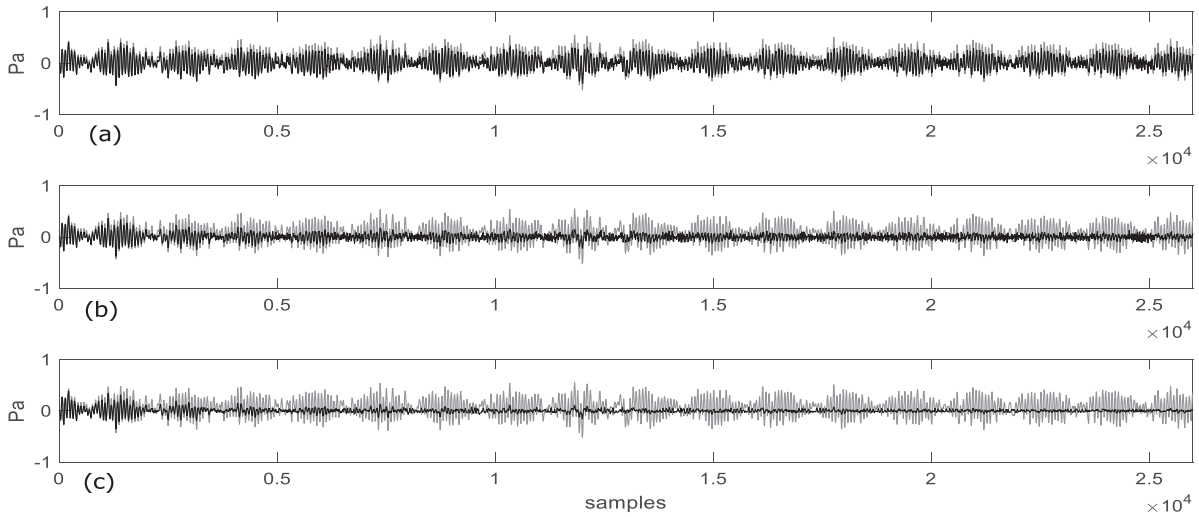

Figure 4: Error (black) and desired (gray) signals for buffer size *BS* (a) 10, (b) 20 and (c) 30 (*ORD*=2, a=10, μ_w=0.01 and μ_a=0.05).

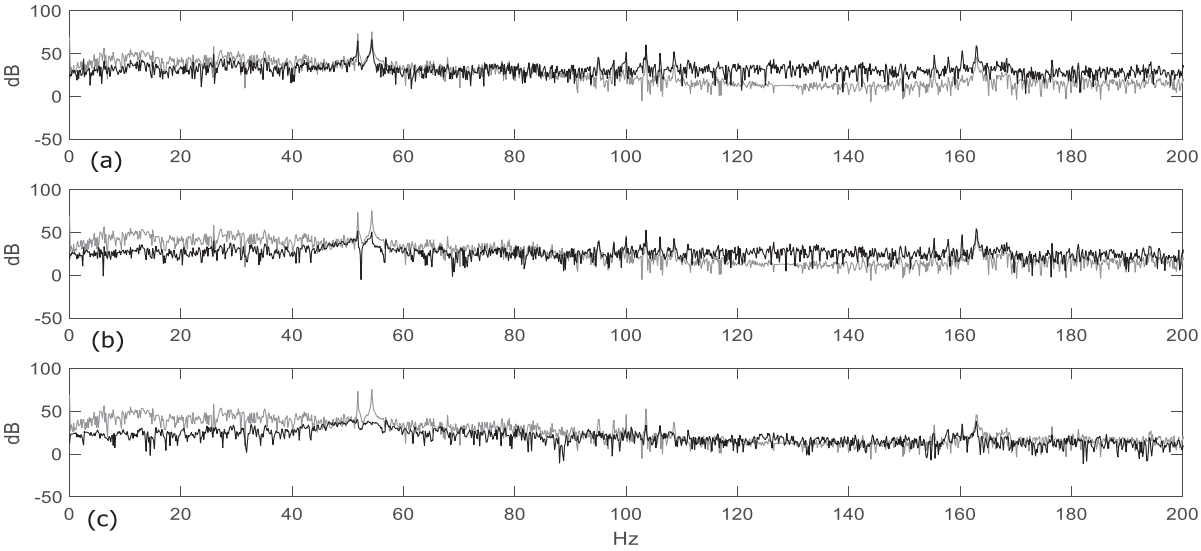

Figure 5: Spectrum of the error (black) and desired (gray) signals for buffer size *BS* (a) 10, (b) 20 and (c) 30 (*ORD*=2, a=10, μ_w=0.01 and μ_a=0.05).

Moreover, it may be noted, as shown in Table 2, that the ANCS using *BS*=30 achieved up to 40 dB noise reduction at the desired 'beat' components f_o and f_1.

Freq. (Hz)	ANC OFF SPL (dB)	ANC ON/SPL (dB)		
		BS=10	*BS*=20	*BS*=30
f_o=52	73.33	64.98	51.77	39.32
f_1=55	75.48	66.32	50.74	34.26

Table 2: AEFLN controller performance in accordance to the buffer size *BS*.

Then, the effect of the step size μ_w on the performance and the convergence behavior of the AEFLN controller is studied with respect to the iterations for fixed values of order *ORD*=2, buffer size *BS*=30 and μ_a=0.05, and initial condition of *a*=10.

Thus, as it is observed in Fig. 6, the MSEs computed over the last 6000 iterations are about -50, -35 and -23 dBs for μ_w 0.01, 0.001 and 0.0001, respectively. This means that the AEFLN approach achieves an improved steady state MSE for μ_w close to 0.01. Thus, the AEFLN-based ANC system has been shown to provide a better performance for step size μ_w greater than 0.01 and smaller than 0.1. Also, the noise cancellation performance of AEFLN controller with respect to step size μ_w is confirmed in the Figs. 7 and 8, and the Table 3.

The measured error signal *e(n)* and its spectrum are shown in Figs. 7 and 8. Again, a high narrowband attenuation and an enhanced convergence behavior of the AEFLN controller is achieved around the 'beat' components and their harmonics for step size μ_w close to 0.01. As shown in Table 3, that the ANCS using μ_w =0.01 achieved up to 37 dB noise reduction at the desired 'beat' components f_o and f_1.

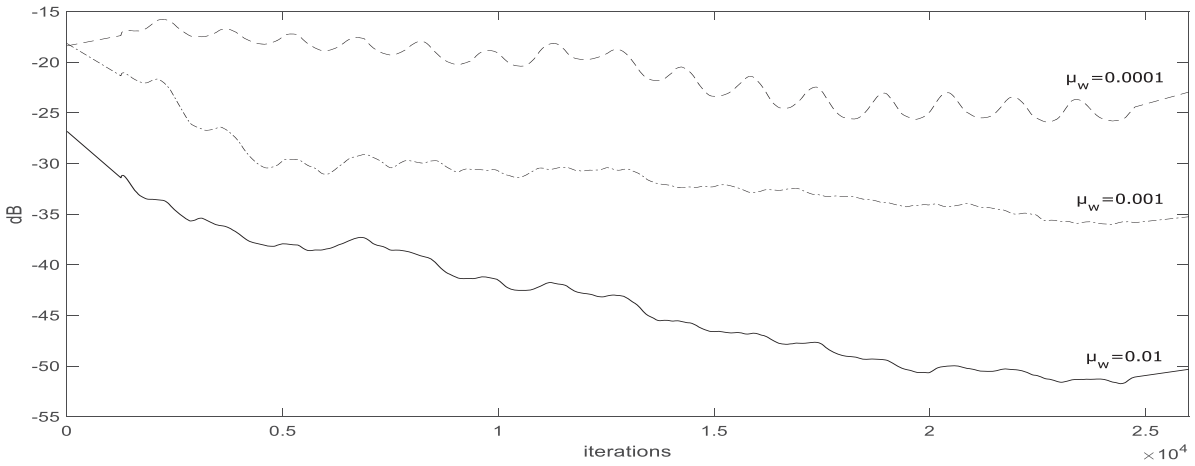

Figure 6: Comparison of convergence characteristics (MSE) obtained for different step sizes μ_w (*ORD*=2, *BS*=30, *a*=10 and μ_a=0.05.

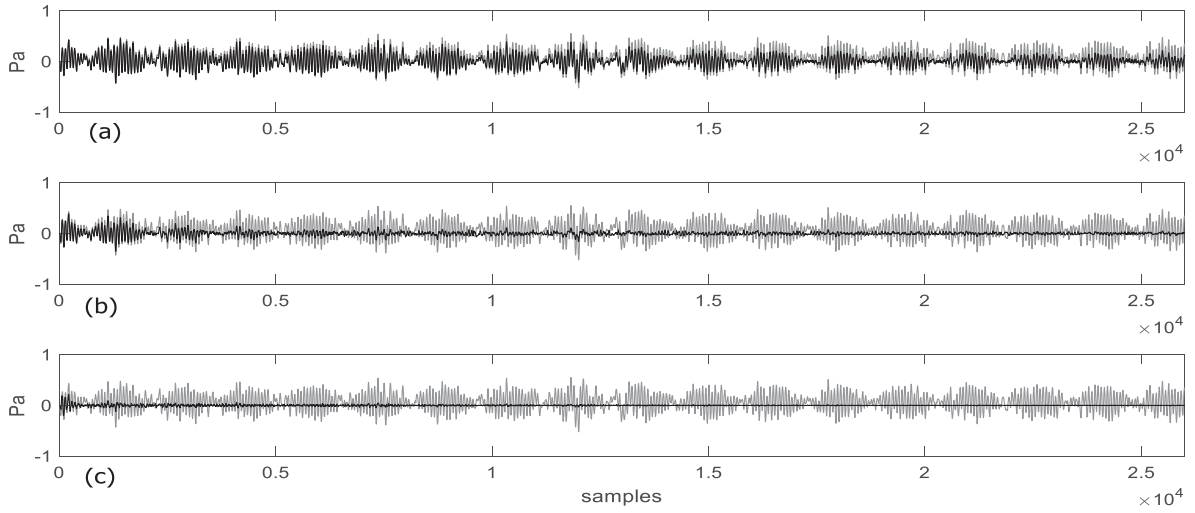

Figure 7: Error (black) and desired (gray) signals for step size μ_w (a) 0.0001, (b) 0.001 and (c) 0.01 (*ORD*=2, *BS*=30, *a*=10, μ_a=0.05).

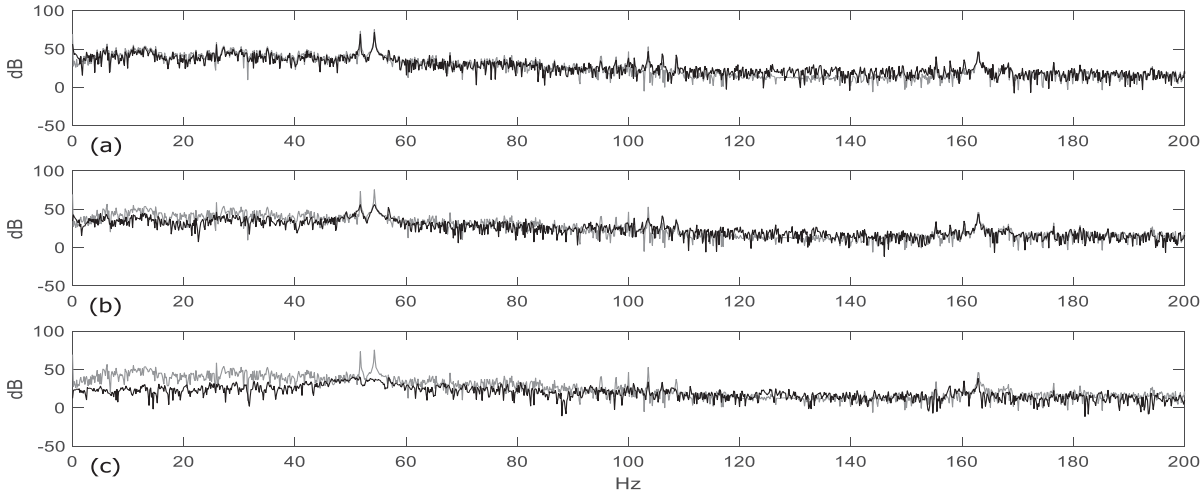

Figure 8: Spectrum of error (black) and desired (gray) signals for step size μ_w (a) 0.0001, (b) 0.001 and (c) 0.01 (*ORD*=2, *BS*=30, a=10, μ_a=0.05).

Freq. (Hz)	ANC OFF SPL (dB)	ANC ON/SPL (dB)		
		μ_w=0.0001	μ_w=0.001	μ_w=0.01
f_o=52	73.33	69.38	55.94	39.32
f_1=55	75.48	71.41	56.02	34.26

Table 3: AEFLN controller performance in accordance to the step size μ_w.

In addition, as presented in Fig. 9, the step size μ_w affects the steady state and the convergence of the exponential factor a. The attempt to study the convergence behavior of a has been achieved considering fixed values of order *ORD*=2, buffer size *BS*=30 and μ_a=0.05, and initial condition of a=10. Thus, a fast and steady convergence speed and behavior of a can be expected increasing the value of μ_w close to 0.01.

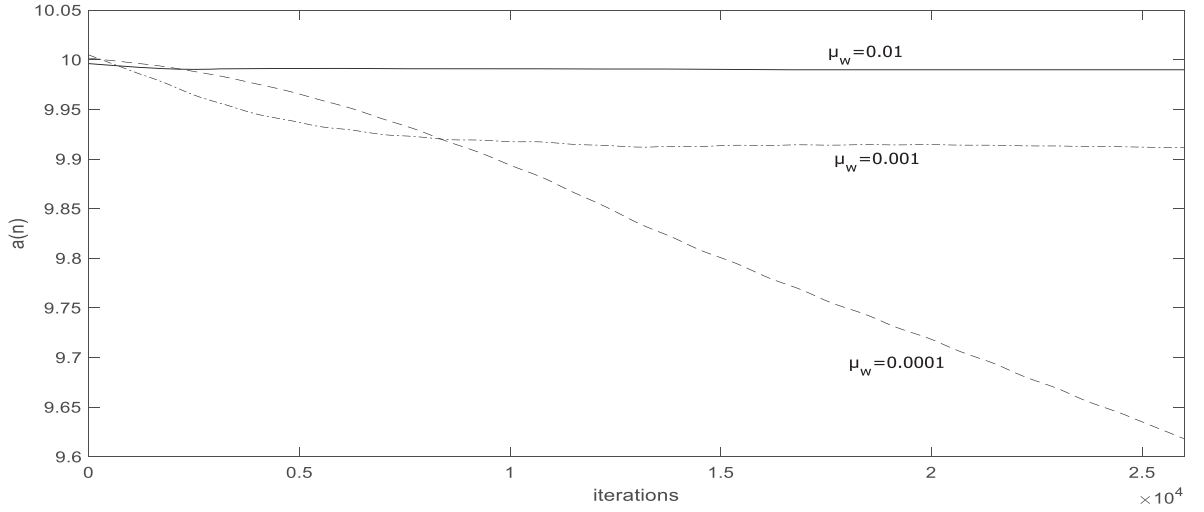

Figure 9: Exponential factor a(n) convergence for different step sizes μ_w (*ORD*=2, *BS*=30, a=10, μ_a=0.05).

Moreover, a study of the AEFLN convergence behavior in respect of the initial condition of a has been achieved considering fixed values of order ORD=2, buffer size BS=30, μ_w=0.01 and μ_a=0.05.

As it is observed in Fig. 10, the MSEs computed over the last 3000 iterations are about -60, -52, -45, -50 and -55 dBs for a equal to -1, 0, 2, 10 and 20, respectively. Thus, the convergence speed and AEFLN performance are slightly affected by the initial condition of a.

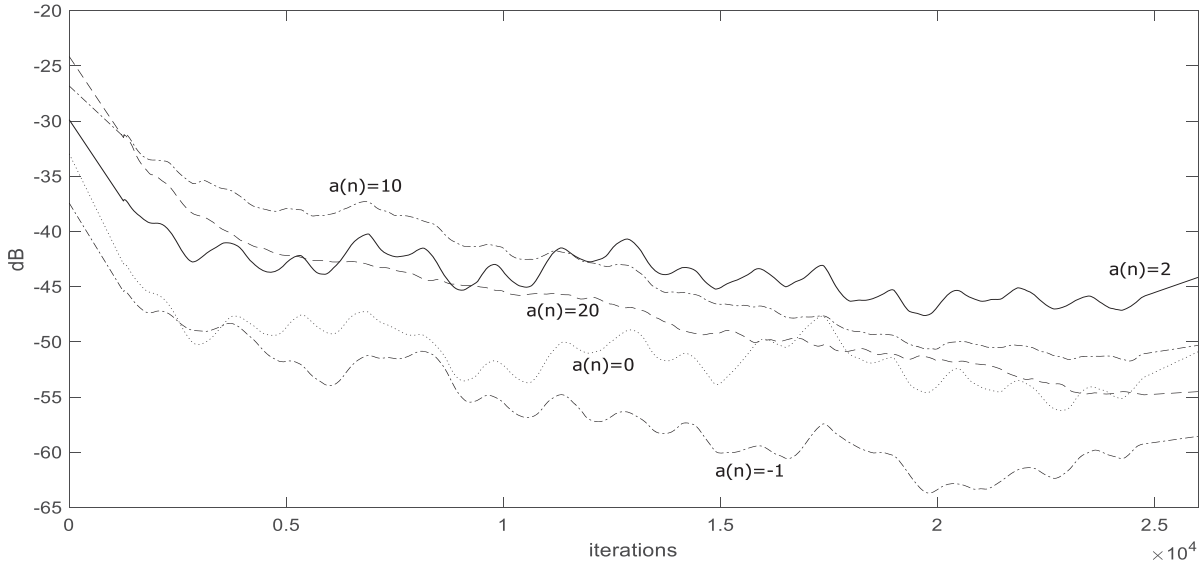

Figure 10: Comparison of convergence characteristics (MSE) obtained for different adaptive exponential parameters $a(n)$ (ORD=2, BS=30, μ_w=0.01 and μ_a=0.05).

In contrast to the buffer size and the step size μ_w, the order of the AEFLN controller in this case does not affect the convergence speed and performance of AEFLN and exponential factor a. The following results illustrated in Figs. 11 and 12 confirm the above conclusion.

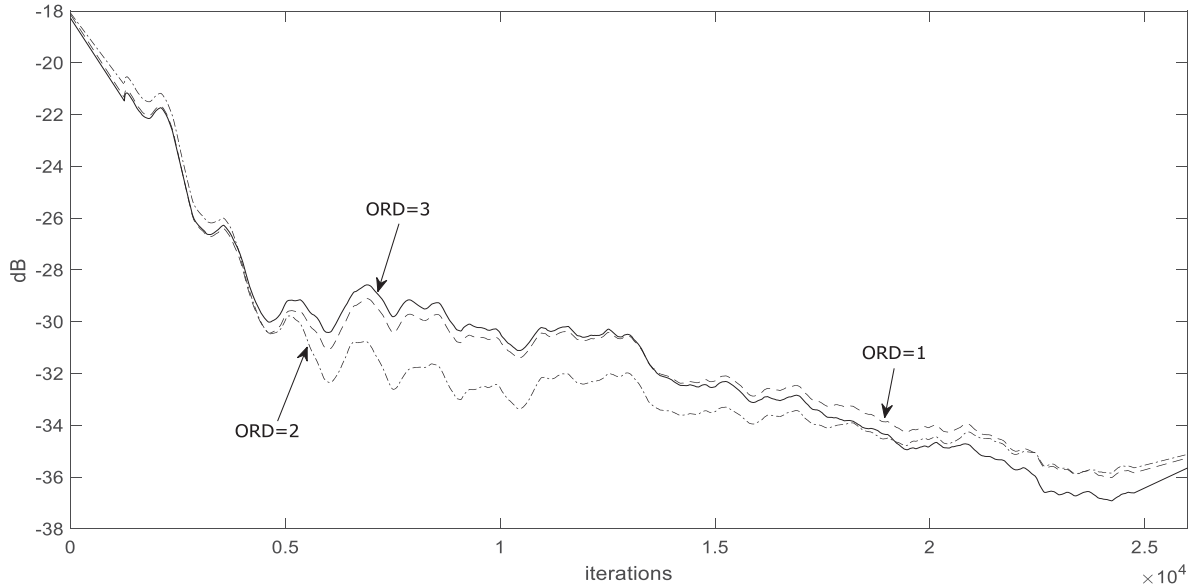

Figure 11: Comparison of convergence characteristics (MSE) obtained for different AEFLN orders (a=10, μ_w=0.01 and μ_a=0.05).

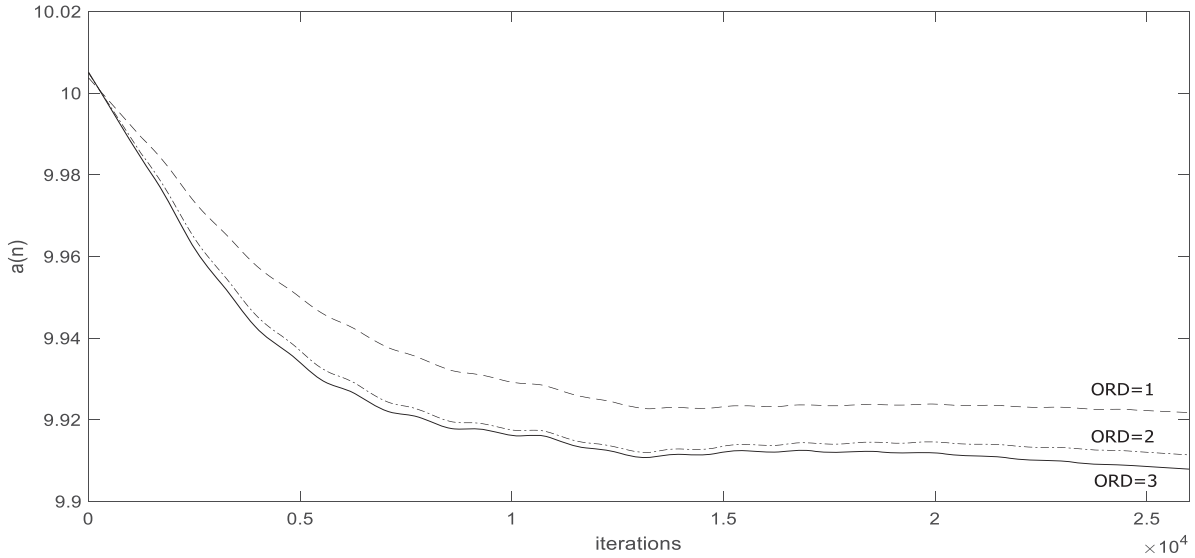

Figure 12: Exponential factor a(n) convergence for different AEFLN orders *ORD* (a=10, μ_w=0.01 and μ_a=0.05).

Next, another attempt has been made to study the effect of the buffer size *BS* on the performance and the convergence behavior of the TFLN-based controller.

Fig. 13, shows the variations of MSE with respect to the iterations for fixed values of order *ORD*=2 and learning rate μ_t=0.001. As illustrated in Fig. 13, the MSEs computed over the last 12000 iterations are about -45, -34, -23 and -20 dBs for *BS* 30, 20, 10 and 5, respectively. It is obvious that the TFLN controller provides a better performance for buffer size close to 30. Also, the Figs. 14 and 15 confirm the enhanced noise cancellation performance of TFLN controller with respect to *BS*. Figs. 14 and 15 present the error signal *e(n)* and its spectrum, respectively. The plots of Figs. 14 and 15 confirm that significant levels of narrowband attenuation achieved around the 'beat' components and their harmonics for *BS* greater than 30 samples. In the Fig. 14, it is also interesting to observe the enhanced convergence behavior of the TFLN controller.

Moreover, as shown in Table 4, the ANC system using *BS*=30 can achieve up to 45 dB noise reduction at the desired 'beat' components f_o and f_1.

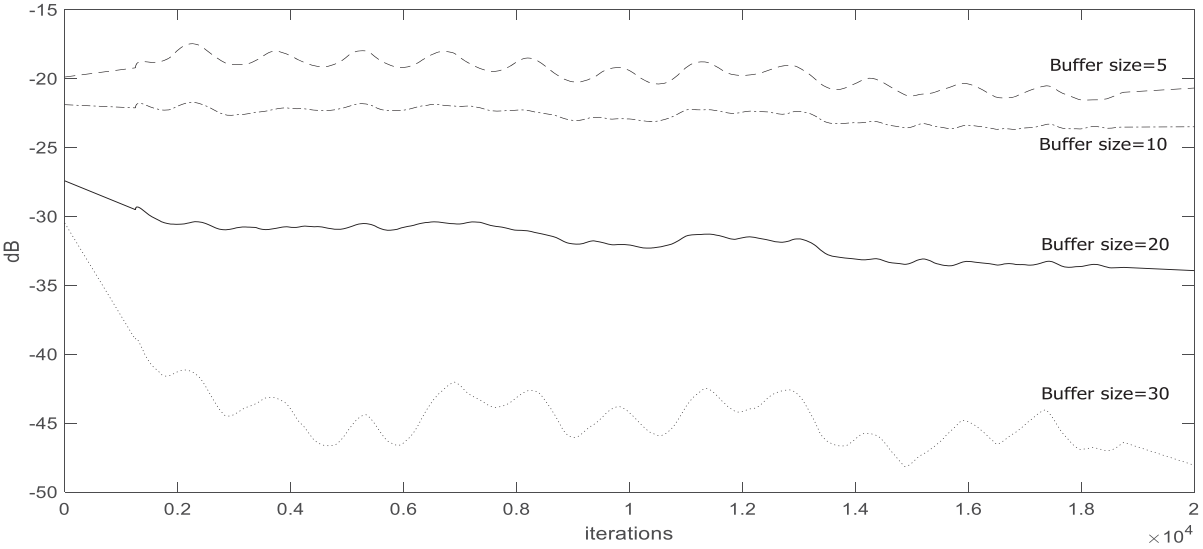

Figure 13: Comparison of convergence characteristics (MSE) obtained for different buffer sizes *BS* and TFLN order *ORD*=2, and μ_t=0.001.

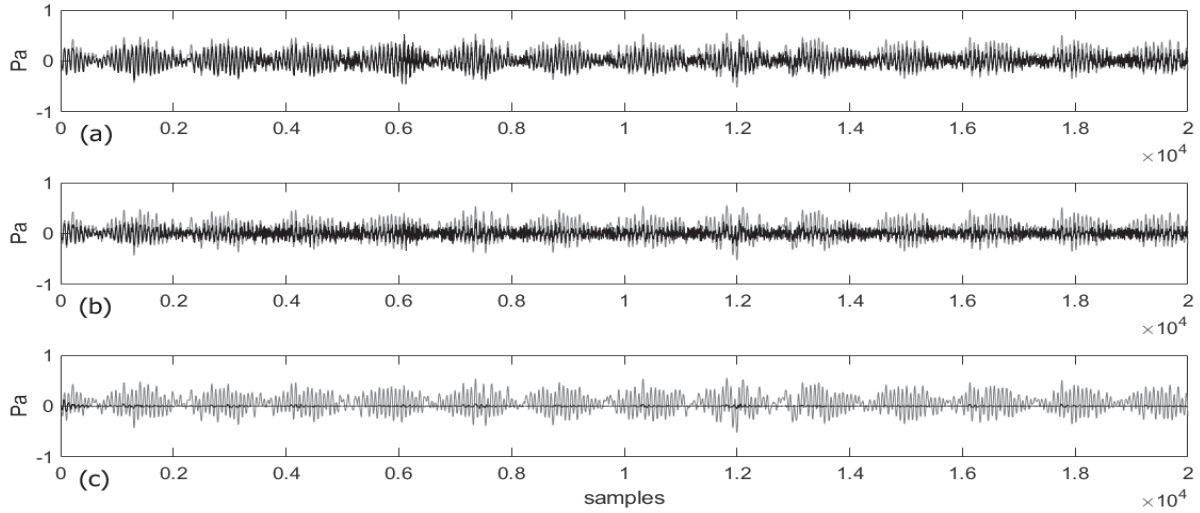

Figure 14: Error (black) and desired (gray) signals for buffer size *BS* (a) 5, (b) 10 and (c) 30 (*ORD*=2 and μ_t=0.001).

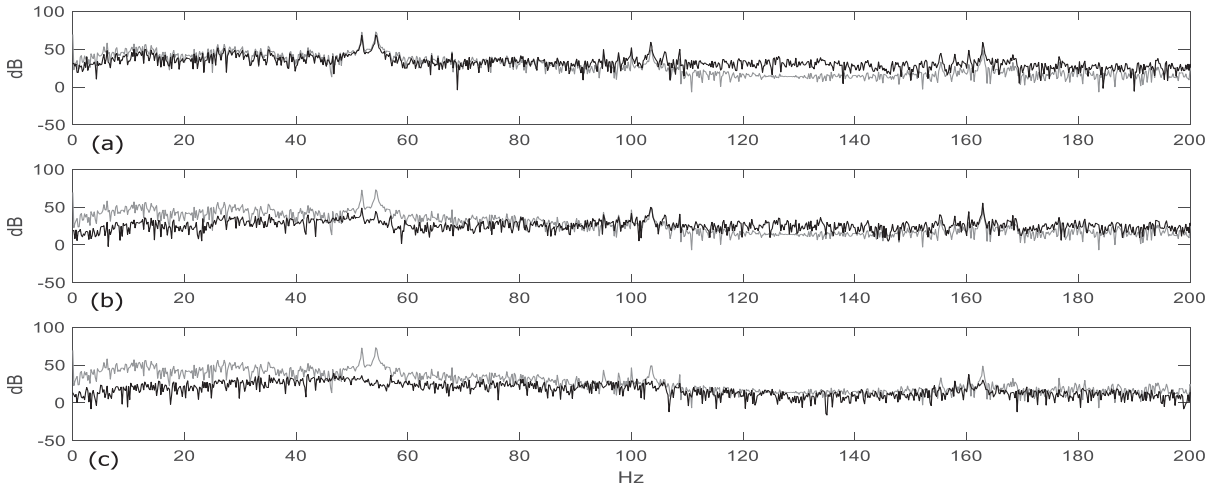

Figure 15: Spectrums of error (black) and desired (gray) signals for TFLN buffer size *BS* (a) 5, (b) 20 and (c) 30 (*ORD*=2 and μ_t=0.001).

Freq. (Hz)	ANC OFF SPL (dB)	ANC ON/SPL (dB)		
		BS=5	*BS*=20	*BS*=30
f_o=52	73.33	68.41	48.81	35.98
f_1=55	75.48	68.92	44.31	25.93

Table 4: TFLN controller performance in accordance to the buffer size *BS*.

Similarly to the AEFLN controller, the order of the TFLN controller does not affect the convergence speed and performance. The following results illustrated in Figs. 11 and 12 confirm the above conclusion.

Fig. 16, shows the variations of MSE with respect to the iterations for fixed values of buffer size *BS*=2 and learning rate μ_t=0.001. As illustrated in Fig. 16, the TFLN controller performance has slight variations in accordance to the order. Also, the Figs. 17 and 18, and the Table 5 confirm the performance and convergence speed of TFLN controller with respect to *ORD*.

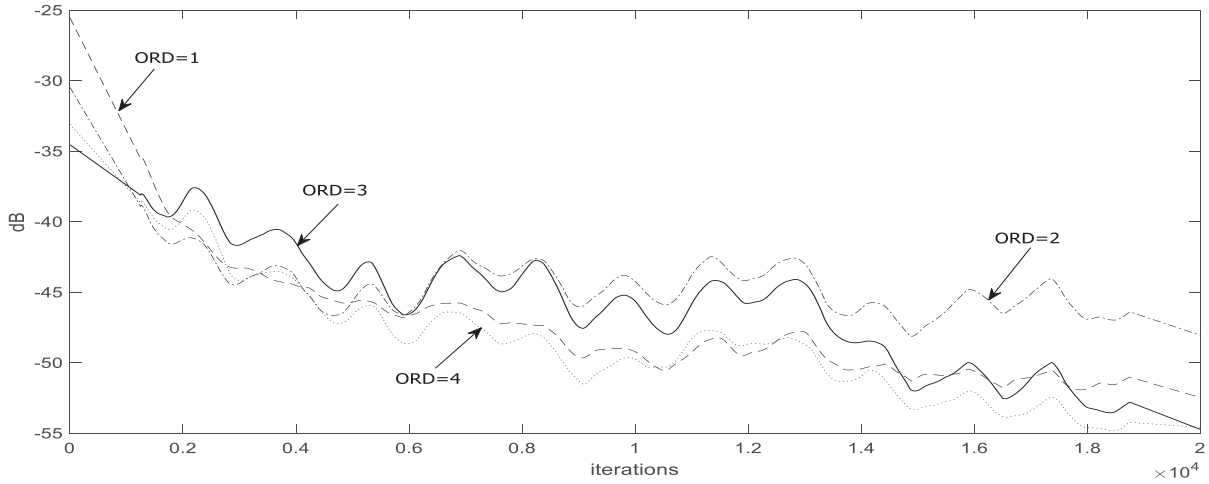

Figure 16: Comparison of convergence characteristics (MSE) obtained for different TFLN orders (μ_t=0.001 and buffer size *BS*=30).

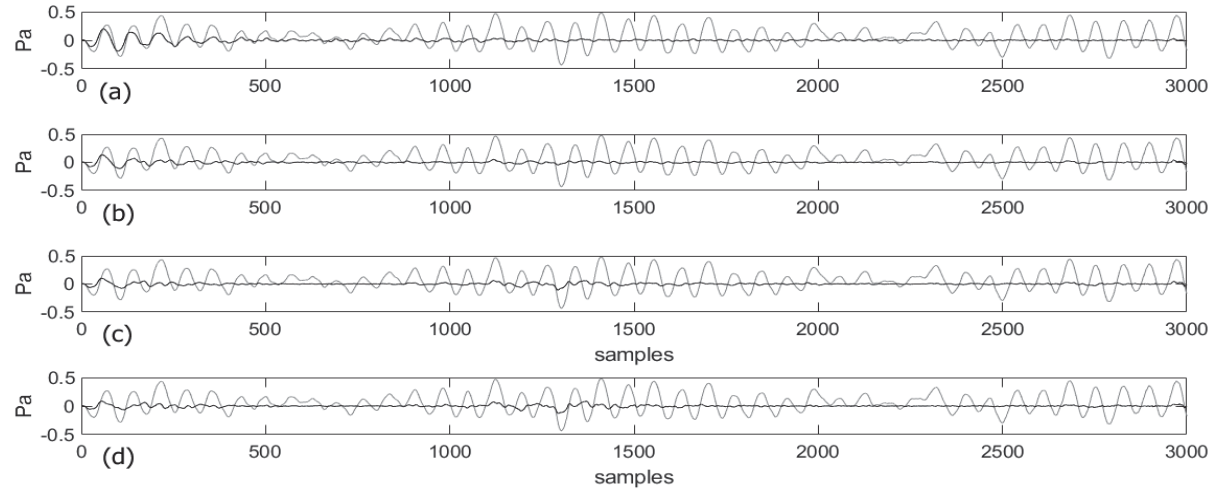

Figure 17: Error (black) and desired (gray) signals for TFLN order size (a) 1, (b) 2, (c) 3 and (d) 4 (μ_t=0.001 and *BS*=30).

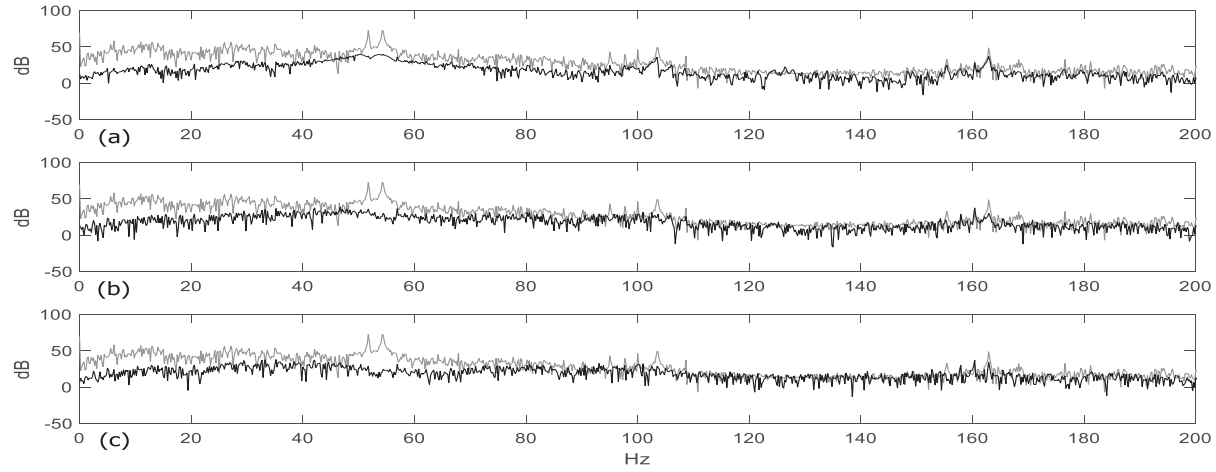

Figure 18: Spectrums of error (black) and desired (gray) signals for TFLN order size (a) 1, (b) 2 and (c) 3 (μ_t=0.001 and *BS*=30).

Freq. (Hz)	ANC OFF SPL (dB)	ANC ON/SPL (dB)		
		ORD=1	*ORD*=2	*ORD*=3
f_o=52	73.33	37.51	35.98	28.96
f_1=55	75.48	38.47	25.93	27.00

Table 5: TFLN controller performance in accordance to the order *ORD*.

Finally, the effect of the step size μ_t on the performance and the convergence behavior of the TFLN approach is studied for fixed values of order *ORD*=2 and buffer size *BS*=30.

Thus, as it is observed in Fig. 19, the MSEs computed over the last 15000 iterations are about -50, -48 and -40 dBs for μ_t 0.01, 0.001 and 0.0001, respectively. This means that the TFLN approach achieves an improved steady state MSE for μ_w close to 0.01. Also, the noise cancellation performance of TFLN controller with respect to step size μ_w is confirmed in the Table 6. As shown in Table 6, that the ANCS using μ_w =0.01 achieved up to 23 dB noise reduction at the desired 'beat' components f_o and f_1.

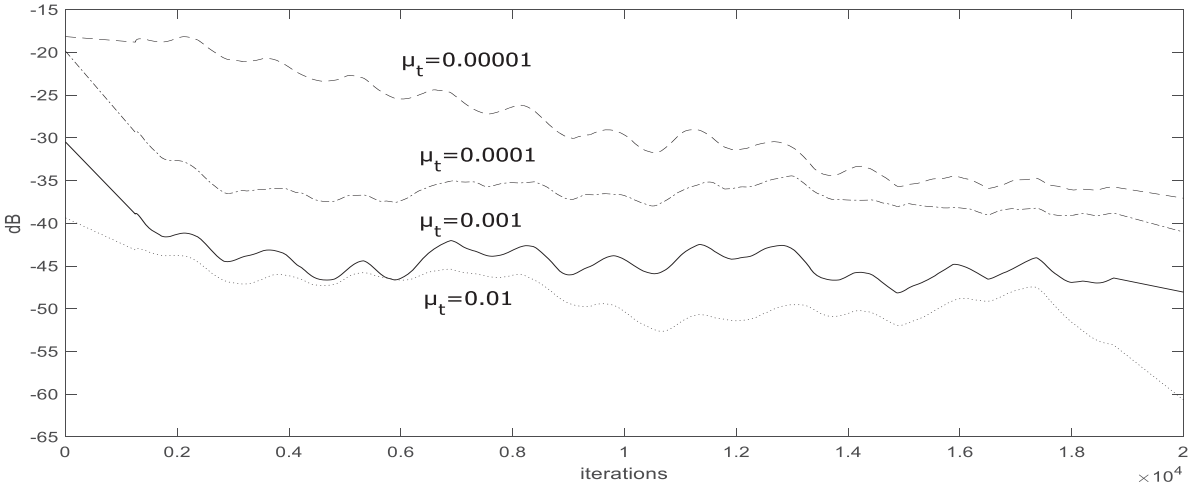

Figure 19: Comparison of convergence characteristics (MSE) obtained for different step sizes μ_t (*ORD*=2, and *BS*=30).

Freq. (Hz)	ANC OFF SPL (dB)	ANC ON/SPL (dB)		
		μ_t=0.0001	μ_t=0.001	μ_t=0.01
f_o=52	73.33	46.66	35.98	24.30
f_1=55	75.48	43.83	30.34	19.25

Table 6: TFLN controller performance in accordance to the step size μ_t.

5 CONCLUSIONS

In this paper the potential of applying a nonlinear active noise control system to reduce the levels of noise produced by two asynchronous diesel generators in the twin cabin of a luxury yacht has been investigated. It is difficult to control this using passive control treatments due to both weight and size limitations. Global active noise control is also not feasible due to the relatively wideband frequency content and the modally dense nature of the master cabin. Therefore, a practical active control system has been implemented which focuses a zone of

control at the head of the bed, where the generator noise is most disturbing when occupants are trying to sleep.

It has been shown that, due to the 'beat' components and their harmonics present in the disturbance noise spectrum, it is necessary to control multiple tones in order to achieve a significant level of narrowband attenuation. Therefore, a feedforward nonlinear control system has been investigated. It has been shown that this controller achieves significant narrowband attenuation in the sound pressure level at the error microphone located at the head of the bed. The performance, the stability as well as convergence of AEFLN and TFLN algorithms are dependent on the proper selection of the buffer size (*BS*) and the learning rates.

ACKNOWLEDGMENT

This research has been co-financed by the European Union and Greek national funds through the Operational Program Competitiveness, Entrepreneurship and Innovation, under the call RESEARCH – CREATE – INNOVATE (project code:T1EDK-3427)

REFERENCES

[1] S. Elliott, P. Nelson, I. Stothers, C. Boucher, In-flight experiments on the active control of propeller-induced cabin noise, *Journal of Sound and Vibration* 140(2), 219–38, 1990.

[2] LPR. de Oliveira, K. Janssens, P. Gajdatsy, H. Van der Auweraer, PS. Varoto, P. Sas, et al., Active sound quality control of engine induced cavity noise, *Mechanical Systems and Signal Processing* 23, 476–88, 2009.

[3] J. Cheer, SJ. Elliott, Multichannel control systems for the attenuation of interior road noise in vehicles, *Mechanical Systems and Signal Processing* 60–61, 753–769, 2015.

[4] K. Chen, R. Paurobally, J. Pan, X. Qiu, Improving active control of fan noise with automatic spectral reshaping for reference signal, *Applied Acoustics* 87, 142–152, 2015.

[5] S-P. Moon, JW. Lee, T-G. Chang, Performance analysis of an adaptive feedback active noise control based earmuffs system, *Applied Acoustics* 96, 53–60, 2015.

[6] T. Pamies, J. Romeu, M. Genesca, R. Arcos, Active control of aircraft fly-over sound transmission through an open window, *Applied Acoustics* 84, 116–121, 2014.

[7] P. Belanger, A. Berry, Y. Pasco, O. Robin, Y. St-Amant, S. Rajan, Multi-harmonic active structural acoustic control of a helicopter main transmission noise using the principal component analysis, *Applied Acoustics* 70(1), 153–164, 2009.

[8] J. Cheer, SJ. Elliott, Active noise control of a diesel generator in a luxury yacht, *Applied Acoustics* 105, 209–214, 2016.

[9] M. Wu, G. Chen, XJ. Qiu, An improved active noise control algorithm without secondary path identification based on the frequency domain subband architecture, *IEEE Transactions on Audio, Speech and Language Processing* 16(8), 1409–1419, 2008.

[10] S. Veena, SV. Narasimhan, Improved active noise control performance based on Laguerre lattice, *Signal Processing* 84(4), 695–707, 2004.

[11] SM. Kuo, DR. Morgan, Active noise control systems, algorithms and DSP implementations, *New York: Wiley*, 1996.

[12] OJ. Tobias, R. Seara, Performance comparison of the FXLMS, nonlinear FXLMS and leaky FXLMS algorithms in nonlinear active noise applications, Volume 1, 155–158: *Proceedings of the 11th European Signal Processing Conference*, 2004.

[13] NV. George, G. Panda, Advances in active noise control: a survey, with emphasis on recent nonlinear techniques, *Signal Processing* 93, 363–377, 2013.

[14] L. Lu, H. Zhao, Adaptive Volterra filter with continuous lp-norm using a logarithmic cost for nonlinear active noise control, *Journal of Sound and Vibration* 364, 14–29, 2016.

[15] Y. Pao, Adaptive Pattern Recognition and Neural Networks, Reading, *MA, USA: Addison-Wesley*, 1989.

[16] J. C. Patra, R. N. Pal, B. N. Chatterji, G. Panda, Identification of nonlinear dynamic systems using functional link artificial neural networks, *IEEE Transactions on Systems, Man, and Cybernetics, Part B* 29(2), 254–262, 1999.

[17] J C. Patra, Chebyshev neural network-based model for dual-junction solar cells, *IEEE Transactions on Energy Conversion* 26(1), 132–139, 2011.

[18] D. Comminiello, M. Scarpiniti, L. A. Azpicueta-Ruiz, J. Arenas-Garcia, A. Uncini, Functional link adaptive filters for nonlinear acoustic echo cancellation, *IEEE/ACM Transactions on Audio, Speech and Language Processing* 21(7), 1502–1512, 2013.

[19] JC. Patra, AC. Kot, Nonlinear dynamic system identification using Chebyshev functional link artificial neural networks, *IEEE Transactions on Systems, Man, and Cybernetics, Part B* 32(4), 505–511, 2002.

[20] JC. Patra, PK. Meher, G. Chakraborty, Nonlinear channel equalization for wireless communication systems using Legendre neural networks, *Signal Processing* 89(11), 2251–2262, 2009.

[21] P. Vinal, G. Vaibhav, H. Shashank, VG. Nithin, Design of Adaptive Exponential Functional Link Network-Based Nonlinear Filters, *IEEE Transactions on Circuits and Systems* 63(9), 2016.

[22] J. Jensen, S. Jensen, E. Hansen, Exponential sinusoidal modeling of transitional speech segments, Volume 1, 473–476: *Proceedings of IEEE International Conference of Acoustics, Speech and Signal Processing*, 1999.

[23] J. Jensen, J. H. Hansen, Speech enhancement using a constrained iterative sinusoidal model, *IEEE Transactions on Speech and Audio Processing* 9(7), 731–740, 2001.

EURODYN 2020
XI International Conference on Structural Dynamics
M. Papadrakakis, M. Fragiadakis, C. Papadimitriou (eds.)
Athens, Greece, 23–26 November 2020

TUNING STRATEGIES AND PLACEMENTS FOR DISTRIBUTED MULTIPLE TUNED MASS DAMPERS FOR WIND-INDUCED VIBRATION CONTROL IN HIGH-RISE BUILDINGS

A. Abed[1] **and O. Moustachi**[1]

[1]Laboratory of Civil, Hydraulic and Environmental Engineering, Mohammadia School of Engineering, Mohammed V University, Rabat, Morocco.
e-mail: ahmed abed@um5.ac.ma, moustachi@emi.ac.ma

Keywords: Vibration, Control, Distributed MTMD, Wind, Differential Evolution.

Abstract. *Tuning frequency and TMD placement have a great impact of the effectiveness of a control device. A comparative study between three tuning and placement strategies for distributed multiple tuned mass dampers for vibration control in high-rise buildings was conducted. A new design approach based on Differential Evolution was introduced and used to optimize damping, stiffness and placement for a controller with known mass. The proposed approach implemented an iterative optimization of the MTMD by updating structural parameters and the tuning frequency after every iteration. The Designs produced by the three methods were evaluated. A frequency response analysis was performed, and the effectiveness of the control systems was measured through their ability to reduce average and maximum RMS and peak displacement and acceleration time responses.*

1 INTRODUCTION

With the recent advancements in construction technologies and materials, buildings are becoming taller and lighter. As such, multiple systems for mitigating the effects of earthquakes and wind induced loads were invented and developed. Since then, Tuned Mass Damper (TMD), a relatively easy to implement vibration absorber, has known a huge success and was adopted in multiple real world situations. In fact, Soong and Dargush [1] concluded that a TMD is very effective in controlling buildings with a dominant first vibration mode, which is typically the case for high-rise buildings. In a research conducted by Tsai and Lin [2], they showed that the TMD was able to reduce the effects of resonance, however, in some cases, they noticed response amplification under low frequency excitations. Furthermore, while a single TMD is able to control structural vibration, it is very sensitive to changes and identification errors in structural parameters, which can reduce its effectiveness. As a solution, Xu and Igusa [3] showed that using Mutiple TMDs (MTMD) improves the robustness of the control system, and its effectiveness in reducing structural response.

MTMD tuning and placement greatly affect their ability to control vibrations. In this regard, multiple researchers studied the effects of tuning and placement strategies of MTMDs on their effectiveness. Xu and Igusa [3] researched equally spaced MTMDs under wide-band random excitation. Bakre and Jangid [4] looked for optimal parameters of MTMD under harmonic base excitation .Elias and Matsagar [5] showed that distributed absorbers are more effective than non-distributed absorbers placed at the top floor. Moreover, they concluded that as the number of controllers increases, the difference in effectiveness increases. Moon [6] stated that the loss of effectiveness is minimal if placement is based on modal shape. As for tuning, Han and Li [7] concluded that uniformly distributed tuning frequencies produce an effective control system.

In this paper, we studied three different tuning and placement strategies for distributed MTMDs. The first strategy consisted of tuning and placing the absorbers according to natural frequencies and modal shapes. The second, used natural frequencies for tuning, and an algorithm based on differential evolution to find the optimal placement. The third and proposed strategy, relied on differential evolution [8] to tune and place the controllers. We also considered the maximum gain of the controlled building, calculated using the transfer matrix of the structure, as the cost function that is subject to minimization. We conducted a comparison between the resulting frequency response curves, and evaluated the performance of every control system using 8 different criteria.

2 FORMULATION

In this study, we considered a 76-story benchmark building with a total mass of 150,000t. The structure is sensitive to wind load since it presents an aspect ratio of height to base width of 7.3. A detailed description of the building's model was given by Yang et al. [9], where they removed rotational degrees of freedom by the means of static condensation. All data about the structure and across-wind load is available at the website [10]. The results of wind tunnel tests can be found in the paper by Samali et al. [11].

The equations of motion for the controlled structure using p controllers is written as

$$\mathbf{M}\ddot{\mathbf{X}} + \mathbf{C}\dot{\mathbf{X}} + \mathbf{k}\mathbf{X} = \mathbf{F} \tag{1}$$

where $\mathbf{M}$, $\mathbf{C}$ and $\mathbf{K}$ are the mass, damping and stiffness matrices for the controlled structure, respectively. $\ddot{\mathbf{X}}$, $\dot{\mathbf{X}}$, $\mathbf{X}$ are the acceleration, velocity and displacement vectors, respectively. $\mathbf{F}$

is the wind load vector.

$$\mathbf{M} = \begin{bmatrix} \mathbf{M_s} & 0 \\ 0 & 0 \end{bmatrix} + \sum_{i=1}^{p} m_{d,i} \mathbf{r_i} \mathbf{r_i}^T, \quad \mathbf{C} = \begin{bmatrix} \mathbf{C_s} & 0 \\ 0 & \mathbf{c_d} \end{bmatrix}, \quad \mathbf{K} = \begin{bmatrix} \mathbf{K_s} & 0 \\ 0 & \mathbf{k_d} \end{bmatrix} \tag{2}$$

where $\mathbf{M_s}$, $\mathbf{C_s}$ and $\mathbf{K_s}$ are the mass, damping and stiffness matrices of the uncontrolled structure, respectively. For $i \in \{1, 2, \ldots, p\}$, $m_{d,i}$ is the mass of the controller and $\mathbf{r_i}$ is the controller location column vector. $\mathbf{c_d}$ and $\mathbf{k_d}$ are diagonal matrices containing the dampings and stiffnesses of the controllers.

The transfer matrices for displacement $\mathbf{G_X}$ and acceleration $\mathbf{G_{\ddot{X}}}$ of the controlled system at input frequency ω can be extracted from Eq. (1) and are expressed as

$$\mathbf{G_X}(\omega) = (-\omega^2 \mathbf{M} + j\omega \mathbf{C} + \mathbf{K})^{-1} \tag{3}$$

$$\mathbf{G_{\ddot{X}}}(\omega) = -\omega^2 \left(-\omega^2 \mathbf{M} + j\omega \mathbf{C} + \mathbf{K}\right)^{-1} \tag{4}$$

where $j^2 = -1$.

The gain of the system at frequency ω is defined as the ratio of output over input, and is represented by the maximum singular value σ of the transfer matrix. The proposed approach aims to reduce the maximum system gain for all input frequencies, thus, reducing dynamical effects and structural response. Hence, the cost function f_c of the considered optimisation problem is subject to minimization and is defined as

$$f_c = \frac{\max\left\{\sigma_X \quad / \, \omega \geq 0\right\}}{\sigma_{Xo}} + \frac{\max\left\{\sigma_{\ddot{X}} \quad / \, \omega \geq 0\right\}}{\sigma_{\ddot{X}o}} \tag{5}$$

where $\sigma_X = \max\left\{\frac{\|G_X(\omega)u\|}{\|u\|} \quad / \, \|u\| \neq 0\right\}$ and $\sigma_{\ddot{X}} = \max\left\{\frac{\|G_{\ddot{X}}(\omega)u\|}{\|u\|} \quad / \, \|u\| \neq 0\right\}$. σ_{Xo} and $\sigma_{\ddot{X}o}$ are the maximum displacement and acceleration frequency responses for the uncontrolled structure.

3 METHODS

3.1 Five modes control strategy

Elias and Matsagar [5] considered the first five modes of vibrations to design the controllers, since the total modal mass contribution of the first five modes is more than 90% of the mass of the building. The first five natural frequencies of the building are 0.16, 0.77, 1.99, 3.79 and 6.40 Hz. The mass ratio of the whole control system is 0.82%, which is the optimal mass ratio for the considered structure as suggested by Patil and Jangid [12]. Elias and Matsagar used five TMDs to mitigate the effects of wind on the benchmark building, such that

$$f_i = \frac{\omega_i}{\Omega_i} = 1, \quad k_i = \frac{m}{\sum_{j=1}^{5} (1/\omega_j)^2} \quad \text{for } i \in \{1, 2, 3, 4, 5\} \tag{6}$$

where f_i, ω_i and k_i are the frequency ratio, natural frequency and stiffness of the i-th controller. Ω_i is the i-th natural frequency of the uncontrolled structure. m is the total mass of the control system.

$$m_i = \frac{k_i}{\omega_i^2}, \quad \xi_i = 0.05, \quad c_i = 2\xi_i m_i \omega_i \quad \text{for } i \in \{1, 2, 3, 4, 5\} \tag{7}$$

where m_i, ξ_i and c_i are the mass, damping ratio and damping of the i-th controller.

The controllers' placement was decided as follows: the i-th controller is placed at the floor which exhibits the highest modal shape amplitude for the i-th vibration mode without taking into account the floors where a controller is already installed. Using this rule, the first TMD was placed at the 76th floor, the second at the 75th floor, the third at the 74th floor, the fourth at the 61st floor and the fifth at the 65th floor.

3.2 Proposed approach

The proposed approach uses an evolutionary meta-heuristic search algorithm, called Differential Evolution, to optimize damping, stiffness and placement for a TMD with known mass. Differential Evolution (DE) is a meta-heuristic evolutionary algorithm for global optimization over continuous spaces proposed by Storn and Price [13]. Unlike other evolutionary algorithms, DE uses mutation as the main search mechanism and a greedy selection process to direct the search. Moreover, it employs a non-uniform crossover operation. Therefore, it can successfully find the true global optimal solution regardless of initial values [8]. DE is fast, easy to implement and uses few control parameters. Additionally, it is self-adaptive and can be used in constrained, multi-objective, continuous or discrete optimization problems [8]. With its superiority to other search algorithms, it has been successfully and widely applied in multiple engineering fields. DE has three control parameters, the population size NP, differential weight F and crossover probability CR. The population size greatly affects the search efficiency. A higher NP is recommended and should be proportional to the number of parameters to optimize. F controls new solutions generation which is based on weighted differences between two randomly selected solutions and the updated best solution. Randomizing F every iteration accelerates the convergence. CR determines, at recombination (crossover), which solution's components are more favoured, (i.e., whether more of the components of old or new solutions are kept). DE consists of three operations: mutation, recombination and selection, that are performed in succession until the stop condition is met.

The population of solutions can be represented by a set of NP vectors of size 2.

$$population = \{\mathbf{x}_1,\ \mathbf{x}_2,\ \cdots,\ \mathbf{x}_{NP}\} \tag{8}$$

where $\mathbf{x_k} = \{\xi_k,\ f_k\}$ is the state of solution k, ξ_k and f_k are the damping and frequency ratios.

For every parent vector $\mathbf{x_k}$, a solution vector $\mathbf{x_i}$ is chosen, and a mutant vector $\mathbf{v_i}$ is created by

$$\mathbf{v_i} = \mathbf{x_{best}} + F\left(\mathbf{x_{r1}} - \mathbf{x_i}\right) \tag{9}$$

where $i, r1 \in \{1, 2, \cdots, NP\}$ are randomly selected and different form each other, and $\mathbf{x_{best}}$ is the best solution found so far.

Next, a trial vector $\mathbf{u_k}$ is produced. The j-th component $u_{k,j}$ of the trial vector is selected randomly based on

$$u_{k,j} = \begin{cases} v_{i,j}, & \text{if } rnd_j \leq CR \text{ or } j = rn_i \\ x_{k,j}, & \text{if } rnd_j > CR \text{ and } j \neq rn_i \end{cases} \quad \text{for } j \in \{1,\ 2\} \tag{10}$$

where $rnd_j \in [0, 1]$ is a random number and $rn_i \in \{1,\ 2\}$ is a randomly selected.

The best possible placement for the trial vector is determined by trying all possible placement whithin the search domain. The trial vector $\mathbf{u_k}$ is then evaluated using the cost function and

compared to the parent $\mathbf{x_k}$, the best of the two is retained as an individual for the next generation, the state of the parent vector is updated.

$$\mathbf{x_k} = \text{best}(\mathbf{x_k}, \mathbf{u_k}) \tag{11}$$

The best solution is compared to the new produced vector and both optimal placement and optimal solution are updated if necessary. This process is repeated NP times. Afterwards, the convergence condition in Eq. (12) is checked, in case it is verified, the algorithm returns $\mathbf{x_{best}}$ and optimal placement, otherwise the process is run again for the new population of solutions.

After every generation, the population of solutions converges to an optimal solution, as a result, the variation and diversity in the population decreases. Therefore, the condition for convergence can be expressed as a function of the standard deviation (std) of the population, and is written

$$\frac{tol}{\text{std}(population)} \geq 1 \tag{12}$$

where tol is the maximum acceptable standard deviation for the population.

The proposed approach consists of using the described algorithm to optimize a single TMD. Structural matrices are then updated to take into account the new TMD. The new tuning frequency which corresponds to the new fundamental frequency is calculated. The floor which contains the new controller is removed form the placement search domain. Afterwards, the algorithm is used again to design the next TMD, but this time to control the system composed of the structure and the previous TMD. This process is repeated p times, until all controllers are optimized. The proposed method is illustrated in Figure 1.

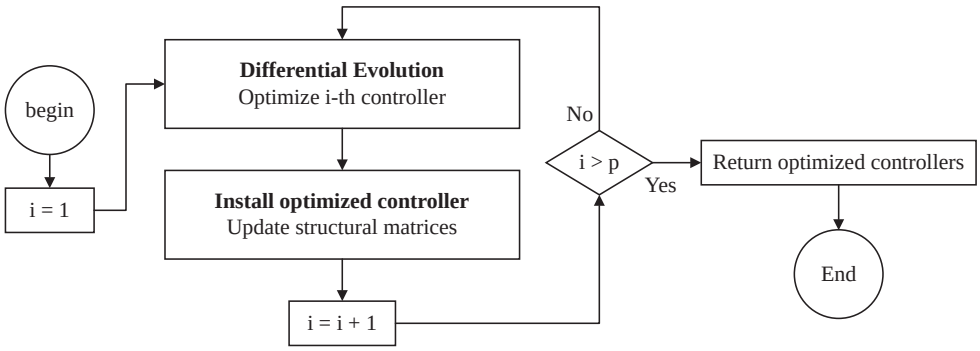

Figure 1: Proposed approach flow chart

4 RESULTS

Three tuning and placement strategies were compared. The first is the one proposed by Elias and Matsagar. The second used the controllers proposed by the first strategy, however, optimal placement was decided using the proposed algorithm. The third strategy employed our approach to optimize five controllers with equal mass considering the updated natural frequency of the building. After optimizing and installing a controller, the tuning frequency for the next controller is chosen to be the new fundamental frequency of the controlled structure using the already designed TMDs. For the second strategy, the algorithm proposed installing the controllers on the 76th, 75th, 74th, 73rd and 72nd floors. The optimized TMDs for the third strategy are shown in Table 1.

TMD	μ (%)	ξ	f	floor	ω_{tuning} (rad/s)
1	0.164	0.066	0.996	76	1.01
2	0.164	0.100	1.039	75	0.96
3	0.164	0.111	1.072	74	0.95
4	0.164	0.324	1.070	73	0.94
5	0.164	0.177	1.055	72	0.93

Table 1: Optimization results for the third strategy

Given the three proposed systems of controllers, we performed a frequency response analysis. Figures 2 and 3 show the displacement and acceleration response curves. Where ω_s is the fundamental frequency of the building.

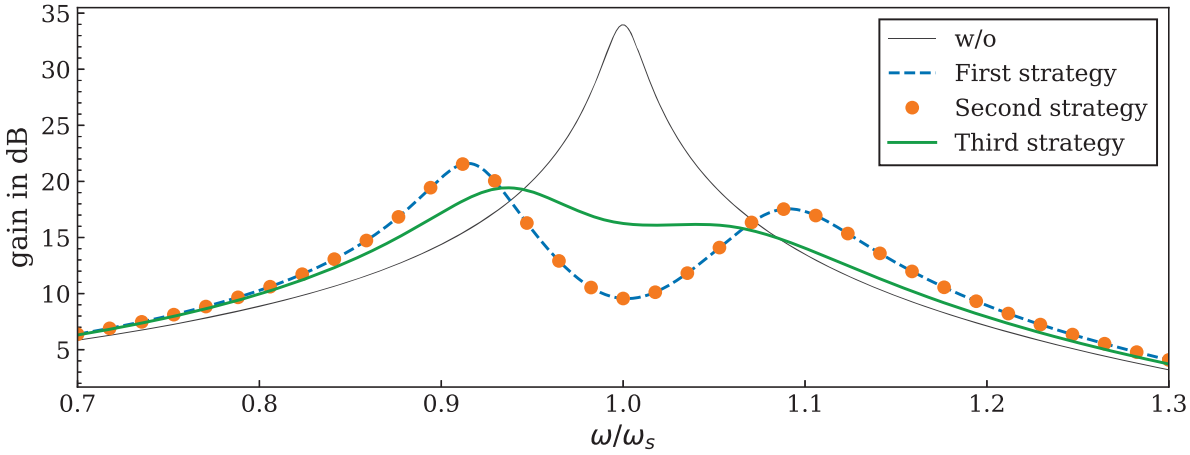

Figure 2: Displacement frequency response

For both displacement and acceleration frequency responses, the third strategy, which used our approach, was successful in reducing peak gain and also in reducing response amplification that usually occurs for low input frequencies. For the first and second strategies, although the controllers placements aren't the same, they produced the same frequency response.

In order to evaluate the performance of the proposed TMDs, Yang et al. [9] introduced 8 performance indices. The first four indices describe the controllers' ability to reduce Root Mean Square (RMS) displacement and acceleration, while the last indices four measure the reduction in peak floor displacement and acceleration.

The first index measures the reduction in maximum floor RMS acceleration and is written as

$$J_1 = \frac{\max\left(\sigma_{\ddot{X}1}, \sigma_{\ddot{X}30}, \sigma_{\ddot{X}50}, \sigma_{\ddot{X}55}, \sigma_{\ddot{X}60}, \sigma_{\ddot{X}65}, \sigma_{\ddot{X}70}, \sigma_{\ddot{X}75}\right)}{\sigma_{\ddot{X}75o}} \tag{13}$$

where $\sigma_{\ddot{X}i}$ is the RMS acceleration of the i-th floor and $\sigma_{\ddot{X}75o}$ is the RMS acceleration of the 75th without control.

The second index measures the average reduction in RMS acceleration and is defined as

$$J_2 = \frac{1}{6}\sum_i \frac{\sigma_{\ddot{X}i}}{\sigma_{\ddot{X}io}} \text{ for } i = 50,\ 55,\ 60,\ 65,\ 70,\ 75 \tag{14}$$

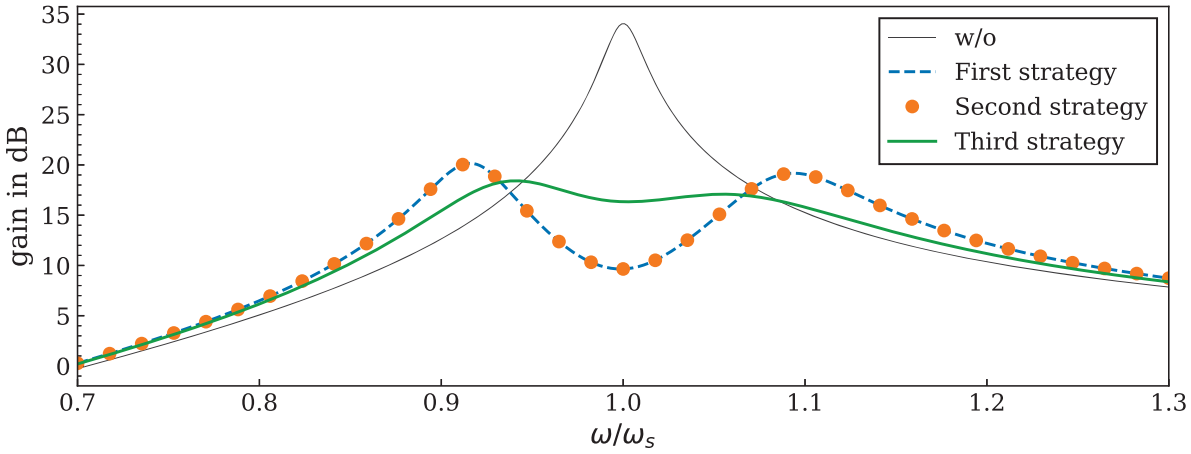

Figure 3: Acceleration frequency response

where $\sigma_{\ddot{X}io}$ is the RMS acceleration of the i-th in absence of control.

The third and fourth indices describe the reduction in maximum and average RMS floor displacement and are expressed as

$$J_3 = \frac{\sigma_{X76}}{\sigma_{X76o}} \tag{15}$$

$$J_4 = \frac{1}{7}\sum_i \frac{\sigma_{Xi}}{\sigma_{Xio}} \text{ for } i = 50,\ 55,\ 60,\ 65,\ 70,\ 75,\ 76 \tag{16}$$

where σ_{Xi} and σ_{Xio} are the RMS displacement of the i-th floor with and without control, respectively.

The last four indices are defined the same as the first ones while replacing RMS values with peak values.

$$J_7 = \frac{\max\left(\ddot{X}_{p1}, \ddot{X}_{p30}, \ddot{X}_{p50}, \ddot{X}_{p55}, \ddot{X}_{p60}, \ddot{X}_{p65}, \ddot{X}_{p70}, \ddot{X}_{p75}\right)}{\ddot{X}_{p75o}} \tag{17}$$

$$J_8 = \frac{1}{6}\sum_i \frac{\ddot{X}_{pi}}{\ddot{X}_{pio}} \text{ for } i = 50,\ 55,\ 60,\ 65,\ 70,\ 75 \tag{18}$$

$$J_9 = \frac{X_{p76}}{X_{p76o}} \tag{19}$$

$$J_{10} = \frac{1}{7}\sum_i \frac{X_{pi}}{X_{pio}} \text{ for } i = 50,\ 55,\ 60,\ 65,\ 70,\ 75,\ 76 \tag{20}$$

where $\ddot{X}_{pi}$ and $\ddot{X}_{pio}$ are the peak acceleration of the i-th floor with and without control, respectively. X_{pi} and X_{pio} are the peak displacement of the i-th floor with and without control, respectively.

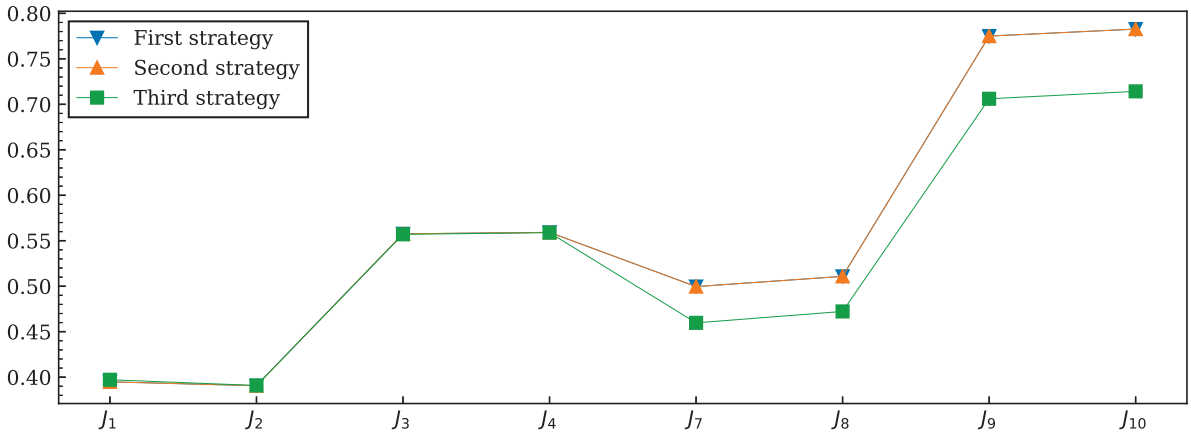

Figure 4: Performance indices

Using the generalized-α method and a time step of $1ms$, a forced time response under across-wind load was performed, and the performance indices were calculated for the three strategies. The results are shown in Figure 4.

Considering displacement and acceleration RMS reduction, indicated by the first four indices, all three strategies were able to reduce RMS response and performed equally. Looking at peak displacement and acceleration reduction, indicated by the last four indices, all three strategies succeeded in mitigating the effects of wind on the benchmark building, however, our approach produced a better reduction, especially for average and peak displacement, we noticed a bigger improvement.

5 CONCLUSION

A comparative study between tuning and placement strategies for MTMDs for the benchmark building was conducted. Tuning based on the first five vibration modes and on the updated fundamental frequency were both considered. In the first method, frequency ratio was similar between the TMDs, while in the second, TMDs shared the same mass ratio. For placements, a distributed TMD scheme was adopted. Optimal placement based on maximal modal shape was considered for the first tuning strategy. The proposed algorithm based on DE, which minimized peak displacement and acceleration frequency responses, was employed, first to find optimal placements for the previously tuned DTMDs, and second to tuned and place controllers for the second tuning strategy. Frequency response and time history analyses were conducted and the effectiveness of the designed MTMDs were compared.

First, all strategies were successful in producing an MTMD design that was effective in controlling the wind-induced vibration in the benchmark building. We observed a noticeable reduction in peak and mean RMS displacement and acceleration, and in mean and peak acceleration.

Second, while the first two strategies were different in terms of placement, the performance of the control systems were similar. This suggests that, for the first tuning strategy, MTMD placement based on modal shape is a good approximation for optimal placement for the considered cost function.

Finally, the proposed strategy improved the effectiveness of the control. Both displacement and acceleration peak frequency responses were reduced. Furthermore, while peak and mean

RMS responses were similar to the other strategies, the proposed design improved peak and mean displacement and acceleration reduction for the benchmark building. This shows that the proposed method enhanced the control effectiveness with no cost in terms of RMS response.

While the present paper compared the three control systems in terms of effectiveness in structural response reduction, it could be interesting to consider analyzing the robustness of the proposed MTMDs in comparison to other approaches.

REFERENCES

[1] T. T. Soong and G. F. Dargush, Passive energy dissipation systems in structural engineering. *Wiley*, ISBN: 9780471968214, 1997.

[2] H. C. Tsai and G. C. Lin, Explicit formulae for optimum absorber parameters for force-excited and viscously damped systems, *Journal of Sound and Vibration*, **176**, 585–596, 1994.

[3] K. Xu and T. Igusa, Dynamic characteristics of multiple substructures with closely spaced frequencies, *Earthquake Engineering & Structural Dynamics*, **21**, 1059–1070, 1992.

[4] S. V. Bakre and R. S. Jangid, Optimum multiple tuned mass dampers for base-excited damped main system, *International Journal of Structural Stability and Dynamics*, **4**, 527–542, 2004.

[5] S. Elias and V. Matsagar, Distributed Multiple Tuned Mass Dampers for Wind Vibration Response Control of High-Rise Building, *Journal of Engineering (United Kingdom)*, **2014**, 2014.

[6] K. S. Moon, Vertically distributed multiple tuned mass dampers in tall buildings: Performance analysis and preliminary design, *Structural Design of Tall and Special Buildings* , **19**, 347–366, 2010.

[7] B. Han and C. Li, Characteristics of linearly distributed parameter-based multiple-tuned mass dampers, *Structural Control and Health Monitoring*, **15**, 839–856, 2008.

[8] Karaboğa, Derviş and Selçuk Ökdem, A Simple and Global Optimization Algorithm for Engineering Problems: Differential Evolution Algorithm. *Turkish Journal of Electrical Engineering and Computer Sciences*, **12**, 53–60, 2004.

[9] J. N. Yang, A. K. Agrawal, B. Samali, and J. C. Wu, Benchmark problem for response control of wind-excited tall buildings, *Journal of Engineering Mechanics*, **130**, 437–446, 2004.

[10] SSTL, Structural Control: Benchmark Comparisons, Smart Structures Technology Laboratory, 2002.

[11] B. Samali, K. C. S. Kwok, G. S. Wood, and J. N. Yang, Wind tunnel tests for wind-excited benchmark building, *Journal of Engineering Mechanics* , **130**, 447–450, 2004.

[12] V. B. Patil and R. S. Jangid, Optimum multiple tuned mass dampers for the wind excited benchmark building, *Journal of Civil Engineering and Management*, **17**, 540–557, 2011.

[13] Storn, Rainer and Price, Kenneth, Differential Evolution - A Simple and Efficient Heuristic for Global Optimization over Continuous Spaces, *Journal of Global Optimization*, **11**, 341–359, 1997.

EURODYN 2020
XI International Conference on Structural Dynamics
M. Papadrakakis, M. Fragiadakis, C. Papadimitriou (eds.)
Athens, Greece, 23–26 November 2020

OPTIMUM DESIGN OF A TUNED-INERTER-HYSTERETIC-DAMPER (TIHD) FOR BUILDING STRUCTURES SUBJECTED TO EARTHQUAKE BASE EXCITATIONS

Predaricka Deastra[1], David J. Wagg, [2], and Neil D. Sims[2]

[1]PhD Student, Department of Mechanical Engineering, The University of Sheffield
Sir Frederick Mappin Building, Mappin Street, Sheffield S1 3JD
e-mail: pdeastra1@sheffield.ac.uk

[2] Professor, Department of Mechanical Engineering, The University of Sheffield
Sir Frederick Mappin Building, Mappin Street, Sheffield S1 3JD
e-mail: {david.wagg,n.sims}@sheffield.ac.uk

Keywords: Tuned-inerter-hysteretic-damper, hysteretic damping, seismic response, Self-adaptive Differential Evolution (SADE) algorithm, optimisation, time domain.

Abstract. *This paper discusses optimum design approaches for a novel tuned-inerter-hysteretic-damper (TIhD) which is a passive vibration suppression device for building structures subject to earthquake base excitations. The TIhD has a linear hysteretic damping element connected in series with an inerter. This device exploits the advantage of linear hysteretic damping which can reduce the structural response amplification at frequencies above resonance, due to the frequency dependent damping. In the present study, the effectiveness of this device in reducing seismic response of building structures is assessed and the optimum tuning of the device parameters is explored. In particular, eight different earthquakes are selected for a case study. The optimum parameters of the TIhD are obtained numerically by using the Self-Adaptive Differential Evolution (SADE) algorithm. The optimisation criterion is the minimum root-mean-square (RMS) value of the top-storey displacement response of the structure. The performance of this tuning configuration is then compared to that of a classically tuned device. The tuning performance is also compared across a range of simulated earthquakes, giving new insight into the challenges of optimising inerter designs that involve hysteretic damping.*

1 INTRODUCTION

In earthquake engineering practice, the use of inerters for suppressing structural vibration due to earthquakes has received a significant attention recently. An inerter is a two terminal mechanical device that generates forces proportional to the relative acceleration between its two terminals. In most studies, the inerter is combined with a spring and dashpot to form an inerter-based-damper (IBD). Several IBD concepts have been proposed in literature. Three of the most popular ones are the tuned-inerter-damper (TID), tuned-mass-damper-inerter (TMDI) and tuned-viscous-mass-damper (TVMD).

The TID was first introduced by Lazar et al. [1] in 2014. The layout of the TID is very similar to a classical tuned mass damper (TMD), but the mass m_d is replaced by an inerter element with inertance constant b_d. It has been shown to have a similar behavior with TMD. For example, the optimum tuning of the TID shows two equal peaks in the host structure frequency response assuming harmonic case. However, the presence of an inerter makes it possible to achieve a large mass ratio with a small physical mass. Furthermore it has been proven that the optimum location of the TID in a multi-storey building structure is on the base [1]. This is another benefit of the TID compared to the TMD, whose optimum location is on the top storey of a structure.

A study to enhance the TMD performance by employing an inerter led to a concept called tuned-mass-damper-inerter (TMDI) [2]. It is basically a TMD with an inerter connected in series. The TMDI can be considered as an ideal TID with the TMDI mass element m_d representing the physical mass of the inerter. When the inerter mass is zero ($m_d = 0$), the TMDI becomes a TID.

The first IBD introduced in the literature was the TVMD [3]. It consists of a parallel connected inerter and dashpot in series with a spring. A simple design method of the TVMD for MDOF structures can be found in [4]. The TVMD proposed in [4] combines a device called viscous-mass-damper (VMD) with a chevron bracing. The VMD is a combined inerter and dashpot in parallel. The inerter is given by a flywheel driven by a ball-screw mechanism and the dashpot is given by fluid flow. Another reaslisation of the TVMD can be found in [5], where a rack-and-pinion type of inerter was combined with an viscous damper in parallel. The spring element is given by a chevron bracing.

Recently, research on the IBD has been focused on three main areas: (1) The application and optimisation of IBD for different systems and condition, for examples see [6–8]; (2) Experimental validation, for examples see [9–11]; (3) studies of the IBD considering different layout or different type of inerter, stiffness and damping, for examples see [12–15]. From these three areas of research, one common discussion is about the IBD optimisation. Mostly, the optimisations of the IBD are based on the fixed-point theory (FPT) of Den Hartog [16]. However this is limited to the harmonic excitation case. For random and nonstationary signals such as earthquakes, often numerical approaches are used, for example see [8].

In this paper, an optimisation of a novel tuned-inerter-hysteretic-damper (TIhD) is discussed. The TIhD is the case when a material damper is connected in series with an inerter. In this case the material damper is represented by a linear hysteretic damping or complex stiffness. An extensive discussion about this concept has been discussed by the authors in a separate paper [17]. In the present work, a particular emphasis is given to the TIhD optimisation for building structures subject to earthquake base excitations. Specifically, a self-adaptive-differential-evolution (SADE) algorithm [18] is used to obtain the TIhD optimum parameters.

2 STRUCTURAL SYSTEM

To assess the structural performance with an optimized TIhD, a SDOF structure is selected as shown in Figure 1. Here m and k are the structural mass and stiffness respectively, and b_d is the

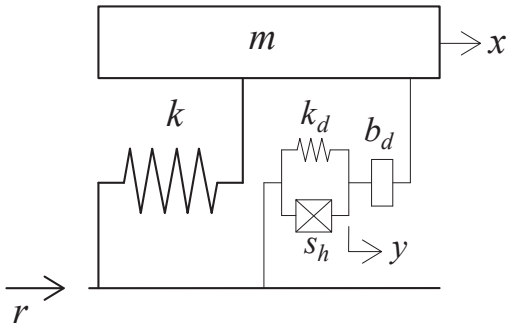

Figure 1: SDOF structure with a TIhD

TIhD inertance. For a numerical example in this paper, m and k are assumed to be 1tonne and 10kN/m. The hysteretic damping of the TIhD is represented by a complex stiffness $k_d(1+j\eta)$, where $j=\sqrt{-1}$. k_d and s_h are the real and imaginary stiffness terms so that the loss factor is $\eta = s_h/k_d$. The structure is subjected to earthquake base displacement $r(t)$. The equation of motion of the structure is given by

$$\begin{cases} m\ddot{x}(t) + k(x(t)-r(t)) + b_d(\ddot{x}(t)-\ddot{y}(t)) = 0 \\ b_d(\ddot{x}(t)-\ddot{y}(t)) = k_d(1+j\eta)(y(t)-r(t)) \end{cases} \tag{1}$$

where $x(t)$ and $y(t)$ are the displacement response of the lumped mass, m, and the TIhD displacement repectively.

It is important to note that the complex stiffness $k_d(1+j\eta)$ is a noncausal model meaning physically it is not realisable. However, this model has been widely accepted in analysis [19] to accurately represent a class of nonlinear damping [20], as well as the phenomena of energy dissipation in a variety of materials such as rubber and viscoelastic polymers [21–24]. Due to its noncausality, it is common in practice to simplify the damping as a viscous damping via an equivalent viscous damping. This is in fact not accurate, especially at frequencies away from the resonance. Therefore a special time domain method is required to analyze such structure in the time domain as has been extensively discussed by the authors in [17].

3 OPTIMISATION PROCEDURE

In this paper, the time domain technique was adopted to optimize the TIhD parameters for a seismic application. Firstly, the TIhD was optimized based on an extended FPT adopted from Hu et al. [25] with an additional fine tuning procedure as discussed in [17]. For a given mass ratio, $\mu = \frac{b_d}{m} = 0.9$, the result is shown in Figure 2. In earthquake engineering practice this approach is not appropriate due to the broad band nature of the earthquakes, but it is often used for a preliminary design due to its simplicity.

Secondly, a SADE algorithm [18] was adopted to find the TIhD optimum parameters for some different earthquakes. The objective function is the minimum root-mean-square (RMS) value of the structural response $x(t)$. For one specific earthquake it is expressed by

$$\begin{gathered} b_{d_{min}} \le b_d \le b_{d_{max}}; k_{d_{min}} \le k_d \le k_{d_{max}}; \eta_{min} \le \eta \le \eta_{max} \\ min|\text{RMS}(x(t))| \end{gathered} \tag{2}$$

It is important to set a feasible limitation for b_d, k_d and η as shown in Eq.2 to reduce the computational cost. In this study, the limitations are $0.1 \leq b_d \leq 0.9; 0.1 \leq k_d \leq 10; 0.1 \leq \eta \leq 2$. Another important note is that the use of the SADE algorithm to obtain the RMS value of the structural response requires a time domain analysis. In this case, it has been made possible because of the time domain analysis proposed by the authors [17] for structures with linear hysteretic damping.

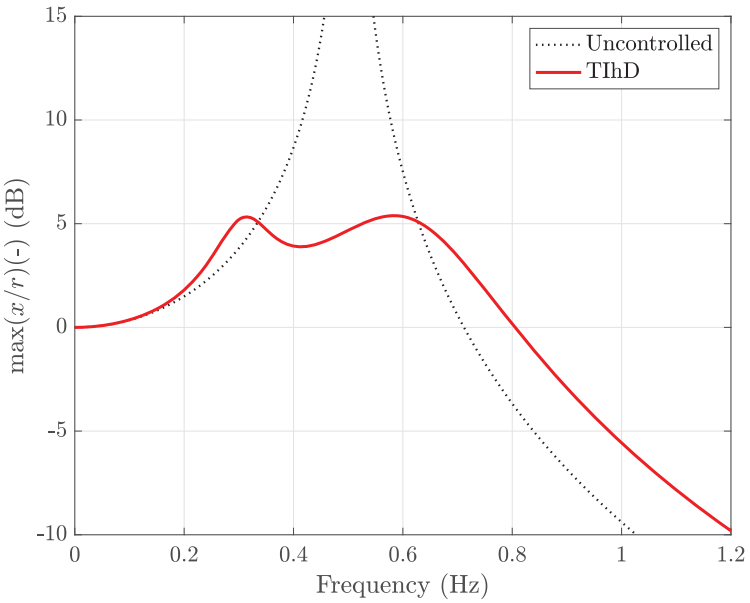

Figure 2: Maximum absolute displacement for $\mu = 0.9$, $k_d = 3.47$kN/m and $\eta = 1.26$

4 RESULTS AND DISCUSSION

In order to asses the effectiveness of the SADE algorithm against the FPT for minimizing a structural response subject to seismic excitations, eight different earthquakes were selected as shown in Figure 3.

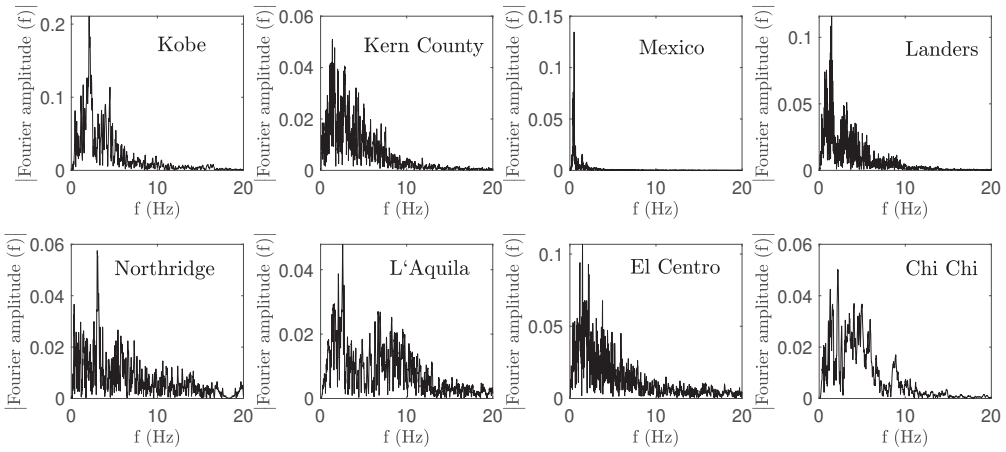

Figure 3: Fourier spectrum of the considered earthquakes ground motion

Figure 4 shows the RMS of the structural displacement response comparison between the

optimised TIhD obtained by the FPT and by the SADE algorithm given by the Eq. 2. In this Figure, the RMS value of each earthquake is normalised against the RMS value from the FPT which is set to 100%. It is obvious that the SADE algorithm gives better reduction of the RMS value for all of the selected earthquakes. This is however not a practical solution because it leads to many inertance-stiffness-loss factor (ISL) configurations as shown in Table 1. For a realistic implementation, one configuration must be chosen, without prior knowledge of the specific earthquake excitation.

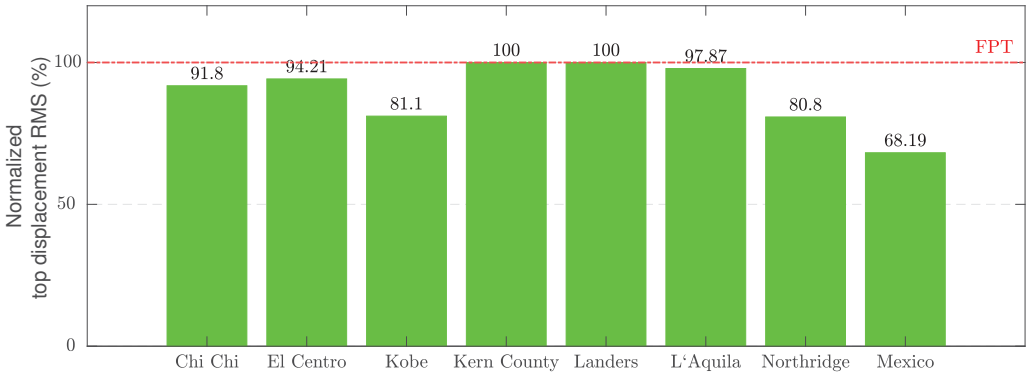

Figure 4: Normalised root mean square of the structural displacement response, SADE - Eq. 2

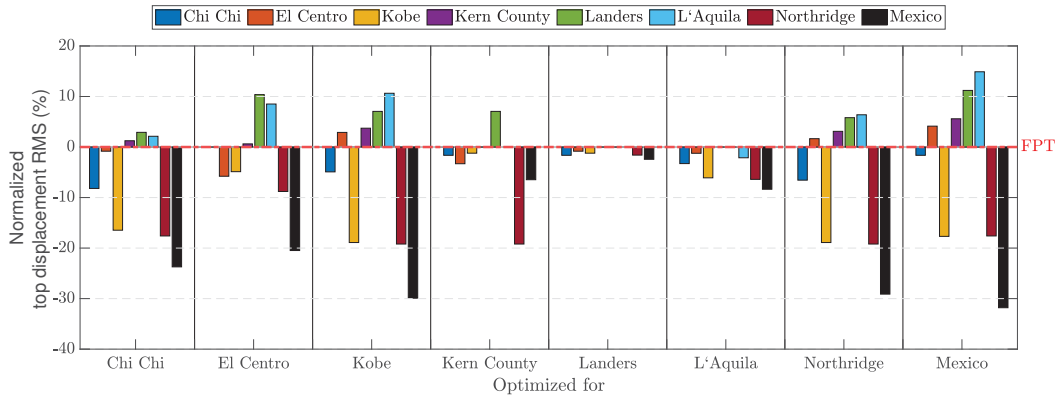

Figure 5: Cross-optimisation, SADE - Eq. 2

Figure 5 shows a cross-optimisation, meaning one configuration was selected from one particular earthquake to be used for simulation of other earthquake cases. For example, the first group of bars shows the structural response subjected to the eight considered earthquakes using one ISL configuration optimized for Chi Chi earthquake. The structural performance is being compared with the FPT which is set to 0%. Hence any negative values means a reduction on the structural response, on the other hand, any positive values means an amplification on the structural response relative to the FPT. For example, the group of bars for Landers implies that using one ISL configuration optimised for Landers earthquake for all other considered earthquakes makes the structural performance better than the one obtained via the FPT.

The group of bars for L'Aquila and Landers in Figure 5 in this case are the best result of this cross-optimisation since all other groups of bars show both positive and negative values. This

simulation also implies that a correct formulation to chose or obtain the best ISL configuration is required. For this reason, a method that is based on the SADE algorithm was developed to find the best ISL configuration that gives minimum average RMS values of the structural performance subjected to a number of ground motions. It is expressed as

$$b_{d_{min}} \leq b_d \leq b_{d_{max}}; k_{d_{min}} \leq k_d \leq k_{d_{max}}; \eta_{min} \leq \eta \leq \eta_{max}$$
$$min \left| \frac{\sum_{i=1}^{n} \text{RMS}(x_i(t))}{n} \right| \tag{3}$$

where n is the number of considered earthquake input signals.

Figure 6 shows the structural performance comparison between the two approaches against the FPT. The second approach is (although not strictly better than the first approach) almost as good and clearly still superior than the FPT. It is in fact is more practical than the first approach because, as shown in Table 1, it has only one ISL configuration as in the case of the FPT. Two

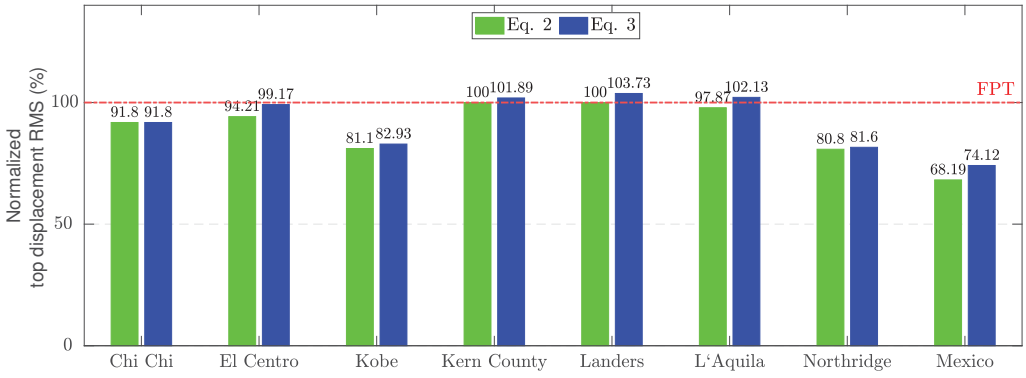

Figure 6: Normalised root mean square of the structural displacement response, SADE - Eq. 2 and 3

.

examples of the displacement response time history of the considered structure are given in Figure 7.

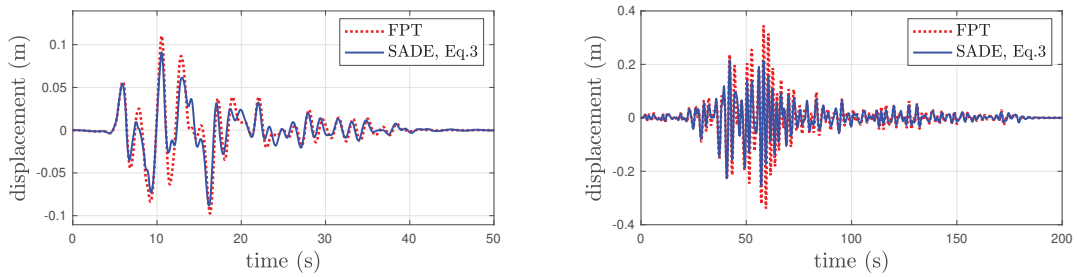

Figure 7: Examples of time history displacement response of the considered structure subjected to displacement ground motions (a) Kobe (b) Mexico

.

Table 1: TIhD optimum parameters

Earthquake	Fixed-point-theory (FPT)			SADE - Eq. 2			SADE - Eq. 3		
	b_d (Tonne)	k_d (kN/m)	η	b_d (Tonne)	k_d (kN/m)	η	b_d (Tonne)	k_d (kN/m)	η
Chi Chi	0.9	3.47	1.26	0.9	6.58	0.71	0.9	6.88	0.63
El-Centro				0.9	5.66	0.42			
Kobe				0.9	8.01	0.50			
Kern County				0.9	4.22	0.80			
Landers				0.9	3.71	1.14			
L'Aquila				0.9	4.30	1.06			
Northridge				0.9	7.68	0.54			
Mexico				0.9	8.16	0.39			

5 CONCLUSION

This paper presents the optimum design of the TIhD for long-period structures subjected to seismic ground motions. The optimisation method is based on the combined SADE algorithm and the time domain method for the TIhD to obtain the best ISL configuration of the TIhD.

There are two approaches presented in this study. The first approach is to find the minimum RMS value of the structural response for each of the considered earthquakes. Although the results show a superior benefit compared to the fixed point theory, it is however not practical because there is one ISL configuration obtained for one specific earthquake. As a result, there are many ISL configurations obtained depending on the number of the considered earthquake. The second approach is to find the best ISL configuration that gives minimum average RMS value of the structural response for all of the considered earthquakes. The second approach is considered to be a more practical solution and can be directly compared to the fixed point theory.

It has been shown that numerically optimised designs of TIhD can outperform those design using the classical fixed point theory. This is because the numerical method accommodates frequency independency, relying on a recently developed time-domain solution algorithm for hysteretic damping [17]. However this obviously requires a priori knowledge of the seismic excitation. Consequently further work should extend this approach to consider more formal earthquake design methodologies as part of the time-domain optimisation.

6 ACKNOWLEDGEMENT

PD would like to acknowledge the funding support from Indonesia Endowment Fund For Eduction (LPDP).

REFERENCES

[1] I.F. Lazar, S.A. Neild, D.J. Wagg, Using an inerter-based device for structural vibration suppression, *Earthquake Engineering & Structural Dynamics*, **43**,1129–1147, 2014.

[2] L. Marian, A. Giaralis, Optimal design of a novel tuned mass-damper-inerter (TMDI) passive vibration control configuration for stochastically support-excited structural systems,

Probabilistic Engineering Mechanics, **38**,156–164, 2014.

[3] K. Saito, Y. Sugimura, S. Nakaminami, H. Kida, N Inoue, *Vibration Tests of 1-story Response Control System Using Inertial Mass and Optimized Soft Spring and Viscous Element. Proceedings of the 14th World Conference on Earthquake Engineering*, 2008.

[4] K. Ikago, Y. Sugimura, K. Saito, N Inoue, *Simple Design Method for a Tuned Viscous Mass Damper Seismic Control System. Proceedings of the 15th World Conference on Earthquake Engineering*, 2012.

[5] R.M. Hessabi, O. Mercan, Investigations of the application of gyro-mass dampers with various types of supplemental dampers for vibration control of building structures, *Engineering Structures*, **126**,174–186, 2016.

[6] A. Di Matteo, C. Masnata, A. Pirrotta, Simplified analytical solution for the optimal design of Tuned Mass Damper Inerter for base isolated structures, *Mechanical Systems and Signal Processing*, **134**,106337, 2019.

[7] Z Zhao, Q. Chen, R. Zhang, C. Pan, Y. Jiang, Optimal design of an inerter isolation system considering the soil condition, *Engineering Structures*, **196**,109324, 2019.

[8] D. De Domenico, P. Deastra, G. Ricciardi, N.D. Sims, D.J. Wagg, Novel fluid inerter based tuned mass dampers for optimised structural control of base-isolated buildings, *Journal of the Franklin Institute*, **356**,7626–7649, 2019.

[9] X. Liu, B. Titurus, J.Z. Jiang, Generalisable model development for fluid-inerter integrated damping devices, *Mechanism and Machine Theory*, **137**,1–22, 2019.

[10] E.D.A John, D.J. Wagg, Design and testing of a frictionless mechanical inerter device using living-hinges, *Journal of the Franklin Institute*, **356**,7650–7668, 2019.

[11] C. Málaga-Chuquitaype, C. Menendez-Vicente, R. Thiers-Moggia, Experimental and numerical assessment of the seismic response of steel structures with clutched inerters, *Soil Dynamics and Earthquake Engineering*, **121**,200–211, 2019.

[12] S. Zhou, C. Jean-Mistral, S. Chesne, Influence of inerters on the vibration control effect of series double tuned mass dampers: Two layouts and analytical study, *Structural Control & Health Monitoring*, **26**,e2414, 2019.

[13] A. Javidialesaadi, N.E. Wierschem, Optimal design of rotational inertial double tuned mass dampers under random excitation, *Engineering Structures*, **165**,412-421, 2018.

[14] X. Shi, S. Zhu, A comparative study of vibration isolation performance using negative stiffness and inerter dampers, *Journal of the Franklin Institute*, **356**,7922-7946, 2019.

[15] Z. Zhao, R. Zhang, Y. Jiang, C. Pan, A tuned liquid inerter system for vibration control, *International Journal of Mechanical Sciences*, **164**,105171, 2019.

[16] J.P. Den Hartog, (1956) Mechanical Vibrations (4th edition), Dover: New York.

[17] P. Deastra, D.J. Wagg, N.D. Sims, M. Akbar, Tuned-inerter-dampers with linear hysteretic damping. (*under review*).

[18] A.K. Qin, P.N. Suganthan, *Self-adaptive Differential Evolution Algorithm for Numerical Optimization, 2005 IEEE Congress on Evolutionary Computation,* **2**, 1785–1791, 2005.

[19] C.F. Beards, (1996) Structural Vibration: Analysis and Damping, Halsted Press: New York-Toronto.

[20] J.A. Inaudi, M. Kelly, A friction mass damper for vibration control, *Report No. UCB/EERC-92/18, Earthquake Engineering Research Center, University of California at Berkeley, 1992*.

[21] R.M. Joseph, A.B. Kirsten, C.P. Scott, *Complex stiffness measurement of vibration damped structural elements. Proceedings of the International Modal Analysis Conference, Vol. 1, p. 391-397.*, 2000.

[22] D.R. Mohan, G. Scott, G. Dave, *Measurement of dynamic parameters of automotive exhaust hangers. SAE Technical Papers, Noise and Vibration Conference and Exposition, Vol. 1, p. 1-8.*, 2001.

[23] B. Bloss, D.R. Mohan, Measurement of damping in structures by the power input method, *Experimental Techniques*, **26**, Issue 3, 30–32, 2002.

[24] E.O. Lu, M.R. Zaidi, Dynamic stiffness and loss factor measurement of engine rubber mount by impact test, *Materials and Design*, **32**, 1880–1887, 2011.

[25] Y. Hu, M.Z.Q Chen, Z. Shu, L. Huang, Analysis and optimisation for inerter-based isolators via fixed-point theory and algebraic solution, *Journal of Sound and Vibration*, **346**,17–36, 2015.

EURODYN 2020
XI International Conference on Structural Dynamics
M. Papadrakakis, M. Fragiadakis, C. Papadimitriou (eds.)
Athens, Greece, 23–26 November 2020

RESPONSE CONTROL OF BUILDINGS USING TMDI UNDER WIND AND EARTHQUAKES

Said Elias[1], Rajesh Rupakhety[2], and Simon Olafsson[2]

[1] Post PhD Scholar at Earthquake Engineering Research Centre, Faculty of Civil and Environmental Engineering, School of Engineering and Natural Sciences, University of Iceland,
Austurvegur 2a, 800 Selfoss, Iceland
e-mail: said@hi.is

[2] Professor at Earthquake Engineering Research Centre, Faculty of Civil and Environmental Engineering, School of Engineering and Natural Sciences, University of Iceland,
Austurvegur 2a, 800 Selfoss, Iceland
{rajesh,simon}@hi.is

Keywords: Earthquake, High-rise building, TMDi, Wind forces

Abstract. The objective of this article is to investigate vibration mitigation technique of a reinforced concrete (RC) building subjected to wind or earthquake ground motion. Numerical analysis of a RC building controlled by inerter tuned mass damper (TMDi) is conducted under independent action of wind forces and earthquake ground motion. The performance of the control devices is evaluated in terms of reduction in response parameters such as floor acceleration and displacements. The results show that vibration mitigation achieved from the TMDi system employed in the RC building varies significantly with the type of excitation. Nevertheless, the TMDi system is found to be more reliable than a TMD system.

1 INTRODUCTION

Tall buildings are exposed to natural hazards such as wind and earthquakes during their lifetime. Tuned mass damper (TMD) is commonly recommended for vibration control of tall structures [1-8]. A detailed literature survey is presented by Elias and Matsagar [9]. It is well-established that heavier TMDs are more effective than lighter ones. However, heavier TMDs are not practically efficient as they exert additional loads on the floors they are placed on. Dividing the total mass of the TMD and distributing over different floors is an option to reduce excessive loads on a single floor [10-16]. The other attractive solution is use of inerters combined with a TMD (TMDi) [17-22]. Inerters can generate very large inertial force with very small physical mass. The application of TMD and TMDi on base-isolated (BI) structures have been reported in the literature [23-29]. Such control strategies often consider a single type of hazard, often seismic ground motion or wind action, and studies covering multiple hazards are limited in the literature. Some studies have addressed multi hazard issues in structural vibration control [30-35]. Recently, Elias et al. [36] reported the performance of TMDs in response control of a tall building subjected to wind and earthquakes. They showed that a system designed for earthquakes may not be as effective for wind forces. They also proposed a solution that is optimal considering both the hazards. This study extends the work of Elias et al. [36] to TMDi devices.

2 MATHIMATICAL MODELLING

The building considered in this study is a 76-story benchmark building, which is very sensitive to wind [36-38]. Detailed information of the building can be found elsewhere [38]. Figure 1 shows the schematic models of the benchmark building equipped by a) TMD and b) TMDi. The optimum frequency and damping ratio of the TMD is calculated from the formulation given in Sadek et al. [39], whereas the optimal frequency and damping ratio of TMDi is based on formulations given in Giaralis and Petrini [18]. By assuming a mass (m_1) for TMD, its stiffness (k_1) and damping (c_1) are calculated from the optimal frequency of the TMD which is tuned to the first mode of vibration of the building. The physical mass of the TMDi is the same as that of the TMD. The TMDi contains an additional inertial device, an inerter, whose inertance is denoted by b. The stiffness (k_{TMDi}) and damping (c_{TMDi}) are estimated from the optimal tuning frequency. The position of the inerter is varied in different floors to find its optimal location. Many studies report benefits of attaching the inerters to the lower floors, however, a thorough study about the optimal placement of inerters is lacking in the literature. Three different models are created: uncontrolled (NC), controlled with TMD (TMD), and controlled with TMDi (TMDi). The models are subjected to wind and earthquake forces. I

3 NEWMERICAL STUDY

The building in this study has a height of 306.1 m and width of 40 m, and this ratio is 7.6525>5. This confirms that the building is wind sensitive. It is assumed that the building lies in a seismic area and might experience strong ground shaking. Wind forces are by varied by using mean velocity at the top of the building from 14 m/sec to 66 m/sec by an incremental value of 1 m/sec. A set of 100 ground motions used by Saha et al. [40] are used as seismic action.

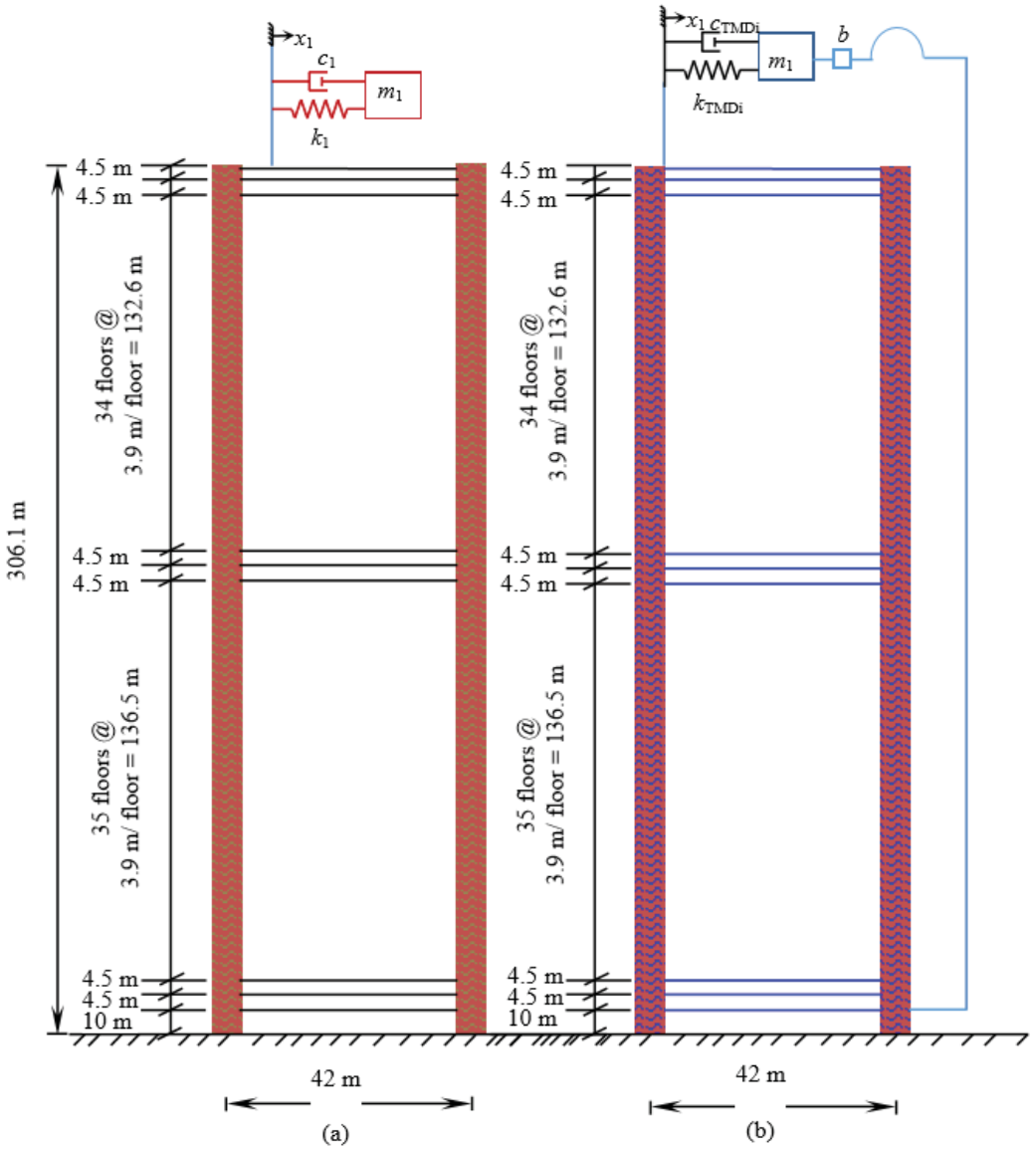

Figure 1: Schematic models of benchmark building equipped by a) TMD, b) TMDi.

In this study mass (m_1) is assumed to be 0.0082 times the total mass of the building. The corresponding value of generalized mass used in the formulation of Sadek et al. [39] is 0.01123. The b value of the inerter is assumed to be 0.3.

3.1 Optimal Placement of Inerter

Figures 2 and 3 show the response of the building equipped by a TMDi while subjected to wind and ground motions. The location of inerter is varied from first floor to the top floor under both hazards. Optimal location is identified based on displacement response. Figure 2 shows lower floors are not necessarily the optimal location for the inerter. While the response to wind forces seems relatively independent of the inerter location for low wind velocity, floor 65 seems to be the best location when the wind velocity is high.

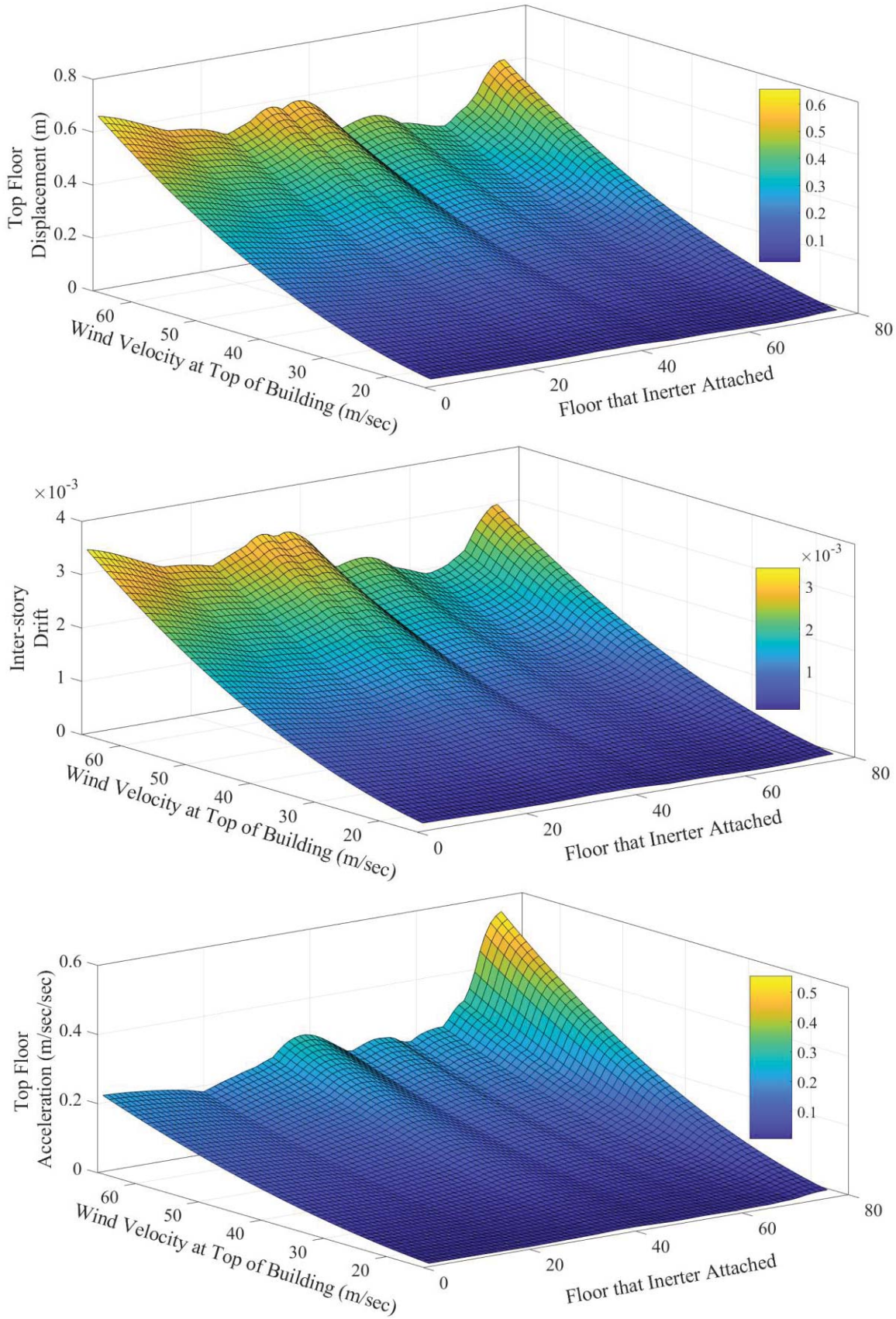

Figure 2: Response of the building equipped by a TMDi with inerter connected at different floors under wind forces.

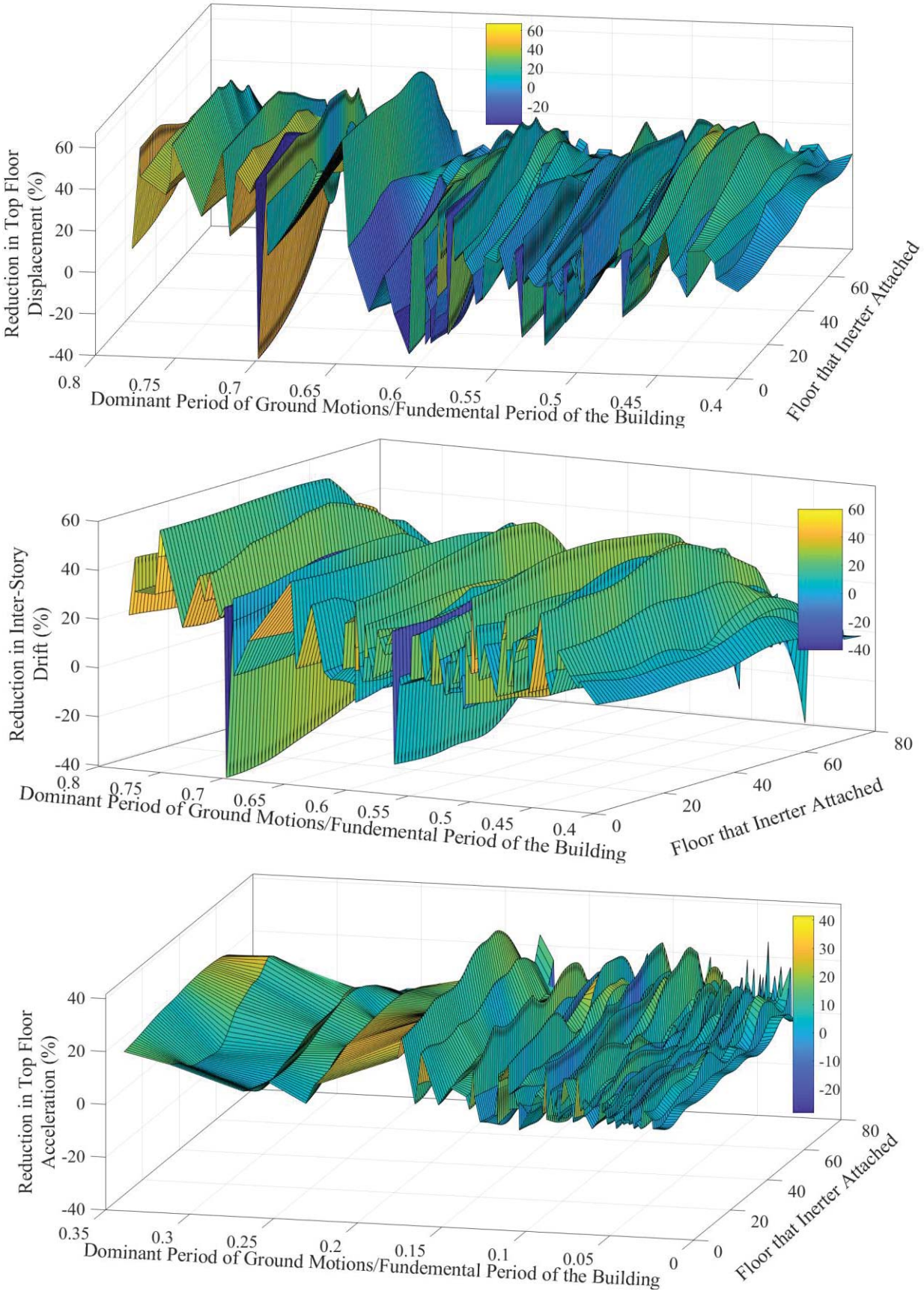

Figure 3: Response of the building equipped by a TMDi, inerter connected at different floors under earthquakes.

Optimal response in terms of interstory is attained by placing the inerter at floor number 63 and. These locations are, however, not optimal for controlling floor acceleration. Selection of the inerter floor for optimal control of floor acceleration results in poor performance in controlling displacement and interstory drift. It therefore seems that the optimal location depends on the response parameter being controlled. In this study, floor number 65 is selected as the best location. Figure 3 shows that the performance of the device is greatly variable depending on the frequency content of ground motion (measured by its dominant period) and the location of the inerter. For a given ground motion, the response is fairly independent of the location of the inerter. However, the optimal location of the inerter is highly dependent on the ground motion. By maximizing the average displacement reduction across all the ground motions, floor 45 is selected as the optimal position in this study. It is, however, important to note that the designer/analyst might choose other criteria for such optimization. Other options such as optimization for the worst-case ground motion, or scenario hazard at a given site might be selected based on the performance requirements of the building. Comparative study between TMD and TMDi

In this section the performance of the TMD and TMDi are compared. Figure 4 shows the response of the NC and building equipped with a TMD and TMDi to winds of different velocities. The peak response corresponding to the largest wind velocity and different locations of the inerters is shown in the inset plots. The response shown in the main plots correspond to the inerter device connected at floor 65. It is observed that the TMDIs provide slightly better response reduction that the TMDs. For the largest wind velocity considered here, which is 66 m/s, displacement response at the top of the building is reduced by 32% and 42%, respectively by the TMD and TMDI.

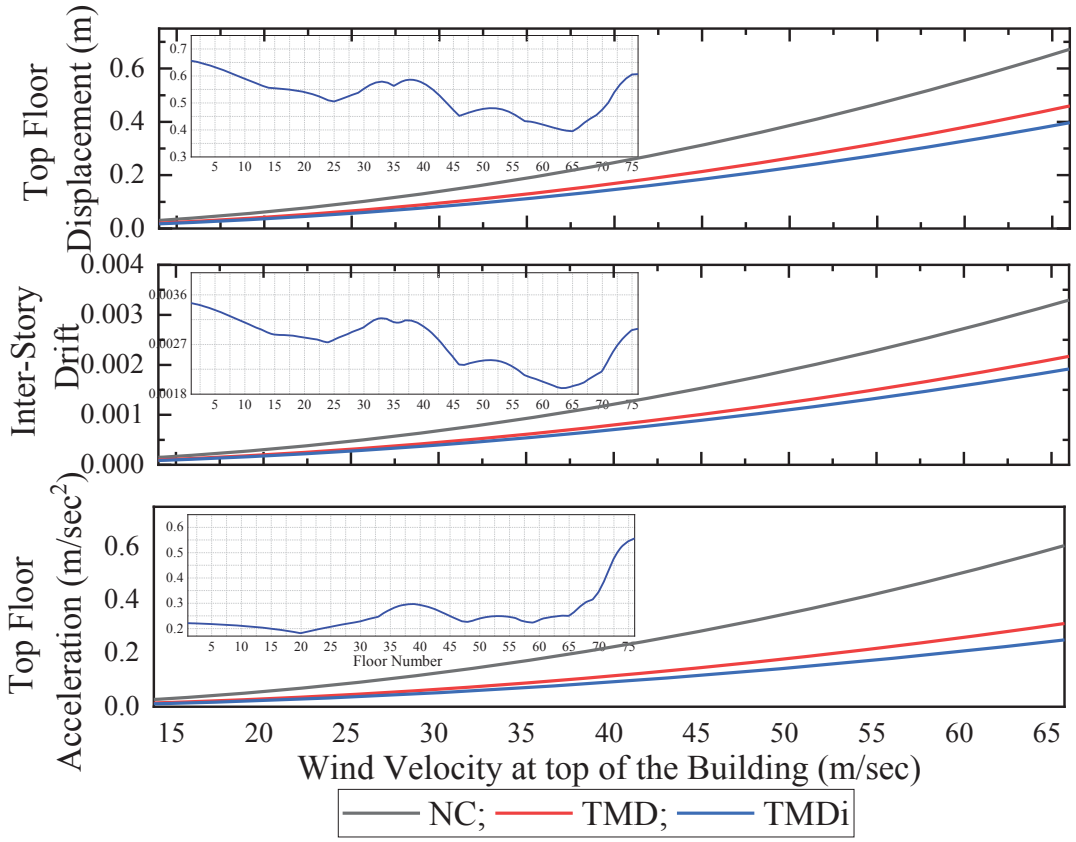

Figure 4: Response of the NC and building equipped by a TMD and TMDi, inerter connected at different floors under wind forces.

In case of earthquakes the response reduction is highly dependent on earthquake ground motion. The plots in the left panel show response reduction as a function of the ratio dominant period of ground motion to the fundamental period of the building. For each ground motion, the maximum reduction achieved by varying the location of the inerter is shown with the grey line while the blue line corresponds to the inerter placed at floor 45. The results show that the maximum reduction is not very different from the reduction obtained by placing the inerter at floor 45. It is also noticed that the TMDi provides very good response reduction while the TMDs are mostly ineffective. It is also interesting to note that the performance of the TMDi is highly dependent on the frequency content of the ground motion. The plots in the right panel of Figure 5 show the variation in response reduction with the location of inerter when subjected to the ground motion against which the TMDi is the most effective. The results show that response reduction is fairly independent of the inerter location up to floor number 55-60, but installing the inerter at higher floors reduces the effectiveness significantly. The overall results show that placement of the inerter is more critical for wind forces than seismic excitation for this building. Some practical issues for connection of inerter is provided by Giaralis and Petrini [18]. However, optimal location of the inerter and the practical difficulties associated in their installation requires further investigation.

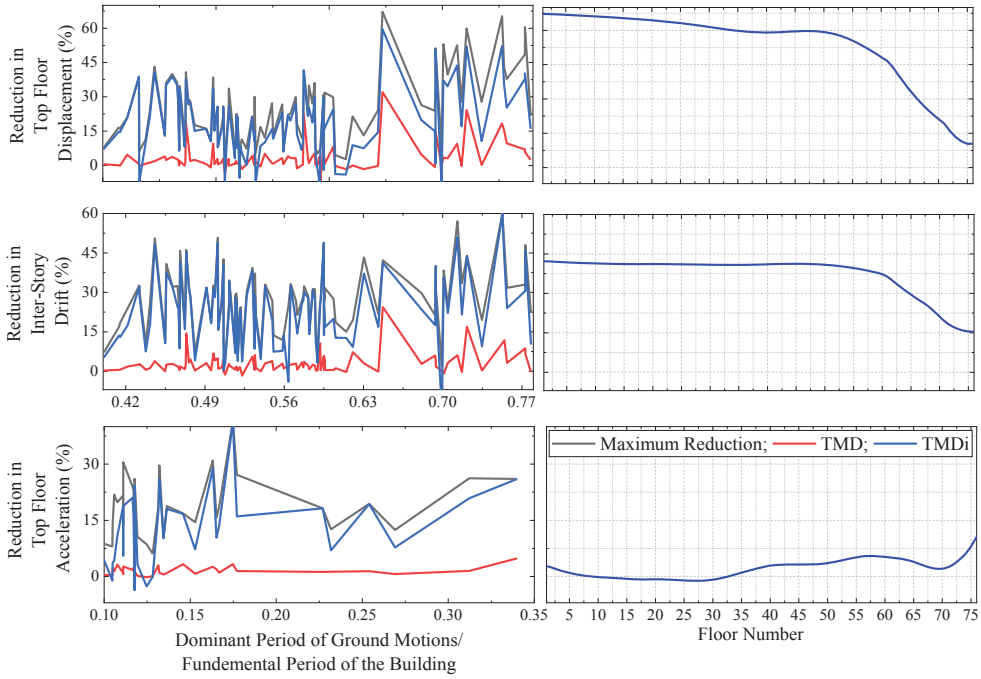

Figure 5: Response of the NC and building equipped by a TMD and TMDi, inerter connected at different floors under earthquakes.

4 CONCLUSIONS

The following conclusions can be made from the results presented in this study.

- Lower floors are not necessarily better for the location of inerter devices used to control wind-induced response of tall buildings like the one studied here. The optimal floor for the inerter depends on the response parameter to be controlled, especially when the wind velocity is high. Therefore, optimal location is expected to be structure and excitation dependent.

- The performance of TMDi when subjected to ground motion is highly dependent on the frequency content of ground motion. An optimal inerter location for one ground motion might be adverse for another ground motion. In this sense, the optimal location for seismic excitation is more critical than that for wind excitation. However, for a given ground motion, the optimal location is not very variable across the height of the building, as long as it is not near the top of the building. In this respect, optimal location of the inerter needs to consider frequency content of expected ground motion based on the site-specific seismic hazard. As the frequency content of ground motion changes with earthquake magnitude, a performance-based framework seems essential for optimizing TMDi devices for seismic response control.
- TMDIs provide much better response control seismic response of this building than TMD.
- Optimal parameters and locations of inerters for controlling response to different types of environmental actions might be different, and a more rigorous procedure for multi-hazard scenarios needs to be developed.

REFERENCES

[1] Gaur, S., Elias, S., Höbbel, T., Matsagar, V. A., & Thiele, K. (2020). Tuned mass dampers in wind response control of wind turbine with soil-structure interaction. Soil Dynamics and Earthquake Engineering, 132, 106071.

[2] Elias, S., & Matsagar, V. (2019). Seismic response control of steel benchmark building with a tuned mass damper. Asian Journal of Civil Engineering, 1-14.

[3] Taha, A. E., Elias, S., Matsagar, V., & Jain, A. K. (2019). Seismic response control of asymmetric buildings using tuned mass dampers. The Structural Design of Tall and Special Buildings, 28(18), e1673.

[4] Elias, S. (2019). Effect of SSI on vibration control of structures with tuned vibration absorbers. Shock and Vibration, 2019.

[5] Elias, S., Matsagar, V., & Datta, T. K. (2019). Along‐wind response control of chimneys with distributed multiple tuned mass dampers. Structural Control and Health Monitoring, 26(1), e2275.

[6] Elias, S., & Matsagar, V. (2018). Wind response control of tall buildings with flexible foundation using tuned mass dampers. In Wind Engineering for Natural Hazards: Modeling, Simulation, and Mitigation of Windstorm Impact on Critical Infrastructure (pp. 55-78).

[7] Elias, S., Matsagar, V., & Datta, T. K. (2017). Distributed multiple tuned mass dampers for wind response control of chimney with flexible foundation. Procedia engineering, 199, 1641-1646.

[8] Elias, S., Matsagar, V., & Datta, T. K. (2016). Effectiveness of distributed tuned mass dampers for multi-mode control of chimney under earthquakes. Engineering Structures, 124, 1-16.

[9] Elias, S., & Matsagar, V. (2017). Research developments in vibration control of structures using passive tuned mass dampers. Annual Reviews in Control, 44, 129-156.

[10] Elias, S., Matsagar, V., & Datta, T. K. (2019). Distributed tuned mass dampers for multi-mode control of benchmark building under seismic excitations. Journal of Earthquake Engineering, 23(7), 1137-1172.

[11] Gill, D., Elias, S., Steinbrecher, A., Schröder, C., & Matsagar, V. (2017). Robustness of multi-mode control using tuned mass dampers for seismically excited structures. Bulletin of Earthquake Engineering, 15(12), 5579-5603.

[12] Elias, S., & Matsagar, V. (2019). Seismic vulnerability of a non-linear building with distributed multiple tuned vibration absorbers. Structure and Infrastructure Engineering, 15(8), 1103-1118.

[13] Elias, S., & Matsagar, V. (2014). Distributed multiple tuned mass dampers for wind vibration response control of high-rise building. Journal of Engineering, 2014.

[14] Elias, S., Matsagar, V., & Datta, T. K. (2019). Dynamic response control of a wind-excited tall building with distributed multiple tuned mass dampers. International Journal of Structural Stability and Dynamics, 19(06), 1950059.

[15] Elias, S. (2018). Seismic energy assessment of buildings with tuned vibration absorbers. Shock and Vibration, 2018.

[16] Elias, S., & Matsagar, V. (2014). Wind response control of 76-storey benchmark building with distributed multiple tuned mass dampers. Journal of Wind and Engineering, 11(2), 37-49.

[17] Marian, L., & Giaralis, A. (2014). Optimal design of a novel tuned mass-damper–inerter (TMDI) passive vibration control configuration for stochastically support-excited structural systems. Probabilistic Engineering Mechanics, 38, 156-164.

[18] Giaralis, A., & Petrini, F. (2017). Wind-induced vibration mitigation in tall buildings using the tuned mass-damper-inerter. Journal of Structural Engineering, 143(9), 04017127.

[19] Giaralis, A., & Taflanidis, A. A. (2018). Optimal tuned mass‐damper‐inerter (TMDI) design for seismically excited MDOF structures with model uncertainties based on reliability criteria. Structural Control and Health Monitoring, 25(2), e2082.

[20] Marian, L., & Giaralis, A. (2017). The tuned mass-damper-inerter for harmonic vibrations suppression, attached mass reduction, and energy harvesting. Smart structures and systems, 19(6), 665-678.

[21] Giaralis, A., & Petrini, F. (2017). Optimum design of the tuned mass-damper-inerter for serviceability limit state performance in wind-excited tall buildings. Procedia engineering, 199, 1773-1778.

[22] Cao, L., & Li, C. (2019). Tuned tandem mass dampers‐inerters with broadband high effectiveness for structures under white noise base excitations. Structural Control and Health Monitoring, 26(4), e2319.

[23] Stanikzai, M. H., Elias, S., Matsagar, V. A., & Jain, A. K. (2019). Seismic response control of base-isolated buildings using tuned mass damper. Australian Journal of Structural Engineering, 1-12.

[24] Stanikzai, M. H., Elias, S., Matsagar, V. A., & Jain, A. K. (2019). Seismic response control of base‐isolated buildings using multiple tuned mass dampers. The Structural Design of Tall and Special Buildings, 28(3), e1576.

[25] Stanikzai, M. H., Elias, S., & Rupakhety, R. (2020). Seismic Response Mitigation of Base-Isolated Buildings. Applied Sciences, 10(4), 1230.

[26] De Domenico, D., & Ricciardi, G. (2018). An enhanced base isolation system equipped with optimal tuned mass damper inerter (TMDI). Earthquake engineering & structural dynamics, 47(5), 1169-1192.

[27] De Domenico, D., & Ricciardi, G. (2018). Earthquake-resilient design of base isolated buildings with TMD at basement: application to a case study. Soil Dynamics and Earthquake Engineering, 113, 503-521.

[28] De Domenico, D., & Ricciardi, G. (2018). Improving the dynamic performance of base‐isolated structures via tuned mass damper and inerter devices: A comparative study. Structural Control and Health Monitoring, 25(10), e2234.

[29] De Domenico, D., & Ricciardi, G. (2018). Optimal design and seismic performance of tuned mass damper inerter (TMDI) for structures with nonlinear base isolation systems. Earthquake engineering & structural dynamics, 47(12), 2539-2560.

[30] Chulahwat, A., & Mahmoud, H. (2017). A combinatorial optimization approach for multi-hazard design of building systems with suspended floor slabs under wind and seismic hazards. Engineering Structures, 137, 268-284.

[31] Aly, A. M., & Abburu, S. (2015). On the design of high-rise buildings for multihazard: fundamental differences between wind and earthquake demand. Shock and Vibration, 2015.

[32] Chapain, S., & Aly, A. M. (2019). Vibration attenuation in high-rise buildings to achieve system-level performance under multiple hazards. Engineering Structures, 197, 109352.

[33] Roy, T., & Matsagar, V. (2019). Effectiveness of passive response control devices in buildings under earthquake and wind during design life. Structure and Infrastructure Engineering, 15(2), 252-268.

[34] Rezaee, M., & Aly, A. M. (2018). Vibration control in wind turbines to achieve desired system‐level performance under single and multiple hazard loadings. Structural Control and Health Monitoring, 25(12), e2261.

[35] Nikellis, A., Sett, K., & Whittaker, A. S. (2019). Multihazard Design and Cost-Benefit Analysis of Buildings with Special Moment–Resisting Steel Frames. Journal of Structural Engineering, 145(5), 04019031.

[36] Elias, S., Rupakhety, R., & Olafsson, S. (2019). Analysis of a Benchmark Building Installed with Tuned Mass Dampers under Wind and Earthquake Loads. Shock and Vibration, 2019.

[37] Patil, V. B., & Jangid, R. S. (2011). Optimum multiple tuned mass dampers for the wind excited benchmark building. Journal of Civil Engineering and Management, 17(4), 540-557.

[38] Yang, J. N., Agrawal, A. K., Samali, B., & Wu, J. C. (2004). Benchmark problem for response control of wind-excited tall buildings. Journal of engineering mechanics, 130(4), 437-446.

[39] Sadek, F., Mohraz, B., Taylor, A. W., & Chung, R. M. (1997). A method of estimating the parameters of tuned mass dampers for seismic applications. Earthquake Engineering & Structural Dynamics, 26(6), 617-635.

[40] Saha, S. K., Matsagar, V., & Chakraborty, S. (2016). Uncertainty quantification and seismic fragility of base-isolated liquid storage tanks using response surface models. Probabilistic Engineering Mechanics, 43, 20-35.

EURODYN 2020
XI International Conference on Structural Dynamics
M. Papadrakakis, M. Fragiadakis, C. Papadimitriou (eds.)
Athens, Greece, 23–26 November 2020

SUPPRESSION OF VIBRATION TRANSMISSION BETWEEN OSCILLATORS COUPLED WITH AN INERTER-BASED JOINT

Zhuang Dong[1], Jian Yang[1*], Han Meng[2] and Dimitrios Chronopoulos[2]

[1] Department of Mechanical, Materials and Manufacturing Engineering, University of Nottingham Ningbo China, Ningbo 315100, PR China.
Zhuang.Dong@nottingham.edu.cn
Jian.Yang@nottingham.edu.cn

[2] Institute for Aerospace Technology & The Composites Group, University of Nottingham, Nottingham, NG8 1BB, UK.
Han.Meng@nottingham.ac.uk
Dimitrios.Chronopoulos@nottingham.ac.uk

Keywords: Vibration transmission, Inerter, Vibration power flow, Force transmissibility

Abstract. *This paper investigates the dynamic characteristics and vibration transmission behaviour of harmonically forced oscillators coupled via an inerter-based joint. The inerter is a recently proposed passive mechanical element that can be used for vibration suppression purpose. The coupled oscillators represent simplified models for the dominant modes of engineering structures such as beams and plates, while the inerter-based joint serves as the vibration transmission path between the two subsystems. The effects of the inerter on the level of vibration transmission are examined for enhanced design of suppression devices. The steady-state dynamic responses of the oscillators and vibration power flow between them are derived analytically. Vibration transmission between the two subsystems is evaluated by both the force transmissibility and time-averaged vibration power flow transmission. It is shown that the use of the inerter in the joint can reduce force and vibration power flow transmission over a large band of excitation frequencies. It is found that the addition of the inerter can also introduce anti-resonances in the frequency-response curves and in the curves of the force transmissibility, where the vibration transmission can be suppressed at specific excitation frequencies. It is shown that force transmissibility reduces at low frequencies and tends to an asymptotic value as the excitation frequency decreases. These findings provide a better understanding of the effects of inerters in the joint on vibration transmission and benefit future designs of mechanical joints of coupled structures for vibration mitigation purpose.*

1 INTRODUCTION

There has been a growing demand for high performance vibration control devices that change the vibration transmission behaviour of dynamical systems to meet specific requirements [1]. Some work considers the use of metamaterials for vibration suppression purpose [2-6]. Recently, a passive mechanical element, the inerter, which can be used to provide inertial coupling such as to modify the dynamic behaviour was proposed [7]. The forces applied to the two terminals of the inerter are proportional to the relative accelerations of the two ends, i.e., $F_b = b(\dot{V}_1 - \dot{V}_2)$, where F_b is the coupling inertial force, b is an intrinsic parameter of the inerter named inertance, $\dot{V}_1$ and $\dot{V}_2$ are the accelerations of the two terminals. Since the introduction of the inerter concept, it has been applied to aircraft landing gear shimmy suppression [8], vehicle suspension systems [9] and building vibration control system [10]. Some studies have also been reported on the performance of inerter-based single degree-of-freedom (DOF) vibration isolators [11], dual-stage isolator [12] and nonlinear inerter-based isolator [13].

In many mechanical systems and engineering structures, subsystems are connected via mechanical or structural joints, the design of which is important to reduce vibration transmission between different parts of the integrated system. For the evaluation of vibration transmission level, the force transmissibility and time-averaged vibration power flow quantities may be used. Vibration power flow analysis (PFA) method is a widely accepted tool to characterize the dynamic behaviour of coupled systems and complex structures [14]. Various PFA approaches have been developed to investigate linear vibration control systems. The power flow characteristics of single-DOF inerter-based isolators [11] and two-DOF inerter-based isolators [12] were also investigated. In recent years, this dynamic analysis approach has been developed to investigate vibration power flow in nonlinear vibration isolation systems [15], in oscillators coupled with a nonlinear interface[16], in coupled nonlinear oscillators [17], nonlinear systems with bilinear stiffness and bilinear damping [18] and in impact oscillator systems [19]. It is accordingly beneficial to examine the effects of inerters from a vibration power flow viewpoint for enhanced designs of inerter-based vibration suppression systems.

This paper investigates the influence of introducing the inerter to a mechanical joint on vibration transmission between coupled oscillators. The steady-state response amplitude, force transmissibility and vibration power flow quantities are obtained. The remaining content of the paper is organized as follows. In Section 2, the coupled oscillator system will be briefly introduced and modelled. Then the force transmissibility of the system will be derived in Section 3. The vibration power flow variables and maximum kinetic energies of the system will be formulated in Section 4. Conclusions are drawn in at the end of the paper.

2 THE COUPLING OSCILLATORS MODEL

In this section, the effects of including an inerter in the joint of coupled oscillators on the dynamics and vibration transmission behaviour are investigated. Figure 1 provides a schematic presentation of the model comprising two subsystems coupled with a mechanical joint characterized by an inerter with inertance b and a spring with stiffness coefficient k_0. Subsystem one is a single-DOF system consisting of a mass m_1 subject to an external harmonic excitation of amplitude f_0 with frequency ω, a viscous damper of damping coefficient c_1, and a linear spring with stiffness coefficient k_1. Subsystem two is another single-DOF system having mass m_2, a viscous damper with damping coefficient c_2, and a linear spring with stiffness coefficient k_2. It is assumed that the masses both move horizontally without frictions and their static equilibrium positions, where $x_1 = x_2 = 0$ and the springs are unstretched, are taking as the reference. The dynamic governing equations of the system could be written as

$$m_1\ddot{x}_1 + c_1\dot{x}_1 + k_1x_1 + f_b + k_0(x_1 - x_2) = f_0e^{i\omega t}, \tag{1a}$$

$$m_2\ddot{x}_2 + c_2\dot{x}_2 + k_2x_2 - f_b - k_0(x_1 - x_2) = 0, \tag{1b}$$

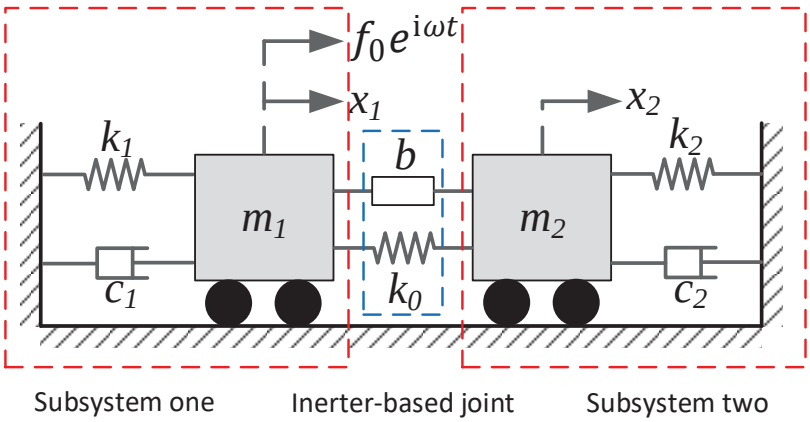

Figure 1: A schematic representation of the coupled oscillator coupled with an inerter-based joint.

where $f_b = b(\ddot{x}_1 - \ddot{x}_2)$, m_i, c_i and k_i $(i = 1, 2)$ are the masses, damping coefficients and spring stiffness coefficients respectively. $x_i, \dot{x}_i$ and $\ddot{x}_i$ $(i = 1, 2)$ represent the displacements, velocities and accelerations respectively. To facilitate later derivations of the response and vibration transmission, the following parameters are introduced

$$\omega_1 = \sqrt{\frac{k_1}{m_1}}, \omega_2 = \sqrt{\frac{k_2}{m_2}}, \mu = \frac{m_2}{m_1}, l_0 = \frac{m_1 g}{k_1}, X_1 = \frac{x_1}{l_0}, X_2 = \frac{x_2}{l_0}, \gamma = \frac{k_2}{k_1}, \delta = \frac{k_0}{k_1},$$

$$\xi_1 = \frac{c_1}{2m_1\omega_1}, \xi_2 = \frac{c_2}{2m_2\omega_2}, \lambda = \frac{b}{m_1}, F_0 = \frac{f_0}{k_1 l_0}, \Omega = \frac{\omega}{\omega_1}, \tau = \omega_1 t,$$

where ω_1 and ω_2 are the undamped natural frequencies of thee subsystems one and two, μ is the mass ratio, l_0 is the characteristic length, X_1 and X_2 are the nondimensional displacements of m_1 and m_2, γ is stiffness ratio of the springs, ξ_1 and ξ_2 are damping ratios, λ is nondimensional inertance ratio, F_0 is nondimensional force amplitude, Ω is the dimensionless excitation frequency and τ is the dimensionless time. Thus, Eq. (1a) and (1b) can be rearranged into the following nondimensional form

$$X_1'' + 2\xi_1 X_1' + X_1 + F_b + \delta(X_1 - X_2) = F_0e^{i\Omega\tau}, \tag{2a}$$

$$X_2'' + 2\xi_2 X_2' + X_2 - \frac{1}{\gamma}F_b - \frac{\delta}{\gamma}(X_1 - X_2) = 0, \tag{2b}$$

where $F_b = \lambda(X_1'' - X_2'')$. By introducing $X_1 = X_0e^{i\Omega\tau}, X_2 = Y_0e^{i\Omega\tau}$, Eq. (2) can be transformed as

$$-\Omega^2 X_0 + 2\xi_1 X_0 i\Omega + X_0 + \lambda(\Omega^2 Y_0 - \Omega^2 X_0) + \delta(X_0 - Y_0) = F_0, \tag{3a}$$

$$-\Omega^2\gamma Y_0 + 2\xi_2\gamma Y_0 i\Omega + \gamma Y_0 - \lambda(\Omega^2 Y_0 - \Omega^2 X_0) - \delta(X_0 - Y_0) = 0. \tag{3b}$$

The response amplitudes may be written in the non-dimensional form

$$Y_0 = \frac{\frac{\delta}{\gamma} - \frac{\lambda}{\gamma}\Omega^2}{1 + 2\xi_2 i\Omega - \Omega^2 - \frac{\lambda}{\gamma}\Omega^2 + \frac{\delta}{\gamma}} X_0, \tag{4a}$$

$$X_0 = \frac{F_0}{1+2\xi_1 \mathrm{i}\Omega-\Omega^2-\frac{1+2\xi_2 \mathrm{i}\Omega-\Omega^2}{1+2\xi_2 \mathrm{i}\Omega-\Omega^2-\frac{\lambda}{\gamma}\Omega^2+\frac{\delta}{\gamma}}(\lambda\Omega^2-\delta)}. \tag{4b}$$

Figure 2 shows the influence of adding the inerter to the mechanical joint on the the response amplitudes of the oscillator masses. Four different values of inertance ratio with $\lambda = 0, 0.5, 1$ and 2 are selected and the corresponding results are shown by solid, dashed, dash-dot and dotted lines. The other parameters are set as $\xi_1 = \xi_2 = 0.02, \gamma = 1, \delta = 1, F_0 = 1$. In the figure, $X = |X_0|$ and $Y = |Y_0|$, denoting the response amplitudes of masses m_1 and m_2, respectively. When the inerter is not included in the joint, two resonant peaks are observed in each curve of X and Y, one of which moves to the lower frequency range with the increase of inertance ratio λ. However, the other peak remains at the same frequency when the inertance ratio λ changes. The anti-peak in Figure 2(a) also moves to low frequency range with the increase of inertance ratio λ. When $\lambda = 1$, two peaks in Figure 2(a) become close with an anti-peak at $\Omega \approx 1$, which indicates the benefit of using inerter for vibration suppression at high frequencies. In Figure 2(b), the addition of inerter introduces an anti-peak in each curve, which can be used to reduce vibration level of mass m_2 at a prescribed excitation frequency.

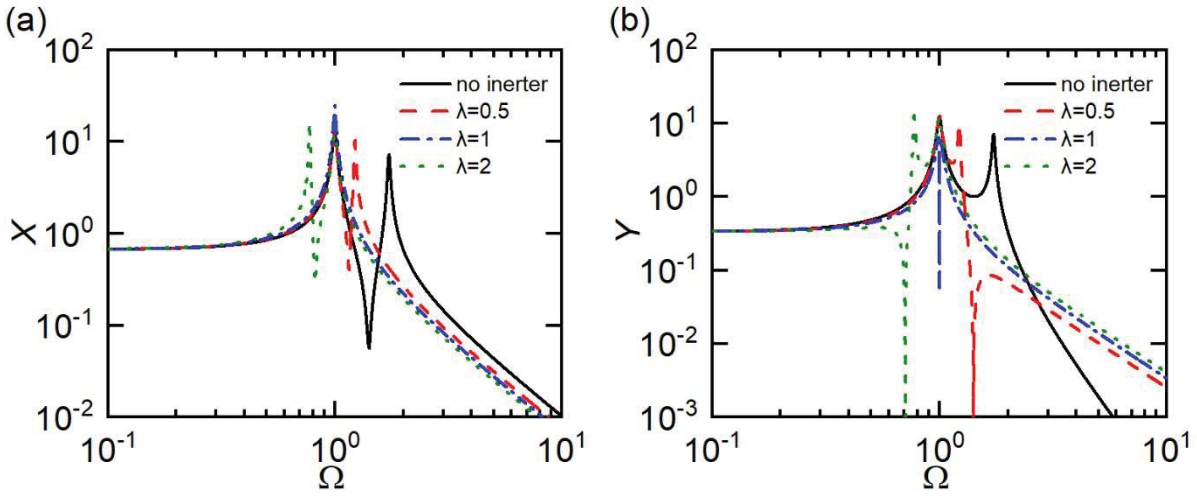

Figure 2: Response amplitude of (a) mass m_1 and (b) mass m_2 ($\xi_1 = \xi_2 = 0.02, \gamma = \delta = F_0 = 1$).

3 FORCE TRANSMISSIBILITY

The force transmissibility has been widely used to evaluate the level of vibration transmission between different subsystems of an integrated structure. It is used here to access the performance of inerter-based mechanical joint in reducing the force transmission. For the current system, the force transmitted to the second mass can be expressed as

$$F_t = F_b + \delta(X_1 - X_2) = \lambda(X_1'' - X_2'') + \delta(X_1 - X_2) = F_{t0}e^{\mathrm{i}\Omega\tau}. \tag{5}$$

As the fore transmissibility is defined as the ratio between the amplitude of the transmitted force and that of the external force, we have

$$TR = \left|\frac{F_{t0}}{F_0}\right| = \left|\frac{\delta-\lambda\Omega^2}{F_0}(X_0 - Y_0)\right|. \tag{6}$$

Figure 3 shows the force transmissibility characteristics of the system with parameters set as $\xi_1 = \xi_2 = 0.02, \gamma = \delta = F_0 = 1$. The figure shows that the use of inerter introduces an anti-peak in each curve, which moves to lower frequency range with the increase of the inertance ratio λ. Figure 3 shows that with the use of inerter in the joint, the force transmissibility TR

remains smaller than 1 in a large range of excitation frequencies. This characteristic can be used to reduce the transmitted force at low excitation frequencies.

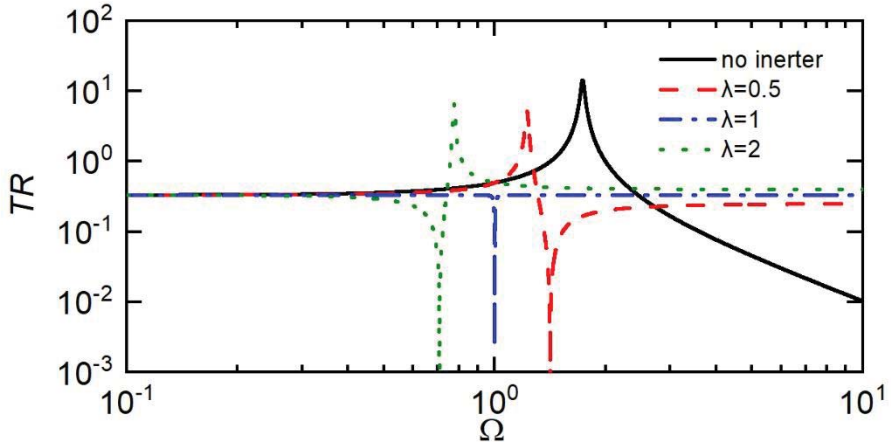

Figure 3: Force transmissibility between oscillators coupled with an inerter-based joint ($\xi_1 = \xi_2 = 0.02, \gamma = \delta = F_0 = 1$).

4 VIBRATION POWER FLOW ANALYSIS

In this section, the vibration transmission behaviour of the inerter-based coupled oscillator system is examined from the perspective of vibration power and energy. The non-dimensional instantaneous input power of the system is the product of the excitation force and the corresponding velocity of the mass

$$P_{in} = F_0 e^{\mathrm{i}\Omega\tau} X_1', \tag{7}$$

where X_1' is the non-dimensional velocity of the mass m_1, which can be expressed as

$$X_1' = \mathrm{i}\Omega X_0 e^{\mathrm{i}\Omega\tau}. \tag{8}$$

Thus, the non-dimensional steady-state time-averaged input power over an excitation cycle is

$$\bar{P}_{in} = \frac{1}{T}\int_{\tau_0}^{\tau_0+T} P_{in}\,\mathrm{d}\tau = \frac{1}{2}\mathrm{Re}\{F_0{}^* X_0 \mathrm{i}\Omega\}, \tag{9}$$

where Re indicates the real part of a complex value and * denotes the complex conjugate. Based on Eq. (4b), the input power for the system can be expressed as

$$\bar{P}_{in} = \frac{1}{2}|F_0^2|\mathrm{Re}\left\{\frac{\mathrm{i}\Omega}{1+2\xi_1\mathrm{i}\Omega-\Omega^2-\frac{1+2\xi_2\mathrm{i}\Omega-\Omega^2}{1+2\xi_2\mathrm{i}\Omega-\Omega^2-\frac{\lambda}{\gamma}\Omega^2+\frac{\delta}{\gamma}}(\lambda\Omega^2-\delta)}\right\}. \tag{10}$$

The corresponding time-averaged transmitted power $\bar{P}_t$ to mass m_2 is

$$\bar{P}_t = \frac{1}{T}\int_{\tau_0}^{\tau_0+T} P_t\,\mathrm{d}\tau = \frac{1}{2}\mathrm{Re}\{F_{t0}{}^* Y_0 \mathrm{i}\Omega\}, \tag{11}$$

The power transmission ratio R_t to mass m_2 may be defined as the ratio between the time-averaged transmitted power $\bar{P}_t$ and the time-averaged input power $\bar{P}_{in}$

$$R_t = \frac{\bar{P}_t}{\bar{P}_{in}}. \tag{12}$$

As the velocity amplitude of mass m_1 in the steady-state motion is $X\Omega$, the non-dimensional maximum kinetic energy of mass m_1 in the steady-state motion is

$$K_{max} = \frac{1}{2}X^2\Omega^2. \tag{13}$$

Based on those formulas, Figure 4 investigates the effects of introducing an inerter-based coupled oscillator on the power flow behaviour. The system parameter values are set as $\xi_1 = \xi_2 = 0.02, \gamma = \delta = F_0 = 1$, the same as those used in Figure 2. Two peaks can be observed in each curve of $\bar{P}_{in}$ and $\bar{P}_t$, Figure 4(a) shows that the use of inerter moves the second peak of $\bar{P}_{in}$ to the low-frequency range with the increase of inertance ratio λ, but corresponding peak value changes little. The first peak frequency and value of $\bar{P}_{in}$ remain almost the same despite of the variations of the inertance ratio λ. The effect of inerter on the time-averaged input power $\bar{P}_{in}$ is relatively small at low and high excitation frequencies. Figure 4(b) shows that the addition of inerter introduces an anti-peak in the curve of time-averaged transmitted power $\bar{P}_t$. The first peak in $\bar{P}_t$ is little affected by the changes of λ. The second peak of $\bar{P}_t$ moves to low frequency range with the increase of inertance ratio λ, but the corresponding peak value remains almost the same. Figure 4(c) plots the variations of the maximum kinetic energy of mass m_1. It shows that for the mechanical joint with inerter, the anti-peak as well as the second peak in the curve without inerter move to the low-frequency range. When $\lambda = 1$, two peaks and one anti-peak merge together as one peak with a higher peak value. This indicates the system in this case is beneficial at high frequencies. The effect of the inerter is little when the frequency is low.

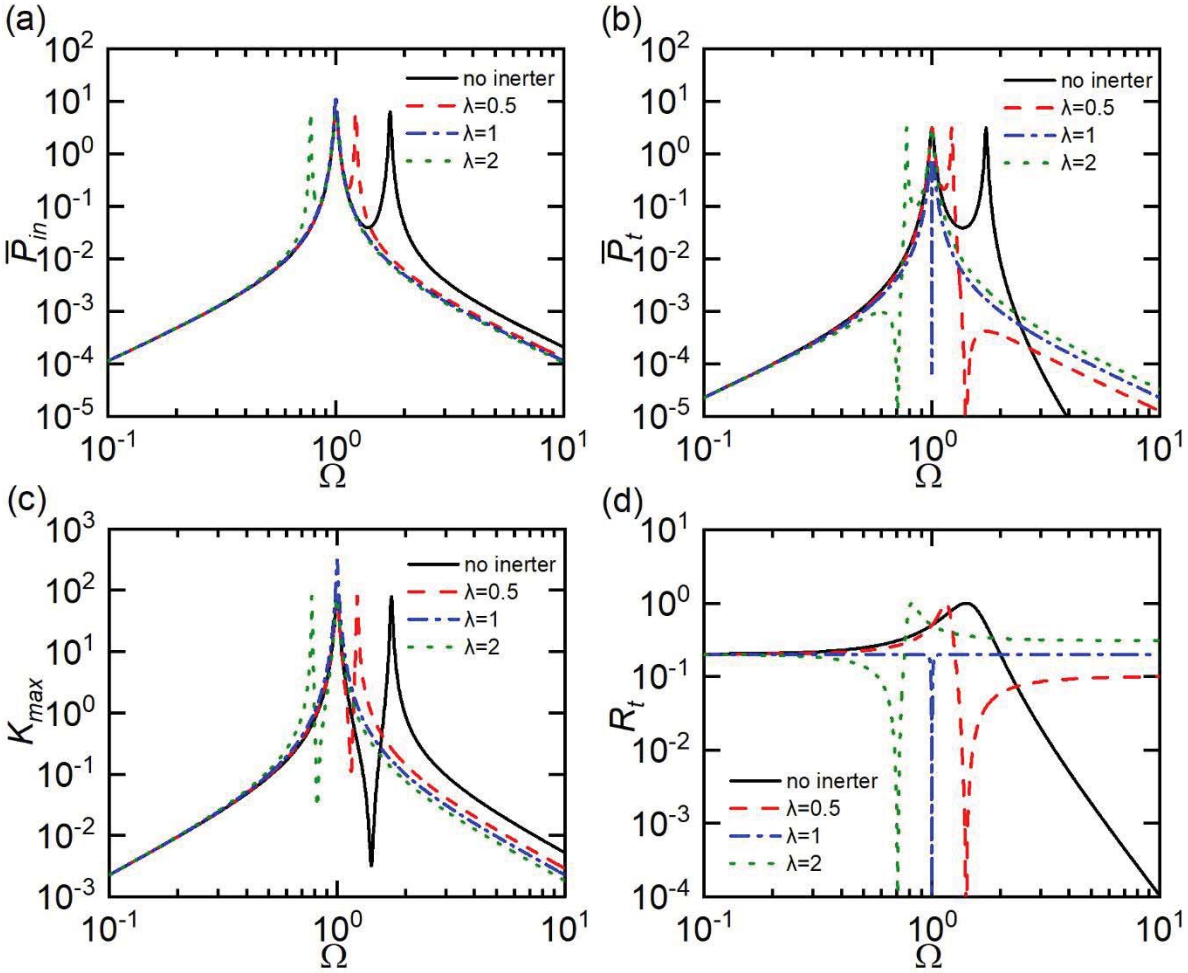

Figure 4: Power flow behaviour of oscillators coupled with an inerter. (a) Time-averaged input power (b) time-averaged transmitted power (c) maximum kinetic energy and (d) power transmission ratio

Figure 4(d) illustrates the influence of inerter in the joint on vibration transmission in terms of the power transmission ratio R_t. An anti-peak is introduced in the curve of R_t, and the peak of the curve moves to the low-frequency range with the increase of inertance ratio λ. When $\lambda = 1$, there is a local minimum point. This characteristic shows the benefits of adding the inerter to the joint at specific excitation frequencies. When Ω is small, the effect of inerter is little, and there is an increase of power transmission ratio R_t with the increase of inertance ratio λ in high frequency range.

5 CONCLUSIONS

The dynamics and performance of an inerter-based mechanical joint between coupled oscillators were investigated in this paper. The force transmissibility and vibration power flow characteristics of the system were examined to evaluate the effects of the inclusion of inerter on the suppression of vibration transmission. It was shown that a larger inertance value leads to a shift of response peaks of the two masses to the low-frequency range. Adding the inerter to the joint results in increases in the force transmission at high excitation frequencies but less time-averaged input power and lower maximum kinetic energy of one of the subsystems. It was found that the inclusion of inerters can provide benefits to vibration mitigation by creating a large frequency band where the force transmissibility and power transmission ratio are relatively low. By properly setting the inertance value, anti-peaks may be created in curves of force transmissibility and power transmission ratio so that their values can be substantially reduced. Based on this property, vibration transmission between the two coupled oscillators can be greatly suppressed at pre-determined excitation frequencies. Asymptotic behaviour of force transmission and power transmission was found when the excitation frequency extends to high frequencies.

ACKNOWLEDGEMENT

This work was supported by National Natural Science Foundation of China (Grant number 51605233) and by Ningbo Science and Technology Bureau under Natural Science Programme (Grant number 2019A610155).

REFERENCES

[1] J. Yang, Y. Xiong and J. Xing (2013). Dynamics and power flow behaviour of a nonlinear vibration isolation system with a negative stiffness mechanism. *Journal of Sound and Vibration*, 332(1), pp.167-183.

[2] H. Meng, D. Chronopoulos, A.T. Fabro, W. Elmadih, I. Maskery, Rainbow metamaterials for broadband multi-frequency vibration attenuation: Numerical analysis and experimental validation, *Journal of Sound and Vibration*, 465, 115005, 2020.

[3] H. Meng, D. Chronopoulos, A.T. Fabro, I. Maskery, Y. Chen, Optimal design of rainbow elastic metamaterials, *International Journal of Mechanical Sciences*, 165, 105185, 2020.

[4] W. Elmadih, D. Chronopoulos, W. Syam, I. Maskery, H. Meng, R. Leach, Three-dimensional resonating metamaterials for low-frequency vibration attenuation, Scien-tific Reports, 9, 1-8, 2019.

[5] O. McGee, H. Jiang, F. Qian, Z. Jia, L. Wang, H. Meng, D. Chronopoulos, Y. Chen, L. Zuo, 3D printed architected hollow sphere foams with low-frequency phononic band gaps, *Additive Manufacturing*, 30, 100842, 2019.

[6] H. Meng, D. Chronopoulos, A.T. Fabro, Numerical simulation data for the dynamic properties of rainbow metamaterials, *Data in brief*, 28, 104772, 2020.

[7] M. Smith (2002). Synthesis of mechanical networks: the inerter. *IEEE Transactions on Automatic Control*, 47(10), pp.1648-1662.

[8] Y. Li, J. Jiang and Neild, S. (2017). Inerter-Based Configurations for Main-Landing-Gear Shimmy Suppression. *Journal of Aircraft*, 54(2), pp.684-693.

[9] J. Jiang, A. Matamoros-Sanchez, R. Goodall and M. Smith (2012). Passive suspensions incorporating inerters for railway vehicles. *Vehicle System Dynamics*, 50(sup1), pp.263-276.

[10] S. Zhang, J. Jiang and S. Neild (2016). Optimal configurations for a linear vibration suppression device in a multi-storey building. *Structural Control and Health Monitoring*, 24(3).

[11] J. Yang, Force transmissibility and vibration power flow behaviour of inerter-based vibration isolators, *Journal of Physics: Conference Series*, 2016, 744(1): 012234.

[12] J. Yang, J. Jiang, X. Zhu and H. Chen (2017). Performance of a dual-stage inerter-based vibration isolator. *Procedia Engineering*, 199, pp.1822-1827.

[13] J. Yang, J. Jiang and S. Neild (2019). Dynamic analysis and performance evaluation of nonlinear inerter-based vibration isolators. *Nonlinear Dynamics*. [online] Available at: https://doi.org/10.1007/s11071-019-05391-x.

[14] H. Goyder and R. White (1980). Vibrational power flow from machines into built-up structures, part III: Power flow through isolation systems. *Journal of Sound and Vibration*, 68(1), pp.97-117

[15] J. Yang, Y. Xiong and J. Xing (2016). Vibration power flow and force transmission behaviour of a nonlinear isolator mounted on a nonlinear base. *International Journal of Mechanical Sciences*, 115-116, pp.238-252.

[16] J. Yang, B. Shi and C. Rudd (2018). On vibration transmission between interactive oscillators with nonlinear coupling interface. *International Journal of Mechanical Sciences*, 137, pp.238-251.

[17] B. Shi and J. Yang (2019). Quantification of vibration force and power flow transmission between coupled nonlinear oscillators. *International Journal of Dynamics and Control*, https://doi.org/10.1007/s40435-019-00560-7.

[18] B. Shi, J. Yang and C. Rudd (2019). On vibration transmission in oscillating systems incorporating bilinear stiffness and damping elements. *International Journal of Mechanical Sciences*, 150, pp.458-470.

[19] W. Dai, J. Yang and B. Shi (2020). Vibration transmission and power flow in impact oscillators with linear and nonlinear constraints. *International Journal of Mechanical Sciences*, 168, p.105234.

EURODYN 2020
XI International Conference on Structural Dynamics
M. Papadrakakis, M. Fragiadakis, C. Papadimitriou (eds.)
Athens, Greece, 23–26 November 2020

SEISMIC PROTECTION OF MULTI-STOREY ROCKING STRUCTURES WITH INERTERS

Rodrigo Thiers-Moggia[1], **Christian Málaga-Chuquitaype**[2]

[1]Imperial College London
address
e-mail: r.thiers16@imperial.ac.uk

[2] Imperial College London
address
e-mail: c.malaga@imperial.ac.uk

Keywords: Rocking structures, Inerter, Seismic control, Pulse-like ground motion.

Abstract. *Recent studies on seismic control of rocking structures have proposed the use of inerters, mechanical devices that develop resisting forces proportional to the relative acceleration between their terminals. Analytical analyses have shown that these devices effectively reduce the frequency parameter of a rocking block resulting in lower seismic demands and enhanced stability due to the well-known size effect of the rocking behaviour. As with most of such strategies, the efficiency of the inerter has been assessed for perfectly rigid bodies in the first place. However, in real practical applications, rocking structures will exhibit some degree of flexibility. Moreover, some of the underlying assumptions of the analytical models used to study rigid bodies imply that the structures are slender, and therefore more likely to deform during the rocking motion. In this paper, the dynamic response of multi-mass flexible rocking bodies equipped with inerters is examined. Firstly, a numerical model is formulated and implemented in OpenSees. This model is then validated against analytical analyses of single-mass flexible structures. Subsequently, the responses of buildings ranging from 3 to 9 stories are studied and compared in terms of elastic deformations, base rotations and floor accelerations. The effect of increasing levels of flexibility in the efficiency of the inerter is also assessed.*

1 INTRODUCTION

The uplifting and rocking of free-standing structures can significantly reduce the seismic shear and moment demands at their base [1]. During the last decades, this concept has been widely studied and applied to the protection of earthquake resistant structures [2, 3]. While allowing the base to rock can help to control structural damage by reducing deformations, previous studies suggest that it can also induce higher inter-storey drifts that may be associated with unacceptable non-structural damage [4].

Seismic control systems for rocking structures have been mainly oriented to the protection of museum artefacts and non-structural equipment. Early strategies were based on simple measures, such as lowering the centre of mass or anchoring the object to a fixed support, and are usually not practical [5]. On the other hand, traditional strategies used in building structures, such as base isolation, have been shown not to be effective for a wide range of rocking structures [6]. In this context, recent studies have proposed the use of inerters, mechanical devices that develop resisting forces proportional to the relative acceleration between their terminals. This strategy effectively reduces the frequency parameter of a rocking block leading to lower seismic demands and enhanced stability due to the well-known size effect of the rocking behaviour [7]. As with most of such strategies, the efficiency of the inerter has only been assessed for perfectly rigid bodies. However, in real building applications, rocking structures will exhibit some degree of flexibility. Moreover, some of the underlying assumptions of the analytical models used to study rigid bodies imply that the structures are slender, and therefore more likely to deform during the rocking motion.

In this paper, the dynamic response of multi-mass flexible rocking bodies equipped with inerters is studied considering configurations representative of real building structures. Firstly, a numerical model for the rocking structure-inerter system is formulated and implemented in OpenSees [8]. This model is then validated against analytical responses of single-mass flexible structures. Subsequently, the dynamic response of three buildings ranging from 2 to 9 stories subjected to acceleration pulses is studied and compared in terms of elastic deformations, base rotations and floor accelerations. The effect of increasing levels of flexibility on the efficiency of the protective system is also assessed.

2 DEFINITION OF THE NUMERICAL MODELS

2.1 Model parameters

The dynamic response of multi-mass rocking structures equipped with inerters can be studied considering the system illustrated in Figure 1a. In this model, the rocking body is represented by n lumped masses, m_i, connected by elastic beam-column elements of flexural stiffness EI_i, and supported by a rigid base allowed to uplift. Two degrees of freedom per level are considered, namely, lateral displacement and rotation. The geometry of the structure is characterized by the radial distance between the pivot points and the masses, R_i, and the corresponding slenderness, α_i. Accordingly, the frequency parameter of the multi-mass structure can be defined as [9]:

$$p_n = \sqrt{\frac{\underline{1}^t[M]\underline{H}\,g}{J_p}} \tag{1}$$

where [M] corresponds to the mass matrix, $\underline{H}$ to the heights vector and J_p is the rotational

inertia of the system obtained as:

$$J_p = \underline{R}^t \, [M] \, \underline{R} \tag{2}$$

where $\underline{R}$ is the radial distances vector. Finally, a grounded inerter of inertance $m_{r,1}$ is connected to the horizontal displacement of the first level mass. The apparent mass ratio is defined as $\sigma = m_r / \sum_{n=1}^{n_{levels}} m_i$.

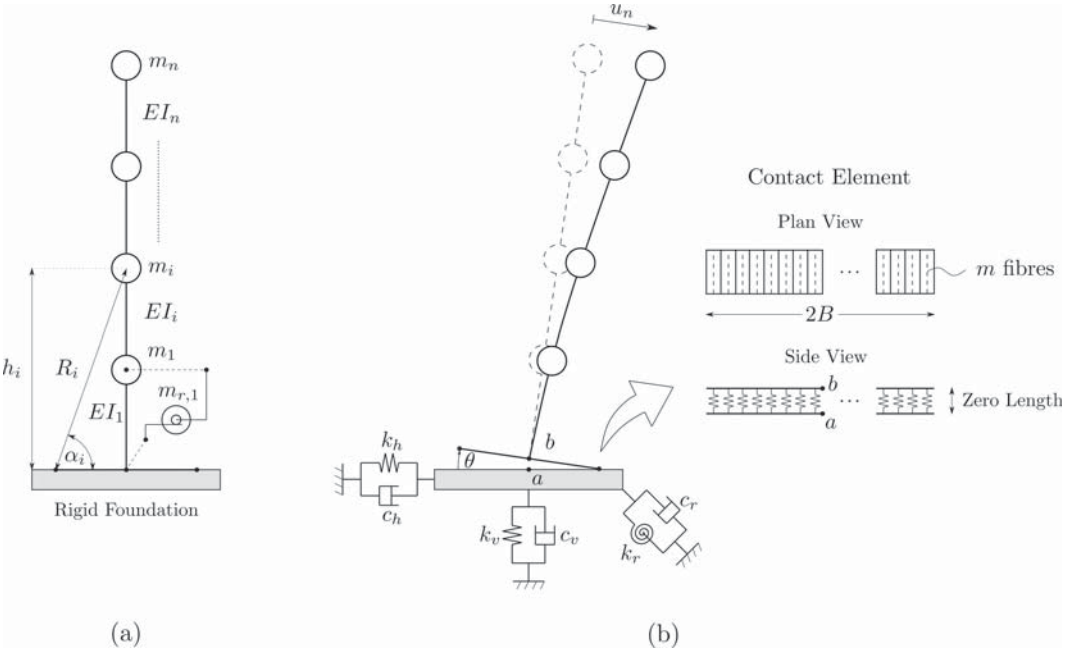

Figure 1: Schematic diagram of the numerical model of the rocking structure-inerter system.

2.2 Numerical model of the rocking structure

The modelling strategy adopted in this study is based on the finite element model for flexible rocking structures proposed by Vassiliou et al. [10]. The model, illustrated in Figure 1b, consists of 3 components: The deformable body, the rocking surface and the underlying soil. Linear-elastic beam-column elements are used to represent the flexible structure, whereas a zero-length element with 2048 sectional fibres is considered for the rocking surface. A non-dissipative compression-only material is assigned to the rocking section, so the system is free to rotate about the pivot points. Unless otherwise stated, the stiffness of the fibres is set at very high values in order to represent a rigid rocking surface. Energy loss during impact is incorporated by taking into account the energy radiated into the underlying ground. Accordingly, the soil underneath the rigid foundation is represented by a set of vertical, horizontal and rotational springs and dashpots whose mechanical properties are determined according to machine vibration theory [11]:

$$\begin{aligned} K &= k \, K_{st} \\ C &= c \, K_{st} \, \frac{R_f}{V_s} \end{aligned} \tag{3}$$

with

$$K_{st,v} = \frac{4 \, \rho \, V_s^2 \, R_f}{1 - \nu} \qquad K_{st,h} = \frac{8 \, \rho \, V_s^2 \, R_f}{2 - \nu} \qquad K_{st,r} = \frac{8 \, \rho \, V_s^2 \, R_f^3}{3(1 - \nu)} \tag{4}$$

where K_{st} is the static stiffness, ρ, ν and V_s are the density, Poisson's ratio and shear wave velocity of the supporting soil, k and c are dynamic amplification factors given in [11], and R_f is the foundation's radius. The values of the dynamic amplification factors $k_v = k_h = k_r = 1$, $c_v = 0.75$, $c_h = 0.6$ and $c_r = 0$ are obtained considering a stiff soil of $V_s = 1000\,[m/s]$, $\rho = 2\,[ton/m^3]$ and $\nu = 0.3$. The foundation, on the other hand, is assumed to be circular with a radius of $R_f = 2B$.

2.2.1 Energy dissipation in the deformable structure

Several analytical and experimental studies have suggested that the addition of viscous damping to rocking models may lead to a significant overestimation of the energy dissipated in the uplifted state [1, 12, 13]. In order to address this shortcoming, a variable damping ratio is introduced to the model presented in the pevious section. Inherent structural damping during the full contact phase is modelled using Rayleigh's classical damping, assigning a prescribed damping ratio, ξ_{fc}, to the first and third vibration modes of the fixed base structure [14]. Once the base uplifts, the analysis is halted and the damping ratio is adjusted before continuing, so that the resultant uplifted damping agrees with experimental observations [13]. The effect of considering different levels of uplifted damping ratios in single-mass rocking oscillators is illustrated in Figure 2. For the first structure (black line), a constant damping ratio of $\xi_{fc} = \xi_{up} = 0.01$ is considered. In the second case (red line), the uplifted damping ratio is modified as outlined above so that the resultant damping corresponds to that of a 1% damped oscillator. In the final case (blue line), no damping is considered during the rocking phase (numerically very small).

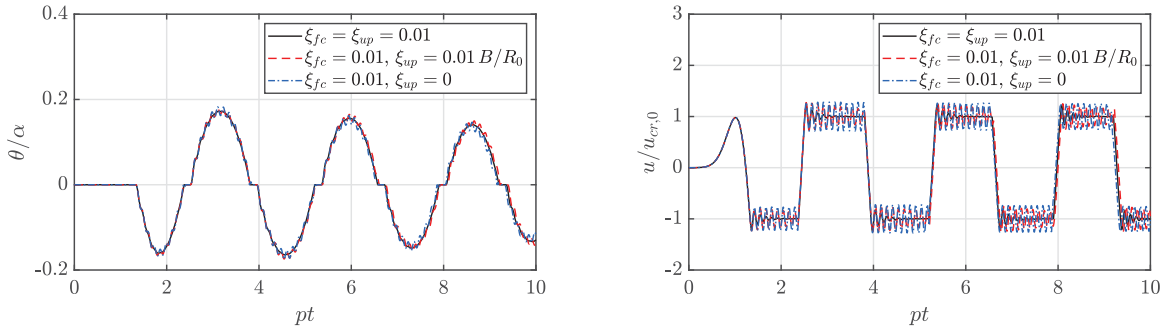

(a) Rotation and deformation responses for different levels of damping ratio.

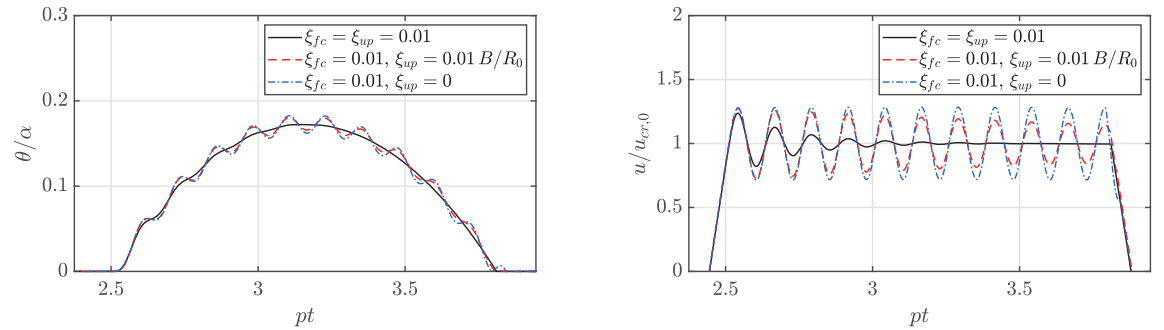

(b) Detailed view of the rotation and deformation responses during a rocking cycle.

Figure 2: Response of a single-mass rocking structure of $\omega_n/p = 5$, $\alpha = 0.1$, and different values of damping ratio, subjected to a single Ricker pulse of $\omega_g/p = 5$ and $a_g = 1.5\,g\tan\alpha$.

The results presented in Figure 2 confirm that the use of a constant damping ratio (black line) results in significantly higher dissipative forces which quickly attenuate the oscillations in the uplifted state. This, in turn, leads to a smother and slightly lower rotation response, as it can be observed in the detailed view of Figure 2b. On the other hand, the difference between the maximum responses of the small damping ($\xi_{up} = 0.01B/R_0$) and no damping cases ($\xi_{up} = 0$) is not significant. Consequently, a conservative assumption of no damping during the rocking phase is adopted in this study, unless otherwise stated.

2.2.2 Validation of the structural model

The structural model described in the previous section is implemented in the open-source finite element framework OpenSees [8] and validated against experimental data published in [13]. Based on this experimental evidence, a variable damping ratio is consider for the models, so that the resultant uplifted damping matches the one of the full contact phase (red line case in Figure 2). Four single-mass rocking oscillators of natural frequencies ranging from 1[Hz] to 4[Hz] are selected for the validation process. The properties of the structures are summarized in Table 1. For further details about the specimens and the experimental program, the reader is referred to [13].

Specimen	f_{fix} $[Hz]$	ξ $[\%]$	α $[rad]$	p $[Hz]$
1 Hz Long Base	0.94	0.26	0.159	3.22
2 Hz Long Base	2.07	0.28	0.160	3.23
3 Hz Short Base	3.12	0.35	0.081	3.25
4 Hz Long Base	3.84	1.32	0.081	3.24

Table 1: Description of the single-mass rocking specimens selected for the validation process (Truniger et al. [13]).

Figure 3 compares the predicted and measured rotation and elastic deformation responses of the specimens when subjected to single-pulse ground motions. One of the main difficulties in the prediction of rocking time history responses is related to the fact that small errors in the rotation amplitude lead to accumulative errors in the phase. This situation can be clearly observed in the 1[Hz], 2[Hz] and 4[Hz] specimens. Nevertheless, very good agreement is observed in the amplitude of the base rotation for the whole range of flexibilities under consideration. On the other hand, accurate predictions of the maximum elastic deformation response are also obtained for the more flexible oscillators, however, results show that the numerical model tends to overestimate the deformation as the structures become more rigid.

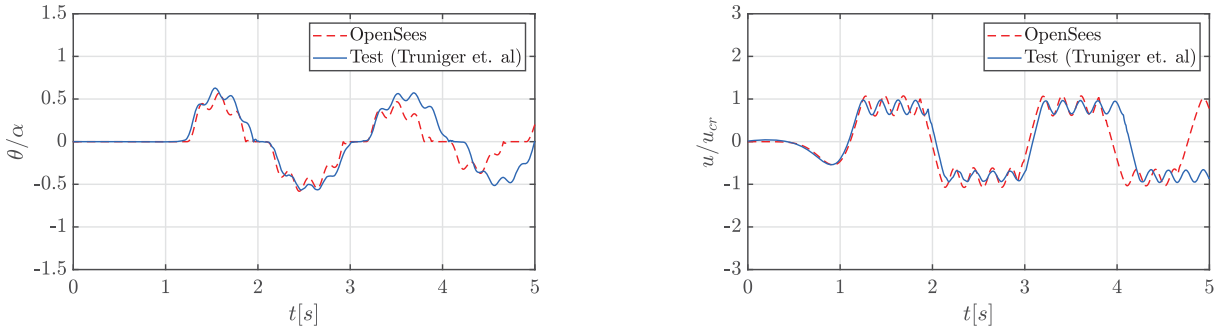

(a) 1 [Hz] Long Base (Test 3)

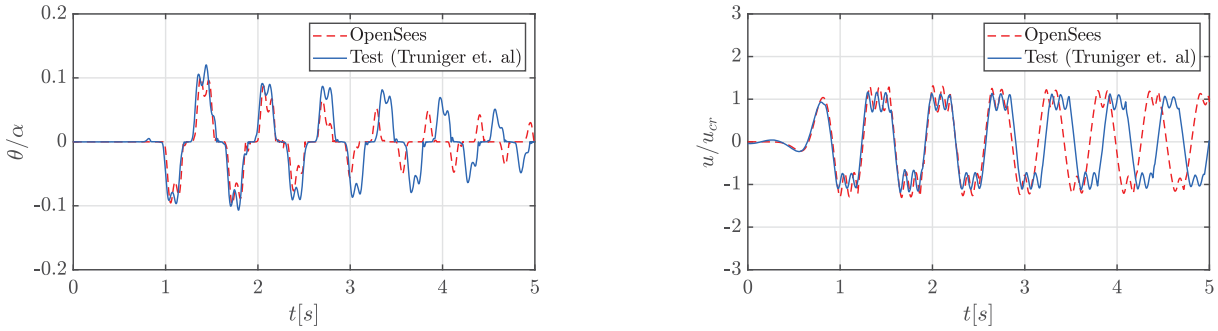

(b) 2 [Hz] Long Base (Test 14)

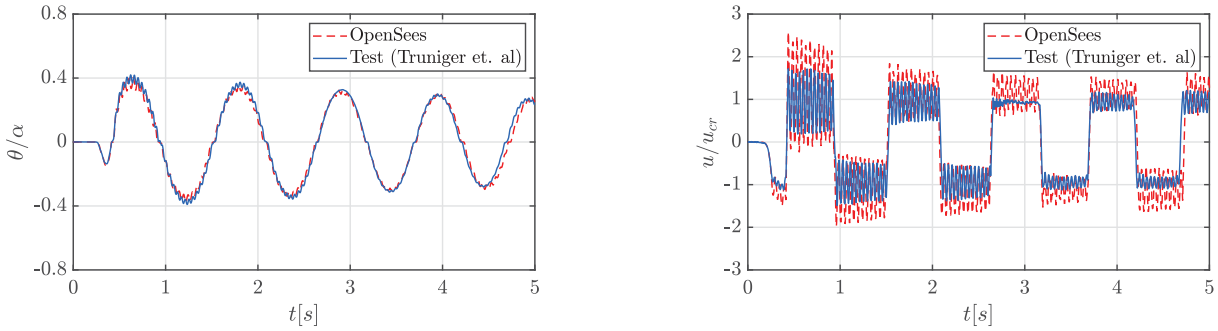

(c) 3 [Hz] Short Base (Test 47)

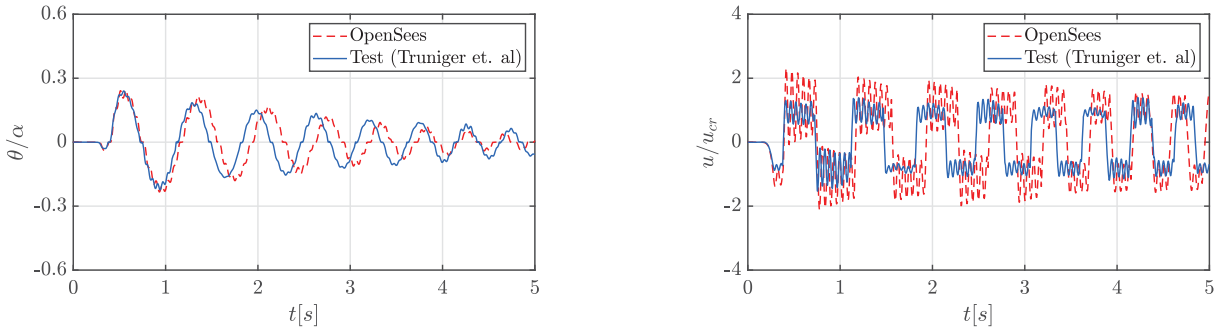

(d) 4 [Hz] Long Base (Test 52)

Figure 3: Comparison of the OpenSees numerical model with experimental results from Truniger et al. [13]

2.3 Numerical model of the inerter

In this section, a numerical model for the inerter is presented and validated against theoretical results. The proposed model, schematized in Figure 4, consists of two nodes connected through a rigid link, and an angular mass, J, assigned to the rotational degree of freedom of the system.

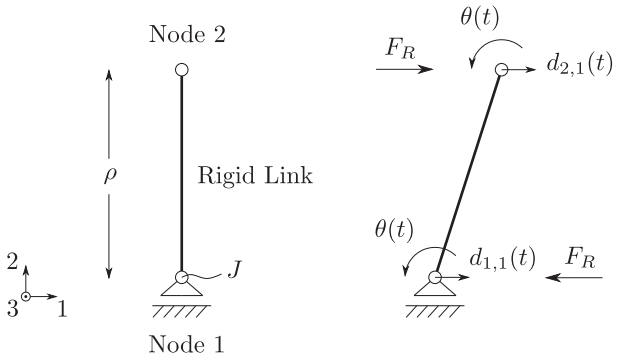

Figure 4: Schematic diagram of the numerical model of the inerter

The relative lateral displacement between the nodes is transformed into a rotation in Node 1 through a rigid link. Since a linear geometric transformation is considered for the link element, the relative displacement and rotation of the system are related according to:

$$d_r = d_{2,1}(t) - d_{1,1}(t) = -\rho\theta \tag{5}$$

The force couple required to impose this relative displacement, $F_R(t)$, can then be obtained evaluating the rotational equilibrium about Node 1:

$$F_R(t) = \frac{J\,\ddot{d}_r(t)}{\rho^2} = m_r\,\ddot{d}_r(t) \tag{6}$$

Therefore the reactive force developed by the model is proportional to the horizontal relative acceleration between Node 1 and Node 2. The parameters of the model, J and ρ, are then defined in terms of the inertance, m_r, according to Equation 6.

When the structure-inerter system is subjected to a ground excitation, part of the energy is transferred to the inerter and accumulated as angular momentum. As the translating mass of the structure tends to move slower, the rotating flywheels might drive the mass and induce undesirable deformations. Makris et al. [15] proposed the use of a clutch mechanism in order to ensure the system can only resist the motion of the structure. As a clutch-inerter device can only oppose one sense of motion, a parallel pair of inerters is necessary for this configuration. Additionally, a dissipative mechanism is needed to decelerate the flywheels once disengaged. The sequential engagement of the two parallel inerters that can only resist the motion is modelled redefining the rotational mass, J, after each time step according to:

$$F_R(t) = \begin{cases} m_r\,\ddot{d}_r, & \left[\frac{\ddot{d}_r}{\dot{d}_r}\right] > 0 \\ 0, & \left[\frac{\ddot{d}_r}{\dot{d}_r}\right] < 0 \end{cases} \tag{7}$$

2.3.1 Validation of the inerter model

The proposed numerical model was implemented in OpenSees [8] and validated against the analytical model developed by Makris et al [15]. The responses obtained with the numerical model and the corresponding solution of the equation of motion for a SDOF structure of period $T = 1[s]$ and $\sigma = 0.5$, subjected to a single sinusoidal pulse, are presented in Figure 5.

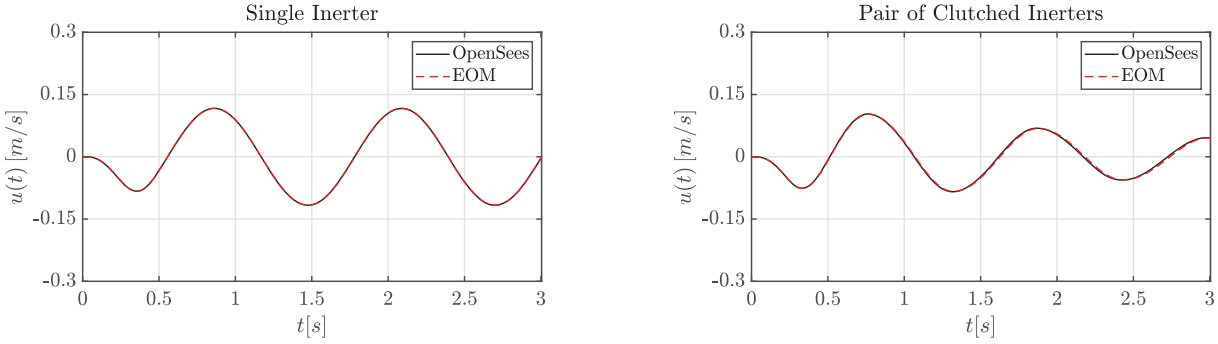

(a) Displacement response.

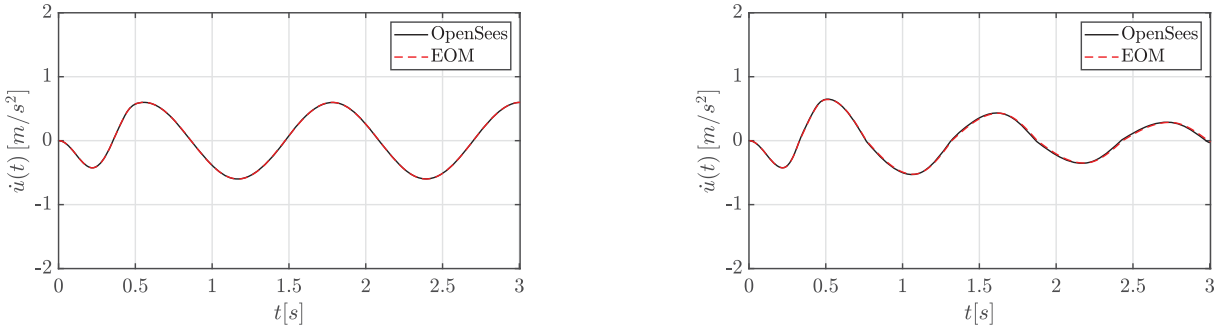

(b) Velocity response.

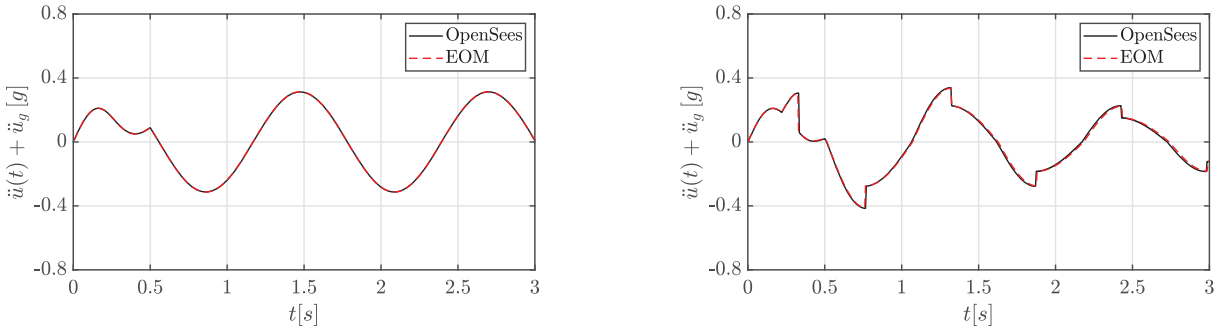

(c) Absolute acceleration response.

Figure 5: Comparison of the inerter numerical model and the solution of the equation of motion for a SDOF structure equipped with inerters of $\sigma = 0.5$, subjected to a single sine pulse of $T_0/T_g = 2$ and acceleration amplitue $a_g = 0.5[g]$.

2.4 Validation of the rocking structure-inerter model

As a final validation, the numerical models described in the previous sections are combined and compared with the analytical model for single-mass rocking structures equipped with inerters developed by Thiers-Moggia and Málaga-Chuquitaype [4]. This formulation, referred as VVEL, considers large rotations for the base and small deformations for the oscillator. The

numerical model, on the other hand, considers a corrotational transformation for the rocking body. In order to make both formulations comparable, the natural frequency of the OpenSees model is obtained considering P-Δ effects in the lateral stiffness of the system.

$$\omega_{n,OS} = \sqrt{\frac{3EI/h^3 - N/h}{m}} \tag{8}$$

Figure 6 compares the responses obtained for three structures of different levels of flexibilities and apparent mass ratios, subjected to single Ricker pulses of frequency ω_g and acceleration amplitude a_g.

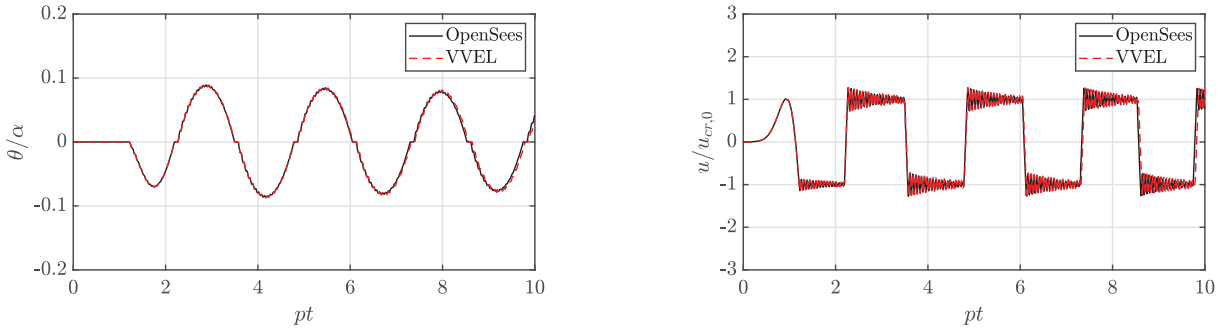

(a) $\omega_n/p = 10$, $\omega_g/p = 5$, $a_g = 1.5\,g\tan\alpha$, $\alpha = 0.1$, $\xi_{fc} = 0.01$, $\xi_{up} = 0.01\,B/R_0$ and $\sigma = 1$.

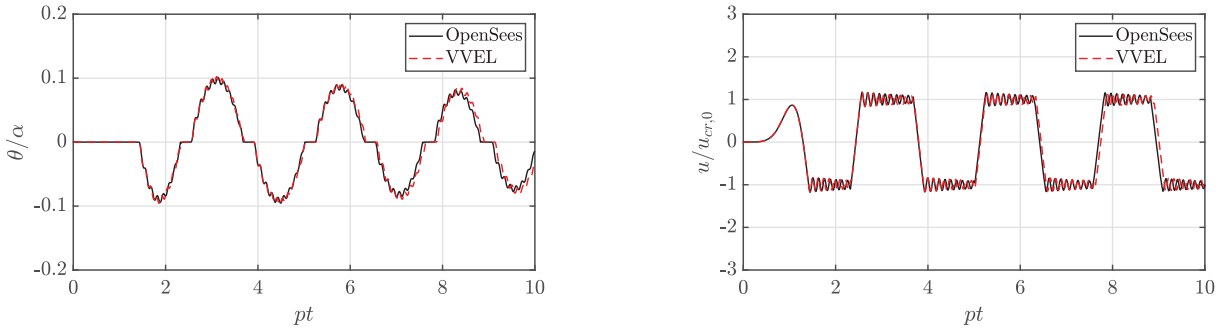

(b) $\omega_n/p = 5$, $\omega_g/p = 5$, $a_g = 1.5\,g\tan\alpha$, $\alpha = 0.1$, $\xi_{fc} = 0.01$, $\xi_{up} = 0.01\,B/R_0$ and $\sigma = 0.5$.

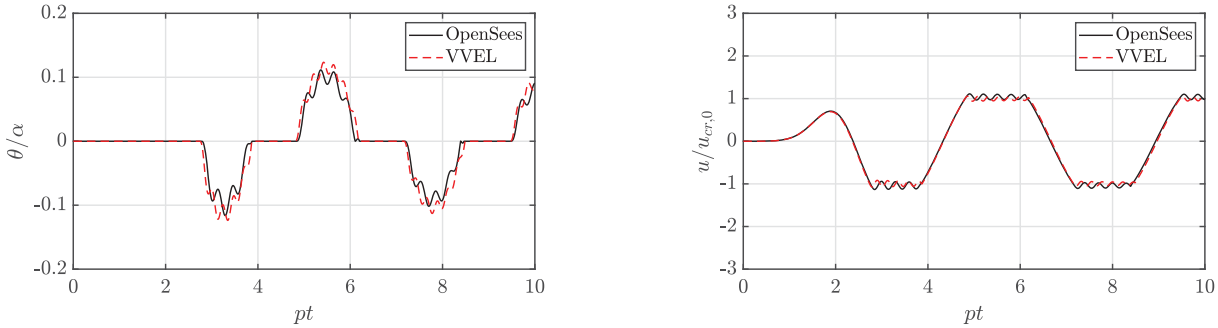

(c) $\omega_n/p = 2$, $\omega_g/p = 3$, $a_g = 1.5\,g\tan\alpha$, $\alpha = 0.1$, $\xi_{fc} = 0.01$, $\xi_{up} = 0.01\,B/R_0$ and $\sigma = 0.5$.

Figure 6: Comparison of the OpenSees numerical model and VVEL analytical model for rocking structures equipped with single inerters.

Excelent agreement between the two models is observed for the stiffer structures. However, small differences emerge in the amplitude of the rotation and elastic deformation responses as the oscillators become more flexible. This difference is partially explained by the variation of

the axial load, N, during the rocking motion which alters the lateral stiffness of the oscillator in the numerical model, an effect that becomes more significant in more flexible structures.

3 RESPONSE UNDER PULSE GROUND MOTIONS

Assuming a uniform distribution of stiffness and masses along the height of the structure, the rotation and deformation responses of the system shown in Figure 1a are a function of 10 parameters involving three fundamental dimensions:

$$[\theta, \underline{u}] = \phi \left(EI\,, m\,, m_r\,, \xi\,, n_{levels}\,, \alpha_{cg}\,, R_{cg}\,, \omega_g\,, a_g\,, g\,, t \right) \tag{9}$$

where α_{cg} and R_{cg} are the slenderness and radial distance of the centre of gravity, and ω_g and a_g are the excitation's frequency and acceleration amplitude, respectively. According to Vaschy-Buckingham's Π-theorem [16, 17], the response of the system can be described by $10 - 3 = 7$ dimensionless parameters:

$$\left[\frac{\theta}{\alpha_{cg}}, \frac{\underline{u}\,\omega_{n1}^2}{g \tan \alpha_{cg}} \right] = \phi \left(\frac{\omega_{n1}}{p_n}\,, \sigma\,, \xi\,, n_{levels}\,, \alpha_{cg}\,, \frac{\omega_g}{p_n}\,, \frac{a_g}{g \tan \alpha_{cg}}\,, p_n t \right) \tag{10}$$

where ω_{n1} is the first frequency of the MDOF oscillator, and $\omega_{n1}^2 / g \tan \alpha_{cg}$ represents the critical displacement of an equivalent SDOF oscillator of frequency ω_{n1} and slenderness α_{cg}. Figure 7 compares the dimensionless response of a 3-storey rocking structure of $\omega_{n1}/p_n = 35$, $\alpha_{cg} = 0.165$, $\xi = 0.01$, with and without inerters, subjected to a single Ricker pulse of frequency $\omega_g/p_n = 10$ and acceleration amplitude $a_g = 2\,g \tan \alpha_{cg}$.

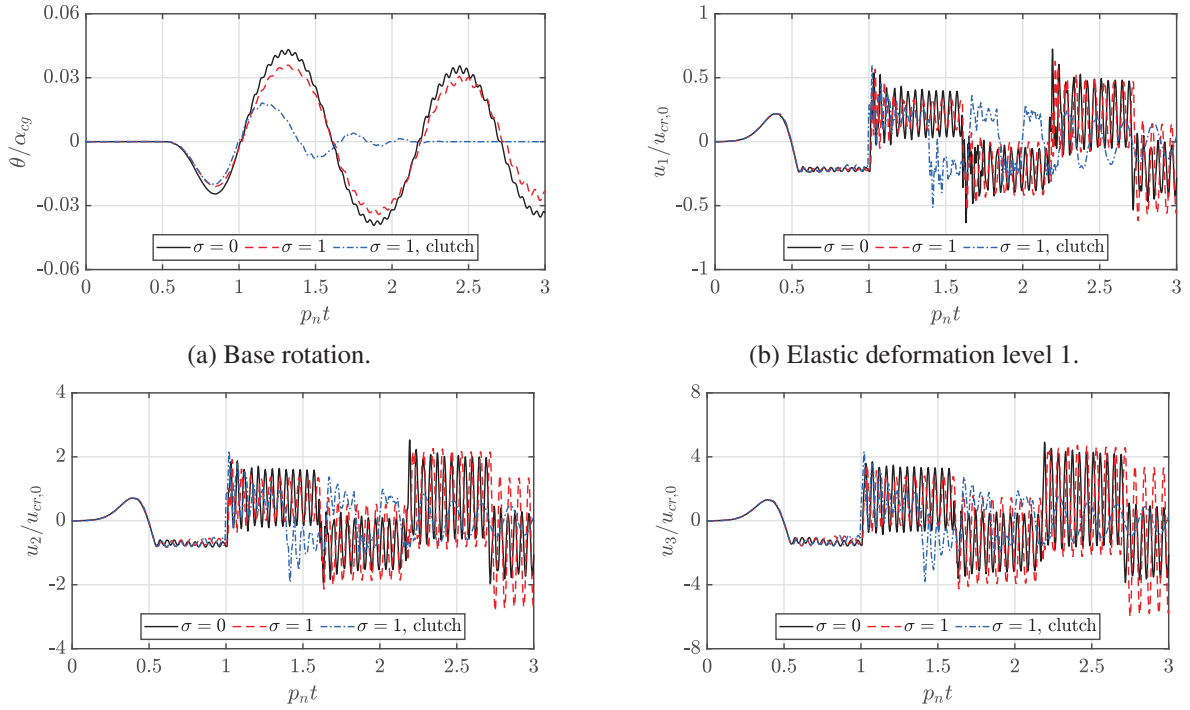

(a) Base rotation.

(b) Elastic deformation level 1.

(c) Elastic deformation level 2.

(d) Elastic deformation level 3.

Figure 7: Response of a 3-storey rocking structure of $\omega_{n1}/p_n = 35$, $\omega_g/p_n = 10$, $\alpha_{cg} = 0.165$, $\xi = 0.01$ and $a_g = 2\,g \tan \alpha_{cg}$ with and without inerters.

While the inclusion of the inerters considerably reduced the maximum base rotation, little effect is observed on the amplitude of the elastic deformations. This observation agrees with conclusions obtained in previous studies involving single-mass rocking oscillators [4]. Importantly, the introduction of the clutch significantly improves the efficiency of the inerter in reducing the rotation response. The effect of the clutch can be better examined by inspecting the total energy of the structure-inerter system, given by:

$$E_T = \frac{1}{2}\sum_{n=1}^{n_{levels}} m(\dot{x_i}^2 + \dot{y_i}^2) + \sum_{n=1}^{n_{levels}} mg(y_i - h_i) + \int_0^H \frac{M(y)^2}{2EI}dy + \frac{1}{2}\, m_r\, \dot{x_i}^2 \qquad (11)$$

where $\dot{x}_i$ and $\dot{y}_i$ are the horizontal and vertical velocities of the mass at the ith-level, and $M(y)$ corresponds to the bending moment at a height equal to y. Figure 8 shows the total energy of the same structure with different configurations of inerter devices normalized by $E_{ref} = mgR_{cg}(1 - cos\alpha_{cg})$, where E_{ref} represents the difference in potential energy of a rigid rocking structure between its unstable ($\theta = \alpha_{cg}$) and stable ($\theta = 0$)) equilibrium positions. Impact in each case is indicated with a solid circle.

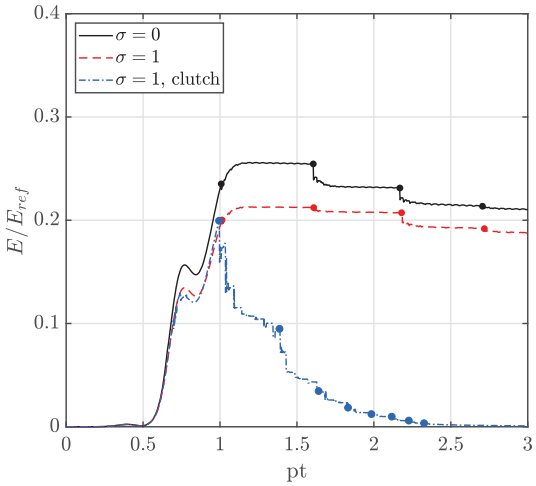

Figure 8: Total Energy of the structure-inerter systems.

It is clear from Figure 8 that the inclusion of the inerter limits the total energy absorbed by the system, while at the same time it reduces the amount of energy dissipated during each impact. This results in the lower peak rotation observed in Figure 7, with similar amplitudes in the later cycles of the rocking response. Such increase in the restitution coefficient is also predicted by conservation of moment of angular momentum equations [7].

Part of the total energy absorbed by the system is stored in the inerter device, as shown in the close-up view of Figure 9a. As the structure rocks and oscillates this energy is transferred back and forth, with the inerter alternately opposing and driving the motion. When the clutch is introduced, the inerter disengages from the structure and the energy stored in it is not transferred back to the oscillator. Assuming that the disconnected inerter is then able to dissipate this energy, every engagement-disengagement cycle removes energy from the structural system, increasing the speed at which the rotation and deformation responses are attenuated. Experimental analyses conducted by Málaga-Chuquitaype et al. [18] suggest that friction within the inerter can effectively dissipate part of the energy, while other researchers have suggested the addition of viscous fluids [15, 19]. This behaviour is illustrated in Figure 9b., where the engagement and disengagement of the inerter is indicated with blue and white backgrounds respectively.

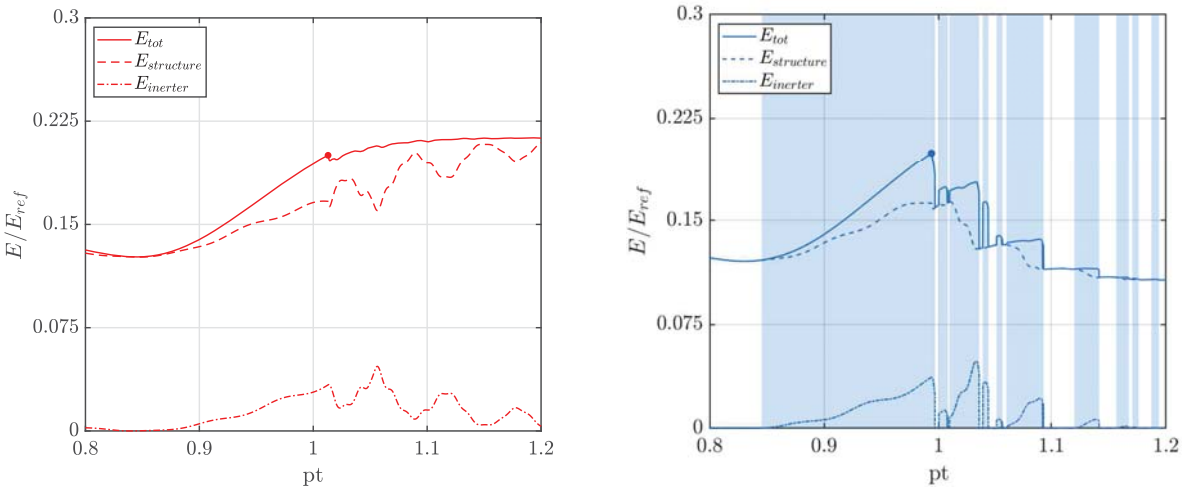

(a) Single inerter.

(b) Pair of clutched inerters.

Figure 9: Energy transfer between the inerter and the structure.

3.1 Response spectra

This section examines the response of multi-mass rocking structures equipped with inerters under a wider range of Ricker pulse ground motions. Figure 10, 11 and 12 summarize the response of a set of 3, 5 and 9-storey structures representative of walled buildings of $2B = 2\,[m]$ by $H = 9\,[m]$, $2B = 3\,[m]$ by $H = 15\,[m]$ and $2B = 3\,[m]$ by $H = 27\,[m]$, respectively.

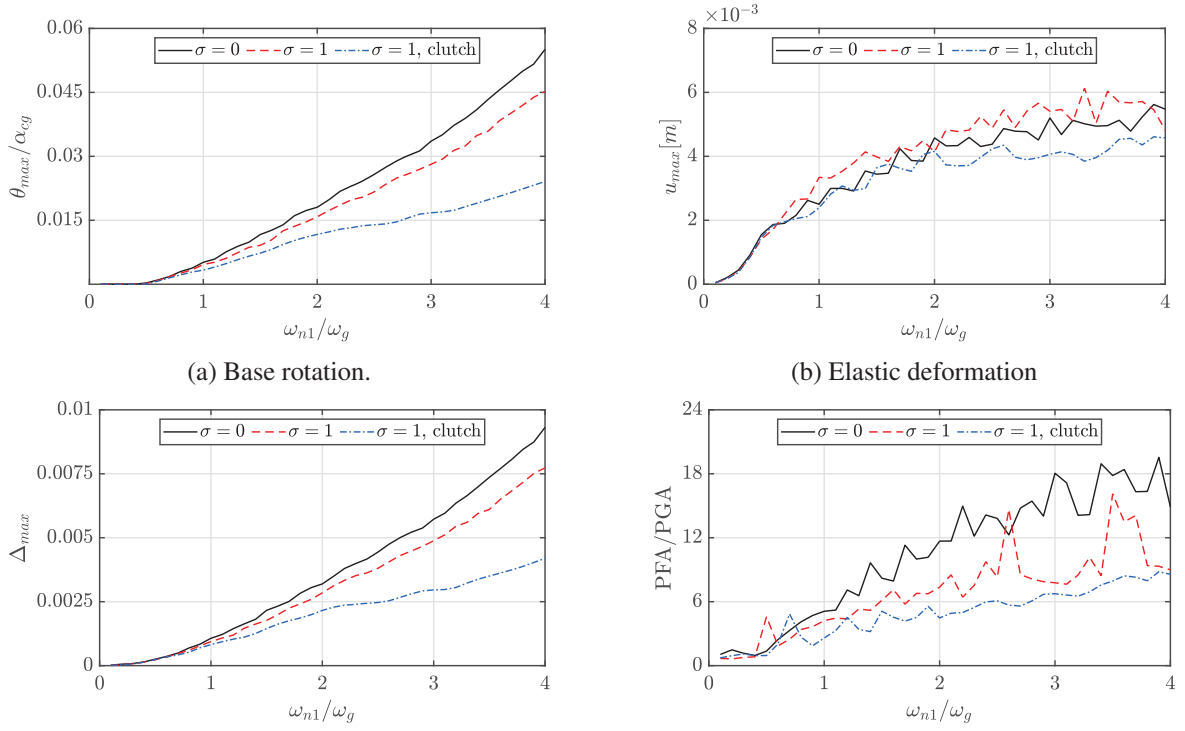

(a) Base rotation.

(b) Elastic deformation

(c) Drift

(d) Floor acceleration

Figure 10: Response of a 3-storey rocking structure of $\omega_{n1}/p_n = 35$, $\alpha_{cg} = 0.165$, $\xi = 0.01$, with and without inerters, under Ricker pulses of $a_g = 2\,g\tan\alpha_{cg}$.

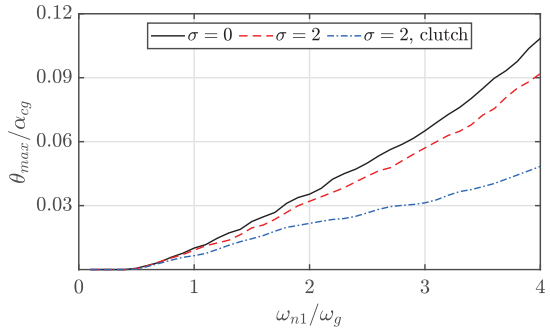

(a) Base rotation.

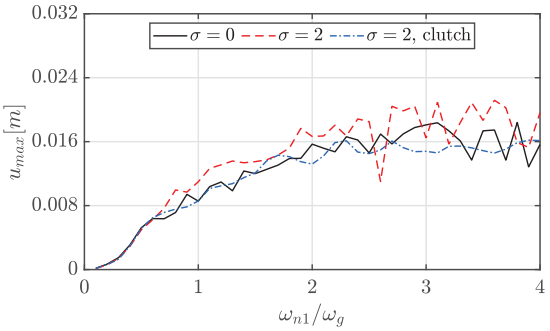

(b) Elastic deformation.

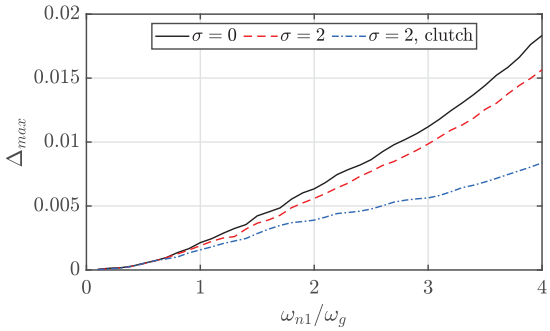

(c) Drift.

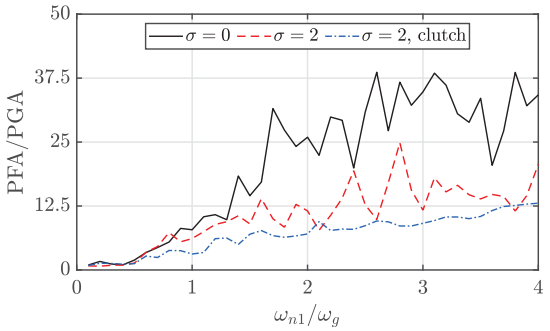

(d) Floor acceleration.

Figure 11: Response of a 5-storey rocking structure of $\omega_{n1}/p_n = 25$, $\alpha_{cg} = 0.12$, $\xi = 0.01$, with and without inerters, under Ricker pulses of $a_g = 2\,g\tan\alpha_{cg}$.

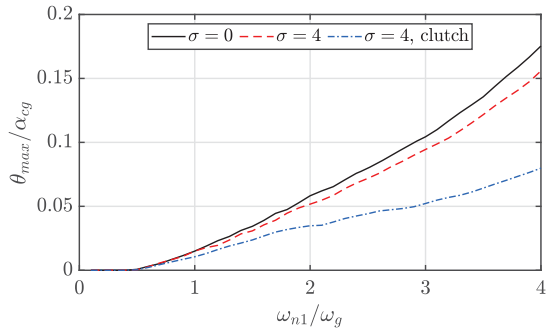

(a) Base rotation.

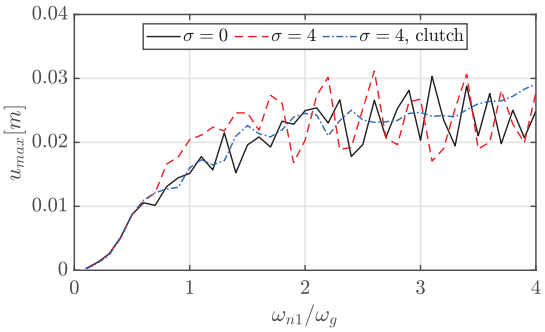

(b) Elastic deformation.

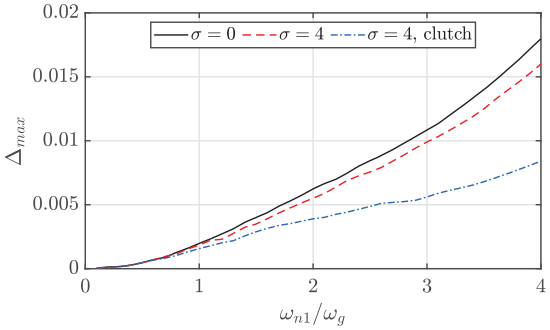

(c) Drift.

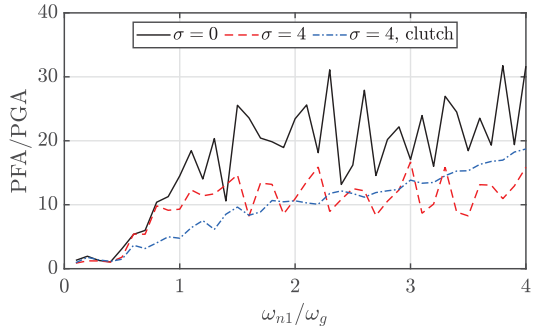

(d) Floor acceleration.

Figure 12: Response of a 9-storey rocking structure of $\omega_{n1}/p_n = 20$, $\alpha_{cg} = 0.1$, $\xi = 0.01$, with and without inerters, under Ricker pulses of $a_g = 2\,g\tan\alpha_{cg}$.

In all three cases, the addition of the inerter has very little effect on the rotation and elastic deformation responses for high frequency excitations ($\omega_{n1}/\omega_g < 1$). As the duration of the pulses increases, the rotation demands grow and the effect of the inerter becomes more significant, reaching reductions between 15% and 20% for $\omega_{n1}/\omega_g = 4$. Although this improvement happens at the expense of inducing slightly higher elastic deformations, this drawback does not translate into higher drifts, since the total lateral deformation is mainly controlled by the base rotation. On the other hand, the introduction of the clutch significantly improves the performance of the inerter, reducing also the elastic deformation response for the cases where uplift and rocking occurs. It is also important to note that, as the structure becomes taller, higher levels of inertances are required to obtain similar levels of response suppression. However, the actual mass of the inerter can be reduced thousands of times using amplification mechanisms such as ball-screws [20] or gear systems [21].

The maximum acceleration response in rocking structures is often controlled by impact forces. When a rigid elastic rocking surface is considered, these forces can cause significant spikes in the acceleration history. This behaviour can be clearly identified in Figure 10d, 11d and 12d, where considerably higher acceleration amplification ratios are registered once the rocking motion is triggered ($\omega_{n1}/\omega_g > 0.65$). The inclusion of the inerter consistently reduces these spikes, with further improvements when the clutch is added. Nevertheless, in very limited cases the protected structures may experience peak accelerations of slightly higher magnitude.

A sensitivity analysis is carried out in order to evaluate the effect of the rocking surface stiffness on the peak floor accelerations and the efficiency of the inerter in reducing them. Four stiffness values are considered: Rigid (10^{10}[GPa]), Steel (200[GPa]), Concrete (25[GPa]) and Timber (10[GPa]), while a depth of 0.3[m] is assumed for the rocking element.

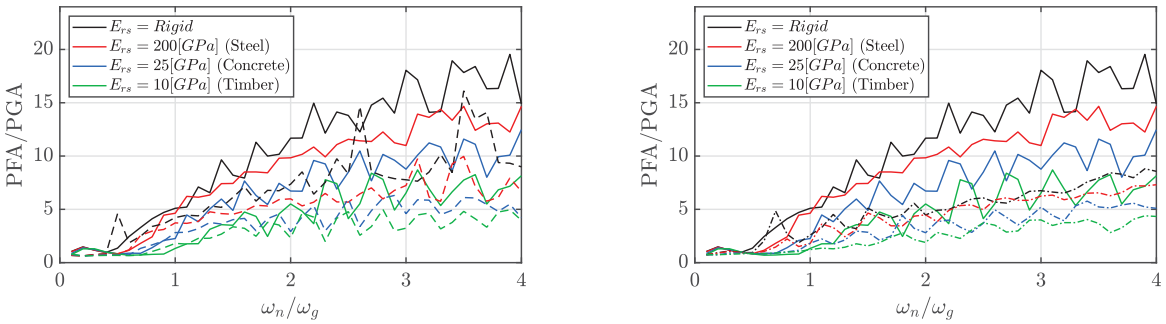

(a) Single inerter.

(b) Pair of clutched inerters.

Figure 13: Effect of the rocking base stiffness on the peak floor accelerations in a 3-storey building of $\omega_{n1}/p_n = 35$, $\alpha_{cg} = 0.12$, $\xi = 0.01$ and $a_g = 2g \tan \alpha_{cg}$ with and without inerters (dashed and continue lines respectively).

The results summarized in Figure 13 show that more rigid rocking surfaces are associated to larger floor accelerations . On the other hand, the efficiency of the inerter in reducing peak floor accelerations is not significantly affected by the flexibility of the rocking surface.

4 CONCLUSIONS

This paper investigated the alternative of using inerters to improve the seismic response of multi-mass rocking structures. Firstly, the numerical model proposed by Vassiliou et al. [10] was modified in order to account for experimental evidence related to the energy dissipated by

the rocking oscillator during the uplifted phase. Additionally, the study presented a numerical strategy to represent the inerter in finite element frameworks, such as OpenSees. The model of the full structure-inerter system was then validated against an analytical model of a single-mass rocking oscillator. Both formulations showed very good agreement for different levels of flexibility and excitation frequencies.

The proposed model was subsequently used to assess the dynamic response of a set of 3, 5 and 9-level structures subjected to analytical pulse excitations. Two inerter configurations were considered; a single inerter connected to the first level diaphragm, and a pair of clutched inerters that can only oppose the motion of the mass. The analyses showed that the inerter increasingly reduces the amplitude of the base rotation as the demands grow, with very little effect for high frequency excitations. Although this improvement happened at the expense of inducing slightly higher elastic deformations, this was not reflected on the total drift, as the lateral deformation of the system is mainly controlled by the base rotation. On the other hand, the introduction of the clutch consistently reduced both the rotation and elastic deformations demands. It was shown that this improvement is caused by the disengagement of the inerter which prevents the transference of the energy stored in it back into the structure. Finally, a sensitivity analysis was conducted in order to examine the influence of the rocking surface stiffness on the acceleration demands. The analyses showed that the efficiency of the inerter in reducing floor accelerations is not affected by the level of flexibility of the rocking interface.

REFERENCES

[1] A. Chopra and Y. SCS, "Simplified Earthquake Analysis of Structures with Foundation Uplift," *Journal of Structural Engineering*, vol. 111, no. 4, pp. 906–930, 1985.

[2] M. Priestley, "An overview of PRESSS research program," *PCI Journal*, vol. 36(4), 1991.

[3] A. Iqbal, S. Pampanin, A. Palermo, and A. H. Buchanan, "Performance and design of lvl walls coupled with ufp dissipaters," *Journal of Earthquake Engineering*, vol. 19, no. 3, pp. 383–409, 2015.

[4] R. Thiers-Moggia, *Seismic Protection of Rocking Structures with Inerters*. PhD thesis, Imperial College London, 2020.

[5] N. Makris and J. Zhang, "Rocking Response and Overturning of Anchored Equipment under Seismic Excitation," *Pacific Earthquake Engineering ResearchCentre, Berkeley*, 1999.

[6] M. Vassiliou and N. Makris, "Analysis of the rocking response of rigid blocks standing free on a seismically isolated base," *Earthq Eng Struct Dyn*, vol. 41, pp. 177–196, 2012.

[7] R. Thiers-Moggia and C. Malaga-Chuquitaype, "Seismic protection of rocking structures with inerters," *Earthquake Engng Struct Dyn*, vol. 48, pp. 528–547, 2019.

[8] S. Mazzoni, F. McKenna, M. Scott, and G. Fenves, *Open Systems for Earthquake Engineering Simulation User Command-Language Manual - OpenSees version-2.1.0*. Pacific Earthquake Engineering Research Center, University of California, Berkeley, CA, 2009.

[9] S. Acikgoz and M. J. DeJong, "Analytical modelling of multi-mass flexible rocking structures," *Earthquake Engineering & Structural Dynamics*, vol. 45, no. 13, pp. 2103–2122, 2016.

[10] M. F. Vassiliou, K. R. Mackie, and B. Stojadinović, "A finite element model for seismic response analysis of deformable rocking frames," *Earthquake Engineering & Structural Dynamics*, vol. 46, no. 3, pp. 447–466, 2017.

[11] G. Gazetas, "Analysis of machine foundation vibrations: state of the art," *International Journal of Soil Dynamics and Earthquake Engineering*, vol. 2, no. 1, pp. 2–42, 1983.

[12] S. Acikgoz and M. J. DeJong, "The interaction of elasticity and rocking in flexible structures allowed to uplift," *Earthquake Engineering & Structural Dynamics*, vol. 41, no. 15, pp. 2177–2194, 2012.

[13] R. Truniger, M. Vassiliou, and B. Stojadinovic, "An analytical model of a deformable cantilever structure rocking on a rigid surface: experimental validation," *Earthq Eng Struct Dyn*, vol. 44, no. 15, pp. 2795–2815, 2015.

[14] A. Chopra, *Dynamics of structures: Theory and applications to earthquake engineering*. International Series in Civil Engineering and Engineering Mechanics, Prentice Hall, Upper Saddle River, NJ, 2000.

[15] N. Makris and G. Kampas, "Seismic Protection of Structures with Supplemental Rotational Inertia," *Journal of Engineering Mechanics*, vol. 142, no. 11, pp. 1–11, 2016.

[16] A. Vaschy, " Sur les lois de similitude en physique," *Annales Telegraphiques*, vol. 19, pp. 25–28., 1892.

[17] E. Buckingham, "On physically similar systems; illustrations of the use of dimensional equations," *Phys. Rev.*, vol. 4, pp. 345–376, Oct 1914.

[18] C. Málaga-Chuquitaype, C. Menendez-Vicente, and R. Thiers, "Experimental and numerical assessment of the seismic response of steel structures with clutched inerters," *Soil Dynamics and Earthquake Engineering*, vol. 121, pp. 200–211, 03 2019.

[19] J. Hwang, J. Kim, and Y. Kim, "Rotational Inertia Dampers with Toggle Bracing for Vibration Control of a Building Structure," *Engineering Structures*, vol. 29, pp. 1201–1208, 2007.

[20] K. Ikago, K. Saito, and N. Inoue, "Seismic control of single-degree-of-freedom structure using tuned viscous damper," *Earthquake Engineering and Structural Dynamics*, vol. 41, no. 3, pp. 436–474, 2012.

[21] M. Smith, "Synthesis of mechanical networks: The Inerter," *IEEE Trans. Autom. Control*, vol. 47(10), pp. 1648–1662, 2002.

EURODYN 2020
XI International Conference on Structural Dynamics
M. Papadrakakis, M. Fragiadakis, C. Papadimitriou (eds.)
Athens, Greece, 23–26 November 2020

THE EFFECTS OF PARASITIC MASS ON THE PERFORMANCE OF INERTER-BASED DYNAMIC VIBRATION ABSORBERS

Hakan Dogan, Neil D. Sims, and David J. Wagg

University of Sheffield
Department of Mechanical Engineering, University of Sheffield, S1 3JD, UK
e-mail: {hdogan1, n.sims, david.wagg}@sheffield.ac.uk

Keywords: Inerter, Parasitic mass, Inerter-based dynamic vibration absorber.

Abstract. *This study investigates the effects of parasitic mass on the performance of inerter-based dynamic vibration absorbers (IDVAs). IDVAs have been increasingly employed to suppress vibrations in applications of civil engineering structures and vehicle suspension systems. While the masses of the components in a traditional dynamic vibration absorber can be easily compensated for due to its simple layout, the masses of the components in an IDVA can act as parasitic mass and might affect the performance of IDVAs. This can lead to the loss of benefits which is provided by the IDVAs. The negative effect of a parasitic mass in an IDVA can be observed in applications which have smaller inertance values. In such cases, it is important to consider masses of the components while selecting optimal parameters to maximize the performance improvement which can be obtained by an IDVA. In this study, a milling operation is modelled and its machining stability is increased by utilizing an IDVA. The negative effect of a parasitic mass on the performance is shown, and the performance improvement is regained by considering the parasitic mass in the tuning strategy.*

1 INTRODUCTION

Tuned mass dampers (TMDs) have been successfully employed to suppress vibration since the concept was introduced by Frahm [1] in the early 20th century. The device which was proposed by Frahm, the so-called dynamic vibration absorber (DVA), consists of an auxiliary mass and a spring. It targets the natural frequency of the system that is required to be controlled. Although it can successfully suppress vibrations at the resonance frequency, it allows high amplitude vibrations near the resonance frequency. This drawback of the DVA was modified by adding a viscous damper in the work of Den Hartog [2]. The resulting tuned mass damper (TMD) has the capability to suppress vibration at a wider range of frequencies. The tuning methodology was also developed by Den Hartog [2] using the fixed-points-theory.

To increase the performance of the TMD, a relative-acceleration-dependent-inertial element in conjunction with a spring and a damper, was studied by Kuroda [3]. This concept was analysed by many authors, for example Saito [4] investigated how it could be used to control seismic response of the structures. Similarly, the inerter, which was first introduced by Smith [5] by using the force-current analogy between mechanical and electrical networks, applies forces proportional to the relative acceleration between the two terminals. There are three types of inerter which have been mostly studied in the literature: the ball-screw inerter [6], the rack and pinion inerter [5, 6], and the fluid inerter [7]. Recently, the frictionless mechanical inerter that consists of a disc as flywheel and the living-hinges was presented to eliminate the friction that is caused by gears or ball-screw interaction [8]. Inerter-based vibration absorbers have been studied to improve the vibration performance of the system in vehicle suspensions [9, 10], civil engineering applications [11, 12, 13], landing-gear systems [14] and machining applications [15, 16].

Tuning parameters of the components of the inerter-based device plays an important role in the their vibration suppression performance. Lazar et al. [11] proposed a tuning strategy based on Den Hartog's fixed-points-theory for a tuned inerter damper (TID). Hu and Chen [17] used a direct search method to obtain design parameters of inerter-based dynamic vibration absorbers (IDVAs) for H_2 and H_∞ optimisations. Shen et al. [18] utilized a genetic algorithm to find the optimal parameters for the vibration suppression of the vehicle body controlled by an IDVA. Barredo et al. [19] presented an analytical methodology to obtain close-form solutions of three inerter-based configurations for an undamped primary system. Generally, the mass of the inerter is neglected in the mathematical model of the system during the process of finding the optimal parameters. This is because the inertance value of the inerter is generally very large compared to the mass of the inerter. However, for instance, the optimal inertance value for a small-primary-mass application can be small so that the mass of the inerter cannot be constructed small enough to neglect. In such cases, the mass of the inerter can act as a parasitic mass and lower the vibration suppression performance of the system being controlled.

This study investigates the effect of the parasitic mass caused by the mass of the components of the inerter. The novelty is that this parasitic mass is considered in the mathematical model and included in the evaluation of the performance of an IDVA. The effect of the parasitic mass is shown with two scenarios: the vibration suppression of a structure and the chatter stability of a milling operation. The effects of the parasitic mass are evaluated in the discussion section and finally the conclusions are presented.

2 PARASITIC MASS DUE TO AN INERTER

The inerter is a mechanical device which generates equal and opposite inertial forces proportional to the relative acceleration applied at the two nodes [5]. An ideal inerter can be represented as shown in Figure 1(a) and the schematic view of a physical realisation of the inerter [8] can be seen in Figure 1(b). The inerter in Figure 1(b) consists of a disc, which is the flywheel, in the middle and two legs that are the nodes of the inerter. The connections between the legs and the flywheel can be established by living-hinges to eliminate the friction and the backlash or by simple pin joints. The inertance of the inerter can be calculated as [8]

$$b = \frac{I_{disc}}{l_a^2} \tag{1}$$

where I_{disc} is the moment of inertia of the disc and l_a^2 is the distance between the points where the two legs are connected to the flywheel disc. Hence the inertial force generated by the inerter is

$$F_{inerter} = b(\ddot{x}_2 - \ddot{x}_1) \tag{2}$$

Equation 1 gives the inertance of an ideal inerter using a disc as a flywheel in Figure 1(b). The inertance values for the different types of inerters are calculated in a similar manner [5, 7, 20]. Once again, these inertance values are for an ideal inerter so the masses of the components of the inerter (e.g. the mass of the housing in a ballscrew inerter, the mass of the rack in a rack and pinion inerter or the mass of the legs in an inerter as shown in Figure 1(b)) are neglected. This is because the inertia of these parts is typically small compared with the inertance of the inerter device. Intrinsically, an inerter works as a kind of an inertia amplifier in most cases. Thus, it has higher inertance and the inertial increment in the device allows one to neglect the inertia of those which do not contribute this increment.

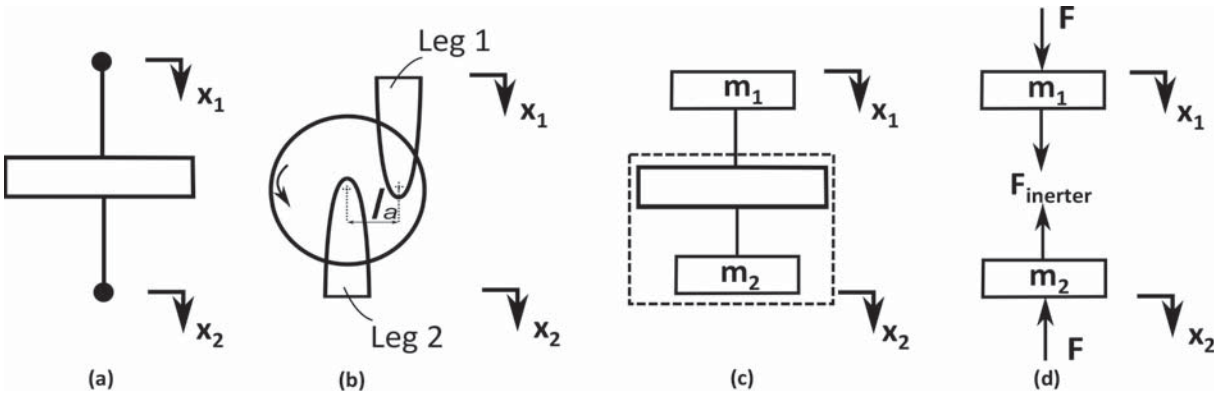

Figure 1: (a) Mathematical model of an ideal inerter, (b) schematic view of a small-scale mechanical inerter, (c) mathematical model of the inerter including the masses of legs and disc (the inertance value of the inerter involves only the rotational inertia of the disc.), (d) free body diagram of the inerter.

If the inertia of all components is considered, the mathematical model of an inerter becomes as shown in Figure 1(c) rather than in Figure 1(a). Leg 2 in Figure 1(b) is connected to the centre of the mass of the disc. The living-hinges or the pin joints, which are considered in the realisation, allow only rotational motion so that the disc and Leg 2 can be considered as rigidly connected in the translation motion. Hence, m_2 is the sum of the mass of the disc and the mass of Leg 2 while m_1 is equal to the mass of the Leg 1. The inertia of the inerter in Figure 1(c)

involves only the rotational inertia of the disc as expressed in Equation 1. Two inertial elements (m_1 and m_2) appear on the two nodes of the inerter in Figure 1(d) and induce the forces $m_1\ddot{x}_1$ and $m_2\ddot{x}_2$.

If the node with the inertial element is mounted on a spring or a damper, the inertial element (mass) acts as a parasitic mass between the inerter and the spring or the damper. The parasitic mass can be neglected in two cases where (1) the node with the inertial element has a ground connection or is mounted to another mass, and (2) the inertance value of the inerter is too large compared with the inertial element. Otherwise, the parasitic mass must be considered in the calculations.

3 MATHEMATICAL MODEL WITH A PARASITIC MASS

A tuned inerter damper consists of a spring which is connected to a damper in parallel, and an inerter which is in a series connection with the spring and the damper. Since one of the terminals of the inerter is connected to the spring and the damper, the parasitic mass can be observed in this configuration. The mathematical model of the TID with an ideal inerter is represented in Figure 2.

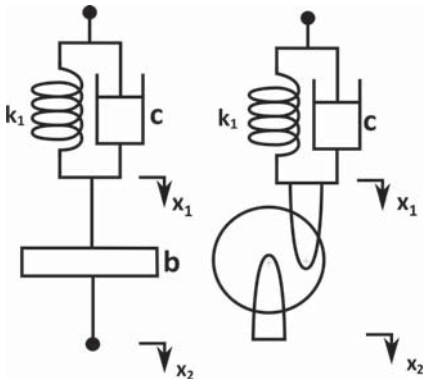

Figure 2: Mathematical model of a tuned mass damper with an ideal inerter, where the masses of the body of the inerter and the legs are neglected.

The TID can be employed to suppress a single-degree-of-freedom system which is under an excitation. The TID in a series connection with a spring, which is an IDVA, can be mounted to the primary system with a spring in series connection as shown in Figure 3(a). In reality, depending on the location of the inerter, either of the mathematical models in Figures 3(b) and 3(c) is a better representation than the model in Figure 2 due to the parasitic mass as discussed in the previous section. The upper nodes in Figures 3(b) and 3(c) are connected to the primary mass in Figure 3(a), and the bottom nodes are fixed to the auxiliary mass. Therefore, the inertial elements on these nodes can be neglected as the inertial element can be simply added to the mass which the nodes are connected to. Both of the mathematical models in Figure 3(b) and Figure 3(c) involve the parasitic mass m_p owing to the mass of the inerter as well as the masses of the spring and damper.

The location of the inerter, whether it is located in the bottom or the upper side, is not important if there is no parasitic mass between the inerter, and the spring and the damper. It matters if there is a parasitic mass since the equations of motion of the whole system will differ. The equations of motion for Figure 3(b), where the inerter is connected to the auxiliary mass (This layout is named in this paper as $icma$), can be written as

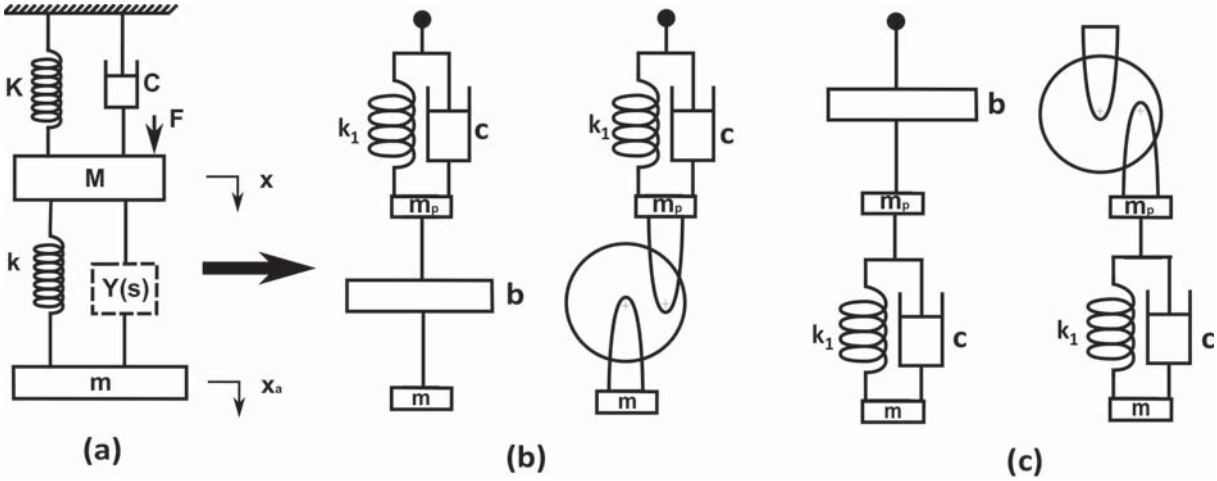

Figure 3: (a) Mathematical model of a structure controlled by an IDVA. Y(s) represents the impedance of the configuration in series connection with a spring. (b) Mathematical model of the case where the inerter is connected to the auxiliary mass,m (the $icma$). (c) Mathematical model of the case where the inerter is connected to the primary mass,M (the $icmp$).

$$\begin{aligned} M\ddot{x} + (C+c)\dot{x} + (K+k_1)x - c\dot{x}_p - k_1 x_p &= F \\ -c\dot{x} - k_1 x + (m_p+b)\ddot{x}_p + c\dot{x}_p + k_1 x_p - b\ddot{x}_a &= 0 \\ -b\ddot{x}_p + (m_a+b)\ddot{x}_a &= 0 \end{aligned} \tag{3}$$

where x, x_p and x_a are the displacements of the primary, parasitic and auxiliary masses, respectively. The equations of motion for Figure 3(c), where the inerter is connected to the primary mass (this layout is named in this paper as $icmp$), can be written as

$$\begin{aligned} (M+b)\ddot{x} + C\dot{x} + Kx - b\ddot{x}_p &= F \\ -b\ddot{x} + (m_p+b)\ddot{x}_p + c\dot{x}_p + k_1 x_p - c\dot{x}_a - k_1 x_a &= 0 \\ -c\dot{x}_p - k_1 x_p + m_a\ddot{x}_a + c\dot{x}_a + kx_a &= 0 \end{aligned} \tag{4}$$

The inertia of the parasitic mass is always added to the inertance of the inerter as seen Equations 3 and 4. Hence, the mass of the inerter is neglected if the inertance is too high.

4 THE EFFECT OF THE PARASITIC MASS

The system considered in this study to investigate the effect of the parasitic mass on the performance of a tuned inerter damper is depicted in Figure 3(a). A TID in series with a spring is mounted to the primary mass in a single-degree-of-freedom system to examine three mathematical models: No parasitic mass, the $icma$, and the $icmp$ cases. The effect of the parasitic mass on the vibration and chatter suppression performances is analysed.

4.1 Vibration Suppression Case

The study of Hu and Chen [17] has already shown that the inerter-based configuration which is presented in this work improved the vibration suppression performance of an undamped system. Therefore, a parasitic mass in this configuration can be considered to observe the effect

of the parasitic mass. The system with a parasitic mass is governed by either Equations 3 or 4, depending on the position of the inerter. The frequency response function (FRF) is given in the form as

$$H_i(j\omega) = \frac{X(jw)}{F(jw)} = \frac{R_{Ni} + jI_{Ni}}{R_{Di} + jI_{Di}}, \quad i = 1, 2, 3 \tag{5}$$

where $i = 1$, $i = 2$ and $i = 3$ represent for three mathematical models: No parasitic mass, the $icma$ and the $icmp$ cases, respectively.

The primary mass and the natural frequency of the primary system were taken as $M = 5\ kg$ and $f_n = 200\ Hz$. The primary system considered an undamped system and thus, $\zeta_{primary} = 0$. In order to obtain optimal design parameters (k, k_1, c and b), Self-adaptive Differential Evolution (SaDE) algorithm [21] can be utilized as a numerical optimisation method. The objective function for a constant mass ratio ($\mu = m/M$) can be written as

$$min_{k,k_1,c,b}\Big(max_{\omega}\big(|H_i(j\omega)|\big)\Big), i = 1, 2, 3 \tag{6}$$

since the minimisation of the maximum absolute value of the FRF is desired.

The optimal design parameters were found for mass ratio $\mu = 0.1$ and the case with no parasitic mass. The optimal inertance value for the case with no parasitic mass was found $b = 0.0965\ kg$. 5% and 10% of the inertance value, which are $4.8\ g$ and $9.6\ g$, were added as the parasitic mass to examine the two cases. For 5% parasitic mass, the optimal design parameters was obtained. The optimal parameters are given in Table 1 and the results are demonstrated in Figures 4 and 5.

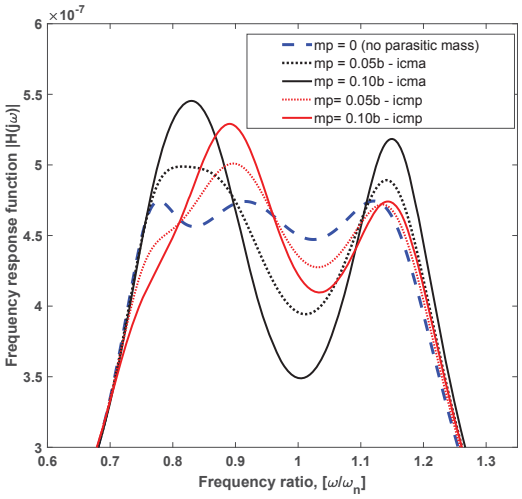

Figure 4: The magnitude of the FRF obtained from three cases: No parasitic mass, the $icma$ and the $icmp$ for parasitic masses of 5% and 10% of the optimal inertance value.

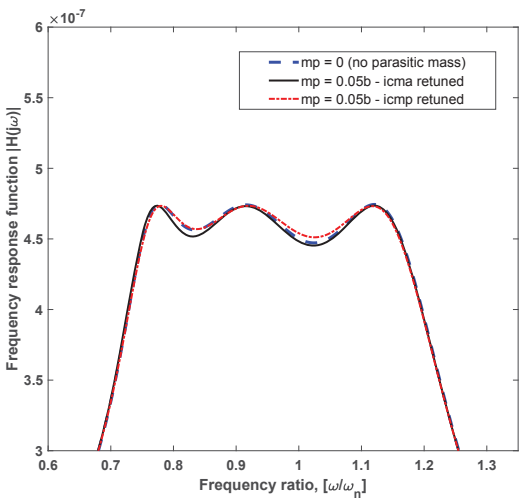

Figure 5: The magnitude of the FRF after retuning the optimal parameters considering a parasitic mass of 5% of the optimal inertance value.

The results show that both of the parasitic masses increased the amplitude of the vibration. The higher parasitic mass added caused the higher amplitude as shown in Figure 4. The $4.8\ g$ parasitic masses increased the amplitude of the displacement by 4.84% for the $icma$ and 5.39% for the $icmp$ After retuning the parameters for $4.82\ g$ parasitic mass, Figure 5 shows that the

Configurations	$m_p\ [g]$	$k\ [kN/m]$	$k_1\ [kN/m]$	$b\ [kg]$	$c\ [Ns/m]$
No parasitic mass	0	712.4	11.7	0.0965	60.3
$icma$	4.8	709.0	121.5	0.0999	64.5
$icmp$	4.8	721.5	115.2	0.0950	63.6

Table 1: Optimal design parameters obtained to suppress the vibrations in Figure 3(a) for $\mu = 0.1$.

same level of vibration suppression was provided again. Furthermore, the amplitude of the displacement was decreased by 0.2% compared to the case with no parasitic mass.

5 CASE STUDY ON MACHINING STABILITY

One potential application of inerters is in the suppression of vibrations during machining [15, 16]. Here, alternative methods for passive vibration control have already been proposed [22], and it has been shown that such approaches can improve the productivity by avoiding the onset of unstable self-excited vibrations known as chatter.

Consequently, this section provides a brief numerical case study to demonstrate how inerter systems can be used to suppress chatter. For simplicity, a turning configuration is chosen in order to demonstrate the concept without recourse to detailed theoretical analysis.

The mechanism which leads to regenerative chatter for a turning operation is briefly given here and explained comprehensively in [23, 24]. The cutting force which is applied to a flexible cutting tool leads to the waviness on the surface of the workpiece as shown in Figure 6. The phase difference (ε) between the waviness of the previous and the current cuts which are induced by the previous and the current displacements of the cutting tool, $y(t)$ and $y(t-T)$, causes a change in the instantaneous chip thickness. This variation in the instantaneous chip thickness induces a variation in the cutting force as the cutting force is proportional to the cross-sectional area of the chip and thus, the chip thickness. The variation in the cutting force leads to the waviness on the surface of the workpiece again. This regenerative mechanism can cause instability in the cutting operation.

The delay term T in the displacement in the previous cut $y(t-T)$ is introduced by the spindle rotation. Hence, for a machinist, two parameters which define the cutting force and accordingly a stable cut in a machining operation are the depth of cut and the spindle speed. The chatter stability of a machining process is generally evaluated over stability lobe diagrams (SLDs), which give the stability boundary in terms of the depth of cut for each spindle speed. The results for this study case will be presented as SLDs.

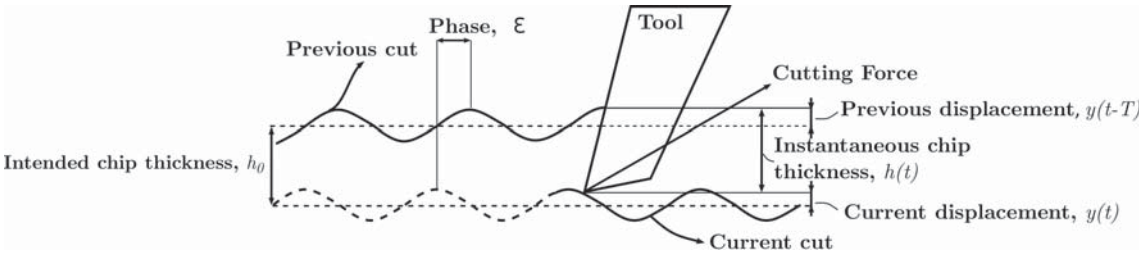

Figure 6: Depiction of a regenerative chatter mechanism

A chatter stability condition can be defined as the limiting depth of cut b_{lim}, which can be

simply expressed as [23]

$$b_{lim} = -\frac{1}{2K_s\Re\{H(j\omega)\}} \tag{7}$$

where K_s is specific cutting coefficient, which can be accepted as a constant term in this case and $Re\{H(j\omega)\}$ is the real part of the FRF of the system. The limiting depth of cut b_{lim} gives the stability boundary so the system becomes unstable beyond this value. The stability boundary can be increased by maximising the negative real part of the FRF when considering the depth of cut as a positive real number. Although Equation 6 is derived basing on a turning operation, it is approximately valid for a milling operation [22].

A milling operation can be reduced in a single-degree-of-freedom system so that Figure 3(a) can be used as the mathematical model of a machining operation controlled by a passive control device. Similar to the previous analysis, a parasitic mass can be added to the structure and the effects of the parasitic mass can be evaluated.

A similar analysis to the previous section was conducted. The primary mass, the natural frequency of the primary system and the damping ratio were taken as $M = 5\ kg$, $f_n = 200\ Hz$ and $\zeta_{primary} = 0.0035$. The milling operation parameters are presented in Table 2. The objective function for this case can be defined to maximise the negative minimum real part of the FRF of the system. Therefore, the objective function can be written as

$$max_{k,k_1,c,b}\left(min_{\omega}\big(\Re\{H_i(j\omega)\}\big)\right), i = 1, 2 \tag{8}$$

subject to $\Re\{H_i(j\omega)\} > 0$ and where $i = 1$, $i = 2$ and $i = 3$ represent for three mathematical models of no parasitic mass, the $icma$, and the $icmp$ cases, respectively.

Tool diameter	16 mm
Number of teeth	4
Radial immersion	4 mm
Tangential cutting stiffness	796.1 N/mm^2
Radial cutting stiffness	168.8 N/mm^2

Table 2: Milling simulation parameters

The optimal design parameters were found for mass ratio $\mu = 0.1$ and the case with no parasitic mass. The optimal inertance value for the case with no parasitic mass was almost the same as the previous case. Only 10% of the inertance value was added as the parasitic mass in the other two cases and the optimal design parameters were retuned. The optimal parameters are presented in Table 3. The stability boundaries are presented in Figures 7 and 8. The region under the stability boundary/curve represents a stable cutting condition. Thus, the higher curve means higher stability and hence improved productivity from the machining operation.

The stability lobe diagrams were compared with the stability diagram of the one controlled with a TMD whose optimal design parameters were obtained by Sims' tuning methodology [22]. It can be seen that the parasitic mass added into the configuration, whether the $icma$ or the $icmp$, removed the benefit of using an inerter as the stability boundary lowered to the level of one obtained with the TMD. The parasitic mass of $9.6\ g$ decreased the limiting depth of cut (the stability boundary) by 34.4% for the $icma$ and 17.6% for the $icmp$ configuration. After retuning the parameters considering the parasitic mass, the improvement obtained by using an inerter was regained as shown in Figure 8.

Configurations	m_p	$k\ [kN/m]$	$k_1\ [kN/m]$	$b\ [kg]$	$c\ [Ns/m]$
No parasitic mass	0	974.1	152.3	0.0956	69.2
$icma$	9.6 g	970.2	181.5	0.1048	82.7
$icmp$	9.6 g	996.6	157.6	0.0893	72.3

Table 3: Optimal design parameters obtained to increase machining chatter stability for $\mu = 0.1$.

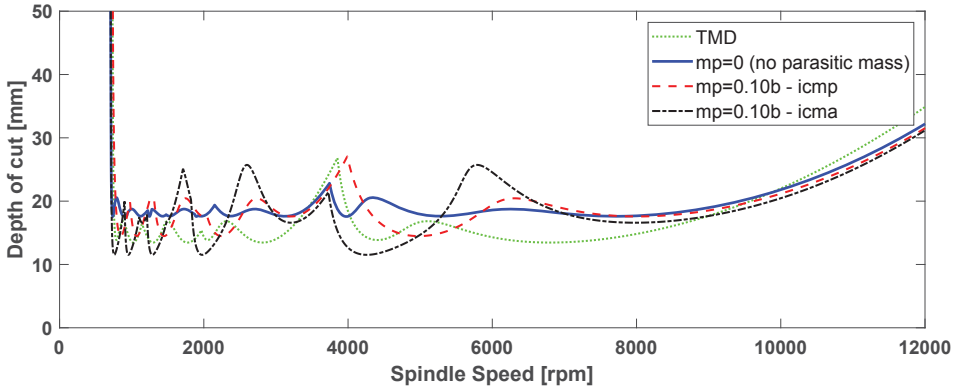

Figure 7: Stability lobe diagram obtained for three cases: No parasitic mass, the $icma$ and the $icmp$ by considering a parasitic mass of 10% of the optimal inertance value.

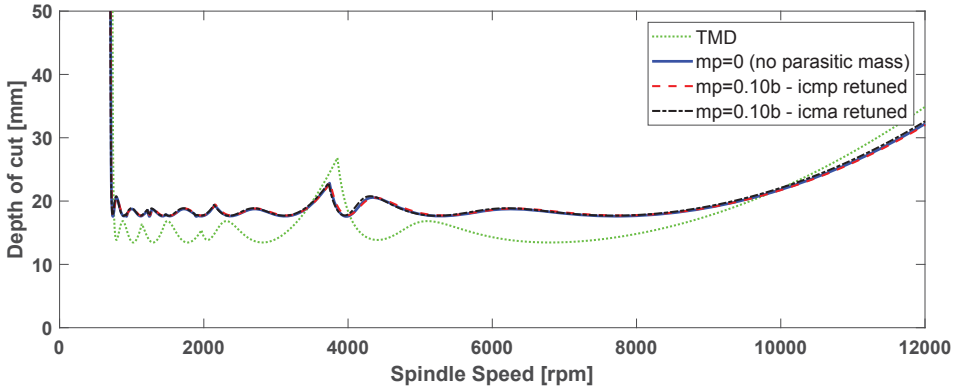

Figure 8: Stability lobe diagram after retuning the optimal parameters considering a parasitic mass of 10% of the inertance value.

6 Discussion

The results have shown that neglecting the mass of the inerter leads to a decrease in the vibration suppression and machining chatter stability performances since the optimal design parameters were obtained for the ideal condition, where the mass of the inerter is assumed as zero. For high ratios of the mass of the inerter to the inertance, the inertial effect of the mass of the inerter becomes insignificant as it is always coupled to the inertance (m_p+b) in the equations of motion. The structural mass of the inerter is generally designed to be small compared to the inertance but this cannot be always the case, especially for the applications where the modal mass of the primary system is small. It can be noted that the two cases for the location of the inerter the $icma$ and the $icmp$, had different behaviours. This should be considered in the design of the control device if the parasitic effect is inevitable.

Finally, it has seen that the improvement which is provided by using an inerter can be gained again by retuning the optimal parameters considering the parasitic mass. After the retuning the parameters, the results were slightly better than the result for an ideal inerter. The reason for this can be commented that the overall mass of the control device is increased by the parasitic mass. This can be seen as equal to the increase in the mass ratio. Therefore, it demonstrates slightly better performance.

7 Conclusion

The effects of the mass of the inerter on the performance of a system controlled by a inerter-based device was investigated for a generic vibration suppression scenario and also for the specific case of a machining dynamics problem. The mass of the inerter was assumed to be a lumped mass in the mathematical model and the FRFs were derived. Using the FRFs, the vibration suppression and machining stability performances of the system were examined. The result showed that if the ratio of the mass of the inertance to the inertance is not small enough, the mass of the inerter reduces the vibration performance of the system. However, the vibration performance was regained by retuning the optimal design parameters considering the parasitic mass.

REFERENCES

[1] H. Frahm, *Device for Damping Vibrations of Bodies*, 989,958 (1911).

[2] J. P. Den Hartog, Mechanical Vibrations, *McGraw-Hill, New York*, 1956.

[3] H. Kuroda, F. Arima, K. Baba, Y. Inoue, *Principles and characteristics of viscous damping devices (gyro-damper), the damping forces which are highly amplified by converting the axial movement to rotary one, 12th World Conference on Earthquake Engineering*, 2000.

[4] K. Saito, K. Yogo, Y. Sugimura, S. Nakaminami, K. Park, *Application of rotary inertia to displacement reduction for vibration control system, 13th World Conference on Earthquake Engineering*, 2004.

[5] M. C. Smith, *Synthesis of mechanical networks: the inerter, Proceedings of the 41st IEEE Conference on Decision and Control*, 2002.

[6] M. Z. Q. Chen, C. Papageorgiou, F. Scheibe, F. Wang, M. C. Smith The missing mechanical circuit element, *IEEE Circuits and Systems Magazine*, **9**, 10-26, 2009.

[7] F. Wang, M. Hong, T. Lin, Designing and testing a hydraulic inerter, *Journal of Mechanical Engineering Science*, **225**, 66-72, 2010.

[8] E. D. A. John, D. J. Wagg, Design and testing of a frictionless mechanical inerter device using living-hines, *Journal of the Franklin Institute*, **356** 7650-7668, 2019.

[9] M. C. Smith, F. Wang, Performance benefits in passive vehicle suspensions employing inerters, *Vehicle System Dynamics*, **42**, 235-257, 2004.

[10] Y. Hu, M. Q. Chen, Z. Shu, Passive vehicle suspensions employing inerters with multiple performance requirements, *Journal of Sound and Vibration*, **33**, 2212-2225, 2014.

[11] I. F. Lazar, S. A. Neild, D. J. Wagg, Using an inerter-based device for structural vibration suppression, *Earthquake Engineering and Structural Dynamics*, **43(8)**, 1129-1147, 2014.

[12] F. Wang, M. Hong, C. Chen, Building suspensions with inerters, *Proceedings IMechE, Journal of Mechanical Engineering Science*, **224**, 1605-1616, 2009.

[13] Y. Hu, J. Wang, M. Z. Q. Chen, Z. Li, Y. Sun, Load mitigation for a barge-type floating offshore wind turbine via inerter-based passive structural control, *Engineering Structures*, **177**, 198-209, 2018.

[14] Y. Li, J. Z. Jiang, S. Neild Inerter-based configurations for main-landing-gear shimmy suppression, *Journal of Aircraft*, **54(2)**, 684-693, 2017.

[15] F. Wang, C. Lee, R. Zheng, Benefits of the inerter in vibration suppression of a milling machine, *Journal of the Franklin Institute*, **356(14)**, 7689-7703, 2019.

[16] H. Dogan, N. D. Sims, D. J. Wagg, Investigation of the inerter-based dynamic vibration absorber for machining chatter suppression, *Journal of Physics: Conference Series*, **1264**, 2019.

[17] Y. Hu, M. Z. Q. Chen, Performance evaluation for inerter-based dynamic vibration absorbers, *International Journal of Mechanical Sciences*, **99**, 297-307, 2015.

[18] Y. Shen, L. Chen, X. Yang, D. Shi, J. Yang, Improved design of dynamics vibration absorber by using the inerter and its application in vehicle suspension, *Journal Sound and Vibration*, **361**, 148-158, 2016.

[19] E. Barredo, A. Blanco, J. Colin, V. M. Penagos, A. Abundez, L. G. Vela, V. Meza, R. H. Cruz, J. Mayen, Closed-form solutions for the optimal design of inerter-based dynamic vibration absorbers, *International Journal of Mechanical Sciences*, **144**, 41-53, 2018.

[20] F. Wang, M. Liao, B. Liao, W. Su, H. Chan, The performance improvements of train suspension systems with mechanical networks employing inerters, *Vehicle System Dynamics*, **47**, 805-830, 2009.

[21] A. K. Qin, P. N. Suganthan, *Self-adaptive differential evolution algorithm for numerical optimization, IEEE Congress on Evolutionary Computation*, 2005.

[22] N. D. Sims, Vibration absorbers for chatter suppression: a new analytical tuning methodology, *Journal of Sound and Vibration*, **301**, 592-607, 2007.

[23] T. L. Schmitz, K. S. Smith, Machining Dynamics: Frequency Respoonse to Improved Productivity, *Springer*, e-ISBN: 978-0-387-09645-2, 2009.

[24] Y. Altintas, Manufacturing Automation: Metal Cutting Mechanics, Machine Tool Vibration, and CNC Design, *Cambridge University Press*, ISBN: 978-0-521-17247-9, 2012.

EURODYN 2020
XI International Conference on Structural Dynamics
M. Papadrakakis, M. Fragiadakis, C. Papadimitriou (eds.)
Athens, Greece, 23–26 November 2020

VIBRATION CONTROL OF STEEL LIQUID STORAGE TANKS EQUIPPED WITH INERTER-BASED ISOLATION SYSTEMS

Daniele Zahedin Labaf[1], Maurizio De Angelis[1], and Daniele Pietrosanti[1]

[1]Sapienza, Università di Roma
Via Eudossiana 18- 00184- Roma
e-mail: {daniele.zahedinlabaf,maurizio.deangelis,daniele.pietrosanti}@uniroma1.it

Keywords: Vibration control; Base isolation; Inerter; cylindrical tanks; multiobjective optimal design; seismic response.

Abstract. *Base isolation represents a very widely used strategy to mitigate the effects of earthquake excitation on structures. However, it can induce high displacements between the isolation layer and the ground, which may cause serious damage, and even heavy and dangerous consequences in case of industrial components. Among them, big steel tanks for storage of petroleum or other chemical products, should be considered very carefully. Moreover, isolation technique doesn't seem to be effective in the control of the sloshing modes, due to the length of their periods of vibration. This fact can imply severe negative effects on the free surface of the storage tank, where the sloshing wave can exceed the upper limit of the tank, overtopping it, or inducing breaking on the floating roof.*

Moving from the results available in the Literature, in which the introduction in civil applications of a two terminal device, named inerter, able to generate an inertial mass much greater than its gravitational mass, is proposed; the force produced by the inerter is proportional to the difference of acceleration between its terminals. This work concerns the evaluation, through numerical models, of the seismic performance of a passive base isolation system involving a ground inerter system, called IBIS in the following, connecting the isolation layer of a steel liquid storage tank to the ground. The model considered in the numerical analysis consists in a reduced 2DOF linear system. The first degree of freedom is represented by the first sloshing mode; the second is relative to the base isolation system, whose mass includes the basement, the tank and the impulsive component of liquid mass.

The aim is to gain a reduction of the response in terms both of isolation layer displacement and of sloshing height.

The effectiveness of the control strategy proposed has been evaluated considering both a random white noise process and earthquakes (near-fault and far-field) as base input, achieving strong reduction of the response, in terms of sloshing height and isolation displacement.

1 INTRODUCTION

The seismic response of liquid storage tanks has been extensively studied by authors in the past decades [5, 6, 11]. The growth of interest in the engineering field is essentially due to the extremely severe consequences of accidents involving tanks, often occurring in petrochemical plants.

The seismic traditional base isolation has been the topic of both theoretical and experimental works, and its employment in the mitigation of the response of storage tanks has been already proposed, both in passive and semi-active control [7, 16]. Base isolation represents, in fact, a consolidated strategy, commonly used in passive structural control, as it is founded on modifying the structural stiffness of a structure, connecting the basement to the ground by deformable layer of isolators, able to create a flexible level in which the deformation is concentrated, uncoupling the structural displacement from the shaking ground. Therefore, the isolation technique typically acts on the structural stiffness, increasing the fundamental period of the structure, with the result of reducing both the base shear and the overturning moment of the tank, cutting the transfer of the earthquake-induced forces to the superstructure [1].

The employment of this technique presents two main drawbacks. One is related to the onset of the deformable layer, which can experience high displacements. The second one is due to the fact that the isolation period may draw a value comparable to the period of the sloshing modes, implying the incapability of controlling the convective response, or even increasing it.

This paper concerns the optimal design and effectiveness investigation of an isolation system arranged in parallel with a two-terminal device named inerter.

This device has been proposed by Smith and developed in the past years in mechanical engineering with the aim to suppress vibrations in vehicles. In fact, it is able to establish a difference in acceleration between its two terminals, so to produce an amplification mass effect, making the inertial mass much greater than the gravitational mass. This feature makes its use particularly interesting in passive vibration control. The constant of proportionality between the force produced by this device and the relative acceleration takes the name of inertance and has the dimensions of a mass.

The introduction of this device in Civil Engineering has been object of a series of theoretical [3, 4, 9, 10, 12] and experimental [13, 14] research studies. In fact, adding to a conventional TMD -small auxiliary mass- an inerter device- small gravitational mass but large inertial mass- it is possible to obtain a new system, named in literature TMDI, with high inertial mass ratio. This new system manages to combine positive features of a conventional TMD- small mass ratios- with those of an unconventional TMD- high mass ratio: lightness, due to a small auxiliary gravitational mass, and high efficacy and robustness, due to a high inertial mass ratio.

The introduction of inerter-based systems for the mitigation of the response of storage tanks has been already proposed in studies available in the Literature [8, 17]. For instance, Luo et al. proposed to introduce, in parallel with the isolation system, modeled as a linear visco-elastic, a system, called VMD, through which reductions of the sloshing response are achieved. Zhang et al. compared the performances of two different auxiliary control systems, which they plan to place in parallel, with respect to the linear visco-elastic isolation system, respectively a series or a parallel of an inerter and a linear viscous damper.

This work aims at proposing an optimization procedure used for the design of a novel non-conventional isolation system, based on a multi-objective approach, in order to achieve, concurrently, an effective control of the behaviour of both the convective and the impulsive part. Each of them represents a SDOF system, according to the model with lumped masses available in

literature. It is worth noticing that the problem the authors dealt with in this paper is similar to a procedure for the optimal tuning of a Tuned Mass Damper system [2, 7, 15], with the difference that the superstructure is here assigned and the aim of the design procedure is the identification of the optimal substructure, whose dissipative capacity, stiffness and inertance have to be found through the multi-objective optimization procedure.

The focus is mainly represented by broad tanks with a large radius, which are widespread throughout the country and typically characterized by a little ratio between the impulsive and the convective masses and by a great first sloshing period.

The paper is organized as follows. The mechanical model is illustrated and the governing equations of motion are derived in the next section. A multi-objective optimization problem is then set in section 3. The main results, in terms of Pareto fronts, frequency response functions and time-history analyses, are discussed in section 4.

2 MECHANICAL MODEL AND EQUATIONS OF MOTION

2.1 Mechanical model

Due to the complexity of the exact mathematical procedure to describe the complete model, an equivalent model, based on lumped masses and stiffnesses, can be introduced, assuming the fluid stored in the tank to be non viscous, incompressible and homogeneous and the flow field to be irrotational. Introducing hypotheses on the distribution of the hydrodynamic pressures, according to the model proposed by Housner for cylindrical tanks and developed by others, the liquid can be considered constituted by three components. The first one, known as impulsive, moves rigidly with the tank walls; the second one represents the interaction between the liquid stored in the tank and the walls; the last one experiences the sloshing motion.

Considering a cylindrical broad tank with circular shape, radius R, filled with a liquid of density ρ_L till a height H, the mass of the $i{-}^{th}$ convective mode can be expressed as:

$$m_U^i = m\frac{2}{s\lambda_i(\lambda_i^2-1)}tanh(s\lambda_i) \tag{1}$$

where m is the total liquid mass, calculated as $m = \pi\rho_L HR^2$, $s = \frac{H}{R}$ is the aspect ratio and λ_i is the $i{-}^{th}$ zero of the first derivative of the Bessel function of the first kind. The $i{-}^{th}$ circular frequency is represented by:

$$\omega_U^i = \sqrt{\frac{\lambda_i g tanh(s\lambda_i)}{R}} \tag{2}$$

The mass and the circular frequency of the first sloshing mode can be obtained substituting λ_1 = 1.8412 in Eqs.1-2. The component related to the liquid-walls interaction has been neglected. Furthermore, only the first sloshing mode is taken into account. The impulsive mass m_L can be derived as:

$$m_L = m - m_U^1 \tag{3}$$

The mechanical model of the proposed isolated reduced order 2DOF system is sketched in Fig.1. A traditional linear base isolation system, called BIS in the following, represented by a SDOF system, whose mass, stiffness and viscous damping coefficients are denoted by m_L, k_L and c_L, is combined with an inerter. Therefore, the connection between the basement and the ground is modeled as a parallel of a Kelvin-Voigt viscoelastic element and a linear inerter.

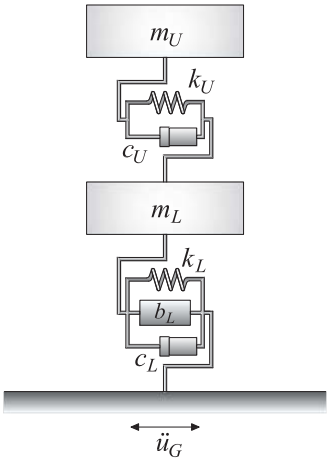

Figure 1: Mechanical model of the 2DOF system.

Table 1: Dimensionless parameters involved in the proposed model.

Description	Symbol	Definition
Isolation damping ratio	ξ_L	$\frac{c_L}{2\sqrt{k_L m_L}}$
Convective damping ratio	ξ_U	$\frac{c_U}{2\sqrt{k_U m_U}}$
Mass ratio	μ	$\frac{m_U}{m_L}$
Frequency ratio	δ	$\frac{\omega_L}{\omega_U}$
Inertial mass ratio	β	$\frac{b_L}{m_L}$

2.2 Equations of motion

The equations of motion of the reduced 2 DOFs for the Inerter Base Isolated System (IBIS), written in terms of the dimensionless parameters listed in Tab.1, result:

$$\begin{gathered}\ddot{u}_L(t) + 2\mu\xi_U\omega_U(\dot{u}_L(t) - \dot{u}_U(t)) + \mu\omega_U^2(u_L(t) - u_U(t)) + \frac{f_c(t)}{m_L} = -\ddot{u}_g(t) \\ \mu\ddot{u}_U(t) + 2\mu\xi_U\omega_U(\dot{u}_U(t) - \dot{u}_L(t)) + \mu\omega_U^2(u_U(t) - u_L(t)) = -\mu\ddot{u}_g(t) \\ \frac{f_c(t)}{m_L} = [\beta\ddot{u}_L(t) + 2\xi_L\delta\omega_U\dot{u}_L(t) + \delta^2\omega_U^2 u_L(t)]\end{gathered} \tag{4}$$

where $u_L(t)$ and $u_U(t)$, collected in $\mathbf{u}(t)$, respectively represent the displacement of the lower (L) and upper (U) oscillators with respect to the ground, the overdot indicates differentiation with respect to time t and where $\omega_U = \sqrt{\frac{k_U}{m_U}}$ and $\omega_L = \sqrt{\frac{k_L}{m_L}}$. Then, the dimensionless sloshing height, with respect to R, can be calculated as:

$$h(t) = \frac{2(\ddot{u_U}(t) + \ddot{u_g}(t))}{g(\lambda_1^2 - 1)} \tag{5}$$

The Equations which govern the problem of a base isolated system without involving the linear inerter can be obtained from the Eq.4 equaling to zero the inertance contribution. In fact, if the inertance is null, the control system falls back in a base isolation system.

Taking into account the probabilistic nature of the earthquake excitation, neglecting instead the dependence on the excitation frequency, the ground acceleration $\ddot{u}_g(t)$ is firstly modeled

as a Gaussian zero mean white noise random process with power spectral density $S_{\ddot{u}_g} = S_0$. Therefore the stochastic properties are assumed to describe the system response. Rewriting the governing equations of motion in the first-order state space form:

$$\dot{z}(t) = \mathbf{A}\mathbf{z}(t) + \mathbf{B}a(t) \tag{6}$$

where

$$\mathbf{z}(t) = \left[\begin{array}{cc} \mathbf{u}(t) & \dot{\mathbf{u}}(t) \end{array} \right]^{\mathrm{T}} \tag{7}$$

is the state vector, $a(t)$ is the applied input process, the matrices **A** and **B** are the state matrix and the input vector, respectively. Since the stationary input process has zero mean and the initial conditions are zero, the response is fully represented by the covariance matrix $\mathbf{G}_{zz}$, that satisfies, by virtue of the stationarity of $\mathbf{z}(t)$, the Lyapunov Equation:

$$\mathbf{A}\mathbf{G}_{zz} + \mathbf{G}_{zz}\mathbf{A}^T + 2\pi S_0 \mathbf{B}\mathbf{B}^T = \mathbf{O} \tag{8}$$

The variances of the displacements of the two oscillators in the controlled configuration, found solving numerically the Eq.8, respectively σ_L^2 and σ_U^2, have been normalized by dividing each of them by σ_{U0}^2, which represents the variance of the displacement of the upper mass with respect to the ground in absence of control, obtaining:

$$I_U = \sqrt{\frac{\sigma_U^2}{\sigma_{U0}^2}} \quad \text{and} \quad I_L = \sqrt{\frac{\sigma_L^2}{\sigma_{U0}^2}} \tag{9}$$

3 MULTI-OBJECTIVE OPTIMIZATION OF THE IBIS

In this section the optimal design of the control system is discussed.

Not all the dimensionless parameters listed in Tab.1 get involved in the optimization procedure as design parameters. In fact, in this work, the sloshing damping factor ξ_U and the mass ratio μ have been supposed known; whereas the three dimensionless parameters referred to the IBIS, i.e. the frequency ratio δ, the damping factor ξ_L and the inertial ratio β, assume the role of design parameters to be optimized. Therefore the proposed procedure aims at designing the optimal connection between the basement of the tank and the ground.

Aiming at achieving the overall protection of both the sub-structures, preserving both the primary and the secondary structures, a multi-objective design criterion has been adopted. Two objective functions have been selected to be minimized: these are the displacement of the upper system relative to the basement- the sloshing displacement- and the lower system displacement relative to the ground- basement displacement. These two functions are in conflict. It is in fact worth noticing that a more effective reduction of the secondary system displacement inevitably corresponds to a worse control of the response of the impulsive displacement. The identification of a solution which corresponds to a minimum- optimal value- for all the objective functions is allowed if they do not conflict with each other.

Therefore, in this case, none of the objective functions can be improved without negative consequences on the other one. Thus, the problem can be stated in the form:

$$\text{find} \qquad min \quad [\mathbf{F}(\mathbf{x})] \qquad \text{subjected to } \mathbf{x}^{min} \leq \mathbf{x} \leq \mathbf{x}^{max} \tag{10}$$

In other terms, the multi-objective optimization procedure consists in finding the design vector **x**, which components vary in a space, capable to minimize the vector of the objective functions **F**(**x**). As a consequence the identification of a unique solution is no longer possible, instead a set of solutions which constitute the Pareto front can be detected.

Table 2: Geometrical and mechanical tank properties [1].

Radius	$R\ [m]$	27.43
Maximum filling level	$H\ [m]$	13.71
Elastic modulus of the tank	$E\ [MPa]$	210000
Steel density	$\rho_s\ [\frac{kg}{m^3}]$	7900
Liquid density	$\rho_L\ [\frac{kg}{m^3}]$	1000
Total liquid mass	$m\ [kg]$	3.24e+07
Convective mass	$m_U\ [kg]$	2.14e+07
Impulsive mass	$m_L\ [kg]$	1.10e+07

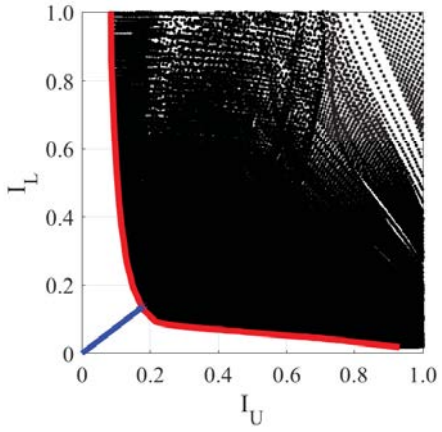

Figure 2: Optimal design of the control system by the Pareto Front.

4 NUMERICAL INVESTIGATIONS

The procedure explained in the previous section has been adopted assuming a case study, whose geometrical and mechanical properties are collected in Tab.2. The results are discussed in this section.

The sloshing damping factor ξ_U = 0.005 and the mass ratio μ = 2.0 have been fixed (see Tab. 1-2) .The three dimensionless design parameters vary in the ranges shown in Tab.3.

4.1 Multi-objective optimization

The problem stated in the previous section can be fitted to the case under consideration substituting in **x** the vector containing the three design parameters:

$$\mathbf{x} = \left[\begin{array}{ccc} \xi_L & \delta & \beta \end{array} \right]^{\mathrm{T}} \tag{11}$$

and considering the following vector of the objective functions:

$$\mathbf{F}(\mathbf{x}) = \left[\begin{array}{cc} I_U(\mathbf{x}) & I_L(\mathbf{x}) \end{array} \right]^{\mathrm{T}} \tag{12}$$

The results obtained applying to the system a base motion, modeled as a white noise random input, are illustrated in this section. Both the Pareto front and the performance of the proposed

Table 3: Space of the dimensionless design parameters.

Description	Symbol	$\mathbf{x}^{min}$	$\mathbf{x}^{max}$
Isolation damping ratio	ξ_L	0.01	0.50
Frequency ratio	δ	0.10	10.0
Inertial mass ratio	β	0	10.00

Table 4: Optimal dimensionless parameters found through the multi-objective procedure.

Description	Symbol	Optimal value
Isolation damping ratio	ξ_L	0.50
Frequency ratio	δ	2.24
Inertial mass ratio	β	5.10

IBIS are shown in Fig.2, from which the achievement of a meaningful reduction of the structural response in a large portion of the plan can be deduced.

Moreover the existence of a limit curve, the Pareto front, which delimits a region to whom the access is denied, is highlighted. Among all the points belonging to the Pareto front, the point of minimum distance- blue line in Fig.2- from the origin of the axes has been chosen as the point of the optimality.

At least a triplet of specific values of the dimensionless parameters ξ_L, δ, β can be associated to each point on the plan in Fig.2. Depending on both the ranges of variation of parameters and the number of steps assumed in the analysis, a complete filling of the plan (I_U, I_L) can be achieved, except for the forbidden area.

The triplet of dimensionless parameters associated to the point of optimal performance is listed in Tab.4. Some comments on the optimal values obtained should be done. It is, in fact, worth noticing that ξ_L attains the maximum value ξ_L^{max}, β^{opt} falls in the middle of the range of variation, taking a fairly high value, attesting the inertance beneficial contribution, and δ^{opt} is greater than one, which implies that the period of the control isolation system is lower than the convective period. Instead, values of δ lower than one stand for sloshing mode period stiffer than the isolation system. With the aim of avoiding the onset of crises due to static actions, the adoption of a too flexible isolation system, i.e. the assumption of small values of δ, should be also excluded.

4.2 Sensitivity analyses

Dealing with the issue of establishing the robustness of the proposed seismic mitigation strategy, sensitivity analyses have been performed in order to evaluate the influence of each dimensionless parameter pertinent to the control system on the reduction of the response, paying attention to the system behaviour in a neighborhood of the optimal point.

Denoting with I the ratio between the distance of the current point on the plan (I_U, I_L) from the origin of the axes and the distance of the point of optimal performance, the contour plots obtained fixing $\delta = \delta^{opt}$ and varying the other two parameters around the optimal values are illustrated in Fig.3. The values of the dimensionless parameters divided by the corresponding values in Tab.4 take the superscript N.

The red point in the middle of Fig.3 (B) represents the point of optimality (see Tab.4). It can be noticed that a better control of the response can be achieved increasing ξ_L, suggesting that ξ_L increments induce an advancement of the Pareto Front towards the origin of the axes. Refer, e.g., to the green (D) and red (B) points in Fig.3, which are associated to the same value

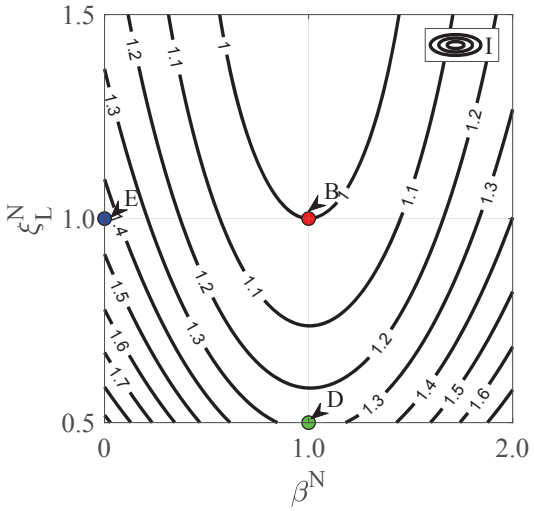

Figure 3: Contour plots of I, assuming δ^{opt}.

Table 5: Optimal dimensionless parameters found through the multi-objective procedure selected for the analyses performed in time and frequency domain.

Description	Symbol	A	B	C
Isolation damping ratio	ξ_L	0.15	0.50	0.50
Frequency ratio	δ	2.56	2.24	1.55
Inertial mass ratio	β	6.8	5.1	0

of β but to different values of ξ_L. Moving on a vertical line, it is also shown in Fig.3 that further increasing ξ_L beyond the optimal value does not lead to a meaningful improvement of the performance. Furthermore, the existence of a minimum for β is well stressed, implying that the selection of a β value should be done carefully.

Fig.3 can be used in order to compare the performance of a IBIS - red point- with respect to a BIS- blue point (E), characterized by the same ξ_L, highlighting the achievement of a reduction of I thanks to the employment of the inertance.

4.3 Evaluation of the IBIS seismic performance

The frequency transfer function curves of sloshing displacement and isolation displacement are represented. The values of the parameters are listed in (Tab.5).

In (Fig.4) the effectiveness of the optimally designed IBIS is shown, through the representation of the frequencydomain transfer function curves, from which an effective response mitigation for both sloshing height and isolation displacement can be deduced. For comparative purposes, the responses of an optimized system characterized by a lower xi_L value (A) and of an optimized BIS (C) are shown.

In order to evaluate and assess the seismic effectiveness of the designed control system object of this work, numerical simulations have been carried out, assuming different base motion histories. Time-history analyses have been carried out on the 2DOF system both in the fixed

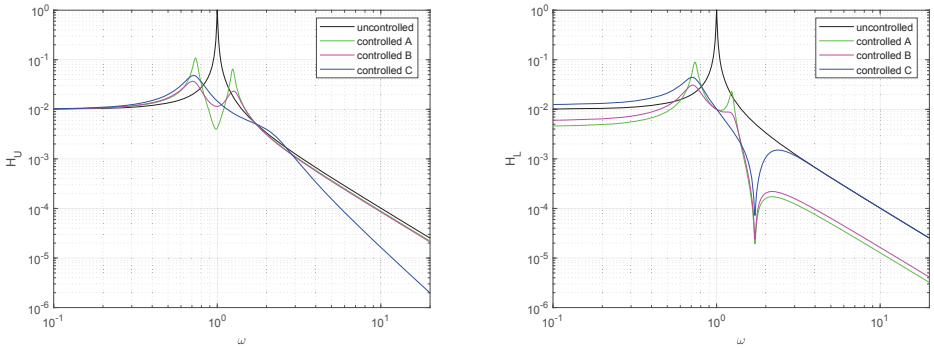

(a) (b)

Figure 4: Frequency transfer functions of a) sloshing height and b) isolation displacement.

base tank configuration and in the IBIS.

Two quantities have been monitored in order to evaluate the response, i.e. sloshing heights and basement displacements relative to the ground. The responses in time domain in terms of sloshing heights and isolation displacement are illustrated. The values are normalized by dividing the sloshing height and the basement displacement by the peak value of the sloshing height in the uncontrolled configuration. The dimensionless indices obtained make the interpretation of the results easier, in the sense that a value smaller than one means an effective reduction of the response quantities, whereas a value greater than one implies an amplification of the response with respect to the reference configuration. The results shown refer to a system involving the optimal set of parameters.

5 CONCLUSIONS

A novel strategy for controlling the sloshing response of seismically excited liquid storage tanks with rigid walls based on an inerter- based isolation system has been developed in this paper. The studies are carried on a reduced 2DOF system. With the aim of controlling at the same time the displacements of the two coupled oscillators- one pertinent to the sloshing part of liquid mass, the second one comprehensive of the impulsive part of the total liquid mass- the design parameters of the inerter- based isolation system, that is, its damping coefficient, its stiffness and its inertial mass, called inertance, are optimized by stating a Pareto multi-objective optimization problem, minimizing the two objective functions related to the displacements of the two oscillators, assuming as a base input a ground acceleration modeled as a Gaussian stochastic process with white noise power spectral density. On the basis of the defined design method an optimized system, able to effectively control both the sloshing and the isolation response, has been obtained.

Sensitivity analyses, in which the influence of the dimensionless parameters selected as representative of the added vibration control system is investigated, have been conducted. Thus, the role of the design parameters in the deployment of points in the plan depicted has been extensively investigated.

Results obtained by subjecting the system to a series of near fault and far field earthquakes as well as synthetic accelerograms were subsequently reported, showing the gaining of mean-

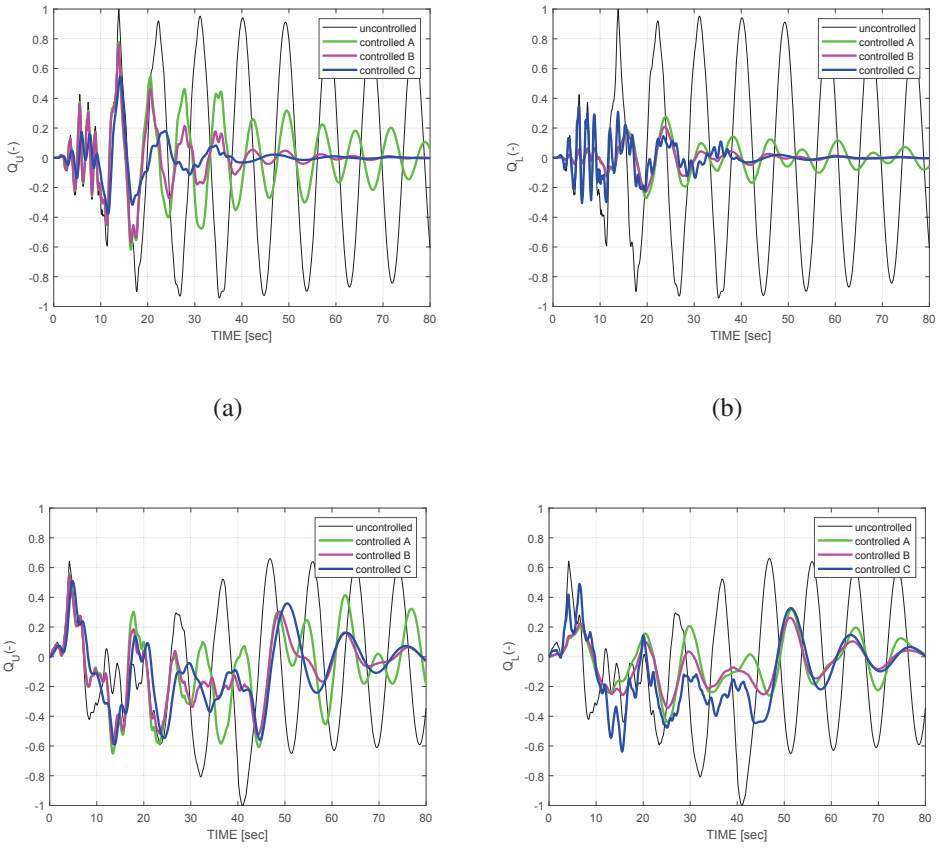

Figure 5: Time histories of: a) normalized sloshing height, b) normalized isolation displacement for Kobe earthquake; c) normalized sloshing height, d) normalized isolation displacement for Hachinohe earthquake.

ingful reductions of the response.

Further developments will involve a TMDI system in order to study any beneficial effects of its employment in such kind of problems.

REFERENCES

[1] De Angelis M, Giannini R, Paolacci F, Experimental investigation on the seismic response of a steel liquid storage tank equipped with floating roof by shaking table tests. *Earthquake Engineering and Structural Dynamics*, **39**, 377–396, 2010.

[2] De Angelis M, Perno S, Reggio A, Dynamic response and optimal design of structures with large mass ratio TMD. *Earthquake Engineering and Structural Dynamics*, **41**, 41–60, 2012.

[3] De Angelis M, Giaralis A, Petrini F, Pietrosanti D, Optimal tuning and assessment of inertial dampers with grounded inerter for vibration control of seismically excited base-isolated systems. *Engineering Structures*, **196**, 1–19, 2019.

[4] De Domenico D, Ricciardi G, An enhanced base isolation system equipped with optimal Tuned Mass Damper Inerter (TMDI). *Earthquake Engineering and Structural Dynamics*, **47**, 1169–1192, 2018.

[5] Haroun MA. Vibration studies and tests of liquid storage tanks. *Earthquake Engineering and Structural Dynamics*, **11**, 179–206, 1983.

[6] Haroun MA, Ellaithy HM. Model for flexible tanks undergoing rocking. *Journal of Engineering Mechanics*, **111**, 143–157, 1985.

[7] Housner GW, Bergman LA, Caughey TK, Chassiakos AG, Claus RO, Masri SF, Skelton RE, Soong TT, Spencer BF, Yao JTP. Structural Control: Past, Present and Future. *Journal of Engineering Mechanics*, **123**, 897–971, 1997.

[8] Luo H, Zhang R, Weng D. Mitigation of liquid sloshing in storage tanks by using a hybrid control method. *Soil Dynamics and Earthquake Engineering*, **90**, 183–195, 2016.

[9] Marian L, Giaralis A. The tuned mass-damper-inerter for harmonic vibrations suppression, attached mass reduction, and energy harvesting. *Smart Structures and Systems*, **6**, 665–678.

[10] Marian L, Giaralis A. Optimal design of a novel tuned mass-damper-inerter (TMDI) passive vibration control configuration for stochastically support-excited structural systems. *Probabilistic Engineering Mechanics*, **38**, 156–164, 2014.

[11] Matsui T. Sloshing in a cylindrical liquid storage tank with a single-deck type floating roof under seismic excitation. *Journal of Pressure Vessel*, **131**, 1–10, 2009.

[12] Pietrosanti D, De Angelis M, Basili M. Optimal design and performance evaluation of systems with Tuned Mass Damper Inerter (TMDI). *Earthquake Engineering and Structural Dynamics*, **46**, 1367–1388, 2017.

[13] Pietrosanti D, De Angelis M, Giaralis A. Experimental study and numerical modeling of nonlinear dynamic response of SDOF system equipped with tuned mass damper inerter (TMDI) tested on shaking table under harmonic excitation. *International Journal of Mechanical Sciences*, https://doi.org/10.1016/j.ijmecsci.2020.105762

[14] Pietrosanti D, De Angelis M, Giaralis A. Shake table testing of a tuned mass damper inerter (Tmdi)- equipped structure and nonlinear dynamic modeling under harmonic excitations. *Lecture Notes in Mechanical Engineering*, 1512–1521, 2020.

[15] Reggio A, De Angelis M. Optimal energy-based seismic design of nonconventional Tuned Mass Damper (TMD) implemented via inter-story isolation. *Earthquake Engineering and Structural Dynamics*, **44** 1623–1642, 2015.

[16] Renzi E, De Angelis M. Optimal semi-active control and non-linear dynamic response of variable stiffness structures. *Journal of Vibration and Control*, **11** 1253–1289, 2005.

[17] Zhang R, Zhao Z, Pan C. Influence of mechanical layout of inerter systems on seismic mitigation of storage tanks. *Soil Dynamics and Earthquake Engineering*, **114** 639–649, 2018.

EURODYN 2020
XI International Conference on Structural Dynamics
M. Papadrakakis, M. Fragiadakis, C. Papadimitriou (eds.)
Athens, Greece, 23–26 November 2020

INERTER-BASED VIBRATION ABSORBERS FOR ROTATING WIND TURBINE BLADES

Zili Zhang[1]

[1]Department of Engineering, Aarhus University
8000 Aarhus, Denmark
e-mail: zili_zhang@eng.au.dk

Keywords: Inerter, Vibration absorber, Wind turbine blades, Closed-form expressions.

Abstract. *Rotating wind turbine blade is lightly damped in the edgewise mode due to low aerodynamic damping. Adding damping into edgewise mode becomes an important design consideration for protecting the wind turbine blades from damage during the design period. This paper proposes the use of two novel inerter-based vibration absorbers, the tuned mass-damper-inerter (TMDI) and the rotational inertia double tuned mass damper (RIDTMD), for mitigation of edgewise blade vibrations. A 2-DOF model is established for the rotating blade-TMID system, and a 3-DOF model is established for the blade-RIDTMD system. Closed-form expressions for the optimal tuning and damping ratios of the blade-mounted TMDI and RIDTMD are derived, as well as for a classic tuned mass damper (TMD). Performance of the TMD, TMDI and RIDTMD are compared in terms of the blade vibration mitigation and the damper stroke, in both frequency domain and time domain. Results indicate that comparing with TMD, TMDI has the advantage of significantly less damper stroke at the cost of slight degradation in blade vibration control performance. On the other hand, RIDTMD achieves better vibration control performance comparing with an optimal TMD, with slightly increased stroke. The results indicate encouraging prospects for the use of TMDI and RIDTMD in the control of vibrations of wind turbine blades.*

1 INTRODUCTION

The increased size of wind turbines results in more flexible blades and tower that are more susceptive to dynamic loads due to turbulent winds and irregular sea waves. Structural vibrations of the wind turbine tower and blades negatively affect both the fatigue life of the structure and the power production.

The modes of vibrations in wind turbine blades are classified as flapwise and edgewise modes, representing vibrations out of the rotor plane and in the rotor plane, respectively. The flapwise vibration is highly damped under normal operational conditions because of the very high aerodynamic damping [1, 2], and thus is mainly quasi-static. On the other hand, edgewise vibration is associated with negligible aerodynamic damping [1, 2], and is dominated by dynamic response instead of quasi-static. There is also risk of aeroelastic instability in the edgewise mode for some combinations of blade properties and operational conditions, where the sum of structural damping and aerodynamic damping becomes negative. Therefore, adding damping into edgewise mode becomes an important design consideration for protecting the wind turbine blades from damage during the design period.

Structural control of wind turbine blades has received much attention in the literature in recent years. Comparing with active control [3, 4], passive and semi-active control technologies are more cost-effective and simple to implement, thus more applicable for applications in wind industry. Various types of pendulum-like passive vibration absorbers have been proposed for damping edgewise vibrations [5, 6, 7, 8], where nonlinear equations of motion have been derived for these devices (coupled to the rotating blade). Due to the inherent nonlinearities of these devices, the dampers can only be optimized through numerical optimization. On the other hand, the classic tuned mass damper (TMD) and the inerter-based vibration absorbers [9, 10, 11] provide the possibility for optimal design using closed-form formulas, since their behavior is rather linear. Furthermore, using the inerter in a smart way can improve the performance of the inerter-based vibration absorbers, thus resulting in devices that are more promising to be employed for wind turbine blades.

This paper proposes the use of two novel inerter-based vibration absorbers, the tuned mass-damper-inerter (TMDI) [10] and the rotational inertia double tuned mass damper (RIDTMD) [11], for mitigation of edgewise blade vibrations. A 2-DOF model is established for the rotating blade-TMID system, and a 3-DOF model is established for the blade-RIDTMD system. Closed-form expressions for the optimal frequency tuning and damping ratios of the blade-mounted TMDI and RIDTMD are derived, as well as for a classic TMD. Results indicate that comparing with TMD, TMDI has the advantage of significantly less damper stroke at the cost of slight degradation in blade vibration control performance. On the other hand, RIDTMD achieves better vibration control performance comparing with an optimal TMD, with slightly increased damper stroke.

2 FORMULATION OF EQUATIONS OF MOTION

2.1 Problem definition

The model of a rotating blade equipped with a vibration absorber (TMD or TMDI or RIDTMD) is shown in Figure 1. The blade is modelled as a rotating Euler-Bernoulli beam in the rotating (x_1, x_2, x_3)-coordinate system, with a rotational speed Ω. So the azimuthal angle $\Psi(t)$ of the blade becomes $\Psi(t) = \Omega t$. The blade edgewise vibration is described by the local degree of freedom (DOF) $q(t)$, representing the tip displacement in the negative x_2- direction. Assuming the blade vibration to be dominated by its fundamental mode, the local edgewise displacement

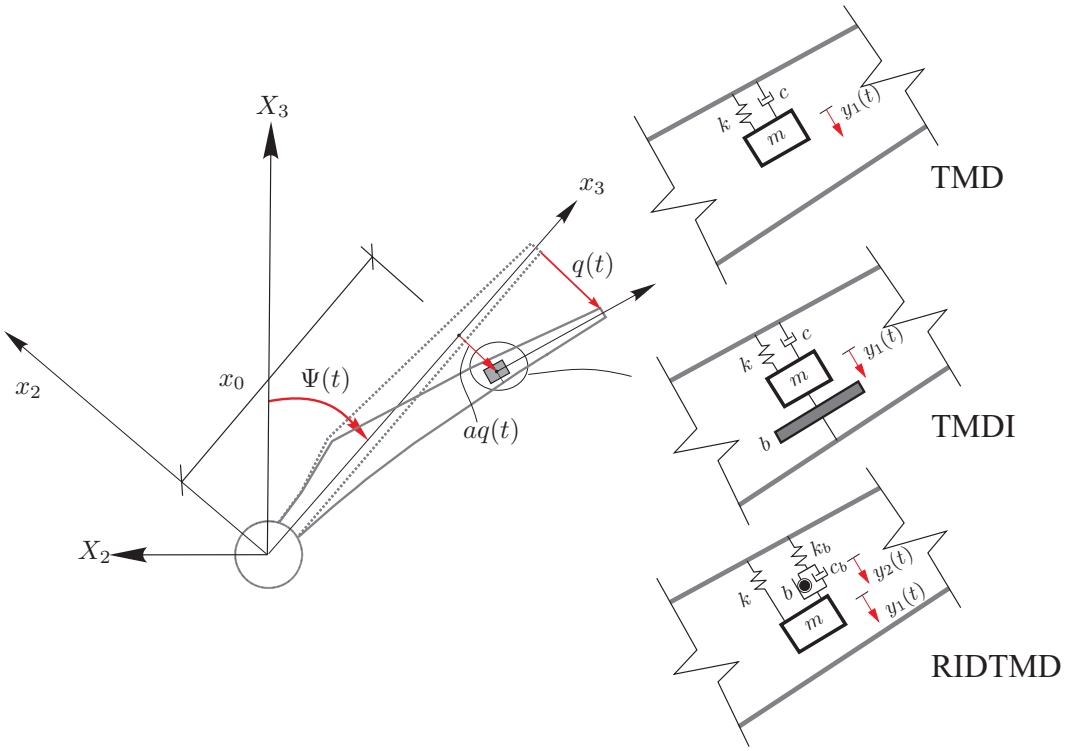

Figure 1: Definition of coordinate systems, layout of the three vibration absorbers, and degrees of freedom.

field $u_2(x_3,t)$ of the blade can be written as $u_2(x_3,t) = -\Phi(x_3)q(t)$, where $\Phi(x_3)$ is the fundamental edgewise eigenmode that is normalized to unit at the blade tip.

The vibration absorbers are assumed to be installed at the coordinate $x_3 = x_0$. So the local displacement of blade at the damper location becomes $u_2(x_0,t) = -aq(t)$, with $a = \Phi(x_0)$ being a design parameter representing the damper location. For TMD or TMDI, only one DOF, $y_1(t)$, is needed to model the device. $y_1(t)$ indicates the displacement of the TMD block mass m relative to the deformed blade. On the other hand, for RIDTMD, two DOFs, $y_1(t)$ and $y_2(t)$, are needed to model the device. $y_1(t)$ again indicates the displacement of the TMD absorber mass m relative to the deformed blade, while $y_2(t)$ indicates the displacement of the inerter b with respect to the deformed blade. Therefore, $q(t)$ and $y_1(t)$ make up the 2 DOFs of the rotating blade-TMDI (or blade-TMD) system, while $q(t)$, $y_1(t)$ and $y_2(t)$ make up the 3 DOFs of the rotating blade-RIDTMD system.

2.2 Equations of motion based on analytical dynamics

Take the blade-TMDI system as an example, the velocity components of the vibrating blade described in the local (x_2, x_3)-coordinate system are:

$$\begin{aligned} v_2(x_3,t) &= -\Omega x_3 - \Phi(x_3)\dot{q}(t) \\ v_3(x_3,t) &= -\Omega\Phi(x_3)q(t) \end{aligned} \tag{1}$$

Described in the fixed global (X_2, X_3)-coordinate system, the components of the velocity vector of the TMDI absorber mass become:

$$\begin{aligned} V_{2,d}(t) &= -\left(x_0\Omega + a\dot{q} + \dot{y}_1\right)\cos\Psi + \left(aq + y_1\right)\Omega\sin\Psi \; v_3(x_3,t) \\ V_{3,d}(t) &= -\left(x_0\Omega + a\dot{q} + \dot{y}_1\right)\sin\Psi - \left(aq + y_1\right)\Omega\cos\Psi \end{aligned} \tag{2}$$

The total kinetic energy of the system (i.e. one blade and one TMDI including the absorber mass and the inerter) becomes:

$$T(t) = \frac{1}{2}\int_0^L \mu(x_3)\Big(v_2^2(x_3,t) + v_3^2(x_3,t)\Big)dx_3 + \frac{1}{2}m\Big(V_{2,d}^2(t) + V_{3,d}^2(t)\Big) + \frac{1}{2}b\dot{y}_1^2 \tag{3}$$

where $\mu(x_3)$ is the mass per unit length of the blade. The total potential energy of the system is:

$$U(t) = mg\left(x_0\cos\Psi - aq\sin\Psi - y_1\sin\Psi\right) + \frac{1}{2}k_0q^2 + \frac{1}{2}ky_1^2 \tag{4}$$

where $k_0(\Omega)$ is the modal stiffness of the blade including the geometric stiffness effect from centrifugal acceleration [12].

Inserting Eqs. (3) and (4) into Lagrange's equation, the equations of motion of the blade-TMDI system becomes:

$$\begin{bmatrix} m_0 + a^2m & am \\ am & m+b \end{bmatrix}\begin{bmatrix}\ddot{q}\\ \ddot{y}_1\end{bmatrix} + \begin{bmatrix}0 & 0\\ 0 & c\end{bmatrix}\begin{bmatrix}\dot{q}\\ \dot{y}_1\end{bmatrix} + \begin{bmatrix} k_0 - (m_0 + a^2m)\,\Omega^2 & -am\Omega^2 \\ -am\Omega^2 & k - m\Omega^2\end{bmatrix}\begin{bmatrix}q\\ y_1\end{bmatrix} = \begin{bmatrix} f(t) + amg\sin\Psi \\ mg\sin\Psi\end{bmatrix} \tag{5}$$

where structural damping has been neglected for the following derivation of closed-form expressions. $m_0 = \int_0^L \mu(x_3)\,\Phi^2(x_3)dx_3$ is the modal mass of the blade. Hence, $\omega_0 = \sqrt{k_0/m_0}$ is the angular eigenfrequency of the blade. Further, $f(t)$ is the modal load on the blade from turbulence and gravity.

By setting $b = 0$ in the above equation, the equations of motion for the blade-TMD system [12] is recovered.

Using a similar analytical dynamics approach, the equations of motion of the 3-DOF blade-RIDTMD become:

$$\begin{bmatrix} m_0 + a^2m & am & 0 \\ am & m+b & -b \\ 0 & -b & b\end{bmatrix}\begin{bmatrix}\ddot{q}\\ \ddot{y}_1\\ \ddot{y}_2\end{bmatrix} + \begin{bmatrix}0 & 0 & 0\\ 0 & c_b & -c_b\\ 0 & -c_b & c_b\end{bmatrix}\begin{bmatrix}\dot{q}\\ \dot{y}_1\\ \dot{y}_2\end{bmatrix} +$$

$$\begin{bmatrix} k_0 - (m_0 + a^2m)\,\Omega^2 & -am\Omega^2 & 0 \\ -am\Omega^2 & k - m\Omega^2 & 0 \\ 0 & 0 & k_b\end{bmatrix}\begin{bmatrix}q\\ y_1\\ y_2\end{bmatrix} = \begin{bmatrix} f(t) + amg\sin\Psi \\ mg\sin\Psi \\ 0\end{bmatrix} \tag{6}$$

3 Closed-form expressions for optimal tuning

Based on Eq. (5) or Eq. (6), closed-form expressions for optimal parameter tuning can be performed. The fixed-point method [13] has been used for blade-mounted TMDI (also TMD), while the pole placement method [14] has been used for the blade-mounted RIDTMD.

3.1 Optimal tuning of the bladed-mounted TMDI

Representing the responses $q(t)$ and $y_1(t)$ and the load $f(t)$ to be harmonic varying with angular frequency ω, the normalized (by the static response f_0/k_0 with f_0 being the amplitude of the load) complex structural response q_0 can be obtained. $\frac{q_0}{f_0/k_0}$ is a function of ω and the following normalized parameters:

$$\mu = \frac{m}{m_0}, \quad \beta = \frac{b}{m_0}, \quad \gamma = \frac{b}{m} = \frac{\beta}{\mu}, \quad \omega_{\text{TMDI}} = \sqrt{\frac{k}{m+b}}, \quad \zeta_{\text{TMDI}} = \frac{c}{2\sqrt{k\,(m+b)}} \tag{7}$$

where μ and β are the mass ratio and inertance ratio, respectively. ω_{TMDI} and ζ_{TMDI} are the angular eigenfrequency and damping ratio of the TMDI, respectively.

It turns out that the two fixed points also exit in the present case, i.e. rotating blade with a TMDI. Following the similar procedure in [13], by equalizing the dynamic amplification (absolute value of the normalized complex amplitude) at these two fixed frequencies, the optimal frequency tuning formula becomes:

$$\left(\omega_{\text{TMDI}}\right)_{opt} = \sqrt{\frac{\left(1+\gamma+a^2\beta\right)\omega_0^2 - \left(1+a^2\mu\right)\left(\gamma+a^2\beta\right)\Omega^2}{\left(1+\gamma\right)\left(1+a^2\mu\right)^2}} \tag{8}$$

which not only depends on the mass ratio and inertance ratio, but also is dependent on the rotational speed Ω.

The optimal TMDI damping ratio is chosen to ensure that the dynamic amplifications are equal at the two fixed-frequencies and ω_∞ (the natural frequency of the blade with a locked TMDI) [13]. The closed-form formula for the optimal TMDI damping ratio tuning becomes:

$$\left(\zeta_{\text{TMDI}}\right)_{opt} = \sqrt{\frac{1}{2}\frac{\left(a^2\mu+a^2\beta+a^4\mu\beta\right)}{\left(1+\gamma\right)\left(1+a^2\mu\right)}\frac{\omega_0^4}{\left(1+\gamma+a^2\beta\right)\omega_0^4 - \left(1+a^2\mu\right)\left(1+2\gamma+2a^2\beta\right)\omega_0^2\Omega^2 + \left(1+a^2\mu\right)^2\left(\gamma+a^2\beta\right)\Omega^4}} \tag{9}$$

By setting $\beta = 0$ (and thus $\gamma = 0$) in Eqs. (8) and (9), the optimal tuning formulas for the blade-mounted TMD [12] are recovered:

$$\left(\omega_{\text{TMD}}\right)_{opt} = \frac{\omega_0}{1+a^2\mu} \tag{10}$$

$$\left(\zeta_{\text{TMD}}\right)_{opt} = \sqrt{\frac{1}{2}\frac{a^2\mu}{1+a^2\mu}\left(\frac{\omega_0^2}{\omega_0^2 - \left(1+a^2\mu\right)\Omega^2}\right)} \tag{11}$$

3.2 Optimal tuning of the bladed-mounted RIDTMD

Again, the normalized complex structural amplitude q_0 can be obtained by assuming all responses and the load to be harmonically varying. The expression becomes much more lengthy because the system has 3 DOFs now. For the RIDTMD, four parameters (instead of two for the TMDI) need to be optimized, i.e. k, k_b, b and c_b.

The idea is to optimally place the poles of the system [14], i.e. the complex roots of the sextic characteristic equation (the denominator of the complex structural amplitude), in order to obtain the optimal damper parameters. The mathematical derivations are rather exhaustive, and will be detailed in a separate publication. The general steps are: 1) Choose the mass ratio μ. 2) The two springs k and k_b are optimally tuned so that two of the three poles are inverse points with respect to a quarter circle (resulting in equal modal damping ratio), while the other pole is placed on this circle. 3) The inertance b and the damping coefficient c_b are optimally calibrated based on the triple-root bifurcation point together with two scaling parameters. The closed-form expressions indicate that the optimal parameters all depend on the rotational speed.

4 Results

Data from the NREL 5 MW reference turbine [15] were employed to calibrate the structural model of the wind turbine blade. Each blade has a length of 61.5 m and an overall mass of 17740 kg, with the edgewise bending stiffness, the mass per unit length and the fundamental edgewise mode shape given by [15]. The rated rotational speed of the rotor is Ω_0=1.27 rad/s.

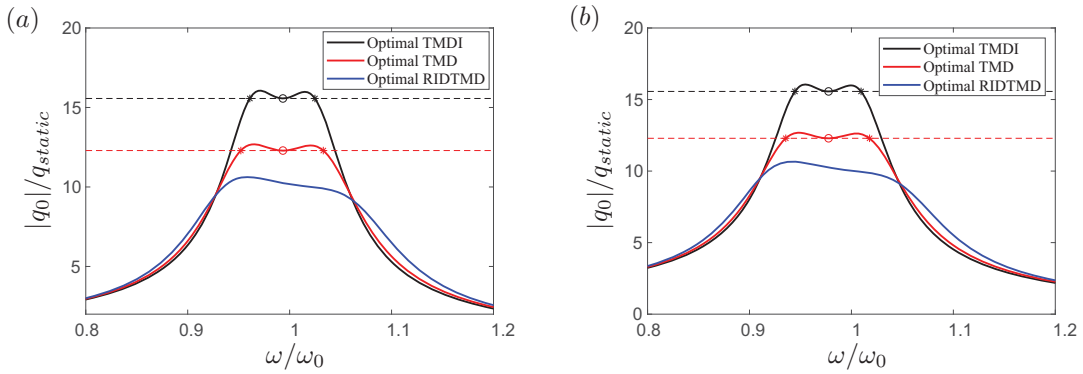

Figure 2: Dynamic amplification of the structural response, $x_0 = 45$ m and $\mu = 0.05$ for all three dampers. $\beta = 0.03$ has been chosen for TMDI. Asterisk: the fixed-point frequencies. Circle: ω_∞. (a) $\Omega = 0$ (non-rotating blade). (b) $\Omega = \Omega_0$ (1.27 rad/s).

Figure 2 shows the dynamic amplification of the structural response, with the three optimally-tuned dampers attached. Both cases of $\Omega = 0$ (non-rotating blade) and $\Omega = \Omega_0$ have been considered. The dampers are located at the location of $x_0 = 45$ m, and the mass ratio of the TMD absorber for all of them is kept at $\mu = 0.05$. For TMDI, the inertance ratio should also be chosen in advance, here β is chosen to be $\beta = 0.03$. It is seen that the optimal RIDTMD has the best performance in reducing the blade response comparing with the optimal TMD and the optimal TMDI. The TMDI has the least reduction effect. Furthermore, for the optimal TMDI or optimal TMD, the dynamic amplifications at the two fixed frequencies and ω_∞ are on the same horizontal line. This is as expected since the optimal tuning formulas for TMDI or TMD have been derived exactly based on this criterion. It is also seen that for the optimal RIDTMD, the dynamic amplification curve is skewed, which is in agreement with the finding in [14] and is due to the fact that equal modal damping ratio does not guarantee the equal height of dynamic amplifications.

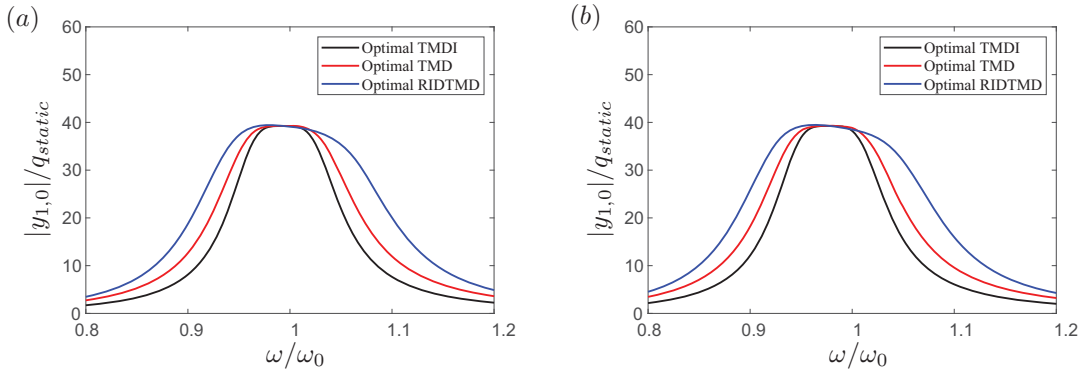

Figure 3: Dynamic amplification of the damper stroke, $x_0 = 45$ m and $\mu = 0.05$ for all three dampers. $\beta = 0.03$ has been chosen for TMDI. (a) $\Omega = 0$ (non-rotating blade). (b) $\Omega = \Omega_0$ (1.27 rad/s).

Correspondingly, Figure 3 shows the dynamic amplification of the relative absorber motion (the damper stroke). Even though the peak heights of the three curves are similar, the curve corresponding to optimal RIDTMD is the most broad-banded, while the optimal TMDI is the most narrow-banded. This implies that the optimal TMDI performs best in terms of the smallest damper stroke, while the optimal RIDTMD has the largest stroke. The finding from Figure 3 is in contrary to that from Figure 2, which makes sense because the improvement of one performance indicator is normally at the cost of worsening another indicator. Comparing with TMD,

both TMDI and RIDTMD improve one certain type of the damper performance. It is up to the designer to decide which performance indicator is more important.

5 CONCLUSIONS

Closed-form expressions have been derived for optimal tuning of the blade-mounted TMDI and the blade-mounted RIDTMD, the former based on fixed-point method and the latter based on pole-placement method. Using the NREL 5-MW wind turbine as the numerical example, it is observed that comparing with the optimal TMD, the optimal TMDI has the advantage of less damper stroke at the cost of slight degradation in blade vibration control performance. On the other hand, the optimal RIDTMD is superior in damping blade vibrations comparing with the optimal TMD, with slightly increased stroke. This work provides rigourous theoretical formulations as well useful design formulas for the blade-mounted inerter-based vibration absorbers.

REFERENCES

[1] M.H. Hansen, Aeroelastic instability problems for wind turbines, *Wind Energy*, **10**, 551–577, 2007.

[2] Z. Zhang, Passive and Active Vibration Control of Renewable Energy Structures. Ph.D. thesis, Aalborg University, Denmark. 2015.

[3] A. Staino, B. Basu, S.R.K. Nielsen, Actuator control of edgewise vibrations in wind turbine blades, *Journal of Sound and Vibration*, **331**, 1233–1256, 2012.

[4] B. Fitzgerald, B. Basu, Cable connected active tuned mass dampers for control of in-plane vibrations of wind turbine blades, *Journal of Sound and Vibration*, **333**, 5980–6004, 2014.

[5] Z. Zhang, J. Li, S.R.K. Nielsen, B. Basu, Mitigation of edgewise vibrations in wind turbine blades by means of roller dampers, *Journal of Sound and Vibration*, **333**, 5283–5298, 2014.

[6] Z. Zhang, B. Basu, S.R.K. Nielsen, Tuned liquid column dampers for mitigation of edgewise vibrations in rotating wind turbine blades, *Structural Control and Health Monitoring*, **22**, 500–517, 2015.

[7] B. Basu, Z. Zhang, S.R.K. Nielsen, Damping of edgewise vibration in wind turbine blades by means of circular liquid dampers, *Wind energy*, **19**, 213–226, 2016.

[8] Z. Zhang, S.R.K. Nielsen, B. Basu, J. Li, Nonlinear modeling of tuned liquid dampers (TLDs) in rotating wind turbine blades for damping edgewise vibrations, *Journal of Fluids and Structures*, **59**, 252–269, 2015.

[9] M.C. Smith, Synthesis of mechanical networks: the inerter, *IEEE Transactions on automatic control*, **47**, 1648–1662, 2002.

[10] L. Marian, A. Giaralis, Optimal design of a novel tuned mass-damper–inerter (TMDI) passive vibration control configuration for stochastically support-excited structural systems, *Probabilistic Engineering Mechanics*, **38**, 156–164, 2014.

[11] H. Garrido, O. Curadelli, D. Ambrosini, Improvement of tuned mass damper by using rotational inertia through tuned viscous mass damper, *Engineering Structures*, **56**, 2149–2153, 2013.

[12] Z. Zhang, Optimal tuning of the tuned mass damper (TMD) for rotating wind turbine blades, *Engineering Structures*, **207**, 110209, 2020.

[13] S. Krenk, Frequency analysis of the tuned mass damper, *Journal of Applied Mechanics*, **72**, 936–942, 2005.

[14] J. Høgsberg, Vibration control by piezoelectric proof-mass absorber with resistive-inductive shunt, *Mechanics of Advanced Materials and Structures*, **20**, 1–13, 2019.

[15] J. Jonkman, S. Butterfield, W. Musial, G. Scott, Definition of 5-MW reference wind turbine for offshore system development, *National Renewable Energy Laboratory, Technical Report*, 2009.

EURODYN 2020
XI International Conference on Structural Dynamics
M. Papadrakakis, M. Fragiadakis, C. Papadimitriou (eds.)
Athens, Greece, 23–26 November 2020

MOTION CONTROL PERFORMANCE OF TUNED MASS DAMPER INERTER (TMDI) IN CONTINUOUS WHITE-NOISE EXCITED CANTILEVERED BEAMS WITH VARIOUS SHAPES

Zixiao Wang[1], Agathoklis Giaralis[2]*

[1] PhD Candidate, Department of Civil Engineering, City University of London
Northampton Square, London EC1V 0HB, UK
e-mail: Zixiao.Wang@city.ac.uk

[2] Senior Lecturer, Department of Civil Engineering, City University of London
Northampton Square, London EC1V 0HB, UK
e-mail: agathoklis.giaralis.1@city.ac.uk

Keywords: Tuned mass damper inerter, optimal passive vibration control, white-noise excitation, low-order modelling.

Abstract. The tuned mass-damper-inerter (TMDI) is a linear passive dynamic vibration absorber for motion control of dynamically excited building (primary) structures. It couples the classical tuned mass damper (TMD), comprising a secondary mass attached to the top building floor via a spring and dashpot, with an inerter, a mechanical element resisting relative acceleration, which links the secondary mass to a lower floor. Recent studies demonstrate that TMDI motion control effectiveness is influenced by the vibration modes of the uncontrolled primary structure. Herein, this influence is quantified through a parametric investigation considering a wide range of white-noise excited primary structures modelled as cantilevered continuous beams with various shapes and, therefore, different vibration modes. This quantification is facilitated by considering a low-order model of TMDI-equipped flexural cantilever which accounts for the effect of flexural rigidity and mass distribution of the primary structure as well as the influence of the fundamental mode shape to the location that the inerter connects the secondary mass to the primary structure. The investigation is further supported by optimal H_2 tuning of TMDI aiming to minimize the free-end primary structure displacement under white noise excitation. It is shown that the TMDI achieves enhanced structural performance as the inerter links the secondary mass further away from the top of the primary structure where the mass is attached to for all primary structure shapes. Moreover, it is found that improved TMDI performance and reduced stroke (relative secondary mass displacement with respect to the primary structure) are achieved for primary structure shapes with stiffness and mass distribution weighted heavier towards the base of the structure (i.e., when most of material is concentrated towards the bottom end of the structure) either through appropriate shaping or through increase of base to free-end depth ratio for fixed non-uniform shapes.

1 INTRODUCTION

In recent years the use of the inerter, defined in [1] as a mechanical element that resists relative acceleration through the inertance constant, has been widely considered in various linear passive dynamic vibration absorber configurations for enhanced motion control in dynamically excited structures [2]. Among these absorbers, the tuned mass damper inerter (TMDI) introduced in [3] attracted significant attention in the literature and its potential to achieve improved vibration suppression compared to the standard tuned mass damper (TMD) has been verified in various applications including for the seismic protection of building structures [3-5] as well as for safeguarding occupants' comfort in wind excited slender tall buildings [6-8]. In the TMDI configuration for building (primary) structures, an inerter is used to link a secondary mass attached to one building floor (commonly the top floor) through a spring in parallel with a viscous damper (dashpot) to a different (lower) floor.

Giaralis and Taflanidis [9] were the first to demonstrate for a seismically excited TMDI-equipped 10-storey shear frame structure that the more floors the inerter spans (i.e., the further lower the floor that the inerter connects the secondary mass) the more improved vibration suppression is furnished by an optimally tuned TMDI. This observation was more recently confirmed for seismically and wind excited real-life benchmark multi-storey structures [5,7]. Further, recognizing that spanning several floors may not be economically feasible in routine practical applications, Wang and Giaralis [8] proposed a local primary structure modification namely top-floor softening, which leads to an increased local difference in the primary structure mode shapes and was shown to have a similar beneficial effect with spanning more floors in wind-excited buildings equipped with a top-floor TMDI. This result suggests that the mode shapes of the uncontrolled primary structure and, hence, the mass and stiffness distribution of the primary structure influences the motion control potential of the TMDI. To this end, this paper aims to quantify this influence through a parametric investigation considering a wide range of white-noise excited primary structures modelled as cantilevered continuous beams with various shapes and, therefore, different vibration modes. This quantification is facilitated by considering a low-order model of TMDI-equipped flexural cantilever which accounts for the effect of flexural rigidity and mass distribution of the primary structure as well as the influence of the fundamental mode shape to the location that the inerter connects the secondary mass to the primary structure. The investigation is further supported by optimal H_2 tuning of TMDI aiming to minimize the free-end primary structure displacement under white noise excitation. The presentation starts from the definition of the simplified model and the derivation of frequency response functions used in random vibration analyses.

2 SIMPLIFIED 2-DOF DYNAMIC MODELLING AND ANALYSIS OF TMDI-EQUIPPED CONTINUOUS FLEXURAL CANTILEVERED BEAMS

2.1 Model description and equations of motion

Consider the TMDI-equipped continuous flexural cantilever beam (primary structure) depicted in Figure 1(a). The beam height is H and has distributed flexural rigidity $EI(x)$ and distributed mass $m(x)$, with $0 \leq x \leq \mathrm{H}$, while it is taken as undamped. A TMDI is attached to the free-end of the primary structure to control its lateral motion due to horizontal distributed dynamic load $p(x,t)$. Specifically, the TMDI consists of a secondary mass, m_{TMDI}, attached to the free-end of the primary structure through a linear spring with stiffness k_{TMDI} in parallel with dashpot with damping coefficient c_{TMDI} and further connected to the primary structure at height $x=\chi$ through an inerter with inertance b.

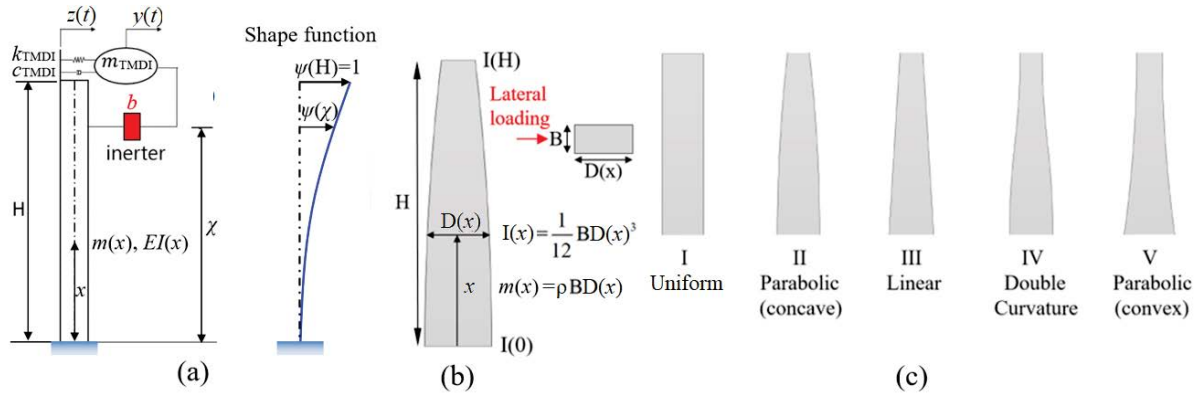

Figure 1 (a) Primary structure (cantilevered beam) equipped with TMDI and assumed mode shape, (b) Parametric variation of the primary structure, and (c) Considered primary structure geometrical shapes.

Let the lateral motion of the uncontrolled primary structure be governed by a single time-invariant shape function $\psi(x)$ which complies to the fixed support conditions at x=0 and, without loss of generality, is normalised such that ψ(H)=1 as shown in Figure 1(a). Under this assumption, the primary structure can be modelled as a generalized single degree of freedom (SDOF) system [10] and its lateral deflection can be written as $u(x,t)=\psi(x)z(t)$ where $z(t)$ is the tip displacement of the primary structure. In this setting, a simplified two degree of freedom (2-DOF) model is herein employed to approximate the lateral deflection of the TMDI-equipped cantilever beam in terms of its tip displacement $z(t)$ and the TMDI mass displacement $y(t)$ written in matrix form as

$$\mathbf{M}\ddot{\mathbf{q}}+\mathbf{C}\dot{\mathbf{q}}+\mathbf{K}\mathbf{q}=\mathbf{p}\,. \tag{1}$$

In the above equation, the displacement and forcing vectors are defined as

$$\mathbf{q}=\begin{Bmatrix} z(t) \\ y(t) \end{Bmatrix} \quad \text{and} \quad \mathbf{p}=\begin{Bmatrix} p^*(t) \\ 0 \end{Bmatrix}, \tag{2}$$

respectively, while the mass, damping, and stiffness matrix are

$$\mathbf{M}=\begin{bmatrix} m^*+b\psi(\chi)^2 & -b\psi(\chi) \\ -b\psi(\chi) & m_{TMDI}+b \end{bmatrix}, \mathbf{C}=\begin{bmatrix} c_{TMDI} & -c_{TMDI} \\ -c_{TMDI} & c_{TMDI} \end{bmatrix}, \text{and } \mathbf{K}=\begin{bmatrix} k^*+k_{TMDI} & -k_{TMDI} \\ -k_{TMDI} & k_{TMDI} \end{bmatrix}, \tag{3}$$

respectively and a dot over a symbol signifies differentiation with respect to time. Further, in the above expressions, $p^*(t)$, m^*, and k^* are the generalized load, mass, and stiffness of the generalized SDOF representation of the primary structure defined as [Clough and Penzien 1993]

$$p^*(t)=\int_0^H p(x,t)\psi(x)dx, \quad m^*=\int_0^H m(x)\psi(x)^2dx, \quad \textit{and} \quad k^*=\int_0^H EI(x)\psi''(x)^2dx\,, \tag{4}$$

where a prime over a symbol denotes differentiation with respect to x.

Notably, in the herein considered 2-DOF model the assumed (single) mode shape of the primary structure, $\psi(x)$, is explicitly accounted for in defining the primary structure generalized properties in Eq.(4) as well as the inerter force through the expression

$$F_b(t)=b\left(\psi(\chi)\ddot{z}(t)-\ddot{y}(t)\right). \tag{5}$$

In the above equation, it is clearly seen that the inerter force depends on the mode shape coordinate at location $x=\chi$ (i.e., where the inerter links the attached mass to the primary structure), including the limiting case of $\psi(\chi=0)=0$ for which the inerter is grounded and the mass

matrix in Eq.(3) becomes diagonal [11]. Moreover, the 2-DOF model can also treat TMD-equipped primary structures as a special case for which b=0. In this regard, the 2-DOF model in Eq.(1) can be effectively used as a vehicle to study the response of TMD(I)-equipped cantilevered beams with different assumed uncontrolled dominant vibration modes as well as different inerter connecting location to the primary structure.

2.2 Frequency domain random vibration analysis for white noise excitation

In the ensuing numerical part of this work, three dynamic response quantities of practical interest are monitored under the assumption of uniformly distributed zero-mean spatially uncorrelated white noise excitation. These are the root mean square (RMS) values of the free-end primary structure displacement, $z(t)$, of the TMDI stroke, $z(t)$-$y(t)$ (i.e., relative displacement of the secondary mass with respect to the free-end of the primary structure), and of the inerter force in Eq.(5). These quantities are readily determined using frequency domain analysis via the expressions

$$\sigma_z = \sqrt{\int_0^{\omega_{\max}} \left| p_o^* H(\omega) \right|^2 W_o d\omega},$$

$$\sigma_{y-z} = \sqrt{\int_0^{\omega_{\max}} \left| p_o^* G(\omega) \right|^2 W_o d\omega}, \quad \text{and} \tag{6}$$

$$\sigma_{F_b} = b\sqrt{\int_0^{\omega_{\max}} \left| p_o^* B(\omega) \right|^2 W_o d\omega}.$$

In the above expressions, ω is angular frequency, $\omega_{\max}$ is a cut-off frequency above which the frequency response functions in the arguments of the integrals attain negligible values, W_o is the amplitude of the white noise power spectral density function and $p_o^* = \int_0^H \psi(x)dx$. Further, $H(\omega)$, $G(\omega)$, and $B(\omega)$ are given as

$$H(\omega) = \frac{Z(\omega)}{P^*(\omega)} = \frac{k_{22} - \omega^2 m_{22} + i\omega c_{22}}{(k_{11} - \omega^2 m_{11} + i\omega c_{11})(k_{22} - \omega^2 m_{22} + i\omega c_{22}) - (k_{12} - \omega^2 m_{12} + i\omega c_{12})(k_{21} - \omega^2 m_{21} + i\omega c_{21})},$$

$$G(\omega) = \frac{Z(\omega) - Y(\omega)}{P^*(\omega)} = \left(1 + \frac{k_{21} - \omega^2 m_{21} + i\omega c_{21}}{k_{22} - \omega^2 m_{22} + i\omega c_{22}}\right) H(\omega), \quad \text{and} \tag{7}$$

$$B(\omega) = \frac{\omega^2 \left[\psi(\chi) Z(\omega) - Y(\omega)\right]}{P^*(\omega)} = \omega^2 \left[\psi(\chi) + \frac{k_{21} - \omega^2 m_{21} + i\omega c_{21}}{k_{22} - \omega^2 m_{22} + i\omega c_{22}}\right] H(\omega),$$

respectively, where $i = \sqrt{-1}$, and m_{mn}, c_{mn} and k_{mn}, with m,n=1,2 are the elements of the matrices in Eq. (3).

3 OPTIMAL TMDI DESIGN USING THE SIMPLIFIED 2-DOF MODEL

To support meaningful discussion on motion control performance of TMDI-equipped structures, it is deemed essential to optimally design/tune the TMDI to minimize primary structure response. To this aim, an optimization problem is formulated to tune TMDI stiffness and damping properties such that the RMS displacement of the primary structure free-end under white noise excitation, taken as the objective function (OF), is minimized. That is,

$$\text{OF}=\sigma_z \,. \tag{8}$$

The design problem has 5 non-dimensional design variables (DVs), namely the inerter connectivity ratio CR, the mass ratio μ, the inertance ratio β, the TMDI frequency ratio υ_{TMDI}, and the TMDI damping ratio ξ_{TMDI} defined as

$$\text{CR}=\frac{\text{H}-\chi}{\text{H}},\quad \mu=\frac{m_{TMDI}}{m^*},\quad \beta=\frac{b}{m^*},\quad \upsilon_{TMDI}=\frac{\sqrt{\dfrac{k_{TMDI}}{(m_{TMDI}+b)}}}{\omega_1},\ \text{and}\ \xi_{TMDI}=\frac{c_{TMDI}}{2\sqrt{(m_{TMDI}+b)k_{TMDI}}}, \tag{9}$$

where ω_1 is the first natural frequency of the uncontrolled primary structure. Then, optimal primary DVs, υ_{TMDI} and ξ_{TMDI}, are sought that minimize the OF given values of the secondary DVs: CR, μ, and β. The optimization problem is numerically solved in the ensuing numerical work using a pattern search algorithm [12] with iteratively updated search range of the primary variables hard-coded in MATLAB®.

4 PERFORMANCE ASSESSMENT OF TMDI-EQUIPPED CANTILEVERED BEAMS WITH DIFFERENT GEOMETRIC SHAPES

4.1 Parametric variation of primary structure geometric shape

As seen in section 2, the dominant vibration mode of the uncontrolled primary structure $\psi(x)$ enters explicitly in the definition the generalized primary structure properties as well as in the mass matrix of the simplified 2-DOF model used to capture the response of TMDI-equipped cantilevered beams. Given that in many practical applications the first mode, $\varphi_1(x)$, of the primary structure dominates its dynamic response, the choice of $\psi(x)= \varphi_1(x)$ is meaningful. However, $\varphi_1(x)$ depends heavily on the stiffness (flexural rigidity) and mass distribution along the height of the primary structure. To this end, the influence of the dominant vibration mode to the motion control potential of the TMDI is herein studied by varying parametrically the geometric shape (profile) of the primary structure as shown in Figure 1(b). Specifically, primary structures with fixed width B along the height of the structure but varying depth $D(x)$ within the direction of the lateral load are considered which further influence the flexural rigidity and mass distribution as specified in Figure 1(b). The five different primary structure shapes plotted in Figure 1(c) are considered. Shape I (uniform) has constant cross-section along the primary structure height and slenderness ratio H/D= 20, whereas two different depth ratios defined as R=D(0)/D(H), i.e., R=2 and R=5, are considered for the remaining four non-uniform shapes. Importantly, all 9 considered primary structures have the same total area/volume and, thus, total mass which is taken as a practical reference criterion in the herein undertaken comparative study.

4.2 Numerical derivation of fundamental mode shapes and optimal TMDI tuning

The fundamental mode shape of each of the 9 in total different uncontrolled primary structures herein considered is obtained numerically using finite element (FE) discretization. Specifically, each primary structure is discretized using 40 tapered equal-length beam elements. A 41-DOF planar dynamic system is then derived involving only one lateral translational DOF per FE node grid along the horizontal load direction in terms of a diagonal mass matrix and a full stiffness matrix. The mass matrix is formed by lumping the own-mass of the elements at the nodes while the stiffness is constructed using standard static condensation to eliminate vertical and rotational DOFs at each FE node. Next, standard modal analysis is conducted to obtain the first mode shape vector with 41 elements. The central difference method is used to obtain the second derivative of the fundamental mode shapes. Next, the standard trapezoid quadrature rule is used to calculate the integrals defining the generalized primary structure properties in Eq.(4) for each of the 9 primary structures. Finally, the optimization problem described in section 3 is solved to find optimal k_{TMDI} and c_{TMDI} from the non-dimensional frequency and damping ratios in Eq.(9) for each primary structure. Given that the focus of this paper is to investigate the influence of mode shapes to TMDI performance, fixed values for the mass ratio and inertance ratio are herein assumed taken equal to μ= 0.1% and β=16% and the average generalised mass from all 13 primary structures is used in the numerator of these ratios in Eq.(9). However, the CR in Eq.(9) is parametrically investigated as its influence is coupled with the influence of the fundamental mode shape through the modal coordinate $\psi(\chi)= \varphi_1(\chi)$ affecting the mass matrix of the mode in Eq. (3). In this regard, CR is let to vary within the range [0 1], where CR=1 corresponds to grounded inerter (χ=0).

4.3 Influence of depth ratio R

The influence of fundamental mode shape variation due to different depth ratio R=D(0)/D(H) values of the primary structure to the TMDI motion control potential is firstly investigated. This is facilitated by plotting the RMS free-end displacement of optimal TMDI-equipped primary structures against CR for fixed R separately for each of the geometric shapes II-V of Figure 1(c). These plots are presented in Figure 2 where the free-end TMDI-equipped primary structure displacement is normalized by the corresponding TMD-equipped primary structure obtained by solving the optimization problem in section 3 for b=0. In all plots the same R=1 curve corresponding to the uniform section shape (I) is included as a base-line.

It is evidenced that improved vibration suppression is achieved, though at a decreasing rate, as CR increases (i.e., as the further away from the free-end the inerter links the secondary mass to the primary structure) irrespective of the geometric shape and, thus, the mode shape of the primary structure. Further, for relatively small CR values the TMD outperforms the TMDI. These results agree with previous numerical studies addressing different structures and dynamic loads [4,5,7] which confirms the validity of the herein considered simplified 2-DOF model for optimal TMDI design. More interestingly, it is seen that for all the considered primary structure shapes TMDI performance improves as the depth ratio increases for any fixed CR and this improvement is more substantial for lower CR values. This observation suggests that the TMDI becomes more effective in mitigating lateral vibrations in cantilevered beam-like primary structures (such as tall buildings, and chimneys) as their upper part becomes more flexible through upwards tapering. In this regard, the critical CR value for given host structure geometric shape and inertial TMDI parameters (i.e., mass m_{TMD} and inertance b), that needs to be exceeded for TMDI to outperform TMD depends heavily on the depth ratio R. For instance, for double curvature shape (IV) shown in Figure 2(c), the critical CR values are 7.4%, 5.1%, and 2.75% for

depth ratios R 1, 2, and 5, respectively. Hence, the requirement to the inerter span reduces as the primary structure tapering rate towards reduced cross-section with height increases.

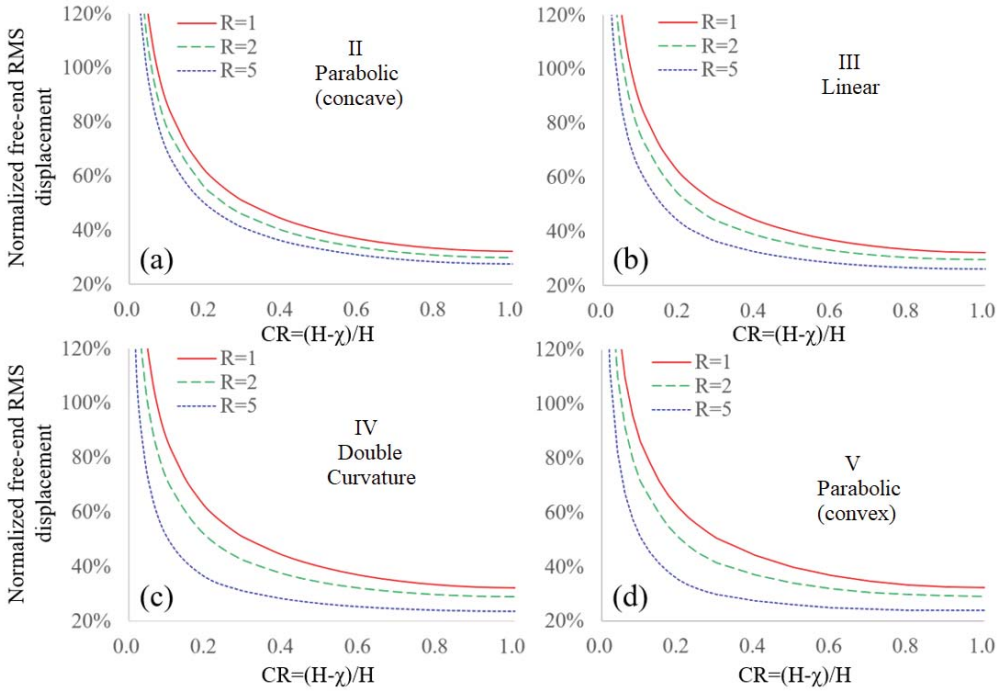

Figure 2. Free-end RMS displacement performance of optimal TMDI-equipped primary structures as function of the inerter connectivity ratio (CR) for various depth ratios R=D(0)/D(H).

4.4 Influence of depth profile D (primary structure shape)

Here, attention is firstly focused on exploring the influence of fundamental mode shape variation due to different primary structure shaping (see Figure 1(c)) to the TMDI motion control potential. This is facilitated by bar-plotting the RMS free-end displacement of TMDI-equipped primary structures with different shapes for CR=2.5%, 5.0%, and 7.5%, and for all different depth ratios in the upper row of panels in Figure 3. The same normalization of the RMS displacement as in Figure 2 applies. A consistent trend in these plots appears: the TMDI motion control potential increases for fixed CR and R as the primary structure shape changes from type "II" towards type "V". With reference to the shapes in Figure 1(c), this trend ultimately confirms again that better TMDI motion control is achieved as mass and stiffness distribution is heavier weighted towards the fixed-end of the primary structure. Interestingly, worst performance is noted for uniformly distributed mass and stiffness. For example, for depth ratio R=2 and CR= 5.0%, the TMDI with β=16% achieves gradually improved performance compared to the TMD by 0.5%, 2.7%, 4.7%, and 5.3% for primary structure shapes II, III, IV, and V respectively. As discussed before, for the relatively low CR=2.5% value in Figure 3(a), the TMD always outperforms the TMDI, but as CR increases (compare e.g. Figure 3(b) with 3(c) and note the difference in the y-axis scale) improvement of TMDI versus TMD become more substantial. The improved TMDI performance as the upper part of primary structure becomes more flexible is readily attributed to smaller values of $\psi(\chi)$ as the mode shape curvature increases (i.e., as the difference of ψ(H)- $\psi(\chi)$ increases). Nevertheless, the improvement achieved through increase of R is less significant for shapes II and III compared to shapes IV and V. This

result demonstrates that careful design/shaping of the primary structure is required to achieve increased TMDI control performance.

Moreover, the second row of panels in Figure 3 furnishes bar-plots of RMS stroke values σ_{y-z} computed from Eq.(6) for the same cases as the first row of panels of Figure 3 and normalized by the RMS stroke for the TMD. As has been reported in several previous studies [6,7], the inclusion of the inerter to the TMD reduces dramatically the secondary mass stroke (relative displacement of secondary mass with the primary structure free-end) with higher reductions achieved as CR increases. For all the herein considered primary structures and CRs, the reduction is more than 80%. Here, a novel observation is that mode shape differences due to either the shape of the primary structure or its depth ratio do not influence as much the stroke as they influence the free-end displacement. Still, it is important to note that stroke demands follow consistently the same reduction trend as free-end displacement demand with mode shape variation: as R increases for the same primary structure shape or as shapes go from type II to type V for fixed R the normalized stroke reduces by about 1% irrespective of the CR. This is a quite welcoming result as stroke is proportional to TMDI cost in several practical applications [5,6].

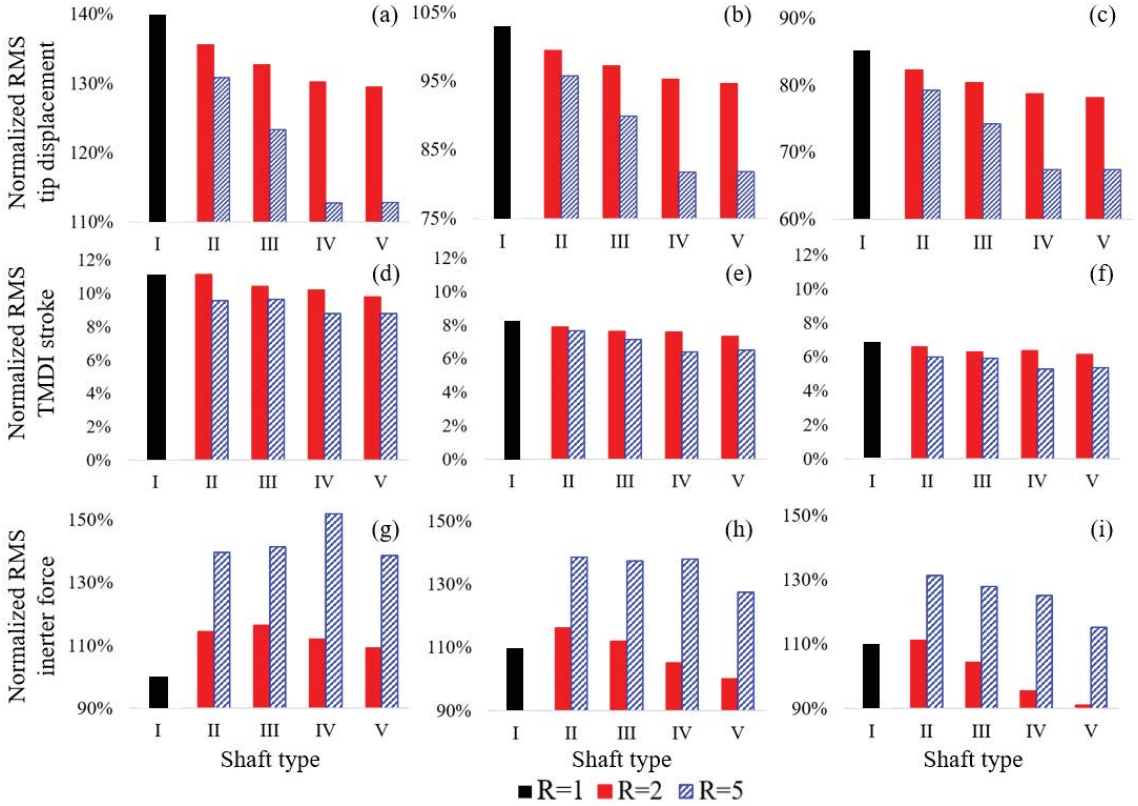

Figure 3. Free-end RMS displacement performance (upper panels), RMS TMDI stroke performance (middle panels) and RMS inerter force (lower panels) for different primary structure shape, depth ratio R and connectivity ratio CR. Values in the first two rows of panels are normalized with respect to TMD case (b=0) and values in the last row of panels are normalized with the respect to R=1, CR=2.5% TMDI case.

Lastly, considering that modal information affects explicitly the magnitude of the inerter force exerted to the primary structure at x=χ location, it is deemed practically important to gauge the influence of mode shapes variation to the inerter force in the last row of panels of Figure 3. In these plots, inerter force values are normalized by the inerter force developing at the uniform cantilever with CR=2.5%. Interestingly, it is seen that lower force develops at the uniform shaped primary structure compared to all the other shapes for the relatively large depth ratio

R=5. On the other hand, inerter force decreases for R=2 and 5 as shapes vary from type II to type V for relatively large CRs, e.g., CR=5.0% and 7.5%. One may be tempted to interpret this decrease of inerter force as the cause of TMDI achieving improved vibration suppression with primary structure shape variation seen in the first row of panels in Figure 3. However, this trend changes for a given primary structure shape with increasing depth ratio R: inerter force increases significantly as R increases from 2 to 5 for all primary structure shapes considered. Thus, the inerter force is not necessarily consistent with TMDI performance in terms of free-end displacement which, ultimately, is mostly related to the control force exerted at the free-end of the cantilever through the spring and dashpot. However, with reference to the upper row of panels in Figure 3, the increase in inerter force is accompanied with enhanced TMDI performance through increasing the depth ratio R. In this respect, it can be concluded that modifying the primary structure fundamental mode shape through more elaborate primary structure shaping rather than through increasing the depth ratio R is more advantageous in enhancing TMDI performance as it does not lead to increased inerter force exerted at the primary structure.

5 CONCLUDING REMARKS

The influence of the geometric shape of cantilevered primary structures to the TMDI performance for suppressing vibrations due to white noise external loading has been parametrically investigated. Five different shapes of primary structure have been considered with different base to free-end depth ratio with a TMDI attached to their free-end. Parametric analysis has been facilitated by a simplified 2-DOF in which the primary structure is represented by a generalized SDOF system whose properties account for the geometric shape of the structure through the mass and stiffness distribution along the structure height as well as through the fundamental mode shape of the structure. Further, the adopted 2-DOF model explicitly accounts for the location of the primary structure to which the inerter links the secondary mass. Since the primary structure modal coordinate at this location multiplies the inertance and depends on the shape on the shape of the primary, the inerter connection location was also varied in the parametric investigation. TMDI performance has been evaluated in terms of RMS free-end displacement for which the TMDI was optimally tuned. It is found that TMDI performance improves monotonically but at a reduced rate as the inerter connecting location to the primary structure moves away from the free end for all nine different primary structure shapes. Moreover, it was shown that improved TMDI performance as well as stroke are achieved for primary structure shapes with stiffness and mass distribution weighted heavier towards the base of the structure (i.e., when most of material is concentrated towards the bottom end of the structure) either through appropriate shaping or through increase of base to free-end depth ratio for fixed shape. Lastly, numerical data suggest that the primary structure shaping (i.e., considering more "pointy" primary structure geometry/shape) is practically most beneficial as it does not create increased inerter force exerted to the primary structure. Overall, the herein investigation point to the importance of primary structure design to enhance the dynamic performance of optimal TMDI-equipped structures.

REFERENCES

[1] M.C. Smith, Synthesis of Mechanical Networks: The Inerter, *IEEE Transactions On Automatic Control* 47(10), 1648-1662, 2002.

[2] A.A. Taflanidis, A. Giaralis, D, Patsialis, Multi-objective optimal design of inerter-based vibration absorbers for earthquake protection of multi-storey building structures, *Journal of the Franklin Institute* 356, 7754-7784, 2019.

[3] L. Marian, A. Giaralis, Optimal design of inerter devices combined with TMDs for vibration control of buildings exposed to stochastic seismic excitations, *Proc,.11th ICOSSAR Int. Conf. on Structural Safety and Reliability*, 1025-1032, 2013.

[4] A. Giaralis, A.A. Taflanidis, Optimal tuned mass-damper-inerter (TMDI) design for seismically excited MDOF structures with model uncertainties based on reliability criteria, *Struct. Control Health Monit.* 25, e2082, 2018.

[5] R. Ruiz, A.A. Taflanidis, A. Giaralis, D. Lopez-Garcia, Risk-informed optimization of the tuned mass-damper-inerter (TMDI) for the seismic protection of multi-storey building structures, *Eng. Struct.* 177, 836-850, 2018.

[6] A. Giaralis, F. Petrini, Wind-induced vibration mitigation in tall buildings using the tuned mass-damper-inerter (TMDI), *J. Struct. Eng.*, DOI: 10.1061/(ASCE)ST.1943-541X.0001863, 2017.

[7] F. Petrini, A. Giaralis, and Z. Wang, Optimal tuned mass-damper-inerter (TMDI) design in wind-excited tall buildings for occupants' comfort serviceability performance and energy harvesting, *Eng. Struct.* 204, 109904, 2020.

[8] Z. Wang, A. Giaralis, Top-storey softening in optimal tuned mass damper inerter (TMDI)-equipped wind-excited tall buildings for enhanced serviceability performance under vortex shedding effects, *J. Struct. Eng.*, DOI: 10.1061/(ASCE)ST.1943-541X.0002838, 2020.

[9] A. Giaralis, A.A. Taflanidis, Reliability-based design of tuned-mass-damper-inerter (TMDI) equipped stochastically support excited structures, *In: Proceedings of the 12th International Conference on Applications of Statistics and Probability in Civil Engineering- ICASP12*, 2015.

[10] R.W. Clough, J. Penzien, *Dynamics of Structures*, ISBN-13: 978-8123926636, 1993.

[11] L. Marian, A. Giaralis, Optimal design of a novel tuned mass-damper–inerter (TMDI) passive vibration control configuration for stochastically support-excited structural systems. *Prob. Eng. Mech.* 38, 156–164, 2014.

[12] A. Charles, J.E. Dennis Jr., Analysis of Generalized Pattern Searches, *SIAM Journal on Optimization* 13(3), 889–903, 2003.

EURODYN 2020
XI International Conference on Structural Dynamics
M. Papadrakakis, M. Fragiadakis, C. Papadimitriou (eds.)
Athens, Greece, 23–26 November 2020

EXPERIMENTAL STUDY OF RAILWAY BRIDGES OF SEVERAL STRUCTURAL TYPOLOGIES

P. Galvín[1], E. Moliner[2], A. Romero[1] and M.D. Martínez-Rodrigo[2]

[1] Escuela Técnica Superior de Ingeniería, Universidad de Sevilla
Camino de los Descubrimientos s/n, ES-41092 Sevilla, Spain
e-mail: {pedrogalvin,aro}@us.es

[2] Department of Mechanical Engineering and Construction, Universitat Jaume I
Avda. Sos Baynat s/n, ES-12071 Castellón, Spain
e-mail: {lola.martinez,molinere}@emc.uji.es

Keywords: Railway bridges, experimental measurements, traffic induced vibrations, bridge dynamics.

Abstract. *This work is devoted to the experimental evaluation of the dynamic response of railway bridges with common typologies in short-to-medium spans. An extensive experimental campaign is performed in several railway bridges belonging to the High-Speed (HS) and conventional Spanish railway network. The main objectives are to (i) characterise the structures main features affecting their dynamic behaviour, (ii) determining the soil properties at the structures respective locations; and analysing the bridge dynamic responses under different operating conditions. All the bridges are composed by simply-supported (S-S) bays with different steel, concrete and steel-concrete composite typologies. Five bridges have been experimentally investigated: i) Old Guadiana Bridge: a double-track simply-supported bridge with two $13\,m$ equal spans composed by two adjacent single-track decks with continuous ballast; ii) Jabalón High-Speed Bridge: an isostatic bridge of three S-S bays of $20\,m$ equal spans composed by a double-track pre-stressed concrete girders deck; iii) Algodor Bridge: an isostatic double-track bridge with three S-S bays of $10\,m$ equal spans and a pseudo-slab concrete deck; iv) Jabalón Conventional Line Bridge: a steel truss single-track structure composed by three $25\,m$ equal spans; and v) Tinajas Bridge: a steel-concrete composite single-track bridge with three bays of 25, 35 and $22\,m$ spans, respectively. The first four bridges are nowadays at full operation while the latter is under its construction final stage. The study includes the identification of bridge modal parameters and dynamic soil properties, a discussion on the identified structural damping in all the bridges, the measurement of vibration levels induced by railway traffic under operational conditions in the first four bridges and under construction operation machinery in the fifth case, and an analysis of the differences found in the structural behaviour of different bridge typologies for the same traffic. This paper summarizes a vast experimental campaign.*

1 Introduction

The dynamic effects in railway bridges have become an issue of interest and concern for scientists and engineers in the last decades, especially since the advent of High-Speed [1]. An excessive level of vertical accelerations on the deck platform (greater than 3.5 or $5\,\mathrm{m/s^2}$ in ballast or slab track bridges, respectively), can lead to misalignment of the rails as a result of premature deconsolidation of the ballast layer, to the loose of contact between wheel and rail with the subsequent increase of the risk of derailment, to fatigue problems in the structures in the long term or to an increase of the maintenance costs in the best scenario. Consequently, the Serviceability Limit States for Traffic Safety and, in particular, the vertical acceleration of the deck has become one of the most restrictive requirements in the design of new bridges. The bridges composed by simply-supported spans with short to medium span lengths are especially critical in this regard, due to their natural frequencies and usually low mass and damping associated levels. This problem of high accelerations is particularly relevant at resonance [2, 3].

A comprehensive experimental campaign in five railway bridges in Spain is presented in this work. The tests include the identification of the modal parameters of the structures, the characterization of the soil at the respective sites and the measurement of the bridge dynamic responses under railway traffic. Five bridges were tested: i) Old Guadiana Bridge: a double-track S-S bridge with two $13\,\mathrm{m}$ equal spans composed by two adjacent single-track decks sharing a continuous ballast layer; ii) Jabalón High-Speed Bridge: an isostatic bridge with three S-S bays of $20\,\mathrm{m}$ equal spans composed by a double-track pre-stressed concrete girders deck; iii) Algodor Bridge: a double-track bridge with three S-S bays of $10\,\mathrm{m}$ equal spans and a filler beam concrete deck; iv) Jabalón Conventional Line Bridge: a steel truss single-track structure composed by three $25\,\mathrm{m}$ equal spans; and v) Tinajas Bridge: a steel-concrete composite single-track continuous bridge with three spans of 25, 35 and $22\,\mathrm{m}$, respectively.

The outline of the paper is as follows. In Section 2, a general description of the experimental tests performed during the campaigns is included. The results of the experimental measurements on each particular bridge are given in the different subsections of Section 3. A final analysis on the differences found in the structural behaviour of the different typologies for similar traffic is included in Section 4.

2 Experimental set-up

In April and May 2019, the authors performed an experimental campaign on several railway bridges with the purpose of characterizing the structure and soil dynamic properties along with the bridge dynamic response under railway traffic. As per the acquisition equipment, a portable acquisition system LAN-XI of Brüel & Kjaer was used. The acquisition system fed the sensors (accelerometers) and an instrumented impact hammer in the case of the soil tests. It also performed the Analog/Digital conversion (A/D). The A/D was carried out at a high sampling frequency that avoided aliasing effects using a low-pass filter with a constant cut-off frequency. The sampling frequency was $f_s = 4096\,\mathrm{Hz}$. The acquisition equipment was connected to a laptop for data storage. Endevco model 86 piezoelectric accelerometers were used with a nominal sensitivity of $10\,\mathrm{V/g}$ and a lower frequency limit of approximately $0.1\,\mathrm{Hz}$. The acquisition system was configured to avoid the sensors overload. Nevertheless, in some cases, the signals were overloaded. In the case of Tinajas Bridge, Etna stations of Kinemetrics were used with internal triaxial accelerometers with a nominal sensitivity of $1.25\,\mathrm{V/g}$. Here, the sampling frequency was $f_s = 250\,\mathrm{Hz}$.

The modal parameters of the bridges were identified from ambient vibration data by the

(a)

(b)

Figure 1: (a) Location of the bridges in Spain and (b) experimental set-up.

stochastic subspace identification technique [4]. The ambient vibration response was acquired during the tests while the trains were not crossing the bridges. Data were decimated to carry out data analysis in the frequency range of interest ($0 - 30$ Hz). The signals were filtered applying two third-order Chebyshev filters with high-pass and low-pass frequencies of 1 Hz and 30 Hz, respectively.

The dynamic characterisation of the soil was carried out by the seismic refraction and the Spectral Analysis of Surface Waves (SASW) tests. The seismic refraction test allowed the identification of the P-wave velocity (C_p) of the soil layers. The SASW test was used to determine the S-wave velocity (C_s), and the material damping ratio of the soil layers (β) was estimated by the half-power bandwidth method [5]. 100 hammer impacts were applied to a 50 cm $\times$ 50 cm $\times$ 8 cm aluminium foundation anchored to the soil surface (Figure 2). The instrumented hammer included a PCB 086D50 force sensor. The vertical free field response was recorded by means of accelerometers anchored to the soil surface every 2 m (from 2 m to 72 m). Steel stakes of cruciform section and 30 cm of length were driven into the ground surface and the accelerometers were screwed to these stakes. After each impact, a time signal of 16348 samples (4 s) was stored. The force channel was used as a trigger, a pre-trigger of 1 s, and a post-trigger of 3 s. In this case, the signals were decimated (order 4), filtered with a third-order

Chebyshev filter with a high-pass frequency of 1 Hz and a low-pass frequency of 100 Hz.

Figure 2: Soil test set-up close to one of the bridges under study.

3 Railway Bridges

In what follows, the specificities of the experimental set-ups and the experimental measurements recorded in Old Guadiana, Jabalón HSL, Jabalón, Algodor and Tinajas bridges are outlined.

During the recordings, several RENFE trains (S100, S102, S104, S112, S120, S130, S449, S599, Altaria and freight trains) crossed the bridges. Figure 3 includes the axle schemes and coach distributions of series S100, S102, S104, S120 and Altaria trains. Also the axle distances d and axle loads P are provided. More information in this regard can be found in Reference [6].

3.1 Old Guadiana Bridge

3.1.1 Description of the structure

This first bridge under study crosses Old Guadiana River in the conventional railway line Madrid-Alcázar de San Juan-Jaén, in the Alcázar de San Juan-Manzanares section (see Figure 4). It is a double-track concrete bridge composed by two identical simply-supported bays. The horizontal structure is formed by two structurally independent although adjacent decks, one for each track, sharing the ballast layer. Each deck is composed of a concrete slab resting on five pre-stressed concrete $0.75\,\text{m} \times 0.3\,\text{m}$ rectangular girders with no transverse stiffening elements (see Figure 5). The longitudinal girders rest on the two abutments and on a central pile support through neoprene bearings. Each deck accommodates a ballasted eccentric track with Iberian gauge (1668 mm), UIC60 rails and mono-block concrete sleepers separated $0.60\,\text{m}$.

The vertical acceleration response was measured at 18 points of the lower flange lower horizontal face of the pre-stressed concrete girders (points $1 - 18$ in Figure 6). The accelerometers were attached to the girders using circular aluminium plates with $9\,\text{cm}$ of diameter and $6\,\text{mm}$ of thickness fixed with epoxy resin to the concrete surface (see Figure 1.(b)) which was previously treated for proper adherence. The response at points of the two decks in both spans was recorded.

Renfe Class 100

Renfe Class 102

Renfe Class 104

Renfe Class 120

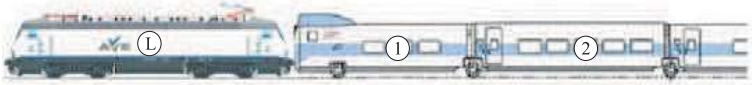

Renfe Altaria

Train	Renfe S100		Renfe S102		Renfe S104		Renfe S120		Altaria-13	
	d [m]	*P* [kN]	*d* [m]	*P* [kN]	*d* [m]	*P* [kN]	*d* [m]	*P* [kN]	*d* [m]	*P* [kN]
Axle 1	3.78	174	4.585	170	3.85	153	4.11	153		225
Axle 2	3	174	2.65	170	2.7	153	2.8	153	3	225
Axle 3	11	174	8.35	170	16.3	153	16.2	150	7.5	225
Axle 4	3	174	2.65	170	2.7	153	2.8	150	3	225
Axle 5	3.1	140	5.735	156	4.2	153	3.613	161	6.74	70
Axle 6	3	140	10.52	161	2.7	153	2.8	161	9.84	140
Axle 7	15.595	160	13.14	170	16.3	153	16.2	162	13.14	140
Axle 8	3	160	13.14	167	2.7	153	2.8	162	13.14	140
Axle 9	15.7	160	13.14	161	4.2	153	3.613	155	13.14	140
Axle 10	3	160	13.14	159	2.7	153	2.8	155	13.14	140
Axle 11	15.7	160	13.14	166	16.3	153	16.2	159	13.14	140
Axle 12	3	160	13.14	166	2.7	153	2.8	159	13.14	140
Axle 13	15.7	172	13.14	170	4.2	153	3.613	158	13.14	140
Axle 14	3	172	13.14	166	2.7	153	2.8	158	13.14	140
Axle 15	15.7	160	13.14	170	16.3	153	16.2	157	13.14	140
Axle 16	3	160	13.14	166	2.7	153	2.8	157	13.14	140
Axle 17	15.7	160	10.52	163					13.14	140
Axle 18	3	160	5.735	170					9.84	70
Axle 19	15.7	160	2.65	170						
Axle 20	3	160	8.35	170						
Axle 21	15.595	140	2.65	170						
Axle 22	3	140								
Axle 23	3.1	174								
Axle 24	3	174								
Axle 25	11	174								
Axle 26	3	174								

Figure 3: Trains coach distribution and axle distances.

3.1.2 Modal parameters identification

Ten modes with natural frequencies below 30 Hz are identified from the ambient vibration recorded during 3600 s. In Figure 7 the first ten mode-shapes are represented.

In Table 1 the identified natural frequencies and the damping ratios from the ambient response are included for the first ten modes. In the fundamental mode the identified damping ratio reaches 2.3%, higher than the value prescribed by standards for design purposes for this particular length and bridge typology (1.5% as per [7]).

The bridge response under operational conditions strongly depends on structural damping. Obtaining a realistic value of modal damping representative of the bridge dynamic response

Figure 4: Old Guadiana Bridge (39°17'37.8"N 3°12'22.5"W).

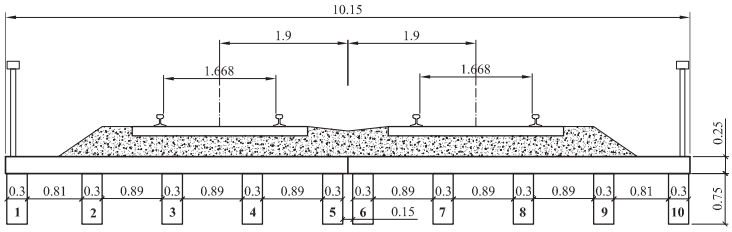

Figure 5: Old Guadiana Bridge deck cross section (Dimensions in [m]).

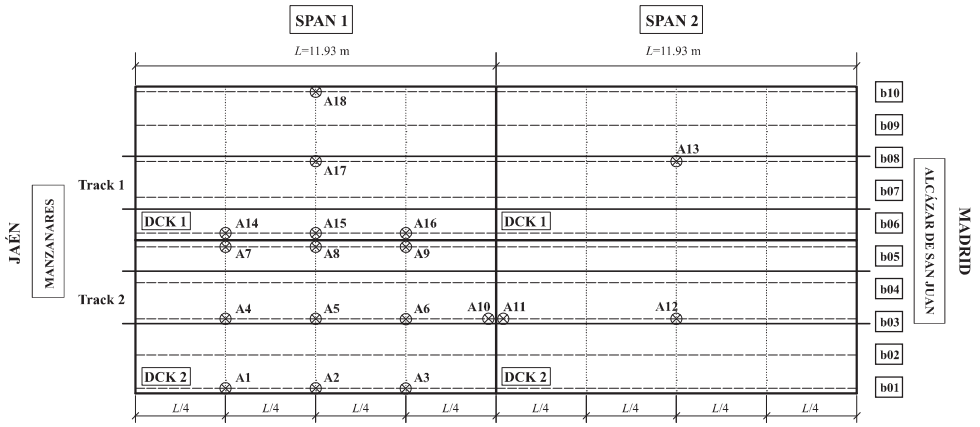

Figure 6: Location of the sensors at Old Guadiana Bridge.

under forced vibration is complicated, partially due to the dependency of this parameter with the amplitude of vibration. For this reason, modal damping has been also identified from the free vibration response recorded after the train passages indicated in section 3.1.4, using 10 s of free vibration. The modal damping ratios are extracted by the methodology presented by Kim et al. [8].

The damping ratio estimations are presented in Figure 8 and Table 1. The values of damping estimated from ambient vibration are represented with solid circles and compared to the values obtained from the train passages. The obtained results for the same vehicle crossing the bridge along the same track are consistent. As a general conclusion, it can be mentioned that the damping ratios from the train passages were considerably higher than those obtained from

Mode	f [Hz]	ξ_{AV} [%]
1	9.8	2.3
2	11.0	0.9
3	12.8	1.0
4	16.5	0.3
5	17.9	0.1
6	21.0	1.0
7	22.2	1.2
8	23.7	0.4
9	27.8	1.1
10	28.7	0.1

Mode	$\overline{\xi}_{TP}$ [%]	σ_{TP} [%]
1	2.9	0.6
2	2.5	0.5
3	1.5	0.3
4	1.9	0.1
5	1.7	0.1
6	1.3	0.2
7	1.4	0.2
8	1.2	0.1
9	1.2	0.2
10	1.0	0.2

Table 1: (left) Identified natural frequencies and damping ratios from ambient vibration and (right) mean and standard deviation of the identified damping ratios from free vibration after train passages in Old Guadiana Bridge.

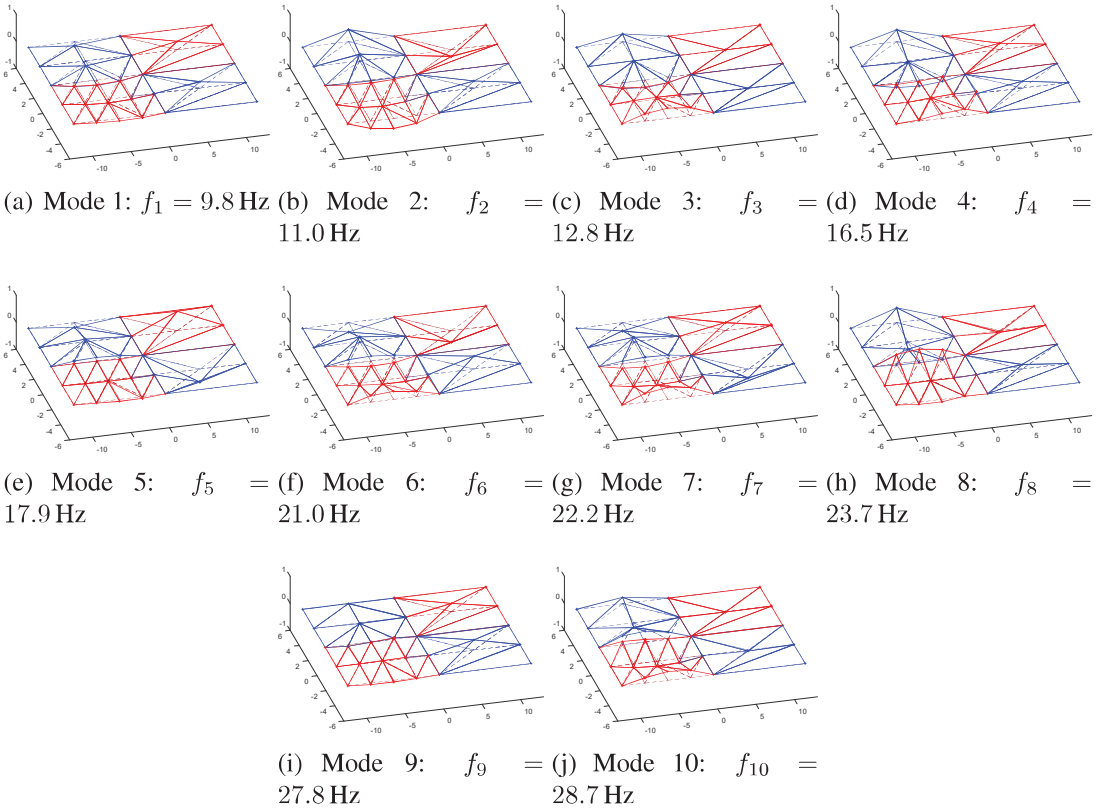

(a) Mode 1: $f_1 = 9.8$ Hz (b) Mode 2: $f_2 = 11.0$ Hz (c) Mode 3: $f_3 = 12.8$ Hz (d) Mode 4: $f_4 = 16.5$ Hz

(e) Mode 5: $f_5 = 17.9$ Hz (f) Mode 6: $f_6 = 21.0$ Hz (g) Mode 7: $f_7 = 22.2$ Hz (h) Mode 8: $f_8 = 23.7$ Hz

(i) Mode 9: $f_9 = 27.8$ Hz (j) Mode 10: $f_{10} = 28.7$ Hz

Figure 7: Identified mode shapes in Old Guadiana Bridge.

ambient vibration (factors of 1.3, 2.8 and 1.5 can be detected considering the mean value for all the trains in modes from 1 to 3). Notwithstanding the uncertainties, the estimations from the railway traffic were done under operational conditions of the bridge and can represent better the actual behaviour of the structure.

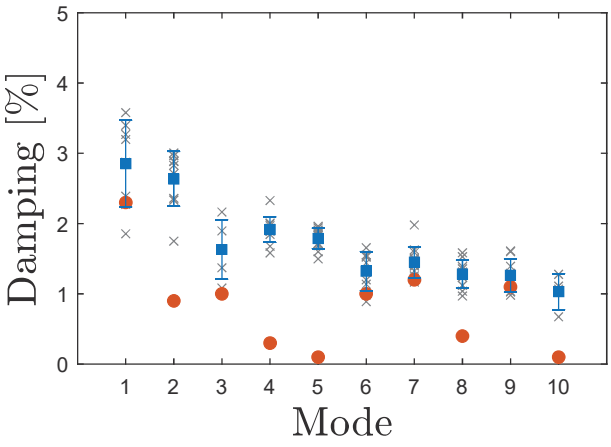

Figure 8: Old Guadiana bridge: estimated damping ratios from (red circle) ambient vibration and (grey crosses) train passages. The (blue square) mean value and (blue line) the mean value $\pm$ the standard deviation (σ) are also presented.

3.1.3 Soil properties identification

Following the procedure described in Section 2, the main dynamic properties of the soil are identified in the proximities of Old Guadiana Bridge. Figure 9 shows the resulting dispersion curve. The maxima in the spectrum are due to the Rayleigh waves. Table 2 shows the soil properties obtained from the resolution of the inverse problem using the elastodynamics toolbox (EDT) from Schevenels et al. [9].

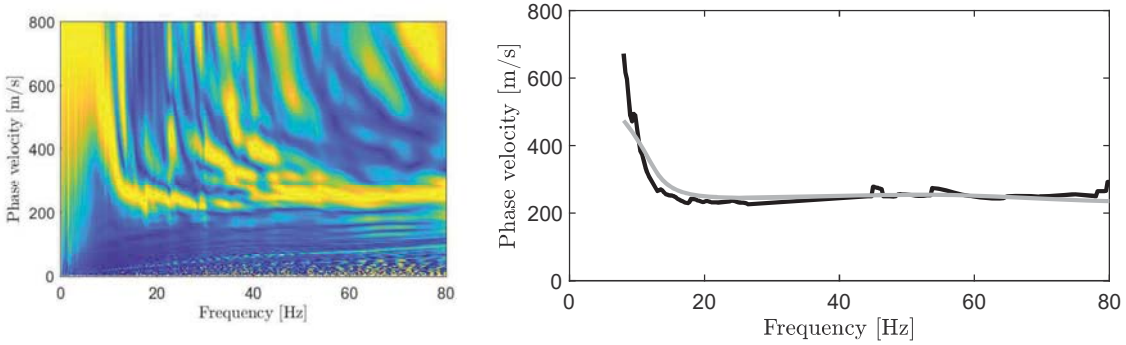

(a) (b)

Figure 9: Old Guadiana Bridge: (a) experimental dispersion curve and (b) solution of the inverse problem: experimental (black line) and numerical (grey line).

Layer	h [m]	C_p [m/s]	C_s [m/s]	ρ [kg/m^3]	β [-]
1	2	499	298	1900	0.08
2	4.5	350	207	1900	0.05
3	3.6	1300	719	1900	0.05
4	∞	500	250	1900	0.09

Table 2: Identified soil properties at Old Guadiana Bridge.

The soil presents two upper layers with a shear wave velocity lower than 300 m/s on a half-space with $C_s = 250$ m/s. The bridge supports at the abutments consist of spread footings. Therefore, in this case, SSI could affect to a certain extent the dynamic properties of the structure and its structural behaviour [10, 11].

3.1.4 Response due to train passages

The bridge response under thirteen circulations was recorded on May 6^{th} between 12:18 and 17:38 hours. In Table 3 the following information is included for each passage: train type, track number according to Figure 6, traffic direction, travelling speed, coaches scheme (L: locomotive, C: carriage) and average axle load P_k for the passenger coaches. Altaria trains, composed by a Talgo 252 locomotive and either 9 or 13 passenger coaches, are regular trains with a characteristic distance between shared axles of 13.14 m. S449 trains are articulated trains with distributed power, five coaches in total and a distance between shared bogies in the central carriages of 17.75 m. Trains S599 are conventional trains composed by two external power cars and a central carriage, and present a car length of approximately 25 m. Only one of the trains was a freight train with a conventional scheme as well. All passenger trains were commercial RENFE medium distance trains. Except for the second circulation, all the trains crossed the bridge at speeds in the interval $[140, 160]$ km/h.

Passage	Train	Track	Ride	Speed [km/h]	Scheme	$P_k/axle$ [kN]
1	Altaria-9	2	M-A	160	L-9C	140
2	S599	2	M-A	80	L-C-L//L-C-L	131
3	Altaria-13	2	M-A	160	L-13C	140
4	S449	1	A-M	160	L-3C-L	161
5	S449	1	A-M	160	L-3C-L	161
6	S449	2	M-A	160	L-3C-L	161
7	S599	1	A-M	143	L-3C-L	131
8	Altaria-13	1	A-M	157	L-13C	140
9	Altaria-9	1	A-M	155	L-9C	140
10	Freight train	1	A-M	-	L-13C	-
11	S449	2	M-A	160	L-3C-L	161
12	S449	1	A-M	160	L-3C-L	161
13	S449	2	M-A	160	L-3C-L	161

Table 3: Train passages recorded at Old Guadiana Bridge. M: Manzanares and A: Alcázar de San Juan.

In Figure 10 the acceleration response at two pair of sensors located at midspan of either span is represented in the frequency domain for train passages #1, #3, #5, #6, #9, #11, #12 and #13. One of the sensors is located under the loaded track and the other one under the unloaded track in all the cases. The maximum static load acting simultaneously on each of the spans, taking into account the span length, the particular axle loads, and the bogie and axle distances for the three types of trains is quite different: 140 kN for Altaria Talgo trains (one axle), 322 kN for S449 (two axles) and 524 kN for S599 trains (four axles). This may be the reason why many of the sensors were overloaded during train passages #2 and #7. In all the cases the response presents peaks associated to the excitation (i.e. ratio of train speed v to bogie and axle distances v/d_{bogie} and v/d_{axle}, respectively, and corresponding multiples) and to the bridge lowest natural

frequencies. In the case of Altaria Talgo trains, the acceleration amplitude in the vicinity of the bridge fundamental frequency stands out considerably in comparison to the peaks associated to the excitation. This is not the case for the S449 or the S599 trains. This is partially related to the fact that the former trains with a characteristic distance of $13.14\,\mathrm{m}$ travel at a velocity close to the theoretical third resonant speed of the fundamental mode of the bridge: $v_{1,3} = 9.8 \times 13.14/3 \times 3.6 = 154\,\mathrm{km/h}$, in combination with the high number of passenger coaches. The maximum overall acceleration measured during the train passages for frequency contents below $30\,\mathrm{Hz}$ reaches $1.61\,\mathrm{m/s^2}$, close to one half of the limit established by the Serviceability Limit State for traffic safety $3.5\,\mathrm{m/s^2}$ for bridges with ballasted tracks [12]. This maximum takes place under Altaria train with 9 passenger coaches crossing the bridge along track 2 northbound (circulation #1). Similar amplitudes of the vertical acceleration are measured for the second circulation. Nevertheless, it should be said that the actual maximum acceleration most probably took place in an overloaded sensor and is higher than the previously mentioned value. In the plots included in Figure 10 the acceleration response in the sensor located in the unloaded deck is, in some cases, of the same order of magnitude than that measured in the loaded deck. For sensors 5 and 17 (centre of the decks) the response at the unloaded sensor is relevant at the fundamental frequency (first longitudinal bending mode); and for sensors 2 and 18 (external borders of the decks) the unloaded sensor response has also important contributions at other identified frequencies, indicating an important coupling between the two decks of the same span through the ballast layer. This issue was already detected under ambient vibration and seems to be also important under the circulation of trains, despite the much higher vibration amplitudes of the structure in this case. The coupling between the adjacent decks is analysed in more detail for the Altaria trains in what follows.

Figure 11 shows the bridge response at sensors 5, 17, 8 and 15 due to a Renfe Altaria train travelling along tracks 1 (red trace) and 2 (black trace) at $v = 160\,\mathrm{km/h}$ and $v = 155\,\mathrm{km/h}$, respectively (circulations #1 and #9). Therefore, this figure shows the response of the two adjacent decks in the first span under the circulation of two identical trains travelling at very similar speeds in the two opposite directions. As mentioned before, the resonant speeds for the fundamental mode and third resonance is $v_{1,3} = 154\,\mathrm{km/h}$, very close to the actual speeds. The damping ratios for the first mode obtained from the free vibration response after the trains left the structure were in these cases 2.2% and 2.8%, respectively. The response measured at points 5 and 17 (Figure 6) presents a very high similarity when the trains cross the bridge along either of the two tracks (i.e. the unloaded and loaded sensor responses are very similar no matter what is the train direction). This shows that both decks dynamic responses are very similar and that the coupling effect is bidirectional. The contribution of mode 1 clearly prevails in all the sensors and that of the third mode (transverse bending mode) is clearly visible at points 8 and 15. Moreover, the characteristic vehicle frequency $v/d = 160/3.6/13.14 = 3.4\,\mathrm{Hz}$ and its second harmonic can also be observed at the sensors installed at the loaded deck (and are almost imperceptible at the unloaded one). When the Altaria train crosses the bridge along track 2 induces a higher acceleration response in deck 2 (sensors 5 and 8), as expected. Nevertheless, the levels of the amplitudes measured at deck 1 (sensors 15 and 17) are considerable. The maximum acceleration amplitude in deck 1 is in that case approximately 45% of the highest acceleration measured in deck 2. Among the four selected sensors the one exhibiting the highest response is sensor 8, at the longitudinal edge of deck 2, in the loaded case, showing an important contribution of the fourth mode. Again, the coupled responses of the decks through the ballasted track are significant.

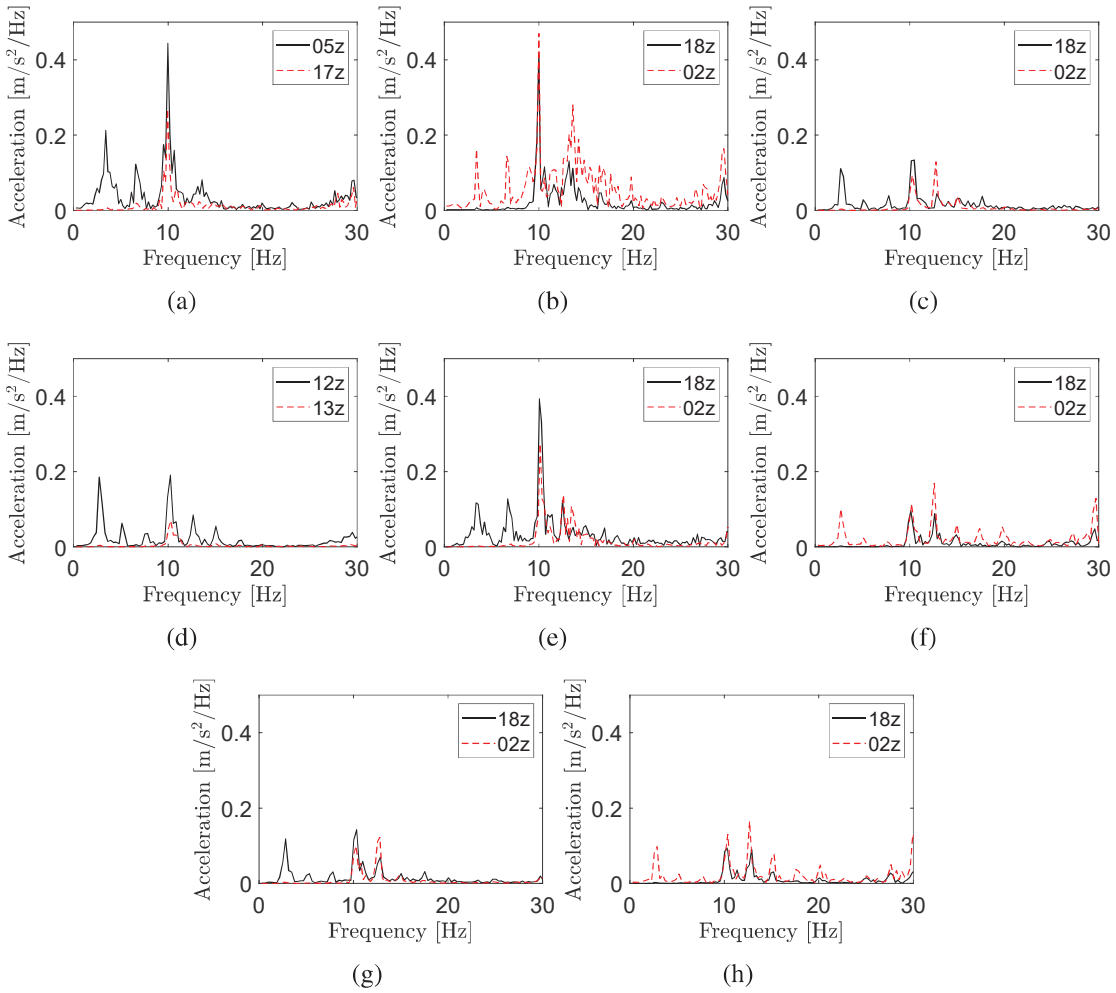

Figure 10: Old Guadiana Bridge: frequency content of the structural acceleration induced by train (a) #1, (b) #3, (c) #5, (d) #6, (e) #9, (f) #11, (g) #12 and (h) #13

3.2 Jabalón HSL Bridge

3.2.1 Description of the structure and properties identification

Jabalón HSL Bridge (Figure 12), is a railway bridge composed by three identical S-S bays of 24.9 m equal spans. The structure crosses Jabalón River with a 134° skew angle. Each deck consists of a cast-in-situ concrete slab with dimensions 11.6 m × 0.3 m (wide × thickness). The slab rests over five prestressed concrete I girders with a height of 2.05 m separated 2.625 m (see Figure 13). The girders lean on the supports through laminated rubber bearings. The slab carries two ballasted tracks with UIC gauge (1435 mm), UIC60 rails and mono-block concrete sleepers every 0.60 m. The substructure consists of two outer reinforced concrete abutments and two inner wall piers. Figure 14 shows the measurement points, all of them located at span 1. Unfortunately, it was only possible to record the response of the first span due to the piers height and the river flow.

Table 4 presents the identified modal parameters of the structure.

Table 5 presents the identified dynamic soil properties. The experimental procedure described in section 3.1.3 is reproduced at this bridge site. The soil in the surroundings of Jabalón HSL bridge is composed of an upper layer of limestone of approximately 2 m with a shear wave

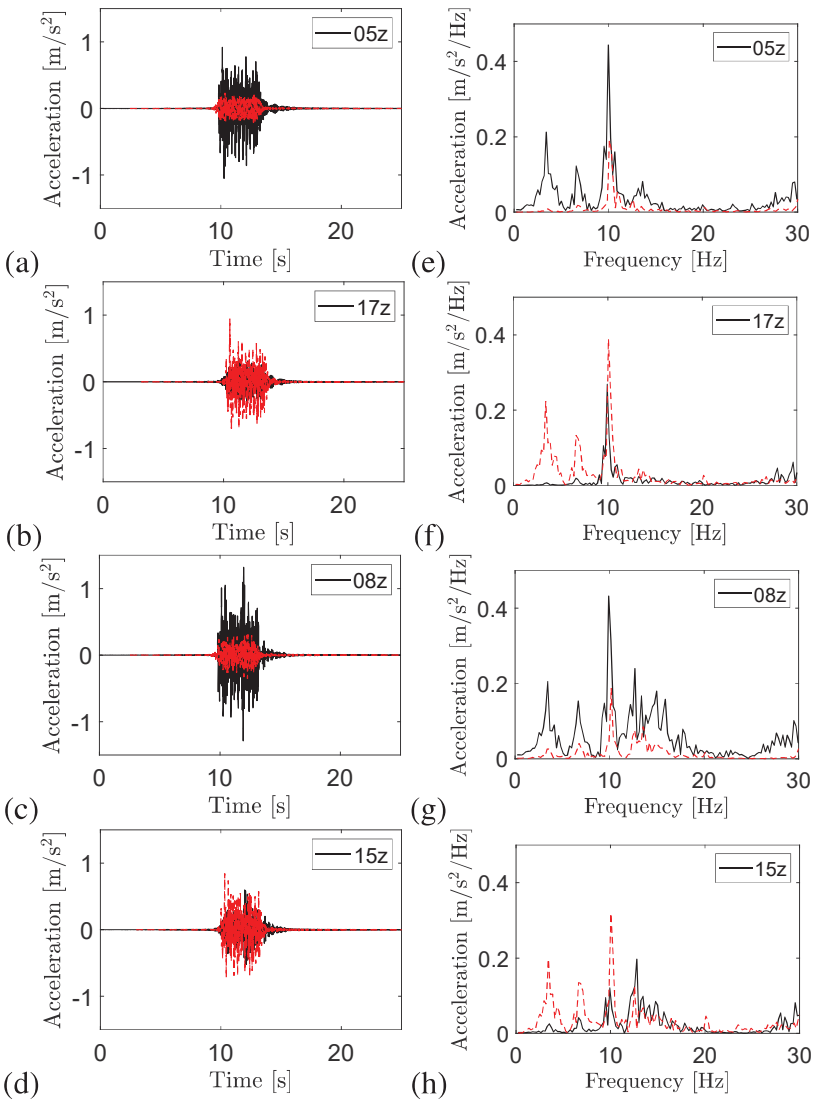

Figure 11: Old Guadiana Bridge: (a-d) time history and (e-h) frequency content of the acceleration at points 5, 17, 8 and 15 induced by Renfe Altaria train with 9 coaches (black line) at $v = 160$ km/h circulating on track 2 and (red line) at $v = 155$ km/h circulating on track 1.

Figure 12: HSL bridge over Jabalón River (38°53'51.3"N 3°57'53.0"W).

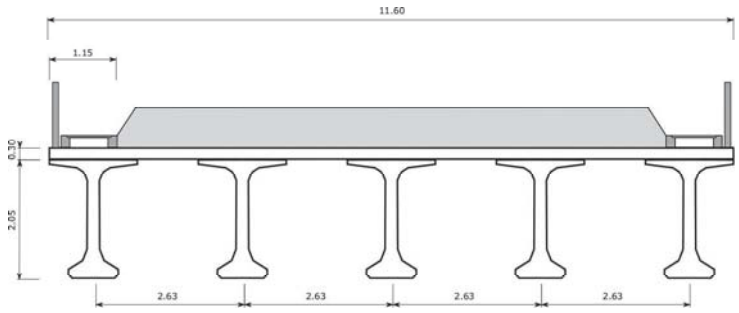

Figure 13: Jabalón HSL deck cross section (Dimensions in [m]).

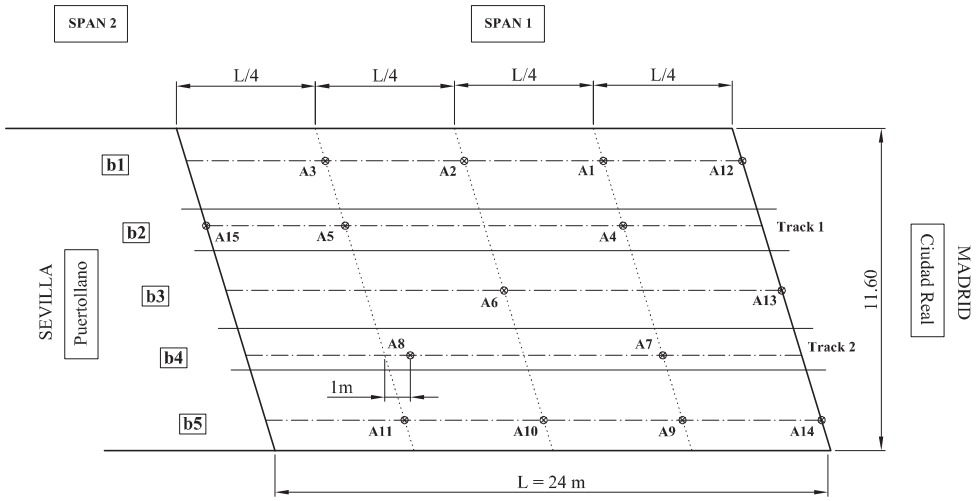

Figure 14: Location of the sensors on Jabalón HSL Bridge.

Mode	f [Hz]	ξ_{AV} [%]
1	6.3	3.2
2	7.2	1.6
3	9.3	0.7
4	14.8	0.6
5	24.0	1.2
6	24.5	0.8

Mode	$\overline{\xi}_{TP}$ [%]	σ_{TP} [%]
1	3.5	0.9
2	3.3	0.8
3	2.4	0.7
4	2.0	0.2
5	1.1	0.1
6	1.2	0.2

Table 4: (left) Identified natural frequencies and damping ratios from ambient vibration and (right) mean and standard deviation (σ) of the identified damping ratios from train-induced vibrations of Jabalón HSL Bridge.

velocity of $C_s = 321$ m/s, a layer of clay gravel of approximately 2 m and $C_s = 176$ m/s on a sand-clay halfspace with $C_s = 225$ m/s. The profile from the SASW test is consistent with that provided by a geotechnical analysis performed at the site prior to the bridge construction [13].

3.2.2 Response due to train passages

Table 6 summarizes the train passages recorded at Jabalón HSL Bridge. The dynamic response of the bridge under the circulation of 20 passenger trains was recorded on May 8^{th} 2019

Layer	h [m]	C_p [m/s]	C_s [m/s]	ρ [kg/m^3]	β [-]
1	2	800	321	2000	0.1
2	2	715	176	2000	0.1
3	∞	500	225	2000	0.1

Table 5: Identified soil properties at Jabalón Bridge.

between 11.52 and 15.24 hours. All the trains that travelled over the bridge in both directions were RENFE High-Speed services. In particular articulated S100 trains, regular S102, S112 and S130 trains, and conventional S104 trains crossed the bridge in single and duplex configurations. The identified travelling velocities are comprised between 236 and 290 km/h and are included in Table 6 along with the trains schemes and average axle loads of the passenger coaches.

The trains inducing the lowest dynamic response on Jabalón HSL bridge are S104 trains. These trains are composed by only two passenger coaches and their maximum speed is 250 km/h. The overall maximum acceleration reaches 1.8 m/s^2 (calculated after the signal is filtered under 30 Hz), and happens for the ninth circulation (S102 duplex at 265 km/h). A similar maximum level of the acceleration is obtained for circulations #4 and #12 for a similar and for the same train. S102 trains are regular Talgo trains with a short characteristic distance (13.14 m) and a high number of axles. Therefore this trains are prone to excite the participation of low frequency modes of the bridge. Again, one should be cautious with this value as some of the sensors overloaded and are not considered in the analysis. Sensors that particularly experienced overload are those close to the supports of the deck under the loaded track (13 and 15 when the trains travel along track 1, and 13 and 14 when they travel along track 2). A non symmetric dynamic behaviour is detected when comparing the responses between accelerometers 10 and 2, which may be related to the deck obliquity. In all the cases the response measured close to the abutments and to the intermediate pile are considerably lower in terms of accelerations than at the intermediate sections.

Figures 15, 16 and 17 compare the bridge response at four sensors under the circulation of three trains Renfe S104, Renfe S102 and Renfe S100 crossing the bridge a two similar (yet non-resonant) speeds. The first figure corresponds to train S104 travelling along track 1 southbound. The response at the sensors close to the loaded track (accelerometers 1 and 2) exhibits contributions in the frequencies v/d_i and corresponding harmonics, being d_i the characteristic length or distance between axles and between bogies of the trains. This train, in particular, does not excite the bridge natural frequencies to a big extent compared to S102 or S100, which are composed by a much higher number of passenger coaches. The responses for two travelling speeds are superimposed: 249 and 255 km/h. The responses are almost identical despite the small difference in the speeds. It should be said that the second and third theoretical resonant speeds for the fundamental mode associated to the coaches lengths are 196 and 294 km/h, far from the actual velocities. For this reason the response is not very sensitive to this parameter.

3.3 Algodor Bridge

The third bridge under study, Algodor Bridge, belongs to the Madrid-Sevilla High-Speed railway line as well. It is a railway bridge composed by three S-S bays with 10.25 m, 10.00 m and 10.25 m spans (distance between centres of neoprene bearings). The bridge crosses Algodor river with a skew angle of $114.3°$ (Figure 18). Algodor Bridge presents a filler beam deck,

Passage	Train	Track	Ride	Speed [km/h]	Scheme	$P_k/axle$ [kN]
1	S102	1	M-C	290	L-12C-L	165
2	S102	2	C-M	266	L-12C-L	165
3	S104	2	C-M	251	L-2C-L	153
4	S112-Duplex	1	M-C	267	L-12C-L//L-12C-L	172
5	S102	1	M-C	240	L-12C-L	165
6	S102-Duplex	2	C-M	263	L-12C-L//L-12C-L	165
7	S100	1	M-C	290	L-8C-L	156
8	S112	1	M-C	269	L-12C-L	172
9	S102-Duplex	2	C-M	265	L-12C-L//L-12C-L	165
10	S130	1	M-C	236	L-11C-L	165
11	S102	2	C-M	274	L-12C-L	165
12	S102-Duplex	1	M-C	267	L-12C-L//L-12C-L	165
13	S130	2	C-M	237	L-11C-L	165
14	S104	1	M-C	249	L-2C-L	153
15	S100	2	C-M	262	L-8C-L	156
16	S130	1	M-C	236	L-11C-L	165
17	S100	1	M-C	290	L-8C-L	156
18	S102	2	C-M	273	L-12C-L	165
19	S104	1	M-C	255	L-2C-L	153
20	S104	2	C-M	236	L-2C-L	153

Table 6: Train passages recorded at Jabalón HSL Bridge. M: Madrid and C: Ciudad Real.

composed by a 0.65 m thick and 11.6 m wide concrete slab longitudinally reinforced with 20 inverted T pre-stressed concrete girders enclosed within the depth of the slab and with the required steel rebars for transverse reinforcement (see Figure 19). The girders lean on the supports through laminated rubber bearings. The slab carries two ballasted tracks with UIC gauge (1435 mm), UIC60 rails and mono-block concrete sleepers every 0.60 m, and with an equal eccentricity of 2.15 m measured from its longitudinal axis. The bridge deck is supported on reinforced concrete abutments in its outermost sections and the inner sections of both bays lean on a 0.6 m thick and 12.3 m wide concrete pier. Figure 20 shows the measurement points. In this case, two of the three spans were monitored.

Five modes were identified from the ambient vibration response with frequencies up to 30 Hz. Table 7 and Figures 21 and 22 show the identified modal parameters. The first two modes correspond to the first longitudinal bending mode of each span vibrating out of phase and in phase, respectively. In modes 3 and 4 the deck deforms under torsion: in the former each span deforms independently and, in the latter, the torsional deformations of both spans are coupled. The last mode corresponds to the transverse bending deformation of one the spans. Modal damping is again identified both from ambient vibration and from the free vibration after the train passages. It should be mentioned in this case that modes 1 and 2, and modes 3 and 4 present very similar natural frequencies, which could bias the estimation of this parameter [8]. The identified damping for the fundamental mode from the train passages is 2.1%, higher than the ambient vibration estimation (1.5%) and than the value recommended by Eurocode (1.7%).

Table 8 shows the dynamic soil properties. The soil in the surroundings of Algodor Bridge is composed of an upper layer of gravel of approximately 2 m with $C_s = 314$ m/s on a clay on

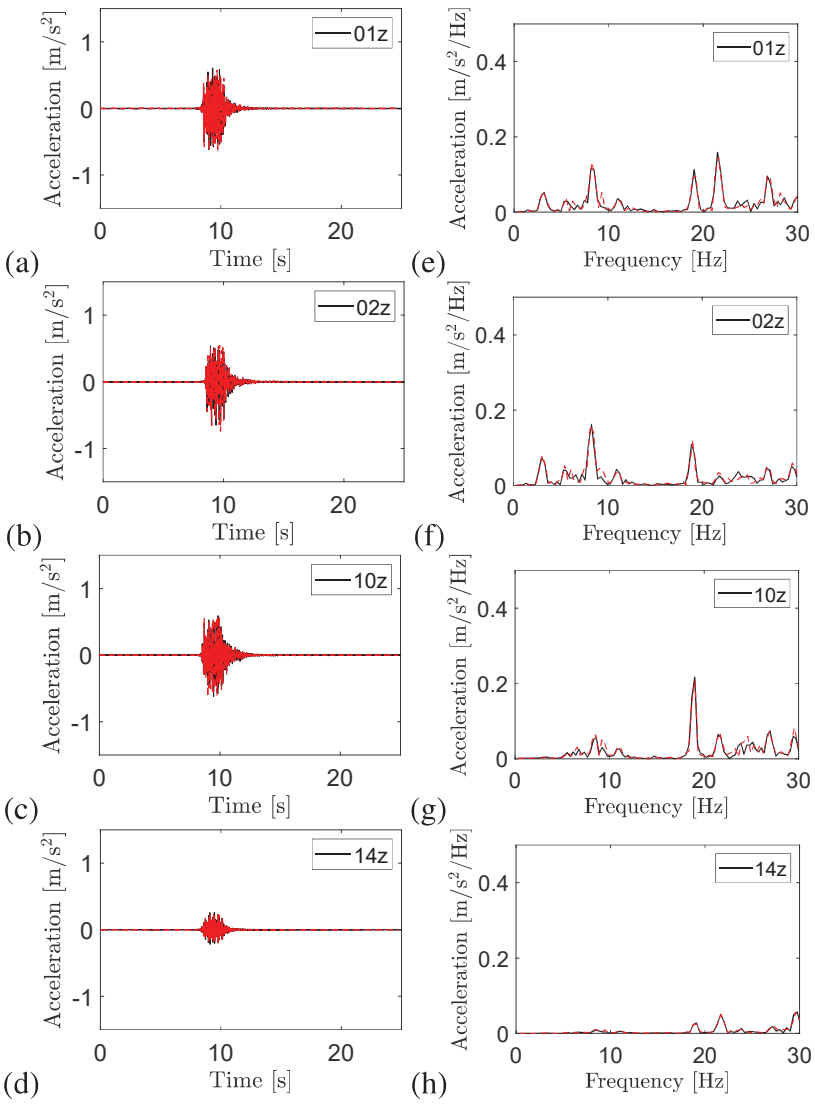

Figure 15: Jabalón HSL Bridge: (a-d) time history and (e-h) frequency content of the acceleration at points 1, 2, 10 and 14 induced by Renfe S104 train circulating on track 1 at (black line) $v = 249$ km/h and (red line) $v = 255$ km/h.

a slate halfspace with $C_s = 800$ m/s. The high identified value of the P-wave velocity indicates that the soil is saturated. The profile is consistent with that provided by a geotechnical analysis performed at the site prior to the bridge construction [14].

Mode	f [Hz]	ξ [%]
1	11.6	1.5
2	11.7	2.9
3	13.7	1.0
4	13.9	0.6
5	19.6	0.9

Mode	$\overline{\xi}_{TP}$ [%]	σ_{TP} [%]
1	2.1	0.4
2	1.9	0.4
3	1.8	0.5
4	1.8	0.6
5	1.1	0.2

Table 7: (left) Identified natural frequencies and damping ratios from ambient vibration and (right) mean and standard deviation (σ) of the identified damping ratios from train-induced vibrations in Algodor Bridge.

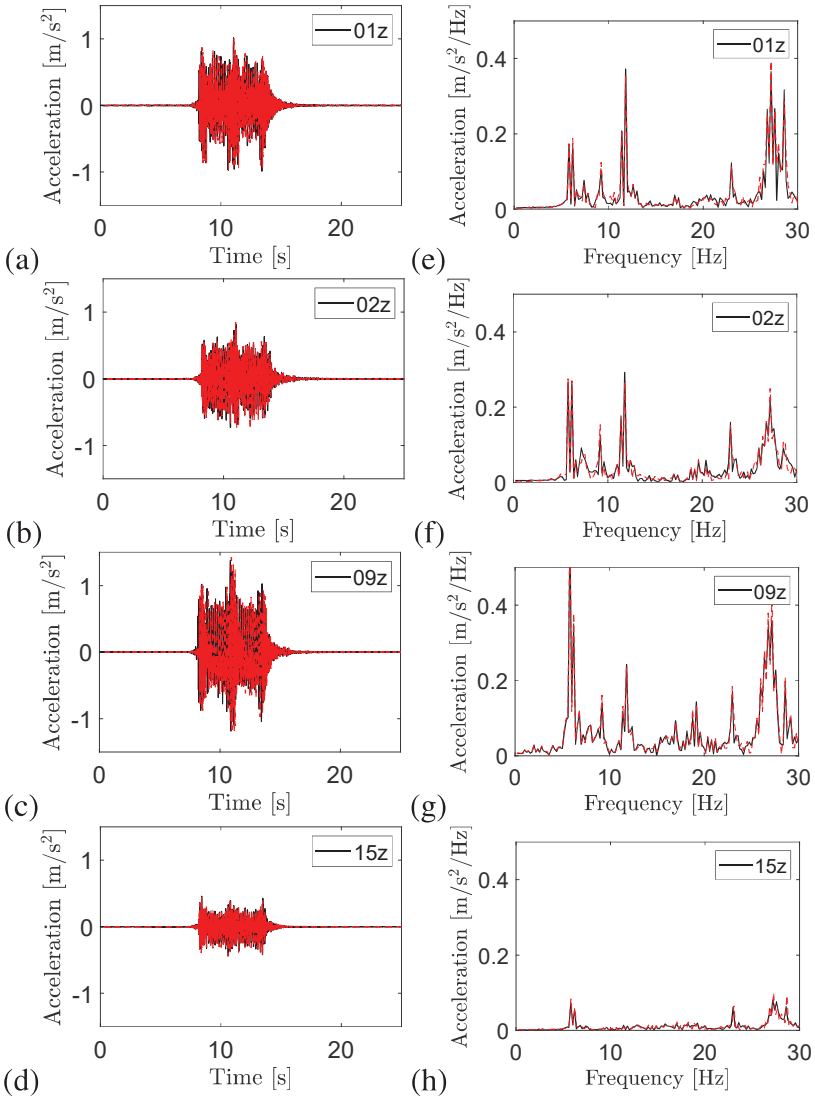

Figure 16: Jabalón HSL Bridge: (a-d) time history and (e-h) frequency content of the acceleration at points 1, 2, 9 and 15 induced by Renfe S102 duplex train circulating on track 2 at (black line) $v = 263$ km/h and (red line) $v = 265$ km/h.

Layer	h [m]	C_p [m/s]	C_s [m/s]	ρ [kg/m^3]	β [-]
1	2	554	314	2000	0.09
2	∞	1600	800	2000	0.07

Table 8: Identified soil properties at Algodor Bridge.

3.3.1 Response due to train passages

On May 5^{th} 2019 the response of Algodor Bridge under the circulation of 13 passenger trains was recorded. The particular trains were Renfe S102, S130 and S120, in single and duplex configurations, and Renfe S100. S102 and S130 are regular trains, S120 is a conventional train and S100 is articulated. Table 9 presents information in relation with these train passages. The travelling speeds were comprised between 228 and 307 km/h. The overall maximum acceleration measured was 2.96 m/s^2 under passages #2 and #3 of the S102 train at 304 km/h. This value was measured at accelerometer 1 (central span, central section border girder closest to the

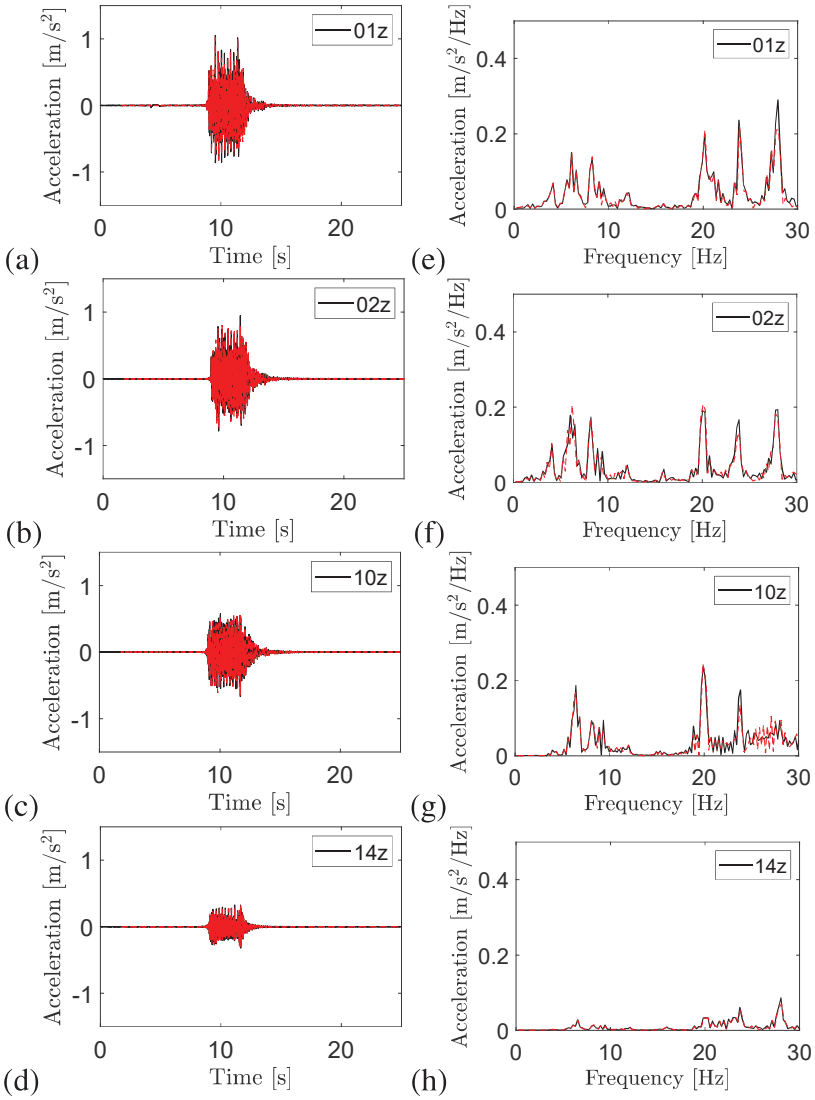

Figure 17: Jabalón HSL Bridge: (a-d) time history and (e-h) frequency content of the acceleration at points 1, 2, 10 and 14 induced by Renfe S100 train circulating on track 1 at (black line) $v = 290$ km/h and (red line) $v = 290$ km/h.

Figure 18: Bridge over Algodor River (39°31'55.5"N 3°49'25.3"W).

loaded track). Some sensors were overloaded in some cases. In particular accelerometer 4, in

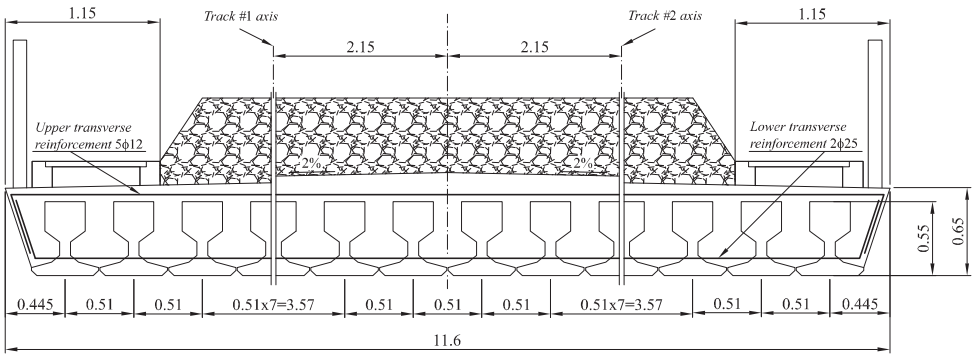

Figure 19: Algodor Bridge deck cross section (Dimensions in [m]).

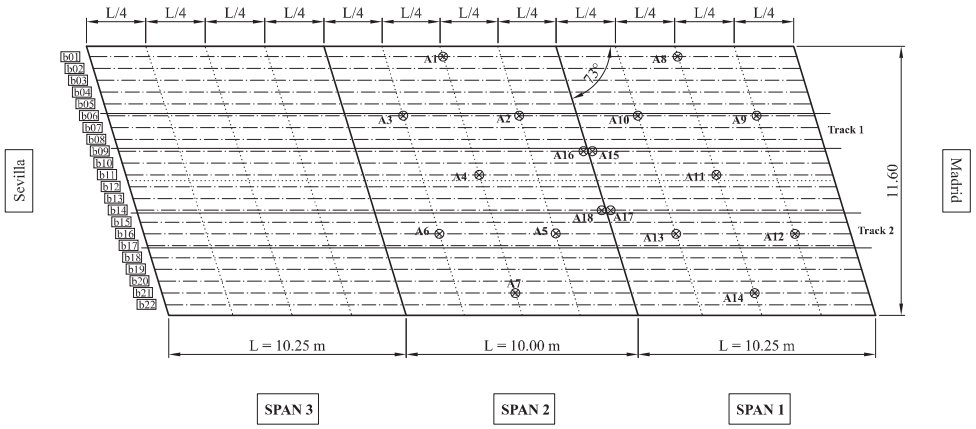

Figure 20: Location of the sensors on Algodor Bridge.

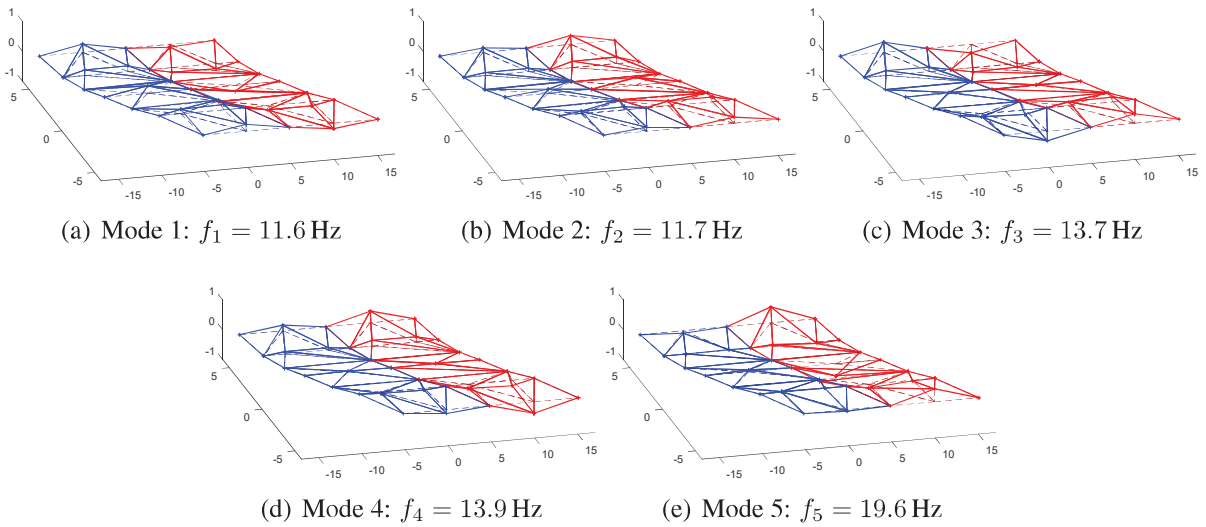

(a) Mode 1: $f_1 = 11.6\,\text{Hz}$ (b) Mode 2: $f_2 = 11.7\,\text{Hz}$ (c) Mode 3: $f_3 = 13.7\,\text{Hz}$

(d) Mode 4: $f_4 = 13.9\,\text{Hz}$ (e) Mode 5: $f_5 = 19.6\,\text{Hz}$

Figure 21: Identified mode shapes of Algodor Bridge: (red) span 1 and (blue) span 2.

the very centre of the second span, was overloaded under most of the circulations. Therefore, the maximum acceleration of the deck could be somewhat higher than the referred value.

Figure 23 shows the structural response induced by the fourth and ninth trains passages.

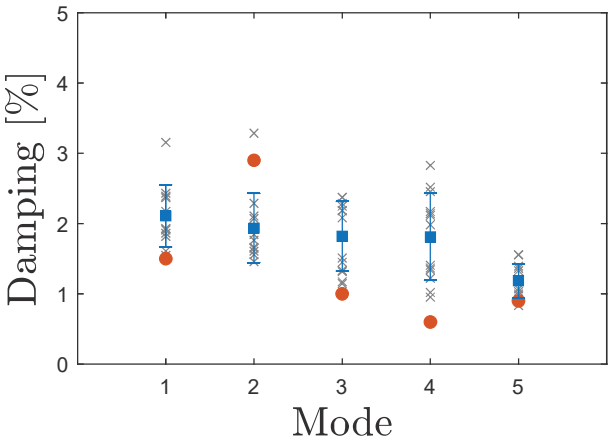

Figure 22: Algodor bridge: estimated damping ratios from (red circle) ambient vibration and (grey crosses) train passages. The (blue square) mean value and (blue line) the mean value $\pm$ the standard deviation (σ) are also presented.

These correspond to the circulation of two Renfe S102 trains travelling at $v = 304$ km/h along track 1 (black trace) and at $v = 306$ km/h along track 2 (red trace). The responses are compared at sensors 1 and 7 (mid section of the central span) and 8 and 11 (mid section of first span). The contribution of torsion modes (with frequencies close to 14 Hz) and transverse bending mode (with frequency close to 20 Hz) are the most relevant regardless of the train direction. In each span the decks of Algodor Bridge present very similar length and width dimensions. Also, the flexural and torsional stiffnesses are uniformly distributed due to the filler-beam typology of the deck. This justifies the plate-type dynamic response that this bridge in particular exhibits. The S102 trains velocities are far from any resonant condition of the longitudinal bending and torsion modes ($v_{1,2} = 274.4$ and $v_{3,2} = 324$ km/h for $f_1 = 11.6$ and $f_3 = 13.7$ Hz, respectively) but the third resonant frequency of the fifth mode (transverse bending mode) is induced by this train travelling at $v_{3,3} = 13.14 \times 19.6 \times 3.6/3 = 309$ km/h. This may be the reason why an important amplification happens close to 20 Hz.

Passage	Train	Track	Ride	Speed [km/h]	Scheme	P_k/axle [kN]
1	S102-Duplex	1	M-C	298	L-12C-L//L-12C-L	165
2	S130-Duplex	2	C-M	228	L-11C-L//L-11C-L	165
3	S102	1	M-C	304	L-12C-L	165
4	S102	1	M-C	304	L-12C-L	165
5	S102-Duplex	2	C-M	252	L-12C-L//L-12C-L	165
6	S120	2	C-M	250	L-2C-L	160
7	S102-Duplex	2	C-M	260	L-12C-L//L-12C-L	165
8	S120-Duplex	1	M-C	238	L-2C-L//L-2C-L	160
9	S102	2	C-M	306	L-12C-L	165
10	S130-Duplex	1	M-C	237	L-11C-L//L-11C-L	165
11	S130	2	C-M	229	L-11C-L	165
12	S102	1	M-C	298	L-12C-L	165
13	S100	2	C-M	307	L-8C-L	156

Table 9: Train passages recorded at Algodor Bridge. M: Madrid and C: Ciudad Real.

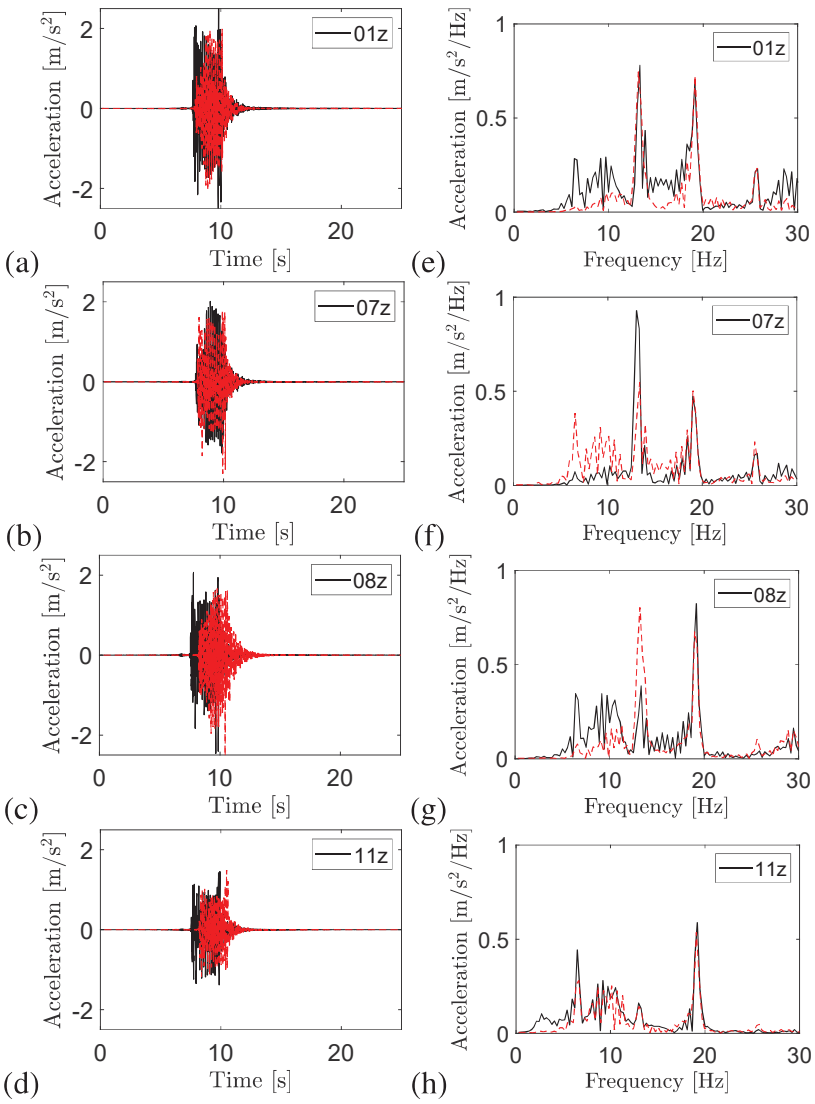

Figure 23: Algodor Bridge: (a-d) time history and (e-h) frequency content of the acceleration at points 1, 7, 8 and 11 induced by Renfe S102 train circulating (black line) on track 1 at $v = 304$ km/h and (red line) on track 2 at $v = 306$ km/h.

3.4 Jabalón Bridge

Jabalón Bridge (Figure 24), is a steel truss railway bridge composed by three S-S bays of 25 m of span. This bridge also crosses Jabalón river but it belongs to the conventional railway line Alcázar de San Juan-Ciudad Real-Badajoz. In this section nowadays the traffic is very limited and most of the circulations are freight trains and maintenance vehicles. Jabalón and Jabalón HSL are only 200 m apart and one set of tests were performed in the area in order to identify the soil properties (see section 12). Jabalón Bridge carries only one ballastless track (Figure 25 left) with Iberian gauge, UIC60 rails and wooden sleepers. Due to the absence of ballast and direct contact between the rail and the steel structure, unfortunately, several accelerometers were unstuck due to the high level of vibrations induced by the train passages. In what follows a few remarks are included in relation to the behaviour of this particular structure but the information available is much less than in the previous cases.

Figure 26 shows the measurement points. The accelerometers were glued directly at the truss

connections in different orientations (see Figure 25 right). Three modes were clearly identified from ambient vibration (see Table **??**). In increasing frequency order these modes correspond to first lateral bending, first longitudinal bending and first torsion modes. In this case, only damping values identified from ambient vibration are available. The fundamental mode exhibits very low damping, typical in steel structures but the values obtained for the second and third modes are comparable to the values identified in previous bridges. The modal damping value proposed by Eurocode [7] for this steel bridge is 0.5%.

Figure 24: Bridge over Jabalón River (38°53'51.2"N 3°57'44.7"W).

Figure 25: (left) Track in the Bridge over Jabalón River and (right) accelerometer at the truss connection.

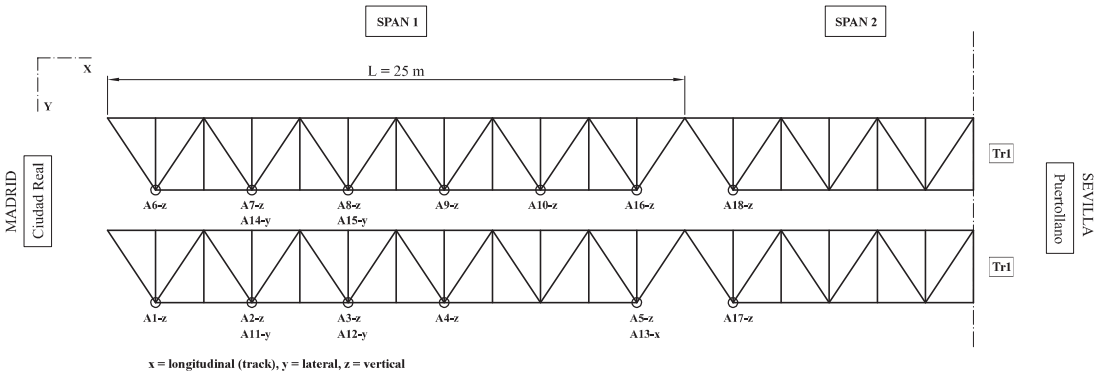

Figure 26: Location of the sensors on Jabalón Bridge.

3.5 Tinajas Bridge

The bridge over the Tinajas Stream (Figure 27) is a three-span continuous bridge with span lengths of 25 m, 35 m and 25 m. At the moment of the experimental campaign this bridge was under construction. It belongs to the conventional railway line between Bobadilla and Algeciras. The bridge presents a steel-concrete composite section formed by two main steel I beams and an upper concrete slab. The slab is 8.6 m wide allowing the installation of a single-track with Iberian gauge, UIC60 rails and mono-block concrete sleepers every 0.60 m (Figure 28). The height of the I beams is 1.8 m. The concrete slab presents variable thickness from 0.20 m to 0.38 m. Close to the intermediate supports the section is completed with a lower concrete slab with a thickness of 0.20 m. The two main steel beams are reinforced with sheets of variable thickness in the lower flange ($30 - 60$ mm) and web ($15 - 20 - 25$ mm), and with steel plates of constant thickness (25 mm) in the upper flange. The beams are braced every 5 m with H-shaped transverse frames. The deck is supported on two abutments at the outermost sections and on two concrete piles at the inner supports, all of them with micropiles. The deck rests on eight POT bearings positioned under each beam longitudinal axis at the piles and abutments. Transversely the deck movement is restricted by seismic supports installed at each pile and abutment. The longitudinal moving support is materialized at one of the abutments. The rectangular concrete piles have a cross section of 4.50 m $\times$ 1.50 m and heights of 16.60 m and 16.01 m, respectively.

Figure 27: Bridge over Tinajas River (37°01'41.0"N 4°45'26.6"W).

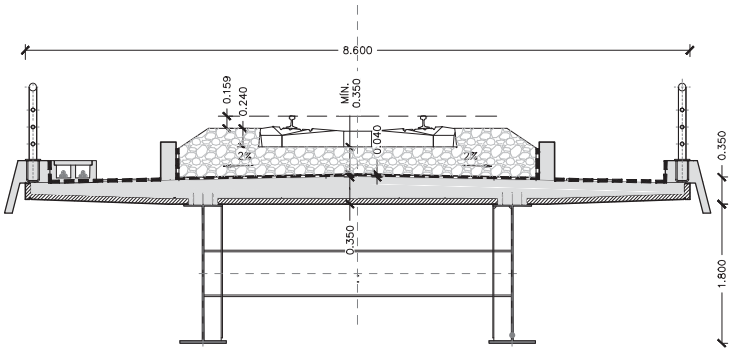

Figure 28: Tinajas Bridge deck cross section (Dimensions in [m]).

The ambient response of the bridge deck was measured at 18 points using triaxial accelerometers (Figure 29). Table 10 and Figure 30 present the identified modal parameters. In the first

five mode shapes the deck deforms under lateral bending (mode 1), longitudinal bending (modes 2 and 5) and torsion (modes 3 and 4). Very low damping values, in the range $[0.4 - 0.7]\%$, were identified for the five modes in ambient vibration, close to the Eurocode recommendation of 0.5% for spans longer than $20\,\mathrm{m}$ in the case of steel-concrete composite bridges. Modal parameters were not identified in free vibration as the bridge was not operational during the measurements. In this case, soil tests were not performed.

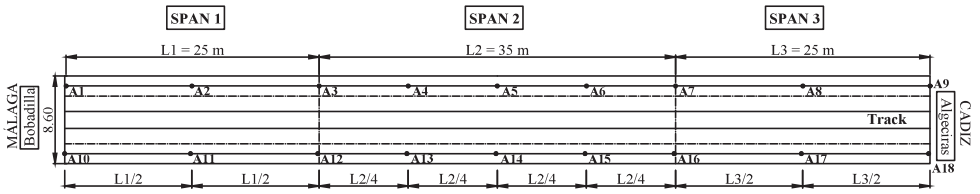

Figure 29: Location of the sensors on Tinajas Bridge.

Mode	f [Hz]	ξ [%]
1	3.0	0.7
2	3.7	0.6
3	6.0	0.4
4	10.5	0.6
5	11.7	0.5

Table 10: Identified natural frequencies of Tinajas Bridge: (red) span 2 and (blue) spans 1 and 3.

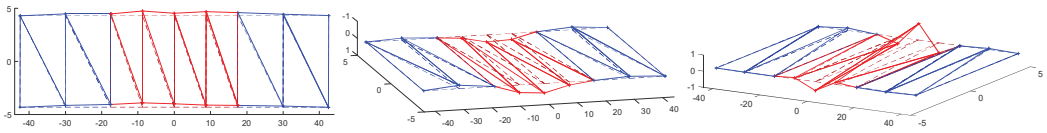

(a) Mode 1: $f_1 = 3.0\,\mathrm{Hz}$ (b) Mode 2: $f_2 = 3.7\,\mathrm{Hz}$ (c) Mode 3: $f_3 = 6.0\,\mathrm{Hz}$

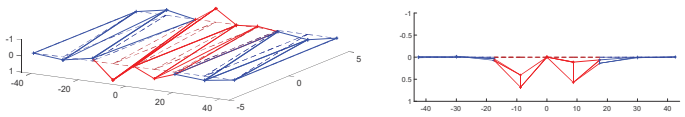

(d) Mode 4: $f_4 = 10.5\,\mathrm{Hz}$ (e) Mode 5: $f_5 = 11.7\,\mathrm{Hz}$

Figure 30: Identified mode shapes of Tinajas Bridge: (blue) spans 1 and 3 and (blue) span 2.

3.5.1 Response due to ballast distributing and profiling and stabilisation machines passages

The objective of this test, unlike the previous, was to measure the bridge behaviour under track construction operations: ballast distribution, profiling and stabilisation . Plasser & Theurer Unimat 08-475/4S ballast distributing machine has two bogies with two axles separated $14\,\mathrm{m}$. The distance between axles is $1.8\,\mathrm{m}$ and the axle load is $198\,\mathrm{kN}$. Plasser & Theurer DGS

62N profiling and stabilisation machine consists of two bogies with two axles each one. The distance between bogies is 12 m and the distance between axles of the same bogie is 1.5 m. The front axle load is 140 kN and the rear axle load is 145 kN in this case. The total load is approximately 570 kN. Moreover, Plasser & Theurer DGS 62N applies a maximum vertical load of 356 kN. Both machines are used to maintain the geometry and good condition of the track. The stabilization is done immediately after the tamping operations [15].

Figure 31 shows the longitudinal (x), lateral (y) and vertical (z) acceleration at points 4 and 11 due to the Plasser & Theurer DGS 62N operating at 40 Hz and the Plasser & Theurer Unimat 08-475/4S operating at 35 Hz with a nominal pressure of 20 bar. The frequency content is represented in logarithmic scale. In the case of the profiling and stabilisation machine, the contribution of the load frequency can be clearly observed in the response.

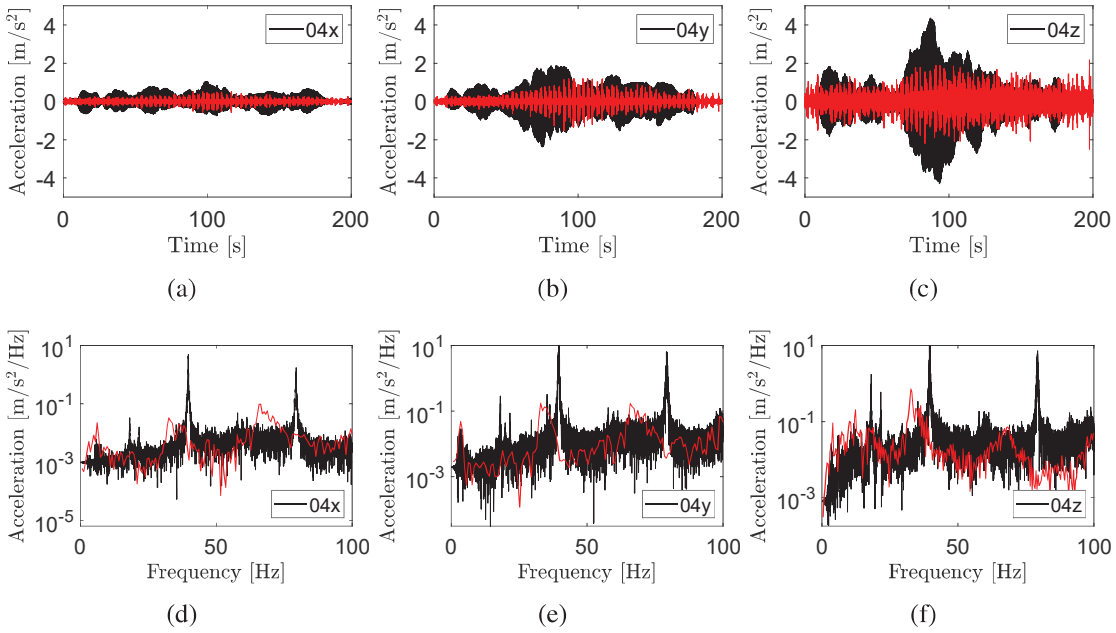

Figure 31: Tinajas bridge: (a-c) time history and (d-f) frequency content of the acceleration at point 4 induced by (black line) Plasser & Theurer DGS 62N profiling and stabilisation machine operating at 40 Hz and (red line) Plasser & Theurer Unimat 08-475/4S ballast distributing machine operating at 35 Hz.

4 Conclusions

The experimental campaign presented in this paper is aimed at analysing the dynamic behaviour of railway bridges. The tests were performed on five bridges with different structural typologies: i) a bridge with spans composed by two adjacent single-track decks sharing a continuous ballast track; ii) a three-span bridge composed by a double-track pre-stressed concrete girders deck; iii) a three-span S-S bridge with a filler-beam concrete deck; iv) a three-span S-S steel truss bridge with a single ballastless track, and v) a steel-concrete composite continuous three-span bridge. The bridge dynamic behaviour, the soil properties and the response under operational and maintenance conditions have been studied in the previous sections.

This work also shows that damping identification is difficult and depends on the chosen methodology. According to previous studies [8] it depends on the time span and bandpass filter applied but, despite that, it can be concluded that the estimated damping ratios in free vibration under operational conditions were always greater than the values obtained in ambient vibration.

The analysis of the acceleration response of the bridges due to train traffic shows, in the frequency domain, clear peaks associated to the excitation (bogie and axle passages, and even its corresponding harmonics) and also to the bridge lowest natural frequencies. The maximum overall acceleration measured is lower (yet significant), than the Serviceability Limit State prescribed by European Standards [12], limited to $3.5\,\mathrm{m/s^2}$ for bridges with ballasted tracks.

The coupling effect between adjacent decks of the same span caused by the continuity of the ballast layer is clearly perceptible in the train-induced vibrations of Old Guadiana bridge, which can be also identified under ambient vibrations. A similar observation was previously reported by Rauert at al. [16] in a S-S bridge formed by one span with two separated decks. Therefore, for an accurate prediction of the dynamic response of bridges composed by several S-S spans and/or structurally independent decks at each span, the consideration of the coupling effect induced by the ballast continuity in the numerical models may become important.

Acknowledgements

The acquisition of the experimental data on which this paper is based was made possible thanks to ADIF. The authors would like to acknowledge the financial support provided by (i) the Spanish Ministry of Economy and Competitiveness under the research project [BIA2016-75042-C2], (ii) the Spanish Ministries of Science, Innovation and Universities through the project US-126491 funded by the FEDER Andalucía 2014-2020 Operational Program, (iii) Generalitat Valenciana under the research project [AICO2019/175] and (iv) the Andalusian Scientific Computing Centre (CICA).

REFERENCES

[1] L. Frýba, Dynamic behaviour of bridges due to high-speed trains, in: Bridges for High-Speed Railways, CR Press, London, 2008, pp. 137–158.

[2] W. Hoorpah, Dynamic calculations of high-speed railway bridges in france – some case studies, in: Dynamics of High-Speed Railway Bridges, CR Press, London, 2008, pp. 133–145.

[3] M. Zacher, M. Baeßler, Dynamic behaviour of ballast on railway bridges, in: Dynamics of High-Speed Railway Bridges, CR Press, London, 2008, pp. 99–112.

[4] E. Reynders, System identification methods for (operational) modal analysis: Review and comparison, Archives of Computational Methods in Engineering 19 (1) (2012) 51–124. doi:10.1007/s11831-012-9069-x.

[5] S. A. Badsar, M. Schevenels, W. Haegeman, G. Degrande, Determination of the material damping ratio in the soil from SASW tests using the half-power bandwidth method, Geophysical Journal International 182 (3) (2010) 1493–1508. doi:10.1111/j.1365-246X.2010.04690.x.

[6] Renfe, Our trains.
URL https://www.renfe.com/EN/viajeros/nuestros_trenes/index.html

[7] CEN/TC250, Eurocode: Basis of structural design. Annex A2: Application for bridges. Final version, European Committee for Standardization, Brussels, 2005.

[8] B. H. Kim, N. Stubbs, T. Park, A new method to extract modal parameters using output-only responses, Journal of Sound and Vibration 282 (1) (2005) 215 – 230. doi:https://doi.org/10.1016/j.jsv.2004.02.026.

[9] M. Schevenels, S. François, G. Degrande, EDT: An elastodynamics toolbox for MATLAB, Computers & Geosciences 35 (8) (2009) 1752 – 1754. doi:http://dx.doi.org/10.1016/j.cageo.2008.10.012.

[10] A. Doménech, M. Martínez-Rodrigo, A. Romero, P. Galvín, On the basic phenomenon of soil-structure interaction on the free vibration response of beams: Application to railway bridges, Engineering Structures 125 (2016) 254 – 265. doi:http://dx.doi.org/10.1016/j.engstruct.2016.06.052.

[11] M. Martínez-Rodrigo, P. Galvín, A. Doménech, A. Romero, Effect of soil properties on the dynamic response of simply-supported bridges under railway traffic through coupled boundary element-finite element analyses, Engineering Structures 170 (2018) 78 – 90. doi:https://doi.org/10.1016/j.engstruct.2018.02.089.

[12] CEN, EN 1991-2, Eurocode 1: Actions on Structures - Part 2: Traffic loads on bridges, European Committee for Standardization, Brussels, 2002.

[13] Ministerio de transporte, turismo y comunicaciones, Nuevo acceso ferroviario a Andalucía. Tramo: Ciudad Real - Brazatortas. Proyecto de infraestructura y vía. Estudio geológico y geotécnico, Gobierno de España, 1987.

[14] Ministerio de transporte, turismo y comunicaciones, Proyecto de infraestructura y vía del tramo Mascaraque-El Emperador. Modificación nº 1. Documento nº 1. Memoria y anejos II., Gobierno de España, 1987.

[15] Indian Railways Institute of Civil Engineering, Mechanised Tamping & Stabilisation Pune - 411 001, Tech. rep. (November 2016).

[16] T. Rauert, H. Bigelow, B. Hoffmeister, M. Feldmann, On the prediction of the interaction effect caused by continuous ballast on filler beam railway bridges by experimentally supported numerical studies, Engineering Structures 32 (12) (2010) 3981–3988.

EURODYN 2020
XI International Conference on Structural Dynamics
M. Papadrakakis, M. Fragiadakis, C. Papadimitriou (eds.)
Athens, Greece, 23–26 November 2020

DYNAMIC RESPONSE OF CORRUGATED STEEL CULVERTS FOR RAILWAY LINES

A. Andersson[1] **and R. Karoumi**[2]

[1]Royal Institute of Technology
Brinellvägen 23, SE-100 44 Stockholm
e-mail: adde@kth.se

[2] Royal Institute of Technology
Brinellvägen 23, SE-100 44 Stockholm
e-mail: raidk@kth.se

Keywords: Railway bridge, high-speed train, soil-structure interaction, frequency response function.

Abstract. *Corrugated steel culverts are sometimes used as an alternative to portal frame bridges for small and medium crossings under railway lines. From a static point of view, the corrugated steel culverts are rather flexible structures and the load capacity relies on the confinement from the surrounding soil. From a dynamic point of view, especially for potential use on high-speed lines, the structural manner of action is not yet fully explored.*

This paper presents the result from full-scale experimental testing of a corrugated steel culvert, including both forced vibration tests and response from passing trains. The aim is to estimate the dynamic characteristics of the bridge, especially the interaction with the surrounding soil and how that will influence the response at the track level. From the forced vibration tests, the results show that the structure has a high inherent damping owing to the surrounding soil and that both the natural frequency and damping change with load amplitude. The experimental frequency response functions are used for updating numerical models to further understand the dynamic behaviour of these structures.

1 INTRODUCTION

Corrugated steel culverts consist of corrugated pipes or aches, often assembled by bolted curved sheets. The corrugation itself is rather weak but can withstand significant loads when properly confined by backfilling, therefore often denoted soil-steel composite bridges, SSCB. They are built for both road and railway applications and can reach spans up to 20 m. A typical cross-section of a SSCB is illustrated in Figure 1 and a typical corrugation is shown in Figure 2.

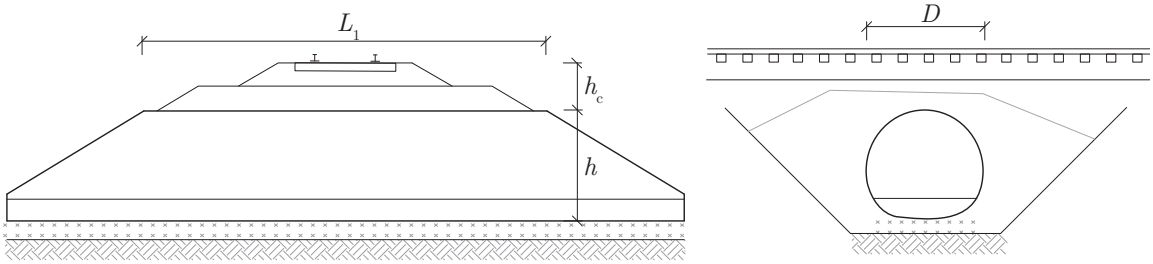

Figure 1: Typical cross-section of a SSCB.

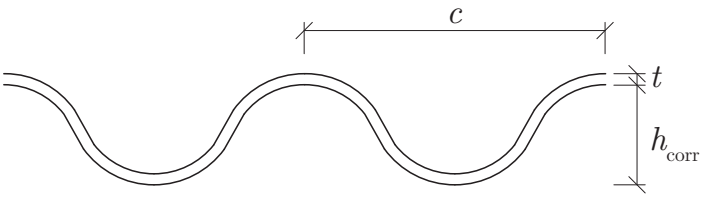

Figure 2: Basic profile of the corrugated plate.

As an example, the Swedish railway network contains about 4200 railway bridges whereof 75 are SSCB. The rate of construction has been relatively constant since the 1960ies. Most bridges have a closed elliptic culvert profile and the average diameter D = 3.3 m. The height of cover h_c is usually not less than 1.1 m. The data from the Swedish bridges is presented in Figure 3. More detailed description of different culvert profiles and corrugation sections can be found in [1] and [2].

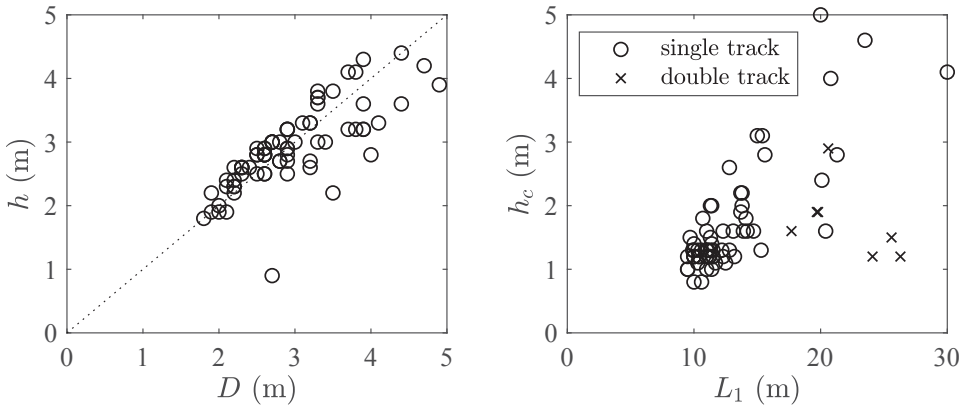

Figure 3: Geometrical data for soil-steel composite bridges in Sweden.

1.1 Previous studies

There is a relatively vast amount of literature on the topic of soil-steel composite bridges, mostly devoted to different aspects of static design and construction methods. Several experimental campaigns are also published, comprising static load tests to failure, fatigue tests and dynamic tests. In this paper however, only work related to dynamic analysis and tests on soil-steel composite bridges for railway traffic is included.

Skivarpsån, Sweden

One of the earlier work the dynamic performance of SSCB for railways is the bridge over Skivarpsån in South of Sweden. It consists of a semi-circular corrugated arch with D = 11 m, h = 4.3 m and h_c = 1.8 m that was installed outside of an existing concrete arch bridge in 2003. The new bridge is founded on separate supports and does not transfer any load to the old bridge that is still in place. A SuperCor S37 corrugation with c = 380 mm, h_{corr} = 140 mm and t = 7.0 mm was used.

The first experimental campaign is reported in [3], comprising the construction stage followed by static and dynamic load tests with trains. Strain gauges were installed on the intrados of the corrugation, at quarter point and the crown. An LVDT was installed at the crown, measuring the relative displacement between the new and the old bridge. The result from a passing freight train showed about 1 mm vertical crown displacement and about 13 MPa stress in the corrugation. The same tests were later published in [4].

More comprehensive dynamic tests were performed in two following campaigns, reported in [5] and [6]. A 78 tonne RC4 locomotive was used, running at different speeds from 10 to 125 km/h. The measured response showed a crown displacement from 0.7 to 0.9 mm and about 11-15 MPa stress in the culvert. Both tests were performed with similar test schedule, in May and October 2004.

The results was later published in [7] and [8]. It was concluded that there was no significant difference between the two tests and that the ballast acceleration was less than 0.5 m/s^2. The work on the bridge over Skivarpsån is also compiled in [9].

Märsta, Sweden

In 2009 and 2010, experimental testing was performed on a double track closed arch culvert in Märsta outside of Stockholm, Sweden, first reported in [10]. The geometry is D = 3.7 m, h = 4.1 m and h_c = 1.9 m and a VE-profile with c = 150 mm, h_{corr} = 50 mm and t = 5.5 mm.

The culvert was instrumented with strain gauges, accelerometers and LVDTs and the response from passing trains was recorded with a top speed of 175 km/h. The results showed a peak displacement of about 0.5 mm, acceleration of 0.8-1.4 m/s^2 and 6 MPa stress in the culvert. Accelerometers were also installed in the track area before, on and after the bridge. The peak ballast acceleration was in the range of 0.5-3.5 m/s^2.

2D and 3D models were developed with relatively good agreement compared to experimental results, reported in [11]. The load distribution from the track to the culvert was found to have a significant importance and the 2D-models were partly based on a best-fit 3D-model in that aspect. Simulations of high-speed trains indicated potential exceedance of the accelerations for train speeds above 250 km/h. It was pointed out however that the models were afflicted with great uncertainties. In [12] a best fit 3D model was found for a soil E-modulus of 120 MPa and simulations indicated that the acceleration limit was reached at about 300 km/h.

A hydraulic system for forced vibration tests on railway bridges was later developed and first

tested in [13]. This equipment was used when performing new tests on the culvert in 2017 and on two additional bridges in 2018.

Culverts in Poland

Experimental testing of a double track twin culvert is reported in [14]. The closed arch culvert has the geometry D = 4.4 m, h = 2.8 m and h_c = 2.4 m and the centre distance between the two culverts is 5.9 m. The corrugation has a geometry with c = 150 mm, h_{corr} = 50 mm and t = 3.0 mm.

The vertical crown displacement was measured using an interferometric radar sensor and a total of 40 trains with speed from 20 to 120 km/h was recorded. The results showed a vertical peak displacement of about 0.6 mm. Based on the same data, further analysis reported in [15] showed a dynamic amplification factor ranging from 1.1 to 1.4. It should be noted however that the resolution and accuracy of the measurement system was rather limited. The same bridge was later instrumented with strain gauges, accelerometers and LVDTs, reported in [16]. The results confirmed previous displacements of about 0.6 mm. In addition, a peak stress of 11 MPa was recorded. From a passing train at 120 km/h the peak acceleration was 0.7 m/s^2 in the culvert and 1.2 m/s^2 in the ballast.

Experimental testing of a similar bridge but with a single span is reported in [17]. The geometry was D = 4.7 m, h = 2.9 m and h_c = 2.4 m and with the same corrugation as the previous bridge. Trains passing at 40 to 130 km/h was recoded during 24h and relatively similar results were obtained as the previous tests; 0.65 mm vertical crown displacement, a peak stress of 13 MPa and 0.7 and 1.3 m/s^2 in the culvert and the track respectively.

1.2 Aim and scope

The aim of this paper is to estimate the dynamic characteristics of an existing SSCB, by means of experimental testing and numerical simulation. Of special interest is the interaction with the surrounding soil and how that influence the response at the track level. By using forced vibration testing, amplitude dependent properties are explored.

2 EXPERIMENTAL TESTING

2.1 The bridge

The experimental testing was performed on a single track close arch bridge at Hårestorp, about 400 km South of Stockholm, Sweden. The geometry is D = 4.9 m, h = 3.9 m and h_c = 1.2 m and an MP 150 profile with c = 150 mm, h_{corr} = 50 mm and t = 5.0 mm. A photo of the bridge is shown in Figure 4. Experimental tests were performed in September 2018.

Figure 4: View of the Hårestorp bridge, during field tests in 2018. Passage of an X14 passenger train.

2.2 Instrumentation

The bridge was instrumented with 16 uniaxial accelerometers (SiFlex SF1500S), two strain gauges (120Ω from HBM) and two displacement transducers (HBM WA10 LVDT). The instrumentation is illustrated in Figure 5 and Figure 6, accelerometers are denoted a1-a16, strain gauges e1-e2 and displacement transducers d2-d3.

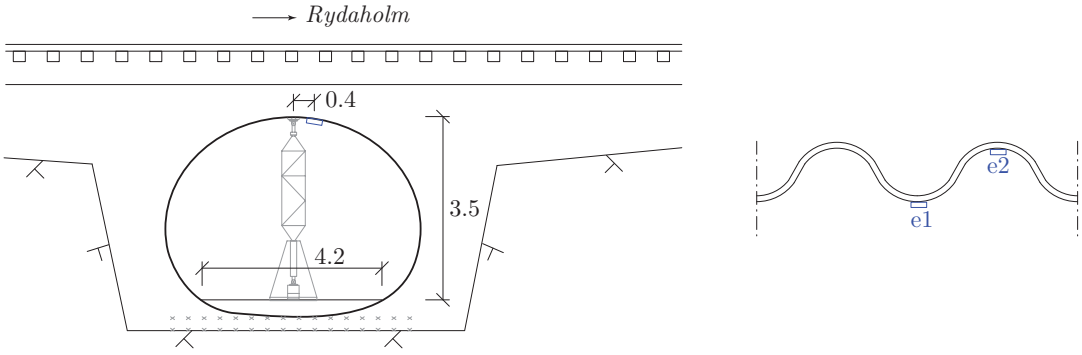

Figure 5: Instrumentation of the bridge at Hårestorp in 2018, section and detail of corrugation.

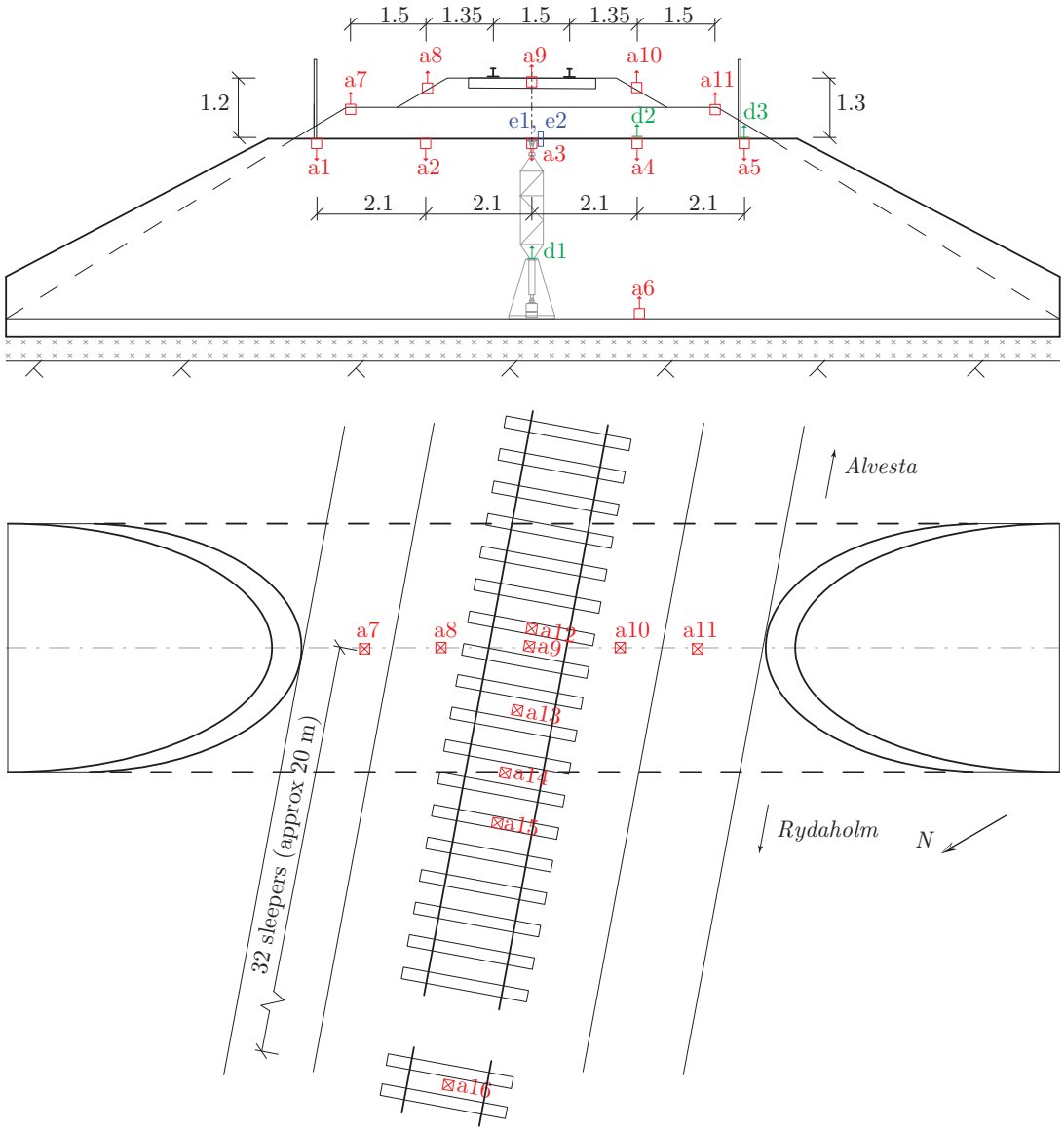

Figure 6: Instrumentation of the bridge at Hårestorp in 2018, plan and elevation.

2.3 The actuator system

The main part of the experimental equipment consists of the actuator system for forced vibration tests. The schematics is illustrated in Figure 7. It consists of a 50 kN MTS load actuator that is powered by an oil pump with a peak pressure of 210 bar and flow rate of 120 litre/min, powered by an integrated 40 hp diesel engine. The total mass of the oil pump is about 1000 kg. The actuator is placed inside the bridge and the load is transmitted to the crown by an aluminium truss system that can be rebuilt to adjustable heights. A load cell is placed on top of the truss and both the lower and upper points of the system is hinged. Load controlled harmonic sweeps are performed by using an MTS FlexTest SE controller. The data is collected by an MGCPlus data acquisition system, consisting of the input force, actuator displacement and the sensors on the bridge.

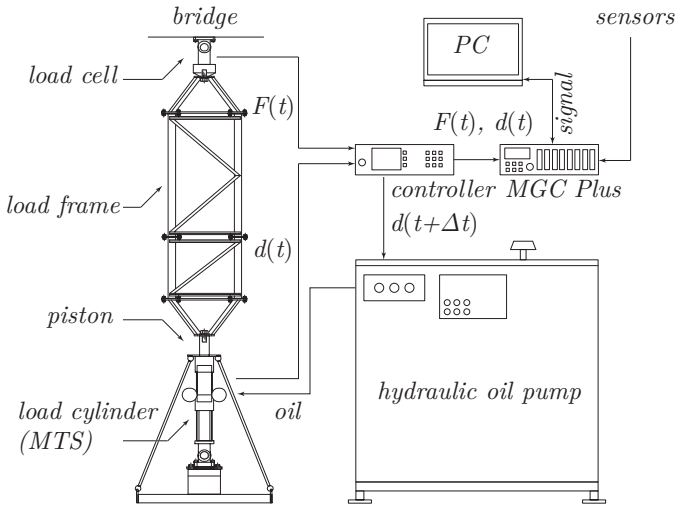

Figure 7: Illustration of the actuator system used during the experimental testing.

2.4 Train passages

A total of 8 train passages were recorded, running at a speed ranging from 120 to 150 km/h. The allowable speed at the location is 160 km/h. The peak vertical displacement during train passage is about 0.8 mm. By integrating the accelerometer a1 to a5, the displacement along the culvert is presented in Figure 8.

The peak acceleration from the culvert and the track during train passages is presented in Figure 9. The results highly depends on the frequency content and a comparison is made between a 30 Hz and 100 Hz LP-filter. The relatively large scatter in results become less when comparing individual sensors for the same type of trains at similar speed.

An example of the stress in the crown during train passage is shown in Figure 10. The largest bending stress is about 7 MPa. The combination of axial and bending stress results in a peak stress of about 4 MPa in tension at e1 and 12 MPa in compression at e2.

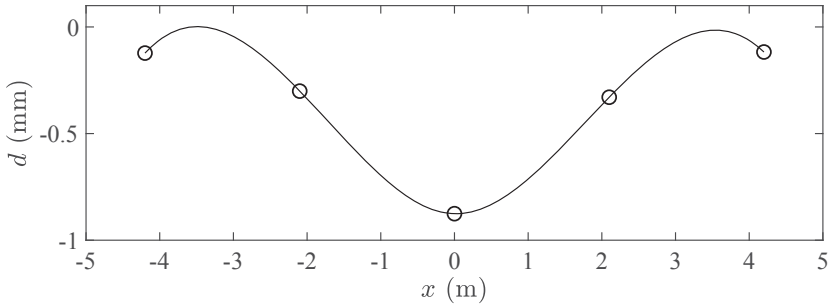

Figure 8: Vertical peak displacement of the culvert estimated from accelerometer a1-a5, X14 train passage.

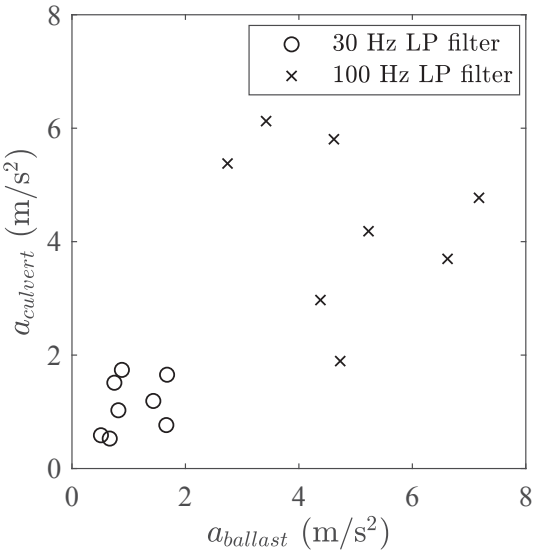

Figure 9: Peak acceleration with 30 Hz and 100 Hz filter, all trains.

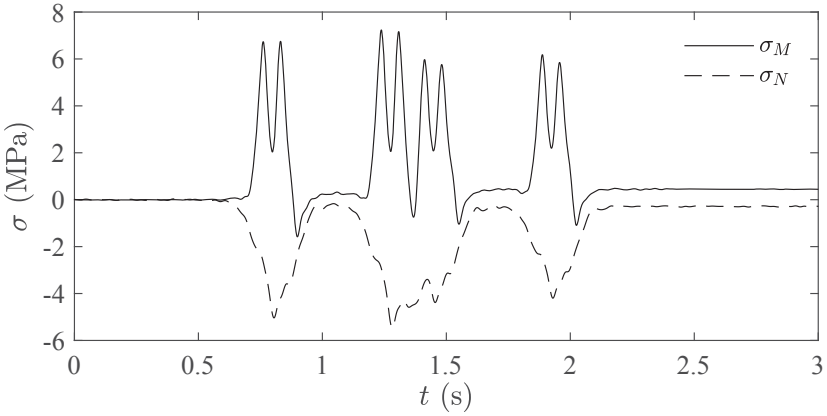

Figure 10: Stress in the crown of the culvert, X14 train passage.

2.5 Forced vibration tests

Forced vibration tests were performed with the actuator in the centre of the bridge near sensor a3. Harmonic frequency sweeps were performed from 1-40 Hz with a rate of Δf = 0.05 Hz/s. Test were performed with load amplitudes from 1-20 kN. The complex-values transfer function $\mathbf{H}(\omega)$ is calculated based on the Fourier transform of the output acceleration $a(t)$ and input force $F(t)$ according to Equation 1. Further in this paper the FRF will have the unit kN/m/s^2.

$$\mathbf{H}(\omega) = \mathbf{A}(\omega)/\mathbf{F}(\omega) \tag{1}$$

The results show that the vibration of the culvert and the track seems to be in phase up to about 30 Hz, as illustrated in Figure 11 for accelerometer a3 and a9. When comparing the FRFs for different load amplitudes, Figure 12, increasing the load amplitude results in a clear decrease in natural frequency, ranging from 16.4 Hz to 14.4 Hz. At the same time the estimated damping increase from 3.8% to 6.5%, using the half-Power Bandwitdh method.

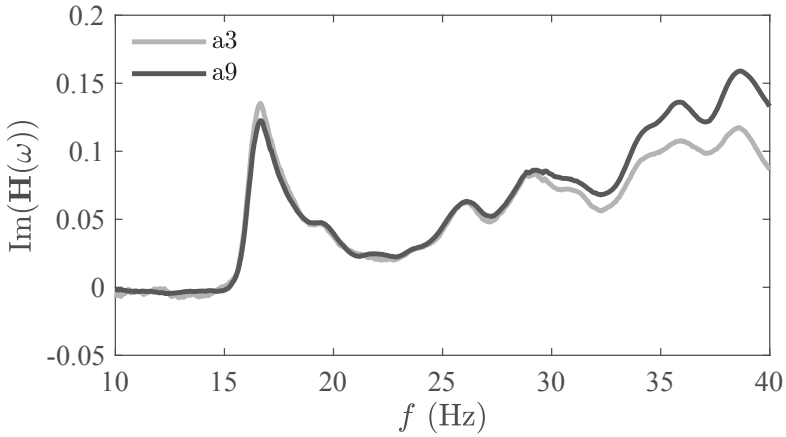

Figure 11: FRF, compare response in culvert and track, F_{amp} = 1 kN.

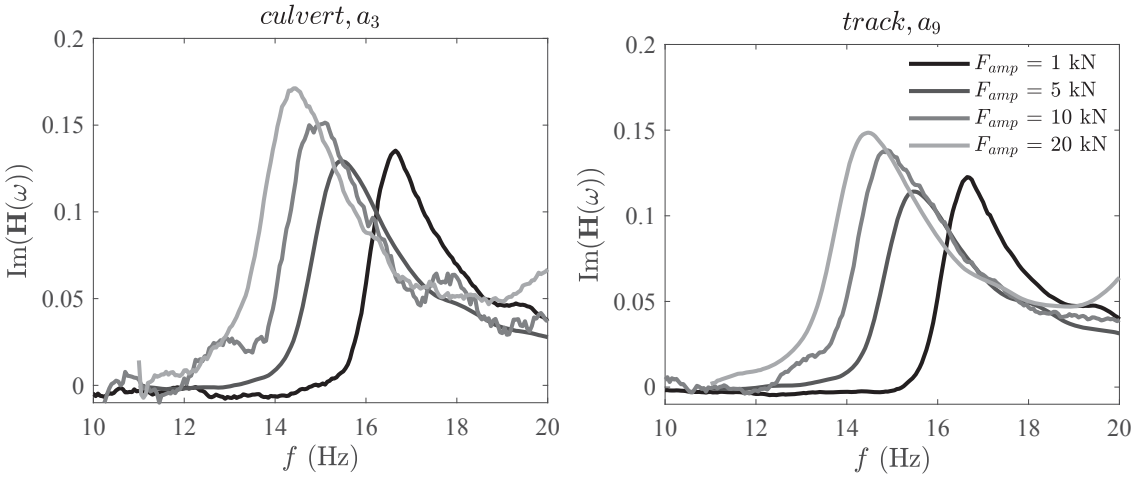

Figure 12: FRF, compare response in culvert and track for different load amplitudes.

3 NUMERICAL SIMULATIONS

A 3D finite element model of the SSCB has been developed, illustrated in Figure 13. The rails are modelled with beam elements but the rail pads, sleepers, ballast and subgrade are modelled with 20-noded quadratic brick elements (C3D20R). The total length of the model is 20 m and each end is modelled with infinite elements (CIN3D12R), h = 4 m. The corrugated steel culvert is modelled with orthotropic shell elements to represent the stiffness of the corrugation in the tangential and radial direction.

An example of calculated FRF is presented in Figure 14. The input is E_b = 160 MPa, E_s = 300 MPa, ν_b = 0.20, ν_s = 0.25, ρ_b = 1800 kg/m^3, ρ_s = 1800 kg/m^3 and ζ = 5%.

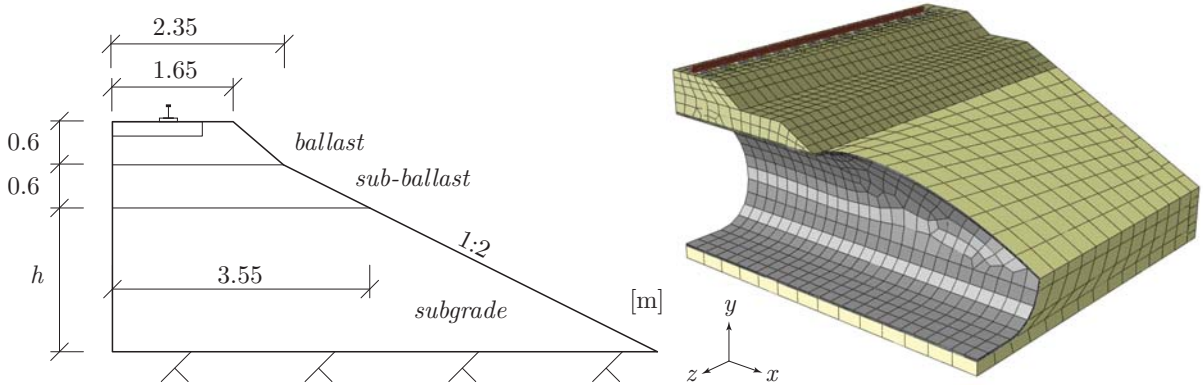

Figure 13: 3D model of the SSCB.

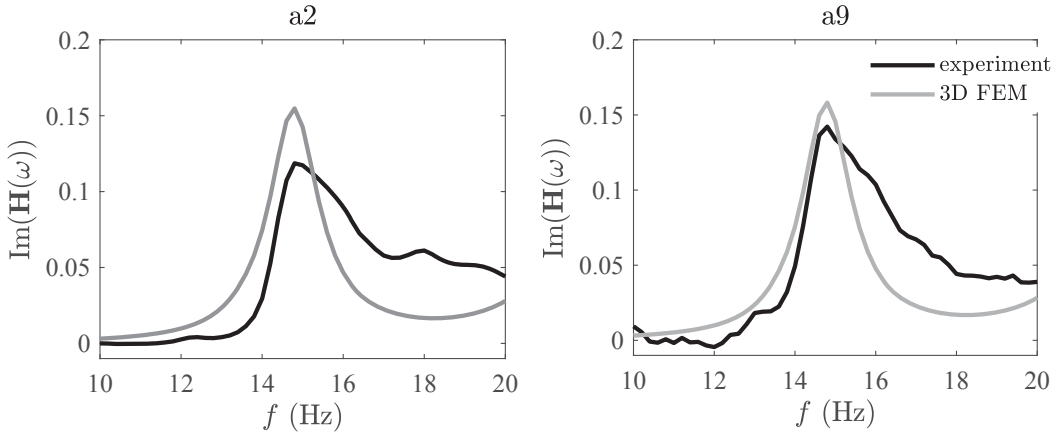

Figure 14: FRF, comparison between experiments and the 3D-model.

4 CONCLUSIONS

From the results presented in this paper the following is concluded.

- The experimental results with forced vibration response shows a significant influence of the load amplitude; higher loads results in lower natural frequency and higher damping.
- The recorded train passages show a vertical crown displacement of about 1 mm and a peak stress of about 6 MPa. The peak acceleration depends on the cut-off frequency, at 30 Hz the peak acceleration is in the order of 2 m/s^2.
- A preliminary FE-model shows a frequency response in the same order of magnitude as the experiments, but may need to be refined for increased performance.

ACKNOWLEDGEMENTS

The research presented in this paper was funded by ViaCon Sp z o.o. The experimental testing was performed by KTH division of Structural Engineering and Bridges.

REFERENCES

[1] L. Pettersson, Full Scale Tests and Structural Evaluation of Soil Steel Flexible Culverts with low Height of Cover, *Doctoral thesis, KTH, Struct. Eng. and Bridges*, 2007.

[2] L. Pettersson, H. Sundquist, Design of soil steel composite bridges, *Technical report, KTH, Struct. Eng. and Bridges*, 2014.

[3] E. Bayoğlu Flener, Field Tesing of a Long-Span Arch Steel Culvert Railway Bridge over Skivarpsån, Sweden (Part I), *Tehnical report, KTH, Struct. Eng. and Bridges*, 2003.

[4] E. Bayoğlu Flener, R. Karoumi, H. Sundquist, Field testing of a long-span arch steel culvert during backfilling and in service, *Structure and Infrastructure Engineering*, **1**, 181-188, 2005.

[5] E. Bayoğlu Flener, Field Tesing of a Long-Span Arch Steel Culvert Railway Bridge over Skivarpsån, Sweden (Part II), *Tehnical report, KTH, Struct. Eng. and Bridges*, 2004.

[6] E. Bayoğlu Flener, Field Tesing of a Long-Span Arch Steel Culvert Railway Bridge over Skivarpsån, Sweden (Part III), *Tehnical report, KTH, Struct. Eng. and Bridges*, 2005.

[7] E. Bayoğlu Flener, R. Karoumi, Dynamic testing of a soil-steel composite bridge, *Engineering Structures*, **31**, 2803-2811, 2009.

[8] E. Bayoğlu Flener, R. Karoumi, Testing of a soil-steel bridge under static and dynamic loads, *Bridge Engineering*, **163**, 19-29, 2010.

[9] E. Bayoğlu Flener, Static and dynamic behaviour of soil-steel composite bridges obtained by field testing, *Doctoral thesis, KTH, Struct. Eng. and Bridges*, 2009.

[10] A. Andersson, H. Sundquist, R. Karoumi, Full scale tests and structural evaluation of soil-steel flexible culverts for high-speed railways, *Archives of the Institute of Civil Engineering*, 43-53, 2012.

[11] P. Mellat, A. Andersson, L. Pettersson, R. Karoumi, Dynamic behaviour of a short span soil-steel composite bridge for high-speed railways - Field measurements and FE-analysis, *Engineering Structures*, **69**, 49-61, 2014.

[12] A. Andersson, R. Karoumi, A soil-steel bridge under high-speed railways, *Archives of the Institute of Civil Engineering*, 45-52, 2017.

[13] A. Andersson, M. Ülker-Kaustell, R. Borg, O. Dymén, A. Carolin, R. Karoumi, Pilot testing of a hydraulic bridge exciter, *MATEC Web of Conferences, EVACES 2015*, 1-6, 2015.

[14] D. Beben, Application of the interferometric radar for dynamic tests of corrugates steel plate (CSP) culvert, *NDT & E International*, **44**, 405-412, 2011.

[15] D. Beben, Experimental Study on the Dynamic Impacts of Service Train Loads on a Corrugated Steel Plate Culvert, *Journal of Bridge Engineering*, **18**, 339-346, 2013.

[16] D. Beben, Corrugated Steel Plate Culvert Response to Service Train Loads, *Journal of Performance of Constructed Facilities*, **28**, 376-390, 2014.

[17] D. Beben, Experimental Testing of Soil-Steel Railway Bridge Under Normal Train Loads, *MATEC Web of Conferences, EVACES 2017*, 805-815, 2018.

EURODYN 2020
XI International Conference on Structural Dynamics
M. Papadrakakis, M. Fragiadakis, C. Papadimitriou (eds.)
Athens, Greece, 23–26 November 2020

DYNAMIC SOIL-STRUCTURE INTERACTION IN RESONANT RAILWAY BRIDGES WITH INTEGRAL ABUTMENTS

Abbas Zangeneh[1,2], Andreas Andersson[1,3], Costin Pacoste[1,2] and Raid Karoumi[1]

[1] Division of Structural Engineering and Bridges, KTH
S-100 44 Stockholm, Sweden
{abbaszk, adde, costin, raidk}@kth.se

[2] ELU Konsult AB
S-102 51 Stockholm, Sweden

[3] Swedish Transport Administration, Trafikverket
S-171 54 Solna, Sweden

Keywords: Dynamic soil-structure interaction, High-speed railway bridges, Integral abutments, Resonant response, Simplified method

Abstract.

In this work, the effect of the surrounding soil condition on the fundamental modal characteristics and dynamic response of railway bridges with integral abutments is studied. Due to the computational cost of the full FE models and the lack of reliable simplified models, the effect of the soil-structure interaction is usually neglected in the vibration analysis of the high-speed railway bridges. In the present study, an efficient simplified numerical model is employed to evaluate the modal characteristics of the railway bridge–soil systems. After verifying the accuracy of the simplified numerical model against rigorous models, the effect of the span length and abutment/soil stiffness on the dynamic response of the studied bridges is investigated through a comprehensive parametric study. Several case studies which covers different span lengths and abutment conditions are chosen. It is shown that the SSI has substantial effect on the dynamic response of the short and stiff bridges while its effect decreases as the ratio between the deck stiffness and the abutment/soil stiffness decreases. The results may lead to review the recommended modal damping ratios for this type of bridges in the code provisions and design manuals.

1 INTRODUCTION

The frequency content and amplitude of the vibrations in the resonant response of railway bridges is governed by the fundamental modal characteristics (natural frequency and damping ratio) of the structural system [1, 2]. Hence, to predict the resonant response with reasonable accuracy, it is important to properly estimate the modal characteristics of the structural system, considering the effect of the flexibility and dissipation capacity of the surrounding soil [1]. Bridges with integral abutments and culverts are one of the most common type of underpasses along modern railway lines. This type of bridge is designed as a reinforced concrete rigid frame and is surrounded by backfill soil. Presence of backfill soil may provide an additional stiffness to the system which leads to an increase in the fundamental natural frequency and thus shifts the critical resonant speed to a higher value [3, 4]. The dissipation capacity of the backfill soil could also lead to an increase in the global damping of the system and consequently reduce the amplitude of the resonant response of the bridge [3, 4]. In the field of train-induced vibration analysis of railway bridges, limited results have been published on the bridge with integral abutments considering the effect of soil-structure interaction [4-7]. To study the influence of soil-structure interaction on the modal properties of railway bridges with integral abutment in a systematic manner, implementing simple and accurate models to calculate the natural frequency and modal damping ratio of the bridge-soil system is helpful. In this paper, an efficient and simple approach to model the effect of the surrounding soil on the modal characteristics and resonant response of the railway bridges with integral abutment is proposed. The dynamic soil-structure interaction problem is modelled through a 2D finite element (FE) of the portal frame bridge in which the side walls are surrounded by series of spring/dashpot sets. The merit of using efficient simplified models is that the key factors governing the dynamic response of the studied system can be identified. The accuracy of the proposed analytical expressions will be verified through comparison with the finite element solutions. Then, the variation of the fundamental frequency and modal damping ratio of bridge-soil systems are analyzed through a comprehensive parametric study. This gives valuable information on how SSI can affect dynamic characteristics of railway bridges with integral abutment and when the effect of SSI is negligible.

2 NUMERICAL MODEL

The general configuration of the proposed 2D model for a bridge with integral abutments which is surrounded by backfill soil is shown in Figure 1a. In order to investigate the importance of the backfill soil and to understand the effect of abutment-backfill interaction, the effect of the supporting subsoil is neglected. Thus, it is assumed that the supporting subsoil is rigid and consequently the bottom nodes of the model are fixed.

The structural domain Ω_b is modelled with Euler-Bernoulli beam elements while the surrounding soil domain Ω_s is replaced by its dynamic impedance at the interface nodes. Taking dynamic soil-structure interaction into account, the equation of motion for the coupled soil-structure system in the frequency domain can be expressed as follows:

$$\left[\mathbf{K_b} + \lambda\mathbf{C_b} + \lambda^2\mathbf{M_b} + \mathbf{K_s}(\lambda) + \lambda\mathbf{C_s}(\lambda)\right]\mathbf{u}(\lambda) = \mathbf{p}(\lambda) \tag{1}$$

where $\lambda = i\omega$ is the complex frequency, $\mathbf{u}(\lambda)$ is the nodal displacement vector, $\mathbf{p}(\lambda)$ is the nodal force vector and $\mathbf{K}_b$, $\mathbf{C}_b$ and $\mathbf{M}_b$ are respectively the stiffness, damping and mass matrices of the viscoelastic bridge structure. Finally, $\mathbf{K}_s(\lambda)$ and $\mathbf{C}_s(\lambda)$ represents the frequency dependent dynamic stiffness and damping contribution of the surrounding soil at interface nodes.

2.1 Proposed model for backfill-wall interaction

The wall–backfill interaction behaviour in the normal direction is modelled by using distributed spring/dashpots, k_s and c_s over the whole area of the walls evaluated using Eq. (2) and 3 [8] (see Figure 1a). The spring and dashpot coefficients are chosen based on the recommended values by Veletsos and Yonan [8]. It is well-known that at frequencies below the cut-off frequency of the soil layer, $f_s = V_s/4H$ [9], the radiation damping is negligible and consequently the damping originates only from the hysteretic damping of the soil medium. However, at frequencies higher than the f_s, the radiation damping capacity of the stratum is gradually approaches the maximum value, as shown in Figure 1c [9]. It should be noted that, the frequency dependency of the spring stiffness is disregarded and the average value of the recommended static stiffness by Veletsos and Yonan [8] for the 1st two vibration modes of wall-soil system is considered. As it will be shown in section 3.2, this assumption results in a good agreement between the proposed model and the reference solution.

$$k_s = \frac{2\pi}{\sqrt{2(1-\nu_s)}} \frac{\rho_s V_s^2}{H} \tag{2}$$

$$\begin{cases} c_s(\omega) = c_{s,m}(\omega) = 2\xi_s k_s / \omega_1 & \phi \le 1 \\ c_s(\omega) = c_{s,m}(\omega) + c_{s,rad}(\omega) = 2\xi_s k_s / \omega_1 + \rho_s . V_p \sqrt{1-(1/\phi)^2} & \phi > 1 \end{cases} \tag{3}$$

where ϕ is the relative frequency parameter as defined by Eq. 4 and V_s, V_p , ρ_s, ξ_s , ν_s and H respectively represents shear and compression wave velocities, density, hysteretic damping, Poisson ratio and height of the soil layer.

$$\phi = f_1 / f_s = \omega_1 / (\pi V_s / 2H) \tag{4}$$

2.2 Complex eigenvalue analysis

The complex modal characteristics of the coupled soil-structure system can be found as the solution of the following quadratic eigenproblem:

$$\left[(\mathbf{K_b} + \mathbf{K_s}(\lambda_m) + \lambda_m [\mathbf{C_b} + \mathbf{C_s}(\lambda_m)] + \lambda_m^2 \mathbf{M_b} \right] \varphi_m = 0 \tag{5}$$

where λ_m and φ_m are the complex-valued eigenvalue and corresponding eigenvector of mode m (m = 1, …,n) and n denotes the number of degrees of freedom. Provided that the system is underdamped, the undamped eigenfrequency ω_m and modal damping ratio ξ_m of the system for the m-th mode is calculated by Eq. (5).

$$\omega_m = |\lambda_m|, \quad \xi_m = -\Re(\lambda_m) / \omega_m \tag{6}$$

Following the procedure by Tisseur et al. (2001) [10], the quadratic eigenproblem in Eq. (1) is converted into a bigger equivalent linear matrix pencil that has the same eigenvalues as the original problem. Rearranging Eq. (1) and using the auxiliary vectors, the following linear matrix pencil can be used where $\tilde{\varphi}_m^T = \left\{ \varphi_m^T, \lambda_m \varphi_m^T \right\}$.

$$\left(\begin{bmatrix} \mathbf{K}_b + \mathbf{K}_s(\lambda_m) & \mathbf{0} \\ \mathbf{0} & \mathbf{I} \end{bmatrix} - \lambda_m \begin{bmatrix} -[\mathbf{C}_b + \mathbf{C}_s(\lambda_m)] & -\mathbf{M}_b \\ \mathbf{I} & \mathbf{0} \end{bmatrix} \right) \tilde{\varphi}_m = \mathbf{0} \tag{7}$$

Then, the eigenpairs of the linear matrix pencil in Eq. (6) can be computed by applying a standard linear eigensolver. Since the damping matrix of the surrounding soil $\mathbf{C}_s(\lambda)$ is fre-

quency-dependent, an iterative procedure is used to compute the modal properties of the system, considering the natural frequency of the bridge without SSI, ω_m, as the initial guess.

In non-proportionally damped systems as is the case here, the computed eigenvectors φ_m are complex-valued, implying that the mode shape components will move with different phase angles [11]. The overall phase coherence between the n elements of a complex eigenvector φ_m can be measured by using the modal collinearity factor (MCF) [11] defined as:

$$\mathrm{MCF} = 1 - A_p / A_c \tag{8}$$

where A_p is the convex polygon in the complex plane defined by the extremities of each element in the eigenvector and A_c is the area of a circle whose radius corresponds to the largest magnitude of the eigenvector as shown in Figure 2a. The MCF takes values from 0 to 1 with a value equal to 1 indicating a real-valued mode corresponding to a standing wave.

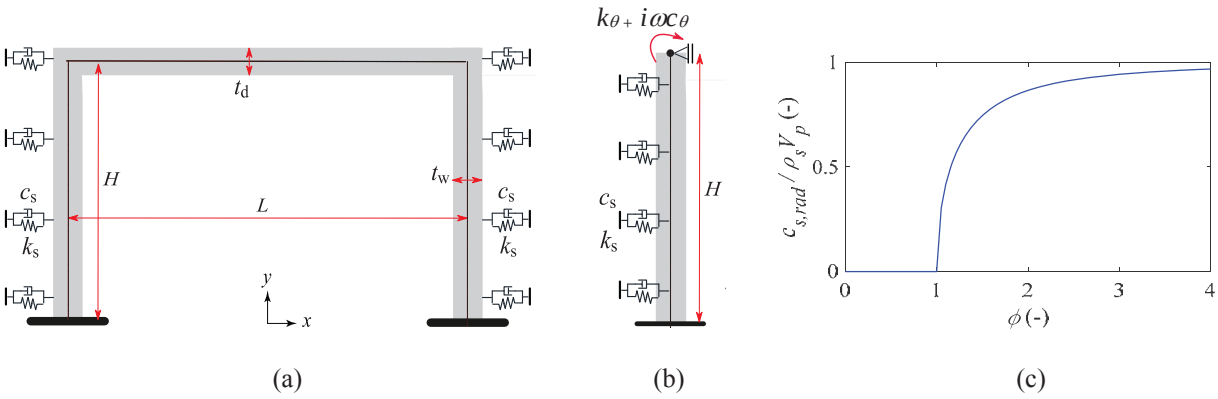

(a) (b) (c)

Figure 1: (a) Configuration of the 2D simplified model of the frame, (b) computational 2D model for rotational impedance function of abutment-backfill system, (c) Radiation damping coefficient $c_{s,rad}$

3 PARAMETRIC STUDY

3.1 Definition of case studies

The parametric study focuses on short to medium size portal frame bridges. Referring to Figure 1a, the parametric variables of four case study bridges are summarized in Table 1. The thickness of the frame bridge ($t = t_f = t_w$) is assumed to vary with the span length L and estimated based on collected data from existing single-track ballasted concrete bridges in Sweden [15]. The height, width, mass density and modulus of elasticity of all four case study bridges are assumed constant at H = 7 m, B = 6 m, ρ_b = 2300 kg/m^3 and E_b = 30 GPa, respectively. No structural damping is assigned to the bridge itself. Eliminating the internal damping of the structure allows a better understanding of the effect of SSI on the global damping of the coupled system. In this simulations, mass of the ballast layer is assumed to be 750 kg/m^2 and added to the deck nodes. Table 2 summarize the parameters of the surrounding soil. The sensitivity of the fundamental modal characteristics of the bridges with respect to the shear wave velocity of the backfill soil is investigated.

Table 1. Geometrical properties of bridges

L	[m]	7	9	11	15
$t_f = t_w$	[m]	0.65	0.75	0.85	1.0
$f_{1,n}$*	[Hz]	24.6	18.9	15.0	10.6

* Natural frequency of the bridge without SSI

Table 2. Backfill soil properties

H (m)	V_s (m/s)	ξ_s (%)	ν_s (-)	ρ_s (t/m^3)
7	{0,...,1000}	2.5	0.2	1.8

As the response of the bridge-soil system is governed by the viscoelastic properties of the bridge and surrounding soil, the following dimensionless parameters are defined to study the sensitivity of the modal properties of the coupled systems:

(a) The relative frequency parameter, ϕ, defined by Eq. (4) which represents the ratio of the coupled-soil-structure eigenfrequency to the resonant frequency of the backfill stratum. This parameter is used to study the sensitivity of the modal properties of the system to the cut-off frequency of the stratum.

(b) The relative stiffness parameter, κ, defined as the ratio of the flexural rigidity of the frame structure to the static stiffness of the backfill soil.

$$\kappa \approx \frac{32EI(H/L+2)/(L^2H)}{2\rho_s V_s^2 B} \tag{9}$$

(c) The abutment impedance ratio, χ, defined as the ratio between the real and imaginary parts of the rotational dynamic stiffness at the top node of the abutment (see Figure 1b).

$$\chi = k_\theta(f_1)/f_1 c_\theta(f_1) \tag{10}$$

3.2 Verification

In this section, the accuracy of the proposed simplified model is verified through comparison with the results of a full 3D FE-PML model. The computed modal properties of some case studies using proposed simplified model are compared to results of full 3D FE-PML model. The configuration of the 3D FE model is shown in Figure 2b. For this comparison, the shear wave velocity of the backfill soil is assumed constant at V_s =300 m/s and the modal properties of the frame-soil system for the 1st vertical bending are calculated for two different span lengths. In each case, the thickness of the wall and deck is assumed to be similar and varied between 0.2 to 1.2 m in increments of 50 mm. The 3D FE model of the wall and backfill soil is discretized using 8-noded shell and 20-noded hexahedral solid elements, respectively. According to the shear wave velocity of the backfill soil layer, the element size in the soil medium is chosen in such a way that there are at least 8 quadratic elements per wavelength at 50 Hz [11]. For the finite element mesh configuration of Figure 2b, the PML parameters are tuned to properly absorb evanescent and propagating waves [13].

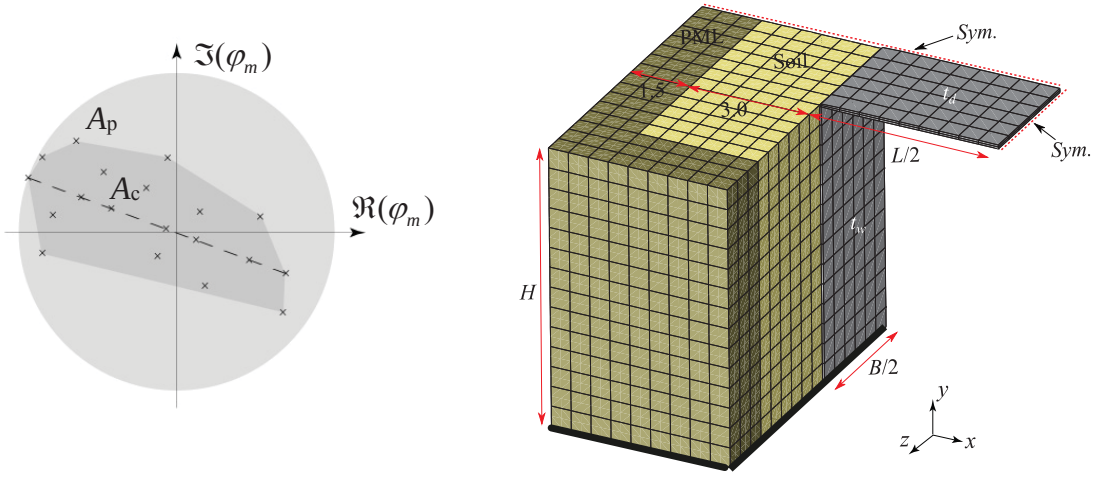

(a) (b)

Figure 2: (a) Definition of modal collinearity factor (MCF), (b) Configuration of 3D FE-PML model (units in m).

The comparison between the calculated complex modal parameters of the 1st vertical bending mode of the studied cases are presented in Figure 3. As can be seen, the calculated natural frequencies and modal damping ratios using the proposed simplified model are in a very good agreement with the results of the 3D FE-PML analyses. It should be noted that modal characteristics of the reference 3D FE-PML model have been computed using the procedure in [14].

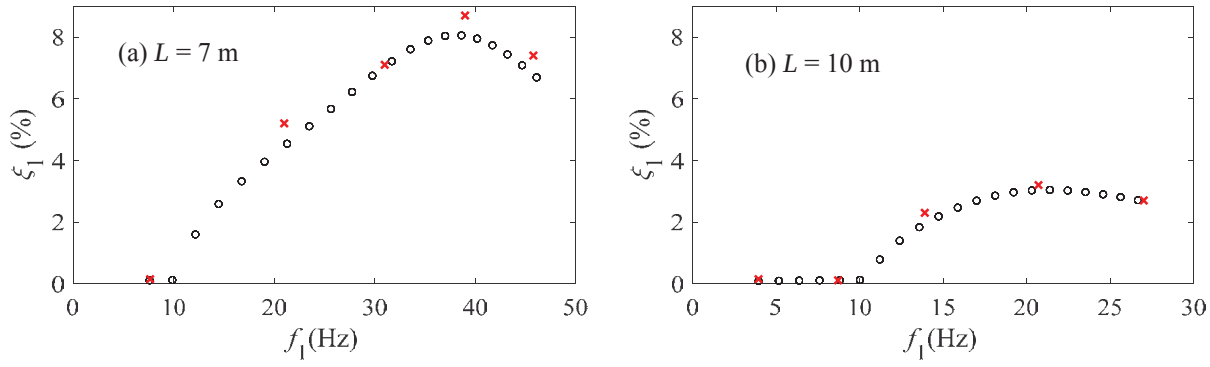

Figure 3: Comparison between computed modal characteristics using 2D simplified model (black o) and 3D FE-PML model (red ×), (a) L = 7 m, (b) L = 10 m.

3.3 Results of parametric studies

The variation of the frequency lengthening $f_1/f_{1,n}$, modal damping ratio ξ_1, MAC_1 and MCF_1 values for the 1st vertical bending mode of the studied cases a function of the shear wave velocity are presented in Figure 4a-d, respectively. As the structure is modeled without any material damping, the increase in modal damping ratios is solely attributed to radiation and material damping of the surrounding soil.

The dynamic stiffness of the backfill leads to an increase in the fundamental frequency of the coupled system and the frequency lengthening due to SSI becomes higher as the backfill soil becomes stiffer (see Figure 4a). The dissipation capacity of the backfill soil generally results in higher modal damping ratios for the coupled soil-structure system. The results in Figure 4b indicates that there exists a critical value V_s in which the fundamental damping ratio reaches its maximum value. The value of $V_{s,crit}$ is found to occur, when MCF_1 (Figure 4d) and the abutment impedance ratio χ_1 (Figure 4e) reach their minimum values. In this case, the maximum modal complexity occurs and the mode shape is most different from a standing wave. Clearly, by increasing the shear wave velocity toward infinity, the natural frequency of the studied system gradually converges to the fundamental frequency of a clamped-clamped beam and consequently, the modal damping ratio approaches zero.

The variation of the modal damping ratio ξ_1 for the studied system as a function of the relative frequency parameter ϕ and the relative stiffness parameter κ are presented in Figure 5a and 5b, respectively. In this Figure, the variation of the shear wave velocity is limited to the range of reasonable values in practice (e.g. V_s =100 to 500 m/s). The results show that the amount of additional damping due to SSI is principally governed by the following two factors:

- The relative frequency parameter which is the ratio between the fundamental frequency of the bridge-soil system and the cut-off frequency of the backfill layer. Theoretically, at frequencies lower than the cut-off frequency of the backfill layer ($\phi < 1$), the radiation damping capacity of the backfill soil is zero. However, at frequencies higher than the cut-off frequency of the backfill layer ($\phi > 1$), the radiation damping capacity of the backfill layer is restored and approaches its maximum capacity with a logarithmic growth (see also Figure 1c).

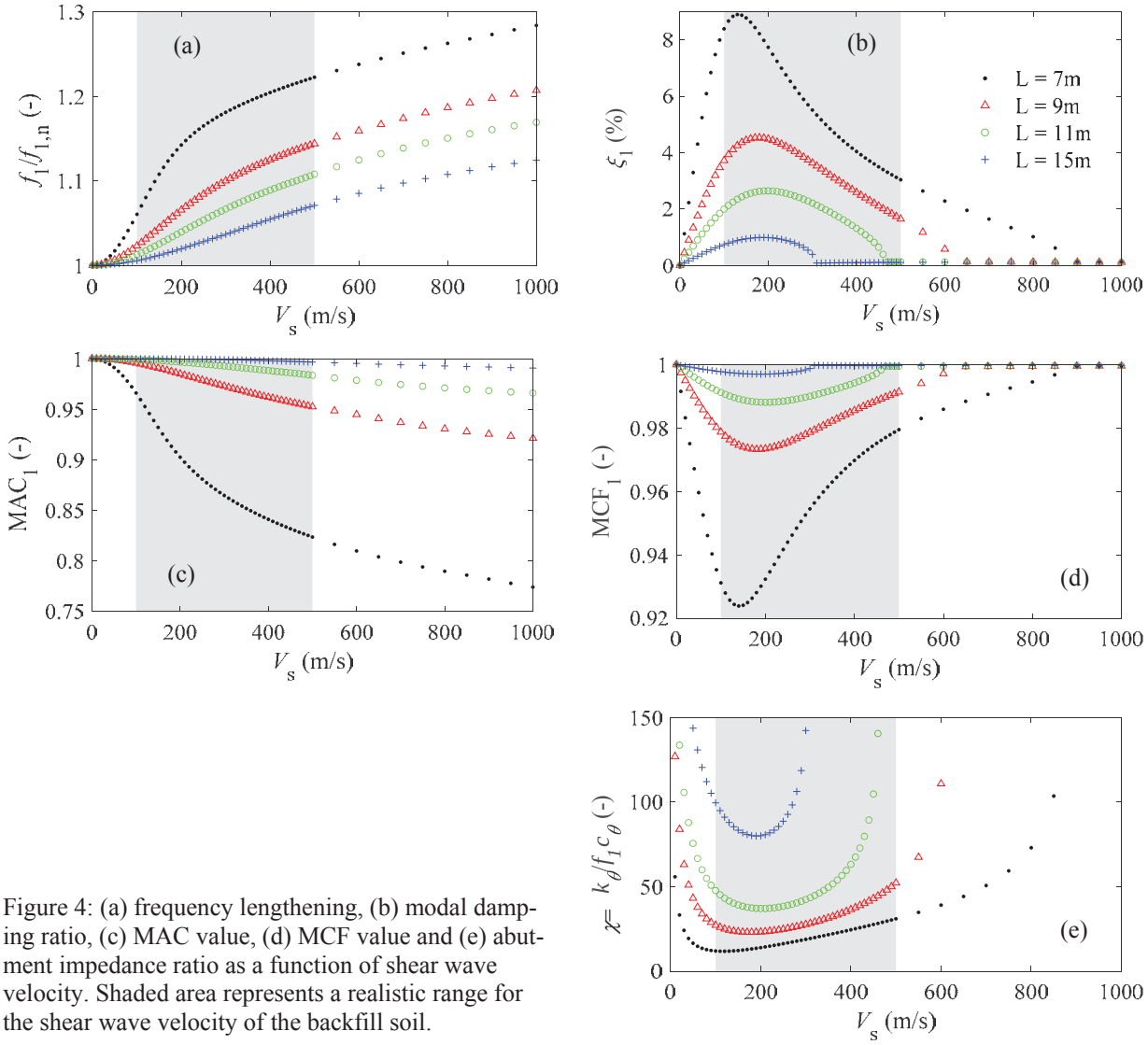

Figure 4: (a) frequency lengthening, (b) modal damping ratio, (c) MAC value, (d) MCF value and (e) abutment impedance ratio as a function of shear wave velocity. Shaded area represents a realistic range for the shear wave velocity of the backfill soil.

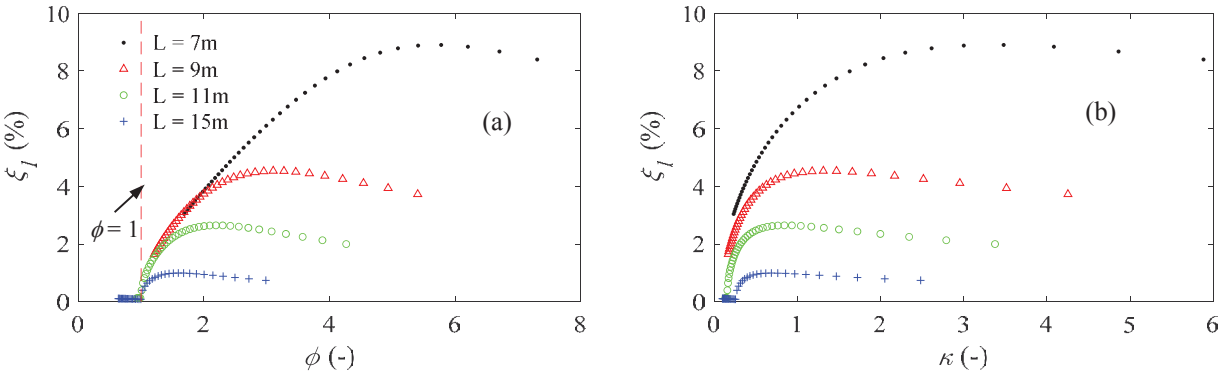

Figure 5: (a) Variation of modal damping ratio as a function of relative frequency parameter, (b) Variation of modal damping ratio as a function of relative stiffness parameter. Results were presented for V_s = 100-500 m/s.

- The relative stiffness parameter which is defined as the ratio between the stiffness of the structure and the backfill soil. The dissipation capacity of the backfill soil is negligible for a flexible structure surrounded by very stiff soil. Generally, there is a critical value for the relative stiffness parameter in which the additional damping of the system due to SSI becomes maximum. This is the case when the ratio between the real and imaginary parts of the abutment impedance reaches its minimum value, as shown in Figure 4e. After this turning point, the additional damping due to SSI is gradually decreased as the relative stiffness parameter increases.

4 CONCLUSIONS

In this paper, a simplified Winkler-based model is proposed for modeling the abutment-backfill soil interaction. Using this model, the effect of dynamic soil-structure interaction on the resonant response of portal frame bridges founded on a rigid base is studied. The fundamental modal characteristics of the short to medium span case study bridges are computed for a wide range of shear wave velocities of the backfill soil. The following remarks can be concluded from the presented results:

- Generally, dynamic soil-structure interaction results in higher eigenfrequencies, modal damping ratios and modal complexities for the studied coupled soil-structure system with the inf uence getting more intense for shorter (stiffer) bridges. The presence of backfill soil provide an additional stiffness and damping to the structural system.
- The dynamic stiffness of the backfill leads to an increase in the fundamental frequency of the system and thus shifts the critical resonant speed to a higher value. The frequency lengthening due to SSI is essentially controlled by the ratio between the stiffness of the frame bridge and the backfill soil.
- The amount of additional damping due to SSI (foundation damping) is principally governed by the following factors: (a) ratio between the fundamental frequency of the coupled system and the cut-off frequency of the backfill layer and (b) ratio between the stiffness of the frame bridge and the backfill soil. The additional damping may lead to a considerable increase in the global damping of the system and consequently reduce the amplitude of the resonant response of the bridge.

REFERENCES

[1] ERRI D-214, 1999b. Rail bridges for speeds over 200Km/h, Final Report. European Rail Research Institute (ERRI).

[2] H. Xia, N. Zhang, W. Guo, 2006, Analysis of resonance mechanism and conditions of train–bridge system. Journal of Sound and Vibration 297 (3), 810–822.

[3] P. Museros, M.L. Romero, A. Poy, E. Alarcón, Advances in the analysis of short span railway bridges for high-speed lines. Comput Struct 2002;80:2121–32.

[4] A. Zangeneh, C. Svedholm, A. Andersson, C. Pacoste, R. Karoumi, Identification of Soil-Structure Interaction Effect in a Portal Frame Railway Bridge through Full-Scale Dynamic Testing, Engineering Structures 159 (2018) 299-309

[5] A. Romero, M. Solís, J. Domínguez, P. Galvín, Soil-structure interaction in resonant railway bridges, Soil Dynamics and Earthquake Engineering 47 (2013) 108-116.

[6] M. Ülker-Kaustell, R. Karoumi, C. Pacoste, Simplifed analysis of the dynamic soil-structure interaction of a portal frame railway bridge, Engineering structures 32 (11) (2010) 3692-3698.

[7] M. F. Báez H., A. Fraile, J. Fernández, L. Hermanns, A vibration prediction model for culvert-type railroad underpasses, Engineering Structures 172 (2018) 1025–1041.

[8] A.S. Veletsos, A.H. Younan, 1997, Dynamic response of cantilever retaining walls, J.Geotech Engrg., ASCE, 123 (2) 1090-0241

[9] G. Gazetas, Formulas and charts for impdances of surface and embedded foundations, J. of Geo. Eng., 117(9) (1991), p. 1363-1381

[10] F. Tisseur, K. Meerbergen, The quadratic eigenvalue problem. SIAM Rev 2001;43:235-286.

[11] D. J. Ewins, 2000, Modal testing: Theory, practice and application, 2nd Ed., Research Studies Press Ltd., Baldock, Hertfordshire, U.K.

[12] R.L. Kuhlemeyer, J. Lysmer, Finite element method accuracy for wave propagation problems, Journal of the Soil Mechanics and Foundations Division, Vol. 99, No. 5. (May 1973), pp. 421-427

[13] A. Fathi, B. Poursartip, L. Kallivokas, Time-domain hybrid formulations for wave simulations in three-dimensional PML-truncated heterogeneous media. Int J Numer Methods Eng 2015;101:165–98.

[14] M. Papadopoulos, R. Van Beeumen, S. François, G. Degrande, G. Lombaert. Modal characteristics of structures considering dynamic soil-structure interaction effects. Soil Dynamics and Earthquake Engineering, 105:114-118, 2018.

[15] C. Johansson, A. Andersson, C. Pacoste, R. Karoumi, 2013, Järnvägsbroar på Botniabanan: Dynamiska kontroller för framtida höghastighetståg - Steg 1.(In Swedish)

EURODYN 2020
XI International Conference on Structural Dynamics
M. Papadrakakis, M. Fragiadakis, C. Papadimitriou (eds.)
Athens, Greece, 23–26 November 2020

A NEW APPROACH TO MODEL ROCKING MOTION OF POST-TENSIONED SEGMENTAL COLUMNS

Ehsan Ahmadi[1] **and Mohammad M. Kashani**[2]

[1] Postdoctoral Research Associate
University of Southampton, United Kingdom
e-mail: e.ahmadi@soton.ac.uk

[2] Associate Professor
University of Southampton, United Kingdom
mehdi.kashani@soton.ac.uk

Keywords: Post-tensioned segmental columns, Rocking motion, Accelerated bridge construction, Numerical modelling

Abstract. *Application of post-tensioned segmental columns are increasing in accelerated bridge construction, where rocking motion of the segments results in lateral displacement of the column and the post-tensioning tendon provides self-centering capacity of the system. Analytical solution of such system is very complex as the equations of rocking motion are highly nonlinear, and it is almost impossible to solve such systems for seismic excitations. Furthermore, using finite element-based software such as ABAQUS and ANSYS make the dynamic analysis very time consuming and, so computationally inefficient. Therefore, this paper introduces a new technique for modelling of post-tensioned segmental columns in OpenSees program, which is computationally efficient, and exhibits a good agreement with analytical approaches and experimental results. Using the developed model, the frequency response function and seismic response of an exemplary column are extracted which exhibits a lower and an upper branch around the resonance.*

1 INTRODUCTION

Bridges are crucial parts of any transportation system, and any disruption in their functionality can result in tremendous economic and life losses. In particular, lateral seismic effects can cause permanent structural damage. Traditional reinforced concrete (RC) columns are integrally connected to the underlying foundation. Thus, plastic hinges, and consequently permanent plastic deformations are generated in RC columns under lateral seismic loadings. As an excellent alternative to RC columns, precast post-tensioned segmental (PPS) columns are recently used in accelerated bridge construction. The PPS columns are manufactured offsite, which improves concrete quality and shortens construction time. Furthermore, the rocking mechanism of the segments and self-centering property of the post-tensioned tendon substantially decrease the residual drift of the column after the lateral loading events. However, the segments might still be prone to local damages at their contact interfaces.

Many experimental works have been conducted to investigate performance of the PPS columns subject to static cyclic and dynamic loading testing protocols [1].To increase energy-dissipating capacity of the PPS columns, different strategies were recommended ([2-6]). In a series of different studies, high-damping material layers were placed between the segments in small-scale columns inspired by mechanics of the human spine, and damping level of the system was highly increases ([7-10]).

Many numerical studies have been also done to model static and dynamic behavior of the PPS columns. 3D continuum finite element (FE) models ([2, 11]) and fibre-based FE models ([12, 13]) have been employed to capture seismic response of the PPS columns. Complex continuum FE models can capture local damages generated in contact surfaces at the compression zones. However, such models have low calculation efficiency particularly in case of parametric studies when a large number of simulations are required. Fibre-based FE models have been extensively used in seismic response evaluation of RC columns ([14-16]). Unlike continuum FE models, fibre-based FE models are computationally efficient. However, they cannot model the contact surface between segments of PPS columns, i.e. rocking joints and compression zones, as good as continuum FE models. Simplified analytical models ([1, 2]) were also proposed to predict lateral force-displacement behavior of the PPS columns. Therefore, this paper summarizes a computationally efficient approach for modelling the rocking motion of the PPS columns already published in [17]. A new modelling in OpenSees program [18] is developed, and both experimental and analytical results are used to validate the proposed model. Finally, frequency response function of an exemplary column is generated and discussed using the proposed modelling method.

2 THE MODELLING DESCRIPTION

The finite element program OpenSees [18] is adopted to create a model for simulation of rocking motion of the PPS columns shown in Figure 1. A generic two-dimensional (2D) column model is developed with three degrees-of-freedom per node consisting of horizontal and vertical translations as well as a rotational displacement (see Figure 1b).

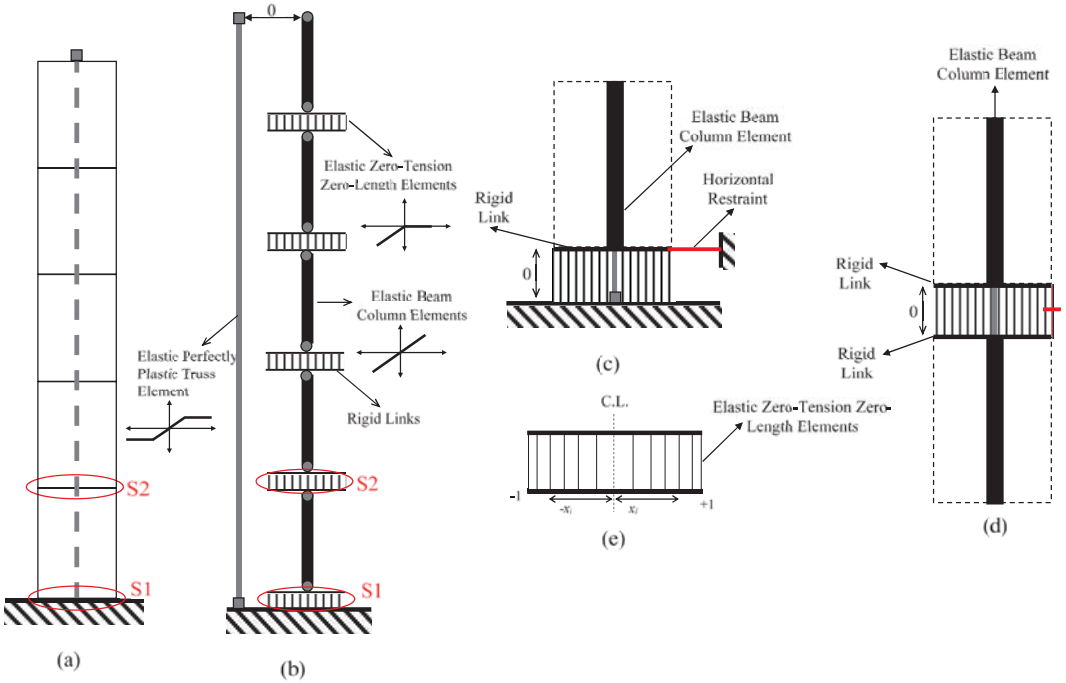

Figure 1: (a) the PPS column, (b) the segments and tendon modelling, (c) detailed modeling of base surface, (d) detailed modelling of the intermediate surfaces, and (c) weighting and positioning of the gap elements.

Uniaxial Elastic Beam-Column elements are used to simulate the segments. The post-tensioning tendon is simulated with a Truss Element with an Elastic Perfectly Plastic uniaxial material. The axial shortening of the post-tensioning tendon is taken into account using an initial strain in the material model. Geometric nonlinearities of the segments and the tendon are accounted for using the Corotational geometric transformation. The axial load at the top of the column is modelled as a vertical force on the topmost node of the column. Further, inertial effects of the bridge deck is incorporated in to the model assigning lumped horizontal and vertical masses to the top node of the column. The modelling details of the compression zones between the segments of the PPS column are shown in Figures 1c and 1d. Given the experimental testing results reported [19], the contact surface between the segments segments are not completely rigid, and thus, it is best modelled with a flexible contact surface with an appropriate stiffness distribution. The Lobatto Quadrature integration scheme [20] is used to spread the normal stiffness of the contact surfaces over the width of each surface. Each surface is modelled as a number of vertical zero-length gap elements. An elastic zero-tension uniaxial material model is used to model flexibility at the contact surfaces. The weight of the stiffness (w_i) and position of each gap element (x_i) determined from Lobatto Quadrature integration scheme.

12 number of gap elements was found to be sufficient to model the contact surfaces. Rigid links are used between adjacent top and bottom nodes of each rocking surface. Linear geometric transformation is used for rigid links. All degrees-of-freedom of the bottom node of the gap elements at the base surface are restrained to simulate a fixed base under the base segment. The horizontal degree-of-freedom of top node of the end gap element is also restrained to avoid sliding at the base (Figure 1c). A horizontal zero-length gap element between top and bottom nodes of the end vertical gap element with an elastic uniaxial material of very large stiffness is used to allow for shear transfer at the intermediate rocking surfaces (shown by red in Figure 1d). Furthermore, to allow for shear transfer between rigid links and adjacent segments, equal degree-of-freedom constraints were adopted.

3 MODELLING VALIDATION

3.1 Analytical approach

Analytical moment-rotation relationship of a single post-tensioned rigid rocking block is used to validate the OpenSees model of the PPS columns. Consider a single post-tensioned rigid block of width b and height h rocking on a rigid surface around its edges. Taking a moment around the pivot point, using kinematic of rigid bodies, and applying the equilibrium rule, the static moment-rotation relationship for a single post-tensioned rigid block is obtained [21]:

$$M(\theta) = \lambda kB\cos(\theta/2)\left[2\lambda B\sin(\theta/2) + F_0/k\right] - WR\sin(\beta+\theta) \tag{1}$$

where λ is 0.5 and -0.5 respectively for positive and rocking motions; k is the elastic stiffness of the post-tensioning tendon; F_0 is the initial post-tensioning force of the tendon, and W is the weight of the block. The clockwise rocking is taken positive, and the block angle, β, and rocking radius, R, are defined as follows:

$$\beta = -\tan^{-1}(2\lambda b/h); \quad R = \sqrt{\lambda^2 b^2 + h^2/4} \tag{2}$$

To reach a rigid segment and a rigid surface at the base, large values are assigned to the bending stiffness of the segment and axial stiffness of the gap elements. Figure 2 shows the static

moment-rotation graphs of a single post-tensioned rigid block obtained from the OpenSees model and the analytical approach. The moment is normalised to the moment due to the gravitational force, i.e. weight of the segment times the width of the segment, bW. As illustrated in Figure 2, the graphs are very similar, which numerically validates the static behavior of the OpenSees model. Note that in Figure 2b, the result of OpenSees model is different from the analytical solution at high base rotation values, which is because of the yielding of the post-tensioning tendon.

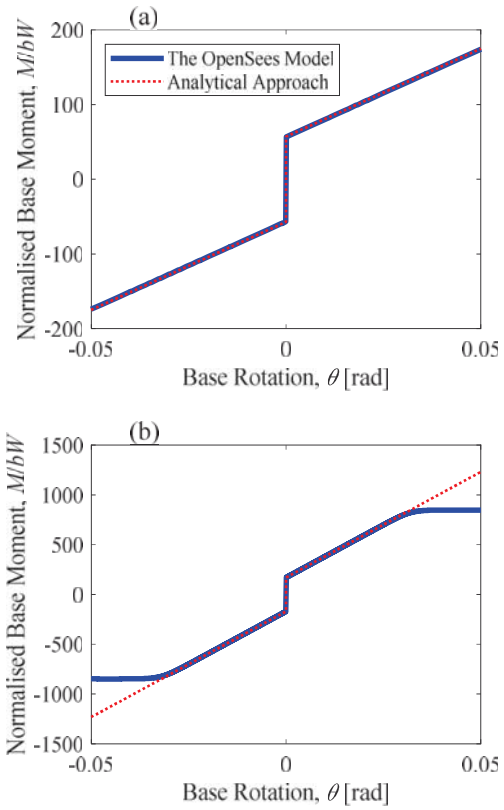

Figure 2: Analytical validation of the PPS model, normalised static moment-rotation relationship for a post-tensioned rigid block on a rigid surface: (a) $h/b = 6$, and (b) $h/b = 2$.

3.2 Experimental approach

In this section, the results of an experimental testing and a reduced-order analytical model already reported in [8] are used to verify the PPS model. The experimental column is a post-tensioned segmental column consisting of 50 mm square wooden segments. The segments are tied together by a 1 mm high-strength stainless steel cable. The elastic modulus of the wooden blocks and stainless steel cable are 12.5 GPa and 118 GPa respectively. To simulate the inertia force of the top deck, a 2.5 kg lump mass is installed at the top of the column. The self-centring mechanism is provided by the cable with a 300N post-tensioning force. Moreover, a reduced-order mode with detailed description in [8], simulates the column as a single-degree-of-freedom (SDOF) systems based only on the base rotation. Figure 3 shows base moment-rotation of the PPS model, the experimental column as well the analytical SDOF model for both static and dynamic tests. For the dynamic analysis of the OpenSees model, a constant stiffness-proportional Rayleigh damping is used for all elements of the model. As seen in Figure 3, the proposed PPS model can reliably simulate both nonlinear static and dynamic behaviors of the PPS columns. For the dynamic modelling, a constant stiffness-

proportional Rayleigh damping well duplicates the damping of the PPS columns (Figure 3b). Note that the damping of the PPS columns mostly come from the behavior of the contact surfaces between the segments, and is dependent on the ground motion amplitude [8],]. Thus, a combination of viscous and Coulomb damping is more appropriate, and this may cause the difference between the PPS model and the experiment results.

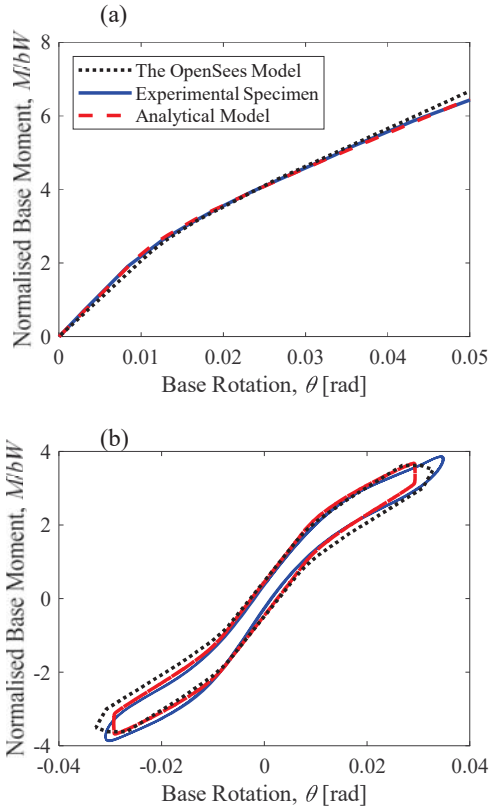

Figure 3: Normalised base moment-rotation from the OpenSees model, experimental specimen, and analytical model: (a) 9 blocks and static behavior, and (b) 6 blocks and dynamic behavior.

4 FREQUENCY RESPONSE FUNCTION AND SEISMIC RESPONSE OF AN EXEMPLARY COLUMN

In this section, an exemplary column of height 3 m and width 0.5 m is presented. To extract frequency response function (FRF) of this column, increasing and decreasing frequency sine-sweep base excitations with varying amplitudes are used to capture possible lower and upper branches due to instability of the dynamic behavior of the column around the resonance. Figure 4 shows frequency response functions of the column. The horizontal axis is the excitation frequency normalised by the first natural frequency of the column at very small vibration amplitudes. For very small excitation amplitudes, the column has not started its rocking motion yet and hence, the resonance occurs at the same frequency as the natural frequency, i.e. normalized excitation frequency of 1. For higher vibration amplitudes, the rocking motion of the column is started, and thus, the FRF curve exhibits a lower and an upper branch. In addition, after the rocking initiation, the natural frequency of the column drops, and is dependent on the excitation amplitude.

The backbone curve clearly shows dynamic softening of the column. The column's frequency drop with the increase in the excitation amplitude demonstrates the reduction in the column's stiffness after initiation of the columns rocking. Further, some subharmonic compo-

nents are seen at low excitation frequencies for high excitation amplitudes. The FRFs also show that the model faces dynamic instability around the resonance frequency of the column.

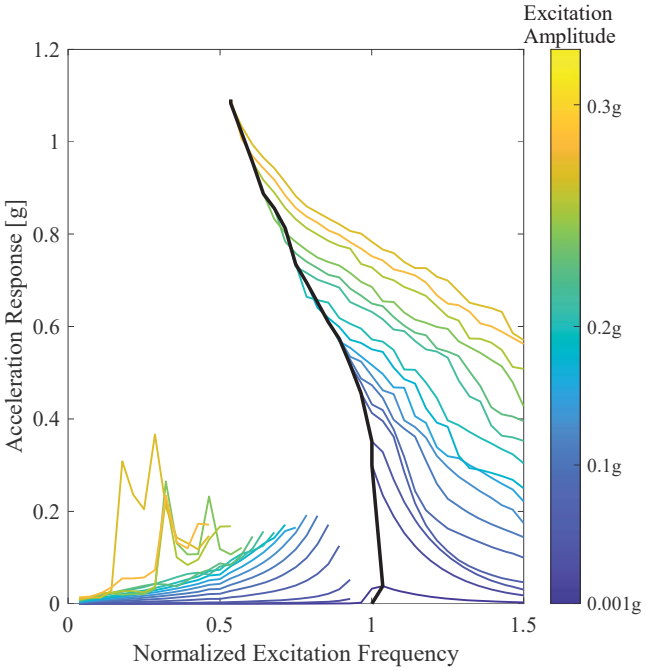

Figure 4: Frequency response function and backbone curve of an exemplary column.

Figure 5 shows hysteretic base shear, V, versus displacement, Δ, of the top of the exemplary column subject to an earthquake ground motion. The base shear is normalised by the total weight of the pier, W, (i.e. weight of the segments and the deck), and the top displacement is normalised by the height, H, of the column, i.e. top drift. The figure highlights the self-centering property and low-damping capacity of the post-tensioned segmental columns.

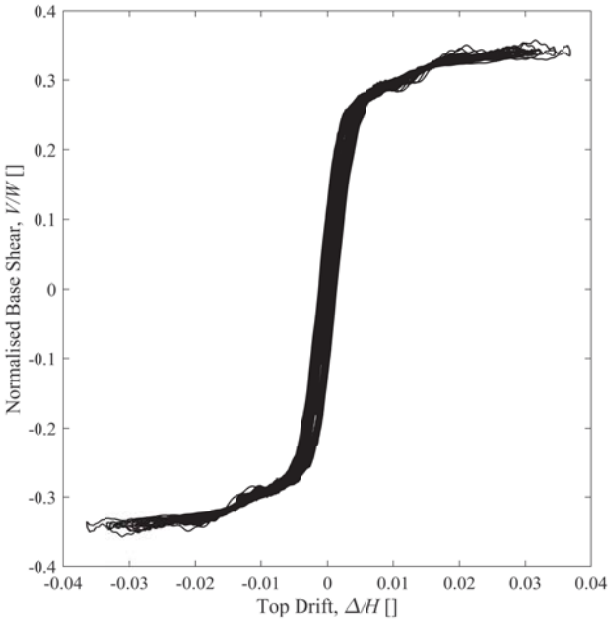

Figure 5: Normalised base shear versus top drift of the column subject to an earthquake ground motion.

5 CONCLUSIONS

In this paper, a new approach is developed in OpenSees program to simulate nonlinear static and dynamic behaviors of post-tensioned segmental columns. In this approach, the segments are modeled as elastic Beam-Column elements, and the post-tensioning tendon is modeled using an elastic-plastic Truss element. More importantly, the contact surfaces at the rocking joints are simulated using elastic zero-tension segments.

The proposed modelled is validated using two approached. First, the analytical static moment-rotation relationship of a post-tensioned rigid block on a rigid base is used and compared with the results of the model. Afterwards, the static and dynamic results of an experimental specimen as well as a reduced-order SDOF model of post-tensioned multi blocks are employed to validate the proposed model. The comparison between the results of the proposed model with those from the analytical and experimental approaches demonstrates the reliability of the proposed model to predict nonlinear static and dynamic behavior of the PPS columns. Frequency response function curve of an exemplary column is also presented using the developed modelling strategy where it shows a two-branch behavior around the resonance. The seismic response of the column also demonstrates low damping capacity of such columns.

6 ACKNOWLEDGEMENT

The first author acknowledges the support received by the UK Engineering and Physical Sciences Research Council (EPSRC) for a Prosperous Nation [grant number EP/R039178/1]: SPINE: Resilience-Based Design of Biologically Inspired Columns for Next-Generation Accelerated Bridge Construction].

REFERENCES

[1] JT. Hewes, Seismic design and performance of precast concrete segmental bridge columns, *PhD Thesis*, University of California, San Diego, 2002.

[2] YC. Ou, M. Chiewanichakorn, AJ. Aref, GC. Lee, Seismic Performance of Segmental Precast Unbonded Posttensioned Concrete Bridge Columns, *Journal of Structural Engineering*, 133,1636–47, 2007.

[3] CC. Chou, YC. Chen, Cyclic tests of post-tensioned precast CFT segmental bridge columns with unbonded strands, *Earthquake Engineering and Structural Dynamics*, 35, 159–75, 2006.

[4] D. Marriott, S. Pampanin, A. Palermo, Quasi-static and pseudo-dynamic testing of unbonded post-tensioned rocking bridge piers with external replaceable dissipaters. *Earthquake Engineering and Structural Dynamics*, 38, 331–54, 2009.

[5] MA. ElGawady, A. Sha'lan A, Seismic Behavior of Self-Centering Precast Segmental Bridge Bents, *Journal of Bridge Engineering*,16, 328–39, 2011.

[6] S. Motaref, M. Saiidi, D. Sanders,Experimental Study of Precast Bridge Columns with Built-In Elastomer. *Transportation Research Record: Journal of the Transportation Research Board*, 2202, 109–16, 2010.

[7] MM. Kashani, A. Gonzalez-Buelga, Nonlinear dynamics of self-centring segmental composite rocking column, *Procedia Engineering*, 199, 441–6, 2017.

[8] MM. Kashani, A. Gonzalez-Buelga, RP. Thayalan, AR. Thomas, NA. Alexander, Experimental investigation of a novel class of self-centring spinal rocking column, *Journal of Sound and Vibration*, 437, 308–24, 2018.

[9] MM. Kashani, E. Ahmadi, A. Gonzalez-Buelga, D. Zhang, F. Scarpa, Layered composite entangled wire materials blocks as pre-tensioned vertebral rocking columns, *Composite Structures*, 214, 153–63, 2019.

[10] E. Ahmadi, MM. Kahshani, On the use of entangled wire materials in pre-tensioned rocking columns, *Journal of Physics: Conference Series*, 1264, 012007, 2019.

[11] YC. Ou, MS. Tsai, KC. Chang, GC. Lee, Cyclic behavior of precast segmental concrete bridge columns with high performance or conventional steel reinforcing bars as energy dissipation bars, *Earthquake Engineering and Structural Dynamics*, 39, 1181–98, 2010.

[12] S. Motaref, Seismic Response of Precast Bridge Columns with Energy Dissipating Joints, *PhD Thesis*, University of Nevada, Reno, 2011.

[13] N. Zhang, Dynamic properties and application of steel fiber reinforced self-consolidating concrete to segmental bridge columns in moderate-to-high seismic regions, *PhD Thesis*, University at Bufallo, 2014.

[14] WK. Lee, SL. Billington, Modeling Residual Displacements of Concrete Bridge Columns under Earthquake Loads Using Fiber Elements, *Journal of Bridge Engineering*, 15, 240–249, 2010.

[15] SE. Abdel Raheem, Pounding mitigation and unseating prevention at expansion joints of isolated multi-span bridges, *Engineering Structures*, 31, 2345–56, 2009.

[16] B. Shrestha, H. Hao, K. Bi, Effectiveness of using rubber bumper and restrainer on mitigating pounding and unseating damage of bridge structures subjected to spatially varying ground motions, *Engineering Structures*, 79, 195–210, 2014.

[17] E. Ahmadi, MM. Kashani, Numerical investigation of nonlinear static and dynamic behaviour of self-centring rocking segmental bridge piers, *Soil Dynamics and Earthquake Engineering*, 128, 105876, 2020.

[18] F. McKenna, OpenSees: A framework for earthquake engineering simulation, *Computing in Science and Engineering*, 13, 58–66, 2011.

[19] LT. Kibriya, C. Málaga-Chuquitaype, MM. Kashani MM, NA. Alexander, Nonlinear dynamics of self-centring rocking steel frames using finite element models, *Soil Dynamics and Earthquake Engineering*, 115, 826–37, 2018.

[20] HA. Spieth, AJ. Carr, AG. Murahidy, D. Arnolds, M. Davies, JB. Mander, Modelling of post-tensioned precast reinforced concrete frame structures with rocking beam-column connections, *New Zealand Society of Earthquake Engineering Conference*, 2004.

[21] E. Ahmadi, MM. Kahshani, Nonlinear rocking dynamics of pre-tensioned single rigid blocks under harmonic base excitation. *Journal of Physics: Conference Series*, 1265, 012006, 2019.

EURODYN 2020
XI International Conference on Structural Dynamics
M. Papadrakakis, M. Fragiadakis, C. Papadimitriou (eds.)
Athens, Greece, 23–26 November 2020

STOCHASTIC DYNAMIC ANALYSIS OF HIGH-SPEED MAGLEV GUIDEWAY COUPLED SYSTEM CONSIDERING VEHICLE PARAMETER

Peng zhang[1,2], **Zhi-wu Yu**[1,2], **and Jian-feng Mao**[1,2]

[1] School of Civil Engineering, Central South University
address
[2] National Engineering Laboratory for High Speed Railway Construction
address
pzhang1119@csu.edu.cn; zhwyu@csu.edu.cn; csumjf@csu.edu.cn;

Keywords: Maglev, Stochastic Vibration, Probability Density Evolution, Monte Carlo Method

Abstract. *The maglev guideway coupling system is a complex random system, it is worth clarifying the stochastic dynamic vibration of maglev system caused by random vehicle parameters. In this paper, a stochastic vibration analytical approach based on probability density evolution method (PDEM), which can consider multiple stochastic structure parameters, is employed to calculate stochastic vibration. The maglev-guideway coupling stochastic time-dependent equation is established, considering the stochastic vehicle load, the stiffness and damping of second suspension. Then, the Wilson-θ method and the finite deference method with Total Variation Diminishing (TVD) schemes are used to calculate the stochastic dynamic responses. Meanwhile, the validity of proposed method is compared with Monte Carlo Method (MCM). The results show, the proposed random dynamic model is available for dynamic vibration analysis of maglev system with good calculation efficiency. When the same integral step is adopted, the PDEM reduce computing time by 1-2 order of magnitudes compared with MCM. The stochastic vehicle loads have a significant effect on the dynamic deflection of guideway, while both the random damping and stiffness of second suspension have a little effect on deflection of guideway. The stochastic vehicle loads act a more sensitive effect on the car body acceleration than the other two parameters.*

1 INTRODUCTION

Maglev train is a modern advanced technological ground transport tool, which realizes the suspension and guidance between the train and the guideway through non-contact electromagnetic force. There are two types maglev system according to the running speed: high-speed maglev traffic [1, 2] and medium-low-speed maglev traffic [3]. The high-speed maglev train is suitable for long-distance intercity transportation, and has broad application prospects.

The vibration of maglev guideway system has drawn a great attention of researchers over the past few decades [4-9]. In the early research of maglev-guideway system dynamics, Hullender[4] began to pay attention to the influence of track irregularity on guideway. Wang[10] simplified the maglev vehicle as moving uniform force, and simplified the guideway structure as Euler-Bernoulli beam-uniform spring-Euler-Bernoulli beam. He analyzed the influence of structure parameter to the natural frequency of guideway. With the development of maglev vehicle manufacturing technology, the vehicle model is become more complex [11]. To study the high-speed maglev vehicle guideway coupled vibration, Zhao and Zhai [6] established a 10 degree of freedom vehicle model by rigid body dynamics and three types guideway model by modal superposition method. They analyzed the responses of vehicle and guideway and the vehicle ride quality index under different deterministic irregularity. Shi [9] present a EMS maglev vehicle-controller-guideway model, and developed a simulation program. He verified the model by measurement data and investigated the responses of maglev system under irregularity. Yang and Yau [8] presented a iterative method and established a two dimension vehicle-guideway-pier-soil coupled model, in which the PID controller is used to control the maglev force. They analyzed the effect of ground wave propagation on system dynamic. To study the medium-low-speed maglev vehicle guideway vibration, Han [12] present a UTM-02 maglev vehicle model with controller. He analyzed the some factor that affect the natural frequency of guideway. Lee [13] developed a medium-low speed numerical maglev vehicle model with a LQG controller and investigated the effect of some parameters on the vibration of maglev system.

From the above research results, there are little research about the stochastic vibration of maglev system, the stochastic vibration research framework of maglev vehicle guideway system has not been established. Vehicle parameters is an important random source of maglev system due to the boarding and alighting of passengers and manufacturing error [14, 15], which may have a great impact on running safety and smoothness, it is worth clarifying the stochastic dynamic vibration of maglev system caused by random vehicle parameters, however, relevant research has not been done yet.

In this paper, a stochastic vibration analytical approach based on probability density evolution method is employed to calculate stochastic vibration. The maglev-guideway coupling stochastic time-dependent equation is established, considering the stochastic vehicle load, stiffness and damping of second suspension, stiffness and damping of primary suspension. Then, the Wilson-θ method and finite difference method with TVD schemes are used to calculate the stochastic dynamic responses. Meanwhile, the validity of proposed method is compared with MCM.

2 N-DIMENSIONAL REPRESENTATIVE POINT SELECTION OF STOCHASTIC VEHICLE PARAMETER

Due to the boarding and alighting of passengers, the change weight of luggage and backpack, etc., the mass of car body is a stochastic parameter, which may has a great influence of dynamic responses. Due to the microstructure of the material and the manufacturing error, etc.,

the stiffness and damping of secondary suspension also stochastic parameter. Selection of representative parameters is an important part of probability density evolution analysis. The number theory method (NTM) is employed to select the multidimensional representative point of system parameters. Considering the randomness of the mass of car body m_c, the stiffness of second suspension k_s, the damping of second suspension c_s. The stochastic variable space $\boldsymbol{\phi}$ can be expressed as the function of random vehicle parameter:

$$\boldsymbol{\phi} = f(\mathrm{m}_{c1}, \mathrm{m}_{c2}, \ldots, \mathrm{m}_{cN}, \mathrm{k}_{s1}, \mathrm{k}_{s2}, \ldots \mathrm{k}_{sN}, \mathrm{c}_{s1}, \mathrm{c}_{s2}, \ldots, \mathrm{c}_{sN}) \ (i = 1,2, \ldots, \mathrm{N}) \tag{1}$$

$f(\cdot)$ is the transform function of maglev vehicle random parameters, N is the total number of random multidimensional points.

According to research result of NTM [16], a point set can be generate by applying the N-dimensional hypercube distribute C^N. The random variables of the normal distribution are usually symmetric, to generate the representative point set, the ball screening hypercube method is used to filter the point, then an affine transformation is employed to map the representative point set in probability distribution space, it can be expressed as:

$$\boldsymbol{\Theta}_k = \{\theta_{k,1}, \theta_{k,2}, \ldots, \theta_{k,q}\}, k = 1,2, \ldots, n_{sel} \tag{2}$$

The probability subdivision of representative point set are divided with Voronoi Cells. $\mathrm{V}(\boldsymbol{\Theta}_q) = V_q$, $\cup_{p=1}^{n_{sel}} \mathrm{V}(\boldsymbol{\Theta}_q) = \cup_{p=1}^{n_{sel}} V_q$ and $V_i \cap V_j = 0, i \neq j$. The joint probability density of the total subdivision space meets the requirements:

$$\sum_{q=1}^{n_{sel}} P_q = \sum_{q=1}^{n_{sel}} \int_{V_q} P_{\boldsymbol{\Theta}}(\theta)\, d\theta = \int_{\cup_{p=1}^{n_{sel}} V_q} P_{\Theta}(\theta)\, d\theta = 1 \tag{3}$$

P_q is the probability value of representative point.

3 MAGLEV VEHICLE GUIDEWAY COUPLED MODEL

A maglev vehicle guideway coupled model is proposed. The vehicle model is established by multi rigid-body dynamics, which contains one car body, four magnet bogie, and second suspension, the vehicle model is shown in Fig. 1. The model contains 10 independent degree of freedom (DOF), the vertical displacement (z_c) and vertical pitching (β_c) of car body, the vertical displacement ($z_{bi}(i = 1,2,3,4)$) and vertical pitching of magnet bogie ($\beta_{ci}(i = 1,2,3,4)$). The dynamic vibration equation of the maglev system can be established by applying the principle that the total potential energy of the elastic system is constant and "set-in-right-seat" rule. The dynamic motion of vehicle can be written as:

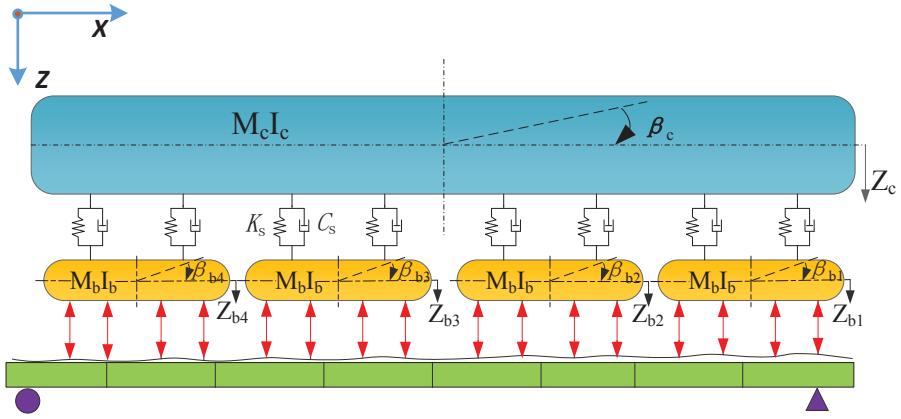

Fig. 1 Maglev vehicle model

$$\begin{bmatrix}\mathbf{M}_{cc} & \\ & \mathbf{M}_{bb}\end{bmatrix}\begin{Bmatrix}\ddot{\mathbf{U}}_{cc}\\ \ddot{\mathbf{U}}_{bb}\end{Bmatrix}+\begin{bmatrix}\mathbf{C}_{cc} & \mathbf{C}_{cb}\\ \mathbf{C}_{bc} & \mathbf{C}_{bb}\end{bmatrix}\begin{Bmatrix}\dot{\mathbf{U}}_{cc}\\ \dot{\mathbf{U}}_{bb}\end{Bmatrix}+\begin{bmatrix}\mathbf{K}_{cc} & \mathbf{K}_{cb}\\ \mathbf{K}_{bc} & \mathbf{K}_{bb}\end{bmatrix}\begin{Bmatrix}\mathbf{U}_{cc}\\ \mathbf{U}_{bb}\end{Bmatrix}=\begin{Bmatrix}0\\ \mathbf{F}_{bb}(\mathrm{t})\end{Bmatrix} \tag{4}$$

Where the subscript cc, bb represent the car body, magnet bogie respectively. **M**, **C**, **K**, **U** are the mass matrix, damping matrix, stiffness matrix and displacement vector vehicle system respectively [17]. The force vector $\mathbf{F}_{bb}(\mathrm{t})$ can be written as:

$$\mathbf{F}_{bb}(\mathrm{t})=\sum_{m=1}^{4}\sum_{k=1}^{4}\frac{\mu_0 N^2 A}{4}\left(\frac{i_0+\Delta i(t)}{c_0+\Delta c_k(t)}\right)^2\boldsymbol{R}_{\boldsymbol{lm}} \tag{5}$$

In which, $\frac{\mu_0 N^2 A}{4}$ is the electromagnetics parameter of levitation magnet. μ_0 is the permeability, N is number of turns in the magnet winding, A is pole area of iron-core. i_0 is the rated current, c_0 is the initial air gap. $\Delta i(t)$ is increment of current, $\Delta c_k(t)$ is the increment of air gap in the kth magnet wheel of mth magnet bogie. Both of Δi and Δc are time-dependent and they will change with the change of vehicle running position. $\boldsymbol{R}_{\boldsymbol{lm}}$ is a transform vector, which can distribute the force to the vertical and pitching of the magnetic bogie.

The guideway is recognized as an Euler-Bernoulli beam, the finite element method is applied to establish the vibration equation of guideway so that local vibration of the guideway could be considered accurately. The dynamic motion of guideway can be expressed as:

$$\begin{bmatrix}\mathbf{M}_{gg} & \\ & \mathbf{M}_{pp}\end{bmatrix}\begin{Bmatrix}\ddot{\mathbf{U}}_{gg}\\ \ddot{\mathbf{U}}_{pp}\end{Bmatrix}+\begin{bmatrix}\mathbf{C}_{gg} & \mathbf{C}_{gp}\\ \mathbf{C}_{pg} & \mathbf{C}_{pp}\end{bmatrix}\begin{Bmatrix}\dot{\mathbf{U}}_{gg}\\ \dot{\mathbf{U}}_{pp}\end{Bmatrix}+\begin{bmatrix}\mathbf{K}_{gg} & \mathbf{K}_{gp}\\ \mathbf{K}_{pg} & \mathbf{K}_{pp}\end{bmatrix}\begin{Bmatrix}\mathbf{U}_{gg}\\ \mathbf{U}_{pp}\end{Bmatrix}=\begin{Bmatrix}\mathbf{F}_{gg(\mathrm{t})}\\ 0\end{Bmatrix} \tag{6}$$

Where the subscript gg, pp represent guideway and pier respectively. **M**, **C**, **K**, **U** are the mass matrix, damping matrix, stiffness matrix and displacement vector of guideway system respectively. $\mathbf{F}_{gg(\mathrm{t})}$ is the force vector of guideway.

4 PROBABILITY DENSITY EVOLUTION METHOD

Based on Eq. (4)and Eq. (6) , we can established the coupled dynamic equation of vehicle and guideway system. Considering the randomness of vehicle parameters, the coupled equation can be simplified as:

$$\mathbf{M}(\boldsymbol{\Theta})\{\ddot{\mathbf{U}}\}+\mathbf{C}(\boldsymbol{\Theta})\{\dot{\mathbf{U}}\}+\mathbf{K}(\boldsymbol{\Theta})\{\mathbf{U}\}=\mathbf{F}(\boldsymbol{\Theta},t) \tag{7}$$

When considering the randomness of vehicle parameters, the mass matrix, damping matrix, stiffness matrix and force vector are all random, which can be uniformly described by random variables $\boldsymbol{\Theta}$.

The step by step integral method Wilson-θ method is used to calculate the stochastic dynamic responses. For the maglev system, the dynamic responses can be determined by displacement and velocity responses. Taking $\Psi = \{\Psi_v, \Psi_g\}^T$ to unified characterize the stochastic responses of structure, they can be expressed as:

$$\Psi = H_\Psi(\boldsymbol{\Theta}, \mathrm{t}) \tag{8}$$

$$\dot{\Psi} = \frac{d(\{\Psi_v, \Psi_g\}^T)}{dt} = \{\dot{\Psi}_v, \dot{\Psi}_g\}^T = h_\Psi(\boldsymbol{\Theta}, \mathrm{t}) \tag{9}$$

In which, the subscript v and g represent the vehicle and guideway respectively. $H_\Psi(\boldsymbol{\Theta}, \mathrm{t})$ and $h_\Psi(\boldsymbol{\Theta}, \mathrm{t})$ replace the system displacement responses and velocity responses. Assuming $\mathbf{U}$ as the response to be calculated, and its first-order differential can be written as:

$$\dot{U} = \mathrm{G}(\Psi, \dot{\Psi}) = \mathrm{G}(H_\Psi(\boldsymbol{\Theta}, \mathrm{t})\ h_\Psi(\boldsymbol{\Theta}, \mathrm{t}))^T \tag{10}$$

$G(\cdot)$ is the transform equation.

Taking $p_{U\boldsymbol{\Theta}}(u, \theta, t)$ as the joint probability density function of $(\boldsymbol{U}, \boldsymbol{\theta})$. Eq. (10) satisfied the general probability density evolution equation[18]:

$$\frac{\partial p_{U\boldsymbol{\Theta}}(u, \boldsymbol{\theta}, t)}{\partial t} + \dot{U}(\boldsymbol{\theta}, t)\frac{\partial p_{U\boldsymbol{\Theta}}(u, \boldsymbol{\theta}, t)}{\partial u} = 0 \tag{11}$$

The initial responses is $U(\mathrm{t}_0) = u_0$, $\boldsymbol{\Theta} = \theta_q$, $(q = 1,2,3, \ldots, n)$, considering the initial probability condition of Eq. (11), two side difference method with Total Variation Diminishing (TVD) scheme are used to solve the partial differential equation (11), then, we can get the probability solution $p_{U\boldsymbol{\Theta}}(u, \boldsymbol{\theta}, t)$, the probability density function can be expressed as:

$$p_U(u, t) = \int_{V_\Theta} p_{U\Theta}(u, \theta, t) d\theta \tag{12}$$

5 CASE STUDY

5.1 Verification of Accuracy and efficiency

To consider the stochastic vehicle parameters, each vehicle has 3 independent random variables $\bar{m}_{ci}$, $\bar{k}_{si}$ and $\bar{c}_{si}$ $(i = 1,2, \ldots,10)$. The point selection method introduced in section 1 is used to select representative points. In this article, there are 300 discrete representative point set have been taken into considered. The three-dimension of PDF and matching contour of acceleration of first car body at center of mass under stochastic vehicle loads are shown in Fig. 2, where it is seen that the real-time probability density function seems like the shape of mountains.

To assess the accuracy and efficiency of the proposed method, the result of PDEM running 500 samples are compared to those of MCM running 8000 samples, the comparison of PDEM and MCM are shown in Fig. 3, where it is seen that the both the mean value and standard deviation of acceleration obtained by PDEM are accord well with MCM. Further, to complete those calculation, the PDEM took only 242min, while the MCM needs 8910 min. Therefore, it could be concluded the proposed method improves 1~2 orders of magnitudes and is of high accuracy and efficiency.

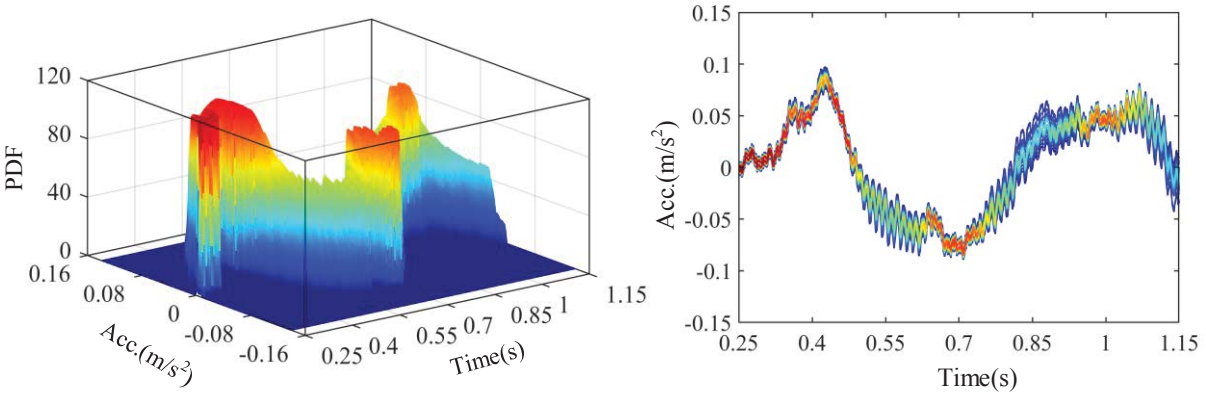

Fig. 2 Acceleration of first car body at center of mass under stochastic vehicle load (CV=0.25)

(a) PDF (b) contour of PDF

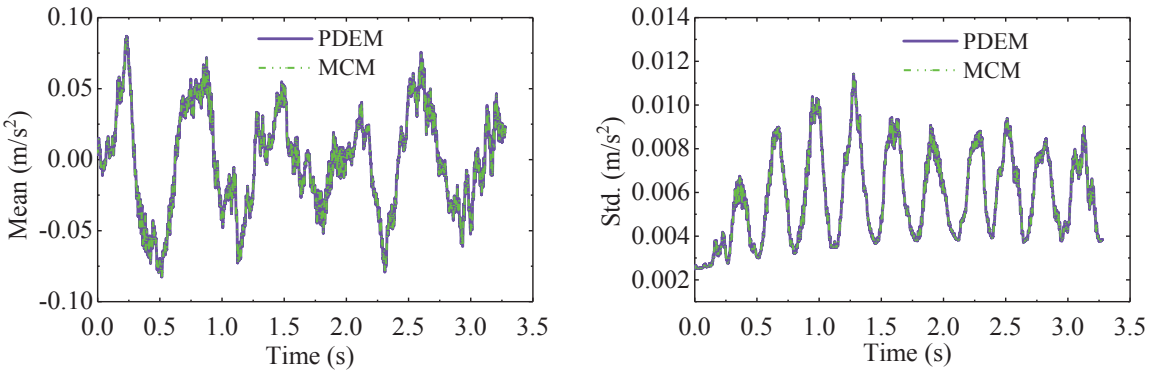

Fig. 3 Mean value and standard deviation of acceleration of the first car body at center of mass under stochastic vehicle load (CV=0.25) (a) mean value (b) standard deviation

5.2 Effect of the level of different vehicle parameters

5.2.1. Dynamic responses analysis of vehicle

Acceleration of car body is important for running safety and riding quality. To study the influence of different vehicle parameters on dynamic responses of the coupled system, the coefficient of variation (COV) are divided into 9 sets, which ranging from 0.05 to 0.25, with an interval of 0.025. Assuming the mean of vehicle mass $\bar{m}_c = 5000kg$, the stiffness of second suspension $\bar{k}_{smean} = 5\%\bar{k}_s$; the damping of second suspension $\bar{c}_{smean} = 5\%\bar{c}_s$. A larger vertical coordinate COV value indicate a greater influence on the dynamics of the corresponding dynamic index, such as acceleration of car body, deflection of guideway, etc.. Fig. 4 shows the vertical acceleration of the first vehicle under the stochastic second suspension stiffness with the COV of 0.25. Clearly, it can be seen that the maximum mean value is $7.88 \times 10^{-2}\mathrm{m/s^2}$, and the maximum value of standard deviation is $4.81 \times 10^{-3}\mathrm{m/s^2}$. Fig. 5 shows the COV of acceleration of the first car body under different vehicle parameters. It can be seen that the COV of acceleration of the car body increase in varying degree with the increases of COV. The maximum value of COV car body acceleration reaches about 0.122, 0.061, 0.059 affected by stochastic vehicle loads, stiffness of second suspension, damping of second suspension respectively. Among the stochastic vehicle loads, stiffness of second suspension, damping of second suspension, the COV curves affected by stochastic vehicle loads the increases steeper

but is not linear increase, while those increase slowly affected by stochastic stiffness and damping of second suspension. It means that the stochastic vehicle loads act a more sensitive effect on the car body acceleration than the other two parameters.

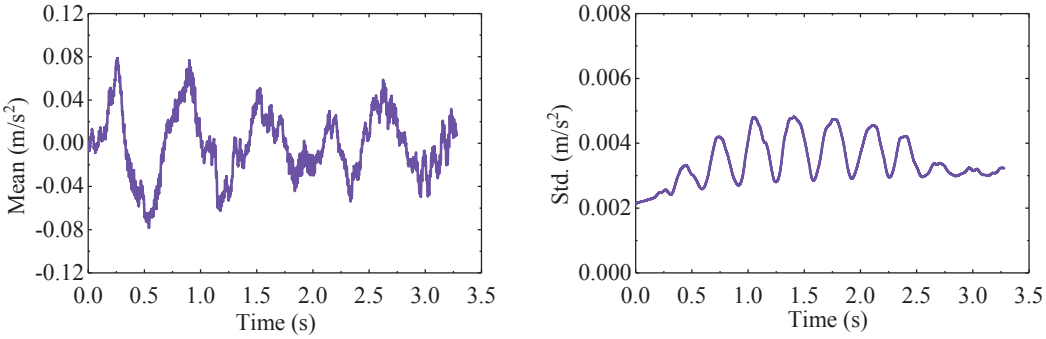

Fig. 4 Acceleration of the first vehicle under stochastic stiffness of second suspension: (a) mean value (b) standard deviation

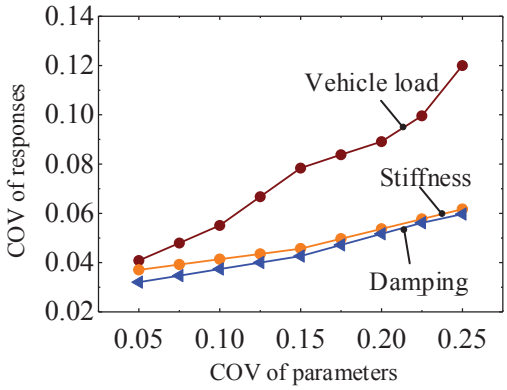

Fig. 5 Variables of coefficient for acceleration of the first car body under different vehicle parameters

5.2.2. Dynamic responses analysis of guideway

The dynamic deflection is an important index of guideway. For the same way, Fig. 6 shows the vertical deflection of guideway in the mid-point of the first span, under the stochastic second suspension stiffness with the COV=0.25. Clearly, it can be seen that the maximum mean value is approximate 1.65mm, and the maximum value of standard deviation is approximate 4.89×10^{-2}mm. The COV of dynamic responses of the deflection is 2.96%, which is less than the COV of second suspension stiffness.

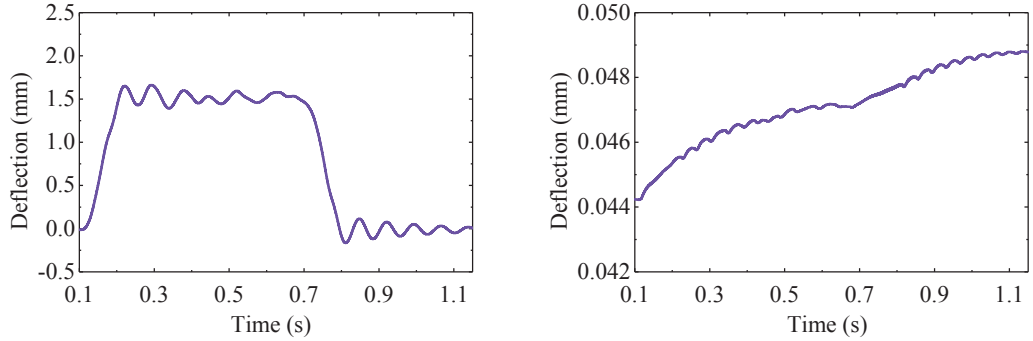

Fig. 6 Deflection of guideway in the mid-point of the first span: (a) mean value (b) standard deflection

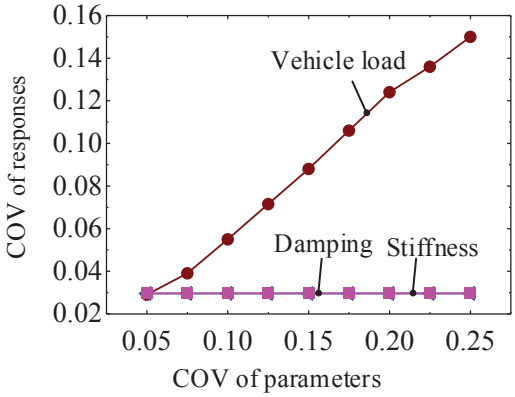

Fig. 7 Variables of coefficient of deflection of first span mid-point under different vehicle parameters

Fig. 7 shows the COV of dynamic deflection of first span mid-point under different vehicle parameters. It can be seen that the COV curves of guideway deflection rise rapidly with the increases of COV of stochastic vehicle loads, while the COV curves affected by stochastic stiffness and damping of second suspension almost do not changes. When the stochastic vehicle loads considered, the maximum value of COV of guideway deflection reaches about 0.151, while the maximum value of COV is 0.028 and 0.029 when the stochastic damping and stiffness of second suspension are considered respectively. This means that the stochastic vehicle loads has a great influence of the deflection of guideway, and the stochastic stiffness of second suspension and the stochastic damping of second suspension have a little influence on the deflection of guideway.

6 CONCLUSIONS

This paper proposed a stochastic vibration analytical approach to calculate maglev vehicle guideway system vertical stochastic vibration. The maglev-guideway coupled stochastic time-dependent equation is established, Wilson-θ method and finite deference method with TVD schemes are used to calculate the stochastic dynamic responses. The results calculated by MCM are compared with the proposed method. Meanwhile, the effects of the stochastic vehicle load, the stiffness and damping of second suspension on maglev vehicle and guideway are investigated and discussed. The conclusion of following can be summarized

(1) The proposed random dynamic model is available for dynamic vibration analysis of maglev system with good accurate and efficient. It can reduce computing time by 1-2 order of magnitudes compared with MCM.
(2) For the vehicle parameters, stochastic vehicle load has a significant effect on the dynamic deflection of guideway, while both the random damping and stiffness of second suspension have a little effect on deflection of guideway.
(3) The acceleration of car body seems to be affected by many factor, the maximum value of COV car body acceleration reaches about 0.122, 0.061, 0.059 affected by stochastic vehicle loads, stiffness of second suspension, damping of second suspension respectively. The stochastic vehicle loads act a more sensitive effect on the car body acceleration than the other two parameters.

7 ACKNOWLEDGMENTS

This work is supported by the National Natural Science Foundation of China (Grant No. 51578549, 51708558), the Joint Fund of the National Natural Science Foundation of China

(Grant No. U1934217), and Hunan Provincial Innovation Foundation for Postgraduate (No. CX20190129).

REFERENCES

[1] J.D. Yau, Aerodynamic vibrations of a maglev vehicle running on flexible guideways under oncoming wind actions, Journal of Sound and Vibration, 329 (2010) 1743-1759.

[2] J.D. Yau, Interaction response of maglev masses moving on a suspended beam shaken by horizontal ground motion, Journal of Sound and Vibration, 329 (2010) 171-188.

[3] J.B. Han, H.S. Han, S.S. Kim, S.J. Yang, K.J. Kim, Design and validation of a slender guideway for Maglev vehicle by simulation and experiment, Vehicle System Dynamics, 54 (2016) 370-385.

[4] D.A. Hullender, Analytical Models for Certain Guideway Irregularities, Journal of Dynamic Systems Measurement & Control, 97 (1975) 417.

[5] C. Y, vehicle/guideway interaction for high speed vehicle on a flexible guideway, Journal of Sound and Vibration, 175 (1994) 22.

[6] C.F. Zhao, W.M. Zhai, Maglev vehicle/guideway vertical random response and ride quality, Vehicle System Dynamics, 38 (2002) 185-210.

[7] D.J. Min, M.R. Jung, M.Y. Kim, J.W. Kwark, Dynamic Interaction Analysis of Maglev-Guideway System Based on a 3D Full Vehicle Model, International Journal of Structural Stability & Dynamics, 17 (2017) 647-670.

[8] Y.B. Yang, J.D. Yau, An iterative interacting method for dynamic analysis of the maglev train–guideway/foundation–soil system, Engineering Structures, 33 (2011) 1013-1024.

[9] J. Shi, Q.C. Wei, Y. Zhao, Analysis of dynamic response of the high-speed EMS maglev vehicle/guideway coupling system with random irregularity, Vehicle System Dynamics, 45 (2007) 1077-1095.

[10] H.P. Wang, J. Li, K. Zhang, Vibration analysis of the maglev guideway with the moving load, Journal of Sound and Vibration, 305 (2007) 621-640.

[11] Z.L. Wang, Y.L. Xu, G.Q. Li, Y.B. Yang, S.W. Chen, X.L. Zhang, Modelling and validation of coupled high-speed maglev train-and-viaduct systems considering support flexibility, Vehicle System Dynamics, 57 (2018) 161-191.

[12] H.S. Han, B.H. Yim, N.J. Lee, Y.C. Hur, S.S. Kim, Effects of the guideway's vibrational characteristics on the dynamics of a Maglev vehicle, Vehicle System Dynamics, 47 (2009) 309-324.

[13] J.S. Lee, S.D. Kwon, M.Y. Kim, I.H. Yeo, A parametric study on the dynamics of urban transit maglev vehicle running on flexible guideway bridges, Journal of Sound & Vibration, 328 (2009) 301-317.

[14] Z.W. Yu, J.F. Mao, Probability analysis of train-track-bridge interactions using a random wheel/rail contact model, Engineering Structures, 144 (2017) 120-138.

[15] J.F. Mao, Z.W. Yu, Y.J. Xiao, C. Jin, Y. Bai, Random dynamic analysis of a train-bridge coupled system involving random system parameters based on probability density evolution method, Probabilistic Engineering Mechanics, 46 (2016) 48-61.

[16] K.F. Fang, Y.Wang, Application of number theory method in statistics, Science Press China, 1996.

[17] Z.h. Zhu, P. Zhang, T.T. Zhao, Z.J. Li, L.Y. Zhou, Driving dynamic response analysis of the steel-concrete composite trussed girder bridge considering the effect of nodal rigid zone, Journal of Hunan University(Natural Sciences), 45 (2018) 19-28.

[18] J. Li, J.B. Chen, Stochastic dynamic of structures, John Wiley & Sons(Asia) Pte Ltd, Singapore, 2009.

EURODYN 2020
XI International Conference on Structural Dynamics
M. Papadrakakis, M. Fragiadakis, C. Papadimitriou (eds.)
Athens, Greece, 23–26 November 2020

RAIL-BRIDGE INTERACTION EFFECTS IN SINGLE-TRACK MULTI-SPAN BRIDGES. EXPERIMENTAL RESULTS VERSUS NUMERICAL PREDICTIONS UNDER OPERATING CONDITIONS

M.D. Martínez-Rodrigo[1], P. Galvín[2], E. Moliner[1] and A. Romero[2]

[1] Universitat Jaume I, Mechanical Engineering and Construction Department
Avda. Sos Baynat s/n, 12071 Castellón, Spain
e-mail: {mrodrigo, molinere}@uji.es

[2] Universidad de Sevilla, Escuela Técnica Superior de Ingeniería
Camino de los Descubrimientos s/n, 41092 Sevilla, Spain
{pedrogalvin, aro}@us.es

Keywords: Railway bridges, rail-bridge interaction, experimental measurements

Abstract. *This paper is devoted to the analysis of rail-bridge interaction effects in railway bridges under the circulation of moving trains. In a first approach, a bidimensional Finite Element model is implemented. The rail and the bridge are represented as Bernouilli-Euler beams, and a three-layer discrete track model accounting for the damping and flexibility of rail pads, ballast and subgrade is considered. In the model, several elastically supported spans are included, coupled by the presence of the track. First a sensitivity analysis is performed on the track parameters. A numerical receptance test is simulated on the rails showing that the track damping parameters influence the response only in the vicinity of the track natural frequencies, which are much higher than the bridge's. Then, the maximum acceleration of the bridge is evaluated under equidistant trains and consistent conclusions are extracted regarding the track parameters. Last, the number of spans included in the model is evaluated showing that limiting the model to one span does not necessarily lead to the highest response in terms of the bridge acceleration. Finally, the response of an existing two-span single-track bridge belonging to a conventional Spanish line is evaluated under the circulation of the Altaria Talgo train. Numerical predictions are compared to experimental results obtained in a recent campaign. The prediction of the vertical acceleration at the sensors located along the longitudinal symmetry axis is adequate. From the experimental results the coupling effect between the adjacent decks in each span is evident suggesting the need of analyzing this phenomenon with more sophisticated models.*

1 INTRODUCTION

Railway induced vibrations are a matter of concern for engineers and authorities in recent societies. In many countries, nowadays High-Speed services allow intense mobility between distant highly populated urban areas. The crescent density of traffic and the train operational speeds require, nonetheless, an outstanding response of railway infrastructures in order to ensure traffic safety, passenger comfort and adequate environmental conditions in the surrounding areas.

Comprising an important proportion of the railway infrastructure, railway bridges have received considerable attention in the last years and, to ensure traffic safety and passenger comfort, their design must accomplish strict requirements [1]. In particular, short-to-medium span simply-supported (SS) bridges with ballasted tracks are prone to experience high deck vertical accelerations which may lead to ballast deconsolidation, rail misalignment and other related problems [2]-[11]. In this context, a deep understanding of train-track-bridge interaction mechanisms is essential in order to be able to predict and assess the dynamic response of such structures. A state-of-the-art review on the evolution of numerical models and experimental tests focusing on validation, safety assessment and long-term performance investigation of train-track-bridge systems was recently presented by Zhai et al. [5].

Railway axle loads and bridges interact through the track infrastructure. The track distributes the axle loads and may exert a restraining effect on the bridges' boundary conditions [6] and a coupling effect among consecutive spans of the same viaduct [7], or between adjacent single-track decks [8]. Nevertheless, in many publications these effects are disregarded and the influence of the super-structure composed by the rails, sleepers and ballast, in ballasted tracks, is still not well known.

In this contribution, the dynamic behavior of multi-span single-track bridges is investigated with the aim of evaluating the effect of the continuity of the track on the bridge vertical response. In section 2 an existing bridge object of study is described, along with the numerical model. In section 3, the results of a preliminary sensitivity analysis on a few track parameters is presented. In section 4, the results of an experimental campaign recently performed on the bridge are compared with numerical predictions. Finally, some conclusions are extracted regarding the effect of the track super-structure on the bridge acceleration response.

2 BRIDGE DESCRIPTION AND NUMERICAL MODEL

2.1 Bridge description

The bridge under study is a bridge crossing the Old Guadiana River in the conventional railway line Madrid-Alcázar de San Juan-Jaén in the Alcázar de San Juan-Manzanares section (see Fig. 1). It is a double track concrete bridge composed by two identical SS bays. In each span, the horizontal structure is formed by two structurally independent decks, one for each track. Each deck is composed by a concrete slab resting on five pre-stressed concrete rectangular girders with no transverse stiffening elements (see Fig. 2). The longitudinal girders rest on the two abutments and on a central support through neoprene bearings. Each deck accommodates a ballasted track with Iberian gauge UIC60 rails and mono-block concrete sleepers with a spacing of 0.60 m.

2.2 Numerical model

In a first approach, the numerical model described in what follows is used. Only one single-track deck is represented in both bays as two successive Bernoulli-Euler (B-E) beams resting on elastic supports, accounting for the neoprene bearings elastic vertical stiffness. The two rails

are treated as an equivalent single B-E beam as well. A three layer discrete track model (see Fig. 3) as the one proposed by Zhai [9] is implemented, where the damping and stiffness of rail pads, ballast and subgrade are included at the sleepers positions.

Figure 1: Old Guadiana Bridge photographs.

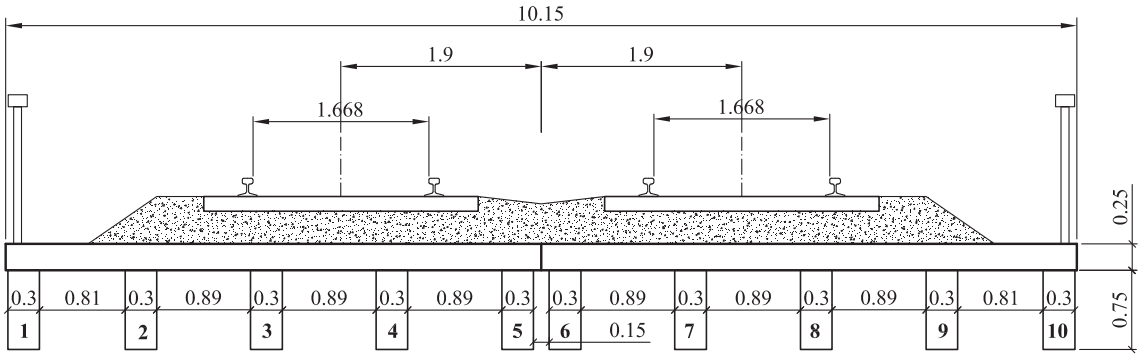

Figure 2: Old Guadiana Bridge cross-section.

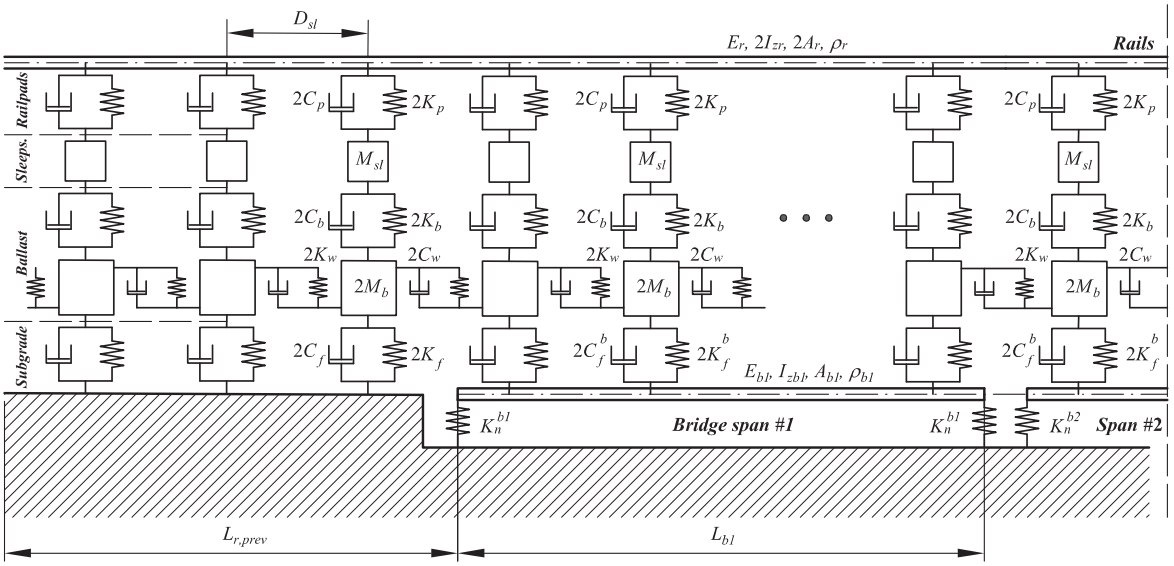

Figure 3: Numerical track-bridge interaction model.

In order to simulate the axle vertical forces, a constant moving load model is selected, therefore neglecting vehicle-structure interaction effects. The model, as described above, is generated using Finite Elements in Ansys software. Then, the equations of motion of the complete system are integrated in the time domain applying Newmark-Betta constant acceleration algorithm programmed in Matlab.

2.3 Parameter selection and model updating

In the last years, different authors have proposed discrete track models for the analysis of railway induced vibrations. Fig. 4 shows the evident dispersity in the values of four parameters admitted in previous publications: the rail pads and ballast vertical stiffness and damping K_p, C_p, K_b and C_b. First, a set of nominal or reference values for all the track parameters is selected on the basis of the literature review. Then, the bridge parameters, assumed identical in both bays, (Modulus of Elasticity E_{bi}, moment of inertia I_{zbi} and linear mass m_{bi}) are adjusted in order to reproduce static and dynamic tests performed on the structure right before its opening [23]. In Table 1 the bridge and track reference parameters are included. These will be the ones used in the experimental validation (section 4). The fundamental frequency of the track-bridge system for these parameters equals 10.07 Hz. A damping ratio of 1.565% is assigned to any mode as per [24] for pre-stressed concrete bridges of the particular span length.

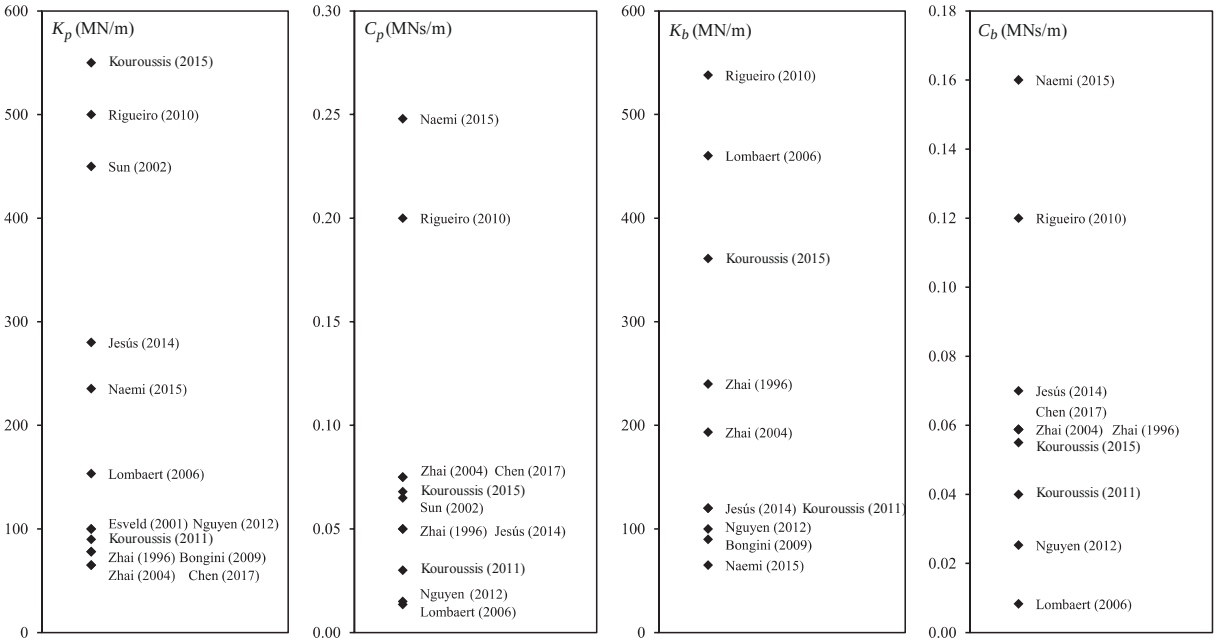

Figure 4: Rail pad and ballast layer stiffness and damping values admitted by different authors in the past for comparable ballast layers thicknesses and sleepers distances [6],[9]-[20].

Rail and bridge parameters		Track parameters per rail seat	
A_r (m^2)	76.86E-4	K_p (N/m)	1E8
E_r (Pa)	2.1E11	C_p (Ns/m)	7.5E4
I_{zr} (m^4)	3055E-8	M_{sl} (kg)	300
ρ_r (m^3)	7850	K_b (N/m)	1.933E8
D_{sl} (m)	0.60	C_b (Ns/m)	5.88E4
L_{bi} (m), N_{sp}	11.93, 2 spans	M_b (kg)	317.91
$(I_z \cdot E)_{bi}$ (Nm^2)	7.09E9	K_f (N/m)	7.3987E7
m_{bi} (kg/m)	8727	C_f (Ns/m)	3.115E4
ζ_{bi} (%)	1.565	K_w (N/m)	7.84E7
$K_{n,bi}$ (N/m) st/dyn	11.165E8 / 22.33E8	C_w (Ns/m)	8E4

Table 1: Bridge-track reference parameters

As per the subgrade stiffness and damping coefficients inside the bridge, 100 K_f and 0 Ns/m have been assigned as it is assumed that the ballast layer rests directly on the concrete slab.

A track length of 20 m is included before and after the two-span bridge, equivalent to more than 30 times the sleeper distance, which is considered adequate attending to previous publications [21], [22]. A convergence analysis is performed on this length ensuring the adequacy of this value.

3 SENSITIVITY ANALYSIS

3.1 Track receptance

Fist, the track dynamic response is evaluated numerically. To this end a harmonic test is performed on approximately 50 m of track (in the absence of bridge). A vertical harmonic load of 210 kN is applied at the central section of the double rail and the vertical displacement amplitude is determined in the same location. The forcing frequency varies between 1 and 2000 Hz in increments of 0.5 Hz. Fig. 5 shows the results for individual variations of C_p, C_b, C_f and C_w with respect to the reference values included in Table 1.

Two resonance frequencies are clearly detected in the proximities of 170 and 1350 Hz. The variations in the damping parameters affect the response only close to resonance. As the maximum frequency of interest in the bridge acceleration response is 60 Hz, the effect of these parameters on the bridge response should be very small. In the following section this particular issue is checked.

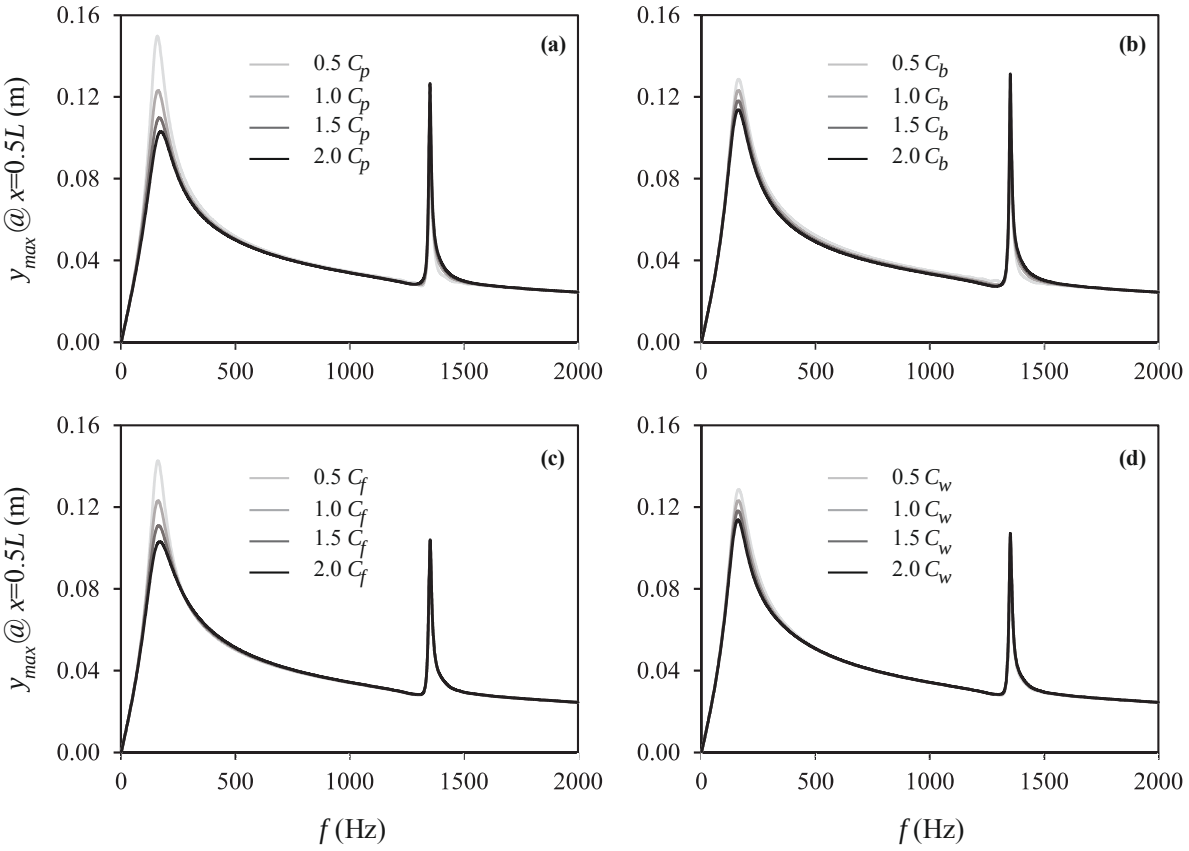

Figure 5: Receptance numerical test performed on the track model for independent variations of C_p, C_b, C_f and C_w.

3.2 Bridge maximum acceleration under train of equidistant loads

Second, the effect of the variations on four track parameters: the stiffness and damping coefficients of the rail pads, K_p and C_p, and of the ballast, K_b and C_b on the bridge maximum acceleration response is investigated. To this end, the response of the bridge is obtained under the circulation of an artificial train of 20 equidistant loads of 210 kN separated 18 m, with the aim of inducing two clear resonances on the structure. The bridge time-history response in terms of displacements and accelerations is obtained for 60 velocities of circulation in the range [40,100] m/s. A Chebyshev order 3 filter is applied to the acceleration response filtering contributions below 1 Hz and above 60 Hz. After filtering, maximum response envelopes are obtained for values of the track parameters:

$$[0.5,1,2,4]\cdot K_p \quad [0,0.5,1,2]\cdot C_p \quad [0.5,1,2,4]\cdot K_b \quad [0,0.5,1,2]\cdot C_b \tag{1}$$

where the values of K_p, C_p, K_b and C_b are those in Table 1. Fig. 6 shows the evolution of the maximum acceleration, which always takes place in the center of the second span, in absolute value in terms of the velocity for individual variations of each track parameter.

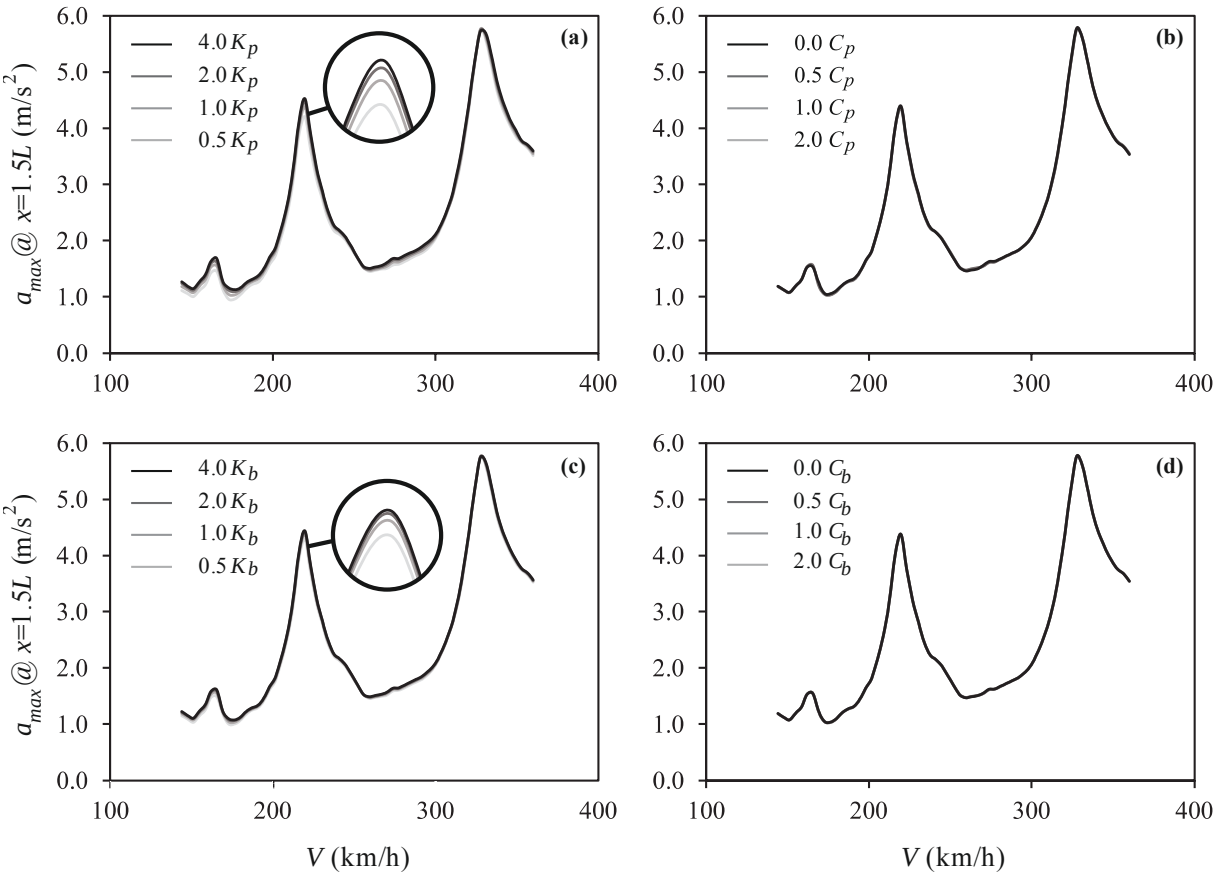

Figure 6: Maximum acceleration vs. velocity for individual variations of K_p, K_b, C_p, and C_b.

In all the plots shown in Fig. 6 three resonant peaks can be detected, corresponding to second, third and fourth resonances of the fundamental mode of the bridge, which in the reference case presents a frequency f_1 = 10.07 Hz. These theoretical resonant speeds can be calculated as:

$$V_1^{r,j=2} = \frac{df_1}{2}3.6 = 326.27\,\frac{km}{h}\; V_1^{r,j=3} = 217.5\,\frac{km}{h}\; V_1^{r,j=4} = 163.1\,\frac{km}{h} \tag{2}$$

The individual variations considered in the track do not affect significantly the reference fundamental frequency. From the observation of Fig. 6 (c)-(d) it may be concluded that the

influence of the variations in the rail pads and ballast damping constants is negligible on the maximum acceleration response of the bridge for the reference values of the remaining parameters, as expected from the results of the receptance study. The parameter that seems to affect the most the acceleration envelope at the most critical section is the rail pad stiffness K_p, leading to a decrease in the maximum acceleration at resonance as K_p reduces (for more flexible rail pads). This effect is more visible for higher resonance orders. The same tendencies, although in a less pronounced manner, are observed in terms of the variations considered in the ballast stiffness K_b.

3.3 Influence of the number of spans

Last in the sensitivity analysis, the effect of including a different number of spans in the numerical model on the maximum bridge response is investigated. Due to the longitudinal coupling exerted by the track on the structurally independent decks, the maximum response could differ depending on the number of spans. The analysis is performed in two cases: including and neglecting the decks neoprene bearings. In Fig. 7 the maximum acceleration at mid-span is represented for the same train of equidistant loads used in the previous subsection. All the bridge and track parameters adopt the reference values. Fig. 7(a) corresponds to the simply-supported (SS) case, i.e. no neoprene bearings , while Fig. 7(b) represents the elastically supported case, i.e. considering the neoprene bearings vertical flexibility. Colors red, black and grey are selected to represent results computed with one, two and three spans, respectively. Then, solid, dashed and dotted lines correspond to the response at mid-span of the first, second and third spans, respectively.

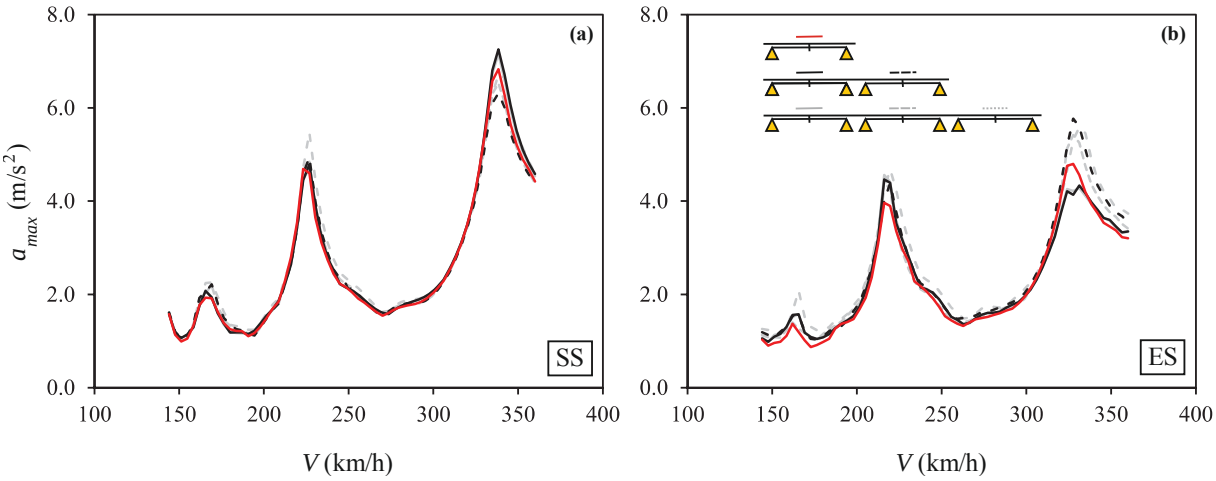

Figure 7: Maximum acceleration vs. velocity for models with one, two and three spans. (a) Simply-supported and (b) elastically-supported decks.

From the analysis of Fig. 7 one may conclude that: (i) the model leading to the maximum predicted acceleration and the most critical section depend on the maximum velocity considered; (ii) the difference between the three models is more relevant at resonance; (iii) in the particular case under study considering just one span does not predict the maximum response at any resonant peak. From the previously said, if the rail is included in the model and computational time is not an issue, including all the spans in the model may be on the safety side when it comes to predicting the maximum vertical acceleration response.

4 EXPERIMENTAL VALIDATION

4.1 Description of experimental campaign

In May 2019 the authors performed an experimental campaign on Old Guadiana Bridge with the purpose of characterizing the structure and soil dynamic properties along with the bridge dynamic response under railway traffic (see Fig. 8). As per the acquisition equipment, a portable acquisition system LAN-XI of Brüel & Kjaer was used. The acquisition system fed the sensors (accelerometers) and an instrumented impact hammer in the case of the soil tests. It also performed the Analog/Digital conversion (A/D). The A/D was carried out at a high sampling frequency that avoided aliasing effects using a low-pass filter with a constant cut-off frequency. The sampling frequency was $f_s = 4096$ Hz. The acquisition equipment was connected to a laptop for data storage. Endevco model 86 piezoelectric accelerometers were used with a nominal sensitivity of 10 V/g and a lower frequency limit of approximately 0.1 Hz. The acquisition system was configured to avoid the sensors' overload.

Figure 8: Experimental campaign photographs.

From the dynamic characterization of the soil, which was carried out by the by Spectral Analysis of Surface Waves test a rather stiff soil was identified with a shear wave velocity higher than 250 m/s in the upper soil layer. The bridge response depends on soil-structure interaction (SSI) and soil stratigraphy. However, due to the high soil stiffness identified, in a first approach these effects are disregarded.

As per the bridge structure, eighteen accelerometers were connected to the lower horizontal surface of the decks longitudinal girders in the locations indicated in Fig. 9.

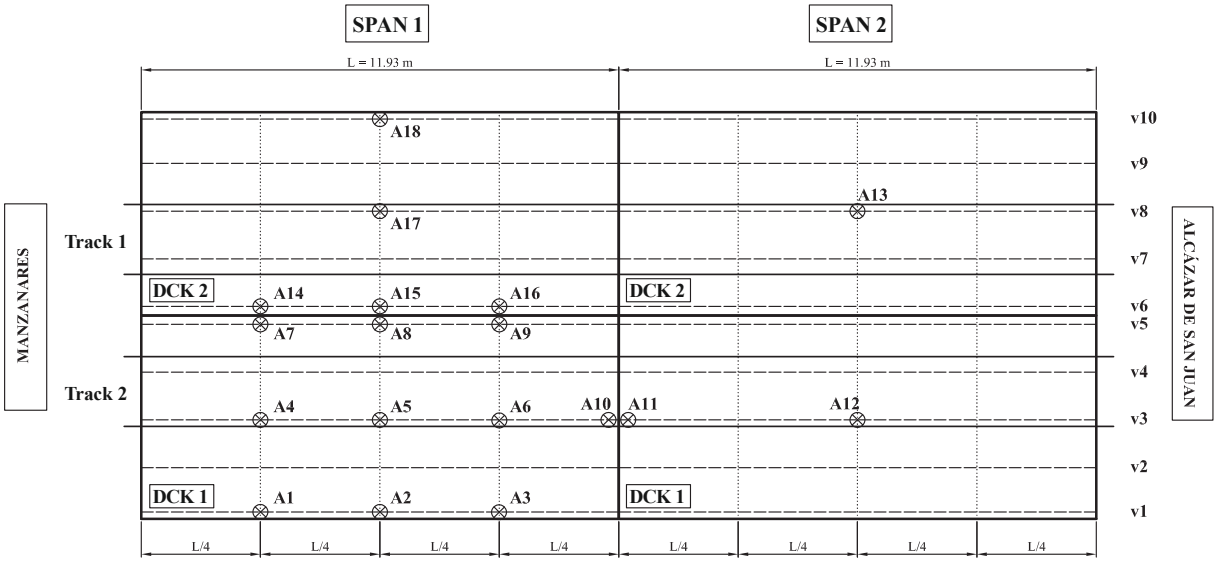

Figure 9: Sensors placement in experimental campaign.

4.2 Numerical predictions vs. experimental measurements

During the campaign the response of the structure was recorded under the circulation of different trains. Two of these circulations are included in this section. Both correspond to the medium distance Renfe Altaria Talgo VI train travelling along tracks 2 and 1 (see Fig. 9) in the directions South-North (Manzanares-Alcázar de San Juan) and North-South, respectively. Fig. 10 and Fig. 11 show photographs of the trains and a scheme of the axles distances. Also, Table 2 includes the train axles arrangement and loads.

First, the speeds were identified from the frequency associated to the bogie distance leading to approximately 155 km/h in both cases. Then, the response of the bridge was calculated using the numerical model described in section 2.2 with the properties included in Table 1, with the exception of structural damping which was assumed as 3.1% for the fundamental frequency, 10.065 Hz, and 1.56% for 90 Hz (Eurocode value). The first value was identified during the proof load test. The numerical response, integrated in the time domain using the full FE model, is also filtered between 1 and 30 Hz, applying the same procedure as with the experimental records. Given the bidimensional nature of the numerical model, only the response at sensors installed underneath beams 3 and 8 is compared with the numerical predictions.

Figure 10: Renfe Altaria Talgo VI trains crossing Old Guadiana Bridge.

It has been verified that the bridge maximum acceleration did not exceed the limit established by the Serviceability Limit State for traffic safety in the case of ballasted tracks [1] according to the measurements in all the sensors.

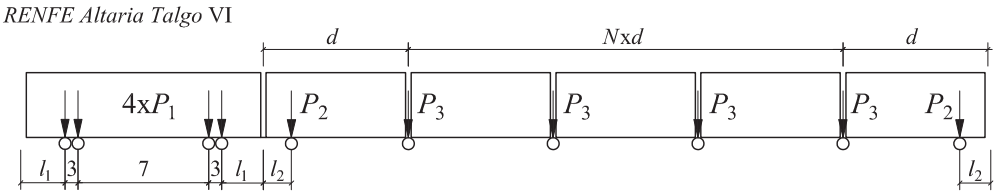

Figure 11: Renfe medium distance Altaria Talgo VI train axle scheme.

Train	N	d(m)	d_1 (m)	l_1 (m)	l_2 (m)	P_1 (kN)	P_2 (kN)	P_3 (kN)
Altaria	7	13.14	--	3.44	3.3	225	70	140

Table 2: RENFE Altaria Talgo VI features

Fig. 12 shows an experimental vs. numerical comparison of the vertical acceleration at sensors 5 and 6 under the circulation of the northbound train, in the time (a)-(b) and frequency (c)-(d) domains. The Talgo passenger coaches present a distance between shared axles of 13.14 m. The theoretical resonant speed associated to this length for the third resonance of the

fundamental mode is approximately 159 km/h, which is close to the real speed. This can be detected in the time-history plots where two oscillations of decreasing amplitude take place between the passage of consecutive axles.

$$V_1^{r,j=3} = \frac{df_1}{3} 3.6 = 158.7 \frac{km}{h} \approx 154.8 \frac{km}{h} = V \tag{3}$$

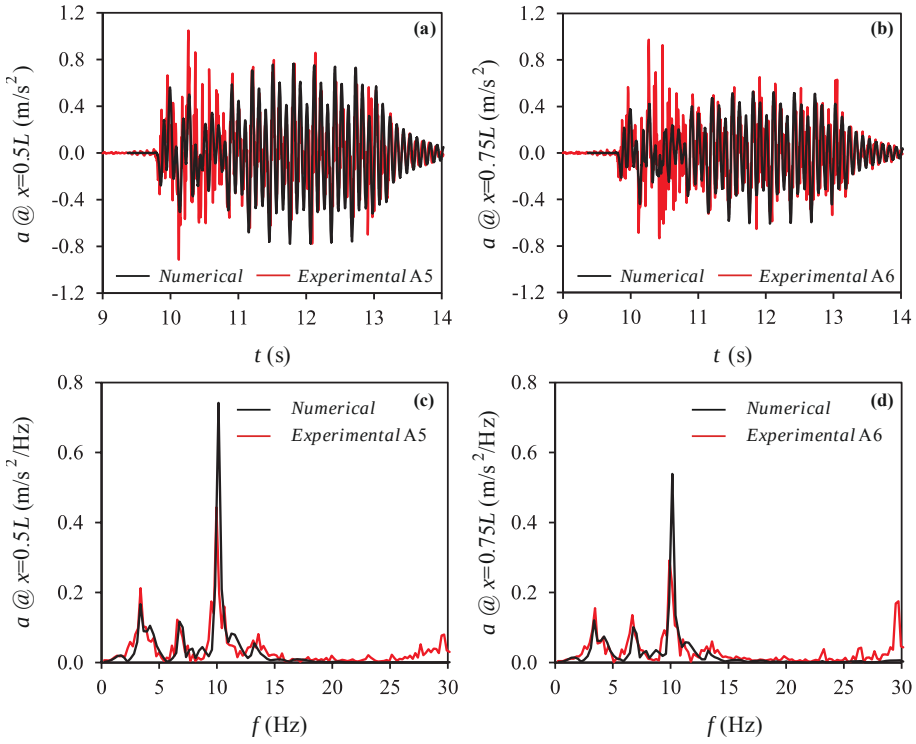

Figure 12: (a)-(b) Time history and (c)-(d) frequency content of the acceleration response at sensors 5 and 6 induced by Altaria Talgo VI train. Numerical prediction (black trace) vs. experimental measurements (red trace). Northbound train (track #2).

The accuracy of the numerical model is found reasonable up to 30 Hz, both at $L/2$ and $3L/4$ of the first span, although the numerical model overpredicts the acceleration for contributions close to the bridge fundamental frequency. This can be associated to vehicle-structure interaction which is not taken into account and can be of importance, specially at resonance; or to other energy dissipation mechanisms amplitude dependent such as the interaction between the adjacent decks, etc.

Fig. 13 shows the same type of comparative for the southbound train. In this case the acceleration is compared at sensors 13 and 17, located at mid-span of the second and first spans, respectively. Again, the time-history response is well reproduced, especially after the passage of the locomotive. In the frequency domain again, a predominant peak is detected showing the important contribution of the fundamental mode with a certain overprediction of the acceleration in the numerical case.

4.3 Coupling effect between adjoining decks

Finally, the coupling effect between the adjacent decks in each span is evaluated in forced vibration. Figs. 14(a)-(c) represent for the northbound train travelling along track #2 the experimental response measured at sensor 5 (at mid-span under the loaded track) and, simultaneously, at sensor 17 (at mid-span under the adjacent unloaded track).

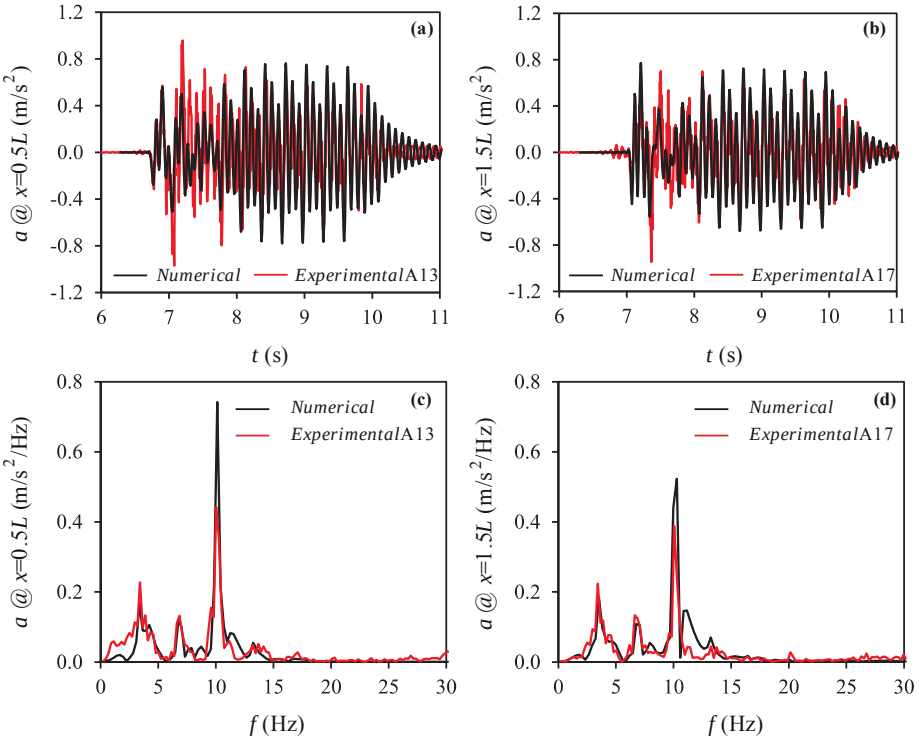

Figure 13: (a)-(b) Time history and (c)-(d) frequency content of the acceleration response at sensors 13 and 17 induced by Altaria Talgo VI train. Numerical prediction (black trace) vs. experimental measurements (red trace). Southbound train (track #1).

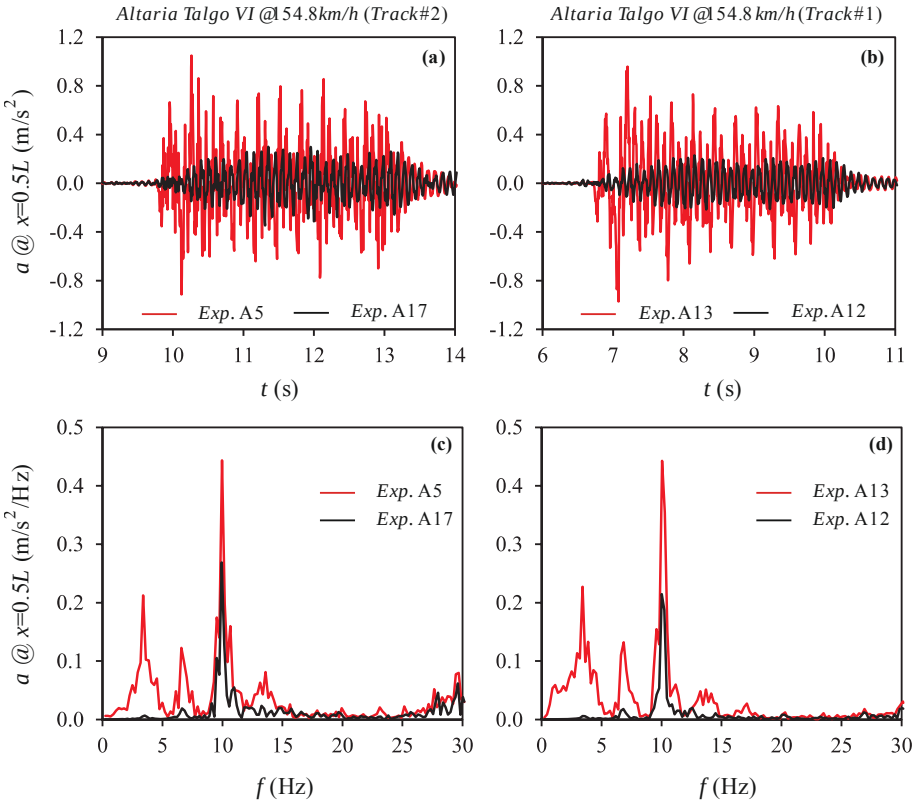

Figure 14: (a)-(b) Time history and (c)-(d) frequency content of the acceleration response at sensors 5 and 17 induced by the northbound train, and at sensors 13 and 12 induced by the southbound train.

The transmission of vibrations between the two decks is evident, even though these are only connected by the continuous ballast layer. At the unloaded sensor the frequency peaks associated to the excitation (e.g. bogie distance) which are visible in the low frequency range in the loaded sensor, are almost not perceptible; but the acceleration at the fundamental frequency reaches 60.6% de value in the loaded sensor. The same effect may be observed under the circulation of the southbound train when one compares the response between sensors 13 (under loaded track) and 12 (adjacent deck at symmetrical position). In this case the maximum acceleration in the unloaded sensor at the fundamental frequency in the frequency domain attains 48.5% the same maximum measured at sensor 13. This vibration transmission can be caused both by the continuous ballast layer and by the common foundations shared by the decks. In the opinion of the authors this phenomenon deserves further investigation. Implementing a 3D model of the bridge-track system would permit to evaluate the vibration transmitted between the decks close to the shared border in the frequency range of interest.

5 CONCLUSIONS

The present article constitutes a preliminary analysis on the longitudinal and transverse coupling effects exerted by the track on simply-supported bridges with independent single-track decks. From this study, the following can be concluded:

- There is a very high dispersion in the track parameters admitted by different authors for similar track infrastructures. The rail pad stiffness seems to affect the most the bridge maximum acceleration specially at high-order resonances, leading to lower amplitudes for higher flexibilities of this parameter. The ballast stiffness affects in a similar way, although to a lower extent. The damping parameters of the track do not seem to affect the bridge maximum response below 60 Hz. These parameters do affect the track response but at much higher frequencies.
- Considering one span in multi-span bridges may not lead to the maximum predicted acceleration when the track is included in the numerical model. The effect of the number of spans gains importance at resonance. The model leading to the maximum dynamic response as well as the most critical section depend on the maximum velocity of interest.
- The experimental vs. numerical predictions in the case of Old Guadiana bridge are reasonable in the sensors located along the longitudinal axis of the decks, as there is no contribution of the torsion mode at those locations. The numerical model tends to overestimate the real response close to the bridge natural frequency.
- The transmission of vibrations from the loaded deck to the unloaded deck is relevant. This may be caused by the continuous ballast layer but also by the shared foundations of the two decks. In the authors' opinion this effect is not well known and should be investigated using a 3D model of the complete bridge.

ACKNOWLEDGEMENTS

The authors would like to acknowledge the financial support provided by (i) Generalitat Valenciana under AICO/2019/175 research project, (ii) the Spanish Ministry of Economy and Competitiveness under research project [BIA2016-75042-C2], and Universitat Jaume I annual research plan under action [UJI/A2018/06].

REFERENCES

[1] CEN EN-1990, Eurocode: Basis of structural design. Annex 2: Application for bridges, (2002).

[2] ERRI D214: Rail bridges for speeds > 200 km/h. final report. Part a. Synthesis of the results of d 214 research. European Rail Research Institute (1999).

[3] W. Hoorpah, Dynamic calculations of high-speed railway bridges in France –some case studies, *Dynamics of High-Speed railway bridges*, Taylor & Francis, 2008.

[4] M. Zacher, M. Baeßler, Dynamic behaviour of ballast on railway bridges, *Dynamics of High-Speed Railway Bridges*, Taylor & Francis, 2008.

[5] W. Zhai, Z. Han, Z. Chen, L. Ling, S. Zhu, Train-track-bridge dynamic interaction: a state-of-the-art review, *Vehicle System Dynamics* 7, 984-1027, 2019.

[6] C. Rigueiro, C. Rebelo, L. Simões da Silva, Influence of ballast models in the dynamic response of railway viaducts, *Journal of Sound and Vibration* 329, 3030-3040, 2010.

[7] K. Liu, G. Lombaert, G. De Roeck, Dynamic analysis of multispan viaducts with weak coupling between adjacent spans, *Journal of Bridge Engineering* 19(1), 83-90, 2014.

[8] C. Rebelo, L. Simões da Silva, C. Rigueiro, M. Pircher, Dynamic behaviour of twin single-span ballasted railway viaducts. Field measurements and modal identification, *Engineering Structures* 30, 2460-2469, 2008.

[9] W. Zhai, K. Wang, J. Lin, Modelling and experiment of railway ballast vibrations, *Journal of Sound and Vibration* 270, 673-683, 2004.

[10] G. Kouroussis, D.P. Connolly, G. Alexandrou, K. Vogiatzis, The effect of railway local irregularities on ground vibration. *Transportation Research Part D* 39, 17-30, 2015.

[11] Y.Q. Sun, M. Dhanasekar, Influence of the railway track parameters to the vertical and lateral impact, *Conference on Railway Engineering*, Wollongong, 2002.

[12] A.H. Jesús, Z. Dimitrovová, M.A.G. Silva, A statistical analysis of the dynamic response of a railway viaduct, *Engineering Structures* 71, 244-259, 2014.

[13] M. Naemi, J.A. Zakeri, M. Esmaeili, M. Mehrali, Dynamic response of sleepers in a track with uneven rail irregularities using a 3D vehicle–track model with sleeper beams, *Archives of Applied Mechanics* 85,1679-1699, 2015.

[14] G. Lombaert, G. Degrande, J. Kogut, S. François, The experimental validation of a numerical model for the prediction of railway induced vibrations, *Journal of Sound and Vibration* 297, 512-535, 2006.

[15] G. Kouroussis, G. Gazetas, I. Anastasopoulos, C. Conti, O. Verlinden, Discrete modelling of vertical track–soil coupling for vehicle–track dynamics, *Soil Dynamics and Earthquake Engineering* 31, 1711-1723, 2011.

[16] C. Esveld, Modern railway track, Delft University of Technology, 2001.

[17] K. Nguyen, J.M. Goicolea, F. Gabaldón, Comparison of dynamic effects of high-speed traffic load on ballasted track using a simplified two-dimensional and full three-dimensional model, *Journal of Rail and Rapid Transit* 228(2), 128-142, 2012.

[18] W.M. Zhai, Two simple fast integration methods for large-scale dynamic problems in engineering, *International Journal for Numerical Methods in Engineering* 39, 4199-4214, 1996.

[19] E. Bongini, F. Poisson, Ground vibrations simulation cases parameters, *Technical report*, SNCF, France, 2009.

[20] Z. Chen, W. Zhai, K. Wang, A locomotive-track coupled vertical dynamics model with gear transmissions, *Vehicle System Dynamics* 55(2), 244-267, 2017.

[21] P. Lou, A vehicle-track-bridge interaction element considering vehicle's pitching effect, *Finite Elements in Analysis and Design* 41, 397-427, 2005.

[22] R.A. Clark, P.A. Dean, J.A. Elkins, S.G. Newton, An investigation into the dynamic effects of railway vehicles running on corrugated rails, *Journal of Mechanical Engineering Science* 24(2), 65-76, 1982.

[23] M.D. Martínez-Rodrigo, J. Lavado, P. Museros, Dynamic performance of existing high-speed railway bridges under resonant conditions retrofitted with fluid viscous dampers, *Engineering Structures* 32, 808-828, 2010.

[24] CEN EN-1991-2, Eurocode 1. Actions on structures. Part 2: Traffic loads on bridges, 2003.

EURODYN 2020
XI International Conference on Structural Dynamics
M. Papadrakakis, M. Fragiadakis, C. Papadimitriou (eds.)
Athens, Greece, 23–26 November 2020

VERTICAL COUPLING EFFECT OF THE BALLASTED TRACK ON THE DYNAMIC BEHAVIOR OF MULTITRACK RAILWAY BRIDGES COMPOSED BY ADJACENT DECKS

E. Moliner[1], A. Romero[2], J.C. Sánchez-Quesada[1], M.D. Martínez-Rodrigo[1] and P. Galvín[2]

[1]Universitat Jaume I
Av. Sos Baynat s/n, 12006 Castellón, Spain
e-mail: molinere@uji.es, jquesada@uji.es, mrodrigo@uji.es

[2] Universidad de Sevilla
Escuela Técnica Superior de Ingeniería
Camino de los Descubrimientos s/n, 41092 Sevilla, Spain
e-mail: aro@us.es, pedrogalvin@us.es

Keywords: railway bridge dynamics, ballasted track, vertical acceleration, moving-loads

Abstract. *In the present contribution the effect of the continuity of the ballasted track on the dynamic response of simply-supported railway bridges composed by structurally independent adjacent slabs at each span is addressed. Previous research works and experimental campaigns performed on simply-supported structures have shown that the presence of the ballast layer and other track components (rails, sleepers) may induce a dynamic coupling effect between the bridge spans or adjacent decks. In this study the influence of this effect on the train-induced vibrations is assessed. With this purpose a preliminary three-dimensional finite element (FE) model that includes the track components as a set of discrete mass, stiffness and damping elements has been implemented to numerically evaluate the influence of the continuity of the track components on the prediction of the bridge acceleration response under the passage of railway vehicles. The numerical model is calibrated with the load test results performed on a simply-supported railway bridge composed by several adjacent slabs. Finally the measured structural response of the bridge under train induced vibrations is compared with the numerical predictions. Preliminary conclusions regarding the importance of considering the continuity of the track components for the prediction and the assessment of the Serviceability Limit State of vertical acceleration in ballasted simply-supported railway bridges are presented.*

1 INTRODUCTION

The evaluation of the dynamic performance of railway bridges under the passage of the modern railway transportation systems is an issue of main concern to guarantee structural integrity and traveling comfort. In particular, for short-to-medium simply-supported (SS) bridges the Serviceability Limit State of vertical acceleration, limited to 3.5 m/s^2 for ballasted tracks according to Eurocode (EC) [1], is one of the most demanding requirements for their design or upgrading to new traffic requirements, since they are especially susceptible of experiencing considerably high vibration levels at circulating speeds above 200 km/h due to their low associated structural damping and mass [2, 3]. Therefore, the development of reasonably accurate numerical models becomes crucial in practical applications.

However, the dynamic response of these structures can be difficult to predict during the design or upgrading stages, since there is a main source of uncertainty in what concerns the modeling of the super-structure components, formed by ballast, sleepers and rails in ballasted tracks. In many publications and practical applications the effect of the track is disregarded, and the coupling effect exerted by its continuity along SS spans of the same bridge, and also by the shared ballast layer between structurally independent decks that form one span in certain bridges, can be significant. Also the track distributes the axle loads and may exert a restraining effect on the boundary conditions at the end supports of the bridge. Previous studies have already suggested the importance of the coupling and restraining effect induced by the ballasted track [4, 5, 6, 7], but this effect is not yet well known and requires further research.

In this regard a preliminary study of the influence of the track components and its continuity on the bridge acceleration response under the passage of railway convoys, was performed by the authors in a previous work [8]. In this study, the bridge spans were represented by Bernouilli-Euler (B-E) beams resting on elastic supports, and a three layer discrete track model consisting of a set of springs and dampers representing the track components (sleepers, railpads, etc.) as the one proposed by Zhai was used [9]. With this preliminar model a sensitivity analysis over the stifness and damping coefficients of the track parameters was performed, showing that the variation of track damping constants has a negligible effect on the maximum vertical acceleration response induced by train passage. This prelimilar observation is also in accordance with previous works which consider that the dynamic response of the track structure occurs only for frequencies considerably higher that those of the vehicle and the bridge deck, of the order of 100 Hz or above [10]. For this reason, the use of Mode Superposition analysis for solving the dynamic equilibrium equatios of the bridge is a reasonable strategy to reduce computational cost in the prediction of train-induced vibrations. Previous studies apply this technique, therefore neglecting the damping introduced by the track elements at discrete positions but including global damping ratios instead. [5, 11, 12]

In this contribution, the dynamic behavior of multi-span SS bridges formed by structurally independent single-track decks at each span is investigated, in order to evaluate the effect of the continuity of the ballasted track on the vertical acceleration response under train-induced vibrations. As the object of study, a bridge belonging to the spanish railway network is used, which is described in Section 2. The results of an experimental campaign performed by the authors in this bridge are used to calibrate the thtree-dimensional finite element model described in Section 3. In Section 4 the results of the comparison between numerical predictions and experimental measurements are shown, in terms of both natural frequencies and mode shapes and railway-induced vibrations. Finally, some conclusions are extracted regarding the effect of the track superstructure on the dynamic response of the bridge.

2 CASE STUDY: OLD GUADIANA RIVER BRIDGE

2.1 Bridge description

In a view to evaluate the vertical coupling effect of the ballasted track on the bridge dynamic response, an existing double-track bridge composed by two simply-supported (SS) identical bays (span length L=11.9 m) with separated single-track decks is used as the object of study. This bridge belongs to the conventional railway line Madrid-Alcázar de San Juan-Jaén, in Spain (Fig.1).

Figure 1: Old Guadiana river bridge.

As can be seen in Fig.1 the two structurally independent decks that form each span are composed by a reinforced concrete slab resting on five pre-stressed concrete rectangular girders. Each deck accommodates a ballasted track with Iberian gauge UIC60 rails and mono-block concrete sleepers at regular distances of 0.60 m. The longitudinal girders of the decks rest on the two abutments and on a central support through laminated rubber bearings. A cross-section of the bridge is shown in Fig.2.

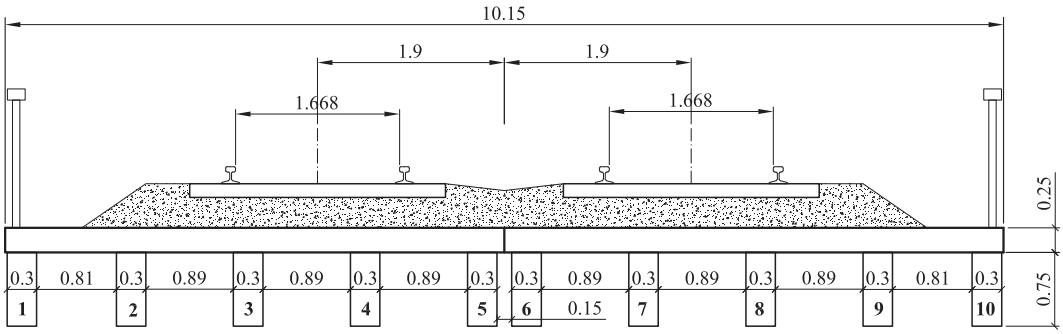

Figure 2: Cross section of the bridge.

2.2 Experimental campaign

In May 2019 the authors performed an experimental campaign on the bridge which included a dynamic characterisation of the soil and of the structure. As per the acquisition equipment, a portable acquisition system LAN-XI of Brüel & Kjaer was used. The Analog/Digital conversion (A/D) was carried out at a high sampling frequency that avoided aliasing effects using a low-pass filter with a constant cut-off frequency. The sampling frequency was fs = 4096 Hz. As

regards the soil characterisation, which was carried out by the by Spectral Analysis of Surface Waves test, a rather stiff soil was identified with a shear wave velocity higher than 250 m/s in the upper soil layer.

For the characterisation of the structure the acceleration response was measured under ambient and train-induced vibrations at 18 points of the lower flange of the pre stressed concrete girders (points 1-18 in Fig.3). Endevco model 86 piezoelectric accelerometers with a nominal sensitivity of 10 V/g and a low frequency limit of 0.1 Hz were installed in the aforementioned locations.

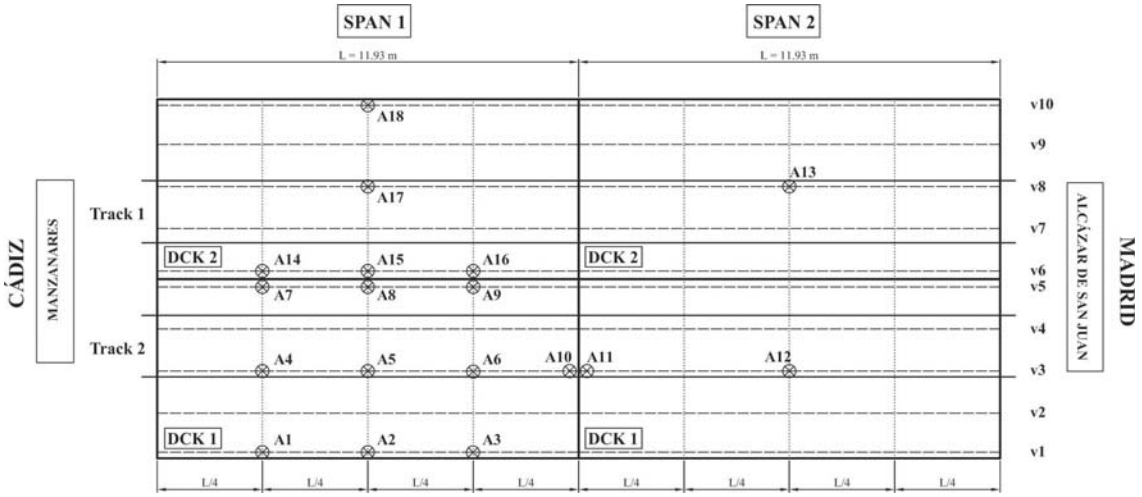

Figure 3: Location of the sensors at Old Guadiana river Bridge.

The ambient vibration data recorded during 3600 s was used for the identification of the modal parameters of the bridge by state-space models, using MACEC software [13]. Table 2 (top) shows the damping ratios and natural frequencies of the first 6 identified modes (fexp) and their mode shapes are shown in Fig.4 in solid black trace. As can be seen the lowest one in frequency order corresponds to the first longitudinal bending of each bay where the two adjacent decks vibrate in phase. The second mode corresponds to the typical first torsion mode of a continuous deck in each span, where the two independent slabs that share the ballast layer deform accordingly. In the third mode, the two adjacent decks in a span deform under independent torsion but out of phase such that they conform a typical first transverse bending mode of a continuous slab. In the aforementioned modes, the deck coupling caused by the ballast layer is very evident. In the higher frequency modes the decks deform under combinations of torsion, longitudinal and transverse bending.

3 NUMERICAL ANALYSIS

3.1 Finite element model

The finite element (FE) model shown in Fig.5 has been implemented in the commercial code ANSYS to obtain preliminary conclusions about the vertical coupling effect of the ballast layer on the dynamic behaviour of Old Guadiana bridge. The main features of the model are:

- The reinforced concrete slabs that form each span are simulated by means of isotropic thin plates discretised with shell elements with 6 degrees of freedom (dof) per node.

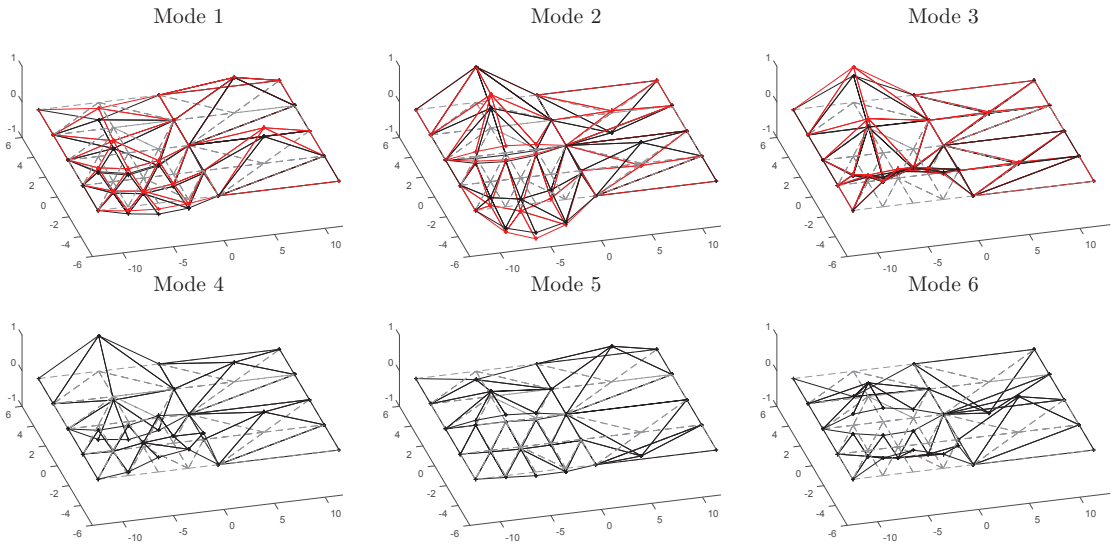

Figure 4: Experimental (black solid line) vs. numerical with coupled spans and decks (red solid line) first six identified mode shapes. Undeformed shape (dashed grey line).

The element size is chosen to adequately reproduce the wavelengths of the modes with frequencies up to 30 Hz as per EC [1].

- For each slab, different mass density elements are defined in order to concentrate the weight of the handrails, sidewalks and concrete slab selfweigth in its corresponding position over the plattform area.

- The vertical interaction effect induced by the ballast layer on the two separated decks at each span is simulated in a first approach by discrete longitudinal springs with vertical constant stiffness K_{wL}, that are distributed along the free longitudinal border of the adjacent slabs.

- A three layer two-dimensional (2D) discrete track model as the one proposed by Zhai [9] is implemented to include the distributive effect of the train axle loads exerted by each rail, as well as the vertical coupling effect among the bridge spans. In this model, the rails are simulated as Bernoulli-Euler beam elements with 6 dof per node, and the damping and stiffness of rail pads, ballast and subgrade are included at the sleepers positions as seen in Fig.5.

- The longitudinal girders are included in the model as beam elements with 6 dof per node. These nodes are connected to those of the upper plate right above them by means of rigid kinematic constraints. The distance between the plate and the beams nodes equals the real separation between the slab neutral plane and the center of mass of the girders.

- The laminated rubber bearings of the bridge are introduced in discrete positions by means of longitudinal springs with vertical constant stiffness $K_{v,dyn}$.

- A point load model is adopted for the railway excitation, therefore neglecting vehicle-structure interaction effects according to Eurocode 1 [14]. In this regard, some previous works also reveal that the incorporation of interaction effects in the design of new high-speed simply supported bridges or in the assessment of existing ones is not well justified,

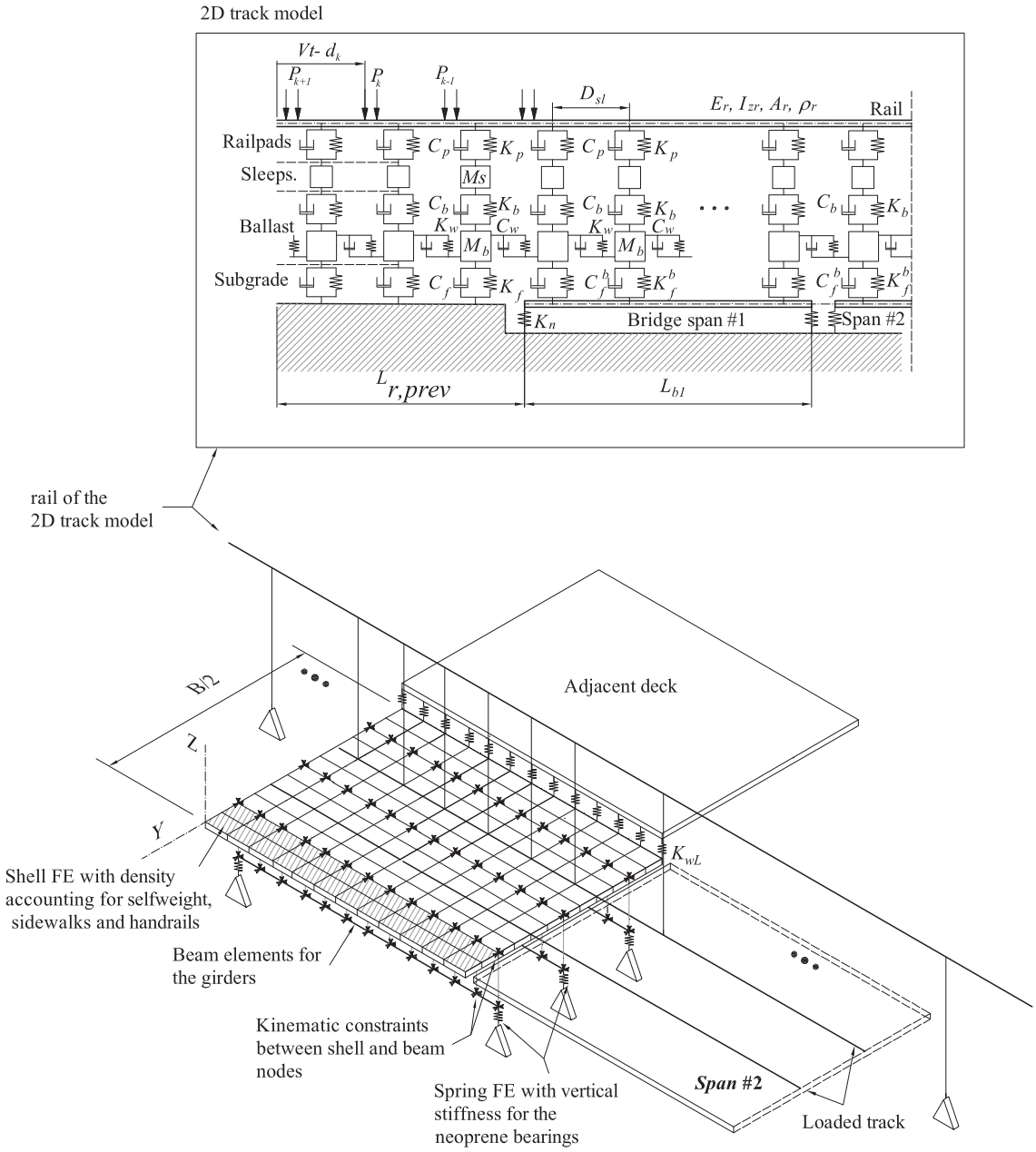

Figure 5: FE model.

since they can be very low due to the marked variability of the vehicle suspension characteristics, the mass and frequency ratios between the bridge and the vehicles suspension systems parameters and coaches masses [15, 16, 17, 18, 19]. Therefore, the use of a point load model in this study seems a reasonable approach to provide essential information concerning the track coupling effect.

- The dynamic equations of motion are transformed into modal space and numerically integrated by the Newmark-Linear Acceleration algorithm. Therefore, in a first approach the additional damping introduced by the track components is neglected for the calculation of the deck acceleration response under train induced vibrations and the modal damping ratios identified in the experimental campaign are used instead. This is in accordance

with the conclusions derived from a sensitivity analysis performed by the authors in a previous work, showing a negligible influence of this parameter on the vertical acceleration response of the deck [8]. The time-step is defined as 1/25 times the smallest period used in the analysis (mode contributions up to 30 Hz as per European Standards [1]).This value avoids period elongation errors and enables to capture properly the oscillations of the modal loading functions and the peak responses obtained by the summation of all modal contributions.

3.2 Description of the analysis procedure

The effect of the continuity of the ballasted track on the dynamic behaviour of railway bridges formed by SS decks is evaluated in this work by comparison with the test results of Old Guadiana bridge.

In a first step, the numerical model described in section 3.1 is calibrated in order to reproduce the static tests performed on the structure right before its opening and also the dynamic results obtained in the experimental campaign performed by the authors in May 2019. The calibration of the model is made considering three different approaches, which are:

(i) Single-deck single-span (SDSS): the 2D discrete track model is not included. Therefore, the four structurally independent decks that form Guadiana Old bridge are not coupled, and the axle railway loads move along the discretised slab following the loaded track position. In order to consider the weight of the track components (rails, ballast, sleepers), the density of the FE located at the position of the track plattform is modified accordingly. Since the track is not included in the model, when a load enters or exits the bridge a transient phenomenon takes place which leads to unrealistic high-frequency modal contributions of the plate. This numerical problem is solved in the model including the distributive effect of rails, sleepers and ballast during the application process of the wheel loads when they are close to the abutments. To this end, the value of each axle load is modulated throughout a load-print distributive function based on the Zimmerman-Timoshenko solution for an infinite beam on Winkler foundation, as described in [20].

(ii) Single-deck double-span (SDDS): in this approach the 2D track model is included but the effect of the transverse continuity of the ballast is neglected by setting the vertical constant stiffness between adjacent decks, K_{wL}, to zero.

(iii) Double-deck double-span (DDDS): the model shown in Fig.5 is fully implemented to simulate the dynamic behaviour of old Guadiana bridge.

For the calibration of the FE model assuming the previously mentioned approaches, a set of nominal or reference values for the track parameters K_p, C_p, K_b, C_b, K_f , C_f , K_{bf}, C_{bf} and M_s, is defined on the basis of the literature review. These parameters remain constant while the main track parameters affecting deck coupling, which are K_w and K_{wL}, and other bridge parameters, such as the deck and girders elastic modulus, vertical stiffness of the rubber bearings $K_{v,dyn}$, thickness of the ballast layer (which affects directly to the ballast mass) are varied in a realistic range until a satisfactory correspondence between numerical and experimental results in terms of natural frequencies and mode shapes is achieved. Table 1 shows the calibrated properties of the three different approaches considered in the numerical model of Guadiana bridge. As regards the ballast shear stiffness between adjacent decks, K_{wL}, it is provided per unit of span length. As per the subgrade stiffness K_f^b and damping coefficients inside the bridge C_f^b, the

values $100K_f$ and 0 Ns/m have been assigned as it is assumed that the ballast layer rests directly on the concrete slab inside the bridge. All these values will be the ones used in Section 4.

		SDSS	SDDS	DDDS
Slabs	ρ [kg/m^3]		2500	
	E_{slab} [MPa]		25200	
Girders	I_h [m^4]		0.011	
	J[m^4]		0.00505	
	ρ [kg/m^3]		2500	
	E_{girder} [MPa]		28800	
Track parameters	K_p [N/m]	–	1E8	1E8
	C_p [Ns/m]	–	7.5E4	7.5E4
	M_s [kg]		300	
	K_b [N/m]	–	1.933E8	1.933E8
	C_b [Ns/m]	–	5.88E4	5.88E4
	M_b [kg]		672.2	
	K_f [N/m]	–	7.9387E7	7.9387E7
	C_f [Ns/m]	–	7.5E4	7.5E4
	K_w [N/m]	–	7.84E5	7.84E5
	C_w [N/m]	–	8E4	8E4
	k_{wL} [N/m^2]	–	–	4.07E6
Supports	$K_{v,dyn}$ [N/m]		1.95E8	

Table 1: Calibrated properties of the FE model.

Secondly, a sensitivity analysis is performed to evaluate the influence of the ballast shear stiffness parameters for longitudinal and transverse coupling between the bridge decks (K_w and K_{wL}), on the natural frequencies and mode shapes of the structure. And finally, the vertical acceleration response of the deck predicted with the calibrated numerical model assuming the three different approaches is compared with the experimental measurements at several sensor locations under the passage of real trains at resonant and non resonant speeds.

4 RESULTS

4.1 Ballasted track coupling effect on the natural frequencies and mode shapes

Table 2 (bottom) shows the numerical natural frequencies and the Modal Assurance Criterion (MAC) values [21] of the paired mode shapes obtained with the calibrated FE models. In this table, only the numerical modes that exhibit MAC values higher than 0.7 with a frequency difference with respect to the experimental value below 10% are shown. For a better comparison between the numerical models, the MAC values provided in the table have been calculated with the measurements of the same number of sensors (sensors A1 to A10 of Fig.3).

As can be seen the total number of paired modes that meet this criterion is scarce. However, it should be mentioned that in the remaining identified modes above the third one not all of them could be fully described due to the limited number and spatial distribution of sensors installed. Therefore, a satisfactory correspondence of these mode shapes with the experimental measurements was not expected.

Among the three different modeling approaches used in this work, the better correspondence with the experimental values is achieved with the model that considers the coupling effect be-

Mode		1	2	3	4	5	6
f_{exp} [Hz]		9.82	11.05	12.86	16.53	17.93	21.05
ς_{exp} [Hz]		2.3	0.9	1.0	0.3	0.1	1.0
Numerical approach							
SDSS	f_{num} [Hz]	9.98	–	12.21	–	–	–
	MAC [-]	0.98	–	0.99	–	–	–
SDDS	f_{num} [Hz]	9.97	–	12.75	–	–	–
	MAC [-]	0.98	–	0.99	–	–	–
DDDS	f_{num} [Hz]	9.97	11.05	12.75	–	–	–
	MAC [-]	0.98	0.97	0.99	–	–	–

Table 2: (top) First six experimental frequencies, their corresponding modal damping ratios and (bottom) frequencies and AutoMAC of the paired numerical modes.

tween both the bridge spans and the adjacent decks induced by the continuity of the ballasted track. The prediction of the fundamental mode is less affected by the coupling and the restraining effect on the bridges' boundary conditions exerted by the ballasted track, since the three approaches reach a satisfactory correspondence with the measurements. In the third mode, the consideration of the span coupling with the introduction of the track in the numerical model improves the prediction of the natural frequency, while the MAC value remains unaffected when compared to the other numerical approaches. And finally, the second mode corresponding to a first torsion mode of the double track deck in each span, is only predicted when the coupling caused by the ballast layer that is shared between the two adjacent decks is considered.

Fig. 4 shows, in solid red trace, the paired numerical modes predicted with the DDDS FE model. When the MAC values are calculated considering all the measurement points (A1 to A18) the values change to 0.95, 0.74 and 0.99 for the first three modes, respectively. The MAC of the second mode worsens significantly, and it is caused by the measurements of the sensors A12 and A13 located in the other span.

For a better understanding of the effect of the ballasted track coupling parameters, K_w and K_{wL}, on the natural frequencies and MAC values of the first three experimental modes, a sensitivity analysis has been performed considering variations of each of the cited parameters while the others remain constant according to the values provided in table 1. The proposed variations are: [1/100 1/50 1/10 1/5 1/2 1 10 50 100 10000]$\cdot K_w$ and [1/100 1/50 1/10 1/5 1/2 1 10 50 100 100]$\cdot K_{wL}$.

The results in terms of frequency difference, calculated as $(f_{num} - f_{exp})/f_{exp} \times 100$ and MAC values are shown in Fig.6. The results corresponding to variations of the coupling between spans K_w are shown in black trace, while the coupling between adjacent spans K_{wL} is shown in red trace. As can be seen, there exists an optimum value that ensures the best fitting with the experimental measurements .

4.2 Bridge response under railway traffic

During the experimental campaign performed by the authors in In May 2019 a number of trains crossed the bridge at different speeds. The forced bridge vibrations were recorded showing that the maximum acceleration levels did not exceed the Serviceability Limit State for traffic safety in ballasted tracks, limited to 3.5 m/s^2 as per European Standards [1]. The circulation of one of these trains, the medium distance Renfe Altaria Talgo VI train, is included in this section. It is a regular train with a characteristic distance between axles of the passenger cars of 13.14 m.

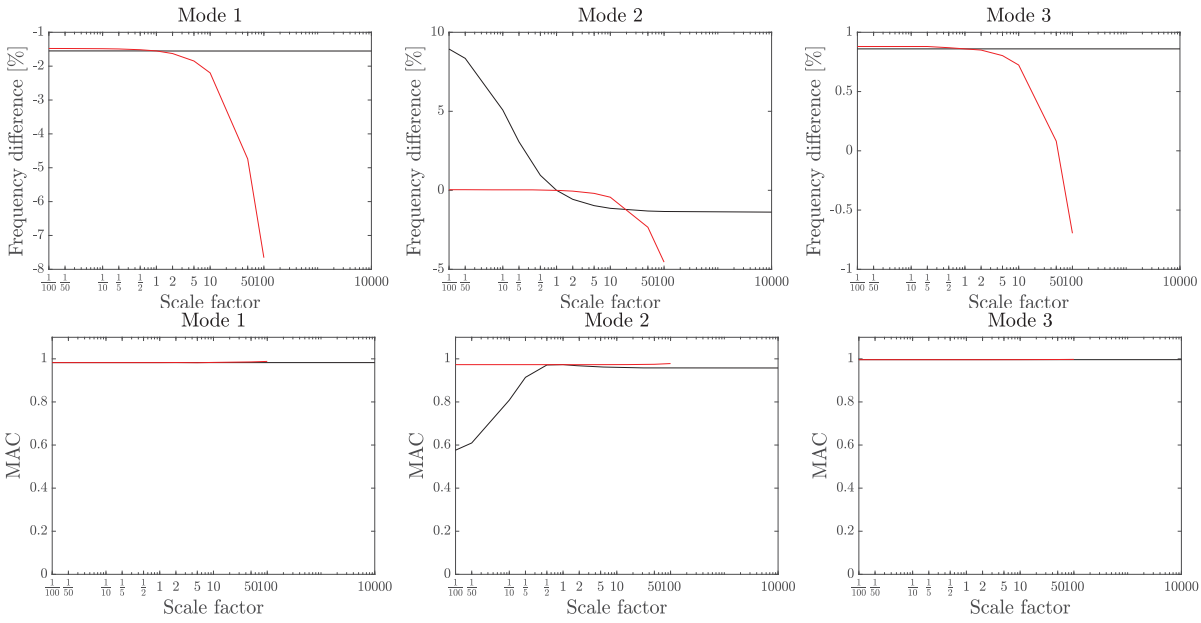

Figure 6: Sensitivity analysis of the influence of K_w (black) and K_{wL} (red trace) on the natural frequencies and MAC values

Figure 7 and Table 3 show the axle scheme and loads. More information about the train can be found in [22]. It travels along track 2 in the direction South-North (Manzanares-Alcázar de San Juan). Its circulation speed was identified from the frequency associated to the bogie distance leading to approximately 155 km/h, which is very close to the theoretical speed associated to a third resonance of the fundamental mode (159 km/h, approximately).

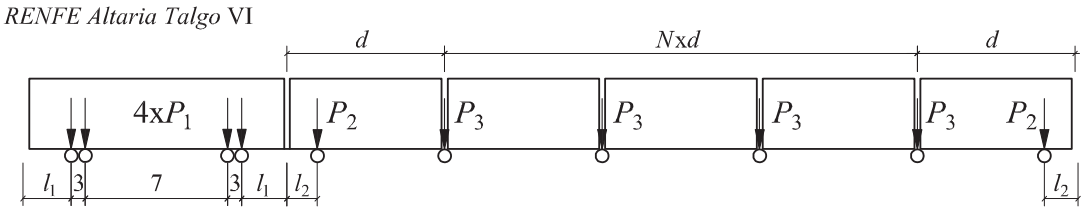

Figure 7: RENFE Altaria Talgo VI axle scheme

Train	N	d [m]	l_1 [m]	l_1 [m]	P_1 [kN]	P_2 [kN]	P_3 [kN]
Altaria	7	13.14	3.44	3.3	225	70	140

Table 3: RENFE Altaria Talgo VI features.

The response of the bridge was calculated using the numerical model described in section 3.1 with the properties included in table 1 by Mode Superposition, including modal contributions up to 30 Hz as per European Standards [1]. A track length of 20 m is included before and after the two-span bridge, a sensitivity analysis of this length was previously performed to guarantee the convergence of the dynamic results.

In a first approach the additional damping introduced by the track elements is therefore neglected, which is also in accordance with previous works [5, 11, 12]. The modal damping

obtained in the experimental campaign was assigned to the paired numerical modes, for the other modes of frequencies up to 30 Hz a value of 1.56% is assumed (Eurocode value [1]).

Fig.8 shows the vertical acceleration response under the passage of the train at different points of the deck, in particular points 2, 5 and 18. The sensors 2 and 5 are located under the loaded decks and the other one under the unloaded deck. The response is plotted in the time domain (first row of the figure) and frequency domain (last row of the figure). In all the plots the experimental signal, plotted in solid black trace, is filtered applying a two third-order Chebyshev filter with high-pass and low-pass frequencies of 1 Hz and 30 Hz. The numerical predictions are plotted with different colours: red line is used for the SDSS model, blue for the SDDS model and green for the DDDS model. Concerning numerical predictions, results at point 18 are only available in the DDDS model, since decks 1 are 2 are uncoupled in the remaining ones and therefore, the acceleration results are zero in the unloaded deck.

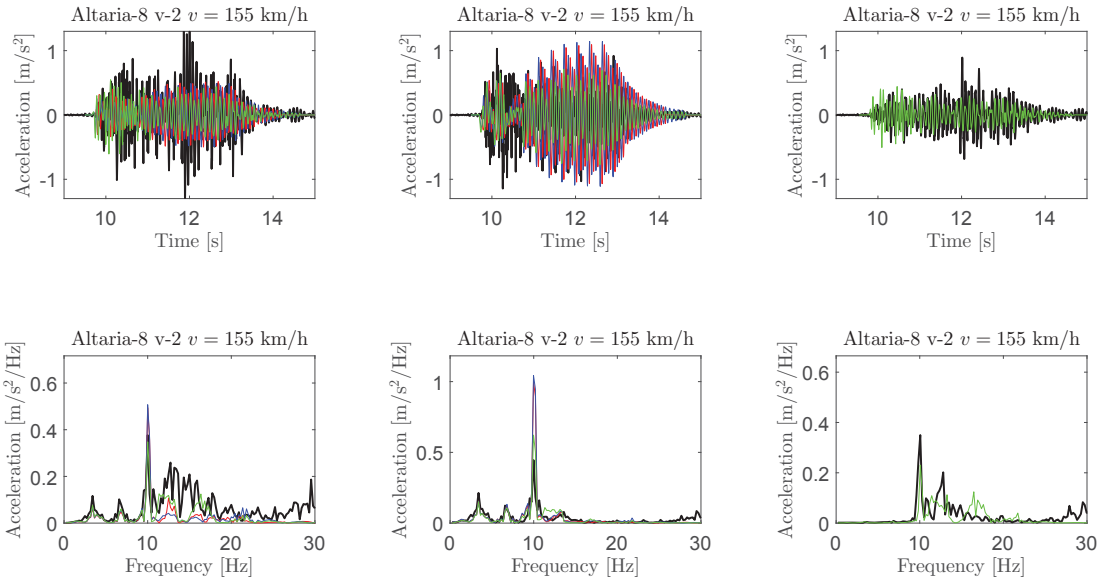

Figure 8: Time history (top) and frequency content (bottom) of the acceleration at point 2 (left), point 5 (center) and point 18 (right) induced by Renfe Altaria: experimental (black line), SDSS model (red line), SDDS model (blue line) and DDDS model (green line)

As can be seen from the frequency domain plots the vertical acceleration response of the bridge is caused by several mode contributions apart from the longitudinal bending one. However, the peak amplitude associated to the fundamental mode predominates when compared to the other frequency contributions, as expected in a resonance situation. This is especially clear at point 5, and is in accordance with the sensor location (at mid-span under the loaded track). The response also presents peaks at low frequencies (in the vicinity of 3 Hz and 6 Hz) associated to the excitation and corresponding to the axle passing frequency (i.e. ratio of train speed v to axle distances v/d_{axle}, respectively, and corresponding multiples). For sensor 18, located in the unloaded deck, the response is still relevant, showing an important coupling between adjacent decks of the same span through the ballast. This effect was also detected under ambient vibration in the mode shapes and seems to be also important under forced vibrations, despite the higher level of vertical vibrations in this case. This coupling effect could be also associated to the shared foundation between both decks.

Regarding the comparison between the response predicted by the three numerical approaches, it is noticeable that the model that considers both the longitudinal and transverse coupling between decks (DDDS model) predicts the frequency contributions in the range [10-15] Hz with higher accuracy, but the three of them overestimate the contribution of the fundamental mode in the response. The authors consider that the additional damping induced by the track elements, that is neglected in this preliminary study and also the effect of the train-bridge interaction, could be responsible of the differences and needs to be investigated in a future work. At frequencies above 15 Hz the predictions worsen, which is in accordance with the model updating, since only the first three experimental modes were successfully identified in the numerical models. In the time domain response, the models tend to underestimate the amplitude of the vibration at points 2 and 18, where the contribution of modes above 15 Hz play a more significant role than at point 5 due to the sensor location. The damping associated to the high frequency modes in the numerical calculations and also the unsuccessful mode pairing with the ones predicted by the numerical models, can be an issue and require further research.

5 CONCLUSIONS

In this work a preliminary evaluation of the effect of the ballasted track continuity on the dynamic response of railway bridges formed by simply-supported spans with structurally independent adjacent decks at each span, is addressed. First, a preliminary FE model that considers the track and therefore, the coupling between adjacent decks and spans has been implemented. The numerical results are compared with the experimental measurements performed on a real bridge formed by several independent decks, and the following conclusions can be extracted:

- The coupling effect exerted by the ballasted track between consecutive spans and adjacent decks that form the same span in railway bridges is clear. In the particular bridge of study, the coupling effect between adjacent decks of the same span predominates over the coupling between different spans. This issue can be detected under both ambient and train-induced vibrations despite the different level of vibration amplitude induced by these excitations. In this regard, the shared foundations of the two decks may also have an important role on this coupling.

- The transmission of vibrations from the loaded deck to the unloaded deck is relevant. The numerical predictions reveal that a more accurate model updating can be achieved if both coupling effects are considered. In terms of natural frequencies and mode shapes, the sole introduction of the coupling between SS spans in the numerical model does not improve the predictions when compared to the ones obtained when the track is neglected for this particular bridge.

- The three implemented numerical approaches overestimate the contribution of the fundamental mode in the response, thus the prediction is more accurate when both couplings effects are considered. The additional damping induced by the track elements, that is neglected in this preliminary study and also the effect of the train-bridge interaction require further research. Also the shared foundation between decks belonging to the same span can have an influence on the deck coupling that is not well known up to date.

- The three implemented numerical approaches overestimate the contribution of the fundamental mode in the response, thus the prediction is more accurate when both couplings

effects are considered. The additional damping induced by the track elements, that is neglected in this preliminary study and also the effect of the train-bridge interaction, could be responsible of the differences and require further research. Also the shared foundation between decks belonging to the same span can have an influence on the deck coupling that is not well known up to date.

6 ACKNOWLEDGEMENTS

The authors would like to acknowledge the financial support provided by (i) Generalitat Valenciana under AICO/2019/175 research project, and (ii) Universitat Jaume I 2018 Research Program under UJI-A2018-06 research project.

REFERENCES

[1] CEN. Eurocode: Basis of structural design. Annex A2: Application for bridges, *Final version, European Committee for Standardization*, Brussels, 2005.

[2] ERRI-D-214/RP9,Rail bridges for speeds>200km/h. Final report. Part A. Synthesis of the results of D214 research, *European Rail Research Institute*, 1999.

[3] Frýba L., Dynamic behaviour of bridges due to high-speed trains, *In: Workshop bridges for high-speed railways, Porto*, 137–58, 2004.

[4] Rigueiro C., Rebelo C., Simoes da Silva, L., Influence of ballast models in the dynamic response of railway viaducts, *Journal of Sound and Vibration*,**329**, 3030-3040, 2010.

[5] Liu K., Lombaert G., De Roeck G., Dynamic analysis of multispan viaducts with weak coupling between adjacent spans, *Journal of Bridge Engineering-ASCE*, **19(1)**, 83-90, 2014.

[6] Rebelo, C., Simoes da Silva, L., Rigueiro, C., Pircher, M., Dynamic behaviour of twin single-span ballasted railway viaducts, *Field measurements and modal identification*, *Engineering Structures*, **30**, 2460-2469, 2008.

[7] Rauert T., Bigelow H., Hoffmeister B., Feldmann M., On the prediction of the interaction effect caused by continuous ballast on filler beam railway bridges by experimentally supported numerical studies, *Engineering Structures*, **32**, 3981-3988, 2010.

[8] M.D. Martínez-Rodrigo, A. Romero, E. Moliner, J. Chordá, P. Galvín, Influence of ballast track on vertical response of multispan simply-supported bridges under railway traffic, *ICCES 2020 : The 26th International Conference on Computational & Experimental Engineering and Sciences*, 2020.

[9] Zhai W., Wang K., Lin J., Modelling and experiment of railway ballast vibrations, *Journal of Sound and Vibration*, **270**, 673–683, 2004.

[10] Pablo Antolín and Nan Zhang and José M. Goicolea and He Xia and Miguel A. Astiz and Javier Oliva,"Consideration of nonlinear wheel–rail contact forces for dynamic vehicle–bridge interaction in high-speed railways, *Journal of Sound and Vibration*, **332(5)**, 1231-1251, 2013.

[11] C. Boniflácio, D. Ribeiro, R. Calçada and R. Delgado, Dynamic Behaviour of a Short Span Filler-Beam Railway Bridge under High Speed Traffic, *Civil-Comp Press. Proceedings of the Second International Conference on Railway Technology: Research, Development and Maintenance*, 2014.

[12] G. chellini, L. Nardini, W. Salvatore, Dynamical identification and modelling of steel–concrete composite high-speed railway bridges, *Structure and Infrastructure Engineering*, **7(11)**, 823-841, 2011.

[13] Reynders E., System Identification Methods for (Operational) Modal Analysis: Review and Comparison, *Archives of Computational Methods in Engineering*, **28**, 51–124, 2012.

[14] CEN. EN 1991-2. Eurocode 1: Actions on Structures - Part 2: Traffic loads on bridges, , *European Committee for Standardization*, Brussels, 2002.

[15] K. Liu and G. De Roeck and G. Lombaert, The effect of dynamic train–bridge interaction on the bridge response during a train passage, textitJournal of Sound and Vibration, **325**, 240–251, 2009.

[16] Y. Yang, M. Cheng, K. Chang, Frequency variations in vehicle-bridge interaction systems, textit International Journal of Structural Stability and Dynamics, **13(2)**, 1350019, 2013.

[17] A. Doménech, P. Museros and M.D. Martínez-Rodrigo, Influence of the vehicle model on the prediction of the maximum bending response of simply-supported bridges under high-speed railway traffic, textitEngineering Structures, **72**, 123–139, 2014.

[18] T. Arvidsson, R. Karoumi, C. Pacoste, Statistical screening of modelling alternatives in train-bridge interaction systems, textitEngineering Structures, **59**, 693–701, 2014.

[19] J.D. Yau, M.D. Martínez-Rodrigo, A. Doménech, An equivalent additional damping approach to assess vehicle-bridge interaction for train-induced vibration of short-span railway bridges, textitEngineering Structures, **188**, 469–479, 2019.

[20] Martínez-Rodrigo M.D., Lavado J., Museros P., Dynamic performance of existing high-speed railway bridges under resonant conditions retrofitted with fluid viscous dampers, *Engineering Structures*, **32(3)**, 808–828, 2010.

[21] Allemang R.J., Brown D.L., Correlation coefficient for modal vector analysis, *In: Proceedings of international modal analysis I*, 110–6, 1982.

[22] Renfe, Our trains, https://www.renfe.com/EN/viajeros/nuestros_trenes/index.html.

EURODYN 2020
XI International Conference on Structural Dynamics
M. Papadrakakis, M. Fragiadakis, C. Papadimitriou (eds.)
Athens, Greece, 23–26 November 2020

DISPLACEMENT BASED ANALYSIS AND DESIGN OF ROCKING BRIDGES

Michalis F. Vassiliou[1], **Natalia Reggiani Manzo**[2]

[1] Assistant Professor, Chair of Seismic Design and Analysis, IBK, ETH Zürich
Stefano-Franscini-Platz 5, CH-8093 Zürich
e-mail: vassiliou@ibk.baug.ethz.ch

[2] Ph.D. Candidate, Chair of Seismic Design and Analysis, IBK, ETH Zürich
Stefano-Franscini-Platz 5, CH-8093 Zürich
reggianimanzo@ibk.baug.ethz.ch

Keywords: rocking, uplifting structures, dimensional analysis, dimensionality reduction, displacement based design

Abstract. *The response of a rigid rocking block is traditionally described by its tilt angle. This is a correct description, but this paper suggests that describing rocking via displacements is more meaningful, because it uncovers that two geometrically similar blocks of different size will experience the same top displacement, provided that they are not close to overturn. The above is illustrated for both analytical pulse excitations and for recorded ground motions. Thus the displacement demand of a ground motion on a rocking block is only a function of its slenderness; not of its size. This reduces the dimensionality of the problem and allows for the construction of size-independent rocking demand spectra.*

1 INTRODUCTION

The systematic study of the rocking oscillator started with Housner's seminal paper in 1963 [1]. Motivated by the surprising stability that tall slender "golf-ball-on-a-tee" structures presented in the 1960 Chilean earthquake, he showed that (a) out of 2 geometrically similar planar rigid objects, the larger one is harder to overturn dynamically, and (b) the overturning potential of a ground motion increases with its dominant period.

The interest on the rocking oscillator [2-6] sources from its ability to describe systems that cannot be described adequately by the classical elastic oscillator [7]. Indeed, the rocking oscillator can be used to understand the behavior of masonry structures [8-14], the seismic behavior of non-anchored equipment [15-22], as well as to explain the stability of ancient Greco-Roman and Chinese temples that have been standing for more than 2,500 years in earthquake prone regions [23-27]. Rocking motion has also inspired researchers to use inerters as seismic protection devices [28-29]. What is not widely known in the western world, is that rocking has been used since more than 40 years as a seismic isolation method in the USSR (and now in former USSR countries) [30, 31]. The Soviet system comprises an intentionally designed soft rocking story. The uplift of the rocking columns works as a mechanical fuse and limits the forces transmitted to the superstructure.

Rocking walls have been suggested as a resilient design approach for buildings [32, 33 and references therein].

Moreover, a 33-m-tall chimney at the Christchurch airport has been designed to uplift [34], and three 30 to 38-m-tall chimneys in Piraeus, Greece, have been retrofitted by allowing them to uplift in case of an earthquake.

Rocking systems are perfectly compatible with Accelerated Bridge Construction as they comprise prefabricated elements with dry connections. In fact, restrained rocking systems [35-42] have already found their way to practice, with the Wigram-Magdala restrained rocking bridge in New Zealand [43] being the first restrained rocking bridge constructed.

However, several researchers have suggested that the restraining tendon in rocking bridges is not only obsolete, but might unnecessarily decrease the design forces of both the superstructure and the foundation, maybe requiring a pile foundation when it could have been avoided [44-60]. Makris and Vassiliou [61] and Vassiliou and Makris [62] have suggested that as the size of a rocking bridge increases, the restraining system can become obsolete and merely increases the design forces of both the superstructure and the foundation.

A main drawback of unrestrained rocking bridges stems from their response being absolutely uncorrelated to any elastic system. Therefore, the elastic-based research results are not applicable: e.g. intensity measures, response spectra, motion-to-motion variability, design ground motions need to be re-determined. To this end, the rocking oscillator should be described with the minimum parameters needed.

This paper suggests that the current state of the art of using the tilt angle θ as the DOF of a rocking system is, of course, correct, but it is not the optimal. Using the top displacement of the oscillator, u, reduces the dimensionality of the problem. Then, the displacement *demand* on a rocking block becomes only slightly dependent on its size and is a function only of its slenderness [63].

2 ROTATION BASED DIMENSIONAL ANALYSIS OF THE ROCKING OSCILLATOR

The equation of in-plane motion for a rigid rectangular rocking column (Figure 1) with slenderness α and a semi-diagonal of length R (Figure 1) is:

$$\ddot{\theta} = -p^2 \cdot \left(\sin\left(\pm\alpha - \theta\right) + \frac{\ddot{u}_g}{g} \cos\left(\pm\alpha - \theta\right) \right) \tag{1}$$

where

$$p = \sqrt{(3g)/(4R)} \tag{2}$$

is the frequency parameter of the rocking column. The upper sign in front of α corresponds to a positive, and the lower to a negative rocking angle θ with respect to the defined coordinate system (Figure 1).

It is assumed that energy is only dissipated during impact. Housner [1] assumed that (a) the impact is instantaneous and (b) that the impact forces are concentrated on the impacting corner. Under these assumptions the ratio of post to pre impact rotational velocities is

$$r = \frac{\dot{\theta}_{after}}{\dot{\theta}_{before}} = 1 - \frac{3}{2}\sin^2\alpha \tag{3}$$

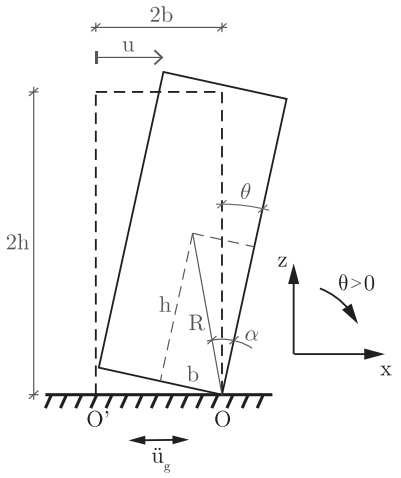

Figure 1: Geometric characteristics of the rigid rocking block.

Researchers (including the senior author of this paper) have critically evaluated the Housner model - especially its damping assumptions [64-68]. Indeed, while assuming the impact to be instantaneous seems a reasonable assumption, there is no evident reason to assume that the impact forces act on the impacting corner. Given the large sensitivity of the time history response of the rocking oscillator to all the parameters that define it, Housner's model might seem simplistic. However, experimental testing shows that even though it cannot predict the response to an individual ground motion, it can predict the statistics of the response to a set of ground motions [69]. Therefore, we consider it adequate within the scope of earthquake engineering [70].

By inspecting Equation (1) and (2) one can conclude that the rotational response of a rocking block to a ground motion is a function of

$$\theta_{\max} = f_1\left(R, \alpha, g, \ddot{u}_g(t)\right) \tag{4}$$

As the gravity acceleration, g, is constant, the rotational response to a given ground motion is a function of 2 parameters α and R, similarly to the elastic oscillator, in which the response is a function of the eigenperiod, T, and damping ratio ζ. Therefore, by keeping one parameter constant (R or α) one can construct rotational spectra for rocking structures. However, unlike

the elastic oscillator, where, for usual structures, one parameter (T) is more influential than the other (ζ), in the case of rocking structures, both R and α strongly influence the rotational response.

Since ground motions containing distinguishable acceleration and/or velocity pulses are particularly destructive [71 and references therein], Zhang and Makris [72] have studied the response of a planar rocking block to acceleration pulses given by analytical expressions. A pulse of a given waveform can be described by two parameters. Zhang and Makris [69] chose the acceleration amplitude a_p and the dominant cyclic frequency ω_p. Then, the response will be a function of

$$\theta_{\max} = f_2\left(R, \alpha, g, a_p, \omega_p\right) \tag{5}$$

Equation (5) involves 6 quantities with 2 reference dimensions (Time and Length). Therefore, according to Vaschy - Buckingham's Π-Theorem of Dimensional Analysis ([73, 74]), the number of dimensionless parameters describing the problem is 6 – 2 = 4. There is not a unique solution for choosing these four parameters. Zhang and Makris [72] suggested describing the problem as

$$\theta_{\max} = \varphi_1\left(\alpha, \frac{\omega_p}{p}, \frac{a_p}{g\tan\alpha}\right) \tag{6}$$

ω_p / p is often called size-frequency parameter and depends on the frequency of the excitation and on the size of the block. $a_p/(g\tan\alpha)$ is usually called non-dimensional acceleration but it can also be perceived as a non-dimensional strength parameter, since $mgR\sin\alpha$ is the moment that withstands uplift ("strength") and is $ma_pR\cos\alpha$ the overturning moment.

Therefore, dimensional analysis reduces the dimensionality of the problem from 6 to 4. Hence, by keeping the slenderness parameter α constant, one can produce contour plots of the maximum tilt angle θ as a function of ω_p / p and $a_p/(g\tan\alpha)$, the so called "rocking spectra". It is worth mentioning that Dimitrakopoulos and DeJong [75] have shown that for small values of α one can drop it as an independent parameter from Equation (6) as long as the coefficient of restitution, r, is treated as an extra independent parameter – however in this section r is not treated independently.

Figure 2 shows the rocking spectra of symmetric and antisymmetric Ricker wavelets. Ricker wavelets are defined as the 2nd and 3rd derivative of the Gaussian:

$$\ddot{u}_g = a_p\left(1 - \frac{2\pi^2t^2}{T_p^2}\right)e^{-\frac{1}{2}\frac{2\pi^2t^2}{T_p^2}} \tag{7}$$

$$\ddot{u}_g = \frac{a_p}{\beta_r}\left(\frac{4\pi^2t^2}{3T_p^2} - 3\right)\frac{2\pi t}{\sqrt{3}T_p}e^{-\frac{1}{2}\frac{4\pi^2t^2}{3T_p^2}} \tag{8}$$

where

$$T_p = \frac{2\pi}{\omega_p} \tag{9}$$

and β_r= 1.3801 to enforce that the function maximum is equal to a_p.

The spectra confirm the remarkable observation that larger structures are harder to overturn dynamically and that higher frequency pulses have a lower overturning potential. Interestingly, they show a heavy dependence of the response on both ω_p/p and $a_p/g\tan\alpha$.

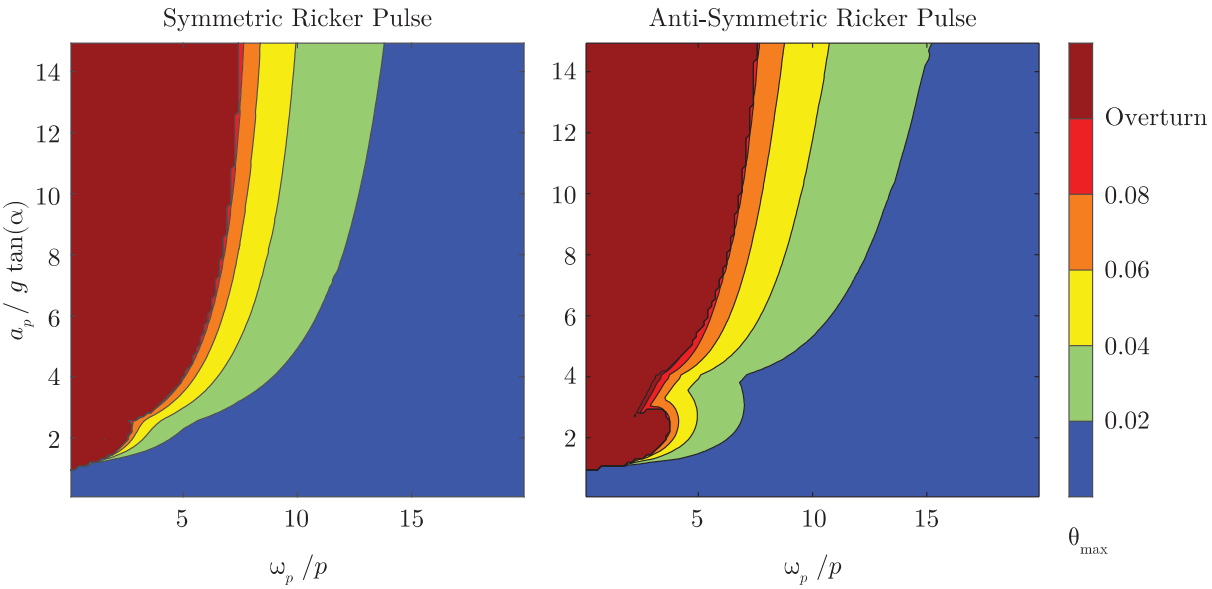

Figure 2: Non-dimensional rocking spectra based on rotations. α = 0.1

3 DISPLACEMENT BASED DIMENSIONAL ANALYSIS OF A ROCKING OSCILLATOR EXCITED BY ANALYTICAL PULSES

3.1 Analysis based on the frequency parameter of the block *p*

The dimensional analysis of the previous section is one of the many correct solutions to describe the problem. It is based on rotations. This section, however, suggests that there is another, displacement based basis of describing the problem, which is also mathematically correct and more convenient. The convenience does not lie only on the fact that earthquake engineers are more used to displacements than rotations: A displacement based analysis further reduces the dimensionality of the problem allowing the construction of 2D rocking spectra.

Indeed, the rotation based analysis of the problem is based on the "recipe for similarity analysis" described in Chapter 5 of the well-known Dimensional Analysis textbook of Barenblatt [76]: "*If the problem has an explicit mathematical formulation, the independent variables in the problem and the constant parameters that appear in the equations, boundary conditions and initial conditions, etc., are adopted as the governing parameters.*" As this section shows, choosing the parameters that appear in the analytical equation might not be the most convenient way of describing this particular problem.

The top displacement of the rocking block can be obtained by a one-to-one mapping on the rotations:

$$u = 2R\sin\left(\pm\alpha\right) - 2R\sin\left(\pm\alpha - \theta\right) \tag{10}$$

The upper sign in front of α corresponds to a positive, and the lower sign to a negative tilt angle θ with respect to the defined coordinate system. If we use the top displacement as the single DOF of the problem, then the maximum response can be described as:

$$u_{\max} = f_3\left(R, \alpha, g, a_p, \omega_p\right) \tag{11}$$

To numerically compute the response of the block, we will resort to Equation (1), which is given in terms of rotation θ. Then, using Equation (10) we compute the displacement response.

Applying Buckingham's Π-theorem on Equation (11), one possible non-dimensionalization is

$$\frac{u_{\max}\omega_p^{\,2}}{a_p} = \varphi_2\left(\alpha, \frac{\omega_p}{p}, \frac{a_p}{g\tan\alpha}\right) \tag{12}$$

Figure 3 shows the contour plots of $\frac{u_{\max}\omega_p^{\,2}}{a_p}$ as a function of ω_p/p and $a_p/(g\tan\alpha)$ for a given α = 0.1. The remarkable observation is that within the non-overturning region the non-dimensional displacement depends heavily (and strongly non-linear) on the non-dimensional strength parameter $a_p/(g\tan\alpha)$ but only loosely on the size-frequency parameter ω_p/p. When the block is not close to overturning, the influence of ω_p/p is practically negligible.

Figure 4 plots $\frac{u_{\max}\omega_p^{\,2}}{a_p}$ as a function of $a_p/(g\tan\alpha)$ for different values of ω_p/p (and a constant slenderness α = 0.1). For reasons of figure clarity, only non-overturning values of $\frac{u_{\max}\omega_p^{\,2}}{a_p}$ are plot, i.e. not plotting $\frac{u_{\max}\omega_p^{\,2}}{a_p}$ means that the block has overturned. Figure 5 plots $\frac{u_{\max}\omega_p^{\,2}}{a_p}$ as a function of ω_p/p for different values of $a_p/(g\tan\alpha)$ (and α = 0.1). Again, it is observed that, as long as the system is away from overturning, the dominant factor that influences $\frac{u_{\max}\omega_p^{\,2}}{a_p}$ is $a_p/(g\tan\alpha)$; not ω_p/p. In fact for small values of non-dimensional acceleration $a_p/(g\tan\alpha)$, the response for all values of size-frequency parameter ω_p/p is practically the same. The response starts to deviate only when the system is close to overturning – or has overturned.

In other words, a small and a large block, geometrically similar to each other and excited by analytical pulses, will have roughly equal top displacement, provided that the displacement is not enough to bring them close to overturn. A given pulse will induce the same *displacement demand*. The larger block is more stable simply because its displacement capacity (i.e. the displacement needed to cause overturn, i.e. its width) is larger.

Therefore, using a displacement basis to describe the problem further decreases the number of parameters needed to define it. Practically, the displacement demand on a rocking oscillator excited by a pulse is only a function of its non-dimensional strength parameter $a_p/(g\tan\alpha)$; not of its size.

The strongly nonlinear nature of rocking motion is also evident in Figures 4 and 5. $\frac{u_{\max}\omega_p^{\,2}}{a_p}$, which expresses the relation of the rocking displacement to the ground motion

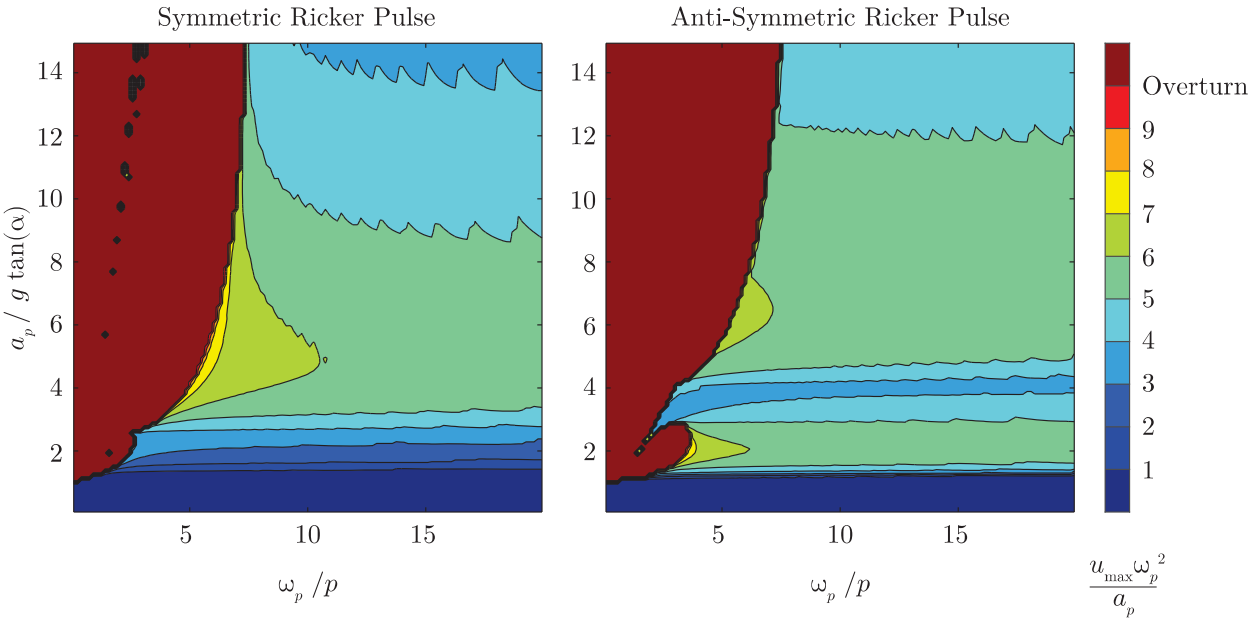

Figure 3: Non-dimensional rocking spectra based on displacements.

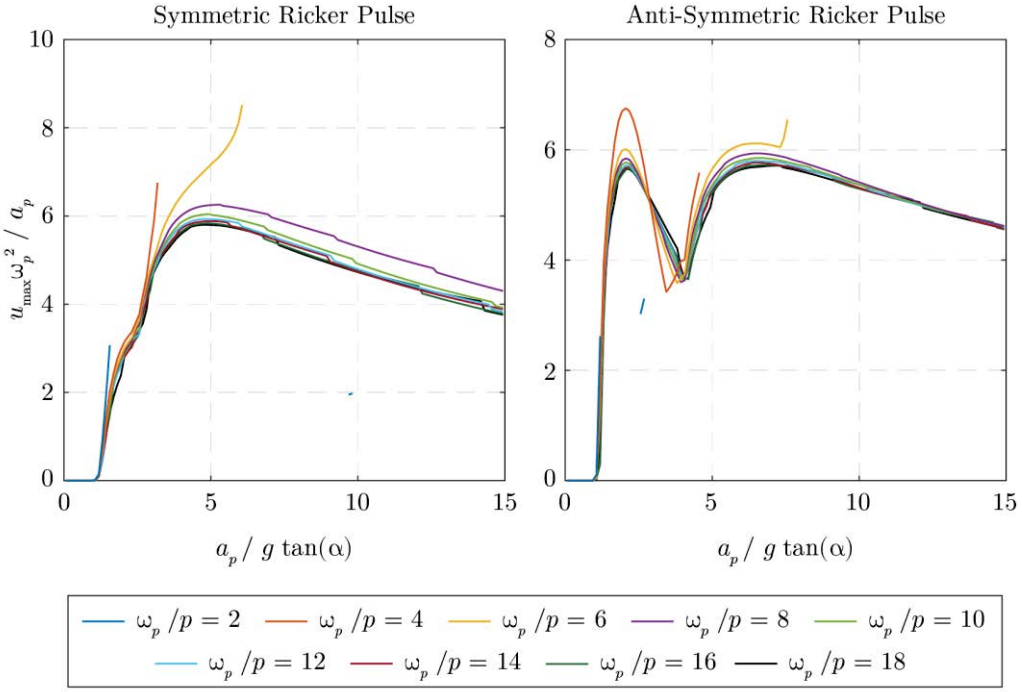

Figure 4: $\frac{u_{max}\omega_p^2}{a_p}$ vs $a_p/(g\tan\alpha)$ plots for constant ω_p/p . $\alpha = 0.1$

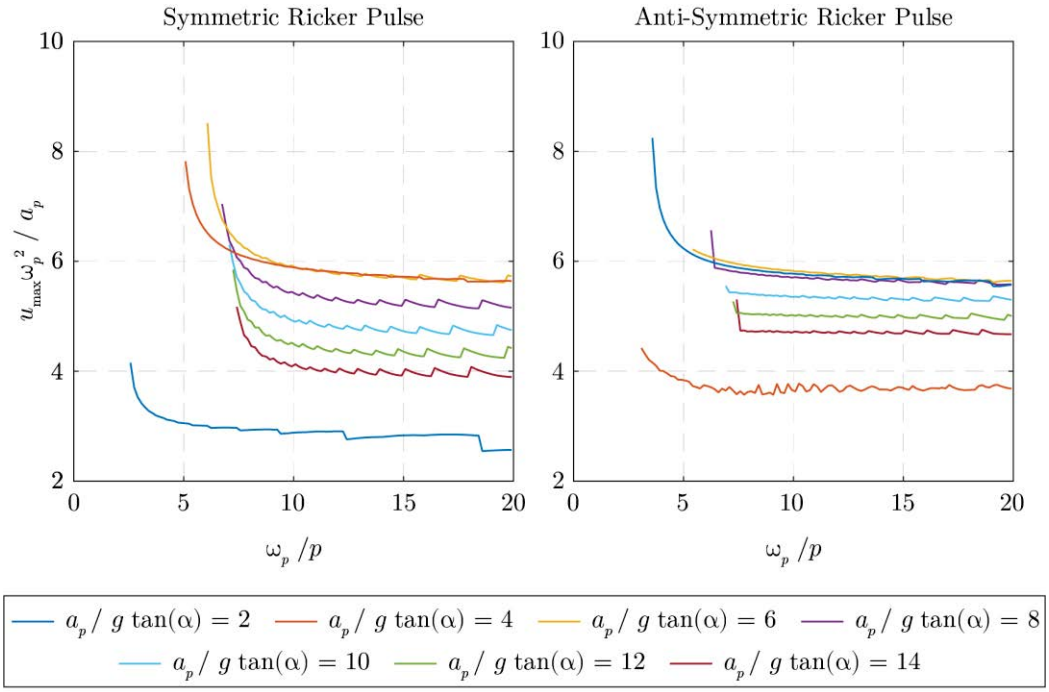

Figure 5: $\frac{u_{max}\omega_p^2}{a_p}$ vs ω_p / p plots for constant $a_p/(g\tan\alpha)$ and $\alpha = 0.1$

displacement, does not depend monotonically on the strength parameter $a_p/(g\tan\alpha)$. In fact, the discontinuities of the $\omega_p/p = 2$ line of Figure 4 convey that a block can survive a stronger pulse and overturn in a weaker one.

Going back to dimensional quantities, Figure 6 plots the displacement response to a symmetric Ricker pulse with a_p = 1g and T_p = 0.5s and to an antisymmetric Ricker pulse with a_p = 1g and T_p = 1s. The plots confirm that the displacement demand only loosely depends on the size, if the block is not close to overturning. The dominant factor is the slenderness. Therefore we can define the displacement demand rocking spectrum of a ground motion as a unary function

$$u_{demand} = f(\alpha) \text{ if } u_{demand} \square\ 2b \tag{13}$$

that is computed via Equations (1) and (10) for a large enough block size. To check the stability of a block, one has to compute the maximum displacement demand via Equation (13) and compare it with the displacement capacity (i.e. the block width).

Therefore the reduction of the dimension of the problem follows two steps: a) Applying Buckingham's theorem and b) Observing that the displacement demand is roughly independent of the size. The first step is exact and follows from dimensional analysis. The second step is approximate and in this section illustrated for analytical pulses. Blöchlinger [77] gave a first indication that the approximation also works for recorded ground motions. Further evidence supporting this approximation and highlighting its limitations are given in a next section of this paper.

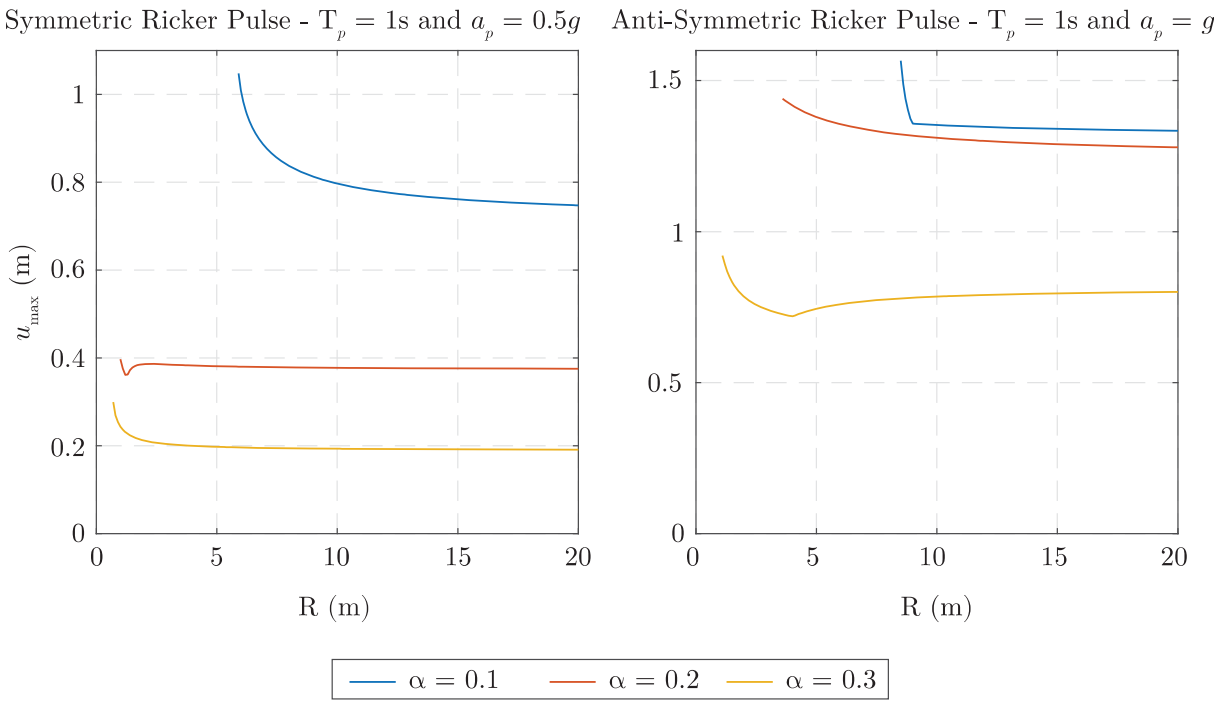

Figure 6: Maximum block displacement as a function of block size for Symmetric and Anti-Symmetric Ricker excitation.

3.2 Analysis based on the base width of the block *b*

The previous section chooses the frequency parameter p and the slenderness of the block, α, as the two parameters to define it. However, p has a physical meaning that is totally unrelated to rocking. It is the natural frequency that the block would have had *if* it was hanging from its corner [75]. But this is merely a coincidence, rocking blocks have no natural frequency [1], and the use of p often creates misunderstandings. In this section we propose to describe the block with two physical parameters that have a clear physical meaning, directly related to the rocking problem. The slenderness α is retained, as it controls the uplift of the structure (and could be parallelized with the strength of a system), but p is replaced by b, which is the half-width of the base and exactly equal to one half of its displacement capacity. Then the displacement response will be:

$$u_{\max} = f_4\left(b, \alpha, g, a_p, \omega_p\right) \tag{14}$$

Using Buckingham's Π theorem we get:

$$\frac{u_{\max}\omega_p^{\,2}}{\alpha_p} = \varphi_3\left(\frac{a_p}{g\tan\alpha}, \frac{b\omega_p^{\,2}}{a_p}, \alpha\right) \tag{15}$$

The term $a_p/(g\tan\alpha)$ would be the reciprocal of the non-dimensional strength, $\left(b\omega_p^{\,2}\right)/a_p$ would be the non-dimensional displacement capacity, and α (taken as an independent parameter) controls damping, because it controls the coefficient of restitution.

Figure 7 plots displacement spectra according to the suggested non-dimensionalization. One can observe that for both pulses a base (i.e a displacement capacity = 2b) of roughly 9

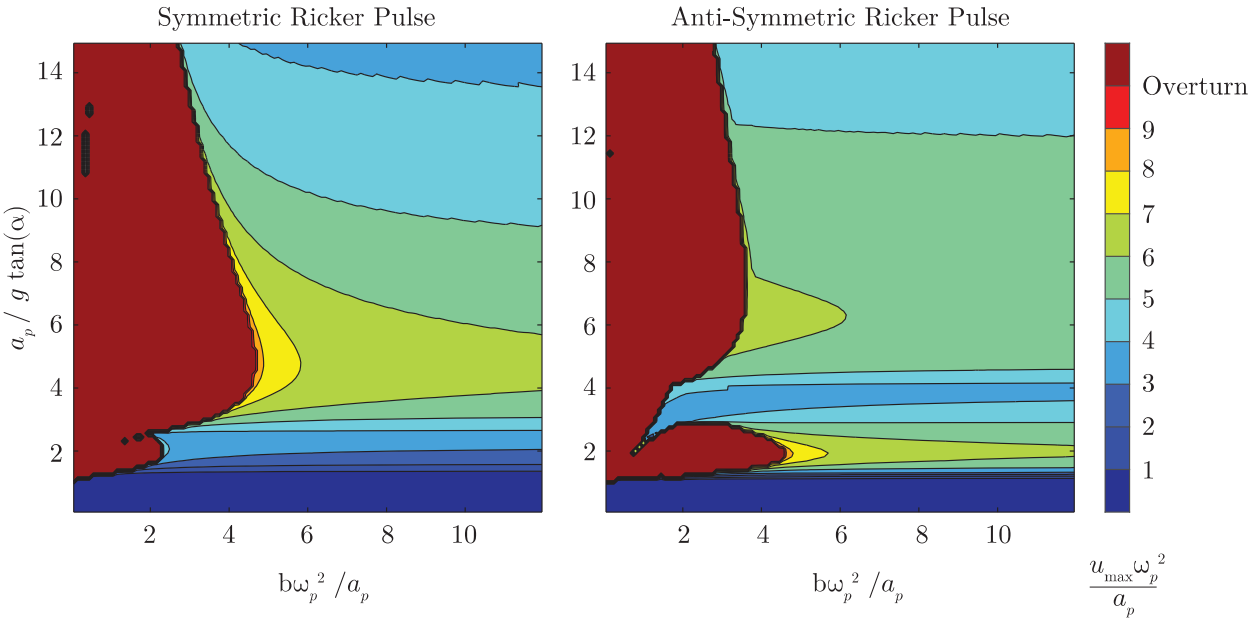

Figure 7: Displacement based non-dimensional rocking spectra using the width of the block to characterize its size.

times the length scale of the pulse $L_e = a_p / \omega_p^2$ is enough to keep the block stable, no matter what the non-dimensional strength parameter is.

4 DISPLACEMENT BASED ANALYSIS OF A ROCKING OSCILLATOR EXCITED BY RECORDED GROUND MOTIONS

Analytical pulses can be used to qualitatively study the rocking oscillator. However, as the rocking problem is very sensitive to all of its parameters, pulses would not suffice to prove that the displacement demand on a rocking structure depends only on its slenderness and not on its size. Therefore, this section examines the displacement response of a rocking block excited by recorded ground motions.

4.1 FEMA P695 Ground motions

There is no consensus in the engineering community on what ground motions should be used in time history analysis. Several approaches exist including using recorded (scaled or unscaled), artificial, or synthetic ground motions. In this paper we choose to use the 3 sets of ground motions proposed by FEMA P695 [79] (far field, near field pulse-like, and near field non-pulse-like) only as a means to illustrate our rocking-related argument, without taking stance on the debate around ground motions. It is evident that any ground motion selection method based on the response of an elastic system is in principle not applicable in the case of the rocking oscillator, as the elastic and rocking oscillator are uncorrelated. More information on the FEMA P695 ground motions can be found in FEMA [79].

4.2 Equal displacement rule for rocking structures and displacements demand spectra

Vassiliou et al. [80] have proven that rigid rocking oscillators of equal height attached to massless foundations of the same size behave identically, no matter what their actual column width is (Figure 8). Therefore, the design question of a rocking structure would be: Find the size, *2B'*, of the foundation for a given oscillator height 2*H*. Hence, it is more meaningful to

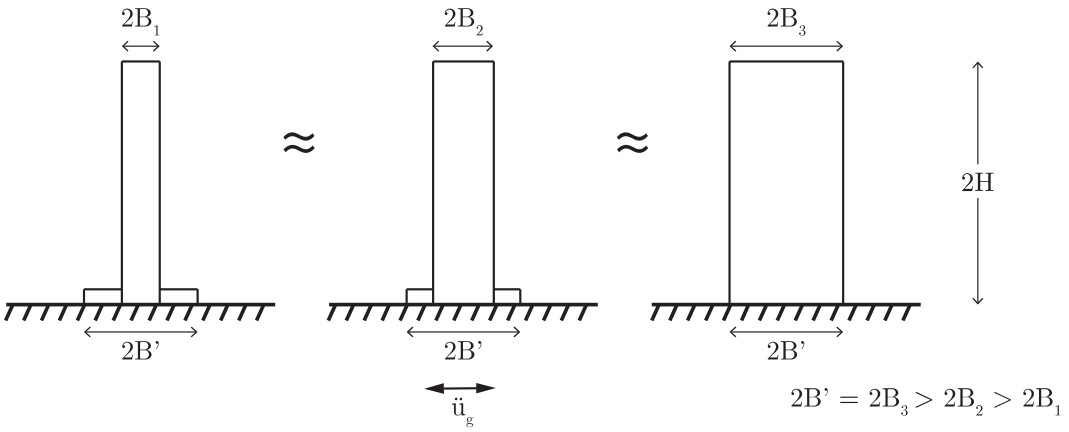

Figure 8: Rocking oscillators of equal height.

use H as a size parameter instead of R, even if the former does not explicitly appear in the equation of motion.

Figure 9 offers the displacement of a rocking oscillator as function of its slenderness α, and for $2H$=*2, 4, 10, 20, 80,* and *1000m*, for a selection of the FEMA P695 ground motions. The $2H$=1000m is offered only for reasons of mathematical completeness, to study the limit case of $H \to \infty$. For reasons of plot clarity, each line is plotted only for $\alpha > \alpha_{\text{crit}}$, where α_{crit} is the minimum slenderness angle for which the block overturns. We observe that all blocks of same slenderness angle present roughly the same displacement, as long as they are not close to overturning. The same observation holds for all the ground motions tested.

As analysis and design of a rocking structure would not involve a single ground motion, but a set of design motions, it makes sense to study the problem by applying sets of multiple excitations and comparing the statistics of the results (e.g. the median displacement among all the ground motions of the excitation set). Figure 10 plots displacement spectra of the median of the displacement for 7 variations of the near-field pulse-like FEMA P695 set: a) Unscaled ground motions, b) scaled so that their PGA is equal to $0.5\overline{PGA}$, or $\overline{PGA}$, or $2\overline{PGA}$, c) scaled so that their PGV is equal to $0.5\overline{PGV}$, or $\overline{PGV}$, or $2\overline{PGV}$, where $\overline{PGA}$, $\overline{PGV}$ are defined as

$$\overline{PGA} = \underset{i=1\ldots N}{median}\left(\sqrt{PGA_{i_x} \times PGA_{i_y}}\right) \tag{16}$$

$$\overline{PGV} = \underset{i=1\ldots N}{median}\left(\sqrt{PGV_{i_x} \times PGV_{i_y}}\right) \tag{17}$$

where N is the number of the ground motions and x and y are the two components of each ground motion. Note that each horizontal component of each ground motion is treated as an independent motion. Figures 11 and 12 plot the same spectra for the far field and near field non-pulse-like ground motions.

The following observations can be made:

a) The median spectra are smoother, likewise design elastic spectra that were derived by statistical processing of elastic spectra of single ground motions are smoother than single ground motion spectra.

b) As long as the system is not close to overturning, the displacement does not depend on the size of the block. For this part of the spectrum, instead of computing a different spectrum for each block size, one can compute the design spectrum for $2H \to \infty$ ($2H$ =

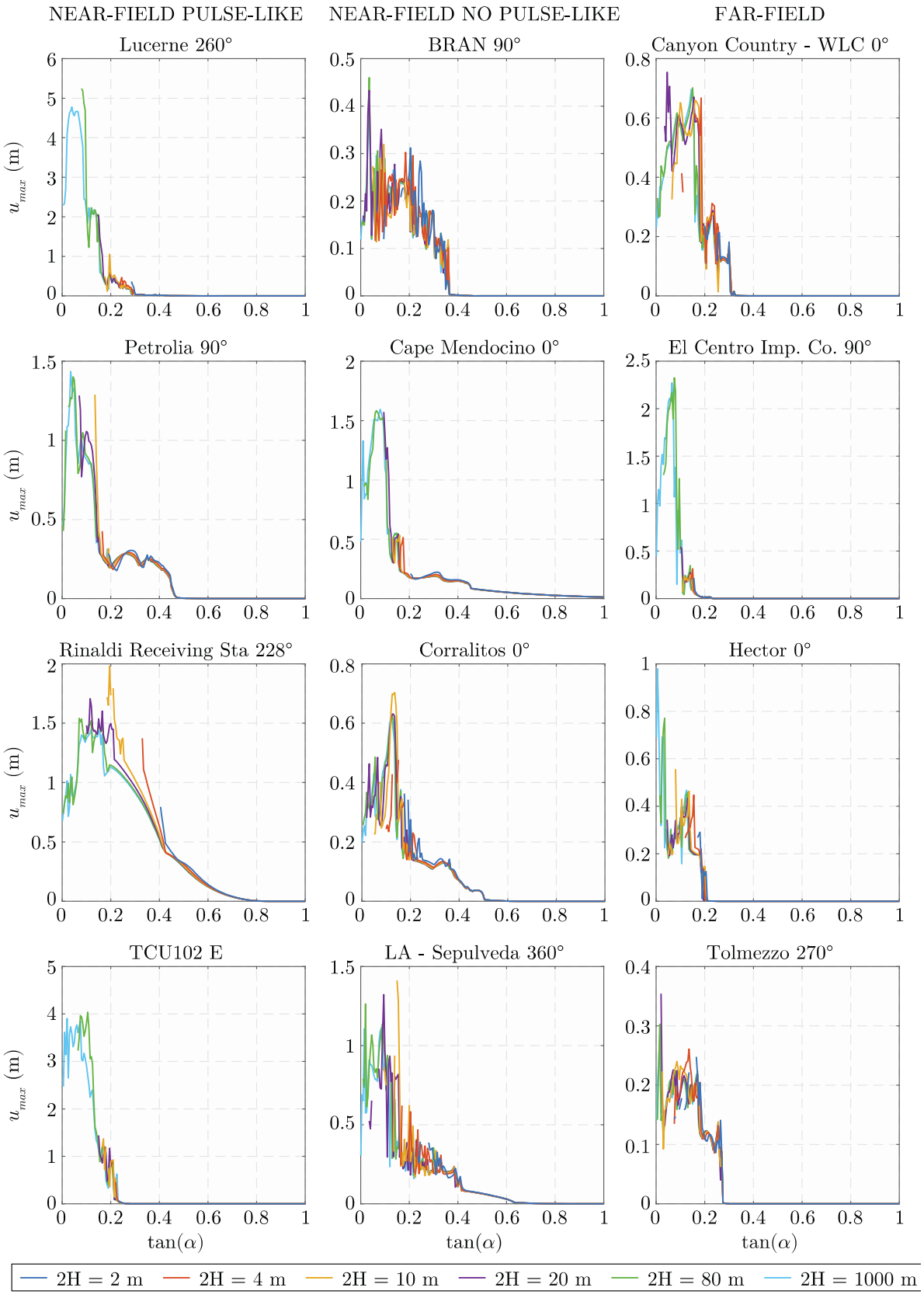

Figure 9: Displacement of a rocking oscillator as function of its slenderness α.

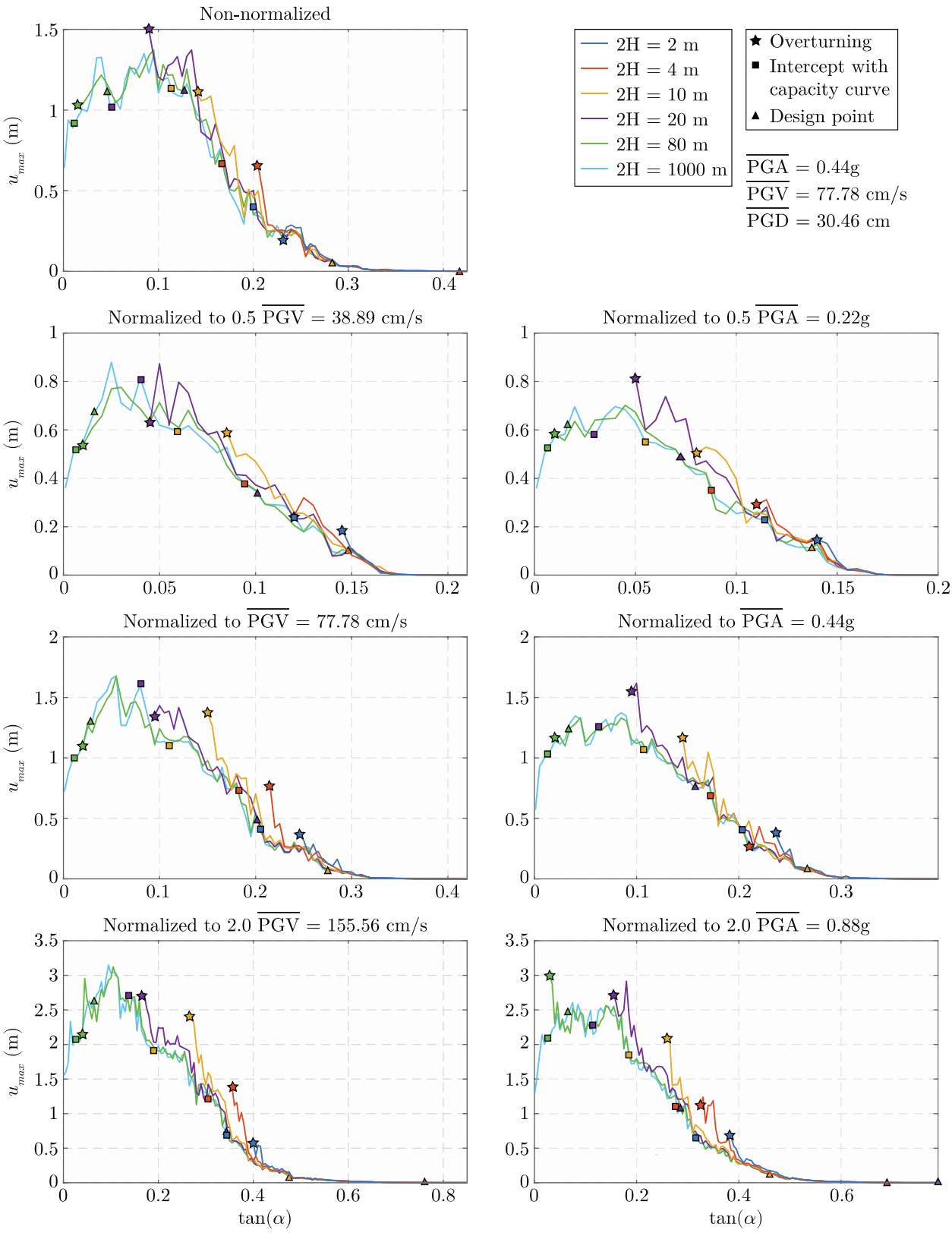

Figure 10: Median Displacement Spectra for Near-Field Pulse-Like Record Set.

1000m seems an adequate value) and use it to calculate the displacement *demand* on any rocking structure (i.e. $u_{max}=f(\alpha)$). We name the above finding "equal displacement rule" for rocking structures.

c) As the system gets closer to overturning the equal displacement rule does not apply: smaller systems present larger displacements than larger ones. Moreover, as the system approaches overturning, the slope of the spectrum increases dramatically i.e. a small decrease in tanα leads to very large increase in displacement. This trend dictates that a rational design of a rocking structure would require that this steep part of the spectrum be avoided. because an earthquake slightly stronger than the design one would cause a tremendous increase in displacement. Therefore, the equal displacement rule applies to the rational design region.

d) The form of the spectrum for all 3 sets of ground motions presents some repetitive pattern:
   i. As α tends to zero, u_{max} tends to a finite value. For spectra of individual ground motions, this value is $\frac{3}{2}PGD$. An explanation for this is offered in the next section.
   ii. As α increases from zero, the displacement demand amplifies 2-2.5 times and reaches a plateau.
   iii. Further increase of α leads to a monotonic decrease of the displacement demand.
   iv. Naturally, when tanα reaches PGA/g, the displacement demand becomes zero, as there is no uplift.

4.3 Preliminary design based on the equal displacement rule

If not for a final design, the equal displacement rule can be used for preliminary calculations. Indeed it is not an exact method, but a preliminary design method that does not aim at being exact, but at providing a tool for initial calculations, that for certain cases and required degree of accuracy can be enough. The same holds for yielding structures, where the "equal displacement rule" is used for many structural systems, while for more complicated systems it is used only for preliminary design and then more refined methods are applied. It could be stated that the findings of this paper constitute the generalization of equal displacement rule from yielding to rocking systems. This section proposes a methodology to design a rocking structure based on the equal displacement rule:

a) On the u_{max} – tanα curve, we plot the capacity line $u_C = 2H\tan\alpha$.
b) We determine the intersection of the capacity line and the $2H = \infty$ line. We define the abscissa of this point as $\tan\alpha_k$.
c) We use a multiplier of 2.5 to determine the design slenderness: $\tan\alpha_D = 2.5\tan\alpha_k$. The multiplier serves as a safety factor to move the design point away from the steep part of the spectrum.

Figure 13 outlines the design procedure applied for a rocking bridge with columns of 6.7m height ($2H$ = 6.7m). Based on Makris and Vassiliou [46] the response of the frame is equal to the response of a solitary block of $2H$ = 10m. For this bridge, twenty one design scenarios are explored, corresponding to the 21 spectra of Figures 10-12. Tables 1-3 and Figure 14 summarize the findings for the 21 design scenarios and compare the displacement predicted

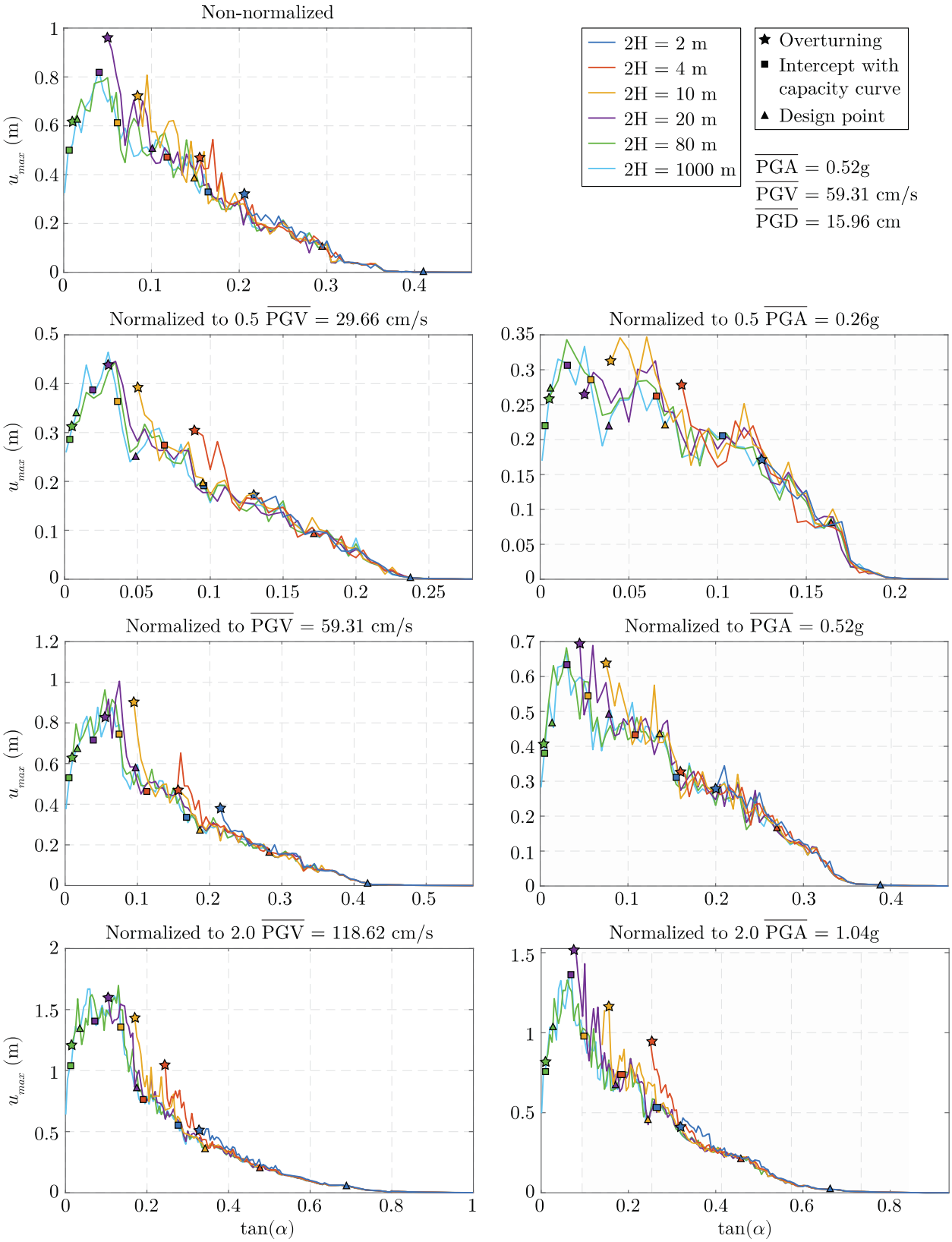

Figure 11: Median Displacement Spectra for Near-Field No Pulse-Like Record Set.

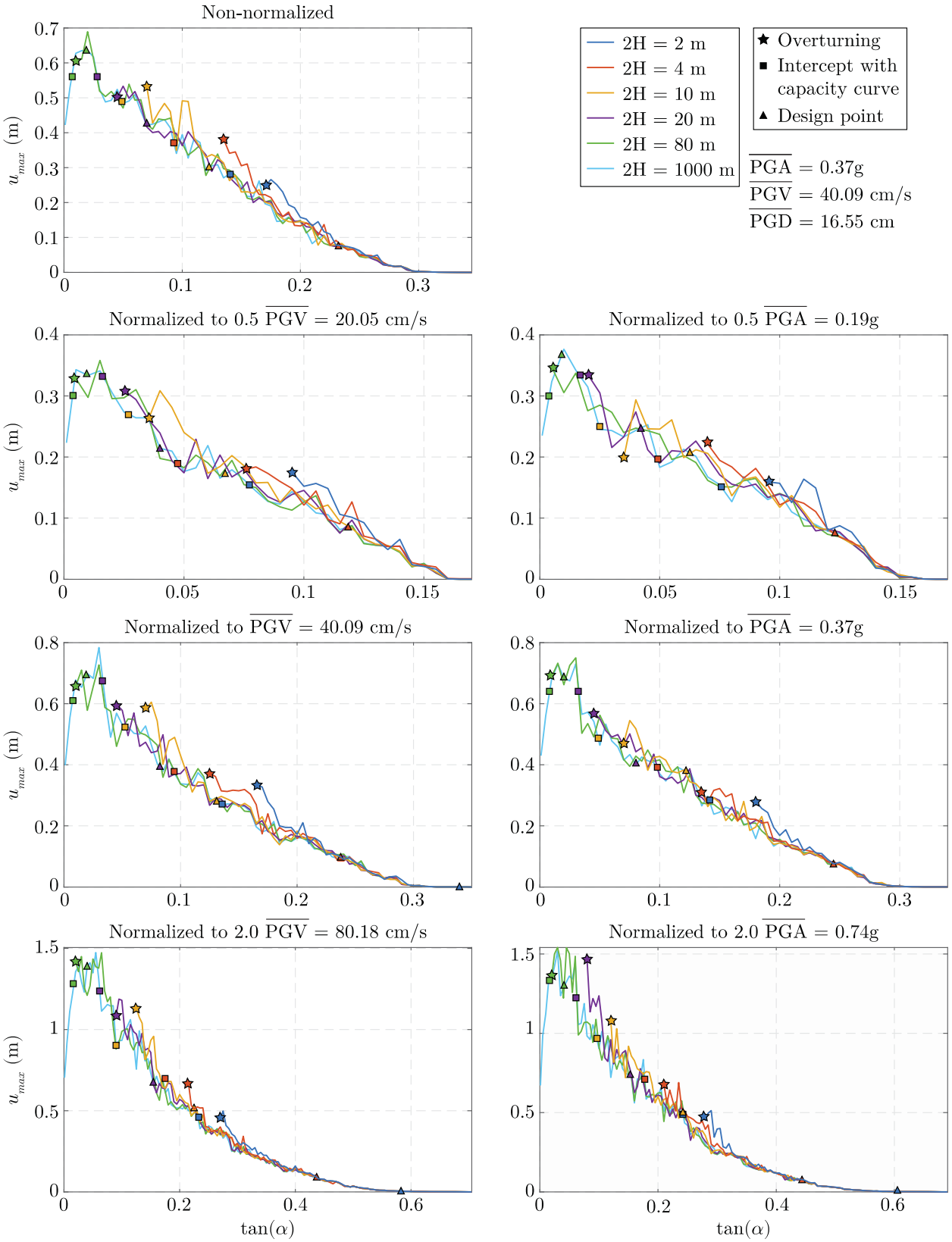

Figure 12: Median Displacement Spectra for Far-Field Record Set.

by the demand spectrum ($2H$ = 1000m) to the displacement predicted by the $2H$=10m spectrum. We observe that in all but two cases (near fault pulse-like scaled to $0.5\overline{PGA}$ and near fault non-pulse-like scaled to $2\overline{PGA}$) the error in predicting the median displacement is less than 20%. In all cases, the error is smaller than 40%, and no system overturned.

	Unscaled	$0.5\overline{PGA}$	$\overline{PGA}$	$2\overline{PGA}$	$0.5\overline{PGV}$	$\overline{PGV}$	$2\overline{PGV}$
$\tan(\alpha_D)$	0.2839	0.1378	0.2671	0.4618	0.0596	0.1094	0.1909
2H = 1000m	0.05	0.11	0.08	0.12	0.10	0.07	0.08
2H = 10m	0.06	0.15	0.07	0.13	0.10	0.10	0.08

Table 1: Near field pulse like FS=2.5.

	Unscaled	$0.5\overline{PGA}$	$\overline{PGA}$	$2\overline{PGA}$	$0.5\overline{PGV}$	$\overline{PGV}$	$2\overline{PGV}$
$\tan(\alpha_D)$	0.1524	0.0708	0.1356	0.2446	0.0916	0.1892	0.3405
2H = 1000m	0.34	0.22	0.44	0.44	0.19	0.27	0.36
2H = 10m	0.41	0.26	0.41	0.69	0.21	0.30	0.38

Table 2: Near field non pulse like FS=2.5.

	Unscaled	$0.5\overline{PGA}$	$\overline{PGA}$	$2\overline{PGA}$	$0.5\overline{PGV}$	$\overline{PGV}$	$2\overline{PGV}$
$\tan(\alpha_D)$	0.1228	0.0620	0.1215	0.2411	0.0675	0.1320	0.2249
2H = 1000m	0.30	0.21	0.38	0.52	0.17	0.28	0.52
2H = 10m	0.33	0.20	0.37	0.50	0.19	0.29	0.49

Table 3: Far field FS=2.5.

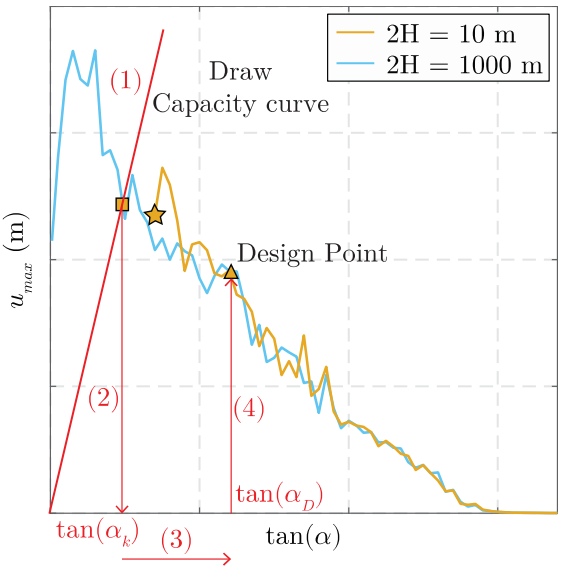

Figure 13: Design procedure.

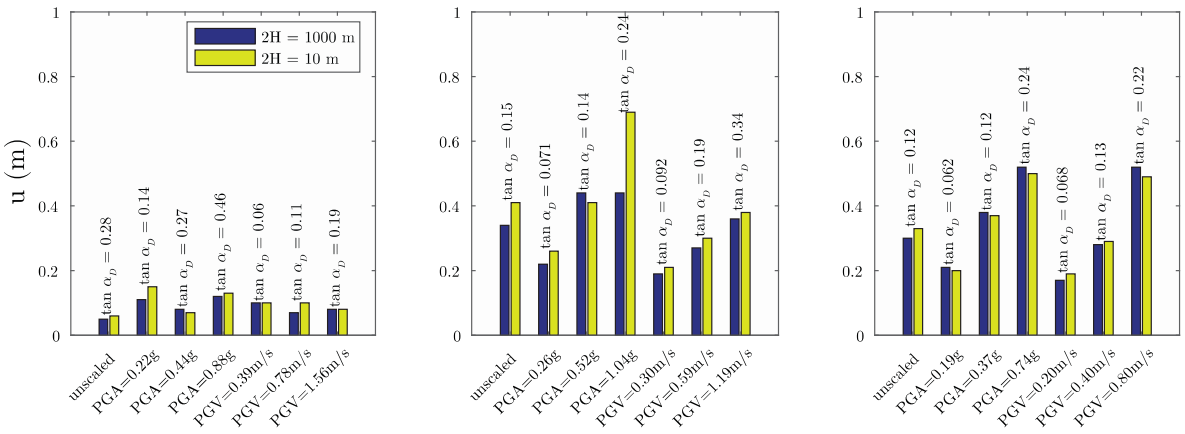

Figure 14: Comparison of the displacement response at the design point. Predictions based on the 2*H*=1000m and on the 2*H*=10m spectra.

5 INTERPRETATION OF THE EQUAL DISPLACEMENT RULE BASED ON THE EQUATION OF MOTION

The equal displacement rule can be interpreted by properly manipulating the equation of motion. Assuming small rotation angles (sin*x*=*x* and cos*x*=1), Equation (1) gives

$$\ddot{\theta} = -\frac{3g}{4H}\cdot\left(\pm\alpha - \theta + \frac{\ddot{u}_g}{g}\right) \tag{18}$$

For small angles, $u = 2H\theta$. Then

$$\ddot{u} = -\frac{3g\alpha}{2}\cdot\left(\pm 1 - \frac{u}{2b} + \frac{\ddot{u}_g}{g\alpha}\right) \tag{19}$$

When $u/2b$ is small (i.e. the block is not close to overturning, the other terms dominate the response and u becomes a function only of α. Furthermore, when $\ddot{u}_g/(g\alpha) \gg 1$, then $\ddot{u} = -3\ddot{u}_g/2$. Therefore, as $\alpha \to 0$ (which can only happen for blocks with $H \to \infty$), $u_{max} \to$ 3/2 PGD.

6 CONCLUSIONS

The widely used description of the rocking block via its rotation is correct, but not optimal. It reveals that larger blocks are more stable and that higher frequency pulses present less overturning potential. However, it does not reveal the "equal displacement rule of rocking structures", namely that a large and a small block of the same aspect ratio will present the same top displacement, if they both are not close to overturning. Not being close to overturning is a design necessity anyway, therefore, for the scope of design, we can claim that the displacement demand is the same and it only depends on the slenderness, not on the size of the block. The above is illustrated for both analytical pulse excitations and for sets of recorded ground motions. As the response of a rocking block away from overturning essentially becomes a unary function, rocking spectra that plot the displacement demand as a function of the slenderness of the block can be developed. The shape of these spectra seem to follow a repetitive pattern, starting for tanα=0 from u=3/2×PGD, reaching a plateau of 2-2.5×3/2×PGD, and then gradually decreasing to zero. More research with more ground motions in needed to better understand the shape of the spectra. Based on the above, a design method that uses a size-

independent rocking spectrum is suggested. This should be taken into account when intensity measures for rocking structures [81-84] designed not to get close to overturning are explored.

ACKNOWLEDGEMENTS

This work was supported by the ETH Zurich under Grant ETH-10 18-1. The methods, results, opinions, findings and conclusions presented in this report are those of the authors and do not necessarily reflect the views of the funding agency.

REFERENCES

[1] GW. Housner, The behavior of inverted pendulum structures during earthquakes, *Bulletin of the seismological society of America* 53 (2), 403-417, 1963.

[2] AK. Chopra, SCS. Yim, Simplified earthquake analysis of structures with foundation uplift, *Journal of Structural Engineering* 111 (4), 906-930, 1985.

[3] IN. Psycharis, Effect of base uplift on dynamic response of SDOF structures, *Journal of Structural Engineering* 117 (3), 733-754, 1991.

[4] G. Oliveto, I. Caliò, A. Greco, Large displacement behaviour of a structural model with foundation uplift under impulsive and earthquake excitations, *Earthquake Engineering & Structural Dynamics* 32 (3), 369-393, 2003.

[5] QTM. Ma, The mechanics of rocking structures subjected to ground motion, Doctoral dissertation, ResearchSpace, Auckland, 2010.

[6] S. Acikgoz, MJ. DeJong, The interaction of elasticity and rocking in flexible structures allowed to uplift, *Earthquake Engineering & Structural Dynamics*, 41 (15), 2177-2194, 2012.

[7] N. Makris, D. Konstantinidis, The rocking spectrum and the limitations of practical design methodologies, *Earthquake Engineering & Structural Dynamics* 32(2), 265-289, 2003.

[8] I. Stefanou, I. Psycharis, IO. Georgopoulos, Dynamic response of reinforced masonry columns in classical monuments, *Construction and Building Materials* 25 (12), 4325-4337, 2011.

[9] MJ. DeJong, Seismic response of stone masonry spires: Analytical modeling. *Engineering Structures* 40, 556-565, 2012.

[10] M. Tondelli, K. Beyer, M. DeJong, M., Influence of boundary conditions on the out-of-plane response of brick masonry walls in buildings with RC slabs, *Earthquake Engineering & Structural Dynamics* 45 (8), 1337-1356, 2016.

[11] C. Casapulla, L. Giresini, PB. Lourenço, Rocking and Kinematic Approaches for Rigid Block Analysis of Masonry Walls: State of the Art and Recent Developments, *Buildings* 7 (3), 69, 2017.

[12] D. Kalliontzis, AE. Schultz, Characterizing the In-Plane Rocking Response of Masonry Walls with Unbonded Posttensioning, *Journal of Structural Engineering* 143 (9), 04017110, 2017.

[13] A. Mehrotra, MJ. DeJong, The influence of interface geometry, stiffness, and crushing on the dynamic response of masonry collapse mechanisms, *Earthquake Engineering & Structural Dynamics* 47 (13), 2661-2681, 2018.

[14] Giresini, L., Sassu, M., & Sorrentino, L. (2018). In situ free-vibration tests on unrestrained and restrained rocking masonry walls. *Earthquake Engineering & Structural Dynamics*, *47*(15), 3006-3025.

[15] D. Konstantinidis, N. Makris, Experimental and analytical studies on the response of 1/4-scale models of freestanding laboratory equipment subjected to strong earthquake shaking, *Bulletin of earthquake engineering* 8 (6), 1457-1477, 2010.

[16] A. Di Egidio, R. Alaggio, A. Contento, M. Tursini, E. Della Loggia, Experimental characterization of the overturning of three-dimensional square based rigid block, *International Journal of Non-Linear Mechanics* 69, 137-145, 2015.

[17] CE. Wittich, TC. Hutchinson, Shake table tests of stiff, unattached, asymmetric structures, *Earthquake Engineering & Structural Dynam*ics 44 (14), 2425-2443, 2015.

[18] A. Dar, D. Konstantinidis, WW. El-Dakhakhni, Evaluation of ASCE 43-05 seismic design criteria for rocking objects in nuclear facilities, *Journal of Structural Engineering* 142 (11), 04016110, 2016.

[19] AG. Sextos, GD. Manolis, N. Ioannidis, A. Athanasiou, Seismically induced uplift effects on nuclear power plants. Part 2: Demand on internal equipment, *Nuclear Engineering and Design* 318, 288-296, 2017.

[20] A. Dar, D. Konstantinidis, W. El-Dakhakhni, Seismic response of rocking frames with top support eccentricity, *Earthquake Engineering & Structural Dynamics* 47 (12), 2496-2518, 2018.

[21] E. Voyagaki, P. Kloukinas, M. Dietz, L. Dihoru, T. Horseman, O. Oddbjornsson, A. Steer, Earthquake response of a multiblock nuclear reactor graphite core: Experimental model vs simulations, *Earthquake Engineering & Structural Dynamics* 47(13), 2601-2626, 2018.

[22] L. Di Sarno, G. Magliulo, D. D'Angela, E. Cosenza, Experimental assessment of the seismic performance of hospital cabinets using shake table testing, *Earthquake Engineering & Structural Dynamics* 48 (1), 103-123, 2019.

[23] HP. Mouzakis, IN. Psycharis, DY. Papastamatiou, PG. Carydis, C. Papantonopoulos, C. Zambas, Experimental investigation of the earthquake response of a model of a marble classical column, *Earthquake Engineering & Structural Dynamics* 31 (9), 1681-1698, 2002.

[24] C. Papantonopoulos, IN. Psycharis, DY. Papastamatiou, JV. Lemos, HP. Mouzakis, Numerical prediction of the earthquake response of classical columns using the distinct element method, *Earthquake Engineering & Structural Dynamics* 31 (9), 1699-1717, 2002.

[25] L. Papaloizou, P. Komodromos, Planar investigation of the seismic response of ancient columns and colonnades with epistyles using a custom-made software, *Soil Dynamics and Earthquake Engineering* 29 (11), 1437-1454, 2009.

[26] MF. Vassiliou, N. Makris, Analysis of the rocking response of rigid blocks standing free on a seismically isolated base, *Earthquake Engineering & Structural Dynamics* 41(2), 177-196, 2012.

[27] Ž. Nikolić, L. Krstevska, P. Marović, H. Smoljanović, Experimental investigation of seismic behaviour of the ancient Protiron monument model, *Earthquake Engineering & Structural Dynamics* 48 (6), 573-593, 2019.

[28] N. Makris, G. Kampas, Seismic protection of structures with supplemental rotational inertia, *Journal of Engineering Mechanics* 142 (11), 04016089, 2016.

[29] R. Thiers-Moggia, C. Málaga-Chuquitaype, Seismic protection of rocking structures with inerters. *Earthquake Engineering & Structural Dynamics* 48 (5), 528-547, 2019.

[30] JA. Bachmann, MF. Vassiliou, B. Stojadinović, Dynamics of rocking podium structures, *Earthquake Engineering & Structural Dynamics* 46 (14), 2499-2517, 2018.

[31] Bachmann, J. A., Vassiliou, M. F., & Stojadinovic, B. (2019). Rolling and rocking of rigid uplifting structures. *Earthquake Engineering & Structural Dynamics*, *48*(14), 1556-1574.

[32] N. Makris, M. Aghagholizadeh, The dynamics of an elastic structure coupled with a rocking wall, *Earthquake Engineering & Structural Dynamics* 46 (6), 945-962, 2017.

[33] M. Aghagholizadeh, N. Makris, Earthquake response analysis of yielding structures coupled with vertically restrained rocking walls, *Earthquake Engineering & Structural Dynamics* 47(15), 2965-2984, 2018.

[34] RD. Sharpe, RI. Skinner, The seismic design of an industrial chimney with rocking base. *Bulletin of the New Zealand National Society for Earthquake Engineering* 16 (2), 98-106, 1983.

[35] JB. Mander, CT. Cheng, Seismic resistance of bridge piers based on damage avoidance design, Technical Report NCEER-97-0014, State University of New York, Buffalo, NY, 1997.

[36] Palermo, A., Pampanin, S., & Calvi, G. M. (2004). The use of controlled rocking in the seismic design of bridges. *Doctate Thesis, Technical Institute of Milan, Milan*, (1), 1-5.

[37] Marriott, D., Pampanin, S., & Palermo, A. (2009). Quasi-static and pseudo-dynamic testing of unbonded post-tensioned rocking bridge piers with external replaceable dissipaters. *Earthquake engineering & structural dynamics*, *38*(3), 331-354.

[38] Motaref, S., Saiidi, M. S., and Sanders, D. (2010). "Experimental study of precast bridge columns with built-in elastomer." Transportation Research Record, 2202, 109–116.

[39] Sideris, P., Aref, A. J., & Filiatrault, A. (2014). Large-scale seismic testing of a hybrid sliding-rocking posttensioned segmental bridge

[40] Sideris, P., Aref, A. J., & Filiatrault, A. (2015). Experimental seismic performance of a hybrid sliding–rocking bridge for various specimen configurations and seismic loading conditions. *Journal of Bridge Engineering*, *20*(11), 04015009.

[41] T. Thonstad, IM. Mantawy, JF. Stanton, MO. Eberhard, DH. Sanders, Shaking table performance of a new bridge system with pretensioned rocking columns, *Journal of Bridge Engineering* 21 (4), 04015079, 2016.

[42] AI. Giouvanidis, EG. Dimitrakopoulos, Seismic performance of rocking frames with flag-shaped hysteretic behavior, *Journal of Engineering Mechanics* 143 (5), 04017008, 2017.

[43] PJ. Routledge, MJ. Cowan, A. Palermo, Low-damage detailing for bridges - a case study of Wigram-Magdala bridge, *Proceedings of New Zealand society for earthquake engineering 2016 Conference*, 2016.

[44] I. Anastasopoulos, G. Gazetas, M. Loli, M. Apostolou, N. Gerolymos, Soil failure can be used for seismic protection of structures, *Bulletin of Earthquake Engineering* 8 (2), 309-326, 2010.

[45] Makris N and Vassiliou MF (2012), Sizing the slenderness of free-standing rocking columns to withstand earthquake shaking, *Archive of Applied Mechanics*, 1-15.

[46] N. Makris, MF. Vassiliou, Planar rocking response and stability analysis of an array of free standing columns capped with a freely supported rigid beam, *Earthquake Engineering & Structural Dynamics* 42 (3), 431-449, 2013.

[47] N. Makris, MF. Vassiliou, Are Some Top-Heavy Structures More Stable?, *Journal of Structural Engineering* 140 (5), 2014.

[48] EG. Dimitrakopoulos, AI. Giouvanidis, Seismic Response Analysis of the Planar Rocking Frame, *Journal of Engineering Mechanics* 141 (7), 04015003, 2015.

[49] A. Agalianos, A. Psychari, MF. Vassiliou, B. Stojadinovic, I. Anastasopoulos, Comparative Assessment of Two Rocking Isolation Techniques for a Motorway Overpass Bridge, *Frontiers in Built Environment* 3, 47, 2017.

[50] MF. Vassiliou, KR. Mackie, B. Stojadinović, A finite element model for seismic response analysis of deformable rocking frames, *Earthquake Engineering & Structural Dyn*amics 46, 447–466, 2017.

[51] MF. Vassiliou, S. Burger, M. Egger, JA. Bachmann, M. Broccardo, B. Stojadinovic, The three-dimensional behavior of inverted pendulum cylindrical structures during earthquakes, *Earthquake Engineering & Structural Dynamics* 46 (14), 2261-2280, 2018.

[52] MF. Vassiliou, Seismic response of a wobbling 3D frame, *Earthquake Engineering & Structural Dynamics* 47 (5), 1212-1228, 2018.

[53] Y. Xie, J. Zhang, R. DesRoches, JE. Padgett, Seismic fragilities of single-column highway bridges with rocking column-footing, *Earthquake Engineering & Structural Dynamics* 48, 843–864, 2019.

[54] Sieber, M., Klar, S., Vassiliou, M. F., & Anastasopoulos, I. Robustness of simplified analysis methods for rocking structures on compliant soil (2020). *Earthquake Engineering & Structural Dynamics* DOI: 10.1002/eqe.3294

[55] Thomaidis, I. M., Kappos, A. J., & Camara, A. (2020). Dynamics and seismic performance of rocking bridges accounting for the abutment-backfill contribution. *Earthquake Engineering & Structural Dynamics*. DOI: 10.1002/eqe.3283

[56] Giouvanidis, A., & Dong, Y. (2020). Seismic loss and resilience assessment of single-column rocking bridges. *Bulletin of Earthquake Engineering*, https://doi.org/10.1007/s10518-020-00865-5

[57] Aghagholizadeh, M. (2020). A finite element model for seismic response analysis of vertically-damped rocking-columns. *Engineering Structures*, *219*, 110894.

[58] Avgenakis, E., & Psycharis, I. N. (2019). Determination of the nonlinear displacement distribution of the semi-infinite strip–application to deformable rocking bodies. *International Journal of Solids and Structures*, *170*, 22-37.

[59] Avgenakis, E., & Psycharis, I. N. An integrated macroelement formulation for the dynamic response of inelastic deformable rocking bodies. *Earthquake Engineering & Structural Dynamics*.

[60] Avgenakis, E., & Psycharis, I. N. (2020). Modeling of inelastic rocking bodies under cyclic loading. *Journal of Engineering Mechanics*, *146*(4), 04020020.

[61] N. Makris, MF. Vassiliou, Dynamics of the rocking frame with vertical restrainers, *Journal of Structural Engineering* 141 (10), 04014245, 2014.

[62] MF. Vassiliou, N. Makris, Dynamics of the Vertically Restrained Rocking Column. *Journal of Engineering Mechanics* 141(12), 04015049, 2015.

[63] Reggiani Manzo, N., & Vassiliou, M. F. (2019). Displacement-based analysis and design of rocking structures. *Earthquake Engineering & Structural Dynamics*, *48*(14), 1613-1629.

[64] MF. Vassiliou, R. Truniger, B. Stojadinović, An analytical model of a deformable cantilever structure rocking on a rigid surface: development and verification, *Earthquake Engineering & Structural Dynamics* 44 (15), 2775-2794, 2015.

[65] R. Truniger, MF. Vassiliou, B. Stojadinović, An analytical model of a deformable cantilever structure rocking on a rigid surface: experimental validation, *Earthquake Engineering & Structural Dynamics* 44 (15), 2795-2815, 2015.

[66] AI. Giouvanidis, EG. Dimitrakopoulos, Nonsmooth dynamic analysis of sticking impacts in rocking structures, *Bulletin of Earthquake Engineering* 15 (5), 2273-2304, 2017.

[67] MN. Chatzis, MG. Espinosa, AW. Smyth, Examining the energy loss in the inverted pendulum model for rocking bodies, *Journal of Engineering Mechanics* 143 (5), 04017013, 2017.

[68] D. Kalliontzis, S. Sritharan, Characterizing Dynamic Decay of Motion of Free-Standing Rocking Members, *Earthquake Spectra* 34 (2), 843-866, 2018.

[69] JA. Bachmann, M. Strand, MF. Vassiliou, M. Broccardo, B. Stojadinović, Is rocking motion predictable?, *Earthquake Engineering & Structural Dynamics* 47 (2), 535-552, 2018.

[70] Del Giudice, L., Wrobel, R., Leinenbach, C., & Vassiliou, M. F. (2020). Static Testing of Additively Manufactured Microreinforced Concrete Specimens for Statistical Structural Model Validation at a Small Scale. In *8th International Conference on Advances in Experimental Structural Engineering (8AESE)*.

[71] MF. Vassiliou, N. Makris, Estimating time scales and length scales in pulse-like earthquake acceleration records with wavelet analysis. *Bulletin of Seismological Society of America* 101 (2), 596-618, 2011.

[72] J. Zhang, N. Makris, Rocking response of free-standing blocks under cycloidal pulses, *Journal of Engineering Mechanics*, 127(5), 473-483.

[73] A. Vaschy, Sur les lois de similitude en physique, *Annales Télégraphique*s 19, 25–28, 1892.

[74] E. Buckingham, On physically similar systems; illustrations of the use of dimensional equations, *Physical Review* 4 (4), 345–376, 1914.

[75] EG. Dimitrakopoulos, MJ. DeJong, Revisiting the rocking block: closed-form solutions and similarity laws, *Proceedings of Royal Society A* 468 (2144), 2294-2318, 2012.

[76] GI. Barenblatt, Scaling, self-similarity, and intermediate asymptotics: dimensional analysis and intermediate asymptotics, *Cambridge University Press*, 1996.

[77] Blöchlinger, Rigid body rocking spectra for recorded earthquake ground motions, Master's Thesis, ETH Zurich, 2016.

[78] MJ. DeJong, EG. Dimitrakopoulos, Dynamically equivalent rocking structures, *Earthquake Engineering & Structural Dynamics* 43 (10), 1543-1563, 2014.

[79] FEMA P695, Quantification of Building Seismic Performance Factors, Washington, D.C: Rep. FEMA P695, Federal Emergency Management Agency, 2009.

[80] MF. Vassiliou, KR. Mackie, B. Stojadinović, Dynamic response analysis of solitary flexible rocking bodies: modeling and behavior under pulse-like ground excitation, *Earthquake Engineering & Structural Dynamics* 43, 1463–1481, 2014.

[81] EG. Dimitrakopoulos, TS. Paraskeva, Dimensionless fragility curves for rocking response to near-fault excitations, *Earthquake Engineering & Structural Dynamics* 44 (12), 2015-2033, 2015.

[82] A. Pappas, A. Sextos, F. Da Porto, C. Modena, Efficiency of alternative intensity measures for the seismic assessment of monolithic free-standing columns, *Bulletin of Earthquake Engineering* 15 (4), 1635-1659, 2017.

[83] AI. Giouvanidis, EG. Dimitrakopoulos, Rocking amplification and strong-motion duration, *Earthquake Engineering & Structural Dynamics* 47 (10), 2094-2116, 2018.

[84] IE. Kavvadias, GA. Papachatzakis, KE. Bantilas, LK. Vasiliadis, A. Elenas, Rocking spectrum intensity measures for seismic assessment of rocking rigid blocks, *Soil Dynamics and Earthquake Engineering* 101, 116-124, 2017.

EURODYN 2020
XI International Conference on Structural Dynamics
M. Papadrakakis, M. Fragiadakis, C. Papadimitriou (eds.)
Athens, Greece, 23–26 November 2020

SEISMIC PERFORMANCE OF BRIDGES ISOLATED WITH DCFP DEVICES

P. Castaldo[1], G. Amendola[2], D. Gino[3], E. Miceli[4]

[1] Department of Structural, Geotechnical and Building Engineering (DISEG), Politecnico di Torino
Turin, Italy
e-mail: paolo.castaldo@polito.it

[2] Department of Structural, Geotechnical and Building Engineering (DISEG), Politecnico di Torino
Turin, Italy
e-mail: guglielmo.amendola@polito.it

[3] Department of Structural, Geotechnical and Building Engineering (DISEG), Politecnico di Torino
Turin, Italy
e-mail: diego.gino@polito.it

[4] Department of Structural, Geotechnical and Building Engineering (DISEG), Politecnico di Torino
Turin, Italy
e-mail: elena.miceli@studenti.polito.it

Keywords: seismic isolation, double concave friction pendulum (DCFP) isolator, bridge, pier-abutment-deck interaction, non-dimensional form, optimal friction coefficient.

Abstract. *The paper analyzes the influence of double concave friction pendulum (DCFP) isolator properties on the seismic performance of isolated bridges. The behavior of these systems is analyzed by employing an eight-degree-of-freedom model accounting for the first five vibrational modes of the pier and the presence of a rigid abutment, whereas the DCFP isolator behaviour is described combining two single FPSs in series. The uncertainty in the seismic input is taken into account by considering a set of natural records with different characteristics. The variation of the statistics of the response parameters relevant to the seismic performance is investigated through an extensive parametric study carried out for different system properties.*

1 INTRODUCTION

Seismic isolation has emerged as one of the most powerful techniques in the ensemble of retrofitting methodologies [1]-[5] to improve the safety and resilience of infrastructure systems [6]-[7]. In the more general seismic approach, seismic isolation of bridges permits to obtain the uncoupling of the deck from the horizontal earthquake's components, leading to a significant reduction of the deck acceleration and, as consequence, of the forces transmitted to the pier.

Several studies [1]-[4] have been carried out in the last decades investigating the effectiveness of the isolation devices and carrying out experimental and analytical studies on the seismic response of bridges isolated by sliding isolation systems finding out as these kind of devices are quite effective and efficiency in the aseismic bridges' design. Ghobarah and Ali [5] and Turkington et al. [8] showed that the presence of lead-rubber bearings shift the natural period of the structure and increases the amount of damping, moreover they permit to distribute the seismic forces approximately evenly between pier and abutment. Jangid [9] studied the seismic response of bridges seismically isolated by lead-rubber bearings (L-RB) to bidirectional earthquakes outlining that the bidirectional interaction of the restoring forces of the L-RB has not negligible effects on the seismic response of the isolated bridges. In [10]-[11], the seismic behaviour of bridges seismically isolated by adopting friction pendulum system (FPS) was studied. When FPS bearings are used, the natural period of the isolated structure becomes independent of the mass of the superstructure and it just has a dependence on the radius of curvature of the sliding surface [12].

Another important feature of this isolation system is mainly related to the energy dissipation mechanism that becomes possible thanks to the velocity dependent friction between the sliding surfaces and the composite material on the slider [13]-[17]. In addition, it has been demonstrated in [18]-[19] that the characteristics of an FPS become more effective by introducing a second sliding surface obtaining the so called double concave friction pendulum (DCFP). In particular, Kim and Yun [20] studied the positive effects of a double concave friction pendulum system on a bridge response considering different combinations of radii of curvature and of friction coefficients.

Other studies [21]-[22] have been more oriented to define design approaches by means of the seismic reliability-based design (SRBD), in which the main uncertainties such as the seismic input and the system properties have been taken into account. In [23] the optimal properties of FPS able to minimize the seismic response of bridge under earthquake having different frequency contents representative of different soil conditions has been evaluated.

This study analyzes the influence of the double concave friction pendulum (DCFP) isolator properties on the seismic performance of isolated bridges taking into account the pier-abutment-deck interaction. The behavior of these systems, as also described in [10]-[24] is analyzed by employing an eight-degree-of-freedom (8dof) model representative of the reinforced-concrete pier flexibility in addition to the presence of a rigid abutment and deck, whereas the DCFP isolator behaviour is described combining two single FPSs in series [18]-[19]. For each sliding surface, a widespread model which considers the variation of the friction coefficient with the sliding velocity is adopted [15]-[16]. The uncertainty in the seismic input is taken into account by means of a set of natural records with different characteristics. The variation of the statistics of the response parameters relevant to the seismic performance of the isolated bridges is investigated through a nondimensionalization of the motion equations, as also implemented in [25]-[28] developing an extensive parametric study.

2 EQUATIONS OF MOTION

An 8-degree-of-freedom (dof) system is employed to model the isolated bridge configuration of Figure 1. Specifically, 5 dof are given by the lumped masses of the pier, 2 dof correspond to the two slider masses of the DCFP isolators, located respectively on the pier and on the abutment, and 1 dof is related to the rigid deck mass [10].

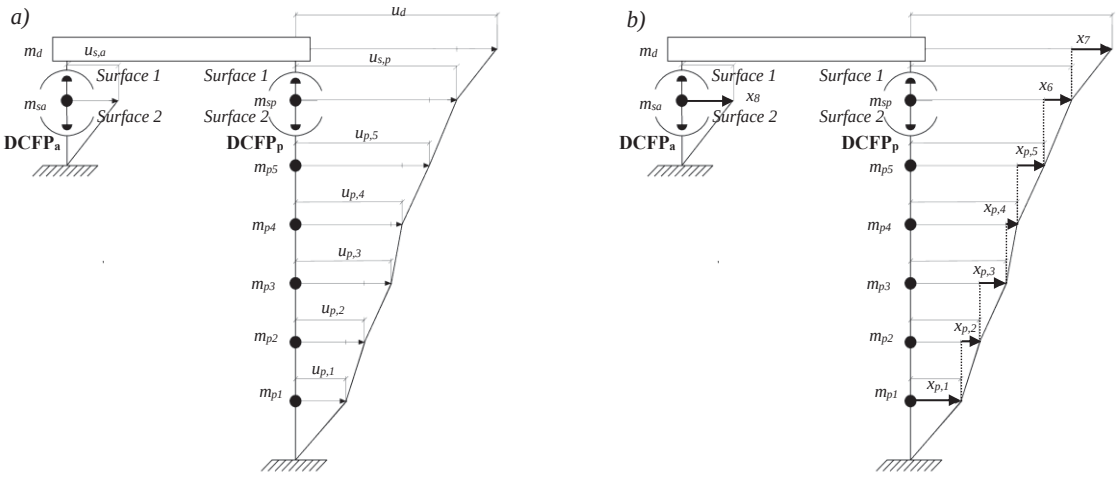

Figure 1: 8dof model of bridge isolated with DCFP bearings: relative displacements with respect to the ground a) and drifts between masses b) .

The equations of motion governing the response of the model representing a bridge on DCFP isolators, in terms of relative displacement with respect to the ground (Figure 1a) subjected to the seismic input $\ddot{u}_g(t)$ is:

$$m_d\left[\ddot{u}_d(t)+\ddot{u}_g(t)\right]+F_{1a}(t)+F_{1p}(t)=0$$

$$m_{sa}\left[\ddot{u}_{sa}(t)+\ddot{u}_g(t)\right]-F_{1a}(t)+F_{2a}(t)=0$$

$$m_{sp}\left[\ddot{u}_{sp}(t)+\ddot{u}_g(t)\right]-F_{1p}(t)+F_{2p}(t)=0 \qquad \text{(1a,b,c,d,e)}$$

$$m_{p5}\left[\ddot{u}_{p5}(t)+\ddot{u}_g(t)\right]+c_{p5}\left[\dot{u}_{p5}(t)-\dot{u}_{p4}(t)\right]+k_{p5}\left[u_{p5}(t)-u_{p4}(t)\right]-F_{2p}(t)=0$$

$$m_{pi}\left[\ddot{u}_{pi}(t)+\ddot{u}_g(t)\right]+c_{pi}\left[\dot{u}_{pi}(t)-\dot{u}_{pi-1}(t)\right]+k_{pi}\left[u_{pi}(t)-u_{pi-1}(t)\right]+$$
$$-c_{pi+1}\left[\dot{u}_{pi+1}(t)-\dot{u}_{pi}(t)\right]-k_{pi+1}\left[u_{pi+1}(t)-u_{pi}(t)\right]=0 \quad for \quad i=1,...,4$$

where u_d denotes the displacement of the superstructure relative to the ground, u_{sp} the displacement of the slider of the DCFP device on the pier with respect to the ground, u_{sa} the displacement of the slider of the DCFP device on the abutment with respect to the ground, u_{pi} (i=1,..,4,5) the displacement of pier i-th mass relative to the ground, m_d , m_{sp} and m_{sa} respectively the mass of the deck and of the two DCFP devices respectively on the pier and on the

abutment, m_{pi} (i=1,..,4,5) the mass the i-th lumped mass of the pier, k_{pi} and c_{pi} (i=1,..,4,5) respectively the stiffness and inherent viscous damping constant for each dof of the pier, t the time instant, the dot differentiation over time, $F_{ja}(t)$ and $F_{jp}(t)$ denote the reaction of the DCFP bearings on the abutment and on the pier, respectively, for the upper (j = *1*) and lower surface (j = *2*). The deck isolated by DCFP isolators is herein considered without any viscous capacities [28].
A DCFP can be modeled as a serial combination of two single FPS. Thus, according with [18]-[19], when the inertial force associated with the movement of the small slider mass is neglected, the reaction forces (F_2 and F_1) at the lower and upper surface become the same and can be readily obtained as follows:

$$F = F_1 = F_2 = \frac{m_d g}{R_1 + R_2}(u) + \frac{m_d g\left(R_1 \mu_1\left(\dot{u}_1\right)\mathrm{sgn}\left(\dot{u}_1\right) + R_2 \mu_2\left(\dot{u}_2\right)\mathrm{sgn}\left(\dot{u}_2\right)\right)}{R_1 + R_2} \tag{2}$$

where u is related to the total deformation of the double concave friction pendulum, u_1 to the deformation of the upper surface and u_2 to the lower one. The first part of the right hand side of Eq.s (2) represents the restoring stiffness (k_{comb}) of the combined DCFP from which the restoring natural period can be obtained as follows:

$$k_{comb} = \frac{m_d g}{R_1 + R_2} \tag{3}$$

$$T_d = 2\pi\sqrt{\left(R_1 + R_2\right)/g} \tag{4}$$

where g is the gravity constant, R_1 and R_2 are the radii of curvature of the DCFP.

In Eq.(2), $f_j\left(\dot{u}_j(t)\right)$ (j=*1,2*) is the coefficient of sliding friction, which depends on the slider slip velocity along one of the two bearing internal surfaces, indicated with $\dot{u}_j(t)$, and $\mathrm{sgn}\left(\dot{u}_j\right)$ (j=*1,2*) with *sgn*(·) denoting the sign function. Note that the subscript 1 refers to the upper surface whereas the subscript 2 refers to the lower surface. On the other hand, the second part of the Eq.s (2a,b), under the hypothesis that sliding occurs on both surfaces and in the same direction, represents the equivalent friction coefficient of the DCFP [18]:

$$\mu_{eqv} = \frac{\mu_1 R_1 + \mu_2 R_2}{R_1 + R_2} \tag{5}$$

In the above discussion, it is also assumed that the DCFP bearings used to isolate the deck and placed, respectively, on the pier and on the abutment have the same characteristics, so that it's obvious they move simultaneously.
Moreover, experimental results [14]-[16] suggest that, for each sliding surface, the coefficient of sliding friction of Teflon-steel interfaces obeys to the following equation:

$$\mu_j\left(\dot{u}_j\right) = \mu_{j,\max} - \left(\mu_{j,\max} - \mu_{j,\min}\right)\cdot\exp\left(-\alpha\left|\dot{u}_j\right|\right) \quad for \quad j = 1,2 \tag{6}$$

in which $\mu_{j,\max}$ represents the maximum value of friction coefficient attained at large velocities of sliding, and $\mu_{j,\min}$ represents the value at zero velocity. To further simplify the problem,

in the following analyses it is assumed that $\mu_{j,\max} = 3\mu_{j,\min}$ based on a regression of the experimental results, whereas the exponent α is assumed equal to 30 [14]-[16].

3 NON-DIMENSIONALIZATION OF THE EQUATIONS OF MOTION

In order to analyze the role of each characteristic parameter controlling the seismic behaviour of the system under investigation, the results obtained solving the equations of motion are reduced to a non-dimensional form as discussed in [26]-[28].
To easily obtain the deformation of the isolators along each sliding surface, Eq.(1) can be rewritten in terms of drifts between the masses of the system instead of displacement respect to the ground:

$$m_d\ddot{x}_7(t)+m_d\ddot{x}_6(t)+m_d\ddot{x}_{p5}(t)+m_d\ddot{x}_{p4}(t)+m_d\ddot{x}_{p3}(t)+m_d\ddot{x}_{p2}(t)+$$
$$+m_d\ddot{x}_{p1}(t)+c_d\dot{x}_d(t)+F_{1a}(t)+F_{1p}(t)=-m_d\ddot{u}_g(t)$$

$$m_{sp}\ddot{x}_6(t)+m_{sp}\ddot{x}_{p5}(t)+m_{sp}\ddot{x}_{p4}(t)+m_{sp}\ddot{x}_{p3}(t)+m_{sp}\ddot{x}_{p2}(t)+$$
$$+m_{sp}\ddot{x}_{p1}(t)-F_{1p}(t)+F_{2p}(t)=-m_{sp}\ddot{u}_g(t)$$

$$m_{sa}\ddot{x}_8(t)-F_{1a}(t)+F_{2a}(t)=-m_{sa}\ddot{u}_g(t)$$

$$m_{p5}\ddot{x}_{p5}(t)+m_{p5}\ddot{x}_{p4}(t)+m_{p5}\ddot{x}_{p3}(t)+m_{p5}\ddot{x}_{p2}(t)+m_{p5}\ddot{x}_{p1}(t)-c_d\dot{x}_d(t)+$$
$$+c_{p5}\dot{x}_{p5}(t)+k_{p5}x_{p5}(t)-F_{2p}(t)=-m_{p5}\ddot{u}_g(t)$$

$$m_{p4}\ddot{x}_{p4}(t)+m_{p4}\ddot{x}_{p3}(t)+m_{p4}\ddot{x}_{p2}(t)+m_{p4}\ddot{x}_{p1}(t)-c_{p5}\dot{x}_{p5}(t)-k_{p5}x_{p5}(t)+$$
$$+c_{p4}\dot{x}_{p4}(t)+k_{p4}x_{p4}(t)=-m_{p4}\ddot{u}_g(t)$$

$$m_{p3}\ddot{x}_{p3}(t)+m_{p3}\ddot{x}_{p2}(t)+m_{p3}\ddot{x}_{p1}(t)-c_{p4}\dot{x}_{p4}(t)-k_{p4}x_{p4}(t)+$$
$$+c_{p3}\dot{x}_{p3}(t)+k_{p3}x_{p3}(t)=-m_{p3}\ddot{u}_g(t) \qquad \text{(7a,b,c,d,e,f,g,h)}$$

$$m_{p2}\ddot{x}_{p2}(t)+m_{p2}\ddot{x}_{p1}(t)-c_{p3}\dot{x}_{p3}(t)-k_{p3}x_{p3}(t)+c_{p2}\dot{x}_{p2}(t)+k_{p2}x_{p2}(t)=-m_{p2}\ddot{u}_g(t)$$

$$m_{p1}\ddot{x}_{p1}(t)-c_{p2}\dot{x}_{p2}(t)-k_{p2}x_{p2}(t)+c_{p1}\dot{x}_{p1}(t)+k_{p1}x_{p1}(t)=-m_{p1}\ddot{u}_g(t)$$

where:

$$F_{1a}=\frac{m_d g}{2}\left[\frac{1}{R_{1a}}\left(\sum_{i=1}^{5}x_{pi}+x_6+x_7-x_8\right)+\mu_{1a}\left(\operatorname{sgn}\left(\sum_{i=1}^{5}\dot{x}_{pi}+\dot{x}_6+\dot{x}_7-\dot{x}_8\right)\right)\right]$$
$$F_{2a}=\left(\frac{m_d}{2}+m_{sa}\right)g\left[\frac{1}{R_{2a}}(x_8)+\left(\mu_{2a}(\dot{x}_8)\right)\left(\operatorname{sgn}(\dot{x}_8)\right)\right] \qquad \text{(8a,b,c,d)}$$
$$F_{1p}=\left(\frac{m_d g}{2}\right)\left[\frac{1}{R_{1p}}(x_7)+\left(\mu_{1p}(\dot{x}_7)\right)\left(\operatorname{sgn}(\dot{x}_7)\right)\right]$$
$$F_{2p}=\left(\frac{m_d}{2}+m_{sp}\right)g\left[\frac{1}{R_{2p}}(x_6)+\left(\mu_{2p}(\dot{x}_6)\right)\left(\operatorname{sgn}(\dot{x}_6)\right)\right]$$

After that, dividing all the equations by m_d , Eq.(7) applies:

$$\ddot{x}_7(t)+\ddot{x}_6(t)+\ddot{x}_{p5}(t)+\ddot{x}_{p4}(t)+\ddot{x}_{p3}(t)+\ddot{x}_{p2}(t)+\ddot{x}_{p1}(t)+2\xi_d\omega_d\dot{x}_d(t)+$$
$$+\frac{g}{2}\left[\frac{1}{R_{1a}}\left(\sum_{i=1}^{5}x_{pi}+x_6+x_7-x_8\right)+\mu_{1a}(v)\left(\operatorname{sgn}\left(\sum_{i=1}^{5}\dot{x}_{pi}+\dot{x}_6+\dot{x}_7-\dot{x}_8=v\right)\right)\right]+$$
$$+\frac{g}{2}\left[\frac{1}{R_{1p}}(x_7)+\left(\mu_{1p}(\dot{x}_7)\right)\left(\operatorname{sgn}(\dot{x}_7)\right)\right]=\ddot{u}_g(t)$$

$$\lambda_{sp}\left(\ddot{x}_6(t)+\ddot{x}_{p5}(t)+\ddot{x}_{p4}(t)+\ddot{x}_{p3}(t)+\ddot{x}_{p2}(t)+\ddot{x}_{p1}(t)\right)+$$
$$-\frac{g}{2}\left[\frac{1}{R_{1p}}(x_7)+\left(\mu_{1p}(\dot{x}_7)\right)\left(\operatorname{sgn}(\dot{x}_7)\right)\right]+\left(\frac{1}{2}+\lambda_{sp}\right)g\left[\frac{1}{R_{2p}}(x_6)+\left(\mu_{2p}(\dot{x}_6)\right)\left(\operatorname{sgn}(\dot{x}_6)\right)\right]=-\lambda_{sp}\ddot{u}_g(t)$$

$$\lambda_{sa}\ddot{x}_8(t)-\frac{g}{2}\left[\frac{1}{R_{1a}}\left(\sum_{i=1}^{5}x_{pi}+x_6+x_7-x_8\right)+\mu_{1a}(v)\left(\operatorname{sgn}\left(\sum_{i=1}^{5}\dot{x}_{pi}+\dot{x}_6+\dot{x}_7-\dot{x}_8=v\right)\right)\right]+$$
$$+\left(\frac{1}{2}+\lambda_{sa}\right)g\left[\frac{1}{R_{2a}}(x_8)+\left(\mu_{2a}(\dot{x}_8)\right)\left(\operatorname{sgn}(\dot{x}_8)\right)\right]=-\lambda_{sa}\ddot{u}_g(t)$$

$$\lambda_{p5}\left(\ddot{x}_{p5}(t)+\ddot{x}_{p4}(t)+\ddot{x}_{p3}(t)+\ddot{x}_{p2}(t)+\ddot{x}_{p1}(t)\right)-2\xi_d\omega_d\dot{x}_d(t)+2\xi_{p5}\omega_{p5}\lambda_{p5}\dot{x}_{p5}(t)+\omega_{p5}^2\lambda_{p5}x_{p5}(t)+$$
$$-\left(\frac{1}{2}+\lambda_{sp}\right)g\left[\frac{1}{R_{2p}}(x_6)+\left(\mu_{2p}(\dot{x}_6)\right)\left(\operatorname{sgn}(\dot{x}_6)\right)\right]=-\lambda_{p5}\ddot{u}_g(t)$$

$$\lambda_{p4}\left(\ddot{x}_{p4}(t)+\ddot{x}_{p3}(t)+\ddot{x}_{p2}(t)+\ddot{x}_{p1}(t)\right)-2\xi_{p5}\omega_{p5}\lambda_{p5}\dot{x}_{p5}(t)-\omega_{p5}^2\lambda_{p5}x_{p5}(t)+$$
$$+2\xi_{p4}\omega_{p4}\lambda_{p4}\dot{x}_{p4}(t)+\omega_{p4}^2\lambda_{p4}x_{p4}(t)=-\lambda_{p4}\ddot{u}_g(t)$$

(9a,b,c,d,e,f,g,h)

$$\lambda_{p3}\left(\ddot{x}_{p3}(t)+\ddot{x}_{p2}(t)+\ddot{x}_{p1}(t)\right)-2\xi_{p4}\omega_{p4}\lambda_{p4}\dot{x}_{p4}(t)-\omega_{p4}^2\lambda_{p4}x_{p4}(t)+2\xi_{p3}\omega_{p3}\lambda_{p3}\dot{x}_{p3}(t)+$$
$$+\omega_{p3}^2\lambda_{p3}x_{p3}(t)=-\lambda_{p3}\ddot{u}_g(t)$$

$$\lambda_{p2}\left(\ddot{x}_{p2}(t)+\ddot{x}_{p1}(t)\right)-2\xi_{p3}\omega_{p3}\lambda_{p3}\dot{x}_{p3}(t)-\omega_{p3}^2\lambda_{p3}x_{p3}(t)+2\xi_{p2}\omega_{p2}\lambda_{p2}\dot{x}_{p2}(t)+$$
$$+\omega_{p2}^2\lambda_{p2}x_{p2}(t)=-\lambda_{p2}\ddot{u}_g(t)$$

$$\lambda_{p1}\ddot{x}_{p1}(t)-2\xi_{p2}\omega_{p2}\lambda_{p2}\dot{x}_{p2}(t)-\omega_{p2}^2\lambda_{p2}x_{p2}(t)+2\xi_{p1}\omega_{p1}\lambda_{p1}\dot{x}_{p1}(t)+\omega_{p1}^2\lambda_{p1}x_{p1}(t)=-\lambda_{p1}\ddot{u}_g(t)$$

and the following ratios are introduced:

$$\lambda_{pi}=\frac{m_{pi}}{m_d},\ \lambda_{sa}=\frac{m_{sa}}{m_d},\ \lambda_{sp}=\frac{m_{sp}}{m_d},$$
$$\omega_d=\sqrt{\frac{k_{comb}}{m_d}},\ \omega_{pi}=\sqrt{\frac{k_{pi}}{m_{pi}}},\ \xi_{pi}=\frac{c_{pi}}{2m_{pi}\omega_{pi}} \tag{10a,b,c,d,e,f}$$

where the first three terms are the mass ratios, the third and the fourth terms are the circular frequency of vibration of the isolated deck and of the *i*-th dof of the pier and the one denotes the damping factor of the *i*-th dof of the pier.

Inspired from [26]-[28], let us introduce the time scale $\tau=t\omega_d$ in which ω_d is the fundamental circular frequency of the isolated system with infinitely rigid superstructure, considering

the equivalent stiffness of the DCFP isolator k_{comb}, and the seismic intensity scale a_0, expressed as $\ddot{u}_g(t) = a_0 \ell(\tau)$ where $\ell(\tau)$ is a non-dimensional function of time describing the seismic input time-history, the following non-dimensional equations can be obtained:

$$\ddot{\psi}_7(\tau)+\ddot{\psi}_6(\tau)+\ddot{\psi}_{p5}(\tau)+\ddot{\psi}_{p4}(\tau)+\ddot{\psi}_{p3}(\tau)+\ddot{\psi}_{p2}(\tau)+\ddot{\psi}_{p1}(\tau)+2\xi_d\dot{\psi}_7(\tau)+\frac{g}{2}\left[\frac{1}{R_{1p}}\frac{1}{\omega_d^{\,2}}\psi_7(\tau)+\frac{\mu_{1p}(\dot{\psi}_7)}{a_0}\operatorname{sgn}(\dot{\psi}_7)\right]+$$
$$+\frac{g}{2}\left[\frac{1}{R_{1a}}\frac{1}{\omega_d^{\,2}}\left(\sum_{i=1}^{5}\psi_{pi}(\tau)+\psi_6(\tau)+\psi_7(\tau)-\psi_8(\tau)\right)+\right.$$
$$\left.+\left(\frac{\mu_{1a}}{a_0}\left(\sum_{i=1}^{5}\dot{\psi}_{pi}(t)+\dot{\psi}_6(\tau)+\dot{\psi}_7(\tau)-\dot{\psi}_8(\tau)\right)\right)\left(\operatorname{sgn}\left(\sum_{i=1}^{5}\dot{\psi}_{pi}(\tau)+\dot{\psi}_6(\tau)+\dot{\psi}_7(\tau)-\dot{\psi}_8(\tau)\right)\right)\right]=-\ell(\tau)$$

$$\lambda_{sp}\left[\ddot{\psi}_6(\tau)+\ddot{\psi}_{p5}(\tau)+\ddot{\psi}_{p4}(\tau)+\ddot{\psi}_{p3}(\tau)+\ddot{\psi}_{p2}(\tau)+\ddot{\psi}_{p1}(\tau)\right]-\frac{g}{2}\left[\frac{1}{R_{1p}}\frac{1}{\omega_d^{\,2}}\psi_7(\tau)+\frac{\mu_{1p}(\dot{\psi}_7)}{a_0}\operatorname{sgn}(\dot{\psi}_7)\right]+$$
$$+\left(\frac{1}{2}+\lambda_{sp}\right)g\left[\frac{1}{R_{2p}}\frac{1}{\omega_d^{\,2}}\psi_6(\tau)+\frac{\mu_{2p}(\dot{\psi}_6)}{a_0}\operatorname{sgn}(\dot{\psi}_6)\right]=-\lambda_{sp}\ell(\tau)$$

$$\lambda_{sa}\ddot{\psi}_8(\tau)-\frac{g}{2}\left[\frac{1}{R_{1a}}\frac{1}{\omega_d^{\,2}}\left(\sum_{i=1}^{5}\psi_{pi}(\tau)+\psi_6(\tau)+\psi_7(\tau)-\psi_8(\tau)\right)+\right.$$
$$\left.+\left(\frac{\mu_{1a}}{a_0}\left(\sum_{i=1}^{5}\dot{\psi}_{pi}(t)+\dot{\psi}_6(\tau)+\dot{\psi}_7(\tau)-\dot{\psi}_8(\tau)\right)\right)\left(\operatorname{sgn}\left(\sum_{i=1}^{5}\dot{\psi}_{pi}(\tau)+\dot{\psi}_6(\tau)+\dot{\psi}_7(\tau)-\dot{\psi}_8(\tau)\right)\right)\right]+$$
$$\left(\frac{1}{2}+\lambda_{sa}\right)g\left[\frac{1}{R_{2a}}\frac{1}{\omega_d^{\,2}}\psi_8(\tau)+\frac{\mu_{2a}(\dot{\psi}_8)}{a_0}\operatorname{sgn}(\dot{\psi}_8)\right]=-\lambda_{sa}\ell(\tau)$$

$$\lambda_{p5}\left[\ddot{\psi}_{p5}(\tau)+\ddot{\psi}_{p4}(\tau)+\ddot{\psi}_{p3}(\tau)+\ddot{\psi}_{p2}(\tau)+\ddot{\psi}_{p1}(\tau)\right]-2\xi_d\dot{\psi}_d(\tau)+2\xi_{p5}\lambda_{p5}\frac{\omega_{p5}}{\omega_d}\dot{\psi}_{p5}(\tau)+\frac{\lambda_{p5}\omega_{p5}^2}{\omega_d^2}\psi_{p5}(\tau)+$$
$$-\left(\frac{1}{2}+\lambda_{sp}\right)g\left[\frac{1}{R_{2p}}\frac{1}{\omega_d^{\,2}}\psi_6(\tau)+\frac{\mu_{2p}(\dot{\psi}_6)}{a_0}\operatorname{sgn}(\dot{\psi}_6)\right]=-\lambda_{p5}\ell(\tau)$$

$$\lambda_{p4}\left[\ddot{\psi}_{p4}(\tau)+\ddot{\psi}_{p3}(\tau)+\ddot{\psi}_{p2}(\tau)+\ddot{\psi}_{p1}(\tau)\right]-2\xi_{p5}\lambda_{p5}\frac{\omega_{p5}}{\omega_d}\dot{\psi}_{p5}(\tau)+2\xi_{p4}\lambda_{p4}\frac{\omega_{p4}}{\omega_d}\dot{\psi}_{p4}(\tau)-\lambda_{p5}\frac{\omega_{p5}^2}{\omega_d^2}\psi_{p5}(\tau)+$$
$$+\lambda_{p4}\frac{\omega_{p4}^2}{\omega_d^2}\psi_{p4}(\tau)=-\lambda_{p4}\ell(\tau)$$

$$\lambda_{p3}\left[\ddot{\psi}_{p3}(\tau)+\ddot{\psi}_{p2}(\tau)+\ddot{\psi}_{p1}(\tau)\right]-2\xi_{p4}\lambda_{p4}\frac{\omega_{p4}}{\omega_d}\dot{\psi}_{p4}(\tau)+2\xi_{p3}\lambda_{p3}\frac{\omega_{p3}}{\omega_d}\dot{\psi}_{p3}(\tau)-\lambda_{p4}\frac{\omega_{p4}^2}{\omega_d^2}\psi_{p4}(\tau)+$$
$$+\lambda_{p3}\frac{\omega_{p3}^2}{\omega_d^2}\psi_{p3}(\tau)=-\lambda_{p3}\ell(\tau)$$

$$\lambda_{p2}\left[\ddot{\psi}_{p2}(\tau)+\ddot{\psi}_{p1}(\tau)\right]-2\xi_{p3}\lambda_{p3}\frac{\omega_{p3}}{\omega_d}\dot{\psi}_{p3}(\tau)+2\xi_{p2}\lambda_{p2}\frac{\omega_{p2}}{\omega_d}\dot{\psi}_{p2}(\tau)-\lambda_{p3}\frac{\omega_{p3}^2}{\omega_d^2}\psi_{p3}(\tau)+ \qquad \text{(11 a,b,c,d,e,f,g,h)}$$
$$+\lambda_{p2}\frac{\omega_{p2}^2}{\omega_d^2}\psi_{p2}(\tau)=-\lambda_{p2}\ell(\tau)$$

$$\lambda_{p1}\ddot{\psi}_{p1}(\tau)-2\xi_{p2}\lambda_{p2}\frac{\omega_{p2}}{\omega_d}\dot{\psi}_{p2}(\tau)+2\xi_{p1}\lambda_{p1}\frac{\omega_{p1}}{\omega_d}\dot{\psi}_{p1}(\tau)-\lambda_{p2}\frac{\omega_{p2}^2}{\omega_d^2}\psi_{p2}(\tau)+\lambda_{p1}\frac{\omega_{p1}^2}{\omega_d^2}\psi_{p1}(\tau)=-\lambda_{p1}\ell(\tau)$$

Furthermore, the following non-dimensional parameters that control the bridge system of Figure 1 have been adopted:

$$\Pi_{\omega i}=\frac{\omega_{pi}}{\omega_d},\ \Pi_{\lambda i}=\lambda_{pi}=\frac{m_{pi}}{m_d},\ \Pi_{\lambda sa}=\lambda_{sa},\ \Pi_{\lambda sp}=\lambda_{sp},$$
$$\Pi_{\mu a}\left(\dot{\psi}_d\right)=\frac{\mu_a\left(\dot{\psi}_d\right)g}{a_0},\quad \Pi_{\mu p}\left(\dot{\psi}_d\right)=\frac{\mu_p\left(\dot{\psi}_d\right)g}{a_0},\ \Pi_{\xi_{pi}}=\xi_{pi} \tag{12a,b,c,d,e,f,g}$$

$\Pi_{\lambda,}\,\Pi_{\lambda sa,}\,\Pi_{\lambda sp,}$ are the previously defined mass ratios, Π_{ξ_p} describes the viscous damping inherent respectively to the pier dof. Regarding the control parameters of the pier, indeed, the parameters ω_{pi} are related to the fundamental vibration pulsation ω_p (the first vibration mode) as well as the sum of the mass ratios is related to the overall mass ratio $\Pi_\lambda=\lambda_p=\frac{\sum_{i=1,5} m_{pi}}{m_d}$ and, finally, all the damping factors are assumed equal to $\Pi_{\xi_p}=\xi_p$.

The non-dimensional parameters $\Pi_{\mu a,}\,\Pi_{\mu p}$ measure the isolator strengths, provided by the friction coefficients of the two isolators, respectively. Since these parameters depend on the response through the velocities, the following parameters are used in their steads:

$$\Pi^*_{\mu a}=\frac{\mu_{\max,a}g}{a_0},\quad \Pi^*_{\mu p}=\frac{\mu_{\max,p}g}{a_0} \tag{13a,b}$$

It is important to observe that the normalized response of the dynamic system does not depend on the seismic intensity level a_0. Conversely, the seismic response depends also on the function $\lambda(\tau)$ and also on the isolation circular frequency ω_d (or period $T_d=2\pi/\omega_d$).

The non-dimensional response parameters that describe the dynamic response of the deck and of the *i*-th dof for the pier and the two sliders are, respectively:

$$\psi_{u_d}=\frac{u_{d,\text{peak}}\omega_d^2}{S_A(T_d)}\quad,\ \psi_{x_d}=\frac{x_{d,\text{peak}}\omega_d^2}{S_A(T_d)}=\frac{(x_6+x_7)_{\text{peak}}\omega_d^2}{S_A(T_d)},$$
$$\psi_{u_p}=\frac{u_{p,\text{peak}}\omega_d^2}{S_A(T_d)}=\frac{u_{p5,\text{peak}}\omega_d^2}{S_A(T_d)},\ \psi_{x_i}=\frac{x_{i,\text{peak}}\omega_d^2}{S_A(T_d)}\quad \text{with}\ i=1,\ldots,8 \tag{14a,b,c,d}$$

4 PARAMETRIC STUDY

This section presents the results of an extensive parametric study carried out on the bridge system of Fig. 1 to evaluate the performance of bridges isolated with DCFP bearings.

Seismic input description

The evaluation of the seismic performance of any engineered systems should account for the variability of the intensity, frequency content, and duration of the records at the site. Coherently with the performance-based earthquake engineering (PBEE) approach [29]-[30], this study separates the uncertainties related to the seismic input intensity from those related to the characteristics of the record (record-to-record variability) by introducing a scale factor, a_0, i.e. an intensity measure (*IM)*. By this way, the randomness in the seismic intensity can be described by a hazard curve, whereas the ground motion randomness for a fixed intensity level

can be described by selecting a set of ground motion realizations characterized by a different duration and frequency content, and by scaling these records to the common a_0 value. In line with the criteria of efficiency, sufficiency, and hazard computability [34]-[35], in this study, the spectral pseudo-acceleration, $S_A(T_d)$, at the isolated period of the system, $T_d = 2\pi / \omega_d$, is assumed as intensity measure. This *IM* is related to the spectral displacement S_d by the relation $S_A(T_d) = \omega_d^2 S_d(T_d)$. Many studies (e.g., [34]-[35]) demonstrated that S_A is more efficient than the peak ground acceleration, and its use permits to reduce the response dispersion for the same number of ground motion considered and to obtain more confident response estimates for a given number of records employed.

#	Year	Earthquake Name	Recording Station Name	Vs_{30} [m/sec]	Source (Fault Type)	M [-]	R [km]	PGA_{max} [g]
1	1994	Northridge	Beverly Hills - Mulhol	356	Thrust	6.7	13.3	0.52
2	1994	Northridge	Canyon Country-WLC	309	Thrust	6.7	26.5	0.48
3	1994	Northridge	LA – Hollywood Stor	316	Thrust	6.7	22.9	0.36
4	1999	Duzce, Turkey	Bolu	326	Strike-slip	7.1	41.3	0.82
5	1999	Hector Mine	Hector	685	Strike-slip	7.1	26.5	0.34
6	1979	Imperial Valley	Delta	275	Strike-slip	6.5	33.7	0.35
7	1979	Imperial Valley	El Centro Array #11	196	Strike-slip	6.5	29.4	0.38
8	1995	Kobe, Japan	Nishi-Akashi	609	Strike-slip	6.9	8.7	0.51
9	1995	Kobe, Japan	Shin-Osaka	256	Strike-slip	6.9	46	0.24
10	1999	Kocaeli, Turkey	Duzce	276	Strike-slip	7.5	98.2	0.36
11	1999	Kocaeli, Turkey	Arcelik	523	Strike-slip	7.5	53.7	0.22
12	1992	Landers	Yermo Fire Station	354	Strike-slip	7.3	86	0.24
13	1992	Landers	Coolwater	271	Strike-slip	7.3	82.1	0.42
14	1989	Loma Prieta	Capitola	289	Strike-slip	6.9	9.8	0.53
15	1989	Loma Prieta	Gilroy Array #3	350	Strike-slip	6.9	31.4	0.56
16	1990	Manjil, Iran	Abbar	724	Strike-slip	7.4	40.4	0.51
17	1987	Superstition Hills	El Centro Imp. Co.	192	Strike-slip	6.5	35.8	0.36
18	1987	Superstition Hills	Poe Road (temp)	208	Strike-slip	6.5	11.2	0.45
19	1987	Superstition Hills	Westmorland Fire Stat.	194	Strike-slip	6.5	15.1	0.21
20	1992	Cape Mendocino	Rio Dell Overpass	312	Thrust	7.0	22.7	0.55
21	1999	Chi-Chi, Taiwan	CHY101	259	Thrust	7.6	32	0.44
22	1999	Chi-Chi, Taiwan	TCU045	705	Thrust	7.6	77.5	0.51
23	1971	San Fernando	LA - Hollywood Stor	316	Thrust	6.6	39.5	0.21
24	1976	Friuli, Italy	Tolmezzo	425	Thrust	6.5	20.2	0.35
25	1980	Irpinia	Bisaccia	496		6.9	21.3	0.94
26	1979	Montenegro	ST64	1083	Thrust	6.9	21.0	0.18
27	1997	Umbria Marche	ST238	n/a	Normal	6.0	21.5	0.19
28	2000	South Iceland	ST2487	n/a	Strike-slip	6.5	13	0.16
29	2000	South Iceland (a.s.)	ST2557	n/a	Strike-slip	6.5	15.0	0.13
30	2003	Bingol	ST539	806	Strike-slip	6.3	14.0	0.30

Table 1. Selected ground motions for time history analysis.

In this specific study, the choice of $S_A(T_d)$ as *IM* is motivated by the fact that if all the records are normalized to $S_A(T_d)$, then the normalized displacement response of a system with

period T_d, rigid superstructure and mounted on a frictionless isolator is equal to 1 for each record and it is not affected by the record-to-record variability. Thus, this system can be assumed as reference case for evaluating the influence of the isolator friction and of the isolation period on the response statistics. The record-to-record variability is described through a set of 30 real ground motion records reported in Table 1.

Seismic performance description

This study considers the following set of response parameters relevant to the performance of the isolated system (Eq. (10)): the peak isolator deformation between the two devices $u_{d,\max}$ and $x_{d,\max}$, the peak displacement of pier's top relative to the ground $u_{p,\max}$ and the peak relative displacement along the pier $x_{pi,\max}$. These parameters have be expressed in non-dimensional form according to Eq.s (11) and (13).
By repeatedly solving Eqn. (9) for the ground motions records reported in Table 1, a set of samples is obtained for each output variable used to monitor the seismic performance.
In this paper, the response parameters are assumed to follow a lognormal distribution as widely employed in PBEE [29]-[30] and in many parametric studies concerning the performance of structural systems also since the log-normality assumption permits to estimate, with a limited number of samples, the response at different percentile levels, which is very useful for system reliability assessment [25],[31]-[41].
A lognormal distribution can be fitted to the generic response parameter *D* (i.e., the extreme values $\psi_{u_d}, \psi_{x_d}, \psi_{u_p}$, ψ_{x_i} of Eq.s (11) and (12) by estimating the sample geometric mean, $GM\left(D\right)$, and the sample dispersion, $\beta\left(D\right)$, defined as follows:

$$GM\left(D\right) = \sqrt[N]{d_1 \cdot \ldots \cdot d_N} \tag{15}$$

$$\beta\left(D\right) = \sigma_{\ln}\left(D\right) = \sqrt{\frac{\left(\ln d_1 - \ln\left[GM\left(D\right)\right]\right)^2 + \ldots\ldots + \left(\ln d_N - \ln\left[GM\left(D\right)\right]\right)^2}{N-1}} \tag{16}$$

where d_i denotes the *i*-th sample value of *D*, and *N* is the total number of samples. The sample geometric mean is an estimator of the median of the response and its logarithm coincides with the lognormal sample mean $\mu_{\ln}\left(D\right)$ [26].

Parametric study results

This section shows the results of the parametric study carried out to evaluate the relation between the isolation and bridge properties and the system performance, for the reference seismic input described through the ground motion records of Table 1.
Note that any model uncertainty is considered in the numerical analyses [43]-[45]. The configuration of Table 2 has been used for the DCFP bearings properties.
The two DCFP devices on the abutment and on the pier are identical. So, it follows that $\Pi^*_{\mu a} = \Pi^*_{\mu p} = \Pi^*_{\mu}$ as well as $\Pi_{\lambda sa} = \Pi_{\lambda sp} = \Pi_{\lambda s}$. The parameter $\Pi_{\xi_p} = \xi_p$ is assumed equal to 5%, the isolated bridge period T_d is varied in the range between 2s, 2.5s, 3s, 3.5s and 4s, the pier period T_p in the range between 0.05s, 0.1s, 0.15s and 0.2s. Assuming that each of the pier masses are equal, $\Pi_{\lambda} = \lambda_p$ has been considered varying in the range between 0.1, 0.15 and 0.2, Π^*_{μ} in the range between 0 (no friction) and 2 (very high friction). For numerical reasons, the

ratio $\Pi_{\lambda s}$ is assumed equal to 0.005. Therefore, numerical investigations have been carried out on several different systems by varying the main dynamic parameters and for two different DCFP bearing configurations for 30 different time history seismic input.
For each value of the parameters of interest in the parametric study, the differential equation of motion, i.e., Eqn. (9), has been repeatedly solved for the different ground motion considered. The Bogacki-Shampine integration algorithm available in Matlab-Simulink [42] has been employed choosing a variable step to improve the solution accuracy. The probabilistic properties of the normalized response have been evaluated by estimating the geometric mean, *GM*, and the dispersion, β, of the parameters of interest through Eqns. (15) and (16).

	R_1/R_2	$\mu_{1,max}/\ \mu_{2,max}$	μ_{eqv}
Case 1	2	4	3 μ_2

Table 2. DCFP bearings properties within the parametric analysis.

Figs. 2-5 show the statistics (*GM* and β values) of the response parameters considered, obtained for different values of the system parameters varying in the range of interest. Each figure contains three surface plots, corresponding to different values of Π_λ. Only the results corresponding to T_p= 0.1s and T_p= 0.2s are illustrated.

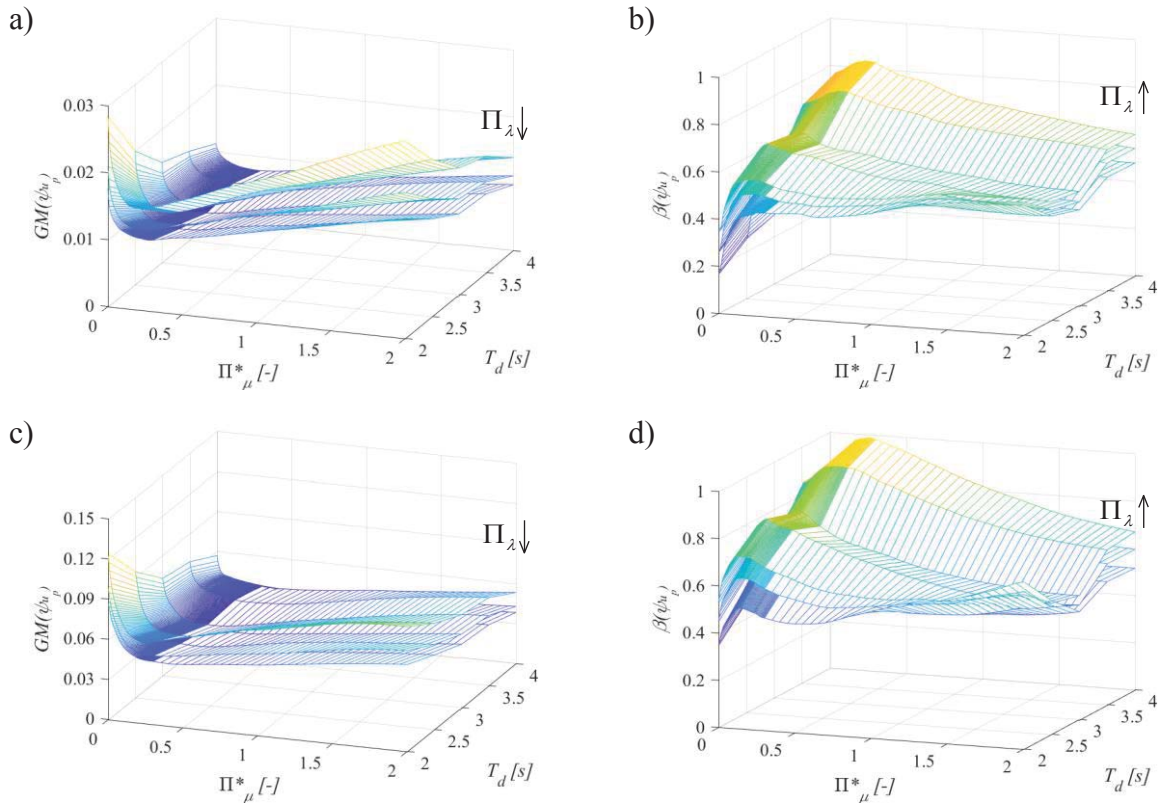

Figure 2. Normalized displacement of pier top vs. Π^*_μ and T_d: median value and dispersion for T_p = 0.1s (a and b) and T_p = 0.2s (c and d) for different values of Π_λ. The arrow denotes the increasing direction of Π_λ.

Fig. 2 plots the results concerning the normalized displacement of pier top ψ_{u_p} with respect to the ground. It is noteworthy that for very low Π_μ^* values, $GM\left(\psi_{u_p}\right)$ decreases by increasing Π_μ^*, whereas for high Π_μ^* values it increases by increasing Π_μ^*. Thus, there exists an optimal value of Π_μ^* such that the displacement of pier top is minimized. This critical value is in the range between 0 and 0.5 depending on the values of T_d, T_p and Π_λ. In addition to that, $GM\left(\psi_{u_p}\right)$ decreases significantly with increasing Π_λ and decreasing T_p, which control directly the main modal period of the pier (for higher ω_d^2, smaller will be the displacement of the pier top). T_d has an influence on $GM\left(\psi_{u_p}\right)$ leading to a general decrease for its increase. The dispersion $\beta\left(\psi_{u_p}\right)$ shows a maximum value approximatively at the same value of Π_μ^* that gives the minimum value of $GM\left(\psi_{u_p}\right)$. The response dispersion increases with increasing vibration period T_p and mass ratio Π_λ. From low to high values of T_d, the dispersion $\beta\left(\psi_{u_p}\right)$ tends to increase.

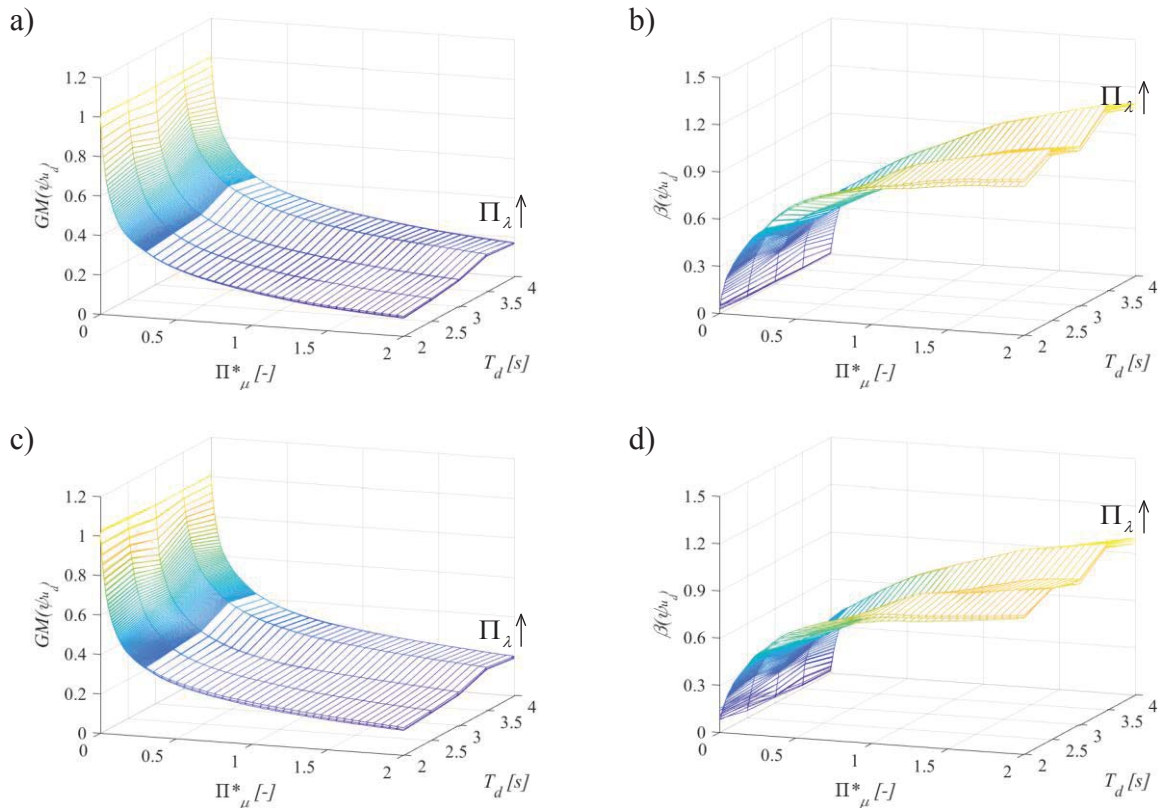

Figure 3. Normalized deck displacement vs. Π^*_μ and T_d: median value and dispersion T_p = 0.1s (a and b) and T_p = 0.2s (c and d) for different values of Π_γ. The arrow denotes the increasing direction of Π_γ.

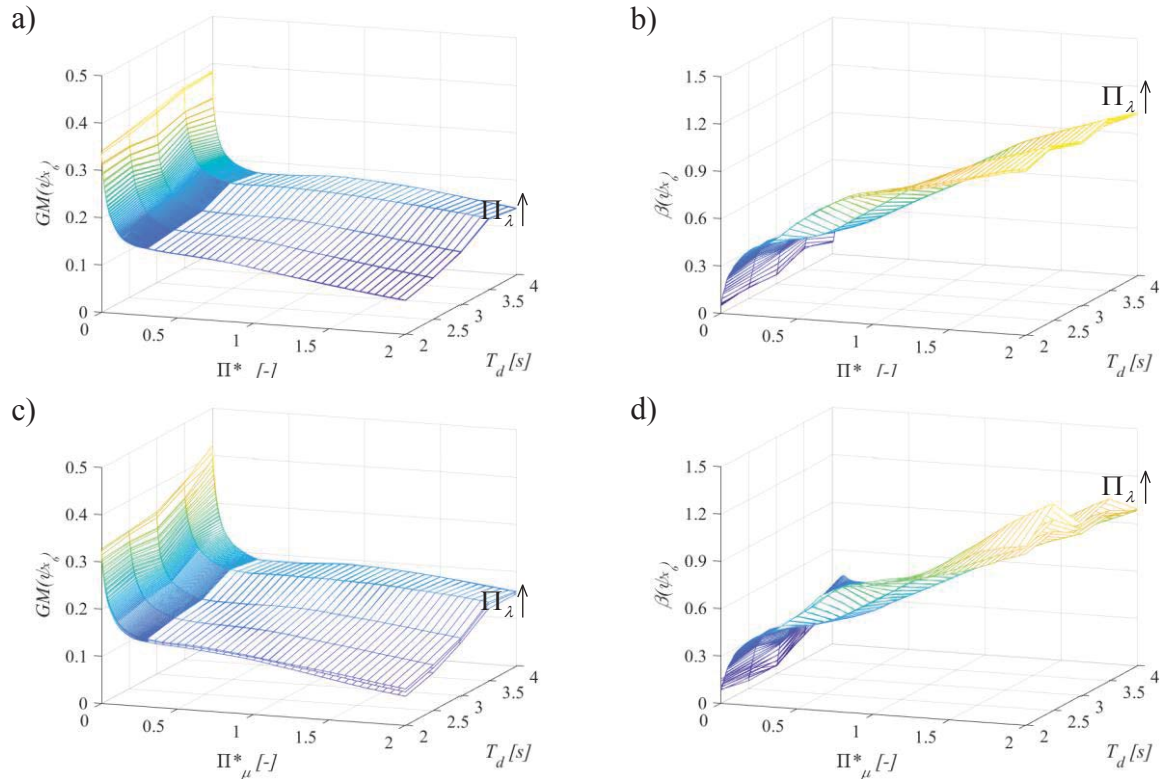

Figure 4. Normalized pier bearing deformation along the lower surface vs. Π^*_μ and T_d: median value and dispersion for T_p = 0.1s (a and b) and T_p = 0.2s (c and d) for different values of Π_λ. The arrow denotes the increasing direction of Π_λ.

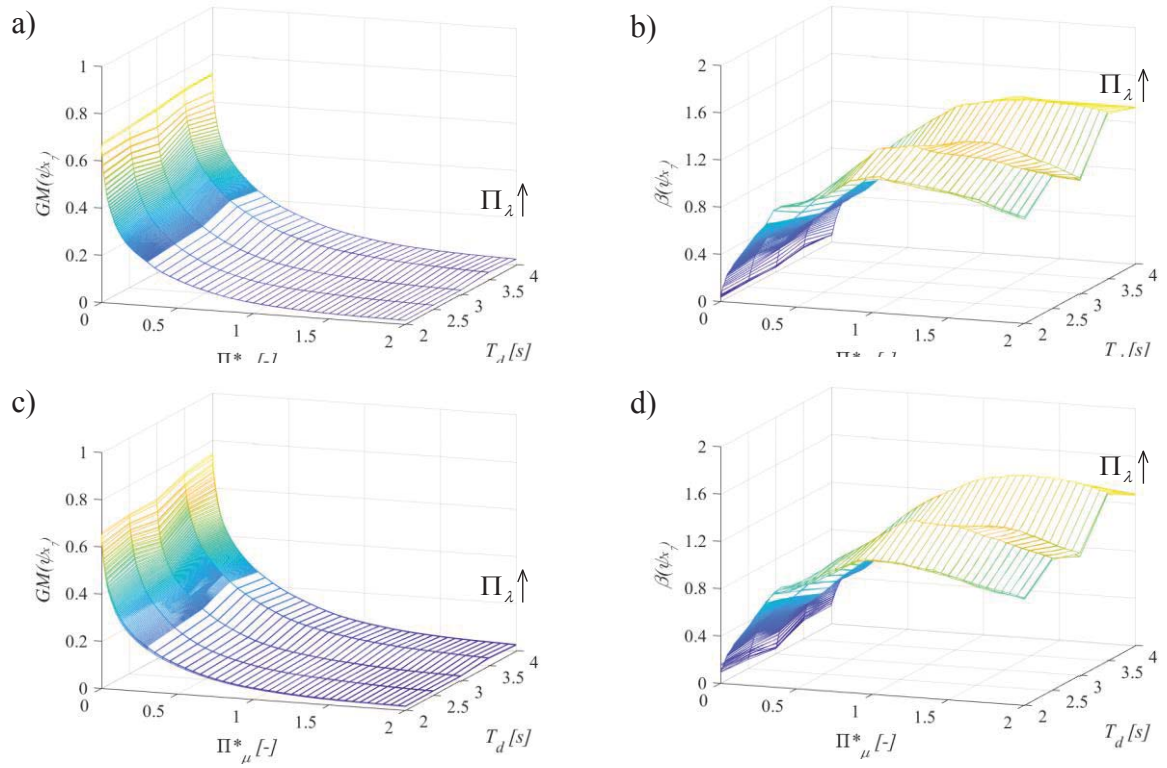

Figure 5. Normalized pier bearing deformation along the upper surface vs. Π^*_μ and T_d: median value and dispersion for T_p = 0.1s (a and b) and T_p = 0.2s (c and d) for different values of Π_λ. The arrow denotes the increasing direction of Π_λ.

Fig. 3 (a,c) shows the response statistics of the normalized deck displacement ψ_{u_d}, which corresponds to the overall deformation of the bearing placed on the abutment, since this latter is the peak value with respect to the displacement relative to the pier top of the other device due to the flexibility of the pier. Obviously, $GM\left(\psi_{u_d}\right)$ decreases significantly as Π^*_μ increases. In general, the values of $GM\left(\psi_{u_d}\right)$ increase slightly for increasing values of T_d and of Π_λ, and they are not affected significantly by T_p. The values of the dispersion $\beta\left(\psi_{u_d}\right)$, plotted in Figs. 3(b,d), are very low for low Π^*_μ values due to the high efficiency of the *IM* employed in the study, and attain their peak for high values of Π^*_μ. The other system parameters have a reduced influence on $\beta\left(\psi_{u_d}\right)$ compared to the influence of Π^*_μ.

Fig. 4(a) and (c) show the variation with the system parameters of the geometric mean of the normalized pier bearing deformation along the lower surface $GM(\psi_{x_6})$, for T_p=0.1s and T_p=0.2s. This parameter decreases at first quickly, and then slightly increases after values of Π^*_μ close to 0.5, reaching a maximum for Π^*_μ close to 1. The values of the dispersion $\beta\left(\psi_{x_6}\right)$, plotted in Figs. 4 (b,d), are very low for low Π^*_μ values, and increase monotonically with Π^*_μ. The other system parameters have a negligible influence on $\beta\left(\psi_{x_6}\right)$ compared to the influence of Π^*_μ.

Fig. 5(a) and (c) show the variation with the system parameters of the geometric mean of the normalized pier bearing deformation along the upper surface $GM(\psi_{x_7})$, for T_p = 0.1s and T_p = 0.2s. This parameter decreases hyperbolically with increasing Π^*_μ. The values of the dispersion $\beta\left(\psi_{x_7}\right)$, plotted in Figs. 5(b,d), are very low for low Π^*_μ values, and show a maximum for $\Pi^*_\mu \approx 1$, reaching very high values close to 1.5. Once again, the other system parameters have a no significant influence on $\beta\left(\psi_{x_7}\right)$ compared to the influence of Π^*_μ.

These last figures demonstrate the highest influence of the upper surface, characterized by higher values of the sliding friction coefficient and of the radius of curvature to define the global response of the seismic DCFP device as shown by the both statistic in Fig. 3. In fact, it is the upper surface that plays a crucial role for high intensity to elongate the isolated period and to dissipate more energy.

5 OPTIMAL VALUES

The existence of an optimal value of the friction coefficient able to minimize the displacement of pier top is the result of counteracting effects that occur for increasing values of the friction coefficient as already highlighted in [23]: increase of the isolator strength with increase of the equivalent stiffness and with a reduction of the corresponding equivalent fundamental vibration period; increase of participation of higher vibration modes as well as transfer of forces towards the superstructure; increase of energy dissipation (equivalent damping).

Fig. 6 reports the variation of $\Pi^*_{\mu,optimum}$ with Π_λ and T_p for T_d = 2s (Fig. 6 a) and T_d = 3s (Fig. 6 b) obtained by considering the minimization of the median (i.e., 50th percentile) of the normalized displacement of pier top ψ_{u_p} in the range of Π^*_μ between 0 and 0.5. It is ob-

served that $\Pi^*_{\mu,optimum}$ generally increases along with Π_λ, T_p and T_d. According to Eqn. (13), the optimal friction coefficient of the upper surface can be easily calculated as $f_{1,\max,opt} = \frac{\Pi^*_{\mu,opt} \cdot S_A(T_d)}{g}$ and of lower surface since the ratio is assumed equal to 4 (Table 2). Thus, it increases linearly with the *IM* level.

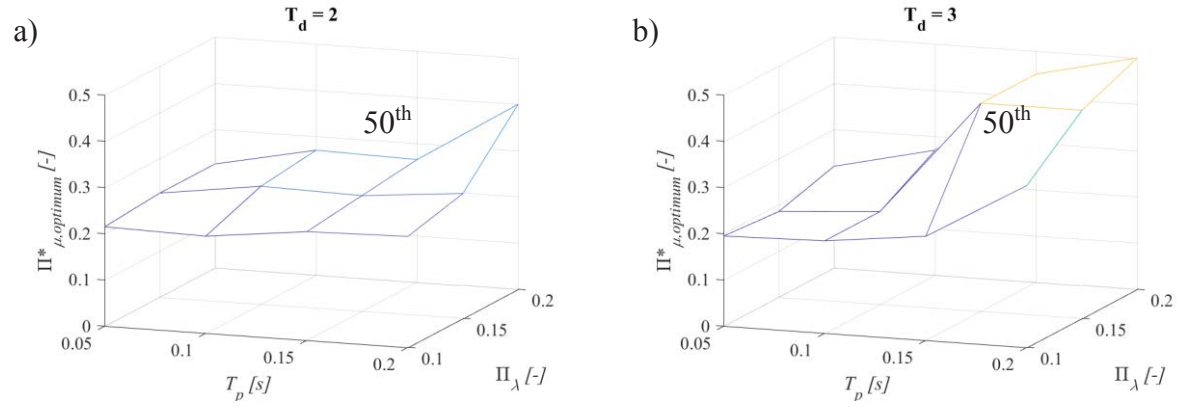

Figure 6. Critical values of normalized friction vs. Π_λ and T_p for T_d =2s (a) and T_d =3s (b).

6 CONCLUSIONS

This paper investigates the seismic performance of bridges isolated with double concave friction pendulum (DCFP) isolators considering the pier-abutment-deck interaction. They are illustrated the results of a parametric study for different isolator and bridge properties and various response parameters that are of interest for monitoring the seismic behavior. The behavior of these systems is analyzed by employing an eight-degree-of-freedom model accounting for the pier flexibility.

An ensemble of ground motions is considered to simulate the record-to-record variability effects, and a nondimensionalization of the results of the equation of motion is proposed to unveil the parameters controlling the problem.

The influence of dynamic and DCFP system properties are evaluated by considering the geometric mean (GM) and dispersion of each normalised response parameter, assumed to follow a lognormal distribution.

The results demonstrate that the increase of the normalized friction coefficient leads to a decrease of the deck response whereas the normalized response of the pier presents a particular trend showing the existence of an optimal value able to minimize this curve. The value of the optimal non-normalised friction coefficient depends on the structural properties. Specifically higher values are required for high pier period combined to high isolated deck period.

REFERENCES

[1] M. C. Constantinou, A. Kartoum, A. M. Reinhorn, P. Bradford , Sliding isolation system for bridges: Experimental study, *Earthquake Spectra* 1992; 8(3): 321-344.

[2] A. Kartoum, M. C. Constantinou, A. M. Reinhorn, Sliding isolation system for bridges:

Analytical study, *J. Struct. Eng.* 1992; 8(3): 345-372.

[3] P. Tsopelas, M. C. Constantinou, Y. S. Kim, S. Okamota, Experimental study of FPS system in bridge seismic isolation, *Earthquake Eng. Struct. Dyn.* 1996a; 25(1): 65-78.

[4] P. Tsopelas, M. C. Constantinou, S. Okamota, S. Fujii, D. Ozaki, Experimental study of bridge seismic sliding isolation systems, *Eng. Struct.* 1996b; 18(4): 301-310.

[5] A. Ghobarah, H. M. Ali, Seismic performance of highway bridges, *Eng. Struct.* 1988; 10(3): 157-166

[6] Troisi R., Alfano G. 2019. Towns as Safety Organizational Fields: An Institutional Framework in Times of Emergency. *Sustainability*, 11: 7025, 2019, doi:10.3390/su11247025.

[7] Troisi R., Alfano G. 2020. Firms'crimes and land use in Italy. An exploratory data anlysis. New Metropolitan Perspectives, International Symposium – 4th edition, 27-30 May 2020, pp 10.

[8] D. H. Turkington, A. J. Carr, N. Cooke, P. J. Moss, Seismic design of bridges on lead-rubber bearings, *J. Struct. Eng.* 1989; 115(12): 3000-3016.

[9] R. S. Jangid, Seismic response of isolated bridges, *J. Bridge Eng.* 2004; 9(2): 156-166.

[10] R. S. Jangid, Stochastic Response of Bridges Seismically Isolated by Friction Pendulum System, *J. Bridge Eng*. 2008; 13(4): (319).

[11] Y. P. Wang, L. L. Chung, W. H. Liao, Seismic response analysis of bridges isolated with friction pendulum bearings, *Earthquake Eng. Struct. Dyn.* 1998; 27(10): 1069-1093.

[12] VA. Zayas, SS. Low, SA. Mahin, A simple pendulum technique for achieving seismic isolation. *Earthquake Spectra* 1990; 6:317–33.

[13] L. Su, G. Ahmadi , IG. Tadjbakhsh, Comparative study of base isolation systems. *Journal of Engineering Mechanic* 1989; 115:1976–92.

[14] A. Mokha , MC. Constantinou, AM. Reinhorn, Teflon Bearings in Base Isolation. I: Testing. *J. Struct. Eng.* 1990; 116(2): 438-454.

[15] M. C. Constantinou, A. Mokha, A. M. Reinhorn, Teflon Bearings in Base Isolation. II: Modeling. *J. Struct. Eng*. 1990; 116(2):455-474.

[16] M. C. Constantinou, AS. Whittaker, Y. Kalpakidis, DM. Fenz, GP. Warn, Performance of Seismic Isolation Hardware Under Service and Seismic Loading. Technical Report, 2007.

[17] J. L. Almazàn, J. C. De la Llera, Physical model for dynamic analysis of structures with FPS isolators. *Earthquake Engineering and Structural Dynamics* 2003; 32:1157–1184.

[18] D. M. Fenz, M. C. Constantinou, Behaviour of the double concave friction pendulum bearing, *Earthquake Engineering and Structural Dynamics*, 2006; 35:1403-1424.

[19] M. C. Constantinou, Friction pendulum double concave bearings, technical report. University of Buffalo NY, October 29, 2004.

[20] Y. S. Kim, C. B. Yun, Seismic response characteristics of bridges using double concave friction pendulum bearings with tri-linear behavior. *Engin. Struct*. 29, 2007, 3082-3093.

[21] P. Castaldo, B. Palazzo, P. Della Vecchia, Life-cycle cost and seismic reliability analy-

sis of 3D systems equipped with FPS for different isolation degrees, *Engineering Structures*, 2016; 125: 349–363.

[22] P. Castaldo, G. Amendola, B. Palazzo , Seismic fragility and reliability of structures isolated by friction pendulum devices: Seismic reliability-based design (SRBD), *Earthquake Engineering and Structural Dynamics*, 2017, 46(3); 425–446, DOI: 10.1002/eqe.2798.

[23] P. Castaldo, M. Ripani, R. Lo Piore, Influence of soil conditions on the optimal sliding friction coefficient for isolated bridges, *Soil Dynamics and Earthquake Engineering*, 2018, 111; 131–148, https://doi.org/10.1016/j.soildyn.2018.04.056.

[24] Y. P. Wang, L. Chung, H. L. Wei, Seismic response analysis of bridges isolated with friction pendulum bearings, *Earthquake Eng. Struct. Dyn.*, 27(10); 1069-1093.

[25] E. Tubaldi E, L. Ragni, A. Dall'Asta, Probabilistic seismic response assessment of linear systems equipped with nonlinear viscous dampers, *Earthquake Engineering & Structural Dynamics* 2014; DOI: 10.1002/eqe.2461.

[26] P. Castaldo, E. Tubaldi, Influence of FPS bearing properties on the seismic performance of base-isolated structures, *Earthquake Engineering & Structural Dynamics*, 2015; 44(15): 2817-2836.

[27] P. Castaldo, M. Ripani, Optimal design of friction pendulum system properties for isolated structures considering different soil conditions, *Soil Dynamics and Earthquake Engineering*, 2016, 90:74–87, DOI: 10.1016/j.soildyn.2016.08.025.

[28] P. Castaldo, E. Tubaldi, Influence of ground motion characteristics on the optimal single concave sliding bearing properties for base-isolated structures. *Soil Dynamics and Earthquake Engineering*, 2018, 104: 346–364.

[29] RD. Bertero, VV. Bertero, Performance-based seismic engineering: the need for a reliable conceptual comprehensive approach. *Earthquake Engineering and Structural Dynamics,* 2002;31:627–652 (DOI: 10.1002/eqe.146).

[30] H. Aslani, E. Miranda, Probability-based seismic response analysis. *Engineering Structures* 2005; **27**(8): 1151-1163.

[31] P. Castaldo, B. Palazzo, T. Ferrentino T., Seismic reliability-based ductility demand evaluation for inelastic base-isolated structures with friction pendulum devices, *Earthquake Engineering and Structural Dynamics*, 2017, 46(8): 1245-1266, DOI: 10.1002/eqe.2854.

[32] Castaldo P., Alfano G. Seismic reliability-based design of hardening and softening structures isolated by double concave sliding devices, *Soil Dynamics and Earthquake Engineering*, 129: 105930, 2020.

[33] P. Castaldo, B. Palazzo, G. Alfano, MF. Palumbo, Seismic reliability-based ductility demand for hardening and softening structures isolated by friction pendulum bearings, 2018, *Structural Control and Health Monitoring*, e2256. https://doi.org/10.1002/stc.2256.

[34] N. Shome, C. A. Cornell, P. Bazzurro, J. E. Carballo, Earthquake, records, and nonlinear responses. *Earthquake Spectra*, 1998, 14(3); 469-500.

[35] N. Luco, C. A. Cornell, Structure-specific scalar intensity measures for near-sorce and ordinary earthquake ground motions. *Earthquake Spectra*, 2007, 23(2); 357-392.

[36] Garzillo C., Troisi R. Le decisioni dell'EMA nel campo delle medicine umane. In EMA e le relazioni con le Big Pharma - I profili organizzativi della filiera del farmaco, G. Giappichelli, 85-133, 2015.

[37] Golzio L. E., Troisi R. The value of interdisciplinary research: a model of interdisciplinarity between legal re-search and research in organizations. *Journal For Development And Leadership*, 2: 23-38, 2013.

[38] Nese A.; Troisi R. Corruption among mayors: evidence from Italian Court of Cassation judgments, *Trends In Organized Crime*, 1-26, 2018. DOI:10.1007/s12117-018-9349-4.

[39] Troisi R., Golzio, L. E. Legal studies and organization theory: a possible cooperation. *Manageable cooperation* - European Academy of Management: 16th EURAM Conference, Paris, 1-2, 1-4 June 2016.

[40] Troisi R., Guida V. Is the Appointee Procedure a Real Selection or a Mere Political Exchange? The Case of the Italian Health-Care Chief Executive Officers. *Journal of Entrepreneurial and Organizational Diversity*, 7 (2): 19-38, 2018, DOI:10.5947/jeod.2018.008.

[41] Troisi R. Le risorse umane nelle BCC: lavoro e motivazioni al lavoro. In Progetto aree bianche. Il sistema del credito cooperativo in Campania, 1: 399-417, 2012.

[42] Math Works Inc. MATLAB-High Performance Numeric Computation and Visualization Software. User's Guide. Natick: MA, USA, 1997.

[43] Castaldo, P., Gino, D., Bertagnoli, G. & Mancini, G. Resistance model uncertainty in non-linear finite ele-ment analyses of cyclically loaded reinforced concrete systems, *Engineering Structures*, 211: 110496, 2020, https://doi.org/10.1016/j.engstruct.2020.110496.

[44] P. Castaldo, D. Gino, G. Mancini, Safety formats for non-linear analysis of reinforced concrete structures: discussion, comparison and proposals. *Engineering Structures*, 193,136-153, 2019.

[45] P. Castaldo, D. Gino, G. Bertagnoli, G. Mancini, Partial safety factor for resistance model uncertainties in 2D non-linear finite element analysis of reinforced concrete structures. *Engineering Structures,* 176:746-762, 2018.

EURODYN 2020
XI International Conference on Structural Dynamics
M. Papadrakakis, M. Fragiadakis, C. Papadimitriou (eds.)
Athens, Greece, 23–26 November 2020

MEASUREMENTS OF AMBIENT VIBRATIONS FOR A CABLE-STAYED BRIDGE INCLUDING THE SOIL-FOUNDATION SYSTEM

Vanni Nicoletti[1], **Davide Arezzo**[1], **Sandro Carbonari**[1], **Francesca Dezi**[2] **and Fabrizio Gara**[1]

[1] Dept. of Construction, Civil Engineering and Architecture, DICEA, Univ. Politecnica delle Marche, Via Brecce Bianche, 60131, Ancona, Italy.

[2] Dept. of Economics, Science and Law, DESD, University of the Republic of San Marino, Via Consiglio dei Sessanta, 99, 47891, Republic of San Marino.

e-mails: v.nicoletti@pm.univpm.it, d.arezzo@pm.univpm.it, s.carbonari@univpm.it, francesca.dezi@unirsm.sm, f.gara@univpm.it

Keywords: bridge dynamic testing, bridge proof load test, cable-stayed steel bridge, modal identification, ambient vibration tests, soil-structure interaction.

Abstract. *This paper deals with the dynamic characterization of a cable-stayed steel-concrete composite bridge located on the Saline river, close to Pescara in central Italy, carried out during the static proof load test. The bridge is 189 m long and is composed by 4 inclined steel pipe pylons that sustain a steel-concrete composite deck by means of 40 stay cables. During the proof test, an extensive experimental campaign is carried out to check the overall structural performance before the bridge openings to traffic. In detail, the main girder deflections, the axial loads on strands, the pylons displacements, and the bearings displacements were monitored through conventional and non-conventional techniques, such as the laser scanner technique. In addition, an accelerometer array is installed during the proof test to evaluate the dynamic characteristics of the structure in its loaded and unloaded conditions through ambient vibration measurements. Sensors are positioned on the deck, on two pylons and on the foundation system, in order to characterize the whole structural dynamic behavior, including the contribution of the soil-foundation compliance. With reference to the unloaded bridge, the latter issue is analyzed in this paper, focusing on the different restraint condition exerted by the soil-foundation system of the pylons, because of the different embedment of the reinforced concrete basements. It is shown that the soil-foundation compliance has greater effects on higher modes for the bridge at hand and that possible non-symmetries due to the different foundation degree of restraint can be suitably captured through ambient vibration tests. Data from experimental tests are crucial not only to check consistency between the design and the real structure before the opening to traffic, but also to calibrate refined finite element models to be used for the structural health monitoring of the bridge. In this sense, a reliable evaluation of the contribution of the soil-foundation system is mandatory, considering that the bridge, having foundations located in the riverbed, is prone to the scour hazard.*

1 INTRODUCTION

System modal identification and structural health monitoring of structures have recently drawn attention within the civil engineering community for developing real time assessment tools and for reducing uncertainties in the design and modelling of structures. In these fields, the estimation of structural dynamic properties through ambient vibration measurements play an important role since such tests are fast and easy to perform [1]. In the case of bridges, ambient vibration tests are usually performed focusing the attention of the deck accelerations, by positioning sensors over the superstructure in correspondence of piers and at midspans [2-3]. This approach generally allows a satisfactory identification of resonance frequencies but provides inaccurate information about mode shapes since displacements at the deck level may be due to both the pier deflection, the bearing compliance (which may be important in the case of isolated bridges) and the deformability of the soil-foundation system [4-6]. The latter, depending on the geotechnical context, may be relevant especially in case of scour phenomena.

This paper deals with the dynamic monitoring of a cable-stayed steel bridge performed during the proof load tests required for the bridge opening to traffic. Firstly, the overall experimental campaign scheduled during the proof load test is described, then results of the performed dynamic tests are presented. The bridge dynamic identification, achieved through ambient vibration tests performed on the unloaded bridge, is presented and results are shown in terms of modal parameters. The latter are compared with those obtained with numerical model developed for design purposes.

Finally, the contribution of the soil-foundation compliance on the bridge dynamics is investigated extending ambient measurements to the foundation system.

2 THE "FILOMENA DELLI CASTELLI" BRIDGE

The "Filomena Delli Castelli" bridge is a 189 m long cable-stayed steel-concrete composite bridge newly built over the Saline river in Pescara, central Italy (Fig. 1), which allows road and cycle-pedestrian connections between the Municipalities of Montesilvano and Città Sant'Angelo.

The bridge has 3 spans of length 42.6, 103.4 e 42.6 m and is composed by a twin girder directly supporting cross-beam composite deck, supported by 40 stay cables anchored in semi-fan system to two pylons made with concrete filled steel tubes. All the stay cables, composed by up to 37 seven-wire parallel-strands with an extruded HDPE sheath, are anchored to the upper flange of the main girders, excepting the four external ones, which are fixed to the concrete abutments to limit displacements of pylons. One strand of each stay is equipped with a load cell. The deck has variable width from 19.2 to 22.8 m, which includes a cycle-pedestrian path on the downstream side, and is composed by two 14.1 m spaced and 1.2 m high I shaped girders, and 4.5 m spaced cross-beams with cantilevers, both supporting a 25 cm thick concrete slab.

Each pylon has two inclined steel tubes of different height and diameter 1.9 m, filled with concrete in the lower part (16 m) and connected by a box steel cross-beam under the deck level; pylons on the upstream side are 34 m high, while those on the downstream side are 37 m high. Each pylon is fixed over a conical trunk shape r.c. basement by means of Dywidag steel anchor bolts and supported by a piled raft foundation. The upstream and downstream pylon foundations are connected to each other through a r.c. tie beam. The seismic protection of the bridge is achieved through Lead Rubber Bearings (LRB) located at the 2 pylon cross-beams in the middle position. The remaining support devices are multidirectional negative load pot bearings.

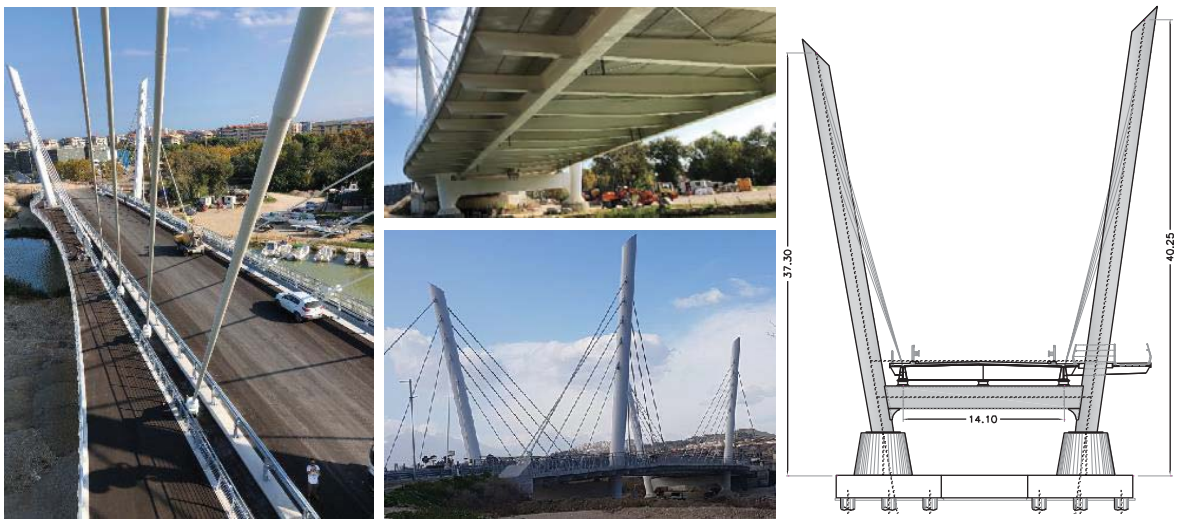

(a) (b)

Figure 1: Filomena Delli Castelli bridge in Pescara: (a) general views, (b) transverse scheme.

3 EXPERIMENTAL PROGRAMME

The final proof test of the bridge was executed in October 2019; 12 fully loaded trucks were used, and two load configurations were considered to get the design bending moments at Serviceability Limit State in the most stressed cross-sections of the deck. The load test allows comparison between theoretical displacements (obtained from the design numerical model) and the experimental ones and the evaluation of the residual deflection of the deck after load removal. Moreover, dynamic tests were executed to compare numerical and experimental modal parameters of the bridge at both unloaded and loaded conditions.

The following response parameters were monitored during the different phases of the load tests to evaluate the overall static and dynamic behavior of the bridge:
i) deflections of the main girders, through a topographic measurement station;
ii) axial load of strands, through load cells;
iii) deck and pylons displacements through a Laser Scanner (LS) technology;
iv) horizontal displacements of some support devices, through centesimal comparators;
v) tracking of the modal parameters (frequencies, damping ratios and mode shapes) of the bridge during test, through Ambient Vibration Tests (AVTs);
vi) resonant frequencies from impact tests (obtained by a truck passing over an artificial bump);
vii) resonant frequencies of a typical truck to exclude possible bridge-truck interactions;
viii) continuous measurement of the air temperature and the temperature of the road pavement.

This paper addresses results of the dynamic identification of the overall structure at unloaded conditions, focusing on the contribution of the soil-foundation compliance on the interpretation of the bridge dynamics.

4 DYNAMIC IDENTIFICATION OF THE OVERALL BRIDGE

The bridge dynamic identification is obtained through AVTs performed before the proof load test. The vibrations are due to environment effects, i.e. microtremors, wind, river waves, and anthropic activities, i.e. car and train traffic close to the structure. The latter are measured through low noise uniaxial piezoelectric accelerometers, connected to a data acquisition system by means of coaxial cables. A laptop equipped with a LabVIEW [7] software is used to control and store the data. Sensors are located on the structure according to the arrangement

shown in Fig. 2. As for the superstructure (Fig. 2a), 15 accelerometers are placed on the deck in 5 representative cross sections to identify the bending, transverse and torsional deck modes while 4 accelerometers are positioned on the downstream pylons (2 at each pylon) to measure the longitudinal and transverse accelerations and to capture their contribution on the overall vibration modes of the bridge.

Additionally, 10 sensors are located on the conical r.c. basements of the two downstream side pylons (Fig. 2b): for each basement, 3 sensors are oriented to measure the vertical accelerations in order to identify the foundation rocking, while the remaining 2 sensors are oriented to measure the transverse and longitudinal accelerations, respectively, to capture the translational components of the motion. During the test, 30 minutes long records with 2048 Hz frequency sampling rate are acquired. This time length provides enough data to obtain modal parameters with a good accuracy, as reported in [8], where a length of the acquired time window of about 1000-2000 times the period of the fundamental mode is recommended. In AVTs the input is neither controlled nor known, and it is assumed to have a flat spectrum such as a white noise; therefore, to identify the bridge modal parameters the output-only technique working in the time domain called Covariance-driven Stochastic Subspace Identification (SSI-COV) [9] is used.

The data post-processing provides the natural frequencies, damping ratios and mode shapes of the investigated structure; in detail, Fig. 3 shows the first 6 bridge vibration modes together with the relevant resonant frequency and damping ratio of the bridge at unloaded conditions. The first three modes represent the first bending, the first torsional and the second bending mode of the deck, respectively; the fourth and fifth modes are both typical of the second deck torsional mode, however, mode shapes are also characterized by a significant bending of the edge spans that, in turn, governs the response of the lateral spans more than the torsion. Finally, the sixth mode is the typical third bending deck mode.

Fig. 4 shows the stabilization diagram through which modes have been identified; in detail, a mode is assumed to be stable if the frequency variation Δf, the damping ratio variation $\Delta\xi$ and the Modal Assurance Criterion (MAC) between two subsequent model order are less than 1 and 2% for Δf and $\Delta\xi$, respectively, and higher than 99% for the MAC. The first Singular Value (SV) line is also reported for completeness.

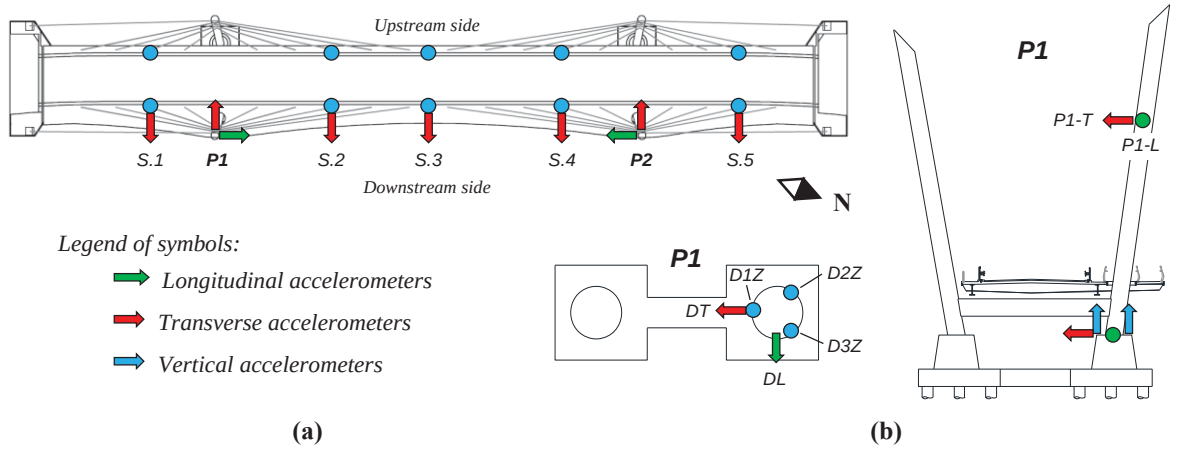

Figure 2: Sensors layout: (a) arrangement on the deck and (b) on the basements.

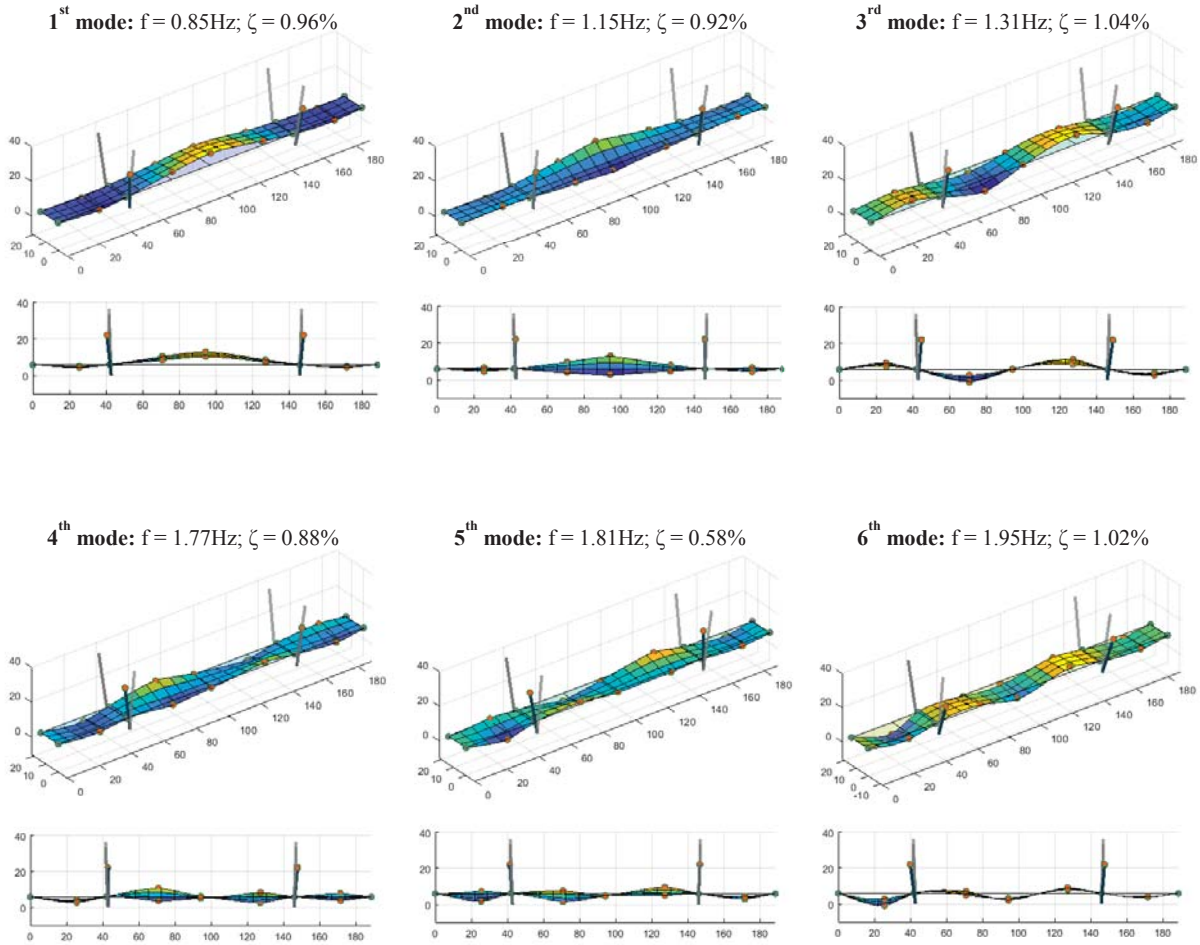

Figure 3: Experimental modal parameters of the unloaded bridge.

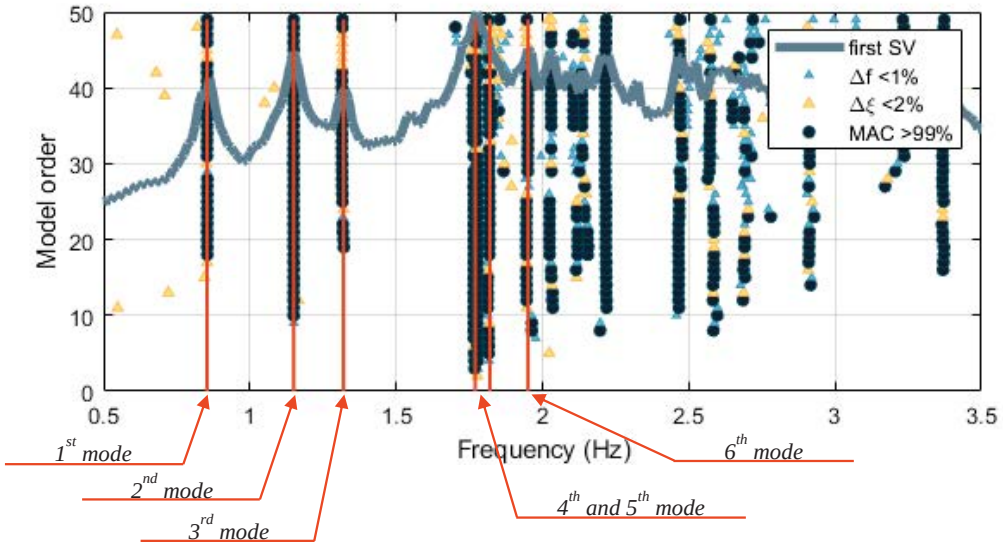

Figure 4: Stabilization diagram.

5 COMPARISON BETWEEN EXPERIMENTAL AND NUMERICAL RESULTS

The experimental modal parameters obtained from AVTs are compared with the numerical ones achieved from the finite element (f.e.) model of the whole bridge developed for design purposes (Fig. 5). All the structural components are modelled as frame elements and the concrete deck slab is included considering the relevant effective widths above the steel members (both girders and cross-beams). The model, which was adopted for the design of the superstructure, neglects the foundation system, and the pylons are clamped at the base. The two girders are supported by multidirectional supports and links simulating the dissipative devices, consistently with the real restraint scheme of the bridge. An eigenvalue analysis is performed, and the first four numerical natural frequencies obtained are listed in Tab. 1 together with the experimental ones previously described. As can be seen, the numerical model provides natural frequency values lower than the experimental ones (from 9% for the 1st mode to around 30% for the 4th mode) meaning that the global stiffness of the real structure is higher than the expected one, as usually expected from the outcomes of proof static and dynamic load tests. In particular, the torsional stiffness of the real deck is higher than the one captured by the model, which foresees the use of beam element. Indeed, for a more reliable prediction of the contribution of the warping torsion, a more accurate model should be developed adopting shell elements for the steel members.

To compare the mode shapes, the Modal Assurance Criterion (MAC) index is calculated and reported in Fig. 6. It can be observed that the first four numerical mode shapes are very similar to the first four experimental ones, as can be deduced from the matrix diagonal entry values which are close to 100% (MAC = 100% perfect matching, MAC = 0% no matching). However, although numerical and experimental mode shapes are very similar, the experimental and numerical frequency values are not very close. Accordingly, a bridge f.e. model refinement and calibration is suggested to obtain a numerical model able to accurately capture the dynamic behavior of the real bridge not only in terms of mode shapes but also of natural frequency values; this could be useful, for example, as starting point for a Structural Health Monitoring (SHM) system. Research is moving in this direction.

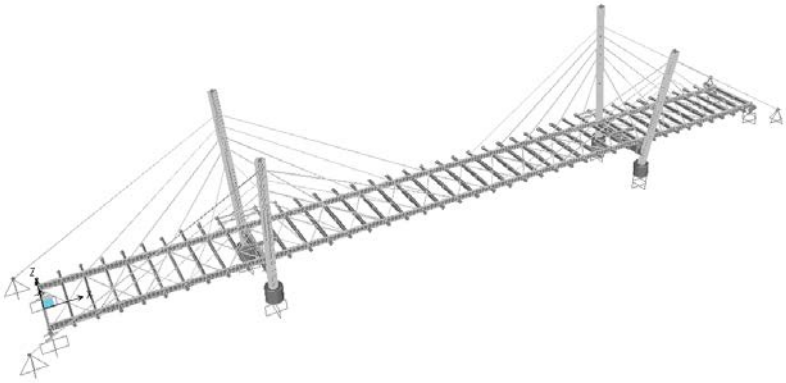

Figure 5: Design f.e. model of the bridge (concrete slab excluded from the view).

Mode	Frequency [Hz]	
	Numerical	Experimental
1st	0.77	0.85
2nd	0.96	1.15
3rd	0.88	1.31
4th	1.47	1.77

Table 1: Comparison between experimental and numerical natural frequencies.

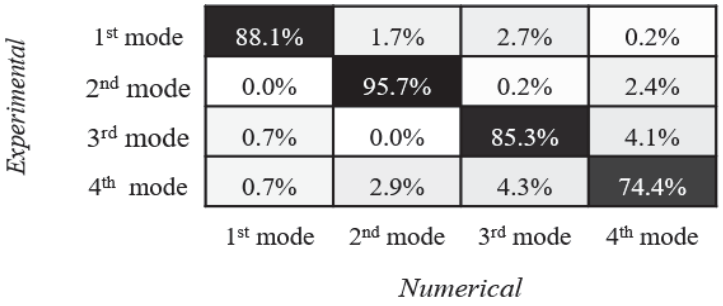

Figure 6: Comparison between experimental and numerical mode shapes (MAC indexes).

6 INVESTIGATION OF THE FOUNDATION DEFORMABILITY

In order to provide useful information for the model refinement and calibration, the contribution of the soil-foundation deformability on the overall bridge dynamics is investigated, extending measurements of vibrations to the foundation basements. As previously stated, pylons are fixed on conical r.c. basements founded on piled raft foundations, which have the same geometry (Fig. 7a).

However, during the execution of the AVTs, the basements were differently embedded in the soil, as can be observed in Fig. 7b from which it is evident that one of the pylon foundations is located within the riverbed. The different foundation embedment can provide different restraint conditions to the basements, as will be analyzed and discussed in this section. In order to verify this assumption, the modal displacements obtained from accelerometers placed on the pylons are analyzed.

A first clue to the fact that the restraint conditions of south pylons may be different is provided by the absolute values of the pylons modal displacements shown in Tab. 2. Indeed, it can be observed that displacements relevant to pylon P1 (with a lower basement embedment) are greater than those relevant to pylon P2, indicating an overall higher deformability of the element. For modes 1, 2 and 6, which are supposed to be symmetric according to the structural geometry, the average modal displacements evaluated experimentally at P1 are about 37% higher than those at P2 in the longitudinal direction (data of P#-L) and about 92% in the transverse direction (data of P#-T). Previous percentages are largely dominated by the contribution of the 6th mode for which an evident larger deformability of the south edge span is evident in Fig. 3.

The soil-foundation compliance is further investigated through the analysis of signals recorded by sensors located at the foundation basements. Fig. 8 shows the Power Spectral Density (PSD) of the sensors together with the first SV line obtained from sensors located on the deck; the superposition of data is useful to address the significance of the soil-foundation compliance on the identified resonance frequencies and mode shapes. Unfortunately, some signals are very noisy (DL, D2Z, D3Z) so that a complete and reliable evaluation of modal displacements at the foundation level is difficult to be obtained.

However, some interesting considerations can be done. Firstly, as expected, the soil foundation compliance produces greater effects on higher modes as demonstrated by high peaks in the PSD of signals registered at the foundation basements that locate mainly in correspondence of the 4th, 5th and 6th modes of the bridge. Furthermore, data confirm the hypothesis of the larger deformability of the soil-foundation system P1 with respect to P2; indeed, accelerations registered at the foundation of P1 are sensibly higher than those registered at the foundation of P2.

Accelerometer (Fig. 2)	Modal displacement					
	Mode 1	Mode 2	Mode 3	Mode 4	Mode 5	Mode 6
P1-L	0.229	0.090	0.379	0.111	0.105	0.264
P1-T	0.096	0.048	0.080	1.000	1.000	0.775
P2-L	0.194	0.085	0.348	0.173	0.015	0.141
P2-T	0.057	0.032	0.072	0.196	0.590	0.299

Table 2: Pylons modal displacements in longitudinal (L) and transverse (T) direction.

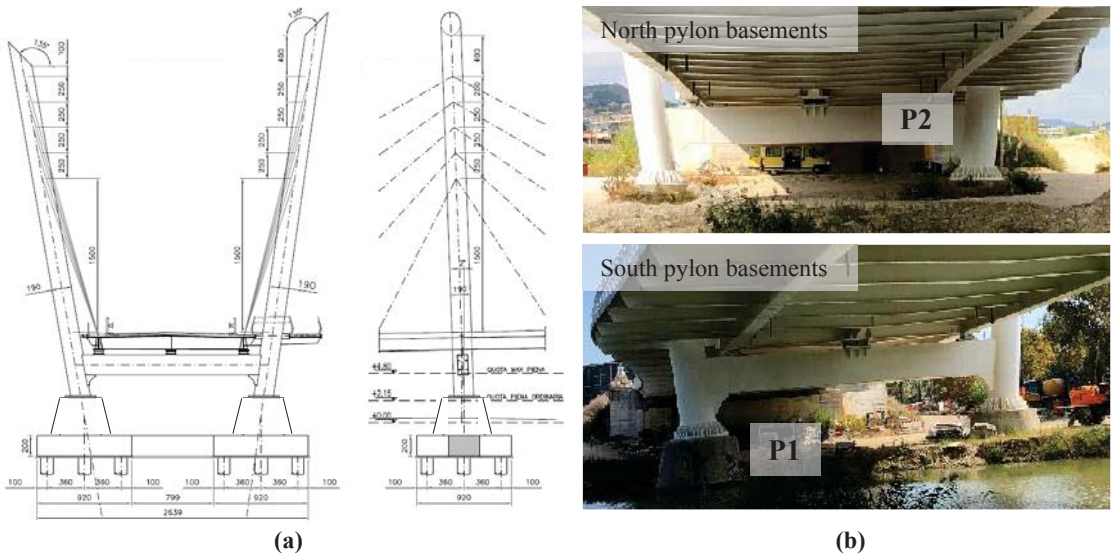

Figure 7: Pylon foundation systems: (a) schematic layout, (b) north and south basement pictures.

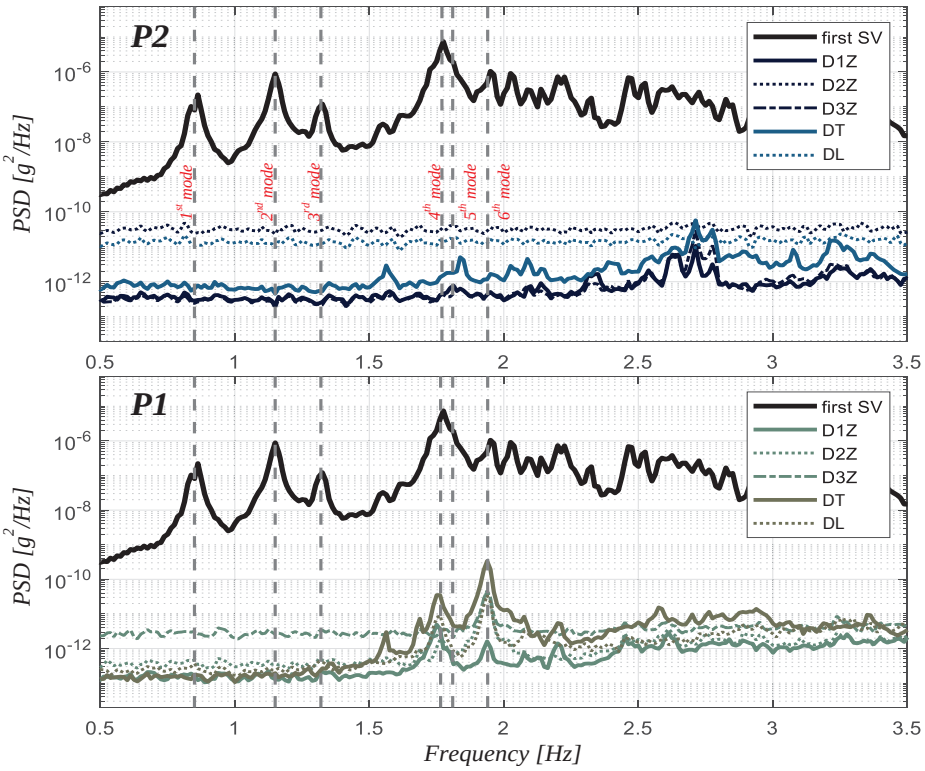

Figure 8: PSD of the sensors placed on the basements.

7 CONCLUSIONS

The dynamic characterization of a cable-stayed steel-concrete composite bridge in central Italy carried out during the static proof load test has been presented in this paper. The bridge is 189 m long and is composed by 4 inclined steel pipe pylons that sustain a steel-concrete composite deck by means of 40 stay cables. Sensors have been installed on the deck, on two pylons and on the foundation system, in order to characterize the whole structural dynamic behavior, including the contribution of the soil-foundation compliance. With reference to the unloaded bridge, the latter issue has been analyzed focusing on the different restraint condition exerted by the soil-foundation system of the pylons, because of the different embedment of the reinforced concrete basement.

Although some signals acquired at the foundations resulted to be very noisy, making it difficult to obtain a reliable and complete evaluation of the effects of the soil-foundation compliance on mode shapes, important considerations arise from the signal analyses, which may be crucial to calibrate refined f.e. models for the SHM of the bridge at hand. Finally, ambient vibration tests extended to foundations revealed capable to capture and to monitor the soil-foundation system compliance, which may be important for bridges subjected to pier scour hazard.

REFERENCES

[1] R. Astroza, H. Ebrahimian, J.P. Conte, J.I. Restrepo, T.C. Hutchinson, Influence of the construction process and nonstructural components on the modal properties of a five-story building, *Earthquake Engineering & Structural Dynamics*, 2015.

[2] J. Brownjohn, P. Xia, Dynamic assessment of curved cable-stayed bridge by model updating, *Journal of Structural Engineering*, 126:2(252), pp. 252-260, 2000.

[3] C. Bedon, A. Morassi, Dynamic testing and parameter identification of a base isolated bridge, *Engineering Structures*, 60, pp. 85-99, 2014.

[4] P. Faraonis, A. Sextos, E. Chatzi, V. Zabel, Model updating of a bridge-foundation-soil-system based on ambient vibration data, *UNCECOMP*, 2015.

[5] F. Gara, M. Regni, D. Roia, S. Carbonari, F. Dezi, Evidence of coupled soil-structure interaction and site response in continuous viaducts from ambient vibration tests, *Soil Dynamics and Earthquake Engineering*, 120, pp 408-422, 2019.

[6] W. Zheng, W. Yu, Probabilistic approach to assessing scoured bridge performance and associated uncertainties based on vibration measurements, *J. Bridge Eng*, DOI: 10.1061/(ASCE)BE.1943-5592.0000683, 2014.

[7] National Instruments, LabVIEW Signal Processing Course Manual, National Instruments Corporate Headquarters, 2019.

[8] R. Canteni, Experimental methods used in system identification of civil engineering structures, *Proceedings of the 1st Int. Conf. on OMA*, Copenhagen, Denmark, 2005.

[9] P. Van Overschee, B. De Moor, Subspace identification for linear systems: theory–implementation–applications. Dordrecht, The Netherlands: Kluwer Academic Publishers, 1996.

EURODYN 2020
XI International Conference on Structural Dynamics
M. Papadrakakis, M. Fragiadakis, C. Papadimitriou (eds.)
Athens, Greece, 23–26 November 2020

PERFORMANCE OF INERTIAL MASS CONTROLLERS FOR ULTRA-LIGHTWEIGHT FOOTBRIDGES: A CASE STUDY

Carlos M. C. Renedo [1], Iván M. Díaz[1], Justin M. Russell[2] and Stana Živanović [3]

[1] Universidad Politécnica de Madrid, Department of Continuum Mechanics and Theory of Structure,
ETSI Caminos, Canales y Puertos.
Madrid, Spain
e-mail: carlos.martindelaconcha@upm.es, ivan.munoz@upm.es

[2]University of Warwick, School of Engineering
Coventry, United Kingdom
e-mail: J.Russell.3@warwick.ac.uk

[3] University of Exeter, College of Engineering, Mathematics and Physical Sciences
Exeter, United Kingdom
e-mail: S.Zivanovic@exeter.ac.uk

Keywords: Structural control, inertial vibration controllers, lightweight structures, human-structure interaction.

Abstract. *The increasing use of lightweight materials in construction, such as fiber reinforced polymer (FRP) composites or aluminum, together with rising architectural tendencies towards slender and stunning layouts are enabling to dramatically decrease the weight of contemporary structures. This fact involves a positive reduction of the structural carbon footprint, but it poses a challenge to complying with vibration serviceability limit state (VSLS) under human-induced loading. Indeed, ultra-lightweight structures (with relatively low inherent mass and damping) may undergo vertical vibration in a broader frequency band than those built in the past and be prone to human-structure interaction (HSI), which should be considered when assessing VSLS of these structures.*

Instead of adding structural mass or performing expensive structural stiffening to rectify the vibration problem, the integration of smart damping strategies could be an optimum solution that has additional benefits of preserving lightweight nature of these structures. This paper presents a case study of vibration control of an ultra-lightweight FRP truss footbridge. This work investigates the influence of three types of inertial mass controllers (passive, semi-active and active) on the vibration control of the bridge in the presence, as well as in the absence, of HSI. It was found that active vibration control was the less deteriorated when considering HSI in comparison with passive and semi-active control strategies.

1 INTRODUCTION

The contemporary structural design framework is evolving towards a state of greater creative freedom. Nowadays, designers can make use of a wide variety of tools in order to satisfy the increasingly demanding requirements for new structures. The use of lightweight materials such as fiber reinforced polymers (FRP) or aluminium, have enabled development of "minimum weight" structures. Sizing of structures types with moderate strength demands and strict vibration serviceability requirements (e.g. footbridges and composite floor systems) is now governed by vibration criteria rather than ultimate limit state [1]. However, substantial reduction of structural self-weigh, is to be achieved, requires integration of vibration control measures in the design stage in order to satisfy VSLS under Human-induced loading.

Up to now, human-induced vibrations of lightweight structures were mainly caused by resonant behaviours of certain vibration modes located within the high-energy frequency content of dynamic loading generated by humans. For example, traditionally, lightweight steel footbridges with vertical natural frequencies up to 5 Hz were considered prone to excessive vibration in resonance excitation by one of the first two harmonics of dynamic force generated by humans. In the case of lightweight steel floor systems, this resonant vibration has been usually related to the third harmonic of the human loading [2].

Ultra-lightweight structures may additionally undergo undesired vibrations due to either non-resonant responses excited by lower harmonics of the human loading, or resonant loading related to higher and less energetic harmonics of the human loading. Hence, for FRP or aluminium structures even higher modes up to or above 10 Hz could respond considerably [3]. Furthermore, whilst the mass of a human in classic steel lightweight structures is much lower than the structural modal mass, this is no longer the case in ultra-lightweight structures. Indeed, human body mass cannot be simply modelled as equivalent dead load. Instead, their interaction with the structural vibration have to be accounted for. Thus, to properly asses the VSLS in ultra-lightweight structures, it is necessary to model humans as interactive dynamic systems. A simple way to achieve this is to model the human as a Mass-Spring-Damper-Actuator system connected to the structure [4].

Future structures will need to be sustainable in terms of material usage and maintenance, and serviceable in terms of static deflection and dynamic comfort. Fortunately, there are many strategies to minimize the dynamic response of a structural system. Among these strategies, inertial controllers are the most widespread damping technology applied to "lively" civil engineering structures [5]. They consist of an inertial mass that applies counteract forces on the structure. They have an advantage of not needing a reference support to react so they can be simply placed on the structural point to be controlled. In practice, inertial controllers can be implemented in three different ways according to the nature of the control: passive, semiactive or active. The passive devices, most commonly known as Tuned Vibration Absorbers (TVAs), are able to damp resonant vibrations when tuned to a single problematic natural frequency of the structure [6]. The Semi-active Tuned Vibration Absorbers (STVAs) are able to adjust the stiffness or damping properties of the controller in real time, by means of smart dampers (usually magneto-rheological dampers). They can control several closed vibration modes as well as vibration modes with time-varying modal parameters [7]. Active Vibration Absorvers (AVAs) make use of actuators for introducing counteract control forces to the lively structure in real time, allowing to mitigate both resonant and non-resonant responses, even over a relatively broad frequency range [8].

These three control systems can be studied and designed as a feedback system, so the design problem is set to be a closed-loop system. Up to now, many design strategies based on feedback control have been proposed, however, from the authors knowledge, none of them have yet considered the influence of the HSI as another element which also feeds back the structure to be controlled. When considering HSI, the dynamic properties of the structure, change, an so, the inertial controllers which were designed without taking into account this effect could be degraded. This paper intends to asses the influence of the HSI on the performance of three inertial controllers applied to an existing FRP laboratory footbridge, designed to be as lively as possible under human-induced dynamic loading [3].

The remainder of the paper is organized as follows. First the structure will be described in Section 2. Section 3 outlines the closed-loop system model that incorporates HSI. Section 4 provides selected results on the performance of the three inertial mass controllers in presence and absence of HSI. Finally, Section 5 provides conclusions.

2 STRUCTURE

The main aims of designing the studied FRP bridge was to produce a laboratory facility exceptionally responsive to dynamic excitation by human walking and enable research in pedestrian-structure dynamic interaction (Figure 1). To achieve this aim, it was set that the bridge should withstand vibration amplitude of up to 100 mm, on top of the static deflection (of 47.5 mm for the adopted design solution) due to self-weight.

Figure 1: FRP Laboratory Footbridge.

The truss structure with 16.8 m span and 1.4 m overhangs at both ends, is made of three types of FRP structural elements as depicted in Figure 2. The bottom chords are simply supported using four steel bearings, including a roller at one end. All connections are executed using stainless steel bolts. Total mass of the bridge is 1400 kg only. More detailed description of the bridge is available in the paper by Russell et al. 2019 [3].

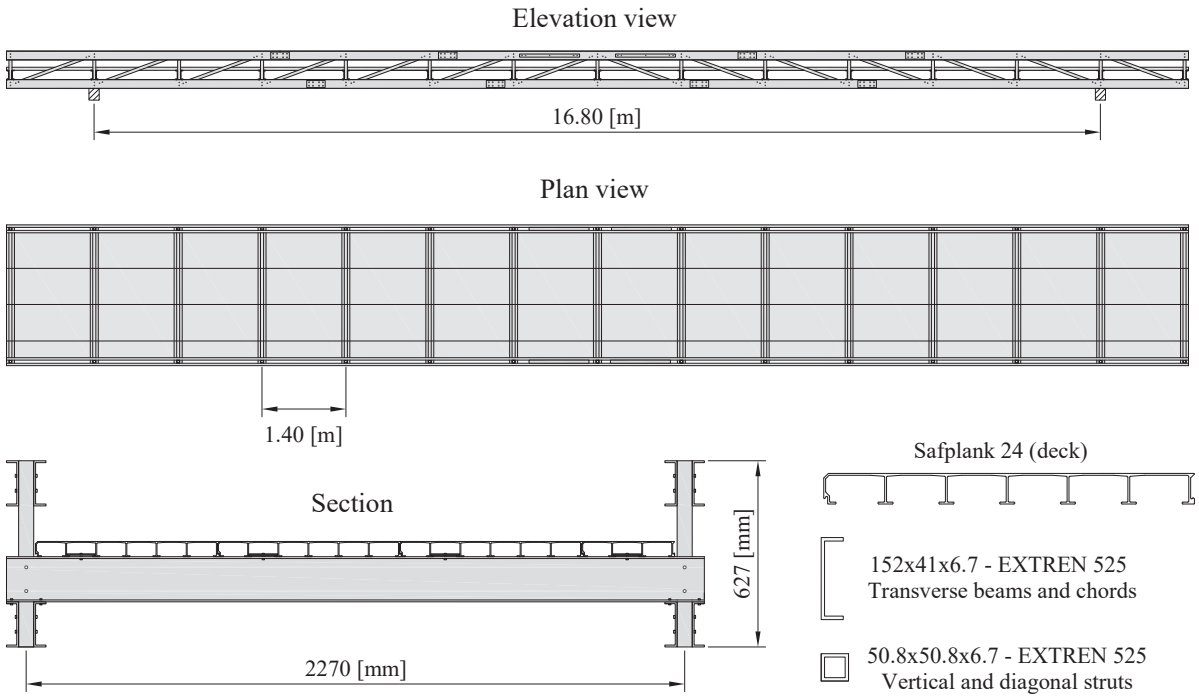

Figure 2: GFRP Laboratory Footbridge: geometrical layout.

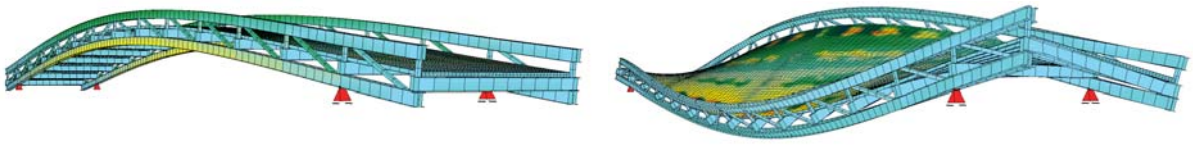

(a) Flexural Mode at 2.5 Hz. (b) Torsion Mode at 3.4 Hz

Figure 3: First two vibration modes of the structure.

The first two vibration modes have natural frequencies at 2.5 Hz (first vertical flexural mode) and at 3.4 Hz (first torsion mode), as shown in Figure 3. It is expected this bridge can achieve vertical acceleration up to around 10 $\mathrm{m/s^2}$ under a single pedestrian walking to excite resonance in the first vibration mode at 2.5 Hz. Indeed, the maximum permitted dynamic deflection of 100 mm (span/170) at 2.5 Hz would correspond to a peak acceleration of almost 25 $\mathrm{m/s^2}$. In practice, these vibrations are likely to be much lower due to vibration attenuation effects caused by walker-footbridge interaction. Therefore, the primary aim of designing a bridge that can resist the stress under single walker exciting the resonance and, at the same time, be lively was executed successfully [10].

Note that the bridge has not been designed to fulfil the usual design requirement of satisfying the Ultimate Limit State under a live load of 5 $\mathrm{kN/m^2}$, as loading of about 500 $\mathrm{kg/m^2}$ by people is not representative for this (and many other) footbridges. The bridge can accommodate several people working on the deck to set up the tests. The deflection due to a single 75 kg person standing at mid-span is 6.5 mm, and therefore deflection due to a few people walking on the bridge at the same time is much less than the 100 mm limit.

This laboratory facility employs much less material than a structure that would comply with VSLS. For this study, an acceleration of 1 $\mathrm{m/s^2}$ has been considered the target value for the control systems. To computationally test the implemented control measures, a single person bouncing loading scenario is utilised.

3 INERTIAL MASS CONTROLLERS AND HUMAN-STRUCTURE INTERACTION

This paper focus on the control of the most responsive first flexural vibration mode at 2.5 Hz. This simplification means that this is only a first step in our study known that ultra-lightweight structures tend to display multi-mode dynamic responses excited by several resonant and non-resonant harmonics. The model for general control scheme considered can be divided in three parts: the structure, the human and the inertial controller.

The human and the inertial controller can be modelled as two different elements feeding back to the main structure and changing the system's dynamic properties (and consequently the dynamic response). In this section, the three parts of the dynamic model are described in detail.

3.1 The structural model

The case study footbridge has been modelled as an equivalent mass-spring-damper system, which represents the vertical dynamic response of the first flexural mode at mid span, with a mass of 650 kg, a natural frequency of 2.5 Hz, and a damping ratio of 0.94 % [10]. The transfer function between the acceleration response and the excitation force is as follows:

$$G_s(s) = \frac{s^2\, X(s)}{F_h(s)} = \frac{1/m_s\; s^2}{s^2 + 2\,\omega_s\,\zeta_s\,s + \omega_s^2}, \tag{1}$$

where $s = j\omega$ is the Laplace variable, $\omega_s = 2f\pi f_s$ is the circular natural frequency of the structure (rad/s), f_s is the responding natural frequency in Hz and m_s and ζ_s are the mass (kg) and damping ratio of the first vibration mode at mid-span. Moreover, $F_h(s)$ is the Laplace transform of the external human force acting on the structure and $s^2 X_s(s)$ is the Laplace transform of the structural acceleration, Where $X_s(s)$ denotes the Laplace transform of the structural displacement. Figure 4 shows the structure block diagram.

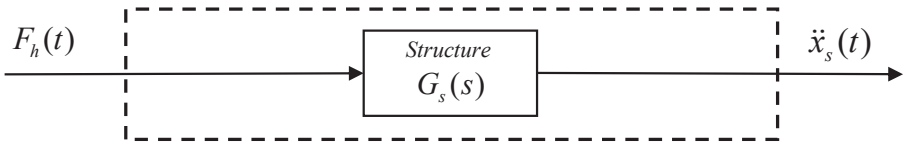

Figure 4: Block diagram of the structure without HSI.

3.2 The human model

First, a non-interactive human model is considered. Given the high accelerations expected (as shown in Section 4), it is reasonable to think that the interaction between the human and the

structure will have significant influence on structural vibration. To account for this, the second model is an interactive model that includes the dynamics of the human.

For the non-interactive model, a dynamic bouncing force measured using a laboratory force plate is used to represent the human on the structure as depicted in Figure 4.

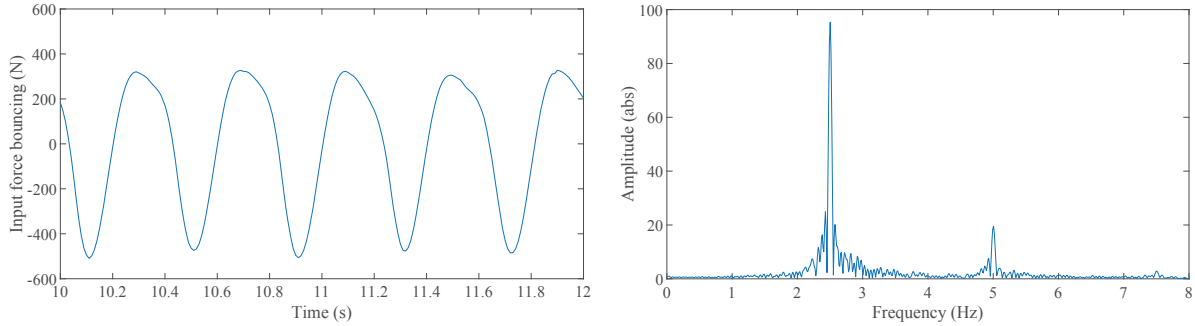

(a) Non-interactive bouncing force at 2.5 Hz. (b) Non-interactive bouncing force spectrum.

Figure 5: Dynamic component of non-interactive bouncing force F_h at 2.5 Hz measured in a laboratory force plate.

Two force waveforms have been applied in the non-interactive simulations: one at resonance conditions of 2.5 Hz (Figure 5) and the other, out of resonance at 2 Hz. Each force record is 20 s long.

The interactive model considers the dynamics of the human body using a Mass-Spring-Damper-Actuator system attached to the structure [11]. Thus, the human is defined by means of its body's natural frequency f_h, damping ratio ζ_h and mass m_h. In addition, a harmonic force generated by the human muscles is also accounted for via a pair of action-reaction forces acting simultaneously on both the footbridge and the human, here named as human interactive force or F_{hi}.

When considering HSI, the dynamic analysis of the new system (structure + human) is performed assuming that this interaction can be modelled as a closed-loop in which the human feeds back to the main structure. This feedback loop is easily deducted from the force balance illustrated in Figure 6, which is governed by the following equations:

$$F_t = k_h(x_h - x_s) + c_h(\dot{x_h} - \dot{x_s}) \tag{2}$$

$$-m_h\ddot{x_h} = (F_t - F_{hi}) \tag{3}$$

$$m_s\ddot{x_s} + c_s\dot{x_s} + k_s x_s = (F_t - F_{hi}) \tag{4}$$

where x_h is the human displacement, $k_h = \omega_h^2 m_h$ is the stifness of the human model, $w_h = 2\pi f_h$ is the natural circular frequency of the human and $c_h = 2\omega_h m_h \zeta_h$ is the viscous damping of the human. Additionally, x_s is the structural displacement, $k_s = \omega_s^2 m_s$ is the structure's stiffness and $c_s = 2\omega_s m_s \zeta_s$ is the viscous damping of the structure. F_t is the transmitted passive force between the structure and the human.

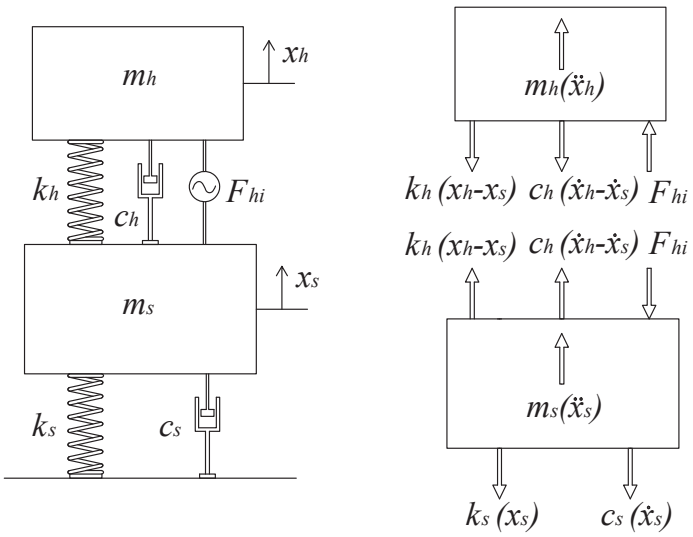

Figure 6: Interactive human model and force equilibrium for each degree of freedom.

The human parameters considered are: mass m_h of 66 kg, natural frequency f_h of 2.3 Hz and a damping ratio ζ_h of 25 %. Additionally, the muscle force generated by the human modeled as an actuator force F_{hi} has a forcing frequency of either 2.5 Hz or 2.0 Hz while its amplitude is 25 % of the human weight:

$$F_{hi}(t) = Q\alpha \sin(2\pi f t), \tag{5}$$

where Q is the human weight taken of 660 N and $\alpha = 0.25$.

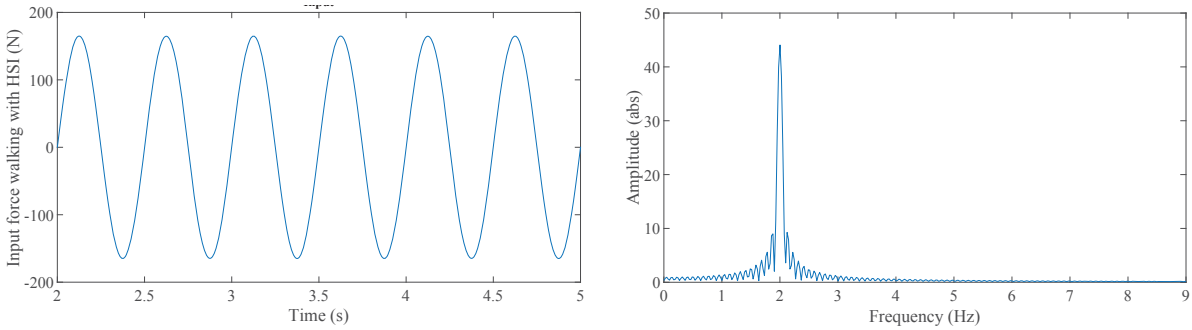

(a) Dynamic interactive bouncing force at 2.5 Hz.

(b) Dynamic interactive bouncing force spectrum.

Figure 7: Human-actuator bouncing force model F_{hi} at 2.5 Hz.

Figure 7 shows the force exerted by the human actuator for bouncing at resonance when accounting for HSI. Note that the amplitude of F_{hi} is lower than the amplitude of F_h used for the non-interactive loading model (Figure 5). Finally, the block diagram for the described system is shown in Figure 8. This diagram makes use of the structure's transfer function described in Equation 1 apart from two additional transfer functions used for modelling the interaction:

$$G_h(s) = \frac{s^2 X_{hi}(s)}{F_{hi}(s)} = \frac{s^2}{m_h s^2 + c_h s + k_h} = \frac{1/m_h\ s^2}{s^2 + 2\,\omega_h\,\zeta_h\,s + \omega_h^2} \tag{6}$$

$$G_{HSI}(s) = \frac{s^2 X_{h-HSI}(s)}{s^2 X_s(s)} = \frac{c_h s + k_h}{m_h s^2 + c_h s + k_h} = \frac{2\,\omega_h\,\zeta_h\,s + \omega_h^2}{s^2 + 2\,\omega_h\,\zeta_h\,s + \omega_h^2} \tag{7}$$

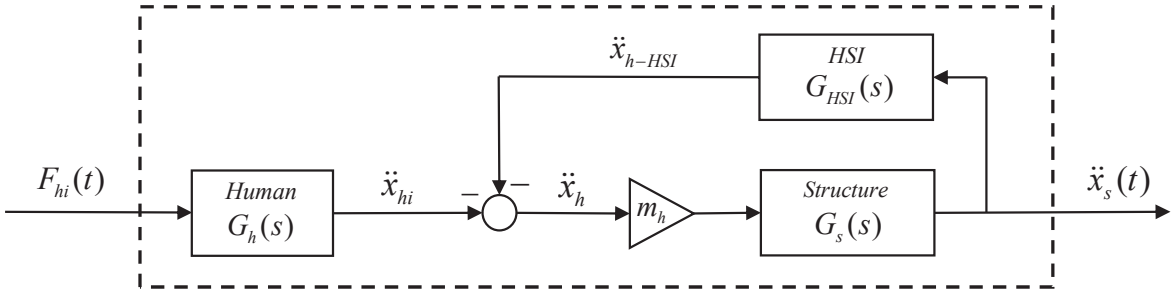

Figure 8: Closed-loop scheme for modelling HSI.

The main idea under this formulation is that the external force entering the structural system is equal to the inverse of the inertial force experienced by the human in real time. Thus, the human acceleration can be decomposed into two different components, one due to its motion $\ddot{x}_{hi}$, and a second human acceleration caused by the structural motion $\ddot{x}_{h-HSI}$. The first one can be directly obtained from the human actuator force by using the transfer function $G_h(s)$. The second is obtained using the transfer function $G_{HSI}(s)$ from the structural acceleration. By summing up the two components and multiplying them by the negative human mass, the external force on the structural system is derived, and so, the interaction loop is closed.

3.3 Tuned Vibration Absorber

The TVA can also be modelled as a closed feedback loop. The same idea used to model the HSI is now applied to the TVA. Hence, the external force entering the structural system due to the TVA is equal to the inverse of the inertial force of the TVA. The following transfer function similar to the one used for the HSI is defined as:

$$G_{TVA}(s) = \frac{s^2 X_T(s)}{s^2 X_s(s)} = \frac{c_T\,s + k_T}{m_T s^2 + c_T\,s + k_T} = \frac{2\,\omega_T\,\zeta_T\,s + \omega_T^2}{s^2 + 2\,\omega_T\,\zeta_T\,s + \omega_T^2} \tag{8}$$

where $\omega_T = 2f\pi f_T$ is the circular natural frequency of the TVA (rad/s), f_T is the respective natural frequency in Hz and m_T, k_T and ζ_T are the mass (kg), stiffness (N/m) and damping ratio of the TVA and $c_T = 2\omega_T\zeta_T m_T$.

The dynamic system is now composed of a two-closed loops scheme, as shown in Figure 9.

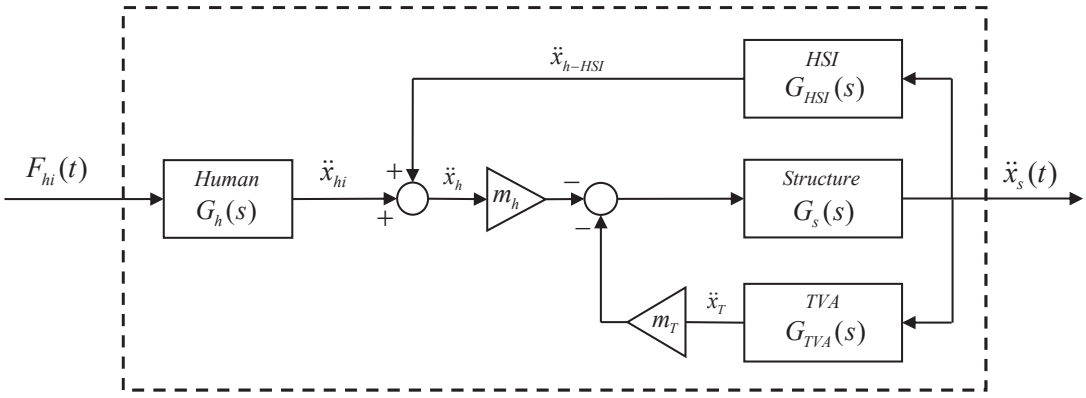

Figure 9: Double closed-loop scheme to model the structure with a TVA and HSI.

The TVA parameters have been designed using the approximation provided by Asami and Nishihara [12], based on the H_∞ for primary structural systems with negligible damping. The following expressions provide the optimal ω_T and ζ_T which minimizes the structure acceleration for a given m_T:

$$\eta = \sqrt{\frac{1}{1+\mu}} \tag{9}$$

$$\zeta_{\mathrm{T}} = \sqrt{\frac{3\mu}{8(1+\mu)^3}} \cdot \sqrt{1+\frac{27}{32}\mu}, \tag{10}$$

where $\mu = m_{_T}/m_{_S}$ is the absorber-to-the-primary-system mass ratio. A mass ratio of 2 % which corresponds to $m_T = 13kg$ has been selected. Parameter $\eta = \omega_{_T}/\omega_{_S}$ is the absorber-to-the-primary-system frequency ratio, in this case 0.99. Finally, ζ_T is 8.7%. The TVA has been designed following an optimum law which does not consider the influence of the HSI.

3.4 Semi-Active Tuned Vibration Absorber

The STVA has been designed using an on-off phase control-strategy [13]. This control strategy has been adopted due to its simplicity for implementing it in practical applications. Indeed, the real-time parameters required for this phase control are easy to measure: the structure acceleration, instead of the displacement, and the inertial mass velocity. The structural response is minimised when the velocity of the inertial mass $\dot{x}_{_T}$ and the structural acceleration $\ddot{x}_{_s}$ have opposite phases. Thus, the inertial controller objective is to facilitate a mass motion as close as possible to this phase. The aforementioned behaviour is equivalent to a 90º phase lag between the structural acceleration and the control force. Thus, when the whole system behaves as desired, the viscous damping of the STVA should be small (ideally zero), however when the phase behaviour is not the correct one, the damper is blocked introducing a control force into the system [14]. The following phase control is summed up as follows:

$$\begin{cases} \ddot{x}_{_S} \cdot \dot{x}_{_T} \leq 0 & \Rightarrow \quad c_{_T} = c_{\min} \quad \text{(normal functioning)} \\ \ddot{x}_{_S} \cdot \dot{x}_{_T} > 0 & \Rightarrow \quad c_{_T} = c_{\max} \quad \text{(blocking functioning)}, \end{cases} \tag{11}$$

where c_{min} is the minimum viscous damping given the minimum damper force when the STVA is working properly. The lower c_{min} results in better performance of STVA. Parameter c_{max} is the maximum viscous damping providing the maximum damper force which corresponds to the state of damper blocked. The magnitude $\ddot{x}_S$ needs to be measured using an accelerometer and $\dot{x}_T$ might be estimated from the integration of an accelerometer signal installed on the inertial mass. Both signals are low-pass filtered in order to avoid control instabilities related to the on-off control law. Note that the design parameters of the STVA correspond to those calculated for the TVA except for c_{min} and c_{max} that are equal to 0.1 and 50 times the value of the c_T for the TVA, respectively. Figure 10 illustrates the non-linear closed loop used to model the STVA, in presence of HSI. Note that if c_T is constant, then block diagrams of Figures 9 and 10 become the same.

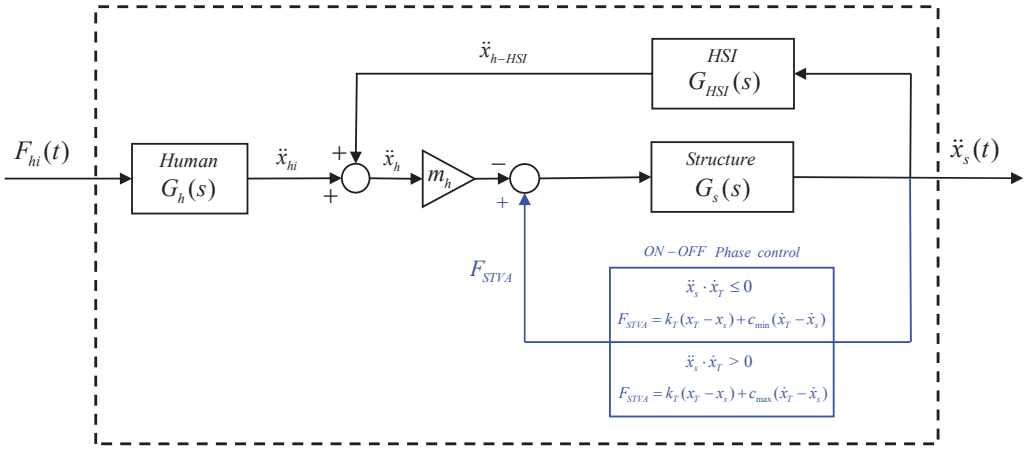

Figure 10: Double closed-loop scheme to model the structure with a STVA considering the HSI.

3.5 Active Vibration Absorber

Direct Velocity Feedback (DVF) control strategy has been used for the AVA. This means that the control force introduced into the system using an actuator is in phase with structure's velocity. Although DVF is, by its nature, unconditionally stable, when accounting for the actuator dynamics, the closed-loop system becomes conditionally stable and the stability margin has to be studied prior to the implementation [15]. The velocity estimated is multiplied by a control gain K_C producing a command signal in terms of voltage to the actuator. Firstly, the limit control gain for stability is derived by classical root locus techniques, $K_{C_{\text{lim}}} \simeq 70$. Finally, a control gain K_C equal to $K_{C_{\text{lim}}}/2$ has been chosen providing enough stability gain margin and leading to a safe implementation [16]. The actuator transfer function between the transmitted control force and the control voltage is considered as a second-order proof-mass actuator model:

$$G_{AVA}(s) = \frac{150\ s^2}{s^2 + 5.7\ s + 8.2^2} \tag{12}$$

where the circular natural frequency of the actuator is $\omega_A = 8.2$ rad/s (1.3 Hz) and $2\zeta_a\omega_a = 5.7$, ζ_a being the actuator damping ratio. The chosen AVA has an inertial mass equal of 13 kg, the same as the one used for the TVA and STVA. The natural frequency of the actuator is a critical parameter when controlling low-frequency vibrations. The lower the natural frequency of the

actuator is, the closer to linear the behaviour of the actuator is. A sufficiently small, but realistic, value for the actuator passive behaviour in terms of natural frequency has been chosen. Note that the shaker's natural frequency can be changed by means of changing the passive stiffness or by the use of more sophisticated control laws [17]. Figure 11 depicts the feedback scheme for the AVA.

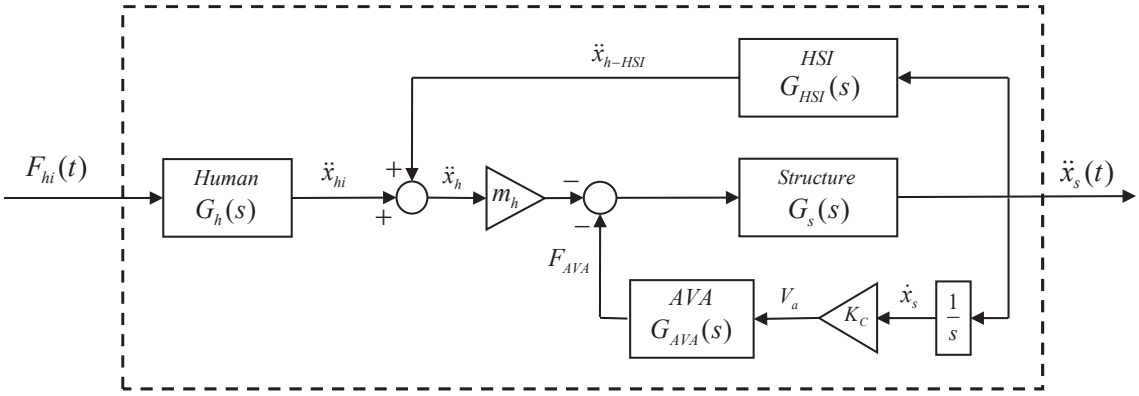

Figure 11: Double closed-loop scheme to model the structure with a AVA considering the HSI

4 RESULTS

Figures 12 and 13 provide the resonant response of the structural system under bouncing action without and with HSI, respectively. Three serviceability indicators are calculated: the Peak acceleration value, the maximum value of the running 1 s root mean square acceleration (often refered to as Maximum Transient Vibration Value or MTVV) and the cumulative Vibration Dose Value (VDV).

When assessing the structural response at resonance, the accelerations reached without considering HSI are not only excessive but also unlikely to be achieved. Once the HSI is taken into account, the dynamic response decreases significantly. In both cases, the structure exceeds the vibration serviceability limit of 1 $\mathrm{m/s^2}$ for peak acceleration. Therefore there is a need to apply inertial vibration controllers to reduce the structural vibration.

When including HSI into the dynamic analysis, the system to be controlled is no longer the structure.The human is a new element to be considered as is influences the dynamic properties of the system to be controlled. The inertial vibration controllers reduce their damping capacity at resonance (especially the TVA and STVA), due to part of the energy introduced into the structure is damped by the very human system which generates it. This fact can be observed in Figure 14 where the VDV of all the dynamic loading cases are compared. The VDV is a suitable vibration serviceability parameter to use for this comparison because of its cumulative nature. To explain the controllers performance out of resonance is a bit more complicated and would require an overall and deep comprehension of the interaction phenomena between all the elements that compound the dynamic system.

The AVA is by far the most effective of the three inertial controllers considered, and it is the only solution capable of reducing the peak acceleration at resonant bouncing below the established threshold of 1 $\mathrm{m/s^2}$ (Figure 13d). Therefore, active control is the most promising damping technique for controlling ultra-weight structures, as it is able to effectively cancel complex dynamic responses compound of resonant and non-resonant harmonics.

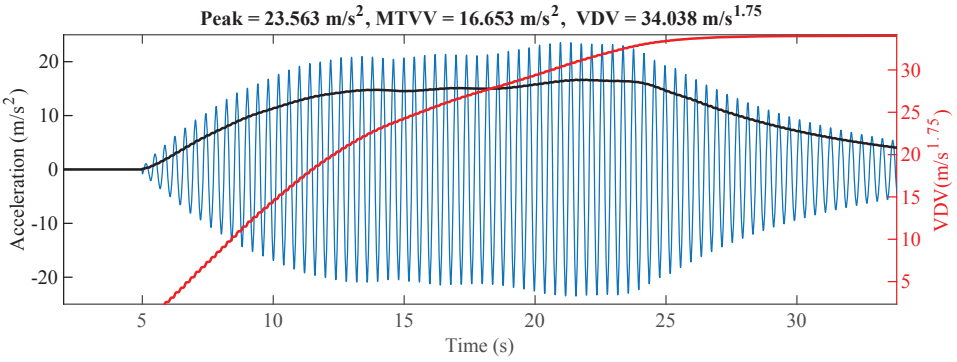

(a) Uncontrolled.

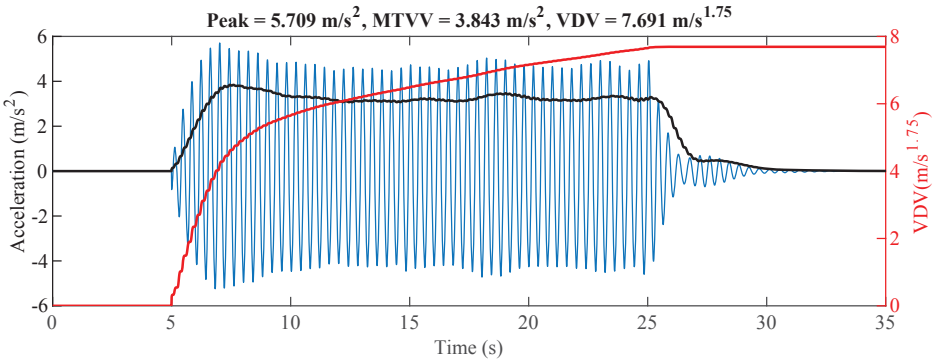

(b) Passive.

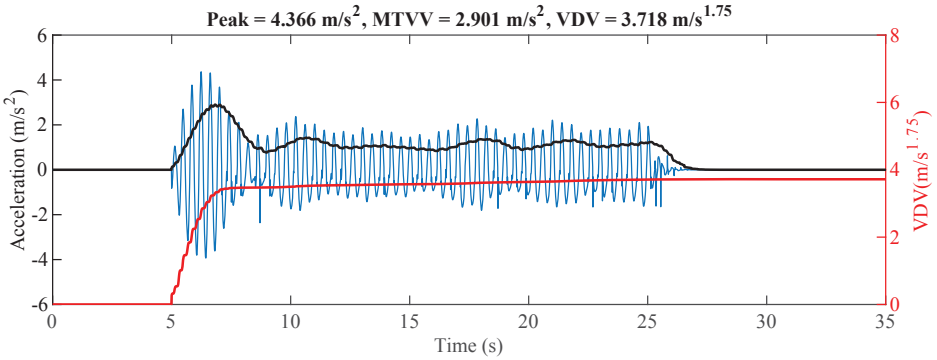

(c) Semi-active.

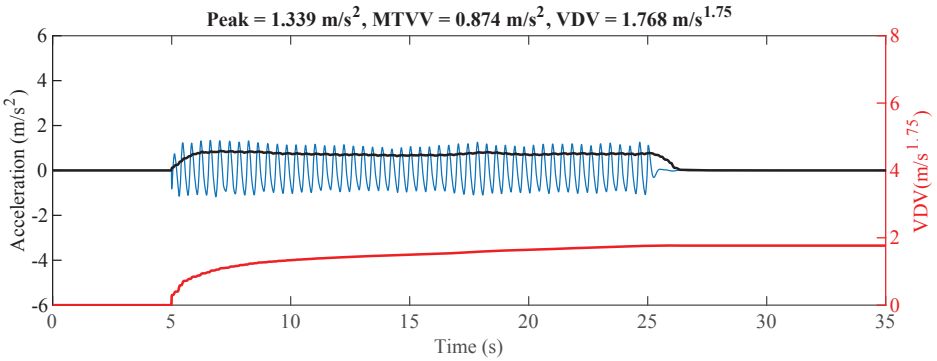

(d) Active.

Figure 12: Resonance response of the structure without HSI under bouncing loading.

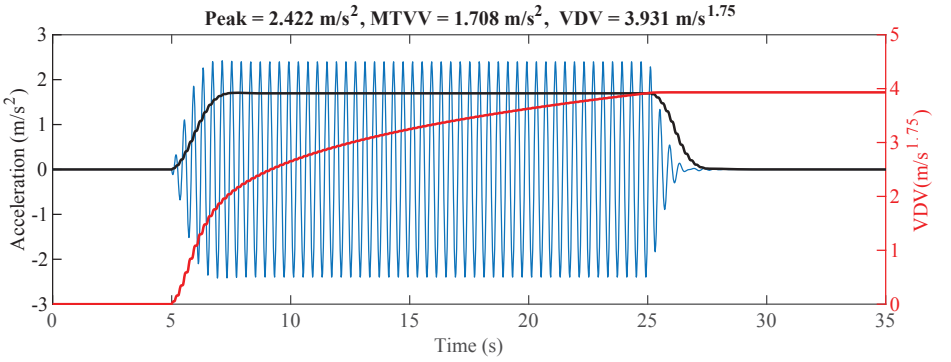

(a) Uncontrolled.

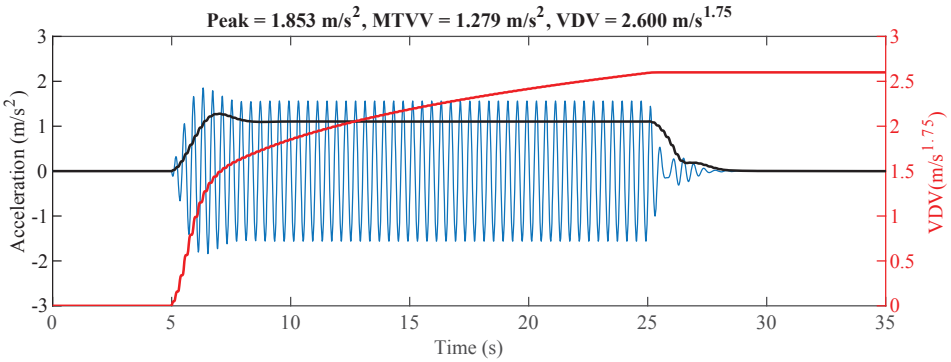

(b) Passive.

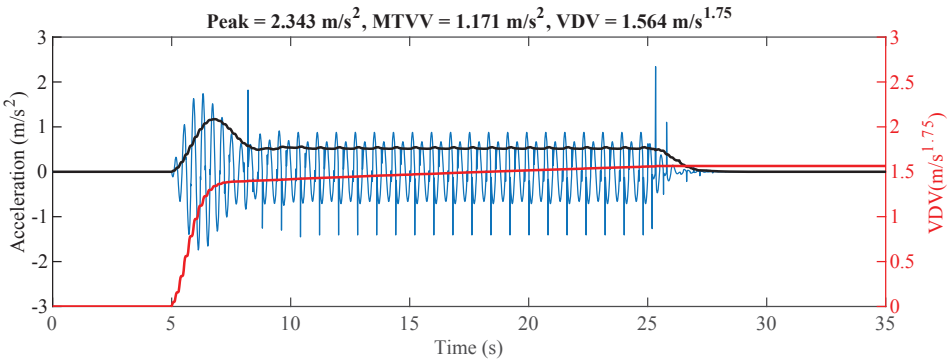

(c) Semi-active.

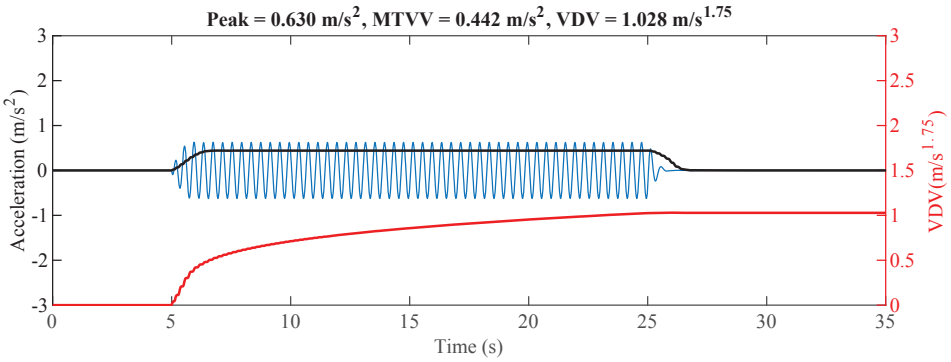

(d) Active.

Figure 13: Resonance response of the structure with HSI under bouncing loading.

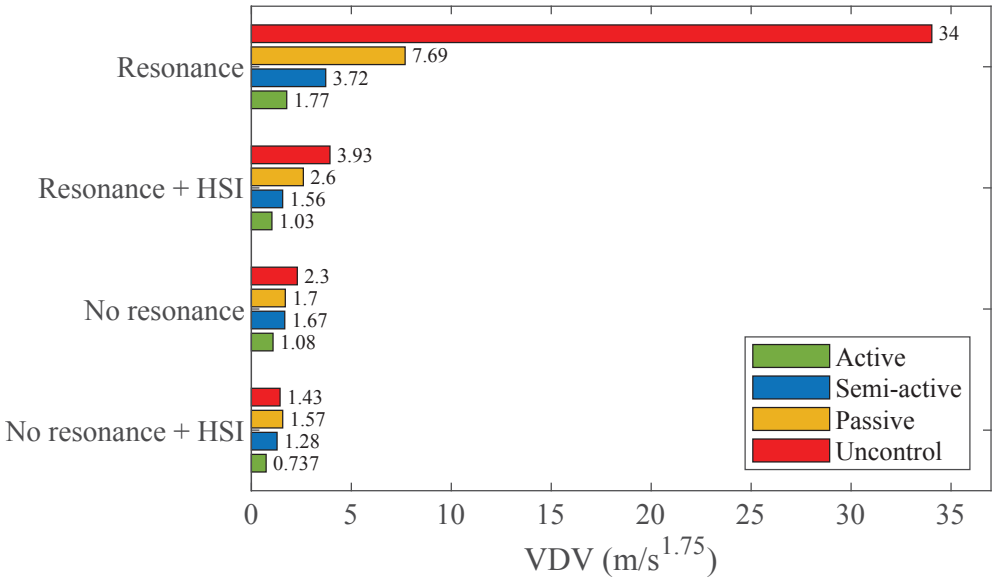

Figure 14: VDV of the structural response for all loading cases.

5 CONCLUSIONS

In this paper, three types of inertial controllers (Passive, Semi-active and Active) have been applied to an ultra-lightweight FRP footbridge conceived as a unique laboratory facility to investigate the HSI. The dynamic response of the first flexural vibration mode of the structure and the controllers' performance have been numerically studied in the presence and absence of HSI.

The uncontrolled case without HSI leads to an unrealistic acceleration of 23.5 $\mathrm{m/s^2}$. However, when the HSI is included the acceleration is reduced to a realistic value of 2.4 $\mathrm{m/s^2}$. Moreover, when HSI is included, the controllers reduce drastically their performance, mainly due to the fact that they were designed without taking into account the HSI. The improvements for the resonant case (with interaction) were 34%, 60% and 74% for passive, semi-active and active, respectively in terms of VDV. However for non-resonant excitation, the only controller able to mitigate vibration was the AVA with a 50 % of improvement.

This paper is a first study on the performance of inertial controllers for human-induced excitation of structures prone to show HSI. Future works on the design of inertial controllers should include the HSI and the resulting human-structure model should be carefully analyzed in order to propose new controller design strategies for these unexplored systems.

6 ACKNOWLEDGEMENTS

The authors acknowledge the financial support provided by the UK's Engineereing and Physical Sciences Reasecrh Council (project EP/M021505/1: Characterising dynamic performance of fibre reinforced polymer structures for resilience and sustainability) and the Spanish Ministry of Science, Innovation and Universities through the project SEED-SD (RTI2018-099639-B-I00). Dr Iván M. Díaz would like to acknowledge the financial support provided by Fundación José Entrecanales Ibarra to carry out a Research Stay at University of Exeter. Carlos M. C. Renedo would like to thank Universidad Politécnica de Madrid for the financial support through a PhD research grant.

REFERENCES

[1] D. Kendall, *Next Generation of footbridges in FRP composites, Proceedings of Footbridge 2014 - Past, present and future, 16-18 July, London, United Kingdom,* 1-11, 2014.

[2] C. M. C. Renedo, I. M. Díaz and J. H. García-Palacios, *High performance dynamically-loaded structures: integrating smart dampers, Proceedings of International fib Symposium on Conceptual Design of Structures, 26-28 September, Madrid, Spain,* 33-40, 2019.

[3] J. Russell, J. T. Mottram, S. Živanović and X. Wei, *Design and Performance of a lively FRP footbridge, Volume 2: Proceedings of the 37th IMAC, A Conference and Exposition on Structural Dynamics, 28-31, January, Orlando, Florida*, 125-128, 2019.

[4] J. F. Jímenez-Alonso, A. C. Sáez, E. Caetano and F. Magalhaes, Vertical crowd-structure interaction model to analyze the change of the modal properties of a footbridge, *Journal of bridge Engineering*, **21(8)**, 1-19, 2016.

[5] D. Nyawako and P. Reynolds, Technologies for mitigation of human-induced vibrations in civil engineering structures. *The Shock and Vibration Digest,* **39 (6)**,465-493, 2007.

[6] H. Bachmann and B. Weber, Tuned Vibration Absorbers for Damping of "Lively Structures", *Structural Engineering International*, **95 (1)**, 31-37, 1995.

[7] M. Setareh, Floor vibration control using semi-active tuned mass dampers, *Canadian Journal of Civil Engineering* **29**, 76–84, 2002.

[8] L. Hanagan and T. Murray, Active control approach for reducing floor vibrations, *Journal of Structural Engineer* **123 (11)**, 1497-1505,1997.

[9] X. Wei, J. Russell, S. Zivanovic and J.T. Mottram, Measured dynamic properties for FRP footbridges and their critical comparison against structures made of conventional construction materials, *Composite Structures*, **223**, 1-16, 2019.

[10] S. Živanović, J. Russell and V. Racic, *Vibration performance of a lightweight FRP footbridge under dynamic excitation by pedestrians, Volume 2: Proceedings of the 37th IMAC, A Conference and Exposition on Structural Dynamics, 28-31, January, Orlando, Florida*, 111-114, 2019.

[11] J. W. Dougill, J. R. Wright, J. G. Parkhouse and R. E. Harrison, Human structure interaction during rhythmic bobbing, *The Structural Engineer*, **84 (22)**, 32–39, 2006.

[12] T. Asami, and O. Nishihara, Closed-form exact vibration absorbers (Application to different transfer functions) and damping systems, *Journal of Vibration and Acoustics-Transactions of the Asme*, **125 (3)**, 398-405, 2003.

[13] C. Moutinho, Testing a simple control law to reduce broadband frequency harmonic vibrations using semi-active tuned mass dampers, *Smart Materials and Structures*, **24 (5),** 05507, 2015.

[14] J. M. Soria, I. M. Díaz and J. H. García-Palacios, Further steps towards the tuning of inertial controllers for broadband-frequency-varying structures, *Structural Control and Health Monitoring,* **27**, 10.1002/stc.2461, 2020.

[15] I. M. Díaz and P. Reynolds, Robust saturated control of human-induced vibrations via a proof-mass actuator, *Smart Material and Structures*, **18 (12)**, 125024-125033, 2009.

[16] X. Wang, E. Pereira, J. H. García-Palacios and I. M. Díaz, A general vibration control methodology for human induced vibrations, *Structural Control and Health Monitoring*, **26 (10)**, 10.1002/stc.2406, 2019.

[17] I. M. Díaz, E. Pereira, M. J. Hudson and P. Reynolds, Enhancing active vibration control of pedestrian structures using inertial actuators with local feedback control, *Engineering Structures,* **41**, 157-166, 2012.

EURODYN 2020
XI International Conference on Structural Dynamics
M. Papadrakakis, M. Fragiadakis, C. Papadimitriou (eds.)
Athens, Greece, 23–26 November 2020

INTERVAL SERVICEABILITY ASSESSMENT OF FOOTBRIDGES

Roberta Santoro[1], Alba Sofi[2], and Federica Tubino[3]

[1] University of Messina
Villaggio S.Agata, 98166, Messina, Italy,
e-mail: roberta.santoro@unime.it

[2] University "Mediterranea" of Reggio Calabria
Via dell'Università 25, 89124, Reggio Calabria, Italy
e-mail: alba.sofi@unirc.it

[3] University of Genoa
Via Montallegro 1, 16145, Genova, Italy
e-mail: federica.tubino@unige.it

Keywords: Footbridges; Human-induced vibration; Interval Analysis; Serviceability

Abstract. *This paper studies serviceability assessment of footbridges through a non-deterministic approach. The parameters defining pedestrian-induced loading and the structural dynamic properties are characterized through possible ranges of variation. Starting from analytical expressions for the spectral moments of the structural response, the improved interval analysis is applied together with an optimization strategy that allows us to obtain the bounds of the standard deviation of the footbridge acceleration and of the mean value and cumulative distribution function of its maximum value. Based on this approach, a possible interval of variation of the structural response is evaluated, rather than a single deterministic value. Thus, an interval level of comfort can be defined.*

1 INTRODUCTION

Serviceability assessment of footbridges is commonly carried out, based on current guidelines (e.g., [1]), by comparing a deterministic value of the expected maximum acceleration and suitable thresholds defining different comfort classes. Actually, the problem should be tackled through a non-deterministic approach due to the uncertainties characterizing both pedestrian-induced loading (i.e. dynamic loading factor, pedestrian weight and step frequency) and the structural dynamic properties (i.e. modal damping ratios, natural frequencies and modal masses). An approach accounting only for the errors connected with the estimate of structural parameters has been introduced through a fuzzy analysis [2]. Based on the characterization of the coefficient of variation of both the loading and the structural uncertain parameters, the propagation of uncertainties on the serviceability assessment of footbridges has been studied adopting the Taylor series expansion technique [3]. Furthermore, Monte Carlo simulations have been performed assuming plausible probability distributions of the uncertain parameters, and the probability distribution of the mean value of the maximum acceleration has been estimated numerically [3].

Actually, probability distributions of the loading and structural parameters are not available, but the literature analysis in [3] provides possible ranges of variation of these parameters. Thus, a suitable tool for taking into account uncertainties in serviceability assessment of footbridges is interval analysis (e.g., [4], [5]). In this paper, starting from the analytical expression for the spectral moments of the structural response [6], the *improved interval analysis* [4] is applied together with an optimization strategy (see e.g., [7]) that allows us to obtain the bounds of the maximum footbridge acceleration. Based on this approach, serviceability assessment is carried out within a non-probabilistic framework, and an interval level of comfort is estimated.

2 ANALYTICAL FORMULATION

The force exerted on footbridges in multi-pedestrian traffic condition is commonly schematized in the time domain as the sum of moving harmonic loads with random amplitude, frequency and velocity. Based on this force model, serviceability assessment has to be carried out through Monte Carlo simulations.

According to the Equivalent Spectral Model (ESM) [6], multi-pedestrian loading can be modelled as an equivalent Gaussian stationary random process. Considering the first mode shape of a simply-supported beam of length L, $\varphi_j(x)=\sin(\pi x/L)$, the power spectral density function (PSDF) of the modal force $F_j(t)$ is given by:

$$S_{F_j}(\omega) = \frac{N_p}{4}(\alpha G)^2 \, p_\Omega(\omega) \tag{1}$$

where N_p is the number of pedestrians, α is the mean value of the dynamic loading factor, G is the mean value of the weight of pedestrians, $p_\Omega(\omega)$ is the probability density function (PDF) of the circular step frequency of pedestrians, assumed as normally-distributed with mean value $\mu_{\omega p}$ and standard deviation $\sigma_{\omega p}$. The spectral moments of zero- and second-order of the acceleration of the j-th principal coordinate $p_j(t)$ can be approximated as follows:

$$\lambda_{0,\ddot{p}_j} \approx \frac{\pi \omega_j S_{F_j}(\omega_j)}{4\xi_j M_j^2} = \sigma_{\ddot{p}_j}^2; \qquad \lambda_{2,\ddot{p}_j} \approx \frac{\pi \omega_j^3 S_{F_j}(\omega_j)}{4\xi_j M_j^2} \tag{2}$$

where M_j, ω_j and ξ_j are, respectively, the j-th modal mass, natural circular frequency and damping ratio of the structure. The maximum acceleration of the j-th principal coordinate in the time interval T is then defined as the following random process:

$$\ddot{p}_{j,\max}(T) = \max_{0\le t\le T} \left| \ddot{p}_j(t) \right| \tag{3}$$

where the time interval T can be conventionally defined as a multiple of the average crossing time of pedestrians ($T=NL/c_m$, N=10, c_m=0.9 $\mu_{\omega p}/2\pi$).

Under the Poisson's assumption of independent up-crossings of a prescribed threshold, the cumulative distribution function (CDF) of the maximum acceleration is defined as follows:

$$L_{\ddot{p}_{j,\max}}(b,T) = \Pr\left[\ddot{p}_{j,\max}(T) \le b \right] \approx \exp\left[-2\ \nu_{\ddot{p}_j} T \exp\left(-\frac{b^2}{2\sigma_{\ddot{p}_j}^2} \right) \right] \tag{4}$$

where $\nu_{\ddot{p}_j}$ is the expected frequency of the acceleration of the j-th principal coordinate, given by:

$$\nu_{\ddot{p}_j} = \frac{1}{2\pi} \sqrt{\frac{\lambda_{2,\ddot{p}_j}}{\lambda_{0,\ddot{p}_j}}} = \frac{\omega_j}{2\pi}. \tag{5}$$

The mean value of the maximum mid-span acceleration can be approximated according to Davenport's formulation ([8], [9]) as follows:

$$\ddot{q}_{\max} = \mathrm{E}\left[\ddot{p}_{j,\max} \right] = g_{\ddot{p}_j} \sigma_{\ddot{p}_j};\quad g_{\ddot{p}_j} = \sqrt{2\ln(2\nu_{\ddot{p}_j} T)} + \frac{0.5772}{\sqrt{2\ln(2\nu_{\ddot{p}_j} T)}} \tag{6}$$

3 INTERVAL SERVICEABILITY ASSESSMENT

Interval serviceability assessment is based on the assumption of uncertain loading and structural parameters, represented as interval variables [10] according to the interval model of uncertainty:

$$\mathbf{x}^I = \left\{ \mu_{\omega p}^I \quad \sigma_{\omega p}^I \quad \alpha^I \quad G^I \quad \omega_j^I \quad \xi_j^I \quad M_j^I \right\}^{\mathrm{T}} \tag{7}$$

where the apex denotes interval variables. Each component of the vector $\mathbf{x}^I$, i.e. the k-th interval variable x_k^I, is defined as:

$$x_k^I = x_{0,k} \left(1 + \Delta x_k \hat{e}_k^I \right) \tag{8}$$

where $\hat{e}_k^I = [-1,1]$ is the so-called *extra unitary interval* [4], $x_{0,k}$ and Δx_k are the midpoint and normalized deviation amplitude, defined as follows:

$$x_{0,k} = \frac{\overline{x}_k + \underline{x}_k}{2}; \qquad \Delta x_k = \frac{\overline{x}_k - \underline{x}_k}{2x_{0,k}} \tag{9}$$

being $\underline{x}_k$ and $\overline{x}_k$ the lower bound (LB) and upper bound (UB) of the interval variable x_k^I.

Based on the interval representation of the involved quantities, the PSDF of the modal force is an interval function:

$$S_{F_j}^I(\omega) = \frac{N_p}{4}(\alpha^I G^I)^2 \, p_\Omega^I(\omega). \tag{10}$$

As a consequence, also the spectral moments of zero- and second-order of the acceleration of the *j*-th principal coordinate are interval variables:

$$\lambda_{0,\ddot{p}_j}^I = \frac{\pi\omega_j^I S_{F_j}^I(\omega_j^I)}{4\xi_j^I \left(M_j^I\right)^2} = \left(\sigma_{\ddot{p}_j}^2\right)^I; \qquad \lambda_{2,\ddot{p}_j}^I = \frac{\pi\left(\omega_j^I\right)^3 S_{F_j}^I(\omega_j^I)}{4\xi_j^I \left(M_j^I\right)^2}. \tag{11}$$

The interval CDF is defined as:

$$L_{\ddot{p}_{j,\max}}^I(b,T) = \exp\left[-2\ \nu_{\ddot{p}_j}^I T^I \exp\left(-\frac{b^2}{2\left(\sigma_{\ddot{p}_j}^2\right)^I}\right)\right] \tag{12}$$

where the interval expected frequency is:

$$\nu_{\ddot{p}_j}^I = \frac{1}{2\pi}\sqrt{\frac{\lambda_{2,\ddot{p}_j}^I}{\lambda_{0,\ddot{p}_j}^I}} = \frac{\omega_j^I}{2\pi}. \tag{13}$$

Finally, the interval mean value of the maximum acceleration process is defined as follows:

$$\ddot{q}_{\max}^I = g_{\ddot{p}_j}^I \sigma_{\ddot{p}_j}^I; \qquad g_{\ddot{p}_j}^I = \sqrt{2\ln(2\nu_{\ddot{p}_j}^I T^I)} + \frac{0.5772}{\sqrt{2\ln(2\nu_{\ddot{p}_j}^I T^I)}}. \tag{14}$$

The LB and UB of the standard deviation of the acceleration are given by:

$$\underline{\sigma}_{\ddot{p}_j} = \min_{\mathbf{x}\in\mathbf{x}^I}\left\{\sqrt{\frac{\pi\omega_j S_{F_j}(\omega_j)}{4\xi_j M_j^2}}\right\}; \qquad \overline{\sigma}_{\ddot{p}_j} = \max_{\mathbf{x}\in\mathbf{x}^I}\left\{\sqrt{\frac{\pi\omega_j S_{F_j}(\omega_j)}{4\xi_j M_j^2}}\right\}. \tag{15}$$

Analogously, the LB and UB of the CDF of the maximum acceleration are:

$$\begin{aligned}
\underline{L}_{\ddot{p}_{j,\max}}(b,T) &= \min_{\mathbf{x}\in\mathbf{x}^I}\left\{\exp\left[-2\ \nu_{\ddot{p}_j} T \exp\left(-\frac{b^2}{2\sigma_{\ddot{p}_j}^2}\right)\right]\right\}; \\
\overline{L}_{\ddot{p}_{j,\max}}(b,T) &= \max_{\mathbf{x}\in\mathbf{x}^I}\left\{\exp\left[-2\ \nu_{\ddot{p}_j} T \exp\left(-\frac{b^2}{2\sigma_{\ddot{p}_j}^2}\right)\right]\right\}.
\end{aligned} \tag{16}$$

The LB and UB of the maximum mid-span acceleration are given by:

$$\begin{aligned}
\underline{\ddot{q}}_{\max} &= \min_{\mathbf{x}\in\mathbf{x}^I}\left\{\left[\sqrt{2\ln(2\nu_{\ddot{p}_j} T\ )} + \frac{0.5772}{\sqrt{2\ln(2\nu_{\ddot{p}_j} T\ )}}\right]\sigma_{\ddot{p}_j}\right\}; \\
\overline{\ddot{q}}_{\max} &= \max_{\mathbf{x}\in\mathbf{x}^I}\left\{\left[\sqrt{2\ln(2\nu_{\ddot{p}_j} T\ )} + \frac{0.5772}{\sqrt{2\ln(2\nu_{\ddot{p}_j} T\ )}}\right]\sigma_{\ddot{p}_j}\right\}.
\end{aligned} \tag{17}$$

Finally, the *coefficients of interval uncertainty* (*c.i.u.*) for the two response quantities of interest can be defined as the ratio between their deviation amplitude and their midpoint as follows:

$$c.i.u.[\sigma^I_{\ddot{p}_j}] = \frac{\overline{\sigma}_{\ddot{p}_j} - \underline{\sigma}_{\ddot{p}_j}}{\overline{\sigma}_{\ddot{p}_j} + \underline{\sigma}_{\ddot{p}_j}}; \qquad c.i.u.[\ddot{q}^I_{\max}] = \frac{\overline{\ddot{q}}_{\max} - \underline{\ddot{q}}_{\max}}{\overline{\ddot{q}}_{\max} + \underline{\ddot{q}}_{\max}}. \tag{18}$$

4 NUMERICAL APPLICATION

Current guidelines require to perform serviceability assessment of footbridges by comparing a deterministic value of the expected maximum acceleration and suitable thresholds defining different comfort classes. Table 1 reports the threshold values as defined by SETRA [1].

Comfort class	Min [m/s^2]	Max [m/s^2]
Maximum	0	0.5
Medium	0.5	1
Minimum	1	2.5
Unacceptable	2.5	

Table 1: Comfort classes (SETRA).

In this Section, serviceability assessment of an ideal footbridge is carried out. Results of a conventional evaluation are compared with those deriving from interval analysis. In particular, at first interval analysis is carried out assuming fixed normalized deviation amplitudes of the parameters based on [3]. Then, an increasing degree of uncertainty is considered according to the following definition of the interval variables:

$$x^I_k(\beta) = x_{0,k}\left(1 + \beta \Delta x_k \hat{e}^I_k\right), \qquad 0 \le \beta \le 1. \tag{19}$$

Furthermore, three different interval analyses are carried out: considering all the parameters as uncertain, i.e. full uncertainty analysis (FU), taking into account only the uncertainties in the structural parameters (SU), and taking into account only uncertainties in the loading parameters (LU).

An ideal, steel, simply-supported beam with span length L=50 m, a deck width b=2 m is analyzed [3]. Considering load category III, sparse crowd [1], a pedestrian density ρ=0.5 pedestrians/m^2 is assumed, i.e. N_p=50, and the predicted maximum acceleration applying SETRA procedure is $\ddot{q}_{\max}$ =2.15 m/s^2, falling into a minimum comfort class according to Table 1. Interval analysis is carried out assuming the midpoint and the normalized deviation amplitude of the uncertain parameters in Table 2.

Parameter	$x_{0,k}$	Δx_k
$\mu_{\omega p}$ [rad/s]	2 π 1.88	0.03
$\sigma_{\omega p}$ [rad/s]	2 π 0.17	0.17
α	0.35	0.20
G [N]	700	0.10
ω_j [rad/s]	2 π 1.88	0.10
ξ_j [%]	0.42	0.60
M_j [kg]	50000	0.10

Table 2: Midpoint and normalized deviation amplitude of interval variables (Example 1).

The nominal solutions for the standard deviation and the mean value of the maximum acceleration are $\sigma_{\ddot{p}_j} = 0.50$ m/s^2 (Eq.(2)), $\ddot{q}_{\max} = 1.94$ m/s^2 (Eq. (6)). Table 3 reports the LB and UB of $\sigma^I_{\ddot{p}_j}$ (see Eq.(15)) and $\ddot{q}^I_{\max}$ (see Eq. (17)) together with their *c.i.u.* (see Eq. (18)), obtained in the three analyses. The significant deviation amplitudes of the uncertain parameters (Table 2) lead to very large *c.i.u.*, especially if all the parameters (structural and loading) are considered as uncertain (FU). However, the uncertainty in the dynamic response is mainly governed by the uncertainties in the structural parameters. When only loading parameters are assumed as uncertain (LU), the deviation amplitude of the response is significantly reduced. It should be remarked that the maximum acceleration obtained applying SETRA procedure is higher than the nominal value and it is close to the UB provided by interval analysis if only loading uncertainties are accounted for (LU). In all the other cases (FU and SU), SETRA prediction is well below the UB provided by interval analysis, and it can be non-conservative.

Analysis	$\underline{\sigma}_{\ddot{p}_j}$	$\overline{\sigma}_{\ddot{p}_j}$	$c.i.u.[\sigma^I_{\ddot{p}_j}]$	$\underline{\ddot{q}}_{\max}$	$\overline{\ddot{q}}_{\max}$	$c.i.u.[\ddot{q}^I_{\max}]$
FU	0.13	1.29	0.82	0.49	5.02	0.82
SU	0.25	0.88	0.56	0.97	3.42	0.56
LU	0.32	0.72	0.38	1.26	2.81	0.38

Table 3: LB, UB and *c.i.u* of the standard deviation of the response and of the maximum acceleration (Example 1).

Figure 1 provides the UB and LB of $\sigma^I_{\ddot{p}_j}$ (a) and its *c.i.u.* (b) versus the coefficient β which measures the degree of uncertainty according to Eq. (19): results obtained for the three different analyses (FU, SU, LU) are reported. Fig. 1(a) shows that the interval of variation of the standard deviation of the response is very wide, especially if both loading and structural uncertainties are taken into account (FU). From Fig. 1(b) it can be deduced that the *c.i.u.* is almost proportional to the degree of uncertainty β. Furthermore, the *c.i.u.* takes values lower than 10% only if a small degree of uncertainty of the parameters is assumed, or at least structural parameters are assumed as deterministic. When all the parameters are assumed as uncertain, the *c.i.u.* is very large.

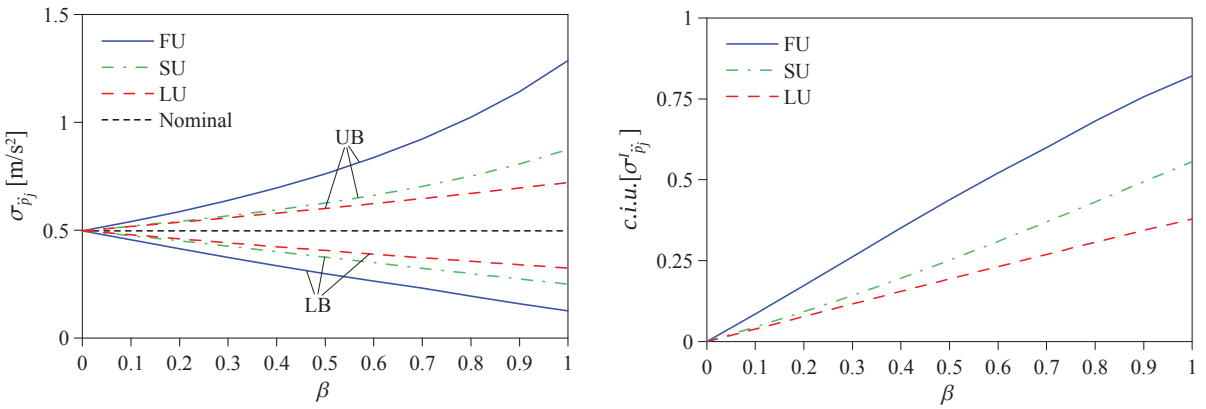

Figure 1: UB and LB of standard deviation of the acceleration (a) and its *coefficient of the interval uncertainty* (b) for increasing degree of uncertainty (Example 1).

Figure 2 provides the LB and UB of the CDF of the maximum acceleration for β=1, for the full uncertainty analysis (FU), taking into account only the uncertainties in the structural parameters (SU), and taking into account only uncertainties in the loading parameters (LU). From Fig. 2, the LB and UB of the probability of falling within each comfort class can be estimated. It can be deduced that, if the nominal values of the parameters are assumed, the footbridge will surely fall within a minimum comfort class. When all the parameters are considered as uncertain, the UB and LB of the CDF are extremely far from each other: considering the LB of the CDF, the maximum footbridge acceleration is surely higher than 4 m/s^2, and thus the comfort level is unacceptable, while considering the UB of the CDF, the maximum acceleration is almost surely lower than 0.5 m/s^2 and the maximum comfort level is assured. When only the structural or the loading parameters are considered as uncertain, the interval of variation of the CDF becomes narrower. For example, if only loading parameters are considered as uncertain, the LB of the CDF falls within unacceptable comfort class and the UB of the CDF falls within a minimum comfort class.

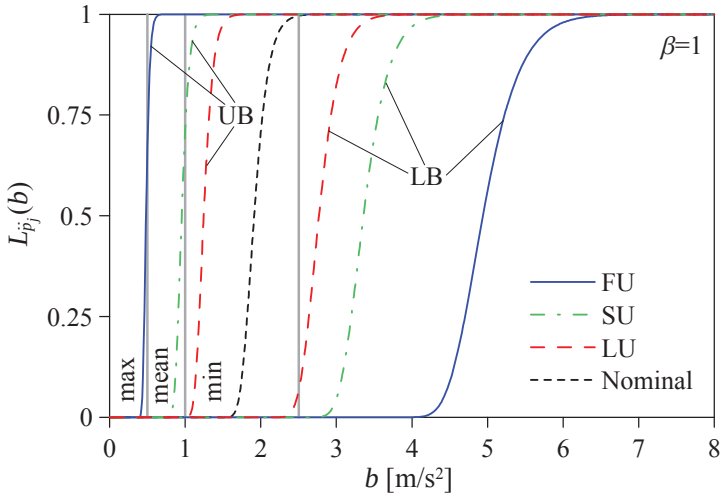

Figure 2 UB and LB of the CDF of the maximum acceleration (β=1) (Example 1).

Figure 3 provides the UB and LB of $\ddot{q}^I_{\max}$ compared with the comfort limits provided by SETRA (a) and its *c.i.u.* (b) for increasing degree of uncertainty. Figure 3(a) shows that, if all the parameters are considered as uncertain and the maximum degree of uncertainty is assumed, then the interval of variation of the response is so wide that the footbridge could fall in any comfort class (from unacceptable to maximum comfort). If only the uncertainties of the loading are considered, the footbridge is almost surely in a minimum comfort class, as predicted by SETRA guideline. As regards structural uncertainties, if the degree of uncertainty is small then interval serviceability assessment provides a minimum comfort class, while for large degree of uncertainty a comfort level ranging from minimum to unacceptable can be obtained. From Fig. 3(b), it can be deduced that the *c.i.u.* of the maximum acceleration has the same trend as the one of the standard deviation of the response (Fig. 1(b)). Also from a quantitative point of view, the two *c.i.u.* are almost coincident: the uncertainty in the maximum acceleration is then governed by the uncertainty in the standard deviation.

In order to assess the influence of uncertainties on serviceability assessment of footbridges less sensitive to human-induced vibrations, a second footbridge is analyzed. The same parameters listed in Table 2 are considered, except for the natural circular frequency ω_j: its nominal value is not coincident with the nominal value of the mean step circular frequency,

but it is assumed 2 π 2.17 rad/s. Figure 4 is analogous to Figure 3, but it is referred to this second example. Results are similar to the ones obtained for Example 1 from a qualitative point of view. From a quantitative point of view, Figure 4(a) shows that the comfort level of this footbridge is surely higher than the one of Example 1. In particular, if the degree of uncertainty is small (β<0.25) the footbridge comfort class can range between mean and minimum. However, if all the parameters are considered as uncertain and the maximum degree of uncertainty is assumed, then the interval of variation of the response is so wide that also this footbridge could fall in any comfort class (from unacceptable to maximum comfort). Figure 4(b) shows that the coefficient of interval uncertainty is even larger than in Example 1. In particular, if all the uncertainties are taken into account, for high degree of uncertainty the *c.i.u.* tends to an asymptotic value.

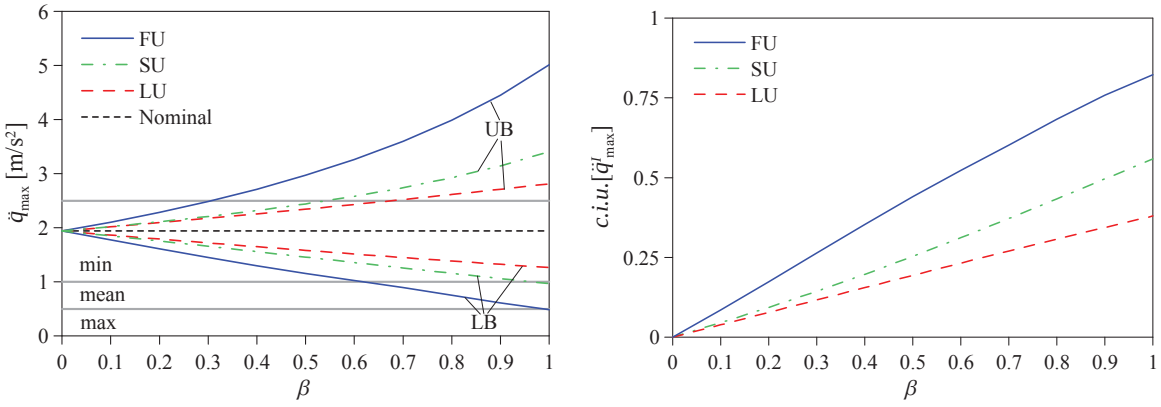

(a) (b)

Figure 3: UB and LB of mean value of the maximum acceleration (a) and its *coefficient of the interval uncertainty* (b) for increasing degree of uncertainty (Example 1).

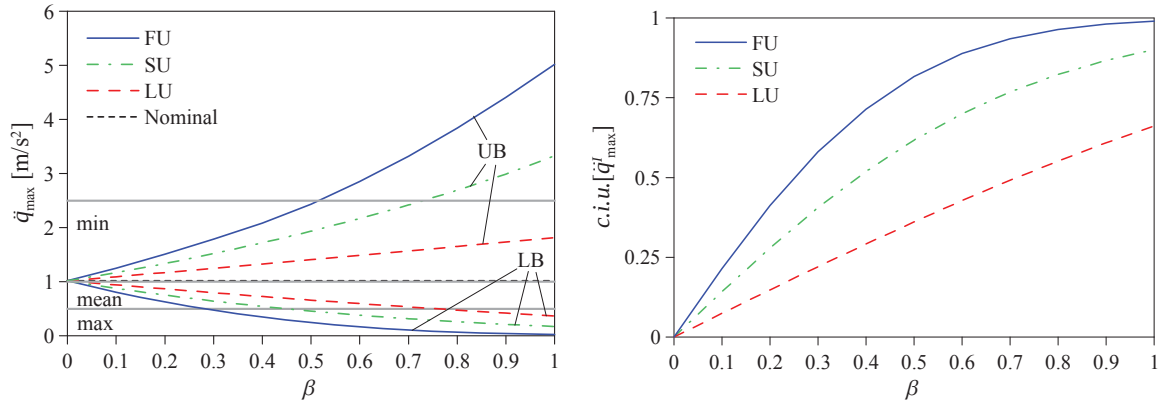

(a) (b)

Figure 4: Non resonant case: UB and LB of mean value of the maximum acceleration (a) and its *coefficient of the interval uncertainty* (b) for increasing degree of uncertainty (Example 2).

5 CONCLUSIONS

Serviceability assessment of footbridges is studied through a non-deterministic approach, modelling structural and loading parameters as interval variables. Based on this approach, the standard deviation of the footbridge acceleration and the mean value of the maximum accel-

eration are also interval variables, while the cumulative distribution function of the maximum acceleration is an interval function.

The application to an ideal case study has shown that the high degree of uncertainty in the loading and structural parameters leads to very large intervals of variation of the response. If all the parameters are considered as uncertain and the maximum degree of uncertainty is assumed, then the interval of variation of the response is so wide that the footbridge could fall in any comfort class (from unacceptable to maximum comfort). The separate analysis of the role of the structural and loading parameters has shown that uncertainty in the structural parameters provides a determinant contribution to the variation of the response. In order to obtain narrow intervals of variation of the response, a reliable characterization of the loading and of the structural properties is mandatory.

REFERENCES

[1] SETRA (2006). *Footbridges – Assessment of vibrational behaviour of footbridges under pedestrian loading*. Paris: Technical Department for Transport, Roads and Bridges Engineering and Road Safety. Ministry of Transport and Infrastructure.

[2] K. Lievens, G. Lombaert, G. De Roeck, P. Van den Broeck, Robust design of a TMD for vibration serviceability of a footbridge, *Engineering Structures* 123, 408-414, 2016.

[3] F. Tubino, L. Pagnini, G. Piccardo, Uncertainty propagation in the serviceability assessment of footbridges, *Structure and Infrastructure Engineering* 16(1), 123-137, 2020.

[4] G. Muscolino, A. Sofi, Stochastic analysis of structures with uncertain-but-bounded parameters via improved interval analysis, *Probabilistic Engineering Mechanics* 28, 152-163, 2012.

[5] G. Muscolino, R. Santoro, A. Sofi, Reliability assessment of structural systems with interval uncertainties under spectrum-compatible seismic excitations, *Probabilistic Engineering Mechanics* 44, 138-149, 2016.

[6] G. Piccardo, F. Tubino, Equivalent spectral model and maximum dynamic response for the serviceability analysis of footbridges, *Engineering Structures* 40, 445-456, 2012.

[7] R. Santoro, G. Muscolino, I. Elishakoff, Optimization and anti-optimization solution of combined parameterized and improved interval analyses for structures with uncertainties, *Computers & Structures*, 149, 31-42, 2015.

[8] G. Davenport, Note on the distribution of the largest value of a random function with application to gust loading, *Proceedings of the Institution of Civil Engineering*, 28, 187-196, 1964.

[9] F. Tubino, G. Piccardo, Serviceability assessment of footbridges in unrestricted pedestrian traffic conditions, *Structure and Infrastructure Engineering*, 12(12), 1652-1662, 2016.

[10] R.E. Moore, R.B. Kearfott, M.J. Cloud, Introduction to Interval Analysis, *SIAM*, Philadelphia, ISBN:978-0-89871-669-6, 2009.

EURODYN 2020
XI International Conference on Structural Dynamics
M. Papadrakakis, M. Fragiadakis, C. Papadimitriou (eds.)
Athens, Greece, 23–26 November 2020

CLOSED—FORM SOLUTION OF THE RESPONSE OF SINGLE PEDESTRIAN INDUCED LOAD FOR CLAMPED—CLAMPED BRIDGES

Daniel Colmenares[1], **Andreas Andersson**[2], **and Raid Karoumi**[2]

[1]KTH Royal Institute of Technology
Brinellvägen23
e-mail: dancol@kth.se

[2,3] KTH Royal Institute of Technology
Brinellvägen23
e-mail: {andreas.andersson@byv.kth.se,raid.karoumi@byv.kth.se}

Keywords: dynamic performance, pedestrian loading, footbridge, resonance vibration.

Abstract. *This paper presents an analytical approximation to describe the vertical and horizontal vibrations of clamped-clamped beams subjected to a single pedestrian induced load. No intra—person variability is considered and only a single crossing is taken into account. This approximation is performed by choosing a suitable trigonometric function that well estimates the dynamic properties and mode shape of the system. Moreover, the approximation enables to find the relationship between the loading parameters such as the step frequency and velocity and, the dynamic properties of the system as the natural frequency and damping. Furthermore, approximation formulas are presented for peak displacements, velocities and accelerations in the damped, low damped and undamped cases. Finally, amplifications factors and minimum design mass curves are defined using non dimensional parameters, aiming to contribute to a fast pedestrian bridge dynamic assessment for systems whose mode shapes reassemble the mode shape of a clamped—clamped beam, for both walking and running pedestrian load cases.*

1 INTRODUCTION

As high strength materials become more readily available, lightweight structures and slender structures are more commonly produced, having well aesthetic design whilst less material is being used. Consequently, new lightweight and lively structural systems may exhibit larger deformations than old heavy structures, making them susceptible to a dynamic excitation. This is the case for many newly constructed footbridges.

The behaviour of footbridges are heavily dependent on the natural frequency of the structure itself. In this way, the dynamic effects need to be considered due to the high levels of accelerations obtained when the frequencies associated with pedestrian loading are within the range of the fundamental natural frequencies of the structural system. Additionally, the pedestrians introduce both vertical and horizontal forces meaning that, structural systems may become vulnerable in different directions and serviceability criteria of lightweight structures of pedestrian bridges can be easily exceeded.

Different load case scenarios are considered in the design stage and assessment of footbridges. Consider the Sétra design code for footbridges [1], in which by finding the equivalent number of pedestrians synchronized in a footbridge, gives a procedure to address the walking crowd scenario in order to assess serviceability levels of the system. However, no specific procedure is given for the running load event like marathons nor the cases in which a single or few runners excite the structural system while walking or standing pedestrians are present, exceeding the serviceability levels required. This is the case of [2], in which a single runner was able to surpass the acceleration limit. To this aim, fast and reliable tools for design and assessment aiming to address the running load case in footbridges are necessary as well as more research on the subject is required.

In the present work, the moving harmonic load problem is studied in the context of pedestrian bridge dynamics for a clamped—clamped beam system. The interest in this subject relies on the fact that, the symmetric mode shape of vibration of tied arch bridges and frame type bridges, which are typical structural topologies found in footbridges, can be approximated and reassembled to the first mode of vibration of a clamped—clamped beam. In this way, the aforementioned approximation is here presented focusing on the comparison between the influence of walking and running in the response of footbridges.

2 PROBLEM FORMULATION

Consider a theoretical model of a clamped—clamped beam subjected to a single time varying force $F(t)$, moving with a constant velocity v from the left side to the right-hand side of the continuous system shown in Figure 1.

In this work, it is considered $y(x,t)$ as the deflection of the beam along the vertical axis y, evaluated at the horizontal position x in the time t, m is the linear density of the beam, E is the elastic modulus of the beam, I the inertia of the system, c_e the external damping coefficient and c_i the internal damping coefficient as considered in [3]. The span length L of the clamped–clamped beam model is considered as the effective length of the typical symmetric mode shape of a tied arch bridge. The equation of motion of the system is set as:

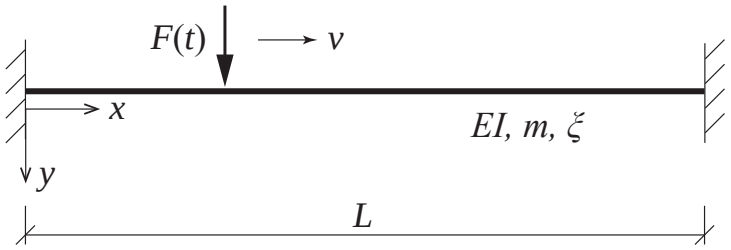

Figure 1: Clamped–clamped beam

$$m\ddot{y} + c_e\dot{y} + c_iI\dot{y}'''' + EIy'''' = F(t)\delta(x - vt), \;\; 0 \leq vt \leq L \tag{1}$$

In which dots $(\dot{})$ represent a time derivative, primes $(')$ indicate a spatial derivative respect to the horizontal coordinate x of the system, δ is the Dirac function. For a clamped—clamped beam, the boundary conditions are:

$$\begin{aligned} y(0,t) &= 0 \\ y(L,t) &= 0 \\ y'(0,t) &= 0 \\ y'(L,t) &= 0 \end{aligned} \tag{2}$$

Initial conditions considered as:

$$\begin{aligned} y(x,0) &= 0 \\ \dot{y}(x,0) &= 0 \end{aligned} \tag{3}$$

And the time varying force $F(t)$ defined as [1]:

$$F(t) = G_0 + \sum_{i=1}^{3} G_i \sin(2\pi f_{step}\, i\, t) \tag{4}$$

Where G_0 denotes the weight of the pedestrian and $G_i = DLF_i \cdot G_0$, in which DLF_i refers to the dynamic load factor i of the pedestrian load in accordance to the activity performed by the pedestrian.

Let us consider, as an approximation, the first vibration mode ϕ_1 of the beam as a linear combination of assumed functions that satisfy boundary conditions as a ”shape function” that well suits the problem as:

$$\phi_1(x) = 1 - \cos^2\left(\frac{\pi x}{L}\right) = 1/2\left(1 - \cos\left(\frac{2\pi x}{L}\right)\right) \tag{5}$$

Considering the modal superposition method, the response of the beam can be approximated by its first mode of vibration as:

$$\begin{aligned} y(x,t) = \sum_{n=1}^{m} \phi_n(x)\, q_n(t) \cong \phi_1(x)\, q_1(t) \\ \dot{y}(x,t) \cong \phi_1(x)\, \dot{q}_1(t) \\ \ddot{y}(x,t) \cong \phi_1(x)\, \ddot{q}_1(t) \end{aligned} \tag{6}$$

Where q_n represents the generalized coordinate of the nth mode. Equation (6) applies under the hypothesis that the first mode of vibration very well suits and represents the system's behaviour under a moving harmonic load with an exciting frequency f_{step} closed to the natural frequency of the system f_1. Substituting (6) in (1), multiplying the resulting equation by the assumed mode shape function ϕ_1 and integrating along the beam axis, one obtains:

$$\begin{aligned} m\ddot{q}_1(t) \int_0^L (\phi_1(x))^2 dx + \dot{q}_1(t) \left[c_e \int_0^L (\phi_1(x))^2 dx + c_i I \int_0^L (\phi_1(x))^{<4>} \phi_1(x) dx \right] + \\ EI q_1(t) \int_0^L (\phi_1(x))^{<4>} \phi_1(x) dx = \int_0^L F(t)\delta(x - vt)\phi_1(x) dx \end{aligned} \tag{7}$$

In which the natural frequency of vibration of the system becomes:

$$\omega_1^2 = \frac{EI}{m} \frac{\int_0^L (\phi_1(x))^{<4>} \phi_1(x) dx}{\int_0^L (\phi_1(x))^2 dx} \tag{8}$$

In this way, the numerator and the denominator of equation (8) denote the modal stiffness and the modal mass of the first mode of vibration, respectively. Solving the integrals one gets:

$$K_1 = EI \int_0^L (\phi_1(x))^{<4>} \phi_1(x) dx = \frac{2\pi^4 EI}{L^3} \tag{9}$$

$$M_1 = m \int_0^L (\phi_1(x))^2 dx = \frac{3}{8} mL \tag{10}$$

And the natural frequency is then defined as:

$$\omega_1^2 = \frac{K_1}{M_1} = \frac{16\pi^4 EI}{3L^4 m} \tag{11}$$

Under the hypothesis of Rayleigh's damping in which $c_e = \alpha_e m$ and $c_i = \alpha_i E$, the damping coefficient ξ_1 is defined as:

$$\xi_1 = \frac{1}{2}\left(\frac{\alpha_e}{\omega_1} + \alpha_i \omega_1\right) \tag{12}$$

And, equation (7) is reduced to the equivalent dynamic equation in the modal coordinates $q_1(t)$ as:

$$\ddot{q}_1(t) + 2\xi_1\omega_1\dot{q}_1(t) + \omega_1^2 q_1(t) = \frac{F(t)\phi_1(vt)}{m\int_0^L (\phi_1(x))^2 dx} \tag{13}$$

$$\ddot{q}_1(t) + 2\xi_1\omega_1\dot{q}_1(t) + \omega_1^2 q_1(t) = \frac{8F(t)\phi_1(vt)}{3mL}$$

Substituting the assumed mode shape function ones gets:

$$\ddot{q}_1(t) + 2\xi_1\omega_1\dot{q}_1(t) + \omega_1^2 q_1(t) = \frac{8}{3mL}F(t)\frac{1}{2}\left(1 - \cos\left(\frac{2\pi vt}{L}\right)\right) \tag{14}$$

By neglecting G_0 and considering a general harmonic component i in the load model presented in equation (4), it follows that:

$$\ddot{q}_{1,i}(t) + 2\xi_1\omega_1\dot{q}_{1,i}(t) + \omega_1^2 q_{1,i}(t) = \frac{8}{3mL}G_i \sin(2\pi f_{step}\, i\, t)\,\frac{1}{2}\left(1 - \cos\left(\frac{2\pi vt}{L}\right)\right) \tag{15}$$

And, using the principle of superposition and trigonometric identities the general problem can be reduced to the summation of the threefold components:

$$q_{1,i}(t) = z_{1,i}(t) + z_{2,i}(t) + z_{3,i}(t) \tag{16}$$

In which $z_{1,i}(t)$, $z_{2,i}(t)$ and $z_{3,i}(t)$ correspond to the following threefold problems:

$$\ddot{z}_{1,i}(t) + 2\xi_1\omega_1\dot{z}_{1,i}(t) + \omega_1^2 z_{1,i}(t) = \frac{8}{3mL}\frac{G_i}{2}\sin(2\pi f_{step}\, i\, t) \tag{17}$$

$$\ddot{z}_{1,i}(t) + 2\xi_1\omega_1\dot{z}_{1,i}(t) + \omega_1^2 z_{1,i}(t) = -\frac{8}{3mL}\frac{G_i}{4}\sin\left(2\pi f_{step}\, i - \frac{2\pi v}{L}\right)t$$

$$\ddot{z}_{3,i}(t) + 2\xi_1\omega_1\dot{z}_{1,i}(t) + \omega_1^2 z_{1,i}(t) = -\frac{8}{3mL}\frac{G_i}{4}\sin\left(2\pi f_{step}\, i + \frac{2\pi v}{L}\right)t$$

From equations (17), a beating phenomena can be identified as a consequence of the definition of the load in terms of harmonic components and the spatial wave that defines the mode shape of vibration. Finally, the solution of the aforementioned equations can be found in [3] and it is here adapted:

$$z_{1,i}(t) = \frac{G_i L^3}{4\pi^4 EI} \frac{1}{(1-S_{1,i}^2)^2 + (2\xi_1 S_{1,i})^2} \Big\{ (1-S_{1,i}^2)\, \sin(\Omega_{1,i} t) - 2\xi_1 S_{1,i}\, \cos(\Omega_{1,i} t) + \\ \mathrm{e}^{-\xi_1 \omega_1 t} \left[2\xi_1 S_{1,i} \cos(\omega_{d1} t) + \frac{S_{1,i}}{\sqrt{1-\xi_1^2}} (2\xi_1^2 + S_{1,i}^2 - 1) \sin(\omega_{d1} t) \right] \Big\} \tag{18}$$

$$z_{2,i}(t) = -\frac{G_i L^3}{8\pi^4 EI} \frac{1}{(1-S_{2,i}^2)^2 + (2\xi_1 S_{2,i})^2} \Big\{ (1-S_{2,i}^2)\, \sin(\Omega_{2,i} t) - 2\xi_1 S_{2,i}\, \cos(\Omega_{2,i} t) + \\ \mathrm{e}^{-\xi_1 \omega_1 t} \left[2\xi_1 S_{2,i} \cos(\omega_{d1} t) + \frac{S_{2,i}}{\sqrt{1-\xi_1^2}} (2\xi_1^2 + S_{2,i}^2 - 1) \sin(\omega_{d1} t) \right] \Big\}$$

$$z_{3,i}(t) = -\frac{G_i L^3}{8\pi^4 EI} \frac{1}{(1-S_{3,i}^2)^2 + (2\xi_1 S_{3,i})^2} \Big\{ (1-S_{3,i}^2)\, \sin(\Omega_{3,i} t) - 2\xi_1 S_{3,i}\, \cos(\Omega_{3,i} t) + \\ \mathrm{e}^{-\xi_1 \omega_1 t} \left[2\xi_1 S_{3,i} \cos(\omega_{d1} t) + \frac{S_{3,i}}{\sqrt{1-\xi_1^2}} (2\xi_1^2 + S_{3,i}^2 - 1) \sin(\omega_{d1} t) \right] \Big\}$$

Where $\Omega_{1,i}$, $\Omega_{2,i}$ and $\Omega_{3,i}$ are the loading frequencies defined as:

$$\begin{aligned} \Omega_{1,i} &= 2\pi f_{step}\, i \\ \Omega_{2,i} &= 2\pi f_{step}\, i - \frac{2\pi v}{L} \\ \Omega_{3,i} &= 2\pi f_{step}\, i + \frac{2\pi v}{L} \end{aligned} \tag{19}$$

The factors $S_{1,i}$, $S_{2,i}$ and $S_{3,i}$ are:

$$\begin{aligned} S_{1,i} &= \frac{\Omega_{1,i}}{\omega_1} \\ S_{2,i} &= \frac{\Omega_{2,i}}{\omega_1} \\ S_{3,i} &= \frac{\Omega_{3,i}}{\omega_1} \end{aligned} \tag{20}$$

And ω_{d1} represents the damped frequency of the system:

$$\omega_{d1} = \omega_1 \sqrt{1-\xi_1^2} \tag{21}$$

Furthermore, magnification factors of the components of each solution in (18) can be defined as:

$$\Phi_{1,i} = \frac{1}{(1-S_{1,i}^2)^2 + (2\xi_1 S_{1,i})^2} \Big\{ (1-S_{1,i}^2)\ \sin(\Omega_{1,i}t) - 2\xi_1 S_{1,i}\ \cos(\Omega_{1,i}t) + \\ \mathrm{e}^{-\xi_1\omega_1 t}\left[2\xi_1 S_{1,i}\cos(\omega_{d1}t) + \frac{S_{1,i}}{\sqrt{1-\xi_1^2}}(2\xi_1^2 + S_{1,i}^2 - 1)\sin(\omega_{d1}t) \right] \Big\} \tag{22}$$

$$\Phi_{2,i} = \frac{1}{(1-S_{2,i}^2)^2 + (2\xi_1 S_{2,i})^2} \Big\{ (1-S_{2,i}^2)\ \sin(\Omega_{2,i}t) - 2\xi_1 S_{2,i}\ \cos(\Omega_{2,i}t) + \\ \mathrm{e}^{-\xi_1\omega_1 t}\left[2\xi_1 S_{2,i}\cos(\omega_{d1}t) + \frac{S_{2,i}}{\sqrt{1-\xi_1^2}}(2\xi_1^2 + S_{2,i}^2 - 1)\sin(\omega_{d1}t) \right] \Big\}$$

$$\Phi_{3,i} = \frac{1}{(1-S_{3,i}^2)^2 + (2\xi_1 S_{3,i})^2} \Big\{ (1-S_{3,i}^2)\ \sin(\Omega_{3,i}t) - 2\xi_1 S_{3,i}\ \cos(\Omega_{3,i}t) + \\ \mathrm{e}^{-\xi_1\omega_1 t}\left[2\xi_1 S_{3,i}\cos(\omega_{d1}t) + \frac{S_{3,i}}{\sqrt{1-\xi_1^2}}(2\xi_1^2 + S_{3,i}^2 - 1)\sin(\omega_{d1}t) \right] \Big\}$$

Then, the solution of the modal coordinates for a given harmonic component i can be written as follows:

$$q_{1,i}(t) = \frac{G_i L^3}{4\pi^4 EI}\left(\Phi_{1,i} - \frac{\Phi_{2,i}}{2} - \frac{\Phi_{3,i}}{2}\right) \tag{23}$$
$$\dot{q}_{1,i}(t) = \frac{G_i L^3}{4\pi^4 EI}\left(\dot{\Phi}_{1,i} - \frac{\dot{\Phi}_{2,i}}{2} - \frac{\dot{\Phi}_{3,i}}{2}\right)$$
$$\ddot{q}_{1,i}(t) = \frac{G_i L^3}{4\pi^4 EI}\left(\ddot{\Phi}_{1,i} - \frac{\ddot{\Phi}_{2,i}}{2} - \frac{\ddot{\Phi}_{3,i}}{2}\right)$$

And, the final solution becomes:

$$y(x,t) = \frac{L^3}{4\pi^4 EI}\left(1 - \cos\left(\frac{2\pi x}{L}\right)\right)\sum_{i=1}^{3} G_i\left(\Phi_{1,i} - \frac{\Phi_{2,i}}{2} - \frac{\Phi_{3,i}}{2}\right) \tag{24}$$
$$\dot{y}(x,t) = \frac{L^3}{4\pi^4 EI}\left(1 - \cos\left(\frac{2\pi x}{L}\right)\right)\sum_{i=1}^{3} G_i\left(\dot{\Phi}_{1,i} - \frac{\dot{\Phi}_{2,i}}{2} - \frac{\dot{\Phi}_{3,i}}{2}\right)$$
$$\ddot{y}(x,t) = \frac{L^3}{4\pi^4 EI}\left(1 - \cos\left(\frac{2\pi x}{L}\right)\right)\sum_{i=1}^{3} G_i\left(\ddot{\Phi}_{1,i} - \frac{\ddot{\Phi}_{2,i}}{2} - \frac{\ddot{\Phi}_{3,i}}{2}\right)$$

3 ACCELERATION RESPONSE

This section considers the response at the mid point $x = L/2$ of the beam. In order to evaluate the acceleration response of the system, the second derivative of equations (22) are computed as the following:

$$\ddot{\Phi}_{j,i} = \frac{\omega_1^2}{(1-S_{j,i}^2)^2 + (2\xi_1 S_{j,i})^2} \Big\{ (1-S_{j,i}^2) S_{j,i}^2 \, \sin(\Omega_{j,i} t) - 2\xi_1 S_{j,i}^3 \, \cos(\Omega_{j,i} t) + \\ \mathrm{e}^{-\xi_1 \omega_1 t} \cos(\omega_{d1} t) \Big[2\xi_1 S_{j,i} (2\xi_1^2 - 1) - 2\xi_1 S_{j,i} (2\xi_1^2 + S_{j,i}^2 - 1) \Big] + \\ \mathrm{e}^{-\xi_1 \omega_1 t} \sin(\omega_{d1} t) \Big[4 S_{j,i} \xi_1^2 \sqrt{1-\xi_1^2} + (2\xi_1^2 - 1) \Big(S_{j,i} / \sqrt{1-\xi_1^2} \Big) (2\xi_1^2 + S_{j,i}^2 - 1) \Big] \Big\} \tag{25}$$

Where $j = 1, 2, 3$. If low damping is assumed, equation (25) can written as:

$$\ddot{\Phi}_{j,i} = \frac{\omega_1^2}{(1-S_{j,i}^2)^2 + (2\xi_1 S_{j,i})^2} \Big\{ (1-S_{j,i}^2) S_{j,i}^2 \, \sin(\Omega_{j,i} t) - 2\xi_1 S_{j,i}^3 \, \cos(\Omega_{j,i} t) + \\ -\mathrm{e}^{-\xi_1 \omega_1 t} \cos(\omega_1 t) \Big[2\xi_1 S_{j,i}^3 \Big] - \mathrm{e}^{-\xi_1 \omega_1 t} \sin(\omega_1 t) \Big[S_{j,i} (S_{j,i}^2 - 1) \Big] \Big\} \tag{26}$$

And, if no damping is considered one gets:

$$\ddot{\Phi}_{j,i} = \frac{\omega_1^2}{(1-S_{j,i}^2)^2} \Big\{ (1-S_{j,i}^2) S_{j,i}^2 \, \sin(\Omega_{j,i} t) - \sin(\omega_1 t) \, S_{j,i} (S_{j,i}^2 - 1) \Big\} \tag{27}$$

Considering a single harmonic i the response is approximated as:

$$\ddot{y}_i(t) = \frac{L^3}{4\pi^4 EI} G_i \left(\ddot{\Phi}_{1,i} - \frac{\ddot{\Phi}_{2,i}}{2} - \frac{\ddot{\Phi}_{3,i}}{2} \right)$$

Finally, by taking in ${\omega_1}^2$ as a common factor from equation (25) and considering equation (11), the response due to a single harmonic i component can be written as:

$$\ddot{y}_i(t) = \frac{G_i/2}{3/8mL} \Theta_i(S_{j,i}\,, \Omega_{j,i}\,, \omega_1\,, \xi_1, t) \\ \ddot{y}_i(t) = \frac{G_i/2}{M_1} \Theta_i(S_{j,i}\,, \Omega_{j,i}\,, \omega_1\,, \xi_1, t) \tag{28}$$

Where Θ_i can be defined as the magnification factor of the dynamic response, that is a function dependent on the frequency ratio ($S_{j,i}$ between the input frequency $\Omega_{j,i}$ and the natural frequency ω_1 of the system, damping ratio ξ_1 and the loading time t.

3.1 ESTIMATION OF MAXIMUM RESPONSE

In order to evaluate the importance of the position of the load, parameters $\Omega_{2,i}$ and $\Omega_{3,i}$ from equation (19) can be written as the following:

$$\Omega_{2,i} = \frac{2\pi v}{L}(i\,k - 1) \qquad (29)$$
$$\Omega_{3,i} = \frac{2\pi v}{L}(i\,k + 1)$$

Where k denotes the number of cycles or steps applied to the system by the pedestrian. The aforementioned equation, when multiply by time t, it allows to evaluate the magnification factor as function of the non-dimensional position vt/L in accordance with $S_{j,i}$, where $j = 1, 2, 3$. Also, equations (29) can be written as follows:

$$\Omega_{2,i} = 2\pi f_{step}\left(i - \frac{1}{k}\right) \qquad (30)$$
$$\Omega_{3,i} = 2\pi f_{step}\left(i + \frac{1}{k}\right)$$

In this way, equations (30) indicate that, as the number of cycles increases the velocity term can be neglected, approaching the steady state response. In this regard, it is important to mention that the equations here exposed, will correctly approximate the response when the step frequency f_{step} is close to the natural frequency f_1 rather than exactly the natural frequency of the bridge. This is understood from the fact that, the differential equation (13) changes when perfect resonance is addressed. Furthermore, the system will achieve its maximum response when the $S_{j,i}$ parameter is close to the unity, meaning that the step frequency f_{step} is at resonance with the natural frequency f_1. This is a consequence of the presence of the velocity term that originates the beating of the system response components as shown in equations (17) and (18). From equation (30), it can be seen that for very short span bridges the velocity term has a greater influence on the $S_{j,i}$ parameter. However, if the pedestrian bridge is short there will not be enough cycles to achieve high amplification in the system's response. Finally, considering the first harmonic component, the envelope of the magnification factor Θ_1 can be evaluated, as shown in Figure 2. The envelop is made by evaluating the magnification factor as a function of different frequency ratios $S_{j,i}$, respect to the non-dimensional position vt/L, given a number of cycles k and damping ratio ξ_1. The maximum values of the magnification factor were taken and plotted in Figure 2, which correspond to the case of a resonant loading case, i.e. $S_{j,i} \cong 1$. This is a consequence of the presence of the velocity term. The obtained magnification factor curves, are consistent with results published by [4, 5, 6, 7, 8], taking into account the modal mass and modal stiffness of the clamped–clamped beam system. It can be seen from from Figure 2 that, the response is highly dependent of the damping ratio of the system; a small change in the damping characteristics of the system has the effect of drastically reducing its dynamic response, even reducing the order of magnitude of the expected accelerations. This exposes the disproportional trade-off between the dissipation capacities of the system and its corresponding response given a resonant input, in regards to a transient event.

Equation (26) has been validated since it produces the same magnification factor curves as the complete solution in equation (25), for the presented damping levels. Then, the maximum response due to the ith harmonic component of the pedestrian load can be estimated as:

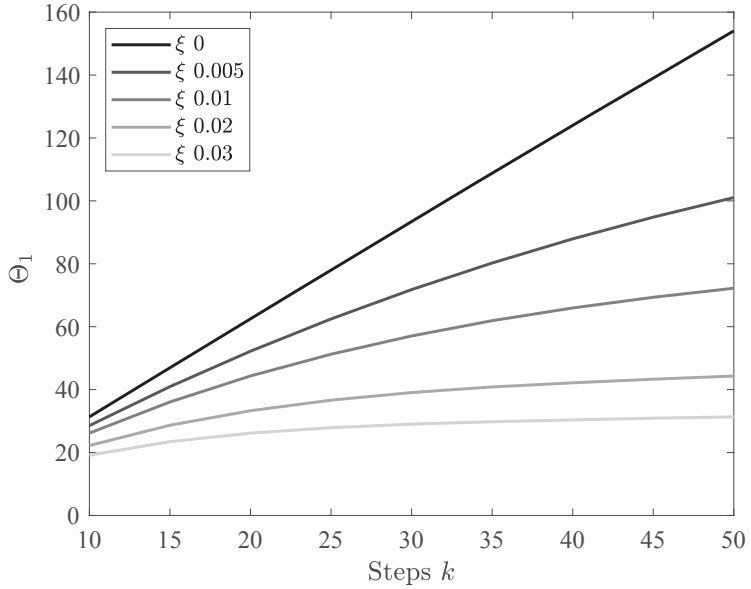

Figure 2: Magnification factor

$$\ddot{y}_i = \frac{G_i/2}{3/8mL}\Theta_i(k,\xi) \tag{31}$$

Finally, equation (31) can be normalized by taking into account the equivalent steady state response of the prescribed single crossing pedestrian $\overline{\ddot{y}}$, i.e. the steady state response produced by a harmonic load placed in the centre of the beam as:

$$\frac{\ddot{y}_i}{\overline{\ddot{y}}} = \Theta_i(k,\xi)\,\xi, \qquad \ddot{y}_i = \Lambda\,\overline{\ddot{y}} \tag{32}$$

In which Λ is defined as $\Lambda = \Theta_i(k,\xi)\,\xi$. The parameter Λ represents the fraction of the transient structural response respect to the equivalent steady state response, quantifying how representative the transient event is in respect to the steady state. Results are shown in Figure 3, in which normal walking and normal running defined with a stride length of 0.75 m and 1.25 m as in [9] have been taken into account. In Figure 3, normal running has plotted with a dash line while normal walking with a continuous line. From the results it can be seen that, due to the difference of the stride length and its immediately consequence in the number of cycles applied to the system between the aforementioned activities, for a given bridge length L and a damping ratio ξ, it is easier to achieve an steady state response for normal walking than normal running. This effect is emphasized as damping increases.

3.2 MINIMUM MASS DESIGN CURVES

By the use of equation (31) , it is possible to generate design curves for minimum mass needed for a single running and a single walking load cases in pedestrian bridges. Given a

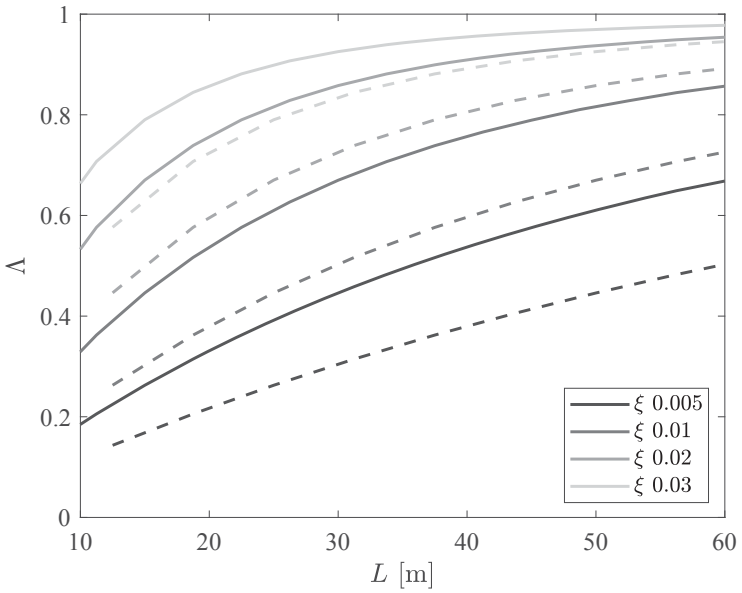

Figure 3: Λ (- - normal running — normal walking)

specific acceleration limit a_{limit} one gets:

$$m = \frac{G_i/2}{3/8\, a_{limit}\, L}\Theta_i(k,\xi) \tag{33}$$

By selecting a specific stride length l_s as reference value and considering $L = k\, l_s$, the minimum linear mass needed can be defined as:

$$m = \frac{G_i/2}{3/8\, a_{limit}\, k\, l_s}\Theta_i(k,\xi) = \frac{G_i/2}{3/8\, a_{limit}\, L}\Theta_i(L/l_s,\xi) \tag{34}$$

It is considered that normal walking and normal running are defined with a stride length of 0.75 m and 1.25 m, respectively [9]. For a given a_{limit}, a general minimum mass design curve can be developed for any given value of a_{limit}, as shown in Figure 4, in which normal running has been plotted with a dash line and normal walking with continuous line. It can be seen in equation (34) that the minimum linear mass is inversely proportionally to the length L of the bridge system and proportional to the magnification factor $\Theta_i(k,\xi)$. In this way, by studying the minimum linear mass m it is possible to appreciate which effect dominates in the verification of the serviceability limit state.

It can be seen from Figure 4 that, under the same levels of damping, running is always more critical than walking, which exposes the need of addressing the running load case scenario for pedestrian bridges. The high differences between normal running and normal walking are explained by the combined effect of the differences in their corresponding dynamic load factors DLF_i and the different magnification factors Θ_i for a given bridge length L, i.e. the number load cycles applied. The importance of the aforementioned results lies on its generality, solved for

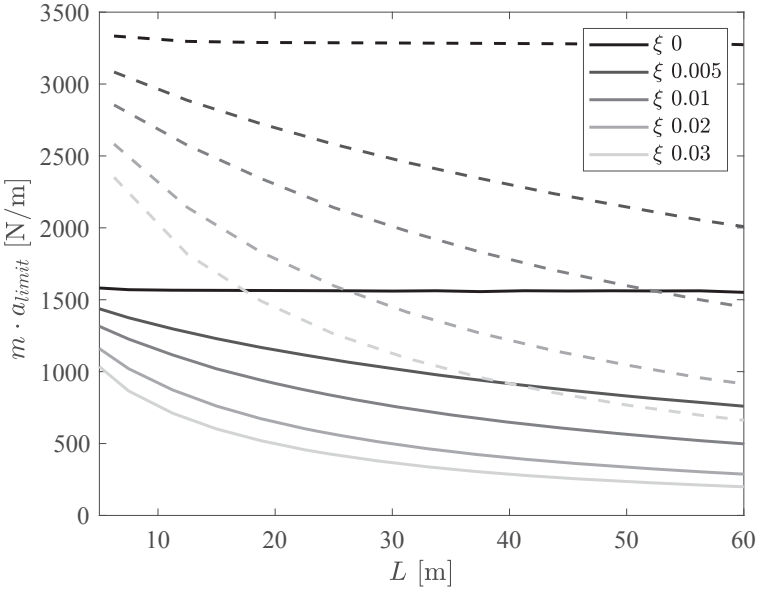

Figure 4: Minimum linear mass (- - normal running — normal walking)

any prescribed acceleration limit a_{limit} in regards to vertical vibrations. Finally, it is important to remark that the equations developed can be used for any type of bridge that reassembles the first mode of a vibration of a clamped—clamped beam, as found in tied arch bridges, portal frame bridges and frame type bridges.

4 CONCLUSIONS

This paper presents an analytical approximation to describe the vertical vibrations of clamped-clamped beams subjected to a single pedestrian induced load, and the following can be concluded.

- A magnification factor is presented and quantified in a closed—form equation. And, the low damping assumption has been introduced and validated for the single passing pedestrian load case scenario. The magnification factor exposes the disproportional trade-off between the dissipation capacities of the system and its corresponding dynamic response given a resonant input, which indicates how pedestrian bridges can be susceptible to experience a large acceleration response.

- It has been quantified how the number load cycles influence the transient response to reach its equivalent steady state response for both normal running and normal walking, in which due to the differences in the stride length, it is easier to achieve steady state under a normal walking regime load than normal running.

- By studying the minimum linear mass parameter, it has been demonstrated that running is more critical than walking for a given damping ratio, exposing the need to address its corresponding load case scenario in the design codes. To this aim, a design chart is given in the present paper in order to perform fast design and assessment of pedestrian bridges for a single crossing pedestrian load case scenario.

- The high differences between normal running and normal walking regarding the minimum mass parameter are explained by the combined effect of the differences in their corresponding dynamic load factors DLF_i and the different magnification factors Θ_i for a given bridge length L, i.e. the number load cycles applied. The importance of this result lies on its generality, since it has been solved for any prescribed acceleration limit a_{limit} in regards to vertical vibrations.

Finally, the moving harmonic load problem applied to clamped—clamped beams has been addressed and it is explained how it can be used for structures that reassemble the mode shape of the studied system such as frame-type bridges and tied arch bridges, exposing the utility and generality of the present work.

REFERENCES

[1] Sétra, Guide methodologique passerelles pietonnes (Technical guide Footbridges: assessment of vibrational behaviour of footbridges under pedestrian loading), 2006.

[2] E. Zäll, J. Garmendia Purroy, A. Andersson, M. Ülker-Kaustell, *The effect of runners on footbridges - A case study, FOOTBRIDGE Proceedings*, 2017.

[3] Y.B. Yang, J.D.Yau, Y.S. Wu, Vehicle-bridge interaction dynamics with applications to high-speed railways ,*World Scientific*, ISBN: 981-238-847-8, 2004.

[4] J.H. Rainer, G. Pernica, D.E. Allen, *Dynamic Loading and Response of Footbridges, Volume 2: Proceedings C.S.C.E. Second International Conference on Short and Medium Span Bridges*, 1986.

[5] H. Bachman, W. Ammann, Vibrations in Structures Induced by Man and Machines, *IABSE-AIPC-IVBH*, ISBN: 3-85748-052-X, 1987.

[6] F. Ricciardelli, C. Briatico, Transient Response of Supported Beams to Moving Forces with Sinusoidal Time Variation, *Journal of Engineering Mechanics*, **137(6)**, 422–430, 2011.

[7] F. Ricciardelli, C. Demartino, Design of Footbridges against Pedestrian-Induced Vibrations, *Journal of Bridge Engineering*, **21(8)**, C4015003, 2016.

[8] R. Pimentel, H. Braga Fernandes, Simplified expressions for the vibration serviceability of beam-like footbridges, *Bridge Structures*, **5(1)**, 3–16, 2009.

[9] Guidelines for the design of footbridges, *International Federation for Structural Concrete (fib)*, ISBN: 2-88394-072-X ,2005.

EURODYN 2020
XI International Conference on Structural Dynamics
M. Papadrakakis, M. Fragiadakis, C. Papadimitriou (eds.)
Athens, Greece, 23–26 November 2020

NUMERICAL VALIDATION OF THE GENERALIZED EQUIVALENT SPECTRAL MODEL THROUGH CROWD DYNAMICS SIMULATIONS

Fiammetta Venuti[1], **Federica Tubino**[2]

[1] Politecnico di Torino
Viale Mattioli, 39, 10125 Torino, Italy
e-mail: fiammetta.venuti@polito.it

[2] Università di Genova
Via Montallegro, 1, 16145 Genova, Italy
e-mail: federica.tubino@unige.it

Keywords: Crowd Modelling, Footbridges, Pedestrian Loading, Spectral Model

Abstract. *This paper aims to provide a validation of the Generalized Equivalent Spectral Model of pedestrian-induced loading through numerical simulations of crowd dynamics. Pedestrian flows with varying density are numerically simulated based on the social force model. The instantaneous step frequency of each pedestrian is obtained from his instantaneous velocity. Results obtained from numerical simulations are statistically analyzed to obtain probability density functions of the step frequency. Then, each pedestrian is modelled as a moving harmonic load, whose trajectory and velocity are obtained from crowd simulations. The power spectral density function of the modal force obtained from numerical simulations is then compared with the analytical expression provided by the Generalized Equivalent Spectral Model. Possible modifications of the original formulation are analyzed, in order to fit numerical results.*

1 INTRODUCTION

Vibration serviceability assessment of footbridges under human-induced excitation requires the availability of suitable and reliable load models. Several walking load models have been proposed in the last decades, but so far none of them has been fully validated and recognized as the most reliable. Recently, increasing attention has been devoted to stochastic load models, which allow considering the inherent randomness of walking parameters, also known as inter-subject variability. A possible approach is the modelling of pedestrian loading as a stationary random process through the definition of a suitable spectral model (e.g. [1], [2]). Most spectral models proposed so far refer to unrestricted pedestrian traffic, i.e. to very low pedestrian density, so that pedestrians are free to walk at their desired speed. To the authors' knowledge, the only extension to crowded conditions has been proposed by Ferrarotti and Tubino [3]. In the Generalized Equivalent Spectral Model (GESM), the effects of human-human interaction are taken into account in two ways: (1) the mean step frequency of pedestrians is expressed as a function of the crowd density; (2) a coherence function is introduced to model the increasing correlation of the loading at different locations for increasing crowd density. Due to the lack of experimental data, the coherence function has been defined in a qualitative physically-based way. Thus, a numerical and/or experimental validation of the model is needed.

The aim of the proposed work is to numerically validate the GESM through crowd dynamics simulations. These are carried out with the commercial software MassMotion [4], which is based on a microscopic description of pedestrian dynamics, i.e. each pedestrian is modelled as a single agent, whose velocity is determined by the interactions with the environment and the surrounding pedestrians. The simulations are performed on an ideal footbridge, crossed by unidirectional flow of pedestrians with crowd densities varying in the range 0.3-1.5 ped/m^2. The pedestrian trajectories and velocities obtained from crowd simulations are used to derive the pedestrian-induced forces. The power spectral density function of the modal force obtained from numerical simulations is then compared with the analytical expression provided by the GESM to evaluate whether the proposed coherence function is suitable to correctly model human-human interaction effects. A critical analysis is provided, and possible modifications of the original formulation are proposed in order to fit numerical results.

2 PEDESTRIAN-INDUCED FORCES: ANALYTICAL FORMULATION

In this Section, the Generalized Equivalent Spectral Model (Section 2.1) and the time-domain force model (Section 2.2) are introduced.

2.1 Generalized Equivalent Spectral Model

The Generalized Equivalent Spectral Model (GESM) [3] of pedestrian-induced forces is based on the definition of the cross-power spectral density function (cpsdf) of the force per-unit-length $S_{ff}(x,x',n)$, which, under the assumption of uniform equivalent loading, is given by:

$$S_{ff}\left(x,x';n\right)=S_f\left(n\right)Coh_{ff}\left(x,x';n\right) \tag{1}$$

where $S_f(n)$ is the power spectral density function (psdf) of the force per-unit-length, and $Coh_{ff}(x,x',n)$ is its coherence function, given by:

$$S_f\left(n\right)=\frac{\left(\alpha_m G_m\right)^2}{\varepsilon L}\frac{N_p}{4}p_N\left(n\right) \tag{2}$$

$$Coh_{ff}\left(x,x';n\right)=\begin{cases}1 & \text{if} \quad \left|x-x'\right|<\varepsilon \\ \exp\left[-C\left(\left|x-x'\right|-\varepsilon\right)\right] & \text{otherwise}\end{cases} \tag{3}$$

In Eq. (2), α_m and G_m are, respectively, the mean value of the DLF and of pedestrian weight, N_p is the mean number of pedestrians on the footbridge, $p_N(n)$ is the probability density function (pdf) of the step frequency n, ε is interpreted as the separation distance that each pedestrian interposes with others to avoid contact, assumed as ε= 4 m. The exponential decay coefficient in Eq. (3), is expressed as a function of the mean step frequency n_m, $C = \exp(C_1 n_m + C_2)$, (C_1 = 22.7, C_2=-41). The mean step frequency n_m can be obtained as a function of the mean walking velocity v_m [5]:

$$n_m = 0.35v_m^3 - 1.59v_m^2 + 2.93v_m \tag{4}$$

The mean step velocity v_m is related to pedestrian density ρ through the fundamental law:

$$v_m\left(\rho\right)=v_{\max}\left\{1-\exp\left[-\gamma\rho_{\max}\left(\frac{1}{\rho}-\frac{1}{\rho_{\max}}\right)\right]\right\} \tag{5}$$

with $\rho_{\max}$=5.4 ped/m^2, γ=0.354, v_{max}=1.34 m/s according to Buchmueller and Weidmann [6].

Based on the GESM, the psdf of the modal force for a generic mode shape $\varphi_j(x)$ is given by:

$$S_{F_j}\left(n\right)=S_f\left(n\right)\chi_j\left(n\right) \tag{6}$$

where $\chi_j(n)$ is the admittance function, defined as follows:

$$\chi_j\left(n\right)=\int_0^L\int_0^L Coh_{ff}\left(x,x';n\right)\varphi_j\left(x\right)\varphi_j\left(x'\right)dxdx' \tag{7}$$

being L the length of the structure. Under the assumption of unrestricted traffic, and considering the first mode shape of a simply-supported beam $\varphi_j(x)$=sin($\pi x/L$), the psdf of the modal force is given by [3]:

$$S_{F_j\mathrm{unr}}\left(n\right)=\left(\alpha_m G_m\right)^2\frac{N_p}{4}p_N\left(n\right) \tag{8}$$

2.2 Time-domain force model

Pedestrian-induced force is commonly schematized as a moving load. The force per unit length exerted by N_p pedestrians can be expressed as the sum of the forces exerted by each single pedestrian as follows:

$$f\left(x,t\right)=\sum_{i=1}^{N_p}f_i\left(t\right)\delta\left[x-x_i\left(t\right)\right] \tag{9}$$

where t and x are the time and the abscissa along the structure, $x_i(t)$ and $f_i(t)$ are, respectively, the instantaneous position and the force exerted by the i-th pedestrian, and $\delta(\bullet)$ is the Dirac delta function.

If pedestrian traffic is simulated numerically in order to take into account interaction among pedestrians, then the instantaneous position x_i and velocity v_i of the i-th pedestrian are the output of the simulation, and the step frequency n_i can be derived from the step velocity v_i through a suitable law (e.g. Eq. (4)). Since the pedestrian step frequency $n_i(t)$ is time variant during

footbridge crossing, the pedestrian force exerted by the *i*-th pedestrian can be modelled as a sinusoidal carrier signal, whose base frequency $n_{m,i}$ is modulated, as follows:

$$f_i(t) = \alpha_i G_i \sin\left[2\pi n_{m,i} t + 2\pi \int_0^{T_i} \left(n_i(t) - n_{m,i}\right) \mathrm{d}t\right] \tag{10}$$

where $n_{m,i}$ is the mean value of the instantaneous step frequency during footbridge crossing time T_i. Furthermore, α_i and G_i are the dynamic load factor (DLF) and the weight of the *i*-th pedestrian, respectively.

Starting from Eq. (9), the modal force for a generic mode shape $\varphi_j(x)$ can be expressed as:

$$F_j(t) = \int_0^L f(x,t)\varphi_j(x)\,\mathrm{d}x = \sum_{i=1}^{N_p} f_i(t)\varphi_j\left[x_i(t)\right] \tag{11}$$

3 CROWD DYNAMICS NUMERICAL SIMULATION

Numerical simulations of crowd dynamics are carried out on an ideal footbridge, whose dimensions in plan recall the ones of the De Gasperi footbridge in Milan: length L=60 m, width B=2.7 m [7]. Pedestrian initial positions are randomly distributed in a "starting area" before the footbridge entrance, ten times longer than the footbridge length: this assures that pedestrians are initially uniformly distributed with a crowd density ρ. Hence, the total number of generated pedestrians N is set equal to $10\rho BL$. Four values of crowd density, [0.3 0.7 1.1 1.5] ped/m^2, from unrestricted to extremely dense pedestrian traffic, are considered. For each crowd density, 100 simulations are performed to obtain statistical reliability.

For each simulation, mean values of the pedestrian density and velocity are calculated during the period of full occupancy T_{full}. The lower and upper boundaries of T_{full} are determined as the first and last time instant when the 95% of the mean number of pedestrians N_p are on the footbridge [8]. The obtained mean values are then averaged over 100 simulations.

Figure 1 plots the v_m-ρ relation resulting from crowd simulations (MM), together with a fitting law and the fundamental law in Eq. (5). It can be observed that for pedestrian densities below around 1.7 ped/m^2 the mean walking velocities obtained from numerical simulations are lower than those estimated with the Weidmann law in Eq. (5).

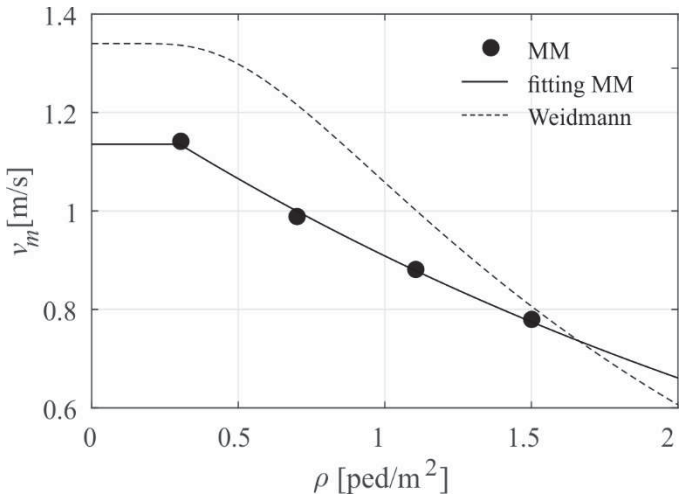

Figure 1: Comparison between v_m-ρ relation obtained with MM and proposed by Weidmann.

Time histories of step frequencies are derived from walking velocities through Eq. (4). Moreover, in order to account for the reaction time needed by pedestrians to adapt their step frequency to variations of the walking velocity, the step frequency is estimated as the 5s-moving average of the instantaneous values.

Table 1 reports the obtained mean value and standard deviation of step frequencies for the four crowd densities.

ρ [ped/m^2]	0.3	0.7	1.1	1.5
n_m [Hz]	1.786	1.676	1.588	1.492
n_{std} [Hz]	0.1083	0.0962	0.0752	0.0598

Table 1: Mean and standard deviation of step frequencies obtained from numerical simulations.

Pdfs of the mean step frequencies during footbridge crossing are estimated from each simulation. Figure 2 plots the obtained numerical mean pdfs and their Gaussian fitting, together with the model adopted in [3]. The numerical pdf is well approximated by a Gaussian fitting, especially for densities below 1.5 ped/m^2, while the pdf in [3], assuming n_{std}=0.18 Hz, does not fit the simulation results.

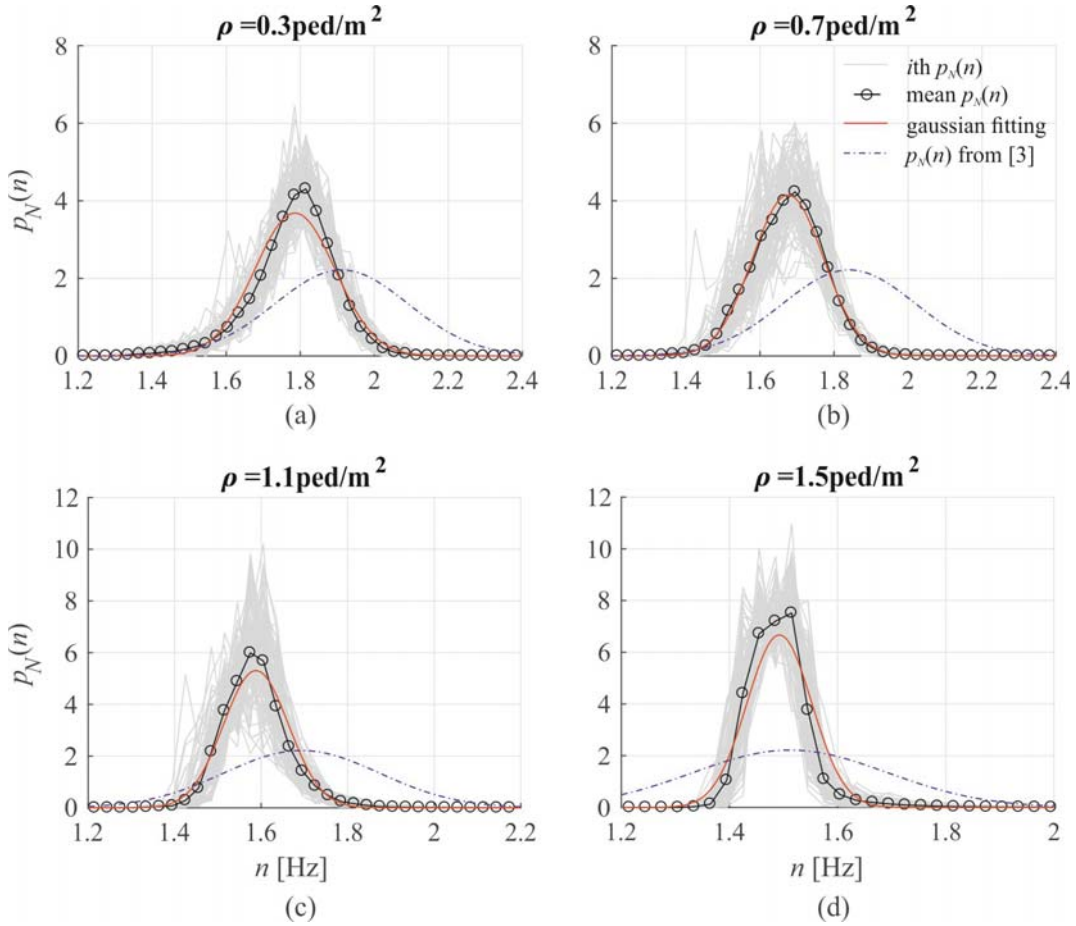

Figure 2: Numerical PDFs of the mean step frequencies and Gaussian fitting.

Figure 3 shows the mean and standard deviation (std) of step frequencies obtained from the fitting of numerical pdfs for each crowd density, compared with the mean step frequencies estimated through Eqs (4), (5). In line with the v_m-ρ trend in Figure 1, numerical mean step

frequencies decrease on increasing crowd density and numerical values are lower than those estimated from Eqs. (4), (5). Standard deviation values also show a decreasing trend for increasing crowd density, meaning that in crowded conditions pedestrians tend to walk at step frequencies closer to the mean value.

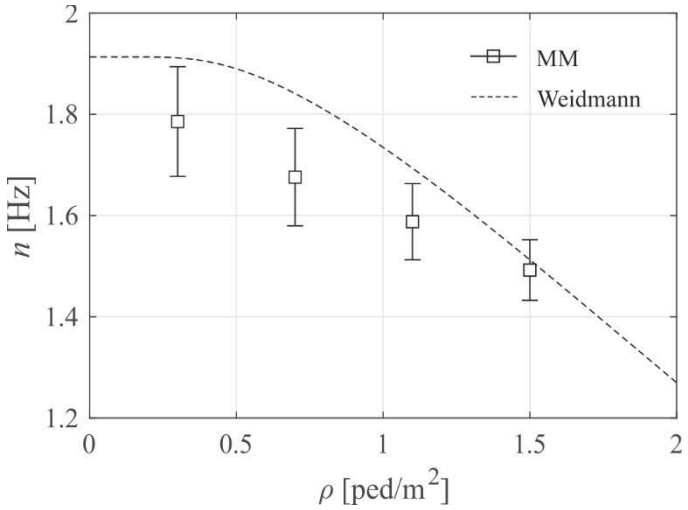

Figure 3: Numerical mean and std of step frequencies in comparison with those estimated from Eqs (4), (5).

The forces induced by each pedestrian are then calculated according to Eq. (9), with each contribution given by Eq. (10), and the modal force is calculated as in Eq. (11), assuming $\alpha_i G_i = \alpha_m G_m = 280$ N. Figure 4 plots an example of the time history of the modal force obtained from a simulation.

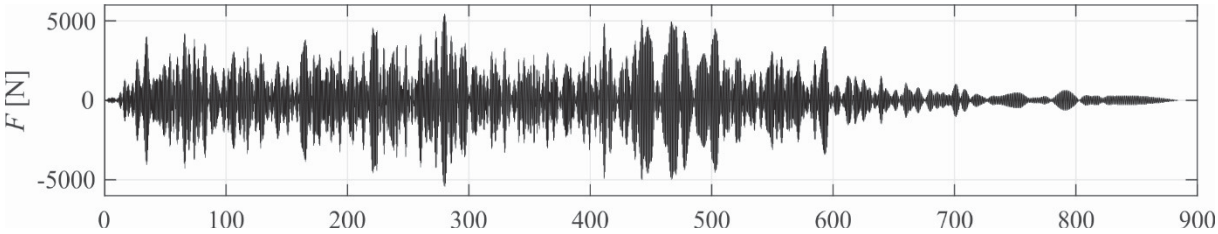

Figure 4: Time history modal force for a simulation with 0.7 ped/m^2.

4 PSDF OF THE MODAL LOAD AND GESM VALIDATION

This section is devoted to the comparison between the numerical psdfs and the analytical expressions provided by the GESM. For each value of the crowd density, the numerical psdfs of the modal force are calculated for each simulation and then averaged over 100 simulations. Concerning GESM, three different psdfs are considered:

- the psdf obtained from Eq. (6), assuming $p_N(n)$ in Eq. (2) as a normal distribution, with mean value from Eq. (4) and std corresponding to 0.18 Hz [3] (GESM);
- the psdf obtained from Eq. (6), assuming $p_N(n)$ as a normal distribution, with mean value and std obtained from numerical simulations in Table 1 ($GESM_{sim}$);
- the psdf obtained from Eq. (8), valid for unrestricted pedestrian traffic, assuming $p_N(n)$ as a normal distribution, with mean value and std obtained from numerical simulations in Table 1 ($GESM_{unr}$).

Figure 5 plots the comparison between the modal psdfs obtained from numerical simulations and the analytical estimates obtained from the GESM. From Figure 5, it can be deduced that

the original formulation (GESM) provides a psdf of the modal force which is far from the one obtained numerically from crowd simulations: the difference comes mainly from the significant difference between the mean step frequency obtained from crowd numerical simulations and the ones provided by Eq. (4), already remarked in Figure 4; furthermore, Table 1 shows that the numerically obtained standard deviation of the step frequency is much smaller than the value assumed in the GESM. The analytical prediction provided by the GESM with mean and std of the step frequency obtained from numerical simulations ($GESM_{sim}$) is in accordance with the numerical result for low crowd density (unrestricted pedestrian traffic), while it greatly overestimates the numerical results for higher crowd densities. The analytical solution that provides results in better accordance with numerical simulations is the one obtained from GESM with numerically estimated mean and std of the step frequency under the hypothesis of unrestricted pedestrian traffic ($GESM_{unr}$). Thus, it seems that interaction among pedestrians can be globally modelled assuming a psdf of the modal load provided by the GESM for unrestricted traffic, adopting a pdf of the step frequency coherent with simulations, i.e. taking into account the reduction of its mean value and std on increasing crowd density.

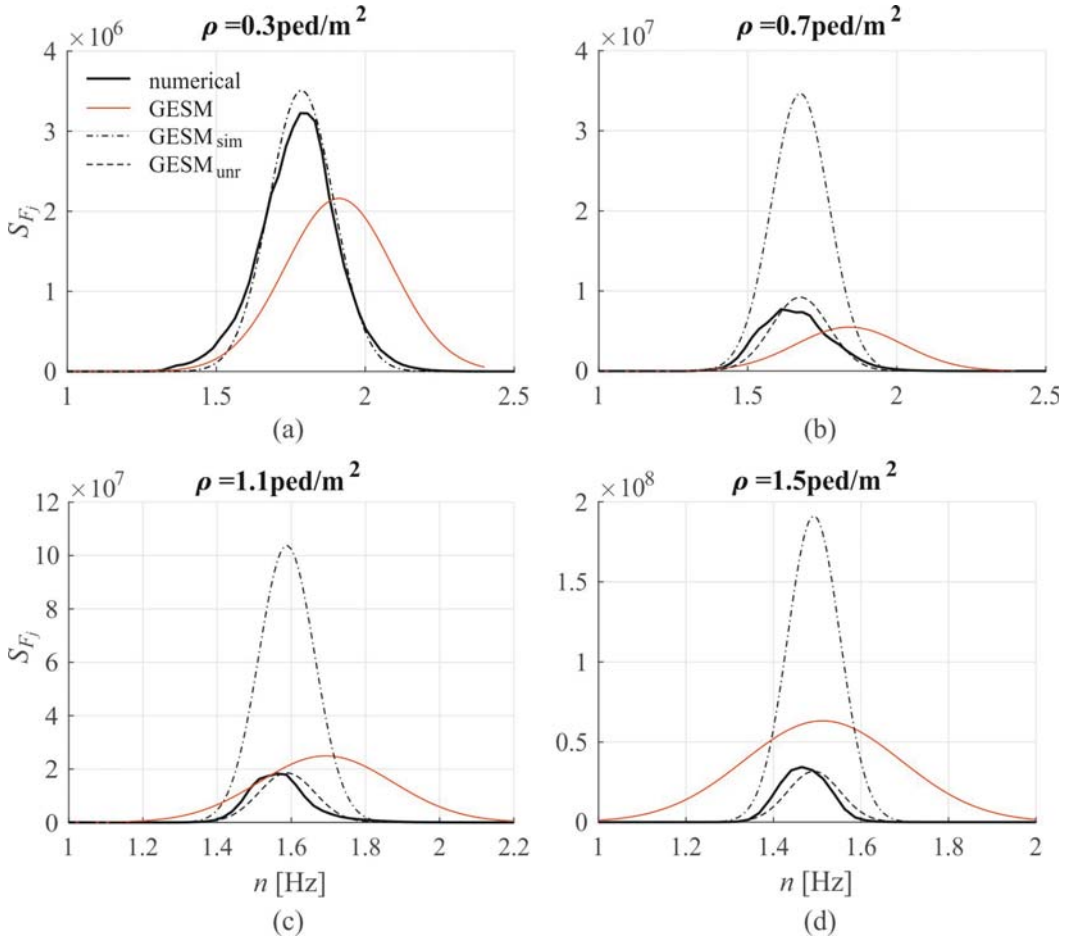

Figure 5: Comparison between psdfs of the modal force obtained from numerical simulations and GESM predictions.

5 CONCLUSIONS AND PROSPECTS

This paper has studied pedestrian-induced forces on footbridges in different traffic conditions. Pedestrian flows have been simulated numerically with the commercial software MassMotion, based on the social force model, and the instantaneous step frequency of pedestrians has been

derived from their velocity. The probabilistic analysis of the step frequency has revealed that, in accordance with the Weidmann law, the mean step frequency tends to decrease on increasing crowd density but numerically obtained walking velocities are lower. Furthermore, also the standard deviation of the step frequency tends to decrease in crowded conditions.

The comparison between the power spectral density function of the modal force obtained from numerical simulations and the analytical expression provided by the GESM has shown that the correlation among pedestrians can be modelled through the GESM including density-dependent values of the mean and standard deviation of the step frequency. The coherence model originally proposed highly overestimates the correlation among pedestrians and provides very large values of the modal force, if compared with numerical simulations. Assuming the coherence model proposed by the GESM for unrestricted pedestrian traffic provides results in accordance with numerical simulations.

The results here obtained are referred to a single deck geometry. Further analyses investigating the influence of the deck width on the equivalent loading spectral properties are necessary. Furthermore, the attention is here focused on the spectral properties of the modal load: a strategy to directly characterize the coherence function of the equivalent distributed loading is under investigation.

ACKNOWLEDGEMENTS

F. Venuti wishes to thank Oasys ltd for having provided free license of the software MassMotion.

REFERENCES

[1] J.M.W. Brownjohn, A. Pavic, P.A. Omentzetter, Spectral density approach for modelling continuous vertical forces on pedestrian structures due to walking. *Canadian Journal of Civil Engineering* 31(1), 65-77, 2004.

[2] G. Piccardo, F. Tubino, Equivalent spectral model and maximum dynamic response for the serviceability analysis of footbridges, *Engineering Structures* 40, 445-456, 2012.

[3] A. Ferrarotti, F. Tubino, Generalized Equivalent Spectral Model for serviceability analysis of footbridges, *Journal of Bridge Engineering* 21(12), 04016091, 2016.

[4] Mass Motion. Oasys Ltd, 2017.

[5] F. Venuti, L. Bruno, An interpretative model of the pedestrian fundamental relation, *Comptes Rendus Mecanique* 335(4), 194-200, 2007.

[6] S. Buchmueller, U. Weidmann, Parameters of pedestrians, pedestrian traffic and walking facilities. Report n. 132. ETH. Zürich, 2006.

[7] F. Tubino, L. Carassale, G. Piccardo, Human-induced vibrations on two lively footbridges in Milan, *Journal of Bridge Engineering ASCE* 21(8), 2016.

[8] F. Venuti, A. Reggio, Mitigation of human-induced vertical vibrations of footbridges through crowd flow control, *Structural Control and Health Monit*oring 25, e2266, 2018.

EURODYN 2020
XI International Conference on Structural Dynamics
M. Papadrakakis, M. Fragiadakis, C. Papadimitriou (eds.)
Athens, Greece, 22–26 June 2020

VALIDATION OF A NOVEL VIRTUAL REALITY PLATFORM FOR INVESTIGATING PEDESTRIAN-PEDESTRIAN INTERACTION IN THE CONTEXT OF STRUCTURAL VIBRATION SERVICEABILITY

Artur A. Soczawa-Stronczyk[1], Mateusz Bocian[1,2]

[1] School of Engineering, University of Leicester, UK
e-mail: {aamss1, m.bocian}@leicester.ac.uk

[2] Biomechanics & Immersive Technology Laboratory, University of Leicester, UK

Keywords: Virtual reality, Pedestrian-pedestrian interaction, Crowd dynamics, Gait synchronisation, Stepping behaviour

Abstract. *Pedestrian-pedestrian interaction (PPI) is one of the fundamental mechanisms purported to influence the amplitudes of structural response under the action of a walking crowd. This is because a pedestrian is likely to alter their gait due to the presence of other pedestrians, which in turns alters the magnitude of structural loading. However, little empirical data are currently available to assess the effect of PPI in the context of vibration serviceability. This is mainly due to logistical challenges in assembling and instrumenting a crowd of walking pedestrians, and the associated cost. To this end, a novel virtual reality platform is developed for experimental investigation of pedestrian-pedestrian interaction. In comparison to real-world crowd testing, the platform enables experimental protocols to be implemented repeatedly in a highly controlled environment while collecting a rich set of data on pedestrian behaviour. The platform incorporates state-of-the-art technology for motion capture, artificial intelligence and three-dimensional computer modelling, and comprises of three core modules: (i) the environment, (ii) the crowd and (iii) the user interface enabling real walking behaviour. To assess the validity of the platform for investigating PPI, tests were conducted to quantify gait synchronisation between a pair of walking pedestrians. The pair of pedestrians consisted of either two real humans or a real human and an avatar generated within a fully immersive VR environment. The test subject was either not explicitly asked to or specifically asked to synchronise their gait while walking side-by-side or front-to-back. It was found that walking with an avatar yields qualitatively the same results as walking with a real person, whether that is with or without the instruction to synchronise gait. However, the results differ quantitatively in terms of the synchronisation strength and the directionality.*

1 INTRODUCTION

In recent years, the industry-wide trend of pushing boundaries in terms of sleek and slender design using light materials often leads to reduced mass, stiffness and damping [1] of the newly built structures. As a consequence, several footbridges failed to satisfy the vibration serviceability criteria when occupied by a crowd of people [2–11]. A number of dynamic force models were put forward to account for the adaptation of pedestrian's stepping behaviour due to the presence other walkers [12–15], known as pedestrian-pedestrian interaction (PPI). However, very few studies attempted to uncover the underlying network of complex dynamic interactions present in a crowd of walking pedestrians and quantify the strength of PPI in the context of structural dynamics [16–18]. This is predominantly due to many uncertainties associated with a full-scale crowd testing, but also low repeatability of experimental conditions and a significant logistical challenge of gathering and instrumenting a group of walkers together with the accompanying costs.

To alleviate these issues, a novel experimental platform is proposed to limit the logistical efforts in investigating PPI whilst providing an accurate representation of real-life environment. This is achieved by employing the latest developments in motion capture, three-dimensional modelling and virtual reality (VR) technology, and by using artificial intelligence (AI) - driven virtual pedestrians capable of simulating complex social interactions present in real crowds.

This paper is structured as follows: Section 2 describes the development of the VR experimental platform for PPI investigation, Section 3 details the validation procedure of the platform, followed by the data analysis process, Section 4 presents the validation results together with the discussion, and Section 5 provides the conclusions.

2 DEVELOPMENT OF THE VIRTUAL-REALITY PLATFORM

A construction of biomechanically representative, virtual reality-based experimental platform for investigating PPI consisted of the following stages. Firstly, an optical motion capturing system was employed to record multiple gait cycles of a real person walking with various speeds along a straight line as well as along an arc of circles with various radiuses, with the procedure repeated at multiple walking speeds. Secondly, the recorded motions were used to create an animation controller which would drive the motion of a realistic humanoid character in VR, referred to as an agent. Lastly, a novel AI system was employed to steer the agent in the virtual setting.

2.1 Motion capture

A twenty-five years old male performer (height 182.5 cm, weight: 80 kg) was recruited from the university cohort. He was outfitted with a motion capture equipped with thirty-seven reflective markers placed on body landmarks. The performer was asked to complete four different types of walks at pacing frequencies ranging from 1.3 Hz to 2.0 Hz at 0.1 Hz increments. The walks consisted of walking along a straight line, and around small, medium and large circles with the radiuses of 63.5 cm, 27 cm and 254 cm (25 in, 50 in and 100 in) respectively. A metronome was used to ensure the consistent pacing frequency of the performer throughout the motion recording process.

The gait cycles were recorded using a set of eight OptiTrack Prime 13 cameras, which provided near real-time tracking data at the sampling rate of 120 Hz. The raw tracking data were transferred over to the processing unit over the IEEE 802.3 compliant, gigabit network. The

data were recorded and post-processed using OptiTrack's proprietary software, Motive:Body 2.0.

The initial post-processing consisted of interpolation of missing markers' trajectories due to occlusions and light reflections. Based on the characteristics of the specific marker's trajectory, this was done by employing a first or third-degree polynomial interpolation algorithm. Furthermore, any noise in the raw tracking data was removed by using a fourth-order two-way Butterworth low-pass filter with the cut off frequency at 6 Hz. The primary noise source was markers' vibration, as they were not directly attached to the bones. Also, changes in air temperature and lighting conditions contributed to the decrease in the tracking quality.

The actual processing of the motion capture data was conducted in Autodesk MotionBuilder 2018. During this stage, the original data were down sampled to 30 frames per second. Furthermore, details such as feet's floor contact and fingers positions were adjusted. Finally, from multiple recordings of the same kind, gait cycles were extracted and stitched together to minimise the repeatability of the avatar's motions.

2.2 Avatars creation

Adobe Fuse CC 1.2 was used to create three-dimensional models of humanoid characters employed in VR. The software allowed physical and visual features of virtual avatars to be adjusted, i.e. dimensions of body parts, facial expression and clothing. In order to create the bone structure of the virtual characters, the models were exported to Adobe Mixamo where they were rigged. This created a puppet-like animation mechanism by tying the skeleton to the skin mesh.

Rigged avatars were then exported to Unity 2018.4.0f1 – a game engine used throughout this project. Unity was chosen predominantly due to its C# scripting API and a vast Asset Store collection compared to other game engines.

The next step consisted of retargeting motion-captured gait cycle animations onto the avatars and creating an animation controller. The animation controller employed two-dimensional linear animation blending to create smooth transitions between recorded animations based on two input parameters: (i) selected pacing frequency and (ii) the desired direction of progression.

Footsteps sound effects were added to avatars to provide realistic auditory ques based on the walking surface. The sound effects were programmed to be triggered by every heel strike.

2.3 Steering system

Polarith AI system was implemented to navigate the avatar around the virtual environment by feeding input parameters into the animation controller. It is an artificial-intelligence navigation system which is fully programmable and operates based on a multi-objective optimisation algorithm. The system works in two stages. Firstly, it samples the surrounding to detect the position of the objective and any obstacles. Secondly, it uses an optimisation algorithm to find the local solution to the optimisation problem [19]. The solution takes the form of the desired direction of movement, which is then fed to the animation controller to move the avatar.

For the purpose of experimental platform validation, a path-follow behaviour was programmed without any obstacles present.

3 PLATFORM VALIDATION

To validate the virtual reality platform, one healthy male test subject (age: 30, height: 191.6 cm, weight: 80.1 kg) was recruited from the cohort of students at the University of Leicester.

Prior to taking part in the experiment, he was asked to: (i) familiarise himself with the participant's information letter, (ii) complete the physical activity readiness questionnaire, and (iii) sign the informed consent form. He was asked to wear flat sole shoes and casual clothing.

The study was approved by the University of Leicester Ethics of Research Committee.

3.1 Location

Due to the space requirement, the Charles Wilson Sports Hall was selected as a suitable location for the validation study. The sports hall is located within the main campus of the University of Leicester, UK. It is 16.7 m wide and 33.5 m long with the clear ceiling height of 5.6 metres at the highest point. To minimise the effect of light reflections on tracking quality, the parquet floor was covered with a dark monotone carpet. This also eliminated visual reference cues offered by the floor markings, which otherwise might have influenced the test subject's movements.

3.2 Experimental protocol

The test subject was provided with a habituation time to familiarise himself with the virtual environment. He was asked to perform a total of sixteen walks around a path consisting of two 10 m long straights and two turns 5 m in diameter. Each walk consisted of 8 laps, resulting in a total distance of 285 m travelled per walk. During each walk, the test subject walked next to (side-by-side; SbS) or behind (front-to-back; FtB) a pacer. The walks were performed in two settings: (i) in the virtual environment (VR), where the pacer was previously created, virtual agent or (ii) in the real environment (RL), where the male performer employed to record virtual agent's motion served as a pacer.

To avoid any directional bias in test subject's behaviour, each walk was performed twice, in a clockwise and an anticlockwise direction around the path. During the first eight walks, the test subject was only directed to maintain his assigned position relative to the pacer, hereafter referred to as uninstructed synchronisation experimental conditions (US). During the last eight walks, the test subject was explicitly asked to walk in step with the pacer, in such manner that the timing of their ipsilateral footsteps was perfectly matched, hereafter referred to as instructed synchronisation experimental conditions (IS).

In order to control real pacer's stepping behaviour, he was equipped with Pioneer SE-M521 over-ear headphones connected to KORG MA-1 metronome. The pacing frequency of the virtual pacer was controlled in the game engine through the animation controller.

The pacing frequency of pacers was based on test subject's height and calculated using the following formula:

$$FR = \frac{v}{gl} \tag{1}$$

where v is the walking velocity, g is the gravitational acceleration, l is a leg length, and FR is the Froude number which was set to 0.15. The leg length l was estimated by using test subject's height, and gender relationship derived by Pheasant [20], and explicitly given by Bocian et al. [21]:

$$l = 0.7028h - 0.3091 \tag{2}$$

where h is the test subject's height. The walking velocity v was converted to the pacing frequency f_p using the Eq. 3, which was derived from experimental data in Soczawa-Stronczyk et al. [22].

$$f_p = 0.66v + 0.99 \tag{3}$$

As a consequence, virtual pacer's pacing frequency was set to 1.81 Hz and the metronome beat for the real pacer was set to 108 BPM.

3.3 Instrumentation

A motion capture system (mocap system) made up of twenty-four OptiTrack Prime 17W and ten OptiTrack Prime 13 cameras was set up in the sports hall. During walks performed in the virtual environment, the test subject was equipped with Oculus Rift CV1 head-mounted display (HMD) together with the MSI VR One 7RE backpack PC used to generate the environment. The HMD had reflective markers affixed to it in order to track its position and rotation using the mocap system. The positional data were wirelessly streamed to the backpack PC from the dedicated mocap processing PC using the NatNet server broadcast protocol version 3.0, through IEEE 802.11n-2009 wireless network.

The virtual environment used during the validation experiment was created using building information modelling (BIM) software - ARCHICAD 23. A high-detail, realistic representation of the Charles Wilson Sports Hall was created.

During all walks, the test subject was instrumented with two APDM Opal™ wireless attitude and heading reference systems (AHRS). One AHRS was attached to the lower back, at the level of fifth lumbar vertebra (L5), whereas the other was strapped to the right ankle, using elastic straps. The data recorded by AHRSs were sampled at 128 Hz and time locked. For the purpose of the subsequent analysis, three-dimensional acceleration signal recorded in the local coordinate system (i.e. sensor) was extracted and resolved to the global coordinate system by means of the quaternion algebra. This allowed the vertical component of the acceleration vector (i.e. that aligned with the gravity vector) to be extracted for further analysis.

The real pacer was outfitted with a set of AHRS of the same type and positioned at the same body locations as in the case of the test subject. This enabled synchronisation to be easily quantified based on a set of compatible signals.

Only the data from the sensor strapped to the ankle were used, as the data were sufficient to describe a gait cycle fully.

Figure 1: A person wearing HMD (right) walking next to the pacer in the virtual environment (left).

As it was impossible to instrument the virtual pacer, the displacement of the right ankle was recorded in the game engine, at a sampling frequency of circa 50 Hz. Considering that the

displacement signal was not time-locked with the AHRS's data, the following time alignment procedure was implemented. An AHRS was fastened to a rigid body with three reflective markers, which were tracked by the motion capture system. The position of the rigid body was isometrically mapped (i.e. preserving distances and rotation angles) onto an unrendered virtual cube, of which displacement was recorded together with the displacement of the virtual pacer's ankle. Before and after each test, the AHRS-rigid body couple was slowly waved using a sinusoidal motion to create a reference signal subsequently used to time-align the data from the game engine and the AHRS.

3.4 Data analysis

The subsequent quantification of the synchronisation strength was performed in MATLAB R2019b and was based on vertical velocity signals from the ankle. This is due to the need to reconcile the displacement signals from the game engine (expressed in m) with the acceleration signals from AHRS (expressed in m/s^2) to a common physical quantity before further processing. In order to minimise the impact of the data loss inherent to the numerical differentiation (high frequency noise), as well as to lessen the signal drift rising from the numerical integration (low frequency noise), it was decided to differentiate game engine's displacement signals and integrate the AHRS' acceleration signals to achieve compatible velocity signals (expressed in m/s), as shown in Figure 2.

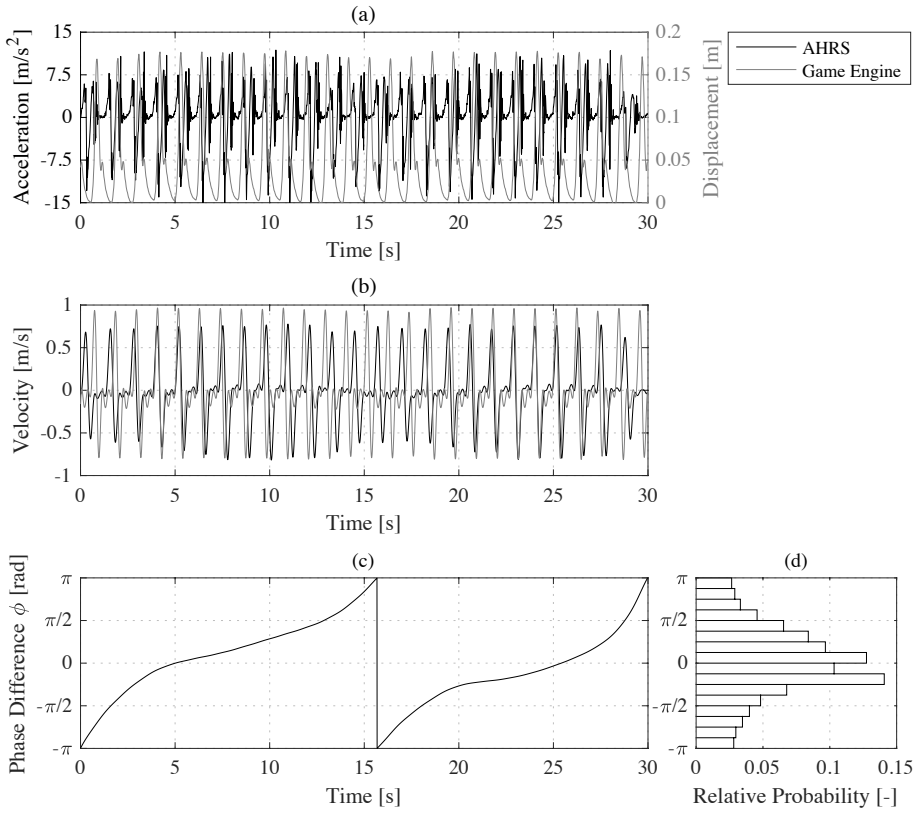

Figure 2: Examples of (a) the raw AHRS acceleration signal and the resampled game engine displacement signal from the ankle, (b) the corresponding velocity signals, (c) the corresponding phase difference signal and (d) the relative probability distribution.

At the start, the displacement signals were upsampled from the variable sampling rate of circa 50 Hz to the uniform sampling rate of 128 Hz to match the sampling rate of AHRS acceleration signals. The upsampling was performed using shape-preserving piecewise cubic interpolation algorithm implemented in MATLAB's *resample* function [23].

In order to differentiate the game engine's displacement signals, a one-dimensional gradient of the vertical displacement vector was calculated and then divided by the numerical gradient of the corresponding time vector. The ensuing velocity vector was post-filtered using the fourth-order two-way Butterworth band-pass filter with the frequency band set to preserve the first three harmonics of the original signal.

The numerical integration of AHRS acceleration signal was proceeded by the pre-filtering of original signals with the fourth-order two-way Butterworth band-pass filter with the same frequency band as in the case of numerical differentiation. The integration was performed by employing the cumulative trapezoidal numerical integration method [24] and post-filtering the resulting velocity signals with the fourth-order two-way Butterworth high-pass filter with the cut-off frequency equal to half of the frequency of the first harmonic.

Finally, with all signals representing the same physical quantity, the two velocity signals derived from the AHRS-rigid body were used to find the delay between AHRS and the game engine's signals for each walk. Using MATLAB's *finddelay* function [25], the cross-correlation between the two velocity signals was calculated at all viable lags. Subsequently, the cross-correlation was normalised, and the estimated delay was given as the negative lag characterised by the largest absolute value of the normalised cross-correlation, which allowed game engine's and AHRS signals to be time-aligned.

3.5 Synchronisation quantification

Before the quantification of pairwise gait synchronisation strength between the test subject and the pacer, analytic representations of velocity signals had to be calculated first. For this purpose, each pair of velocity signals (velocities of test subject's and pacer's right ankles from each walk) was band-pass filtered by utilising the fourth-order two-way Butterworth band-pass filter with a frequency band ranging from 0.70 times the minimum signal (stride) frequency to 1.25 times the maximum stride frequency, as suggested in van Ulzen et al. [26].

For each of the velocity signals $v_i(t)$, the Hilbert transform was then used to obtain the instantaneous phase information contained within the analytic signal $v_i^a(t)$, defined as [27]:

$$v_i^a(t) = v_i(t) + \frac{i}{\pi} P.V. \int_{-\infty}^{+\infty} \frac{v_i(\tau)}{t-\tau} d\tau \tag{4}$$

where $P.V.$ is the Cauchy principal value of the integral. The instantaneous phase angle of the velocity signals $\phi_i(t)$ was calculated by taking the four-quadrant inverse tangent of the imaginary, $\Im$, and real, $\Re$, parts of the analytical signal:

$$\phi_i(t) = \tan^{-1} \frac{\Im[v_i^a(t)]}{\Re[v_i^a(t)]} \tag{5}$$

The phase angle difference of the considered pair of signals $\phi_{p,s}(t)$ was calculated by subtracting test subject's phase angle time series (denoted by subscript s) from the one of the pacer (denoted by subscript p).

$$\phi_{p,s}(t) = \phi_p(t) - \phi_s(t) \tag{6}$$

The synchronisation strength between test subject's and pacer's gait cycles was determined based on the Shannon entropy $E_{p,s}$ of the phase difference distribution, defined as [28]:

$$E_{p,s} = -\sum_{k=1}^{N} P_{p,s}^{k} \ln P_{p,s}^{k} \tag{7}$$

where $P_{p,s}^{k}$ is the probability of the phase difference $\phi_{p,s}(t)$ falling into a k^{th} bin of $\pi/8$ in size, and N is the total number of bins. In order to be able to compare the values of the synchronisation strength across different walks, the synchronisation strength index $\rho_{p,s}$ was then calculated by normalising by the maximum achievable Shannon entropy in the case of the perfect frequency synchrony:

$$\rho_{p,s} = \frac{\ln N - E_{p,s}}{\ln N} \tag{8}$$

The index takes values ranging from 0 to 1, with 0 corresponding to a complete lack of gait synchronisation (i.e. a uniform distribution of phase difference) and 1 representing a perfect gait synchronisation (i.e. a Dirac-like distribution of phase difference).

4 RESULTS AND DISCUSSION

4.1 Stride frequency

In order to assess the influence of the experimental environment on the pacing rate, stride frequency of both pacers and the test subject was calculated using fast Fourier transform for each of the walks. Subsequently, the difference between pacers' and test subject's stride frequencies was quantified. Under US experimental conditions, the mean (± standard deviation) difference was equal to $\bar{\mathrm{f}}_{p-s}^{RL.US} = 0.060 \pm 0.011$ Hz and to $\bar{\mathrm{f}}_{p-s}^{VR.US} = 0.037 \pm 0.008$ Hz during walks in the RL and VR environments, respectively. Similarly, the same comparison made for walks under IS experimental conditions showed an average difference of $\bar{\mathrm{f}}_{p-s}^{RL.IS} = 0.004 \pm 0.005$ Hz and $\bar{\mathrm{f}}_{p-s}^{VR.IS} = 0.003 \pm 0.002$ Hz, respectively. Moreover, the overall increase of test subject's stride frequency in the virtual environment was equal to 2.81% and 0.13%, under US and IS experimental conditions, respectively. Those results show a high level of affinity between the two tested environments and indicate that test subject's stride frequency remained unaltered in the virtual environment, compared to the real equivalent.

4.2 Gait variability

To evaluate the compatibility of the walking stimulus between the real and virtual environments, the gait cycle variability of both pacers was quantified and assessed through the coefficient of variation (CoV) of the stride frequency.

The mean gait variability attained by the real pacer was $\overline{\mathrm{CoV}}_{p}^{RL} = 1.09 \pm 0.09\%$, with the maximum recorded value of $\mathrm{CoV}_{p}^{RL} = 1.26\%$. The virtual pacer achieved the maximum gait variability of $\mathrm{CoV}_{p}^{VR} = 0.56\%$ with the mean of $\overline{\mathrm{CoV}}_{p}^{VR} = 0.52 \pm 0.03\%$. Even though the average gait variability of the real pacer was double the value achieved by the virtual counterpart, the real pacer's variability was deemed acceptable to provide consistent visual and auditory cues to the test subject. A certain level of discrepancy between the two pacers' gait variabilities was expected due to the inherent inability of the real human to replicate their stepping behaviour perfectly, and the finite number of gait cycles available to drive the virtual pacer.

Under the US experimental conditions, the mean gait variability of the test subject was $\overline{\mathrm{CoV}}_s^{RL.US} = 3.63 \pm 1.44\%$ and $\overline{\mathrm{CoV}}_s^{VR.US} = 3.32 \pm 2.00\%$ during walks in the real and virtual environments, respectively, with the corresponding maximum values $\mathrm{CoV}_s^{RL.US} = 5.43\%$ and $\mathrm{CoV}_s^{RL.US} = 5.75\%$.

The walks performed under IS experimental conditions were characterised by test subject's lower gait variability. The maximum gait variability attained during walks performed in the real and virtual environment, respectively, was $\mathrm{CoV}_s^{RL.IS} = 4.24\%$ and $\mathrm{CoV}_s^{VR.IS} = 3.10\%$, with the mean values of $\overline{\mathrm{CoV}}_s^{RL.IS} = 3.01 \pm 0.95\%$ and $\overline{\mathrm{CoV}}_s^{VR.IS} = 2.31 \pm 0.58\%$ respectively.

The instruction to synchronise steps with the pacer resulted in a decrease in the gait cycle variability in both environments. A more considerable increase in the consistency of the gait cycle was observed during the VR walks, which was pronounced under the IS experimental conditions. This can be attributed to the more isolated conditions offered by the virtual environment. Although the virtual environment was constructed to mimic the sports hall's interior where the tests took place, it secluded the test subject from some of the peripheral stimuli present in the real environment. As a consequence, the test subject's cognitive load was relieved, which might have resulted in more cognitive resources being spent on the execution of gait control. In addition, several studies have reported that the virtual environment alters the distance perception while walking [29–33], resulting in shorter strides [34] and more careful feet placement.

4.3 Synchronisation strength

Synchronisation strength index values achieved during walks under US experimental conditions were comparably low, with the mean synchronisation strength index of $\bar{\rho}^{RL.US} = 0.005 \pm 0.004$ and $\bar{\rho}^{VR.US} = 0.015 \pm 0.014$ during walks performed in the real and virtual environments, respectively, with the corresponding highest index values of $\rho^{RL.US} = 0.012$ and $\rho^{VR.US} = 0.037$.

The synchronisation strength index values recorded under US experimental conditions were below the proposed synchronisation threshold of $\rho = 0.2$ [35]. These results are consistent with previous findings for a pair of walkers [26,36] and a group of pedestrians walking on a rigid ground [22] and a bridge [16], and reflect the transient nature of the unprompted gait adaptation mechanism.

The synchronisation strength index values achieved in IS experimental conditions are presented in Figure 3 (represented by the vector magnitude) and are accompanied by the mean circular direction (represented by the corresponding vector angle) to indicate the directionality of the synchronisation phenomenon. The mean circular direction $\bar{r}$ was calculated by transforming all phase difference values into a two-dimensional vector $\bar{r} = (\cos\alpha, \sin\beta)$ and averaging over the number of data points [37]. According to the adopted sign convention, positive values represent test subject’s leading the pacer, and the negative values indicate the test subject lagging the pacer.

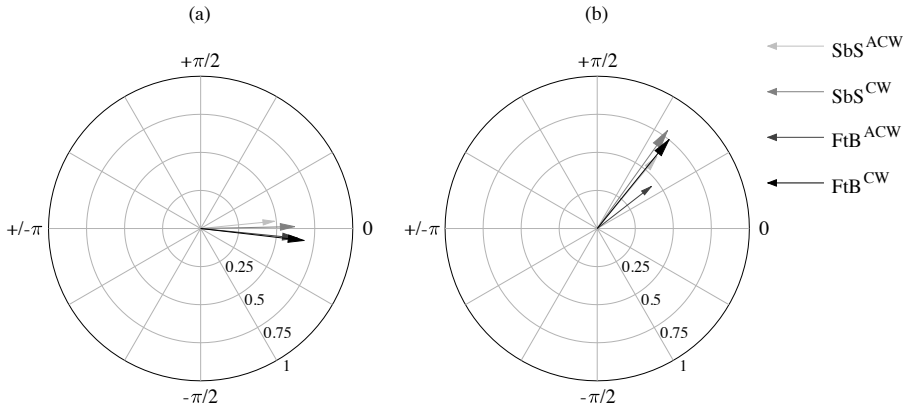

Figure 3: The synchronisation strength index values (magnitude) together with the corresponding mean circular direction (angle) recorded during walks in (a) the real and (b) virtual environments under IS experimental conditions.

The instruction given to the test subject to synchronise his gait cycle with the pacer led to a similar increase in the synchronisation strength values in both environments. The mean synchronisation strength index of $\bar{\rho}^{RL.IS} = 0.605 \pm 0.074$ and $\bar{\rho}^{VR.IS} = 0.650 \pm 0.134$ was attained during walks in the real and virtual environment, respectively. This was the result of the test subject exhibiting increased control over the stepping behaviour in comparison to US walks.

The mean circular direction of the walks performed in the real environment took near-zero values with the front-to-back walks recording slightly negative values, and the side-by-side walks slightly positive values. Negative values of the directionality during front-to-back walks were the result of the test subject reaction to the pacer's action. On the other hand, during side-by-side walks, the pacer was positioned within test subject's horizontal far peripheral vision [38], which might have prompted the emergence of test subject's anticipatory stepping behaviour.

The aforementioned mechanism responsible for the anticipatory behaviour was amplified during the side-by-side walks performed in the virtual environment. This is because of the head-mounted display limiting test subject's horizontal field of view by circa. 110^{o} [39,40], and thus effectively eradicating far peripheral vision. The test subject attempted to compensate for this by falling slightly behind the pacer so that the pacer was within his field of view.

The virtual reality gave rise to an additional mechanism prompting the anticipatory behaviour, as the gait anticipation was also present during the front-to-back walks, where the pacer was no longer positioned in the test subject's far horizontal peripheral but rather in the centre of his gaze. In the front-to-back collocation, the rear walker would attempt to arrive at the double stance phase of gait faster than the person positioned in front in order to allow for a more natural collision avoidance corrections [41].

In the case of side-by-side and front-to-back collocations, the repetitiveness of virtual pacer's gait cycle might have laid grounds for greater predictability of its gait cycle, especially given the more isolated conditions offered by the virtual environment.

5 CONCLUSIONS

This paper presents the development and validation of a novel virtual reality platform for investigating pedestrian-pedestrian interaction and crowd dynamics. The platform utilises the most recent advancements in three-dimensional modelling, motion capturing and virtual reality technology. It comprises of a highly detailed representation of the real environment and an AI-driven virtual pedestrian capable of exhibiting complex social interactions found in real

crowds. The validation process involved a 30 years old male test subject covering the distance in excess of 4 km in the real and virtual environments, walking next to or behind a pacer, that being either a real person or an animated virtual agent. Sixteen walks were recorded in total, including eight without and eight with the instruction to synchronise steps.

No disimilarities were found between test subject's stride frequencies attained in the RL and VR environments, as the stride frequency values increased by a total of 1.42% in the VR. This subsequently resulted in the relationship between test subject's and pacers' stride frequencies being compatible across the two tested environments.

The assessment of the difference between test subject's and pacers' stride frequencies yielded compatible results in both, the real and virtual environments. Furthermore, no significant differences in gait parameters of the tested subject were found between the two tested environments.

The analysis of pacers' gait variability showed that the average difference between real and virtual pacers' gait variability is equal to 0.57%, which ensures the compatibility of the visual and auditory cues provided by the walking stimulus across the two environments. The test subject's gait variability was lower in the virtual environment by 8.5% under US experimental conditions, and by 23.3% under IS experimental conditions. The more consistent stepping behaviour was likely the result of a smaller number of peripheral stimuli offered by the virtual environment, which subsequently allowed for a greater focus on pacer's motion.

Under US experimental conditions, the synchronisation strength index achieved in the virtual reality platform was compatible with the real environment, yielding values not exceeding 0.04. This is consistent with previous results obtained for a pair of walkers [26,36] and during walking in a group [16,22].

The instruction given to the test subject to synchronise his gait with that of the pacer resulted in an increase of the synchronisation strength index in both environments beyond 0.2. The effect of the instruction was stronger in the virtual environment, where the synchronisation strength index was higher by 7.4%. The directionality of gait synchronisation revealed that in the real environment, the test subject was reacting to pacer's stepping behaviour during walks in the front-to-back arrangement and anticipating pacer's footsteps during side-by-side walks. The anticipatory behaviour was further amplified in the virtual environment and also emerged during front-to-back walks.

Overall, the preliminary results presented herein indicate that the developed experimental platform has the potential to become a viable solution for investigating crowd dynamics, within and beyond the context of vibration serviceability.

ACKNOWLEDGEMENTS

The authors acknowledge: Mr Allan Rankin, Mr Harry Piercy and Target3D Ltd. for providing the optical system used in the validation study and their generous hands-on assistance during the experiments; Mr Maksat Kalybek for support in the run-up and in the aftermath of the experimental campaign and Dr Niamh Hynes for assistance in the data collection.

REFERENCES

[1] Venuti F, Bruno L. Crowd-structure interaction in lively footbridges under synchronous lateral excitation: A literature review. Phys Life Rev 2009;6:176–206. https://doi.org/10.1016/j.plrev.2009.07.001.

[2] Dallard P, Fitzpatrick T, Flint A, Low A, Smith RR, Willford M, et al. London Millennium Bridge: Pedestrian-Induced Lateral Vibration. J Bridg Eng 2001;6:412–7. https://doi.org/10.1061/(ASCE)1084-0702(2001)6:6(412).

[3] Dallard P, Fitzpatrick AJ, Flint A, Le Bourva S, Low A, Ridsdill Smith RM, et al. The London Millennium Footbridge. Struct. Eng., 2001.

[4] Brownjohn JMW, Fok P, Roche M, Moyo P. Long span steel pedestrian bridge at Singapore Changi Airport - Part 1: Prediction of vibration serviceability problems. Struct Eng 2004.

[5] Brownjohn JMW, Fok P, Roche M, Omenzetter P. Long span steel pedestrian bridge at Singapore Changi Airport - Part 2: Crowd loading tests and vibration mitigation measures. Struct Eng 2004.

[6] Caetano E, Cunha Á, Magalhães F, Moutinho C. Studies for controlling human-induced vibration of the Pedro e Inês footbridge, Portugal. Part 1: Assessment of dynamic behaviour. Eng Struct 2010;32:1069–81. https://doi.org/10.1016/j.engstruct.2009.12.034.

[7] Caetano E, Cunha Á, Moutinho C, Magalhães F. Studies for controlling human-induced vibration of the Pedro e Inês footbridge, Portugal. Part 2: Implementation of tuned mass dampers. Eng Struct 2010;32:1082–91. https://doi.org/10.1016/j.engstruct.2009.12.033.

[8] Kawasaki T, Nakamura S, Ohno K. Field measurement of lateral vibration of a suspension bridge induced by pedestrians. Doboku Gakkai Ronbunshu 2004;2004:97–107. https://doi.org/10.2208/jscej.2004.777_97.

[9] Nakamura S ichi, Kawasaki T. Lateral vibration of footbridges by synchronous walking. J Constr Steel Res 2006;62:1148–60. https://doi.org/10.1016/j.jcsr.2006.06.023.

[10] Hoorpah W, Flamand O, Cespedes X. The Simone de Beauvoir Footbridge between Bercy Quay and Tolbiac Quay in Paris: Study and measurement of the dynamic behaviour of the structure under pedestrian loads and discussion of corrective modifications. In: Caetano E, Cunha Á, Hoorpah W, Raoul J, editors. Footbridge Vib. Des. 1st Editio, Leiden, The Netherlands: CRC Press/Balkema; 2017, p. 202.

[11] Bocian M, Burn JF, Macdonald JHG, Brownjohn JMW. From phase drift to synchronisation – pedestrian stepping behaviour on laterally oscillating structures and consequences for dynamic stability. J Sound Vib 2017;392:382–99. https://doi.org/10.1016/j.jsv.2016.12.022.

[12] Grundmann H, Kreuzinger H, Schneider M. Dynamic calculation of footbridges. Bauingenieur 1993;68:215–25.

[13] Piccardo G, Tubino F. Parametric resonance of flexible footbridges under crowd-induced lateral excitation. J Sound Vib 2008. https://doi.org/10.1016/j.jsv.2007.09.008.

[14] Newland DE. Pedestrian excitation of bridges. Proc Inst Mech Eng Part C J Mech Eng Sci 2004. https://doi.org/10.1243/095440604323052274.

[15] Venuti F, Bruno L, Napoli P. Pedestrian Lateral Action on lively Footbridges: A New Load Model. Struct Eng Int 2007;17:236–41. https://doi.org/10.2749/101686607781645897.

[16] Bocian M, Brownjohn JMW, Racic V, Hester D, Quattrone A, Gilbert L, et al. Time-dependent spectral analysis of interactions within groups of walking pedestrians and vertical structural motion using wavelets. Mech Syst Signal Process 2018;105:502–23. https://doi.org/10.1016/j.ymssp.2017.12.020.

[17] Pimentel RL, Araújo MC, Brito HMBF, de Brito JLV. Synchronization among Pedestrians in Footbridges Due to Crowd Density. J Bridg Eng 2013;18:400–8. https://doi.org/10.1061/(ASCE)BE.1943-5592.0000347.

[18] Van Nimmen K, Lombaert G, Jonkers I, De Roeck G, Van den Broeck P. Characterisation of walking loads by 3D inertial motion tracking. J Sound Vib 2014;333:5212–26. https://doi.org/10.1016/J.JSV.2014.05.022.

[19] Polarith UG. Polarith AI Documentation 2019. http://docs.polarith.com/ai/index.html (accessed January 29, 2020).

[20] Pheasant ST. Anthropometric estimates for british civilian adults. Ergonomics 1982;25:993–1001. https://doi.org/10.1080/00140138208925060.

[21] Bocian M, Macdonald JHG, Burn JF. Probabilistic criteria for lateral dynamic stability of bridges under crowd loading. Comput Struct 2014;136:108–19. https://doi.org/10.1016/j.compstruc.2014.02.003.

[22] Soczawa-Stronczyk AA, Bocian M, Wdowicka H, Malin J. Topological assessment of gait synchronisation in overground walking groups. Hum Mov Sci 2019;66:541–53. https://doi.org/10.1016/j.humov.2019.06.007.

[23] MathWorks. Resample uniform or nonuniform data to new fixed rate - MATLAB resample 2019. https://uk.mathworks.com/help/signal/ref/resample.html (accessed February 20, 2020).

[24] Venkateshan SP, Swaminathan P. Numerical Integration. Comput. Methods Eng., Elsevier; 2014, p. 317–73. https://doi.org/10.1016/b978-0-12-416702-5.50009-0.

[25] MathWorks. Estimate delay(s) between signals - MATLAB finddelay 2019. https://uk.mathworks.com/help/signal/ref/finddelay.html (accessed January 14, 2020).

[26] van Ulzen NR, Lamoth CJC, Daffertshofer A, Semin GR, Beek PJ. Characteristics of instructed and uninstructed interpersonal coordination while walking side-by-side. Neurosci Lett 2008;432:88–93. https://doi.org/10.1016/j.neulet.2007.11.070.

[27] Rosenblum MG, Pikovsky AS, Kurths J. Phase synchronization of chaotic oscillators. Phys Rev Lett 1996;76:1804–7. https://doi.org/10.1103/PhysRevLett.76.1804.

[28] Tass P, Rosenblum MG, Weule J, Kurths J, Volkmann J, Schinitzler A, et al. Detection of n: m phase locking from noisy data: application to magnetoencephalography. Phys Rev Lett 1998;81:3291–4.

[29] Janeh O, Langbehn E, Steinicke F, Bruder G, Gulberti A, Poetter-Nerger M. Walking in virtual reality: Effects of manipulated visual self-motion on walking biomechanics. ACM Trans Appl Percept 2017;14. https://doi.org/10.1145/3022731.

[30] Steinicke F, Bruder G, Jerald J, Frenz H, Lappe M. Estimation of detection thresholds for redirected walking techniques. IEEE Trans Vis Comput Graph 2010. https://doi.org/10.1109/TVCG.2009.62.

[31] Knapp J, Loomis J. Visual Perception of Egocentric Distance in Real and Virtual Environments. Virtual Adapt. Environ., CRC Press; 2003, p. 21–46. https://doi.org/10.1201/9781410608888.pt1.

[32] Renner RS, Velichkovsky BM, Helmert JR. The Perception of Egocentric Distances in Virtual Environments - A Review. ACM Comput Surv 2013;46. https://doi.org/10.1145/2543581.2543590.

[33] Willemsen P, Colton MB, Creem-Regehr SH, Thompson WB. The effects of head-mounted display mechanics on distance judgments in virtual environments. Proc. 1st Symp. Appl. Percept. Graph. Vis. - APGV '04, New York, New York, USA: ACM Press; 2004, p. 35. https://doi.org/10.1145/1012551.1012558.

[34] Mohler BJ, Campos JL, Weyel MB, Bülthoff HH. Gait parameters while walking in a head-mounted display virtual environment and the real world. Proc. 13th Eurographics Symp. Virtual Environ., 2007. https://doi.org/10.2312/PE/VE2007Short/085-088.

[35] Zivotofsky AZ, Gruendlinger L, Hausdorff JM. Modality-specific communication enabling gait synchronization during over-ground side-by-side walking. Hum Mov Sci 2012;31:1268–85. https://doi.org/10.1016/j.humov.2012.01.003.

[36] van Ulzen NR, Lamoth CJC, Daffertshofer A, Semin GR, Beek PJ. Stability and variability of acoustically specified coordination patterns while walking side-by-side on a treadmill: Does the

seagull effect hold? Neurosci Lett 2010;474:79–83. https://doi.org/10.1016/J.NEULET.2010.03.008.

[37] Berens P. CircStat: A MATLAB toolbox for Circular Statistics. J Stat Softw 2009;31:1–21. https://doi.org/10.18637/jss.v031.i10.

[38] Simpson MJ. Mini-review: Far peripheral vision. Vision Res 2017;140:96–105. https://doi.org/10.1016/j.visres.2017.08.001.

[39] Rakkolainen I, Raisamo R, Turk M, Hollerer T, Palovuori K. Extreme field-of-view for head-mounted displays. 3DTV-Conference, vol. 2017- June, IEEE Computer Society; 2018, p. 1–4. https://doi.org/10.1109/3DTV.2017.8280417.

[40] Howell HW. Medical Physiology and Biophysics. London, UK: Sounders; 1960.

[41] Repp BH, Su Y-H. Sensorimotor synchronization: A review of recent research (2006–2012). Psychon Bull Rev 2013;20:403–52. https://doi.org/10.3758/s13423-012-0371-2.

EURODYN 2020
XI International Conference on Structural Dynamics
M. Papadrakakis, M. Fragiadakis, C. Papadimitriou (eds.)
Athens, Greece, 23–26 November 2020

MEASURING THE DYNAMIC RESPONSE OF A LIVELY FOOTBRIDGE TO AMBIENT AND WALKING EXCITATION

Alfredo Cigada[1], Carmelo Gentile[2], Giulia Lastrico[3] and Maria Gabriella Mulas[3]

[1] Dept. of Mechanical Engineering (DMEC), Politecnico di Milano
Via La Masa 1 Milano, Italy
e-mail: alfredo.cigada@polimi.it

[2] Dept. of Architecture, Built Environment and Construction Engng. (DABC), Politecnico di Milano,
Piazza Leonardo da Vinci 32, 20133 Milano, Italy
e-mail: carmelo.gentile@polimi.it

[3] Department of Civil and Environmental Engineering (DICA), Politecnico di Milano
Piazza Leonardo da Vinci 32, 20133 Milano, Italy
e-mail: giulia.lastrico@polimi.it; mariagabriella.mulas@polimi.it

Keywords: Lively footbridge; ambient vibration tests, forced vibration tests; walking pedestrians; resonant conditions.

Abstract. *The paper presents selected results of a first experimental campaign on a footbridge over-passing the Lambro River near Milano (Italy). The 3-span footbridge, for a bicycle-pedestrian mixed use, has a reinforced concrete deck supported by a steel structure. The footbridge, 107 m long and with a constant width of 4.4m, is roughly symmetric about both mid-span and the longitudinal axis. As a part of proof tests performed in March 2016, ambient vibration tests identified the footbridge modal properties, detecting at 1.75 Hz the fundamental bending mode with the maximum amplitude recorded at mid-span, a finding confirmed by an ANSYS FE model of the footbridge. A series of forced vibration tests, performed in July 2017, investigated the response of the bridge under different loading conditions. Groups of pedestrians, in number of 1, 2, 3, 4, 6, 8 and 12, crossed the bridge, walking with a step frequency as close as possible to the first fundamental frequency. Different spatial configurations were explored for each number of pedestrians, investigating the spread in data related to different walking people/groups and their formation. Pedestrians followed straight trajectories and their spatial configuration was symmetric about the longitudinal axis of the bridge; single pedestrians walked along the footbridge axis. This paper focuses on a few results related to: (a) single pedestrians; (b) groups of multiple pedestrians in the same configuration, a longitudinal row; (c) 12 pedestrians in different spatial configurations. Experimental results highlight the effect of both intra-subject and inter-subject variability and the influence of spatial configuration on the maximum measured acceleration. The bridge performance is discussed by comparison between experimental results and limit values of the vertical acceleration according to HiVoSS guideline.*

INTRODUCTION

In the last two decades, dynamic testing of bridges has been widely adopted for several purposes, as in identification of dynamic properties in proof tests, validation of FE models, and detection of excessive vibrations for lively footbridges [1]-[5]. Very often, aesthetic aspects have motivated the structural conception of recent footbridges, characterized by significant slenderness. For this reason, a significant amount of research work has been devoted to the problem of their serviceability assessment [6], also because slender structures are prone to a modification of modal properties due to the increase of mass when pedestrians are present [7]. In addition, the problem of human-structure interaction requires the derivation of proper pedestrian models and procedures of analysis [8], [9].

This paper presents selected results of a research work that covers many of the above aspects with reference to a footbridge located in Northern Italy. Ambient vibration tests (AVTs) performed during proof tests provided the footbridge modal properties, indicating that the first flexural mode was at a frequency of 1.75 Hz, well within the critical range of excitation due to walking pedestrians. A FE model confirmed this finding. Subsequently, the experimental response of the footbridge to crossing pedestrians was determined for different groups of pedestrians walking at the first mode frequency. The outcome of these tests provides both an experimental assessment of the serviceability conditions and useful insights on the different footbridge response due to the inter- and intra-subject variability.

In the following, Section 1 describes the case study. Section 2 presents the results of operational modal analysis and structural identification, while Section 3 is devoted to the numerical finite element (FE) modelling. Section 4 presents and discusses the forced vibration tests with walking pedestrians. A few conclusions are drawn in Section 5.

1 DESCRIPTION OF THE FOOTBRIDGE

The footbridge, shown in Figure 1, overpasses the Lambro River (Cerro al Lambro, Italy), and runs parallel to a 3-arch masonry Canal Bridge built on 1806. The straight footbridge, 107 m long and 4.4 m wide, is subdivided into a central span, 58 m long, and two side spans, each 24 m long. Two welded double-T longitudinal beams, 2 m high and located at the two sides of the footbridge are its main resisting elements.

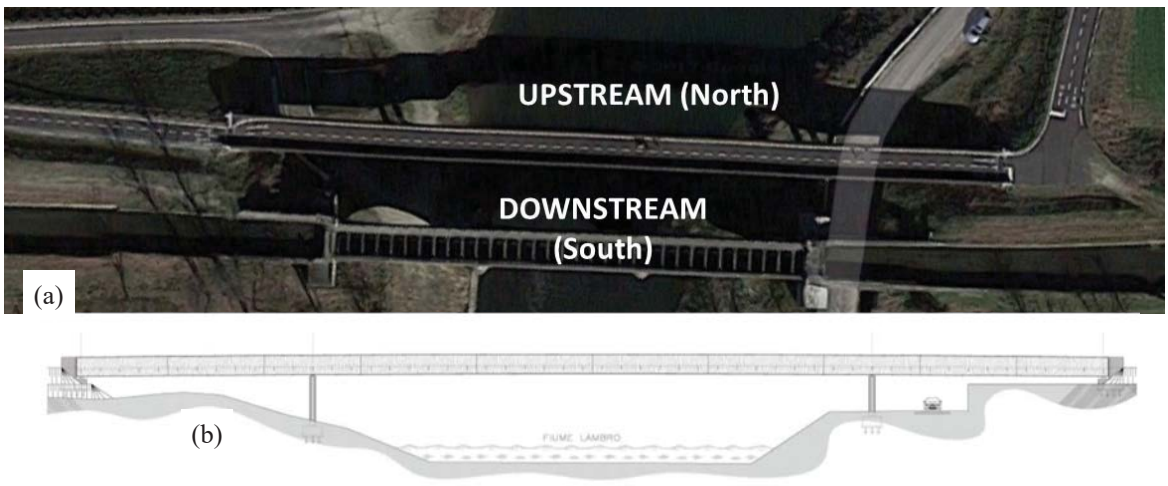

Figure 1: Lambro footbridge: (a) aerial view; (b) side view.

Each longitudinal beam is subdivided in ten on-site welded segments, whose geometry is symmetric about the longitudinal axis and the transverse axis at mid-span. A view from below

of the footbridge and its typical cross-section at an intermediate support are shown in Figure 2a and 2b, respectively. The cross brace system in Figure 2a is made of steel L90×8 profiles bolted at the bottom flange of the longitudinal beams. The same figure also shows the transverse beams and the secondary beam, an IPE100, connecting the mid-span of transverse beams. Figure 2b shows the transverse beam, made of the steel profile IPE240 in the mid-span and of HEA240 on the piles and at the side spans. Transverse beams connect the longitudinal beams and support the deck, where a reinforced concrete (RC) slab with an overlying bituminous conglomerate pavement is cast on a metal corrugated sheet. The deck has an inclination of 2%. As shown in Figure 1b, two couples of circular RC columns provide the intermediate supports subdividing the bridge into three spans. Foundation of columns is on piles. At all supports, the bottom flange of longitudinal beams rest on elastomeric bearings SI-H 300/52. At intermediate supports, a RC 45×45 cm pile cap is interposed between column and beam (Figure 2b).

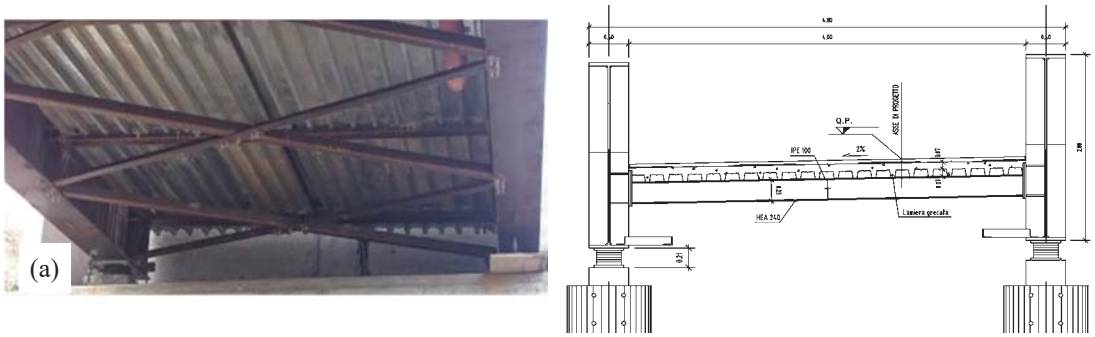

Figure 2: Lambro footbridge: (a) view from below; and (b) cross-section.

With the same corrugated sheet profile A 75/P750 in Figure 3a (units: mm), two cross-sections of the deck are present. In the central span, the sheet thickness is 7/10 mm and the cast in situ slab is 75 mm thick, for a total deck thickness of 150 mm (Figure 3b). At the two ends, for a length of 4.5 m starting from the abutments, the sheet thickness is 15/10 mm and the cast in situ slab is 305 mm thick, for a total thickness of 380 mm. In these zones, where the deck works as a ballast for the central span, the metal sheet is directly connected to the lower flanges of the double-T profiles. Further details on the footbridge geometry can be found in [10].

All steel profiles are made of S335 steel while corrugated sheet is made of S235 steel. Deck is made of concrete of class *C30/37,* having Young's modulus E_c=33 GPa. The class of concrete for columns is *C32/40*, with Young's modulus E_c=33.6 GPa.

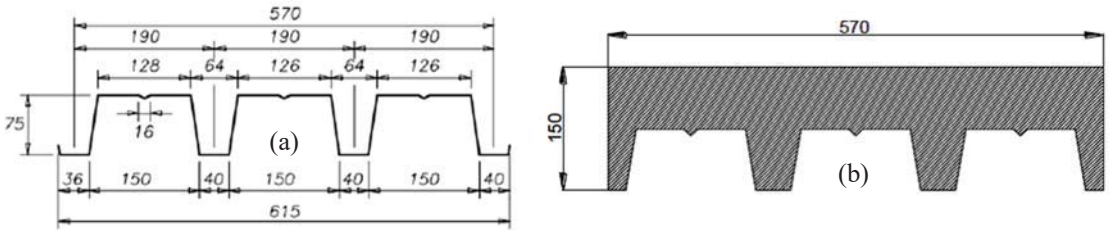

Figure 3: Cross-section of the deck: (a) corrugated sheet A75/P 570; (b) central span, with cast-in-situ concrete.

2 OPERATIONAL MODAL ANALYSIS AND STRUCTURAL IDENTIFICATION

Ambient vibration tests were performed on the footbridge in March 2016 to evaluate its dynamic characteristics. The vertical response was measured in 10 selected points installed on the main side beams (Figure 4), by using high sensitivity piezoelectric accelerometers (WR

model 731A, 10 V/g sensitivity and ±0.50g of peak acceleration). A short cable (1m) connected each sensor to a power unit/amplifier (WR model P31). Two-conductor cables connected the amplifiers to a 24-channel data acquisition system (24-bit resolution, 102 dB dynamic range).

The adopted sampling frequency, in presence of anti-aliasing filters, is equal to 200 Hz, which is fairly larger than that required for the investigated footbridge, as the significant frequency content of collected signals is below 12 Hz (Figure 5). Hence, apart from the already mentioned anti-aliasing filters, the identification tools application was preceded by a second digital step: the time series were low-pass filtered, using a 7th order Butterworth filter with cut-off frequency of 20 Hz, and down-sampled to 40 Hz.

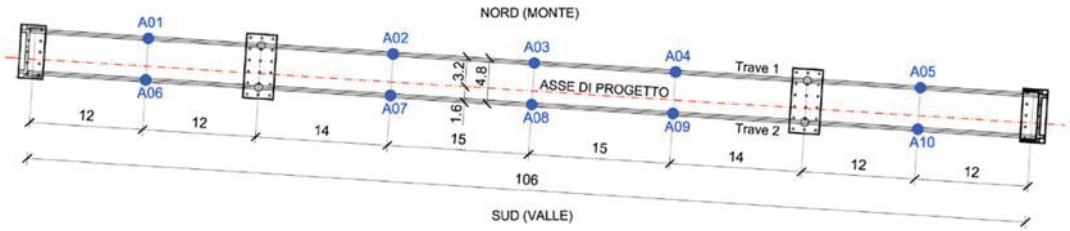

Figure 4: Accelerometer positions on the deck and associated numbers

The modal identification was performed using a time window of 3600 s and applying well-known output-only algorithms, such as the Frequency Domain Decomposition (FDD) [11] and the data-driven Stochastic Subspace Identification (SSI-data) [12] techniques available in the commercial software ARTeMIS [13]. The stabilization diagram, obtained applying the SSI-data algorithm, is shown in Figure 5, along with the first Singular Value (SV) lines of the spectral matrix. The alignments of the stable poles in the stabilization diagram (SSI-data) technique provide a clear indication of the structural modes. Table 1 compares the modal estimates obtained by applying the FDD and the SSI-data techniques through: (a) the identified natural frequencies, f_{FDD} and f_{SSI}; (b) the modal damping ratio and its standard deviation (ζ_{SSI}, σ_ζ) identified by the SSI method and (c) the MAC [14] of the corresponding mode shapes.

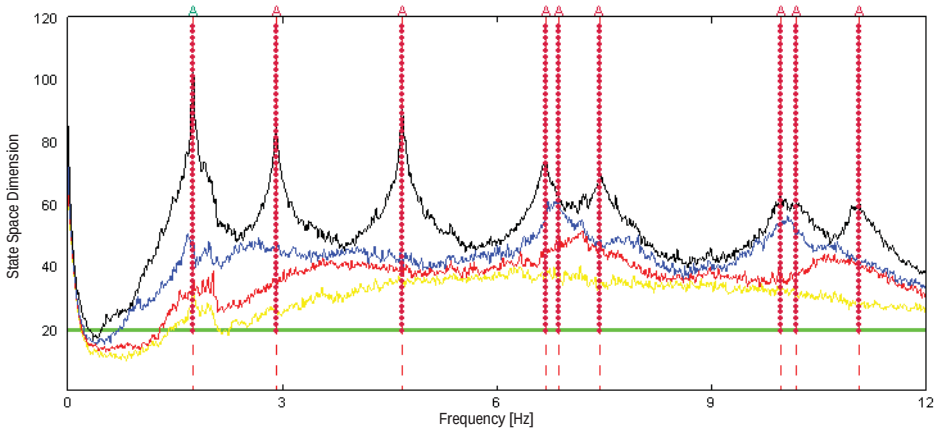

Figure 5: Stabilization diagram (SSI-data) and automatic (A) identification of natural frequencies.

The inspection of Table 1 confirms that the natural frequencies estimated by the two different methods are practically coincident. A similar correspondence was found for most mode shapes (MAC value larger than 0.98), except for the 5th mode (torsion), for which the MAC is about 0.80 and the SSI-data algorithm conceivably provides a better estimation of the mode shape. Figure 6 shows the measurement-based mode shapes identified using the SSI-data technique.

Mode Id.	f_{FDD} (Hz)	f_{SSI} (Hz)	ζ_{SSI} (%)	σ_ζ (%)	MAC
1 (B)	1.748	1.749	0.135	0.83×10^{-3}	1.000
2 (T)	2.910	2.912	0.758	0.81×10^{-2}	1.000
3 (B)	4.668	4.675	0.249	0.13×10^{-2}	1.000
4 (B)	6.660	6.676	1.001	0.35×10^{-2}	0.998
5 (T)	6.797	6.862	3.084	0.34×10^{-2}	0.801
6 (B)	7.441	7.443	1.389	0.79×10^{-2}	0.993
7 (T)	9.954	9.956	1.373	0.16×10^{-1}	0.984
8 (B)	10.190	10.190	1.774	0.71×10^{-2}	0.998
9 (T)	11.030	11.060	1.172	0.21×10^{-1}	0.998

Table 1: Summary of the modal parameters identified by FDD and SSI-data methods (B=bending; T= Torsion).

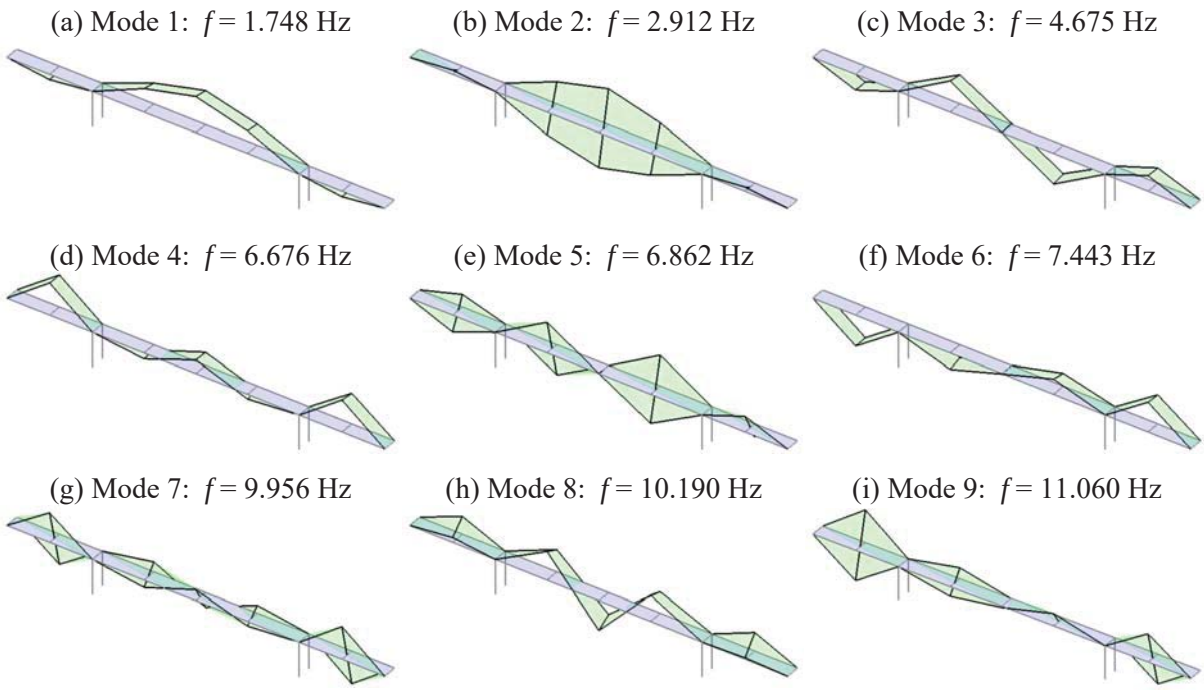

Figure 6: Vibration modes identified from ambient vibration measurements (SSI-data).

3 FINITE ELEMENT MODEL

The finite element (FE) model of the bridge (Figure 7) is based on the as-built design data extracted from the blueprints. The origin of the reference system for the mesh nodes is on the exterior node of the first segment of the upstream side: *x*- and *y*-axis are the transverse and longitudinal axis, respectively, while the *z*-axis is vertical upwards. Within the ANSYS [15] framework, the steel elements are modeled with two-node Timoshenko elements named BEAM188. Shell elements named SHELL181 describe the deck, with a mesh grid of 1m × 1m. Consistent mass option is adopted for all these elements. A BEAM188 element is adopted also for elastomeric bearings, fixed at its lower end and free to rotate differently from the longitudinal beam node it is connected to. Since the deck in the central span is simply supported by

transverse beams, nodes of the shells and nodes of the transverse beams share the same translational degrees of freedom but can have different rotations. The situation is slightly different at the end spans, where the transverse beam are included within the slab thickness and also rotations are constrained.

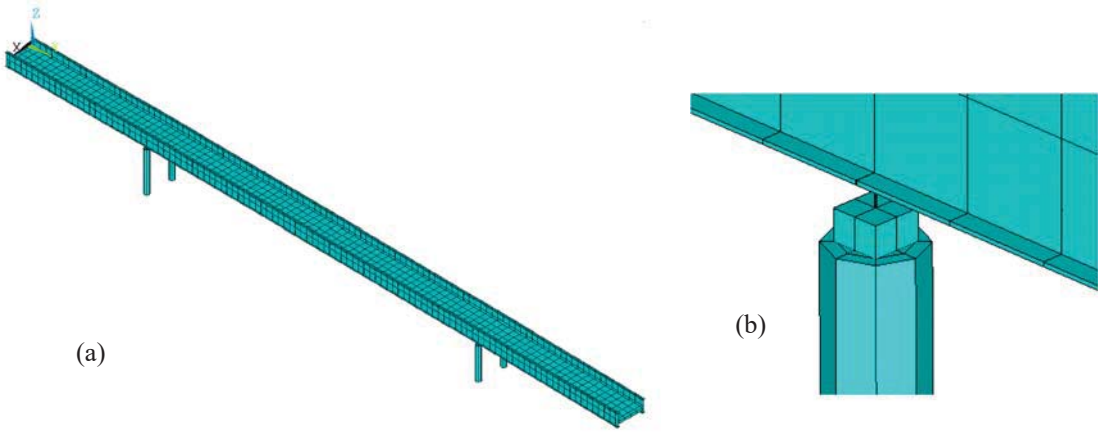

Figure 7: FE model: (a) general view; (b) detail of column with pedestal and elastomeric bearing.

The mesh nodes are located on three different layers, due to the offset among the axes of longitudinal beams, deck, transverse beams and bracing. Thus, in spite of the relatively simple structural scheme, the FE mesh is made complex by the need to account for both offsets and internal releases between adjacent elements. A further problem arises from the orthotropy of the deck, with different values of moments of inertia in longitudinal and transverse direction, due to the shape of the corrugated metal sheet (see Figure 3). SHELL181 elements are characterized by a rectangular cross-section, with a unique value of thickness, density and elastic modulus in both directions. Hence, with a preliminary calibration of these parameters for the two typical cross-sections, an effective shell thickness t_e was determined - equal to 122 mm in the central span and 347 mm for the two side spans - as the one of a rectangular cross-section providing the same moment of inertia of the existing section about the transverse axis. From the t_e value, an effective value of density ρ_e is computed, equal to 3400.7 kg/m^3 in the central span and to 3086.0 kg/m^3 for the two side spans, able to reproduce the total mass of each element, also accounting for dead load. Materials properties have the values defined in Section 1.

3.1 Model updating

A preliminary dynamic analysis on the FE model just presented was performed to check the similarity between experimental and numerical modal parameters. The correlation between the dynamic characteristics of the initial model and the experimental results is shown in column (3) of Table 2 via the frequency discrepancy $\varepsilon_f = (f_{FEM} - f_{SSI})/ f_{SSI}$. Column (4) list the number of order of the numerical mode and a descriptor of the mode shape: bending in the vertical plane (B) or torsional (T). Table 2 shows one-to-one correspondence between the mode shapes and fairly good correlation also in terms of frequency. Only the frequency discrepancy of the second mode is 9.13%, whereas it ranges between –0.76% and 3.35% for the other modes. Hence, the correlation between numerical and experimental behavior seems to provide a sufficient verification of the main assumptions adopted in the initial model.

As previously pointed out, the main uncertainties in the numerical model are related to the footbridge deck and, more specifically, to the Young's modulus of the cast-in-situ concrete (E_{deck}) and to the effective thickness of the shell elements along the span (t_{e1}) and near the

supports (t_{e2}). In order to improve especially the main difference (on the frequency of second mode), the three uncertain parameters of the deck (E_{deck}, t_{e1} and t_{e2}) were updated and their optimal values were identified by minimizing the difference between numerical and experimental natural frequencies. After the updating, a complete correlation analysis was carried out between numerical and experimental modal parameters. The MAC index [14] in column (7) of Table 2 shows an excellent correlation for all the modes. Discrepancy in terms of frequency has a different trend for bending vertical modes, correctly reproduced, and for torsional modes, still affected by an error up to 7.73% for the second mode. Figure 8 shows the numerical counterpart of Figure 6 after updating. The first three numerical modes are "quasi-rigid" modes, transversal, longitudinal and rotational, respectively, involving the bearings deformability. Modes 5 and 9 (f = 1.903 and 6.411 Hz) are lateral/torsional modes and were not identified experimentally.

Exp.	Initial Model			Updated Model		
f_{SSI} (Hz)	f_{FEM} (Hz)	ε_f (%)	Mode #	f_{FEM} (Hz)	ε_f (%)	MAC
1.749	1.749	–	4/B	1.749	–	0.995
2.912	3.178	9.13	6/T	3.137	7.73	0.999
4.675	4.676	0.02	8/B	4.672	–0.06	0.998
6.676	6.702	0.39	10/B	6.683	0.10	0.999
6.862	6.968	1.54	11/T	6.782	–1.17	0.990
7.443	7.508	0.87	12/B	7.483	0.54	0.995
9.956	9.880	–0.76	13/T	9.575	–3.83	0.964
10.190	10.188	–0.02	18/B	10.107	–0.81	0.945
11.060	11.430	3.35	36/T	11.318	2.33	0.974

Table 2: Correlation between experimental and numerical (initial and updated model) dynamic characteristics.

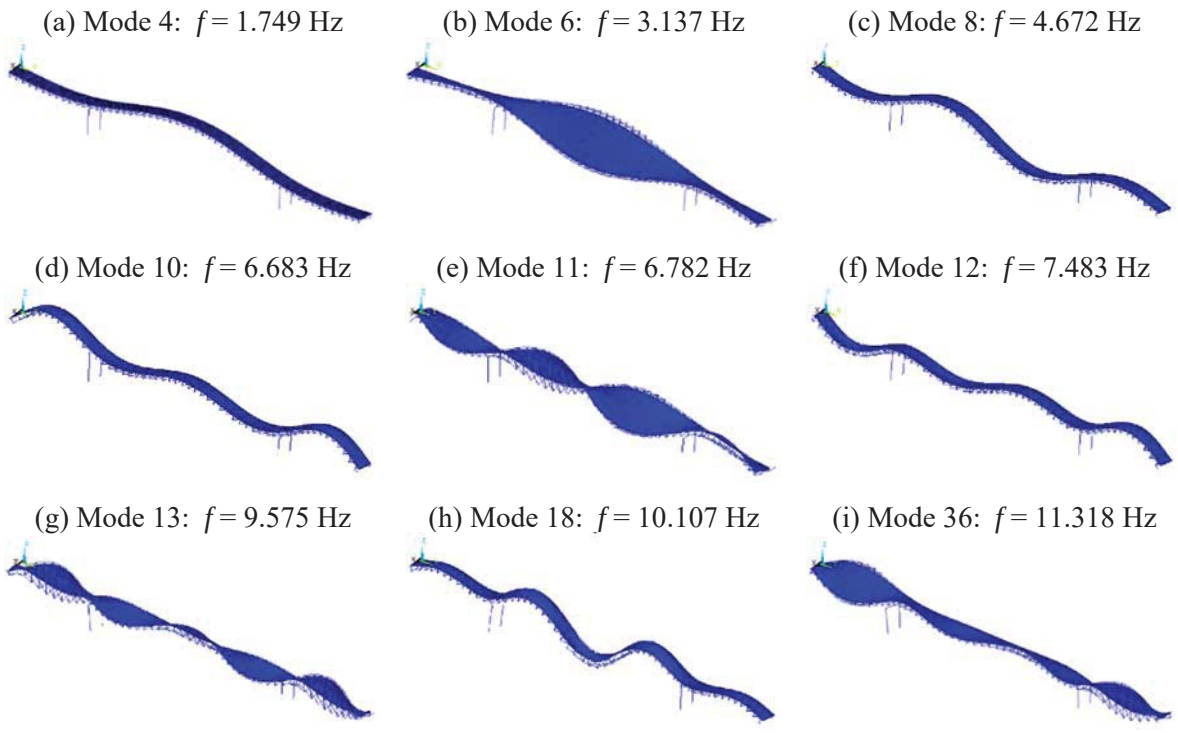

Figure 8: Natural frequencies and mode shapes of the updated FE model.

4 FORCED VIBRATION TESTS

After the proof tests of 2016 and the development of the FE model, a series of forced vibration tests under walking pedestrians were performed on July 20, 2017. Tests aimed to assess the extreme values of the bridge response to different pedestrians' configurations, and the effect of pedestrians' inter-subject variability. Table 3 presents the ID, sex, mass *M* and height *H* of the twelve volunteers involved in the tests (including also two Authors). All TSs are young people, with an age between 22 and 30, but TS5 and TS8, whose age is in the range 50-60. Fifty-two tests with different configurations were performed, involving either single pedestrians or groups with different numbers of people, as detailed in Table 4. Configurations differ either in space or in the Test Subjects (TSs) involved, as it is the case for the twelve configurations with a single pedestrian.

ID	TS1	TS2	TS3	TS4	TS5	TS6	TS7	TS8	TS9	TS10	TS11	TS12
Sex	M	M	F	F	M	F	F	M	M	M	M	M
M [kg]	65	86	59	53	70	65	62	84	76	72	73	70
H [cm]	172	182	164	158	181	173	170	177	185	183	175	175

Table 3: General data of test subjects (TS) involved in the walking tests.

Pedestrians #	1	2	3	4	6	8	12
Configurations	12	6	6	9	4	4	11

Table 4: Number of configurations adopted for each of the different numbers of pedestrians crossing the bridge.

To detect the extreme values of the bridge response, the overall layout of the test was designed to excite mainly the fundamental mode. Hence, for all tests, the target walking frequency of pedestrians was 1.75Hz and spatial configurations were either aligned along or symmetric about the longitudinal axis of the bridge. The first tests involved single pedestrians walking on the bridge, to investigate the uncertainty related to the excitation provided by each individual walking on the bridge. Differences concerns coordination, capability to adapt and follow a predefined rhythm on the 100m distance of the bridge length, as well as the capability to adapt to a lock-in condition when the bridge is vibrating in a perceptible way. In the subsequent tests, the maximum acceleration amplitudes given by groups of walking people arranged in different configurations were investigated. Pedestrians, in groups of 2, 3, 4, 6 or 12 people, were aligned either along the bridge axis, or in a transverse row (with a maximum of 4 people) or in staggered formations with one or more transverse rows and at least two people in each row.

The output produced by the walking people in each configuration was detected in terms of vibration measurements at several points. Figure 9 shows the accelerometer layout. In addition to the sensors used for the modal analysis (see Figure 4), there are four vertical sensors located at the intermediate supports and five horizontal sensors in the central span. The measurement set-up adopted the high sensitivity accelerometers and the data acquisition system of the AVTs.

Individuals or groups of pedestrians crossed the whole bridge, entering from the left side in Figure 9 and exiting on the opposite side. Each crossing corresponded to a single record with multiple channels. Recording of the bridge vibrations started a few instants before the entrance of pedestrians on the bridge and stopped when free vibrations following the transit decayed significantly. To detect the time instant at which each pedestrian started to cross the bridge in the records, each volunteer gave a heel strike while entering the bridge.

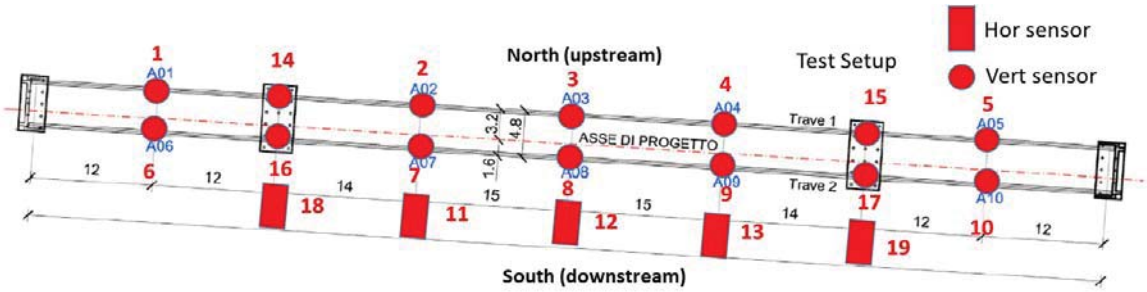

Figure 9: Accelerometer layout during the tests with walking people.

Records of the 19 sensors for the 52 tests show a general trend. The bridge response, in terms of vibration time history, reflects the quasi-symmetry of the bridge. Records on the first half of the bridge almost overlap those on the second half, but the latter show larger acceleration, denoting a resonant phenomenon that builds up during the bridge crossing. Downstream records are similar to but slightly exceed upstream records, possibly due to the effect of the torsional mode. In the following, the presentation of a few results will focus on basic aspects, providing a clear indication of the extreme values of vertical acceleration. A more detailed analysis will concern tests with a single pedestrian, highlighting the effect of intra- and inter-variability.

4.1 Single pedestrian tests

This series of tests aimed at evaluating differences in the excitation produced by each TS. Figure 10 depicts, for each pedestrian, the extreme values recorded by the vertical sensors aligned along the downstream edge during the bridge crossing in the sense from A6 to A10 (see Figure 9). These 12 tests confirm the general trend of the bridge response: the peak values in A6 and A10 are similar but not equal. Values in A10, towards the end of the bridge crossing, exceed those in A6, at the bridge entrance, showing that the resonance phenomenon builds up during the bridge crossing. Sensor A8 at mid-span detects the overall extreme value of the bridge response, reaching 0,30 m/s^2, a value within the comfort range according to Hyvoss Guideline [16]. In addition, the minimum peak value in A8, around 0.06 m/s^2, indicates a wide spread in extreme values produced by different TSs, also visible in the dispersion about the average value (dotted line in Figure 10). The standard deviation (solid lines in Figure 10) has the same pattern of the average value, denoting that dispersion increases as the vibration levels.

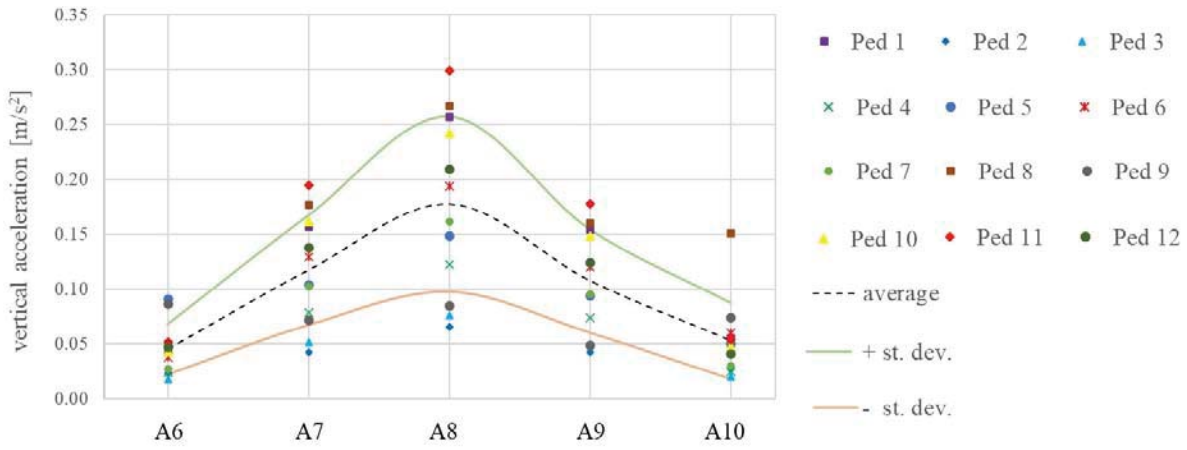

Figure 10: Single pedestrian tests, peak values and standard deviation of vertical downstream acceleration.

Figure 11 shows, for two pedestrians crossing the bridge (TS1 and TS2), the time history of acceleration at the seven downstream vertical sensors, superposed in a single graph. Even though walking at the same frequency, each person has his/her own step speed and, in the three graphs, equal time does not necessarily imply equal position on the bridge. In each graph, the signals of the different sensors differ in amplitude but are eminently in phase. While graph in Figure 11a appears dominated by the first natural mode, more frequency components are visible in Figure 11b where a "beating" phenomenon is appreciated. Largest values are found in the first case. Differences can be justified by the person's capability to keep a constant rhythm (and possibly a centered trajectory) and therefore to excite resonance on the first mode. The excitation under resonant conditions requires some time for the bridge vibrations to reach the maxima, followed by a certain time required for a complete decay, after the person left the bridge.

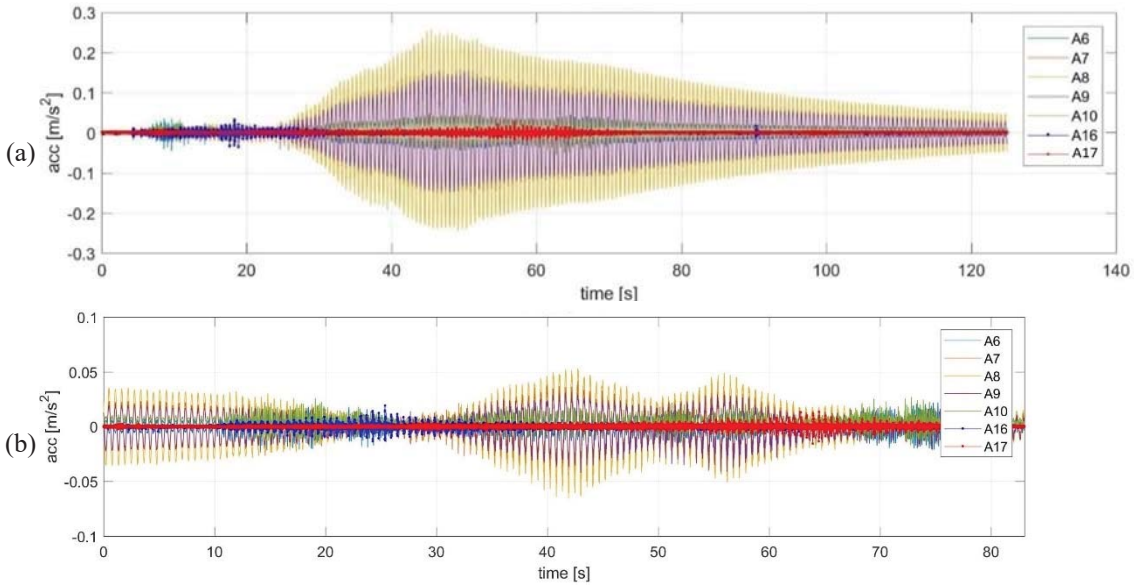

Figure 11: Downstream records for single pedestrians: (a) TS1; (b) TS2.

The trends shown in Figure 10 and Figure 11 can be associated with the different capability of the TSs to lock to the first mode bridge vibration. To investigate this aspect, the time (measured from the beginning of the records) of peak occurrence in downstream sensors is depicted in Figure 12. Two different patterns are apparent: a few pedestrians excite the bridge to high levels while walking on the shorter side spans, while others produce the maximum vibration level in all sensors only when walking close to mid span, where the modal shape allows for the maximum energy input.

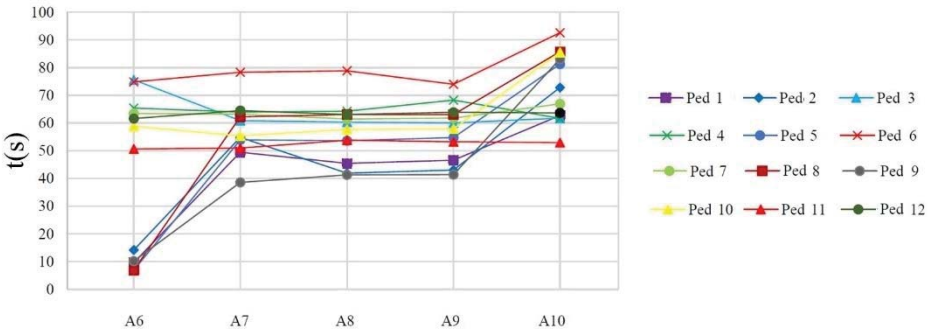

Figure 12: Time at which maxima are reached during each time record (downstream).

Figure 13 and Figure 14 present a time frequency relation for pedestrians TS1 and TS2 at sensors A6 (side span) and A8 (midspan), respectively. Fourier spectra are computed with a moving window, 6 s long, overlapped by 5/6 of the window length. The first natural frequency of the bridge is clearly visible for both people and for both sensors. For both pedestrians the spectral response of the side span includes many higher order harmonics, coherently with the modal shapes at the side span and with the fact that the build up under resonant conditions needs some time to develop fully. The energy dispersion in TS2's response leads to lower values of energy on each frequency and a limited value of vibration (Figure 11b).

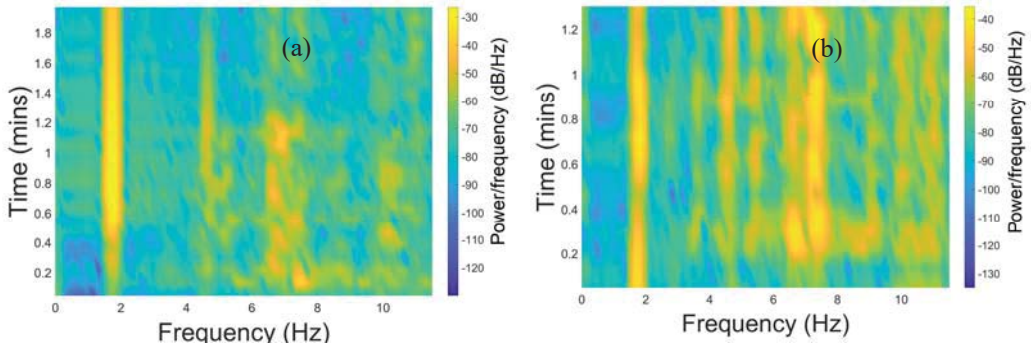

Figure 13: Time frequency representation at sensor A6: (a) TS1; (b) TS2.

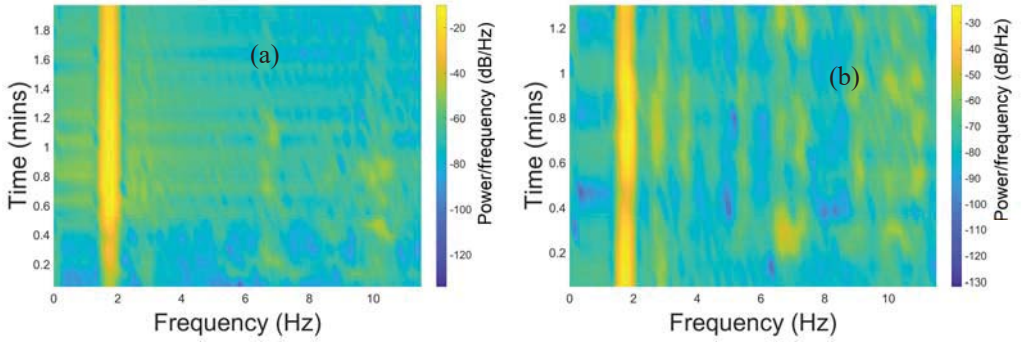

Figure 14: Time frequency representation at sensor A8: (a) TS1; (b) TS2.

A similar pattern is detected at mid-span (Figure 14), where the energy transmitted by TS1 is practically all on the first mode frequency and is associated to significant levels of vibration (see Figure 11a). TS2's response still shows a certain degree of dispersion, even though more limited than that visible in Figure 13b. Again, dispersion is associated to lower values of both energy per frequency and levels of vibration dominated by the first mode.

4.2 Groups

Forty tests concerned groups of two or more pedestrians, as detailed in Table 4. In longitudinal direction, pedestrians were spaced apart of a target distance of 60 cm. In transverse direction, inter distance was not constant, depending on the number of pedestrians involved. For each space configuration of a given group of pedestrians, at least two tests were performed varying the TSs involved. The presentation of these tests is beyond the scope of this paper, and only two aspects are discussed here. First, the average peak value of vertical acceleration at midspan (sensor A8) is investigated in Figure 15, as a function of the number of crossing pedestrians in the same space configuration, a longitudinal row along the bridge axis. The average

is computed for each group of tests concerning the same number of pedestrians. Vertical acceleration increases when the number of pedestrians varies between one and eight, and slightly decreases when pedestrians are 12. The values in Figure 15 can be assumed as a measure of the serviceability conditions of the footbridge.

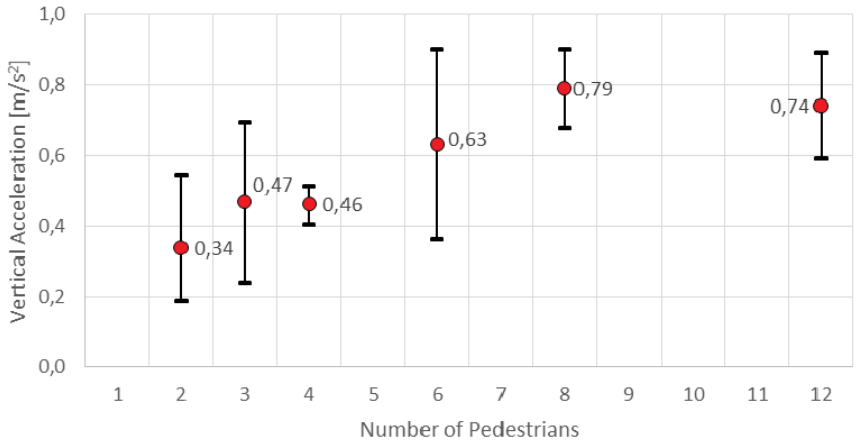

Figure 15 : Average and extreme values of peak acceleration and as a function of the number of pedestrians.

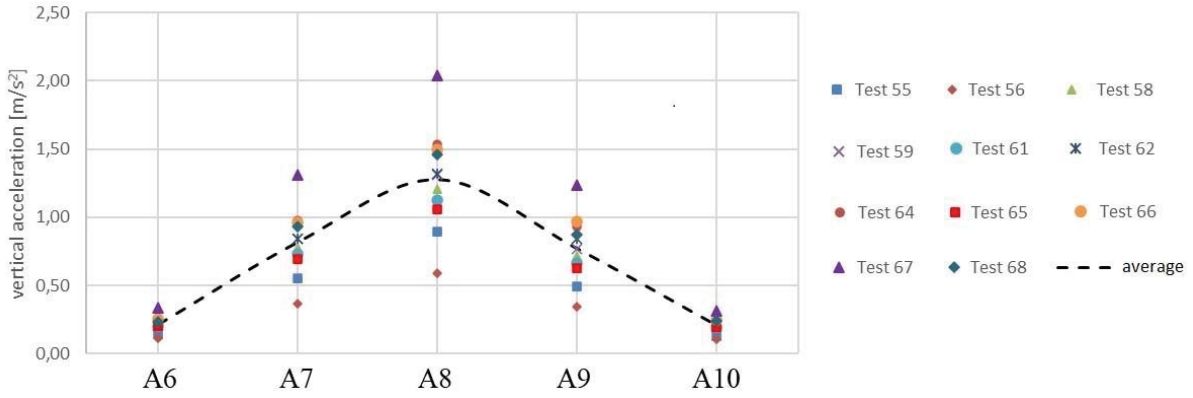

Figure 16: Downstream sensors, peak values for groups of 12 people in different space configurations.

Second, the outcome of the 11 tests with twelve pedestrians in different space configurations is shown in Figure 16 in terms of peak acceleration at downstream sensors. Test 55 and 56 involved a longitudinal row of 12 people. Test 58 and 59 involved two transverse rows of 6 people while Test 61 and 62 had six transverse rows of 2 people. Test 64, 65 and 66 involved four transverse rows of 3 people while Test 67 and 68 had three transverse rows of 4 people.

The most severe load case was generated by Test 67, whose results, however, are quite different from those of Test 68, sharing the same space configuration even though with different positions of pedestrians. While the compact space configuration is able to excite significantly the first mode when all the pedestrians are around midspan where the mode shape has its maximum, the lack (or presence) of synchronization among pedestrians is able to explain both the peak values reached and the difference between Tests 67 and 68.

5 CONCLUSIONS

Aim of this paper was the presentation of selected results on the dynamic testing of a footbridge located in Northern Italy. Experimental tests were performed with different purposes at different times. First, AVT's were carried out in 2016, to identify modal properties, as a part of

proof tests necessary to the footbridge opening. Subsequently, after the derivation of a FE model able to simulate with accuracy the modal properties, forced vibration tests were performed within a sponsored research program. The positive novelty of this work is the link between the two series of tests, where the results of AVTs have driven the subsequent FE modeling and walking tests. The availability of a validated FE model of the footbridge is the base for a future numerical simulation of the walking tests, providing a reliable numerical model of a real structure in the coupled problem of human-structure interaction. Hence, these tests can be adopted to evaluate and validate modelling strategies for pedestrians as mechanical systems moving with a given gait.

The results of numerical modelling showed a problem in reproducing the experimentally detected behavior, relieved but not solved by an optimization procedure. Since vertical bending modes are simulated with an excellent agreement, it appears that the footbridge possesses separated resisting mechanisms in bending and torsion, an aspect that must be tackled in future research works. Foundations on piles, not accounted for in this work, could be the cause of the experimental frequency lower than the numerical one. Their effect is currently under study.

Tests on a limited sample of single pedestrian under similar conditions outlined a meaningful but large spread in their behavior, when trying to walk under resonant conditions. The different response generated by TS1 and TS2, in terms of both peak value and frequency content of vertical acceleration, evidences a dissimilar behavior of the two TSs. Differently from TS2, TS1 locks in to the footbridge vibration, an aspect that should be taken into account when modeling human-structure interaction.

Among the tests performed with groups of pedestrians, in this work only two types of tests are considered. Tests with pedestrians on a single line provides an indirect serviceability assessment, showing an increasing trend with a maximum value as the number of pedestrian increases. Even though in these tests, as in single pedestrian tests, all the peak values are within the range of maximum or medium comfort according to the Hyvoss Guideline [16], it is noticed that a very limited number of pedestrians is able to produce high values of acceleration.

Finally, the results in terms of peak values for the different space configurations of 12 people are analyzed, taking into account that more than one test was performed for each configuration, by varying the position of TSs. At mid-span, the same configuration (the most compact in longitudinal direction) but with different TSs' position produced the overall maximum peak acceleration of the whole test set and the minimum with reference to the configurations of 12 pedestrians. Hence, also in this case two different aspects are brought to the light. First, the importance of the inter-subject variability and of the correlation existing among pedestrians' motion. Second, the need for a numerical serviceability assessment following [16] is confirmed, and is currently under way.

It can be concluded that the experimental research strategy adopted here provided interesting results, opening the way to future numerical and experimental studies.

ACKNOWLEDGEMENTS

The first and last Authors gratefully acknowledge the financial contribution of MIUR (Italian Ministry of Higher Education) under grant PRIN 2015-2018, Project 2015TTJN95, "Identification and monitoring of complex structural systems" for the forced vibration tests of July 2017. The work presented here is based on the MS thesis of G. Lastrico, under the guidance of the other three Authors. AVTs were performed by C. Gentile and forced vibration tests by A. Cigada, with the participation of G. Lastrico and M.G. Mulas. The contribution of V. Racic in devising the pedestrians' configurations is gratefully acknowledged.

REFERENCES

[1] E. Caetano, Á. Cunha, F. Magalhães, C. Moutinho. Studies for controlling human-induced vibration of the Pedro e Inês footbridge, Portugal. Part 1: Assessment of dynamic behaviour, *Engineering Structures*, (32), 1069-1081, 2010.

[2] F. Benedettini, C. Gentile, Operational modal testing and FE model tuning of a cable-stayed bridge, *Engineering Structures*, (33), 2063-2073, 2011.

[3] A. Gheitasi, O. E. Ozbulut, S. Usmani, M. Alipour, D. K. Harris, Experimental and analytical vibration serviceability assessment of an in-service footbridge, *Case Studies in Nondestructive Testing and Evaluation*, (6), 79-88, 2016.

[4] E. Lai, C. Gentile, M.G. Mulas, Experimental and numerical serviceability assessment of a steel suspension footbridge, *J. of Constructional Steel Research*, (132), 16-28, 2017.

[5] I. A. Ribeiro de Silva, J. G. Santos de Silva, Experimental and numerical dynamic structural analysis of footbridges when subjected to pedestrians walking loads, *Journal of Civil Structural Health Monitoring*, 8: 585-595, 2018.

[6] K. Van Nimmen, G. Lombaert, G. De Roeck, P. Van den Broeck, Vibration serviceability of footbridges: evaluation of current codes of practice, *Engineering Structures*, (59), 448-461, 2014.

[7] G. Busca, A. Cappellini, S. Manzoni, M. Tarabini, M. Vanali, Quantification of changes in modal parameters due to the presence of passive people on a slender structure, *J. of Sound and Vibration*, (333), 5641-5652, 2014.

[8] C. C. Caprani, E. Ahmadi, Formulation of human-structure interaction system models for vertical vibration, J. of Sound and Vibration, (377), 346-367, 2016.

[9] M.G. Mulas, E. Lai, G. Lastrico "Coupled Analysis of Footbridge-Pedestrian Dynamic Interaction", *Engineering Structures*, 176C (2018), 127-142.

[10] G. Lastrico, Studio numerico e sperimentale della risposta dinamica di una passerella pedonale, MS Thesis in Civil Engineering, Politecnico di Milano, 2017 (in Italian).

[11] R. Brincker, L.M. Zhang, P. Andersen, Modal identification from ambient responses using Frequency Domain Decomposition, *Proceedings of the 18th IMAC*, 2000.

[12] B. Peeters, G. De Roeck, Reference-based stochastic subspace identification for output-only modal analysis, *Mechanical Systems and Signal Processing* 13(6), 855-878, 1999.

[13] SVS, ARTeMIS Extractor 2011, http://www.svibs.com/, 2012.

[14] R.J. Allemang, D.L. Brown, Correlation coefficient for modal vector analysis, *Proceedings of the 1st IMAC*, 1983.

[15] ANSYS, Online Manuals Release 5.5, http://mostreal.sk/html/guide_55/GBooktoc.html2015.

[16] Research Fund for Coal and Steel. HiVoSS: Design of footbridges, Guideline EN03, 2008.

[17] S. Živanović, A. Pavic, P. Reynolds, Vibration serviceability of footbridges under human-induced excitation: a literature review, *J. Sound Vib*. 279 (1-2) (2005) 1-74.

EURODYN 2020
XI International Conference on Structural Dynamics
M. Papadrakakis, M. Fragiadakis, C. Papadimitriou (eds.)
Athens, Greece, 23–26 November 2020

DYNAMIC PROPERTIES OF TWO PEDESTRIAN WOODEN BRIDGES INCLUDING SEASONAL EFFECTS

John Hallak Neilson[1], Aida Ibisevic[1], Hasanhüseyin Ugur[1], Jean-Marc Battini[1], Roberto Crocetti[1], Costin Pacoste[2], Maria D. Martinez-Rodrigo[3]

[1] Affiliation of John Hallak Neilson, Aida Ibisevic, Hasanhüseyin Ugur, Jean-Marc Battini, Roberto Crocetti
KTH, Royal Institute of technology, Division of Structural Engineering and Bridges, Stockholm, Sweden
e-mail: jphneilson@gmail.com
{aidaib,hugur,jeanmarc,crocetti}@kth.se

[2] Affiliation of Costin Pacoste
ELU Konsult, Stockholm, Sweden
costin.pacoste@elu.se

[3] Affiliation of Maria D. Martinez-Rodrigo
Universitat Jaume I, Department of Mechanical Engineering and Construction, Castellón, Spain
mrodrigo@uji.es

Keywords: Pedestrian wooden bridges, Dynamic properties, FE model

Abstract. *The dynamic properties of two pedestrian wooden bridges situated in the Stockholm area have been determined experimentally. The main purpose was to investigate if these properties are season dependent. For that, tests were performed during the winter and the spring. 17 accelerometers were used to measure both vertical and horizontal vibrations. An impact hammer was used to excite the bridges. For the Vega bridge, a large variation for the lowest natural frequencies was observed, both for the first vertical and for the first transversal mode. For the Hägernäs bridge, a large variation was observed for the first transversal mode but not for the first vertical mode. With exception for the first transversal mode for the Hägernäs bridge, no significant differences regarding the damping between winter and spring were observed. Finite element models of the two bridges have also been implemented and a good agreement with experimental results have been obtained. The numerical models have shown that the connections between the different components of the bridges have a significant influence on the dynamic properties. The models have also shown that the variation of the stiffness for the asphalt layer may explain the differencies for the natural frequencies between spring and winter. However, due to the incertainties in the modelling of the asphalt, this conclusion must be taken with caution.*

1 INTRODUCTION

Due to its ecological benefits wood is an attractive alternative for pedestrian bridges. However, the combination of a slender and a light wooden structure may result in uncomfortable vibrations for crossing pedestrians and therefore accurate dynamic analyses are often required in the design process.

Whereas simple finite element models can often be used for static analyses of wooden pedestrian bridges, for dynamic analyses more advanced models are often necessary. The main reason is that the connections between the different structural elements must be modelled carefully in dynamic analyses [1-3]. Another difficulty is related to the stiffness of the asphalt layer, which is due to the stiffness of the asphalt itself but also to the degree of shear action between the asphalt and the timber deck. These effects have been studied by several researchers through dynamic experiments both in laboratory [4,5] and on existing bridges [5-7]. All these works show that the effect of the stiffness of the asphalt pavement on the natural frequencies is low in summer and high in winter. This is due to the viscoelastic properties of the asphalt which change with the temperature but also to the shear action between the asphalt and the deck which is low in summer and high in winter.

The purpose of this paper is to study experimentally and numerically the dynamic properties of two pedestrian wooden bridges. Experimental tests were performed both in winter and in spring in order to investigate the influence of the temperature on the dynamic properties. A finite element model was implemented for each bridges. Two key aspects are the modelisation of the connections and the material parameters for the asphalt layer.

2 VEGA BRIDGE

2.1 Description

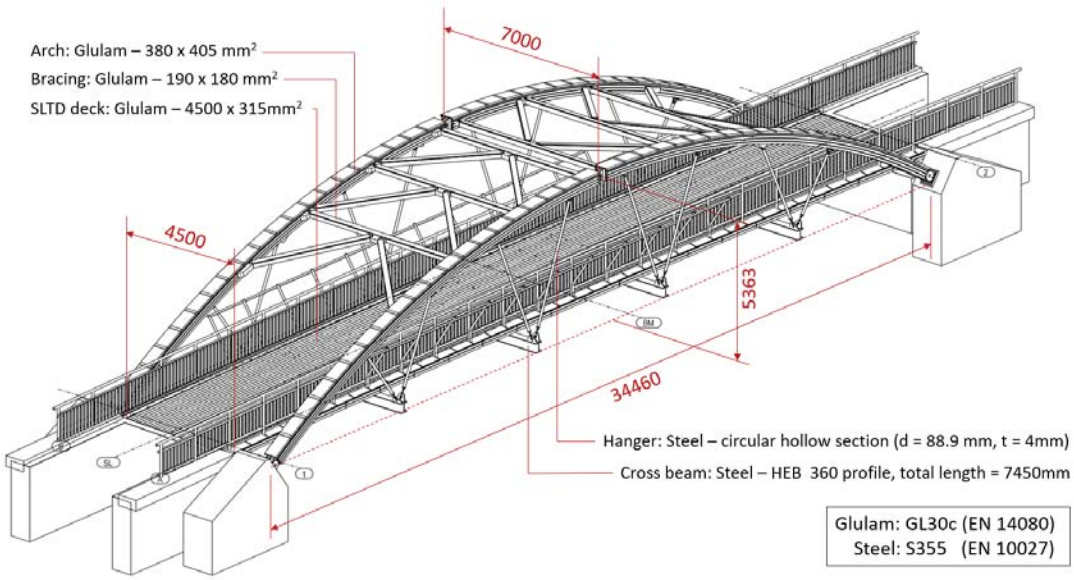

Figure 1 –Vega bridge: dimension, material and cross-sections

The bridge, see Figure 1, is based on a 3-hinged arch. It was prefabricated and hoised in place. The deck consists of Stress Laminated Timber Deck (SLTD), made of a number of glulam beams (each with a 142 × 315 mm^2 cross-section) that are transversally prestressed by steel rods every 60 cm. The deck is covered by an asphalt layer with a thickness of 85 mm. The V-shaped disposition of the steel hangers has been chosen in order to increase the buckling capacity. The deck is supported by four steel cross beams. The two arches are connected through six K-shaped braces. Both the arch and the braces are made of glulam.

2.2 Experimental setup

Experimental testing was performed during cold (March 11th, 2019: -6°C) and warm (May 15th, 2019: 15°C) weather. 17 accelerometers were placed on the deck and measured vertical and transversal accelerations. An accelerometer was also attached to the lowest transverse brace in order to measure the lateral acceleration of the arch. The bridge was excited by using two methods: an impact hammer and a free falling from an 80 kg person from a height of 30 cm. The results were then processed using a low-pass Butterworth filter with a cut-off frequency of 20 Hz and Fast Fourier Transformations in order to identify the natural frequencies and eigenmodes. The damping coefficients were obtained using the half power bandwidth method.

2.3 Finite element model

The finite element model was implemented in Abaqus. It consists of the following parts: arch, braces, hangers, cross beams, deck and asphalt layer.The arch and the bracings were modelled using 3D beam elements. The dimension of the rectangular cross-sections are given in Figure 1. The material parameters of the Glulam were taken as E = 13 GPa, ν = 0.2, ρ = 440 kg/m^3. The hangers and the cross-beams, were also modelled using 3D beam elements. The material parameters for steel were taken as E = 210 GPa, ν = 0.3, ρ = 7850 kg/m^3. The SLTD deck consists of timber beams of height 0.315 m that are prestressed transversally, thus carrying load mainly through friction. It was modelled using 4 node orthotropic shell elements with E_x = 13 GPa, E_y = 0.26 GPa, G_{xy} = G_{xz} = 0.78 GPa, G_{yz} = 0.078 GPa. The asphalt layer, that has a height of 85 mm, was modelled with 4 node isotropic shell elements with ν = 0.3, ρ = 2243 kg/m^3. Two values for the elastic modulus was taken: 3 GPa in warm conditions and 25 GPa in cold conditions.

A hinge at the crown of the arch was introduced by allowing only the rotation around the transversal axis. The interactions arch/bracing, arch/hanger and hanger/cross beams were simulated by using tie constraints that permit rotations and by introducing offsets so that the connections are modelled at the exact positions. The interaction between the cross beams and the deck is performed through steel plates that are welded to the cross beams and inserted in the timber deck. For each steel beams, coupling constraints were defined at three points, with vertical and transversal translational restraints for the middle point and vertical and longitudinal translational restraints for the two other points. A full shear interaction between the asphalt layer and the timber was assumed by using offsets corresponding to half of the thickness for both the deck and the asphalt and by using tie constraints between both surfaces.

The boundary conditions were introduced at the arch springings and at the deck abutments. The arches are connected to a concrete block by a steel device that, ideally, only allows for rotation around the y axis. However, rotational springs around x and z axes were introduced in order to match the experimental results. The deck is supported continuously along the abut-

ment length through steel plates which are embedded in the abutment's concrete in one end and inserted into the deck on the other. The outermost plates are oriented in a way to prevent longitudinal displacement, whereas the one on the center prevents transversal displacement. These boundary conditions were introduced in the deck by defining reference points with an offset of half the deck height. Vertical translations were restrained along the width of the deck and longitudinal or transverse translations, depending on the orientation of the respective plate, were restrained at the location of the steel plates. Longitudinal restraints are present at only one abutment.

2.4 Experimental and numerical results

The experimental and numerical results are presented in Tables 1 and 2 and Figure 2. The experimental results show clearly that the temperature has a significant influence on the natural frequencies and that a decrease of the temperature leads to an increase of the stiffness. Compared to warm conditions, the natural frequencies in cold conditions are 44% higher for the first transversal mode and 22% higher for the first vertical mode. The high impact of the temperature change for the first transversal mode was expected since the change in the stiffness of the asphalt with the temperature affects especially this mode. A change of the damping ratios due to the temperature cannot be identified. However, it can be observed that the values of the damping were almost all higher than the one suggested by the Eurocode (1.5% for structures with mechanical joints).

With exception for the torsional mode, good agreement between experimental and numerical natural frequencies are obtained. The differences for the natural frequencies between Models 2 and 1, which differ only by the *E* value of asphalt, are 39% for the first transverse mode and 17% for the first vertical mode, which is closed to the experimental values given above. Therefore, it seems that the differences in the experimental frequencies between warm and cold conditions can be explained to a large extent by the effect of the asphalt. However, this conclusion must be taken with caution since both the adopted values for the asphalt stiffness and the adopted full shear connection between the deck and asphalt layers can be debated.

Vibration mode	Exp. freq. (15°C)	Exp. freq. (-6°C)	Model 1 (15°C)	Model 2 (-6°C)
1st vertical	2.88	3.50	2.80	3.27
2nd vertical	3.51	3.86	3.69	4.03
3rd vertical	5.13	6.27	5.26	6.17
1st transversal	4.53	6.53	4.62	6.41
1st torsional	4.57	5.44	5.68	6.43

Table 1: Vega bridge: experimental and numerical natural frequencies.

Vibration mode	Damping ratio (15°C)	Damping ratio (-6°C)
1st vertical	3.2	3.4
2nd vertical	1.5	3.1
3rd vertical	2.8	3.0
1st transversal	4.0	4.5
1st torsional	2.4	2.0

Table 2: Vega bridge: experimental damping ratios.

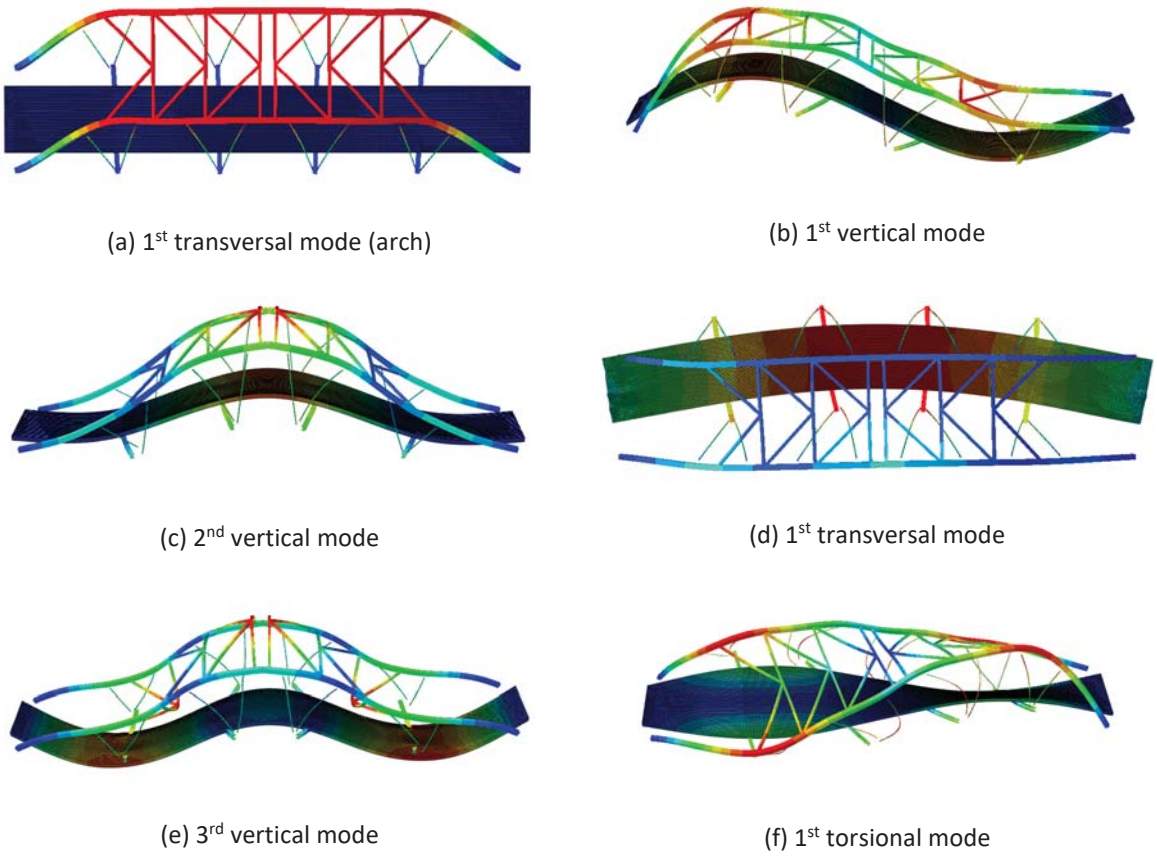

Figure 2 –Vega bridge: numerical mode shapes

3 HÄGERNÄS BRIDGE

3.1 Description

The bridge, see Figure 2, is based on a 3-hinged arch. The deck, 42 m long, consists of two laminated veneer lumber (LVL) plates glued and screwed together. Below the deck lies a grid consisting of 5 longitudinal and 13 transversal glued laminated timber beams. The 5 longitudinal beams support the deck. The longitudinal beams rest on concrete abutments at their ends as well as on four steel beams. Two of the steel beams are attached to the glued laminated timber arches. The other two steel beams are attached to steel hangers which in turn are attached to the arches. The two arches are laterally stabilized through 4 cross braces placed between the concrete abutment of the arches and the steel beams. The deck is covered by an asphalt layer with a thickness of 75 mm.

Figure 3 –Hägernäs bridge

3.2 Experimental setup

Experimental testing was performed during cold (March 5th, 2019: -10°C) and warm (May 17th, 2019: 17°C) weather. 16 accelerometers were placed on the deck and measured vertical and transversal accelerations. 2 accelerometers were also attached to the vertical hangers in order to measure the lateral acceleration of the arch. The same two sources of excitation as for the Vega bridge and also the same processing of the measured signals were used.

3.3 Finite element model

The deck was modelled using 4 node orthotropic shell elements with a thickness of 126 mm. This approach is valid since a full interaction between the two (LVL) plates can be assumed. The material parameters are E_x = 10.5 GPa, E_y = 2.4 GPa, G_{xy} = 0.6 GPa, G_{xz} = 0.12 GPa, G_{yz} = 0.22 GPa, ρ = 550 kg/m^3. The arches as well as the 5 longitudinal and 13 transversal beams were modelled using 3D beam elements. The material parameters were taken as E = 10.4 GPa, ν = 0.2, ρ = 440 kg/m^3. The steel beams and the hangers were also modelled with 3D beam elements whereas the cross braces were modelled using 3D truss elements. The material parameters of steel were taken as E = 210 GPa, ν = 0.3, ρ = 7850 kg/m^3. The asphalt layer with a height of 75 mm was modelled in the same way as for the Vega bridge, with the same material parameters.

The connections between the different parts were modelled as they are expected to work for small amplitudes of vibration. A hinge at the crown of the arch was introduced by allowing only the rotation around a transversal axis. The interactions steel beam/hanger, steel beam/arch, longitudinal beam/transverse beam and longitudinal beam/deck were simulated by using tie constraints for both displacements and rotations. The bolted connection between the hangers and the arches allows a certain rotation in two directions, around the vertical and transversal axes. To model this behaviour a rigid body constraint with two connectors was used.

The longitudinal timber beams are resting on the steel beams and are placed between two steel plates welded to the steel beams. The steel plates have slotted holes to accomodate the difference in thermal expansion between steel and timber. The two beams are connected with steel rods that go through the elongated holes. These connections allow small rotations around the three axes and also some vertical translation. Each connection is modelled using a rigid

body constraint between the midsurface of both beams and the two connectors. A vertical spring was placed at the connector situated at the steel beam.

The bridge rests on concrete foundations. The cross-bracings are fixed in all translations at their ends. At the supports, the arches are connected with hinges that allow only for the rotation around the transversal axis. At the abutments, for each longitudinal beam two steel plates with holes are cast into the concrete. The beam is placed between the plates and screwed to it. At one abutment, the holes in the steel plates allow no movements whereas at the other abutment the holes permit the longitudinal displacement. In the model, reference points with an offset of half the deck height were created at both ends of all the longitudinal beams. At one end, only the rotations around the transversal axis was allowed whereas at the other end, the rotation around the transversal axis and the longitudinal translation were allowed.

3.4 Experimental and numerical results

The experimental and numerical results are presented in Tables 3 and 4 and Figure 4. The experimental results show that the temperature has a significant influence on the natural frequency for the first transversal mode (the difference between cold and warm conditions is 26%) but not for the first vertical mode (the difference between cold and warm condition is 5%). Except for the first transversal mode, no differences regarding the damping coefficients were observed between warm and cold conditions. It can also be noted that almost all the values of the damping were slightly lower than the one suggested by the Eurocode.

The differences for the natural frequencies between Models 2 and 1 are 18% for the first transverse mode and 4% for the first vertical mode, which is closed to the experimental values given above. Therefore, and as for the Vega bridge, it seems that the differences in the experimental frequencies between warm and cold conditions can for a large part be explained by the stiffness of the asphalt. However, as for the Vega bridge, this conclusion must be taken with caution.

Vibration mode	Exp. freq. (17°C)	Exp. freq. (-10°C)	Model 1 (17°C)	Model 2 (-10°C)
1st vertical	5.13	5.37	5.46	5.66
2nd vertical	5.71	6.14	5.79	6.08
3rd vertical	6.18	6.56	6.97	7.11
1st transversal	4.36	5.50	5.13	6.04
1st torsional	6.71	7.18	7.28	7.59

Table 3: Hägernäs bridge: experimental and numerical natural frequencies.

Vibration mode	Damping ratio (17°C)	Damping ratio (-10°C)
1st vertical	1.0	1.0
2nd vertical	1.2	1.2
3rd vertical	1.1	1.4
1st transversal	2.0	0.8
1st torsional	1.2	1.0

Table 4: Hägernäs bridge: experimental damping ratios.

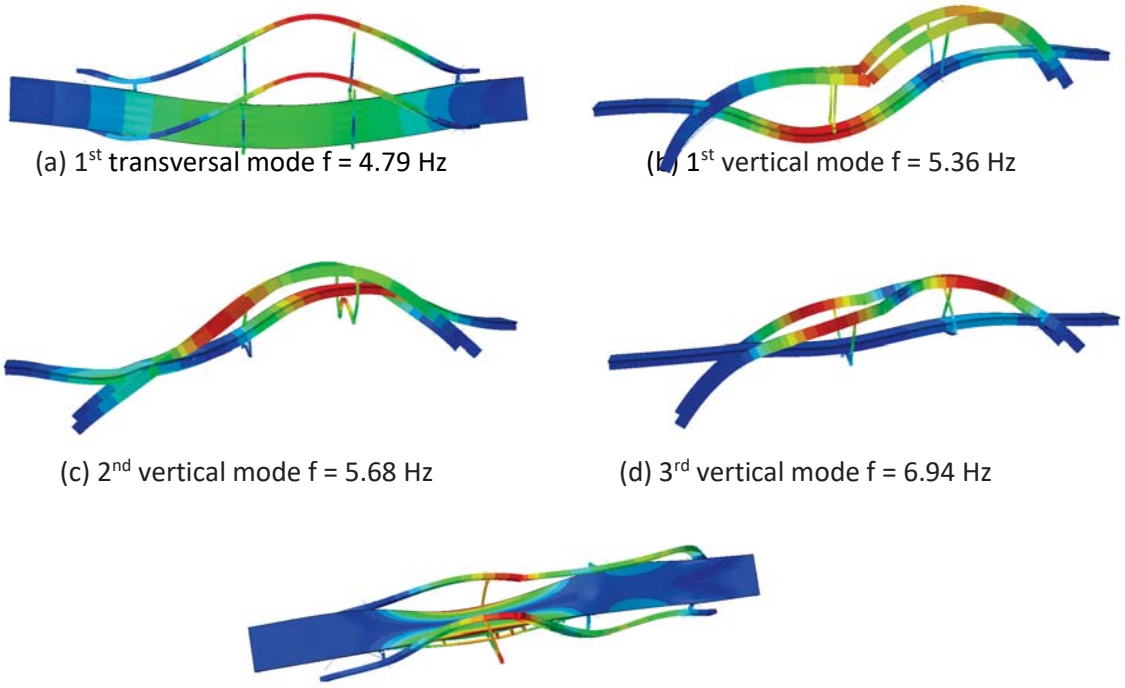

Figure 4 –Hägernäs bridge: numerical mode shapes

4 CONCLUSIONS

In this paper experimental and numerical analyses of two timber pedestrian bridges have been presented. Both bridges are about 40 m long and consist of a timber deck supported by two timber arches. Experimental tests were performed in warm and cold conditions. The experimental results show that the temperature has a significant influence on the natural frequencies of the bridges, especially for the first transversal mode and that a decrease of the temperature leads to an increase of the stiffness. For the Vega bridge, the natural frequencies in cold conditions are 44% higher for the first transversal mode and 22% higher for the first vertical one compared to warm conditions. For the Hägernäs bridge, the corresponding values are 26% and 6%. For both bridges, no significant differences regarding the damping between winter and spring were observed. However, and compared to the values suggested by the Eurocode, higher damping coefficients were measured for the Vega bridge and slightly lower ones for the Hägernäs bridge.

A finite elements model was implemented for each bridge. These models show that the connections between the different components of the bridge must be considered carefully in order to obtain accurate results compared to the experimental natural frequencies. The numerical results tend to show that the differences in the experimental frequencies between warm and cold conditions can for a large part be explained by the stiffness of the asphalt. However, this conclusion must be taken with caution since both the adopted values for the asphalt stiffness and the adopted full shear connection between the deck and asphalt layers can be debated.

REFERENCES

[1] Cecháková, V., Rosmanit, M., Fojtik, R. FEM modeling and experimental tests of timber bridge structure. Procedia Engineering 40, 79–84 (2012) .

[2] Cruz, P. J. S., Salgado, R., Branco, J. Dynamic analysis and structural evaluation of gois footbridge. Mecânica Experimental 17, 129–137 (2009).

[3] Rønnquist, A., Wollebaek, L., Bell, K. Dynamic behavior and analysis of a slender timber footbridge. Norwegian University of Science and Technology, Trondheim (2015).

[4] Schubert, S., Gsell, D., Steiger, R., and Feltrin, G. Influence of asphalt pavement on damping ratio and resonance frequencies of timber bridges. Engineering Structures 32, 3122–3129 (2010).

[5] Feltrin, G., Schubert, S., Steiger, R. (2011). Temperature effects on the natural frequencies and modal damping of timber footbridges with asphalt pavement. EVACES ’11, 4th International Conference on Experimental Vibration Analysis for Civil Engineering Structures (2011)

[6] Hamm, P. Ein beitrag zum schwingungs- und dämpfungsverhalten von fussgängerbrücken aus holz. Report, Civil Engineering, TU München, Germany (2007).

[7] Gülzow, A., Steiger, R., Gsell, D., Wilson, W., Feltrin, G. Dynamic field performance of a wooden trough bridge. EMPA - Swiss Federal Laboratories for Materials Science and Technology, 441–450 (2015).

EURODYN 2020
XI International Conference on Structural Dynamics
M. Papadrakakis, M. Fragiadakis, C. Papadimitriou (eds.)
Athens, Greece, 23–26 November 2020

EVALUATION OF HUMAN INDUCED VIBRATIONS IN KJÆRRA BRIDGE

Thomas T. Tenev[1], **Ole A. Kristiansen**[1] **and Emrah Erduran**[2]

[1] Dept. of Civil Engineering, Technical University of Denmark - DTU
Brovej, Building 118, DK-2800 Kgs. Lyngby, Denmark
e-mail: tenev.thomas@gmail.com / olekri95@gmail.com

[2] Dept. of Civil Eng. and Building Technology, Oslo, Norway Metropolitan University
Pilestredet 35, 0166 Oslo
e-mail: emrah.erduran@oslomet.no

Keywords: Human induced vibrations, Modal analysis, Lock-in effects, Footbridge, Field Measurements

Abstract. *The users of the 132-meter-long Kjærra Bridge in Larvik, Norway, noticed severe lateral vibrations due to pedestrian loading on the opening day in 2001. During the period that the bridge was designed, there were no clear guidelines to minimize pedestrian induced vibrations in footbridges. This article aims to explain severe vibrations induced by pedestrians on the Kjærra Bridge, and to highlight the importance of clear guidelines to prevent similar cases in the future. To this end, a series of vibration measurements, both free and forced, are conducted on the Kjærra Bridge. The free- and forced-vibration tests are supplemented by numerical analysis for several different loading scenarios. Field measurements and numerical analysis results are compared with the current guidelines to evaluate the design of the bridge. The analyses results show vibration levels in the unacceptable range put forth by current design guidelines for several loading scenarios indicating that these guidelines can successfully predict human-induced vibrations on footbridges.*

1 INTRODUCTION

The Kjærra Bridge is a 132m long timber footbridge with a free span of 92 metres across the Numedalslågen river in Larvik, Norway. The structure is based on two concrete bridgeheads, each supporting a triangular console. The consoles support a double, undertensioned structural system with laminated timber compression members and steel wires taking the tensional forces. The lateral load carrying system consists of a horizontal steel truss between the laminated timber arches and was designed for wind loads. The width of the bridge is 2.4m and, architecturally, it was designed to fit in its environment which is surrounded by woods and waterfalls leading to a very slender structure; see Figure 1. The bridge was opened to the public on the 5th of July 2001 [1] and the users of the bridge noticed severe lateral vibrations due to pedestrian loading on the opening day of the bridge. The slender structure and the lateral vibrations observed in the bridge were similar to those observed in the London Millenium Bridge, which had been designed in the same period as the Kjærra Bridge.

During the design and construction of the Kjærra Bridge, there were no standards or guidelines available in Norway to minimize human-induced vibrations. Although some dynamic analysis had been conducted during the design stage, these analysis had no effect on the final design mainly due to lack of such guidelines.

The aim of this article is two-folds: (1) to investigate the reasons of the human-induced vibrations observed in the Kjærra Bridge and (2) to investigate whether the current design guidelines such as HIVOSS [2] and Sétra [3] can successfully predict the excessive vibrations observed. To achieve these goals, free- and forced-vibration tests were carried out on the bridge and dynamic analyses were conducted using a detailed numerical model in Autodesk Robot.

Figure 1: The Kjærra Bridge has a total span of 132m and a free span of 92m across the Numedalslågen River in Lardal, Norway. Photo: Lisbeth Michelsen

2 DESIGN LAYOUT

The bridge was designed as part of a municipal effort to improve access to the public riverbanks. The bridge structure consists of two triangular consoles supported by concrete foundations on each riverbank. These consoles are made of three main components: Two 13 metre long side spans with an elaborate truss brackets made of glulam, and a 92 metre long mid-span

with a lower span cable construction system.

The main span is constructed as a truss, consisting of arched glulam girders, compression members made of glulam cigar beams and steel cables to absorb tensile forces. The truss system is jointed at the middle as a variant of the Polonceau system first designed by French railway engineer Jean-Barthélémy Camille Polonceau (1813 - 1859) [4].

The distance between the extremes of the console beams carrying the main span is 66 metres resulting in a maximum free span of 92 meters. The cantilever console-structure is made of beams and compression members in glulam timber, as well as diagonal steel cross-bracing in the transverse direction leading the forces from the main span to triangular concrete foundations. Furthermore, the two console-structures are anchored at reinforced concrete abutments on each riverbank. Figure 2 shows the elevation view of the bridge.

A wind bracing made of steel L-beams are bolted to the primary beams along the bridge main axis. Horizontal forces are obtained by the wind bracing and transferred down to the foundations through cross bracing.

3 CHARACTERISTICS OF DYNAMIC PEDESTRIAN LOADING

The severe vibrations on the Kjærra Bridge normally occurs when relatively dense flows of people cross the bridge simultaneously. Pedestrian loadings are complex loadings that are challenging to carefully define. This dynamic loading is affected and modified by many parameters. However, studies show that the average frequency of the loading, i.e. the number of steps per second, for normal walking is somewhere between 1.6 and 2.4 Hz. For the same walk, the transverse loading frequency is equal to half of the vertical loading, i.e. the transverse loading frequency for normal walking is somewhere between 0.8 and 1.2 Hz [3].

The phenomenon of ***lock-in*** of a pedestrian crowd is defined as "a pedestrian crowd, with frequencies randomly distributed around an average value and with random phase shifts, will gradually coordinate at a common frequency (that of the footbridge) and enters in phase with the footbridge motion". [3]. To compensate for the imbalance from the vibrational behaviour in the structure, crowds tend to instinctively follow the footbridge motion frequency. As soon as the amplitude of the movements are perceptible, crowd behaviour is no longer random and a motion synchronized with the vibrations of the bridge is developed. Thus, the vibrations tend to amplify as crowd-motion synchronizes with the transverse vibrations in the footbridge, ultimately leading to resonance to the accelerations. These vibrations may reach a critical acceleration if a critical number of pedestrians provoke the vibrations [3].

4 GUIDELINES FOR HUMAN INDUCED VIBRATIONS IN FOOTBRIDGES

At the time of construction, there were no clear guidelines in Norway concerning design for human-induced vibrations in footbridges. Currently, EN-1990:2002 [5] is the relevant standard in Norway that sets the criteria for comfort of the pedestrians on footbridges. According to EN-1990:2002, all footbridges that has a frequency lower than 5 Hz in the vertical direction and 2.5 Hz in the horizontal should be verified for comfort criteria. The comfort criteria is further defined in terms of the maximum acceleration created by groups of 8 to 15 walking normally (persistent design situation). The maximum allowed accelerations are 0.7 m/s^2 in the vertical direction and 0.2 m/s^2 in the horizontal direction. For exceptional crowd conditions, i.e. when the number of pedestrians is significantly over 15, the maximum allowed horizontal acceleration is 0.4 m/s^2. Further, EN-1990:2002 also suggests that, due to uncertainty and complexity of the calculations, it may be necessary to make provisions in the design such as use of dampers unless

the comfort criteria is cleared by a substantial margin.

Although EN-1990:2002 [5] provides guidelines and criteria to avoid severe vibrations in footbridges, these guidelines are not very detailed and can be regarded as imprecise. On the other hand, two guidelines, Sétra [3] and HIVOSS (Human-Induced Vibrations of Steel Structures) [2] provide more detailed and precise requirements to minimize human-induced vibrations in footbridges. According to Sétra [3], the critical eigenfrequencies are 0.3-2.5 Hz and 1-5 Hz in horizontal and vertical directions, respectively. HIVOSS [2] sets these critical eigenfrequencies at 0.5-1.2 Hz and 1.25-2.3 Hz, respectively. According to these two documents, the structures whose predominant vibration frequencies fall into these ranges must undergo a more detailed evaluation. This evaluation requires the evaluation of the comfort level based on the maximum expected acceleration in both vertical and horizontal directions computed via dynamic analysis under pedestrial loading [2, 3]. Table 1 presents the range of accelerations in vertical and horizontal directions for different comfort classes. It should be noted that the range of accelerations given in Table 1 are valid for both Sétra and HIVOSS guidelines [2, 3].

Class	Degree of Comfort	a_{limit}-vertical	a_{limit}-lateral
CL1	Maximum	< 0.50 m/s^2	< 0.10 m/s^2
CL2	Medium	0.50 - 1.00 m/s^2	0.10 - 0.30 m/s^2
CL3	Minimum	1.00 - 2.50 m/s^2	0.30 - 0.80 m/s^2
CL4	Unacceptable	> 2.50 m/s^2	> 0.80 m/s^2

Table 1: Defined comfort class with common acceleration ranges for Sétra and HIVOSS

5 FIELD MEASUREMENTS

Free-vibration and forced-vibration measurements were conducted on the bridge in the spring of 2019 in order to understand the vibration characteristics of the bridge. The measurements were done using a one triaxial accelerometer, Diciducer Model 333D01, at a rate of 800 Hz, on various locations on the bridge. Figure 2 presents the elevation view of the bridge and the five points where the measurements were taken. Point 3 in Figure 2 is the mid-point of the bridge and points 1 and 5, and 2 and 4 are symmetric with respect to the mid-point. As expected, the measurements at the symmetrical points gave very similar response. Therefore, results are only presented for points 1 and 2 for brevity.

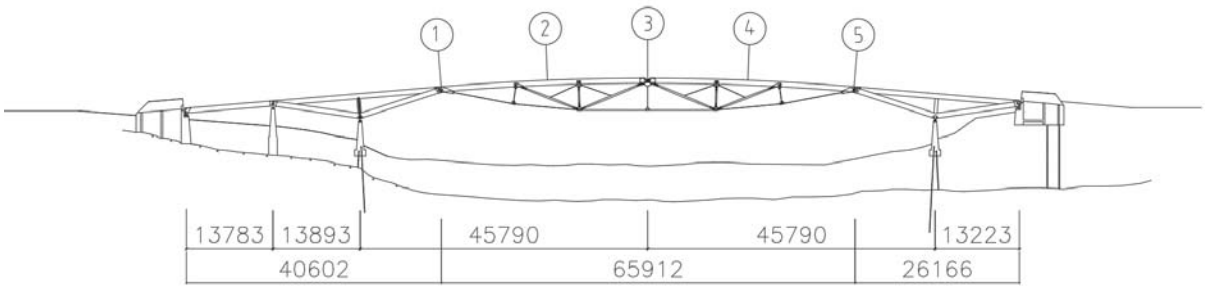

Figure 2: Elevation view: Kjærra Bridge with points of measurements (all dimensions in mm)

The measured acceleration time histories from the free-vibration analyses were converted to

frequency domain using Fast Fourier Transformation (FFT) for the measurements at points 1, 2 and 3. The results plotted in Figure 3 shows that the predominant frequencies in the horizontal and vertical directions are 0.88 Hz and 1.43 Hz, respectively. Measurements at points 1 and 2 also show the frequencies of the higher modes that are suppressed at point number 3. The predominant frequencies fall into the critical range in EN-1990:2002 [5], Sétra and HIVOSS [2, 3] guidelines.

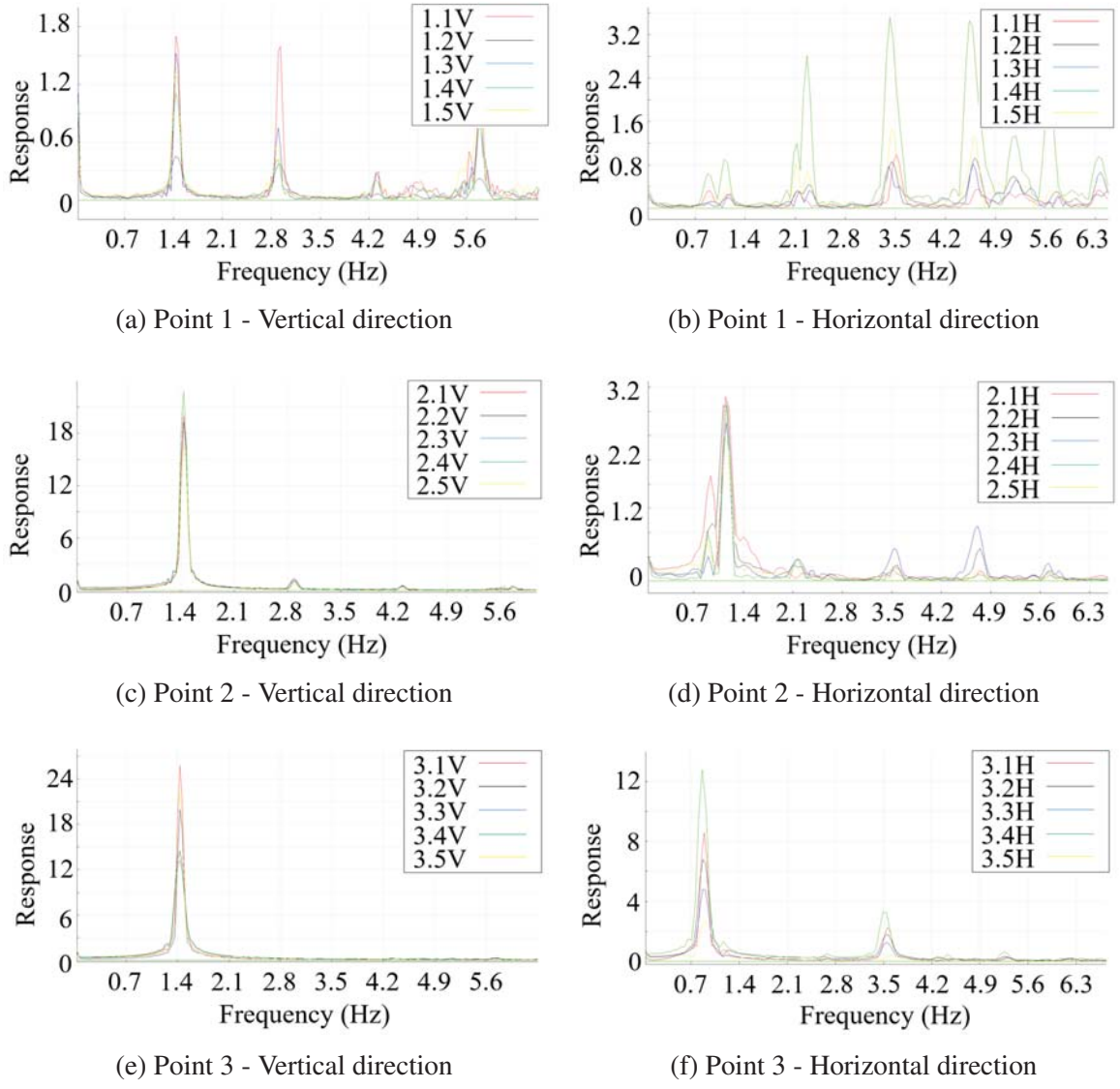

(a) Point 1 - Vertical direction

(b) Point 1 - Horizontal direction

(c) Point 2 - Vertical direction

(d) Point 2 - Horizontal direction

(e) Point 3 - Vertical direction

(f) Point 3 - Horizontal direction

Figure 3: Frequency response function at the mid-span measured from free vibration analyses

In addition to the free vibration measurements, forced-vibration measurements induced by up to three people were conducted to measure the level of accelerations. Around hundred measurements were made on different locations on the bridge to understand the characteristics of the vibrations. However, in this article, we will only focus on the critical results, which are the measurements made at the middle of the main span (point 3 in Figure 2). This area on the bridge shows the highest response to the lowest vibration frequencies on the structure for both horizontal- and vertical vibrations.

The forced-vibration tests conducted on the bridge show that, as expected, the accelerations increase linearly by the number of people inducing the vibrations. By first introducing vibrations induced by one, and then two and three people to amplify the vibrations on the bridge, it is measured that the accelerations (associated to the dominating frequencies) increase by approximately 0.11 m/s^2 for vertical vibrations and 0.28 m/s^2 for horizontal vibrations per person. As a result, maximum horizontal and vertical accelerations were recorded as 0.34 m/s^2 and 0.80 m/s^2 in the vertical and horizontal directions, respectively when the forced-vibrations are introduced by three people; Figure 4 and 5. This shows that, even for a load of three persons, the maximum accelerations recorded on the bridge get fairly close to the *Medium* degree of comfort set forth by Sétra and HIVOSS guidelines; Table 1.

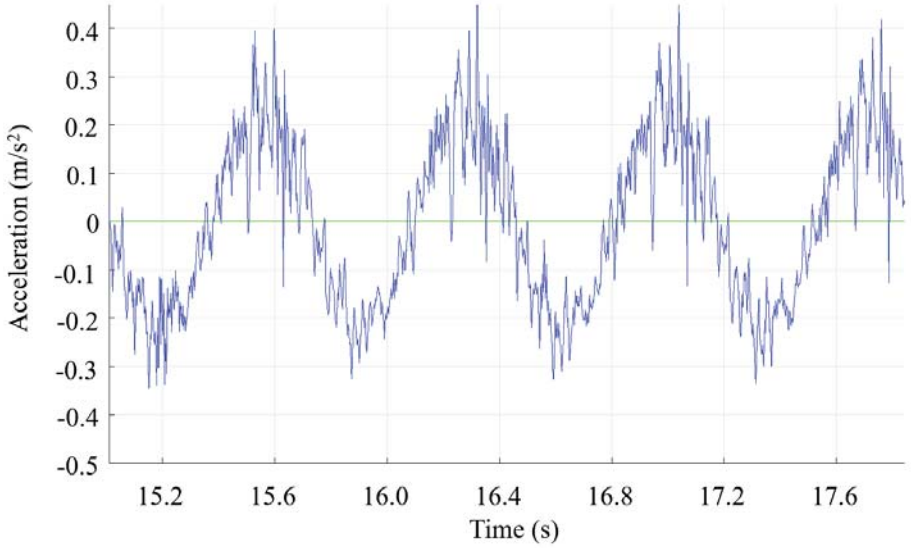

Figure 4: Acceleration measurements for induced vibrations in vertical direction

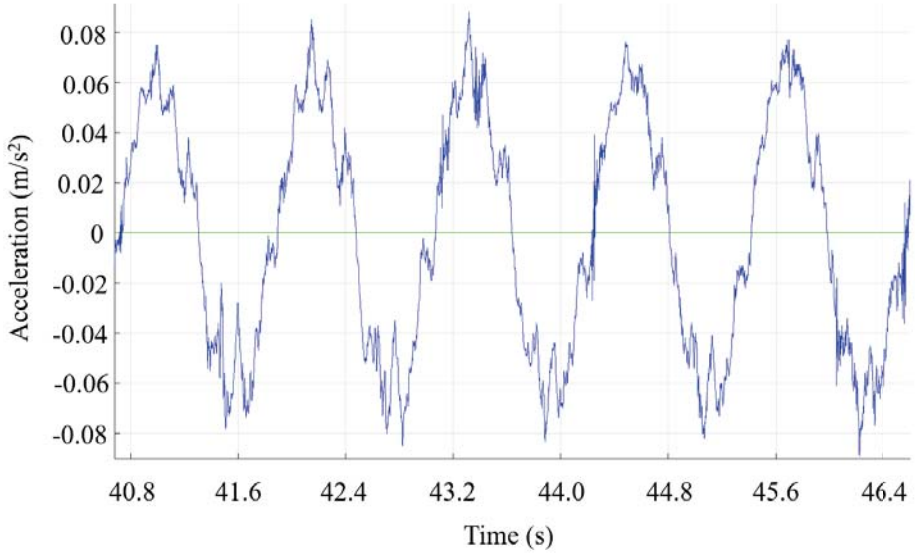

Figure 5: Acceleration measurements for induced vibrations in horizontal direction

6 NUMERICAL ANALYSIS

A detailed finite element model of the bridge was created in the Autodesk® Robot™ Structural Analysis environment to conduct a dynamic analysis of the bridge structure. Both modal analysis and *Footfall Harmonic Analysis (FHA)* of the structure was performed to investigate the free-vibration and forced-vibration behaviour of the bridge. When establishing the dynamic model, the nodal stiffnesses were carefully assessed and modelled, among other things by defining rigid links, master nodes and slave nodes. Furthermore, the hand railing was modelled as imposed load, converted to structural mass prior to the modal analysis, assuming negligable contribution to the overall stiffness of the structure.

A modal analysis of the structure was performed to investigate the dynamic behaviour. The results from the modal analysis show low natural frequencies both in the vertical- and lateral directions. Table 2 presents these frequencies together with the percentage of total mass vibrating in each mode in lateral (UY) and vertical (UZ) directions.

Mode shape [-]	Frequency [Hz]	Period [Sec]	Cur.mas.UY [%]	Cur.mas.UZ [%]
1	1.06	0.94	31.4	0.0
2	1.33	0.75	24.9	0.0
3	1.80	0.56	0.0	42.4

Table 2: Results of the modal analysis for the first five modes

The results of the modal analysis (Table 2) are in quite a good agreement with the free-vibration tests (Figure 3) although the numerical model seems to slightly overestimate the frequencies of the structure. Figure 6 and 7 depict the mode shapes of the predominant lateral and vertical modes obtained from modal analysis. The vibration frequencies in both the horizontal and vertical directions (1.06 Hz and 1.80 Hz, respectively), similar to the frequencies from the free-vibration measurements, fall into the critical range according to all three documents considered. As such, evaluation of maximum expected accelerations is necessary to assess the level of human-induced vibrations in the bridge.

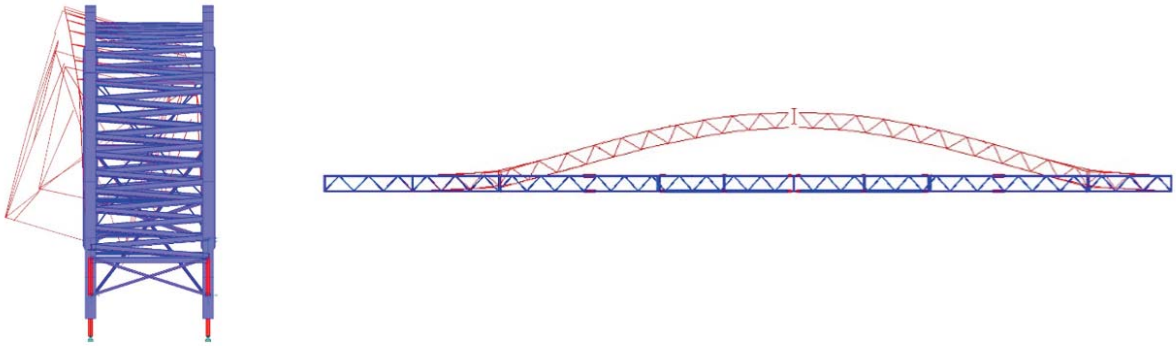

Figure 6: Mode shape of the first lateral mode; f=1.06 Hz

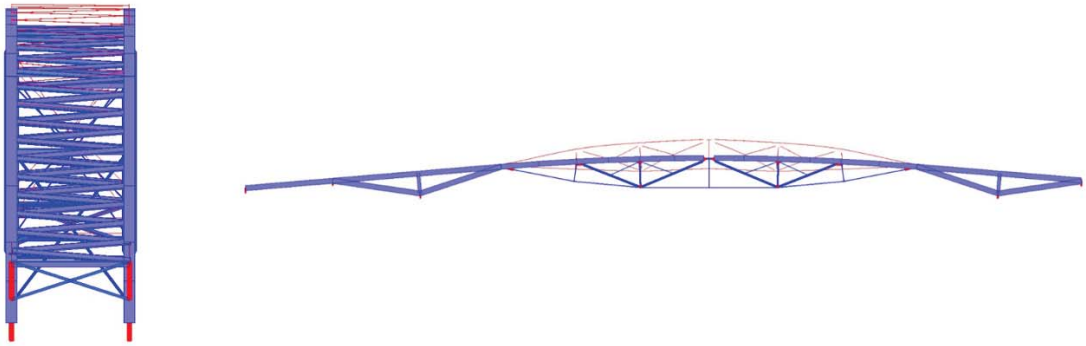

Figure 7: Mode shape of the first vertical mode; f=1.80 Hz

For this, a *footfall harmonic analysis* (FHA) was performed, examining the effect of human footsteps interpreted as a harmonic load at a specific range of frequency on the structure. Due to the limitation of the software used, only vertical direction response was investigated through the FHA. The frequency of movement of the harmonic load was set to be between 0.5 Hz - 5.0 Hz and the number of steps was set to 100. Furthermore, the damping ratio was modelled as 5% of the critical damping and the harmonic load was set to 70 kg based on the average weight of a person.

The FHA has been repeated to simulate different number of people crossing the bridge simultaneously. Figure 8 shows the response of the bridge when the number of people crossing the bridge is set to ten. As expected, the most severe response is observed at 1.80 Hz, which is the predominant frequency in the vertical direction. The footfall analysis show that the maximum acceleration levels in the vertical direction can reach 1.6 m/s^2, which is much higher than the comfort criteria set forth by EN-1990:2002 [5] for groups of 8 to 15 people; 0.7 m/s^2. This level of acceleration also places the comfort level of the bridge at *Minimum* according to Sétra and HIVOSS guidelines.

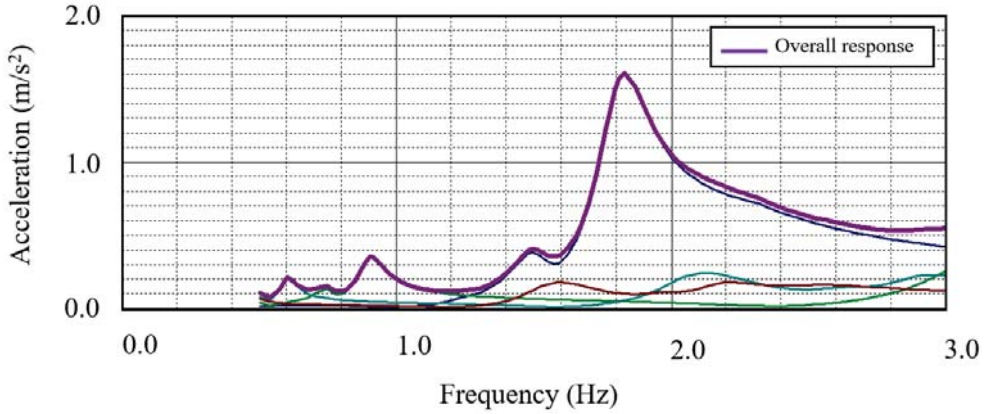

Figure 8: Results of Footfall Harmonic Analysis

Table 3 summarizes the results of the FHA for different number of pedestrians crossing the bridge including the estimated maximum acceleration for all cases. The variation of maximum acceleration with the number of pedestrians computed using FHA is also depicted in Figure 9

together with the maximum accelerations obtained from forced-vibration measurements. Also plotted in Figure 9 is the linear extrapolation of the maximum observed accelerations in the forced-vibration tests. Although the measurements are limited to three people, linear extrapolation of the observed maximum accelerations up to 15 people can be regarded as realistic considering that the behaviour of the bridge most likely remain elastic for a pedestrial load of up to 15 persons.

The maximum acceleration levels presented in Table 3 and Figure 9 show that the human-induced vibrations in the Kjærra Bridge exceeds the comfort criteria of EN-1990:2002 [5] already for five pedestrians. According to the Sétra and HIVOSS guidelines, the comfort level of the bridge reduces from *Maximum* to *Medium* at four pedestrians and further down to *Minimum* at seven pedestrians. Extrapolating the results of the FHA suggests that the threshold of *Unacceptable* vibrations will be exceeded when a group of 16 people cross the Kjærra Bridge at the same time.

$n_{pedestrians}$ [-]	$F_{harmonic}$ [kg]	Accel. [m/s^2]
1	70	0.16
2	140	0.31
3	210	0.47
4	280	0.63
5	350	0.79
10	700	1.60
15	1050	2.40

Table 3: Dynamic response of Kjærra Bridge obtained from FHA

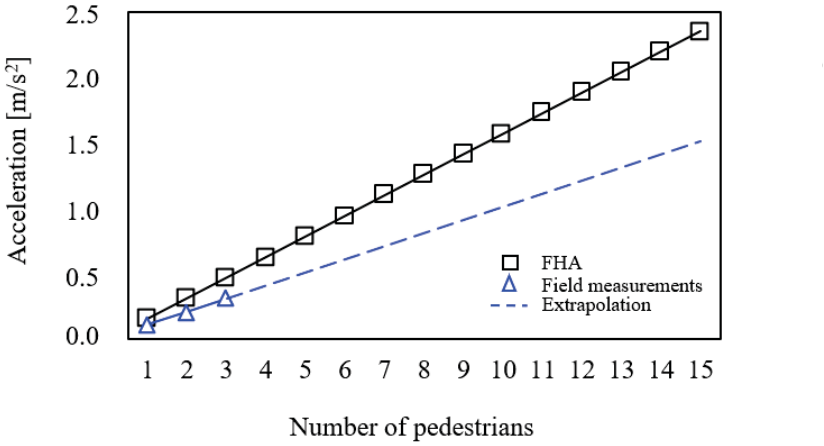

Figure 9: Measured and computed maximum accelerations for Kjærra Bridge

7 CONCLUSION

Kjærra Bridge had been designed and constructed at the beginning of the 21^{st} century, when there were no clear guidelines or standards that has focused on human-induced vibrations on footbridges. As a result of the slender geometry of the bridge, the pedestrians crossing the

bridge in groups have been experiencing severe vibrations. This paper has investigated the dynamic behavior of the bridge through field measurements and numerical analysis. The conclusions drawn from the results of free- and forced-vibration measurements conducted on the Kjærra Bridge and the numerical analysis performed can be summarized as follows:

- The free-vibration measurements indicate that the predominant frequencies in both horizontal and vertical directions are in the critical range according to all three prominent documents that focus on comfort criteria for vibrations in footbridges [2, 3, 5] .
- The forced-vibration measurements show that, even for three persons, the acceleration levels get close to the comfort level *Medium* according to Sétra and HIVOSS guidelines.
- The modal analysis results can be deemed to be in good agreement with free-vibration measurements although the former seems to slightly overestimate the vibration frequencies in both horizontal and vertical directions.
- The footfall harmonic analysis conducted for different number of pedestrians show that the comfort level of the Kjærra Bridge is not acceptable according to EN-1990:2002 [5] for pedestrian groups five or more people. The acceleration level falls into *Minimum* comfort level when the number of pedestrians exceed seven and becomes *Unacceptable* for 16 people according to Sétra and HIVOSS [3, 2] guidelines.
- The results of this study suggest that both EN-1990:2002 [5] and HIVOSS [2] and Sétra [3] guidelines can effectively predict that the human-induced vibrations in Kjærra Bridge can exceed acceptable levels for a relatively small group of pedestrians. As such, it can be argued that any future design that follow the aforementioned guidelines can be expected to have a satisfactory behavior as far as human-induced vibrations are concerned.
- On the other hand, the problems associated with human-induced vibrations for Kjærra Bridge demonstrate the need for a theroetically-sound and precise standard to avoid such problems in future designs.

ACKNOWLEDGEMENT

The work presented herein was supported by Dr. Techn. Kristoffer Apeland A/S (K. Apeland) and Oslo Metropolitan University. The authors gratefully acknowledge their generous support.

REFERENCES

[1] Kjærra Fossepark *Official Website*, Reached on the 13th of February 2020 from: https://www.kjaerra.no/kjrrabrua.

[2] Directorate General for Research and Innovation. Design of Footbridges - Guidelines: *Human-Induced Vibrations of Steel Structures (HIVOSS)*, EU publications, 2010.

[3] The Technical Department of Transportation, Sétra, Techincal guide: *Footbridges: Assessment of vibrational behaviour of footbridges under pedestrian loading*, 2006.

[4] B. N. Sandaker, *The Structural Basis of Architecture*, page 20, ISBN-13: 978-0415415477, 2011.

[5] European Committee for Standadization. NS-EN 1990:2002+A1:2005+NA:2016: *Basis of Structural Design*, 2016.

EURODYN 2020
XI International Conference on Structural Dynamics
M. Papadrakakis, M. Fragiadakis, C. Papadimitriou (eds.)
Athens, Greece, 23–26 November 2020

PERFORMANCE OF BIODYNAMIC MODELS TO REPRESENT THE ACTION OF A PEDESTRIAN IN THE VERTICAL DIRECTION

Rafaela L. Silva[1], Roberto L. Pimentel[2], and Aleksandar Pavic[3]

[1]Postgraduate Research Programme in Civil and Environmental Engineering
Federal University of Paraíba
UFPB/CT-Campus Universitário, s/n, João Pessoa-PB, Brazil
rafaela-lopess@hotmail.com

[2]Department of Civil and Environmental Engineering
Federal University of Paraíba
UFPB/CT-Campus Universitário, s/n, João Pessoa-PB, Brazil
r.pimentel@uol.com.br

[3]College of Engineering, Mathematics and Physical Sciences
University of Exeter
Harrison Building, Streatham Campus, University of Exeter, North Park Road, Exeter, UK EX4 4QF
A.Pavic@exeter.ac.uk

Keywords: Footbridges, Human-structure interaction, Walking, Vibration, SDOF models

Abstract. *The last two decades saw an increase in the number of studies investigating the problem of excessive structural vibration due to pedestrian dynamic loads. Several models to represent the pedestrian action on the structure have been developed. The simplest model (used in most guidelines) consists of applying a moving force on the structure to predict its dynamic behaviour. However, it is now well known that this model cannot accurately estimate the dynamic response of the structure under human action. This is chiefly because the human body has its own dynamic properties, depending on the activity and posture, and the simplest model does not consider this when modelling a pedestrian. This way, single degree of freedom (SDOF) models considering stiffness, mass and damping of an individual have been initially presented. Such models have been compared with the simplest moving force model in terms of accuracy of the structural response. However, challenges remain in terms of dealing with its mathematical modelling, and validation with experimental measurements. In this context, this paper presents a discussion about the formulations of such SDOF models, in order to clarify conceptual and mathematical similarities and differences between such formulations. A basic formulation was identified to compare values that have been proposed for the body parameters, using as a reference experimental data obtained from tests carried out in resonance condition on a lively footbridge. The SDOF model and, generally, the values of body parameters proposed in the literature, performed well against experimental data. There was evidence that lower natural frequencies of the pedestrian body adopted in one of the formulations led to less accurate results, but further studies are needed to confirm this.*

1 INTRODUCTION

Structures have become increasingly lighter and slender, and consequently more susceptible to excessive vibrations. Thereby, loads that generally did not cause structural problems in the past, for example, human activity (running, walking, bouncing etc.), are now of interest for serviceability limit states. This way, the last two decades has concentrated an increased number of studies that aim to investigate the dynamic behaviour of structures under human loads [1].

To deal with this, for design purposes, several ways of applying these loads on the structure have been presented [2]. Focusing on the vertical direction and walking movement, the simplest model consists in applying a moving periodic force (MF) over the structure, mathematically expressed by a Fourier series [3].

Currently included in most standards and guidelines [e.g., 4-6], it is now well known that the MF model cannot estimate precisely the dynamic properties of the system under human action, and sometimes can result in overestimated responses, as shown by Caprani *et al.* [7].

This is because the dynamics of the pedestrian body is not considered in the MF model. Indeed, Shahabpoor *et al.* [1] and Caprani & Ahmadi [2] emphasized that human-structure interaction (HSI) is the key to understand and estimate the effect of human induced loads in structures, particularly in resonance condition. Thus, biodynamic models have been introduced to model pedestrians, the simplest one being a single degree of freedom spring-mass-damper (SMD model).

However, even among the SMD models, there are significant differences in the formulations, ranging from the absence of an analytical formulation [8-10], to the adoption of additional energy input that generates the pedestrian up and down movement by different means (e.g., actuators [11-13], heel movement [14], additional velocity term [15]), or else none of these additions [7,16,17].

Another aspect regarding the SMD models are the values adopted for the parameters mass, stiffness and damping, and several proposals can be found [10,15,17-20], in which such values were obtained in different ways. However, comparisons of performance of SMD models and associated parameters among each other and against the same experimental data are scarce or even non-existent.

In this context, the aim of this paper is twofold. First, an analysis is presented regarding the formulations of SMD models, as a way of clarifying their similarities and differences in conceptual and mathematical terms. The target is to identify a basic analytical formulation for the SMD model and adopt it to compare different formulations. Then, and adopting this basic formulation, parameters proposed in the literature for stiffness, mass and damping of the SMD models were compared, employing experimental data from a pedestrian crossing of a very lively footbridge that had the first vertical mode easily excited. It should be mentioned that the test was carried out in resonance condition, so as to enhance differences in the response between the MF and several SMD models.

2 ANALYSIS OF SMD MODELS

In this section, SMD models of the literature are critically analysed, and a basic analytical formulation is identified and adopted for further comparison against experimental data. Following this, values for the SMD parameters are presented.

2.1 Formulation of SMD models

The first model known to the authors that proposed the modelling of a moving pedestrian as a dynamic system when calculating footbridge vibrations was proposed in Archbold [8],

see also Fanning *et al.* [9]. Being called later on in the literature as a Moving Oscillator, this model consists of applying a ground reaction force $F(t)$ produced from walking on a rigid surface, simultaneously with a SMD model, the latter representing the dynamics of the pedestrian body.

The ground reaction force is usually assumed to be periodic and represented in terms of a Fourier series. For a rigid surface, this time varying force $F(t)$ is shown in Eq. (1), considering only the first harmonic, as this usually suffices for analyses of typical footbridges in resonance condition. In Eq. (1), W is the weight of the pedestrian ($W = Mg$, in which M is the pedestrian total mass, and g is the acceleration due to gravity), f_p is the pacing rate, and DLF stands for dynamic load factor [3].

$$F(t) = W\,(1 + DLF\ \sin\,(2\,\pi f_p\ t)) \tag{1}$$

It should be noted that there is no specific analytic formulation presented in Archbold [8] and Fanning *et al.* [9] to represent the interaction between pedestrian and footbridge. This proposal is, thus, just a procedure to include the dynamics of pedestrian. This same procedure was adopted by Silva *et al.* [10].

A first analytical formulation to account explicitly for the interaction between pedestrian and footbridge can be found in the work of Caprani *et al.* [7]. It is considered that the ground reaction force produced by the pedestrian is the sum of elastic spring and dissipative forces, that is, the force is transmitted to the mass of the pedestrian through the spring and damper, while walking on a rigid or on a flexible surface.

The outcome of this formulation is that the ground reaction force is equal to the respective inertia force in each case, as will be shown later. Venuti *et al.* [16] adopted the formulation of Caprani *et al.* [7], but with a difference that the former opted to express the interaction force as the sum of the elastic spring and damping forces instead of the inertia force, which led to a different arrangement of terms in the formulation. Shahabpoor *et al.* [17] also adopted this formulation, for investigating the action of a pedestrian flow, which was assumed as continuous and stationary.

This formulation was employed with some modifications by Pfeil *et al.* [14]. First, a function was introduced to represent the up and down movement of the heels. One can think of this function as a conceptual cause of the up and down movement of the pedestrian. However, in the development of the formulation, it can be inferred that this function could be suppressed without affecting the equations of motion.

This way, by omitting this function for the sake of clarity, the model adopted by Pfeil *et al.* [14] can be seen in Figure 1: a walking person represented as a SMD model, with respective modal mass (m_p), damping (c_p) and stiffness (k_p). By considering the equilibrium at the pedestrian's centre of mass (COM) and at contact point, the equation of motion of the pedestrian can be expressed in Eqs. (2) and (3), while walking on rigid and flexible surfaces, respectively.

$$F(t) = \ - c_p\ \dot{u}_{pr} - k_p\ u_{pr} = m_p\ \ddot{u}_{pr} \tag{2}$$

$$F_{int}(t) = -\ c_p\,(\dot{u}_{pr} + \dot{u}_p - \dot{u}_s)\ -\ k_p\,(u_{pr} + u_p - u_s)\ =\ m_p\,(\ddot{u}_{pr} + \ddot{u}_p) \tag{3}$$

In Eqs. (2) and (3), u_{pr} is the vertical displacement of the pedestrian's COM while walking on a rigid surface; u_p is the vertical displacement while walking on flexible surface which takes into account the pedestrian-structure interaction; and u_s is the vertical displacement of the structure at the contact point. It should be noted, as indicated in Figure 1, that the forces $F(t)$ and $F_{int}(t)$ represented in these equations act on the pedestrian. Equal and opposite forces are acting on the structure.

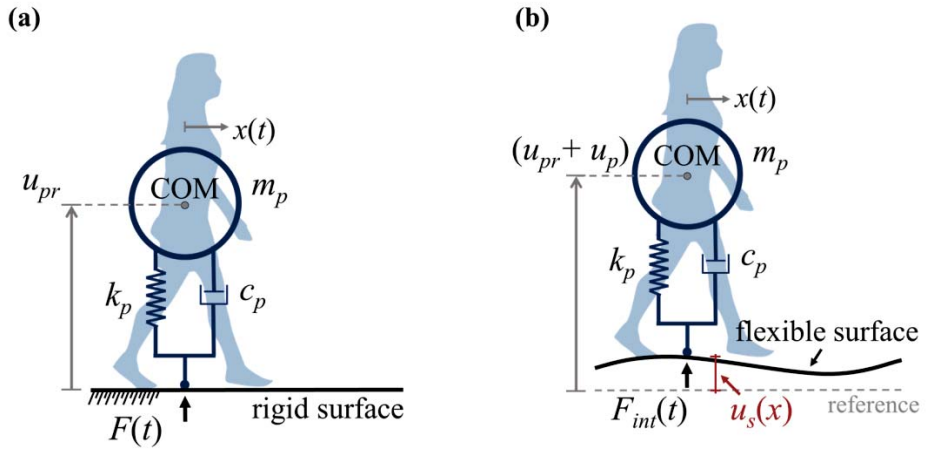

Figure 1: The SMD model (a) on a rigid surface and (b) on a flexible surface, after [14].

Considering all this, Pfeil *et al.* [14] explicitly showed that the ground reaction force from the rigid surface $F(t)$ could be introduced into the expression of the interaction force $F_{int}(t)$ while walking on a flexible surface. This is directly obtained by manipulating Eqs. (2) and (3). Then, by turning around $F(t)$ and $F_{int}(t)$, in order to apply them at the structure, Eq. (4) is obtained:

$$F_{int}(t) = c_p\,(\dot{u}_p - \dot{u}_s) + k_p\,(u_p - u_s) + F(t) \tag{4}$$

The introduction into the formulation of the interaction displacement u_p as a part of the total displacement of the pedestrian's COM while walking on flexible surfaces, led to a difference in this formulation when compared to the ones adopted by the aforementioned authors [7,16,17]. Adoption of u_p is necessary if the ground reaction force from walking on the rigid surface is to be employed into the formulation of walking on the flexible surface. The outcome is that the total displacement of the COM of the pedestrian while walking on a flexible surface ($u_p + u_{pr}$) differs from that adopted by Caprani *et al.* [7].

The equation of motion of the pedestrian body, in terms of the interaction displacement u_p, can be obtained by combining Eqs. (2) and (3):

$$m_p\,\ddot{u}_p \;+\; c_p\,(\dot{u}_p - \dot{u}_s) \;+\; k_p\,(u_p - u_s) = 0 \tag{5}$$

Now, by using the concept of modal superposition, a coupled system (pedestrian-structure) with two degrees of freedom is formulated. For this purpose, the structure displacement (u_s) at the contact point, assuming a single mode structural response, can be expressed as:

$$u_s(x) \;=\; \phi_i(x)\,y_i \tag{6}$$

where y_i is the general coordinate corresponding to the i^{th} mode with the respective mode shape $\phi_i(x)$, and x stands for the pedestrian position at the structure.

Remembering that modal superposition equation is given by:

$$m_i\,\ddot{y}_i \;+\; c_i\,\dot{y}_i \;+\; k_i\,y_i \;=\; P_i \tag{7}$$

where m_i, c_i and k_i are the modal mass, damping and stiffness of the i^{th} mode of the structure, and P_i is the generalized force, given by:

$$P_i = \phi_i(x)\,F_{int}(t) \tag{8}$$

The equation of motion of the joint pedestrian-structure system (unknowns y_i and u_p) can be expressed by Eq. (9), obtained by substituting Eq. (8) into (7), and considering Eqs. (4) and (6).

$$m_i \ddot{y}_i + (c_i + \phi_i^2 c_p)\dot{y}_i + (k_i + \phi_i^2 k_p) y_i - \phi_i c_p \dot{u}_p - \phi_i k_p u_p = \phi_i F(t) \tag{9}$$

The coupled pedestrian-structure system can be also written in a matrix form, as stated by Pfeil *et al.* [14]:

$$\mathbf{M}\,\ddot{\mathrm{U}} + \mathbf{C}\,\dot{\mathrm{U}} + \mathbf{K}\,\mathrm{U} = \mathrm{F} \tag{10}$$

where,

$$\mathbf{M} = \begin{bmatrix} m_i & 0 \\ 0 & m_p \end{bmatrix}, \quad \mathbf{C} = \begin{bmatrix} c_i + \phi_i^2 c_p & -\phi_i c_p \\ -\phi_i c_p & c_p \end{bmatrix}, \quad \mathbf{K} = \begin{bmatrix} k_i + \phi_i^2 k_p & -\phi_i k_p \\ -\phi_i k_p & k_p \end{bmatrix},$$

$$\mathrm{F} = \begin{Bmatrix} \phi_i F(t) \\ 0 \end{Bmatrix} \quad \text{and} \quad \mathrm{U} = \begin{Bmatrix} y_i \\ u_p \end{Bmatrix}$$

Note that the equations are similar to the ones presented by Venuti *et al*. [16]. However, the variable representing the displacement of the pedestrian's COM herein consists only of the interaction displacement u_p of the COM while walking on a flexible surface.

A slight modification of this formulation was introduced by Jiménez-Alonso & Sáez [19] by placing a small part of the pedestrian mass at feet level and in permanent contact with the structure. By doing this, the interaction force $F_{int}(t)$ differs from the expression present in Eq. (3). Nonetheless, bearing in mind that the fraction of the total mass M of the pedestrian that is included in the SMD model (as a modal mass m_p) varies among proposals found in the literature (values will be discussed later), the modification introduced by Jiménez-Alonso & Sáez [19] did not differ much from the previous formulations.

Finally, Gomez *et al.* [15] conceived the source of external energy that caused the pedestrian up and down movement as an initial velocity condition applied to the SMD model, when the heel hits the ground. By comparing their formulation with the one from Pfeil *et al.* [14], this initial velocity condition replaced the use of the ground reaction force $F(t)$ (applied on a rigid surface) when formulating the equations for walking on flexible surfaces.

However, this is more a matter of preference about using or not the ground reaction force from walking on a rigid surface into the formulation. It should be noted that using $F(t)$ has advantages since expressions for it are very deeply studied in the literature [1, 2].

The formulation from Pfeil *et al.* [14], slightly modified by the suppression of the function representing the heel movement, was, thus, selected as a basic one in this paper, and is adopted for the analysis of the values of the SMD parameters.

2.2 SMD parameters

There are studies that proposed values for the SMD parameters based on experimental tests with walking subjects.

One of the first studies was conducted by Silva & Pimentel [18]. Values were determined based on tests with twenty subjects walking on a rigid surface, in which acceleration was measured at waist level only. Regression expressions were then proposed for the modal mass, stiffness and damping, as a function of the total mass and pacing rate of the pedestrian. In a

subsequent work, Silva *et al.* [10] presented additional linear expressions to obtain stiffness and damping.

The study of Toso *et al.* [20] also obtained SMD parameters from walking subjects. In this case, the ground reaction force from a rigid surface was measured simultaneously with the body acceleration for thirty-five subjects and used as an input to determine a set of regression expressions for the SMD parameters.

The main feature for obtaining the SMD parameters in these three studies was a formulation in which the equation of motion of the pedestrian assumed that all forces were applied at the pedestrian's COM, including the ground reaction force.

Gomez *et al.* [15] applied the same test setup as Silva & Pimentel [18], but enrolling only three subjects and employing a different formulation for the equation of motion (see Section 2.1), which led to values for stiffness and damping for each test subject. In addition, they also considered the modal mass as the respective total mass of the test subject.

In all these aforementioned works, the SMD parameters were determined directly from measurements on each individual, walking alone. However, a different approach is reported in other studies, where the values of the SMD parameters were obtained indirectly through measurements of the structural response. This line of reasoning was presented by Jiménez-Alonso & Sáez [19], and they obtained values for the SMD parameters based on experimental results carried out by Geogarkis & Jorgensen [21], in which test subjects walked in group (in varied density scenarios) across a simply supported beam.

By using a genetic algorithm, average values for the SMD parameters for each scenario were obtained, and Jiménez-Alonso & Sáez [19] concluded that there was no significant variability in the sprung mass, equivalent damping ratio and body natural frequency for different scenarios.

Shahabpoor *et al.* [17] also employed tests with group of pedestrians. They assumed that the modal mass was the total mass of the pedestrian and identified a range of values for the body natural frequency and damping.

A synthesis of all of these findings is presented in Tables 1 and 2, where ξ_p and f_{np} are respectively damping ratio and natural frequency of the pedestrian body.

	Silva & Pimentel [18]	**Silva *et al.* [10]**
$m_p(M, f_p)$	$97.082 + 0.275\,M - 37.52\,f_p$ (kg)	$97.082 + 0.275\,M - 37.52\,f_p$ (kg)
$c_p(m_p)$	$29.041\,m_p^{0.883}$ (N.s/m)	$107.455 + 16.208\,m_p$ (N.s/m)
$k_p(c_p)$	$30351.744 - 50.261\,c_p + 0.035\,c_p^2$ (N/m)	$5758.441 + 11.103\,c_p$ (N/m)
	Toso *et al.* [20]	
$m_p(M, f_p)$	$-231.34 + 3.69\,M + 154.06\,f_p - 1.97\,M f_p + 0.005\,M^2 - 15.25\,f_p^2$ (kg)	
$c_p(M, m_p)$	$-1115.69 + 92.56\,M - 108.94\,m_p + 2.91\,M\,m_p - 1.33\,M^2 - 1.30\,m_p^2$ (N.s/m)	
$k_p(M, f_p)$	$75601.45 - 1295.32\,M - 33786.75\,f_p + 506.44\,\mathrm{M}\,f_p + 3.59\,M^2 + 539.39\,f_p^2$ (N/m)	

Table 1: Proposed expressions for the SMD parameters

	Jiménez Alonso & Sáez [19]	**Gomez *et al.* [15]**	**Shahabpoor *et al.* [17]**
m_p **(kg)**	83.97% of total mass	total mass	total mass
ξ_p **(%)**	47.18	12 – 18	27.5 – 30
f_{np} **(Hz)**	2.76	2.29 – 2.52	2.75 – 3.00

Table 2: Proposed values for the SMD parameters

3 TEST STRUCTURE AND EXPERIMENTAL RESULTS

The test structure is the Aberfeldy glass reinforced plastic cable-stayed footbridge, in Scotland (Figure 2a). More details about the test structure can be found elsewhere [14, 22].

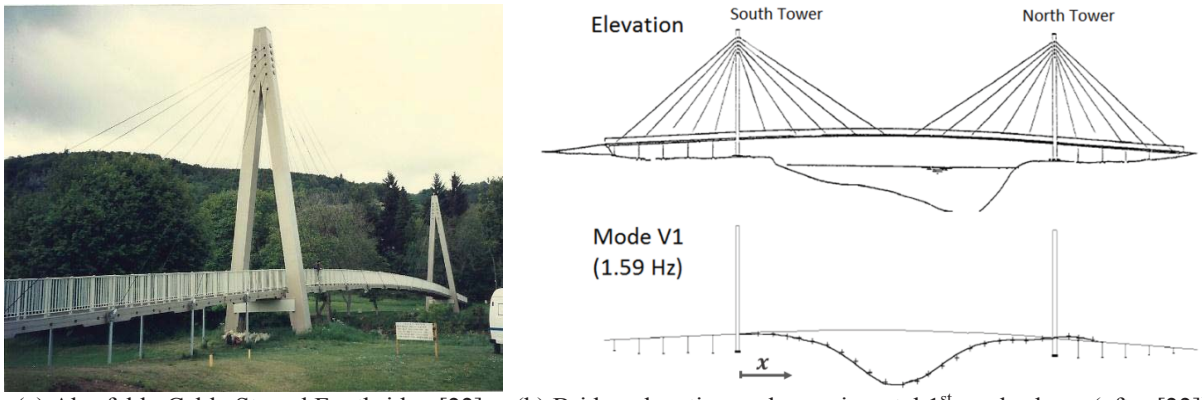

(a) Aberfeldy Cable Stayed Footbridge [22] (b) Bridge elevation and experimental 1st mode shape (after [22])

Figure 2: Test structure and mode shape of interest

The test result of interest is the filtered vertical acceleration response at mid span due to the crossing of a pedestrian walking in resonance with the first vertical mode of the structure, in which the maximum acceleration (a_{max}) and root mean square acceleration (a_{rms}) was respectively 2.14 m/s² and 0.89 m/s². The whole measured time response signal was available for comparison with the numerical predictions.

As observed in Pfeil *et al.* [14], even with the control of the pedestrian gait with a help of a metronome, the strong deck vibrations led to a pace losing, causing disturbances in the response signal. This was taken into account in this work.

On the other hand, by analysing the experimental mode shape in Figure 2b, it is clear that the relevant response occurs while walking between the towers and in order to be used in Eq. (10), a mathematical expression for unity scaled $\phi_i(i=1)$ given in Eq. (11) was fit to the experimental mode shape.

$$\phi_1(x) = 0.11867 - \frac{1845.64}{4\pi(x - 31.881)^2 + 513.413\pi} \tag{11}$$

Finally, the absence of some information from the experimental side led to a need of adopting values from the literature. The step length of the pedestrian was assumed as 0.90 m [13]. The DLF of the pedestrian was not experimentally determined; and an initial value of 0.25 was defined based on Young [23] and adjusted in the analysis, as will be shown later on. All information gathered for the analysis is presented in Table 3.

Test structure (1st mode)		**Test Pedestrian**	
Modal mass (m) (calculated)	2547 kg	Total mass (M)	80 kg
Damping ratio (ξ)	0.84 %	Pacing rate (f_p)	Average of 1.56 Hz
Natural frequency (f_n)	1.59 Hz	Step length (assumed)	0.90 m

Table 3: First mode dynamic parameters of the structure and pedestrian characteristics, based on experimental data except where indicated.

4 RESULTS AND DISCUSSIONS

The performance of the SMD parameters was investigated by comparing numerical results obtained adopting the interaction model of Pfeil *et al.* [14] against the experimental result (see

Table 4). The results were compared in terms of the maximum (a_{max}) and root mean square (a_{rms}) acceleration, as well as the fit to the experimentally measured acceleration response time history (see Figures 3 and 4). For conciseness, only the best results obtained for each of the formulations are shown in these Figures. However, Table 4 contains the whole range of results obtained for all formulations. It can be noted that a range of values was proposed in some formulations for the pedestrian parameters [15,17], and this is the reason why some combinations of these values (in particular, damping and natural frequency of the pedestrian body) were performed (see sets (1) to (4) in Table 4). On the other hand, for the formulations in which regression expressions or average values were proposed [10,18-20], the body parameters were obtained by employing the body parameters of the test subject.

	Gomez *et al.* [15]				**Shahabpoor *et al.* [17]**			
Set	(1)	(2)	(3)	(4)*	(1)	(2)	(3)	(4)*
m_p **(kg)**	80	80	80	80	80	80	80	80
ξ_p **(%)**	12	18	12	18	27.5	30	27.5	30
f_{np} **(Hz)**	2.29	2.29	2.52	2.52	2.75	2.75	3.00	3.00
DLF	0.27	0.27	0.26	0.26	0.26	0.26	0.25	0.25
a_{max} **(m/s²)**	2.19	2.08	2.25	2.17	2.18	2.17	2.16	2.15
a_{rms} **(m/s²)**	0.93	0.90	0.95	0.93	0.94	0.93	0.93	0.92

	MF model	**Jiménez Alonso & Sáez [19]**	**Silva & Pimentel [18]**	**Silva *et al.* [10]****	**Toso *et al.* [20]**
m_p **(kg)**	-	67.18	60.18 - 61.68	60.18 - 61.68	52.71 - 54.75
ξ_p **(%)**	-	47.18	53.11 - 53.58	52.34 - 52.46	55.42 - 57.76
f_{np} **(Hz)**	-	2.76	2.67 - 2.69	2.72 - 2.74	1.74 - 1.81
DLF	0.26	0.26	0.27	0.27	0.29
a_{max} **(m/s²)**	2.40	2.16	2.15	2.17	1.88
a_{rms} **(m/s²)**	1.03	0.94	0.94	0.95	0.86

* Best result obtained for the range of the proposed values.
** Values from [10] were close to the ones from [18], and were not shown in Figure 4.
Obs.: The variation in the SMD parameters from [10, 18, 20] was due to the dependence of such parameters with the varied pacing rate throughout the crossing.

Table 4: Results obtained employing different values for the pedestrian parameters

For each case, the unknown *DLF* of the test subject was adjusted to produce a best fit, based on a trial and error process. However, it can be seen from Table 4 that this is not a significant issue since the best value of the *DLF* obtained for each formulation varied very little, around the value 0.27 stated in Pfeil *et al.* [14].

Regarding the values of the SMD parameters, it is noted that despite the wide range of values of the parameters, no great difference was identified among the results (Figure 4).

However, some discrepancies were noted about the proposed values of the natural frequency f_{np} of the pedestrian body. Toso *et al.* [20] values for this parameter are below all the other works and the results with their parameters were the least accurate among the whole set of SMD parameters investigated (Figure 3b). This requires further studies, with a larger sample of experimental data, to confirm or not the relevance of this parameter, since the natural frequency f_{np} may not be the sole cause of the discrepancy.

In general, despite the different ways of obtaining the SMD parameters, the results were in very good agreement with the experimental one and presented a much better performance against MF model (Figure 3a), which overestimated the bridge response. The difference in

peak and RMS values between MF and biodynamic models might be small (see values in Table 4), but this was for a single pedestrian crossing. Actual design cases consider group or streams of pedestrians crossing the structure, which deserves further investigation.

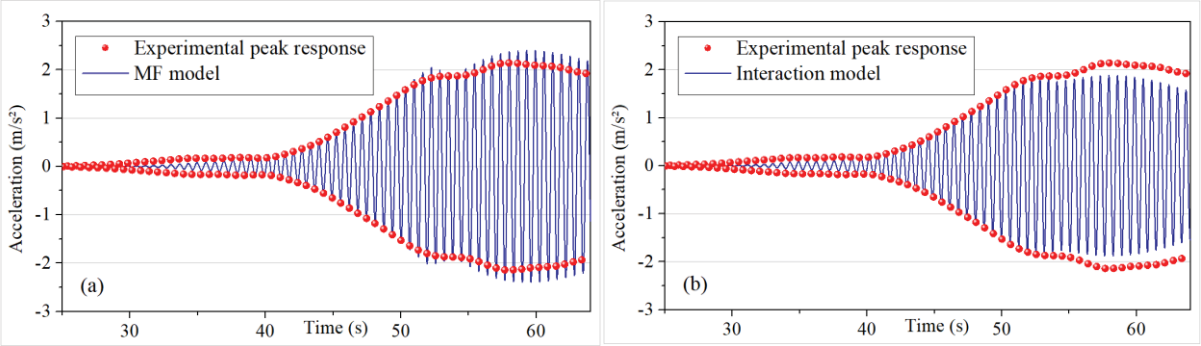

Figure 3: Acceleration at the mid span of the footbridge - (a) Experimental x MF model; (b) Experimental x Interaction Model using the set of parameters from Toso *et al.* [20]

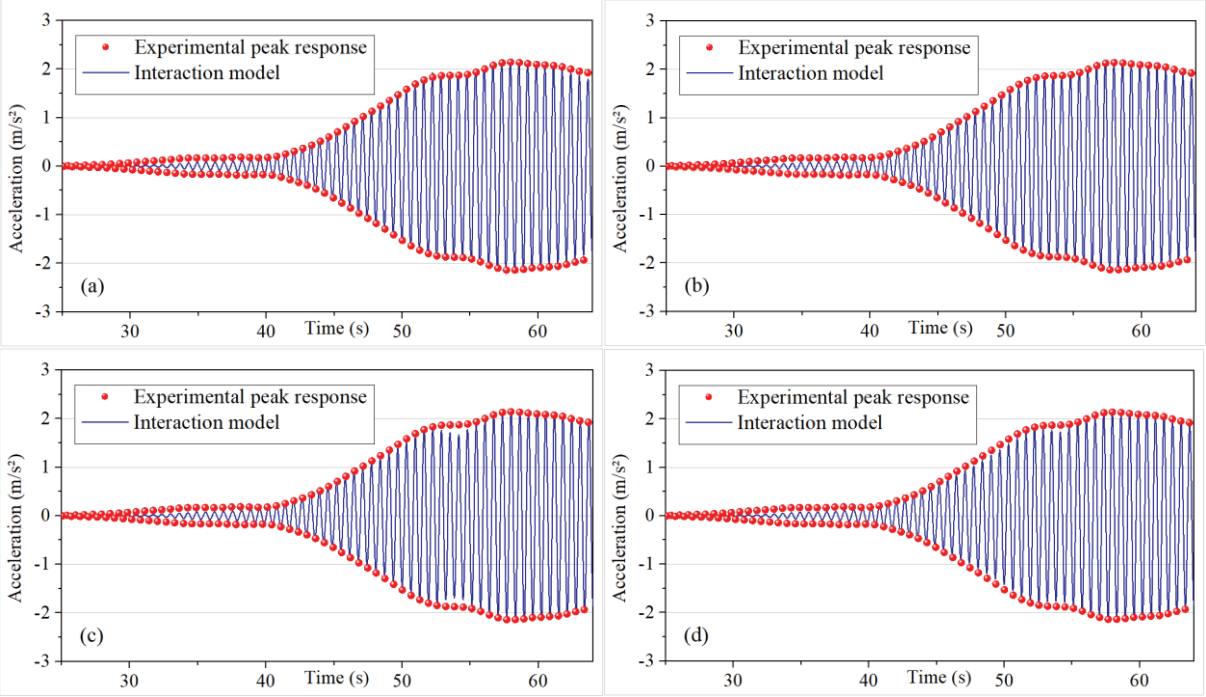

Figure 4: Acceleration at the mid span of the footbridge - Experimental versus Interaction Model using the set of parameters from (a) Silva & Pimentel [18]; (b) Jiménez-Alonso & Sáez [19]; (c) Gomez *et al.* [15]; (d) Shahabpoor *et al.* [17]

5 CONCLUSIONS

A discussion of SDOF spring-mass-damper models proposed in the literature to model pedestrians in HSI studies was presented. It was shown that the formulations proposed to account for HSI were based on the same concept that the ground reaction force, either on a rigid or on a flexible surface, is equal to the inertia force of the pedestrian body. In general, this led to an analytical formulation to represent the coupled pedestrian-structure system.

The formulation presented by Pfeil *et al.* [14] made it clear that the ground reaction force obtained from rigid surfaces (widely used in the literature) can be inserted into the equations that consider the deformability of the structure. With a slight modification, this so called

'interaction model' [14] was adopted to compare the performance of various SMD parameters proposed in the literature and obtained through experimental measurements with walking subjects, albeit each set of parameters was obtained in different and independent ways.

Despite of the different ways in obtaining the SMD parameters, the different proposals generally resulted in quite good agreement with the experimental result obtained from a pedestrian crossing a lively footbridge. However, a less accurate response was obtained from one of the formulations, when the proposed value for the natural frequency of the pedestrian body was lower, which requires attention and further studies.

In spite of the good performance of the simple SMD models and respective parameters in this case, a more in-depth analysis is required with well instrumented pedestrians. This way, the performance of the SMD models could also be compared against more elaborated biodynamic models currently proposed in the literature. In addition, evaluations employing a larger number of test subjects crossing simultaneously a structure are required, so as to comply with the design cases of current standards.

ACKNOWLEDGEMENTS

The authors acknowledge the financial support from CAPES/BR for this research project.

REFERENCES

[1] E. Shahabpoor, A. Pavic, V. Racic, Interaction between walking Humans and Structures in Vertical Direction: A Literature Review, *Shock and Vibration*, 2016, Article ID 3430285.

[2] C.C. Caprani, E. Ahmadi, Formulation of human-structure system models for vertical vibration, *Journal of Sound and Vibration* 377, 346–367, 2016.

[3] H. Bachmann, W. Ammann, *Vibration in structures induced by man and machines*, Structural Engineering document n.3, International Association for bridge and Structure Engineering, Zurich, Switzerland, 1987.

[4] Technical Department for Transport, Roads and Bridges Engineering, and Road Safety/French Association of Civil Engineering (SETRA/AFGC), *Footbridges: assessment of vibrational behaviour of footbridges under pedestrian loading, Technical Guide 0611*, SETRA/AFGC, Paris, France, 2006.

[5] M. Feldmann, Ch. Heinemeyer, M. Lukic et al., *Human-Induced Vibration of Steel Structures (Hivoss)*, Research Fund for Coal and Steel, European Commission, 2008.

[6] British Standards Institution (BSI), *UK national annex to Eurocode 1: Actions on structures. Part 2: Traffic loads on bridges,* NA to BS EN 1991-2:2003*,* London, 2008.

[7] C.C. Caprani, J. Keogh, P. Archbold, P. Fanning, Characteristic vertical response of a footbridge due to crowd loading, *Proceeding of the 8th International Conference on Structural Dynamics (Eurodyn'11)*, 978–985, Leuven, Belgium, 2011.

[8] P. J. Archbold, *Interactive load models for pedestrian footbridges* [Ph.D. thesis], National University of Ireland, University College Dublin, 2004.

[9] P. J. Fanning, P. Archbold, A. Pavic, A novel interactive pedestrian load model for flexible footbridges, *Proceedings of the SEM Annual Conference and Exposition on Experimental and Applied Mechanics*, 573–580, Portland, Ore, USA, June 2005.

[10] F.T. Silva, H.M.B.F. Brito, R.L. Pimentel, Modelling of crowd load in vertical direction using biodynamic model for pedestrians crossing footbridges, *Canadian Journal of Civil Engineering*.40, 1196–1204, 2013.

[11] M. Zhang, C. Geogarkis, J. Chen. Biomechanically Excited SMD Model of a Walking Pedestrian, *Journal of Bridge Engineering* 21(8): C4016003, 2016.

[12] M.A. Toso, H.M. Gomes. A coupled biodynamic model for crowd-footbridge interaction, *Engineering Structures* 177, 47-60, 2018.

[13] H. Dang, S. Živanović, Modelling pedestrian interaction with perceptibly vibrating footbridges, *FME Transactions* .41, 271–278, 2013.

[14] M. Pfeil, N. Amador, R. Pimentel, and R. Vasconcelos. Analytic-numerical model for walking person – footbridge structure interaction, *Proceedings of the 9th International Conference on Structural Dynamics (Eurodyn'14)*, 1079–1086, Porto, Portugal, 2014.

[15] D. Gomez, S.J. Dyke, S. Rietdyk, Experimental Verification of a Substructure-Based Model to Describe Pedestrian–Bridge Interaction, *Journal of Bridge Engineering*, 23(4): 04018013, 2018.

[16] F. Venuti, V. Racic, A. Corbetta, Modelling framework for dynamic interaction between multiple pedestrians and vertical vibrations of footbridge, *Journal of Sound and Vibration* 379, 245–263, 2016.

[17] E. Shahabpoor, A. Pavic, V. Racic, Identification of mass–spring–damper model of walking humans, *Structures* 5, 233–246, 2016.

[18] F.T. Silva, R.L. Pimentel, Biodynamic walking model for vibration serviceability of footbridges in vertical direction, *Proceedings of the 8th International Conference on Structural Dynamics (Eurodyn' 11)*, 1090–1096. Leuven, Belgium, 2011.

[19] J. F. Jiménez Alonso, A. Sáez, A direct pedestrian structure interaction model to characterize the human induced vibrations on slender footbridges, *Informes de la Construcción* 66, n.1, article m007, 2014.

[20] M.A. Toso, H.M. Gomes, F.T. Silva, R.L. Pimentel, Experimentally fitted biodynamic models for pedestrian-structure interaction in walking situations, *Mechanical Systems and Signal Processing* 72–73, 590–606, 2016.

[21] C.T. Georgakis, N.G. Jorgensen, Change in mass and damping on vertically vibrating footbridges due to pedestrians, *Proceedings of the 31st Conference on Structural Dynamics (IMAC '13)* 3, 37–45, 2013.

[22] R.L. Pimentel, *Vibration performance of pedestrian bridges due to human-induced loads* [Ph.D. thesis], University of Sheffield, Sheffield, UK, 1997.

[23] P. Young, Improved floor vibration prediction methodologies, *ARUP Vibration Seminar*, 2001.

EURODYN 2020
XI International Conference on Structural Dynamics
M. Papadrakakis, M. Fragiadakis, C. Papadimitriou (eds.)
Athens, Greece, 23–26 November 2020

PEDESTRIAN LATERAL FOOT PLACEMENT AND LATERAL DYNAMIC INSTABILITY OF BRIDGES

Mateusz Bocian[1,2], Jeremy F. Burn[3], John H.G. Macdonald[4]

[1] School of Engineering, University of Leicester, Leicester LE1 7RH, UK
[2] Department of Bridges and Railways, Faculty of Civil Engineering,
Wrocław University of Science and Technology, 50-370 Wrocław, Poland
e-mail: m.bocian@leicester.ac.uk

[3] Department of Mechanical Engineering, University of Bristol, Bristol BR8 1TR, UK
e-mail: J.F.Burn@bristol.ac.uk

[4] Department of Civil Engineering, University of Bristol, Bristol BR8 1TR, UK
e-mail: John.Macdonald@bristol.ac.uk

Keywords: human-structure interaction, bridge dynamics, inverted pendulum model, pedestrian loading, lateral instability

Abstract. *The most often purported mechanism causing the lateral dynamic instability of the London Millennium Footbridge is the synchronisation of footsteps to the lateral structural motion. However, evidence from full-scale measurements and treadmill tests has challenged this notion. Instead, an active control of foot placement is advocated to be the source of destabilising forces to the structure, occurring even without synchronisation. This is to say that, while walking on a laterally oscillating surface, pedestrians maintain their balance primarily by controlling the position of their feet, rather than adjusting the timing. Similar behaviour was previously observed in experimental tests measuring the response of pedestrians to an impulsive perturbation of gait. The analysis of the collected data suggested a simple linear foot placement control law, whereby the position of the foot at the instant of foot placement immediately following the perturbation depends on the instantaneous lateral velocity of the centre of mass and a constant offset. However, it is has been uncertain whether the same foot placement control law applies while walking on laterally oscillating structures. To test this proposition, an experimental campaign was conducted on a laterally oscillating treadmill with a test subject monitored with an optical motion capture system. The motion of the body centre of mass and the position of the feet were identified and analysed. It was found that a simple linear foot placement control law applies. Further tests were conducted to test the influence of the visual information on pedestrian stepping behaviour using virtual reality delivered via a head mounted display. It was found that the identified foot placement control law is very robust for different walking surface conditions and visual environments.*

1 INTRODUCTION

Lateral dynamic instability under the loading from a walking crowd has been observed on many bridges around the world [1-8]. Despite intensive research in the last two decades to uncover the nature of this phenomenon, a consensus has not yet been reached. The paradigm still dominating in the field is that, in the presence of perceptible bridge motion, pedestrians adjust their stride frequency to match the vibration frequency of the bridge, hence a direct resonance will occur. This is supposedly amplified by a tendency of pedestrians to synchronise their footsteps to one another. However, some measurements from full-scale structures [5, 6] and laboratory environments [9, 10] have challenged the notion of prevalence of the direct resonance, while the natural tendency of pedestrians to synchronise their footsteps with other pedestrians has been found to be quite weak [11, 12]. Meanwhile, it has been shown that destabilising forces to the bridge can arise from simple mechanics of walking, whereby pedestrians adjust the lateral position of their stepping foot in response to perturbations from the oscillating bridge, even in the absence of synchronisation [13]. This analysis was accomplished by employing an inverted pendulum model (IPM) to idealise the dynamics of pedestrian motion in the frontal plane, i.e. the vertical plane perpendicular to the direction of progression. The IPM consists of a mass supported by a rigid massless leg. The transition between steps is instantaneous and the position of foot placement for the stepping leg, u, is assumed to follow the law proposed by Hof *et al.* [14]:

$$u = x_{\mathrm{CoP}} - x_{\mathrm{CoM}} = \frac{\dot{x}_{\mathrm{CoM}}}{\Omega_p} \pm b_{\min} \tag{1}$$

where x_{CoP} and x_{CoM} is the lateral distance, measured from the same arbitrary reference point on the surface, to the centre of pressure (CoP) and the vertical projection of the centre of mass (CoM), respectively, a dot over the symbol represents differentiation with respect to time, $\Omega_p = \sqrt{g/l_{\mathrm{eq}}}$ is the angular pendulum frequency in which g is the gravitational acceleration and l_{eq} is the equivalent pendulum length, the ± sign accounts for the bipedal nature of human gait (i.e. changing point of support from step to step) and $b_{\min}$ is a constant termed the margin of stability. The IPM based on Eq. (1) has been shown to be capable of explaining the forces generated by a pedestrian on a laterally oscillating bridge [13, 15], with good qualitative agreement with experiments involving unimodal [16, 17] and multi-modal [18] bridge motion. However, little direct experimental evidence has been presented to date to specifically support the adopted foot placement control law [19, 20]. Moreover, it is currently unclear whether $\dot{x}_{\mathrm{CoM}}$ in Eq. (1) should be taken relative to the moving bridge, $\dot{x}^{\mathrm{rel}}_{\mathrm{CoM}}$, or some stationary point outside of the bridge relative to which the bridge is moving, $\dot{x}^{\mathrm{abs}}_{\mathrm{CoM}}$ [9].

Considering the gaps in the current state of knowledge, the aim of this study is to verify whether a foot placement control law of the type proposed by Hof *et al.* [14] applies for walking on an oscillating bridge. To this end, tests were conducted on a self-paced treadmill capable of lateral oscillation. Gait kinematics of a test subjects were recorded using an optical motion capture system to obtain an instantaneous position of the body centre of mass (CoM) and feet. Motivated by the form of the Hof *et al.*'s [14] foot placement control law in Eq. (1), a simple linear regression model was fitted to the data relating the step width and lateral velocity of the CoM at the instant of foot placement. To tests the robustness of the pedestrian stepping behaviour, three types of visual environment were provided to the test subject.

2 METHODOLOGY

A 21 year-old healthy female with body mass of 51kg and height 1.64m was recruited for the tests. The test subject wore gym-type clothing and flat-sole shoes. Prior to participating in the tests, the subject familiarised herself with the information letter for participants, completed a physical readiness questionnaire and signed an informed consent form. The tests were approved by the University of Bristol Ethics of Research Committee.

Six tests were conducted in total. The subject walked on the treadmill when stationary (i.e. non-oscillating), denoted NLTM (no lateral treadmill motion), and on the treadmill with it oscillating in the lateral direction with sinusoidal motion of amplitude 10mm and frequency 0.9Hz, denoted LTM (lateral treadmill motion). The test subject was subjected to three visual conditions, including that of the laboratory environment, denoted RL (real life), and two virtual reality environments delivered via a head mounted display, denoted VR1 and VR2. The details of the instrumentation used during the tests and data analysis are given in this section.

2.1 Treadmill

A custom-built treadmill mounted on a shaking table capable of providing lateral motion was used during the tests. A generous walking area of 2m by 1.5m was provided to facilitate the operation of a treadmill speed feedback control mechanism, enabling automatic adjustment of the treadmill speed to that of the user, and to facilitate adaptive pedestrian stepping behaviour.

2.2 Virtual reality

An immersive and interactive virtual reality (VR) environment was delivered via an nVisor SX111 head mounted display, offering a 76 degrees horizontal and 64 degrees vertical field of view and 1280 by 1024 resolution per eye. The VR environment was developed in NetBeans 7.01 IDE using the Jogl platform providing 3D graphics based on the OpenGL® API for applications written in Java™. It consisted of three main elements, (i) the bridge, (ii) the substratum, i.e. stationary objects rendered below the bridge, providing height reference, and (iii) the superstratum, i.e. objects rendered around the bridge, above the substratum. Two VR scenes were built, differing in terms of the number and type of visual reference cues available to the user. In both scenes, the virtual bridge was translating together with the treadmill belt thus providing optical flow as for normal overground walking, i.e. motion of the objects perceived due to self-motion – here realized by walking on a treadmill. In both scenes, the lateral movement of the virtual bridge was enabled by coupling it with the lateral treadmill motion. The first scene, hereafter referred to as VR1, presented in Figure 1 (a), contained visual information enabling motion parallax, i.e. the perception of relative motion of objects against the rest of the visual field caused by self-motion of the observer. This was achieved by inclusion of stationary objects set in the scene, i.e. the substratum (water beneath the bridge) and red posts positioned alongside the bridge, and also bridge railings moving with the bridge and the deck being rendered in a pattern resembling wood. The second scene, hereafter referred to as VR2, presented in Figure 1 (b), was built by stripping VR1 of most of the information facilitating the perception of self-motion to the point that the only object left in the scene was the deck, rendered in a low contrast pattern, surrounded by dense fog.

(a) (b)

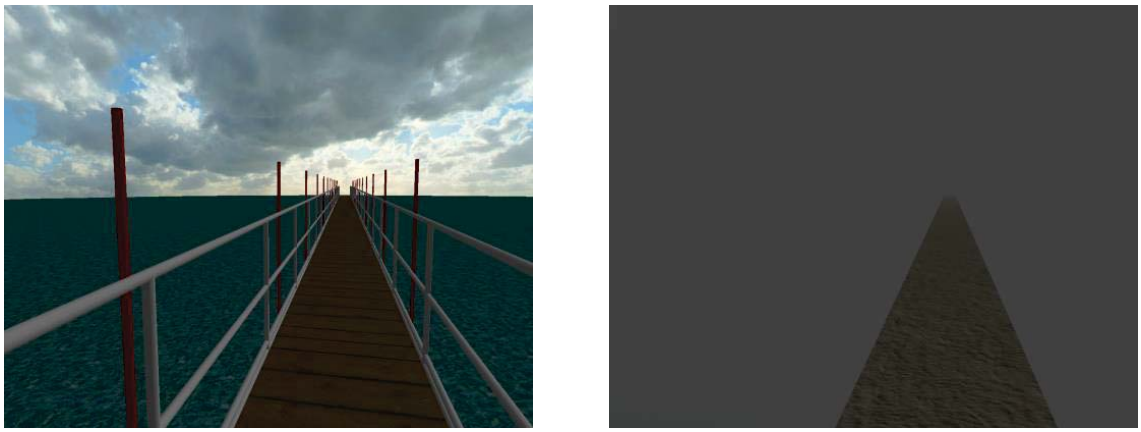

Figure 1: Virtual reality environments projected onto the left-eye screen of head mounted display, (a) VR1, (b) VR2.

2.3 Data capture and analysis

An optical motion capture system consisting of six Qualisys cameras was used to record, at the sampling frequency of 128Hz, the motion of fourteen retroreflective markers attached to the body landmarks of the test subject. This enabled the position of the CoM to be determined using the linked-segments modelling procedure [21]. One marker was attached to the lateral malleolus (i.e. ankle) of each foot to determine the pseudo step width, defined here as the lateral distance between the projections of the position of the CoM and the ankle marker onto the surface at the instant of foot placement. The term *pseudo step width* is used herein, since in the original formulation of the IPM [14] the step width is defined using the centre of pressure (CoP) and the transfer from one leg to the other is instantaneous. However, the CoP was not measured during the tests and the double-support phase of gait is not negligibly short. Therefore, it was assumed herein that (i) the ankle marker, due to anatomical constraints, gives a representative point of reference for the step width in the spatial reference frame, and that (ii) the instant of foot placement gives a representative point of reference for the step width in the temporal reference frame. That instant was determined from the vertical velocity of the ankle markers according to the procedure proposed in [22].

The following function was fitted to the pseudo step width data, compatible with the IPM and lateral foot placement control law in Eq. (1):

$$u^* = x_{\mathrm{ANKLE}} - x_{\mathrm{CoM}} = \rho_1 \dot{x}_{\mathrm{CoM}} \pm \rho_2 \tag{2}$$

where u^* is the pseudo step width, x_{ANKLE} is the lateral position of the ankle marker attached to the stepping foot, $\dot{x}_{\mathrm{CoM}}$ is the lateral velocity of CoM at the instant of heel strike, and ρ_1 and ρ_2 are the coefficients of the fit. Note ρ_1 and ρ_2 in Eq. (2) correspond to the inverse of the IPM angular frequency, Ω_p, and the margin of stability, b_{min}, respectively, from Eq. (1), and have physical units of time and displacement, respectively. The outstanding problem is the definition of the lateral velocity of the CoM, $\dot{x}_{\mathrm{CoM}}$, for LTM tests. Note this ambiguity does not exist for NLTM tests, since $\dot{x}^{\mathrm{rel}}_{\mathrm{CoM}}$ is then equal to $\dot{x}^{\mathrm{abs}}_{\mathrm{CoM}}$. This issue will be taken into consideration in the discussion of the results in Section 3.

The displacement signal of the CoM was differentiated to obtain lateral the CoM velocities $\dot{x}_{\mathrm{CoM}}^{\mathrm{abs}}$ and $\dot{x}_{\mathrm{CoM}}^{\mathrm{rel}}$. A fourth-order two-way Butterworth low-pass filter with cut off frequency of 6Hz was applied to all the data.

3 RESULTS AND DISCUSSION

The empirical data relating pseudo step width, u^*, with the absolute lateral velocity of the CoM, $\dot{x}_{\mathrm{CoM}}^{\mathrm{abs}}$, for all the conducted tests are shown in Figure 2.

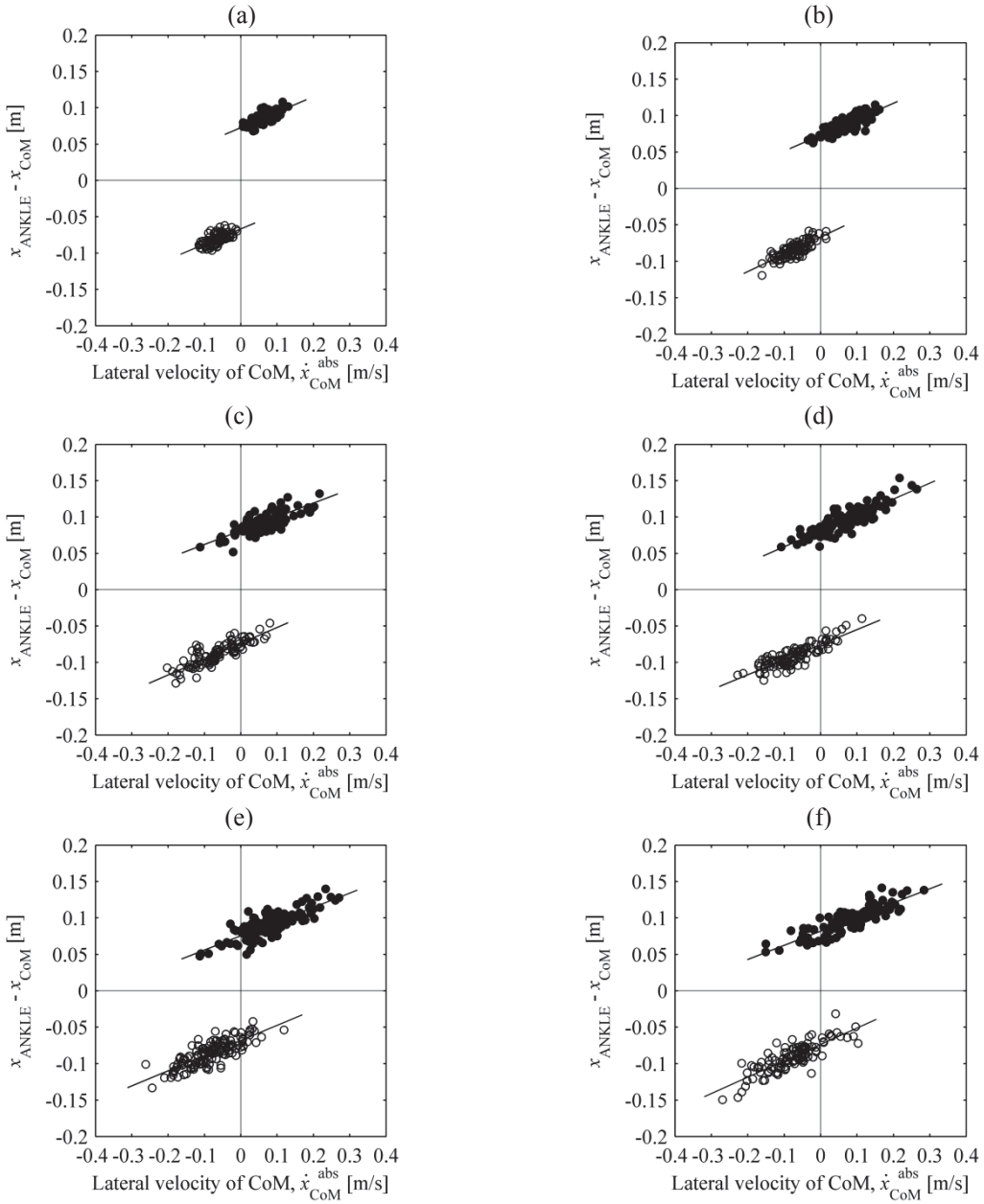

Figure 2: Relationship between the pseudo step width and the absolute lateral velocity of the CoM at the instant of heel strike for (a) RL NLTM, (b) RL LTM, (c) VR1 NLTM, (d) VR1 LTM, (e) VR2 NLTM and (f) VR2 LTM. The data for the right and left leg are denoted by ● and ○ in the top and bottom parts of the plots, respectively.

The least spread of data can be seen in Figure 2 (a) & (b) for walking in the visual environment of the laboratory (RL), without and with lateral treadmill oscillation (NLTM & LTM), respectively. The greatest spread of data can be seen in Figure 2 (e) & (f) for walking in VR2 in NLTM & LTM, respectively. Despite the differences in data variability, the gradients and intercepts (with the vertical axes) of the best linear fits, found separately for the right and left leg data, seem to be compatible.

During all the tests, except for NLTM RL, some steps were taken in which the CoM was travelling towards the stance leg in the frontal plane at the instant of touchdown of the stepping leg. These steps are shown as points in Figure 2 for which $\dot{x}_{\mathrm{CoM}}^{\mathrm{abs}}$ is negative for the right leg or positive for the left leg. No excursion of the foot to the contralateral (i.e. abnormal) side of the CoM can be directly observed from the data in Figure 2. This would be evident if u^* was negative for the right leg or positive for the left leg. However, since the ankle markers were not aligned with the CoP, it is possible that this situation occurred for some steps, when the magnitude of u^* (on the vertical axes) was below 0.05m.

The results of fitting a linear function (i.e. simple linear regression) to the experimental data according to Eq. (2), based on the absolute and relative lateral velocity of the CoM, $\dot{x}_{\mathrm{CoM}}$, are given in Table 1. Note ρ_2 takes positive and negative values depending on the stepping leg. Goodness of fit statistics are quantified in terms of the root mean square (RMS) error, denoted as standard error in Table 1, and degrees-of-freedom adjusted R-square, denoted as adjusted R-square in Table 1.

Experimental condition	$\dot{x}_{\mathrm{CoM}}$ [m/s]	Figure 2 reference	Leg	ρ_1 [s]	ρ_2 [m]	Standard error [m]	Adjusted R-square
RL NLTM	abs	(a)	right	0.2071	0.0787	0.0052	0.5381
RL NLTM	abs	(a)	left	0.2003	–0.0748	0.0055	0.4341
RL LTM	abs	(b)	right	0.1985	0.0796	0.0064	0.6654
RL LTM	abs	(b)	left	0.2229	–0.0742	0.0059	0.6768
RL LTM	rel	N/A	right	0.1065	0.0858	0.0096	0.2386
RL LTM	rel	N/A	left	0.0964	–0.0828	0.0091	0.2467
VR1 NLTM	abs	(c)	right	0.1874	0.0824	0.0086	0.6532
VR1 NLTM	abs	(c)	left	0.2217	–0.0746	0.0080	0.7448
VR1 LTM	abs	(d)	right	0.2144	0.0819	0.0090	0.7444
VR1 LTM	abs	(d)	left	0.2044	–0.0762	0.0081	0.7339
VR1 LTM	rel	N/A	right	0.1659	0.0854	0.0139	0.3903
VR1 LTM	rel	N/A	left	0.1252	–0.0824	0.0125	0.3649
VR2 NLTM	abs	(e)	right	0.1895	0.0811	0.0094	0.6525
VR2 NLTM	abs	(e)	left	0.2058	–0.0728	0.0087	0.7044
VR2 LTM	abs	(f)	right	0.1893	0.0814	0.0099	0.7217
VR2 LTM	abs	(f)	left	0.2215	–0.0729	0.0111	0.6931
VR2 LTM	rel	N/A	right	0.1564	0.0771	0.0138	0.4955
VR2 LTM	rel	N/A	left	0.1646	–0.0692	0.0153	0.4355

Table 1: Results of fitting a linear function to experimental data.

A simple linear regression based on the absolute velocity of the CoM, $\dot{x}_{\mathrm{CoM}}^{\mathrm{abs}}$, provides overall better fit to the data than using the relative velocity of the CoM, $\dot{x}_{\mathrm{CoM}}^{\mathrm{rel}}$. The mean adjusted R-square obtained using $\dot{x}_{\mathrm{CoM}}^{\mathrm{abs}}$ is 0.71 for LTM. In comparison, the mean adjusted R-square

obtained using $\dot{x}_{\mathrm{CoM}}^{\mathrm{rel}}$ for LTM is only 0.36. The values of adjusted R-square obtained using $\dot{x}_{\mathrm{CoM}}^{\mathrm{abs}}$ show that a linear foot placement control law can explain 71% of pseudo step width variance for LTM. In the world of biology, and considering the data come from testing a human, this indicates a strong functional relationship between the variables. Therefore, all further discussion is based on the results obtained using $\dot{x}_{\mathrm{CoM}}^{\mathrm{abs}}$ only.

The mean gradients of the fit, ρ_1, for the right and left legs are 0.2s and 0.21s, respectively. The mean intercepts of the fit, ρ_2, for the right and left legs are 0.08m and –0.07m, respectively. The difference in sign reflects the bipedal nature of human gait. The values are consistent throughout all the tests, except RL NLTM, indicating a simple linear foot placement control law is robust against surface oscillation and modifications to the visual field.

The higher variability of data for VR tests visible in Figure 2 is reflected in the higher values of the standard error in Table 1, quantifying the dispersion of the pseudo step width around the fit. This is the case for NLTM and LTM tests. The highest variability in data is observed for VR2. The test subject was then provided the least amount of visual information which, it appears, led to greater variation of the gait.

The values of ρ_1 and ρ_2 differ from the values previously assumed in the use of the IPM [13-15], as defined in Eq. (1). The gradient of the linear foot placement control law is in this case the inverse of the pendulum angular frequency, which for the test subject employed for the test would be 0.34s. This is greater than all of the values from the experiments in Table 1. The intercept is the margin of stability, which for unperturbed walking was assumed to take a value of 0.016m [13-15]. These discrepancies were expected considering the definition of the pseudo step width, stated in Section 2, in particular the difference in the spatial and temporal reference frames used in the formulation of the IPM compared with those used in the experiments.

Overall, it is concluded that the foot placement control law of the type proposed by Hof *et al.* [14], based on lateral velocity of the CoM at heel strike, applies for walking on laterally oscillating bridges. This gives supporting evidence for the assumptions made in the IPM [13,15,19]. Further work will attempt to reconcile the discrepancies between IPM predictions and the experimental data presented in this study.

4 CONCLUSIONS

- A foot placement control law of the form proposed by Hof *et al.* [14] applies for walking on laterally oscillating structures.
- The step width depends on the absolute rather than relative lateral velocity of the centre of mass at the instant of foot placement onto the walking surface.
- The foot placement control law is robust against modifications to the visual environment as well as motion of the walking surface.
- The presented data can help in the calibration of the inverted pendulum pedestrian model for walking on laterally oscillating structures.

REFERENCES

[1] Y. Fujino, B.M. Pacheco, S. Nakamura, P. Warnitchai, Synchronization of human walking observed during lateral vibration of a congested pedestrian bridge, *Earthquake Engineering & Structural Dynamics* 22, 741-758, 1993.

[2] P. Dallard, A.J. Fitzpatrick, A. Flint, S. Le Bourva, A. Low, R.M. Ridsdill Smith, M. Willford,, The London Millennium Footbridge, *The Structural Engineer* 79, 17-33, 2001.

[3] S. Nakamura, Field measurements of lateral vibration on a pedestrian suspension bridge, *The Structural Engineer* 81(22), 22-26, 2003.

[4] J.M.W. Brownjohn, P. Fok, M. Roche, P. Omenzetter, Long span steel pedestrian bridge at Singapore Changi Airport - Part 2: Crowd loading tests and vibration mitigation measures, *The Structural Engineer* 82(16), 28-34, 2004.

[5] F. Danbon, G. Grillaud, Dynamic behaviour of a steel footbridge. Characterisation and modelling of the dynamic loading induced by a moving crowd on the Solferino Footbridge in Paris, *Proceedings of Footbridge 2005 – 2nd International Conference*, Venice, Italy, 2005.

[6] J.H.G. Macdonald, Pedestrian-induced vibrations of the Clifton Suspension Bridge, UK, *Proceedings of the Institution of Civil Engineers - Bridge Engineering* 161, 69-77, 2008.

[7] E. Caetano, Á. Cunha, F. Magalhaes, C. Moutinho, Studies for controlling human-induced vibration of the Pedro e Inês footbridge, Portugal. Part 1: Assessment of dynamic behaviour, *Engineering Structures* 32, 1069-1081, 2010.

[8] R.E. White, N.A. Alexander, J.H.G. Macdonald, M. Bocian, Characterisation of crowd lateral dynamic forcing from full-scale measurements on the Clifton Suspension Bridge, *Structures* 24, 415-425, 2020.

[9] E.T. Ingólfsson, C.T. Georgakis, F. Ricciardelli, J. Jönsson, Experimental identification of pedestrian-induced lateral forces on footbridges, *Journal of Sound and Vibration* 330, 1265-1284, 2011.

[10] M. Bocian, J.F. Burn, J.H.G. Macdonald, J.M.W. Brownjohn, From phase drift to synchronisation - pedestrian stepping behaviour on laterally oscillating structures and consequences for dynamic stability, *Journal of Sound and Vibration* 392, 382-399, 2017.

[11] M. Bocian, J.M.W. Brownjohn, V. Racic, D. Hester, A. Quattrone, L Gilbert, R. Beasley, Time-dependent spectral analysis of interactions within walking pedestrians and vertical structural motion using wavelets, *Mechanical Systems and Signal Processing* 105, 502-523, 2018.

[12] A.A. Soczawa-Stronczyk, M. Bocian, H. Wdowicka, J. Malin, Topological assessment of gait synchronisation in overground walking groups, *Human Movement Science* 66, 541-553, 2019.

[13] J.H.G. Macdonald, Lateral excitation of bridges by balancing pedestrians, *Proceedings of the Royal Society A - Mathematical, Physical and Engineering Sciences* 465, 1055-1073, 2009.

[14] A.L. Hof, R.M. van Bockel, T. Schoppen, K. Postema, Control of lateral balance in walking - Experimental findings in normal subjects and above-knee amputees, *Gait & Posture* 25, 250-258, 2007.

[15] M. Bocian, J.H.G. Macdonald, J.F. Burn, Biomechanically inspired modelling of pedestrian-induced forces on laterally oscillating structures, *Journal of Sound and Vibration* 331, 3914-3929, 2012.

[16] S.P. Carroll, J.S. Owen, M.F.M. Hussein, Reproduction of lateral ground reaction forces from visual marker data and analysis of balance response while walking on a laterally oscillating deck, *Engineering Structures* 49, 1034-1047, 2013.

[17] M. Bocian, J.H.G. Macdonald, J.F. Burn, D. Redmill, Experimental identification of the behaviour of and lateral forces from freely-walking pedestrians on laterally oscillating structures in a virtual reality environment, *Engineering Structures* 105, 62-76, 2015.

[18] M. Bocian, J.H.G. Macdonald, J.F. Burn, Determination of pedestrian loads in the presence of multi-modal bridge vibrations, *Proceedings of Eurodyn 2014 - 9th International conference on Structural Dynamics*, Porto, Portugal, 2014.

[19] S.P. Carroll, J.S. Owen, M.F.M. Hussein, Experimental identification of the lateral human-structure interaction mechanism and assessment of the inverted-pendulum biomechanical model, *Journal of Sound and Vibration* 333, 5865-5884, 2014.

[20] D. Claff, M.S. Williams, A. Blakeborough, The kinematics and kinetics of pedestrians on a laterally swaying footbridge, *Journal of Sound and Vibration* 407, 286-308, 2017.

[21] D.A. Winter, Biomechanics and motor control of human movement, 4th ed., John Wiley & Sons, Hoboken, USA, 2009.

[22] C.M. O'Connor, S.K. Thorpe, M.J. O'Malley, C.L. Vaughan, Automatic detection of gait events using kinematic data, *Gait & Posture* 25, 469-474, 2007.

EURODYN 2020
XI International Conference on Structural Dynamics
M. Papadrakakis, M. Fragiadakis, C. Papadimitriou (eds.)
Athens, Greece, 23–26 November 2020

MOTION-BASED DESIGN OF ACTIVE TUNED MASS DAMPERS TO CONTROL PEDESTRIAN-INDUCED VIBRATIONS IN FOOTBRIDGES UNDER UNCERTAINTY CONDITIONS

Javier Fernando Jiménez-Alonso[1], José Manuel Soria[2], Carlos Martín de la Concha Renedo[3] and Francisco Guillen González[4]

[1-3] Department of Continuum Mechanics and Structures. Universidad Politécnica de Madrid
Profesor Aranguren, 3, 28040 Madrid (Spain)
e-mail: {jf.jimenez, jm.soria, carlos.martindelaconcha@upm.es

[4] Department of Differential Equations and Numerical Analysis. Universidad de Sevilla
Calle Tarifa, s/n, 41002 Seville (Spain)
guillen@us.es

Keywords: Motion-based design, Human-induced vibrations, Structural control, Active tuned mass dampers, Footbridges, Uncertainty conditions

Abstract. *Two key aspect must be considered for the design of modern footbridges: (i) their sensitivity to human-induced vibrations; and (ii) the influence of the variation of the operational and environmental conditions on their modal properties. One possible option, to guarantee an adequate behavior of these structures under both conditioning factors, is the installation of a control system. Among the different systems, active damping devices have shown a great effectiveness when they are used to control the dynamic response of civil engineering structures under uncertainty conditions. Different design algorithms have been proposed to guarantee that structures, controlled by these damping devices, meet the design requirements without compromising the budget. Among these proposals, the motion-based design method has shown a high performance when it has been implemented to design passive damping devices for footbridges under uncertainty conditions. Herein, this design method has been adapted and further implemented for the robust optimum design of active tuned mass dampers when they are employed to control the human-induced vibrations in slender footbridges. According to this method, the design problem can be transformed into two coupled sub-problems: (i) a multi-objective optimization sub-problem; and (ii) a reliability analysis sub-problem. Thus, the main objective is to find the parameters of the active damping device which guarantee an adequate comfort level without compromising its cost. The compliance of this vibration serviceability limit state is computed via a reliability index (related to the probability of failure), which takes into account the effect of the variation of the operational and environmental conditions on the modal properties of the structure.*

1 INTRODUCTION

Modern footbridges have experienced an increase in their slenderness due to both the improvement of the strength of the construction materials and the aesthetic requirements of the current societies [1]. Accordingly, this higher slenderness has enhanced the sensitivity of these structures to two phenomena: (i) the human-structure interaction [2]; and (ii) the variability of their modal properties due to the modification of the operational and environmental conditions [3].

In order to overcome these limitations, external damping devices have been widely installed on these structures to guarantee their robust structural behavior during their overall life cycle [4]. Among these damping devices, active control systems have shown a high effectiveness when they have been used to control the dynamic response of civil engineering structures under stochastic conditions [5]. Different algorithms and control laws have been proposed to perform successfully the design process of these damping devices [6]. Among the different approaches, the motion-based design method [7] under a stochastic approach is presented and further implemented herein to design active tuned mass dampers (ATMD) when they are used to control the human-induced vibrations in slender footbridges under uncertainty conditions. Thus, the main contribution of this study is to adapt the abovementioned method, which has been previously implemented for the design of passive tuned mass dampers [8], for the design of ATMDs.

According to this method, the design problem may be transformed into two coupled sub-problems: (i) a multiple-objective optimization sub-problem [9]; and (ii) a reliability analysis sub-problem [10]. The multiple-objective function of the first sub-problem is defined in terms of two different elements: (i) the parameters of the ATMD, which are needed to be determined; and (ii) the design requirements of the structure which are needed to be met [2]. As the main objective of this design process is to control the human-induced vibrations in footbridges, the design requirements may be defined in terms of the comfort level of the structure. Thus, these design requirements are met if the maximum acceleration of the structure is lower than an allowable acceleration established by the designer [2]. Additionally, the aforementioned design requirements have been re-formulated based on a probabilistic approach due to the sensitivity of the modal properties of the structure to the variation of the operational and environmental conditions [11]. According to this approach, the design requirements are met if a reliability index, β, which reflects the probability of compliance of the mentioned vibration serviceability limit state (VSLS), is greater than an allowable reliability index, β_{lim} [10]. Sampling techniques are usually considered to compute this reliability index [10]. Herein a conventional Monte Carlo simulation has been considered [10]. Finally, the performance of the proposed algorithm has been validated via the analysis of a numerical case-study [2]. Concretely, the VSLS of a steel footbridge under uncertainty conditions has been met via the installation of an ATMD designed according to the proposed algorithm.

The paper is organized as follows. In section 2, the mathematical model of the ATMD-footbridge interaction system is formulated and its dynamic response under pedestrian action is computed numerically in time domain. Subsequently, in section 3, the motion-based design method under a stochastic approach is described in detail. Later, in section 4, a numerical case-study is presented to assess the performance of the proposed method when it is implemented for the design of an ATMD used to control the dynamic response of a steel footbridge under pedestrian action. Finally, some concluding remarks are included in section 5 to finish the paper.

2 ACTIVE TUNED MASS DAMPER-FOOTBRIDGE INTERACTION MODEL UNDER PEDESTRIAN LOAD

In order to design an active damping device, according to the mentioned proposal, the dynamic response of an ATMD-footbridge interaction system under pedestrian action must be computed numerically. Thus, four steps must be given: (i) the formulation of the ATMD-footbridge interaction model; (ii) the definition of the pedestrian load; (iii) the selection of the control law which defines the driving force; and (iv) the numerical integration of the equations of motion which governs the ATMD-footbridge interaction model.

For the formulation of the ATMD-footbridge interaction model, the following assumptions have been considered herein: (i) the dynamic response of the structure may be approached (modal coordinates) by a single vibration mode [6], since it is assumed that only a vibration mode is prone to suffer from human-induced vibrations; (ii) the ATMD is modelled via a single degree of freedom system (physical coordinates) [5]; (iii) the pedestrian load is simulated by an equivalent harmonic load [2]; and (iv) the ATMD is located at the point with the maximum modal displacement. Figure 1 shows a scheme of the ATMD-footbridge interaction model.

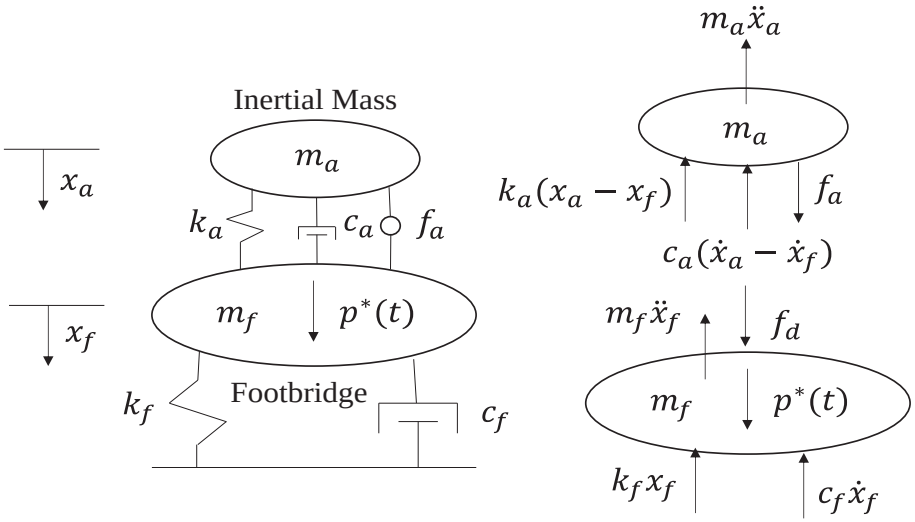

Figure 1: The ATMD-footbridge interaction model.

Thus, the equations of motion of the ATMD-footbridge interaction model can be obtained via the implementation of the second Newton's law to the two masses (ATMD and equivalent modal mass). These equations may be expressed as follows:

$$m_f\ddot{x}_f(t) + c_f\dot{x}_f(t) + k_f x_f(t) = p^*(t) + f_d(t) \quad (1)$$

$$m_a\ddot{x}_a(t) + c_a\left(\dot{x}_a(t) - \dot{x}_f(t)\right) + k_a\left(x_a(t) - x_f(t)\right) = f_a(t) \quad (2)$$

$$f_d(t) = c_a\left(\dot{x}_a(t) - \dot{x}_f(t)\right) + k_a + k_a\left(x_a(t) - x_f(t)\right) - f_a(t) = -m_a\ddot{x}_a(t) \quad (3)$$

where m_f [kg], c_f [sN/m] and k_f [N/m] are respectively the mass, damping and stiffness of the considered vibration mode of the footbridge; $p^*(t) = \phi^T p(t)$ [N] is the projection of the pedestrian load on the considered vibration (being $p(t)$ the pedestrian load [N], ϕ the considered vibration mode and ^{T} the transpose function); $\ddot{x}_f(t)$ [m/s^2], $\dot{x}_f(t)$ [m/s] and $x_f(t)$ [m] are respectively the acceleration, velocity and displacement of the footbridge; m_a [kg], c_a [sN/m] and k_a [N/m] are respectively the mass, damping and stiffness of the ATMD; $\ddot{x}_a(t)$

[m/s^2], $\dot{x}_a(t)$ [m/s] and $x_a(t)$ [m] are respectively the acceleration, velocity and displacement of the ATMD; $f_a(t)$ [N] is the driving force generated by the actuator of the ATMD; and $f_d(t)$ [N] is the control force generated by the ATMD.

These equations can be re-organized in matrix form as follows:

$$\begin{bmatrix} m_f & 0 \\ 0 & m_a \end{bmatrix} \begin{Bmatrix} \ddot{x}_f(t) \\ \ddot{x}_a(t) \end{Bmatrix} + \begin{bmatrix} c_f + c_a & -c_a \\ -c_a & c_a \end{bmatrix} \begin{Bmatrix} \dot{x}_f(t) \\ \dot{x}_a(t) \end{Bmatrix} + \begin{bmatrix} k_f + k_a & -k_a \\ -k_a & k_a \end{bmatrix} \begin{Bmatrix} x_f(t) \\ x_a(t) \end{Bmatrix} = \begin{Bmatrix} 1 \\ 0 \end{Bmatrix} p^*(t) + \begin{Bmatrix} -1 \\ 1 \end{Bmatrix} f_a(t) \quad (4)$$

$$[M]\{\ddot{x}(t)\} + [C]\{\dot{x}(t)\} + [K]\{x(t)\} = \{B_0\}p^*(t) + \{B_c\}f_a(t) \quad (5)$$

where $[M] = \begin{bmatrix} m_f & 0 \\ 0 & m_a \end{bmatrix}$ is the mass matrix; $[C] = \begin{bmatrix} c_f + c_a & -c_a \\ -c_a & c_a \end{bmatrix}$ is the damping matrix; $[K] = \begin{bmatrix} k_f + k_a & -k_a \\ -k_a & k_a \end{bmatrix}$ is the stiffness matrix; $\{B_0\}$ is the input vector associated with the pedestrian load; $\{B_c\}$ is the input vector associated with the driving force; $\{\ddot{x}(t)\}$ is the acceleration vector; $\{\dot{x}(t)\}$ is the velocity vector and $\{x(t)\}$ is the displacement vector.

In order to integrate this equation system and make easier the determination of the driving force, $f_a(t)$, the abovementioned equation system must be transformed into a state space formulation [6]. According to this formulation, the dynamic behavior of a linear invariant system may be expressed by the following differential equation system with initial conditions ($\{z(0)\} = z_0$):

$$\{\dot{z}(t)\} = [A]\{z(t)\} + [B]\{p^*(t)\} + [B]\{f_a(t)\} \quad (6)$$

$$\{y(t)\} = [E]\{z(t)\} + [D]\{f_a(t)\} \quad (7)$$

where $\{z(t)\}$ is the state vector; $\{y(t)\}$ is the output vector; $[A]$ is the system matrix; $[B]$ is the input matrix; $[E]$ is the output matrix; and $[D]$ is the feedthrough matrix [6]. It is possible via matrix transformations to convert the abovementioned equation system into its state space formulation [6]. The state space matrices can be defined as:

$$[A] = \begin{bmatrix} 0 & I \\ -[M]^{-1}[K] & -[M]^{-1}[C] \end{bmatrix} \quad (8)$$

$$[B] = \begin{bmatrix} 0 \\ -[M]^{-1}\{B_i\} \end{bmatrix} \text{ where } \{B_i\} = \begin{cases} \{B_0\} & \text{for } p^*(t) \\ \{B_c\} & \text{for } f_a(t) \end{cases} \quad (9)$$

$$[E] = -[E_a][[M]^{-1}[K] \quad [M]^{-1}[C]] \quad (10)$$

$$[D] = [E_a][M]^{-1}[B] \quad (11)$$

where the state vector $\{z(t)\} = \{x_f(t) \quad x_a(t) \quad \dot{x}_f(t) \quad \dot{x}_a(t)\}$ is defined in terms of the displacements and velocities of both the footbridge and the ATMD; and the output vector, $\{y(t)\}$, is defined in terms of the accelerations experienced by the footbridge (being $[E_a]$ the acceleration matrix which indicates the elements in which the acceleration is computed).

In order to obtain the response of this state space equation system both the pedestrian force, $p(t)$, and the driving force, $f_a(t)$, which simulates the behavior of the actuator of the ATMD, must be defined.

The pedestrian force, $p(t)$, has been simulated based on the recommendations of the French guidelines [2]. Only the vertical contribution of the walking pedestrian action has been considered herein. According to these guidelines, the walking pedestrian action, $p(t)$, can be determined via an equivalent harmonic force defined as follows:

$$p(t) = 280 \cdot \cos(2\pi \cdot f_f \cdot t) \cdot n_{eq} \cdot \psi \tag{12}$$

where f_f [Hz] is the natural frequency of the considered vibration mode of the structure; n_{eq} [-] is the equivalent number of pedestrians; and ψ is a reduction factor which takes into account the probability that the natural frequency is within the range which characterizes the human-structure interaction in vertical direction ($1.25 \leq f_f \leq 2.3$ Hz) [2].

The driving force, $f_a(t)$, is determined via the implementation of a feedback controller to the above mentioned system in the state space [6]. Figure 2 shows the general layout of the feedback controller considered.

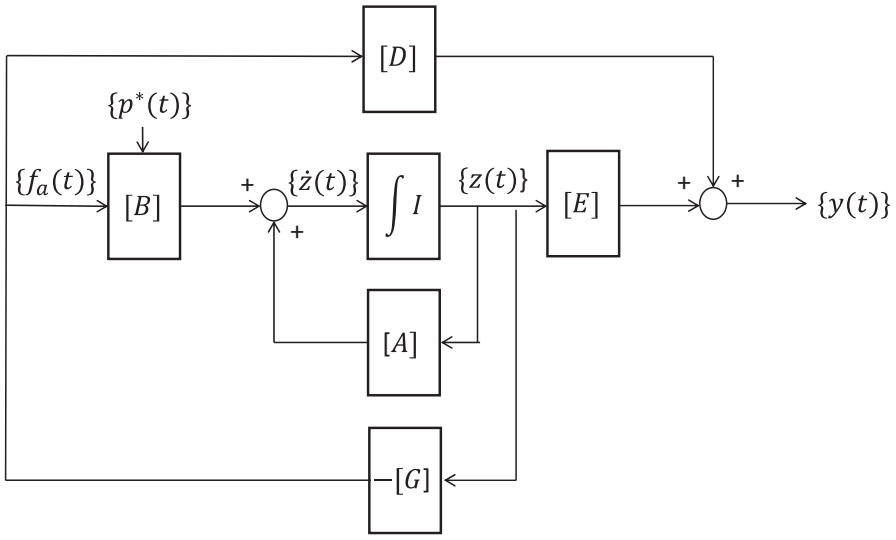

Figure 2: Design of a feedback controller in a state space formulation [6].

The implementation of this feedback controller allows modifying the system equation as follows:

$$\{\dot{z}(t)\} = [A]\{z(t)\} + [B_0]\{p^*(t)\} + [B_c]\{f_a(t)\}] \tag{13}$$

where $[B_0]$ and $[B_c]$ are obtained from equation (9) considering as pattern load vectors $\{B_0\}$ and $\{B_c\}$respectively.

Thus, according to the feedback controller (Figure 2), the driving force, $f_a(t)$, may be determined in terms of a gain matrix, $-[G]$, and the state vector, $\{z(t)\}$. Thus, the system equation may be expressed as:

$$\{\dot{z}(t)\} = [A]\{z(t)\} + [B_0]\{p^*(t)\} - [B_c][G]\{z(t)\} \tag{14}$$

$$\{\dot{z}(t)\} = ([A] - [B_c][G])\{z(t)\} + [B_0]\{p^*(t)\} \tag{15}$$

There are several algorithms [6] to determine the value of the gain matrix, $-[G]$. Among these algorithms, the linear quadratic regular (LQR) method [6] has been considered herein due to its extensive use for practical engineering applications [5]. According to this method, the

value of the gain matrix, $-[G]$, is obtained via the minimization of the following performance-index function, J:

$$J = \int_0^\infty \left[\{z(t)\}^T[Q]\{z(t)\} + \left\{[G]\{z(t)\}\right\}^T[R]\left\{[G]\{z(t)\}\right\}\right]dt \tag{16}$$

where $[Q]$ and $[R]$are two weighting matrices which may be computed in terms of the mass, $[M]$, and stiffness, $[K]$, matrices of the interaction model [6]. According to the recommendations of several authors [6], the weighting matrices may be determined as follows:

$$[Q] = \alpha_d \begin{bmatrix} [K] & 0 \\ 0 & [M] \end{bmatrix} \tag{17}$$

$$[R] = \beta_d [I] \tag{18}$$

where α_d [-] and β_d [-] are the weighting factors; and $[I]$ is the identity matrix. In this manner, once the value of these factors has been fixed, the value of the different element of the gain matrix, $-[G]$, which minimizes the value of the performance-index function, J, is obtained.

Subsequently, the response of the ATMD-footbridge interaction model has been obtained via the integration of the abovementioned state space system using a Runge-Kutta method, as it is implemented in the Matlab software [12].

Therefore, an adequate value of the driving force, $f_a(t)$, is obtained via the adjustment of the value of the weighting factors, α_d and β_d. For this purpose, the following iterative process must be addressed: (i) to develop a linear model of the ATMD-footbridge interaction model in the state space domain (where the value of the mass and stiffness of the ATMD are fixed); (ii) to adjust the value of the weighting matrices, $[Q]$ and $[R]$ in terms of an original value of the weighting factors, α_d and β_d; (iii) to determine an optimum value of the driving force, $f_a(t)$, via the minimization of the performance-index function, J; (iv) to simulate numerically the response of the linear system; and (v) to modify the values of the weighting factors, α_d and β_d, and repeat the steps (ii) to (iv) until the dynamic response of the footbridge meets the design requirements established by the designer [2].

3 MOTION-BASED DESIGN UNDER UNCERTAINTY CONDITIONS

The aforementioned control algorithm has been hybridized with the motion-based design method under uncertain conditions [8] to improve the performance of the design process of active damping devices. The performance-based design method [13] transforms the design problem into two coupled sub-problems: (i) a multi-objective optimization sub-problem; and (ii) a reliability analysis sub-problem. Thus, the main objective of this design problem is to determine the parameters of the ATMD that, minimizing its cost, ensures the compliance of the design requirements [2]. As the design requirements, which need to be accomplished, are defined in terms of the accelerations of the structure, $\ddot{x}_f(t)$, this design process may be understood as a motion-based design optimization method [7].

Therefore, the general formulation of the proposed method may be expressed as follows [13]:

$$\begin{gathered} \text{Find } \theta_i \; i = 1,..,n_d \\ \text{Minimizing } \mathbf{f}(\theta_i) = [f_1(\theta_i) \quad ... \quad f_j(\theta_i) \quad ... \quad f_{n_f}(\theta_i)] \\ \text{Subjected to } \theta_i^l \le \theta_i \le \theta_i^u \end{gathered} \tag{19}$$

where $\mathbf{f}(\theta_i)$ is the multi-objective function; $f_j(\theta_i)$ is the j^{th} terms of the multi-objective function; n_f is the number of terms of multi-objective function; θ_i is the i^{th} design variable; θ_i^l is the lower bound of the ith design variable; θ_i^u is the upper bound of the ith design variables, and n_d is the total number of design variables.

For this case, the design of an ATMD, the above multi-objective function may be formulated in terms of two aspects: (i) the different parameters of the ATMD; and (ii) the compliance of the VSLS of the footbridge. According to the most advances guidelines [2], the VSLS is met if the maximum acceleration of the structure, $\ddot{x}_f(t)$, is lower than an allowable value, $\ddot{x}_{lim}$, established by the designer [2].

Additionally, in order to take into account the random character of the modal properties of the footbridge, which are sensitive to the variation of the operational and environmental conditions [3], the VSLS is re-formulated via a probabilistic approach [10]. According to this approach, the modal properties of the footbridge are assumed to be random variables which follow a normal probability distribution function. Hence, the response of the system is also a random variable, and it is possible to determine the probability of failure associated with the compliance of the different design requirements (in this case, the VSLS). According to this, the VSLS is defined in terms of a reliability index, β, which reflects the probability of failure associated with the compliance of this limit state. Thus, the limit state is met if this reliability index, β, is greater than an allowable value, β_{lim}, established by the design guidelines [14]. In order to compute the reliability index, β, analytical and numerical method can be used [11]. Among these methods, a Monte Carlo simulation has been considered herein [10].

In order to establish the formulation of this design problem, based on the motion-based design, the design parameters must be determined. For this particular case, five are the design variables: (i) the mass ratio of the ATMD, $\mu = m_a/m_f$ [-]; (ii) the frequency ratio of the ATMD, $\delta = f_d/f_f$ [-] (where f_d [Hz] is the natural frequency of the ATMD); (iii) the damping ratio of the ATMD, ζ_a; and (iv) the weighting factors, α_d and β_d (which characterize the driving force, $f_a(t)$). In order to reduce the number of design variables, simplifying the problem, a hybrid strategy has been considered herein [2]. Thus, both the frequency, δ, and damping, ζ_a, ratios of the ATMD have been established according to a conventional criterion for the design of passive tuned mass dampers [2]. According to this, the frequency ratio of the ATMD is set as, $\delta = 1/(1+\mu)$; and the damping ratio of the ATMD is set as, $\zeta_a = \sqrt{3\mu/(8(1+\mu))}$.

In this manner, the formulation of the motion-based design method under uncertainty conditions for this particular problem can be formulated as follows:

$$\begin{aligned} &\text{Find } \mu,\ \alpha_d,\ \beta_d \\ &\text{Minimizing } \{\mathbf{f}(\mu,\alpha_d,\beta_d)\} = \{f_1(\mu) \quad f_2(\mu,\alpha_d,\beta_d)\} = \{\mu \quad \tfrac{\beta_{lim}}{\beta}\} \\ &\text{Subjected to } \mu \in [0.01\ 0.10]\ \alpha_d \in [10\ 1000]\ \beta_d \in [10^{-5}\ 10^{-8}] \end{aligned} \tag{20}$$

Subsequently, in order to solve this optimization problem, global optimization algorithms are normally employed due to their good efficiency to find optimum solutions in nonlinear optimization problems [13]. Among these computational algorithms, a nature-inspired computational algorithm, genetic algorithms, has been considered herein [9]. As result of this optimization process, a set of non-dominated solutions is obtained [9]. This set of solutions may be represented in a functional space, generating the so-called Pareto front [9]. Finally, a subsequent decision-making problem must be addressed, the selection of the best solution among the dif-

ferent elements of the Pareto front. Therefore, an additional condition, β_{lim}/β, has been included herein to select the best element of the Pareto front. Figure 3 illustrates the additional condition considered to solve the decision-making problem.

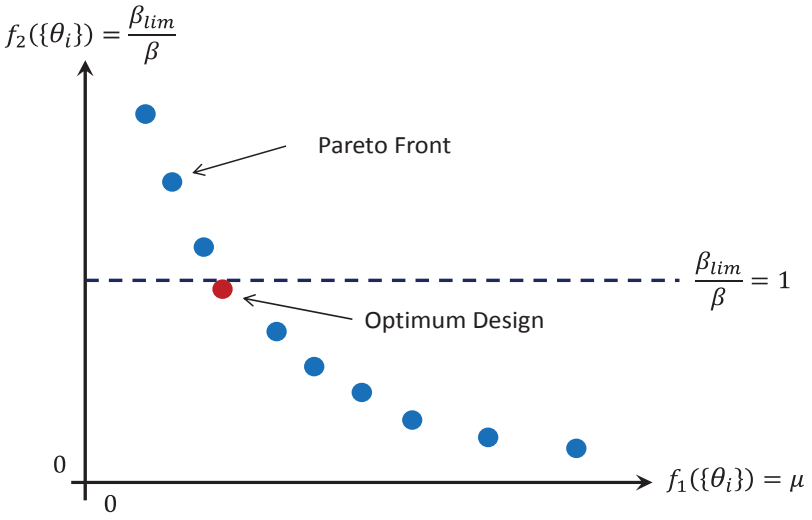

Figure 3: Additional condition considered to solve the decision-making problem.

4 APPLICATION EXAMPLE: MOTION-BASED DESIGN OF AN ATMD FOR A VIBRATING FOOTBRIDGE UNDER UNCERTAINTY CONDITIONS

In order to illustrate the performance of the motion-based design method, when it is implemented to design ATMDs for vibrating footbridges under uncertainty conditions, the following numerical case-study is presented. Thus, the compliance of the VSLS of a numerical footbridge is guaranteed via the installation of an ATMD. A detailed description of this numerical footbridge can be found in the French guidelines [2]. The structural behavior of the structure has been simulated via the finite element (FE) method. The FE package Ansys [15] has been used for this purpose. A numerical model using 646 beam elements and 540 shell elements (BEAM188 and SHELL181 respectively) has been built (Figure 4). A structural damping ratio of $\zeta_f = 0.6$ % has been considered [2]. The numerical modal parameters of the footbridge have been obtained via a numerical modal analysis. As result of this analysis, it was checked that the first vertical vibration mode ($f_f = 2.14$ Hz) is prone to vibrate under pedestrian action (Figure 4). The modal mass, m_f, of this vertical vibration mode is about 34706 kg.

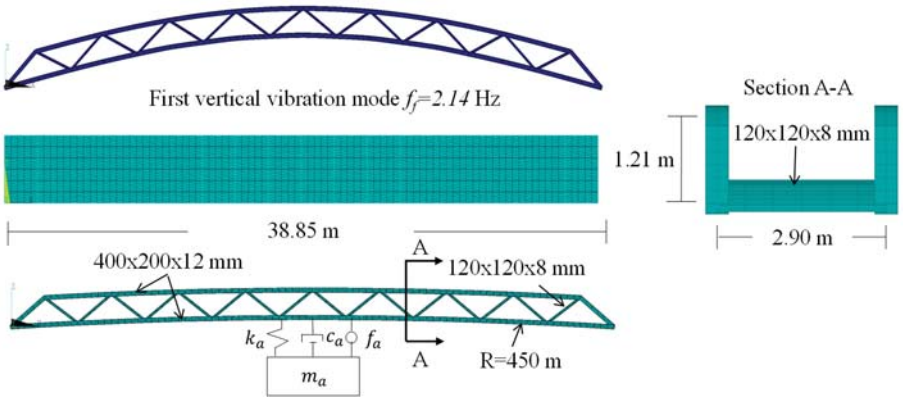

Figure 4: FE model of the benchmark footbridge and first vertical vibration mode.

In order to check the VSLS of this footbridge, the recommendations of the French guidelines [2] have been considered herein. Thus, one design scenario has been taken into account with the following design parameters: (i) a pedestrian traffic of 1 P/m^2 [2]; (ii) an allowable vertical acceleration, $\ddot{x}_{lim}$, of 1.00 m/s^2 [2]; and (iii) an allowable reliability index, β_{lim}, of 1.5 [14]. If this requirement is not met, an ATMD must be installed to reduce the amplitude of the human-induced vibrations according to the mentioned thresholds. According to the results provided by several researchers [3], a range of variation of ± 10 % has been considered for both the first vertical natural frequency of the footbridge and its associated damping ratio. Consequently, it has been checked that the VSLS term of the multi-objective function is a random variable which follows a log-normal probability distribution. In order to obtain the reliability index, β, associated with the VSLS of the footbridge, a Monte Carlo simulation has been performed [10]. For the selection of the sample size (50000 simulations), a convergence analysis has been carried out. The mathematical package Matlab [12] has been employed for this study.

As result of this study, Table 1 shows the reliability index, β, associated with the VSLS without and with the ATMD. As Table 1 shows, the motion-based design method allows control the dynamic response of the footbridge under uncertainty conditions without compromising the cost of the control system. Additionally, the parameters of the ATMD designed according to this method have been included in Table 1.

ATMD	$\ddot{x}_f$ [m/s^2]	β [-]	α_d [-]	β_d x 10^{-8} [-]	m_a [kg]	c_a [sN/m]	k_a x 10^5 [N/m]	f_a [N]
No	---	-0.53	---	---	---	---	---	---
Yes	1.00	1.50	511.30	344.19	625	1343	1.09	286

Table 1: Reliability index, β, of the VSLS of the footbridge (without and with ATMD)..

5 CONCLUSIONS

In this manuscript, the motion-based design method has been presented and further implemented for the design of ATMDs when they are used to mitigate the human-induced vibrations in footbridges under uncertainty conditions. According to this method, the design problem may be formulated via two coupled sub-problems: (i) a multi-objective optimization sub-problem; and (ii) a reliability analysis sub-problem. Thus, the multi-objective function is defined in terms of two aspects: (i) the parameters of the ATMD which are needed to be determined; and (ii) a reliability index, which establishes the probability of compliance of the VSLS of the structure. Sampling techniques, as the Monte Carlos simulation method, can be employed to estimate numerically this reliability index. As application example, a steel footbridge, which is prone to vibrate due to walking pedestrian action, has been selected. In order to mitigate the pedestrian-induced vibrations, an ATMD has been installed at its mid-span. The ATMD parameters have been obtained via the implementation of the aforementioned method. As result of this study, the performance of the proposed method has been shown up. In spite of its good performance, further studies are needed, both to better characterize the probabilistic distribution function of the different modal properties of the structure; and to assess experimentally the performance of structures controlled by active damping devices designed according to this proposal.

ACKNOWLEDGEMENTS

This work was partially funded by two research projects: (i) research project RTI2018-094945-B-C21 (Ministerio de Economía y Competitividad of Spain and the European Regional

Development Fund) and (ii) research project SEED-SD RTI2018-099639-B-I00 (Ministerio de Ciencia, Innovación y Universidades of Spain).

REFERENCES

[1] K. Van Nimmen, G. Lombaert, G. De Roeck and P. Van den Broeck. Vibration serviceability of footbridges: evaluation of the current codes of practice. *Engineering Structures*, 59: 448-461, 2014.

[2] Setra/AFGC Guide méthodologique passerelles piétonnes (Technical Guide Footbridges: Assessment of vibration behaviour of footbridge under pedestrian loading), 2006.

[3] W.-H. Hu, C. Moutinho, E. Caetano, F. Magalhães, A. Cunha. Continuous dynamic monitoring of a lively footbridge for serviceability assessment and damage detection. *Mechanical System and Signal Processing*, 33: 38-55, 2012.

[4] F. Weber, G. Feltrin, O. Huth. Guidelines for Structural Control. Structural Engineering Re-search Laboratory. Swiss Federal Laboratories for Materials Testing Research. Dübendort, Switzerland, 2006.

[5] A. Preumont, K. Seto. Active Control of Structures, 1st edn. *John Wiley & Sons, Ltd*., ISBN: 978-0-470033-93-7, 2008.

[6] Z.-D. Xu, Y.-Q. Guo, J.-T. Zhu, F.-H. Xu. Intelligent Vibration Control in Civil Engineering Structures. *Zhejang Universtiy Press Co. Ltd*. ISBN: 978-0-124058-74-3, 2017.

[7] J.J. Connor. Introduction to Structural Motion Control. *Pearson Mit-Prentice Hall,*. ISBN: 978-0-130091-38-3, 2003.

[8] J.F. Jimenez-Alonso, A. Saez. Motion-based design of TMD for vibrating footbridges under uncertainty conditions. *Smart Structures and Systems*, 21(6): 727-740, 2018.

[9] K. Deb, A. Pratap, S. Agarwal, T. Meyarivan. A fast and elitist multi-objective genetic algorithm: NSGA-II. *Evolutionary Computation*, 6(2): 182-197, 2002.

[10] M. Holický. Reliability Analysis for Structural Design, *1st edn. Sun Media*, ISBN: 978-1-920338-11-4, 2009.

[11] A.K. Rathi, A. Chakraborty. Reliability-based performance optimization of TMD for vibration control of structures with uncertainty in parameters and excitation. *Structural Control and Health Monitoring*, 24(1): e1857, 2016.

[12] Matlab (2020) R2020a. http://www.mathworks.com/.

[13] Q.Q. Liang. Performance-Based Optimization: A review. *Advances in Structural Engineering*, 10(6): 739-753, 2007.

[14] EN 1990 Eurocode 0: Basis of Structural Design; European Committee for Standardization, Brussels, 2002.

[15] Ansys (2020) Mechanical Release http://www.ansys.com/

EURODYN 2020
XI International Conference on Structural Dynamics
M. Papadrakakis, M. Fragiadakis, C. Papadimitriou (eds.)
Athens, Greece, 23–26 November 2020

CONTACT FORCE RECONSTRUCTION ON VIBRATING SURFACES

J. Van Hauwermeiren[1], K. Van Nimmen[1], B. Vanwanseele[2] and P. Van den Broeck[1]

[1]KU Leuven, Department of Civil Engineering, Structural Mechanics,
B-3001 Leuven
[2]KU Leuven, Department of Movement Sciences, Human Movement Biomechanics Research Group,
B-3001 Leuven
e-mail: {jeroen.vanhauwermeiren, katrien.vannimmen, benedicte.vanwanseele,
peter.vandenbroeck}@kuleuven.be

Keywords: Human-induced vibrations, inertial motion tracking, force reconstruction, human-structure interaction.

Abstract. *Current load models describing the effect of crowd-induced loading require further development and validation. To this end, detailed full-scale operational loading data is required. The Eeklo Footbridge Benchmark Dataset considers loading scenarios up to 0.50 pers./m^2 (148 pers.). The data set comprises a digital twin of the structure and the simultaneous registration of the trajectories of the pedestrians using a camera setup, the body acceleration using low-cost accelerometers attached to the lower back and the structural acceleration using a sensor network. The low-cost accelerometers are subject to higher measurement noise than conventional techniques. The goal is to verify to what extent the low-cost sensors can be used for the contact force reconstruction in vibrating-surface conditions and, more importantly, the quantification of human-structure interaction effects in case of the Eeklo Benchmark Dataset.*

First, a data set is collected comprising the simultaneous registration of contact forces and lower-back accelerations in rigid-surface conditions. The latter are obtained using the low-cost sensors. The measurement noise characteristics of the low-cost sensors are determined. It is found that the signal-to-noise ratio of the human body acceleration at the lower back during walking in rigid-surface conditions is very high. Therefore, the employed sensors are suited for force reconstruction based on the lower-back accelerations in rigid-surface conditions.

Second, the additional accelerations of the human body in case of walking on a vibrating surface are examined by a numerical example. The quantities of the example are set to be representative for the loading scenarios of the Eeklo Benchmark Dataset. The signal-to-noise ratio of the additional human body accelerations is low. As a consequence, it is inaccurate to use the total human body accelerations for the total contact force reconstruction of the participant. Instead, it is found that an inverse approach is more suited. The total human body accelerations are a good approximation of the internally-driven ones. The conclusions of this numerical example are case-specific while the presented methodology is generic and can be readily extended to virtually any other footbridge.

1 Introduction

As a result of ever increasing lighter and stronger materials, footbridge design today is often dominated by its vibrations serviceability [1]. On the other hand, the human-structure interaction (HSI) effects comprising the combined added mass and damping effect, are more prominent for footbridges for increasing ratios of the crowd mass to the structural mass [2]. Normative design codes neglect the effect of HSI [3, 4]. This is in turn a result of the absence of full-scale validation of this phenomenon [2]. Such a validation requires detailed information on the loading data during realistic walking scenarios comprising the simultaneous registration of the induced loads and the structural response [5]. The Eeklo Benchmark Dataset provides, for the first time ever, such a detailed dataset. The trajectories of each pedestrian are registered using a camera setup. The induced loads of the crowd are characterized by the registered body acceleration of each individual. Given the scale of the application, low-cost sensors are employed instead of the conventional measurement systems. Their measurement noise variance is higher compared to their more expensive alternatives.

Multiple strategies exist for the experimental validation, analysis and calibration of HSI phenomena. A first category directly analyzes the induced contact forces [6, 7, 8, 9, 10] or body locomotion [11] during walking on vibrating conditions. A second category consists of inverse techniques. In this case, the governing parameters of the HSI models are determined such that the discrepancy between the reconstructed and measured structural response is minimized [12, 13, 14].

The goal of the present study is to verify that the employed low-cost sensors are suited for the characterization of the human body motion. Furthermore, it is investigated which techniques are suited for the validation and calibration of HSI models given the specific load-structure conditions of the Eeklo Benchmark Dataset and the employed low-cost sensors.

This contribution starts with a discussion of the dynamics of the coupled crowd-structure system (Section 2). Next, the contact force reconstruction using low-cost sensors on rigid surface conditions is verified (Section 3). Furthermore, the contact force reconstruction on vibration surfaces is investigated (Section 4). The most important conclusions are summarized in Section 5.

2 Dynamics of the coupled crowd-structure system

2.1 Human body dynamics

The human body is in reality composed of a large number of body segments [15]. It is common practice to lump all the activated masses in one single activated mass m_{H1} and all the non-activated masses into a single non-activated mass m_{H0} [16, 17, 18]. Obviously, the sum equals the body weight of the pedestrian: $m_{\mathrm{ped}} = m_{\mathrm{H0}} + m_{\mathrm{H1}}$. The activated mass m_{H1} is driven by an internal driving term $G(t)$ while the connection between the non-activated mass m_{H0} and activated mass m_{H1} is modeled by an internal reaction force $\mathcal{G}(t)$ (Fig. 1-a).

Expression of the force equilibrium at the contact plane and applying Newton's second law gives:

$$F(t) = m_{\mathrm{H0}}\ddot{u}_{\mathrm{s}}(t) + m_{\mathrm{H1}}\ddot{u}_{\mathrm{H1}}(t) = (1-\mu_{\mathrm{H1}})m_{\mathrm{ped}}\ddot{u}_{\mathrm{s}}(t) + \mu_{\mathrm{H1}}m_{\mathrm{ped}}\ddot{u}_{\mathrm{H1}}(t) \tag{1}$$

where F is called the contact force and $\mu_{\mathrm{H1}} = m_{\mathrm{H1}}/m_{\mathrm{ped}}$ the ratio of the activated mass to the total mass of the pedestrian.

In case of walking on a rigid surface, the kinetics of the supporting surface are zero ($u_{\mathrm{s}} = 0$)

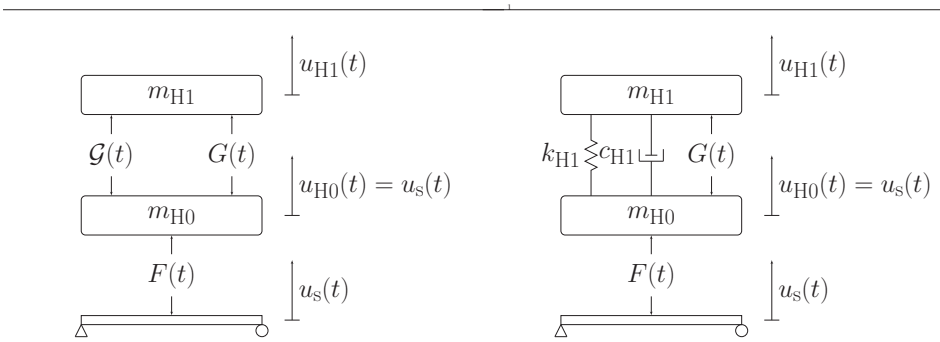

Figure 1: Schematic representation of the human body dynamics modeled by a non-activated (m_{H0}) and activated mass (m_{H1}). Connection with the supporting surface modeled (left) generically and (right) by a spring and viscous damper.

yielding the following simplifications: $G = G^{\mathrm{RS}}$, $F = F^{G} = F^{G^{\mathrm{RS}}}$ and $u_{\mathrm{H1}} = u_{\mathrm{H1}}^{G} = u_{\mathrm{H1}}^{G^{\mathrm{RS}}}$ where the subscript RS denotes that it concerns rigid-surface conditions. The subscript G^{RS} denotes that the contact force and human body kinetics are purely a result of the internally-driven force G^{RS}. The contact force in this case reads:

$$F^{G^{\mathrm{RS}}}(t) = m_{\mathrm{H1}}\ddot{u}_{\mathrm{H1}}^{G^{\mathrm{RS}}}(t) = \mu_{\mathrm{H1}} m_{\mathrm{ped}} \ddot{u}_{\mathrm{H1}}^{G^{\mathrm{RS}}}(t) \tag{2}$$

For walking on vibrating surfaces, it is obvious that $u_{\mathrm{s}} \neq 0$. In this study, it is assumed that the internal driving term G is unaltered with respect to the rigid-surface conditions: $G = G^{\mathrm{RS}}$. This corresponds to the assumption that there is no active human-structure interaction. Moreover, in case of walking on vibrating surfaces the human body kinetics do not only consist of the internally-driven kinetics $u_{\mathrm{H1}}^{G^{\mathrm{RS}}}(t)$ but an additional mechanical interaction term $u_{\mathrm{H1}}^{\mathrm{int}}(t)$, resulting from the mechanical interaction of the human body with the vibrating surface. In this study it is assumed that the superposition principle holds i.e. $u_{\mathrm{H1}}^{\mathrm{tot}}(t) = u_{\mathrm{H1}}^{G^{\mathrm{RS}}}(t) + u_{\mathrm{H1}}^{\mathrm{int}}(t)$. Combining the total human body kinetics with Eq. (1) allows to write the contact force in the following form:

$$F^{\mathrm{tot}}(t) = \underbrace{m_{\mathrm{H1}}\ddot{u}_{\mathrm{H1}}^{G^{\mathrm{RS}}}(t)}_{=F^{G^{\mathrm{RS}}}(t),\ \mathrm{Eq.\ (2)}} + \underbrace{m_{\mathrm{H0}}\ddot{u}_{\mathrm{s}}(t) + m_{\mathrm{H1}}\ddot{u}_{\mathrm{H1}}^{\mathrm{int}}(t)}_{=F^{\mathrm{int}}(t)} \tag{3}$$

and illustrates how the **total contact force** (F^{tot}) is the combination of the **internally-driven contact force** equal to the contact force on a rigid surface ($F^{G^{\mathrm{RS}}}$) and an additional **mechanical interaction contact force** (F^{int}).

2.2 Equations of motion of the coupled crowd-structure system

The structural response to the walking excitation of a crowd composed of n_{p} pedestrian is calculated using the well-known equations of motions in modal coordinates of the reduced-order finite element (FE) model:

$$\ddot{\mathbf{Z}}(t) + \mathbf{\Gamma}\dot{\mathbf{Z}}(t) + \mathbf{\Omega}^2\mathbf{Z}(t) = \mathbf{\Phi}^{\mathrm{T}}\mathbf{S}_{\mathrm{p}}(t)\mathbf{F}^{\mathrm{tot}}(t) = \mathbf{\Phi}^{\mathrm{T}}\mathbf{S}_{\mathrm{p}}(t)\left[\mathbf{F}^{G^{\mathrm{RS}}}(t) + \mathbf{F}^{\mathrm{int}}(t)\right] \tag{4}$$

where $\mathbf{Z}(t) \in \mathbb{R}^{n_{\mathrm{m}}}$ are the modal displacements of the n_{m} retained modes, $\mathbf{\Omega}^2 \in \mathbb{R}^{n_{\mathrm{m}} \times n_{\mathrm{m}}}$ a diagonal matrix containing the squared circular eigenfrequencies in increasing order, $\mathbf{\Gamma} \in \mathbb{R}^{n_{\mathrm{m}} \times n_{\mathrm{m}}}$ a diagonal matrix containing the modal damping ratios in corresponding order, $\mathbf{\Phi} \in$

$\mathbb{R}^{n_{\text{DOF}} \times n_{\text{m}}}$ the matrix containing the corresponding mode shape values at each degree of freedom (DOF) of the structure as columns, $\mathbf{S}_{\text{p}}(t) \in \mathbb{R}^{n_{\text{DOF}} \times n_{\text{p}}}$ the force-selection matrix containing the time-varying position of the n_{p} pedestrians and thus relating each position to a corresponding degree of freedom of the system, $\mathbf{F}^{\text{tot}}(t) \in \mathbb{R}^{n_{\text{p}}}$ the matrix containing the total contact force of each pedestrian which is the combination of the internally-driven contact forces $\mathbf{F}^{G^{\text{RS}}}(t) \in \mathbb{R}^{n_{\text{p}}}$ and the mechanical interaction contact forces $\mathbf{F}^{\text{int}}(t) \in \mathbb{R}^{n_{\text{p}}}$.

As the interaction contact forces depend on the surface vibrations, it is convenient to place $\mathbf{F}^{\text{int}}(t)$ at the left-hand side of Eq. (4), allowing for a closed-form solution of the structural response. To this end, it is necessary to make an assumption on how the internal reaction force $\mathcal{G}(t)$ is modeled. A popular approach is to model the connection of the activated mass m_{H1} with the supporting surface by a linear spring and linear viscous damper (Fig. 1-b) [19, 20, 8, 10, 17]. The internal reaction force reads: $\mathcal{G}(t) = c_{\text{H1}}[\dot{u}_{\text{s}}(t) - \dot{u}_{\text{H1}}(t)] + k_{\text{H1}}[u_{\text{s}}(t) - u_{\text{H1}}(t)]$ where k_{H1} and c_{H1} respectively denote the spring and damping coefficient. The operator is linear this case. The spring-mass-damper is often characterized in terms of its natural frequency f_{H1} and damping ratio ξ_{H1} [2]. Eq. (4) is rewritten to:

$$\mathbf{M}_{\text{HB}}(t) \begin{bmatrix} \ddot{\mathbf{Z}}(t) \\ \ddot{\mathbf{U}}^{\text{int}}_{\text{H1}}(t) \end{bmatrix} + \mathbf{C}_{\text{HB}}(t) \begin{bmatrix} \dot{\mathbf{Z}}(t) \\ \dot{\mathbf{U}}^{\text{int}}_{\text{H1}}(t) \end{bmatrix} + \mathbf{K}_{\text{HB}}(t) \begin{bmatrix} \mathbf{Z}(t) \\ \mathbf{U}^{\text{int}}_{\text{H1}}(t) \end{bmatrix} = \begin{bmatrix} \mathbf{\Phi}^{\text{T}} \mathbf{S}_{\text{p}}(t) \mathbf{F}^{G^{\text{RS}}}(t) \\ \mathbf{0} \end{bmatrix} \tag{5}$$

where $\mathbf{M}_{\text{HB}}(t)$, $\mathbf{C}_{\text{HB}}(t)$ and $\mathbf{K}_{\text{HB}}(t)$ are the system matrices of the coupled crowd-structure system. Their derivation and definition is given in [2]. For a certain loading scenario ($\mathbf{S}_{\text{p}}(t)$ and $\mathbf{F}^{G^{\text{RS}}}(t)$) Eq. (5) is solved for the response of the coupled crowd-structure system ($\left[\mathbf{Z}(t)\ \mathbf{U}^{\text{int}}_{\text{H1}}(t)\right]^{\text{T}}$) using a discrete-time state space approach [2].

3 Experimental study of the contact force reconstruction on rigid surfaces

3.1 Measurement protocol and experimental results

Fifteen healthy Belgian adults (age: 21-51 years, weight: 54-85 kg, height: 1.66-1.90 m, females: 2, males: 13) participated in the experimental program in the Movement and posture Analysis Laboratory Leuven (MALL) at the Department of Kinesiology of KU Leuven [21]. The participants provided informed consent in accordance with the ethical guidelines for research involving human participants at the University of KU Leuven.

An instrumented treadmill with two separate belts (Forcelink) is used to register the tri-axial contact forces with a sampling rate of 1 kHz. Three different speeds per pedestrian are considered (between 4 km/h and 6 km/h). The walking speeds were randomized to avoid a bias due to fatigue or psychological adaptation of the walking gait. Each test duration is approximately 2 minutes. The first 15 seconds are removed in the further analysis as this is considered to be the time to adapt to the walking speed of the treadmill. The test results of pedestrian 7, trial 1 and pedestrian 12, trial 1 are discarded in the further analysis due to the presence of severe measurement errors.

Besides the contact force, the human body acceleration is registered near the 5$^{\text{th}}$ lumbar vertebrae using a low-cost tri-axial USB accelerometer of the type GCDC X-16D (range $\pm 16\ g$, LSB 4.8828 $10^{-4} g$ [22]) with a sampling rate of 200 Hz. This sensor is identical to the one used in the Eeklo Benchmark Dataset.

The force plate data is decimated to 200 Hz. To mitigate the effect of measurement noise, all signals are low-pass filtered using a 4$^{\text{th}}$ order Butterworth filter with a cutoff frequency of

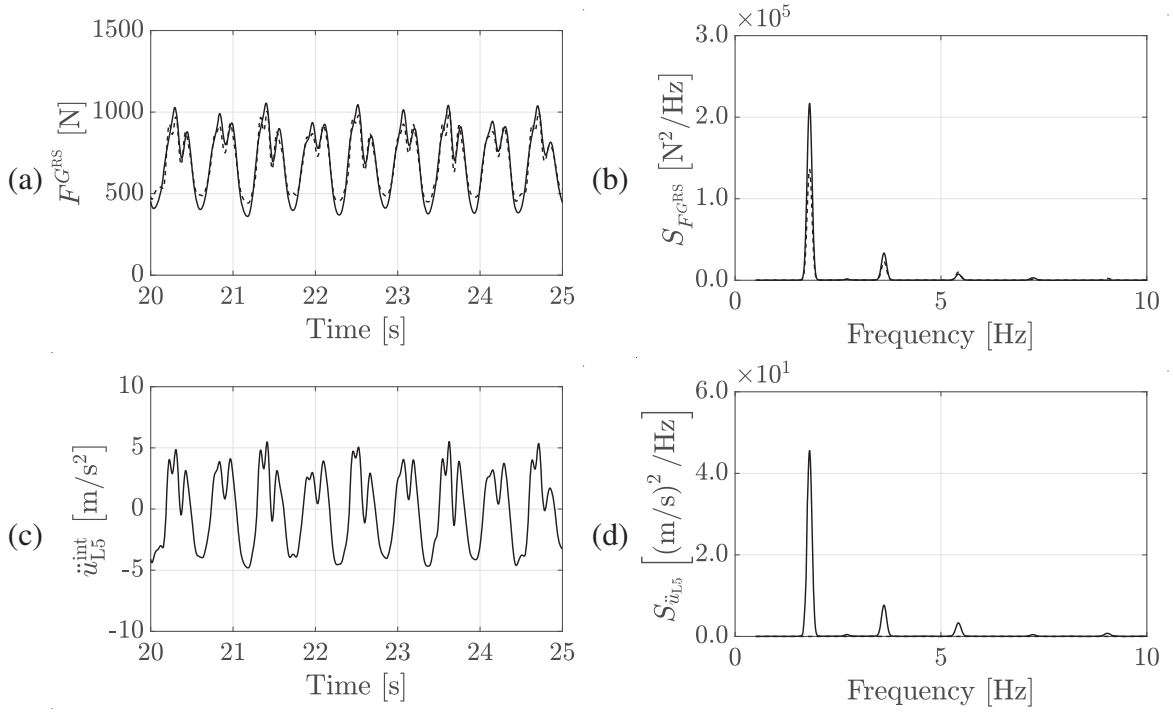

Figure 2: The reference pedestrian during the instrumented treadmill laboratory measurements. Internally-driven contact force: measured (solid) versus reconstructed (dashed): (a) time series and (b) PSD. Measured internally-driven human body acceleration: (c) time series and (d) PSD with indication of the measurement noise of the low-cost sensors (dashed line).

12 Hz. As such, the relevant frequency content (0 Hz-10 Hz) for the vibration serviceability assessment of footbridges (scope of application) is retained [23]. The force plate data and low-cost accelerometer data are synchronized offline using a common trigger event.

To characterize the measurement noise of the low-cost sensors, long-term duration measurements ($>$ 20 hours) are performed on a rigid surface. It is found that the measurement noise can be characterized as bandpass-limited white Gaussian noise comprised between 0 Hz and 70 Hz with a 95% percentile value of the variance of 0.0124 $(\mathrm{m/s^2})^2$.

A typical time series and amplitude spectrum of the reference pedestrian (pedestrian 2 during trial 2) is shown in Fig. 2. The signal-to-noise ratio in the frequency range 0.5 Hz-10 Hz is very high $3286 \approx 35.17$ dB and therefore it is concluded that the low-cost sensors are sufficiently accurate compared to the conventional measurement methods.

3.2 Relating the lower-back acceleration and the contact force

The internally-driven contact force is reconstructed using Eq. (2): $\tilde{F}^{G^{\mathrm{RS}}}(t) = m_{\mathrm{H1}} \ddot{u}_{\mathrm{H1}}^{G^{\mathrm{RS}}}(t)$. The tilde denotes that it concerns a reconstructed quantity. The vertical acceleration measured at the lower back is assumed to be a good approximation of the acceleration of the activated human body mass [24]. Moreover, in [24] it is found that the fraction of the activated body mass compared to the total body mass is $\mu_{\mathrm{H1}} = 0.76$ which is adopted in the present work. An example of the reconstructed internally-driven contact force is shown in Fig. 2. The reconstruction inevitably yields some reconstruction error. This is a combined result of the modeling assumption of the human body dynamics (Section 2.1) and the fact that the measured acceleration at the lower back does not perfectly coincide with the acceleration of the actived human

body mass. The latter stems from the measurement error of the sensors, but also the soft tissue artifacts [25]. Moreover, the factor μ_{H1} is subject to inter-person variability and depends on the walking speed [24].

4 Contact force reconstruction on vibrating surfaces

4.1 Framework of the numerical-experimental example

The contact force reconstruction procedure on vibrating surfaces is illustrated by a numerical example. The quantities of the example are chosen such that a representative scenario of the Eeklo Benchmark Dataset is obtained.

The modal parameters of the Eeklo footbridge of the corresponding benchmark dataset are considered and stored in $\mathbf{\Phi}$, $\mathbf{\Omega}^2$, $\mathbf{\Gamma}$. The structure consists of 14 modes below 12 Hz and are calculated with a detailed FE model which is calibrated using experimental operational modal analysis data [26]. The digital twin describing the dynamic behavior of the footbridge, is part of the open access benchmark dataset (See accompanying paper: 'An open access benchmark dataset on pedestrian-induced vibrations collected on the Eeklo footbridge'). A flow $\mathbf{S}_{\text{p}}(t)$ consisting of 148 persons (≈ 0.50 pers./m^2) is considered where the trajectories of the participants correspond to those as registered in the Eeklo Benchmark Dataset (total duration of 20 minutes). The HSI is modeled by a moving spring-mass-damper at each location of the pedestrian occupying the bridge (see also Fig. 1-b). The values are adopted from [17]: $f_{\text{H1}} = 3.25$ Hz and $\xi_{\text{H1}} = 0.30$.

The crowd-induced loading and related of response of the numerical study is established by the following steps:

1. The internally-driven contact forces $\mathbf{F}^{G^{\text{RS}}}(t)$ are selected from the registered trials during the laboratory measurements on rigid surfaces (Section 3.1). As the total test duration is longer than the typical trial duration, the contact force and lower-back acceleration vector are repeated. As trials are selected multiple times, they are assigned a random uniformly-distributed time shift (outer values $\pm$ the average step duration) to avoid an artificial correlation between the pedestrians in the crowd.

2. The corresponding part of the lower-back acceleration as registered during the laboratory experiments is selected and stored in the matrix $\ddot{\mathbf{U}}_{\text{H1}}^{G^{\text{RS}}}(t)$. This quantity is later used for the contact force reconstruction (Section 4.2) and to determine the total human body accelerations (step 5).

3. The reference response is calculated by plugging in the internally-driven contact forces $\mathbf{F}^{G^{\text{RS}}}(t)$ in Eq. (5). The equation is solved for the modal accelerations $\ddot{\mathbf{Z}}(t)$ and the interaction human body accelerations $\ddot{\mathbf{U}}_{\text{H1}}^{\text{int}}(t)$.

4. The modal accelerations $\ddot{\mathbf{Z}}(t)$ are used to calculate the vertical acceleration at the middle of the central span $\ddot{u}_{\text{midspan}}(t)$ (Fig. 3). This structural acceleration quantity is hereafter referred to as the reference response.

5. The interaction human body accelerations are assumed to correspond to the additional kinetics that a pedestrian registers in case of walking on a vibrating surface as a result of the HSI. The total acceleration registered at the lower back is: $\ddot{\mathbf{U}}_{\text{H1}}^{\text{tot}}(t) = \ddot{\mathbf{U}}_{\text{H1}}^{G^{\text{RS}}}(t) + \ddot{\mathbf{U}}_{\text{H1}}^{\text{int}}(t)$. This quantity is later used for the contact force reconstruction (Section 4.2).

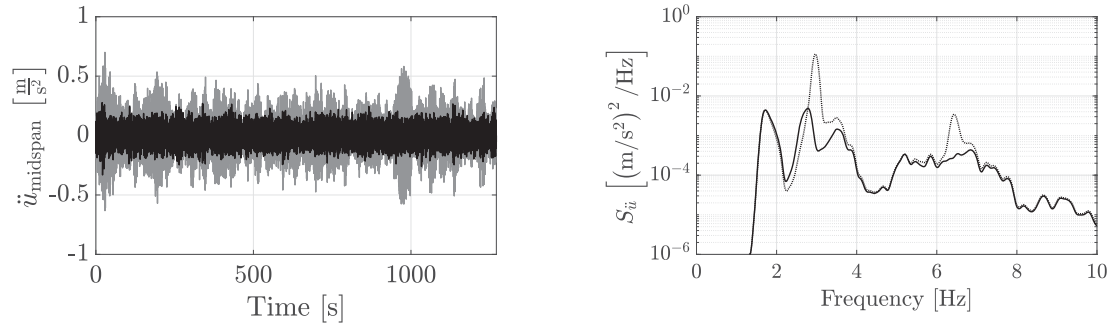

Figure 3: Structural accelerations at midspan of the reference response with (black) and without (gray) consideration of HSI: time series (left) and PSD (right).

An example of the interaction contact force and interaction human-body acceleration (Fig. 4) illustrates that the interaction components are very small compared to their internally-driven counterparts (Fig. 2). The reference structural response is additionally calculated without considering HSI (Fig. 3). The comparison shows that the structural response is highly sensitive to the presence of HSI, despite the low amplitudes of the interaction contact forces and related interaction human body accelerations. This can be explained by the fact that a part of the frequency content of the interaction contact forces is near-resonant with modes 2 ($f_2 = 2.97$ Hz) and mode 5 ($f_5 = 5.68$ Hz) which are characterized by a low modal mass (See also accompanying paper: 'An open access benchmark dataset on pedestrian-induced vibrations collected on the Eeklo footbridge').

Compared to the measurement noise of the low-cost sensors (frequency band 0.5 Hz-10 Hz), a signal-to-noise ratio of the mechanical interaction human body accelerations of $1.58 \approx 1.99$ dB is found, which is very low.

The difference in PSD of the structural response with and without the incorporation of HSI is expressed in terms of the relative difference in power spectra density (PSD). The considered frequency range is 0.5 Hz to 10 Hz. The relative difference in PSD of a time series $\ddot{u}_{\text{B}}(t)$ relative to a the PSD of a time series $\ddot{u}_{\text{A}}(t)$ is defined as:

$$\Delta S_{\ddot{u}} = \frac{\int_{f=0.5\text{ Hz}}^{f=10\text{ Hz}} |S_{\ddot{u}_{\text{A}}}(f) - S_{\ddot{u}_{\text{B}}}(f)| df}{\int_{f=0.5\text{ Hz}}^{f=10\text{ Hz}} S_{\ddot{u}_{\text{A}}}(f) df} \tag{6}$$

The relative difference of the reference response without incorporation of HSI to the reference response with HSI is 4.71. This value is a measure for the sensitivity of the reference response to HSI. This high difference indicates that HSI has a prominent influence on the structural response. This indicates the potential of the Eeklo Benchmark Dataset for the identification and quantification of HSI effects.

4.2 Contact force reconstruction from the human body accelerations

The reconstruction of the contact forces based on the lower-back accelerations yields some reconstruction error, even in rigid-surface conditions (Section 3.2). It is first investigated how this reconstruction error propagates to the related reconstructed response. The internally-driven contact forces of each pedestrian is reconstructed as $\tilde{F}^{G^{\text{RS}}}(t) = m_{\text{H1}} \ddot{u}_{\text{H1}}^{G^{\text{RS}}}(t)$ (Section 3.2) and

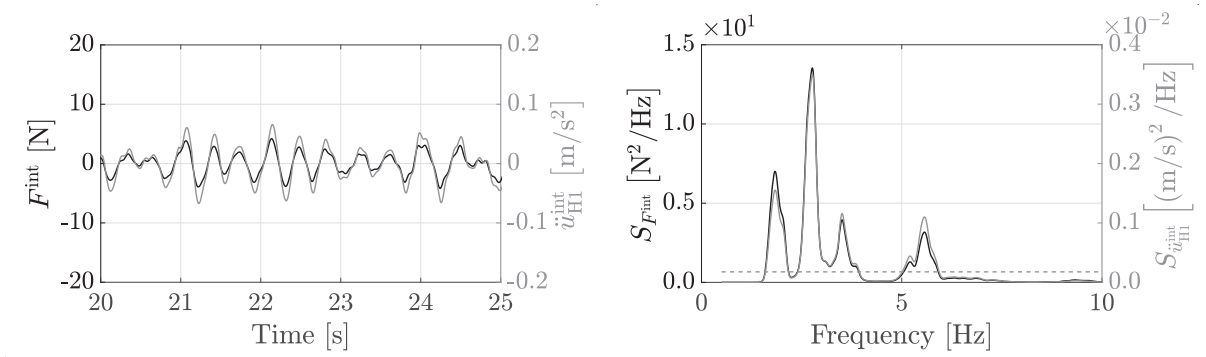

Figure 4: The interaction contact force (black) and interaction human body acceleration (gray) of reference pedestrian during the numerical example: relevant zoom of the time series (left) and PSD (right) with indication of the measurement noise of the low-cost sensors (dashed line).

stored in $\tilde{\mathbf{F}}^{G^{\mathrm{RS}}}(t)$. This matrix is applied on the equations of motion of the coupled crowd-structure system (Eq. (5)). The results (Fig. 5) show that the reconstructed response has a relative difference in PSD with respect to the reference response of 0.51 (calculated with Eq. (6)). This corresponds to 0.51/4.71 = 11% of the sensitivity of the reference response to HSI. It is noteworthy that this is a purely theoretical situation as in reality one always registers the total human body accelerations in measurement campaigns which cannot be separated into the internally-driven and interaction component.

Since the total human body accelerations are the ones that are registered during an experimental campaign, the most logical choice is to reconstruct the total contact forces as $\tilde{F}^{\mathrm{tot}}(t) = m_{\mathrm{H0}}\ddot{u}_{\mathrm{s}}(t) + m_{\mathrm{H1}}\ddot{u}^{\mathrm{tot}}_{\mathrm{H1}}(t)$ where $\ddot{u}_{\mathrm{s}}(t)$ are the structural vibrations at the position of the pedestrian. The reconstructed total contact forces are substituted into Eq. (4) to reconstruct the structural response. The results (Fig. 5) show that the relative difference in PSD increases from 0.51 to 2.13 (= 45% of the sensitivity). This can be explained by the low signal-to-noise ratio of the interaction human body accelerations (Fig. 4) while their importance is high (Fig. 3). In this theoretical example, the structural accelerations at the position of the pedestrian are easily obtained as $\ddot{u}_{\mathrm{s}}(t) = S_{\mathrm{p}}^{\mathrm{T}}(t)\boldsymbol{\Phi}\ddot{\mathbf{Z}}(t)$. In reality, however, the structural accelerations are measured at a limited number of points. Estimates of the structural accelerations at the contact points of pedestrians could be made using for instance techniques such as joint input-state estimation [27] but will slightly deviate from the true accelerations. As such, an additional reconstruction error is introduced leading to an even higher relative difference in PSD of the structural response. Therefore, it is concluded that a direct total force reconstruction is not suited in case of the Eeklo Benchmark Dataset.

Given the small power of the interaction human body acceleration compared to the internally-driven ones (Figs. 2 and 4), it could be opted to neglect the interaction accelerations. As such, it is assumed that the total human body accelerations is as a good approximation of the internally-driven ones: $\ddot{u}^{G^{\mathrm{RS}}}_{\mathrm{H1}}(t) \approx \ddot{u}^{\mathrm{tot}}_{\mathrm{H1}}(t)$. As such, the internally-driven contact forces can be estimated as: $\tilde{F}^{G^{\mathrm{RS}}}(t) = m_{\mathrm{H1}}\ddot{u}^{\mathrm{tot}}_{\mathrm{H1}}(t)$. The reconstructed structural response is obtained by plugging in the reconstructed internally-driven contact force into the equations of motion of the coupled crowd-structure system (Eq. (5)). The results (Fig. 5) show that the response is more accurately reconstructed compared to the previous case. The relative difference in PSD increases from 0.51 to 0.87. This is only a fraction of the sensitivity of the response to human-structure interaction (0.87/4.71 = 18%). This difference can be exploited for the estimation of the parameters of the

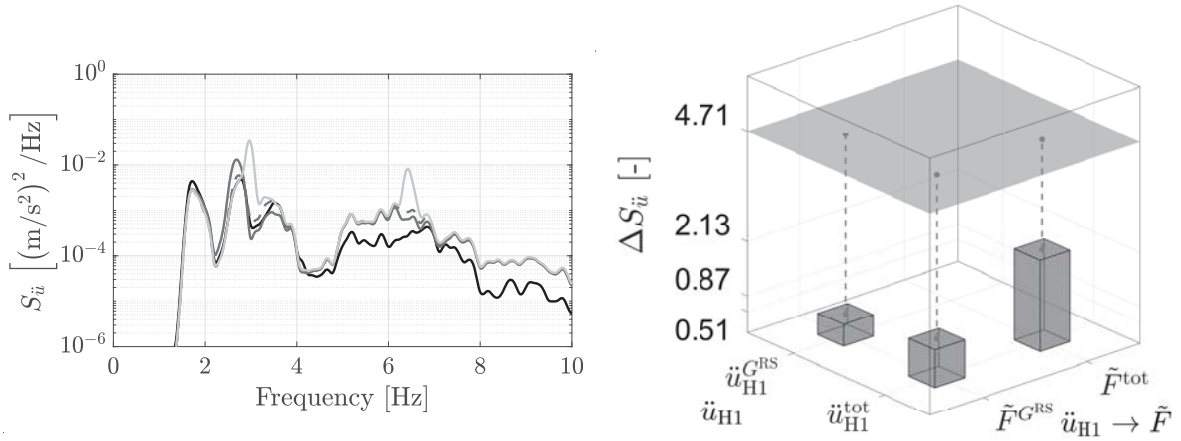

Figure 5: Assessment of the different reconstruction techniques based on the structural accelerations at midspan. Left: PSD of the reference response (black solid), the reconstructed response using either the total human body accelerations (solid) to reconstruct the total (light gray) or internally-driven (dark gray) contact forces or using the internally-driven human body accelerations to reconstruct the internally-driven contact forces (dashed). Right: relative difference in PSD of the reconstructed response to the reference response for the different reconstruction scenarios (bars) and sensitivity of the reference response to HSI (gray-patched plane).

governing HSI in an inverse way where the internally-driven contact forces are reconstructed using the total human body accelerations.

5 Conclusions

The present contribution focuses on the human body dynamics and the HSI that occurs in case a walking crowd occupies a vibration structure. It is shown how the registration of the human body accelerations can be exploited to reconstruct the contact forces.

An experimental dataset using an instrumented treadmill and comprising 43 trials is collected. The internally-driven contact forces and internally-driven human body accelerations are simultaneously registered. The human body accelerations are collected using sensors which are identical to the ones used in the Eeklo Benchmark Dataset. It is found that the signal-to-noise ratio of the internally-driven human body accelerations during walking is very high compared to the noise characteristics of the low-cost sensors. Hence the employed sensors are competitive with the sensor equipment conventionally used for the registration of the human body acceleration.

Next, a numerical study of the Eeklo footbridge is considered where the applied internally-driven contact forces are the ones as registered in the laboratory setup and the HSI is modeled using a popular approach with parameter values established in the literature. The structural response is sensitive to the presence of HSI. This confirms the potential of the Eeklo Benchmark Dataset for the quantification of HSI effects. The signal-tot-noise ratio of the interaction human body accelerations to the low-cost sensor's noise characteristics is found to be low, suggesting the inadequacy to directly reconstruct the total contact forces using the registered total human body accelerations.

The first approach reconstructs the total contact force using the total human body accelerations. Due to the low signal-to-noise ratio of the interaction human body accelerations, a large

reconstruction error is found indeed confirming the inadequacy for a direct total contact force reconstruction. Instead, it is found that a more accurate reconstruction of the structural response is found if the internally-driven contact forces are reconstructed by considering the total human body accelerations as a good approximation of the internally-driven ones. This means that for the specific case of the Eeklo footbridge, an inverse approach to estimate the governing HSI parameters is advised.

While the obtained conclusions are case-specific and depend on the modeling strategy and related parameters of the HSI model, the methodology to determine the optimal reconstruction method is generic as it can be applied on virtually any structure in combination with any HSI model.

REFERENCES

[1] K. Van Nimmen, G. Lombaert, G. De Roeck, and P. Van den Broeck, "Vibration serviceability of footbridges: Evaluation of the current codes of practice," *Engineering Structures*, vol. 59, pp. 448–461, 2014.

[2] K. Van Nimmen, G. Lombaert, G. De Roeck, and P. Van den Broeck, "The impact of vertical human-structure interaction on the response of footbridges to pedestrian excitation," *Journal of Sound and Vibration*, vol. 402, pp. 104–121, 2017.

[3] Association Française de Génie Civil, Sétra/AFGC, *Sétra: Evaluation du comportement vibratoire des passerelles piétonnes sous l'action des piétons (Assessment of vibrational behaviour of footbridges under pedestrian loading)*, 2006.

[4] C. Heinemeyer, C. Butz, A. Keil, M. Schlaich, A. Goldack, M. Lukić, B. Chabrolin, A. Lemaire, P. Martin, A. Cunha, and E. Caetano, *Design of Lightweight Footbridges for Human Induced Vibrations - Background document in support to the implementation, harmonization and further development of the Eurocodes*. JRC-ECCS 2009, 2009.

[5] S. Živanović, "Benchmark footbridge for vibration serviceability assessment under vertical component of pedestrian load," *Journal of Structural Engineering*, vol. 138, pp. 1193–1202, 2012.

[6] E. Ahmadi, C. Caprani, S. Živanović, and A. Heidarpour, "Assessment of human-structure interaction on a lively lightweight GFRP footbridge," *Engineering Structures*, vol. 199, p. 109687, 2019.

[7] E. Ahmadi, C. Caprani, S. Živanović, and A. Heidarpour, "Vertical ground reaction forces on rigid and vibrating surfaces for vibration serviceability assessment of structures," *Engineering Structures*, vol. 172, no. June, pp. 723–738, 2018.

[8] E. Ahmadi, C. Caprani, S. Živanović, N. Evans, and A. Heidarpour, "A framework for quantification of human-structure interaction in vertical direction," *Journal of Sound and Vibration*, vol. 432, pp. 351–372, 2018.

[9] K. Van Nimmen, K. Maes, P. Van den Broeck, and G. Lombaert, "Identification of human-induced loading using a joint input-state estimation algorithm," in *Proceedings of the 35th International Modal Analysis Conference Series*, (California, USA), January 2017.

[10] M. A. Toso, H. M. Gomes, F. T. Da Silva, and R. L. Pimentel, "Experimentally fitted biodynamic models for pedestrian-structure interaction in walking situations," *Mechanical Systems and Signal Processing*, vol. 72-73, pp. 590–606, 2016.

[11] H. V. Dang and S. Zivanovic, "Influence of Low-Frequency Vertical Vibration on Walking Locomotion," *Journal of Structural Engineering*, vol. 142, no. 12, pp. 1–12, 2016.

[12] E. Shahabpoor, A. Pavic, and V. Racic, "Identification of walking human model using agent-based modelling," *Mechanical Systems and Signal Processing*, vol. 103, pp. 352–367, 2018.

[13] K. Van Nimmen, P. Van den Broeck, and G. Lombaert, "Inverse identification of the pedestrian characteristics governing human-structure interaction," in *Proceedings of the 10th International Conference on Structural Dynamics, EURODYN 2017* (F. Vestroni, F. Romeo, and V. Gattulli, eds.), (Rome, Italy), pp. 2889–2894, September 2017.

[14] K. Van Nimmen, K. Maes, P. Van den Broeck, G. De Roeck, and G. Lombaert, "Inverse identification of pedestrian-induced loads," in *Proceedings of ISMA 2016 International Conference on Noise and Vibration Engineering* (P. Sas, D. Moens, and A. van de Walle, eds.), (Leuven, Belgium), September 2016.

[15] D. A. Winter, *The Biomechanics and Motor Control of Human Gait*, vol. 74. Waterloo, Ontario, Canada: University of Waterloo Press, 1988.

[16] J. M. W. Brownjohn, "Energy dissipation from vibration floor slabs due to human-structure interaction," *Journal of Shock and Vibration*, vol. 8, pp. 315–323, 2001.

[17] Y. Matsumoto and M. J. Griffin, "Mathematical models for the apparent masses of standing subjects exposed to vertical whole-body vibration," *Journal of Sound and Vibration*, vol. 260, no. 3, pp. 431–451, 2003.

[18] X. Zheng and J. M. W. Brownjohn, "Modelling and simulation of human-floor system under vertical vibration," in *Proceedings of SPIE: Smart Structures and Material* (L. Davis, ed.), 4327, pp. 513–520, 2001.

[19] E. Shahabpoor, A. Pavic, and V. Racic, "Interaction between Walking Humans and Structures in Vertical Direction: A Literature Review," *Shock and Vibration*, vol. 2016, no. June, pp. 1–22, 2016.

[20] K. Van Nimmen, G. Lombaert, G. De Roeck, and P. Van den Broeck, "The impact of vertical human-structure interaction on the response of footbridges to pedestrian excitation," *Journal of Sound and Vibration*, vol. 402, pp. 104–121, 2017.

[21] J. Duysens, I. Jonkers, and S. Verschueren, *MALL: Movement & posture Analysis Laboratory Leuven*. Interdepartmental research laboratory at the Faculty of Kinisiology and Rehabilitation Sciences - KU Leuven.

[22] G. C. D. Concepts, *X16-1D: User manual rev B*. 2016.

[23] S. Živanović, A. Pavic, and P. Reynolds, "Vibration serviceability of footbridges under human-induced excitation: A literature review," *Journal of Sound and Vibration*, vol. 279, no. 1-2, pp. 1–74, 2005.

[24] K. Van Nimmen, G. Zhao, A. Seyfarth, and P. Van den Broeck, "A Robust Methodology for the Reconstruction of the Vertical Pedestrian-Induced Load from the Registered Body Motion," *Vibration*, vol. 1, no. 2, pp. 250–268, 2018.

[25] V. Racic, J. M. W. Brownjohn, and A. Pavic, "Reproduction and application of human bouncing and jumping forces from visual marker data," *Journal of Sound and Vibration*, vol. 329, pp. 3397–3416, 2010.

[26] K. Van Nimmen, G. Lombaert, I. Jonkers, G. De Roeck, and P. Van den Broeck, "Characterisation of walking loads by 3D inertial motion tracking," *Journal of Sound and Vibration*, vol. 333, no. 20, pp. 5212–5226, 2014.

[27] K. Maes, A. W. Smyth, G. De Roeck, and G. Lombaert, "Joint input-state estimation in structural dynamics," *Mechanical Systems and Signal Processing*, vol. 70–71, pp. 445–466, 2016.

EURODYN 2020
XI International Conference on Structural Dynamics
M. Papadrakakis, M. Fragiadakis, C. Papadimitriou (eds.)
Athens, Greece, 23–26 November 2020

AN OPEN ACCESS BENCHMARK DATASET ON PEDESTRIAN-INDUCED VIBRATIONS COLLECTED ON THE EEKLO FOOTBRIDGE

P. Van den Broeck[1], **J. Van Hauwermeiren**[1], **and K. Van Nimmen**[1]

[1] KU Leuven, Department of Civil Engineering, Structural Mechanics
B-3001 Leuven, Belgium
e-mail: {peter.vandenbroeck, jeroen.vanhauwermeiren, katrien.vannimmen}@kuleuven.be

Keywords: footbridge, pedestrian-induced vibrations, dataset, open access.

Abstract. *This paper presents a new and publicly available full-scale dataset collected specifically for the further development and validation of models for crowd-induced loading. The dataset is collected on a real footbridge, with multiple modes sensitive to pedestrian-induced vibrations and with a digital twin available. Video cameras are used to capture the walking trajectories of the pedestrians. The bridge and pedestrian motion are registered simultaneously using wireless tri-axial accelerometers on the deck and the lower back of the pedestrians. Two data blocks are collected involving pure ambient excitation. Four data blocks are collected involving two pedestrian densities, 0.25 persons/m^2 and 0.50 persons/m^2, representing a total of more than one hour data for each pedestrian density. Analysis of the structural response shows that the different data blocks can be considered representative for the involved load case. The identified distribution of step frequencies in the crowd indicate a significant contribution of (near-)resonant loading with multiple modes of the footbridge. Furthermore, the dataset displays clear signs of human-structure interaction, suggesting a significant increase in effective modal damping ratios due to the presence of the crowd.*

1 INTRODUCTION

The vibration serviceability under crowd-induced loading has become a key design criterion for footbridges. Although increased research efforts are put into the characterization of crowd-induced loading including related interaction phenomena, a major challenge lies in the further development and validation of these load models. Full-scale benchmark datasets that simultaneously register the structural and crowd motion make an invaluable contribution to meeting this need by providing detailed information on representative operational loading and response data. Currently available datasets either (1) involve a (too) low number of pedestrians [1, 2, 3, 4, 5], (2) do not involve the simultaneous registration of pedestrian and bridge motion [1, 2, 6, 7, 8, 9], (3) do not involve a footbridge with multiple modes sensitive to walking excitation [3, 10, 11] and/or (4) for which a suitable digital twin is available, or (5) are not open access. To the knowledge of the authors, only the dataset collected by Živanović [10] and Gómez et al. [11] are publicly available.

In this paper, a novel publicly-available full-scale dataset is introduced, documenting a comprehensive experimental study involving pedestrian-induced vibrations on the Eeklo footbridge. The experimental study is unique and suitable for comprehensive validation purposes as it involves multiple pedestrian densities, the synchronous and detailed registration of the pedestrians' body motion and footbridge vibrations, a duration of the tests sufficient to be representative for the involved load cases, and a structure for which a reliable digital twin is available.

2 EEKLO FOOTBRIDGE

The Eeklo footbridge has three spans, a main central span of 42 m and two side spans of 27 m. In total, 14 modes were identified with a frequency up to 12 Hz (Figure 1). An excellent agreement is found between the experimentally identified modal characteristics and the ones calculated by the calibrated FE model. For more information related to the footbridge and the model calibration, the reader is referred to [12]. The corresponding digital twin describing the dynamic behavior of the footbridge, is part of the open access benchmark dataset.

3 EXPERIMENTAL STUDY

The bridge deck accelerations were measured using 10 wireless tri-axial acceleration sensors (GeoSIG GMS sensors [13]) with a sample rate of 200 Hz. The accelerations at the lower back of each participant was registered by a wireless inertial sensor [14] with a sample rate of 100 Hz. 21 cameras were used to capture the entire bridge deck at 30 frames per second. The acceleration signals registered on the bridge deck and at the lower back of the pedestrians are synchronized off-line using regular synchronization events. The cameras are synchronized off-line based on common events captured in adjacent cameras.

The experimental study considered ambient excitation of the empty footbridge and multiple tests with a duration of about 10 up to 20 minutes involving the pedestrian densities 0.25 persons/m^2 and 0.50 persons/m^2, and amounting to a total of more than one hour test data for each pedestrian density.

4 OBSERVATIONS

4.1 Distribution of step frequencies

Based on the measurements of all USB sensors, the time-variant pacing rate for each pedestrian is determined, using the procedure detailed in [15]. Figure 2-a shows the histogram of the

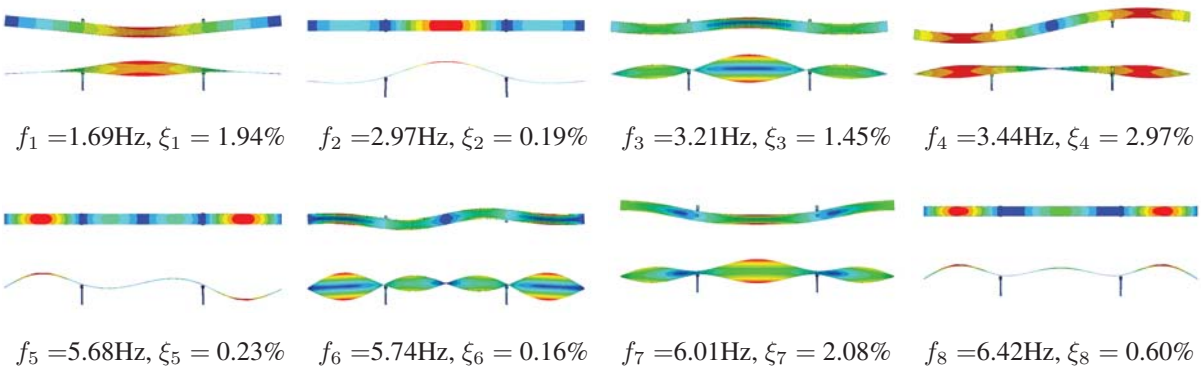

Figure 1: Top and side view of the first eight modes of the Eeklo footbridge (cfr. digital twin).

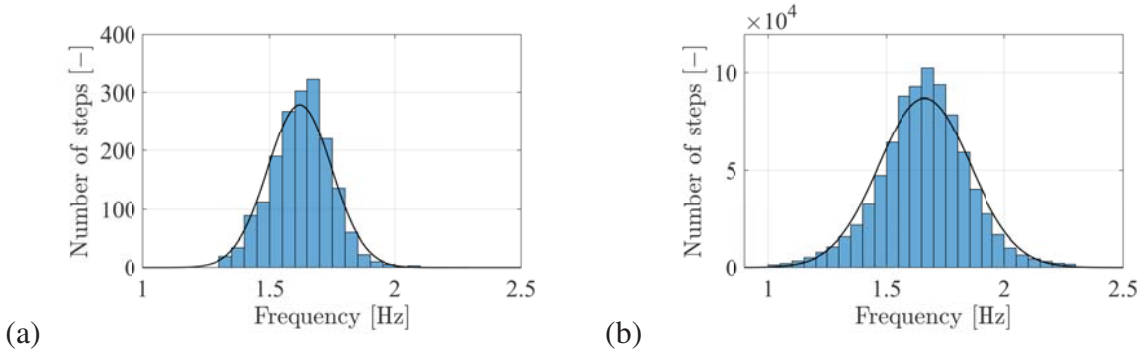

Figure 2: Histogram with fitted Gaussian distribution of the identified pacing rates (a) for a single pedestrian and (b) the corresponding aggregated distribution for all 148 pedestrians for a pedestrian density of 0.50 persons/m^2.

identified pacing rates for pedestrian 1 during free walking. This figure shows that the distribution of steps can be well fitted by a Gaussian distribution. A goodness of fit (chi-squared or χ^2 test) of 84% is found. Similar observations are made for the other pedestrians in the crowd.

Figure 2-b presents the histogram and fitted Gaussian distribution of the experimentally identified pacing rates of all pedestrians for pedestrian density of 0.50 persons/m^2. These results show that the distribution of step frequencies can again be well fitted by a Gaussian distribution. The distribution of step frequencies is characterized by $\mathcal{N}(1.66, 0.19)$ Hz (χ^2 test of 87%). Similarly, for a pedestrian density of 0.25 persons/m^2, a good fit is found with the distribution $\mathcal{N}(1.77, 0.13)$ Hz (χ^2 test of 94%). These results show that as the pedestrian density increases from 0.25 persons/m^2 to 0.50 persons/m^2, the mean walking speed slightly decreases [16, 17]. This, in turn, results in a decrease of the mean step frequency from 1.77 Hz to 1.66 Hz. It is also observed that the standard deviation in step frequency increases with the pedestrian density, from 0.13 Hz to 0.19 Hz. This phenomenon could be attributed to the impact of human-human interaction that increases with the pedestrian density: as the number of interactions between pedestrians increases, the pedestrians display more variations in their walking behavior, as also observed in [18].

4.2 Pedestrian trajectories

The video footage is used to obtain the pedestrian trajectories by a sequence of pedestrian detection and tracking, as comprehensively described in [19]. The time-averaged spatial dis-

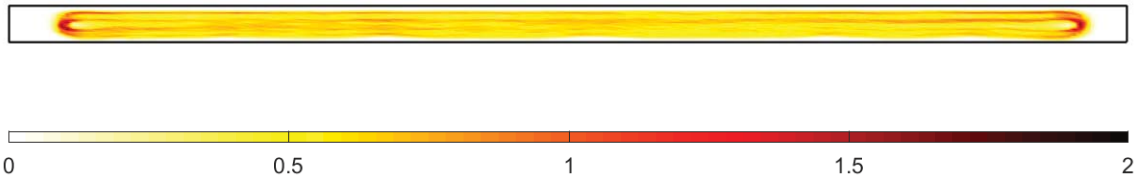

Figure 3: (Top) Heat map of the pedestrians during a test involving a pedestrian density of 0.50 persons/m^2 and (bottom) the corresponding color bar expressed in persons/m^2.

tribution of the pedestrians of a test involving a pedestrian destiny of 0.5 persons/m^2 is shown by means of a heat map in Figure 3. This figure shows that the spatial distribution is (slightly) non-uniform. This is the case for both pedestrian densities. Further analysis also shows that the spatial distribution (slightly) varies over consecutive time blocks, indicating that the spatial distribution is non-stationary. Also, during all tests the formation of 4 lanes over the width of the bridge deck is observed. This so-called lane-formation is a natural phenomenon in pedestrian flows [20].

The average speed of the pedestrians is calculated, resulting in the following distributions for the densities 0.25 and 0.50 persons/m^2: $\mathcal{N}(1.28, 0.02)$ m/s and $\mathcal{N}(1.10, 0.03)$ m/s.

4.3 Structural response

The structural response is low-pass filtered with a cut-off frequency of 10 Hz. Figure 4 presents the full time series and a 10-second zoom of the structural accelerations induced by ambient excitation and a pedestrian density of $0.50\ \mathrm{pedestrians/m^2}$. The Power Spectral Density (PSD) of the structural response is calculated considering consecutive time windows of length $T = 25$ s, with 50% overlap. Figure 5 presents the PSD of the structural accelerations induced by ambient excitation and a pedestrian density of $0.50\ \mathrm{pedestrians/m^2}$. It is noted that ambient excitation is also present when pedestrian excitation is considered. The following observations are made:

- When comparing the time series for ambient excitation to those involving pedestrian excitation, the vibration levels appear to be in the same order of magnitude.
- For ambient excitation, the PSD shows that the vertical structural accelerations are dominated by the contributions of the first (1.69 Hz) and the second (2.97 Hz) mode of the footbridge.
- For the entire frequency range up to 10 Hz, with the exception of a small interval around 2.97 Hz (structural mode 2), the PSD corresponding to pedestrian excitation is significantly larger than the one corresponding to ambient excitation. This observation indicates that pedestrian excitation is the dominant source of vibrations for the tests involving walking persons.
- The peak value of the PSD close to the fundamental mode of the footbridge (f_1 =1.69 Hz) is about 20 times larger when excited by a pedestrian density of $0.50\ \mathrm{pedestrians/m^2}$, compared to the peak value for ambient excitation. This observation indicates that the pedestrian excitation clearly prevails over the impact of ambient excitation. This observation is furthermore confirmed by the identified distributions of step frequencies (Figure 2)

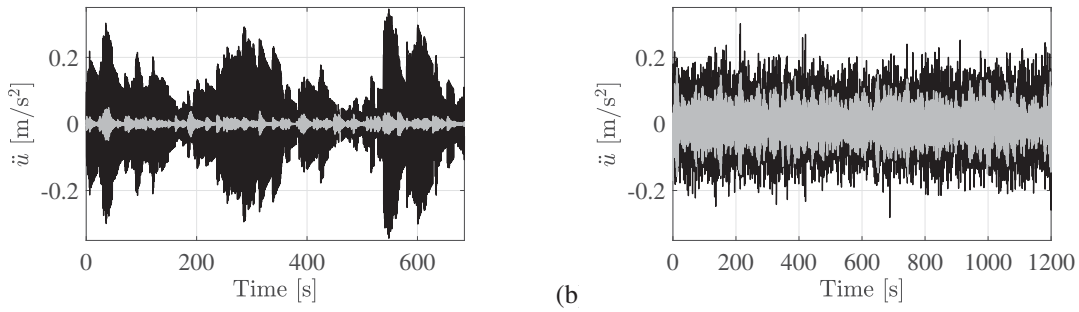

Figure 4: Time series of the structural accelerations induced by (a) ambient excitation and (b) a pedestrian density of $0.50\ \mathrm{pedestrians/m^2}$, low-pass filtered with a cut-off frequency of 10 Hz: the vertical (black) and lateral (gray) component in the middle of the center span.

which shows that a considerable fraction of the pedestrians is walking at (near-)resonance with the fundamental mode.

- The peak value of the PSD close to the second mode of the footbridge (2.97 Hz), is about 20 times *smaller* when excited by a pedestrian density of $0.50\ \mathrm{pedestrians/m^2}$, with respect to the peak value due to ambient excitation. Considering the second harmonic of the walking load, it is clear that also in this case a considerable fraction of the pedestrians is walking at (near-)resonance with the second mode of the footbridge (see Figure 2). In addition, the second mode is highly sensitive to (near-)resonant excitation, much more even than the fundamental mode, because of its very low modal damping ratio (0.2%) and modal mass. Therefore, it can be assumed that also in this frequency range, pedestrian excitation dominates the structural response. The fact that the peak value of the PSD close to the second mode is considerably smaller than when only ambient excitation is considered, can be assumed to be attributed to HSI. This is in line with recent studies [21, 22, 23, 24, 25] indicating that the effective damping ratio of the coupled crowd-structure system increases considerably for increasing crowd to structure mass ratios and for natural frequencies of the empty structure close to that of the human body of a pedestrian. This presumed increase in effective damping ratio is also in line with the observation that the peak in the PSD in figure 5 around the second mode (2.97 Hz) is considerably wider for the tests involving pedestrian excitation in comparison to the peak due to ambient excitation. Evidence of the increase in effective damping due to the presence of persons on the Eeklo footbridge, in particular for the second mode, has also been reported in [12].

5 CONCLUSIONS

This paper presents the benchmark full-scale dataset on pedestrian-induced vibrations collected on the Eeklo footbridge, involving the simultaneous registration of pedestrian and bridge motion. The Eeklo footbridge is a lightweight steel structure characterized by multiple low-frequent modes that lie within the dominant spectrum of pedestrian excitation. The structural vibrations are registered by wireless tri-axial accelerometers. The 3D body motion of each pedestrian is registered using a wireless tri-axial accelerometer, securely fixed close to the body center of mass, and the position along the bridge deck is captured by video cameras. The experimental study considered multiple tests involving the pedestrian densities 0.25 persons/m^2 and 0.50 persons/m^2, as well as two tests involving pure ambient excitation.

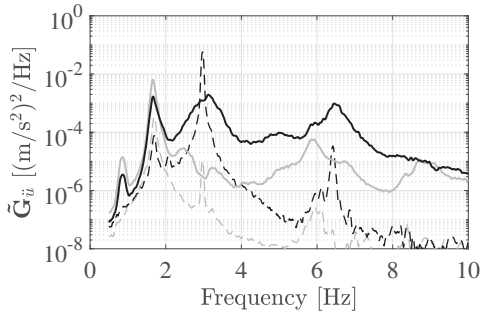

Figure 5: The average PSD of the structural accelerations due to ambient (dashed) and pedestrian (solid) excitation for a pedestrian density of 0.50 pedestrians$/\mathrm{m}^2$, low-pass filtered with a cut-off frequency of 10 Hz: the vertical (black) and lateral (gray) component in the middle of the center span.

Analysis shows that the different tests involving the same load case, can be considered representative for that involved load case. It is shown that pedestrian excitation dominates over ambient excitation when walking persons are involved. The dataset displays clear signs of HSI, suggesting a significant increase in effective modal damping ratio(s) due to the presence of the crowd, in particular for modes with a natural frequency close to that of the human body.

6 Data availability

The Eeklo footbridge benchmark dataset is freely available upon request to the corresponding author(s) and at (`www.kuleuven.be/structural-mechanics-ghent`, Tools and Downloads).

REFERENCES

[1] P. Fanning, P. Healy, and A. Pavic, "Pedestrian bridge vibration serviceability: A case study in testing and simulation," *Advances in Structural Engineering*, vol. 13, no. 5, pp. 861–873, 2010.

[2] F. Tubino, L. Carassale, and G. Piccardo, "Human-induced vibrations on two lively footbridges in Milan," *Journal of Bridge Engineering*, vol. 21, no. 8, 2016.

[3] P. Dey, A. Sychterz, S. Narasimhan, and S. Walbridge, "Performance of pedestrian-load models through experimental studies on lightweight aluminium bridges," *Journal of Bridge Engineering*, vol. 21, no. 8, 2016.

[4] K. Van Nimmen, P. Verbeke, G. Lombaert, G. De Roeck, and P. Van den Broeck, "Numerical and experimental evaluation of the dynamic performance of a footbridge with tuned mass dampers," *Journal of Bridge Engineering*, 2016.

[5] M. Bocian, J. Brownjoh, V. Racić, D. Hester, A. Quattrone, L. Gilbert, and R. Beasley, "Time-dependent spectral analysis of interactions within groups of walking pedestrians and vertical structural motion using wavelets," *Mechanical Systems and Signal Processing*, vol. 105, pp. 502–523, 2018.

[6] E. Caetano, A. Cunha, F. Magalhães, and C. Moutinho, "Studies for controlling human-induced vibration of the Pedro e Inês footbridge, Portugal. Part 1: Assessment of dynamic behaviour," *Engineering Structures*, vol. 32, pp. 1069–1081, 2010.

[7] S. P. Carroll, J. S. Owen, and M. F. M. Hussein, "A coupled biomechanical discrete element crowd model of crowd-bridge dynamic interaction and application to the clifton suspension bridge," *Engineering Structures*, vol. 49, pp. 58–75, 2013.

[8] J. Brownjohn and C. Middleton, "Efficient dynamic performance assessment of a footbridge," *Proceedings of the Institution of Civil Engineers*, vol. 158, no. 4, 2005.

[9] A. Gheitasi, O. Ozbulut, S. Usmani, M. Alipour, and D. Harris, "Experimental and analysitcal vibration serviceability assessment of an in-service footbridge," *Case Studies in Nondestructive Testing and Evaluation*, vol. 6, pp. 79–88, 2016.

[10] S. Živanović, "Benchmark footbridge for vibration serviceability assessment under vertical component of pedestrian load," *Journal of Structural Engineering*, vol. 138, pp. 1193–1202, 2012.

[11] S. Gomez, J. Marulanda, P. Thomson, J. Garcia, D. Gomez, A. Ortiz, S. Dyke, J. Caicedo, and S. Rietdyk, "Benchmark problem for assessing effects of human-structure interaction in footbridges," in *Proceedings of IMAC 35, the International Modal Analysis Conference*, (Garden Grove, CA, USA), Springer International Publishing, January – February 2017.

[12] K. Van Nimmen, G. Lombaert, I. Jonkers, G. De Roeck, and P. Van den Broeck, "Characterisation of walking loads by 3D inertial motion tracking," *Journal of Sound and Vibration*, vol. 333, pp. 5212–5226, 2014.

[13] GeoSIG GMS 18 24, *User Manual*. GeoSIG Ltd, 2012.

[14] Gulf Coast Data Concepts, *User Manual X16-1D USB Accelerometer Data Logger*. Gulf Coast Data Concepts, 2016.

[15] K. Van Nimmen, G. Zhao, A. Seyfarth, and P. Van den Broeck, "A robust methodology for the reconstruction of the vertical pedestrian-induced load from the registered body motion," *Vibration*, vol. 2, pp. 250–268, 2018.

[16] U. Weidmann, "Transporttechnik der fussganger (Transport technology of the pedestrian)," *Schriftenreihe IVT-Berichte*, vol. 90, 1993.

[17] F. Venuti and L. Bruno, "An interpretative model of the pedestrian fundamental relation," *Comptes Rendus - Mecanique*, vol. 335, no. 4, pp. 194–200, 2007.

[18] X. Wei, P. Van den Broeck, G. De Roeck, and K. Van Nimmen, "A simplified method to account for the effect of human-human interaction on the pedestrian-induced vibrations of footbridges," in *Proceedings of the 10th International Conference on Structural Dynamics, EURODYN 2017* (F. Vestroni, F. Romeo, and V. Gattulli, eds.), (Rome, Italy), September 2017.

[19] J. Van Hauwermeiren, P. Van den Broeck, K. Van Nimmen, and M. Vergauwen, "Vision-based methodology for characterizing the flow of a high-density crowd," in *Proceedings of the 9th InternationalConference on Bridge Maintenance, Safety and Management*, (Melbourne, Australia), Taylor and Francis Group, CRC Press, July 2018.

[20] D. Helbing and P. Molnar, "Social force model for pedestrian dynamics," *Physical Review*, vol. 51, no. 5, pp. 4282–4286, 1995.

[21] W. Dong, M. Kasperski, and G. Shiqiao, "Change of the dynamic characteristics of a pedestrian bridge during a mass event," in *Proceedings of the 8th International Conference on Structural Dynamics of EURODYN*, (Leuven, Belgium), July 2011.

[22] K. Salyards and Y. Hua, "Assessment of dynamic properties of a crowd model for human-structure interaction modelling," *Engineering Structures*, vol. 89, pp. 103–110, 2015.

[23] E. Shahabpoor, A. Pavić, and V. Racić, "Interaction between walking humans and structures in vertical direction : A literature review," *Shock and Vibration*, pp. 12–17, 2016.

[24] K. Van Nimmen, G. Lombaert, G. De Roeck, and P. Van den Broeck, "The impact of vertical human-structure interaction on the response of footbridges to pedestrian excitation," *Journal of Sound and Vibration*, vol. 402, pp. 104–121, 2017.

[25] F. Tubino, "Probabilistic assessment of the dynamic interaction between multiple pedestrians and vertical vibrations of footbridges," *Journal of Sound and Vibration*, vol. 417, pp. 80–96, 2018.

EURODYN 2020
XI International Conference on Structural Dynamics
M. Papadrakakis, M. Fragiadakis, C. Papadimitriou (eds.)
Athens, Greece, 23–26 November 2020

IDENTIFICATION OF HUMAN-STRUCTURE INTERACTION BASED ON FULL-SCALE OBSERVATIONS

K. Van Nimmen[1], J. Van Hauwermeiren[1], and P. Van den Broeck[1]

[1] KU Leuven, Department of Civil Engineering, Structural Mechanics
B-3001 Leuven, Belgium
e-mail: {katrien.vannimmen, jeroen.vanhauwermeiren, peter.vandenbroeck}@kuleuven.be

Keywords: footbridge, pedestrian-induced vibrations, human-structure interaction, full-scale observations.

Abstract. *The further development and improvement of prediction models for crowd-induced vibrations of footbridges requires detailed information on representative operational loading data. This paper uses an inverse method to estimate the parameters that govern human-structure interaction from the resulting structural response. The parameters of interest concern the dynamic characteristics of a single-degree-of-freedom (SDOF) system, applied to describe the mechanical interaction between the pedestrian and the structure. The parameter estimation procedure assumes that the dynamic behavior of the empty structure, the average pedestrian weight and the distribution of step frequencies in the crowd are known. The dynamic characteristics of the mechanical interaction model are estimated by minimizing the discrepancy between the observed and the simulated power spectral density of the structural response.*

The approach is applied to the Eeklo Footbridge Benchmark Dataset where the pedestrian and bridge motion are registered simultaneously using wireless tri-axial accelerometers, involving pedestrian densities up to 0.5 persons/m^2. A digital twin of the Eeklo footbridge, the average weight of the pedestrians and the distribution of step frequencies, identified from the accelerations registered on the lower back of each pedestrian, are used as input for the proposed parameter estimation procedure. The results show that an estimate of the natural frequency and damping ratio of the mechanical interaction model is obtained that is in line with recent findings in the literature. These estimates are, however, for the first time ever based on a comprehensive set of full-scale observations.

1 INTRODUCTION

Footbridges are often sensitive to human excitation. Although the dynamic performance under high crowd densities is often imperative for the design, these loading conditions have virtually never been verified [1]. The need for the validation of load models for crowd-induced loading is high, in particular due to the impact of human-structure interaction (HSI) that is predicted to play a vital role in the vibration serviceability assessment [2, 3, 4, 5].

In-field observations are the only way to obtain detailed and accurate information on representative operational loading data. As direct force measurements are in this case practically infeasible, inverse methods, where the unknown input parameters are identified from the resulting vibration response and a dynamic model of the structure, constitutes a promising alternative.

This paper uses a parameter estimation procedure to estimate the parameters that govern HSI from the resulting structural response. This procedure is applied to a dataset of in-field observations on a slender footbridge involving a pedestrian density of 0.5 persons/m^2.

2 METHODOLOGY

2.1 Coupled crowd-structure model

The mathematical framework introduced in [4] is used. In this framework, each pedestrian in the crowd is modeled as the superposition of an autonomous force term, corresponding to the forces induced on a rigid surface, and a linear SDOF system used to simulate the mechanical interaction with the supporting structure. This SDOF system is composed of a rigid and an activated mass, representing respectively 5% and 95% of the total mass of the pedestrian. The dynamic behavior of the supporting structure, which in this study is referring to a footbridge, is represented by its modal parameters. The equations of motion of the coupled crowd-structure model read:

$$\dot{\mathbf{x}}(t) = \mathbf{A_c}\mathbf{x}(t) + \mathbf{B_c}\mathbf{S_p}(t)\mathbf{p}_{\text{F}}(t) \tag{1}$$

$$\text{with} \quad \mathbf{x}(t) = \begin{bmatrix}\mathbf{z}(t) & \mathbf{u}_{\text{H}}(t) & \dot{\mathbf{z}}(t) & \dot{\mathbf{u}}_{\text{H}}(t)\end{bmatrix}^\top \tag{2}$$

$$\mathbf{A_c} = \begin{bmatrix}\mathbf{0} & \mathbf{I} \\ -\bar{\mathbf{M}}_{\text{HS}}^{-1}\bar{\mathbf{K}}_{\text{HS}} & -\bar{\mathbf{M}}_{\text{HS}}^{-1}\bar{\mathbf{C}}_{\text{HS}}\end{bmatrix} \tag{3}$$

$$\mathbf{B_c} = \begin{bmatrix}\mathbf{0} \\ \mathbf{T_p}\end{bmatrix} \tag{4}$$

with $\mathbf{x}(t) \in \mathbb{R}^{n_s}$ the state vector and $n_s = 2(n_m + n_{\text{H}})$, $\mathbf{z}(t) \in \mathbb{R}^{n_m}$ the modal coordinate vector, n_m the number of modes, $\mathbf{u}_{\text{H}} \in \mathbb{R}^{n_{\text{H}}}$ the vector of displacements of SDOF interaction models, n_{H} the number of pedestrians, $\mathbf{p}_{\text{F}}(t) \in \mathbb{R}^{n_{\text{H}}}$ is the force vector collecting the time history of the autonomous force term $p_{\text{F},k}(t)$ of each pedestrian k of the n_{H} pedestrians as rows and $\mathbf{S_p}(t) \in \mathbb{R}^{n_{\text{DOF}} \times n_{\text{H}}}$ a selection matrix which transfers the forces to the corresponding n_{DOF} DOFs of the model of the structure. $\bar{\mathbf{M}}_{\text{HS}}$, $\bar{\mathbf{K}}_{\text{HS}}$ and $\bar{\mathbf{C}}_{\text{HS}}$ are the generalized mass-, stiffness and damping matrices of the coupled crowd-structure system and $\mathbf{T_p}$ is the generalized input transformation matrix, as defined in [4]. The autonomous force term $p_{\text{F},k}(t)$ depends on the weight and the step frequency ($f_{s,k}$) of the pedestrian and is modeled using the probabilistic single-person force model developed by Živanović et al. [6].

2.2 Parameter estimation problem

The parameter estimation problem is highly similar to the one introduced in [7]. The objective is to identify the parameters that determine the effect of HSI on the resulting structural

response: the dynamic characteristics of the linear mechanical systems representing the pedestrians in the crowd. The following inputs are assumed to be known:

1. The dynamic behavior of the empty footbridge.
2. The structural response induced by the pedestrians at one or more locations on the footbridge.
3. The average (total) mass of the pedestrians.
4. The distribution of step frequencies in the crowd: $f_s = \mathcal{N}(\mu_{f_s}, \sigma_{f_s})$ [Hz].

The first three items can be obtained using conventional techniques or tests. The fourth item can, for example, be identified from acceleration measurements performed at the lower back of each pedestrian (See accompanying paper: 'An open access benchmark dataset on pedestrian-induced vibrations collected on the Eeklo footbridge').

In [7] it is shown that when a sufficiently long duration of the structural response induced by a pedestrian density d is considered, the statistical effect of the autonomous force term (resulting from the random arrival times and the intra-person variabilities) on the power spectral density (PSD) of the resulting structural response can be averaged out.

The optimization problem is now formulated where the objective function measures the difference between the PSD of the experimentally observed ($\tilde{\mathbf{G}}_{\ddot{u}}$) and the numerically simulated ($\mathbf{G}_{\ddot{u}}$) structural response within a frequency range defined by a lower (ω_{l} [rad/s]) and upper bound (ω_{u} [rad/s]). The residuals are computed at discrete frequencies ω_k [rad/s]: $\omega_k = \omega_{\mathrm{l}} + k\Delta\omega \quad \text{for} \quad k = 0, ..., N$, with $N + 1 = (\omega_{\mathrm{u}} - \omega_{\mathrm{l}})/\Delta\omega + 1$ the number of samples and $\Delta\omega$ the selected frequency resolution. The parameters of the SDOF model are assumed identical for the different persons on the structure. The average total mass of the pedestrians is a known input, determining the rigid (5%) and activated mass (95%) of the SDOF model. The decision variables in this optimization problem are the natural frequency f_{H1} and the modal damping ratio ξ_{H1}, and are subject to the following physical constraints: $f_{\mathrm{H1}} > 0$ and $\xi_{\mathrm{H1}} > 0$. The problem, subject to two inequality constraints, is formulated in standard form:

$$\underset{f_{\mathrm{H1}},\, \xi_{\mathrm{H1}}}{\text{minimise}} \quad \frac{\| \tilde{\mathbf{G}}_{\ddot{u}} - \mathbf{G}_{\ddot{u}}(f_{\mathrm{H1}}, \xi_{\mathrm{H1}}) \|_2^2}{\| \tilde{\mathbf{G}}_{\ddot{u}} \|_2^2} \tag{5}$$

$$\text{subject to} \quad f_{\mathrm{H1}} > 0 \tag{6}$$

$$\xi_{\mathrm{H1}} > 0 \tag{7}$$

and can be categorized as a nonlinear programming problem due to the nature of the objective function. The inequality constrained optimization problem is solved using the lsqnonlin-solver (MATLAB®) by means of the trust-region-reflective algorithm.

3 EEKLO FOOTBRIDGE

The Eeklo footbridge has three spans, a main central span of 42 m and two side spans of 27 m. The dynamic behavior of the footbridge is characterized by 14 modes with a frequency up to 12 Hz. The corresponding digital twin describing the dynamic behavior of the footbridge, is part of the open access benchmark dataset (See accompanying paper: 'An open access benchmark dataset on pedestrian-induced vibrations collected on the Eeklo footbridge').

3.1 Numerical verification

In this numerical verification section, the objective is to verify the parameter optimization procedure for the Eeklo footbridge. In addition, the impact of modeling errors on the solution of the parameter estimation problem is investigated.

In this numerical verification example, the pedestrian density is set to match the one considered in the in-field tests (see next section): 148 persons (≈ 0.5 persons/m^2). The distribution of step frequencies is set to follow a Gaussian distribution: $f_s = \mathcal{N}(1.89, 0.18)$ [Hz]. The weight of the pedestrians is set to 70 kg. The corresponding PSD of the pedestrian load is defined based on the procedure detailed in [8], using the dynamic load factors for the main and sub-harmonics of the walking load defined in [6]. The PSD of the pedestrian load is presented in Figure 1.

The natural frequency (f_{H1}) and the modal damping ratio (ξ_{H1}) of the interaction model are set to respectively 3 Hz and 30%. Figure 2 visualizes the FRF of the Eeklo footbridge, empty and with HSI. This figure shows that the impact of HSI is high for mode 2 ($f_2 = 2.97$ Hz), mode 5 ($f_5 = 5.68$ Hz) and mode 8 ($f_8 = 6.42$ Hz). These modes are bending modes characterized by a low modal mass (22×10^3 kg – 26×10^3 kg) and a low damping ratio ($0.2\% - 0.6\%$). The highest impact is found for mode 2, as the natural frequency of the interaction model is in this case close to the optimal tuning frequency for accelerations [9].

When no modeling errors are assumed, the parameter estimation procedure converges to the true minimum. This was also illustrated for a hypothetical example in [7]. This contribution in addition analyses the influence of modeling errors. These modeling errors ($\epsilon_{\square}$) are related to the inputs that the parameter estimation procedure assumes to be known. Given the high accuracy with which the structural response can be measured, and the ease with which the total mass of the pedestrians can be determined, the impact of related errors is not investigated. Also, it is assumed that the impact of (correlated) measurement noise, e.g. related to the sensor placement, is negligible. The modeling errors considered in this study are related to:

- The dynamic behavior of the empty structure, or thus the structural modal parameters: Given the uncertainty bounds on the modal parameters identified using state-of-the-art system identification techniques [10, 11], it is reasonable to assume errors of ϵ_f =1% and ϵ_ξ =10% on respectively the experimentally identified natural frequencies and modal damping ratios. The corresponding modal masses can be calculated using a (preferably calibrated) FE model of the structure. For the calculated modal mass, an error of ϵ_m =2% is considered reasonable. Less satisfactory results may be characterized by errors of 5%, 30% and 5% (upper bound error) on respectively the natural frequencies, modal damping ratios and modal masses.

- The distribution of step frequencies in the crowd: Assuming that the distribution of step frequencies follows a Gaussian distribution, the impact of an error of 2% and 5% on the mean value (ϵ_μ) and standard deviation (ϵ_σ) of the step frequencies is investigated.

The parameter estimation procedure now uses the PSD of the vertical and lateral acceleration levels calculated at the center of the main and the side span of the footbridge (close to the parapet). Analysis shows that as little information on HSI is contained in the PSD of the lateral acceleration levels, including these PSDs in the objective function (Eq. 5) has a negligible impact on the obtained optimal solution. These PSDs can therefore be excluded from the selected input data.

For the sake of conciseness, this paper only reports the joint impact of the modeling errors on the solution of the parameter estimation problem (estimation error). The estimation error

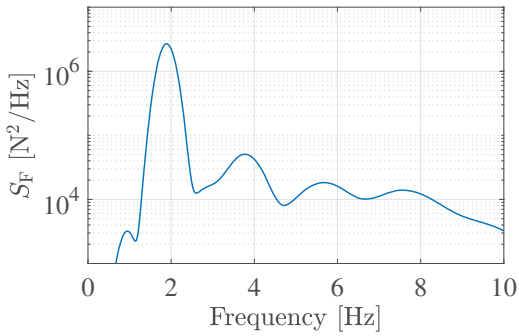

Figure 1: PSD of the pedestrian load (S_F) for 148 persons.

($\Delta_\square$) is expressed in terms of the percentage of difference with the true optimal solution of the parameter estimation problem ($f^\star_{H1} = 3$ Hz, $\xi^\star_{H1} = 30$ %). The following results are found:

- $\Delta_{f^\star_{H1}} = 3\%$ and $\Delta_{\xi^\star_{H1}} = 9\%$ for ϵ_f =1%, ϵ_ξ =10%, ϵ_m =2%, $\epsilon_\mu = \epsilon_\sigma = 2\%$.
- $\Delta_{f^\star_{H1}} = 5\%$ and $\Delta_{\xi^\star_{H1}} = 20\%$ for ϵ_f =2%, ϵ_ξ =30%, ϵ_m =5%, $\epsilon_\mu = \epsilon_\sigma = 5\%$.

These results show that the impact of the reasonable range of modeling errors that can be expected for the present case, have a small impact on the estimated natural frequency of the interaction model (5%). The impact on the estimated damping ratio is higher (20%), but is still reasonable given that the structural response is less sensitive to changes in this parameter. Further analysis shows that in this case, the errors on the distribution of step frequencies (ϵ_μ and ϵ_σ) have the largest impact on the estimation error. The low impact of the relatively large modeling errors assumed on the modal damping ratios, stems from the fact that the modal damping ratios of the dominant modes are very low in relation to the damping added by HSI. By consequence, the impact of these inherent structural modal damping ratios on the corresponding effective damping of the coupled crowd-structure system is very low.

However, it is noted that the low impact of the modeling errors, in particular those related to the modal parameters of the footbridge, on the estimated parameters is in this case due to the high impact of HSI on multiple modes of the footbridge (mode 2, mode 5 and mode 8). This is, in turn, due to the involved low modal masses, low damping ratios and natural frequencies of these modes. These results are highly case-specific and should be investigated for each case prior to the application of the parameter estimation procedure. Furthermore, this investigation does not consider the impact of other modeling errors, such as for example lateral mechanical HSI that is neglected here or errors in the load model that is used to describe the autonomous force term.

3.2 Application to full-scale data

The inputs for the parameter estimation procedure are set to match the conditions of the in-field observations involving 148 pedestrians (See accompanying paper: 'An open access benchmark dataset on pedestrian-induced vibrations collected on the Eeklo footbridge'):

1. The digital twin of the Eeklo footbridge is used to describe the dynamic behavior of the empty footbridge.

2. The structural response measured at the center of the main and the side span is used (close to the parapet). As the numerical verification section has shown that HSI is most relevant

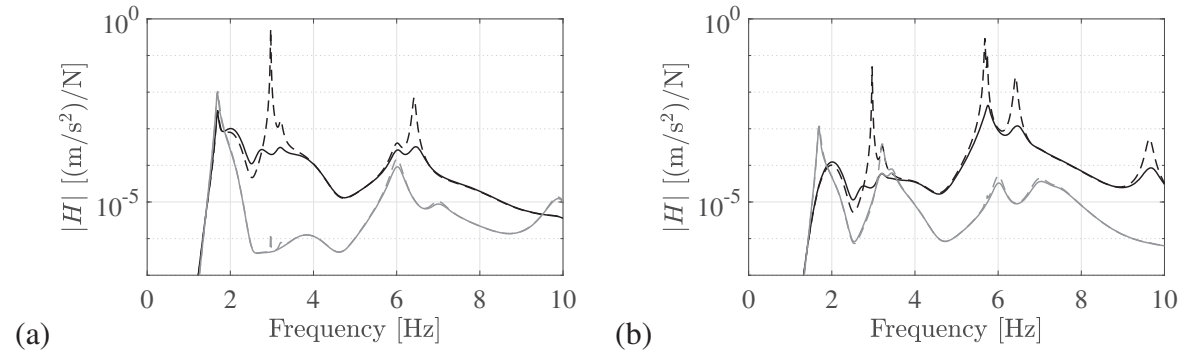

Figure 2: The FRF for a (black) vertical and (gray) lateral input and output acceleration at the center of the (a) central and (b) side span of the Eeklo footbridge, (dashed) empty and (solid) with HSI, for a pedestrian density of 0.50 persons/m^2.

for the vertical output, only the acceleration levels registered in the vertical direction are used. The Power Spectral Density (PSD) of the structural response is calculated considering consecutive time windows of length $T = 25$ s, with 50% overlap.

3. The average body mass of the pedestrians is 73.2 kg.

4. The distribution of step frequencies in the crowd: $f_s = \mathcal{N}(1.66,\ 0.19)$ [Hz].

Given that the highest impact of HSI is expected for mode 2, mode 5 and mode 8, the frequency range [2.5, 8.0] Hz is taken into account for the parameter estimation procedure.

In Figure 3, the objective function defined in Eq. 5 is evaluated for a realistic range of the two decision variables: the natural frequency $1 \leq f_{\text{H}} \leq 5$ [Hz] and the modal damping ratio $0.2 \leq \xi_{\text{H}} \leq 0.6$ [-]. This figure shows that the objective function, and thus the impact of HSI, is mainly sensitive to changes in the natural frequency f_{H} of the interaction model. Figure 3 illustrates a generally low sensitivity of the objective function to the modal damping ratio ξ_{H} of the interaction model.

The following optimal solution is found for the interaction model:

- $f^{\star}_{\text{H1}} = 3.02$ Hz
- $\xi^{\star}_{\text{H1}} = 46$ %

Figure 4 compares the PSD of the measured output with the one calculated for the footbridge with and without HSI, whereby HSI is modeled with the fitted interaction model. In turn, Figures 5 and 5 present the measured and calculated (with and without HSI) vertical acceleration levels at respectively the midspan and the sidespan. These figures show that when HSI is disregarded, the structural response is significantly overestimated. More importantly, this figure shows that the fitted interaction model allows to arrive at a good fit with the measurements. Based on the insights gained in the numerical verification section, an indicative uncertainty bound of 5% and 20% on respectively the estimated natural frequency and modal damping ratio is assumed, where this uncertainty in this case mainly stems from the modeling errors related to the distribution of the step frequencies in the crowd. These uncertainty bounds are also indicated on Figure 3.

Finally, it is noted that the identified natural frequency ($f_{\text{H1}} = 3.02 \pm 0.15$ Hz) and damping ratio ($\xi_{\text{H1}} = 0.46 \pm 0.10$) of the interaction model are in line with recent findings in the literature [3, 4].

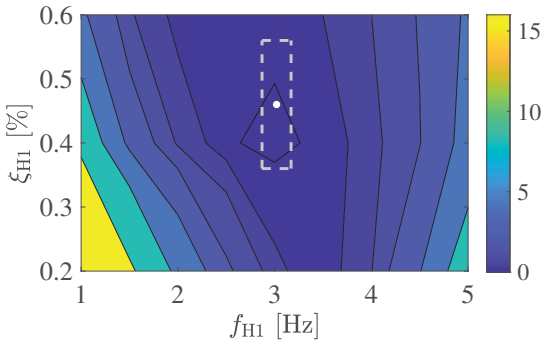

Figure 3: Evaluation of the objective function in terms of the natural frequency f_{H1} and the damping ratio ξ_{H1} of the interaction model, and the indicative uncertainty bounds (dashed lines) on the optimal solution (•).

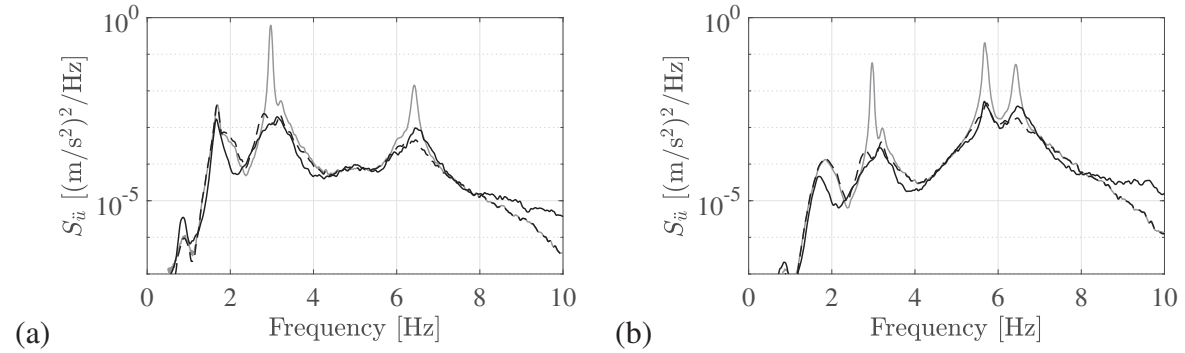

Figure 4: The PSD of the vertical acceleration levels at the center of the (a) central and (b) side span of the Eeklo footbridge for a pedestrian density of 0.50 persons/m^2: (black, solid) measurements, and numerically simulated (gray, solid) without HSI and (black, dashed) with HSI based on the fitted interaction model.

4 CONCLUSIONS

This paper estimates the natural frequency and damping ratio of an SDOF interaction model, applied to describe the mechanical interaction between the pedestrian and the structure, by minimizing the discrepancy between the observed and the simulated power spectral density of the structural response. The approach is applied to the Eeklo Footbridge Benchmark Dataset where the pedestrian and bridge motion are registered simultaneously using wireless tri-axial accelerometers and video cameras, involving a pedestrian density of 0.5 persons/m². A digital twin of the Eeklo footbridge, the average weight of the pedestrians and the distribution of step frequencies, identified from the accelerations registered on the lower back of each pedestrian, are used as input for the proposed parameter estimation procedure. A natural frequency of 3 Hz and a damping ratio of 46% are identified for the mechanical interaction model. These results are in line with recent findings in the literature and are, for the first time ever, based on full-scale observations.

REFERENCES

[1] C. T. Georgakis and E. Ingólfsson, "Recent advances in our understanding of vertical and lateral footbridge vibrations," in *Proceedings of the 5th International Footbridge Conference*, (London, UK), July 2014.

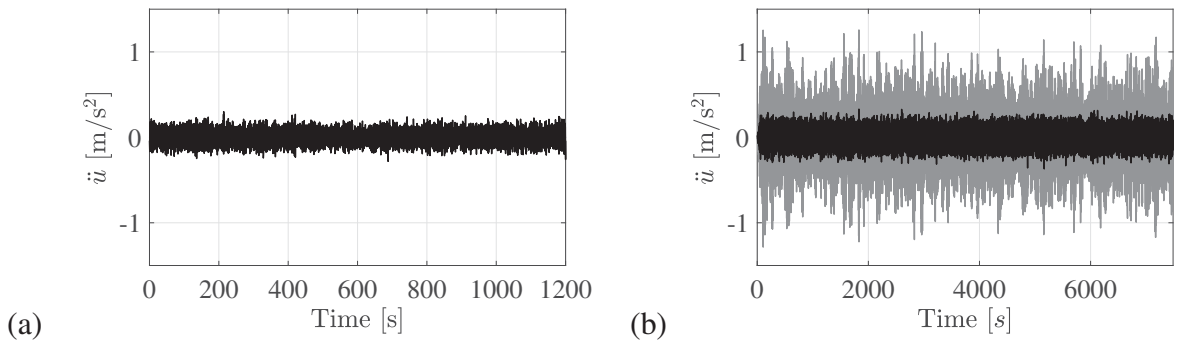

Figure 5: The vertical acceleration levels at the center of the central span of the Eeklo footbridge for a pedestrian density of 0.50 persons/m^2: (a) measurements, (b) numerically simulated (gray) without HSI and (black) with HSI based on the fitted interaction model.

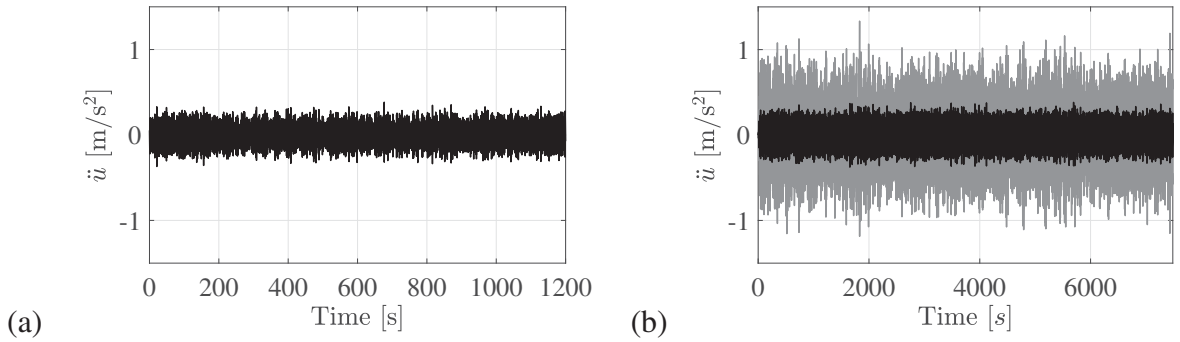

Figure 6: The vertical acceleration levels at the center of the side span of the Eeklo footbridge for a pedestrian density of 0.50 persons/m^2: (a) measurements, (b) numerically simulated (gray) without HSI and (black) with HSI based on the fitted interaction model.

[2] K. Salyards and Y. Hua, "Assessment of dynamic properties of a crowd model for human-structure interaction modelling," *Engineering Structures*, vol. 89, pp. 103–110, 2015.

[3] E. Shahabpoor, A. Pavić, and V. Racić, "Interaction between walking humans and structures in vertical direction : A literature review," *Shock and Vibration*, pp. 12–17, 2016.

[4] K. Van Nimmen, G. Lombaert, G. De Roeck, and P. Van den Broeck, "The impact of vertical human-structure interaction on the response of footbridges to pedestrian excitation," *Journal of Sound and Vibration*, vol. 402, pp. 104–121, 2017.

[5] F. Tubino, "Probabilistic assessment of the dynamic interaction between multiple pedestrians and vertical vibrations of footbridges," *Journal of Sound and Vibration*, vol. 417, pp. 80–96, 2018.

[6] S. Živanović, A. Pavić, and P. Reynolds, "Probability-based prediction of multi-mode vibration response to walking excitation," *Engineering Structures*, vol. 29, no. 6, pp. 942–954, 2007.

[7] K. Van Nimmen, P. Van den Broeck, and G. Lombaert, "Inverse identification of the pedestrian characteristics governing human-structure interaction," in *Proceedings of the 10th International Conference on Structural Dynamics, EURODYN 2017* (F. Vestroni, F. Romeo, and V. Gattulli, eds.), (Rome, Italy), pp. 2889–2894, September 2017.

[8] K. Van Nimmen, P. Van den Broeck, G. Lombaert, and F. Tubino, "Pedestrian-induced vibrations of footbridges: An extended spectral approach," *Journal of Bridge Engineering, Forthcoming, 10.1061/(ASCE)BE.1943-5592.0001582*, 2020.

[9] T. Asami, O. Nishihara, and A. Baz, "Analytical solutions to h-infinity and h-2 optimization of dynamic vibration absorbers attached to damped linear systems," *Journal of Vibration and Acoustics - ASME*, vol. 124, no. 2, pp. 284–295, 2002.

[10] B. Peeters and G. De Roeck, "Reference-based stochastic subspace identification for output-only modal analysis," *Mechanical Systems and Signal Processing*, vol. 13, no. 6, pp. 855–878, 1999.

[11] E. Reynders and G. De Roeck, "Reference-based combined deterministic-stochastic subspace identification for experimental and operational modal analysis," *Mechanical Systems and Signal Processing*, vol. 22, no. 3, pp. 617–637, 2008.

EURODYN 2020
XI International Conference on Structural Dynamics
M. Papadrakakis, M. Fragiadakis, C. Papadimitriou (eds.)
Athens, Greece, 23–26 November 2020

A NOVEL METHOD FOR INDIRECT MEASUREMENT OF GROUND REACTION FORCES ON VIBRATING STRUCTURES

Andrei Firus[1], Roman Kemmler[2], Hagen Berthold[1], Steven Lorenzen[1] and Jens Schneider[1]

[1]Technical University of Darmstadt, Institute of Structural Mechanics and Design
Franziska-Braun-Str. 3, 64287 Darmstadt, Germany
e-mail: firus,berthold,lorenzen,schneider@ismd.tu-darmstadt.de

[2]HTWG Konstanz – University of Applied Sciences, Department of Civil Engineering
Alfred-Wachtel-Str. 8, 78462 Konstanz, Germany
e-mail: roman.kemmler@htwg-konstanz.de

Keywords: Ground reaction forces, human induced vibrations, human-structure interaction, footbridges, vibration serviceability, inverse problems.

Abstract. *This paper presents a novel method for the indirect determination of the ground reaction forces (GRF) induced by a pedestrian during forward locomotion on a vibrating structure. It is based on the formulation of an inverse problem for the identification of the unknown time dependent moving load, which is solved by means of a gradient-based optimization algorithm. The force identification is performed in the time domain using accelerations and/or displacement time histories recorded at different locations on the structure as input data. The practicability and accuracy of the method is evaluated using both simulated measurements and real experimental data recorded on the HUMVIB experimental footbridge on the campus of the Technical University of Darmstadt, Germany. For the validation of the reconstructed forces, an array of biomechanical force plates as well as classical load cells at the supports of the test structure were used. The results show that the proposed method allows a very accurate estimation of the GRF induced by a subject during walking on the experimental structure.*

1 INTRODUCTION

Classical direct measurement methods of ground reaction forces (GRF) induced by pedestrians on rigid surfaces usually imply either force plates [1] or treadmills instrumented with force sensors [2], which are commonly used in biomechanical studies of the human gait. The GRFs can also be directly acquired by means of foot pressure insoles, i.e. instrumented shoes [3, 4]. Their main advantage is that the subject does not have any locomotion constraints, such as targeting the force plates [5], allowing thus the execution of a natural gait. Besides the direct measurement methods, there are also indirect approaches, which try to reconstruct the GRF by means of three dimensional recordings of the body motion and an assumed distribution of the body mass under consideration of the second Newton's law of motion [6, 7, 8, 9, 10]. Extensive literature overviews on the measurement methods of GRFs are given in [5] and [11].

When it comes down to the direct GRF measurement during walking on vibrating structures, only few methods are feasible with justifiable effort. The installation of classical force plates on vibrating structures is possible, it implies however high costs and is rather only feasible for laboratory experiments [12, 13]. In case of laboratory structures, it is also possible to install conventional load cells at the supports [12, 13]. However, both in case of the force plates and the the load cells, the measured forces are "polluted" by a significant component generated by the inertia of the force plate or of the vibrating structure itself, which leads to additional analysis effort and to certain inaccuracies [13, 14]. A good alternative for GRF measurement on vibrating structures are the in-shoe pressure sensors, which have already been used in civil engineering applications [13, 15]. However, they present a limited accuracy of the force amplitudes, which are obtained by integrating the distributed pressure over the foot insole area [5].

In comparison to the drawbacks of the aforementioned direct measurement methods, the time histories of the structural displacements and accelerations can be recorded with high accuracy and reasonable effort. In this sense, this paper addresses a novel method for the indirect determination of the GRF induced by a pedestrian on a vibrating structure, which is based on conventional measurements of structural responses, avoiding thus the use of costly and sensitive biomechanical equipment. The method implies the formulation of an inverse problem for the identification of the unknown time dependent moving load, whose solution is addressed by means of a gradient-based optimization algorithm. The force reconstruction is executed in the time domain using accelerations and/or displacement time histories recorded at different locations on the structure as input data. The practicability and accuracy of the method is evaluated using real experimental data recorded on the HUMVIB experimental footbridge at the Technical University of Darmstadt, Germany. For the validation purposes, an array of biomechanical force plates as well as classical load cells at the supports were used. The method aims to facilitate the analysis of the human-structure interaction effects on bridges in operation.

2 FORMULATION OF THE PROBLEM

2.1 The forward problem

The computation of the motion quantities for a damped linear system containing n_{dof} degrees of freedom can be performed by solving the differential equation of motion:

$$\boldsymbol{K} \cdot \boldsymbol{u}(t) + \boldsymbol{D} \cdot \dot{\boldsymbol{u}}(t) + \boldsymbol{M} \cdot \ddot{\boldsymbol{u}}(t) = \boldsymbol{P}(t) \tag{1}$$

where $\boldsymbol{K}^{n_{\mathrm{dof}} \times n_{\mathrm{dof}}}$, $\boldsymbol{D}^{n_{\mathrm{dof}} \times n_{\mathrm{dof}}}$ and $\boldsymbol{M}^{n_{\mathrm{dof}} \times n_{\mathrm{dof}}}$ are the stiffness, damping and mass matrix, respectively, while $\boldsymbol{P}^{n_{\mathrm{dof}} \times 1}$ represents the vector of external forces at each time instant. $\boldsymbol{u}$, $\dot{\boldsymbol{u}}$ and

$\ddot{\boldsymbol{u}}$ denote the vectors of motion quantities (displacement, velocity and acceleration, respectively). In order to achieve the solution of Eq. 1, it can either be directly integrated or it can be solved by means of the modal superposition principle [16]. The force reconstruction method of the present study is based on the latter one, whereas the modal equations are solved using the time step integration method of Newmark [16].

2.2 The inverse problem

The inverse problem of GRF reconstruction on a vibrating structure formulated within this work implies that the entries of the load vector $\boldsymbol{P}(t)$ are considered to be unknown, while the system matrices $\boldsymbol{K}$, $\boldsymbol{D}$ and $\boldsymbol{M}$ in Eq. 1 are given and assumed to be constant. In addition, it is considered that a set of n_{md} displacement and n_{ma} acceleration time histories are acquired over a finite number n_{t} of discrete time points through experimental investigations. Basically, the inverse problem seeks to find an optimal time-dependent force vector $\boldsymbol{P}(t)$, which caused the measured motion quantities. This can be expressed by means of an unconstrained and unbounded optimization problem:

$$\begin{aligned}\min_{\boldsymbol{s}} \mathcal{F}(\boldsymbol{s}) = & w_{\mathrm{d}} \cdot \sum_{h=1}^{n_{\mathrm{md}}} \sum_{i=1}^{n_{\mathrm{t}}} (u_{h,i} - \bar{u}_{h,i})^2 + w_{\mathrm{a}} \cdot \sum_{h=1}^{n_{\mathrm{ma}}} \sum_{i=1}^{n_{\mathrm{t}}} (\ddot{u}_{h,i} - \bar{\ddot{u}}_{h,i})^2 + \\ & \underbrace{w_{\mathrm{p1}} \cdot \left\| \left(\overbrace{\boldsymbol{Q}_{\mathrm{loc}}^{n_{\mathrm{var}} \times n_{\mathrm{var}}} - \boldsymbol{Q}_{\mathrm{glo}}^{n_{\mathrm{var}} \times n_{\mathrm{var}}}}^{\boldsymbol{Q}_{\mathrm{p1}}} \right) \cdot \boldsymbol{s}^{n_{\mathrm{var}} \times 1} \right\|_2^2}_{\text{Penalty function 1}} + \\ & \underbrace{w_{\mathrm{p2}} \cdot \left\| \left(\overbrace{\boldsymbol{I}^{n_{\mathrm{var}} \times n_{\mathrm{var}}} - \boldsymbol{Q}_{\mathrm{loc}}^{n_{\mathrm{var}} \times n_{\mathrm{var}}}}^{\boldsymbol{Q}_{\mathrm{p2}}} \right) \cdot \boldsymbol{s}^{n_{\mathrm{var}} \times 1} \right\|_2^2}_{\text{Penalty function 2}}\end{aligned} \tag{2}$$

here, $\boldsymbol{s} \in \mathbb{R}^{n_{\mathrm{var}}}$ comprises the n_{var} load values s_k, each of them denoting the value of the moving force at a certain time step t_k, while k represents the index of the n_{var} time steps, in which the force is present on the bridge. $\bar{u}_{h,i}$ and $\bar{\ddot{u}}_{h,i}$ denote the measured displacement and acceleration in the i-th time step for the h-th measurement point. $u_{h,i}$ and $\ddot{u}_{h,i}$ represent the corresponding motion quantities resulting from the numerical analysis (forward problem). The formulation of Eq. 2 implies that the force location is known for each time step. The weighing factors w_{d} and w_{a} are introduced to control the importance of each term in the multiobjective optimization problem described by Eq. 2. The objective function includes also two penalty functions, whose weights are defined by the factors w_{p1} and w_{p2}. They will be discussed in the following.

The first penalty function accounts for a special feature of traffic loads on bridges, which states that their dynamic components vary around the static weight of the pedestrian or vehicle passing the structure, denoted as discrete finite signal with a stable average value (DFS-SAV) [17]. Practically, this means that the local (moving) average values of the force time history to be identified lie not too far from their global average values. This can be expressed mathematically by minimizing the squared differences between the vectors of local and global average values of the force vector $\boldsymbol{s}$. The local and global average values are obtained using a local and a global average matrix $\boldsymbol{Q}_{\mathrm{loc}}$ and $\boldsymbol{Q}_{\mathrm{glo}}$. They are constructed in such a way, that their multiplication by the load vector $\boldsymbol{s}$ delivers the local or the global average value. It is to be mentioned that the

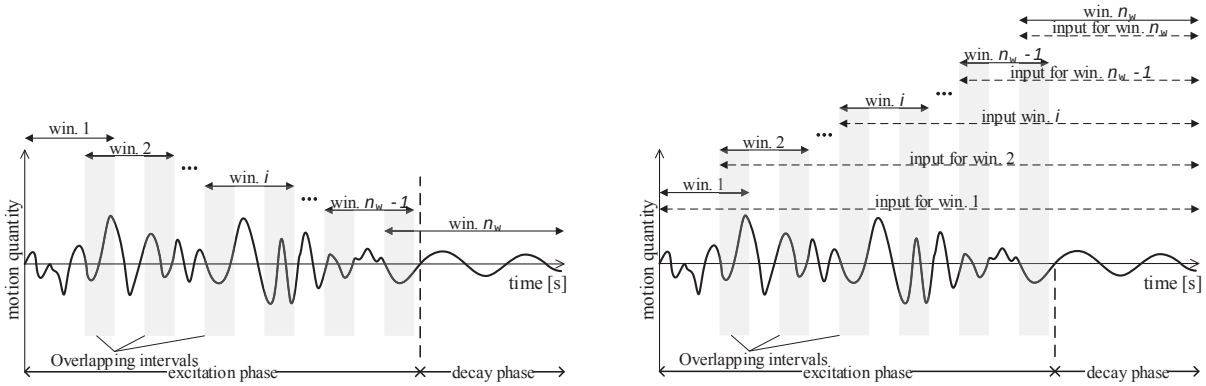

Figure 1: Moving window: forward optimization (left) and backward optimization (right)

local averaging in this study is formulated using a moving window of five samples. The second penalty function controls the smoothness of the solution by minimizing the distance between each value in the solution vector $\boldsymbol{s}$ and the local average of the force. $\boldsymbol{I}$ is the identity matrix, its multiplication with $\boldsymbol{s}$ delivers the unchanged vector $\boldsymbol{s}$.

In order to allow the solution of large problems, the inverse problem in Eq. 2 is addressed using a forward sliding window approach with a certain overlapping interval (Fig. 1 left). It implies that an optimization problem acc. to Eq. 2 has to be formulated and solved for each of the n_w windows. By selecting a reasonable window length, the computational efficiency can be significantly increased in comparison to the direct solution for the whole time frame. After terminating the forward optimization, a subsequent backward optimization problem is enabled (Fig. 1 right). It allows the optimization of the load values in each window under consideration of a more extensive set of input data, which stretches from the starting point of the time window to the end of the decay phase (Fig. 1 right).

The solution the optimization problem elaborated above is obtained using a trust region optimization algorithm, which achieves super-linear convergence when it is supplied with exact sensitivity information (gradient and Hessian) [18].

2.3 Sensitivity analysis

The total derivative of the objective function with respect to a load value s_k can be determined using the the chain rule:

$$\frac{\mathrm{d}\mathcal{F}}{\mathrm{d}s_k} = \underbrace{\sum_{h=1}^{n_\mathrm{md}} \frac{\partial \mathcal{F}}{\partial \boldsymbol{u}_h} \cdot \frac{\partial \boldsymbol{u}_h}{\partial s_k} + \sum_{h=1}^{n_\mathrm{ma}} \frac{\partial \mathcal{F}}{\partial \ddot{\boldsymbol{u}}_h} \cdot \frac{\partial \ddot{\boldsymbol{u}}_h}{\partial s_k}}_{\text{implicit}} + \underbrace{\frac{\partial \mathcal{F}}{\partial s_k}}_{\text{explicit}} \tag{3}$$

The implicit component of the sensitivity expression in Eq. 3 is determined by analytical differentiation the first two terms on the right side of Eq. 2, while the explicit dependencies of the objective function on the load values are given solely by the analytical differentiation of the penalty functions with respect to s_k. The determination of the sensitivity of displacement and accelerations of the h-th measured point with respect to the load value s_k ($\partial \boldsymbol{u}_h / \partial s_k$ and $\partial \ddot{\boldsymbol{u}}_h / \partial s_k$) was also performed analytically. It implies the differentiation of Eq. 1 on both sides with respect to s_k. Considering constant (and thus load independent) system matrices $\boldsymbol{K}$, $\boldsymbol{D}$ and $\boldsymbol{M}$, the differentiation yields:

$$\boldsymbol{K} \cdot \frac{\partial \boldsymbol{u}(t)}{\partial s_k} + \boldsymbol{D} \cdot \frac{\partial \dot{\boldsymbol{u}}(t)}{\partial s_k} + \boldsymbol{M} \cdot \frac{\partial \ddot{\boldsymbol{u}}(t)}{\partial s_k} = \frac{\partial \boldsymbol{P}(t)}{\partial s_k} \tag{4}$$

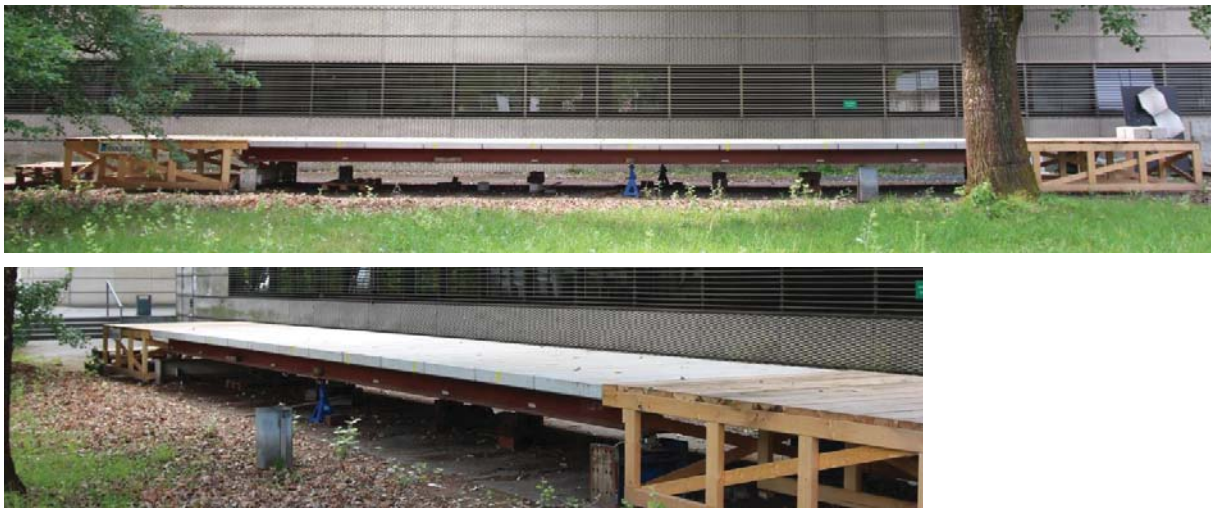

Figure 2: HUMVIB experimental pedestrian bridge (the middle support was removed during the experimental investigations)

where $\partial \boldsymbol{u}/\partial s_k$, $\partial \dot{\boldsymbol{u}}/\partial s_k$, $\partial \ddot{\boldsymbol{u}}/\partial s_k$ denote sensitivity vectors. Evidently, Eq. 4 has a similar form as Eq. 1, if the term $\partial \boldsymbol{P}/\partial s_k$ on the right hand side is considered as an equivalent force vector. Therefore, the unknown sensitivity vectors can be obtained through forward analysis using the mode superposition principle and the time-stepping integration method of Newmark. $\partial \boldsymbol{P}/\partial s_k$ represents the derivative of the vector of external forces with respect to one force in a certain time step. It contains only one value of 1, corresponding to the entry s_k, while all the other values are zero. The entries of the analytical Hessian can be determined by differentiating Eq. 4 with respect to another load value s_i.

3 INVESTIGATIONS ON AN EXPERIMENTAL PEDESTRIAN BRIDGE

3.1 Investigation object

The experimental HUMVIB-Bridge (Fig. 2) is a simply supported pedestrian bridge with a span of $l = 13.24$ m, consisting of two longitudinal steel beams (steel type S235JR) with HEB240 cross section (Fig. 3). The deck plate is made of 13 precast reinforce concrete stripes having the dimensions $250 \times 100 \times 12$ cm. The concrete elements and the steel beams are separated by an elastomeric interlayer with a thickness of 5 mm. The total mass of the experimental pedestrian bridge is about 12 tons, leading to a fundamental frequency of the structure

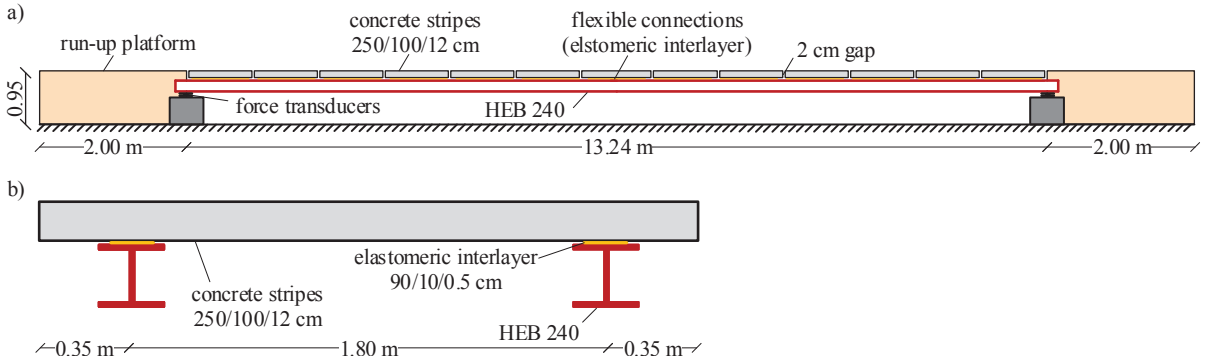

Figure 3: Experimental pedestrian bridge HUMVIB: a) side view; b) cross section

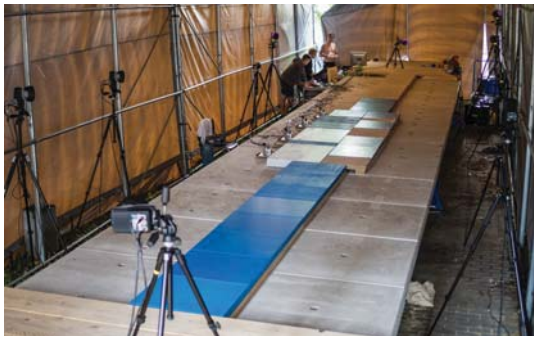

Figure 4: Measurement set-up used in the experimental investigation

of 2.04 Hz. The first five mode shapes and their frequencies were determined experimentally using the reference based combined deterministic-stochastic subspace identification algorithm [19, 20] (s. Fig. 7).

3.2 Measurement set-up

The measurement set-up used in the present investigation is shown in Fig. 4 and schematically illustrated in Fig. 5. The structural responses in vertical direction were recorded at 12 different measurement points (MP) disposed along the steel beams. MP1 to MP4 were instrumented with both acceleration and displacement sensors, while only accelerations were recorded at the locations of MP5 to MP12. Besides the measurement of the motion quantities, the reaction forces at the four supports (MP13 to MP16) were acquired using a set of load cells. In addition, a set of five force plates (FP1 to FP 5) of type KISTLER 9260AA6 ($600\times500\times50$ mm) and two force plates (FP6 and FP7) of type KISTLER 9287CA ($900 \times 600 \times 100$ mm) were installed on the bridge for recording the pedestrian induced GRFs. In order to ensure proper conditions for a natural gait and to reduce the tripping hazard of the subjects, the walking path was leveled using dummy plates with a thickness of 100 mm.

3.3 Structural model

The finite element software ANSYS 2020 R1 was used to generate a numerical model of the experimental pedestrian bridge (Fig. 6a). The steel beams were modeled using beam elements (BEAM188), while the concrete elements were represented through shell elements (SHELL181). Typical (deterministic) material parameters were assigned to the steel beams

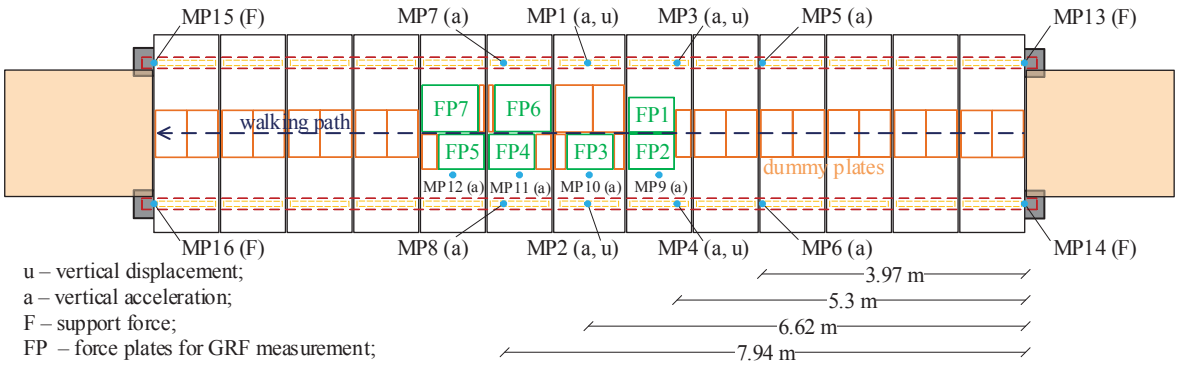

Figure 5: Measurement set-up of the HUMVIB-Bridge

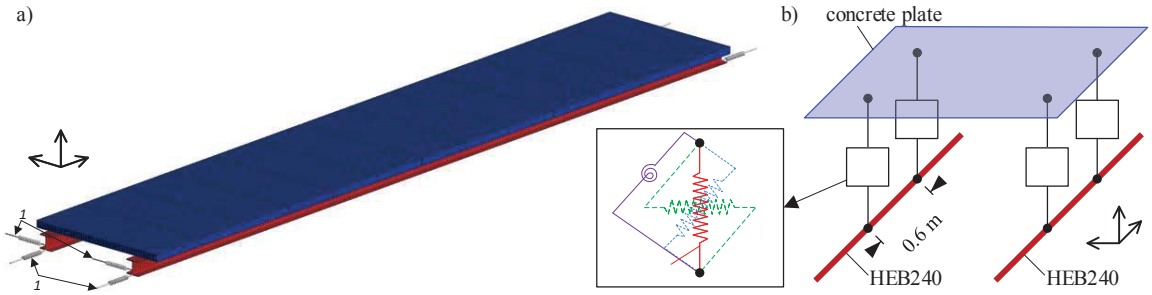

Figure 6: a) Finite element model of the HUMVIB-Bridge; b) Idealized connection between the steel beams and concrete plates

(density $\rho = 7850\ \mathrm{kg/m^3}$, Young's modulus $E = 2.1 \cdot 10^8\ \mathrm{kN/m^2}$ and Poisson ratio $\nu = 0.3$) and the concrete plates ($\rho = 2500\ \mathrm{kg/m^3}$, $E = 3 \cdot 10^7\ \mathrm{kN/m^2}$ and $\nu = 0.2$). The elastomeric interlayer connecting the concrete elements and the steel structure was idealized using a group of three translational springs ($k_{\mathrm{t},2,x}$, $k_{\mathrm{t},2,y}$ and $k_{\mathrm{t},2,z}$ along the x, y and z axis, respectively) and one rotational spring ($k_{\mathrm{r},2,x}$ around the longitudinal x-axis) (Fig. 6b). The beam supports were disposed at the lower flanges and are assumed to be rigid in vertical direction, while horizontal displacements at the supports (in x and y directions) are permitted. In this sense, a set of two translational springs, $k_{\mathrm{t},1,x}$ and $k_{\mathrm{t},1,y}$, were defined at each support (Fig. 6a).

The values of the rotational and translational springs were determined by solving an optimization problem, which seeks to minimize the sum of squared differences between the measured and computed natural frequencies for the first three bending modes and first two torsional modes. The optimization process delivered the following set of optimized stiffness coefficients: $k_{\mathrm{t},1,x} = 12.64 \cdot 10^3\ \mathrm{kN/m}$, $k_{\mathrm{t},1,y} = 10.72 \cdot 10^3\ \mathrm{kN/m}$, $k_{\mathrm{t},2,x} = 11.14 \cdot 10^3\ \mathrm{kN/m}$, $k_{\mathrm{t},2,y} = 2.52 \cdot 10^3\ \mathrm{kN/m}$, $k_{\mathrm{t},2,z} = 18.22 \cdot 10^3\ \mathrm{kN/m}$ and $k_{\mathrm{r},2,x} = 11.95 \cdot 10^3\ \mathrm{kNm}$. The resulting mode shapes and their frequencies are shown in Fig. 7 together with the results obtained from the experimental investigations. The MAC (Modal Assurance Criterion) values determined using the measured and computed values of the five considered mode shapes are 0.9998 (1st mode), 0.9981 (2nd mode), 0.9933 (3rd mode), 0.9959 (4th mode) and 0.9618 (5th mode). Thus, a very good agreement of the results is achieved both on frequency and mode shape level.

3.4 Testing with simulated measurements

In order to generate simulated measurement data, the reference force time history shown in Fig. 10 was applied to the finite element model presented in Section 3.3. The response was evaluated by a forward analysis under consideration of the five modes of vibration shown in Fig. 7. The results of the forward analysis were subsequently polluted with an inconvenient (rather unrealistic) amount of artificial noise, in order to obtain the simulated measurements used for the inverse analysis. Fig. 8 shows exemplarily simulated measurements of displacement and acceleration at the measurement location MP2.

A time step $\Delta t = 0.00333\ \mathrm{s}$, a window size of 400 samples and an overlapping interval of $1/3$ of the window length (s. Fig. 10) were selected. The weighting factors w_{p1} and w_{p2} were determined by means of a parametric study to $w_{\mathrm{p1}} = 5.5 \cdot 10^{-8}$ and $w_{\mathrm{p2}} = 1.0 \cdot 10^{-4}$ (s. Fig. 9). Its aim was to determine the optimal combination of weighting factors, which leads to the lowest error between the reference and the identified forces with simulated measurement data:

$$P_{\mathrm{err}} = \frac{\|\boldsymbol{P}_{\mathrm{identified}} - \boldsymbol{P}_{\mathrm{reference}}\|_1}{\|\boldsymbol{P}_{\mathrm{reference}}\|_1} \cdot 100\ \% \tag{5}$$

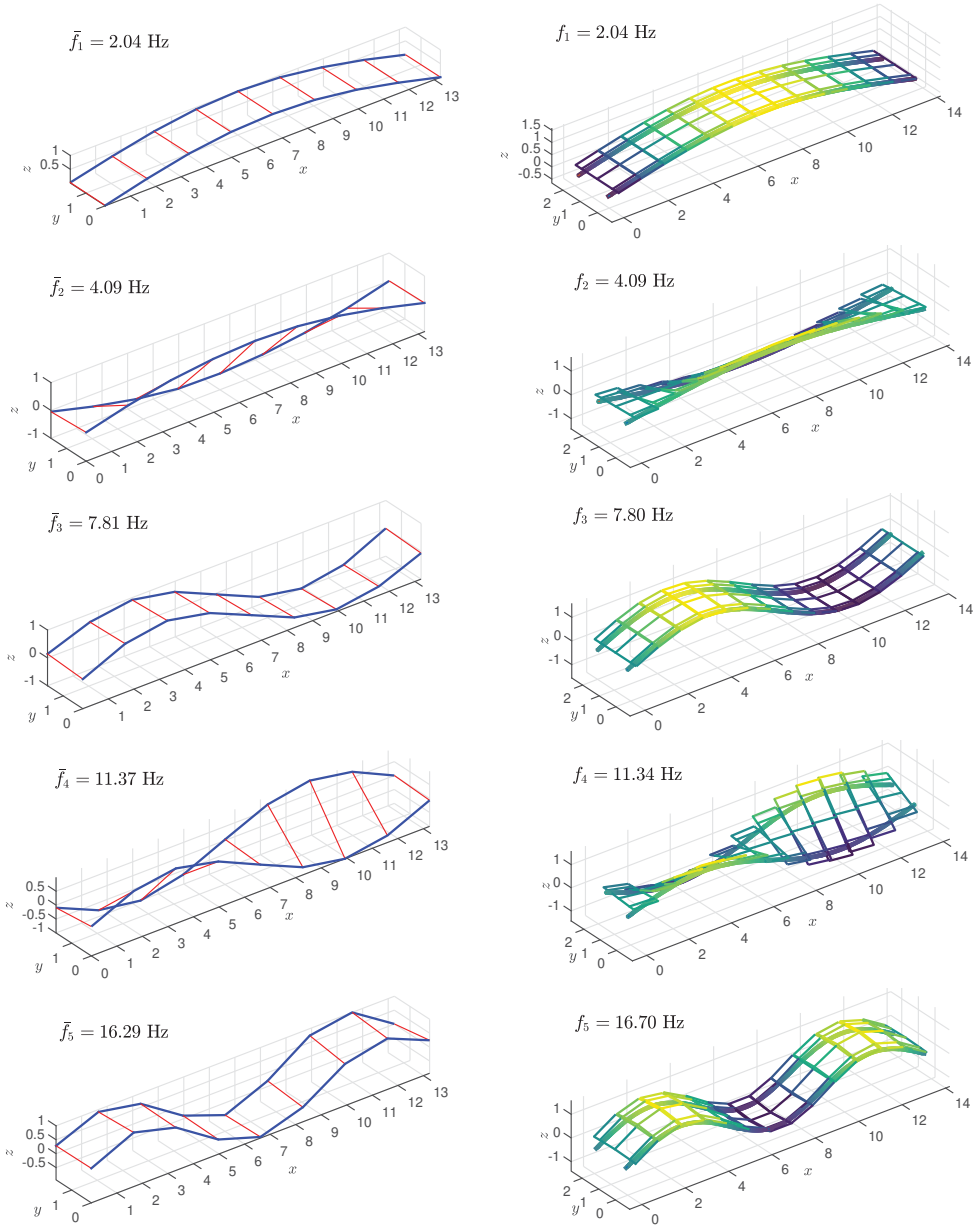

Figure 7: Measured (left) and computed (right) mode shapes and the corresponding natural frequencies

Input data from eight accelerations (MP1 to MP8) and four displacements (MP1 to MP4) was considered. The corresponding weighing factors are $w_\mathrm{a} = 1$ and $w_\mathrm{d} = 5 \cdot 10^5$. The latter seeks to balance the order of magnitude of the displacement and acceleration measurements and ensures a dominant contribution of the displacement term within the objective function.

The result of the optimization problem is shown in Fig. 10. The iteration in each window is terminated when the relative drop of the value of the objective function between two subsequent iterations is less than 10^{-8}. The relative error evaluated according to Eq. 5 at the end of the backward optimization is $4.72\ \%$. This result indicates a very good global agreement between the reference and the identified force time history. A slightly lower accuracy can be only observed for the rather short intervals, in which the force is located in the proximity of the supports (at the beginning and the end of the bridge). This effect occurs most likely due to the low sensitivities of acceleration and displacement at the measurement points with respect to forces acting at the

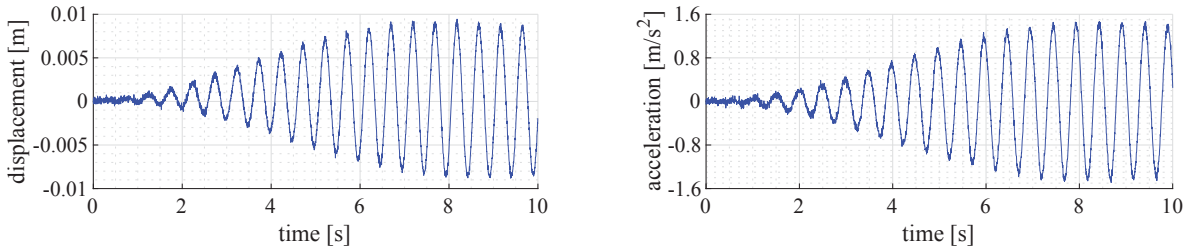

Figure 8: Simulated measurements at MP2: displacement (left) and acceleration (right)

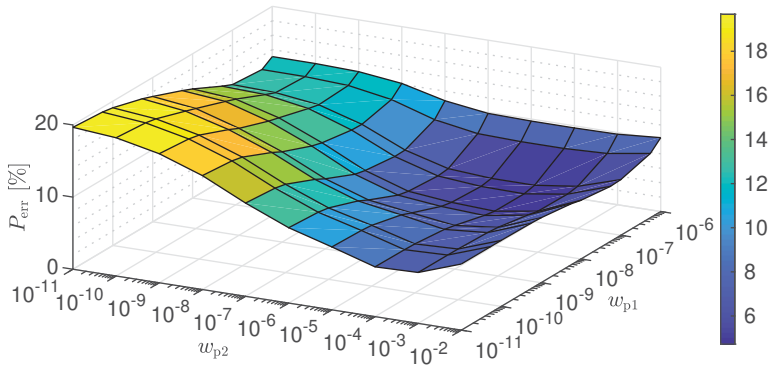

Figure 9: Parametric study for determination of the weighing factors w_{p1} and w_{p2}

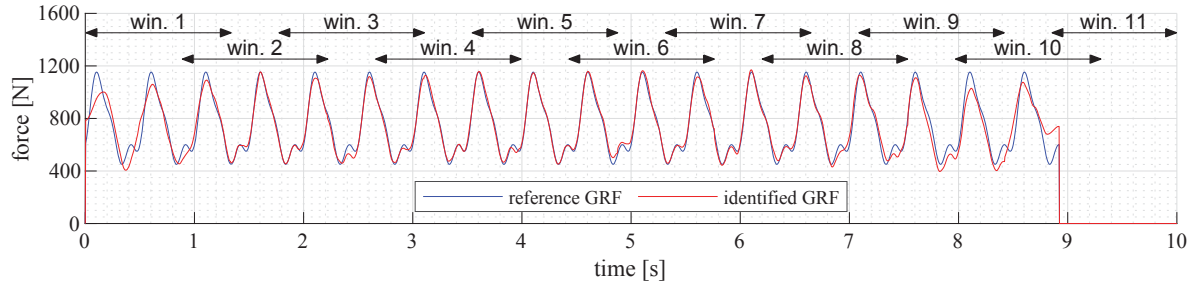

Figure 10: Comparison of the reference force used to simulate the measurement data with the result of the inverse computation

beginning and the end of the bridge. However, the penalty functions ensure stable results even at these locations. A further computation with consideration of only four sensors as input data (accelerations and displacements at MP3 and MP4) delivers an error of $7.16\ \%$, confirming thus the robustness of the method also with a more practicable number of sensors.

3.5 Testing with real measured data

The validation procedure with real measurements implies the acquisition of the measurement data during the passage of a subject weighting $747\ \mathrm{N}$ with a predefined step frequency of $2\ \mathrm{Hz}$. Fig. 11 shows exemplarily the measured displacement and acceleration time histories at MP2. The measured data was filtered using a lowpass filter with a cut-off frequency of $18\ \mathrm{Hz}$, in order to adapt the frequency content of the measurement to the frequency content of the computation. It is to be mentioned that all computational parameters (time step, weighting factors, window size, convergence criteria etc.) were adopted from Section 3.4. In this sense a resampling of

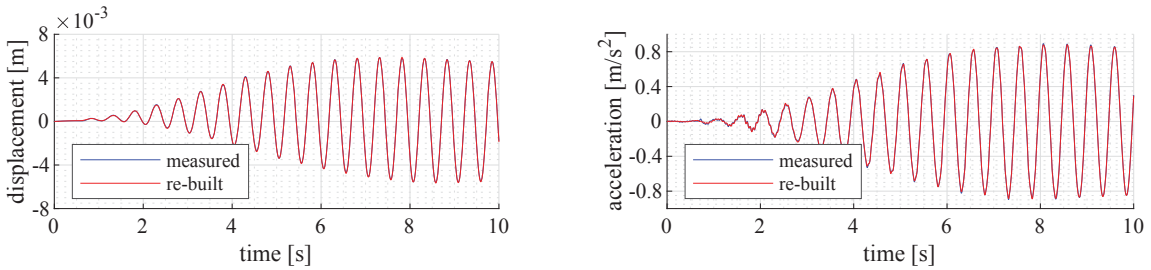

Figure 11: Measured and re-built responses at MP2: displacement (left) and acceleration (right)

the measured signals was carried out, because the measurements were recorded at a sample frequency of 1200 Hz. Also in this case signals of eight acceleration (MP1 to MP8) and four displacement (MP1 to MP4) sensors were used as input data.

In order to use the load cell and force plate signals as reference values for the validation of the GRF reconstruction, the inertial effects of the bridge (in case of load cells) and of the force plate masses had to be removed from the measured force signals [13]. The results after the correction are shown in Fig. 12. Furthermore, in order to account for a possible imperfect walking behavior (e.g. unequal step lengths), the time dependent location of the subject was determined by means of static equilibrium, using the signals of the load cells signals (free of dynamic components) at the two ends of the bridge.

Due to the system changes arising because of the additional mass of the biomechanics equipment, a new model adaptation was necessary for the validation process with real measurement data. In this sense, an additional mass of about 60 $\mathrm{kg/m}$ was applied to the numerical model described in Section 3.3. This leads to a first natural frequency of 1.98 Hz (first bending mode), confirmed also by Fourier analyses of the free decay phases measured during different trials. The further computational natural frequencies are: 3.97 Hz (1st torsional mode), 7.56 Hz (2nd bending mode), 11.02 Hz (2nd torsional mode) and 16.02 Hz (3rd bending mode).

The results of the optimization problem based on real measured data are shown in Fig. 12 together with the reference force time histories from the load cells and the force plates. The relative error $P_{\mathrm{err,LC}}$ of the identified force with respect to the load cell signals (support forces) is 10.18 %. Considering that there are still various uncertainties in the problem definition (e.g. with respect to the modeling, subject velocity, measurement inaccuracies etc.), the result can be interpreted as very satisfactory. However, the quantitative evaluation of the force reconstruction method based on comparisons with the signals of the support forces has to be done with caution,

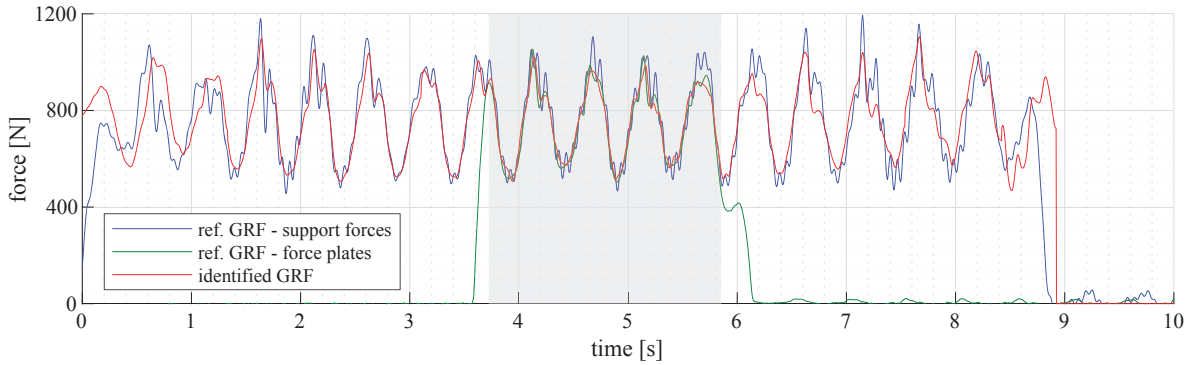

Figure 12: Measured and identified GRF time historie of a subject walking over the HUMVIB-Bridge

since $P_{\mathrm{err,LC}}$ is highly uncertain due to the inexact elimination of the inertial forces from the measured load cell signals (s. interval between 9 and 10 s in Fig. 12). Nevertheless, the load cell signals provide a valuable tool for the general comparison of the GRFs along the bridge. A more reliable validation of the identified GRF is expected when analyzing the relative error $P_{\mathrm{err,FP}}$ of the identified force with respect to the force plate signals for the time interval of passing the force plate array (grey area in Fig. 12). The result is $P_{\mathrm{err,FP}} = 3.20\ \%$, indicating an excellent agreement of the two force signals.

In order to emphasize the efficiency of the method, a forward analysis was performed with the identified force time history. The displacement and accelerations at MP2 (Fig. 11) revealed a nearly perfect match between the real measured data and the re-built structural responses. A further great achievement of the method is the successful qualitative and quantitative reconstruction of the imperfect GRF time history, which shows lower force amplitudes when the pedestrian is located around the middle of the bridge than in case of a location towards the supports. This effect is thought to occur because of the passive and active HSI effects, which are expectedly higher at locations with higher amplitudes, i.e. towards the middle of the bridge. The computation under consideration of accelerations and displacements measured and MP3 and MP4 (total of four sensors) resulted in $P_{\mathrm{err,LC}} = 10.13\ \%$ and $P_{\mathrm{err,FP}} = 3.48\ \%$, indicating a similar results quality as for the configuration with 12 sensors.

4 CONCLUSIONS

- A novel method for an indirect determination of ground reaction forces on vibrating structures was presented. It implies the formulation of an inverse problem in time domain, which is based on the minimization of the difference between a set of computed and a set of measured displacement and acceleration time histories. An important boundary condition of the method is that the location of the force in each time step has to be provided.

- In order to enable the solution of large problems at reasonable computational cost, an approach based on a forward and backward sliding window was developed. It implies the splitting of the total time of analysis into different windows of given length with a certain overlap. An optimization problem of pre-defined dimensions has to be solved in each window both during the forward and backward sliding.

- The tests with simulated measurements under consideration of a worst case noise level indicated that the developed method achieved an accuracy of the identified GRFs of about $5-7\ \%$ with respect to the reference forces, indicating thus a very satisfactory agreement of the results. A slightly lower accuracy was revealed solely for the time intervals, where the force enters and leaves the bridge. This is an effect of the low sensitivities of the measured quantities with respect to the forces acting at those locations.

- The method was subsequently tested using real measurement data recorded during walking trials on the experimental HUMVIB-Bridge on the campus of Technical University of Darmstadt. The measurement set-up included load cells at the supports and an array of biomechanical force plates, which were used as reference values for the validation of the method. The reconstructed forces revealed a very good accuracy of about $10\ \%$ with respect to the highly uncertain load cell measurements and $3\ \%$ related to the more accurate force plates signals. These results were obtained for both a configuration with 12 sensors and a configuration with four sensors as input data, confirming thus the robustness of the method for practical applications. Moreover, the experimentally recorded

trend of decreasing force amplitudes towards the middle of the bridge (correlated with higher response amplitudes) could be successfully reproduced by the developed method. The re-built responses using the identified forces revealed a nearly perfect match with the measured time-histories.

- The developed method can be used for the study of HSI effects by means of ground reaction forces induced by a pedestrian during walking on a vibrating structure. So far, the method was tested on a full-scale experimental structure. The promising results indicate that the method is suitable also for the use within field experiments on real footbridges, as long as a relatively accurate structural model is available.

- The force identification method presented in this paper can be adapted and used for different applications, e.g. the reconstruction of the dynamic axle loads of a complete railway vehicle passing a bridge structure [21].

ACKNOWLEDGMENTS

The authors would like to thank Prof. André Seyfarth and Dr. Guoping Zhao for their support related to the biomechanical measurements.

REFERENCES

[1] Kistler (company), *Product catalogue: Force plates and accessories. Biomechanics measuring systems for performance diagnostics, gait analysis, rehabilitation, and ergonomics.*, Winterthur, Switzerland, 2017.

[2] A. Belli, P. Bui, A. Berger, A. Geyssant, J.R. Lacour, A treadmill ergometer for three-dimensional ground reaction forces measurement during walking, *Journal of Biomechanics*, **34**(1), 105-112, 2001.

[3] A. Forner Cordero, H.J.F.M. Koopman, F.C.T. van der Helm, Use of pressure insoles to calculate the complete groundreaction forces, *Journal of Biomechanics*, **37**(11), 1427-1432, 2004.

[4] D.T.-P. Fong, Y.-Y. Chan, Y. Hong, P.S,-H. Yung, K.-Y. Fung, K.-M. Chan, Estimating the complete ground reaction forces with pressure insoles in walking, *Journal of Biomechanics*, **41**(9), 2597-2601, 2008.

[5] V. Racic, A. Pavic, J.M.W. Brownjohn, Modern facilities for experimental measurement of dynamic loads induced by humans: A literature review, *Shock and Vibration*, **20**, 53-67, 2013.

[6] M. Bocian, J.M.W. Brownjohn, V. Racic, D. Hester, A. Quattrone, R. Monnickendam, A framework for experimental determination of localised vertical pedestrian forces on full-scale structures using wireless attitude and heading reference systems, *Jurnal of Sound and Vibration*, **376**, 217-243, 2016.

[7] K. Van Nimmen, G. Lombaert, I. Jonckers, G. De Roeck, P. Van den Broeck, Characterisation of walking loads by 3D inertial motion tracking, *Jurnal of Sound and Vibration*, **333**, 5212-5226, 2014.

[8] K. Van Nimmen, G. Zhao, A. Seyfarth, P. Van den Broeck, A Robust Methodology for the Reconstruction of the Vertical Pedestrian-Induced Load from the Registered Body Motion, *Vibration*, **2018**, 250-268, 2018.

[9] V. Racic, J.M.W. Brownjohn, A. Pavic, Reproduction and application of human bouncing and jumping forces from visual marker data, *Journal of Sound and Vibration*, **329**, 3397-3416, 2010.

[10] E. Shahabpoor, A. Pavic, Estimation of vertical walking ground reaction force in real-life environments using single IMU sensor, *Journal of Biomechanics*, **79**, 181-190, 2018.

[11] V. Racic, A. Pavic, J.M.W. Brownjohn, Experimental identification and analytical modelling of human walking forces: Literature review, *Journal of Sound and Vibration*, **326**, 1–49, 2009.

[12] A. Firus, J. Schneider, H. Berthold, A. Seyfarth, M. Albinger, *Parameter identification of a biodynamic walking model for human-structure interaction, Proceedings of the 9th International Conference on Bridge Maintenance, Safety and Management (IABMAS 2018)*, Melbourne, Australien, 2018.

[13] E. Ahmadi, C.C. Caprani, S. Zivanovic, A. Heidarpour, Vertical ground reaction forces on rigid and vibrating surfaces for vibration serviceability assessment of structures, *Engineering Structures*, **172**, 723-738, 2018.

[14] H. Werkle, A. Firus, W. Francke, Einfluss personeninduzierter Schwingungen auf die Messgenauigkeit in Ganglaboren, *Bauingenieur*, **90**, 110-119, 2016.

[15] E. Ahmadi, C.C. Caprani, S. Zivanovic, N. Evans, A. Heidarpour, A framework for quantification of human-structure interaction in vertical direction, *Journal of Sound and Vibration*, **432**, 351-372, 2018.

[16] C. Petersen, H. Werkle, *Dynamik der Baukonstruktionen*, 2nd Edition, Springer-Vieweg, Wiesbaden Germany, ISBN: 9783834814593, 2017.

[17] C.-D. Pan, Y. Ling, H.-L. Liu Identification of moving vehicle forces on bridge structures via moving average Tikhonov regularization, *Smart Materials and Structures*, **26**, 1-16, 2017.

[18] J. Nocedal, S.J. Weight, *Numerical Optimization*, 2nd Edition, Springer Science + Business Media LLC, New York, USA, 2006.

[19] E. Reynders, G. De Roeck, Reference-based combined deterministic-stochastic subspace identification for experimental and operational modal analysis, *Mechanical Systems and Signal Processing*, **22.3**, 616-637, 2008.

[20] K. Van Nimmen, K. Lievens, P. Van den Broeck, *TU Darmstadt HUMVIB Bridge - Experimental modal analysis*, tech. rep., KU Leuven, Technology Campus Ghent, 2017.

[21] A. Firus, R. Kemmler, J. Schneider, *A time domain approach for reconstruction of moving loads acting on bridges from dynamic response data, Proceedings of the 10th International Conference on Bridge Maintenance, Safety and Management (IABMAS 2020)*, Sapporo, Japan, 2020.

EURODYN 2020
XI International Conference on Structural Dynamics
M. Papadrakakis, M. Fragiadakis, C. Papadimitriou (eds.)
Athens, Greece, 23–26 November 2020

SIMPLIFIED COMPUTATION OF TIMBER FLOOR VIBRATIONS LEVEL DUE TO HUMAN ACTIVITIES

Thomas Catterou[1], **Jean-Baptiste Castaing**[1], **and Patrice Garcia**[1]

[1]FCBA Bordeaux
address : Alle du Boutaut 33000 Bordeaux, France
e-mail: thomas.catterou@fcba.fr
e-mail: {jean-baptiste.castaing,patrice.garcia}@fcba.fr

Keywords: Structural dynamics, timber floor, human induced vibration

Abstract. *Timber floors are sensitive to vibrations because of their lightweight. Walking on this type of floor could cause motion sickness for the walkers or the other people in the room. Timber floors have to be designed correctly to ensure a good comfort, especially in countries like France where people are used to the vibration comfort level of concrete floors. This paper proposes new methods to assess the dynamical properties of timber floors, and the accelerations due to the walk of an individual. Experimental and numerical tests are made to evaluate the relevance of the method.*

1 Introduction

1.1 Problematic

Due to timber buildings lightweight, their dynamical properties must be studied carefully. Vibration comfort level is an important aspect of the quality of a building. Discomfort is dependent of the sensitivity of each person, their activities and mainly of vibration physical values (frequencies, accelerations, velocities and displacements). These physical quantities have to be assessed to design correctly timber floors. This paper presents a methodology to predict the frequency of the first floor mode and assess the vibration level from walking of individual.

1.2 State of the art

The ISO-10137 norm [1] gives some clues to size floors and footbridges against vibrations. The main point of this norm is to assess the vibration effects due to different sources on the comfort of users. A criterion based on the root mean square (RMS) acceleration is proposed which depends on the building use (figure 1).

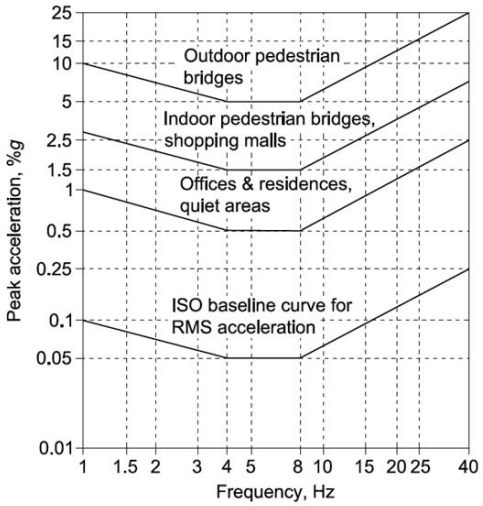

Figure 1: Comfort criterion depending of the frequency and the acceleration of the floor

The Eurocode 5 [2] gives also criteria to assess the comfort of wooden floors. Those criteria are different from ISO ones. This norm focuses on only wooden floors with resonance frequency higher than 8Hz. The other ones have to be evaluated differently. The criteria given are based on the Ohlsson works [4] and depends on the floor velocity due to a theoretical impulsive shock and the floor stiffness. The next edition of the Eurocode will provide criteria for each kind of floors and estimations of the floor acceleration due to the walking of a person. Beyond these norms, a large number of guides exist to design floors regarding vibrations and comfort, including the guide from the American Institute of Steel [3]. This guide gives a method to compute floor acceleration by considering a simplified theoretical model and the average frequency content of load due to walking. This acceleration is confronted to the criteria given by the ISO-10137 [1].

In Europe, HIVOSS guidelines [5] aims to assess the floor comfort with a method called OS-RMS90 (one step, root mean square) [6] . The maximal RMS response of a floor is given

for 90% of kind of walking. Some similar guidelines exist for footbridges, which are also very sensitive to vibrations [7, 8].

Recently, specific studies on wooden floor show that every physical values (displacement, velocity, acceleration and frequency) can be used to judge the comfort of floors. Hu and Chui [9] suggest a empiric criterion based on the ratio between the floor displacement and its frequency. Several kinds of criteria have been reviewed and used on CLT (Cross Laminated Timber) by Weckendorf [10]. Patricia Hamm [11] puts forward that the floor frequency is not a discriminatory factor to provide comfort because some high frequencies floor are evaluated uncomfortable. Then, in 2018, a research group has summarized experimental tests on floors in order to determine an ISO criterion [12]. No consensus has actually been built up on a comfort threshold but in order to be able to use a comfort criterion, the dynamic behavior of timber floors must be well known. Few studies estimate accurately the resonance frequency of timber floors considering their boundaries conditions and orthotropy. Then, Eurocode 5 gives a formula to compute acceleration of a low frequency floor. However, a formula for high frequency floor is missing.

1.3 Objectives and methodology

The purpose of this paper is to define a simplified methodology which can be used by professionals or design department to assess the vibration levels on floors due to human activities. The physical values obtained will have to be compared to a comfort criterion. The assessment of vibration levels requires to identify the floor dynamic properties. First, the frequency of the first floor mode is computed, taking into account wood specificities. Then, according to the properties of the walker (weight, walking frequency), the floor acceleration is determine under theoretical assumptions for low and high frequency floors.

2 Modal frequencies assessment

The knowledge of the floor dynamical properties is necessary to assess its dynamical response due to human activities, like resonance frequency and modal mass. The first frequency mode of wooden floors can be difficult to estimate because of the wood orthotropy and boundary conditions. A method is suggested introducing some scalars deduced from analytical and numerical studies in order to take into account specificities of wooden floors.

2.1 Basic formulas

Leissa has analyzed the vibrational response of rectangular plates with different boundary conditions [13]. In civil engineering, two combinations of boundary conditions occur frequently : two opposite simply supported sides and two free side (SS-F-SS-F) or four simply supported sides (SS-SS-SS-SS). In situ experiments show that boundary conditions on the sides of floors are more likely simply supported than clamped conditions, but it exists a rotational stiffness which will be discussed further.

The formula for the (SS-SS-SS-SS) boundary conditions can be determined analytically [13] :

$$f_{1_{4SS}} = \frac{\pi}{2a^2}\sqrt{\frac{D}{\rho h}}(1+(\frac{a}{b})^2) \tag{1}$$

$f_{1_{4SS}}$ is the resonance frequency of the first mode in the (SS-SS-SS-SS) condition. $D = Eh^3/12(1-\nu^2)$ is the flexural rigidity, E is Young modulus, h is plate thickness, ν is Poisson's

ratio, ρ is mass density per volume, a and b are respectively the largest and smallest dimensions of the studied rectangular floor.

For the (SS-F-SS-F) conditions, the solution has to be estimated from an analytical equation [13]:

$$\begin{aligned} f_{1_{2SS-2F}} &= \frac{C}{2\pi a^2}\sqrt{\frac{D}{\rho h}} \\ C &= 0.051(\frac{a}{b})^2 - 0.28\frac{a}{b} + 9.86 \end{aligned} \tag{2}$$

The equations 1 and 2 are standard results for an isotropic plates with ideal boundary conditions. It is the reference frequency f_{ref} for the rest of the computation. The first step is to homogenize the wooden floor and find the equivalent plate. In most cases, wooden floors are strongly orthotropic. The mechanical parameters in the stiffest direction are the only ones considered in the previous formulas. The effect of orthotropy will be considered further.Then, three coefficients will be added to take into account the wood specificities :

$$f_1 = R_c R_\lambda R_F f_{ref} \tag{3}$$

f_1 is the 'real' frequency of the floor. R_c represents the effect of a continuous floor on several supports on the resonance frequency. R_λ represents the effect of orthotropy. This coefficient is always inferior or equal to 1. R_F describes the effect of the added torsional stiffness due to the load at the extremities of the floor. This coefficient is always superior or equal to 1.

2.2 Orthotropy

Several authors have worked on the vibration properties of orthotropic plates [14, 15]. The Jayaraman results [16] have been used in this paper. For several set of boundary conditions with at least two parallel sides simply supported, it is possible to find complex relationship between the resonance frequencies and the flexural rigidity D_x and D_y (describing respectively the flexural rigidity on the strongest and the weakest direction).

A numerical resolution has been realized for several ratio of orthotropy D_x/D_y, and ratios of floor dimensions a/b. The first observation is that for a (SS-F-SS-F) configuration, the orthotropy has a minor influence on the resonance frequency value : the frequency decreases just by 2% for $a/b = 2$ and $D_x/D_y = 20$. Difference are larger for the following modes. For a (SS-SS-SS-SS) configuration, the impact of orthotropy is major. For the same conditions ($a/b = 2$ and $D_x/D_y = 20$), the frequency falls by 39%.

A statistical resolution has been made to establish the factor R_λ. For a (SS-F-SS-F) configuration, it is possible to consider $R_\lambda = 1$ whereas for a (SS-SS-SS-SS) configuration, R_λ is expressed as followed

$$R_\lambda = 1 - (1 - e^{-0.4\frac{D_x}{D_y}} + 0.4)(0.25\frac{a}{b} - 0.021(\frac{a}{b})^2) \tag{4}$$

2.3 Continuous floors

Floors are usually supported on more than two supports. The continuity of the floor can influence its dynamic behavior. In short, the frequency of a span of continuous floor is higher

than its isostatic equivalent if the neighboring span are shorter and inversely. Then, if one of the support can not be considered as rigid (like a wood joist assembly), it has to be considered in the computation by considering a spring instead of a rigid support. Two situations are presented in this paper.

- **One span floor supported by a rigid support and by a spring**.

Figure 2: One span floor

The spring stiffness can be estimated with the average stiffness of a beam resting on two flat supports separated by a length of L.

$$k = \frac{120EI}{L^3} \tag{5}$$

Thanks to numerical computations, it is possible to compute the ratio R_c which linked the frequency of the beam on rigid support and spring with the frequency of a beam on two rigid supports (figure 3).

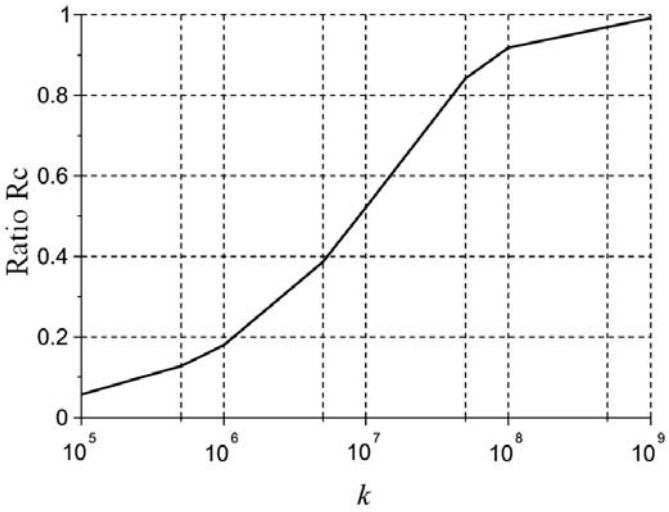

Figure 3: Impact of the spring stiffness on the reatio R_c for a one span floor supported by a rigid support and a spring

The ratio R_c drops when the spring stiffness decreases and moves toward 1 when stiffness increases.

- **Two-spans floor supported on two rigid support and one spring**

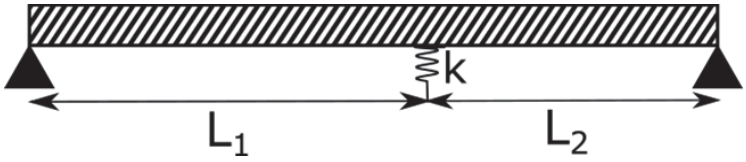

Figure 4: Two spans floor

This configuration is very usual when a floor is supported by two walls at its extremities and a wood joist (figure 4). Considering the first span of length L_1, the ratio R_c corresponds to the resonance frequency of this span divided by the resonance frequency of a equivalent isostatic span with the same length supported on two rigid support. Results are given in figure 5.

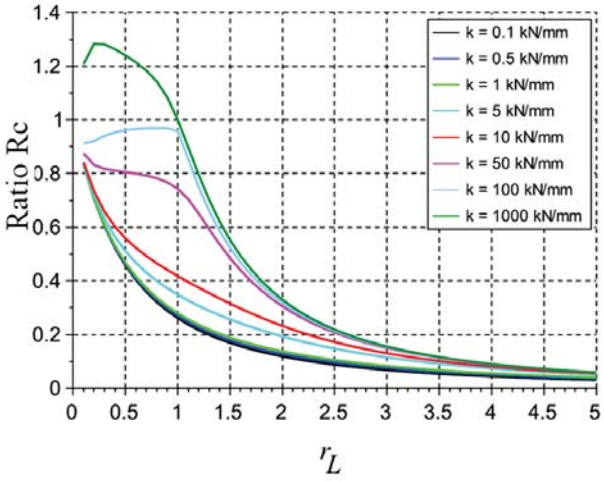

Figure 5: Impact of k and r_L on the ratio R_c for a two spans floor with a spring support in the middle

The ratio R_c will be dependent of the stiffness of the joist, symbolized by a spring and the ratio between the length of the span $r_L = L_2/L_1$. When the stiffness of the spring is very high, $R_c > 1$ for $r_L < 1$ and $R_c < 1$ for $r_L > 1$. It illustrates the fact that a short span next to a large span increases the rigidity of the large span. Then, when spans have the same length, the ratio R_c is equal to one. When the stiffness of the spring decreases, the ratio R_c drops regardless of the r_L value. When the spring stiffness is very low, the continuous floor can be considered as an isostatic floor with a length $L = L_1 + L_2$.

2.4 Wall effect

Loads are often applied on the sides of the floor which can increase its rotational stiffness, and so increase its natural frequency. Experiments have been realized at the FCBA technological institute: natural floor frequency have been measured on CLT or joist-OSB floor while applying an increasing force at their extremities. When the clamping force increases, the floor resonance frequency increases until a threshold. This phenomenon is complex. When a clamped force is imposed on the floor, a rotational stiffness is added but locally, the floor 'crushes' a little in the wall axis. (see figure 6).

This phenomenon depends on several parameters : the ratio a/b, the wall thickness of the

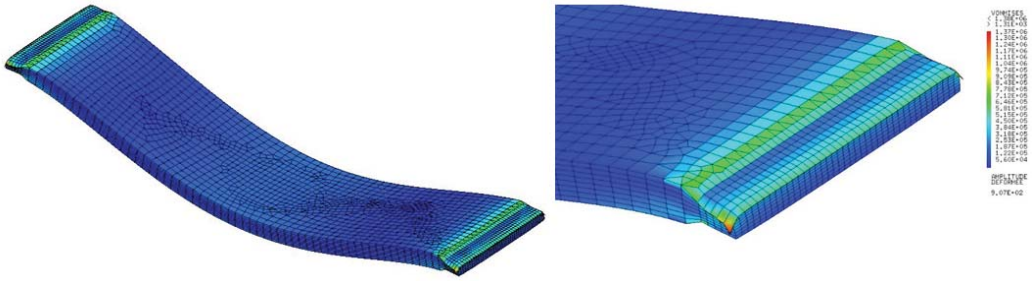

Figure 6: Deflection of a CLT beam with a clamped force at its extremities. The deflection is amplified by 100

wall hw, the floor thickness h, the floor length L, the Young modulus in the direction of the wall load E_z and the force F applied by the wall. A numerical statistical study with finite elements has been made to determine the frequency of a (SS-SS-SS-SS) floor with wall load at its extremity and leads to the following R_F expression.

$$\begin{aligned} R_F &= \sqrt{\frac{1}{\alpha F.10^{-4}}} \text{ if } R_F < \sqrt{\frac{1}{\beta}} \\ R_F &= \sqrt{\frac{1}{\beta}} \end{aligned} \tag{6}$$

with

$$\begin{aligned} \alpha &= (0.87(\frac{a}{b})^{-0.7}(-0.44L+3)\frac{9.2x10^{-2}}{h}\frac{5hw-8.7x10^{-2}}{0.6} \\ \beta &= 0.74((\frac{a}{b})^{-0.2}L^{-0.5}(2h+0.2)hw^{-0.4}E_z^{-0.09} \end{aligned} \tag{7}$$

Several parameters are involved in this phenomenon. In pratical terms, it will be difficult to assess precisely these values. Furthermore, even if the wall load can affect the floor frequency, this effect seems limited as illustrated by in situ measures in a building [17]. Our recommendation is to consider $R_F = 1$. The real frequency should be a little be higher than the calculated one.

2.5 Modal mass

The modal mass can be computed with the following formula [18] :

$$M_{mod} = \frac{M}{ab}\int_S \delta^2(x,y)dS \tag{8}$$

with M the floor total mass and δ the floor modal displacement. In case of isostatic floors with rectangular shapes, it is possible to compute easily the modal mass of the first mode :

$$\begin{aligned} M_{mod} &= \frac{M}{2} \text{ in the SS-F-SS-F configuration} \\ M_{mod} &= \frac{M}{4}(2-\frac{a}{b}) \text{ in the SS-SS-SS-SS configuration} \end{aligned} \tag{9}$$

In case of complex floor shapes, continuous floors or stiff partition, the modal mass can be strongly altered and more often its value will be lower that the one predicted by equation 9.

3 Acceleration on floor due to walking

3.1 Footstep model

A simplified model is considered to represent the floor first mode (figure 7). The mass M is equal to the modal mass M_{mod} of the first mode and the stiffness $K = \omega_1^2 M$ with the first resonance pulse $\omega_1 = 2\pi f_1$.

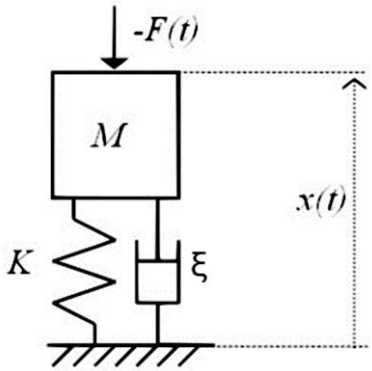

Figure 7: Spring-dashpot system

The HIVOSS guide [5] proposes to model the force load due to a footstep as below:

$$\frac{F(t)}{Q} = \sum_{i=1}^{8} K_i t^i \tag{10}$$

With $F(t)$ the footstep load, Q the weight of the walker in Newton and K_i a parameter defined in [5]. With this formulation, the ratio $F(t)/Q$ is given on the figure 8.

The AISC guide [3] formulates a series of footstep load with the following formula :

$$F(t) = \sum_{i=1}^{4} Q\alpha_i sin(i\omega_1 t) \tag{11}$$

With α_i a parameters different for the walking frequency and its harmonics. For the walk, Murray gives the values of α_i : $\alpha_1 = 0.4, \alpha_2 = 0.07, \alpha_3 = 0.06, \alpha_4 = 0.05$. The decrease of the parameters α_i broadly follows the function $\alpha(f) = e^{-0.4f}$.

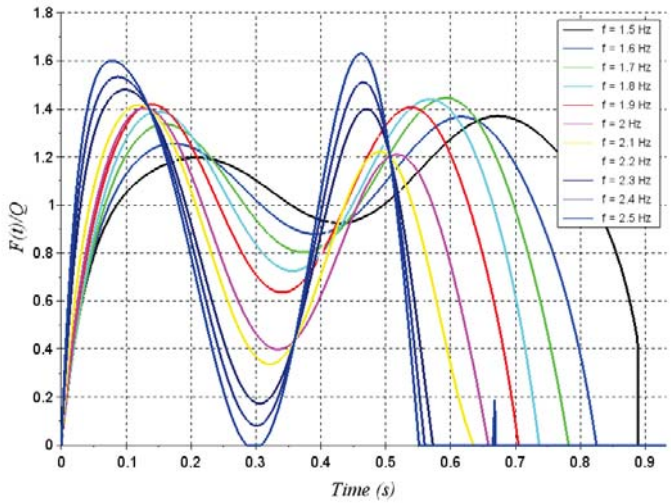

Figure 8: Ratio $F(t)/Q$ for different walking frequencies. The first peak correspond to the load produced by the heels and the second to the load induced by the toes

3.2 Low frequency floor

The next version of Eurocode 5 proposes a formula to compute the acceleration of a low frequency floor subjected to walking loads. Several assumptions are made :

- Only the first mode is considered, the floor is reduced to a simple spring-dashpot system as presented on figure 7.
- The main acceleration is due to the floor solicitation at its resonance frequency. The effect of the other frequencies are neglected.

Under these assumptions, the system acceleration for a walking load can be written :

$$a_{Lf} = \frac{\alpha(f_1)Q}{2\xi\sqrt{2}M_{mod}} \tag{12}$$

ξ is the first modal damping of the floor. $Q/(2\xi M_{mod})$ is the response of a spring damping system to a harmonic oscillation with an amplitude Q at its resonance frequency. α is the amplitude of the footsteps signal at the floor resonance frequency and is equal to $\alpha(f_1) = e^{-0.4f_1}$. The factor $1/\sqrt{2}$ takes into account the responsiveness of the walker to the effective acceleration. The expression is multiplied by a factor 0.4 in Eurocode to take into account that the walker is rarely in the center of the floor span. The factor has not be used here.

3.3 High frequency floor

For an high-frequency floor, the second EUROCODE 5 assumption which was previously presented is invalid. The load at the resonance frequency of the floor is marginal, but the effect of the other frequency of the load can not be neglected. In fact, the load can be considered as quasi-static regarding to the floor resonance frequencies and the floor accelerations are then induced by the floor free vibrations.

By using the formulation of the footstep load proposed by HIVOSS (equation 10), it is possible to determine the maximal load during a walk F_{max}.

$$F_{max} = Q(0.5 f_{step} + 1.5) \tag{13}$$

With f_{step} the frequency of the footstep load.

By considering the simplified spring-dashpot system and a quasi-static response of the system during the load increase, the displacement of the mass can be written :

$$\Delta u = \frac{F_{max}}{K} \tag{14}$$

Then, at the end of the load increase, the system freely oscillates and the mass acceleration is equal to :

$$a = -\frac{F_{max}}{K}\omega_1^2 cos(\omega_1 t) e^{-\xi\omega_1 t} = -\frac{F_{max}}{M_{mod}} cos(\omega_1 t) e^{-\xi\omega_1 t} \tag{15}$$

Generally, persons have a walking frequency inferior to $2.3Hz$. A conservative simplification can be made by considering $F_{max}/Q = 2.4$.

The ISO 2631-1 norm [20] proposes to compute the effective acceleration as the maximal RMS value of 1s of the signal, to take into account the load variability. To obtain the effective acceleration on 1s of a sinus which decreases exponentially, the maximal acceleration have to be multiplied by a factor :

$$V_{eff} = \frac{1}{2}\sqrt{\frac{((2\xi^2+1)e^{2\xi\omega_1} - 1)e^{-2\xi\omega_1}}{\omega_1\xi^3 + \omega_1\xi}} \tag{16}$$

By the way, the maximal effective acceleration for a high frequency floor can be written :

$$a_{Hf} = F_{max} V_{eff} \frac{Q}{M_{mod}} \tag{17}$$

3.4 Validation

The equations 12 and 17 can be used to determine the acceleration due to a walker whatever the floor resonance frequencies. The expression 12 should be used when the frequency of the floor is under 8Hz, otherwise the expression 17 is more appropriate.

The formula 10 has been used to create a representative load of ten footsteps with a footstep frequency of 2Hz. The dynamic response of a spring-dashpot system to this load has been computed for different values of system frequency and for a damping of 2%. The maximum of acceleration computed during the test is confronted with formulas 12 and 17 (figure 9).

In this theoretical example, these formulas allow to conservatively predict system maximal effective acceleration. They have also been confronted to experimental tests.

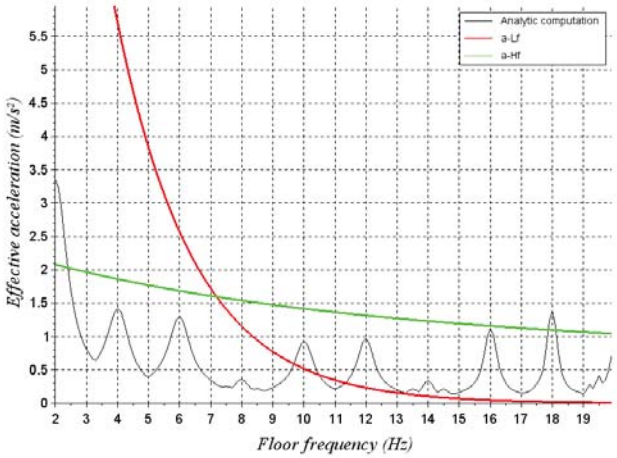

Figure 9: Comparison between accelerations predicted by equations 12 and 17 and the maximal effective acceleration of a spring-dashpot systems with different resonance frequencies subjected to a sequel of ten footsteps with $f_{step} = 2Hz$

Figure 10: Test floors : Joist-OSB floor (left) and CLT floor (right)

4 Experimental and numerical analysis

4.1 Presentation of the experiments

Two floors have been designed and tested, a squared joist-OSB floor and a squared CLT floor of 4.5 metres in length (figure 10). They have been nailed to a piece of wood to ensure a simply supported condition at two of their extremities in order to be in a (SS-F-SS-F) configuration.

Experimental modal analysis have been done on test floors. With a grid of accelerometers and a CMIF (complex mode indicator function), the mode shapes and the mode frequencies have been identified. The most important modes have been discriminated by using an AutoMAC [19]. The two floors are high frequency floors with a resonance frequency of 17.5Hz for the joist-OSB floor and 13.8Hz for the CLT floor.

Walking experiments have been done on each of the test floors. Around 30 persons have walked along the center span of the floors with several accelerometers located on the displacements peaks of the first five modes (figure 11).

The weights, the average step frequencies and the kind of shoes of each person participating to the experiments have been recorded. The floor maximal effective acceleration during the test

Figure 11: People walking on instrumented test floor

has been computed with the method recommended by ISO 2631-1 norm [20] for a transient solicitation:

$$a_{RMS}(t_0) = \sqrt{\frac{1}{T}\int_{t_0-T}^{t_0} a(t)^2 dt} \tag{18}$$

The effective acceleration is computed for short windows of width $T = 1s$.

4.2 Numerical model

A numerical model using shell or cubic finite elements has been created for each test floors in order to understand phenomena occuring during the walk and to make a sensitivity analysis. The measured parameters (Young's modulus and density) of each joist have been considered. Its accuracy has been estimated by confronting numerical modal analysis and experimental modal analysis. An example is given on figure 12.

The numerical model and the experimental results have a very good correlation on a MAC analysis for the first six modes. Dynamical computations are realized using a footsteps load along the center of the floors span. The system is reduced on the first 30 modes to reduce computation times and then solved with an explicit integration scheme. The HIVOSS footstep load (equation 10) is used with randomly generated mass and frequency chosen through a representative distribution law. The maximal effective acceleration is computed just as the experimental tests, with the equation 18.

4.3 Campaign results and interpretation

The effective acceleration identified experimentally and computed numericaly can be plotted according to different factors. The most relevant ones seem to be the weight of the walkers and their walking frequencies (figure 13 and 14).

Results are similar for CLT floor. The numerical and the experimental results have the same order of magnitude (figures 13 and 14). Numerical results are broadly superior to experimental

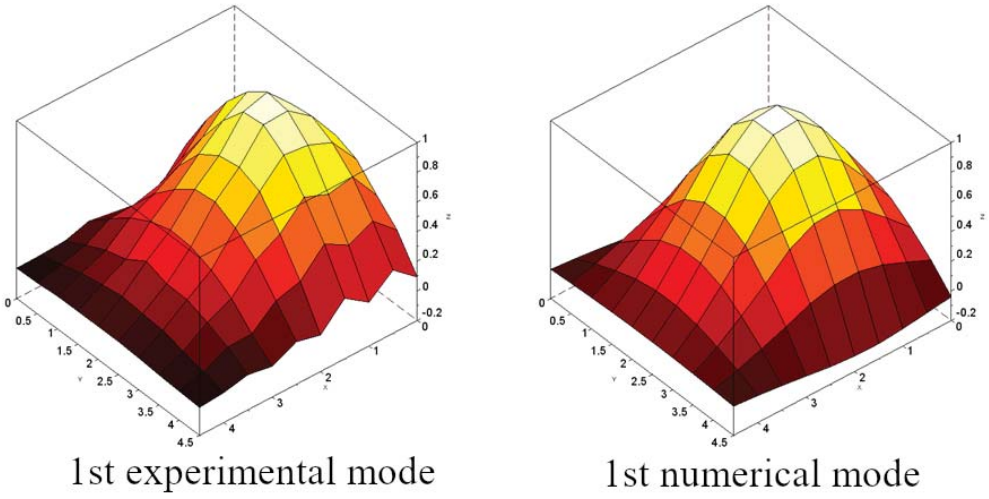

Figure 12: First mode computed numerically and identified experimentally for the joist-OSB floor

ones. It can be explained by the fact that, in the numerical model, the footsteps are very regular with a constant walking frequency whereas during experimental test, the walking frequency varied slightly which induced a lower impact of the harmonics of walking frequency. With the numerical model, the effective acceleration increases with the weight of the walker (figure 13). The uncertainties are greater experimentally and it is difficult to extract a tendency. The same observation can be made by confronting the effective acceleration with the walking frequency (figure 14).

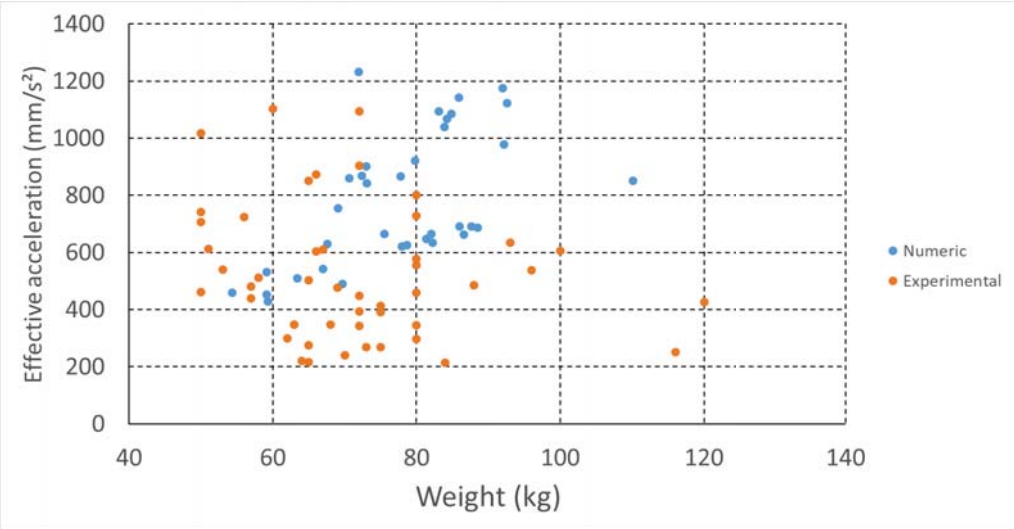

Figure 13: Maximal effective acceleration depending on the weights of the walkers on the joist-OSB floor

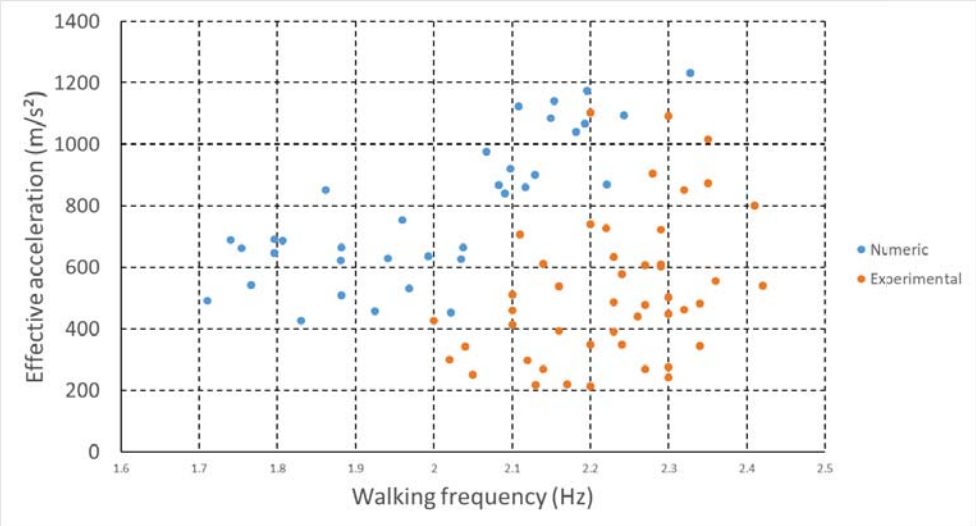

Figure 14: Maximal effective acceleration depending on the walking frequency of the walkers on the joist-OSB floor

4.4 Confrontation to simplified computation

The equation 17 enables a conservative estimation of the acceleration due to the walk of an individual. This formula has been confronted to experimental results. Figure 15 gives an example of results for a 80kg person walking on the joist-OSB floor.

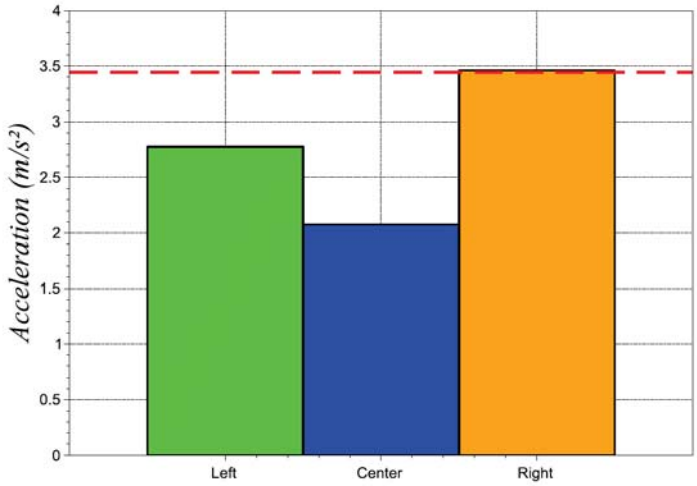

Figure 15: Maximal acceleration measured during the walk by 3 accelerometer on each side of the floor. The dashed line in red correspond to the maximal acceleration predicted by the formula 17

Note that in this figure, the peak of acceleration is considered, so the coefficient V_{eff} of the equation 17 has not been used. This equation gives an accurate value of the acceleration peak, without overestimating it. Based on all the experiments, a margin coefficient has been created, which links the effective acceleration predicted by the formula 17 with the effective acceleration measured experimentally. Results are given in the form of a boxplot on figure 16.

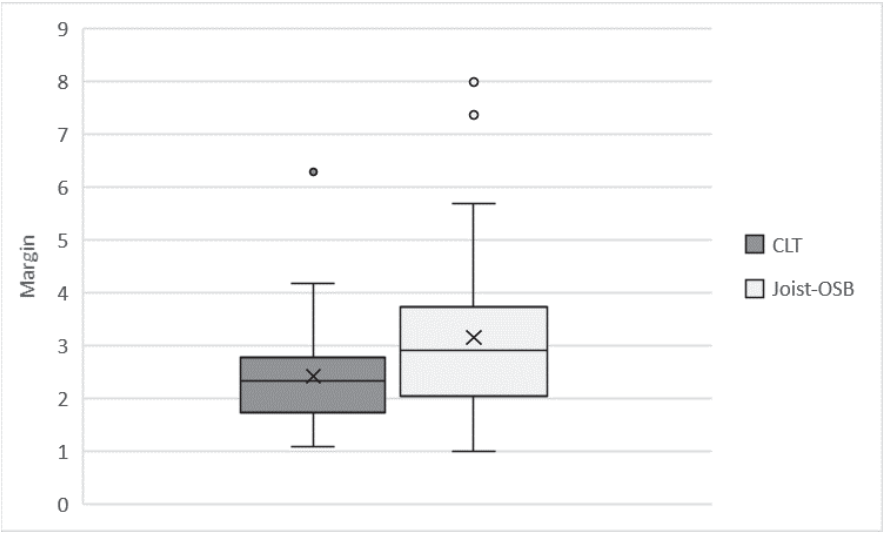

Figure 16: Boxplot of the margin coefficients between simplified formulation and experimental results

The results remain always conservative : the margin coefficient is always superior or very close to 1. On average, the simplified formulation overestimates the floor response, probably because the theory used to build this formula considers an homogeneous floor and a constant walking frequency. By the way, the average coefficient is higher for a joist-OSB floor than for a CLT floor. The joist-OSB floor is very heterogeneous, the joists have different densities and stiffnesses. Moreover, the connections can dissipate some energy. It explains why the joist-OSB floor has a better behavior regarding vibration than the one predicted with the theory.

5 Conclusion

This article presents a new simplified method to compute resonance frequency for a timber floor and its acceleration during walking of an individual. This method is based under theoretical assumptions and numerical computations. The simplified method has been confronted to experimental results on two kind of floors and gives conservative results with a moderate overestimation. This method has to be applied for in situ floors in order to validate its relevance.

Thereafter, the influence of a group of persons on the floor vibrations will be studied, depending on their activities. Then several ways to mitigate floor vibrations, with construction method adjustment or passive system should be conceived. However, one of the most important step is to define criteria to assess the comfort level of timber floors depending on the physical values of the vibration.

6 Acknowledgements

Financial support was provided by the region Nouvelle Aquitaine.

REFERENCES

[1] International Organization for Standardization, Bases for design of structures Serviceability of buildings and walkways against vibrations, 2007

[2] European Committee for Standardization, Eurocode 5: design of timber structure, 1994

[3] T. Murray, Design Guide 11: Vibrations of Steel-Framed Structural Systems Due to Human Activity, American Institute of Steel Construction,2016

[4] S.Ohlsson, Springiness and Human-induced Floor Vibrations: A Design Guide, Swedish Council for Building Research, 1988

[5] E. Caetano and A. Cunha, Human induced vibrations in floors design Guidelines and Background Documentation, HIVOSS Project, European Commission, 2008

[6] Galanti, F., Heinemeyer, C., Feldmann, M., et Lentzen, S., Assessment of floor vibration using the OS-RMS90 method, *University of Southampton, Institute of Sound Vibration and Research*, 2011

[7] Setra, Assessment of vibrational behaviour of footbridges under pedestrian loading ,2006

[8] J. Kala, V. Salajka, et P. Hradil, Footbridge response on single pedestrian induced vibration analysis, *World Acad. Sci. Eng. Technol.*, 2009

[9] L. J. Hu et Y. Chui, Development of a design method to control vibrations induced by normal walking action in wood-based floors, *Proceedings of the 8th World Conference on Timber Engineering*, 2004

[10] J. Weckendorf, T. Toratti, I. Smith, T. Tannert, Vibration serviceability performance of timber floors, *European Journal of Wood and Wood Products*, 2015

[11] P.Hamm, Floor vibration - new results, *WCTE conference*, 2010

[12] L. Hu, Y. Chui, P.Hamm, T.Torrati and T.Orskaug, Development of ISO baseline vibration design method for timber floors, *WCTE conference*, 2018

[13] A.W. Leissa, The free vibration of rectangular plates, *Journal of Sound and Vibration*, 1973

[14] Y.F. Xing, B. Liu, New exact solutions for free vibrations of thin orthotropic rectangular plates, *Composite Structures*, 2009

[15] H.Ghashochi-Bargh, S.Razavi, A simple analytical model for free vibration of orthotropic and functionally graded rectangular plates, *Alexandria Engineering Journal*, 2018

[16] G. Jayaraman, P. Chen, V.W. Snyder, Free vibrations of rectangular orthotropic plates with a pair of parallel edges simply supported, *Computers & Structures*, 1990

[17] K. Jarner, A. Brandt, A. Olsson, In situ testing of timber floor vibration properties, *WCTE 2010*, 2010

[18] V. Giurgiutu, Structural Health Monitoring with Piezoelectric Wafer Active Sensors, Chapter 3 - Vibration Fundamentals, *Academic Press - Oxford*, 2014

[19] M. Pastor, M. Binda, T. Harcarika, Modal Assurance Criterion, *MMaMS*, 2012

[20] International Organization for Standardization, Mechanical vibration and shock Evaluation of human exposure to whole-body vibration Part 1, 1997

EURODYN 2020
XI International Conference on Structural Dynamics
M. Papadrakakis, M. Fragiadakis, C. Papadimitriou (eds.)
Athens, Greece, 23–26 November 2020

SYSTEM IDENTIFICATION OF HUMAN LEG SPRING STIFFNESS DURING RHYTHMIC JUMPING ON A PERCEPTIBLY MOVING SURFACE

R.E.White[1], N.A.Alexander[2], J.H.G.Macdonald[3]

[1]Department of Civil Engineering, Queen's Building, University of Bristol, UK, BS8 1TR
Rory.White@bristol.ac.uk
[2]Department of Civil Engineering, Queen's Building, University of Bristol, UK, BS8 1TR
Nick.Alexander@bristol.ac.uk
[3]Department of Civil Engineering, Queen's Building, University of Bristol, UK, BS8 1TR
John.Macdonald@bristol.ac.uk

Keywords: pedestrian-loading, biomechanics, non-linear dynamics, human-structure interaction, jumping, experimental system identification

Abstract. In recent years, various man-made structures, such as grandstands and footbridges, have shown significant vibration problems during human jumping causing concern for maintenance and serviceability. To understand the interactions observed between a human and a structure, a 5.5m timber beam was constructed and instrumented. This was designed to simulate a cantilever tier of a grandstand, with similar natural frequency and damping ratio to the full-scale structure and with a similar mass ratio of a single human to the beam as for a crowd to the full-scale structure. Measurements of accelerations and displacements of both the jumper and beam, and of the contact force between them, were acquired. Tests for a range of target jumping frequencies, from below to above the structure's natural frequency, were performed to identify the jumper's dynamics and the induced vibrations of the structure and to observe interactions. System identification techniques were performed to evaluate and model the human leg mechanics of a jumper on a vertically oscillating surface. Force-displacement curves, for both relative (jumper to beam) and absolute displacements, have been obtained. The corresponding leg spring stiffness has been evaluated using a linear fit. Variations in the stiffness for different jumping frequencies is discussed.

1 INTRODUCTION

Previous experimentation into human-structure interaction (HSI) during rhythmic jumping and bobbing on a perceptibly moving surface has shown that periodic jumping close to the natural frequency of the structure was not possible [1,2,3]. A simple reduced-order model [4] was presented to provide an explanation for this problematic jumping. The model assumes an approximate linear spring-mass-damper-actuator system, as an approximation, that is included in IStructE guidelines [4] and other literature [5,6]. Unfortunately, the values of the parameters of the system, are uncertain. Furthermore, a frequency-invariant linear model may not be sufficient. In this paper, force-displacement curves, for absolute and relative displacement, are presented to characterise the leg stiffness from direct measurements of force and displacement. This is performed for low-and high jumping frequencies, above and below a structure's natural frequency. A linear polynomial is applied, using regression analysis, to capture and model the leg stiffness. The evaluated coefficients are observed to be frequency-dependent.

2 EXPERIMENTAL MODELLING

To investigate the interactions of a human jumping rhythmically on a perceptibly moving surface a small beam section was constructed. This was assembled to simulate an oscillating cantilever tier of a grandstand structure due to human jumping loads. These have been known to contain low frequency resonant modes in the region of 1-6Hz with low damping ratios as a result of the long, thin slender structures [7]. This makes them susceptible to significant vertical excitation from humans jumping at various jumping frequencies.

2.1 Beam construction & instrumentation

The beam was designed to be cost effective and simple to construct. The main beam span was constructed from five 150mm x 47mm x 5500mm C24 structural timber beams fixed together side-by-side using thirteen 750mm x 20mm x 100mm plywood slats evenly and symmetrically distributed. This is displayed in Figure 1(a) and 1(b). The beam was clamped at both supports, 75mm from the ends. The clamps were formed from scaffolding pipe tubes, 50mm cross-sectional diameter, cut a length of 900mm. This is shown in Figure 1(c). 10mm holes were drilled into the top and bottom to allow secure fastening of the clamps to the beam using M8 threaded rods. The beam was built into a simple scaffolded system to raise it to provide a clearance of 300mm from the underside of the beam to the finished floor level. This was to ensure that the beam would not make contact with the floor during experimentation. An AMTI OR6-7 force-plate was mounted in the centre of the beam. The total mass of the beam was approximately 170kg. Handrails were constructed for safety of the test subjects. The linear natural frequency and damping ratio of the first bending mode were measured as $f_1=1.89Hz$ and ς_1=0.11%.

Direct measurements of displacement and acceleration of the beam were acquired using two Sétra uniaxial accelerometers and reflective motion capture markers. These were positioned either side of the force plate, across the width of the beam section, at mid-span. The generalised beam dynamics were evaluated by averaging the measurements from each pair of sensors, to evaluate a single measurement for acceleration and displacement respectively.

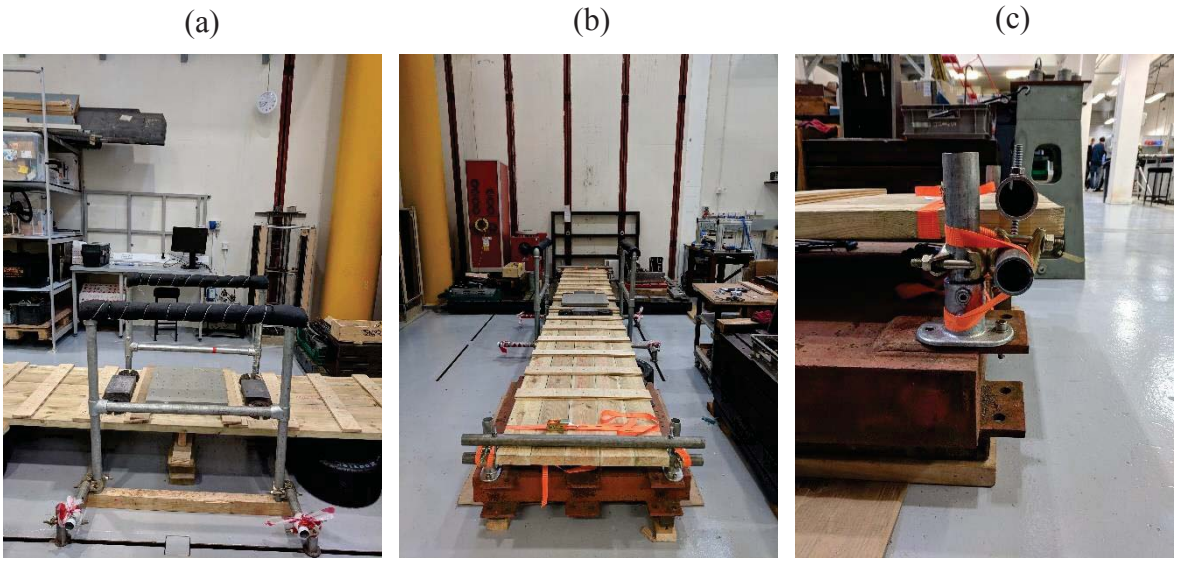

Figure 1 Breakdown of constructed bridge (a) Central jumping zone; (b) Length of bridge; (c) Bridge beam end-fixtures

2.2 Procedure and human instrumentation

Biomechanical jumping experiments on the beam were performed for a single male test subject, age 26, mass 74.5kg, height 189cm, leg length 114cm. The test subject's bodyweight corresponded to a human-structure mass ratio of 0.44. Experimental tests were performed above and below the beam's natural frequency. The test subject was given a two-minute rest between each jumping test to ensure that fatigue or physical exhaustion did not occur. Each test were performed over a 50s window with a rhythmic jumping period of 30s. 20s was allowed for the person to step on and off the beam comfortably. Jumping tests were performed at multiple frequencies above and below the beam's natural frequency, (f_1=1.89Hz):1.25Hz, 1.50Hz, 2.70Hz and 3.00Hz.

A 14-marker body system was adopted for the tracking of the human jumping kinematics using Qualisys motion capture software. Markers were fastened using double-sided medical (hypo-allergenic) tape. The test subject wore fitted gym attire to minimise any soft tissue artefacts. From the marker setup, a nine – segment body model was defined following the procedure illustrated by Winter [8] to locate the human body centre of mass (COM) during the tests. This is common practice within the biomechanics research field.

3 DATA PROCESSING

During acquisition of force plate and accelerometer measurements an anti-aliasing low-pass Butterworth filter with a cut-off frequency of 1400Hz was used. The force plate and accelerometer sensor measurements were down-sampled and decimated to the motion capture system's sampling frequency of 100Hz for data processing and analysis. A fourth order low-pass Butterworth filter with a cut-off frequency of 20Hz was applied to all measurements to mitigate any high-frequency noise effects, whilst still capturing higher harmonic responses. Using the 30s jumping record, for each test, a 20s record was extracted for analysis of displacement, acceleration and force data measurements.

The force plate instrumented on the beam measured the loading induced by a human jumper for each target jumping frequency test performed. To quantify the contact force, the inertial force of the force plate itself was first evaluated from a free vibration test. This provided the

'dynamic mass' of the force plate which was found to be 15.3kg. The contact force of the test subject was evaluated as follows:

$$F_{\mathrm{GRF}} = F_{\mathrm{meas}} - m_{fp}\ddot{x}_b \tag{1}$$

where F_{GRF} is the contact force exerted between the test subject and beam, F_{meas} is the directly measured force from the force plate, m_{fp} is the dynamic mass of the force plate, $\ddot{x}_b$ is the measured acceleration at midspan of the beam.

The three-dimensional coordinates of the subject body COM were calculated as follows:

$$\begin{Bmatrix} x_{\mathrm{COM}} \\ y_{\mathrm{COM}} \\ z_{\mathrm{COM}} \end{Bmatrix} = \frac{1}{m_p} \sum_{i=1}^{N_s} m_{\mathrm{seg},i} \begin{Bmatrix} x_{\mathrm{seg},i} \\ y_{\mathrm{seg},i} \\ z_{\mathrm{seg},i} \end{Bmatrix} \tag{2}$$

where x_{COM}, y_{COM}, and z_{COM} are three-dimensional coordinates of the position of the COM of the subject's body, m_p is the subject's total body mass, N_s is the total number of body segments (nine in this case), i is the segment index, $m_{\mathrm{seg},i}$ is the mass of the i-th segment and $x_{\mathrm{seg},i}$, $y_{\mathrm{seg},i}$, and $z_{\mathrm{seg},i}$ are three-dimensional coordinates of the position of the COM of the i-th segment.

Considerable variability in loading/displacement from cycle to cycle was observed in these jumping tests. This is a direct result of the oscillating surface affecting the jumper to be slightly in or out-of-phase with the beam. One consequence was a difficulty in defining, based on period, the flight and contact phases. In order to distinguish the flight and contact phases of the jump cycle, and to allow for noise on the force measurements, the times of take-off and landing were defined as when the contact force equalled 5% of the bodyweight. Smaller values were zeroed as they were assumed to be during the flight phase.

Figure 2 depicts a time-history breakdown for the test subject's dynamics of a test at their preferred jumping frequency. Figure 2(a) indicates the jumper's body segments and centre-of-mass trajectories, as described in Eq.2. This is detailed as grey and black respectively. Figure 2(b) shows the processed contact force to distinguish clear contact and flight phases, normalised to the person's bodyweight. Figure 2(c) displays the beam mid-span displacement. The positive sign convention for the jumper COM and beam displacements are defined as the downward displacement corresponding to a positive contact force indicating compression. The reference (zero) displacement for the jumper is defined as the static COM displacement. These measurements are processed further into overlaid cycle-by-cycle time-histories to signify the jumper's variability performing rhythmic jumping on the oscillating beam, as shown in Figure 3.

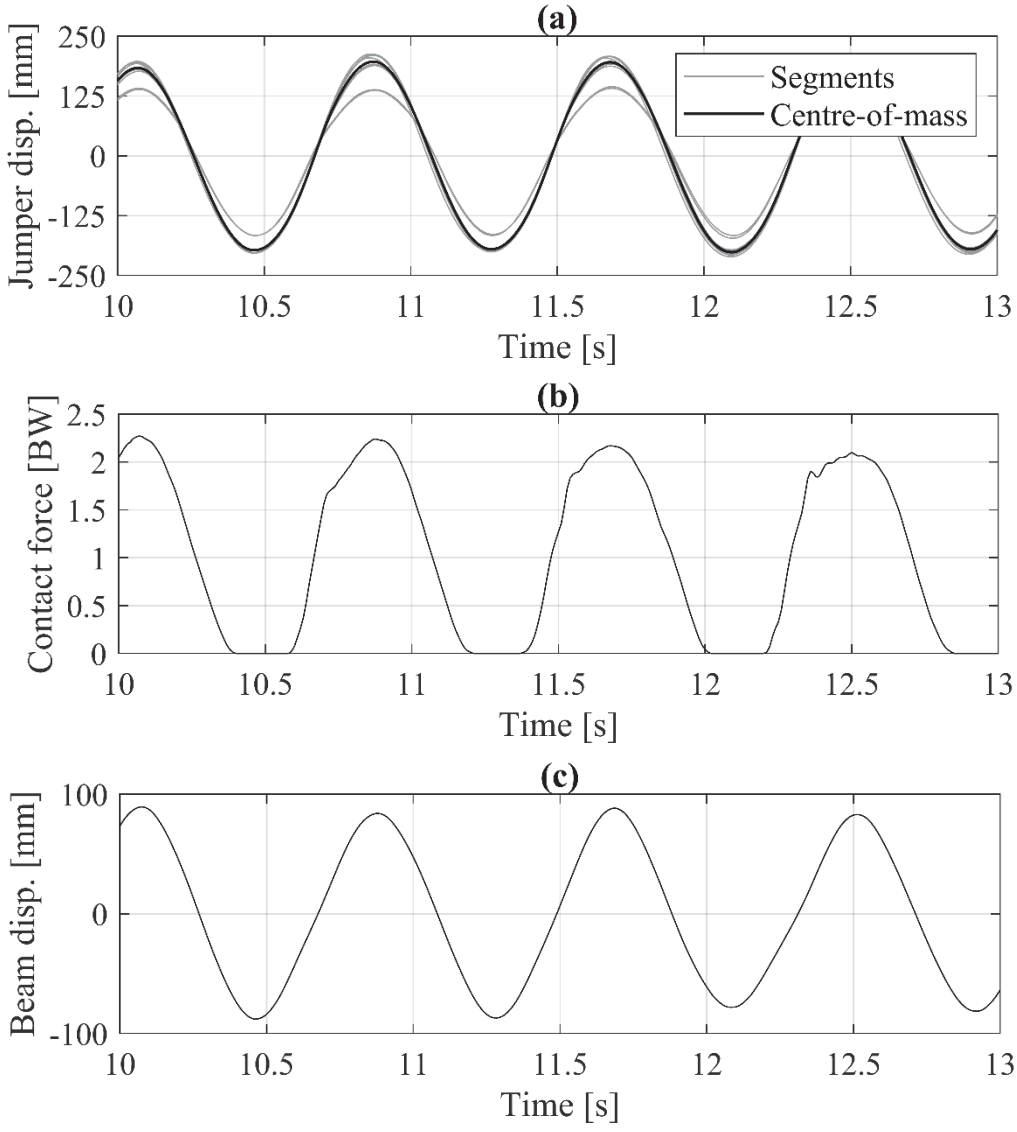

Figure 2 Example time-histories of test subject's dynamics jumping at their preferred frequency (a) jumper COM (grey indicates the defined body segment trajectories and black indicates the evaluated centre-of-mass); (b) Contact force; (c) Beam mid-span displacement

Figure 3 displays the time-histories of the contact force (a), relative displacement (b), jumper to bridge, jumper COM displacement (c) and beam displacement (d) for a test at the test subject's preferred jumping frequency. The relative displacement is defined as the jumper COM to bridge displacement. The mean achieved jumping frequency for this test was found to be 1.26 ± 0.05Hz. A jumping cycle is characterised by the contact and flight phases. These are indicated in Figure 3 as a comparative measure of the time spent and response shape for each phase. The dashed grey lines indicate approximate contact and flight phases. For this specific test, the contact phase is observed to be the majority of the period of oscillation and displays significant deflection of both the jumper and beam resulting in a large relative displacement (leg compression).

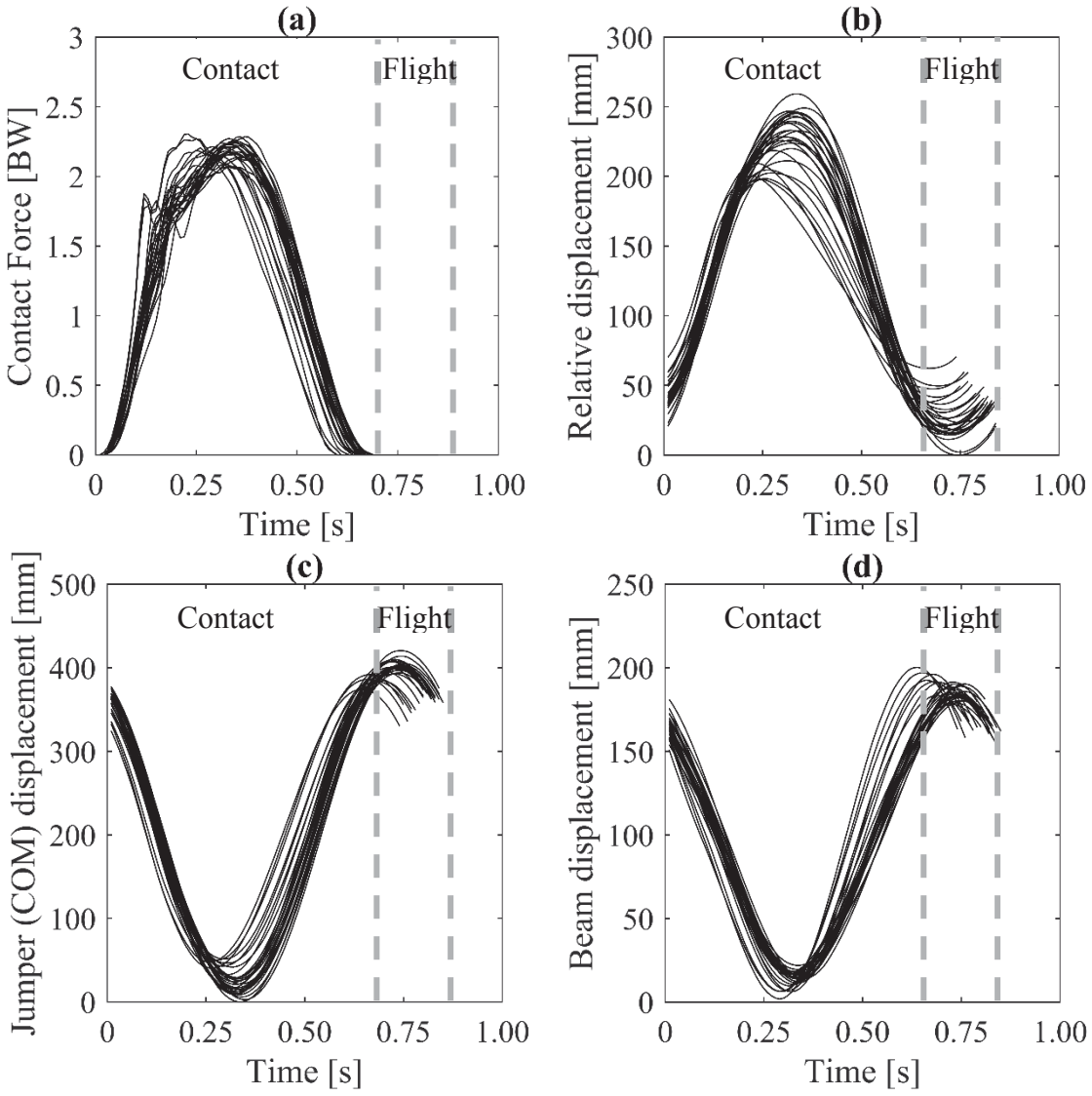

Figure 3 Example time-histories of test subject jumping at their preferred frequency, mean 1.26Hz (a) Contact force; (b) Relative displacement; (c) Jumper centre-of-mass displacement; (d) Beam centre-of-mass displacement

Table 1 summarises the dynamics observed during jumping tests above and below the structure's natural frequency. These are evaluated as the mean peak values observed for each test case. The peak contact force is normalised to the test subject's bodyweight, BW.

Jumping frequency [Hz]	Displacement (mm)			Beam acceleration (m/s^2)	Peak contact force (BW)
	Jumper centre-of-mass	Beam	Relative		
1.26	216	106	125.42	9.56	2.36
1.50	172	151	321.25	14.21	2.91
2.70	105	55.8	137	12.7	3.00
3.00	52.9	37.8	91.9	13.97	3.05

Table 1 Summary of mean peak values of dynamics measured for jumping frequency test cases above and below the structure's natural frequency (f_1=1.89Hz)

4 FORCE-DISPLACEMENT CURVES

Force-displacement curves for the coupled oscillating jumper and beam system have been plotted for the absolute (jumper's COM) and relative displacement (jumper to bridge). This is performed as a comparison to explore the leg stiffness effects for each case to understand the underlying interactions.

The compressing and extending stages of the contact phase were identified for each jumping test case to examine the loading and unloading relationships. These are overlaid in Figures 4 and 5. The red dots denote compressing, whilst blue indicates extending. This was important to understand any subtle changes in the leg stiffness during each stage of the contact phase. In order to distinguish the compressing and extending stages during the contact phase, the velocity was evaluated, for each displacement measurement, to identify the loading conditions. To be consistent with the positive sign convention of downward displacement, corresponding to a positive contact force, compressing was defined as positive velocity, whilst extending was defined as negative velocity.

A simple linear relationship, Eq.(5), was applied to each jumping test case, for both displacements, to characterise the leg stiffness profile during the compression and extension stages of the contact phase.

$$F_{GRF} = kZ \tag{3}$$

Where k is the linear stiffness coefficient of Eq.(5) and Z is the displacement of interest (absolute or relative). These were found using regression analysis.

4.1 Relative displacement

Figure 4 displays the force-displacement curves for jumping at 1.25Hz, 1.50Hz, 2.70Hz and 3.00Hz, using the measured relative displacement. Below the structure's natural frequency (f_1=1.89Hz), the 1.25Hz and 1.50Hz test cases indicate large relative displacements with similar contact forces. The shapes are observed as being approximately linear with the compressing and extending stages following very similar paths indicating similar stiffness. For the 1.50Hz test case, the compressing stage of the cycle is seen to be considerably variable. Table 1 indicates that the beam displacement amplitude is largest at the 1.50Hz which could be due to a jumping frequency near resonance.

Above the structure's natural frequency, the 2.70Hz and 3.00Hz cases indicate less deflection (approximately 200mm max displacement corresponding to 2kN of force, 2.36BW). Interestingly, both curves of these test cases display hysteresis loops indicating that the energy exchanged during the leg compression and extension is significantly different. The stiffness

profiles during each stage of contact are observed to be considerably different suggesting a larger stiffness spring during compression in comparison to extension.

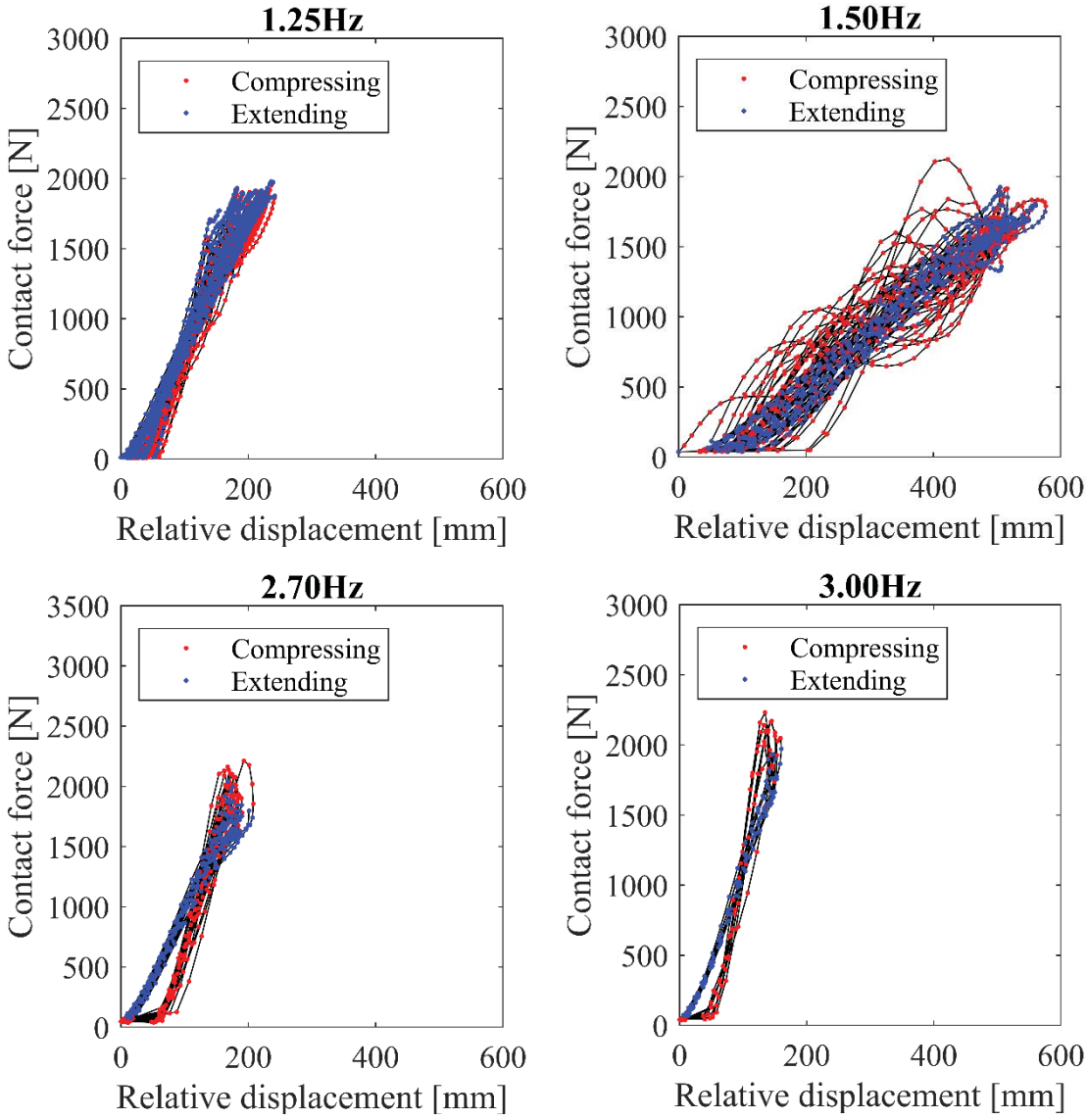

Figure 4 Contact force - relative displacement relationships for jumping frequencies above and below the structure's natural frequency (f_1=1.89Hz). Red dots denote compression, whilst blue indicates extension.

4.2 Absolute displacement

Figure 5 displays the force-displacement curves for jumping at 1.25Hz, 1.50Hz, 2.70Hz and 3.00Hz, using the measured jumper's COM displacement. Below the structure's natural frequency (f_1=1.89Hz), the jumper's COM observes large displacements, approximately 300mm max deflections corresponding to 2kN of force (a bodyweight factor of 2.36). The 1.25Hz test case shows a clear linear trend with the compressing and extending stages following very similar paths. The 1.50Hz jumping is rather variable, particularly during compression, suggesting the test subject found this frequency difficult to periodically jump at. The extension is observed to be clearly linear.

The force-displacement relationship, for the absolute displacement at 2.70Hz jumping, is observed to be linear. The evaluation of the compressing and extending stages, of the contact phase, indicates slightly different leg stiffnesses. This suggests tentative evidence of a hysteresis loop like the relative displacement case. At 3.00Hz, the force-displacement curve observes a subtle hysteresis loop, mirroring the effects of the relative displacement case. The compressing and extending stages follow distinctly different paths corresponding to distinctive stiffness profiles. The relationship during extension is observed to be linear in comparison to compression which is clearly complex in nature.

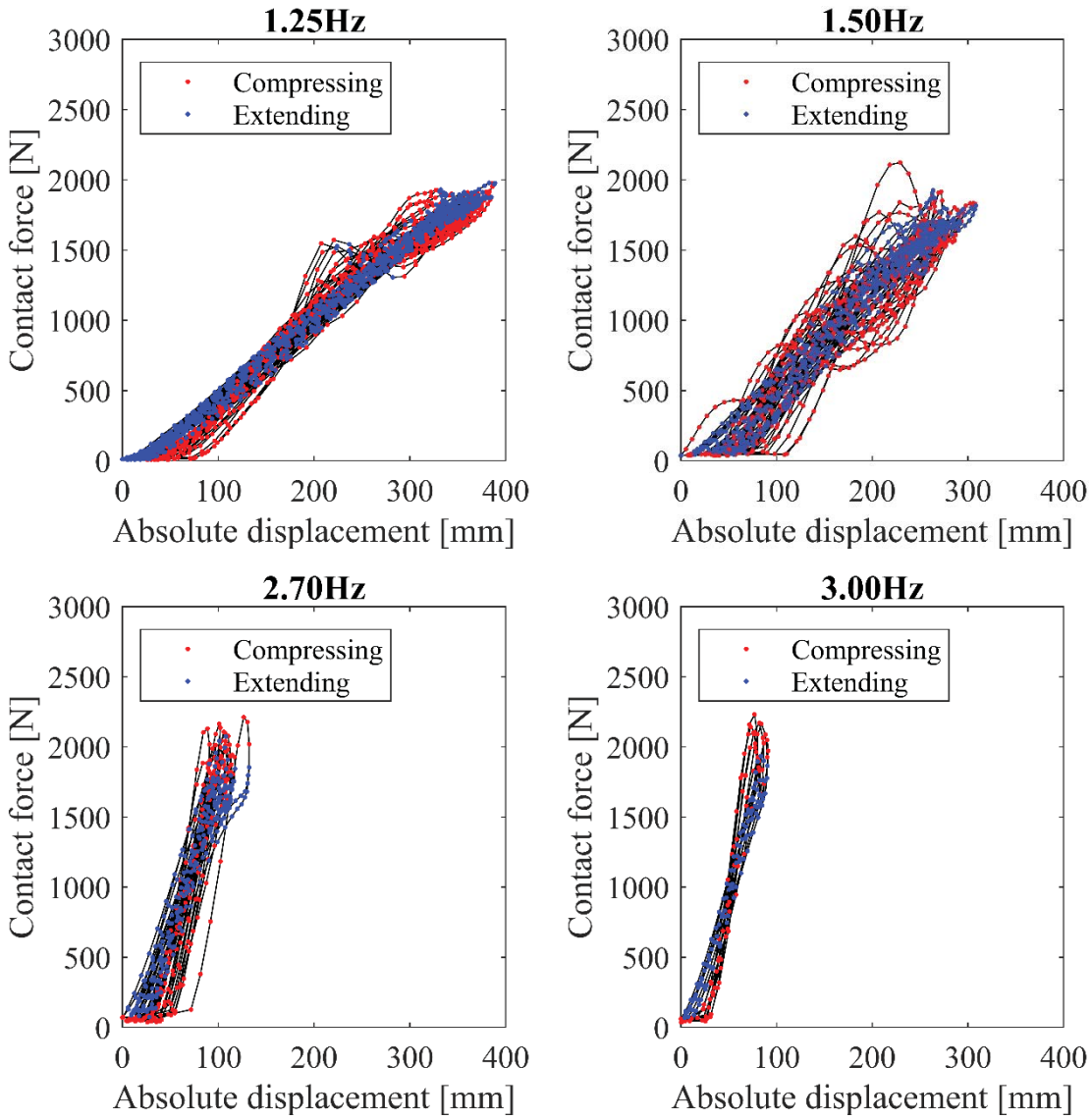

Figure 5 Contact force - absolute displacement relationships for jumping frequencies above and below the structure's natural frequency (f_1=1.89Hz). Red dots denote compression, blue dots indicate extension.

5 LEG STIFFNESS

Figure 6 displays the frequency-dependency of the linear fits. The compression stiffness coefficients are indicated as red crosses whilst the extension stiffness coefficients are presented as blue circles. The leg stiffness coefficients, displayed in Figure 6, are computed using the calculated stiffness coefficients, in Figures 4 and 5, divided by the test subject's body mass. The stiffness coefficients evaluated from the relative and absolute displacements are represented in Figure 6(a) and 6(b) respectively. In Figure 6(a), the compressing and extending stiffness are seen to increase at high frequency jumping whilst the stiffness indicates a decrease from 1.25Hz to 1.50Hz. The rates of increase for the stiffness coefficients are suggestive of being non-linear. Figure 6(b) displays an increase in stiffness from 1.25Hz to 1.50Hz followed by an increase in 2.70Hz to 3.00Hz. The compressing stiffness at these frequencies increase significantly in comparison to the extending stiffness. At low jumping frequencies, the stiffness coefficients for the two stages, obtained for both absolute and relative displacement, are approximately the same in value. Above the structure's natural frequency (f_1=1.89Hz), the compressing and extending stiffness coefficients are observed to differ considerably indicating a complex stiffness mechanism of the leg. This is more evident in the case of the absolute displacement, Figure 6(b).

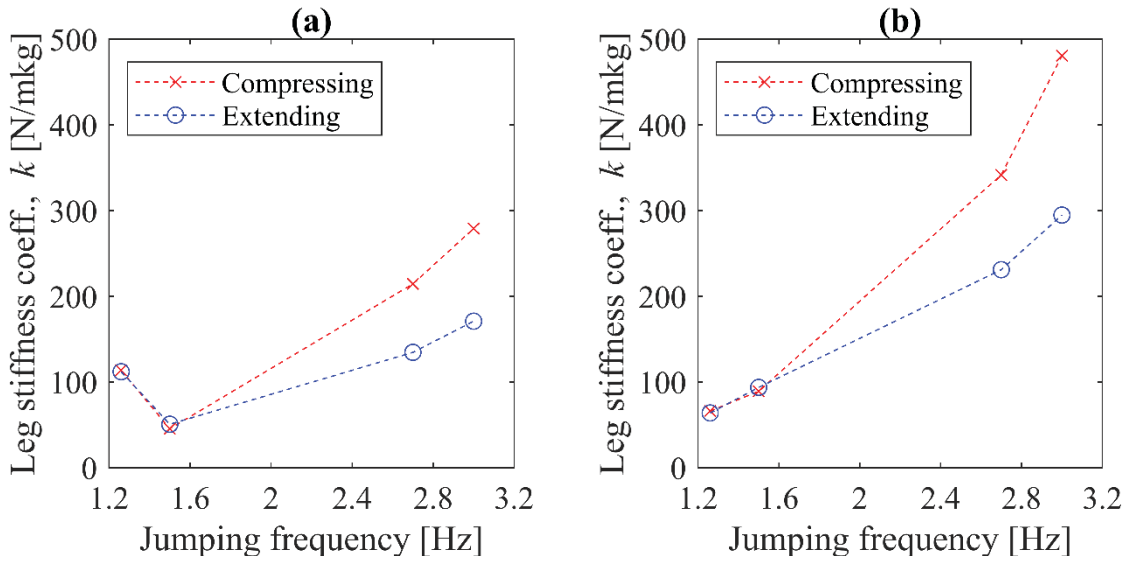

Figure 6 Frequency dependency of linear stiffness coefficients (a) relative displacement; (b) absolute displacement

6 CONCLUSIONS

Force-deflection curves for absolute and relative displacement measurements have been presented with the corresponding stiffness profile being explored. At low jumping frequencies, the force-displacement relationships are observed to be close to pseudo-linear. However, at high jumping frequencies, the relationships are observed to be more complex. The relative displacement exhibits hysteresis loops, indicating a complex energy exchange at high frequency jumping. Hysteresis is subtly mirrored in the absolute displacement case for the 3.00Hz jumping case. The frequency-dependencies of the stiffness coefficients suggest that at low jumping frequencies the stiffness profile during compression and extension are extremely similar. At high jumping frequencies, the stiffness is observed to be larger and complex during

compression in comparison to extension. This suggests that the leg stiffness mechanism is considerably more complex at high jumping frequencies.

REFERENCES

[1] Yao S, Wright JR, Pavic A, Reynolds P. Experimental study of human-induced dynamic forces due to jumping on a perceptibly moving structure. Journal of Sound and Vibration. 2006;296(1-2):150-65.
[2] Yao S, Wright JR, Pavic A, Reynolds P. Experimental study of human-induced dynamic forces due to bouncing on a perceptibly moving structure. Canadian Journal of Civil Engineering. 2004;31(6):1109-18.
[3] Harrison RE, Yao S, Wright JR, Pavic A, Reynolds P. Human jumping and bobbing forces on flexible structures: effect of structural properties. Journal of Engineering Mechanics. 2008;134(8):663-75.
[4] IStructE, Dynamic performance requirements for permanent grandstands subject to crowd action, The Institution of Structural Engineers, London, 2008
[5] Alexander NA, Macdonald JHG, Champneys AR. Numerical investigation of a simple model of human jumping on an oscillating structure. Procedia engineering. 2017 ;199:2844-9.
[6] N.A. Alexander, Theoretical treatment of crowd-structure interaction dynamics, Proceedings of the Institution of Civil Engineers - Structures and Buildings, 2006, 159(6), 329-338
[7] J.W. Dougill, J.R. Wright, J.G. Parkhouse and R.E. Harrison, Human structure interaction during rhythmic bobbing, The Structural Engineer, 2006, 84:32-39
[8] Winter DA. Biomechanics and motor control of human movement. John Wiley & Sons; 2009

EURODYN 2020
XI International Conference on Structural Dynamics
M. Papadrakakis, M. Fragiadakis, C. Papadimitriou (eds.)
Athens, Greece, 23–26 November 2020

ENVIRONMENTAL IMPACT OF STRUCTURAL MODIFICATIONS IN OFFICE FLOORS TO SATISFY VIBRATION SERVICE ABILITY

Márcio S. Gonçalves[1] **and Aleksandar Pavic**[1]

[1] Vibration Engineering Section, College of Engineering, Mathematics, and Physical Sciences, University of Exeter, Kay Building, North Park Road, Exeter, EX4 4QF, U.K.
{ms892, a.pavic}@exeter.ac.uk

Keywords: Vibration, serviceability, floor, office, structural modification, embodied energy, embodied carbon.

Abstract. *Modern office floors (featuring slender slabs, longer spans, open-plan spaces, less furniture) are increasingly susceptible to walking-induced excessive vertical vibrations. Therefore, vibration serviceability has become the governing design criterion for office floor structures. Structural modifications are normally performed to tackle this problem, but they considerably increase the amount of construction materials needed, which is directly linked to the embodied energy (EE) and embodied carbon (EC) in floor design. In fact, reduction of EE and EC is becoming a necessary feature in building construction due to urgent global sustainability issues.*

However, structural modifications are frequently carried out with no optimisation analysis, resulting in reduced sustainability of office floor design. This paper investigates the environmental impact of structural modifications to satisfy vibration serviceability, in terms of embodied energy and carbon, for a finite element model of a steel-concrete composite office floor, featuring a trapezoidal steel deck supported by downstanding steel beams. The original floor design has minimal structural dimensions to comply with all design criteria (i.e. strength, thermal comfort, acoustic insulation, fire protection, maximum deflection), except for vibration serviceability under walking-induced loads.

The desktop study was performed by employing structural modifications in the slab depth and beam profiles until the response factor of 4 was achieved over the whole floor area, for pacing frequencies from 1.4 Hz to 2 Hz. Results showed that the compliant floor design nearly features 14 %, 27 % and 37 % extra EE, EC and structural weight (SW), respectively, compared with their counterparts in the original design. This is one of very few studies in the public domain demonstrating the huge financial and environmental costs of meeting current vibration serviceability criteria for office floors.

1 INTRODUCTION

The built environment is responsible for nearly 40% of CO_2-related energy globally consumed and construction of the built environment accounts for 13% of the international gross domestic product (GDP) [1]. Also, as rigorous goals for minimisation of the overall energy (i.e. embodied and operational) consumption have been established for the near future [2] and the operational energy of buildings has been successfully reduced, embodied energy (including carbon footprint) is becoming crucial to minimise in the life cycle of modern buildings [1].

Related to this, vibration serviceability is well known as the floor design criterion that frequently leads to structural modifications that is increasing embodied energy in modern office floors.

Modern office floors are frequently long-span supporting open-plan paperless working environments. This feature has led to lowering of the vertical fundamental natural frequency of the floor to below 10 Hz [3], reduced modal damping ratios (lower than 2%) and lightweight structure (lower than 150 kg/m^2). These characteristics, in turn, have made modern office floors more susceptible to excessive near-resonant walking-induced vibrations.

Structural modifications are commonly carried out to make office floors vibration serviceable, especially steel-concrete composite slabs. Such modifications are normally carried out by increasing the slab depth and placing heavier downstanding beam profiles. These modifications can substantially increase the amount of embodied energy (EE), embodied carbon (EC), and structural weight (SW) per unit area of the floor.

This paper, therefore, presents a parametric study of structural modifications in a modern steel-concrete composite office floor design to meet vibration serviceability requirements. The vibration performance of the floor design was assessed and compared with different potential structural solutions. The EE, EC, and SW of each redesign were evaluated for their energy consumption, carbon footprint, and material usage.

2 PROTOTYPE OFFICE FLOOR STRUCTURE

A steel-concrete composite office floor was sized to just about satisfy all floor design criteria apart from vibrations (i.e. strength, thermal comfort, acoustic insulation, fire protection, maximum deflection). The floor was then assessed against the criterion for vibration serviceability under walking-induced loads.

The structure was a 30 m x 44.1 m floor composed of seven spans of 6.1 m length and three bays of 10 m width (21 panels in total) supported by a composite slab (8 cm deep concrete deck and an 1 mm thick 6 cm deep steel deck profile), as shown in Figure 1.

The floor was modelled using finite element (FE) software ANSYS [4]. Each panel was supported by I-profiled universal steel beams: two secondary beams (UB 356 x 171 x 51) in the x-direction, spaced by 2.1 m; two secondary beams, between columns, in the x-direction (UB 356 x 171 x 57); and two primary beams in the y-direction (UB 406 x 140 x 53). The primary beams were connected to 3 m high I-profiled universal steel columns (UC 203 x 203 x 60).

The floor area was modelled using SHELL181 (isotropic, four-noded) elements. Beams and columns were modelled using BEAM189 (three-noded) elements. Both shell and beam elements featured six degrees of freedom (translations and rotations relative to X, Y, and Z axes) in all nodes. The FE model featured 4,186 nodes, forming a 70 x 70 cm grid. For vibration serviceability assessment purposes, the columns were modelled assuming fixed end supports (Figure 1).

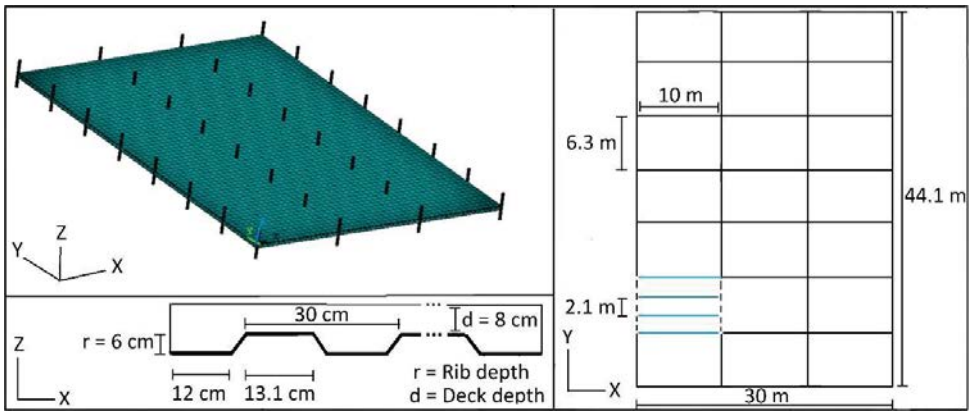

Figure 1: Office floor FE model (top left) and floor slab cross section (bottom left). Floorplan dimensions (right) with example secondary beams (solid blue) and primary beams (dashed red). Columns present at line intersections.

Modal analysis was performed and 36 modes of vibration, up to 15 Hz, were calculated. The first four unit-scaled modes of vibration are shown in Figure 2.

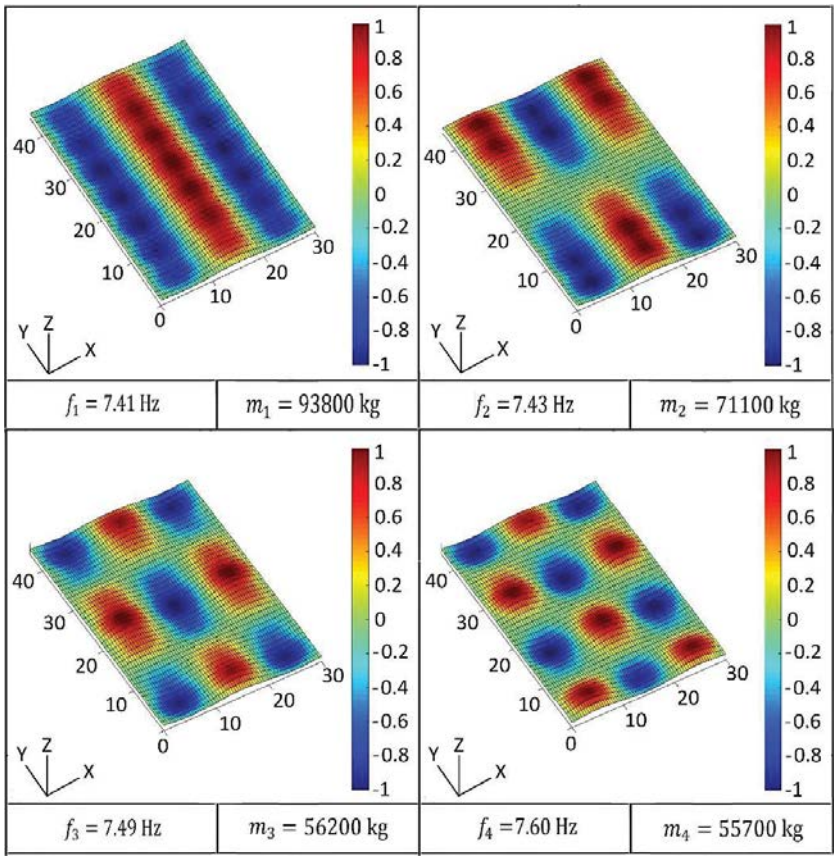

Figure 2: First four modes of vibration of the office floor Model 1 (floor dimensions in meters).

3 ANALYSIS APPROACH

The goal was to design a modern steel-concrete composite office floor compliant with all design criteria, including vibration serviceability, using as little steel and concrete as possible. The vibration serviceability assessment procedure of the CCIP-016 design guide [5] was used in this study.

The excitation was placed at each node of the floor area, and the response was calculated at the same location. The R factor was then calculated and assessed over the whole floor area, for walking frequencies from 1.4 Hz to 2 Hz, in steps of 0.005 Hz. A damping ratio of 2% was assumed for all modes. The starting office floor configuration (Model 1), in turn, did not comply with the assessment criterion (Figure 3).

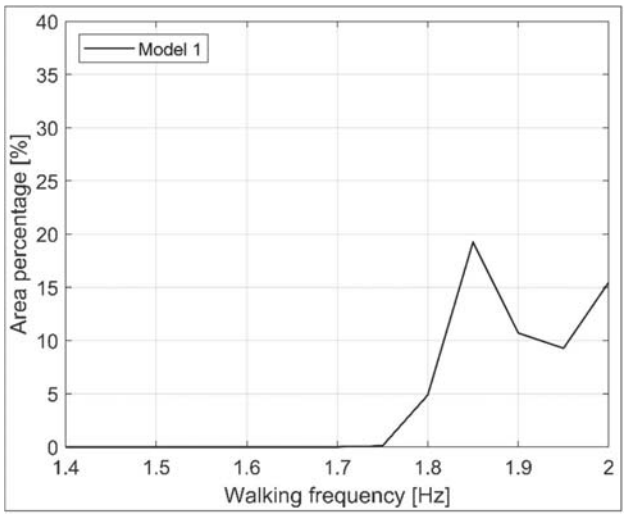

Figure 3: Percentage of the floor area that exceeded R factor of 4 at different walking frequencies.

A contour plot of the response factors calculated over the floor area, for a walking frequency of 1.85 Hz (that corresponds to the highest percentage in Figure 3), is shown in Figure 4.

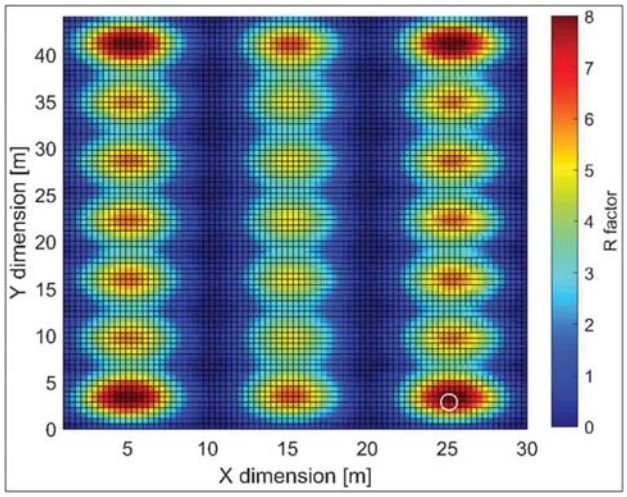

Figure 4: Contour plot of R factors over the floor area at the walking frequency of 1.85 Hz. White circle indicates the most responsive location.

In Figure 4, an adequate floor vibration performance across the whole floor would be represented by a flat line at 0% from 1.4 Hz to 2 Hz, which means that no floor area exceeds R factor of 4. Nearly 20% of the floor area of Model 1 exceeded the R factor of 4, which meant the need for redesign.

Different redesigns were carried out (generating FE models 2 to 10), by modifying the slab depth and both primary and secondary steel beam profiles, until a response factor of less than 4 was achieved for the whole floor area. Table 1 shows all redesigns and their corresponding structural modifications of primary beams (PUB), secondary universal beams (SUB), secondary universal beams between columns (SUBC), relative to Model 1. All models feature the same column profiles (UC 203x203x60).

Model	Slab depth [cm]	PUB	SUB	SUBC
1	8	406x140x53	356x171x51	356x171x57
2	9	406x140x53	356x171x51	356x171x57
3	10	406x140x53	356x171x51	356x171x57
4	8	406x140x53	356x171x57	356x171x57
5	9	406x140x53	356x171x57	356x171x57
6	11	406x140x53	356x171x57	356x171x57
7	12	406x140x53	356x171x57	356x171x57
8	13	406x140x53	356x171x57	356x171x57
9	11	406x140x53	406x140x53	406x140x53
10	13	406x140x53	406x140x53	406x140x53

Table 1: Structural dimensions of all office floor designs (Models 1 to 10).

Table 2 shows the first four natural frequencies of all floor designs.

Model	f_1 (Hz)	f_2 (Hz)	f_3 (Hz)	f_4 (Hz)
1	7.41	7.43	7.49	7.60
2	7.26	7.30	7.38	7.53
3	7.13	7.18	7.29	7.49
4	7.59	7.61	7.67	7.79
5	7.58	7.60	7.66	7.77
6	7.16	7.23	7.36	7.59
7	7.06	7.14	7.30	7.58
8	6.97	7.06	7.26	7.57
9	7.62	7.67	7.80	8.01
10	7.38	7.47	7.65	7.67

Table 2: First four natural frequencies of office floor redesigns (Models 2 to 10).

A comparison of the floor vibration performance of all designs is shown in Figure 5.

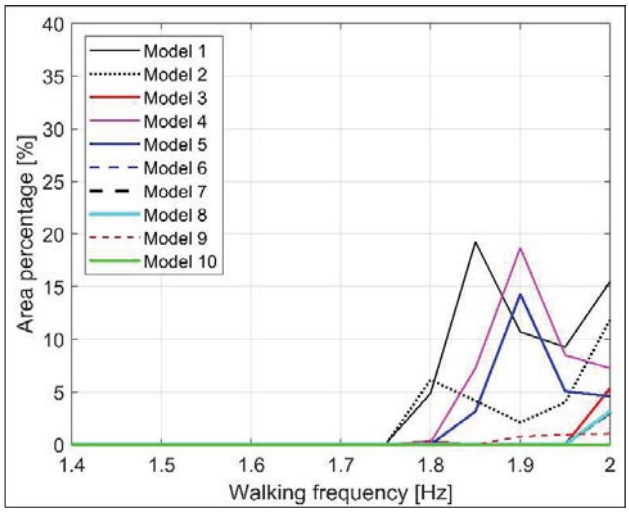

Figure 5: Vibration serviceability assessment of all office floor designs.

It is important to mention here that structural modifications can make the office floor susceptible to near-resonant vibrations at other walking frequencies without solving the problem: Models 4 and 5 became more susceptible to frequencies close to 1.9 Hz (instead of 1.85 Hz, in Model 1) and still have nearly 20% and 15% of the floor area, respectively, exceeding R factor of 4. Therefore, modifications of this kind should be carefully interpreted, as increasing weight and stiffness will not always improve the vibration serviceability performance of the floor.

Once the vibration serviceability was achieved in floor Model 10, the next stage was the quantification of the structural weight of each floor design relative to Model 1 (Table 3).

Model	Concrete %, floor SW	Steel %, floor SW	Total SW [t]	SW relative to Model 1
1	81 %	19 %	341.1	-
2	82 %	18 %	366.2	+7 %
3	83 %	17 %	391.4	+15 %
4	80 %	20 %	343.6	+1 %
5	82 %	18 %	368.6	+8 %
6	84 %	16 %	419.0	+23 %
7	85 %	15 %	444.2	+30 %
8	85 %	14 %	469.3	+38 %
9	84 %	16 %	416.6	+23 %
10	86 %	14 %	466.9	+37 %

Table 3: Comparison of structural weight for office floor designs.

The embodied energy (EE) and embodied carbon (EC) were calculated based on the amount of concrete (2 GJ per ton, 1 tCO_2 per ton) and steel (20 GJ per ton, 3 tCO_2 per ton) used [6]. Values, relative to Model 1, are also shown in Table 4.

Model	EE [GJ]	Relative EE	EC [tCO_2]	Relative EC
1	1858	-	471.8	-
2	1908	+3 %	496.9	+5 %
3	1959	+5 %	522.0	+11 %
4	1909	+3 %	479.3	+2 %
5	1955	+5 %	503.9	+7 %
6	2059	+11 %	554.7	+18 %
7	2110	+14 %	579.9	+23 %
8	2160	+16 %	605.0	+28 %
9	2059	+11 %	554.7	+18 %
10	2111	+14 %	597.7	+27 %

Table 4: Comparison of embodied energy and embodied carbon among office floor designs.

The structural modifications converted the original office floor design (Model 1) into a vibration serviceable floor (Model 10). However, the whole redesigning process was very time-consuming: nine attempts were made to get the structural design needed. Relative to Model 1, Model 10 had 14%, 27%, and 37% extra EE, EC, and SW, respectively, just to satisfy the vibration serviceability criterion.

The structural weight also increased substantially and resizing of structural elements of lower storeys, as well as building foundations, may be required, resulting in further structural modifications. All these implications can indicate the need for a more efficient design process for a sustainable vibration serviceable office floor.

4 CONCLUSIONS

Structural modifications were carried out in the design of a modern steel-concrete composite office floor to make the structure vibration serviceable. The structure was initially sized to just about satisfy all typical floor design criteria (i.e. strength, thermal comfort, acoustic insulation, fire protection, maximum deflection), except for the vibration serviceability requirement. Subsequently, structural redesigns were carried out through gradual structural modifications: increase of slab depth and changes of primary and secondary steel beam profiles.

The fully compliant office floor design met vibration serviceability criteria but required 14%, 27%, and 37% extra embodied energy, embodied carbon and structural weight, respectively, which is quite a lot just to satisfy vibration serviceability.

5 ACKNOWLEDGEMENTS

This study was financed in part by the Coordenação de Aperfeiçoamento de Pessoal de Nível Superior - Brasil (CAPES) - Finance Code 001.

REFERENCES

[1] J. Orr, M.P. Drewniok, I. Walker, T. Ibell, A. Copping, S. Emmitt. Minimising energy in construction: Practitioners' views on material efficiency. *Resources, Conservation and Recycling* 140, 125-136, 2019. doi: https://doi.org/10.1016/j.resconrec.2018.09.015

[2] HM Government. Construction 2025. Industrial Strategy: government and industry in partnership. London, 2013.

[3] P. Reynolds, A. Pavic. Effects of False Floors on Vibration Serviceability of Building Floors. II: Response to Pedestrian Excitation. *Journal of Performance of Constructed Facilities* 17(2), 87–96, 2003. doi: https://doi.org/10.1061/(ASCE)0887-3828(2003)17:2(87).

[4] ANSYS Inc. Release 17.1 Documentation for ANSYS, 2016.

[5] M.R. Willford, P. Young. A Design Guide for Footfall Induced Vibration of Structures - CCIP-016. *The Concrete Centre*, 2006.

[6] J. Allwood, J. Cullen. Sustainable Materials - with Both Eyes Open: Future Buildings, Vehicles, Products and Equipment - Made Efficiently and Made with Less New Material. UIT Cambridge Ltd 2012.

EURODYN 2020
XI International Conference on Structural Dynamics
M. Papadrakakis, M. Fragiadakis, C. Papadimitriou (eds.)
Athens, Greece, 23–26 November 2020

ANALYSIS THE LATERAL VIBRATION SERVICEABILITY OF TEMPORARY GRANDSTAND AND HUMAN COMFORT BASED ON EXPERIMENT

Suhui Yu[1], Jian Yuan[1], Wei Wang[1], Chengqiang Gao[1], Weili Wang[1], Cong Liu[2]

[1] Academy of Combat Support, Rocekt Force University of Engineering, Street 2 Tongxin Road

Baqiao District Xi'an, 710025, China

[2] School of Civil Engineering, Suzhou University of Science and Technology, Suzhou 215011, PR China
e-mail: yuanjian_850809@.163.com

Keywords: Human comfort, Vibration serviceability, Temporary grandstand, Lateral vibration experiment.

Abstract. *Excessive vibrations of temporary grandstand due to crowds who had rhythmic motions can cause human in panic, which have been attracted increasing attention in recent years. This paper based on an experiment that a temporary steel grandstand occupied 20 participants is oscillated by crowd with rhythmic swaying motions at lateral direction. And then a series of vibration perception questionnaires about crowd reactions are obtained. Evaluation of annoying level derives from concept of degree of membership and annoying rate method is proposed, then the human comfort of vibration serviceability of temporary grandstand is assessed with acceleration vibration dose value (VDV). The result shows that standing crowds have more tolerant to vibration than seated crowds. The measured vibrations generated by crowd activities on temporary grandstand can cause panic in crowd. New relationship between the annoyance rate and structural acceleration VDV at logarithmic coordinate is proposed. The findings of this study may be utilized to manage the vibration of temporary grandstand and assess the human comfort when structure was oscillated at lateral excitations.*

1 INTRODUCTION

The problems of vibration serviceability of structure such as in long-span floor structures[1], footbridges[2] and grandstands[3,4], have become more prevalent in recent years, because the structures can gather large crowd. It is different in the safety of structure due to the failure of structural component; excessive vibration of structure can cause crowd discomfort or panic. Vibration serviceability of grandstand relates to the comfort of spectators, and human perception is of primary importance with any tendency to panic or feeling of discomfort being related to the dynamic response of the structure[5]. This seems to be a common problem in temporary demountable grandstands (TDGs), the lightweight structural components of TDG can be rapidly assembled, easily dismantled and reused that result in low stiffness of structure at lateral direction, so it can be susceptible to vibrations that caused by active crowds.

It is a fact that human can feel the vibration from structure, the degrees of perception for structural vibration but cannot be measured with any direction assessment methods or instruments. Studying the relationship between human perception and spur belongs to the branch of psychophysics subject. Vibration environments, in terms of human sensation of vibration levels, need to be quantified by psychological research. Introspection is used to describe an experimental technique that was first developed by psychologist Wilhelm Wundt, in Wundt's lab, there were two key components that make up the contents of the human mind: sensations and feelings, and Wundt believed that researchers needed to do more than simply identify the structure or elements of the mind, instead, it was essential to look at the processes and activities that occur as people experience the world around them[6]. Therefore, it is necessary to conduct a psychophysical experiment survey by means of a category judgment method[7]. Although evaluation and assessment of vibration serviceability is a complicate task, it is a reasonable and available method that using experimental introspection with questionnaire to evaluate the reaction of human perception. So from the early years such as in 1931 Reiher and Mesiter used a shaking platform[8], 1971 Khan and Parmelee used a rotating display table[9], 1972 Chen and Roberts experimented human at a wheeled windowless test room[10] and 1974 Wiss and Parmelee measured human at a rise floor[11], all of them used this method to investigate the vibration serviceability of structure.

A number of research projects have, to date, largely focused on producing load models to accurately represent the dynamic crowd load and the human-structure interaction, however, the vibration response of grandstand structure is becoming better understood, the question arises as to what level of dynamic response is acceptable to the users[12]. There have been few findings on the subject of serviceability of grandstands, for example Kasperski has carried out full scale test on one bay of a permanent cantilevered stand[3]; Browning determined the key factors of influencing human perception and acceptability of vibrations in permanent grandstands through by synchronized crowd loading with 17 persons[12]. Meanwhile, a resemblance grandstand occupied 15 spectators that attached to a motion simulator located on each corner has been experimented, in order to investigate human vibration perception and comfort states[13]. In particular, Setareh proposed new relationships between the current vibration evaluation parameters along with guidance for the assessment of human exposure to vibration owing to rhythmic activities[4]. What these reviews have highlighted is that vibrations were induced by human have vertical motions and few research analyzed the human vibration perception in the TDG. And what's more, lateral vibration is more likely to be induced than vertical vibration happen in reality for TDG[14]. This remains an open problem in the area, the aim here is to investigate the vibration serviceability of TDG.

So with this aim in mind, this paper presents a new experiment that a TDG occupied 20 persons which vibrations derived from crowd motions, to investigate the human horizontal vibrations perception with vibration questionnaires. Based on these experimental results, the vibration acceptability of the TDG is analyzed by a annoyance rate method that the fuzzy logic method and the probability theory was combined with the signal detecting theory of psychophysics[15-17]. As alluded to earlier, this method has been available for appraising the vibration comfort of vehicle suspension system[18,19], high-speed train[20], pedestrian bridge[21], floor structure[22,23], and noise annoyance[24,25].

The next section presents the lateral oscillation experiment in this study. In Section 3, the evaluation method is introduced and the relationships of evaluation parameters of structural vibration are analyzed. New relationship between annoyance rate and structural acceleration VDV is proposed, and the main findings and discussions are outlined in Section 4. The conclusions will be presented in the final chapter.

2 LATERAL VIBRATION EXPERIMENTS OF TEMPORARY GRANDSTAND

Experimenting was executed on the basis of a rigorous risk assessment and approval of the experiment program by the University's research ethics committee, using its standard procedures for protect the safety of participants and acquired sensible data. For simulating the lateral vibration of temporary grandstand, structural vibration derived in the active crowd when they have rhythmic movements on the test temporary grandstand, and it is considered as internal excitation to investigate the passive and/or active crowd annoying levels of vibration.

2.1 Ethics statement

This study was approved by the School of Civil Engineering and the Key Lab of Structures, Dynamic Behavior and Control of the Ministry of Education at the Harbin Institute of Technology. All participants provided written informed consent, and agreed to put their photos with no argument.

2.2 Test condition

The details of test structure and instruments can be found in the document[35]. For crowds excitation, there are 11 experiment conditions that crowd has swaying activities at temporary grandstand, the detail of swaying person's number, test conditions and crowd swaying frequencies are shown in the Table 1. For the first and second condition twenty persons finished nine frequencies swaying movements, some of them finished six frequencies swaying movements in the rest conditions. In order to follow the tempo of swaying more better for participants, they were asked to sway the hips to the left on one beat and then to the right on the next which guided by a constant metronome beat, just as the Fig.1 depicts crowd followed the one beat at the time of t_1 and next beat at the time of t_3, so participants completed a sway cycle that will need two beats, and the frequency $f_{\text{metronome}}$ was inspired by metronome which is twice the frequency of participant swaying f_{crowd}. All participants moved in a way that was natural to him or her according to the frequency of metronome.

Test condition number	Test conditions	$f_{metronome}$ (Hz)
1	All standing persons swaying	0.5,0.75,1.0,1.1,1.25,1.4,1.5,1.7,1.8
2	All seated persons swaying	0.5,0.75,1.0,1.1,1.25,1.4,1.5,1.7,1.8
3	Number 6-20 person standing swaying, 1-5 person seated	0.5,0.75,1.0,1.1,1.25,1.4
4	Number 11-20 person standing swaying, 1-10 person seated	0.5,0.75,1.0,1.1,1.25,1.4
5	Number 16-20 person standing swaying, 1-15 person seated	0.5,0.75,1.0,1.1,1.25,1.4
6	Number 6-20 person standing swaying, 1-5 person standing	0.5,0.75,1.0,1.1,1.25,1.4
7	Number 11-20 person standing swaying, 1-10 person standing	0.5,0.75,1.0,1.1,1.25,1.4
8	Number 16-20 person standing swaying, 1-15 person standing	0.5,0.75,1.0,1.1,1.25,1.4
9	Number 6-20 person seated swaying, 1-5 person seated	0.5,0.75,1.0,1.1,1.25,1.4
10	Number 11-20 person seated swaying, 1-10 person seated	0.5,0.75,1.0,1.1,1.25,1.4
11	Number 16-20 person seated swaying, 1-15 person seated	0.5,0.75,1.0,1.1,1.25,1.4

Table 1: Details of crowd rhythmic activities

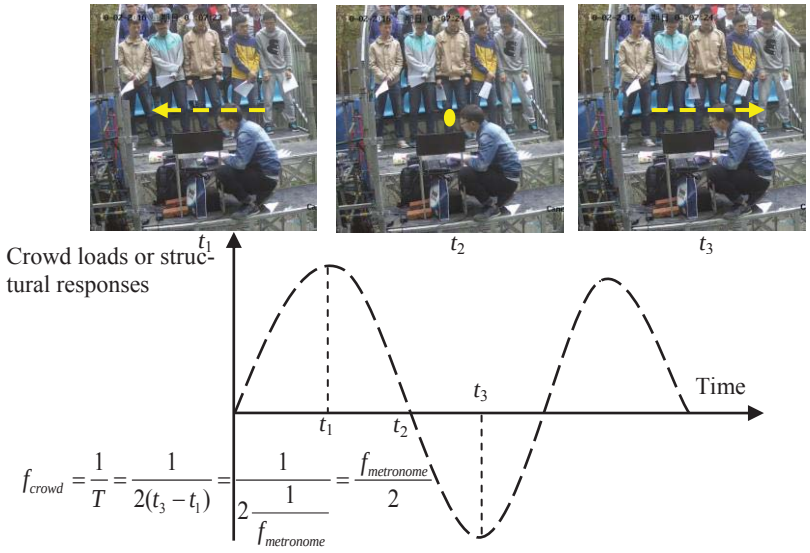

Figure 1: The relationship between metronome frequency and crowd swaying frequency

2.3 Vibration perception questionnaire

As mentioned previously, no standard or code can provide specific clause on the assessment of human vibration acceptability for TDG, even not to mention the vibration comfort when the excitation main from lateral direction. But, a series of classic experiments about human perception that participants rate their feeling of the vibration were carried out[3,8,9,12,13]. All these researchers classed the human perception and vibration level three to six categories, which based on the concept of equidistance followed human psychological changes. Some achievements have been adopted by BS6472-1[27] and ISO2631-1[28] standards. So, according to these findings, the level of vibration perception (Six categories) and comfort are provided with vibration perception questionnaires, which require participants to select their subjective perception and/or levels of comfort during exposure to vibration are used in this paper. The questionnaires contain the level of vibration perception with the level comfort and shows in the Table 2.

Ordinal	Perception Category	Subjective Response
1	Imperceptible	No response(Not uncomfortable)
2	Litter Perception	Normal(A little uncomfortable)
3	Clear Perception	Accept(Fairly uncomfortable)
4	Little Strong Perception	Litter nervous(Uncomfortable)
5	Strong Perception	Nervous(Very Uncomfortable)
6	Very Strong Vibration	Panic(Extreme Uncomfortable)

Table 2: Human perception and comfort category

3 EVALUATION METHOD

According to record the human sensation of vibration levels from participant's perception and comfort, the basic evaluation methods for measuring vibration is calculated using three forms of acceleration: peak acceleration limits(was cited in NBCC[29]); acceleration root mean square (RMS) of weighted frequency; vibration dose value (VDV). The latter two are acceptable by most standards (BS7085[30], BS6472[31] and ISO10137[32]) to quantify vibration levels. They are calculated by the Eq.(1).

$$a_w(t) = W(f) \cdot a(t)$$

$$a_{wp} = \max\left|a_w(t)\right|$$

$$a_{wrms} = [\int_0^T a_w^2(t)dt]^{0.5} (\lim_{\lambda \to 0} \sum_{i=1}^{n} a_w^2(\zeta_i) \cdot \Delta t_i)^{0.5} = (\sum_{i=1}^{n} [W(f)a(t_i)]^2 \cdot f')^{0.5}, \lambda = \max\{\Delta x_1, \Delta x_2, \cdots, \Delta x_n\} \quad (1)$$

$$a_{wvdv} = \left[\int_0^T a_w^4(t)\mathrm{d}t\right]^{0.25} = (\lim_{\lambda \to 0} \sum_{i=1}^{n} a_w^4(\zeta_i) \cdot \Delta t_i)^{0.25} = (\sum_{i=1}^{n} [W(f)a(t_i)]^4 \cdot f')^{0.25}, \lambda = \max\{\Delta x_1, \Delta x_2, \cdots, \Delta x_n\}$$

With $a_w(t)$=frequency weighted acceleration in $m \cdot s^{-2}$;
$W(f)$=the overall frequency weighting function from ISO2631-1[28];
$a_{wp}(t)$=frequency weighted peak acceleration in $m \cdot s^{-2}$;
$a_{wrms}(t)$=frequency weighted RMS of acceleration in $m \cdot s^{-2}$;
$a_{wvdv}(t)$=frequency weighted VDV of acceleration in $m \cdot s^{-1.75}$;
f'=sample frequency in s;
T=vibration duration in s.

3.1 Annoyance rate method

Although the limit acceleration value was given in some standards like ISO2631-1[28], the membership between the limit value and comfortable level was not reasonable extrapolated. The result of questionnaires includes the ambiguity of seismesthesia and the sensitivity randomness existing in participants' response to vibration environment. All these uncertainties need to be analyzed from a view psychophysics. So firstly the seismesthesia of membership function and corresponding conditional probability distribution[14] is calculated by Eq.(2) based on the Table 1 and questionnaires.

$$v_j = \frac{j-1}{K-1}, j = 1,2,...,K \quad (2)$$

With v_j=the seismesthesia of membership value of the jth type of the unacceptable range;
K=the class number of the subjective response, according to Table 2, K=6.

So the subjective response corresponding to the value of the membership value can be shown in the Table 3.

Subjective response	Membership value
j=1 No response	0.0
j=2 Normal	0.2
j=3 Acceptable	0.4
j=4 Litter nervous	0.6
j=5 Nervous	0.8
j=6 Panic	1.0

Table 3: Seismesthesia membership values

Secondly, a new evaluation index annoyance rate method is presented, which is a fuzzy stochastic model for participant response to vibrations. The method considers these uncertainties with the fuzzy logic method and the probability theory, combined the objective experimental data statistics. So, annoyance rate is the proportion of some kind of subjective response under certain external stimulus intensity, which considers synthetically response ambiguity and randomness with fuzzy membership value. It is useful as a benchmark to determine the annoyance threshold for vibration serviceability criteria, that threshold indicates the ration of people who cannot accept the vibration to the statistical that total number. Under discrete distribution, the annoyance rate can be calculated by Eq.(3):

$$R(x=i)=\frac{\sum_{j=1}^{K} v_{ij} n_{ij}}{\sum_{j=1}^{K} n_{ij}} \tag{3}$$

With $R(x=i)$=Annoyance rate of the ith vibration intensity;

v_{ij}=the membership of value is calculated by Eq. (2) at the ith vibration intensity;

n_{ij}=the number of subjective response of the jth type of the ith vibration intensity;

K=The class number of the subjective response, K=6 (see Table 3).

3.2 Relationship of structural vibration evaluation parameters

For human induced vibration experiment, the results are investigated. For example, Fig.2(a) shows one of the time history of structural acceleration which was oscillated by twenty persons when they have rhythmic movements. Then the peak acceleration, RMS and VDV of each test condition (Table 1) results are calculated, and the scatter plots the three measures plotted against crowd swaying frequencies is shown in Fig.2(b). In this Figure, also the hollow dots stand for peak accelerations, square dots stand for RMS values and diamond dots stand for VDV. It is found that RMS values are higher than peak value and VDV, the max value is about 13.49m/s^2, which is out of the limits were given by Kasperski[3], Setaerh[4], Nhleko[13], BS6841[26], BS6472[27], and BRE[34]. According to these above results, when enquired the vibration serviceability of these participant, they are in panic.

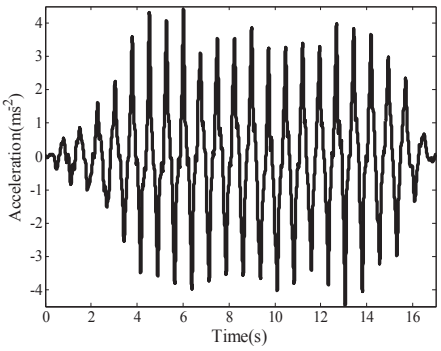

(a) Structural acceleration curve of seated crowd with 1.6Hz swaying

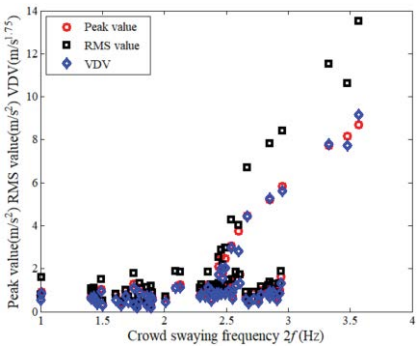

(b) Three measures acceleration against crowd swaying frequencies

Fig.2 The structural acceleration peak acceleration、RMS and VDV relationship with crowd swaying frequencies

When the scatter a_{wp}, a_{wrms} plotted against a_{wvdv} respectively, as shown in Fig.3, both of them have a linear relationship with a_{wvdv} and the fitting curve is Eq.(4):

$$a_{wvdv} = 0.9995a_{wp} - 0.1486$$
$$a_{wvdv} = 0.6873a_{wrms} - 0.0316 \tag{4}$$

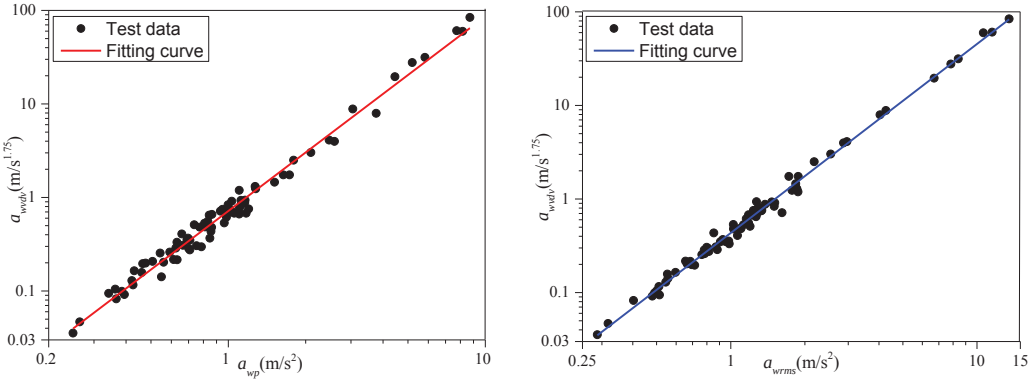

Fig.3 a_{wvdv} plotted against a_{wp} and a_{wrms} from human induced measured data

Bearing all this in mind, the structure was oscillated by crowd have rhythmic activities with linear increasing swaying frequencies, the structural acceleration VDV have a linear relationship with RMS and peak acceleration at Logarithmic coordinate system. And what's more, crowd swaying movements can induce structure has more than 1g acceleration, which can cause crowd have panic.

4 ASSESSMENT OF THE EXPERIMENT RESULTS

4.1 Acceptable VDV limits

Due to VDV is versatility than RMS that has been calculated to quantify human reaction to numerous types of vibration, and VDV will be used for finding the relationship with annoyance ratio in this paper.

Active crowd induced structure vibration experiment results are also investigated to find the relationship between annoyance rate and structural VDV. Due to when the VDV is high than 2.8m/s$^{1.75}$, the crowd have in panic, and the annoyance rate is 1.0, So only the corresponding value which the annoyance rate is lower than 1.0 are shown in Fig.4(a). It may indi-

cates standing crowd can tolerate more strong structural vibration than seated crowd when the structural vibration was induced by swaying crowd, this finding consistent with Nhleko's research[13].In order to demonstrate the nonlinear relationship between VDV and annoyance rate, the two kinds of data were fitted by a 3-rd degree polynomial formula respectively, and shown in Eq.(5):

$$\begin{aligned} R''_{seated} &= 0.0777a^3_{wvdv} - 0.4280a^2_{wvdv} + 0.9642a_{wvdv} + 0.0041 \\ R''_{standing} &= 0.0585a^3_{wvdv} - 0.3224a^2_{wvdv} + 0.7594a_{wvdv} + 0.0430 \end{aligned} \tag{5}$$

With R''_{seated} is the annoyance rate of seated crowd at human induced vibration experiments; $R''_{standing}$ is the annoyance rate of standing crowd at human induced vibration experiments.

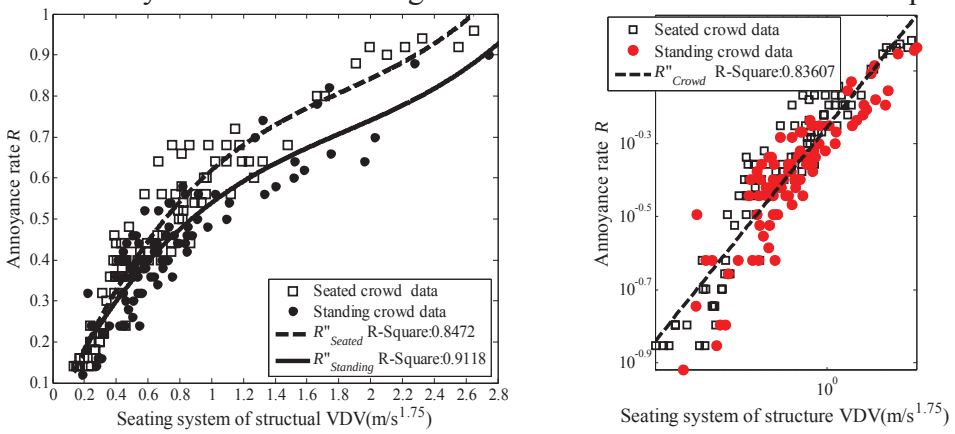

(a) Cartesian coordinate system (b) Logarithmic coordinate system

Fig.4 The distribution of crowd annoyance rate at human induced structural vibration

Also, a linear relationship between structural VDV and annoyance rate at Logarithmic coordinate system is fitted by Eq.(6)when considered the seated crowd data and standing crowd data as a whole sample, and the fitting curve is shown in Fig.4(b):

$$\log_{10}(R''_{crowd}) = 0.67556\log_{10}(a_{wvdv}) - 0.25358 \tag{6}$$

With R''_{crowd} is the annoyance rate of crowd at human induced vibration experiment.

In this paper, when R is lower than 0.4, which indicates crowd in comfort at structure; R varies at 0.4 to 0.6 means some persons in crowd have uncomfortable feelings; R varies at 0.6 to 0.8 means most of them in crowd have uncomfortable feelings; and when R is larger than 0.8 that shows crowd in panic. Based on this annoyance levels of vibration and according to the Eq.(6), the structural acceleration VDV 1.11m·s$^{-1.75}$ that corresponding to R=0.6 as the serviceability limit, and 1.71m·s$^{-1.75}$ that corresponding to R=0.8 as the serviceability limit of the upper boundary.

4.2 Discussion with other standards or guides and research

The obtained comfort levels data in this paper are compared with the limits recommended in the provisions of BS6841[26], which are mainly for vibrations encountered in transportation and industrial activities. This standard used RMS as the limit and given five vibration levels. According to the annoyance rate with structural vibrations of the experiment data in this paper, the VDV can be calculated by Eq.(6) at each value of annoyance rate R firstly, and then the corresponding RMS can be calculated by Eq.(4). So on the basis of the conversion procedure, the level of comfortable corresponding to R=0.2 and RMS is 0.365m·s^{-2}; the level of little uncomfortable corresponding to R=0.4 and RMS is 0.936m·s^{-2}; the level of fairly

uncomfortable corresponding to R=0.6 and RMS is 1.661 m·s^{-2}; the level of very uncomfortable corresponding to R=0.8 and RMS is 2.186m·s^{-2}; and the level of extremely uncomfortable corresponding to R>0.8 and assumed RMS is greater than 2.186m·s^{-2}. It is found that the experiment data is slightly higher than the design criteria when the specified level under fairly uncomfortable and the data 2.29-3.69m·s^{-2} appear in the specified limits when the level is very uncomfortable. This means that the limits for temporary grandstand appear upper the design criteria for public facilities such as permanent concrete structure, that is reasonable for believe temporary structures can allow to with big displacement or vibration.

The standard BS6472[31] has given some acceleration limit curves for labs, residential, office building and workshops. Nhleko[13] used 25 times the base curve and 50 times the base curve specified in this standard as a basis and the upper boundary of acceleration limit for grandstand design (shown as two purple broken lines), respectively. In addition, NBCC2005[29] specifies serviceability acceleration limits at 0.4-0.7m·s^{-2} for grandstand, and IStructE2008[33] also recommends values of 0.3m·s^{-2}, 0.75m·s^{-2} and 2.0m·s^{-2} for grandstand hosting predominantly seated crowd, pop music concerts and extreme events(crowd has strong rhythmic activities)，respectively. If the mean of the 'fairly uncomfortable' of comfortable obtained in this study is used to defined the serviceability limit state for temporary grandstand, the value of limit is 2.18m·s^{-2}, which is higher than Nhleko's[13] research and NBCC2005[29] limits, but it remains in the range of IStructE2008[33]specifies limits.

When the VDV as serviceability limit, the guide BRE[34] based on the standard BS6841[26]and BS6472[31]given the limit with human perception of vibration, and Setaerh[4]based on Kasperski's[3] experiment results also gives the limits. It is noticeable that the published standards and literatures have given the limits for permanent grandstand, and the structure was induced by vertical human motions. So the serviceability limits are different from the results in this paper. It may be possible that the vibration direction and more flexible temporary grandstand have larger effects on crowd reactions than they occupied at stiffness permanent grandstand when subjected to excitations which mainly derived from vertical vibration and using different frequency weighting value may also influence the results. Due to the participants are just only young individuals, not including children and/or old persons, the distribution of annoyance rate may be different when participants are a typical population sample, and although the experiment environment is quiet, the vibration annoyance may be influenced by the noise, it is need to focus on combined or interactive effect of noise and vibration exposures on annoyance for TDGs, so it will be researched in the future work. Also, more research is needed to investigate different and bigger temporary grandstands with different crowds, along with better identification of human reactions.

5 CONCLUSION

This paper addresses the annoyance levels of lateral vibration on temporary grandstand. A temporary grandstand occupied 20 participants was induced by crowd with rhythmic swaying activities, meanwhile the vibration questionnaires of participants are obtained. Occupant comfort was evaluated by annoyance rate method and assessed by the RMS and VDV of structure. There are some conclusions are obtained.

- Crowd annoyance rate has not a linear relationship with vibration, and indicated crowd may adjust their reaction for comfort when they under a certain range of vibration intensity.
- Standing crowd may have more tolerant to vibration than seated crowd.

- The serviceability limit of 1.11m·s$^{-1.75}$ and the upper boundary of 1.71m·s$^{-1.75}$suggested by VDV are obtained.
- It may be useful for analyzing the vibration serviceability of temporary grandstand.

ACKNOWLEDGMENTS: This work was financially supported by Youth Fund of Rocket-Force University of Engineering 2019QNJJ005.

REFERENCES

[1] H.Bachmann. Vibrations of building structures caused by human activities, case study of a gymnasium. National Research Council of Canada, Ottawa, Ont., Technical Translation 2077, 1984.

[2] P.Dallard, A.Fitzpatrick, A.Flint, et al. London millennium bridge: pedestrian- induced lateral vibration. ASCE, Journal of Bridge Engineering, 6(6), 412-417, 2001.

[3] Actual Problems with Stand Structures due to Spectator Induced Vibrations. Proceedings of the 3rd European Conference on Structural Dynamics: EURODYN 96, Florence, Italy. Rotterdam: Balkema, 1, 455-461, 1996.

[4] M. Setareh. Evaluation and assessment of vibrations owning to human activity. Structures and Buildings, 165(SB5), 219-230, 2012.

[5] Interim guidance on assessment and design. Dynamic performance requirements for permanent grandstands subject to crowd action. The Institution of Structural Engineers, 2001.

[6] K. Cherry. A look at Introspection Wundt's Experimental Technique. https://www.verywell mind.com/what-is-introspection-2795252. 2018(Updated March 15 2018).

[7] J. P. Guidford. Psychometric methods, McGraw-Hill, New York.1954.

[8] H. Reiher, F. J. Mister. Die empfindlichkeit des menschen gegenerschutterungen (The Effect of Vibrations on People). Forschung auf dem Gebiete des Ingenieurwesens 2. Jahrang der ZeitschriftTechnischeMechanik und Thermodynamik, (Research in the Areas of Engineering 2nd Year of the Journal of Applied Mechanics and Thermodynamics) Berlin. 2(11), 381-386, 1931.

[9] F. Khan, R. Parmelee. Service Criteria for Tall Buildings for Wind Loading. Proceedings of the 3rd International Conference on Wind Effects on Buildings and Structures. Tokyo, Japan, 1971.

[10] P. Chen, I. L. Robertson. Human Perception Thresholds of Horizontal Motion. Journal of the Structural Division, Proceedings of the American Society of Civil Engineers, 98(ST8), 1681-1695, 1972.

[11] J. F. Wiss, M. Parmelee. Human Perception of Transient Vibrations. Journal of the Structural Division, Proceedings of the American Society of Civil Engineers, 100(ST4), 773-787, 1974.

[12] G. G. Browning. Human perception of vibrations due to synchronised crowd loading in grandstands. The University of Bath, UK, 2011.

[13] S Nhleko. Human-induced lateral excitation of public assembly structures. The University of Oxford, 2011.

[14] B. R. Ellis, T. Ji, J. D. Littler. The response of grandstands to dynamic crowd loads. Proceedings of the Institution of Civil Engineers: Structures and Buildings, 140(4), 355-365, 2000.

[15] Z. G. Song, W. L. Jin. A fuzzy-stochastic model for human response to vibrations. Journal of Basic Science and Engineering, 10(3), 287-294, 2002.

[16] Z. G. Song. A new annoyance-based vibration comfort design theory on engineering structures. Zhejiang University, 2003.

[17] Z.G. Song, W. L. Jin. Serviceability design of ice induced platform vibration based on ice zoning map of bohai sea-acceptable acceleration levels. The Ocean Engineering, 123(12), 61-65, 2005.

[18] C. Y. Tang, T. X. Zhang, J. Q. Song. Evaluation of comfortability during vibration on basis of annoyance rate. Journal of Northeastern University (Natural Science), 27(7), 802-805, 2006.

[19] C. Y. Tang, T. X. Zhang, G. Y. Zhao, et al. Annoyance rate evaluation method on ride comfort of vehicle suspension system. Journal of Mechanical Engineering, 27(2), 296-303, 2014.

[20] Y. P Guo, G. Q. Song. Dynamic comfort evaluation of high-speed train based on annoyance rate model. Journal of Northeastern University (Natural Science), 34(11), 1620-1624, 2013.

[21] A. M Yuan, W. X Wu, M. Xu, et al. Study on pedestrian bridge's vibration comfort evaluation based on annoyance rate. Journal of Water Resources and Architectural Engineering, 11(4), 135-140, 2013.

[22] X. Z Shen, J. Teng. Vibration serviceability assessment method for floor structures based on random walking force and annoyance rate. Journal of Vibration and Shock, 31(22), 71-75,95, 2012.

[23] J. Wei, R. S Chen, J. G. Wu, et al. Appraisement of the vibration serviceability for a long-span pre-stressed floor based on annoyance rate. Zhejiang Construction, 32(1), 19-23, 2015.

[24] Y. F. Huang, G. Q. Di, Y. T. Zhu, et al. Pair-wise comparison experiment on subjective annoyance rating of noise samples with different frequency spectrums but same a-weighted level. Science of the Total Environment, 69(12), 1205-1211, 2008.

[25] R. H. Bakker, E. Pedersen, G. P. Van Den Berg, et al. Impact of wind turbine sound on annoyance, self-reported sleep disturbance and psychological distress. Science of the Total Environment, 425(5), 42-51, 2012.

[26] BS 6841. Guide to Measurement and Evaluation of Human Exposure to Whole Body Mechanical Vibration and Repeated Shock. British Standards Institution, 1987.

[27] BS 6472-1. Guide to Evaluation of Human Exposure to Vibration in Buildings-Part 1: Vibration Sources other than Blasting. British Standards Institution. 2008.

[28] ISO 2631-1. Mechanical Vibration and Shock–Evaluation of Human Exposure to Whole-body Vibration. Part 1: General Requirement, 1997

[29] NBCC. User's Guide National Building Code of Canada 2005, Structural Commentaries (Part 4 of Division B) Commentary D. National Building Code of Canada (NBCC). 2005.

[30] BS 7085. Medical contra-indications to participation in experiments involving whole-body mechanical vibration. British Standards Institution, 1987.

[31] BS 6472. Guide to Evaluation of Human Exposure to Vibration in Buildings (1Hz to 80Hz). British Standards Institution. 1992.

[32] ISO 10137. Basis for the design of structures-Serviceability of buildings against vibration. International Organization for Standardization (ISO), 2007.

[33] Institution of Structural Engineers. Dynamic Performance Requirements for Permanent Grandstands Subject to Crowd Action: Recommendations for Management, Design and Assessment. London, IStructE, 2008.

[34] BRE Digest 426. The Response of Structures to Dynamic Crowd Loads, 2nd End. BRE, 2004.

[35] Jian Y, Lin H, Feng F, et al. The Dynamic Parameters of Passive Human at Temporary Demountable Grandstands During Exposure to Lateral Vibration, Journal of Civil Engineering and Management, 24(4), 265-283, 2018.

EURODYN 2020
XI International Conference on Structural Dynamics
M. Papadrakakis, M. Fragiadakis, C. Papadimitriou (eds.)
Athens, Greece, 23–26 November 2020

LARGE-SCALE AEROELASTIC TESTING TO INVESTIGATE THE RESILIENCY OF TRANSMISSION INFRASTRUCTURE TO HURRICANE STORMS

Ziad Azzi[1], **Amal Elawady**[2], **and Arindam G. Chowdhury**[2]

[1] Department of Civil and Environmental Engineering, Florida International University
10555 W Flagler St., Miami, FL, 33174
e-mail: zazzi001@fiu.edu

[2] International Hurricane Research Center of Extreme Events, Florida International University
11200 SW 8th St., Miami, FL, 33199
{aelawady,chowdhur}@fiu.edu

Keywords: Aeroelastic, Wall of Wind, Transmission Lines, Vibrations, Vortex Shedding

Abstract. *An aeroelastic experimental study is ongoing at the NSF designated Experimental Facility Wall of Wind (WOW) aiming at advancing the knowledge pertaining to the dynamic behavior of power transmission infrastructure during strong windstorms including hurricanes. The WOW is a large open jet wind testing facility capable of simulating hurricane winds at different wind speeds and up to 70 m/s (Category 5 hurricane). The study is motivated by the increasing storms including hurricanes which recently are reported to cause substantial losses to the U.S. energy infrastructure. A multi-spanned aeroelastic transmission line system is designed and constructed at the WOW using a length scale of 1:50 for the tower and a distorted length scale of 1:150 for the conductors. The selected length scales enable considering several test configurations including various wind directions ranging between 0° to 90°. While adopting the Froude number scaling, the tests are conducted at speeds ranging between 5 m/s to 10 m/s, representing full-scale wind speeds ranging between 35 m/s to 70 m/s. The aeroelastic test results are analyzed in order to assess the dynamic response of the transmission towers during the simulated hurricane conditions. This includes an investigation of the modal properties, the development of a new technique to estimate structural and aerodynamic damping, and comparison of the resulting drag coefficients with values specified in ASCE 7-16.*

1 INTRODUCTION

Electric power grids in the United States are constantly threatened by wind-induced loads caused by hurricanes, tornadoes and downbursts. Generation, supply and delivery of power to several areas of the country have been severely impacted by these wind hazards. Between 2003 and 2012, 87% of all power outages were triggered by severe weather, making it the leading cause of blackouts in the United States [1]. Weather-related power outages exacted huge losses on the U.S economy, with figures ranging between $20 to $55 billion [1]. Therefore, it is of the utmost importance to improve the resiliency of the transmission grid against threats from strong winds including hurricanes.

Support towers, conductors, ground wires and insulators are the main components of overhead transmission lines systems. Electricity is transported from the generation station to different cities through conductors that span for kilometers. Conductors are attached to the towers using porcelain insulators. The function of ground wires is to protect the line from possible lightning strikes [2]. In general, many structures are not designed to withstand hurricane or tornado loads because of the very low probabilities of occurrence and exposure to them. However, that is not the case for transmission systems due to the fact that they are long span structures and extend for kilometers. Therefore, in the event of occurrence of high intensity winds coming from a hurricane or tornado, their probability to hit one of the towers become significantly larger. Subsequently, the failure of one tower can lead to cascading failures of other towers due to the unbalanced forces triggered by the snapping of one or more conductors [3, 4, 5, 6]. The responses of transmission lines to wind-induced dynamic loading can be divided into three phenomena: galloping, vortex shedding and buffeting from incoming turbulence [2, 7, 8]. On the one hand, the tower's natural frequency is typically higher than 1 Hz, leading to insignificant resonant tower responses. On the other hand, the tower's conductors have a frequency ranging between 0.2 and 0.3 Hz. This range could be very close to the natural frequency of the turbulent winds. Various studies have reported that, at high wind speeds, the conductor's behavior increases the aerodynamic damping, thus, rendering the resonant effect almost negligible [3, 7, 9, 10, 11, 12]. In general, wind tunnel experiments on transmission structures can be grouped into aerodynamic testing and high-frequency force balance testing. For the latter, by carefully estimating aerodynamic coefficients from the previous methods and combining them with analytical approaches, one can estimate the dynamic responses of a certain system [10, 11]. However, such tests do not consider the aeroelastic forces induced by motions of the structure and its various components. In addition, the response of transmission towers and conductors as one system was barely examined by previous wind tunnel studies due to the complexity of satisfying basic scaling laws concerning geometric, dynamic and kinematic similitudes [12, 13]. Other experimental studies on tower-conductor systems only considered a single span system and did not properly model the boundary effects caused by the presence of adjacent spans when a multi-span system is subjected to turbulent winds [14, 15].

The aim of this research is to advance the current knowledge by conducting an extensive experimental program to study the aeroelastic response of a multi-spanned transmission line system subjected to hurricane winds. These tests will provide deeper insights into the highly complex coupled dynamic behavior at system levels.

2 METHODOLOGY

2.1 Wall of Wind Experimental Facility

The aeroelastic model was designed, constructed and tested at the NSF Natural Hazards Engineering Research Infrastructure (NHERI) Wall of Wind Experimental Facility (WOW EF). The WOW EF is designated as an open-jet testing facility capable of testing full- and large-scale structures using a powerful 12-fan system. The 12 fans are arranged in two arced rows, which can generate wind speeds up to 70 m/s along with specified turbulence characteristics of terrain exposures [16]. Figure 1 depicts the WOW intake side along with the 12-fan system.

Figure 1: WOW intake side and 12-fan system

2.2 Full-Scale Model

For this project, the transmission tower illustrated in Figure 2 is selected. This tower is classified as double circuit vertical self-supported steel lattice tower with a height of 27.5 m, and a rectangular base having a length of 7.6 m and a width of 2.7 m. The tower has three different levels of identical cross-arms. Such a configuration allows the attachment of six bundles of conductors, two at each vertical level. The conductors span a horizontal length of 180 m between supporting transmission towers and have a diameter of 0.028 m. Moreover, the conductors are sagged at midspan by around 3.6 m and they are attached to the towers by porcelain insulators having a length of 1.5 m and diameter of 0.08 m.

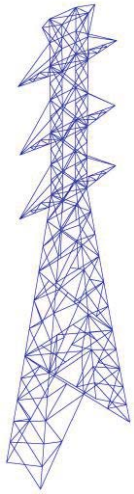

Figure 2: Three-dimensional view of the transmission tower

2.3 Aeroelastic Model Design and Construction

Whenever the geometry and physical properties of a prototype have to be reproduced as a model at a smaller scale, great care needs to be taken in order to reproduce the same dynamic behavior. For aeroelastic modelling, this scaling exercise becomes more tedious. This means that the scaling relationship between elastic, inertia, viscous, gravity and damping forces needs to be maintained. While preserving the geometry is essential for the reproduction of the aerodynamic loads, maintaining the mass and stiffness is vital for the dynamic loads associated with the response of the model [18]. Some of the advantages of using aeroelastic models include: (i) the proper simulation of turbulence effects and wind-structure interaction, (ii) the subtle interactions between the coupled modes of vibration of the system and (iii) local, topographical as well as three-dimensional effects can be investigated [19]. Generally, for any quantity Q_p measured on the prototype, Equation 1 can be used to calculate its model counterpart Q_m, where λ_Q is the scaling factor:

$$Q_m = Q_p \times \lambda_Q \tag{1}$$

Normally, it is preferred to use prototype material in the construction of the aeroelastic model to maintain the structural damping which is crucial in the dynamic responses of the system [20]. However, since lattice towers are lightweight structures, it is challenging to satisfy the mass scaling using prototype steel material. Therefore, a different metal such as aluminum is usually selected to satisfy the mass scaling requirement. In addition, it is worthwhile mentioning that the damping ratio of aluminum is close to that of its steel counterpart.

For this project, a length scale λ_L of 1:50 is selected. Moreover, Froude number scaling is maintained in the model as that in the prototype. This means that the ratio between the inertial and gravitational forces is preserved. This is simply achieved by linking the velocity scale λ_U to the square root of the length scale λ_L, i.e., the velocity scale is equal to 1:7.07. Some of the essential parameters required to correctly design the aeroelastic model along with their scaling ratios are presented in Table 1.

Quantity Q	Scaling factor λ_Q
Length L	1:50
Velocity U	1:7.07
Mass m	$1:50^3$
Mass moment of inertia I	$1:50^5$
Time t	1:7.07
Acceleration a	1
Damping ζ	1
Elastic stiffness EI	$1:50^5$
Elastic stiffness EA	$1:50^3$
Force F	$1:50^3$
Bending and torsional moments M, T	$1:50^4$

Table 1: Essential scaling parameters required for aeroelastic design

The system of this experimental program consists of three transmission towers, two rigid end frames and six conductors spanning in between (Figure 3). This means that four full spans are considered. This is an improvement over previous synoptic wind tunnel testing on transmission lines that considered single spans and did not consider the boundary effects caused by the presence of adjacent spans [11, 17]. However, in order to accommodate the entire system

on the WOW turntable, a distorted length scale of 1:150 will be used for the span length only. This new approach of horizontally distorting the cable length by a factor of three while maintaining the properties of the non-distorted model, i.e. frequency, drag and mass along with the conductor sag does not significantly alter the behavior of the conductors [21]. This approach is reinforced by the idea that conductors' natural frequencies are controlled by their sags when the tension they carry is not high, such as the case of transmission lines. All other parameters are kept the same, i.e. scaled down to a length scale λ_L of 1:50, including wind tunnel simulation [21]. Figure 3 shows a CAD drawing of the entire system to be constructed at the WOW.

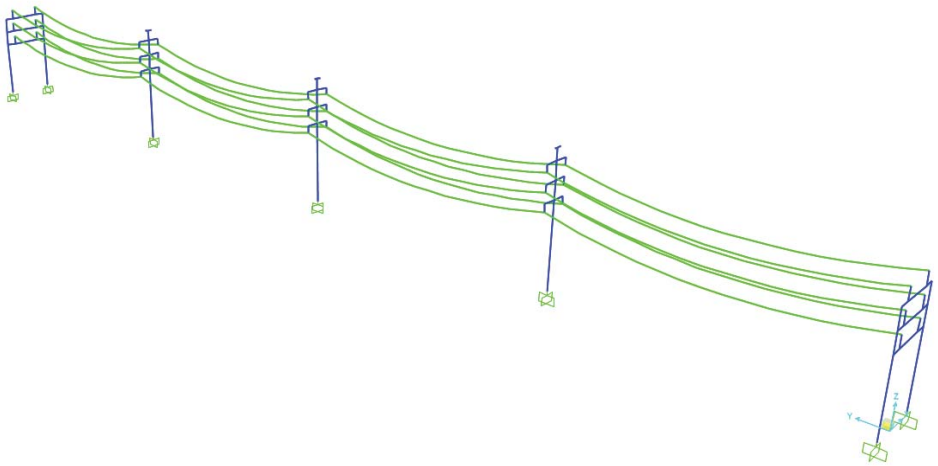

Figure 3: CAD drawing showing the entire system

In order to replicate the behavior of its full-scale counterpart, the aeroelastic transmission tower is designed and constructed in two parts: (i) an aluminum rectangular spine that encompasses the structural properties of the lattice structure and (ii) non-structural cladding elements that replicate the exact shape of the tower angle members to maintain its geometry and aerodynamics. The spine has a height of 55 cm and is embedded inside an aluminum bearing plate at the bottom to create a fixity. Furthermore, the spine has cross-sectional dimensions of 5.6 mm depth and 14.7 mm width. The previous dimensions were calculated using the factors stated in Table 1. This ensured the replication of the along-wind, across-wind and torsional behavior of the prototype. The non-structural cladding elements are 3D printed using a plastic like material and are glued to the spine. For the conductors, a steel wire having a diameter of 0.56 mm was utilized. Likewise, non-structural foam rods were attached over the entirety of the spans to maintain the same drag, distributed weight and average diameter over the entire length as the prototype. The insulators are represented by aluminum cylindrical rods with lengths of 3 cm and diameter of 0.25 mm. The insulators are connected to the cross-arms at their top and conductors at their bottom using 3D printed sections. Finally, aluminum rigid frames constructed from hollow rectangular tubes are used as end supports to the system to carry unbalanced tensile forces in the conductors. Figures 4a, 4b and 4c portray the single tower, the entire system and the insulator along with its connections, respectively.

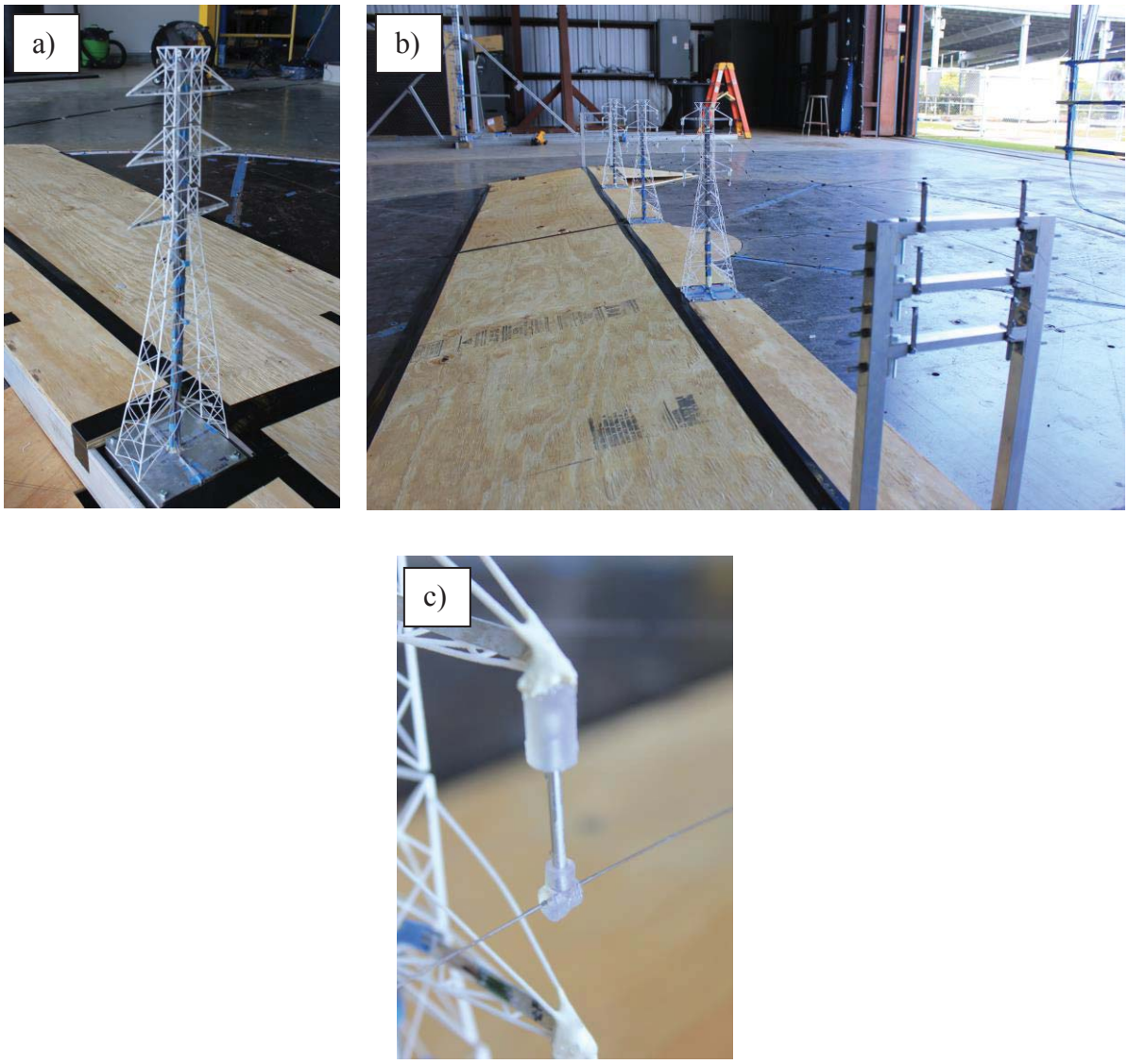

Figure 4: Models constructed at the WOW; a) Transmission tower with no insulators, b) Entire system, and c) Insulator with top and bottom connections

2.4 Instrumentation and Testing Protocol

To measure the complex and coupled response of the system to synoptic winds, the model was carefully instrumented. At the base of each tower (total of three), one six-degrees-of-freedom (6-DOF) load cell was mounted to capture the base shears and moments. In addition, three 3-DOF accelerometers were attached on the middle transmission tower to collect accelerations and subsequently, system frequencies. Lastly, a total of twenty strain gauges were applied at different parts of the spines and cross-arms to record forces and stresses. Strain gauges mounted on cross-arms allow the collection of drag forces experienced by the conductors.

The testing protocol consisted of varying wind speeds ranging between 5 m/s and 10 m/s at model height (0.55 m), representing full-scale speeds of approximately 35 m/s and 71 m/s at prototype height (27.5 m). The model was exposed to various wind directions ranging between 0^o (wind normal to conductors) and 90^o (wind parallel to conductors) at 15^o increments. The duration of each test case was about 2 min (equal to 14 min, full-scale) and the exposure

simulated was open terrain. Figures 5a and 5b depict some of the instrumentation used in the testing.

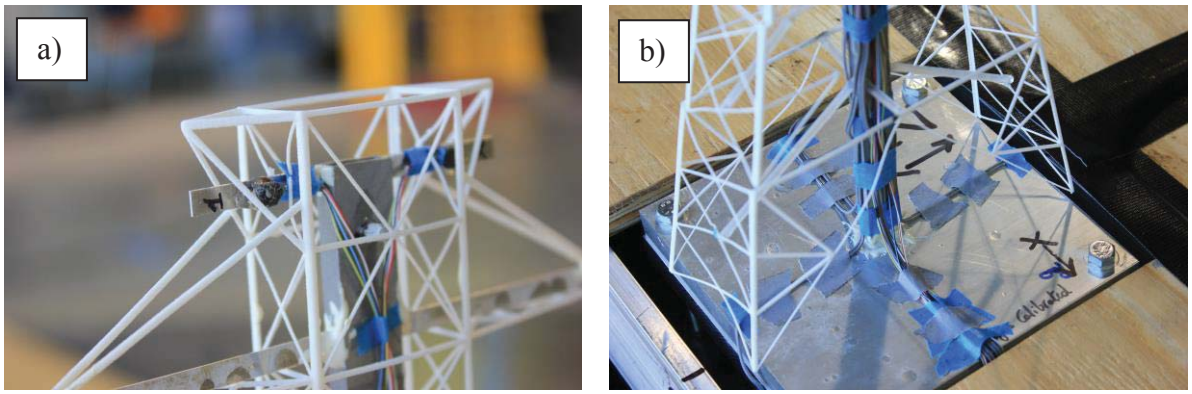

Figure 5: Some of the instrumentation used; a) Accelerometers mounted on the top cross-arm, and b) 6-DOF load cell installed at the base of the spine

3 VALIDATION OF THE AEROELASTIC MODEL

Two layers of validation are conducted. First, the generation of the aeroelastic model on a Finite Element Method (FEM) software allows the checking of selected materials and sections for design purposes. Second, a free vibration test is conducted inside the WOW facility for the test model. Such testing will ensure the accuracy of the construction and material selection since human errors are inherent in any experiment, especially at such a small-scale. For both validation procedures, the model natural frequencies of the system are compared with the target ones, which are obtained from their scaled prototype counterparts.

System	Mode of vibration	Prototype frequency f_p (Hz)	Target frequency f (Hz)	Model frequency f_m (Hz) (design)	Model frequency f_m (Hz) (construction)	Percent difference (%) (design, construction)
Single tower	Longitudinal	2.25	15.88	15.56	16.01	2.02, 0.82
	Transverse	5.10	36.08	35.82	35.10	0.72, 2.72
Full model	Conductor only	0.25	1.80	1.77	1.61	1.67, 10.56
	Longitudinal	2.28	16.10	16.45	17.52	2.17, 8.82
	Torsional	5.11	36.11	36.1	32.22	0.03, 10.74
	Transverse	5.12	36.24	37.1	39.95	2.37, 10.24

Table 2: Target and aeroelastic model frequencies

For the validation of the aeroelastic model design, a FEM replica is generated using the scaled down sections and materials selected in section 2.3, above. The software used for design validation in terms of frequency comparison is SAP2000 [22]. Concerning the validation of the construction, the aeroelastic model is carefully and meticulously assembled together. The tower-insulator and insulator-conductor connections are reproduced to depict the realistic boundary conditions and behavior in prototype transmission lines systems. Subsequently, a free vibration test is conducted to evaluate the natural frequencies of the model. The latter are obtained from the peaks in the power spectral density (PSD) of the acceleration responses when the system is excited in its natural modes of vibration. Table 2 shows the modes of vi-

bration of interest for two models: a single lattice tower with no insulators and the complete aeroelastic model previously described. As indicated in Table 2, the model frequencies for both design and construction phases are in good agreement with the target ones for the single tower system. Obtained frequencies for the design of the full model system are also well in agreement with a maximum difference of around 2.37%. However, the frequencies obtained from the free vibration tests yielded a maximum difference of about 10.74% with the target ones. This could be due to some discrepancies in the distribution of the masses along the model during construction. Another reason for the minor discrepancies could be attributed to unequal sags in the conductors of the transmission lines system, which could alter the behavior of the model during dynamic loading since the sags greatly contribute to the frequency of the conductors. Nevertheless, the obtained results and percent differences gave enough confidence for the team to carry on with the wind tunnel testing and subsequent data analysis.

4 DAMPING ESTIMATION

The self-supported transmission tower can be compared to a single-degree-of-freedom (SDOF) system. For approximation purpose, the system consists of a particle of mass M concentrated at the top of the tower. The tower has a linear elastic behavior and negligible mass with the particle being subjected to an aeroelastic force $F_{ae}(t)$. The displacement at the top of the tower $x(t)$ is opposed by: (i) a restoring force $-kx$ where k is the stiffness of the tower, and (ii) a damping force $-c\dot{x}$ where is c is the damping coefficient [22]. Equation 2 shows Newton's second law of motion of the system, which states that the product of the particle's mass M by its acceleration $\ddot{x}$ is equal to the total aeroelastic force applied to the particle above:

$$M\ddot{x} = - c\dot{x} - kx + F_{ae}(t) \tag{2}$$

Assigning n (= $\sqrt{(k/M)}/(2\pi)$) and ζ_{eff} (= $c/(2\sqrt{(kM)})$) as the frequency of vibration and the effective damping ratio in the direction of the motion respectively, Equation 2 can then be re-written as Equation 3:

$$\ddot{x} + 2\zeta_{eff}(2\pi n)\dot{x} + (2\pi n)^2 x = F_{ae}(t)/M \tag{3}$$

In case of free vibrations of a SDOF system in one direction, the damping ratio ζ_{eff} becomes the structural damping of the system ζ_{st} and the term on the right side of Equation 3 becomes zero. Chowdhury et al. [24] developed a new system identification technique, called the Iterative Least Squares (ILS) approach in order to obtain all eighteen flutter derivatives for a streamlined bridge deck from free vibrations displacement time histories. In order to obtain the flutter derivatives using the ILS approach, it is imperative to first find the aeroelastically modified effective damping C^{eff} and stiffness K^{eff} matrices, respectively, which include the aeroelastic vector component [25, 26]. In this case, the latter component in the aeroelastic drag force D_{ae}. Subsequently, if the free vibrations tests are done twice, with and without the WOW fans turned on, then one can obtain the structural and effective damping ratios ζ_{st} and ζ_{eff}, correspondingly. Hence, the aeroelastic damping ratio ζ_{aero} can be calculated by subtracting ζ_{st} from ζ_{eff}. However, Equation 3 needs to be represented as the state-space model shown in Equation 4:

$$\dot{\underline{X}} = \underline{A}\underline{X} \text{ with, } \quad \underline{X} = \begin{Bmatrix} \underline{y} \\ \dot{\underline{y}} \end{Bmatrix}, \underline{A} = \begin{bmatrix} \underline{0} & \underline{I} \\ -\underline{K}^{eff} & -\underline{C}^{eff} \end{bmatrix} \tag{4}$$

The $\underline{A}$ matrix is a $2n$ x $2n$ square matrix, where n is the number of degrees of freedom for the dynamic system and $\underline{I}$ is the identity matrix of size n x n. Consequently, the $\underline{A}$ matrix in Equation 4 can be determined if the acceleration $\underline{\ddot{y}}$, the velocity $\underline{\dot{y}}$ and the displacement $\underline{y}$ can be recorded for all n degrees of freedom (n = 1 in the case of the transmission tower) for at least $2n$ different instants of time [24, 27].

A mechanism was constructed at the WOW using steel supports and electromagnets in order to free vibrate the transmission tower by giving it an initial displacement in both strong and weak axes (0° and 90°). The three accelerometers previously used in the wind testing were also utilized in this set of experiments in order to record the acceleration time histories of the transmission tower at its topmost point. Subsequently, a MATLAB [28] code was developed in order to integrate the acceleration data and obtain the subsequent velocity and displacement time histories using the Newmark integration method [29]. Last but not least, the ILS method was adopted along with the obtained time histories until the convergence of $\underline{A}$ matrix was determined to be sufficient. Hence, C^{eff} and K^{eff} are determined and the damping ratios, both structural and effective, could be estimated.

For the purpose of this paper, the ILS algorithm will be applied to a no wind loading case in order to extract the structural damping ζ_{st}. Consequently, the transmission tower was given an initial displacement of 2 cm, then the structure was allowed to freely oscillate until reaching its rest position, with the WOW fans turned off. The time histories of acceleration data at the top of the tower were recorded. This exercise was repeated five times for each direction (0° and 90°) and the values were averaged. This paper will only tackle the 0° direction (displacement along the weak axis). Then, the obtained results of the variable were the following: K^{eff} = 9,350 N/m and C^{eff} = 0.56. The mass of the aeroelastic transmission tower is around 1.1 kgs. By using the equations of the natural frequency n and damping ratio ζ previously stated, the obtained values are: n = 14.7 Hz and ζ = 0.25% for mode shape 1. Figure 6 shows the acceleration time history of the free vibration test conducted along the weak axis.

$$\zeta = (1/(2\pi j)) \times ln\,(\ddot{x}_1/\ddot{x}_{j+1}) \tag{5}$$

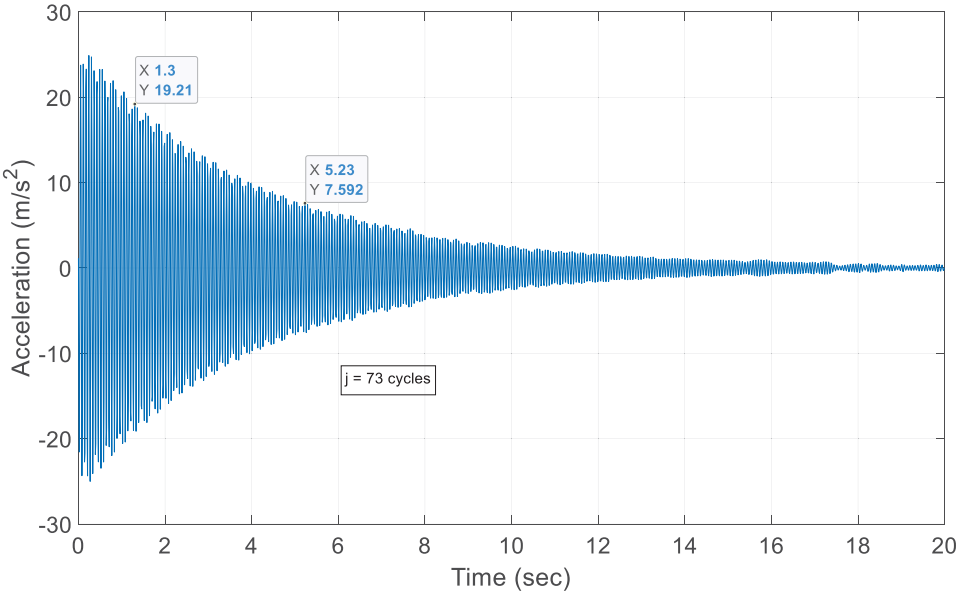

Figure 6: Acceleration time history of free vibration test

By comparison with Table 2, the obtained frequency for mode 1 is well in agreement with its design counterpart (14.7 Hz compared to 15.9 Hz). Furthermore, and by comparison with

the estimation of the damping coefficient using the decay of motion (Figure 6), the obtained structural damping ζ_{st} using the ILS approach is also well in agreement. From Figure 6, the estimated structural damping using the decay of motion (Equation 5) is around 0.21%. The previous results show the accuracy of the ILS approach in obtaining the stiffness and the damping ratio of the system in any direction. This approach will be used later to estimate the damping ratio in the strong axis. Moreover, the ILS approach will be adopted to obtain the effective damping ratio (experiment repeated with the WOW fans turned on) and therefore, propose values for the subsequent aerodynamic damping for along- and across-wind directions at different wind speeds.

5 DRAG COEFFICIENT COMPARISON

This section tackles the determination of the drag coefficients from the aeroelastic transmission tower model and compares the values to the ones suggested in the ASCE 7-16 [30] standard. Note that during the design stage of the model and more specifically the cladding elements, the tower geometry was divided into seven zones. Each zone had its own drag coefficient, based on its solidity ratio. For the sake of this paper, the drag coefficients of the entire tower are assessed with respect to both wind speeds and directions. The drag coefficients are calculated based on the data collected from the strain gauges installed on different parts of the spine and cross-arms, as shown in Equation 6:

$$C_D = 2\varepsilon EI/bM \tag{6}$$

In Equation 6, ε is the strain in the direction of loading, E is the modulus of elasticity of the material in N/m^2, I is the moment of inertia of the section in m^4, b is the distance to the centroid and M is the measured bending moment at the point of location of the strain gauge. Likewise, M is given in Equation 7:

$$M = \sum F_{Di} d_i = \sum 0.5\rho A_i C_D U^2 d_i \tag{7}$$

In Equation 7, i represents the zone number (total of seven zones), U is the wind speed at the height of the zones in m/s, A_i is the area of the elements in the plane perpendicular to the wind direction in zone i in m^2 and d_i is the distance from the strain gauge to the point of application of the force on zone i in m. Figure 7 shows a schematic of the forces on the spine.

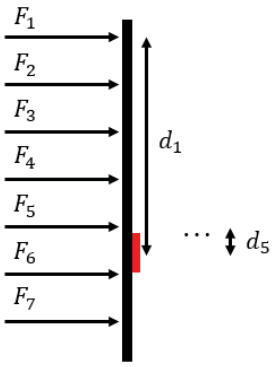

Figure 7: Schematic of forces applied on the seven zones of the spine

Similarly, and for squared trussed towers as in the case of the aeroelastic transmission tower, ASCE 7-16 [30] suggests Equation 8 for the calculation of the force coefficients (or drag coefficients per zone). Equation 8 presents C_D as a function of the solidity ratio ϕ, which is defined as the ratio of the solid area to the gross area of the tower zone, in the direction of

loading. Figure 8 showcases the comparison between values of C_D calculated using Equation 6 using experimental data and ASCE 7-16 [30] recommended ones (Equation 8).

$$C_D = 4\phi^2 - 5.9\phi + 4 \tag{8}$$

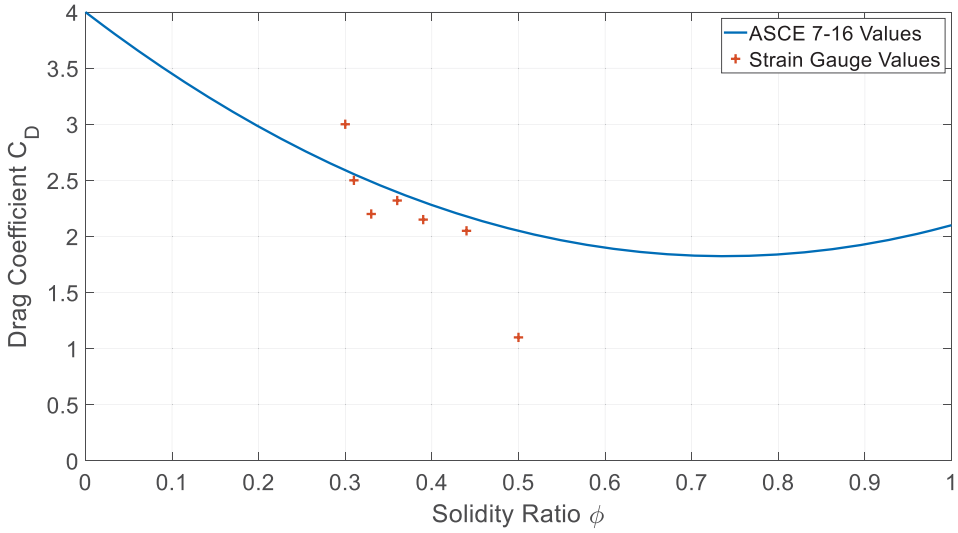

Figure 8: Comparison between experimental and ASCE 7-16 C_D values for 0° wind direction

By inspecting Figure 8, it can be noted that the experimental values of C_D obtained using strain gauge data are well in agreement with values suggested in ASCE 7-16 [29] using Equation 8. This trend is seen for all experimental values besides one. For a solidity ratio ϕ of 0.5, and at a wind direction of 0° (across conductors), the drag coefficient C_D obtained from the experiment was almost half the value suggested in the standard. This could possibly be explained by a large vibration in the across-wind direction, leading to bending moments M higher than the expected ones (Equation 7). This would lead to a decrease in the value of C_D. Nevertheless, for the rest of the wind directions, the C_D values were well in range of the theoretically suggested ones. Further data analysis is required in order to obtain force and moment coefficients C_F and C_M, respectively, and compare them with values suggested in ASCE 7-16 [30] for truss structures.

6 CONCLUSION

An aeroelastic model for a multi-spanned transmission line system was designed and constructed at the NSF NHERI WOW EF. This paper only discussed the behavior of a single self-supported lattice tower to synoptic winds. The geometric scale of the tower model was selected to be 1:50. A detailed description of the design, instrumentation and construction of the aeroelastic model is presented in this paper. The specimen was validated for both design and construction by comparing the subsequent natural frequencies to their prototype counterparts. The results were well in agreement. An ILS method was introduced in order to suggest values for the aerodynamic damping of lattice towers for both along- and across-wind directions. Last but not least, drag coefficient values obtained from experimental data were in good agreement with the ones suggested in the ASCE 7-16 [30] standard. In the future, more detailed data analysis will be conducted to obtain force and moment coefficients for the transmission tower and the entire system.

REFERENCES

[1] R. J. Campbell, Weather-Related Power Outages and Electric System Resiliency, *Congressional Research Service*, Library of Congress, R42696, 2012.

[2] H. Aboshosha, A. Elawady, A. El Ansary, and A. El Damatty, Review on Dynamic and Quasi-Static Buffeting Response of Transmission Lines under Synoptic and Non-Synoptic Winds, *Engineering Structures*, 112, 23-46, 2016.

[3] H. Aboshosha, and A. El Damatty, Effective Technique to Analyze Transmission Line Conductors under High Intensity Winds, *Wind and Structures*, Vol. 18, No. 3, 2014.

[4] H. Ahmed, Numerical and Experimental Studies of Transmission Lines Subjected to Tornadoes, *University of Western Ontario – Electronic Thesis and Dissertation Repository*, Paper 2479, 2014.

[5] F. Yang, and H. Zhang, Two Case Studies on Structural Analysis of Transmission Towers under Downburst, *Wind and Structures*, Vol. 22, No. 6, 685-701, 2016.

[6] A. Elawady, and A. El Damatty, Longitudinal Force on Transmission Towers Due to Non-Symmetric Downburst Conductor Loads, *Engineering Structures*, 127, 206-226, 2016.

[7] S. Haddadin, H. Aboshosha, A. M. El Ansary, and A. El Damatty, Sensitivity of Wind Induced Dynamic Response of a Transmission Line to Variations in Wind Speed, *Resilient Infrastructure,* London, June 1-4, 2016.

[8] H. Matsumiya, and T. Nishihara, Wind Tunnel Tests for Simulating Large-Amplitude, Low-Frequency Galloping on Overhead Transmission Lines, *The Seventh International Colloquium on Bluff Body Aerodynamics and Applications (BBAA7)*, Shanghai, China; September 2-6, 2012.

[9] H. Aboshosha, A. M. Ibrahim, A. A. El Damatty, and A. Hamada, Dynamic Behavior of Transmission Lines Structures under Synoptic Wind Loads, *2016 CIGRE-IEC Colloquium*, May 9-11, Montréal, QC, Canada, 2016.

[10] A. M. Loredo-Souza, and A. G. Davenport, A Novel Approach for Wind Tunnel Modelling of Transmission Lines, *Journal of Wind Engineering and Industrial Aerodynamics*, Vol. 90, no. 4, pp. 407-414, 2002.

[11] W. E. Lin, E. Savorya, R. P. McIntyre, C. S. Vanderlaarb, and J. P. C. King, A Single-span Aeroelastic Model of an Overhead Electrical Power Transmission Line with Guyed Lattice Towers, *13th International Conference on Wind Engineering (ICWE)*, Amsterdam, 2011.

[12] A. Elawady, H. Aboshosha, A., El Damatty, G., Bitsuamlak, H., Hangan, and A. Elatar, Aero-Elastic Testing of Multi-Spanned Transmission Line Subjected to Downbursts, *Journal of Wind Engineering and Industrial Aerodynamics*, Vol. 169, pp. 194-216, 2017.

[13] Y. Chen, and L. Pan, Dynamical Response of Transmission Line Towers Subjected to Thunderstorm Downbursts Based on Experimental Study, *2014 World Congress on Advances in Civil, Environmental and Materials Research (ACEM14)*, Busan, Korea, August 24-28, 2014.

[14] T. G. Mara, J. K. Galsworthy, and E. Savory, Assessment of Vertical Wind Loads on Lattice Frame-Work with Application to Thunderstorm Winds, *Wind and Structures*, Vol. 13, no.5, pp. 413-431, 2010.

[15] F. Cluni, V. Gusella, and G. Bartoli, Wind Tunnel Scale Model Testing of Suspended Cables and Numerical Comparison, *Journal of Wind Engineering and Industrial Aerodynamics*, Vol. 96, no. 6, pp. 1134-1140, 2008.

[16] A. G. Chowdhury, I. Zisis, P. Irwin, G. Bitsuamlak, J.-P. Pinelli, B. Hajra, and M. Moravej, Large-Scale Experimentation Using the 12-Fan Wall of Wind to Assess and Mitigate Hurricane Wind and Rain Impacts on Buildings and Infrastructure Systems, *Journal of Structural Engineering*, 143(7), 2017.

[17] S. Liang, L. Zou, D. Wang, and H. Cao, Investigation on Wind Tunnel Tests of a Full Aeroelastic Model of Electrical Transmission Tower-line Systems, *Engineering Structures*, Vol. 85, pp. 63-72, 2015.

[18] A. Elawady, H. Aboshosha, A. El Damatty, and Bitsuamlak, G., Wind Tunnel Testing of a Multiple Span Aeroelastic Transmission Line Subjected to Downburst Wind, *Resilient Infrastructure*, London, June 1-4, 2016.

[19] P. A. Irwin, Full Aeroelastic Model Tests, *Aerodynamics of Large Bridges*, A. Larsen (ed.), Balkema, Rotterdam, 1992.

[20] N. Isyumov, Wind Tunnel Methods for Evaluating Wind Effects on Buildings and Structures, *International Symposium on Experimental Mechanics*, The University of Waterloo, Waterloo, June 12-16, 1972.

[21] A. M. Loredo-Souza, The Aeroelastic Wind Tunnel Modeling of Transmission Lines and Their Behavior under Severe Boundary Later Winds, *Proceedings of the 9th International Conference on Structural Dynamics*, EURODYN 2014, Porto, Portugal, 30 June – 2 July, 2014.

[22] SAP2000 Version 20.0.0, Structural Analysis Program, *Computers and Structures, Inc.*, www.csiamerica.com, 2018.

[23] E. Simiu, and D. Yeo, Wind Effects on Structures, *John Wiley & Sons*, 4th Edition, 2019.

[24] A. G. Chowdhury, and P. P. Sarkar, Identification of Eighteen Flutter Derivatives of an Airfoil and a Bridge Deck, *Wind and Structures*, Vol. 7, No. 3, pp. 187-202.

[25] P. P. Sarkar. New-Identification Methods Applied to the Response of Flexibles Bridges to Wind. *PhD Thesis*, The John Hopkins University, Baltimore, MD, 1992.

[26] P. P. Sarkar, N. P. Jones, and R. H. Scanlan, Identification of Aeroelastic Parameters of Flexible Bridges, *ASCE Journal of Engineering Mechanics*, 120(8), pp. 1718-1742, 1994.

[27] S. R. Ibrahim, and E. C. Mikulcik, The Experimental Determination of Vibration Parameters from Time Responses, *The Shock and Vibration Bulletin*, Vol. 46, pp. 187-196, 1976.

[28] MATLAB and Statistics Toolbox Release 2019b, *The MathWorks Inc.*, Natick, Massachussets, United States, 2019.

[29] N. M. Newmark, A Method of Computation for Structural Dynamics, *ASCE Journal of Engineering Mechanics*, pp. 67-94, 1959.

[30] ASCE 7, Minimum Design Loads for Buildings and Other Structures, *American Society for Civil Engineers / Structural Engineering Institute (ASCE/SEI)*, Reston, Virginia, United States, 2016.

EURODYN 2020
XI International Conference on Structural Dynamics
M. Papadrakakis, M. Fragiadakis, C. Papadimitriou (eds.)
Athens, Greece, 23–26 November 2020

A STUDY ON THE EVALUATION OF WIND INDUCED VIBRATION OF LONG-SPAN SUSPENSION BRIDGES WITH ARTIFICIAL NEURAL NETWORKS

Dario R. Fernandez[1], **Aksel Fenerci**[1], **and Ole A. Øiseth**[1]
[1] Department of Structural Engineering, NTNU
{dario.r.f.castellon,aksel.fenerci,ole.oiseth}@ntnu.no

Keywords: Long span bridges, Wind Induced Vibrations, Machine Learning.

Abstract. *The Hardanger bridge is a long span suspension bridge located in western Norway and it is subjected to wind-induced-vibrations (WIV). Since the existing methods for WIV simulation demand high computational effort, it is appealing to use Machine Learning models to perform faster analyses. Therefore, this study applies Artificial Neural Network (ANN) and Support Vector Regression (SVR) algorithms to the analytical buffeting response predictions of the Hardanger bridge. The aim is to develop a strategy for training Machine Learning models that can be extended to real datasets. The samples of WIV features were analyzed with three different models: the single hidden layer perceptron, the multilayer perceptron and the support vector regression. Using the Normalized Root Mean Square Error as the performance metric, it was possible to obtain similar results with the different models.*

1 INTRODUCTION

The Hardanger bridge is by now the longest suspension in Norway and among the slenderest bridges in the world. It has been the subject to several research campaigns focusing on wind-induced-vibrations (WIV), on which high computational effort in analytical predictions was a constant [1] [2] [3] [4]. Thus, the deployment of a surrogate model for faster WIV assessment in real datasets is required to extend the experience gained with the Hardanger bridge not only for structural health monitoring applications, but also, for design of structures with similar characteristics. Nevertheless, the application of Machine Learning to datasets of WIV on long span bridges has not been well documented yet, and the comparable studies do not cover the specific category of structure and/or dynamic effect [5] [6].Therefore, this document presents the application of Machine Learning algorithms, specifically Artificial Neural Network (ANN) and Support Vector Regression (SVR), to the Hardanger Bridge WIV simulations with the purpose of developing a training strategy that could be extended to real datasets. This development involved the construction of a training dataset with simulated WIV of the Hardanger bridge which was fed into a group of Machine Learning models. Successively, the models' predictions were tested using a new dataset. The quality of the predictions was verified and compared using the Normalized Root Mean Squared Error (NRMSE). Finally, the training and testing procedure were repeated for different noise conditions added to the structural response fields.

2 MATERIALS & METHODS

2.1 Artificial neural network

An ANN is an assembly of connected and layered sets of units, where: the unit (also known as neuron or node) is an operational entity that stores and distributes information, the layers are the set of neurons, and the connections are the arrays governing the transformation rule between nodes in the contiguous layers. The neurons in a generic layer are stimulated by numeric values or signals coming from those of the previous layer. Then, a neuron is said to be activated or "fired" whenever the algebraic sum of the incoming signals overcomes a certain threshold [8]. To generalize the concept of the linear discriminant involved in the algebraic sum [9], a non-linear activation function, $f(\blacksquare)$, is applied to the result as shown in Equation (1).

The type of neural network used in this study was the so-called Multilayer Perceptron, schematically shown in Figure 1. This type of model overcomes the limitations of the single layered network by allowing the representation of higher complexity functions with their consecutive transformations of the input signals [9]. Nevertheless, to avoid feedback loops, they must be restricted to a feed-forward information flow only.

Equation (1) shows the output of a *j-th* node in the arbitrary *k-th* layer of a Multilayer Perceptron (MLP), where y_j^k is related to an activation threshold, ϑ_j^k and with, $w_{i,j}^{k-1}$ are the connection weight and x_i^{k-1} is the incoming stimulus from the *i-th* node of the previous layer. Subsequently, Equation (2) presents the operations in matrix notation. Combining these operations until the *M-th* layer corresponding to the model physical output, it is possible to obtain an estimation of the of the same $\hat{\boldsymbol{y}}$ as shown in Equation (3).This process is known as feed-forward mapping.

$$y_j^k = f\left(\sum_{i=1,j=j}^{N} w_{i,j}^{k-1}\, x_i^{k-1} + \vartheta_j^k\right) \tag{1}$$

$$y^k = f\{(w^{k-1})^T * x^{k-1} + \vartheta^k\} \tag{2}$$

$$\hat{\boldsymbol{y}}^{k=M} = f\{(w^{M-1})^T \ldots f\{(w^1)^T x^1\} + \vartheta^M\} \tag{3}$$

In the training step of the analysis, the actual output of the network is known. Therefore, a measure in the accuracy of the network can be obtained as shown in Equation (4).

$$\varepsilon = L(\hat{y}_j, y_j) \tag{4}$$

Where ε denotes the actual error and $L(\blacksquare)$ denotes the "loss" or "cost" function.

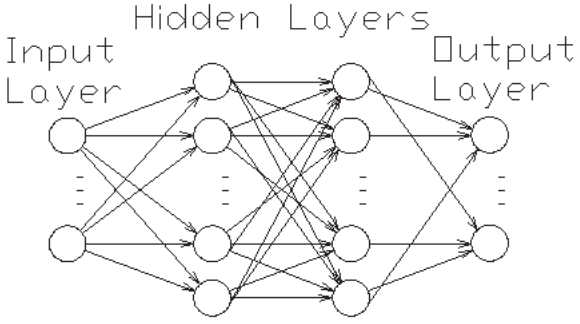

Figure 1: Architecture of ANN

The learning process consists of minimizing the loss function. For multilayered models, this is achieved by transmitting the error through all the layers within the network resulting in an

iterative optimization procedure which is known as backpropagation [10]. It is worth noting that the backpropagation procedure refers only to the error feeding and it is independent of the optimization algorithm used. Since the initial input signal, or origin, is fixed to the dataset, the only parameters to be updated in each iteration are the network weights and the neuron thresholds. Thus, the optimization problem can be written as Equation (5).

$$find\ (W_k\ \&\ \theta_k) \therefore L(\hat{y}_j, y_j) = \min(\varepsilon) \tag{5}$$

2.2 Supporting vector regression

Supporting vector regression is a machine learning tool developed by Vapnik et al. and its historical background can be found in [11]. It is the application of the supporting vector approximation to a regression problem using a ε-insensitive loss function [12]. Given a dataset with corresponding input and output features $\{x_i, y_i| \ldots |x_n, y_n\}$, the idea is to find a function $f(x)$ that approximates y_i with a certain tolerance ε. The regression estimation can be obtained with the linear function shown in Equation (6).

$$f(x) = x'w + \vartheta \tag{6}$$

Introducing the ε-insensitive loss function $L(\blacksquare)$ equal to zero when the difference of the estimation $f(x)$ and the target is less than ε, the constraint shown Equation (7) is added.

$$L(y_i - f(x,w) = \begin{cases} 0 & if|y_i - f(x,w)| \le \varepsilon \\ |y_i - f(x,w)| & otherwise \end{cases} \tag{7}$$

The best estimation minimizes the loss function and thus, the problem can be written as a convex optimization problem shown in Equation (8).

$$\begin{aligned} &minimize && \frac{1}{2}\|w\|^2 \\ &with\ constraints: && y_i - f(x,w) \le \varepsilon \quad f(x,w) - y_i \le \varepsilon \end{aligned} \tag{8}$$

To make the solution more feasible, the tolerance margin is softened by adding a set of slack variables ξ_i, ξ_i^*. The optimization then becomes as shown in Equation (9), where C is the so-called box constraint, a positive valued parameter that balances the accuracy of the model by imposing the penalty of the estimations outside the ε-margin.

$$\begin{aligned} &minimize && \frac{1}{2}\|w\|^2 + C\sum_{i=1}^{N} \xi_i + \xi_i^* \\ &with\ constraints: && \begin{cases} y_i - f(x,w) \le \varepsilon + \xi_i \\ f(x,w) - y_i \le \varepsilon + \xi_i^* \\ \xi_i, \xi_i^* \ge 0 \end{cases} \end{aligned} \tag{9}$$

Solving the posted optmization problem with inequality constraints is equivalient to finding the saddle point in the Lagrange functional of Equation (10).

$$L(\alpha) = \frac{1}{2}\sum_{i=1}^{N}\sum_{j=1}^{N}(\alpha_i - \alpha_i^*)(\alpha_j - \alpha_j^*)\, x_i' x_j + \varepsilon\sum_{i=1}^{N}(\alpha_i + \alpha_i^*) + \sum_{i=1}^{N} y_i(\alpha_i^* - \alpha_i) \tag{10}$$

Where α_n and α_n^* are the Lagrange multipliers with following constraints:

$$\sum_{n=1}^{N}(\alpha_n^* - \alpha_n) = 0;\ 0 \le \alpha_n \le \mathrm{C}\ \&\ 0 \le \alpha_n^* \le \mathrm{C} \tag{11}$$

The w-parameters may be found by:

$$w = \sum_{i=1}^{N} (\alpha_i - \alpha_i^*) x_i \tag{12}$$

Finally, the estimate is found by the expansion of the supporting vectors:

$$f(x) = \sum_{i=1}^{N} (\alpha_i - \alpha_i^*)(x_i{}' x) + \vartheta \tag{13}$$

The parameters ϑ can be obtanied by exploiting the Karush Kun Tuker (KKT) conditions [13] [14], which state that the product between dual variables and constraints vanishes at the optimal solution. Thus, the constraints shown in Equation (14) are added to the problem.

$$\begin{gathered} \alpha_i(\varepsilon + \xi_i - y_i + x_i' w + \vartheta) = 0 \\ \alpha_i{}^*(\varepsilon + \xi_i^* + y_i - x_i' w - \vartheta) = 0 \\ \xi_i(C - \alpha_i) = 0 \\ \xi_i^*(C - \alpha_i{}^*) = 0 \end{gathered} \tag{14}$$

To extend the formulation to nonlinear regression problems, it is required to replace the dot product $(x_i' x)$ with a nonlinear mapping function, known as the kernel function $K(x_i' x)$

$$f(x) = \sum_{i=1}^{N} (\alpha_i - \alpha_i^*) K(x_i{}' x) + \vartheta \tag{15}$$

In this study, a polynomial kernel function of degree d is chosen as shown in Equation (16).

$$K(x_i{}' x) = (1 + x_i{}' x_j)^d \tag{16}$$

2.3 Dataset simulations

The simulations of the structural response were carried out using the multimode theory in the frequency domain, more details in [15].The along-wind turbulent spectrum (S_u) on the bridge girder was obtained from a Kaimal-type spectrum [16] given in Equation (17), where the frequency axis is represented by f, the wind field is characterized by its mean and standard deviation $V\ and\ \sigma$, respectively. The subscript u indicates the along-wind turbulent components and the term A represents the spectral quantity related to the turbulence length scale at a reference height z.

$$\frac{S_u f}{\sigma_u^2} = \frac{\mathrm{A_u} f_z}{(1 + 1.5\mathrm{A_u} f_z)^{5/3}}, f_z = \frac{zf}{V} \tag{17}$$

The inputs for the dataset were the first two statistical moments of the random wind field. Therefore, several realizations of the couples (V, σ_u) were generated and introduced in Equation (17) to obtain the wind turbulence spectra. Further, the CPSD of the structure's response for each generation was computed. Finally, by numerical integration, the output features, namely the standard deviation of the lateral, vertical and torsional responses at the midspan $(\sigma_y, \sigma_z, \sigma_\vartheta)$ were obtained.

According to the observations of the Hardanger bridge measurement campaign reported in [1] (Figure 2), most of the data points lay in a central region. This uneven spread of the samples over the variable-space leads to a strong challenge for training the machine learning models. Therefore, the couples of input features in the training dataset were generated from a uniform linearly spaced function (Figure 3) which evenly distribute the samples. On the other hand,

those of the testing set were random numbers generated from two independent normalized functions (Figure 4) which represent a behavior closer to the real observations. The parameters for the numeric generation are reported in Table 1.

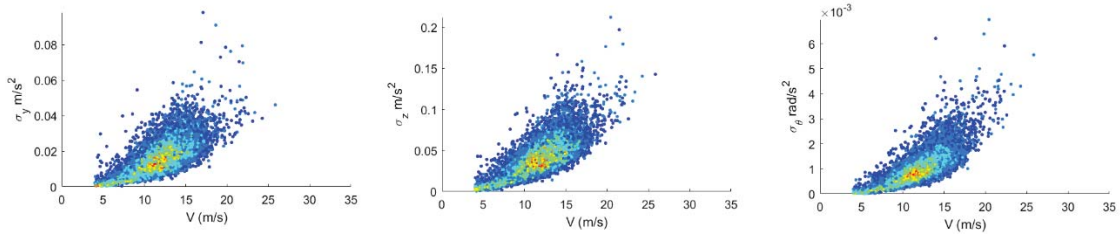

Figure 2: Structural response at midspan

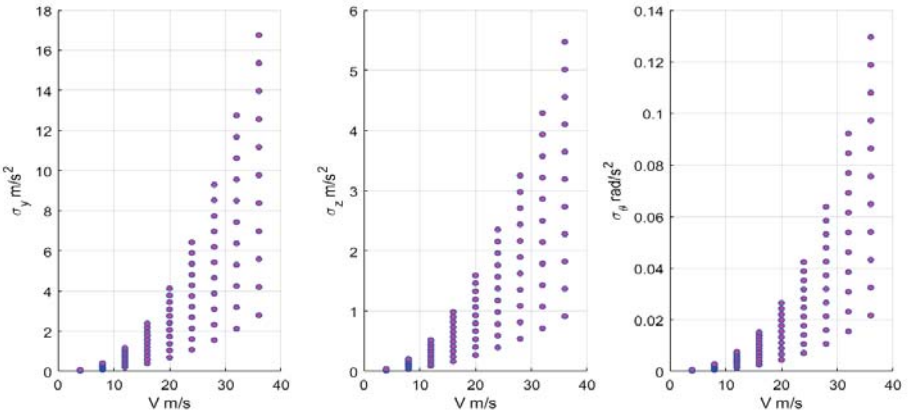

Figure 3: Training dataset

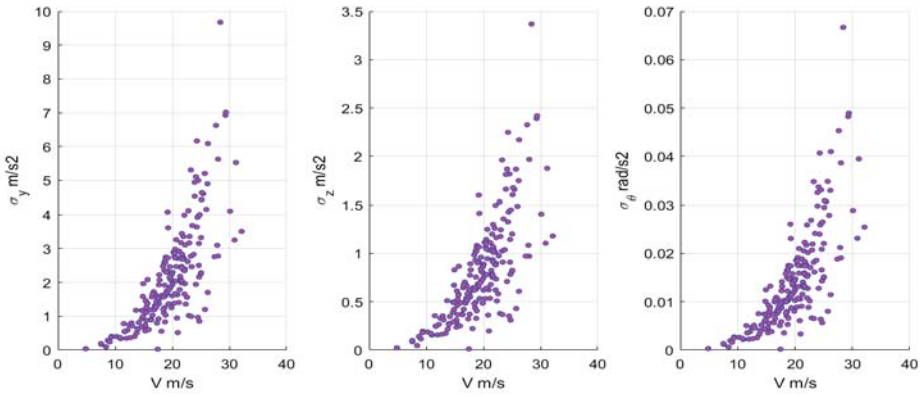

Figure 4: Validation dataset

Set	Function	Mean velocity	Turbulence Intensity	Size
Training set	Uniform Linear Spaced	[4: Δ=3.44:35].	[0.05: Δ=0.27:0.3].	100
Testing set	Rnd. Normal	$\mu = 20\ \sigma = 5$	$\mu = 0.15\ \sigma = 0.05$	200

Table 1: Dataset input generation.

2.4 Noise addition

With the aim of reproducing the challenges found on the measurement campaign, the training procedure was modified by adding a white noise to the output. The mean noise levels were of 2, 15 and 20% added to the structural responses. Nevertheless, since a decrease in the prediction's accuracy is expected with the addition of noise, a strategy for increasing the dataset size was adopted. First, several sets of random numbers were generated from a uniform

distribution according to Equation(18). Then, the different *N-terms* were added independently to the original output and stacked together to create a new larger dataset, Equation(19). The original dataset input was stacked *N-times* to match the size of the noise-output.

$$\begin{gathered} seed_i = Rand\{magnitude: [-0.5 \div 0.5] | size: OutputSet_{original}\} \\ output_{noise}(seed_i) = OutputSet_{original} \otimes \left[1 + \frac{Noise\ level}{25} seed_i\right] \\ Noise\ level \cong mean(output_{noise} - output_{original}) \\ where\ \otimes\ stands\ for\ point\ wise\ multiplication \end{gathered} \tag{18}$$

$$DataSet_{new} = \begin{bmatrix} InputSet_{original} & OutputSet_{original} + output_{noise}(seed_1) \\ InputSet_{original} & OutputSet_{original} + output_{noise}(seed_2) \\ \vdots & \vdots \\ InputSet_{original} & OutputSet_{original} + output_{noise}(seed_n) \end{bmatrix} \tag{19}$$

2.5 Models

Two ANN models were trained and validated: A Single Hidden Layer (SHL) and a Multi-layer Perceptron (MLP). The MLP model is as introduced before and the SHL perceptron model is obtained when the maximum layer index, k, in Equation (1) is equal to 2. The main challenge facing ANN training is the so-called hyperparameter setting. Equation (5) can only find the optimal weights and thresholds (parameters of the problem) as functions of the given network settings. Therefore, the size of the networks, the number of nodes, the learning rate and the selection of the networks functions (activation and loss) were tuned in advance and reported in Table 2.

Setting	SHL	MLP
Activation function	Sigmoid	Relu
Cost function	Mean Squared error	Mean Squared error
Optimization	Bayesian	Bayesian-Adaptative moment
Layers	1	2
Size	64	32-32
Learning rate	-	Min=1e-7
Number of cycles	-	1000

Table 2: Networks settings.

The main challenge for training SVR models is that Equation (15) must be solved separately for each output feature. Therefore, three different models, one for each component of the structural response, were trained with the settings presented in Table 3. The numerical values reported correspond to the hyperparameter optimization result.

Setting	SVR-σ_y	SVR-σ_z	SVR-σ_ϑ
Box constrained	0.1689	0.5511	1.1781
Epsilon	0.0010	0.0016	0.0013
Kernel Function	Polynomial degree:4 scale:2.1438		
Solver	Sequential Minimal Optimization SMO		

Table 3: SVR settings.

3 RESULTS

For each sample point in the testing set, a prediction was obtained. A comparison plot of the standard deviation of the lateral response component σ_y is shown in Figure 5 where the stars represent the model predictions while the dots show the simulated data. The global performance of the models in terms of their NRMSE are as reported in Table 4. The results indicate that the SVR and MLP models showed better performance than the SHL model.

Error	σ_y	σ_z	σ_ϑ
SVR	4,528e-05	4,101e-05	8,682e-04
SHL	5,686e-05	4,487e-05	2,738e-04
MLP	6,481e-06	1,235e-05	2,035e-04

Table 4: NRMSE.

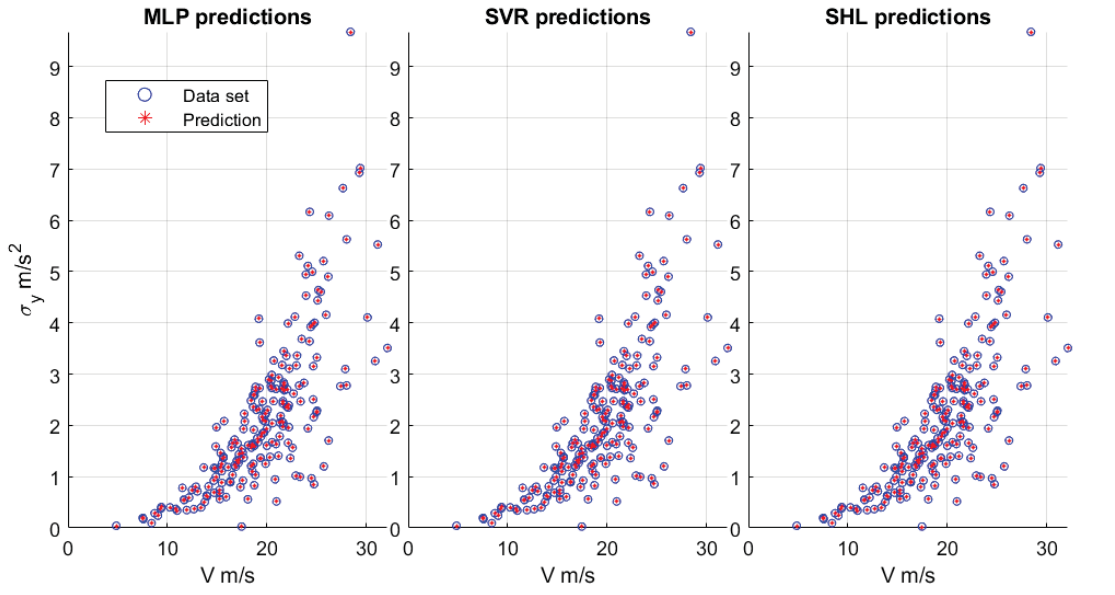

Figure 5: Prediction Scatter plot for σ_y

The performance comparison was extended to the experiment with the noise addition. The dataset creation followed Equation (19). Table 5 reports the Mean Average Percentual Error (MAPE) for the σ_y response component estimated with SVR and MLP models and with noise levels ranging from 2 to 20%. Further, Figure 6 shows a graphical comparison of the target and the estimation of the quantities for noise levels of (a) 2% and (b) 20 %. The MAPE was used for the accuracy metrics because it has comparable units with the added noise level.

Noise	*SVR*	*MLP*
2	1,02	1,12
15	10,95	6,86
20	26,97	6,91

Table 5: σ_y MAPE for different noise levels.

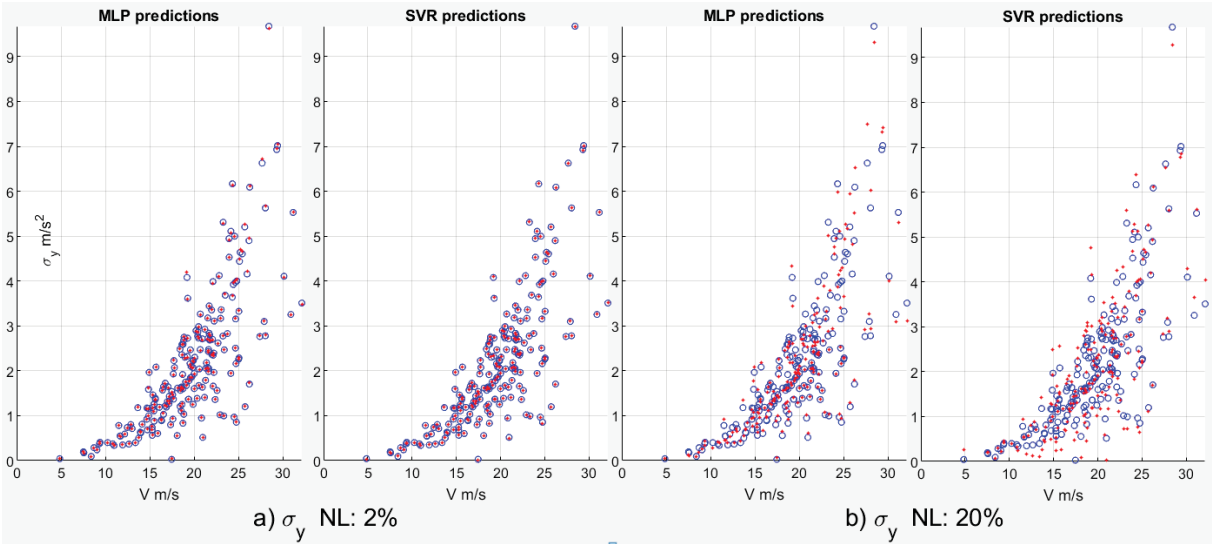

Figure 6: σ_y for: a) NL Noise level 2% b) Noise level 20%

The 27% error reported for a noise level of 20% in the case of the SVR model is particularly high. Nevertheless, after applying the dataset size-increasing strategy (Figure 7) the accuracy improves significantly. Table 6 reports the evolution of the MAPE-σ_y for the different noise levels as the dataset size is increased.

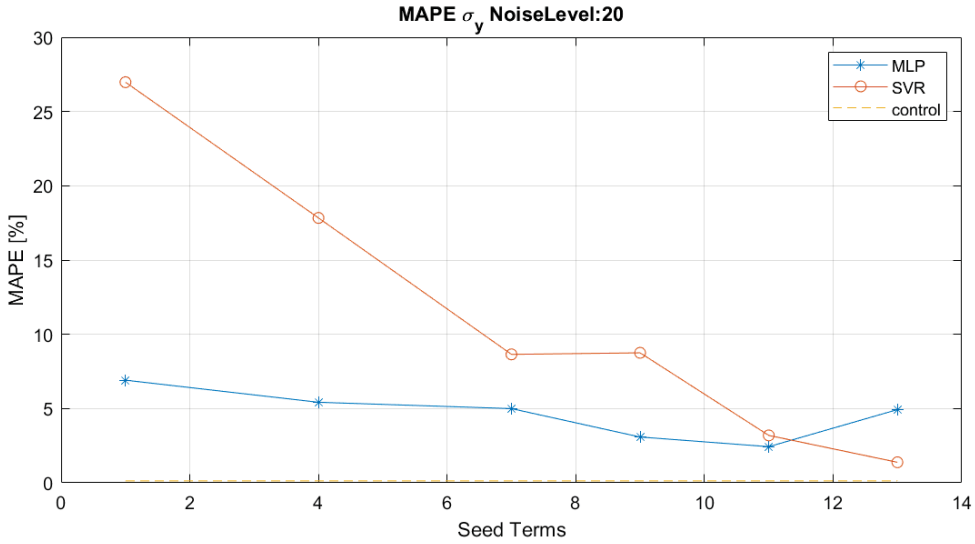

Figure 7: σ_y MAPE evolution with data size increase for 20% noise level

Random Terms	Dataset Size	Noise Level 2%		Noise Level 15%		Noise Level 20%	
		SVR	*MLP*	*SVR*	*MLP*	*SVR*	*MLP*
1	100	1.0246	1.1211	10.9553	6.8677	26.9745	6.9103
4	400	0.7315	1.6877	8.4082	3.5602	17.8352	5.4231
7	700	2.4348	1.7832	3.6389	3.8424	8.6487	4.9967
11	1100	3.2335	0.8224	3.4141	6.2085	3.1915	2.4334
13	1300	0.7284	1.5060	3.4606	9.8955	1.3829	4.9280

Table 6: σ_y MAPE evolution for different Random terms.

4 DISCUSION

The scatter plots from Figure 5 show that the methods can describe the behavior of the structural response in the testing set with reasonable accuracy. This is supported by the NRMSE reports in Table 4. The predictions of the Multilayer perceptron model gave the lowest error for all three response components; however, the other two methods also described the behavior reasonably well.

With the addition of noise to the response, an increase in the MAPE of the predictions were observed. In particular Table 5 reported that for a 20% noise level the error in the SVR model was 27% while that of the MLP model was around 7%. Therefore, the MLP model seems to be more resilient to noise addition than SVR. However, by increasing the size of the dataset the SVR model performance becomes better than the MLP model. According to Table 6, after adding 13 random terms to the dataset with 20% noise level the SVR model showed 25% reduction in the MAPE compared to almost 1% for the MLP. It is also remarkable that for the low noise level i.e. 2%, no appreciable improvement was obtained by increasing the data size. Additionally, the MAPE was almost half of magnitude of the added noise. It is worth noting that the MAPE does not necessarily descreases with increasing data size. For the MLP model an increase in the error was observed for all the noise levels. This behavior implies overtraining phenomena in this type of model.

5 CONCLUSION

The paper showed that it is possible to train machine learning models with the simulated wind induced vibrations of the Hardanger bridge dataset and obtain accurate results. The testing procedure showed a good match between the predictions and the simulations, confirmed by the low NRMSE values. The Multilayer perceptron algorithm implemented in the study gave better results mainly because of the tuning of the hyper parameters. However, to apply the methods to real datasets further analysis must be performed by adding noise to the training samples and checking the accuracy of the predictions.

The MLP model is more resistant to noise for reduced data sizes. Nevertheless, the SVR model improves with increasing data size. Additionally, the MLP model shows a tendency to overtraining as the data size increases. Therefore, extending this experience to the measurement campaigns, it is recommended to use ANN models, specifically MLP, for small datasets with high noise level and SVR models for larger datasets.

REFERENCES

[1] A. Fenerci, O. Øiseth and A. Rønnquist, "Long-term monitoring of wind field characteristics and dynamic response of a long-span suspension bridge in complex terrain," *Engineering Structures,* vol. 147, pp. 269-284, 2017.

[2] A. Fenerci and O. Øiseth, "Site-specific data-driven probabilistic wind field modelling for wind-induced response predeiction of cable-supported bridges," *Journal of Wind Engineering and Industrial Aerodynamics,* vol. 181, pp. 161-179, 2018.

[3] X. Yuwang, O. Øiseth, T. Moan and A. Naess, "Predition of long-term extreme load effects due to wave and wind actions for cable-supported birdges with floating pylons," *Engineering Structures,* pp. 321-333, 2018.

[4] Ø. W. Petersen, O. Øiseth and E.-M. Lourens, "Estimation of the dynamic response of a slender suspension bridge using measured acceleration data," in *X International conference oon Structural Dynamics, EURODYN 2017*, Rome, 2017.

[5] B. Xu, Z. S. Wu and K. Yokoyama, "Neural Networks for decentralized Control fo Cable-Stayed Bridge," *Journal of Bridge Engineering ASCE,* vol. 8, no. 4, pp. 229-236, 2003.

[6] S. Chang, K. Dookie and C. Chang, "Active response control of an offshore strucutre under wave loads using a modified probabilistic neural network," *Journal of Marine Science and Technology Springer,* vol. 14, pp. 240-247, 2009.

[7] X. Yuwang, O. Øiseth and T. Moan, *Artificial Neural Netwroks and support vector machines in the analysis of the lon-term extreme load effects of cable-supported bridges,* Trondheim: Doctoral theses at NTNU 2018:229, 2018.

[8] F. Rosenblatt, "The perceptron: a probabilisitc model for information storage and organization in the brain," *Psychological Review,* vol. 65, no. 6, pp. 386-408, 1958.

[9] C. M. Bishop, Neural Networks for Patter Recognition, New York: Oxford University Press, Inc., 1994.

[10] D. E. Rumelhart, G. E. Hinton and R. J. Williams, "Learning representations by back-propagating errors," *Letters to nature,* vol. 323, no. 9, pp. 533-536, 1986.

[11] A. J. Smola and B. Scholkopf, "A tutorial on support vector regression," NeuroCOLT2 , Berlin, 1998.

[12] V. N. Vapnik, The Nature of Statistical Learning Theory, New York: Springer, 1995.

[13] K. William, *MInima of several variables with inequalities as side conditions,* Chicago: Thesis (S.M.) University of Chicago, 1939.

[14] H. Kuhn and A. Tuker, "Nonlinear Programing," in *Proceedings of the Second Berkeley Symposium on Mathematical Statistics and Probability*, Berkeley, 1951.

[15] O. Øiseth, A. Ronnquist and R. Sigbjornsson, "Simplified prediction of wind-induced response and stability," *Journal of Wind Engineering,* vol. 98, pp. 730-741, 2010.

[16] J. C. Kaimal, J. C. Wyngaard, Y. Izumi and O. R. Cote, "Spectral characteristics of surface-layer turbulence," *Quaterly Journal of Royal Meteorological Society,* vol. 98, no. 417, pp. 563-589, 1972.

EURODYN 2020
XI International Conference on Structural Dynamics
M. Papadrakakis, M. Fragiadakis, C. Papadimitriou (eds.)
Athens, Greece, 23–26 November 2020

AUTHORIAL METHOD OF EVALUATING VIBRATIONAL COMFORT OF OCCUPANTS OF HIGH-RISE BUILDINGS BASED ON AEROELASTIC MODEL TESTS

Aleksander Pistol[1], **Łukasz Flaga**[1], **Piotr Krajewski**[1] **and Andrzej Flaga**[1]

[1] Wind Engineering Laboratory of Cracow University of Technology
ul. Warszawska 24
31-155 Kraków, Poland
e-mail: {aleksander.pistol,lukasz.flaga,piotr.krajewski2,aflaga}@pk.edu.pl

Keywords: wind engineering, aeroelastic model, vibrational comfort, high-rise buildings

Abstract. *Wind-induced vibrations are an issue not only for the structure safety, but also for the comfort of its occupants, especially in residential buildings. This paper provides the setup, methodology and results of wind tunnel aeroelastic model tests of twin high-rise (95 m high) residential buildings located in Warsaw, Poland. The aim of the tests was to assess the degree in which vibrations may be uncomfortable or harmful to the occupants of these buildings. The evaluation of vibrational comfort was conducted according to the general rules provided in ISO 6897. Measurements during both the tuning and the wind tunnel tests were performed with a system of accelerometers which allowed for direct measurement of structure accelerations, comparable with threshold values provided in the standard. The tests for each building were performed for 12 different angles of wind attack. Main non-dimensional dynamic numbers considered in the analysis were the ratios of corresponding natural frequencies in model and real-life scales, Strouhal numbers, mass scales and logarithmic decrements of damping. A mathematical model was developed which allowed for addressing the problem of coupling between the vibrations in the two main directions for angles of wind attack that are not perpendicular to the main axes of the building. As the buildings are located in dense urban development with many even taller neighbors, the influence of aerodynamic interference was crucial for the tests. Moreover, performing the tests on two buildings with a similar shape allows for comparison and assessment of the scale of influence of this interference. Besides the direct results which could be applied by the designers, these tests show the practical aspects of scaling and dimensional analysis for model tests of complicated physical phenomena, which can be used for solving actual technical and engineering problems.*

1 INTRODUCTION

The aim of this paper is to present aeroelastic wind tunnel model tests of a complex of two high-rise buildings connected with a lower link. The purpose of the tests was to assess the level of wind-induced vibrations in the buildings and compare the results with thresholds for human discomfort. This allowed to identify potential uncomfortable or unhealthy conditions at the stage of construction design, when such problems can still be mitigated to great effect through the inclusion of mechanical or mass dampers, or structural stiffening elements.

1.1 Subject of model tests

Subject of the model tests is a complex of two high-rise (95 m high) buildings connected with a lower link. The buildings are located in the inner center of Warsaw, where they will be surrounded by other buildings of similar height (or even higher), of which *The Hub* (complex of three buildings of 86-130 m high) and *Skyliner* (195 m high) are the most notable. The visualization of the buildings can be seen in Figure 1, while their location in plan is shown in Figure 2.

Figure 1. Visualization of the twin high-rise buildings

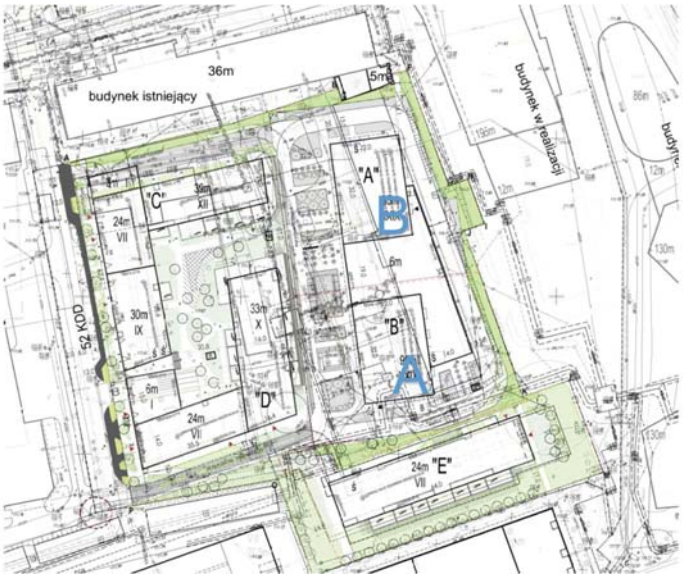

Figure 2. Location in plan of the subject buildings

1.2 Criteria of evaluation

Evaluation of perceptibility degree of horizontal vibrations by residents of high buildings was conducted in accordance with ISO/6897 91983 [1]. This document only takes into account the influence of horizontal vibrations of the building in the limited frequency range: $f \in (0{,}063;\ 1)$ Hz. The limit values of vibrations (criteria of vibrations perceptibility, levels of vibrations perception) for residents are presented on the charts in logarithmic rectangular co-ordinate system: standard deviation of acceleration σ_a – frequency of vibrations *f*.

Criteria of vibrations perceptibility depends on buildings type (general buildings, special buildings, maritime constructions) and on the nature of dynamic action (non-frequently repetitive, frequently repetitive). Charts of levels (thresholds) of vibrations perceptibility by residents are presented in Figure 3.

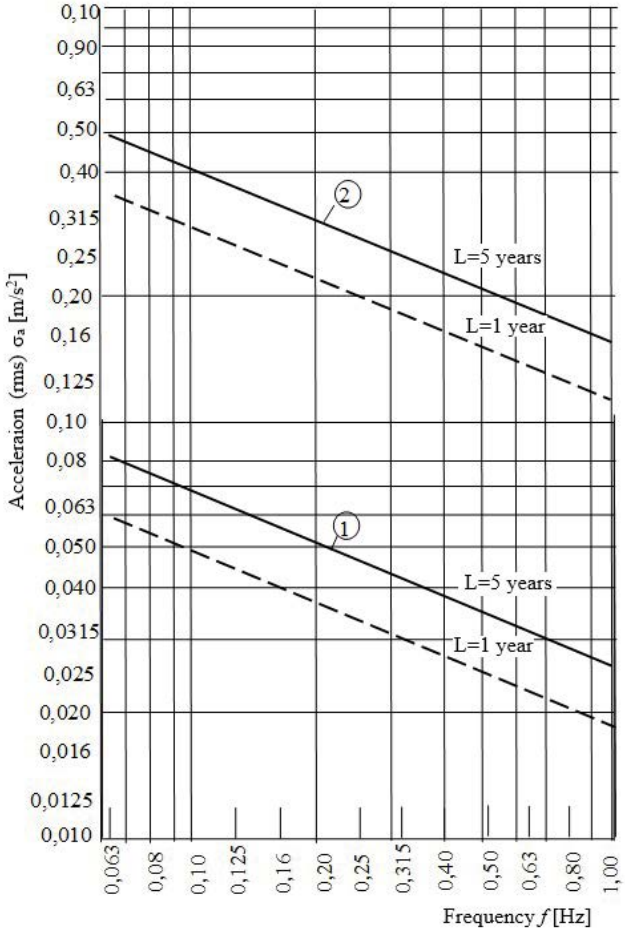

Figure 3. Limit values of horizontal vibrations of general buildings 1 and maritime constructions 2 in the case of non-frequently repetitive dynamic actions [1]

The criteria of vibrations perceptibility cannot be applied in the case of specific dynamic actions, such as earthquakes, explosions, etc. or in the case of coastal floating buildings.

Level of vibrations perception by occupants concerns people of so-called normal, mature population. No other correction factors considering age, sex, etc. were introduced.

Moreover, the influence of the following factors on the level of vibrations perception was not taken into account: body position (vertical, sitting, horizontal, aslant), visual sensations during building movements (horizontal or torsional vibrations of the building, minimal displacements of the objects inside the building). However, it should be mentioned that even minimal torsional vibrations of the building can reduce permissible level of vibrations perception significantly [2].

Level of vibrations perceptibility in the case of non-frequently repetitive vibrations depends on return period L of special intensity events and duration time of each of special intensity event; the shorter return period L, the lower limit level of vibrations perceptibility.

Criterion of vibrations perception by occupants in general buildings can be characterised as follows: vibrations causing complaints or unfavourable comments (concerning the influence of vibrations on residents comfort) in no more than 2% of residents who are in these parts of buildings where the highest vibrations appear, are considered as permissible. The considered time of vibrations are the worst 10 minutes of strong wind (storm) with return period $L = 5$ years (or more).

Available data which is necessary to determine criterion of vibrations permissibility usually concerns return periods shorter than 5 years. Regarding to this, the additional criterion of vibrations permissibility for return period of $L = 1$ year was introduced in ISO document [1]. It should be mentioned that values of permissible acceleration in the case of frequently repetitive loads (of everyday nature) are four times lower for special buildings (where precision and routine work is performed) than for general buildings.

The highest values of acceleration for high buildings appear mostly in their higher parts and usually refer to basic natural frequency of buildings vibrations f1. However, considering the level of vibrations permissibility by the buildings occupants, it may happen that accelerations related to second (or higher) natural frequency of building vibrations are more dangerous/uncomfortable for people.

Investigations of the level of vibrations perceptibility by residents were conducted in wind tunnel, where acoustic effects were not taken into account. It should be emphasised that air flows in the nature can cause infrasounds effects or noise, which influence on the level of vibrations perception by residents of buildings.

2 EXPERIMENTAL SETUP

2.1 Similarity criteria and their fulfilment

The most important similarity criteria for aeroelastic models of buildings and resulting similarity scales which were taken into account in wind tunnel model tests are presented below [3]:

Geometrical similarity scale

Wind tunnel tests were conducted using the models in scale of 1:300, hence geometrical similarity scale:

$$k_D = \frac{D_{ref,M}}{D_{ref,P}} = \frac{1}{300} \tag{1}$$

where indexes: „*M*" and „*P*" concern model and prototype, respectively. Moreover, external surfaces of aeroelastic models were accurately simulated comparing with the prototype (real life scale). Considering above, it can be concluded that geometrical similarity criteria were fulfilled in wind tunnel model tests.

Similarity criteria for inflowing air

Basic similarity criteria for inflowing air are the most commonly the following quantities:

- exponent α of power-law profile of mean wind velocity;
- the level of turbulence intensity I_v and profile of turbulence intensity;
- direction of inflowing air defined by mean angle of wind attack $\bar{\theta}$;
- Reynolds number $Re = \frac{v_{ref} D_{ref}}{\nu}$, where: ν – kinematic viscosity of air.

Profiles of mean wind velocity and turbulence intensity, obtained from wind tunnel tests, are shown in Fig. 4. and Fig. 5., respectively. They correspond to the profiles in nature with sufficient accuracy. Discrete values of angle $\bar{\theta}$, with increment of 30°, were adopted during wind tunnel tests to take into account the influence of mean wind direction. The analysed buildings are low flow bodies, so the influence of Reynolds number is negligible in this case.

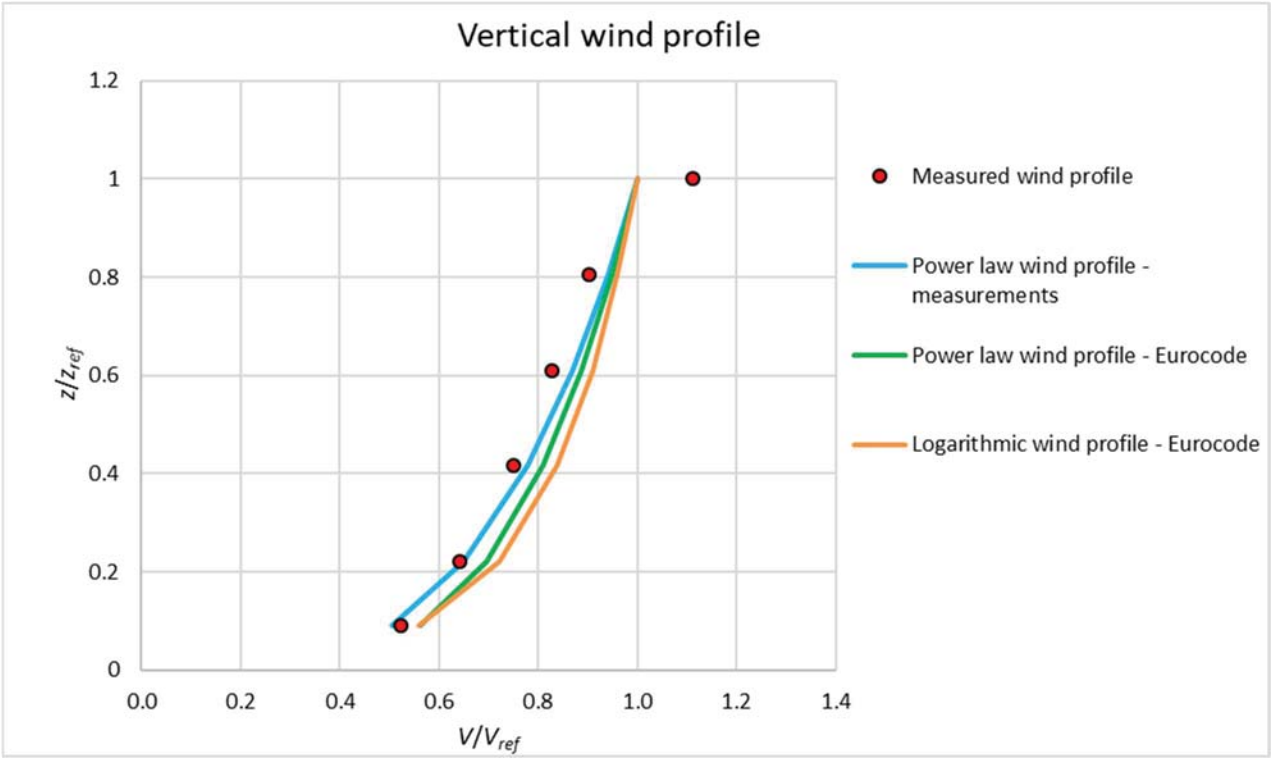

Figure 4. Vertical wind profile obtained in wind tunnel for the measurements

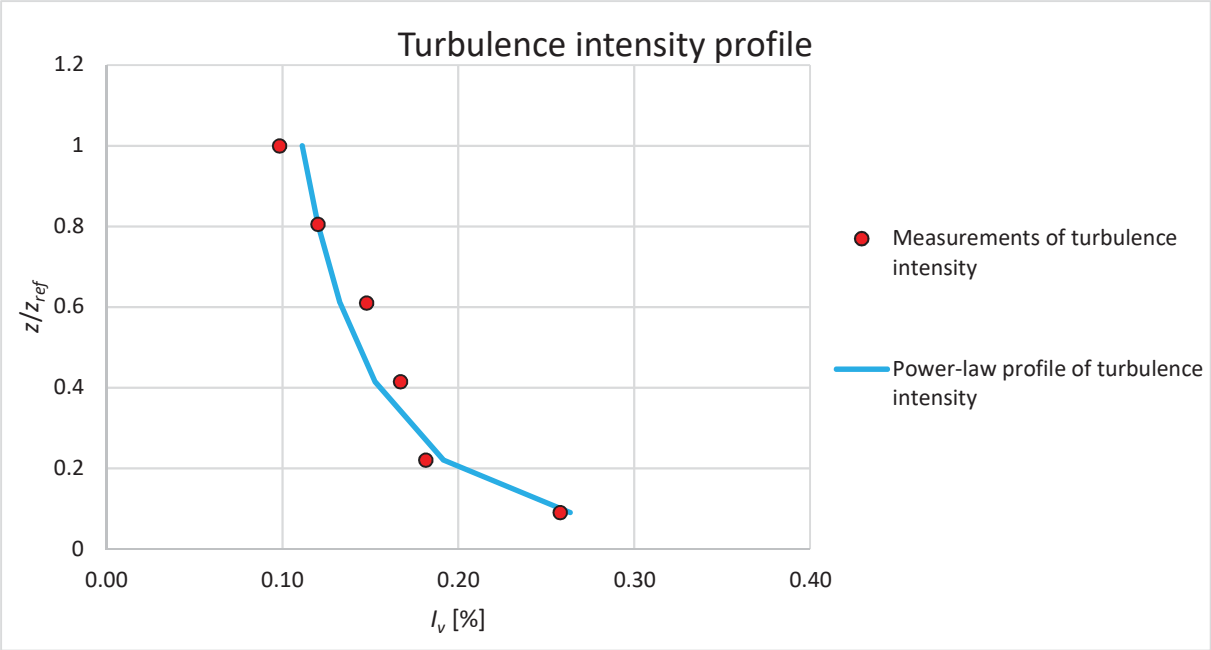

Figure 5. Vertical turbulence intensity profile obtained in wind tunnel for the measurements

Summing up, it can be concluded that basic similarity criteria of inflowing air were almost fully fulfilled in wind tunnel tests.

Mechanical similarity criteria

Similarity criterion of mass (inertia forces)

Similarity criterion of mass can be expressed by the formula:

$$M_{\rho M} = M_{\rho P} \tag{2}$$

or:

$$\frac{M_{\rho M}}{M_{\rho P}} = k_{M\rho} = \frac{\left(\rho D_{ref}^2 \frac{H}{M_{total}\breve{M}}\right)_M}{\left(\rho D_{ref}^2 \frac{H}{M_{total}\breve{M}}\right)_P} = \left(\frac{H_M}{H_P}\right)^3 \frac{(M_{total}\breve{M})_P}{(M_{total}\breve{M})_M} = 1.0 \tag{3}$$

where:

ρ – density of atmospheric air; M_{total} – total mass of aboveground part of the building; $\breve{M}$ – dimensionless generalized mass, taking into account free vibrations modes of the building.

Assuming that free vibrations modes of the buildings and their models corresponding to frequencies of free vibrations f_{1X} and f_{1Y} are similar and that equivalent masses of above-ground part of the buildings and their models on the unit of height are distributed uniformly – it can be adopted that: $\breve{M}_M \cong \breve{M}_P$. Then:

$$k_{M\rho} \cong \left(\frac{H_M}{H_P}\right)^3 \frac{M_{total,P}}{M_{total,M}} = 1.0 \tag{4}$$

which results in the following relationship:

$$\frac{M_{total,M}}{M_{total,P}} = \left(\frac{H_P}{H_M}\right)^3 = 300^3 = 27 \cdot 10^6 \tag{5}$$

Similarity criterion of vibrations damping (damping forces)

Mean logarithmic decrements of vibrations damping $\Delta_{mean,X}, \Delta_{mean,Y}$ (or decrements of critical damping $\gamma_{mean,X}, \gamma_{mean,Y}$) for equivalent systems of one degree of freedom for directions X and Y, respectively, can be defined as follows:

$$\Delta_{mean,X} = \frac{1}{N} \ln \frac{A_{1,X}}{A_{N+1,X}} \tag{6}$$

$$\Delta_{mean,Y} = \frac{1}{N} \ln \frac{A_{1,Y}}{A_{N+1,Y}} \tag{7}$$

where: N – number of the consecutive amplitudes of damped free vibrations adopted to determine mean values of Δ_{mean}.

Quantities $\Delta_{mean,X}$ and $\Delta_{mean,Y}$ are dimensionless quantities constituting another similarity criteria, hence:

$$\frac{(\Delta_{mean,X})_M}{(\Delta_{mean,X})_P} = k_{\Delta_{mean,X}} = 1; \frac{(\Delta_{mean,Y})_M}{(\Delta_{mean,Y})_P} = k_{\Delta_{mean,Y}} = 1 \tag{8}$$

Similarity criteria of vibrations frequency (elastic forces)

Similarity criteria of vibrations frequency $f_{1,X}$ and $f_{1,Y}$ result from respective kinematic Strouhal numbers St_X and St_Y :

$$St_{X,M} = St_{X,P}; St_{Y,M} = St_{Y,P} \tag{9}$$

$$\left(\frac{f_{1,X} D_{ref}}{v_{ref}}\right)_M = \left(\frac{f_{1,X} D_{ref}}{v_{ref}}\right)_P \tag{10}$$

$$\left(\frac{f_{1,Y} D_{ref}}{v_{ref}}\right)_M = \left(\frac{f_{1,Y} D_{ref}}{v_{ref}}\right)_P \tag{11}$$

or:

$$\left(\frac{f_{1,Y}}{f_{1,X}}\right)_M = \left(\frac{f_{1,Y}}{f_{1,X}}\right)_P \tag{12}$$

It results in the following similarity criteria:

$$k_{f1,X} = \frac{f_{1,X,M}}{f_{1,X,P}} = \frac{D_{ref,P}}{D_{ref,M}} \frac{v_{ref,M}}{v_{ref,P}} \tag{13}$$

$$k_{f1,X,Y} = \frac{f_{1,Y,M}}{f_{1,Y,P}} = \frac{f_{1,X,M}}{f_{1,X,P}} \tag{14}$$

Assessment of fulfilment of similarity criteria for aeroelastic models

Aeroelastic model for each of the buildings was created and calibrated taking into account fulfilment of the most important mechanical similarity criteria with iterative method. The assessment of fulfilment of mechanical similarity criteria, considering the parameters of adopted aeroelastic model, can be characterised as follows:

Total mass of aboveground part of model: $M_{total,M} = 0.149$ kg
Hence:

$$\frac{M^{*}_{\rho,M}}{M_{\rho,P}} = \varkappa = \left(\frac{1}{300}\right)^{3} \frac{29.113^{6}\ kg}{0.149\ kg} = 7.25 \neq 1 = \frac{M_{\rho,M}}{M_{\rho,P}} \tag{15}$$

According to above, it can be concluded that criterion of similarity of masses is not fulfilled. Taking this into account, if other similarity criteria were fulfilled with enough approximation, the results of measurements of the response of such aeroelastic model (eg. vibrations acceleration) should be decreased $\varkappa$ times (in this case, divided by 7.25).

Mean logarithmic decrements of vibrations damping

Time series of free vibrations along *X* and *Y* axes is presented in Fig. 6. and 7.

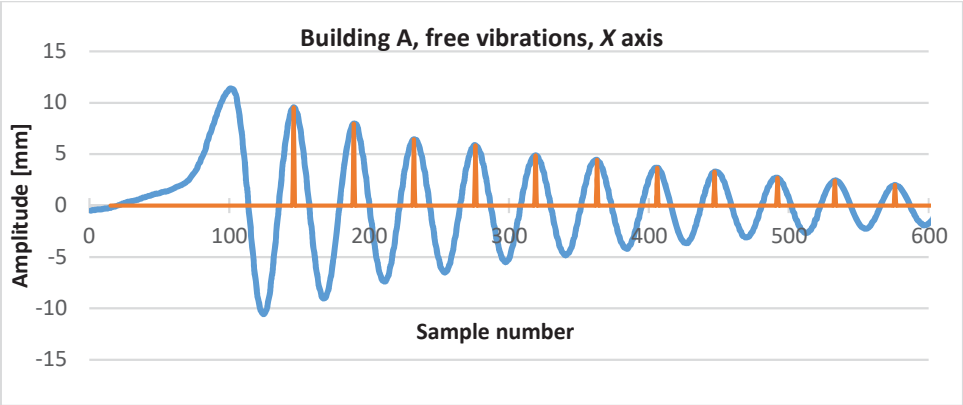

Figure 6. Free vibrations of model of building A along *X* axis

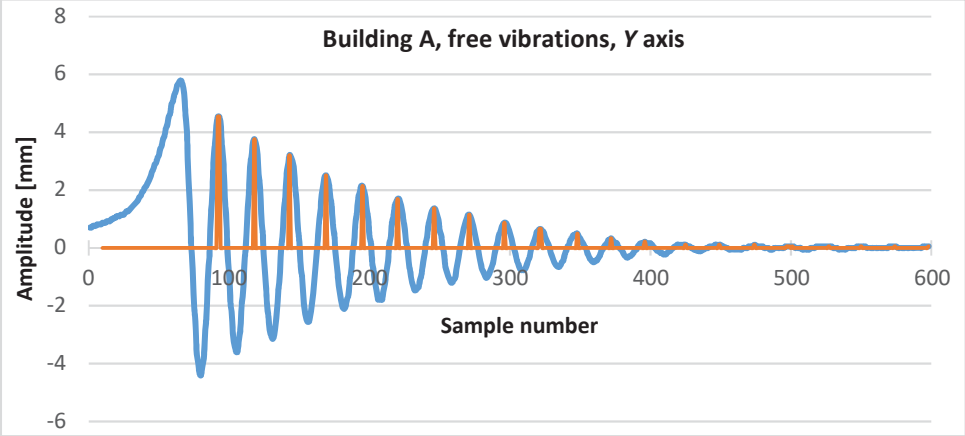

Figure 7. Free vibrations of model of building A along *Y* axis

Basing on above time series, mean decrements of damping vibrations were assessed: $\Delta_{mean,X,M} = 0.15$ and $\Delta_{mean,Y,M} = 0.09$. Taking into account real value of $\Delta = (0.08 \div 0.15)$, it can be concluded that similarity criteria of damping forces are fulfilled with a good approximation.

Frequency of model free vibrations: $f_{1X} = 11.66$ Hz; $f_{1Y} = 18{,}34$ Hz.

From criterion of kinematic Strouhal number (1.11) for first frequency of free vibrations in *X* direction it results that:

$$k_{f1,X} = \frac{11.66}{0.27} = 300\frac{v_{ref,M}}{18.8} \tag{16}$$

hence:

$$v_{ref} = \frac{11.66 \cdot 18.8}{0.27 \cdot 300} = 2.71 \frac{\mathrm{m}}{\mathrm{s}} \tag{17}$$

Wind tunnel tests should be conducted at mean wind velocity v_{ref}. However, this velocity was increased to value of $v_{ref}^{*} = 3.4 \frac{\mathrm{m}}{\mathrm{s}}$ because of small vibrations amplitudes at lower velocity (amplitudes were close to measurement range of measuring instruments). Because of this measurements results should be scaled with the use of respective factor.

When increasing $v_{ref,M}$ from 2.7 m/s to 3.4 m/s fluctuations of wind velocity are increased from v_M' to $v_M'^{*}$ as well. It can be assumed with a good approximation that $\frac{v_{ref,M}^{*}}{v_{ref,M}} \cong \frac{v_M'^{*}}{v_M'}$. Therefore, dimensionless dynamic component of wind action, appearing on the right side of the motion equation of models is almost unchanged. Nevertheless, kinematic Strouhal number changes as follows: $\frac{St_{ref,M}^{*}}{St_{ref,M}} = \frac{v_{ref,M}}{v_{ref,M}^{*}} = \frac{2.7}{3.4} = 0.79$. In turn, this change causes that model responses in resonance zones increase by the factor resulting from the following relation:

$$\mu = \frac{\frac{1}{St_{ref,M}^{*}}}{\frac{1}{St_{ref,M}}} = \frac{v_{ref,M}^{*}}{v_{ref,M}} = \frac{3.4}{2.7} = 1.26 \tag{18}$$

The second similarity criterion for vibrations frequency has the following form:

$$\frac{f_{1,Y,M}}{f_{1,X,M}} = \frac{18.34}{11.66} = 1.57 \tag{19}$$

$$\frac{f_{1,Y,P}}{f_{1,X,P}} = \frac{0.47}{0.27} = 1.74 \tag{20}$$

Taking into account uncertainties given above (concerning real values of frequencies of buildings free vibrations $f_{1,X,P}$ and $f_{1,Y,P}$), it can be concluded that above similarity criterion regarding ratio of frequency of free vibrations is fulfilled with a good approximation.

Relationships for other similarity scales

Assuming that:

- geometrical scale k_D is:

$$k_D = \frac{D_{ref,M}}{D_{ref,P}} = \frac{1}{300} \tag{21}$$

- frequency scale k_f is:

$$k_f = k_{f1,X} = \frac{11.66}{0.27} = 43.18, \qquad k_{f1,X}^{*} = \frac{D_{ref,P}}{D_{ref,M}} \frac{v_{ref,M}^{*}}{v_{ref,P}} = \frac{300}{1} \frac{3.4}{18.8} = 54.25 \tag{22}$$

- time scale k_t is:

$$k_t = \frac{1}{k_f} = \frac{0.27}{11.66} = 0.023, \qquad k_t^{*} = \frac{1}{k_f} = \frac{1}{54.25} = 0.01843 \tag{23}$$

Then velocity scale k_v is:

$$k_v = \frac{k_D}{k_t} = \frac{\frac{1}{300}}{0.023} = 0.145, \qquad k_v^{*} = \frac{k_D}{k_t^{*}} = \frac{\frac{1}{300}}{0.01843} = 0.181 \tag{24}$$

and acceleration scale k_a is:

$$k_a = \frac{k_D}{k_t^2} = \frac{\frac{1}{300}}{0.023^2} = 6.30, \qquad k_a^* = \frac{k_D}{k_t^{*2}} = \frac{\frac{1}{300}}{0.01843^2} = 9.814 \tag{25}$$

Hence, due to unfulfilment of criterion of kinematic Strouhal number, relationships between accelerations of building models a_M^* and prototypes a_P are as follows:

$$a_M^* = k_a^* a_P = \mu \cdot k_a \cdot a_P \tag{26}$$

Moreover, taking into account remarks about unfulfilment of similarity criteria of mass for buildings models and their prototypes, relationships between accelerations measured on the buildings models a_M^{**} and on their prototypes a_P can be defined as:

$$a_M^{**} = \varkappa \cdot \mu \cdot k_a \cdot a_P \tag{27}$$

or in another form:

$$a_P = \frac{a_M^{**}}{\varkappa \cdot \mu \cdot k_a} = \frac{a_M^{**}}{7.25 \cdot 1.26 \cdot 9.814} = 0.0112 \cdot a_M^{**} \tag{28}$$

2.2 Wind tunnel parameters and apparatus

Wind tunnel tests were conducted for 12 angles of wind inflow, with increment of 30°. The accelerometers, placed in upper parts of the model, were used to register building accelerations in X and Y direction. The measurement results were processed using narrow-band filter for first frequencies of free vibrations for directions X and Y. Then, the results of this process were multiplied by scale factors resulting from similarity criteria. Finally, they were compared with limit accelerations.

Model tests were conducted at the boundary layer aerodynamic tunnel of Wind Engineering Laboratory of Cracow University of Technology. The dimensions of the working section are 1.6 m height and 2.2 m width; however, with adjacent compensation chambers bordered by slotted walls on both sides, the width is about 3.5 m. Such design allows for a significant reduction of boundary layer disturbances during partially blocked flow, enabling for investigations on larger model while minimizing the errors resulting from blockage effect. Details of the wind tunnel are shown in Fig. 8 and Fig. 9.

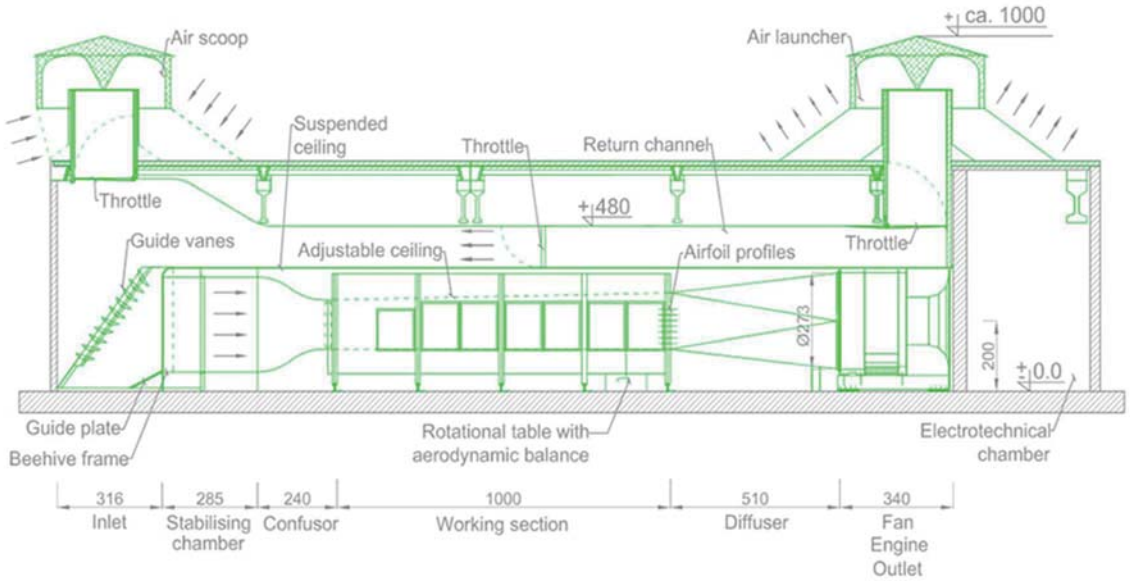

Figure 8: Longitudinal cross section of Wind Engineering Laboratory of Cracow University of Technology wind tunnel (all dimensions in [cm]).

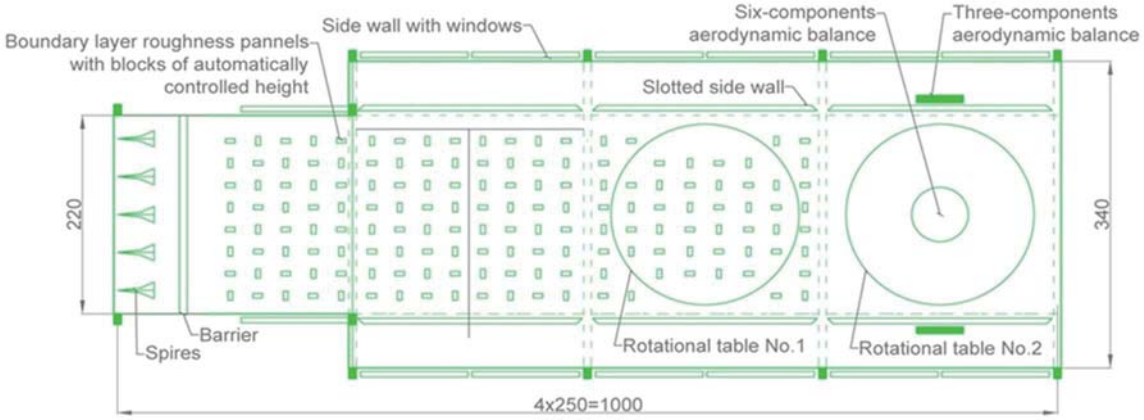

Figure 9: Top view of Wind Engineering Laboratory of Cracow University of Technology wind tunnel working section (all dimensions in [cm]).

The working section is ended with a cascade of horizontal airfoil profiles that reduces the influence of vortices generated by the fan on an air flow in the area of the rotational table. Guide vanes, inlet, beehive frame, stabilization chamber, confusor are the elements designed to take over the stream either returning through the return channel or taken from above the building roof by external air scoop and direct it respectively, making the stream homogeneous and of a very low turbulence before the inflow to the working section. The diffuser which is behind the working section is of a rectangular shape at the beginning part and of a circular shape at the end part (cross-section of the fan) and its length is equal to 5 m.

The axial fan, single-stage of efficiency 0.8 – 0.9, the outer diameter 2.72 m and the velocity of the end of the fan blade up to 100 m/s, is located on the suction side of the wind tunnel. The engine of the alternate current, shorted, driving the fan with a power of 200 kW, of nominal revolutions 750 rpm and supply voltage 220 V, controlled by inverter. Maximum mean flow velocity in the working section is 40 m/s.

The vibrations of aeroelastic model were measured with *Brüel & Kjær* Type 3050-B-060 module with DeltaTron Accelerometers Type 4507 B 002. This allowed for direct measurement of amplitudes of model accelerations under the effect of strong wind.

2.3 Wind and dynamic characteristics adopted in model tests and in analysis of tests results for subject buildings

Wind characteristics of inflowing air according to [4] and dynamic characteristics of the analysed buildings which were adopted in model tests and in analysis of tests results are as follows:

- Category of terrain roughness: IV; exponent of power law wind profile: $\alpha = 0.24$;
- Basic wind velocity: $v_b = 22$ m/s;
- Reference height in the nature: $z_{ref} = 102.5\ m$;
- Mean wind velocity at the reference height:

$$v_{ref} = v_m(102.5) = 22.0 \cdot 0.62 \left(\frac{102.5}{10}\right)^{0.24} = 23.8 \text{ m/s} \tag{29}$$

- Reference velocity for 5-years return period:

The following denotations are used: v_L – mean wind velocity with L years return period, v_k – characteristic wind velocity (i.e. mean wind velocity with $L = L_k = 50$ years return period). Assuming Gumbel distribution and averaged values of the parameters of this distribution in European conditions, the following relationships can be written [3]:

$$v_L = U - \frac{1}{a}\ln\left[-\ln\left(1-\frac{1}{L}\right)\right];\ \frac{1}{a} \approx (0.1 \div 0.3);\ \text{on average: } \frac{1}{a} \approx 0.13U \tag{30}$$

$$\frac{v_L}{v_k} \approx \frac{1-0.13\ln\left[-\ln\left(1-\frac{1}{L}\right)\right]}{1-0.13\ln\left[-\ln\left(1-\frac{1}{L_k}\right)\right]} \tag{31}$$

Assuming $L_k = 50$ years, values of $\frac{v_L}{v_k}$ were calculated using different values of L. This value can be calculated for return period of $L = 5$ years:

$$v_{ref,L(5year\ )} = v_{ref,L(50years)}(0.79) = 23.8 \cdot 0.0.79 = 18.8\ \frac{m}{s} \tag{32}$$

Above relationship concerns mean wind velocity in open agricultural area at the height of 10 m above ground. However, it can be assumed (due to lack of data) that this relationship can also be adopted for mean wind velocity at any height z above terrain of other type and, in consequence, for dynamic component of wind action $w(z,t)$ which linearly depends on mean wind velocity $\bar{v}(z)$ and its fluctuations $v'(z,t)$. Fluctuations $v'(z,t)$ depend on mean wind velocity $\bar{v}(z)$ and decrease with decreasing of mean wind velocity $\bar{v}(z)$. Then, it can be assumed that dynamic component of wind action corresponding to v_5 (ie. $L = 5$ years) is $(0.79)^2$ times smaller than this component in the case if $v_k = v_{50}$.

- Building height: $H_A = H_B = 102.5$ m;
- Total mass of aboveground part of each building: $M_{total,P} = 29.113 \cdot 10^6$ kg;
- Total mass of aboveground part of each model: $M_{total,M} = 0.149$ kg;
- Basic frequencies of free vibrations of the buildings for direction *X* and *Y*, received from the consulting engineers basing on the calculations of free vibrations of these buildings, are as follows: $f_{1X} = 0.27$ Hz; $f_{1Y} = 0.47$ Hz. It is worth to mention that adopted frequencies f_{1X} and f_{1Y} can differ from these for real objects because of the following reasons:

  1. Stiffness of so called non-structural elements of the buildings are not taken into account;

  2. Mass of the buildings resulting from variable payload of the buildings can be different;

  3. Material and mechanical characteristics of structural elements of the buildings adopted in dynamic calculations can differ from these for real objects;
- Basic frequencies of free vibrations of the buildings models in direction *X* and *Y* are: $f_{1X} = 11.66$ Hz; $f_{1Y} = 18.34$ Hz
- Logarithmic decrements of vibrations damping for each building relating to frequencies f_{1X} and f_{1Y} should be in the range of: $\Delta \in (0.08 \div 0.15)$ [5].

2.4 Models for the tests

The models for the aeroelastic tests were created in the scale of 1:300. Such scale allowed for recreation of the surroundings of the subject buildings in a radius of 300 m. Due to its close

proximity to the subject buildings and towering height, possibly impacting the results, also the *Warsaw Spire* building (180 m) was added to the model, despite its location outside of the surroundings radius. Fig. 10 shows the computer model of the buildings and their surroundings, while the physical model in the working space of wind tunnel is presented in Fig. 11.

Figure 10: Computer model of the analyzed buildings (marked in red) and their surroundings.

Figure 11: Physical model of the analyzed buildings and their surroundings in the working space of wind tunnel.

On the contrary of the rest of the model which was made as rigid models from PVC, ABS and HIPS plastics, the aeroelastic models of the two subject buildings were made from light plywood (cover) and steel or aluminum core (depending on the variant of the model). Three different variants were created with different structural design (see Fig. 12). For each of the variants, dynamic characteristics were investigated, which allowed for the comparison and final choice of the model which best corresponds to the real life characteristics of the buildings.

Model shown in Fig. 12c was chosen. Subsequently, this model has been tuned and calibrated to the real life dynamic characteristics of the buildings (mostly concerning the ratio of first two natural frequencies and damping).

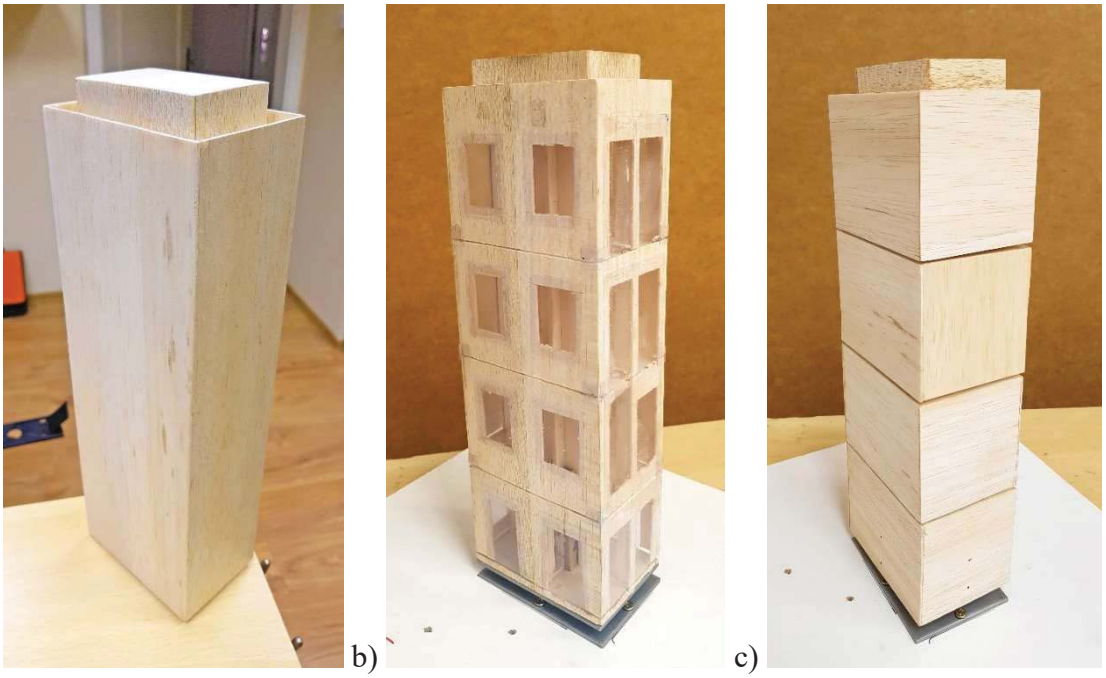

Figure 12: Different variants of aeroelastic model of the subject buildings.

3 RESULTS AND ANALYSIS

3.1 Results of aeroelastic tests

Basing on the results of wind tunnel model tests conducted on aeroelastic models of buildings A and B, RMS values of filtered signals of vibrations acceleration in natural scale were determined. The appropriate similarity scales were taken into account. Then, RMS values were compared with limit values of vibrations acceleration RMS_{dop} in accordance with Fig. 3.

RMS values obtained for directions X and Y (RMS_X and RMS_Y) and values of $RMS_{max} = \sqrt{RMS_X^2 + RMS_Y^2}$ as well as limit values of RMS_{lim} were summarised in Tab. 1, 2 and were presented in Fig. 13 and 14.

Building A, $v_{ref,L(5\ years)} = 18.8$ m/s					
Filtration X1					
Angle $\bar{\theta}$	Central frequency [Hz]	RMS_X	RMS_Y	RMS_{max}	RMS_{lim}
0°	0.22	0.014	0.004	0.015	0.050
30°	0.22	0.005	0.003	0.006	0.050
60°	0.22	0.007	0.005	0.008	0.050
90°	0.22	0.004	0.003	0.005	0.050
120°	0.22	0.005	0.002	0.005	0.050
150°	0.22	0.009	0.001	0.009	0.050
180°	0.22	0.007	0.001	0.007	0.050
210°	0.22	0.005	0.001	0.005	0.050
240°	0.22	0.005	0.001	0.005	0.050
270°	0.22	0.008	0.001	0.008	0.050
300°	0.22	0.013	0.002	0.013	0.050
330°	0.22	0.010	0.002	0.010	0.050
Building A, $v_{ref,L(5\ years)} = 18.8$ m/s					
Filtration Y1					
Angle $\bar{\theta}$	Central frequency [Hz]	RMS_X	RMS_Y	RMS_{max}	RMS_{lim}
0°	0.35	0.009	0.005	0.011	0.042
30°	0.35	0.004	0.004	0.006	0.042
60°	0.35	0.006	0.006	0.008	0.042
90°	0.35	0.004	0.004	0.006	0.042
120°	0.35	0.005	0.006	0.008	0.042
150°	0.35	0.007	0.004	0.008	0.042
180°	0.35	0.006	0.004	0.007	0.042
210°	0.35	0.004	0.003	0.005	0.042
240°	0.35	0.005	0.004	0.006	0.042
270°	0.35	0.007	0.004	0.008	0.042
300°	0.35	0.010	0.005	0.011	0.042
330°	0.35	0.008	0.004	0.008	0.042

Table 1: RMS values of vibrations acceleration due to vibration comfort of residents for building A, in [m/s2]

Building B, $v_{ref,L(5\ years)} = 18.8$ m/s					
Filtration X1					
Angle $\bar{\theta}$	Central frequency [Hz]	RMS_X	RMS_Y	RMS_{max}	RMS_{lim}
0°	0.27	0.009	0.004	0.010	0.046
30°	0.27	0.008	0.004	0.009	0.046
60°	0.27	0.008	0.004	0.009	0.046
90°	0.28	0.005	0.004	0.007	0.045
120°	0.24	0.007	0.004	0.008	0.048
150°	0.24	0.006	0.004	0.007	0.048
180°	0.24	0.005	0.004	0.006	0.048
210°	0.28	0.004	0.003	0.005	0.045
240°	0.28	0.006	0.003	0.007	0.045
270°	0.28	0.006	0.003	0.006	0.045
300°	0.28	0.006	0.003	0.007	0.045
330°	0.27	0.007	0.003	0.007	0.046
Building B, $v_{ref,L(5\ years)} = 18.8$ m/s					
Filtration Y1					
Angle $\bar{\theta}$	Central frequency [Hz]	RMS_X	RMS_Y	RMS_{max}	RMS_{lim}
0°	0.37	0.005	0.007	0.009	0.041
30°	0.37	0.005	0.007	0.008	0.041
60°	0.37	0.005	0.007	0.008	0.041
90°	0.37	0.005	0.006	0.008	0.041
120°	0.37	0.002	0.007	0.008	0.041
150°	0.37	0.002	0.008	0.009	0.041
180°	0.37	0.002	0.007	0.007	0.041
210°	0.37	0.003	0.005	0.006	0.041
240°	0.37	0.005	0.005	0.007	0.041
270°	0.37	0.004	0.005	0.007	0.041
300°	0.37	0.005	0.006	0.007	0.041
330°	0.37	0.005	0.007	0.008	0.041

Table 2: RMS values of vibrations acceleration due to vibration comfort of residents for building B, in [m/s2]

a)

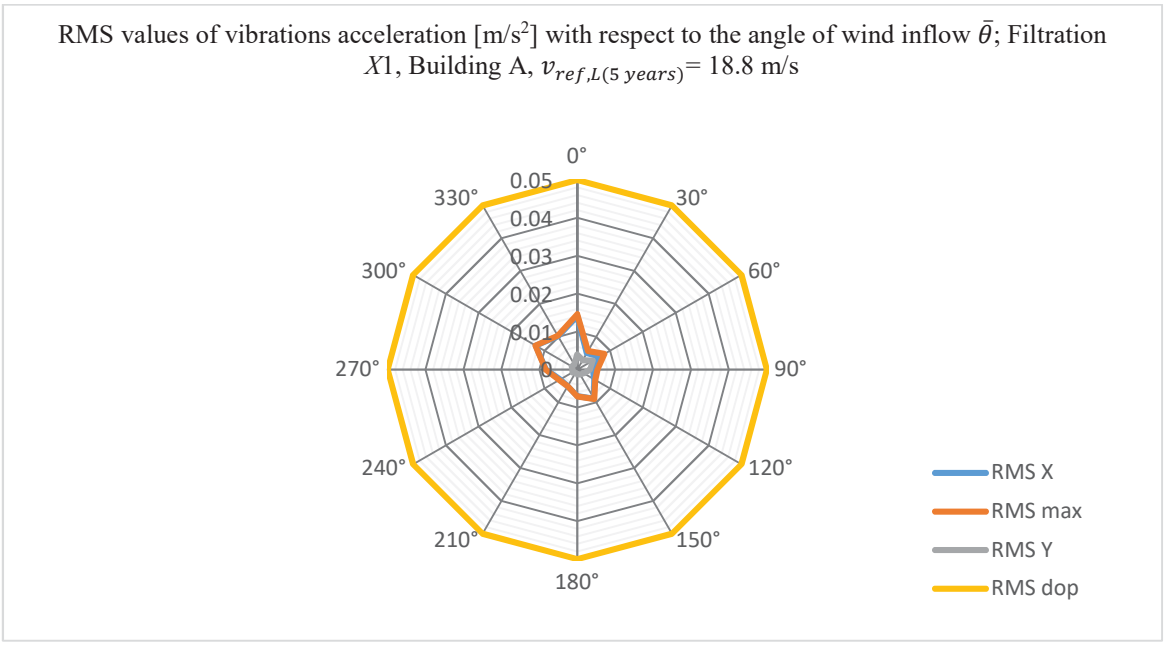

b)

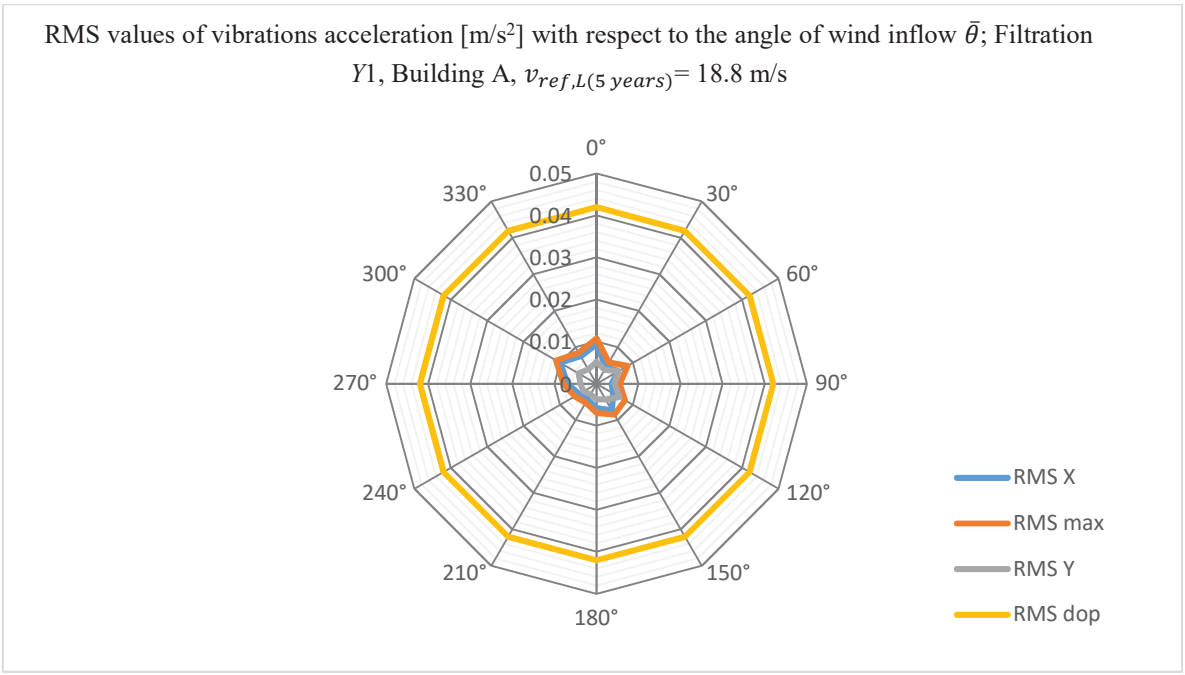

Figure 13. RMS values of vibrations acceleration due to vibration comfort of residents of building A: a) filtration $X1$, b) filtration $Y1$

a)

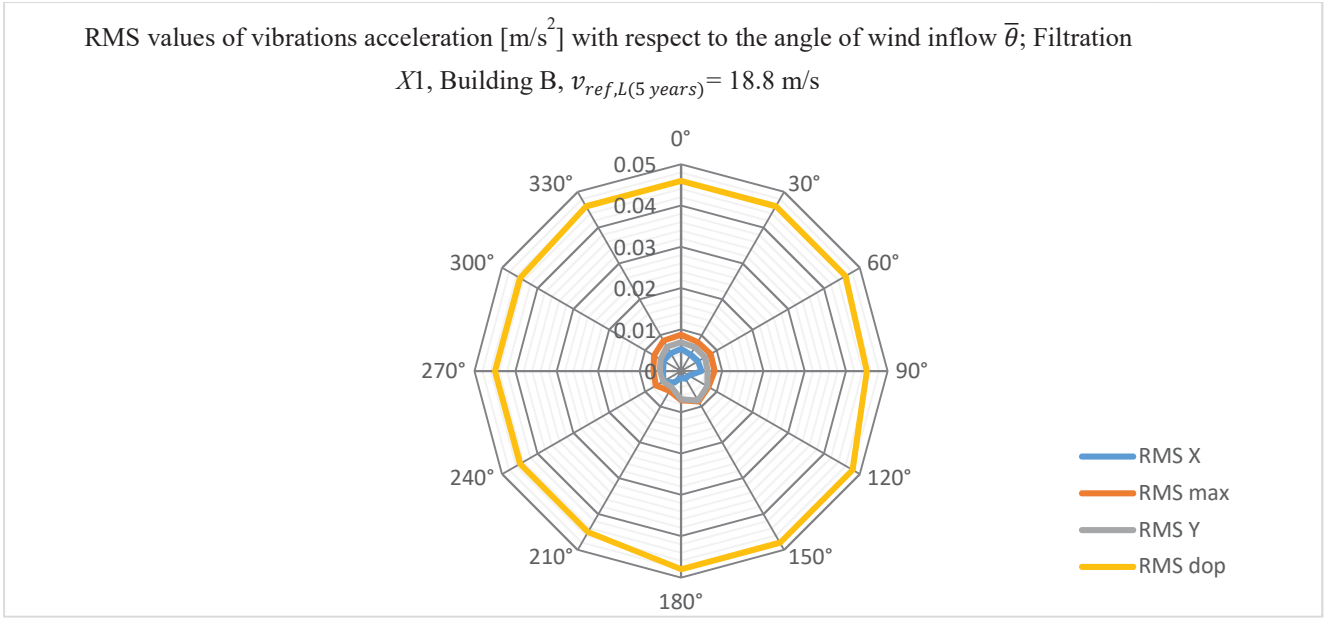

b)

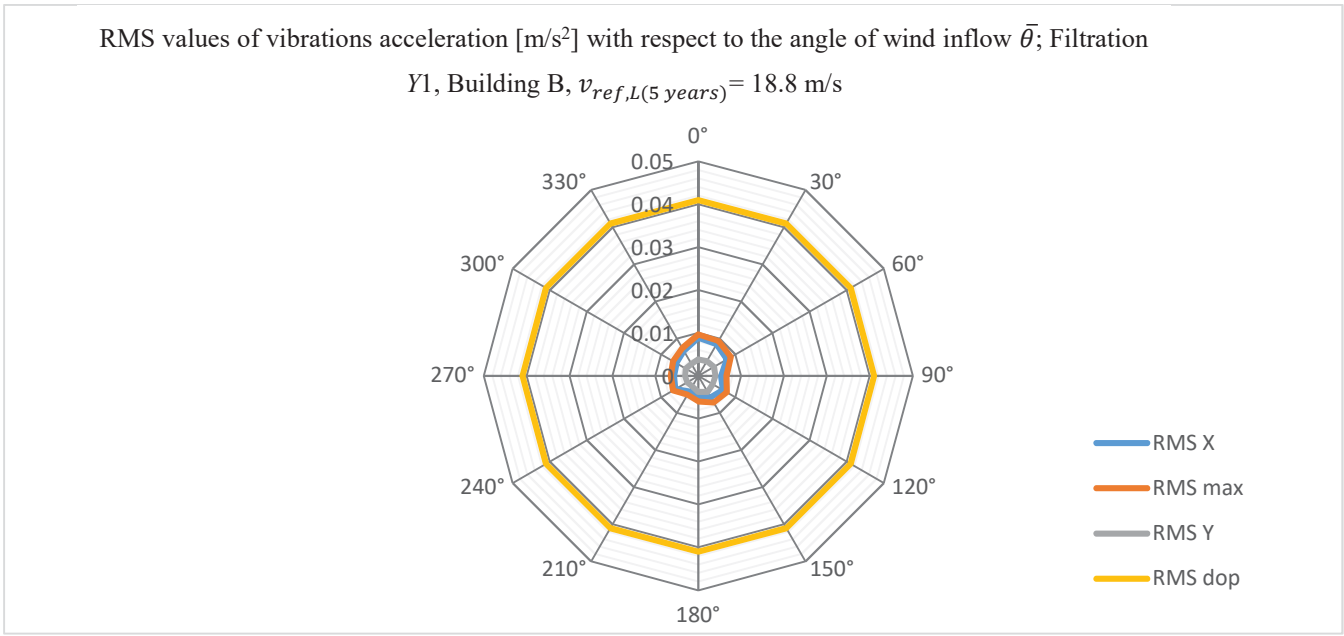

Figure 14. RMS values of vibrations acceleration due to vibration comfort of residents of building B: a) filtration $X1$, b) filtration $Y1$

3.2 Results analysis and evaluation of vibrational comfort

RMS values of vibrations acceleration meet the requirement of vibration comfort in all considered cases:

$$RMS_{max} \leq RMS_{lim}$$

which proves there is sufficient stiffness of the analysed buildings.

It should be mentioned that one can observe unevenness of vibrations level with respect to the angle of wind inflow in the Figure 5 and 6. It may be the result of significant aerodynamic

interference appearing between the analysed buildings and the neighbouring buildings (mainly from the east). However, the observed phenomena are not dangerous for the analysed buildings.

It can be concluded that the stiffness of the building is sufficient and the building meets requirements of vibrational comfort.

4 CONCLUSIONS

The proposed method allowed for obtaining reliable results, which could be implemented in practical engineering design. Combining the deeply developed mathematical model based on similarity criteria with tests in wind tunnel on physical models proved to be a good solution of the problem. The authors are planning to extend this approach in further works by also including the torsional mode of vibrations along with two basic axial ones. In this case the torsional frequency was much higher, but in taller slender buildings it also plays an important role in the evaluation of the vibrations as it can have values which are even below 1 Hz.

The obtained results are what can be expected for buildings of this height and massing. The problems with vibrational comfort of building's occupants occur mostly in taller buildings with lower natural frequencies. In this case, there clearly should be no problem with harmful wind-induced vibrations (in light of employed evaluation criteria) as the measured and calculated values are much below the limit thresholds. However, the buildings – due to their regular shape and similarity – provided to be a good way of validating the used method. Furthermore, the differences of vibration acceleration RMS values, which can be noticed between Fig. 13 and Fig. 14 for each of the buildings, highlight the significant role of aerodynamic interference of surrounding buildings. The location between two other tall buildings (comp. Fig. 10) of building B seems to be having a significant impact on the values of its vibrations along *X* axis, which are considerably smaller than what can be observed for building A.

5 ACKNOWLEDGMENTS

The authors acknowledge the support of the PROM programme no.PPI/PRO/2019/1/00018/U/00001 which is co-financed by the European Social Fund under the Knowledge Education Development Operational Programme.

REFERENCES

[1] Irwin A. ISO/6897 91983: *Guide to the Evaluation of the Response of Occupants of Fixed Structures, Especially Buildings and Off-shore Structures, to Low-frequency Horizontal Motion* (0.063 *to* 1 *Hz*), 1983.

[2] Ciesielski R., Flaga A.: *Evaluation of the level of the perceptibility of low frequency* ($f \leq 1\ Hz$) *horizontal vibrations by occupants with the consideration of new ISO standards*. Polish Science Academy, Cracow Department, Commission of Civil Engineering, 1987, 5-19 [in Polish].

[3] Flaga A.: *Wind Engineering. Fundamentals and Applications*, Arkady, Warsaw 2008 [in Polish].

[4] PN-EN 1991-1-4. *Eurocode* 1 – *Actions on structures – Part* 1-4: *General actions – Wind Actions*.

[5] Council on Tall Buildings – Committee 24: *Stiffness, Deflections and Cracking, Charter CB*-9, vol. CB of Monograph on Planning and Design of Tall Building. ASCE, New York, 1978.

EURODYN 2020
XI International Conference on Structural Dynamics
M. Papadrakakis, M. Fragiadakis, C. Papadimitriou (eds.)
Athens, Greece, 23–26 November 2020

WIND TUNNEL TESTS ON MOTION-INDUCED VORTEX VIBRATION

Kazutoshi Matsuda[1], Kusuo Kato[2] and Nade Cao[3]

Department of Civil Engineering and Architecture, Kyushu Institute of Technology
1-1, Sensui-cho, Tobata-ku, Kitakyushu, Fukuoka 804-8550 JAPAN
[1]e-mail: matsuda@civil.kyutech.ac.jp
[2]e-mail: kato.kusuo78o@mail.kyutech.jp
[3]e-mail: cao.nade133@mail.kyutech.jp

Keywords: Motion-induced vortex vibration, Wind tunnel tests, Separated vortex from leading edge, Secondary vortex at trailing edge, Spring-supported tests, Flow visualization tests

Abstract. *In 2009, a crack was discovered in the bracing member around the intermediate pier of Ikitsuki Bridge, a truss bridge in Nagasaki Prefecture, Japan. As a result of a field oscillation measurement by Nagasaki University, the main cause of the crack was identified as the Kármán vortex-induced vibration. However, aerodynamic vibrations were also observed even in the wind speed range lower than the resonance wind speed of the Kármán vortex-induced vibration. Conventionally, according to the result of a wind tunnel test using side ratios of B/D=2.0-8.0 (B: along-wind length, D: cross-wind length), the motion-induced vortex vibration caused by unification of the separated vortex from leading edge and the secondary vortex at trailing edge was recognized. However, considering the fact that the side ratio of the section of the bracing member of Ikitsuki Bridge is B/D=1.18, there has been a little past research on motion-induced vortex vibration on a rectangular cross section of B/D of less than 2. Therefore, the authors moved forward with a research of the motion-induced vortex vibration, focusing on the rectangular cross sections with small side ratios including B/D= 1.18. In order to clarify the generation of motion-induced vortex vibration, a spring-supported test and a smoke flow visualization test were conducted on the said cross sections. A possibility was shown that without the formation of the secondary vortex at trailing edge, a motion-induced vortex vibration might occur. Based on the wind tunnel test results, this research aimed to verify whether or not the secondary vortex at trailing edge is essential for the generation of motion-induced vortex vibration. As a result, it was found that it is considered that the secondary vortex at trailing edge is not always necessary not only for rectangular cross-sections with less than a side ratio of B/D=2, but also for a cross section similar to the rectangular cross section at both small amplitude range at the onset reduced wind speed of motion-induced vortex vibration and a comparatively large amplitude range where the maximum response amplitude of motion-induced vortex vibration occurs.*

1 INTRODUCTION

The vortices separated from rectangular cross sections are broadly classified into Kármán vortices and motion-induced vortices (separated vortices from leading edge) [1, 2]. The former are those that are accompanied by the interferences of two separated shear layers at both the top and bottom surfaces of the structures. The latter are the ones that are shedding separately from the leading edges of the top and bottom surfaces caused by the separated shear layers at the top and bottom surfaces excited alternately due to the vibration of the rectangular cross section. The vibration caused by the latter vortices was found in the past wind tunnel tests [3, 4]. The vibration is known as either motion-induced vortex vibration [1, 2] or impinging-shear-layer instability [5-8]. The onset wind speed of this vibration depends on the side ratio of the rectangular cross section and this relation was schematically clarified [1, 8]. The mechanisms of the motion-induced vortex vibration of the rectangular section and H-shaped section cylinders were also revealed [9-12]. This research is involved in the motion-induced vortex vibration generated in a bracing member of a real truss bridge in Japan.

In 2009, Ikitsuki Bridge, a truss bridge in Nagasaki Prefecture with a center span length of 400 m, was discovered to have a crack in the bracing member of the bridge [13]. As a result of the subsequent vibration measurement at the site, the main cause of the crack was identified as Kármán vortex-induced vibration. However, vibrations were also observed in the wind speed range of 7-8 m/s, which was lower than the resonance wind speed of Kármán vortex-induced vibration. Conventionally, according to the results from a wind tunnel test using a side ratio of B/D=2-8, the motion-induced vortex vibration was confirmed [1]. However, the side ratio of the section of the bracing member is B/D=1.18, and there has been a little past research on motion-induced vortex vibration on a rectangular cross section of B/D of less than 2. Therefore, in the past research, a spring-supported test was carried out targeting a rectangular cross section of B/D=1.18. Furthermore, unsteady aerodynamic lift measurement and flow field visualization were performed and the results of the spring-supported test were discussed. It was found in the past research that it is considered that the secondary vortex at trailing edge is not always essential for the generation of the motion-induced vortex vibration for the cross section of B/D=1.18 at the onset reduced wind speed region.

The purpose of this research is to further assure the conclusions of past research. Specifically, in this research, the necessity of a secondary vortex at trailing edge not only at the onset reduced wind speed region, but also at the reduced wind speed region where the maximum response amplitude of motion-induced vortex vibration occurs were discussed through spring-supported tests and flow visualization tests using the models of three kinds of cross-sectional shapes where a secondary vortex at trailing edge is considered less likely to occur.

2 PAST RESEARCH RESULTS

Figure 1 shows the result of the spring-supported test of the cross section of B/D=1.18 for an angle of attack of 0 degrees [14]. Vibrations were confirmed from the neighborhoods of reduced wind speed Vr=2 and 8. Because the reduced wind speed at motion-induced vortex vibration is calculated as Vr=1.67B/D=1.67×1.18=2.0 [1], vibrations around Vr=2 were considered to be motion-induced vortex vibrations. The effects of the existence or non-existence of flange on the maximum response amplitude of motion-induced vortex vibration are extremely small.

The Strouhal number measured on the cross-section with flanges was St=0.124 [14]. Its inverse number is the critical reduced wind speed of the beginning of the Kármán vortex-induced vibration. In other words, because Vr=1/St=1/0.124=8.1, a vibration beginning in the neighborhood of a reduced wind speed of 8 can be judged as Kármán vortex-induced vibra-

tion. However, from the fact that the Scruton number in this experiment's case was small at *Sc*=1.32, it was found that Kármán vortex-induced vibration was changed to a galloping along with the increase in wind speed.

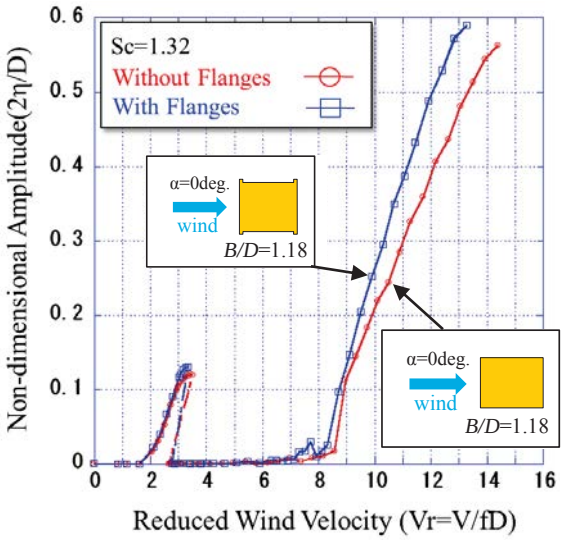

Figure 1: Spring-supported test result (*B/D*=1.18, angle of attack, α=0 deg.) [14]

Figure 2 shows unsteady aerodynamic lift coefficients $C_{L\eta i}$ in the wind speed range of *Vr*=0-5. $C_{L\eta i}$ in the ranges of the wind speed of motion-induced vortex vibration are positive values and they correspond to the responses in Figure 1. This shows the same tendency as the result that was confirmed by Yagi et al [15] that unsteady aerodynamic force coefficient H_1^* of rectangular cross-section with a side ratio of *B/D*=1 becomes a positive value in the neighborhoods of *Vr*=1.67*B/D*=1.67 and *Vr*=1/*St*. Furthermore, Nakamura and Mizota suggested the existence of low speed instability from the results of measuring unsteady aerodynamic lifts using a rectangular cross section of *B/D*=1 [16,17].

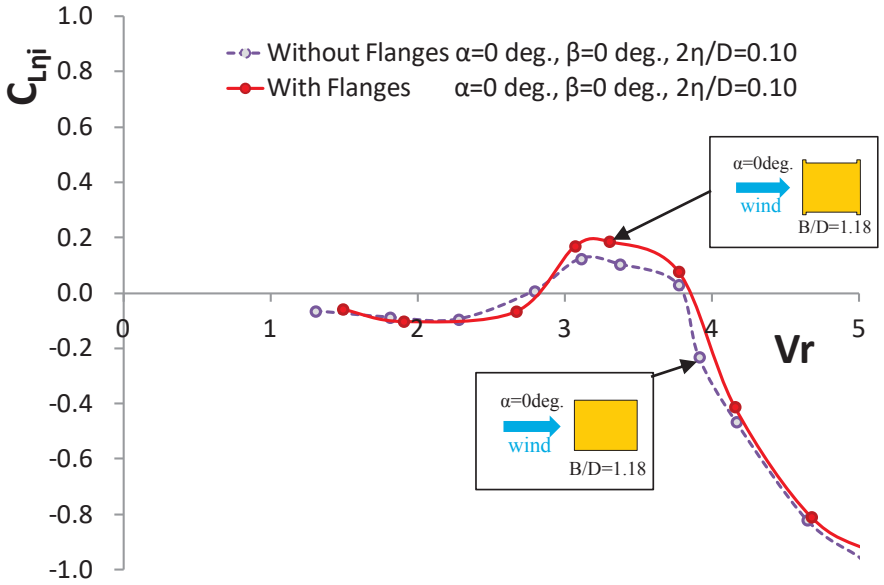

Figure 2: Unsteady aerodynamic lift coefficients [14]

Figures 3(a) shows the relation between the amplitude of forced-oscillation and the generation probability of the secondary vortex at trailing edge, regarding a model of B/D=1.18. The generation probability of the secondary vortex at trailing edge is defined as (the number of secondary vortex at trailing edge/20) ×100(%). Figures 3(b) shows the relation between reduced wind speed, Vr and non-dimensional double amplitude, $2\eta/D$ which is obtained on a time-averaged basis. Figures 3(c) shows the results of the flow visualizations. Additionally, the generation of the secondary vortex at trailing edge for the model with a side ratio of B/D=1.18 is usually recognized when the amplitude of oscillation is more than $2\eta/D$=0.05, shown in Figure 3(a). However, according to the result of the spring-supported test of this model, shown in Figure 3(b), the motion-induced vortex vibration was observed to form in the amplitude below $2\eta/D$ =0.05 at a reduced wind speed of Vr=2.0. There was a hysteretic behavior observed in between Vr=2.6 and Vr=3.3.

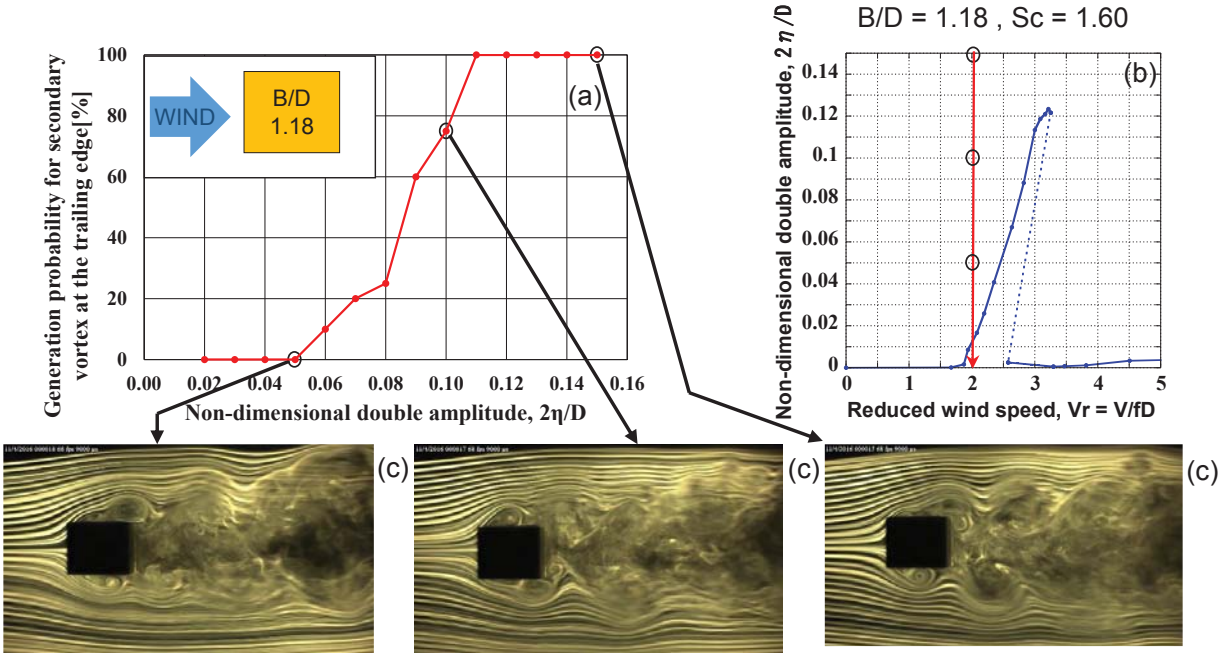

Figure 3: B/D=1.18, (a) Generation probability for secondary vortex at trailing edge at Vr=2.0, (b) Relation between Vr and $2\eta/D$, (c) Flow visualization test results of forced-oscillating model at the top displacement in $2\eta/D$=0.05 and 0.15, at the bottom displacement in $2\eta/D$=0.10 [18].

3 EXPERIMENTAL SETUP

3.1 Section models

Cross-sectional shapes where a secondary vortex at trailing edge is considered not to occur or to be less likely to occur during vibration were selected, as shown in Figure 4. The gradient θ was provided in a mainstream direction at the downstream side of a rectangular cross-section of a side ratio of B/D=2, and θ was changed to θ=5 degrees, 10 degrees and 15 degrees. In addition to that, a rectangular cross section with a side ratio of B/D=2 was added for a spring-supported test for comparison, and the wind-tunnel tests were conducted in a smooth flow for four cross-sections in total.

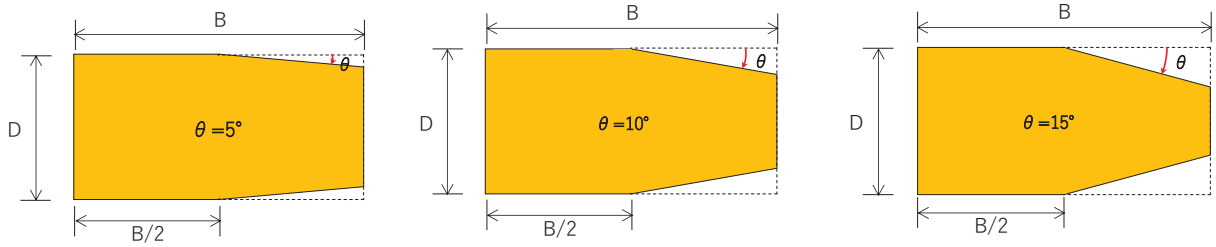

Test	B(mm)	D(mm)
Spring-supported tests	180	90
Flow visualization tests	40	20

Figure 4: Model cross sections.

3.2 Spring-supported tests

The spring-supported test was conducted in the middle-sized wind tunnel (cross-section: 1.8m high×0.9m wide) at Kyushu Institute of Technology. Main experimental conditions for the model were: mass per unit length=2.82-5.43 kg/m, natural frequency of heaving vibration=5.25-7.29 Hz, logarithmic decrement of structural damping=0.004-0.008 and Scruton number=4.7. Table 1 shows the conditions for the spring-supported tests. Figure 5 shows a photo of the section model installed in the wind tunnel.

Table 1: Spring-supported test conditions.

θ (deg.)	D (m)	Air density ρ (kg/m^3)	Natural frequency f (Hz)	Mass per unit length m (kg/m)	Logarithmic decrement δ	Scruton Number $Sc=2m\,\delta/\rho D^2$
0*)	0.09	1.21	5.25	5.43	0.00428	4.75
5		1.19	7.23	2.87	0.00791	4.73
10		1.20	7.27	2.83	0.00812	4.73
15		1.19	7.29	2.82	0.00796	4.67

*) Rectangular cross section of B/D=2

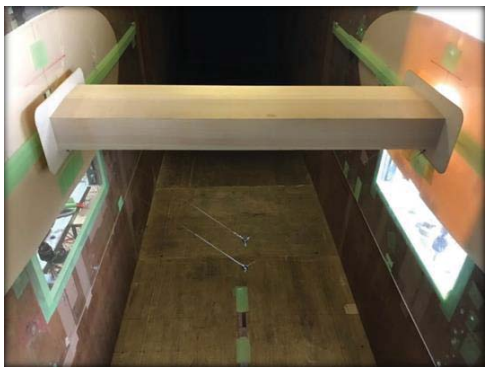

Figure 5: Section model for a spring-supported test mounted in Kyushu Institute Technology wind tunnel.

3.3 Flow visualization tests

Figure 6 shows the experimental system of the flow visualization test. The flow field visualizations around the model during forced-oscillating times were conducted using a small-sized wind tunnel (0.4m high×0.4m wide) at Kyushu Institute of Technology. It was considered that the wind speeds in the wind tunnel of V=0.6-1.0 m/s are good for visualization, so that eventually V=0.6 m/s was selected. As for the forced-oscillating amplitude η, because the

peak of aerodynamic response in the range of low wind speed is $2\eta/D$=0.30 approximately, the non-dimensional double amplitudes were set up as $2\eta/D$=0.02-0.35 in accordance with the spring-supported test results. Figures 7 and 8 show the forced oscillation system and the installation status of a model, respectively. Table 2 shows the conditions for the flow visualization tests.

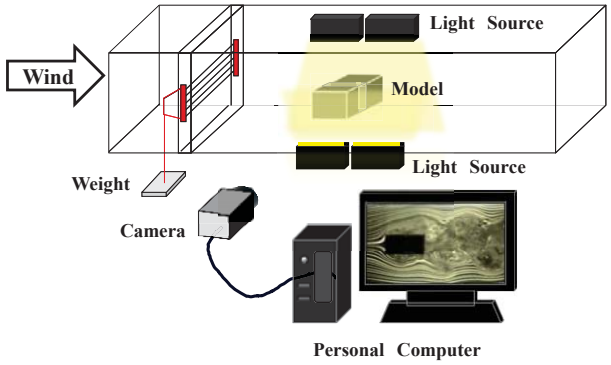

Figure 6: Flow visualization test system.

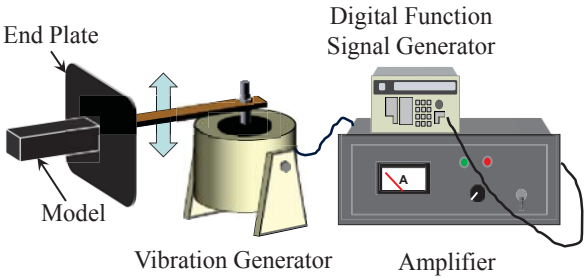

Figure 7: Forced oscillation system for flow visualization tests.

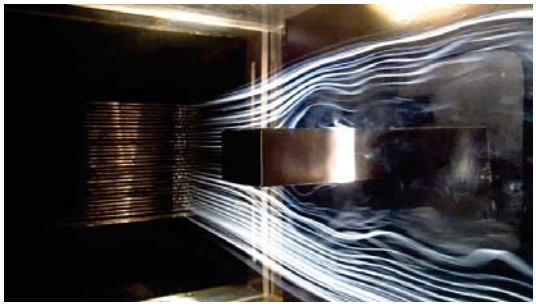

Figure 8: Section model for flow field visualization test mounted in Kyushu Institute Technology wind tunnel.

Table 2: Flow visualization test conditions

θ (deg.)	Reduced wind speed $Vr=V/fD$	Frequency of forced oscillation method f (Hz)	Forced-oscillating non-dimensional amplitudes $2\eta/D$	Frame rate (fps)
5	3.9	7.69	0.02-0.30 (every 0.02 intervals), 0.35	69.2
	5.2	5.77		51.9
10	4.0	7.50		67.5
	5.2	5.77		51.9
15	4.6	6.52		58.7
	5.2	5.77		51.9

V: Wind speed, V=0.6m/s

4 EXPERIMENTAL RESULTS AND DISCUSSION

Figure 9 shows the results of the spring-supported tests of the three kinds of cross-sections and a rectangular cross-section of *B/D*=2. The onsets of vortex-induced vibrations were confirmed at the approximate reduced wind speed *Vr*=4.0, in all cross-sections. These vibrations are considered to be motion-induced vortex vibrations because the onset reduced wind speed of the motion-induced vortex vibration of a rectangular cross-section of a side ratio, *B/D* = 2, is approximately *Vr* =1.67*B/D*=3.34, which is close to the values of the onset wind speeds of these vortex-induced vibrations. In the four kinds of cross-sections, it was confirmed that Kármán vortex vibrations were generated at the approximate reduced wind speed *Vr*=13, and shifted to galloping along with wind speed increase. It was confirmed that the maximum amplitudes of the three kinds of motion-induced vortex vibrations on the cross sections which have the gradient θ are just about the same even if the gradient θ of the downstream side cross section changes. It was confirmed that in the cross section of θ = 15 degrees, compared with other cross-sections, the onset wind speed range of motion-induced vortex vibration shifts to the side of high wind speed.

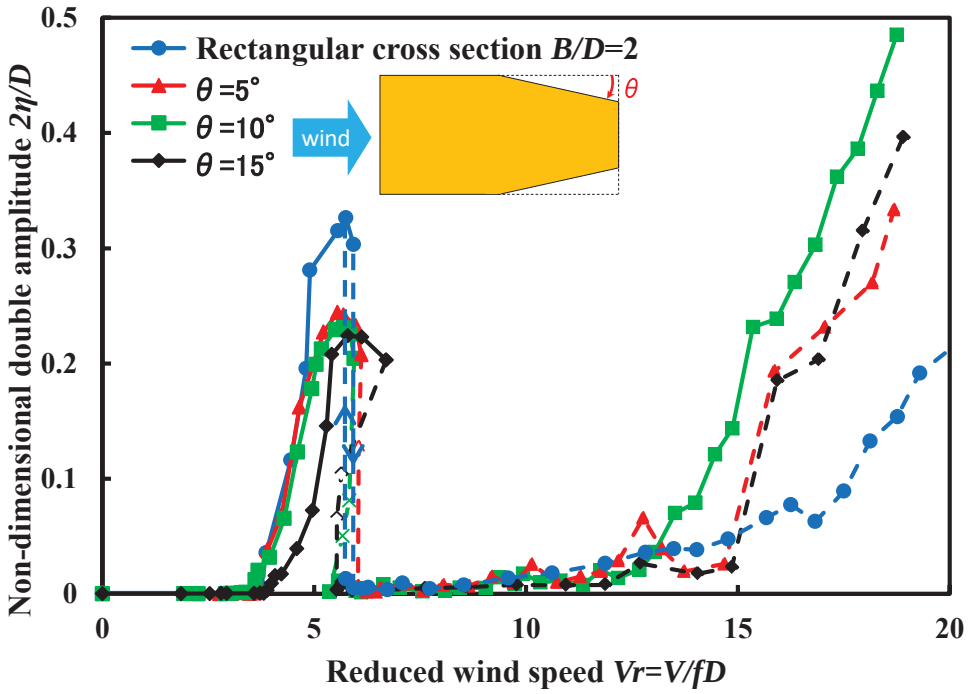

Figure 9: Spring-supported test result (angle of attack: α=0 deg., Scruton number: *Sc*=4.7).

4.1 Onset reduced wind speed region

Figure 10 shows the measuring results of the generation probability of a secondary vortex at trailing edge of the three kinds of cross-sections having the gradient θ and a rectangular cross-section with a side ratio of *B/D*=2 [19] at the onset reduced wind speed of motion-induced vortex vibration. Figure 11 shows the visualized images of the flows at the neighborhood of the onset reduced wind speed of motion-induced vortex vibration. From Figure 10, it was confirmed that a secondary vortex at trailing edge at the onset reduced wind speed in the three cross-sections, compared with a rectangular cross-section of *B/D*=2, is less likely to occur if the gradient θ becomes larger. Furthermore, in the cross section of θ=15 degrees, almost no generation of a secondary vortex at trailing edge was confirmed until non-dimensional double amplitude $2\eta/D$=0.35. Although from Figure 11, the generation of a secondary vortex

at trailing edge was confirmed at non-dimensional double amplitude $2\eta/D$=0.20, in the cross sections of θ =5 degrees and 10 degrees, no generation of a secondary vortex at trailing edge was confirmed in the cross section of gradient θ=15 degrees. Therefore, it was confirmed that the larger the gradient θ is, the less the secondary vortex at trailing edge is likely to occur. By comparing the results of the spring-supported tests of Figure 9 and those of the generation probability of a secondary vortex at trailing edge at the approximate onset reduced wind speed of motion-induced vortex vibration of Figure 10, it was confirmed that no secondary vortex at trailing edge was generated in all three kinds of cross sections having the gradient θ at the small amplitude range of $2\eta/D \leqq 0.04$ at the onset of motion-induced vortex vibration. From this fact, as with the case of the experimental result of a rectangular cross section of a side ratio B/D = 2 of the past research [19], a secondary vortex at trailing edge is not always necessary for the onset of motion-induced vortex vibration relating to the three kinds of cross sections having the gradient θ.

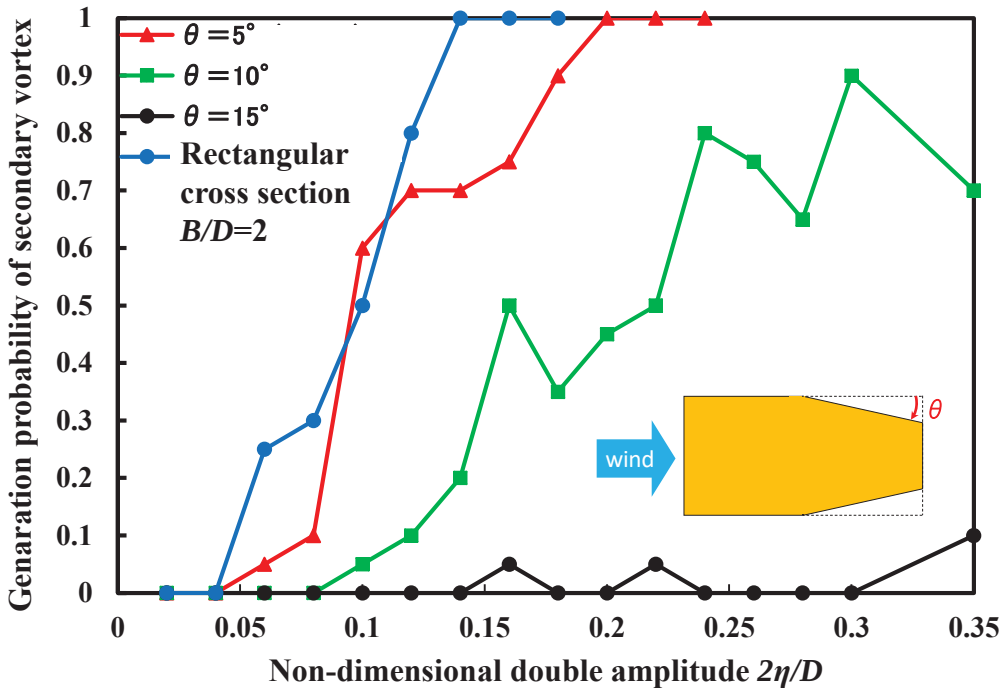

Figure 10: Generation probability for secondary vortex at the trailing edge at onset reduced wind speed region Vr=3.9-4.6

4.2 Reduced wind speed region where the maximum response amplitude of motion-induced vortex vibration occurs

Figure 12 shows the results of the measurements of the generation probability of a secondary vortex at trailing edge of the three kinds of cross-sections having the gradient θ and a rectangular cross section with a side ratio of B/D=2 [19] at the reduced wind speed of Vr=5.2 where the maximum response amplitude of motion-induced vortex vibration occurs. Figure 13 shows the visualized images of the flows at the reduced wind speed with maximum amplitude of motion-induced vortex vibration. As shown in Figure 12, it was confirmed that as with the case of the generation probability of a secondary vortex at trailing edge at the onset wind speed, the greater the gradient θ is, the less the secondary vortex at trailing edge is likely to be

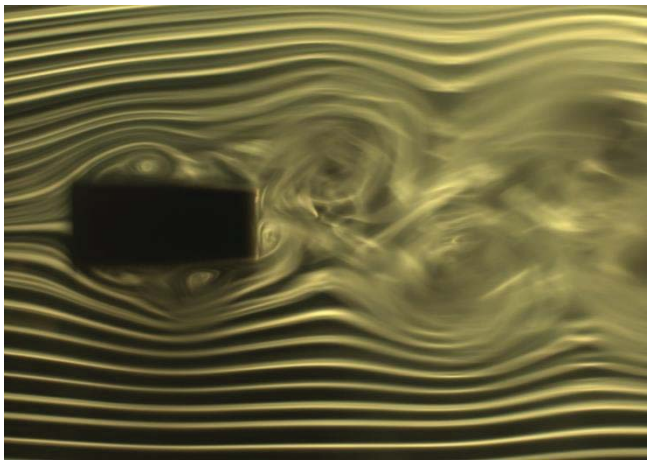

(a) θ = 5 degrees, Vr=3.9, generation probability=100%

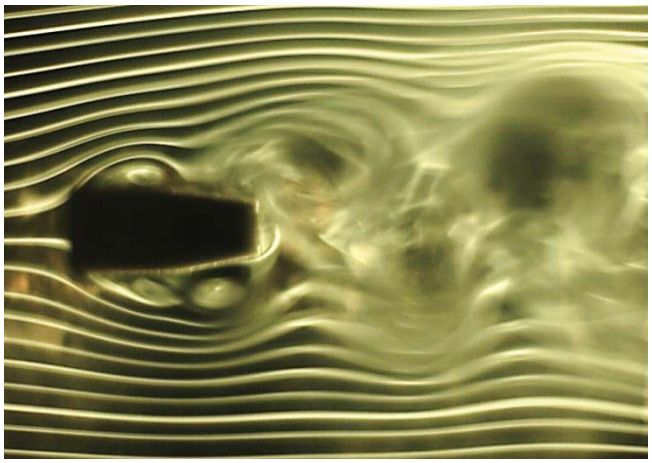

(b) θ = 10 degrees, Vr=3.9, generation probability=45%

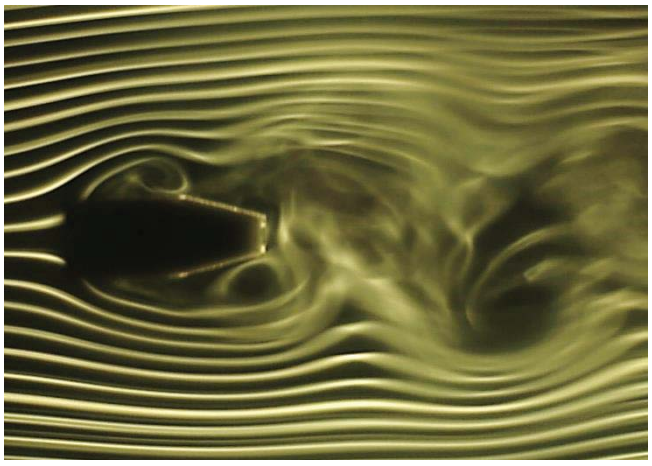

(c) θ = 15 degrees, Vr=4.6, generation probability=0%

Figure 11: Flow visualization test results at onset reduced wind speed region ($2\eta/D$ = 0.20 at the maximum downward speed).

generated. From the visualized images of the flows shown in Figure 13, the generation of a secondary vortex at trailing edge could be confirmed at trailing edge of a cross section in each cross section of gradient θ= 5 degrees and 10 degrees; however, that could not be confirmed in the case of the cross section of gradient θ=15 degrees. In the cross sections of gradient θ=10 degrees and θ=15 degrees, the generation probability of a secondary vortex at trailing edge was 15% at maximum at the non-dimensional double amplitude range less than $2\eta/D$ = 0.26, where motion-induced vortex vibration occurred, it was confirmed that a secondary vortex at trailing edge is not generated strongly enough.

Furthermore, the maximum amplitude of each motion-induced vortex vibration in the cross section of gradient θ=5 degrees where the generation probability of a secondary vortex at trailing edge at the non-dimensional double amplitude $2\eta/D$=0.26 is 60% and in the cross-section of θ=15 degrees where the generation probability of a secondary vortex at trailing edged at the non-dimensional double amplitude $2\eta/D$=0.26 is 0% is approximately the same. From this fact, it is considered that after the onset of motion-induced vortex vibration, a secondary vortex at trailing edge does not contribute enough to the exciting force of motion-induced vortex vibration at the stage where the maximum response amplitude of motion-induced vortex vibration occurs.

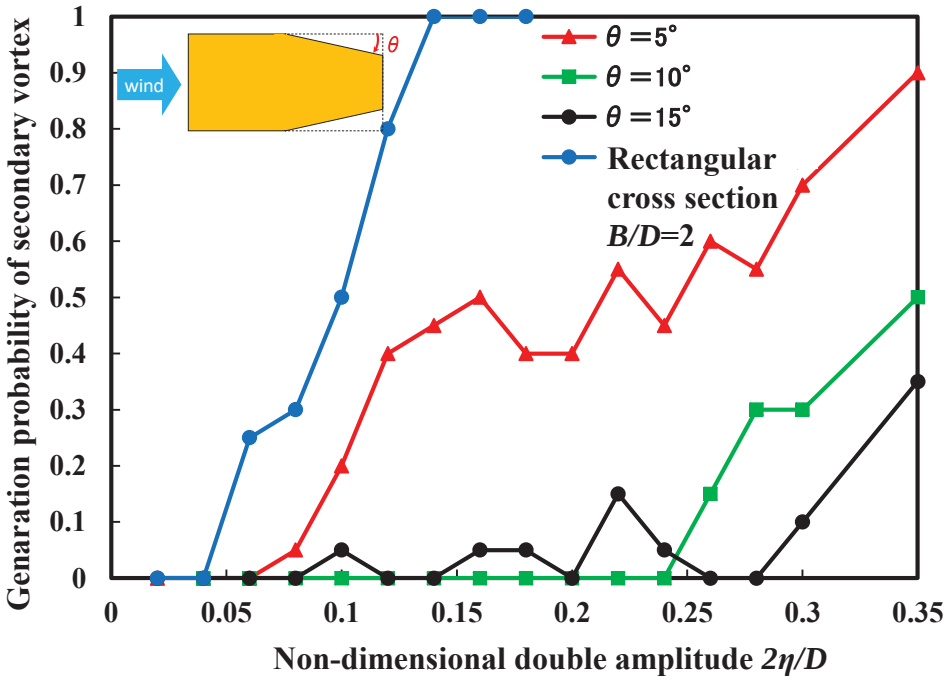

Figure 12: Generation probability for secondary vortex at the trailing edge at reduced wind speed region where maximum response amplitude of motion-induced vortex vibration occurs, Vr=5.2

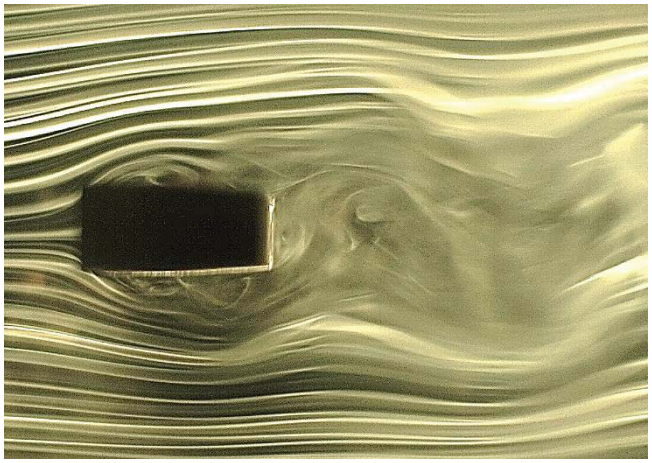

(a) θ = 5 degrees, Vr=5.2, generation probability=60%

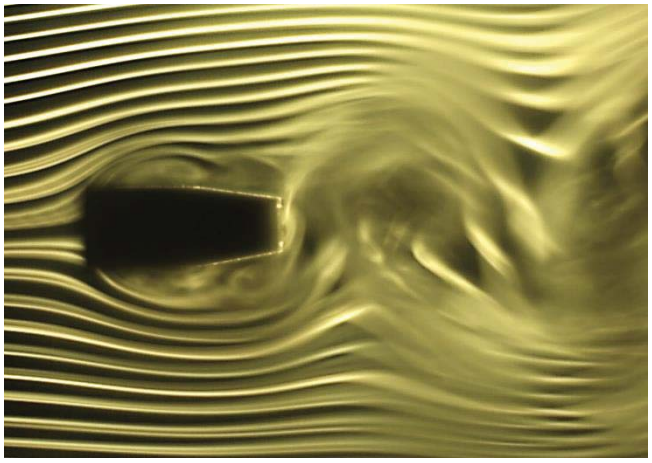

(b) θ = 10 degrees, Vr=5.2, generation probability=15%

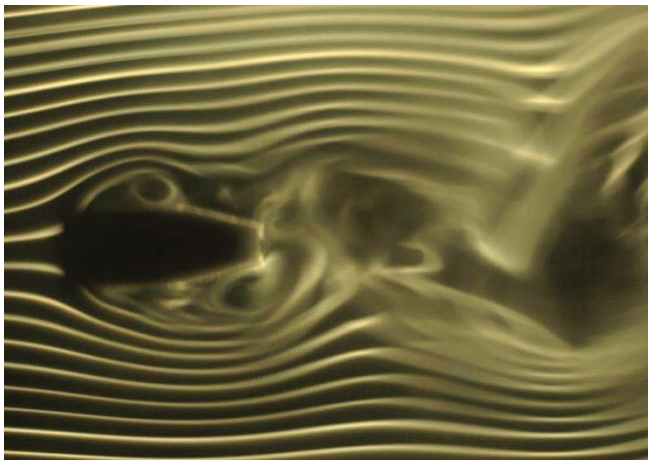

(c) θ = 15 degrees, Vr=5.2, generation probability=0%

Figure 13: Flow visualization test results at reduced wind speed region where maximum response amplitude of motion-induced vortex vibration occurs ($2\eta/D$ = 0.26 at the maximum downward speed).

5 CONCLUSIONS

It was found that it is considered that the secondary vortex at trailing edge is not always necessary not only for rectangular cross-sections with less than a side ratio of $B/D = 2$, but also for a cross section similar to the rectangular cross section at both small amplitude range at the onset reduced wind speed of motion-induced vortex vibration and a comparatively large amplitude range where the maximum response amplitude of motion-induced vortex vibration occurs.

ACKNOWLEDGEMENTS

The authors are grateful to Mr. Mitsushi Imamura and Mr. Tomoya Yanase, who carried out wind tunnel tests at Kyushu Institute of Technology.

REFERENCES

[1] N. Shiraishi, M. Matsumoto: On classification of vortex-induced oscillation and its application for bridge structures, *Journal of Wind Engineering and Industrial Aerodynamics*, Vol.14, Nos.1-3, pp.419-430, 1983.

[2] S. Komatsu and H. Kobayashi: Vortex-induced oscillation of bluff cylinders, *Journal of Wind Engineering and Industrial Aerodynamics*, Vol.6, pp.335-362, 1980.

[3] M. Novak: Galloping and vortex induced oscillations of structures, *Proceedings of the Third International Conference on Wind Effects on Buildings and Structures*, Tokyo, Japan, pp.799-809, 1971.

[4] Y. Otsuki, K. Washizu, H. Tomizawa, A. Ohya and K. Fujii: Experiments on the aeroelastic instability of prismatic bars with rectangular sections, *Proceedings of the Third International Conference on Wind Effects on Buildings and Structures*, Tokyo, Japan, pp.891-898, 1971.

[5] D. Rockwell and E. Naudascher: Review- Self-sustaining oscillations of flow past cavities, *Transactions of the ASME, Journal of Fluids Engineering*, Vol.100, pp.152-165, 1978.

[6] Y. Nakamura, Y. Ohya and H. Tsuruta: Experiments on vortex shedding from flat plates with square leading and trailing edge, *Journal of Fluid Mechanics*, Vol. 222, pp.437-447, 1991.

[7] Y. Ohya, Y. Nakamura, S. Ozono, H. Tsuruta and R. Nakayama: A numerical study of vortex shedding from flat plates with square leading and trailing edges, *Journal of Fluid Mechanics*, Vol. 236, pp.445-460, 1992.

[8] E. Naudascher and Y. Wang: Flow-induced vibrations of prismatic bodies and grids of prisms, *Journal of Fluids and Structures*, Vol.7, pp.341-373, 1993.

[9] M. Matsumoto, N. Shiraishi, H. Shirato, S. Stoyanoff, and T. Yagi: Mechanism of, and turbulence effect on vortex-induced oscillations for bridge box girders, *Journal of Wind Engineering and Industrial Aerodynamics*, Vol. 49, Issues 1-3, pp.467-476, 1993.

[10] Y. Kubo, K. Hirata and K. Mikawa: Mechanism of aerodynamic vibrations of shallow bridge girder sections, *Journal of Wind Engineering and Industrial Aerodynamics*, Vol.41-44, pp.1297-1308, 1992.

[11] R. Mills, J. Sheridan, K. Hourigan and M.C. Welsh: The mechanism controlling vortex shedding from rectangular bluff bodies, *Proceedings of the twelfth Australasian Fluid*

Mechanics Conference, Sydney, pp.227-230, 1995.

[12] R. Mills, J. Sheridan and K. Hourigan: Particle image velocimetry and visualization of natural and forced flow around rectangular cylinders, *Journal of Fluid Mechanics*, Vol. 478, pp.299-323, 2003.

[13] S. Nakamura, K. Shintomi, S. Tanaka, T. Nishikawa and T. Okumatsu: A survey on wind conditions at the Ikitsuki Bridge, *Proceedings of the 67th annual meeting of JSCE*, No.67, I-323, pp.645-646, 2012. (in Japanese)

[14] K. Matsuda, K. Kato, K. Hisadomi and K. Harada: Low speed instability of two-dimensional rectangular prisms, *Proceedings of the ASME 2013 Pressure Vessels and Piping Conference (PVP2013)*, 97353, 2013.

[15] T. Yagi, K. Shinjo, S. Narita, T. Nakase and H. Shirato: Interferences of vortex sheddings in galloping instability of rectangular cylinders, *Journal of Structural Engineering*, JSCE, Vol.59A, pp.552-561, 2013. (in Japanese)

[16] Y. Nakamura and T. Mizota: Unsteady lifts and wakes of oscillating rectangular prisms, *Journal of the Engineering Mechanics Division, ASCE*, Vol.101, No.EM6, Proc. Paper 11813, pp.855-871, 1975.

[17] T. Mizota and A. Okajima: Experimental studies of flow patterns around oscillating rectangular prisms and their unsteady aerodynamic forces, *Proceedings of the Japan Society of Civil Engineers*, Vol.327, pp.49-60, 1982. (in Japanese)

[18] K. Matsuda, K. Kato, K. Arise and H. Ishii. Study on the relation between side ratios of rectangular cross sections and secondary vortices at trailing edge in motion-induced vortex vibration, *Proceedings of the ASME 2017 Pressure Vessels & Piping Division Conference*, PVP2017, 65565, 2017.

[19] K. Matsuda, K. Kato, N. Cao and R. Higashimura, Experimental study on the effect of secondary vortices at the trailing edge on motion-induced vortex vibration, *Proceedings of XV Conference of the Italian Association for Wind Engineering*, Napoli, Italy, 10-12 September, 2018.

EURODYN 2020
XI International Conference on Structural Dynamics
M. Papadrakakis, M. Fragiadakis, C. Papadimitriou (eds.)
Athens, Greece, 23–26 November 2020

DYNAMIC STUDY OF PORT CRANES SUBJECTED TO STOCHASTIC WIND ACTIONS

L. Solazzi

Department of Mechanical and Industrial Engineering
University of Brescia
Via Branze, 38 - 25123 Brescia (Italy)
luigi.solazzi@unibs.it

Keywords: container crane, lifting equipment, wind actions, stochastic wind field design, dynamic behavior, dynamic analyses, finite element analysis.

Abstract. *The focus of this research is to evaluate and compare the mechanical behaviour of three different big cranes (low profile container crane, ship to shore container crane and derrick crane) subjected to wind actions, which are schematized in two different ways: the first considering the constant actions over time and the second considering that changing over time. Regarding this second point, it was assumed a Kaimal, Wingaarard, Izumi and Cotè [1] model, and the actions were determined by developing a specific Mathcad program. After a preliminary analytical cranes design, the successive steps regards the solid model and the numerical analyses performed by finite element method. The numerical results show that, if the wind actions were schematized like variable in time, the maximum displacement is greater respect the one obtained with the constant actions. This gain is important and it is not constant, but changes with the cranes type and the geometrical configurations. For low profile container crane, the increment is approximatively three time while for the derrick crane with the arm at 5° position this value is only about 20%. The research is still in progress primarily in order to extend this methodology to other lifting equipment.*

1 INTRODUCTION

The scope of this research is to analyze the dynamical behaviour of three different crane types subjected to wind actions. In particular, the goal of this study is to analyze the wind effects on three different geometrical crane considering different wind actions schematizations.

The cranes can be subjected to many different actions, dead load and inertia actions due to moving loads or crane parts [2,3,4,5,6], moving trolley [7,8], impulse loading [9], wind [10,11,12], earthquake [13,14]. Earthquake actions can be very dangerous, in fact, for example during Kobe earthquake, (17/1/1995) [15, 16] different cranes collapsed causing considerable damage also on the economic point of view. In this case, the principal failure modes for these structures are local or global buckling phenomena.

The wind actions are one of the main load conditions that act on lifting equipment like crane. These actions can lead the structures to collapse (for example due the overturning moment, buckling phenomena local or global, and so on) [17, 18, 19, 20]. In general, and according to the several standards (as, for example, EN 13000), the wind action and the relative load can be estimated assuming a constant force.

The magnitude of this load is correlated to the wind velocity, the area interested by the wind and some aerodynamical coefficients. However, it is important to underline that, compared to the civil structures, the mechanical ones in general are more flexible and composed by many different elements (like beam, or truss elements). Based on this point of view, assuming a constant load action applied to the structure can be unsafe for the structure. For the components, it is important to study the interaction between wind action and the dynamical behaviour of the whole crane or its parts.

In this research three different crane types (low profile container crane with retractable boom, container crane with lift arm and derrick crane) were analyzed in order to study the mechanical behaviour of the structures subjected to stochastic wind load actions.

The reason of this research is to study, evaluate and compare the results obtained by numerical analyses on crane subjected to two different wind loads schematizations i.e. constant and variable in time.

2 WIND ACTIONS

The wind actions applied to the crane produce a force that acts in two directions: one in the wind direction, and one in orthogonal direction (figure 1). The forces intensity can be evaluated by equations1 and 2.

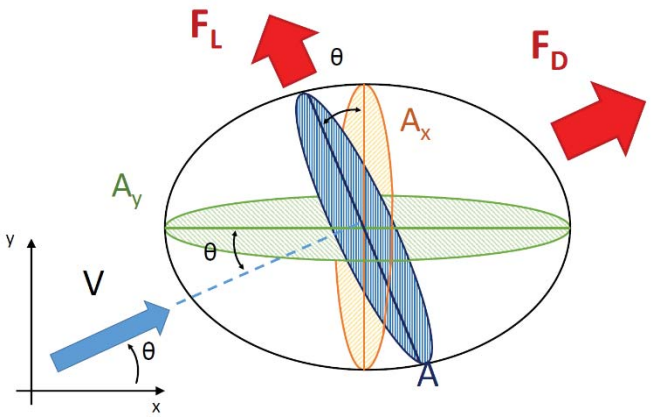

Figure 1: Actions on the structure by wind.

$$F_D = \frac{1}{2}\rho[V(x,y,z,t)]^2 c_D A \quad (1)$$

$$F_L = \frac{1}{2}\rho[V(x,y,z,t)]^2 c_L A \quad (2)$$

Where:
ρ =air density;
$V(x,y,z,t)$=field velocity;
$c_L$and c_D= lift and drag coefficients;
$A = |A_x * \cos\vartheta| + |A_y * \sin\vartheta|$ is area and $\vartheta$is the yaw angle.

The numerical analyses were carried out considers two different wind action schematizations. The first schematization considering the wind action varying in time; the second one considering the action constant over time. In general, the first approach was studied by stochastic method [21, 22, 23].

2.1 Kaimal's model [1.]

The wind field velocity can be expressed by formula (3):

$$V(x,y,z,t) = V_m(z) + v(x,y,t) \quad (3)$$

Where:
$V_m(z)$= is the mean velocity, it is independent of space and time but only varies along the height of the structure (z) by formula (4):

$$V_m(z) = V_g\left(\frac{z}{Zg}\right)^{\alpha} \quad (4).$$

Assuming:
V_g =20 m/s; $Z_g = 7.5\ m$; $\alpha = 1/7$.
$v(x,y,t)$= is the component variable over time i.e. the fluctuating wind speed.

By summarizing as much as possible in [1, 24, 25, 26], the fluctuating part of wind velocity can be evaluated by power spectrum method (point j) (5):

$$S_u(\omega,z) = \frac{1}{2}\frac{1}{2\cdot\pi}\cdot 200\cdot u(z_j)^2\cdot\frac{z_j}{V_m(z_j)}\cdot\frac{1}{\left[1+50\left(\frac{|\omega|z_j}{2\pi V_m(z_j)}\right)\right]^{\frac{5}{3}}} \quad (5)$$

.

With these expression it is possible to evaluate the coherence function between two points and the fluctuating part of the wind speed (v) by formula (6) which consider a random variable in $B(\omega, j, k)$ function.

$$v(j,\frac{t}{\Delta t}) = \mathrm{Re}\left[\sum_{k=0}^{j}\sum_{l=2}^{M} B(\omega,j,k)e^{ilp2\frac{\pi}{2N}}\right] \quad (6)$$

3 NUMERICAL PROCEDURE

For all the cranes analyzed, the main points developed are reported below.

Design a crane considering the "classical" actions: dead load, working load or payload, inertia loads and wind loads. For this point it was assumed a classical structural high strength steel (S460M or S460ML according to European standard EN 10025:2004).

After a preliminary analytical design, a solid model (Solid Works® software) and finite element analyses were carried out (Autodesk Simulation ® software).

Through a specific developed Matchcad ® program, the wind velocity (equation 6), the power spectrum (equations 5) and the wind forces (equations 1 and 2) were evaluated.

Each crane was divided in different sub-structures, characterized by area, position (z), and drag and lift coefficients; on each one the forces calculated at previous point were applied. It is important to underline that the number of sub-structures was chosen considering two parameters i.e. the convergence solution to the maximum crane displacement and the computational cost. In general, each fem model was composed by 5000 quadratic beam elements and by 8000 nodes. The numerical procedure adopted for fem analyses is direct integration method. For this technique, the most important parameter is the delay time between two steps. The value assumed after some iterations in order to evaluate the convergence solution on the maximum displacement is $\Delta t = 0.05s$.

4 LOW PROFILE CONTAINER CRANE

Figure 2 shows the solid crane model; the main crane parameters are: payload=50 t; lifting velocity (without load) =85 m/min; lifting velocity (with load) =35 m/min; maximum height (under spreader) =30 m; overall height =55 m; boom length =80 m.

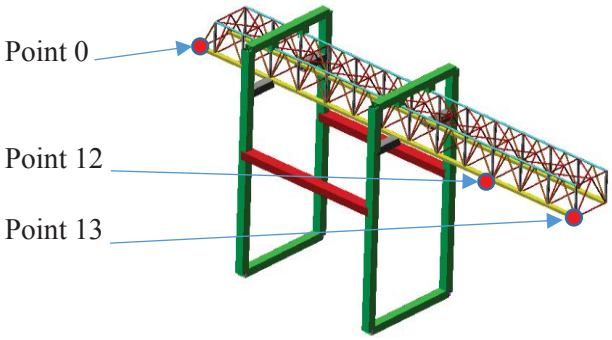

Figure 2: Solid model of low profile container crane with some specific points on main arm.

Figures 3 and 4 show the trend of the wind velocity and the drag and lift forces applied to different points of the crane. Figure 5 shows the crane displacement.

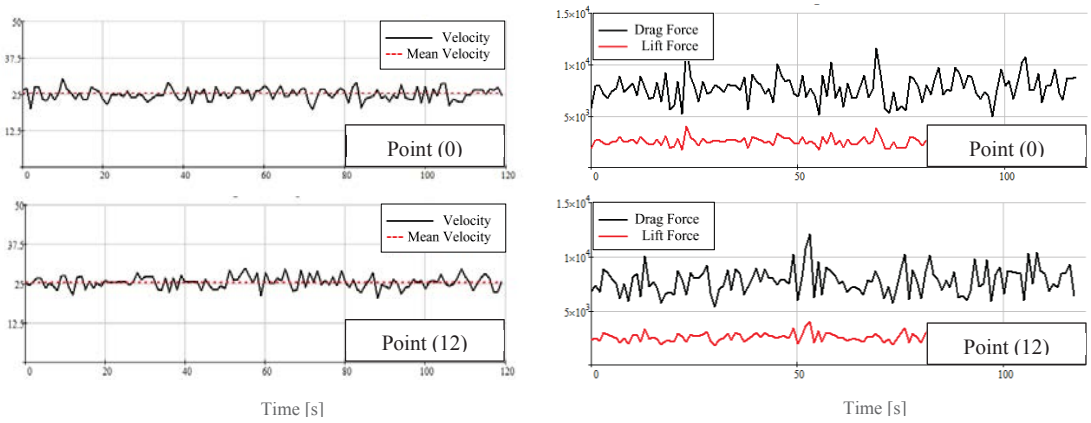

Figure 3 Wind velocity [m/s] and drag and lift forces [N] in different crane points [(0), (12)].

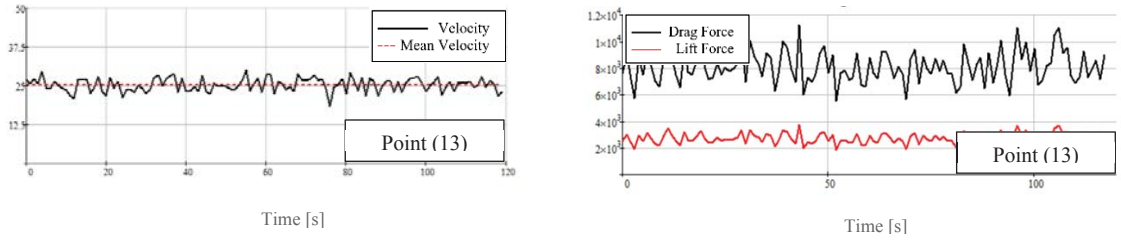

Figure 4 Wind velocity [m/s] and drag and lift forces [N] for the point of crane n°13.

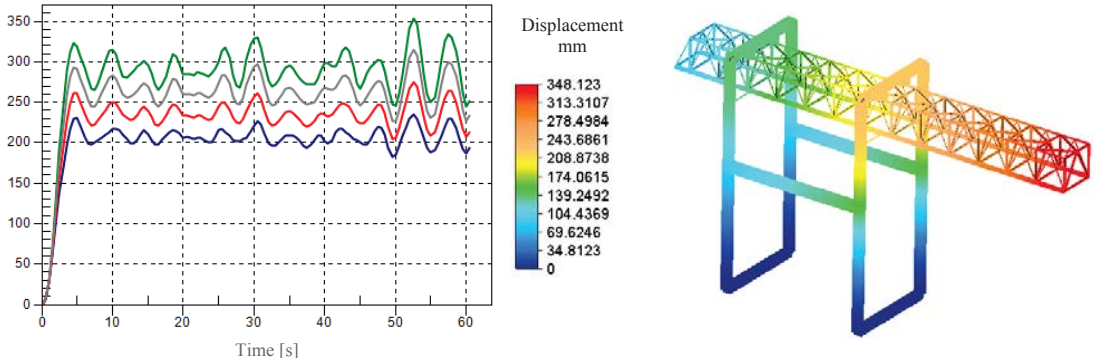

Figure 5 Crane displacement [mm] for low profile container crane (arm at seaside position) subjected to Kaimal wind spectrum actions.

5 CONTAINER CRANE

The main parameters of this crane are payload =45t, total length of the main beam =125 m, and height =74 m. Figure 6 shows the crane solid model and the fem model.

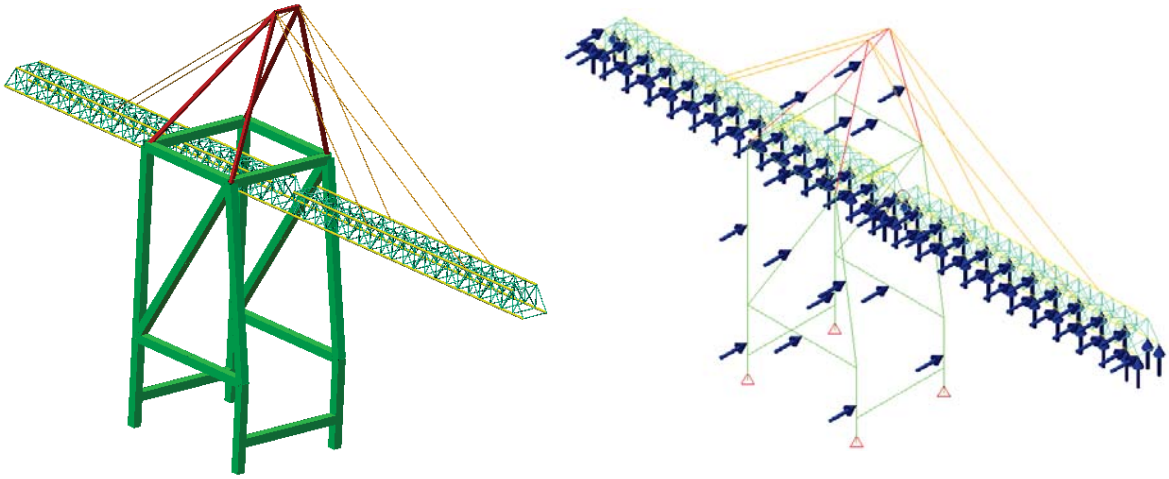

Figure 6 Solid model and fem model for container crane.

Figure 7 shows the crane displacement for different points. It is important to underline that the maximum displacement is located at the arm end and the maximum magnitude is in the wind direction (y direction) i.e. orthogonal to the main beam (the translation in the other direction x and z is very low if comparted with the value in y direction).

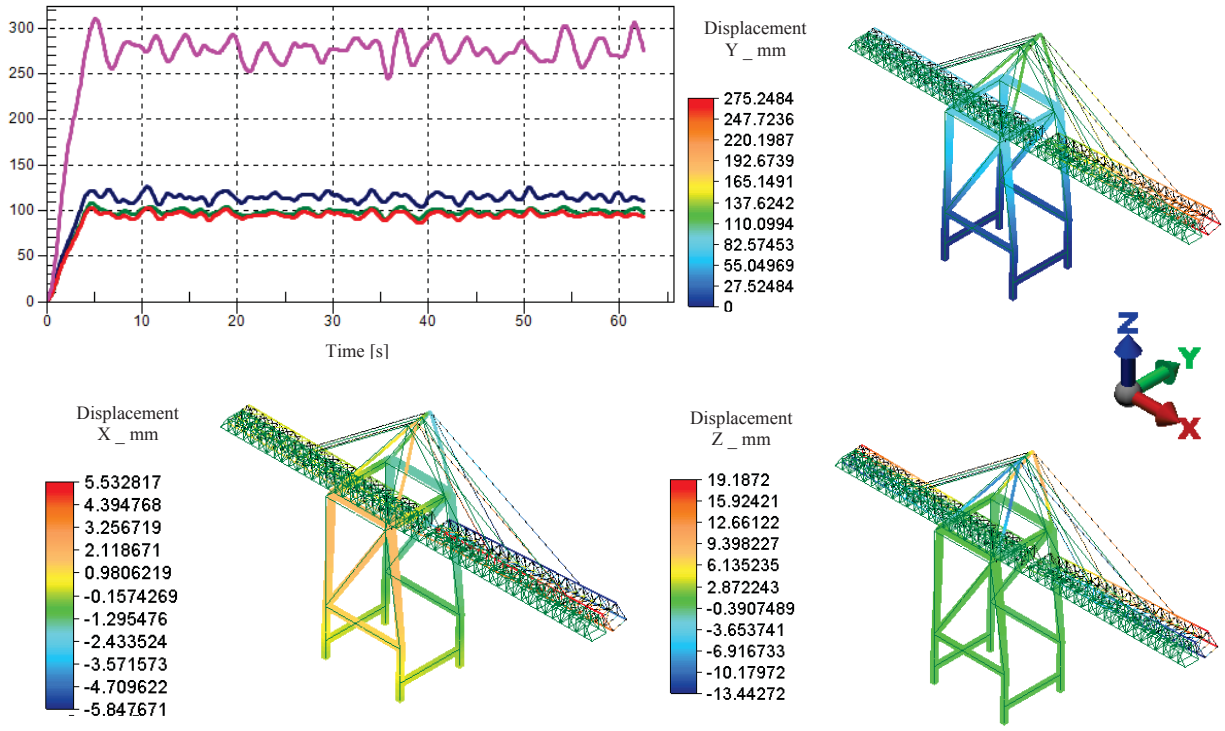

Figure 7 Crane displacements.

6 DERRICK CRANE

The crane parameters considered in this research are an 80-m long arm and a payload equal to 40 t when the inclination of the arm, with respect to the ground, is between 0 ° and 30 °; while the payload equal to 60 t for an inclination of the arm between 30 ° and 85 °. The height of central tower is 45 m. The load lifting speed was assumed equal to vs = 20 m / min; while the arm lifting speed (speed at the height of the arm) was assumed equal to va= 10 m / min. Figure 8 reports the fem model for the two geometrical configurations i.e. 5° ad 85° analyzed. The figures 9 and 10 show the displacement results from numerical analyses.

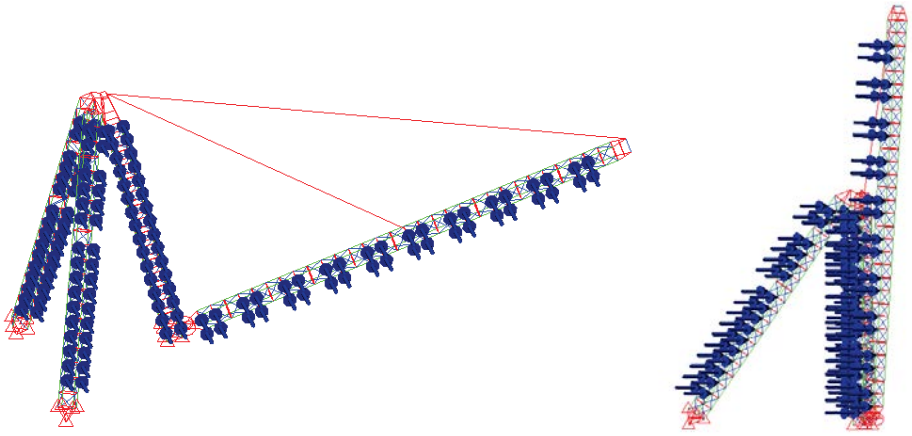

Figure 8 Derrick crane fem model.

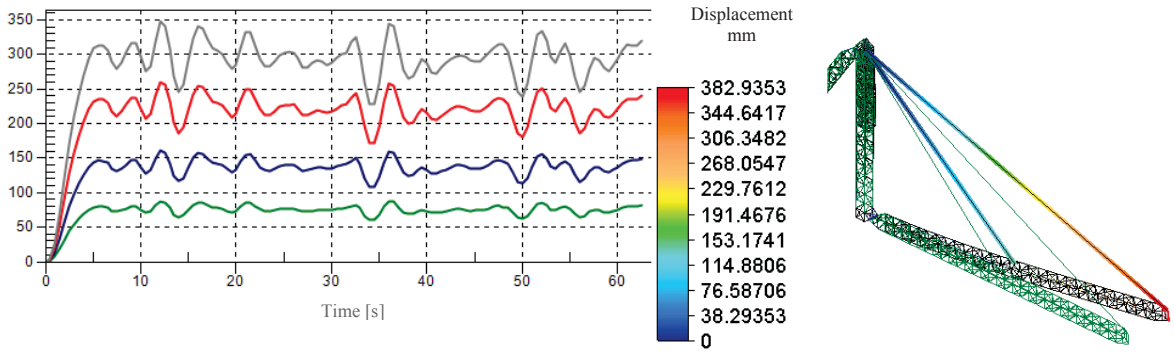

Figure 9 Derrick crane displacement in 5° geometrical configuration for different points on main arm.

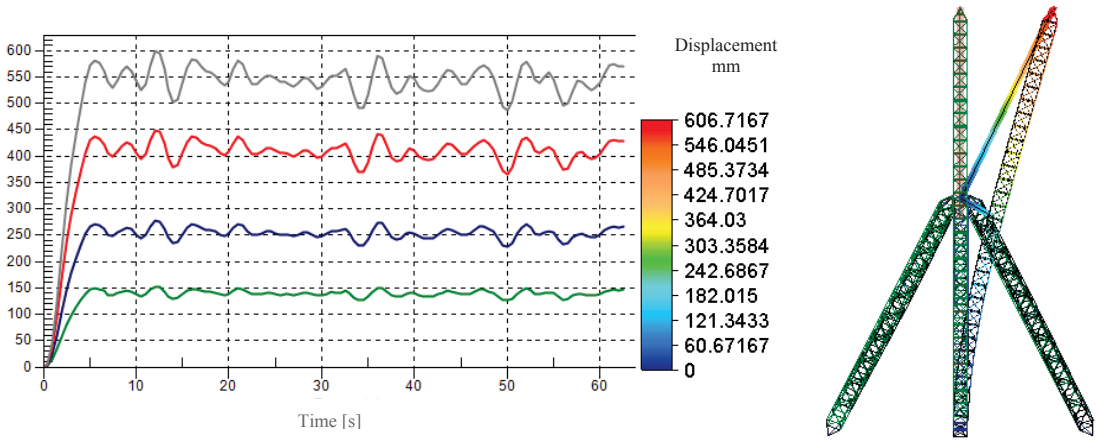

Figure 10 Derrick crane displacement in 85° geometrical configuration for different points on main arm.

7 RESULTS

The main results of this research in order to evaluate the effect of different wind actions schematizations (constant ad variable in time) on crane displacement are summarized in table 1. This table reposts also the perceptual variation with respect to the displacement values obtained considering constant wind action.

Crane /configuration	Wind action=constant (A)	Wind action=variable in time (B).	Variation (B-A)/A*100
Low profile	120.5	348.1	188.9
Container crane	158.7	320.5	101,9
Derrick crane / 5°	310.8	382.9	23,1
Derrick crane / 85°	384.6	606.7	57,7

Table 1: Maximum displacement [mm] for three different cranes and with different wind loads schematizations.

The results show that, for all numerical analyses carried out, the displacements evaluate considering that the forces variable in time are greater than the one evaluated with constant forces.

This result is very important because, correlated to the displacement value, there are three phenomena that must be taken into account in order to avoid the structures damage due to the wind actions, and these are stress state, fatigue phenomenon and the overturning moment.

Another observation is important: the increase displacement value changes with the crane typologies end the geometrical configurations. The aspect that needs further investigations may be correlate to the mechanical behavior of the crane and in particular to the natural frequencies and the mass participations factors involved in the wind load direction.

8 CONCLUSIONS

This research reports the main numerical results for three different port cranes subjected to wind actions. These actions were schematized in two different ways, one considering the velocity constant in time and the second considering the velocity changing in time.

After the design process for all cranes, a specific Mathcad® program was developed in order to evaluate the forces trend (lift and drag). The structures were divided in many different substructures and on each of these, specific actions were applied. The numerical results show that the maximum displacements are quite different and these shifts is not constant but depends on the crane type and geometrical configuration.

These results need more investigation because, correlated to the displacement, there are other phenomena like stress state (and fatigue) and overturning moment that can induce the crane to collapse. The next step of this research regards two points.

The first point concerns the implementation of this methodology to evaluate the structure mechanical behavior on other cranes type. The second point relates to the wind actions schematization and, in particular, this second point want to analyze the effect of different wind schematization or model assumptions, as reported in [27], on the crane response, especially in the displacement values, and compare it to the one obtained in the static load conditions.

REFERENCES

[1] J.C. Kaimal, J. C. Wyngaard, Y. Izumi, O.R. Cotè, Spectral characteristics of surface layer turbulence, *Quaternary journal of royal meteorological society* 98, 563-589, 1972.

[2] L. Solazzi, Experimental and analytical study on elevating working platform, *Procedia Engineering* 199, 2597-2602, 2017.

[3] I. A. Lagerev, Research of dynamics of hydraulic loader crane in case of conjoint movement of sections, *Lecture Notes in Mechanical Engineering* 0, 2283-2293, 2019.

[4] L. Solazzi, N. Zrnic, Design a high capacity derrick crane considering the effects induced by load application and release, Journal of Applied engineering Science 15(1), 15-24, 2017.

[5] L. Solazzi, G. Incerti, C. Petrogalli, Estimation the dynamic effect in the lifting operations of a boom crane, Proceedings - 28th European Conference on Modelling and Simulation, ECMS 2014, 309-315, 2014.

[6] Zrnić, N., Gašić, V., Bošnjak, S. and Đorđević, M.: Moving loads in structural dynamics of crane: bridging the gap between theoretical and practical research, *FME Transactions* 41, 291-297, 2013.

[7] Z. A. Qiao, y. G. Sun, D. S. Dong, Research on Elastic Effect of the Frame Excited by Inertia Load of the Trolley, *8th Annual IEEE International Conference on Cyber Technology in Automation, Control and Intelligent Systems*, CYBER 2018, 10 April 2019, Article number 8688141, 867-872b, 2018.

[8] L. Solazzi, M. Cima, Structural dynamics of big gantry crane subjected to different trolley move, *Journal of Physics: Conference Series* 164 (1), 24 July 2019, Article number 012046, 2019.

[9] L. Solazzi, C.Remino, G. Incerti, Overhead crane subjected to impulse loading, *Journal of Physics: Conference Series* 1264 (1), 24 July 2019, Article number 012045, 2019.

[10] H. Jiang, Y. Li, Dynamic Reliability Analysis of Tower Crane with Wind Loading, *IOP Conference Series: Materials Science and Engineering* 677(5), 2019.

[11] L. Solazzi, Stochastic wind loading applied to container crane, *FME Transaction* 46(3), 299-305, 2018.

[12] L. Solazzi, N. Zrnic, Numerical study of wind actions applied to a low profile container crane, *FME Transaction* 44(1), 29-35, 2016.

[13] P. Wang, L. Yu, W. Han, H. Tang, F. Yan, D. Zhao, Analysis on response of tower crane structures under random earthquake excitations, *Jixie Qiangdu /Journal of Mechanical Strength* 38 (1), 192-196, 2016

[14] L. Solazzi, Ship to shore subjected to earthquake, *Procedia Engineering* 10, 2690-2695, 2011.

[15] M. A. Jordan, The 1995 Kobe Earthquake, *Liftech Consultants Inc.,* 1995.

[16] V. Santiago-Fandiño, S. Sato, N. Maki, K. Iuchi, The 2011 Japan Earthquake and Tsunami: Reconstruction and Restoration, *Springer*, ISBN 978-3-319-58690-8, 2018.

[17] H. K. Dong, C. O. Byung, H.H. Sang, S.S. Jae, S.C. I, S.S. Man, S. J. Ji, Collapse of container cranes at busan port under typhoon maemi, *Proceedings of the 14 International offshore and polar engineering conference*, Toulon , France, 2004.,

[18] C. Klinger, Failures of crane due to wind induced vibrations, *Engineering Failure Analysis* 43, 198-220, 2014.

[19] F. Frendo, Gantry crane derailment and collapse induced by wind load, *Engineering failure analysis* 66, 479-488, 2016.

[20] P. Mc Carthy, E. Soderberg, A. Dix, Wind damage to dockside cranes: recent failure and recommendations, *Proceeding of TCLEE conference*, Okland, 2009

[21] S. Gur, S. Ray-Chaudhuri, Probabilistic assessment of container crane under wind loading, *Proceedings of the international symposium on engineering under uncertainty: safety assessment and management* (ISEUSAM), 2012.

[22] S. Gur, S. Ray-Chaudhuri, Vulnerability assessment of container cranes under stochastic wind loading, *Structure and infrastructure engineering: maintenance, management, life cycle design and performance* 10:12, 1511-1530, 2014.

[23] S. Gur, S. Ray-Chaudhuri, Probabilistic assessment of container crane under wind loading, *Proceedings of the international symposium on engineering under uncertainty: safety assessment and management* (ISEUSAM), 1049-1060, 2012.

[24] R.D. Ambrosini, J.D. Riera, R., F. Danesi, Analysis of structure subject to random wind loading by simulation in the frequencies domain, *Probabilistic engineering mechanics* 17, 233-239, 2002.

[25] Y. Tamura, A. Kareem, Advanced structural wind engineering, *Springer*, ISBN 978-4-431-54336-7, 2013.

[26] E. Simiu, Y. Dong Hun, Wind effects on structures, *John Wiley & Sons*, ISBN 9781119375883, 2019.

[27] J. D. Holmes, Wind loading of structures, *Taylor & Francis Group*, ISBN: 978-1-4822-2922-6, 2015.

EURODYN 2020
XI International Conference on Structural Dynamics
M. Papadrakakis, M. Fragiadakis, C. Papadimitriou (eds.)
Athens, Greece, 23–26 November 2020

ON THE VALIDATION AND USE OF A SIMPLIFIED MODEL OF AEOLIAN VIBRATION OF OVERHEAD LINES FOR PARAMETRIC STUDIES

Emmanuel CIEREN[1], John REDFORD[1], Maxime GUÉGUIN[1], Olivier ALLIX[2], Christine YANG[3], Fikri HAFID[3] and Jean-Michel GHIDAGLIA[4]

[1]Eurobios
61 avenue du président Wilson, 94235 Cachan, FRANCE
{ecieren,mgueguin,jredford}@eurobios.com

[2]LMT, ENS Paris-Saclay, CNRS
Université Paris-Saclay, 94230 Cachan, FRANCE
olivier.allix@ens-paris-saclay.fr

[3]RTE–R&D
Immeuble Window, 7C place du dôme, 92073 Paris La Défense, FRANCE
{christine.yang,fikri.hafid}@rte-france.com

[4]Université Paris-Saclay, ENS Paris-Saclay, CNRS, Centre Borelli
F-91190, Gif-sur-Yvette, FRANCE
jmg@cmla.ens-cachan.fr

Keywords: Overhead power lines, aeolian vibrations, fretting-fatigue.

Abstract. *Several factors are involved in estimating the lifetime of overhead lines. Focusing on the mechanical part, conductor vibrations represent an important contribution to the creation and propagation of cracks, which has led us to investigate the behavior of a suspended cable subject to wind. Among the already available tools, there is either the simple energy balance principle, which is physically less accurate, or a more complete mechanical modelling, which is computationally expensive. In this paper, we present a model that fills this gap: we are able to perform large parametric studies in a moderate amount of time without compromising the physical accuracy of the results. Results from this model compare well with Code_Aster simulation results. We outline a steady state which can be characterized with a few parameters, and demonstrate an example of a parametric study that can be performed.*

1 Introduction

Asset management is a major challenge for RTE (Réseau de Transport d'Electricité), the French TSO (Transmission System Operator), because electrical grid component maintenance and renewal represent important economic issues. Thus, improved lifetime assessment could lead RTE to substantial savings while still assuring a high quality service. Overhead power cables, or conductors, which are stranded wire assemblies, are one of RTE's main assets. It is well known in the overhead lines community that aeolian vibrations cause fretting fatigue in or around the clamp/conductor system and lead to aging of the conductors [1, 2].

Aeolian vibrations are an aero-elastic phenomenon, where the wind induces vortex shedding that causes alternating lift and drag forces. If the structural damping is not sufficient, the conductor can vibrate under low-speed wind conditions (velocities ranging from about one to seven $\mathrm{m\,s^{-1}}$). These vibrations can be quantified by studying the equation of motion of a conductor exposed to wind, where the model for the conductor can be represented as a suspended cable. This system can be solved using the Code_Aster finite-element solver, and the obtained results are found to compare well with experiments [3]. Yet, running this type of simulation for a significant part of RTE's network ($300\,000$ spans) is prohibitively expensive. The Energy Balance Principle (EBP) is a simple model that is widely used in the literature, and this can be used to compute the vibration amplitude. The EBP is reliant on balancing the energy introduced by the wind and the energy dissipated by the conductor [4]. Yet, this method does not adequately cover low wind speeds because it relies on experimental data which is difficult to acquire. This is the motivation for the development of a simpler equivalent model (1D, nonlinear, finite-difference method solution), which is based on the cable dynamics and thus is physically more accurate than the EBP. Compared to Code_Aster, the same vibration amplitudes are found, while the computation is much faster.

Section 2 presents two models, one for the conductor and another for conductor-wind interaction; in section 3 the conductor model is validated before an example parametric study that can be performed with the model is shown in section 4. Finally, in the discussion (section 5) several improvements are outlined that can be made to both models to better capture aeolian vibrations.

2 Models

2.1 Equation of Motion for a Suspended Cable

Let us consider an elastic cable suspended between two poles separated by a distance L_s. We denote m as the cable mass per unit length, H is the equilibrium tension, EA is the axial stiffness of its cross section and g is the standard gravity. At equilibrium, the cable has the shape of a catenary due to its own weight, and its length is given by (1).

$$L \;=\; 2a\,\sinh\left(\frac{L_\mathrm{s}}{2a}\right)\;, \quad \text{with } a \;=\; \frac{H}{mg} \tag{1}$$

The dynamic displacement of the cable from its equilibrium is given by $\mathbf{U} = U_\mathrm{T}\,\mathbf{e}_\mathrm{T} + U_\mathrm{N}\,\mathbf{e}_\mathrm{N} + U_\mathrm{B}\,\mathbf{e}_\mathrm{B}$, where the unit vectors $\mathbf{e}_\mathrm{T}$, $\mathbf{e}_\mathrm{N}$ and $\mathbf{e}_\mathrm{B}$ respectively represent the tangential, normal and binormal directions of the Frenet triad defined by the equilibrium position of the cable (see also figure 1). All U_i components depend on time T and S, which is the curvilinear abscissa along the cable.

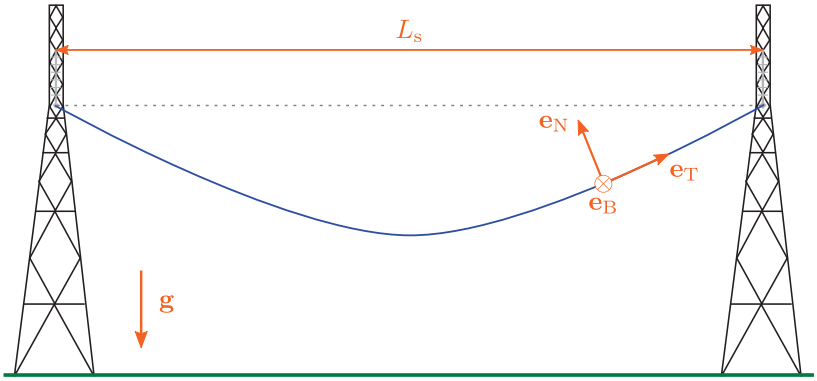

Figure 1: Vibration model notations.

Considering that $H \gg mgL$ (which implies that the equilibrium curvature is small and that the catenary is well approximated by a parabola), and that $EA \gg H$ (such that we have ${}^{EA}/_{H} > {}^{H}/_{mgL}$), the equations of motion when the cable is subject to an external force $\mathbf{F} = F_T\,\mathbf{e}_T + F_N\,\mathbf{e}_N$ regarding the equilibrium are given by [5]

$$\left\{ \begin{array}{rcl} \dfrac{\partial^2 u_N}{\partial t^2} & = & \left(v_t^2 + v_\ell^2 e\right) \dfrac{\partial^2 u_N}{\partial s^2} \; + \; \dfrac{v_\ell^2}{v_t^2} e \; + \; f_N \\ \dfrac{\partial^2 u_B}{\partial t^2} & = & \left(v_t^2 + v_\ell^2 e\right) \dfrac{\partial^2 u_B}{\partial s^2} \; + \; f_B \end{array} \right. , \tag{2}$$

where

$$e(t) = \int_0^1 \left\{ -\frac{u_N}{v_t^2} + \frac{1}{2} \left[\left(\frac{\partial u_N}{\partial s} \right)^2 + \left(\frac{\partial u_B}{\partial s} \right)^2 \right] \right\} \mathrm{d}s \; . \tag{3}$$

All quantities in equations (2) and (3) are dimensionless: we have $s = {}^{S}/_{L}$, $t = {}^{T}/_{\sqrt{L/g}}$, $u_i = {}^{U_i}/_{L}$ and $f_i = {}^{F_i}/_{mg}$; the coefficients v_t and v_ℓ stand for the (non-dimensional) velocity of transverse and longitudinal waves along the cable (4). Since the cable has fixed ends, Dirichlet boundary conditions are used for each component of the displacement.

$$v_t \; = \; \sqrt{\frac{H}{mgL}} \; , \quad v_\ell \; = \; \sqrt{\frac{EA}{mgL}} \tag{4}$$

After solving this system, it is possible to retrieve the u_T component by identifying a function $h(s,t)$ such that $e(t) = \int_0^1 h(s,t)\,\mathrm{d}s$; we then have

$$u_T(s,t) \; = \; e(t)\, s \; - \; \int_0^s h(s,t)\,\mathrm{d}s \; . \tag{5}$$

The system (2) is solved using a finite difference approach with second order approximation in space and a linearized Crank-Nicolson scheme (also second order) in time. The solver has been implemented with Python for its flexibility, but a C/C++ version could also be implemented if performance improvements are necessary.

2.2 Wind Interaction

Aeolian vibrations are attributed to a fluid dynamics phenomenon called vortex shedding. In simple terms, this is when a fluid (*e.g.* air) flowing past a cylindrical body causes vortices to be formed downstream of the cylinder, which then become unstable and detach. The vortices detach periodically from either side of the body, creating a von Karman vortex street, and also inducing an alternating lift force along with an oscillation in the drag force. The detachment frequency is characterized by

$$f_{\mathrm{w}} \;=\; \frac{U}{d}\,\mathrm{S_t}\;, \tag{6}$$

where U is the fluid speed, d the cylinder's diameter and $\mathrm{S_t}$ a dimensionless number (called the Strouhal number) which depends on the shape of the body and the Reynolds number ($\mathrm{S_t} \approx 0.2$ for $\mathrm{Re} \in [10^2, 10^5]$ in the case of a fixed, infinite and smooth cylinder).

No theoretical prediction for vortex shedding exists in the literature, so empirical formulations from experiments in wind tunnels are used. Especially important is the work of Bishop and Hassan [6], who ran experiments with a smooth cylinder subject to a uniform air flowing normal to the cylinder axis, and made detailed force measurements. The force per unit length on the cylinder is given by

$$\begin{cases} F_{\mathrm{L,D}} \;=\; {}^1\!/_2\,\rho_{\mathrm{air}}\,d\,|U|\,U\,\bar{C}_{\mathrm{L,D}}(t) \\ \bar{C}_{\mathrm{L}}(t) \;=\; C_{\mathrm{L}} + C_{\mathrm{L0}}\sin(\;\omega_{\mathrm{w}}t) \\ \bar{C}_{\mathrm{D}}(t) \;=\; C_{\mathrm{D}} + C_{\mathrm{D0}}\sin(2\omega_{\mathrm{w}}t) \end{cases}\;, \tag{7}$$

with $\omega_{\mathrm{w}} = 2\pi f_{\mathrm{w}}$, ρ_{air} being the air volumic mass. Indices L and D correspond to *lift* and *drag* directions: the drag direction is parallel to the air flow, and L is normal to both the air flow and cylinder axis. The dimensionless coefficients C_{D}, C_{D0}, C_{L} and C_{L0} are measured experimentally or can be found with fluid dynamics computations [7]. Bishop and Hassan give the following values for a Reynolds number around 10^4: $C_{\mathrm{D}} = 1.1$, $C_{\mathrm{D0}} = 0.075$, $C_{\mathrm{L}} = 0$ and $C_{\mathrm{L0}} = 0.6$.

When using the force formulation (7) as an input in (2), we consider the wind along the binormal direction, hence $f_{\mathrm{N}} \equiv {}^{F_{\mathrm{L}}}\!/_{mg}$ and $f_{\mathrm{B}} \equiv {}^{F_{\mathrm{D}}}\!/_{mg}$. A geometric correction is not added because the curvature of the cable is assumed to be small. However, as our cylinder will be moving, we do need to modify (7) to take the relative speed of the cable into account. Equation (8) is obtained using projections, but it was chosen to keep the frequency in (6) unchanged.

$$\begin{cases} f_{\mathrm{N}} \;=\; \dfrac{\rho_{\mathrm{air}}dL}{2m}\sqrt{\dot{u_{\mathrm{N}}}^2 + \left(\dfrac{U}{\sqrt{Lg}} - \dot{u_{\mathrm{B}}}\right)^2}\left[-\dot{u_{\mathrm{N}}}\,\bar{C}_{\mathrm{D}}(t) + \left(\dfrac{U}{\sqrt{Lg}} - \dot{u_{\mathrm{B}}}\right)\bar{C}_{\mathrm{L}}(t)\right] \\ f_{\mathrm{B}} \;=\; \dfrac{\rho_{\mathrm{air}}dL}{2m}\sqrt{\dot{u_{\mathrm{N}}}^2 + \left(\dfrac{U}{\sqrt{Lg}} - \dot{u_{\mathrm{B}}}\right)^2}\left[\left(\dfrac{U}{\sqrt{Lg}} - \dot{u_{\mathrm{B}}}\right)\bar{C}_{\mathrm{D}}(t) + \dot{u_{\mathrm{N}}}\,\bar{C}_{\mathrm{L}}(t)\right] \end{cases} \tag{8}$$

3 Validation

3.1 Utilization in Overhead Lines Context

The model in section 2.1 is to be applied to the case of electrical overhead lines, and thus it is necessary to ensure that the conditions are representative. For this a dataset of about $82\,000$ spans from the RTE network is used in which all the required physical properties are well

quantile	$1/vt^4$	v_t^4/v_ℓ^2
0.1	0.0132	0.00253
0.2	0.0192	0.00306
0.3	0.0242	0.00348
0.4	0.0291	0.00387
0.5	0.0338	0.00428
0.6	0.0390	0.00476
0.7	0.0451	0.00533
0.8	0.0531	0.00619
0.9	0.0655	0.00791

Table 1: Quantiles for error terms computed on a sample of spans.

known. Lee's model does not account for height difference, so we remove the spans that have a height difference h larger than 20 m or such that $h/L_\mathrm{s} < 5\%$, which leaves about $65\,000$ spans.

To obtain (2), several Taylor expansions using $k = 1/v_t^2$ as a parameter were performed; the error is $O\left(1/vt^4\right)$ when neglecting terms on the order of k^2 or smaller. The second hypothesis, which compares longitudinal and transverse wave speeds ($v_\ell^2 > v_t^4$), is easier to meet since conductor materials often have high axial stiffness and relatively low tension. Both ratios have been computed on the sample of spans. The results in table 1 show that the curvature error is quite limited (below 7%) for 90% of the spans, and that the error in the wave-speeds is even lower. This would not be the case if we had kept spans with higher height difference.

3.2 Comparison with Code_Aster

Code_Aster open source software is used to solve numerical problems in structural mechanics [8]. It is a continuum mechanics solver based on the finite element method that can be employed for different types of mechanical, thermal or acoustic problems. In our case, we use a three-dimensional large displacement model to compute a cable displacement when it is subject to wind. We performed our comparison using an ASTER570 conductor (m = 1.57 $\mathrm{kg\,m^{-1}}$, EA = 37.6 MN, d = 31.1 mm) on a span of length L_s = 400 m and with tension H = 37 kN; we used ρ = 1.20 $\mathrm{kg\,m^{-3}}$ for the air volumic mass and a wind speed of U = 3.00 $\mathrm{m\,s^{-1}}$; other wind parameters are given in section 2.2. The cable is considered at rest at initial time. In this comparison, we do not take into account the speed correction raised in section 2.2, since it requires deeper modifications in Code_Aster's source code; this is not important here as we only want to compare the cable models. The simulation time is 45 s; discretization parameters are respectively n = 257 and 250 elements for Code_Aster and Lee's model and we use the same time step $\Delta t = 1.0 \times 10^{-3}$ s. Results in figure 2 show near identical vibrations. The comparison between the two approaches remains good if the input parameters are changed, and the best correspondence is observed far from the span ends.

Comparing execution times of a three-dimensional model, such as the one used here in Code_Aster, with a much simpler model is a bit unfair, but this is important when we want to perform numerous simulations for a parametric study. On a standard desktop computer (using an Intel i7-3770 processor and 12 GB of memory), a computation of two and a half hours was necessary to complete a simulation using Code_Aster and about 80 seconds for Lee's model, which gives a time ratio slightly above 100.

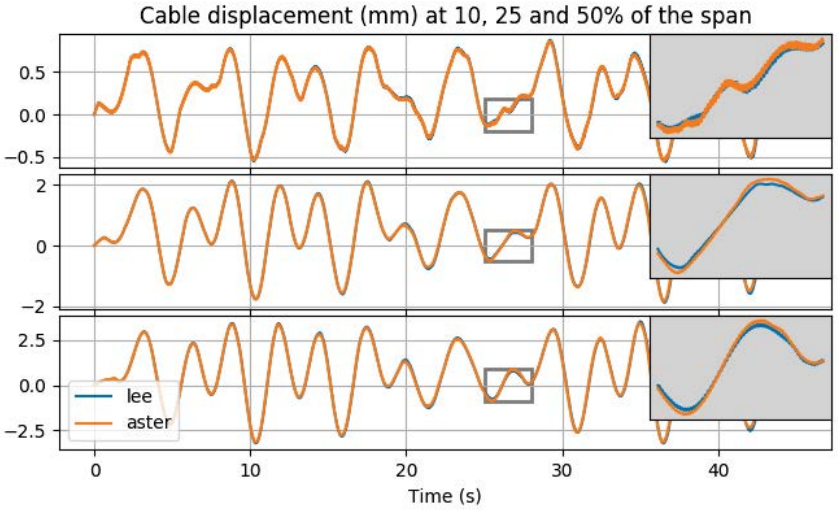

Figure 2: Comparison of displacement with regard to equilibrium position for u_{N} component obtained by solving Lee and Code_Aster models.

3.3 Observations

Let us consider the same cable at the mid-span and with the speed correction taken into account (figures 3 and 4). Focusing on the binormal component (parallel to the wind), we observe damped oscillations that seem to tend to a stationary state. The oscillation frequency matches the natural frequency of the cable $f_1 = \frac{1}{2L_{\mathrm{s}}}\sqrt{\frac{H}{m}}$, and the time constant can be estimated with $\tau = \frac{2m}{\rho_{\mathrm{air}} d U C_{\mathrm{D}}}$. The limiting value for u_{B} can be computed using a static version of (2), but it can be well approximated by a catenary equation using an analogy with the gravity case

$$u_{\mathrm{B}}^{\infty}(s) \;=\; 2\tilde{a}\,\sinh\left(\frac{L_{\mathrm{s}}}{2\tilde{a}}(1-s)\right)\,\sinh\left(\frac{L_{\mathrm{s}}}{2\tilde{a}}s\right)\;, \quad \text{with } \tilde{a} \;\equiv\; \frac{H\tau}{mU}\;, \tag{9}$$

where $s \in [0,1]$ is the curvilinear abscissa along the span. By combining these observations, a good analytical approximation can be written for the binormal component:

$$u_{\mathrm{B}}(s,t) \;\approx\; \left[1 \;-\; \exp\left(-t/\tau\right)\cos\left(2\pi f_1 t\right)\right]\; u_{\mathrm{B}}^{\infty}(s)\;. \tag{10}$$

Focusing on the normal component, damped oscillations are also observed, but these are much less regular than for the binormal component; a steady state is observed after approximately 200 seconds. The frequency of these oscillations is close to, but different to twice the cable natural frequency. In fact, it exactly matches the first out-of plane frequency f_1' defined in [9] using a transcendental equation. The steady-state vibrations have a small amplitude (about $50\ \mu\mathrm{m}$) and their frequency is exaclty f_{w}. Similar to the binormal component, the mean of the steady state vibrations $u_{\mathrm{N}}^{\infty}(s)$ can be computed. However, a good analytical approximation for the oscillation amplitude was not found.

4 Example of a parametric study

Typically, how vertical vibrations vary with span length, tension and wind speed are of interest. Since an expression for the normal component vibration amplitude has not been found, several simulations have been performed to cover the different cases. Considering an ASTER570 cable, most span lengths go from 100 to 800 m, and the tensions between 10 and 60 kN. Two

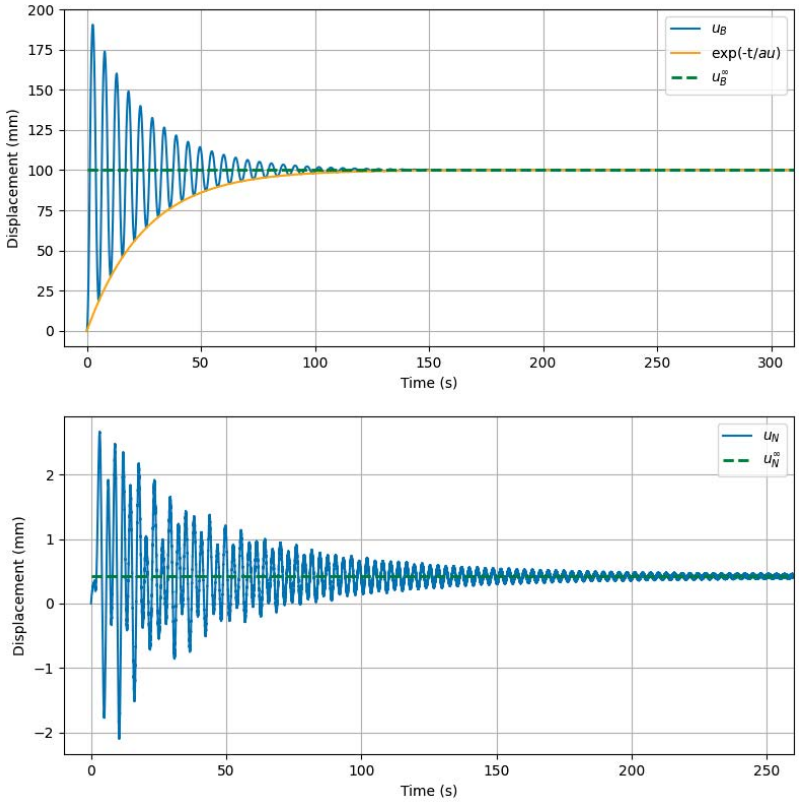

Figure 3: Cable displacement (mm) at mid-span regarding equilibrium position for the binormal (top) and the normal (bottom) component. The green line can be computed by solving a static problem and the orange line outlines the damping in $\exp(-t/\tau)$.

sets of simulations have been performed; one with a small number of points for L_s and H, and several wind speeds (15 lengths, 11 tensions and 11 wind speeds) to cover the wind speed dependency, and another with one wind speed but a greater number of points (56 lengths and 41 tensions) to obtain a more detailed map. The same parameters as in previous section are kept, but only the steady state is considered when performing amplitude measurements.

Figure 5 shows the value of u_N^∞ in the span-length/tension plane for different wind speeds. The same pattern is observed in all cases, with the amplitude increasing with the wind speed. To investigate further, five length/tension points were selected and the variation of the vibration amplitudes with wind speed for these points is shown in figure 6. It appears that all the curves follow the same pattern, which leads us to assume that the expression for the vibration amplitude (for a given type of conductor, *i.e.* a fixed mass, diameter and axial stiffness) can be expressed as the product of two functions; one that depends on span length and tension, and the other that only depends on the wind speed (with other parameters, such as ρ_air, and C_D, being fixed). Thus, we can omit the wind speed factor and only analyze one high-resolution map. This is what has been done in figure 7, where it is observed that larger values of u_N^∞ are obtained for longer span lengths and lower tension cables.

The amplitudes of the steady state vibrations (figure 8) are observed to have very small values for all wind speeds. The amplitude is always below $2.5\ \mathrm{mm}$ at mid-span, whereas cable damage would be expected at higher amplitudes [10].

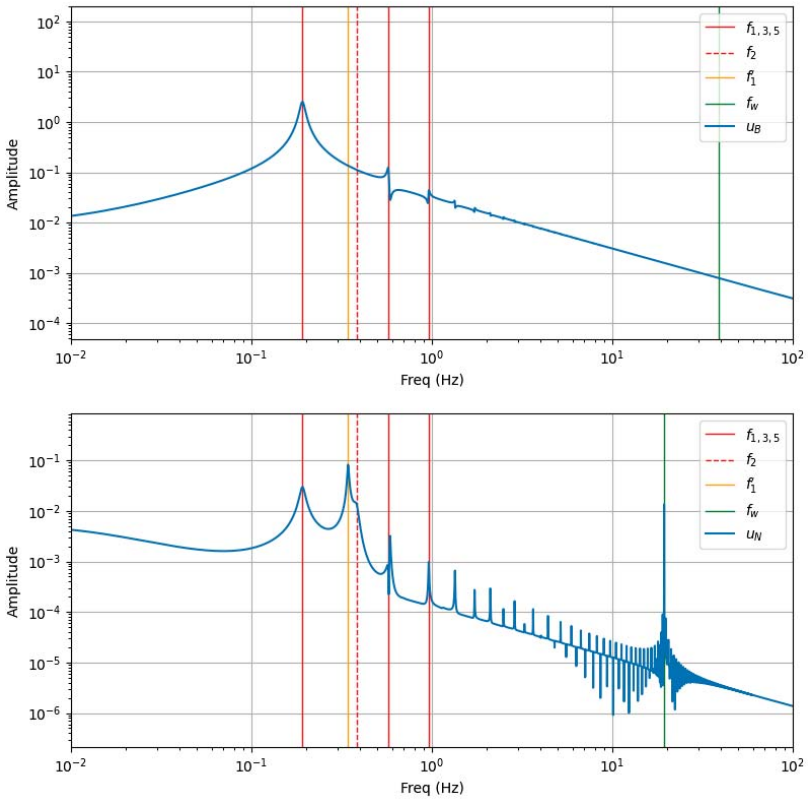

Figure 4: Mid-span vibration spectra for the binormal (top) and the normal (bottom) component. Red lines are natural frequencies of the cable (solid for odd modes, dashed for even), the orange line is the frequency given in [9] and the green one is the wind frequency.

5 Discussion

Several points in Lee's model should be improved: there is currently no consideration of any kind of damping. This explains why vibration amplitudes continue to increase with wind speed, instead of reaching a peak value and then returning lower values, like with the EBP model. A viscous damping term could be added to (2), but it is well known that damping is non-linear in cables due to the friction between wires. Part of our future work consists of evaluating friction in different conductors and its dependence on common parameters, such as span tension or local curvature, before implementing a damping term in Lee's model.

The model does not take height difference between suspension points of the cable into account. Even if the model is already able to perform simulation of a significant fraction of the RTE network, a model that includes this effect would be a improvement. This could be done with [11] for instance.

The wind interaction model used here is also not satisfactory, as the computed amplitudes are too low to explain fretting fatigue close to the suspension points. Several factors can explain these results:

- Use of the Bishop and Hassan model assumes a fixed cylinder, which is an assumption that is not met; therefore, another wind interaction formulation should be used.
- Furthermore, the Bishop and Hassan model includes no influence of the vortex shedding on the cable motion. In reality, the motion of the structure and the vortex shedding interact to increase the possibility of resonance, which is referred to as lock in.

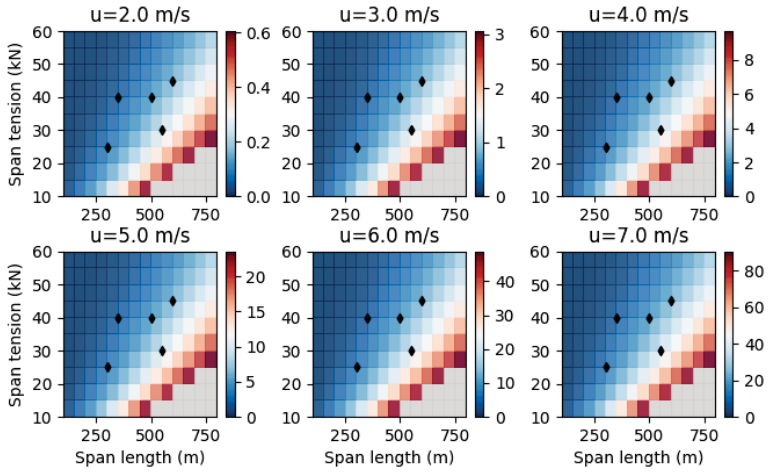

Figure 5: Values of u_N^∞ (mm), ie the mean value of normal steady state vibrations, in the span-length/tension plane for different wind speeds. Black points are a reminder of the points used in figure 6.

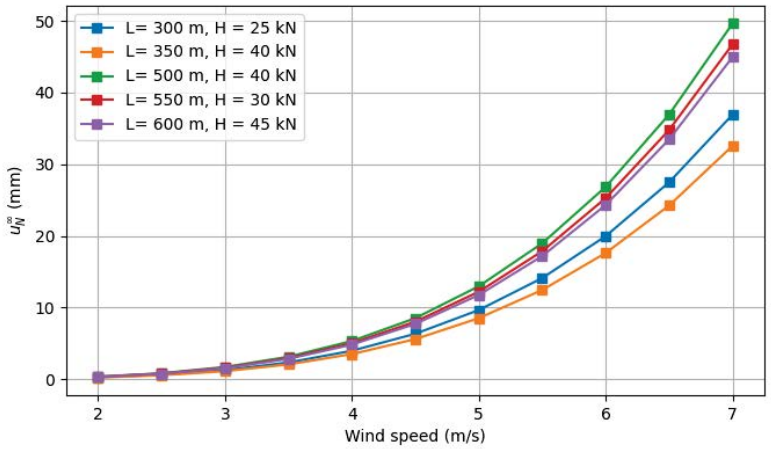

Figure 6: Mean value of normal steady state vibrations (mm) with wind speeds for selected span lengths and tensions.

- A constant wind in space and time is unlikely to occur in the field; the cable motion under dynamic wind loading should be studied.

In order to address these questions, the Bishop and Hassan formulation will be compared with a wake oscillator, like that in [12]. In such a model the vortex shedding is influenced by the cable motion, while the tool is still simple and fast; simulations will also be performed using dynamic wind fields. This appoach will allow confirmation on whether aeolian vibrations are caused by VIV.

6 Conclusion

A simple model is presented to investigate the interaction between a suspended cable and a weak wind. The purpose is to have a model with more physics and parameters than the EBP, but that is also less complicated and computationally demanding than a full three-dimensional structural mechanics simulation. Ideally, computation of a large number of configurations in a short period of time will allow parametric investigation of the RTE network, but without compromising the physical accuracy of the results. The model has been validated using Code_Aster

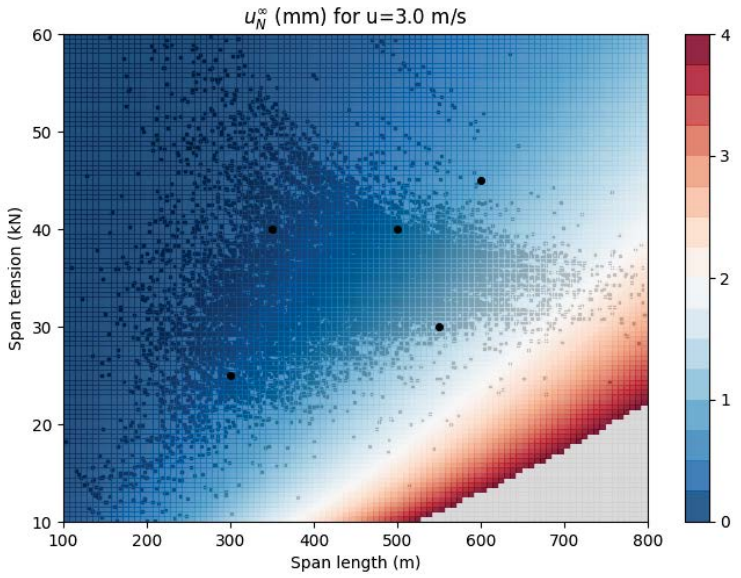

Figure 7: Mean value of normal steady state vibrations (mm) in the span-length/tension plane for a wind speed of $3\ \mathrm{m\,s^{-1}}$ (high resolution). Background points show the ASTER570 spans from the RTE network; black points are the values used in figure 6.

as a reference, which showed little difference in the results from both models while having a factor of 100 improvement in computational performance. A steady state has been outlined that can be characterized by a few parameters (vibration mean, amplitude and frequency). The mean can be recovered with static computations and formulations were obtained for the frequencies, however it was not possible to find a simple expression for the amplitude, which is why a parametric study was performed. Considering vertical vibrations, both mean value and amplitude of the steady state are too small to explain aging of conductors; this will lead us to improve the wind interaction model. Some limitations in the model itself and potential solutions to overcome them have been identified. In future, we intend to evaluate cumulative damage for a span within the simulated vibration histories. This will be done by counting the number of cycles and the related vibration amplitudes, and then combining these with results from simulations at the microscopic scale. The end result will be a crack initiation risk function for the wires at the contact location. This should allow ranking of all spans of the RTE network in order to help and improve maintenance operations.

REFERENCES

[1] Giorgio Diana, Umberto Cosmai, André Laneville, Alessandra Manenti, David Hearnshaw, and Konstantin O. Papailiou. Chapter 2: Aeolian vibration. *EPRI Transmission line reference book: Wind-induced conductor motion*, 2006.

[2] L Cloutier, S Goudreau, and A Cardou. Chapter 3: Fatigue of overhead conductors. *EPRI Transmission line reference book: Wind-induced conductor motion*, 2006.

[3] Sébastien Langlois, Frédéric Lévesque, and Frédéric Legeron. Finite element model of vibrating overhead conductors with variable bending stiffness. In *9th International Symposium on Cable Dynamics*, 2011.

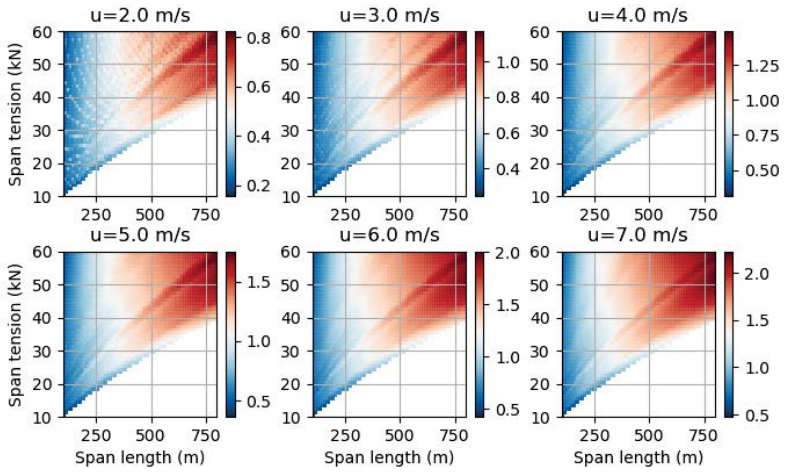

Figure 8: Amplitude of normal steady state vibrations (mm) in the span-length/tension plane for different wind speeds.

[4] Suzanne Guérard. *Power Line Conductors, a Contribution to the Analysis of their Dynamic Behaviour*. PhD thesis, Université de Liège, 2011.

[5] Christopher L. Lee and Noel C. Perkins. Nonlinear Oscillations of Suspended Cables Containing a Two-to-One Internal Resonance. *Nonlinear Dynamics*, 3(6):465–490, 1992.

[6] R. E. D. Bishop and A. Y. Hassan. The lift and drag forces on a circular cylinder oscillating in a flowing fluid. *Proceedings of the Royal Society of London A: Mathematical, Physical and Engineering Sciences*, 277(1368):51–75, 1964.

[7] Lei Zhang, John Redford, Fikri Hafid, Jean-Michel Ghidaglia, and Maxime Guéguin. Viv modelled using simplified cable dynamics coupled to sub-critical cylinder flow simulations in a moving reference frame. *Submited*, 2019.

[8] Electricité de France. Finite element $code\_aster$, analysis of structures and thermomechanics for studies and research. Open source on www.code-aster.org.

[9] Giuseppe Rega. Nonlinear vibrations of suspended cables–Part I: Modeling and analysis. *Applied Mechanics Reviews*, 57(6):443–478, 2004.

[10] R.B. Kalombo, G. Reinke, T.B. Miranda, J.L.A. Ferreira, C.R.M. [da Silva], and J.A. Araújo. Experimental study of the fatigue performance of overhead pure aluminium cables. *Procedia Structural Integrity*, 19:688 – 697, 2019. Fatigue Design 2019, International Conference on Fatigue Design, 8th Edition.

[11] Marco Lepidi and Vincenzo Gattulli. Static and dynamic response of elastic suspended cables with thermal effects. *International Journal of Solids and Structures*, 49(9):1103 – 1116, 2012.

[12] M.L. Facchinetti, Emmanuel De Langre, and F. Biolley. Coupling of structure and wake oscillators in vortex-induced vibrations. *Journal of Fluids and Structures*, 19(2):123–140, 2004.

EURODYN 2020
XI International Conference on Structural Dynamics
M. Papadrakakis, M. Fragiadakis, C. Papadimitriou (eds.)
Athens, Greece, 23–26 November 2020

FATIGUE LIFE ESTIMATION CONSIDERING THE QUASI-PERIODIC CROSS-WIND RESPONSE OF SLENDER STRUCTURES IN THE LOCK-IN RANGE

F. Lupi[1,2], **R. Höffer**[1], **H.-J. Niemann**[2,1]

[1] Ruhr-Universität Bochum
Universitaetsstraße 150, 44801 Bochum
e-mail: {Francesca.lupi, Ruediger.Hoeffer, Hans-juergen.niemann}@rub.de

[2] Niemann&Partner Engineering Consultants
Universitaetsstraße 142, 44799 Bochum

Keywords: Free-vibration wind tunnel tests, Fatigue, Rainflow Cycle Counting, Quasi-Periodicity

Abstract. *The paper presents free-vibration wind tunnel tests on the aeroelastic model of a free-standing tower that shows vortex-induced vibrations in the lock-in range. Previous research by the authors focused on the investigation of the negative aerodynamic damping through forced-vibration tests. This knowledge allowed a realistic prediction for the maxima of the cross-wind oscillation amplitudes. In view of fatigue analysis, however, not only the maxima, rather a proper characterization of the cross-wind response is needed to determine the actual damage accumulation. Depending on the reduced wind velocity and the Scruton number of the vibrating structure, the experiments on the aeroelastic model in free vibrations show evidence of an intermittent – mathematically speaking quasi-periodic – behavior. It results from a beating effect between the natural oscillation frequency of the structure and the vortex shedding load, which may lock-in and lock-out in consequence of low frequency turbulence fluctuations. In addition, the frequency of the vortex shedding load along the height of the structure varies due to the varying mean velocity according to the wind profile and the varying Strouhal number. This exhibits smaller values close to the tip region. Outcomes of this investigation are the estimation of the negative aerodynamic damping through free-vibration wind tunnel tests and the estimation of the fatigue lifetime considering the quasi-periodic aeroelastic response through a rainflow fatigue load cycle counting.*

1 INTRODUCTION

Slender structures subjected to vortex-induced vibrations (VIV) experience an aeroelastic interaction in the lock-in range. The negative aerodynamic damping, interpreted as energy transferred from the flow into the structure, is the governing parameter for the onset of self-induced vibrations. However, available literature models still lack of a unified behavior of the aerodynamic damping as a function of the oscillation. This is also reflected in codified methods to design slender structures in view of cross-wind actions. This evidence applies firstly for the maxima of the oscillation amplitudes, i.e. the maxima of the structural stresses. Additionally, concerning the modelling of load processes for the analysis of fatigue strength, theoretical deficiencies cause even larger deviations between the prediction of fatigue life and its actual value.

A deeper knowledge about the non-linear behavior of the negative aerodynamic damping for a circular cylinder was gained by the authors from two-dimensional wind tunnel experiments in forced vibrations. The experiments were performed at the WISt Boundary Layer Wind Tunnel at Ruhr-Universität Bochum, Germany [10]. The experimental model of the aerodynamic damping developed in [10] was implemented in the spectral method originally proposed by Vickery&Basu [14] and applied to 27 full-scale steel chimneys collected from literature. This novel spectral method, known also as "Damping Modified Spectral Method" (DMSM), allows the calculation of the largest oscillation of structures in the lock-in range [9]. Compared to other codified methods for structural analysis (e.g. [12], [13], [14]), DMSM provides a safe but more realistic prediction of the maxima of the cross-wind oscillation amplitudes. In view of fatigue analysis, however, not just one amplitude determines the damage, rather a proper characterization of the cross-wind response is needed to determine the actual damage accumulation.

Wind tunnel experiments on an aeroelastic model of a full-scale tower immersed in uniform, low-turbulent flow (I_v = 4,5%) are analyzed in this paper. The wind tunnel tests are performed at WISt Boundary Layer Wind Tunnel at Ruhr-Universität Bochum, Germany. First, the concept of the negative aerodynamic damping developed in [10] with the support of forced-vibration tests is now assessed in case of free-vibration experiments. Furthermore, the experiments on the aeroelastic model in free-vibrations demonstrate an intermittent – mathematically speaking quasi-periodic – behavior [11]. It results from a beating effect between the natural oscillation frequency of the structure and the vortex shedding load, which may lock-in and lock-out in consequence of low frequency turbulence fluctuations. Additionally, the frequency of the vortex shedding load along the height of the structure may vary due to varying mean velocity and varying Strouhal number, which exhibits smaller values close to the tip region.

For the purpose of fatigue calculations, current design models usually assume that the resonant vibration always occurs in the lock-in range with its largest value (see [5], [13]). This may lead, however, to an excessively conservative estimation of the fatigue damage.

In this paper, the contribution of the intermittent oscillations to fatigue life can be assessed from the aeroelastic measurements with the help of a rainflow load cycle counting. The load collectives that are determined from the time histories of the tower responses in the lock-in range for different Scruton numbers are then applied to a full-scale chimney sample, thereby allowing a realistic prediction of fatigue life. The result is then compared to the prediction of fatigue life by applying the standard procedure of the Eurocode [5].

2 WIND TUNNEL EXPERIMENTS

2.1 Setup of free-vibration wind tunnel tests

Free-vibration wind tunnel tests on a free-standing, aeroelastic model with circular cross-section are performed at WISt Boundary Layer Wind Tunnel at Ruhr-Universität Bochum, Germany. It is an open circuit wind tunnel with a test section of 1.8 m in width and 1.6 m in height (Figure 1). The tests are performed in uniform flow, with turbulence intensity Iv = 4.5%.

Figure 1: WISt Wind tunnel at Ruhr-Universitaet Bochum, Germany (left) and wind tunnel model (right)

The aeroelastic model for the free-vibration wind tunnel tests is a cantilever beam with circular cross-section (Figure 1). The model is fabricated with a carbon tube (external diameter 32 mm and internal diameter 29 mm) that arises above the wind tunnel floor up to the height of 775 mm (measured from the wind tunnel floor). Below the wind tunnel, the carbon tube is connected to a steel bar (length = 210 mm, diameter 15 mm). The steel bar provides the necessary stiffness to the model and benefits from small damping dissipation. The steel bar is fixed to a force balance located at the model foot. Being the model surface smooth and the wind velocity below ca. 10 m/s, the Reynolds number of the investigation is subcritical ($Re < 2{,}1 \cdot 10^4$).

The structural characteristics of the model that are relevant for the dynamic investigation such as the mode shape, the modal mass and the equivalent mass, are calculated through a finite element model of the wind tunnel prototype. It results the modal mass $M_1 = 0.0630$ kg and equivalent mass $m_{eq} = 0.2286$ kg/m. The finite element model also serves for a preliminary estimation of the natural frequencies and thus of the critical velocity of vortex resonance. The actual natural frequency of the model is measured through wind tunnel experiments in still air and in existence of wind. In addition, the snap-back tests in still air (free-decay tests) allow the estimation of structural damping. The behavior of the model in still air is described in the next section.

The reactions at the base of the model are measured by a 6-component force balance of the type K6D154 (ME-Meßsysteme). The measuring range is up to 200N for the forces and up to 20Nm for moments. The force balance is composed by six independent sensors, which are equipped with strain gauges. The three forces along the axes x, y and z (named F_x, F_y, F_z) and the three bending moments around same axes (M_x, M_y, M_z, respectively) can be calculated in time-domain through a calibration matrix applied to the volt signals measured by the sensors. The sampling frequency is set to 2000 Hz. Every measurement lasts for 98,304 s.

The stiffness of the wind tunnel model is measured through static calibration tests with increasingly higher horizontal forces of known value applied at the top of the model. At the same time, the static displacement of the tip of the model is measured by a laser sensor. The stiffness of the model is linear. By means of the model flexibility, during dynamic tests the oscillation

at the top of the model can be calculated from the forces or the bending moments measured at the base.

2.2 Behavior of the model in still air

Snap back tests are performed in still air to test the natural frequency of the model and its structural damping. The latter also includes the contribution of the still air damping. Figure 2 (left) shows a free-decay tests. The natural frequency in still air is about 22,3 Hz. The structural damping is evaluated from the oscillation amplitudes as logarithmic decrement:

$$\delta_s \cong \frac{1}{m} ln\left(\frac{A_n}{A_{n+m}}\right) \tag{1}$$

The reversals considered for the evaluation of the structural damping are marked in blue in Figure 2 (left). The overall value of the damping, calculated considering the first and the last reversals in the free-decay time history, is $\delta_s = 0{,}018$. Additionally, a sensitivity study has been performed concerning the proper number m of cycles to be counted between two amplitudes in equation (1), in order to capture the non-linear behavior of the structural damping. Figure 2 (right) shows the behavior of the structural damping in case m = 25. The structural damping varies nonlinearly with the amplitude of oscillation between $\delta_s = 0{,}010$ and $\delta_s = 0{,}030$.

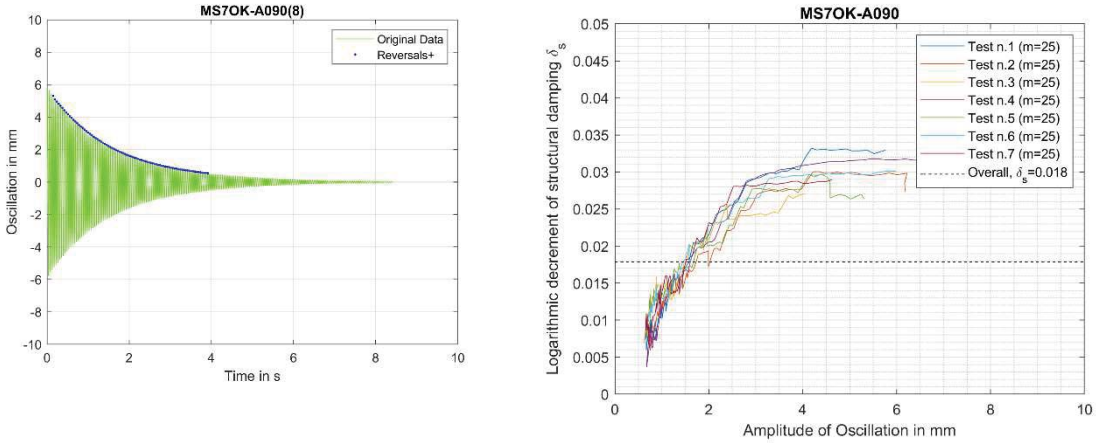

Figure 2: Snap back test and non-linear evaluation of the structural damping

2.3 Resonant vibrations in the lock-in range

The aeroelastic model of the tower is excited in the lock-in range for different wind velocities. Figure 3 shows the spectrum of the base force in the lift direction in case $V_H/V_{cr} = 0{,}85$. V_H is the wind velocity referred to the height of the model. The natural frequency of the model remains substantially unchanged with respect to still air tests: $f_l = 22{,}22$ Hz. The Strouhal number is St = 0,203 and this follows: $V_{cr} = 3{,}50$ m/s.

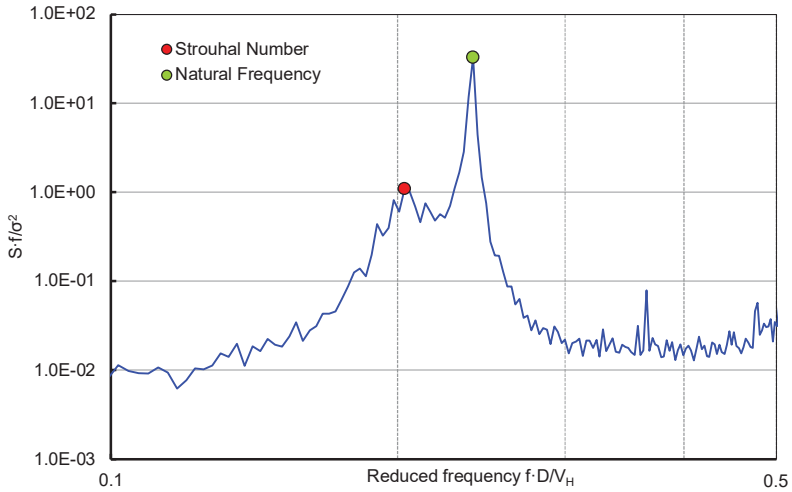

Figure 3: Spectrum of the base force in the lift direction, V_H = 2,99 m/s, V_H/V_{cr} = 0,85

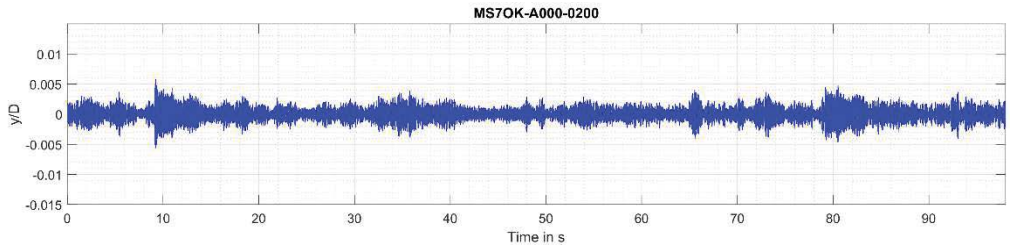

Figure 4: Time history of the response y/D at V_H/V_{cr} = 0,85

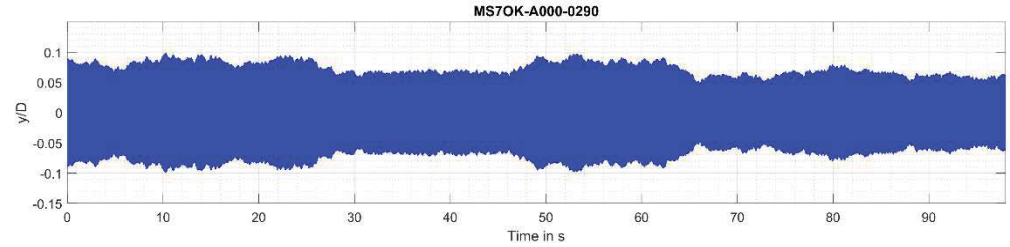

Figure 5: Time history of the response y/D at V_H/V_{cr} = 1,13 (max)

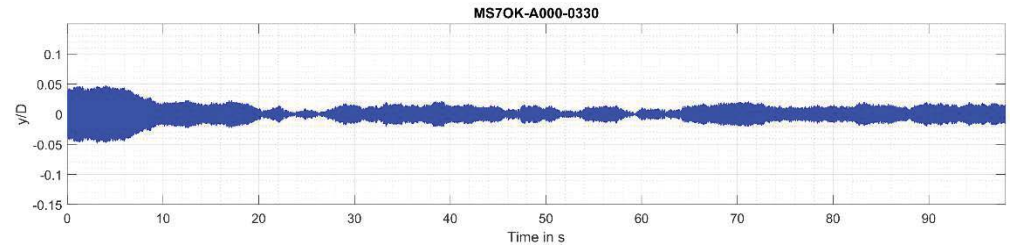

Figure 6: Time history of the response y/D at V_H/V_{cr} = 1,25

Figure 4, Figure 5 and Figure 6 show the time histories of the nondimensional response y/D for different velocities in the lock-in range. Because of the intermittency of the response, a question arises: is the response stationary, i.e. is the standard deviation a suitable parameter to describe the VIV response in the lock-in range? This issue is particularly important especially in view of the spectral analysis presented in the following sections, which considers the standard deviation of the response as governing parameter for the structural design.

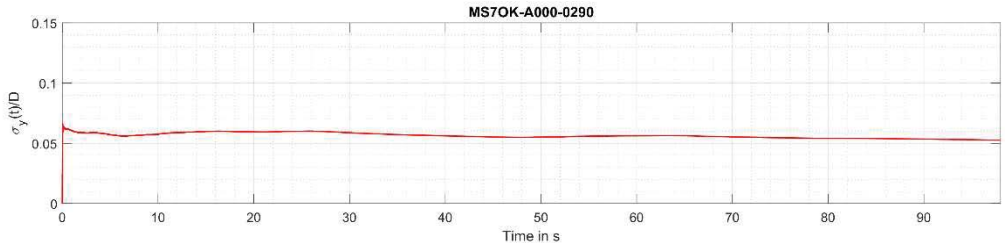

Figure 7: Convergence of the standard deviation of the response at V_H/V_{cr} = 1,13 (max)

First, the convergence of standard deviation of the response for increasingly higher time intervals is investigated. Figure 7 shows that the recorded signal is long enough to ensure a robust estimation of standard deviation of the response.

Second, the stationarity of the response is investigated by dividing the time history in blocks of 10-min events in full-scale. The full-scale similarity considers a full-scale frequency $f_{1,FS}$ = 0,629 Hz, as it will be explained later in Table 2. Being the natural frequency in the wind tunnel experiments $f_{1,WT}$ = 22,22 Hz, it follows that the frequency scale is λ_F = 35,33 and the time scale is its inverse, i.e. $\lambda_T = 1 / \lambda_F$ = 0,028. Therefore, 600 seconds in full-scale correspond to 16,98 seconds in the wind tunnel. Each of the recorded time histories includes five 10-min events in full-scale. For each event, the maximum amplitude and the standard deviation of the oscillation are calculated. Then, a statistical analysis of the maxima is performed to evaluate the mean value of the peak amplitudes among different events and the mean value of the standard deviations among different events. These two last parameters represent the statistical maximum and the statistical standard deviation, respectively, and they will be referred to in the following analysis. Their ratio allows calculating a statistically representative peak factor for the time history. Figure 8 shows the result for the case V_H/V_{cr} = 1,13. In particular:

Mean value of maxima, $y_{max} / D = 0{,}0932$
Mean value of standard deviation, $\sigma_y / D = 0.0536$
$k_p = y_{max} / \sigma_y = 1.74$

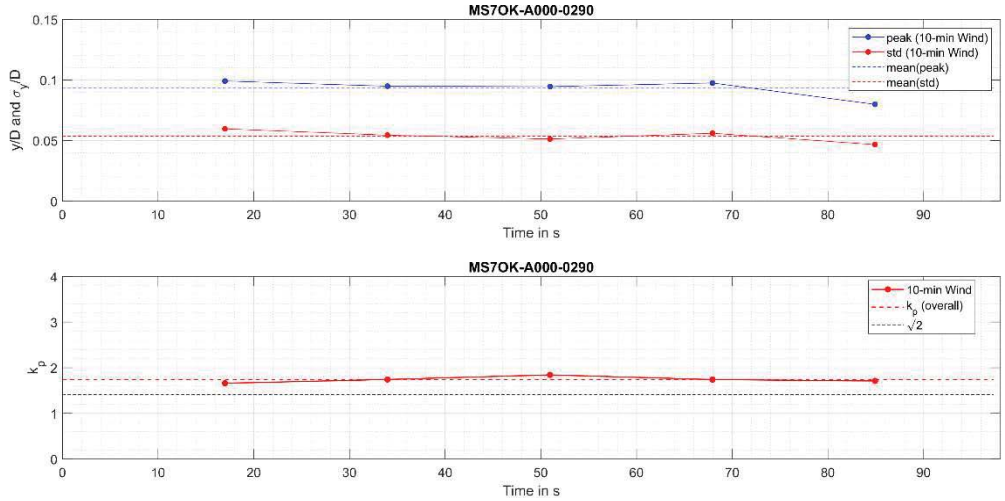

Figure 8: Analysis of peak amplitudes, standard deviations, peak factors k_p for 10-min events and for the overall time history (V_H/V_{cr} = 1,13 (max))

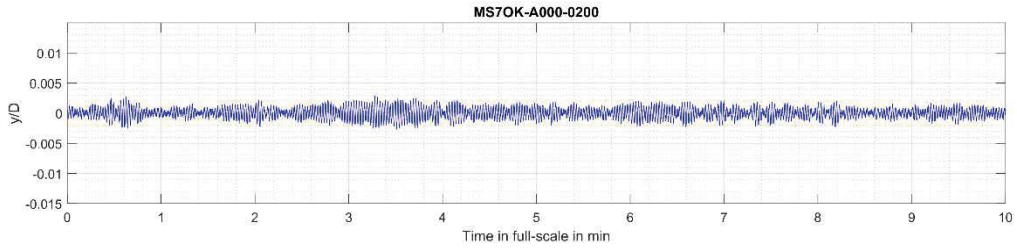

Figure 9: Time history of the response y/D in 10-min full-scale interval at V_H/V_{cr} = 0,85

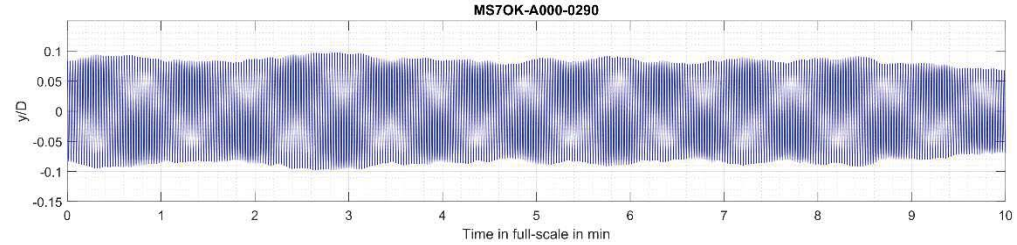

Figure 10: Time history of the response y/D in 10-min full-scale interval at V_H/V_{cr} = 1,13 (max)

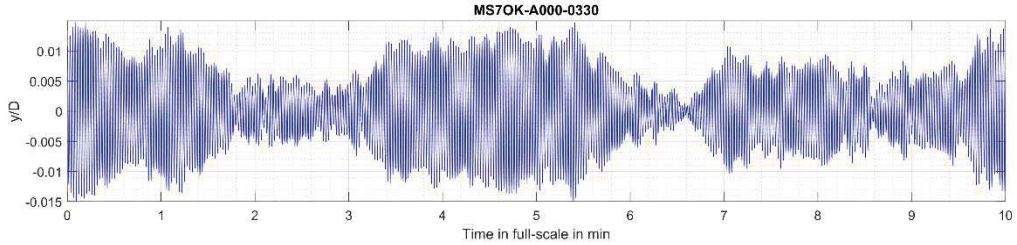

Figure 11: Time history of the response y/D at V_H/V_{cr} = 1,25

Furthermore, Figure 9, Figure 10 and Figure 11 show the time history of the response in a selected 10-min full-scale interval. For the sake of clarity, the y-axis is scaled 10 times in Figure 9 and Figure 11 with respect to Figure 10.

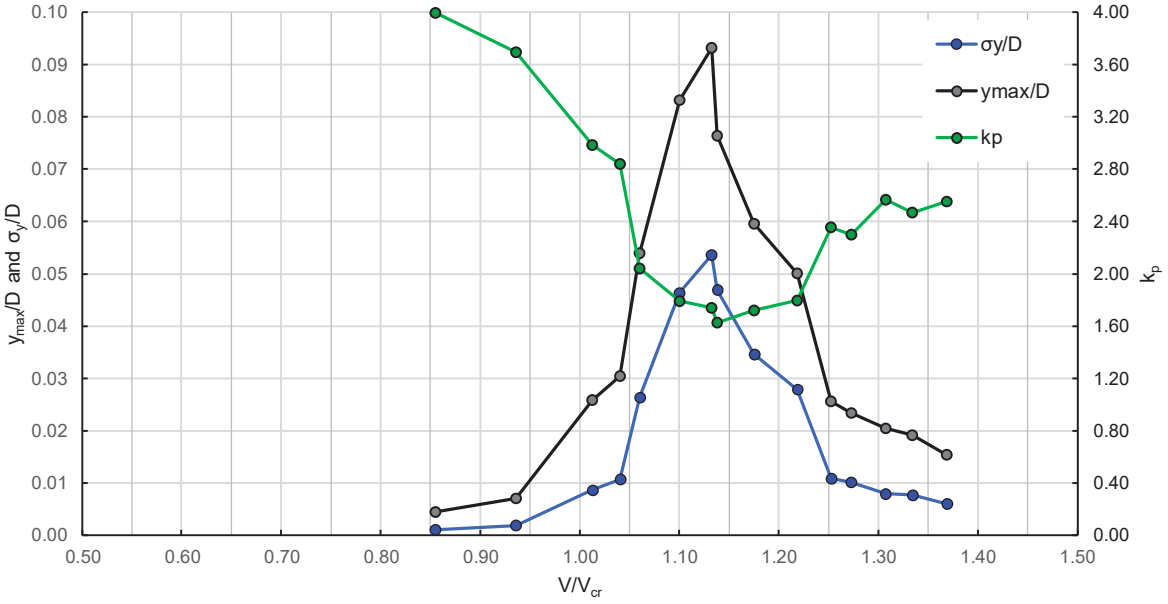

Figure 12: Statistical maxima of the oscillation, standard deviations and peak factors in the lock-in range

Figure 12 shows the lock-in phenomenon. As it often occurs, the largest oscillation occurs for $V > V_{cr}$. The right-hand side of the figure shows, instead, the distribution of the peak factors in the lock-in range. As expected, at the beginning and at the end of the lock-in range the stochastic behavior predominates and the peak factor increases. In full resonance, due to the predominant harmonic character, the peak factor is reduced. The ideal value $\sqrt{2}$ corresponds to the peak factor of a pure harmonic signal.

3 ESTIMATION OF THE NEGATIVE AERODYNAMIC DAMPING FROM FREE-VIBRATION WIND TUNNEL TESTS

Previous work of the authors allowed the measurement of negative aerodynamic damping K_a in vortex-induced vibrations through forced vibration wind tunnel tests [10]. The behavior of the negative aerodynamic damping as a function of rms oscillation is described by the following curve:

$$K_a = a \cdot e^{-b \cdot \frac{\sigma_y}{D}} \cdot \left(\frac{\sigma_y}{D}\right)^c \tag{2}$$

with a = 0,3464, b = 5,808 and c = 0,3582.

With regard to Equation (2), the largest oscillation in the lock-in range can be predicted by the following model, which originates from a modification of the Vickery&Basu model [14]:

$$\sigma_y^2 = \frac{S_{L1}(f_n)}{\left(\omega_1^2 \cdot M_1\right)^2} \cdot \frac{\omega_1}{\frac{4}{\pi}(\delta_s + \delta_a)} = \frac{S_{L1}(f_1)}{\left(\omega_1^2 \cdot M_1\right)^2} \cdot \frac{\omega_1}{8 \cdot \frac{\rho \cdot d^2}{m_{eq}} \cdot \left(\frac{Sc}{4\pi} - K_a\right)} \tag{3}$$

The background of equation (3) is explained in [9] and goes back to the evaluation of the resonant response to stochastic load in the first mode shape. The stochastic load is the vortex shedding load, which has a spectral density centered around the Strouhal frequency:

$$S_{L1}(f_1) \cong 2\lambda \cdot \int_0^H \left(\frac{1}{2}\rho V_m(z)^2\right)^2 \cdot D(z)^3 \cdot \frac{\sigma_{cL}^2}{\sqrt{\pi} \cdot St(z) \cdot \frac{V_m(z)}{d(z)} \cdot B(z)} \cdot \exp\left(-\left(\frac{1 - \frac{f_1}{St(z) \cdot \frac{V_m(z)}{d(z)}}}{B(z)}\right)^2\right) \cdot \Phi_n(z)^2 \cdot dz \tag{4}$$

By definition, the Vickery&Basu model considers the load on the non-vibrating structure and includes all aeroelastic effects in the negative aerodynamic damping. Although this assumption may be questionable, it has little effect on the response prediction, as long as the response is predominantly governed by the motion-induced forces. This condition happens in the case of sufficiently small Scruton numbers, i.e. pronounced lock-in range. In this case, the major role in the response prediction is played by the accurate estimation of both structural and aerodynamic damping terms.

A further remark to equation (4), which follows from the assumption of the Vickery&Basu model to consider load on the non-vibrating structure, is the absence of lock-in effect for $V \neq V_{cr}$, i.e. $f_s = St \cdot V_m/d \neq f_1$. For example, the largest oscillation occurs for $V / V_{cr} = 1{,}13$ in the present experiment (see Figure 12). This is a typical behavior particularly for sufficiently small Scruton numbers. According to the equation (4), $S_{L1}(f_1)$ calculated for $V_m = 1{,}10 \cdot V_{cr}$ is smaller than $S_{L1}(f_1)$ calculated for $V_m = V_{cr}$, due to the negative exponential function. Since the Strouhal law is violated in the lock-in range, it would be more reasonable not to apply any reduction to $S_{L1}(f_1)$ caused by the exponential term in the lock-in range, especially for $y = y_{max}$. However,

no further correction to the Vickery model is applied in this paper. Additional experimental evidence would be needed.

In present case, the nonlinear behavior of the structural damping needs to be considered, in order to ensure the most accurate estimation of the Scruton number which corresponds to the oscillation amplitude reached in lock-in. Referring to Figure 12 and considering the largest oscillation $y_{max}/D = 0{,}0932$ (i.e. $y_{max} = 2{,}98$ mm), the corresponding structural damping is estimated as $\delta_s = 0{,}028$. The air density during the experiments is 1,16 kg/m^3. It follows Sc = 10,74, being Sc defined as follows:

$$\mathrm{Sc} = \frac{2 \cdot m_{eq} \cdot \delta_s}{\varrho \cdot D^2}$$

Table 1 lists all the model parameters that are applied in this work to solve the equation (3). Unfortunately, some load parameters in equation (4), such as the rms value of the lift coefficient σ_{cL}, the correlation length relative to the diameter λ and the spectral bandwidth B, could not be measured during the experiments and therefore could only be estimated from literature and comparison with the Standard Codes.

Parameter	Symbol	Unit	Value	Reference
Model diameter	D	m	0,032	Wind tunnel model
Model height	H	m	1,016	Wind tunnel model
Model natural frequency	f_1	Hz	22,22	Measured
Structural damping	δ_s	-	0,028	Measured
Modal mass	M_1	kg	0.0630	Calculated from FE model
Equivalent mass	m_{eq}	kg/m	0.2286	Calculated from FE model
$\int_0^H \Phi_n(z)^2 \cdot dz = M_1 / m_{eq}$	-	-	0,276	Calculated from FE model
Scruton number	Sc	-	10,74	Calculated
Rms lift coefficient	σ_{cL}	-	0,7	EN 1991-1-4 [5]
Correlation length related to diameter	λ	-	1 (i.e. 1·d)	Estimated [2]
Spectral bandwidth	B	-	0,145	Estimated through 0,1 + Iv [2]
Strouhal number	St	-	0,203	Measured
Critical velocity	V_{cr}	m/s	3,50	Calculated from $V_{cr} = f_1 \cdot D/St$
Wind velocity at $y = y_{max}$ (uniform profile)	V_m	m/s	3,97	Measured at $y = y_{max}$
Velocity ratio at $y = y_{max}$	V_m / V_{cr}	-	1,13	Result
Air density	ρ	kg/m^3	1,16	Measured
Max amplitude of oscillation	y	mm	2,98	Measured (Figure 12)
Rms of the oscillation at max	σ_y	mm	1,72	Measured (Figure 12)

Table 1: List of model parameters

Considering all the parameters in Table 1, it is clear that the only unknown in equation (3) is the aerodynamic damping parameter K_a, which could be calculated. The result is $K_a = 0{,}82$. Considering the K_a-curve proposed in [10] (equation (2)), the agreement is satisfying, as shown in Figure 13. On the other hand, the well-known Vickery curve

$$K_a = K_{a0}\left(1 - \left(\frac{\sigma_y}{a_L \cdot D}\right)^2\right) \tag{5}$$

would give $K_a = 1{,}97$ at $\sigma_y/D = 0.054$ by assuming $K_{a0} = 2$ and $a_L = 0{,}4$ in accordance with [5] for the subcritical range of Reynolds number.

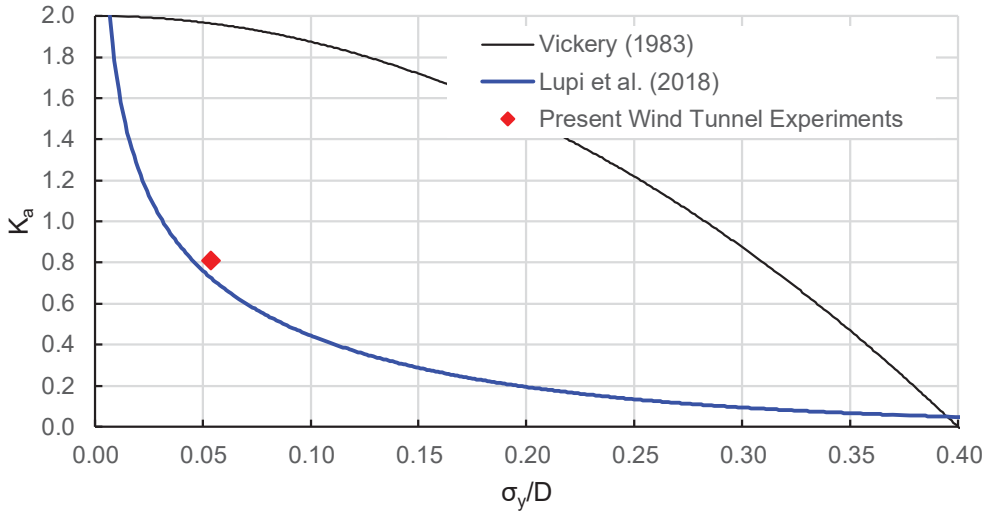

Figure 13: Estimation of negative aerodynamic damping parameter K_a from free-vibration tests and comparison with literature

4 PREDICTION OF FATIGUE LIFE

4.1 Case study

For the purpose of fatigue life prediction, wind stresses caused by vortex excitation need to be calculated on a sample structure. For this purpose, the full-scale chimney in Skjern (Denmark), described in [8] and [3] and investigated by the authors in [9] is chosen as case study. The governing parameter is the similar Scruton number used. In details, the structural parameters of the full-scale chimney applied for this work are reported in Table 2.

Parameter	Symbol	Unit	Value	Reference
Tower diameter (constant)	$D^{(FS)}$	m	1.1	[8]
Tower height	$H^{(FS)}$	m	45	[8]
Tower natural frequency	$f_1^{(FS)}$	Hz	0,629	[8]
Structural damping	$\delta_s^{(FS)}$	-	0,034	[8]
Modal mass	$M_1^{(FS)}$	kg	2218 kg	Calculated from FE model
Equivalent mass	$m_{eq}^{(FS)}$	kg/m	246,4	based on the mass distribution
$\int_0^H \Phi_n(z)^2 \cdot dz = M_1 / m_{eq}$	-	-	9,00	in [8] considering a parabolic mode shape
Scruton number	$Sc^{(FS)}$	-	11,078	Calculated

Table 2: Full-scale chimney in Skjern (Denmark) [3], [8]

4.2 Fatigue life estimation according to the Eurocode Method

The Eurocode EN 1991-1-4 [5] proposes a method to calculate the fatigue life of a structure subjected to vortex excitation, which was originally developed in [13]. The method is based on the calculation of the number of load cycles around $V = V_{cr}$ according to the Weibull distribution of the wind velocity. It further assumes that the vibration in the lock-in range is harmonic and its amplitude corresponds to the maximum resonant oscillation. The method is suitable for practical applications and generally provides safe results. The procedure is briefly described here and applied to the sample chimney in Table 2, in order to compare the results with a more sophisticated rainflow analysis for cycle counting, which is later applied to the wind tunnel measurements.

The Weibull probability distribution of the wind velocity is characterized by two parameters, the shape parameter k and the scale parameter A. The probability density function is:

$$f(V) = \frac{k}{A} \cdot \left(\frac{V}{A}\right)^{k-1} \cdot e^{-\left(\frac{V}{A}\right)^{k}} \tag{6}$$

The cumulative distribution function is the probability when the wind velocity V assumes a value less than or equal to V_i:

$$F(V) = P(V \leq V_i) = 1 - e^{-\left(\frac{V_i}{A}\right)^{k}} \tag{7}$$

It follows that the probability when the wind velocity assumes values comprised between V_1 and V_2 is expressed as:

$$P(V_1 \leq V \leq V_2) = F(V_2) - F(V_1) = e^{-\left(\frac{V_1}{A}\right)^{k}} - e^{-\left(\frac{V_2}{A}\right)^{k}} \tag{8}$$

In absence of wind statistics at the location of the structure, the Eurocode recommends:

- k = 2 (Rayleigh-Distribution)
- $A = \sqrt{2} \cdot V_{mod}$, being V_{mod} the modal value of the Weibull probability distribution. The parameter "A" can be taken as 20% of the mean wind velocity at the height of the cross-section where the vortex shedding occurs [5].

Assuming that the wind velocities V_1 and V_2 mark the beginning and the end of the lock-in range, respectively, the equation (8) describes the probability when the wind velocity excites the structure in the lock-in range. Considering the natural vibration frequency f_1, the number of load cycles in the lock-in range in the whole design lifetime of the structure (T = 50 years = $3{,}1536 \cdot 10^7 \cdot 50$ seconds) amounts to:

$$N = 3{,}1536 \cdot 10^7 \cdot \mathrm{T} \cdot \mathrm{f}_1 \cdot \left(e^{-\left(\frac{V_1}{A}\right)^{k}} - e^{-\left(\frac{V_2}{A}\right)^{k}}\right) \tag{9}$$

For the purpose of simplicity, [13] proposes:

$$e^{-\left(\frac{V_1}{A}\right)^{k}} - e^{-\left(\frac{V_2}{A}\right)^{k}} = f(V_{cr}) \cdot \Delta V = f(V_{cr}) \cdot \varepsilon_0 \cdot V_{cr} = \frac{k}{A} \cdot \left(\frac{V_{cr}}{A}\right)^{k-1} \cdot e^{-\left(\frac{V_{cr}}{A}\right)^{k}} \cdot \varepsilon_0 \cdot V_{cr} \tag{10}$$

[13] recommends $\varepsilon_0 = 0{,}3$, meaning that the lock-in range extends for $0{,}3 \cdot V_{cr}$, (e.g. $V_1 = 0{,}9 \cdot V_{cr}$ and $V_2 = 1{,}2 \cdot V_{cr}$), which is often the case.

For the case under investigation, considering the natural frequency $f_1 = 0{,}629$ Hz (see Table 2), the scale parameter A as $0{,}2 \cdot V_m(H)$, assuming the second terrain category and $v_b = 25$ m/s (see [5] and [6]), it results:

$$A = 0{,}2 \cdot V_m(H) = 0{,}2 \cdot v_b \cdot \left(\frac{H^{(FS)}}{10}\right)^{0{,}16} = 0{,}2 \cdot 25 \cdot \left(\frac{45}{10}\right)^{0{,}16} = 6{,}36\ m/s \tag{11}$$

The critical wind velocity V_{cr} is:

$$V_{cr} = \frac{f_1 \cdot D^{(FS)}}{St} = \frac{0{,}629 \cdot 1{,}1}{0.203} = 3{,}41\ m/s \tag{12}$$

Therefore:

$$N = 3{,}1536 \cdot 10^7 \cdot \mathrm{T} \cdot \mathrm{f}_1 \cdot \frac{k}{A} \cdot \left(\frac{V_{cr}}{A}\right)^{k-1} \cdot e^{-\left(\frac{V_{cr}}{A}\right)^k} \cdot \varepsilon_0 \cdot V_{cr} = 1{,}2823 \cdot 10^8 \tag{13}$$

The Eurocode Method assumes that the resonant vibrations of the structure in the lock-in range are harmonic with constant amplitude. Their amplitude corresponds to the maximum oscillation in the lock-in range. Using y_{max}/d value from the wind tunnel tests (Figure 12), it follows:

$$y_{max}^{(FS)} = \frac{y_{max}}{d} \cdot D^{(FS)} = \frac{y_{max}}{d} \cdot 1{,}1 = 0{,}0932 \cdot 1{,}1 = 0{,}103\ m \tag{14}$$

The wind stresses result from the following distribution of inertial forces along the height of the structure [5]:

$$F_w(z) = m(z) \cdot (2 \cdot \pi \cdot f_1)^2 \cdot \Phi_1(z) \cdot y_{max}^{(FS)} \tag{15}$$

For the purpose of this investigation, the bending moment at the base of the chimney is considered. Referring to the cross-section at the based described in [8] (diameter D = 1,1 m and wall thickness t = 0,016 m), the maximum of the wind stress in resonance corresponds to σ_{max} = 13,91 N/mm^2, i.e. stress range $\Delta\sigma_{max}$ = 27,82 N/mm^2. The stress range corresponds to the difference between two extremes. The relationship between the maximum oscillation on top and the stress range at the base is as follows:

$$\Delta\sigma = 2 \cdot \frac{\int_0^H m(z) \cdot (2 \cdot \pi \cdot f_1)^2 \cdot \Phi_1(z) \cdot z \cdot dz}{W} \cdot y_{max}^{(FS)} \tag{16}$$

The cumulative damage and the fatigue lifetime follow from the assumption of a detail category. Let us consider, for instance, the detail category 45 according to [7]. In this case, according to the Wöhler line, the number of load cycles N_R to cause failure amounts to 1,2019*10^7. From the previously calculated total number of load cycles of stress range $\Delta\sigma_{max}$ during the required design life (equation (13)), it results:

$$D_d = \frac{N}{N_R} = \frac{1{,}28.23 \cdot 10^8}{1{,}2019 \cdot 10^7} = 10{,}67 > 1 \tag{17}$$

Being $D_d > 1$, the structure will be damaged by fatigue during its lifetime of 50 years, i.e. after about 5 years. This result follows from the assumption that the vibration of the structure occurs in the lock-in range with constant amplitude equal to its maximum value. This assumption is particularly convenient for Code applications and is on the safe side. However, a more realistic fatigue lifetime may be estimated by considering the actual variability of the oscillation amplitude in the lock-in range, e.g. through rainflow counting.

4.3 Fatigue life estimation considering rainflow cycle counting

The rainflow analysis is a method to count the number of load cycles and produce a stress range spectrum in case of time histories with varying amplitude. In this work, it is referred to the algorithm for rainflow counting that is described in ASTM E1049-85 [1].

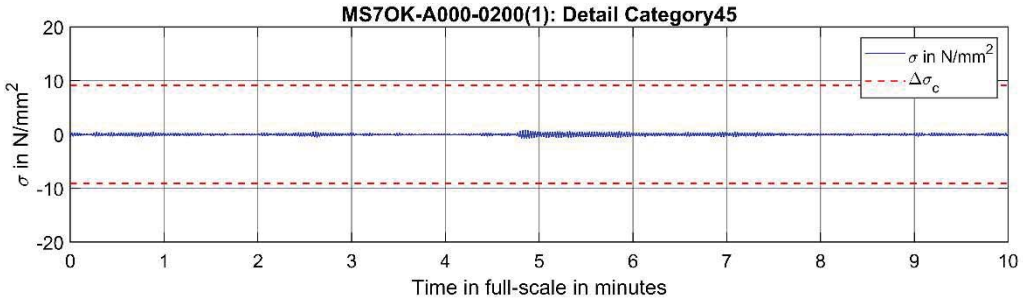

Figure 14: Time history of the stress response in 10-min full-scale interval at V_H/V_{cr} = 0,85

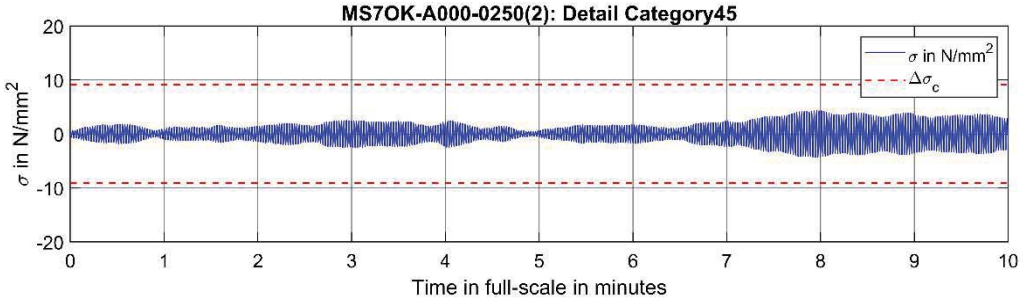

Figure 15: Time history of the stress response in 10-min full-scale interval at V_H/V_{cr} = 1,01

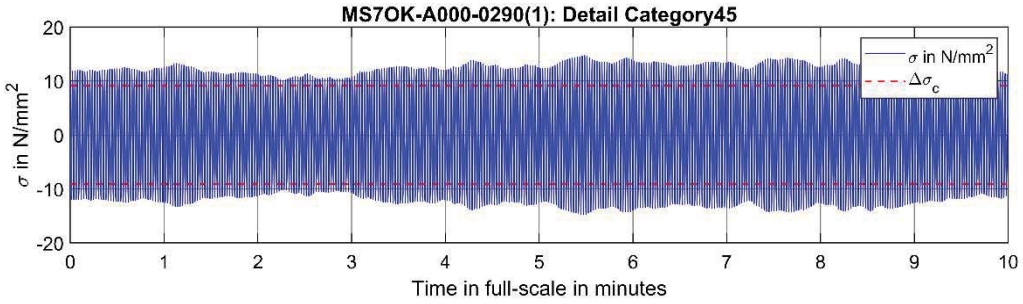

Figure 16: Time history of the stress response in 10-min full-scale interval at V_H/V_{cr} = 1,13 (max). The dashed line indicates the cut-off stress for the Detail Category 45.

Figure 14, Figure 15, Figure 16 show some typical time histories of the stresses at the foot of the chimney in the lock-in range, which are calculated by integration of the inertial forces along the height according to the equation (15). The figures also plot $\Delta\sigma_L$, i.e. the cut-off limit for the given detail category (in this case: DC = 45), i.e.:

$$\Delta\sigma_L = \left(\frac{2}{5}\right)^{\frac{1}{3}} \cdot \left(\frac{5}{100}\right)^{\frac{1}{5}} \cdot DC = 18{,}21\ N/mm^2 \tag{18}$$

For all stress ranges above the $\Delta\sigma_L$ stress range, damage is accumulated.

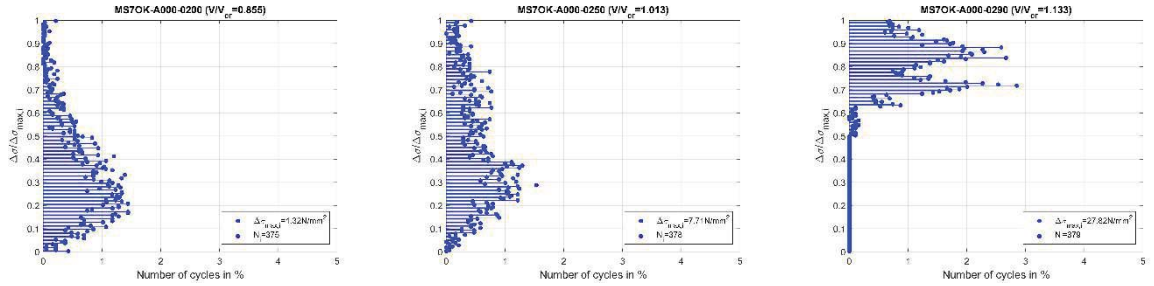

(a) (b) (c)

Figure 17: Stress collectives in the lock-in range by rainflow counting

Figure 17 describes the collectives, i.e. the stress range spectra, which correspond to the time histories in Figure 14, Figure 15, Figure 16, respectively. Figure 17 (a) shows a typical collective shortly before beginning of the lock-in range. In accordance with a stochastic signal, the number of cycles that correspond to the maxima of the oscillation is small compared to the number of cycles for smaller oscillation. A similar pattern is observed in Figure 17 (b). Figure 17 (c) - which corresponds to a fully resonant time history (see Figure 16), where the largest oscillation in the lock-in range is reached - indicates another behavior. Due to the predominant harmonic component, most of load cycles occur with the larger oscillations.

The calculation of the stress collectives from the experiments at different V/V_{cr} through rainflow cycle counting allows the calculation of actual cumulative damage in the structure. For each ratio V/V_{cr}, a velocity class can be identified such that $V_1 \leq V/V_{cr} < V_2$. For each velocity class, depending on the Weibull distribution defined in equation (6), the probability when the wind velocity assumes values within the velocity class can be calculated (equation (8)). In this way, the number of load cycles for each velocity class can be calculated (N_i) according to the equation (9).

Table 3 shows the calculation of the cumulative damage by considering largest stress range $\Delta\sigma_{max,i}$ for each velocity class and attributing it to the number of cycles N_i. The calculation assumes that the vibration in each velocity class is harmonic and its amplitude corresponds to $y_{max,i}/D$ in the lock-in curve shown in Figure 12. The rainflow counting is not considered in this calculation. The cumulative damage then results:

$$D_d = 1{,}752 > 1 \text{ (considering the lock-in range but without rainflow counting)}$$

It means a reduction of the fatigue lifetime to about 28,5 years. On the other hand, if the intermittent behavior is considered through rainflow analysis and each stress collective such as those in Figure 17 is considered for each velocity class, the cumulative damage results smaller than 1, i.e. the structure will not be damaged by fatigue during the whole lifetime (50 years):

$$D_d = 0{,}659 < 1 \text{ (considering rainflow counting)}$$

Finally, given the cumulative damage calculated through rainflow analysis, the equivalent stress ranges which correspond to the cumulative damage can be calculated for each velocity class (Table 5). From that, equivalent oscillation amplitudes and equivalent peak factors for fatigue analysis in the lock-in range are developed. Figure 18 shows the peak factors for the ultimate limit state (already shown in Figure 12), which provide the maxima in the lock-in range. The peak factors for fatigue analysis, which provide equivalent stresses that give the same cumulative damage as the rainflow analysis, are also shown in the figure.

Velocity classes	V_a [m/s]	V_b [m/s]	V_i [m/s]	V_i / V_{cr}	N_i = Number of load cycles (Weibull)	$y_{max,i}/D$ [-]	$\Delta\sigma_{max,i}$ = stress range [N/mm²]	N_{Ri} = Number of load cycles to failure	$D_d = N_i/N_{Ri}$ = Cumulative Damage
1	2.78	3.05	2.91	0.855	3.20E+07	0.004	1.325	Inf	0.000
2	3.05	3.32	3.19	0.936	3.27E+07	0.007	2.117	Inf	0.000
3	3.32	3.50	3.45	1.013	2.24E+07	0.026	7.705	Inf	0.000
4	3.50	3.58	3.55	1.041	1.04E+07	0.030	9.088	Inf	0.000
5	3.58	3.68	3.62	1.061	1.31E+07	0.054	16.114	Inf	0.000
6	3.68	3.81	3.75	1.101	1.59E+07	0.083	24.832	2.12E+07	0.751
7	3.81	3.87	3.86	1.133	8.47E+06	0.093	27.822	1.20E+07	0.705
8	3.87	3.95	3.88	1.139	9.63E+06	0.076	22.805	3.25E+07	0.296
9	3.95	4.08	4.01	1.176	1.80E+07	0.060	17.786	Inf	0.000
10	4.08	4.21	4.15	1.219	1.74E+07	0.050	14.959	Inf	0.000
11	4.21	4.30	4.27	1.253	1.23E+07	0.026	7.665	Inf	0.000
12	4.30	4.40	4.34	1.273	1.25E+07	0.023	6.966	Inf	0.000
13	4.40	4.50	4.46	1.308	1.41E+07	0.020	6.107	Inf	0.000
14	4.50	4.61	4.55	1.335	1.39E+07	0.019	5.703	Inf	0.000
15	4.61	4.72	4.67	1.369	1.55E+07	0.015	4.595	Inf	0.000
Sum					2.485E+08				**1.752**

Table 3: Cumulative damage in the lock-in range without rainflow counting

Velocity classes	V_a [m/s]	V_b [m/s]	V_i [m/s]	V_i / V_{cr}	N_i = Number of load cycles (Weibull)	N_{Ri} = Number of load cycles to failure = N_i/D_d	D_d = Cumulative damage through Rainflow
1	2.78	3.05	2.91	0.855	3.20E+07	Inf	0.000
2	3.05	3.32	3.19	0.936	3.27E+07	Inf	0.000
3	3.32	3.50	3.45	1.013	2.24E+07	Inf	0.000
4	3.50	3.58	3.55	1.041	1.04E+07	Inf	0.000
5	3.58	3.68	3.62	1.061	1.31E+07	Inf	0.000
6	3.68	3.81	3.75	1.101	1.59E+07	6.80E+07	0.234
7	3.81	3.87	3.86	1.133	8.47E+06	3.03E+07	0.279
8	3.87	3.95	3.88	1.139	9.63E+06	6.64E+07	0.145
9	3.95	4.08	4.01	1.176	1.80E+07	Inf	0.000
10	4.08	4.21	4.15	1.219	1.74E+07	Inf	0.000
11	4.21	4.30	4.27	1.253	1.23E+07	Inf	0.000
12	4.30	4.40	4.34	1.273	1.25E+07	Inf	0.000
13	4.40	4.50	4.46	1.308	1.41E+07	Inf	0.000
14	4.50	4.61	4.55	1.335	1.39E+07	Inf	0.000
15	4.61	4.72	4.67	1.369	1.55E+07	Inf	0.000
Sum					2.48E+08		**0.659**

Table 4: Cumulative damage in the lock-in range by rainflow counting

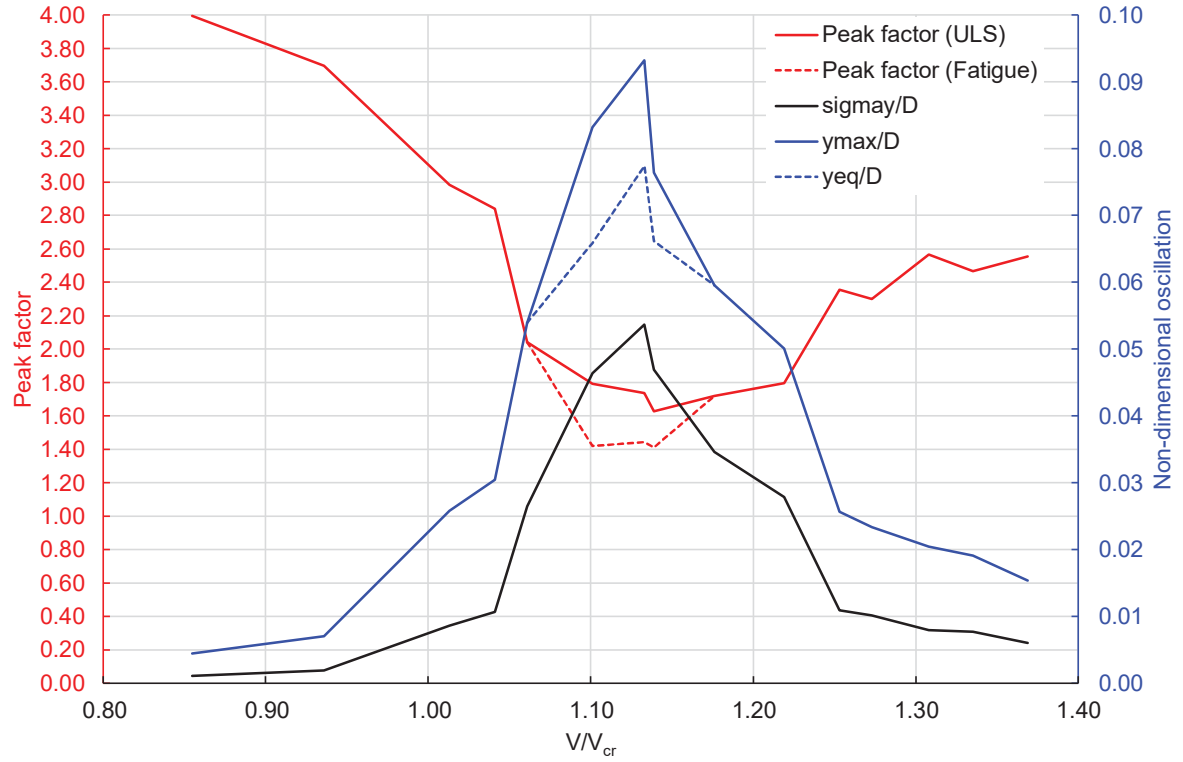

Figure 18: Peak factors for ultimate limit state (ULS) and equivalent peak factors in the lock-in range for fatigue analysis

Velocity classes	V_i / V_{cr}	$y_{max,i} / D$ (Figure 12a)	$\sigma_{,i} / D$ (Figure 12a)	$k_{pi} = y_{max,i} / \sigma_{,i}$ (Figure 12b)	D_d = Cumulative damage through Rainflow	$\Delta\sigma_{eq,i}$ = equivalent stress range [N/mm^2]	$y_{eq,i} / D$ = equivalent amplitude	$k_{pi,eq}$ = equivalent peak factor for fatigue analysis
1	0.855	0.004	0.001	3.995	0.000	≤ 18.212	≤ 0.061	n/a
2	0.936	0.007	0.002	3.696	0.000	≤ 18.212	≤ 0.061	n/a
3	1.013	0.026	0.009	2.985	0.000	≤ 18.212	≤ 0.061	n/a
4	1.041	0.030	0.011	2.838	0.000	≤ 18.212	≤ 0.061	n/a
5	1.061	0.054	0.026	2.042	0.000	≤ 18.212	≤ 0.061	n/a
6	1.101	0.083	0.046	1.792	0.234	19.675	0.066	1.420
7	1.133	0.093	0.054	1.737	0.279	23.123	0.077	1.444
8	1.139	0.076	0.047	1.627	0.145	19.765	0.066	1.411
9	1.176	0.060	0.035	1.720	0.000	≤ 18.212	≤ 0.061	n/a
10	1.219	0.050	0.028	1.795	0.000	≤ 18.212	≤ 0.061	n/a
11	1.253	0.026	0.011	2.357	0.000	≤ 18.212	≤ 0.061	n/a
12	1.273	0.023	0.010	2.300	0.000	≤ 18.212	≤ 0.061	n/a
13	1.308	0.020	0.008	2.566	0.000	≤ 18.212	≤ 0.061	n/a
14	1.335	0.019	0.008	2.466	0.000	≤ 18.212	≤ 0.061	n/a
15	1.369	0.015	0.006	2.554	0.000	≤ 18.212	≤ 0.061	n/a
Sum					**0.659**			

Table 5: Equivalent peak factors for fatigue analysis

5 CONCLUSIONS

The paper analyzes the negative aerodynamic damping in vortex-induced vibrations through free-vibration tests on an aeroelastic model. The result is compared with the curve previously gained by the authors through forced-vibration tests and shows a good agreement. Then, fatigue analysis through rainflow cycle counting is applied to the time histories measured in the wind tunnel experiments, which show a quasi-periodic behavior in the lock-in range. In view of fatigue, not the maxima, but rather the stress distribution needs to be considered for the evaluation of the fatigue lifetime. The rainflow analysis allows the calculation of equivalent stresses which produce the same cumulative damage as the actual time histories with varying amplitude. In this way, a peak factor for fatigue analysis can be defined. Similarly, using the ultimate limit state peak factor that is applied to the standard deviation of the response, the largest oscillation in the lock-in range is calculated.

6 ACKNOWLEDGEMENTS

This work is part of a research project funded by the Deutsche Forschungsgemeinschaft (DFG, German Research Foundation) – Project number 426322127. The support is gratefully acknowledged.

REFERENCES

[1] ASTM E1049-85 Standard Practices for Cycle Counting in Fatigue Analysis, *ASTM International.* 2017

[2] CICIND Model Code for Steel Chimneys, The CICIND Chimney Standard, 2010.

[3] Dyrbye C., Hansen S.O., *Wind Loads on Structures*, John Wiley & Sons Ltd, 1997.

[4] Ehsan F., Scanlan R.H. Vortex-Induced Vibrations of Flexible Bridges. *Journal of Engineering Mechanics*, Vol. 116, No 6, 1990.

[5] EN 1991-1-4. Eurocode 1: Actions on Structures, Part 1-4: General actions - Wind actions, 2010.

[6] DIN EN 1991-1-4/NA German National Annex to Eurocode 1. Actions on Structures, Part 1-4: General actions - Wind actions, 2010.

[7] EN 1993-1-9: Eurocode 3: Design of Steel Structures - Part 1-9: Fatigue, 2005.

[8] Frandsen S., RISO kontraktrapport: Tvaersvingninger af stalskorstene. Feltmalinger. Roskilde (in Danish), 1979.

[9] Lupi F., Niemann H.-J., Höffer R., A novel spectral method for cross-wind vibrations: Application to 27 full-scale chimneys. *Journal of Wind Engineering and Industrial Aerodynamics*, 171, pp. 353-365, 2017.

[10] Lupi F., Niemann H.-J., Höffer R., Aerodynamic damping model in vortex-induced vibrations for wind engineering applications. *Journal of Wind Engineering and Industrial Aerodynamics*, 174, pp. 281-295, 2018.

[11] Náprstek J., Fischer C. Analysis of the quasiperiodic response of a generalized van der Pol nonlinear system in the resonance zone. *Computers and Structures*, 207, pp. 59-74, 2018.

[12] Ruscheweyh H.; Sedlacek G., 1988. Crosswind vibrations of steel stacks. - critical comparison between some recently proposed codes. *Journal of Wind Engineering and Industrial Aerodynamics*, Volume 30, Issues 1–3, 173-183.

[13] Ruscheweyh H., Ein verfeinertes, praxisnahes Berechnungsverfahren wirbelerregter Schwingungen von schlanken Baukonstruktionen im Wind. *Beiträge zur Anwendung der Aeroelastik im Bauwesen*, Heft 20. Innsbruck Lausanne, 1986

[14] Vickery B.J., Basu R.I., Across-wind Vibrations of Structures of Circular Cross-section. Part I: Development of a mathematical model for two-dimensional conditions. *Journal of Wind Engineering and Industrial Aerodynamics*, Vol. 12, 49–73, 1983.

EURODYN 2020
XI International Conference on Structural Dynamics
M. Papadrakakis, M. Fragiadakis, C. Papadimitriou (eds.)
Athens, Greece, 23–26 November 2020

MODELING THE INTERACTION OF GALLOPING AND VORTEX INDUCED VIBRATION OF STEEL-CONCRETE COMPOSITE BRIDGES IN LAUNCHING PHASE

Cong Chen, Niccolo Wieczorek, Julian Unglaub, and Klaus Thiele

Institute of Steel Structures, Technische Universität Braunschweig, Beethovenstr. 51, Brunswick, Germany

e-mail: {c.chen, n.wieczorek, j.unglaub, k.thiele}@ stahlbau.tu-braunschweig.de

Keywords: Galloping; Vortex induced vibration; steel-concrete composite bridge; Wind tunnel tests; wake-oscillator model

Abstract. *Aeroelastic galloping instability and vortex induced vibration can be both relevant during the launching phase of steel-concrete composite bridges, due to the light weight and bluff shape of the normally first-launched steel box. A bridge deck sectional model with an open cross section, which is typical during the construction phase of steel-concrete composite bridges, was tested by means of wind tunnel techniques in smooth flow. Strong interaction between galloping and vortex induced vibration was observed for this bridge deck at a wind angle of attack of 4°， being the actual galloping onset fixed at the Kármán-vortex-resonance wind speed up to a high value of the mass-damping parameter. Tamura's wake-oscillator model was selected to model the interaction phenomenon observed for this bridge deck, following a recently proposed parameter identification method. For a wide range of the mass-damping parameter examined, satisfying agreements were found between the solutions of the mathematical model and the wind tunnel aeroelastic test results. This mathematical model was then applied to a full-scale case study, which is a 7-span continuous steel-concrete bridge during the critical launching phase.*

1 INTRODUCTION

Slender structures with special cross sections, like square and D shapes, can be susceptive to both galloping instability and vortex induced vibration (VIV) in the across wind direction. Under certain circumstances, these two phenomena are supposed to interact with each other, promoting a combined VIV-galloping instability [1]. The mass-damping parameter, namely the well-known Scruton number (*Sc*), plays a key role in this complex behavior [2]. And a high value of *Sc*, dependent on the cross section geometry, is usually needed to well separate these two phenomena. Otherwise, the complex behavior of the VIV-galloping instability is unable to be predicted by either the classical quasi-steady galloping theory or the VIV theory.

Two important mathematical models aiming at capturing the interaction mechanics of VIV and galloping were proposed by Corless and Parkinson [3] and Tamura and Shimada [4], by coupling an equation modelling the dynamics of the vortex-shedding force to the classical nonlinear equation describing the transverse motion of the cylinder according to the quasi-steady theory. In describing the self-excited and self-limited characteristics of the vortex shedding force, the former adopted the lift-oscillator model which is a Rayleigh-type oscillator, while the latter adopted the wake-oscillator which is a Van der Pol-type oscillator. In particular, the model proposed by Tamura and Shimada [4] was deduced based on physical considerations of the near-wake [5], rather than simply with an empirical approach. Recently, the wake-oscillator model was slightly modified and applied to a 3:2 rectangular cylinder, showing good agreements with the experimental results in a wide range of Scruton number [6].

For engineering practice, this combined VIV-Galloping instability may occur when the Scruton number of the structure is not high enough. In particular, this combined instability seems very relevant for the modern launching of steel-concrete composite bridges, since the steel box girder, which is normally launched first, could feature light weight, low damping and bluff cross section. A typical case should be mentioned is the Aftetal Bridge (in Germany), since its 90-m steel box girder was totally modified during the construction phase with temporary wind fairings to eliminate the risk of transverse galloping [7], as shwon in Figure 1.

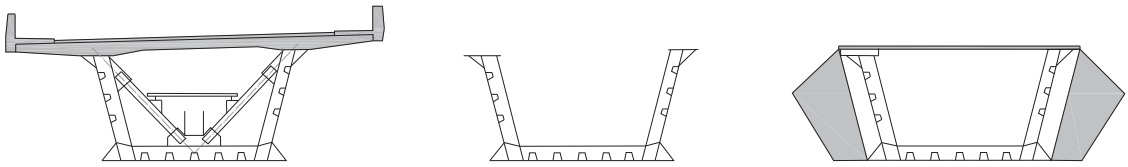

Figure 1. Cross-section modification of the Aftetal bridge, Germany, during the launching phase: (a) complete steel-concrete composite deck in service; (b) original steel box, and (c) modified steel box with temporary wind fairings during the launching phase [7].

In our previous work [8], a bridge deck model with typical open cross section was experimentally tested in smooth flow, showing a strong VIV-galloping tendency at its mean wind angle of attack of 4° (see the velocity-amplitude curve replotted in Figure 4). There, the actual galloping onset is fixed at the Kármán-vortex-resonance reduced critical wind speed V_r for Scruton number up to at least 70.

In this work, additional wind tunnel static tests were supplemented for the bridge deck model particularly at its 4° flow incidence, aiming at clarifying the dependence of the vortex shedding force coefficient C_{L0} on Reynolds number that reported in [8]. Mathematical modeling for the VIV-galloping instability of the bridge deck is firstly carried out on the wind tunnel sectional model. Then, the wake oscillator model with the parameters obtained from wind

tunnel tests was applied to a full-scale case study, which is a 7-span continuous steel-concreted bridge during its critical launching phase.

2 WIND TUNNEL TESTS

The extra wind tunnel static tests were carried out with the same wind tunnel model in the same wind tunnel facility as reported in [8], except that the static setup was re-mounted after one year later. More measures were added for the 4° angle of attack at various Reynolds number ($Re = \rho Ud/\mu$, being μ the dynamic viscosity of air). Details about the geometry of the bridge deck model is given in Figure 2. The length of the bridge deck model between two end-plates is l_e = 1300 mm.

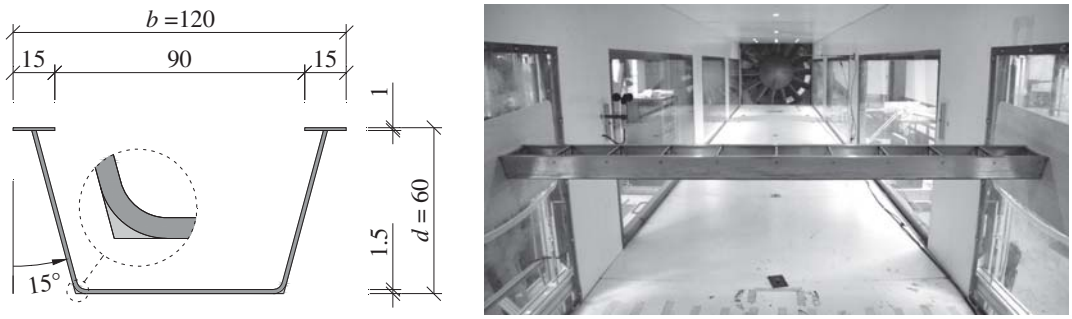

Figure 2. (a) Geometry of the open cross section, and (b) photo of the bridge deck model mounted in the wind tunnel (dimensions in mm).

The method of calculating the sinusoidal equivalent amplitude of the fluctuating lift coefficient C_{L0} was also improved. In [8], the C_{L0} coefficient was obtained by integrating the power spectral density of the fluctuating lift with a narrow band around the Strouhal frequency n_{st}, then square-rooting, normalizing with $0.5\rho U^2 dl_e$ and finally timing $\sqrt{2}$. However, the C_{L0} obtained in this way is affected by the dynamic amplification effect, unless the first bending natural frequency of the model is very high compared to the vortex-shedding frequency. To correct this bias, the classical dynamic amplification factor for a single-degree-of-freedom system was employed. First, a sensitivity analysis showed that for damping ratios up to 5% the amplification factor exhibits negligible variations, if the ratio of the vortex-shedding frequency to the model natural frequency is lower than 0.84 (this is the maximum frequency ratio encountered during the static tests). Consequently, since for an aluminum model rigidly mounted in the static setup, the damping ratio of the first bending mode is unlikely to be higher than 5%, a null damping ratio was therefore considered to calculate the amplification factor and to correct the C_{L0} values.

Finally, the main results in our previous work were given here again, which is supposed to facilitate the mathematical modeling work that is to be presented in the following. Figure 3 shows the mean drag and lift coefficients for the bridge deck model, respectively defined as $C_D = D/(0.5\rho U^2 dl_e)$ and $C_L = L/(0.5\rho U^2 dl_e)$, being D and L respectively the mean drag and lift over records of 100 s. C_D and C_L will be used to calculate the C_{Fy}^{QS} coefficient in the mathematical modeling work. Figure 4 shows the aeroelastic response of the bridge deck at its 4° mean flow incidence, with various Scruton number considered. The natural frequency of the model in still-air is n_0 = 9.63 Hz and n_0 = 9.53 Hz respectively for test case #a1-a6 and #a7-a9. y_{rms} represents the root mean square value of the across wind displacement y in the steady or statistically steady oscillation state. $V_r = 1/(2\pi St)$ denotes the Kármán-vortex-resonance wind

speed in reduced form. And for the bridge deck model at 4° flow incidence, the static test reports a Strouhal number St = 0.102. Finally, Scruton number is defined as $Sc = 4\pi M\zeta_0/\rho d^2 l_e$, with ζ_0 the damping ratio and M the effective oscillation mass (3.6 kg for test case #a1-a6 and 3.67 kg for test case #a7-a9).

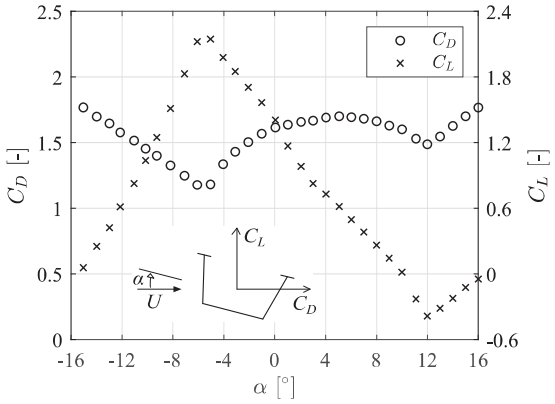

Figure 3. Mean drag and lift coefficient for various wind angle of attack of the bridge deck model at $Re = 6.0 \cdot 10^4$.

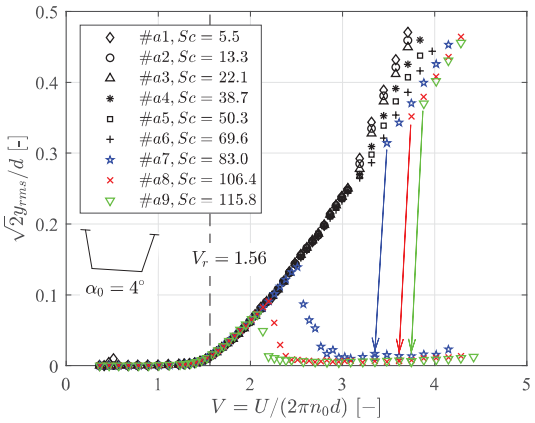

Figure 4. Effect of the Scruton number on the dynamic response of the bridge deck model at $\alpha_0 = 4°$.

3 WAKE OSCILLATOR MODEL FOR SECTIONAL MODEL

3.1 The wake oscillator model

The wake-oscillator nonlinear model proposed by Tamura and Shimada [4] was selected to simulate the VIV-galloping interaction for the bridge deck at 4° mean flow incidence. The near-wake lamina is supposed to pivot about the centroid of the bridge deck (following the modified form of wake oscillator in [6]), as schematized in Figure 5. The transverse motion of the bridge deck y and the rotation of the wake lamina ϑ are respectively governed by the two coupled equations in a dimensionless form:

$$Y'' + 2\zeta_0 Y' + Y = \frac{V^2}{m^*} f \cdot \left(\vartheta - \frac{Y'}{V} \right) + \frac{V^2}{m^*} C_{Fy}^{QS}(\alpha) \tag{1}$$

$$\vartheta'' - 2\beta v \vartheta' \cdot \left(1 - \frac{4f^2}{C_{L0}^2} \vartheta^2 \right) + v^2 \vartheta = \lambda Y'' + v^2 \frac{Y'}{V} \tag{2}$$

where $Y = y/d$ is the normalized displacement, $m^* = M/(0.5\rho d^2 l_e)$ the mass ratio, $C_{Fy}^{QS}(\alpha)$ the quasi-steady transverse force coefficient, $\upsilon = n_{st}/n_0$ the frequency ratio. f is a parameter relating the rotation of the wake ϑ to the resulting unsteady lift coefficient. $(\cdot)'$ represents differentiation with respect to non-dimensional time $\tau = 2\pi n_0 t$. The expression of β and λ are:

$$\beta = \frac{4\sqrt{2}}{\pi} St^2 h^* f \tag{3}$$

$$\lambda = 8\pi St^2 h^* \tag{4}$$

The restoring force F_L on the wake lamina is supposed to act at 1/4 of its chord, as suggested in [6], resulting in following relationship representing an additional restriction between the St, h^* and l^*:

$$St = \frac{n_{st} d}{U} = \sqrt{\frac{1}{8\pi l^* h^*}} \tag{5}$$

being $h^* = h/d$ and $l^* = l/d$ are the normalized wake width and semi-length.

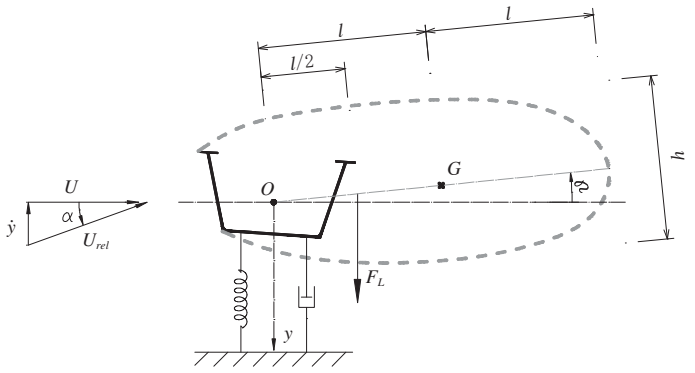

Figure 5. Schematic of the wake oscillator implemented for the bridge deck. G is the centroid of the equivalent near-wake lamina, and O is the pivot position of the wake, which is assumed to coincide with the centroid of the bridge deck.

3.2 Parameter setting

The parameters that need to be set in the equations are h^*, f, C_{Fy}^{QS}, C_{L0} and St. In particular, the last three can be obtained from the static test results. Figure 6(a) shows the cubic spline interpolation of the experimental $C_{Fy}^{QS}(\alpha)$ data measured at $Re = 6.0 \cdot 10^4$, obtained by applying:

$$C_{Fy}^{QS}(\alpha) = -\sec(\alpha)\left[C_L(\alpha) + C_D(\alpha)\tan(\alpha)\right] \tag{6}$$

The coefficient was shifted by resetting $\alpha = 4°$ as a new null wind angle of attack and neglecting the part of C_{Fy}^{QS} inducing only static deformation. A proper linear extrapolation of the experimental data was necessary for large α to ensure stable numerical solutions for large-amplitude oscillation. Given the extra static test results and the improved calculation method of the C_{L0}, the dependence of C_{L0} on Re is clearer for Re up to about $4.9 \cdot 10^4$, as shown in Figure 6(b). The experimental C_{L0} was therefore interpreted by piecewise-linear approximation in the range of Re between $1.6 \cdot 10^4$ and $8.0 \cdot 10^4$, corresponding to the wind speed range in which the aeroelastic tests were conducted. For $Re < 1.6 \cdot 10^4$, C_{L0} was assumed constant due to the accuracy problem of the instruments for very low wind speeds. Finally, a constant $St = 0.102$ was adopted.

A constant $h^* = 1.8$ was assumed for the bridge deck, kept the same as for a square cylinder in [4] and for a 3:2 rectangular cylinder in [6], where it also shows the solution of the wake-oscillator model is not sensitive to the h^*. To obtain the value of f parameter, the method recently proposed in [6] was adopted, calibrating the parameter f in the VIV range with a set of experimental results for a high value of the Scruton number. The calibration process is shown in Figure 7 with the experimental data of test case #a9, especially aiming at a good match of the amplitude-velocity curve slope between the experimental results and the numerical solutions. A good match of the numerical solution and the experiment was obtained when the value of f is set about 15.

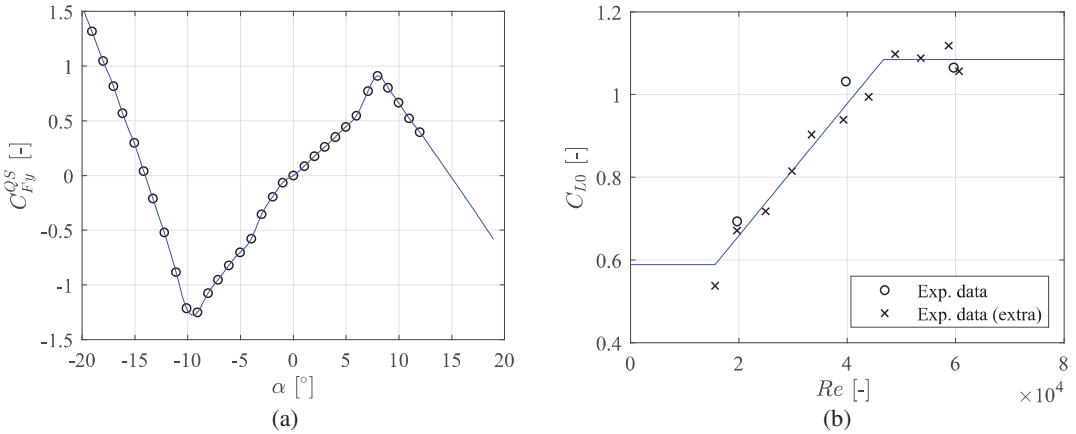

Figure 6. (a) Cubic spline interpolation and linear extrapolation of the experimental $C_{Fy}^{QS}(\alpha)$ data (Re =6.0·10^4) after the shift of the coefficient for α = 4°; (b) piecewise-linear approximation of the experimental $C_{L0}(Re)$ data.

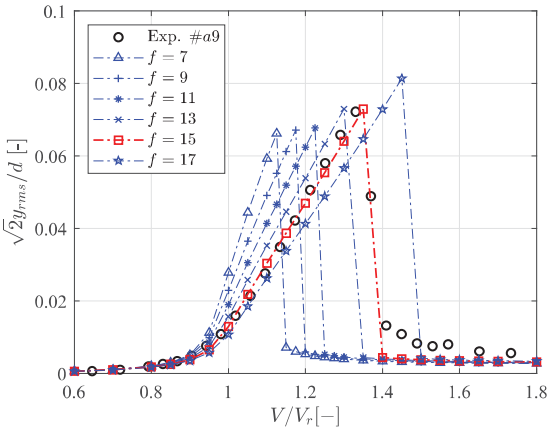

Figure 7. Calibration of the f parameter with experimental results for test case #a9, being the initial condition for numerical integration set as [Y, Y', ϑ, ϑ'] = [0.001, 0, 0, 0].

3.3 Numerical results for the wind tunnel sectional model

The equations were numerically solved by the ODE45 function of Matlab®. The relative and absolute error tolerance of the solver were respectively set to 10^{-6} and 10^{-8}, well balancing computational cost and accuracy (several tests with lower tolerances were also carried out). The performance of the mathematical model was examined by comparing the solution with the experimental results for a wide range of Sc, in terms of the amplitude-velocity curves shown in Figure 8. The QS galloping solutions are also reported as a reference.

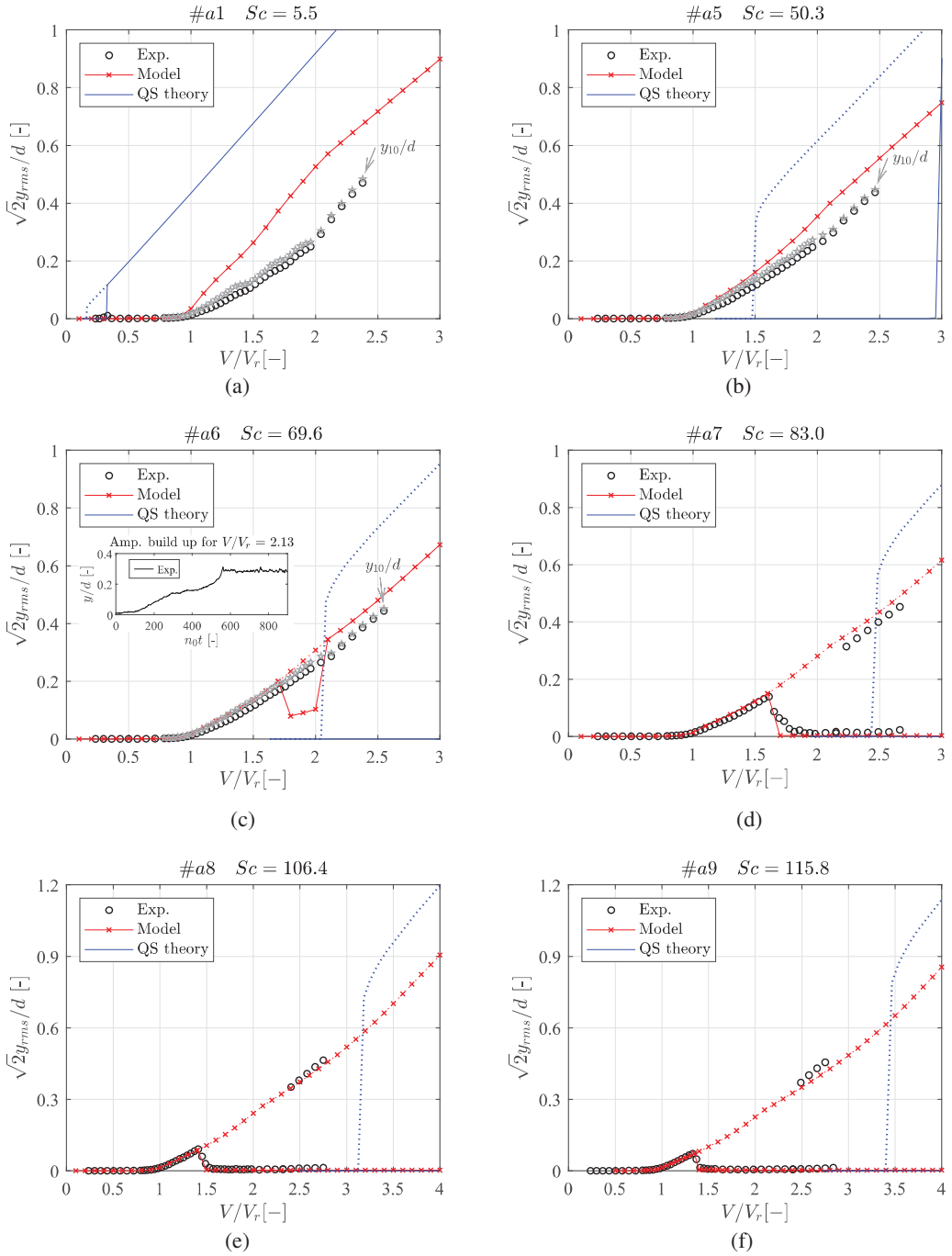

Figure 8. Numerical solution of wake-oscillator model equations for various *Sc*. Solid and dotted lines indicate steady-state solutions respectively for initial conditions [Y, Y', ϑ, ϑ'] = [0.001, 0, 0, 0] and [tan(15°)·V, 0, 0, 0].

For very low *Sc* values, such as in test case #a1, the mathematical model is able to successfully predict the onset of galloping at V_r, as observed in the experiments. The calculated amplitude is higher than the measured one, especially for V close to V_r. Even considering the average of the 10% largest peaks in the time histories (y_{10}), which represents a

statistical maximum amplitude for the experimental results, the agreement with the solutions of the mathematical model is not significantly improved. Increasing Sc up to 50.3 (test case #a5), the numerical solution gradually approaches the experimental data, the galloping onset remaining fixed at V_r. For a slightly higher Sc (test case #a6), the mathematical model starts to show a "drop and recover" of the steady-state amplitude around $V/V_r = 1.9$, when the solution is attained from a small initial condition. In contrast, a branch with higher amplitude can be found when a much larger initial condition is imposed. The existence of the moderate-amplitude branch around $V/V_r = 1.9$, which is not predicted by the quasi-steady theory, must be related to the strong nonlinearity of the Van der Pol wake equation in the model [9]. During the experiments for test case #a6, the wind tunnel model was released from rest for $1.63 \leq V/V_r \leq 2.55$, but no second branch was found. However, a careful inspection of the time records shows that the amplitude build-up at $V/V_r = 2.13$ is different from those at different reduced wind speeds. This amplitude build-up pattern is reported in Figure 8 (c). Two inflection points can be seen in the build-up envelop, revealing the tendency of the system to exhibit a lower-amplitude branch. This branch is unstable in the considered case but may become stable for a slightly larger Scruton number. For $Sc \geq 83.0$, the mathematical model shows a classical VIV response when the solution is attained from a small initial condition. The lock-in wind speed range, the maximum amplitude and the shape of amplitude-velocity curve are all well predicted (Figure 8 (d)-(f)). Nevertheless, a second branch with larger amplitudes can also be found just after the end of the lock-in range. It represents the extension of the VIV response branch and it tends to approach the QS solution, spanning a wind speed range where no vibration is expected according to the QS theory. Interestingly, such a branch was also found during the wind tunnel tests by releasing the wind tunnel model from a large displaced position, though it does not extend down to the lock-in range.

In general, the mathematical model provides satisfying predictions on the VIV-galloping behaviors of the bridge deck model at its 4° mean flow incidence.

3.4 Sensitivity study

Before applying the wake-oscillator model to full-scale structure, it is to check the sensitivity of the wake-oscillator model to the unmatched mass ratio m^* between the wind tunnel tests and the full-scale condition. The mass ratio is about $m^* = M/(0.5\rho d^2 l_e) = 1300$ for the wind tunnel model, while this is about 510 for bridge deck like the Aftetal bridge in full scale (510 is calculated according to the open cross section of Aftetal bridge [7], which has a similar side ratio $b/d = 2$, a height about $d = 5$ m and a mass about 7.7 ton/m). Therefore, the mass ratio in the full scale is about 40% of the wind tunnel model. In the wake oscillator model, this sensitivity study was implemented by manually setting the mass ratio of the bridge deck 40% of its original value, and increasing the damping ratio to maintain an unchanged Scruton number for each test case. The numerical solutions attained from small initial conditions are provided in Figure 9, for test case #a1 and test case #a7. It is clear that the wake oscillator is not sensitive to the mass ratio difference between the wind tunnel model and the full scale case.

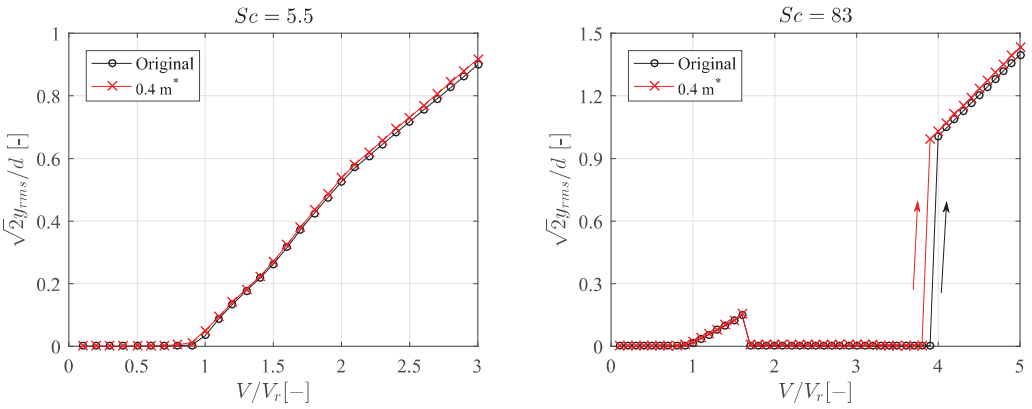

Figure 9. Checking the sensitivity of the wake oscillator model to mass ratio m^* for two maintained Scruton number (solution obtained from mall initial condition).

4 APPLICATION OF THE WAKE-OSCILLATOR MODEL FOR CONTINUOUS BEAM BRIDGE

4.1 Extending the wake-oscillator model for slender continuous structures.

For slender structures in the natural wind field, the turbulence in incoming flow and many three-dimensional conditions play important roles in the flow-structure interaction. To apply the wake oscillator model to predict the VIV-galloping instability for continuous flexible structure, at this stage, assumptions have to be made: (i) Two- dimensional flow is maintained at each point along the axis of the continuous structure; (ii) Only the mean component of the approaching air flow is considered, namely ignoring the turbulent parts.

In [10], Tamura's wake oscillator was used for the vortex induced vibration of the continuous system with circular cross section. There, the wake rotation angle and the across wind displacement are considered as a $\vartheta(x, t)$ and $y(x, t)$, which depends right now on the along-axis position x. By considering a single mode shape for the continuous system, the controlling equation for $\vartheta(x, t)$ and $y(x, t)$ were finally expressed by a single differential equation of order of 4, with the normalized mode shape and the mean wind profile collected in several constants. This method is not used here, because the quasit-steady force coefficient C_{Fy}^{QS} for non-circular cross section is much more complicated (for circular cross section this can be simply expressed as $C_D \cdot (Y'/V)$ as in [10]).

As an alternative way, multiple discrete wake oscillators were considered here for the continuous system, and the dynamics of the continuous system is described by finite element method. Figure 10 illustrates the idea, where wake oscillators were coupled on the continuous system by every two nodes. As an example, the wake oscillator at node N_{2i} will be only excited by the transverse motion y at N_{2i}, and the reference length to calculate the aerodynamic force on node N_{2i} is the distance between node N_{2i-1} and N_{2i+1}. Such a measure is just to facilitate the practical programming. The equations for the dynamics of the continuous system is first written in matrix form, applying the classical 2-d beam element and considering only the bending deformation. The discrete wake oscillators were expressed also in matrix form and combined together with structural matrix to form new matrixes (including both the degree of the freedom of nodes and the wake oscillators), with the coupled items expressed in submatrix of the new matrix. For brevity, these matrixes are not given here.

With this way, multiple mode shapes can be included in the calculation, and it is easy to take into account when the cross section of the continuous system is changed, for example,

the launching nose in the following case study. The disadvantage is that more computational cost is needed, due to the increased number of wake oscillators.

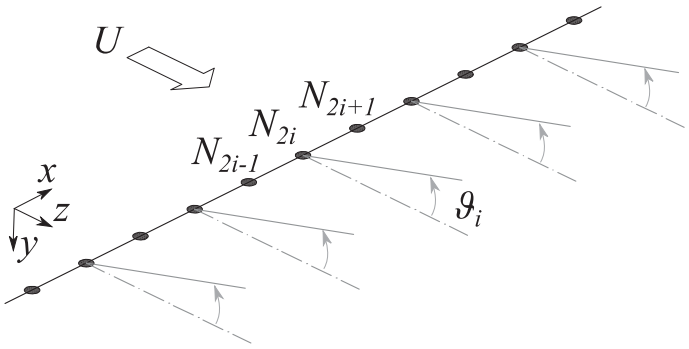

Figure 10. Discrete wake oscillators on continuous system.

4.2 The case study

The Aftetal bridge [7] during its critical launching is considered here as a case study. The span arrangement is shown in Figure 11. For the 5m high steel open box (assumed here the same aerodynamic shape as our wind tunnel model), the mass per unit length is assumed 7.7 ton/m, the moment of inertia of the cross section I_{zz} = 4.89 m^4, Young's-modulus 210·10^9 N/m^2 and Poisson's ratio 0.3.

For the launching nose, due to the lack of the wind tunnel test results, we simply assumed here a lattice structure with a solidity ratio of 0.334 as shown in Figure 12. The mass of this launching nose is assumed half of the open cross section, and the bending stiffness is assumed the same as the open cross section. The length of the launching nose is 30m.

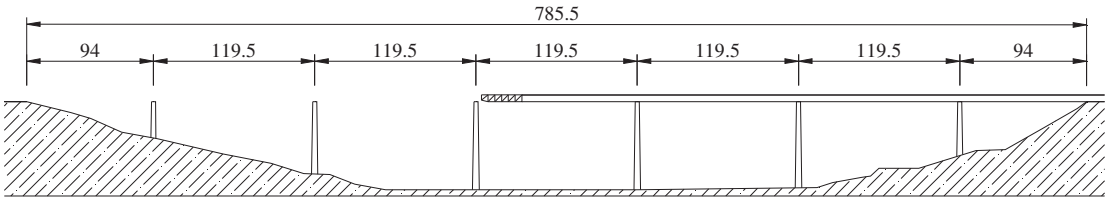

Figure 11. Span arrangement of the Aftetal bridge [7] (during the critical launching phase, dimension in m).

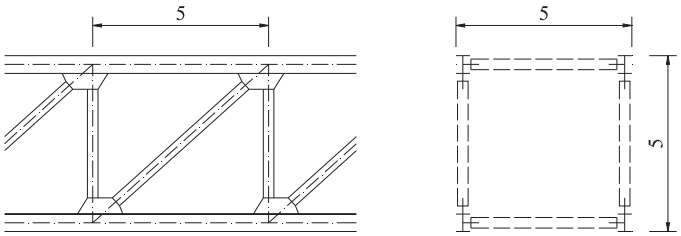

Figure 12. Assumed lattice structures for the launching nose (dimension in m).

The continuous structural system is discrete into 92 elements and 93 nodes, shown in Figure 13. Fini. Depending on whether the launching nose is used or not during the launching phase, the total number of implemented wake oscillators is 43 or 46. In the case of with the launching nose, the quasi-steady aerodynamic force of the lattice structure is still taken into

account, although no wake oscillator is applied. The structural damping matrix is calculated using the classical Rayleigh damping, assuming the same damping ratio for the first mode and second mode shape.

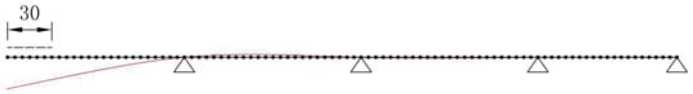

Figure 13. Finite element discrete of the structure and its first mode shape.

The natural wind is assumed to attack at a mean angle of 4° of the bridge deck, leading to the oscillation of the structure not strictly in the across-wind direction. However, considering the attack angle is still very small, this influence is ignored. Therefore, the aerodynamic parameters for the open cross section and the wake-oscillator are kept the same as in Chapter 3. For the launching nose, the drag and lift coefficient is calculated according to [11], shown in Figure 14. It is to note that the lattice launching nose is able to introduce positive aerodynamic damping into the structural system due to the drag force.

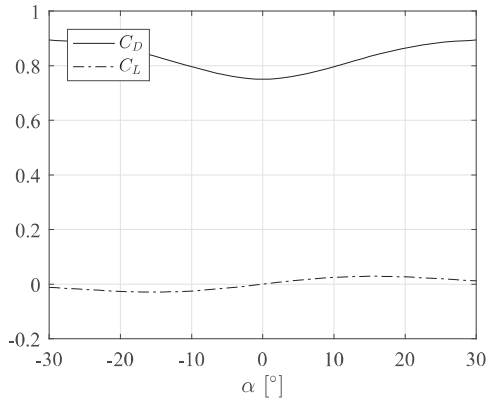

Figure 14. Drag and lift coefficients for the lattice launching nose (referred to the enclosed area $A = 5\text{m} \cdot$ per unit length).

Finally, the first bending frequency is 0.3671Hz or 0.3045 Hz depending on whether the launching nose is used or not (corresponding mode shape shown in Figure 13. Fini). For both cases, the second bending frequency is higher than 4 times the first one. Therefore, the VIV-galloping instability is only considered for the first mode. The critical wind speed for the vortex induced vibration is 18.0m/s or 14.9 m/s, taking $St = 0.102$ and the height of the bridge deck $d = 5$ m.

4.3 Results

4.3.1. Effect of the mode shape

First of all, the effect of the mode shape is examined here without considering the launching nose. The numerical results for the wind tunnel sectional model are re-computed with the same mass ratio as the full-scale one, C_{L0} was also set constant as 1.085 which is the value for high Reynolds number. Therefore, the only difference between the sectional model and the continuous system is the mode shape. The numerical results are shown in Figure 15, with the amplitude at the tip of the cantilever (see Figure 13. Fini) representing the response of the continuous system. According to the numerical results, the effect of the mode shape is mainly reflected by the oscillation amplitude. The onset wind speed for galloping and the lock-in

wind speed range for vortex induced vibration is not significantly influenced by the mode shape. On the other hand, the ratio of the oscillation amplitude between the continuous system and the sectional model seems dependent on the wind speed, rather than a constant value. Taking the results of Sc =83 for example, the oscillation amplitude ratio is 1.59, 1.36 and 1.25 for V/V_r = 1.1, 1.6 and 5.0.

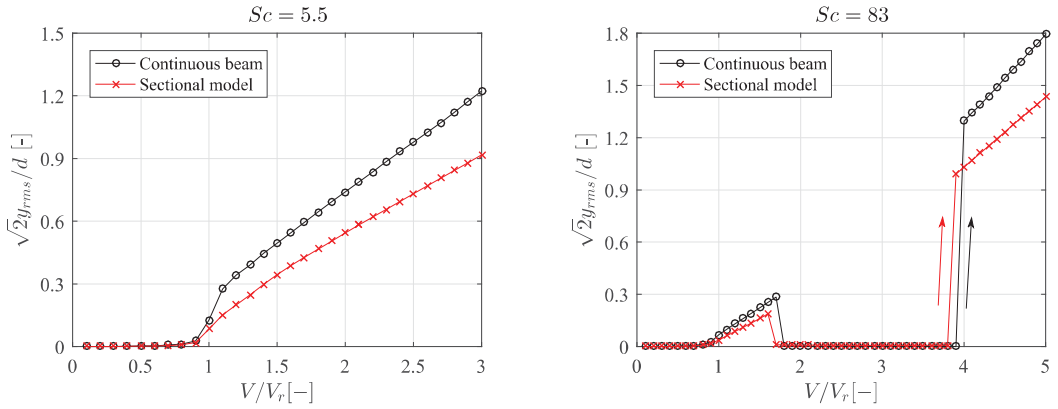

Figure 15. Effect of the mode shape: (a) for a low Scruton number; (b) for a high Scruton number. Solutions are obtained with small initial conditions.

4.3.2. Effect of the launching nose

For bridge construction with launching method, the use of a light-weight launching nose will not only increase the first bending frequency in the critical launching phase, but also could contribute to stabilizing the possible wind induced vibration if the launching nose is well-designed. Figure 17 shows the effect of launching nose considering a very low damping ratio for the first mode. There, "TS" stands results of the wake oscillator model, "QS" the results according to quasi-steady theory and "L. N." the launching nose. With or without launching nose, the equivalent mass m_e is = 5.3 ton/m or 7.7 ton/m in the first mode. Quasi-steady solution is also provided for comparison. From the quasi-steady solution, it is clear that the one with launching nose features a much higher galloping onset though the Scruton number in this case is even lower (due to a lower equivalent mass). This is because the launching nose locates at the tip of the cantilever. The positive aerodynamic damping due to a low value of drag coefficient can still influence the dynamics of the structural system a lot. Nevertheless, the wake-oscillator will still predict a galloping onset at the critical wind speed for vortex induced vibration.

The damping value is further increased, and the results from the wake-oscillator model with or without launching nose are shown in Figure 17. The solutions of the wake-oscillator model right now also show the benefits of the launching nose. At a damping ratio of 1.17% (logarithmic damping δ = 0.074), the response with launching nose turns into a VIV response rather than a galloping starting at V_r. This is still not reached for the one without launching nose up to a damping ratio of 1.54% (logarithmic damping δ = 0.097). Finally, it is worth stating that, in Figure 17 (a), the quasi-steady theory predicted galloping onset for the damping ratio 0.67% is already about 4 times the vortex resonance wind speed. However, the wake-oscillator model still predicts a galloping response starting at V_r.

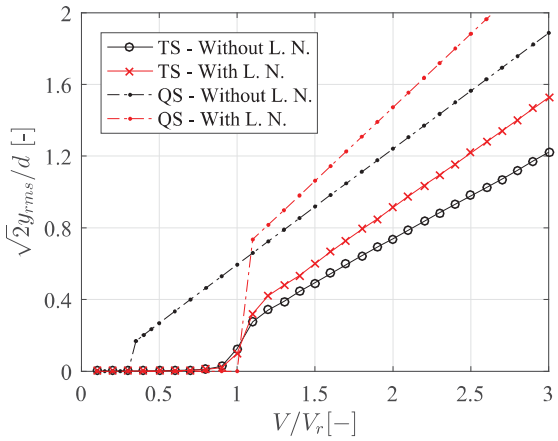

Figure 16. Effect of the launching nose for a very low damping ratio of 0.17% (logarithmic damping $\delta = 0.011$). Solutions are obtained with small initial conditions.

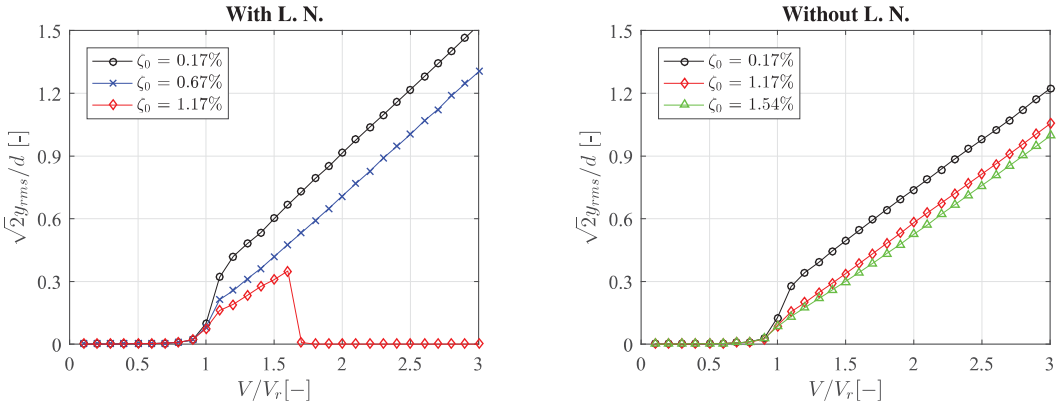

Figure 17. Comparison of the response with or without launching nose by increasing damping ratio. Solutions are obtained with small initial conditions.

5 CONCLUSIONS

- Tamura's wake oscillator model was used to capture the VIV-galloping instability of a bridge deck with open cross section. Compared with the wind tunnel test results, satisfying predictions were obtained with this wake oscillator model. In particular, the galloping onset wind speed was well captured for a wide range of Scruton number.
- The wake oscillator model was then extended to continuous system, and a 7-span continuous bridge during its critical launching phase was considered as a case study. Due to the effect of mode shape, the wake oscillator model predicts a larger amplitude response at the cantilever tip, compared with the predictions for the wind tunnel sectional model. But the critical wind speed seems not affected.
- The launching nose was found able to make an important contribution in stabilizing the VIV-galloping instability if its aeroelastic effect is well taken into account. This also implies that particular aerodynamic optimization made on the launching nose could be a more efficient way in suppression the vibration, due to the special location of the launching nose.

- Finally, the predictions provided by the wake oscillator model for the continuous system need to be verified by future wind tunnel tests.

ACKNOWLEDGEMENT

The first author wishes to thank the China Scholarship Council (CSC) for the funding support (No. 201506260188).

REFERENCES

[1] C. Mannini, A.M. Marra, G. Bartoli, VIV-galloping instability of rectangular cylinders: review and new experiments, *J. Wind Eng. Ind. Aerod.*, 132, 109-124, 2014.

[2] C. Mannini, A.M. Marra, T. Massai, G. Bartoli, Interference of vortex-induced vibration and transverse galloping for a rectangular cylinder, *J. Fluids Struct.*, 66, 403-423, 2016.

[3] Corless, R.M., Parkinson, G.V., A model of the combined effects of vortex-induced oscillation and galloping. *J. Fluids Struct.*, 2, 203–220, 1988.

[4] Y. Tamura K. Shimada, A mathematical model for the transverse oscillations of square cylinders, *Proc. 1st Int. Conf. on Flow Induced Vibrations*, Bowness-on-Windermere, UK, Springer-Verlag, pp. 267-276, 1987.

[5] Tamura, Y., Matsui, G., Wake-oscillator model of vortex-induced oscillation of circular cylinder. *In: Proceedings of the 5th International Conference on Wind Engineering*, Jul. 8-14, 1979. Elsevier, Forth Collins, US, pp. 1085–1094, 1979.

[6] C. Mannini, T. Massai, A.M. Marra, Modeling the interference of vortex-induced vibration and galloping for a slender rectangular prism, *J. Sound Vib.*, 419, 493-509, 2018.

[7] Hanswille, G., Anwendung der Teile 2 der Eurocodes 3 und 4 für Stahl- und Verbundbrücken. *Stahlbau*, 83, 217–226, 2014. (in German).

[8] Chen, C., Mannini, C., Bartoli, G., Thiele, K., Unsteady galloping of a bridge deck with open cross section: wind tunnel tests and mathematical modeling. *In: Proceedings of the 15th International Conference on Wind Engineering*, Sep. 1-6, Beijing, China, 2019.

[9] Mannini, C., Asymptotic analysis of a dynamical system for vortex-induced vibration and galloping. *In: Lacarbonara W., Balachandran B., Ma J., Tenreiro Machado J., Stepan G. (eds) Nonlinear Dynamics of Structures, Systems and Devices*, pp. 389-397, Springer, Cham, 2020.

[10] Tamura, Y., Amano, A.., mathematical model for vortex-induced oscillations of continous systems with circular cross section, *J. Wind Eng. Ind. Aerod.*, 14, 431-442, 1983.

[11] Engineering Sciences Data Unit (ESDU). Lattice structures Part 2: mean fluid forces on tower-like space frames. Wind Engineering Sub-Series, Data Item 81028, London 1988.

EURODYN 2020
XI International Conference on Structural Dynamics
M. Papadrakakis, M. Fragiadakis, C. Papadimitriou (eds.)
Athens, Greece, 23–26 November 2020

WIND TUNNEL VIV TESTING OF HELICAL STRAND CABLE MODELS

Arsenii Trush[1,2], **Stanislav Pospíšil**[1], **and Hrvoje Kozmar**[3]

[1] Institute of Theoretical and Applied Mechanics of the Czech Academy of Sciences
Prosecka 809/76, 19000 Prague, Czech Republic
{trush, pospisil}@itam.cas.cz

[2] Faculty of Civil Engineering, Czech Technical University
Thakurova 7, 16629 Prague, Czech Republic

[3] Faculty of Mechanical Engineering and Naval Architecture, University of Zagreb
Ivana Lučića 5, 10000 Zagreb, Croatia
hkozmar@fsb.hr

Keywords: Air turbulence, Bridge cables, Vortex shedding, Wind tunnel experiments.

Abstract. *Structural cables have been commonly used as tension members for both high-rise and long-span structures. Wind-induced vibrations along with the traffic loads are the main factors causing fatigue damages of cables. Moreover, the vibration of these essential supporting elements can influence the response of the superstructure (and vice versa) in the form, e.g., of parametric vibration, damage, or the consequent destructive vibration of the superstructure itself. The most common cable types for guyed masts, roofs, cable stayed and suspension bridges are: parallel wire strand, helical wire strand, locked-coil cable. Each of them has its own advantages, such as: corrosion resistance, fatigue endurance, and low production cost. Cables have a characteristic surface and roughness depending on the production technology and design. The surface modifications have a major effect on aerodynamic properties. This presented work aims at determining the functionality of the open wire helical strand cable construction in various turbulence conditions via experimental investigation in a wind tunnel. According to the results in moderately turbulent conditions, the surface roughness of helical strand cables reduces the lock-in range compared to the reference smooth model. The hysteresis character of resulting amplitude at an increased/decreased flow velocity was observed for all models. The most pronounced effect was for the case of a model with bigger surface roughness and higher lay angle. This trend was observed also for the more turbulent flows. Vibration also starts at the lower critical flow velocities indicating an increase of the Strouhal number.*

1 INTRODUCTION

Wind related aerodynamic forces can be divided into the following groups: forces originating directly from the impact of wind on a cable (drag forces, buffeting), and so-called aeroelastic phenomena resulting from the interaction between a cable and air flow (vortex shedding, galloping, rain-wind induced vibrations, etc.) that pose a particular risk due to a large number of loading cycles.

Oscillations of cylindrical structural elements are in most cases induced by the wind, which forms regions of disturbed flow around such structures. Usually, four regions are distinguished:

- a region of retarded flow upstream of the body,
- boundary layer regions attached to the cylinder,
- regions above and below the cylinder characterized by an accelerated flow,
- a wake with a separated flow, e.g., [1].

The flow conditions in each of the regions affect the vibration: fluctuating in-plane pressures called buffeting, vortices shed at the cable surface imposing the out-of-plane pressures, and the oscillating wake flow, see, e.g. [2]. The vibration can affect the stability of the supported structure; it may also cause high stresses in the cables (or the individual strands of a cable) and high internal forces in structural members. The fatigue damage caused by the cyclic loads, leading to normal stress in the cables or to fretting friction damage is significant [3]. This is one of the disadvantages of using steel cables with high tensile strength, as it is accompanied by a reduction in ductility and an increase in the susceptibility of cable wires to brittle fatigue failure [4], [5]. During inspection of bridge suspension cables, defects of various types were observed, e.g., cracking, pitting, fretting, fatigue, etc., see [6], [7]. vortex-induced vibration (VIV) can occur at moderate wind speeds and produce a large number of loading cycles, potentially causing serious problems.

VIV is a result of the fluid-structure interaction. It is due to alternating vortices shed at the cylinder surface, which produce the periodic forcing. If the damping and structure-air mass relations, expressed by the non-dimensional parameter called Scruton number (*Sc*) is low, the structural motion influences the flow field. analysis of the cylinder response requires knowledge of the vortex shedding frequency, which is commonly expressed as the non-dimensional Strouhal number (*St*). This expression helps to transfer the results among different experiments and studies on vibrating bluff cross-sections with different geometries and fluid properties. Knowledge of *St* is necessary for determination of the critical wind velocity at which the resultant vibration of the cylinder is at, or near to, resonance. The *St* value depends on the shape (geometry) of the cylinder, surface roughness of the cylinder, turbulence intensity, and on the Reynolds number (*Re*) which determines the flow regimes for structures with both circular cross-sections and non-circular ones.

For both theoretical and computational investigations, structural cables are often assumed to have perfectly circular cross-sections. In contrast to aerodynamic bodies (wings) and bodies with sharp edges (rectangular profiles), cylinders, which may be classified as semi-aerodynamic, can have their flow separation point at varying positions along the body surface. The position of this point depends on the free-stream velocity, turbulence intensity, and roughness of the body surface [8]. Not even dry, wrapped or coated bridge cables have ideally smooth surfaces. Roughness on the surface commonly influences turbulence characteristics in the proximity of the body surface.

The location of the flow separation point is important especially for cables manufactured using individual steel wires with no coated protection as in the case of guy ropes. In the case of steel strands covered with polyethylene (HDPE) tubing, local alterations of the inherent

surface roughness, resulting from mechanical damage, manufacturing, creep, and exposure to atmospheric pollution and solar activity, are expected. Such geometrical deviations, corrosion and other types of surface changes can be defined as technological roughness. Such microscopic variations on the body surface can induce macroscopic changes in the flow around it [9], and therefore they require analysis. The Reynolds number is closely related to the flow separation on the cable surface, as it is the governing parameter of the transitions (critical state) occurring in the disturbed regions, i.e. the wake, the free shear layers, and the boundary layers [10]. This critical state in the boundary layer has attracted the most attention, as it is within this range of the Reynolds numbers that one can expect significant variations in the aerodynamic coefficients. They are provoked by changes in the flow and by the occurrence of flow instabilities which are expressed as a drop in the drag coefficient and a simultaneous appearance of a steady lift. A theoretical and experimental work focused on the wind-induced response of a full-scale yawed bridge cable section model for varying Reynolds numbers and wind angles-of-attack was addressed in [11]. The study also demonstrated the influence of cable surface roughness and wind incidence angle on the force coefficients. Roughness produced using sand paper, a wire mesh screen, and ribs were investigated in [12]. The drag coefficient for rough cylinders and the related change in the critical Reynolds number were reported in [13], [14], [15]. In [16], two types of cylinder roughness were classified and tested. In [17], alterations in surface roughness were observed to shift the vortex shedding to post-critical regimes.

A large number of television broadcasting and meteorological masts in the Czech Republic were built in the 70-90s of the 20th century. At the moment, guys of these masts are at the end of their life cycle and the problem of assessing their residual life and replacement is actual. The idea to improve the aerodynamic and fatigue performance of cables by selecting the optimal surface parameters of cable for specific turbulence conditions at a construction site is very attractive. This presented work aims at determining the functionality of the open wire helical strand cable construction in various turbulence conditions via experimental investigation in a wind tunnel.

2 EXPERIMENTAL SETUP

Experiments were carried out in the climatic wind tunnel of the Institute of Theoretical and Applied Mechanics in Czech Republic. The aerodynamic section equipped with the turntable has a 1.9 m wide and 1.8 m high rectangular cross section. The total length of the test section is 11.0 m.

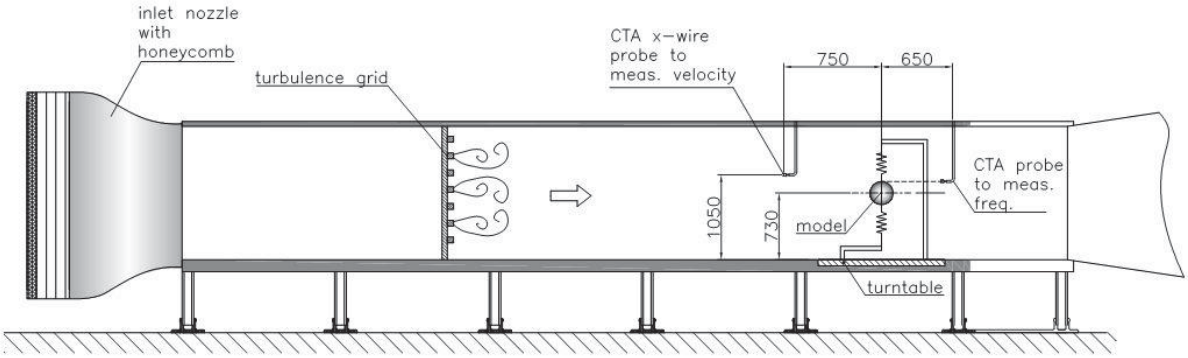

Figure 1: Arrangement of the experiment in the aerodynamic test section of the climatic wind tunnel.

2.1 Structural models for wind tunnel testing

Open wire helical strand cables were selected as the structural models for the experimental study in the wind tunnel. In order to evaluate separately an impact of the lay angle and surface roughness factors, the structural model with next parameters were manufactured:

- Model of helical strake cable (construction 1x61 according ISO 17893:2004) with relative surface roughness $k/D = 5.6\%$ and lay length $l = 12 \cdot D$;
- Model of helical strake cable (construction 1x61), $k/D = 5.6\%$, $l = 24 \cdot D$;
- Model of helical strake cable (construction 1x91), $k/D = 4.5\%$, $l = 12 \cdot D$;
- Circular cylinder as a reference model.

All models were made from polystyrene, polished and varnished. The length of the models was 1.27 m with diameter $D = 0.13$ m. The length-to-diameter ratio was approximately equal to 10. A rigid carbon fiber tube with the outer diameter of 13 mm and the wall thickness of 2 mm was used as an axis that can be fixed to the experimental stand, [18].

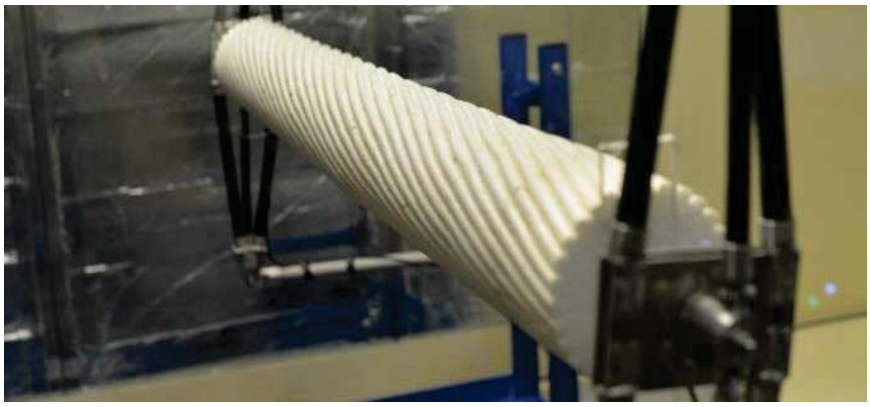

Figure 2: Model of 1x91 cable on the dynamic force balance stand.

The logarithmic decrement of structural damping obtained from the vibration decay is $\delta = 0.035$ and $Sc = 6.4$. The duration of each measurement was 120 seconds. The measurement of the response was carried out in the range of the reduced velocity $U/(f_n \cdot D) = 2 \div 8$ and $Re = 1.12 \cdot 10^4 \div 4.5 \cdot 10^4$. The lock-in range was measured in two directions. The flow velocity increased in steps from the value lower than the theoretically predicted critical flow velocity until the resonant (lock-in) vibrations were obtained. After the end of the lock-in range, the flow velocity was changed in the opposite direction. The Plexiglas screens were installed on both sides of the structural models to create two dimensional (2D) flow conditions.

2.2 Turbulence generation in the wind tunnel

All configurations were tested in the low turbulent flow at the free stream turbulence $I_u = 0.75\%$ and in turbulent flows generated by using the square mesh arrays of rectangular bars placed upstream of the structural models.

Figure 3: Wooden grid used for turbulent flow generation.

To obtain detailed characteristics of turbulence in the wind tunnel test section, the flow profiles were measured at a step of 75 mm along the model axis using x-wire CTA probe. The exponential autocorrelation method was used to obtain the integral length scales of turbulence, see Figure 4.

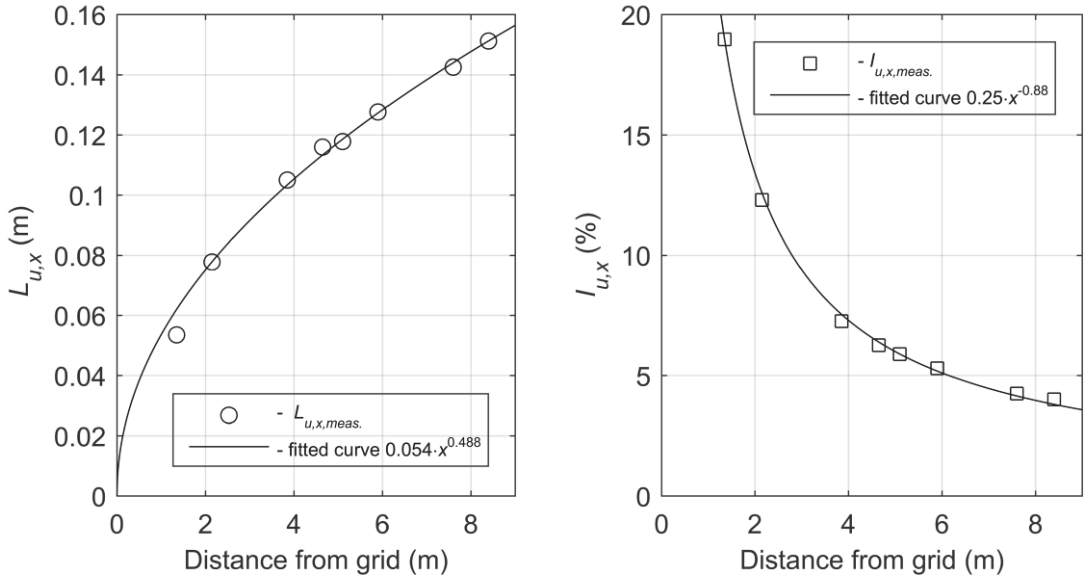

Figure 4: Turbulence integral length scale (left) and turbulence intensity (right) dependency on the distance from grid.

Distance from the grid (m)	Turbulence intensity $I_{u,x}$ (%)	Turbulence length scale $L_{u,x}$ (m)
7.1	4.5	0.141
4.6	6.5	0.114
2.1	12.3	0.078

Table 1: Turbulence intensity and integral length scale of turbulence (obtained by exponential method) at the location used in the mechanical response experiments.

The same x-wire probe was installed to measure flow velocity during mechanical response tests at 0.75 m upstream of the models and the sampling rate was 1000 Hz.

3 RESULTS

The experimental results obtained on the smooth circular cylinder are shown in graphs of dimensionless amplitude vibration Amp_{red} versus reduced wind velocity U_{red} in Figure 5, the model of 1x61 cable with lay length $l = 12 \cdot D$ in Figure 6, 1x61 cable with the lay length $24 \cdot D$ in Figure 7, 1x91 cable with the lay length $12 \cdot D$ in Figure 8. The results taken during a step-wise increase of the flow velocity are indicated by the empty markers, and the results taken during a stepwise decrease of the flow velocity by the filled markers.

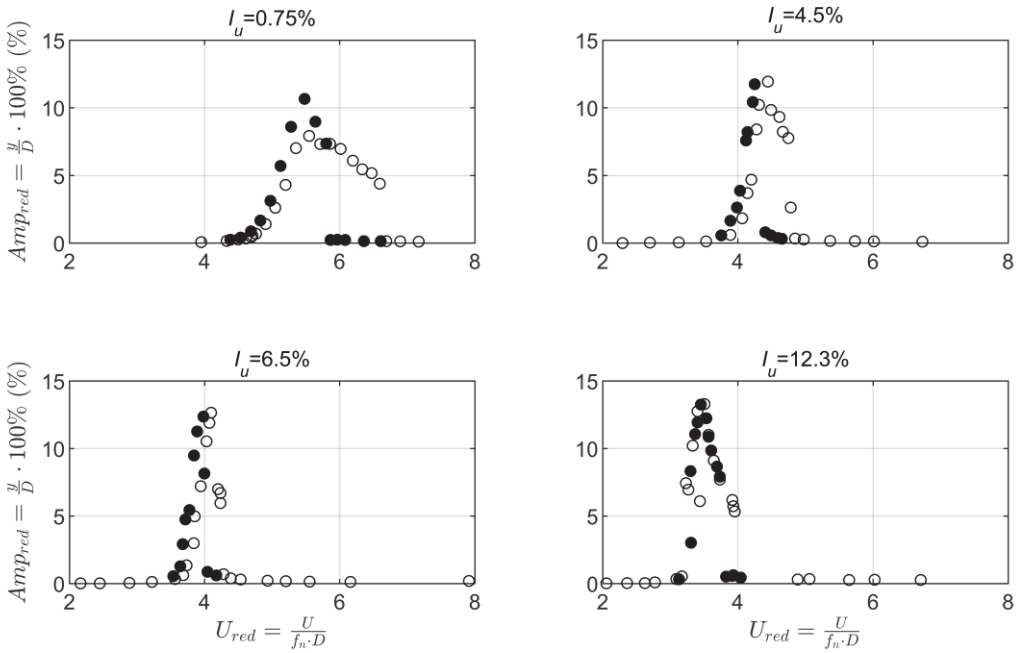

Figure 5: Amplitude response plot of smooth surface cable model.

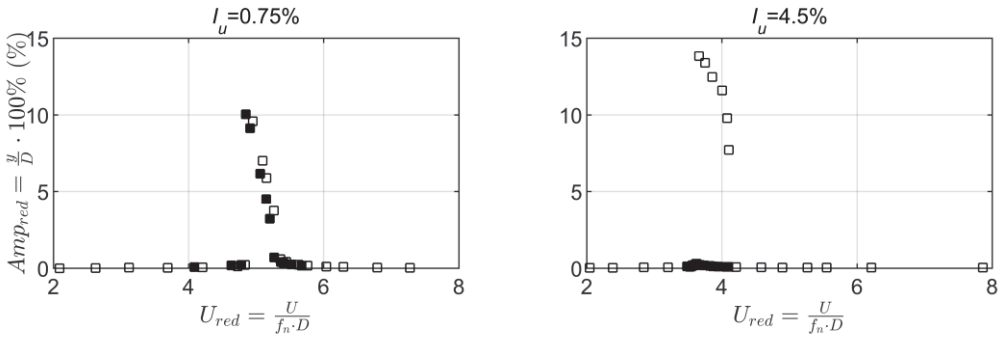

Figure 6: Amplitude response plot of helical cable 1x61-12.

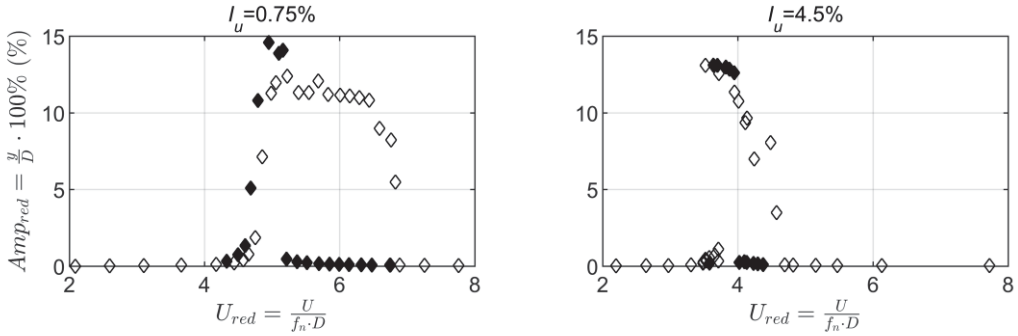

Figure 7: Amplitude response plot of helical cable 1x61-24

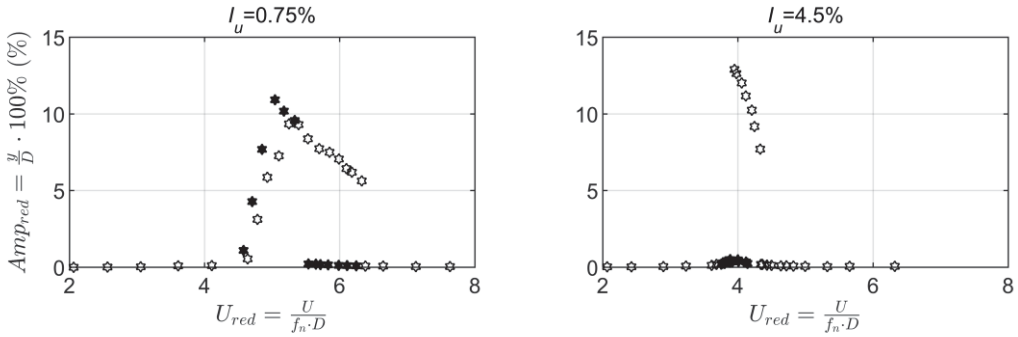

Figure 8: Amplitude response plot of helical cable 1x91-12 model.

Test results showed the hysteresis character of the `increased/decreased velocity trend lines` for the response of all the structural models and all turbulence intensities. The trend obtained by reducing the flow velocity has a peak amplitude approximately equal to or higher than for the case of the increasing velocity. The lock-in range for the cases of stepwise increasing of the flow velocity is wider. In low turbulent flow the helical surface roughness can lead to an increase in the peak amplitude and widening of the lock-in range for the case of stepwise velocity increasing compared to the smooth reference model. Higher values of surface roughness and turbulence intensity lead to a reduction of the lock-in range. The most pronounced effect was observed for the case of the cable model characterized by larger lay angle. This trend remains present in more turbulent flows where the vibrations start at lower critical flow velocities. This yields an increase in *St*. For the helical cable models, no vibrations at the dimensionless amplitude exceeding 2% in the lock-in range were observed in turbulent flows at turbulence intensities 6.5% and 12.3%.

4 CONCLUSIONS

The rationality of using cables with a smooth or rough surface is determined by the turbulent wind conditions at the construction site and the arrangement of structural elements. Smooth circular shape is optimal for single or widely spaced cable in open areas, where wind turbulence is low. Cables with the helical shape are optimal for moderate to strong turbulence wind conditions, while preference should be given to higher values of surface roughness and lower lay lengths. The present work has practical results, which could improve the knowledge of the complex wind loading of bridge cables, cables of the mast towers as well as the loading on the broadcast towers with tubular structural elements.

ACKNOWLEDGEMENTS

The activity presented in the paper is part of the research grant No. 19-04695S of the Czech Science Foundation (GAČR).

REFERENCES

[1] M. Zdravkovich, Flow around circular cylinders, *Oxford University Press*, ISBN: 9780198563969, 1997.

[2] J. Gerrard, The wakes of cylindrical bluff bodies at low Reynolds number, *Philosophical Transactions of the Royal Society of London* 288, 351-382, 1978.

[3] J. Dowd, M. Poser, K. Frank, S. Wood and E. Williamson, Bending Fatigue of Cable Stays, *Journal of Bridge Engineering* 6, 639-644, 2001.

[4] K. Mahmoud, Fracture strength for a high strength steel bridge cable wire with a surface crack, *Theoretical and Applied Fracture Mechanics* 48, no. 2, 152-160, 2007.

[5] K. Gjerding Smith, R. Johnsen, H. Lange, B. Leinum, G. Gundersen, B. Isaksen and G. Naerum, Wire fractures in locked coil cables, *Bridge Structures* 2, no. 2, 2006.

[6] H. Li, W. Chen, F. Xu, F. Li and J. Ou, A numerical and experimental hybrid approach for the investigation of aerodynamic forces on stay cables suffering from rain-wind induced vibration, *Journal of Fluids and Structures* 26, no. 7-8, 1195-1215, 2010.

[7] D. Dan, W. Cheng, L. Sun and Y. Guo, Fatigue durability study of high density polyethylene stay cable sheathing, *Construction and Building Materials* 111, 474-481, 2016.

[8] H. Niemann and N. Hölscher, A review of recent experiments on the flow past circular cylinders, *Journal of Wind Engineering & Industrial Aerodynamics* 33, no. 1-2, 197-209, 1990.

[9] G. Schewe, On the force fluctuations acting on a circular cylinder in crossflow from subcritical up to transcritical Reynolds numbers, *Journal of Fluid Mechanics* 133, no. 1, 265-285, 1983.

[10] G. Schewe, Reynolds-number effects in flow around more-or-less bluff bodies, *Journal of Wind Engineering & Industrial Aerodynamics* 89, 1267-1289, 2001.

[11] G. Matteoni and C. T. Georgakis, Effects of surface roughness and cross-sectional distortion on the wind induced response of bridge cables in dry conditions, *Journal of Wind Engineering and Industrial Aerodynamics* 136, 89-100, 2015.

[12] J. Ribeiro, Effects of Surface Roughness on the two dimensional flow past circular cylinders 1: mean forces and pressures, *Journal of Wind Engineering & Industrial Aerodynamics* 37, 299-309, 1991.

[13] A. Fage and J. Warsap, The effects of turbulence and surface roughness on the drag of a circular cylinder, *British Aeronautical Research Council* 1179, 248-255, 1929.

[14] E. Achenbach, Influence of surface roughness on the cross-flow around a circular cylinder, *Journal of Fluid Mechanics* 46, 321-335, 1971.

[15] O. Guven, C. Farell and V. C. Patel, Surface-roughness effects on the mean flow past circular cylinders, *Journal of Fluid Mechanics* 98, 673-701, 1980.

[16] Y. Nakamura and Y. Tomonari, The effects of surface roughness on the flow past circular cylinders at high Reynolds numbers, *Journal of Fluid Mechanics* 124, 363-378, 1982.

[17] G. Diana, M. Belloli, S. Giappino and S. Muggiasca, Vortex induced vibrations at high Reynolds numbers, *Proceedings of 6th. International Colloquium on Bluff Bodies Aerodynamics and Applications*, Milano, Italy, 2008.

[18] R. Král, S. Pospíšil and J. Náprstek, Experimental set-up for advanced aeroelastic tests on sectional models, *Experimental Techniques* 40, no. 1, 3-13, 2016.

EURODYN 2020
XI International Conference on Structural Dynamics
M. Papadrakakis, M. Fragiadakis, C. Papadimitriou (eds.)
Athens, Greece, 23–26 November 2020

NUMERICAL AND EXPERIMENTAL STUDY OF A SLENDER CATENARY BRIDGE WITH A NOVEL TENSIONING SYSTEM

Gergely Szabó[1], **Gábor Hochrein**[2]

[1] Bridge design engineer
1031 Budapest, Hungary, Silvanus stny. 45.
e-mail: drszabo@pontterv.hu

[2] Bridge design engineer
1119 Budapest, Hungary, Than Karoly u. 3-5
e-mail: hid@pontterv.hu

Keywords: catenary bridge, geometrically non-linear dynamics, iso-tensioning

Abstract. *Catenary pedestrian bridges are apparently spreading all over the world. These structures are highly popular as they can form the landscape and provide the pedestrians with excitement and adventure. Consequently, there is a strong need to increase the span length, which might call for the reconsideration of the conventional approaches. A novel concept was proposed with special focus on feasibility and proper static and dynamic performance of slender catenary bridges. A dedicated physical model was built and measured in order to demonstrate the advantages. A long span catenary bridge designed in the framework of a feasibility study was also considered as an ideal candidate for our proposed method.*

1 INTRODUCTION

1.1 Catenary bridge structures

The main elements of these bridges are the catenary cables that are fixed at both ends. These cables carry the vertical loads, such as the self-weight or ice loading. When necessary, wind cables and connecting cables are also involved in order to provide extra stiffness to the whole structure, which was studied in detail in [1]. The problem with these bridges is that the connecting cables are complicated to tension evenly due to their mutual interaction. There can be loose cables that may vibrate, and the others can be overloaded. On top of all, the overall structural behavior is strongly temperature dependent. The novel approach has been first introduced at the WIBE (World Innovation in Bridge Engineering) prize competition. In this paper a more detailed introduction is addressed.

1.2 The proposed iso-tensioning system

To overcome the above mentioned problems, a novel concept is proposed shown in Figure 1. In contrast to conventional catenary bridges, the evenly distributed and temperature independent connecting cable forces can be conveniently ensured by adopting pulleys that are used for railway overhead electric wires for instance. Post-tensioning cables on both sides of the catenary with ballasts at their end points are used to adjust the desired pre-stressing to the structure.

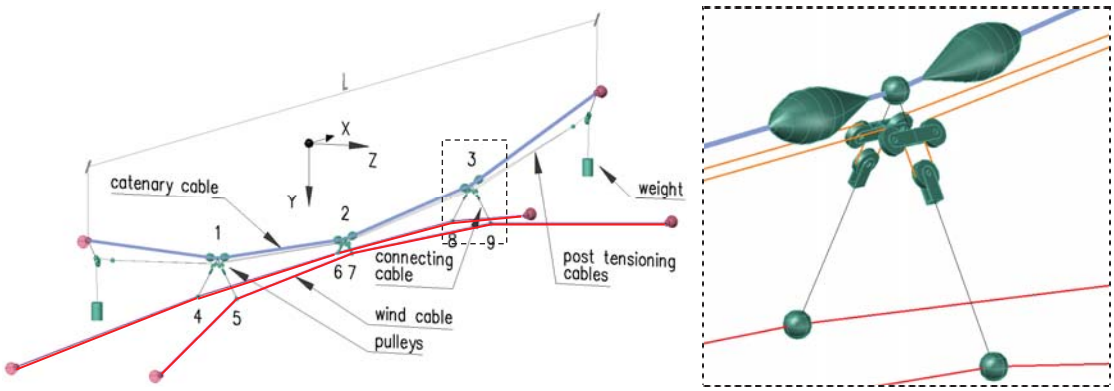

Figure 1: Structural setup of the proposed system.

2 PRELIMINARY PHYSICAL MODEL

The structural behavior was investigated by using physical models that are most common in wind engineering [2]. A preliminary model was created in order to qualitatively demonstrate that the proposed system behaved according to our expectations; the connecting cables were indeed evenly pre-stressed, no loose cables were observed. A horizontal load test was also carried out. All the cables were modeled by using fishing line, with lead as weight. The proposed configuration consists of three pulleys in a group belonging to each connecting cable; two of them are joined together and to the catenary, and the third one is fixed to the upper end of the connecting cable. Two post-tensioning cables were driven through the corresponding pulleys with ballast weights at their end points providing the desired internal forces in the connecting cables, resulting in a spatial pre-stressed structure. Although the results were in line with the expectations as to the structural behavior, the unpredictable material of the applied fishing line hindered a precise comparison with numerical results. Therefore, a detailed physical model was constructed based on the experiences gained on this preliminary model.

3 DETAILED PHYSICAL MODEL

3.1 Model fabrication

In order to carry out quantitative validation, steel wire ropes were used for the main catenary cable as well as the wind cables. Despite the fact that fishing line found to be improper due to its nonlinear material properties, it was still used for the post-tensioning and the connecting cables with respect to the moderate cable forces in these elements; the strain remained in the linear range. Besides, a multi-strand fishing line is advantageous due to its bending flexibility, which reduces the overall friction of the pulley system. The structure is shown in Figure 2 with coloring the different cable types for better visibility, which will be used later where necessary. The span of the main catenary cable is L=14 m. The diameter of the catenary cables is 3.0 mm (EA=560 kN), and that of the wind cables is 1.0 mm (EA=75 kN). The fishing line diameter of the post-tensioning and the connecting cables is 0.40 mm (EA=2 kN). When the bridge was ready and the ballasts were released, the spatial pre-stressed structure was qualitatively studied; the connecting cable forces were indeed close together as desired, loose cables were not found.

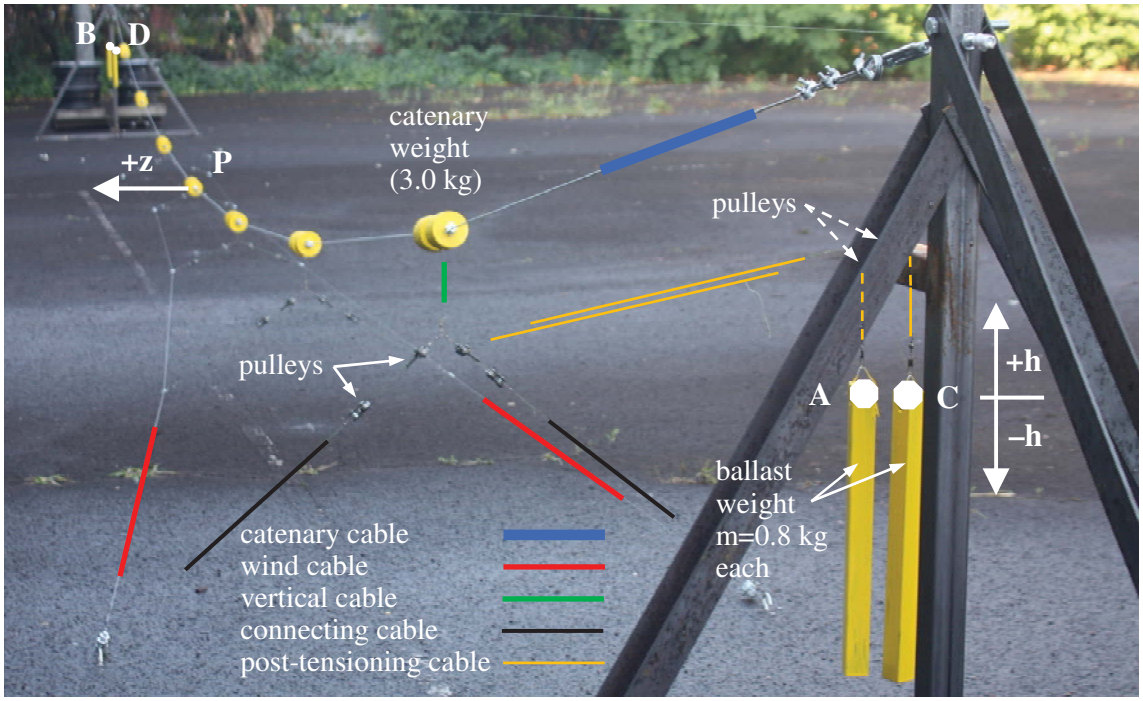

Figure 2. View of the 14 m long physical model with the monitored points and the colored cable types.

The projected schematic top view of the original and the proposed structural configuration is shown in Figure 3. In case of the conventional structure, the connection between the main catenary cable and the wind cables is made by using connecting cables. The desired internal forces can be adjusted by pre-stressing the wind cables and the connecting cables, which is tedious to carry out precisely due to the mutual interaction of the cables. The connecting cable force distribution depends on the stiffness properties of the whole structure and the pre-stress applied to the cables. The original system is referred to as model v1.

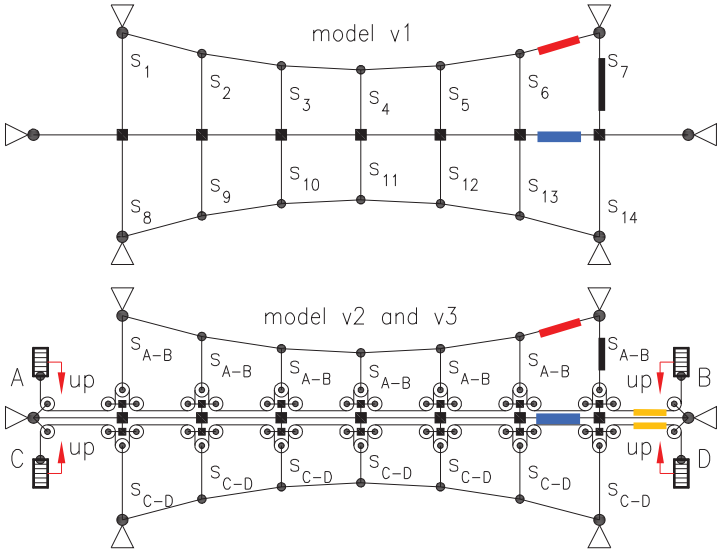

Figure 3: Conventional (top) and the proposed structural system with the connecting cable forces (s).

The proposed system requires ballast weights in order to set the desired cable forces. In contrast to model v1, the connecting cables do not connect the wind cables and the catenary directly, but two post-tensioning cables are included in the whole system belonging to the two wind cables on the two sides of the catenary.

The post-tensioning cables are referred to as A-B and C-D, according to the points on the ballast weights (Figure 3). The whole system of a post-tensioning cable and the belonging connecting cables are referred to as branches A-B and C-D. There are two versions of the proposed system; in case of model v2 all the four ballast weights move independently from each other. Model v3 is different, as the neighboring ballasts are connected together; the motion of ballasts A and C is not independent, instead a common upward or downward motion is allowed only. The same applies to ballasts B and D. Model v2 and v3 both produce equal connecting cable forces within a branch if the friction of the pulleys is neglected. For model v2 the connecting cable forces of the two branches are equal, that is $s_{A\text{-}B}=s_{C\text{-}D}$.

The pulley system gives an additional flexibility to the system, which may reduce the horizontal stiffness of the main catenary. Therefore, it was of utmost importance to compare the static and dynamic behavior of the proposed models v2 and v3 to the original one of v1. The physical model was constructed with special attention to this need; the pulley system was equipped with a constraint that was capable of fixing the post-tensioning cable, which made it feasible to investigate and compare the behavior of model v1, v2 and v3. The structural details of the physical model are shown in Figure 4.

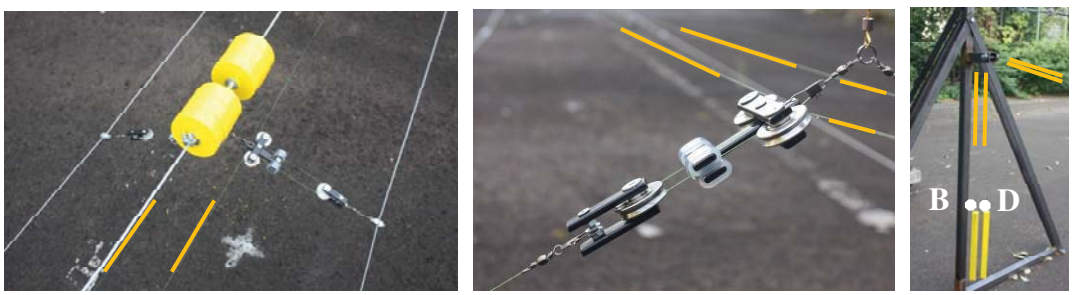

Figure 4: Structural details of the physical model: catenary node, pulleys and ballast weights.

3.2 Measurements

The slender catenary bridges are sensitive to wind loading; therefore the behavior due to horizontal static loading was studied and compared. The catenary nodes were loaded horizontally at each node. The load test can be seen in Figure 5. All the three configurations were tested. Model v1 was set by fixation of the post-tensioning cables around the pulleys. The connecting cable forces are independent from each other in this case. For model v2 the above mentioned fixation was released. Model v3 was set by joining the neighboring ballasts together. The pulley friction can be an important factor in the proposed system; therefore the initial friction value was measured by applying force difference onto the two ends of a test cable hanging on the two sides of a solo V-groove ball bearing. The force difference reached 5 % at the boundary of stall and motion, but drops to 1-2 % when even moderate motion appears. Time-dependent behavior was also observed, which was explained by the presence of grease in the bearings. Due to the high friction and viscous properties of the pulleys, the whole structure was given slight vibration at each static measurement in order to help the pulleys and the post-tensioning cables arrange and approach to the ideal frictionless state. This was particularly important for model v2. In case of model v1 the ballast weights do not move and there is no pulley rotation either. In case of model v2, on the side the horizontal force pushes the structure toward, the ballasts move downwards as the distance between the catenary and the wind cable decreases. The post-tensioning cable releases ballasts A and B down. On the opposite side, the ballasts C and D are lifted upwards. The horizontal displacement of the catenary and the corresponding vertical displacement of ballasts A and C can be seen in Figure 5. In case of model v3 the neighboring ballasts are joined together, therefore no significant ballast motion was observed.

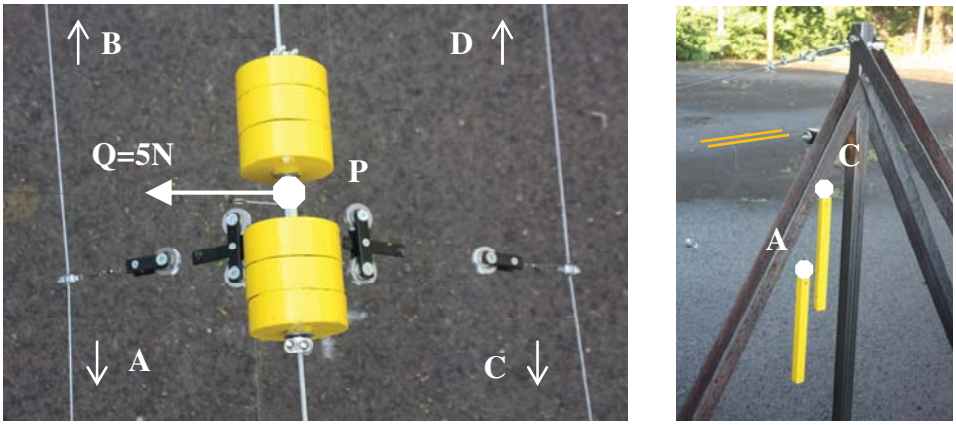

Figure 5: Horizontal static deflection of the catenary and the vertical displacement of the ballasts for model v2.

The dynamic properties were studied by using an accelerometer attached to the middle catenary point P (see Figure 2 and 5). The first vibration mode of the bridge was considered only, which was excited simply by hand. The symmetrical sway mode was the same for every model. In case of model v2, the sway motion of the catenary was accompanied by the vertical motion of the ballasts with small amplitudes of 1-2 cm only, nevertheless. In case of model v1 and v3 there were no ballast motion amplitudes observed.

4 STATIC NUMERICAL MODEL

4.1 Introduction of the numerical approach

The static behavior was studied on a 72 DOFs numerical model, which was written in Octave (Figure 6). The model consists of two-node spatial truss elements with tension capabilities only. The structural elements are the main catenary cable (blue), the wind cables on both sides (red), the connecting cables (black) and the vertical elements (green). The post-tensioning cables and the ballasts are not shown in this model, but their effect is included as described below.

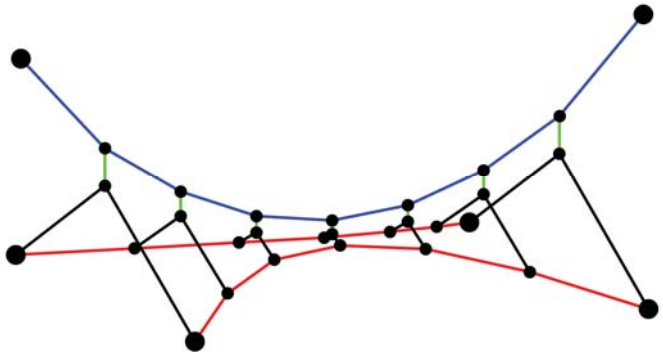

Figure 6: Geometry of the numerical model.

4.2 Static equations with geometrical non-linearity

The considered mechanical system involves geometrical non-linearity; therefore the (load control) New-ton-Raphson iterative approach was applied to find static equilibrium. The key step of the process is solving the $\mathbf{K}_i(\mathbf{x}_i)\Delta\mathbf{x}_i=\Delta\mathbf{q}_{red,i}$ matrix-equation for the $\Delta\mathbf{x}_i$ displacement error vector due to the reduced force error vector of $\Delta\mathbf{q}_{red,i}=-\mathbf{G}_i\mathbf{F}^{-1}d\mathbf{t}_i+\Delta\mathbf{q}_i$. The iterative process is to be continued until the $\Delta\mathbf{t}_i=\mathbf{t}-(\mathbf{l}_i-\mathbf{l}_0-\mathbf{F}\mathbf{s}_i)$ and $\Delta\mathbf{q}_i=\mathbf{q}-(-\mathbf{G}_i\mathbf{s}_i)$ unbalanced kinematic and force vector norms are smaller than a tolerance. In the equations above $\mathbf{x}_i$ = displacement vector of the 24 nodes (see Figure 6); $\mathbf{l}_i$ = stressed cable length vector; $\mathbf{l}_0$ = stress-free cable length vector; $\mathbf{t}$ = kinematic load vector; $\mathbf{q}$ = external force vector; $\mathbf{G}_i$ = geometry matrix containing the direction unit vectors of each cable; $\mathbf{K}_i$ = tangential stiffness matrix; $\mathbf{F}$ = flexibility matrix. All the matrices and vectors are to be updated at each i^{th} iteration step. The above detailed Newton-Raphson iteration was carried out in two steps. At the first construction stage the main catenary cable was activated with its vertical loading, which was complemented by the wind cables and the connecting cables at the second stage. Therefore, the sizes of the matrices and vectors are different in these two construction stages. The results of the first stage (e.g. cable length and forces, geometry and stiffness matrices) are used as initial condition for the second one. The first stage is the same for the three models. In case of model v1 the prestressing is defined onto the wind cables and the connecting cables as kinematic loads, i.e. cable shortening. The connecting cable force distribution strongly depends on how the kinematic loads are defined. In case of model v2 and v3, however, the connecting cable forces are the same in every cable and depend on the ballast weight only. The additional horizontal forces are applied at stage two.

4.3 Formulation of stiffness matrices

The key step during the Newton-Raphson process is the formulation of the tangential stiffness matrix that belongs to the actual state of the structure, which can be assembled from the element stiffness matrices. Spatial truss elements were used with an element stiffness matrix:

$$\mathbf{K}_e = \left[k - \frac{s}{L}\right]\mathbf{e}\cdot\mathbf{e}^T + \frac{s}{L}\mathbf{I} \tag{1}$$

The spring stiffness is k = EA/L, with EA = normal stiffness; L = cable length; **e** = cable orientation unit vector; s = cable force; **I** = identity matrix. The element matrix takes structural and geometrical stiffness into account. For model v1 the formulation of the element matrices is straightforward, the internal force variation of the j^{th} connecting cable is $\Delta s_j = f(\Delta L_j)$, which is the function of the length variation. For model v2 and v3, however, special further considerations have to be made. The force of the j^{th} connecting cable depends not only on the displacement of the nodes of its two end points, but of every connecting cable. Therefore, a compatibility equation of the coupled system of the post-tensioning and connecting cables has to be solved at each iteration step in order to obtain the cable force changes based on the displacement variation vector Δx_i. The arrangement of branch A-B can be seen in Figure 7.

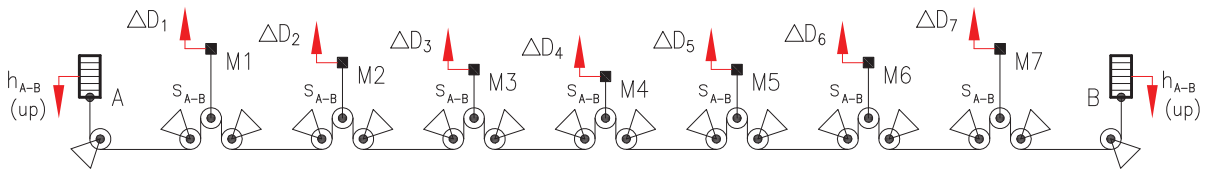

Figure 7: Schematic projected arrangement of branch A-B (D and h are displacement, s is the cable force).

The forces in the connecting cables of a branch are equal, provided that pulley friction is neglected, which leads to the analogy of serial coupling in electricity. By using this principle, the system shown in Figure 7 was reduced into an inhomogeneous spring, which includes all the connecting cables and the tensioning cable of branch A-B (see Figure 8). The points M_j were merged into point M, and points A and B into A-B. The total displacement variation onto point M is calculated as $\Delta x_{A\text{-}B} = \Sigma \Delta D_j$, where ΔD_j = end points distance variation (see Figure 8 and 9) of the j^{th} connecting cable of branch A-B. The linear reduced stiffness can be calculated by using a reciprocal formula for the serially coupled linear springs of a branch as:

$$k_{red,A-B} = \frac{1}{\sum \frac{L_j}{EA_j} + \frac{L_{A-B}}{4EA_{A-B}}} \tag{2}$$

L_j = length of a connecting cable; EA_j = normal stiffness of a connecting cable, $L_{A\text{-}B}$ = length of the post-tensioning cable, $EA_{A\text{-}B}$ = normal stiffness of the post-tensioning cable. Branch C-D can be handled likewise. Symmetrical horizontal loading was considered only.

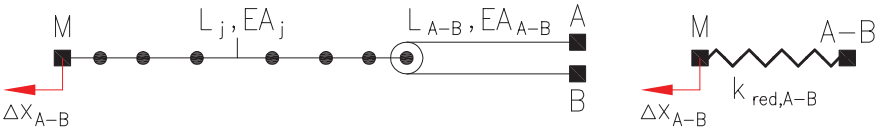

Figure 8: Construction of the idealized spring (left) and its reduced model (right).

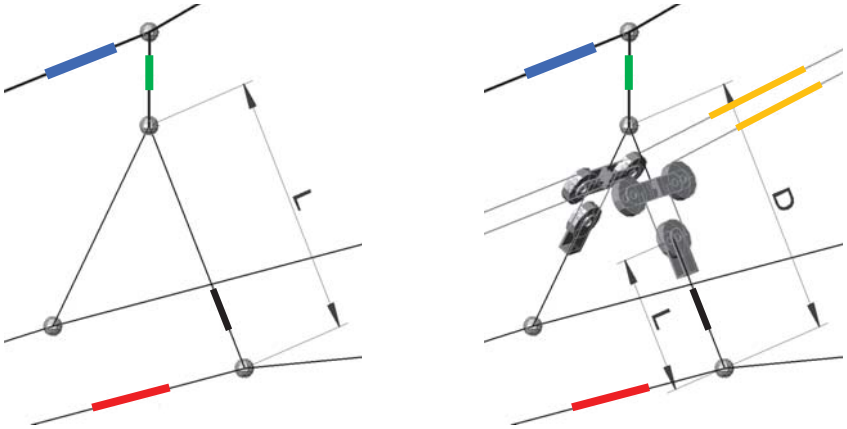

Figure 9: Connecting cables of model v1 (left) and v2-v3 (right) with connecting and post-tensioning cables.

If there is no horizontal load, models v2 and v3 are the same as the force is s=2mg in every connecting cable, where m = weight of one ballast and g=9.81 m/s. The behavior of these two models, however, is different if horizontal load is also applied, which is illustrated in Figure 10. In case of model v2, branches A-B and C-D are independent; therefore the ballast weights can move freely. Consequently the connecting cable forces do not change due to any structural displacement field, that is $\Delta s_{A\text{-}B}=0$ and $\Delta s_{C\text{-}D}=0$. This can be modeled by simply eliminating term k in the element stiffness matrix of the connecting cables (1), which means that the geometrical stiffness belonging to the constant connecting cable forces exists only. It should be noted, however, that instead of using zero value for k, a small nonzero value is better to use for faster convergence. In case of model v3 points A-C and B-D are connected together; the two inhomogeneous springs belonging to the branches A-B and C-D are now coupled in a parallel way.

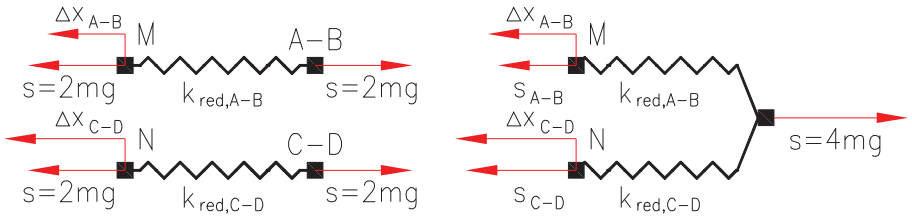

Figure 10: Difference between the behavior of model v2 (left) and v3 (right).

The internal force variation for branch A-B is $\Delta s_{A\text{-}B}=f(\Delta D_j, j=1..2n)$ and that for the branch C-D is $\Delta s_{C\text{-}D}=g(\Delta D_j, j=1..2n)$, where n = number of the connecting cables on one side, namely 7 in our case. Unlike model v2, the connecting cable forces are not invariant of the reduced displacement variation in case of model v3. If the reduced displacement variation of $\Delta x_{A\text{-}B}$ and $\Delta x_{C\text{-}D}$ are not equal, a difference will appear between the connecting cable forces of the two branches.

The reduced displacement variations for branch A-B is $\Delta x_{red,A\text{-}B}=\Delta x_{A\text{-}B}-(\Delta x_{A\text{-}B}+\Delta x_{C\text{-}D})/2$ and for branch C-D is $\Delta x_{red,C\text{-}D}=\Delta x_{C\text{-}D}-(\Delta x_{A\text{-}B}+\Delta x_{C\text{-}D})/2$. If symmetrical horizontal forces are applied, the connecting cable force variations is be calculated as $\Delta s_{A\text{-}B}=\Delta x_{red,A\text{-}B}\cdot k_{red,A\text{-}B}$ and $\Delta s_{C\text{-}D}=\Delta x_{red,C\text{-}D}\cdot k_{red,C\text{-}D}$. Compared to model v2, stiffness k in the element stiffness matrix is not zero. The normal stiffness k for each connecting cable of branch A-B and C-D were selected as $n\cdot k_{red,A\text{-}B}$ and $n\cdot k_{red,C\text{-}D}$, respectively. This intuitive stiffness approximation of the connecting cables gave fast convergence in case of symmetrical total horizontal loading.

5 DYNAMIC NUMERICAL MODEL

The dynamic behavior of the three models was studied by extending the static equations with the inertia and damping forces. A non-iterative incremental time advancement version of leap-frog scheme was used. Also, a nested Newton-Raphson scheme can also be developed.

Model v1 required to solve Equation (3):

$$\mathbf{M}\Delta\mathbf{a}_t + \mathbf{C}\Delta\mathbf{v}_t + \mathbf{K}_t(\mathbf{x}_t)\Delta\mathbf{x}_t = \Delta\mathbf{Q}_t \tag{3}$$

In (3) **M** = mass matrix; **C** = damping matrix; **a** = acceleration vector; **v** = velocity vector; **x** = displacement vector; **Q** = external load vector. As the structure is geometrically non-linear, the stiffness matrix had to be updated at each time step based on the geometrical position of the nodes (see Figure 6) and the cable forces. Although the explicit scheme was easy to implement, the time step for a stable and accurate solution was typically 10 times less than usual in linear dynamics.

Model v2 required the modification of the equation (3) into (4):

$$\mathbf{M}\Delta\mathbf{a}_t + \mathbf{C}\Delta\mathbf{v}_t + \mathbf{K}_t(\mathbf{x}_t)\Delta\mathbf{x}_t + \Delta\mathbf{P}(a_t, v_t) = \Delta\mathbf{Q}_t \tag{4}$$

The elements of vector $\Delta\mathbf{P}_t$ are determined by solving $\Delta\mathbf{P}_t=\mathbf{G}_t\Delta\mathbf{s}_t$, where $\Delta\mathbf{s}_t$ = internal force vector increment belonging to the connecting cables. Unlike static behavior, the connecting cable forces do change due to inertia and damping forces accompanied by the ballast weight motion, therefore $\Delta\mathbf{P}_t$ is the function of $\mathbf{a}_t$ and $\mathbf{v}_t$ of the structural nodes. In Figure 11 the coupled system of the post-tensioning cable and the connecting cables is shown for model v2, which was reduced into an idealized spring system. The two ballasts of a branch move identically due to symmetrical horizontal loading. The spring representing branch A-B is excited at point M with displacement increment of $\Delta x_{A\text{-}B}=\Sigma\Delta D_j$, where D is illustrated in Figure 9. The spring of branch C-D is derived likewise. In order to improve the performance of model v2, each ballast can be equipped with a linear hydraulic damper (c) and a nonlinear spring that is inactive until a prescribed displacement (δ) is reached. The dynamic equation of motion is solved for the vertical ballast displacement variation Δh, from which the cable force change in the reduced spring of a branch is $\Delta s=(\Delta x-\Delta h)\cdot k_{red}$, which is equal to the connecting cable force increments of the same branch. Based on the connecting cable force increments, $\Delta\mathbf{P}_t$ can be compiled, and the displacement, velocity and acceleration increments of the 24 structural nodes and the four ballasts can be calculated at a time step.

Model v3 is simpler than v2 in case of horizontal loading, as the vertical motion of the ballast and the consequent dynamic forces can be neglected. Instead, the principles introduced at the static numerical modeling apply here. The difference is that the internal forces of the connecting cables are taken into consideration in the $\Delta\mathbf{P}_t$ vector rather than in the term $\mathbf{K}_t\Delta\mathbf{x}_t$, which means that the internal forces are handled as external loadings. This is important with respect to the explicit time advancement scheme as there is no internal iteration within a time step. The nonlinear dynamic calculation was tested by applying quasi-static test loading; the results were in good agreement with that of the nonlinear static calculations for all the three models.

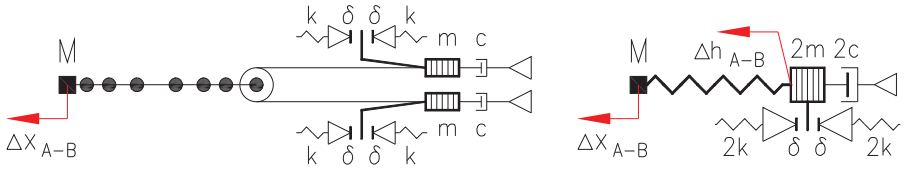

Figure 11: Dynamic model of the idealized spring for branch A-B (left) and its reduced model (right).

6 VALIDATION

In the previous chapters the proposed structural system was investigated by means of physical and numerical approaches. The input for the numerical simulation was set in accordance with the measured physical model; the normal stiffness of the steel wires and the multi-strand fishing line were measured through tensional tests. The weight of each structural part was also determined. Neither hydraulic damping, nor nonlinear springs were applied to the ballasts. A horizontal static load of 5 N was applied to the catenary nodes. The horizontal displacement showed linear tendency for every model for this load. In Table 1 the measured and calculated horizontal displacement in mm of point P (see Figure 12) and vertical displacement of ballast points A and C are compared. The measured and simulated displacement values are in good agreement for model v1 and v3. The results of model v1 and v3 are close together, showing that there is no significant loss in the overall stiffness due to the dominant horizontal loading by applying the proposed post-tensioning system of model v3. Model v2, however, gave 2-3 times larger displacement, which can be explained by the unconstrained vertical displacement of the ballasts and the consequently constant connecting cable forces. The connecting cables with constant forces need to change spatial orientation in order to balance the horizontal load, which is the source of the significantly larger horizontal displacement. The measured horizontal displacement is lower by 35 percent than the calculated one due to the friction of the pulleys. The ballast displacement shows the difference between models v2 and v3; points A and C move in the opposite direction and so do points B and D in case of model v2. On the other hand, in case of model v3, points A-C and B-D are connected together, resulting in a small common displacement, which constrains the horizontal displacement of the catenary.

Models	Physical			Numerical		
	P_hor	A_vert	C_vert	P_hor	A_vert	C_vert
v1	21	-	-	22	-	-
v2	50	-190	178	67	-276	276
v3	28	3	3	29	8	8

Table 1: Horizontal displacement of point P and vertical displacement of points A and C [mm].

The developed dynamic numerical method was also validated. The natural frequencies were determined by FFT analysis of the time series of the geometrically non-linear time stepping method. The simulation was started on the completed bridge structure as a result of the nonlinear static calculation. The time dependent horizontal load was applied to each catenary node; it was ramped up in a quasi-steady manner and then set to zero in one time step, obtaining a free decay oscillation to study.

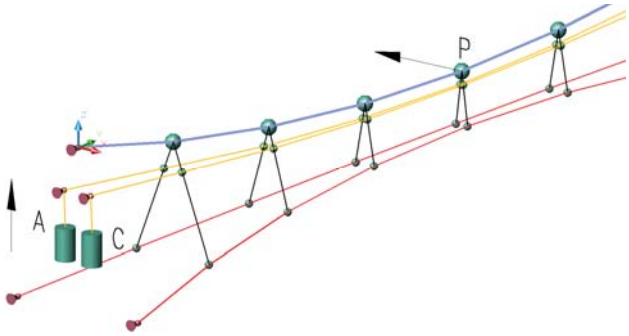

Figure 12: Investigated points and displacement directions.

The results are shown in Table 2 for the three models and with stage1 for the catenary alone state. The measured and simulated natural frequencies of the sway mode are in good agreement. According to expectations, model v1 has the highest frequency as it has the highest stiffness. Model v3 showed higher static deflection and the frequency is consequently lower. Model v2 is interesting as the sway mode has a frequency close to that of models v1 and v3. On the other hand, the extra freedom of the ballasts provided a slow vibration mode that belongs to the vertical motion of the ballasts and the horizontal motion of the catenary. The frequency is around 0.30 Hz, which is shown in Table 2 in parentheses. This mode was spotted numerically but did not show up in the measurements, which is explained by the behavior of the pulleys; the bearings of this size give relatively high friction and viscosity, which might hinder the whole pulley system from accommodating this vibration mode.

Models	Physical	Numerical
stage1	0.68	0.66
v1	1.50	1.44
v2	1.37	1.30(0.30)
v3	1.38	1.28

Table 2: Natural frequencies of the symmetrical sway mode.

7 INDUSTRIAL APPLICATION

7.1 The considered long-span catenary bridge

In this chapter an L=700 m main span catenary is considered that has been designed by Pont-TERV Ltd in the framework of a feasibility study in 2017 (see Figure 13). The bridge geometry is similar to the physical model that was studied earlier. The proposed novel tensioning system and the adequate numerical approach were adopted to this bridge structure. It is highlighted that this span length maximization is under research in case of road bridges [4].

Figure 13: The considered long span catenary structure (Feasibility study, courtesy of Pont-TERV Ltd, 2017).

7.2 Application of the proposed iso-tensioning system

At first, the horizontal displacement of the structure due to horizontal loading on the catenary is illustrated in Figure 14. It can be seen that the catenary together with the wind cables moves sideways.

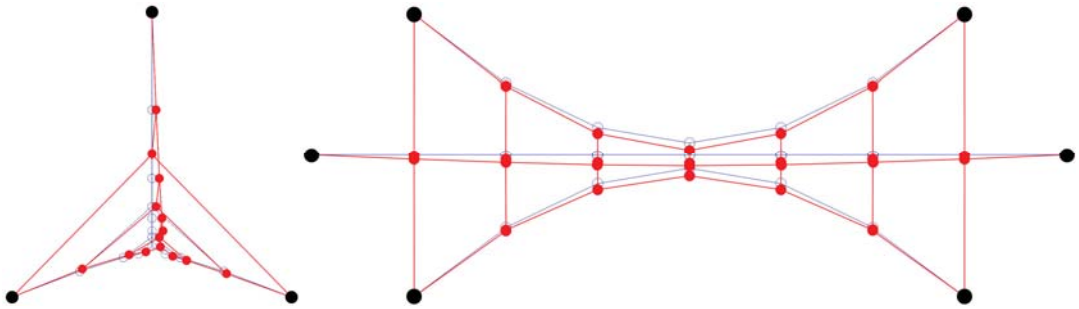

Figure 14: Horizontal deflection of the catenary.

The selected ballast weight is 4 t each. The static test loading was horizontal Q_{top}=14 kN at the nodes of the catenary, and Q_{bottom}=31 kN at the nodes representing the bridge walkway. The horizontal loading was ramped up within 20 seconds and then was kept constant. The horizontal displacement of point P for models v1, v2 and v3 is shown in Figure 15. Both models are common in reach a horizontal displacement around 60-80 cm when the ramped load reaches its maximum value. This displacement belongs to the spatial deformation of the whole bridge structure (see Figure 14).

The displacement values remain constant except for model v2, which shows increasing tendency with time. This creep-like behavior is due to the ballast motion pulled by the post-tensioning cables, which is explained in Figure 15 (right hand side); z_0 is the deflection due to short-term load, z_t is the long-term deflection. The displacement growth speed can be decreased by involving dampers shown in Figure 11. In our calculations a value of c=10 kNs/m was selected. The maximum displacement of model v2 was reached when the orientation of the connecting cables changed in order to reach equilibrium. It is important to note that there is a limit for the static horizontal loads to be balanced by the connecting cables, as the forces in these cables are constant under any external load conditions. To overcome this problem, the ballast motion was constrained by using supports that were activated after a prescribed vertical motion (h), which restricted the horizontal displacement of the catenary as well. At each ballast, a spring with k=10000 kN/m was defined that was activated when the ballast vertical displacement exceeded δ=2.00 m. With this non-linear constraint the creep-like behavior could be well controlled. In Figure 15 (left hand side), the results of model v2 both with and without constraint are shown (red and green curves).

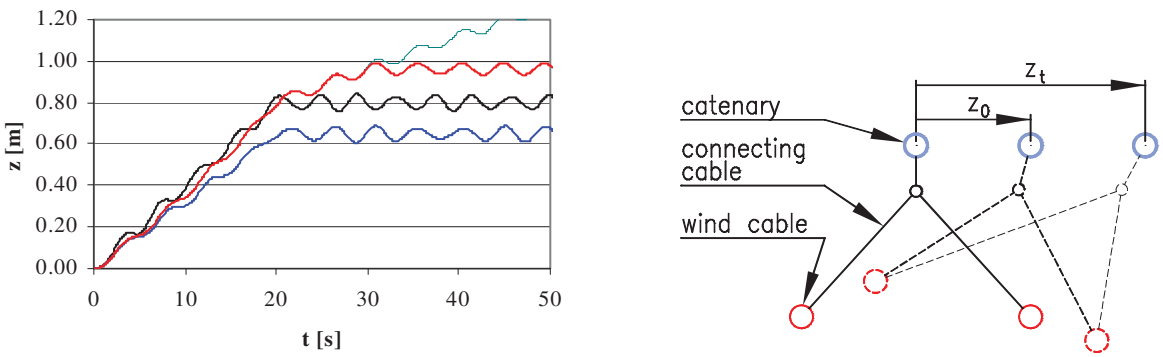

Figure 15: Horizontal displacement due to static load (v1: black, v2-constrained: red, v2: green, v3: blue).

In Figure 16 the dynamic performance of the three models are compared. The model v2 is investigated with the above mentioned constraint, the no-constrain condition is not shown now. The test load is the same as the quasi-static one, but when its maximum was reached, the load was dropped to zero in one time step, leading to a free decay oscillation. The results of model v1 and v3 are close together. Model v2 shows larger damping, which can be explained by the damped motion of the ballasts; the horizontal displacement of the walkway are transferred by the post-tensioning cables to the ballasts that can move freely making the dampers work. The neighboring ballasts are prevented from moving in the opposite direction in case of model v3; therefore the hydraulic dampers do not increase the overall damping at all.

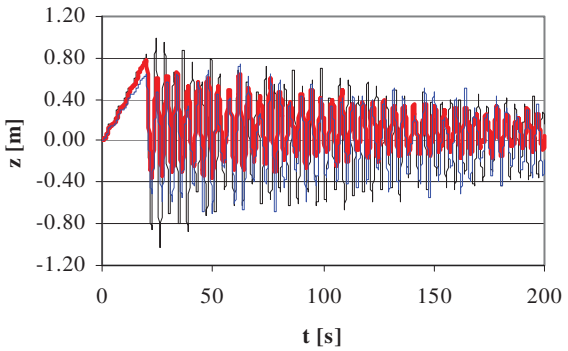

Figure 16: Horizontal displacement due to sudden load (v1: black, v2-constrained: red, v3: blue).

Having studied the structural behavior of the three different models due to ideal loads, a real test was also carried out. An along-wind time series was generated based on the turbulent spectrum proposed by the Eurocode. By using the wind speed values at each time step, the loading to the catenary and walkway nodes was determined. Unlike nonlinear aerodynamic load models, a simplified along-wind loading of $q_x=0.5\rho U^2 c_x A$ was chosen, where ρ = air density; U = wind velocity; c_x= static force coefficient of the certain structural element; A = reference area. The effect of the displacement and velocity of the bridge on the aerodynamic forces is neglected. The structural logarithmic damping value of $\delta=0.22$ was selected as a sum of the inherent structural damping ($\delta=0.02$) and the aero-dynamic damping.
All the parameters were chosen in accordance with Eurocode (terrain category: III, height over ground: 80 m). Due to the high reduced wind speed, the simplified aerodynamic load model is justified; therefore advanced three-dimensional fluid-structure interaction model [2] can be omitted for this problem. The results are shown in Figure 17. For model v2 each ballast was equipped with a hydraulic damper and a non-linear spring that was introduced earlier. The dynamic displacement values of model v1 and v3 show the same tendency, but that is apparently lower in case of model v2 due to the additional effect of the dampers of the ballasts.

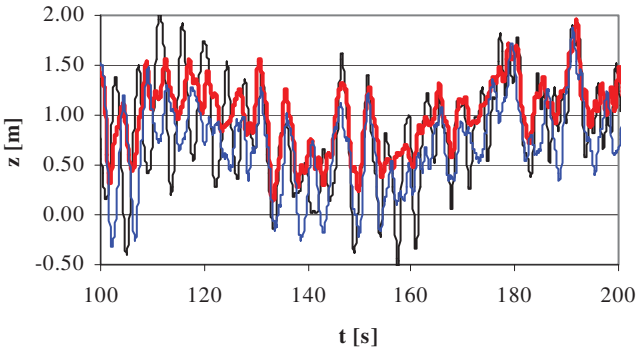

Figure 17: Horizontal displacement of point P due to buffeting (v1: black, v2-constrained: red, v3: blue).

8 CONCLUSIONS

- In this paper a novel post-tensioning method was proposed for long span catenary bridges. The system involves pulleys that has a number of advantages. First of all, the prestressing is temperature-independent. Seconly, the connecting cable forces are evenly distributed, therefore any vibration of a loose cable is unlikely. The proposed structural configuration was tested on a physical model. The evenly distributed connecting cable forces were indeed observed, which was our main goal to achieve. An adequate numerical model was also developed. Three configurations were investigated; a conventional one named model v1, and the novel pulley based system with and without fixing the neighboring ballasts together, which are models v3 and v2, respectively. The measured and calculated results were in good agreement.
- The friction of the pulleys were not considered in the numerical models. Their effect will be studied in our advanced models in the future.
- The validated numerical model was tested on a catenary bridge of real sizes as well. It was found that model v2 and v3 worked properly due to buffeting forces, as the dynamic responses did not exceed that of model v1, which indicated that the loss in the horizontal stiffness of the proposed systems can be avoided. The novel configuration v2 and v3 are basically different in nature; v3 is simpler as the neighboring ballasts are connected together, which results in a stiffness close to model v1 and a consequently similar static and dynamic behavior. The more sophisticated v2, however, requires special treatment in order to preserve stiffness; a constraint is necessary to the ballasts that controls the displacement. On the other hand, applying hydraulic dampers too, the overall damping of the bridge can be increased. The choice between model v2 and v3 therefore requires profound design and economic considerations.
- To conclude, the main goal of a temperature-independent and evenly distributed connecting cable forces has been achieved by the proposed structural configuration(s) with at least equivalent static and dynamic performance compared to the conventional catenary bridges. The additional damping experienced in case of model v2 is beyond our expectations, which will be further investigated as it can be essential in span length maximization.

REFERENCES

[1] M.H. Huang, D.P. Thambiratnam, N.J. Perera, Vibration Characteristics of Shallow Suspension Bridger with Pre-tensioned Cables, *Engineering Structures 27(8)*, 1220-1233, 2005.

[2] S. Stoyanoff, P. Irwin, Flutter Analysis of Lions' Gate Bridge during Deck Replacement, *Proceedings of the 6th Asia-Pacific Conference on Wind Engineering*, 2005.

[3] G. Szabó, J. Györgyi, G. Kristóf, Advanced flutter simulation of flexible bridge decks, *Coupled Systems Mechanics 1(2)*, 133-154, 2012.

[4] Y.J. Ge, Aerodynamic challenge and limitation in long-span cable-supported bridges, *Proceedings of Advances in Civil, Environmental, and Materials Research*, 2016.

EURODYN 2020
XI International Conference on Structural Dynamics
M. Papadrakakis, M. Fragiadakis, C. Papadimitriou (eds.)
Athens, Greece, 23–26 November 2020

PREDICTION OF THE WIND-INDUCED FATIGUE OF SLENDER STRUCTURES

M. Damele[1], **and M. P. Repetto**[1]

[1] University of Genoa – Civil, Chemical and Environmental Engineering Department
Via Montallegro 1 Genova 16145
michela.damele@edu.unige.it, repetto@dicca.unige.it

Keywords: Fatigue damage, Slender structures, Wind-induced fatigue, Fatigue standard methods, Antenna masts.

Abstract. *A major shortcoming in the structural and wind engineering sectors concerns wind-induced fatigue design and verification procedures. Despite wind-induced fatigue is a critical phenomenon which may lead many slender structures to damage and collapses, suitable engineering and standards procedures are still fragmentary and almost lacking. Structural typologies sensitive to this problem are, for example, wind turbines, bridges, cranes, poles and towers. A method was proposed by one of the authors, which allows to evaluate in closed form the mean damage in the unit time induced by alongwind turbulence effect on steel slender structures or steel structural elements. The procedure is suitable for engineering calculations and code provisions. The present paper describes the more recent advance in generalizing the procedure for determining the wind-induced fatigue damage of slender structures, taking into account simultaneous alongwind and crosswind structural responses due to turbulence and discussing the main analytical features and the simplifying hypotheses adopted. The set of input parameters is coherent with standard format. An application of the proposed generalized procedure to a real case study is reported and discussed, showing the capability of the proposed method to catch the main feature of the fatigue damage phenomenon with quite simple calculation procedure.*

1 INTRODUCTION

Fatigue is a critical phenomenon producing localized and progressive damage and subsequent weak structural collapses, due to moderate but repeated loading conditions. Metallic elements often experience this process in the welded or bolted joints. Such phenomenon may determine failures under cyclic actions of amplitude lower than design loads, thus without exceeding ultimate strength and without appreciable plastic deformations. Ultimate verification methods provided by standards and codes are therefore not suitable for fatigue analysis.

The fatigue analysis under variable amplitude stress histories implies the application of a suitable accumulation rule because fatigue damage increases in a cumulative manner. The fatigue failure occurs when the total accumulated damage reaches a critical value. The cumulative damage rate depends both on the amplitude of the cycles and on their sequence, as well as many other aspects. In 1945 the Palmgren-Miner linear accumulation rule was proposed, according to which one block of cycles of n_j constant amplitude Δ_j produces a fraction of damage $d_j(\Delta_j)$ proportional to the ratio n_j/N_j. The total cumulative damage D is expressed linearly adding the fractional damages due to different stress cycles amplitude [1]. The Palmgren-Miner rule, which remains the most commonly adopted accumulation law so far, basically disregards the loading sequence. The critical total damage value, corresponding to failure, is conventionally defined as equal to one; the fatigue life is defined as the time in which D reaches the unit.

Existing literature and codes provide information on structural fatigue resistance of structures through *S-N* experimental curves in the bi-logarithmic diagram, which associate to every constant stress amplitude Δ the number of cycles that leads to collapse N, giving different shapes of curves depending on different materials and cyclic loading applications. Adopting the commonly used nominal stress approach, *S-N* resistance curves are given for classified structural details and the level of stress analysis adopted corresponds to the global stress calculated in the cross-section under consideration, assuming a linear elastic behaviour of the material and disregarding the local stress raising effects of the welded joint [2, 3, 4].

Wind actions may produce large vibrations of exposed slender structures and repeated stress cycles in critical details during the whole structural life. The dynamic response of structure to turbulence actions or to the vortex shedding phenomenon can be critical for moderate and frequent wind velocities, inducing the propagation of fatigue crack. Thus, wind-induced fatigue is a frequent reason of structural damages and collapses [5, 6]. Slender structures or slender structural elements are particularly sensitive to this phenomenon. Poles, masts and antennas supports are typical kinds of structures sensitive to wind induced fatigue, strongly affected by dynamic response due to turbulence action. Vortex shedding actions usually are negligible for these kinds of structures, unless particular shapes are used [6].

Despite a wide research literature addressed to this problem, standards and codes related to wind-induced fatigue are still fragmentary. Eurocode [7] provides a calculation procedure for alongwind fatigue assessment based on very simplified assumptions [8], furnishing results than can be high uncertain. This code also provides methods for evaluating vortex shedding-induced response and fatigue. Other international standards are addressed to particular kinds of structures, such as steel chimneys [9], poles and infrastructural supporting constructions [10] and wind turbines [11], adopting different approaches. A wide research project aimed at formulating and calibrating a procedure for determining wind-induced fatigue has been carried out by the authors. This paper presents an overview of the proposed procedure, focusing on more advanced generalizations to alongwind and crosswind buffeting actions and different resistance curves. The procedure is finally applied to a monopole antenna mast.

2 BASES OF THE PROPOSED METHOD

Time is conventionally subdivided into successive ΔT time intervals of 10 minutes – 1 hour, falling in the spectral gap, which separates the macro-meteorological and the micro-meteorological peaks. Wind velocity at a reference height above the ground is schematized, in each ΔT interval, through its mean value $\bar{u}$, its direction, and the three zero-mean fluctuating orthogonal components, *u'*, *v'*, *w'*, referred to, respectively, as longitudinal, lateral and vertical turbulence; these are modelled as stochastic stationary Gaussian processes. The mean wind velocity at the structural site is linked with the mean wind velocity at a reference site, namely the mean wind velocity at a reference height on a reference terrain, probabilistically characterized by the Weibull distribution parameters.

Let us consider a slender structure or structural element whose length l is much greater than the reference size b of its cross-section. Let x, y, and z be a local Cartesian reference system with origin at o; z coincides with the structural axis, x is aligned with the mean wind direction, o lies on the face of the structure with $z = 0$. The wind loading is schematized as a three-variate two-dimensional random stationary Gaussian process, whose i-th component ($i = x, y, \theta$) is given by:

$$F_i(z,t) = \bar{F}_i(z) + F'_i(z,t) \tag{1}$$

where $0 \le z \le l$; t = time; F_x, F_y, F_θ = alongwind force, crosswind force and torsional moment around z per unit length; $\bar{F}_i$ = mean value of F_i ; and F'_i = nil mean fluctuation of F_i around $\bar{F}_i$. Using a quasi-steady theory and dealing with the structure as a linear system, the wind-induced stress at a coordinate z of the structure in a ΔT time interval is a stochastic stationary Gaussian process given by the sum of the mean static stress caused by the mean wind action and the fluctuating stress components, caused by the buffeting and vortex shedding actions. Therefore, the wind-induced stress at a coordinate z of the structure in a ΔT time interval is given by:

$$s_i(z,t) = \bar{s}_i(z) + s'_i(z,t) \tag{2}$$

where $\bar{s}_i$ is the mean static stress and s'_i is the fluctuating stress. The fluctuating stress, varying on time, may produce fatigue phenomenon. In alongwind direction, the stress process is caused by the buffeting actions due to turbulence and it can be schematized as a bi-modal process [12, 13], with a low frequency quasi-static component and a high frequency resonant component. Crosswind fluctuating part of the response is due to the joint action of the oncoming wind turbulence and of the vortex wake. Resonant response to vortex shedding actions occur at critical wind velocity, corresponding to the condition in which the shedding frequency is equal to the fundamental mode of vibration of the structure.

In order to verify a structural component with regard to wind-induced fatigue, a cycle histogram has to be determined, which provides the number of cycles associated with every stress amplitude on varying of mean wind velocity. The cycle histogram evaluation is not trivial, requiring the application of a suitable cycles counting method to the wind-induced response processes associated to the whole range of wind velocity loading conditions [14, 15, 16]. As the response due to wind is dealt with as a random stationary process in frequency-domain, definition of cycle counting for random loads and definition of the mean fatigue damage or mean fatigue life are required. The analysis is strongly dependent from random process characteristics [17, 18].

In order to obtain the cycle histogram, structural response must be evaluated at a large number of wind velocity values, usually at intervals of 1 m/s up to the reference mean veloci-

ty with 50 years return period, then the number of cycles that stresses the structure is identified by the bi-modal counting method [12, 13]. From the cycle histogram it is possible to evaluate the damage histogram and then the total cumulative damage, expressed by means of the linear accumulation law [1]. Finally, the fatigue life is defined by $T_F = 1/\bar{D}(1)$, where $\bar{D}(1)$ is the cumulated mean damage in the unit time. Then, a refined closed-form solution of the alongwind turbulence-induced fatigue has been obtained [19, 20], expressing $\bar{D}(1)$ in analytical form as the product of a basic "0 level" solution, multiplied by three corrective factors:

$$\bar{D}(1) = \bar{D}_0(1) C_{BM} C_M C_{SN} \tag{3}$$

where the "0 level" solution of damage adopts three classic simplifications: 1) the stress process is narrow band; 2) the stress process is zero mean; 3) the *S-N* fatigue curve is a straight line on a bi-logarithmic diagram, with constant slope equal to 3. The corrective factors have been provided analytically by removing independently the three simplifications one by one: the bi-modal factor C_{BM} considers the process as bi-modal, with a quasi-static and a resonant component; the mean stress factor C_M takes into account the non-null value of the mean stress; the fatigue curve factor C_{SN} regards the tri-linear trend adopted for steel structural details subjected to normal stresses according to the Eurocode [2].

This achievement allows to evaluate the mean total fatigue damage due to alongwind turbulence in closed-form computing the structural response just for two values of wind velocity. In order to reach this aim, three hypotheses have been assumed. The first main simplifying hypothesis is that basic stress parameters of the random process are expressed as functions of the mean wind velocity by the power law approximation. This rule was first introduced by Holmes [5] limited to the standard deviation and later generalized by Repetto and Solari [19, 20] to any stress parameter due to alongwind loadings. It is possible to estimate the exponent of the power law in function of two different values of wind velocity, conventionally the "reference" mean wind velocity, that is the velocity with 50 years return period in the site at a fixed reference height adopted for ULS analysis, and a "fatigue" velocity, which represents the wind velocity that produces the maximum fatigue damage. The second hypothesis is that the density function of the mean wind velocity is represented by the hybrid Weibull model [21]. The third hypothesis assumes that the considered *S-N* resistance curve follows the tri-linear trend adopted in the mechanical and structural practice for steel details subjected to normal stresses, according to the nominal approach [2].

Two classes of formulas at different level of calculation, simplified and detailed calculations, has been defined [22]. The first one provides preventive values of fatigue damage and fatigue life, strongly on the safe side, to detect whether the structure is sensitive to fatigue or not; the second one gives reliable values of fatigue evaluation. The alongwind-induced fatigue assessment method has been completed discussing input parameters and defining their expressions in accordance with Eurocode standards format for wind induced Ultimate Limit State (ULS) analysis [22]. This preliminary work has allowed to introduce the alongwind method in new reviewed CNR [23].

3 THE GENERALIZED MODEL

Starting from the model outlined in Section 2, the method is generalized considering a wide range of *S-N* fatigue resistance curves shapes, in order to evaluate different materials affected by fatigue damage and to evaluate structures susceptible to normal or shear stress conditions. Then the generalization has taken into account both alongwind and crosswind buffeting-induced fatigue; since vortex shedding induced vibrations are generally negligible in cross-

wind response of structures like slender supports and antenna masts, in this paper vortex induced fatigue is not considered. The whole procedure is therefore reformulated, also defining input parameters expressions totally coherent with current Eurocode standards.

3.1 *S-N* fatigue resistance curves

One of the most evident limit of the model described Section 2 is that is valid only for fatigue due to normal stresses in steel structural elements, referring to a particular type of fatigue resistance curve. *S-N* curves in standards and recommendations may assumes different shapes depending on the material, the type of loading application and the stress condition. Linear curves in the bi-logarithmic diagram are provided for some particular materials such as some types of glasses, composites and concretes. Bilinear curves may be distinct in two families, characterized by a cut-off limit and by two different slopes, respectively. Examples of bilinear *S-N* curves are related to shear stresses in steel elements and to aluminium details. Finally, trilinear curves (e.g. *S-N* curves for normal stresses in steel elements) have two different slopes and a cut-off limit, but they are going to be adapted to bilinear shape [4].

In the method proposed in 2012 [20], the total annual mean damage (3) takes account of *S-N* curves trend through the fatigue curve factor C_{SN}, which reduces the "0 level" solution of damage considering only the particular trilinear *S-N* curves for normal stresses in steel details. The generalization of the whole formulation, and in particular of fatigue curve factor C_{SN}, has been carried out, expressing this corrective factor in a more general format, on varying the characteristics of the concerned bilinear *S-N* curve. Indeed, different bilinear shapes in bi-logarithmic diagram may represent fatigue resistance of a wide range of structural details of different materials affected by normal or shear stress processes. Furthermore, two particular cases have been analysed, in accordance with the generalized formulation. These are the case of fatigue due to cyclic normal stresses in steel details, completely coherent with the one proposed in [20], and the case of fatigue due to cyclic shear stresses in steel details. The simplified and detailed calculations have been also defined for the latter particular case.

3.2 Alongwind and crosswind buffeting-induced fatigue

Since the power law approximation for the basic stress input parameters is effective for alongwind and crosswind turbulence induced response, if vortex shedding contribution is neglected the analytical formulation is formally equal for alongwind and crosswind buffeting-induced fatigue analysis. Coherently, the closed-form solution of wind-induced cumulated mean damage in the unit time can be again expressed as the product of the "0 level" solution, multiplied by the corrective factors (3). The stress input parameters have been defined analytically starting from the method recently proposed by Solari [24], which allows to determine the simultaneous alongwind, crosswind, and torsional loading and response of slender structures by means of calculations suitable for standard verifications, within the gust factor technique framework [25, 26]. The generalized formulation of terms in (3) are then given by:

$$\begin{aligned}\bar{D}_0(1) &= 31.536 \cdot 2^{\left(\frac{3m_1-1}{2}\right)} \sqrt{\pi} \cdot \Gamma\left(\frac{m_1}{2}+1\right) \frac{\sigma_{i,ref}^{m_1}}{\Delta_C^{m_1}} \nu_{i,ref} \\ &\times \left(0.2k-0.12\right)^{m_1\alpha_{\sigma,i}} \left(\frac{m_1\alpha_{\sigma,i}}{k}+1\right)^{\left(\frac{m_1\alpha_{\sigma,i}}{k}+0.5\right)} \exp\left[-\left(\frac{m_1\alpha_{\sigma,i}}{k}+1\right)\right]\end{aligned} \tag{4}$$

$$C_{BM} = \frac{\nu_{i,Q,ref}}{\nu_{i,ref}} + \frac{n_{i1}}{\nu_{i,ref}} \lambda_{i,ref}^{\frac{m_1}{2}} \left(0.2k - 0.12\right)^{\frac{m_1}{2}\alpha_{\lambda,i}} \left(\frac{m_1 \alpha_{\sigma,i}}{k} + 1\right)^{\frac{m_1 \alpha_{\lambda,i}}{2k}} \tag{5}$$

$$C_M = \left[\frac{s_u}{\left(s_u - \overline{s}_P\right)}\right]^{m_1} \left[1 + \frac{\overline{s}_{i,ref}}{\left(s_u - \overline{s}_P\right)} m_1 \left(0.2k - 0.12\right)^2 \left(\frac{m_1 \alpha_{\sigma,i}}{k} + 1\right)^{\left(\frac{2}{k}\right)}\right] \tag{6}$$

$$C_{SN} = 1 - \exp\left\{-\left\{\left[\left(a^I \left(m_1 + \frac{N_L - 10^7}{45 \cdot 10^6}\right) + a^{II}\right)^{\frac{1}{k}} \left(0.2k - 0.12\right)\right]^{\alpha_{\sigma,i}} \times \left(\frac{\sigma_{i,ref}}{\Delta_C}\right)\right\}^{\left[\frac{k}{\alpha_{\sigma,i}}\left(0.15\left(m_1 + \frac{N_L - 10^7}{45 \cdot 10^6}\right) + 1.55\right)\right]}\right\} \tag{7}$$

where "*i*" is the directional index, with $i = D, L$ for alongwind and crosswind structural response parameters, respectively; m_1, Δ_C and N_L are parameters of the considered *S-N* fatigue curve; a^I, a^{II} are constant values depending on the shape of the considered *S-N* fatigue curve, in particular $a^I = 7.44$, $a^{II} = -3.81$ for bilinear *S-N* curves with cut-off limit, $a^I = 6.33$, $a^{II} = 2$ for bilinear *S-N* curves without cut-off limit; $\Gamma(\bullet)$ is the gamma function; k is the shape parameter of the Weibull probability distribution of the current values of the wind velocity in situ [27]; $\nu_{i,Q,ref}$ is the expected frequency of the *i*-component of turbulence [26]; n_{i1} is the first mode of vibration frequency in the *i*-direction; s_u is the material failure characteristic stress; $\overline{s}_P$ is the permanent loadings-induced stress in the examined section (calculated at serviceability); parameters of the response process in *i*-direction at reference wind velocity are $\overline{s}_{i,ref}$, $\sigma_{i,ref}$, $\nu_{i,ref}$, $\lambda_{i,ref}$, which are the mean value, standard deviation, expected frequency and normalized variance of the resonant part of the process in the critical section, respectively; $\alpha_{\sigma,i}$ is the exponent of the power law expressing the standard deviation of the fluctuating stress, σ_i, on varying wind velocity; $\alpha_{\lambda,i}$ is the exponent of the power law expressing the normalized variance of the stress resonant part, λ_i, on varying wind velocity [22, 24]. Only the exponents of power laws parameters, $\alpha_{\sigma,i}$ and $\alpha_{\lambda,i}$, require the calculation of the structural response at reference and fatigue wind velocity values.

4 ANTENNA MAST CASE STUDY

Antenna mast structures are built in such a large and growing number. They are characterized by increasing height, lightness, slenderness and complicated shape that make them extremely sensitive to complex aeroelastic phenomena and wind-excited vibrations, such as to require refined analyses in order to capture their physical behaviour. An impressive number of damage and collapses that increasingly involved these structures, often due to wind-excited fatigue, but in many cases not so well understood, emphasizes their susceptibility to wind actions and their potentially dangerous role in the anthropogenic territory.

A case study concerning a real antenna mast, taken from existing literature [28], is analyzed. This structure is a telecommunication antenna mast composed by two steel shafts with tubular circular section, whose total height is $H = 30$ m (Fig. 1). The first shaft is 24 m long; the outer diameter of its section, whose thickness is constant and equal to 5 mm, varies from

950 mm at the bottom to 350 mm at the top; the cables attached along this shaft have a distributed mass per unit length 5 kg/m. The second shaft, put above the first one, is 6 m long and carries 6 antennas. Its section has constant outer diameter 193.7 mm and constant thickness 7.1 mm; the total mass of the shaft is 540 kg. A stair is placed along the whole structure and has a mass per unit length 7 kg/m. The additional components, namely the stair, the cables and the antennas, give rise to a distributed mass eccentricity; however, they are assumed to be ineffective with regard to the structural stiffness. The pole is located in a terrain characterized by a roughness length z_0 = 0.3 m and a basic reference wind velocity u_{ref} = 25 m/s (i.e. the mean wind velocity at 10 m height above ground, in a flat homogeneous terrain with roughness length z_0 = 0.05 m and return period 50 years); the mean wind velocity profile is logarithmic. Assuming that the reference height is z_e = 24 m, i.e. the top of the main shaft, the design mean wind velocity at such a height is $\bar{u}(z)$ = 23.6 m/s. The aerodynamic characteristics of the structure have been determined by static wind tunnel experiments [28]. The first natural (flexural) frequency in both alongwind and crosswind directions is n_{i1} = 0.77 Hz. The test-case clearly points out the importance of mechanical and aerodynamic eccentricities; in fact, the presence of external devices such as cables and stairs substantially changes the drag coefficient, which results deeply dependent on the direction of the oncoming flow; in addition, large lift forces arise that rapidly change on varying the wind direction.

The proposed procedure to evaluate alongwind and crosswind-induced fatigue results easy to apply from an engineering point of view. The considered *S-N* fatigue curve corresponds to steel detail category 36 provided by IIW [4], so that m_1 = 3, Δ_C = 36 and $N_L = 10^7$; a^I = 7.44 and a^{II} = -3.81. The shape parameter of the Weibull probability distribution of wind velocities k is taken equal to 1.15; the expected frequencies of turbulence components are $\nu_{D,Q,ref}$ = 0.058 Hz and $\nu_{L,Q,ref}$ = 0.078 Hz [26]; the steel failure characteristic stress is s_u = 510 MPa; the permanent loadings-induced stress in the examined section is calculated as $\bar{s}_P$ = 1.818 MPa; parameters of the response process in the critical section at reference wind velocity are evaluated as $\bar{s}_{D,ref}$ = 39.066 MPa, $\sigma_{D,ref}$ = 29.263 MPa, $\nu_{D,ref}$ = 0.567 Hz, $\lambda_{D,ref}$ = 0.543 in alongwind direction [22] and $\bar{s}_{L,ref}$ = 10.162 MPa, $\sigma_{L,ref}$ = 32.349 MPa, $\nu_{L,ref}$ = 0.727 Hz, $\lambda_{L,ref}$ = 0.892 in crosswind direction [24]; the exponents of power laws parameters are assessed as $\alpha_{\sigma,D}$ = 2.321 and $\alpha_{\lambda,D}$ = 0.920 in alongwind response analysis [22] and $\alpha_{\sigma,L}$ = 2.558 and $\alpha_{\lambda,L}$ = 0.221 in crosswind response analysis [24].

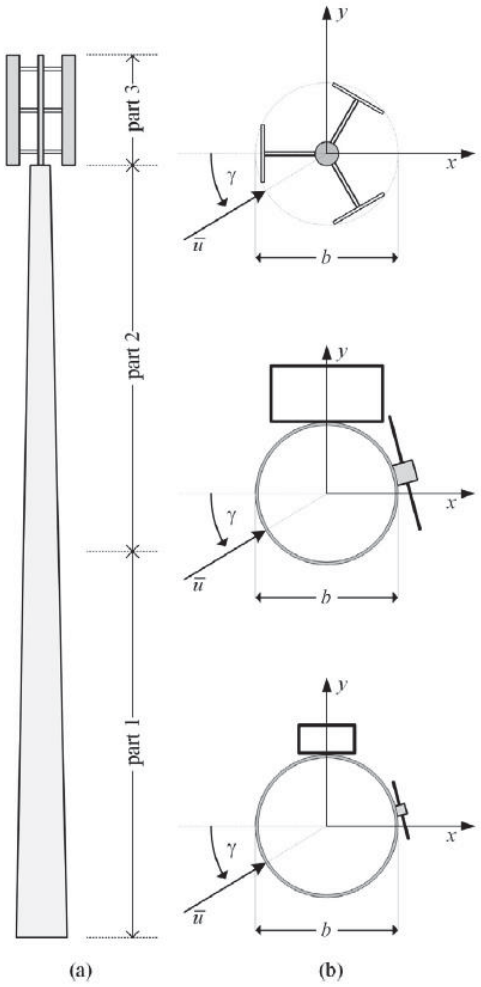

Figure 1: Schematic representations of the antenna mast (a) and of cross-sections at different heights (b).

Dealing with alongwind fatigue analysis, Eqs. (4)-(7) are applied obtaining values in the first column of Tab. I, leading to a mean total damage in the unit time equal to $\bar{D}(1) = 0.0081$ (Eq. (3)), therefore the fatigue life of the structure is predicted as 124 years. On the other hand, dealing with crosswind fatigue analysis, values in the second column of Tab. I are obtained, leading to a mean total damage in the unit time equal to $\bar{D}(1) = 0.0225$, therefore the fatigue life of the structure is predicted as 44 years. In both analyses, the 0 level solutions results comparable, with a slightly larger value in crosswind direction, due to larger standard deviation of crosswind response. The bi-modal factor C_{BM} reduces the 0 level damage taking into account the quasi-static part of the response spectrum; in alongwind assessment the quasi-static part of the response has a high role, strongly reducing the total damage; on the contrary, in crosswind assessment the role of quasi-static part of the response is reduced, prevailing the resonant contribution, thus also the reduction of the total damage is lower. The mean stress corrective factor C_M slightly increases the total damage in both analysis, meaning that the mean response to wind loading is not all that important. Finally, the fatigue curve factor C_{SN} reduces the damage in both cases to the almost same extent, taking into account the cut-off limit of fatigue resistance in steel details. All these considerations highlight that, due to the difference between alongwind and crosswind response spectral characteristics, crosswind turbulence-induced fatigue is widely more critical than alongwind-induced fatigue. In general,

the procedure outlines outcomes in accordance with [28] about the critical issue of exceptional large lift forces on this structure due to mechanical and aerodynamic eccentricities, showing that this also propagates fatigue damage.

	Alongwind buffeting-induced fatigue analysis	Crosswind buffeting-induced fatigue analysis
$\bar{D}_0(1)$	0.0241	0.0286
C_{BM}	0.3705	0.8785
C_M	1.0951	1.0456
C_{SN}	0.8247	0.8566
$\bar{D}(1)$	0.0081	0.0225
Fatigue life	124 years	44 years

Table 1: Outcomes of the application of the procedure to the antenna mast.

5 CONCLUSIONS AND PERSPECTIVES

The resulting model proposed in the paper is a general method of wind-induced fatigue assessment of slender structures, suitable for engineering applications. The proposed procedure can be applied in general situations, concerning different kinds of slender structures of different materials with different possible loading conditions. The model allows to evaluate both alongwind and crosswind turbulence-induced fatigue of structures, leading to reasonable values of fatigue life. A case study is analyzed adopting the proposed procedure, showing its ease of use and effectiveness and highlighting the potential sensitivity of this kind of structures to wind induced fatigue. Crosswind turbulence-induced response and fatigue is actually disregarded in antenna mast structural typology. Engineering calculations idealize antenna masts as polar symmetric structures, even if this is usually not correct due to several peculiar features such as stairs, cable bundles, solar panels, lighting devices, top balcony, antennas and parabolas, and cylinder hulls covering the transmission devices. One or the whole of these elements gives rise to mass and shape eccentricities, which make these structures complex both in mechanical and aerodynamic terms. Such an aspect greatly contributes to make antenna masts sensitive to potential instabilities caused by aeroelastic phenomena and exposed to intense and non-conventional wind-excited vibrations. The proposed method allows to catch the main feature of the fatigue damage phenomenon also in non-conventional situations with quite simple calculation procedure.

Future perspectives are to examine the significance of different contributions to crosswind-induced fatigue damage accumulation, due to the joint action of the oncoming wind turbulence and of the vortex wake. As regards crosswind response of slender structures, engineering procedures estimates separately crosswind maximum response to gust buffeting and to critical vortex shedding conditions. This is reasonable for ULS analysis, but there's no guarantee such assumption would provide reliable outcomes in fatigue analysis (superposition principle does not apply due to the strong non-linearity of the fatigue damage phenomenon). The possibility of separating the effects of the vortex shedding also in fatigue analysis needs to be further investigated, as well as the role of parameters uncertainties in response and in fatigue evaluations.

REFERENCES

[1] M. Miner, Cumulative Damage in Fatigue, *Trans. A.S.M.E.*, 67, A159, 1945.

[2] Eurocode 3: Design of steel structures – Part 1-9: Fatigue, EN 1993-1-9, 2005.

[3] Eurocode 9: Design of aluminium structures – Part 2: Structures susceptible to fatigue, ENV 1999-2, 1998.

[4] IIW, International Institute of Welding, Recommendations for fatigue design of welding joints and components, document XIII / XV revision, 2016 edition.

[5] J.D. Holmes, Fatigue under along-wind loading - closed-form solutions, *Engineering Structures* 24, 109-14, 2002.

[6] M.P. Repetto, G. Solari, Wind-induced fatigue collapse of real slender structures, *Engineering Structures* 32, 3888-3898, 2010.

[7] Eurocode 1: Actions on structures - Part 1-4: General actions - Wind actions, UNI EN 1991-1-4, 2005.

[8] F.H. Kemper, M. Feldmann, Fatigue life prognosis for structural elements under stochastic wind loading based on spectral methods, Part I: Linear structures, *Proceedings of the 8th International Conference on Structural Dynamics*, EURODYN 2011, July 4-6, Leuven, Belgium, 2011.

[9] CICIND, International Committee on Industrial Chimneys, Model Code for Steel Chimneys, Revision 1, Amendment A, December 1999.

[10] AASHTO, American Association of State Highway and Transportation Officials, Standard Specifications for Structural Supports for Highway Signs, Luminaires, and Traffic Signals, 2018 edition.

[11] IEA, International Energy Agency, Recommended practices for wind turbine testing and evaluation – Part 3 – FATIGUE, 1990.

[12] M.P. Repetto, Cycles counting methods for bi-modal stationary Gaussian processes, *Probabilistic Engineering Mechanics* 20(3), 229–238, 2005.

[13] M.P. Repetto, G. Solari, Bimodal alongwind fatigue of structures, *Journal of Structural Engineering* 132(6), 899–908, 2006.

[14] N.E. Dowling, Fatigue Failure Prediction for Complicated Stress-Strain Histories, *Journal of Materials*, JMLSA, 7(1), 71-87, 1972.

[15] I. Rychlik, A new definition of the rainflow cycle counting method, *International Journal of Fatigue* 9, 119-121, 1987.

[16] I. Rychlik, Characterization of random fatigue loads, *Stochastic Approach to Fatigue, CISM Course and Lectures n. 334*, Ed. K. Sobczyk, Springer-Verlag, Wienn-New York, 1993.

[17] T. Dirlik, Application of computer in fatigue analysis, PhD Thesis, University of Warwick, United Kingdom, 1985.

[18] D. Benasciutti, R. Tovo, Fatigue life assessment in non-Gaussian random loadings, *International Journal of Fatigue* 28(7), 733-746, 2006.

[19] M.P. Repetto, G. Solari, Closed form solution of the alongwind-induced fatigue damage to structures, *Engineering Structures* 31(10), 2414–2425, 2009.

[20] M.P. Repetto, G. Solari, Closed-Form Prediction of the Alongwind-Induced Fatigue of Structures, *Journal of Structural Engineering* ASCE 138, 1149-1160, 2012.

[21] E.S. Takle, J.M. Brown, Note on the use of Weibull statistics to characterize wind speed data, *Journal of Applied Meteorology* 17, 556-559, 1978.

[22] M.P. Repetto, M. Damele, Wind-Induced Fatigue Verification Standard Methods, In Ricciardelli F., Avossa A. (eds) *Proceedings of the XV Conference of the Italian Association for Wind Engineering*. IN VENTO 2018, Lecture Notes in Civil Engineering, vol 27. Springer, Cham, 573-586, 2019.

[23] CNR_DT_207, Istruzioni per la valutazione delle azioni e degli effetti del vento sulle costruzioni, Roma, 2008 (Review 2018).

[24] G. Solari, Gust Buffeting of Slender Structures and Structural Elements: Simplified Formulas for Design Calculations and Code Provisions, *Journal of Structural Engineering* ASCE 144(2), 2018.

[25] G. Piccardo, G. Solari, 3-D wind-excited response of slender structures: Closed form solution, *Journal of Structural Engineering* 126(8), 936–943, 2000.

[26] G. Piccardo, G. Solari, 3-D gust effect factor for slender vertical structures, *Probabilistic Engineering Mechanics* 17(2), 143–155, 2002.

[27] L.C. Pagnini, G. Solari, Joint Modeling of the Parent Population and Extreme Value Distributions of the Mean Wind Velocity, *Journal of Structural Engineering* ASCE 142(2), 1-10, 2016.

[28] C.H. Nguyen, A. Freda, G. Solari, F. Tubino, Aeroelastic instability and wind-excited response of complex lighting poles and antenna masts, *Engineering Structures* 85, 264–276, 2015.

EURODYN 2020
XI International Conference on Structural Dynamics
M. Papadrakakis, M. Fragiadakis, C. Papadimitriou (eds.)
Athens, Greece, 23–26 November 2020

A STOCHASTIC AND CONTINUOUS MODEL OF AEOLIAN VIBRATIONS OF CONDUCTORS EQUIPPED WITH STOCKBRIDGE DAMPERS

Francesco Foti[1], Vincent Denoël[2], Luca Martinelli[1], and Federico Perotti[1]

[1] Department of Civil and Environmental Engineering, Politecnico di Milano, Italy
e-mail: francesco.foti@polimi.it, luca.martinelli@polimi.it, federico.perotti@polimi.it

[2] Structural & Stochastic Dynamics, University of Liège, Belgium
Allée de la Découverte 1, 4000 Liège, Belgium
email: v.denoel@uliege.be

Keywords: Aeolian vibrations, Cable dynamics, Overhead power lines, Stockbridge dampers.

Abstract. *Suspended conductors and guard wires of overhead electrical transmission lines (OHL) are prone to aeolian vibrations, resulting from the alternate shedding of vortices in the wake of the cable. These vibrations can occur under light to moderate wind and, whenever not properly controlled, can induce wear damage and fatigue failures of the cables. Nonlinear passive control devices such as Stockbridge dampers, hence, are often installed along the line spans to reduce the vibration severity. The technical approach to the assessment of aeolian vibrations is based on the Energy Balance Method (EBM) and relies on the simplifying assumption of mono-modal oscillations. Typical aeolian vibration records, however, clearly show that several modes can be simultaneously excited due to wind variations in time and along the span. Aiming at overcoming the mono-modal vibration assumption of the EBM, in the present paper wind forces are modeled as a narrow band stochastic process, centered around the Strouhal frequency of the conductor and with arbitrary cross-correlation in space. A new approach, based on the well-known smooth endochronic Bouc-Wen model, is developed to describe the hysteretic dynamic response of Stockbridge dampers. An iterative solution strategy based on a stochastically equivalent linear damper model is then developed to investigate aeolian vibrations of a suspended cable with a Stockbridge damper attached along its length.*

1 INTRODUCTION

Suspended conductors and guard wires of overhead electrical transmission lines (OHL) are prone to aeolian vibrations, resulting from the alternate shedding of vortices in the wake of the cable. These vibrations can occur under light to moderate wind and are characterized by small-amplitude (typically less than one diameter) transverse oscillations in the cross-wind direction. Vibration frequencies can be in the broad range of 3-200 Hz, depending on the geometry and axial load of the cable (see e.g. [3, 10, 11, 17]). Whenever not properly controlled, aeolian vibrations can induce wear damage and fatigue failures of the cables (e.g. [11]). Nonlinear passive control devices such as Stockbridge dampers, hence, are often installed along the line spans to reduce the vibration severity (e.g. [9]).

The technical approach currently adopted to assess the aeolian vibration level is based on the Energy Balance Method (EBM) and relies on the simplifying assumption of mono-modal oscillations (see e.g. [13]). Typical aeolian vibration records, however, clearly show that several modes can be simultaneously excited due to wind variations in time and along the span [5]. Aiming at overcoming the mono-modal vibration assumption of the EBM, Hagedorn and coworkers [15, 16] developed a promising analytical model to evaluate aeolian vibrations of overhead electrical transmission lines within a probabilistic framework. Wind forces were modeled as a narrow band stochastic process, centered around the Strouhal frequency of the conductor and with arbitrary cross-correlation in space. Aeolian vibrations of damped conductors, then, were rigorously studied under the simplifying assumption of linear behavior of the attached passive control devices.

Stockbridge dampers, however, are characterized by a markedly hysteretic dynamic behavior [28, 27]. In the present paper, the formulation proposed by Hagedorn and coworkers is extended to fully account for the nonlinearities related to the damper mechanical response. A new approach, based on the well-known smooth endochronic Bouc-Wen model [23, 6], is first developed to describe the hysteretic dynamic response of Stockbridge dampers. An iterative solution strategy based on a stochastically equivalent linear damper model is then developed to investigate aeolian vibrations of a suspended cable with a Stockbridge damper attached along its length. Finally, the main features and the potential drawbacks of the proposed formulation are illustrated with reference to a simple yet meaningful benchmark case.

2 FORMULATION OF THE PROBLEM

2.1 The cable model

Let us consider a cable suspended to horizontal supports and with a Stockbridge damper attached at a distance x_d from its left end-section (see Figure 1). The cable is subject to the combined action of a constant axial force H and a dynamic load $f = f(x,t)$, where x is a coordinate spanning the free length l of the cable and t is the time. Consistently with classic approximate "externally forced models" for VIV of bluff bodies (see e.g. [25]), the force f is herein introduced to describe the fluctuating lift force induced by the alternate shedding of vortices in the wake of the cable. By neglecting both sag-extensibility effects and bending stiffness terms, small planar vibrations are governed by the linear partial differential equation:

$$-H\partial_x^2 w + \beta\partial_t w + \gamma\partial_t^2 w = f - F_d\delta(x - x_d), \quad x, x_d \in (0, l) \tag{1}$$

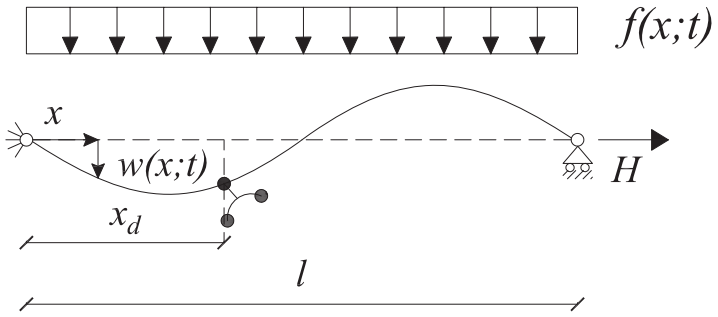

Figure 1: Schematic representation of a suspended cable with length l subject to a constant axial force H and a fluctuating lift force $f(x,t)$. A passive vibration control device is attached at $x = x_d$.

where $w = w(x,t)$ is the transverse displacement of the cable centerline, γ is the mass per unit of length, β is a viscous damping coefficient, F_d is the force exerted by the damper on the cable and the symbol $\delta(\cdot)$ denotes the delta Dirac's function. It is worth noting that the herein adopted viscous damping model is frequently adopted in practical applications and research works, in spite of not being fully compliant with experimental evidence and theoretical arguments (see e.g. [7, 8]). This is felt as a possible drawback of the proposed formulation that will be dealt with in the future.

By neglecting the flexibility of the cable supports, Eq. (1) can be solved for prescribed initial conditions under the homogeneous boundary conditions:

$$w(x=0,t) = w(x=l,t) = 0, \quad \forall t \tag{2}$$

Consistently with the previously stated modeling assumptions, the distributed external force acting on the cable can be defined as:

$$f(x,t) = \frac{1}{2}\rho d U^2 q(x,t) \tag{3}$$

where ρ is the air density, d is the cable diameter, U is the mean wind velocity and $q = q(x,t)$ can be regarded as a space- and time-variable lift coefficient. The lift coefficient can be conveniently modeled (see e.g. [29, 15, 16]) as a stationary stochastic field process with correlation function:

$$R(x_1, x_2, t) = \Psi(x_1, x_2)\, k(t) \tag{4}$$

where $\Psi(x_1, x_2)$ and $k(t)$ are, respectively, a space correlation function and the auto-correlation function of a narrow-band process, centered around the Strouhal frequency

Ω_s, with uni-lateral power spectral density:

$$G_q(\omega) = \frac{1}{2\pi} \int_0^{+\infty} k(t) \exp(-j\omega t)\, dt = \frac{C_{L,rms}^2}{B\Omega_s\sqrt{\pi}} \exp\left[-\left(\frac{1-\frac{\omega}{\Omega_s}}{B}\right)^2\right], \quad \omega \in \mathbb{R}^+ \tag{5}$$

where $C_{L,rms}$ is the root mean square (r.m.s.) value of the lift coefficient (cf. [29]), and B is a parameter controlling the bandwidth of the spectral peak. By denoting as S_t the Strouhal number of the cable, the frequency Ω_s reads:

$$\Omega_s = 2\pi \frac{S_t U}{d} \tag{6}$$

The Strouhal number can be assumed equal to $S_t = 0.185$ for Reynolds numbers and wind conditions typical of overhead electrical line (OHL) conductors [10, 3]. On the other hand, reference values of the r.m.s. lift coefficient $C_{L,rms}$ and the bandwidth parameter B typical of OHL conductors, are site-dependent and have not been explicitly reported in the literature, to the authors' knowledge. They could be, however, obtained through in-situ experimental campaigns (e.g. [5]) or wind tunnel tests on scaled models (e.g. [29]). An aperçu of the expected order of magnitude of the model parameters $C_{L,rms}$ and B can be obtained by looking at the values reported by Vickery and Clark [29] for a slightly tapered cylindrical stack model: $C_{L,rms} = 0.2$ and $B = 0.08 - 0.32$, where the smaller value is associated to smooth flow conditions and the larger one to a turbulence intensity equal to about 10%.

Both Hagedorn and coworkers [15, 16] and Vickery and Clark [29] adopt an exponentially decaying space correlation function $\Psi(x_1, x_2)$ (see Eq. (4)). Hagedorn and coworkers introduce the following definition:

$$\Psi = \Psi_H(x_1, x_2) = \psi(x_1)\,\psi(x_2) \exp\left[-\left(\frac{x_1 - x_2}{\delta_x}\right)^2\right] \tag{7}$$

without providing, however, experimental information on both the function $\psi(x)$ and the space correlation coefficient δ_x . Based on the fitting of experimental measurements on a tapered cylindrical stack model, Vickery and Clark [29] propose the following definition:

$$\Psi = \Psi_{VC}(\bar{r}(x_1, x_2)) = \cos\left(\frac{\eta_2}{\eta_1}\bar{r}\right) \exp\left[-\left(\frac{\bar{r}}{\eta_1}\right)^2\right] \tag{8}$$

where $\eta_1 = 3$, $\eta_2 = 2$ and $\bar{r}$ is the non-dimensional distance between two points of the cable identified by the coordinates x_1 and x_2:

$$\bar{r} = \frac{|x_1 - x_2|}{d} \tag{9}$$

In the absence of experimental information explicitly referred to OHL conductors, the space correlation function proposed by Vickery and Clark [29] will also be adopted in the present work to model the lift forces acting on the suspended cable (Eq. (4)).

Figure 2(a) shows the uni-lateral power spectral density of the lift coefficient, $G_q(\omega)$, obtained through Eq. (5) under the assumption: $C_{L,rms} = 0.2$. The results are shown for two different values of the bandwidth parameter B (i.e. $B = 0.1, 0.3$) and of the Strouhal

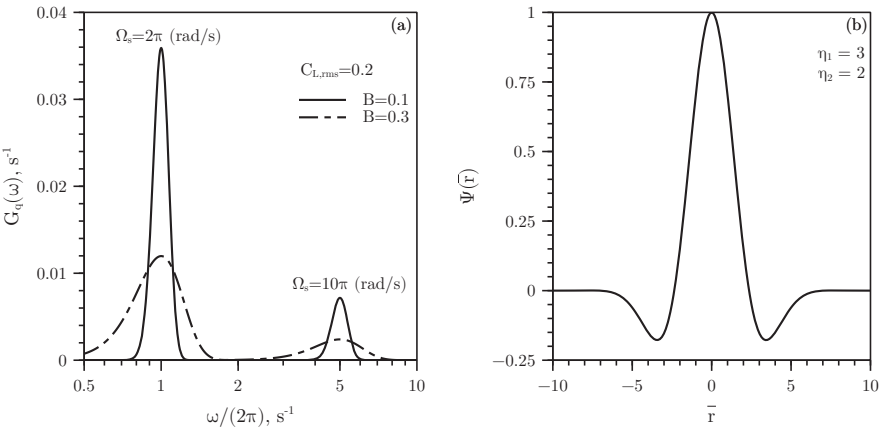

Figure 2: (a) Uni-lateral power spectral density of the lift coefficient, $G_q(\omega)$ (see Eq. (5)). The root mean square value of the lift coefficient is assumed equal to $C_{L,rms} = 0.2$. The function $G_q(\omega)$ is shown for different values of the bandwidth parameter B (i.e. $B = 0.1,\ 0.3$) and of the Strouhal frequency (i.e. $\Omega_s = 2\pi,\ 10\pi$ rad/s). (b) Space coherence function $\Psi(\bar{r})$ (see Eq. 8). Parameters η_1 and η_2 are respectively set equal to $\eta_1 = 3$ and $\eta_2 = 2$.

frequency (i.e. $\Omega_s = 2\pi,\ 10\pi$ rad/s). Increasing values of the bandwidth parameter B, physically related to increasing values of wind turbulence [29], affect the power spectral density of the lift coefficient yielding lower and broader peaks. It is however worth noting that the total energy content of the function $G_q(\omega)$ is not affected by the parameter B, since $\int_{-\infty}^{+\infty} G_q(\omega)\, d\omega = C_{L,rms}^2$.

It is also worth noting that, not only the total energy content is insensitive to the intensity of turbulence, but also so is the space correlation function $\Psi(\bar{r})$ (depicted in Figure 2(b)) due to the definition herein adopted. These aspect do not appear fully consistent with experimental evidences (e.g. [7, 8]). A thorough experimental testing campaign would be necessary to further assess the validity of these assumptions.

2.2 The damper model

The most common type of Stockbridge dampers is made of a metallic clamp, a short metallic strand, also known as "messenger cable," with two inertial bodies attached at its end-sections [10, 9]. The clamp is rigidly attached to the messenger cable and allows connecting the damping device along the span of the OHL conductor. Whenever the clamp undergoes a vertical translation, the two sides of the messenger cables behave as uncoupled flexible cantilevers with lumped translational and rotational masses attached at their ends. Differently than classic linear tuned mass dampers [4], Stockbridge dampers are characterized by a markedly hysteretic dynamic behavior due to the frictional dissipation mechanisms activated by the bending of the messenger cable [28, 9].

In the present work, we will focus on the special, but practically meaningful case, of symmetric Stockbridge dampers (see Figure 3) under the following simplifying assumptions: (i) the clamp can only undergo vertical translations $w_d(t) = w(x = x_d, t)$, and (ii) the rotational inertia of the rigid bodies attached to the end-sections of the messenger cable is neglected. By denoting as $v = v(t)$ the vertical displacement of the tip of the messenger cable with respect to the clamp, the force F_d exerted by the damper on the

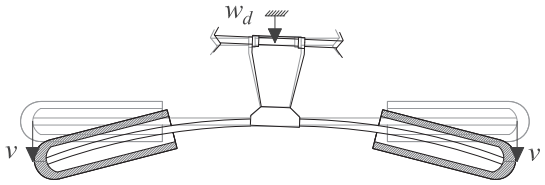

Figure 3: Schematic representation of a symmetric Stockbridge damper. Symbols w_d and v denote, respectively, the vertical translation of the clamp and the relative displacement of the tip of the messenger cable with respect to the clamp.

cable (also see Eq.(1)) can be expressed as [9]:

$$F_d = (2m_d + m_c)\,\ddot{w}_d + 2m_d\ddot{v} \tag{10}$$

where m_d is the mass of each rigid body attached at the tips of the messenger cable, m_c is the mass of the clamp and a dot denotes derivation with respect to time t. The mass of the clamp is often significantly smaller than the total mass of the damper and Eq. (10) can be approximately re-written as:

$$F_d = 2m_d\,(\ddot{w}_d + \ddot{v}) \tag{11}$$

The relative motion of the tip of the messenger cable is governed by the nonlinear ordinary differential equation:

$$m_d\ddot{v} + F_R = -m_d\ddot{w}_d \tag{12}$$

where F_R is the hysteretic restoring force exerted by the messenger cable on the damper mass. Inspired by the work of Pivovarov and Vinogradov [26], a phenomenological modeling approach is adopted to characterize the restoring force F_R based on an application of the well known smooth endochronic Bouc-Wen hysteretic model [23, 6]. To this aim, the five-parameter Bouc-Wen model summarized by Ikhouane and coworkers [20, 21, 22] is herein re-stated in a slightly modified form:

$$\begin{cases} F_R = \alpha k_d v + (1-\alpha)\,k_d v_0 z \\ \dot{z} = \frac{1}{v_0}\left[\dot{v} - \sigma\,|\dot{v}|\,|z|^{n-1}\,z + (\sigma-1)\,\dot{v}\,|z|^n\right] \end{cases} \tag{13}$$

where $z\,(t) \in [-1,1]$ is a non-dimensional hysteretic variable, $k_d > 0$ is the initial stiffness of the first-loading branch of the load-displacement curve $F_R = F_R\,(v(t), z\,(t))$, $\alpha > 0$ is the ratio between the minimum theoretical value of the post-yielding tangent stiffness of the of the first-loading branch and k_d, v_0 is a non-negative parameters with the units of a displacement. Finally, σ and n are non-dimensional parameters controlling the shape of the hysteresis cycles. It is worth noting that, to ensure the stability and the thermodynamic admissibility of the Bouc-Wen model (13), the parameters σ and n should satisfy

the following inequalities: $\sigma \geq 1/2$ and $n \geq 1$ [22]. In order to avoid cumbersome calculations and to keep the model as simple as possible, in the present work the parameters σ and n are both set equal to the unity and the second Eq. in (13) is re-written as:

$$\dot{z} = \frac{1}{v_0} \left(\dot{v} - |\dot{v}| \, z \right) \tag{14}$$

2.3 Non-dimensional formulation

In the following, the governing equations of the problem introduced in Sections 2.1 and 2.2 will be re-stated in a more convenient non-dimensional form. To this aim, let us introduce the non-dimensional space (ξ) and time (τ) variables:

$$\xi = \frac{x}{l} \in [0, 1] \, , \quad \tau = \Omega_c t \in \mathbb{R}^+ \tag{15}$$

where Ω_c is the characteristic frequency of the cable:

$$\Omega_c = \sqrt{\frac{H}{\gamma l^2}} \tag{16}$$

Substitution of Eqs. (15) and (16) in Eq. (1) yields the non-dimensional equation of motion:

$$-\partial_\xi^2 \bar{w} + 2\zeta_c \partial_\tau \bar{w} + \partial_\tau^2 \bar{w} = \bar{f} - \bar{F}_d \delta \left(\xi - \xi_d \right) , \quad \xi, \xi_d \in (0, 1) \tag{17}$$

where $\bar{w} = \frac{w(x(\xi), t(\tau))}{d}$, $\zeta_c = \frac{l^2 \Omega_c}{2H} \beta$, $\bar{f} = \frac{l^2}{Hd} f \left(x \left(\xi \right), t \left(\tau \right) \right) = \frac{\rho l^2 U^2}{2H} q \left(x \left(\xi \right), t \left(\tau \right) \right)$, $\bar{F}_d = \frac{l}{dH} F_d$, and $\xi_d = \frac{x_d}{l}$. The non-dimensional counterpart of the homogeneous boundary conditions (2) reads:

$$\bar{w} \left(\xi = 0, \tau \right) = \bar{w} \left(\xi = 1, \tau \right) = 0, \quad \forall \tau \tag{18}$$

Starting from Eq. (11), the non-dimensional force $\bar{F}_d$ exerted by the damper on the cable can be expressed as:

$$\bar{F}_d = \mu \left(\frac{d^2 \bar{w}_d}{d\tau^2} + \frac{d^2 \bar{v}}{d\tau^2} \right) \tag{19}$$

where $\bar{v} = \frac{v(x(\xi), t(\tau))}{d}$, $\bar{w}_d = \frac{w_d}{d} = \bar{w} \left(\xi = \xi_d, \tau \right)$ and μ is the mass ratio:

$$\mu = \frac{2 m_d}{\gamma \, l} \tag{20}$$

The relative motion of the tip of the messenger cable (see Eqs. (12), (13)-a and (14)), then, is governed by the non-dimensional equations:

$$\begin{cases} \frac{d^2 \bar{v}}{d\tau^2} + \alpha \Theta^2 \bar{v} + (1 - \alpha) \, \Theta^2 \bar{v}_0 \bar{z} = -\frac{d^2 \bar{w}_d}{d\tau^2} \\ \frac{d\bar{z}}{d\tau} = \frac{1}{\bar{v}_0} \left(\frac{d\bar{v}}{d\tau} - \left| \frac{d\bar{v}}{d\tau} \right| \bar{z} \right) \end{cases} \tag{21}$$

where $\Omega_d = \sqrt{\frac{k_d}{m_d}}$, $\Theta = \frac{\Omega_d}{\Omega_c}$, $\bar{v}_0 = \frac{v_0}{d}$ and $\bar{z} = z \left(t \left(\tau \right) \right)$.

3 PROPOSED SOLUTION STRATEGY

In this Section, the response of a bare suspended cable (i.e. a cable without attached damper) to the stochastic wind model defined in Section 2.1 is first considered (Section 3.1). The solution is then extended to the case of a cable equipped with a linear passive damping device (Section 3.2), by following the same approach proposed by Hagedorn and coworkers [15, 16]. Finally, the solution strategy is generalized to deal with the non-linearities that characterize the Stockbridge damper model presented in Section 2.2.

3.1 Response of a bare cable

Let us preliminary consider the response of a bare suspended cable subject to a concentrated force $F_1 = \frac{dH}{l}\exp(j\omega t)$ applied at the generic abscissa $x = x_1$. The non-dimensional equation of motion (see Section 2.3), hence, reads:

$$-\partial_\xi^2\bar{w} + 2\zeta_c\partial_\tau\bar{w} + \partial_\tau^2\bar{w} = \delta(\xi-\xi_1)\exp(j\bar{\omega}\tau), \quad \xi,\xi_1 \in (0,1), \quad \bar{\omega} = \frac{\omega}{\Omega_c} \tag{22}$$

Stationary oscillatory solutions of Eq. (22) satisfying the homogeneous boundary conditions (18) can be expressed as $\bar{w}(\xi,\tau) = \phi(\xi)\exp(j\bar{\omega}\tau)$, where ϕ is the solution of the boundary value problem ("Green's function", see e.g. [18]):

$$\begin{cases} -\phi'' + 2\zeta_c j\bar{\omega}\phi - \bar{\omega}^2\phi = \delta(\xi-\xi_1) \\ \phi(0) = \phi(1) = 0 \end{cases} \tag{23}$$

and an apex denotes derivation with respect to ξ.

Solution of (23) is straightforward and can be expressed, by explicitly highlighting its dependence on both ξ_1 and $\bar{\omega}$,as:

$$\phi(\xi,\xi_1,\bar{\omega}) = \begin{cases} \frac{\sin[\nu(\bar{\omega})\,\xi]\sin[\nu(\bar{\omega})\,(1-\xi_1)]}{\nu(\bar{\omega})\sin[\nu(\bar{\omega})]} & 0 \le \xi \le \xi_1^- \\ \frac{\sin[\nu(\bar{\omega})\,(1-\xi)]\sin[\nu(\bar{\omega})\,\xi_1]}{\nu(\bar{\omega})\sin[\nu(\bar{\omega})]} & \xi_1^+ \le \xi \le 1 \end{cases} \tag{24}$$

with the definition:

$$\nu = \sqrt{\bar{\omega}^2 - 2\zeta_c j\bar{\omega}} \tag{25}$$

Let us consider now a bare cable subject to the the stochastic wind model fully detailed in Section 2.1. Knowledge in closed form of the Green function $\phi = \phi(\xi,\xi_1,\bar{\omega})$ allows one to easily evaluate (see e.g. [24]) the uni-lateral cross power spectral density function $G_w(x_1,x_2,\omega)$ of the transverse displacements ($w = w(x,t)$) as:

$$G_w(x_1,x_2,\omega) = \left(\frac{1}{2}\rho d U^2\right)^2 \frac{l^4}{H^2}\,\bar{C}\left(\xi_1(x_1),\xi_2(x_2),\bar{\omega}(\omega)\right) G_q(\omega) \tag{26}$$

where $G_q(\omega)$ is defined in Eq. (5) and $\bar{C}$ is the two-dimensional integral:

$$\bar{C}(\xi_1,\xi_2,\bar{\omega}) = \int_0^1\int_0^1 \phi^*(\zeta_1,\xi_2,\bar{\omega})\,\phi(\xi_1,\zeta_2,\bar{\omega})\,\bar{\Psi}(\zeta_1,\zeta_2)\,d\zeta_1 d\zeta_2 \tag{27}$$

where an asterisk is adopted to denote complex conjugate values. Finally, the variance of the displacement is a function of the arc-length coordinate x and reads:

$$\sigma_w^2(x) = \int_0^{+\infty} G_w(x, x, \omega)\, d\omega \tag{28}$$

3.2 Response of a cable equipped with a linear damper

By following the same approach adopted in Section 3.2, let us preliminary consider the response of a suspended cable with a damper attached at $x = x_d$ and subject to a concentrated force $F_1 = \frac{dH}{l}\exp(j\omega t)$ applied at the generic abscissa $x = x_1$. The non-dimensional equation of motion (see again Section 2.3), hence, reads:

$$\begin{gathered} -\partial_\xi^2 \bar{w} + 2\zeta_c \partial_\tau \bar{w} + \partial_\tau^2 \bar{w} = -\bar{F}_d \delta(\xi - \xi_d) + \delta(\xi - \xi_1)\exp(j\bar{\omega}\tau), \\ \xi, \xi_d, \xi_1 \in (0,1), \quad \bar{\omega} = \frac{\omega}{\Omega_c} \end{gathered} \tag{29}$$

where $\bar{F}_d$ is the non-dimensional counterpart of the force exerted by the damper on the cable.

Under the assumption of linear behavior of the attached damper, the non-dimensional force of the damper and clamp displacement can be respectively expressed as:

$$\bar{F}_d(\tau) = \hat{F}_d \exp(j\bar{\omega}\tau) \quad \text{and} \quad \bar{w}_d(\tau) = \hat{W}_d \exp(j\bar{\omega}\tau) \tag{30}$$

Moreover, the following linear relation can always be introduced:

$$\hat{F}_d = Z_{d,FW}(\bar{\omega})\, \hat{W}_d \tag{31}$$

where $Z_{d,FW} = Z_{d,FW}(\bar{\omega})$ is the non-dimensional frequency response function of the linear damper. Substitution of Eqs. (30) and (31) in Eq. (29) yields:

$$\begin{gathered} -\partial_\xi^2 \bar{w} + 2\zeta_c \partial_\tau \bar{w} + \partial_\tau^2 \bar{w} = \left[-Z_{d,FW}(\bar{\omega})\, \hat{W}_d\, \delta(\xi - \xi_d) + \delta(\xi - \xi_1)\right] \exp(j\bar{\omega}\tau), \\ \xi, \xi_d, \xi_1 \in (0,1), \quad \bar{\omega} = \frac{\omega}{\Omega_c} \end{gathered} \tag{32}$$

Stationary oscillatory solutions of Eq. (32) satisfying the homogeneous boundary conditions (18) can be expressed as $\bar{w}(\xi, \tau) = \phi_d(\xi)\exp(j\bar{\omega}\tau)$, where ϕ_d is the solution of the boundary value problem ("Green's function"):

$$\begin{cases} -\phi_d'' + 2\zeta_c j\bar{\omega}\phi_d - \bar{\omega}^2\phi_d = -Z_{d,FW}(\bar{\omega})\, \hat{W}_d \delta(\xi - \xi_d) + \delta(\xi - \xi_1) \\ \phi_d(0) = \phi_d(1) = 0 \end{cases} \tag{33}$$

and an apex denotes derivation with respect to ξ. By exploiting the definition of the Green's function $\phi = \phi(\xi, \xi_1, \bar{\omega})$ introduced in the previous Section (Section 3.1, Eq. (23)) and the superposition principle, it can be easily shown that:

$$\hat{W}_d = \frac{\phi(\xi_d, \xi_1, \bar{\omega})}{1 + \phi(\xi_d, \xi_d, \bar{\omega})\, Z_{d,FW}(\bar{\omega})} \tag{34}$$

and

$$\phi_d\left(\xi,\xi_1,\xi_d,\bar{\omega}\right)=\frac{-Z_{d,FW}\left(\bar{\omega}\right)\phi\left(\xi_d,\xi_1,\bar{\omega}\right)\phi\left(\xi,\xi_d,\bar{\omega}\right)}{1+\phi\left(\xi_d,\xi_d,\bar{\omega}\right)Z_{d,FW}\left(\bar{\omega}\right)}+\phi\left(\xi,\xi_1,\bar{\omega}\right) \tag{35}$$

The response of the suspended cable subject to the stochastic wind model, defined in Section 2.1, then, can be calculated through Eqs. (26)-(28) by simply replacing the Green function ϕ with ϕ_d.

3.3 Response of a cable equipped with a Stockbridge damper

Let us now consider the case of a suspended cable with a Stockbridge damper attached at $x=x_d$. The dynamic behavior of the damper is described through the non-linear model detailed in Section 2.2, based on an application of the Bouc-Wen hysteretic model. The response of the coupled cable+damper system subject to the stochastic wind model defined in Section 2.1 can be sought through an iterative solution strategy based on: (i) the definition of a stochastically equivalent damper model and (ii) the solution strategy already developed in Section 3.2 under the simplifying assumption of linearity of the damper behavior.

The motion of the Stockbridge damper subjected to a prescribed clamp displacement $w_d\left(t\right)=w\left(x=x_d,t\right)$ is governed by the non-dimensional system of Eqs. (21). Under a stochastic loading, the motion of the clamp is a stochastic process with uni-lateral power spectral density $G_{wd}=G_{wd}\left(\omega\right)=G_w\left(x_1=x_d,x_2=x_d,\omega\right)$ (see Eq. (26)) and variance $\sigma_{wd}^2=\sigma_w^2\left(x=x_d\right)$ (Eq. (28)). A stochastically equivalent linear system of equations describing the motion of the Stockbridge damper, then, can be defined by replacing the second equation in (21) with a linear evolution law for the hysteretic variable $\bar{z}$, i.e.:

$$\begin{cases}\frac{d^2\bar{v}}{d\tau^2}+\alpha\Theta^2\bar{v}+\left(1-\alpha\right)\Theta^2\bar{v}_0\bar{z}=-\frac{d^2\bar{w}_d}{d\tau^2}\\ \frac{d\bar{z}}{d\tau}=\frac{1}{\bar{v}_0}\left(c_e\frac{d\bar{v}}{d\tau}+k_e\bar{z}\right)\end{cases} \tag{36}$$

The linearization coefficients c_e and k_e can be evaluated in order to minimize the expectation of the squared error $\epsilon^2=\left(\frac{d\bar{v}}{d\tau}-\left|\frac{d\bar{v}}{d\tau}\right|\bar{z}-c_e\frac{d\bar{v}}{d\tau}-k_e\bar{z}\right)^2$. By assuming a joint gaussian probability density function for the variables $\left(\bar{v},\frac{d\bar{v}}{d\tau},\bar{z}\right)$, the coefficients c_e and k_e can be evaluated as a special case of the more general expressions proposed by Hurtado and Barbat [19] and read:

$$c_e=1-\frac{2\sqrt{2}}{\pi}\Gamma\left(\frac{3}{2}\right)\sigma_z\rho_{\dot{v}z} \tag{37}$$

$$k_e=-\frac{2\sqrt{2}}{\pi}\Gamma\left(\frac{3}{2}\right)\sigma_{\dot{v}} \tag{38}$$

where σ_z, $\sigma_{\dot{v}}$ and $\rho_{\dot{v}z}$ denote the standard deviations and the correlation coefficient of the variables $\bar{v}$ and $\bar{z}$. The variables σ_z, $\sigma_{\dot{v}}$ and $\rho_{\dot{v}z}$ can be evaluated, for a prescribed motion of the clamp, by solving the linear system of equations (36). By following the approach proposed by Giaralis ([14], Section 6.2.3, pp. 151-157) the following equations can be easily derived:

$$\sigma_{\dot{v}}^2=\int_0^{+\infty}A\left(\bar{\omega}\right)A^*\left(\bar{\omega}\right)\bar{\omega}^6\frac{\Omega_c G_{wd}\left(\omega\left(\bar{\omega}\right)\right)}{d^2}d\bar{\omega} \tag{39}$$

$$\sigma_z^2 = \int_0^{+\infty} B\left(\bar{\omega}\right) B^*\left(\bar{\omega}\right) \bar{\omega}^4 \frac{\Omega_c G_{wd}\left(\omega\left(\bar{\omega}\right)\right)}{d^2} d\bar{\omega} \tag{40}$$

$$\rho_{\dot{v}z} = -\frac{k_e}{c_e} \cdot \frac{\sigma_z}{\sigma_{\dot{v}}} \tag{41}$$

with the definitions:

$$A\left(\bar{\omega}\right) = \frac{\frac{-k_e}{\bar{v}_0} + j\bar{\omega}}{\left(\alpha\Theta^2 - \bar{\omega}^2\right)\left(\frac{-k_e}{\bar{v}_0} + j\bar{\omega}\right) + j\bar{\omega}\left(1-\alpha\right)\Theta^2 c_e} \tag{42}$$

$$B\left(\bar{\omega}\right) = \frac{j\bar{\omega}c_e}{\left(\alpha\Theta^2 - \bar{\omega}^2\right)\left(\frac{-k_e}{\bar{v}_0} + j\bar{\omega}\right) + j\bar{\omega}\left(1-\alpha\right)\Theta^2 c_e} \tag{43}$$

Finally, after some straightforward calculations, herein omitted for the sake of conciseness, the non-dimensional frequency response function of the stochastically equivalent linear damper (see Eq. (31)) can be expressed as:

$$Z_{d,FW}\left(\bar{\omega}\right) = -\mu\bar{\omega}^2\left(1 + A\left(\bar{\omega}\right)\right) \tag{44}$$

Once $Z_{d,FW}\left(\bar{\omega}\right)$ is known, a chain substitution into Eqs. (35), (27), (26) and(28) allows one to find a new uni-lateral power spectral density $G_{wd}\left(\omega\right)$ and variance σ_{wd}^2. The process is iterated until convergence on $\sigma_w^2\left(x\right)$ is obtained within a prescribed tolerance. This fixed point algorithm is known to be less efficient than a Newton-Raphson approach [2] but has been sufficiently efficient to solve the problem at hand without any big convergence issues.

4 APPLICATION

In the following, the proposed modeling procedure is used to investigate the dynamic response of a benchmark OHL span already studied elsewhere (see e.g. [12, 13]). The length of the span is 450 m and the cable is a ACSR Bersfort 48/7 conductor (diameter $d = 35.6$ mm, mass per unit of length $\gamma = 2.375$ kg/m, Rated Tensile Strength $RTS = 180$ kN) subject to an axial force $H = 0.2\,RTS = 36$ kN. The non-dimensional viscous damping coefficient ζ_c, that approximately account for both the aerodynamic and internal damping of the cable, is assumed equal to $\zeta_c = 0.001$. It is worth noting that, although the order of magnitude of this value seems to be consistent with some experimental data reported in the literature (e.g. [1]), as already noticed in Section 2.1 the adopted viscous damping model is not expected to be fully compliant with all experimental evidences and theoretical arguments of the literature (see e.g. [7, 8]).

A symmetric Stockbridge damper that was experimentally tested by Sauter and Hagedorn [27, 28] is assumed to be applied at the 5% and 10% of the span (i.e. at the non-dimensional arc-length coordinate $\xi_d = 0.05$ and $\xi_d = 0.10$). The mass attached at the both tips of the messenger cable is equal to $m_d = 0.856$ kg, leading to a mass ratio $\mu = 8 \cdot 10^{-4}$ (Eq. (20)).

Sauter and Hagedorn [27, 28] tested the damper on a shaker with sweep tests in frequency at two different constant values of the clamp velocity ($\dot{w}_d$), namely 0.05m/s and 0.2 m/s. From these tests the parameter of the proposed Bouc-Wen model of the damper (see Section 2.2) were identified to match the experimental data obtained for the clamp velocity 0.2 m/s. The identified model parameters are: $k_d = 8$ N/mm, $\alpha = 0.25$ and

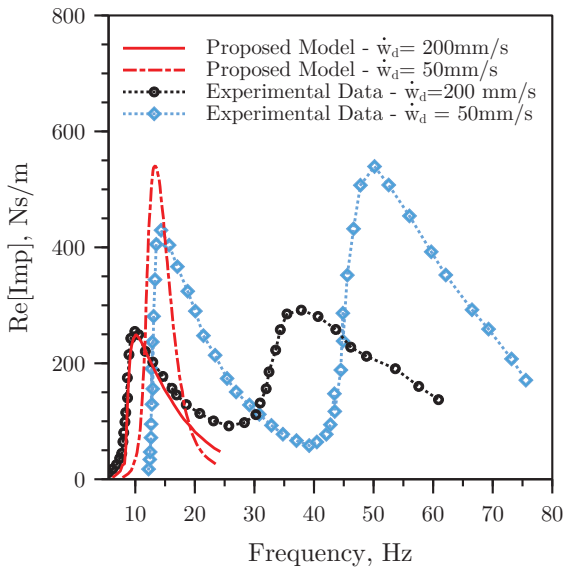

Figure 4: Real part of the impedance curve of the Stockbridge damper tested on a shaker for sweep tests in frequency with an imposed vertical translation of the clamp having a constant value of the clamp velocity equal to $\dot{w}_d = 0.05$ m/s and$\dot{w}_d = 0.2$ m/s. Comparison between the results of the proposed non-linear damper model (see Section 2.2) and experimental data from [27].

$v_0 = 2$ mm. The required numerical simulations were performed by applying a sinusoidal motion of the clamp with a frequency undergoing a linear sweep from 0 to 50 Hz during a total duration of 100 s. The non-linear equations of motion of the damper, then, were numerically integrated at constant time step $\Delta t = 10^{-5}$ s with a Newmark constant acceleration time-stepping strategy. Iterative corrections were performed through a standard Newton-Raphson scheme at each step.

Figure 4 shows the comparison between experimental results and numerical results in terms of the real part of the impedance function of the damper. It is worth noting that the predictions of the proposed damper model match very well the experimental results not only for the clamp velocity used in the BW identification process ($\dot{w}_d = 0.2$ m/s), but also for $\dot{w}_d = 0.05$m/s.

Based on the input data listed above, application of the proposed procedure leads to the results depicted in Figure 5.

Figure 5(a) reports for a line without dampers the standard deviation of the displacement ad the line midspan, expressed as a fraction of the conductor diameter, as a function of the mean wind velocity. Results are reported for two different values of the bandwidth parameter B. Figure 5(b) reports the same quantities for $B = 0.1$ and a line with a damper located at 5% the span (grey broken line), 10% the span (grey solid line). The results referred to the base cable (black solid line) are also reported to facilitate compartison. From this figure some comments can be drawn. As it can be appreciated, (a) in spite the damper was not optimized, it is nevertheless effective over a wide range of wind velocities; (b) at higher wind velocities, the damper is less effective, as it was expected since the proposed model does not account for the second resonance peak shown in Figure 4 (e.g. at 37 Hz and 55 Hz for the 50 mm/s and 200 mm/s clamp velocity values, respectively).

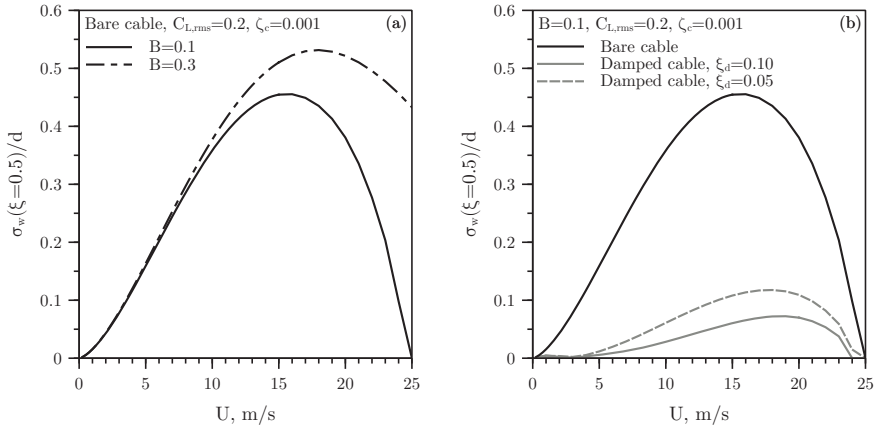

Figure 5: Standard deviation of the cable response at midspan, expressed as a fraction of the cable diameter (a) without attached Stockbridge damper, (b) with attached Stockbridge damper. The curve $B = 0.1$ is similar in both plots to facilitate comparison.

5 CONCLUSIONS

A stochastic and continuous model of aeolian vibrations of overhead electrical line conductors equipped with Stockbridge dampers has been presented in this paper. Focusing on small-amplitude planar transverse vibrations, suspended cables were modeled through the classic taut-string model. Consistently with classic approximate "externally forced models" for vortex induced vibrations (VIV) of bluff bodies, the wind forces acting on the continuous cable model were described as a narrow band stochastic process, centered around the Strouhal frequency of the conductor and with arbitrary cross-correlation in space. A new approach, based on the well-known smooth endochronic Bouc-Wen model, was developed to describe the hysteretic dynamic response of Stockbridge dampers. An iterative solution strategy based on a stochastically equivalent linear damper model, then, was presented to investigate aeolian vibrations of a suspended cable with a Stockbridge damper attached along its length. Finally, the main features and the potential drawbacks of the proposed formulation were illustrated with reference to a simple yet meaningful benchmark case.

REFERENCES

[1] D. Brika, A. Laneville, Vortex-induced vibrations of a long flexible circular cylinder, *Journal of Fluid Mechanics*, **250**, 481–508, 1993.

[2] T. Canor, N. Blaise, V. Denoel, An asymptotic expansion-based method for a spectral approach in equivalent statistical linearization, *Probabilistic Engineering Mechanics*, **38**, 1–12, 2014.

[3] CIGRE, In: G. Diana (Ed.), An asymptotic expansion-based method for a spectral approach in equivalent statistical linearization, *CIGRE Green Books, Springer*, 2018.

[4] J.P. Den Hartog, Mechanical Vibrations, *Dover Publications, New York, NY, USA, 14th edition*, 1985.

[5] V. Denoel, T. Andrianne, Real-scale observations of vortex induced vibrations of stay-cables in the boundary layer, *Procedia Engineering*, **199**, 3109–3114, 2017.

[6] M. Domaneschi, Simulation of controlled hysteresis by the semi-active Bouc-Wen model, *Computers & Structures*, **106-107**, 245–257, 2012.

[7] F. Foti, L. Martinelli, A unified analytical model for the self-damping of stranded cables under aeolian vibrations, *Journal of Wind Engineering & Industrial Aerodynamics*, **176**, 225–238, 2018.

[8] F. Foti, L. Martinelli, An enhanced unified model for the self-damping of stranded cables under aeolian vibrations, *Journal of Wind Engineering & Industrial Aerodynamics*, **182**, 72–86, 2018.

[9] F. Foti, L. Martinelli, Hysteretic behaviour of Stockbridge dampers: modelling and parameter identification, *Mathematical Problems in Engineering*, **Volume 2018**, Article ID 8925121, 17 pages, 2018.

[10] CIGRE, EPRI - Electric Research Power Institute, Transmission Line Reference Book: Wind- induced Conductor Motion, *EPRI, Palo Alto, USA*, 2006.

[11] M. Ervik, et al., Report on aeolian vibrations, *Electra*, **124**, 40–77, 1986.

[12] C. Gazzola, F. Foti, L. Martinelli, F. Perotti, An efficient semi-analytical procedure for assessing aeolian vibrations of overhead transmission lines, *In: Advances in Engineering Materials, Structures and Systems: Innovations, Mechanics and Applications – Zingoni (Ed.), Taylor & Francis Group, London*, 37–42, 2019.

[13] C. Gazzola, F. Foti, L. Martinelli, F. Perotti, An Appraisal of Modelling Strategies for Assessing Aeolian Vibrations of Transmission Lines, *In: In: Carcaterra A., Paolone A., Graziani G. (eds) Proceedings of XXIV AIMETA Conference 2019 (AIMETA 2019)*, 1522–1534, 2020.

[14] A. Giaralis, Wavelet based response spectrum compatible synthesis of accelerograms and statistical linearization based analysis of the peak response of inelastic systems, *Rice University (Doctoral Dissertation), Houston, Texas, USA*, 2008.

[15] P. Hagedorn, Wind-excited vibrations of transmission lines: a comparison of different mathematical models, *Mathematical Modelling*, **8**, 352–358, 1987.

[16] P. Hagedorn, J. Schmidt, N. Nascimento, Stochastic field processes in the mathematical modelling of damped transmission line vibrations, *Mathematical Modelling*, **8**, 359–363, 1987.

[17] C. Hardy, P. Van Dyke, Field observations on wind-induced conductor motions, *Journal of Fluid and Structures*, **9**, 43–60, 1995.

[18] W. Hurewicz, Lectures on ordinary differential equations, *14th edition, Dover Publications, New York, NY, USA*, 2014.

[19] J.E. Hurtado, A.H Barbat, Equivalent linearization of the Bouc-Wen hysteretic model, *Engineering Structures*, **22**, 1121–1132, 2000.

[20] F. Ikhouane, J. Rodellar, J.E. Hurtado, Analytical characterization of hysteresis loops described by the Bouc-Wen model, *Mechanics of Advanced Materials and Structures*, **13**, 463–472, 2006.

[21] F. Ikhouane, V. Manosa, J. Rodellar, Dynamic properties of the hysteretic Bouc-Wen model, *Systems and Control Letters*, **56**, 197–205, 2007.

[22] F. Ikhouane, J.E. Hurtado, J. Rodellar, Variation of the hysteresis loop with the Bouc-Wen model parameters, *Nonlinear Dynamics*, **48**, 361–380, 2007.

[23] M. Ismail, F. Ikhouane, J. Rodellar, The hysteresis Bouc-Wen model, a survey, *Archives of Computational Methods in Engineering: State-of-the-Art Reviews*, **16**, 161–188, 2009.

[24] D.E. Newland, An Introduction to: Random Vibrations, Spectral and Wavelet Analysis, *Third Edition, Dover Publications, New York, NY, USA*, 2005.

[25] M.P. Paidoussis, S.J. Price, E. De Langre, Fluid-structure interactions: cross-flow-induced instabilities, *Cambridge University Press*, 2010.

[26] I. Pivovarov, O.G. Vinogradov, One application of Bouc's model for non-linear hysteresis, *Journal of Sound and Vibration*, **118**, 209–216, 1987.

[27] D. Sauter, Modeling the dynamic characteristics of slack wire cables in Stockbridge dampers, *Technische Universitat Darmstadt (Dissertation), Darmstadt, Germany*, 2003.

[28] D. Sauter, P. Hagedorn, On the hysteresis of wire cables in Stockbridge dampers, *International Journal of Non-Linear Mechanics*, **37**, 1453–1459, 2002.

[29] B.J. Vickery, A.W. Clark, Lift or across-wind response of tapered stackss, *Journal of Structural Division (ASCE)*, **98**, 1–20, 1972.

EURODYN 2020
XI International Conference on Structural Dynamics
M. Papadrakakis, M. Fragiadakis, C. Papadimitriou (eds.)
Athens, Greece, 23–26 November 2020

ENHANCED SERVICEABILITY PERFORMANCE IN WIND-EXCITED TALL BUILDINGS EQUIPPED WITH OPTIMAL TUNED MASS DAMPER INERTER VIA TOP-STOREY SOFTENING

Zixiao Wang[1], **Agathoklis Giaralis**[2]*

[1] PhD Candidate, Department of Civil Engineering, City University of London
Northampton Square, London EC1V 0HB, UK
e-mail: Zixiao.Wang@city.ac.uk

[2] Senior Lecturer, Department of Civil Engineering, City University of London
Northampton Square, London EC1V 0HB, UK
e-mail: agathoklis.giaralis.1@city.ac.uk

Keywords: Tuned mass damper inerter, optimal passive vibration control, wind-excited tall buildings, vortex shedding, occupants' comfort, floor acceleration.

Abstract. A local structural modification, namely top-storey softening, is herein considered in conjunction with optimally tuned top-floor tuned mass damper inerter (TMDI) for improved serviceability performance in mid-to-high rise buildings (host structures). The focus is to reduce floor accelerations on typical core-frame host structures with rectangular footprint due to wind-induced vortex shedding (VS) effects causing occupants' discomfort. This aim is achieved by formulating an optimal TMDI tuning problem in which TMDI inertial and top-storey host structure properties (i.e., attached mass and inertance, and top-storey height) are treated as design variables, to a case-study building aiming to minimize peak floor acceleration in the across-wind direction. The optimal TMDI tuning problem is numerically solved for a wide range of design variables for a 34-storey composite core-frame building subject to stochastic spatially-correlated wind-force field accounting for VS effects. A planar low-order dynamical model capturing faithfully modal properties of the 34-storey building is developed to facilitate computational work and parametric investigation. It is found that top-storey stiffness reduction, herein regulated through storey height, not only relaxes attached TMDI mass/weight requirements, but also reduces TMDI stroke, and inerter force for fixed performance and inertance. It is concluded that by leveraging inertance and top-storey stiffness, the considered solution can efficiently control VS-induced floor acceleration with small additional gravitational (added weight) and horizontal damping forces to the satisfaction of standard code requirements for occupants comfort.

1 INTRODUCTION

Passive dynamic vibration absorbers, including tuned mass-dampers (TMDs), have been widely used for mitigating wind-induced vibrations in tall buildings (e.g., [1,2]). A typical linear TMD comprises a mass attached towards the top of the building (host structure) via linear stiffeners and dampers [3]. The TMD is tuned to the first natural frequency of the building aiming to dampen the fundamental lateral mode shape which tends to be mostly excited due to resonance with the frequency of wind-induced forces. Such forces typically develop in the across-wind direction of tall buildings with rectangular foot-print due to vortex shedding (VS) [4] and may induce large floor accelerations causing occupants' discomfort [5] and, consequently, serviceability structural failure. This consideration becomes critical for slender tall buildings and governs their design [6]. Meanwhile, the applicability of passive TMDs for wind-induced vibration suppression is limited by structural and economical considerations. This is because their motion control potential relies on the attached mass (i.e., the larger it is, the more effective the TMD becomes [7]), but constraints apply to the TMD weight that can be safely accommodated at the top floor of slender/tall buildings while TMD up-front cost increases proportionally with its mass [8].

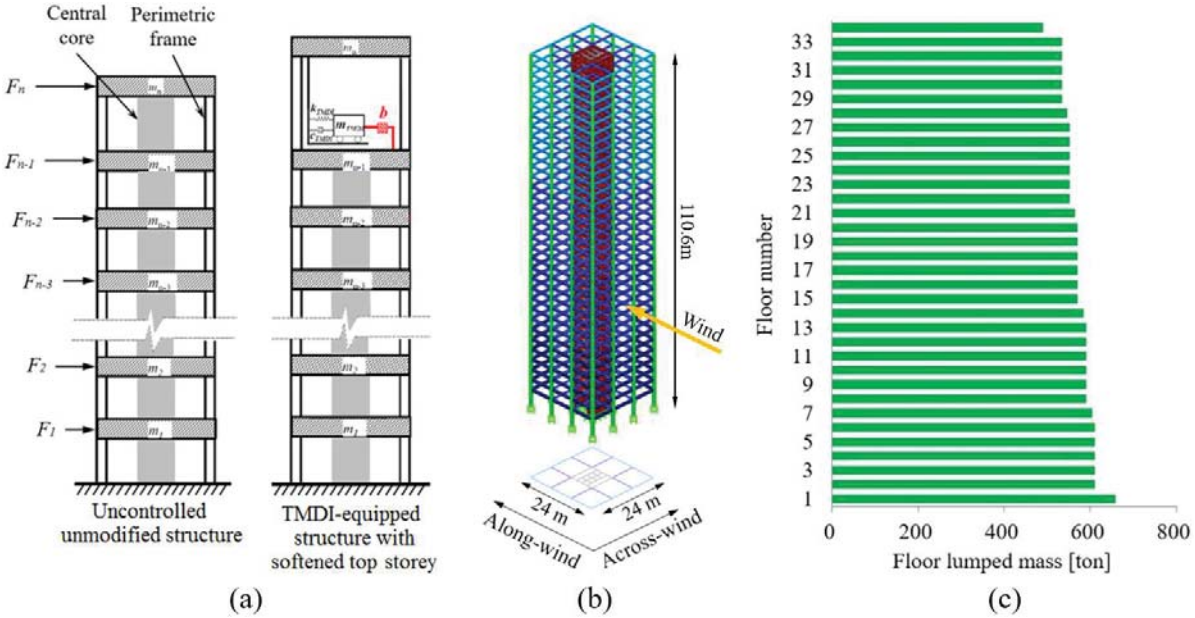

Figure 1 (a) Schematic of a TMDI-equipped planar coupled core-frame building with soft top-storey, (b) case-study 34-storey building, and (c) lumped floor mass distribution.

Recently, it has been shown [9,10] that the incorporation of an inerter to TMD-equipped tall buildings in the so-called tuned mass damper inerter (TMDI) configuration enhances serviceability performance against VS-induced wind forces without increasing the required attached weight, thus overcoming the above TMD limitations. Specifically, the inerter is defined as a linear mechanical element that resists relative acceleration through the inertance constant assuming mass units (kg) [11]. In the TMDI, originally proposed for seismic protection of building structures [12-14], an inerter element is used to link the TMD attached mass to a different floor from the one that the TMD is attached to. It is then found [9,10] that improved floor acceleration mitigation is achieved in tall wind-excited TMDI-equipped buildings by increasing the inertance, which scales-up independently of physical mass in prototyped inerter devices [15,16], and, even more so, by letting the inerter span more than one storey. Nevertheless, for

routine slender mid-to-high-rise buildings with 20-40 storeys, TMDI configuration with inerter spanning more than one floor is not as practical as in the case of tall landmark structures (e.g., [2]) since occupying high-premium space across several upper floors of such structures for accommodating a control device is not cost effective. To this end, this paper explores the potential of a local structural modification, top-storey softening, in conjunction with top-storey TMDI placement as shown in Figure 1(a), to mitigate floor accelerations in the across-wind direction of VS-sensitive buildings with no more than 40 stories. Notably, the above vibration mitigation solution is practically meritorious for such buildings in which standard coupled core-frame systems are used for lateral wind load resistance [17]. This is because: (1) the considered solution does not utilize premium space since the TMDI is fully contained within a single (last) floor which is commonly reserved for accommodating various building services, and (2) top-storey softening can be readily achieved by simple local modifications such as discontinuation of the core at the last floor as well as increasing the top-storey height as depicted in Figure 1(a).

Herein, the effectiveness of top-storey softening to improve TMDI motion control efficiency is numerically illustrated with the aid of a 34-storey composite core-frame building structure shown in Figure 1(b) subject to a parametrically defined stochastic across-wind force model accounting for VS effects. An optimal TMDI design problem is formulated and numerically solved to minimize floor acceleration (i.e., occupants' comfort criterion) of the case-study building in which top-floor height along with TMDI inertial properties (i.e., mass and inertance) are explicitly taken into consideration. Optimal TMDI-equipped structure performance is assessed in terms of floor acceleration, TMDI stroke, and damping and inerter forces and attention is focused to quantify gains in the required attached mass and to check for occupants' comfort criteria. The presentation begins with a brief description of the case-study building and its numerical modelling enabling efficient TMDI incorporation and dynamic analysis.

2 CASE-STUDY BUILDING STRUCTURE AND NUMERICAL MODELLING

The adopted structure is 110.6m high and has square 24m-by-24m footprint as shown in Figure 2(b). The lateral load-resisting structural system is composite consisting of a perimetric three-bay per side steel moment resisting frame (MRF) and a central reinforced concrete (r/c) core. MRF members are rigidly connected and have hollow rectangular sections with varying dimensions along the building height. The r/c core has 8m-by-8m plan-view dimensions and consists of outer wall segments whose thickness reduces progressively with building height and inner (stiffening) wall segments with same thickness along the building height. Hinged primary beams are used to couple the MRF with the core at each floor level which do not participate in resisting lateral loads and floor slabs behave as rigid diaphragms. The total mass of the structure accounting for dead and live loads, M_{tot}, is 92830tons and is distributed at each floor level as shown in Figure 1(c). To expedite computational work required in TMDI optimal design, a planar dynamic model with 34 degrees of freedom (DOFs) corresponding to the uncoupled lateral in-plane translations of rigid slabs along the across-wind direction of the case-study building is defined in terms of a diagonal mass matrix, $\mathbf{M}_s \in \mathbb{R}^{34\times34}$, and full stiffness and damping matrices, $\mathbf{K}_s \in \mathbb{R}^{34\times34}$ and $\mathbf{C}_s \in \mathbb{R}^{34\times34}$, respectively. The main diagonal of the $\mathbf{M}_s$ matrix is populated with the lumped floor masses of Figure 1(c). Further, the stiffness matrix $\mathbf{K}_s$ is obtained from a detailed linear finite element (FE) model of the lateral load-resisting structural system of the building developed in SAP2000® software package. The accuracy of the modal properties (mode shapes and natural frequencies) of the 34-DOF dynamic model is verified against modal analysis results from the detailed FE model. Lastly, the inherent structural damping is incorporated in the modelling through a full damping matrix $\mathbf{C}_s$ obtained by assuming

modal damping ratios $\xi_j = 1\%$ for $j = 2,3,4$; $\xi_j = 2\%$ for $j = 5,6,7$; $\xi_j = 4\%$ for $j = 8,9,10$; $\xi_j = 8\%$ for $j = 11,...,20$; and $\xi_j = 16\%$ for $j = 21,...,34$.

3 WIND EXCITATION MODEL

The input wind action to the 34-DOF dynamic model capturing the across-wind dynamics of the case-study building is herein represented by the stochastic across-wind force model developed in [2] for buildings with rectangular footprint. This wind forcing model is based on wind tunnel testing data and accounts for both the turbulence and the VS components of the wind force in the across-wind direction. It is defined by a zero-mean stationary Gaussian spatially correlated random field represented in frequency domain by a full power spectral density (PSD) matrix. For the 34-DOF dynamic model, a $\mathbf{S}_{\mathbf{FF}}^{34} \in \mathbb{R}^{34\times 34}$ wind force PSD matrix is determined upon spatial discretization of the wind random field at each building floor. The assumed mean wind velocity profile is plotted in Figure 2(a). It follows the Eurocode-compliant logarithmic law [18] and terrain category IV (i.e., area in which at least 15% of the surface is covered with buildings and their average height exceeds 15 m) and is defined for basic wind velocity of 22m/s (i.e., 10mins mean wind velocity at 10m height above open flat terrain). For illustration, wind force PSDs computed by the model in [2] at four different floor slab heights are plotted in Figure 2(b) following the assumed mean wind velocity profile.

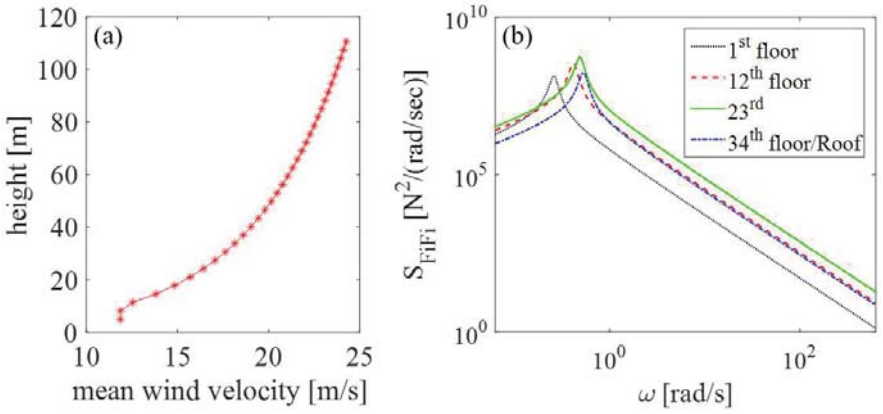

Figure 2. Assumed wind excitation model: (a) mean wind velocity profile, (b) power spectral density functions (PSDs) of across-wind forces acting at different floor levels of the case-study building.

4 TMDI-EQUIPPED STRUCTURE AND FREQUENCY DOMAIN ACROSS-WIND RESPONSE ANALYSIS

Mathematically, a top-floor TMDI is added to the 34-DOF system model following [9,10] to yield a 35-DOF augmented model with mass, $\mathbf{M} \in \mathbb{R}^{35\times 35}$, damping, $\mathbf{C} \in \mathbb{R}^{35\times 35}$, and stiffness, $\mathbf{K} \in \mathbb{R}^{35\times 35}$, matrices written as

$$\mathbf{M} = \begin{bmatrix} m_1 & 0 & \cdots & \cdots & \cdots & 0 \\ & m_2 & \cdots & \cdots & \cdots & \vdots \\ & & \ddots & 0 & 0 & 0 \\ & & & m_{33}+b & 0 & -b \\ & SYM & & & m_{34} & 0 \\ & & & & & m_{TMDI}+b \end{bmatrix}, \quad \mathbf{C} = \begin{bmatrix} c_{1,1} & c_{1,2} & \cdots & \cdots & c_{1,34} & 0 \\ & c_{2,2} & \cdots & \cdots & \vdots & \vdots \\ & & \ddots & c_{32,33} & c_{32,34} & 0 \\ & & & c_{33,33} & c_{33,34} & 0 \\ & SYM & & & c_{34,34}+c_{TMDI} & -c_{TMDI} \\ & & & & & c_{TMDI} \end{bmatrix}, \quad (1)$$

$$\text{and } \mathbf{K} = \begin{bmatrix} k_{1,1} & k_{1,2} & \cdots & \cdots & k_{1,34} & 0 \\ & k_{2,2} & \cdots & \cdots & \vdots & \vdots \\ & & \ddots & k_{32,33} & k_{32,34} & 0 \\ & & & k_{33,33} & k_{33,34} & 0 \\ & SYM & & & k_{34,34}+k_{TMDI} & -k_{TMDI} \\ & & & & & k_{TMDI} \end{bmatrix},$$

in which $m_k = \mathbf{M}_s[k,k]$, $c_{k,l} = \mathbf{C}_s[k,l]$, and $k_{k,l} = \mathbf{K}_s[k,l]$ where k,l=1,2,…,34 are the elements of the mass, damping, and stiffness matrices of the uncontrolled host structure, respectively, while the 35-th DOF corresponds to the lateral TMDI mass displacement. Further, in the previous expressions, m_{TMDI} is the TMDI mass attached to the top (34th) floor via a spring with k_{TMDI} stiffness in parallel with a linear dashpot with damping coefficient c_{TMDI}, and b is the inertance of the inerter element highlighted in red in Fig. 1(a), connecting the TMDI mass to the penultimate (33rd) floor.

Response displacement, velocity, and acceleration PSD matrices of the TMDI-equipped structure subject to the wind force PSD matrix defined in section 3 can be obtained as

$$\mathbf{S}_{\mathbf{xx}}(\omega) = \mathbf{B}(\omega)^{*}\,\mathbf{S}_{\mathbf{FF}}(\omega)\mathbf{B}(\omega), \quad \mathbf{S}_{\dot{\mathbf{x}}\dot{\mathbf{x}}}(\omega) = \omega^2\mathbf{S}_{\mathbf{xx}}(\omega), \quad \text{and} \quad \mathbf{S}_{\ddot{\mathbf{x}}\ddot{\mathbf{x}}}(\omega) = \omega^4\mathbf{S}_{\mathbf{xx}}(\omega) \tag{2}$$

respectively. In Eq. (2), $\mathbf{S}_{\mathbf{FF}}(\omega) \in \mathbb{R}^{35\times 35}$ is the wind force PSD matrix $\mathbf{S}_{\mathbf{FF}}^{34}$ augmented by a bottom zero row and a right-most zero column corresponding to the TMDI displacement DOF as the TMDI is internally housed and not subjected to any wind load. Further, the "*" superscript denotes complex matrix conjugation, and the transfer matrix **B** is given as

$$\mathbf{B}(\omega) = \left[\mathbf{K} - \omega^2\mathbf{M} + i\omega\mathbf{C}\right]^{-1} \tag{3}$$

where, $i = \sqrt{-1}$, and the "-1" superscript denotes matrix inversion. Next, response displacement, velocity, and acceleration variance of the k-th floor are obtained as

$$\sigma_{x_k}^2 = \int_0^{\omega_{\max}} S_{xx}[k,k]\,d\omega, \quad \sigma_{\dot{x}_k}^2 = \int_0^{\omega_{\max}} S_{\dot{x}\dot{x}}[k,k]\,d\omega, \quad \text{and} \quad \sigma_{\ddot{x}_k}^2 = \int_0^{\omega_{\max}} S_{\ddot{x}\ddot{x}}[k,k]\,d\omega, \tag{4}$$

respectively, where $\omega_{\max}$ is a cut-off frequency above which the energy of the underlying processes is negligible. Moreover, the variance of the relative response displacement, velocity, and acceleration between floors/DOFs k and l are obtained by

$$\begin{aligned} \sigma_{x_{k,l}}^2 &= \sigma_{x_k}^2 + \sigma_{x_l}^2 - 2\int_0^{\omega_{\max}} S_{xx}[k,l]\,d\omega, \\ \sigma_{\dot{x}_{k,l}}^2 &= \sigma_{\dot{x}_k}^2 + \sigma_{\dot{x}_l}^2 - 2\int_0^{\omega_{\max}} S_{\dot{x}\dot{x}}[k,l]\,d\omega, \text{ and} \\ \sigma_{\ddot{x}_{k,l}}^2 &= \sigma_{\ddot{x}_k}^2 + \sigma_{\ddot{x}_l}^2 - 2\int_0^{\omega_{\max}} S_{\ddot{x}\ddot{x}}[k,l]\,d\omega. \end{aligned} \tag{5}$$

Ultimately, peak response quantities are estimated by multiplying the square root of the variances in Eqs. (4) and (5) with the peak factor g given by the empirical formula [18]

$$g = \sqrt{2ln(\eta T_{wind})} + \frac{0.577}{\sqrt{2ln(\eta T_{wind})}}, \tag{6}$$

where $\eta=2\pi/\omega_{n(1)}$ and T_{wind} is the time duration of exposure to the wind action. In the ensuing numerical work, T_{wind} is taken equal to 3600s (i.e., one hour of stationary wind excitation is assumed).

5 OPTIMAL TMDI DESIGN WITH TOP-STOREY SOFTENING FOR SERVICEABILITY PERFORMANCE

To investigate the potential of top-storey softening in TMDI-equipped buildings for enhanced serviceability performance under wind excitation, the properties of the TMDI in Fig. 1(a) are optimally designed to mitigate floor accelerations in the case-study building subject to the wind forces defined in section 3. To this aim, an optimal TMDI tuning problem is formulated taking as the objective function (OF) to be minimized the peak floor acceleration of the highest occupied of the case-study building (i.e., the 32nd floor). That is,

$$\text{OF}=g\sigma_{\ddot{x}_{32}}. \tag{7}$$

The problem has 5 design variables (DVs), namely the top-storey height H_{top}, the mass ratio μ, the inertance ratio β, the TMDI frequency ratio υ_{TMDI}, and the TMDI damping ratio ξ_{TMDI}. The last four DVs are defined as

$$\mu=\frac{m_{TMDI}}{M_{tot}},\ \beta=\frac{b}{M_{tot}},\ \upsilon_{TMDI}=\frac{\sqrt{\frac{k_{TMDI}}{(m_{TMDI}+b)}}}{\omega_1}\ \text{and}\ \xi_{TMDI}=\frac{c_{TMDI}}{2\sqrt{(m_{TMDI}+b)k_{TMDI}}}, \tag{8}$$

where ω_1 is the first natural frequency of the uncontrolled structure. Then, optimal primary DVs, υ_{TMDI} and ξ_{TMDI}, are sought that minimize the OF given values of the secondary DVs, H_{top}, μ, and β. (secondary design parameters). The optimization problem is numerically solved for the case-study structure using a pattern search algorithm [19] with iteratively updated search range of the primary variables hard-coded in MATLAB®.

6 PERFORMANCE ASSESSMENT OF OPTIMAL TMDI-EQUIPPED STRUCTURE WITH SOFTENED TOP-STOREY

In this section, numerical results are furnished to demonstrate the effectiveness of optimally designed TMDI in containing VS induced vibrations in the case-study building exposed to the PSD wind force matrix as top-floor lateral stiffness reduces. To this aim, TMDIs with different inertance ratios (β = 0% (TMD), 2%, and 10%) are examined for fixed attached mass μ=0.1% while the top-storey of the case-study building is softened laterally by discontinuing the r/c core at the penultimate (33rd) storey (see Fig. 1(a)) and by varying its height within H_{top}= [4.0, 6.0] (m) interval.

Figure 3(a) reports percentage reduction factor (RF) of peak floor acceleration at the 32nd floor of optimal TMDI-equipped structure with respect to the uncontrolled case-study building with coreless top-storey for three different inertance ratios as a function of top-storey lateral stiffness. The latter is given as a percentage of the top-storey stiffness of the case-study structure without r/c core at the 33rd storey and H_{top}=3.2m. It is observed that optimal TMDI capability to suppress floor accelerations increases appreciably and monotonically as the top-storey stiffness reduces for fixed inertance. On the antipode, for the TMD case (i.e., no inerter and β = 0%) acceleration RFs remain practically constant with top-storey flexibility. These results reveal that the presence of the inerter enables improved TMDI vibration control potential as top-storey stiffness reduces. This fact is attributed to the coupling of the acceleration of the attached mass to the acceleration of the 33rd floor achieved by the inerter mathematically manifested through

the non-diagonal terms in the mass matrix **M** in Eq. (1). And the herein advocated host-structure modification (i.e., top-storey softening) leverages the positive effect of this coupling in reducing floor accelerations below the top-storey. Nevertheless, when no such coupling exists (i.e., conventional TMD case), top-storey flexibility has no effect to the overall motion control level achieved. In this regard, top-storey lateral stiffness becomes a critical TMDI design parameter. Moreover, it is seen that for given β there is a limiting top-storey stiffness reduction defined by the intersection of the TMD RF curves with the TMDI RF curves, above which the TMD outperforms TMDI. This limiting value increases as inertance increases. Thus, top-storey softening reduces demands for large inertance.

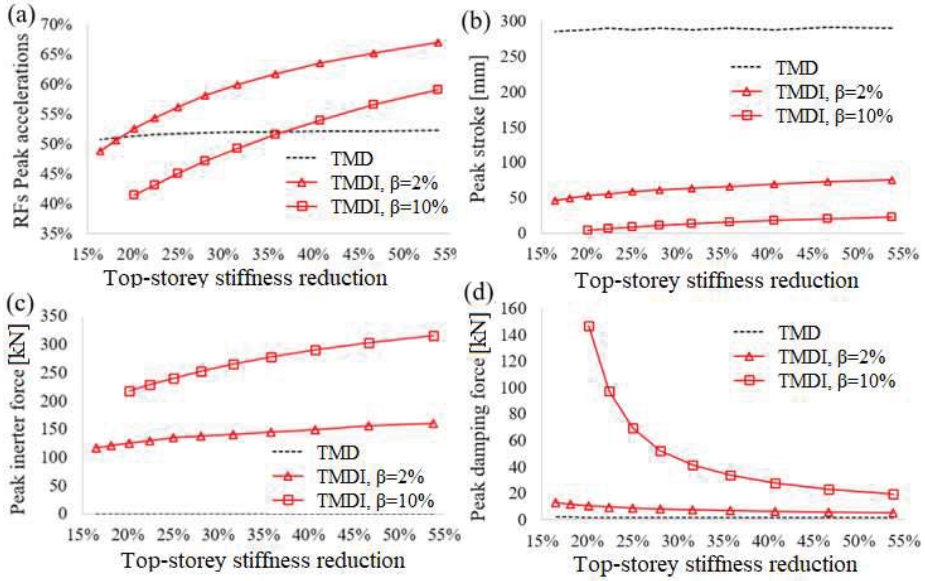

Figure 3. (a) Peak acceleration percentage reduction of 32nd floor, (b) secondary mass stroke, (c) peak inerter force, and (d) peak damping force in TMD(I)-equipped structure for attached mass ratio, μ=0.1%, and inertance ratios, β, against lateral top-storey stiffness reduction.

Turning the attention to the peak stroke of the secondary mass, that is, the peak relative displacement of the TMD(I) mass with respect to the floor that the mass is attached to, $g\sigma_{x_{35,33}}$, Figure 3(b) plots peak TMDI stroke versus top-storey stiffness reduction. It is seen that stroke dramatically reduces with increasing inertance, which is a well-reported effect in the literature [9,10]. Further, stroke demand is positively (though insignificantly) affected by top-storey stiffness reduction. This is quite welcoming result suggesting that the favourable effect of increasing top-storey flexibility to the TMDI effectiveness for suppressing floor accelerations does not come with any increasing cost/demand related to the stroke of the damping device or to the clearance of the secondary mass.

Peak inerter and damping forces developing at the inerter and at the dashpot of optimally designed TMDIs are also deemed essential to check as they need to be economically accommodated locally by the host structure. In this respect, Figures 3(c) and (d) report peak inerter and damping forces, respectively. It is seen that peak inerter force decreases as the top-storey softens at an increasing rate. On the contrary, damping force increases exponentially as the top-storey stiffness reduces for β = 10%. These trends indicate that top-storey stiffness reduction improves TMDI motion control performance through significant increase of the damping force but not of the inerter force.

Numerical results reported in Figure 3(a) suggest that the same structural performance, in terms of peak floor acceleration, can be achieved by using different sets of secondary design

parameters. From practical viewpoint, this is an important consideration as it enables exchanging attached mass to inertance and/or to top-storey stiffness within a performance-oriented design context. To illustrate this point, Figures 4(a) and (b) plot optimal iso-performance curves on the TMDI inertial μ-β plane for fixed top-storey stiffness and for fixed performance, respectively. It is seen that all iso-performance curves have negative slope on the μ-β plane establishing the direct mass reduction/substitution effect endowed by the inertance leading to overall more lightweight inertial dampers. Furthermore, as suggested by Figure 4(b), the same performance can be achieved with reduced average required inertance by approximately 1.6% at μ=0.1%, for every 2% reduction to the top-storey stiffness. As a final remark, top-storey softening further leads to attached mass reduction for fixed inertance to achieve/maintain a preset performance: Figure 4(b) shows that 2% reduction of top-storey stiffness reduces the required mass ratio by about 0.1%, which corresponds to a 20ton TMDI weight reduction for the considered building structure.

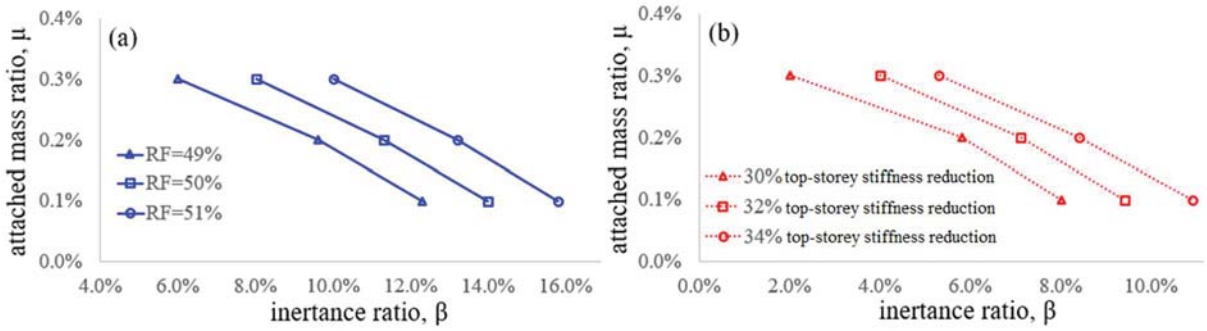

Figure 4. Quantification of mass-inertance-damping coefficient trade-off for (a) fixed normalized stiffness 38%, and (b) fixed performance RF=50%.

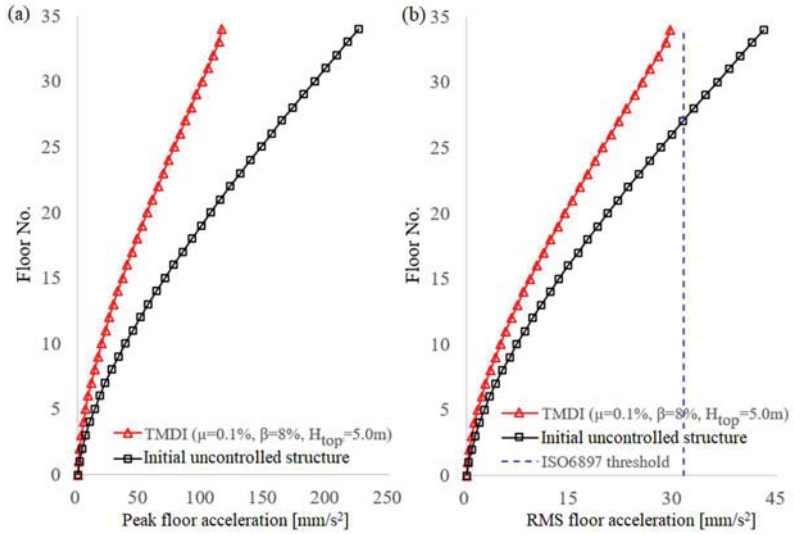

Figure 5. Floor acceleration distribution along the building height and check for occupants' comfort.

As a final check, Figure 5 plots peak and RMS floor accelerations along the building height for the uncontrolled and for a TMDI controlled structure with about 28% top-storey stiffness reduction. The benefit of TMDI is clearly seen and the rationale behind optimal TMDI tuning for minimizing floor acceleration of the 32nd floor is justified as it leads to floor acceleration reductions in all lower floors. More importantly, Figure 5(b) shows that the uncontrolled structure did not meet occupants' comfort threshold according to ISO6897 [5] at floors 26 and above

for the specific wind excitation, while the particular optimally tuned TMDI with top-storey softening meets the ISO6897 criterion for all floors.

7 CONCLUDING REMARKS

The effectiveness of optimally tuned top-storey TMDIs in conjunction with local top-storey softening has been numerically explored for mitigating floor accelerations in the across-wind direction of slender core-frame buildings which become critical for serviceability design associated with occupants' comfort. Numerical results for different TMDI inertance and top-storey stiffness have shown that improved structural performance in terms of peak floor acceleration and attached mass stroke are achieved by increasing inertance and/or by reducing top-storey stiffness for fixed TMDI attached mass. Meanwhile no improved performance is achieved by conventional TMD through top-storey softening. It was further demonstrated that the required TMDI mass/weight can be reduced either by increasing inertance or by softening the top-storey for a preset performance level. Therefore, top-storey softening facilitates practical implementation of TMDI as it relaxes requirements for large inertance.

REFERENCES

[1] A. Kareem, T. Kijewski, Y. Tamura, Mitigation of motions of tall buildings with specific examples of recent applications, *Wind and Structures* 2(3), 201-251, 1999.

[2] Q.S. Li, L.H. Zhi, A.Y. Tuan, C.S. Kao, Dynamic behavior of Taipei 101 Tower: Field measurement and numerical analysis, *J. Struct. Eng.* 137, 143–155, 2011.

[3] S. Elias, V. Matsagar, Research developments in vibration control of structures using passive tuned mass dampers, *Annual Reviews in Control* 44, 129-156, 2017.

[4] S. Liang, S. Liu, Q.S. Li, L. Zhang, M. Gu, Mathematical model of across-wind dynamic loads on rectangular tall buildings. *J. Wind Eng. Ind. Aerodyn.* 90, 201-251, 2002.

[5] Guidelines for the evaluation of the response of occupants of fixed structures to low frequency horizontal motion (0.063 to 1 Hz), *ISO Standard 6897*, 1984.

[6] M. Ciampoli, F. Petrini, Performance-Based Aeolian Risk assessment and reduction for tall buildings, *Prob. Eng. Mech.* 28, 75–84, 2012.

[7] M. De Angelis, S. Perno, A. Reggio, Dynamic response and optimal design of structures with large mass ratio TMD, *Earthquake Eng. Struct. Dyn.* 41, 41–60, 2012.

[8] K. Tse, K. Kwok, Y. Tamura, Performance and Cost Evaluation of a Smart Tuned Mass Damper for Suppressing Wind-Induced Lateral-Torsional Motion of Tall Structures, *J. Struct. Eng.* 138(4), 514-525, 2012.

[9] A. Giaralis, F. Petrini, Wind-induced vibration mitigation in tall buildings using the tuned mass damper-inerter (TMDI), *J. Struct. Eng.* 143(9), 04017127, 2017.

[10] F. Petrini, A. Giaralis, Z. Wang, Optimal tuned mass-damper-inerter (TMDI) design in wind-excited tall buildings for occupants' comfort serviceability performance and energy harvesting, *Eng. Struct.* 204, 109904, 2020.

[11] M.C. Smith, Synthesis of Mechanical Networks: The Inerter, *IEEE Trans. Automat. Control* 47(10), 1648-1662, 2002.

[12] L. Marian, A. Giaralis, Optimal design of inerter devices combined with TMDs for vibration control of buildings exposed to stochastic seismic excitations, *Proc,.11th ICOSSAR Int. Conf. on Structural Safety and Reliability*, 1025-1032, 2013.

[13] L. Marian, A. Giaralis, Optimal design of a novel tuned mass-damper–inerter (TMDI) passive vibration control configuration for stochastically support-excited structural systems, *Prob. Eng. Mech. 38*, 156–164, 2014.

[14] R. Ruiz, A.A. Taflanidis, A. Giaralis, D. Lopez-Garcia, Risk-informed optimization of the tuned mass-damper-inerter (TMDI) for the seismic protection of multi-storey building structures, *Eng. Struct.* 177, 836-850, 2018.

[15] S. Nakaminami, H. Kida, K. Ikago, N. Inoue, Dynamic testing of a full-scale hydraulic inerter-damper for the seismic protection of civil structures, *7th International conference on advances in experimental structural engineering*, 41-54, 2016.

[16] D. Pietrosanti, M. De Angelis, A. Giaralis, Experimental study and numerical modeling of nonlinear dynamic response of SDOF system equipped with tuned mass damper inerter (TMDI) tested on shaking table under harmonic excitation, *Int. J. Mech. Sci.* 184(15), 105762, 2020.

[17] S.B. Taranath, *Tall Building Design, Steel, Concrete, and Composite Systems.* ISBN: 9781466556201, 2017.

[18] A.G. Davenport, Note on the distribution of the largest value of a random function with application to gust loading, *Proc. of the Institution of Civil Engineers* 28(2), 187-196, 1964.

[19] A. Charles, J.E. Dennis, Analysis of Generalized Pattern Searches, *SIAM Journal on Optimization* 13(3), 889–903, 2003.

EURODYN 2020
XI International Conference on Structural Dynamics
M. Papadrakakis, M. Fragiadakis, C. Papadimitriou (eds.)
Athens, Greece, 23–26 November 2020

DYNAMICS OF TENSEGRITY SOLAR FAÇADES OPERATING AS MECHANICAL ENERGY HARVESTERS

Raffaele Miranda[1], Enrico Babilio[2], Narinder Singh[1], Diana P. Villamil[1], Filipe Santos[3] and Fernando Fraternali[1]

[1]Department of Civil Engineering, University of Salerno,
via Giovanni Paolo II, 132, 84084, Fisciano (SA), Italy
{ramiranda,snarinder,f.fraternali}@unisa.it, dianamaritzap@gmail.com

[2]Department of Structures for Engineering and Architecture (DiSt), University of Naples "Federico II",
via Forno Vecchio 36, 80134, Naples, Italy
enrico.babilio@unina.it

[3]CERIS and Departamento de Engenharia Civil da Faculdade de Ciências e Tecnologia,
Universidade NOVA de Lisboa,
Quinta da Torre, 2829-516 Caparica, Portugal
fpas@fct.unl.pt

Keywords: tensegrity structures, dynamic solar façades, energy harvesting, energy efficient buildings.

Abstract. *Deployable sunscreens with tensegrity architecture have been recently proposed for dynamic solar façades of buildings working on low energy consumption. Such structures are aimed at ensuring well-being indoor conditions while using reduced electrical-grid energy. The present paper studies the dynamical response of the tensegrity shading screens recently appeared in the literature, by studying structures formed by modular panels suitably assembled to form an origami pattern. The origami tensegrity façade is activated by stretching or releasing selected cables. Its energy-harvesting ability arises from the action of piezoelectric effects under the opening/closure motion of the origami panels, and wind-induced fluctuations. The dynamic response of the origami panels is simulated through a fully tensegrity model, with the aim of estimating their energy harvesting ability. The given results show that the overall tensegrity façade can daily produce a quantity of electric energy equivalent to the electric power produced by more than 200 squared meters of photovoltaic panels, and about 90 squared meters of rooftop wind turbines.*

1 INTRODUCTION

An energy-efficiency building (EEB) ensures well-being indoor conditions with the least consumption of energy from fossil and non-renewable sources [1]. Design of new constructions to reach performances of so-called nearly zero-energy buildings (nZEB) is introduced by the 2010 European Union Directive for the optimization of the energy performance of buildings [2], which enforces the EU states to provide the minimum requirements for the energy performance of buildings and constructive elements. Indeed, buildings are responsible for approximately 40% of EU energy consumption, so that the challenge for the near future is to drastically reduce energy dependency on fossil sources, while maintaining current living standards. In this direction, the building envelope is among the most important components to take into consideration in design of a EEB [3, 4], since it can significantly help in reducing energy losses. For instance, the building envelope may be exploited to increase energy efficiency in the summer by controlling the incident solar radiation through dynamic shading systems. In recent studies, it has been proposed to exploit the deployment ability of tensegrity structures to design dynamic envelopes [5, 6]. Tensegrity systems are composed of bars, generally under compression, assembled inside a net of strings undergoing tensile stresses, only [7]. Furthermore, it is possible to take advantages from vibratory motion of such systems under environmental actions to harvest energy. The present paper is devoted to a tensegrity-like module merging the function of sunscreen to some harvesting ability.

2 THE LAYOUT OF THE TENSEGRITY SUNSCREEN MODEL

The present contribution briefly details about an origami module based on tensegrity architecture equipped with piezoelectric strings. The module is designed to be mounted in front of or to cover building façades and pursue the two-fold objective to serve both as screen and mechanical energy harvester and enriches a unit introduced in [5] and further studied in [6, 8, 9] named as TABS, acronym of *tensegrity Al Bahar screen*, because of its shape resembling that of shading systems designed by Aedas architects to protect the external façades of the Al Bahar towers, in Abu Dhabi [10, 11]. While Al Bahar screen are piston actuated, motion of TABS depends on its tensegrity architecture. The enriched module, referred as WTABS [12], where 'W' stands for *wind*, introduces as a novelty with respect TABS the addition of six D-bar systems. The basic module of the WTABS system is shown in Fig.1, both through exploded and assembled views. With reference to Fig.1, starting from the top (which indeed does mean from external, i.e. away from the building), WTABS is composed by a macro-triangle, *origami* screen module, subdivided into six micro-triangles made of PTFE (glass fiber), able to generate a rigid motion in space, infilling a tensegrity system formed by 12 bars and 3 external strings. Below, there is a complex made of six D-bar, two elastic restraints (linear springs with stiffness $K = 67$ kN m^{-1}) and a linear actuator (model Rolaram®R2501190 [13]). While three D-bars, the springs and the actuator have axes which are and, during the morphing process, stay in a plane parallel to the rear building, the remaining three D-bars are mounted inclined. The actuator Rolaram®R2501190 (294 kN dynamic loading, 3500 mm maximum stroke [13]) stretches and relaxes cables, thus activating the folding/unfolding mechanism of the system. Bars and strings composing the module are respectively made with 6082-T5 Aluminum profiles and wire ropes composed of a nylon core string with 8.9 mm diameter, wrapped by piezoelectric cables [14].

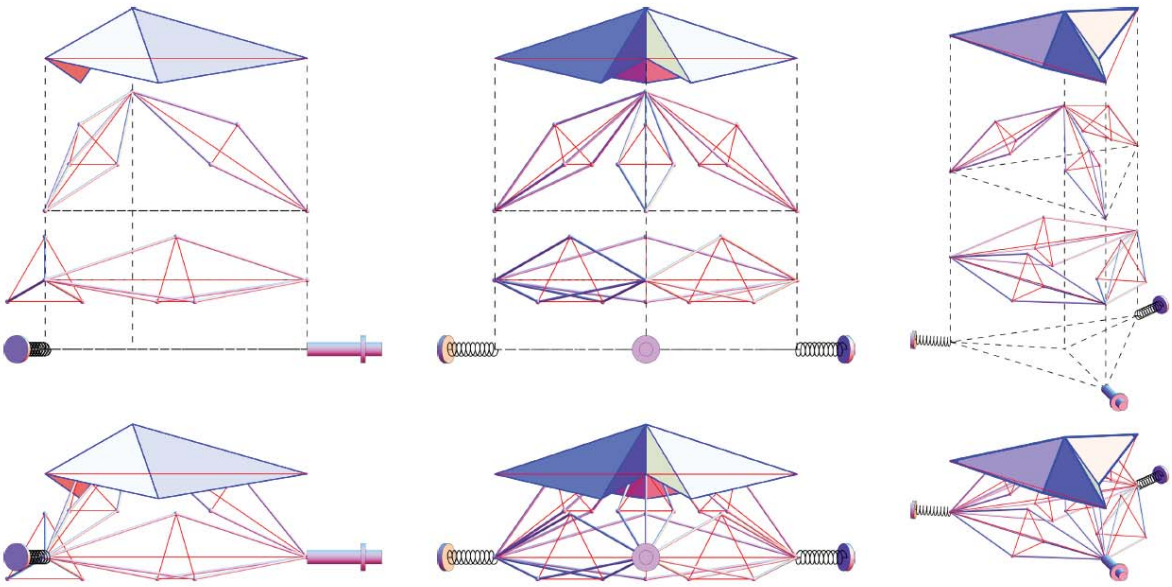

(a) (b) (c)

Figure 1: Three exploded (top panels) and assembled (bottom panels) views of TABS: (a) side view, parallel to the axis of actuator; (b) side view, in front of the actuator; (c) axonometric view. Exploded views allow to recognize the main components of TABS. From top: screen; D-bars inclined with respect to the rear building wall; D-bars parallel to the rear building wall; elastic restraints and actuator.

3 WTABS MOTION EQUATIONS AND LOADS

This section introduce the WTABS equations of motion, in matrix form, and reports about the evaluation of wind pressure to adopt in numerical simulations.

3.1 Matrix form of equation of motion

The WTABS module is a tensegrity network made up of n_n nodes, modeled as frictionless joints, n_b bars, and n_s elastic strings. The generic node i, with $i \in [1, \dots, n_n]$ is located by the vector $\mathbf{n}_i \in \mathbb{R}^3$ and is loaded by the external force $\mathbf{w}_i$. Hence the nodal matrix $\mathbf{N} \in \mathbb{R}^{3\times n_n}$ and load matrix $\mathbf{W} \in \mathbb{R}^{3\times n_n}$ can be written as

$$\mathbf{N} = \begin{bmatrix} \mathbf{n}_1 & \mathbf{n}_2 & \cdots & \mathbf{n}_i & \cdots & \mathbf{n}_{n_n} \end{bmatrix}, \quad \mathbf{W} = \begin{bmatrix} \mathbf{w}_1 & \mathbf{w}_2 & \cdots & \mathbf{w}_i & \cdots & \mathbf{w}_{n_n} \end{bmatrix}. \tag{1}$$

The vectors representing i^{th} bar and string are $\mathbf{b}_i \in \mathbb{R}^3$ and $\mathbf{s}_i \in \mathbb{R}^3$, respectively, and can be stacked in matrices $\mathbf{B} \in \mathbb{R}^{3\times n_b}$ and $\mathbf{S} \in \mathbb{R}^{3\times n_s}$, as

$$\mathbf{B} = \begin{bmatrix} \mathbf{b}_1 & \mathbf{b}_2 & \cdots & \mathbf{b}_i & \cdots & \mathbf{b}_{n_b} \end{bmatrix}, \quad \mathbf{S} = \begin{bmatrix} \mathbf{s}_1 & \mathbf{s}_2 & \cdots & \mathbf{s}_i & \cdots & \mathbf{s}_{n_s} \end{bmatrix}. \tag{2}$$

By introducing the connectivity matrices of bars $\mathbf{C_B} \in \mathbb{R}^{n_b\times n_n}$ and strings $\mathbf{C_S} \in \mathbb{R}^{n_s\times n_n}$, the matrices given by Eqn.(2) are written as

$$\mathbf{B} = \mathbf{N}\mathbf{C}_\mathbf{B}^\mathbf{T}, \quad \mathbf{S} = \mathbf{N}\mathbf{C}_\mathbf{S}^\mathbf{T}. \tag{3}$$

The generic $(i, j)^{\text{th}}$ entry of $\mathbf{C_B}$ (or of $\mathbf{C_S}$) takes value -1 if vector $\mathbf{b}_i$ (or $\mathbf{s}_i$) is directed away from node j^{th}, 1 if vector $\mathbf{b}_i$ (or $\mathbf{s}_i$) is directed toward node j and 0 if vector $\mathbf{b}_i$ (or $\mathbf{s}_i$) does not touch node j. On introducing the class number m of a tensegrity network, we may state that a tensegrity is of class m if the maximum number of the compressive elements concurring in

each node is equal to m [7, 15, 16]. In this case, the tensegrity sunscreen module that we are considering is a tensegrity of class 6.

By introducing the matrices $\mathbf{M} \in \mathbb{R}^{n_n \times n_n}$ and $\mathbf{K} \in \mathbb{R}^{n_n \times n_n}$, respectively defined as

$$\mathbf{M} = \frac{1}{12} \mathbf{C_B}^T \hat{\boldsymbol{m}} \mathbf{C_B} + \mathbf{C_R}^T \hat{\boldsymbol{m}} \mathbf{C_R} \,, \tag{4}$$

$$\mathbf{K} = \mathbf{C_S}^T \hat{\boldsymbol{\gamma}} \mathbf{C_S} - \mathbf{C_B}^T \hat{\boldsymbol{\lambda}} \mathbf{C_B} \,, \tag{5}$$

we can write the equations of motion (of a class 1 tensegrity system) as [17]

$$\ddot{\mathbf{N}}\mathbf{M} + \mathbf{N}\mathbf{K} = \mathbf{W} \,, \tag{6}$$

where $\mathbf{N}$ has been already given by the first of Eqns.(1) and $\ddot{\mathbf{N}}$ stands for its second derivative with respect to time.

Similarly to matrices $\mathbf{C_B}$ and $\mathbf{C_S}$, $\mathbf{C_R} \in \mathbb{R}^{n_b \times n_n}$ in Eqn.(4) is a connectivity matrix. Its i^{th} row corresponds to the bar $\mathbf{b}_i$ and its $(i,j)^{\text{th}}$ entry takes value 1/2 if vector $\mathbf{b}_i$ touches node j, or 0 otherwise [18]. Furthermore, $\hat{\boldsymbol{m}} \in \mathbb{R}^{n_b \times n_b}$, and $\hat{\boldsymbol{\gamma}} \in \mathbb{R}^{n_s \times n_s}$ in Eqns.(4)-(5) are diagonal matrices, whose $(i,i)^{\text{th}}$ entries are, respectively, masses m_i, $i \in [1, \ldots, n_b]$ and force densities along strings γ_i, $i \in [1, \ldots, n_s]$ given by

$$\gamma_i = \begin{cases} \max\left[0, \dfrac{E_{sj} A_{sj}}{L_j}\left(1 - \dfrac{L_i}{s_i}\right) + c_i \dfrac{\mathbf{s}_k^T \dot{\mathbf{s}}}{s_i^2}\right] \,, & \text{if } s_i \geq L_i \,, \\ 0 \,, & \text{otherwise,} \end{cases} \tag{7}$$

being E_{si} the Young's modulus of the material, A_{si} the cross-sectional area and L_j the rest length of the string, c_i the damping coefficient and $s_j = \|\mathbf{s}_j\|$. Finally $\hat{\boldsymbol{\lambda}} \in \mathbb{R}^{n_b \times n_b}$ denotes the diagonal matrix of force densities in bars and is given by

$$-\hat{\boldsymbol{\lambda}} = \frac{1}{12} \left\lfloor \dot{\mathbf{B}}^{\mathbf{T}} \dot{\mathbf{B}} \right\rfloor \hat{\boldsymbol{m}} \hat{\boldsymbol{\ell}}^{-2} + \frac{1}{2} \left\lfloor \mathbf{B}^T \left(\mathbf{W} - \mathbf{S} \hat{\boldsymbol{\gamma}} \mathbf{C_S}\right) \mathbf{C_B^T} \right\rfloor \hat{\boldsymbol{\ell}}^{-2} \,, \tag{8}$$

where $\hat{\boldsymbol{\ell}}^{-2} \in \mathbb{R}^{n_b \times n_b}$ is a diagonal matrix of terms $\ell_k^{-2} = \|\mathbf{b}_k\|^{-2}$ and $\lfloor \mathbf{A} \rfloor$ is a matrix keeping the diagonal terms of the square matrix $\mathbf{A}$, while all the off-diagonal entries are set to zero.

3.2 Modeling of the wind forces

We model the action of wind on WTABS on assuming the wind speed as depending on time and only one space variable, the height (took along the axis y in a three dimensional Cartesian frame), and is given by

$$v(y,t) = v_m(y) + v'(y,t) \,, \tag{9}$$

where v_m is averaged over a time interval of 10 min and v' accounts for high frequency fluctuations. The latter is suitably represented as a single stationary Gaussian random process with zero mean described by the spectral density [19]

$$S_L(y,n) = \frac{6.8\, f_L(y,n)}{\left(1 + 10.2\, f_L(y,n)\right)^{5/3}} \,, \tag{10}$$

where $f_L(y,n)$ is a dimensionless frequency

$$f_L(y,n) = \frac{n\, L(y)}{v_m(y)} \,, \tag{11}$$

$L(y)$ being the turbulence scale, and n the natural frequency. By choosing a frequency step $\Delta n = 0.05$ Hz, and a set of $N = 100$ frequencies $n_k = (k - 1/2)\Delta n$, we obtain [20]

$$v'(y,t) = \sum_{k=1}^{N} \sqrt{2S_L(y,n)\Delta n}\cos\left(2\pi n_k t + \varphi_k\right), \tag{12}$$

φ_k denoting randomly generated phases (in radians) over the angle interval spanning from 0 up to 2π.

Finally, we cast the peak value of the wind kinetic pressure, expressed in Pa, as

$$q(y,t) = \frac{1}{2}\rho\left(v_m(y) + v'(y,t)\right)^2, \tag{13}$$

$\rho = 1.25$ kg m^{-3} being the density of air.

The effect of wind pressure on nodes of WTABS is then computed as follows.

On introducing two vectors $\mathbf{a}_p$ and $\mathbf{b}_p$ lying along the edges of the generic micro-triangle on WTABS, the surface area A_p of such an element and its unit normal are given by

$$A_p = \frac{1}{2}||\mathbf{a}_p \times \mathbf{b}_p||, \quad \mathbf{n}_p = \frac{\mathbf{a}_p \times \mathbf{b}_p}{||\mathbf{a}_p \times \mathbf{b}_p||}. \tag{14}$$

The wind force acting over the panel p, along its normal vector, is computed through

$$\boldsymbol{\omega}_p = q\, A_p(\boldsymbol{n}_p \otimes \boldsymbol{n}_p)\mathbf{k}, \tag{15}$$

$\mathbf{k}$ and $\otimes$ denoting the unit vector along the axis z, towards the building, and the tensor product symbol, respectively. Finally, the wind force acting on the generic node i is

$$\mathbf{w}_i = \frac{1}{3}\sum_{p=1}^{n_i} \boldsymbol{\omega}_p, \tag{16}$$

n_i being the number of panels attached to node i.

4 NUMERICAL APPLICATIONS

The present section is devoted to the dynamic analyses of the WTABS system undergoing the wind forces and actuation motion. The numerical integration of Eqn.(6) is performed applying fourth order Runge-Kutta theory with a time step of 0.025 s.

4.1 Actuation motion

The motion of WTABS is driven by the linear actuator Rolaram®R2501190 [6, 13]. We consider a simulation in which the screen is deployed in 40 s, starting from the folded configuration. Then, the force impressed on the node is held constant for 40 s more. Figure 2 graphically illustrates the simulation. In particular, it is shown how the position of the central point of the module changes over time during the actuation motion. Four top views of deformed configurations, from folded to deployed state, are reported.

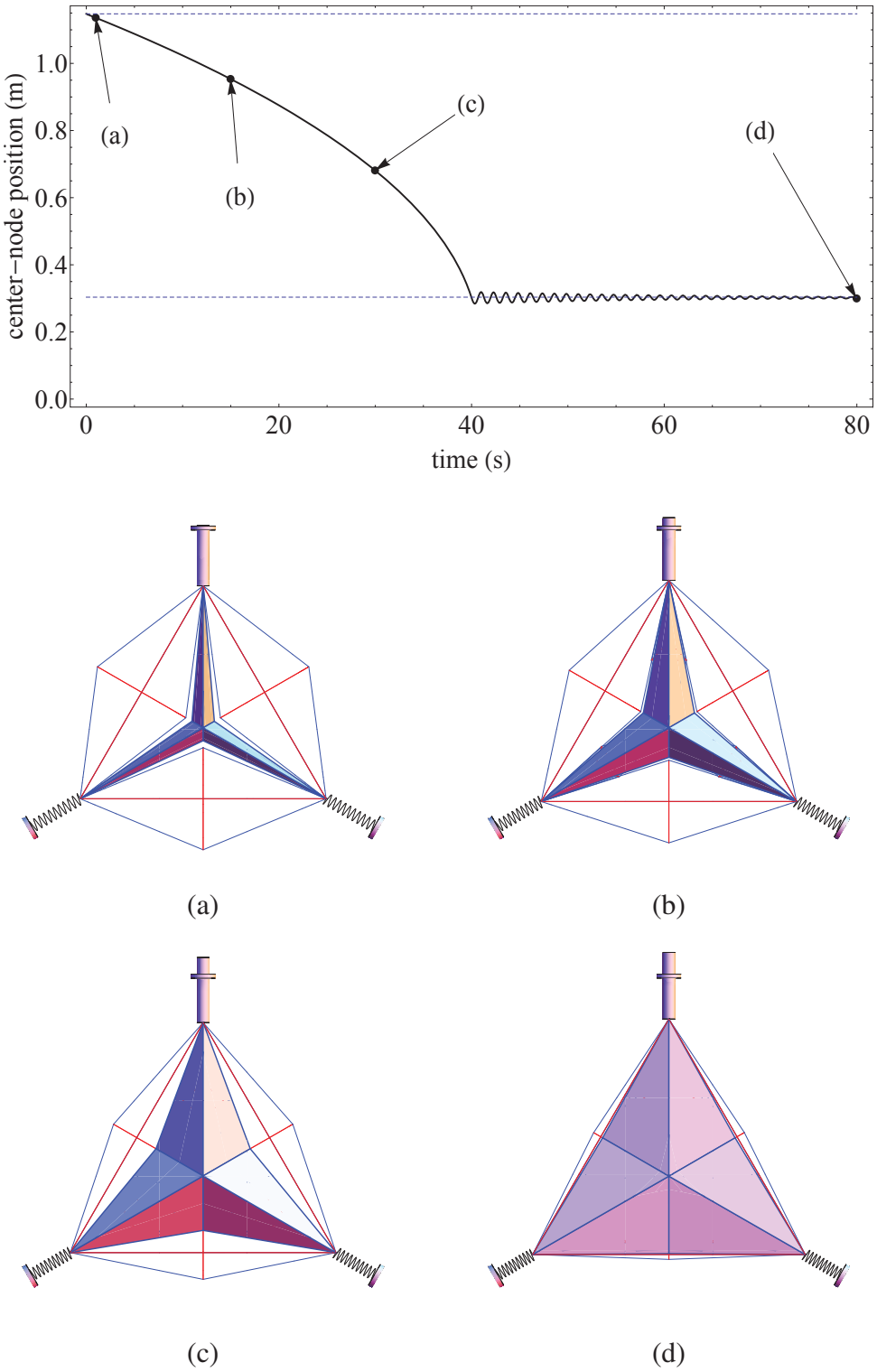

Figure 2: Deployment of WTABS driven by the actuator. Position of center node (top panel) and four top views of selected configurations, namely after 1 (a), 15 (b), 30 (c), and 80 (d) s from actuation start.

4.2 Fluctuations due to wind

The simulate wind pressure we consider environmental characteristics of the Al Bahar Towers and the height of the towers. By considering ??$y^* = 120$ m in a coastal area exposed to wind, we get the turbulence scale value $L(y^*) = 40.1589$ m [19]. As average speed we set $v_m(y^*) = 73.4$ m s^{-1}, which produces a wind pressure of 3.5 kPa, that is the value considered for the real scale prototypes of the towers [11]. Relevant information and results of the simulation are graphically shown in Figure 3.

5 MECHANICAL ENERGY HARVESTING

The WTABS module is equipped with PVDF-coated piezoelectric cables (see [12] for details on the cable structure) that, by virtue of the electromechanical effect, allows energy conversion described by

$$W_E = k_{33}^2 W_M \tag{17}$$

where W_E and W_M stand for electric and mechanical energy and k_{33} is the electromechanical coupling coefficient along the longitudinal axis of the piezoelectric cable. By using the strain history of the cables during the simulations briefly reported in Sect. 4, mechanical energy can be computed as

$$W_M = \frac{1}{2T} \sum_{s=1}^{n_s} \left(E_f A_f L_{is} \int_0^T \varepsilon_s(t)^2 \mathrm{d}t \right) , \tag{18}$$

with reference to the two different implementation hypotheses we obtain [12]

$$W_E^{\text{actuation}} = 321.3 \text{ kJ} , \qquad W_E^{\text{wind}} = 5.749 \times 10^{-4} \text{ kJ} . \tag{19}$$

In [12], it has been observed that, although the amount of energy harvested by a single WTABS is low, the total energy that can be daily generated by a WTABS modules in reference to the size of the towers (composed of over a thousand shading systems) m^2 [10, 11], is considerable and can be employed to power microelectronic devices, WiFi repeaters, cellular phones, and LED lighting systems [21].

6 CONCLUDING REMARKS

This work has dealt with the generalization of the TABS shading system proposed in [6] from the energetic point of view, by integrating such a system with additional D-bar modules equipped with piezoelectric cables for energy harvesting (WTABS design [12]). The dynamics of the WTABS module has been numerically simulated, on accounting for the opening and closure operations of the screens and the dynamic action of wind forces. The obtained results have allowed us to calculate the amount of mechanical energy harvested by the shading system under such loading conditions. Overall, the electric power that can be daily generated by the WTABS modules is equivalent to the power produced by approximatively 200 photovoltaic panels, and nearly 90 microeolic wind turbines with one squared meter surface area. We address the generalization and the experimental identification [22] of the WTABS concept to different façade geometries and a variety of energy harvesting materials to future work.

Acknowledgements

R.M., N.S., and F.F. acknowledge financial support from MIUR under the PRIN 2017 National Grant ‘Multiscale Innovative Materials and Structures’(grant number 2017J4EAYB).

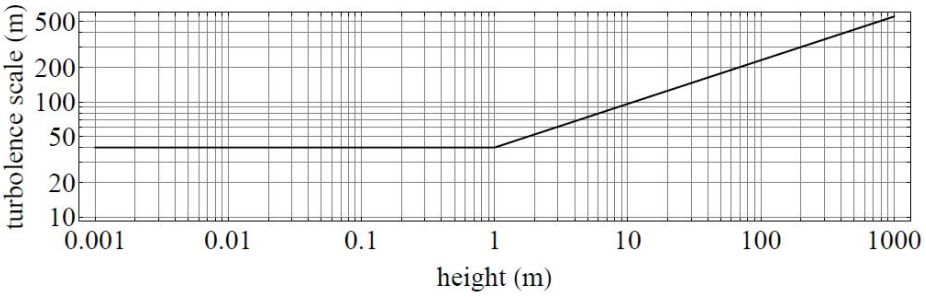

(a)

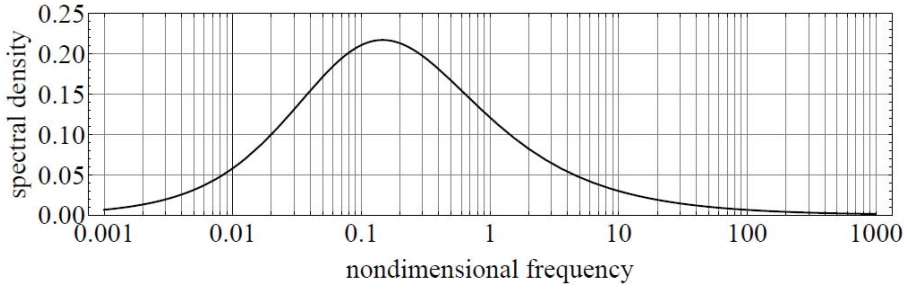

(b)

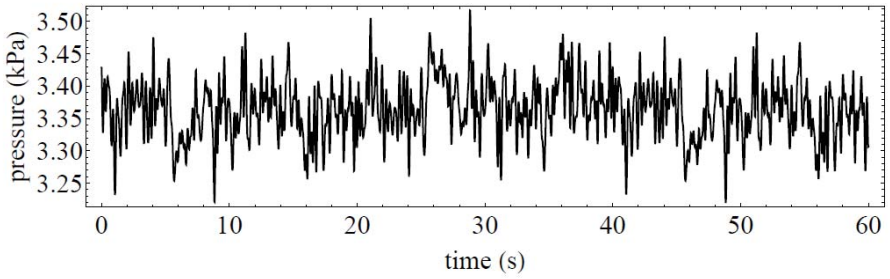

(c)

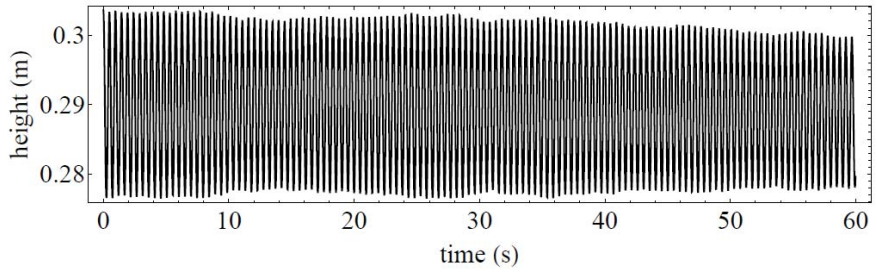

(d)

Figure 3: Turbulence scale (a), spectral density (b), wind pressure (c) and fluctuations of height of the central node of WTABS (d).

REFERENCES

[1] T. Herzog, I. Flagge, V. Herzog-Loibl, A. Meseure. *Thomas Herzog: Architektur + Technologie*. Prestel, 2001.

[2] Directive 2010/31/EU of the European Parliament and of the Council of 19 May 2010 on the energy performance of buildings.

[3] L. Pérez-Lombard, J. Ortiz, and C. Pout. A review on buildings energy consumption information. *Energy and Buildings*, 40(3):394–398, 2008.

[4] European Commission, HORIZON 2020 Work Programme 2014-2015, PART 5.ii, p. 98, 2014.

[5] F. Fraternali, E. De Chiara, and R.E. Skelton. On the use of tensegrity structures for kinetic solar facades of smart buildings. *Smart Materials and Structures*, 24(10), 2015.

[6] E. Babilio, R. Miranda, and F. Fraternali. On the kinematics and actuation of dynamic sunscreens with tensegrity architecture. *Frontiers in Materials*, 6, 2019.

[7] R.E. Skelton and M. de Oliveira. *Tensegrity systems*. Springer US, 2010.

[8] E. Babilio, R. Miranda, G. Carpentieri, and F. Fraternali. Computational modeling of the dynamics of active sunscreens with tensegrity architecture. COMPDYN 2019: 7th International Conference on Computational Methods in Structural Dynamics and Earthquake Engineering. Crete, Greece, 24–26 June 2019. Volume 2, pages 2159–2166. National Technical University of Athens, 2019.

[9] R. Miranda, A. Amendola, I. Mascolo, F. Fraternali, and E. Babilio. Design and control of adaptive tensegrity sunscreens. SEMC 2019: 7th International Conference on Structural Engineering, Mechanics and Computation. Cape Town, South Africa, 2–4 September 2019. Pages 1027–1032. CRC Press/Balkema, 2019.

[10] A. Armstrong, G. Buffoni, D. Eames, R. James, L. Lang, J. Lyle, and K. Xuereb. The al bahar towers: multidisciplinary design for Middle East high-rise. *The Arup Journal*, 2:60–73, 2013.

[11] A. Karanouh and E. Kerber. Innovations in dynamic architecture. *Journal of Façade Design and Engineering*, 3(2):185–221, 2015.

[12] R. Miranda, E. Babilio, N. Singh, , F. Santos, and F. Fraternali. Mechanics of smart origami sunscreens with energy harvesting ability. *Mechanics Research Communications*, 2020. doi:10.1016/j.mechrescom.2020.103503

[13] Power jacks, rolaram, electric linear actuators. Available at: `www.powerjacks.com/perch/resources/brochure/pjlab-rolaram-en-01-1b.pdf`. Date accessed: March 4, 2020.

[14] M.N. Silleto, S.-J. Yoon, and K. Arakawa. Piezoelectric cable macro-fiber composites for use in energy harvesting. *International Journal of Energy Research*, 39(1):120–127, 2015.

[15] K. Nagase and R.E. Skelton. Network and vector forms of tensegrity system dynamics. *Mechanics Research Communications*, 59:14–25, 2014.

[16] C. Sultan, M. Corless, and R.E. Skelton. Linear dynamics of tensegrity structures. *Engineering Structures*, 24(6):671–685, 2002.

[17] R.E. Skelton. Dynamics and control of tensegrity systems. In *IUTAM Symposium on Vibration Control of Nonlinear Mechanisms and Structures*, pages 309–318. Springer Netherlands, 2005.

[18] G. Carpentieri and R.E Skelton. On the dynamics of tensegrity bridges. *Journal of Aerospace Engineering and Mechanics*, 1(1):48–62, 2017.

[19] EN 1991-1-4 (2005) (English): Eurocode 1: Actions on structures, Parts 1-4: General actions. Wind actions. [Authority: The European Union Per Regulation 305/2011, Directive 98/34/2011, Directive 98/34/EC, Directive 2004/18/EC].

[20] F. Amarante dos Santos, P.F. Gonçalves, C. Cismaşiu, and M. Gamboa-Marrufo. Smart glass facade subjected to wind loadings. *Proceedings of the Institution of Civil Engineers - Structures and Buildings*, 167(12):743–752, 2014.

[21] G. De Pasquale. 11 - Energy harvesters for powering wireless systems*. In Deepak Uttamchandani, editor, *Handbook of Mems for Wireless and Mobile Applications*, pages 345–400. Woodhead Publishing, 2013.

[22] F. Fabbrocino, I. Farina, and M. Modano. Loading noise effects on the system identification of composite structures by dynamic tests with vibrodyne. *Composites Part B-Engineering*, 115:376-383, 2017.

EURODYN 2020
XI International Conference on Structural Dynamics
M. Papadrakakis, M. Fragiadakis, C. Papadimitriou (eds.)
Athens, Greece, 23–26 November 2020

TALL OFFSHORE STEEL WIND TURBINE TOWERS UNDER WIND, CURRENT AND WAVE LOADING: AN EXPERIMENTAL AND NUMERICAL STUDY

Yu Hu[1,2], Jian Yang[1,2], Charalampos Baniotopoulos[2], Xinger Wang[1], Xiaowei Deng[1]

[1]School of Naval Architecture, Ocean and Civil Engineering, Shanghai Jiao Tong University, Shanghai 200240, China

[2]School of Civil Engineering, University of Birmingham, Edgbaston, Birmingham, B15 2TT, U.K.

e-mail: huyu1012@hotmail.com e-mail: j.yang.1@sjtu.edu.cn

e-mail: c.baniotopoulos@bham.ac.uk e-mail: dxw913@sjtu.edu.cn

Keywords: Wind turbine tower, Offshore Wind Turbines, Monopiles, Dynamic analysis, Current-wave-wind interaction

Abstract. *In the present paper the dynamic response of tall offshore monopile steel wind turbine towers under wind, wave and current during the erection stage is studied. In particular, in the present paper the effect of current-wave-wind interaction as dynamic loading on the dynamic response of offshore wind turbine towers is for first time studied experimentally. A statistical analysis of the dynamic displacements of the model is conducted to study the effect of various loading states on the respective dynamic response. As outcome of the present study it was confirmed that the current field strongly affects the dynamic response of offshore monopoles and in particular, more significantly than the wave field. In the final part, an advanced finite element model is proposed for the efficient study of the structural response of the tower model during erection under current, wave and wind interaction.*

1 INTRODUCTION

In marine environment there are more complicated environmental actions on offshore wind turbine towers (e.g. wind, wave and current loadings) than on the onshore ones. In engineering practice, the wind turbine towers as monopiles need to be constructed during the erection stage in marine environments where current and waves interact. Several researchers have studied the structural characteristics of wind turbine towers during the erection stage by using numerical simulation methods. Tziavos *et al*. [1, 2] studied current practice in terms of engineering methods used for the determination of loads acting on monopile offshore towers and the numerical methods used for the investigation of its structural behaviour. With respect to hydrodynamic loads on monopile wind turbines, the popular linear wave theory along with the Morison equation can be used to model normal sea states, whereas higher-order wave models are necessary to investigate severe events such as wave breaking. Offshore monopile wind turbine towers during the construction stage in marine environment have to resist wind, waves and currents. In this paper the effect of the current action on the dynamic behavior of offshore monopile wind turbine towers is first considered experimentally and then, an appropriate numerical model to study the respective structural dynamic response of the tower is proposed.

2 EXPERIMENTAL SETUP

2.1 Test facility

The experiment of a monopile subjected to wind, waves and current was performed at the Wind Tunnel and Circulating Water Channel Lab, Shanghai Jiao Tong University in China. The Lab consists of two large-scale facilities, the multifunctional wind tunnel and the circulating water channel with the capability to create an environment of currents, waves and sea wind. In particular, the channel is able to simulate various marine environments including current, waves, sea wind and stratified flow. For the specific experimental setup, wind field and current field at a uniform velocity along the tower height and periodic regular wave was provided.

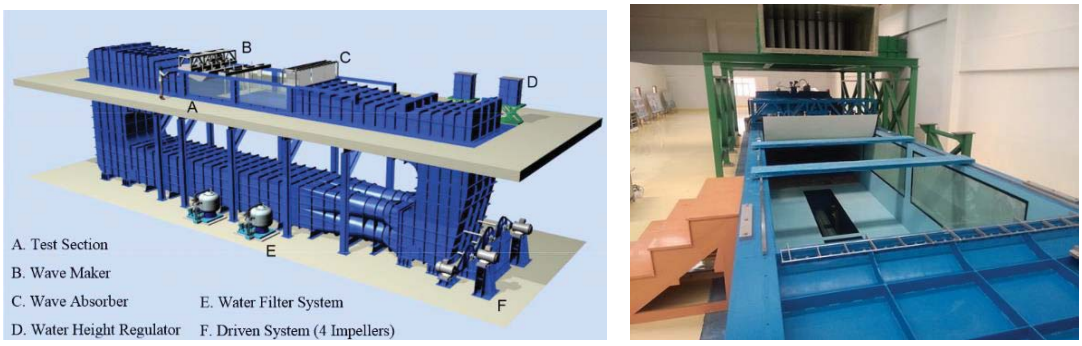

a. A full image b. Actual test section

Figure 1. The facilities at the Wind Tunnel and Circulating Water Channel Lab, SJTU.

2.2 Description of the tower model

The prototype monopile structure is a 75m height offshore wind turbine tower during the erection stage. Figure 2 depictes that experimental measurement setup and the dimensions of the tower model. The experimental model is installed in the Wind Tunnel and Circulating Water Tank as shown in Figure 2. The prototype is located at a site with a water depth of 23m, its external radius on the base is 7m and that on the top is 3.75m. The monopile is fixed in the

seabed, whilst the model was manufactured with a geometrical scaling of 1:75. The dimensions of the tower model are displayed in Figure 2b. The height of the scaled down tower is 1.3m, 1.0m height above the water surface level and 0.3m height under water depth respectively. The diameter of the tower model varies linearly along its height from 190mm at the bottom to 100mm at the top as shown in Figure 2b. The thickness of the tower model is 0.5mm and the tower is fixed by four Φ12 bolts. As is well-known in an actual wind tunnel or water tank test to balance Froude and Reynolds numbers is a hard task and to this end, the Froude laws of similitude had been used for the physical modelling of the properties of the tower model.

The monopile response was measured by using one accelerometer at 90cm height of point B on the leeside of the tower model in x-axis direction and one sensor head at the 80cm height of the point C in cross section direction in z-axis direction and the other one at the 90cm height of the point A in cross section direction to measure the velocity values in z-axis direction. All the transducers were connected with their corresponding data acquisition instruments. The wave gauge is employed to measure the wave elevation when applying wave loads in the Circulating Water Tank.

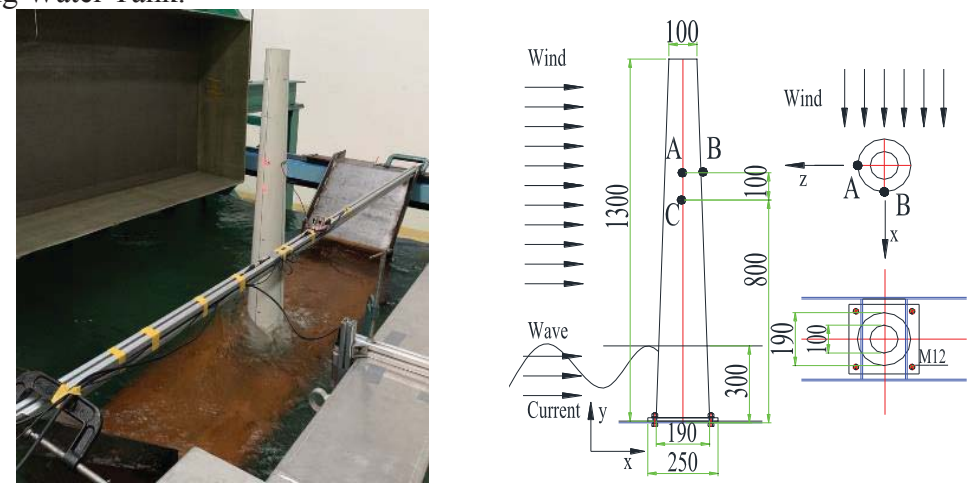

a. Actual experiment setup b. Dimensions of the tower model (in mm)

Figure 2. Experimental setup and dimension of tower model

2.3 Loading states

In the experiment various loading cases were considered to study the effect of wind, waves and current loadings on the dynamic response of offshore wind turbine towers. For the wind loading, the wind speed was gradually increased from 5m/s to 28m/s in the wind tunnel. For the current loading, its velocity with a stepwise increase was performed in the range of 0.3m/s to 2m/s. For wave loading, as wave elevation was ranged from 20mm to 50mm for wave periods from 0.5s to 1.25s in the water tank, the corresponding wave heights at the wave periods of 0.5s, 0.75s, 1s and 1.25s being respectively 44mm, 32mm, 25mm and 22mm. The wave shape was the most stable one when wave maker was initially launched, then the new wave was taken to break gradually due to the reflection of the previous wave in the water tank, and therefore, the experimental results should be tested in the beginning of the step of wave generation for the loading states that involve waves.

As the lower edge of the air outlet of the wind tunnel is 10cm higher than the still water level in the water tank, current field and wave field could not be affected individually by wind field when wind tunnel is running stably (Figure 2a). For wind-current, wind-wave and wave-current loading states, the three loading states can be performed by combining wind loading and current loading, wind loading and wave loading, wave and current loading. For the wind-

current-wave loading states, the wind field should be first flow in the velocity range of 7.5m/s to 20m/s until a stable state, then, current field is adjusted in the speed range of 0.3m/s to 0.8m/s up to its steady stage and finally wave field is provided in the periods of 0.5s, 0.75s and 1.0s.

3 EXPERIMENTAL RESULTS

Aiming to investigate the effect of various marine loadings on the dynamic characteristics of offshore wind turbine towers during construction, during the present experimental test the following loading states had been separated into four groups a) wind-wave; b) wind-current; c) wind-wave-current; d) wave-current.

3.1 Wind, wave and current

For the loading states of wind only, wind-wave, wind-current and wind-wave-current, the wind speed was gradually increased in the range of 5m/s to 28m/s. In each case, the velocity, acceleration and displacement at points A, B and C were respectively measured in the steady wind field. For the current only, its speed is set in a uniform speed at one loading state varying from 0.3m/s to 2m/s. For wave only, the still water level was 30cm. For each loading case, the period of wave maker is first determined at 0.4s, 0.5s, 0.75s, 1s and 1.25s, and then the wave height had been monitored by wave gauge. Figure 3 shows time histories of wave elevations and displacement responses when wave period is 0.75s and wave height is 28mm. According to Figure 3a, for wave height 28mm, the wave period is 1s. According to Figure 3b, it can be observed that as there are two peaks and one valley within each second, the time histories of displacement response exhibit periodicity and the respective periods are equal to the input period of the wave maker.

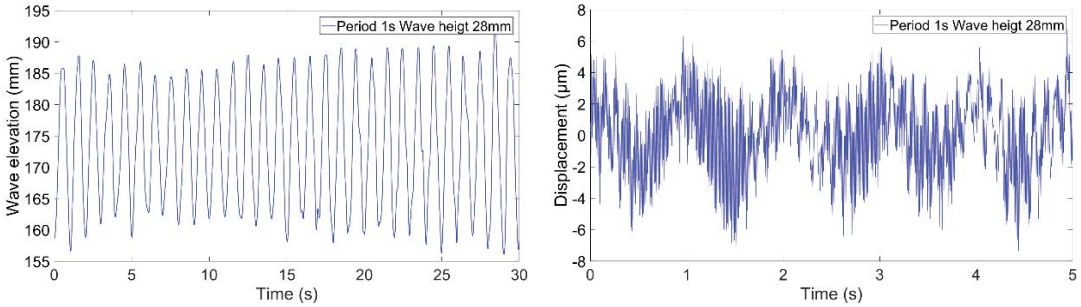

a. Time histories of wave elevations b. Time histories of displacement responses

Figure 3 Time histories of wave elevations and displacement response of the model under wave only at period of 1s and at wave height of 28mm

The displacement response of the tower model at point C under various loading states is depicted in Figure 4. According to Figure 4, there is regular dynamic response of the tower under wind speeds of 11m/s in the four loading states. Specifically, for the loading states of wind only, the regular dynamic response of the tower at point C exists only at wind speed 11m/s. For the loading of wind-wave and wind-current, the regular dynamic response of the tower under low current speeds and low wave periods respectively are depicted in Figures 4b and 5c, where the dynamic response of the tower becomes irregular gradually as soon as the current speed and the wave period increase. For the loading states of wind-wave-current, the regular dynamic response of the tower under the combination of low current speed and low wave period still occur, they however disappear as soon as current speed and wave period increase. For the loading states of wave only and current only, the dynamic responses of the tower were both irregular in the present experiment.

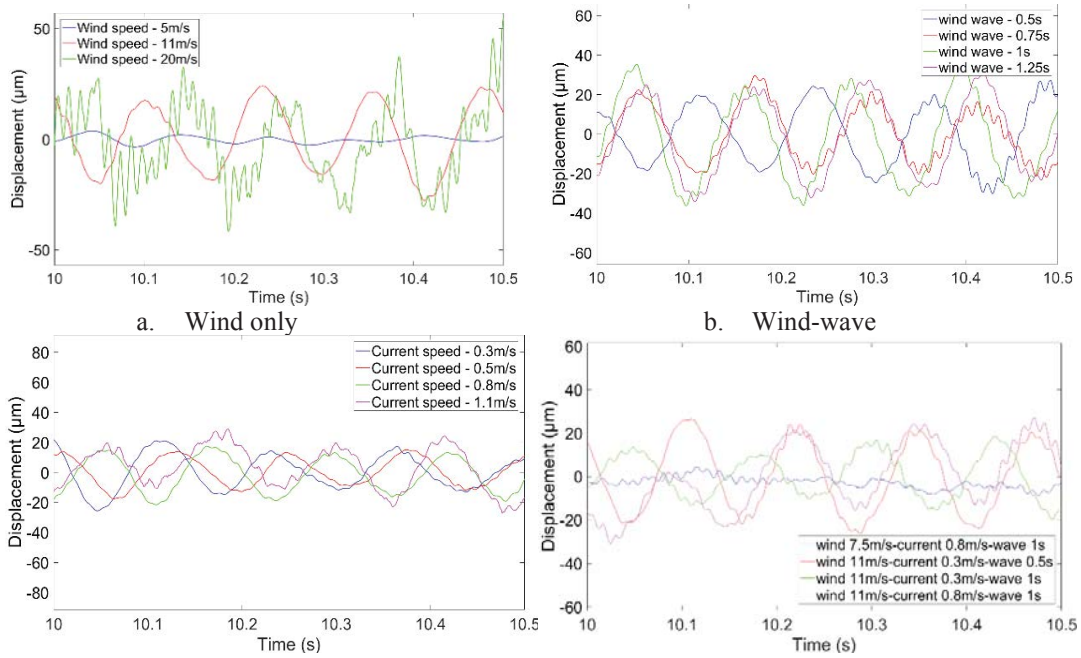

a. Wind only b. Wind-wave

c. Wind-current d. Wind-wave-current

Figure 4 Displacement response of the tower model at point C under various loading states

For the wind-wave loading cases, wind loading was chosen at wind speeds of 7.5m/s, 11m/s, 20m/s and 25m/s and the wave maker produced wave loadings at the periods of 0.5s, 0.75s, 1s and 1.25s with wave heights 44mm, 32mm, 28mm and 22mm respectively. Figure 5 shows the standard deviation of the displacement of the tower model at various wind speeds under wind only, wave only and wind-wave at various periods of 0.5s, 0.75s, 1s and 1.25s. According to Figure 5a, the standard deviation of the displacement of the tower model declines when wind speed increases from 0m/s to 7.5m/s, and the standard deviations of the displacement of the tower model are less than that of tower model under wave only. Then the standard deviation of displacement of tower model rises with wind speed increasing being greater than that of the tower model under wave only. Therefore, it is concluded that wave loading dominates the structural responses of tower model at a low wind speed loading state, whilst wind loading controls the structural responses of tower model at a high wind speed. Figure 5b provides the standard deviation of the displacement of the tower model under various loading states at wind speeds 7.5m/s and 20m/s and at periods 0.5s, 0.75s, 1s and 1.25s. Thus, for the 7.5m/s wind loading case, wave significantly affects the dynamic responses, whilst for the 20m/s wind loading case, wind predominantly controls the dynamic response of the monopile with the wave period varying. For the loading case of wind-current, a similar tendency can be observed where current only affects the dynamic response of the tower at low wind speed, whilst wind controls the dynamic response of the tower in the case that wind speed increases.

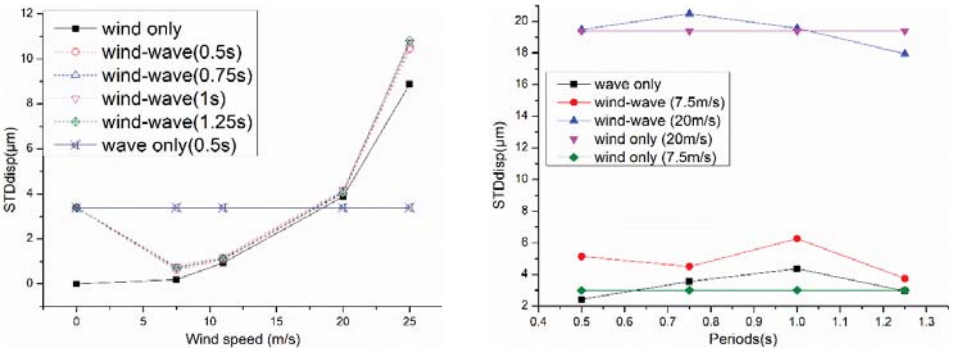

a. STD displacement versus wind speed b. STD displacement versus periods

Figure 5 Standard deviation of the model displacements under wind only, wave only and wind-wave

For the wind-wave-current loading state, wind loadings correspond to wind speeds of 7.5m/s, 11m/s and 20m/s, current loadings are set at current velocities of 0.3m/s, 0.5m/s and 0.8m/s, wave loadings are provided at wave periods of 0.5s, 0.75s and 1s. The wind field first runs at a stable state and then, current field is stabilized and at a final stage the wave field is made by using wave maker. Acceleration response of model under wind-wave-current and wave-current loading states at wind speed of 7.5m/s, 11m/s and 20m/s when current speed is 0.3m/s and wave period is 0.5s is depicted in Figure 6.

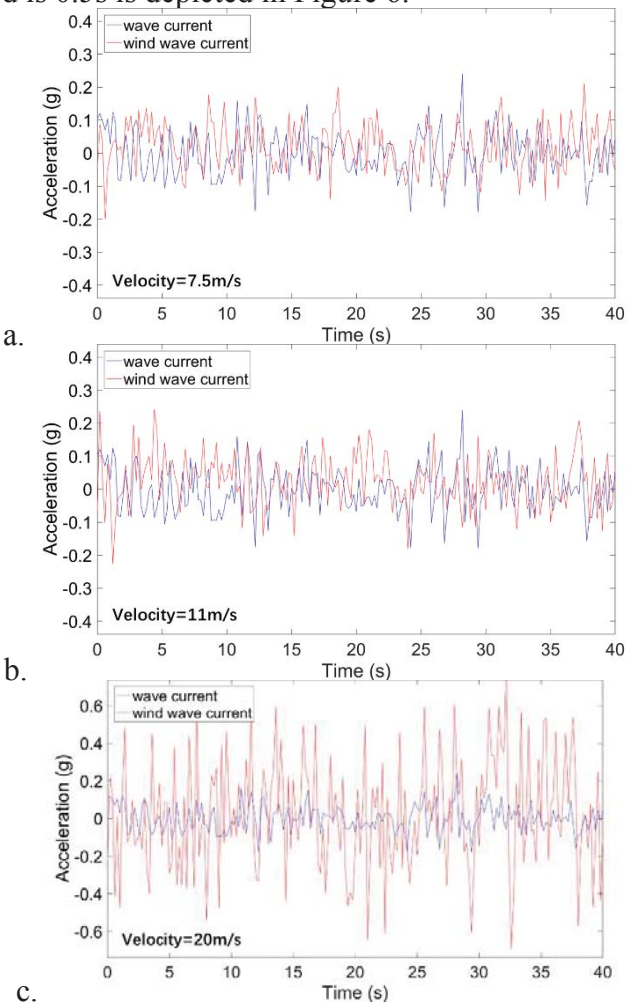

a.

b.

c.

Figure 6 Accelerations of the tower model under wind-wave-current and wave-current loading states

It was found that the combination of wave and current action only affects the dynamic response of the model in a low and medium wind speed; for a strong wind speed, wind still controls the dynamic responses of the tower.

3.2 Wave and current

With reference to the loading states of wave and current, loading states including wave only, current only and wave-current were considered to study the effect of wave and current on the dynamic response of the model. In this loading case, the current speed was 0.3m/s, 0.5m/s, 0.8m/s and 1.1m/s respectively and wave periods were set at 0.5s, 0.75s, 1s and 1.25s.

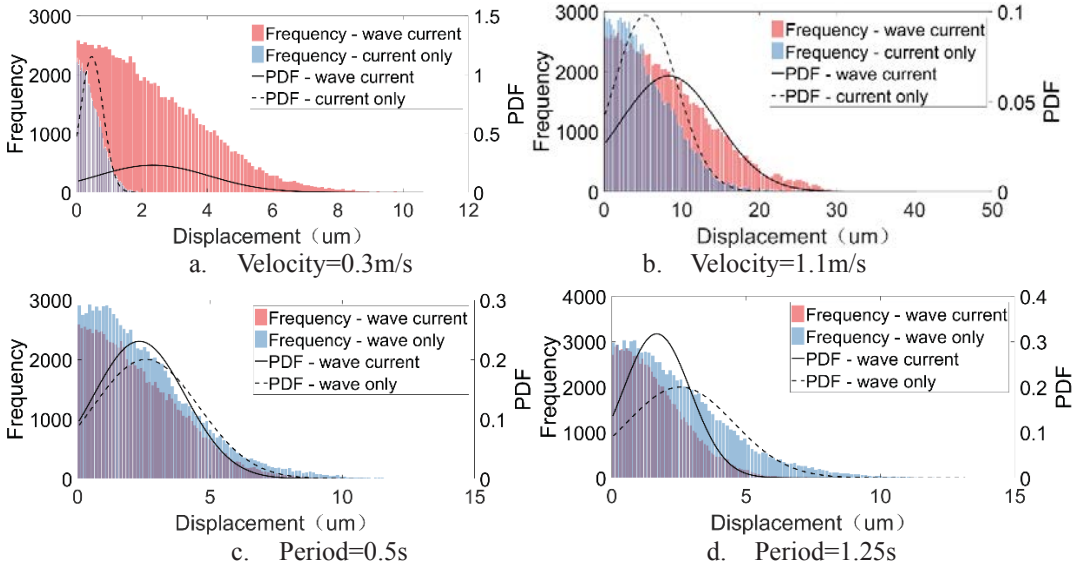

Figure 7 Probability characteristics of the displacements at point C under current speeds of 0.3m/s and 1.1m/s (wave period=0.5s) and wave periods of 0.5s and 1.25s (current speed=0.3m/s)

The probability characteristics of the displacements at point C under current speeds of 0.3m/s and 1.1m/s and wave period of 0.5s and 1.25s appear at Figure 7. The frequency in these figures is the number of any displacement value of the tower under various loading states. For the loading case at current speed of 0.3m/s, the probability function of displacement of the model under wave-current ranges in a wider displacement amplitude than that of the tower model under current only (shown in Figure 7a), which means that the wave dominates the structural response of the tower at this low current speed.

For the loading case at current speed of 1.1m/s, displacement amplitudes under wave-current and current only increase whilst probability functions move closer in the sense that current field principally controls the dynamic response of the monopile at current speed of 1.1m/s. According to Figures 7c and 7d, the value of displacements of the tower under wave only can always surpass that of the tower model under current-wave with the wave period increasing from 0.5s to 1.25s, the two PDFs only move slightly each other which indicate that wave period increase could not affect very significantly the dynamic response of the tower model under wave-current loading state.

4 NUMERICAL SIMULATION

4.1 Loadings

In marine environment the offshore monopile wind turbine towers during the erection stage are subjected to wind, current and wave loadings.

4.1.1 Wind and current loading

Wind loading can be applied to the tower wall as pressure around the tower cross section. The wind flow created at the wind tunnel is a uniform wind field at different wind speeds and the wind pressure on the tower model is related to the wind speed based on the Bernoulli equation as follows:

$$P_w = 0.5\rho_a v_a^2 \tag{1}$$

where P_w is the wind pressure, ρ_a is the air density (1.25kg/m^3) and v_a is the wind speed.

According to EN 1991-1- 4 [3], the external wind pressure corresponds to different profiles with reference to the circular cylinder. Reynolds number are respectively given by the equation:

$$R_e = vD/\nu \tag{2}$$

where R_e is the Reynolds number, v is the fluid speed, D is the diameter of the tower and ν is the kinematic viscosity of fluid.

With reference to the current loading, this is transferred into pressure according to the Bernoulli equation:

$$P_c = 0.5\rho_w v_c^2 \tag{3}$$

where P_c is the current pressure, ρ_w is the water density (1000kg/m^3) and v_c is the current speed.

4.2.2 Wave loading

For the wave loading, this is obtained by the Morrison's equation as the offshore monopile is a slender cylindrical structure fixed in the seabed. According to Morrison's equation [4],

$$dF = \rho_w \frac{\pi D^2}{4} dz C_M a + \frac{\rho_w}{2} C_D D dz |u| u \tag{4}$$

where wave moves along the x-direction as shown in Figure 2, a and u is the acceleration and the velocity of undisturbed wave in x-direction, respectively. C_M and C_D are respectively the mass and the drag coefficient for a smooth tubular section (respectively 2.0 and 1.2 in this experiment). For the situation of finite water depth, u and a can be obtained as the equations (5) and (6) [5]:

$$a = \omega^2 A \frac{coshk(y+h)}{sinhkh} \cos(\omega t - kx) \tag{5}$$

$$u = \omega A \frac{coshk(y+h)}{sinhkh} \sin(\omega t - kx) \tag{6}$$

$$\lambda = \frac{g}{2\pi} T^2 tanh \frac{2\pi}{\lambda} h \tag{7}$$

where $\omega=2\pi/T$, $k=2\pi/\lambda$, T is the period of the wave, λ is the wave length, A is the amplitude of the wave, t is the time, x is the wave motion direction, y is the vertical coordinate and its positive direction is upwards from water level to the tower top, h is the water depth in the water tank equal to 1.6m in this experiment and g is the gravitational acceleration.

4.2 Validation of the numerical model

The wind turbine tower model was created by the finite element software ABAQUS using the S4R shell element [6]. The tower was considered as fixed at its bottom and manufactured by Q235 steel. Its density and elastic modulus were respectively 7.85g/cm^3 and 206GPa and the Poisson's rate is 0.3. Wind, current and wave loading profiles of the offshore wind turbine tower are shown in Figure 8. In this model, as wind and current loadings are applied as uniform velocity on the slender cylindrical tower structure for each loading state, according to the equations (1, 3), the wind loading can be simplified in accordance to the inventory data [3, 7] and the current loading can be simplified as shown in Figure 8. In the tests the wind speed

was kept in the range of 7.5m/s to 20m/s, therefore, the Reynolds number of wind field varies from 0.5×10^5 to 1.5×10^5 being less than 2.0×10^5. The current speeds were varying from 0.3m/s to 2m/s in the Circulating Water Tank during the test. According to equation (2), the Reynolds numbers of current range from 0.3×10^5 to 2×10^5. Therefore, according to the inventory data [3, 4, 5], the distributions of wind and current load coefficients around the circumference can be divided into four parts. The angles of the wind pressure and current pressure around the circumference of the tower cross section were respectively decided to be 60°, 85°, 130° and 85° in this loading states as shown in Figure 8. The wind pressure had been simplified into uniform pressure along the tower height over the water level as wind field is applied as one constant velocity in a stepwise way whilst the current pressure was considered as uniform pressure along the tower height under the water level. For the wave loading, it had been considered as a periodic compressive loading applied on the half section of the tower wall under the water level as shown in Figure 8.

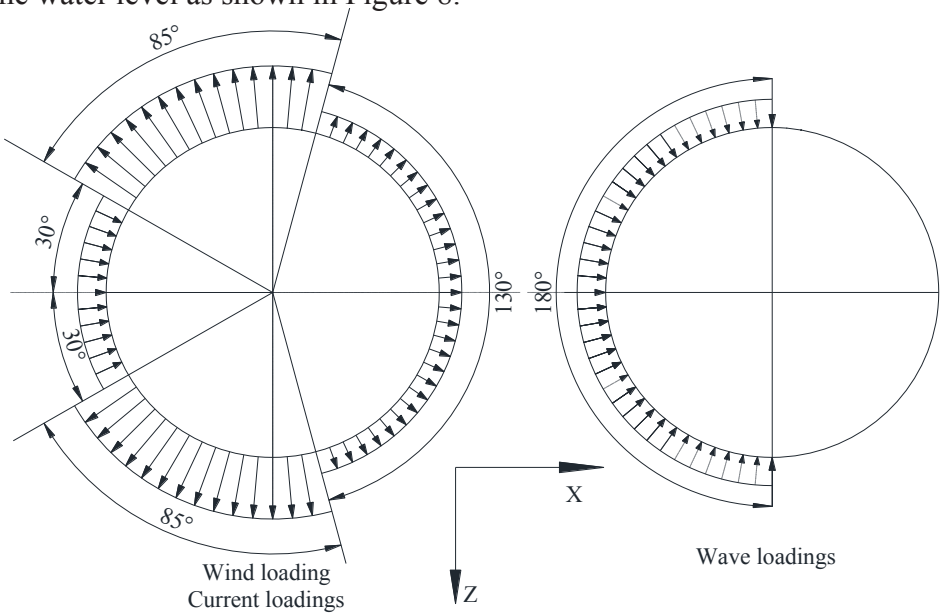

Figure 8 Wind, current and wave loading profile of offshore wind turbine tower

For the loading states of wind speed of 11m/s, current speed of 0.3m/s and wave periods of 0.5s and wave elevation of 44mm, the corresponding wind pressure, current pressure and wave force are calculated by the equations (1)-(7), and therefore, the displacement response at point C of the tower model under wind, current and wave loadings can be obtained from the numerical model. Figure 9 depicts the laboratory test and the numerical results with reference to the displacements at point C of the tower. It is noted that a good agreement between numerical and experimental results had been achieved.

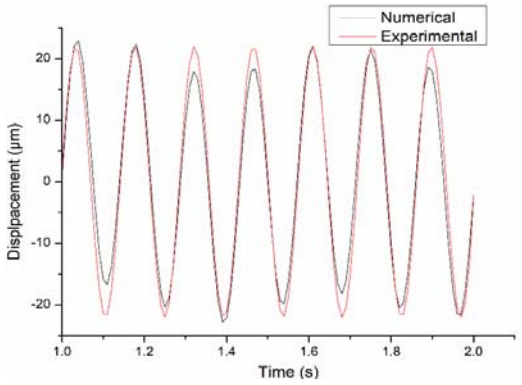

Figure 9 Comparison of time histories of displacement responses of the tower model at point C

5 CONCLUSIONS

In the present paper a Wind Tunnel and Circulating Water Channel was employed to study the dynamic response of offshore wind turbine tower during the erection stage in a marine environment. In this experiment, the loading states of wind-wave, wind-current, wave-current and wind-wave-current were applied to explore their effect on the dynamic response of the offshore tower model. To this end, the later with a geometrical scaling of 1:75 was manufactured and tested under wind, wave and current loadings. Three points A, B and C had been chosen to measure the velocity, displacement and acceleration respectively under the aforementioned selected loading cases. The numerical model of the monopile under wind, wave and current was validated by comparing its results with the experimental ones.

According to the laboratory test results, for the wave loading at low periods and current loading at low speeds, the dynamic response of the monopile under wind-wave, wind-current still occurs regularly, and the dynamic response of the tower is only slightly affected by the wave loading at high periods and current loading at high speeds under the wind speed of 11m/s. For the wind-wave-current loading case, the effect of combination of wave and current on the dynamic response of the tower is significant as displacements of the tower happen irregularly with the wave period and current speed increase. The loading states of wind-wave, wind-current, wind-wave-current and wind only control the dynamic response of the tower as soon as the wind speed increases. For the loading states of wave-current, the effect of the current loading is more significant than that of wave loading on the dynamic response of the tower. Therefore, current loading should not be ignored when the dynamic response of offshore towers in the marine environment is investigated.

6 ACKNOWLEDGEMENTS

The financial support of the present research activity by the European Union's Horizon 2020 Research and Innovation Programme under the Marie Sklodowska-Curie Grant Agreement No 793316 is gratefully acknowledged. The first author acknowledges with thanks the support of his research provided by the National Natural Science Foundation of China (No. 51808335); the third author acknowledges with thanks the IGI Global Challenges funding Scheme of the University of Birmingham (Project Nr 3035). All authors would like also to thank Mr. Fei Wang, member of the technical staff at Wind Tunnel and Circulating Water Channel at Shanghai Jiao Tong University for his patient work in the laboratory tests.

REFERENCES

[1] N. Tziavos, H. Hemida, N. Metje, C. Baniotopoulos. Non-linear Finite Element Analysis of Grouted Connections for Offshore Monopile Wind Turbines, *Ocean Engineering* 171: 633-645, 2018.

[2] N.I. Tziavos, H. Hemida, S. Dirar, M. Papaelias, N. Metje, C.C. Baniotopoulos, Structural health monitoring of grouted connections for offshore wind turbines by means of acoustic emission: An experimental study, *Renewable Energy* 147: 130-140, 2019.

[3] ENV 1991-01-04: *Actions on structures*, CEN, Brussels 1991.

[4] J.R. Morison, J.W. Johnson, S.A. Schaaf. The force exerted by surface waves on piles. *Journal of Petroleum Technology* 5: 149-154, 1950.

[5] J.N. Newman. *Marine Hydrodynamics* [M]. Cambridge: The MIT Press. 1977.

[6] ABAQUS/Standard and ABAQUS/Explicit-Version 6.8-1. *Abaqus Theory Manual*, Dassault System. 2008.

[7] A. Roshko. Experiments on the flow past a circular cylinder at very high Reynolds number. *Journal of Fluid Mechanics* 10: 345-356, 1961.

EURODYN 2020
XI International Conference on Structural Dynamics
M. Papadrakakis, M. Fragiadakis, C. Papadimitriou (eds.)
Athens, Greece, 23–26 November 2020

SPATIAL DISTRIBUTED CHARACTERISTICS OF DYNAMIC RESPONSE OF JACKET SUPPORTED OFFSHORE WIND TURBINE UNDER HURRICANE INDUCED ENVIRONMENTAL LOADS

Bowen Jiang[1], Qingshan Yang[1], Guoqing Huang[1] and Min Liu[1]

[1] School of Civil Engineering, Chongqing University
No.174 Shazhengjie, Shapingba, Chongqing, China
jbw1991222@163.com

Keywords: Offshore wind turbines, Hurricane, Dynamic responses, Spatial distribution

Abstract. *During extreme tropical cyclones such as hurricanes and typhoons, although offshore wind turbines (OWTs) are parked and feathered to mitigate loads on the turbine blades, failures may happen to OWTs due to hurricane induced environmental loads or errors of the control systems. In this study, attempts are made to investigate the spatial distributed characteristics of hurricane induced response of OWTs considering the influence of the misalignment between local wind and wave. The dynamic responses of the jacket supported OWT are computed via implementing coupled aero-servo-hydro elastic analysis based on the hurricane-related wind and wave fields. Parametric models are adopted to simulate the spatial dependent turbulent wind fields and uni-directional irregular wave fields induced by hurricanes. Based on a series of coupled aero-servo-hydro elastic analyses, the spatial distributed characteristics of dynamic response such as tower-top and platform displacement, structural stress in tower and substructure and axial force on cross-section of the legs are investigated by comparing their maximum, mean and standard deviation values. In addition, focusing on the points where maximum responses occur, the time history curves of response are obtained and analyzed to illustrate their temporal characteristics.*

1 INTRODUCTION

As a widely concerned renewable energy, offshore wind energy undoubtedly provides a solution to the environmental problems encountered in the process of energy utilization. However, the harvest of wind resource is companied with potential risks due to extreme tropical cyclones such as typhoons and hurricanes. In southeast coastal area of China where many offshore wind farms are located, there is a high risk that OWTs are exposed by tropical cyclones. From 2003 to 2008, a number of wind turbine failure cases during tropical cyclone activities were reported and attracted the attention of some scholars [1-3]. These failure events all happened to onshore wind turbines in the Asia-Pacific region and can be characterize as structural failure and blade failure. According to Li's study [3], the cause of the failures during hurricane events are correlated with extreme wind speed, drastic change of wind direction, intense turbulence in the inflow wind and fail of control system. During hurricane events, extreme wind and waves are generated causing the bearing loads more complicated than that on onshore wind turbines, which may lead to failures of OWTs although there is no record of these events.

Based on the above considerations, environmental loads due to hurricanes should be considered in the design future turbines. One of the major problems in analyzing the characteristics of OWT response caused by hurricanes is modelling spatio-temporal correlated wind and wave fields. In the past few decades, some sophisticated numerical models such as WAVEWATCH III, UMCM and SWAN [4-6] have been used to predict the wind and wave within hurricanes based on the physics of wave generation. However, due to the high computational cost and limited resolution, these numerical models are not appreciable for the dynamic analysis of OWTs. To this end, some parametric models were proposed to characterize hurricane generated wind and waves. For hurricane wind field model, Holland model [7] has been extensively used to characterize the hurricane radial profiles due to its simplicity and effectiveness. Some other parametric models for hurricane winds have been proposed taking into account the effect of surface friction and storm translation [8-11]. Attempts have also been made to provide parametric wave models generated by hurricanes [12-19]. The spatial distributed characteristic of significant wave height and local wave directions are investigated in these works.

Inspired by the failure cases of wind turbines reported before (although these failure events all happened to onshore wind turbines), the control system, turbine parking strategy and blade azimuthal configuration have vital influence on the aerodynamic load of a wind turbine. Kim and Manuel [5] investigated the hurricane induced loads on a monopole supported 5-MW OWT with considerations for nacelle yaw and blade pitch control and validated the most unfavorable yaw angle during hurricanes. For OWTs supported by substructures such as jackets and tripods, the structural bearing capacities are different when being loaded in different directions. Wei et al [20] investigated the bearing capacities of a jacket supported OWT in different directions. The lowest loading capacity at 45° is verified based on a static nonlinear pushover analysis of the jacket structure under wind and wave loads. Furthermore, attentions have been paid to hurricane risk assessment of OWTs and directional effects of environmental loads on OWTs [21-23].

In summary, the wind fields and wave fields induced by hurricanes are spatial distributed due to the characteristics of hurricane wind and physical mechanism of wave generation. Therefore both the amplitude and the direction of environmental loads vary with the spatial location. Despite the studies above, limited studies have been conducted on characteristics of hurricane induced dynamic response of jacket supported OWTs focusing on the spatial correlated wind and wave fields generated by hurricanes.

2 MODELING OF WIND AND WAVE INDUCED BY HURRICANES

The dynamic responses of OWTs depend on the environmental loading which is remarkably correlated with the wind fields and wave fields induced by hurricanes. However, due to the movement and intensity variation of storm, the hurricane induced wind fields and wave fields evolve over time. Therefore, the wind speed or the wave elevation at any specified point can be modeled as non-stationary processes. Despite the time-varying characteristics, the wind speed or the wave elevation can be characterized by stationary processes during a short interval (10 min) based on the slow-change characteristic of hurricane wind fields. Thus, parametric models are adopted to simulate the spatial dependent wind field and wave field during hurricanes.

2.1 Modeling of hurricane wind

The near-surface hurricane wind field, namely the mean wind speed at height of 10 m can be decomposed into an axisymmetric component of the storm vortex and an axially asymmetric component of the surface background wind [11]. The schematic for calculation of the near-surface hurricane wind at any specified point is shown in Figure 1. As is defined in Figure 1, storm track is assumed to be aligned with the horizontal axis and the storm center is fixed to the coordinate origin. r and φ are radial distance from storm center to observation point P and azimuth of vector OP which is defined counter-clockwise from the horizontal axis. The coordinate of the observation point P is $\left(X_P, Y_P\right)$, where Y_P represents the offset distance of point P from the storm track; X_P represents the horizontal distance of point P from the storm center O. The near-surface hurricane wind speed equals the vector sum of the component of the storm vortex and the component of the surface background wind. Meanwhile, a deceleration effect and a rotational effect are caused by the surface friction therefore the gradient wind and background wind should be modified by reduction factor (α_r and α_t) and rotation angle (α and β).

$$\vec{U}=\alpha_r\vec{V}_r+\alpha_t\vec{V}_t \tag{1}$$

Where $\vec{U}$ is the mean wind speed at height of 10 m; α_r and α_t are surface wind reduction factor (SWRF) of gradient wind speed V_r and background wind speed V_t.

In the present study, the gradient wind and the background wind are converted to the surface level with SWRF $\alpha_r=0.8$ and $\alpha_t=0.5$. The rotation angle of background wind $\beta=20^\circ$ while the rotation angle of gradient wind α is given by the National Weather Service's expression [8]

$$\alpha=\begin{cases}10^\circ\left(1+r/R_m\right), 0\le r<R_m\\ 20^\circ+25^\circ\left(r/R_m-1\right), R_m\le r<1.2R_m\\ 25^\circ, r\ge 1.2R_m\end{cases} \tag{2}$$

Where R_m is radius to maximum wind.

The value of the axisymmetric component of the storm vortex can be calculated based on the Holland model [7].

$$V_r(r)=\left\{\left(\frac{R_m}{r}\right)^B \frac{100B\Delta P\exp\left[-\left(\frac{R_m}{r}\right)^B\right]}{\rho}+\frac{r^2 f_c^2}{4}\right\}^{0.5}-\frac{f_c r}{2} \tag{3}$$

Where ρ is air density; $f_c = 2\Omega\sin\Phi$ is the Coriolis parameter, in which $\Omega = 7.292\times10^{-5}$ and Φ is lattice; ΔP is central pressure deficit; B is the Holland parameter which is determined as

$$B=\frac{V_m^2 e\rho + f_c V_m R_m e\rho}{100\Delta P} \tag{4}$$

Where e is base of natural logarithms; V_m is maximum mean wind speed.

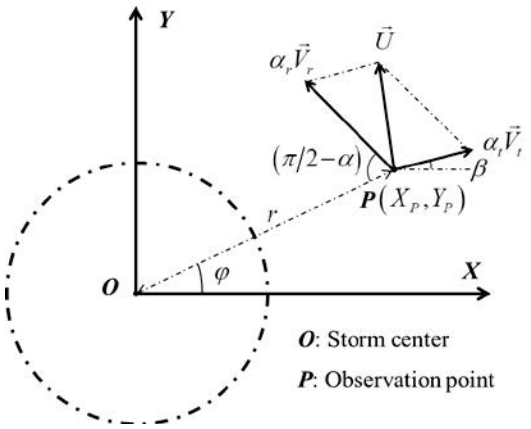

Figure 1: Schematic for calculation of the near-surface hurricane wind at any specified point

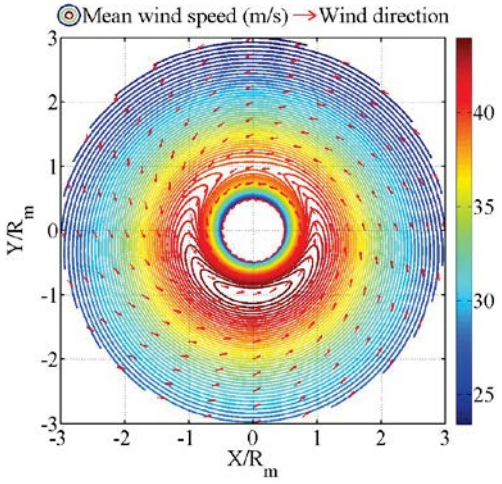

Figure 2: Contour of hurricane wind field at height of 10 m

Parameters	values
Latitude	30.8 deg
Storm central pressure deficit	52 mb
Radius to maximum winds	74 km
Forward movement speed	4.5 m/s
Air density	1.15 kg/m^3

Table 1: Parameters of a measured hurricane

Using the hurricane wind model mentioned above, the spatial distribution of mean wind speed at height of 10 m can be simulated according to the parameters of a measured hurricane listed in Table 1. The contour of hurricane wind field at height of 10 m is shown in Figure 2.

As is shown in Figure 2, due to the background wind, a peak occurs at the point where $r = R_m$ and $\varphi = 270^\circ$.

2.2 Modeling of hurricane wave

In early studies, wind generated seas are characterized by wave spectra based on measured data which are related with the steady wind speed over the sea [24, 25]. However, during meteorological forcing events such as tropical clones, hurricanes and typhoons, destructive waves are generated by time-varying wind fields correlated with the vortex structure. To this end, the concept of an extended fetch was proposed by Young [12-14] to reflect to the relationship between significant wave height, maximum wind velocity in the storm and velocity of the forward movement of the storm. More recently, fetch- or duration-limited wave growth functions [16-19] have been proposed according to the datasets from the National Aeronautics and Space Administration (NASA) and National Oceanic and Atmospheric Administration (NOAA) combined hurricane hunter missions during Bonnie 1998 [15, 26] and Ivan 2004 [27]. The fetch-limited wave growth function can be expressed as:

$$\begin{cases} H_s = 8.10\times10^{-4} U_{10}^{1.19} x_\eta^{0.405} \\ T_p = 9.28\times10^{-2} U_{10}^{0.526} x_\omega^{0.237} \end{cases} \tag{5}$$

Where H_s is significant wave height; T_p is spectral peak wave period; U_{10} is mean wind speed at height of 10 m; x_η and x_ω are effective fetch corresponding to H_s and T_p respectively.

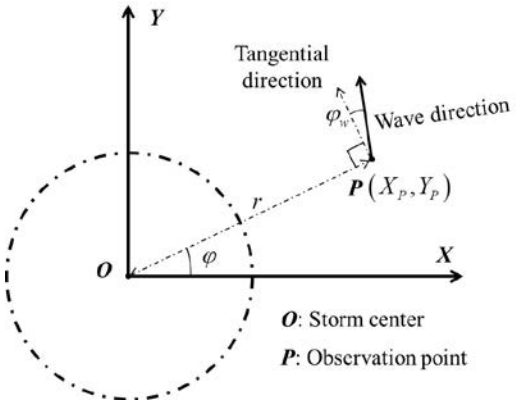

Figure 3: Schematic of azimuthal dependent wave direction

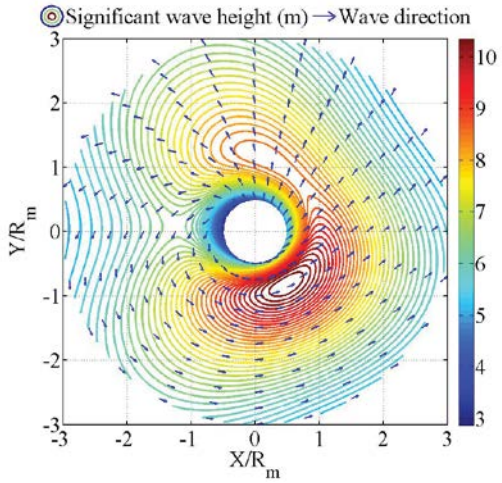

Figure 4: Contour of significant wave height

In this model, the variables x_η and x_ω in fetch-limited wave growth function as well as the angle between wave direction and tangential direction φ_w are azimuthal dependent as is shown in Figure 3. In Figure 3, the storm track is assumed to be aligned with the horizontal axis and the storm center is fixed to the coordinate origin. The detailed method to determine these variables can be found in Hwang's studies [18, 19]. In present study, Hwang's model was adopted to simulate hurricane wave field according to the hurricane wind field presented

in Section 2.1. The spatial distributed significant wave height, spectral peak wave period and directions of wind and waves are shown in Figures 4-6.

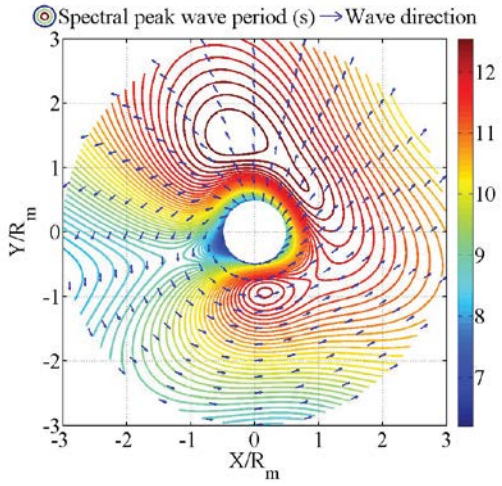

Figure 5: Contour of spectral peak wave period

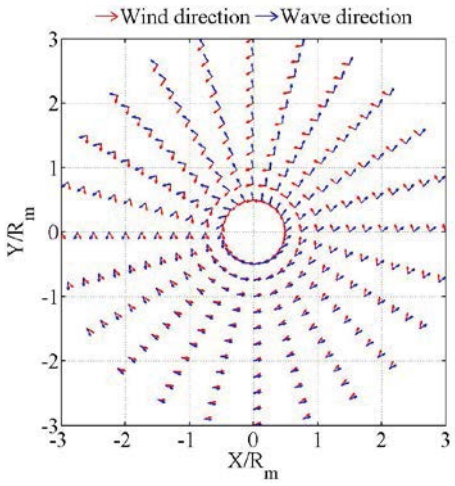

Figure 6: Azimuthal dependent wind and wave directions

3 NUMERICAL SIMULATION

3.1 Modeling of OC4-jacket OWT

In this study, a jacket design, namely OC4-jacket is considered to support the NREL 5-MW baseline turbine [28, 29]. The main dimensions and properties of OC4-jacket and NREL 5-MW baseline turbine are listed in Table 2. The schematic of the OC4-jacket support structure is shown in Figure 7. As shown in Figure 7, the supporting structural system of OC4-jacket is designed to be deployed in the site with 50-m water depth with the rotor-nacelle assembly (RNA) being mounted 90 m above mean sea level (MSL). In order to realize the rigid connection between tower and substructure, a rigid platform is employed. Moreover, the effect of nonlinear soil-pile interaction is neglected, in other words, the 4 legs of the jacket are assumed clamped at the seabed.

To simulate the parked wind turbine during hurricanes, the turbine blades were pitched to 90 and the RNA was yawed to be aligned with the local wind direction (shown in Figure 8). As a compromise of save computing cost, the wind turbine was assumed to be located within the range of $0.5R_m \sim 3.0R_m$ from the storm center.

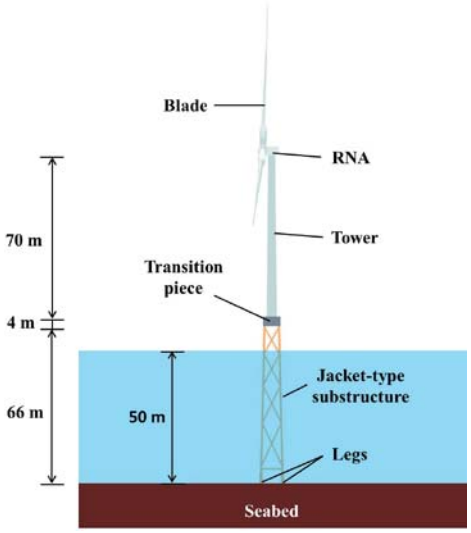

Figure 7: Schematic of an OC4-jacket OWT

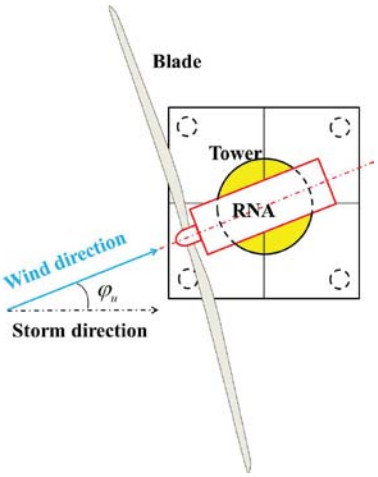

Figure 8: Schematic of nacelle yaw angle

Properties	values
Rated power	5 MW
Cut in wind speed, rated wind speed, cut out wind speed	3 m/s, 11.3 m/s, 25 m/s
Rotor diameter, hub diameter	126 m, 3 m
Hub height above MSL	90 m
Deck height above MSL	16 m
Tower length	68 m
Transition-piece length	4 m
Tower-base outer diameter	6 m
Tower-base thickness	0.032 m
Tower-top outer diameter	4 m
Tower-top thickness	0.03 m
RNA mass	350000 kg
Jacket mass	581256 kg
Transition piece mass	666000 kg
Tower mass	229812 kg
Structural damping ratio	1%

Table 2: Main properties of OC4-jacket and NREL 5-MW baseline turbine

3.2 Environmental loads

The inflow wind can cause aerodynamic load on OWTs including drag and lift force on blades and drag force on towers. With the hurricane wind field determined in Section 2.1, the Frøya wind profile and spectral model [30] were adopted to calculate the time series of inflow wind speed at different locations. The Frøya wind profile is expressed as

$$\overline{u}\left(z\right)=U_{ref}\left(1+0.0573\sqrt{1+U_{ref}}\right)\ln\left(z/H_{ref}\right) \tag{6}$$

Where $\overline{u}\left(z\right)$ is mean wind speed at height z; U_{ref} is the 1-hour mean wind speed at H_{ref}, $H_{ref}=10\,\mathrm{m}$.

The Frøya spectral model was developed for neutral conditions over water in the Norwegian Sea. It can be expressed as

$$S_u\left(f\right)=\frac{320\left(\frac{U_{ref}}{10}\right)^2\left(\frac{z}{10}\right)^{0.45}}{\left(1+\tilde{f}^{\,n}\right)^{\frac{5}{3n}}} \tag{7}$$

Where $n=0.468$ and

$$\tilde{f}=172f\left(\frac{z}{10}\right)^{2/3}\left(\frac{U_{ref}}{10}\right)^{-0.75} \tag{8}$$

In practice, blade element momentum (BEM) theory is one of most commonly used methods for calculating aerodynamic load on wind turbine blades. According to this method, two-dimensional airfoil tables of lift and drag coefficient are included as a function of the angle of attack, thus a set of equations can be iteratively solved for the induced velocities on each blade element. For parked turbines, the rotor wake/induction effects can be ignored. Thus, the aerodynamic load on blades and tower can be directly calculated based on the tables of lift and drag coefficient and instantaneous inflow wind speed.

The hydrodynamic load on OWTs is related to local wave kinematics. The linear Airy wave theory [31] is used to predict the kinematics of two-dimensional waves of small height in deep water. In order to reflect the stochasticity of sea states, irregular waves can be modelled as the linear superposition of sinusoidal wave components. Thus, the distribution of wave energy at different frequencies is characterized by specifying a wave spectrum. For a developing sea, the JONSWAP (the Joint North Sea Wave Project) spectrum was proposed and adopted by IEC standard [25, 32]. The IEC JONSWAP spectrum is expressed as

$$S_{JS}\left(f\right)=0.3125H_s^2T_p\left(\frac{f}{f_p}\right)^{-5}\exp\left[-1.25\left(\frac{f}{f_p}\right)^{-4}\right]\left(1-0.287\ln\gamma\right)\gamma^{\exp\left[-0.5\left(\frac{\frac{f}{f_p}-1}{\sigma}\right)^2\right]} \tag{9}$$

Where $S_{JS}\left(f\right)$ is IEC JONSWAP spectrum; f_p is spectral peak wave frequency, $f_p=1/T_p$; $\sigma=0.07$ for $f\le f_p$, $\sigma=0.09$ for $f>f_p$; γ is peak-shape parameter:

$$\gamma\begin{cases}5, \dfrac{T_p}{\sqrt{H_s}} \le 3.6 \\ \exp\left(5.75-1.15\dfrac{T_p}{\sqrt{H_s}}\right), 3.6 < \dfrac{T_p}{\sqrt{H_s}} \le 5 \\ 1, \dfrac{T_p}{\sqrt{H_s}} > 5\end{cases} \tag{10}$$

Based on the wave kinematics determined by JONSWAP spectrum as a function of significant wave height H_s and spectral peak wave period T_p, the wave force on slender members can be calculated by Morison's equation [33]

$$f_H = f_D + f_I = \frac{1}{2}C_D\rho_w D\left(u_x - \dot{x}\right)\left|u_x - \dot{x}\right| + C_M\rho_w\frac{\pi D^2}{4}\frac{\mathrm{d}u_x}{\mathrm{d}t} - \left(C_M - 1\right)\rho_w\frac{\pi D^2}{4}\ddot{x} \tag{11}$$

Where f_H is hydrodynamic force of a small size cylinder per unit length; f_I and f_D are the inertia force and drag force per unit length; C_M and C_D are the inertia coefficient and drag coefficient; u_x is the horizontal velocity component of water particle; ρ_w is water density; D is the diameter of cylinder; $\mathrm{d}u_x/\mathrm{d}t$ is the horizontal acceleration component of water particle; $\dot{x}$ and $\ddot{x}$ are the horizontal velocity component and horizontal acceleration component of the cylinder.

3.3 Dynamic analysis

The structural response of OWTs subjected to simultaneous wind and wave is nonlinear and influenced by the interaction of aerodynamic, hydrodynamic, structural, operational, and geotechnical effects. The open-source software for turbine dynamic simulation, FAST [34], developed at National Renewable Energy Laboratory (NREL) are used in calculating the structural response of OWTs subjected to simultaneous wind and wave, where aerodynamic load and hydrodynamic load are obtained as described in previous steps. In this case, six 700-s simulations were conducted assuming that the OWT is located in different positions within the range of $0.5R_m \sim 3.0R_m$ from the storm center with the first 100 s of dynamic responses removed.

Through numerical calculation, the maximum, mean, and standard deviation values of dynamic responses in key components were extracted. To reveal spatial distributed characteristics of dynamic response, the contour of maximum dynamic responses with respect to normalized spatial coordinates X/R_m and Y/R_m were obtained and analyzed.

Assuming that the storm intensity and the forward movement speed of the storm remains constant, the spatial distributed hurricane wind and wave field can be converted to time varying hurricane wind and wave field. As the storm track is aligned with the horizontal axis and the storm center is fixed to the coordinate origin, the observation point *P* moves in the negative direction of the horizontal axis with an offset distance Y_P. Thus, the time series of mean wind speed, significant wave height and maximum value of dynamic response can be obtained by extracting points from contours of dynamic response on line $Y = Y_{P\max}$. It should be noticed that $Y_{P\max}$ is offset distance of the point where maximum response occurs (Fig 9 (a)).

4 RESULTS AND ANALYSIS

4.1 Tower-top and platform displacement

Figure 9 shows contours of maximum, mean and standard deviation value of tower-top displacement and platform displacement. In Figs 9 (a-f), $d_{T\max}$, $d_{T\text{mean}}$, d_{TSTD} , $d_{P\max}$, $d_{P\text{mean}}$ and d_{PSTD} stand for maximum tower-top displacement, mean tower-top displacement, standard deviation of tower-top displacement, maximum platform displacement, mean platform displacement and standard deviation of platform displacement respectively. As is shown in Figure 9 (c-d), being the reflection of hurricane wind field, $d_{T\text{mean}}$ and $d_{P\text{mean}}$ have almost the same characteristic in spatial distribution. In addition, $d_{T\max}$, d_{TSTD}, $d_{P\max}$, and d_{PSTD} have similar characteristic in spatial distribution: the maximum value locates at the same point where $r = R_m$ and $\varphi = 255^\circ$. The point of maximum displacement has an offset distance $Y_{P\max} = -71.48$ .This is mainly because aerodynamic load has dominant effect on tower-top displacement and platform displacement. Apart from the mean response determined by mean wind load, the azimuth of the maximum response is affected by dynamic response which is related to dynamic loads and structural resistance.

The time history of normalized mean wind speed U_{10} , significant wave height H_s and maximum displacement $d_{\max}$ at the point of maximum displacement are shown in Figure 10. From Figure 10, the maximum displacement occurs near the eyewall after the wind speed reaches the peak value. In addition, similar to the time history curve of mean wind speed, the time history curve of maximum displacement shows unimodal characteristic. However, even if the aerodynamic load has dominant effect on tower-top displacement and platform displacement, the time history curve of maximum displacement is asymmetric while the time history curve of mean wind speed is of high symmetry due to the low forward movement speed of the storm. This phenomenon is correlated with non-axisymmetry of supporting substructure and temporal correlated wind-wave misalignment angle.

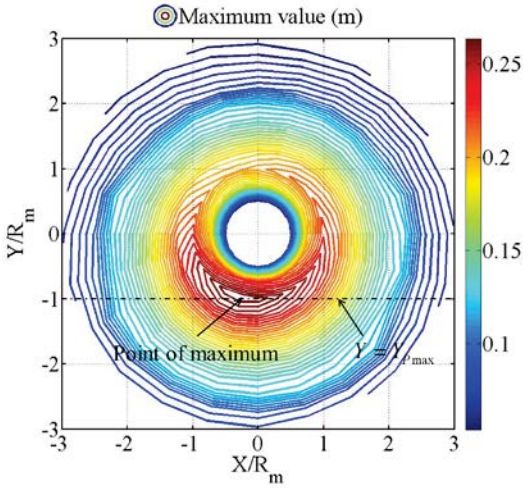

(a) $d_{T\max}$

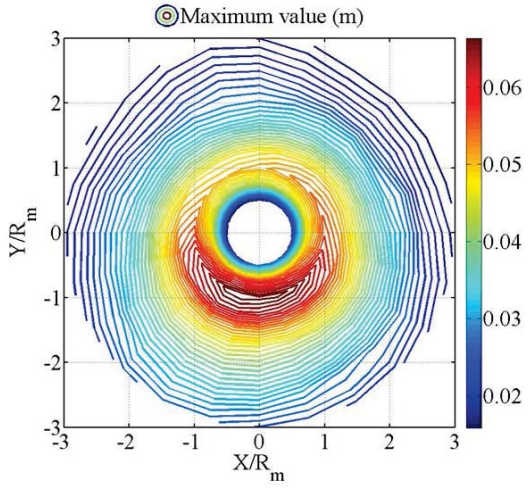

(b) $d_{P\max}$

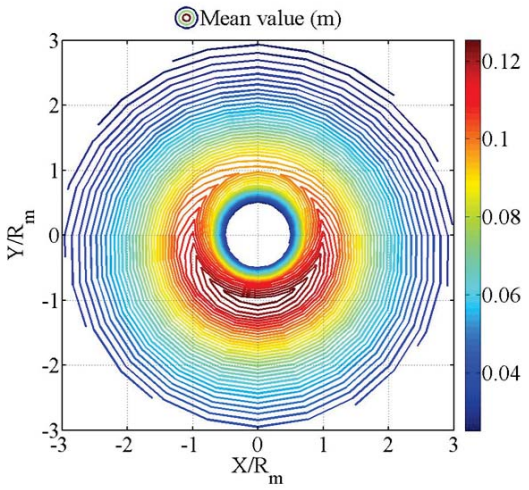

(c) $d_{T\,\mathrm{mean}}$

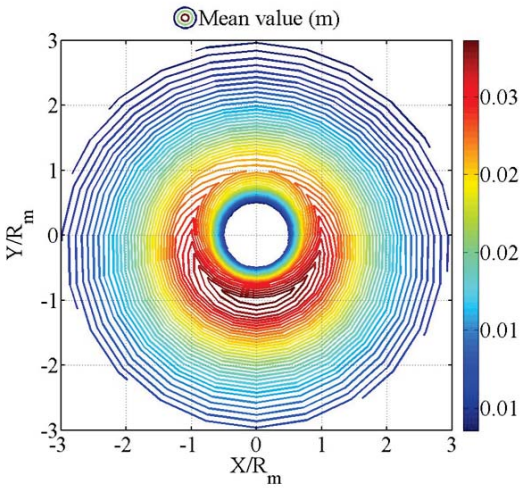

(d) $d_{P\,\mathrm{mean}}$

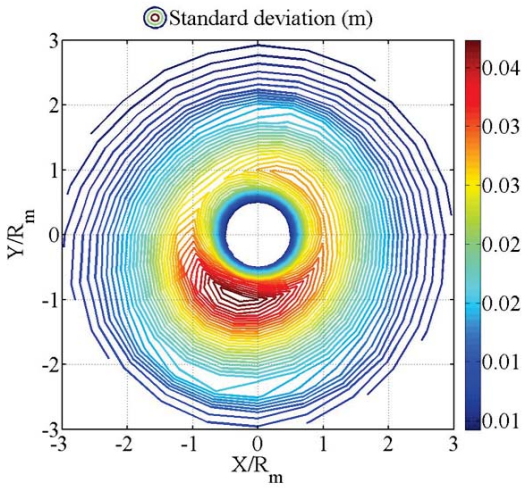

(e) d_{TSTD}

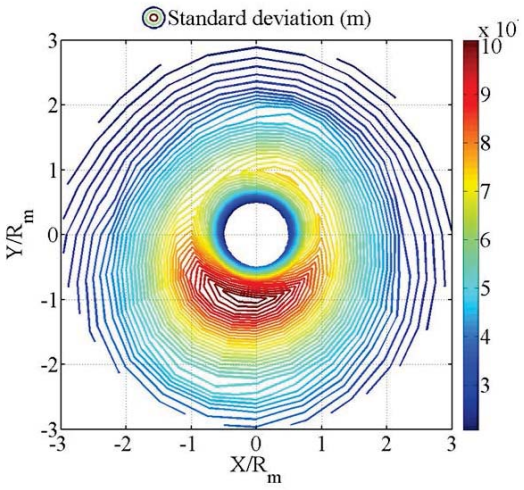

(f) d_{PSTD}

Figure 9: Contours of maximum, mean and standard deviation value of tower-top displacement and platform displacement

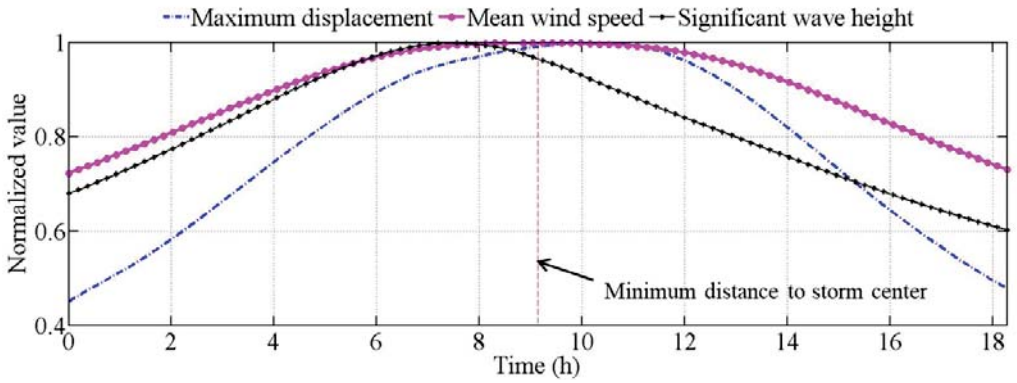

Figure 10: Time history of normalized mean wind speed, significant wave height and maximum displacement

4.2 Stress in tower and substructure

Contours of maximum normal stress and maximum shear stress in tower and substructure are shown in Figure 11 (a-d). In Figure 11 (a-d), $\sigma_{NT\max}$, $\sigma_{NJ\max}$, $\sigma_{ST\max}$ and $\sigma_{SJ\max}$ stand for maximum tower normal stress, maximum normal stress in substructure, maximum tower shear stress, maximum shear stress in substructure respectively. From Figure 11 (a-d), the distribution characteristic of $\sigma_{NT\max}$ and $\sigma_{ST\max}$ are similar to those of $d_{T\max}$. However, $\sigma_{NJ\max}$ and $\sigma_{SJ\max}$ show different characteristic in spatial distribution. The maximum value of $\sigma_{NJ\max}$ and $\sigma_{SJ\max}$ can be found at the point where $r = R_m$ and $\varphi = 285^\circ$. This point is almost coincident with the point where maximum significant wave height occurs. Meanwhile, another peak of $\sigma_{NJ\max}$ and $\sigma_{SJ\max}$ locates near the point where maximum value of $d_{T\max}$ occurs. Therefore, conclusion can be made that the maximum values of $\sigma_{NJ\max}$ and $\sigma_{SJ\max}$ should be attributed to hydrodynamic load while the maximum values of $\sigma_{NT\max}$ and $\sigma_{ST\max}$ should be attributed to aerodynamic load.

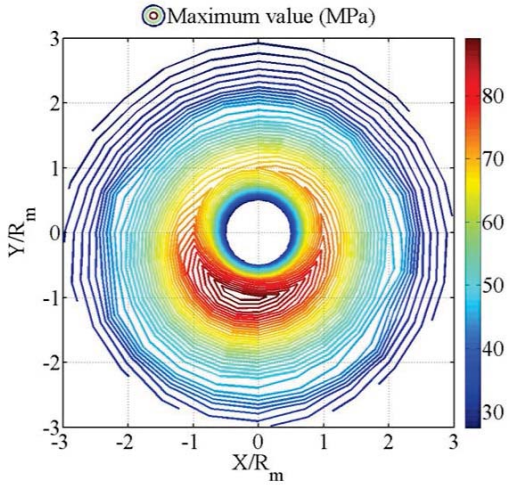

(a) $\sigma_{NT\max}$

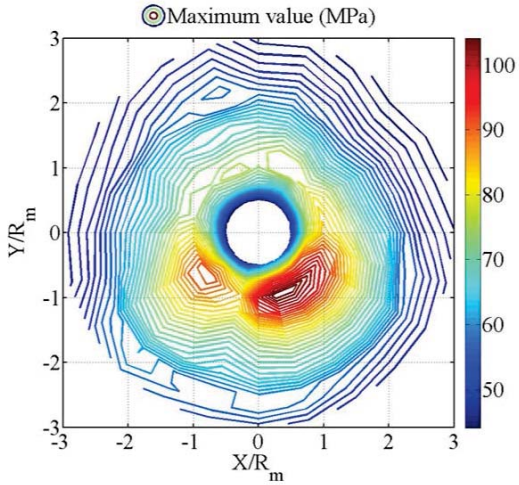

(b) $\sigma_{NJ\max}$

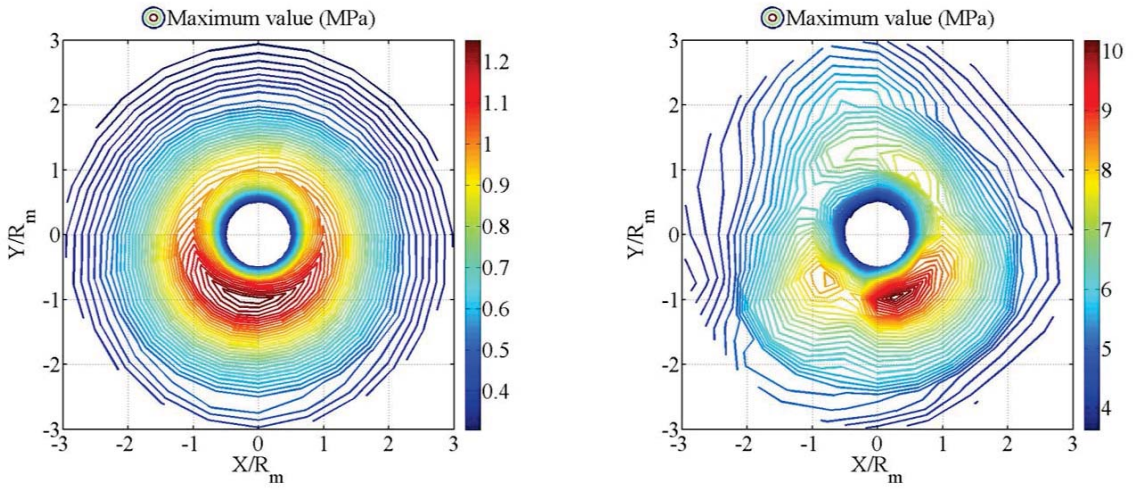

(c) $\sigma_{ST\max}$ (d) $\sigma_{SJ\max}$

Figure 11: Contours of maximum normal stress and maximum shear stress in tower and substructure

According to the same method above, we can obtain the time history curves of normalized maximum normal stress $\sigma_{N\max}$ and normalized maximum shear stress $\sigma_{S\max}$ at the points where maximum values occur (shown in Figures 12-13). It should be noted that the maximum normal stress and maximum shear stress do not locate at the same point. Thus, the time history curves of normalized mean wind speed U_{10} and significant wave height H_s at corresponding points are shown in Figures 12-13. As Figures 12-13 show, the time history curves of normalized maximum normal stress $\sigma_{N\max}$ and normalized maximum shear stress $\sigma_{S\max}$ are bimodal with the maximum values occur before the arrival of minimum distance to storm center. With the intensity of hydrodynamic loads at their maximum values, the points of maximum response coincide with the points of maximum significant wave height.

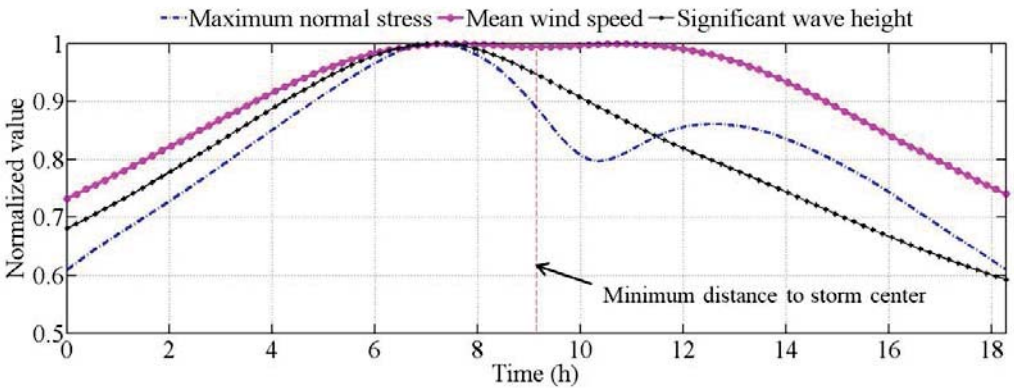

Figure 12: Time history of normalized mean wind speed, significant wave height and maximum normal stress

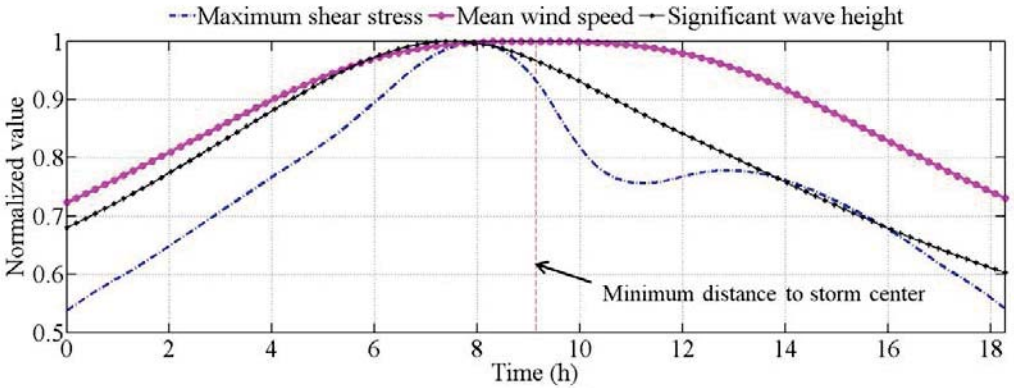

Figure 13: Time history of normalized mean wind speed, significant wave height and maximum shear stress

4.3 Uplift and downward axial force on legs

A part from the failure induced by excessive displacement and structural stress, the ultimate limit state of an OWT can also be determined by foundation uplift and yielding of underlying soil. Therefore, the contours of maximum uplift axial force $N_{U\max}$ and downward axial force $N_{D\max}$ on legs were checked (shown in Figure 14). From Figure 14 (a-b), the distribution characteristic of $N_{U\max}$ and $N_{D\max}$ are same as those of $\sigma_{NJ\max}$ and $\sigma_{SJ\max}$ except that the maximum values of $N_{U\max}$ and $N_{D\max}$ locate at the same point.

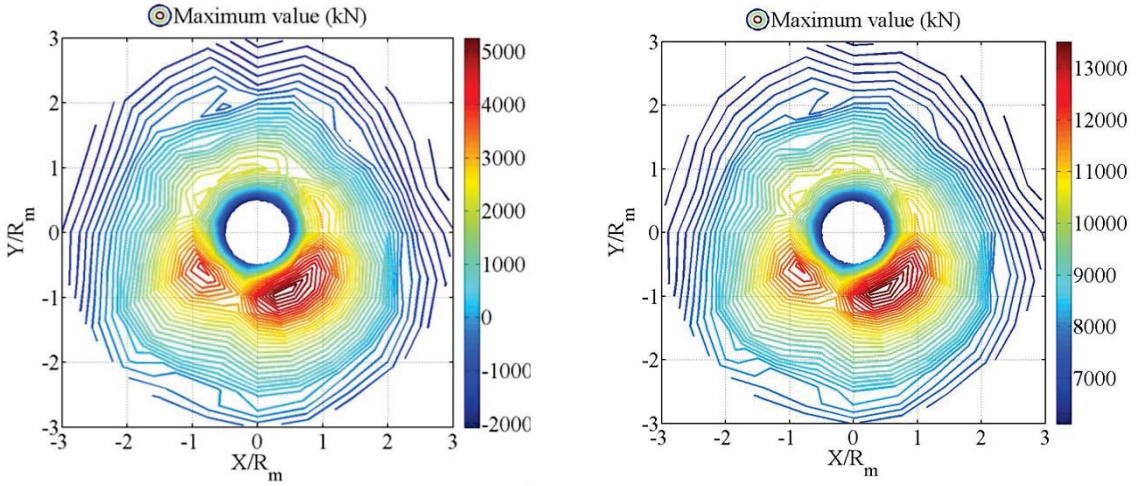

(a) $N_{U\max}$ (b) $N_{D\max}$

Figure 14: Contours of maximum uplift axial force and downward axial force on legs

The time history of normalized maximum uplift axial force $N_{U\max}$ and downward axial force $N_{D\max}$ at the points where maximum values occur are shown in Figure 15. From Figure 15, the time history of normalized maximum uplift axial force $N_{U\max}$ and downward axial force $N_{D\max}$ are bimodal in shape with the maximum values occur before the arrival of mini-

mum distance to storm center. Except for the specific value, the time history curve of $N_{U\max}$ shows the same trend as that of $N_{U\max}$.

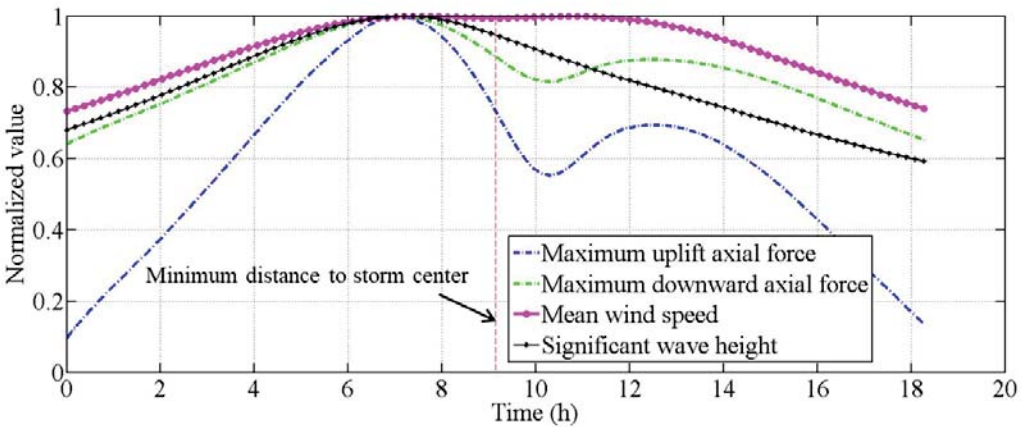

Figure 15: Time history of normalized mean wind speed, significant wave height, maximum uplift axial force and maximum downward axial force

5 CONCLUSIONS

In this paper, a series of coupled aero-servo-hydro elastic analyses have been conducted to investigate the spatial distributed characteristics of hurricane induced response of OWTs , by checking the tower-top and tower base displacement, normal stress and shear stress in tower and substructure , uplift and downward axial force of legs, etc. From this study, the following conclusions can be drawn:

(1) As tower-top and platform displacement are dominated by aerodynamic load, the spatial distribution and time history curve of maximum displacement show similar characteristics as mean wind speed. The maximum displacement occurs near the eyewall where the time history curve of maximum displacement shows unimodal characteristic. Moreover, time history curve shows that the maximum displacement occurs before the arrival of minimum distance to storm center.

(2) For structural stress, the spatial distributions of maximum normal stress and shear stress in tower show different characteristics from those in substructure. The spatial distributions of maximum normal stress and shear stress in tower are similar to those of maximum tower-top displacement while the maximum normal stress and shear stress in substructure can be found at the point near the point of maximum significant wave height. Besides, even if the time history curves of mean wind speed and significant wave height are unimodal in shape, the time history curves of normalized maximum normal stress and normalized maximum shear stress are bimodal with the maximum values occur before the arrival of minimum distance to storm center

(3) Being dominantly affected by hydrodynamic load, the spatial distributions of maximum uplift axial force and downward axial force share the same characteristic with those of maximum normal stress and shear stress in substructure. In addition, the time history curves of normalized maximum uplift axial force and downward axial force are bimodal in shape with the maximum values occur before the arrival of minimum distance to storm center.

REFERENCES

[1] T. Ishihara, et al， An analysis of damaged wind turbines by Typhoon Maemi in 2003, Sixth Asia-Pacific Conference on Wind Engineering (APCWE VI), 2005.

[2] J. Chou & W. Tu, Failure analysis and risk management of a collapsed large wind turbine tower, Engineering Failure Analysis 18(1), 295-313, 2011.

[3] Z. Li, et al, Design defect of wind turbine operating in typhoon activity zone, Engineering Failure Analysis 27, 165-172, 2013.

[4] Q. Liu, et al, Numerical simulations of ocean surface waves under hurricane conditions: As-sessment of existing model performance, Ocean Modelling 118, 73-93, 2017.

[5] E. Kim, & L. Manuel, Hurricane-induced loads on offshore wind turbines with considerations for nacelle yaw and blade pitch control, Wind Engineering 38(4), 413-423, 2014.

[6] J. T. Ta & G. S. Dwarakish, Numerical wave modelling–A review, Aquatic procedia 4, 443-448, 2015.

[7] G. J. Holland, An analytic model of the wind and pressure profiles in hurricanes, Monthly weather review 108 (8), 1212-1218, 1980.

[8] A. C. Phadke, et al, Modeling of tropical cyclone winds and waves for emergency management, Ocean Engineering 30(4), 553-578, 2003.

[9] H. E. Willoughby & M. E. Rahn, Parametric representation of the primary hurricane vortex. Part I: Observations and evaluation of the Holland (1980) model, Monthly Weather Review 132 (12), 3033-3048, 2004.

[10] K. Emanuel, et al, A statistical deterministic approach to hurricane risk assessment, Bulletin of the American Meteorological Society 87(3), 299-314, 2006.

[11] N. Lin, Ning & D. Chavas, On hurricane parametric wind and applications in storm surge modeling, Journal of Geophysical Research: Atmospheres 117(D9), 2012.

[12] I. R. Young & J. Vinoth, An “extended fetch” model for the spatial distribution of tropical cyclone wind–waves as observed by altimeter, Ocean Engineering 70, 14-24, 2013.

[13] I. R. Young, A review of parametric descriptions of tropical cyclone wind-wave generation, Atmos-phere 8(10), 194, 2017.

[14] I. R. Young & J. Vinoth, A parametric model for tropical cyclone waves, ASME 2013 32nd International Conference on Ocean, Offshore and Arctic Engineering, American Society of Mechanical Engineers Digital Collection, 2013.

[15] I. J. Moon, et al, Numerical simulation of sea surface directional wave spectra under hurricane wind forcing, Journal of physical oceanography 33(8), 1680-1706, 2003.

[16] P. A. Hwang, Fetch-and duration-limited nature of surface wave growth inside tropical cyclones: With applications to air–sea exchange and remote sensing, Journal of Physical Oceanography 46(1), 41-56, 2016.

[17] P. A. Hwang & E. J. Walsh, Azimuthal and radial variation of wind-generated surface waves inside tropical cyclones, Journal of Physical Oceanography 46(9), 2605-2621, 2016.

[18] P. A. Hwang & Y. Fan, Effective fetch and duration of tropical cyclone wind fields estimated from simultaneous wind and wave measurements: Surface wave and air–sea exchange computation, Journal of Physical Oceanography 47(2), 447-470, 2017.

[19] P. A. Hwang, et al, Ocean surface wave spectra inside tropical cyclones, Journal of Physical Oceanography 47(10), 2393-2417, 2017.

[20] K. Wei, et al, Directional effects on the reliability of non-axisymmetric support structures for offshore wind turbines under extreme wind and wave loadings, Engineering Structures 106, 68-79, 2016.

[21] E. Kim & L. Manuel, A framework for hurricane risk assessment of offshore wind farms, ASME 2012 31st international conference on ocean, offshore and arctic engineering, American Society of Mechanical Engineers Digital Collection, 2013.

[22] K. Wei, S. R. Arwade & A. T. Myers, Incremental wind-wave analysis of the structural capacity of offshore wind turbine support structures under extreme loading, Engineering Structures 79, 58-69, 2014.

[23] S. T. Hallowell, et al, Hurricane risk assessment of offshore wind turbines, Renewable energy 125, 234-249, 2018.

[24] W. J. Pierson Jr & L. Moskowitz, A proposed spectral form for fully developed wind seas based on the similarity theory of SA Kitaigorodskii, Journal of geophysical research 69(24), 5181-5190, 1964.

[25] K. Hasselmann, et al, Measurements of wind-wave growth and swell decay during the Joint North Sea Wave Project (JONSWAP), Ergänzungsheft 8-12, 1973.

[26] C. W. Wright, et al, Hurricane directional wave spectrum spatial variation in the open ocean, Journal of Physical Oceanography 31(8), 2472-2488, 2001.

[27] Y. Fan, et al, Numerical simulations and observations of surface wave fields under an extreme tropical cyclone, Journal of Physical Oceanography 39(9), 2097-2116, 2009.

[28] J. Jonkman, et al. Definition of a 5-MW reference wind turbine for offshore system development, No. NREL/TP-500-38060. National Renewable Energy Lab.(NREL), Golden, CO (United States), 2009.

[29] R. R. Damiani, et al, Assessing the importance of nonlinearities in the development of a substructure model for the wind turbine CAE tool FAST, ASME 2013 32nd International Conference on Ocean, Offshore and Arctic Engineering, American Society of Mechanical Engineers Digital Collection, 2013.

[30] B. J. Jonkman, TurbSim User's Guide v2. 00.00, Natl. Renew. Energy Lab, 2014.

[31] M. J. Tucker & E. G. Pitt. Waves in ocean engineering. No. Volume 5. 2001.

[32] International Electrotechnical Commission, IEC 61400-3 Wind Turbines Part3: Design Requirements for Off-shore Wind Turbines, International Electrotechnical Commission: Geneva, Switzerland, 2009.

[33] J. R. Morison, J. W. Johnson, & S. A. Schaaf, The force exerted by surface waves on piles, Journal of Petroleum Technology, 2(05), 149-154, 1950.

[34] J. M. Jonkman & M. L. Buhl Jr, FAST user's guide, National Renewable Energy Laboratory, Golden, CO, Technical Report No. NREL/EL-500-38230, 2005.

EURODYN 2020
XI International Conference on Structural Dynamics
M. Papadrakakis, M. Fragiadakis, C. Papadimitriou (eds.)
Athens, Greece, 23–26 November 2020

SURROGATE MODEL FORMULATION FOR STOCHASTIC FLUTTER ANALYSIS OF WIND TURBINE BLADES UNDER UNCERTAIN AERODYNAMICS LOADS

Luca Caracoglia[1]

[1] Department of Civil and Environmental Engineering, Northeastern University
360 Huntington Avenue, Boston, Massachusetts 02115, USA
e-mail: lucac@coe.neu.edu

Keywords: Wind energy, Horizontal-axis wind turbine blades, Random aerodynamics modeling, Stochastic flutter

Abstract. *The problem of flow-induced stability of wind turbine blades has been recognized by the literature for quite some time. Traditionally, the issue of flutter for a standard-size wind turbine blade has been avoided either because the rotor's operational angular speeds are low, or the blades are appropriately parked during high-wind events. Nevertheless, it has been recently shown that critical flutter rotor speed can still be an issue during operational stages for very long blades, such as the ones typical of off-shore wind turbines [1]. In these cases, the flutter probability, influenced by various sources of uncertainty, can be non-negligible from the point of view of structural reliability. Consequently, it is of interest to examine the non-deterministic flutter problem along with the prediction of the flutter probability.*

In contrast with previous work on the estimation of flutter probability of wind turbine blades, this study proposes a new, theoretically-based and numerically-implemented model to identify the conditions for stochastic stability of wind turbine blades. The model is based on implementation of stochastic calculus methods. Dynamic stability in a non-deterministic context depends on a specific definition. In the context of long-span bridge aerodynamics this problem has been examined in the recent past through implementation of the theory of (largest) Moment Lyapunov Exponent for dynamical systems, which may be used to test the statistical moment stability. The same approach is utilized in this paper to formulate and solve a suitable reduced-order model of the blade dynamics. The model is inspired by an analogous model used for rotorcraft stability under inflow turbulence perturbations [2, 3]. Soil-structure interaction and its effects on the stability of the blades, for example simulated through imperfect boundary conditions at the root, are not addressed in the manuscript but may be included in future formulations.

Description of the model will be presented, followed by results and discussion. Numerical results analyze the flutter of the reference NREL (National Renewable Research Laboratory) 5-MW wind turbine blade.

1 INTRODUCTION

Flow-induced stability of wind turbine blades has been examined by researchers for several years [4-6]. The issue of flutter for a standard-size wind turbine blade has been avoided either because the rotor's operational angular speeds are low, or the blades are appropriately parked when high wind speeds are observed. This author has recently demonstrated that critical flutter rotor speed can still be an issue during operational stages for very long blades, such as the ones employed for last-generation off-shore wind turbines [1]. In fact, flutter probability, influenced by various sources of uncertainty, can be of the order of 10^{-4} to 10^{-3}, a non-negligible value from the point of view of structural reliability. Consequently, it is of interest to examine the non-deterministic flutter problem along with prediction of flutter probability.

Contrary to ongoing work on the estimation of flutter probability of wind turbine blades [7, 8], this paper examines a new model to identify the conditions for stochastic stability of the rotor blades. The model is based on implementation of stochastic calculus methods [9] and stochastic dynamic stability, which depends on its definition (e.g. almost-sure stability, etc. [10, 11]). In the context of long-span bridge aerodynamics this problem has been examined [12] through implementation of the theory of (largest) Moment Lyapunov Exponent (MLE) for dynamical systems, which may be employed to study statistical moment stability [10]. The same approach is utilized in this paper to formulate and solve a surrogate, reduced-order model that mimics the blade dynamics. The model is derived from an analogous model used for rotorcraft stability under inflow turbulence perturbations [2, 3]. A short description of the model is presented in the next section, followed by preliminary results and brief discussion.

The issue of soil-structure interaction and its effects on the stability of the blades, for example simulated through imperfect boundary conditions at the root, is not addressed in the manuscript. For example, an indicative study that considers soil-structure interaction effects on the reduction of offshore wind turbine stochastic response due to a series of flaps installed on the rotor blades is discussed, for example, by Thakur et al. [13]. Formulation of this effect is not included herein and will possibly be considered in future studies.

2 THEORETICAL BACKGROUND

Figure 1 illustrates a schematic of a wind turbine blade of length R, i.e. its radius measured from the rotor plane center, rotating at an angular speed Ω (rad/s). Inflow conditions are also displayed. The generic cross section of the blade is located at a distance x from the rotor center. The figure also explains two main differences compared to standard aeroelastic theory of translating airfoil wings [14]: the reference inflow speed is not constant but linearly varies along the axis x; the reference chord length of each section of the blade also varies depending on the cross-section's geometry. Consequently, standard flutter theory cannot be used.

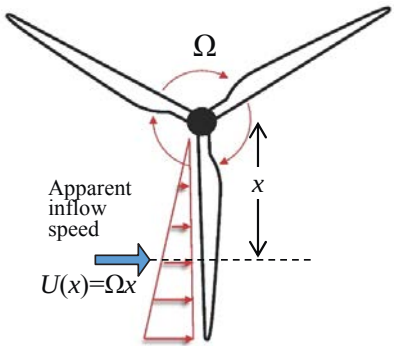

Figure 1: Schematic of rotating wind turbine blade with indication of relative inflow velocity $U(x)$ with $0 \leq x \leq R$.

Equations of motion are based on a continuous formulation of loads and response along blade's longitudinal axis x. The model exploits the model by Hodges and Dowell [15] and previous results [1]. The reference inflow velocity $U(x)$ is defined under the condition of "still-air" wind, i.e. blades rotate at no wind speed, and zero initial twist. This hypothesis is acceptable since inflow velocity is mainly controlled by blade rotation and attached flow conditions are needed to ensure that standard aeroelastic formulation can be applied.

The dynamic response of the blade is represented by modal superposition of the flap-wise, bending deflections h and torsional angles α, rewritten in terms of dimensionless time $\tau=t\omega_{0j}$ (with ω_{0j} a reference frequency) and span-wise coordinate $\eta=x/R$ as:

$$h(\eta,\tau)=\sum\nolimits_q \xi_q(\tau)c_o h_q(\eta)\approx \xi_j(\tau)c_0 h_j(\eta) \tag{1}$$

$$\alpha(\eta,\tau)=\sum\nolimits_q \xi_q(\tau)\alpha_q(\eta)\approx \xi_k(\tau)\alpha_k(\eta) \tag{2}$$

In the previous equation modal superposition is employed, with c_0 a reference chord length of the blade and $h_q(\eta)$, $\alpha_q(\eta)$ dimensionless mode shape functions of generic mode q. If flutter analysis is restricted (truncated) to the combination of a reference flap-wise mode (bending only, jth mode with natural angular frequency ω_{0j}) and torsional mode (torsional only, kth mode with angular frequency ω_{0k}), the two-mode reduced order model equations of the blade rotating at angular rotor speed Ω are, in dimensionless form:

$$\xi_j''(\tau)+2\zeta_j\xi_j'(\tau)+\xi_j(\tau)+\varepsilon_j\chi^2\xi_j(\tau)=Q_j(\tau)\Big/\left(\omega_{0j}^2 I_{0j}\right) \tag{3}$$

$$\xi_k''(\tau)+2\zeta_k\Delta\omega\xi_k'(\tau)+\left(\Delta\omega\right)^2\xi_k(\tau)+\varepsilon_k\chi^2\xi_j(\tau)=Q_k(\tau)\Big/\left(\omega_{0j}^2 I_{0k}\right) \tag{4}$$

In the previous equations the flap-wise mode j is taken as the reference and the flutter frequency ratio is defined as $\chi=\Omega/\omega_{0j}$, whereas the modal frequency ratio is $\Delta=\omega_{0k}/\omega_{0j}$. The derivation with respect to dimensionless time $\tau=t\omega_{0j}$ is designated by the prime symbol; the terms ε_j and ε_k indirectly measure the effects of the centrifugal forces on the rotating blade. The generalized forces Q_j and Q_k are computed according to unsteady aeroelastic airfoil theory via indicial functions [16], i.e. the Wagner function describing the (C) circulatory flow effects [17], and accounting for (NC) non-circulatory effects [18, 19]. It is interesting to note that using the standard dimensionless time $s=Ut/c$ (with U tangential inflow speed and c chord length, Fig. 1) is unsuitable for the purposes of derivation of a closed-form equation, since this quantity varies with x and depends on each specific blade cross section. Furthermore, since the relative tangential speed U varies along x, the convolution integral needed by the unsteady aeroelastic force formulation cannot be resolved in closed form. Therefore, the exponential term of the indicial function in the R.T. Jones' formula [17] below:

$$\Phi(s)=1-\sum\nolimits_{r=1,2} c_r\left\{\mathrm{e}^{-d_r s}\right\} \tag{5}$$

with c_r and d_r being suitable constants and s dimensionless time, must be represented by Taylor series to enable model derivation. The order of the Taylor series expansion of $\Phi(\tau)$ is N. After suitable manipulation, the generalized force of the reference flap-wise mode j is:

$$\frac{Q_j(\tau)}{\left(\omega_{0j}^2 I_{0j}\right)}=\Gamma_j^C C_L^*\left\{\begin{array}{l}\dfrac{\Phi_0 c_0}{2R\chi}G_{h_jh_j}^{(-1)}\xi_j'+\displaystyle\sum_{n=0}^{N}\frac{G_{h_jh_j}^{(n)}}{n!}\left(\frac{2R\chi}{c_0}\right)^n\left[c_1 d_1^{n+1}+c_2 d_2^{n+1}\right]\hat{\mu}_{ae,j}^{(n)}\\ +\Phi_0 G_{h_j\alpha_k}^{(0)}\xi_k+\displaystyle\sum_{n=0}^{N}\frac{G_{h_j\alpha_k}^{(n+1)}}{n!}\left(\frac{2R\chi}{c_0}\right)^{n+1}\left[c_1 d_1^{n+2}+c_2 d_2^{n+2}\right]\hat{\nu}_{ae,j}^{(n)}\end{array}\right\}+\Gamma_j^{NC}\left\{\begin{array}{l}G_{h_jh_j}^{(-1)}\xi_j''+\dfrac{R\chi}{c_0}G_{h_j\alpha_k}^{(-1)}\xi_k'\\ -\dfrac{a}{2}G_{h_j\alpha_k}^{(m)}\xi_k''\end{array}\right\} \tag{6}$$

In the previous equation the first set of braces is related to the C terms of the lift force whereas the second one to the NC, "added mass" effect. The quantity C_L^* is the derivative of the lift coefficient with respect to angle of attack (assumed as a constant along the blade), Γ_j^C and Γ_j^{NC} are dimensionless modal inertias, $G_{hj\alpha k}^{(.)}$ are "modal integral" terms. Finally, $\hat{\mu}_{ae,j}^{(n)}$ and $\hat{\nu}_{ae,j}^{(n)}$ are "partial" aeroelastic states. A similar expression can be derived to describe the generalized force of the mode k; it is not shown for the sake of conciseness.

Following previous work [12], propagation of aeroelastic load uncertainty that accounts for wind tunnel errors and modeling simplifications, is enforced by perturbing the term d_r (with r=2) of $\Phi(\tau)$ as $d_2 = d_{2m} + \delta_2$ with d_{2m} being its mean value and δ_2 a zero-mean random error parameter. The previous equations can be re-cast into a stochastic differential system, Itô-type, depending on a dimensionless scalar Wiener process $B(\tau)$ [9]. This vector equation includes the effect of random error δ_2 by state augmentation, as follows:

$$\mathrm{d}\,\mathbf{Z}(\tau) = \mathbf{a}_{NL}(\mathbf{Z}(\tau))\,\mathrm{d}\,\tau + \sqrt{2\pi}\,\mathbf{d}_u\,\mathrm{d}\,B(\tau) \tag{7}$$

In the previous equation, the drift function $\mathbf{a}_{NL}$ is nonlinear because of δ_2 whereas the diffusion vector $\mathbf{d}_u$ is zero since the forcing function is aeroelastic, i.e. turbulence effects are neglected in this first implementation. The previous equation is solved numerically through Euler-Monte Carlo algorithm, i.e. through sampling [12]. The pth order MLE is approximated, with time τ_l sufficiently large, as:

$$\Lambda_{\Xi}(p) = \lim_{\tau\to\infty} \log\left(\mathrm{E}\left[\left\|\Xi(\tau)\right\|^p\right]\right)\Big/\tau \approx \log\left(\mathrm{E}\left[\left\|\Xi(\tau_l)\right\|^p\right]\right)\Big/\tau_l\,, \tag{8}$$

and with $\Xi = [\xi_j, \xi_k, \mathrm{d}\xi_j/\mathrm{d}\tau,\ \mathrm{d}\xi_k/\mathrm{d}\tau]^T$.

3 EXAMINATION OF TAYLOR SERIES REPRESENTATION OF AIRFOIL INDICIAL FUNCTION

The derivation of the surrogate model requires the representation of the circulatory aeroelastic load, i.e. indicial function [Eq. (5)] by Taylor series expansion. A parametric study is carried out to examine the influence of the expansion order N on the accuracy of the representation. Apart from Eq. (5) (R.T. Jones' formula [17]) the use of the rational function below, as a first approximation to Eq. (5), has also been considered [16]:

$$\Phi(s) \approx \Phi_{\mathrm{rf}}(s) = \frac{s+2}{s+4} \tag{9}$$

The generalized aeroelastic force [Eq. (6)] in the proposed formulation strictly depends on the first derivative of Φ (or Φ_{rf}) with respect to dimensionless time s. The derivatives of Eqs. (5) and (9), using the Taylor expansion truncated at order N, respectively become

$$\frac{\mathrm{d}\,\Phi}{\mathrm{d}\,s} = \sum_{r=1,2} c_r d_r \left\{\mathrm{e}^{-d_r s}\right\} \approx \sum_{r=1,2} c_r d_r \left\{\sum_{n=0}^{N} \frac{(-s)^n (d_r)^n}{n!}\right\}, \tag{10}$$

$$\frac{\mathrm{d}\,\Phi_{\mathrm{rf}}}{\mathrm{d}\,s} = \frac{2}{(s+4)^2} \approx 2\left\{\sum_{n=0}^{N} (-1)^n (n+1)\, 4^{-(n+2)} s^n\right\} \tag{11}$$

Eq. (11) is obtained by suitable expansion of the expression $(s+4)^{-2}=y^{-2}$.

Figure 2 presents the results of this parametric study. In Figure 2a, the two expressions of the indicial functions, Eq. (5) and Eq. (9), are depicted; the main difference is related to the

range of dimensionless time larger than 4. Figure 2b examines the ability of the Taylor expansion to replicate the first derivative of the indicial function, $d\Phi/ds$ or $d\Phi_{rf}/ds$. The Taylor expansion in Eq. (10) is truncated at order N=5 whereas the one in Eq. (11) at order N=30.

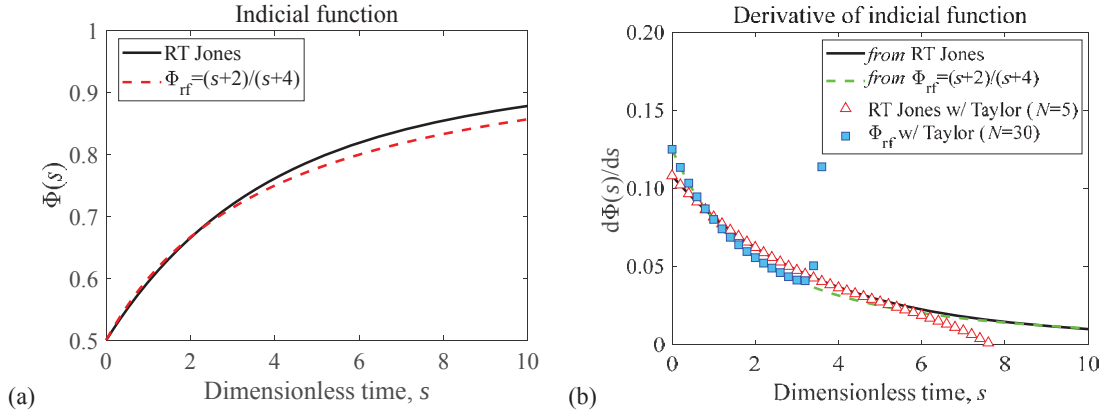

Figure 2: Taylor series representation of airfoil indicial function as a function of expansion order N - RT Jones' formula vs. rational function formula; (a) indicial function $\Phi(s)$, (b) first derivative of indicial function $d\Phi/ds$.

Even though the R.T. Jones' formula has been criticized since it may lead to less accurate results for large s [16], Figure 2b suggests that the ability of replicating the derivative of the function $d\Phi/ds$ is achieved with a lower order N. This feature is preferable from the point of view of the derivation of the surrogate model since N controls the number of partial aeroelastic states, $\hat{\mu}_{ae,j}^{(n)}$ and $\hat{\nu}_{ae,j}^{(n)}$, and consequently the complexity of the model in Eq. (7). Therefore, Eq. (10) is employed as the basis for the expression in Eq. (6).

4 SIMULATION RESULTS

The stochastic coupled-mode flutter of the NREL 5-MW wind turbine blade is examined (rotor radius R=61.5 m). The main structural and aerodynamic properties are derived from the literature [20]. The reduced-order model in Eq. (6) is based on the third flap-wise mode (mode j, natural frequency 4.34 Hz) and the first torsional mode (mode k, natural frequency 5.39 Hz) [1, 20]. Figure 3 illustrates the mode shapes of the two fundamental modes, employed for flutter analysis; in the panels both flap-wise (h) and torsional modal components (α) are displayed; edge-wise terms (p) are not shown.

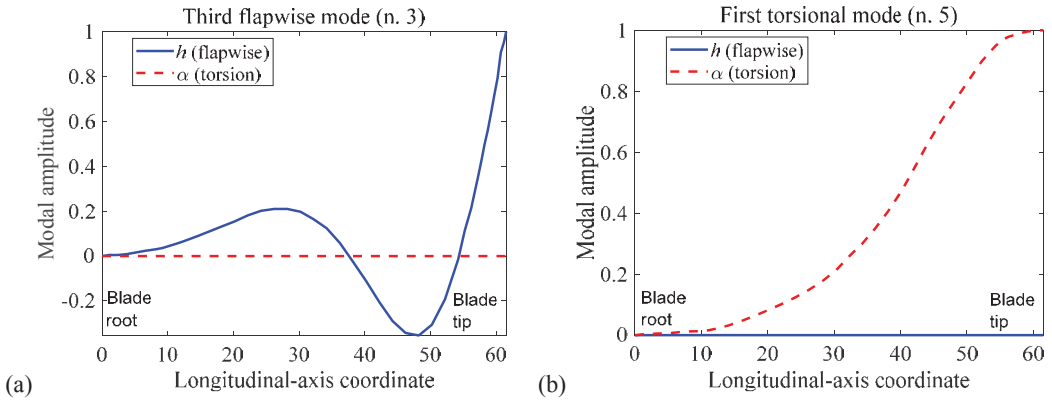

Figure 3: Mode shapes of the two fundamental modes used for flutter analysis; (a) third flap-wise mode (mode j), (b) first torsional mode (mode k). Data are derived from [1, 20].

The edgewise component (p) was neglected in the model. Modal similarity is evident from the panels, confirming that modal integrals $G_{hj\alpha k}^{(\cdot)}$ are non-zero and are responsible for the aeroelastic coupling.

The deterministic flutter problem is solved by setting δ_2=0; the system in Eq. (7) becomes linear in terms of state vector **Z** and flutter is examined by computing the system's eigenvalues as a function of Ω or χ, and by locating zero-damping critical condition. Results are illustrated in Figure 4. The critical flutter rotor speed is estimated as 16.7 rpm (against 20.7 rpm found in previous work [6]). The flutter frequency is 4.5 Hz (against 3.6 Hz). Differences are attributed to the fact that flutter solution of the NREL 5-MW wind turbine blade is also influenced by the 2nd flap-wise mode, neglected in this formulation. Furthermore, a constant C_L^* is employed in Eq. (5), whereas the lift slope varies along x as the cross section of the blade changes [20]. Results are, however, acceptable in the context of this simulation.

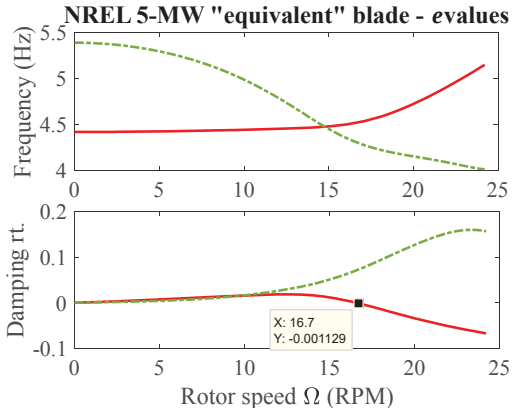

Figure 4: Eigenvalue analysis of the NREL 5-MW wind turbine blade; 3rd flap-wise mode (solid line) and 1st torsional mode (dashed-dotted line) as a function of angular rotor speed Ω (rpm). Flutter solution is highlighted; a positive damping rt. (ratio) in the figure is related to a stable system.

Figure 5 illustrates the stochastic flutter analysis of the system by presenting the estimation of Eq. (8) through numerical solution of Eq. (7) at Ω=16.94 rpm. The example includes non-zero random initial conditions and modeling error δ_2 in the aeroelastic loading of about 8% with respect to the nominal value d_{2m}.

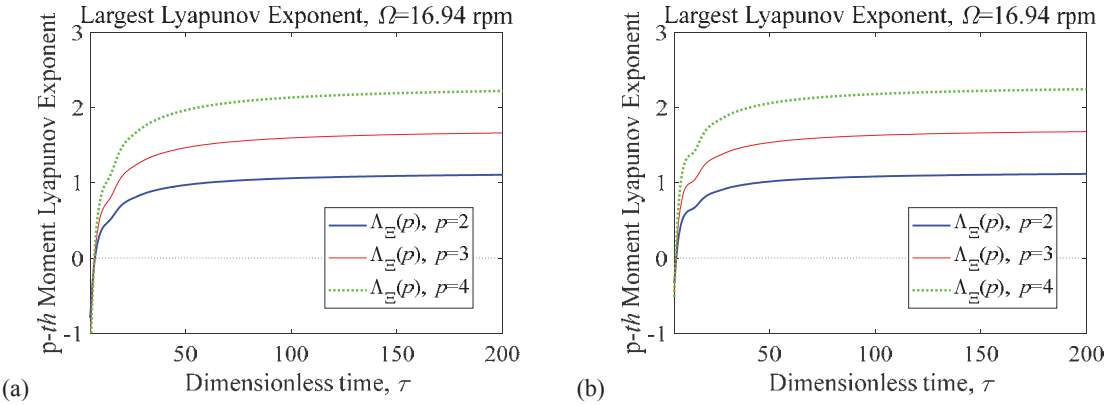

Figure 5. Stochastic flutter analysis of the NREL 5-MW wind turbine blade with random d_2; initial random conditions with (a) moderate zero-mean amplitudes, $E[\xi_{j0}^2]=E[\xi_{k0}^2]=0.01$; (b) large amplitudes, $E[\xi_{j0}^2]=E[\xi_{k0}^2]=0.10$.

Non-zero initial conditions are necessary to examine the onset of stochastic flutter. Two cases are presented: small initial dimensionless modal amplitudes with zero mean and variances $E[\xi_{j0}^2]=E[\xi_{k0}^2]=0.01$, and moderate amplitudes with $E[\xi_{j0}^2]=E[\xi_{k0}^2]=0.10$. The figure confirms that, since the stochastic problem is non-linear, it is amplitude dependent. In particular, for both small and moderate initial amplitudes an unstable system is obtained at Ω=16.94 rpm (negative MLE, asymptotically) suggesting that introduction of modeling error in the loading leads to a de-stabilizing effect in comparison with Figure 4.

5 DISCUSSION AND CONCLUSIONS

The study has demonstrated that it is possible to derive an analytical, closed-form formulation to describe the dynamics of rotating wind turbine blades under the influence of wind loads, contaminated by modeling variability and simplifications. The proposed formulation was employed to examine stochastic flutter of a reference offshore wind turbine blade. Numerical results (Figure 5) are, however, influenced by the solution algorithm, which may numerically introduce an unstable behavior. This aspect requires additional investigation. More discussion and a more detailed parametric investigation, by varying the properties of the input random variables, will be necessary in the future along with soil-structure interaction.

6 ACKNOWLEDGMENTS

This research was supported in part by the National Science Foundation of the USA, Award CMMI-1462774. Collaboration of Prof. Yahya Modarres-Sadeghi from the University of Massachusetts, Amherst (USA) is gratefully acknowledged.

REFERENCES

[1] P. Pourazarm, L. Caracoglia, M. Lackner, Y. Modarres-Sadeghi, Stochastic analysis of flow-induced dynamic instabilities of wind turbine blades, *J. Wind. Eng. Ind. Aerod.* 137, 37–45, 2015.

[2] Y.K. Lin, Y. Fujimori, S.T. Ariaratnam, Rotor blade stability in turbulent flows-part I, *AIAA J.* 17(6), 545-552, 1979.

[3] Y. Fujimori, Y.K. Lin, S.T. Ariaratnam, Rotor blade stability in turbulent flows-part II, *AIAA J.* 17(7), 673-678, 1979.

[4] M.H. Hansen, Aeroelastic instability problems for wind turbines, *Wind Energy* 10, 551-577, 2002.

[5] V.A. Riziotis, S.G. Voutsinas, E.S. Politis, P.K. Chaviaropoulos, Aeroelastic stability of wind turbines: the problem, the methods and the issues, *Wind Energy* 7, 373-392, 2004.

[6] P. Pourazarm, Y. Modarres-Sadeghi, M. Lackner, A parametric study of coupled-mode flutter for MW-size wind turbine blades, *Wind Energy* 19, 497-514, 2016.

[7] S. Li, L. Caracoglia, Surrogate Model Monte Carlo simulation for stochastic flutter analysis of wind turbine blades, *J. Wind. Eng. Ind. Aerod.* 188, 43-60, 2019.

[8] S. Li, L. Caracoglia, Wind tunnel experimental variability of aerodynamic loads for wind turbine blades, *Proceedings of the WindTEch 2019 Conference*, University of Massachusetts, Amherst, (electronic proceedings), 2019.

[9] M. Grigoriu, Stochastic calculus. Applications in science and engineering, *Birkhäuser*, Boston, MA, USA, 2002.

[10] W.-C. Xie, Dynamic stability of structures, *Cambridge University Press*, New York, NY, USA, 2006.

[11] Y.K. Lin, G.Q. Cai, Probabilistic structural dynamics, *McGraw-Hill*, New York, New York, USA, 1995.

[12] L. Caracoglia, An Euler–Monte Carlo algorithm assessing Moment Lyapunov Exponents for stochastic bridge flutter predictions, *Computers & Structures* 122, 65-77, 2013.
[13] S. Thakur, K.A. Abhinav, N. Saha, Stochastic response reduction on offshore wind turbines due to flaps including soil effects, *Soil Dynamics and Earthquake Engineering* 114, 174-185, 2018.
[14] T. Theodorsen, General theory of aerodynamic instability and the mechanism of flutter, Technical Report 496, *National Advisory Committee for Aeronautics*, 1935.
[15] D.H. Hodges, E.H. Dowell, Nonlinear equations of motion for the elastic bending and torsion of twisted nuniniform rotor blades, Techincal Note D-7818, *National Aeronautics and Space Administration (NASA)*, 1974.
[16] R.L. Bisplinghoff, H. Ashley, R.L. Halfman, Aeroelasticity, *Dover Publications Inc.*, Mineola, NY, USA, 1955.
[17] R.T. Jones, The unsteady lift of a finite wing, Technical Note 682, *NACA*, 1939.
[18] J.G. Leishman, Challenges in modelling the unsteady aerodynamics of wind turbines, *Wind Energy* 5, 85-132, 2002.
[19] A.A. Singapore Wala, E.Y.K. Ng, S. Narasimalu, A Beddoes-Leishman–type model with an optimization-based methodology and airfoil shape parameters, *Wind Energy* 21(7), 590-603, 2018.
[20] J. Jonkman, S. Butterfield, W. Musial, G. Scott, Definition of a 5-MW reference wind turbine, Technical Report NREL/TP-500-38060, *National Renewable Research Laboratory*, 2009.

EURODYN 2020
XI International Conference on Structural Dynamics
M. Papadrakakis, M. Fragiadakis, C. Papadimitriou (eds.)
Athens, Greece, 23–26 November 2020

A SYSTEMATIC INVESTIGATION OF COMMON GRADIENT BASED MODEL UPDATING APPROACHES APPLIED TO HIGH-FIDELITY TEST-DATA OF A WIND TURBINE ROTOR BLADE

Johannes Knebusch[1], **Janto Gundlach**[1], **and Yves Govers**[1]

German Aerospace Center (DLR)
Institute of Aeroelasticity
Bunsenstraße 10, 37073 Göttingen
Germany

johannes.knebusch@dlr.de
janto.gundlach@dlr.de
yves.govers@dlr.de

Keywords: Windenergy, Rotorblade, High-Fidelity, Model Updating

Abstract. *Within the context of the "SmartBlades2"-project, a wind turbine rotor blade was designed and extensively tested. The rotor-blade uses a lightweight composite structure and bend-twist coupling. The bend-twist coupling facilitates a passive load-reduction by changing the angle of attack under load. Due to a high sensor-density of 265 accelerometers in the experimental modal test of the blade, the sophisticated structural dynamics of the model are captured. Apart from the commonly measured first flapwise-, edgewise-bending and torsion mode, 35 modes up to a frequency of 60 Hz are identified. Unlike in many other wind turbine rotor blade investigations, the Finite Element (FE) model uses shell elements instead of beam elements and is directly based on production drawings. This experimental and simulative setup is particularly relevant, since a significant number of mode shapes exhibit a distinct local behavior which was in previous studies not accounted for. The differences between experimental and simulated results are minimized using computational model updating procedures. In this case-study, two formerly underrepresented aspects of the updating of large-scale FE models are examined. One is the use of different parameterizations and the other is the possibility of insufficient experimental data. The parametrizations are based on well-established criteria like error-localization and sensitivity. Moreover, the updating is performed with different (i.e. reduced) subsets of the modal data and the results are then compared to the model updating results achieved with the entire dataset. This in-depth investigation of the model updating of a composite structure allows the deduction of general guidelines in the model updating of industrial-sized FE models.*

1 INTRODUCTION

1.1 Model updating of rotor blades

In recent years a large number of wind-turbines were installed [14, 16, 19]. While the total installed power increased significantly, the output per wind turbine was also improved. This was reached by a number of measures. Aside from higher towers and efficiency improvements of the drivetrain, one important aspect is the aerodynamic improvement of the rotor blade [27]. Two closely related main trends govern this aerodynamic improvement. One is the aerodynamic optimization of the shape of the blade, and the other is the increasing length of the blades [15, 17, 27].
In general the aerodynamic optimization of the blade leads to mechanically more complex behavior [26]. The mechanical behavior of optimized rotor blades can, unlike the behavior of previously designed rotor blades not sufficiently be described with simple beam theory and requires more sophisticated models [25]. In addition to this, longer blades lead to higher loads and therefore a more considerate mechanical approach becomes necessary.
The wind turbine rotor blade that will be investigated in the following was designed with the intention of a geometrical bend-twist coupling to passively reduce loads during operation. Modal data from experimental vibration testing and finite element (FE) simulations usually lead to different results. In order to get reliable experimental data, various measures were taken [18]. To get an overview of the structural behavior, broadband random excitation signals are used. To check for specific properties, this is followed by tuned sine excitation. Different excitation levels are chosen, to identify possible nonlinearities. The modal parameters from all excitation runs (high force, low force, random, sine sweep - each in edge-wise as well as flap-wise direction) are compared with each other to extract the ”best” modes for the experimental modal model. Modeling errors in simulations can be classified in three main categories: idealization errors, discretization errors and erroneous parameters assumptions [22]. Neither idealization errors nor discretization errors are within the scope of conventional computational model updating [22]. Assuming these errors are negligible, a tuning (updating) of the parameters, so that similar results are achieved is reasonable [5]. The model updating is relying on previously acquired high-fidelity test-data described in [11, 13] and an existing FE model of the wind turbine rotor blade [30, 31]. From Figure 1 an impression of the fixed-free experimental set-up as well as the corresponding FE model can be gained. The model updating in this study is achieved

a) rotor blade attached to test-rig b) FE model of rotor blade and test-rig

Figure 1: Experimental setup and FE model

with FEMtools and MSC Nastran.
A simulation model that closer resembles reality will allow for better strain and deflection predictions and therefore offers several advantages. In operations, having better strain estimates leads to better fatigue and life-cycle estimations. Furthermore structural improvements of the mechanical behavior of new blades in the future can be based on a more precise predecessor model. This allows for reduced security margins, as the certainty in the mechanical behavior

of the precursor is higher. Increasing the validity of the deflection predictions enables better assessment of loads on the blade as well as on the entire wind turbine. Finally having more accurate deflection predictions also leads to better estimates of the output electrical power.
Numerous publications deal with iterative gradient-based model updating in the aerospace sector whereas only a few publications deal with the model updating of wind turbine blades. One reason for that appears to be, that the security requirements in the aerospace industry are higher than in the wind turbine industry. This is reflected in the certification process. Ground Vibration Tests are necessary for new aircraft prototypes, whereas they are not explicitly recommended for new wind turbine blades [2]. In this context the following publication presents a case study of the updating of a helicopter frame [22], [6] describes the updating of a full scale aircraft and among many others [7, 12, 21, 28] deal with small scale model updating problems. MOGRAVE and FRIBERG treat both a small scale and an industrial sized example [21]. Herein small refers to the dimensions of the model and not necessarily to the number of elements in the FE model. In recent years, some authors dealt with model updating of wind turbine blades. Amongst them [8, 9, 29] focused on a few modes and static deflection data. LUCZAK et al. investigated a blade section and chose a response surface based approach, that led to slightly improved correlation between test and analysis [20]. GROSS et al. updated a small scale wind turbine rotor blade (i.e. small in terms of rotor length) iteratively and sensitivity based [10]. The wind turbine rotor blade is tested under different boundary conditions. The exact improvements achieved with the model updating in terms of correlation between measured and simulated mode shapes remain unclear. In [5] the importance of having fewer parameters than responses and thus creating an (over-) determined system of equations is underlined. While DASCOTTE acknowledges the advantages of such a parameterization, the benefits of using more parameters than responses are described [1].

1.2 Methodology and Structure

The aim of this work is to improve and validate an existing FE model which is directly based on production drawings. In order to achieve this, high fidelity experimental results are used. A brief overview over the existing theoretical foundation for the techniques used in this work is given in Section 2. After an initial comparison of experimental and simulated results, it becomes apparent, that the compliance of the test-rig used during the experiments is non negligible, the model is thus (successfully) manually adapted (Section 3). The global similarity between experimental and simulated results ought to be minimized by adapting material parameters, while reflecting the true properties of the material as close as possible. This is firstly examined with the full set of sensors. A particular focus is laid on minimizing differences between experimental and simulated eigenfrequencies. Furthermore, two different parameterizations are investigated. These parameterizations are used and compared with respect to their advantages and disadvantages (Section 4.1). The parameterization which yields better results is used in the following computational model updating of the wind turbine rotor blade with subsets of sensors. The results of this are compared to the reference case that uses a full set of sensors (Section 4.2). Due to the comprehensive previously acquired experimental data [11], the updated wind turbine rotor blade models can be validated by changing the respective boundary conditions to ”free-free” and comparing the results to the respective experimental data set (Section 4.3). In Section 5 the results are summarized and an outlook is given. Section 6 acknowledges the support of different partners, without whom this study would not have been possible. The present work relies on a previously created simulation-model [30] as well as experimental data [11, 13] and is directly based on the study described in [18].

2 Iterative gradient-based model updating

The exact relation between changes in physical quantities like mass and stiffness (i.e. parameters) and the resulting changes in modal properties (i.e. responses) is simple to derive for very small systems but becomes increasingly difficult and practically impossible for industrial sized models. In light of this, the functional relation between parameters and responses is approximated with a TAYLOR series limited to the first two terms

$$\boldsymbol{r}_{\text{fe}}\left(\boldsymbol{p}\right) = \boldsymbol{r}_{\text{fe}}\left(\boldsymbol{p}_{\text{n}}\right) + \underbrace{\left.\frac{\partial \boldsymbol{r}_{\text{fe}}}{\partial \boldsymbol{p}}\right|_{\boldsymbol{p}=\boldsymbol{p}_{\text{n}}}}_{:=\boldsymbol{S}} \left(\boldsymbol{p} - \boldsymbol{p}_{\text{n}}\right). \tag{1}$$

In this $\boldsymbol{r}_{\text{fe}}$ is the response dependent on the parameters. Responses are chosen by the analyst and comprise (in the context of this work) of mode shapes and derived metrics, eigenfrequencies, mass and center of gravity resulting from the simulation model. $\boldsymbol{p}$ are the parameters (e.g mass and stiffness) and $\boldsymbol{p}_{\text{n}}$ are the parameter values at which the TAYLOR series is evaluated. $\boldsymbol{S}$ stands for the sensitivity of the numerical model. Evaluating $\boldsymbol{r}_{\text{fe}}$ at, yet to determine, new parameter values $\boldsymbol{p}_{\text{n+1}}$, the difference between experimental and numerical responses is

$$\boldsymbol{\varepsilon} = \boldsymbol{r}_{\text{exp}} - \boldsymbol{r}_{\text{fe}}\left(\boldsymbol{p}_{\text{n+1}}\right) \tag{2}$$

using the TAYLOR series for $\boldsymbol{r}_{\text{fe}}\left(\boldsymbol{p}_{\text{n+1}}\right)$ leads to the error term

$$\boldsymbol{\varepsilon} = \underbrace{\boldsymbol{r}_{\text{exp}} - \boldsymbol{r}_{\text{fe}}\left(\boldsymbol{p}_{\text{n}}\right)}_{:=\Delta\boldsymbol{r}} - \boldsymbol{S}\underbrace{\left(\boldsymbol{p}_{\text{n+1}} - \boldsymbol{p}_{\text{n}}\right)}_{:=\Delta\boldsymbol{p}}. \tag{3}$$

The objective function is then defined as

$$J(\Delta\boldsymbol{p}) = \boldsymbol{\varepsilon}^T\boldsymbol{W}_r\boldsymbol{\varepsilon} + \Delta\boldsymbol{p}^T\boldsymbol{W}_p\Delta\boldsymbol{p}. \tag{4}$$

It is dependent on the parameter changes $\Delta\boldsymbol{p} = \left(\boldsymbol{p}_{\text{n+1}} - \boldsymbol{p}_{\text{n}}\right)$. By additionally introducing diagonal weighting matrices for the parameters ($\boldsymbol{W}_p$) and the responses ($\boldsymbol{W}_r$) confidence in both experimental results and numerical model assumptions can be expressed [1]. The weighting matrices furthermore have a regularizing effect, which is comparable to a TIKHONOV-regularization [5]. Minimizing (4) leads to the calculation formulae for the new parameter $\boldsymbol{p}_{\text{n+1}}$ as defined in [1] and given in the following. According to DASCOTTE [1], if the number of parameters is less than or equal to the number of responses the new parameter values are calculated as

$$\boldsymbol{p}_{\text{n+1}} = \boldsymbol{p}_{\text{n}} + \left(\boldsymbol{W}_p + \boldsymbol{S}^T\boldsymbol{W}_R\boldsymbol{S}\right)^{-1}\boldsymbol{S}^T\boldsymbol{W}_R\Delta\boldsymbol{r}, \tag{5}$$

if the number of parameters is larger than the number of responses the new parameters are calculated with the equation

$$\boldsymbol{p}_{\text{n+1}} = \boldsymbol{p}_{\text{n}} + \left(\boldsymbol{W}_P\right)^{-1}\boldsymbol{S}^T\left(\boldsymbol{W}_R^{-1} + \boldsymbol{S}\boldsymbol{W}_P^{-1}\boldsymbol{S}^T\right)^{-1}\Delta\boldsymbol{r}. \tag{6}$$

2.1 Unification of measurements and simulations

In preparation of the updating, measurements and simulations have to be unified in many respects, which will be described in the following. Within this work all mode shapes (i.e experimental mode shapes $\boldsymbol{\psi}_r$ and simulated mode shapes $\boldsymbol{\phi}_r$) are scaled to largest component one. In the following damping is not considered and therefore the numerically calculated mode

shapes are entirely real valued. As the blade is lightly damped [18] using the magnitude and an appropriate sign for the experimental results as described in [1] is reasonable. In order to compare measurements and numeric calculations a common set of measurement points and degrees of freedom (DOFs) must be chosen. The numeric results can be reduced to the measurement points and DOFs, or the measurements can be expanded to the numerical calculated points and degrees of freedom. Expanding the measurement results implies interpolation between measurement points and can for example be achieved with the system equivalent reduction and expansion process (SEREP as described in [24]). To reduce the simulation results, the measurement points of the structure are mapped to nearby FE nodes. This means, that the results at DOFs, that are not close to a measurement point are omitted. As there are usually significantly more nodes than measurement points, the number of deleted results is large. The results (i.e. mode shapes) will be reduced to the measurement points.

2.2 Metrics for comparison

After measurements and simulations are unified, the similarity of measurement and simulation results can be quantified. This similarity quantification is helpful in the manual model adaptation and necessary for the computational model updating procedure. In the computational model updating select pairs are formed between experimental modes and simulated modes that have a high initial congruence.
In the derivation of most metrics, model assumptions and mathematical properties, like mass orthogonality or linear independence of eigenvectors are exploited. While the indicators described hereafter are rather similar, an important distinction is whether they refer to every DOF or they are giving a value for all DOFs. The same normal mode shapes have to be collinear and different mode shapes must be orthogonal with respect to the mass matrix [3]. This is supposed to be true for (normalized) experimental modes, numerical modes and between numerical and (normalized) experimental modes. Due to inaccurate and incomplete measurements, this relation is in practice not entirely fulfilled. Besides using Mass $\boldsymbol{M}$ as a weighting factor one can also directly check the orthogonality of mode shapes. The Mass Matrix $\boldsymbol{M}$ can (like any model of the real world) only be approximately correct. It is therefore reasonable to use no weighting factor instead of using a potentially wrong weighting factor. One then calculates the modal-assurance-criterion (MAC) for the simulated mode $\boldsymbol{\phi}_k$ (with the numbering k) and the experimental mode $\boldsymbol{\psi}_m$ (with the numbering m):

$$\mathrm{MAC}(\boldsymbol{\phi}_k, \boldsymbol{\psi}_m) = \frac{\left(\boldsymbol{\phi}_k^T \cdot \boldsymbol{\psi}_m\right)^2}{\left(\boldsymbol{\phi}_k^T \cdot \boldsymbol{\phi}_k\right)\left(\boldsymbol{\psi}_m^T \cdot \boldsymbol{\psi}_m\right)}. \tag{7}$$

The resulting value is 100 % for collinear modes and 0 % for orthogonal modes [1]. MAC values between simulated mode shapes of the same simulation are, as MAC value between experimental mode shapes of the same dataset, referred to as AUTOMAC values. As a measure of orthogonality for every degree of freedom l, over N mode shapes (with the numbering k) the coordinate-modal-assurance-criterion (COMAC) is introduced [1]

$$\mathrm{COMAC}(l) = \frac{\left(\sum_{k=1}^{N} (\boldsymbol{\phi})_k^l \, (\boldsymbol{\psi})_k^l\right)^2}{\left(\sum_{k=1}^{N} (\boldsymbol{\phi})_k^l \, (\boldsymbol{\phi})_k^l\right)\left(\sum_{k=1}^{N} (\boldsymbol{\psi})_k^l \, (\boldsymbol{\psi})_k^l\right)}. \tag{8}$$

The COMAC gives a sum (and therefore allows for fast checks) for multiple modes. The COMAC takes values between zero and one hundred percent. For brevity, the percentage signs are oftentimes omitted in the following.

3 Comparison of initial results and manual model adaptation

In Figure 2 the eight initially paired mode shapes are shown. In this figure, the experimental results are shown in red, while the simulated results are shown in blue. Their medium MAC value of 92 and medium frequency deviation of 8.8 % is detailed in Figure 6. It is noteworthy that mode shape 2.) has a MAC value of 98 inspite of its dissimilar appearance in Figure 2 2.). This is due to the fact, that sensors in edge-wise direction are only installed on the leading edge (Fig. 13 2.)), therefore the test-model (red) is not deformed in edge-wise direction at the other positions. It becomes apparent, that for all mode shape pairs apart from the first one, the experimentally determined eigenfrequency is higher than the simulated eigenfrequency. Furthermore the overall MAC values are high, but decrease slightly for modes with higher frequency.

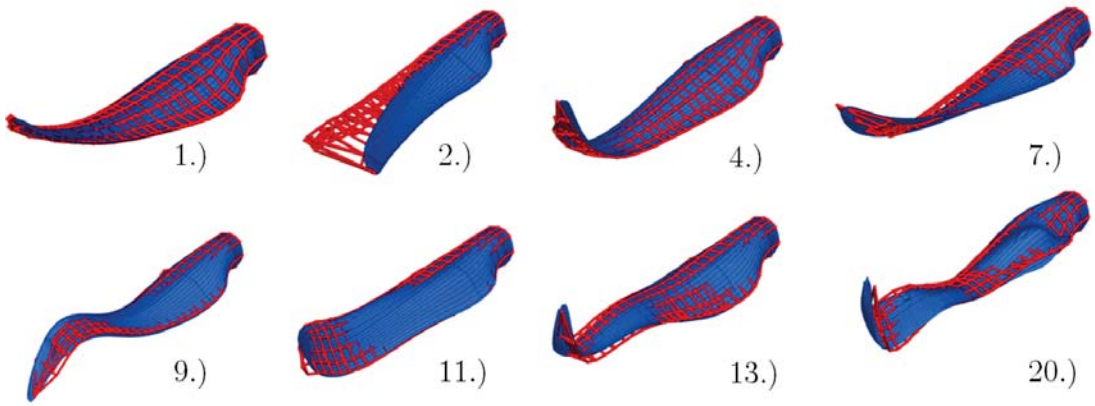

Figure 2: Initially paired mode shapes (numbered according to experimental mode shape number)

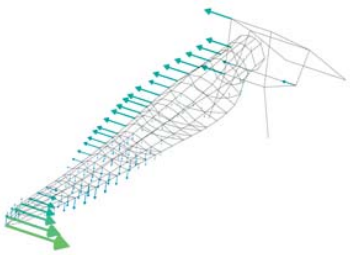

Figure 3: rig-mode at 7.2 Hz

The blade is tested while being clamped to a test-rig Figure 5 a). In a first approach a fixed-boundary condition is applied (i.e. displacement and rotations in all directions are suppressed) at the first nodal line on the blade root. An inspection of the COMAC values displayed in Fig. 4 a) and Fig. 4 b shows, that the local correlation gets significantly lower towards the root of the blade. Herein the gray markers indicate COMAC values below 50. In Figure 3 the first (experimental) rig-mode is depicted. Since this is the fifth experimental mode, it is concluded that the compliance of the test-rig is non negligible and therefore an FE model of the test-rig is created. The FE model of the blade is then rigidly attached to the FE model of the test-rig. The test-rig is made out of steel. The exact sort of the steel is unknown to the authors, S335 with its properties given in e.g. [4] is used in the model. To efficiently simulate the behavior of the test-rig, small features, like chamfers, holes and bolts are removed from the model. The simplified geometry of the test-rig is shown in Figure 5 b. Based on the simplified geometry, with unstructured meshing an FE model that consists of 58398 CTETRA-elements is constructed. The test-rig is estimated to have total mass of 23.5 tons. Removing holes, bolts and chamfers leads to an increase in mass of 1.5 tons and an (not quantified) increase in stiffness. The test-rig is fixed to the ground at four corner points with threaded rods. Nonetheless, the test-rig is assumed to move in lateral direction. This assumption is backed by the width of the support surface of the H beam (as depicted in the bottom

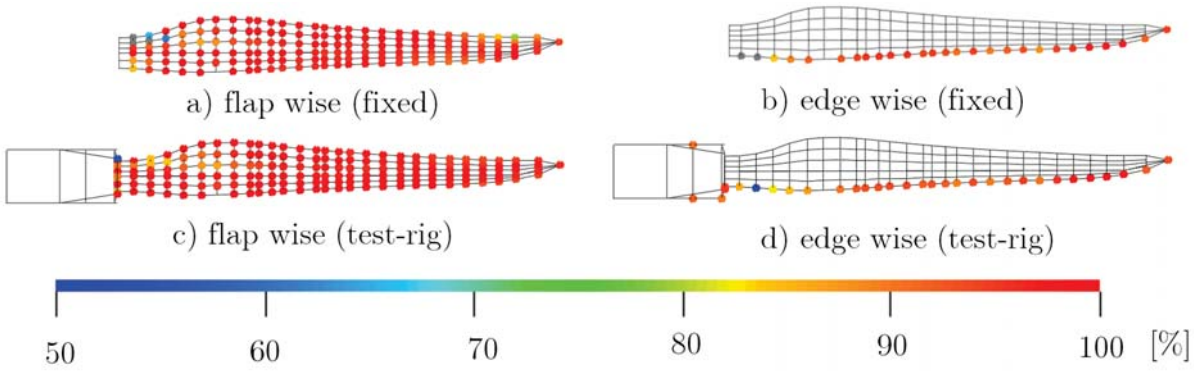

Figure 4: COMAC for 8 initially paired mode shapes

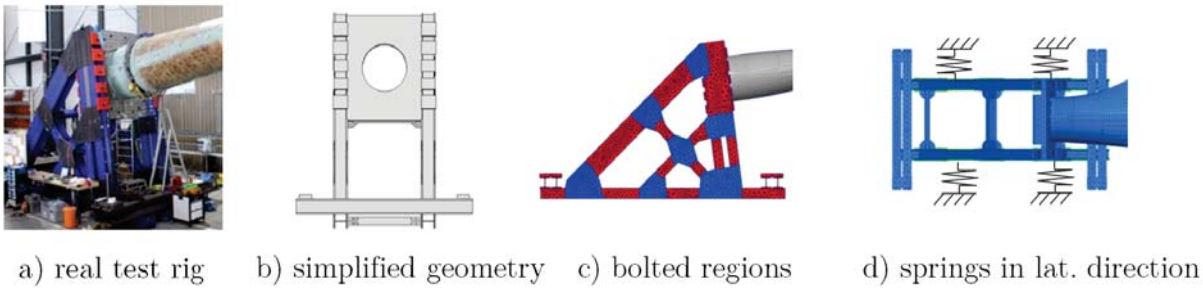

Figure 5: Test-rig: from reality to FE-model

of Fig. 5 a) and Fig. 5 b)) on which the test-rig stands (1 cm for each surface, therefore 4 cm in total). This assumed lateral movement is described in the model, by attaching springs in lateral direction at every node on the bottom surfaces of the H beams (as symbolized in Fig. 5 d). The spring constants as well as the stiffness of the test-rig in areas of bolted connections shown in blue in Figure 5 c) are adjusted to reproduce the first rig-mode. With a stiffness reduction in these areas to 10 % of the nominal stiffness, a MAC value of 85 % and a frequency deviation of 1.64 % deviation is reached for the simulated mode and the experimental mode displayed in Figure 3. Furthermore, significantly higher COMAC values are reached for the initially paired mode shapes in both flap wise (Fig. 4 c)) and edge wise direction (Fig. 4 d)). Since the COMAC is calculated over all initially paired mode shapes, the increased COMAC values indicate, that the test-rig describes the reality more closely, than a fully fixed boundary condition. In Figure 6, MAC values as well as frequency deviations between simulated and experimental results for both the initial configuration (i.e. fully fixed) and the configuration with the auxiliary test-rig are shown. From this, it becomes clear, that the simulation model with the auxiliary test-rig not only leads to increased MAC values (compared to the initial configuration) but also three mode shapes (5.) 18.) 19.)) that where previously not paired (n.p.) and are now paired. Despite the slightly increased deviations in eigenfrequency for the model with the auxiliary test-rig (Fig. 6 c)), the overall similarity between experiment and simulation is increased with the above described manual model adaptation.

4 Computational Model updating

In order to further improve the global similarity between simulated and experimental results the model of the blade is computationally updated as described in the following. In this process the above described auxiliary model of the test-rig is used but not further adapted.

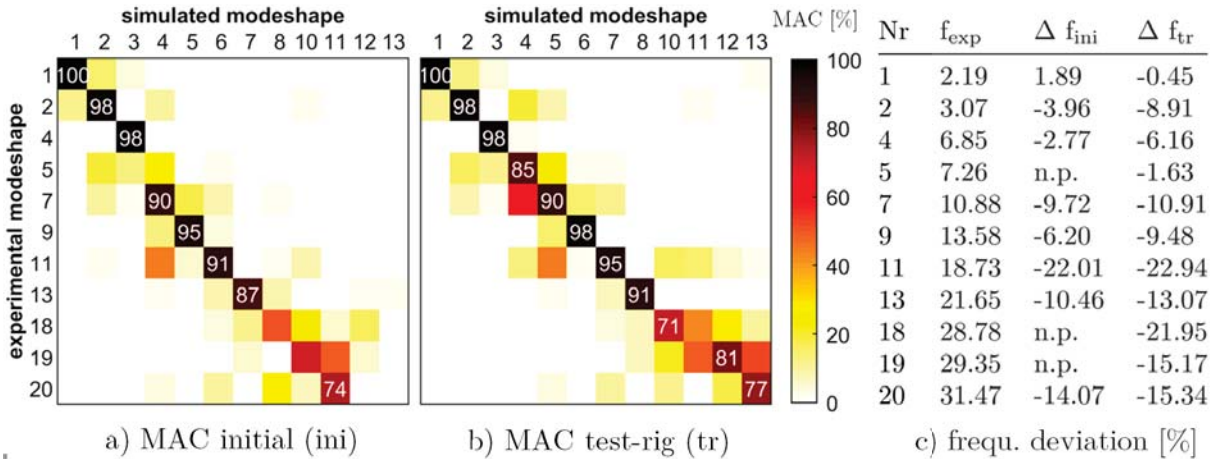

Nr	f_{exp}	Δf_{ini}	Δf_{tr}
1	2.19	1.89	-0.45
2	3.07	-3.96	-8.91
4	6.85	-2.77	-6.16
5	7.26	n.p.	-1.63
7	10.88	-9.72	-10.91
9	13.58	-6.20	-9.48
11	18.73	-22.01	-22.94
13	21.65	-10.46	-13.07
18	28.78	n.p.	-21.95
19	29.35	n.p.	-15.17
20	31.47	-14.07	-15.34

Figure 6: MAC and deviation in eigenfrequency for initial and manually adapted model

4.1 Updating based on full set of sensors - reference configuration

4.1.1 Responses

The magnitude of the relative deviation in eigenfrequency $|\Delta f| = |(f_{fe}\text{-}f_{exp})/f_{exp}|$ between a simulated (fe) and an experimental mode (exp) is used as one measure for pairing respective modes. This is due to the fact that, in conjunction with similar mode shapes, this deviation is a good indicator of similarity and therefore helps in relating models in terms of their dynamic behavior. In the following, experimental and simulated modes are considered to be paired, if they have MAC value above 70 % and an absolute frequency deviation of less than 30 %.
As responses MAC values (11) and frequency deviations (11) of paired mode shapes as well as the center of gravity (1) in spanwise direction (COG) and the mass (1) are used. This results in a total number of 24 responses. The responses are weighed differently. The diagonal response weighting matrices $\boldsymbol{W}_R$ are built from the weights as given in the following. The frequency responses are, as oppose to all other responses which are given a weighting of 1, given different weights in the objective function (Tab. 4.1.1). Responses with higher weights are emphasized in the objective function, while responses with a lower weight are not. The weighting is based on the premise, that in the updating of this rotorblade, large initial discrepancies in frequency (in particular for torsional modes) ought to be minimized, while mode shape correlation should improve.

Table 1: response weighting

Experimental Mode Shape	1.)	2.)	4.)	5.)	7.)	9.)	11.)	13.)	18.)	19.)	20.)
frequency weighting	1	2	1	1	2	1	4	1	2	2	4

4.1.2 Initial sensitivities

To tune the global dynamic behavior of the simulation model, two types of parameters are used. A scaling factor on the membrane stiffness as well as a scaling factor on the density. In preparation of the parameterization, sensitivities are calculated for every shell element with respect to each response. The summed normalized initial sensitivities are displayed in Figure

7. Herein the scale is limited to allow the detection of relevant regions. For a small number of elements the magnitude of the sensitivities is larger than shown in Figure 7. With this, it becomes apparent that different regions are particularly sensitive. It is worth noting, that apart from the areas marked in red and blue in Figure 7, the beginning of the spar (not visible in the figure) is highly sensitive to changes in density as well as in membrane stiffness.

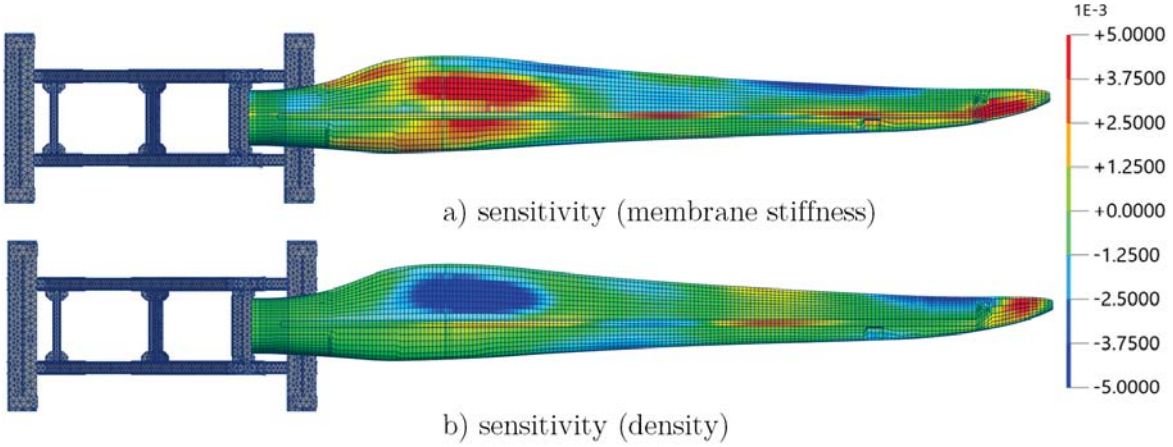

Figure 7: Initial summed normalized sensitivities (limited scale)

4.1.3 Parameterization

The model is parameterized in two different ways. In the first approach 12 design fields are used. Using one scaling factor on the membrane stiffness and one scaling factor on the density as parameters for each design field leads to 24 parameters in total. The design fields are equally spaced from root to tip and numbered consecutively from left to right, beginning in the upper left and ending in the lower right (Fig. 8 a)). The spar is included in the lower 6 design fields (i.e. design field number 7 to design field number 12). In the second approach 40 design fields as shown in Figure 8 b) are used and numbered according to the same scheme as in the other parameterization. Additionally 19 design fields are equally spaced along the spar (from root to tip) leading to a total number of 59 design fields and thus 118 parameters. The first parameterization has the advantage of using the same number of parameters (24) as responses (24) and therefore leading to a determined system of equations. In spite of this drawback, the parameterization with 118 parameters has the advantage of a finer spatial resolution and furthermore accounts for differences in sensitivities on the spar as oppose to the outer hull of the blade. Since the second parameterization uses fewer responses than parameters, the parameter changes are additionally constrained to their initial value in order to ensure a deterministic updating procedure. Because the model is directly based on production drawings, the maximum

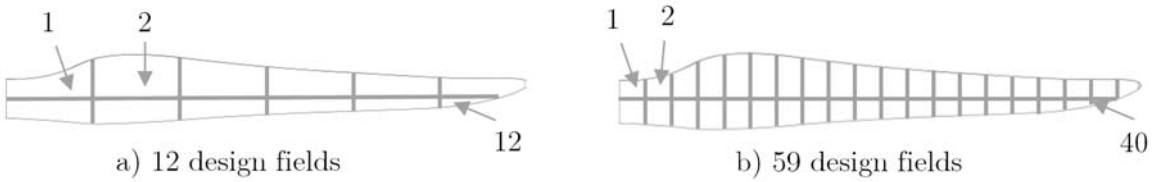

Figure 8: Design fields leading to parameterizations

parameter change is set to 15%. While the exact number is based on engineering judgment, the general limitation of parameter changes is due to the notion, that the updated model should not just reproduce the experimental results but also reflect the true material properties as close as possible [23]. The parameter change per iteration is limited to 0.5 % in order achieve a smooth convergence of parameters. All parameters are weighed equally with a value of 1 (i.e. $\boldsymbol{W}_P$ is the identity matrix). This is due to the fact, that there is no indication of particular uncertainty on select parameters.

4.1.4 Adaptations

The parameters are adjusted in 150 iteration steps. The final parameter values are shown in Figure 9. Both models are adapted similarly. This is particularly the case for the membrane stiffness (Fig. 9 c), Fig. 9 d)) where the membrane stiffness in large regions is increased by the set maximum of 15 %. Figure 9 b) shows, that the density at the tip of the blade is changed significantly differently in the two neighboring design fields 19 and 20. The discrepancy of more than 20 % shows that using a finer spatial resolution is particularly reasonable in this area. Furthermore, the differences between the adaptations of the spar as oppose to the outer hull of the blade (Figure 9 b) Figure 9 d)) indicates, that the sensitivities throughout the updating process differed. Since, in the parameterization with 12 design fields, the spar is included in the design fields towards the leading edge, the adaptations to the spar shown in Fig. 9 a) b) are equal to the respective parameter changes for the outer hull of the blade. Figure 10 shows

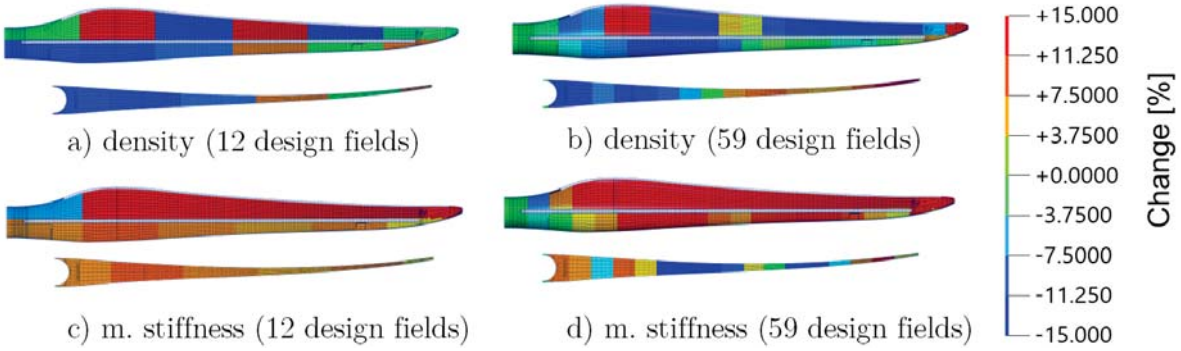

Figure 9: Parameter adaptations after 150 iteration steps

the parameter evolution over 150 iteration steps. Numerous parameters are increased to the set magnitude limit of 15% change after a comparatively small number of iterations. Besides this, parameters do not visibly change slope of change (i.e. parameters that decrease in the beginning continue to decrease and parameters that increase in the beginning continue to increase).

4.1.5 Results

Oposing Figure 6 and Figure 11 highlights, that updating the FE model (while using the FE model of the test-rig) leads to increased MAC values and decreased frequency deviations. Figure 11 a) and b) show that the MAC values are improved with both parameterizations. The parameterization with 118 parameters leads to an (overall) higher similarity (i.e. increased MAC values and decreased frequency deviations) than the parameterization with 24 parameters (Fig. 11) . From Figure 12 it becomes clear, that the parameter adaptations lead to an improvement

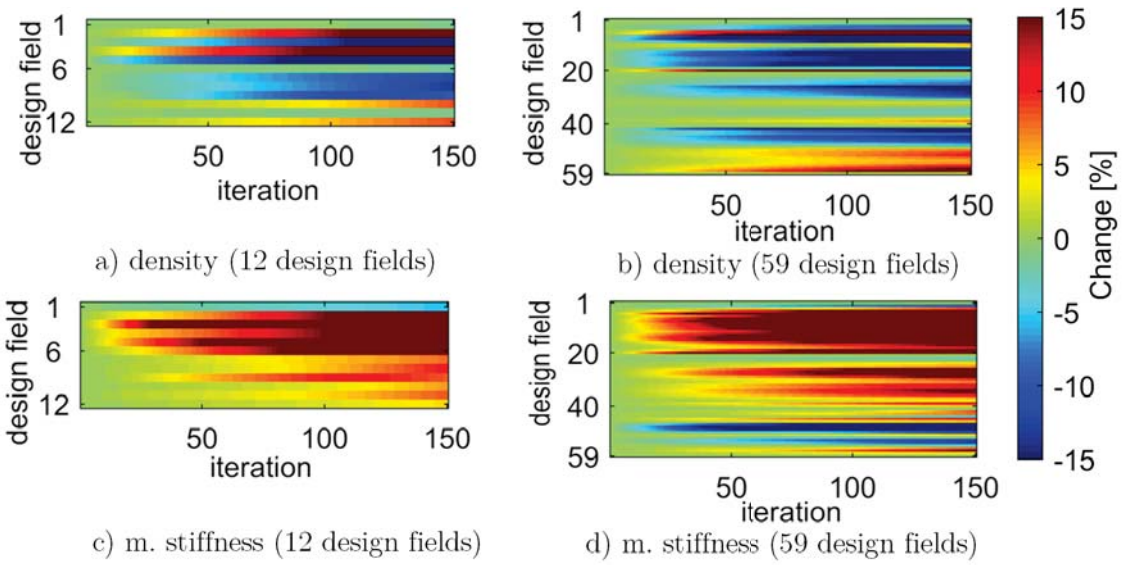

Figure 10: Evolution of iteratively adapted parameters

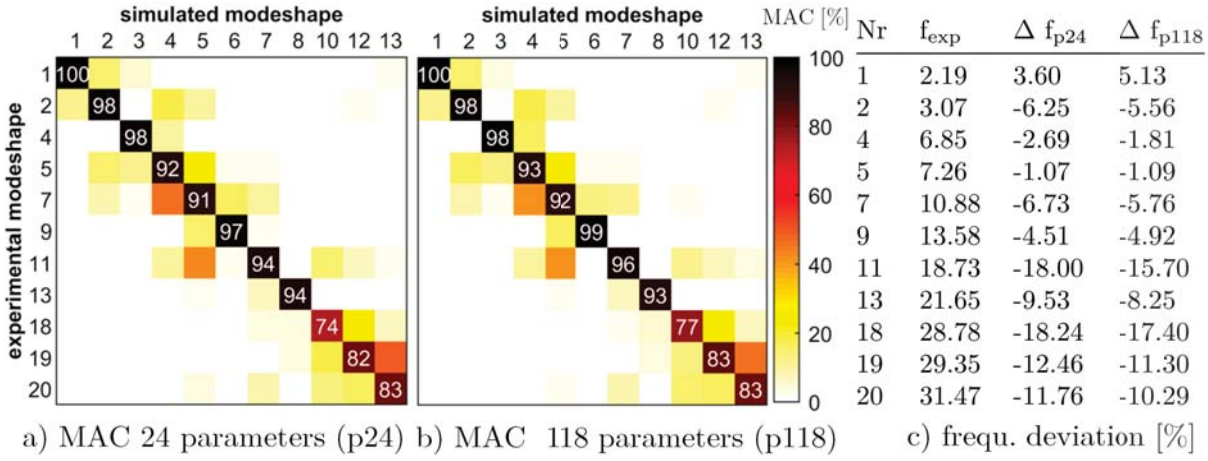

Nr	f_{exp}	Δf_{p24}	Δf_{p118}
1	2.19	3.60	5.13
2	3.07	-6.25	-5.56
4	6.85	-2.69	-1.81
5	7.26	-1.07	-1.09
7	10.88	-6.73	-5.76
9	13.58	-4.51	-4.92
11	18.73	-18.00	-15.70
13	21.65	-9.53	-8.25
18	28.78	-18.24	-17.40
19	29.35	-12.46	-11.30
20	31.47	-11.76	-10.29

Figure 11: MAC and deviation in eigenfrequency for updated models

in mean MAC value and decreasing discrepancy in frequency. Furthermore Figure 12 shows, that these similarity indicators are better for the parameterization with 118 parameters than for the parameterization with 24 parameters. It ought to be noted, that, while frequency deviations are still decreasing after iteration 100 mean MAC values are slightly deteriorating.

4.2 Updating based on reduced set of sensors

The updating with the reduced set of sensors uses the sensor locations shown in Figure 13 and is performed with the second parameterization (i.e. 118 parameters), which yielded better results in the reference case. The updating is performed with different sets of sensors selections. While the number of sensors used in the updating is reduced, the modal model is not changed, i.e. the modal identification is not repeated with the reduced sensor sets. The full set of sensors is displayed in green in the upper part of Figure 13. The total number of paired sensors on the wind turbine rotor blade and the test-rig is 272, 237 sensors are in flap wise direction while 35 are in edge wise direction (at the leading edge). The number of sensors is iteratively reduced. In each step one sensor is removed based on the notion, that the sum over the off-diagonal values of

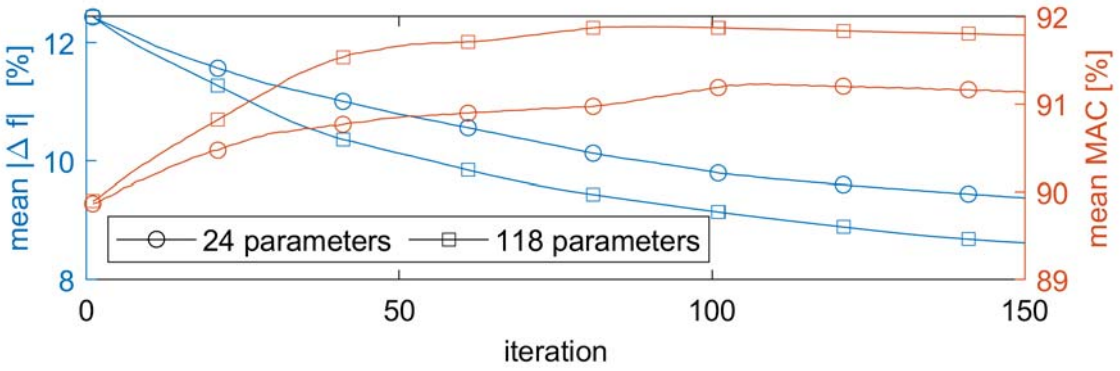

Figure 12: Evolution of medium MAC value and frequency deviation

the AUTOMAC-matrix for the Finite-Element (FE) mode shapes 1 to 20 evaluated at the sensor positions is minimized. Three configurations with reduced sensor sets will be investigated. The number of sensors is reduced to 1/2 (red. sens (1/2)), 1/4 (red. sens. (1/4)) and 1/8 (red. sens. (1/8)). The remaining sensors for these configurations are marked on the lower test-model in Figure 13. In the first configuration, sensors are located at all color-marked positions (red. sens (1/2)), the second configuration uses only the sensors at the positions marked in yellow and red (red. sens. (1/4). The third configuration uses only sensors at the locations marked in yellow (red. sens (1/8)). From Figure 14 it becomes clear, that potentially hard to distinguish mode shapes e.g. 11 and 12 are hard to distinguish for all configurations. Overall the AUTOMAC matrices lead to the impression, that most mode shapes up to the 20th mode are well distinguishable for all configurations. The evolution of the mean similarity indicators

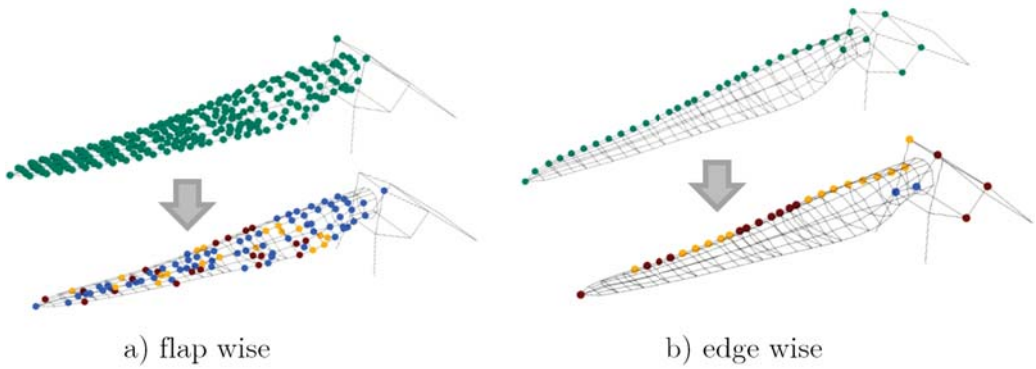

Figure 13: Full and reduced sensor selection

for the updating of these reduced configurations are displayed in Figure 15. It becomes clear, that the frequency discrepancy for all reduced sensor configurations is minimized as well as for the full sensor configuration. In contrast to this, the MAC improvements for the reduced configurations (red. sens. (1/4) and (red. sens. (1/8))) are smaller than for the full set of sensors or nonexistent (red. sens. (1/2)).

4.3 Verification

The boundary condition of the updated models is changed to ”free-free” and compared to the experimental ”free-free” modal-data described in [11]. An overview of these verification results can be gained from Figure 16. In this, the similarity metrics are calculated for mode

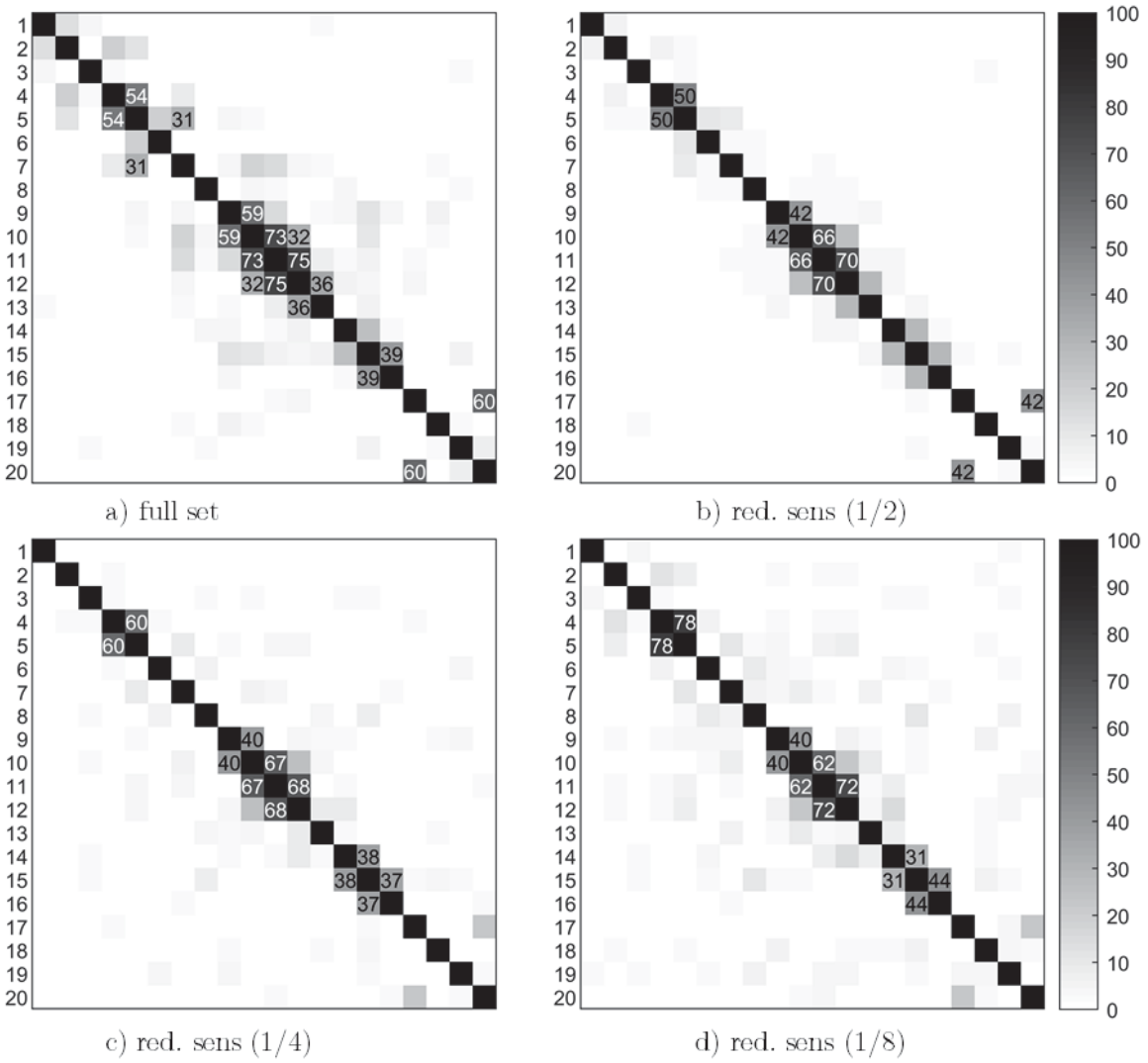

Figure 14: FE-AUTOMAC matrices in [%] evaluated for full and reduced sensor sets

shape pairs that occur in all configurations. It becomes clear, that the mean frequency deviation is improved for all configurations and all mean MAC values are marginally aggravated. The improvements are slightly better in terms of the MAC values for the parameterization with 24 parameters as oppose to the parameterization with 118 parameters. With respect to the mean frequency deviation, the parameterization with 118 parameters leads to slightly better results.

5 Summary and Outlook

In the present work, several aspects of the model updating of an industrial-sized FE model of a wind turbine rotor-blade were investigated. The more accurate representation of the boundary condition by creation of an auxiliary FE model led to the largest improvement in MAC values and slightly worsened the frequency deviation. In this case study, a parameterization with a number of parameters that exceeds the number of responses led to better results, than a parameterization in which the number of parameters is equal to the number of responses (Fig. 11). Furthermore it was shown, that with a reduced number of sensors, the frequency deviation can be minimized well, while the correlation of the MAC values was not significantly improved

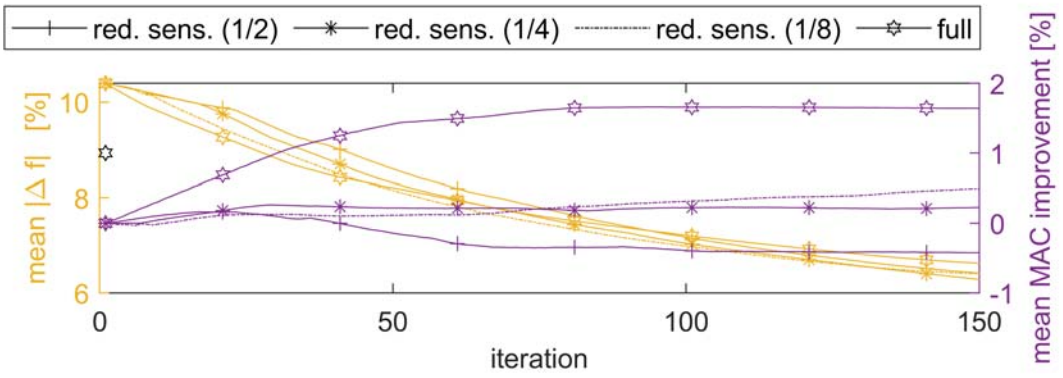

Figure 15: Evolution of similarity criteria for reduced sensor sets

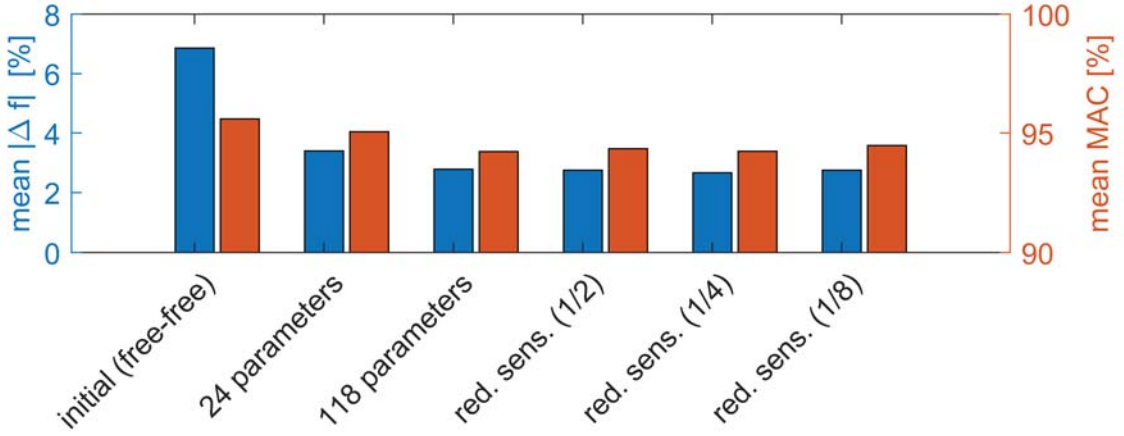

Figure 16: Verification of Updating results under altered boundary condition

(Fig. 15). The evolution of parameters showed no obvious ripple effects, which indicates, that the step-size for the parameter adjustments was chosen to be small enough. A large number of parameters was at the set global limit of 15%. Relevant parameter changes where observed for almost all parameters. While the observed improvements are in line with the focus on decreasing frequency deviations, it becomes apparent, that the parameter adaptations do not fully represent the true material characteristics. In light of this, future works should use different parameterizations and judge the respective results. If mode shape correlation improvements are of interest, a large number of sensors should be used. The effects of response-weighting are assumed to be relevant and will be examined in future works.

6 Acknowledgments

This publication relies upon previous works especially [11, 13, 18] and was partially funded by the German Federal Ministry for Economic Affairs and Energy (BMWi) in the SmartBlades2 project (0324032A-H). The authors are much obliged to all members of the DLR modal test team. The updating procedure was implemented within FEMtools (Dynamic Design Solutions) with the very appreciated technical assistance of its leader Eddy Dascotte.

References

[1] E. Dascotte. FEMtools Model Updating Theoretical Manual. June 2019.

[2] DIN EN 61400-23:2014-12;VDE 0127-23:2014-12. Wind energy generation systems - part 23: rotor blades, 2019.

[3] D. Ewins. *Modal testing: theory and practice*, volume 15. Research studies press Letchworth, 1984.

[4] U. Fischer. *Tabellenbuch metall (mit Formelsammlung)*. Europa-Lehrmittel, 2011.

[5] M. Friswell and J.E. Mottershead. *Finite Element Model Updating in Structural Dynamics*. Solid Mechanics and Its Applications. Springer Netherlands, 2013. ISBN 9789401585088.

[6] D. Göge. Automatic updating of large aircraft models using experimental data from ground vibration testing. *Aerospace Science and Technology*, 7(1):33 – 45, 2003. ISSN 1270-9638. doi:https://doi.org/10.1016/S1270-9638(02)01184-7.

[7] Y. Govers. *Parameter identification of structural dynamic models by inverse statistical analysis*. PhD thesis, Universitätsbibliothek Kassel, 2012.

[8] D. Griffith and T. Carne. Experimental modal analysis of 9-meter research-sized wind turbine blades. In *Structural Dynamics and Renewable Energy, Volume 1*, pages 1–14. Springer, 2011.

[9] T. Griffith, J. Paquette, and T. Carne. Development of validated blade structural models. In *46th AIAA Aerospace Sciences Meeting and Exhibit*, page 1297, 2008.

[10] Johann Gross, Tobias Oberhardt, Pascal Reuss, and Lothar Gaul. Model updating of the ampair wind turbine substructures. In *32nd International Modal Analysis Conference (IMAC XXXII)*, 2014.

[11] J. Gundlach and Y. Govers. Experimental modal analysis of aeroelastic tailored rotor blades in different boundary conditions. In *Journal of Physics: Conference Series*, volume 1356, page 012023. IOP Publishing, 2019.

[12] A. Gupta, C. Moreno, H. Pfifer, B. Taylor, and G. Balas. Updating a finite element based structural model of a small flexible aircraft. In *AIAA Modeling and Simulation Technologies Conference*, page 0903, 2015.

[13] B. Haller. Smartblades2 - deliverable del 1.2.2.1 del 1.2.2.2 del 1.2.2.3 rev. 0.0. 2018.

[14] R. Hara. Chapter 5 - prediction of wind power generation output and network operation. In Toshihisa Funabashi, editor, *Integration of Distributed Energy Resources in Power Systems*, pages 109 – 131. Academic Press, 2016. ISBN 978-0-12-803212-1. doi:https://doi.org/10.1016/B978-0-12-803212-1.00005-2.

[15] C. Hernández, T. Telsnig, and A. Pradas. Jrc wind energy status report 2016 edition. *Market, Technology and Regulatory Aspects of Wind Energy*, 2017.

[16] International Renewable Energy Agency IRENA. Installed capacity trends. https://www.irena.org/win, 2019. Last accessed on 27th of August 2019.

[17] J. Kaldellis and D. Zafirakis. The wind energy (r) evolution: A short review of a long history. *Renewable energy*, 36(7):1887–1901, 2011.

[18] J. Knebusch. Finite element model updating of wind turbine rotor blades using modal data aquired with attached load frames. Master's thesis, Technical University Berlin, 2019.

[19] D. Leung and Y. Yang. Wind energy development and its environmental impact: A review. *Renewable and sustainable energy reviews*, 16(1):1031–1039, 2012.

[20] M. Luczak, S. Manzato, B. Peeters, Kim. Branner, P. Berring, and M. Kahsin. Updating Finite Element Model of a Wind Turbine Blade Section Using Experimental Modal Analysis Results. *Shock and Vibration*, 2014:1–12, 2014. ISSN 1070-9622, 1875-9203. doi:10.1155/2014/684786.

[21] P. Mograve and O. Friberg. Updating large finite element models in structural dynamics. *AIAA journal*, 36(10):1861–1868, 1998.

[22] J. Mottershead, M. Link, and M. Friswell. The sensitivity method in finite element model updating: A tutorial. *Mechanical Systems and Signal Processing*, 25(7):2275–2296, October 2011. ISSN 08883270. doi:10.1016/j.ymssp.2010.10.012.

[23] H. Natke. *Einführung in Theorie und Praxis der Zeitreihen- und Modalanalyse: Identifikation schwingungsfähiger elastomechan. Systeme*. Grundlagen der Ingenieurwissenschaften. Vieweg, Braunschweig, 2., verb. aufl edition, 1988. ISBN 978-3-528-18145-1. OCLC: 246837170.

[24] J. O'Callahan and P. Li. A non smoothing serep process for modal expansion. In *Proceedings of the 12th International Modal Analysis*, volume 2251, page 232, 1994.

[25] W. Ostachowicz, M. McGugan, J. Schröder-Hinrichs, and M. Luczak. *MARE-WINT: new materials and reliability in offshore wind turbine technology*. Springer, 2016.

[26] S. Scott, M. Capuzzi, D. Langston, E. Bossanyi, G. McCann, P. Weaver, and A. Pirrera. Gust response of aeroelastically tailored wind turbines. In *Journal of Physics: Conference Series*, volume 753, page 042006. IOP Publishing, 2016.

[27] J. Serrano-González and R. Lacal-Arántegui. Technological evolution of onshore wind turbines—a market-based analysis. *Wind Energy*, 19(12):2171–2187, 2016.

[28] J. Sinha and M. Friswell. Model updating: a tool for reliable modeling, design modification and diagnosis. *The Shock and Vibration Digest*, 34(1):27–35, 2002.

[29] J. White, D. Adams, and M. Rumsey. Modal analysis of cx-100 rotor blade and micon 65/13 wind turbine. In *Structural Dynamics and Renewable Energy, Volume 1*, pages 15–27. Springer, 2011.

[30] C. Willberg. Smartblades 2 finite element reference wind turbine blade model, 2020. URL `https://doi.org/10.5281/zenodo.3628356`.

[31] C. Willberg. Validation of a 20m wind turbine blade model. *Wind Energy Science*, 2020. Currently under review.

EURODYN 2020
XI International Conference on Structural Dynamics
M. Papadrakakis, M. Fragiadakis, C. Papadimitriou (eds.)
Athens, Greece, 23–26 November 2020

PLATFORM OPTIMIZATION OF LARGE FLOATING OFFSHORE WIND ENERGY STRUCTURES

G. Ferri[1], E. Marino[1] and C. Borri[1]

[1] Department of Civil and Environmental Engineering, University of Florence
via di Santa Marta 3, Florence
giulio.ferri@unifi.it

enzo.marino@unifi.it, claudio.borri@unifi.it

Keywords: Floating Offshore Wind Turbines, Semisubmersible platform, 10MW Wind Turbines, Large floating platform, Platform optimization.

Abstract. *The increasing demand of energy is leading to continue innovation in the renewable energy sector. Wind energy harvesting hit a milestone placing wind farm offshore, firstly in shallow water, using fixed bottom supporting technologies and now moving to deep sea areas, where floating platforms are needed. With floating technologies, construction and service costs exponentially grow; therefore, structural and mechanical optimizations have a primary role in the design of a floating offshore wind turbine (FOWT). Optimizations may involve the stabilizing principle, platform shape and size, mooring lines geometry and positioning. In the present work, attention is focused on structural aspects and an optimization procedure for a large wind turbine supported by semisubmersible-like platforms is proposed. In this study, platform is optimized with the intent to enhance the structural performances of the whole system.*

.

1 INTRODUCTION

Floating Offshore Wind Turbines (FOWT) are complex structural systems exposed to multiple stochastic loading conditions. Optimal platform design is crucial to ensure appropriate reliability levels at the lowest possible cost. Past studies compared different platform stability classes. Wayman and Sclavounos [1] investigated stability and response of a barge-like platform and a Tension Leg Platform (TLP). They developed a simplified Frequency Domain (FD) model to evaluate the coupling interaction between the wind turbine and the floating system. With the increasing of rotor size, above 200m diameter and 10MW rated power, rational upscaling technique [2] based on power ratios were adopted to directly design platforms for larger turbines. New typologies of platforms, for example the tri-spar floater [3], have also been studied. However, there is still lack in design optimization for such large turbines. Brommundt et al. [4] performed a design optimization on mooring lines of a 5MW FOWT for two targeted environmental conditions. Karimi et Al. [5] performed a multi-objective design optimization of a 5MW WT supported by a semisubmersible platform and a TLP. Both cost and structural performances were considered as targets. Optimization is usually performed in the frequency domain, with the overall objective of reducing cost and increasing structural performances. Design variables are usually the geometrical properties of the platform, whereas a widely adopted objective function is the nacelle acceleration Response Amplitude Operators (RAO).

In the present work, the optimal dimensions of a semisubmersible-like platform, similar to the OC4 NREL platform [6], but suitable for a 10MW WT are investigated. The analysis is performed in the frequency domain, adopting a validated in-house developed model [7] coupled with FAST-v7 [8]. The effect of the mooring lines and the wind turbine are accounted for through additional mass, damping and stiffness matrices computed through a linearization analysis performed with FAST.

In the following, firstly the adopted FD model is briefly described. Then, results obtained from a parametric study of a semisubmersible platform suitable for a 10 MW WT are presented and compared with an upscaled 10 MW WT model [2]. In conclusion, future developments for a wider FD-based optimization procedure will be presented.

2 FREQUENCY DOMAIN MODEL

FOWTs can be analysed either in the time domain or in the frequency domain. In the first case, nonlinear dynamic interaction of the whole structure with wind, waves and control system can be possibly captured. Moreover, the time domain approach allows to simulate extreme load conditions, such as breaking waves impacts [9], [10], shutdown, or system failure. In an optimization context, where a large number of simulations are required, the time domain approach may lead to an unaffordable computational cost. FD models neglect or approximate nonlinear effects and allow to consider only steady load conditions. Despite these simplifications, their efficiency may still offer valuable guidance in the pre-screening phase of an optimization-based design. Most of the proposed FD approaches superimpose the turbine contribution in terms of mass, damping and stiffness matrices to the hydrodynamic contribution due to the floating platform. The description of the FD model adopted in this work, together with a code-to-code verification using benchmark results obtained from time domain simulations [11] [12], is available in [7]. The ANSYS AQWA potential solver [13] is adopted to evaluate radiation/diffraction hydrodynamic contributions to the equation of motion of the floating platform, while Morison's equation [14] is used for slender elements. The model considers approximated nonlinear viscous drag term and heave plates damping.

Mooring lines and wind turbine contribution to the equation of motion are evaluated through a linearization analysis around the operational point performed with FAST_v7. The linearized equation of motion is solved for the six rigid body platform degrees of freedom (DoFs). Finally, the RAOs are calculated.

3 10MW FOWT OPTIMIZED SEMISUBMERISBLE PLATFORM

In this section, a new semisubmersible-like platforms, suitable for the 10 DTU WT [15] is studied. The effect of two key design variables, namely the outer column diameter d and platform radius r (Figure 1), on the dynamic response of the platform is investigated.

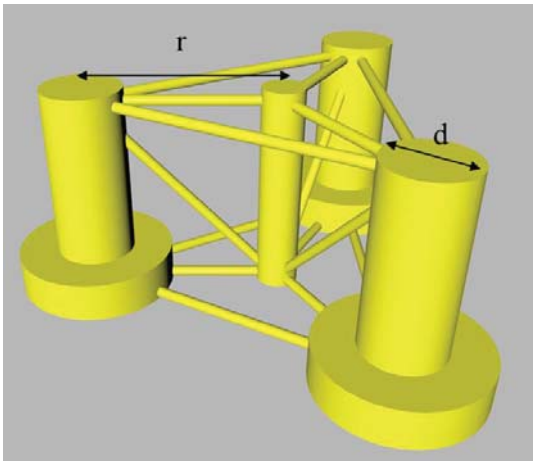

Figure 1: Semisubmersible-like platform design viariables.

The ratio between heave plates and side columns diameters is set to 2. Heave plates length is set to 6m. Draft is kept constant to 28m by modifying the concrete ballast.

The length of the mooring lines is rearranged to maintain the same stiffness matrix on the whole set of possible solutions [7]. Eight different column diameters and platform radii are chosen in order to create a grid of 32 combinations. The grid spacing for d and r are 1 m and 5 m, respectively. The results for all 32 combinations are then interpolated using spline surfaces. Although only parked state condition is presented in this paper, for each combination (d, r), the mean pitch rotation angle is checked as to whether it is suitable for a power production state. A rotation of 5° is considered the maximum allowable pitch angle [1].

Two quantities of heave and pitch motions are chosen as target to be minimized: RAO peaks and integral RAO in the range of frequency excited by the constant 1 m^2/Hz white noise (0 to 0.2 Hz). Both heave and pitch are also indicators of turbine performance as discussed in [12] and [1]. Results are presented in Figures 2-5 and compared with those of an upscaled platform from the 5MW DeepWind semisubmersible (identified by a red dot in Figures 2 and 3). Heave and pitch RAO peaks for the investigated platforms are presented in Figure 2. From Figure 2a, a minimum region of heave RAO peak (parked case) can be identified for outer columns diameter between 16-17m and for almost all platform radii considered. Figure 2b presents the pitch RAO peaks (parked state). The minimum region between 13 m and 14 m for the column diameters and a platform radius of 35 m has to be discarded since the maximum allowable pitch angle of 5° is violated. A minimum region for a smaller and lighter solution with respect of the upscaled one (marked as a red dot in the figure) can be found between 16 m and 17 m for the column diameters and a platform radius of 35 m. Platforms with 16–17 m column diameters and 35 m radii appear to be the best choice, which minimizes both heave and pitch peaks.

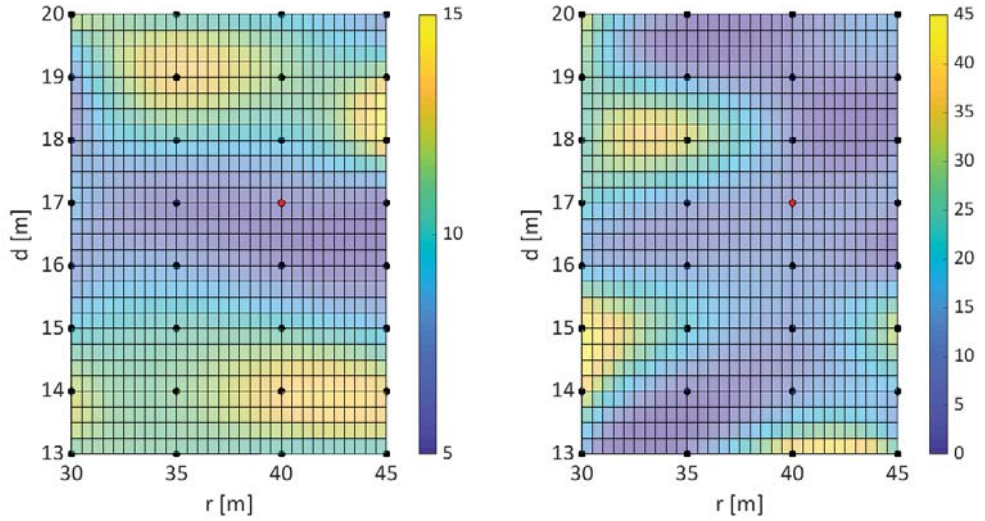

(**a**) (**b**)

Figure 2: Parked condition; RAO peaks of heave (m/m) (a) and pitch (deg/m) (b). Red dots refer to the upscaled configuration.

In Figure 3, RAO integrals of heave (Figure 3a) and pitch (Figure 3b) DOFs are presented. Figure 3a and 3b reveal a lower minimum region between 16 m and 17 m for the outer column diameters. Local maxima in the bottom and upper part of the domain are caused by an increasing of the eigenfrequency peak and by heave–pitch coupling.

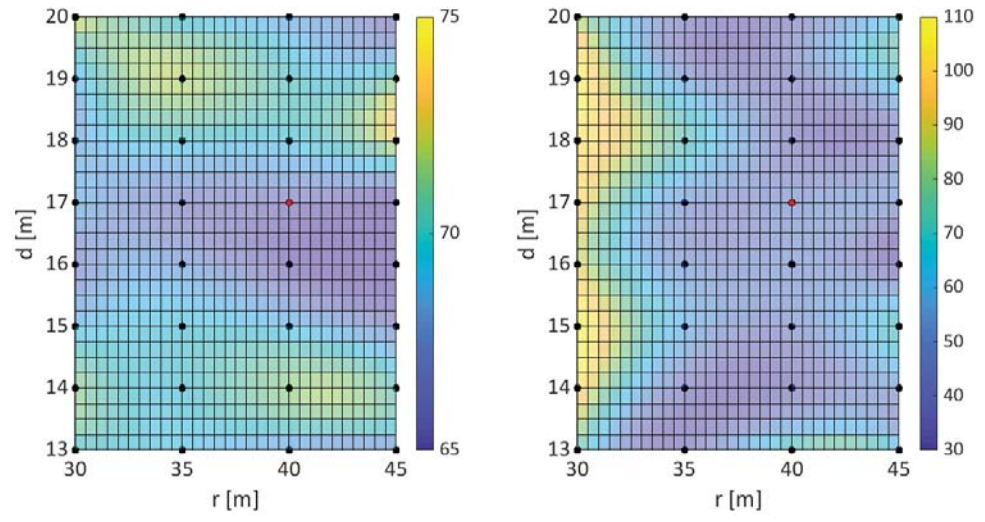

(**a**) (**b**)

Figure 3: Parked condition; RAO integral of heave (a) and pitch (b). Red dots refer to the upscaled configuration.

Considering the platforms analysed, and that the platform response in pitch would affect more the fatigue behaviour of both turbine tower and mooring lines than the response in heave, the configuration with a 16 m column diameter and 35 m platform radius is preferred to the 17 m, 35 m.

In Table 4, the numerical values of the RAO peaks of the upscaled and the optimized platform are compared. As it is possible to observe, a low reduction is achieved in surge because

the dynamic behaviour is mainly dominated by mooring lines, which are not optimised in this study.

	Surge Peak	Heave Peak	Pitch Peak
Upscaled	26.12	14.74	15.31
Optimised	24.08	7.27	9.62
Reduction [%]	7.78	50.69	37.12

Table 4. Comparisons of RAO peak values between the upscaled and optimised platforms.

4 CONCLUSION AND FUTURE WORKS

In the present work, a frequency domain optimization procedure for a semisubmersible-like platform is discussed. The optimized procedure is performed by considering 2 variables, namely the outer columns diameter d, and the platform radius r. An optimal configuration is achieved for d=16m and r=35m. Future works will be focused on considering more variables, such as draft and heave plates height. Moreover, different targets to be minimized will be considered, such as nacelle acceleration RAO and the difference between the platform draft windward and the local free surface wave elevation [16]. This is a fundamental quantity that must be considered to prevent bottom-slamming and, therefore, to reduce fatigue loads on mooring lines and turbine tower. To increase the efficiency of the optimization procedure, the next step will be the evaluation of multidimensional fitted functions for the hydrodynamic parameters (added mass, radiation damping and diffraction forces). This procedure will allow not to call the potential flow solver at every run in the optimization algorithm, leading to a drastic reduction of the computational time. The proposed procedure is also enforced by the fact that the hydrodynamic parameters are relatively smooth functions as it is possible to see in Figure 4.

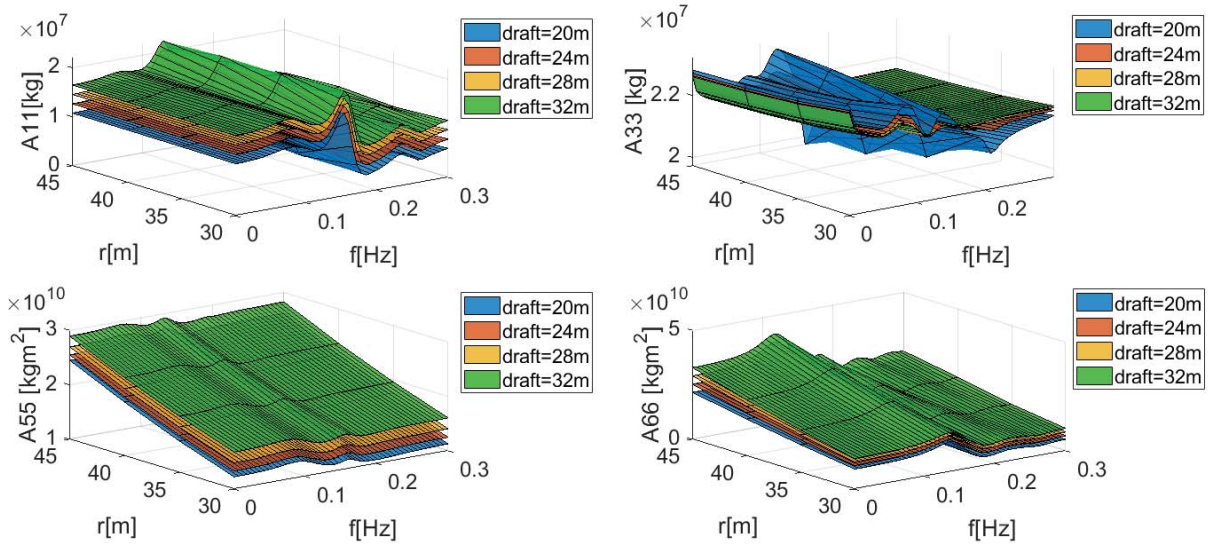

Figure 4: Added mass coefficients for a semisubmersible-like platform of 14 m side column diameter, varying platform radius (y axis), frequency (x axis) and platform draft from 20 m to 32 m.

REFERENCES

[1] E. N. Wayman and P. D. Sclavounos, “Coupled Dynamic Modeling of Floating Wind

Turbine Systems Preprint," *Offshore Technol. Conf. 1–4 May 2006, Houston, TX*, 2006.

[2] M. Leimeister, E. E. Bachynski, M. Muskulus, and P. Thomas, "Rational Upscaling of a Semi-submersible Floating Platform Supporting a Wind Turbine," in *Energy Procedia*, 2016, vol. 94, pp. 434–442.

[3] J. Azcona, F. Vittori, U. Schmidt, and F. Savenije, "Design Solutions for 10MW Floating Offshore Wind Turbines Document information," vol. 308974, no. 308974, 2017.

[4] M. Brommundt, L. Krause, K. Merz, and M. Muskulus, "Mooring system optimization for floating wind turbines using frequency domain analysis," *Energy Procedia*, vol. 24, no. January, pp. 289–296, 2012.

[5] M. Karimi, M. Hall, B. Buckham, and C. Crawford, "A multi-objective design optimization approach for floating offshore wind turbine support structures," *J. Ocean Eng. Mar. Energy*, vol. 3, no. 1, pp. 69–87, 2017.

[6] A. Robertson and J. Jonkman, "Definition of the Semisubmersible Floating System for Phase II of OC4," no. September, 2014.

[7] G. Ferri, E. Marino, and C. Borri, "Optimal Dimensions of a Semisubmersible Floating Platform for a 10 MW Wind Turbine," *Energies 2020, Volume 13, Issue 12, 3092*, 2020.

[8] J. Jonkman and M. L. Buhl, "FAST User's Guide," vol. 123, no. 6, pp. 407–8, 2007.

[9] E. Marino, C. Borri, and U. Peil, "A fully nonlinear wave model to account for breaking wave impact loads on offshore wind turbines," *J. Wind Eng. Ind. Aerodyn.*, vol. 99, no. 4, pp. 483–490, Apr. 2011.

[10] E. Marino, C. Lugni, and C. Borri, "A novel numerical strategy for the simulation of irregular nonlinear waves and their effects on the dynamic response of offshore wind turbines," *Comput. Methods Appl. Mech. Eng.*, vol. 255, 2013.

[11] A. Robertson *et al.*, "Offshore code comparison collaboration continuation within IEA wind task 30: Phase II results regarding a floating semisubmersible wind system," *Proc. Int. Conf. Offshore Mech. Arct. Eng. - OMAE*, vol. 9B, no. March 2014, 2014.

[12] N. Robertson *et al.*, "OC5 Project Phase II: Validation of GLobal Loads of the DeepCwind FLoating Semisubmersible Wind Turbine," *Energy Procedia*, vol. 137, pp. 38–57, 2017.

[13] "AQWA User Manual," vol. 15317, no. October, pp. 724–746, 2012.

[14] J. R. Morison, J. W. Johnson, and S. A. Schaaf, "The force exerted by surface waves on piles," *J. Pet. Technol.*, vol. 2, no. 05, pp. 149–154, 1950.

[15] C. Bak *et al.*, "Design and performance of a 10 MWwind turbine," *J. Wind Energy*, no. July, pp. 1–138, 2013.

[16] P. Sclavounos, C. Tracy, and S. Lee, "Floating offshore wind turbines: Responses in a seastate Pareto optimal designs and economic assessment," *Proc. Int. Conf. Offshore Mech. Arct. Eng. - OMAE*, vol. 6, pp. 31–41, 2008.

EURODYN 2020
XI International Conference on Structural Dynamics
M. Papadrakakis, M. Fragiadakis, C. Papadimitriou (eds.)
Athens, Greece, 23–26 November 2020

DYNAMIC FIELD DATA FROM OFFSHORE MONOPILE WIND TURBINES – ASSESSMENT OF NATURAL FREQUENCIES AND DAMPING

Karin Norén-Cosgriff[1] and Amir M. Kaynia[1]

[1] Norwegian Geotechnical Institute, NGI, Oslo, Norway
e-mail: Karin.Noren-Cosgriff@ngi.no, Amir.M.Kaynia@ngi.no

Keywords: offshore wind energy; pile foundation; measurements; acceleration; strain; natural frequencies.

Abstract. *The dynamic characteristics of offshore wind turbines are heavily affected by the ambient excitations (e.g. wave excitations and wind excitations) and nonlinear soil behaviour. For monopile structures, the fatigue design for the wind and wave loading is one of the most important problems to consider. Since the fatigue damage is sensitive to the foundation stiffness and damping, increasing the accuracy of analysis tools used in the design and optimization process can improve the reliability of the design and reduce conservatism, thereby leading to a more cost-efficient design. In this context, analysis of field data is important for calibrating and verifying purposes.*

This paper presents analysis of measured accelerations and strains in two offshore wind turbines in the North Sea with monopile foundations. One of the turbines is in a site that is dominated by sand and the other by clay. Field data during idling conditions, collected over long periods of operation, are analysed and the natural frequencies and estimates of damping are determined. Further, the effect of load (wave, wind and dynamic bending moment) on the natural frequencies is investigated and clear correlation between load level and natural frequency is demonstrated, which points to the importance of soil nonlinearity.

1 INTRODUCTION

According to [1] soil structure interaction (SSI) effects can reduce the fixed-base fundamental frequency more than 15% in the frequency range above > 0.25 Hz. Therefore, analysis tools need to include an accurate description of the soil. In this context, analysis of field data is important for calibrating and verifying purposes. However, only measurements from a few installations are reported in the literature. Some of these are mentioned below.

In [2] analyses of more than 1500 "rotor-stop" tests performed on offshore wind turbines founded on monopiles in four wind parks are described. In [3] analyses of measurement data from one offshore wind turbine structure on a monopile foundation in Horns Reef II wind farm are presented. In [4] results are presented from analyses of 'rotor stop' tests performed on one offshore wind turbine on a monopile in Burbo Banks wind farm. Research in [5] presents results from a load measuring campaign on one offshore wind turbine on a monopile in Horns Rev 1 Wind Farm. Studies carried out in [6] report measurements of overall damping from "rotor-stop" test in the Horns Rev 1 and the Burbo offshore wind farms. Finally, [7] and [8] present data from a long-term monitoring campaign and overspeed stops performed at the Belwind wind farm.

In the present study, analyses of measurement data from two wind farms in the North Sea with monopile foundations are presented. Measured acceleration and strain data collected over several periods of idling conditions are analysed. The objectives of these analyses are twofold. First, to determine the natural frequencies to be used in validation of developed foundation models, and second, to observe any sensitivity of the measured natural frequencies to the intensity of loading, which in turn would point to the role of soil nonlinearity. This paper describes the analyses performed at these sites and the main results.

2 SITE CONDITIONS, TURBINE STRUCTURE AND INSTRUMENTATION

Both sites are located in the North Sea. The ground conditions at the first site are sand-dominated, while the second site is predominantly clay. Measurement data from one tower at each site are used in this study. The tower at the sandy site is equipped with strain gauges at four levels on the inner wall of the monopile (MP) and the inner wall of the transition piece (TP). In this study, measured vertical strain in TP are analysed and in addition, information about wind speed from measurement at the tower is used. The tower at the clayey site is equipped with horizontal and vertical accelerometers close to the tower bottom, and strain gauges at several levels in the tower, the transition piece and the monopile. In this study, measured accelerations in the horizontal X and Y directions and foundation vertical strain are analysed. In addition, information about wind speed and wind direction measured at the tower are used. For both sites, information about significant wave height (Hs) and wave direction are collected from nearby metmasts. For the sandy site, no information about nacelle direction was available from measurements at the tower due to sensor error. The nacelle direction is therefore assumed to be about equal to the wind direction measured at the nearby metmast. Figure 1 shows the monopiles and the location of the instruments. Table 1 gives further information about the sites, the installations and the instrumentation. For the clayey site, for which both strain and accelerometer data are available, the determination of natural frequencies and damping are based on acceleration, since these data have the best quality. For the sandy site, the determination of the natural frequencies and damping are based on measured strain. Assessment of load through dynamic bending moment, is based on measured strain for both sites.

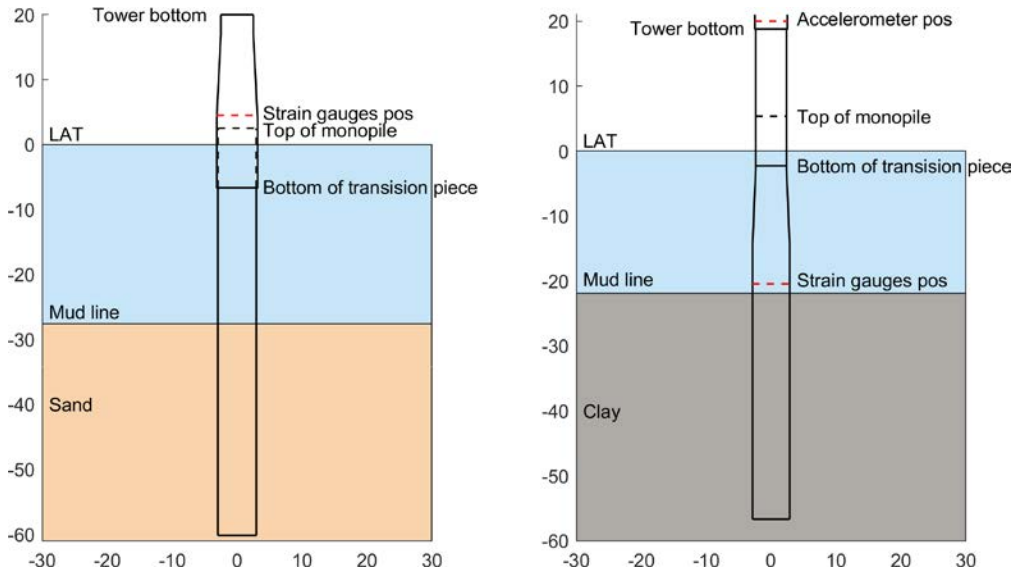

Figure 1: Ground conditions, monopile layout and sensor location, left: sandy site, right: clayey site.

	Site 1	Site 2
Ground conditions	Sand dominated	Clay dominated
Water depth	27 m	22 m
Turbine power	3.6 MW	3.6 MW
Monopile diameter	5.95 m	5.70 m
Instrumentation	4 vertical strain gauges in TP EL +4.5	3 vertical strain gauges in MP EL -20.45. 1 horizontal (X and Y) accelerometer in tower El +20
Sampling frequency	10 Hz	25 Hz

Table 1: Ground conditions, OWT and instrumentation

3 WIND AND WAVE INFORMATION

The response in idling periods are more affected by the foundation stiffness and damping than the response during production, which is primarily influenced by aerodynamic damping and stiffness. Therefore, the focus in this study is on idling periods. For the sandy site, the turbine is idling throughout all time periods from which data were received, while for the clayey site, the turbine is idling in between periods of production. Some of these idling periods lasted only a few minutes, while others lasted for several days. For data used in this study, a requirement is set for a minimum idling period of 24 minutes, with the first and last two minutes discarded to avoid influence from start-up and shut-down of the turbine. Figure 2 shows the distribution of the analysed time periods over wind speeds, wave heights, and wind and wave directions, described as averages in 20-minutes periods. The length of the red bins in the Rose diagrams corresponds to the number of 20-minutes periods with this observation, e.g. about hundred 20-minutes periods with wind direction between 265 and 270 degree for the sandy site.

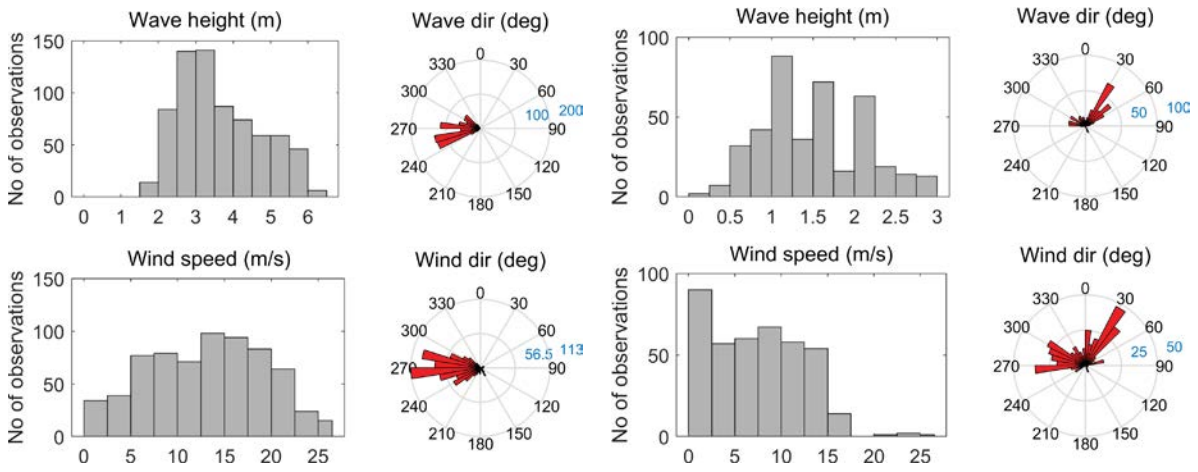

Figure 2: Distribution of average (in 20-minutes periods) wind speed, wave height and wind and wave direction for the analysed time periods, left: sandy site, right: clayey site.

4 DETERMINATION OF NATURAL FREQUENCIES

The natural frequencies are determined using the following FFT based methodology:

- The idling periods are divided into 20-minutes segments and FFT is performed on each segment using a 10-minutes analysis period and 50 % overlap, resulting in one Power Spectrum Density (PSD) for each segment with a frequency resolution of 0.0017 Hz.
- To determine the overall natural frequencies, an average PSD is calculated from all PSDs for the individual time periods, and the natural frequencies are identified from the peaks in the average PSD.
- To study a possible effect of the load on the natural frequencies, the first natural frequencies are determined from the PSDs for all individual 20-min segments and plotted against average wind speed, wave height and calculated dynamic bending moment in the respective 20-min period. Averaging by use of overlaps have the disadvantage of reducing the frequency resolution. Therefore, each determination of the first natural frequency in this part of the study is based on results from FFT analysis of 20-minutes segments without averaging.

The response of an offshore wind turbine is directional dependent due to the thrust on the rotor [3], i.e. there may be a small difference in the natural frequencies in the yaw direction (Fore-aft) and perpendicular to yaw direction (Side-side). Before applying the above methodology, the two directions are therefore analysed separately by transforming the measured accelerations and strains to a local coordinate system determined by the nacelle direction using the following equation:

$$\begin{bmatrix} Side-side \\ Fore-aft \end{bmatrix} = \begin{bmatrix} \cos\theta & -\sin\theta \\ \sin\theta & \cos\theta \end{bmatrix} \begin{bmatrix} X \\ Y \end{bmatrix} \quad (1)$$

where θ is the nacelle direction from North-Y.

Figure 3 shows the overall PSD (average of PSDs from all 20-min periods) with the identified natural frequencies below 2 Hz. The first bending modes can be seen at 0.30 Hz and 0.33 Hz and the second bending modes at 1.70 Hz and 1.59 Hz for the sandy and clayey sites respectively. The peaks in between the 1st and second bending modes are believed to correspond to blade bending modes.

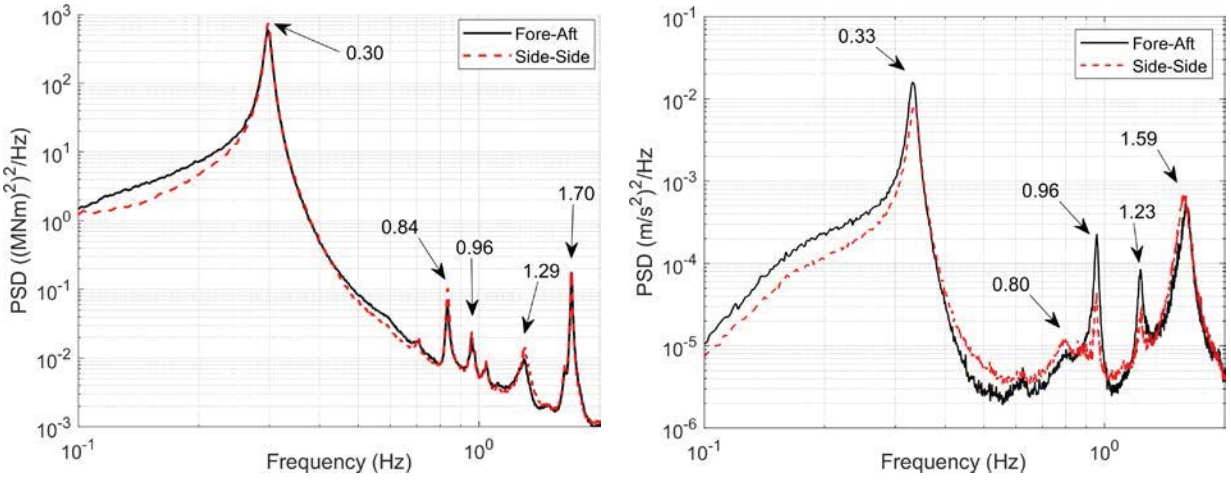

Figure 3: Overall PSD (average of all 20-min periods) with identified natural frequencies below 2 Hz, left: sand dominated site, right: clay dominated site.

Figure 4 shows the first natural frequencies in fore-aft and side-side direction determined for all individual 20-min segments and plotted versus load, i.e. wind speed, significant wave height and total dynamic bending moment (calculated from measured strain) for the two sites. Linear fits to data are also shown in the figures.

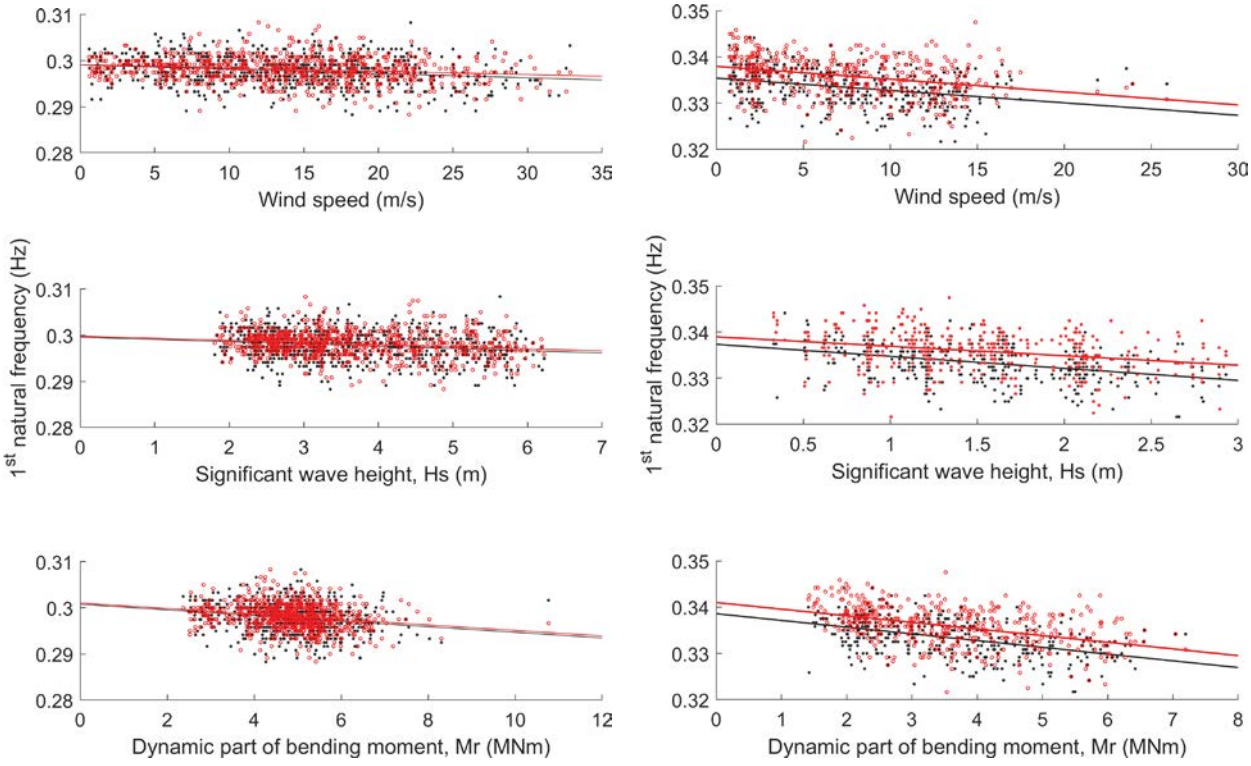

Figure 4: First natural frequency from FFT in side-side direction (red) and fore-aft direction (black) plotted against wind speed, wave height and total dynamic bending moment, left: sandy site, right: clayey site.

The results show that the first natural frequency decreases with increased load, which points to influence of soil nonlinearity. This is most evident for first natural frequency plotted versus the bending moment, which directly represents the load acting on the monopile.

However, Figure 4 also shows quite a large spread in data at the same time as the variation in the natural frequencies with load is very small. To reduce the spread of data and get a clearer trend, it may be considered to increase the frequency resolution by extending the length of the time series used in the FFT. Nevertheless, the wind and wave load are changing with time and the variation in load for each observation will therefore increase if the length of the time series are increased. As an alternative, other methods such as the time domain Multichannel AutoRegressive Moving Average (MARMA) method may be used to yield more accurate spectra with higher resolution compared to FFT. Further, Figure 4 shows that the two modes for the sandy site are not resolved. Methods like MARMA, which are based on analysis of the covariance function and takes advantage of cross information between all channels, will also be much better at identifying closely spaced natural frequencies compared to the FFT method. The MARMA method was successfully tried in the current study and resulted in a clear separation between the two modes and less spread in data compared to FFT.

5 ASSESSMENT OF DAMPING

Damping can be assessed from the measured data both in the frequency domain and in the time domain. Common for all methods is that they estimate the overall damping of the system, which for the first bending modes consists of a combination of aerodynamic damping, damping due to constructive devices, such as a tuned mass dampers, and additional damping, e.g. structural, hydrodynamic and soil damping [8]. When the turbine is parked or idling the aeroelastic damping is very low and it is therefore disregarded in this study.

In the frequency domain, the half-power bandwidth method can be used to estimate the damping ratio. By assuming that the damping ratio ζ is small (less than about 10%), the damping ratio is estimated using the following equation:

$$\zeta \approx \frac{f_2 - f_1}{2f_n} \tag{2}$$

where f_2 and f_1 are the upper and lower half-power frequencies, and f_n is the natural frequency.

For structures with closely spaced modes, possible mode coupling may lead to errors in the damping estimate [9]. For Offshore wind turbine (OWT) structures on monopiles, the first modes in the fore-aft and side-side direction are very closely spaced and a mode coupling is therefore possible. If mode coupling occurs, vibrational energy will be transferred from the highest to the lowest damped mode [2]. Damping determined with the half power bandwidth method should therefore only be considered as estimates of the real damping. Further, to obtain reasonably good estimate of the damping, it is important that the frequency resolution is fine enough for the shapes of the peaks to be correctly represented in the PSD, since a too coarse resolution will make the peaks wider and lower and hence over-estimate the damping. On the other hand, averaging is necessary to obtain peaks smooth enough such that the half power bandwidth method can be applied. In this study the half power bandwidth method is applied to the overall PSD as shown in Figure 3. A single degree of freedom (SDOF) system is fitted to the measured PSD by use of least squares estimation in the frequency range from f_1 to f_2. The damping is thereafter determined from the parameters of the SDOF system. Table 2 tabulates the first natural frequencies and overall damping ratios in fore-aft and side-side direction.

Direction	Sandy site		Clayey site	
	f_n (Hz)	ζ	f_n (Hz)	ζ
Fore-aft	0.298	0.019	0.333	0.021
Side-side	0.298	0.017	0.336	0.025

Table 2: First natural frequencies ($f_{n)}$ and damping ratio (ζ) determined by the half-power bandwidth method

The measurements at the clayey site show a larger overall damping than at the sandy site. It is assumed that the difference in damping ratio between the two sites is due to the differences in soil properties. However, the tower at the sandy site is equipped with a tuned mass damper, which contributes to the overall damping, while the tower at the clayey site has no damper. Therefore, the real difference in damping between the two sites is probably larger than shown in Table 2. The estimated damping ratios in Table 2 are somewhat lower than reported from rotor stop tests in [4] and [2]. However, in [10] even lower damping ratios was reported from an overspeed test when the tuned mass damper in top of the tower was turned off.

6 CONCLUSIONS

In this study, the first natural frequencies and associated damping are determined from measured dynamic field data from two wind farms in the North Sea with monopile foundations. At the first site, the ground conditions are dominated by sand, and at the second by clay. Only measurement data from periods when the turbines are idling are included in the analyses.

A clear correlation is demonstrated between load level and frequency, which points to the importance of soil nonlinearity. The estimated damping ratio for time periods when the turbine is idling is about 1.7-2.5 %, with higher damping for the clayey site compared to the sandy site. The estimated damping ratios are somewhat lower than reported from other field tests.

ACKNOWLEDGEMENTS

This study was performed with support from the research project REDWIN (Reducing cost of offshore wind by integrated structural and geotechnical design), funded by the Research Council of Norway, Grant Agreement 243984. This support is highly appreciated.

REFERENCES

[1] G.M. Álamo, J.J. Aznárez, L.A. Padrón, A.E. Martínez-Castro, R. Gallego, O. Maeso, Dynamic soil-structure interaction in offshore wind turbines on monopiles in layered seabed based on real data, *Ocean Engineering* 156, 14–24, 2018.

[2] M. Damgaard, L.B. Ibsen, L.V. Andersen, J.K.F. Andersen, Cross-wind modal properties of offshore wind turbines identified by full scale testing, *J. Wind Eng. Ind. Aerodyn* 116, 94–108, 2013.

[3] D. Kallehave, C.L. Thilsted, A. Troya, Observed variations of monopile foundation stiffness, *Frontiers in Offshore Geotechnics* III, 717–722, 2015.

[4] W.G. Versteijlen, A.V. Metrikine, J.S. Hoving, E. Smid, W.E. De Vries, Estimation of the Vibration Decrement of an Offshore Wind Turbine Support Structure Caused by its Interaction with Soil, http://resolver.tudelft.nl/uuid:608f979a-d199-463e-899c-0007103cfdb0, 2011.

[5] T. Hald, C. Mørch, L. Jensen, C. LeBlanc Bakmar, K. Ahle, Revisiting monopile design using p-y curves Results from full scale measurements on Horns Rev, *EWEA* 09, 2009.

[6] N.J. Tarp-Johansen, L.C. Andersen, E. Damgaard, C. Mørch, S. Frandsen, B. Kallesøe, Comparing Sources of Damping of Cross-Wind Motion, *In European Offshore Wind: Conference & Exhibition The European Wind Energy Association,* 2009.

[7] R. Shirzadeh, W. Weijtjens, P. Guillaume, C. Devriendt, The dynamics of an offshore wind turbine in parked conditions: a comparison between simulations and measurements, *Wind Energ* 18, 1685-1702, 2015.

[8] R. Shirzadeh, C. Devriendt, M.A. Bidakhvidi, P. Guillaume, Experimental and computational damping estimation of an offshore wind turbine on a monopile foundation, *Journal of Wind Engineering and Industrial Aerodynamics* 120, 96-106, 2013.

[9] G.A. Papagiannopoulos, G.D. Hatzigeorgiou, On the use of the half-power band width method to estimate damping in building structures, *Soil Dynamics and Earthquake Engineering* 31, 1075–1079, 2011.

[10] C. Devriendt, M. El-Kafafy, G. De Sitter, P.J. Jordaens, P. Guillaume, Continuous dynamic monitoring of an offshore wind turbine on a monopile foundation, *Proceedings of ISMA,* 2012.

EURODYN 2020
XI International Conference on Structural Dynamics
M. Papadrakakis, M. Fragiadakis, C. Papadimitriou (eds.)
Athens, Greece, 23–26 November 2020

MONITORING OF OFFSHORE WIND TURBINES UNDER WAVE AND WIND LOADING DURING INSTALLATION

Aljoscha Sander[1], **Christian Meinhardt**[2], **and Klaus-Dieter Thoben**[1]

[1] University of Bremen
Badgaststeiner Strasse 1, 28359 Bremen, Germany
e-mail: {aljoscha.sander,thoben}@uni-bremen.de

[2] GERB Schwingungsisolierungen GmbH & Co. KG
Roedernallee 174-176 13407 Berlin, Germany
e-mail: christian.meinhardt@gerb.com

Keywords: oscillations, offshore installation, tuned mass damper

Abstract. *During the single blade installation of offshore wind turbines, relative motion between the blade root and turbine hub can cause a delay in the progression of the installation. This contribution presents the results of a monitoring campaign conducted during the installation of an offshore wind park in the North Sea. The campaign covered different states of the turbines: without rotor blades, with rotor blades, without supplementary damping system and with an installed, tuned mass damper system. The objective of the campaign was to determine the dynamic behaviour of the turbines in correlation with wind and wave data and to determine modal parameters. Accordingly, the turbines have been instrumented with sensors to record accelerations at three different positions. The modal parameters were then obtained using SSI/FDD algorithms. Structural damping is additionally determined with an RDM algorithm, and the results are being compared. The analysis of the data will be presented, including the different stages of the structural damping and the corresponding changes in movement patterns. The results shall be used to verify the load models and the predicted response of the structure.*

1 INTRODUCTION

Offshore wind turbines are steadily increasing in size in order to meet the rising demand for green electricity. This increase in accompanied with increasing water depths of offshore wind farms. Additionally, monopiles have become the economic foundations of choice. This current state of offshore wind farms results in eigenfrequencies between 0.2 Hz and 0.3 Hz, making the offshore wind turbines more susceptible for wind and wave induced loads. The response of these turbines is dependent on geometrical as well as structural parameters, among which the structural damping is essential for fatigue loads. Therefore it is of paramount importance to accurately predict the damping of a turbine in the design phase. Offshore wind turbines have generally a low damping ratio, with typical values around 1 %. Different types of damping can be distinguished in a offshore wind turbine: structural, soil, hydrodynamic and aerodynamic damping. Additionally, for a fully operational turbine, a directional dependency of their structural behaviour due to the damping effect of aerodynamic thrust generated by the blades can be observed. Hence, side-side deflection is in general more prone to large deflection amplitudes.

Damgaard et al. (2013) [1] and Guillaume et al. (2013) [2] used acceleration measurements conducted on operational wind turbines to calculate structural damping for the different modes of tower oscillations seen in offshore wind turbines. Both oscillations due to rotor stop tests as well as oscillations under ambient conditions proved to be sufficient to get accurate enough estimates of damping ratios. As the different modes of a wind turbine are spaced very close to each other, a coupling of the two lowest eigenmodes can be assumed and therefore pure fore-aft and side-side modes are not to be expected as energy will be transformed from one mode to another. This can results in a orbit like motion, where the turbines switches oscillation directions. In order to reduce fatigue loads and subsequently increase reliability, different types of damping systems have been proposed to reduce loads in offshore wind turbines, among which are: passive, semi-active and active tuned mass dampers (TMD), tuned liquid column damper, viscous fluid dampers & magnetorheological dampers [3].

Brodersen et al. [4] investigated an active tuned mass damper implemented into HAWC2 simulations, exploring the influence of the damper on structural responses. They showed, that fore-aft oscillations behave differently compared to lateral oscillations as the blades act as 'aerodynamic dampers'. They concluded, that an active tuned mass damper needs less mass to achieve high damping, however, the damper needs to be properly tuned in order to achieve maximum efficiency. A limiting factor of the active mass damper is the displacement velocity of the damper's mass. The authors address the tuning problem, by presenting a tuning algorithm. However, external loads in offshore wind turbines are complicated by wind-wave misalignment. One mitigation might be a tuned mass damper. Steward and Lackner [5] used simulations to demonstrate that an optimally tuned mass damper can reduce fore-aft and side-side fatigue loads by 5 % and 40 % respectively for the 5 MW NREL Turbine. These results were obtained by implementing a custom-written extension of FAST to include the modelling of TMDs. The authors further investigated two different orientation patterns of the TMDs. They conclude, that TMDs are cost-efficient and simple and conclude, that due to reduced loads, an increase in reliability can be expected.

Oscillations are not only critical regarding fatigue loads; relative motion between rotor hub and blade root during single blade installation can cause severe delays and thus increase cost significantly. Relative motion can be cause by aerodynamically induced movement of the blade dangling from the crane hook or by tower oscillations which in turn are caused by wind and wave loading and are thus a stochastic processes by nature. Recent work has investigated the

aerodynamic behaviour of turbine blades during craning operations in order to better understand limitations imposed by external factors such as wind speed and direction. For wind speeds between 8 - 12 m/s single blade installation was found to be feasible [6]–[9].

Jiang et al. [10] modelled the overall system consisting of a Tower-Nacelle-Hub assembly subjected to metocean loads as well as a blade under wind loading during single blade installation using HAWC2. Adapting a custom, integral criteria to assess likelihood of an installation attempt to succeed. The authors concluded, that during the final mating process between blade root and hub, tower oscillations are more dominant than blade root movements if significant resonance responses of the structure due to wave loading are present. Subsequently Jiang (2018) [3] proposed to use TMDs during the installation of offshore wind turbines at the tower top of an offshore wind turbine to reduce relative motion between blade root and nacelle hub [3]. Adapting the simulations from the previous study, the author found a 50 % reduction in relative motion when only considering the hub movement and an overall reduction of 30 % when considering both hub and blade root motion. First to demonstrate the theoretical application of an TMD for single blade installation.

Within this work, we present first measurements of a tuned mass damper used to reduce tower oscillations during single blade installation in the North Sea. Different states of the turbine undergoing installation were monitored: Tower (T), Tower, Nacelle and Hub (TNH) and Tower, Nacelle and Hub with the blades added consecutively (TNHB1, TNHB2 and TNHB3, where the number corresponds to the number of blades installed). The objective of the campaign was to monitor overall dynamic system behaviour and to obtain modal parameters.

2 MATERIAL AND METHODS

2.1 Wind farm details

A wind farm consisting of 32 multi-megawatt offshore wind turbines was installed during the time period of one year in the North Sea. The turbines have a hub height of approximately 110 m and were installed using a state of the art installation jack-up unit (IJU). The turbines are of hard-soft type and were installed in water depths between 35 m and 40 m.

The general installation procedure is as follows: (1) the IJU reaches the installation site, jacks up and connects to the previously installed transition piece atop the monopile with a gangway. (2) Following preparation on the transition piece, the tower is lifted from the IJU and placed on the transition piece. (3) The tower is followed by the nacelle-hub assembly. (4) If the conditions are favourable the blades are then installed using a specialized yoke, henceforth denoted as single blade installation tool (SBIT) with a net mass of approx. 70 t. (4.1) The SBIT is hooked onto the crane and grabs a blade from the blade rack aboard the IJU. (4.2) The SBIT and the blade are lifted to hub height and slowly manoeuvred such that the blade main axis and the generator axis are perpendicular towards each other. (4.3) Using a guiding pin, the blade root is then slowly mated with the hub flange. This processes is then repeated for each blade. It is within this phase of installation, where relative motions between blade root and hub must be at a minimum.

As this process is highly sensitive to relative motions between blade root and rotor hub a tuned mass damper was installed inside the nacelle. The TMD has two degrees of freedom and a damping mass of 10 tonnes. Using spring elements and viscous damping, the TMD was tuned to match the eigenfrequency of the turbines during single blade installation.

As the tuned mass damper was only available during the second half of the installation campaign, measurements of single blade installation with and without a TMD were conducted.

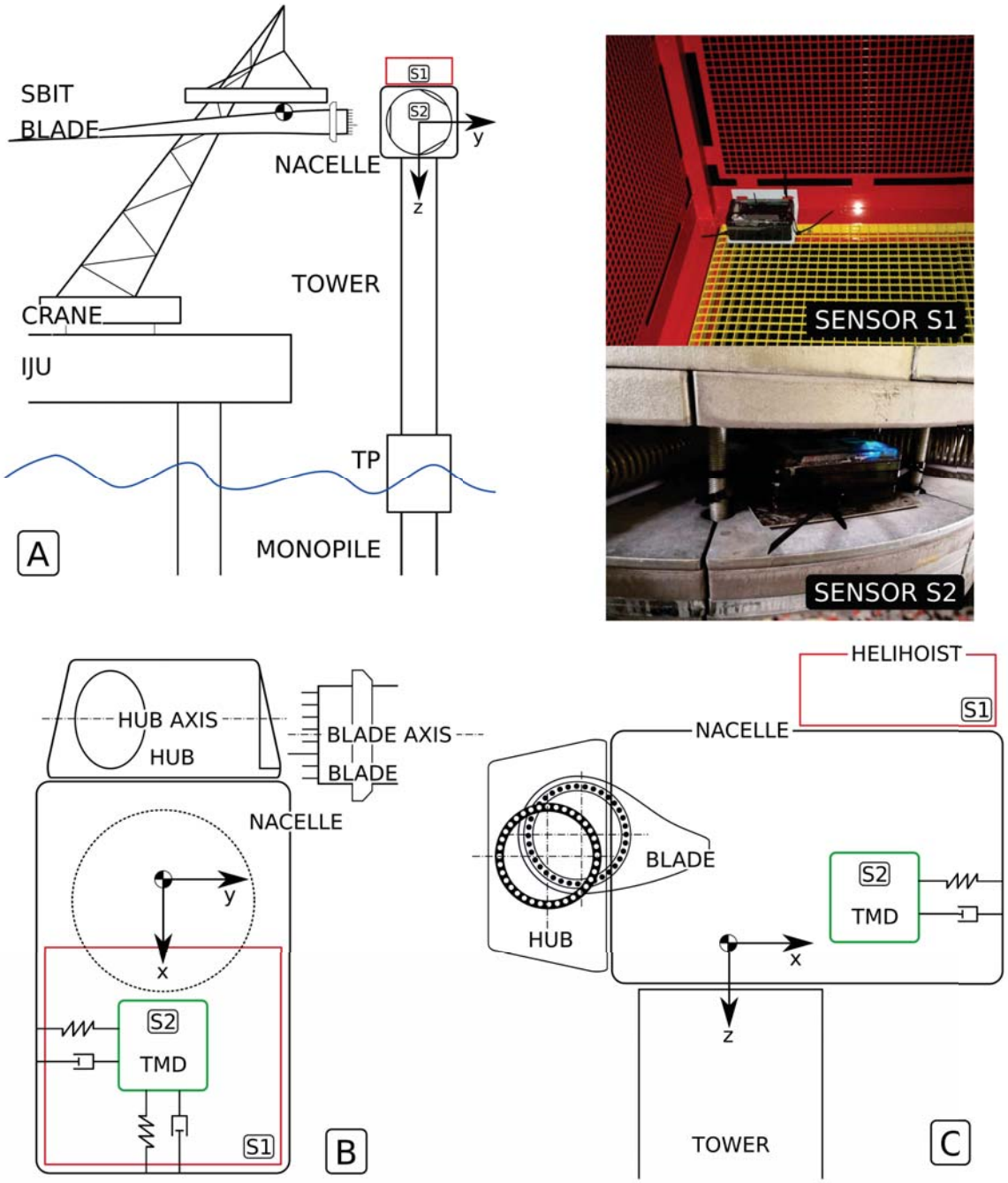

Figure 1: Typical setup of a single blade installation. (A) Installation Jack Up Unit (IJU) next to the Tower-Nacelle-Hub Assembly with the blade being attached to a Single Blade Installation Tool (SBIT), typically a yoke-like structure. The red square indicated the helicopter hoisting platform. S1 and S2 correspond to the sensors used within this study to determine dynamic behaviour of the turbine. (B) Top view of the single blade installation process. The green structure represents the tuned mass damper, deployed during single blade installation. (C) Side view of the installation process. Upper right figures: Sensors S1 and S2 mounted on the helicopter hoisting platform and the tuned mass damper respectively.

2.2 Measurements

In order to monitor the dynamic behaviour of the turbines during installation, custom build sensor boxes were deployed at two different positions: one sensor box is placed on the topmost position of the nacelle: the helicopter hoisting platform (short: helihoist). A second sensor box is placed on the tuned mass damper during installations where a tuned mass damper was present.

Sensor boxes contained a lead battery and electronics in a water proof containment (box) with a weight of approximately 3 kg and the measurements of 0.2 m x 0.06 m x 0.1 m. A LSM9DS1 (SparkFun Electronics, Colorado, USA) 9-Degrees-of-Freedom inertial measurement sensor capable of measuring linear acceleration, linear angular acceleration and the magnetic field was combined with a GPS-Sensor (GP-20U7; SparkFun Electronics, Colorado, USA), providing accurate time stamps as well as altitude information to form the sensory core of the sensor boxes. A real time clock (RS3231) provided back up temporal information in case of lack of GPS signal. A 32 GiB micro-SD-Card was used to store measurements. As a microcontroller, an ESP32 (Espressif Systems, Shanghai, China) was used. A sample frequency of 33 Hz was used, yielding accurate temporal resolution while allowing for good battery run time.

A LiDAR aboard the IJU provided high spatial and temporal resolution wind field information (measurement return period 1 s / 1 Hz). Additionally, a wave buoy in the vicinity of the installation site provided wave data, including significant wave height, peak period, zero upcrossing period and wave direction. The measurement return period was 30 min. / 0.00055 Hz.

In total, 15 turbines without a TMD and 4 turbines with a TMD were monitored during installation.

2.3 Data processing

All data post-processing has been implemented utilizing Python3 as well as it's rich set of scientific data analysis frameworks. As a fundamental data structure Pandas DataFrames (version 0.24.2) [11] was used. Numerical calculations were carried out using NumPy version 1.16.4 [12] and SciPy, version 1.3.0 [13]. All figures were generated using Matplotlib version 3.1.0.

Post-processing of measurement data starts with the subtraction of the mean for each acceleration component. Accelerations were then resampled using a linear interpolation scheme to a constant frequency of 30 Hz and filtered using a Butterworth Bandpass filter of third order. Lower and upper cut off frequencies were set to 0.1 and 1 Hz respectively. Accelerations were then integrated twice to yield velocity and position of the sensors during installation. Integration was carried out by applying a second order trapezoid scheme utilizing SciPy's integation module.

Based upon the positional vector, the instantaneous tower deflection D was calculated:

$$D = \sqrt{x^2 + z^2} \tag{1}$$

Where x and z are the instantaneous position vector components. The second component of the positional vector has been omitted, as it is aligned parallel to the tower axis and therefore it's contribution to the tower top deflection can be neglected.

To obtain a measure for the current state of the turbine and to allow for correlations with environmental data, 10 minute means of D were calculated, denoted as D_{10}. To maintain OEM privacy, all data has been normalised by the turbine tower diameter d_T, such that: $d = D/D_T$

and $d_{10} = D_{10}/D_T$. To further enhance privacy all dates presented in this study have been reset such that all measurements start at 01.01.1970 at 00:00 UTC. Temporal information is therefore only relative.

Wind data was binned into 10 minute windows and the window average was calculated. For wave measurements, data was first upsampled to 10 minute periods utilizing a forward interpolation scheme and subsequently merged with the wind data. Figure 2 depicts the data processing steps.

Figure 2 shows the data processing pipeline. Raw data is resampled, filtered and integrated twice to yield both velocity and position of the sensor in space and time. Using the postion vector, the deflection of the Nacelle can be calculated by employing Equation 1. Combining these measurements with metocean data and applying temporal averaging allows for scatter plots of mean deflection and metocean parameters such as significant wave height.

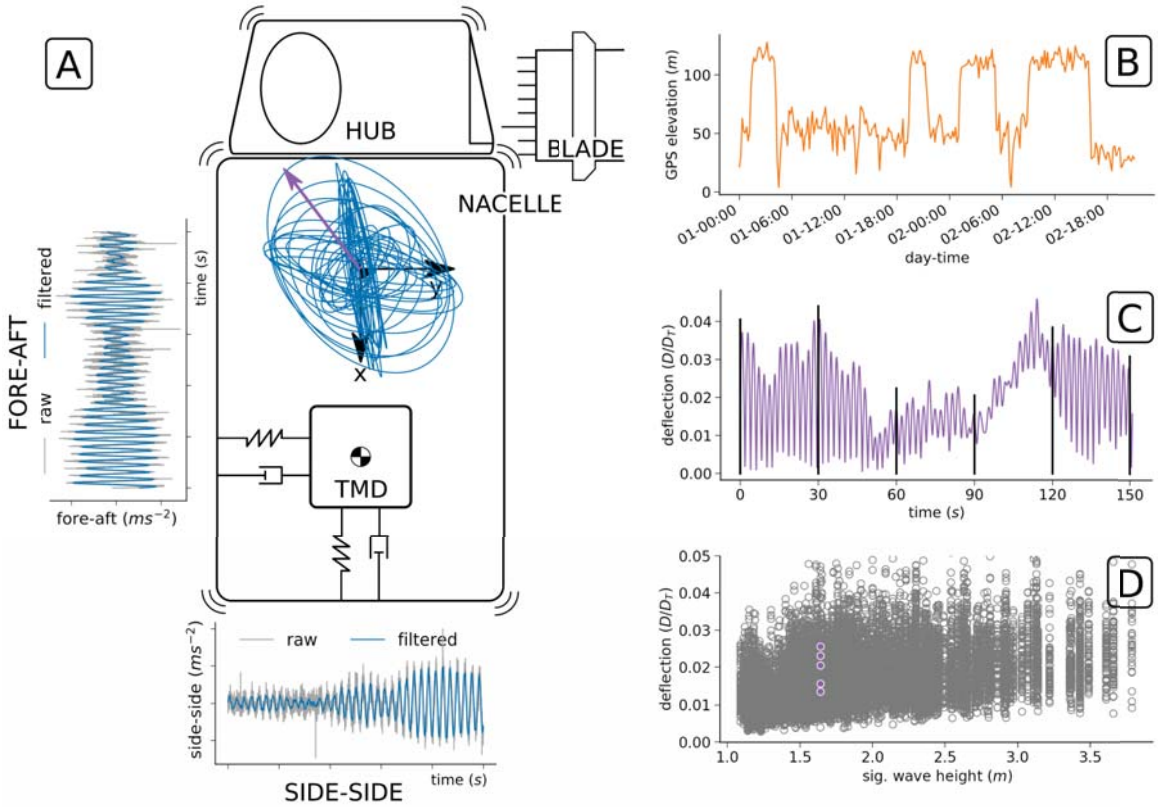

Figure 2: Data acquisition and processing: (A) Fore-aft and side-side accelerations are recorded by the sensors, resulting in a trajectory which can swiftly change direction. (B) GPS-Profile of the single blade installation process captured by another sensor mounted on the single blade installation tool. This allowed accurate tracking of the process in both space and time. (C) Integration of accelerations yields the trajectory of the orbit, from which the absolute deflection, a measure of how much the nacelle diverges from its base position can be obtained. (D) Applying a 60 s average of the deflection allows for the correlation of the deflection with external parameters, such as sig. wave height or wind speed.

2.4 Modal parameters

The monitoring campaign, which covered the states where the tuned mass damper system was either disabled (blocked) or activated was also used to identify the effectiveness of the TMD system by continuously determining the overall structural damping of the Tower-Nacelle-Hub assembly. To determine the structural damping ratio from the accelerations with unknown input (output only data), system identification techniques are applied such as the Random Decrement Method (RDM) as well as Stochastic Subspace Identification (SSI) and Enhanced Frequency Domain Decomposition (EFFD).

Random Decrement Method Figure 3a schematically shows the principle behind the random decrement method. Based on the assumption that the random excitation consists of a deterministic component which corresponds to free vibration terms and a random component which corresponds to forced vibrations, the random part can be eliminated by averaging a large number of blocks extracted from the time domain signal with a length τ. The blocks are chosen with the help of a threshold level. The Random Decrement Signature (RDS) (Figure 3b and Figure 3c) results the averaged time segments and the resulting damping ratio can be derived from the logarithmic decrement whereas the quality of the RDS strongly depends on the selection of the segment duration τ and the threshold y_S.

The random decrement method has been approved for system identification analyses of structures and buildings ([14]–[16]). Since the results of the damping are depending on the threshold and the segment duration, these parameters were varied to gain stochastic certainty. A window length of 2 and 3 periods (based on the determine natural frequency of the main structure) was analysed as well as a threshold level of 30 %, 50 % and 60 % of the max value of the investigated time history.

Figure 3b and Figure 3c show exemplary random decrement signatures from which the structural damping of the TNH was determined by analysing the decaying curve. This process was automated and applied for the complete time series that were recorded.

Operational Modal Analysis The stochastic subspace identification method is considered as a robust output-only identification technique compared to other available methodologies [17]. SSI algorithms identify a stochastic state-space model of the structure. The resulting model can then be translated into a more convenient structural model form for engineering interpretation of the results. The state-space model can be related to both modal model and Finite Element (FE) model formulations. The method works in the time domain and is based on a state space description of the dynamic problem assuming a linear behavior of the structure and a time-invariant dynamic response of the system due to a white-noise excitation. The system identification results at different model orders are compared to distinguish true structural modes from spurious modes in so-called stabilization diagrams. The time domain based SSI technique together with additional techniques such as the Enhanced Frequency Domain Decomposition (EFDD) techniques are often combined in algorithms for commercial Operational Modal Analysis software packages. The EFDD method relies on computation of response spectra. Long records are, therefore, required to keep low the error on spectrum estimation and to extract modal parameters in a reliable way. The software ARTEMIS from SVIBS (Structural Vibration Solutions) was used to identify the vibration modes of the TNH and to determine the structural damping. The results are plotted as stabilization cards and the estimated modal parameters are listed together with information about the probabilistic uncertainty.

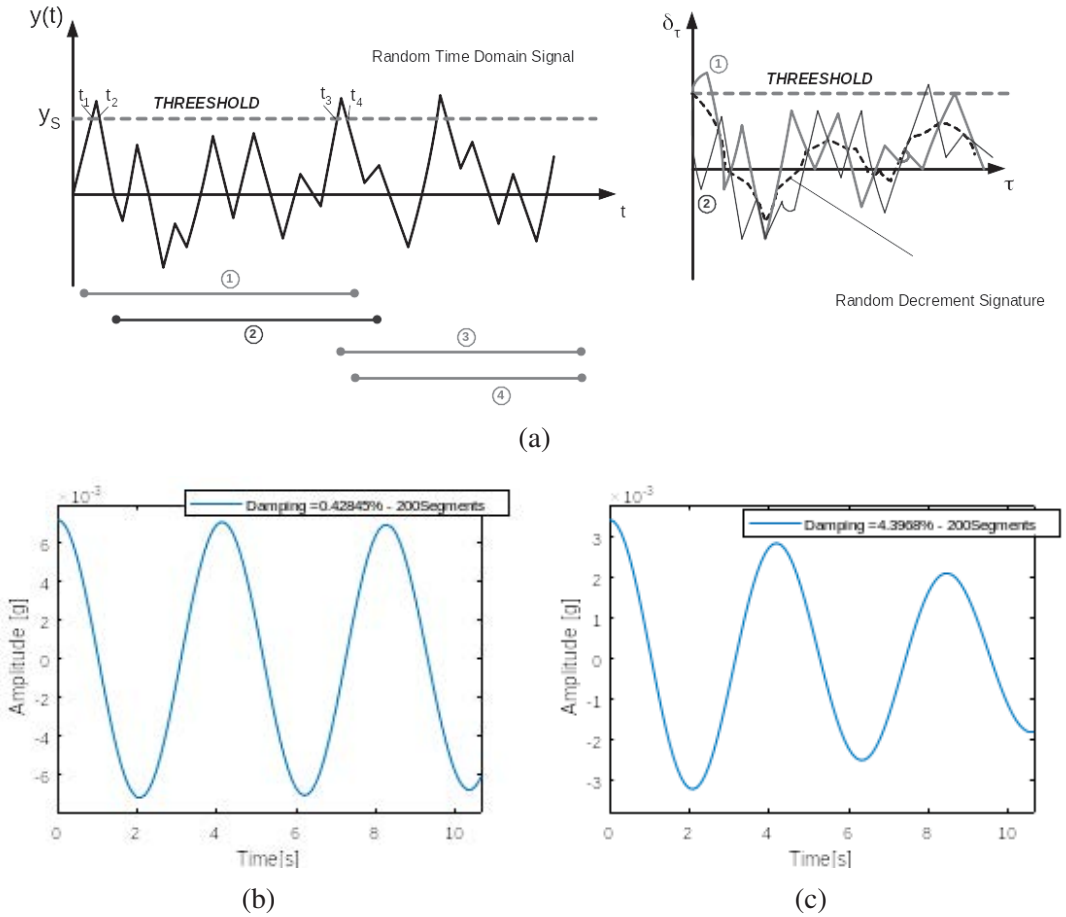

Figure 3: Principle of the Random Decrement Method (a). (b) Random Decrement Signature (RDS) of a 10 minute time history segment with blocked TMD – (c) (RDS) of a 10 minute time history segment with activated TMD

Identification of TMD parameters A two-measuring point acquisition, for which the vibrations of the wind turbine tower structure and the vibrating mass of the TMD are recorded can be used to determine the TMD parameters. But since this method will only provide the absolute vibrations of main structure and TMD a certain post-processing effort is required. Direct information regarding the relative TMD displacements can be gained when the relative vibrations of the TMD mass in addition to the vibrations of the main structure are getting obtained to derive the TMD parameters directly.

3 RESULTS

3.1 Nacelle deflections during single blade installation

Figure 4 shows exemplary two time series of nacelle deflection during the installation of two offshore wind turn turbines during single blade installation, where one turbine was equipped with a tuned mass damper. Both instantaneous deflection as well as the 10 min. mean of the deflection is shown (white line). A black horizontal line indicates the limit for single blade installation as learned during previous installations. For the installation without a TMD (Figure 4a), this limit is exceeded multiple times, Though the 10 min. average remains well below the limit. The time series shown starts after the finalised nacelle installation, spans an intermediate time period of about two hours within which the single blade installation tool (yoke) is picked up by the crane and then includes the three consecutive blade installations. Total blade installation spanned approx. 62 h with installation attempts made at each window where the deflection dropped below 3 % tower diameter. Six attempts at blade installation were made, for each blade two, where each of the first attempts failed.

During single blade installation with a TMD (Figure 4b) deflection was almost entirely above the threshold. With the beginning of the blade installation, the TMD was activated. This is indicated by the hatched area. An immediate response in nacelle deflection can be observed with the instantaneous deflection dropping below the installation limit with the exception of four spikes. The 10 min. mean of the nacelle deflection assumes a near constant value at when compared to the prior time period. The total blade installation installation duration was approx. 13 h, a significant reduction when compared to the previous installation duration without a TMD. To compare the two installations and to correlate the observed behaviour with metocean parameters, time series were divided into 10 min. segments and a temporal average was applied. This is shown in Figure 4c, where the 10 min. mean nacelle deflection is shown for the two previous installations as a function of the significant wave height.

During the installation without a TMD, significant wave height was between 0.75 m and 1.8 m. For the installation with a TMD, the wave range was between 1.25 m and 1.9 m. A clear reduction in mean deflection can be observed. Furthermore, while for the installation without a TMD mean deflection spread for a constant sig. wave height, spreading is significantly reduced with a TMD present.

Figure 5 shows 10 min. mean deflections for all captured installations with (red) and without (blue) a TMD present. The 10 min. mean deflection as a function of the significant wave height (Figure 5a), the wave peak period (Figure 5b) and the 10 min. mean wind speed (Figure 5c) are shown. Additionally, to give a simple model, a linear function is fitted using linear regression to both data sets.

The linear functions for both installations with and without TMD converge at a min. mean deflection of 0.5 %. For the installations with the TMD activated, the slope of mean deflection with significant wave height and wind speed is greatly reduced compared to the installations without a TMD present. As in Figure 4c, the spreading for a given wind speed Figure 5c or wave height Figure 5a is reduced as well. No clear correlation between mean deflection and wave peak period can be observed.

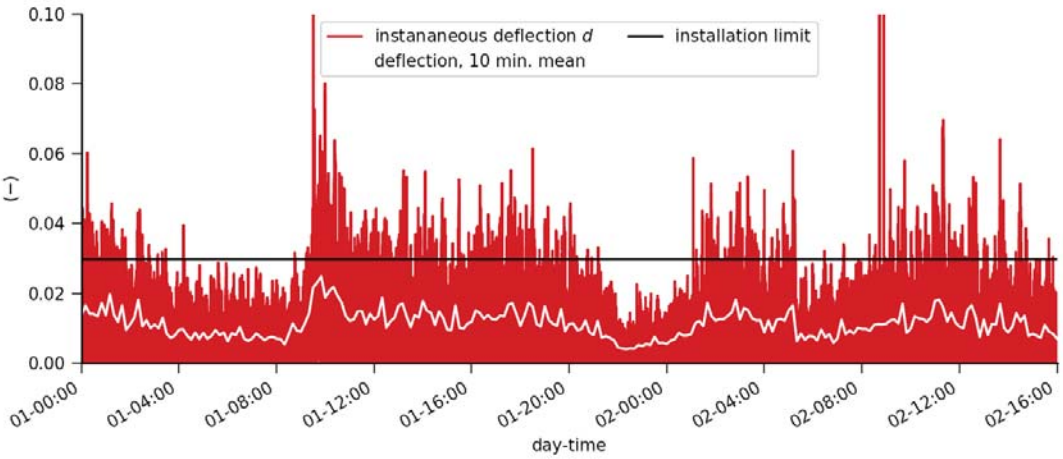

(a)

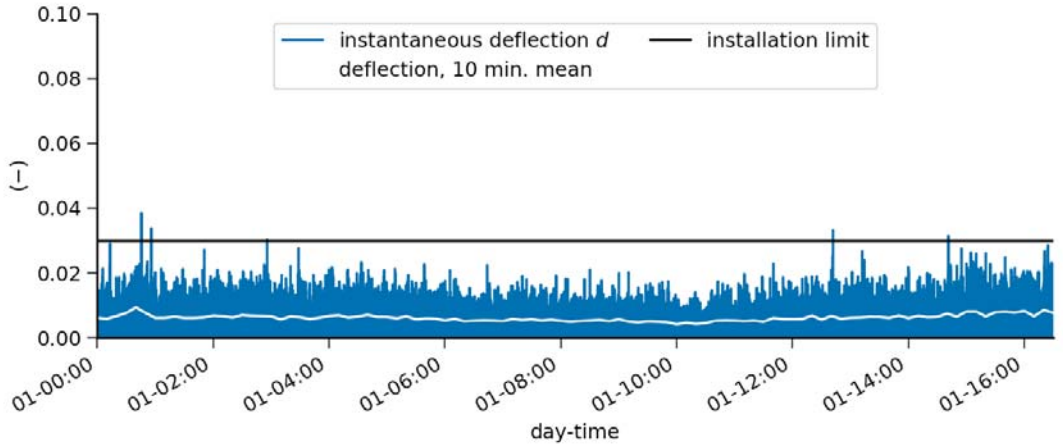

(b)

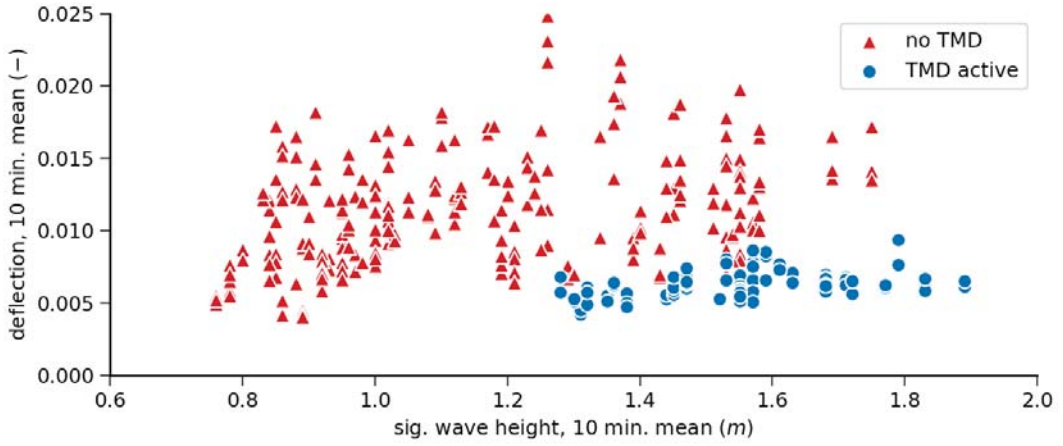

(c)

Figure 4: Time series of the nacelle deflection during single blade installation without a tuned mass damper (TMD) (a) and with TMD present (b). The white lines indicate the 10 min. mean of the deflection. The black line represents the empirically determined single blade installation limit of the deflection above which most installation attempts fail. (c) shows a scatter diagram of the 10 min. mean deflections from the two installations as a function of significant wave height.

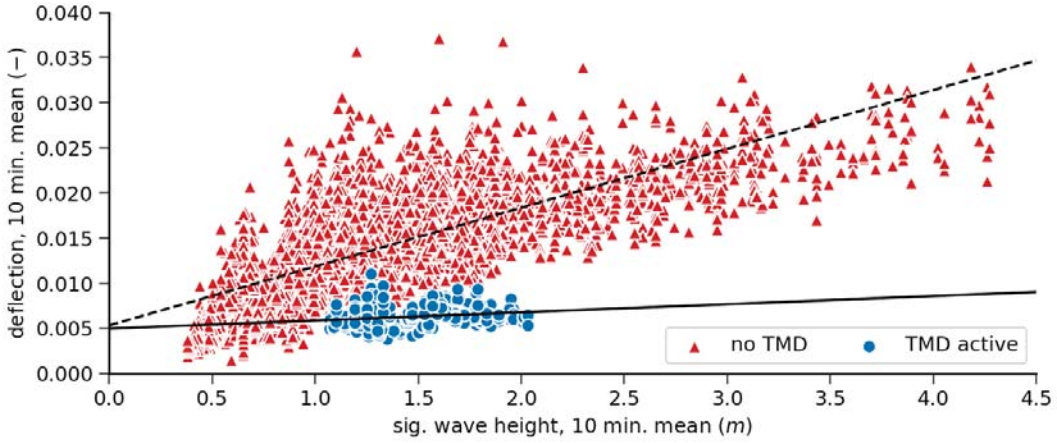

(a)

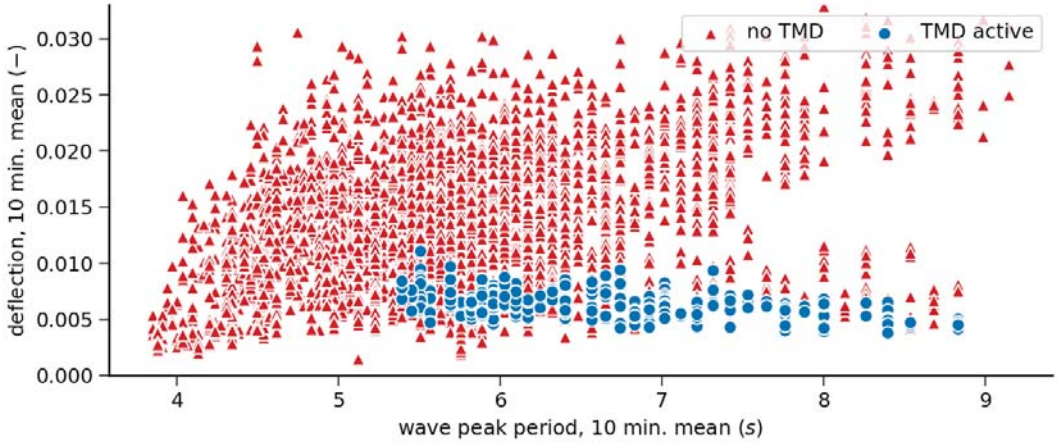

(b)

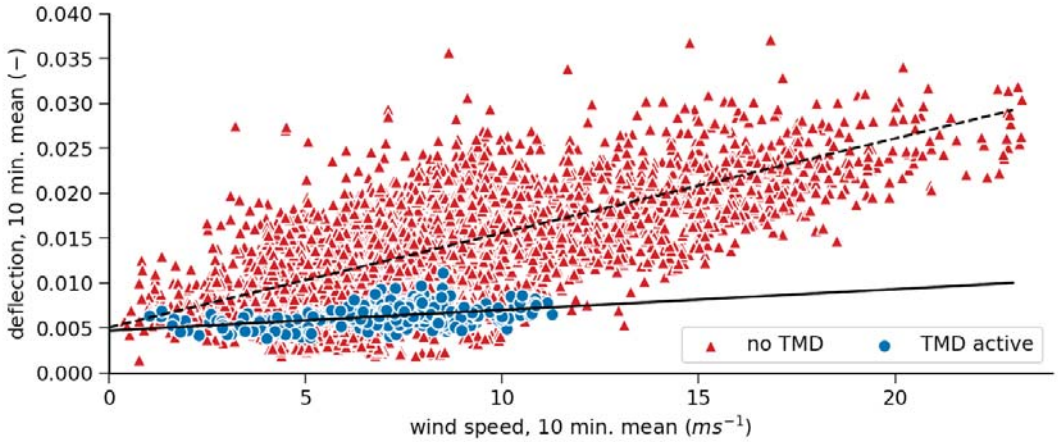

(c)

Figure 5: Scatter diagrams for the 10 min. mean deflection as a function of significant wave height H_S (a), wave peak period T_P (b) and the 10 min. mean wind speed U (c). Red indicates installations without a tuned mass damper (TMD), blue corresponds to installations with an active TMD.

3.2 Modal parameters

Figure 6 shows recorded time series of fore-aft and side-side accelerations of the wind turbine in different configurations (TNH, THNB1, TNHB2 and TNHB3) as well as the corresponding spectrograms (lower row, left and right hand side) which show the Auto Power Spectra of 10 minute - time segments plotted vs. the entire time of the monitoring campaign for the examined structure. The spectrogram not only indicates the times of the rotor blade installation for which a shift of the natural frequency can be detected but also the reduced acceleration values of the Auto-Power-Spectra and the much wider peaks indicating the increase of structural damping.

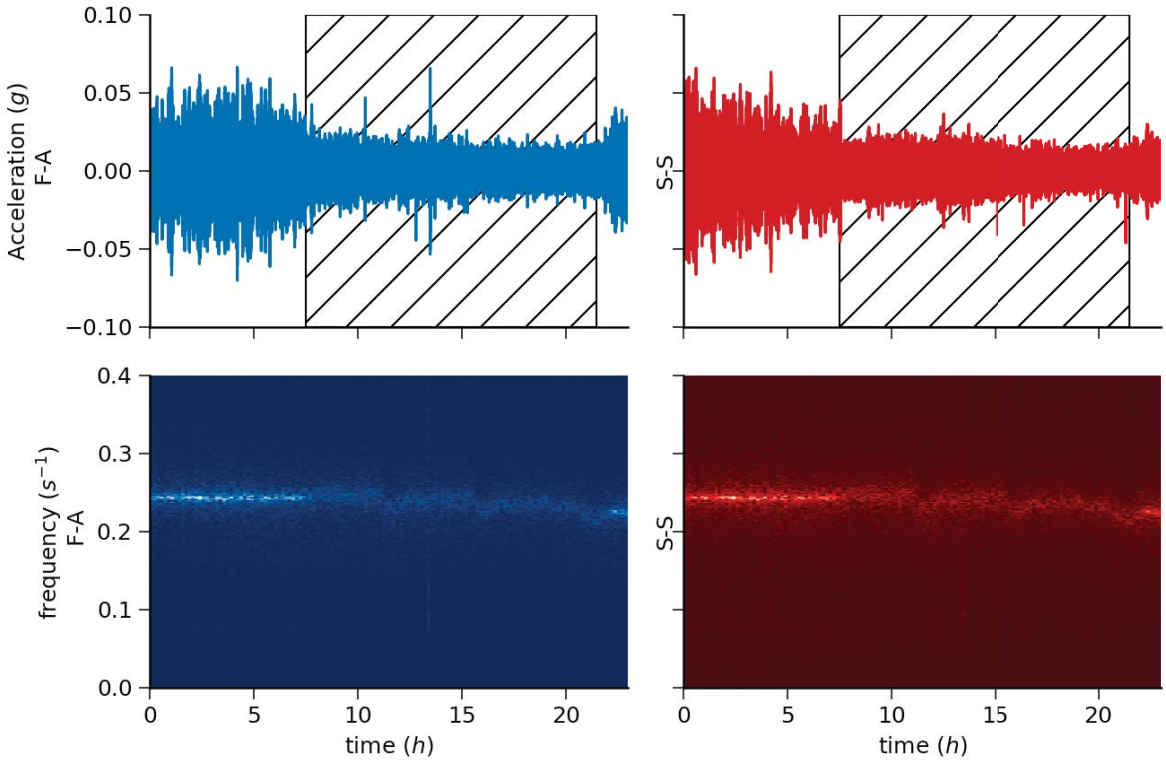

Figure 6: Top: Measured acceleration time series (fore-aft and side-side direction) of the wind turbine tower with Nacelle during single blade installation. The hatched area indicates the TMD being unlocked, resulting in an immediate reduction in accelerations. Bottom: Spectrogram (APS for 10 min time segments vs. recorded time). With each installed blade, a shift in frequency can be observed.

Figure 7 shows the determined damping ratios for time series with a length of 10 minutes, obtained via RDM. The time periods for which the TMD has been activated can clearly be identified. With the TMD deactivated, the damping ratio remains mostly below 1 %. With the activation of the TMD, damping ratio increases to values between 2 % and 4 %.

Figure 8a and Figure 8b show the resulting stabilization diagrams for a time period with blocked TMD and with activated TMD. It can be seen that for the state with blocked TMD the identified modal parameters coincide with structural damping determined with the Random Decrement Method. The damping estimation with the SSI algorithm revealed smaller structural damping ratios than determined with the RDM (TMD active: 2,52 %, no TMD: 0.57 %).

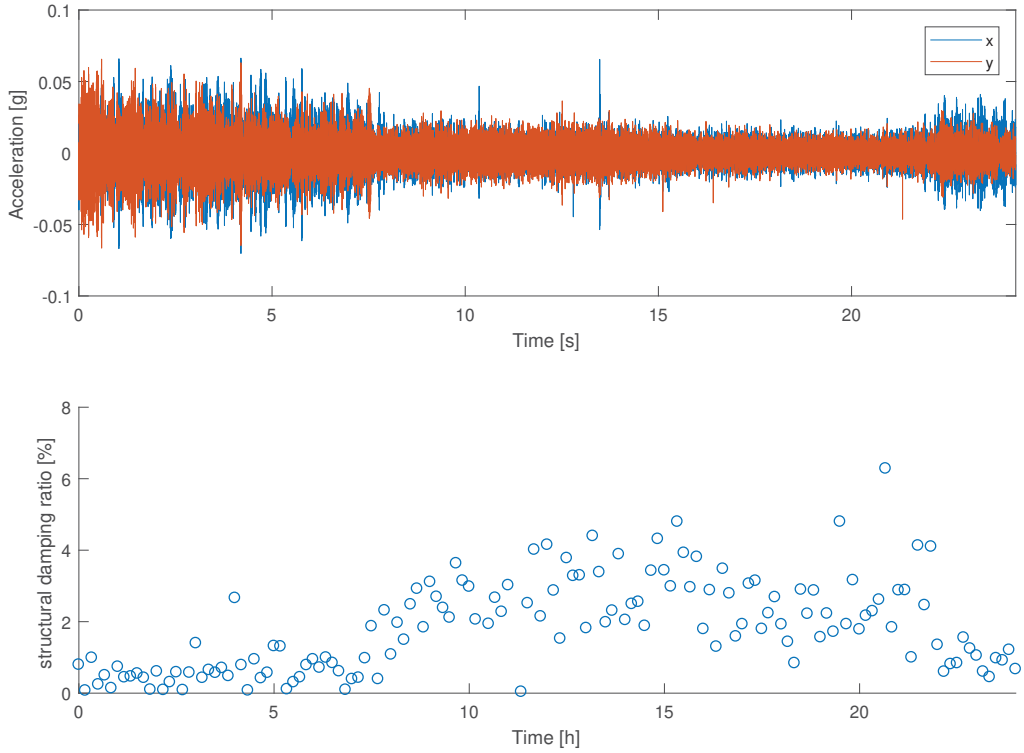

Figure 7: Above: Measured acceleration time histories of the wind turbine tower with Nacelle during rotor blade installation (x: fore-aft and y: side-side). Below: Determined Structural Damping ratio for time segments of 10 minutes using the Random Decrement Method

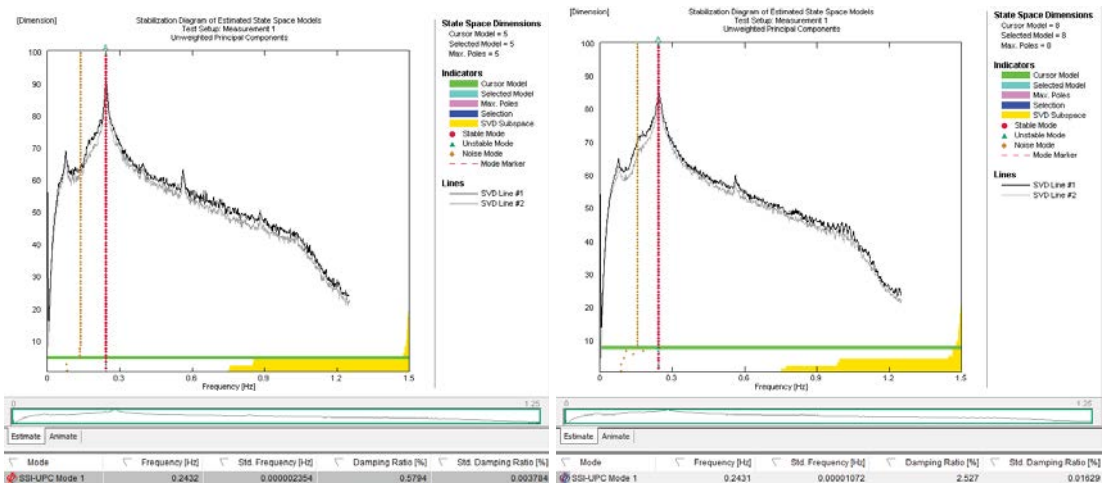

(a) (b)

Figure 8: Resulting Stabilization Diagrams from the Operational Modal Analysis (SSI Method) using the recorded ambient accelerations of TNH during single blade installation – (a): with blocked TMD – (b): with TMD – tuning frequency higher than optimum

3.3 Behaviour of the Tuned Mass Damper

Figure 9 shows the FFT spectra of 5 minute time segments of the accelerations measured at he nacelle (left) and the TMD mass (right). Initially (Time $\leq$ 1h) the FFTs of the Nacelle and the TMD mass show the same acceleration amplitudes and similar narrow peaks, which indicates, that the TMD is blocked. Later the FFT spectra of the Nacelle shows much smaller acceleration amplitudes with wider peaks, indicating that the TMD is active.

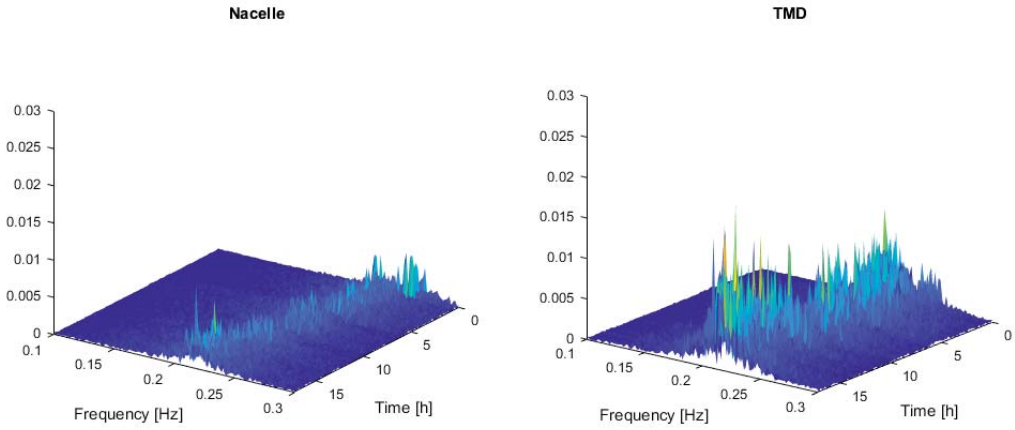

Figure 9: FFT Spectra of the acceleration time histories (5 minute segments) at Nacelle and TMD mass plotted for the entire monitoring time

The transfer function (shown for the measured accelerations of the nacelle in Figure 10) corresponds to a Frequency Response Function of the TMD system without the interaction with the main structure. From this function the tuning frequency and TMD damping ratio can is obtained by comparison with a single-degree of freedom approximation.The tuning frequency is 0.227 Hz while the TMD damping ratio is determined to be 10 %.

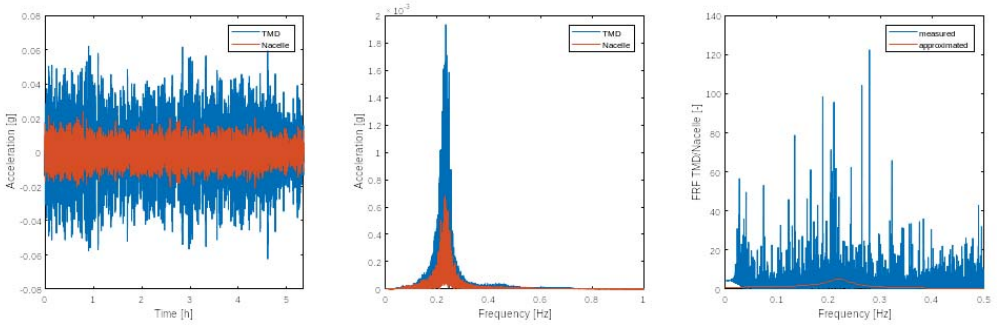

Figure 10: Left: Recorded Time Histories of the accelerations at Nacelle and TMD – Center: FTT Spectra of the entire time – Generated Transfer function and approximated signle degree of freedom - frequency response function with a tuning frequency of 0.227 Hz and a TMD damping ratio of 10 %.

4 DISCUSSION

The results presented here indicate that a TMD might indeed be a cost-effective and robust measure to improve single blade installation. However, much remains to be learned about the correlations and causalities of observed effects during single blade installation. While the measurements showed, that relative motions are indeed driven by wind and waves, the strong correlation between wind and waves - at least in the North Sea - does not allow to discern whether one of the two loads is the main driver.

While the TMD reduced deflections by more than 50 % compared to deflections observed during installations without a TMD at similar sea states other factors may still have a significant influence on the success of the single blade installation process. Among these are wind loads on the blade lifting device, wave loads on the ship and human influence as the installations are carried out manually. Structural damping increased significantly, independent on calculation method. Nevertheless more measurement with a higher precision are needed to gain more insight into the dynamic behaviour of offshore wind turbines in general and during installation in particular.

Apart from a reduction in relative motion and an increase in structural damping, the tuned mass damper increases the predictability of turbine behaviour during planning and execution of single blade installation and thus leads to a significant reduction in (financial) project risk.

Furthermore, the reduction in relative motion also leads to a reduction in HSE risks as well as a reduction in component damage. The unpredictable nacelle motions during the mating of the blade root and the hub pose a significant risk to technicians and can also lead to collisions between the hub/nacelle and the blade/lifting device.

While intended as a cost-efficient manner of measuring in dynamic behaviour of the turbines during installation, it has become apparent, that the MEMS-based sensor devices are fully capable of measuring relevant parameters with the needed precision and therefore present a novelty as well. In future studies the data obtained during this measurement campaign should be used to verify design load models as well as structural responses obtain via numerical simulations.

With regards to the operational modal analysis: a trial to determine the frequency response function for shorter time periods and detect variations of the TMD parameters with varying excitation levels and characteristics was not possible, since the time periods have to be long enough to generate the transfer function for TMD and Nacelle. While measuring the accelerations of the vibrating mass of a TMD system only provides an absolute vibration value, the direct acquisition of the relative displacement between TMD mass and main structure enables to determine the resulting TMD displacement directly but again not the TMD parameters such as tuning frequency and damping. To assess these values a comparison with a calculation model is still required.

We hypothesize, that the success rate of single blade installation is also dependent on the direction of oscillations, e.g. the shape of the orbit. This has yet to be investigated in future studies, where installation times should be correlated not only with nacelle deflection but also deflection direction and changes thereof.

5 ACKNOWLEDGEMENT

We thank our partners from the industry for enabling this research. We thank Andreas Haselsteiner, Carolina Gomez Rodriguez, Michael Janssen and for valuable discussions and proofreading.

Part of this work is part of the project SKILLS (funding code 0325934B). SKILLS is funded by the Federal Ministry of Economy and Energy, following a decision of the German Bundestag.

Funding Data: Bundesministerium fuer Wirtschaft und Energie (0325934B, Funder ID. 10.13039/501100006360).

References

[1] M. Damgaard, L. B. Ibsen, L. V. Andersen, and J. K. F. Andersen, "Cross-wind modal properties of offshore wind turbines identified by full scale testing," en, *Journal of Wind Engineering and Industrial Aerodynamics*, vol. 116, pp. 94–108, May 2013. DOI: 10.1016/j.jweia.2013.03.003.

[2] P. Guillaume, G. De Sitter, P. J. Jordaens, and C. Devriendt, "Damping estimation of an offshore wind turbine on a monopile foundation," en, *IET Renewable Power Generation*, vol. 7, no. 4, pp. 401–412, Jul. 2013. DOI: 10.1049/iet-rpg.2012.0276.

[3] Z. Jiang, "The impact of a passive tuned mass damper on offshore single-blade installation," English, *Journal of Wind Engineering and Industrial Aerodynamics*, vol. 176, pp. 65–77, May 2018, WOS:000432502100006. DOI: 10.1016/j.jweia.2018.03.008.

[4] M. L. Brodersen, A.-S. Bjørke, and J. Høgsberg, "Active tuned mass damper for damping of offshore wind turbine vibrations," *Wind Energy*, vol. 20, no. 5, pp. 783–796, 2017.

[5] G. M. Stewart and M. A. Lackner, "The impact of passive tuned mass dampers and wind–wave misalignment on offshore wind turbine loads," *Engineering Structures*, vol. 73, pp. 54–61, 2014.

[6] M. Gaunaa, L. Bergami, S. Guntur, and F. Zahle, "First-order aerodynamic and aeroelastic behavior of a single-blade installation setup," en, *Journal of Physics: Conference Series*, vol. 524, p. 012 073, Jun. 2014. DOI: 10.1088/1742-6596/524/1/012073.

[7] M. Gaunaa, J. Heinz, and W. Skrzypiński, "Toward an Engineering Model for the Aerodynamic Forces Acting on Wind Turbine Blades in Quasisteady Standstill and Blade Installation Situations," en, *Journal of Physics: Conference Series*, vol. 753, p. 022 007, Sep. 2016. DOI: 10.1088/1742-6596/753/2/022007.

[8] Y. Wang, D. Tian, and W. He, "Computation of hoisting forces on wind turbine blades using computation fluid dynamics," *Applied Mechanics and Materials*, vol. 446-447, pp. 452–457, 2014. DOI: 10.4028/www.scientific.net/AMM.446-447.452.

[9] L. Kuijken, "Single Blade Installation for Large Wind Turbines in Extreme Wind Conditions," en, Master of Science Thesis, European Wind Energy Master - TU Delft and DTU, 2015.

[10] Z. Jiang, Z. Gao, Z. Ren, Y. Li, and L. Duan, "A parametric study on the final blade installation process for monopile wind turbines under rough environmental conditions," English, *Engineering Structures*, vol. 172, pp. 1042–1056, Oct. 2018, WOS:000445440300076. DOI: 10.1016/j.engstruct.2018.04.078.

[11] W. McKinney, "Data Structures for Statistical Computing in Python," 2010, pp. 51–56.

[12] S. van der Walt, S. C. Colbert, and G. Varoquaux, "The NumPy Array: A Structure for Efficient Numerical Computation," *Computing in Science Engineering*, vol. 13, no. 2, pp. 22–30, Mar. 2011. DOI: 10.1109/MCSE.2011.37.

[13] SciPy 1.0 Contributors, P. Virtanen, R. Gommers, T. E. Oliphant, M. Haberland, T. Reddy, D. Cournapeau, E. Burovski, P. Peterson, W. Weckesser, J. Bright, S. J. van der Walt, M. Brett, J. Wilson, K. J. Millman, N. Mayorov, A. R. J. Nelson, E. Jones, R. Kern, E. Larson, C. J. Carey, İ. Polat, Y. Feng, E. W. Moore, J. VanderPlas, D. Laxalde, J. Perktold, R. Cimrman, I. Henriksen, E. A. Quintero, C. R. Harris, A. M. Archibald, A. H. Ribeiro, F. Pedregosa, and P. van Mulbregt, "SciPy 1.0: Fundamental algorithms for scientific computing in Python," en, *Nature Methods*, Feb. 2020. DOI: 10.1038/s41592-019-0686-2.

[14] H. A. Cole, "On-line failure detection and damping measurement of aerospace structures by random decrement signatures," Tech. Rep., Mar. 1973.

[15] J. C. Asmussen, S. R. Ibrahim, and R. Brincker, *Random decrement : Identification of structures subjected to ambient excitation*, en, Library Catalog: www.semanticscholar.org, 1998.

[16] B. Peeters and G. De roeck, "REFERENCE-BASED STOCHASTIC SUBSPACE IDENTIFICATION FOR OUTPUT-ONLY MODAL ANALYSIS," en, *Mechanical Systems and Signal Processing*, vol. 13, no. 6, pp. 855–878, Nov. 1999. DOI: 10.1006/mssp.1999.1249.

[17] M. Döhler, P. Andersen, and L. Mevel, "Operational Modal Analysis Using a Fast Stochastic Subspace Identification Method," en, in *Topics in Modal Analysis I, Volume 5*, R. Allemang, J. De Clerck, C. Niezrecki, and J. Blough, Eds., Series Title: Conference Proceedings of the Society for Experimental Mechanics Series, New York, NY: Springer New York, 2012, pp. 19–24. DOI: 10.1007/978-1-4614-2425-3_3.

EURODYN 2020
XI International Conference on Structural Dynamics
M. Papadrakakis, M. Fragiadakis, C. Papadimitriou (eds.)
Athens, Greece, 23–26 November 2020

EXPERIMENTAL EVALUATION OF BENDING MOMENTS AT THE TOWER OF AN ONSHORE WIND TURBINE

João Pacheco[1], **Francisco Pimenta**[1], **Álvaro Cunha**[1], **and Filipe Magalhães**[1]

[1] CONSTRUCT-VIBEST, Faculty of Engineering, University of Porto
Rua Dr. Roberto Frias, s/n 4200-465, Porto, Portugal
e-mail: {ec11142, ec09176, acunha, filipema}@fe.up.pt

Keywords: Wind turbine, Continuous monitoring system, Fatigue assessment, Strain gauge

Abstract. *The main goal of the WindFarmSHM research project is the development, validation and optimization of a monitoring strategy to be applied at the level of the wind farm, which should be able to evaluate the structural condition of a set of wind turbines and their consumed fatigue life. The accomplishment of this goal implies the development of an experimental campaign, the construction of numerical models and the implementation of new data processing methodologies.*

The experimental campaign is being performed at Tocha wind farm (an onshore wind farm located in Portugal) and includes the monitoring of three wind turbines, loaded by winds with different turbulence intensities motivated by the neighboring wind turbines, during a period of about 2 years. The instrumentation includes strain gauges, clinometers and accelerometers distributed in the tower and rotor.

As a first step in the development of tools to assess the fatigue condition of wind turbine towers, this work describes the data processing needed to obtain an accurate experimental estimation of the bending moments applied in the tower of the already fully instrumented wind turbine (WT1) and the validation of the obtained results using complementary monitoring components.

The experimental results reported in this contribution are also being used for calibration of advanced numerical models developed in FAST, which are very relevant for a better understating of the experimental data.

1 INTRODUCTION

Wind energy has experienced a truly remarkable evolution during the last two decades in terms of installed capacity and technological developments. In the EU, wind was the fastest growing energy source between 2005 and 2017, surpassing coal in 2016 as the second largest total installed power generation capacity [1]. 2017 was a record year for onshore and offshore installations that grew, respectively, 14.3% and 101% compared to 2016. It is expected that this capacity will continue to grow and that it will even double in a minimum interval of 10 years (taking the most optimistic forecast) [2].

Based on this scenario, it is possible to identify some of the present challenges, highlighting the concerns of the wind operators that need to manage the existing infrastructure Wind turbines were designed to operate 20 years, so it is estimated that about one half of the accumulated capacity currently installed in the EU will reach the end of design life in 2030 [2]. It is therefore essential to create a regulatory framework that defines the rules for the actions to be taken when the expected design life of the structures is exhausted.

Considering this background, the main goal of the WindFarmSHM research project is the development, validation and optimization of new methodologies to continuously assess the structural elements of wind turbines: tower, blades and foundation. This implies the development of innovative algorithms for data processing in order to:

i) Evaluate the remaining fatigue life of the main structural components based on the direct measurement of strains with strain gages, curvature measurements using pairs of clinometers or/and adopting a virtual sensors approach [3, 4];

ii) Extrapolate results obtained for instrumented wind turbines to non-instrumented wind turbines of the same wind farm, using SCADA data.

As a first step, this work describes the methodology and its validation for experimental estimation of the bending moments applied in the tower.

2 TOCHA WIND FARM

Tocha wind farm is located in the central region of Portugal approximately 3 km from the coastline, inserted in a coastal area with plain sandy terrain. It consists of five VESTAS wind turbines, model V100 with 1.8 MW of rated power, totaling 9.0 MW of installed power. This wind farm is owned by EDP Renewables and started its operation in May 2012.

Figure 1 shows the geographic location of the wind farm, the distribution of the five wind turbines (identified with numbers that will be used throughout this work)

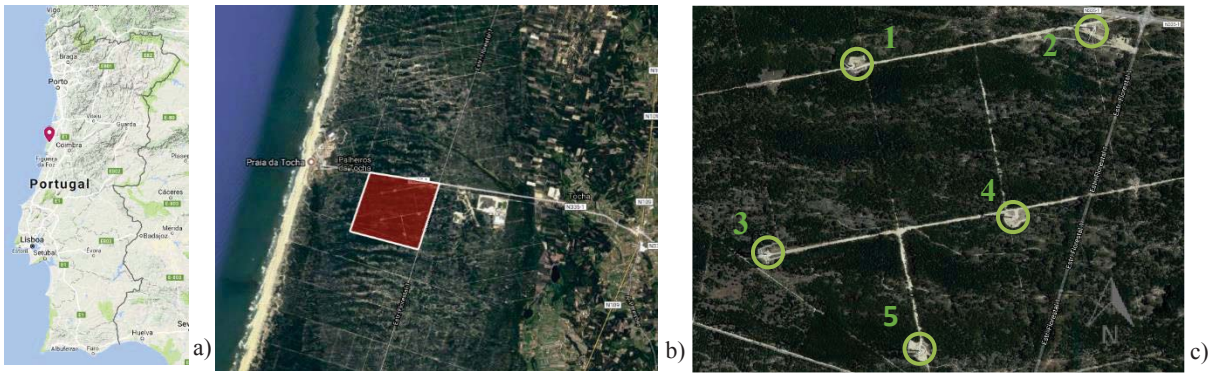

Figure 1: Tocha wind farm: a) Geographic location in Portugal [5]; b) Implantation area [6]; c) Wind turbines [7].

The Vestas V100-1.8 MW is a wind turbine designed for low wind onshore sites, so it features a larger rotor diameter, enabling it to deliver higher output at low wind speeds. It is a 3-bladed upwind turbine with a rotor diameter of 100 m (sweep an area of 7850 m^2) and a generator rated at 1.8 MW. The turbine operates at variable speeds from 9.3 to 16.6 rpm with a pitch control system. The hub is placed at a height of 95 m and is supported by a steel tower, of variable diameter, composed of four segments that are linked by bolted connections. Since the soil is sand, the steel tower is connected to a 14 by 14 m concrete slab supported by sixteen concrete piles with 1 m diameter.

As show in Figure 2, the power production increases gradually from cut-in wind speed (4 m/s) to rated wind speed (12 m/s) and is stable up to cut-out wind speed (20 m/s).

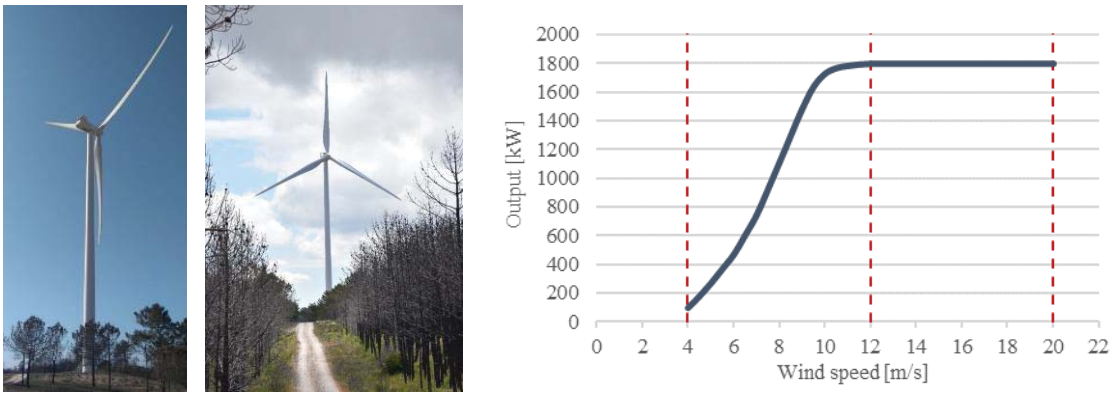

Figure 2: Wind turbines at Tocha wind farm and power curve of V100-1.8MW (https://en.wind-turbine-models.com).

3 MONITORING SYSTEMS

The experimental campaign in Tocha wind farm involves the simultaneous monitoring of several wind turbines during a period of about two years, which includes three instrumentation layout. However, only the tower monitoring systems comprehending acceleration and strain recording installed in wind turbine 1 are briefly described in this paper. A detailed description of the Tocha wind farm experimental campaign as well as some preliminary results can be found in [8].

The accelerations measurement system installed in the tower is based on a central acquisition system to witch all sensors are connected. It is composed by six force-balance accelerometers distributed along the tower height, measuring accelerations along two orthogonal horizontal directions at three sections, according to the scheme presented in Figure 3. In order to limit the length of the GPS signal cable (GPS antenna located in the nacelle), the central acquisition system (KMI) is located at the top platform, around 87 m.

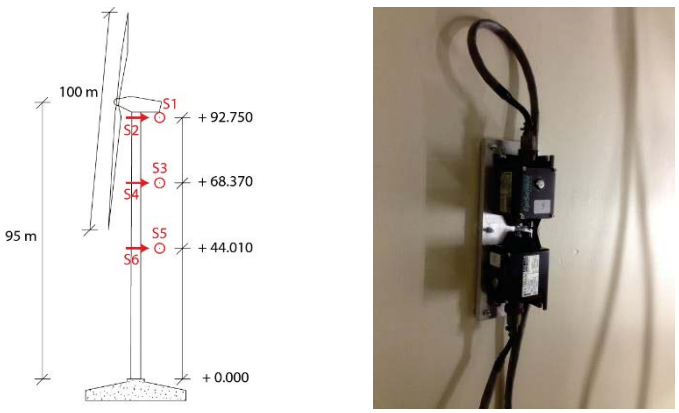

Figure 3: Sections instrumented with force balance sensors accelerometers (left). Photo of the force balance sensors (right).

In order to evaluate alternative procedures for estimating static and dynamic bending moment diagrams along the tower, two alternative monitoring systems were considered: using strain and rotation measurements (not covered in this work), combined with accelerometers.

The strains system is composed of six 2D rosette strain gages, which measure the strain in two orthogonal directions and four temperature sensors Pt100.

In order to estimate the static bending moments diagram along the entire length of the tower the six strain gauges are distributed in two cross sections: four sensors at 6.5 m from the base of the tower (bottom section) and two sensors at 7.7 m (top section) as shown in Figure 4. The four temperature sensors are located in the bottom section, next to the strain gauges.

As will be demonstrated in the next section, measuring deformation in the direction perpendicular to the tower axis and temperatures is important to allow the evaluation of alternative procedures to minimize the influence of temperature on the measured longitudinal deformations.

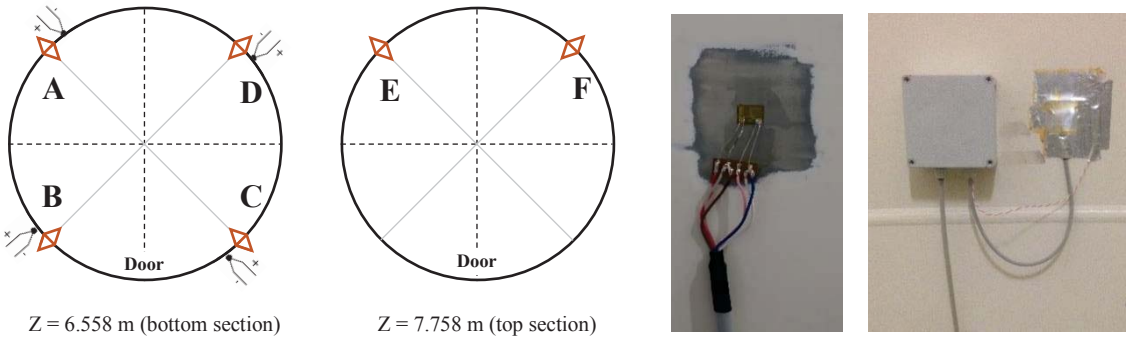

Z = 6.558 m (bottom section) Z = 7.758 m (top section)

Figure 4: Locations of the strain gages (◊) and temperature sensors ( ); photo of a 2D rosette strain gage before protection; and photo of the strain rosette and temperature sensor after protection and box for signal conditioning.

These two monitoring components are connected to a National Instruments digitizer and processor, installed at the base of the tower. The acquisition frequency is 50 Hz for the strains measurements and 1 Hz for temperature measurements. A program developed in LabView for this specific application ensures data acquisition and recording.

Figure 5 shows the position of the strain gauges and clinometers along the vertical alignment formed by strain gauges A and E.

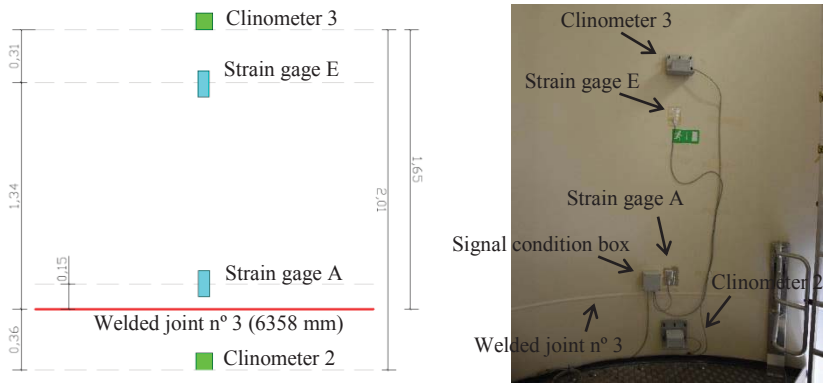

Figure 5: Scheme and photo of the position of the clinometers and strain gauges along the same vertical alignment.

In order to process the data collected from the described monitoring systems, it is essential to have SCADA data that accurately characterize the environmental and operational conditions of the wind turbine. In this study, the owner of the wind farm provides SCADA data with two types of sample rates: mean, maximum and minimum values from 10 min periods (SCADA 10 min) and data with a sampling interval of 15 sec (SCADA high resolution), of several operational and environmental parameters.

The data acquired with a higher sampling frequency is very useful as it allows accurately monitoring the rapid variations of some parameters, such as wind speed and direction, rotor speed, yaw angle and blades pitch angle, which is not possible to follow from the average values.

As shown in the Table 1, the monitoring of the tower is composed by three independent monitoring systems that adopt different timing protocols. In this way, it is necessary to synchronize all these systems in a common time frame to permit the join processing of different sensors datasets.

Acquisition system	Sensors type	Timing protocols
KMI	Force-balance Accelerometers	Global Positioning System time (GPS)
cRIO	Strain gauges Clinometers Temperature	Internal clock
SCADA	SCADA sensors	Network Time Protocol (NTP)

Table 1: Summary of installed monitoring systems at the tower of WT1 and corresponding timing protocols.

Global Positioning System time protocol was chosen as the reference from which all other systems were synchronized, so the force-balance accelerometers system is the reference time.

The synchronization of the cRIO acquisition system was performed by comparing the time series of extensions with the time series of accelerations measured by the force-balance sensors (Figure 6 left). The delay between the two systems identified over time is variable due to the limited accuracy of the internal clock of the cRIO system, so the time shift between the two systems is continuously updated. In a second phase, in order to make this synchronization

mora accurate are easy to automate, a low cost accelerometer placed next to one of the force balance sensors was connected to the cRIO.

The synchronization of SCADA data was performed by comparing the evolution of the yaw angle (SCADA high resolution) with the time series of strains over a variation of yaw angle of the nacelle (the eccentricity of the nacelle and rotor mass generates a sinusoidal signal in the strains gauges as shows in Figure 6 right). A constant delay of approximately 50 seconds was observed between the two systems.

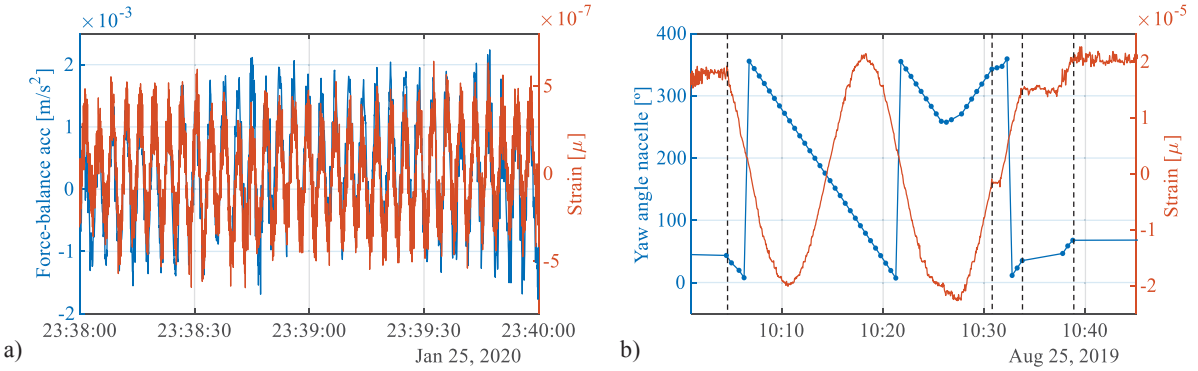

Figure 6: Synchronization of the monitoring systems: a) KMI (force-balance S3) and cRIO (strain gauge B) ; b) cRIO (strain gauge A) and SCADA (yaw angle) (the vertical dashed lines correspond to the singular points used for synchronization).

4 PROCESSING METHODOLOGY, CALIBRATION AND VALIDATION

Strain gauges are very sensitive sensors and many factors can easily preclude accurate measurements. All potential sources of errors need to be identified and it is necessary to implement a methodology for the signal processing according to the precision of the intended results.

Thus, the experimental determination of bending moments in the tower requires the acquired raw data to be pre-processed to obtain the real deformation. In the present application, as a first trial, the methodology presented in [9] with some upgrades is being followed. In a general way, this methodology consists of the following three steps: i) correction of the effect of temperature on strain gauges; ii) signal correction based on the average value of the extensions recorded on diametrically opposed sensors; iii) signal calibration according to guideline [10]. In the following sections, the steps of the implemented methodology are presented and validated.

4.1 Orientation Calibration

The first step is to determine the exact position of the sensors in the instrumented section of the tower (despite the care used in the sensor gluing there are always inaccuracies in sensor position), taking into account a local coordinate system where the y-axis coincides with the position of the entrance door. The nacelle angle defines the fore-aft and site-side axis for which the bending moments will be estimated.

As shown in Figure 7, the full rotation of the nacelle generates a sinusoidal signal in the strains gauges due the eccentricity of the nacelle and rotor mass. The values of the yaw angle for which the minimum value of the signals occurs correspond to the radial position of each sensor. In a good installation, the maxima and minima of diametrically installed sensors

should happen for the same time instant and for that same time instant the other two sensors should be close to zero. Please note that the strains presented in Figure 7 were pre-processed to have zero mean.

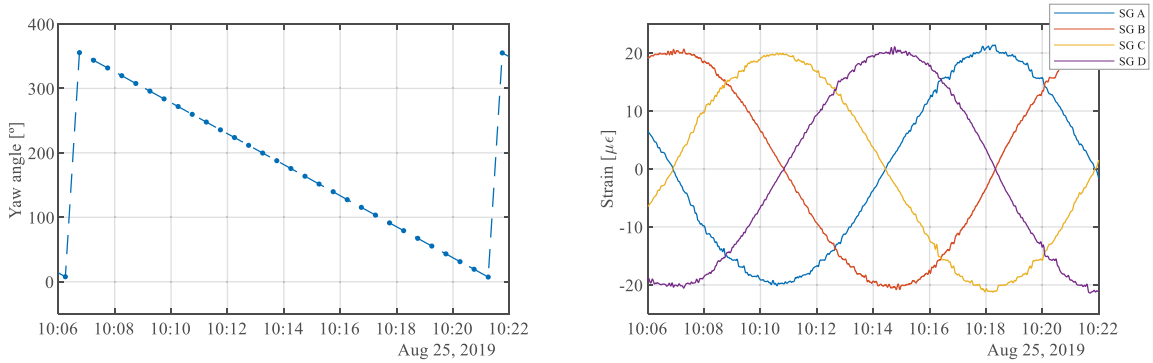

Figure 7: Yaw angle nacelle (left) and strain gauges signals (right) during nacelle full rotation at Aug 25, 2019 (see sensor positions in Figure 4 and Figure 5).

4.2 Correction of temperature effects

Many factors can easily distort strain measurements, but temperature is the most frequent source of errors. Temperature can influence the measurement of strains in two ways: thermal output and non-linear temperature gradient.

Thermal output is caused by variation of the electrical resistivity of the grid conductor with temperature and the differential thermal expansion between the grid conductor and the steel of the tower. This effect is minimized using the thermal output compensation curve provided by the manufacturer and the temperature measured on the steel surface.

The local heating of the sun can also influence the measured strains, as the temperature gradient may become non-linear. This parasite strains are minimized by averaging the two signals provided by the gauge couple installed at 180°.

Strain gauges are connected to the acquisition system using a ¼-bridge configuration with three wires in order to avoid effects of temperature on the cables.

In order to demonstrate in a practical example the influence of the temperature on the strain measurements, Figure 8 a) represents four strain signals measured at the bottom section, after being zeroed during the nacelle full rotation performed at around 07:00 (without compensation of the temperature effects). The same signals but with temperature effects minimized is shows at Figure 8 b). Comparing these figures, it is observed that in the first one the signals provided by the gauge couple installed at 180° are not perfectly symmetric, whereas in the second there is a perfect symmetry with respect to the x axis.

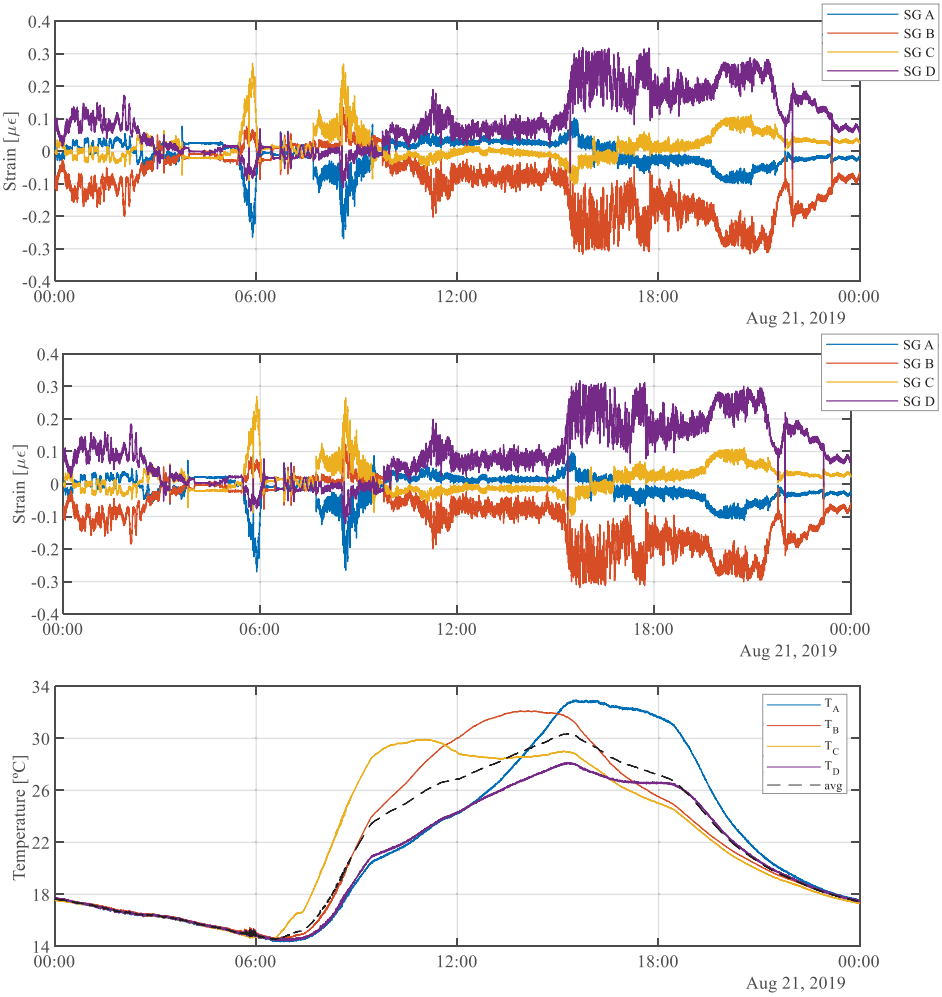

Figure 8: Daily temperature effects on strains measurements at the bottom section: a) Strains signals zeroed during the nacelle rotation; b) Strains signals zeroed during the nacelle rotation with compensation of the temperature effects; c) Temperature measurements

4.3 Drift correction

A significant drift is observed on the strains signals over time [11]. The correction of this drift is based on the procedure defined by the International Electrotechnical Commission (IEC) standards called calibration check [10]. The mean of the signals generated by yawing the nacelle through 360º represents the zero point (Figure 7).

A total of 10 full rotation of the nacelle, that met all the requirements, were observed in the period of 01-Aug-2019 to 01-Dez-2019 and were used to the calibration process (Figure 9).

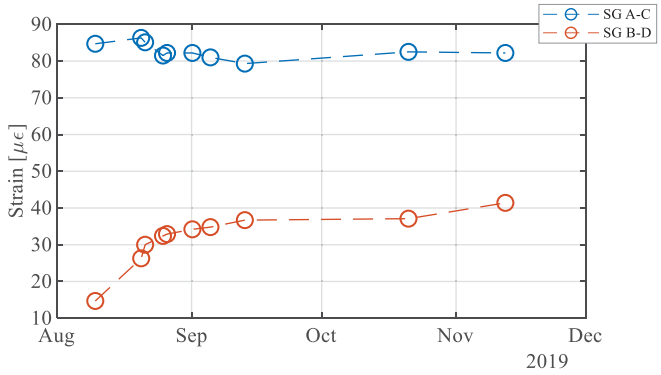

Figure 9: Mean value of the full rotation signals observed at August-2019 to December-2019 (see sensor positions in Figure 4 and Figure 5).

It appears that in the first months the drift remains close to 85 με for couple A-C. For the couple B-D, there is an initial 15 με drift with a linear evolution up to about 35 με over the first month. In the following months, the drift remains approximately constant.

4.4 Amplitude validation

The last validation consists of checking if the values of the strains measured in the structure and processed according to the procedure just presented correspond to real values of deformation of the structure due to applied loads.

In this sense, the average values of strains observed in all the recorded 10 min setups (total of 14720 setups) are shown in the Figure 10 as a function of the yaw angle. These values are compared with the theoretical strain curve that would be obtained for the maximum thrust force applied at the rotor level. It should be noted that the maximum drag force applied at the hub level is approximately 280 kN (calculated from the drag coefficients presented in [12]).

There is a good agreement between theoretical and experimental values. However, it should be noted that maximum strain values are not obtained for all directions. This is because prevailing conditions of wind action exist. These results also allow validating the calibration of the sensor orientation in section 4.1.

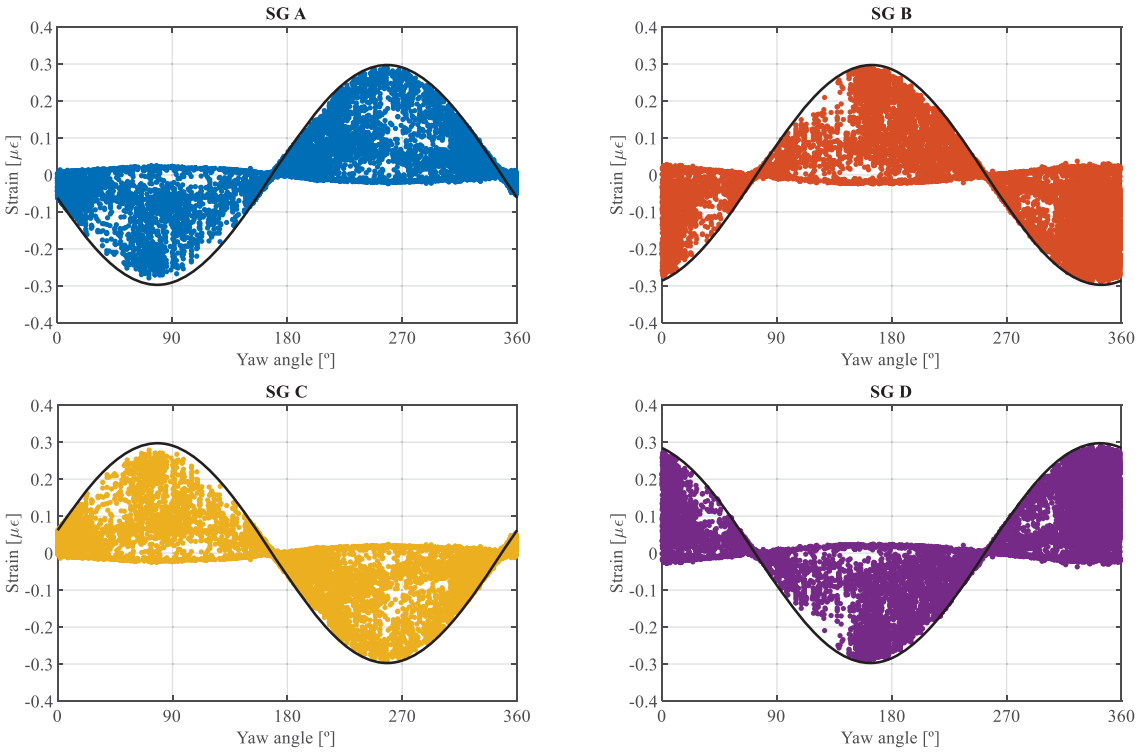

Figure 10: Average measured strains of strain gauges A, B, C and D (August-2019 to January-2020).

The bending moments estimated from the measurement of strains were also compared with those that can be obtained from the measurement of accelerations. Considering a rotor stop event (in which only the first vibration mode of the tower explains the structure's response) the displacement of the tower at the level of the accelerometer S1 was determined by double integration of the acceleration (Figure 11 left). Using a stiffness matrix provided by a simple numerical model developed in Robot [13], it was possible to determine the equivalent modal force applied at the S1 sensor level and the associated bending moment at the section instrumented with strain gages. The method followed to determine the response of structures in displacement from the measurement of accelerations is further developed in [3, 4].

For the same rotor stop event the strain time series measured at strains gauge D is represented in Figure 11 right.

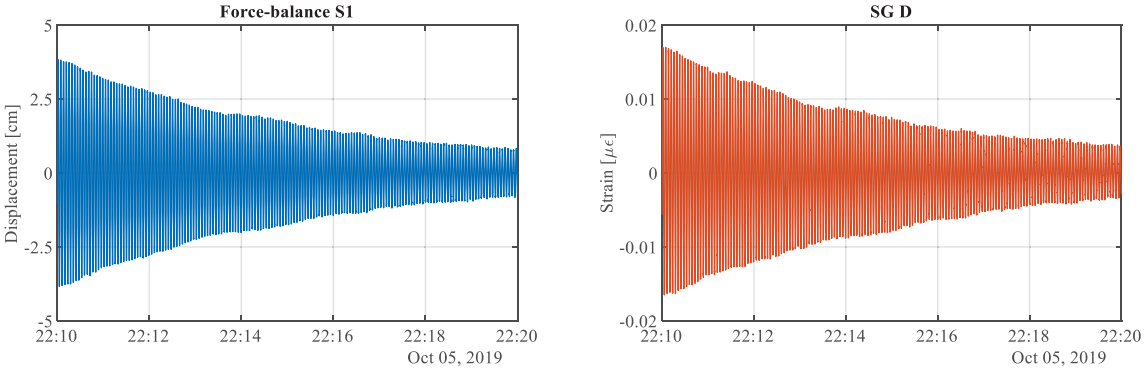

Figure 11: Rotor stop event on Oct, 5 2019: Time series of displacements at the top of the tower estimated from accelerations measured at sensor S1 (left) and strains at strain gauge D (right)

The bending moments at the base of the tower estimated from accelerations and strains are shown in the Figure 12. There is an excellent similarity between the bending moments estimated with the two methods. The error is less than 10% and can be explained by the difficulty in accounting for the exact stiffness of the tower.

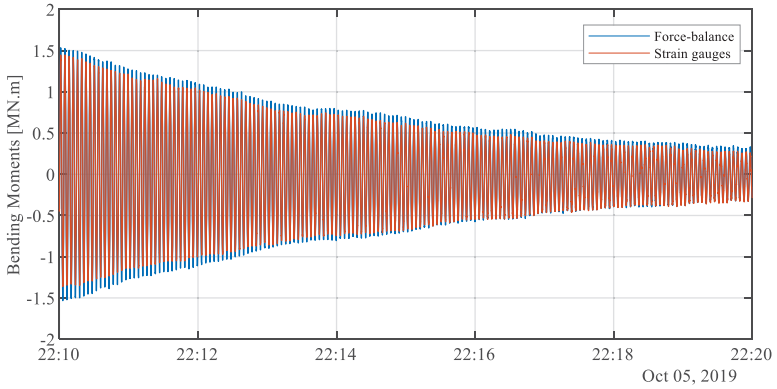

Figure 12: Bending moments at the base of the tower estimated from accelerations and strains time series.

5 RESULTS

After the calibration and validation of the methodology to estimate the bending moments at the base of the tower, some final results are presented.

Applying the described data processing to the recorded series, in Figure 13 the temporal evolutions of the bending moments observed in the bottom instrumented section are presented, for the two main directions, considering two alternative turbine operation scenarios. The experimental results are compared with numerical counterparts, obtained from a model developed in FAST [14] and calibrated using the methodology described in [15].

It is possible to verify a good agreement between the numerical and experimental results. It should be noted that the simulated wind loads respect the mean and standard deviations observed in the field measurements, but the time series are different. In both analyzed situations, the mean values and scatter of the FA bending moments are very similar.

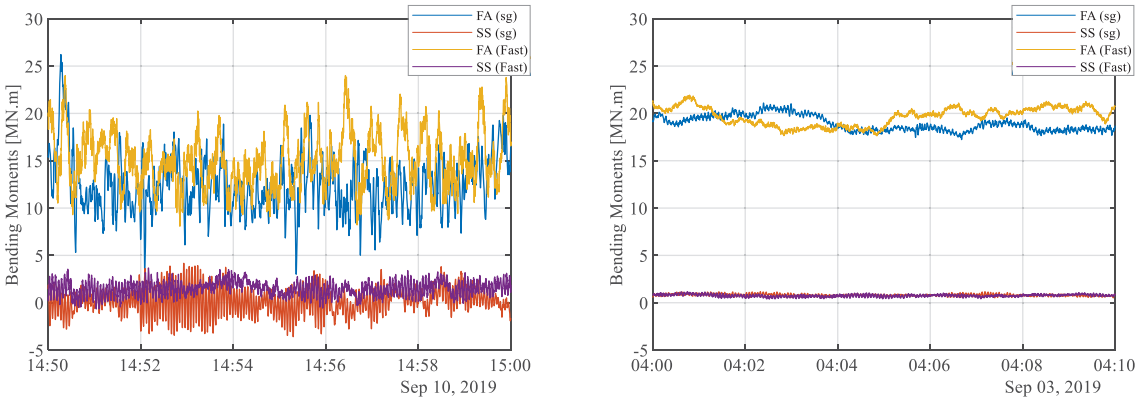

Rotor speed = 14.9 rpm; Wind speed = 13.0 m/s; TI = 14.6 %
$M_{FA,sg}$ = 12524 kN; $M_{FA,Fast}$ = 15043 kN

Rotor speed = 13.0 rpm; Wind speed = 7.9 m/s; TI = 4.4 %
$M_{FA,SG}$ = 18922 kN; $M_{FA,Fast}$ = 19684 kN

Figure 13: Experimental and numerical bending moments time series for FA and SS directions in the bottom instrumented section of the tower considering two operating conditions (TI: turbulence intensity; M_{xx}: bending moment average).

A very interesting in wind turbine towers is to express the evolution of the stresses as a function of wind speed. Figure 14 shows the 10 min average bending moment at the tower base for the fore-aft direction versus the 10 min average wind speed provided by the SCADA system during normal operation, considering different turbulence intensities.

Despite the short period of analysis, the results are quite promising. The drag force that is acting on the rotor and is responsible for the tower deflection is reduced above 10 m/s due the starting of the pitch control to keep the lift force and rotor speed constant. It is also verified that for wind speeds between 8 and 12 m/s the bending moment decreases as the turbulence intensity increases.

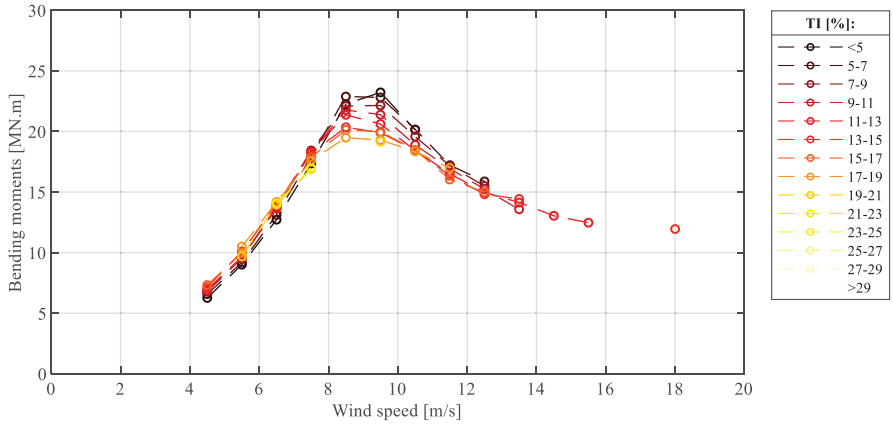

Figure 14: 10min average bending moment at the tower base for fore-aft direction versus the 10min average wind speed during normal operation, considering different turbulence intensities (August-2019 to January-2020).

6 CONCLUSIONS

This paper presents the methodology followed for the experimental evaluation of bending moments at the tower of a wind turbine. The quite extensive monitoring camping that is being conducted in Tocha wind farm is described, with particular attention for the strains monitoring system.

Special attention is given to the signal processing of the strain gauges, taking into account that temperature is known to be the major cause of signal perturbation. In this way, it is presented a procedure to minimize de daily temperature effects and also the long-term effects on the strain gauges. The post-processed strain signal are validated with theoretical and other experimental results.

Although the amount of data is still small, the results obtained are very promising. They are the starting point for fatigue calculation under development.

ACKNOWLEDGEMENTS

The support of EDP Renewables and VESTAS in greatly acknowledged. This work was also financially supported by: PhD Grant SFRH/BD/129688/2017, UID/ECI/04708/2019-CONSTRUCT - Instituto de I&D em Estruturas e Construções and the project PTDC/ECI-EST/29558/2017, all funded by national funds through the FCT/MCTES (PIDDAC).

REFERENCES

[1] EWEA, Wind in power 2017 - Annual combined onshore and offshore wind energy statistics. Brussels, Belgium, 2018.

[2] EWEA, Wind energy in Europe: Scenarios for 2030. Brussels, Belgium, 2017.

[3] G. Oliveira, F. Magalhães, Á. Cunha, E. Caetano, Dynamic monitoring system for utility scale wind turbines: damage detection and fatigue assessment, *Journal of Civil Structural Health Monitoring* 7, 657-668, 2017.

[4] H. P. Hjelm, R. Brincker, J. Graugaard-Jensen, K. MunchK, Determination of Stress Histories in Structures by Natural Input Modal Analysis. *Paper presented at the XXIII International Modal Analysis Conference (IMAC)*, Florida, USA, 2005.

[5] Google. (n.d.). [Google Maps location of Tocha Wind Farm, Tocha, Cantanhede, Coimbra, Portugal]. Retrieved March 21, 2018, from https://www.google.com/maps/@39.5170771,-9.4259083,7.5z.

[6] Google. (n.d.). [Google Maps location of Tocha Wind Farm, Tocha, Cantanhede, Coimbra, Portugal]. Retrieved March 21, 330 2018, from https://www.google.com/maps/@40.3195058,-8.8204938,1387m/data=!3m1!1e3.

[7] Google. (n.d.). [Google Maps location of Tocha Wind Farm, Tocha, Cantanhede, Coimbra, Portugal]. Retrieved March 21, 2018, from https://www.google.com/maps/@40.3244121,-8.8220541,7848m/data=!3m1!1e3.

[8] F. Magalhães, J. Pacheco, C. Moutinho, S. Guimarães, L. Noites, A. Cunha, M. Marques, J. C. Matos, Monitoring campaign in an onshore wind farm: installation description and preliminary results, *8th International Operational Modal Analysis Conference,* Copenhagen, Denmark, 2019.

[9] C. T. Loraux, Long-term monitoring of existing wind turbine towers and fatigue performance of UHPFRC under compressive stresses. École Polytechnique Fédérale de Lausanne, Lausanne, 2018.

[10] IEC 61400-13, IEC 61400-13 Wind energy generation systems - Part 13: Measurement of Mechanical Loads, *International Electrotechical Commission (IEC)*, 2015.

[11] K Hoffmann, An introduction to stress analysis and transducer design using strain gauges. *HBM Test and Measurement*, 2012.

[12] Morrison Hershfield Limited, Wind Turbine Specification Report, HAF Wind Energy Project (1104037.00), 2012.

[13] Autodesk, Robot Structural Analysis Professional (Version 29.0.05650(x64)), 2016.

[14] M. Sprague, J. M. Jonkman, B. Jonkman, FAST Modular Framework for Wind Turbine Simulation: New Algorithms and Numerical Examples. In: Proc. 33rd Wind Energy Symposium. Kissimmee, Florida, 2015.

[15] F. Pimenta, C. M. Branco, C. M. Teixeira, F. Magalhães, Calibration of onshore wind turbine numerical model using experimental data, *15th EAWE PhD Seminar on Wind Energy*, Nantes, France, 2019.

EURODYN 2020
XI International Conference on Structural Dynamics
M. Papadrakakis, M. Fragiadakis, C. Papadimitriou (eds.)
Athens, Greece, 23–26 November 2020

WIND TURBINE ROTOR BLADE VIBRATION – APPLICATION OF TWO ALTERNATIVE MODAL DECOMPOSITION PROCEDURES

Evgueni Stanoev[1]

[1] Chair of Wind Energy Technology, Faculty of Mechanical Engineering and Marine Technology
University of Rostock, Albert-Einstein-Str. 2, 18059 Rostock, Germany
e-mail: evgueni.stanoev@uni-rostock.de

Keywords: modal decomposition, complex eigenvalue problem, vibration of wind turbine rotor blade, non-proportional damping

Abstract: *Two alternative modal decomposition procedures are applied to the vibration of a generic WT rotor blade, subjected to wind thrust loads. The first one, published first in [7] and [16], is based on a state-space-formulation of the equations of motion with symmetric damping matrix, which represents non-proportional damping. By use of the complex right eigenvectors of the associated quadratic eigenvalue problem a modal transformation matrix in real space is assembled, combining two complex transformations. The proposed procedure retains all common advantages of the classic modal decomposition of the equations of motion.*

The second applied procedure, known as a "phase synchronisation method", is presented in [14], [15]. The equations of motion here are formulated in the Lancaster state space form. Beside this the associated complex conjugated eigenvector and eigenvalue pairs are combined in separated modal resp. spectral matrices – this is another major difference to the first procedure. The assembling of the final real-space transformation matrix is based on the notion of "phase synchronization". The development of both procedures is described briefly, differences and advantages are discussed and pointed out in details.

Both presented methods are demonstrated on numerical example - vibration of a wind turbine rotor blade subjected to wind thrust loads. The presumed symmetric non-proportional damping matrix is derived by an aerodynamic damping approach, applied on the level of the differential equations of the beam element.

1 INTRODUCTION

The solution of the classic linear eigenvalue problem, associated to the equations of motion of multi-degree-of-freedom-systems (MDOFS), consists of real eigenvalues (natural frequencies) and real eigenvectors. The inclusion of viscous damping in the equations of MDOFS leads to a quadratic eigenvalue problem with corresponding complex conjugate pairs of eigenvalues and eigenvectors.

Starting point of our considerations are the equations of motion of a damped MDOFS in configuration space

$$\boldsymbol{M}\ddot{\boldsymbol{V}} + \boldsymbol{D}\dot{\boldsymbol{V}} + \boldsymbol{K}\boldsymbol{V} = \mathbf{p}(t)\ , \tag{1.1}$$

where $\boldsymbol{M}, \boldsymbol{D}$ and $\boldsymbol{K}$ are, respectively the (n x n) mass, damping and stiffness matrix, and $\boldsymbol{V}, \dot{\boldsymbol{V}}, \ddot{\boldsymbol{V}}$ are respectively the (n x 1) displacement, the velocity and the acceleration vectors and **p**(t) is the (n x 1) excitation vector.

In structural mechanics problems the matrices $\boldsymbol{M}, \boldsymbol{D}$ and $\boldsymbol{K}$ are considered to be real, symmetric and positive definite, excluding the presence of rigid body modes. In the classic modal analysis $\boldsymbol{D} = \mathbf{0}$, in this case Eq. (1.1) can be decoupled by use of the real right eigenvectors $\mathbf{X}_j$ of the undamped system:

$$\left(\lambda_j^2\, \boldsymbol{M} + \boldsymbol{K}\right) \mathbf{Q}_j = \mathbf{0} \tag{1.2}$$

In the case of classically damped system with $\boldsymbol{D} \neq \mathbf{0}$ Eq. (1.1) can also be decoupled by the real eigenvectors of the undamped system. According to [2] the necessary and sufficient condition for classical damping is:

$$\boldsymbol{D}\boldsymbol{M}^{-1}\boldsymbol{K} = \boldsymbol{K}\boldsymbol{M}^{-1}\boldsymbol{D} \tag{1.3}$$

The proportional damping assumption

$$\boldsymbol{D} = \alpha\boldsymbol{M} + \beta\boldsymbol{K}\ , \tag{1.4}$$

the so-called *Rayleigh damping*, is a particular case of classic damping – Eq. (1.4) satisfies the condition (1.3).

The associated quadratic eigenvalue problem to Eq. (1.1) is

$$\left(\boldsymbol{M}\lambda_j^2 + \boldsymbol{D}\lambda_j + \boldsymbol{K}\right)\boldsymbol{Q}_j = \mathbf{0} \tag{1.5}$$

where

$$\lambda_j = \alpha_j + i\omega_{Dj} \ \rightarrow\ \boldsymbol{Q}_j\ ; \qquad \overline{\lambda}_j = \alpha_j - i\omega_{Dj} \ \rightarrow \overline{\boldsymbol{Q}}_j \tag{1.6}$$

are complex conjugate eigenvalues with associated complex eigenvector pairs $\boldsymbol{Q}_j, \overline{\boldsymbol{Q}}_j$.

This paper presents the simpliest variant of a general modal decomposition method, presented in some variants in [7] and [16]-[19]. The method is used to transform in real-space the equations of motion of multi-degree-of-freedom-systems (MDOFS) with symmetric damping matrix, representing non-proportional damping. The equations of motion are stated in state-space formulation. The variant, presented in Section 3, is described in comparison with a similar technique for decoupling of non-classically damped system equations, referred to as *phase synchronization*, presented in earlier publications [4], [14], [15]. This approach has been described in [13] and [14] for free and forced vibrations in configuration space formulation. In [15] it has been shown the interpretation of the decoupling transformation by phase synchronization on the basis of state space formulation.

The problem of decoupling the homogenous problem in Eq. (1.5) can also be addressed as a reduction of the quadratic pencil $Q(\lambda) = \boldsymbol{M}\lambda^2 + \boldsymbol{D}\lambda + \boldsymbol{K}$. In [8], [9] and [4], [5] have been proposed the notion of *structure-preserving transformations* in diagonalizing $Q(\lambda)$. In [15] it has been shown the interpretation of the decoupling transformation by phase synchronization on the basis of state space formulation, under the assumption that all the eigenvalues λ_j , $\overline{\lambda}_j$ are complex and distinct.

In order to introduce to the method presented in Section 3, we will first briefly review in Section 2 the phase synchronization procedure on the basis of state space formulation according to [14], [15].– for the case of forced vibrations with n distinct complex conjugated eigenvalues λ_j.

2 THE PHASE SYNCHRONIZATION PROCEDURE IN STATE SPACE

All eigenvalues λ_j , $\overline{\lambda}_j$ in Eq. (1.6) are supposed to be complex conjugated and distinct, i.e. the quadratic eigenvalue problem is non-defective.

First of all, Eq. (1.1) should be written in state space in the *symmetric Lancaster form*, see [12]:

$$\begin{bmatrix} \boldsymbol{D} & \boldsymbol{M} \\ \boldsymbol{M} & \end{bmatrix} \begin{bmatrix} \dot{\boldsymbol{V}} \\ \ddot{\boldsymbol{V}} \end{bmatrix} + \begin{bmatrix} \boldsymbol{K} & \\ & -\boldsymbol{M} \end{bmatrix} \begin{bmatrix} \boldsymbol{V} \\ \dot{\boldsymbol{V}} \end{bmatrix} = \begin{bmatrix} \mathbf{p}(t) \end{bmatrix} \tag{2.1}$$

The associated state space eigenvalue problem takes the form

$$\left(\begin{bmatrix} \boldsymbol{D} & \boldsymbol{M} \\ \boldsymbol{M} & \end{bmatrix} \lambda_j + \begin{bmatrix} \boldsymbol{K} & \\ & -\boldsymbol{M} \end{bmatrix} \right) \begin{bmatrix} \boldsymbol{X}_j \\ \lambda_j \boldsymbol{X}_j \end{bmatrix} = L(\lambda_j) \begin{bmatrix} \boldsymbol{X}_j \\ \lambda_j \boldsymbol{X}_j \end{bmatrix} = \mathbf{0}$$

$$\rightarrow \begin{bmatrix} \boldsymbol{K} & \\ & -\boldsymbol{M} \end{bmatrix} \begin{bmatrix} \boldsymbol{X}_j \\ \lambda_j \boldsymbol{X}_j \end{bmatrix} = -\lambda_j \begin{bmatrix} \boldsymbol{D} & \boldsymbol{M} \\ \boldsymbol{M} & \end{bmatrix} \begin{bmatrix} \boldsymbol{X}_j \\ \lambda_j \boldsymbol{X}_j \end{bmatrix} \tag{2.2}$$

The symmetrically linearized pencil $L(\lambda_j)$ is referred to as the *Lancaster structure*.

A first complex modal transformation is defined by

$$\begin{bmatrix} \boldsymbol{V} \\ \dot{\boldsymbol{V}} \end{bmatrix} = \begin{bmatrix} \boldsymbol{X} & \overline{\boldsymbol{X}} \\ \boldsymbol{X}\boldsymbol{\Lambda} & \overline{\boldsymbol{X}}\,\overline{\boldsymbol{\Lambda}} \end{bmatrix} \begin{bmatrix} \boldsymbol{a} \\ \boldsymbol{b} \end{bmatrix} \tag{2.3}$$

where

$$\boldsymbol{a} = [a_1 \quad a_2 \quad \cdots \quad a_n]^T, \quad \boldsymbol{b} = [b_1 \quad b_2 \quad \cdots \quad b_n]^T \tag{2.4}$$

are new complex modal coordinates,

$$\boldsymbol{X} = [\boldsymbol{X}_1 \quad \boldsymbol{X}_2 \quad \cdots \quad \boldsymbol{X}_n], \quad \overline{\boldsymbol{X}} = [\overline{\boldsymbol{X}}_1 \quad \overline{\boldsymbol{X}}_2 \quad \cdots \quad \overline{\boldsymbol{X}}_n] \tag{2.5}$$

are modal matrices built by the complex $\boldsymbol{X}_j$ resp. the conjugate complex eigenvectors $\overline{\boldsymbol{X}}_j$, and

$$\boldsymbol{\Lambda} = \mathrm{diag}[\lambda_1, \lambda_2, \cdots, \lambda_n], \quad \overline{\boldsymbol{\Lambda}} = \mathrm{diag}[\overline{\lambda}_1, \overline{\lambda}_2, \cdots, \overline{\lambda}_n] \tag{2.6}$$

are the associated spectral matrices. The transformation (2.3) implies that the j-th damped mode of vibration $\boldsymbol{s}_j(t)$ is expressed as a linear combination

$$\boldsymbol{s}_j(t) = \boldsymbol{X}_j \underbrace{\left(c_j e^{\lambda_j t}\right)}_{a_j} + \overline{\boldsymbol{X}}_j \underbrace{\left(\overline{c}_j e^{\overline{\lambda}_j t}\right)}_{b_j} \tag{2.7}$$

The eigenvectors $\mathbf{X}_j, \overline{\mathbf{X}}_j$ may be normalized with respect to the mass matrix $\boldsymbol{M}$, which leads to the relationships

$$\begin{aligned} &2\lambda_j \mathbf{X}_j{}^T \boldsymbol{M} \mathbf{X}_j + \mathbf{X}_j{}^T \boldsymbol{D} \mathbf{X}_j = 2i\omega_{Dj} = \lambda_j - \overline{\lambda}_j \quad \text{resp.} \\ &2\lambda_j \overline{\mathbf{X}}_j{}^T \boldsymbol{M} \overline{\mathbf{X}}_j + \overline{\mathbf{X}}_j{}^T \boldsymbol{D} \overline{\mathbf{X}}_j = -2i\omega_{Dj} = \overline{\lambda}_j - \lambda_j \end{aligned} \tag{2.8}$$

Substitute Eq. (2.3) into (2.1) and pre-multiply by $\begin{bmatrix} \boldsymbol{X} & \overline{\boldsymbol{X}} \\ \boldsymbol{X}\boldsymbol{\Lambda} & \overline{\boldsymbol{X}}\,\overline{\boldsymbol{\Lambda}} \end{bmatrix}^T$ to obtain

$$\underbrace{\begin{bmatrix} \boldsymbol{X} & \overline{\boldsymbol{X}} \\ \boldsymbol{X}\boldsymbol{\Lambda} & \overline{\boldsymbol{X}}\,\overline{\boldsymbol{\Lambda}} \end{bmatrix}^T \begin{bmatrix} \boldsymbol{D} & \boldsymbol{M} \\ \boldsymbol{M} & \end{bmatrix} \begin{bmatrix} \boldsymbol{X} & \overline{\boldsymbol{X}} \\ \boldsymbol{X}\boldsymbol{\Lambda} & \overline{\boldsymbol{X}}\,\overline{\boldsymbol{\Lambda}} \end{bmatrix}} \begin{bmatrix} \dot{\boldsymbol{a}} \\ \dot{\boldsymbol{b}} \end{bmatrix} + \underbrace{\begin{bmatrix} \boldsymbol{X} & \overline{\boldsymbol{X}} \\ \boldsymbol{X}\boldsymbol{\Lambda} & \overline{\boldsymbol{X}}\,\overline{\boldsymbol{\Lambda}} \end{bmatrix}^T \begin{bmatrix} \boldsymbol{K} & \\ & -\boldsymbol{M} \end{bmatrix} \begin{bmatrix} \boldsymbol{X} & \overline{\boldsymbol{X}} \\ \boldsymbol{X}\boldsymbol{\Lambda} & \overline{\boldsymbol{X}}\,\overline{\boldsymbol{\Lambda}} \end{bmatrix}} \begin{bmatrix} \boldsymbol{a} \\ \boldsymbol{b} \end{bmatrix} = \begin{bmatrix} \boldsymbol{X}^T \mathbf{p}(t) \\ \overline{\boldsymbol{X}}^T \mathbf{p}(t) \end{bmatrix}$$

$$\begin{bmatrix} \boldsymbol{X}^T \boldsymbol{D} \boldsymbol{X} + 2\boldsymbol{\Lambda}(\boldsymbol{X}^T \boldsymbol{M} \boldsymbol{X}) & \\ & \overline{\boldsymbol{X}}^T \boldsymbol{D} \overline{\boldsymbol{X}} + 2\overline{\boldsymbol{\Lambda}}\left(\overline{\boldsymbol{X}}^T \boldsymbol{M} \overline{\boldsymbol{X}}\right) \end{bmatrix} \begin{bmatrix} \dot{\boldsymbol{a}} \\ \dot{\boldsymbol{b}} \end{bmatrix} + \begin{bmatrix} \boldsymbol{X}^T \boldsymbol{K} \boldsymbol{X} + \boldsymbol{\Lambda}(\boldsymbol{X}^T \boldsymbol{M} \boldsymbol{X})\boldsymbol{\Lambda} & \\ & \overline{\boldsymbol{X}}^T \boldsymbol{K} \overline{\boldsymbol{X}} + \overline{\boldsymbol{\Lambda}}\left(\overline{\boldsymbol{X}}^T \boldsymbol{M} \overline{\boldsymbol{X}}\right)\overline{\boldsymbol{\Lambda}} \end{bmatrix} \begin{bmatrix} \boldsymbol{a} \\ \boldsymbol{b} \end{bmatrix} = \begin{bmatrix} \boldsymbol{X}^T \mathbf{p}(t) \\ \overline{\boldsymbol{X}}^T \mathbf{p}(t) \end{bmatrix} \tag{2.9}$$

Accounting for the normalization (2.8), the left side of Eq.(2.9) can be reformulated:

$$\begin{bmatrix} \boldsymbol{\Lambda} - \overline{\boldsymbol{\Lambda}} & \\ & \overline{\boldsymbol{\Lambda}} - \boldsymbol{\Lambda} \end{bmatrix} \begin{bmatrix} \dot{\boldsymbol{a}} \\ \dot{\boldsymbol{b}} \end{bmatrix} + \begin{bmatrix} \left(\overline{\boldsymbol{\Lambda}} - \boldsymbol{\Lambda}\right)\boldsymbol{\Lambda} & \\ & \left(\overline{\boldsymbol{\Lambda}} - \boldsymbol{\Lambda}\right)\overline{\boldsymbol{\Lambda}} \end{bmatrix} \begin{bmatrix} \boldsymbol{a} \\ \boldsymbol{b} \end{bmatrix} = \begin{bmatrix} \boldsymbol{X}^T \mathbf{p}(t) \\ \overline{\boldsymbol{X}}^T \mathbf{p}(t) \end{bmatrix} \tag{2.10}$$

The state space form (2.1) is now decoupled in the complex form (2.10). Note that although Eq. (2.1) has been decoupled in state space, the new introduced complex variables $\begin{bmatrix}\boldsymbol{a}\\ \boldsymbol{b}\end{bmatrix}$, see Eq. (2.3), cannot be classified as displacements and velocities.

In the next step a purely real 2n-dimensional vector $[\boldsymbol{x}^T \quad \boldsymbol{y}^T]^T$ is defined:

$$\begin{bmatrix}\boldsymbol{x}\\ \boldsymbol{y}\end{bmatrix} = \begin{bmatrix}\boldsymbol{I} & \boldsymbol{I}\\ \boldsymbol{\Lambda} & \overline{\boldsymbol{\Lambda}}\end{bmatrix}\begin{bmatrix}\boldsymbol{a}\\ \boldsymbol{b}\end{bmatrix} \tag{2.11}$$

The inverse relationship of (2.11) is

$$\begin{bmatrix}\boldsymbol{a}\\ \boldsymbol{b}\end{bmatrix} = \begin{bmatrix}\boldsymbol{I} & \boldsymbol{I}\\ \boldsymbol{\Lambda} & \overline{\boldsymbol{\Lambda}}\end{bmatrix}^{-1}\begin{bmatrix}\boldsymbol{x}\\ \boldsymbol{y}\end{bmatrix} = \underbrace{\begin{bmatrix}\left(\overline{\boldsymbol{\Lambda}}-\boldsymbol{\Lambda}\right)^{-1}\overline{\boldsymbol{\Lambda}} & \left(\boldsymbol{\Lambda}-\overline{\boldsymbol{\Lambda}}\right)^{-1}\\ \left(\boldsymbol{\Lambda}-\overline{\boldsymbol{\Lambda}}\right)^{-1}\boldsymbol{\Lambda} & \left(\overline{\boldsymbol{\Lambda}}-\boldsymbol{\Lambda}\right)^{-1}\end{bmatrix}}_{\boldsymbol{S}}\begin{bmatrix}\boldsymbol{x}\\ \boldsymbol{y}\end{bmatrix} = \boldsymbol{S}\begin{bmatrix}\boldsymbol{x}\\ \boldsymbol{y}\end{bmatrix} \tag{2.12}$$

The reason of the definitions (2.11) and (2.12) is better clarified by looking at Sec. 3, Eq. (3.2), (3.4), (3.19).

Finally, we substitute Eq.(2.12) into (2.10) and then pre-multiply the resulting equation by $\boldsymbol{S}^T$ to obtain the real-space relationship (2.13)

$$\underbrace{\begin{bmatrix}\left(\overline{\boldsymbol{\Lambda}}-\boldsymbol{\Lambda}\right)^{-1}\left(-\overline{\boldsymbol{\Lambda}\boldsymbol{\Lambda}}+\boldsymbol{\Lambda}\boldsymbol{\Lambda}\right) & \boldsymbol{I}\\ \boldsymbol{I} & \boldsymbol{0}\end{bmatrix}}_{\begin{bmatrix}\boldsymbol{D_1} & \boldsymbol{I}\\ \boldsymbol{I} & \boldsymbol{0}\end{bmatrix}}\cdot\begin{bmatrix}\dot{\boldsymbol{x}}\\ \dot{\boldsymbol{y}}\end{bmatrix} + \underbrace{\begin{bmatrix}\left(\overline{\boldsymbol{\Lambda}}-\boldsymbol{\Lambda}\right)^{-1}\left(\overline{\boldsymbol{\Lambda}}\,\boldsymbol{\Lambda}\,\overline{\boldsymbol{\Lambda}}-\boldsymbol{\Lambda}\,\overline{\boldsymbol{\Lambda}}\,\boldsymbol{\Lambda}\right) & \boldsymbol{0}\\ \boldsymbol{0} & -\boldsymbol{I}\end{bmatrix}}_{\begin{bmatrix}\boldsymbol{\Omega_1} & \boldsymbol{0}\\ \boldsymbol{0} & -\boldsymbol{I}\end{bmatrix}}\cdot\begin{bmatrix}\boldsymbol{x}\\ \boldsymbol{y}\end{bmatrix} = \underbrace{\begin{bmatrix}\left(\overline{\boldsymbol{\Lambda}}-\boldsymbol{\Lambda}\right)^{-1}\left(\overline{\boldsymbol{\Lambda}}\boldsymbol{X}^T-\boldsymbol{\Lambda}\overline{\boldsymbol{X}}^T\right)\mathbf{p}(t)\\ \left(\overline{\boldsymbol{\Lambda}}-\boldsymbol{\Lambda}\right)^{-1}\left(\overline{\boldsymbol{X}}^T-\boldsymbol{X}^T\right)\mathbf{p}(t)\end{bmatrix}}_{\begin{bmatrix}\boldsymbol{T_1}^T\,\mathbf{p}(t)\\ \boldsymbol{T_2}^T\,\mathbf{p}(t)\end{bmatrix}} \tag{2.13}$$

where $\boldsymbol{D_1}, \boldsymbol{\Omega_1}, \boldsymbol{T_1}$ and $\boldsymbol{T_2}$ are real-space matrices (what can easy be checked):

$$\boldsymbol{D_1} = \left(\overline{\boldsymbol{\Lambda}}-\boldsymbol{\Lambda}\right)^{-1}\left(-\overline{\boldsymbol{\Lambda}\boldsymbol{\Lambda}}+\boldsymbol{\Lambda}\boldsymbol{\Lambda}\right) = -diag\left[\lambda_1+\overline{\lambda}_1,\cdots,\lambda_j+\overline{\lambda}_j,\cdots,\lambda_n+\overline{\lambda}_n\right] = -diag\left[2\alpha_1,\cdots,2\alpha_j,\cdots,2\alpha_n\right] \tag{2.14}$$

$$\boldsymbol{\Omega_1} = \left(\overline{\boldsymbol{\Lambda}}-\boldsymbol{\Lambda}\right)^{-1}\left(\overline{\boldsymbol{\Lambda}}\,\boldsymbol{\Lambda}\,\overline{\boldsymbol{\Lambda}}-\boldsymbol{\Lambda}\,\overline{\boldsymbol{\Lambda}}\,\boldsymbol{\Lambda}\right) = diag\left[\lambda_1\overline{\lambda}_1,\cdots,\lambda_j\overline{\lambda}_j,\cdots,\lambda_n\overline{\lambda}_n\right] = diag\left[\alpha_1^2+\omega_{D1}^2,\cdots,\alpha_n^2+\omega_{Dn}^2\right] \tag{2.15}$$

$$\boldsymbol{T_1} = \left(\boldsymbol{X}\overline{\boldsymbol{\Lambda}}-\overline{\boldsymbol{X}}\boldsymbol{\Lambda}\right)\left(\overline{\boldsymbol{\Lambda}}-\boldsymbol{\Lambda}\right)^{-1} \tag{2.16}$$

$$\boldsymbol{T_2} = \left(\overline{\boldsymbol{X}}-\boldsymbol{X}\right)\left(\overline{\boldsymbol{\Lambda}}-\boldsymbol{\Lambda}\right)^{-1} \tag{2.17}$$

Eq. (2.13) is the transformed uncoupled real-space form of the original equations of motion (2.1), the introduced n-dimensional vector $\boldsymbol{x}$ can be referred to as modal coordinates. The matrix equation (2.13) can be solved by expressing $\boldsymbol{y}$ from the second equation, see Eq. (2.19), and replacing it in the first one to get

$$\ddot{\boldsymbol{x}} + \boldsymbol{D_1}\dot{\boldsymbol{x}} + \boldsymbol{\Omega_1}\boldsymbol{x} = \boldsymbol{T_1}^T\,\mathbf{p}(t) + \boldsymbol{T_2}^T\,\dot{\mathbf{p}}(t) \tag{2.18}$$

Eq. (2.18) represents n uncoupled single-mass oscillator equations, which can be solved numerically by any time step integration operator. Having the time series $\boldsymbol{x}(t)$, $\dot{\boldsymbol{x}}(t)$ and $\ddot{\boldsymbol{x}}(t)$, the modal coordinates $\boldsymbol{y}(t)$ can be expressed from Eq. (2.13) to:

$$\boldsymbol{y} = \dot{\boldsymbol{x}} - \boldsymbol{T_2}^T\,\mathbf{p}(t) \tag{2.19}$$

The relationship between the modal coordinates $\begin{bmatrix} \boldsymbol{x} \\ \boldsymbol{y} \end{bmatrix}$ and the original state space variables $\begin{bmatrix} \boldsymbol{V} \\ \dot{\boldsymbol{V}} \end{bmatrix}$ from (2.1) can be derived by combining the first complex transformation (2.3) with the complex transformation introduced by (2.12):

$$\begin{bmatrix} \boldsymbol{V} \\ \dot{\boldsymbol{V}} \end{bmatrix} = \begin{bmatrix} \boldsymbol{X} & \overline{\boldsymbol{X}} \\ \boldsymbol{X}\boldsymbol{\Lambda} & \overline{\boldsymbol{X}}\,\overline{\boldsymbol{\Lambda}} \end{bmatrix} \begin{bmatrix} \boldsymbol{a} \\ \boldsymbol{b} \end{bmatrix} = \begin{bmatrix} \boldsymbol{X} & \overline{\boldsymbol{X}} \\ \boldsymbol{X}\boldsymbol{\Lambda} & \overline{\boldsymbol{X}}\,\overline{\boldsymbol{\Lambda}} \end{bmatrix} \begin{bmatrix} \boldsymbol{I} & \boldsymbol{I} \\ \boldsymbol{\Lambda} & \overline{\boldsymbol{\Lambda}} \end{bmatrix}^{-1} \begin{bmatrix} \boldsymbol{x} \\ \boldsymbol{y} \end{bmatrix} \tag{2.20}$$

The upper half of (2.20) is

$$\boldsymbol{V} = \left(\boldsymbol{X}\overline{\boldsymbol{\Lambda}} - \overline{\boldsymbol{X}}\boldsymbol{\Lambda}\right)\left(\overline{\boldsymbol{\Lambda}} - \boldsymbol{\Lambda}\right)^{-1}\boldsymbol{x} + \left(\overline{\boldsymbol{X}} - \boldsymbol{X}\right)\left(\overline{\boldsymbol{\Lambda}} - \boldsymbol{\Lambda}\right)^{-1}\boldsymbol{y} = \boldsymbol{T_1 x} + \boldsymbol{T_2 y} \tag{2.21}$$

and accounting for Eq.(2.19):

$$\boldsymbol{V} = \boldsymbol{T_1 x} + \boldsymbol{T_2}\left(\dot{\boldsymbol{x}} - \boldsymbol{T_2^T}\,\mathbf{p}(t)\right) \tag{2.22}$$

By use of Eq. (2.19) the real-space solution (2.20) can be rewritten in state space form:

$$\begin{bmatrix} \boldsymbol{V}(t) \\ \dot{\boldsymbol{V}}(t) \end{bmatrix} = \begin{bmatrix} \boldsymbol{X} & \overline{\boldsymbol{X}} \\ \boldsymbol{X}\boldsymbol{\Lambda} & \overline{\boldsymbol{X}}\,\overline{\boldsymbol{\Lambda}} \end{bmatrix} \begin{bmatrix} \boldsymbol{I} & \boldsymbol{I} \\ \boldsymbol{\Lambda} & \overline{\boldsymbol{\Lambda}} \end{bmatrix}^{-1} \begin{bmatrix} \boldsymbol{x}(t) \\ \dot{\boldsymbol{x}}(t) - \boldsymbol{T_2^T}\,\mathbf{p}(t) \end{bmatrix} \tag{2.23}$$

The inverse transformation of (2.23) is

$$\begin{bmatrix} \boldsymbol{x}(t) \\ \dot{\boldsymbol{x}}(t) \end{bmatrix} = \begin{bmatrix} \boldsymbol{I} & \boldsymbol{I} \\ \boldsymbol{\Lambda} & \overline{\boldsymbol{\Lambda}} \end{bmatrix} \begin{bmatrix} \boldsymbol{X} & \overline{\boldsymbol{X}} \\ \boldsymbol{X}\boldsymbol{\Lambda} & \overline{\boldsymbol{X}}\,\overline{\boldsymbol{\Lambda}} \end{bmatrix}^{-1} \begin{bmatrix} \boldsymbol{V}(t) \\ \dot{\boldsymbol{V}}(t) \end{bmatrix} + \begin{bmatrix} \mathbf{0} \\ \boldsymbol{T_2^T}\,\mathbf{p}(t) \end{bmatrix} \tag{2.24}$$

3 MODAL ANALYSIS PROCEDURE BASED ON THE STIFFNESS NORMALIZED RIGHT EIGENVECTORS

In this section is described a procedure, similar to the phase synchronization method in state space formulation, presented in Sec. 2. We will consider the case of forced vibrations with n distinct complex conjugated eigenvalues λ_j, see Eq. (3.12), what is the most relevant case in structural mechanics based on finite element formulation. The detailed development of the procedure differs in some points from the decomposition method based on the *Lancaster form* (2.1). The description of the differences in details, compared to the development steps in Section 2, aims to outline the structural mechanics background of the utilized mathematical transformations.

In order to derive the modal transformation for a MDOFS we will first consider the viscously damped single-degree-of-freedom-system (SDOFS).

3.1 The single mass oscillator

The equation of motion of a SDOFS is written in the extended form

$$\underbrace{\begin{bmatrix}1 & \\ & -\omega^2\end{bmatrix}}_{\boldsymbol{m}}\underbrace{\begin{bmatrix}\ddot{v}(t)\\ \dot{v}(t)\end{bmatrix}}_{\dot{\boldsymbol{q}}}+\underbrace{\begin{bmatrix}2\eta\omega & \omega^2\\ \omega^2 & \end{bmatrix}}_{\boldsymbol{k}}\underbrace{\begin{bmatrix}\dot{v}(t)\\ v(t)\end{bmatrix}}_{\boldsymbol{q}}=\underbrace{\begin{bmatrix}p(t)\\ \end{bmatrix}}_{\boldsymbol{p}}$$

$$\boldsymbol{m}\dot{\boldsymbol{q}}+\boldsymbol{k}\boldsymbol{q}=\boldsymbol{p} \tag{3.1}$$

where $\ddot{v}$ is acceleration, $\dot{v}$ – velocity, $v(t)$ – displacement, $\omega=\sqrt{\frac{k}{m}}$ – free vibration frequency and $\eta=\frac{c}{2m\omega}$ – Lehr's damping ratio.

The corresponding quadratic eigenvalue problem leads to two complex conjugate right eigenvectors $\boldsymbol{q}_j$, $(j=1,2)$

$$\dot{\boldsymbol{q}}+\underbrace{(\boldsymbol{m}^{-1}\boldsymbol{k})}_{\boldsymbol{a}}\boldsymbol{q}=\boldsymbol{0}\ \rightarrow\ \boldsymbol{q}_1=\begin{bmatrix}\lambda_r+\ i\lambda_i\\ 1\end{bmatrix},\ \boldsymbol{q}_2=\begin{bmatrix}\lambda_r-\ i\lambda_i\\ 1\end{bmatrix} \tag{3.2}$$

where $\lambda_r=-\eta\omega=\alpha$, $\lambda_i=\omega\sqrt{1-\eta^2}=\omega_D$ are the real resp. imaginary part of the associated complex conjugate eigenvalues $\left(\lambda=\lambda_r+i\lambda_i,\ \overline{\lambda}=\lambda_r-i\lambda_i\right)$.

The eigenvectors $\boldsymbol{q}_j$ are normalized with respect to the stiffness matrix $\boldsymbol{k}$, Eq. (3.1), and denoted by $\boldsymbol{\varphi}_j$:

$$[\boldsymbol{q}_1\quad\boldsymbol{q}_2]^T\cdot\boldsymbol{k}\cdot[\boldsymbol{q}_1\quad\boldsymbol{q}_2]=\begin{bmatrix}h_{11} & \\ & h_{22}\end{bmatrix}\quad\rightarrow\ \boldsymbol{\varphi}_j=\frac{\boldsymbol{q}_j}{\sqrt{h_{jj}}}\qquad(j=1,2) \tag{3.3}$$

The (2 x 2) modal matrix $\boldsymbol{\varphi}$, associated to the eigenvalue problem (3.2), is cast:

$$\boldsymbol{\varphi}=[\boldsymbol{\varphi}_1\quad\boldsymbol{\varphi}_2] \tag{3.4}$$

The normalization (3.3) leads to the orthogonality relationships (3.5), (3.6):

$$\boldsymbol{\varphi}^T\,\boldsymbol{m}\,\boldsymbol{\varphi}=\boldsymbol{\varphi}^T\begin{bmatrix}1 & \\ & -\omega^2\end{bmatrix}\boldsymbol{\varphi}=\begin{bmatrix}-\frac{1}{\lambda} & \\ & -\frac{1}{\overline{\lambda}}\end{bmatrix}\ \leftrightarrow\ (\boldsymbol{\varphi}^T)^{-1}\begin{bmatrix}-\frac{1}{\lambda} & \\ & -\frac{1}{\overline{\lambda}}\end{bmatrix}\boldsymbol{\varphi}^{-1}=\begin{bmatrix}1 & \\ & -\omega^2\end{bmatrix} \tag{3.5}$$

$$\boldsymbol{\varphi}^T\,\boldsymbol{k}\,\boldsymbol{\varphi}=\boldsymbol{\varphi}^T\begin{bmatrix}2\eta\omega & \omega^2\\ \omega^2 & \end{bmatrix}\boldsymbol{\varphi}=\begin{bmatrix}1 & \\ & 1\end{bmatrix}\ \leftrightarrow\ (\boldsymbol{\varphi}^T)^{-1}\begin{bmatrix}1 & \\ & 1\end{bmatrix}\boldsymbol{\varphi}^{-1}=\begin{bmatrix}2\eta\omega & \omega^2\\ \omega^2 & \end{bmatrix} \tag{3.6}$$

In Sec. 3.2 there will be used the analytical expression for the inverse of the complex modal matrix $\boldsymbol{\varphi}(\omega,\eta)$:

$$\boldsymbol{\varphi}^{-1}=\frac{1}{2\sqrt{1-\eta^2}}\begin{bmatrix}W_2-iW_1 & Q+iP\\ W_2+iW_1 & Q-iP\end{bmatrix} \tag{3.7}$$

where

$$W_1=\sqrt{\omega\sqrt{1-\eta^2}\left(1-2\eta\sqrt{1-\eta^2}\right)},\quad W_2=\sqrt{\omega\sqrt{1-\eta^2}\left(1+2\eta\sqrt{1-\eta^2}\right)} \tag{3.8}$$

$$P=\omega\left(W_2\sqrt{1-\eta^2}-\eta W_1\right),\qquad Q=\omega\left(W_1\sqrt{1-\eta^2}+\eta W_2\right) \tag{3.9}$$

3.2 Modal transformation of the MDOFS equations

At first the equations of motion (1.1) are recast to first order equations in state space:

$$\underbrace{\begin{bmatrix} \boldsymbol{M} & \\ & -\boldsymbol{K} \end{bmatrix}}_{\boldsymbol{M_G}} \underbrace{\begin{bmatrix} \ddot{\boldsymbol{V}} \\ \dot{\boldsymbol{V}} \end{bmatrix}}_{\dot{\boldsymbol{Q}}} + \underbrace{\begin{bmatrix} \boldsymbol{D} & \boldsymbol{K} \\ \boldsymbol{K} & \end{bmatrix}}_{\boldsymbol{K_G}} \underbrace{\begin{bmatrix} \dot{\boldsymbol{V}} \\ \boldsymbol{V} \end{bmatrix}}_{\boldsymbol{Q}} = \underbrace{\begin{bmatrix} \boldsymbol{p}(t) \\ \end{bmatrix}}_{\boldsymbol{P}} \tag{3.10}$$

where $\boldsymbol{M_G}$ and $\boldsymbol{K_G}$ are, respectively the (2n x 2n) symmetric generalized mass and the generalized stiffness matrices. The formulation in state space (3.10) doesn't use the Lancaster form (2.1), but retains the symmetry in the generalized matrices.

The associated quadratic eigenvalue problem can be written in the 2n-dimensional form

$$\left(\lambda_j \boldsymbol{M_G} + \boldsymbol{K_G}\right) \begin{bmatrix} \lambda_j \boldsymbol{X}_j \\ \boldsymbol{X}_j \end{bmatrix} = \boldsymbol{0} \tag{3.11}$$

where

$$\lambda_j = \lambda_{rj} + i\lambda_{ij} \;\rightarrow \begin{bmatrix} \lambda_j \boldsymbol{X}_j \\ \boldsymbol{X}_j \end{bmatrix}, \quad \overline{\lambda}_j = \lambda_{rj} - i\lambda_{ij} \;\rightarrow \begin{bmatrix} \overline{\lambda}_j \overline{\boldsymbol{X}}_j \\ \overline{\boldsymbol{X}}_j \end{bmatrix}, \quad (j = 1, \dots, n) \tag{3.12}$$

are the corresponding n complex conjugate eigenpairs. Each j[th] eigenvector-pair $\left(\boldsymbol{X}_j, \overline{\boldsymbol{X}}_j\right)$ can be normalized (index (j) omitted) with respect to the general stiffness matrix $\boldsymbol{K_G}$:

$$\begin{bmatrix} \lambda \boldsymbol{X} \\ \boldsymbol{X} \end{bmatrix}^T \begin{bmatrix} \boldsymbol{D} & \boldsymbol{K} \\ \boldsymbol{K} & \end{bmatrix} \begin{bmatrix} \lambda \boldsymbol{X} \\ \boldsymbol{X} \end{bmatrix} = A + iB \;\rightarrow\; \boldsymbol{\Phi} = \frac{\boldsymbol{X}}{\sqrt{A+iB}} = \boldsymbol{\Phi_r} + i\boldsymbol{\Phi_i} \tag{3.13a}$$

$$\begin{bmatrix} \overline{\lambda \boldsymbol{X}} \\ \overline{\boldsymbol{X}} \end{bmatrix}^T \begin{bmatrix} \boldsymbol{D} & \boldsymbol{K} \\ \boldsymbol{K} & \end{bmatrix} \begin{bmatrix} \overline{\lambda \boldsymbol{X}} \\ \overline{\boldsymbol{X}} \end{bmatrix} = A - iB \;\rightarrow\; \overline{\boldsymbol{\Phi}} = \frac{\overline{\boldsymbol{X}}}{\sqrt{A-iB}} = \boldsymbol{\Phi_r} - i\boldsymbol{\Phi_i} \tag{3.13b}$$

Due to the normalization (3.13a-b) the orthogonality relationships (3.14), (3.15) hold – expressed in terms of the j[th] eigenvector-pair (index (j) omitted):

$$\begin{bmatrix} \lambda \boldsymbol{\Phi} & \overline{\lambda \boldsymbol{\Phi}} \\ \boldsymbol{\Phi} & \overline{\boldsymbol{\Phi}} \end{bmatrix}^T \begin{bmatrix} \boldsymbol{M} & \\ & -\boldsymbol{K} \end{bmatrix} \begin{bmatrix} \lambda \boldsymbol{\Phi} & \overline{\lambda \boldsymbol{\Phi}} \\ \boldsymbol{\Phi} & \overline{\boldsymbol{\Phi}} \end{bmatrix} = \begin{bmatrix} -\frac{1}{\lambda} & \\ & -\frac{1}{\overline{\lambda}} \end{bmatrix} \tag{3.14}$$

$$\begin{bmatrix} \lambda \boldsymbol{\Phi} & \overline{\lambda \boldsymbol{\Phi}} \\ \boldsymbol{\Phi} & \overline{\boldsymbol{\Phi}} \end{bmatrix}^T \begin{bmatrix} \boldsymbol{D} & \boldsymbol{K} \\ \boldsymbol{K} & \end{bmatrix} \begin{bmatrix} \lambda \boldsymbol{\Phi} & \overline{\lambda \boldsymbol{\Phi}} \\ \boldsymbol{\Phi} & \overline{\boldsymbol{\Phi}} \end{bmatrix} = \begin{bmatrix} 1 & \\ & 1 \end{bmatrix} \tag{3.15}$$

Then the (2n x 2n) complex modal matrix $\boldsymbol{\Phi_G}$ can be built up:

$$\boldsymbol{\Phi_G} = \begin{bmatrix} \lambda_1 \boldsymbol{\Phi}_1 & \overline{\lambda}_1 \overline{\boldsymbol{\Phi}}_1 & \cdots & \lambda_n \boldsymbol{\Phi}_n & \overline{\lambda}_n \overline{\boldsymbol{\Phi}}_n \\ \boldsymbol{\Phi}_1 & \overline{\boldsymbol{\Phi}}_1 & \cdots & \boldsymbol{\Phi}_n & \overline{\boldsymbol{\Phi}}_n \end{bmatrix} \tag{3.16}$$

Note the difference to the form of Eqs. (2.3), (2.5) – the complex eigenvectors $\boldsymbol{X}$ and the conjugated complex $\overline{\boldsymbol{X}}$ are split, but in (3.16) they remain in pairs.

By the aid of the modal matrix $\boldsymbol{\Phi_G}$ and with account for (3.14), (3.15), the modal decomposition of the equations of motions (3.10) is performed to:

$$\underbrace{\boldsymbol{\Phi}_G^T \begin{bmatrix} \mathbf{M} & \\ & -\mathbf{K} \end{bmatrix} \boldsymbol{\Phi}_G}_{\begin{bmatrix} -\frac{1}{\lambda} & & \\ & \cdots & \\ & & -\frac{1}{\overline{\lambda}_n} \end{bmatrix}} \dot{\mathbf{A}} + \underbrace{\boldsymbol{\Phi}_G^T \begin{bmatrix} \mathbf{D} & \mathbf{K} \\ \mathbf{K} & \end{bmatrix} \boldsymbol{\Phi}_G}_{\begin{bmatrix} 1 & & \\ & \cdots & \\ & & 1 \end{bmatrix}} \mathbf{A} = \boldsymbol{\Phi}_G^T \begin{bmatrix} \mathbf{p}(t) \\ \end{bmatrix} \tag{3.17}$$

where the new complex modal coordinates **A** are introduced by Eq. (3.18):

$$\begin{bmatrix} \dot{\boldsymbol{V}} \\ \boldsymbol{V} \end{bmatrix} = \boldsymbol{\Phi_G}\, \boldsymbol{A}(t) = \boldsymbol{\Phi_G} \begin{bmatrix} a_1(t) & b_1(t) & \cdots & a_n(t) & b_n(t) \end{bmatrix}^{\boldsymbol{T}} \tag{3.18}$$

According to the assembly of the global modal matrix $\boldsymbol{\Phi_G}$ in (3.16), the complex coordinates (a_j, b_j) in the definition (3.18) remain in pairs, corresponding to the eigenvalue pair $(\lambda_j, \overline{\lambda}_j)$, whereas in the definition (2.4) in Sec. 2 they are separated. In comparison to the analogous decoupling transformation (2.10) the uncoupled modal equations (3.17) have – due to the normalization (3.13) – a very clear and more simple form of the modal stiffness matrix (equal to unity matrix) and of the modal mass matrix (equal to the inverse spectral matrix).

In a next step a second transformation of the complex modal equations (3.17) will be introduced in order to get $(j = 1, \ldots, n)$ uncoupled single oscillator equations in real space. The complex modal coordinates $[a_j \quad b_j]^T$, Eq. (3.18), will be replaced by new real coordinates $[x_j \quad y_j]^T$ for each j-th eigenpair, introduced by the definition:

$$\begin{bmatrix} a_j(t) \\ b_j(t) \end{bmatrix} = \left(\boldsymbol{\varphi}^{(j)}\right)^{-1} \begin{bmatrix} x_j(t) \\ y_j(t) \end{bmatrix}, \qquad \begin{bmatrix} \dot{a}_j \\ \dot{b}_j \end{bmatrix} = \left(\boldsymbol{\varphi}^{(j)}\right)^{-1} \begin{bmatrix} \dot{x}_j(t) \\ \dot{y}_j(t) \end{bmatrix} \tag{3.19}$$

Taking into account (3.19), the modal equations (3.17) can be transformed **in pairs** into the real form of SDOFS-equation (index (j) omitted), with regard to the inverse relationships (3.5), (3.6):

$$\begin{array}{cccccc} \underbrace{(\boldsymbol{\varphi}^T)^{-1} \begin{bmatrix} -\frac{1}{\lambda} & \\ & -\frac{1}{\overline{\lambda}} \end{bmatrix} \boldsymbol{\varphi}^{-1}}_{\begin{bmatrix} 1 & \\ & -\omega^2 \end{bmatrix}} & \cdot \begin{bmatrix} \dot{x} \\ \dot{y} \end{bmatrix} & + & \underbrace{(\boldsymbol{\varphi}^T)^{-1} \begin{bmatrix} 1 & \\ & 1 \end{bmatrix} \boldsymbol{\varphi}^{-1}}_{\begin{bmatrix} 2\eta\omega & \omega^2 \\ \omega^2 & \end{bmatrix}} & \cdot \begin{bmatrix} x \\ y \end{bmatrix} & = & \underbrace{(\boldsymbol{\varphi}^T)^{-1} \begin{bmatrix} \lambda \boldsymbol{\Phi}^T \boldsymbol{p}(t) \\ \overline{\lambda} \overline{\boldsymbol{\Phi}}^T \boldsymbol{p}(t) \end{bmatrix}}_{\begin{bmatrix} g(t) \\ h(t) \end{bmatrix}} \end{array} \tag{3.20}$$

Note that the matrix $(\boldsymbol{\varphi})^{-1}$ can be expressed according to Eq. (3.7)-(3.9) simply by the real and imaginary parts $(\lambda_{rj}, \lambda_{ij})$ of the corresponding eigenvalue pair $(\lambda_j, \overline{\lambda}_j)$.

Combining the two complex transformations (3.18), (3.19), a new (2n x 2n) transformation basis **Y** can be defined:

$$\begin{bmatrix} \dot{\boldsymbol{V}} \\ \boldsymbol{V} \end{bmatrix} = \boldsymbol{\Phi_G} \underbrace{\begin{bmatrix} \left(\boldsymbol{\varphi}^{(1)}\right)^{-1} & & \\ & \cdots & \\ & & \left(\boldsymbol{\varphi}^{(n)}\right)^{-1} \end{bmatrix}}_{\boldsymbol{\Psi}^{-1}} \underbrace{\begin{bmatrix} x_1 \\ y_1 \\ \cdots \\ x_n \\ y_n \end{bmatrix}}_{\mathbf{X}} = \underbrace{(\boldsymbol{\Phi_G} \boldsymbol{\Psi}^{-1})}_{\mathbf{Y}} \mathbf{X} = \mathbf{Y}\, \mathbf{X} \tag{3.21}$$

Finally, by the aid of the relationship (3.21), see also (3.17) and (3.20), the equations of motion (3.10) can be transformed into n real uncoupled SDOFS block equations as follows:

$$\underbrace{\mathbf{Y}^{\mathrm{T}}\cdot\begin{bmatrix}\mathbf{M} & \\ & -\mathbf{K}\end{bmatrix}\cdot\mathbf{Y}}_{\begin{bmatrix}1 & & & & \\ & -\omega_1^2 & & & \\ & & \cdots & & \\ & & & 1 & \\ & & & & -\omega_n^2\end{bmatrix}}\cdot\underbrace{\begin{bmatrix}\dot{x}_1\\ \dot{y}_1\\ \cdots\\ \dot{x}_n\\ \dot{y}_n\end{bmatrix}}_{\dot{\mathbf{x}}}+\underbrace{\mathbf{Y}^{\mathrm{T}}\cdot\begin{bmatrix}\mathbf{D} & \mathbf{K}\\ \mathbf{K} & \end{bmatrix}\cdot\mathbf{Y}}_{\begin{bmatrix}2\eta_1\omega_1 & \omega_1^2 & & & \\ \omega_1^2 & 0 & & & \\ & & \cdots & & \\ & & & 2\eta_n\omega_n & \omega_n^2\\ & & & \omega_n^2 & 0\end{bmatrix}}\cdot\underbrace{\begin{bmatrix}x_1\\ y_1\\ \cdots\\ x_n\\ y_n\end{bmatrix}}_{\mathbf{x}}=\underbrace{\mathbf{Y}^{\mathrm{T}}\cdot\begin{bmatrix}\mathbf{p}\\ \end{bmatrix}}_{\begin{bmatrix}g_1\\ h_1\\ \cdots\\ g_n\\ h_n\end{bmatrix}} \tag{3.22}$$

It can be shown that the **Y**-matrix and all „load"-vector component $[g(t) \quad h(t)]^T$ in Eq. (3.22) are purely real. After component multiplication of the analytically expressed terms of $\boldsymbol{\Phi_G}$ and of $\boldsymbol{\Psi^{-1}}$ all imaginary parts cancel each other, see details in [16], [19].

The components of two columns in the real-space matrix **Y**, belonging to the j[th] eigenvector-pair, may be denotes as

$$\mathbf{Y}=\begin{bmatrix}\cdots & \mathbf{Y}_{\mathrm{x1}}^{(\mathrm{j})} & \mathbf{Y}_{\mathrm{y1}}^{(\mathrm{j})} & \cdots\\ \cdots & \mathbf{Y}_{\mathrm{x2}}^{(\mathrm{j})\mathbf{V}} & \mathbf{Y}_{\mathrm{y2}}^{(\mathrm{j})} & \cdots\end{bmatrix} \tag{3.23}$$

Analytical expressions for the components in (3.23) can be derived as functions of the corresponding ω, η and the real and imaginary parts of the $\boldsymbol{\Phi}_j$, accounting also for (3.7)-(3.9), (index (j) omitted):

$$\mathbf{Y}_{x1}^{(\mathrm{j})}=\frac{\omega}{\sqrt{1-\eta^2}}\left[\left(-\eta\,W_2+\sqrt{1-\eta^2}\,W_1\right)\boldsymbol{\Phi}_{\mathbf{r}j}-\left(\eta\,W_1+\sqrt{1-\eta^2}\,W_2\right)\boldsymbol{\Phi}_{\mathbf{i}j}\right]$$
$$\mathbf{Y}_{y1}^{(\mathrm{j})}=\frac{\omega^2}{\sqrt{1-\eta^2}}\left[\left(-\eta\,Q-\sqrt{1-\eta^2}\,P\right)\boldsymbol{\Phi}_{\mathbf{r}j}+\left(\eta\,P-\sqrt{1-\eta^2}\,Q\right)\boldsymbol{\Phi}_{\mathbf{i}j}\right]$$
$$\mathbf{Y}_{x2}^{(\mathrm{j})}=\frac{1}{\sqrt{1-\eta^2}}\left[W_2\boldsymbol{\Phi}_{\mathbf{r}j}+W_1\boldsymbol{\Phi}_{\mathbf{i}j}\right]$$
$$\mathbf{Y}_{y2}^{(\mathrm{j})}=\frac{\omega}{\sqrt{1-\eta^2}}\left[Q\boldsymbol{\Phi}_{\mathbf{r}j}-P\boldsymbol{\Phi}_{\mathbf{i}j}\right] \tag{3.24a-d}$$

Similarly, the two components of the associated "load" vector are analytically:

$$g(t)=\frac{\omega}{\sqrt{1-\eta^2}}\left[\left(-\eta\,W_2+\sqrt{1-\eta^2}\,W_1\right)\boldsymbol{\Phi}_{\mathbf{r}j}^{\mathbf{T}}-\left(\eta\,W_1+\sqrt{1-\eta^2}\,W_2\right)\boldsymbol{\Phi}_{\mathbf{i}j}^{\mathbf{T}}\right]\mathbf{p}(t)$$
$$h(t)=\frac{\omega^2}{\sqrt{1-\eta^2}}\left[\left(-\eta\,Q-\sqrt{1-\eta^2}\,P\right)\boldsymbol{\Phi}_{\mathbf{r}j}^{\mathbf{T}}+\left(\eta\,P-\sqrt{1-\eta^2}\,Q\right)\boldsymbol{\Phi}_{\mathbf{i}j}^{\mathbf{T}}\right]\mathbf{p}(t) \tag{3.25a-b}$$

3.3 Comparison to the "phase synchronization" procedure

The transformation in Sec.2, analogously to (3.19), is given by Eq. (2.12). The advantage of the (2 x 2) transformation used in (3.20) is that it is done on the level "SDOFS-equation", employing stiffness normalization for the modal matrix **φ** – see Eq.(3.3). In contrast to this in the relationship (2.12) a (2n x 2n) matrix $\begin{bmatrix}\boldsymbol{I} & \boldsymbol{I}\\ \boldsymbol{\Lambda} & \overline{\boldsymbol{\Lambda}}\end{bmatrix}$ has to be inverted. Besides the analytical

inversion of the simple (2 x 2) matrix $\boldsymbol{\varphi}^{(j)}$ in (3.7), the definition (3.19) seems quite natural in order to transform the complex modal equations (3.17) back to the real form of uncoupled SDOFS – as seen in (3.20).

The mechanical reason of the relationship (2.11) and the inverse form (2.12) is clarified by looking at the eigenvectors (3.2) of the SDOFS. Due to the inverse order of displacements and velocities $\begin{bmatrix} \boldsymbol{V} \\ \dot{\boldsymbol{V}} \end{bmatrix}$ in the Lancaster form (2.1) in compare to the formulation (3.10), the meaning of the modal coordinates (x_j, y_j) here is interchanged, compare Eq. (2.18) and (3.27).

3.4 Solution of the modal equations and back transformation

Each SDOFS block equation in (3.22) can be solved eliminating the modal coordinate x_j to obtain the usual form of the SDOFS equation of motion (index (j) omitted):

$$x(t) = \dot{y} + \frac{1}{\omega^2} h(t) \tag{3.26}$$

$$\ddot{y}(t) + 2\eta\omega\, \dot{y}(t) + \omega^2 y(t) = g(t) - \frac{2\eta}{\omega} h(t) - \frac{1}{\omega^2} \dot{h}(t) \tag{3.27}$$

A usual numerical step-by-step integration of Eq. (3.27) yields the modal response $y_j(t)$, the modal coordinate $x_j(t)$ is calculated then according to (3.26). The back transformation to the original 2n state variables $\begin{bmatrix} \dot{\boldsymbol{V}}(t) \\ \boldsymbol{V}(t) \end{bmatrix}$ is done by superposition in accordance to (3.21) of the modal time series $x_j(t),\ y_j(t)$ (assembled in $\boldsymbol{X}$, Eq. (3.22)).

The final SDOFS equations from type (3.27) for each j-th eigenpair can be rebuilt in the uncoupled diagonal form (2.18) for the MDOFS – note that $y(t)$ in (3.27) corresponds to $x(t)$ in (2.18). The right sides of both equations clearly correspond to each other.

4 NUMERICAL APPLICATION TO A ROTOR BLADE VIBRATION

The numerical example considers the vibrations of a generic rotor blade subjected to wind thrust load. The equations of motion in the Lancaster form (2.1) and in the state space form (3.10) are solved applying resp. the "phase synchronization" technique, described in Sec.2 , and the proposed modal decomposition method in Sec. 3. In both cases have been employed only the first four lowest natural frequencies and the associated four complex eigenmodes.

4.1 Structural data, geometry and loads

All structural data for the reference rotor blade – geometry, mass, stiffness data etc. - have been taken from [23]. The blade model with 288 DOF is built by 48 beam elements, the over-all blade length is 63 m. The finite element stiffness and mass matrices are calculated on the base of numerical integration of the system of differential equations for the Bernoulli-beam, see detailed description of the employed transfer matrix method in [21].

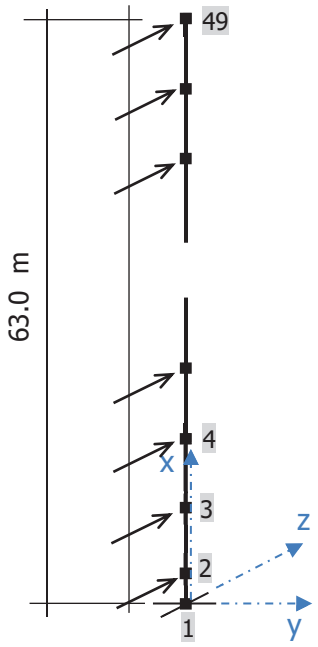

Figure 1: Rotor blade beam model subjected to wind loads

4.2 Wind loads

The wind speed time series $u(t)$, see Fig. 2, used for calculation of the wind thrust force, is an arbitrary 25-sec-cut from a real 10-min wind speed record in an offshore location in Baltic sea. This time series is used to calculate in a simple way realistic wind thrust loads. They are calculated on the basis of the formula for the aerodynamic lift force per unit length of an aerofoil, see [1] p.59:

$$L = \frac{1}{2}\rho \cdot ch(r) \cdot W^2 \cdot C_L \tag{4.1}$$

where:
- W : air velocity relative to the aerofoil
- ρ : air density = 1.225 [kg/m^3]
- $ch(r)$: chord length of the aerofoil
- C_L : lift coefficient $C_L = 2\pi\,\alpha = 2\pi\left(\frac{\pi}{180}6.0\right) = 0.658$, with an assumed constant AoA $\alpha = 6.0$ [deg]

The air velocity W in Eq. (4.1) is the vector sum of the circumferential speed Ωr (with assumed $\Omega = 12$ rpm after the initial four seconds) and the wind speed u, incident on the rotor plane in accordance with the Betz-theory:

$$W = \sqrt{(\Omega\, r)^2 + \left(\frac{2}{3}u\right)^2} \qquad \text{where } \Omega = \left(\frac{12}{30}\pi\right) \text{ in [rad/s]} \tag{4.2}$$

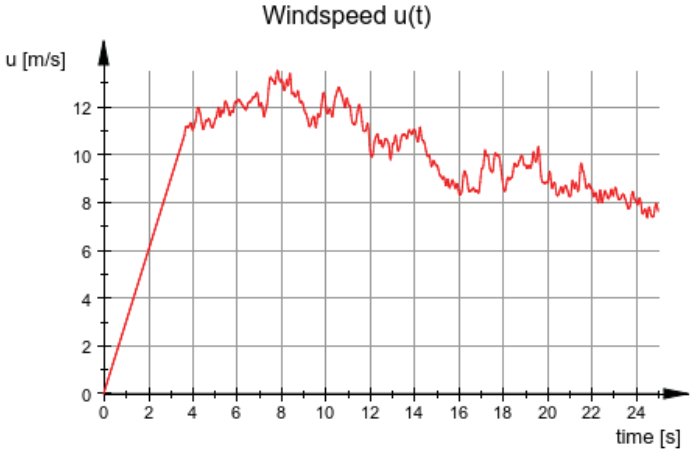

Fig. 2 Wind speed time series

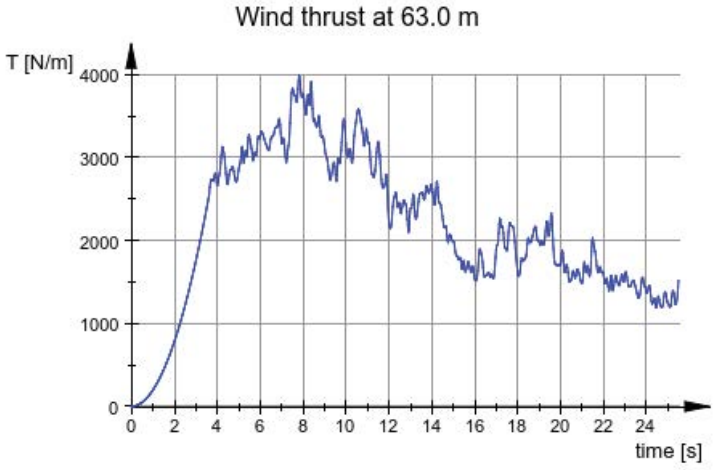

Fig. 3 Wind thrust T(t) on the rotor blade tip at 63.0 m

The resulting wind thrust loads $\mathrm{T}(t)$ per unit length along the x-axis of the rotor blade have been determined as function of the wind speed $u(t)$, see Fig. 3. In the structural model the wind thrust loads are acting as summarized nodal forces – see Fig. 1.

4.3 The non-proportional damping approach

For both procedures, the one described in Sec.2 and the modal decomposition method in Sec. 3, was applied the same system damping matrix. The matrix ***D*,** see Eq. (2.1) and (3.10), which represents non-proportional damping, has been assembled including an stiffness proportional damping part and an aerodynamic damping part.

In order to determine the first damping part the lowest four free-vibration frequencies and associated periods for the undamped system are calculated first to

$$\begin{aligned} f_1 &= 0.6722\ [s^{-1}] & T_1 &= 1.488\ [s] \\ f_2 &= 1.0934\ [s^{-1}] & T_2 &= 0.915\ [s] \\ f_3 &= 1.9177\ [s^{-1}] & T_3 &= 0.521\ [s] \\ f_4 &= 3.9647\ [s^{-1}] & T_4 &= 0.252\ [s] \end{aligned} \tag{4.3}$$

With an assumed damping ratio $\eta = 0.008$ for the first natural period T_1, see [1], p. 249, the stiffness-proportional damping part of $\boldsymbol{D}$, see Eq. (1.4), has been calculated:

$$\boldsymbol{D_p} = \beta\, \boldsymbol{K} \quad , \quad \beta = \frac{2\eta}{\omega_1} = \frac{\eta\, T_1}{\pi} = 0.00379[s] \tag{4.4}$$

The second aerodynamic damping part $\boldsymbol{D_a}$ of the system damping matrix is derived on the basis of a simple approach for the aerodynamic damping coefficient per unit length, given in [1], p. 247:

$$c(r) = \frac{1}{2}\rho \cdot\ \Omega r\ \cdot ch(r) \cdot \frac{dC_L}{d\alpha} \quad \left[\frac{kg}{s}\frac{1}{m}\right], \quad \text{where} \quad \frac{dC_L}{d\alpha} = 2\pi \tag{4.5}$$

The damping coefficients $c(r)$ along the x-axis, which represent the aerodynamic damping, are active for vibration in flapwise direction (z-direction in Fig. 1). In Eq. (4.6) are plotted the calculated $c(r)$-values for the last 12 points along the rotor axis.

r [m]	ch(r) [m]	$c(r)$ [kg/s/m]
56.7	2.28654	783.731
57.7	2.22487	776.044
58.7	2.11651	751.041
59.2	2.03366	727.789
59.7	1.93071	696.783
60.2	1.81172	659.315
60.7	1.68083	616.763
61.2	1.5422	570.555
61.7	1.39997	522.167
62.2	1.25829	473.127
62.7	1.12132	425.014
63.0	1.04312	397.265

(4.6)

Using the relationship (4.5), the damping matrix $\boldsymbol{D_a}$ for the Bernoulli-beam element is derived by analogy with the method used to derive the finite element mass matrix in [21]. The final symmetric system damping matrix $\boldsymbol{D} = \boldsymbol{D_p} + \boldsymbol{D_a}$ is assembled in the usual finite-element manner.

4.4 Rotor blade vibration applying the phase synchronization procedure

The equations of motion in the form (2.1) will be transformed employing only the first four eigenvalues and the associated eigenmodes. The first four lowest angular eigenfrequencies ω_{Dj} of the damped system and the corresponding damping ratios η_j are calculated to

$$\omega_{Dj} = \begin{pmatrix} 4.1399 \\ 6.8696 \\ 12.001 \\ 24.883 \end{pmatrix} \qquad \eta_j = \begin{pmatrix} 0.20484 \\ 0.013013 \\ 0.076374 \\ 0.047186 \end{pmatrix} \tag{4.7}$$

The first four complex conjugate eigenvalue pairs from Eq. (2.2) are combined in the two spectral matrices, see Eq. (2.6):

$$\boldsymbol{\Lambda} = \begin{pmatrix} -0.8664 + 4.14\,\mathrm{i} & 0 & 0 & 0 \\ 0 & -0.0894 + 6.87\,\mathrm{i} & 0 & 0 \\ 0 & 0 & -0.9192 + 12.0\,\mathrm{i} & 0 \\ 0 & 0 & 0 & -1.175 + 24.88\,\mathrm{i} \end{pmatrix} \tag{4.8a}$$

$$\overline{\boldsymbol{\Lambda}} = \begin{pmatrix} -0.8664 - 4.14\,\mathrm{i} & 0 & 0 & 0 \\ 0 & -0.0894 - 6.87\,\mathrm{i} & 0 & 0 \\ 0 & 0 & -0.9192 - 12.0\,\mathrm{i} & 0 \\ 0 & 0 & 0 & -1.175 - 24.88\,\mathrm{i} \end{pmatrix} \tag{4.8b}$$

The corresponding (288x4) mass normalized modal matrix $\boldsymbol{X} = [\boldsymbol{X}_1 \quad \boldsymbol{X}_2 \quad \cdots \quad \boldsymbol{X}_n]$ – Eq. (2.5), is computed to (here only the first twelve rows are printed):

$$[\boldsymbol{X}_1 \quad \boldsymbol{X}_2 \quad \boldsymbol{X}_3 \quad \boldsymbol{X}_4] = \begin{pmatrix} 0 & 0 & 0 & 0 \\ 0 & -0.02737 - 3.329\,10^{-13}\,\mathrm{i} & 0 & -0.03778 + 1.558\,10^{-12}\,\mathrm{i} \\ -0.03531 + 0.0008951\,\mathrm{i} & 0 & -0.04235 - 0.001384\,\mathrm{i} & 0 \\ 0 & 0 & 0 & 0 \\ 0.001415 - 9.58\,10^{-5}\,\mathrm{i} & 0 & 0.004074 - 4.16\,10^{-5}\,\mathrm{i} & 0 \\ 0 & -0.0007704 - 1.154\,10^{-15}\,\mathrm{i} & 0 & -0.002819 + 1.155\,10^{-13}\,\mathrm{i} \\ 0 & 0 & 0 & 0 \\ 0 & -0.0276 - 3.332\,10^{-13}\,\mathrm{i} & 0 & -0.03863 + 1.593\,10^{-12}\,\mathrm{i} \\ -0.03573 + 0.0009239\,\mathrm{i} & 0 & -0.04357 - 0.001372\,\mathrm{i} & 0 \\ 0 & 0 & 0 & 0 \\ 0.001415 - 9.605\,10^{-5}\,\mathrm{i} & 0 & 0.004076 - 4.245\,10^{-5}\,\mathrm{i} & 0 \\ 0 & -0.0007704 - 6.286\,10^{-16}\,\mathrm{i} & 0 & -0.002819 + 1.171\,10^{-13}\,\mathrm{i} \end{pmatrix} \tag{4.9}$$

The two (8 x 8) system matrices in the modal uncoupled equations of motion (2.13) are

$$\begin{bmatrix} \boldsymbol{D_1} & \boldsymbol{I} \\ \boldsymbol{I} & \boldsymbol{0} \end{bmatrix} = \begin{pmatrix} 1.733 & 0 & 0 & 0 & 1.0 & 0 & 0 & 0 \\ 0 & 0.1788 & 0 & 0 & 0 & 1.0 & 0 & 0 \\ 0 & 0 & 1.838 & 0 & 0 & 0 & 1.0 & 0 \\ 0 & 0 & 0 & 2.351 & 0 & 0 & 0 & 1.0 \\ 1.0 & 0 & 0 & 0 & 0 & 0 & 0 & 0 \\ 0 & 1.0 & 0 & 0 & 0 & 0 & 0 & 0 \\ 0 & 0 & 1.0 & 0 & 0 & 0 & 0 & 0 \\ 0 & 0 & 0 & 1.0 & 0 & 0 & 0 & 0 \end{pmatrix} \tag{4.10}$$

$$\begin{bmatrix} \boldsymbol{\Omega_1} & \boldsymbol{0} \\ \boldsymbol{0} & -\boldsymbol{I} \end{bmatrix} = \begin{pmatrix} 17.89 & 0 & 0 & 0 & 0 & 0 & 0 & 0 \\ 0 & 47.2 & 0 & 0 & 0 & 0 & 0 & 0 \\ 0 & 0 & 144.9 & 0 & 0 & 0 & -5.457\,10^{-12} & 0 \\ 0 & 0 & 0 & 620.5 & 0 & 0 & 0 & -3.638\,10^{-12} \\ 1.758\,10^{-12} & 0 & 0 & 0 & -1.0 & 0 & 0 & 0 \\ 0 & 2.648\,10^{-13} & 0 & 0 & 0 & -1.0 & 0 & 0 \\ 0 & 0 & -2.425\,10^{-12} & 0 & 0 & 0 & -1.0 & 0 \\ 0 & 0 & 0 & -4.678\,10^{-12} & 0 & 0 & 0 & -1.0 \end{pmatrix} \tag{4.11}$$

The "right side" vector in the final uncoupled modal equations (2.18) have been calculated as a function of the wind speed time series $u(t)$:

$$\boldsymbol{T}_1^T\,\mathbf{p}(t) + \boldsymbol{T}_2^T\,\dot{\mathbf{p}}(t) = \begin{pmatrix} -19.32\,u^2 \\ -1.951\,u^2 \\ -2.096\,u^2 \\ -0.5554\,u^2 \end{pmatrix} + \begin{pmatrix} 0.02013\,u \\ -1.743\,10^{-12}\,u \\ -0.1791\,u \\ 8.235\,10^{-12}\,u \end{pmatrix} \tag{4.12}$$

The modal vibrations $x_j(t), y_j(t),\ (j = 1,..,4)$ and the resulting time series for the original DOF in the next figures has been determined in the time 0… 25[sec], the time step length for the applied Newmark integration method is 0.02434 s.

The resulting time series of the modal coordinates are shown exemplarily in Figs. 4, 5 and 6.

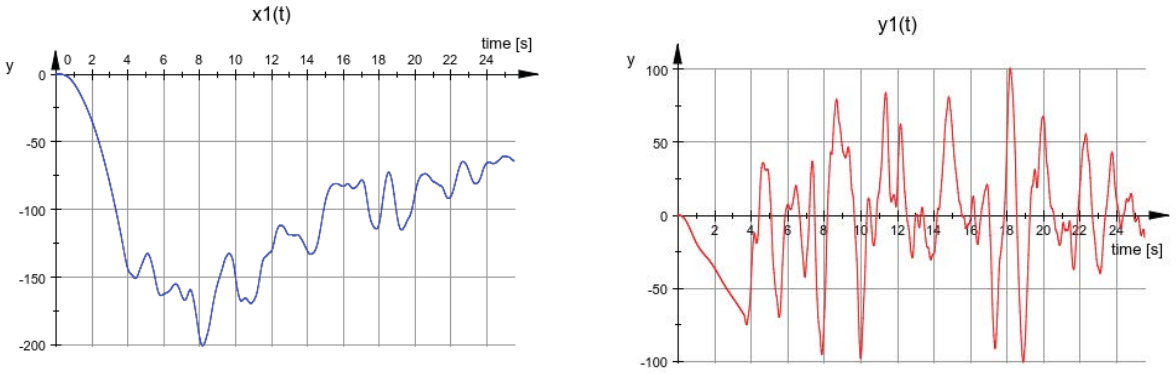

Fig. 4 Time responses of the modal coordinates $x_1(t), y_1(t)$

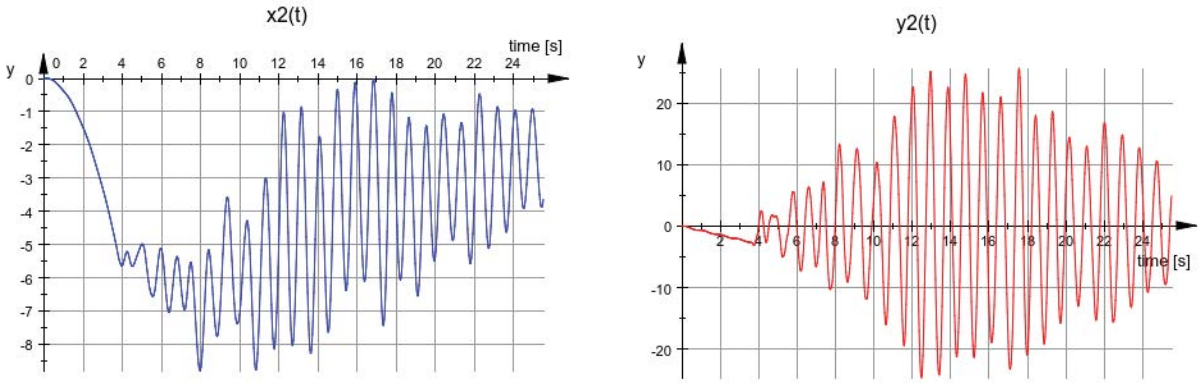

Fig. 5 Time responses of the modal coordinates $x_2(t), y_2(t)$

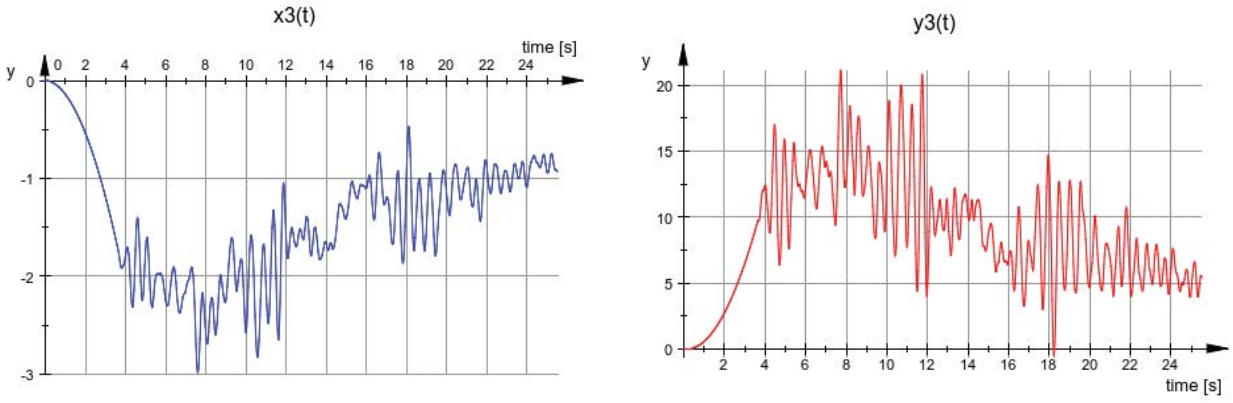

Fig. 6 Time responses of the modal coordinates $x_3(t), y_3(t)$

The back transformation of the modal vibrations to the original DOF in accordance to Eq. (2.23) is done by means of the (576 x 8) real-space transformation matrix, shown in Eq.(4.13) (only the first 18 rows are printed, they correspond to the displacements $\boldsymbol{V}(t)$):

$$\begin{bmatrix} \boldsymbol{X} & \overline{\boldsymbol{X}} \\ \boldsymbol{X}\,\boldsymbol{\Lambda} & \overline{\boldsymbol{X}}\,\overline{\boldsymbol{\Lambda}} \end{bmatrix} \begin{bmatrix} \boldsymbol{I} & \boldsymbol{I} \\ \boldsymbol{\Lambda} & \overline{\boldsymbol{\Lambda}} \end{bmatrix}^{-1} =$$

$$\begin{pmatrix}
0 & 0 & 0 & 0 & 0 & 0 & 0 & 0 \\
0 & -1.195\,10^{-5} & 0 & 4.859\,10^{-5} & 0 & 1.98\,10^{-16} & 0 & 1.203\,10^{-16} \\
-4.156\,10^{-6} & 0 & 1.647\,10^{-5} & 0 & -6.979\,10^{-8} & 0 & 1.503\,10^{-8} & 0 \\
0 & 0 & 0 & 0 & 0 & 0 & 0 & 0 \\
4.858\,10^{-6} & 0 & -1.916\,10^{-5} & 0 & 8.122\,10^{-8} & 0 & -1.715\,10^{-8} & 0 \\
0 & -1.396\,10^{-5} & 0 & 5.623\,10^{-5} & 0 & 8.828\,10^{-17} & 0 & -7.181\,10^{-17} \\
0 & 0 & 0 & 0 & 0 & 0 & 0 & 0 \\
0 & -2.96\,10^{-5} & 0 & 0.0001191 & 0 & 1.863\,10^{-16} & 0 & -1.457\,10^{-16} \\
-1.031\,10^{-5} & 0 & 4.063\,10^{-5} & 0 & -1.723\,10^{-7} & 0 & 3.628\,10^{-8} & 0 \\
0 & 0 & 0 & 0 & 0 & 0 & 0 & 0 \\
7.439\,10^{-6} & 0 & -2.909\,10^{-5} & 0 & 1.234\,10^{-7} & 0 & -2.517\,10^{-8} & 0 \\
0 & -2.13\,10^{-5} & 0 & 8.447\,10^{-5} & 0 & 1.339\,10^{-16} & 0 & -1.163\,10^{-16} \\
0 & 0 & 0 & 0 & 0 & 0 & 0 & 0 \\
0 & -5.45\,10^{-5} & 0 & 0.000217 & 0 & 3.398\,10^{-16} & 0 & -2.773\,10^{-16} \\
-1.916\,10^{-5} & 0 & 7.504\,10^{-5} & 0 & -3.184\,10^{-7} & 0 & 6.543\,10^{-8} & 0 \\
0 & 0 & 0 & 0 & 0 & 0 & 0 & 0 \\
1.024\,10^{-5} & 0 & -3.966\,10^{-5} & 0 & 1.685\,10^{-7} & 0 & -3.294\,10^{-8} & 0 \\
0 & -2.848\,10^{-5} & 0 & 0.000111 & 0 & 1.755\,10^{-16} & 0 & -1.417\,10^{-16}
\end{pmatrix}$$

(4.13)

The total time responses for the original state variables $\boldsymbol{V}(t)$, $\dot{\boldsymbol{V}}(t)$, obtained by a back transformation according to Eq. (2.23), are plotted in Figs. 7-9 for the two bending directions at the rotor blade tip.

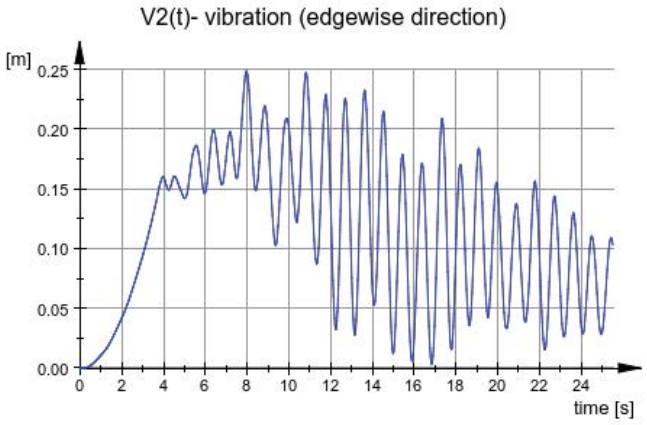

Fig.7 Total vibration $v_2(t)\ [m]$ (in y-direction, see fig.1) at the rotor blade tip - node #49

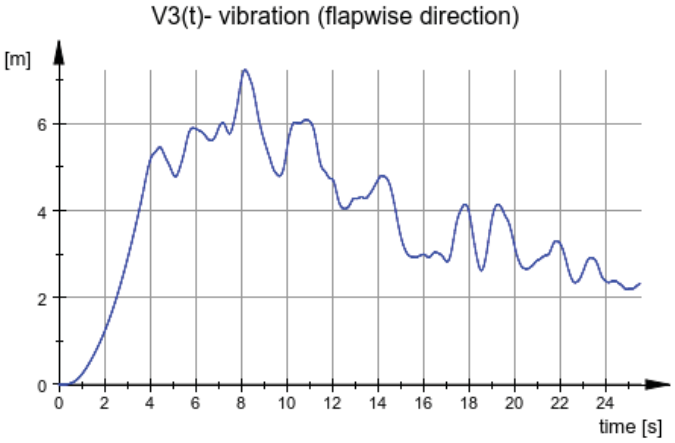

Fig. 8 Total vibration $v_3(t)$ $[m]$ (in z-direction, see fig.1) at the rotor blade tip - node #49

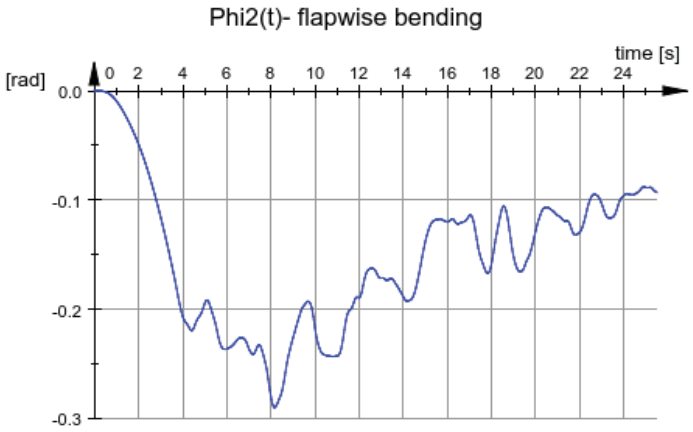

Fig. 9 Total bending angle $\varphi_2(t)$ [rad] (about y-axis, see fig.1) at the rotor blade tip - node #49

4.5 Application of the proposed new modal procedure

In this section the modal procedure based on the stiffness normalized eigenvectors, Sec. 3, is applied to the equations of motion (3.10) for a rotor blade. The geometry, structural data, wind thrust loads and the assembly of the system damping matrix for the rotor blade are described in Sec. 4.1-4.3.

Starting point for the calculations is the eigenvalue problem (3.11). The first four complex conjugate eigenvalue pairs of the matrix $\left(\boldsymbol{M_G}^{-1}\boldsymbol{K_G}\right)$ are

$$\begin{pmatrix} -0.86636+4.13985\,\mathrm{i} \\ -0.86636-4.13985\,\mathrm{i} \\ -0.0894045+6.86957\,\mathrm{i} \\ -0.0894045-6.86957\,\mathrm{i} \\ -0.919237+12.0008\,\mathrm{i} \\ -0.919237-12.0008\,\mathrm{i} \\ -1.17544+24.8831\,\mathrm{i} \\ -1.17544-24.8831\,\mathrm{i} \end{pmatrix} \tag{4.14}$$

The number of modes considered in the modal transformation is limited to the first four eigenvector pairs. Exemplarily the 1-th and the 3-th complex eigenvector pairs are plotted in Fig.10 resp. Fig. 11. Due to the 288 DOF of the beam model, Fig.1, the (576x8) modal matrix $\boldsymbol{\Phi_G}$ with stiffness normalized eigenvectors – Eq.(3.16), is computed to (here only the first twelve rows are printed)

$$\begin{pmatrix}
0 & 0 & 0 & 0 & 0 & 0 & 0 & 0 \\
0 & 0 & 2.28\,10^{-6}+2.28\,10^{-6}\,i & 2.28\,10^{-6}-2.28\,10^{-6}\,i & 0 & 0 & -4.87\,10^{-6}-4.87\,10^{-6}\,i & -4.87\,10^{-6}+4.87\,10^{-6}\,i \\
9.37\,10^{-7}+1.08\,10^{-6}\,i & 9.37\,10^{-7}-1.08\,10^{-6}\,i & 0 & 0 & -2.35\,10^{-6}-2.4\,10^{-6}\,i & -2.35\,10^{-6}+2.4\,10^{-6}\,i & 0 & 0 \\
0 & 0 & 0 & 0 & 0 & 0 & 0 & 0 \\
-1.1\,10^{-6}-1.26\,10^{-6}\,i & -1.1\,10^{-6}+1.26\,10^{-6}\,i & 0 & 0 & 2.73\,10^{-6}+2.79\,10^{-6}\,i & 2.73\,10^{-6}-2.79\,10^{-6}\,i & 0 & 0 \\
0 & 0 & 2.66\,10^{-6}+2.66\,10^{-6}\,i & 2.66\,10^{-6}-2.66\,10^{-6}\,i & 0 & 0 & -5.64\,10^{-6}-5.64\,10^{-6}\,i & -5.64\,10^{-6}+5.64\,10^{-6}\,i \\
0 & 0 & 0 & 0 & 0 & 0 & 0 & 0 \\
0 & 0 & 5.65\,10^{-6}+5.65\,10^{-6}\,i & 5.65\,10^{-6}-5.65\,10^{-6}\,i & 0 & 0 & -1.19\,10^{-5}-1.19\,10^{-5}\,i & -1.19\,10^{-5}+1.19\,10^{-5}\,i \\
2.33\,10^{-6}+2.68\,10^{-6}\,i & 2.33\,10^{-6}-2.68\,10^{-6}\,i & 0 & 0 & -5.79\,10^{-6}-5.92\,10^{-6}\,i & -5.79\,10^{-6}+5.92\,10^{-6}\,i & 0 & 0 \\
0 & 0 & 0 & 0 & 0 & 0 & 0 & 0 \\
-1.68\,10^{-6}-1.93\,10^{-6}\,i & -1.68\,10^{-6}+1.93\,10^{-6}\,i & 0 & 0 & 4.15\,10^{-6}+4.23\,10^{-6}\,i & 4.15\,10^{-6}-4.23\,10^{-6}\,i & 0 & 0 \\
0 & 0 & 4.06\,10^{-6}+4.06\,10^{-6}\,i & 4.06\,10^{-6}-4.06\,10^{-6}\,i & 0 & 0 & -8.47\,10^{-6}-8.47\,10^{-6}\,i & -8.47\,10^{-6}+8.47\,10^{-6}\,i
\end{pmatrix} \tag{4.15}$$

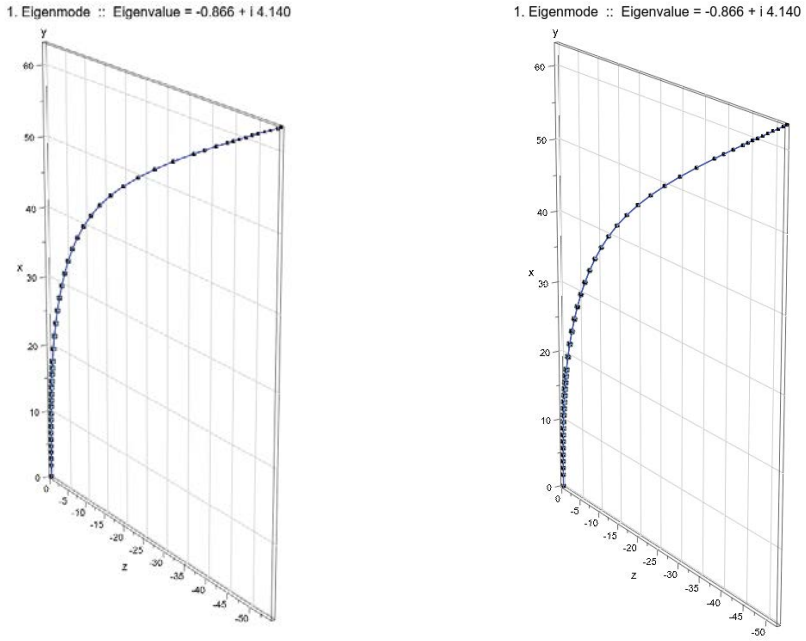

Fig. 10 Real (left) and imaginary (right) part of the 1-th complex eigenvector pair (associated eigenvalue $\lambda = -0.8664 \pm i\,4.140$)

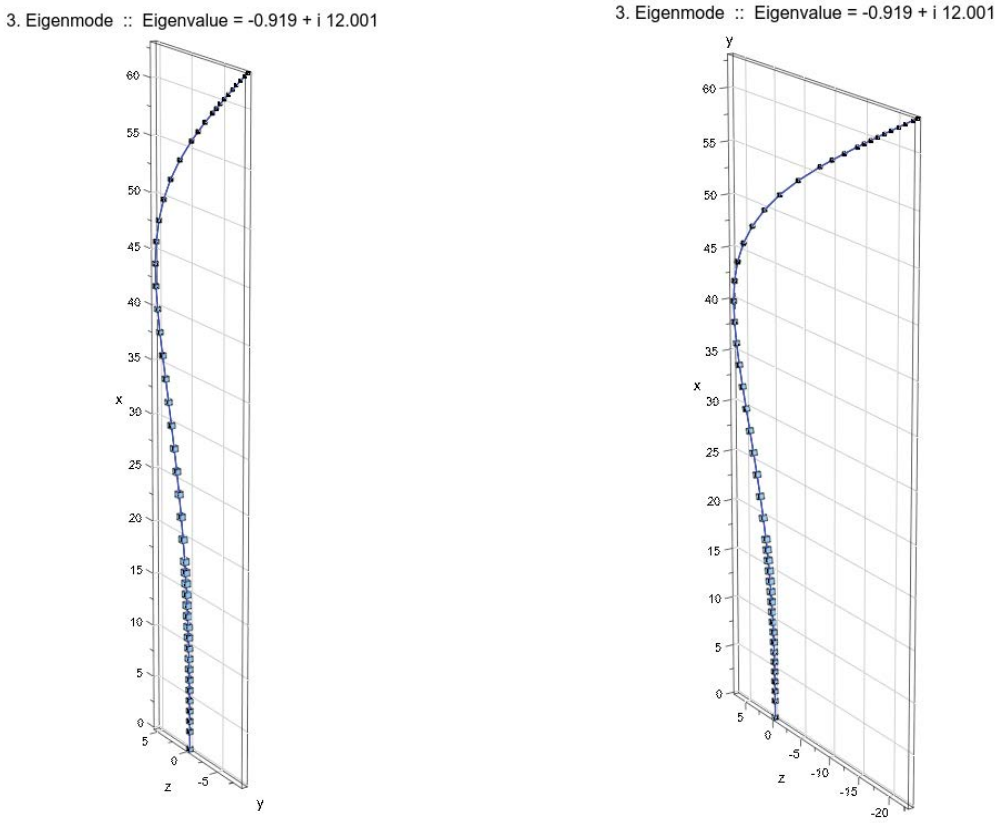

Fig. 11 Real (left) and imaginary (right) part of the 3-th complex eigenvector pair (associated eigenvalue $\lambda = -0.919 \pm i\ 12.001$)

The matrix $\boldsymbol{\Psi}^{-1}$ is calculated for the case of four involved eigenmodes according to Eq. (3.21), (3.7)-(3.9):

$$\boldsymbol{\Psi}^{-1} = \begin{bmatrix} \left(\boldsymbol{\varphi}^{(1)}\right)^{-1} & & & \\ & \left(\boldsymbol{\varphi}^{(2)}\right)^{-1} & & \\ & & \left(\boldsymbol{\varphi}^{(3)}\right)^{-1} & \\ & & & \left(\boldsymbol{\varphi}^{(4)}\right)^{-1} \end{bmatrix} =$$

$$\begin{pmatrix} 1.2302 - 0.80443\,i & 4.396 + 4.396\,i & 0 & 0 & 0 & 0 & 0 & 0 \\ 1.2302 + 0.80443\,i & 4.396 - 4.396\,i & 0 & 0 & 0 & 0 & 0 & 0 \\ 0 & 0 & 1.3275 - 1.2934\,i & 9.0041 + 9.0041\,i & 0 & 0 & 0 & 0 \\ 0 & 0 & 1.3275 + 1.2934\,i & 9.0041 - 9.0041\,i & 0 & 0 & 0 & 0 \\ 0 & 0 & 0 & 0 & 1.8648 - 1.5994\,i & 20.909 + 20.909\,i & 0 & 0 \\ 0 & 0 & 0 & 0 & 1.8648 + 1.5994\,i & 20.909 - 20.909\,i & 0 & 0 \\ 0 & 0 & 0 & 0 & 0 & 0 & 2.612 - 2.3763\,i & 62.2 + 62.2\,i \\ 0 & 0 & 0 & 0 & 0 & 0 & 2.612 + 2.3763\,i & 62.2 - 62.2\,i \end{pmatrix} \tag{4.16}$$

Finally, according to Eq. (3.21) and (3.24), the (576x8) real transformation matrix **Y** is computed, see Eq. (4.17). Here are plotted the first 18 rows starting with row #289 – this part of **Y** corresponds to the $\boldsymbol{V}(t)$-vector of displacements.

$$\mathbf{Y} = \begin{pmatrix}
0 & 0 & 0 & 0 & 0 & 0 & 0 & 0 \\
0 & 0 & 0 & 0.000012 & 0 & 0 & 0 & -0.000049 \\
0 & 4.0\,10^{-6} & 0 & 0 & 0 & -0.000016 & 0 & 0 \\
0 & 0 & 0 & 0 & 0 & 0 & 0 & 0 \\
0 & -5.0\,10^{-6} & 0 & 0 & 0 & 0.000019 & 0 & 0 \\
0 & 0 & 0 & 0.000014 & 0 & 0 & 0 & -0.000056 \\
0 & 0 & 0 & 0 & 0 & 0 & 0 & 0 \\
0 & 0 & 0 & 0.00003 & 0 & 0 & 0 & -0.000119 \\
0 & 0.00001 & 0 & 0 & 0 & -0.000041 & 0 & 0 \\
0 & 0 & 0 & 0 & 0 & 0 & 0 & 0 \\
0 & -7.0\,10^{-6} & 0 & 0 & 0 & 0.000029 & 0 & 0 \\
0 & 0 & 0 & 0.000021 & 0 & 0 & 0 & -0.000084 \\
0 & 0 & 0 & 0 & 0 & 0 & 0 & 0 \\
0 & 0 & 0 & 0.000055 & 0 & 0 & 0 & -0.000217 \\
0 & 0.000019 & 0 & 0 & 0 & -0.000075 & 0 & 0 \\
0 & 0 & 0 & 0 & 0 & 0 & 0 & 0 \\
0 & -0.00001 & 0 & 0 & 0 & 0.00004 & 0 & 0 \\
0 & 0 & 0 & 0.000028 & 0 & 0 & 0 & -0.000111
\end{pmatrix} \tag{4.17}$$

The time-dependent "load" vector in the final uncoupled modal equations (3.22) is calculated to be a function of the wind speed time series, see Fig. 2:

$$\begin{bmatrix} g_1(t) \\ h_1(t) \\ \cdots \\ g_4(t) \\ h_4(t) \end{bmatrix} = \mathbf{Y}^{\mathrm{T}} \cdot \left[\mathbf{p}\right] = \begin{pmatrix} 19.36\,u^2 \\ 0.1812\,u^2 \\ 1.951\,u^2 \\ 0 \\ 1.929\,u^2 \\ -12.95\,u^2 \\ 0.5554\,u^2 \\ 0 \end{pmatrix} \tag{4.18}$$

The (4x4) mass, damping and stiffness matrices of the four final uncoupled modal equations from type (3.27) are resp.

$$\begin{pmatrix} 1.0 & 0 & 0 & 0 \\ 0 & 1.0 & 0 & 0 \\ 0 & 0 & 1.0 & 0 \\ 0 & 0 & 0 & 1.0 \end{pmatrix}, \begin{pmatrix} 1.733 & 0 & 0 & 0 \\ 0 & 0.1788 & 0 & 0 \\ 0 & 0 & 1.838 & 0 \\ 0 & 0 & 0 & 2.351 \end{pmatrix}, \begin{pmatrix} 17.89 & 0 & 0 & 0 \\ 0 & 47.2 & 0 & 0 \\ 0 & 0 & 144.9 & 0 \\ 0 & 0 & 0 & 620.5 \end{pmatrix} \tag{4.19}$$

Compare the numerical evaluations (4.10), (4.11) of the final modal equations from type (2.18) to the final equations (4.19) now – evidently both modal procedures leads to the same final uncoupled modal equations. The Same applies for the "load vectors" in (4.12) resp. (4.18).

Due to the equal final modal equations, as seen above, the time responses of the modal coordinates $y_j(t), x_j(t),\ (j = 1, \ldots, 4)$ are exactly the same. Exemplarily the $y_1(t), x_1(t)$ vibrations are plotted in Fig.12. Compare to Fig. 4 to note the interchanged meaning of y_1 and x_1 in this case, as already mentioned in Sec. 3.3.

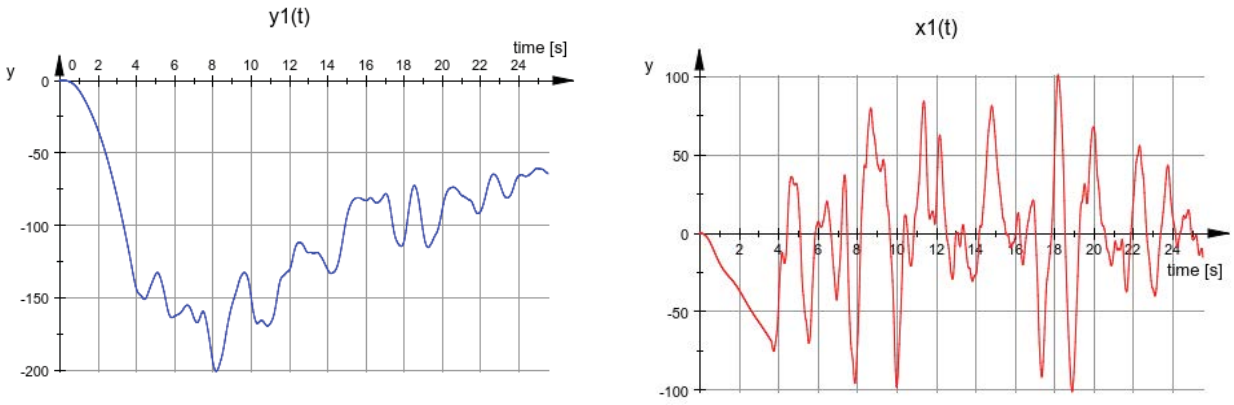

Fig. 12 Time responses of the modal coordinates $y_1(t), x_1(t)$

By a back transformation according to Eq. (3.21) the total responses $\boldsymbol{V}(t)$ is obtained. As a matter of course, all vibration plots in this case are exactly the same like in Figs. 7-9. Exemplarily the plots analogously to Figs. 7,8 is shown in Fig. 13.

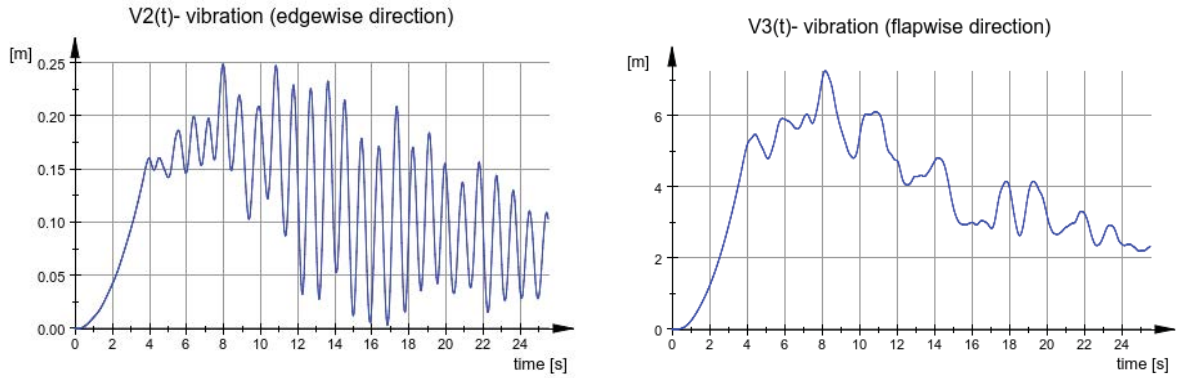

Fig. 13 Total vibrations $v_2(t), v_3(t)$ $[m]$ (y- and z-direction, see fig.1) at the rotor blade tip - node #49

For the sake of validation, the classic equations of motion (1.1) for the rotor blade model were calculated by direct time integration. The parameters used for the applied unconditionally numerically stable Newmark integration method are $\alpha = 0.5,\ \beta = 0.25$. The resulting flap- and edgewise vibrations are practically identical to the vibrations shown in Fig.13.

5 CONCLUSIONS

- The modal decomposition procedure, described briefly in Sec. 2, is well known from the literature, see [13] – [15]. Without any explanations of the notion of "phase synchronization", the presented algorithm leads, starting with a modal transformation in complex space, to an uncoupled, real-space form of modal equations.
- In the proposed modal procedure, presented in Sec. 3, the transformation matrix is assembled employing the right complex conjugate eigenvector pairs, normalized on the SDOFS level and on MDOFS level with respect to the corresponding stiffness matrices.

The real-space modal transformation matrix **Y**, Eq. (3.23), (3.24a-d), is developed by combining of two complex transformations, resulting from the eigenvalue problem of the SDOFS and the MDOFS. There are shown and discussed some advantages and differences in comparison with "phase synchronization" method, Sec. 2, which is based on the "Lancaster" state space form of the equations of motion. The proposed procedure is derived in a quite natural way, but it doesn't base on the notion of "phase synchronization". Both procedures lead in the final form to same uncoupled real-space modal equations, as shown in the numerical example in Sec.4.

- One restrictive condition has to be accounted for: both considered modal procedures implies the existence of distinct complex conjugated eigenvalues, at least for the first lowest natural frequencies.
- Application of the "phase synchronization" and the proposed method implies availability of reliable professional eigensolver software for complex eigenvalue problems. Numerical problems for both procedures in especially this first basic step are to be probably expected in real-life structural models with a high number of DOFS. Another important algorithmic aspect to be accounted for is the assumed order of the eigenvalues and eigenvectors in each complex conjugate pair, Eq. (1.6), (3.12). All complex eigenvectors in the $\boldsymbol{\Phi_G}$ -matrix should be ordered in this way, see Eq. (3.16).
- One important advantage of the classic modal decomposition of the equations of motion is retained in both considered procedures - an uncomplete modal transformation may be performed by use of a few *(k << n)* eigenmodes to get *k* uncoupled SDOFS block equations in real space. This leads with sufficient numerical accuracy to the total time response of all original *n* DOF – as shown in the numerical examples in Sec. 4, employing only the first four complex eigenvalues and associated eigenmodes.
- The presented rotor blade vibration should only be a qualitative demonstration of the numerical performance of both presented modal procedure. For any quantitative conclusions about possible numerical limitations more tests and case studies should be done in future.
- In the numerical example in Sec. 4 was applied a simple approach for the aerodynamic damping in the beam element model. It was used mainly in order to create a symmetric damping matrix on the finite element level, which leads together with the assumed stiffness proportional damping to the damping matrix incorporating non-proportional damping.
- The real-space modal transformation (3.21) could be applied for description of the elastic deformation of a rotor blade beam model, as a part of the multi-body simulation of a wind turbine. In compare to the classic modal superposition, the proposed procedure operates by double number of modal coordinates - (x_j, y_j) , assembled in the modal coordinates vector $\boldsymbol{X}$. The formulation of the integral terms of the mass matrix and the general inertia forces for the flexible rotor blade body by use of this modal transformation is an interesting topic to be investigated in further research.

REFERENCES

[1] Burton T., Jenkins N., Sharpe D., Bossanyi E. 2011. *Wind Energy Handbook*, John Wiley & Sons, 2011, chapters 5.7, 5.8

[2] Caughey T.K., O'Kelly M.E.J. Classical normal modes in damped linear dynamic systems, *ASME Journal of Applied Mechanics* 32 (1965), pp. 583-588

[3] Chorpa A.K. 2007. *Dynamics of Structures. Theory and Applications to Earthquake Engineering*, Pearson Prentice Hall, New Jersey, 2007.

[4] Chu M. T., Buono N. T. 2008. Total decoupling of general quadratic pencils, Part I: Theory, *Journal of Sound and Vibration* 309 (2008) 96–111.

[5] Chu M. T., Buono N. T. 2008. Total decoupling of general quadratic pencils, Part II: Structure preserving isospectral flows, *Journal of Sound and Vibration* 309 (2008) 112-128.

[6] Cramer H., Stanoev E. 2006. Zur modalen Analyse bei gedämpften Mehrmassensystemen, 10. Dresdner Baustatik-Seminar: Neue Bauweisen – Trends in Statik und Dynamik, TU Dresden, Lehrstuhl für Statik, Dresden, 2006, p. 81-90.

[7] Cramer H., Stanoev E. 2008. Ein Verfahren zur modalen Analyse gedämpfter Systeme der Strukturmechanik, *Rostocker Berichte aus dem Institut für Bauingenieurwesen*, Heft 19, Universität Rostock, Institut für Bauingenieurwesen, 2008, ISSN 1438-7638, p. 83-107.

[8] Garvey S.D., Friswell M.I., Prells U. Co-ordinate transformations for second order systems, I: general transformations, *Journal of Sound and Vibration* 258 (2002) 885–909

[9] Garvey S.D., Friswell M.I., Prells U. Co-ordinate transformations for second order systems, II: elementary structure-preserving transformations, *Journal of Sound and Vibration* 258 (2002) 911–930

[10] Géradin M., Rixen D. 1997. *Mechanical vibrations – theory and applications to structural dynamics*, John Wiley & Sons Ltd, 1997.

[11] Kim M.-C., Lee L.-W. Eigenproblems for large structures with non-proportional damping. *Earthquake Engng. Struct. Dyn*, 28, 157-172, 1999

[12] Lancaster P., *Lambda-Matrices and Vibrating Systems*, Pergamon Press, Oxford, United Kingdom, 1966

[13] Ma Fai F., Imam A., Morzfeld M. 2009. The decoupling of damped linear systems in oscillatory free vibration, *Journal of Sound and Vibration* 324 (2009) 408–428.

[14] Ma Fai F., Morzfeld M., Imam A. 2010. The decoupling of damped linear systems in free or forced vibration, *Journal of Sound and Vibration* 329 (2010) 3182–3202.

[15] Ma Fai F., Morzfeld M. 2011. The decoupling of damped linear systems in configuration and state spaces, *Journal of Sound and Vibration* 330 (2011) 155–161.

[16] Stanoev E. 2013. A modified modal analysis method for damped multi-degree-of-freedom-systems in structural mechanics, *Zeitschrift für angewandte Mathematik und Mechanik (ZAMM)*, 2013, 1 – 23 (2013), http://onlinelibrary.wiley.com/ doi/10.1002/zamm.201300061/abstract.

[17] Stanoev E. 2014. A modal analysis method for structural models with non-modal damping. 11th World Congress on Computational Mechanics (WCCM XI) and (ECCM V), 20-25 Juli 2014, Barcelona, ISBN: 978-84-942844-7-2, Tomo IV, p. 3034-3045.

[18] Stanoev E. 2016. A real-space modal analysis method for non-proportional damped structures. ECCOMAS Congress 2016 (VII European Congress on Computational

Methods in Applied Sciences and Engineering), 5-10 June 2016, Crete Island, Greece, https://www.eccomas2016.org/proceedings/ pdf/5682.pdf.

[19] Stanoev E. 2017. Modal analysis procedure using complex left and right eigenvectors of non-proportionally damped structures. COMPDYN 2017 (6th ECCOMAS Thematic Conference on Computational Methods in Structural Dynamics and Earthquake Engineering), 15-17 June, Rhodes, Greece, https://2017.compdyn.org/proceedings/pdf/17160.pdf.

[20] Stanoev, E. 2018. Modal decomposition procedures for FE-based structural models with non-proportional damping. IRF 2018 (6th International Conference Integrity-Reliability-Failure) Lisbon/Portugal 22-26 July 2018. Editors J.F. Silva Gomes and S.A. Meguid, Publ. INEGI/FEUP (2018); ISBN: 978-989-20-8313-1, https://paginas.fe.up.pt/~irf/Proceedings_IRF2018/data/papers/7187.pdf.

[21] Stanoev, E.; Chandrashekhara, S.K. 2019. Determination of Natural Frequencies and Mode Shapes of a Wind Turbine Rotor Blades using Timoshenko Beam Elements: *Wind Energy Science*, 4, 57–69, 2019, https://doi.org/10.5194/wes-4-57-2019.

[22] Stanoev, E.; Modal analysis of wind turbine rotor blades on the basis of a damped eigenvalue problem: Sustainable Development and Innovations in Marine Technologies – Georgiev & Guedes Soares (eds), Proceedings of the 18th International Congress of the Maritime Association of the Mediterranean (IMAM 2019), September 9-11, 2019, Varna, Bulgaria, Taylor & Francis Group, London, 2019, ISBN 978-0-367-40951-7, https://paginas.fe.up.pt/~irf/Proceedings_IRF2018/data/papers/7187.pdf

[23] Jonkman J., Butterfield S., Musual W., Scott G., Definition of a 5-MW Reference Wind Turbine for Offshore System Development, Technical Report NREL/TP-500-38060, National Renewable Energy Laboratory, Colorado, 2009

EURODYN 2020
XI International Conference on Structural Dynamics
M. Papadrakakis, M. Fragiadakis, C. Papadimitriou (eds.)
Athens, Greece, 23–26 November 2020

STATISTICAL PROCESS CONTROL PROCEDURES FOR ONLINE DAMAGE DETECTION OF A MONUMENTAL MASONRY PALACE: THE CONSOLI PALACE IN GUBBIO, ITALY

Enrique García-Macías[1] **and Filippo Ubertini**[2]

[1]Department of Civil and Environmental Engineering, University of Perugia
Via G Duranti 93, Perugia 06125, Italy
enrique.garciamacias@unipg.it

[2] Department of Civil and Environmental Engineering, University of Perugia
Via G Duranti 93, Perugia 06125, Italy
filippo.ubertini@unipg.it

Keywords: Damage identification, Historic buildings, Structural health monitoring, Automated modal identification, Control chart, Machine Learning.

Abstract. *This paper proposes a new semi-supervised two-class pattern classification method for early damage detection of structures. The proposed approach comprises five consecutive steps, including the (i) collection of data samples representing the healthy condition of the structure (training period); (ii) clustering analysis; (iii) outliers elimination; (iv) pattern recognition using local Principal Components Analysis; and (v) pattern classification through control charts. The effectiveness of the proposed approach is demonstrated through two different case studies. These include a benchmark beam simulation model, and the Consoli Palace in Gubbio (Italy). The latter has been monitored for two years using a long-term vibration-based monitoring system, and represents an extraordinary example of a stiff masonry building with complex environmental effects. Analyses and discussion are presented covering the effects of differing structural/environmental behaviour regimes, the presence of outliers in the training period, and the effectiveness of different control charts.*

1 INTRODUCTION

The heightened awareness about the importance of the conservation of heritage structures has fostered the implementation of numerous Structural Health Monitoring (SHM) systems in recent years [14, 9, 5, 10]. In particular, ambient vibration-based SHM systems are becoming particularly popular owing to their capability of performing a non-destructive assessment of the structural integrity with minimum architectural impact and without affecting the normal operating conditions of structures [2, 4, 15]. Through Automated Operational Modal Analysis (A-OMA) techniques, such systems allow the tracking of the modal features of structures and, in turn, it is possible to detect damage-induced anomalies and so enable the decision-making of condition-based rehabilitation [17, 18]. Nevertheless, the development of efficient SHM methodologies for early damage detection still remains an open and active research area.

Specifically, the SHM of masonry structures is specially challenging due to the complex dependence of their intrinsic stiffness on environmental factors (mainly temperature and humidity), often resulting in different behaviour regimes [7, 5, 10]. This is the case, for instance, of masonry structures experiencing freezing conditions during the winter, when the icing of pore water in masonry leads to a dramatic change in temperature/stiffness relationship. Such environmental effects induce both daily and seasonal fluctuations in the modal features of structures, which usually mask damage-induced anomalies. In this regard, the application of advanced statistical process control procedures becomes imperative for early damage detection [3].

In this line, this paper presents a new semi-supervised two-class pattern classification method for early damage detection of structures. The proposed approach comprises five consecutive steps, including the (i) collection of data samples representing the healthy condition of the structure (training period); (ii) clustering analysis; (iii) outliers elimination; (iv) pattern recognition using local Principal Components Analysis; and (v) pattern classification using control charts. The effectiveness of the proposed approach is evaluated through two different case studies. These include a benchmark beam structure model, and the monumental Consoli Palace in Gubbio (Italy). The palace has been continuously monitored since July 2017 with a low-cost mixed static/dynamic/environmental long-term monitoring system [10]. In this work, the monitoring data of three high-sensitivity accelerometers and two thermocouples recording ambient vibrations and environmental temperatures are exploited. On this basis, the resonant frequencies of the palace have been identified and tracked using an A-OMA technique based upon the Covariance-based Stochastic Subspace Identification method (COV-SSI). The experimentally identified resonant frequencies are selected as damage-sensitive features, and the effectiveness of the proposed damage detection approach is evaluated considering artificial damage in the shape of frequency decays. The Consoli Palace represents an exceptional example of a stiff masonry building. Due to the low excitation levels in the building, the identified resonant frequencies present an elevated number of outliers that hinder the damage detection tasks. Additionally, the complex geometry of the palace and its connection with the adjoining buildings originates the existence of highly non-linear environmental effects, making it an outstanding benchmark structure for testing the proposed damage detection approach.

2 TWO-CLASS PATTERN CLASSIFICATION METHOD FOR DAMAGE DETECTION

This paper proposes a five step pattern classification algorithm for two-class damage detection as sketched in Fig. 1. The proposed approach comprises: (I) Characterization of the healthy condition of the structure with an initial training period; (II) Clustering analysis to identify the

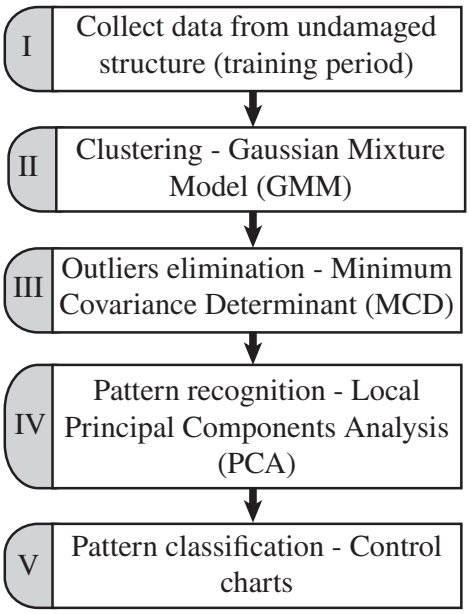

Figure 1: Flow chart of proposed two-class pattern classification algorithm for damage detection.

presence of multiple environmental regimes; (III) Outliers elimination; (IV) Pattern recognition through local PCA; and (V) Patter classification using control charts.

Let us consider that the SHM system performs an automated identification of m resonant frequencies f_i, $i = 1, \ldots, m$ as damage sensitive features. For notational convenience, let us denote the features at an instant n in vector form as $\mathbf{x}_n = \left[f_{(1,n)}, \ldots, f_{(m,n)}\right]$. We assume that the SHM system identifies a total of N sets of modal features, so the observation matrix $\mathbf{Y} \in \mathbb{R}^{N \times m}$ is constructed by collecting the features vectors by rows. In order to statistically characterize the healthy condition of the structure, a subset of tp data samples are selected as the training period. This must be long enough to cover the full range of environmental conditions (both daily and seasonal fluctuations), and typically a one-year period is assumed adequate. Note that the observation matrix $\mathbf{Y}$ represents a multivariate data set which, in principle, is composed of non-linear data.

2.1 CLUSTERING - GAUSSIAN MIXTURE MODEL

In order to take into account different environmental mechanisms, the damage sensitive features in the training period are clustered into different data sets using a GMM model. This approach assumes that the probability density function $p(\mathbf{x})$ of the data set in the training period $\mathbf{X}$ (in general, non-normally distributed) can be represented as a linear superposition of K Gaussian components as [1]:

$$p(\mathbf{x}) = \sum_{k=1}^{K} \pi_k \mathcal{N}\left(\mathbf{x} \,|\boldsymbol{\mu}_k, \boldsymbol{\Sigma}_k\right). \tag{1}$$

Each component of the mixture is defined as a Gaussian distribution $\mathcal{N}\left(\mathbf{x} \,|\boldsymbol{\mu}_k, \boldsymbol{\Sigma}_k\right)$ with mean and covariance matrix denoted by $\boldsymbol{\mu}_k$ and $\boldsymbol{\Sigma}_k$, respectively. The parameters $\boldsymbol{\pi} = [\pi_1, \ldots, \pi_K]^{\mathrm{T}}$ in Eq. (1) are called the mixing coefficients, and they range between 0 and 1 ($0 \leq \pi_k \leq 1$) and sum to one ($\sum_{k=1}^{K} \pi_k = 1$). The model parameters, $\boldsymbol{\mu}_k$,$\boldsymbol{\Sigma}_k$ and π_k, are fitted by minimizing the

log-likelihood function:

$$\ln p(\mathbf{X}\,|\boldsymbol{\pi},\boldsymbol{\mu},\boldsymbol{\Sigma}) = \sum_{n=1}^{t_p} \ln \left\{ \sum_{k=1}^{K} \pi_k \mathcal{N}\left(\mathbf{x}_n\,|\boldsymbol{\mu}_k,\boldsymbol{\Sigma}_k\right) \right\}. \tag{2}$$

The maximum likelihood solution for the parameters ($\boldsymbol{\mu}$,$\boldsymbol{\Sigma}$ and $\boldsymbol{\pi}$) is estimated using the iterative Expectation-Maximization (EM) algorithm. In the expectation (E) step, the parameters (initial guess at the beginning) are held fixed and the posterior probability of assigning $\mathbf{x}_n$ to the k's cluster is given by the so-called responsibilities $\gamma(z_{nk})$ as:

$$\gamma(z_{nk}) = \frac{\pi_k \mathcal{N}\left(\mathbf{x}_n\,|\boldsymbol{\mu}_k,\boldsymbol{\Sigma}_k\right)}{\sum_{j=1}^{K} \pi_j \mathcal{N}\left(\mathbf{x}_n\,|\boldsymbol{\mu}_j,\boldsymbol{\Sigma}_j\right)}, \tag{3}$$

where z_{nk} is an element of a K-dimensional binary random variable $\mathbf{z}$ with a 1-of-K representation. Only one element in $\mathbf{z}$ is equal to 1 and all other elements are 0.

Then, in the maximization (M) step, the parameters are re-estimated using the posterior probability calculated in the previous E step as follows:

$$\boldsymbol{\mu}_k^{new} = \frac{1}{N_k} \sum_{n=1}^{t_p} \gamma(z_{nk}) \mathbf{x}_n, \tag{4}$$

$$\boldsymbol{\Sigma}_k^{new} = \frac{1}{N_k} \sum_{n=1}^{t_p} \gamma(z_{nk}) \left(\mathbf{x}_n - \boldsymbol{\mu}_k^{new}\right) \left(\mathbf{x}_n - \boldsymbol{\mu}_k^{new}\right)^{\mathrm{T}}, \tag{5}$$

$$\pi_k^{new} = N_k/N, \quad N_k = \sum_{n=1}^{t_p} \gamma(z_{nk}). \tag{6}$$

The log-likelihood in Eq. (2) can then be evaluated. Convergence of either the parameters of the log likelihood is checked, and if the criteria are not satisfied, the process is iterated using the updated data values until the criteria are met. Once the K clusters have been defined in the training period, new data samples are assigned to the cluster with the least Mahalanobis distance.

2.2 OUTLIERS ELIMINATION

The Minimum Covariance Determinant (MCD) method [8] is used to minimize the effect of outlier measurements in the training population. The MCD method seeks a sample subset within a multivariate dataset that minimizes the covariance matrix. Specifically, the MCD method is applied in this work to every cluster identified in the training period. Consider an arbitrary cluster $\mathbf{C} = \{\mathbf{x}_1, \ldots, \mathbf{x}_d\}$ containing d samples, and let $H_1 \subset \{1, \ldots, d\}$ be an h-subset, that is $|H_1| = h$. Being $\boldsymbol{\mu}_1$ and $\boldsymbol{\Sigma}_1$ the empirical mean and covariance matrix of the data in H_1, the Mahalobis distances of all the data samples in the cluster read ($\det(\boldsymbol{\Sigma}_1) \neq 0$):

$$d_1(i) = \sqrt{\left(\mathbf{x}_i - \boldsymbol{\mu}_1\right)^{\mathrm{T}} \boldsymbol{\Sigma}_1^{-1} \left(\mathbf{x}_i - \boldsymbol{\mu}_1\right)} \quad \text{for} \quad i = 1, \ldots, d. \tag{7}$$

Now take H_2 another h-subset such that $\{d_1(i); i \in H_2\} := \{(d_1)_{1:d}, \ldots, (d_1)_{h:d}\}$ where $(d_1)_{1:d} \leq (d_1)_{2:d} \leq \ldots \leq (d_1)_{d:d}$ are the ordered distances, and compute $\boldsymbol{\mu}_2$ and $\boldsymbol{\Sigma}_2$ based on H_2. Then $\det(\boldsymbol{\Sigma}_2) \leq \det(\boldsymbol{\Sigma}_1)$ with equality if and only if $\boldsymbol{\mu}_2 = \boldsymbol{\mu}_1$ and $\boldsymbol{\Sigma}_2 = \boldsymbol{\Sigma}_1$. This process, also known as C-step, can be iteratively repeated. If $\det(\boldsymbol{\Sigma}_2) = 0$ or $\det(\boldsymbol{\Sigma}_2) = \det(\boldsymbol{\Sigma}_1)$, the

algorithm stops; otherwise, another C-step is run yielding $\det(\boldsymbol{\Sigma}_3)$, and so on. The sequence $\det(\boldsymbol{\Sigma}_1) \geq \det(\boldsymbol{\Sigma}_2) \geq \det(\boldsymbol{\Sigma}_3) \geq \ldots$ is nonnegative and hence must converge, so there must be an index s such that $\det(\boldsymbol{\Sigma}_s) = 0$ or $\det(\boldsymbol{\Sigma}_s) = \det(\boldsymbol{\Sigma}_{s-1})$. In this work, the fast implementation of the MCD method proposed by Rousseeuw and Driessen [16] has been implemented. The dimension h of the subsets has been selected as $0.8d$. Once the algorithm converges, a certain percentage of the samples with the largest Mahalanobis distances with respect to the converged sample subset are considered as outliers and eliminated.

2.3 PRINCIPAL COMPONENTS ANALYSIS

Once the detected outliers have been eliminated from the clusters, pattern recognition using PCA is conducted for every cluster in the training period. Principal Component Analysis consists of a double change of coordinates, where the original data are first projected in the vectorial space generated by the principal components (PCs) and then remapped back to the original space by retaining only some of the PCs. Let us denote the matrix of observations $\mathbf{X}_{c_k} \in \mathbb{R}^{n_{c_k} \times m}$ in an arbitrary cluster c_k ($k = 1, \ldots, K$) of size n_{c_k} and $\mathbf{X}^*_{c_k} \in \mathbb{R}^{n_{c_k} \times m}$ a matrix whose columns are the centred variables $\mathbf{x}^*_j$ (i.e. $x^*_{ij} = x_{ij} - \overline{x}_j$, where $\overline{x}_j$ denotes the mean value of the observations on variable j). Then, the eigendecomposition of the covariance matrix $\boldsymbol{\Sigma}$ reads:

$$\boldsymbol{\Sigma} = \left(\mathbf{X}^*_{c_k}\right)^{\mathrm{T}} \mathbf{X}^*_{c_k} = \mathbf{U}_{c_k} \mathbf{S}^2 \mathbf{U}^{\mathrm{T}}_{c_k}, \tag{8}$$

where $\mathbf{U}_{c_k} \in \mathbb{R}^{n_{c_k} \times n_{c_k}}$ is the so-called loading matrix. The eigenvalues of the covariance matrix contained in the diagonal matrix $\mathbf{S}^2$ represent the variance contributions of each PC. Assuming that the PCs providing the largest contributions to the variance represent the effects of environmental and operational factors, it is possible to find an approximation $\widehat{\mathbf{X}}^*_{c_k}$ isolating such factors through dimensionality reduction. This can be done by retaining only the first l columns of matrix $\mathbf{U}_{c_k}$ in Eq. (8) into a rectangular reduced loading matrix, $\widehat{\mathbf{U}}_{c_k} \in \mathbb{R}^{l \times m}$. Hence, matrix $\widehat{\mathbf{X}}^*_{c_k}$ is estimated as:

$$\widehat{\mathbf{X}}^*_{c_k} = \mathbf{X}^*_{c_k} \widehat{\mathbf{U}}_{c_k} \widehat{\mathbf{U}}^{\mathrm{T}}_{c_k}, \tag{9}$$

which represents the backward transformation of the original observations in $\mathbf{X}^*_{c_k}$ from a reduced space of the l PCs to the original one. Since the transformation in Eq. (9) provides a representation of the environmental/operational effects, matrix $\widehat{\mathbf{U}}_{c_k}$ allows to predict the resonant frequencies of the structure beyond the training period.

2.4 CONTROL CHARTS

Once the transformation matrices $\widehat{\mathbf{U}}_{c_k}$ are obtained for all the identified clusters c_k ($k = 1, \ldots, K$) in the training period, it is possible to compute a matrix of predicted resonant frequencies $\widehat{\mathbf{Y}} \in \mathbb{R}^{N \times m}$ throughout all the monitoring period. Since the statistical models used to construct $\widehat{\mathbf{Y}}$ are fitted using the training period representing a baseline in-control population where the structure is assumed to remain healthy, the appearance of damage can be inferred from the detection of anomalies in the residual error matrix $\mathbf{E} \in \mathbb{R}^{N \times m}$ computed as:

$$\mathbf{E} = \mathbf{Y} - \widehat{\mathbf{Y}}. \tag{10}$$

Assuming that $\widehat{\mathbf{Y}}$ reproduces the part of the variance in the resonant frequencies related to environmental/operational changes, $\mathbf{E}$ only contains the residual variance stemming from iden-

tification errors, un-modelled environmental/operational effects, and structural defects. Therefore, the presence of damage in the shape of anomalies in the time series of $\mathbf{E}$ can be revealed through control charts. These furnish time series of certain statistical distances between the distribution of the residuals contained in $\mathbf{E}$ and the in-control data base. Specifically, two different control charts are used in this work, including the Hotelling (T^2) and Multivariate Exponentially Weighted Moving Average (MEWMA) control charts. The statistical distances handled by these control charts are positive by definition, so an in-control region can be specified by an interval [0,*UCL*]. The upper control limit (*UCL*) can be estimated as the statistical distance attaining a certain confidence (exceeding) level α in the training database. In this light, the appearance of out-of-control processes violating the in-control region may indicate the appearance of damage.

- *Hotelling's* T^2: The Hotelling's T^2 control chart [6] is defined as:

$$T_i^2 = r\left(\overline{\mathbf{E}} - \overline{\overline{\mathbf{E}}}\right)^{\mathrm{T}} \boldsymbol{\Sigma}_0^{-1}\left(\overline{\mathbf{E}} - \overline{\overline{\mathbf{E}}}\right),\ i = 1, 2, \ldots, N/r, \tag{11}$$

  where r is an integer parameter referred to as subgroup size, $\overline{\mathbf{E}}$ is the mean of the residuals in the subgroup of the last r observations, while $\overline{\overline{\mathbf{E}}}$ and $\boldsymbol{\Sigma}_0$ are the mean values and the covariance matrix of the residuals statistically estimated in the training period.

- *Multivariate Exponentially Weighted Moving Average (MEWMA)*: Originally proposed by Lowry *et al*. [12], the MEWMA control chart represents an intermediate solution between the T^2 and the MCUSUM control charts. Alike the MCUSUM control chart, the MEWMA method also accounts for the information from past observations, although it gives weights decreasing in a geometric progression from the most recent observation to the first one. The statistical distance used in the MEWMA control chart reads:

$$MEWMA_i = \left(r\,\mathbf{z}_i^{\mathrm{T}}\boldsymbol{\Sigma}_{z_i}^{-1}\mathbf{z}_i\right)^{1/2},\ i = 1, 2, \ldots, N/r, \tag{12}$$

  with

$$\begin{aligned} \mathbf{z}_i &= \lambda\left(\overline{\mathbf{E}} - \overline{\overline{\mathbf{E}}}\right) + (1-\lambda)\mathbf{z}_{i-1}, \\ \boldsymbol{\Sigma}_{z_i} &= \lambda\frac{1-(1-\lambda)^{2i}}{2-\lambda}\boldsymbol{\Sigma}_0, \end{aligned} \tag{13}$$

  where λ is a smoothing constant with $0 \leq \lambda \leq 1$. Practically, the most often used value of λ is 0.1.

3 CASE STUDIES

To illustrate the capabilities of the proposed approach for early-damage detection, two case studies are examined in this section. The first one is a numerical beam model which is subjected to changing temperature conditions and varying mass distribution. The second one is a real-life case study, the Consoli Palace in Gubbio (Italy), which was monitored for almost two years.

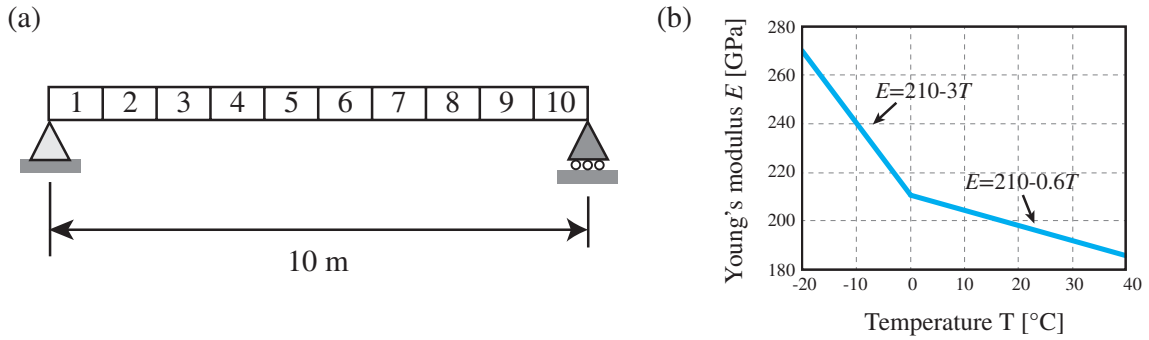

Figure 2: Beam structure model (a) and variations of Young's modulus with temperature for the beam structure model (b).

3.1 Beam structure model

The first case study is the benchmark beam model previously reported in references [11, 20] and sketched in Fig. 2 (a). The model consists of a 10 m long simply supported beam defined by ten 2-nodes beam-bending elements of 1 m each. The beam has constant cross-section, inertia and mass density of 0.08 m^2, 0.0006 m^4, and 7850 kg/m^3, respectively. The Young's modulus of the beam is assumed to be temperature dependent according to the bi-linear relationship shown in Fig. 2 (b).

The first four natural frequencies of the beam are used as damage sensitive features. In particular, seven consecutive set ups are analysed as summarised in Table 1. The training period is defined by the first two data sets (UC-1 and UC-2). The first one includes 800 and 420 observations with temperatures between 0°C and 40°C and between -20°C and 0°C, respectively. In addition, a random variation of $\pm 10\%$ in the mass density of the beam is also considered in order to include some randomness in the observations. The second data set has 400 observations for temperatures between 0°C and 40°C and 210 between -20°C and 0°C. In this case, a larger variation in density of $\pm 25\%$ is considered as a way of simulating the presence of outlier measurements. Afterwards, five damage cases with increasing severities (25%, 30%, 35%, 40% and 45%), labelled from DC-1 to DC-5 in Table 1, are considered. Specifically, damages are simulated through reductions in the bending stiffness of the 4th element. Data from each damaged case are obtained considering 200 samples with temperatures ranging between 0°C and 40°C, and 100 samples between -20°C and 0°C. Moreover, each element is assumed to have a $\pm 10\%$ random variation in density.

	UC-1		UC-2		DC-1		DC-2		DC-3		DC-4		DC-5	
Samples	800	420	400	210	200	100	200	100	200	100	200	100	200	100
ΔT^a	T_1	T_2	T_1	T_2	T_1	T_2	T_1	T_2	T_1	T_2	T_1	T_2	T_1	T_2
$\Delta\rho^b$ [±%]	10	10	25	25	10	10	10	10	10	10	10	10	10	10
Damage^c [%]	0	0	0	0	25	25	30	30	35	35	40	40	45	45

[a] T_1: [0°C,40°C], T_2: [-20°C,0°C].
[b] *$\Delta\rho$ denotes the relative variation of the mass density of the beam.*
[c] *Damage severity defined as a reduction of the bending stiffness of the 4th element.*

Table 1: Data samples considered in the beam structure model.

Figure 3 depicts the plots of environmental temperature versus the four natural frequencies

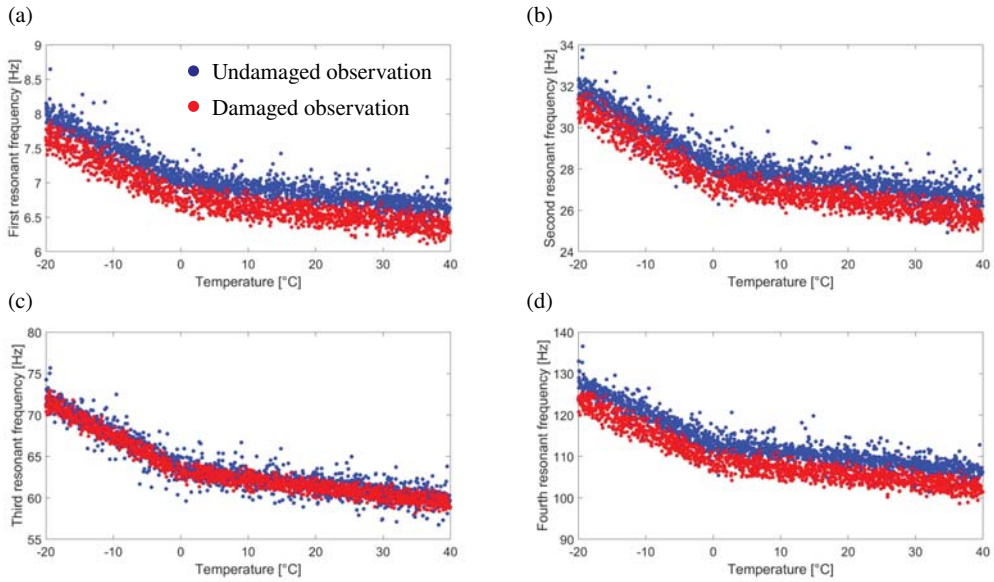

Figure 3: Plot of temperature versus (a) first natural frequency, (b) second natural frequency, (c) third natural frequency and (d) fourth natural frequency of the beam structure model.

of beam structure model. It is interesting to note that the damaged and undamaged observations intermix and can be hardly distinguished from one another in the third resonant frequency. The third mode is relatively insensitive to the presence of damage since the fourth element is located near a node of this mode. In the rest of the modes, some of the damaged observations cluster together with the undamaged cases, specially in the space containing the outlier measurements. Therefore, these outliers need to be identified and removed from the database before applying damage detection methods. To do so, the proposed approach sketched in Fig. 1 is applied herein. Firstly, the GMM model is applied to differentiate the two different environmental regimes in the time series of resonant frequencies. The result, shown in Fig. 4, shows that the GMM model can accurately separate between resonant frequencies obtained with temperatures ranging between -20°C and 0°C (Cold observations) and between 0°C and 40°C (Hot observations). Afterwards, the outliers detection algorithm previously overviewed in Section 2.2 can be applied independently to each cluster. In particular, a percentage of 30% of the data samples with the largest Mahalanobis distances according to Eq. (7) are considered as outliers. The result of the outliers elimination algorithm applied to the training period (UC-1 and UC-2) is shown in Fig. 5. It can be seen that most of the detected outliers surround the clean measurements.

Then, a PCA model can be fitted using the clean training database. In this case, one single PC sufficed to explain more than 95% of the variance of the resonant frequencies in the two clusters. The comparison between the predictions of the resonant frequencies by the PCA model and the numerical ones is presented in Fig. 6. The low scatter of the points around the diagonal line corroborates that the PCA model is formed with accuracy. This model can now be used to detect the appearance of damage beyond the training period according to the approach previously presented in Section 2.3. Specifically, Fig. 7 shows the Hotelling's control charts obtained without applying (a) and applying (b) the outliers elimination algorithm. The effect of the presence of outliers in the training period is clearly exemplified in Fig. 7 (a). In this graph, the presence of outliers between the observation numbers 1020 and 1830 lead to a large UCL (confidence level 95%) and corrupts the estimation of the mean vector $\overline{\overline{\mathbf{E}}}$ and covariance matrix

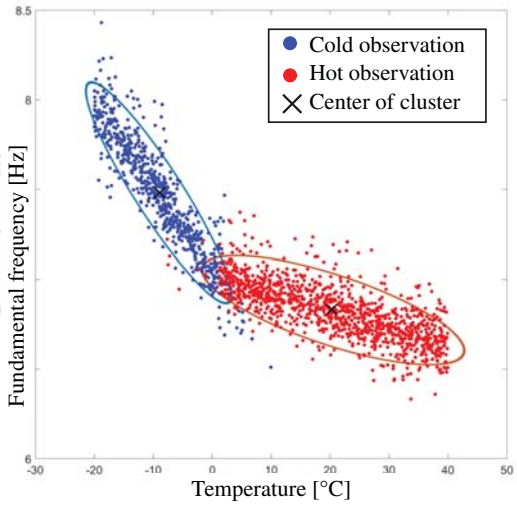

Figure 4: Cluster of the first resonant frequency with temperature of the beam structure model using GMM.

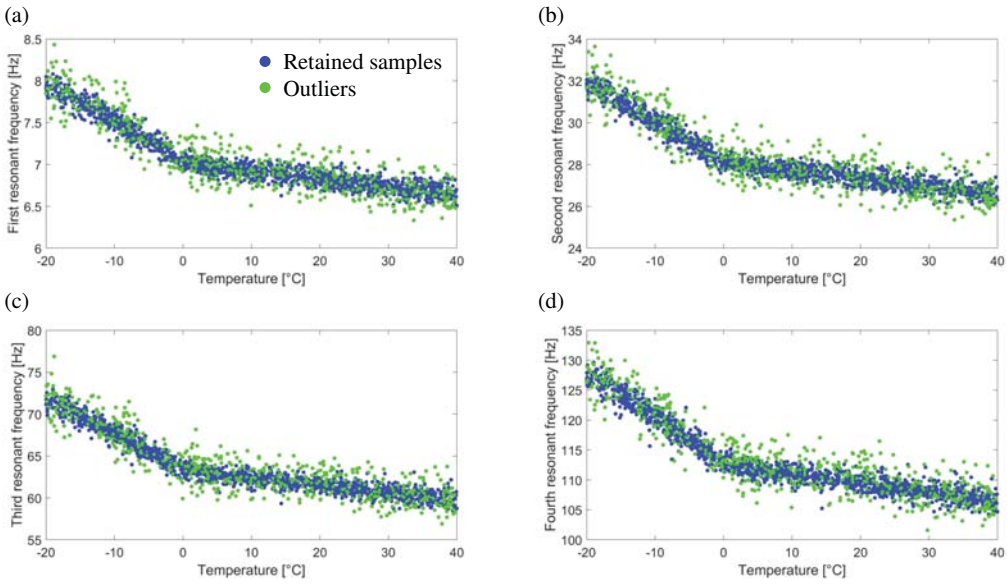

Figure 5: Plot of temperature versus (a) first natural frequency, (b) second natural frequency, (c) third natural frequency and (d) fourth natural frequency of clean undamaged observations, outlier undamaged observations and damaged observations of the beam structure model.

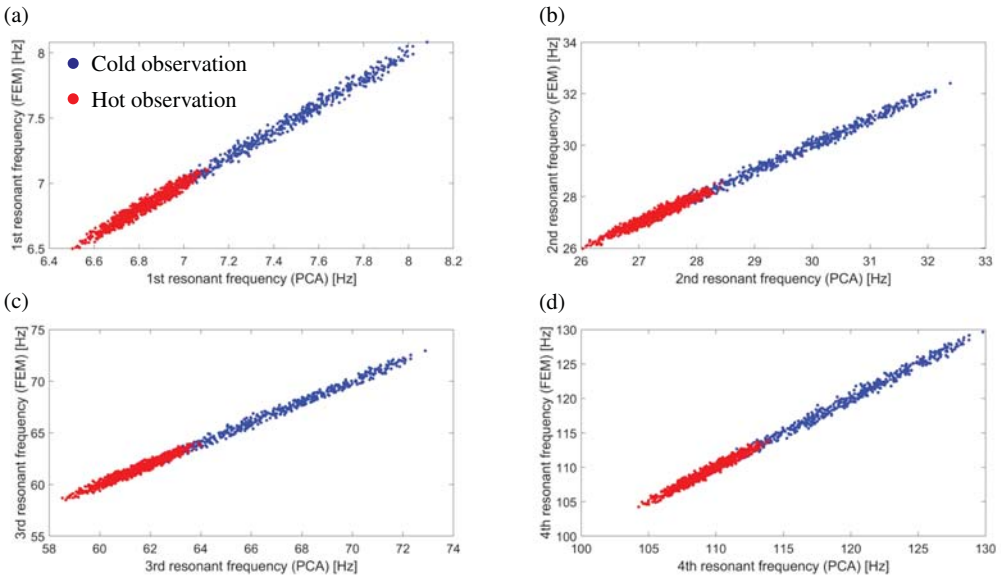

Figure 6: Plot of numerical estimates and predictions of the PCA model in terms of the (a) first natural frequency, (b) second natural frequency, (c) third natural frequency and (d) fourth natural frequency of the beam structure model ($r = 1$)

of the residuals $\boldsymbol{\Sigma}_0$ in the training period. This hinders the detection of mild damage severities, not being possible the identification until the damage severity of 35%-40%. Conversely, the control chart in 7 (b) shows that the outliers elimination algorithm effectively eliminates most of the outliers in the observation numbers between 1020 and 1830. This leads to a considerably smaller UCL and better estimation of $\overline{\overline{\mathbf{E}}}$ and $\boldsymbol{\Sigma}_0$. This allows to accurately detect all the damaged cases.

3.2 Consoli Palace

The Consoli Palace (Fig. 8 (a)), located in the city of Gubbio in Italy, was erected between 1332 and 1349 and currently hosts the Civic Museum of Gubbio. The palace is 60 m high, including a bell-tower and a panoramic loggia, and has a rectangular plan of about 40×20 m. Within the framework of the Horizon 2020 European HERACLES project (2016-2018, heracles-project.eu), a permanent SHM system has been installed in the Consoli Palace since July 2017. Specifically, three PCB 393B12 accelerometers (A1, A2 and A3) were deployed on the roof level of the palace, as well as two K-type thermocouples to monitor the environmental temperature. The sensors are connected to a NI CompactDAQ-9132 data acquisition system with NI 9234 and NI 9219 acquisition modules for accelerations and temperatures, respectively. Ambient accelerations and temperatures were respectively sampled at 100 Hz and 0.1 Hz and stored in consecutive separate files containing 30 min-long recordings. The data files were sent online through the Internet to a remove server, where an in-house code for the management of integrated SHM systems called MOSS was used for automated SHM of the palace.

Figure 9 shows the time series of identified resonant frequencies using an automated version of the SSI-COV. Specifically, five modes corresponding to Fx1 (first global bending mode in the $x-$direction), Fy1 (first global bending mode in the $y-$direction), L1 (first order local mode related to the interaction between the palace and the bell-tower), T1 (global torsional mode), and L3 (third order local mode) were tracked in the Consoli Palace. For more specific information on the adopted A-OMA technique and identification results of the Consoli Palace, readers may

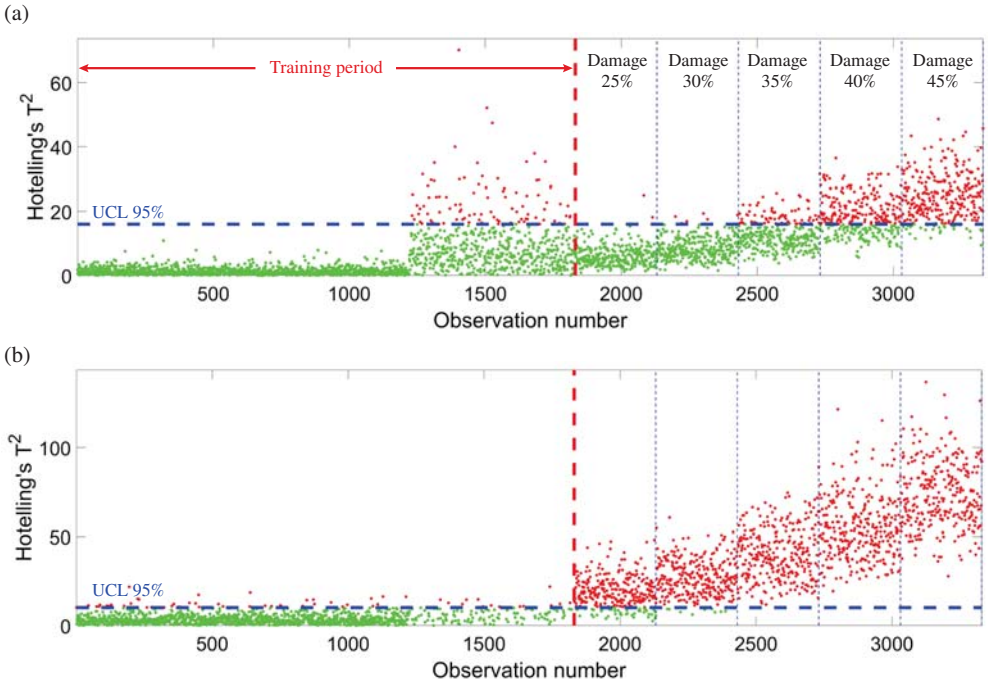

Figure 7: Comparison between the Hotelling's control charts obtained without applying (a) and applying the outliers elimination algorithm (b).

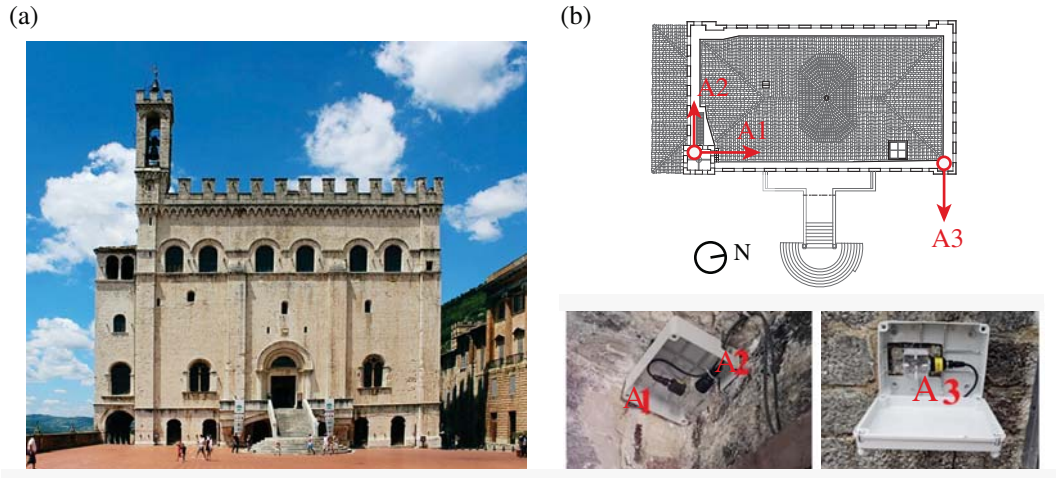

Figure 8: View of the Consoli Palace (a), and sketch of the monitoring system (b).

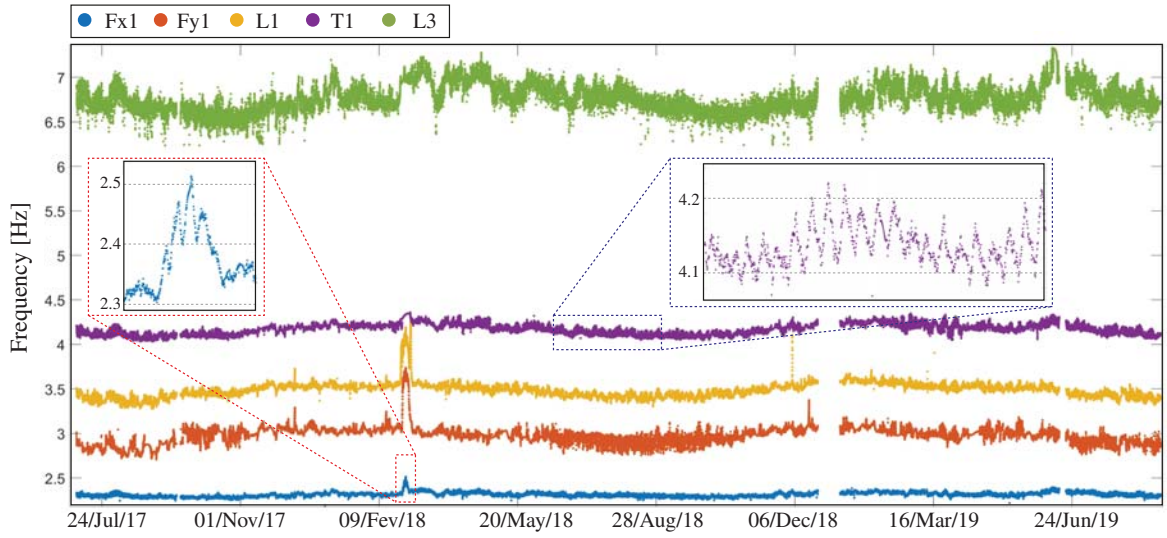

Figure 9: Frequency tracking results of the permanent SHM system installed in the Consoli Palace.

refer to references [13, 19, 10]. It is interesting to note that local sudden increases in the resonant frequencies were found during the time period from February 25$^{\text{th}}$ to March 1$^{\text{st}}$ 2017. Freezing air temperatures were registered during these days, thereby such increases are conceivably due to the formation of ice in the micro porosity of the mortar joints and the consequent stiffening effect.

Figure 10 plots the fundamental frequency versus environmental temperature throughout the training period of one year. In this figure, the presence of freezing conditions is evident in the shape of hasty frequency increases. Moreover, it is noted that the frequency-temperature relationship is not linear, but describes a non-linear behaviour with certain hysteresis. Such a behaviour may be due to the intricate geometry and distribution of volumes of the palace, which presumably originate the presence of complex temperature/humidity gradients throughout the building. In this case, the use of clustering approaches for the discrimination of different environmental regimes becomes imperatives. Specifically, two different GMM models have been investigated, one using 5 clusters in Fig. 10 (a) and a second one only using 2 clusters in Fig. 10 (b). It is noted that the database corresponding to the frequencies under freezing conditions is well captured by both modes. Additionally, it is interesting to note that the GMM model with the largest number of clusters differentiate four clusters in the frequency-temperature hysteresis cycles. Two clusters (cyan and blue) collect the data samples with minimum/maximum temperature values, while two other clusters (green and red) separate the two branches closing the hysteresis cycles. This fact may indicate the existence of distinct cooling and heating mechanisms.

Once the tracked resonant frequencies have been classified into clusters, the outliers elimination algorithm is applied to the database of the training period. Specifically, a percentage of 5% of the data samples with the largest Mahalanobis distances have been eliminated. Additionally, since freezing conditions are only observed in a poorly populated cluster, all the samples corresponding to this cluster have been dismissed. The resulting clean training population has been used to construct the statistical models and so eliminate the effects of environmental factors. Specifically, the GMM model in Fig. 10 (a) has been used to build a four-member PCA model. In all the the sub-models, only 2 PCs have been retained since they sufficed to explain more than

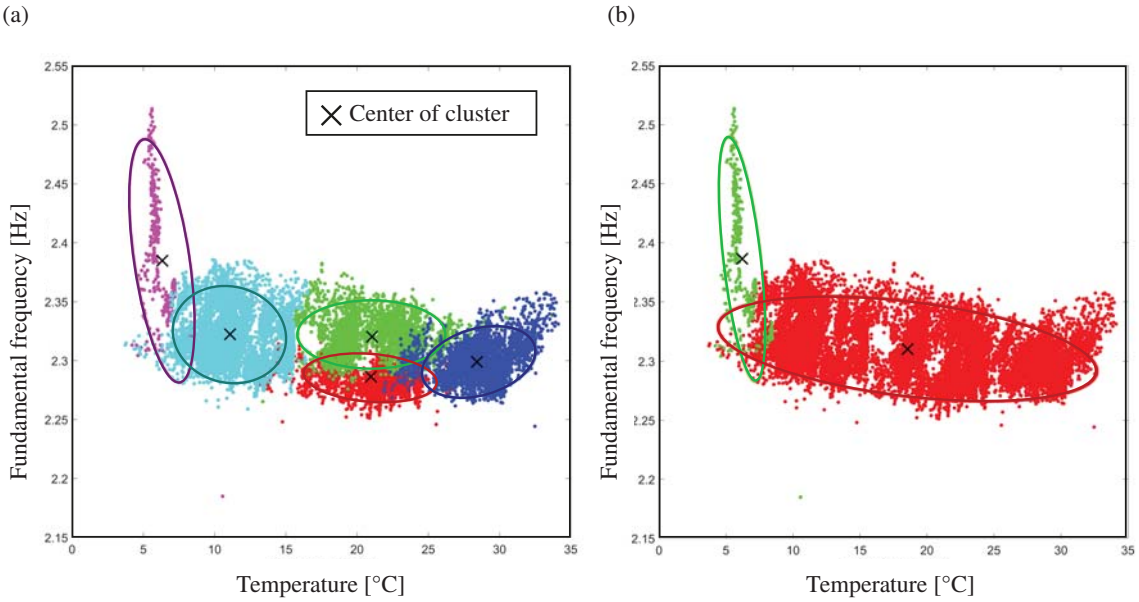

Figure 10: Clustering results of the resonant frequencies of the Consoli Palace using the GMM model considering five clusters (a) and two clusters (b).

95% of the variance of the resonant frequencies of the clusters. On the other hand, for comparison purposes, the GMM model in Fig. 10 (b) has been used to construct an AutoAssociative Neural Network (AANN) [3]. This model is also known as non-linear PCA, and its architecture consists of three hidden layers: mapping, bottleneck, and de-mapping. In this particular work, the mapping, bottleneck, and de-mapping layers have been defined with 5, 3, and 5 neurons, respectively. Hyperbolic tangent sigmoid transfer functions have been selected, and the AANN has been trained using the Levenberg-Marquardt back-propagation method. AANNs have been reported to outperform standard PCA models when dealing with non-linear correlations, so their ability to reproduce the non-linear behaviour observed in Fig. 10 is tested herein by considering the two-cluster GMM model in Fig. 10 (b).

Figures 11 and 12 present the control charts obtained using the PCA and the AANN models, respectively. In these figures, two different cases are analysed, namely the experimentally identified resonant frequencies (undamaged) and a test case including artificial damage. Specifically, the remaining monitoring time after the training period has been divided into three segments, and frequency decays have been applied to the fundamental frequency in the last two segments. The artificial frequency decays have been selected as 0.4% (mild) and 1% (moderate). Additionally, the results obtained using the Hotelling and the MEWMA control charts are also reported. It is noted in all the undamaged cases using the Hotelling's control chart that, although the UCL has been estimated for a confidence level of 95% (5% of outliers), the percentage of outliers is consistently greater than 10% beyond the training period. This fact may indicate limitations of the regression models, frequency tracking errors, or an insufficient training period. Moreover, it is also noticeable that the MEWMA control chart is more sensitive to shifts in the mean values of residuals. Let us focus first on the results obtained with the PCA model in Fig. 11. It is observed that the percentage of outliers in the damaged sections of the Hotelling's control chart goes from 10% and 15.6% (undamaged) to 16% ($\Delta Fx1 = -0.4\%$) and 41.3% ($\Delta Fx1 = -1.0\%$). That is to say, frequency decays of $\Delta Fx1 = -0.4\%$ and $\Delta Fx1 = -1.0\%$ lead to increases in the number of out-of-control samples of 16.0% and 164.74%, respectively. On the other hand, the number of outliers in the damaged sections of the MEWMA control chart

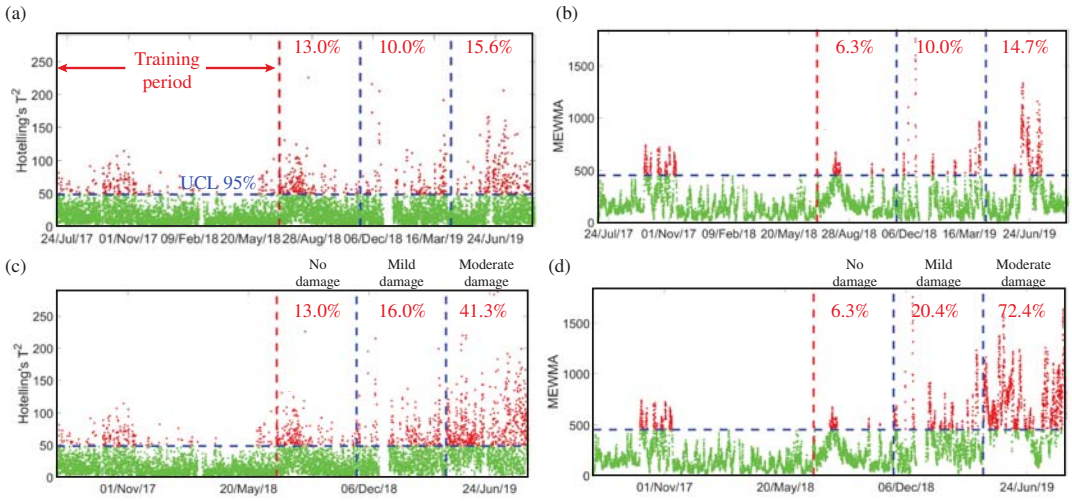

Figure 11: Control charts of the undamaged resonant frequencies of the Consoli Palace (a,b) and considering artificial damages (c,d) using the PCA regression model. The results are obtained using the Hotelling (a,c) and the MEWMA (b,d) control charts ($r = 4$).

goes from 10.0% and 14.7% to 20.4% ($\Delta Fx1 = -0.4\%$) and 72.4% ($\Delta Fx1 = -1.0\%$), that is increases of 104% and 392.517%, respectively. With regard to the results obtained using the AANN model in Fig. 12, it is observed that the number of outliers in the undamaged cases is in general larger that those obtained by the PCA model. This fact may indicate that, despite the superior capability of the AANN model to reproduce non-linear correlations, the consideration of one single cluster for non-freezing conditions may be insufficient. Furthermore, the incorporation of artificial damage in this case leads to increases of -1.89% ($\Delta Fx1 = -0.4\%$) and 219.11% ($\Delta Fx1 = -1.0\%$) in the Hotelling's control chart, and 15.33% ($\Delta Fx1 = -0.4\%$) and 184.43% ($\Delta Fx1 = -1.0\%$) in the MEWMA control chart. Note that even a decrease in the number of outliers is found in the Hotelling's control chart for a mild damage severity. Therefore, it can be concluded that this second model cannot be used to detect early-stage faults, and a larger number of clusters would be necessary to improve its efficiency.

4 CONCLUSIONS

This paper has presented a new semi-supervised two-class pattern classification method for early damage detection of structures. The proposed approach comprises five consecutive steps, including the (i) collection of data samples forming the training period; (ii) clustering analysis using the GMM method; (iii) outliers elimination using the MCD method; (iv) pattern recognition using local Principal Components Analysis; and (v) pattern classification using Hotelling and MEWMA control charts. The effectiveness of the proposed approach has been demonstrated through two different case studies, including a benchmark numerical beam structure and the Consoli Palace in Gubbio (Italy). The presented results and discussion have demonstrated the importance of outliers elimination for the correct statistical analysis of the training population and the construction of statistical models for the elimination of environmental effects. The complex relationships between the resonant frequencies and environmental temperature in the Consoli Palace have highlighted the importance of performing clustering analysis, so that local statistical models can be constructed for the different structural/environmental behaviour regimes.

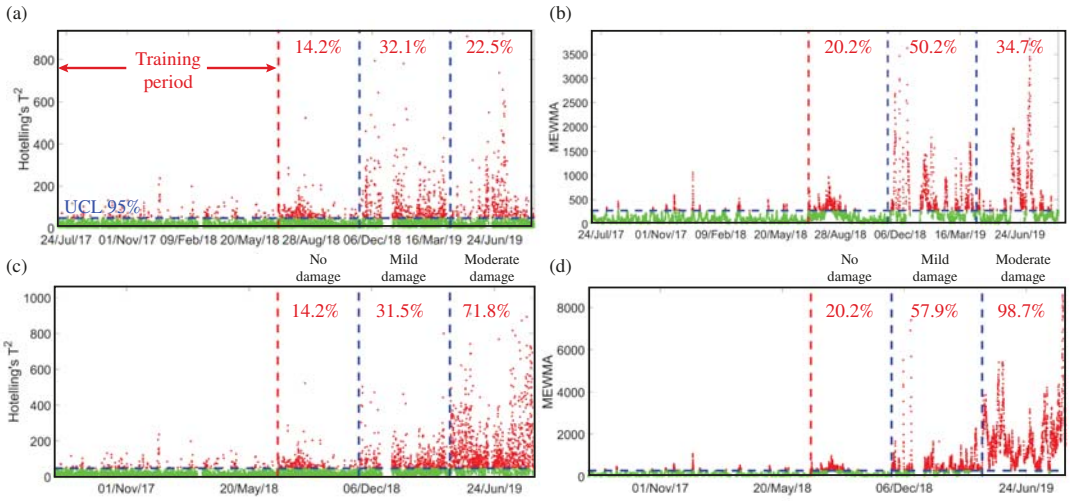

Figure 12: Control charts of the undamaged resonant frequencies of the Consoli Palace (a,b) and considering artificial damages (c,d) using the ANN regression model. The results are obtained using the Hotelling (a,c) and the MEWMA (b,d) control charts ($r = 4$).

ACKNOWLEDGEMENTS

This work was supported by the Italian Ministry of Education, University and Research (MIUR) through the funded Project of Relevant National Interest "DETECT-AGING - Degradation effects on structural safety of cultural heritage constructions through simulation and health monitoring" (protocol no. 201747Y73L).

REFERENCES

[1] C. M. Bishop. *Pattern recognition and machine learning*. springer, 2006.

[2] B. J. A. Costa, F. Magalhães, Á. Cunha, and J. Figueiras. Rehabilitation assessment of a centenary steel bridge based on modal analysis. *Engineering Structures*, 56:260–272, 2013.

[3] C. R. Farrar and K. Worden. *Structural Health Monitoring.: A Machine Learning Perspective*. John Wiley & Sons, 2012.

[4] C. Gentile, M. Guidobaldi, and A. Saisi. One-year dynamic monitoring of a historic tower: damage detection under changing environment. *Meccanica*, 51(11):2873–2889, 2016.

[5] C. Gentile, C. Poggi, A. Ruccolo, and M. Vasic. Vibration-Based Assessment of the Tensile Force in the Tie-Rods of the Milan Cathedral. *International Journal of Architectural Heritage*, pages 1–14, 2019.

[6] H. Hotteling. Multivariate quality control, illustrated by the air testing of sample bombsights. *Techniques of statistical analysis*, pages 111–184, 1947.

[7] W. H. Hu, D. H. Tang, J. Teng, S. Said, and R. Rohrmann. Structural health monitoring of a prestressed concrete bridge based on statistical pattern recognition of continuous dynamic measurements over 14 years. *Sensors*, 18(12):4117, 2018.

[8] M. Hubert, M. Debruyne, and P. J. Rousseeuw. Minimum covariance determinant and extensions. *Wiley Interdisciplinary Reviews: Computational Statistics*, 10(3):e1421, 2018.

[9] S. Ivorra, D. Foti, V. Gallo, V. Vacca, and D. Bru. Bell's dynamic interaction on a reinforced concrete bell tower. *Engineering Structures*, 183:965–975, 2019.

[10] A. Kita, N. Cavalagli, and F. Ubertini. Temperature effects on static and dynamic behavior of Consoli Palace in Gubbio, Italy. *Mechanical Systems and Signal Processing*, 120:180–202, 2019.

[11] J. Kullaa. Distinguishing between sensor fault, structural damage, and environmental or operational effects in structural health monitoring. *Mechanical Systems and Signal Processing*, 25(8):2976–2989, 2011.

[12] C. A. Lowry, W. H. Woodall, C. W. Champ, and S. E. Rigdon. A multivariate exponentially weighted moving average control chart. *Technometrics*, 34(1):46–53, 1992.

[13] F. Magalhães and Á. Cunha. Explaining operational modal analysis with data from an arch bridge. *Mechanical Systems and Signal Processing*, 25(5):1431–1450, 2011.

[14] P. Pachón, R. Castro, E. García-Macías, V. Compan, and E. Puertas. E. Torroja's bridge: Tailored experimental setup for SHM of a historical bridge with a reduced number of sensors. *Engineering Structures*, 162:11–21, 2018.

[15] L. F. Ramos, R. Aguilar, and P. B. Lourenço. Operational modal analysis of historical constructions using commercial wireless platforms. *Structural Health Monitoring*, 10(5):511–521, 2011.

[16] P. J. Rousseeuw and K. V. Driessen. A fast algorithm for the minimum covariance determinant estimator. *Technometrics*, 41(3):212–223, 1999.

[17] W. Soo Lon Wah, Y. T. Chen, G. W. Roberts, and A. Elamin. Separating damage from environmental effects affecting civil structures for near real-time damage detection. *Structural Health Monitoring*, 17(4):850–868, 2018.

[18] F. Ubertini, N. Cavalagli, A. Kita, and G. Comanducci. Assessment of a monumental masonry bell-tower after 2016 Central Italy seismic sequence by long-term SHM. *Bulletin of Earthquake Engineering*, 16(2):775–801, 2018.

[19] F. Ubertini, C. Gentile, and A. L. Materazzi. Automated modal identification in operational conditions and its application to bridges. *Engineering Structures*, 46:264–278, 2013.

[20] W. S. L. Wah, J. S. Owen, Y. T. Chen, A. Elamin, and G. W. Roberts. Removal of masking effect for damage detection of structures. *Engineering Structures*, 183:646–661, 2019.

EURODYN 2020
XI International Conference on Structural Dynamics
M. Papadrakakis, M. Fragiadakis, C. Papadimitriou (eds.)
Athens, Greece, 23–26 November 2020

EFFECT OF NOISE IN THE TIME-FREQUENCY ESTIMATE OF THE PERIDYNAMIC *BOND ELASTIC CONSTANT* PARAMETER

G. Miraglia[1], **R. Ceravolo**[1], **and G. Coletta**[1]

[1] Department of Structural, Geotechnical and Building Engineering, DISEG, Politecnico di Torino, Torino, Italy & Responsible Risk Resilience interdepartmental Centre (R3C), Politecnico di Torino, Torino, Italy
e-mail: gaetano.miraglia@polito.it

{rosario.ceravolo,giorgia.coletta}@polito.it

Keywords: Structural health monitoring, Masonry structures, Peridynamics, Structural features, Gaussian noise.

Abstract. *The Peridynamic (PD) theory is a modern nonlocal (nonlinear, elastic /inelastic, without/with memory) theory able to deal with long-range forces and discontinuity in materials. For this reason the theory is suitable for the monitoring of masonry structures. Starting from a special case of PD formulation, named Bond-Based Peridynamic (BBPD), a feature obtained by the idealization of real systems with BBPD is used for SHM purposes: the bond elastic constant parameter. To characterize the damage (i.e. permanent deterioration of material and/or geometric properties of the systems) occurring in systems idealized with PD models, a joint time-frequency direct estimate of the parameter values is performed using a Short Time Fourier Transform (STFF) of the systems response and the input acceleration at the base of the systems. The method is applied numerically and the effect of noise in the time-frequency evaluation of the parameter values is analyzed. The study concludes that PD can provides simply and strong information on the health of simulated systems, allowing at the same time an easy and scalable parametrization of civil, especially masonry, structures, while the bond elastic constant parameter can be used for the damage characterization, i.e. to detect, quantify and localize the damage in a generic system.*

1 INTRODUCTION

A modern nonlocal theory of continuum established in early 2000 by Stewart Silling [1], [2] and Silling et al. [3], named *Peridynamic* (PD), is recently attracting attention in the field of computational mechanics. The theory replaces the partial differential equations of the classical continuum theory with integral, spatial, equations. This allows to easily overcome problems related to the representation of discontinuities in the matter, which can rise during damage (e.g. cracks), where the differential formulations are not defined. A comprehensive literature review of Peridynamic applications and uses can be found in [4]. Basically, PD theory found its principle in the forces-interaction (*bonds*) of points. The matter is divided in infinitesimal portions characterized by their mass and volume. Each point *k* is then supposed to interact with its neighbours inside a region. The collection of all the points inside this region is named *family* of *k*. The family of *k* is in turn characterized by the *horizon*, i.e. the maximum distance for which the interaction between *k* and the other points of a body occurs. The horizon define the locality of the behaviour of a system; the smaller the horizon the more local the behaviour will be. For further insight on PD theory and its fundamental literature one can refer to the book of Madenci and Oterkus [5].

Despite the huge amount of literature on PD theory and its applications, and the emerging literature on damage simulation in PD, studies on the use of PD theory as a paradigm of SHM are still missing. In particular an interesting field of research in this perspective is the identification of PD model parameters for the damage detection of structural systems, in support to the SHM of the built environment. In this direction, an interesting reference work is the study of Ibrahim [6] on fracture mechanics, which assessed the recent advances of Structural Life Assessment (SLA) and explained the differences between SLA and SHM in PD [4].

On this perspective, the equations of motion written with a special case of PD formulation, the Bond-Based PD (BBPD) [1], reveal a new feature that can be used as control parameter in the monitoring of civil structures. The feature can be extracted thanks to the PD integral equations of motion, which directly relate the internal material state (e.g. internal force field, etc.), with the structural response (e.g. displacements, etc.). This feature is called *bond elastic constant*, and its value should decrease with damage.

In the paper, the method for a direct time-frequency estimate [7], [8], [9] of the values of the bond elastic constant over the joint Time-Frequency (TF) domain is proposed [10] for a single bond, using time-history variables (e.g. displacements, accelerations, etc.) (see Section 2). The method is then demonstrated in Section 3 with numerical simulations on a case study: a single bond is here used to monitor the health of an idealized Single Degree of Freedom (SDOF) system connected to the ground. Conclusions are finally drawn in Section 4.

2 DIRECT TIME-FREQUENCY ESTIMATE OF BOND CONSTANT

The linearized micro-linear viscoelastic BBPD equation of motion can be written in standard form as (bold is herein used for vectors, bold capital for matrices and italic for scalars):

$$\mathbf{M}\ddot{\mathbf{u}}(t) + \mathbf{C}\dot{\mathbf{u}}(t) + \mathbf{K}\mathbf{u}(t) = \mathbf{z}(t)$$

$$\mathbf{M} = \begin{bmatrix} \mathbf{M}_k & \mathbf{O} & \cdots \\ \mathbf{O} & \ddots & \cdots \\ \vdots & \vdots & \ddots \end{bmatrix}; \ \mathbf{C} = \begin{bmatrix} \sum_{\substack{j=1 \\ j\neq k}}^{K} \mathbf{C}_{kj} & -\mathbf{C}_{kj} & \cdots \\ -\mathbf{C}_{kj} & \ddots & \cdots \\ \vdots & \vdots & \ddots \end{bmatrix}; \ \mathbf{K} = \begin{bmatrix} \sum_{\substack{j=1 \\ j\neq k}}^{K} \mathbf{K}_{kj} & -\mathbf{K}_{kj} & \cdots \\ -\mathbf{K}_{kj} & \ddots & \cdots \\ \vdots & \vdots & \ddots \end{bmatrix} \tag{1}$$

where:

$$\begin{gathered}\mathbf{M}_k = m_k \mathbf{I}_3 \\ \mathbf{C}_{kj} = \nu_{kj} \mathbf{K}_{kj} \\ \mathbf{K}_{kj} = c_{kj} V_j V_k \boldsymbol{\Xi}_{kj} \\ \boldsymbol{\Xi}_{kj} = \frac{\boldsymbol{\xi}_{kj} \left(\boldsymbol{\xi}_{kj}{}^{\mathrm{T}}\right)}{\left\|\boldsymbol{\xi}_{kj}\right\|^3} \\ c_{kj} = \begin{cases} c_{kj} \text{ if } \left\|\boldsymbol{\xi}_{kj}\right\| \leq h \\ 0 \text{ if } \left\|\boldsymbol{\xi}_{kj}\right\| > h \end{cases} \\ \boldsymbol{\xi}_{kj} = \mathbf{x}_j - \mathbf{x}_k \end{gathered} \tag{2}$$

In equations (1) and (2) $\mathbf{x}_k = (x_{k,X}, x_{k,Y}, x_{k,Z})^{\mathrm{T}}$ are the coordinates X, Y, Z of point k, c_{kj} is called bond elastic constant, and h is the horizon. V_j and V_k are the volumes associated to the points j and k respectively while ν_{kj} is a bond damping constant; m_k is the mass associated to the point k, $\mathbf{I}_3$ is a 3x3 identity matrix and $\mathbf{O}$ is a 3x3 zero matrix. K is the number of points used to discretize the system. Finally, $\mathbf{u}(t)$ and $\mathbf{z}(t)$ denote the displacement vector and the external force vector respectively, being t the time variable.

The linearized equations of motions can be written in expanded form for each point k as:

$$\begin{gathered}\sum_{\substack{j=1 \\ j \neq k}}^{K} \left[c_{kj} \left(\frac{V_j V_k}{m_k} \frac{\left(\boldsymbol{\xi}_{kj} \left(\boldsymbol{\xi}_{kj}{}^{\mathrm{T}}\right)\right)}{\left\|\boldsymbol{\xi}_{kj}\right\|^3} \boldsymbol{\eta}_{kj} + \nu_{kj} \frac{V_j V_k}{m_k} \frac{\left(\boldsymbol{\xi}_{kj} \left(\boldsymbol{\xi}_{kj}{}^{\mathrm{T}}\right)\right)}{\left\|\boldsymbol{\xi}_{kj}\right\|^3} \dot{\boldsymbol{\eta}}_{kj} \right) \right] = \mathbf{n}_{k,e}(t) \\ \mathbf{n}_{k,e}(t) = -\mathbf{a}_k(t) + \ddot{\mathbf{u}}_k(t) \\ \boldsymbol{\eta}_{kj} = \mathbf{u}_j(t) - \mathbf{u}_k(t) \end{gathered} \tag{3}$$

where $\mathbf{u}_j(t)$ and $\mathbf{u}_k(t)$ are the coordinates X, Y, Z of displacement at point j and k, while $\mathbf{a}_k(t)$ are the coordinates X, Y, Z of the external acceleration at point k. If we write the equations (3) for two points (the first representing the ground and the second representing a SDOF) relativized with respect the response of the first point, we have:

$$c_{21} \left(\frac{V_1 V_2}{m_2} \frac{\left(\boldsymbol{\xi}_{21} \left(\boldsymbol{\xi}_{21}{}^{\mathrm{T}}\right)\right)}{\|\boldsymbol{\xi}_{21}\|^3} \boldsymbol{\eta}_{21} + \nu_{21} \frac{V_1 V_2}{m_2} \frac{\left(\boldsymbol{\xi}_{21} \left(\boldsymbol{\xi}_{21}{}^{\mathrm{T}}\right)\right)}{\|\boldsymbol{\xi}_{21}\|^3} \dot{\boldsymbol{\eta}}_{21} \right) = -\ddot{\mathbf{u}}_1(t) + \ddot{\mathbf{u}}_2(t) \tag{4}$$

In the assumption of all the geometrical quantities known and supposing to know the mass and damping term, we can estimate the time-frequency values of the bond elastic constant as:

$$\begin{gathered} c_{21,d}(f,t) = \frac{\mathrm{T}_{Re}\left(n_{21,d}(t)\right) \mathrm{T}_{Re}\left(n_{2,e,d}(t)\right) + \mathrm{T}_{Im}\left(n_{21,d}(t)\right) \mathrm{T}_{Im}\left(n_{2,e,d}(t)\right)}{\mathrm{T}_{Re}\left(n_{21,d}(t)\right)^2 + \mathrm{T}_{Im}\left(n_{21,d}(t)\right)^2} \\ \mathbf{n}_{21}(t) = \frac{V_1 V_2}{m_2} \frac{\left(\boldsymbol{\xi}_{21} \left(\boldsymbol{\xi}_{21}{}^{\mathrm{T}}\right)\right)}{\|\boldsymbol{\xi}_{21}\|^3} \boldsymbol{\eta}_{21} + \nu_{21} \frac{V_1 V_2}{m_2} \frac{\left(\boldsymbol{\xi}_{21} \left(\boldsymbol{\xi}_{21}{}^{\mathrm{T}}\right)\right)}{\|\boldsymbol{\xi}_{21}\|^3} \dot{\boldsymbol{\eta}}_{21} \\ \mathbf{n}_{2,e}(t) = -\ddot{\mathbf{u}}_1(t) + \ddot{\mathbf{u}}_2(t) \end{gathered} \tag{5}$$

where $c_{21,d}(f,t)$ is the time-frequency estimate of the bond elastic constant obtained with the observations along the direction d (i.e. X, Y, or Z) and the real and imaginary parts of the assumed linear Time-frequency Distribution (TFD), $T_{Re}()$ and $T_{Im}()$, respectively.

3 NUMERICAL APPLICATION

In order to study the effect of noise on the identification of the bond elastic constant, this section demonstrates the identification procedure reported in Section 2 applied on signals corrupted by adding to the original signals, the 7% of uncorrelated random time-histories extracted from Gaussian distributions having the same variance of the uncorrupted signals. The east-west record of the Loma-Prieta earthquake of the October 17, 1989 in the Santa Cruz Mountains (https://it.mathworks.com/help/matlab/matlab_prog/loma-prieta-earthquake.html, sampled at 200 Hz, has been used as input acceleration applied to the assumed SDOF, which was simulated numerically in this section. For the simulation, the following values were assumed:

- $\mathbf{x}_1=(0,0,0)^T$ m;
- $\mathbf{x}_2=(1,0,0)^T$ m;
- $V_1=V_2=1$ m^3;
- $m_2=1$ kg;
- $\nu_{21}=0.0036$ s.

Then, in order to simulate the occurrence of a low level of damage, potentially mistaken for noise in signals, the bond elastic constant has been reduced of a 0.002% each time instant, starting from 16.23 s up to 17.23 s, bringing to a total reduction of about 9.52% in 1 second (corresponding to a reduction in the value of the natural frequency of 4.88%). Figure 1 depicts the imposed acceleration at the base of the SDOF and the acceleration response of the SDOF, while Table 1 reports the reference values of bond elastic constant before and after the application of damage. The explicit forward-backward Euler time integration algorithm has been used to solve the nonlinear dynamic analysis, as suggested by [5].

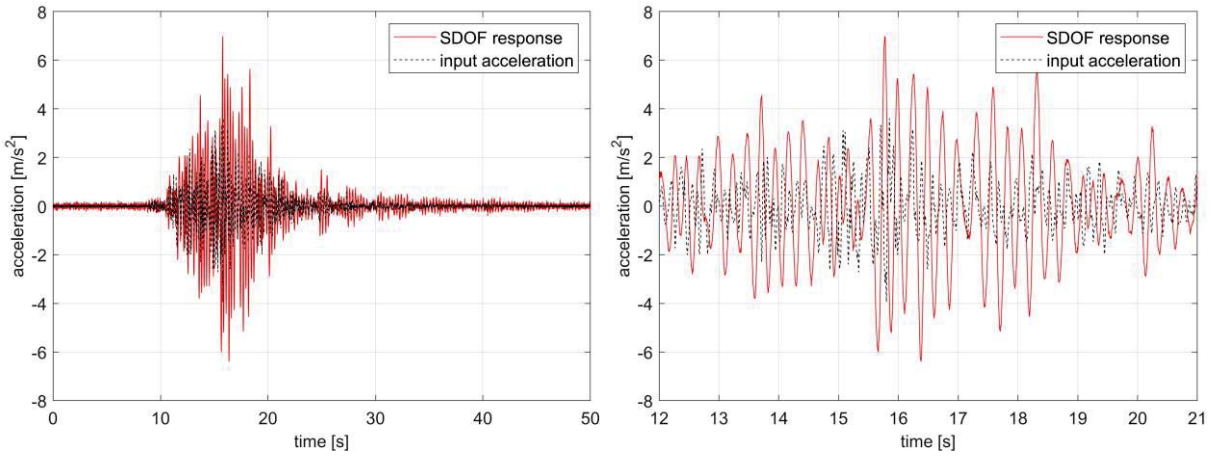

Figure 1: Accelerations obtained from the simulation (left) and zoom of the signals between 12 and 21 s (right).

c_{21} [N/m^6] before damage	c_{21} [N/m^6] after damage
636	575.462

Table 1: Reference values of bond elastic constant before and after the application of damage.

After having simulated the system, the identification procedure described in Section 2 has been applied. The TFD were calculated with a STFT using a periodic Hanning window over 128 points. The following page focuses on the discussion of the results of the procedure.

Figure 2 depicts the estimated bond elastic constant in the case of signals corrupted by 7% of uncorrelated Gaussian noise functions. From the figure is possible to conclude as the parameter estimate is mostly corrupted for joint time-frequency values that are not excited enough. This results is quite interesting because shows as the time-frequency estimate may be used as a tool to identify a time-frequency subdomain that brings the higher quantity of information in the reproduction of a specific signal. In particular, the high frequency values bring to overestimate the true values of the parameters, while the low frequencies bring to underestimate the true c_{21}. Then, it is worth noting that because very high and very low values of the bond elastic constant are associated to low values of probability, the definition of the time-frequency subdomain containing the higher quantity of information is also possible in case of lack of information on the real values of c_{kj}. From Figure 2 it is also possible to note as the estimated values of c_{21} in the area of high information content are almost close to the reference values reported in Table 1, also in case of corrupted signals.

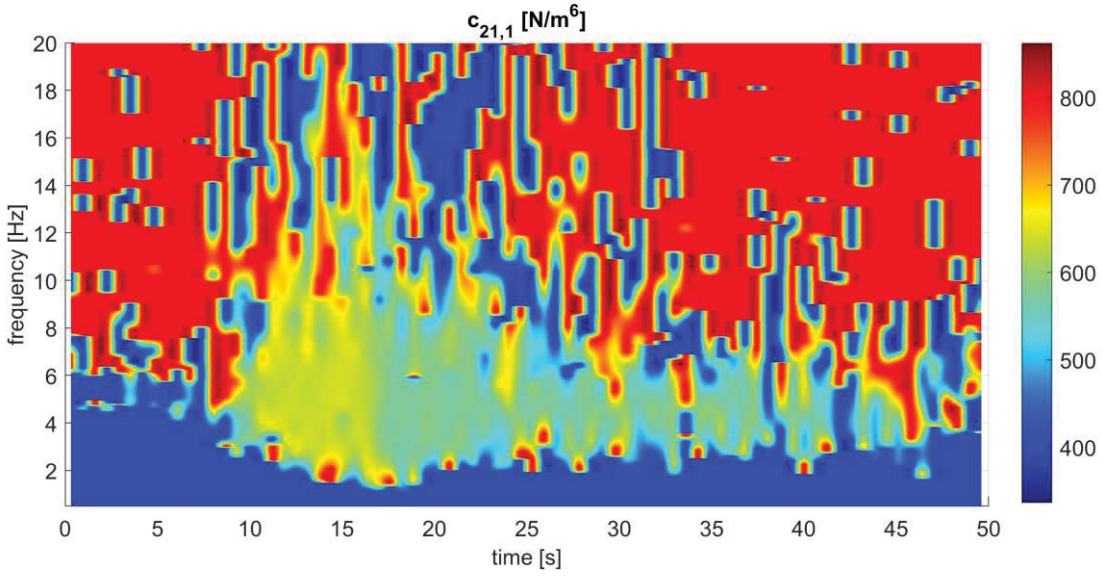

Figure 2: Time-frequency estimate of the bond elastic constant value.

4 CONCLUSIONS

Peridynamic can provides simply and strong information on the health of simulated systems. In the paper, a method to identify the *bond elastic constant* parameter of PD, over the time-frequency domain, has been proposed. The method has been demonstrated numerically on a nonlinear SDOF, whose simulated records has been corrupted by noise. The main results of the analysis are reported hereinafter:

- The method was able to estimate a correct parameter value also in presence of corrupted signals;
- The time-frequency estimate of the parameter reveals the definition of a time-frequency subdomain where the higher quantity of information for a system is located, making its use a potential instrument to define, for example, time-frequency filters specific for a given system.

Finally, it is worth mentioning that given the original aim of PD theory (emulating discontinuities and long-range forces in materials), masonry structures could greatly benefit from this PD idealization, as they are incline to crack under strong external actions, such as those ones due to earthquake.

REFERENCES

[1] S. A. Silling, "Reformulation of elasticity theory for discontinuities and long-range forces," *J. Mech. Phys. Solids*, vol. 48, no. 1, pp. 175–209, 2000.

[2] S. A. Silling, "Peridynamic modeling of the Kalthoff--Winkler experiment," *Submiss. 2001 Sandia Prize Comput. Sci.*, 2001.

[3] S. A. Silling, M. Epton, O. Weckner, J. Xu, and E. Askari, "Peridynamic states and constitutive modeling," *J. Elast.*, vol. 88, no. 2, pp. 151–184, 2007.

[4] A. Javili, R. Morasata, E. Oterkus, and S. Oterkus, "Peridynamics review," *Math. Mech. Solids*, vol. 24, no. 11, pp. 3714–3739, 2019.

[5] E. Madenci and E. Oterkus, *Peridynamic theory and its applications*, vol. 17. Springer, 2014.

[6] R. A. Ibrahim, "Recent advances of structural life assessment and related problems," in *Structural Nonlinear Dynamics and Diagnosis*, Springer, 2015, pp. 1–27.

[7] R. Ceravolo, G. V. Demarie, and S. Erlicher, "Instantaneous identification of degrading hysteretic oscillators under earthquake excitation," *Struct. Heal. Monit.*, 2010, doi: 10.1177/1475921710368202.

[8] R. Ceravolo, S. Erlicher, and L. Z. Fragonara, "Comparison of restoring force models for the identification of structures with hysteresis and degradation," *J. Sound Vib.*, vol. 332, no. 26, pp. 6982–6999, 2013.

[9] O. S. Bursi, R. Ceravolo, S. Erlicher, and L. Zanotti Fragonara, "Identification of the hysteretic behaviour of a partial-strength steel--concrete moment-resisting frame structure subject to pseudodynamic tests," *Earthq. Eng. Struct. Dyn.*, vol. 41, no. 14, pp. 1883–1903, 2012.

[10] G. Miraglia, E. Lenticchia, S. Cecilia, and R. Ceravolo, "Seismic Damage Identification by Fitting the Nonlinear and Hysteretic Dynamic Response of Monitored Buildings," *J. Civ. Struct. Heal. Monit.*, vol. 0, no. 0, p. 0, 2020.

EURODYN 2020
XI International Conference on Structural Dynamics
M. Papadrakakis, M. Fragiadakis, C. Papadimitriou (eds.)
Athens, Greece, 23–26 November 2020

DYNAMIC MODELLING OF TRAM-INDUCED VIBRATION ON THE TEMPLE OF MINERVA MEDICA IN ROME

Fernando Saitta[1], Sara Forliti[2], Alessandro Colucci[2], Angelo Tatì[2] and Ivan Roselli[2]

[1] ENEA, CR Casaccia
Via Anguillarese 301, 00123 Rome, Italy
e-mail: fernando.saitta@enea.it

[2] ENEA, CR Casaccia
Via Anguillarese 301, 00123 Rome, Italy
{sara.forliti,alessandro.colucci,angelo.tati,ivan.roselli}@enea.it

Keywords: Traffic-induced vibration, Historical constructions, Non-stationary processes.

Abstract. *The passage of trams in urban areas is a source of cyclic vibration which can induce damages in buildings close to the track. This aspect is even more relevant in the case of historical buildings and monuments because of their intrinsic fragility and the importance of preserving them as unaltered as possible for the next generations. In this framework, the purpose of this paper is the development of a mathematical modelling, based on experimental measurements, for the numerical simulation of vibration due to tram passages close to the so-called temple of Minerva Medica in Rome. The vibration signals were recorded at some points on ground level and on the structure by the use of GPS synchronized seismographs equipped with triaxial velocimeters. By means of spectral analysis of the acquired data, time windows associated to each tram passage have been assumed as stochastic nonstationary processes characterized in terms of energy and dominant frequencies by an evolutionary power spectral density. The signals acquired at different points due to the same passage define a multivariate process. The model would like to allow the simulation of the input at the base of the monument and the evaluation, through finite element analysis, of the exposure of the structure to cyclic stresses under different amplitudes highlighting the probability and location of damages in time.*

1 INTRODUCTION

Existing monuments in urban areas are subjected to more and more vibration cycles related to the increase in traffic of the last decades. Vibrations induce stresses which could lead to accumulation of micro-damages in time. Therefore, the exposure for a long time of such structures to cyclic loads could be dangerous in the perspective of their conservation.

In this paper a method is presented for the simulation of vibration induced by tram passages near a monument, in order to evaluate the load cycles on the structure, resorting to stochastic dynamics and experimental measurements. In more detail, a relevant case study, the so-called Temple of Minerva Medica in Rome, probably a nymphaeum of an extra-urban residence, was chosen for its peculiarities, i.e. the closeness with tramways, as well as with the main Rome's railway station. The monument was the subject of many studies for its dynamic characterization, before ([1],[2]) and after [3]-[7] the last major rehabilitation intervention that was carried out in 2012-2013. In [7] it was found a much higher effect of the tram passages in the close road with respect to that of the railway trains, whose vibration is more damped. In this context, the recent vibration measures on soil and structure where used to define the model. At each tram passage the acquired time histories in many points served to derive evolutionary spectral densities of the non-stationary processes. The method proposed in [8] is adopted, which in turn integrates the theory of evolutionary processes due to Priestley [9]. In the proposed approach the simulation procedure is particularized to multivariate processes, as was done for stationary cases in [10].

2 THE TEMPLE OF MINERVA MEDICA IN ROME

The temple (Fig. 1) was erected in the 4th century and today is close to the main railway station in Rome. The main chamber is decagonal with a diameter of 25 m and height of about 24 m (originally 32 m, after partial collapse of the dome). Openings are present in the chamber walls at the first level, whereas at the base there are nine apses and the main entrance.

Figure 1: View from South of the Temple of Minerva Medica. The two tramways can be seen (bottom left).

The structure was initially built in *opus latericium*, which was a common construction technique of that time, based on the use of Roman bricks and mortar. As the building started presenting structural problems, in the following centuries the construction was restored and

reinforced. In this context, interventions in *opus mixtum* of tuff bricks and Roman bricks were carried out. In particular, most niches were closed and some walls with the function of buttresses were added on the southeast side of the monument, which testify that a certain structural weakness of this part already arose in ancient times. Also, some major restoration interventions were carried out in the past. In 1846 first floor arcade of the southeast side was reconstructed, while the upper floor arcade of the southeast side was reconstructed in the years 2012-2013.

Close to the building there is the main roman railway station. In addition, the tramways are very close to the South-West side of the building and the effect of tram passages has been shown to be more dangerous for the monument than that of the railway.

3 DYNAMIC MODELLING OF TRAM PASSAGES

3.1 Experimental measurements of vibrations

Several velocity time histories were acquired in different measurement campaigns, in many points on soil and structure. Herein, only data acquired in July 2019 were used. Moreover, only tri-axial signals in point P (Fig. 2) at the base are considered with the purpose of the procedure set-up.

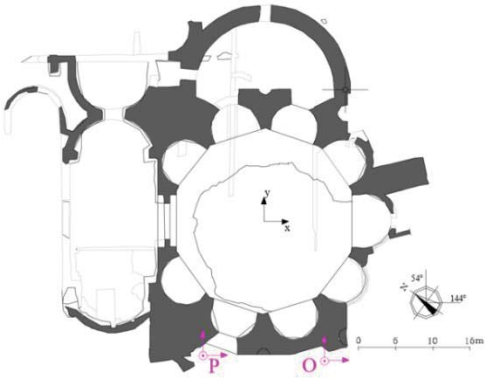

Figure 2: Acquisition points at the base of the structure.

3.2 Mean time arrivals of tram

The simulation of train arrivals in each direction can be obtained by means of a Poisson distribution with parameter λ, defined as follows:

$$p(N,t) = \frac{e^{-\lambda t}(\lambda t)^N}{N!} \tag{1}$$

By means of the data collected in about three hours of experimental measurements, the parameter λ =0.0029 s^{-1} was estimated during day.

3.3 Spectral representation of each passage event

Time histories acquired for 30 passages, 15 per each direction, were used for the definition of evolutionary spectral densities. In more detail, in this initial study the three components recorded in only one point at the base of the structure have been used. In addition, only one direction of tram movement is considered.

Short-time Fourier Transform (SFT) with a window-squared function *h(t)* was adopted [8]:

$$f(t,\omega) = \int_{-\infty}^{\infty} x(\tau)h(t-\tau)e^{-i\omega\tau}d\tau \tag{2}$$

The evolutionary spectral densities have been estimated as follows:

$$S_{x_i x_j}(t,\omega) = E[\int_{-\infty}^{\infty}\int_{-\infty}^{\infty} x_i(\tau_1)x_j^*(\tau_2)h(t-\tau_1)h(t-\tau_2)e^{-i\omega\tau_1}e^{i\omega\tau_2}d\tau_1 d\tau_2] \quad (3)$$

in which $x_i(t)$ and $x_j(t)$ are two signals recorded in different points in space or simply two components at the same points. In this preliminary work only the three components at one point are considered. Therefore spectral density matrix is defined as $\mathbf{S}(t,\omega)=S_{x_i x_j}(t,\omega)$ (i,j=1,..,3). The cross spectra are complex quantities. However, $\boldsymbol{S}$ is Hermitian, so the eigenvalues are real.

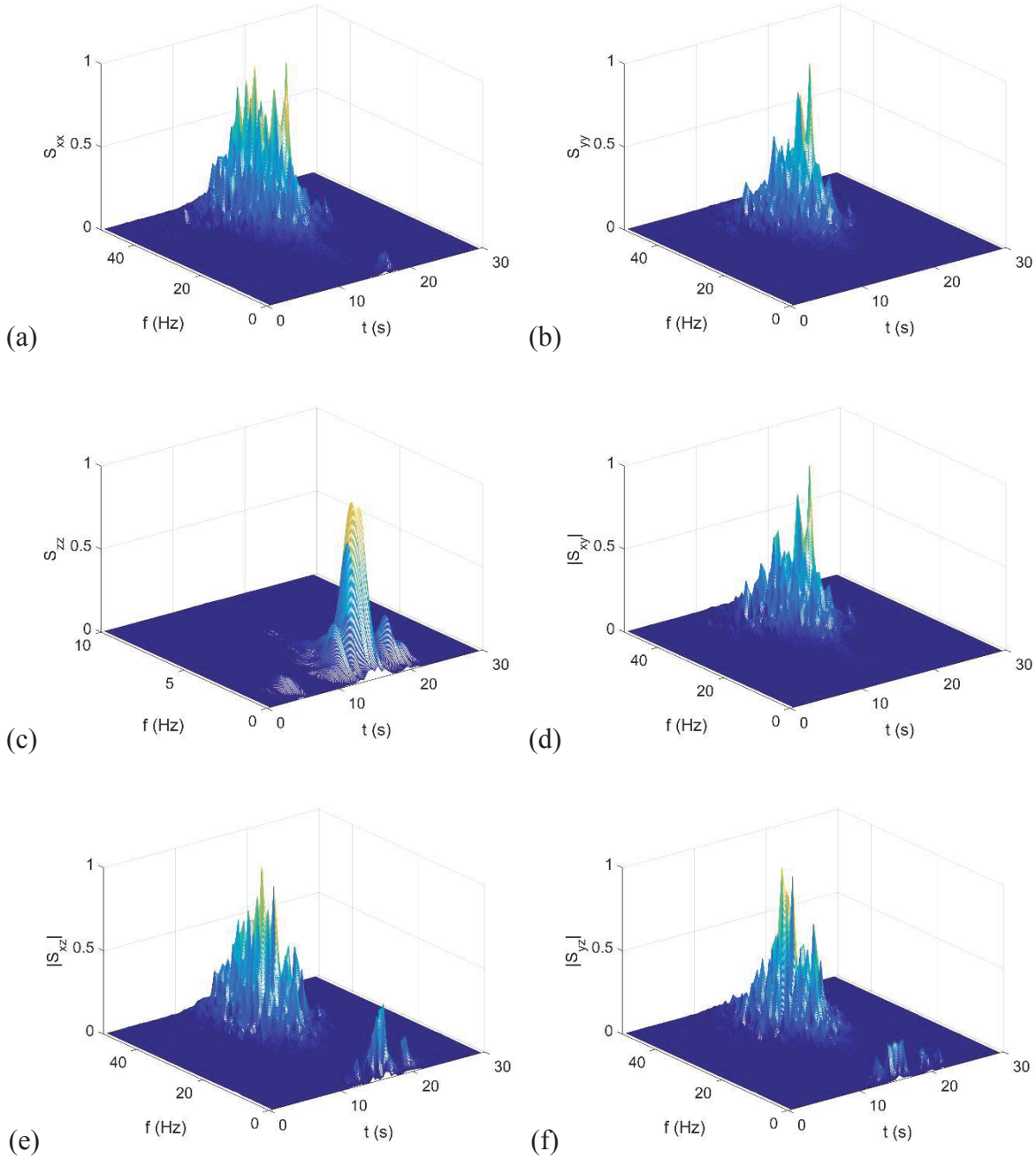

Figure 3: Normalized evolutionary spectral densities, direct (a)-(c) and absolute value of the cross-spectra (d)-(f).

Figs. 3a-f show the obtained spectra, normalized to have unitary maximum amplitude. In the case of cross-spectra which are complex, the absolute value is reported. In addition, the frequency f=$\omega/2\pi$ is considered. Horizontal components present the major energy content at high frequency values, in the range 20-45 Hz, whereas the vertical component has relevant amplitudes for frequencies lower than 5 Hz.

3.4 Simulation

The simulation is performed in the framework of stochastic multivariate processes. In analogy with stationary cases [10], according to [8], with some modification to take into account that eigenvectors are complex, the following simulation formula can be applied:

$$\boldsymbol{x(t)} = \sum_{j=1}^{3} \boldsymbol{X_j(t)} \tag{4}$$

$$\boldsymbol{X_j(t)} = \boldsymbol{2\sum_{k=1}^{N} \mathrm{Re}\left[\psi_j(\omega_k, t)\right] \sqrt{\Lambda_j(\omega_k, t)\Delta\omega} \left[\cos\left(R_{kj}^{(j)}\omega_k t\right) - \sin\left(I_{kj}^{(j)}\omega_k t\right)\right]} \tag{5}$$

Given that $\boldsymbol{S}$ is Hermitian, its eigenvalues are real and eigenvectors respect the following equations: $\boldsymbol{\Psi^* S \Psi = \Lambda}$ and $\boldsymbol{\Psi^* \Psi = I}$. In the previous equations $\boldsymbol{I}$ denotes the identity matrix, the asterisk denotes the transpose and conjugate of the matrix, $\boldsymbol{\Psi}$ is the matrix whose columns are the complex eigenvectors of $\boldsymbol{S}$, and $\boldsymbol{\Lambda}$ is the diagonal matrix of real eigenvalues.

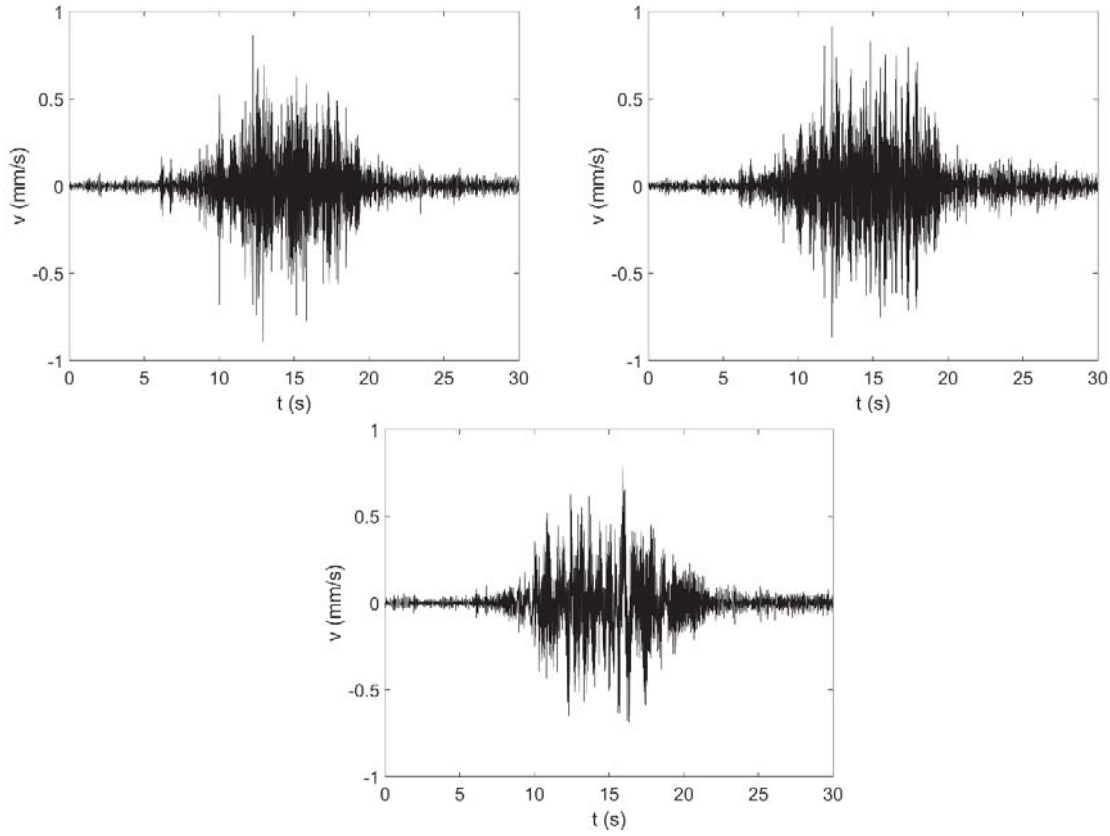

Figure 4: Time histories at one measurement point for one tram passage.

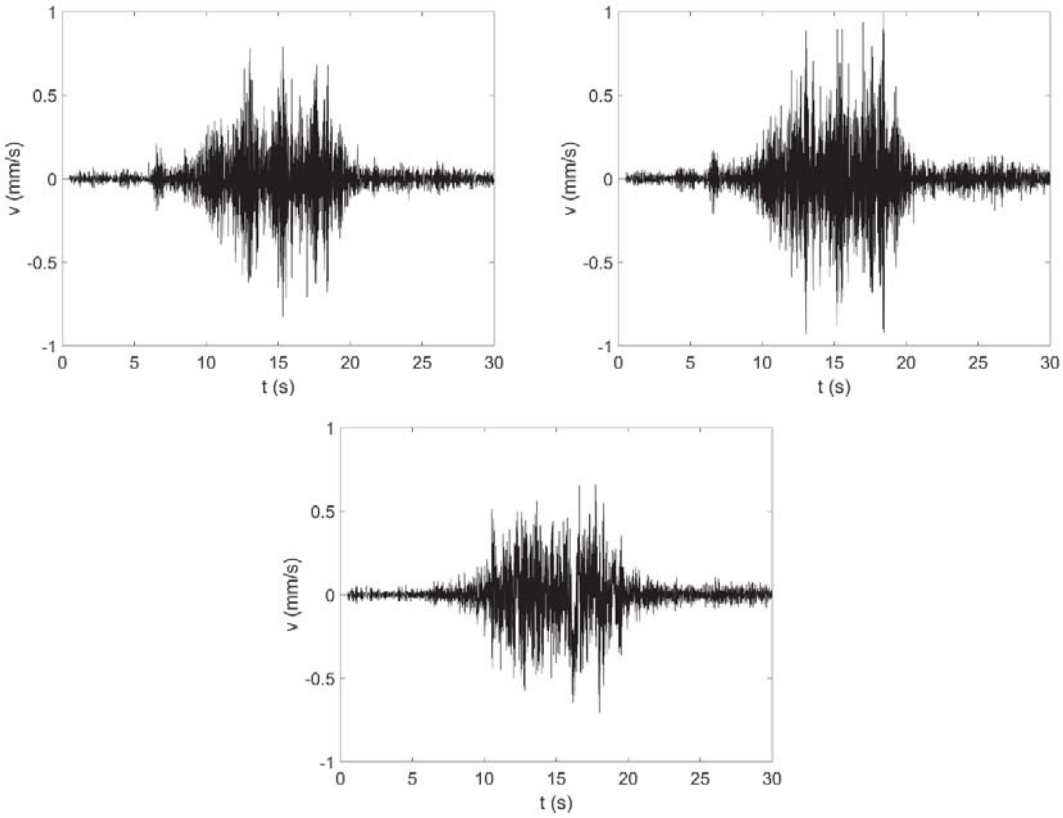

Figure 5: Simulated three-component time history.

Figs. 4 show the time histories acquired at point P of Fig. 2 in one passage event. Figs. 5 show the simulated time histories, which take into account the frequency content and time evolution obtained from 15 tram passages.

4 FINITE ELEMENT MODEL AND STRESS SIMULATION

A finite element model has been developed in Midas Gen code (Fig. 6). The geometry of the monument was largely deduced by laser scanning technique.

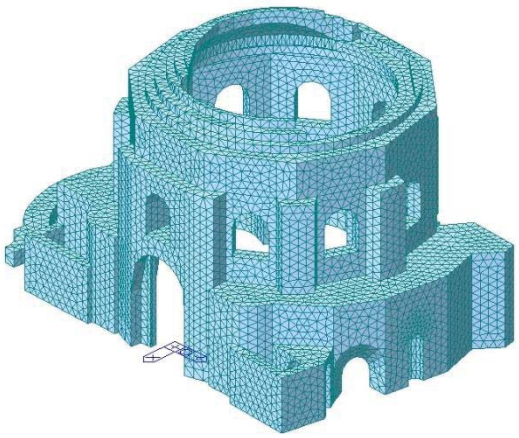

Figure 6: View of the model.

From the initial point cloud, horizontal sections of the monument were obtained and used as

reference to define the volume. 72980 solid elements were used for meshing. The material has been modeled as homogeneous and isotropic with the following parameters: unit weight of 18 kN/m^3, Poisson ratio of 0.2 and 744 MPa of Young modulus. The material properties were calibrated through model updating according to the frequencies obtained through experimental results of ambient vibration testing of the monument [3]. Figs. 7 show the first two modal shapes (f_1=2.070 Hz and f_2=2.392 Hz).

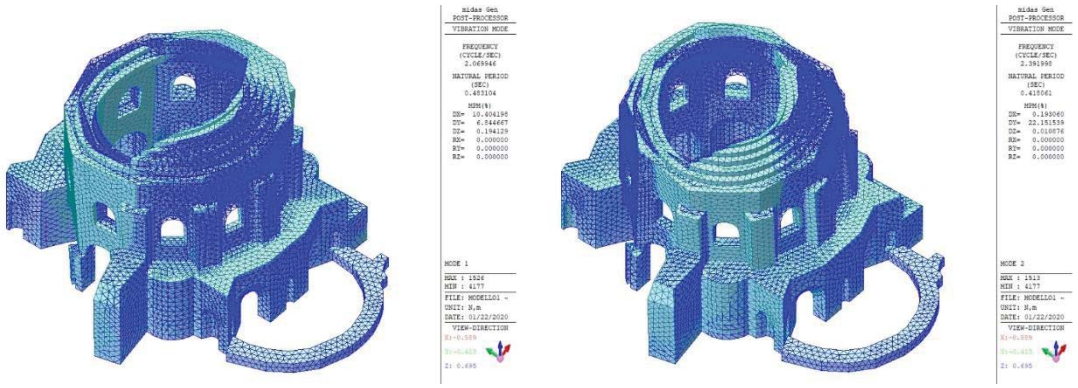

Figure 7: First two modal shapes.

The model has been excited by means of base acceleration obtained by derivative of the simulated time histories of velocity. In order to reduce the order of the model, Ritz vectors were used considering accelerations in three orthogonal directions. Modes up to frequency of about 70 Hz were retained to well describe the spectra content.

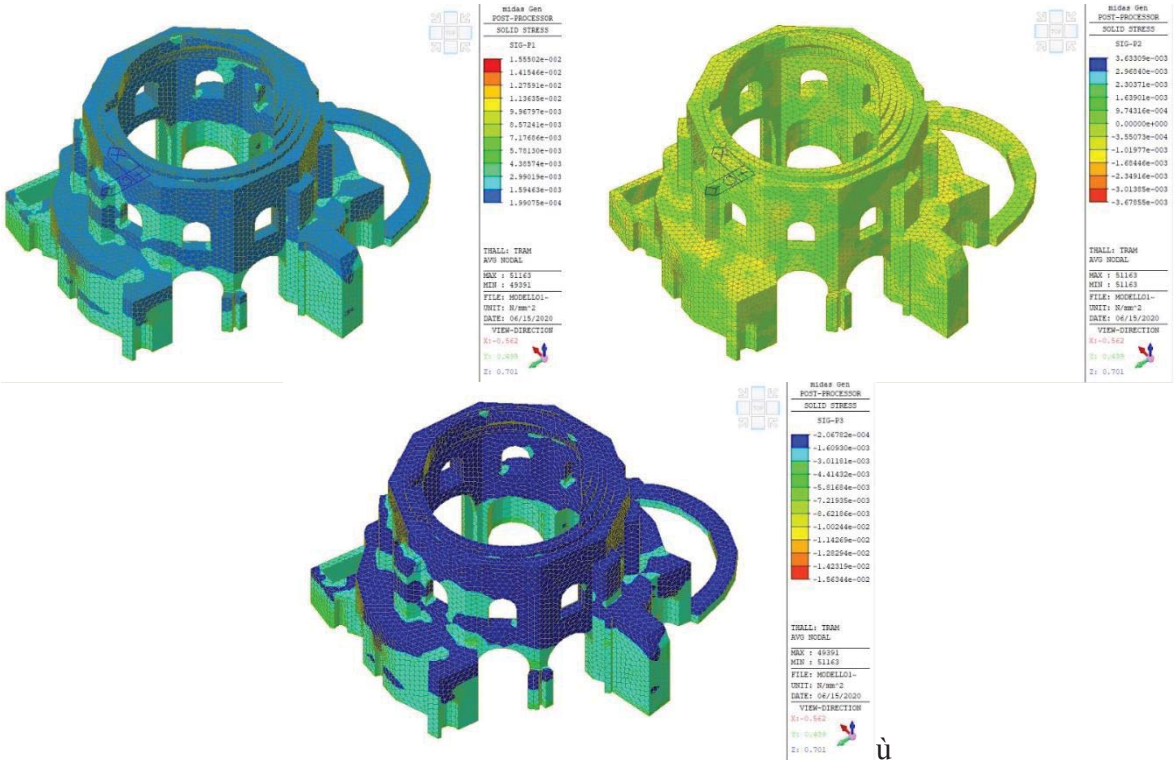

Figure 8: Principal stresses under simulated time accelerations.

Figs. 8 show the principal stresses evaluated on the structure. This preliminary model will be improved considering more than one measurement point to capture the effect of the distance from the tramway and evaluate stresses with a multi-point base input.

5 CONCLUSIONS

A procedure for modelling the vibration due to train passages in the proximity of monuments is proposed in this paper. Resorting to stochastic dynamics, evolutionary spectral densities of each passage event can be defined for each measurement point, as well as the mean time arrival of trams. In this way, time histories of velocities are simulated reflecting time evolution and frequency content of the measure data. In this work the method is applied for data recorded at the base of the Temple of Minerva Medica in Rome. Only one tramway, the closest to the monument, with trams passing in North-West direction, is considered as a preliminary study, defining the mean time arrival of the trains, as well as the evolutionary spectra. Simulation of triaxial velocities in one point is proposed as well as the stress evaluation on the structure. The work would be completed considering more measurement points on the soil, so to have different distances from the tramway and the possibility of simulating a multi-point input on the structure. In this way, load cycles could be evaluated highlighting the portions of the structure much prone to damages.

REFERENCES

[1] P. Clemente, D. Rinaldis, G. Bongiovanni, Dynamic characterization of the 'Tempio della Minerva Medica', *Proceedings of the 10th European Conference on Earthquake Engineering*, 1994.

[2] P. Clemente, Traffic Induced Vibration on Structures, *IABSE Symposium*, San Francisco, 1997.

[3] I. Roselli, V. Fioriti, G. De Canio, Use of the transmissibility function H for ambient vibration measurements of an archeological building, *Proceedings of 2018 IEEE International Conference of Metrology for Archaeology and cultural heritage (MetroArchaeo2018)*, 2018.

[4] V. Fioriti, I. Roselli, G. De Canio, Frequency Domain Analysis of the Minerva Medica Temple by means of the Motion Magnification Methodology, *Proceedings of 2018 IEEE International Conference of Metrology for Archaeology and cultural heritage (MetroArchaeo2018)*, 2018.

[5] I. Roselli, A. Tatì, V. Fioriti, I. Bellagamba, I., M. Mongelli, R. Romano, G. De Canio, M. Barbera, M. Magnani Cianetti, Integrated approach to structural diagnosis by non-destructive techniques: the case of the temple of Minerva Medica, *ACTA IMEKO* 7(3), 13-19, 2018.

[6] I. Roselli, V. Fioriti, M. Mongelli, I. Bellagamba e G. De Canio, Mutual Validation between different Modal Analysis Techniques for Dynamic Identification of the so-called Temple of Minerva Medica, *IOP Conf. Series: Materials Science and Engineering*, 2018.

[7] I. Roselli, V. Fioriti,. I. Bellagamba, M. Mongelli, A. Tatì, M. Barbera, M., Magnani Cianetti, G. De Canio, Urban transport vibrations and cultural heritage sites in Rome: the

cases of the temple of Minerva Medica and of the Catacomb of Priscilla, *WIT Transactions on Ecology and the Environment* 223, 335-343, 2017.

[8] J. Liang, S.R. Chaudhuri, M. Shinozuka, Simulation of Nonstationary Stochastic Processes by Spectral Representation, *Journal of Engineering Mechanics*, 133(6), 616-627, 2007.

[9] M.B. Priestley, Evolutionary Spectra and Non stationary Processes, *J. R. Stat. Soc. Ser. B (Methodol.)*, 27, 204–237, 1965.

[10] M. Di Paola, I. Gullo, Digital generation of multivariate wind field processes, *Probabilistic Engineering Mechanics*, 16, 1-10, 2001.

EURODYN 2020
XI International Conference on Structural Dynamics
M. Papadrakakis, M. Fragiadakis, C. Papadimitriou (eds.)
Athens, Greece, 23–26 November 2020

ENHANCED CONTINUOUS DYNAMIC MONITORING OF A COMPLEX MONUMENTAL PALACE THROUGH A LARGER SENSOR NETWORK

Alban Kita[1], Ilaria Venanzi[1], Nicola Cavalagli[1], Enrique Garcia Macías[1], Filippo Ubertini[1]

[1]Department of Civil and Environmental Engineering, University of Perugia
Via G. Duranti, 93, 06125, Perugia, Italy
{alban.kita, ilaria.venanzi, nicola.cavalagli, enrique.garciamacias, filippo.ubertini}@unipg.it

Keywords: Architectural heritage, Seismic assessment, Dynamic monitoring, Damage detection, Preventive conservation.

Abstract. *After recent seismic events in Italy (Umbria-Marche 1997, L'Aquila 2009, Emilia 2012, Central Italy seismic sequence 2016), there has been a growing scientific interest on the preventive conservation of historic monumental buildings. In this regards, vibration-based low-cost and non-destructive Structural Health Monitoring (SHM) systems provide very useful information on the structural behavior. This information includes both global and local mechanisms and results in more accurate seismic assessments and effective retrofits, also allowing detection of small structural damages developing after far-field earthquakes.*

This paper presents the ongoing research activities regarding the SHM of the Consoli Palace in Gubbio, Italy. A simple and low-cost mixed static-dynamic long-term SHM system has been active since July 2017 with the main purpose of detecting damage-induced anomalies in the time series of the amplitudes of the two major cracks existing in the building and the variation of natural frequencies of global and local vibration modes. The system comprised two crack meters, two temperature sensors and three high sensitivity accelerometers, the latter finalized at the continuous modal identification and modal tracking of the building for damage detection purposes through statistical process control tools. Recently, the SHM system has been integrated with additional sensors, and now comprises 12 accelerometers on three levels of the palace that allow a more detailed detection of the possible vibration modes' variations, 4 crack meters to monitor the openings of two additional cracks and 4 thermocouples to more accurately remove thermal effects by accounting for the effects of the different solar radiation on the buildings' façades. The paper presents preliminary considerations about the first results of the new larger sensor network, including (i) a discussion on the role of an enriched identification of the mode shapes, (ii) a preliminary assessment of environmental effects on modal properties of the structure, both the natural frequencies and mode shapes, and (iii) considerations on the removal of such environmental effects and damage detection based on novelty analysis. The differences between previous and new results and the advantages of the adoption of a larger sensor network are highlighted.

1 INTRODUCTION

Masonry structures, such as towers, palaces and churches, constitute an important part of Cultural Heritage (CH) buildings in Europe, whose preventive conservation against material degradation and natural hazards can be regarded as a societal priority, as well as a scientific and technical challenge. Within the Italian context, most of these buildings are especially exposed to seismic risk, as a consequence of the high seismic hazard of most of the Italian territory and their high seismic vulnerability. This has also been dramatically testified by recent Italian earthquakes, such as those occurred in Emilia in 2012 [1] and Central Italy in 2016-2017 [2], just to mention the most recent ones.

Ambient Vibration Tests (AVT) and Operational Modal Analysis (OMA) [3, 4], as well as long-term vibration-based SHM, are becoming especially popular in application to CH structures, owing to their fully non-destructive and non-invasive nature. Literature counts several applications of vibration-based SHM methods to slender masonry towers based on the continuous identification of natural frequencies from in-service response data collected by a few sensors deployed on the upper part of the structure [5, 6, 7]. In this context, any damage or change in the structural behavior is automatically detected in the form of anomalies in time series of continuously identified natural frequencies, typically using multivariate statistical analysis methods, while the damage localization task can be addressed by solving an inverse problem, with the purpose to identify damage-induced local changes in equivalent elastic properties of the masonry [6, 8]. While suited for slender structures, vibration-based SHM methods are not directly applicable to stiffer masonry buildings, such as churches and palaces, where a mixed static-dynamic monitoring approach is often more informative, using measurements of strains, deformations, tilts and crack amplitudes to derive static signatures [9, 10, 11, 12, 13].

The Consoli Palace is the most representative monument of the medieval town of Gubbio, Italy, and is located in the heart of its historical center. Several studies have been carried out on the Consoli Palace in the framework of Horizon 2020 European HERACLES (HEritage Resilience Against CLimate Events on Site) project, devoted to enhancing the resilience of historic buildings against harmful events [13, 14, 15, 16, 17]. The palace has been under continuous monitoring since July 2017 using a simple mixed static and dynamic long-term SHM system. To the best of the authors' knowledge, the Consoli Palace can be regarded as the first (or one of the first) example(s) in the scientific literature, in which continuous long-term modal identification and SHM based on frequency tracking has been applied to the case of a stiff masonry palace, with the purpose of early detecting any damage or change in its structural behavior following an earthquake, whereby the existing literature limits to slender structures such as towers [5, 6, 7, 18, 19], churches and/or cathedrals [20, 21].

2 THE SHM DAMAGE-DETECTION ALGORITHM

The adopted vibration-based SHM method consists of a Multiple Linear Regression (MLR) model to remove the effects of changes in environmental and operational conditions from time series of natural frequencies and of a control chart based on T^2-statistic to detect deviations from normal conditions possibly related to a structural damage. Tracked modal frequencies are collected in an observation matrix, $\mathbf{Y} \in \mathbb{R}^{n \times N}$, where n is the number of identified frequencies and N is the number of observations. Quantities contained in matrix $\mathbf{Y}$ are affected by

changes in environmental conditions and cannot be directly used as damage sensitive features. Instead, quantities contained in a residual error matrix, $\mathbf{E} \in \mathbb{R}^{n \times N}$, are used for this purpose and computed as

$$\mathbf{E} = \mathbf{Y} - \hat{\mathbf{Y}} \tag{1}$$

where $\hat{\mathbf{Y}}$ are modal frequencies independently estimated through a proper statistical model. Under the assumption that such a model can reproduce the part of the variance in frequency estimates that is associated with changes in environmental and operational conditions, the error matrix only contains the residual variance in the data associated with errors in output-only modal identification and with un-modeled environmental and operational effects on modal frequencies. If a damage pattern develops, this affects data contained in $\mathbf{Y}$ but not those in $\hat{\mathbf{Y}}$. It follows that $\mathbf{E}$ contains quantities that are feasible for damage detection purposes. After computing matrix $\mathbf{E}$ in Eq. (1), a damage condition is identified as an anomaly in the residual errors, under the assumption that damage induces a change in the distribution of $\mathbf{E}$. To this aim, the classic statistical process control tool named *Novelty Analysis* is adopted. It consists of the use of control charts based on properly defined statistical distances or, in other words, on an index able to flag relevant natural frequency shifts (see Fig.1). A well known quantity used for this purpose in SHM is the Hotelling or Shewhart T^2-statistical distance [22], defined as

$$T^2 = r \cdot (\overline{\mathbf{E}} - \overline{\overline{\mathbf{E}}})^T \cdot \Sigma^{-1} \cdot (\overline{\mathbf{E}} - \overline{\overline{\mathbf{E}}}) \tag{2}$$

where r is an integer parameter, referred to as *group averaging size*, $\overline{\mathbf{E}}$ is the mean of the residuals in the subgroup of the last r observations, while $\overline{\overline{\mathbf{E}}}$ and Σ are the mean values and the covariance matrix of the residuals, respectively. Both $\overline{\overline{\mathbf{E}}}$ and Σ are statistically estimated in a reference period, called the *training period* (denoted as t_t), during which the structure is in the healthy state, i.e. it can be considered undamaged and experiences the normal environmental and operational conditions. An anomaly in the data is identified in the form of an outlier in the observed values of the residual errors, which is a value of the statistical distance which lies outside fixed control limits. Changes in T^2 are therefore likely to occur after a seismic event, evidencing the development of a damage pattern in the structure.

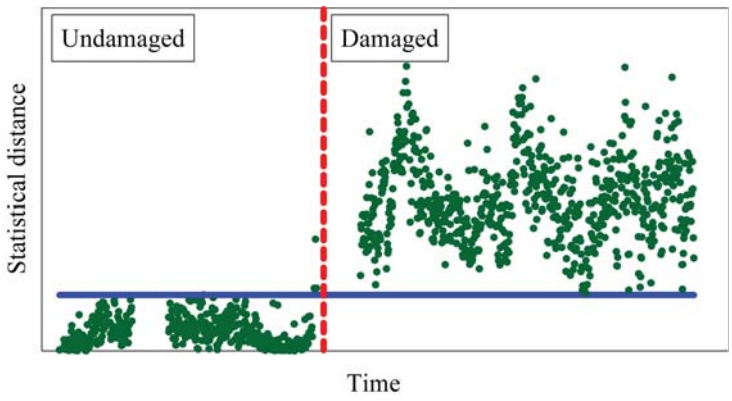

Figure 1: A typical example of control chart.

3 THE CONSOLI PALACE

The Consoli Palace is a very iconic masonry building in the medieval town of Gubbio, Italy. Built in gothic style between 1332 and 1349, it hosted the Consuls who were elected to control both legislative and executive branches of the government of the City. Since 1909 the building has been functioning as the Civic Museum, with a rich collection of art masterpieces, including the Iguvine Tablets dating back to the ancient Umbrian civilization.

AVTs have been carried out in May 2017 allowing identification of the first six modes of vibration within the range from 0 to 10 Hz: three involve vibration of the overall building, being two global flexural modes and one torsional mode, whereas the remaining three modes consist of mixed and/or local modes related to the dynamic interaction between the Palace and the small bell-tower placed on its top.

Significant thermal effects on both crack amplitudes and natural frequencies of the Consoli Palace have been investigated during the first year of monitoring. Negative linear correlations between crack amplitudes and temperature have been observed, while correlations between natural frequencies and temperature are also negative but sometimes non-linear. Also, the simultaneous recordings of static and dynamic data have allowed improving the statistical model used for the prediction of natural frequencies, by including the crack data as predictors, in addition to temperature data as generally found in the literature. More information can be found in [13].

3.1 The monitoring system

A mixed static-dynamic monitoring system has been active since July 2017. It is composed of:

- Three high sensitivity uni-axial piezoelectric accelerometers model PCB 393B12 (10 V/g sensitivity and $\pm$ 0.5 g measuring range) deployed on the roof of the Palace.
- Two crack meters (Linear Variable Displacement Transducers-LVDTs S-Series model with measurement range from 0 to 50 mm and resolution $<0.3\mu$m) permanently installed across two major cracks in the upper portion of the structure and related to possibly activating failure mechanisms, aimed at monitoring their possible opening and closing.
- Two temperature sensors (K-type thermocouples) installed close to each LVDT, in order to measure the surface temperature of the wall aiming at observing its influence on the evolution of the cracking pattern, as well as on global vibration modal properties.
- One data acquisition system (NI cDAQ-9132) with a remote connection to a data analysis server located in the Laboratory of Structural Dynamics of the University of Perugia.

Further details on the monitoring system can be found in [13].

Considering a continuous monitoring period from July 2017 to February 2020, data analysis can be synthesized in Fig.2: (i) results of modal identification and frequency tracking are presented in Fig. 2a, (ii) the recorded time series of crack amplitudes and temperature data are plotted in Figs. 2b, c. Plots versus the most correlated temperature are shown on the right side

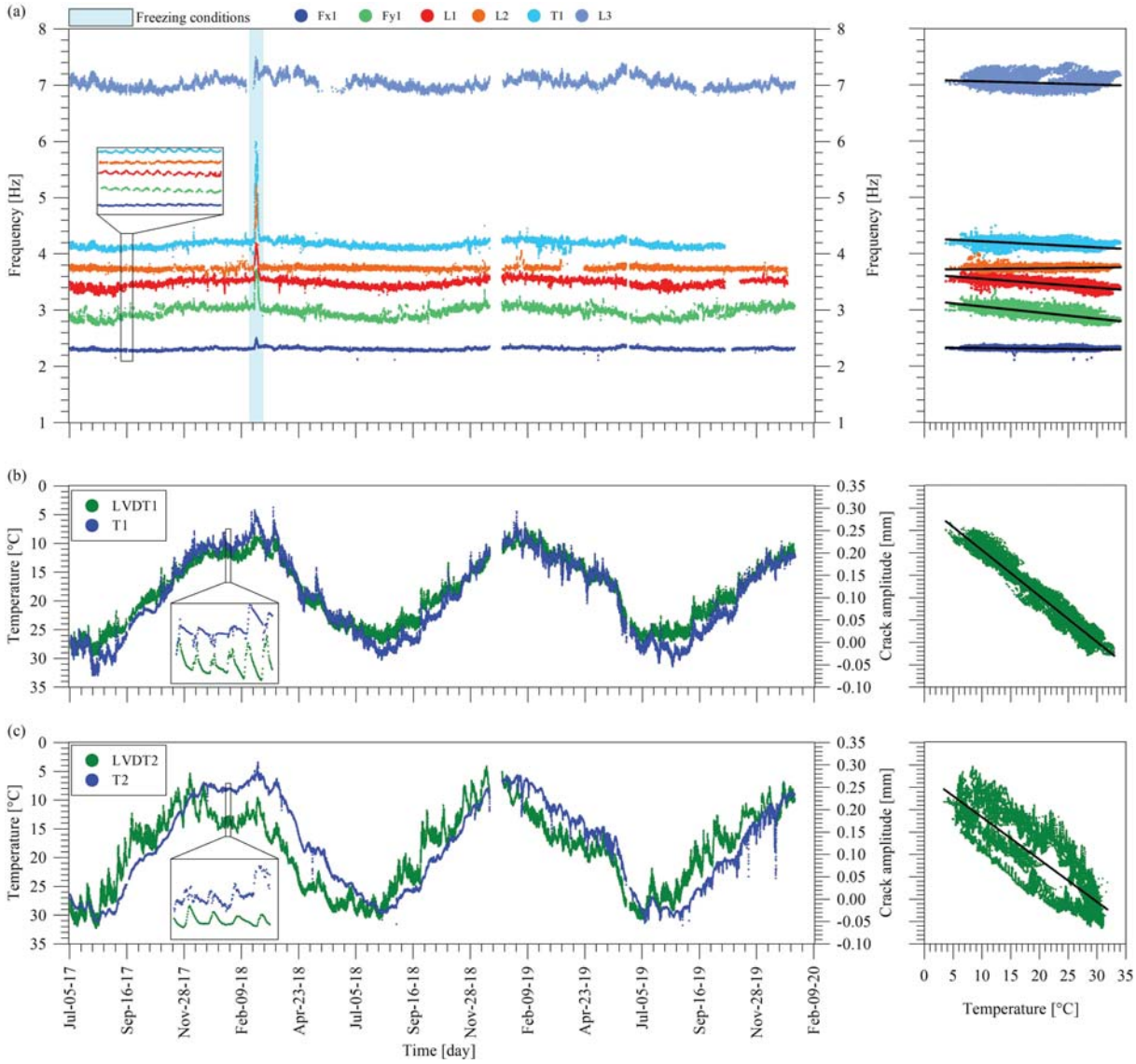

Figure 2: Time series of identified natural frequencies using automated SSI (a) and time evolution of the two monitored crack amplitudes and temperature data of Consoli Palace during more than two years of continuous monitoring (b-c). Their correlation with temperature data is also plotted.

of the figure. These results show that modal tracking is possible with an acceptable continuity for all natural frequencies of the six vibration modes. Also, their seasonal variations and daily fluctuations are evident. However, there are some continuously tracking difficulties. Some natural frequencies are not consistently identified, e.g. Fy1 global and L2 local modes of vibration, exhibiting lower identification success ratios, which might be associated to a lower traffic excitation during night hours, as well as to difficulties in modal tracking due to poor information on the mode shapes which are essential to correctly classify identified poles as belonging to this or that structural mode.

As an alternative solution, a denser sensor network could overcome many of the abovementioned shortcomings of the actual monitoring system.

4 THE NEW PROPOSED MONITORING SYSTEM

The SHM system has been recently enlarged with additional sensors, as depicted in Fig. 3. It now comprises a total of:

- Twelve accelerometers deployed on three levels of the palace that allow a more detailed detection of the possible vibration modes' variations: A1-A3 on the roof are the same sensors as in the previous system, A4-A6 in the Nobili hall, A7-A9 deployed in the Arengo hall and A11, A12 located on the roof and monitoring the top movements of the East and West façades, respectively.
- Four crack meters-LVDTs to monitor the openings of two previous (LVDT1 and LVDT2) and two additional cracks (LVDT3 and LVDT4).
- Four temperature sensors (K-type thermocouples) installed close to each LVDT, allowing a better thermal effects removal by accounting for the effect of the different solar radiation on the North and South façades.
- The same data acquisition system (NI cDAQ-9132) with a remote connection to the laboratory server.

The higher number of accelerometers and their deployment in three levels along the height contributes to improving modal tracking. For instance, natural frequencies of modes Fy1 and L2 can be tracked more regularly. Most importantly, an enriched identification of the mode shapes is considered. In fact, mode shapes can be identified continuously in time and the evolution of Modal Assurance Criterion (MAC) values, calculated with respect to the mode shapes of the calibrated numerical, is possible. On the other hand, considering the characterization of environmental parameters, a more accurate investigation of their effects on modal properties of the structure can be carried out with additional temperature sensors, not limiting it to the natural frequencies but also considering the mode shapes. Two additional crack meters are

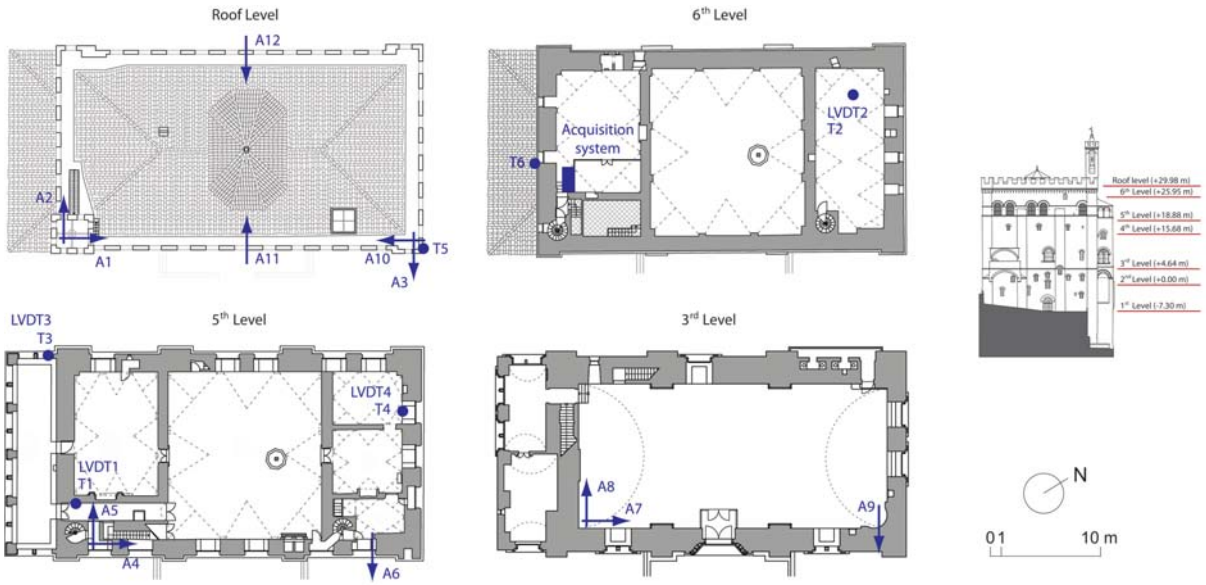

Figure 3: Layout of the new larger sensor SHM network recently installed on the Consoli Palace: (i) 12 accelerometers, (ii) 4 LVDTs, (iii) 4 K-type thermocouples and (iv) the data acqusition system.

installed, considering the main possibly activating failure mechanisms: (i) the overturning of the loggia on the South side of the Palace and (ii) the overturning of the northern part of the West façade. LVDT3 is located in correspondence of a new investigated crack pattern, related to the first mechanism, while LVDT4 is positioned in the medium-lower part of the crack of the North façade, already monitored in the upper level by LVDT2, related to the second mechanism. Finally, after the removal of the environmental effects, damage detection based on novelty analysis can be carried out using the information on variations of both natural frequencies and mode shapes, as well as crack amplitudes. In this context, the purpose of this new larger SHM system is a more accurate early detection of damage-induced anomalies in the time series of the natural frequencies of global and local vibration modes, as well as in the time series of the amplitudes of the major cracks existing in the building.

Based on the very first monitoring days, the differences between previous and new results are under specific attention, highlighting the advantages of the adoption of a larger sensor network. The monitoring data analysis has been carried out using an ad hoc created software tool, called MOSS, allowing continuous automated OMA and damage detection for SHM. The code allows for automatically managing data recordings of ambient vibrations and environmental variables. It also includes multiple regressive models for conducting damage identification, as well as a package of surrogate modeling. A user-friendly graphical interface of the MOSS software is shown in Fig. 4. More information can be found at https://shmlab.weebly.com/ (Research area).

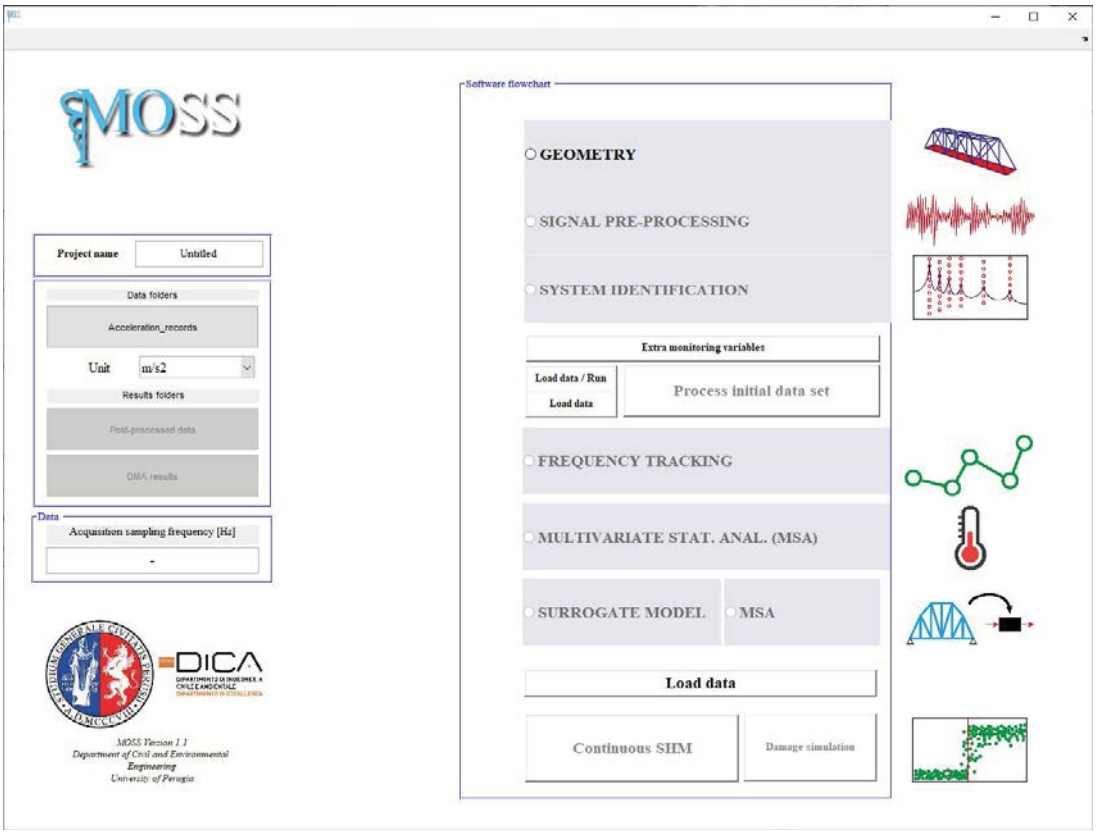

Figure 4: Graphical interface of the MOSS software.

5 CONCLUSIONS

The ongoing research activities regarding the mixed SHM of a monumental palace, the Consoli Palace in Gubbio, Italy, have been presented. A simple and low-cost mixed static-dynamic long-term SHM system has been active from July 2017 to February 2020. A new larger sensor SHM network has been recently installed in the Consoli Palace.

The main advantages of the new system are summarized below:

- An improved natural frequencies tracking and continuous identification of mode shapes.
- A more accurate characterization of environmental parameters and investigation of their effects on the modal properties of the structure.
- A more in-depth investigation of the major crack patterns by using additional crack meters and temperature sensors close to them.
- A more accurate earthquake-induced damage detection based on novelty analysis using the information on variations of both natural frequencies and mode shapes, as well as crack amplitudes.

ACKNOWLEDGEMENTS

This work was supported by the Italian Ministry of Education, University and Research (MIUR) through the funded Project of Relevant National Interest "DETECT-AGING - Degradation effects on structural safety of cultural heritage constructions through simulation and health monitoring" (protocol no. 201747Y73L).

REFERENCES

[1] L. Luzi, F. Pacor, G. Ameri, R. Puglia, P. Burrato, M. Massa, P. Augliera, G. Franceschina, S. Lovati, R. Castro, Overview on the strong-motion data recorded during the May–June 2012 Emilia seismic sequence, *Seismol Res Lett*, **84**, 629—644, 2013.

[2] ReLUIS-INGV Workgroup, Preliminary study on strong motion data of the 2016 central Italy seismic sequence V6, http:// www.reluis.it., 2016.

[3] F. Magalhães, A. Cunha, E. Caetano, Online automatic identification of the modal parameters of a long span arch bridge, *Mechanical Systems and Signal Processing*, **23**, 316-–329, 2009.

[4] F. Ubertini, C. Gentile, A.L. Materazzi, Automated modal identification in operational conditions and its application to bridges, *Engineering Structures*, **46**, 264-–278, 2013.

[5] F. Ubertini, N. Cavalagli, A. Kita, G. Comanducci Assessment of a monumental masonry bell-tower after 2016 Central Italy seismic sequence by long-term SHM, *Bulletin of Earthquake Engineering*, **16**, 775–801, 2018.

[6] I. Venanzi, A. Kita, N. Cavalagli, L. Ierimonti, F. Ubertini Earthquake-induced damage localization in an historic masonry tower through long-term dynamic monitoring and FE model calibration, *Bulletin of Earthquake Engineering*, , 1–28, 2020.

[7] C. Gentile, M. Guidobaldi, A. Saisi One-year dynamic monitoring of a historic tower: damage detection under changing environment, *Meccanica*, **51**, 2873–2889, 2016.

[8] I. Venanzi, A. Kita, N. Cavalagli, L. Ierimonti, F. Ubertini, *Continuous OMA for Damage Detection and Localization in the Sciri tower in Perugia, Italy, 127-136: Proceedings of the 8th International Operational Modal Analysis Conference, Copenhagen, Denmark, May 13th-15th*, 2019.

[9] N. Cavalagli, M. Gioffrè, V. Gusella, *Structural monitoring of monumental buildings: The Basilica of Santa Maria Degli Angeli in Assisi, 2410–2422: Proceedings of 5th ECCOMAS Thematic Conference on Computational Methods in Structural Dynamics and Earthquake Engineering*, 2015.

[10] A. De Stefano, E. Matta, P. Clemente, Structural health monitoring of historical heritage in Italy: some relevant experiences, *Journal of Civil Structural Health Monitoring*, **6**, 83–106, 2016.

[11] V. Gattulli, M. Lepidi, F. Potenza, Dynamic testing and health monitoring of historic and modern civil structures in Italy, *Structural Monitoring and Maintenance*, **3**, 71–90, 2016.

[12] A. Cigada, L. Corradi Dell'Acqua, B. Morlin Visconti Castiglione, M. Scaccabarozzi, M. Vanali, E. Zappa, Structural Health Monitoring of an Historical Building: The Main Spire of the Duomo Di Milano, *International Journal of Architectural Heritage*, **11**, 501–518, 2017.

[13] A. Kita, N. Cavalagli, F. Ubertini, Temperature effects on static and dynamic behavior of Consoli Palace in Gubbio, Italy, *Mechanical Systems and Signal Processing*, **120**, 180–202, 2019.

[14] A. Kita, N. Cavalagli, F. Ubertini, *First results of mixed static-dynamic structural health monitoring of Consoli Palace in Gubbio, 2380–2395: Proceedings of the 10th International Masonry Conference, Milan, Italy, July 9th-11th*, 2018.

[15] N. Cavalagli, A. Kita, V.L. Castaldo, A.L. Pisello, F. Ubertini, Hierarchical environmental risk mapping of material degradation in historic masonry buildings: An integrated approach considering climate change and structural damage, *Construction and Building Materials*, **215**, 998–1014, 2019.

[16] N. Cavalagli, A. Kita, S. Falco, F. Trillo, M. Costantini, F. Ubertini, Satellite radar interferometry and in-situ measurements for static monitoring of historical monuments: the case of Gubbio, Italy, *Remote Sensing of Environment*, **235**, 111453, 2019.

[17] E. Garcia-Macias, A. Kita, F. Ubertini, Synergistic application of operational modal analysis and ambient noise deconvolution interferometry for structural and damage identification in historic masonry structures: three case studies of Italian architectural heritage, *Structural Health Monitoring*, **-**, in press, 2019.

[18] C. Gentile, A. Ruccolo, A. Saisi Continuous Dynamic Monitoring to Enhance the Knowledge of a Historic Bell-Tower, *International Journal of Architectural Heritage*, , 1-13, 2019.

[19] A. Saisi, C. Gentile, A. Ruccolo Continuous monitoring of a challenging heritage tower in Monza, Italy, *Journal of Civil Structural Health Monitoring*, **8**, 77–90, 2018.

[20] C. Gentile, A. Ruccolo, F. Canali Long-term monitoring for the condition-based structural maintenance of the Milan Cathedral, *Construction and Building Materials*, **228**, 117101, 2019.

[21] C. Gentile, A. Ruccolo, F. Canali Continuous monitoring of the Milan Cathedral: dynamic characteristics and vibration-based SHM, *Journal of Civil Structural Health Monitoring*, **9**, 671—688, 2019.

[22] C.R. Farrar, K. Worden, *Structural Health Monitoring: A Machine Learning Perspective*, John Wiley & Sons, 1st edition, 2012.

EURODYN 2020
XI International Conference on Structural Dynamics
M. Papadrakakis, M. Fragiadakis, C. Papadimitriou (eds.)
Athens, Greece, 23–26 November 2020

FE MODEL UPDATING OF MASONRY TOWERS: MODELING AND NUMERICAL ISSUES

R.M. Azzara[1], M. Girardi[2], C. Padovani[2], D. Pellegrini[2], and L. Robol[3,2]

[1]Istituto Nazionale di Geofisica e Vulcanologia (INGV), Osservatorio Sismologico di Arezzo
Via Francesco Redi, 13, 52100, Arezzo, Italy
riccardo.azzara@ingv.it

[2]Institute of Information Science and Technologies "A. Faedo"
Via G. Moruzzi, 1, 56124 Pisa, Italy
{maria.girardi, cristina.padovani, daniele.pellegrini}@isti.cnr.it

[3] Department of Mathematics, University of Pisa
Largo B. Pontecorvo, 5, 56127, Pisa, Italy
leonardo.robol@unipi.it

Keywords: Dynamic monitoring, soil-structure analysis, model updating

Abstract. *The goal of this paper is to investigate the role of soil-structure interaction in modeling the dynamic behavior of masonry towers. The study, conducted on the bell tower of the Basilica of San Frediano in Lucca (Italy), is based on both experimental and numerical results. The former were collected during an experimental campaign carried out on the tower using seismometric stations, while the latter have been obtained via the modal analysis and model updating procedures implemented in the finite element code NOSA-ITACA. Combining experimental and numerical outcomes made it possible to assess the influence of the soil, modeled as a system of elastic springs, on the natural frequencies of the tower. Finite element models of the tower have been calibrated by taking the presence of the adjacent church into account and choosing different unknown parameters, including the soil stiffness.*

1 INTRODUCTION

Finite element (FE) model updating techniques are based on solution of a constrained minimum problem, in which the objective function is generally expressed as the discrepancy between experimental and numerical natural frequencies and mode shapes [1]. Wide application of these techniques to heritage structures is quite recent [2], [3], [4].

An efficient algorithm for model updating based on a modified Lanczos projection strategy and a trust-region scheme has been implemented in NOSA-ITACA, free software developed in house by ISTI-CNR and successfully applied to several case studies [5, 6]. Besides reducing the overall computation time of the numerical process and enabling accurate analysis of large-scale models with little effort, the proposed algorithm allows for obtaining information on both the reliability of the solution and its sensitivity to noisy experimental data.

Recent studies have shown that soil-structure interaction should be taken into account in studying the dynamic behavior of masonry structures [7], [8], [9], [10], [11], [12]. Stemming from the results of a continuous monitoring campaign conducted by the authors on the San Frediano belfry in the historic center of Lucca [13], this paper is aimed at investigating how this interaction influences the results of model updating.

In [13] FE model updating of the tower was conducted, by taking the presence of the adjacent church into account via suitable boundary conditions and considering the tower clamped at the base. In the present paper, the soil-structure interaction is studied by applying at the structure's base a system of elastic springs whose stiffness is varied in order to represent different soil types [14]. Two models of the tower have been analyzed: in the former the tower is free, and the influence of the church neglected, while in the latter the presence of the lateral walls of the church is modelled via elastic springs. The influence of soil stiffness on the tower's natural frequencies has been investigated and the model updating procedure implemented in NOSA-ITACA [5], [6] has been applied to determine the optimal mechanical properties of the tower-springs system.

2 FE MODEL UPDATING

Numerical modeling of a structure is usually characterized by several uncertainties regarding the properties of the constituent materials, the constraining effect of the adjacent buildings, boundary conditions, local soil conditions, etc. Model updating is a procedure aimed at determining some unknown parameters of a FE model in order to match the experimental and numerical dynamic properties of a structure (frequencies and mode shapes) [1]. Assuming that the stiffness and mass matrices of a structure discretized into finite elements depends on a parameter vector x varying in a p-dimensional box Ω, we want to determine the optimal value of x that minimizes, within the box Ω, the objective function

$$\phi(\mathrm{x}) = \sum_{i=1}^{q} w_i^2 [\, f_i^{exp} - f_i(\mathrm{x})]^2, \tag{1}$$

where f_i^{exp} and $f_i(\mathrm{x})$ are the q experimental and numerical frequencies to match (with q not less than p). In particular, numerical frequencies $f_i(\mathrm{x})$ are calculated by solving a generalized eigenvalue problem involving the stiffness matrix K(x) and mass matrix M(x) depending on the parameter vector x. Scalars w_i are the weight that should be given to each frequency in the optimization scheme; in order to obtain satisfactory accuracy on the frequencies, w_i is usually chosen as equal to the inverse of the experimental frequency.

The numerical procedure for model updating, described in detail in [5, 6], has been implemented in the NOSA-ITACA code, a finite element software package developed in house by

ISTI-CNR [15], for performing modal analyses [16] and managing the large-scale problems encountered in applications.

The algorithm implemented in the code is based on construction of local parametric reduced-order models embedded in a trust-region scheme for solving the constrained minimum problem. In particular, the algorithm exploits the structure of the stiffness and mass matrices and the fact that only a few of the smallest eigenvalues have to be calculated in order to solve the problem.

3 THE SAN FREDIANO BELL TOWER

The bell tower of the Basilica of San Frediano (Figure 1), dating back to the 11th century, is one of the best preserved in Lucca's historic center. The tower, whose geometry is sketched in Figure 2 and described thoroughly in [13], is 52 m high, with walls varying in thickness from about 2.1 m at the base to 1.6 m at the top. The San Frediano Basilica adjoins the tower on two sides for about 13 m of its height. The masonry constituting the tower appears to be made of regular stone blocks at the base, while quite homogeneous brick masonry is visible in the upper sections, apart from the central part of the walls, where the masonry between the windows is made up of stone blocks.

In the period 2015-2017 the tower was instrumented with four SARA tri-axial seismometric stations, each made up of a SL06 24-bit digitizer and a SS20 seismometer (electrodynamic velocity transducer, 2.0 Hz eigenfrequency), made available by the Arezzo Seismology Observatory (INGV). The instruments were arranged on the San Frediano bell tower adopting different sensors layouts and data recorded were analyzed via the Covariance Driven Stochastic Subspace Identification method (SSI/Cov) [17], [18] implemented in the MACEC code [19].

Table 1 reports the mean values of the first five frequencies calculated using data recorded in August 2016, with a sampling frequency of 100 Hz. The first and second frequencies correspond to flexural mode shapes along the X and Y direction, respectively. The third frequency is likely related to a torsional mode shape. The last two frequencies correspond once again to flexural model shapes. More details on mode shapes are given in [13].

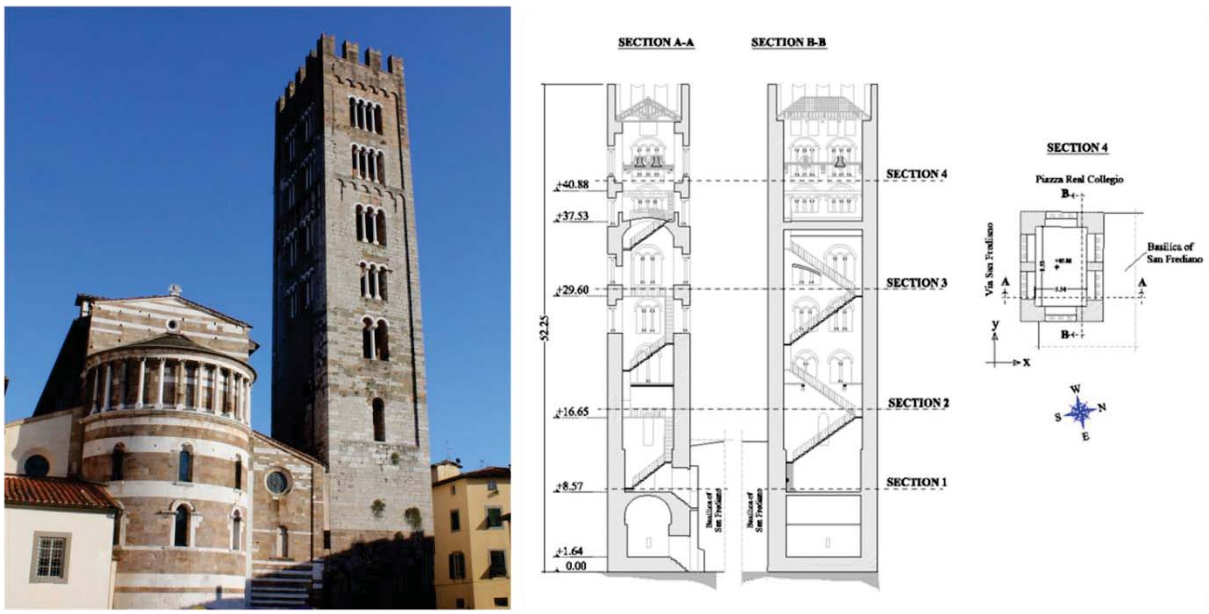

Figure 1: The San Frediano bell tower.

	Frequency [Hz]
Mode 1 (Bending X)	1.11
Mode 2 (Bending Y)	1.39
Mode 3 (Torsional)	3.45
Mode 4 (Bending X)	4.64
Mode 5 (Bending Y)	5.37

Table 1: The first five frequencies of the San Frediano bell tower.

3.1 FE modeling, modal analysis and model updating

This section is devoted to the modal analysis of the bell tower. All numerical analyses presented in this paper have been conducted via the NOSA–ITACA code [5], [6], [16], [15].
The San Frediano bell tower has been discretized into 45935 brick and 673 beam and truss elements (element n. 8, 9 and 35 in [15]) with 60228 nodes, as shown in Figure 2. Beams have been used to model the steel tie rods and the wooden roof elements, while trusses are used for the springs at the base, according to the Winkler model for the soil [14] and to model the adjacent building. In particular, two models have been considered: in the former (Model 1) the presence of the church is neglected, while in the latter (Model 2) elastic spring have been applied 12.50 m above the base to account for the church's adjacent walls (red springs along X and magenta springs along Y in Figure 2). In both cases horizontal displacements of the base are prevented and vertical displacement is constrained by the presence of elastic springs under the tower's base (green in Figure 2).
The masonry has been modeled as an isotropic linear elastic material with Poisson's ratio $\nu = 0.2$, mass density $\rho = 2000$ kg/m^3, and Young's modulus E_m varying from 2.0 GPa to 10.0 GPa. Figures 3 to 7 show the first five frequencies of Model 1 as functions of E_m, with the soil stiffness k_w taking values between 4800 and 128000 kN/m^3, corresponding respectively to loose and dense sand [14]. As expected, for fixed k_w, the frequencies are increasing functions of Young's modulus. The first and second frequencies remain strictly below the corresponding experimental frequencies, likely due to the fact that the real system is considerably stiffer than its numerical model. For fixed E_m, the frequencies increase as soil stiffness k_w increases, but this rise becomes less evident as Young's modulus increases; for example, the first frequency increases by about 44% when E_m=2 GPa and k_w ranges from 4800 kN/m^3 to 128000 kN/m^3, while for E_m=10 GPa the growth of the first frequency is on the order of 18.5%. Furthermore, there is visibly greater influence of the soil stiffness on the two first bending frequencies than on higher-order ones. With respect to the experimental mode shapes, the MAC values [18] are consistently greater than 0.9, and their variation with soil stiffness is not appreciable.

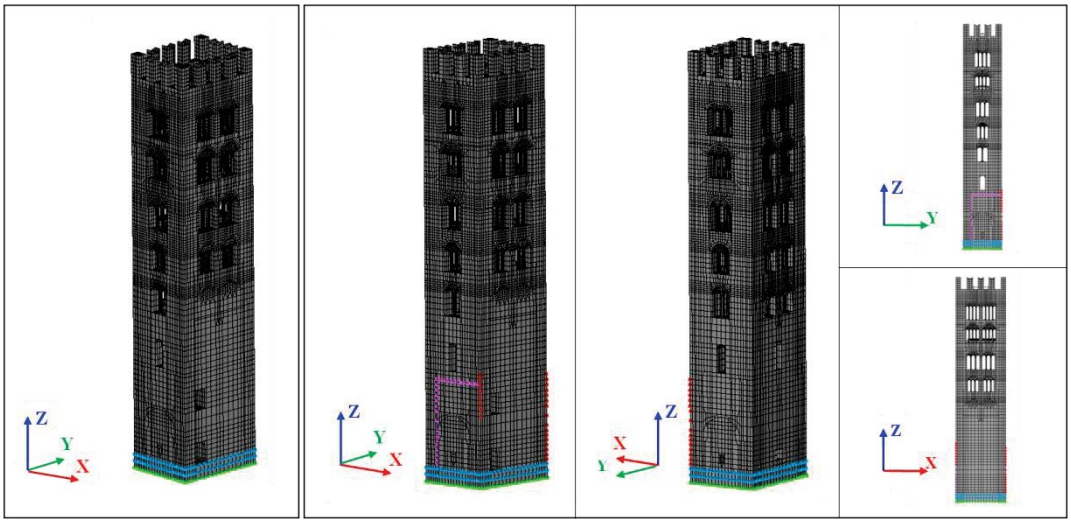

Figure 2: FE discretization of the San Frediano bell tower, model 1 (left) and model 2 (right). In model 1 and model 2 the soil is modeled as vertical springs (green) and the displacements along X and Y are prevented at the base (cyan). In model 2 the presence of the adjacent church is modeled as springs along X (red) and Y (magenta).

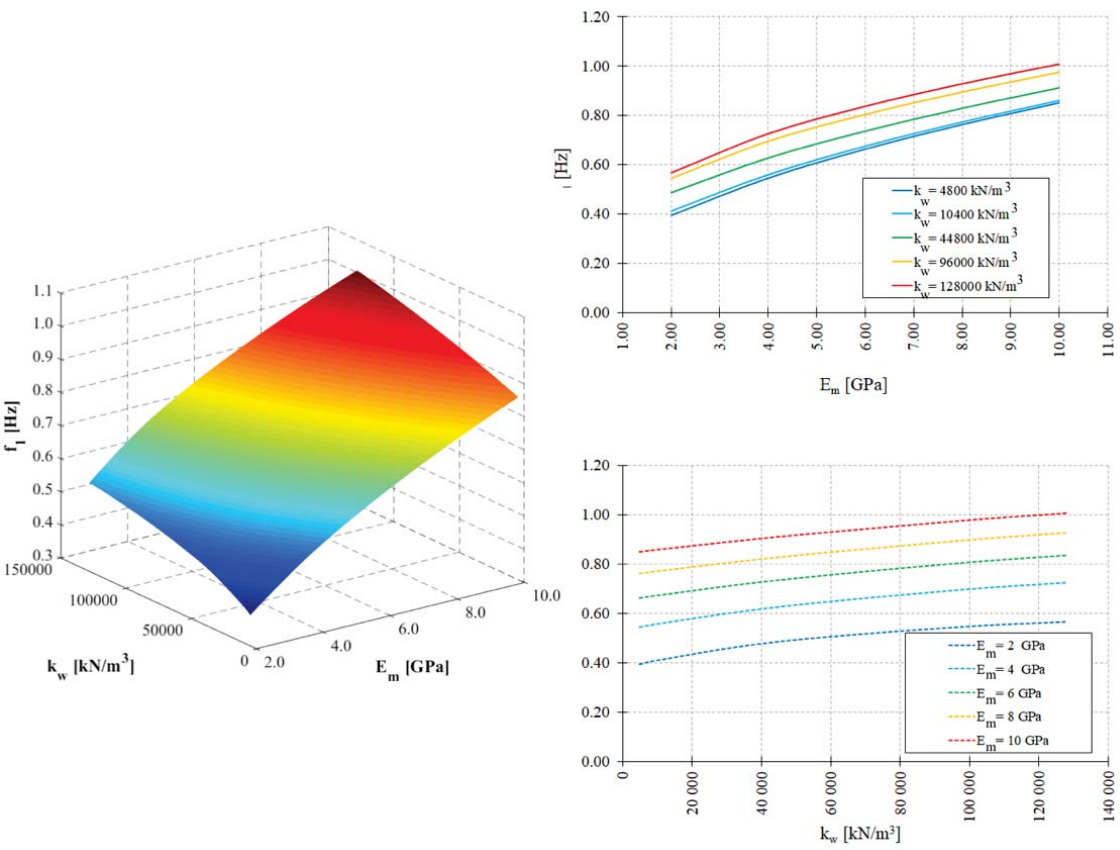

Figure 3: Model 1, first frequency as a function of Young's modulus E_m and soil stiffness k_w.

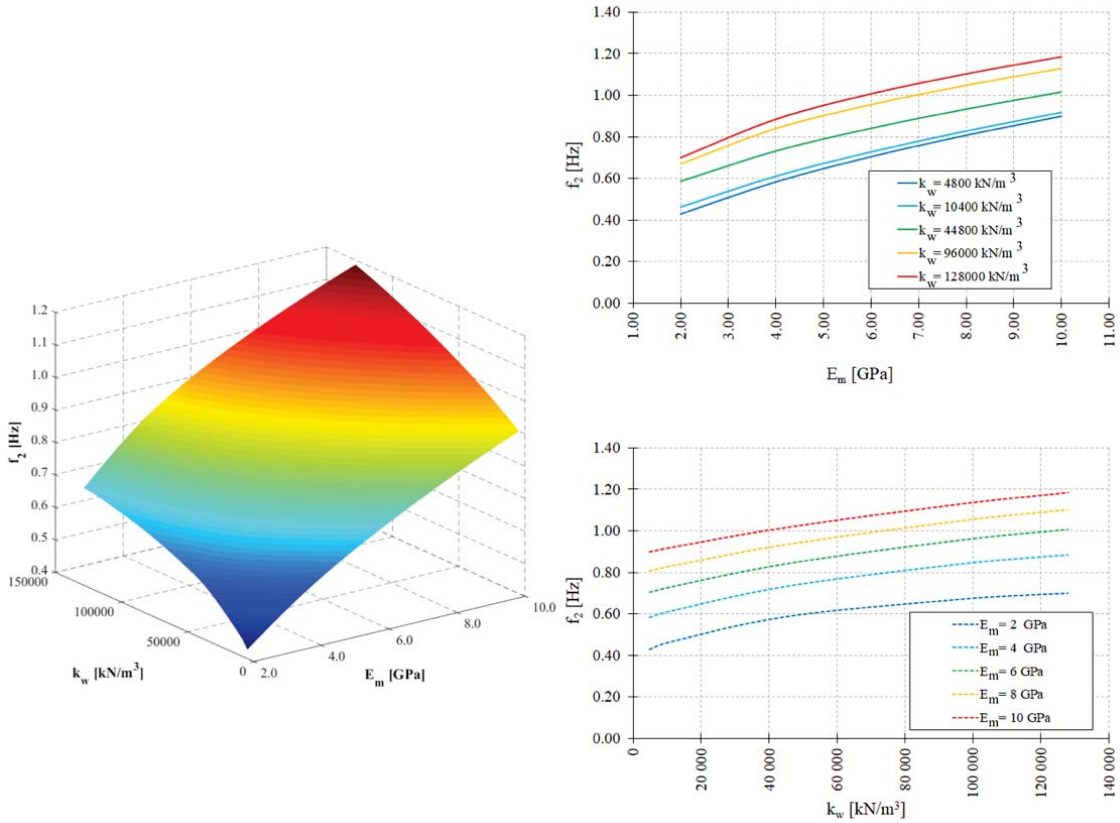

Figure 4: Model 1, second frequency as a function of Young's modulus E_m and soil stiffness k_w.

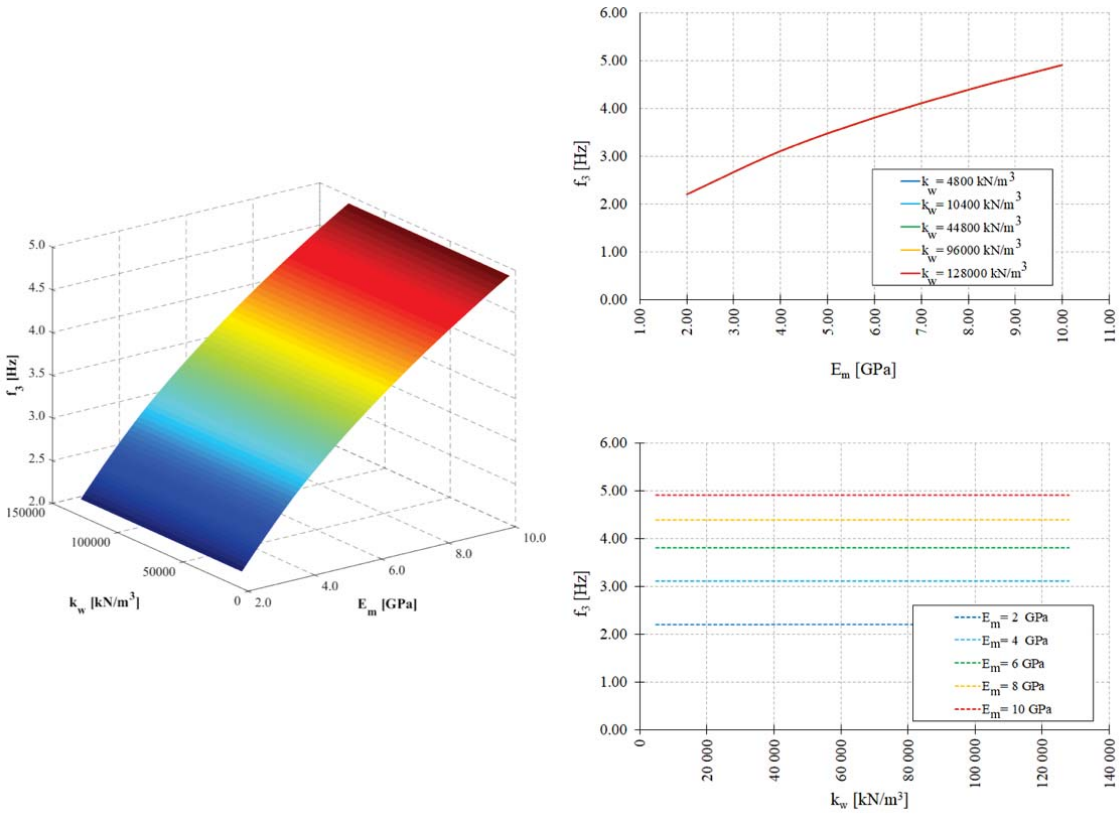

Figure 5: Model 1, third frequency as a function of Young's modulus E_m and soil stiffness k_w.

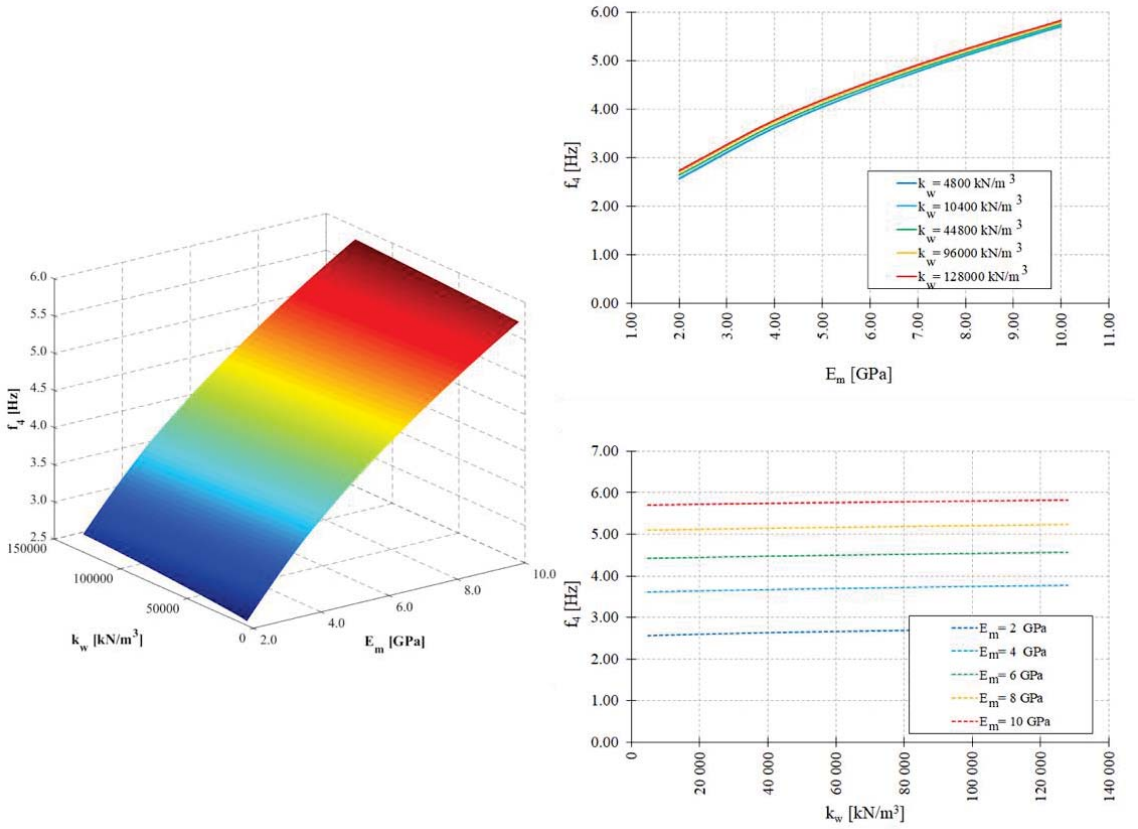

Figure 6: Model 1, fourth frequency as a function of Young's modulus E_m and soil stiffness k_w.

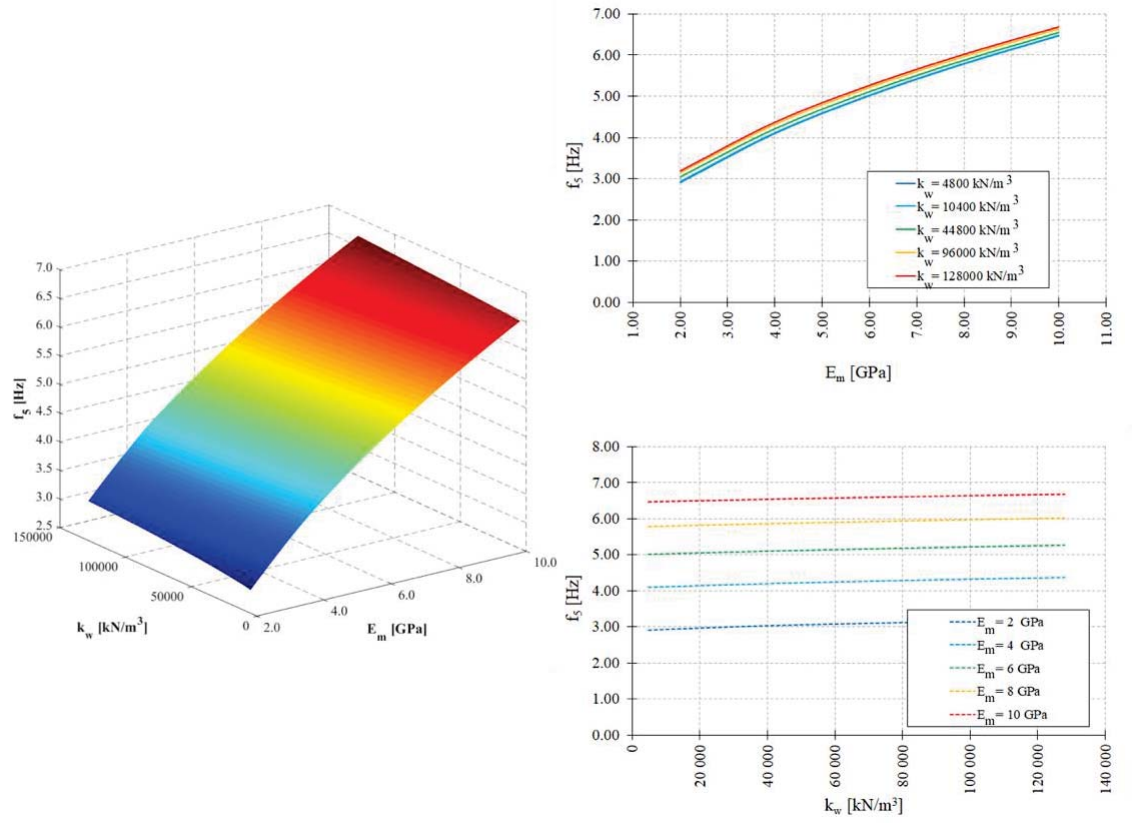

Figure 7: Model 1, fifth frequency as a function of Young's modulus E_m and soil stiffness k_w.

The model updating procedure described in [5] and [6] is conducted on Model 1 considering the unknown parameters masonry's Young's modulus E_m [GPa] and the soil stiffness k_w [kN/m^3] ranging in the intervals

$$E_m \in [1.0, 10.0] \text{ GPa}, \qquad k_w \in [4800.0, 128000.0] \text{ kN/m}^3. \tag{2}$$

The procedure provides the following values

$$E_m^{opt} = 6.61 \text{ GPa}, \quad k_w^{opt} = 1.28\ 10^5 \text{ kN/m}^3, \tag{3}$$

with k_w^{opt} coinciding with the right end of the interval in (2). The corresponding numerical frequencies and the relative errors with respect to the experimental frequencies are summarized in Table 2.

	Exp. freq. [Hz]	Num. freq. [Hz]	Relative error [%]
Mode 1	1.11	0.87	21.62
Mode 2	1.39	1.04	25.18
Mode 3	3.45	3.99	-15.65
Mode 4	4.64	4.78	-3.02
Mode 5	5.37	5.51	-2.61

Table 2: The first five numerical frequencies of Model 1 corresponding to the optimal values in (3) with the relative errors with respect to the experimental values.

The errors shown in the Table demonstrate that Model 1 is not able to capture the dynamic response of the real system.

Model 2 differs from Model 1 in that elastic springs are now applied 12.50 m above the base to account for the adjacent church walls. Let us fix the elastic constants of the springs: k_X = 7.75 10^7 N/m for the springs along X (red in Figure 2) and k_Y = 1.5 10^8 N/m for the springs along Y (magenta in Figure 2). These constants have been determined by considering the presence of the adjacent church, whose walls have a shear stiffness of about 2.4 10^9 N/m in the Y direction and 1.89 10^9 N/m in the X direction. As for the church's constituent material, a shear modulus of 1.25 GPa and a Poisson's ratio of 0.2 have been assumed [20].

Figures 8 to 12 show the first five frequencies of Model 2 as functions of E_m and soil stiffness k_w. Dashed lines represent the experimental frequency values.

As in Model 1, for fixed k_w, the frequencies are increasing functions of Young's modulus and for fixed E_m the frequencies increase with increasing soil stiffness k_w. However, in this case the growth is more or less steady; for example, the first frequency increases by about 6.45% when E_m=2 GPa and the value of k_w is increased from e 4800 kN/m^3 to 128000 kN/m^3, while for E_m=10 GPa the corresponding increase is about of 5.84%.

In this case, unlike in Model 1, the five frequencies of the tower are less influenced by soil stiffness. In fact, the tower's bending stiffness is mainly influenced by the constraint of the adjacent walls, while the vertical deformability of the soil under the base seems to make a negligible contribution to the overall deformability of the system. In this case, also unlike in Model 1, the experimental frequency values intercept the surfaces of the numerical frequencies, thus indicating that Model 2 can provide a good approximation of the actual dynamic behavior of the tower.

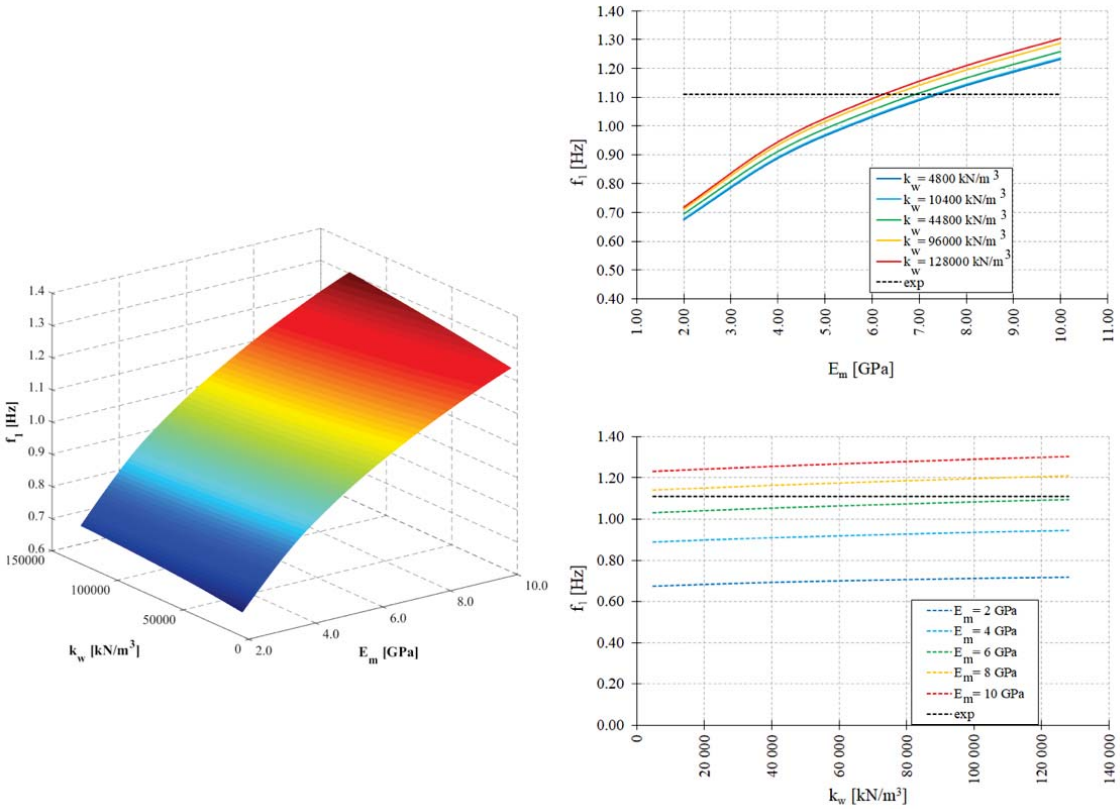

Figure 8: Model 2, first frequency as a function of Young's modulus E_m and soil stiffness k_w.

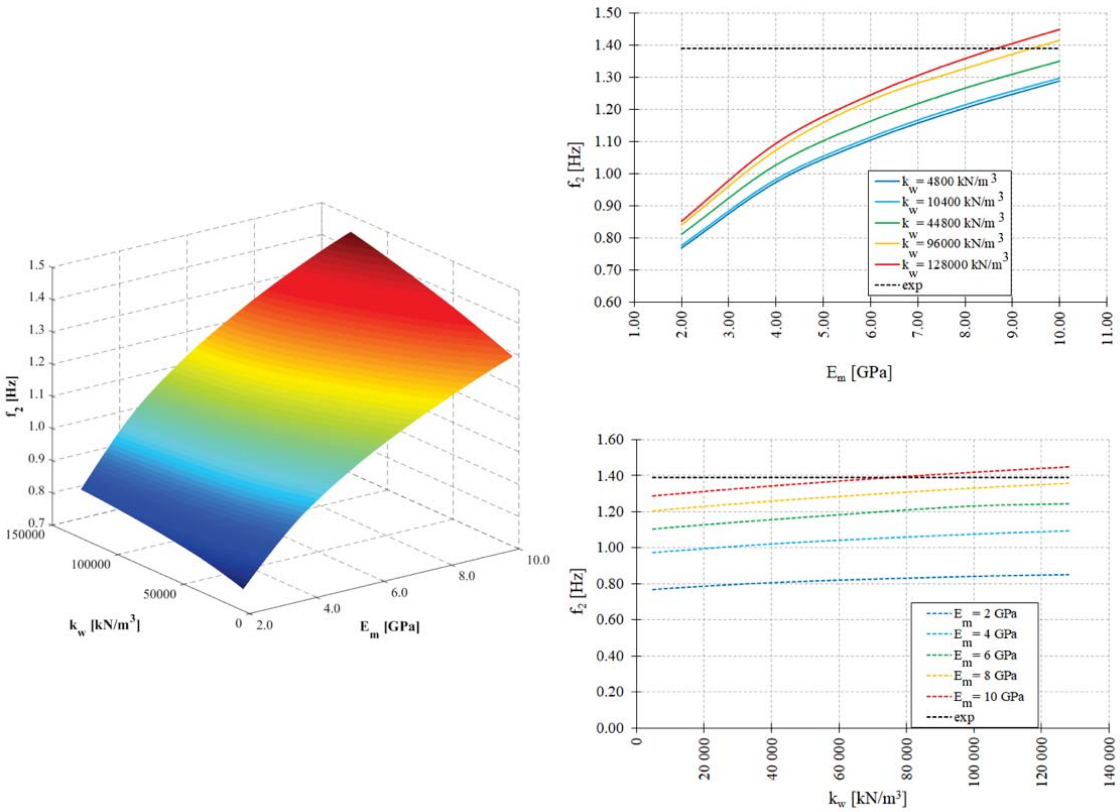

Figure 9: Model 2, second frequency as a function of Young's modulus E_m and soil stiffness k_w.

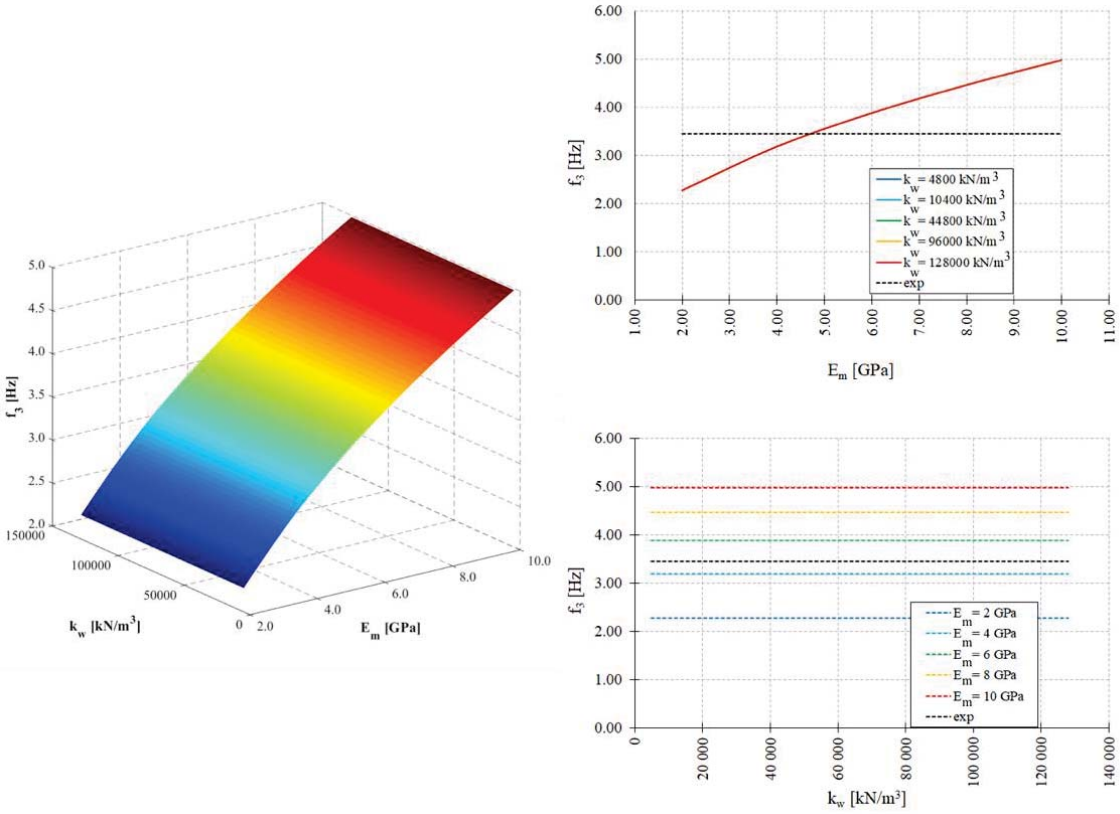

Figure 10: Model 2, third frequency as a function of Young's modulus E_m and soil stiffness k_w.

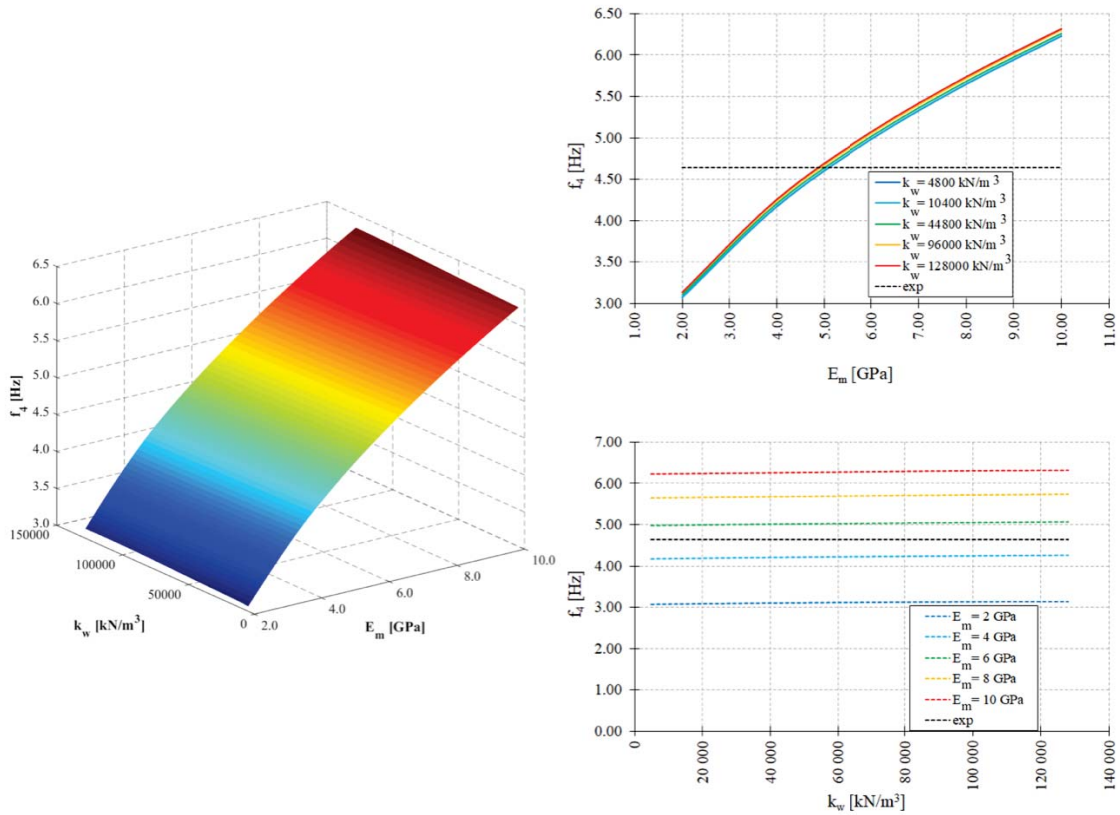

Figure 11: Model 2, fourth frequency as a function of Young's modulus E_m and soil stiffness k_w.

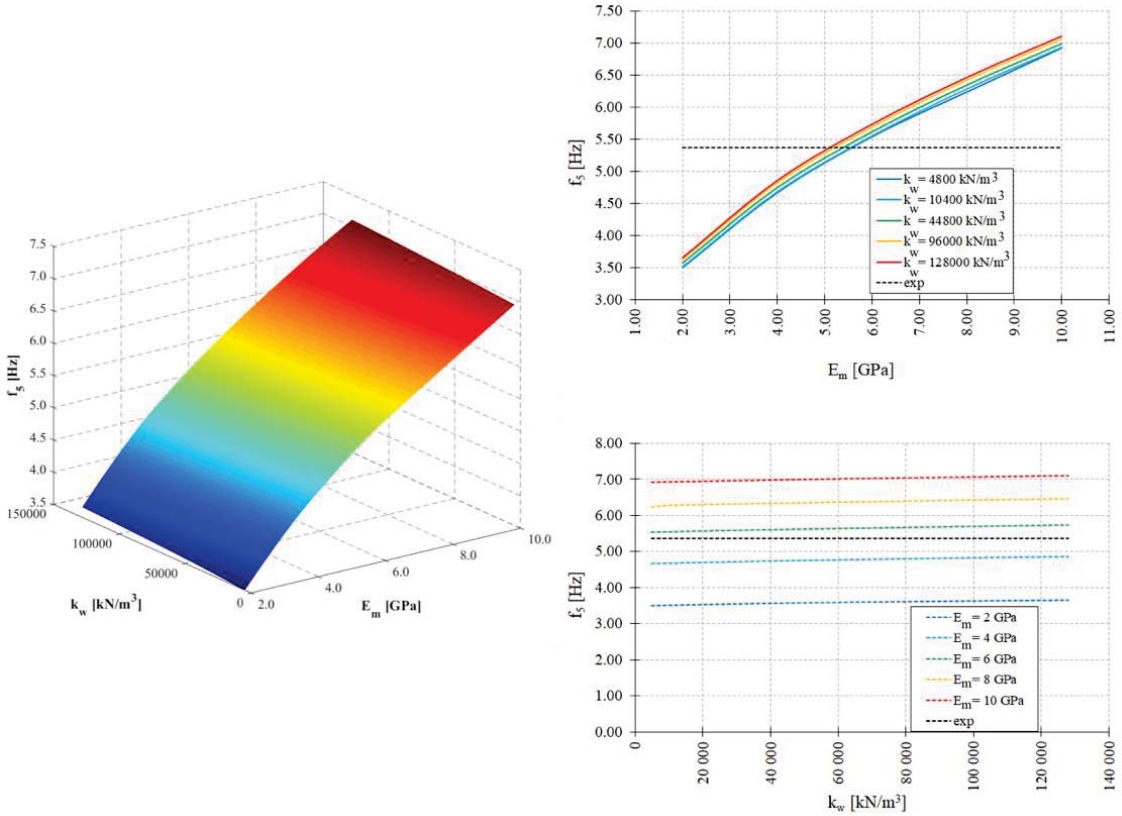

Figure 12: Model 2, fifth frequency as a function of Young's modulus E_m and soil stiffness k_w.

The results of the model updating procedure conducted on Model 2, for E_m [GPa] and k_w [kN/m^3] varying in the intervals given in (2), as in the case of Model 1, are the following

$$E_m^{opt} = 5.327 \text{ GPa}, \qquad k_w^{opt} = 1.28\ 10^5 \text{ kN/m}^3, \tag{4}$$

with k_w^{opt} coinciding with the right end of the interval in (2). The corresponding numerical frequencies and the relative errors with respect to the experimental frequencies are summarized in Table 3.

	Exp. freq. [Hz]	Num. freq. [Hz]	Relative error [%]
Mode 1	1.11	0.98	11.71
Mode 2	1.39	1.29	7.19
Mode 3	3.45	3.65	-5.80
Mode 4	4.64	4.64	0.0
Mode 5	5.37	5.71	-6.33

Table 3: The first five numerical frequencies of Model 2 corresponding to the optimal values in (4) with the relative errors with respect to the experimental values.

The errors in this case are still consistent, but lower (about one half) than those shown in Table 2 for Model 1.

Finally, if model updating is performed considering as unknown parameters E_m, k_w and the elastic constants k_{X1}, k_{X2} and k_Y of the lateral springs as well, for k_{X1}, k_{X2} and k_Y [N/m] varying in the interval [1.0 10^8, 7.0 10^{21}], then the optimal values are

$$E_m^{opt} = 4.53 \text{ GPa}, \quad k_w^{opt} = 0.69389\ 10^5 \text{ kN/m}^3, \quad k_{X1}^{opt} = k_{X2}^{opt} = k_Y^{opt} = 3.5\ 10^{21} \text{ N/m}. \tag{5}$$

The corresponding numerical frequencies and the relative errors with respect to the experimental frequencies are reported in Table 4.

	Exp. freq. [Hz]	Num. freq. [Hz]	Relative error [%]
Mode 1	1.11	1.13	-1.80
Mode 2	1.39	1.39	0.0
Mode 3	3.45	3.50	-1.45
Mode 4	4.64	4.97	-7.11
Mode 5	5.37	6.05	-12.66

Table 4: The first five numerical frequencies of Model 2 corresponding to the optimal values in (5) with the relative errors with respect to the experimental values.

For the sake of comparison, we recall the results obtained in [13] considering the tower clamped at the base and assuming that the horizontal displacements of the points adjacent to the church (magenta and red points in Figure 2) are prevented. The model updating conducted in [13] with E_m as the unknown parameter yielded the following optimal value

$$E_m^{opt} = 4.20 \text{ GPa}, \tag{6}$$

and the frequencies reported in Table 5.

	Exp. freq. [Hz]	Num. freq. [Hz]	Relative error [%]
Mode 1	1.11	1.18	-6.31
Mode 2	1.39	1.43	-2.88
Mode 3	3.45	3.37	-2.32
Mode 4	4.64	4.93	-6.25
Mode 5	5.37	6.00	-11.73

Table 5: The first five numerical frequencies of the tower clamped at the base with the horizontal displacements prevented [13] corresponding to the optimal value in (6) with the relative errors with respect to the experimental values.

Thus, a comparison of Table 4 to Table 5 shows that taking into account both the deformability of the adjacent constraints and the soil–structure interaction allows for appreciably fine-tuning the model and improving the simulation of the experimental results.

4 CONCLUSIONS

This paper is devoted to studying the effects of soil deformability and adjacent buildings on the dynamic behavior of masonry towers. The investigation relies on the use of some experimental results collected during a long-term dynamic monitoring campaign on the San Frediano bell tower in Lucca and an automated model updating procedure implemented in the NOSA-ITACA code.

The paper shows that soil stiffness can significantly affect the dynamic behavior of isolated towers, while in the case of towers connected to other buildings, the model's global stiffness is very sensitive to the kind of connection with the adjacent structures. The use of automated model updating procedures can help fine-tune the FE model, and enables estimating the stiffness of both the soil and the lateral constraints.

REFERENCES

[1] J.E. Mottershead, M.I. Friswell, Model updating in structural dynamics: a survey, *Journal of Sound and Vibration*, 167(2), 347-375, 1993.

[2] Á. Bautista-De Castro, L.J. Sánchez-Aparicio, L.F. Ramos, J. Sena-Cruz, D. González-Aguilera, Integrating geomatic approaches, Operational Modal Analysis, advanced numerical and updating methods to evaluate the current safety conditions of the historical Bôco Bridge, *Construction and Building Materials*, 158, 961-984, 2019.

[3] A. Cabboi, C. Gentile, A. Saisi, From continuous vibration monitoring to FEM-based damage assessment: application on a stone-masonry tower, *Construction and Building Materials*, 156, 252-265, 2017.

[4] R. Ferrari, D. Froio, E. Rizzi, C. Gentile, E.N. Chatzi, Model updating of a historic concrete bridge by sensitivity-and global optimization-based Latin Hypercube Sampling, *Engineering Structures*, 179, 139-160, 2019.

[5] M. Girardi, C. Padovani, D. Pellegrini, L. Robol, A model updating procedure to enhance structural analysis in the FE code NOSA-ITACA, *Journal of Performance of Constructed Facilities*, Vol. 33, Issue 4, 2019.

[6] M. Girardi, C. Padovani, D. Pellegrini, M. Porcelli, L. Robol, Finite element model updating for structural applications, *Journal of Computational and Applied Mathematics*, *370*, 112675, 2020.

[7] R. Lancellotta, D. Sabia, Identification technique for soil-structure analysis of the Ghirlandina tower, *International Journal of Architectural Heritage*, 9(4), 391-407, 2015.

[8] F. Lorenzoni, M.R. Valluzzi, M. Salvalaggio, A. Minello, C. Modena, Operational modal analysis for the characterization of ancient water towers in Pompei, *Procedia engineering*, 199, 3374-3379, 2017.

[9] M. Papadopoulos, R. Van Beeumen, S. François, G. Degrande, G. Lombaert, Computing the modal characteristics of structures considering soil-structure interaction effects, *Procedia engineering*, 199, 2414-2419, 2017.

[10] R.M. Azzara, A. De Falco, M. Girardi, D. Pellegrini, Ambient vibration recording on the Maddalena Bridge in Borgo a Mozzano (Italy): data analysis, *Annals of Geophysics*, 60 (4), S0441, 2017.

[11] G. Zani, P. Martinelli, A. Galli, C. Gentile, M. di Prisco, Seismic Assessment of a 14th-Century Stone Arch Bridge: Role of Soil–Structure Interaction, *Journal of Bridge Engineering*, 24(7), 05019008, 2019.

[12] G. Torelli, D. D'Ayala, M. Betti, G. Bartoli, Analytical and numerical seismic assessment of heritage masonry towers, *Bulletin of Earthquake Engineering*, 18(3), 969-1008, 2020.

[13] R.M. Azzara, G. De Roeck, M. Girardi, C. Padovani, D. Pellegrini, E. Reynders, Assessment of the dynamic behaviour of an ancient masonry tower in Lucca via ambient vibrations, in *Proceedings of the 10th international conference on the Analysis of Historical Constructions-SAHC 2016*, CRC Press, pp. 669-675, 2016.

[14] J.E. Bowles, Foundation analysis and design, McGraw-Hill, USA, 1996.

[15] www.nosaitaca.it/software

[16] M. Porcelli, V. Binante, M. Girardi, C. Padovani, G. Pasquinelli, A solution procedure for constrained eigenvalue problems and its application within the structural finite-element code NOSA-ITACA, *Calcolo*, *52*(2), 167-186, 2015.

[17] R. Brincker, C. Ventura, Introduction to Operational Modal analysis, Wiley, 2015.

[18] E. Reynders, K. Maes, G. Lombaert, G. De Roeck, Uncertainty quantification in operational modal analysis with stochastic subspace identification: Validation and applications, *Mech. Syst. Signal Process* 66-67:13-30, 2016.

[19] E. Reynders, M. Schevenels, G. De Roeck, MACEC 3.3. A Matlab toolbox for experimental and operational modal analysis. http://bwk.kuleuven.be/bwm/macec/, 2014.

[20] Circolare 21 gennaio 2019, n. 7 C.S.LL.PP. Istruzioni per l'applicazione dell'«Aggiornamento delle "Norme tecniche per le costruzioni"», D.M. 17 gennaio 2018.

EURODYN 2020
XI International Conference on Structural Dynamics
M. Papadrakakis, M. Fragiadakis, C. Papadimitriou (eds.)
Athens, Greece, 23–26 November 2020

INFLUENCE OF IMPORTANT STRUCTURAL STRENGTHENING ON THE DYNAMIC PROPERTIES OF A MASONRY ARCH BRIDGE

Chiara Pepi[1], **Nicola Cavalagli** [1], **Massimiliano Gioffré** [1] **and Vittorio Gusella** [1]

[1]Department of Civil and Environmental Engineering, University of Perugia
Via G. Duranti, 93, 06125, Perugia, Italy
e-mail: {chiara.pepi,nicola.cavalagli,massimiliano.gioffre,vittorio.gusella}@unipg.it

Keywords: Masonry arch bridge, Ambient Vibration Tests, Finite Element Analysis.

Abstract. *This paper presents the preliminary results of an ongoing research on a masonry arch bridge in the neighborhood of Todi (Umbria, Italy). Forced and ambient vibration tests (AVTs) were carried out in year 2016 on the masonry arch bridge. High-sensitivity piezoelectric accelerometers, a laser vibrometer and a radar interferometer were used to record the structural response. The structure exhibited typical mechanical deterioration phenomena: longitudinal cracks below the vault, material detachment in the voussoir as well in the spandrel wall and damage of the abutments. The damage level of the masonry was even worsened by vegetation grown between the cracks of the stones. The Enhanced Frequency Domain Decomposition (EFDD) method was used to identify the experimental natural frequencies and mode shapes. The experimental modal properties were finally used to calibrate an accurate Finite Element (FE) numerical model developed using a photogrammetric survey based on high-resolution images provided by UAV (Unmanned Aerial Vehicle) . In 2017 a restoration process was started aimed to strengthen the tested structure. The experimental tests were repeated at the end of the restoration process. In particular, AVTs were carried out using high-sensitivity accelerometers located in the same positions used before the restoration process. In this paper, the comparison of the natural frequencies and the vibration modes, obtained be-fore and after the restoration process, is presented in order to discuss the effect of severe dam-age on the masonry arch bridge. Furthermore, this comparison is used to gather information on the effect of the restoration activities on the dynamic properties of the masonry arch bridge. The obtained results are crucial for calibrating suitable numerical models in both the different stages using a multidisciplinary approach, which uses UAV technology and photogrammetry techniques.*

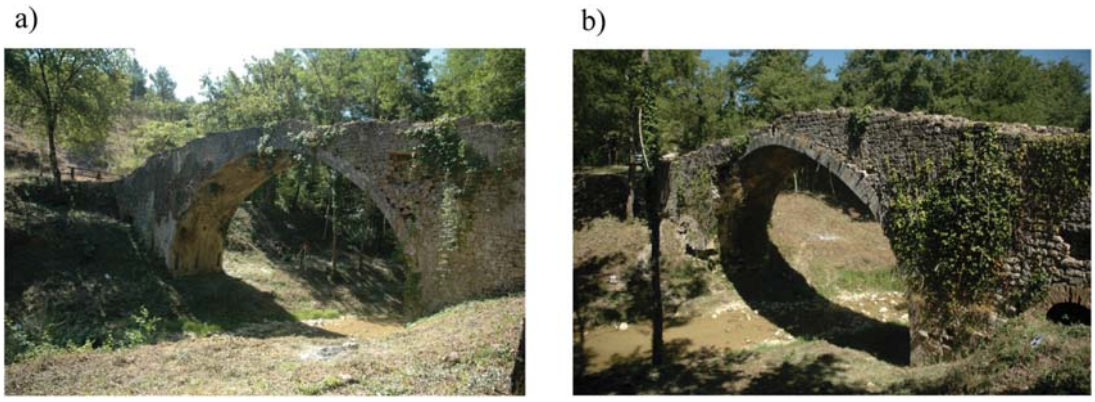

Figure 1: Images of the historic masonry arch bridge before the strengthening: general view of the North (a) and South (b) side.

1 INTRODUCTION

Masonry arch bridges are one of the most common structural typology present in the world-wide cultural heritage. Today many of these ancient constructions are characterized by severe damage conditions due to natural hazards, foundation settlements and inherent degradation with time resulting in loss of strength, stiffness and physical properties [1, 2, 3, 4]. All these factors can affect negatively the structural performance of this kind of constructions often requiring repair and/or strengthening. Over the past decades a large number of experimental studies have been devoted to the investigation of the effectiveness of different strengthening works applied to ancient masonry building but only limited studies used full-scale structures.

Finite element (FE) models can be considered as a predominant tool to investigate the structural performance of historic masonry structures and several contributions can be found in literature [5, 6]. In spite of this, the numerical modeling of historic masonry structures is still a challenging task since they may be characterized by a significant level of complexity in terms of geometry, existing damage and mechanical properties [7, 8, 9, 10]. Modern survey technique such as terrestrial laser scanning and photogrammetry can be suitably used for describing accurately the geometric complexity of the structural members and the irregularities consisting in lacking material volumes due to a severe damage [11, 12, 13]. The proper estimation of the mechanical properties can be performed by means of expensive and invasive procedures, often impossible to be carried out [13]. For this reason, AVTs can be used to extract data on the modal properties of the tested structures [14, 15, 16, 17] and the unknown numerical model parameters can be estimated by solving optimization procedures aimed at minimizing the distance between the model predicted and the measured modal parameters [18, 19, 20, 21, 22, 23, 24].

This work presents the results of an ongoing research on a masonry arch bridge in the neighborhood of Todi (Umbria, Italy). The bridge is characterized by an irregular segmental arch, with a span and a rise higher than 10 m and 4 m, respectively. The structure exhibited typical mechanical deterioration phenomena consisting in cracks below the vault, material detachment in the side walls and the arches and damage of the West and east abutment. The damage level of the masonry was even worsened by vegetation grown between the cracks of the stones (Figure 1(a-b)). In 2017 a restoration process was started mainly consisting in a conservative restoration of the walls (cleaning, coating and grouting) and the planking level and a structural reinforcement of the vault and the masonry walls (Figure 2(a-b)).

The main purpose of this research is to determine the strengthening effects on the dynamic

Figure 2: Images of the historic masonry arch bridge after the strengthening: general view of the South side (a) and wall (b).

properties of this full-scale severely damaged masonry structure before and after strengthening. AVTs were carried out on Case A (i.e. severely damaged bridge) and Case B (i.e. strengthened bridge). Two FE models were developed starting from the digital geometric survey: one derived from photogrammetric survey that accurately describes the damage state (lack of material) and one regularizing the surfaces describing the post-strengthening state. The modal properties identified from both numerical models and the experimental works are compared highlighting the effect of important structural strengthening on the dynamic properties accounting for an accurate geometric description of the geometric irregularities due to severe damage.

2 EXPERIMENTAL MEASUREMENTS

The dynamic characterization of the masonry arch bridge before and after strengthening has been performed by Enhanced Frequency Domain Decomposition (EFDD) [25, 26] using vibration response in operating conditions and classical contact measurements. For the sake of clarity in the following the experimental results obtained before and after strengthening will be referred to as ”Case A”and ”Case B”, respectively.

2.1 Case A: AVTs for severely damaged masonry bridge

AVTs were carried out on the severely damaged masonry arch bridge in 2016 [28]. The dynamic response of the tested structure was measured using nine uni-axial accelerometers (model PCB 3939B12, 10 V/g sensitivity) located in different positions in order to obtain three different setups, to be used for the identification of vertical, horizontal and torsional vibration modes. The three sensor layouts are reported in Figure 3(a-b-c). Three sensors were installed at the keystone section of the arch to be used as a reference system for the analysis: two sensors were placed in the South side, giving measurements in both vertical and transversal directions while the third sensor was placed in the North side giving measurements in the vertical direction (red arrows in Figure 3(a-b-c)).

The testing methodology consisted in three different measurements, each recording 900 s time series with a sampling frequency of 1653 Hz, which is the minimum sampling frequency available for the used system, NI 9234 module with cDAQ 9188, due to inner anti aliasing filter. Since the power spectral density matrix estimated from the raw acceleration data showed a sig-

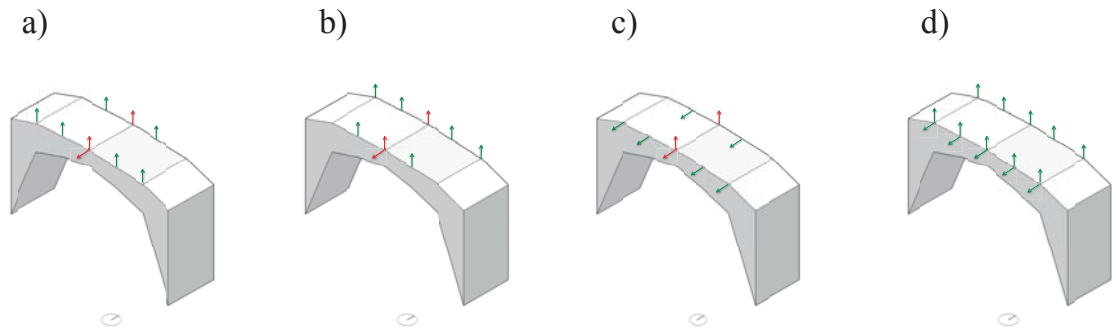

Figure 3: AVTs before strengthening: accelerometers arrangement used in Setup#1 (a), Setup#2 (b) and Setup#3 (c). Accelerometers arrangement for the AVTs after strengthening (d). Reference sensors are indicated in red.

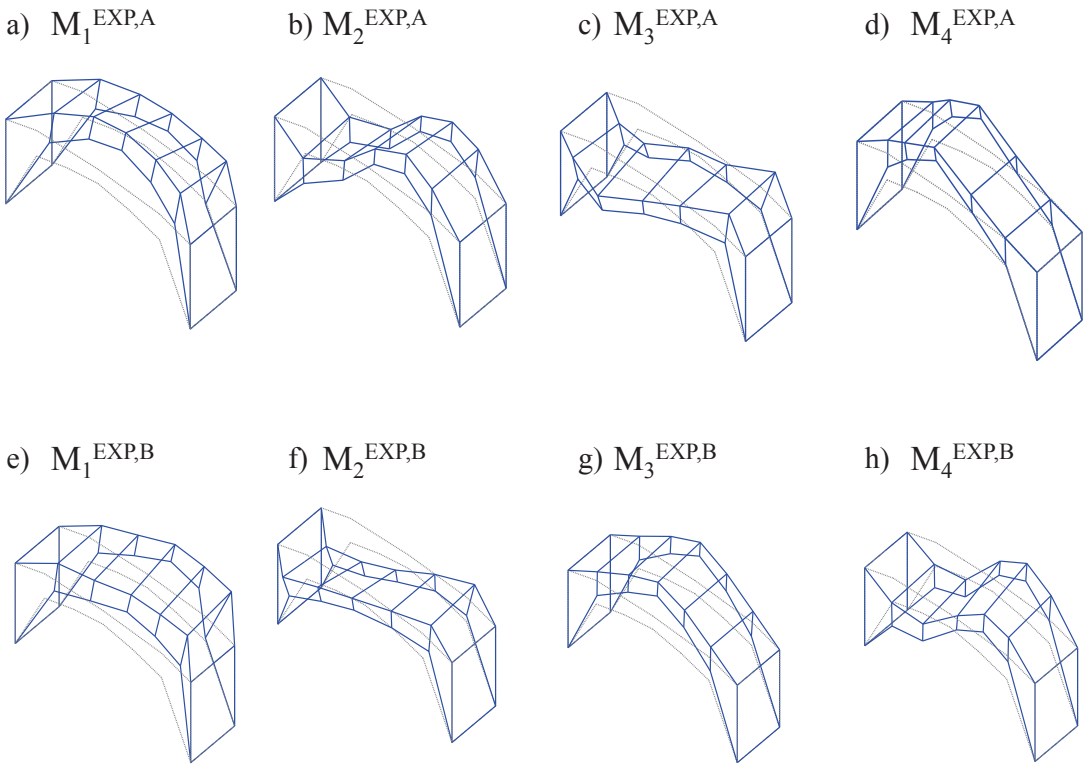

Figure 4: First four vibration modes of the masonry arch bridge before (a-d) and after (e-h) strengthening.

nificant frequency content between zero and 20 Hertz, the recorded data were downsampled to 27.55 Hz, offsets and drifts were removed. A low pass filter of order 3 with a cut-off frequency equal to 27.548 Hz was also applied.

The obtained natural frequencies are summarized in Table 1 and the corresponding vibration modes are reported in Figure 4(a-d). The The first four vibration modes are satisfactory identified from the AVTs. Two Out-of-Plane (OoP) modes ($M_1^{EXP,A}$, $M_3^{EXP,A}$) and two In-Plane (IP) modes ($M_2^{EXP,A}$, $M_4^{EXP,A}$) can be distinguished. Some modes present nearly symmetric configuration ($M_1^{EXP,A}$, $M_4^{EXP,A}$), while others are antisymmetric ($M_2^{EXP,A}$, $M_3^{EXP,A}$).

Given a set of experimental modal vectors it is possible to estimate the auto-MAC matrix

Table 1: Modal features obtained from experimental tests before strengthening.

Mode	$f[Hz]$	Mode's type
$M_1^{EXP,A}$	8.77	1^{st} OoP-Symmetric
$M_2^{EXP,A}$	13.93	1^{st} IP-Antisymmetric
$M_3^{EXP,A}$	14.72	2^{nd} OoP-Antisymmetric
$M_4^{EXP,A}$	17.76	2^{nd} IP-Symmetric

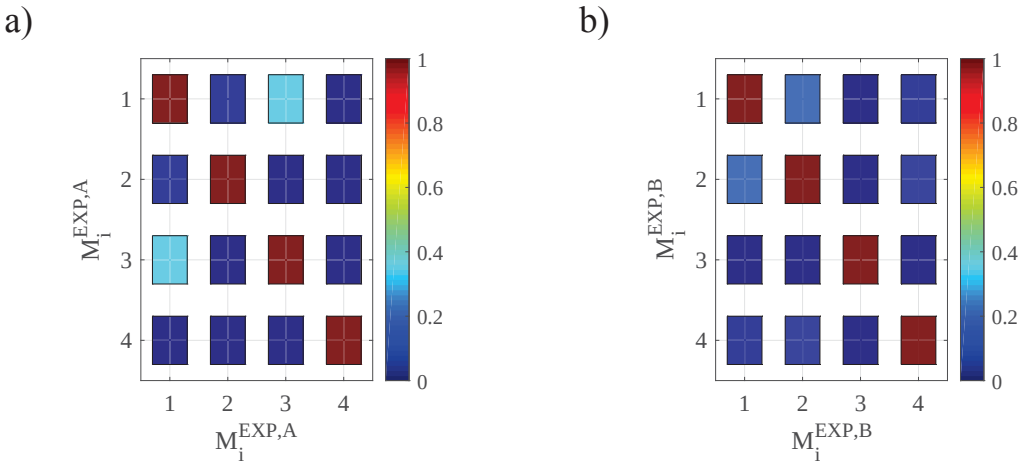

Figure 5: Components of the auto-MAC matrix evaluated on the identified natural mode shapes before (a) and after (b) strengthening.

[27], whose components are the auto-MAC numbers. The auto-MAC numbers are able to measure the degree of correlation between pair of modal vectors, assuming values equal to 1 or 0 for perfect correlation or no correlation, respectively. The auto-MAC numbers are very sensitive to the load non-stationarities and to the noisy reference modal vector. For this reason the auto-MAC is used in order measure the quality of the measurements. The optimal auto-MAC matrix should be characterized by values equal to one on the diagonal and zero otherwise. In this case study, the diagonal terms in diagonal auto-MAC matrix are equal to 1 since each modal vector is paired with itself, while the out-of-diagonal components are not all equal to 0 (Figure 5(a)). It should be noted that the auto-MAC number between the two OoP modes is higher than 0.4, that can be due the low level of vibrations and the related noise in the reference modal vectors, as well as to the combination process of three different setups.

2.2 Case B: AVT for strengthened masonry arch bridge

AVTs were carried out on the strengthened masonry arch bridge in 2017. The dynamic response of the tested structure was measured using fifteen uni-axial accelerometers (model PCB 3939B12, 10 V/g sensitivity).

Accelerometers were placed on both sides of the deck giving measurements in both vertical and transversal direction according to Figure 3(d). The testing methodologies consisted in two different measurements, each recording 1800 s time series with a sampling frequency of 200 Hz. Since the power spectral density matrix estimated from the raw acceleration data showed a significant frequency content between zero and 40 Hertz, the recorded data were downsampled to 50 Hz and offsets and drifts were removed.

Table 2: Modal features obtained from experimental tests after strengthening.

Mode	$f[Hz]$	Mode's type
$M_1^{EXP,B}$	10.96	1^{st} OoP-Symmetric
$M_2^{EXP,B}$	17.78	2^{nd} OoP-Antisymmetric
$M_3^{EXP,B}$	22.62	1^{st} IP-Symmetric
$M_4^{EXP,B}$	32.48	2^{nd} IP-Antisymmetric

The obtained natural frequencies are summarized in Table 2 and the corresponding vibration modes are reported in Figure 4(e-h). The first four vibration modes are satisfactory identified from the AVTs. Two Out-of-Plane (OoP) modes ($M_1^{EXP,B}$, $M_2^{EXP,B}$) and two In-Plane (IP) modes ($M_3^{EXP,B}$, $M_4^{EXP,B}$) can be distinguished. Some modes present nearly symmetric configuration ($M_1^{EXP,B}$, $M_3^{EXP,B}$), while others are clearly antisymmetric ($M_2^{EXP,B}$, $M_4^{EXP,B}$). Figure 5(b) show the auto-MAC matrix characterized by diagonal elements equal to 1 with the out-of-diagonal components all lower than 0.20 indicating good quality measurement.

2.3 Comparison

Figure 6 (a) compares the vibration modes obtained from the AVTs before and after strengthening in terms of MAC matrix. The MAC matrix has a similar meaning of the auto-MAC: the MAC matrix components are the MAC numbers estimated from each pair of vibration modes obtained from the experimental measurements carried out before and after strengthening. The diagonal MAC terms are equal to zero with the exception of the MAC value of the pair given by the first OoP symmetric mode $M_1^{EXP,A}$ and $M_1^{EXP,B}$ (equal to 0.6). The MAC value of the pair given by $M_2^{EXP,A}$ and $M_4^{EXP,B}$ (IP-Antisymmetric) is equal to 0.83; the MAC value of the pair given by $M_3^{EXP,A}$ and $M_2^{EXP,B}$ (OoP-Antisymmetric) is equal to 0.56 and finally the MAC value of the pair given by $M_4^{EXP,A}$ and $M_3^{EXP,B}$ (IP-symmetric) is equal to 0.86. This indicates a shift between the natural frequencies and the corresponding vibration modes caused by the the mass and the stiffness change due to the important structural strengthening.

Figure 6 (b) compares the natural frequencies identified by the measurements before and after strengthening in terms of percentage relative differences $\Delta = (f_i^{EXP,B} - f_i^{EXP,A})/f_i^{EXP,B} \times 100$. These percentage differences have been estimated reordering the natural frequencies such that they correspond to the same mode shape using the maximum MAC number. It should be noted that an increase of the natural frequencies higher than 15 % occur in all cases, with a maximum percentage difference higher than 55 % occurring for the IP-Antisymmetric mode shape (i.e. $f_2^{EXP,A}$ and $f_4^{EXP,B}$).

3 FINITE ELEMENT ANALYSIS

Two preliminary FE models have been set up in ABAQUS [29] environment in order to numerically reproduce the modal behavior of the tested structure before and after strengthening.

The first numerical model will be referred to as "Model A" and it corresponds to the severely damage state (Figure 7(a)). The geometry was carefully defined based on a photogrammetric survey provided by drones as an assembly of five main substructures, namely the arches, the vault, the side walls, the filling and the gallery. It should be noted that the photogrammetric based survey provided an accurate representation of the bridge geometry with respect to its external envelope, allowing to model some important details, such as the lack fo materials in the spandrel, the abutments and the arches. All these volumes were modeled extruding the hole profile obtained from the survey with a constant depth. The initial mechanical characteristics

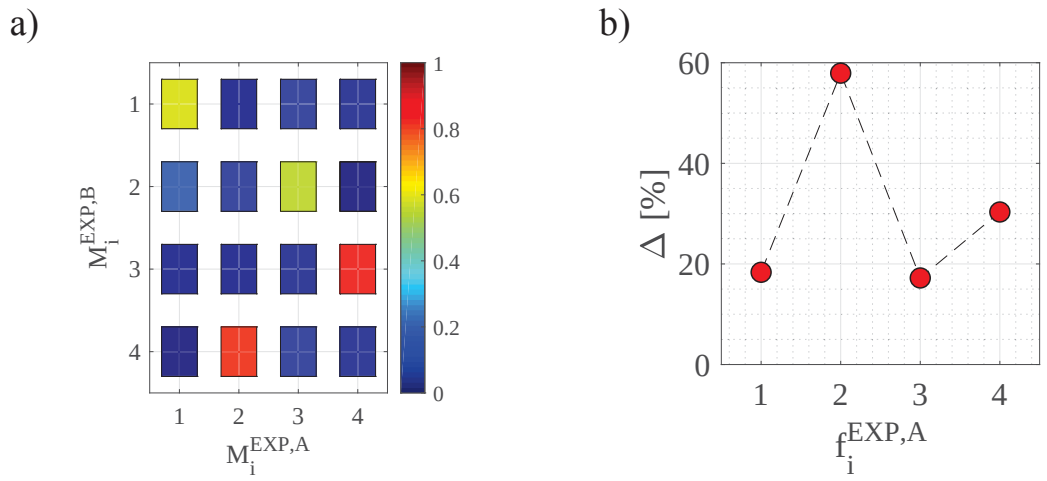

Figure 6: Comparison between the experimental results obtained before and after strengthening: MAC matrix (a) and percentage relative difference in terms of modal frequencies (b).

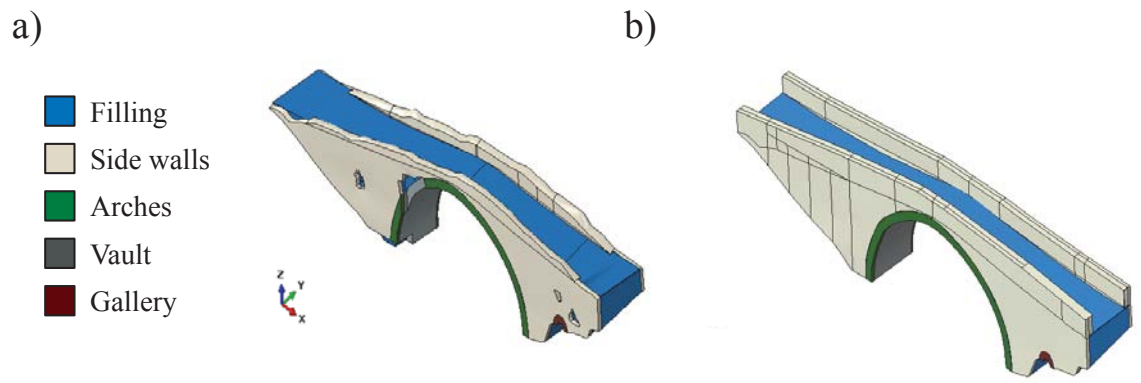

Figure 7: 3D FE models before and after strengthening: Model A (a) and Model B (b).

of all the five substructures are selected according to the prescription of the recent Italian instructions [30, 31, 32]. Table 3 provides a summary of the of the main mechanical properties of the chosen materials in terms of Young's modulus E and mass density ρ. The Poisson's ratio was taken constant for all the materials with a value equal to 0.2. The second numerical model will be referred to as "Model B" and it corresponds to the strengthened state (Figure 7(b)). The geometry was obtained regularizing the external surfaces of Model A. In this case the initial mechanical characteristics of all the five substructures are set according to the prescription of the recent Italian instructions multiplied by a coefficient α, able to account for the good condition of the mortar (Table 3).

The first four mode shapes of the masonry arch bridge in its severely damaged state are shown in Figure 8(a-d). It is worth noting that the second and the third numerical mode shapes ($M_2^{FEM,A}$ and $M_3^{FEM,A}$) are inverted with respect to the experimental modes. This is mainly due to the geometric irregularities considered in the detailed FE model and to the severely damaged state of the vault with several cracks and lacking material. Table 4 compares the natural frequencies identified by the Model A with the measured ones in terms of relative differences

Table 3: Mechanical parameters of the materials used in the FE models: elastic moduli E, mass density ρ and correction coefficient α.

Structural Part	$E[MPa]$	$\rho[t/m^3]$	α
Arches	2800	2.2	1.2
Vault	2400	2.2	1.2
Side walls	1230	2.0	1.4
Filling	870	1.9	1.5
Gallery	1500	1.8	1.5

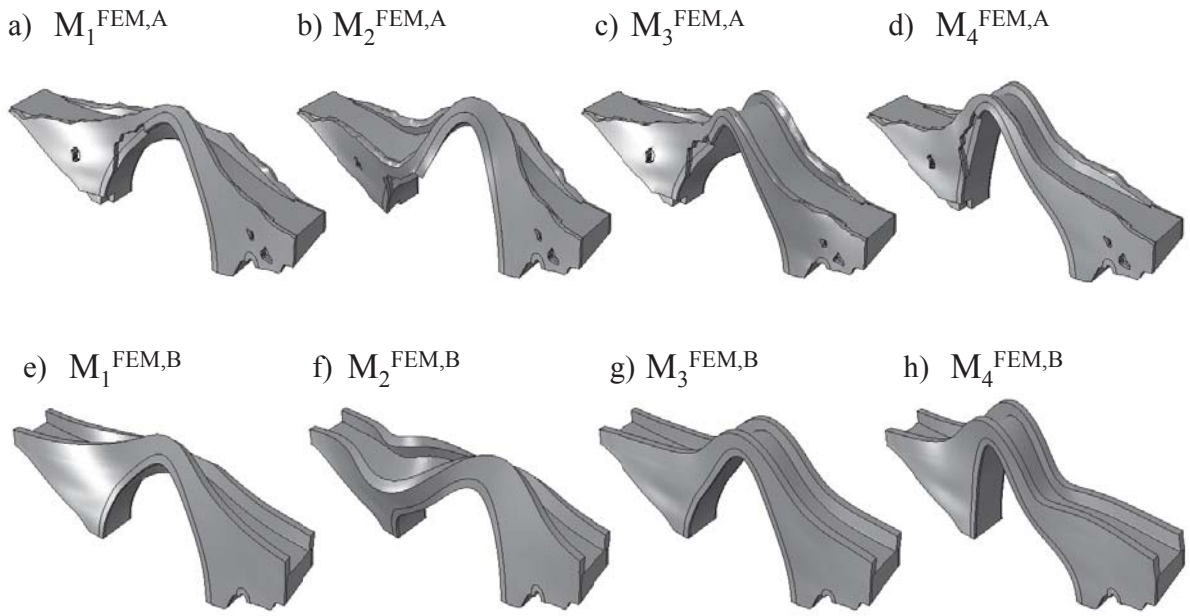

Figure 8: First four numerical mode shapes of the masonry arch bridge estimated from the FE models before (a-d) and after (e-h) strengthening .

$\Delta = (f_i^{EXP,A} - f_i^{FEM,A})/f_i^{EXP,A} \times 100$. Also in this case the natural frequencies are reordered such that that they correspond to the same mode shape accounting for the mode shape/natural frequency switching. It can be seen that the maximum relative difference occur for the second OoP-antisymmetric mode (i.e. $M_3^{EXP,A}$, $M_2^{FEM,A}$).

The first four mode shapes of the masonry arch bridge in its strengthened state are shown in Figure 8(e-h). Figure shows that the mode shapes obtained are the same of those obtained experimentally. Comparison of the numerically and experimentally identified natural frequencies are shown in Table 5 in terms of $\Delta = (f_i^{EXP,B} - f_i^{FEM,B})/f_i^{EXP,B} \times 100$. The maximum error between the natural frequencies is obtained for the second IP-antisymmetric mode, higher than 33 %.

Table 4: Comparison between experimental and initial numerical natural frequencies of Model A.

Mode	$f^{EXP,A}$	$f^{FEM,A}$	$\Delta[\%]$
1^{st} OoP-Symmetric	8.77	8.69	0.82
1^{st} IP-Antisymmetric	13.93	15.31	9.90
2^{nd} OoP-Antisymmetric	14.72	14.70	0.14
2^{nd} IP-Symmetric	15.76	16.01	1.53

Table 5: Comparison between experimental and initial numerical natural frequencies of Model B.

Mode	$f^{EXP,B}$	$f^{FEM,B}$	$\Delta[\%]$
1^{st} OoP-Symmetric	10.96	10.86	0.92
2^{nd} OoP-Antisymmetric	17.78	18.47	3.82
1^{st} IP-Symmetric	22.62	20.20	10.69
2^{nd} IP-Antisymmetric	32.48	21.69	33.22

4 CONCLUSION

The objective of this study was to carry out AVTs on the damaged and the strengthened full-scale masonry arch bridge in order to assess the effect of strengthening on the dynamic properties using both measurements and numerical analyses.

From the experimental measurements four natural frequencies were identified within the range $[8.77 - 17.76]$ Hz and $[10.96 - 32.48]$ Hz respectively for the severely damaged (Case A) and the strengthened (Case B) masonry arch bridge; further two IP and two OoP (symmetric and antisymmetric) vibration modes were identified in both cases. When the dynamic properties obtained from the measurements carried out in the two different cases are compared to each others two majors conclusions can be drawn: first, natural frequencies obtained in Case B were significantly higher than those obtained in Case A; second, after the strengthening the obtained vibration modes were more distinctive and natural frequency/vibration mode switchings were observed for the two IP modes and the second OoP antisymmetric mode.

The results obtained from the measurements were than compared to the results obtained from the numerical analysis starting from two different preliminary FE models: one able to describe the geometric irregularities due to the presence of existing damage and one describing the post strengthened state. It turns out the the adopted simulations are in both cases able to reproduce the modal behavior of the tested structure; natural frequencies and mode shapes match their experimental counterparts although in the post strengthened scenario the model predicted natural frequencies relative to the two IP vibration modes were significantly underestimated.

REFERENCES

[1] V. Sarhosis, S. De Santis and G. De Felice, A review of experimental investigations and assessment methods for masonry arch bridges, *Structure and Infrastructure Engineering*, **12**, 1439-1464, 2016.

[2] P. Zampieri, M.A. Zanini, F. Faleschini, L. Hofer and C. Pellegrino, Failure analysis of masonry arch bridges subject to local pier scour, *Engineering Failure Analysis*, **79**, 371 - 384, 2017.

[3] B. Conde, L. F. Ramos, D. V. Oliveira, B. Riveiro and M. Solla, Structural assessment of masonry arch bridges by combination of non-destructive testing techniques and three-dimensional numerical modelling: Application to Vilanova bridge, *Engineering Structures*, **148**, 621 - 638, 2017.

[4] M.G. Masciotta, D. Pellegrini, M. Girardi, C. Padovani, A. Barontini, P.B. Lourenço, D. Brigante and G. Fabbrocino, Dynamic characterization of progressively damaged segmental masonry arches with one settled support: Experimental and numerical analyses, *Frattura ed Integrita Strutturale*, **14**, 423-441, 2020.

[5] P.B. Lourenço, Computations on historic masonry structures, *Progress in Structural Engineering and Materials*, **4**, 201-319, 2002.

[6] G. Milani and P.B. Lourenco, 3D non-linear behavior of masonry arch bridges, *Computers and Structures*, **110-111**, 133-150, 2012.

[7] B. Conde, P. Eguia, G.E. Stavroulakis and E. Granada, Parameter identification for damaged condition investigation on masonry arch bridges using a Bayesian approach, *Engineering Structures*, **172**, 275-284, 2018.

[8] C. Costa, D. Ribeiro, P. Jorge, R. Silva, A. Arede and R. Calcada, Calibration of the numerical model of a stone masonry railway bridge based on experimentally identified modal parameters, *Engineering Structures*, **123**, 354 - 371, 2016.

[9] F. Clementi, A. Pierdicca, A. Formisano, F. Catinari and S. Lenci, Numerical model upgrading of a historical masonry building damaged during the 2016 Italian earthquakes: the case study of the Podestà palace in Montelupone (Italy), *Journal of Civil Structural Health Monitoring*, **7**, 703-717, 2017.

[10] N. Cavalagli and V. Gusella, Dome of the Basilica of Santa Maria degli Angeli in Assisi: Static and Dynamic Assessment), *International Journal of Architectural Heritage*, **9**, 157-175, 2015.

[11] M. Korumaz, M. Betti, A. Conti, G. Tucci, G. Bartoli, V. Bonora, A.G. Korumaz and L. Fiorini, An integrated Terrestrial Laser Scanner (TLS), Deviation Analysis (DA) and Finite Element (FE) approach for health assessment of historical structures. A minaret case study, *Engineering Structures*, **153**, 224 - 238, 2017.

[12] E. Ridolfi, G. Buffi, S. Venturi and P. Manciola, Accuracy Analysis of a Dam Model from Drone Surveys, *Sensors*, **17**, 1777, 2017.

[13] L.J. Sánchez-Aparicio, A. Bautista-De Castro, B. Conde, P. Carrasco and L. F. Ramos, Non-destructive means and methods for structural diagnosis of masonry arch bridges, *Automation in Construction*, **104**, 360-382, 2019.

[14] D.J. Ewins, Modal testing: theory and practice, *Mechanical engineering research studies: Engineering dynamics series*,1984.

[15] F. Cluni and V. Gusella and M. Gioffré , Performance evaluation of monumental bridges: Testing and monitoring 'Ponte delle Torri' in Spoleto, *Structure and Infrastructure Engineering*, **4**, 95-102, 2008.

[16] M. Gioffré, N. Cavalagli, C. Pepi and M. Trequattrini, Laser doppler and radar interferometer for contactless measurements on unaccessible tie-rods on monumental buildings: Santa Maria della Consolazione Temple in Todi, *Journal of Physics: Conference Series*, **778**, 012008, 2017.

[17] F. Magalhaes, A. Cunha ,E. Caetano and R. Brincker, Damping estimation using free decays and ambient vibration tests, *Mechanical Systems and Signal Processing*, **24**, 1274 - 1290, 2010.

[18] E. Simoen, G. De Roeck, G. Lombaert, Dealing with uncertainty in model updating for damage assessment: A review, *Mechanical Systems and Signal Processing*, **56-57**, 123 - 149, 2015.

[19] C. Pepi and M. Gioffré and M.D. Grigoriu, Bayesian inference for parameters estimation using experimental data, *Probabilistic Engineering Mechanics*, **60**, 103025, 2020.

[20] C. Pepi and M. Gioffré and M.D. Grigoriu and H.G. Matthies, Bayesian updating of cable stayed footbridge model parameters using dynamic measurements, *Proceedings of the 7th ECCOMAS Thematic Conference on Computational Methods in Structural Dynamics and Earthquake Engineering, Crete, Greece*, 2019.

[21] C. Pepi and M. Gioffré and M.D. Grigoriu, Parameters identification of cable stayed footbridges using Bayesian inference, *Meccanica*, **54**, 1403–1419, 2019.

[22] T. Marwala, Finite-element-model Updating Using Computational Intelligence Techniques, *Springer-Verlag,London, UK*, 2007.

[23] C. Gentile and A. Saisi, Ambient vibration testing of historic masonry towers for structural identification and damage assessment, *Construction and Building Materials*, **21**, 1311-1321, 2007.

[24] F. Ubertini, N. Cavalagli, A. Kita and G. Comanducci, Assessment of a monumental masonry bell-tower after 2016 central Italy seismic sequence by long-term SHM, *Bulletin of Earthquake Engineering*, **16**, 775-801, 2018.

[25] R. Brincker, C. Ventura and P. Andersen, Damping estimation by Frequency Domain Decomposition, *Proceedings of the International Modal Analysis Conference - IMAC*, **01**, 964–979, 2001.

[26] R. Brincker and L. Zhang, Frequency domain decomposition revisited, *IOMAC 2009 - 3rd International Operational Modal Analysis Conference*, **01**, 615-626, 2009.

[27] A.J. Allemang, The Modal Assurance Criterion (MAC): Twenty Years of Use and Abuse, *Journal of Sound and Vibrations*, 14-21, 2003.

[28] C. Pepi, M. Gioffrè, G. Comanducci, N. Cavalagl, A. Bonaca and F. Ubertini, Dynamic characterization of a severely damaged historic masonry bridge, *Procedia Engineering*, **199**,3398 - 3403, 2017.

[29] ABAQUS/Standard User's Manual, Version 6.9.

[30] Ministero delle Infrastrutture e dei Trasporti, Decreto Ministeriale 14 Gennaio 2018, Aggiornamento delle Norme tecniche per le costruzioni, Supplemento ordinario alla Gazzetta Ufficiale n. 42 del 20 febbraio 2018 - Serie generale, 2018.

[31] Ministero delle Infrastrutture e dei Trasporti, Istruzioni per l'applicazione dell' Aggiornamento delle Norme tecniche per le costruzioni di cui al decreto ministeriale 17 gennaio 2018, 2018.

[32] CNR-DT 212/2013 Istruzioni per la valutazione affidabilistica della sicurezza sismica di edifici esistenti, 2013.

EURODYN 2020
XI International Conference on Structural Dynamics
M. Papadrakakis, M. Fragiadakis, C. Papadimitriou (eds.)
Athens, Greece, 23–26 November 2020

A MULTIDISCIPLINARY APPROACH INTEGRATING GEOMATICS, DYNAMIC FIELD TESTING AND FINITE ELEMENT MODELLING TO EVALUATE THE CONSERVATION STATE OF THE GUIMARÃES CASTLE'S TOWER KEEP

L.J. Sánchez-Aparicio[1], M.G. Masciotta[2,3], D. Pellegrini[3], B. Conde[4],

M. Girardi[3], C. Padovani[3], L.F. Ramos[5], B. Riveiro[4]

[1] Department of Construction and Technology in Architecture (DCTA), Universidad Politécnica de Madrid
Av. Juan de Herrera 4, 28040 Madrid, Spain
e-mail: lj.sanchez@upm.es

[2] Department of Engineering and Geology, University "G. d'Annunzio" of Chieti-Pescara
Viale Pindaro 42, Pescara, Italy
g.masciotta@unich.it

[3] Institute of Information Science and Technologies "A. Faedo", ISTI-CNR
Via G. Moruzzi 1, Pisa, Italy
{daniele.pellegrini, maria.girardi, cristina.padovani}@isti.cnr.it

[4] Department of Materials Engineering, Applied Mechanics and Construction, University of Vigo
Vigo, Spain
{bconde, belenriveiro}@uvigo.es

[5] ISISE, Department of Civil Engineering, University of Minho, Campus de Azurém
Guimarães, Portugal
lramos@civil.uminho.pt

Keywords: Architectural heritage, geomatics, ambient vibration test, dynamic identification, model updating, numerical simulation

Abstract. *The development of realistic numerical models able to replicate as closely as possible the actual structural behaviour of heritage buildings is crucial for a thorough assessment of their structural performance against exceptional scenarios. In this regard, higher accuracy can be achieved by leveraging a multidisciplinary approach that integrates multiple contributions from different fields, such as geomatics, dynamics and computational modelling. In the present paper, this strategy is applied to the tower keep of the Guimarães castle, in Portugal, a masonry fortified structure dating back to the X century. Starting from an accurate laser scanner survey, a detailed numerical model has been created resorting to efficient algorithms able to represent complex situations. Furthermore, by exploiting the dynamic*

properties extracted from the processing of vibration data collected during field dynamic testing, the mechanical characteristics of the constituent materials of the tower have been estimated by means of a model updating technique embedded in a trust-region scheme implemented in the NOSA-ITACA code. The results obtained so far allowed to establish valuable baseline information that will be of pivotal importance to catch possible changes in the tower's response and to perform more in-depth structural analyses.

1 INTRODUCTION

Heritage structures represent a significant part of our built environment. Besides their cultural and social importance, historical buildings and sites are touristic attractions that positively impact the economy of the cities and countries in which they are located. Thus, the preservation of the built heritage is of primary concern at the local and global scale and goes beyond cultural requirements.

Since ancient constructions have been exposed to aging and deterioration phenomena for centuries, they are particularly vulnerable to new threats and damages. Material aging, pollution impact, long-term effects of ground subsidence, environmental vibrations and extreme events are just some of the main causes of damage in historical structures. If not detected in due time, damage can irreversibly impair the structural performance over time. However, the structural assessment of built heritage does conceal many challenges owing to the geometrical complexity characterizing age-old constructions, the heterogeneity of materials and building techniques adopted as well as the limited knowledge about past events and interventions that might have affected their actual conservation state [1].

In this context, preventive strategies based on regular condition surveys and periodic or continuous structural monitoring are fundamental to obtain a global insight into the behaviour of such non-conventional systems and promptly identify anomalies in order to plan in advance adequate corrective measures and ensure the good conservation of our built heritage [2], [3], [4]. At the same time, the complexity of old constructions requires the use of advanced tools for their accurate documentation and assessment, trying to improve the level of knowledge about the structure and to obtain reference information for post-event analysis in case of unexpected scenarios. A multidisciplinary approach integrating high-resolution surveys, field dynamic testing and finite element modelling is therefore necessary to achieve a full comprehension of historical buildings [5].

In the present work, this strategy is applied to an ancient masonry tower keep located in the hearth of the medieval castle of Guimarães, in Portugal. First, an accurate survey is performed using a terrestrial laser scanner in order to map the existing damages and develop an accurate 3D numerical model. Then, ambient vibration tests are carried out to extract meaningful information about the most significant dynamic parameters of the keep, namely frequencies, mode shapes and damping ratios. Finally, the experimental results are used to calibrate, through a model updating procedure based on a trust-region scheme [6], two refined FE models of the tower in order to estimate the mechanical characteristics of its constituent materials. Research is still in progress to achieve a very accurate simulation of the dynamic behaviour of the keep; however, the obtained results allowed to set baseline information that will be crucial to identify future deviations in the tower's response and to perform more advanced structural analyses.

2 FROM REALITY TO "AS-BUILT" CAD MODELLING

2.1 Guimaraes castle´s tower keep

Located in the historical center of the homonymous city (District of Braga, Portugal), the medieval castle of Guimarães is a five-sided polygonal military fortification erected during the X century (late Romanesque-early Gothic period) on a small hill formed from granite. The castle was primarily built to defend the Monastery of the city and its population from the attacks of Vikings and Moors, becoming nowadays a symbol of the Portuguese national identity. The construction is delineated by thick perimetral walls which give rise to a shape similar to a shield. Eight flanking towers (turrets) can be found along the walls, with height varying from 12 to 20 m. Turrets and walls surround and protect the inner military square together with the most prominent tower therein located: the central tower keep (Figure 1a). This free-standing structure, 25.86 m high and composed of four squared levels with an estimated area of 76 m^2 each, features massive bearing walls made of three-leaf regular granite masonry varying in thickness from about 1.98 m at the 1st floor, to 1.54 m at the 4th one, and is topped by battlements. Centrally, the construction has a squared granite pillar which tapers upwards from about 1.90 x 1.90 m^2 (base) to 1.20 x 1.20 m^2 (top). The pillar and the walls support the double-warped wooden floor of the different levels as well as the wooden trusses and rafters of the tiled four-pitched roof (Figure 1b).

a) b)

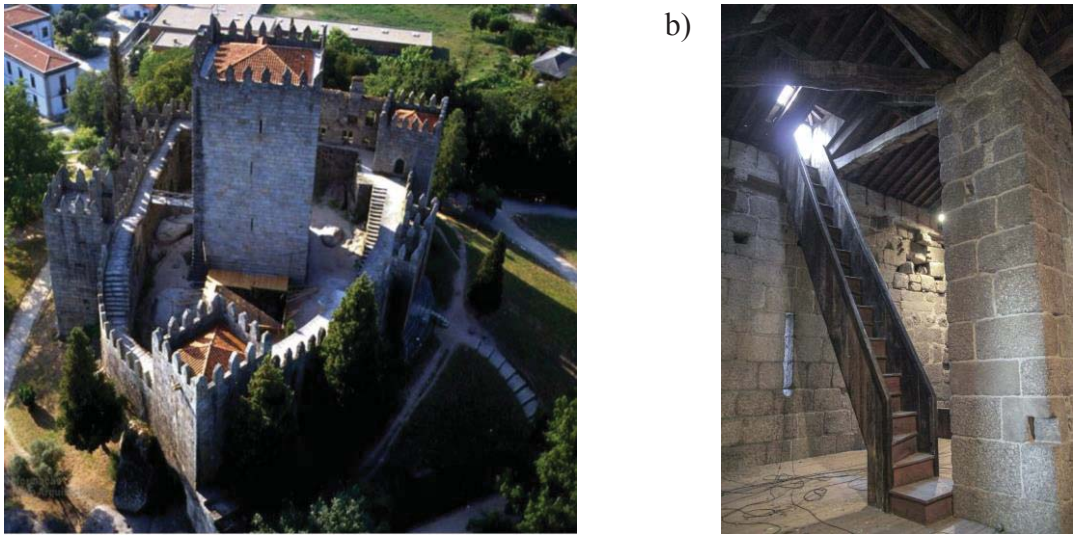

Figure 1: Guimaraes castle: a) outdoor view; and b) detailed view of the central pillar and roof trusses. (First photo source: http://www.monumentos.gov.pt/).

Concerning the state of conservation, the tower keep exhibits typical damages and deterioration processes: moist areas along the walls due to water infiltration and deficiencies in the drainage system; spread biological colonies, especially in the form of lichens, with high concentration on the most exposed parts; longitudinal cracks induced by the out-of-plane deformation of the main façade, likely due to the horizontal thrust of the timber roof structure.

2.2 3D digitalization via TLS technology

The geometrical configuration of the tower, with narrow spaces and unfavorable lighting conditions, made the Terrestrial Laser Scanner (TLS) device the best solution to digitalize the building. The light-weight TLS Faro Focus x330 ® was used for this purpose (Figure 2). Its most relevant features are summarized in Table 1.

Thirty-two scans were needed to capture the whole tower keep (Figure 2): i) eight scan stations to digitalize the façades; ii) sixteen stations to capture the indoor spaces; and iii) eight scans for the roof of the tower. It is worth noting that this large number of scans was due to the necessity of having a good overlap between scan stations in order to carry out a proper cloud-to-cloud alignment.

Specification	Value
Physical principle	Phase shift
Wavelength (nm)	1550
Measurement range (m)	0.60 to 330
Field of view (degrees)	300 V x 360 H
Nominal accuracy value at 25 m (mm)	± 2mm
Capture rage (pts/sec)	122,000 to 976,000
Spatial resolution at 10 m (mm)	6

Table 1: Technical specifications of the TLS Faro Focus.

a) b)

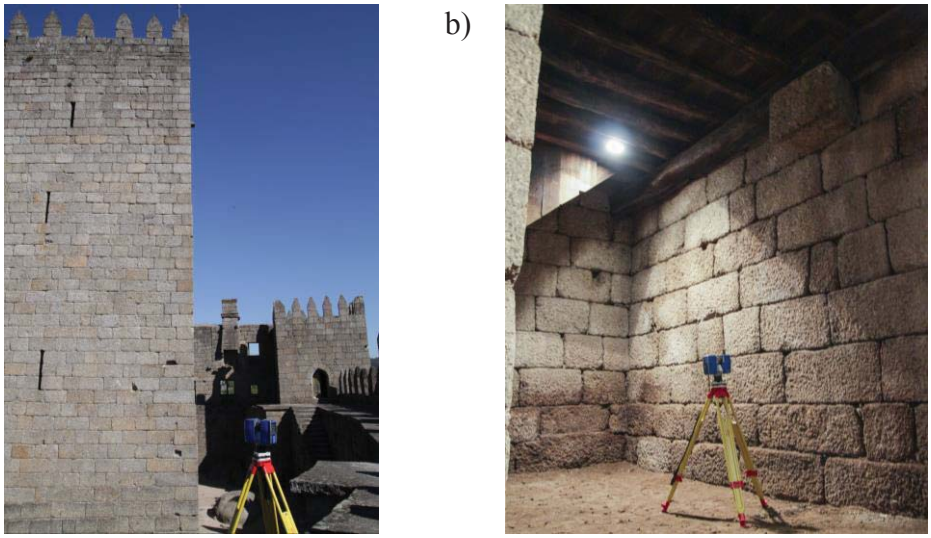

Figure 2: 3D digitization of the tower keep through TLS: a) outdoor; and b) indoor.

2.3 Point cloud processing

All the stations were aligned in a single coordinate system by means of the coarse-to-fine registration proposed in [7]. The approach begins with a pair-wise registration through the ICP (Iterative Closets Point) algorithm [8], followed by the Generalized Procrustes Analysis (GPA) [9], with the aim of minimizing the error accumulation among the different scans. As a result, a complete 3D point cloud of the tower was obtained, with an error of 0.003±0.002 m. The huge amount of captured data, counting about 410,982,656 points, demanded the application of a decimation filter for their manipulation; thus, a curvature-based filter with a threshold of 0.02 m was employed. This filter allows to decimate flat areas while maintaining all the details in curved areas (e.g. edges or timber elements). At the end of the decimation process, the final point cloud contained 32,449,888 points – barely 8% of the original one (Figure 3).

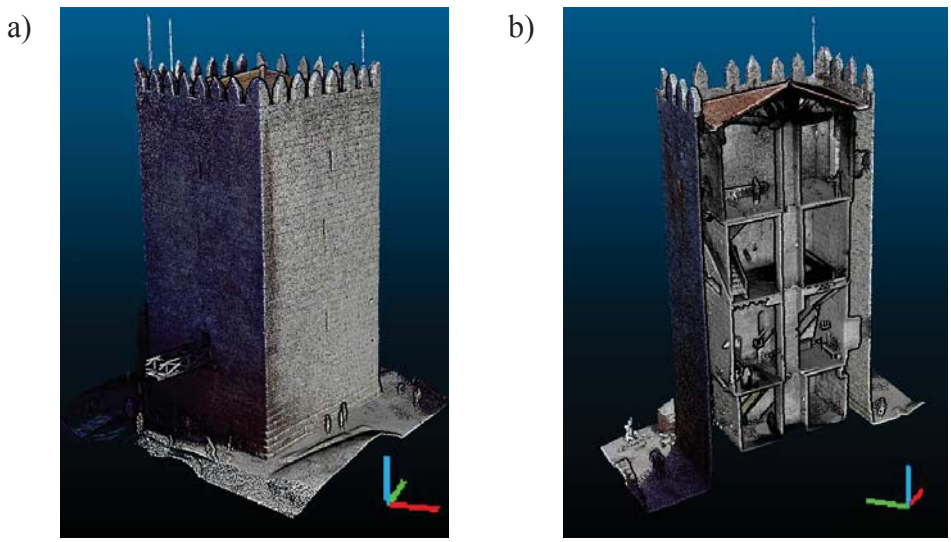

Figure 3: 3D point cloud of the tower keep: a) exterior view; and b) section crossing the center of the tower.

2.4 As-built modelling

As mentioned in Sub-Section 2.1, the main façade of the tower keep suffers visible out-of-plane deformations. With the aim of considering this outward displacement in the numerical analysis of the structure, an as-built CAD modelling stage was carried out, using the reverse engineering workflow proposed by [10]. The approach consists of the following steps: i) 3D Delaunay triangulation; ii) horizontal sections along the z-axis each 2.0 m; iii) b-spline vectorization of each section; iv) creation of surface between b-splines by means of Lofted surfaces; and v) refinement of the model through the use of Boolean operators (Figure 4).

In order to further simplify the subsequent numerical simulation, the timber structure of floors and roof was modelled by means of b-spline curves. To this end, several transversal sections along the different timber elements were extracted; then, a b-spline approximation was computed using as nodes the centroid of each section. This allowed to obtain an accurate as-built CAD model of the tower to be later used as geometrical base for defining the numerical mesh (see Sub-Section 4.2).

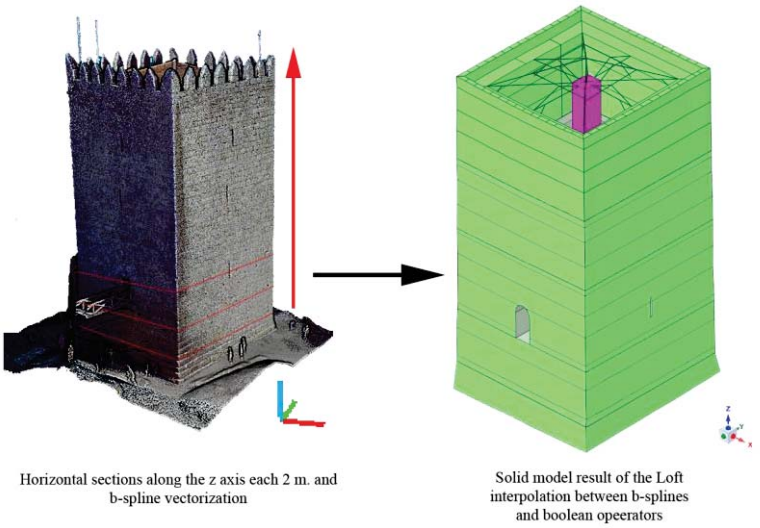

Figure 4: From the point cloud to the CAD model: graphical workflow.

3 OPERATIONAL MODAL ANALYSIS

3.1 Dynamic testing procedure

Dynamic testing can be considered as a global nondestructive tool since it allows to obtain real-time punctual checkups of the structural fitness just by deploying an array of sensors in the structure and recording the corresponding vibration response to random ambient excitations, without resorting to any invasive technique [11]. This aspect represents one of the major strengths of dynamic testing, making it play a leading role in the context of structural health monitoring of historical constructions. From the analysis of vibration signals, it is possible to estimate the dynamic properties of a structural system (frequencies, mode shapes and damping ratios) and use this information for different purposes, including the identification of anomalies and damage mechanisms, the assessment of strengthening needs or the calibration of realistic numerical models for in-depth structural analyses.

As for the Guimarães castle, the dynamic characterization of the tower keep was performed by Operational Modal Analysis (OMA), namely using output-only data acquired from the structure in operating conditions through classical contact vibration sensors. Eleven uniaxial piezoelectric accelerometers (model PCB 393B12, 10 V/g sensitivity, ±0.5 g dynamic range, 8 μg resolution) were distributed across the tower in order to measure its vibration response at strategic locations both in the bearing walls and the central pillar. The testing procedure consisted of two setups, each one recording 600 s acceleration time series sampled at 200 Hz from eleven measurement points; two accelerometers were kept on the top level as reference points for the analysis. In total, records from twenty DOFs (degrees of freedom) were acquired. The complete sensor layout is displayed in Figure 5.

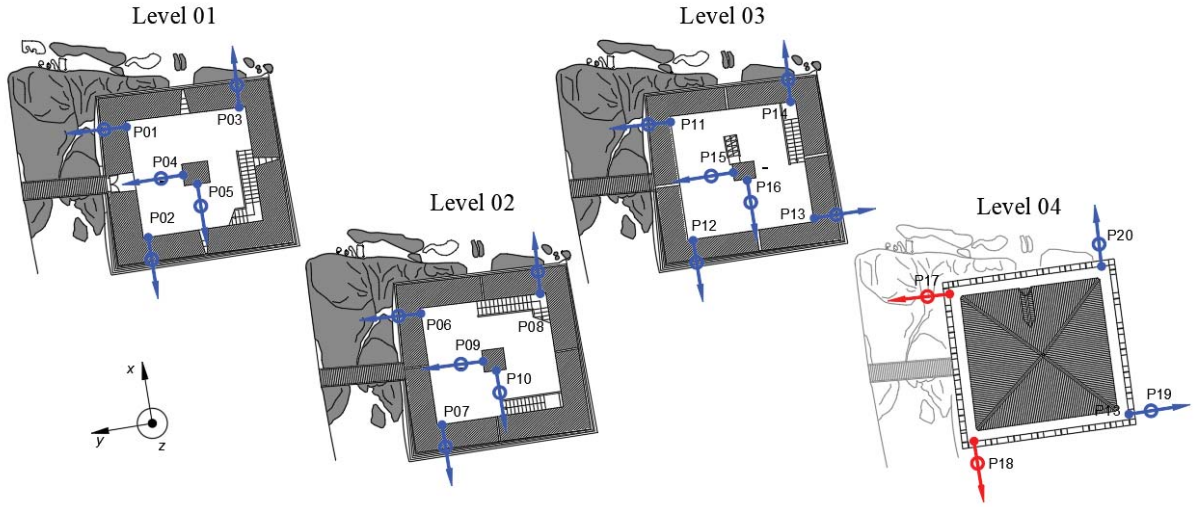

Figure 5: Sensor layout for the dynamic testing (reference sensors are indicated in red).

3.2 Data processing and results

The dynamic properties of the tower keep were estimated using two output-only dynamic identification techniques available in the commercial software ARTeMIS [12], i.e. the Enhanced Frequency Domain Decomposition (EFDD) and the Stochastic Subspace Identification with Extended Unweighted Principal Component (SSI-UPCX). Before elaboration, data were preliminary analyzed to remove trends, down-sample the signals and reduce leakage errors. Indeed, since the power spectral densities of the raw time histories displayed a significant frequency content in the range 2–15 Hz, all data were pre-processed with a decimation of order 5, passing from 102,400 to 20,480 of spectral resolution. Afterwards, both the afore-

mentioned modal estimators were applied, allowing to cross-validate the results of eight out of eleven vibration modes in the frequency and time domains.

The estimated natural frequencies and damping ratios are summarized in Table 2 together with the MAC values indicating the degree of similarity between corresponding mode shapes. Overall, eleven vibration modes were identified for the tower keep: two translation modes at 2.68 Hz (f_1) and 2.74 Hz (f_2) featuring in-phase modal components; one translation mode at 3.88 Hz (f_3) with out-of-phase modal components; one torsion mode at 4.81 Hz (f_4); two bending modes at 5.75 Hz (f_5) and 6.04 Hz (f_6); and five additional higher-order dominant bending modes at 7.22 (f_7), 7.98 (f_8), 9.23 (f_9), 10.22 (f_{10}) and 13.86 Hz (f_{11}).

	f_{EFDD} [Hz]	f_{SSI} [Hz]	$\|\Delta f\|$ [%]	ξ_{EFDD} [%]	ξ_{SSI} [%]	MAC
φ_1	2.67	2.68	0.37	0.66	1.13	0.98
φ_2	2.74	2.74	0.00	0.71	1.15	0.91
φ_3	3.88	3.88	0.00	1.22	1.41	1.00
φ_4	4.82	4.81	0.21	0.63	0.68	0.94
φ_5	5.38	5.75	6.43	0.78	1.99	0.57
φ_6	6.03	6.04	0.17	1.60	2.16	0.99
φ_7	7.16	7.22	0.83	0.51	1.97	0.48
φ_8	7.90	7.98	1.00	1.27	2.10	0.99
φ_9	9.21	9.23	0.22	0.65	2.22	0.98
φ_{10}	10.47	10.22	2.45	0.18	1.75	0.29
φ_{11}	13.91	13.86	0.36	0.38	1.53	0.92

Table 2: Experimental frequencies, damping ratios and MAC values (highlighted in grey the modal vectors featuring a low correlation).

Very low percentage errors in terms of frequency values are found comparing the two modal estimators, and consistent results are obtained as far as the damping ratios are concerned. It is also highlighted that, despite the inherent difficulties associated with the presence of closely spaced frequencies, a high correlation (MAC > 0.90) is found between all comparable vibration modes, except for modes 5, 7 and 10. Figures 6 and 7 show, respectively, the singular value decomposition (SVD) of the spectral density matrices and the first four estimated mode shapes.

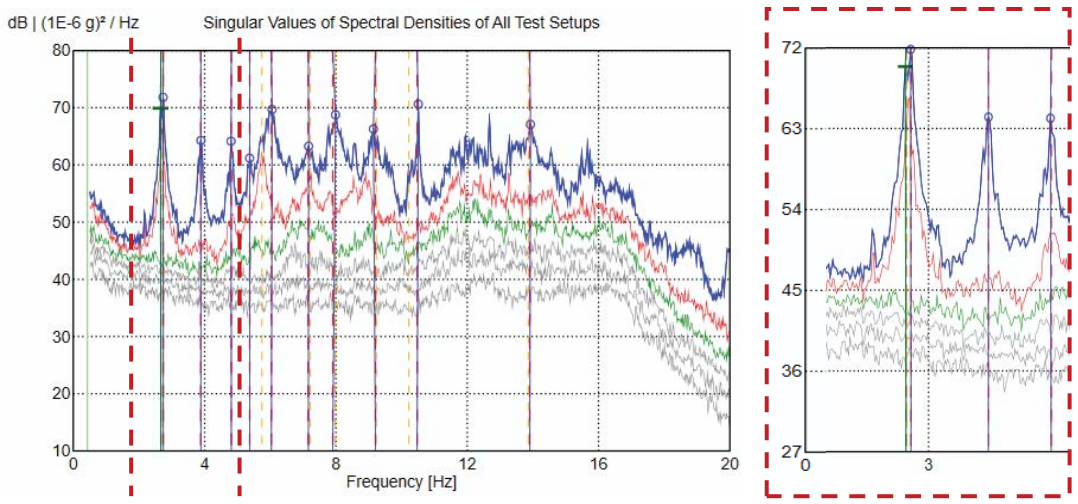

Figure 6: Singular value decomposition: peak picking of dominant frequencies.

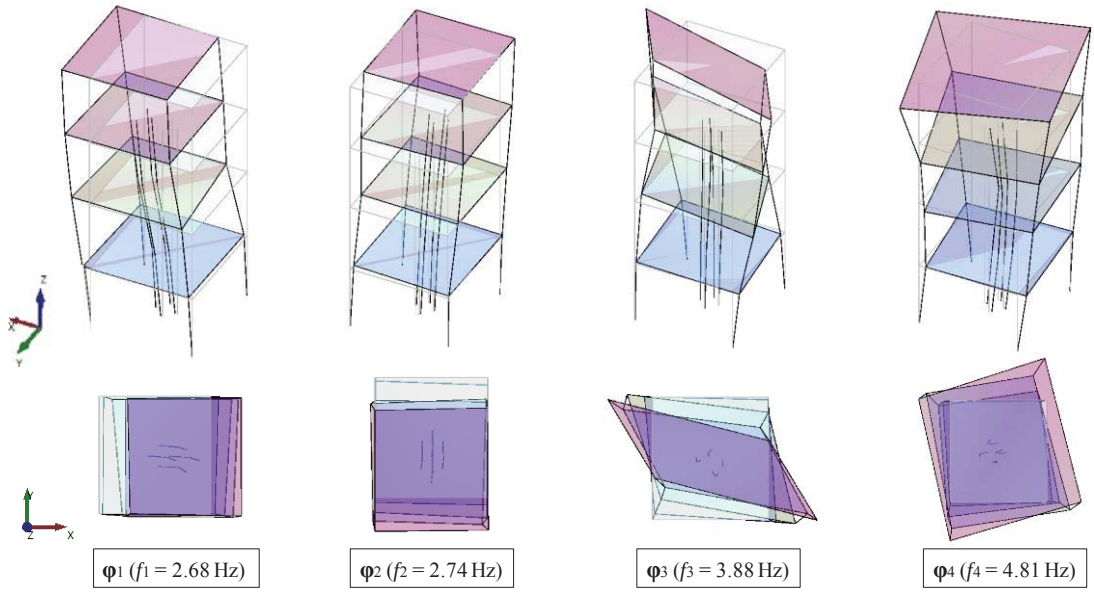

Figure 7: Experimental mode shapes of the tower keep (undeformed shape in light grey).

4 MODAL-BASED FINITE ELEMENT MODEL UPDATING

4.1 Model Updating

Model updating is a procedure aimed at calibrating an FE model in order to match the experimental and numerical dynamic properties (frequencies and mode shapes) of a structure [13]. It is an inverse problem based on modal analysis, which in turn relies on the solution of the generalized eigenvalue problem:

$$\mathbf{Ku} = \omega^2 \mathbf{Mu} \tag{1}$$

where $\mathbf{K}$ and $\mathbf{M} \in \mathrm{R}^{nxn}$ are the stiffness and the mass matrices of the structure discretized into finite elements; $\mathbf{u} \in \mathrm{R}^n$ is the vector of the degrees of freedom, with n being the total number of DOFs. The eigenvalue ω_i^2 is linked to the structure's frequency f_i by the relation $f_i = \omega_i/2\pi$ and the eigenvector $\mathbf{u}^{(i)}$ represents the corresponding mode shape.

The model updating problem can be reformulated as an optimization problem by assuming that the stiffness and mass matrices, $\mathbf{K}$ and $\mathbf{M}$, are functions of a parameter vector x varying in a p-dimensional box Ω. The goal is to determine the optimal value of x that minimizes, within the box Ω, the objective function $\phi(\mathrm{x})$ defined by:

$$\phi(\mathrm{x}) = \sum_{i=1}^{q} w_i^2 [\overline{f_i} - f_i(\mathrm{x})]^2 + w_{i+q}^2 [1 - \gamma_i(\mathrm{x})]^2 \tag{2}$$

where $\overline{f_i}$ and $f_i(\mathrm{x})$ are the q experimental and numerical frequencies to match, scalars γ_i are the square root of the modal assurance criterion (MAC) indicators [14] and measure the correlation between the i-th experimental mode shape and the corresponding numerical one, while scalars w_i encode the weight that should be given to each frequency and mode shape in the optimization scheme. Usually, to obtain relative accuracy on the frequencies, w_i is chosen equal to the inverse of the experimental frequency. As for the eigenmodes, weights are typi-

cally fixed to 0.1; this value respects the accuracy of the information retrieved from the identification phase, where, in general, eigenvectors are obtained with one magnitude lower accuracy than the corresponding frequencies.

The numerical procedure for model updating herein used to obtain the optimal values of the parameter vector x, and described in detail in [15], [6], is implemented in the NOSA-ITACA code [16], a finite element software developed in house by ISTI-CNR (www.nosaitaca.it). The algorithm is based on the construction of local parametric reduced-order models embedded in a trust region scheme for solving the constrained minimum problem. In particular, it exploits the structure of the stiffness and mass matrices and the fact that only a few of the smallest eigenvalues have to be calculated in order to solve the problem. This procedure reduces both the overall computation time of the numerical process and the user's effort.

4.2 FE Model Calibration

With the aim of understanding the dynamic behavior of the tower and the mutual interaction between wooden elements and masonry structure, two detailed FE models, hereinafter referred to as Model A and Model B, were created via the NOSA-ITACA code and calibrated using the experimental results presented in Section 3. The mesh of each model was obtained from the as-built CAD model described in Sub-Section 2.4. Aiming at exploiting all the defined geometrical features, a tetrahedral mesh algorithm with high-order elements was applied, making sure that the thickness of the walls was defined by at least two elements in order to be able to capture stress gradients correctly in future non-linear analyses.

Model A (Figure 8a) counted 220,854 DOFs and was composed of: 45,296 10-node isoparametric tetrahedral elements (element 27 of the NOSA-ITACA library) – used to model the walls and the central pillar of the tower; 1,457 3-node thick shell elements (element 26 of the NOSA-ITACA library) – employed to simulate the wooden slabs; and 1,542 beam elements (element 9 of the NOSA-ITACA library) – used to model the wooden beams of floors and roof. Model B (Figure 8b) was obtained from Model A by removing all shell and beam elements, and replacing them with equivalent masses (m_1, m_2, m_3, m_4).

The masonry was modeled as a homogeneous isotropic material with a Poisson's ratio ν=0.2 and a mass density ρ_m = 2600 kg/m^3 [17], [18]; whereas a Poisson's ratio ν=0.3 and a mass density ρ_w = 1000 kg/m^3 were adopted for the wood. The structure was assumed to be clamped at the base.

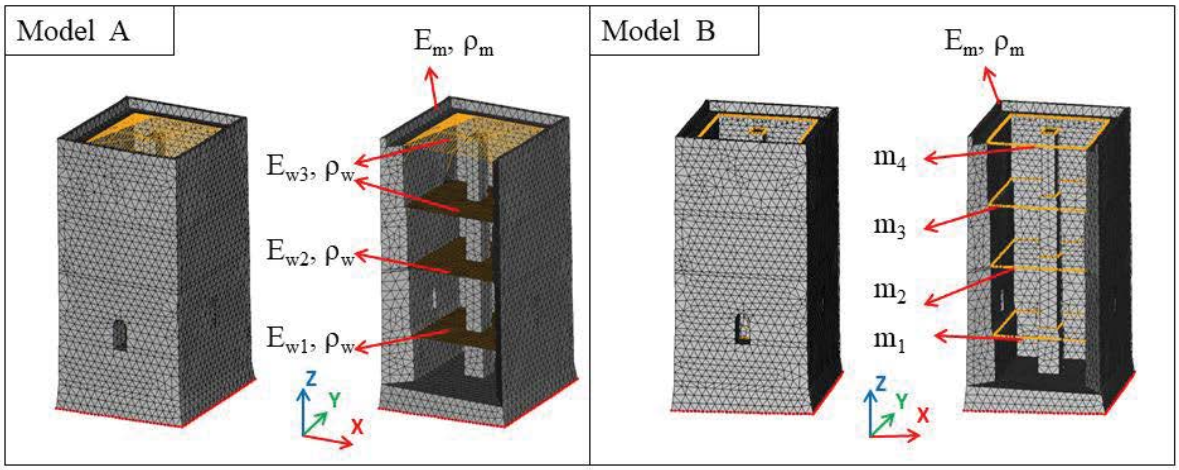

Figure 8: FE modelling of the tower keep: Model A and Model B.

As regards Model A, the numerical procedure recalled in Sub-Section 4.1 was employed to estimate the optimal values for the Young's moduli of masonry E_m, wooden slab and beams E_{w1}, E_{w2}, E_{w3}, assuming for the box Ω the following parameters bounds:

$$1000 \text{ MPa} \leq E_m \leq 8000 \text{ MPa}$$

$$100 \text{ MPa} \leq E_{w1}, E_{w2}, E_{w3} \leq 9000 \text{ MPa}$$

and trying to match the first four experimental frequencies and mode shapes of the tower. The parameter range for the wood material was chosen sufficiently large in order to take into account not only the uncertainties related to the knowledge of the mechanical characteristics of the material itself, but also the possible constraints between the wood elements and the masonry structure. The optimal mechanical parameters obtained through the model updating process are listed below:

$$E_m = 1686.5 \text{ MPa};\ E_{w1} = 290.66 \text{ MPa};\ E_{w2} = 454.76 \text{ MPa};\ E_{w3} = 890.92 \text{ MPa}$$

Table 3 summarizes the results of the optimization algorithm in terms of frequencies, absolute value of relative errors with respect to the experimental frequencies, and MAC values. The numerical mode shapes corresponding to the optimal values of the parameters are shown in Figure 9.

	Exp. [Hz]	Num. [Hz]	$\|\Delta\|$ [%]	MAC
f_1	2.68	2.51	6.34	0.98
f_2	2.74	2.61	4.74	0.99
f_3	3.88	4.26	9.79	0.69
f_4	4.81	4.80	0.21	0.62

Table 3: Model A – experimental frequencies, numerical frequencies, relative percentage errors, MAC values.

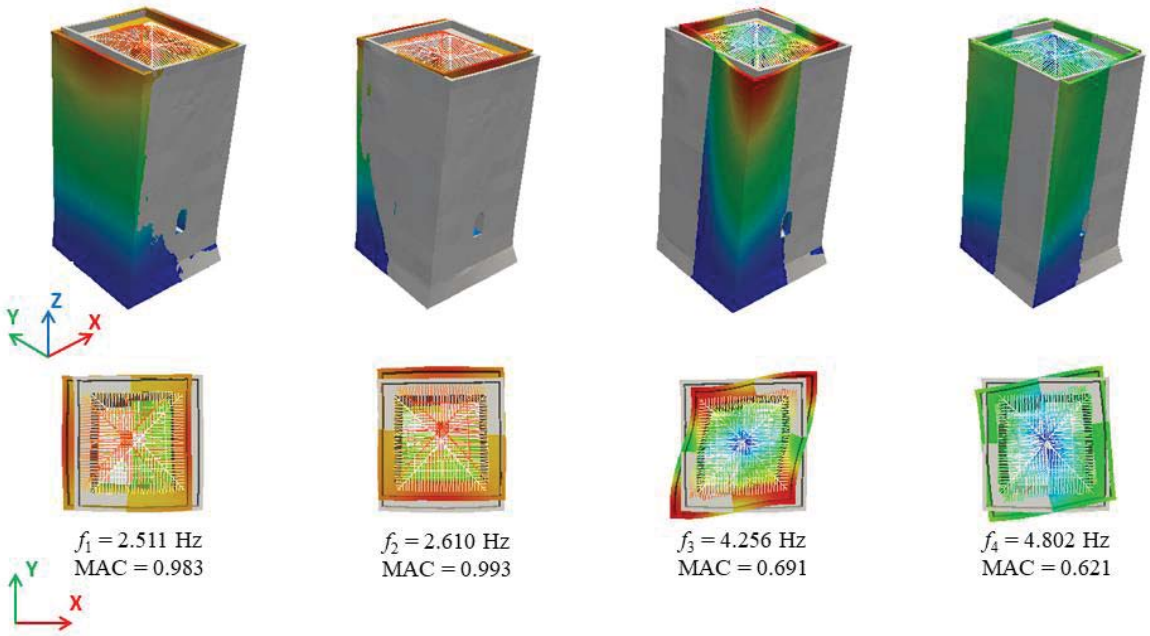

Figure 9: Model A – numerical mode shapes after the updating process (undeformed shape in grey).

In the attempt to improve the tuning with the experimental results, the same procedure was applied to Model B. In this case, the goal was to estimate the optimal values for the Young's modulus E_m and the mass density ρ_m of the masonry, assuming the following box Ω bounds for the parameters:

$$1000 \text{ MPa} \leq E_m \leq 8000 \text{ MPa}$$

$$2000 \text{ kg/m}^3 \leq \rho_m \leq 3000 \text{ kg/m}^3$$

The following parameter values were obtained through the optimization process:

$$E_m = 1955.8 \text{ MPa}; \qquad \rho_m = 2877.14 \text{ kg/m}^3$$

It is interesting to note that the updated Young's modulus and mass density obtained are consistent with the values reported in literature [17], [18].
The overall results in terms of frequencies, absolute value of relative errors between experimental and numerical frequencies, and MAC values are presented in Table 4, while the numerical mode shapes corresponding to the optimal values of the parameters are displayed in Figure 10.

	Exp. [Hz]	Num. [Hz]	$\lvert\Delta\rvert$ [%]	MAC
f_1	2.68	2.61	2.61	0.98
f_2	2.74	2.70	1.46	0.99
f_3	3.88	3.83	1.29	0.69
f_4	4.81	5.08	5.61	0.64

Table 4: Model B – experimental frequencies, numerical frequencies, relative percentage errors, MAC values.

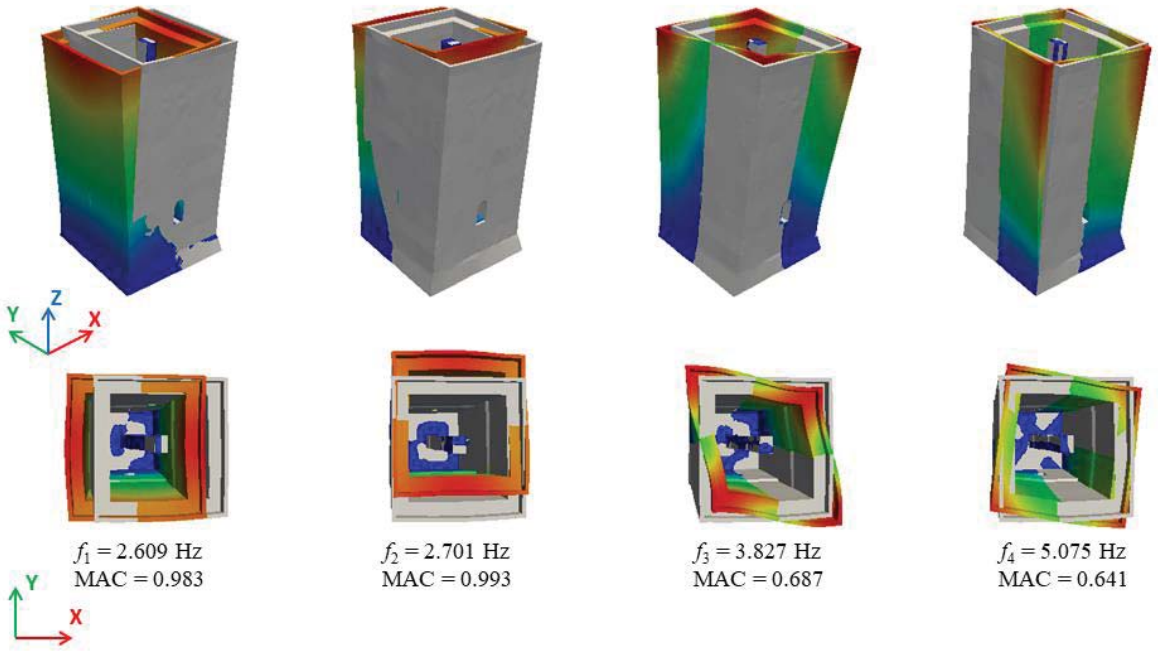

Figure 10: Model B – numerical mode shapes after the updating process (undeformed shape in grey).

Despite the similarities between numerical and experimental mode configurations, a high frequency percentage error is recorded for Model A. The comparison of the results with Model B shows that, if the wooden elements are not considered, the Young modulus of the masonry increases of about 15% and the mass density of nearly 10%; furthermore, the maximum relative error related to the two first frequencies decreases from 6.32% (Model A) to 2.65% (Model B). Regarding the MAC values, a good match between the two first experimental and numerical mode shapes is obtained for both models, while the third and fourth modal vectors are not very well approximated. Using an orthotropic material as done in [19] does not improve the numerical model, since the MAC value related to the third and fourth mode shapes remain unchanged.

5 CONCLUSIONS

The present paper aims to show the capabilities of an integrated and multidisciplinary approach to the complex problem of safeguarding heritage structures. The approach proposed here, encompassing digitalization, monitoring, numerical modelling and simulation, and relying on techniques and tools – either commercial or developed in house – at the disposal of the authors, is tested on the iconic tower keep of the Guimarães castle. The "laser acquisition – 3D digitalization – point cloud processing – CAD modelling – dynamic identification – finite element model updating" chain is described in all its steps, the ultimate goal being an accurate, fine-tuned numerical model of the tower. Such a digital counterpart of the real tower is of fundamental importance, since it constitutes the basis of any eventual finite element simulation aimed to predict the structural behavior of the tower under changing operational and environmental conditions.

REFERENCES

[1] M.G. Masciotta, J.C.A. Roque, L.F. Ramos, P.B. Lourenço, A multidisciplinary approach to assess the health state of heritage structures: The case study of the Church of Monastery of Jerónimos in Lisbon, *Construction and Building Materials,* 116, 169-187, 2016.

[2] R.M. Azzara., G. De Roeck, M. Girardi, C. Padovani, D. Pellegrini, E. Reynders, The influence of environmental parameters on the dynamic of the San Frediano bell tower in Lucca, *Engineering Structures*, 156, 175-187, 2018.

[3] M.G. Masciotta, L.F. Ramos, P.B. Lourenço, The importance of structural monitoring as a diagnosis and control tool in the restoration process of heritage structures: A case study in Portugal, *Journal of Cultural Heritage*, 27, 36-47, 2017.

[4] C. Gentile, A. Ruccolo, F. Canali, Long-term monitoring for the condition-based structural maintenance of the Milan Cathedral, *Construction and Building Materials*, 228 (2019) 117101.

[5] A. Bautista-De Castro, L.J. Sánchez-Aparicio, L.F. Ramos, J. Sena-Cruz, D. González-Aguilera, Integrating geomatic approaches, Operational Modal Analysis, advanced numerical and updating methods to evaluate the current safety conditions of the historical Bôco Bridge, *Construction and Building Materials*, 158, 961-984, 2018.

[6] M. Girardi, C. Padovani, D. Pellegrini, L. Robol, Model updating procedure to enhance structural analysis in the FE code NOSA-ITACA, *Journal of Performance of Constructed Facilities*, 33(4), 2019.

[7] L. J. Sánchez-Aparicio, B. Riveiro, D. Gonzalez-Aguilera, and L. F. Ramos, The combination of geomatic approaches and operational modal analysis to improve calibration of finite element models: A case of study in Saint Torcato Church (Guimarães, Portugal), *Construction and Building Materials*, 70, 118-129, 2014.

[8] P. J. Besl and N. D. McKay, Method for registration of 3-D shapes, in *Sensor fusion IV: control paradigms and data structures*, 586-606, 1992.

[9] R. Toldo, A. Beinat, and F. Crosilla, Global registration of multiple point clouds embedding the generalized procrustes analysis into an ICP framework, *Proceedings of 3DPVT 2010 Conference*, 2010.

[10] L.J. Sánchez-Aparicio, Á. Bautista-De Castro, B. Conde, P. Carrasco, and L.F. Ramos, Non-destructive means and methods for structural diagnosis of masonry arch bridges, *Automation in Construction*, 104, 360-382, 2019.

[11] M.G. Masciotta, L.F. Ramos, Dynamic identification of historic masonry structures, in *Long-term performance and durability of masonry structures,* Woodhead Publishing Series in Civil and Structural Engineering, Woodhead Publishing, 241-264, ISBN: 9780081021101, 2019.

[12] ARTeMIS Modal 5.3.1.1, Structural Vibration Solutions A/S (2018).

[13] J.E. Mottershead, M.I. Friswell, Model updating in structural dynamics: A survey, *Journal of Sound and Vibration*, 167(2) 347-375, 1993.

[14] N.M.M. Maia and J.M.M. Silva, Theoretical and experimental modal analysis. Research Studies Press LTD., Baldock, Hertfordshire, England. ISBN: 0863802087, 1997.

[15] M. Girardi, C. Padovani, D. Pellegrini, M. Porcelli, L. Robol, Finite element model updating for structural applications, *Journal of Computational and Applied Mathematics*, 370 (2020) 112675.

[16] R.M. Azzara, M. Grardi, C. Padovani, D. Pellegrini, Experimental and numerical investigations on the seismic behaviour of the San Frediano bell tower in Lucca, *Annals of Geophysics*, 61C, AC59, 2018.

[17] N. Domede, T. Parent & A. Sellier, Mechanical behaviour of granite: a compilation, analysis and correlation of data from around the world, *European Journal of Environmental and Civil Engineering*, 23:2, 193-211, 2019.

[18] L. M. O. Sousa, A. S. Oliveira, I. M. C. Alves, Influence of fracture system on the exploitation of building stones: the case of the Mondim de Basto granite (north Portugal), *Environ Earth Sci*, 75:39, 2016.

[19] C. Gentile, A. Saisi & A. Cabboi, Structural identification of a masonry tower based on Operational Modal Analysis, *International Journal ofArchitectural Heritage*, 9:2, 98-110, 2015.

EURODYN 2020
XI International Conference on Structural Dynamics
M. Papadrakakis, M. Fragiadakis, C. Papadimitriou (eds.)
Athens, Greece, 23–26 November 2020

ENVIRONMENTAL EFFECTS ON THE DYNAMIC CHARACTERISTICS OF A HISTORIC CATHEDRAL

Carmelo Gentile[1], and Antonello Ruccolo[2]

[1] Politecnico di Milano, Department of Architecture, Built environment and Construction engineering
Piazza Leonardo da Vinci, 32 - 20133 Milan, Italy
e-mail: carmelo.gentile@polimi.it

[2] Politecnico di Milano, Department of Architecture, Built environment and Construction engineering
Piazza Leonardo da Vinci, 32 - 20133 Milan, Italy
antonello.ruccolo@polimi.it

Keywords: Automated modal identification, Cathedral of Milan, Condition-based maintenance, Continuous monitoring, Temperature

Abstract. *The maintenance and preservation of the Milan Cathedral is traditionally performed through well-established and time-scheduled programs of visual inspection and architectural restoration of surfaces, decorations, and statues in Candoglia marble. On the other hand, the structural condition assessment and preservation turns out to be a challenging task due to the dimensions and complexity of the building, the usual uncertainties on the material properties and also the difficulty in inspecting several structural elements. Therefore, a structural monitoring system was recently designed and installed in the Milan Cathedral to assist the condition-based structural maintenance of the monument. The monitoring system includes different sensing technologies to allow appropriate tracking of different long-term structural behavior. The dynamic monitoring of the horizontal response of selected piers is complemented by the static monitoring of the tilt of the same piers and of the strain in selected tie-rods. In addition, the indoor and outdoor environmental parameters are extensively measured as well.*

After a concise historic background on the historic monument and the description of the dynamic monitoring system installed in the Milan Cathedral, the paper focuses on the dynamic characteristics of the monument, that were identified in the first hours of continuous monitoring, Subsequently, the results of the first year of dynamic monitoring are presented and discussed, with special attention being given to the influence of environmental parameters on the variations observed in the resonant frequencies and mode shapes. In more details, the presented results highlight that: (a) 8 global vibration modes are automatically detected in the frequency range 1.0-5.0 Hz; (b) the variations observed in the resonant frequencies are mainly driven by temperature, with the effect of thermal changes being very peculiar; (c) the mode shapes and the related mode complexity do not exhibit appreciable fluctuations associated to the environmental changes, so that an appropriate strategy of SHM should be based also on the time invariance of those parameters.

1 INTRODUCTION

The Milan Cathedral is a world-wide known Heritage monument, whose structural construction took more than 4 centuries, from the apse erection in 1386 until the façade finalization in 1813 [1]. Subsequently, the architectural works continued until the installation of the last iron gate in 1965 and this year is usually indicated as the official completion of the building works. Since 1387 all operational aspects related to the construction, maintenance and restoration of the cathedral are managed by the historic Institution named *Veneranda Fabbrica del Duomo di Milano* [2] and denoted as *Fabbrica* in the following. After the construction of the main structures of the cathedral, the *Fabbrica* main mission moved to continuous inspection, maintenance and preservation of the monument, with those activities being especially related to surfaces, decorations and statues in Candoglia marble.

After the recent assessment of the state of preservation and the tensile force of the metallic tie-rods of the Milan Cathedral [3], the idea of adopting a Structural Health Monitoring (SHM) strategy has been taking shape to continuously assist the structural condition assessment and preservation of the monument. Consequently, a joint research started between the *Fabbrica* and Politecnico di Milano and a structural monitoring system [4] was designed and installed in the cathedral, with the objectives of providing the information needed for the condition-based structural maintenance and the creation of a large archive of experimental data useful to enhance the knowledge of the monument.

The long-term monitoring system [4], fully computer based and with efficient transmission of the collected data, includes static and dynamic measurements. The dynamic monitoring is performed through seismometers (electro-dynamic velocity sensors) installed at the top of 14 selected piers and at 3 levels of the main spire. The static monitoring system consists of: (a) bi-axial tilt-meters installed at the top of selected piers and at 3 levels of the main spire; (b) vibrating wire extensometers mounted on the tie-rods exhibiting tensile stress larger than 100 MPa [3]. Since both the long-term static behavior and the time evolution of dynamic signatures are expected to be sensitive also to environmental changes [5] and especially the temperature might affect the variation of structural parameters in masonry structures [6-11], the indoor and outdoor environmental parameters (temperature and humidity) are extensively measured to establishing correlations with the changes of structural parameters [4-11] and evaluating the risks for the preservation of the main artifacts present in the cathedral [12].

The present paper is mainly aimed at describing the monitoring system installed in the cathedral with emphasis on the dynamic measurements, the processing of the continuously collected time series and the automated extraction of dynamic signatures (i.e. resonant frequencies, mode shapes and mode complexity [13-14]). Since the dynamic response of the church is continuously collected in a well distributed measurement grid (27 channels of data), the features representative of structural condition should include the mode shapes and not only the resonant frequencies. The use of mode shapes and mode complexity within a SHM strategy conceivably exhibit advantages because those modal parameters might be less sensitive than resonant frequencies to exogenous factors and contain information also on the local structural behavior.

In more detail, the paper starts with a concise historic background of the Milan Cathedral and a brief description of the dynamic monitoring hardware and of the software tools developed to process the continuously acquired time series. Subsequently, the dynamic reference characteristics of the cathedral, that were identified in the first hours of dynamic monitoring, are presented and discussed. At last, the evolution in time of the environmental and modal parameters during the first year of monitoring is addressed and comments are given within a SHM perspective.

(a) (b)

Figure 1: Past (a) and present (b) view of the Milan Cathedral (courtesy of *Veneranda Fabbrica del Duomo di Milano*).

(a) (b)

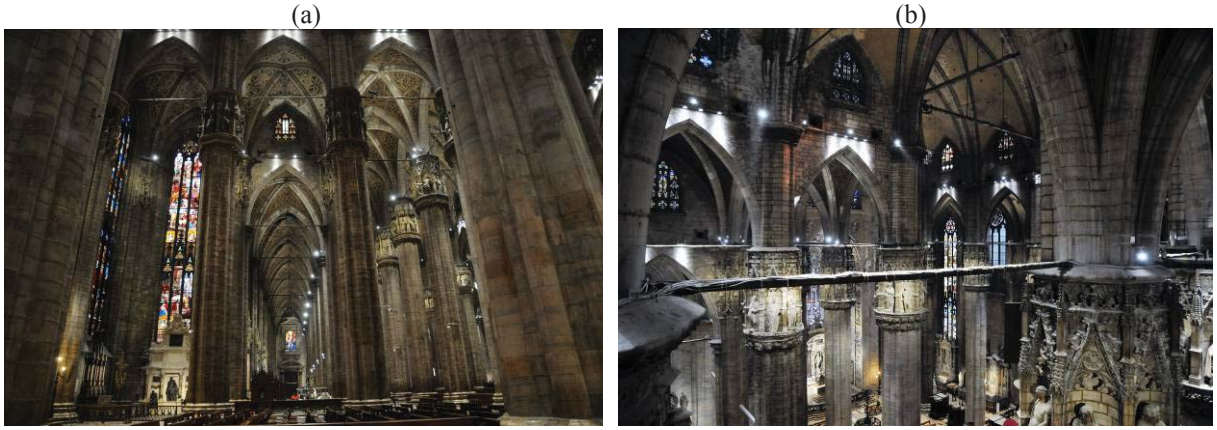

Figure 2: Inner views of piers, arches, vaults and iron tie-rods.

2 THE MILAN CATHEDRAL

The Milan Cathedral (Figs. 1-3) is the most representative landmark of the city of Milan and one of the largest masonry monuments ever built: the building spreads over an area of more than 10400 m^2, with a volume of about 300000 m^3, so that it is the second largest gothic cathedral in the world by volume and area.

The church exhibits a unique style of architecture, which is characterized by a fusion of European Gothic style and Lombardy tradition, also with the presence of neo-classic, neo-gothic and even renaissance influences, due to the long period required by the construction works. The church construction started in 1386 from the half-octagonal apse and East choir, and proceeded with the transept, the main dome, the *tiburio* (i.e., the prismatic structure with octagonal base, which is built around the main dome) and the main spire; subsequently, the five-nave structure over eight bays was built and finalized, in 1813, with a neo-Gothic façade. As previously pointed out, the inauguration of the last gate (January 6h, 1965) is generally assumed as the official ending of the monument building.

When compared with other gothic cathedrals, the Milan Cathedral exhibits a peculiar structural system, with metallic tie-rods being permanently installed under each vault (Fig. 2) and designed to exert an active part in resisting the lateral thrusts [3]. Historical documents [1] testify that the tension bars in the cathedral were permanently installed on the top of the piers during the construction, to reduce the horizontal thrust on the lateral buttresses, as those

buttresses were judged too slender by the French architect Jean Mignot. A total of 122 metallic tie-rods (Fig. 2) is nowadays present in the cathedral and most of them are the original elements dating back to the age of construction.

A longitudinal section of the Milan Cathedral is shown in Fig. 3. The overall dimensions of the Latin cross-shaped plan are about 66 m × 158 m (Fig. 4), with the aisles and the central naves spanning 9.6 m and 19.2 m, respectively.

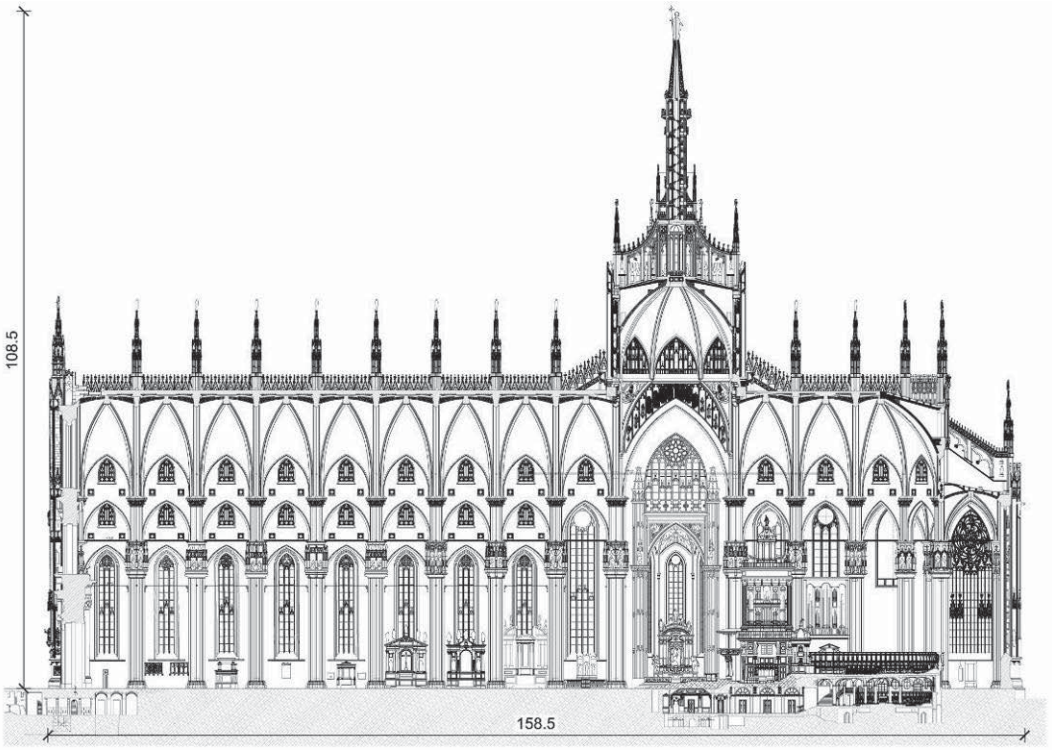

Figure 3: Longitudinal section of the Milan Cathedral
(dimensions in m, courtesy of *Veneranda Fabbrica del Duomo di Milano*).

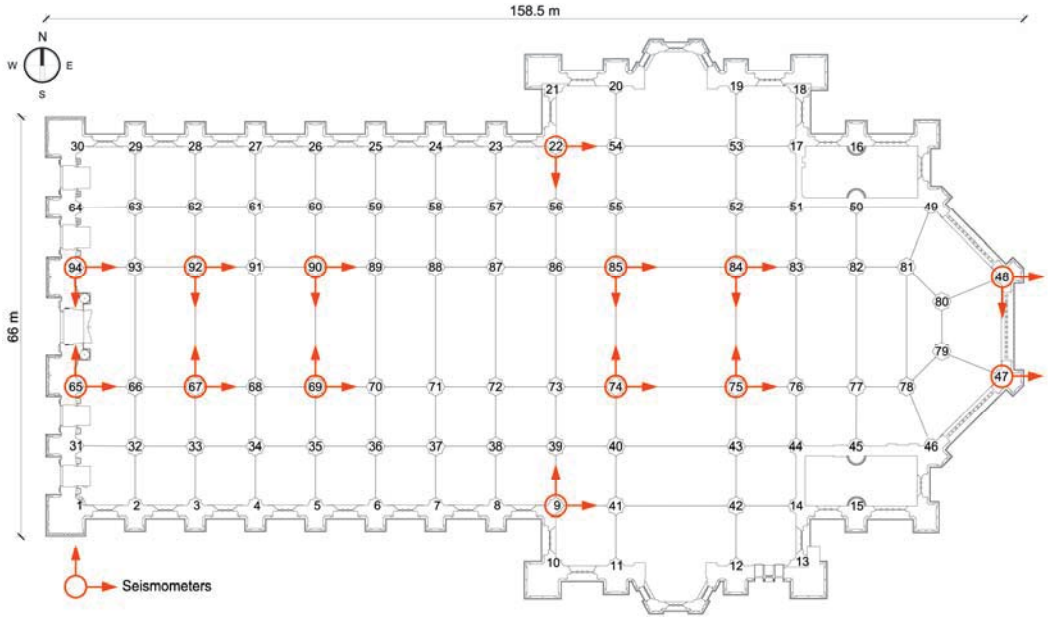

Figure 4: Plan of the Milan Cathedral (dimensions in m) and layout of the seismometers installed in the church.

3 DYNAMIC MONITORING SYSTEM AND DATA ANALYSIS

In order to characterize the health state of the Milan Cathedral and to address its condition-based structural maintenance, the following key parameters are continuously measured or identified from the measurements:

- Bi-axial tilt of the capital of selected piers (i.e., piers 31, 64, 69, 90, 11, 20, 74-75, 84-85 and 47-48 in Fig. 4) and main spire;
- Strain of tie-rods 28-62, 27-61, 26-60, 35-69, 25-59, 7-37, 9-39, 39-40, 56-55, 45-77, 38-72 and 87-57 (Fig. 4);
- Indoor and outdoor environmental parameters. The indoor temperature is measured in the same capitals where the tilts are recorded, whereas the humidity is measured in the neighborhood of instrumented ties. The outdoor parameters are collected through a weather station installed in the main spire;
- Resonant frequencies, mode shapes and damping ratios.

Due to the different technical characteristics of the various sensing devices and sampling rates of the data acquisition, two separated long-term monitoring systems, one static and one dynamic, were installed in the church. Strains, tilts and environmental data are collected at a rate of two samples per hour, whereas the dynamic monitoring is performed with a sampling frequency of 100 Hz. It is further noticed that the monitoring systems are fully computer based and their architecture has been established in order to minimize wiring, as well as the visual impact of the sensing devices inside the church.

The dynamic monitoring system is based on SARA SS45 seismometers (electro-dynamic velocity transducers). Since the electro-dynamic sensors are characterized by high sensitivity of 78 V/(m/s), un-necessity of powering and excellent performance in the low frequency range ($f \leq 100$ Hz), those transducers turn out to be especially suitable for the application in vibration testing or monitoring of civil engineering and cultural heritage [10] structures. The dynamic monitoring system consists of:

- 13 bi-axial seismometers and 1 mono-axial seismometer, installed at the top of selected piers inside the Cathedral (Fig. 4) and measuring the velocity in the two orthogonal N-S (transversal) and E-W (longitudinal) directions. The sensors installed on piers (94, 92, 90), (65, 67, 69), (22, 85, 84), (9, 74, 75) and (47, 48) are grouped and wired to five 24-bit digitizers SARA SL06. Each digitizer is equipped with A/D conversion system, 8 GB memory, synchronization by GPS, back-up battery and UMTS modem for data transfer;
- 3×3 mono-axial seismometers, installed at the same levels of the main spire hosting the biaxial tilt-meters belonging to the static monitoring. The three sensors installed at each level are wired to 24-bit digitizer, with the digitizers being connected to a switch for data transfer.

The velocity data are transferred in real time to the *Fabbrica* workstation and stored in separate files (in compressed mini-seed format) of 1 hour. Every hour, the automatic signal processing involves the following tasks: (a) pre-processing the raw data (to compensate the low-frequency attenuation of the sensor) using the SEISMOWIN commercial software (https://www.sara.pg.it/?lang=en) and subsequent saving of the time series in text format; (b) data analysis to extract the maximum and the root mean square values and creation of a file in Matlab (.mat) format; (c) low-pass filtering and down-sampling (to reduce the sampling frequency from 100 Hz to 20 Hz), and creation of a database of files for the application of the modal identification tools; (d) automated modal estimation and tracking.

After the automated modal parameter estimation, only the hourly evaluated features (i.e. the statistical characteristics of each dataset and the modal parameters) and a few time series corresponding to meaningful events are permanently stored in the *Fabbrica* archives and can be accessed through graphical and reporting tools. It should be noticed that similar tools allow the management and visualization of the static monitoring results.

The modal parameters of the cathedral and of the main spire are independently identified using a fully automated procedure, based on the covariance-driven Stochastic Subspace Identification (SSI-Cov) algorithm [15] and developed in previous research [16]. The length of the time window adopted in the automated identification was set equal to 1 h (3600 s). The automated procedure [16] involves the two main steps of modal parameters estimation (MPE) and modal tracking (MT).

The MPE is performed through an automatic interpretation of the stabilization diagram, based on the sensitivity of frequency and mode shape to the model order variation. For each dataset, after having filtered the spurious poles by checking the associated damping ratio and mode complexity value [13-14], the poles sharing similar frequencies and mode shapes are clustered together, and a set of representative modal parameters (i.e. resonant frequency, damping and mode shape) is estimated for each cluster. It is worth mentioning that the mode complexity is checked by averaging the information provided by both the Modal Phase Collinearity (MPC) [13] and Mean Phase Deviation (MPD) [13-14] through the Modal Complexity Index (MCI = 0.5 × [(1 − MPC) + (MPD/45°)], varying between 0 and 1, with 0 indicating a mono-phase behavior of the identified mode shape).

The MT, aimed at providing the time evolution of the parameters of each mode, is based on frequency and MAC [17] variation with respect to a pre-selected list of baseline modes. It is worth mentioning that this step is performed in an adaptive way, i.e. by updating the MAC and frequency variation threshold of each mode after a new dataset has been analyzed.

In the automated identification of the dynamic characteristics of the cathedral (27 channels of data, Fig. 4), the time lag parameter i was set equal to 60 and the data were fitted using stochastic subspace models of order n varying between 20 and 140; furthermore, in the noise modes elimination step, the maximum allowable damping ratio and MCI was set equal to 8% and 0.15, respectively.

4 DYNAMIC CHARACTERISTICS OF THE CATHEDRAL

The grid of seismometers permanently installed in the cathedral allowed the identification and fairly good spatial description of a relatively large number of key vibration modes. Typical results obtained on the first day of continuous monitoring, in terms of resonant frequencies and mode shapes, are shown in Fig. 5 (where the blue color refers to modes with dominant motion in the N-S direction and the red color refers to modes with dominant deflection in the E-W direction). The inspection of Fig. 5 allows the following comments:

(a) The lower two modes, as expected, are global sway modes of the cathedral along the transverse (N-S, f_{C1}=1.38 Hz, Fig. 5b) and longitudinal (E-W, f_{C2}=1.69 Hz, Fig. 5c) direction;

(b) The subsequent two modes (f_{C3}=1.96 Hz, Fig. 5d and f_{C4}=2.51 Hz, and Fig. 5e) involve dominant motion in the N-S direction and bending of the naves, with the deformed shapes being characterized by one and two changes of sign from apse to façade, respectively;

(c) The higher modes (Figs. 5f-i) are characterized by more complex mode shapes. For example, the 5th mode (f_{C5}=2.65 Hz, Fig. 5f) involves out-of-phase bending of the North and South naves, whereas the 6th mode (f_{C6}=2.76 Hz, Fig. 5g) involves out-of-phase motion of the façade and apse in the E-W direction;

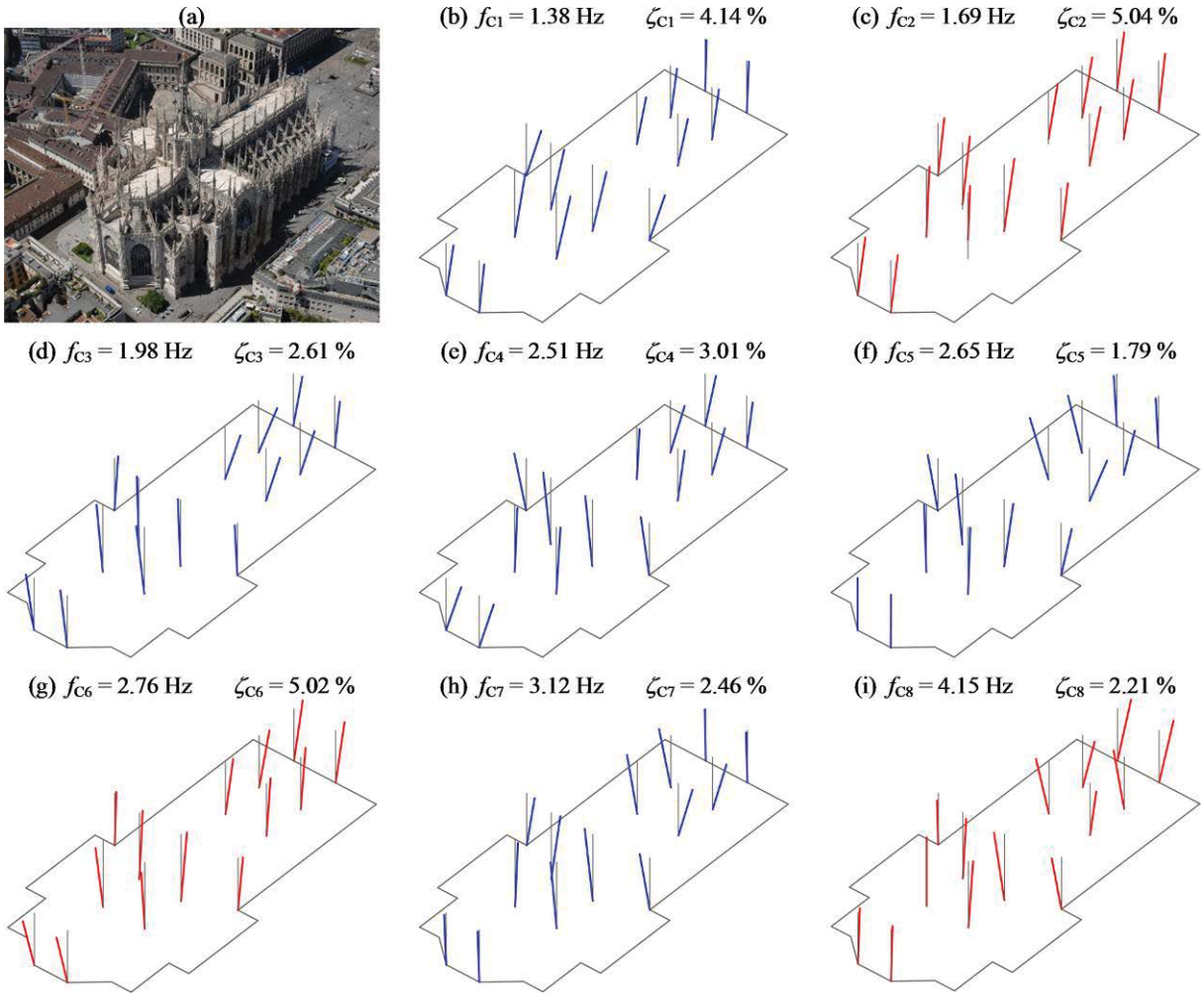

Figure 5: (a) Aerial view of the Milan Cathedral from apse and (b)-(i) identified vibration modes (17/10/2019, h 12:00–13:00).

(d) The N-S modes exhibit damping ratios varying from 1.79% (C5) to 4.14% (C1), whereas the damping of the E-W modes ranges between 2.21% (C8) and 5.04% (C2). It is further noticed that especially the damping of E-W modes seems to be larger than generally observed at the low level of ambient excitation existing on historical buildings.

5 SELECTED RESULTS FROM THE CONTINUOUS DYNAMIC MONITORING

The dynamic monitoring is active in the Milan Cathedral since October 19th, 2018. This section summarizes the main results obtained during the first year of monitoring (from 16/10/2018 to 15/10/2019) and, for the sake of consistency, only the experimental results collected in the cathedral are presented and discussed (with no comments being provided on the data measured on the main spire).

As usual for masonry buildings, the evolution in time of environmental parameters is firstly presented in order to understand the effects of changing environment on the variations observed in the natural frequencies and modal parameters.

5.1 Environmental parameters

As previously pointed out, a quite extended grid of temperature sensors and hygrometers has been installed inside the church, to support both the SHM program and the preservation of

the artifacts, which are kept inside the monument. The variation in time of the average indoor temperature and the outdoor temperature (measured by the weather station) is shown in Fig. 6a, whereas Fig. 6b refers to the average indoor humidity. The orange line in Fig. 6a presents the evolution of the outdoor temperature and highlights changes between −1.7°C and +35.4°C, with remarkable daily variations in sunny days. The corresponding variation of the average indoor temperature is represented by the red line in Fig. 6a and ranges between +8.8°C and +30.6°C: it is further noticed that the availability of a large number of temperature sensors in the church highlights [12] a low temperature gradient in space, with the difference between the extreme values not exceeding 0.5°C. Consequently, the low temperature gradient and the correlation coefficients (always larger than 0.99) between the measured temperatures allow to assume the average indoor temperature (Fig. 6a) as a representative quantity for the SHM correlations. A similar conclusion is drawn for the relative humidity, whose time series are highly correlated [4, 12] and exhibit correlation coefficients of the order of 0.90 or larger.

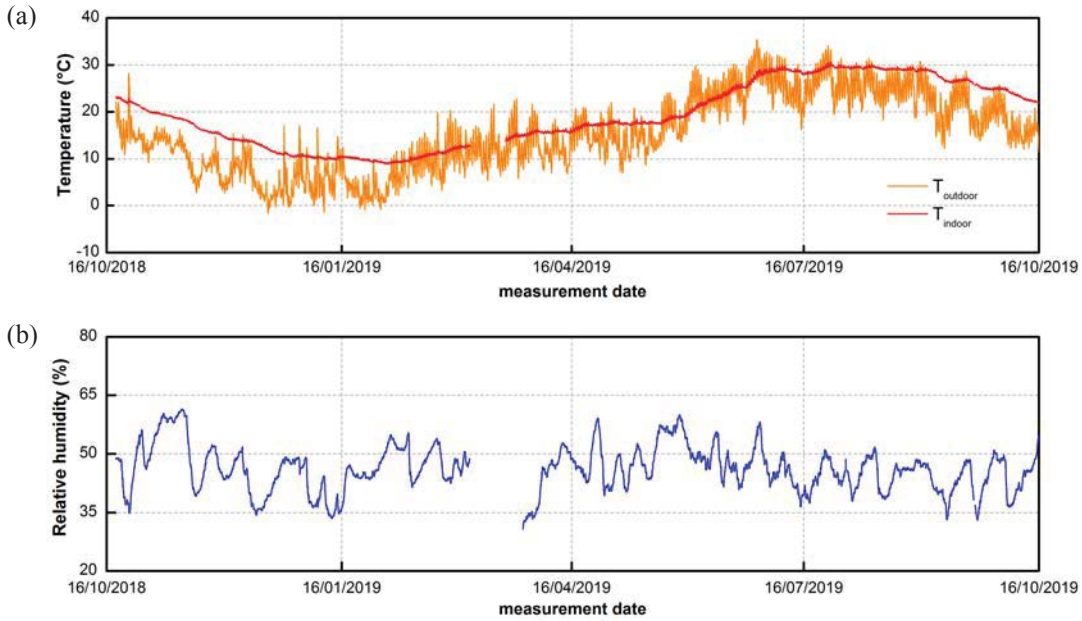

Figure 6: Evolution in time of: (a) average indoor temperature and outdoor temperature; (b) average indoor relative humidity.

5.2 Environmental effects on natural frequencies

The results of automated modal identification and frequency tracking during the first year of monitoring are exemplified in Fig. 7 for the lower 6 modes of the cathedral, exhibiting the higher identification rate. The complete results of automated OMA in terms of natural frequencies and damping ratios are summarized in Table 1 with some statistical information. In more details, Table 1 lists the identification rate, the mean value (f_{mean}) and the standard deviation (σ_f) of the automatically identified frequencies and their extreme values (f_{min}, f_{max}) as well as the mean value (ζ_{mean}) and the standard deviation (σ_ζ) of the damping ratio.

It should be noticed that the identification rate of the frequencies in Fig. 7 ranges between 99.8 % and 88.9 % (Table 1), whereas the higher two frequencies exhibit lower identification success ratios still allowing the tracking with an acceptable continuity.

As expected [5-11], Fig. 7 reveals clear long-term variations as well as daily fluctuations of natural frequencies, that are conceivably associated with changing temperature. In addition, the environmental effects turn out to be very distinctive and this peculiarity is understood, for

example, by carefully inspecting the time evolution of f_{C2} and f_{C4} in Fig. 7. Those modes, whose variation is quite easy to inspect in Fig. 7, are characterized by dominant motion in the longitudinal E-W (f_{C2}) and transverse N-S (f_{C4}) direction (Fig. 5).

Mode	Id. Rate	f_{mean} (Hz)	σ_f (Hz)	f_{min} (Hz)	f_{max}(Hz)	ζ_{mean} (%)	σ_ζ (%)
C1	99.8 %	1.383	0.011	1.359	1.423	3.73	0.24
C2	99.3 %	1.677	0.020	1.605	1.739	5.17	0.81
C3	99.3 %	1.993	0.015	1.956	2.059	3.24	0.42
C4	97.9 %	2.530	0.021	2.477	2.632	3.25	0.42
C5	96.4 %	2.668	0.021	2.609	2.757	1.42	0.32
C6	88.9 %	2.778	0.034	2.683	2.923	5.15	0.55
C7	71.4 %	3.170	0.051	3.066	3.383	2.56	0.53
C8	36.9 %	4.177	0.038	4.094	4.350	1.80	0.31

Table 1: Statistics of the natural frequencies and damping ratios identified in the first year of monitoring.

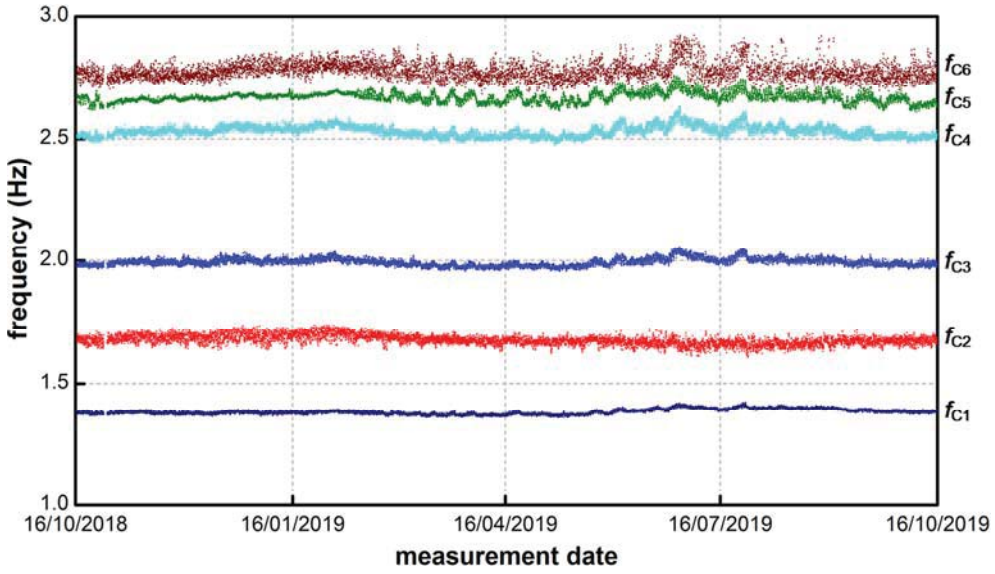

Figure 7: Variation in time of the natural frequencies of the lower 6 modes during the first year of monitoring.

Figure 7 highlights that the frequency of mode C2 clearly increases with decreased indoor and outdoor temperature (Fig. 6a) and decreases with increased temperature: this trend, which is exactly the opposite of what expected for masonry buildings [6-11], is confirmed by plotting the frequency f_{C2} versus the outdoor temperature (Fig. 8a), along with the best fit line: even if for a given temperature a quite remarkable frequency variation is observed, negative temperature correlation is exhibited by frequency f_{C2} during the entire monitoring period. It is worth mentioning that: (a) a negative frequency-temperature correlation is obtained with indoor average temperature and (b) the temperature effect on E-W mode f_{C6} is remarkably similar to what observed for mode f_{C2}, especially in the cold season (Fig. 7).

Even more complicated temperature-driven mechanisms characterize the variation of N-S modes: as shown in Fig. 7, the frequency f_{C4} tends to increase both in the cold and in the hot season and a similar trend is exhibited by N-S modes f_{C1}, f_{C3} and f_{C5}. The correlation between f_{C4} and the outdoor temperature is exemplified in Fig. 8b and, as it has to be expected, a non linear best fit line is obtained.

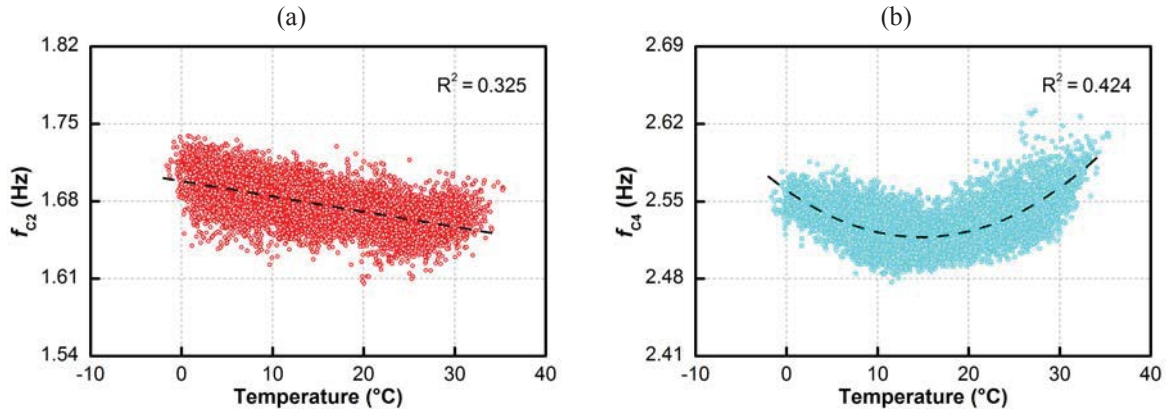

Figure 8: Correlation between outdoor temperature and identified natural frequencies: (a) f_{C2} and (b) f_{C4}.

It is further noticed that, during the cold season, a generalized (tensile) strain increase with decreased temperature is measured by the extensometers installed in the tie-rods [4]. Hence, the corresponding increased forces in the tension bars conceivably exert a stiffening action on the overall structure since the metallic tie-rods form a grid of stiffening elements spread over the entire cathedral (Fig. 2).

In summary, all natural frequencies of the cathedral exhibit a negative dependence on both indoor and outdoor temperatures in the cold season, whereas the correlation changes in the hot season, for the N-S modes only. The negative dependence of natural frequencies on temperature is a distinctive behavior of the Milan Cathedral, with this trend being very different from what generally reported in the long-term studies on masonry structures, either towers [6, 7, 10] or churches [6, 8-9]. Indeed, a negative frequency-temperature correlation is only reported in the literature for a monumental building [11], which is characterized by the presence of metallic tie-rods, as well.

In the authors' opinion, the complex dependence of natural frequencies on temperature observed in the Milan Cathedral results from two temperature-driven opponent effects: the stiffening exerted during the cold season by the increased tensile forces in the metallic grid of tie-rods and the usual thermal expansion of the masonry materials. The former effect turns out to be dominant in the cold season for all modes, whereas the latter tends to overcome in the hot season, for N-S modes.

Notwithstanding the complex temperature-driven behavior of the cathedral and the difference of trend exhibited by N-S and E-W modes, the removal of environmental effects can be performed, for example, by applying the principal component analysis (PCA) [18] to the frequency data collected during an appropriate training period. In the present application, the lower 6 modes (Fig. 7) were considered and the training period includes the first year of monitoring.

Since two latent sources of temperature-driven variability have been suggested by the previous analysis and those sources affect differently the N-S and E-W modes, the first four PCs are retained in order to establish the PCA-based model. As shown in Fig. 9, the PCA provides a very effective removal of the environmental effects.

Once the PCA-based prediction model has been established using the data collected during an appropriate training period, the occurrence of abnormal structural changes not observed during the training period is often detected by using the residual errors (i.e., the difference between the identified frequency and its prediction). Anomaly detection approaches might involve: (a) verifying that each prediction error does not exceed 95% confidence interval [19] or (b) using the prediction errors within the framework of statistical control charts (such as the well-known Hotelling's T^2 control chart [20]).

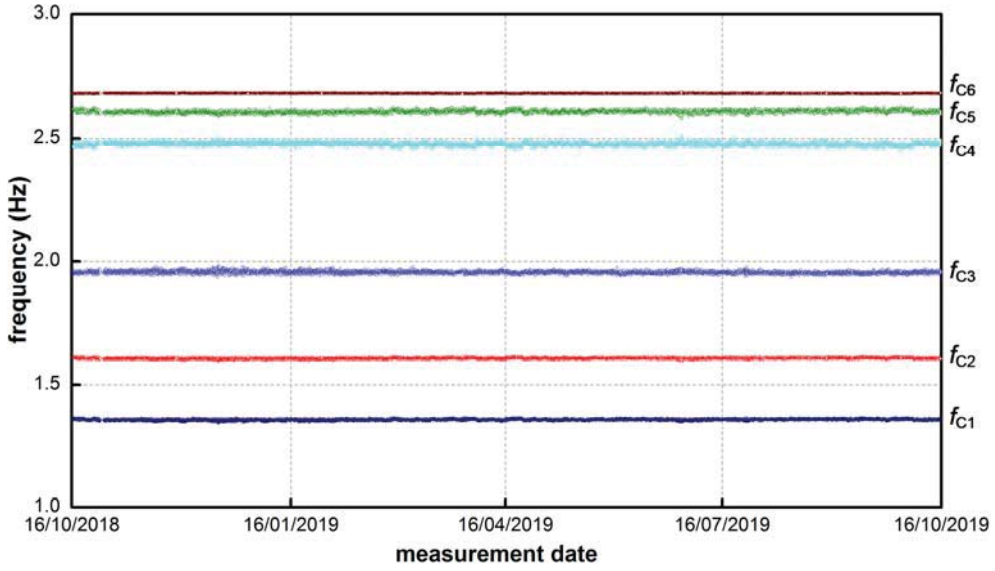

Figure 9: Variation in time of the natural frequencies of the lower 6 modes during the first year of monitoring, after the PCA-based removal of the environmental effects.

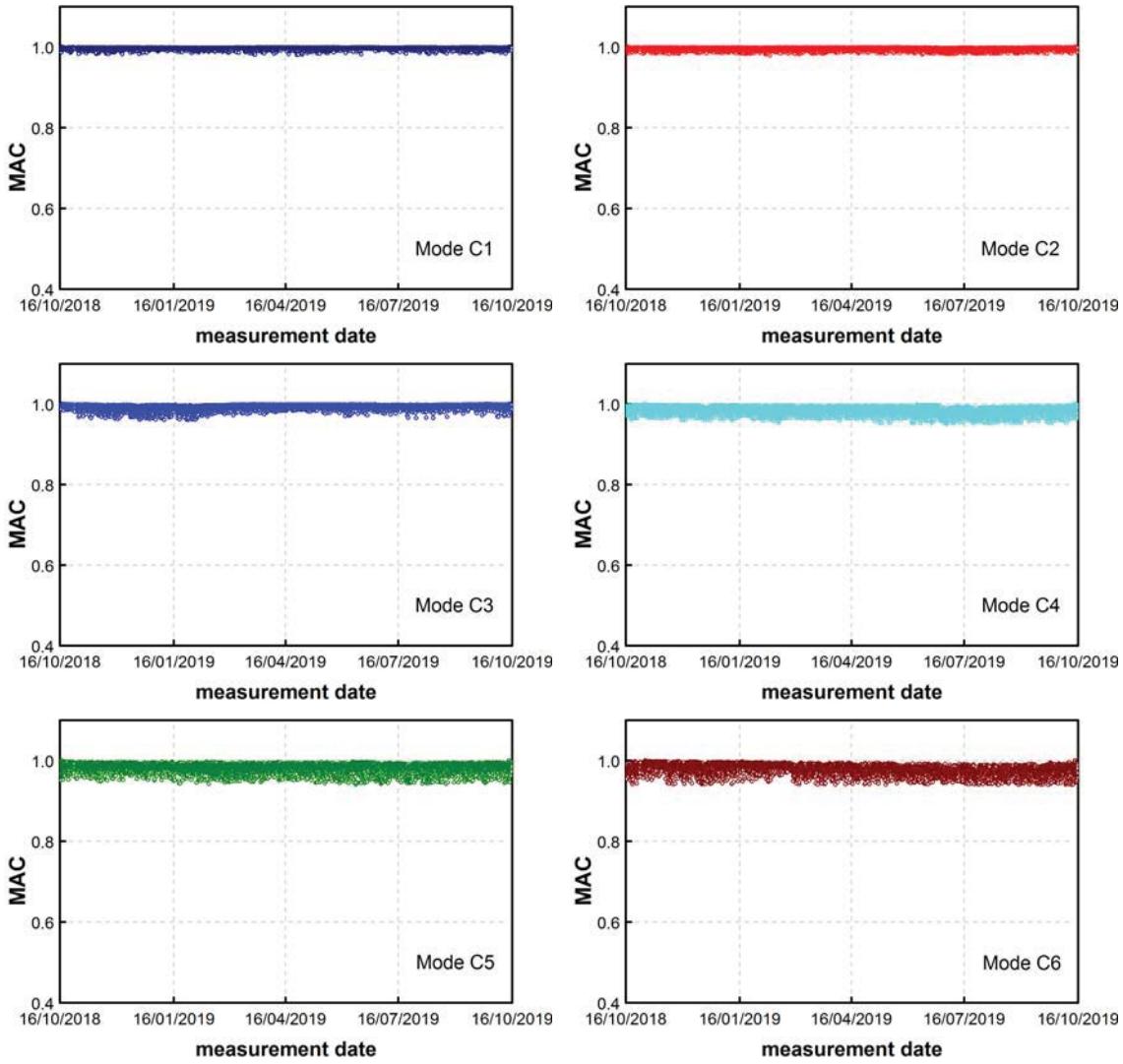

Figure 10: Variation in time of the MAC of the lower 6 modes during the first year of monitoring.

Mode	MAC_{mean}	σ_{MAC}	MAC_{min}	MPC_{mean}	σ_{MPC}	MPC_{min}
C1	0.997	0.002	0.980	0.993	0.003	0.978
C2	0.995	0.003	0.979	0.992	0.004	0.968
C3	0.993	0.006	0.960	0.988	0.010	0.932
C4	0.984	0.008	0.950	0.949	0.024	0.880
C5	0.981	0.011	0.941	0.980	0.017	0.912
C6	0.978	0.012	0.939	0.928	0.024	0.861
C7	0.968	0.020	0.911	0.934	0.028	0.852
C8	0.950	0.019	0.900	0.911	0.033	0.821

Table 1: Statistics of MAC and MPC of modes identified in the first year of monitoring.

5.3 Mode shapes and mode complexity

As previously pointed out, a quite dense network of high quality seismometers is installed in the Milan Cathedral, so that the mode shape variations should be investigated with SHM purposes. Since the environmental changes affect almost uniformly any structural system, the mode shapes are supposed to be less sensitive [10] than natural frequencies to those changes. Consequently, if the mode shapes turn out to be approximately time-invariant during an appropriate observation period (including a statistically representative sample of environmental conditions), any subsequent variation in the mode shapes conceivably provides the evidence of a structural change [21]. On the other hand, even if mode shapes contain also local information on the structure, those parameters might exhibit low sensitivity to local structural changes.

The evolution during the first year of monitoring of the mode shape variation, in terms of MAC, is shown in Fig. 10 for the lower 6 modes. It should be noticed that the MAC index is computed between a pre-selected set of reference mode shapes (corresponding to the same set of baseline modes used in the automated procedure of modal identification, Fig. 5) and the currently identified mode shapes. Figure 10 highlights that the MAC values (i.e., the mode shapes) are approximately independent of temperature and time invariant, even if the standard deviation of the MAC tends to increase with the increasing mode order (i.e., with the increasing spatial complexity of the distribution of modal deformations, Fig. 5). Columns 2-4 of Table 2 summarize the statistical characteristics of the MAC in terms of average value (MAC_{mean}), standard deviation (σ_{MAC}) and minimum value (MAC_{min}).

The investigation on mode shape changes was carried out also by considering the mode complexity, through the MPC (i.e., the collinearity of the mode shape components of each single mode on a straight line in the complex plane). Figure 11 and columns 5-7 of Table 2 demonstrate that also the MPC measure of mode complexity [13] is approximately time invariant, even if the MPC values tend to depart from unity (perfect collinearity) and to exhibit an increased dispersion for the higher modes.

6 CONCLUSIONS

The paper focuses on the monitoring program of the Milan Cathedral. Special emphasis is given on the dynamic measurements, the automated extraction of modal signatures and the influence of environmental changes on the variations observed in the dynamic characteristics of the historic monument. Based on the results collected in the first year of monitoring (i.e., between 16/10/2018 and 15/104/2019), the following main conclusions can be drawn:

- The application of state-of-art tools for automated operational modal analysis allows accurate estimate and tracking of 8 resonant frequencies in the frequency interval 0-5 Hz.

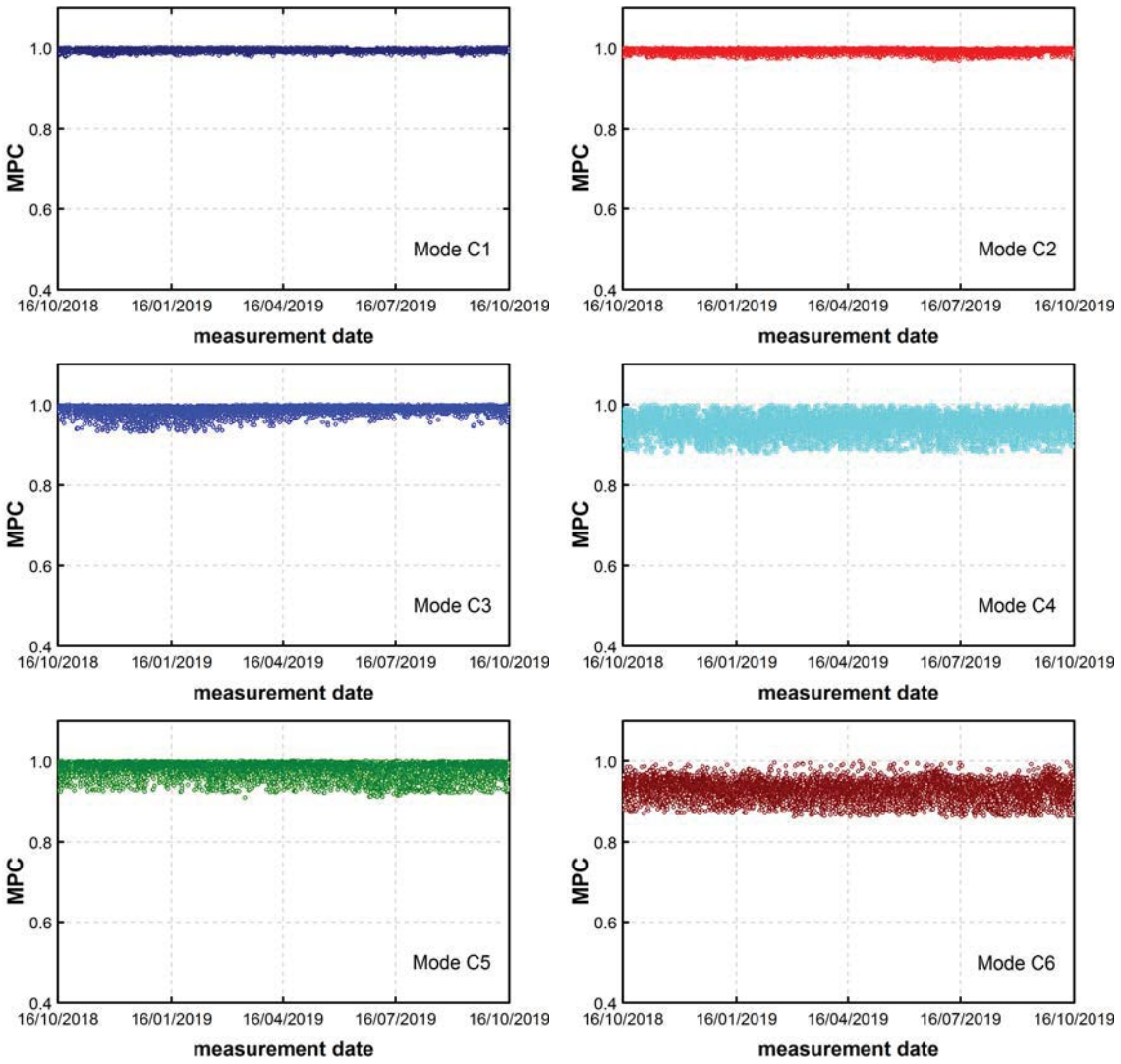

Figure 11: Variation in time of the MPC of the lower 6 modes during the first year of monitoring.

- The automatically identified modes involve dominant motion in the main transverse (N-S) and longitudinal (E-W) direction of the cathedral.
- The (outdoor and indoor) temperature turned out to be a dominant driver of the variations observed in the fluctuation of the resonant frequencies of all modes. The relative humidity seems to slightly affect only the frequency of the first mode [4].
- The frequency-temperature correlations reveal a distinctive trend, which is very different from what reported in almost all long-term studies on historic masonry structures. The natural frequencies of the cathedral exhibit a negative dependence on indoor and outdoor temperature in the cold season, whereas the correlation becomes positive in the hot season, for the N-S modes only.
- The complex dependence of natural frequencies on temperature observed in the Milan Cathedral conceivably results from two temperature-driven opponent effects: the stiffening exerted during the cold season by the increased tensile forces in the metallic tie-rods and the usual thermal expansion of the masonry materials. The former effect turns out to be dominant in the cold season for all modes, whereas the latter tends to rule the frequency variation of N-S modes in the hot season.

- PCA-based regression models are suitable to remove the environmental effects from natural frequencies.
- The mode shapes of the cathedral and the corresponding mode complexity (evaluated via MPC) do not exhibit appreciable fluctuations associated with the environmental effects, so that an appropriate strategy of SHM should be based also on the time invariance of modal deformations.

ACKNOWLEDGEMENTS

The support of *Veneranda Fabbrica del Duomo di Milano* and the precious co-operation of Francesco Canali is gratefully acknowledged. The authors would like to thank the technical staff of AGISCO and *Veneranda Fabbrica del Duomo di Milano* for mounting all monitoring devices, and the technical staff of SARA Electronics Instruments for the assistance during the installation and the initial operational setting of the seismometers.

REFERENCES

[1] Annali della Fabbrica del Duomo di Milano. Dall'origine fino al presente (in Italian), Veneranda Fabbrica del Duomo di Milano, 1885.

[2] C. Ferrari da Passano, Storia della Veneranda Fabbrica (in Italian), Cassa di Risparmio delle Province Lombarde, 1973.

[3] C. Gentile, C. Poggi, A. Ruccolo, M. Vasic, Vibration-based assessment of the tensile force in the tie-rods of the Milan Cathedral, *International Journal of Architectural Heritage* 13(3), 402-415, 2019.

[4] C. Gentile, A. Ruccolo, F. Canali, Long-term monitoring for the condition-based structural maintenance of the Milan Cathedral, *Construction and Building Materials* 228, 117101, 2019.

[5] H. Sohn, Effects of environmental and operational variability on structural health monitoring, *Philosophical Transactions of the Royal Society A* 365, 539-560, 2007.

[6] L.F. Ramos, L. Marques, P.B. Lourenço, G. De Roeck, A. Campos-Costa, J. Roque, Monitoring historical masonry structures with operational modal analysis: two case studies, *Mechanical Systems and Signal Processing* 24(5), 1291-1305, 2010.

[7] A. Saisi, C. Gentile, M. Guidobaldi, Post-earthquake continuous dynamic monitoring of the Gabbia Tower in Mantua, Italy, *Construction and Building Materials* 81, 101-112, 2015.

[8] M.G. Masciotta, J.C.A. Roque, L.F. Ramos, P.B. Lourenço, A multidisciplinary approach to assess the health state of heritage structures: the case study of the Church of Monastery of Jerónimos in Lisbon, *Construction and Building Materials* 116, 169-187, 2016.

[9] A. Elyamani, O. Caselles, P. Roca, J. Clapes, Dynamic investigation of a large historical cathedral, Structural Control and Health Monitoring 24(3), e1885, 2017.

[10] R.M. Azzara, G. De Roeck, M. Girardi, C. Padovani, D. Pellegrini, E. Reynders, The

influence of environmental parameters on the dynamic behaviour of the San Frediano bell tower in Lucca, *Engineering Structures* 156, 175-187, 2018.

[11] A. Kita, N. Cavalagli, F. Ubertini, Temperature effects on static and dynamic behavior of Consoli Palace in Gubbio, Italy, *Mechanical Systems and Signal Processing* 120, 180-202, 2019.

[12] N. Aste, R.S. Adhikari, M. Buzzetti, S. Della Torre, C. Del Pero, H.E. Huerto, C.F. Leonforte, Microclimatic monitoring of the Duomo (Milan Cathedral): risks-based analysis for the conservation of its cultural heritage, Building Environment 148, 240-257, 2019.

[13] R.S. Pappa, K.B. Elliott, A. Schenk, A Consistent-mode indicator for the eigensystem realization algorithm, NASA Technical Memorandum 107607, 1992.

[14] [26] W. Heylen, S. Lammens, P. Sas, Modal Analysis: Theory and Testing, KU Leuven, Belgium, 2007.

[15] B. Peeters, G. De Roeck, Reference-based stochastic subspace identification for output-only modal analysis, *Mechanical Systems and Signal Processing* 13(6), 855-878, 1999.

[16] A. Cabboi, F. Magalhães, C. Gentile, À. Cunha, Automated modal identification and tracking: application to an iron arch bridge, *Structural Control Health Monitoring* 24(1), e1854, 2017.

[17] R.J. Allemang, D.L. Brown, A correlation coefficient for modal vector analysis, *Proceedings of the 1st International Modal Analysis Conference (IMAC-I)*, 1982.

[18] S. Sharma, Applied Multivariate Techniques, John Wiley & Sons, 1995.

[19] Peeters B, De Roeck G. One-year monitoring of the Z24–Bridge: environmental effects versus gamage events. Earthquake Engineering & Structural Dynamics 30, 149-171, 2001.

[20] H. Hotteling, Multivariate quality control, illustrated by the air testing of sample bombsights, Techniques of Statistical Analysis, 111-184, 1947.

[21] A. Cabboi, C. Gentile, A. Saisi, Vibration-based SHM of a centenary bridge: a comparative study between two different automated OMA techniques, *Proceedings of the 9th International Conference on Structural Dynamics*, 2014.

EURODYN 2020
XI International Conference on Structural Dynamics
M. Papadrakakis, M. Fragiadakis, C. Papadimitriou (eds.)
Athens, Greece, 23–26 November 2020

A DAMAGE LOCALISATION PROCEDURE FOR MASONRY TOWERS BASED ON FREQUENCY DATA

Paolo Borlenghi[1], **Carmelo Gentile**[1], **and Antonella Saisi**[1]

[1] Department of Architecture, Built environment and Construction engineering (DABC)
Politecnico di Milano, Milan, Italy
Piazza Leonardo da Vinci, 32 - 20133 Milan, Italy
e-mail: {paolo.borlenghi, carmelo.gentile, antonella.saisi}@polimi.it

Keywords: Masonry tower, Damage localization, Model updating, Operational Modal Analysis, Non-destructive test, Historical constructions

Abstract. *The structural health conditions of masonry towers can be monitored with a few dynamic sensors (e.g. accelerometers or seismometers) placed at the top of the structure. This cost-effective setup provides continuous and reliable information on the natural frequencies of the structure; however, to move from anomaly detection to localisation with such a simplified distribution of sensors, a calibrated numerical model is needed. The paper summarises the development of a Structural Health Monitoring (SHM) procedure for the model-based damage localisation in masonry towers using frequency data. The proposed methodology involves the subsequent steps: (i) preliminary analysis including geometric survey and Ambient Vibration Tests (AVTs); (ii) FE modelling and updating based on the identified modal parameters; (iii) creation of a Damage Location Reference Matrix (DLRM) from numerically simulated damage scenarios; (iv) detection of the onset of damage from the continuous monitoring system performed with state-of-art techniques, and (v) localisation of the anomalies through the comparison between the experimentally identified variations of natural frequencies and the above-defined location matrix, called DLRM. The proposed SHM methodology is exemplified on the ancient masonry tower of Zuccaro in Mantua, Italy. Pseudo-experimental monitoring data were generated and employed to assess the reliability of the adopted algorithm in identifying the damage location. The results show a promise toward the practical applications of the proposed methodology in the monitoring of real structures.*

1 INTRODUCTION

Within the context of Structural Health Monitoring (SHM) of masonry towers, recent experiences [1-4] provided the evidence that the installation of few high-sensitive accelerometers at the top of the structure, combined with automated modal identification tools, can reveal the onset of damage under changing environments. This cost-effective measurement setup provides continuous and reliable information on the natural frequencies of the structure; however, to move from anomaly detection to localisation with such a simplified distribution of sensors, a calibrated numerical model is needed.

One possibility for performing damage localisation of masonry towers is the use of the surrogate-based FE model updating based on cleaned observations [3]. Once the fluctuations from the environmental effects are removed from the identified natural frequencies, the FE model of the structure is updated each time a new observation is available. Consequently, abnormal changes in structural parameters are detected and correlated with their location; in this case, the localisation is performed among the areas involved in the updating. Another way to localise the damage, based on nonlinear dynamic analysis, is shown in [4]: once an anomaly is detected from the monitoring system, a non-linear dynamic analysis is performed with the recorded seismic sequence to identify the areas prone to damage. Subsequently, the frequency decays obtained from the FE analysis, and the one from the monitoring system are compared. The main limitation of the first approach is the detail of the localisation. At the same time, in the latter, the non-linear dynamic analysis is computationally expensive and based on numerous assumptions on material properties.

In the present study, a model-based damage localisation procedure based on previously computed damage scenarios is developed, to increase the capability of real-time damage evaluation after a seismic event. A FE model of the structure is employed to study how damage in a specific location affects the mutual variation between the natural frequencies; accordingly, a damage localisation algorithm based on natural frequency changes is proposed.

The procedure outlined in this paper is summarised in Fig. 1 and involves the following steps: (i) preliminary analysis including geometric survey and ambient vibration tests (AVTs); (ii) FE modelling and updating based on the identified modal parameters; (iii) creation of a Damage Location Reference Matrix (DLRM) from numerically simulated damage scenarios; (iv) detection of the onset of damage from the continuous monitoring system performed with state-of-art techniques, and (v) localisation of the anomalies through the comparison between the experimentally identified variations of natural frequencies and the DLRM location matrix.

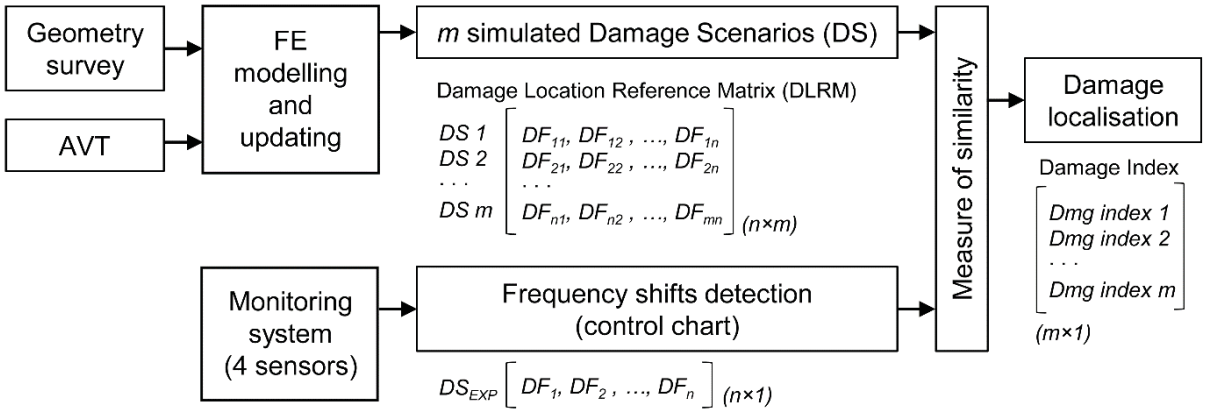

Figure 1: Damage localisation procedure for masonry towers based on the Damage Location Reference Matrix.

The proposed SHM methodology is exemplified on the ancient *Zuccaro*'s tower in Mantua, Italy. Firstly, documentary research, direct on-site inspections, AVTs and FE modelling and updating were performed and are fully reported in [5] and [6]. Subsequently, pseudo-experimental monitoring data are generated from the calibrated model and employed to assess the reliability of the adopted algorithm in identifying the damage location. It is worth mentioning that the investigated structure is of interest due to the quite large number of identified natural frequencies with only four seismometers and the peculiar shape of the last two modes representing a warping distortion of the cross-section.

2 THE DLRM APPROACH FOR DAMAGE LOCALIZATION

The developed DLRM approach is designed to give information on the damage location using only the measured changes in natural frequencies.

It is assumed that a monitoring system with few sensors is available so that the natural frequencies are continuously identified, the environmental effects are removed, and the occurrence of structural anomalies is detected through statistical tools, such as the control charts. Control charts are graphical representations of the evolution over time of a certain process with designed control limits to detect abnormal observations. For SHM purposes, the control limits are based on an initial training period when the structure is assumed to be undamaged. The successful use of control charts in damage detection of ancient constructions has been reported by different scholars [1, 4]. In this paper, the Hotelling multivariate control chart based on the T^2 statistic [7] is adopted.

From a calibrated numerical model, a series of damage scenarios are simulated, and the consequent variations of natural frequencies are collected in a matrix called DLRM. Through a comparison of similarity between the frequency variations in the DLRM and the ones detected from the cleaned observations of the continuous monitoring system, it is possible to locate in which area the anomaly appeared.

To clarify the working principles of the DLRM approach, the model of an idealised masonry tower is employed. Fig. 2 shows the geometry adopted and the *n* vibration modes involved. As demonstrated by different researches [1-4], the first torsion mode (T_1) and four bending modes (B) are often identified with the low-cost monitoring setup.

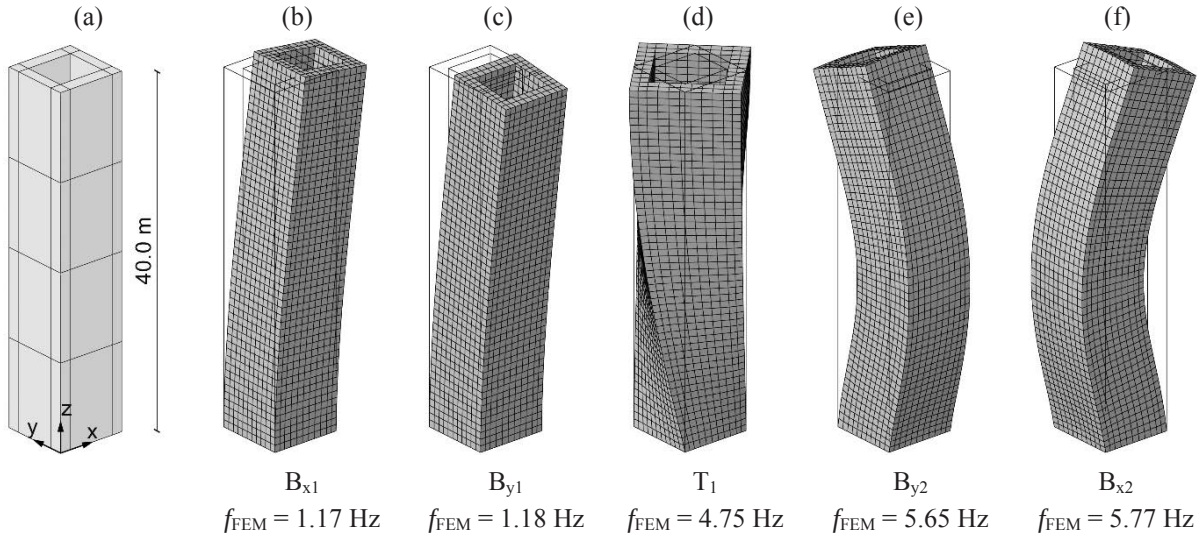

Figure 2: (a) Idealised tower geometry; (b-f) numerical vibration modes employed in the damage localisation.

2.1 Creation of the Damage Location Reference Matrix (DLRM)

The DLRM contains the *m* percentage of variation of the *n* considered natural frequencies. The creation of the DLRM is performed as follow:

(i) the previously calibrated FE model is divided into *m* elements (Fig. 2a), differentiating corners and walls in plan, and floors in height;
(ii) *m* eigenvalue analyses are performed reducing the elastic modulus of each element by a certain quantity (e.g. 40%);
(iii) the changes in the *n* natural frequencies are collected in an *n*-by-*m* matrix called DLRM.

The effects of the different Damage Scenarios (DSs) are measured through the percentage of frequency discrepancy, defined as follow:

$$DF_i = \frac{f_i^u - f_i^d}{f_i^u} \cdot 100 \tag{1}$$

where the *i-th* natural frequencies of the structure before and after the damage are represented by $f_i{}^u$ and $f_i{}^d$, respectively.

To give an example on how the location of damage influences the natural frequencies, Fig. 3 illustrates the comparison between the simulated DS of the idealised tower for the elements of two consecutive floors. The DSs are obtained reducing the elastic modulus of each element by the 40%. As presented in Fig. 1, the DSs are the rows of the DLRM.

From the analysis of this simplified application, it is possible to draw the following observations on the effectiveness of the localisation procedure using the frequency variations:

(a) The DS belonging to different floors gives in all cases different pattern of frequency variations (Fig. 3);
(b) The DS of the four corner elements belonging to the same level (Figs. 3a-b, bars with the same colour) gives the same frequency variations;
(c) The DS on the four wall elements belonging to the same floor (Figs. 3c-d, bars with the same colour) gives the same frequency variations when aligned on the same direction.

2.2 Model-based Damage localisation

Once the onset of damage is detected, it is possible to identify its location analysing the variation of natural frequencies. Comparing the frequency shifts obtained from the monitoring system with the *m* simulated damage scenarios, it is possible to locate the damage among the *m* elements previously identified. The Cosine Similarity is adopted to measure the similarity between the vector of the identified experimental frequency shifts ($\boldsymbol{DS}_{EXP}$) and the *m* vectors of the simulated damage scenarios ($\boldsymbol{DS}_j$):

$$\cos\theta_j = \frac{\boldsymbol{DS}_j \cdot \boldsymbol{DS}_{EXP}}{\left\|\boldsymbol{DS}_j\right\| \cdot \left\|\boldsymbol{DS}_{EXP}\right\|} \tag{2}$$

where θ_j is the *j*-th angle between the two vectors. In the present paper, the adopted Damage Index is expressed as follow:

$$Damage\ Index_j = (\cos\theta_j)^2 \tag{3}$$

where values close to 1 suggest a good correlation with the identified frequency shifts while values lower than 0.8 suggest a poor correlation. The *j*-th Damage Index is then plotted together with the corresponding *j*-th DS – representing the element location – (e.g. Fig. 4). The localisation is then performed considering the location associated with the higher Damage Index.

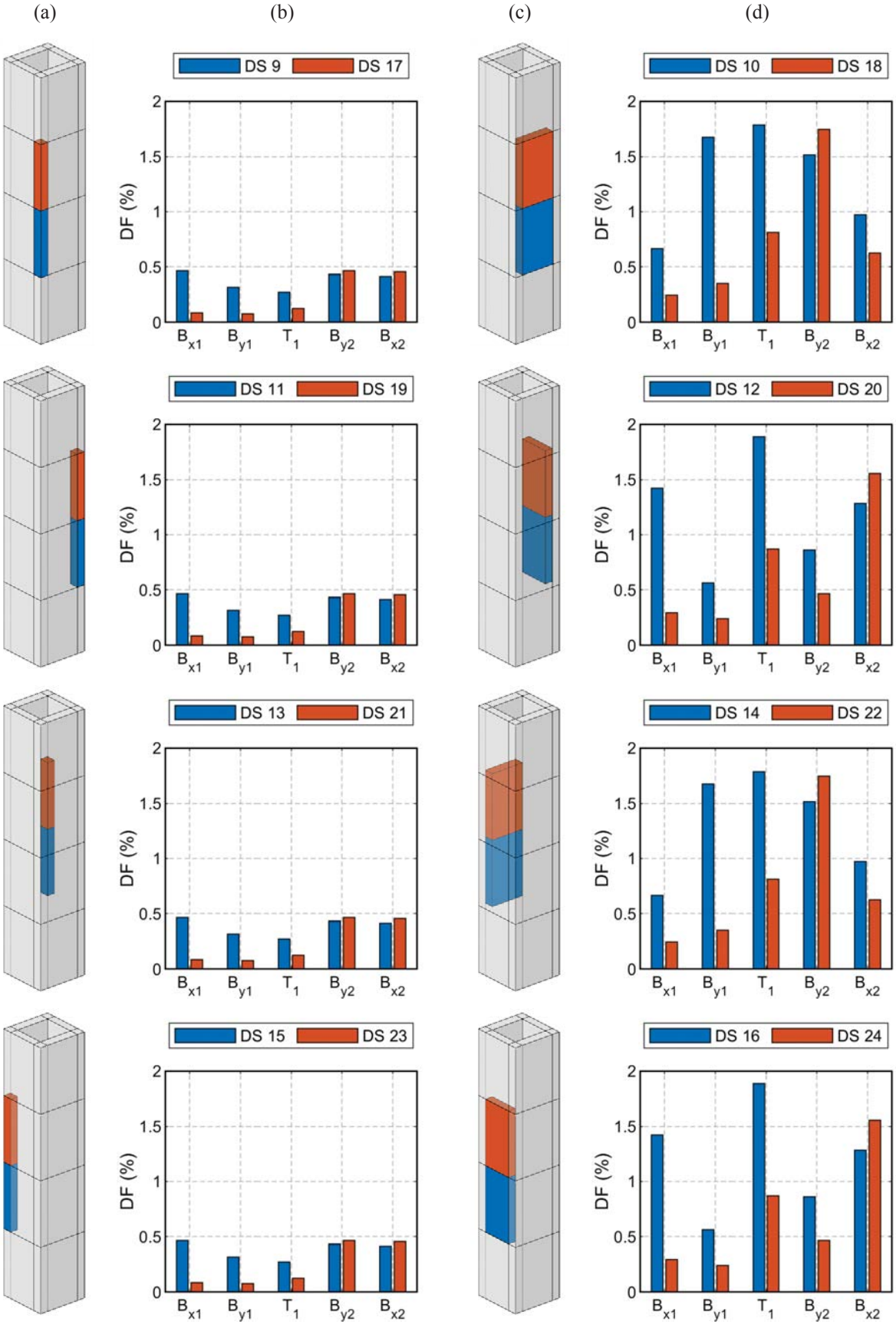

Figure 3: Comparison between the simulated Damage Scenarios (DS) of the first (a-b) and second (c-d) floor in terms of the discrepancy of frequency (DF, Eq. 1).

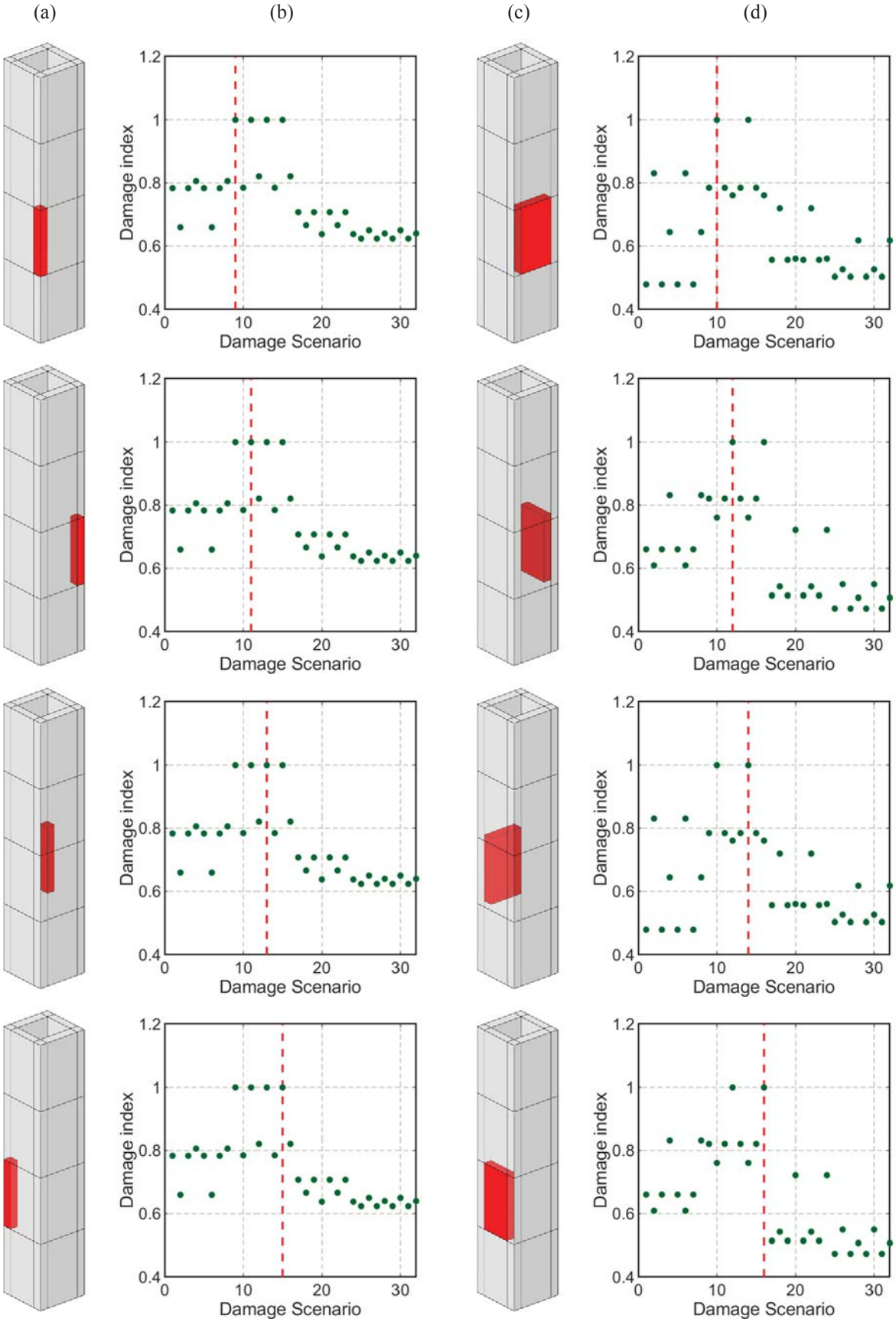

Figure 4: Localisation of simulated frequency shifts obtained by decreasing the elastic moduli of first-floor walls (c-d) and corners (a-b) by the 20% (the red dashed line represents the actual damage location).

The localisation procedure is exemplified on the model of the idealised tower. 8 frequency shifts are simulated reducing the elastic modulus of the 8 elements of the first floor by the 20% (Figs. 4a-c). The simulated DS_{EXP} are then compared with the *j*-th DS of the DLRM. The following observations can be drawn:

(a) As expected, it is not possible to distinguish between a DS on a corner element belonging to the same floor;

(b) Similarly, it is not possible to differentiate between the DS on wall elements belonging to the same level and same direction.

In conclusion, a numerical model of an idealised tower was employed to exemplify the application of the DLRM approach showing promising results. It should be noticed that increasing the number and the type (e.g. bending, torsion, or local) of vibration modes can substantially increase the effectiveness of the localisation capability of the proposed approach.

3 THE ZUCCARO'S TOWER: DESCRIPTION AND DYNAMIC TESTING

The *Zuccaro*'s tower of Mantua (Fig. 5), about 43 m high, is a historical defensive structure built in the Middle Ages [5]. The first record regarding its existence dates back to 1143. The few and small openings and the tower location at the limits of the city Middle Ages fortifications suggest its original defensive role. As shown in Fig. 5, the tower is nowadays included in a building aggregate, surrounded on three-sides by low-rise constructions.

The structure has an approximate squared plan with the side equal to 8.5 m. The load-bearing walls are built in solid brick masonry with a thickness ranging from 1.1 m at the base to 0.8 m at the top. A brick masonry cross vault is covering the ground floor, while a timber staircase is connecting the 8 timber floors distributed along the height of the structure (Fig. 7). It is worth mentioning that the roof and the timber floors were substituted after a fire occurred in 1979 and the related intervention – carried out in the 90s – involved the injection of expanding mortars in several areas.

Due to a large number of uncertainties regarding the evolution of the building and the effectiveness of strengthening interventions, an extensive investigation survey was recently carried out involving visual inspection and Ambient Vibration Testing (AVT). The results of the investigations are reported in [5] and [6]. The survey was aimed at providing details on the geometry of the structure, detect critical areas and irregularities, and identify the dynamic characteristics of the structure (i.e. natural frequencies and mode shapes).

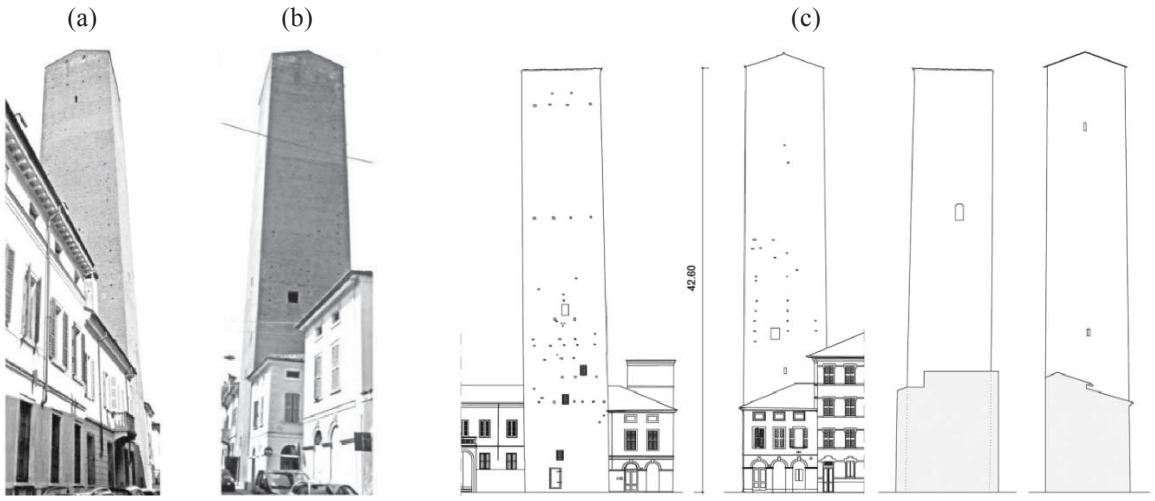

Figure 5: The *Zuccaro*'s tower: views from the west (a) and south corners (b); and geometric survey of the external fronts (c).

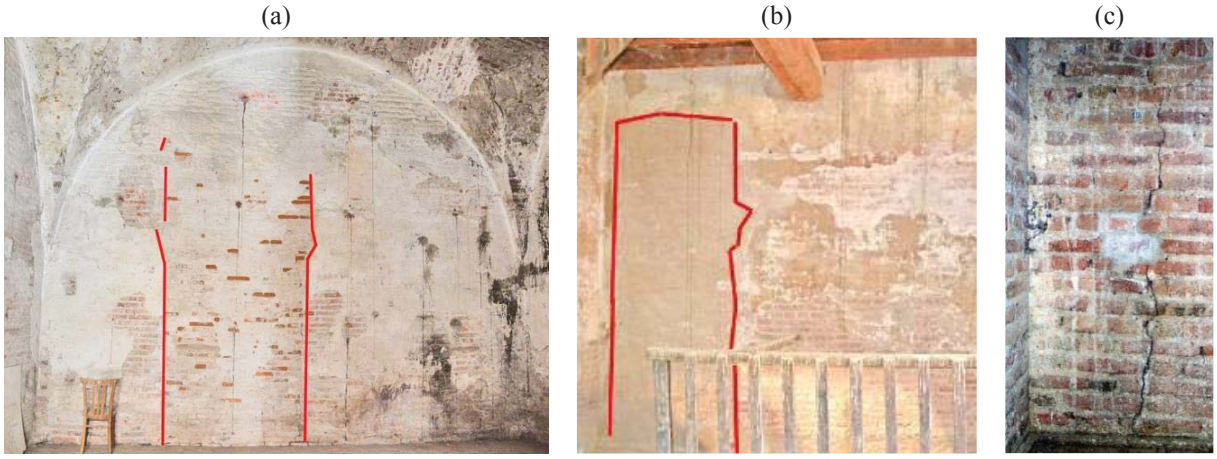

Figure 6: Details of masonry cracks and discontinuities: (a) ground floor, N-E front, (b) 1st floor, S-E front and (c) 3rd floor, S-W front.

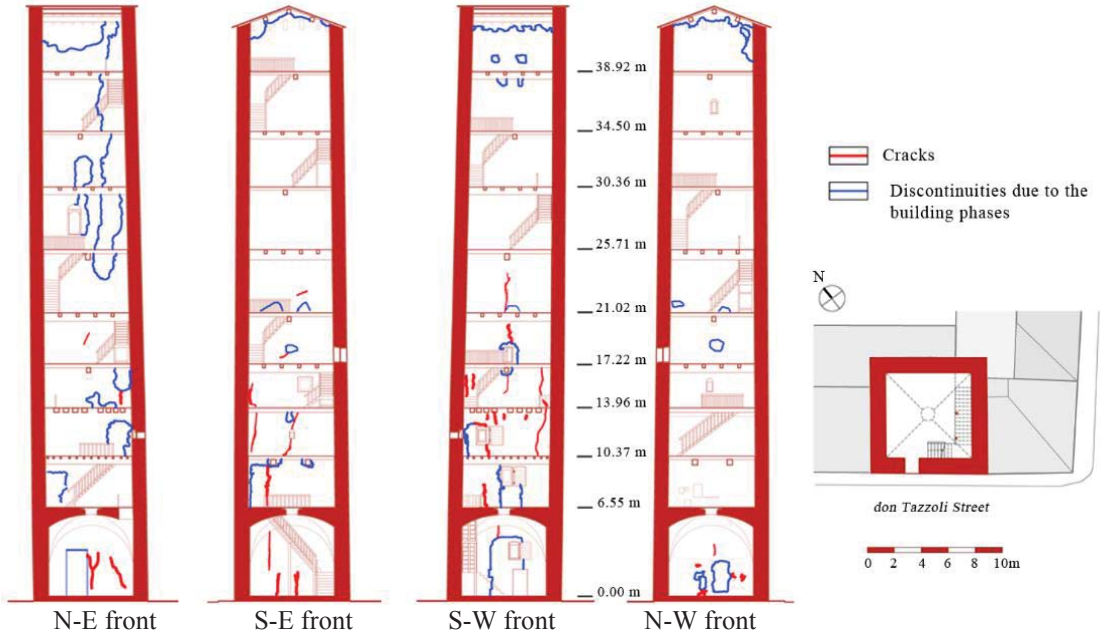

Figure 7: Section of the tower with the survey of the crack patterns and discontinuities due to different building phases.

3.1 On-site inspections

The accurate on-site inspections of the inner fronts of the tower are summarised in Fig. 7. From the stratigraphic survey, the discontinuities due to different building phases or local masonry reconstructions are identified. Furthermore, the on-site inspections highlighted the following aspects:

(a) Sharp discontinuities and deep cracks were found around the corner between the S-W and S-E walls (Fig. 6c) starting from the base up to 17.22 m;
(b) Some deep and thick cracks were identified on the cross vault at the ground level;
(c) The presence of large areas with fragmentary and non-homogeneous masonry was identified starting from the height of 21.0 m on the N-E front (Fig. 7);
(d) Extended dark areas resulting from the fire of 1979 were found in the inner walls.

3.2 Dynamic characteristics of the tower

Two series of AVTs were conducted on the tower involving a different number of sensors. The first test (4 measuring channels) was performed between October 23rd and 24th, 2016 [6] with the twofold objective of identifying the vibration modes of the structure and evaluating the effectiveness of a 4-sensor setup for the future installation of a monitoring system. The second test (28 measuring channels) was performed between December 11th and 12th, 2017 [5] with the objectives of obtaining a complete representation of the mode shapes and roughly assessing the impact of temperature changes on natural frequencies.

During the first test, 2 bi-axial seismometers (electro-dynamic velocity transducers, SARA SS45) were positioned at the opposite corners of the top floor to measure the dynamic response of the structure under ambient excitations. During the second test, high-sensitivity accelerometers (sensitivity of 10 V/g; peak acceleration of 0.5 g) were employed to measure the response of the tower in 14 points belonging to 7 selected cross-sections (Fig. 8a).

The extraction of the modal parameters was performed with two well-known algorithms: the Frequency Domain Decomposition (FDD [8]) and the data-driven Stochastic Subspace Identification (SSI-data [9]). Both algorithms are available in the commercial software ARTeMIS [10]. Overall, 4 bending modes (B), 1 torsion mode (T) and 2 warping distortion modes (W) were identified in the frequency range of 0-9 Hz.

In the present paper only the results of the second test are reported and Fig. 8 summarises the modal parameters identified. The sequence of the first 5 modes is consistent with the results obtained in similar studies [3-4], whereas the last two modes appear to be very peculiar of the investigated structure. From the analysis of the identified dynamic characteristics, the following observations are drawn:

(a) Two closely spaced bending modes in opposite directions (B_{y1} and B_{x1}) are identified between 1.2 and 1.3 Hz;
(b) The third mode is a global torsion mode (T_1) followed by other two higher-order bending modes (B_{y2} and B_{x2});
(c) The last two modes (W_1 and W_2) are associated with cross-section distortion of first and second order. The peculiar shape of these modes is known as warping.
(d) Regardless of the differences in the external temperatures, an excellent correspondence between the first 5 vibration modes was found while W_1 and W_2 exhibit a stronger sensitivity to the environmental conditions.

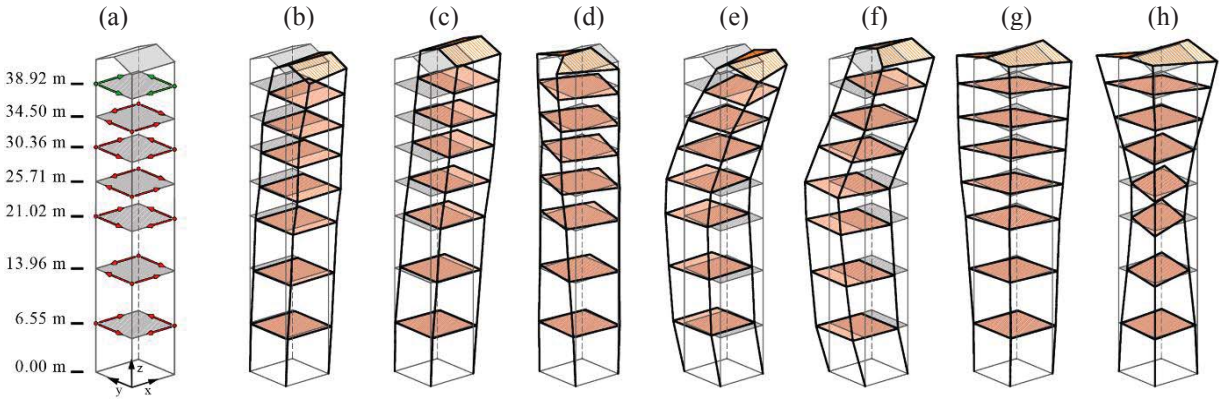

Mode no.	B_{y1}	B_{x1}	T_1	B_{y2}	B_{x2}	W_1	W_2
f_{SSI} (Hz)	1.225	1.280	4.095	4.781	4.977	5.504	7.465

Figure 8: (a) Sensors layout of the AVTs of 11-12 December 2017 (T =2.4°C); (b)-(h) Identified vibration modes.

4 THE ZUCCARO'S TOWER: FE MODELLING AND UPDATING

The 3D model of the tower was developed with the FE code ABAQUS using the eight-node brick elements (C3D8). A relatively large number of elements were employed to obtain a regular distribution of masses, a good description of the opening distribution, and to avoid frequency sensitivity to mesh size. Overall, the numerical model consists of 10582 brick elements with 48438 degrees of freedom and an average mesh size of 0.5m (Fig. 9a).

Once the geometry of the numerical model is established, the selection of the structural parameters to be updated is the next key issue. To prevent the ill-conditioning of the inverse problem and to improve the robustness of the updated parameter estimates the number of updating variables was kept smaller than the experimental parameters used as targets and only the uncertain structural parameters were updated. Consequently, the following assumptions were adopted: (a) the effect of soil-structure interaction was neglected, and the tower was assumed pinned at the base; (b) a linear elastic orthotropic material was adopted for the brick masonry, with constant mass density and Poisson's ratio equal to 17 kN/m^3 and 0.15 respectively; (c) the shear modulus was considered equal to $G = \alpha \cdot E$, where E is the Young's modulus, and α is a constant multiplier.

In addition, to calibrate all the identified vibrations modes, the following aspects were considered:

(a) the presence of the building aggregate was modelled with a uniform distribution of linear elastic translational springs with constants k_x and k_y on the S-E side and N-E side, respectively;
(b) the masonry walls were divided into 2 regions with constant material properties based on successive modelling refinement involving different assumptions on the model uncertainties (the full process is described in [6]);
(c) the presence of timber floors was simulated with a series of rigid beams connected to the vertical walls using linear elastic springs (constant k_{RS}).

Overall, the number of updating parameters was equal to 6: 2 Young's moduli, the ratio α, and the springs constants k_x, k_y and k_{RS}.

The adopted FEMU procedure was implemented in MATLAB environment and it is based on the Douglas-Reid method [11] with the Particle Swarm Optimisation (PSO) algorithm [12]: the updating parameters are iteratively corrected in a constrained range until a stable minimum solution for an objective function is found. Particularly, the following objective function was adopted:

$$J(\boldsymbol{x}) = \frac{100}{n} \sum_{i=1}^{n} \left| \frac{f_i^{AVT} - \widehat{f}_i(\boldsymbol{x})}{f_i^{AVT}} \right| \tag{4}$$

where f_i^{AVT} is the i-th experimentally identified natural frequency and $f_i(\boldsymbol{x})$ is the i-th polynomial approximation [11] of the numerical natural frequencies, expressed as functions of the $\boldsymbol{x}$ updating parameters.

Tab. 2 lists the optimal estimates of the uncertain parameters of the model. The difference between the elastic modulus of the upper and lower part of the tower is motivated by the presence of fragmentary and non-homogeneous masonry starting from the height of 21.0 m (Fig. 7).

In conclusion, an excellent correlation between the numerical and experimental modal parameters is obtained, with the maximum frequency discrepancy (DF_{max}) being equal to 0.71%. Hence, the updated model is capable of accurately representing the experimentally identified modal parameters.

Mode no.	f_{SSI} (Hz)	f_{FEM} (Hz)	DF_i [%]	MAC
B_{y1}	1.225	1.226	-0.08	0.98
B_{x1}	1.280	1.279	0.08	0.98
T_1	4.095	4.096	-0.02	0.92
B_{y2}	4.781	4.782	-0.02	0.84
B_{x2}	4.977	4.977	0.00	0.83
W_1	5.504	5.504	0.00	0.88
W_2	7.465	7.412	0.71	0.83
DF_{ave} [%]	-	-	0.13	-
DF_{max} [%]	-	-	0.71	-

Table 1: Comparison between optimised and experimental (AVT 2017, T=2.4°C) modal frequencies.

Structural parameters	$X_{lower\ bound}$	$X_{optimal\ value}$	$X_{upper\ bound}$
E_L (GPa) height ≤ 21.02m	2.68	3.08	3.62
E_U (GPa) height > 21.02m	1.48	1.73	2.00
α	0.315	0.335	0.349
G_L (GPa) height ≤ 21.02m	0.84	1.03	1.26
G_U (GPa) height > 21.02m	0.47	0.58	0.70
Σk_x (kN/m $\cdot 10^5$)	3.43	13.73	13.75
Σk_y (kN/m $\cdot 10^5$)	0.001	0.001	0.011
k_{RS} (kN/m $\cdot 10^5$)	0.25	0.49	0.74

Table 2: lower bound, optimised values and upper bounds of the identified structural parameters.

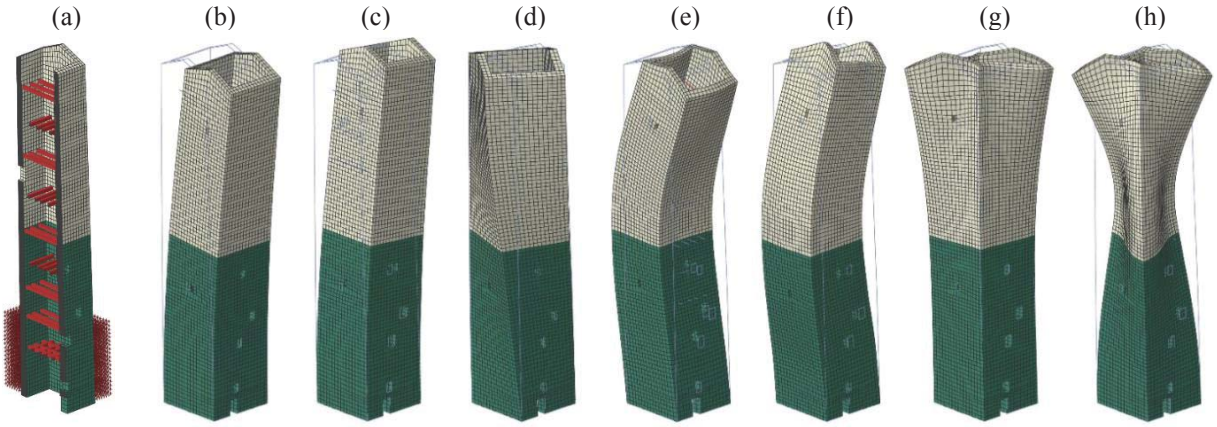

Figure 9: (a) FE model of the *Zuccaro*'s tower and (b-h) vibration modes of the optimal (updated) model.

5 THE ZUCCARO'S TOWER: APPLICATION OF THE DLRM APPROACH

To test the capability of the proposed approach for the damage localisation in masonry towers, three damage scenarios (DS) were simulated, and pseudo-experimental monitoring data were generated for the *Zuccaro*'s tower. The previously updated numerical model was divided into 80 elements (Figs. 10a-b) – 8 elements per floor – to simulate the possible effect of local damages. Fig. 10 shows the selected elements, which belongs to different regions of the tower: lower (DS2), medium (DS44) and upper (DS74) parts.

The damages are simulated in a simplified way through a Young's modulus reduction by 30%. Fig. 11 shows the changes in natural frequencies generated by the three simulated DS. The maximum variation is obtained for the DS2 and it is equal to 0.47% on the first mode (B_{y1}) while in the other two cases the maximum variations are lower than 0.25%.

Since the installation of the monitoring system is ongoing, the monitoring data were generated from the experimentally identified natural frequencies. The environmental effects were not considered at this stage since the procedure is supposed to use the cleaned observations. Consequently, a normal distribution with a defined standard deviation was assumed for each frequency according to literature values (cleansed observations) [3].

Tab. 3 illustrates the adopted mean values and standard deviations for the pseudo-experimental monitoring data and reports the effects of the three DS on the 7 natural frequencies considered. It is worth noting that the DSs have comparable frequency shifts than the selected standard deviations (Tab. 3).

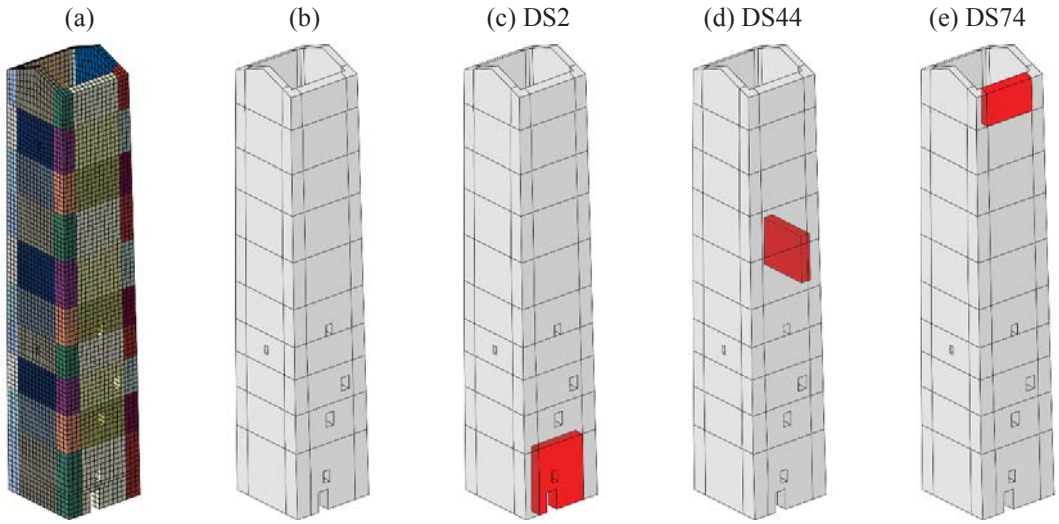

Figure 10: (a-b) FE model of the *Zuccaro*'s tower divided into 80 elements; (c-e) simulated damage scenarios.

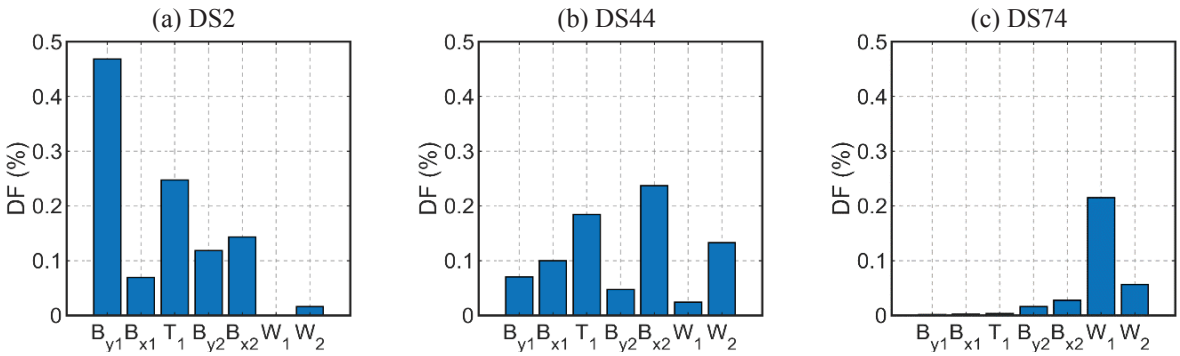

Figure 11: Comparison between the frequency shifts (DF, Eq. 1) of the three introduced damage scenarios.

	f_{mean} (Hz)	σ_f (Hz)	Δf_{DS2} (Hz)	Δf_{DS44} (Hz)	Δf_{DS74} (Hz)
B_{1y}	1.225	0.005	0.006	0.001	0.000
B_{1x}	1.280	0.005	0.001	0.001	0.000
T_1	4.095	0.008	0.010	0.008	0.000
B_{2y}	4.781	0.010	0.006	0.002	0.001
B_{2x}	4.977	0.012	0.007	0.012	0.001
W_1	5.504	0.020	0.000	0.001	0.012
W_2	7.465	0.030	0.001	0.010	0.004

Table 3: Statistic of the pseudo-experimental monitoring data with 3 simulated damage scenarios.

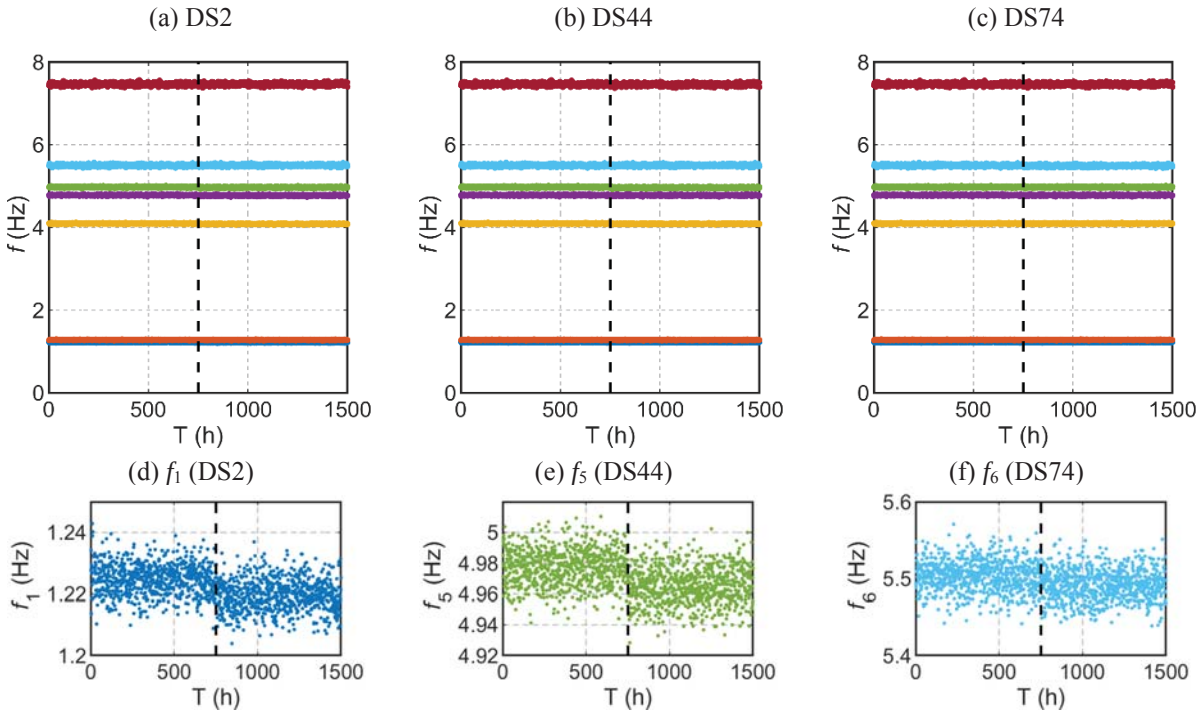

Figure 12: (a-c) Pseudo experimental monitoring data; (d-f) focus on the frequencies with the higher changes.

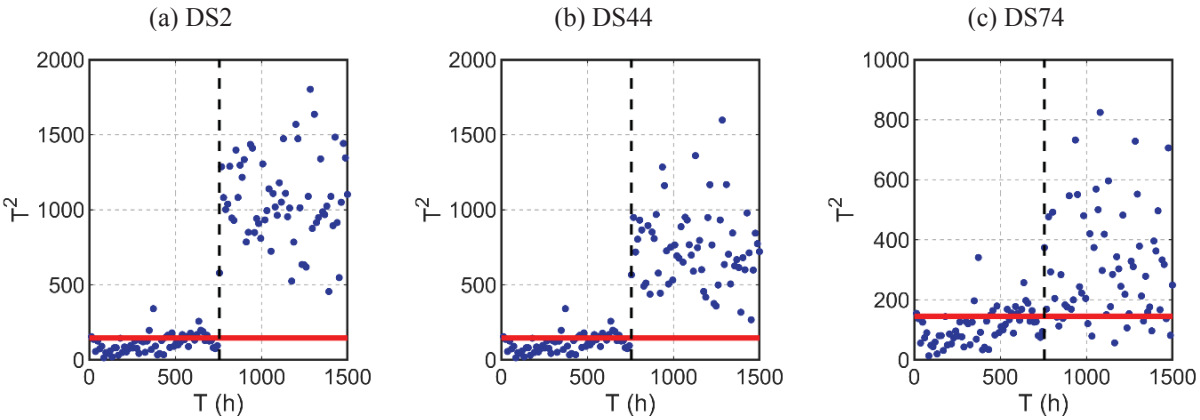

Figure 13: Damage detection through control charts for the 3 damage scenarios.

Overall, 1500 observations are generated (1 observation per hour), and the simulated frequency shifts are introduced in the middle of the generated time history (T=750h; Fig. 12). The frequency shifts are particularly visible on the first mode (B_{y1}; Fig. 12d) for the DS2 and on the fifth mode (B_{x2}; Fig. 12e) for the DS44. Conversely, the effects of the DS74 on f_6 (W_1; Fig. 12f) are less evident; in this case, the standard deviation for the mode W_1 is equal to 0.02 Hz while the considered frequency shift is equal to 0.01 Hz.

To detect the presence of structural anomalies on the generated monitoring data, the control charts based on T^2 – statistic are adopted [7]. A training period of 336 h (14 days) was employed to define the mean values of for the 7 natural frequencies. The residual errors between the mean frequencies of the reference period and the frequencies of each observation are used to define a multivariate control chart (Fig. 13) composed by subgroups of 12 h. The structural anomalies are detected each time an observation lays outside the control limit. The black dashed line in Fig. 13 represents the instance in which the DSs were introduced. Clearly, the three DS are associated with different DFs (see Fig. 11) and consequently the outliers on the control charts are more evident in the DS2 (Fig 13a) where the DFs are higher while are less emphasised in the DS74 (Fig 13c) where the DFs are lower.

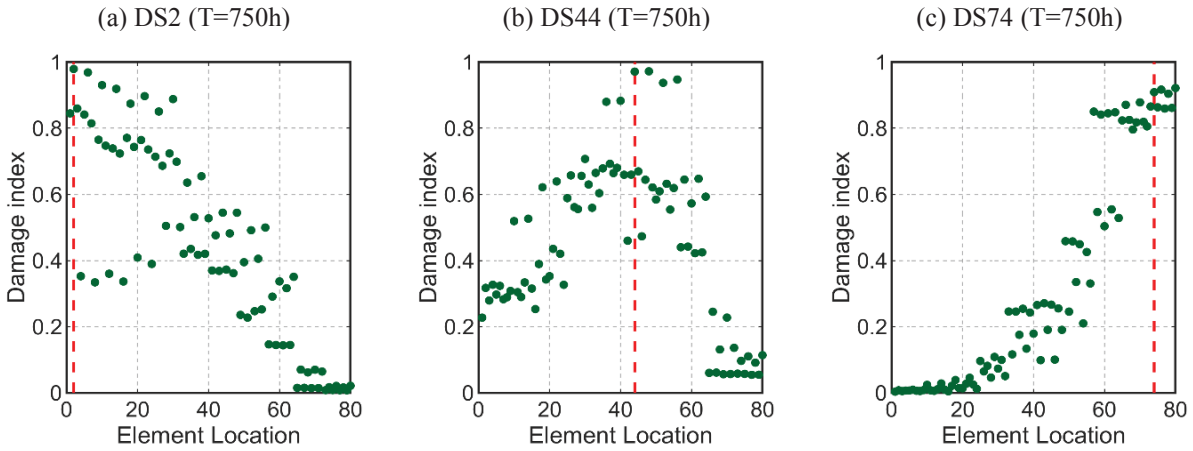

Figure 14: Damage localisation through the DLRM at the time T when the damage was introduced.

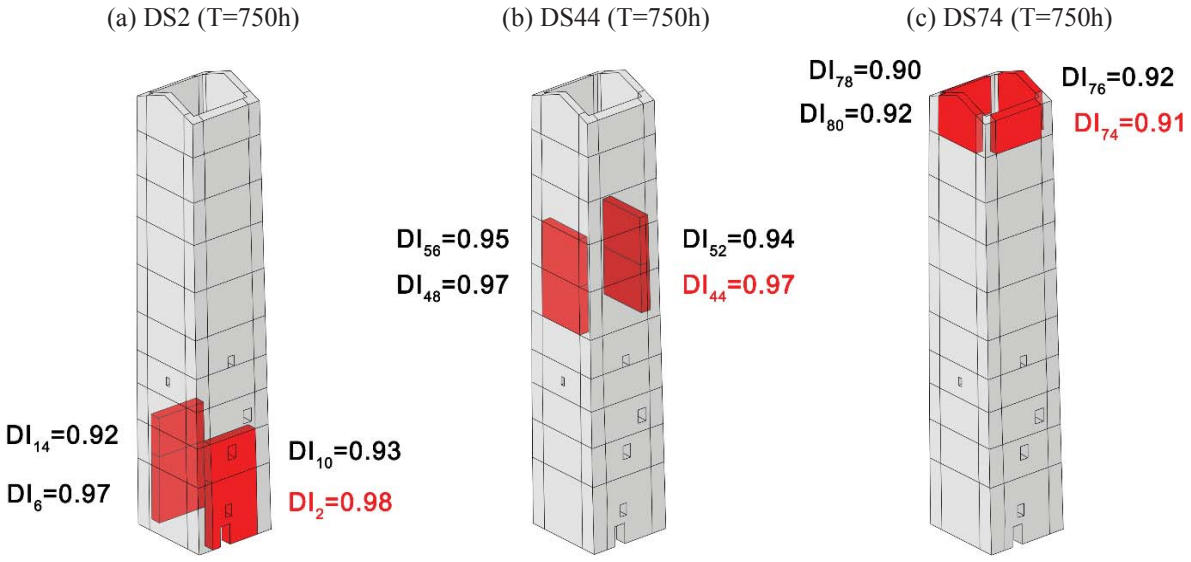

Figure 15: Elements with a damage index higher than 0.90 at the time T=750h (the DI coloured in red indicates the correct position of the simulated damage).

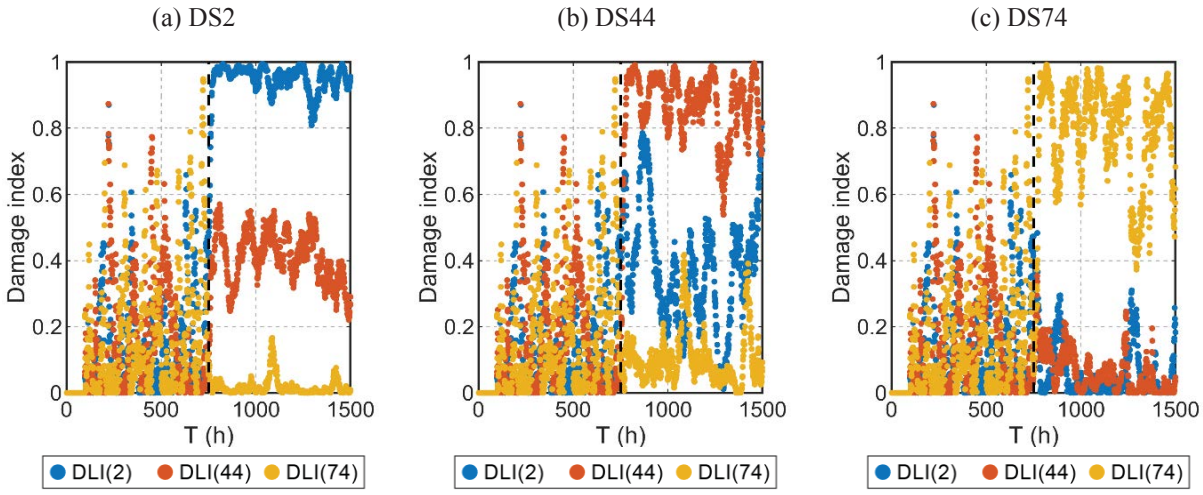

Figure 16: Comparison between the Damage Indexes of three elements over the entire monitoring period.

Once the onset of a damage is verified, the comparison between the pseudo-experimental frequency shifts and the computed DLRM is performed. The DLRM was previously generated from the updated FE model (Fig. 10a) following the procedure explained in Section 2; the adopted elastic modulus reduction was equal to the 50%.

The comparison between the pseudo-experimental frequency shifts and the computed DLRM is provided by Eq. 3 and the results at time T=750h – that is the time when the damage is detected from the control charts – are depicted in Fig. 14. The red dashed line represents the correct damage location while the green dots are the Damage indexes (DIs) of each element. The elements with higher DIs are more likely to be damaged. As it was in the detection stage, the localisation is more evident for DS2 and DS44 since the DFs are higher.

Fig. 15 illustrates the position of the elements with a Damage index higher than 0.90. The following observations can be drawn: (a) the DS2 is correctly localised in the lower part of the tower on the walls along the x-direction; (b) similarly, the DS44 is correctly localised among the 5th and 7th floors on the walls along the y-direction; (c) the DS74 is correctly localised in the top floor of the tower, but it was not possible to distinguish on which wall. Particularly, the localisation of the last DS relies on the induced frequency shift on mode W_1 (see Fig. 11c), which is associated with a cross-sectional distortion. Conversely, the other localisations rely also on bending modes (see Figs. 11a-b) which are characterised by a direction-dominated component of motion.

In conclusion, Fig. 16 illustrates the evolution over time of the DIs of three selected elements. Before the introduction of the structural anomaly at T=750h, the DIs are characterised by random variations; conversely, when the damage occurs, the DIs exhibit a much stable pattern. Notably, the stability is correlated with the magnitude of the frequency shift: bigger for DS2 and lower of DS74.

6 CONCLUSIONS

Prior research has demonstrated the effectiveness of damage localisation for masonry towers based on monitored frequency data and FE modelling [3-4]. In this study, further investigations are carried out to increase the capability of an accurate real-time damage evaluation. Accordingly, a model-based damage localisation procedure using previously computed damage scenarios and continuously identified natural frequencies is illustrated. The proposed approach is exemplified on the *Zuccaro*'s tower; an ancient masonry structure built in the Middle Ages in the city of Mantua, Italy

The results from the investigated structure suggest the following conclusions:

1) In masonry towers, and generally in slender structures, the mutual variation of natural frequencies caused by a structural damage is directly correlated with the damage location;
2) The simulated frequency shifts added to the pseudo-experimental monitoring data were detected and localised with the proposed approach;
3) A cost-effective monitoring setup composed by few sensors placed at the top of the structure and combined with an automated modal identification algorithm and a regression model to filter out the environmental effects can be used not only to detect but also to localise a structural damage.

Promising results suggest future applications of the methodology for monitoring real structures. To expand the capability of the proposed approach, further investigations with multiple damage scenarios should be performed.

ACKNOWLEDGEMENTS

Sincere thanks are due to M. Cucchi (LPMSC, Politecnico di Milano) and A. Ruccolo (PhD candidate, Politecnico di Milano) who assisted the authors in conducting the field tests.

REFERENCES

[1] C. Gentile, M. Guidobaldi, A. Saisi, One-year dynamic monitoring of a historic tower: damage detection under changing environment, *Meccanica* 51(11), 2873-2889, 2016.

[2] R. M. Azzara, G. De Roeck, M. Girardi, C. Padovani, D. Pellegrini, E. Reynders, The influence of environmental parameters on the dynamic behaviour of the San Frediano bell tower in Lucca, *Engineering Structures* 156, 175-187, 2018.

[3] A. Cabboi, C. Gentile, A. Saisi, From continuous vibration monitoring to FEM-based damage assessment: Application on a stone-masonry tower. *Construction and Building Materials* 156, 252-265, 2017.

[4] F. Ubertini, N. Cavalagli, A. Kita, G. Comanducci, Assessment of a monumental masonry bell-tower after 2016 central Italy seismic sequence by long-term SHM, *Bulletin of Earthquake Engineering* 16(2), 775-801, 2018.

[5] A. Saisi, S. Terenzoni, A. Ruccolo, C. Gentile, Safety of the Architectural Heritage: Structural Assessment of the Zuccaro's Tower in Mantua, *in: RILEM Bookseries* 18, 2422-2430, 2019.

[6] C. Gentile, A. Saisi, P. Borlenghi, FE modelling for seismic assessment of an ancient tower from ambient vibration survey, *in: Proceedings of the 8th IOMAC - International Operational Modal Analysis Conference*, 295-305, 2019.

[7] H. Hotelling, Multivariate quality control-illustrated by the air testing of sample bombsights, *in Techniques of Statistical Analysis*, 111-184, 1947.

[8] R. Brincker, L. Zhang, P. Andersen, Modal identification of output-only systems using frequency domain decomposition. *Smart Material and Structures* 10(3), 441-445, 2001.

[9] B. Peeters, System identification and damage detection in civil engineering. Ph.D. Thesis, Katholieke Universiteit Leuven, Belgium, 2000.

[10] Structural Vibration Solutions (SVS). ARTeMIS Extractor 2010. Aalborg, Denmark, 2010.

[11] B. M. Douglas, W. H. Reid, Dynamic tests and system identification of bridges. *Journal of the Structural Division ASCE* 108(10), 2295-2312, 1982.

[12] J. Kennedy, R. Eberhart, Particle Swarm Optimization, *in: Proceedings of IEEE International Conference on Neural Networks*, 1942-1948, 1995.

EURODYN 2020
XI International Conference on Structural Dynamics
M. Papadrakakis, M. Fragiadakis, C. Papadimitriou (eds.)
Athens, Greece, 23–26 November 2020

MODAL PARAMETERS IDENTIFICATION ON ENVIRONMENTAL TESTD OF ANCIENT BELL TOWERS AND VALIDATION OF THEIR NUMERICAL MODELS

F. Clementi[1], G. Standoli[1], E. Giordano[1], A. Ferrante[1] and S. Lenci[1]

[1] Dept. of Civil and Building Engineering, and Architecture,
Polytechnic University of Marche, Ancona, Italy
e-mail: {g.standoli,e.giordano,a.ferrante}@pm.univpm.it, {francesco.clementi,lenci}@univpm.it

Keywords: Structural Health Monitoring, Operation Modal Analysis, Finite Element Model, Tower, Historical Building

Abstract. *Masonry towers are quite widespread in Europe and represent an important portion of the built heritage that must be preserved, especially in high-seismicity regions. Very often, such masonry towers exhibit unique peculiar morphologic and typological characteristics, which might affect their different structural behaviors under horizontal loads. For this reason, accurate knowledge of their dynamical parameters is useful for seismic assessment and the design of risk mitigation interventions.*

In this work, the opportunities provided by dynamic identification techniques for the non-destructive evaluation of heritage structures are discussed with a focus on different bell towers, located in the Marche region (Italy). All of them were stricken by a long seismic sequence (Center Italy earthquakes between August and October 2016), and are investigated in detail in order to have an insight into their dynamic behavior. Furthermore, the experimental investigations and the operational modal analysis results are presented, and they are useful for defining the Finite Element (FE) model of the towers with a continuum approach.

The monitoring system consists of several elements adequately connected. Many operative problems have conditioned the positioning of the instrumentation due to the limited accessibility of the structure, not only to the primary access but also to reach the top.

However, it has been possible to identify with certain confidence the first three frequencies of the towers and their corresponding mode shapes. The results carried out after the updating procedure may be considered very good. The material data values estimated in this way will constitute an important reference for the evaluation of the state of the building.

1 INTRODUCTION

Europe preserves a large part of the Earth's historical and artistic heritage, Italy is one of the European countries that owns the majority of historical buildings, especially palaces and churches. Because of its particular position, the nation is crossed by African and Euro-Asiatic tectonic plates, the seismic risk is very high and continuously endangers the historical structures [1–12]. One of the last examples is the recently Central Italy Earthquakes that hit the areas between Marche, Abruzzo and Umbria Regions causing widespread damages especially at the construction part of the cultural heritage, highlighting, once again, the necessity to find methodologies to take under control their health, in order to intervene before irreparable damages occur. Currently, the most appropriate technique to achieve this purpose is the Structural Health Monitoring (SHM) using the variation of structures dynamic characteristics as frequencies, damping and mode shapes. To obtain these data, accelerometric sensors are placed on specific points of the structure, in order to record, accelerometric time histories only from ambient noise. The data acquired are filtered and processed by appropriate techniques able to extract the dynamic information. These data can be used for two different purposes, depending on the acquisition duration: if there are acquired for a short period (Short-term monitoring) they can be used to identify the current building state and caliber a numerical model [7,13–16], whereas if there are acquired for a long period (Long-term monitoring), such as more than one year, they can be used to the damage identification [17–21], since, the variation of the dynamic characteristics are linked to stiffness or mass variations [22]. In this last case, particular attention must be paid to the ambient conditions because, as many studies showed, they can provoke variation in frequencies, some authors are looking for algorithms to delete them from the signals [23,24].

In this paper, the monitoring and the Finite Element Model (FEM) calibration are presented taking as a case study a complex composed by civic tower a palace and an arcade in Matelica, a village in the hinterland of Marche region Figure 1. This study wants to be an example of applicability the dynamic monitoring for protection of the heritage masonry constructions.

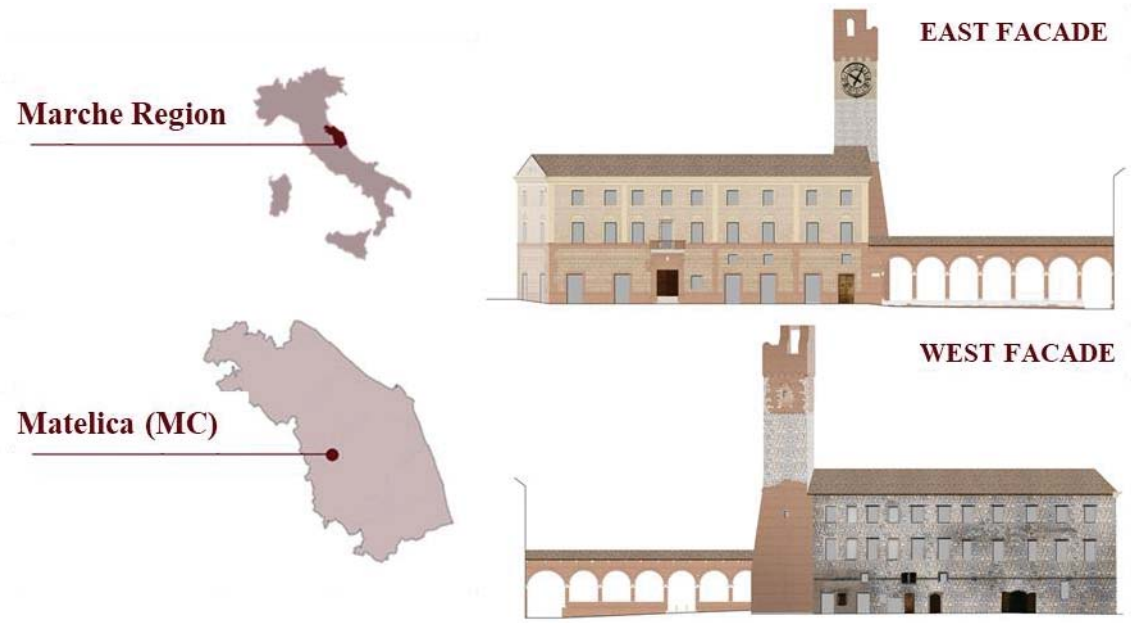

Figure 1 Geographical localization and East and West facades

2 CASE STUDY

2.1. Historical development

At the start, the Governor's Palace was a porticoed structure used as delimitation between the plaza and the open-air market. This structure was destroyed during the gothic war.

The Civic Tower dates to the XII century, it was built on the ruins of a Romanesque structure, in 1209 it became the imperial lieutenant's residence. The actual configuration of the Governator's Palace goes back to 1284, by the work of the Benincasa da Firenze and Bruno da Fabriano. The gallery construction on the tower and the ogival windows closing occurred in the XIV century. In 1511 started the arcade construction, on the right side of the Palace, designed by Costantino and Giovan Battista da Lugano architects, and was initially used as a textile market (Figure 2). The structures were modified several times, between 1670-1830, when they were subjected to the first restoration interventions; however, at their end, the palace was declared unsafe for static problems. To improve the tower stability in 1893 its base was extended. Similar interventions aimed to improve the stability of all the components of the building continued until 1997 when a big restoration was carried out after the Umbria-Marche earthquake.

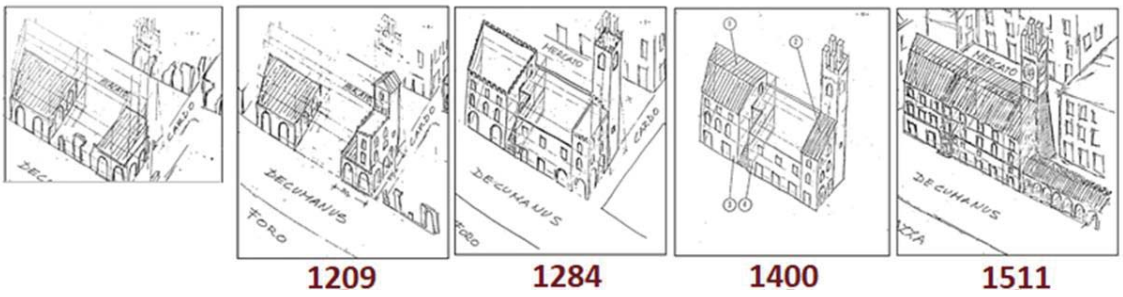

Figure 2 Historical evolution of the complex

2.2. Geometric survey

The palace has a rectangular plant of dimensions 13.30mx37.58m, it has three floors and a mezzanine between the ground and first floor. On the North-West side there is the Civic Tower, it has a rectangular plant 7.25mx7.45m and a height of 35m with eight levels divided by masonry and wood floors. The open gallery is on the North side of the palace. It has a rectangular plant characterized by 14 polygonal columns with ionic capitals that support round arches (Figure 3). The materials used are various. The most visible façades in the South and East are covered by regular masonry, whereas on the others are visible the irregular masonry Figure **1**. The masonry type present are uncut stone for the palace, uncut stone and solid blocks for the tower and solid bricks for the arcade. The roofs are made of wood trusses.

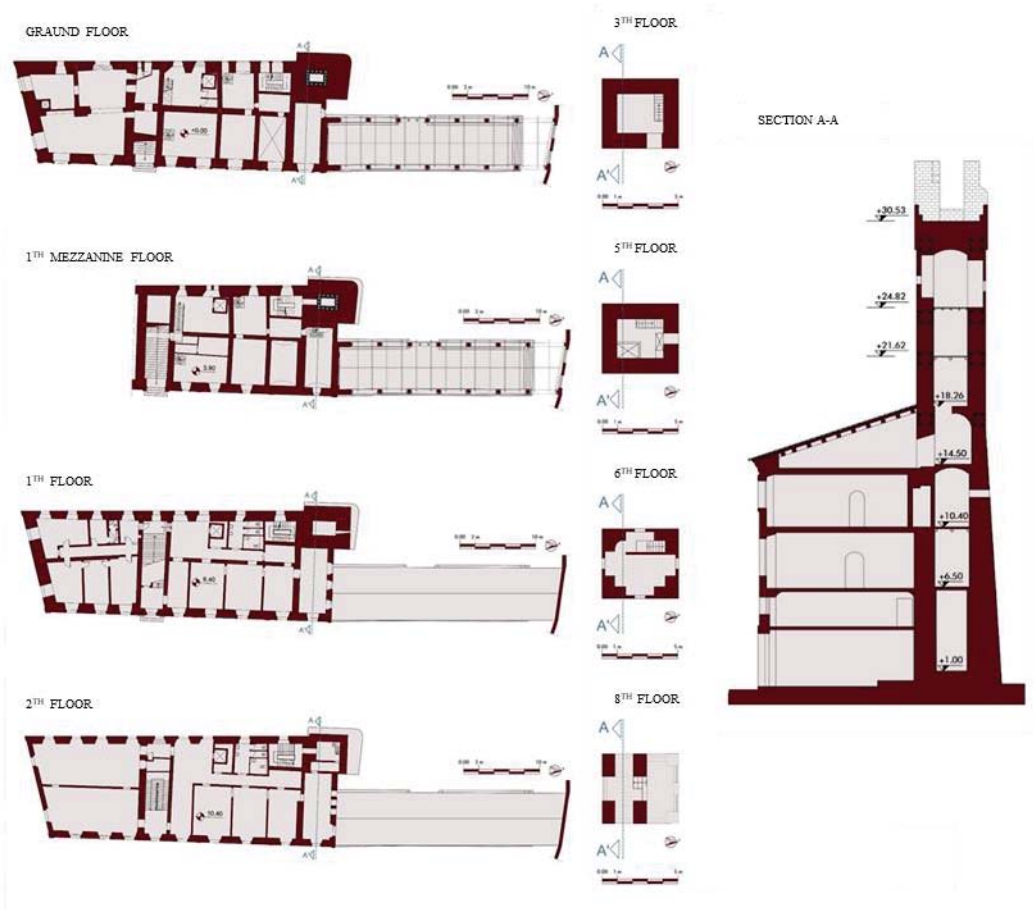

Figure 3 Geometrical configuration of the complex

3 DYNAMIC CHARACTERIZATION

3.1 Ambient Vibration Testing

The study of historical buildings structural behavior is usually carried out through linear or non-linear analysis on FEMs. Being the objective to represent the real structure behavior in the most accurate way, the realization of these Numerical Models (NMs) requires a deep knowledge of the structural parameters, such as materials properties, connections among elements, boundary conditions, etc. Among all the possible methodologies which allows to investigate structural properties, these case study has been approached through a method which has become very popular in the last few years, due to its non-invasiveness and the satisfactory results produced: Ambient Vibration Testing (AVT). This method is based on the monitoring of vibrations produces on the building by ambient effects (like wind, traffic…) and on the extraction of modal properties (natural frequencies, modal damping and mode shapes) from the analysis of these data through modal identification techniques. Then these properties are used to build an Experimental Model (EM), whose response is compared with that of the NM. An iterative process, which consists in the variation of the unknown parameters in the model, like Young Elastic Modulus E and material density ρ, is applied in order to obtain correspondence between both natural frequencies and associated mode shapes of the two types of models [25].

3.2 Monitoring equipment, sensors layout and data

Structural monitoring of the case study has been performed using a wired sensors network, composed of:

- four triaxial accelerometers of GEA System series, with a sensitivity of 1000 mV/g, a measurement range of ± 8g and A/D converter with a resolution of 24 bit;
- hub for synchronization;
- coaxial cables.

Sensors layout has been designed applying the concept of Optimal Sensor Placement (OSP) [26],so that, in the different layouts configured for the acquisitions, sensors have been placed in the most sensitive points of the building (in accordance with the possibility of reaching them), in order to better detect the translational and torsional components of the tower displacement [18]. In order to assure a rigid link between the selected point and the sensor epoxy resin has been used.

The monitoring activity of the tower has been conducted through 6 acquisitions, considering as many sensors layouts, which are shown in Figure 4. Data have been collected with a sample rate of 1024 Hz for periods which vary between 40 and 60 minutes, in order to satisfy Rodriguez condition [27].

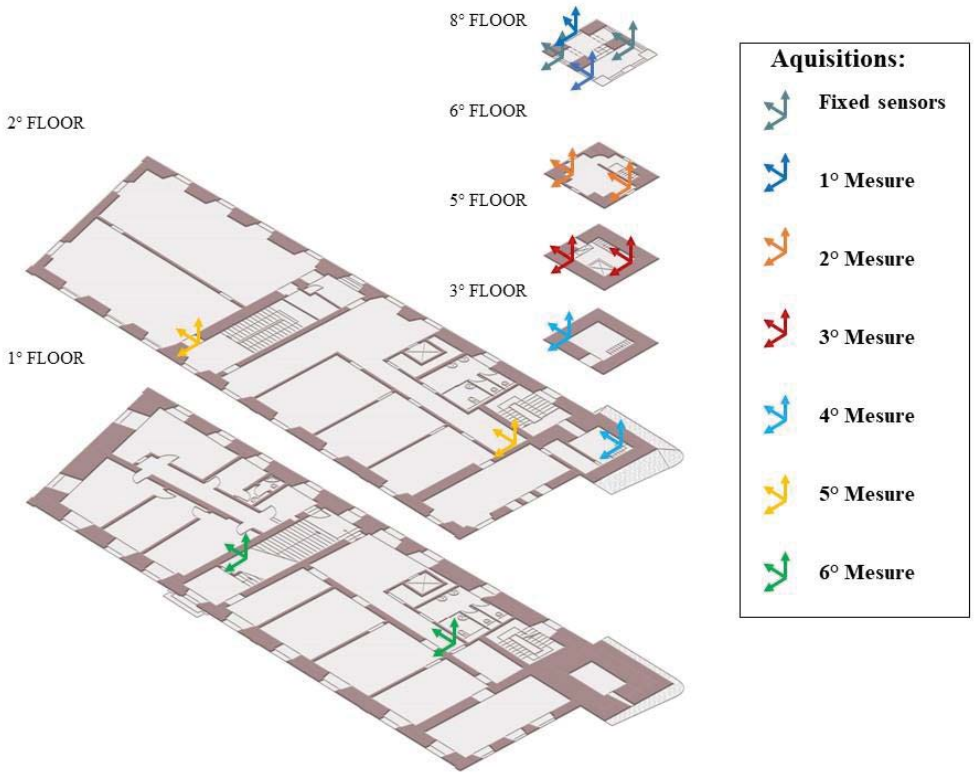

Figure 4 Sensors Layout

3.3 Operational Modal Analysis

3.3.1 OMA identification technique

The acquired data, after a filtering process, have been analyzed through modal identification techniques. Among these methodologies some operates in time domain, while others operate in the frequency domain. For the case study under exam, it was decided to apply a time domain technique, called Stochastic Subspace Identification (SSI) method [28]. This methodology consists in a conversion of the second order differential equation of motion into two first order equations, defined "state equation" and "observation equation", which, for a generic discrete time instant t = kΔt (where Δt is the sampling period and k ϵ N) can be written as:

$$\begin{aligned} \{\hat{x}_{k+1}\} &= [A]\{\hat{x}_k\} + [B]\{u_k\} \\ \{y_k\} &= [C]\{\hat{x}_k\} + [D]\{u_k\} \end{aligned} \tag{1}$$

where:

- $[A]$ is the matrix of input physical information;
- $[B]$ is the matrix of input statistical parameters;
- $[C]$ is the discrete output matrix;
- $[D]$ is the direct output transmission matrix;
- $x_k = x_k(\Delta t)$ is the discrete-time vector containing the sampled displacement and velocities;
- $\{y_k\}, \{u_k\}$ are the vectors of sampled input and output.

Other parameters describing the dynamic system are considered as deterministic and should not be subdued to the variations linked to excitation changes.

At this point, applying a Singular Value Decomposition (SVD) of the [A] matrix, the Eigenvalues, corresponding to the natural frequencies, and the correspondent Eigenvectors, which describe the mode shapes, are extracted.

For the examined case study, acquired data have been decimated into an interval of 12.5 Hz, in order to highlight the first five modes, mainly involving the tower, and their modal parameters. The values of natural frequencies and modal damping, for each mode, are reported in Table 1.

Mode	Frequency [Hz]	Damping [%]
1	1.923	0.679
2	2.007	0.873
3	5.058	2.931
4	6.531	1.569
5	7.629	2.705

Table 1 Modal parameters of Experimental Model

3.3.2 Preliminary FE model

The results of the investigation campaign, carried out to assess the geometrical characteristics of the building and to evaluate status of the materials, allowed to realize a preliminary non calibrated NM, created using Midas FEA© software.

This model, even if the analysis is principally focused on the tower behavior, represents the complete structure, composed of the main building, the tower and the open gallery, due to the importance of considering the effects of interaction between the tower and the connected building [29–31]. The internal elements, like floors and stairs, have been modeled in case they

significantly influence the stiffness of the structure, like in case of the concrete floors built after the restoration works, while, in case of secondary elements, they have been considered only as loads distributed on the walls. As concerns the modeling process, the geometries have been discretized through 4-nodes tetrahedral solid elements, while, for the material properties assigned to the meshes, they have been selected from the tables reported in the Italian Code [32,33], scaled with the appropriate factors to take into accounts the knowledge level (KL1). These preliminary parameters are reported in Table 2.

Position	Types	W [kN/m^3]	E [N/mm^2]
Open Gallery Base	Soft stone masonry	13-16	1440
Open Gallery Walls	Solid bricks masonry	18	1500
Wood	Wood	7.6	1100
Building interior Walls	Solid bricks masonry	18	1500
Interior Arch Walls	Solid bricks masonry	18	1500
Building Perimetric Walls	Rough-hewn masonry	20	1440
Tower Walls (1-2-3-5-6)	Rough-hewn masonry	20	1440
Tower Wall (4)	Rough-hewn masonry	20	1230
Tower Walls (7-8-9)	Solid bricks masonry	18	1500

Table 2 Material parameters of preliminary Numerical Model

The NM, built with these characteristics, has been analyzed using Lanczos method, and has shown the results reported in Table 3, where the values of natural frequencies associated to the first five modes are shown.

Mode	Frequency [Hz]	Damping [%]
1	1.731	5.000
2	1.764	5.000
3	4.953	5.000
4	6.264	5.000
5	7.667	5.000

Table 3 Modal parameters of preliminary Numerical Model

3.3.3 NM calibration

The calibration process of the NM model consists, as already said, in an iterative procedure in which some parameters considered unknown, in particular Young Elastic Modulus and density of materials, are modified, at each step of the procedure, in order to obtain a coincidence, or at least a maximum difference (Δf) of 5%, between the modal frequencies of the experimental and numerical models. Then, also the correspondence between the mode shape, associated to the same mode, is checked and validated, using the CrossMAC criterion [34]. This tool, which is applied in case of complex modes, provides an indication of the consistency of the modal vectors associated to the mode shapes obtained from different models. This indicator is calculated as the normalized scalar product of the modal vector for the r mode of analytical model $\{\varphi_A\}$, and the associated modal vector for the q mode of the test model $\{\varphi_X\}$:

$$MAC(r,q) = \frac{\left|\{\varphi_A\}_r^T\{\varphi_X\}_q\right|^2}{(\{\varphi_A\}_r^T\{\varphi_A\}_r)(\{\varphi_X\}_q^T\{\varphi_X\}_q)} \quad (2)$$

These scalar results are assembled in the CrossMAC matrix, whose optimal configuration is that of a principal diagonal with terms which are near or equal to 1 (which indicate good or perfect correspondence) and with terms outside of the diagonal which are near or equal to 0.

The first comparison in terms of frequencies between the EM and NM is shown in Table 4, which shows a too big difference in the values of frequencies associated to the first two modes.

Mode	Frequency EM [Hz]	Frequency NM [Hz]	Δf [%]
1	1.923	1.731	9.98
2	2.007	1.764	12.11
3	5.058	4.953	2.08
4	6.531	6.264	4.09
5	7.629	7.667	0.50

Table 4 Comparison of EM and preliminary NM modal frequencies

Better correspondence, instead, is obtained comparing the mode shapes, whose direction of displacement are coincident between EM and NM, being the first two mode translational respectively in Y and X direction, the third and the fifth are flexional in Y and X, respectively, while the fourth shows a distorting behavior (Figure 5).

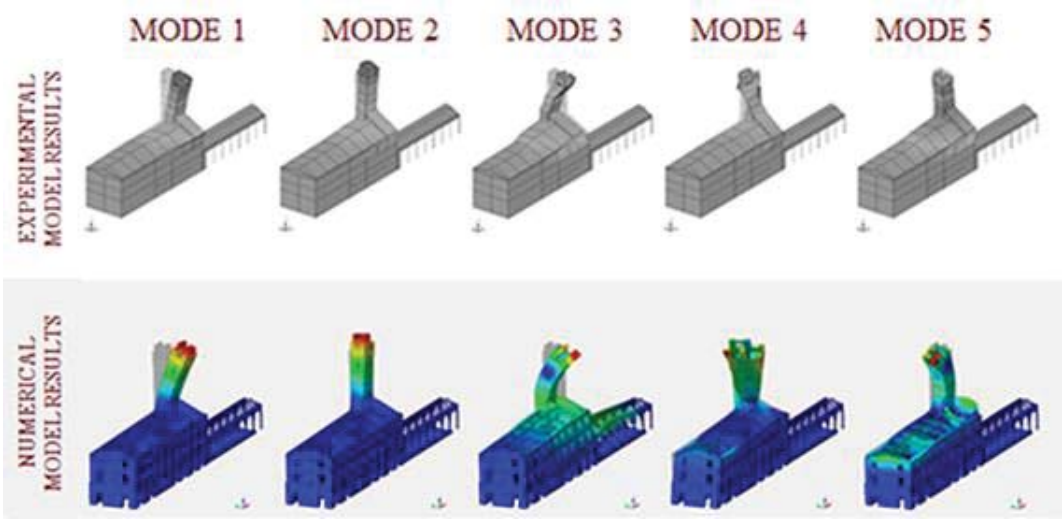

Figure 5 Comparison of mode shapes of preliminary NM and EM

The first step of parameter update has been operated only on the elastic modulus of the materials attributed to the tower elements. The criterion was to increase the stiffness of the element subjected to intervention in 2007 and decrease the density of some other elements, whose characteristics are inferior in respect of the previsions. The result of this operation comported a decrement of the frequencies values difference under the 5%, with the exception of the second mode.

In the second step, also the elastic modulus of elements which were not subdued to interventions has been increased, assuming that their deterioration was not as serious as thought at first. The result comported also a decrement of the difference in the values of frequency for the second mode under 5%.

In the last step it has been decided to intervene on the parameters associated to the building, dividing the perimetric walls in three sections, whose stiffness has been increased for the portion nearer the tower, and decreased for the other two parts. The results in terms of frequencies are reported in Table 5.

Mode	Frequency EM [Hz]	Frequency NM [Hz]	Δf [%]
1	1.93	1.88	2.59
2	2.01	1.92	4.48

3	5.06	5.31	4.94
4	6.53	6.77	3.68
5	7.63	7.82	2.49

Table 5 Comparison of modal frequencies of EM and calibrated NM

This modification allowed a better correspondence between mode shapes, as it is possible to see from Figure 6, and as attested in Table 6, where CrossMAC results are shown.

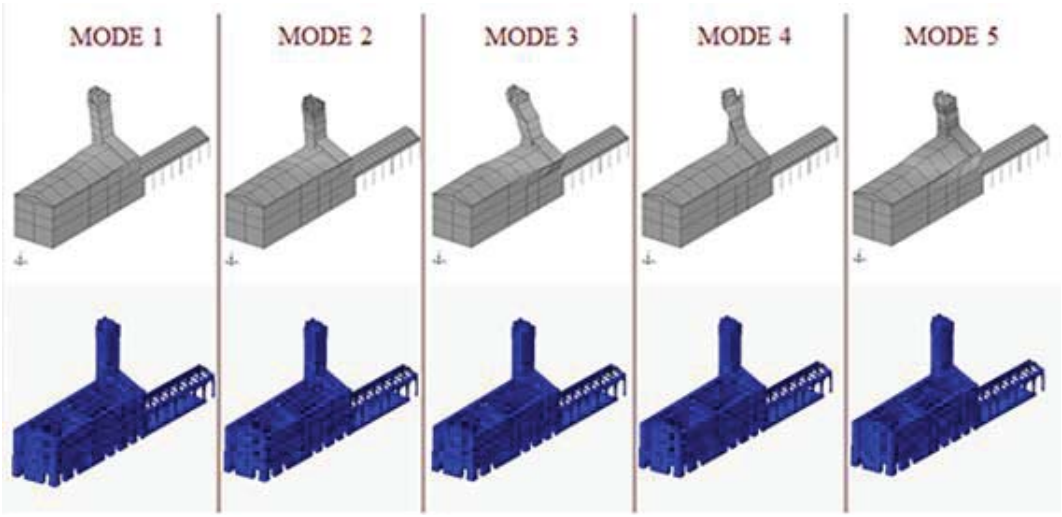

Figure 6 Mode shapes comparison after calibration

CrossMAC		EXPERIMENTAL MODEL				
		MODE 1 1.93 [Hz]	MODE 2 2.01 [Hz]	MODE 3 5.06 [Hz]	MODE 4 6.53 [Hz]	MODE 5 7.63 [Hz]
NUMERICAL MODEL	MODE 1 1.88 [Hz]	0.89	0.03	0.00	0.00	0.01
	MODE 2 1.92 [Hz]	0.00	0.98	0.01	0.04	0.02
	MODE 3 5.31 [Hz]	0.19	0.02	0.70	0.05	0.30
	MODE 4 6.77 [Hz]	0.00	0.02	0.00	0.81	0.16
	MODE 5 7.82 [Hz]	0.00	0.09	0.11	0.10	0.78

Table 6 Cross MAC after calibration

These results highlight the low level of interaction between the tower and the palace, whose dynamic behaviors do not influence each other so much, probably due to the different manufacturing and absence of linking elements. In particular, the disorganic movement of the tower, shown for the higher modes, and especially the distorting behavior of the fourth mode, can be linked to the sectional changes and to the variation of material properties. As concerns the damage propagation, the most damages zones are the ones with low values of Young Elastic Modulus.

4 CONCLUSIONS

The model updating process, operated for the tower and the rest of the Governor Palace structure, produced good results in terms of correspondence with the modal parameters and mode shapes extracted from EM. Moreover, it allowed the observation of an interesting

phenomenon in the tower dynamic behavior, such as the sectional distortion caused by the fourth mode.

Once again, dynamic monitoring and modal identification techniques, confirmed their effectiveness in the evaluation of dynamic behavior and consequently on the health status of historical structures, being the method non-invasive and allowing to produce accurate numerical models, which can be used implement rapid, localized and economically sustainable interventions.

REFERENCES

[1] F. Clementi, A. Ferrante, E. Giordano, F. Dubois, S. Lenci, Damage assessment of ancient masonry churches stroked by the Central Italy earthquakes of 2016 by the non-smooth contact dynamics method, Bull. Earthq. Eng. (2019). doi:10.1007/s10518-019-00613-4.

[2] E. Giordano, F. Clementi, A. Nespeca, S. Lenci, Damage Assessment by Numerical Modeling of Sant'Agostino's Sanctuary in Offida During the Central Italy 2016–2017 Seismic Sequence, Front. Built Environ. 4 (2019). doi:10.3389/fbuil.2018.00087.

[3] G. De Matteis, M. Zizi, Preliminary Analysis on the Effects of 2016 Central Italy Earthquake on One-Nave Churches, in: 2019: pp. 1268–1279. doi:10.1007/978-3-319-99441-3_136.

[4] G. Milani, M. Valente, Failure analysis of seven masonry churches severely damaged during the 2012 Emilia-Romagna (Italy) earthquake: Non-linear dynamic analyses vs conventional static approaches, Eng. Fail. Anal. 54 (2015) 13–56. doi:10.1016/j.engfailanal.2015.03.016.

[5] A. Ferrante, F. Clementi, G. Milani, Dynamic Behavior of an Inclined Existing Masonry Tower in Italy, Front. Built Environ. 5 (2019). doi:10.3389/fbuil.2019.00033.

[6] A. Formisano, G. Vaiano, F. Fabbrocino, G. Milani, Seismic vulnerability of Italian masonry churches: The case of the Nativity of Blessed Virgin Mary in Stellata of Bondeno, J. Build. Eng. 20 (2018) 179–200. doi:10.1016/j.jobe.2018.07.017.

[7] E. Giordano, F. Clementi, A. Barontini, M. Giovanna, E. Chatzi, F. Luís, Damage detection and optimal sensor placement in health monitoring of " Collegiata di Santa Maria " in Visso (Central Italy) Damage detection and optimal sensor placement in health monitoring of " Collegiata di Santa Maria " in Visso (Central Italy), (2019) 44–53.

[8] E. Giordano, A. Ferrante, E. Ribilotta, F. Clementi, S. Lenci, Damage Assessment of San Francesco Church in Amandola Hit by Central Italy 2016-2017 Seismic Event, Key Eng. Mater. 817 (2019) 627–633. doi:10.4028/www.scientific.net/KEM.817.627.

[9] A. Ferrante, E. Ribilotta, E. Giordano, F. Clementi, S. Lenci, Advanced Seismic Analyses of "Apennine Churches" Stroked by the Central Italy Earthquakes of 2016 by the Non-Smooth Contact Dynamics Method, Key Eng. Mater. 817 (2019) 309–316. doi:10.4028/www.scientific.net/KEM.817.309.

[10] E. Ribilotta, E. Giordano, A. Ferrante, F. Clementi, S. Lenci, Tracking Modal Parameter Evolution of Different Cultural Heritage Structure Damaged by Central Italy

Earthquake of 2016, Key Eng. Mater. 817 (2019) 334–341. doi:10.4028/www.scientific.net/KEM.817.334.

[11] A. Ferrante, F. Clementi, G. Milani, Advanced numerical analyses by the Non-Smooth Contact Dynamics method of an ancient masonry bell tower, Math. Methods Appl. Sci. (2020) mma.6113. doi:10.1002/mma.6113.

[12] F. Clementi, G. Milani, A. Ferrante, M. Valente, S. Lenci, Crumbling of Amatrice clock tower during 2016 Central Italy seismic sequence: Advanced numerical insights, Frat. Ed Integrità Strutt. 14 (2019) 313–335. doi:10.3221/IGF-ESIS.51.24.

[13] C. Gentile, A. Saisi, Ambient vibration testing of historic masonry towers for structural identification and damage assessment, Constr. Build. Mater. (2007). doi:10.1016/j.conbuildmat.2006.01.007.

[14] A. De Stefano, E. Matta, P. Clemente, Structural health monitoring of historical heritage in Italy: some relevant experiences, J. Civ. Struct. Heal. Monit. (2016). doi:10.1007/s13349-016-0154-y.

[15] F. Ubertini, G. Comanducci, N. Cavalagli, Vibration-based structural health monitoring of a historic bell-tower using output-only measurements and multivariate statistical analysis, Struct. Heal. Monit. (2016). doi:10.1177/1475921716643948.

[16] F. Clementi, A. Pierdicca, A. Formisano, F. Catinari, S. Lenci, Numerical model upgrading of a historical masonry building damaged during the 2016 Italian earthquakes: the case study of the Podestà palace in Montelupone (Italy), J. Civ. Struct. Heal. Monit. 7 (2017) 703–717. doi:10.1007/s13349-017-0253-4.

[17] I. Venanzi, A. Kita, N. Cavalagli, L. Ierimonti, F. Ubertini, Continuous OMA for Damage Detection and Localization in the Sciri tower in Perugia, Italy, (n.d.).

[18] F. Ubertini, G. Comanducci, N. Cavalagli, A. Laura Pisello, A. Luigi Materazzi, F. Cotana, Environmental effects on natural frequencies of the San Pietro bell tower in Perugia, Italy, and their removal for structural performance assessment, Mech. Syst. Signal Process. (2017). doi:10.1016/j.ymssp.2016.05.025.

[19] N. Cavalagli, G. Comanducci, F. Ubertini, Earthquake-Induced Damage Detection in a Monumental Masonry Bell-Tower Using Long-Term Dynamic Monitoring Data, J. Earthq. Eng. 22 (2018) 96–119. doi:10.1080/13632469.2017.1323048.

[20] P.X. Candeias, A. Campos Costa, N. Mendes, A.A. Costa, P.B. Lourenço, Experimental Assessment of the Out-of-Plane Performance of Masonry Buildings Through Shaking Table Tests, Int. J. Archit. Herit. 11 (2017) 31–58. doi:10.1080/15583058.2016.1238975.

[21] L.F. Ramos, L. Marques, P.B. Lourenço, G. De Roeck, A. Campos-Costa, J. Roque, Monitoring historical masonry structures with operational modal analysis: Two case studies, Mech. Syst. Signal Process. (2010). doi:10.1016/j.ymssp.2010.01.011.

[22] S.W.S. Doebling, C.R.C. Farrar, M.B.M. Prime, D.W.D. Shevitz, Damage identification and health monitoring of structural and mechanical systems from changes in their vibration characteristics: a literature review, Los Alamos Natl. Lab. (1996). doi:10.2172/249299.

[23] C. Gentile, A. Ruccolo, F. Canali, Long-term monitoring for the condition-based structural maintenance of the Milan Cathedral, Constr. Build. Mater. 228 (2019)

117101. doi:10.1016/j.conbuildmat.2019.117101.

[24] L.F. Ramos, P.B. Lourenço, G. De Roeck, A. Campos-Costa, Damage identification in masonry structures with vibration measurements, Struct. Anal. Hist. Constr. Preserv. Saf. Significance - Proc. 6th Int. Conf. Struct. Anal. Hist. Constr. SAHC08. 1 (2008) 311–319. doi:10.1201/9781439828229.ch35.

[25] G. Standoli, E. Giordano, G. Milani, F. Clementi, Model Updating of Historical Belfries Based on Oma Identification Techniques, Int. J. Archit. Herit. (2020) 1–25. doi:10.1080/15583058.2020.1723735.

[26] J. Zhang, K. Maes, G. De Roeck, E. Reynders, G. Lombaert, Experimental verification of optimal sensor placement for multi-setup modal testing, Procedia Eng. 199 (2017) 1068–1073. doi:10.1016/j.proeng.2017.09.063.

[27] J. Rodrigues, Identificação Modal Estocástica: Métodos de Análise e Aplicações em Estruturas de Engenharia Civil, 2004.

[28] M. Systems, K.U. Leuven, Reference-Based Stochastic Subspace Identification for Output-Only Modal Analysis, Mech. Syst. Signal Process. 13 (1999) 855–878.

[29] G. Bartoli, M. Betti, L. Galano, G. Zini, Numerical insights on the seismic risk of confined masonry towers, Eng. Struct. 180 (2019) 713–727. doi:10.1016/j.engstruct.2018.10.001.

[30] A. Cabboi, C. Gentile, A. Saisi, From continuous vibration monitoring to FEM-based damage assessment: Application on a stone-masonry tower, Constr. Build. Mater. 156 (2017) 252–265. doi:10.1016/j.conbuildmat.2017.08.160.

[31] G. Castellazzi, A.M. D'Altri, S. de Miranda, A. Chiozzi, A. Tralli, Numerical insights on the seismic behavior of a nonisolated historical masonry tower, Bull. Earthq. Eng. 16 (2018) 933–961. doi:10.1007/s10518-017-0231-6.

[32] Ministero delle Infrastrutture e dei Trasporti, DM 17/01/2018 - Aggiornamento delle "Norme Tecniche per le Costruzioni" (in italian), (2018) 1–198.

[33] Ministero delle infrastrutture e dei trasporti, Circolare 21 gennaio 2019 n. 7 C.S.LL.PP. Istruzioni per l'applicazione dell'aggiornamento delle "Norme Tecniche per le Costruzioni" di cui al D.M. 17/01/2018 (in Italian), Suppl. Ord. Alla G.U. n. 35 Del 11/2/19. (2019).

[34] M. Pastor, M. Binda, T. Harčarik, Modal assurance criterion, Procedia Eng. 48 (2012) 543–548. doi:10.1016/j.proeng.2012.09.551.

EURODYN 2020
XI International Conference on Structural Dynamics
M. Papadrakakis, M. Fragiadakis, C. Papadimitriou (eds.)
Athens, Greece, 23–26 November 2020

MEASUREMENTS OF THE COLOSSEUM RESPONSE TO ENVIRONMENTAL ACTIONS

Fabrizio Vestroni[1], **Adriano De Sortis**[2] **and Annamaria Pau**[1]

[1] Sapienza University of Rome
Via Eudossiana, Roma
e-mail: vestroni@uniroma1.it, annamaria.pau@uniroma1.it

[2] Department of Civil Protection
Via Vitorchiano 2, Roma
e-mail: adriano.desortis@protezionecivile.it

Keywords: Cultural heritage structures, Monitoring, Modal analysis, Seismic behaviour.

Abstract. *The Colosseum is the most famous monument of ancient Rome. Differential settlements of its foundations, standing partly on alluvial deposits and partly on stiff soil, and various earthquakes are the main causes of collapses that give the Colosseum its present shape. In order to preserve the monument, a number of structural interventions were made during the 19th century. At present, the health status of the monument requires to be monitored against possible degradation phenomena. During the preliminary design stage of a new underground line crossing the center of Rome, at present under construction, further investigations on materials properties and dynamic features have been performed. In particular, twelve accelerometers on two vertical lines in the highest portion of the monument have been installed. In the present paper data gathered with this monitoring system for a long period of time gives the opportunity of a further insight into the health conditions of the structure. The vibration levels induced by road traffic during a long interval of time and frequencies and mode shapes of low modes are identified using ambient vibration. Both these results are compared with the outcomes of an experimental campaign of a few years ago. Finally, the dynamic behaviour recorded during the 2016-2017 Central Italy seismic sequence is analysed and discussed.*

1 INTRODUCTION

Structural Health Monitoring (SHM) has notably increased its importance in the last decades [1, 2, 3]. The spreading of this kind of activity is also due to the updating of instruments and the reduction of their cost; at the same time, theory and techniques of data processing have become more effective [4, 5, 6, 7, 8, 9]. In this field methods based on structural vibration and their evolution are well established, also because information easily obtained using environmental excitations happens to be effective in detecting structural deterioration. In the case of large structures and cultural heritage buildings, SHM should be a must. So, it is natural that the Colosseum, the most famous monument of ancient Rome, is the object of special attention by the Superintendent of Cultural Heritage with a series of activities.

A new underground line crossing the center of Rome, at present under construction [10], run tangentially to the Colosseum; during the design stage a wide campaign of experimental investigations on materials properties and dynamic features have been performed. Moreover, the monument has been instrumented in order to develop both static and dynamic monitoring. In particular, inclinometers and estensometers to measure displacements due to temperature changes and twelve accelerometers on two vertical lines in the zone with greatest height have been installed.

The slow movements produced by temperature induce deformations and stresses, with cycles which are repeated every year. The accelerometric registrations of the ambient vibrations permit to obtain the intrinsic dynamic properties of the structure with a twofold aim. First, the comparison and correlation between experimental modal parameters and those predicted by a finite element model enable us to identify or update an accurate model of the monument; this is an important item especially where buildings of historical interest are involved, since they are often characterized by complex geometry and heterogeneity of materials. Second, the evolution in time of the modal properties gives information on possible degradation phenomena.

In this paper the main attention is devoted to the dynamic response; in particular, the vibration levels induced by road traffic for a long time interval is examined, then ambient vibrations are used to identify frequencies and shapes of low modes by these incomplete data. These results are both compared to available data obtained by the authors during an experimental campaign of a few years ago. Finally, the dynamic response to the 2016-2017 Central Italy seismic sequence is analysed and discussed.

2 THE NEW UNDERGROUND LINE OF ROME

The severe conditions of the surface traffic in Rome highlighted the need to improve the public transportation network. The two existing underground Lines A and B did not reach all the sectors of the city and suburbs. The authority managing the underground lines decided, in such a context, to construct the new Line C crossing the Rome territory along the alignment NW-SE. Figure 1, just for the intermediate part of the line, denoted as Section T3, shows the interference of the new line with some of the most famous monuments in the world. Among the others, the underground line runs near the Colosseum. Further details can be found at [10].

During the design stage, several forecasting activities have been performed, in order to simulate the effects of the underground works and to estimate the possible impacts on the monuments. For the Colosseum, the effects were estimated as negligible and no special provisional measures were provided. Nevertheless, a comprehensive monitoring system has been deployed, in order to study the response of the structure before and during the underground construction.

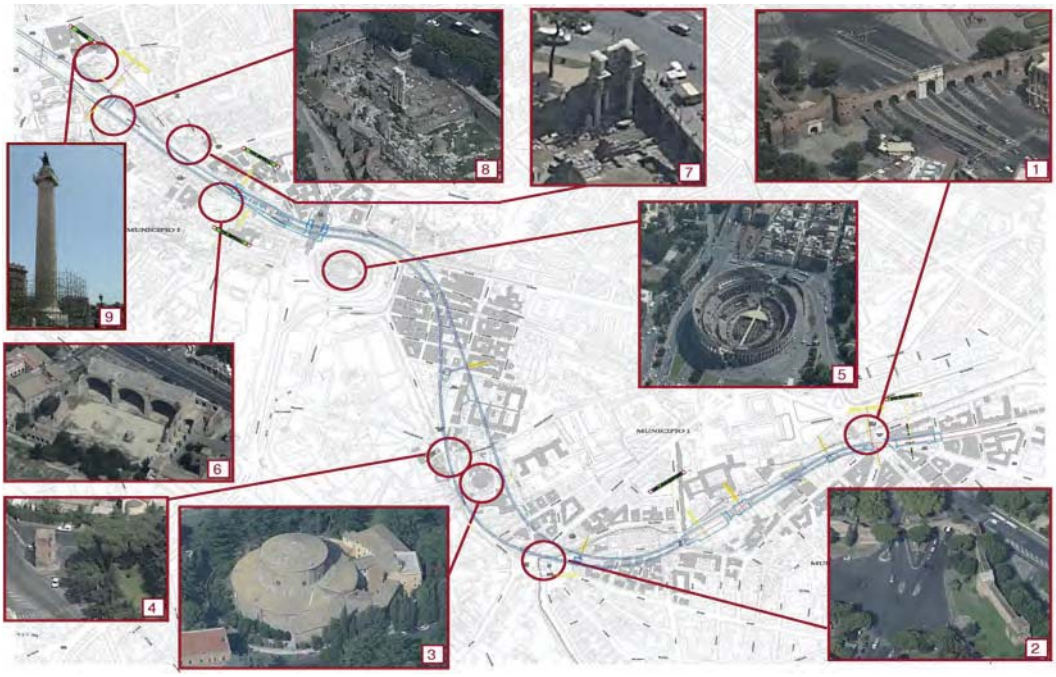

Figure 1: The Section T3 of the new Line C of Rome underground and the interference with monuments: 1) Porta Metronia, 2) Acquedotto Celimontano, 3) Basilica di S. Stefano Rotondo, 4) Porta Asinaria, 5) Colosseum, 6) Basilica di Massenzio, 7) Colonnacce, 8) Foro di Cesare, 9) Colonna Traiana.

3 DESCRIPTION OF THE MONITORING SYSTEM

A general description of the monitoring framework is reported in [11]. For the Colosseum, the monitoring system can be divided into 4 sections:

- topographic monitoring, aimed at gathering absolute displacements and rotations;
- geotechnical monitoring, aimed at gathering soil pore pressure and vertical and horizontal ground displacements;
- structural monitoring, divided into two subsections:

  - static monitoring, aimed at gathering structure and air temperatures, existing cracks openings, relative displacements, rotations;

  - dynamic monitoring, aimed at gathering structural accelerations and velocities.

The static monitoring is composed by 4 thermometers, 7 tiltmeters, 22 crackmeters and 12 wire-crackmeters. The dynamic monitoring is composed by 12 triaxial force-balance accelerometers, located along two vertical alignments, as reported in Fig. 2. The present paper is devoted to the analysis of dynamic measured quantities.

4 ANALYSIS OF DYNAMIC MEASUREMENTS

4.1 Road traffic

The main goal of the accelerometric monitoring system previously described is the survey of the vibration level during the construction of the underground line. Due to the presence of the monitoring system since the end of of 2014 and still functioning, both current vibration level

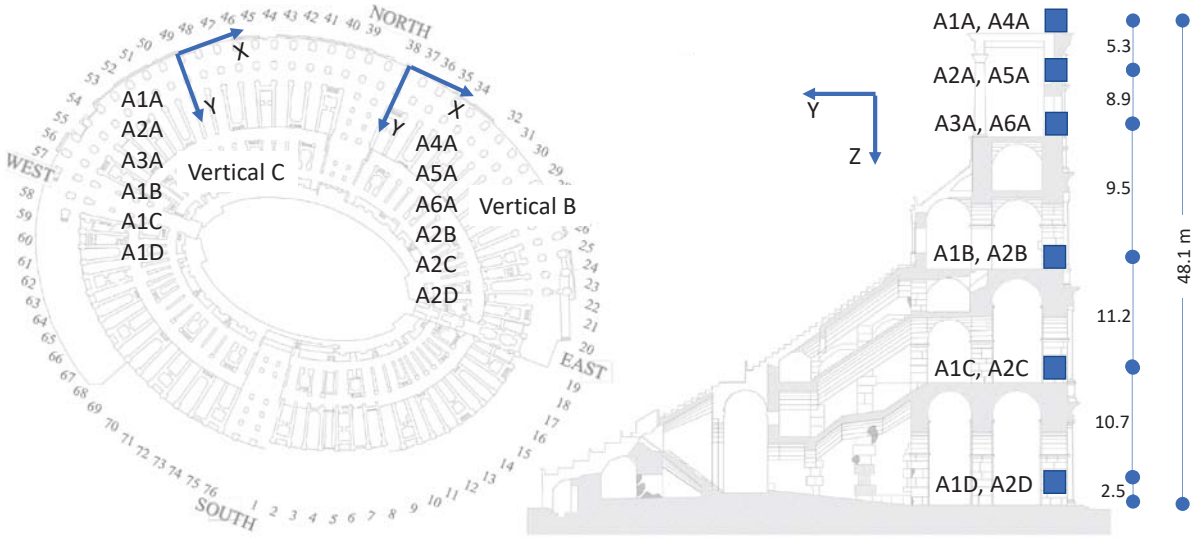

Figure 2: Locations of the accelerometric sensors and channels positive directions.

and peak values can be evaluated. A comprehensive analysis of data is outside the scope of the present paper, nevertheless a short discussion on the vibration level measured during one month (January 2020) is reported here; during this period the construction was inactive. Figure 3 shows the envelopes of the velocity recorded at the base and on the top in each direction. In vertical and circumferential directions at the base the maximum value of the velocity is about 0.15 mm/s, on top is about 0.5 mm/s, with smaller effective values respectively of about 0.02 mm/s at the base and 0.05-0.1 mm/s on top. In radial direction the maximum values of the velocity are similar, while the effective values are respectively of about 0.04 mm/s at the base and 0.15 mm/s on top. With reference to the time interval considered, the vibration level is very similar to that reported in [6] and it does not exceed the limit values reported in [12].

4.2 Modal analysis using ambient vibration

The experimental modal parameters have been evaluated in [6] using a large number of measurement points, under ambient vibration excitation. It was verified that the input at the base of the monument, in the frequency band 1-6 Hz, approximates a white noise. The experimental modal parameters were therefore derived from the response only, under the hypothesis of white noise excitation. In this condition, the output spectrum reaches a maximum at the natural frequencies, where the response of the structure peaks. The vibration frequencies of the first six modes, obtained in [6] by a singular value decomposition of the power spectral density matrix of the responses, are listed in Tab. 1.

Mode	1	2	3	4	5	6
Frequency [6]	1.03	1.30	1.49	1.60	1.66	1.75
Frequency (this study)	1.04	1.28	1.47	1.62	1.71	-

Table 1: Frequencies (Hz) of the first modes evaluated in [6] and in the present study.

Data recorded with the new monitoring system has been used to repeat the experimental modal analysis. In the present setup, few measurements are available, especially on the top

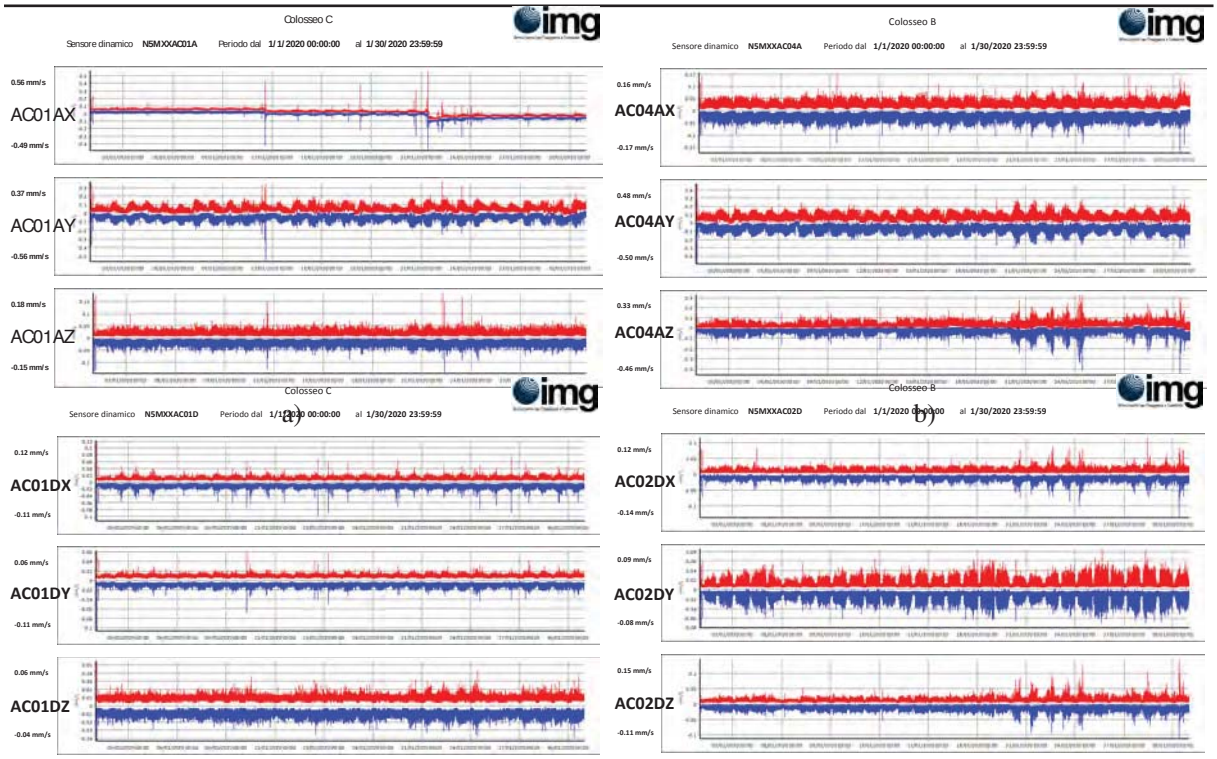

Figure 3: Velocity vibration levels (mm/s) measured during January 2020; a) sensor A1A (top level); b) sensor A4A (top level); c) sensor A1D (base level); d) sensor A2D (base level); for each sensor from top to bottom X (circumferential), Y (radial) and Z (vertical).

of the structure, thus it resulted rather difficult to detect the first two modes, which mainly involve points very far from the sensors. The same techniques applied in [6] have been used. Figure 4 shows the first two singular values of the power spectral density matrix of the response, where the modes identified are indicated with black circles. A comparison between the natural frequencies is reported in Tab. 1, showing a very good agreement. Also the components of the eigenvectors common to both [6] and present test setup have been compared, obtaining an acceptable agreement. Thus, with reference to this limited comparison, it can be argued that the dynamic characteristics of the structure appear stable.

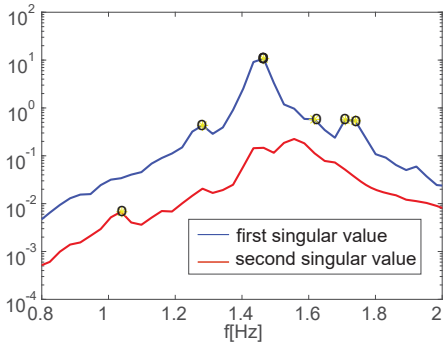

Figure 4: Singular value decomposition of the power spectral density matrix using data from ambient vibration.

n.	year	month	day	hh	mm	ss	M_w	lat	long	depth (km)	dist. (km)	$a_{b,t}$ (g %)	$a_{b,r}$ (g %)	$a_{b,v}$ (g %)
1	2016	8	24	1	36	32	6	42.7	13.2	8	109	0.32	0.35	0.23
2	2016	8	24	2	33	28	5.3	42.7	13.2	8	105	0.24	0.19	0.12
3	2016	10	26	17	10	36	5.4	42.9	13.1	8	122	0.31	0.47	0.17
4	2016	10	26	19	18	7	5.9	42.9	13.1	10	120	0.29	0.39	0.14
5	2016	10	30	6	40	17	6.5	42.8	13.1	10	116	0.95	0.94	0.41
6	2017	1	18	9	25	40	5.1	42.5	13.3	10	97	0.09	0.14	0.08
7	2017	1	18	10	14	9	5.5	42.5	13.3	10	96	0.19	0.36	0.13
8	2017	1	18	10	25	23	5.4	42.5	13.3	9	94	0.24	0.33	0.13
9	2017	1	18	13	33	36	5	42.5	13.3	10	92	0.1	0.2	0.08

Table 2: Events with magnitude $M_w > 5$ during the 2016-2017 Central Italy seismic sequence; the distances are computed between the epicenters and the Colosseum; $a_{b,t}$, $a_{b,r}$ and $a_{b,v}$ (measured in g*100) are the peak base accelerations recorded by the monitoring system respectively along the tangential, radial and vertical directions.

4.3 Response to 2016-2017 Central Italy seismic sequence

The measured response of a structure when it is impacted by a significant earthquake often furnishes significant information about its characteristics and health conditions [13, 14]. During 2016 and 2017, Central Italy has been interested by a significant seismic sequence. The accelerometric monitoring network was already deployed on the monument, thus several records of the structural response are available. Here, only events with magnitude greater than 5 have been considered. The main characteristics of these events are listed in Tab. 2. The epicenters are rather far from the Colosseum, with distances ranging from 92 to 122 km. The maximum value of the acceleration recorded at the base is about 0.01 g in the horizontal direction and 0.004 g in the vertical direction. The event that produced maximum accelerations at the base occurred on 2016, October 30, with a magnitude of 6.5 (event no. 5 in Tab. 2).

Figure 5 shows the 5% damping acceleration response spectra of event no. 5, as recorded at the monument base at two points in two directions. Modes 3 to 6 are located in the maximum amplification range of the spectra. In order to have a rough evaluation of the level of shaking, one could consider that, according to current seismic regulations, the 475-year return period site response spectrum on stiff soil has spectral ordinates respectively of 0.15, 0.23 and 0.1 g at 0, 0.5 and 1s. Thus, in terms of elastic response spectrum, event no. 5 produced about 1/10 of the spectral accelerations expected for the design earthquake.

Table 3 lists maximum accelerations recorded in radial directions. As expected, the peak values have been attained at the top level (about 0.09 g). It is interesting also to note that the dynamic amplification, i.e. the ratio between top and base peak accelerations, decreases when base peak acceleration increases. At any rate, the minimum dynamic amplification in radial direction is about 8.5. Thus, in the hypothesis of linear behaviour, a 475-year earthquake could lead to top accelerations up to about 1.3 g. This highlights the seismic vulnerability of the monument in its actual configuration, which probably requires a study for a mitigation intervention. In circumferential direction (Tab. 3) maximum accelerations of about 0.02–0.03 g have been recorded. Also in this direction the minimum amplification factor is about 3.6, a value rather common for masonry structures. Maximum recorded accelerations in vertical direction, not reported here, exhibits a minimum amplification factor of 2.4.

The configuration of the accelerometric monitoring system allows us to estimate a drift parameter that can be related to the strain level of the structure, i.e. the relative displacement between two sensors on the same vertical divided by their distance. Table 4 lists this quantity

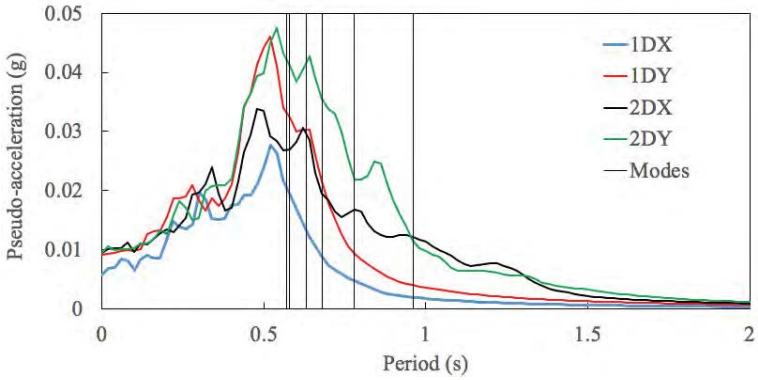

Figure 5: Response spectra at 5% damping of the accelerations recorded at the base during the event n. 5 of Tab. 2; the first letter A of the sensor labels is omitted; the directions X and Y are reported in Fig. 2; the vertical lines correspond to the first 6 modes of the structure.

for both horizontal directions. The graphical representation of Fig. 6 highlights that, in the plane of the facade, a strain concentration occurs on the third order of openings. In the out-of-plane direction, the upper part of the facade exhibits almost constant values. This behaviour is common to all 9 seismic events studied here. With reference to the strongest event no. 5 of Tab. 2, it was verified that the drift parameters of the upper sections are in phase and the maximum values are simultaneously attained, thus the behaviour is that of an almost rigid rotation. The rotation center is located at the base of the third order openings, which can be considered the most stressed part of the structure, both in plane and out of plane, during an earthquake.

5 CONCLUSIONS

The new Line C of Rome underground passes near the Colosseum. Owing to the historical renown of this ancient monument, the General Contractor, on behalf of Superintendent of Cultural Heritage, decided to perform a series of experimental activities to investigate its health conditions; in particular, static and dynamic instruments were used to monitor the structure before, during and after the underground construction.

In this study the focus was on five-year recordings of the dynamic quantities, accelerations and velocities, available to date, considering three different groups of results: the traffic induced vibration, the ambient vibration and the response to a recent seismic sequence in Central Italy.

As far as the velocities caused by the traffic, the levels of the results processed are very similar to those measured in a previous experimental campaign conducted by two of the authors in 2005, and, mainly, the maximum amplitude is below the levels known to cause damage, according to international guidelines.

As far as the ambient vibration, the procedures of the experimental modal analysis are used to identify frequencies and modes components at measurement points. Also in this case the dynamic properties obtained are in good agreement with those determined in 2005, leading to the preliminary conclusion that no overall deterioration phenomena recently occurred.

The registrations of accelerations produced by the seismic sequence of 2016-2017 in Central Italy are of some interest because they are the only available recordings of the earthquake effects on the monument. Notwithstanding the epicenter is far from the Colosseum, around 100 km, the measurements are sufficiently clear, with non-negligible response peaks. For the recorded earthquakes the maximum amplification of the spectrum is observed in a frequency band which

n.	1AY	2AY	3AY	4AY	5AY	6AY	1BY	2BY	1CY	2CY	1DY	2DY
1	3.48	2.28	1.24	5.8	3.09	1.29	0.63	0.8	0.47	0.41	0.35	0.27
2	2.53	1.68	0.81	2.59	1.46	0.87	0.40	0.53	0.25	0.30	0.20	0.19
3	4.04	2.66	1.19	4.88	2.68	1.25	0.81	0.77	0.62	0.51	0.47	0.41
4	3.23	1.96	0.7	5.56	3.13	1.67	0.66	0.88	0.45	0.5	0.34	0.39
5	9.27	3.85	1.71	9.41	6.06	2.52	1.82	1.96	1.25	1.36	0.91	0.94
6	1.42	1.05	0.69	1.24	0.63	0.55	0.28	0.29	0.19	0.16	0.14	0.1
7	2.99	2.01	0.97	2.8	1.34	0.62	0.74	0.59	0.5	0.41	0.36	0.28
8	3.43	2.41	1.52	3.95	1.75	1.1	0.67	0.66	0.47	0.38	0.33	0.24
9	1.05	0.62	0.31	1.7	1.26	0.63	0.35	0.34	0.22	0.24	0.13	0.2

n.	1AX	2AX	3AX	4AX	5AX	6AX	1BX	2BX	1CX	2CX	1DX	2DX
1	0.95	0.87	0.84	1.42	1.25	1.29	0.92	1.35	0.51	0.74	0.27	0.32
2	0.52	0.55	0.55	0.91	0.87	0.81	0.53	0.64	0.31	0.43	0.17	0.24
3	0.89	0.97	0.99	1.1	1.11	1.05	0.73	0.9	0.48	0.57	0.31	0.31
4	0.81	0.81	0.79	1.76	1.45	1.37	0.5	1	0.36	0.64	0.23	0.29
5	2.13	2.16	2.1	3.4	2.99	2.88	1.34	2.56	1.15	1.85	0.57	0.95
6	0.38	0.36	0.33	0.46	0.42	0.42	0.38	0.4	0.19	0.22	0.09	0.08
7	0.96	0.96	0.93	1	0.85	0.86	0.56	0.76	0.28	0.51	0.17	0.19
8	0.87	0.85	0.79	1.22	1.04	1.02	0.91	0.98	0.43	0.52	0.24	0.17
9	0.45	0.45	0.44	0.52	0.44	0.45	0.22	0.44	0.12	0.18	0.07	0.1

Table 3: Maximum accelerations in (g*100) recorded by the monitoring system in radial (Y) and circumferential (X) directions during the events described in Tab. 2; the first letter A of the sensor labels is omitted.

n.	1AY	2AY	3AY	4AY	5AY	6AY	1BY	2BY	1CY	2CY
1	0.145	0.113	0.181	0.227	0.176	0.196	0.009	0.018	0.008	0.008
2	0.103	0.079	0.111	0.113	0.099	0.103	0.007	0.015	0.004	0.006
3	0.14	0.106	0.166	0.175	0.134	0.186	0.01	0.021	0.01	0.01
4	0.11	0.077	0.063	0.208	0.164	0.164	0.009	0.026	0.007	0.011
5	0.329	0.19	0.158	0.472	0.413	0.344	0.026	0.048	0.021	0.028
6	0.046	0.039	0.068	0.044	0.038	0.034	0.005	0.005	0.003	0.003
7	0.094	0.072	0.089	0.099	0.069	0.061	0.011	0.013	0.009	0.007
8	0.117	0.094	0.162	0.143	0.107	0.078	0.014	0.016	0.007	0.009
9	0.03	0.023	0.028	0.067	0.066	0.079	0.005	0.007	0.004	0.004

n.	1AX	2AX	3AX	4AX	5AX	6AX	1BX	2BX	1CX	2CX
1	0.012	0.007	0.096	0.073	0.011	0.106	0.047	0.045	0.02	0.027
2	0.008	0.005	0.078	0.038	0.006	0.075	0.029	0.024	0.014	0.012
3	0.011	0.005	0.082	0.057	0.009	0.108	0.037	0.035	0.016	0.02
4	0.007	0.004	0.046	0.067	0.009	0.105	0.019	0.033	0.009	0.022
5	0.022	0.009	0.128	0.158	0.018	0.309	0.038	0.066	0.025	0.062
6	0.004	0.004	0.039	0.013	0.002	0.025	0.02	0.009	0.009	0.006
7	0.007	0.005	0.061	0.024	0.003	0.064	0.027	0.013	0.011	0.013
8	0.01	0.009	0.128	0.034	0.003	0.073	0.048	0.02	0.024	0.014
9	0.002	0.001	0.023	0.03	0.005	0.04	0.008	0.014	0.004	0.006

Table 4: Maximum relative displacements divided by the distance between two sensors (mm/m) recorded by the monitoring system in radial (Y) and circumferential (X) directions during the events described in Tab. 2; the labels of the columns correspond to the upper sensor; the first letter A of the sensor labels is omitted.

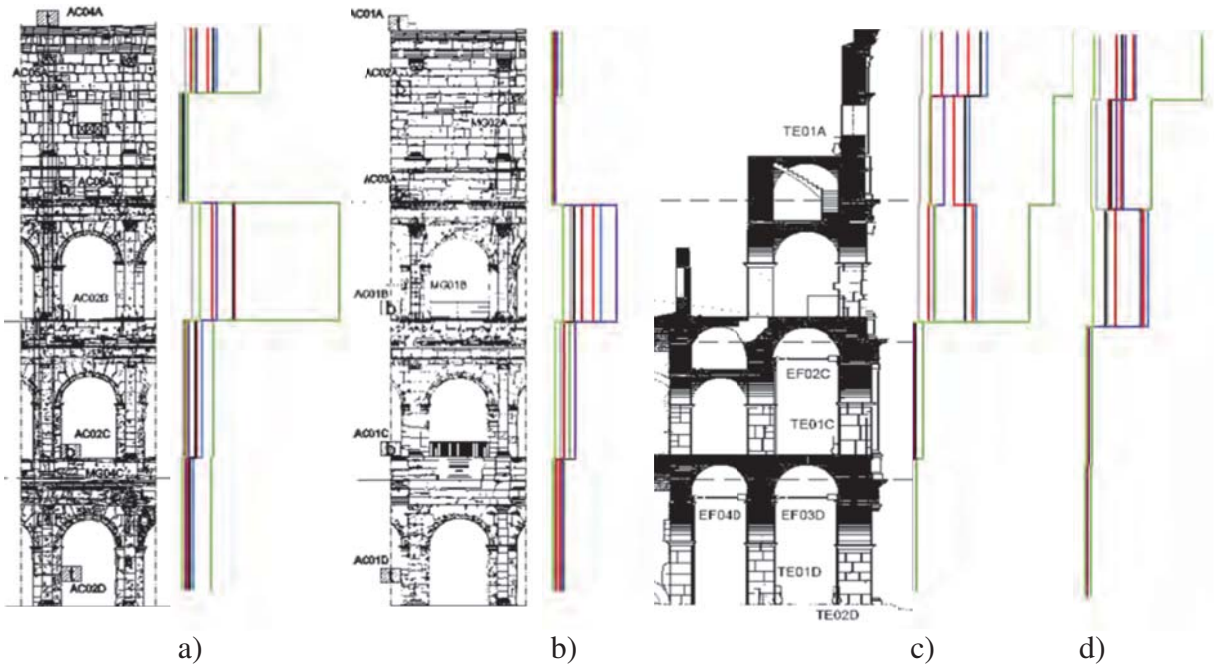

Figure 6: Relative displacements divided by the distance between two sensors recorded by the monitoring system during the events of Tab. 2; a) Vertical B of Fig.2, radial direction ; b) Vertical C, radial direction; c) Vertical B, circumferential direction; d) Vertical C, circumferential direction.

does not involve the first two modes of the monument, localized mainly at Valadier's and Stern's buttresses, which are the most dangerous. These results are important because they make it possible to use an updated finite element model to interpret these data and to predict the response to the expected earthquakes in Rome, evaluating the actual risk of the monument.

6 ACKNOWLEDGEMENTS

The experimental data have been made available by Metro C S.C.p.A., General Contractor of the Line C of the Rome Underground. The cooperation of Design Manager Eliano Romani and Dr. Ivan Mammone are gratefully acknowledged. Moreover, the valuable contribution of Eng. Matteo Ruggeri of IMG S.r.l. that manages the monitoring system is acknowledged.

This work has been partially supported by the MIUR (Ministry of Education, University and Research) under the Project PRIN 2015-2018, P.I. Fabrizio Vestroni, "Identification and Monitoring of Complex Structural Systems".

7 DISCLAIMER

The views and conclusions contained here are those of the authors, and should not be interpreted as necessarily representing official policies, either expressed or implied, of the Italian Government.

REFERENCES

[1] C.R. Farrar, K. Worden, An introduction to structural health monitoring, *Philosophical Transactions of the Royal Society A: Mathematical, Physical and Engineering Sciences*, **365**(1851), 303–315, 2007.

[2] P.C. Chang, A. Flatau, S.C. Liu, Review paper: Health monitoring of civil infrastructure, *Structural Health Monitoring*, **2**(3), 257–267, 2003.

[3] D. Capecchi, F. Vestroni, Monitoring of structural systems by using frequency data, *Earthquake Engineering and Structural Dynamics*, **28**(5), 447–461, 1999.

[4] A. Pau, A. De Sortis, R. Marzellotta, F. Vestroni, Health monitoring of cultural heritage using ambient and forced vibrations, *WIT Transaction on the Built Environment*, **82**, 331-340, 2005.

[5] A. De Sortis, E. Antonacci, F. Vestroni, Dynamic identification of a masonry building using forced vibration tests, *Engineering Structures*, **27**(2), 155–165, 2005.

[6] A. Pau, F. Vestroni, Vibration analysis and dynamic characterization of the Colosseum, *Structural Control and Health Monitoring*, **15**, 1105–1121, 2008.

[7] A. Pau, F. Vestroni, Dynamic characterization of ancient masonry structures, in *Advances in Vibration Analysis Research, Intech, Vienna*, ISBN: 9789533073910, 2011.

[8] A. Pau, F. Vestroni, Vibration assessment and structural monitoring of the Basilica of Maxentius in Rome, *Mechanical Systems and Signal Processing*, **41**(1-2), 454–466, 2013.

[9] G. Bongiovanni, G. Buffarini, P. Clemente, D. Rinaldis, F. Saitta, M. Nicoletti, A. De Sortis, G. Rossi, Dynamic identification of Palazzo Marchesale in S. Giuliano di Puglia, *Proceedings of the 5th International Conference on Structural Engineering, Mechanics and Computation, SEMC*, 81–86, 2013.

[10] http://www.metrocspa.it

[11] E. Romani, I. Mammone, S. Moretti, G. Pezzetti, Rome Metro Line Monitoring System: the C Line experience, *International Symposium on Field Measurements in Geomechanics*, 2018.

[12] UNI 9916:2014 Criteria for the measurement of vibrations and the assessment of their effects on buildings.

[13] V. Gattulli, E. Antonacci, F. Vestroni, Field observations and failure analysis of the Basilica S. Maria di Collemaggio after the 2009 L'Aquila earthquake, *Engineering Failure Analysis*, **34**, 715–734, 2013.

[14] F. Benedettini, A. De Sortis, G. Milana, In field data to correctly characterize the seismic response of buildings and bridges, *Bulletin of Earthquake Engineering*, **15**(2), 643–666, 2017.

EURODYN 2020
XI International Conference on Structural Dynamics
M. Papadrakakis, M. Fragiadakis, C. Papadimitriou (eds.)
Athens, Greece, 23–26 November 2020

ASSESSMENT OF THE TRM REINFORCEMENT OF WINDOWED MASONRY WALLS THROUGH OMA IDENTIFICATION

Salvador Ivorra[1], Domenico Camassa[2], David Bru[1], Ignacio Gisbert[1], Anna Castellano[3], Aguinaldo Fraddosio[2] and Mario Daniele Piccioni[2]

[1] Department of Civil Engineering
University of Alicante
Apartado 99, 03080, Alicante, Spain
sivorra@ua.es, david.bru@ua.es, igisbertsanchez@gmail.com

[2] Department of Civil Engineering Sciences and Architecture
Polytechnique University of Bari
Via Re David, 70125, Bari, Italy
domenico.camassa@poliba.it, aguinaldo.fraddosio@poliba.it, mariodaniele.piccioni@poliba.it

[3] Department of Mechanics, Mathematics and Management
Polytechnique University of Bari
Via Re David, 70125, Bari, Italy
anna.castellano@poliba.it

Keywords: Masonry, seismic vulnerability, TRM, Vibration testing, OMA

Abstract. *Masonry constructions compose the majority of the Architectural Heritage world-wide, thus, their preservation is of great importance. Nevertheless, they usually show a great vulnerability to seismic and dynamic loads. Several reinforcement techniques can be used in order to improve their dynamic behaviour. The Textile Reinforced Mortar (TRM) material appears as very suitable, since it meets the requirements of compatibility and reversibility of the retrofitting. Moreover, it avoids some problems related to permeability. And strongly reduces adhesion and debonding issues. In this paper the effectiveness of the TRM reinforcement for dynamic loads for windowed brick masonry walls is evaluated through vibration testing and operational modal analysis. To this aim, two scaled brick masonry walls were built at the "Laboratorio de Grandes Estructuras" of the University of Alicante. Only one of them was reinforced with the TRM. Both were damaged with a cyclic in-plane lateral force for simulating damage due to seismic actions. Structural vibrations of the two walls were measured in the presence of a white noise excitation. Modal parameters were evaluated through Operational Modal Analysis (OMA) before and after the damage. Finally, changes in modal parameters due to damage were compared and investigated in both the unreinforced and reinforced cases. The results suggest that TRM reinforcement can be considered effective for improving the mechanical behaviour of a brick windowed masonry wall.*

1 INTRODUCTION

Masonry buildings represent a relevant part of constructions all around the world. Indeed, the majority of architectural heritage is made of masonry and a lot of new buildings are still built using masonry materials and traditional techniques. However, masonry buildings usually show a great vulnerability to seismic and dynamic loads [1], mainly due to the properties of the materials and to weak connections between horizontal and vertical structural elements [2-3]. Thus, in order to guarantee the stability and the integrity of the construction, it is of great importance to improve its mechanical behaviour through appropriate strengthening interventions. In addition, the reinforcement of masonry construction may be also aimed at repairing damages induced by unexpected static or dynamic loads, in particular earthquakes, that along with other causes can reduce the mechanical properties of masonry structural elements over time [4-6]. In this document, the assessment of the reinforcement of masonry walls in particular is addressed. Among possible reinforcement materials for masonry, in the recent past Fiber-Reinforced Polymer (FRP) composites [7-11] have been widely employed, but these composites show several drawbacks, mostly related to the stress-transfer mechanisms between reinforcement and masonry supports. More recently, another reinforcement material [12-13], the Textile Reinforced Mortar (TRM), has gained interest since it is particularly suitable for masonry constructions. Indeed, due to the presence of a mortar matrix instead of an epoxy one, it meets the requirements of compatibility and reversibility of the retrofitting. Moreover, it avoids some problems related to permeability and, above all, TRM strongly reduces adhesion and debonding issues. Finally, as it is shown in [14], TRM is effective in recovering the pre-damage stiffness of a scaled masonry building.

For the above, a detailed study on the effectiveness of TRM on different types of wall is of great interest. The main purpose of this study is the evaluation of the effectiveness of TRM reinforcement of a windowed brick masonry walls for dynamic loads. For this purpose, two distinct scaled brick masonry walls were built at the "Laboratorio de Grandes Estructuras" of the University of Alicante (Alicante, Spain). The two walls were constructed with the same geometrical features and with the same materials and technique in such a way that they have about the same mechanical characteristics. Only one of the walls was reinforced with the TRM. A vertical load was applied on both the two walls for reproducing real loading conditions of a bearing masonry wall. Both walls were damaged with a cyclic in-plane lateral force in order to simulate damage due to seismic actions. Finally, in order to evaluate the effectiveness of the TRM reinforcement for brick walls in the presence of windows, modal parameters of the two walls were evaluated through Operational Modal Analysis (OMA) before and after the damage by using ARTeMIS Modal commercial software. Indeed, since modal parameters are function of physical features like mass, stiffness and damping, it is well known that these parameters can be employed for structural assessment and damage identification [15-22].

2 MASONRY WALLS, REINFORCEMENT MATERIAL AND DAMAGE

The two windowed brick walls built for this study are shown in Figure 1a-b. The walls were built using clay bricks laid by means of 10 mm thick lime mortar joints adopting an English bond disposition. The geometric and mechanical characteristics of bricks and lime mortar are reported in Table 1. At the base, the walls were constrained through a steel plate and anchors to the strong floor of the laboratory in such a way that the lateral displacement is hindered. In order to simulate real loading conditions of a masonry wall, two vertical loads of 15000 daN were applied on two points (points P_1 and P_2 in Figure 1c). A steel beam allows for an approximately uniform distribution of the total load (30000 daN) applied on the top of the wall (Figure 1).

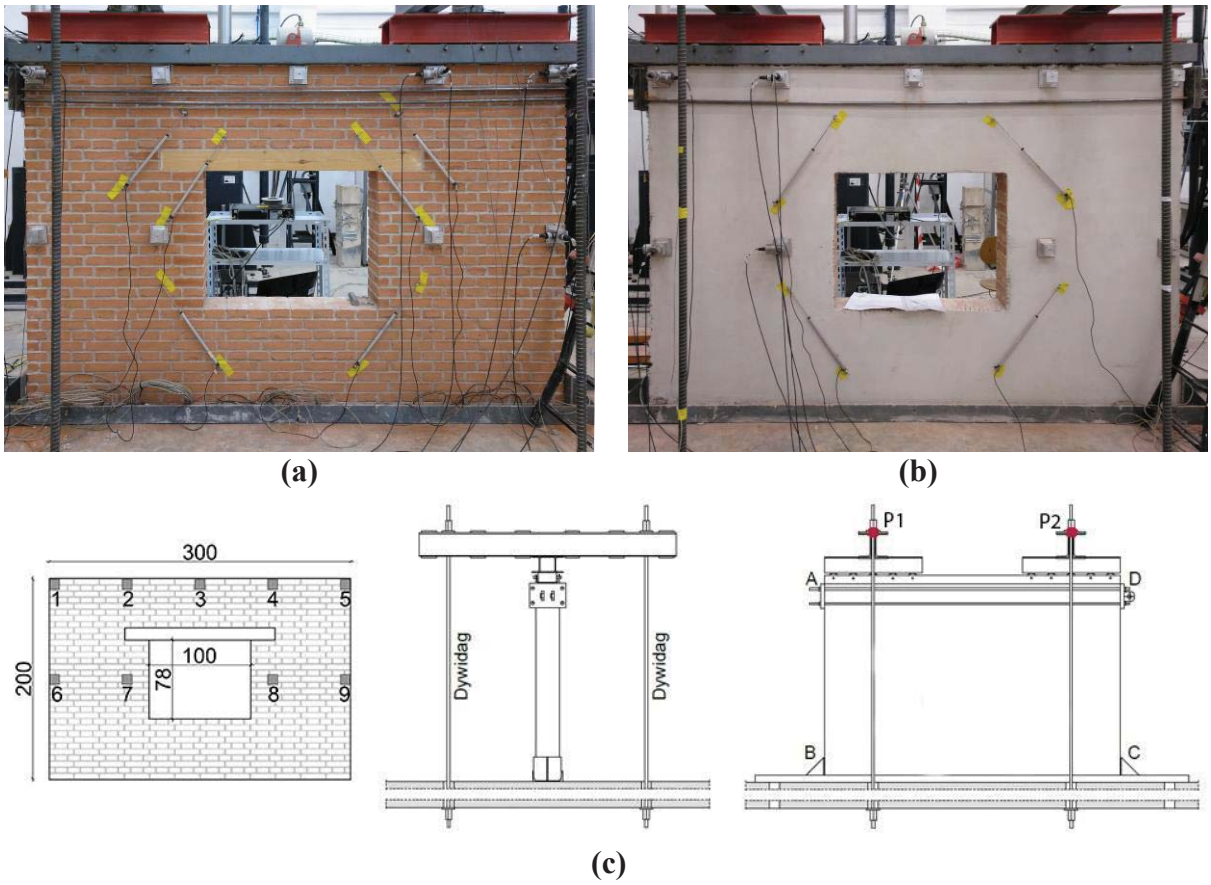

Figure 1: (a) Unreinforced and (b) reinforced windowed masonry walls in the undamaged state; (c) scheme of the experimental setup: preload device and anchorage system.

For the reinforced wall (Figure 1b), a 25x25 mm glass textile mesh embedded into a 10 mm thick cementitious mortar layer was applied on both the two lateral surfaces of the wall. Specifically, the application of the TRM reinforcement occurred in the following steps: (1) a 5 mm thick cementitious mortar layer was applied on the lateral surfaces of the wall; (2) a glass fiber textile grid was located on the cementitious layer; (3) the glass fiber grid was covered with 5 mm thick layer of the cementitious binder. It is worth noting that the first cementitious mortar layer allows for the bond between the masonry support and the glass fiber textile grid. The mechanical properties of the reinforcement are shown in Table 2.

Bricks		Lime mortar	
Dimensions (mm)	230 x 110 x 50	Compression strength at 28 days (MPa)	9.4
Compression strength (MPa)	17.20	Compression strength at 100 days (MPa)	10.1

Table 1: Geometric features and compression strength of bricks and lime mortar.

In order to simulate the effects of a high-intensity seismic action, both the two walls were damaged (Figure 2) by imposing a cyclic in-plane horizontal top displacement with increasing amplitude. Specifically, the horizontal displacement was determined by means of a hydraulic jack with a feedback system capable of producing a displacement control load test.

(a) **(b)**

Figure 2: (a) Unreinforced and (b) reinforced masonry walls after damage.

Mortar		Textile mesh	
Compression strength at 28 days (MPa)	15	Tensile strength (kN/m)	45
Elastic modulus (MPa)	8000	Elastic modulus (MPa)	7200

Table 2: Mechanical properties of the reinforcing materials.

3 MODAL ANALYSIS

Vibration testing and Operational Modal Analysis (OMA) were carried out on the two walls in order to estimate their modal properties (natural frequencies, mode shapes and modal damping) both in the undamaged and damaged state. Schematically, modal properties were estimated in the following four cases: (1) unreinforced and undamaged wall; (2) unreinforced and damaged wall; (3) reinforced and undamaged wall; (4) reinforced and damaged wall. In each of these four cases, the response of the wall was experimentally monitored through accelerometers with respect to 18 DOF. Specifically, a grid of 9 points (Figure 1c) was defined on each wall and, for each point, the in-plane (x-direction) and out-of-plane (y-direction) vibrations were measured. A white noise excitation was generated through a shaker located in the middle of the top of each wall.

For data acquisition, 8 piezoelectric accelerometers of sensitivity 10 V/g, two signal conditioner model PCB 482A22 and two data acquisition devices model Kyowa PCD-320 were employed. The sampling frequency was set to 2000 Hz. Since only 8 accelerometers were available, the two accelerometers located at point 1 (in the x- and y-direction) were adopted as reference sensors. Consequently, it was possible to measure the response of the wall at the considered 18 DOF by three suitable arrangements of accelerometers, thus resulting in 3 data sets.

Finally, vibration data were processed by using the ARTeMIS Modal commercial software. In particular, the Enhanced Frequency Domain Decomposition (EFDD) method was employed for determining natural frequencies, mode shapes and modal damping.

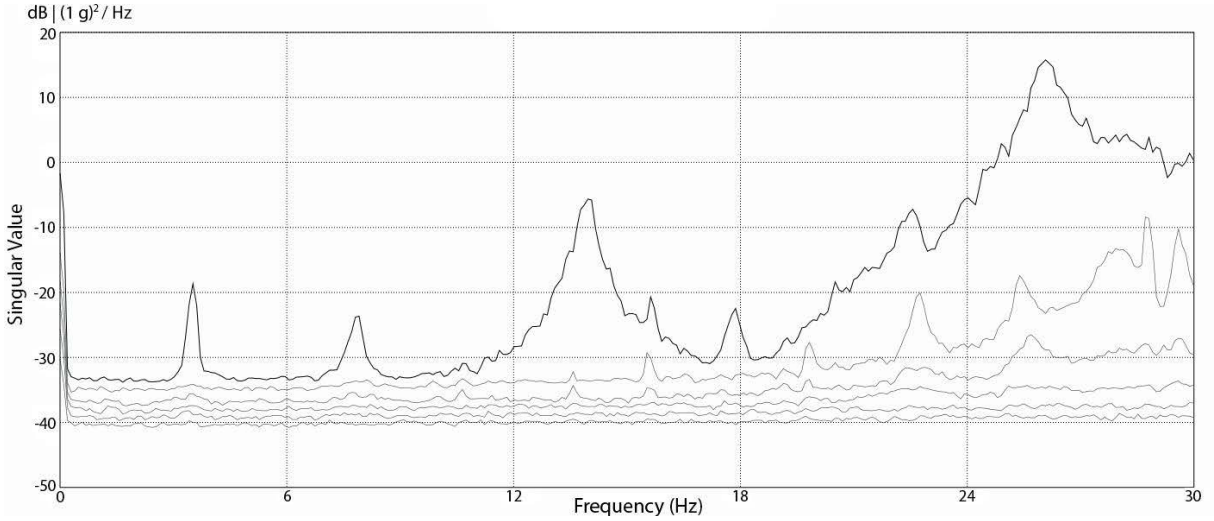

Figure 3: A typical Singular Value Plot obtained by processing acceleration data of the walls through the EFDD technique.

4 RESULTS

Figure 2 shows both the unreinforced and reinforced wall after the damage process. A classical damage pattern with diagonal cracks is visible for the two walls. The horizontal cracks of the reinforced wall are due to the presence of the glass textile grid. In the unreinforced wall, the cracks mainly follow mortar joints, except in some points where they cross one or more bricks. For the unreinforced wall the initial elastic stiffness was 25.2 kN/mm, the ultimate horizontal displacement was 22 mm and the ultimate horizontal load was 143 kN. For the reinforced wall the initial elastic stiffness, the ultimate horizontal displacement and the ultimate horizontal load were 28.7 kN/mm, 33 mm and 351 kN, respectively. Since the two walls were similar to each other, it is evident that the TRM reinforcement improves the stiffness of the wall, its ductility and its ultimate strength to horizontal cyclic loads, and thus to seismic actions.

Regarding operational modal analysis, the first three vibration modes for each wall were identified both in the undamaged and damaged case. Figure 3 shows a typical Singular Value Plot, in the frequency range from 0 to 30 Hz, obtained through the EFDD method. In Table 3, a comparison between natural frequencies estimated in the four cases above listed is reported. Both for the unreinforced and for the reinforced case a noticeable decrease of natural frequencies occurs with damage. In particular, comparing natural frequencies before, f_U, and after, f_D, the damage through the frequency discrepancy parameter $D_f = |(f_D - f_U)/f_U|$, for the unreinforced case a decrease of 24.09 %, 60.00 % and 31.42 % of the natural frequency of the first, second and third vibration mode, respectively, it is observed; the corresponding decreases for the reinforced case are of 44.05 %, 39.20 % and 45.42 %, respectively.

Mode no.	Unreinforced wall			Reinforced wall		
	f_U (Hz)	f_D (Hz)	D_f (%)	f_U (Hz)	f_D (Hz)	D_f (%)
1	5.276	4.005	24.09	6.300	3.525	44.05
2	15.829	6.331	60.00	12.891	7.838	39.20
3	22.415	15.372	31.42	25.551	13.947	45.42

Table 3: Natural frequencies estimated for the unreinforced and reinforced wall both in the undamaged (U) and damaged (D) state.

Since the natural frequency is related to the modal stiffness, a decrease of the natural frequency means that the damage has induced a reduction of the modal stiffness for all the three identified modes. In particular, in the unreinforced wall the damage has mostly affected the second mode, while in the reinforced case it has affected almost uniformly all the three modes. It suggests that the application of TRM reinforcement allows distributing on all vibration modes the negative effects of damage.

Furthermore, it can be observed that, except for the second vibration mode, the reinforced wall has natural frequencies slightly higher than those of the unreinforced wall. Since the two walls are similar to each other, this consideration, together with information about the initial elastic stiffness of the two walls above reported, allows arguing that the TRM reinforcement slightly increase the stiffness of the wall on which it is applied.

Finally, it is worth observing that, even though the ultimate load was much higher for the reinforced wall, the frequency decrease (i.e. the stiffness reduction) due to damage is comparable for the two walls. It means that TRM reinforcement limits the negative effects of the damage on the structural stiffness of the wall.

In Table 4 a comparison between the modal damping ratio estimated for the four considered cases is presented. Both for the unreinforced and for the reinforced case, an increase of modal damping ratio occurs with damage. Comparing modal damping ratio before, ς_U, and after, ς_D, the damage through the discrepancy parameter $D_\varsigma = \left|(\varsigma_D - \varsigma_U)/\varsigma_U\right|$, for the unreinforced case an increase of 1.00 %, 227.39 % and 12.16 % of the modal damping of the first, second and third vibration mode, respectively, it is observed. On the other hand, for the reinforced case an increase of 16.18 %, 87.87 % and 51.95 % of the first, second and third vibration mode, respectively, occur. Since the modal damping is related to energy dissipation, an increase in modal damping means that, as a result of the damage, the energy dissipation increase. As for natural frequencies, modal damping ratio values suggest that the application of TRM reinforcement allows distributing on more vibration modes the negative effects of damage. Indeed, considering the discrepancy parameter D_ς, in the unreinforced wall the damage has mostly affected the second mode, while in the reinforced case the effect is distributed on all the three vibration modes.

Mode no.	Unreinforced wall			Reinforced wall		
	ς_U (Hz)	ς_D (Hz)	D_ς (%)	ς_U (Hz)	ς_D (Hz)	D_ς (%)
1	1.608	1.624	1.00	1.922	2.233	16.18
2	0.449	1.470	227.39	0.907	1.704	87.87
3	0.625	0.701	12.16	0.793	1.205	51.95

Table 4: Modal damping ratio estimated for the unreinforced and reinforced wall both in the undamaged (U) and damaged (D) state.

The estimated mode shapes of the reinforced wall in the undamaged state are represented in Figure 4. The mode shapes estimated in the other three cases are similar. In order to quantitatively compare mode shapes, the Modal Assurance Criterion (MAC) values were calculated. In Table 5 and in Table 6 the MAC values respectively for the unreinforced and the reinforced wall are listed. It can be seen that for both walls, the mode shape of the second vibration mode, which is a bending mode, is the most affected by the damage. Considering the cracking pattern for the two wall (Figure 2), it could be explained by observing that, since the second vibration mode involves opposite transverse displacements of the two free vertexes of the wall (Figure 4b-4e), the friction at crack surface is emphasized for that vibration mode. Further-

more, it is worth observing that the MAC values for the unreinforced case are lower than those for the reinforced case. This can suggest that the TRM reinforcement reduces the negative effects of damage in terms of variation of mode shapes.

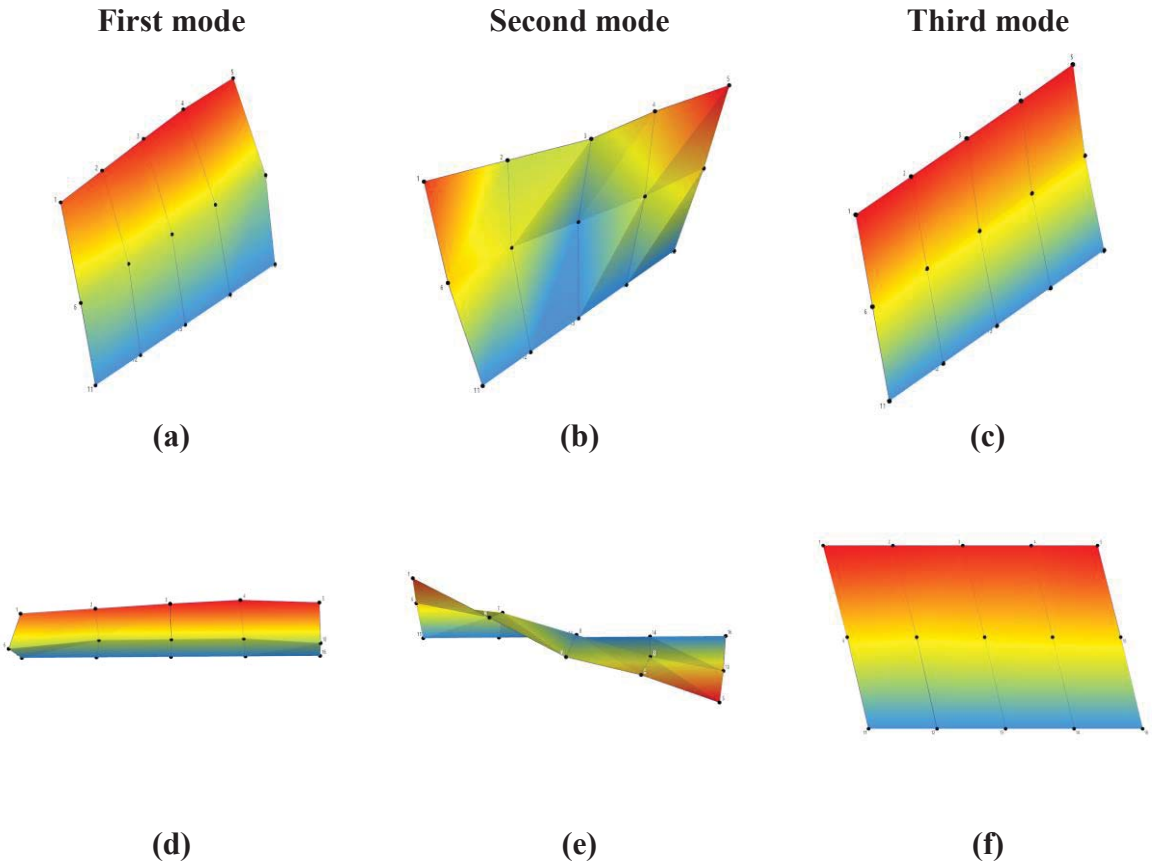

Figure 4: Mode shapes of the unreinforced wall in the undamaged state. General view: (a), (b) and (c). Plan view: (d) and (e). Front view: (f).

Frequency (Hz)	4.005	6.331	15.372
5.276	0.712	0.016	0.017
15.829	0.091	0.531	0.003
22.415	0.001	0.054	0.786

Table 5: MAC values between the mode shapes in the pre and post damage state – unreinforced wall.

Frequency (Hz)	3.525	7.838	13.947
6.300	0.921	0.043	0.001
12.891	0.019	0.842	0.034
25.551	0.001	0.034	0.994

Table 6: MAC values between the mode shapes in the pre and post damage state – reinforced wall.

5 CONCLUSIONS

In this paper, the effectiveness of the TRM reinforcement on scaled windowed brick masonry wall is evaluated through vibration testing and Operational Modal Analysis. In particular, natural frequencies and modal damping are considered as parameters respectively related to the structural stiffness and the energy dissipation. In addition, for both the two walls, mode

shapes are investigated through the calculation of the MAC value both in the undamaged and the damaged state. The results show that, both for the unreinforced and for the reinforced case, for all the three identified modes there is a decrease of natural frequency and an increase of the modal damping. This means that after the damage there is a reduction of structural stiffness and an increase of energy dissipation, respectively. Furthermore, it can be seen that the damage affects the mode shapes mainly for the unreinforced case.

More specifically, the results suggest that the application of TRM reinforcement: (1) improves the stiffness of the wall, its ductility and its ultimate strength to horizontal cyclic loads; (2) allows distributing on more vibration modes the negative effects of damage related to both the structural stiffness and the energy dissipation; (3) limits the effects of damage on mode shapes. This last conclusion remarks that the reinforced wall has at the end of the test higher level of structural integrity than the unreinforced specimen. In conclusion, it can be argued that, with respect to horizontal cyclic load, like seismic actions, TRM reinforcement can improve the mechanical behaviour of windowed brick masonry walls.

REFERENCES

[1] Magenes, G., Calvi, G.M. In-plane seismic response of brick masonry walls, Earthq. Eng. Struct. Dyn. 26 (1996) 1091–1112.

[2] D. Foti, V. Vacca, S. Ivorra, Influence of connections in the seismic behaviour of trilithic large blocks masonry structures, Proc. of the 16th International Brick and Block Masonry Conference (IBMAC 2016), Padova, 26-30 June 2016, p. 195-202.

[3] D. Foti, S. Ivorra, V. Vacca, In plane behavior of a masonry stone wall with hexagonal blocks, Proc. of the 16th International Brick and Block Masonry Conference (IBMAC 2016), Padova, 26-30 June 2016, p. 1587-1591.

[4] CNR-DT 215/2018, Istruzioni per la progettazione, l'esecuzione ed il controllo di interventi di consolidamento statico mediante l'utilizzo di compositi fibrorinforzati a matrice inorganica, National Research Council, Roma, Italy (2019).

[5] Bhattacharya, S., Nayak, S., Dutta, S.C. A critical review of retrofitting methods for unreinforced masonry structures, Int. J. Disaster Risk Reduct. 7 (2014) 51–67. doi:10.1016/j.ijdrr.2013.12.004.

[6] Bru, D., Baeza, F. J., Varona, B., Garcia-Barba, J., Ivorra, S., Static and dynamic properties of retrofitted timber beams using glass fiber reinforced polymers, Materials and Structures 49(1-2) 181-191. doi: 10.1617/s11527-014-0487-0.

[7] S.A. Babatunde, Review of strengthening techniques for masonry using fiber reinforced polymers, Compos. Struct. 161 (2017) 246–255.

[8] ACI 440.2R-17, Guide for the design and construction of externally bonded FRP systems for strengthening concrete structures, American Concrete Institute, ACI Committee 440 (2017).

[9] Triantafillou, T.C., Strengthening of masonry structures using epoxy-bonded FRP laminates, J. Compos. Constr. 2 (1998) 96–104. doi:10.1061/(ASCE)1090-0268(1998)2:2(96).

[10] ACI 549.4R-13, Guide to design and construction of externally bonded fabric-reinforced cementitious matrix (FRCM) systems for repair and strengthening concrete and masonry structures, American Concrete Institute, ACI Committee 549 (2013).

[11] Bilotta, A., Ceroni, F., Lignola, G.P., Prota, A., Use of DIC technique for investigating the behavior of FRCM materials for strengthening masonry elements, Compos. Part B Eng. 129 (2017) 251–270. doi:10.1016/j.compositesb.2017.05.075.

[12] L.A.S. Kouris, T.C. Triantafillou, State-of-the-art on strengthening of masonry structures with textile reinforced mortar (TRM), Constr. Build. Mater. 188 (2018) 1221–1233.

[13] D. Bru, S. Ivorra, F.J. Baeza, Seismic behavior of a masonry chimney retrofitted with composite materials: A preliminary approach, Int. J. Saf. Secur. Eng. 7 (2017) 486–497.

[14] Bru, D., Ivorra, S., Buitrago, M., Bertolessi, E. OMA identification on a scaled masonry building pre and post reinforced with TRM. (2019) 8th IOMAC - International Operational Modal Analysis Conference, Proceedings, pp. 205-212.

[15] S. W. Doebling, C. R. Farrar, M. B. Prime, and D. W. Shevitz, "Damage identification and health monitoring of structural and mechanical systems from changes in their vibration characteristics: A literature review," no. May, 1996, doi: 10.2172/249299.

[16] C. R. Farrar and S. W. Doebling, "An overview of modal-based damage identification methods," 1997, doi: 10.1017/CBO9781107415324.004.

[17] O. S. Salawu, "Detection of structural damage through changes in frequency: A review," *Eng. Struct.*, vol. 19, no. 9, pp. 718–723, 1997, doi: 10.1016/S0141-0296(96)00149-6.

[18] Williams; C. and Salawu; O.S, "Damping as a damage indication parameter," *Proc. 15th Int. Modal Anal. Conf. Int. Soc. Opt. Eng.*, pp. 1531–1536, 1997.

[19] W. M. West, "Illustration of the use of modal assurance criterion to detect structural changes in an Orbiter test specimen," in *Proc. Air Force Conference on Aircraft Structural Integrity*, 1984.

[20] C. H. J. Fox, "The Location of Defects in Structures: A Comparison of the Use of Natural Frequency and Mode Shape Data," in *Proceedings of 10th International Modal Analysis Conference*, 1992.

[21] A. K. Pandey, M. Biswas, and M. M. Samman, "Damage detection from changes in curvature mode shapes," *J. Sound Vib.*, 1991, doi: 10.1016/0022-460X(91)90595-B.

[22] A. Castellano, A. Fraddosio, F. Martorano, G. Mininno, F. Paparella, and M. D. Piccioni, "Structural health monitoring of a historic masonry bell tower by radar interferometric measurements," in EESMS 2018 - Environmental, Energy, and Structural Monitoring Systems, Proceedings, 2018, doi: 10.1109/EESMS.2018.8405824.

EURODYN 2020
XI International Conference on Structural Dynamics
M. Papadrakakis, M. Fragiadakis, C. Papadimitriou (eds.)
Athens, Greece, 23–26 November 2020

MODAL IDENTIFICATION OF THE SAN FRANCESCO CHURCH IN PISA, ITALY

E. Lorenzo[1], F. Canessa[1], G. Chellini[1], A. De Falco[2], C. Resta[2], E. Savelli[1] and G. Sevieri[3]

[1]Department of Civil and Industrial Engineering
University of Pisa, Largo Lucio Lazzarino, Pisa, Italy
e-mail: canessa.francesca@yahoo.it, giuseppe.chellini@ing.unipi.it, emanuele.lorenzo@unifi.it, elena.savelli@gmail.com

[2]Department of Energy, Systems, Territory and Constructions Engineering
University of Pisa, Largo Lucio Lazzarino, Pisa, Italy
e-mail: a.defalco@ing.unipi.it, carlo.resta@posteo.net

[3]Department of Civil, Environmental and Geomatic Engineering
University College London, Gower Street, London, United Kingdom
e-mail: g.sevieri@ucl.ac.uk

Keywords: Structural Health Monitoring, masonry church, dynamic identification, Operational Modal Analysis.

Abstract. *The preservation of Cultural Heritage assets from natural and man-made disasters is of great importance for communities because of their architectural and social value. Lack of any hazard-resisting design, material typology and degradation due to ageing strongly affect the behaviour of Cultural Heritage assets. In this context, Structural Health Monitoring systems can help stakeholders to control the behaviour of heritage constructions, to improve the estimation of their residual life expectancy and to optimize maintenance and retrofitting interventions. This paper presents the preliminary results of the modal identification of the transept of San Francesco church in Pisa. An experimental campaign aimed at measuring the structural response under environmental vibrations was performed, and Operational Modal Analysis was applied to quantify modal properties (frequencies and mode shapes). Data were then used to calibrate the elastic parameters of a refined numerical model. Issues and practical considerations related to the design and installation of dynamic monitoring systems for complex masonry constructions (such as the one under investigation) were derived to provide practitioners with practical guidance.*

1 INTRODUCTION

Cultural Heritage (CH) assets represent a relevant economic resource because of cultural tourism, but their intangible value is also of primary importance since they play a fundamental role in fostering a community's sense of place and belonging. For these reasons, preservation of heritage constructions is a matter of primary importance, though current conservation efforts are too often limited to emergency measures, and designed without a comprehensive intervention plan [1].

In this context, Structural Health Monitoring (SHM) [2] systems can help stakeholders control the behaviour of heritage constructions, while improving the estimation of their residual life expectancy and optimizing maintenance and retrofitting interventions.

Numerical models are commonly used as a tool to assess structural health of CH assets and to predict the buildings response to environmental conditions. Typical CH assets are characterized by the lack of any hazard-resisting design, materials of unknown properties and diffused degradation due to ageing. For this reasons, epistemic uncertainties regarding materials, geometry and boundary conditions [3, 4] strongly affect Finite Element (FE) model results.

Ambient vibration-based modal identification techniques are then key to record and derive information for both model parameter calibration and structural control. Being non-destructive, such techniques perfectly meet the well-known minimum intervention and reversibility criteria for CH assets [5]. Through dynamic identification, vibrational properties of the structure (natural frequencies, modal shapes and damping coefficients) can be deduced and compared to the ones obtained from numerical models [6, 7, 8].

In this paper we present the first steps towards the definition of a robust SHM system for masonry CH assets [10]. The San Francesco church in Pisa, Italy (Figure 1) was chosen as a case study, and dynamic measurements were performed to evaluate the response of its bell tower and transept to ambient vibrations.

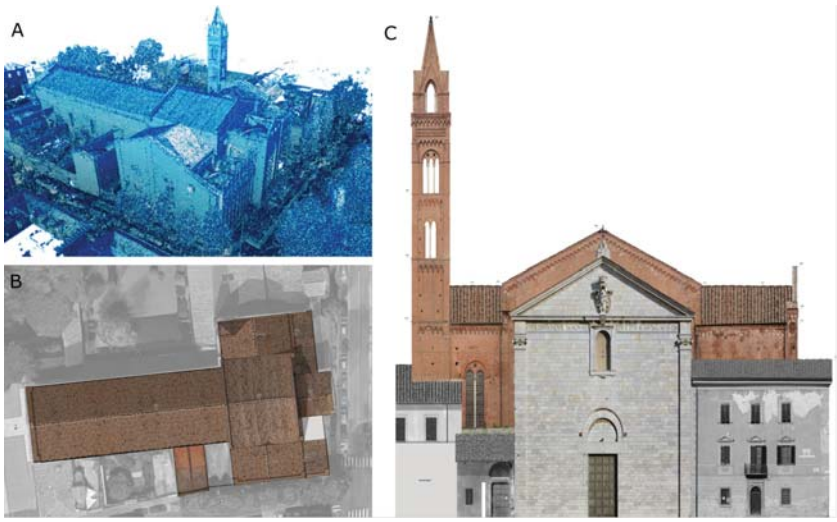

Figure 1: A) Point cloud survey; B) planimetry; C) façade of the San Francesco church.

The results were elaborated through Operation Modal Analysis (OMA) techniques [9] and used to identify natural frequencies and mode shapes. A preliminary dynamic identification of the bell tower alone provided first estimates for the constitutive parameters of the masonry walls. A FE model of the entire church was then built in order to preliminarily choose relevant

mode shapes involving the transept, and to design sensor positioning. After the experimental campaign, the same model was used to perform a manual mode-matching between numerical and experimental results.

2 THE SAN FRANCESCO CHURCH IN PISA

The construction of the San Francesco church in Pisa dates back to the 13^{th} century, and was executed under the direction of architect Giovanni di Simone [11]. It follows the traditional Franciscan canon of sobriety and humbleness, avoiding frescoes and limiting the use of marble to the façade (of later construction), preferring exposed brick on the exterior and painted plaster on the interior.

Its geometry (the nave measures 70.5 m x 17.7 m) makes it the second largest church in the city, after the Cathedral of Pisa. Its peculiarity is a "hanging" masonry tower, resting at a height of 12 m above ground level on two limestone cantilevers embedded in the north transept walls. The dynamic behaviour of the bell tower was already investigated during an experimental campaign in March 2019 by a research group from the University of Pisa lead by Prof. De Falco. The campaign's results are briefly recalled in the following.

A massive restoration work of the San Francesco church is currently underway, thus enabling the self-standing scaffolding system to be used during the dynamic experimental campaign herein presented. It is worth noting that the scaffolding system (Figure 2) is designed to have no contact with the structural system, so that it does not affect dynamic observations. Thanks to this, a diffuse network of sensors over most of the church's transept, including the highest portion of the walls, could be installed, thus obtaining significant data for modal identification.

Figure 2: Self-standing scaffolding system in the nave.

Plans of renovation also envisage the complete removal and restoration of the roof and of the supporting truss structures. This will allow a new experimental campaign to be performed in order to better evaluate the effect of roofing on the overall vibrational behaviour of the building.

3 EXPERIMENTAL CAMPAIGN ON THE BELL TOWER

On the 30^{th} March 2019, an experimental campaign was performed on the San Francesco bell tower in order to identify its modal properties. Accelerometers and velocimeters were placed at different positions along the tower's height (Figure 3), measuring its response to ambient

vibrations. Natural frequencies and mode shapes were derived using the software LMS Test.Lab 8 [12] to perform digital signal processing and to apply the PolyMax algorithm [13] to the data. The first three identified frequencies correspond to two flexural modes (1.10 Hz and 1.32 Hz) and a torsional one (3.55 Hz). Flexural modes are roughly aligned with the main diagonals of the bell tower's cross section.

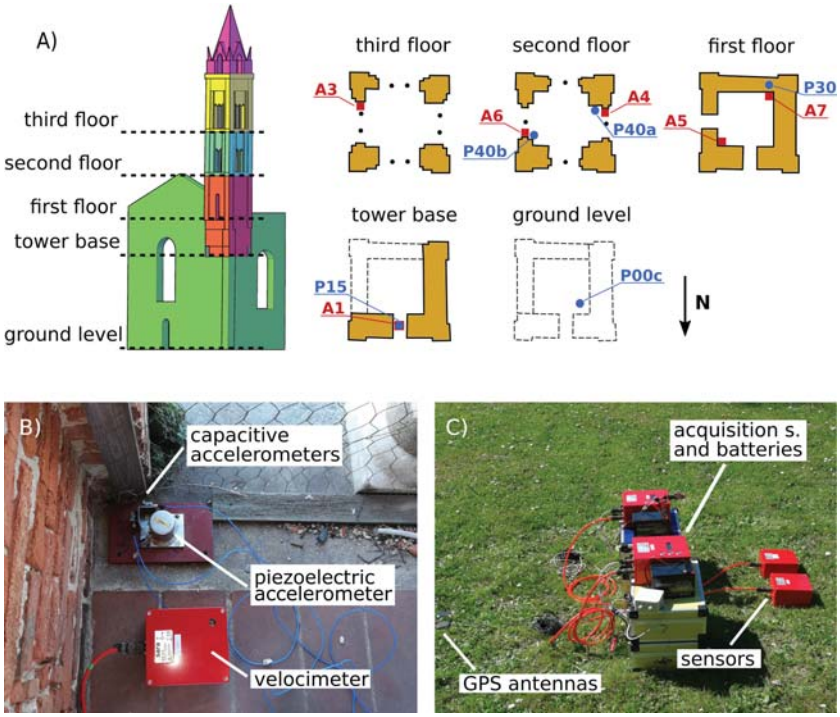

Figure 3: A) Sensor positioning along the bell tower. Accelerometers are indicated with the letter A, velocimeters with the letter P; B) employed sensors; C) velocimeter acquisition system.

A FE model was developed during this phase to simulate the masonry bell tower together with a limited portion of the neighbouring church walls (Figure 10). Experimental results were used to update the value of the elastic material properties of the model. The first three natural frequencies and mode shapes were matched with numerical ones (Figure 4) by varying the values of the Young's moduli of bell tower and church. Good accordance (less than 5% difference) between experimental and numerical data was finally reached for values of 1800 and 1300 MPa for the bell tower and church, respectively.

4 EXPERIMENTAL CAMPAIGN ON THE TRANSEPT

4.1 Instrumentation and acquisition

After the dynamic identification of the bell tower, an experimental campaign was carried out on the church's transept during December 2019 and January 2020. A network of accelerometers was used to record the building's response to ambient vibrations. Nine monoaxial capacitive accelerometers (*PCB DC capacitive accelerometers – Model 3701G3FA3G*) and six monoaxial piezoelectric accelerometers (*PCB ICP accelerometers – Model 393C*) from the Structural Laboratory of the University of Pisa were employed. Technical characteristics of the sensors are summarized in Table 1. Data were recorded and pre-processed through an acquisition system

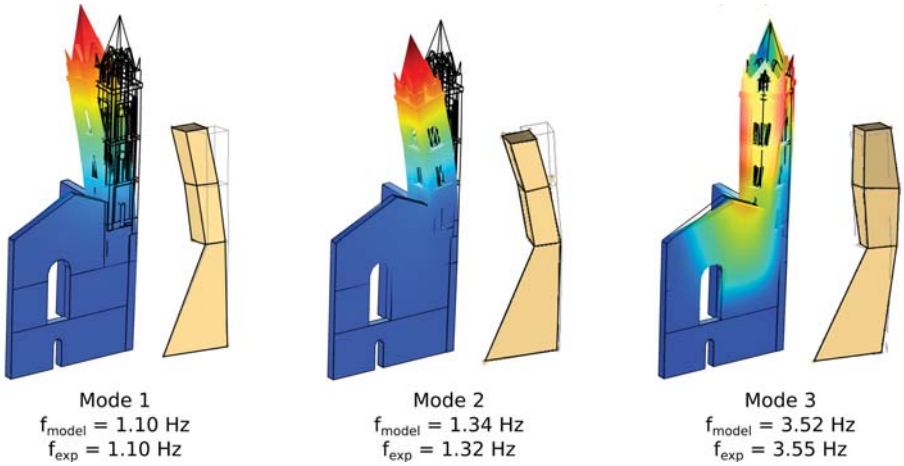

Figure 4: Mode matching for the bell tower.

(*LMS Scadas Mobile*) controlled by a dedicated application (LMS Test.Lab 8). Figure 5 shows the employed sensors and acquisition system.

PCB DC capacitive accelerometers model 3701G3FA3G	
Average sensitivity @ 30 Hz	1000 mV/g
Average eigenfrequency	540 Hz
Frequency range ($\pm$ 5 %)	0 to 100 Hz
PCB ICP piezoelectric accelerometers model 393C	
Average sensitivity @ 100 Hz	1000 mV/g
Average eigenfrequency	5.3 kHz
Frequency range ($\pm$ 5 %)	0.025 to 8¸00 Hz

Table 1: Technical characteristics of the employed sensors.

The sensors were assembled to create two- or three-directional measurement stations by fixing them to rigid metallic plates. Four different device configurations were adopted to perform three 30 minutes records with a sampling frequency of 256 Hz and 8-second average time windows.

Sensor layout was determined beforehand based on the results of a preliminary numerical model. Two main necessities had to be assessed:

1. to identify the modal properties of all reachable transept portions;
2. to gain insight regarding the influence of roof and supporting trusses on the vibrational behaviour of the connected walls.

Figures 6 and 7 show sensor positions, and Table 2 summarizes the configurations with the corresponding instrumented positions. Sensors in positions 1, 6, 8, 14 and 25 were used for each configuration, in order to be able to merge data from the different acquisitions.

Connection between sensors and acquisition system was achieved through cables ranging in length between 50 and 100 m on account of the church's geometry. This required careful

Figure 5: Instrumentation. A) Piezoelectric accelerometer; B) capacitive accelerometer; C) piezoelectric two-directional measurement station; D) acquisition system; E) control station on top of the scaffolding.

POSITION	**1**	2	3	4	5	**6**	7	**8**	9	10	11	12	13
Configuration 1	•	•	•	•	•	•	•	•	•				
Configuration 2	•	•				•	•	•		•	•	•	•
Configuration 3	•					•		•			•		
Configuration 4	•					•		•					

POSITION	**14**	15	16	17	18	19	20	21	22	23	24	**25**	26
Configuration 1	•											•	
Configuration 2	•	•										•	
Configuration 3	•					•			•	•	•	•	•
Configuration 4	•		•	•	•	•	•	•				•	

Table 2: Sensor positions used for the different measurement configurations. In boldface reference positions.

planning in the design of the experimental campaign, to make sure that as few accelerometers as possible had to be moved between a configuration and the following. Nevertheless, logistics often required long procedures, resulting even more complex since operations were carried out on the scaffolding.

Cable length, together with some electrical dissipations which may also have interacted with the scaffolding system, could have been the cause of issues concerning some of the sensors during measurements. This was particularly true in the case of capacitive accelerometers, which required an external power source and for which tripolar power cables were used. Some of the

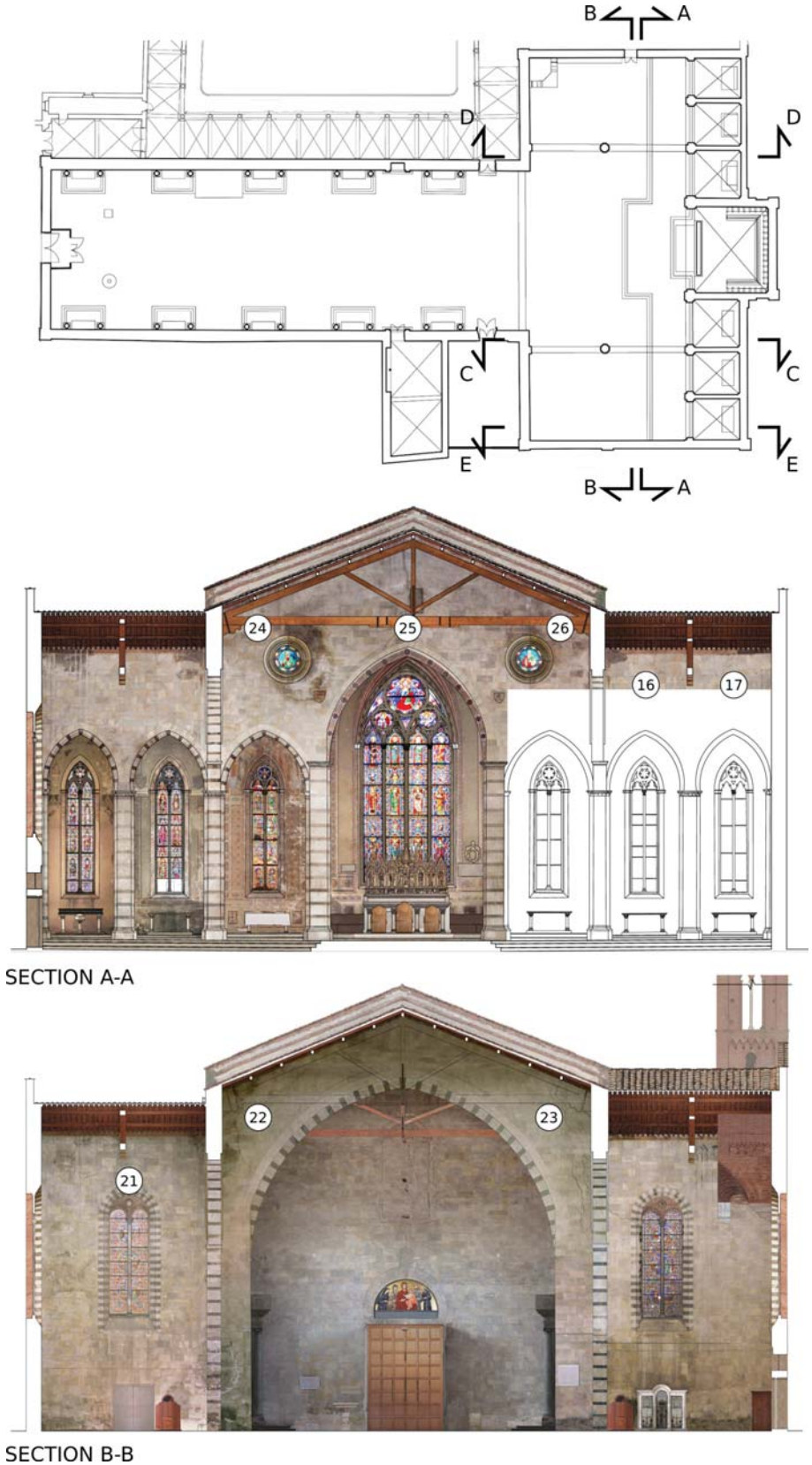

Figure 6: Sensor positioning. Church plan, section AA (east transept wall) and section BB (west transept wall). White portions were impossible to photograph.

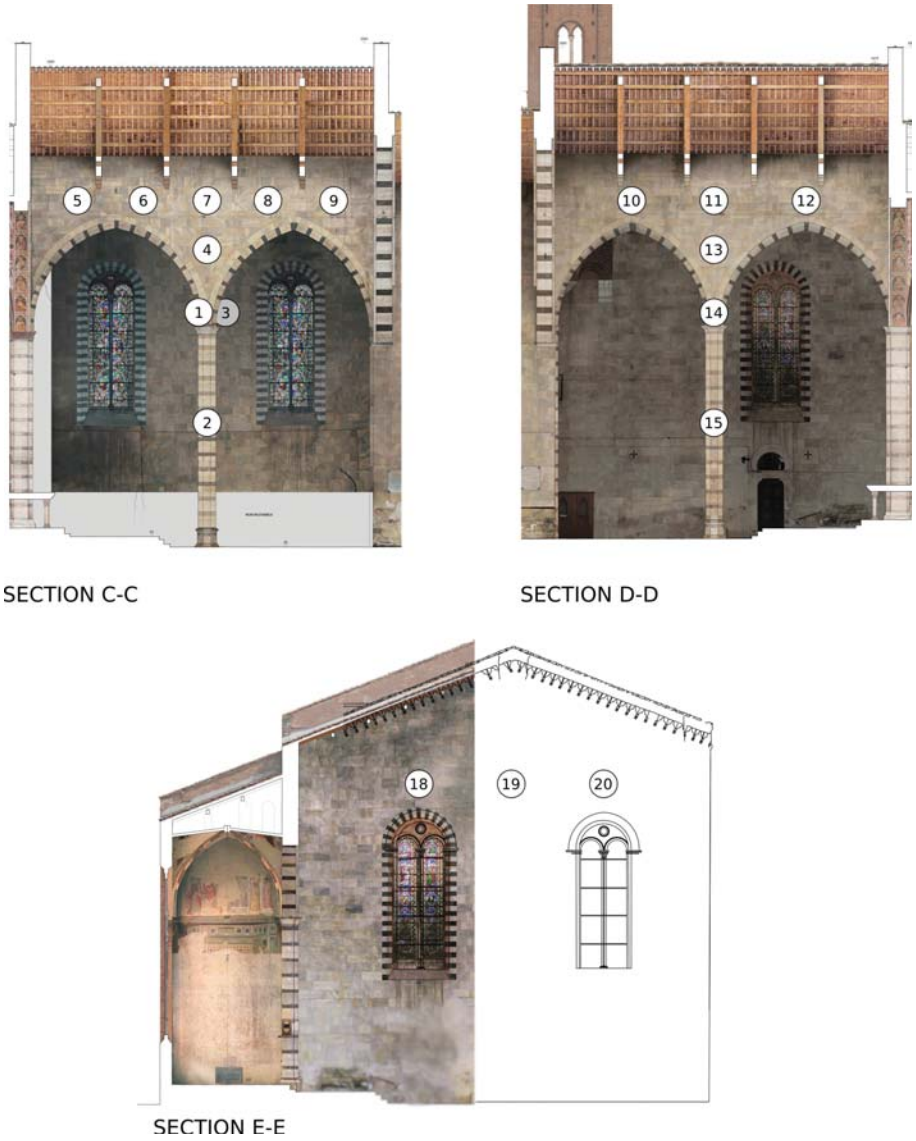

Figure 7: Sensor positioning. Section CC (south partition wall), section DD (north partition wall) and section EE (south transept wall). White portions were impossible to photograph.

longer cables, when used for sensors located closer to the acquisition system, had to be partially stored on cable reels. This may have worsened signal quality through induced electro-magnetic effects. Future testing may benefit from the use of piezoelectric accelerometers only, or from the use of capacitive accelerometers with better insulated cables.

4.2 Data elaboration and discussion

Data from accelerometers were processed using the software LMS Test.Lab, computing the Power Spectral Density function with Hanning windowing at 16768 spectral lines and 10% overlap. To perform a preliminary identification of peaks in the transept's frequency response, selected signals in the frequency domain were grouped based on sensor position: north and south partition walls and east, west and south transept walls. Figure 8 shows the resulting PSDs. Here, the different lines correspond to signals from accelerometers mounted on one wall, and measuring in orthogonal direction. Peaks have been identified through manual peak-picking.

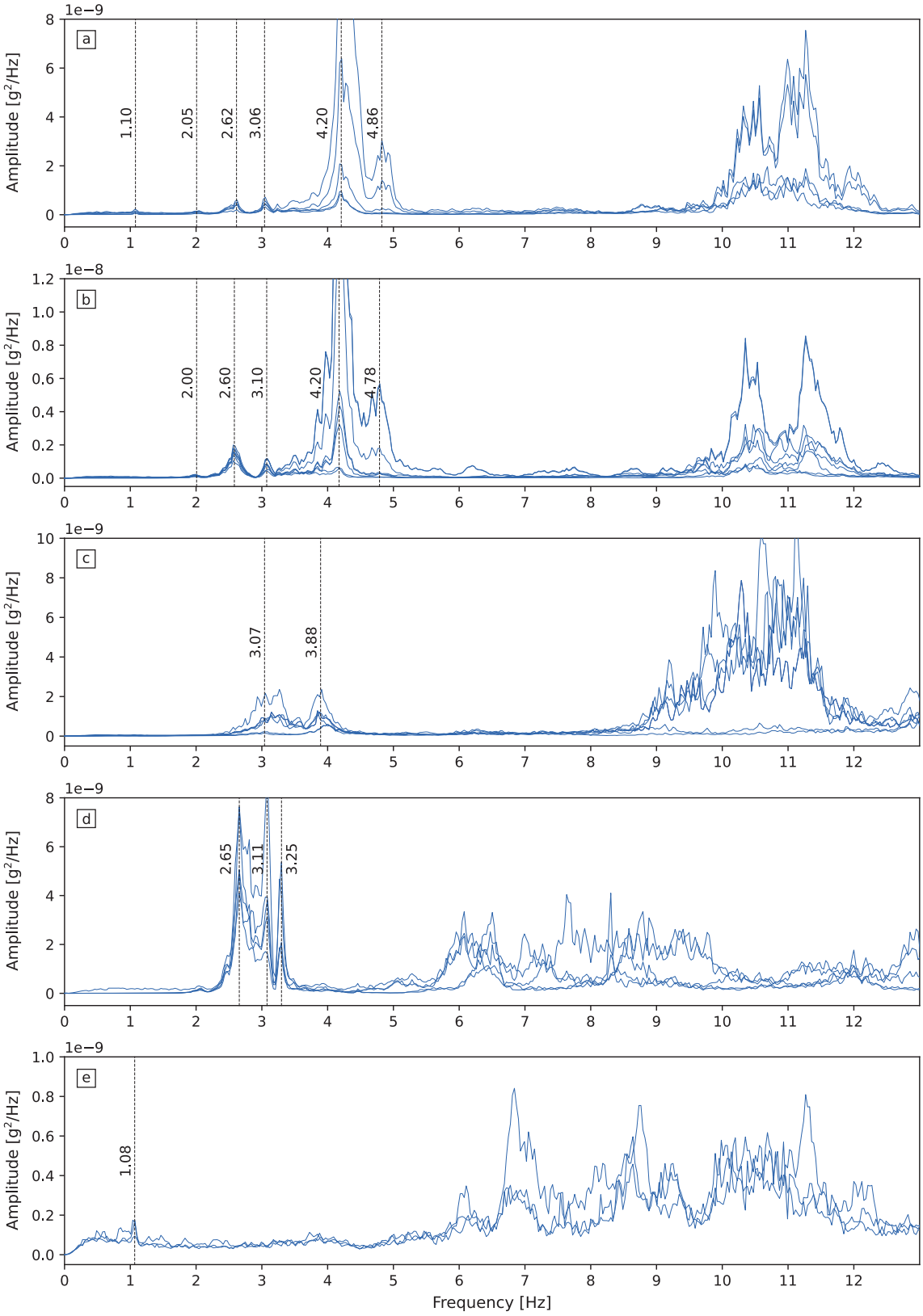

Figure 8: Power Spectral Density of signals recorded from sensors on different transept portions. a) North partition wall; b) south partition wall; c) east transept wall; d) west transept wall; e) south transept wall.

Some observations can be derived:

- frequency responses from the north and south partition walls are very similar. This could be expected since their geometry is roughly the same, even though boundary conditions differ significantly. The north wall is in fact contiguous to the bell tower and to an external vaulted cloister, while the south portion of the transept is free along its height and borders with adjacent roads.
- A peak corresponding to approximately 1.10 Hz can be recognized in the frequency responses of the north partition and west transept walls, and is absent from the response of other walls. This suggests that the first natural frequency of the bell tower, corresponding to its first flexural mode, was identified.
- The vibrational behaviour of the east transept wall is, as expected, quite different from the other walls. This is due to its being horizontally braced by several vaults that cover the altar and the chapels.
- The west transept wall is occupied for the most part by an archway that separates the transept from the nave, as can be seen in Figure 6. Unfortunately, the scaffolding system did not reach the arch's keystone, so that sensors were placed in positions very close to orthogonal walls. The frequency response shown in Figure 8 is detrimentally affected by the lack of sensors in the higher portion of the wall.

The PolyMax algorithm was applied to each single measurement run in order to identify natural frequencies which peaks may have been ignored during manual peak-picking, and the relative partial mode shapes. The results were then combined in LMS Test.Lab to construct global mode shapes, and a multi-run matrix was constructed, grouping together corresponding peaks from different runs (Table 3). Figure 9 shows the mode shapes identified with the PolyMax algorithm, on a simplified 80-point geometry of the church's transept. The northern portion is not shown, since it was not subjected to measurements.

	Configuration 1 [Hz]	Configuration 2 [Hz]	Configuration 3 [Hz]	Configuration 4 [Hz]
Mode 1		1.06	1.08	
Mode 2	2.01	2.00	2.00	
Mode 3	2.62	2.60	2.61	2.58
Mode 4	3.09	3.10	3.06	3.07
Mode 5			3.27	3.51
Mode 6	4.19	4.19	4.19	4.19
Mode 7	4.90	4.87	4.88	4.84
Mode 8	6.19	6.04	6.04	5.98
Mode 9			7.78	7.58
Mode 10	10.07	9.64	10.00	9.84
Mode 11		10.20	10.28	10.20
Mode 12	11.31		11.64	11.57

Table 3: Experimental natural frequencies of the transept.

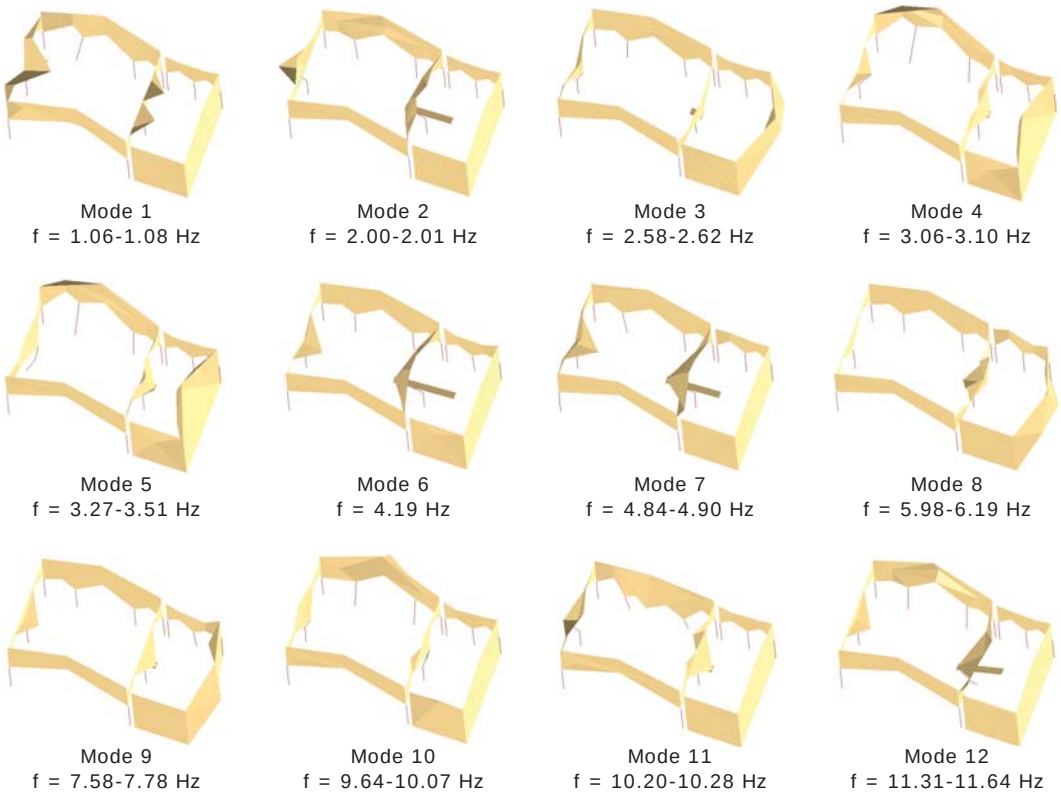

Figure 9: Experimental transept mode shapes extracted with PolyMax algorithm.

The identified mode shapes did not provide useful information regarding the influence of roof and supporting trusses. In particular, at this stage no conclusive answer can be given to the question regarding the eventual rigid-link effect exerted by the roofing system: while some of the mode shapes (e.g., modes 1, 2 and 4) show the two partitioning walls moving in phase, others (e.g., modes 6 and 7) clearly show them moving in opposition of phase. Further measurements, concentrating on the trusses' supports, will help to shed light on the matter.

5 FINITE ELEMENT MODEL

A FE model of the San Francesco church in Pisa was developed using the software Comsol Multiphysics 5.5 [14]. The church's geometry was obtained from a refined point cloud, resulting from a survey fieldwork with laser scanner (Figure 1A). The point cloud was imported in AutoCAD [15] and interpolating solids were defined to assembly the entire geometry of the church.

In Comsol Multiphysics, tetrahedral finite elements with Serendipity quadratic shape functions were used to define a mesh composed of 572991 elements, with maximum dimension set at 1.00 m (Figure 10). A cloister and part of the monastery are contiguous to the northern transept and nave walls (Figure 6). Their presence was considered using displacement boundary conditions to simulate the restraints they exert on the church. Since no conclusive observations could be made regarding the role of the roofing system in the dynamic characterization of the transept, trusses were included in the model because this was thought to represent the most "natural" choice. At this stage, values of Young's moduli for the church's and bell tower's masonry were estimated to be 1300 MPa and 1800 MPa respectively, in accordance with the previous

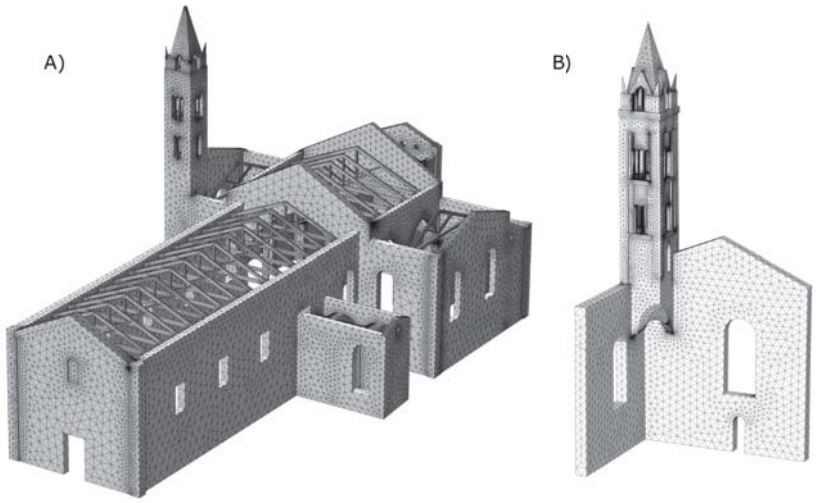

Figure 10: FE models. A) The church; B) preliminary model of the bell tower.

dynamic identification of the bell tower. An automatic updating procedure will be the object of further research work.

Modal analysis resulted in more than 150 mode shapes in the frequency range from 0 to 12 Hz, while only twelve were derived from data analysis (Table 3). Most of the former correspond to natural frequencies of the portions of the church which were not instrumented and therefore not identified, such as the nave and the altar chapels. Sensors used during the acquisition may have not recorded vibrations relative to mode shapes that were not triggered with enough energy by ambient noise.

Mode-matching was performed, and good accordance between experimental and numerical data was reached for some of the modes. Figure 11 shows modal shapes for modes 1, 2, 3 and 7 (according to numbering used in Table 3). Results of the FE model are compared with experimental data. The large number of numerical mode shapes, however, and the presence of many modes with very similar frequencies suggest the necessity to employ an automatic mode-matching procedure such as the Modal Assurance Criterion (MAC) [16]. For this reason, masonry constitutive parameters were not updated using experimental modal information in this case. This will instead be the topic of future research work.

6 CONCLUSIONS

This paper presents preliminary results of the modal identification of the San Francesco Church in Pisa, which is the first step towards the development of a robust SHM system for masonry CH assets. The church's bell tower and transept were subjected to dynamic testing, and operational modal analysis enabled the identification of a limited number of vibrational modes and frequencies. A FE model, preliminarily used to design instrumentation layout, was employed to perform mode matching between experimental and numerical mode shapes, using values for material constitutive parameters resulting from a previous experimental campaign on the bell tower. This first effort allowed us to expand our knowledge regarding practical problems and difficulties arising from performing dynamic testing on a complex structure such as the San Francesco church. Further experimentation will concentrate on specific substructures of the church, and on a dedicated investigation regarding the vibrational influence of roof and supporting trusses.

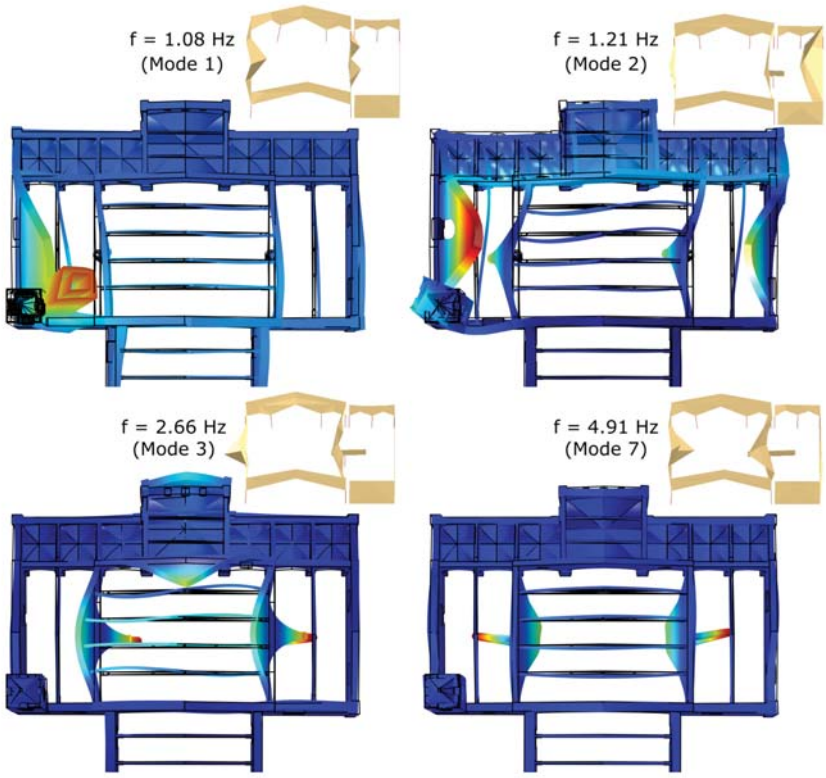

Figure 11: Mode shapes and natural frequencies from the FE model are shown and compared to mode shapes from the experimental campaign.

ACKNOWLEDGEMENTS

For the photographic survey of the San Francesco Church, the authors would like to thank Iole Branca, Gianluca Brocchini, Chiara Cini, Angela Masciangelo and Paola Pellegrino.

REFERENCES

[1] L.F. Ramos, M.G. Masciotta, M.J. Morais, M. Azenha, T. Ferreira, E.B. Pereira, and P.B. Lourenço. HeritageCARE: Preventive conservation of built cultural heritage in the South-West Europe. In Koen Van Balen and Aziliz Vandesande, editors, *Innovative Built Heritage Models*, pages 135–148. CRC Press, 1 edition, January 2018.

[2] Daniel Balageas, Claus-Peter Fritzen, and Alfredo Güemes, editors. *Structural Health Monitoring*. ISTE, London ; Newport Beach, CA, 2006. OCLC: ocm62493224.

[3] Alessandro De Stefano, Emiliano Matta, and Paolo Clemente. Structural health monitoring of historical heritage in Italy: Some relevant experiences. *Journal of Civil Structural Health Monitoring*, 6(1):83–106, February 2016.

[4] Gianni Bartoli, Michele Betti, Antonino Maria Marra, and Silvia Monchetti. A Bayesian model updating framework for robust seismic fragility analysis of non-isolated historic masonry towers. *Philosophical Transactions of the Royal Society A: Mathematical, Physical and Engineering Sciences*, 377(2155):20190024, October 2019.

[5] Alessandra Bonazza, Miloš Drdácký, Christian Hanus, Ingval Maxwell, Ellizabeth Vintzileou, European Commission, and Youth Directorate-General for Education, Sport and Culture. *Study on Safeguarding Cultural Heritage from Natural and Man-Made Disasters: A Comparative Analysis of Risk Management in the EU*. 2018. OCLC: 1111110470.

[6] Donato Sabia, Takayoshi Aoki, Renato Maria Cosentini, and Renato Lancellotta. Model Updating to Forecast the Dynamic Behavior of the Ghirlandina Tower in Modena, Italy. *Journal of Earthquake Engineering*, 19(1):1–24, January 2015.

[7] Riccardo Azzara, Anna De Falco, Maria Girardi, and Daniele Pellegrini. Ambient vibration recording on the Maddalena Bridge in Borgo a Mozzano (Italy): Data analysis. *Annals of Geophysics*, 60(4):9, July 2017.

[8] Antonio Formisano, Gianmaria Di Lorenzo, Lidija Krstevska, and Raffaele Landolfo. Fem Model Calibration of Experimental Environmental Vibration Tests on Two Churches Hit by L'Aquila Earthquake. *International Journal of Architectural Heritage*, pages 1–19, January 2020.

[9] Rune Brincker and Carlos Ventura. *Introduction to Operational Modal Analysis*. John Wiley & Sons, Ltd, 2015.

[10] Carmelo Gentile, Antonello Ruccolo, and Francesco Canali. Continuous monitoring of the Milan Cathedral: Dynamic characteristics and vibration-based SHM. *Journal of Civil Structural Health Monitoring*, 9(5):671–688, November 2019.

[11] Fabio Redi and Gabriella Rossetti. *Pisa Com'era: Archeologia, Urbanistica e Strutture Materiali (Secoli V-XIV)*. GISEM, 1991.

[12] LMS Test.Lab 8 Reference Manual, 2008. www.plm.automation.siemens.com.

[13] Bart Peeters, Geert Lowet, Herman Van der Auweraer, and Jan Leuridan. A new procedure for modal parameter estimation. *Sound and Vibration*, 38(1):24–29, 2004.

[14] Comsol Multiphysics 5.5 Reference manual, 2019.

[15] AutoCAD 2019 Reference Manual. Autodesk.

[16] Miroslav Pastor, Michal Binda, and Tomáš Harčarik. Modal Assurance Criterion. *Procedia Engineering*, 48:543–548, 2012.

EURODYN 2020
XI International Conference on Structural Dynamics
M. Papadrakakis, M. Fragiadakis, C. Papadimitriou (eds.)
Athens, Greece, 23–26 November 2020

DYNAMIC ANALYSIS OF THE INTERACTION BETWEEN BELLS AND MASONRY STRUCTURES

D. Bru[1], S. Ivorra[1], M. Betti[2], G. Bartoli[2], F. J. Baeza[1], and F. B. Varona[1]

[1] Department of Civil Engineering
University of Alicante. Alicante 03690, Spain
david.bru@ua.es, sivorra@ua.es, f.j.baeza@ua.es, borja.varona@ua.es

[2] Department of Civil and Environmental Engineering
University of Florence, Florence I-50139, Italy
mbetti@dicea.unifi.it, Gianni.bartoli@unifi.it

Keywords: Bell tower, Masonry, Dynamic, Damage

Abstract. *This research show the numerical and experimental results evaluated in the Fiesole bell tower in Italy. The aim of this investigation is to increase the knowledge related to the dynamic interaction between the vibration frequencies of the bells and the dynamic behavior of the masonry tower. In particular, in this paper the numerical evaluation focuses on the bell and tower interaction, taking into account the behavior of the tower as an exempt structure. In particular, the study was divided into several phases. The first phase consisted of the geometric definition of the structure, as well as the definition of the mechanical properties of the bells. In the second phase the dynamic properties of the structural system were evaluated and the numerical model was calibrated. In the third phase, lateral restrictions of the tower were released and a parametric study of the interaction of the dynamic forces of the bells with the tower was carried out. Based on these results, the velocity ranges, and swing amplitude of the bells, which could damage the tower, were evaluated according to DIN 4178-2005. The main results show that the biggest bell should not be used for velocity values near 41.53 rpm. regardless of the swing angle. Also, for smaller bells, swing angles between 50º and 95º and speeds between 25-40 rpm. should be avoided.*

1 INTRODUCTION

Masonry towers are very common buildings from the middle ages until now. In particular, many of them have bell towers at the top of the buildings. These bells have been used to advise the population of different events by means of the ringing of the bells [1]. In recent years, interest in the dynamic behavior of such structures has increased, especially through the use of monitoring techniques (structural health monitoring), reporting papers on vibration modes and frequencies [2, 3], as well as studies related to their seismic vulnerability [4]. On the other hand, several authors have published articles related to the dynamic forces generated by the bells ringing [5]. However, there are not many authors who analyze the behavior of these structures under loads in service, such as those due to the swing of the bells.

With the aim of increasing this field of knowledge, in this work the interaction between the vibration frequencies of the bells and the dynamic behavior of the masonry tower, under the consideration of structure exempt is evaluated. In particular, the study is divided into several phases. The first phase consisted of the geometric definition of the structure, as well as the definition of the mechanical properties of the bells. In the second phase the dynamic properties of the structural system are evaluated and the numerical model is calibrated. In the third phase, lateral restrictions of the tower are released and a parametric study of the interaction of the dynamic forces of the bells with the tower is carried out. Based on these results, the velocity ranges, and swing amplitude of the bells, which could damage the tower, are evaluated according to DIN 4150 [6].

2 CASE OF STUDY: FIESOLE BELL TOWER

The tower selected for the analysis is the Fiesole bell tower from the Cathedral of Fiesole (Italy), Figure 1. This structure is a hollow rectangular cross section of 5.10x4.10m². The thickness of the external wall is variable with height. From 0 to 7.25m the thickness of the wall is a constant value of 1m. The thickness for the next section of 15 m length is 0.85m. For the third section of 16m length, the thickness is 0.75m. Finally, for the last section from 38m to the crown at 39.65m, the thickness is equal to 0.25m. Regarding the openings in the external walls of the tower, there are no important elements, except for the access point at the base of the tower, and the openings located in the belfry, at 26.30m and 30.90m. Regarding the lateral constraints, there are tree lateral church walls connected on north, south and west sides with a thickness of 1m. In general, the material of the tower and lateral walls are irregular stone bricks with mortar.

Figure. 1: General and frontal views of bell-tower. From left to right: West, South, East and North Faces.

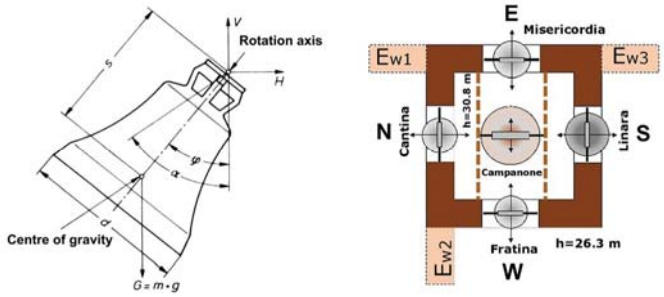

Figure. 2: Left: Simplified bell model. Right: Arrangement of the bells with their swing directions.

3 DYNAMIC BELL FORCES

The belfry of the tower shows five different bells, Figure 2. The first four, Fratina, Cantina, Misericordia and Linara, are located at 26.30m, and the weight of them is 2.452 kN, 2.256 kN, 3.237 kN and 4.395 kN. The last one is the Campanone, located at 30.90m and its weight is 7.142 kN. Table 1 shows the dynamic properties of the bells. These bells swing according to the Central European System [5]. Dynamic horizontal force of the bells, evaluated according of the German standard [10], Equation 1, depends on the mass of the bells, m, the swing velocity, Ω, the geometry coefficient, c, and the swing rotation angle, α. The c coefficient is a function of the inertia and the distance from the bell gravity center to the rotation axis of the bell. Finally, the effect of the rotation angle, α, Figure 2, is taken into account by means of the γ coefficient. Figure 3 shows an example of the dynamic force of the Campanone bell, and the harmonics components of this force. These harmonics change with the swing angle and velocity and they can interact with the vibration frequencies of the tower.

Bell	Geometry coefficient	Weight (kg)	Diameter (mm)	Swing velocity	Swing angle	Dynamic Horizontal Force (kN)
Campanone	0.76	728	1120	29.98	64	5.014
Linara	0.75	448	970	33.52	73	3.645
Misericordia	0.75	330	870	33.04	65	2.289
Cantina	0.75	230	780	34.47	72	1.838
Fratina	0.80	250	670	36.96	69	2.006

Table 1: Dynamic properties of the bells in the Fiesole bell tower.

$$H(t) = c \cdot (m \cdot 981) \cdot \sum \gamma \cdot sin(\Omega \cdot t) \quad (1)$$

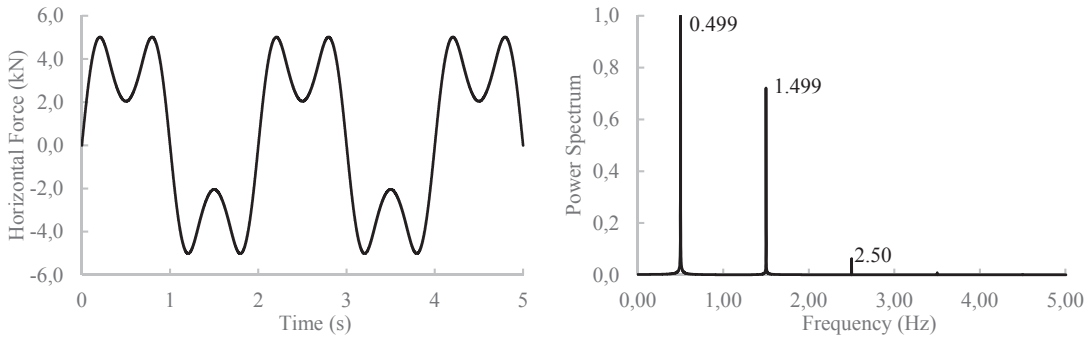

Figure 3: Example of Campanone dynamic loads. Left: Horizontal force; Right: FFT for swing angle of 64°.

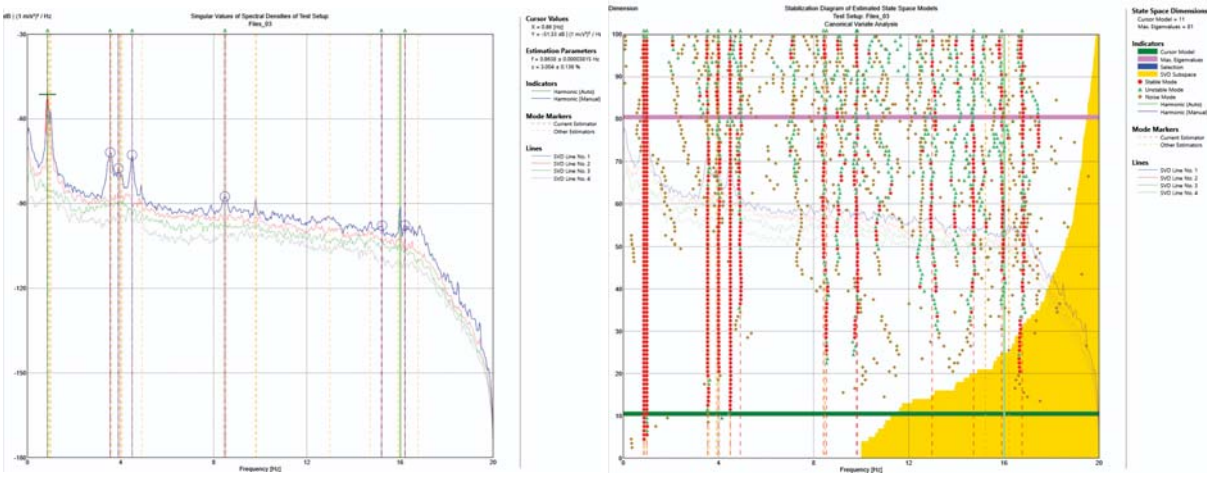

Figure. 4: Left: SVs of PSDs from EFDD analysis. Right: SVs of PSDs from CVA analysis.

4 EXPERIMENTAL TEST

In order to analyze the dynamic properties of the tower six 393 PCB Piezotronics uniaxial accelerometers are placed at 30.9m and 38 m on the internal part of the tower East façade, in a triaxial configuration. By means of this test setup it is possible to evaluate the frequencies in E-W and N-S direction, Figure 2. The range of measurement for these devices is from 0.025 Hz to 800 Hz, with a voltage sensivity of 1V/g. Data acquisition hardware consist of a signal conditioner PCB 482A22 and a data logger HBM Spider8 (SR55). The sample frequency is 400 Hz. Two test are done. During the first one, a signal of 15 minutes is recorded, and the dynamic load used during this test is the ambient noise. In the second test, a signal of 6 minutes is recorded and the dynamic load used in this case is the horizontal force due to the swinging of the Misericordia bell with a swing angle and swing velocity equal to 100º and 30 rpm.

Mode		EFDD		CFDD		CVA	
-	plane	Hz	csv	Hz	csv	Hz	csv
1	zy (N-S)	0.87	*1.22*	0.89	*1.75*	0.86	*0.30*
2	zx (E-W)	0.97	*2.50*	0.98	*0.66*	0.98	*0.59*
3	xy	3.55	*0.11*	3.55	*0.09*	3.54	*0.06*
4	zy (N-S)	3.94	*1.21*	3.98	*1.91*	3.99	*0.19*
5	zx (E-W)	4.48	*0.53*	4.47	*0.51*	4.46	*0.76*

1-2. 1st bending mode. 3. Torsion mode, 4-5. 2nd bending mode.
EFDD: Enhanced Frequency Domain Decomposition; CFDD: Curve-fit Frequency Domain Decomposition; CVA: Canonical Variate Analysis.

Table 2: Statistical analysis of ambient vibration test.

Signals are analyzed using ARTeMIS software for OMA, and Matlab software. Signals are decimated from 400 Hz to 50 Hz, and filtered between 0.1 Hz to 20 Hz. Different techniques are used for the analysis. Table 2 shows the mean frequencies and the standard deviation values for the principal vibration modes according to the Enhanced Frequency Domain Decomposition technique (EFDD) and Curve-fit Frequency Domain Decomposition technique (CFDD) for the analysis in frequency domain, and the parametric technique Canonical Variate Analysis (CVA), for the analysis in time domain. Finally, the global damping of the structure is evaluated using de data of the second test and the logarithmic decay technique. Global damping value is equal to 1.5%, and it is very close to the proposed one by the standard DIN 4178 [7] for masonry buildings.

Finally, with the aim to evaluate the experimental results, the analytical first bending frequency is compared with the proposed in some standards. Table 3 shows the results for the NTC-08 [8], DPCM-11 [9] and NCSE02 [10]. In general, all the results are close to the experimental ones, and they are valid for a preliminary value. Moreover, the results for the Spanish standard shows the best results compared to the experimental data.

Direction	NTC-08	DPCM-11	NCSE-02	Experimental
-	Hz	Hz	Hz	Hz
E-W (zx)	1.307	1.407	1.116	0.976
N-S (zy)	1.307	1.407	0.979	0.873

Table 3: First bending frequency according to different standards.

Figure 5: Frequencies and modal shapes for bell tower without lateral restraints

5 DAMAGE EVALUATION DUE TO BELL SWING

A numerical model has been implemented with ANSYS software with the aim to evaluate the dynamic behavior of the tower, and the dynamic interaction between the tower and the bells. All the elements used are solid 186 elements. Perfect bonded contact is selected between the elements in contact with the tower. The analysis is divided in three phases. The first one consist of the numerical model calibration process. During this phase, a confined model is used, and the optimization process is done using genetic algorithm [11]. The parameters used in GA were, population of 20 chromosomes, elite count and crossover fraction equal to 10% and 80%, and 75 generations. Five variables are evaluated, three variables for the Elastic modulus of the three masonry confinement walls, one for the Elastic modulus of the main body of the tower, and finally, one more for the tower masonry self-weight. Relative error between numerical and experimental data for the first five vibration frequencies is used in the calibration process. Finally, the elastic modulus and the self-weight calibrated values for the tower are 2043 MPa and 1894 kg/m³, and the global error is equal to 3.31%. The second phase consist of the analysis of the bells swing velocity range that could generate resonance problems with the bell tower. In this phase and the next one, the numerical model used is the same as the calibrated one, but the lateral restriction are released. Figure 5 shows the first five modal shapes for the tower without lateral restraints. It has been selected the model without lateral restraints due to the aim of this research is focused on the dynamic interaction between the bell tower and the bells in case of analyzing the tower as exempt structure.

Regarding the critical bell swing velocity range, a preliminary analysis is done taking into account the relationship between the frequency of the tower and the harmonic of the horizontal bell force. Figure 6, shows the amplification factor for the normally used range of bell swing velocities. It is possible to evaluate that the critical bell swing velocities and harmonics for the

first and second mode are 29.34 rpm (1st harmonic) and 36.6 rpm (1st harmonic), for the third mode are 41.53 rpm (3rd harmonic) and 24.93 rpm (5th harmonic), for the fourth mode are 22.55 rpm (7th harmonic) and 31.56 rpm (5th harmonic), and finally, for the fifth mode are 21.2 rpm (9th harmonic), 27.26 rpm (7th harmonic) and 38.16 rpm (5th harmonic). Finally, in the third phase of this research, a parametric study of the interaction between the bell forces and bell tower is done. Figure 6 shows the normalized resultant velocity on the top of the tower for the swing velocities selected, and the normalized standard velocity limitation, for the different bells according to the standard DIN 4150 [6]. For these velocities, a swing angle from 50º to 170º and height equal to 30.9 m in E-W direction, is evaluated.

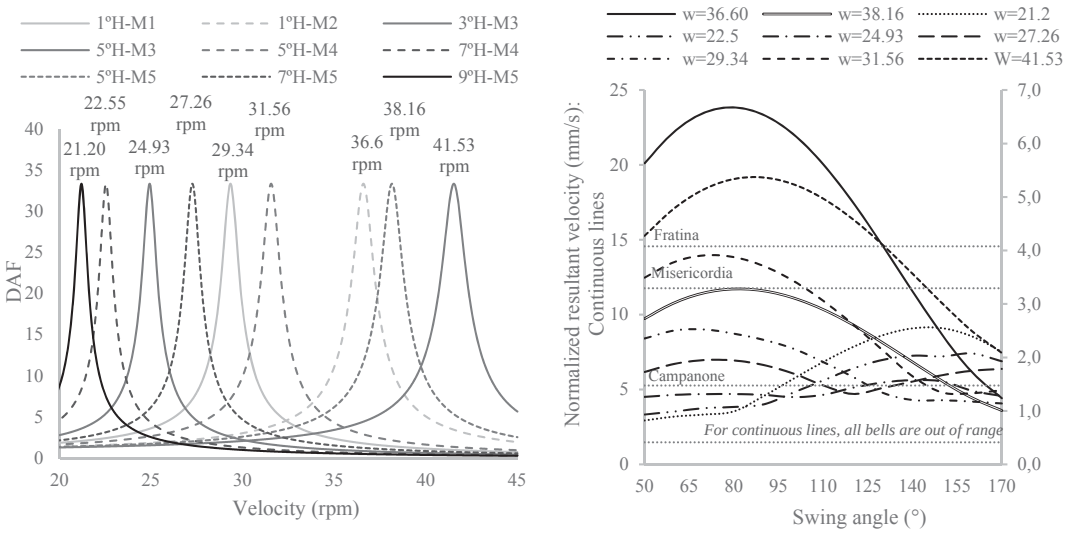

Figure 6: Left: Local sensitivity analysis of the dynamic interaction between bell tower frequencies and bell harmonics. Right: Maximum horizontal velocity of the last floor for bell loads.

The results show that for bells located at 30.9 m none of the three bells in E-W directions could be used for swing velocities equal to 36.60 rpm and 38.16 rpm, with maximum normalized horizontal velocities equal to 23.85 mm/s and 11.72 mm/s. Regarding the others bell swing velocities, for the same location and bell swing direction, it is possible to see that for bells similar to Fratina bell, swing velocity of 41.53 rpm and swing angle from 50º to 130º could damage the tower due to the interaction between the 1st harmonic bell force and the 2nd vibration mode of the tower. However, the results show that there are not resonance problems between the 3rd harmonic of the bell force and the 3rd vibration mode of the tower, although the relationship between these frequencies is close to one. From the point of view of bells similar to the Misericordia bell, damage bell swing velocities are 41.53 rpm and 31.56 rpm for bell swing angles lower than 150º or lower than 110º respectively. Regarding the interaction between the harmonics of the bell forces and the vibration frequencies of the tower for these bell velocities, the problem is focused between the 1st harmonics of the bell forces and the 2nd vibration mode of the tower. In this case the influence of the 3rd and 5th harmonics of the bell forces in the 3rd and 4th vibration mode of the tower is negligible. Finally, Campanone bell shows that only bell swing velocities lower than 25 rpm with bell swing angle lower than 125º could be used without damaging the tower. It is important to note the relevance, for these low bell swing velocities, of the interaction between the higher order harmonics and the higher vibration modes of the tower,

6 CONCLUSIONS

In this paper, the dynamic behavior and the interaction between the Fiesole bell tower and movements of the bells is evaluated. Fist, Operational Modal Analysis is used to evaluate the first five vibration frequencies of the tower by means of three different techniques, EFDD, CFDD, CVA. Second global damping of 1.5% is evaluated using logarithmic decay technique. Third, a numerical model is implemented using ANSYS commercial software, and variables such as bell swing velocity, bell swing angle, and bell dynamic properties are evaluated by means a parametric analysis. The results show that for any bell located at 30.9m height, velocities equal to 36.60 rpm and 38.16 rpm could damage the bell tower. In case of Campanone bell, bell swing velocities higher than 25rpm and bell swing angle higher than 125º could damage the tower. In conclusion, it can be argued that, the dynamic interaction between the bells movements and the bell tower can damage the Fiesole bell tower.

REFERENCES

[1] S. Ivorra, F. J. Pallarés, J.M. Adam, Dynamic behaviour of a modern bell tower – A case study, *Engineering Structures* 31, 1085-1092, 2009.

[2] L.F. Ramos, L. Marques, P.B. Lourenço, G. De Roeck, A. Campos-Costa, J. Roque, Monitoring historical masonry structures with operational modal analysis: Two case studies, *Mechanical Systems and Signal Processing* 24, 1291-1130, 2010.

[3] F. Lorenzoni, F. Casarin, M. Caldon, K. Islami, C. Modena, Uncertainty quantification in structural health monitoring: Applications on cultural heritage buildings, *Mechanical Systems and Signal Processing* 66-67, 268-281, 2016.

[4] G. Bartoli, M. Betti, A. Vignoli, A numerical study on seismic risk assessment of historic masonry towers: a case study in San Gimignano, *Bulletin of Earthquake Engineering*, 14,1475-1518, 2016.

[5] S. Ivorra, M.J. Palomo, G. Verdú, A. Zasso, Dynamic forces produced by swinging bells, *Meccanica*, 41,47-62, 2006.

[6] DIN 4150 – Vibrations in buildings – Part 3: Effects on structures, (1986).

[7] DIN 4178:2005-04. Glockentürme [In German].

[8] Ministerio delle Infrastructure e dei Trasporti. (2008). "Nuove Norme Tecniche per le Costruzioni". NTC 2008, D.M. del Ministero delle 555 Infrastrutture e dei Trasporti del 14/01/2008. G.U. n. 29 del 04.02.2008, S.O. n. 30 (in Italian).

[9] DPCM (Direttiva del Presidente del Consiglio dei Ministri). (2011). "Direttiva del Presidente del Consiglio dei Ministri per la valutazione e riduzione del rischio sismico del patrimonio culturale con riferimento alle NTC 2008". DPCM 2011, G. U. n. 47 del 26.02.2011, Roma (in Italian).

[10] Ministerio de Fomento. (2002). "Norma de Construcción Sismorresistente - Parte General y Edificación (Spanish Standard)". NCSE2002, Madrid, Spain (in Spanish)

[11] C. Chisari, C. Bedon, C. Amadio, "Dynamic and static identification of base-isolated bridges using Genetic Algorithms". *Engineering Structures* 102, 80-92 (2015).

EURODYN 2020
XI International Conference on Structural Dynamics
M. Papadrakakis, M. Fragiadakis, C. Papadimitriou (eds.)
Athens, Greece, 23–26 November 2020

REDUCING IMPACT OF VIBRATIONS FROM COMPACTION ON SLOPE STABILITY

Jörgen A.T. Johansson[1], Joonsang Park[1], Christian Madshus[1], and Carl Wersäll[2]

[1] Norwegian Geotechnical Institute
Sognsveien 72, NO-0866 Oslo, Norway
e-mail: jjo@ngi.no, jp@ngi.no, cm@ngi.no

[2] KTH Royal Institute of Technology
SE-100 44 Stockholm, Sweden
carl.wersall@byv.kth.se

Keywords: Compaction, slope stability, non-linear soil, and equivalent linear frequency domain FE

Abstract. *A tsunami caused by a landslide caused extensive damage at Statland, Norway in 2014. The landslide was probably triggered by man-made vibrations. To understand better how vibrations from vibratory compaction affect slope stability, a frequency domain numerical tool (Comsol Multiphysics) has been extended to account for realistic non-linear soil behaviour. The tool is validated by comparison with field experiments of vibratory compaction. The non-linear analysis is believed to capture the essential behaviour of the vibratory compaction and the response of the slope. The numerical analysis and evaluations indicate vibratory compaction can have contributed to triggering the slide at Statland. To perform compaction in the vicinity of slopes with low stability near the shoreline with vibration susceptible soils we suggest: 1) using lighter equipment and/or higher loading frequencies or performing compaction without vibration, and avoiding excessive jumping of the vibratory roller drum; 2) applying thinner layers and more time between compaction passes, allowing for drainage of potential built up pore pressures; 3) monitoring slope horizontal and vertical displacements at some critical points; and 4) monitor pore pressures at critical points, if possible.*

1 INTRODUCTION

A landslide-induced tsunami caused extensive damage at Statland, Norway in 2014. Only luck prevented any fatalities. The investigation of technical cause [1] concluded the slide was likely triggered by vibratory compaction of a rockfill in the shoreline in connection with development and extension of a near shore recreation cottage area. For safer nearshore developments it is very important to understand better the processes involved in the landslide triggering.

Often ground conditions along the Norwegian fjords consist of loose soil deposits with silt and sensitive clays. In combination with artesian water pressure the stability of such shoreline submarine slopes can be very low. The combination of loose soil and low stability makes these slope extra vulnerable to vibrations.

A tentative procedure on how to account for cyclic- and dynamic effects during vibratory compaction near slopes with vibration sensitive material, was proposed [2]. However, such approach may not always be practical, especially in small projects. Therefore the possibility of establishing a vibration limit has also been investigated in [3]-[4]. Through linear elastic models accounting for soil non-linearity by an ad-hoc reduction of soil stiffness depending on the induced strains. Recently, an equivalent linear numerical tool has been developed which has been validated against data from compaction and pile driving vibration experiments [5]. This tool is applied to the Statland case to better understand how non-linear soil properties affect the dynamic response of the slope. The following section gives a brief description of vibration triggered landslides and soil compaction induced vibrations before describing the numerical model and results for the Statland case.

2 VIBRATION-TRIGGERED LANDSLIDES

It is commonly not considered likely for non-blasting construction vibrations to cause landslides. We have only found the following potential cases in the literature:

- The Trestyckevatten slide south of Uddevalla, Sweden in 1990 [6] was most likely triggered by a heavy vibratory roller which caused the failure of a berm designed to provide additional stability to an embankment for the E6 highway.
- The Åsele-slide in 1983, also in Sweden [7] caused the failure of a road embankment that was partially submerged due to filling up of hydro-electric reservoir. The slide was triggered by tractor- pulled 3.3 ton vibratory roller.
- The 1987 Lake Ackerman slide caused damage to Highway 94 in Michigan, USA [8]. Six 22-ton trucks with vibrator plates generating signals for a seismic refraction study triggered the slide. The road embankment consisted of hydraulic fill of loosely deposited sand. Hryciw et al. estimated the cyclic shear strains induced in the fill of up to 0.06%, which could be enough to generate pore pressure build up and cause failure in loose fine silty sand ([9], [10]).
- The 1994 Skagway landslide reported in [10] have similarities with the Statland case, however there is limited information on the road construction done shortly before the slide. It is not clear if compaction can have contributed to the landslide.

The above cases were all near shoreline submarine landslides with loose ground conditions. For landslides where rock blasting was a potential trigger, the slide occurred in combination with other adverse factor such as low stability prior to blasting, higher than normal ground water level due to high precipitation, artesian pressures, erosion at the slope base, temporary placement of fill masses, etc. In addition, the existence of thin sand or silt layers within the clay are

confirmed in many cases, and are hence assumed to have played a crucial role [12]-[13]. These adverse factors also play an important role, when construction vibrations induce landslides.

3 STATLAND LANDSLIDE

January 29, 2014, a submarine landslide and a resulting tsunami [14] caused damage to port facilities and nearshore infrastructure at Statland, in the county of Nord-Trøndelag, Norway. Some photos of the damage are shown Figure 1. The newly constructed road and part of an old molo was swept away by the landslide. Luckily no humans was in vicinity when the landslide occurred. The tsunami slammed into buildings many of which were totally or partially destroyed. The investigation of the possible slide causes [1] established the slide occurred an hour and half after the filling and compaction work was finished. It further concluded it was very likely the construction work triggered the slide.

Deltaic deposits have accumulated over years along the margin of Namsfjorden outside the small community of Statland. The deposits consist mainly of loose sands and silts overlaying marine and partly sensitive clays (quick clays). The soft and weak soil conditions result in very low static factors of safety for the partially submarine slope [1]. In addition, there are considerable amount of organic material down to depths of 14 m beneath the seabed [1], which originated from sawmill industry in the area during the last 120 years. The sedimentation rate in the area is estimated to be in the order of 12 cm/year. Thus, there are considerable amounts of material still undergoing consolidation.

Such loose silty soils are susceptible to strength degradation due to vibrations, and thus some preliminary analysis of the impact of vibratory compaction on the slope stability was performed in [1]. The analysis indicated that compaction may have contributed to slide triggering in combination with other factors such as low tide and low static stability.

Figure 1 Photos showing damage caused by the Statland landslide. The right hand side photos compare the situation before and after the landslide with yellow dashed line showing the shoreline after the slide.

4 VIBRATIONS FROM VIBRATORY ROLLERS

Ground vibration from vibratory rollers transmits large dynamic loads to the soil in order to compact the fill materials during construction. Such dynamic loads can possibly cause pore pressure build-up and reduce soil strength in vibration susceptible soils such as loose silt and sand, and sensitive clays. This should be considered when carrying out construction work near slopes with such soils. The strength reduction depends on soil conditions, cyclic load amplitude and number of load cycles.

Performing vibratory roller compaction according to guidelines such as the Norwegian standard NS 3458 involves passing over the same area sometimes up to 8 times with the roller. This means a soil element is exposed to a large number of vibration cycles. The number of cycles depends on the speed of the roller and the vibration frequency. Vibratory rollers have vibration frequencies typically between 20-40 Hz and, on some rollers, both the load amplitude and vibration frequency can be varied, depending on the type of soil and the thickness of the compacted layers. The speed of the roller is typically between 0.5 m/s to 1.5 m/s. E.g. for the case of the Statland landslide ([1]) a low estimate of number of cycles indicated the soil in the upper part of the slope had experienced several hundred cycles with strains large enough to build up pore pressure.

The vibration amplitude depends on the vibratory roller's dynamic behaviour and its interaction with the ground during the compaction process (see e.g.[14]and [16]). There are various vibration modes, changing from full contact between drum and the substrate, to the periodic loss of contact during normal operation, to a less desirable chaotic bouncing of the drum as shown in Figure 2. Bouncing occurs when the period for one cycle is longer than the time for loss of contact and is more common at larger load amplitudes and can cause increased vibration amplitudes.

Vibratory compactors can start bouncing when the compacted fill is becoming stiffer after a number of passes over the fill. When this happens the roller drum will lose contact with the soil during a longer part of each vibration cycle and therefor do not vibrate with the same frequency as the compacted fill and soil. When bouncing occurs the soil is subjected to load impulses with a frequency which can be closer to the soil deposit's natural vertical vibration frequency. This can lead to larger vibrations and possibly pore pressure build up further away from the roller. There may be a "double" resonance if the natural frequency of the vibratory roller and the underlying fill is close to the natural vibration frequency of the soil layers in the slope.

Full-scale tests of vibratory compaction [17], [18] indicate the largest vibration amplitude occurs when the drum vibration frequency is about twice of the natural vertical vibration frequency of the system consisting of the drum and underlying fill and soil as shown in Figure 6. This is interpreted as that every other cycle the roller is in the air, and every other cycle it "hits" the compacted fill and soil in phase with the natural vibration frequency between roller and fill.

Jumping reduces the compaction efficiency [17] and is undesired. Therefore, some modern vibratory roller have various types of automatic feedback control systems to avoid such jumping [12]. The jumping is reduced by changing drum vibration amplitude and/or frequency ([19]). Since jumping can cause larger vibrations it is also undesired with respect to slope stability and should be avoided. The lower graph in Figure 2 shows schematically the dynamic behaviour of a vibratory roller drum and the vibration frequency halving which can occur during jumping.

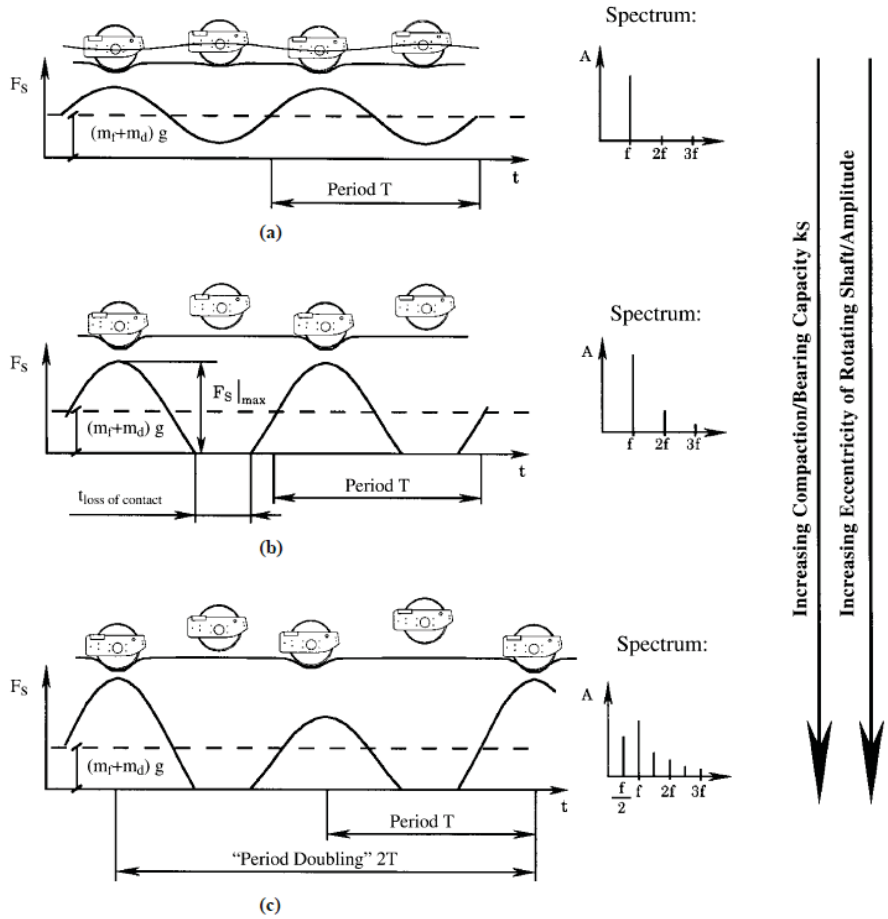

Figure 2 Dynamic behaviour of a vibratory roller drum, a) full contact, b) periodic loss of contact, and c) double-jumping. Spectrum show the period doubling when the drum jumps. From [19].

5 NUMERICAL METHOD

Numerical simulations of effects from vibro-compaction done earlier in [2]-[4] were based on linear elastic material properties. Soil nonlinearity (reduction of stiffness with increased loading) was accounted for by manually reducing the material stiffness in the regions subjected to the largest cyclic strains. Recently we implemented a new feature in Comsol Multiphysics [5], to account directly for soil nonlinearity by means of laboratory measured strain dependent secant stiffness and damping. This extended tool is described in the following sections. The analysis is done in the frequency domain which allows for an equivalent linear soil model to be used to iteratively account for soil non-linearity.

Modelling of nonlinear soil behaviour with the equivalent linear method originates from the analysis of earthquake induced ground vibrations [21][22]. With increasing cyclic strain, the secant soil stiffness decreases, and the damping increases as shown schematically in Figure 3. This behaviour is often represented by curves showing reduction of secant shear modulus and increase of damping as shown in Figure 4.

The input parameters in the model is the initial shear wave speed, mass density, and hysteretic damping. In the frequency domain analysis constant elastic parameters are used, and thus the nonlinear stress-strain variation cannot be followed. Therefore, for each loading frequency, the COMSOL solver iterates until there is shear modulus is compatible with the shear strain in an equivalent linear sense in the whole computational domain. The secant shear modulus and damping vary with the distribution of shear strain amplitude within the soil around the roller

drum. The secant shear modulus, G_s, is expressed as varying with the octahedral shear strain amplitude, γ, according to the hyperbolic relationship in Eq. (1).

$$G_s = G\frac{1}{1+\left(\frac{|\gamma|}{\gamma_{ref}}\right)^n} \tag{1}$$

where G is the initial shear modulus, n and γ_{ref} are material parameters. The octahedral shear strain, γ, is a complex variable when operating in the frequency domain, and therefore the equation was modified in COMSOL to use the amplitude of the shear strain. The material damping is modelled with a frequency independent damping, which is included in the soil stiffness by replacing the shear modulus with a complex shear modulus, $G_s^* = G_s(1+i2D)$, where, D is the material damping factor, and i the imaginary unit.

The above method is not restricted to the hyperbolic law in Eq. (1), other formulations such as presented in [23]-[26], or simple tabulated data points for shear strain versus G/G_s , or damping, for specific materials are also possible. The material damping for the current analysis were given as tabulated values.

The combination of a cyclic and an average shear stress, can have considerable effect on the cyclic stress-strain behaviour and damping [27]-[29], but these effects were not considered in this study. Though the nonlinear cyclic stress-strain and damping-strain behaviour of the clay, silt and sand materials differ to some extent, in this preliminary study, they were modelled with the same stiffness reduction and damping curves, based on the empirical equations in [23] with the soil index input parameters given in Table 1.

Parameter	Value	Unit
Plasticity Index, PI	20	%
OCR	10	1
σ_o'	100	kPa.
n	0.98	1
γ_{ref}	0.075	[%]

Table 1: Input parameters for modulus reduction and damping curves.

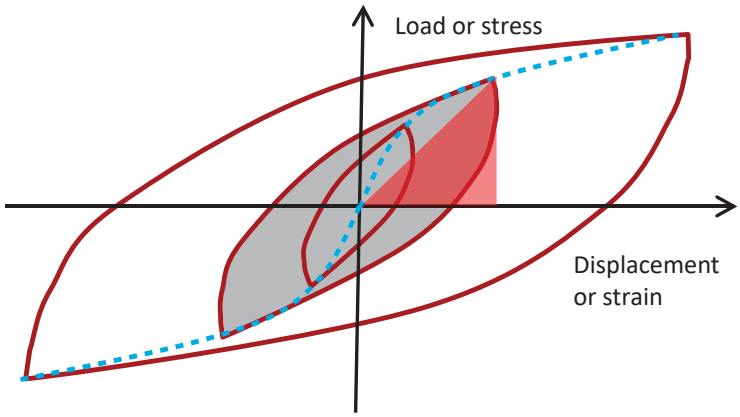

Figure 3 Schematic cyclic stress-strain loops for a soil element. The red triangle and the grey shaded loop shows the definition of elastic energy and hysteretic loss energy respectively in one cycle. The cyclic "back-bone" or "skeleton" curve which controls the shape of the hysteresis loops, is shown by the blue dotted line. Assuming a hyperbolic shape this line is given by Eq. (6).

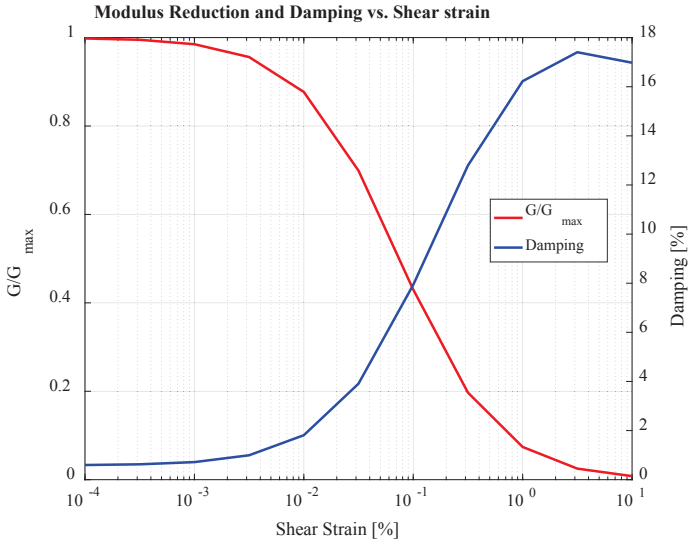

Figure 4 Shear Modulus reduction and damping versus shear strain used in COMSOL analysis.

Absorbing boundaries of the Perfectly Matched Layers (PML) type [30] are used to reduce unwanted wave reflections from the boundaries of the computation domain in the dynamic analysis. This also allows for modelling of radiation damping.

Since the soil strains become large near the vibratory roller it is important to have mesh element size fine enough to resolve the high strain and stress gradients. A comparison between *1st* and 2nd order elements are given in section 7.2. Also the element size should be small enough to resolve the wave lengths appearing for the various stress and strain conditions at the various frequencies analysed. In three dimensions it is most likely faster to adopt the mesh size according to the frequency, i.e. the higher frequency the finer the mesh. In 2D we have found for some models it was faster to use "brute force" and use the same fine mesh for all frequencies.

6 VALIDATION BY COMPARISON WITH FULL SCALE VIBRATORY ROLLER COMPACTION EXPERIMENTS

A qualitative comparison of the vibratory roller drum vertical displacement amplitude is shown in Figure 5. The left figure show measured response in the field [19] and the right figure show simulated response for 3D model as described in section 7, for several load amplitudes constant with frequency. The maximum applied load amplitude is 258 kN shown with light blue line with circle – marked 1 in the legend, the other curves are for lower load amplitudes as indicated by the numbers in the legend. The figure clearly demonstrates that the developed model is able to capture the resonance frequency reduction with increasing load amplitude as it appears due to resonance match with the roller vibration frequency. Some data points are missing in the computation due to lack of convergence in the solver which tends to appear at very large vibration amplitudes. Improved convergence can likely be achieved with a finer mesh.

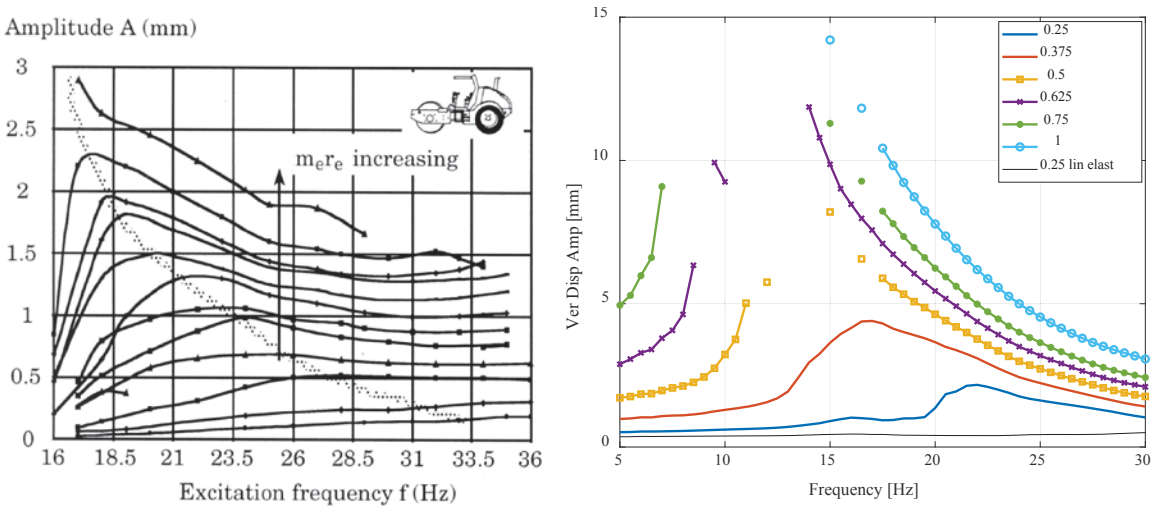

Figure 5 Qualitative comparison vibratory roller drum response to capture the change of resonance frequency due to increasing load amplitude. The left figure is from [19].

To demonstrate quantitatively the equivalent linear method can capture essential features of nonlinear dynamic soil behavior during vibratory compaction, we have compared numerical results with full-scale compaction experiments described in detail in [17] and [18], and in references therein. Several frequency sweep tests were run with the roller passing over an area being compacted. The vertical displacement amplitude of the roller during the sweep tests are shown in Figure 6 a). Within each pass over the compacted area, the frequency is "swept" from 15 to 35 Hz. With increasing number of passes of the vibratory roller, the frequency of the first peak found between 15 and 20 Hz increases due to increasing soil stiffness due to the effect of the compaction. The second peak in each curve at about 30 Hz is due to the drum is bouncing.

An axi-symmetric model was used for quick analysis of the vibro-compaction experiment. The drum, the compacted gravel layer and the underlying rock fill were modelled with 2nd order solid finite elements. Absorbing boundaries was applied on the outer and bottom boundary of the model. A stiff block with a mass of 7600 kg represents the roller drum. The vertical dynamic load on the drum, due to an eccentric moment of 7.3 kgm, is proportional to the square of the rotation frequency giving a load amplitude of 83 kN at 17 Hz increasing to 258 kN at 30 Hz. The depth to bedrock was assumed 5 m in the model.

To account for the densification during compaction, the model was run with different initial shear wave speeds in the gravel fill layer of 160, 180, 200 and 220 m/s. A Poisson's ratio of 0.3 was used in the gravel fill. The rock fill shear wave speed was assumed to vary linearly between from 220 m/s beneath the fill to 270 m/s at 5 m depth. The rock fill density and Poisson's ratio were set to 2000 kg/m^3 and 0.3 respectively.

To model the effect of soil nonlinearity on the response of the drum, the curves for shear modulus reduction and damping versus shear strain shown in Figure 3 were used for the gravel fill. For simplicity, the same curves were used for the rock fill as well.

Varying the initial shear wave speed from 180 m/s to 220 m/s gave a good match with the frequency variation of the first frequency peak observed in the experiment as can be seen in Figure 6 b). The 2nd response peak is due to bouncing of the drum and is not possible to account for in the numerical model due to assumption of full contact between drum and soil.

The experimental response amplitude at the higher frequency of 30 Hz, is not very much higher (~20%) than the response at 15 Hz. Thus the load amplitude experienced by the soil in the experiment when the drum vibrates with 30 Hz and bounces is likely not much larger than the one at 15 Hz.

The analysis show it is necessary to use a nonlinear soil behaviour to obtain a good match with the frequencies observed in the experiments. As shown in Figure 7 the computed shear modulus reduces to less than 10% of its initial value beneath the drum and the material damping factor exceeds 15%. There are many uncertainties in the non-linear modelling in terms of physical input parameters and the numerical model itself. However, the good match with experiments give confidence the method could be used for the analysis of vibro compaction near slopes and other related applications where the nonlinear soil behaviour is important, e.g. foundations subjected to large dynamic loads [5].

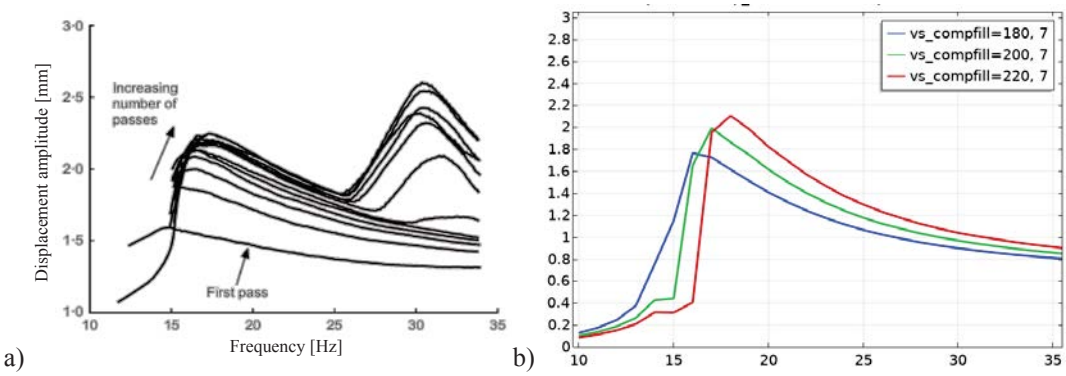

Figure 6 Vertical displacement amplitude of vibratory roller drum in frequency sweep test. a) Experimental result (Modified after [17]). b) Numerical results.

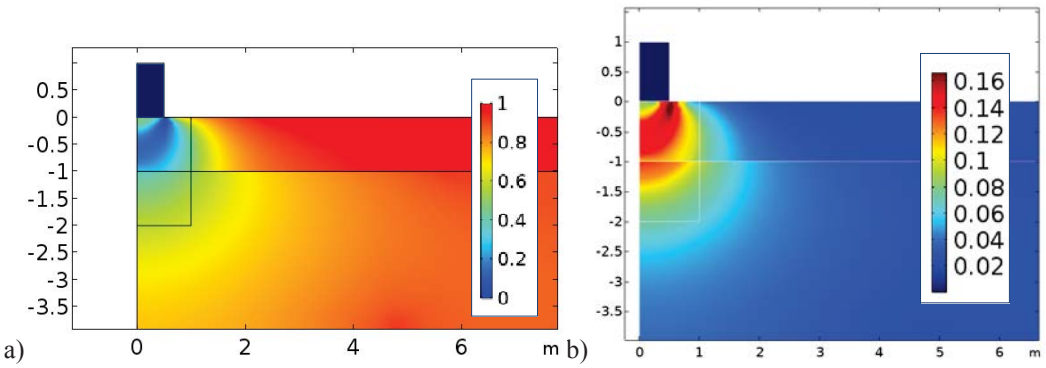

Figure 7 a) Shear modulus reduction and b) soil damping factor beneath vibrating block representing roller drum at 17 Hz for an initial shear wave velocity of 200 m/s in the fill layer.

7 VIBRATION ANALYSIS OF THE STATLAND LANDSLIDE

7.1 Numerical model

A three-dimensional calculation model was established (shown in Figure 8) based on the 2D geometry used in the investigation of the cause of the slide [1]. The colours indicate the shear wave speed as determined from CPT tests made at the site, with interpretation based on empirical equations from [31]. A road was constructed by compacting a rock fill layer (upper most yellow layer) and replacing older loose fills (in turquoise). Older fill material which was not replaced is shown in light green. The old fill contains various materials such as wood chunks etc. The shear wave speed in the replaced masses and in old fills are based on NGI's experience with similar materials [1]. The bed rock is modelled linear elastic with an assumed shear wave speed of 2000 m/s (shown in blue). Above the bedrock there is loose recently deposited material consisting of sand, silt and quick clay with shear wave speeds decreasing with depth from over

200 m/s between of 2 m to 3 m depth beneath the sea floor to about 100 m/s at 25 m depth. This was modelled with three thicker layers in yellow, orange, and red with constant initial shear wave speeds of 150, 120 and 100 m/s respectively. The Poisson's value in the fill mass is set to 0.4 and in soil below ground water level 0.495. The water above the submerged part of the slope has not been modelled. For an analysed vibrating submerged foundation under similar conditions, the water was shown to increase both radiation damping and added soil mass [32][33], thus it will likely have an effect of the dynamic response of the slope, but it is neglected here.

There was no information available about stress-strain curves for the materials at the time of analysis, therefore for simplicity, in the current model the same relative shear modulus reduction versus strain curve was applied to both fill and natural soil. The natural soil is very loose and as such the modulus-reduction curve may give a too stiff response. However, the objective was to estimate the order of magnitude of the induced strains in the soil.

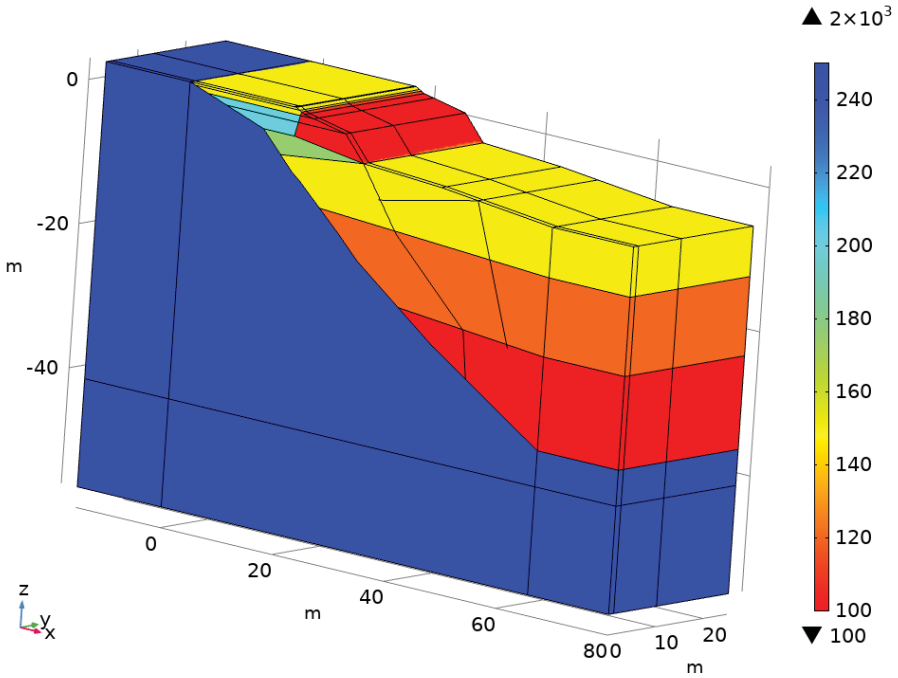

Figure 8 Model used for the vibration analysis of the Statland landslide case. Colours show shear wave speed in the fill and natural soils. The bedrock shear wave speed was set to 2000 m/s (shown in blue).

The vibratory roller used during the compaction work was a Volvo CE SD 115D with a 2.1 m wide and 1.5 m diameter drum. Further technical information about the vibro compactor is available in [34]. The part of the drum in contact with the soil is modelled as a 2.1 m long, 0.3 wide and 5cm thick, rigid plate placed close to the edge of the slope (as shown in Figure 10). The plate mass is equal to the dynamic mass of the whole drum, which was estimated to 3570 kg based on the nominal displacement amplitude of 1.92 mm and load amplitude of 257 kN at a vibration frequency of 30.8 Hz. The Young's modulus of the plate was set to a high value to simulate the drum to be very rigid. The load due to eccentric mass was applied uniformly on the plate and there is no slippage allowed between the plate and the soil. Most vibratory rollers can only operate within a few pre-set frequency values. Here we assumed the load is continuous in the range from 0-30 Hz and proportional to the square of the drum vibration frequency, similar to the load in the full-scale experiments [17].

The static stresses from the weight of the vibratory roller may somewhat increase the stiffness and strength of the soil beneath the drum, but this is not accounted for in analysis. The static load diminishes quickly with depth as opposed to the dynamic loads which penetrate

much deeper. As a verification, the static stresses in the model due to the weight of the plate have been compared with field measurement [35] of a similar vibro compactor. The stresses are of the similar magnitude. Analysis performed in connection with the validation showed the increase in static stress beneath the drum has little effect on the overall vibration response. It was checked by changing low strain shear wave speed with 25% in the layer closest to the drum resulting in 10% change in resonance frequency. This was considered to have little consequence for computing the dynamic effects of vibro compaction on slope stability.

7.2 Effect of soil non-linearity and frequency dependent load

The numerical 3D model is still under development with tuning of mesh size and discretization to handle the large strains in the vicinity of the drum. However, the numerical results are considered to still be informative for engineering purposes and are therefore presented here.

Figure 10 shows the vertical response of the drum with blue curves for a load increasing with the square of the vibration frequency from 10 kN at 5 Hz to 257 kN at 31 Hz. The peak response, taken as average of the two points on the plate, is 3.5 mm at 20 Hz for a load of 109 kN. The drum response increases rapidly when the load frequency approaches 20 Hz due to local resonance between the drum and soil immediately beneath it.

At 4 m below the drum and 10 m further out in the slope (locations indicated with arrows in Figure 10) the vibration amplitude (shown with green and red curve in Figure 9) increases when approaching 15 Hz, which appears to be the natural frequency of the slope. The vibration further away from the drum do not increase above 15 Hz even though the load amplitude and the drum response increases very much at that frequency. This is interpreted due to 1) the soil can only transmit a limited shear stress due to the non-linear soil behavior [31] and 2) the increasing dynamic resistance due inertia of the vibrating plate. This is also indicated by the maximum shear strain plots for 14 Hz and 20 Hz (Figure 10 and Figure 11). For vibration frequencies below 15 Hz there is very low shear strains except in the vicinity of the drum. For vibration frequencies of 20 Hz and above, the shear strain amplitude do not increase very much even though the load amplitude doubles from 20 Hz to 30 Hz. The shear strains reach values for which pore pressure build-up can be expected [9], particularly for a large number of cycles and if the soil cannot dissipate the pore pressure. Such built-up pore pressure may also spread to critical parts of the slope through permeable layers which often exist in quick clay deposits of this kind. ([36]).

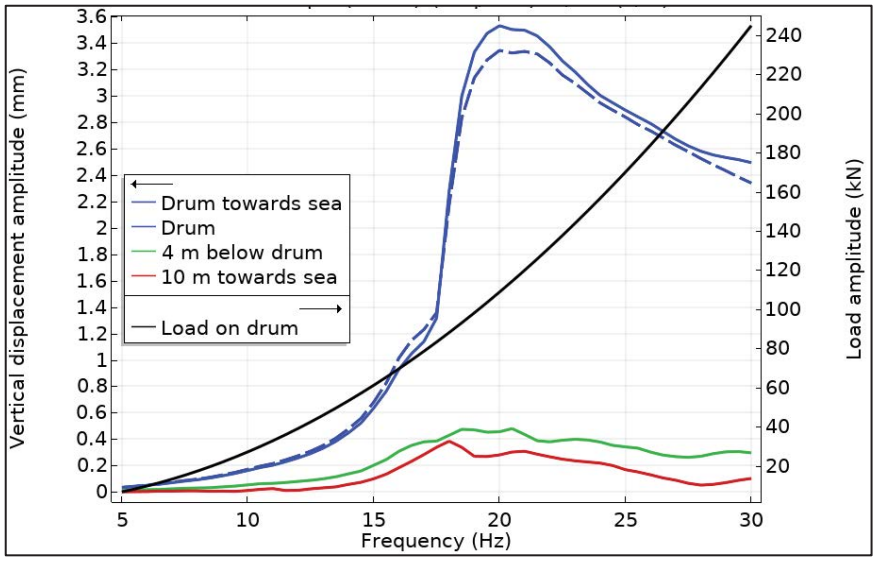

Figure 9 Vertical displacement amplitude (left axis) and load amplitude (right axis) versus loading frequency. Peak drum response at 20 Hz.

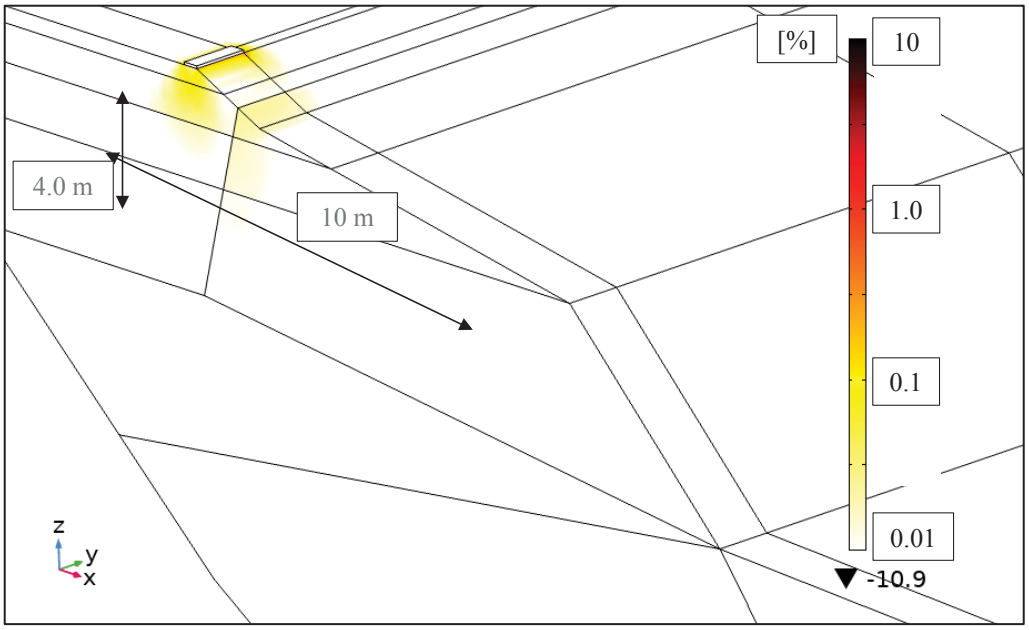

Figure 10 Maximum shear strain at 14 Hz for load amplitude of 53 kN. Colour scale is logarithmic from 0.01 % to 10% shear strain.

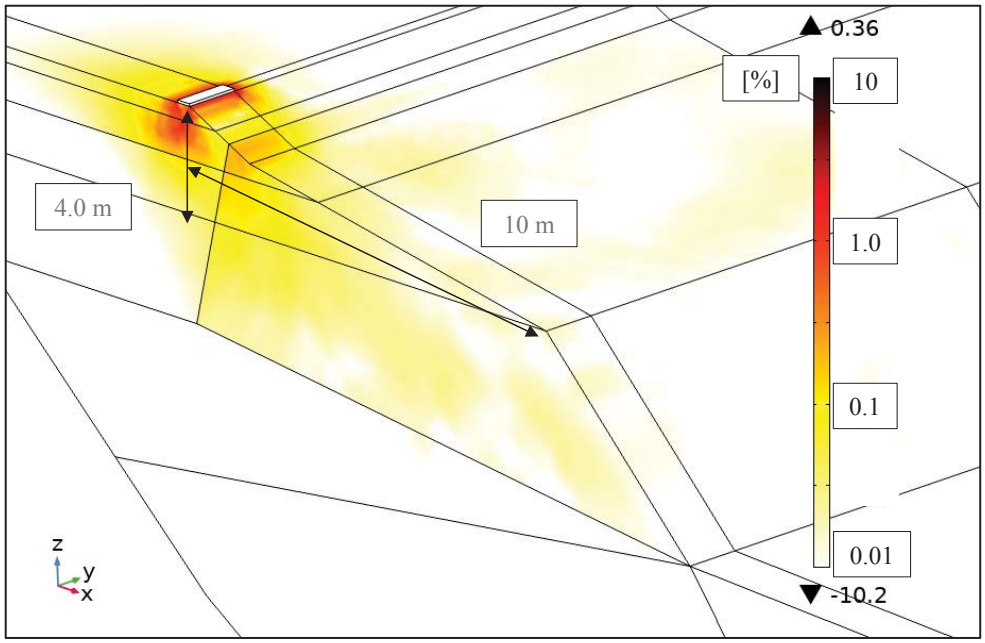

Figure 11 Maximum shear strain at 20 Hz. Colour scale is logarithmic from 0.01 % to 10% shear strain. At 10 m from the drum towards the slope the maximum shear strain reaches 0.025 %.

Using 2nd order elements allows improved capturing of large strain amplitudes around the vibrating plate (drum), and also reduces possible volumetric locking due to high Poisson's values in the submerged part of the slope. Figure 12 shows the response for the same model as in Figure 9, except for the use of 2nd order elements. The peak response of the drum now occurs at 15 Hz compared to 20 Hz for the model with linear element. The vibration amplitude of the drum is approximately the same as for 1st order elements with some increase to the sides of the drum due to local nonlinearity (see solid and dashed blue lines). However, the applied load amplitude on the drum is much lower with 61 kN at 15 Hz, compared to 109 kN at 20 Hz, which indicates the response is to stiff with the 1st order elements.

Using the 2nd order mesh discretization give a softer numerical behavior of the soil, and the frequency at the peak response of the drum-fill now coincides with the slope's natural vibration frequency of about 15 Hz. The vibration amplitude 4 m beneath and 10 m in front of the drum increase rapidly with frequency as shown with green and red curves in Figure 12. 4 m beneath the drum the maximum velocity amplitude is about 35 mm/s and 10 m towards the slope it is 20 mm/s. These velocity amplitudes correspond to shear strains high enough to cause pore pressure build up [9]. The double resonance, i.e. the coincidence of resonance frequency of the drum and compacted fill with the slope's natural vibration frequency likely have contributed to the relatively large shear strains induced.

The difference in response of the slope below and above the resonance frequency is also clearly seen in the plots of shear strains for 13 Hz and 16 Hz as shown in Figure 13 and Figure 14. Figure 14 shows a node-antinode wave pattern with regions of high shear strains surrounding areas with low shear strains.

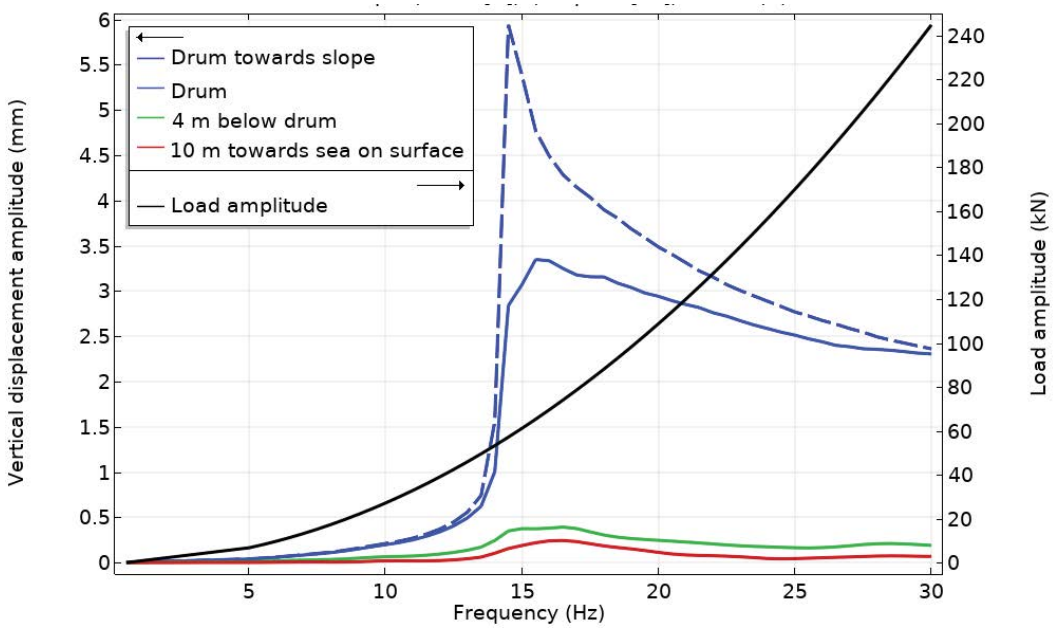

Figure 12 Vertical displacement amplitude (left axis) and load amplitude (right axis) versus loading frequency. Peak drum response at about 15 Hz.

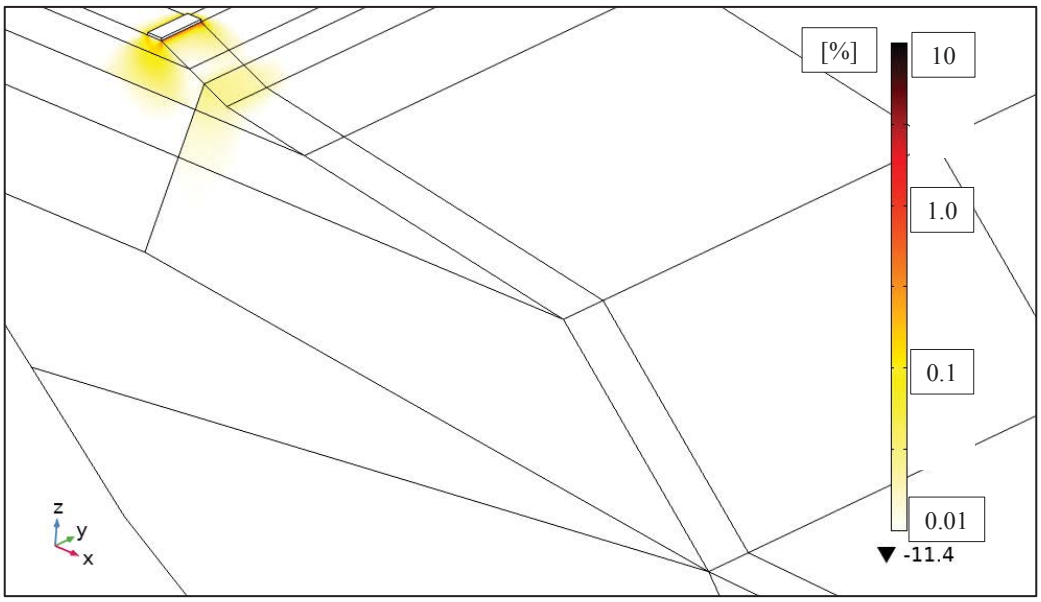

Figure 13 Maximum shear strain at 13 Hz for load amplitude of 46 kN. Colour scale is logarithmic from 0.01 % to 10% shear strain.

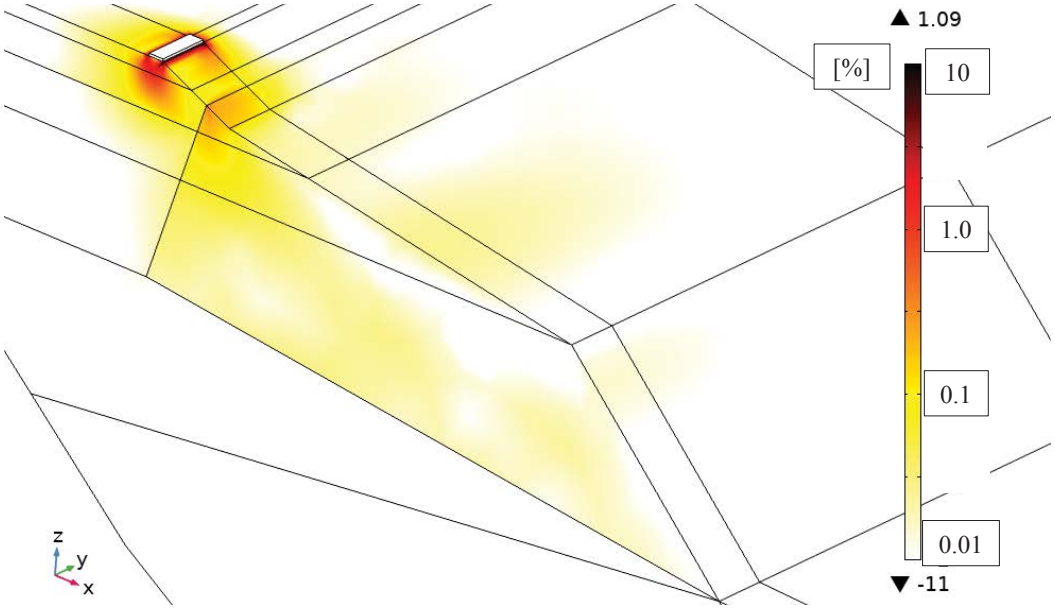

Figure 14 Maximum shear strain at 16 Hz. Colour scale is logarithmic from 0.01 % to 10% shear strain. At 10 m from the drum towards the slope the maximum shear strain reaches 0.025 %.

7.3 Effect of bouncing drum

To understand better the effect of a jumping drum on the slope stability and soil-nonlinearity we have compared the response for four different load amplitudes all at 15 Hz close to the natural frequency of the slope, at which vibrations can propagate out towards the slope surface. This comparison have so far only been done for 1st order elements, but give a qualitative indication.

Comparing static stress due to weight on the drum with dynamic stresses beneath it, indicates the drum may not be in contact with the soil in parts of the vibration cycle (i.e. it is bouncing). The non-contact situation starts at frequencies in the range 12-15 Hz in this analysis. The frequency range will vary with drum mass, load amplitude and the non-linear soil stiffness.

It is not fully correct to apply the equivalent linear method to the problem of a bouncing drum. However, the estimated vibration amplitudes are likely on the high side and thus it would be conservative to use the approach to estimate the effect of compaction on slope stability. As mentioned, the load acting on the drum is proportional to the square of the drum vibration frequency. Thus when the drum is bouncing, the load amplitude applied to the drum is controlled by the drum vibration frequency, even though the soil vibrates with a lower frequency.

The following analysis tries to capture the underlying mechanism causing the second vibration peak around 30 Hz as shown in Figure 6 a). A comparison of stiffness degradation at a vibration frequency of 15 Hz is given in Figure 15 a) - d) for load amplitudes of 67 kN (not bouncing), 101 kN (partial loss of contact), 134 kN (partial loss of contact) and 269 kN (double frequency bouncing at 30 Hz as shown in Figure 2 c) and in the experiment result Figure 6a). 269 kN is the load for a roller vibration frequency of 30 Hz.

For the lower load amplitude (67 kN) there is only stiffness degradation locally beneath the roller and some 30-40% reduction in the upper part of the old fill towards the sea. With increasing load amplitude, the stiffness reduction reaches deeper down, at 100 kN load the reduction is about 60% at a depth of 1.5 m. For a load of 134 kN the stiffness reduction is more than 60% down to 2-meter depth. For the large load amplitude of 269 kN the stiffness degradation is occurring in a larger soil volume down to some 4 meter depth and the old fill sustains larger stiffness degradation down to 2 meter depth.

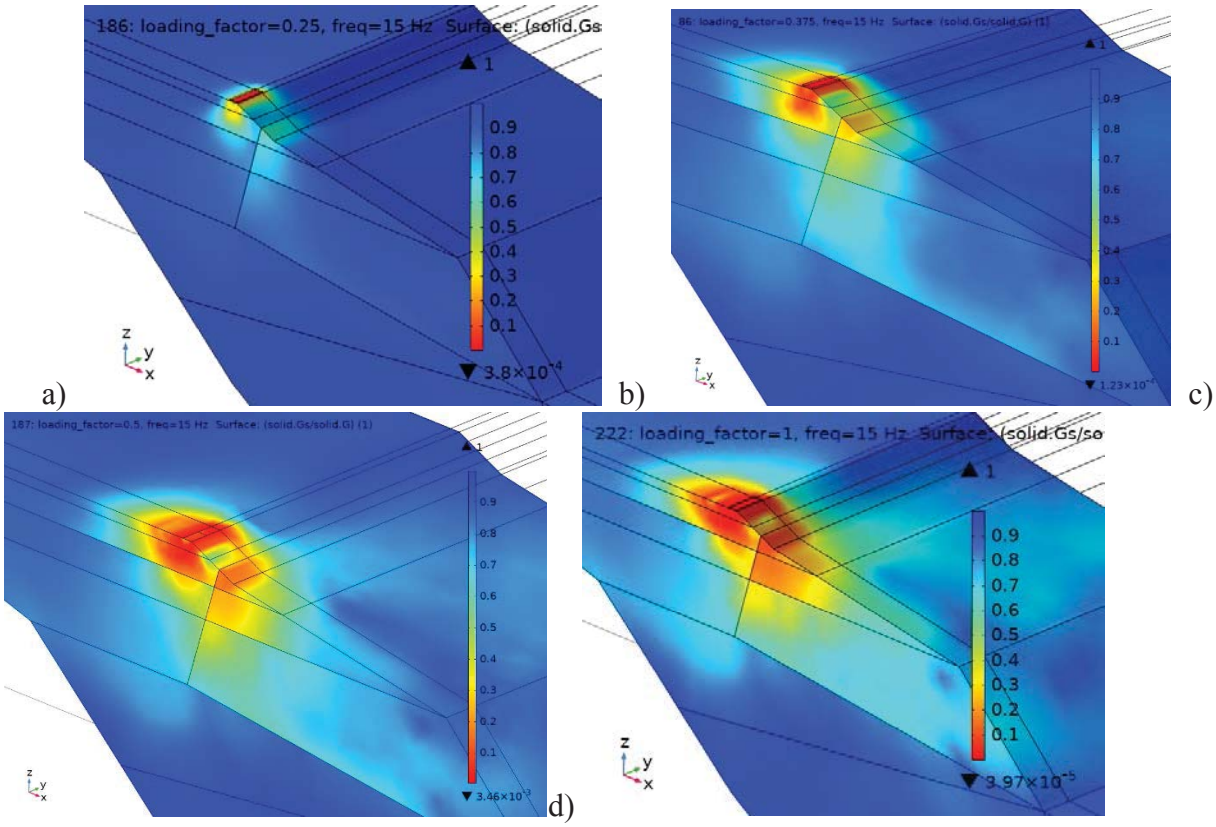

Figure 15 Reduction of shear modulus for a vibration frequency of 15 Hz for a load amplitude of 67 kN in a), corresponding to 25% of maximum load amplitude. In b) the load is 101 kN, in c) 134 kN and in d) the maximum load amplitude of 269 kN is applied.

8 DISCUSSION

There are usually many contributing factors when construction activities cause landslides. These could e.g. be unknown soil conditions, such as the presence of weak soil layers and artesian water pressures resulting in lower actual factors of safety than anticipated by the geotechnical engineer's stability analysis. In the case of vibratory compaction, one should consider the effect of increased weight from the fill, compaction induced increase in lateral pressures, and use of less heavy equipment [37]-[40].

Here we have to tried to understand how vibrations induced by compaction may affect the slope stability. The computed shear strains due to vibrations from compaction for the Statland case are large enough to cause pore pressure build up in the soft soil sediments [9]. Considering the very loose soil conditions as indicated by the post-slide investigation [1] it seems very likely the construction work caused the landslide and probably the vibratory compaction have contributed to the triggering. This confirms the conclusions in [1].

Vibrations were not measured for Statland case. Therefore it is not known how large the vibration amplitude was or how large the dynamic impact on the slope was. The analysis presented in this paper have tried to capture a range of possible load amplitudes and frequencies, to understand the effect of compaction on slope stability and if it is possible to establish a vibration limit to avoid slope failure. For practical reasons such limit values should be related to vibration measured on the ground surface. The vibration amplitude on the ground surface is very high near the vibratory roller, but attenuates quickly with distance. Since the roller is moving around when it operates it may be difficult to establish a vibration limit since the distance

to the roller is not known / varying all the time. Thus, the vibrations could be larger than measured by the vibration sensor. However, if one can measure vibrations on the ground surface at critical locations, e.g. on based slope stability analysis and tentatively keeping them lower than 20 mm/s it seems unlikely the vibrations could have negative effect on slope stability. In general, depending on the ground conditions and computed factor of safety for the slope stability, a slope can tolerate much larger vibration amplitudes than 20 mm/s.

The numerical analysis further indicate for a bouncing roller, i.e. the roller drum is fully in the air during every other soil vibration cycle, the effect on stiffness and strength degradation in the ground can be even larger. Thus avoiding bouncing of the drum is imperative when compacting in the vicinity of vibration sensitive soils. Many modern vibratory compaction rollers can sense and automatically reduce the jumping [15], [19].

The vibration frequency range of many vibratory rollers lies within a range such that when it bounces the frequency of impact on the ground may coincide with global natural vibration frequency of slopes. The performed numerical analysis indicates the global natural frequency of the slope is mainly controlled by the elastic shear wave speeds and geometry. The local soil-nonlinearity around the drum do not affect the global natural frequency. Further analysis is needed to understand the interplay ("double resonance") between the global natural frequency, the local natural frequency of the drum-soil, and how they are affected by soil nonlinear stiffness and slope geometry.

For load amplitudes large enough to cause jumping of the drum, the performed frequency domain analysis does not capture the partial or no-contact between the drum and the soil. Therefore the computed vibration amplitudes are likely on the high side. Further comparison with field measurements and non-linear time domain analysis are needed.

9 CONCLUSIONS AND RECOMMENDATIONS

The numerical analysis indicate vibratory compaction have possibly contributed to triggering the slide at Statland. The nonlinear analysis is believed to have captured the essential behaviour of the vibratory compaction and the response of the slope. The peak response at the frequency is close to the one stated by the operator of the vibratory roller and the manufacturer's data sheet.

To reduce the landslide risk during compaction work in the vicinity of slopes with vibration susceptible soils and low static stability near the shoreline the following is suggested

- Use less heavy equipment and/or higher loading frequencies or perform compaction without vibration. Avoiding excessive bouncing of the vibratory roller drum is imperative.
- Applying thinner layers and more time between compaction passes. Allowing for more time between placing of layers reduces the number of load cycles applied by the soil and allows for drainage of potential built up pore pressures both due to cyclic loading and due to static loading from weight of the fill.
- Monitor slope horizontal and vertical displacements at some critical points.
- Monitor pore pressures at critical points. Locations with artesian pressure have lower stability, any extra pore pressure from the compaction will reduce the stability of the slope.

10 ACKNOWLEDGEMENT

The financial support by the governmental research program "Natural Hazards: Infrastructure for floods and slides (NIFS)" and by the Norwegian Research Council through Remedy

project BegrensSkade II – Risk Reduction of Groundwork Damage Grant No. 267674, is gratefully acknowledged. The equivalent linear dynamic 3D tool sprung out of the collaboration with Prof. Staffan Hintze (NCC), Kenneth Viking (Swedish Transport Administration), and Fanny Deckner (GeoMind) financially supported by NCC and by the Development Fund of the Swedish Construction Industry, which is also highly appreciated.

REFERENCES

[1]NVE The landslide at Nord-Statland. Investigation of technical causes. Report nr. 93-2014. ISBN-nr. 978-82-410-1042-2, http://www.naturfare.no/_attachment/751994/binary/1007572, in Norwegian.

[2]NVE, "Dynamic loading and landslide hazard ", (in Norwegian, title: Dynamiske påkjenninger og skredfare) https://brage.bibsys.no/xmlui/handle/11250/2498527, Report nr. 16-2016, 2016.

[3]Johansson J., Bouchard S. L'Heureux JS. (2017) Vibratory Roller Influence Zone Near Slopes with Vibration Susceptible Soils. In: Thakur V., L'Heureux JS., Locat A. (eds) Landslides inl Sensitive Clays. Advances in Natural and Technological Hazards Research, vol 46. Springer, Cham.

[4]Johansson, J. and L 'Heureux , J.-S. Influence of vibratory compaction on slope stability — an ongoing research topic in Norway, Anniversary Symposium — 40 Years of Roller Integrated Continuous Compaction Control (CCC), D. Adam & S. Larsson (eds.), November 29th, 2018, Vienna, Austria

[5]Johansson, J. and Kaynia, A. M., Equivalent linear pseudostatic and dynamic modelling of vertically vibrating monopile, Marine Structures, accepted manuscript under revision, 2020

[6]Bernander, Stig, Progressive landslides in long natural slopes: Formation, potential extension and configuration of finished slides in strain-softening soils. 2011. 240 p. Doctoral thesis, Luleå University of Technology.

[7]Ekström, A., & Olofsson, T. (1985). Water and frost-stability risks for embankments of fine-grained soils. In From Proceedings of the Symposium on Failures in Earthworks, organized by the Institution of Civil Engineers, held in London, March 6-7, 1985.

[8]Hryciw, R., Vitton, S., and Thomann, T. (1990). ”Liquefaction and Flow Failure During Seismic Exploration.” J. Geotech. Engrg., 116(12), 1881–1899.

[9]Dobry, R., Vasquez-Herrera, A., Mohamad, R., and Vucetic, M. (1985). "Liquefaction flow failure of silty sand by torsional cyclic tests." Proc, Session on Advances in the Art of Testing Soils Under Cyclic Conditions, ASCE, 29-50.

[10]Vucetic, M. (1994). Cyclic Threshold Shear Strains in Soils. Journal of Geotechnical Engineering, 120 (12), 2208–2228. https://doi.org/10.1061/(asce)0733-9410(1994)120:12(2208)

[11]Cornforth, Derek, Landslides in Practice: Investigation, Analysis, and Remedial/Preventative Options in Soils, ISBN: 978-0-471-67816-8 April 2005 624 Pages,

[12] S. Bouchard, J.-S. L’Heureux J. Johansson S. Leroueil and D. LeBoeuf, "Blasting induced landslides in sensitive clays", Landslides and Engineered Slopes. Experience, Theory and Practice – Aversa et al. (Eds), 2016 Associazione Geotecnica Italiana, Rome, Italy, ISBN 978-1-138-02988-0.

[13] Johansson J., Løvholt F., Andersen K.H., Madshus C. and Aabøe R. "Impact of blast vibrations on the release of quick clay slides". ICSMGE 2013, Paris

[14] Glimsdal, S., et al. The 29th January 2014 submarine landslide at Statland, Norway—landslide dynamics, tsunami generation, and run-up. Landslides , 13 (6), 1435–1444. https://doi.org/10.1007/s10346-016-0758-7, 2016

[15] Adam, D., Pistrol, J.: "Dynamic roller compaction for earthworks and roller-integrated continuous compaction control: State of the art overview and recent developments"; Talk: Conferenze di Geotecnica di Torino, XXIV Ciclio, Turin (invited); 02-25-2016 - 02-26-2016; in: "Conferenze di Geotecnica di Torino, XXIV Ciclio", M. Manassero, A. Dominijanni, S. Foti, G. Musso (ed.); (2016), 1 - 41

[16] van Susante, P. J., & Mooney, M. A. (2008). Capturing Nonlinear Vibratory Roller Compactor Behavior through Lumped Parameter Modeling. *Journal of Engineering Mechanics*, *134*(8), 684–693. https://doi.org/10.1061/(asce)0733-9399(2008)134:8(684)

[17] Wersäll, C., Nordfelt, I., & Larsson, S. (2017). Soil compaction by vibratory roller with variable frequency. Géotechnique , 67 (3), 272–278. https://doi.org/10.1680/jgeot.16.p.051

[18] Wersäll, C., Nordfelt, I., & Larsson, S.. Resonant roller compaction of gravel in full-scale tests, Transportation Geotechnics, 14, 93–97, 2018, https://doi.org/10.1016/j.trgeo.2017.11.004

[19] Anderegg, Roland and Kuno Kaufmann Intelligent Compaction with Vibratory Rollers Feedback Control Systems in Automatic Compaction and Compaction Control. Transportation Research Record: Journal of the Transportation Research Board, No. 1868, TRB, National Research Council, Washington, D.C., 2004, pp. 124–134.

[20] Transportation Research Board, Intelligent Soil Compaction Systems, NCHRP report 676, 2010, http://www.trb.org/Publications/Blurbs/164279.aspx.

[21] Lysmer, J., Udaka, T., Tsai, C.F., Seed, H.B., 1975. FLUSH: A computer program for approximate 3-D analysis of soil-structure interaction problems, Report EERC 75-30, Earthquake Engineering Research Center, U.C.Berkeley.

[22] Schnabel, P.B., Lysmer, J., Seed, H.B., 1972. SHAKE: a computer program for earthquake response analysis of horizontally layered sites, Report EERC 72-12, Earthquake Engineering Research Center, U.C.Berkeley.

[23] Darendeli M. B., Development of a new family of normalized modulus reduction and material damping curves, Ph.D. Dissertation, The University of Texas at Austin, August, 2001.

[24] Groholski, D. R.; Hashash, Y. M. A.; Kim, B.; Musgrove, M.; Harmon, J. & Stewart, J. P., Simplified Model for Small-Strain Nonlinearity and Strength in 1D Seismic Site Response Analysis, Journal of Geotechnical and Geoenvironmental Engineering, American Society of Civil Engineers (ASCE), 2016, 142, 04016042

[25] Amir-Faryar, B.; Aggour, M. S. & McCuen, R. H., Universal model forms for predicting the shear modulus and material damping of soils, Geomechanics and Geoengineering, Informa UK Limited, 2016, 12, 60-71

[26] Wichtmann, T. & Triantafyllidis, T. Effect of Uniformity Coefficient on G/Gmax and Damping Ratio of Uniform to Well-Graded Quartz Sands Journal of Geotechnical and

Geoenvironmental Engineering, American Society of Civil Engineers (ASCE), 2013, 139, 59-72

[27]Andersen, K. H., Cyclic soil parameters for offshore foundation design, The Third ISSMGE McClelland Lecture, ISFOG III, Meyer, V. (Ed.), CRC Press, 2015

[28]Blaker, Ø., & Andersen, K. (2015). Shear strength of dense to very dense Dogger Bank sand. In Frontiers in Offshore Geotechnics III (pp. 1167–1172). CRC Press. https://doi.org/10.1201/b18442-175

[29]Løvholt, F., C. Madshus, and K. H. Andersen. "Intrinsic Soil Damping from Cyclic Laboratory Tests with Average Strain Development." Geotechnical Testing Journal 43 (forthcoming). https://doi.org/10.1520/GTJ20170411.[27][27]

[30] Park, J., & Kaynia, A. M. (2017). FE simulation of steady state wave motion in solids combined with a PML approach. Procedia Engineering, 199, 1556–1561. https://doi.org/10.1016/j.proeng.2017.09.054

[31] Robertson, P. K. (2009). Interpretation of cone penetration tests — a unified approach. Canadian Geotechnical Journal, 46 (11), 1337–1355. https://doi.org/10.1139/t09-065

[32] Kaynia, A.M., Kausel, E., and Madshus, C.M. (1998). “Impedances of Underwater Rigid Square Foundations.” Proc. ASCE Spec. Conf. Geotech. Earthquake Engng, Seattle, WA, USA, 1283-1293.

[33] J. Park and A.M. Kaynia, Stiffness matrices for fluid and anisotropic soil layers with applications in soil dynamics, Soil Dynamics and Earthquake Engineering, 115, 169-182, 2018.

[34] Volvo Construction Equipment. Specifications for SD 115 vibrocompactor.

[35] R.V. Rinehart and M.A. Mooney, "Measurement depth of vibratory roller-measured soil stiffness", Géotechnique, Volume 59, Issue 7, 01 September 2009, pages 609 –619.

[36] Hintze et. al., , Report 95. Effect on surrounding during pile and sheet pile installation (Omgivningspåverkan vid pål- och spontslagning), Swedish Pile commission, 1997 (in Swedish). http://www.palkommissionen.org/web/page.aspx?refid=86.

[37] Massarsch, K. R., 2002. ”Effects of Vibratory Compaction”. TransVib 2002 –International Conference on Vibratory Pile Driving and Deep Soil Compaction. Louvain-la-Neuve. Keynote Lecture, pp. 33 – 42.

[38] Chen, T.-J., & Fang, Y.-S. (2008). Earth Pressure due to Vibratory Compaction. Journal of Geotechnical and Geoenvironmental Engineering, 134(4), 437–444. https://doi.org/10.1061/(asce)1090-0241(2008)134:4(437)

[39] Canadian Geotechnical Society, "The Canadian Foundation Engineering Manual", 4th Edition, 2006.

[40] Norwegian Public Roads Administration, (NPRA), Handbook in road construction, N200 (in Norwegian), July 2018.

EURODYN 2020

Proceedings of the
XI International Conference on Structural Dynamics

M. Papadrakakis, M. Fragiadakis, C. Papadimitriou (Eds.)

First Edition, September 2020

ISBN (set): 978-618-85072-2-7
ISBN (vol I): 978-618-85072-0-3

Institute of Structural Analysis and Antiseismic Research
National Technical University of Athens, Greece